PROCEEDINGS OF THE 4TH INTERNATIONAL

CIVIL ENGINEERING & ARCHITECTURE CONFERENCE

Volume 1: Civil Engineering

AHMET CAN ALTUNIŞIK
HASAN BASRİ BAŞAĞA
VOLKAN KAHYA
VEDAT TOĞAN

KTU 1955 KARADENIZ TECHNICAL UNIVERSITY

KARADENİZ TEKNİK ÜNİVERSİTESİ Deprem ve Yapı Sağlığı Uygulama ve Araştırma Merkezi UYGAR

dynamic academy®

golden light publishing®

PROCEEDINGS OF THE 4th INTERNATIONAL CIVIL ENGINEERING & ARCHITECTURE CONFERENCE

17–19 May 2025, Trabzon, Türkiye

Volume 1: Civil Engineering

Editors

Ahmet Can Altunışık

Volkan Kahya

Hasan Basri Başağa

Vedat Toğan

Organized by: Dynamic Academy & Golden Light Publishing

Academic Partner: Karadeniz Technical University

Published: May 2025

ISBN: 978-605-81854-9-4 (Tk) 978-625-96160-0-1 (1.C)

Published by Golden Light Publishing®, a trademark of Dynamic Academy®

Postal Address:	Trabzon Teknoloji Geliştirme Bölgesi Yönetici A.Ş. Üniversite Mahallesi Hastane Caddesi No: 33, 61081 Trabzon, Türkiye
Email:	info@goldenlightpublish.com
Web:	http://www.goldenlightpublish.com http://www.dynaaca.com

TABLE OF CONTENTS

PROCEEDINGS – VOLUME 1: CIVIL ENGINEERING

PREFACE

The 4th International Civil Engineering & Architecture Conference (ICEARC'25) aimed to bring together academics, researchers, and practitioners in the fields of civil engineering and architecture from across the globe. Held in Trabzon, Türkiye on May 17–19, 2025, the conference served as a dynamic platform to review recent achievements, share emerging developments, and address both current and future challenges in these disciplines.

ICEARC'25 has once again demonstrated its truly international character, drawing over **500 participants from 33 countries**. The conference hosted **421 research presentations** delivered in **59 parallel sessions**, and provided participants with excellent networking and collaboration opportunities. In addition to the technical sessions, **four dedicated workshops**—focusing on contemporary themes such as sustainable buildings, hybrid structures, and advanced materials—offered attendees practical insights and knowledge exchange in specialized areas.

The **Proceedings of the 4th International Civil Engineering and Architecture Conference** includes all the accepted and presented papers, compiled in two volumes:

- **Volume 1: Civil Engineering**, comprising 303 papers under major categories such as Structural Mechanics, Earthquake Engineering, Hydraulics & Fluid Mechanics, Geotechnics & Soil Mechanics, Transportation, Structural Materials, Hydrology & Water Resources, Construction Management, and Waste Management.
- **Volume 2: Architecture**, featuring 118 papers grouped under topics such as Architectural Philosophy, Design & Practice, Architecture, Conservation & Restoration, Urban Planning & Landscape, Architectural Engineering, and Interior Design.

We are sincerely grateful to all authors for their valuable contributions. The papers included in these volumes were rigorously reviewed by field experts, and only those that were accepted and presented at the conference have been published. We extend our deepest appreciation to the reviewers for their meticulous evaluations, which significantly contributed to the quality of this publication.

We would also like to express our gratitude for the institutional support provided by **Karadeniz Technical University** and **the Chamber of Civil Engineers (Trabzon Branch)** of the **Union of Chambers of Turkish Engineers and Architects**. We sincerely thank our sponsors:

- **Platinum Sponsor:** Usta Grup
- **Gold Sponsors:** Cengiz İnşaat, Türen İnşaat, Odaş
- **Silver Sponsors:** Es Denizcilik, KCT Yol Yapı İnşaat
- **Bronze Sponsors:** Inosel, YaşarTek, AKM Yapı

Our special thanks go to the **Mayor of Trabzon Metropolitan Municipality**, **Mayor of Ortahisar Municipality**, and **Mayor of Yomra Municipality** for their valuable support.

We also acknowledge the outstanding efforts of the organizing committee, the student volunteers, and all the moderators who chaired our sessions with professionalism and dedication. Their contributions were instrumental in the success of ICEARC'25.

Finally, the conference concluded with a memorable **social tour to the iconic Sümela Monastery and Uzun Göl**, offering participants a taste of the region's rich cultural and natural heritage.

We look forward to welcoming you again at **ICEARC'27**.

Editors

COMMITTEES

ORGANIZATION COMMITTEE

Hamdullah Çuvalcı
Karadeniz Technical University

Ahmet Can Altunışık
Karadeniz Technical University

Cenap Sancar
Karadeniz Technical University

Nilgün Kuloğlu
Karadeniz Technical University

Volkan Kahya
Karadeniz Technical University

Vedat Toğan
Karadeniz Technical University

Hasan Basri Başağa
Karadeniz Technical University

INTERNATIONAL SCIENTIFIC COMMITTEE

Abdullah Avey
İstanbul Ticaret University, Türkiye

Abdussamet Arslan
Gazi University, Türkiye

Abdülkadir Cüneyt Aydın
Atatürk University, Türkiye

Adem Akpınar
Uludağ University, Türkiye

Adem Doğangün
Uludağ University, Türkiye

Afşin Sarıtaş
Middle East Technical University, Türkiye

Ahmet Anıl Dindar
Gebze Teknik University, Türkiye

Ahmet Birinci
Karadeniz Technical University, Türkiye

Ahmet Yakut
Middle East Technical University, Türkiye

Akif Kutlu
İstanbul Technical University, Türkiye

Ali Demir
Manisa Celal Bayar University, Türkiye

Ali Ercan
Middle East Technical University, Türkiye

Ali Fuat Genç
Karadeniz Technical University, Türkiye

Ali Mardini
Bursa Uludağ University, Türkiye

Ali Mortazavi
Izmir Democracy University, Türkiye

Alp Caner
Middle East Technical University, Türkiye

Alper Aldemir
Hacettepe University, Türkiye

Alper İlki
İstanbul Technical University, Türkiye

Alper Polat
Munzur University, Türkiye

Ana Cocho Bermejo
Barcelona Tech, Spain

Arcan Yanık
İstanbul Technical University, Türkiye

Aslı Pelin Gürgün
Yıldız Technical University, Türkiye

Asu Beşgen
Karadeniz Technical University, Türkiye

Atakan Aksoy
Karadeniz Technical University, Türkiye

Atilla Damcı
Istanbul Technical University, Türkiye

Ayhan Nuhoğlu
Ege University, Türkiye

Aynur Kazaz
Akdeniz University, Türkiye

Ayşe Daloğlu
Karadeniz Technical University, Türkiye

Baran Bozyiğit
Dokuz Eylül University, Türkiye

Barbaros Atmaca
Karadeniz Technical University, Türkiye

Gulbin Ozcan-Deniz
Thomas Jefferson University, USA

Gül Polat Tatar
Istanbul Technical University, Türkiye

Gülben Çalış
Ege University, Türkiye

Gürkan Topaloğlu
Karadeniz Technical University, Türkiye

Hakan Tacettin Türker
Bursa Uludağ University, Türkiye

Halil Karahan
Pamukkale University, Türkiye

Hare Kılıçaslan
Karadeniz Technical University, Türkiye

Halil Sezen
Ohio State University, USA

Hasan Biglari
University of Tabriz, Iran

Hasan Murat Tanarslan
Dokuz Eylül Üniversitesi, Türkiye

Hasan Tahsin Öztürk
Karadeniz Technical University, Türkiye

İbrahim Özgür Deneme
Aksaray University, Türkiye

İbrahim Serkan Mısır
Dokuz Eylül Üniversitesi, Türkiye

İlker Kazaz
Erzurum Technical University, Türkiye

İlker Ustabaş
Recep Tayyip Erdoğan University, Türkiye

İrem Dikmen
University of Reading, UK

İsmail Hakkı Çağatay
Çukurova Üniversitesi, Türkiye

İsmail Hakkı Özölçer
Bülent Ecevit University, Türkiye

Johannes Halman
University of Twente, Netherlands

Kadir Güler
İstanbul Technical University, Türkiye

Kemal Beyen
Kocaeli University, Türkiye

Kemal Hacıefendioğlu
Karadeniz Technical University, Türkiye

Kerim Koç
Yıldız Technical University, Türkiye

Korhan Özgan
Karadeniz Technical University, Türkiye

Koshy Varghese
Indian Institute of Technology-Madras, India

Kurtuluş Soyluk
Gazi University, Türkiye

Kutay Orakçal
Boğaziçi Üniversitesi, Türkiye

Kürşat Esat Alyamaç
Fırat University, Türkiye

Leyla Tanaçan
İstanbul Technical University, Türkiye

Low Sui Pheng
National University of Singapore, Singapore

M. Reza Hosseini
The University of Melbourne, Australia

Mahmut Fırat
İnönü University, Türkiye

Mahmut Kılıç
Atatürk Üniversitesi, Türkiye

Majit Ayatollahi
Iran University of Science and Technology, Iran

Maria Giuseppina Limongelli
Politecnico Milano, Italy

Mehmet Aydın Kömür
Aksaray University, Türkiye

Mehmet Emin Arslan
Düzce University, Türkiye

Mehmet Emin Aydın
Necmettin Erbakan University, Türkiye

Mehmet Emin Öncü
Dicle Üniversitesi, Türkiye

Mehmet Emiroğlu
Sakarya University, Türkiye

Mehmet Hakkı Omurtag
İstanbul Medipol University, Türkiye

Metin Hüsem
Karadeniz Technical University, Türkiye

Mohammad Arif Kamal
Aligarh Muslim University, India

Muhammet Karaton
Fırat University, Türkiye

Muhammet Yurdakul
Karadeniz Technical University, Türkiye

Murat Emre Kartal
İzmir Democracy University, Türkiye

Murat Günaydın
Karadeniz Technical University, Türkiye

Murat Kankal
Uludağ University, Türkiye

Murat Yaylacı
Recep Tayyip Erdoğan University, Türkiye

Musa Yetkin
Fırat University, Türkiye

Mustafa Aytekin
University of Bahrain, Bahrain

Mustafa Erol Keskin
Süleyman Demirel University, Türkiye

Mustafa Kubilay Keleşoğlu
İstanbul University, Türkiye

Mustafa Şahmaran
Hacettepe University, Türkiye

Mustafa Tamer Ayvaz
Pamukkale University, Türkiye

Muteber Erbay
Karadeniz Technical University, Türkiye

Mücteba Uysal
Yıldız Technical University, Türkiye

Nemkumar (Nemy) Banthia
The University of British Columbia, UK

Nihal Eratlı
İstanbul Technical University, Türkiye

Nihan Cankabal Ataoğlu
Karadeniz Technical University, Türkiye

Ninel Alver
Ege University, Türkiye

Niyazi Uğur Koçkal
Akdeniz University, Türkiye

Nurcan Öztürk
Karadeniz Technical University, Türkiye

Nuttawit Wattanasakulpong
Walailak University, Thailand

O. Burkan İşgör
Oregon State University

Omar Hamza
University of Derby, England

Onur Behzat Tokdemir
Istanbul Technical University, Türkiye

Onur Onat
İnönü University, Türkiye

Osman Kırtel
Sakarya University, Türkiye

Osman Sivrikaya
Karadeniz Technical University, Türkiye

Osman Tuğrul Baki
Karadeniz Technical University, Türkiye

Osman Üçüncü
Karadeniz Technical University, Türkiye

Ömer Yüksek
Karadeniz Technical University, Türkiye

Önder Halis Bettemir
Inonu University, Türkiye

Özer Çinicioğlu
Boğaziçi Üniversitesi, Türkiye

Özge Cordan
İstanbul Technical University, Türkiye

Özgür Avşar
Eskişehir Technical University, Türkiye

Özgür Özçelik
Dokuz Eylül University, Türkiye

Özlem Aydın
Karadeniz Technical University, Türkiye

Özlem Sağıroğlu Demirci
Gazi University, Türkiye

Parsa Ghannadi
Islamic Azad University, Iran

Ramazan Livaoğlu
Uludağ University, Türkiye

Reyhan Midilli Sarı
Karadeniz Technical University, Türkiye

Reza Maalek
Karlsruhe Institute of Technology, Germany

Rıfat Sönmez
Middle East Technical University, Türkiye

Sabah A. Mushatat
University of Wolverhompton, UK

Sabriye Banu İkizler
Karadeniz Technical University, Türkiye

Sadık Can Girgin
Dokuz Eylül University, Türkiye

Safa Nayır
Karadeniz Technical University, Türkiye

Salman Azhar
Auburn University, USA

Savaş Erdem
İstanbul University-Cerrahpaşa, Türkiye

Selda Al Şensoy
Karadeniz Technical University, Türkiye

Semiha Yılmazer
Bilkent University, Türkiye

Semra Çomu Yapıcı
Bogazici University, Türkiye

Serap Durmuş Öztürk
Karadeniz Technical University, Türkiye

Serkan Bekiroğlu
Yıldız Technical University, Türkiye

Serkan Kıvrak
Eskişehir Technical University, Türkiye

Servet Karasu
Bülent Ecevit University, Türkiye

Seyed Sina Kourehli
Azarbaijan Shahid Madani University, Iran

Sherif Mohamed
University of Southern Queensland, Australia

Sinan Melih Nigdeli
İstanbul University-Cerrahpaşa, Türkiye

Sinan Nacar
Gaziosmanpaşa University, Türkiye

Soroosh Sharifi
University of Birmingham, UK

Süleyman Adanur
Karadeniz Technical University, Türkiye

Şeref Oruç
Karadeniz Technical University, Türkiye

Şevket Ateş
Karadeniz Technical University, Türkiye

Talat Şükrü Özşahin
Karadeniz Technical University, Türkiye

Tayfun Dede
Karadeniz Technical University, Türkiye

Thuc P. Vo
LaTrobe University, Australia

Tuğçe Koç
Karadeniz Technical University, Türkiye

Turhan Bilir
İstanbul University-Cerrahpaşa, Türkiye

Umut Topal
Karadeniz Technical University, Türkiye

Victor Yepes
Universitat Politecnica de Valencia, Spain

Yalçın Yüksel
Yıldız Technical University, Türkiye

Yasin Fahjan
İstanbul Technical University, Türkiye

Yaşar Subaşı Dilek
Van Yüzüncü Yıl University, Türkiye

Yusuf Arayıcı
Northumbria University, UK

Zafer Bozkuş
Middle East Technical University, Türkiye

Zekai Angın
Karadeniz Technical University, Türkiye

Zeynep Işık
Yıldız Technical University, Türkiye

Zeynep Yılmaz
Karadeniz Technical University, Türkiye

ORGANIZERS

KTU 1955 KARADENİZ TECHNICAL UNIVERSITY

dynamic academy®

golden light publishing®

KARADENİZ TEKNİK ÜNİVERSİTESİ İnşaat Mühendisliği

KARADENİZ TEKNİK ÜNİVERSİTESİ Deprem ve Yapı Sağlığı Uygulama ve Araştırma Merkezi UYGAR

KARADENİZ TEKNİK ÜNİVERSİTESİ Mimarlık Bölümü

MAIN CONTRIBUTORS

TRABZON BÜYÜKŞEHİR BELEDİYESİ 1868

TMMOB İNŞAAT MÜHENDİSLERİ ODASI Trabzon Şubesi

CONTRIBUTORS

ORTAHİSAR BELEDİYESİ 2014 TRABZON

YOMRA BELEDİYESİ 1953

TÜRKİYE CUMHURİYETİ ÇEVRE, ŞEHİRCİLİK VE İKLİM DEĞİŞİKLİĞİ BAKANLIĞI

KGM

TRABZON
10. BÖLGE MÜDÜRLÜĞÜ

PLATINUM SPONSOR

USTA GRUP

GOLD SPONSORS

CENGİZ İNŞAAT

TÜREN İNŞAAT Taah.Nak.Tur.Mad.Tic.Ltd.Şti.

odaş

SILVER SPONSORS

ES DENİZCİLİK

KCT KCT YOL YAPI İNŞAAT TİC. A.Ş.

BRONZE SPONSORS

İNOSEL Çimento | Hazır Beton | Enerji

YAŞARTEK İNŞAAT & TAAHHÜT

AKM YAPI Taahhüt San. Ve Tic. A.Ş.

SERVICE SPONSORS

CAFFE HAMBURGER PIZZA & SALAD crakers pizza

KURUKAHVECİ MEHMET EFENDİ

4th International Civil Engineering & Architecture Conference
17-19 May 2025, Trabzon, Türkiye

Nonlinear time-history analysis of a steel-reinforced concrete composite building according to TBEC-2018

Ömer F. Şahin[1*], Süleyman Adanur[2], Hakan T. Türker[3], Ahmet C. Altunışık[2]

[1] *Karadeniz Technical University, The Graduate School of Natural and Applied Sciences, Civil Engineering Graduate Program, 61080 Trabzon, Türkiye*
[2] *Karadeniz Technical University, Department of Civil Engineering, 61080 Trabzon, Türkiye*
[3] *Uludag University, The Graduate, Department of Civil Engineering, 16285 Bursa, Türkiye*

Abstract. Turkey is recognized as one of the most seismically active regions in the world. The 1999 Kocaeli, 1999 Düzce, 2011 Van, 2020 Elazığ-Malatya, 2020 İzmir, and 2023 Kahramanmaraş earthquakes are among the significant seismic events in recent years that have resulted in substantial losses. These earthquakes have revealed that a large portion of the building stock in our country is vulnerable to earthquakes. Chapter 15 of the Turkish Building Earthquake Code-2018 (TBEC-2018) includes guidelines for evaluating existing building systems under seismic effects. In this study, the earthquake performance of a composite building consisting of reinforced concrete (RC) shear walls and steel frames was examined using a nonlinear time-history analysis method in line with the specified rules and calculation principles. Eleven real earthquake records were selected, scaled, and used for the nonlinear time-history analyses. The building under investigation is located in the Iskenderun district of Hatay province, and it sustained no damage during the February 6, 2023, Kahramanmaras earthquakes and is currently in active use. In the final section of the study, ground motion records from the February 6, 2023 Pazarcik (7.7 Mw) earthquake were obtained from two different stations and applied to the building model and the results obtained from the analyses were then examined.

Keywords: Existing Steel-RC Building; Nonlinear Analysis; TBEC-2018; Performance Assessment; February 6 2023 Pazarcik-Kahramanmaraş Earthquake

1. Introduction

Located on a geography where three different tectonic plates intersect, Turkey has a high potential to produce earthquakes in terms of seismic risk. For this reason, many earthquakes occur in this geography. The 1999 Izmit and Düzce earthquakes, 2003 Bingöl, 2011 Van, 2020 Elâzığ, 2020 İzmir and 2023 Kahramanmaraş earthquakes are the events that occurred in Turkey in recent years and caused great losses. On February 6, 2023, two major earthquakes with magnitudes of 7.7 Mw (Pazarcık) and 7.6 Mw (Elbistan) in Kahramanmaraş, Turkey, caused extensive damage and loss of life in 11 provinces in the region. As a result of these earthquakes, more than 700,000 buildings were affected and more than 230,000 were severely damaged or destroyed (Presidency of Strategy and Budget, 2023).

The results of all these earthquakes show that there are still many earthquake resistant structures in our country. Investigation of the structures that have been damaged, collapsed or are still in use and undamaged under the earthquake effect will be beneficial for the design of earthquake resistant structures.

There are guidelines in the literature on earthquake performance assessment of existing structures. Guidelines such as ATC-40 (Applied Technology Council, 1996), FEMA 356 (FEMA, 2000), FEMA 440 (FEMA, 2005), and TBEC 2018 (TBEC, 2018) are some of them.

In this study, the earthquake performance evaluation of Steel's Tower (A Block), which is known to be undamaged after the Kahramanmaraş earthquakes that occurred on February 6, 2023, was carried out according to TBEC 2018 code. This building is located in İskenderun district of Hatay province. The structural system of this building with a height of 52.2 m is composed of steel columns-beams and reinforced concrete walls.

ETABS software was used for nonlinear analysis and 3D modeling in time domain. Plastic rotational hinge are defined at both ends of columns and beams. Fiber hinge model was used for reinforced concrete shear walls. According to TBEC 2018, 22 (2x11) real earthquake records were selected, scaled and used for nonlinear time-history analysis. The earthquake performance level of the building was determined. Then, the ground motion

* Corresponding author, E-mail: sahinfaruk.ins@outlook.com

https://doi.org/10.31462/icearc2025_ce_eqe_020

acceleration records of the February 6, 2023 Pazarcık (7.7 Mw) earthquake, obtained from stations 3112 and 3115 located close to the building, were applied to the analysis model and the results were analyzed.

2. Building properties and seismicity of the region

Built in 2014, Stell Tower's buildings were designed within the scope of TEC-2007 (TEC, 2007) and constructed as three blocks separated by dilatation gaps. This study was carried out on block A. Columns are made of S275 quality HE240A, HE260A, HE300A, HE340A, HE360A, HE400A, HE450A, HE500A, HE550A, HE600A, HE650A, HE700A, HE700B, HE650B profiles. Beams consist of IPE and HEA profiles with different sizes. In the center of the building there is a core consisting of reinforced concrete shear walls. The width of the shear wall members is 30 cm. The shear walls are connected using reinforced concrete beams with dimensions of 30cm x 80cm. The structural slab system is a 12cm high composite slab composed of high strength trapezoidal plate, stud nails and concrete material placed on steel beams. In the analysis model, it is assumed that the floor system has rigid diaphragm behavior. The floor heights are 3 m in the basement, 4.2 m in the ground floor, 3.2 m in the first floor, 2.8 m in the second floor, 3.6 m in the third floor and 3.2 m in all other floors.

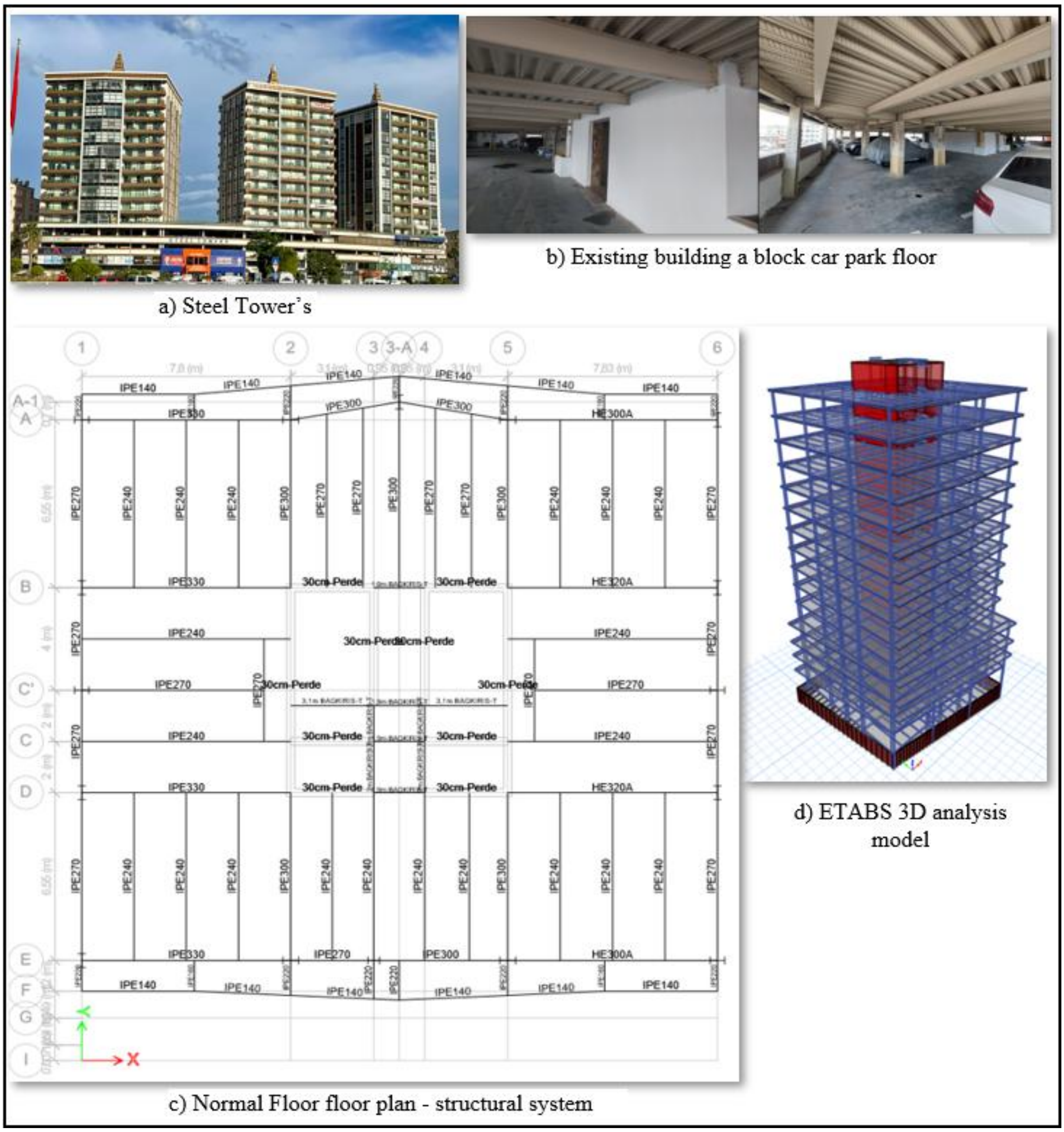

a) Steel Tower's

b) Existing building a block car park floor

c) Normal Floor floor plan - structural system

d) ETABS 3D analysis model

Fig. 1. Steel Tower's building views, floor structural plan and analysis model

Hata! Başvuru kaynağı bulunamadı. Fig. 1 (a) shows the exterior view of the building, (b) shows the structural system images taken from the parking lot floor, (c) shows the normal floor structural system plan and (d) shows the structural analysis model created using ETABS program.

Block A is 23.7 m in X direction and 21.1 m in Y direction and its structural system is geometrically close to a square. Reinforced concrete shear walls are placed to surround the stair and elevator shafts in the center of the building. These shear wall elements were placed in the building with a total of 6 pieces of 3.1 m in X direction, 2 pieces of 8 m and 2 pieces of 4.6 m in Y direction.

According to the geotechnical investigation conducted in 2013, the primary wave velocity (V_p) of the soil was found to be 668 m/s, the shear wave velocity (V_s) was 498 m/s, and the average shear wave velocity in the upper 30 meters ($V_{s(30)}$) was determined to be 474 m/s. The soil subgrade reaction coefficient was calculated as 3000 t/m³. Since the performance analysis of the relevant building will be conducted in accordance with TBEC 2018 within the scope of this thesis, the local soil class has been selected as ZE based on Table 16.1 of TBEC 2018, and the relevant parameters have been determined accordingly.

Hatay province is a city located on the Eastern Anatolian Fault Zone (EAFZ). Fig. 2**Hata! Başvuru kaynağı bulunamadı.** obtained from the Republic of Turkey Ministry of Interior Disaster and Emergency Management Presidency Turkey Acceleration Database and Analysis System, shows the earthquakes (Mw>5.0) that occurred in the region after 2000. The destructive February 6, 2023 Pazarcık 04:17 (7.7 Mw) and February 6, 2023 Elbistan 10:24 (7.6 Mw) earthquakes occurred on the EAFZ. When the ground motion records of the related earthquakes are analyzed, the largest ground acceleration of the Pazarcık earthquake was measured at station 4614 and was 2.005g in the E-W direction.

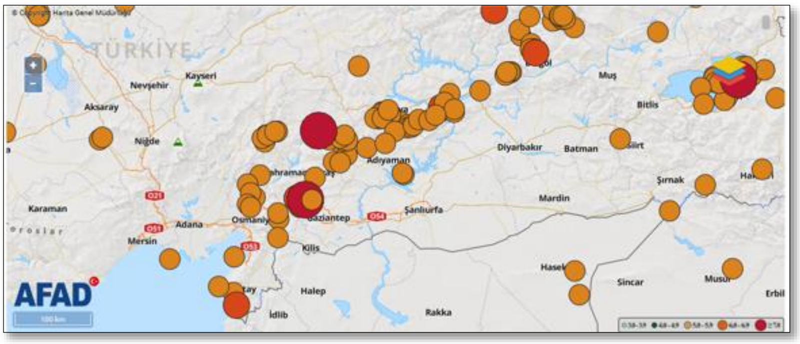

Fig. 2. Earthquakes in the region after 2000 (MW>5.0) (Turkey Strong Motion Database and Analysis System)

The performance analysis was performed using 22 (2x11) earthquake records selected in accordance with TBDY 2018. Then, acceleration records obtained from stations 3112 and 3115, which are the closest stations to the structure, were used in the analysis to examine the effect of the February 6, 2023 Pazarcık (7.7Mw) earthquake that occurred in the region (Fig. 3).

Fig. 3. Station locations 3112-3115

3. Analysis model and earthquake forces

Unconfined concrete, confined concrete and steel material models for reinforced concrete shear wall and beam elements were determined using the relations given in TBEC 2018 (Fig. 4**Hata! Başvuru kaynağı bulunamadı.**). Concrete characteristic compressive strength is defined as 35 Mpa, structural steel quality class is defined as S275 and reinforcing steel quality class is defined as B420C. Reinforced concrete beam section is 30 cm x 80 cm and 5 reinforcements with 18 mm diameter were used as top and bottom reinforcement and 5 reinforcements with 12 mm diameter were used as web reinforcement. Reinforcement with a diameter of 12 mm at 10 cm spacing was used as confined reinforcement. The length of the start-end zone of the shear walls was 60-100 cm and 14 longitudinal reinforcements with a diameter of 22 mm and 16 mm diameter reinforcements with a spacing of 10 cm were used as confined reinforcement. Longitudinal reinforcement with a diameter of 18 mm at 12 cm spacing and reinforcement with a diameter of 16 mm at 12 cm spacing were used as horizontal reinforcement in the middle parts of the wall. The nonlinear material models obtained by using the specified material and section properties were defined in ETABS program (Fig. 5).

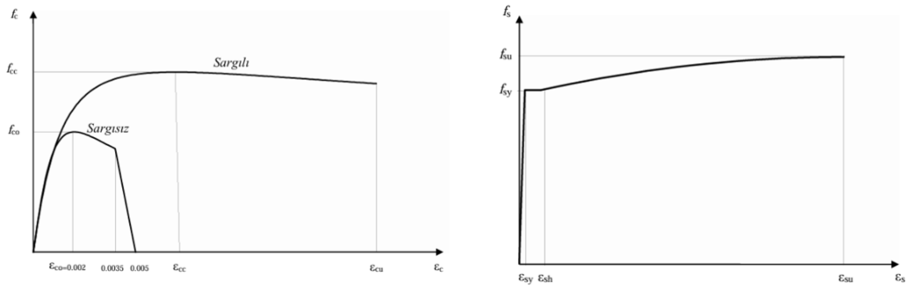

Fig. 4. Confined-unconfined concrate and steel material models *(TBEC, 2018)*

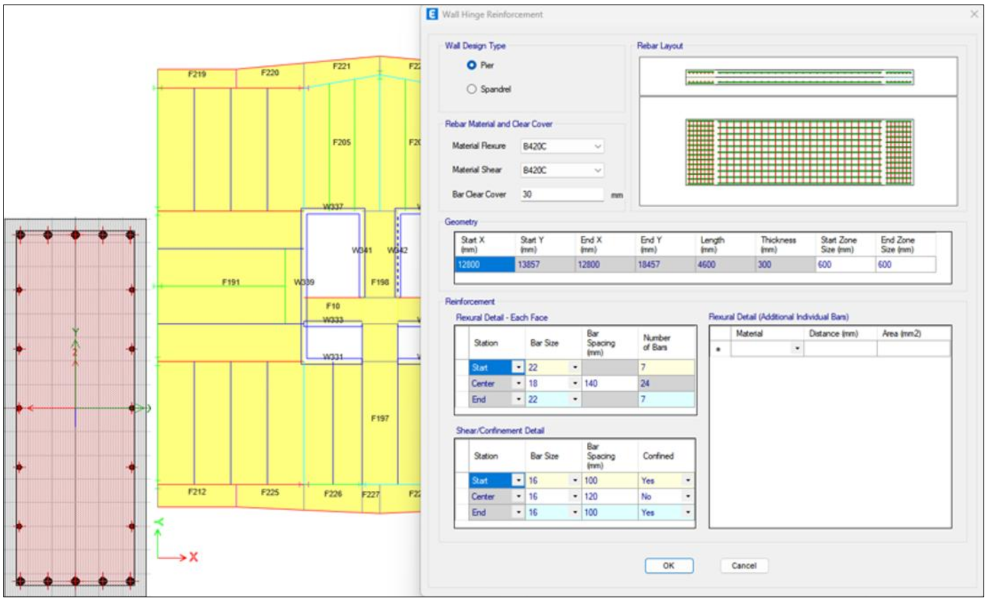

Fig. 5. Beam and shear wall models defined in ETABS program

3.1 Hinge properties

Steel column members are modeled as finite bar elements. In order to represent the nonlinear behavior of these members, lumped plastic hinges were defined at both ends of the members. The axial compressive-tensile strengths of each column section were determined according to the 'Regulation on Design, Calculation and Construction Principles of Steel Structures' (2016) and the interaction diagram (axial force-moment) yield surface was obtained. P-M2-M3 plastic hinge definitions were made through ETABS program.

In the existing structure, single-double angle joint details were used in the connections of steel beam members to shear walls and columns. The moment transfer capacity of this type of connections is very low compared to rigid connections. In this structure, it is assumed that the steel beam members do not transfer moment to the shear walls and columns and the beam ends are modeled as hinged. Since no plastic deformation is expected in hinged joints, no plastic hinge is assigned to the beam members (Fig. 6).

Fig. 6. Steel beam connection details of the existing structure

M3 lumped plastic hinge was defined for reinforced concrete beam elements. SAP2000 program was used to obtain moment-curvature graph for cross-sectional analysis. The yield moment value My=620 kNm and yield curvature value ϕy= 0.0052 were used in the analysis as read from the idealized curve (Fig. 7).

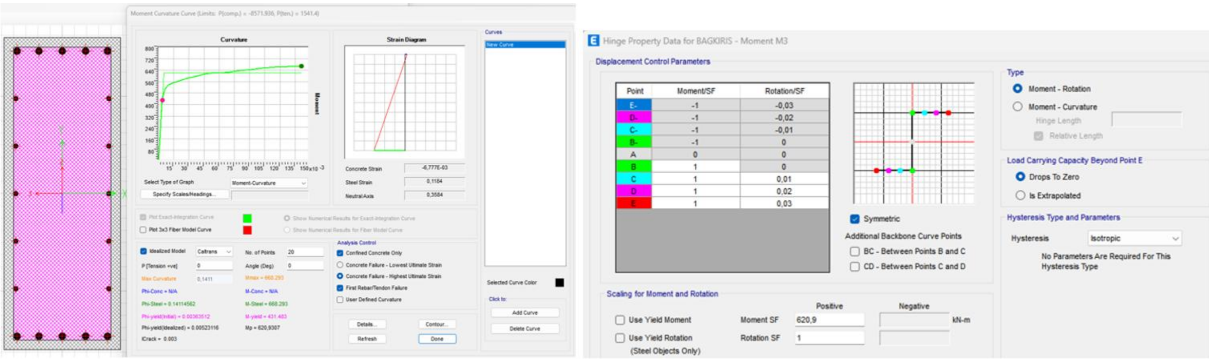

Fig. 7. Cross-sectional analysis and definition of M3 plastic hinge

Reinforced concrete shear walls were assigned fiber P-M3 hinge with the help of ETABS program and shear sections were divided into fiber elements (Fig. 8).

Fiber	Area cm²	Coord2 mm	Material	Color
1	436,7	-2225	C25/30	
2	873,4	-2000	C25/30	
3	436,7	-1775	C25/30	
4	26,6	-2150	B420C	
5	26,6	-1850	B420C	
6	628,6	-1593,8	C25/30	
7	1257,2	-1275	C25/30	
8	1257,2	-850	C25/30	
9	1257,2	-425	C25/30	
10	1257,2	0	C25/30	

Fig. 8. Reinforced concrete shear wall section fiber P-M3 hinge

The effective section stiffnesses of the beam members using lumped plastic hinges are included in the calculations using the equations given in TBEC 2018 (Eq. (1), Eq. (2)).

$$(EI)_e = \frac{M_y}{\theta_y}\frac{L_s}{3} \tag{1}$$

$$\theta_y = \frac{\phi_y L_s}{3} + 0{,}0015\eta\left(1 + 1{,}5\frac{h}{L_s}\right) + \frac{\phi_y d_b f_{ye}}{8\sqrt{f_{ce}}} \tag{2}$$

3.2 Loads and loading cases affecting the structure and seismic loads
The dead loads acting on the structure are as follows;
Slab Loads: Trapezoidal sheet plate under concrete + Slab Concrete (12cm) = 2.1 kN/m^2
Coating + Plaster = 1.6 kN/m^2
Partition Walls = 1 kN/m^2
Total Slab Dead Load = 4.7 kN/m^2
External Walls (20cm) = 4.9 kN/m
Roof Snow Load S = 0.75 kN/m^2
Slab live loads are considered as 2 kN/m^2 and 5 kN/m^2 depending on the floor usage purposes.

The earthquake loads to be applied to the existing structure and the horizontal elastic response spectrum to be used in determining the damage conditions of the structure under these loads were determined according to TBEC 2018 (Fig. 9).

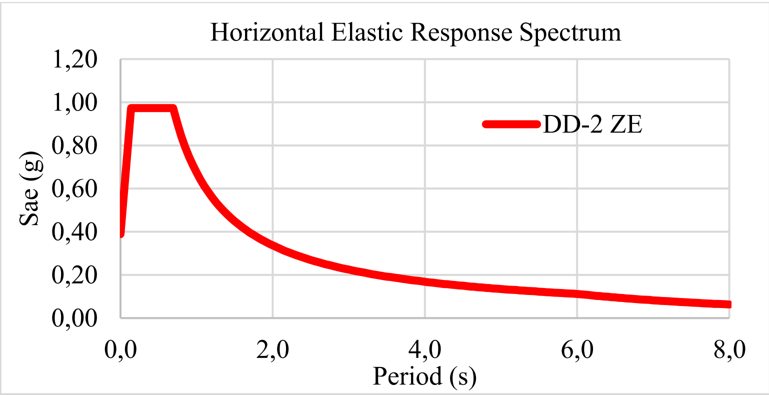

Fig. 9. Horizontal elastic response spectrum

In this study, the Pacific Earthquake Engineering Research Center Ground Motion Database (PEER) NGA West2 Data Bank created by the University of California was used to select the eleven acceleration records required for three-dimensional nonlinear analysis (**Hata! Başvuru kaynağı bulunamadı.**). SeismoMatch (Al-Atik & Abrahamson, 2010) program was used to convert the selected acceleration records to spectral matching (Fig. 10).

Table 1. Selected 11 earthquake acceleration records (PEER)

No	Earthquake	Record Number	Year	Station name	Magnitude	Rrup (km)	Vs30 (m/sn)	Lowest Usable Frequency
1	Imperial Valley-06	178	1979	El Centro Array #3	6.53	12.85	162.94	0.0625
2	Imperial Valley-06	179	1979	El Centro Array #4	6.53	7.05	208.91	0.0625
3	Superstition Hills-02	721	1987	El Centro Imp. Co. Cent	6.54	18.2	192.05	0.0875
4	Superstition Hills-02	728	1987	Westmorland Fire Sta	6.54	13.03	193.67	0.0875
5	Landers	900	1992	Yermo Fire Station	7.28	23.62	353.63	0.07
6	Kobe_ Japan	1101	1995	Amagasaki	6.9	11.34	256.0	0.125
7	Kobe_ Japan	1116	1995	Shin-Osaka	6.9	19.15	256.0	0.125
8	Kocaeli_ Turkey	1158	1999	Duzce	7.51	15.37	281.86	0.1
9	Duzce_ Turkey	1602	1999	Bolu	7.14	12.04	293.57	0.0625
10	Duzce_ Turkey	1605	1999	Duzce	7.14	6.58	281.86	0.1
11	El Mayor-Cucapah_ Mexico	5827	2010	Michoacan De Ocampo	7.2	15.91	242.05	0.0625

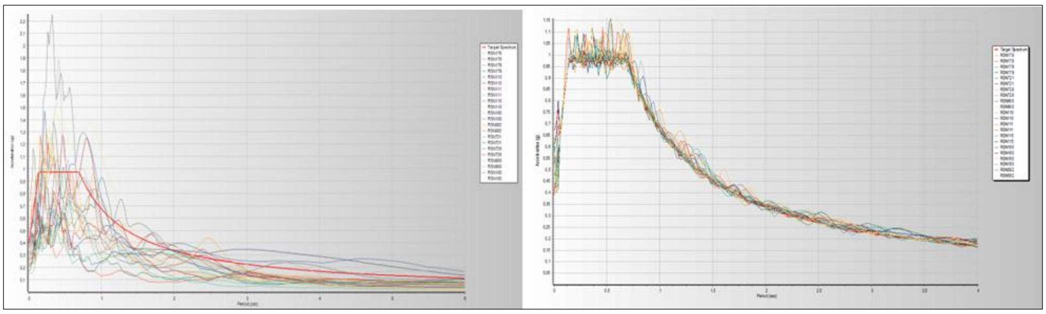

Fig. 10. Match to target spectrum *(SeismoMatch, 2022)*

3.3 Modal analysis results

Dynamic modal analysis of the structure for 50 mode numbers was performed in ETABS program. According to the modal analysis results, the 1st mode has the largest mass participation in the X direction (63.60%) and the 2nd mode has the largest mass participation in the Y direction (63.80%). The dominant mode in X direction is 1st mode with a period value of 2.07 s, and the dominant mode in Y direction is 2nd mode with a period value of 1.510 s.

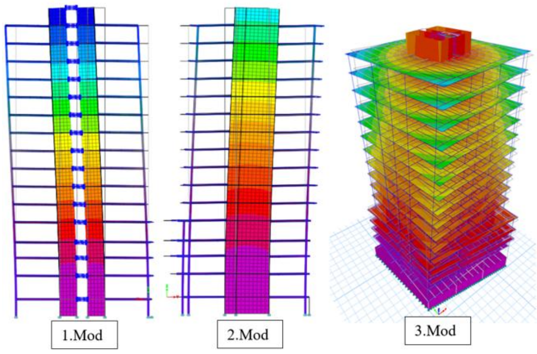

Fig. 11. Mode shapes *(ETABS, 2018)*

4. Nonlinear analysis and evaluation

In TBEC 2018, the condition where inelastic deformation starts significantly and the damage level remains negligible is considered as 'Immediate Occupancy ' (IO) performance level. The condition where the non-linear behaviour stops significantly is called 'Limited Damage' (LD) performance level. After large displacements, the reduction of the earthquake effect indicates that the strength is exhausted and this level is defined as 'Collapse Prevention' (CP) performance level. The limit at which the structural system can safely resist horizontal loads with limited inelastic deformations is defined as the 'Life Safety' (LF) performance level.

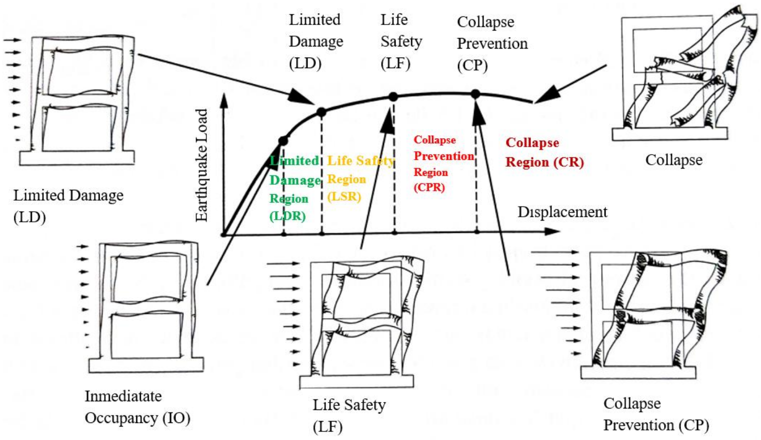

Fig. 12. Damage states TBEC 2018 *(Celep, 2020)*

22 earthquake ground motion acceleration records were used to determine the damage conditions of reinforced concrete beam, reinforced concrete shear wall and steel column elements for each floor level by averaging the maximum strain and rotation values obtained from the analysis results.

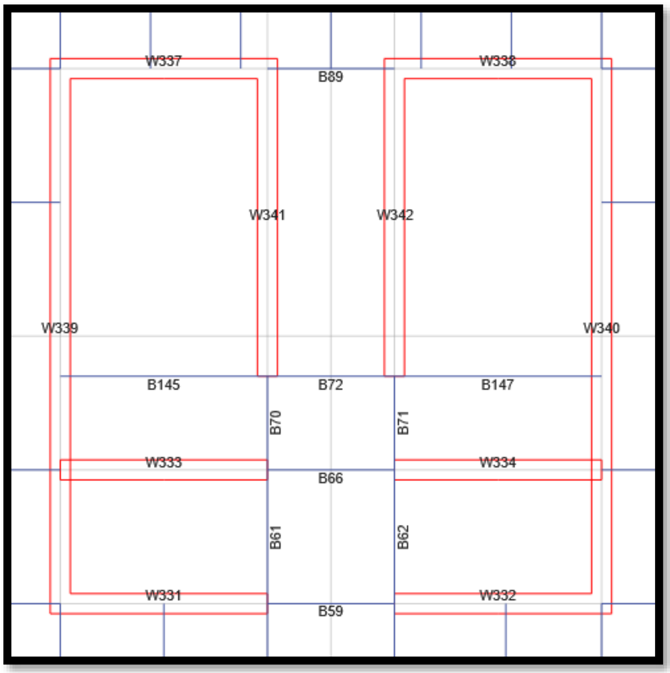

Figure 13. Shear walls and reinforced concrete beams

There are 10 reinforced concrete beams on each floor of the existing building. According to the results of the performance analysis, only the reinforced concrete beam elements in the X direction are damaged. No plastic deformation occurred in the reinforced concrete beam elements in the Y direction. Table 2 shows the proportional distribution of all reinforced concrete beams according to the damage levels.

Table 2. All structure beam damage level percentages

Total			
	Pieces	Ratio	
LDR	105	%LDR	61.76
LSR	43	%LSR	25.29
CPR	8	%CPR	4.71
CR	14	%CR	8.24

Shear force control of reinforced concrete beam elements in the existing structure was performed by following the steps in TBEC 2018 and TS500. In these controls, it was determined that the beam members were designed ductile.

When the flexural damages of reinforced concrete shear walls were analyzed, it was observed that each shear wall remained at 'Limited Damage Region'. The shear capacities of the reinforced concrete shear wall elements were determined using the formulas provided in TBEC 2018 and (Institute) ((Eq. (3), Eq. (4)). Capacity checks were performed by averaging the maximum shear forces obtained from the 22 analyses. It was observed that their shear capacities were sufficient.

$$V_r = A_{ch}\left(0{,}65 + f_{ctd} + \rho_{sh} f_{ywd}\right) \tag{3}$$

$$V_e \leq V_r$$

$$V_e \leq 0{,}85 A_{ch}\sqrt{f_{ck}} \tag{4}$$

$$V_e \leq 0{,}65 A_{ch}\sqrt{f_{ck}}$$

According to the results of the nonlinear analysis, no plastic rotations occurred at the ends of the steel columns. Since the plastic rotation values at the ends of the columns are zero, all columns remain at 'Limited Damage' (SH) performance level.

4.1 February 6, 2023 effects of Kahramanmaraş (Pazarcık) Earthquake on the structure
7.7 Mw Pazarcık earthquake acceleration records were obtained from stations 3112 and 3115 (Fig. *13*) located close to the structure (Fig. 13). The related records were applied to the existing building model and the results such as base shear force values, relative story drifts, peak displacement values were analyzed.

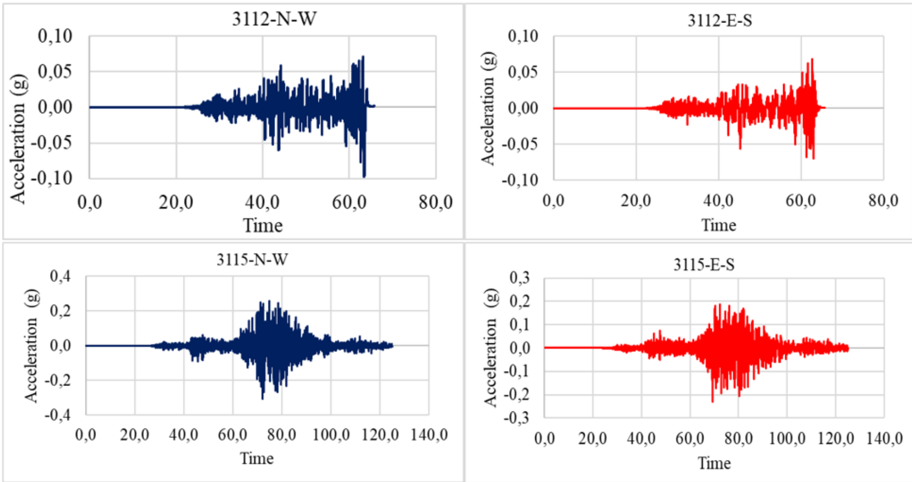

Fig. 13. February 6, 2023 Pazarcık earthquake 3112 and 3115 station acceleration records

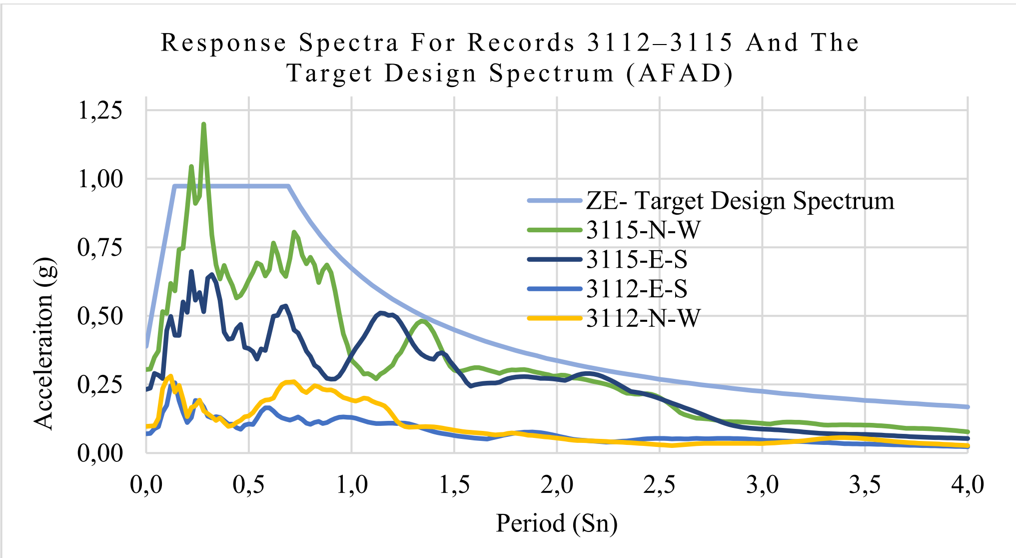

Fig. 14. Response Spectra For Records 3112–3115 And The Target Design Spectrum

When the spectral acceleration values obtained from horizontal ground motion records are compared with the horizontal elastic design spectrum values derived from the Earthquake Hazard Map, it is observed that the actual earthquake at Station 3112 remained below the design spectrum for DD-2 (Design Earthquake) level (Fig. 14). When the spectral acceleration values obtained from the horizontal ground motion records are compared with the horizontal elastic design spectrum values derived from the Earthquake Hazard Map, it is observed that the response spectrum values of the N-W component at Station 3115 exceed the DD-2 target spectrum for period values between 0.20 and 0.26 seconds. On the other hand, the spectral acceleration values of the E-S component remain below the DD-2 target spectrum (Fig. 14).

The earthquake ground motion records of the processed data from stations 3112 and 3115 were defined in ETABS program and loading cases were created. Loading cases were defined to impact the structure from both directions. Then, the directions of the acceleration records were turned 90 and the structure was again affected. The graphs of 'Relative Story Displacement', 'Story Shear Forces' and 'Story Displacements' values are given in (Fig. 15).

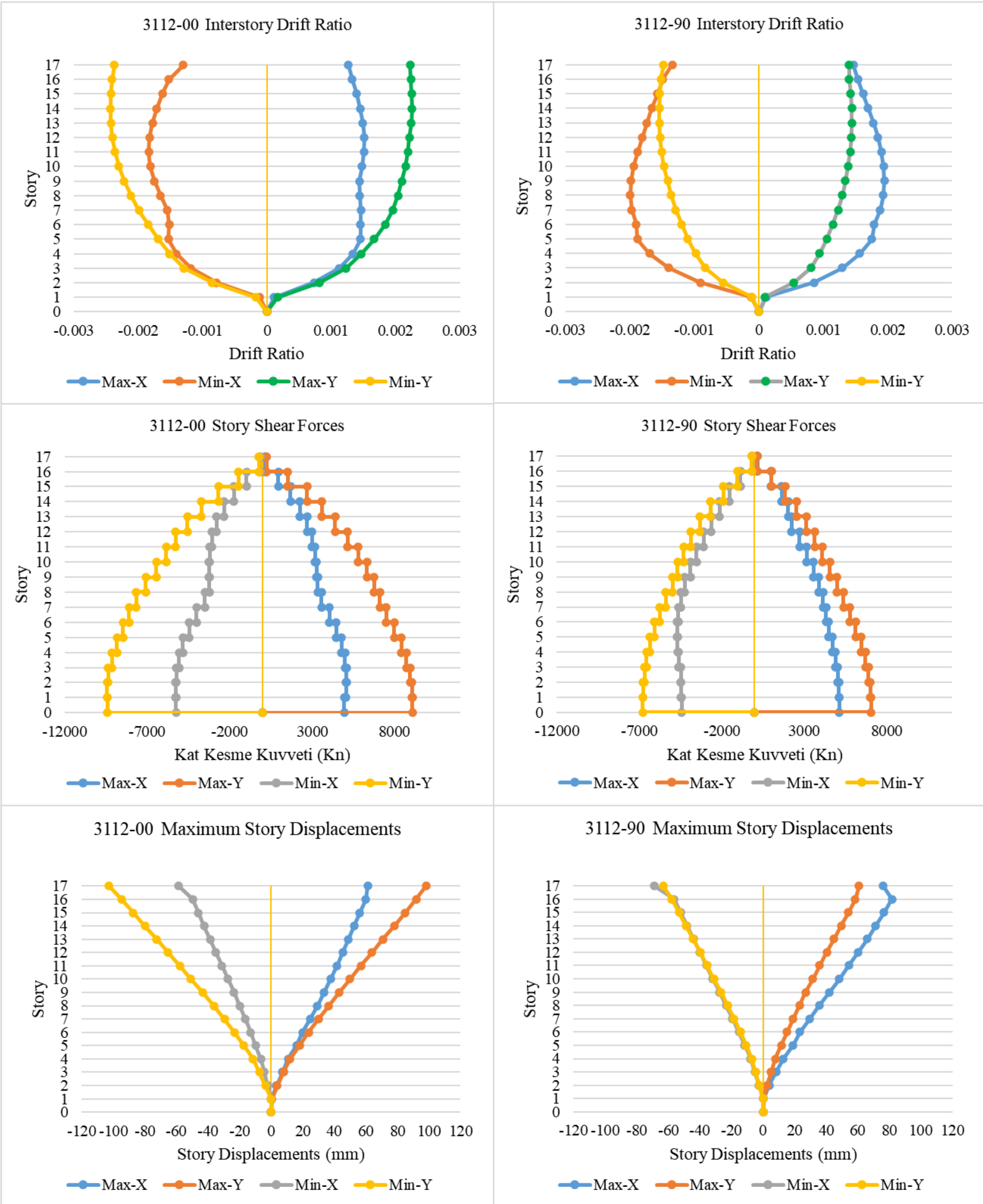

Fig. 15. 'Interstory Drift Ratio', 'Storey Shear Forces' and 'Storey Displacements' graphs for RSN3112-00 / RSN3112-90 loadings

Based on the analysis of ground motion acceleration records from the 3112 station for the February 6 Pazarcık (Kahramanmaraş) earthquake, the maximum peak displacement was observed to be approximately 0.102 meters. The interstory drift ratios remained around 0.2%. According to the records of the Pazarcık earthquake, the maximum base shear force was calculated as 9401.35 kN. As a result of the analyses conducted using the 3112 station records, all steel column, reinforced concrete beam, and shear wall elements in the existing structure remained within the Limited Damage (LD) performance level, and no brittle failure behavior was observed.

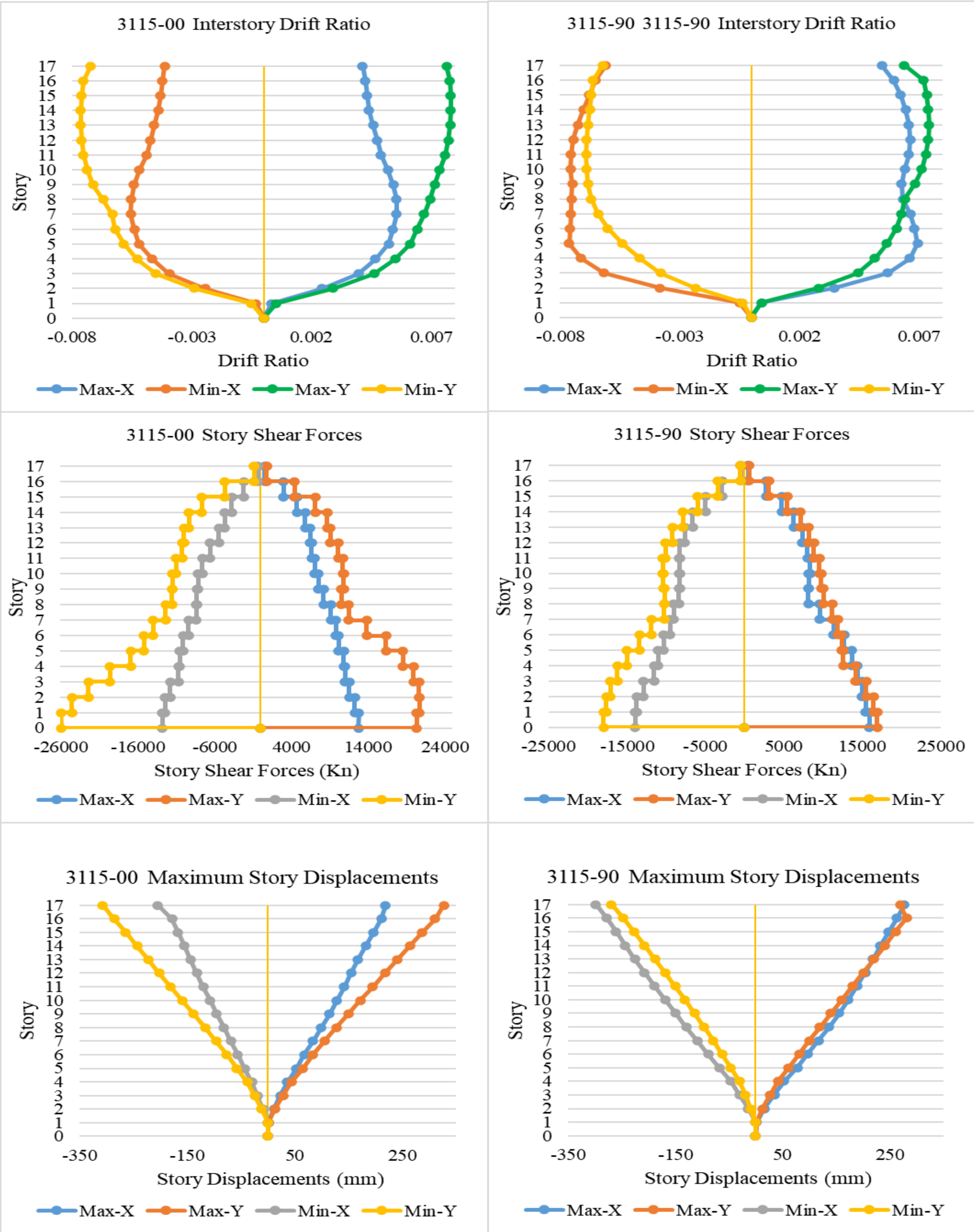

Fig. 16. 'Interstory Drift Ratio', 'Storey Shear Forces' and 'Storey Displacements' graphs for RSN3115-00 / RSN3115-90 loadings

Based on the ground acceleration records obtained from Station 3115 for the February 6 Pazarcık (Kahramanmaraş) earthquake, the maximum peak displacement was observed to be approximately 0.32 meters. The interstory drift ratios remained around 0.7%. According to the records of the Pazarcık earthquake, the maximum base shear force was calculated as 25933 kN.

5. Conclusions

The results obtained from the two stations show noticeable differences. According to the data recorded at Station 3112, no seismic effects significant enough to cause damage were observed in the building. In contrast, the results from Station 3115 indicate that the seismic demand may have caused minor damage specifically in the reinforced concrete beam elements of the structure. However, post-earthquake inspections revealed no visible damage in the building. It is important to recognize that the ground motion records from these stations may not fully represent the actual seismic demands experienced by the building during the February 6 earthquakes, due to factors such as the distance between the stations and the structure, and differences in local site conditions. Station 3112 is located closer to the building, near the coastal area, while Station 3115 is situated further inland compared to Station 3112.

According to the data from Station 3115, the peak ground acceleration (PGA) reached approximately 0.304g, whereas the maximum PGA value recorded at Station 3112 was around 0.101g. In İskenderun district of Hatay province, the level of building damage varied significantly across different areas—while some regions experienced severe structural damage, others were affected much less. One possible reason for this variation could be the differences in ground accelerations, even between nearby locations. The area extending from İskenderun's PAC Square toward the 'Steel Towers', and slightly beyond, contains buildings that suffered heavy damage. Moving from PAC Square toward the coastline, the severity of damage gradually decreases. The building stock between the PAC Square and the coast is notably old, with sandy soil conditions and a high groundwater level. Based on regional damage patterns and the ground motion values recorded by nearby seismic stations, it can be concluded that the February 6 earthquakes caused spatially variable ground accelerations in this region.

References

Al-Atik, L., & Abrahamson, N. (2010). An improved method for nonstationary spectral matching. *Earthquake Spectra, 26*(6), 601-617.

Applied Technology Council. (1996). *Seismic evaluation and retrofit of concrete buildings. ATC-40, CA, 1-2.*

Celep, Z. (2020). *Nonlinear Behavior and Analysis in Reinforced Concrete Structural Systems.* İstanbul: Beta Publishing, Printing, and Distribution Inc.

Disaster and Emergency Management Authority. (2018). *Turkey Strong Motion Database and Analysis System*.

ETABS. (2018). Computer and Structures Inc. *ETABS: Extended Three-dimensional Analysis of Building Systems. Berkeley, CA, USA*.

Federal Emergency Management Agency. (2000). *Prestandard and commentary for the seismic rehabilitation of buildings. FEMA-356.* Washington, DC.

Federal Emergency Management Agency. (2005). *Improvement of nononlinear static seismic analysis procedures. FEMA-440.* Washington, DC.

Institute, T. S. (2000). Design and Construction Rules of Reinforced Concrete Structures. TS-500, Ankara, 75 p.

Ministry of Environment And Urbanization. (2016). *Regulation on the Design, Calculation, and Construction Principles of Steel Structures.*

PEER. (2013). *Peer Ground Motion Database, Pacific Earthquake Engineering Research Center*.

Presidency of Disaster and Emergency Management. (2007). *Turkish earthquake code. TEC.* Ankara.

Presidency of Disaster and Emergency Management. (2018). *Turkish building earthquake code. TBEC.* Ankara.

Presidency of Strategy and Budget. (2023). *Report For Kahramanmaras and Hatay Earthquake.*

SeismoMatch. (2022). *[Computer Software] Seismosoft, Earthquake Engineering Software Solutions*. Messiana, Italy.

Determining the collapse mechanism of a historical minaret under the earthquake effect by finite element simulation

Esin Ertürk Atmaca[1], Ali F. Genç[1], Süleyman Adanur[1], Ahmet C. Altunışık*[1]

[1] Karadeniz Technical University, Department of Civil Engineering, 61080 Trabzon, Türkiye

Abstract. One of the structural parts of the mosques is the minarets, which have a special symbolic significance as well as their functionality. Minarets, which are long and thin in terms of their structure, are very sensitive to earthquake effects compared to the main structures of mosques. They are among the first structures to be damaged or destroyed during and earthquake. In the last century, several devastating earthquakes have occurred in Türkiye and many minarets have been damaged in these earthquakes. One of them is minaret of the historical Yenipazar Mosque. It is narrated that the minaret collapsed in the 1939 Erzincan Earthquake. The purpose of this study is to examine the accuracy of this narration from a technical point of view and determine how the collapse mechanism of the minaret occurred. The finite element (FE) method was used to determine the collapse mechanism of the minaret. The FE model was created in the Abaqus, and nonlinear dynamic analysis was carried out by using 1992 Erzincan Earthquake. It has been observed that the damage mechanism occurred transition segment of the minaret. Tensile stresses occurred locally in this region. This situation can be caused by the difference in stiffness between the slender body and the more rigid pedestal. So, it is very important to determine the collapse mechanisms under the effect of a possible earthquake and take the necessary precautions for this type structures.

Keywords: Collapse mechanism; Finite element simulation; Nonlinear dynamic analysis

1. Introduction

Historical masonry minarets are as enduring icons of architectural and cultural significance across various regions of the world. These magnificent structures, which is primarily associated with Islamic architecture, serving as symbols of religious devotion, architectural mastery, and cultural identity. They are characterized by their towering, slender, and often ornate designs, making them essential components of mosques.

These iconic historical structures have endured for centuries, witnessing various environmental challenges, including seismic events that threaten their structural integrity. Minarets, which are long and thin in terms of their structure, are very sensitive to earthquake effects compared to the main structures of mosques. During an earthquake, they are often among the first structures to be damaged or destroyed. The vulnerability of masonry minarets, which constructed using a variety of materials such as brick, stone, and mortar, lies not only in their height and slender profiles. Also, the intricacy of their designs can cause complex structural behaviour during seismic events. As a matter of fact, understanding the seismic performance of masonry minarets is of importance to safeguard these historical culture and ensure continuity to future. So, it is very important to determine the collapse mechanisms under the effect of a possible earthquake.

In understanding the seismic behaviour of masonry minarets, it has made significant strides in recent years. Studies employing have advanced analytical methods, including finite element analysis and experimental testing, have shed light on their seismic response (Mirtaheri, et al., 2017;Erdoğan et al., 2019;Hökelekli et al., 2020; Hökelekli and Al-Helwani, 2020; Altıok and Demir, 2021a, 2021b; Yurdakul et al., 2021; Işık et al., 2022; Maras et al., 2022; Trešnjo et al, 2023). In addition, innovative retrofitting techniques have been proposed to mitigate seismic risks while preserving their historical and architectural value (Turk, 2013; Bayraktar and Hökelekli, 2021; Şentürk et al., 2022; Demir et al., 2023).

This paper aims to evaluate the seismic performance of a historical masonry minaret, determine the collapse mechanism, and offering insights into the complex behaviour of these type structures, which are located in seismically active regions. Within the scope of this purpose, a historical masonry minaret, which is rumoured to have collapsed in the 1939 Erzincan earthquake, was selected and its seismic behaviour was examined. Modal analysis, and nonlinear dynamic analyses were carried out. The collapse mechanism was evaluated and the results obtained were evaluated according to the relevant guide.

* Corresponding author, E-mail: ahmetcan@ktu.edu.tr

https://doi.org/10.31462/icearc2025_ce_eqe_025

2. Description of historical minaret

Yenipazar Mosque is located in Ordu province of Turkey and was built in 1870 (Fig. 1). It is narrated that the minaret collapsed in the 1939 Erzincan Earthquake. In addition, no study has been carried out on the minaret of the mosque until today. In order to reconstruct the historical minaret, the minaret types of the demolished or standing mosques in its immediate vicinity were determined. Although some of the mosques were destroyed, a restoration project was prepared using the minarets of that period as an example.

Fig. 1. Some views of Yenipazar Mosque and minaret

The pedestal part of the historical minaret has a square geometry and the body part has a circular geometry. The minaret has a total length of 22.17m. The wall thickness is 20cm at the pedestal and 16cm in other sections. The inner diameter of the cylindrical body is 1.26m and the outer diameter is 1.58m. Step length and height of the stairs are 60cm and 22cm, respectively. The minaret is supported on the mosque from one side along the pedestal. Views and sections of survey drawings prepared by taking into account the geometric data of the historical minaret are given in Fig. 2.

3. Evaluation of structural performance

The finite element (FE) method was used to determine the structural behaviour of the historical minaret. The FE model was created in the Abaqus software taking into account the macro modelling technique (Abaqus, 2022) (Fig. 3). Linear tetrahedron C3D4 finite solid element with 4 nodes was used in the FE model. To evaluate the structural behavior of the historical minaret, modal and nonlinear dynamic analysis were carried out.

The collapsed minaret was reconstructed with ashlar stone. Also, rubble stone was used in the filling part of the pedestal of the minaret. As know, the material properties of historical buildings are often difficult to precisely know and destructive and/or non-destructive methods are required to obtain the material properties. In this study, values specified in the guideline called Earthquake Risk Management Guide for Historical Structures were considered in the selection of the material properties (GMERHS, 2017) (Table 1). The guideline, which is published in Turkey, purpose the assessment the seismic performance level of historical masonry structures. On the other hand, Concrete Damage Plasticity (CDP) material model, which is a constitutive model based on a combination of theory of plasticity and damage mechanics, was considered in nonlinear dynamic analysis. The relevant nonlinear parameters (Table 2 and Table 3) considered in the analysis for the masonry units were selected from the literature (Bayraktar and Hökelekli, 2021).

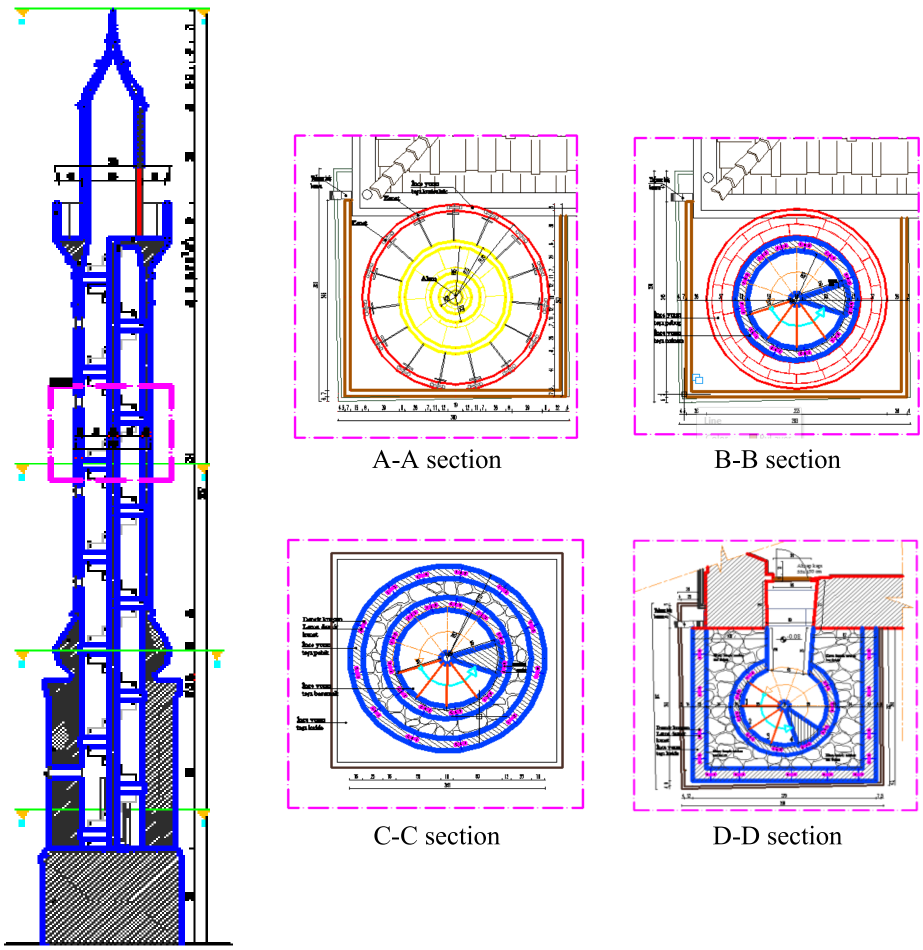

Fig. 2. View and sections of survey drawings prepared for minaret

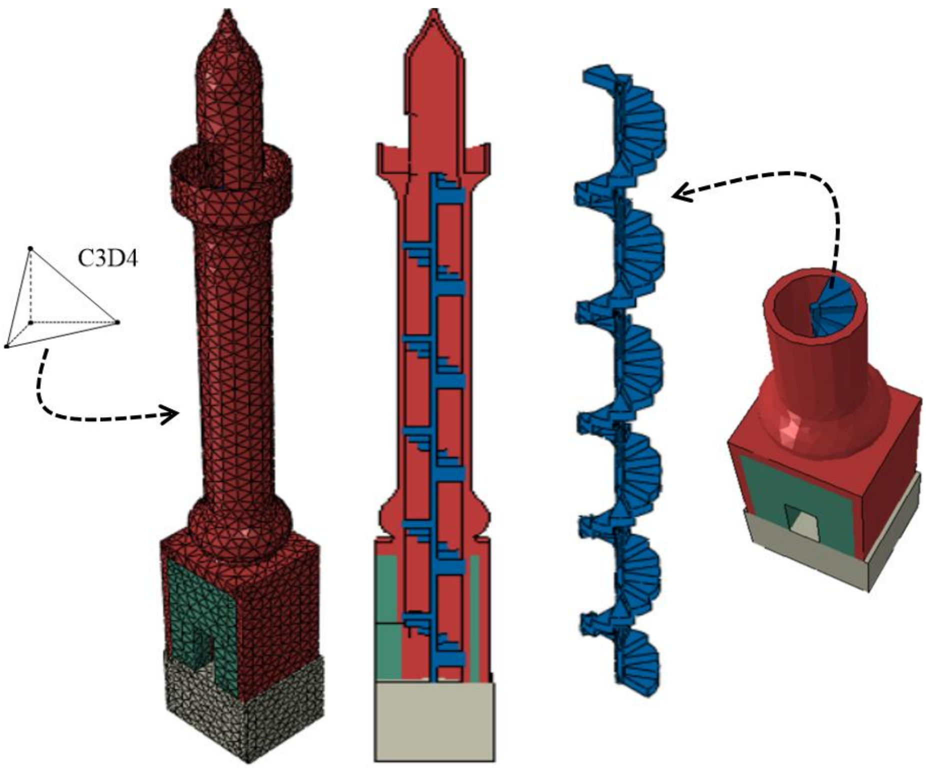

Fig. 3. Some views of the FE model for historical minaret

Table 1. Material properties used in finite element analyses (GMERHS, 2017)

Element	Elasticity modulus (N/m2)	Poisson Ratio (-)
Stone masonry	2.1E9	0.2
Filling part	1.0E9	0.2

Table 2. Mechanical parameters of CDP model for masonry units (Bayraktar and Hökelekli, 2021)

Material	Dilation angle	Eccentricity	f_{bo}/f_{co}	K_c	Viscosity parameter
Stone	10	0.1	1.16	0.667	5E-05

Table 3. Tensile stress–strain values for masonry units (Bayraktar and Hökelekli, 2021)

Tension		Tensile damage parameters	
σ (MPa)	ε^{pl}	dt	ε_t^{pl}
0.2000	0.2000	0.000	0.000
0.0005	0.0005	0.950	0.007
0.0005	0.007		

3.1. Modal response

Modal analysis of the historical minaret was carried out to determine the natural frequencies and mode shapes, called dynamic characteristics. As a result of the analysis, the frequencies of the first five modes were obtained between 1.502-11.391Hz. The first five mode shapes are translational modes in x and y directions, bending modes in x and y directions, and torsional modes, respectively. The first five mode shapes and relevant natural frequency values are given in Fig. 4.

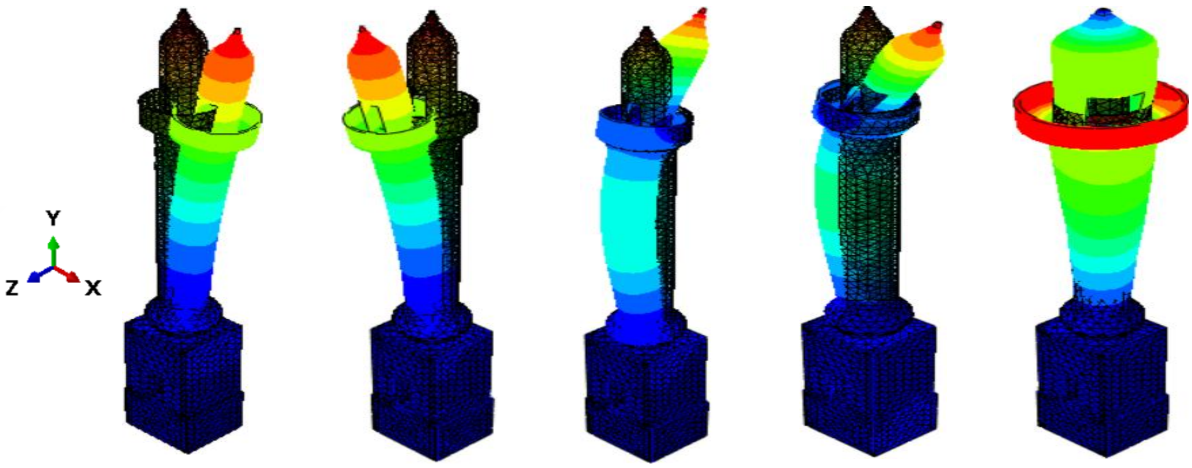

1st mode f1=1.502Hz | 2nd mode f2=1.507Hz | 3rd mode f3=7.812Hz | 4th mode f4=7.956Hz | 5th mode f5=11.391Hz

Fig. 4. The first five mode shapes and relevant frequency values

It is narrated that the historical minaret collapsed in the 1939 Erzincan Earthquake. It is aimed to carried out the nonlinear dynamic analysis to examine the accuracy of this narration from a technical point of view and determine the collapse mechanism of the historical minaret under the earthquake effect. The 1939 Erzincan Earthquake is a very old earthquake and it is very difficult to obtain an acceleration record of the earthquake under the conditions of the time. Only the intensity and magnitude of the earthquake are known. Essentially, since the starting point is to evaluate the collapse mechanism of the historical minaret under dynamic effects, it was approved to use the records of the 1992 Erzincan earthquake, which occurred in the same geography approximately fifty years after the 1939 earthquake and had a high impact. Fig. 5 shows the acceleration components of the 1992 Erzincan Earthquake. In the nonlinear dynamic history analysis, EW component of the earthquake was considered.

The Earthquake Risk Management Guide for Historical Structures sets targeted performance levels based on the order of importance of historical structures. The historical minaret is classified as a local important historical structure, and the Collapse Prevention (CP) performance level is expected at DD-2 seismic ground motion levels, according to the guide. The CP evel is the threshold at which serious damage occurs in structural system elements, the structure is on the verge of partial or total collapse, but migration is prevented. Table 4 and Table 5 show the targeted performance levels as well as the limit values for these performance levels.

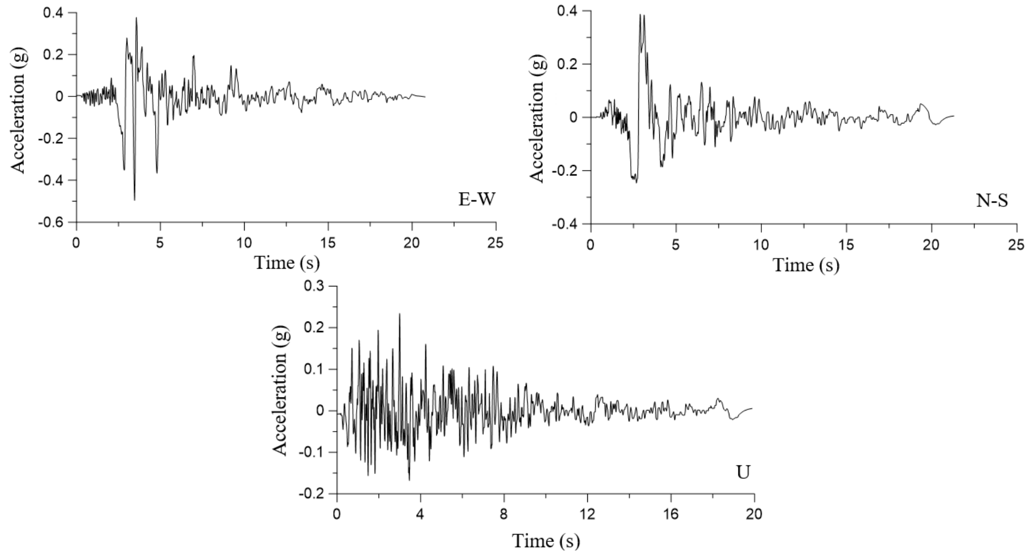

Fig. 5. The acceleration components of the 1992 Erzincan Earthquake

Table 4. Recommended target performance levels (GMERHS, 2017)

Performance Levels to be Selected According to the Importance of Historical Structures	The nationally important historical structure	The internationally important historical structure	
	DD-3 Limited Damage (LD)	DD-2 Limited Damage (LD)	DD-1 Limited Damage (LD)
The locally important historical structure	DD-3 Controlled Damage (CD)	DD-2 Controlled Damage (CD)	DD-1 Controlled Damage (CD)
	DD-3 Collapse Prevention (CP)	DD-2 Collapse Prevention (CP)	DD-1 Collapse Prevention (CP)

Table 5. Calculation methods and limit values related to performance levels (GMERHS, 2017)

Performance Level	Analysis Method/ Limits
Limited Damage Level (LD)	Linear analysis is employed: ✓ Ultimate stresses of the material or ultimate strength of the structural element and joints are not exceeded ✓ Drifts do not exceed 0.3%
Controlled Damage Level (CD)	Linear analysis is employed: ✓ Ultimate stresses of the material or ultimate strength of the structural element and joints are not exceeded, when the structure is subjected to vertical and earthquake loads reduced by Ra≤3 ✓ Drifts do not exceed 0.7% Nonlinear analysis is employed: ✓ Ultimate strains of the material are not exceeded ✓ Drifts do not exceed 0.7%
Collapse Prevention Level (CP)	Linear analysis is employed: ✓ Ultimate stresses of the material or ultimate strength of the structural element and joints can be exceeded with a certain ratio (i.e. 50%), when the structure is subjected to vertical and earthquake loads reduced by Ra≤3 ✓ Drifts do not exceed 1.0% Nonlinear analysis is employed: ✓ Ultimate strains of the material can be exceeded by a certain ratio (i.e., 20%) ✓ Drifts do not exceed 1.0%

*Ra: Seismic Load Reduction Factor

The contour diagram of the horizontal displacement in the moment of the earthquake when the horizontal drift ratio reached 1%, which is specified for CP performance level in Table 5, is given in Fig. 6a. Also, the change of drift ratio with time is shown in Fig. 6b. As can be seen in Fig. 6b, the drift ratio exceed the 1% value first time aproximetly 3.0th seconds of the earthquake record. It can be accepted that the minaret began to be damaged and collapsed after this time.

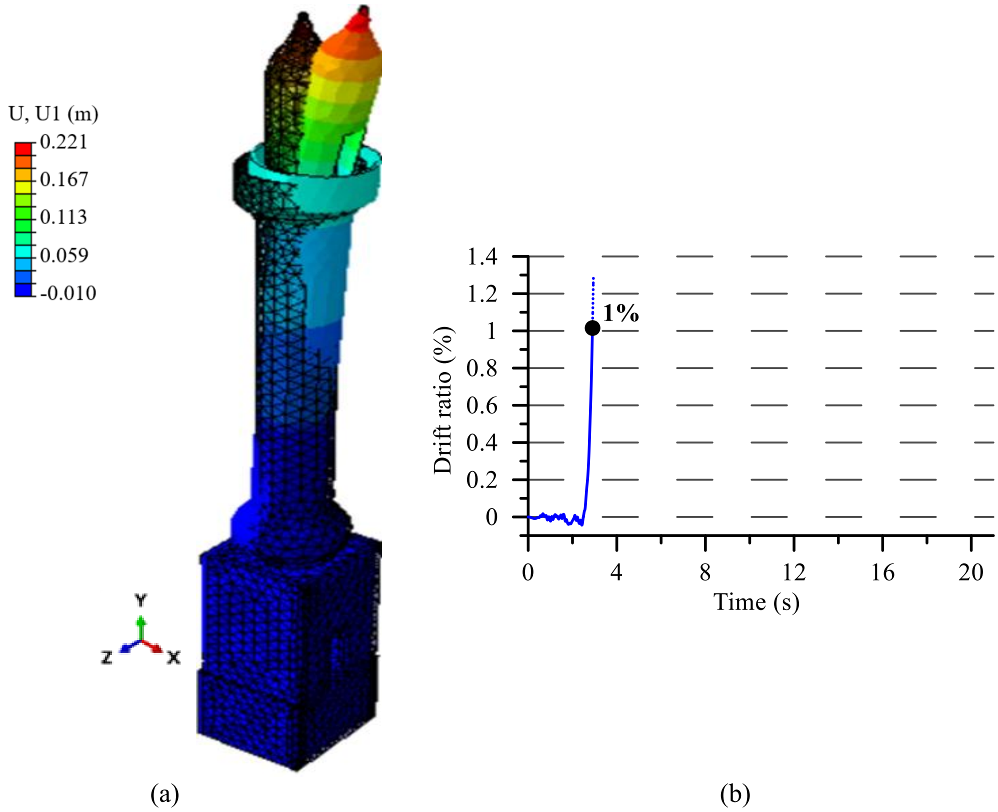

Fig. 6. (a) Displacement contour diagram and (b) time-history graphic of lateral drift ratio

The developing of DamageT contour diagrams under tensile stresses during the earthquake is given in Fig.7. As can be seen in Fig. 7, the transition segment between the pedestal and the cylindrical body of historical minaret started to be damaged at the aproximetly 3.0th second of the earthquake. In the transition segment where the square form of the pedestal transforms into a cylindrical body, damage resulting from horizontal loads such as earthquakes and wind is one of the most common types of damage. The reason for this is the tensile stresses concentration that occurs due to a decrease in cross-section and stiffness at the intersection between the transition segment and the cylindrical body of the minaret. This stiffness reduction results in uneven stress distribution and creates localized points of weakness. The damage mechanism observed in the 4th second of the earthquake is similar to the actual collapse mechanism of the historical minaret (Fig. 8). It was observed that in the following seconds of the earthquake, damage mechanisms also began to occur at the junction of the upper body and the balcony of the historical minaret.

4. Conclusions

This paper presents the evaluation the seismic performance and determinetion the collapse mechanisms of a historical masonry minaret, which is narreted to have collapsed in 1939 Erzincan Earthquake. The following conclusions are drawn from the paper:

- The first five mode shapes are defined as translational modes in x and y directions, bending modes in x and y directions, and torsional modes, respectively. In addition, the frequencies of the first five modes were obtained within 1.502-11.391Hz.
- It was observed that the damage caused by tensile stresses occurred primarily in the transition segment of the historical minaret. It can be stated that this situation arises from the difference in stiffness between the clindirical body and the more rigid In the transition segment where the square form of the pedestal transforms into a cylindrical body, damage resulting from horizontal loads such as earthquakes and wind is one of the most common types of damage. The reason for this is the tensile stresses concentration that occurs due to a decrease in cross-section and stiffness at the intersection between the transition segment

and the cylindrical body of the minaret. This stiffness reduction results in uneven stress distribution and creates localized points of weakness. Also, in this segment, insufficient connections and incorrect design are effective to tensile stress concentration. The geometry and cross-sectional ratios of the pedestal and cylindrical body must be compatible with tensile stresses to spread along the height of the minaret.. The damage mechanism observed in the 4th second of the earthquake is similar to the actual collapse mechanism of the historical minaret.

Minarets, which have long and thin in structural, are very sensitive to earthquake effects in segments where their cross-sections and stiffness differ, and collapse mechanisms generally occur in these regions. So, it can be stated that, it is of great importance to strengthen the minaret walls with rod bars in order to absorb the tensile stresses.

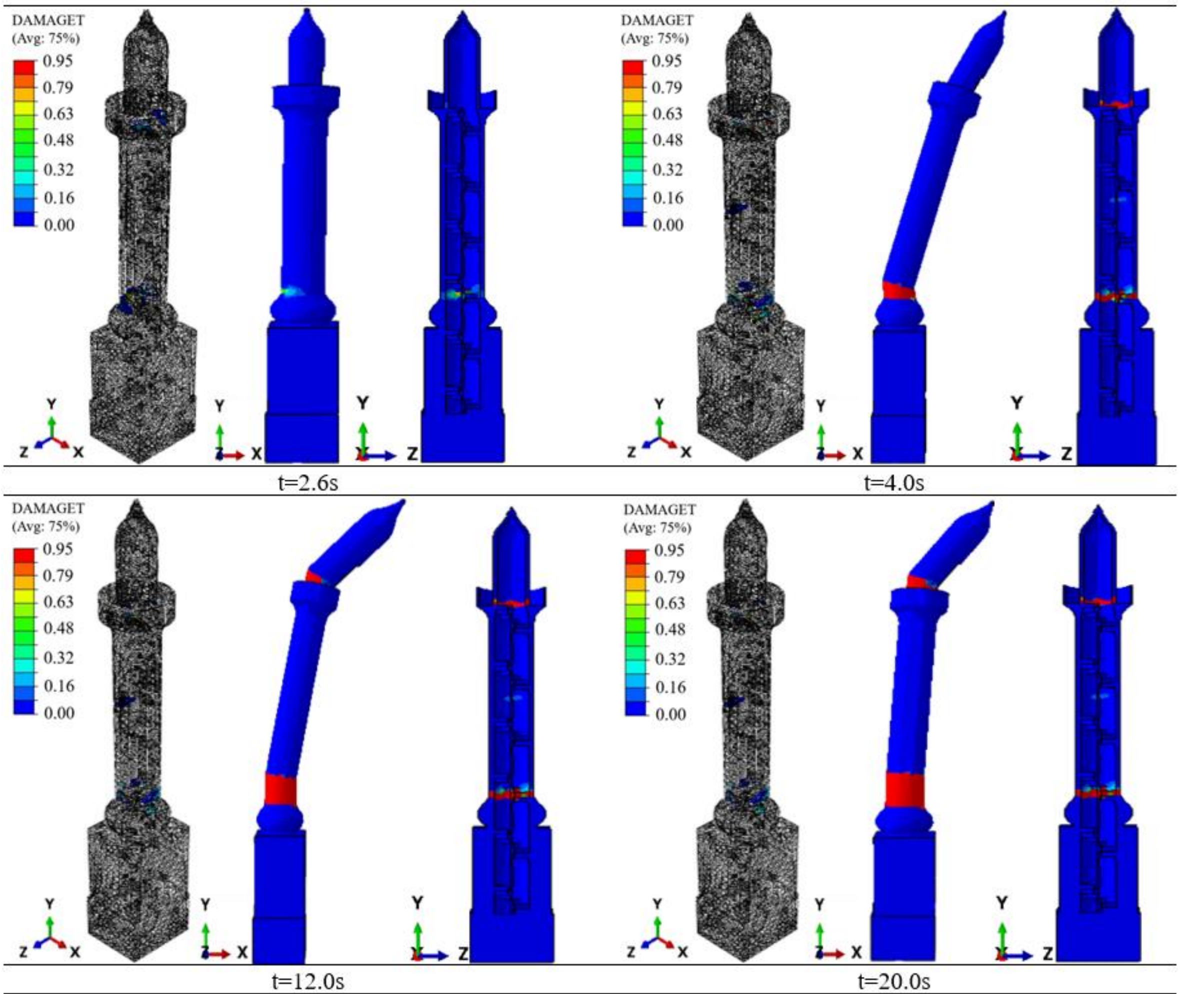

Fig. 7. The evolution of the tension damage during earthquake

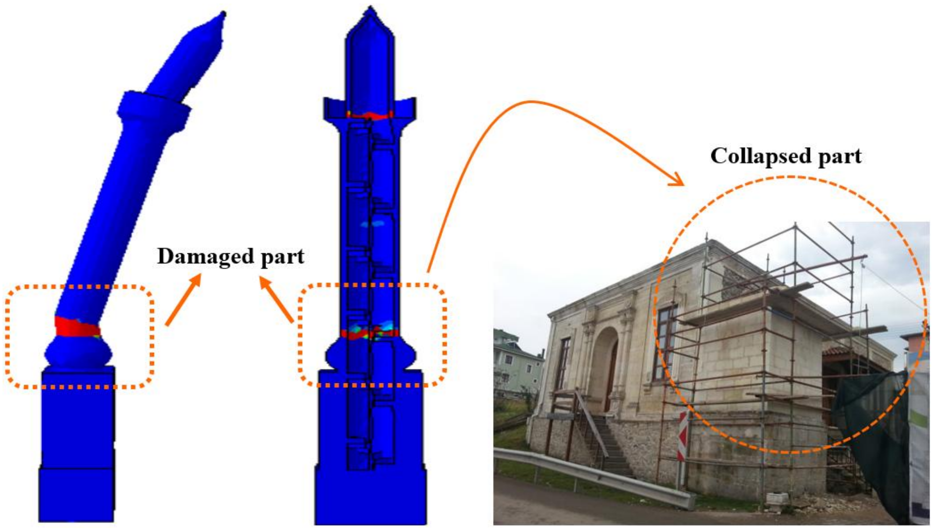

Fig. 8. Comparison of actual collapsed part of historical minaret and tensile damage at t=4th sec of earthquake

References

Abaqus (2022). Dassault Systèmes. Rhode Island, USA.

Altıok, T.Y., & Demir, A. (2021a). Collapse mechanism estimation of a historical masonry minaret considered soil-structure interaction. *Earthquakes and Structures, 21*(2), 161-172

Altıok, T.Y., & Demir, A. (2021b). Seismic damage assessment of a historical masonry minaret considering soil-structure interaction. *Journal of Structural Engineering & Applied Mechanics, 4*(3), 196-212

Bayraktar, A., & Hökelekli E. (2021). A cost-effective FRCM technique for seismic strengthening of minarets. *Engineering Structures, 229*, 111672

Demir, C., Comert, M., Inci, P., Dusak, S., & Ilki, A. (2023). Seismic retrofitting of the 19th century Hirka-i Serif Mosque using textile reinforced mortar. *International Journal of Architectural Heritage, 17*(8), 1634-1387

Erdoğan, Y.S., Kocatürk, T., & Demir, C. (2019). Investigation of the seismic behavior of a historical masonry minaret considering the interaction with surrounding structures. *Journal of Earthquake Engineering, 29*(1), 112-140

GMERHS. Guide to the Management of Earthquake Risks of Historical Structures (2017). General Directorate for Foundations. Ankara, Turkiye.

Hökelekli, E., & Al-Helwani, A. (2020). Effect of soil properties on the seismic damage assessment of historical masonry minaret–soil interaction systems. *The Structural Design of Tall and Special Buildings, 29*(2)

Hökelekli. E., Demir, A., Ercan, E., Nohutçu, H., & Karabulut, A. (2020). Seismic assessment in a historical masonry minaret by linear and non-linear seismic analyses. *Periodica Polytechnica Civil Engineering, 64*(2), 438-448

Işık, E., Avcil, F., Harirchian, E., Arkan, E., Bilgin, H., & Özmen, H.B. (2022). Architectural characteristics and seismic vulnerability assessment of a historical masonry minaret under different seismic risks and probabilities of exceedance. *Buildings, 12*(8), 1200

Maras, M.M., Özmen, A., Sayın, E., & Ayaz, Y. (2022). Seismic assessment of the historical Sütlü Minaret Mosque. *Periodica Polytechnica Civil Engineering, 66*(2), 445-459

Mirtaheri, M., Abbasi, A., & Salari, N. (2017). A seismic behaviour and rehabilitation of the historic masonry minaret by experimental and numerical methods. *Asian Journal of Civil Engineering, 18*(5), 807-822

Nohutcu, H., Hökelekli, E., Ercan, E., & Demir, A. (2017). Collapse mechanism estimation of a historical slender minaret. *Structural Engineering and Mechanics, 64*(5), 653-660

Şentürk, İ., Ergün, M., & Artar, M. (2022). Seismic behavior assessment of historical Alaeddin Bey Mosque and strengthening suggestions by CFRP fabric and steel plate. *Engineering Failure Analysis,* 137, 106242

Trešnjo, F., Humo, M., Casarin, F., & Ademovic, N. (2023). Experimental investigations and seismic assessment of a historical stone minaret in mostar. *Buildings, 13*(2), 536

Turk, A.M. (2013). Seismic response analysis of masonry minaret and possible strengthening by fiber reinforced cementitious matrix (FRCM) materials. *Advances in Materials Science and Engineering,* 952497

Yurdakul, M., Yılmaz, F., Artar, M., Can, Ö., Öner, E., & Daloğlu, A.T. (2021). Investigation of time-history response of a historical masonry minaret under seismic loads. *Structures, 30*(2021), 265-276

Selection of ground motion records considering near field effects for nonlinear time history analysis

Dilara Orhan*[1], Yasin Fahjan[1]

[1] *Istanbul Technical University, Department of Civil Engineering, Istanbul 34469, Turkey*

Abstract. Near-field records exhibit distinct ground motion characteristics compared to far-field records. Assuming these records to have identical characteristics may lead to the oversight of critical near-field effects, such as fling and velocity pulses, which are inherent to near-field records. These effects, however, must be considered during the design process to ensure safety, as they impose additional demands on structural systems. Various design codes propose different solutions to address this issue, with the most common approach involving the application of distinct coefficients to design spectra. Nevertheless, these assumptions often prove either insufficient or overly conservative for certain periods. Additionally, when Time History Analysis is conducted, the aforementioned effects require careful consideration. This is because they are prone to being eliminated during the spectral matching and scaling process or misrepresented in ground motion selection steps. This paper aims to evaluate the perception of near-field effects and compare current methods for selection and scaling of ground motion records for Nonlinear Time History Analysis. To achieve this, different approaches from design codes worldwide are applied within Nonlinear Time History Analysis to Single Degree of Freedom (SDOF) systems of different natural frequencies. The impact of near-field effects across different periods is assessed by examining changes in ductility demands. The results indicate that the inclusion of near-field effects is crucial for certain periods. Thus, these effects must be accurately represented without exaggerating their influence during less critical periods.

Keywords: Ground motion selection; Near-field effects; Nonlinear time history analysis; Ground motion scaling; Ductility

1. Introduction

Near-field ground motions require attention to the dynamics of occurring earthquake waves. Specifically, when rupture propagates toward a site at a velocity close to the shear wave speed, seismic energy concentrates into a single strong velocity pulse at the beginning of the record (Somerville et al., 1997). Besides the mentioned forward directivity, directionality of ground motion record changes the amplitude across periods and distance ranges. For sites at 5 km radius of causative fault maximum spectral accelerations tend to appear closer to 90 degrees (strike-normal orientation) (Shahi & Baker, 2013). These phenomena can significantly influence structural response, highlighting the need for accurate representation in seismic analysis.

However, existing Ground Motion Prediction Models (GMPEs) do not consider near-field effects explicitly and some available design codes only provide rough approximations. UBC-97 was the first design code in United States of America to incorporate near-field effects, applying coefficients to response spectra based on earthquake magnitude and source distance. ASCE introduced the near-fault concept for the first time in its 7.16 version, requiring ground motion record pairs to be rotated to fault-normal and fault-parallel directions while ensuring they are not lower than the maximum considered earthquake spectra. Additionally, ASCE 7-22 modifies the response spectra at longer periods by applying calculated coefficients to address the increased safety demands.

TBDY-2018 was the first design code from Turkiye to state that properly scaled near-field records should be used in nonlinear time history analysis for sites located within 15 km of an earthquake source in the section 5B.3.6(a). In addition to TBDY-2018, the Design of Highway and Railway Tunnels and Geotechnical Structures Under Seismic Effects Code (2020) also imposes restrictions on the selection and scaling of ground motion records for sites near active fault zones in Turkey.

As it is depicted in both ASCE-7-22 and TBDY-2018, selecting the ground motion records is as crucial as processing them. The ground motion records shall be selected to reflect the site conditions at best. Earthquake magnitude, causative source to site distance and site class being the most commonly used factors since they contain the significant information of frequency content, spectral amplitudes, spectral shape and event duration (Beyer &

* Corresponding author, E-mail: orhand19@itu.edu.tr

https://doi.org/10.31462/icearc2025_ce_eqe_031

Bommer, 2007). Additionally, the causative fault mechanism should be similar to the considered event, and the ground motions should contain sufficient energy to accumulate on-site while being recorded within a distance range close to it. Besides these main properties different design codes require certain details to be considered. Those selected ground motions have to be carefully handled in the amplitude scaling process. Since near-field ground motions respond differently at short and longer periods due to variations in spectrum level and magnitude, uniformly scaling a fixed response spectral shape fails to accurately represent them (Somerville, 2003).

Despite the developments in design codes, their coverage and efficiency remain vague. Thus, this study aims to assess ground motion selection methods from ASCE-22 and TBDY-2018 under near field effects. A sample site in Tuzla/Istanbul is selected, which is expected to be affected by the North Anatolian Fault. Ground Motion records are obtained from PEER NGA West2 Ground Motion Database. Nonlinear time history analysis will be performed on a SDOF system while aforementioned codes are applied. As ductility demand outputs of the analysis are compared for that particular site, sufficiency of the methods will be discussed.

2. Influence of near field effects on ground motion records

Prior to investigate the impact of near field effects, it would be more explanatory to show the change in the records themselves. As the most characteristic sign, the velocity pulse is present in the near field records. Even though the pulse can be seen without any procession, it can be clearly shown by extracting from the record itself. The Morgan Hill Earthquake (1984) record from Coyote Lake Dam-Southwest Abutment Station has been used in illustration. Ground motion record is Low-pass Butterworth filtered to get rid of the noise, thus the velocity pulse is more visible. It should be noted that; while filtering the near fault records, especially with high-pass filters, velocity pulses might get lost due to their high frequency characteristics. Filtered results have to be reviewed to avoid such mistakes. Fig. 1 demonstrates the velocity time histories of two perpendicular horizontal components of Morgan Hill Earthquake with properties given in Table 1. The velocity pulse is clearly visible as a full sine wave on both components' velocity time series as highlighted with magenta.

The primary properties of a near field record; magnitude, distance and directionality are examined as they consequentially create the variance in design spectra. To analyze their impact, 56 different near field ground motion records had been chosen from PEER NGA West2 Ground Motion Database which are listed in Table 2. Amplification factors were used to express the change of distance and magnitude caused over spectral period. Following subsections will discuss each factor in detail.

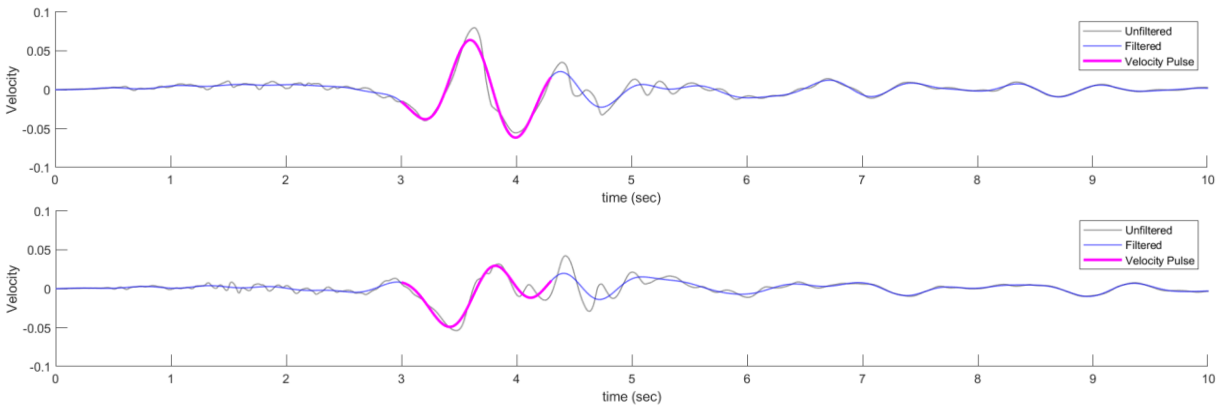

Fig. 1. Velocity time series of horizontal components with low-pass Butterworth filtered, unfiltered and velocity pulse

Table 1. Properties of Morgan Hill Earthquake

Earthquake Name	Year	Station Name	Magnitude (Mw)	Distance (Rjb, km)	Fault Mechanism
Morgan Hill	1984	Coyote Lake Dam - Southwest Abutment	6.19	0.18	Strike Slip

Table 2. List of earthquake events

Earthquake Name	Year	Station Name	Magnitude (Mw)	Distance (Rjb, km)
Chi-Chi_ Taiwan-04	1999	CHY074	6.2	6.02
Coyote Lake	1979	Gilroy Array #2	5.74	8.47

Table 2. Continued

Coyote Lake	1979	Gilroy Array #3	5.74	6.75
Coyote Lake	1979	Gilroy Array #4	5.74	4.79
Coyote Lake	1979	Gilroy Array #6	5.74	0.42
Darfield_ New Zealand	2010	DSLC	7	5.28
Darfield_ New Zealand	2010	GDLC	7	1.22
Darfield_ New Zealand	2010	HORC	7	7.29
Darfield_ New Zealand	2010	LINC	7	5.07
Darfield_ New Zealand	2010	Riccarton High School	7	13.64
Darfield_ New Zealand	2010	ROLC	7	0
Darfield_ New Zealand	2010	Styx Mill Transfer Station	7	20.86
Darfield_ New Zealand	2010	TPLC	7	6.11
Denali_ Alaska	2002	TAPS Pump Station #10	7.9	0.18
Duzce_ Turkey	1999	Bolu	7.14	12.02
Duzce_ Turkey	1999	IRIGM 487	7.14	2.65
El Mayor-Cucapah_ Mexico	2010	El Centro Array #12	7.2	9.98
El Mayor-Cucapah_ Mexico	2010	Westside Elementary School	7.2	10.31
Imperial Valley-06	1979	Agrarias	6.53	0
Imperial Valley-06	1979	Brawley Airport	6.53	8.54
Imperial Valley-06	1979	EC County Center FF	6.53	7.31
Imperial Valley-06	1979	El Centro - Meloland Geot. Array	6.53	0.07
Imperial Valley-06	1979	El Centro Array #10	6.53	8.6
Imperial Valley-06	1979	El Centro Array #3	6.53	10.79
Imperial Valley-06	1979	El Centro Array #4	6.53	4.9
Imperial Valley-06	1979	El Centro Array #5	6.53	1.76
Imperial Valley-06	1979	El Centro Array #6	6.53	0
Imperial Valley-06	1979	El Centro Array #7	6.53	0.56
Imperial Valley-06	1979	El Centro Differential Array	6.53	5.09
Imperial Valley-06	1979	Holtville Post Office	6.53	5.35
Kobe_ Japan	1995	KJMA	6.9	0.94
Kobe_ Japan	1995	Port Island (0 m)	6.9	3.31
Kobe_ Japan	1995	Takarazuka	6.9	0
Kobe_ Japan	1995	Takatori	6.9	1.46
Kocaeli_ Turkey	1999	Arcelik	7.51	10.56
Kocaeli_ Turkey	1999	Yarimca	7.51	1.38
Landers	1992	Yermo Fire Station	7.28	23.62
Morgan Hill	1984	Coyote Lake Dam-Southwest Abutment	6.19	0.18
Morgan Hill	1984	Gilroy Array #6	6.19	9.85
Parkfield-02_ CA	2004	PARKFIELD - EADES	6	1.37
Parkfield-02_ CA	2004	Slack Canyon	6	1.6
Parkfield-02_ CA	2004	Parkfield - Cholame 1E	6	1.66
Parkfield-02_ CA	2004	Parkfield - Cholame 2WA	6	1.63
Parkfield-02_ CA	2004	Parkfield - Cholame 3E	6	4.95
Parkfield-02_ CA	2004	Parkfield - Cholame 3W	6	2.55
Parkfield-02_ CA	2004	Parkfield - Cholame 4W	6	3.3
Parkfield-02_ CA	2004	Parkfield - Fault Zone 1	6	0.02
Parkfield-02_ CA	2004	Parkfield - Fault Zone 9	6	1.22
Parkfield-02_ CA	2004	Parkfield - Fault Zone 12	6	0.88

Table 2. Continued

Parkfield-02_ CA	2004	Parkfield - Stone Corral 1E	6	2.85
San Salvador	1986	Geotech Investig Center	5.8	2.14
San Salvador	1986	National Geografical Inst	5.8	3.71
Superstition Hills-02	1987	Kornbloom Road (temp)	6.54	18.48
Superstition Hills-02	1987	Parachute Test Site	6.54	0.95
Tottori_ Japan	2000	TTR008	6.61	6.86
Westmorland	1981	Parachute Test Site	5.9	16.54

2.1. Effect of directionality and directivity

Directionality becomes an issue where directivity effects, mainly the velocity pulse, change the characteristic of the ground motion record. More specifically, the resultant pulse is directed towards the fault normal direction since surface horizontal shear waves align normal to the fault (Hayden et al., 2014, pp. 2). Consequently, forward directivity pulses typically exhibit the highest peak-to-peak velocity within a 30° range of the fault normal direction, despite considerable scatter (Hayden et al., 2014, pp. 13). Thus, near field records would be underestimated if directionality is not considered in the process.

ASCE 7-22 requires the near field records to be rotated to fault normal and fault parallel directions before applied to the building in the section 16.2.4. While TBDY-2018 does not mention rotation of near field records before application. Thus, assessing the amplification of rotated records would emphasize one of the points those codes differ. To evaluate how much of a difference directionality makes in near field, spectra of records form Table 2 will be rotated to fault normal and fault parallel. And the average ratio to geometric mean of two horizontal components will be plotted over time. Fig. 2 illustrates the average amplification factor of 56 near field records over time. It is clear in Figure 2 that, Fault Normal to Geometric Mean ratio gets even larger after 1.4-1.5 seconds reaching to 1.2 and exceeding 1.35 at longer periods. Which makes longer periods after 1.5 seconds more fragile about directionality of near field records. As expected, fault parallel rotations remain smaller than geometric means with amplification factor smaller than 1 at longer periods, proving velocity pulses concentrate on fault normal direction.

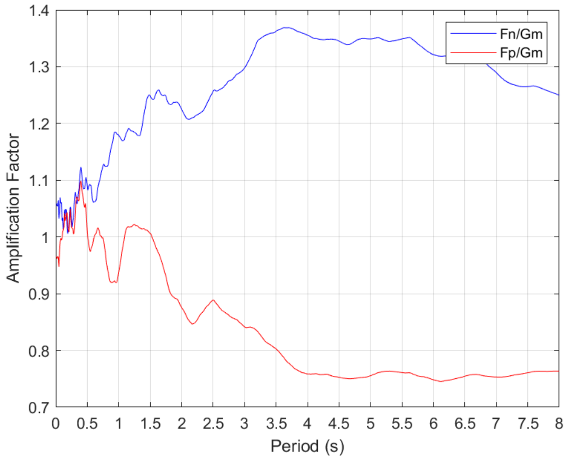

Fig.2. Amplification factor over period graph containing fault normal, fault parallel ratios

2.2. Effect of distance

Spectral acceleration amplitude differs across rotation angles as it is shown in the previous subsection. But it is not the only aspect that near field obliges the designer to be careful of. Meaning that, causative fault-to-site distance plays a crucial role as the spectral amplitude changes with both distance and time. To briefly explain significance over this concept, wave propagation characteristics must be pointed out. Since earthquake waves accumulate in a near field record, high frequency pulses dominate the response. Demanding higher ductility from the structures.

Before investigating the impact on ductility, the most amplificated distance and period couples are to be determined. To accomplish this, the near field events listed in Table 2 are categorized into groups based on Joyner & Boore distance (R_{jb}): less than 5 km, less than 10 km, and more than 10 km. Using the ratios between Fault Normal to Geometric mean and Fault Normal to Maximum Rotated spectra, amplification factors are plotted over period on Fig. 3. Fig. 3 shows that Fault Normal to Geometric Mean spectra ratio has the biggest amplitudes at longer periods for the first 10 km exceeding 1.4. Besides, the factor increases further, nearly reaching 1.5 after

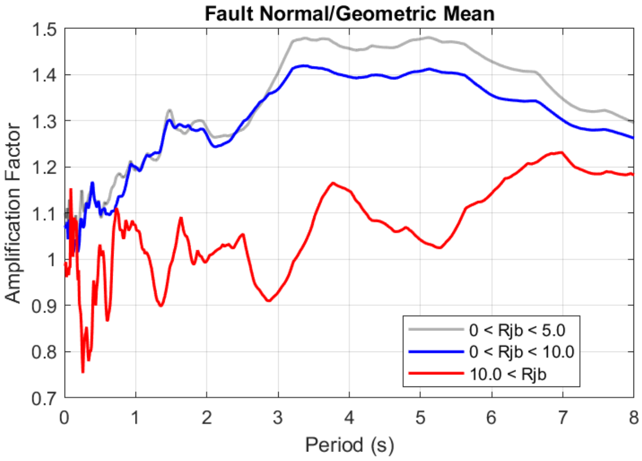

Fig. 3. Amplification factors depending on distance, fault normal to geometric mean spectra ratio over time

3 seconds in the first 5 km. As distance grows larger than 10 km, amplification factor decreases. Yet, Fault Normal spectra remain larger than Geometric Mean spectra for longer periods.

2.3. Effect of magnitude

Another aspect to consider in a possible near field event is the magnitude of the earthquake. Magnitude may seem less relevant in the design process, but a closer look at the components of Moment Magnitude, specifically the Seismic Moment, reveals its significant influence on wave propagation. Seismic Moment quantifies the energy released by a fault during an event, considering the rigidity of the soil, fault area, and slip. Since a fault does not rupture altogether instantaneously, seismic waves accumulate throughout the event. In cases of longer slip, more waves are generated, leading to formation of low-frequency waves. Therefore, smaller magnitude earthquakes lack the frequency content necessary to produce strong near-field effects. Additionally, as the fault area decreases, waves are released bearing less energy, making them easily get damped along the site.

The mentioned relations suggest that as earthquake magnitude increases, near-fault effects have a greater impact on the spectra. Thus, earthquake data from Table 2 are divided into two groups, those with less or more magnitude than Mw 6.5. Average of Fault Normal spectra to Geometric mean spectra ratio of each separate group is plotted over time in Fig. 4. It is clearly shown in Figure 4 that, as the period gets longer, the effect of magnitude on spectra becomes explicitly greater, verifying the suggested relation.

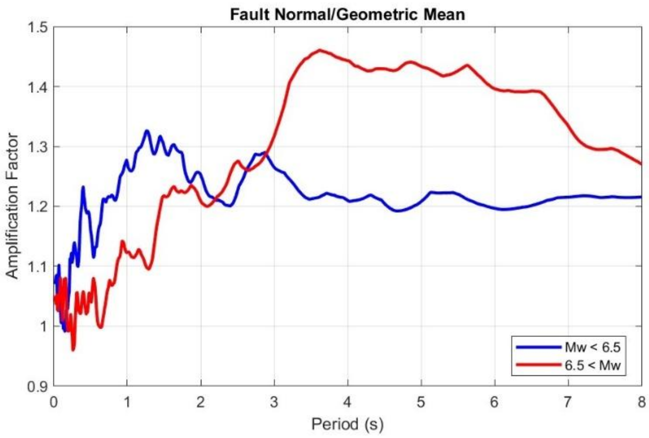

Fig. 4. Amplification factors depending on earthquake magnitude, fault normal to geometric mean spectra ratio over time

3. Ground motion selection

As it is emphasized in earlier sections; properties of ground motion records affect the acceleration spectra due to near field effects. Hence, before conducting a nonlinear time history analysis, selecting proper features to represent near field behavior is essential. The range of features must be defined similarly to the site of interest. These factors can become extensive when more data are available but optimum results can still be obtained with certain features. Mainly, distance to the fault, magnitude of event and Vs_{30} (shear wave velocity of soil) can describe the site conditions effectively. As it has been explained in Section 2, impact of defined range of distance diminishes significantly after 10 km thus, accurate range should be set. Likewise, before and after magnitude of 6.5 spectral amplitudes differ at longer periods making the spectra sensitive to magnitude increment. Also, source mechanism should be similar to the ones that potentially affect the site. Lastly, Vs_{30} of soil is crucial since soil amplifies or deamplifies certain periods. Thus, amplified periods might be amplified again due to soil conditions. Being accurate with these factors leads to a spectrum accounting near field effects decently and resulting in a non-overestimated or underestimated analysis results.

Current codes briefly mention ground motion selection for near fault sites. Besides the magnitude, source characteristics, distance and site conditions; ASCE 7-22 implies in the section 16.2.2 that, MCE_R (Risk based Maximum Considered Earthquake) shall also include the rupture directivity and impulsive characteristics. Although at least 11 records are required, since experiencing pulse-like motions is probabilistic, only a portion of the records (based on pulse probability) has to be pulse-like in the ground motions set. Current code in use in Turkey TBDY-2018, do not put any restrictions considering near fault selection but rather implies that ground motion records should have compatible source to site distance with the site under observation. But Design of Highway and Railway Tunnels and Geotechnical Structures Under Seismic Effects Code adopts a similar approach with ASCE 7-22, making the designer use at least 3 directivity possessing ground motion records with possibility of rupture directivity. Project location is given in Fig. 5 which has at least 10 km distance to the North Anatolian Fault shown with red lines. Considering the possibility of affection of sample site, a range is set for each feature. And the selected 11 ground motion data is given in the Table 3.

Fig. 5. Project location and the North Anatolian Fault

Table 3. List of selected ground motion data

Earthquake Name	Year	Station Name	Magnitude (Mw)	Rjb (km)	Vs30 (m/sec)
Imperial Valley-06	1979	El Centro Array #3	6.53	10.79	162.94
Morgan Hill	1984	Coyote Lake Dam - Southwest Abutment	6.19	0.18	561.43
Superstition Hills-02	1987	Parachute Test Site	6.54	0.95	348.69
Kobe_ Japan	1995	Takatori	6.9	1.46	256
Parkfield-02 CA	2004	Parkfield-Cholame 3E	6.0	4.95	397.36
Duzce_ Turkey	1999	Bolu	7.14	12.02	293.57
Chi-Chi_ Taiwan-04	1999	CHY074	6.2	6.02	553.43
Tottori_ Japan	2000	TTR008	6.61	6.86	139.21
Darfield_ New Zealand	2010	TPLC	7	6.11	249.28
El Mayor-Cucapah_ Mexico	2010	El Centro Array #12	7.2	9.98	196.88
El Mayor-Cucapah_ Mexico	2010	Westside Elementary School	7.2	10.31	242

4. Ground motion scaling

For the last step of ground motion processing, amplitude scaling will be executed in accordance with the ASCE 7-22 and TBDY-2018 instructions. If those codes are to be compared upon their restrictions to amplitude scaling, they both do not put any restriction to preserve the near field characteristics of motions. But ASCE 7-22 forbids the usage of spectral matching unless pulse characteristics are preserved. ASCE 7-22 modifies the response spectra before scaling by coefficients to obtain maximum response spectra rather than geometric mean spectra. To achieve that seismic ground motion maps are increased %10 for short period and %30 for 1 second responses. This modification adequately compensates the growth that velocity pulses create in long period responses. Meanwhile, TBDY-2018 does not embrace such an approach regarding maximum response. But requires the design spectra to be multiplied by 1.3 to close the gap between the component combination methods SRSS and GM, often confused to replace the amplification ASCE 7-22 provides. Besides these coefficients, ASCE 7-22 and TBDY-2018 adopt different approaches with directionality of records. ASCE 7-22 demands the all earthquake records representing nearby causative faults to be rotated to fault normal and fault parallel directions before application. Whereas, TBDY-2018 only demands the seismic components to be orthogonal to the building, overlooking the amplification at fault normal direction.

To compare the differences between ASCE 7-22 and TBDY-2018's methods, selected earthquake records from Table 3 will be scaled to design spectrum that belongs to location in Figure 5. And to compare the difference that near fault makes in rotation of ground motions records, spectra will also be scaled after rotating to fault normal and maximum direction separately. Design spectra of seismic ground motion level with 2% possibility of exceedance in 50 years is obtained which corresponds to the MCE_R spectrum that ASCE 7-22 requires. Ground motion records are rotated by 1 degree to later sort out the maximum of the rotated records. Resultant values of maximum rotation and rotation to fault normal processes are scaled as a group to obtain the best fitting average spectra. Scaling factor of each earthquake record had been picked out as the optimum value as Fahjan (2008) states that in nonlinear analysis scaling factors should be limited between 0.5 and 2. And since, considerably large or small factors alter the physical content of records, excessive factors are intentionally avoided. And the exerted scaling factors are given in the Table 4. In Fig. 6 result of the mentioned processes according to ASCE 7-22 is presented. Fig. 6(a) represents the maximum rotation results. It is obvious that maximum rotated records are well comply with the MCE_R spectrum. Fig. 6(b) represents the fault normal spectrum, showing smaller acceleration values than maximum rotated spectrum. But scaled fault normal spectrum fits the MCE_R spectrum good as well. Figure 7 illustrates the scaling process rooting from TBDY-2018. And in 7(a), maximum rotation process results are presented. Design spectrum lies far below the maximum rotated spectrum after the corner periods, showing that actual ground motion records result in a larger spectrum after scaling. Lastly, Fig. 7(b), shows the resultant spectrum of fault normal records. Even though the spectrum remains smaller than 7(a) similar inference can be made, meaning that fault normal rotated records make a higher spectrum with near field effects. As it is obvious on both Fig. 6(a) and 7(a), maximum rotated spectra catch the amplification on longer periods better contrary to GM and SRSS spectra.

Table 4. List of scaling factors

Earthquake Name	Scaling Factors			
	Maximum Rotated Spectra		Fault Normal Spectra	
	ASCE-7-22	TBDY-2018	ASCE-7-22	TBDY-2018
Imperial Valley-06	3.18	3.85	3.93	3.25
Morgan Hill	1.16	1.39	1.45	1.25
Superstition Hills-02	2.20	2.64	2.64	2.34
Kobe_ Japan	1.20	1.44	1.60	1.33
Parkfield-02_ CA	1.66	2.03	2.12	1.75
Duzce_ Turkey	1.25	1.50	1.67	1.39
Chi-Chi_ Taiwan-04	2.05	2.45	2.71	2.22
Tottori_ Japan	2.40	2.87	2.90	2.45
Darfield_ New Zealand	3.78	4.58	4.81	3.91
El Mayor-Cucapah_ Mexico	2.46	2.96	3.02	2.52
El Mayor-Cucapah_ Mexico	2.71	3.25	3.31	2.77

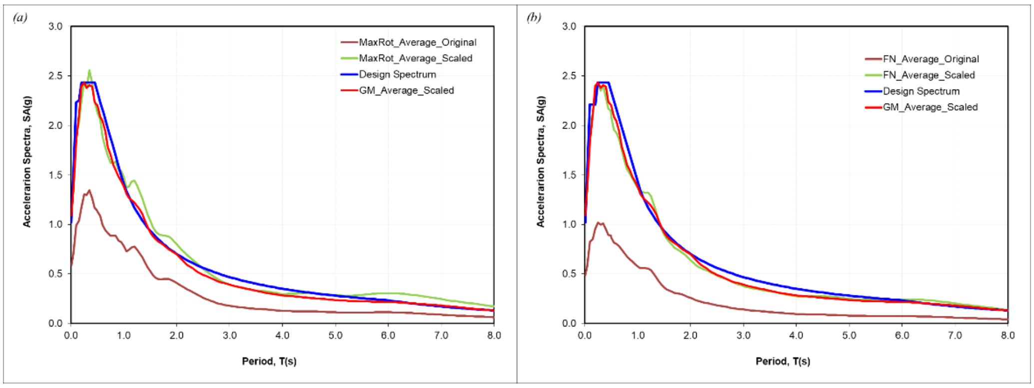

Fig.6. (a) Maximum rotated spectra scaled according to ASCE 7-22,
(b)Fault normal spectra scaled according to ASCE 7-22

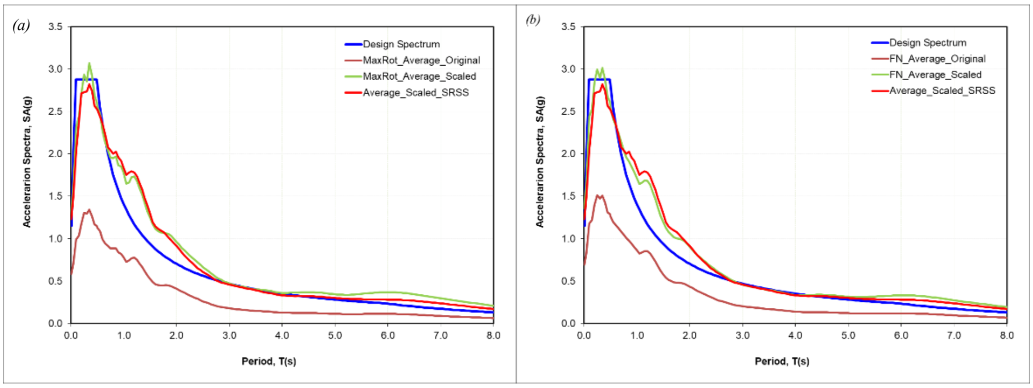

Fig.7. (a) Maximum rotated spectra scaled according to TBDY-2018
(b)Fault normal spectra scaled according to TBDY-2018

5. Nonlinear time history analysis

The low-frequency nature of velocity pulses increases the elastic demand due to the amplification observed at longer periods in the elastic design spectra. However, what truly ensures the safety of a structure is its ability to accommodate plastic deformation and ductility. Therefore, the changes in ductility demands caused by near-field effects will be investigated through nonlinear time history analysis. To compare different methods, the maximum rotated, fault-normal, and fault-parallel time series are scaled according to the factors provided in Table 4. Each pair of scale factors and time series is analyzed separately. The results are then plotted as the average ductility of the selected ground motion series over the period. Fig. 8(a) and 8(b) illustrate the average ductility demand results of the maximum rotated time series scaled according to ASCE 7-22 and TBDY-2018, respectively. Despite differences in the elastic spectrum, the ductility demands show no significant variations based on the dissimilar scale factors provided by ASCE 7-22 and TBDY-2018. Fig. 9(a) and 9(b) present the average ductility demand results of the fault-normal and fault-parallel rotated time series scaled according to ASCE 7-22, respectively. When comparing Fig. 9(a) and 9(b), the anticipated impact of near-field effects becomes evident in Fig. 9(a). It is clear that ductility demands increase significantly in the fault-normal direction compared to the fault-parallel direction, especially between 0.5 and 3 seconds. A similar conclusion can be drawn from Fig. 10(a) and 10(b), which show the fault-normal and fault-parallel ductility demands according to TBDY-2018. To further emphasize the increased ductility demand due to fault-normal rotation, non-rotated horizontal components are plotted in Fig. 11(a) and 11(b). It is clearly evident that near-field effects are overlooked when ground motion records are not rotated. The outcome of the nonlinear time history analysis demonstrates that, regardless of the method provided by the codes regarding spectra, ductility demands are most affected by the orientation and the high-frequency content of pulse-like ground motion records.

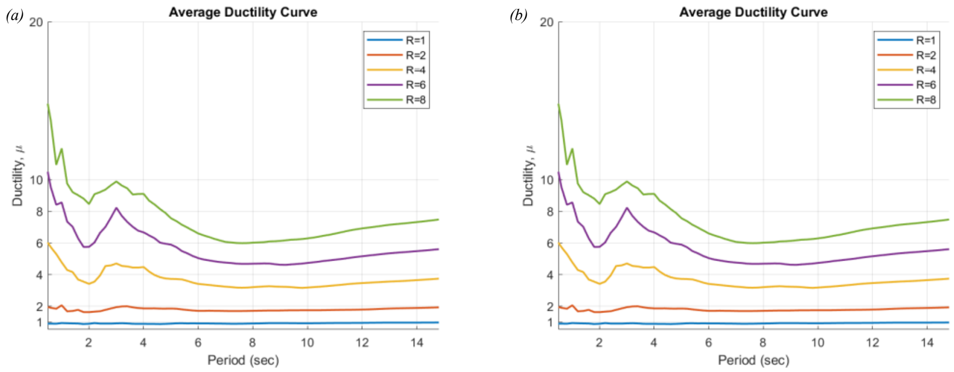

Fig.8. (a) Ductility demand of maximum rotated time series scaled according to ASCE 7-22, (b) Ductility demand of maximum rotated time series scaled according to TBDY-2018

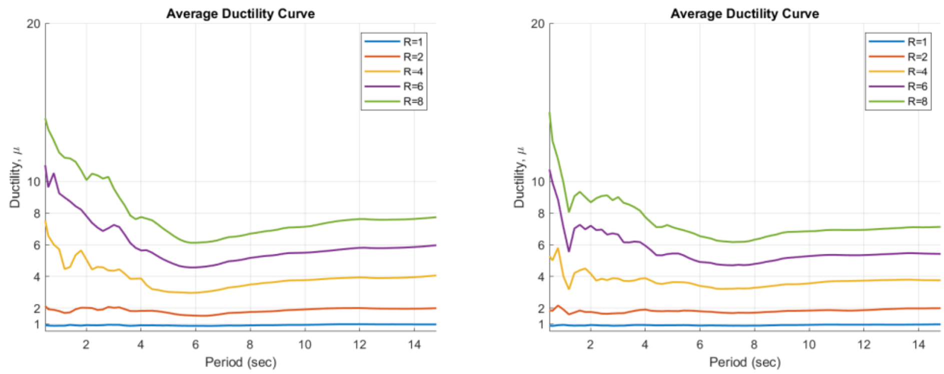

Fig.9. (a) Ductility demand of fault normal time series scaled according to ASCE 7-22, (b) Ductility demand of fault parallel time series scaled according to ASCE 7-22

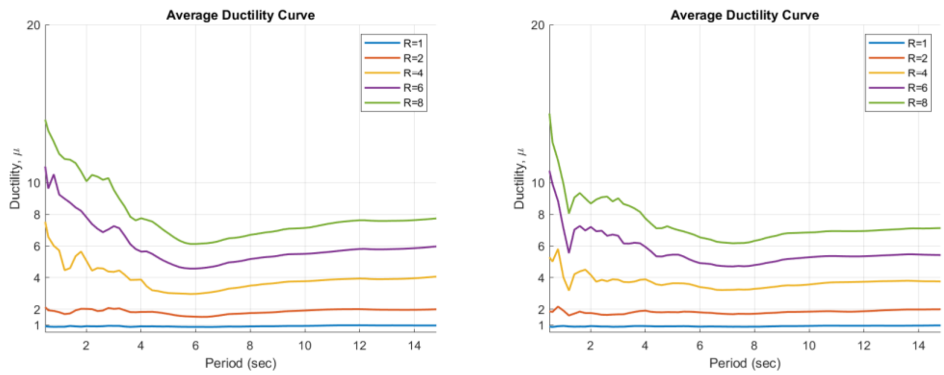

Fig.10. (a) Ductility demand of fault normal time series scaled according to TBDY-2018, (b) Ductility demand of fault parallel time series scaled according to TBDY-2018

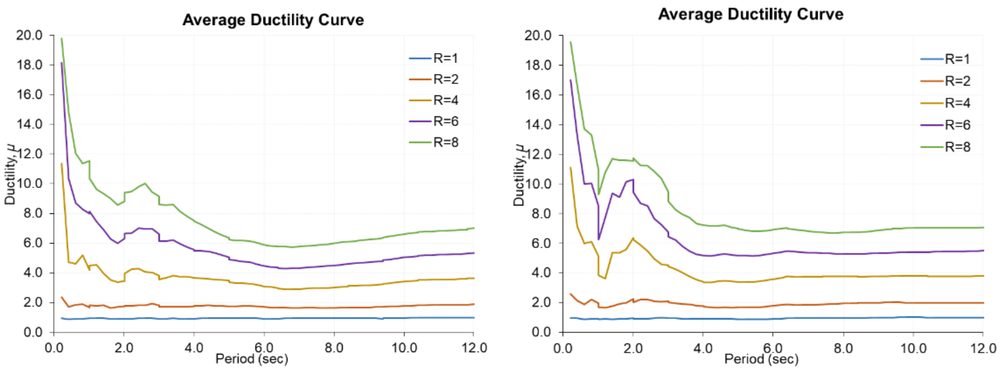

Fig.11. (a) Ductility demand of H1 component time series scaled according to ASCE 7-22, (b) Ductility demand of H2 component time series scaled according to ASCE 7-22

6. Conclusions

Near-field ground motion records inherently contain additional high- and low-frequency waves that differ from those in far-field records. Therefore, this study aims to evaluate the significance of these features, which might be overlooked in current practices. To briefly compare the methods, the impact of near-field motions was investigated through both spectral analysis and nonlinear time history analysis. The results indicate that selecting appropriate ground motions for analysis is crucial to simulate realistic structural responses. Simple scaling method was utilized in this study; however, during the selection and scaling processes, certain near field records resulted in extreme scaling factros. Therefore, acceptable scaling factors must be chosen. For advanced projects, sophisticated scaling methods should consider directivity when dealing with near-field records. The outcome of the spectral analysis shows that the TBDY-2018 design spectrum does not adequately capture the amplification effects caused by near-field motions, remaining approximately 25% to 50% lower than the obtained spectra at longer periods. In contrast, ASCE 7-22 manages to cover the scaled spectra with almost no disparity. However, regarding ductility analysis, both codes provide comparable results, regardless of the orientation of the time series.

- Near-field records tend to exhibit greater amplification within the first 5 km, with the amplification decreasing significantly after 10 km.
- Near-field effects require sufficient energy to become active; thus, as the event magnitude increases, near-field effects grow in intensity and influence the acceleration spectra, particularly after Mw 6.5 events.
- Although ASCE 7-22 addresses the necessary criteria for ground motion selection, TBDY-2018 lacks sufficient requirements beyond source-to-site distance considerations.
- Accumulated earthquake waves do not significantly impact the short-period range of the acceleration spectra; however, low-frequency velocity pulses increase the spectral acceleration at longer periods.
- TBDY-2018 overlooks the orientation of near field records, resulting in a underestimated design spectrum.
- Nonlinear time history analysis results indicate that regardless of the method suggested by design codes, average ductility demand increases and reaches maximum values along the fault-normal direction at short periods.

References

Beyer, K., & Bommer, J. J. (2007). Selection and scaling of real accelerograms for bi-directional loading: A review of current practice and code provisions. *Journal of Earthquake Engineering, 11*(S1), 13–45. https://doi.org/10.1080/13632460701280013

Fahjan, Y. M. (2008). Türkiye Deprem Yönetmeliği (DBYBHY, 2007) Tasarım İvme Spektrumuna Uygun Gerçek Deprem Kayıtlarının Seçilmesi ve Ölçeklenmesi. Teknik Dergi, 19(93), 4423-4444.

Hayden, C. P., Bray, J. D., & Abrahamson, N. A. (2014). Selection of Near-Fault pulse motions. *Journal of Geotechnical and Geoenvironmental Engineering*, *140*(7). https://doi.org/10.1061/(asce)gt.1943-5606.0001129

PEER Ground Motion Database. (2019). *PEER NGA-West2 ground motion records* [Data set]. Pacific Earthquake Engineering Research Center. https://ngawest2.berkeley.edu

Shahi, S. K., & Baker, J. W. (2013). *NGA-West2 models for ground-motion directionality* (PEER Report No. 2013-10). Pacific Earthquake Engineering Research Center, University of California, Berkeley.

Somerville P.G., Smith N.F., Graves R.W., & Abrahamson N.A. (1997). Modification of empirical strong ground-motion attenuation relations to include the amplitude and duration effects of rupture directivity, Seismol. Res. Lett., 68(1), 199-222.

Somerville, P. G. (2003). Magnitude scaling of the near fault rupture directivity pulse. *Physics of the Earth and Planetary Interiors*, *137*(1–4), 201–212. https://doi.org/10.1016/s0031-9201(03)00015-3

4th International Civil Engineering & Architecture Conference
17-19 May 2025, Trabzon, Türkiye

An investigation on the effect of rotational ground motion on seismic behavior precast RC single story industrial building

Yaman Khalbous*[1], Rafet Sisman[1]

[1] Yıldız Technical University, Department of Civil Engineering, 34220 Istanbul, Türkiye.

Abstract. In current engineering practice, seismic design of buildings is realized by considering translational ground motions only. However, for buildings with certain geometrical properties rotational ground motions can be effective. For instance, precast industrial buildings are generally low-rise structures with large plan dimensions. Due to the larger dimensions in the plan, precast industrial buildings can be susceptible to rotational ground motion components. Therefore, the contribution of the rotational ground motion components to the overall seismic behavior of the industrial buildings should be investigated. In this study, it is aimed to perform nonlinear time history analysis for precast industrial buildings by considering rotational ground motion components together with the translational ones. A set of ground motions from the past earthquakes that occurred in Türkiye are utilized in this study. The numerical model of the precast industrial building is developed using a commercial Finite Element Method (FEM) software. In the numerical model, nonlinear elements are modelled using line elements with fiber sections. Appropriate material models are utilized for concrete and reinforcing steel from the material library of the FEM software. The effects of rotational ground motions are evaluated based on the change in the drift ratios of the precast columns. Nonlinear time history analysis results indicate that the contribution of rotational ground motions to the overall seismic performance can be significant.

Keywords: Rotational ground motions; Nonlinear time history analysis; Precast industrial buildings; Seismic structural behavior

1. Introduction

A significant portion of Türkiye lies on active fault lines, making it one of the most seismically active countries in the world. This geographical reality puts millions of people and countless structures at risk, especially in major cities like Istanbul and Balıkesir, where dense populations and vital industrial facilities are concentrated. In these regions, the structural resilience of buildings is not just a matter of engineering it's a matter of public safety and economic stability.

To address this challenge, seismic design standards have been developed and continuously refined over the years. These regulations aim to ensure that buildings can withstand the destructive forces of earthquakes by taking into account the specific seismic characteristics of each region. Traditionally, these codes and engineering practices have focused on translational ground motions those that move the ground horizontally or vertically.

However, growing evidence from recent research suggests that this may not be the full picture. Earthquakes also produce rotational ground motions subtle but potentially influential twists around vertical and horizontal axes that have often been overlooked in conventional analysis. These rotational components can interact with a building's structural system in complex ways, especially in large or irregularly shaped structures like industrial precast buildings.

This study aims to explore this lesser-considered aspect of seismic activity. By using nonlinear time history analysis, which simulates the dynamic response of structures to real recorded ground motions, the research examines how rotational ground motion components influence the behavior of precast industrial buildings. The goal is to provide a deeper understanding of their impact and to highlight the importance of including rotational effects in performance based seismic design, especially for critical infrastructure.

* Corresponding author, E-mail: yaman.khalbous@gmail.com

https://doi.org/10.31462/icearc2025_ce_eqe_038

2. Methodology

2.1. Description of the precast RC industrial building
The building analyzed in this study is a single-story precast reinforced concrete (RC) industrial structure located in Balıkesir, Türkiye. It has a floor plan of 18 by 37.5 meters and has a total height of 12 meters as shown in Fig.1 The structure includes 12 precast concrete columns that carry prefabricated roof beams, trusses, and girders, all designed in accordance with the building codes. The connections between the columns and beams are not rigid they're designed to release moments, so they act like pinned joints. This kind of connection is quite common in precast construction and allows the parts to move slightly without transferring bending forces.

The sandwich panels receive support from precast concrete purlins. Elastic diagonal braces, with pinned connections, were placed between purlins in the numerical model for simulation of the diaphragm effect that was provided by these sandwich panels according to guidelines specified in (TBDY-2018).

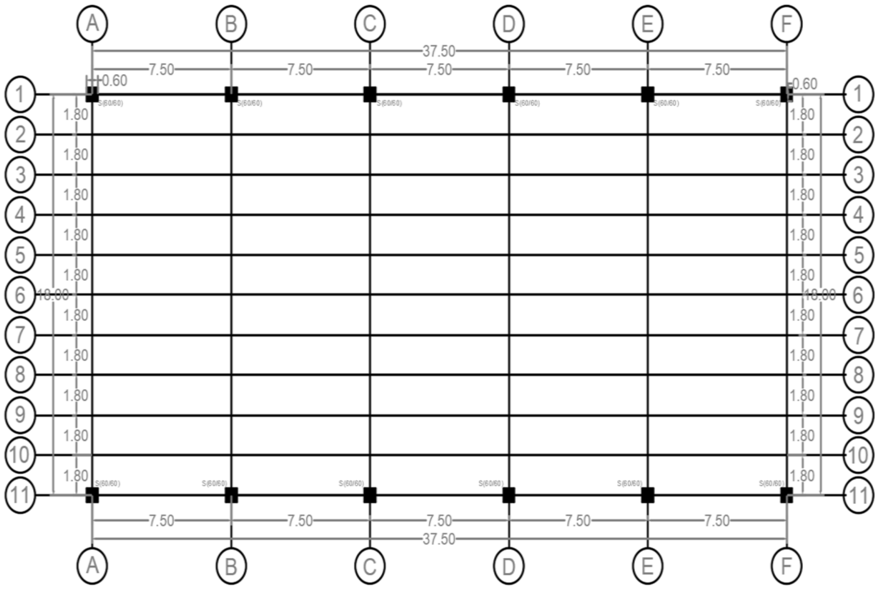

Fig. 1. Plan layout of the structure

$$(\mathrm{EA})_{\mathrm{e}} = 3.5\ \mathrm{t} \tag{1}$$

In this calculation (EA)e. t represents the overall thickness in millimeters of the sandwich panel sheets. As per code requirements, the spacing of purlins in addition to diagonal brace angle was modelled as $\alpha \approx 45°$.

2.2. Numerical modeling approach

2.2.1. Finite element modeling (FEM)
Fig. 2 shows detailed three-dimensional numerical model and it created using (SAP2000, 2025), a widely used software for finite element analysis in structural engineering. The model explicitly captures both translational and rotational seismic excitation responses. Structural columns were modeled with nonlinear frame elements that include plastic hinges defined at potential plastic hinge regions, in accordance with the Turkish Building Earthquake Code (TBDY 2018) requirements. Roof girders, beams, and trusses were idealised as elastic members with pinned connections at the supports.

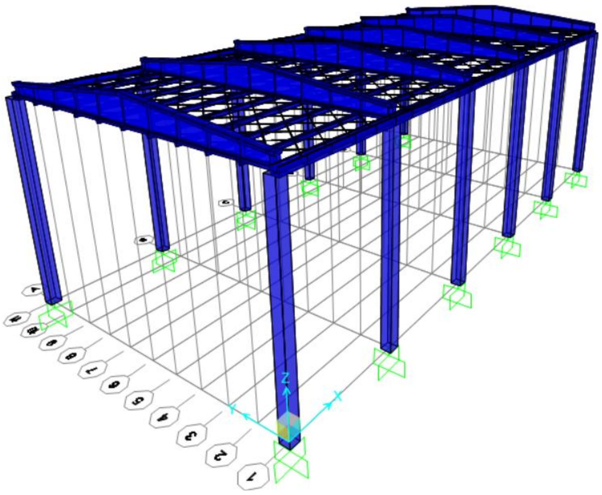

Fig. 2. Three-dimensional modeling of the structure (SAP2000)

2.2.2. Nonlinear material and section modelling

To account for material nonlinearity, fiber hinges are placed at the ends of the columns. These hinges represent the different parts of the cross-section confined concrete, unconfined concrete, and reinforcing steel using individual fibers defined through SAP2000's fiber modeling tool.

The concrete behavior is modeled using (Mander, 1988)'s stress-strain curves, with separate properties for confined and unconfined zones as shown in Fig. 3. In this study, C40 concrete is used, which offers good strength for industrial structures. The reinforcement is B420C grade steel, modeled with an elastoplastic approach to reflect yielding behavior.

The cross-section is divided based on the actual geometry and reinforcement layout, and the hinge length is taken as 10% of the clear column height, following the recommendation in TBDY 2018. This setup allows the model to realistically capture how columns respond during strong earthquakes, especially when they go beyond their elastic limits.

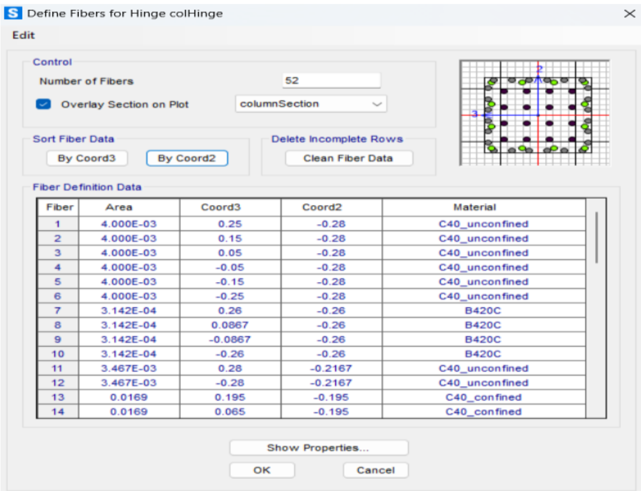

Fig. 3. Fiber section definition for bottom column hinge

2.3. Vertical loading conditions

The vertical loads applied in the structural analysis were determined according to the (TS-498) based on its use and condition of the building. The unit weights of structural elements such as precast concrete columns, roof beams, and roof purlins were directly incorporated into the numerical model through the material definitions transferred to SAP2000. Specifically, the unit weight of reinforced concrete elements was 25 kN/m³ and that of steel elements was 78.5 kN/m³. Table 1 shows the additionally applied dead load and live loads (snow). According to TBDY 2018/Table 4.3, the live load participation factor n=3 was used in the seismic analysis to consider the probability of live loads under seismic conditions.

Table 1. Vertical loads

Loads	Dead/Live	Load Intensity
Covering roof	Dead	0.12 kN/m^3
Snow	Live	0.75 kN/m^3

2.4. Ground motion selection

2.4.1. Translational ground motions

A set of seismic acceleration records of major earthquakes in Turkey was selected from the (AFAD, 2025) database. The criteria for selecting these records included earthquake magnitude, distance from the epicentre to the site, similarity of soil types. This careful selection helps ensure that the ground motions reflect realistic conditions for the area. As a result, the analysis outcomes are more reliable and relevant to the building's actual seismic risk.

The peak ground acceleration (PGA) values for the selected earthquakes in the X, Y, and Z directions are presented in Table 2. An example of the recorded motion, specifically for the 2023 Kahramanmaraş (Elbistan) earthquake, is shown in Fig. 4, which illustrates the translational acceleration time history in the X-direction.

Table 2. Transalational GMs PGA values

Earthquake	PGA_X (g)	PGA_Y (g)	PGA_Z (g)
Mw5.8 Izmit (Kocaeli) 1999	0.324	0.074	0.07
Mw7.1 Duzce (Bolu) 1999	0.523	0.408	0.321
Mw7.7 Kahramanmaras (Elbistan) 2023	0.5	0.549	0.692

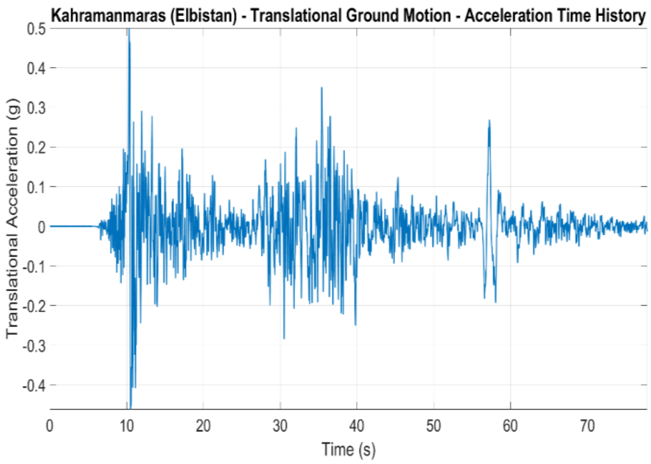

Fig. 4. Translational ground motion time history in X-direction

2.4.2. Rotational ground motion components

In this study, we did not just focus on the usual translational ground movements rotational ground motions also taken into account. These rotational components, which represent twisting around the vertical axis, were estimated using the Single Station Procedure (SSP), this method reconstructs the torsional acceleration histories from the recorded ground translational motions. This method allows the determination of the rotational components by analyzing the wave propagation characteristics of a single recording station.

The rotational motions corresponding to selected seismic events in Turkey are derived and used directly together with the translational motions for nonlinear time history analysis (based on the procedure described in (Şişman & Taciroglu, 2024) paper. When the rotational effects Included it gives us a more realistic picture of how an earthquake might impact large structures, especially those with wide floor plans, like the precast industrial building studied in this project.

The peak rotational acceleration values for the selected earthquakes around Z direction are presented in Table 3. An example of the recorded motion, specifically for the 2023 Kahramanmaraş (Elbistan) earthquake, is shown in Fig. 5.

Table 3. Roatational GMs PGA values

Earthquake	Peak Rotational Acceleration (rad/s²)
Mw5.8 Izmit (Kocaeli) 1999	0.007281837
Mw7.1 Duzce (Bolu) 1999	0.099841712
Mw7.7 Kahramanmaras (Elbistan) 2023	0.100387171

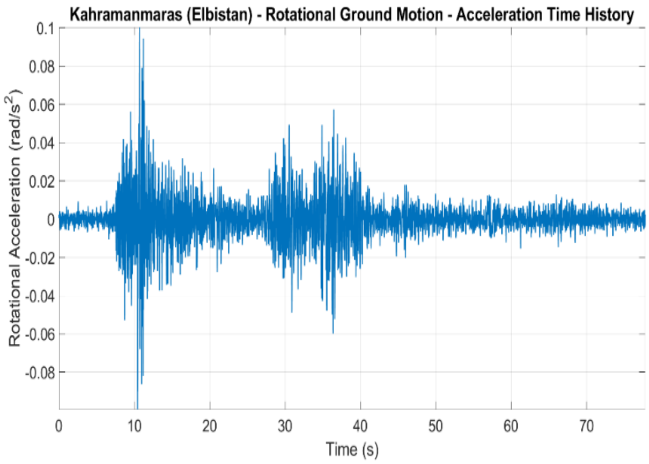

Fig. 5. Rotational ground motion time history

2.5. Nonlinear time history analysis

To better understand how the building will respond to earthquakes, the nonlinear time history analyses are performed. In these analyses, both horizontal (translational) and rotational ground motions applied to the building's finite element model as shown in Fig. 6. The analysis was performed using the Newmark-β method, as described in (Chopra, 2017). with a small time step, typically 0.01, to ensure the seismic input's high frequency content was accurately captured.

The main focus is on how the columns will behave in their drift ratios, and where plastic hinges (potential damage or failure) will form and spread during the earthquake. Two scenarios were examined:

- One where only horizontal and vertical ground motions were applied.
- Another example where both translational and rotational motions were included.

By comparing these two cases, it became clear how rotational ground motions can affect a building's seismic performance. The results of drift ratios and plastic hinge patterns were then evaluated using the performance limits and damage states set by the Turkish Earthquake Code (TBDY 2018), helping us judge whether the current structure meets safety requirements under realistic earthquake conditions.

In the nonlinear time history analysis, the Newmark-β method is used for numerical time integration. The parameters γ=0.5 and β = 0.25 are calculated according to the constant mean acceleration method and β=0.25 is chosen. This method is generally applicable to the analysis of nonlinear structures with large deformations and inelastic behavior.

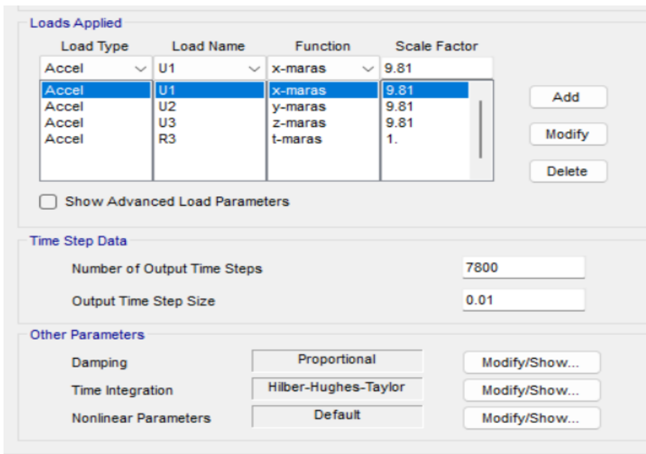

Fig. 6. Time history load case definition for translational and rotational ground motion

Classical proportional damping considered using Rayleigh damping. The damping matrix [c] is defined as the combination of the mass and stiffness matrices:

$$c = \alpha m + \beta k \tag{2}$$

where α and β are the Rayleigh damping coefficients. The modal damping ratio ζ_r for each mode r was calculated as:

$$\zeta_r = \frac{1}{2}\left(\alpha \frac{1}{\omega_r} + \beta \omega_r\right) \tag{3}$$

where ω_r is the circular natural frequency of mode r.

To define appropriate damping across critical vibration modes:

For combined translational and rotational ground motions, the first mode (T = 0.95 sec) and the third mode (T = 0.84 sec) were captured for torsional effects as shown in Fig. 7.

A 5% critical damping ratio (ζ = 0.05) was specified for both selected periods.

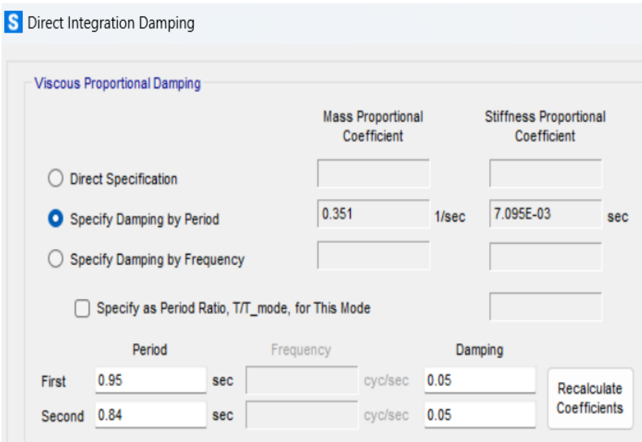

Fig. 7. Damping model

3. Results

The results from the nonlinear time history analysis show that rotational ground motion does not affect every part of the structure in the same way. For example, at Joint 13, as seen in Table 4, there's a slight increase in displacement when rotational ground motion is included—indicating a small rise in drift at this location. Meanwhile, at Joint 145, the opposite occurs: the displacement slightly decreases under rotational input. This pattern is also evident in the Duzce 1999 earthquake results (Table 5) and the Izmit 1999 earthquake results (Table 6). These differences suggest that the effect of rotational motion varies across the building, with certain areas experiencing increased drift while others experience reduced drift depending on the direction and location.

This variation in drift behavior is also illustrated in Fig. 8 and Fig. 9, which compare the X- and Y-axis drift values at Joints 13 and 145 under different ground motion cases.

Table 4. Mw7.7 Kahramanmaras (Elbistan) 2023 maximum drift ratio

Joint	GMs Type	OutputCase	U1	U2	X-axis (Drift)	Y-axis (Drift)
13	Translational	Time History-maras	0.23408	0.19322	1.9507	1.6102
13	Rotational	Time History-T-maras	0.23798	0.19329	1.9831	1.6108
145	Translational	Time History-maras	0.22426	0.18974	1.8689	1.5812
145	Rotational	Time History-T-maras	0.22077	0.18452	1.8397	1.5376

Table 5. Mw7.1 Duzce (Bolu) 1999 maximum drift ratio

Joint	GMs Type	OutputCase	U1	U2	X-axis (Drift)	Y-axis (Drift)
13	Translational	Time History-maras	0.1647	0.1115	1.3725	0.9292
13	Rotational	Time History-T-maras	0.16503	0.1094	1.3753	0.9116
145	Translational	Time History-maras	0.16064	0.1134	1.3387	0.945
145	Rotational	Time History-T-maras	0.15768	0.10969	1.314	0.9141

Table 6. Mw 5.8 Izmit (Kocaeli) 1999 2023 maximum drift ratio

Joint	GMs Type	OutputCase	U1	U2	X-axis (Drift)	Y-axis (Drift)
13	Translational	Time History-maras	0.01797	0.01138	0.14975	0.0948
13	Rotational	Time History-T-maras	0.018	0.01164	0.150017	0.097
145	Translational	Time History-maras	0.01806	0.0132	0.150533	0.11
145	Rotational	Time History-T-maras	0.01811	0.01311	0.150925	0.1093

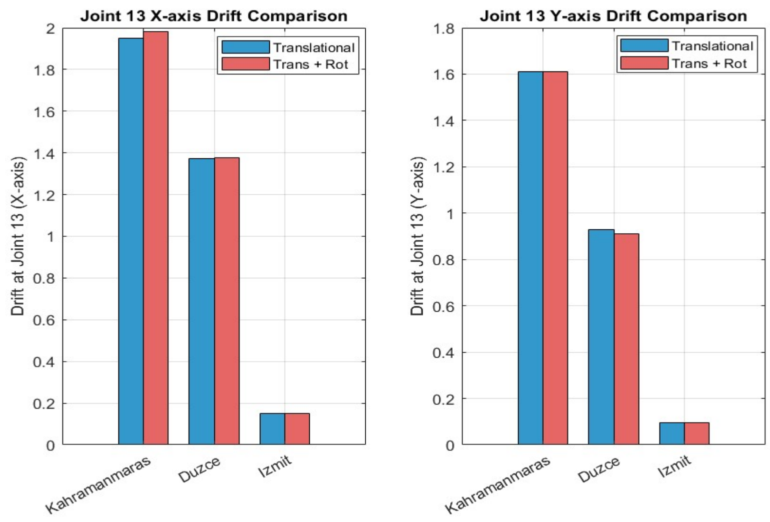

Fig. 8. Joint 13 drift comparison under ground motions

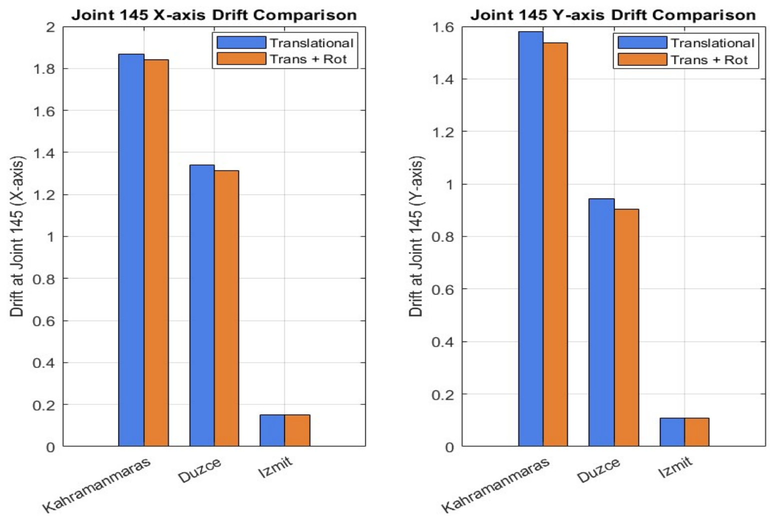

Fig. 9. Joint 145 drift comparison under ground motions

4. Discussion

This study finds that rotational ground motions have relatively little effect on the overall seismic response of the precast industrial building. Rotational effects sometimes caused a drift reduction slightly, such as at Joint 145, but at others, like Joint 13, a slight increase was felt.

This implies that the torsional effect does not function equally and sometimes, aid in the redistribution of forces within to reduce lateral displacement. Despite their little magnitudes compared to translational accelerations, rotational components can even have a slight influence, mainly in large floor plan structures.

However, the findings suggest that for symmetric and regular precast buildings, rotational motion effect is negligible. Therefore, while it may not be necessary to consider rotational movements in all design scenarios, it can improve accuracy in performance analyses, particularly in sensitive or unconventional structural configurations.

5. Conclusions

The research on the influences of rotational ground motions on the seismic response of a single-story precast RC industrial building using nonlinear time history analysis was the object of this research. The study indicated that although the overall influence of rotational components is minor, they can affect structural response by the minimal change of drift values at specific points.

The analyses confirmed that the interaction between translational and rotational motions produces a non-uniform seismic demand, even in ordinary structural configurations. This emphasizes the necessity of considering more than a single component of motion to gain a more complete understanding of structural behavior under earthquake loading.

Lastly, although rotational motions are not critical for all designs, their inclusion provides a more realistic representation of seismic demands. The conclusion is especially beneficial for performance-based design and analysis of industrial facilities where safety and continuity of operations are of utmost importance.

Acknowledgments

I would like to sincerely thank my supervisor, Dr. Rafet Sisman, for his invaluable guidance and support throughout this research.

References

AFAD. (2025). *Earthquake database*. Disaster and Emergency Management Presidency of Turkey (AFAD). Retrieved from https://deprem.afad.gov.tr/

Mander, J.B. (1988). Theoretical stress-strain model for confined concrete. *Journal of Structural Engineering, 114*(8), 1804–1826

Chopra, A.K. (2017). Dynamics of structures: Theory and applications to earthquake engineering. (5th ed., pp. 556–578). Pearson.

Computers and Structures, Inc. (2025). SAP2000: Integrated software for structural analysis and design. Berkeley, California, USA.

Şişman, R., & Taciroglu, E. (2024). Characteristics of torsional ground motions obtained for Turkey and their appraisal against Eurocode 8. *Bulletin of Earthquake Engineering*, *22*(5), 2353-2373

Türkiye Bina Deprem Yönetmeliği (TBDY-2018). (159). Ankara, Türkiye.

Turkish Standards Institution. (1997). TS 498: Design loads for buildings. (7-18). Ankara, Türkiye.

A rapid and hybrid prestressed seismic strengthening system for RC piers using Fe-SMA plates: Experimental breakthrough

Adel Al Ekkawi[1], Raafat El-Hacha[*1]

[1] University of Calgary, Department of Civil Engineering, 2500 University Drive NW, Calgary, Alberta, Canada

Abstract. This study evaluates the efficiency of a rapid and hybrid seismic strengthening technique using prestressed iron-based shape memory alloy (Fe-SMA) plates. Two 1/3-scale RC bridge piers were prepared for this study. The first column remained unstrengthened for baseline comparison. The second column was strengthened with external vertical prestressed Fe-SMA plates on both sides of the column to significantly enhance its flexural and seismic performance. In addition, circumferential Fe-SMA welded plates were utilized around the column for active confinement. All Fe-SMA plates were thermally activated above 250°C, inducing vertical prestressing and active confinement effects in the second column. Under quasi-static lateral cyclic loading, the vertical Fe-SMA plates alone improved the column's lateral strength, energy dissipation, and displacement ductility by 35.97%, 107.29%, and 55.16%, respectively. Thereby, the addition of vertical and lateral prestressed Fe-SMA significantly improved the lateral cyclic response of the second column, alongside with reducing its residual displacements, and effectively suppressing damage in its plastic hinge region. This study pioneers the application of novel prestressed flexural and active confining strengthening systems on RC piers, addressing a significant gap in the area of seismic strengthening. As the first experimental investigation of its kind, it marks a breakthrough in utilizing prestressed Fe-SMA plates as hybrid strengthening to enhance the seismic performance of RC piers. Additionally, the study provides a detailed methodology for the rapid implementation of the proposed hybrid strengthening system, making it highly suitable for scenarios requiring quick bridge rehabilitation and minimal service disruption.

Keywords: Seismic strengthening; Fe-SMA; Prestressed; Plastic hinge; Hybrid

1. Introduction

Previous pioneering studies (ChaiI, Priestley, & Seible 1991; Priestley & Seible 1995) have shown that reinforced concrete (RC) bridge columns built before the 1971 seismic code revisions have suffered from poor ductility and low lateral strength due to inadequate design practices. These issues included widely spaced transverse reinforcement that fails to provide sufficient concrete confinement and short lap splice lengths that prevent full yielding of the columns' longitudinal reinforcements. As a result, such deficiencies posed serious risks to the structural integrity and post-earthquake functionality of bridges. To address these problems, various strengthening systems have been explored, especially focusing on external confinement techniques, which can be classified into passive and active systems. Passive confinement engages only after the column witnesses damage and deforms circumferentially, while active confinement engages instantly after its utilization, thereby providing the deficient RC column with an early increase in strength and enhancement in its performance, even before damage occurs.

Traditional confinement methods like concrete or steel jacketing are labour-intensive, non-durable, and incapable of providing active confinement. Therefore, heavy attempts to use prestressed steel strands, like in (Saatcioglu & Yalcin 2003), or fiber-reinforced polymer (FRP) prestressed belts, like in (Nesheli & Meguro 2006), have been conducted to utilize the great benefits of active confinement and enhance the seismic performance of deficient RC bridge piers. However, such attempts required complex strengthening hardware and installation, and careful design due to challenges like creep rupture in FRP.

In the past three decades, Shape Memory Alloys (SMAs) have emerged as promising materials for seismic strengthening, owing to their unique thermo-mechanical properties (Lagoudas 2008). Notably, (Shin & Andrawes 2011) were the first to introduce Nickel-Titanium-Niobium (NiTiNb) SMA 0.58 mm spirals to apply active confinement around deficient RC columns. Their study showed that the NiTiNb-SMA active confinement

* Corresponding author, E-mail: relhacha@ucalgary.ca

https://doi.org/10.31462/icearc2025.ce.eqe054

https://doi.org/10.31462/icearc2025_ce_eqe_054

significantly increased the column's displacement ductility, energy dissipation, and drift capacity. Consequently, their findings demonstrated the SMA's high potential in enhancing the seismic performance of deficient RC piers.

However, while SMA-based active confinement significantly enhances the ductility and energy dissipation of deficient RC bridge piers (Shin & Andrawes 2011), it contributes little to the column's lateral strength, which is a common observation reported by many researchers (ElGawady, Endeshaw, McLean, & Sack 2010; Saeed, Aules, & Rad 2022; Sause, Harries, Walkup, Pessiki, & Ricles 2004; Shin & Andrawes 2011), whether for actively or passively confined RC columns. As such, flexural strengthening has become important in noticing a significant enhancement in the column's lateral strength and addressing strong-beam weak-column conditions. Countless studies have attempted to utilize flexural strengthening systems on deficient RC columns; however, prestressed flexural strengthening systems have never been attempted before due to its heavy practical challenges in applying prestress forces externally along the column's vertical plane. As a result, passive systems like externally bonded (EB) and near-surface mounted (NSM) reinforcements have gained traction due to their simplicity and ease of use.

In response to the limitations of prestressed flexural strengthening systems utilized on deficient RC bridge columns, the current study builds on prior research by (Al Ekkawi & El-Hacha 2025a) (same authors of this manuscript) who developed recently in 2025, a "*practical and innovative prestressed flexural strengthening technique using iron-based SMA (Fe-SMA) plates*." These plates were anchored on both sides of the column using a welded-bolted system to achieve robust prestressing. Therefore, this study further investigates the performance of this prestressed Fe-SMA flexural strengthening system on another RC column, combining it with active confinement techniques using the same Fe-SMA plates. Correspondingly, two seismically deficient RC columns, representing 1/3-to-scale RC bridge piers, were tested under lateral cyclic loading to assess their lateral cyclic performance in terms of the parameters mentioned in Section 2. The results confirmed the significant benefits of the proposed "active hybrid systems," which integrate flexural and confinement strengthening using prestressed Fe-SMA plates. The findings of this research fill a critical gap in the field of prestressed flexural strengthening and active confinement of RC columns, thereby offering an insightful and better approach for further enhancing the seismic performance of deficient RC bridge columns in the future.

2. Research objective

This study investigates the effectiveness of a novel active hybrid strengthening system using iron-based Shape Memory Alloy (Fe-SMA) as a prestressed flexural external reinforcement and an active confining material to enhance the seismic performance of deficient RC columns. The key performance metrics studied in this research include lateral strength, hysteretic behaviour, displacement ductility, energy dissipation, recentering ability, and accumulated damage. It also explores the benefits of incorporating active confinement using Fe-SMA plates applied through a robust and quick welding approach, highlighting its convenience for emergency applications.

To achieve this, two circular RC columns with low transverse reinforcement – representing seismically vulnerable 1/3-to-scale RC bridge piers – were tested under quasi-static lateral cyclic loading. The two columns are shown in Fig. *1*. One column remained unstrengthened as a control (Fig. *1*a). The second column, named "FlexSMA-CSW," was strengthened and prestressed in flexure using prestressed Fe-SMA plates. In addition, welded Fe-SMA plates were utilized around the column for active confinement (Fig. *1*b). Notably, the aforementioned strengthening elements were applied along the columns' estimated plastic hinge length (determined later in another section). By comparing the performance of these columns, the study demonstrates the effectiveness of the Fe-SMA prestressed flexural strengthening system combined with the confining Fe-SMA welded plates in improving the column's lateral cyclic response.

3. SMA: brief overview

Shape Memory Alloys (SMAs) have gained significant attention in structural strengthening over the past decade due to their unique smart behaviour and superelasticity.

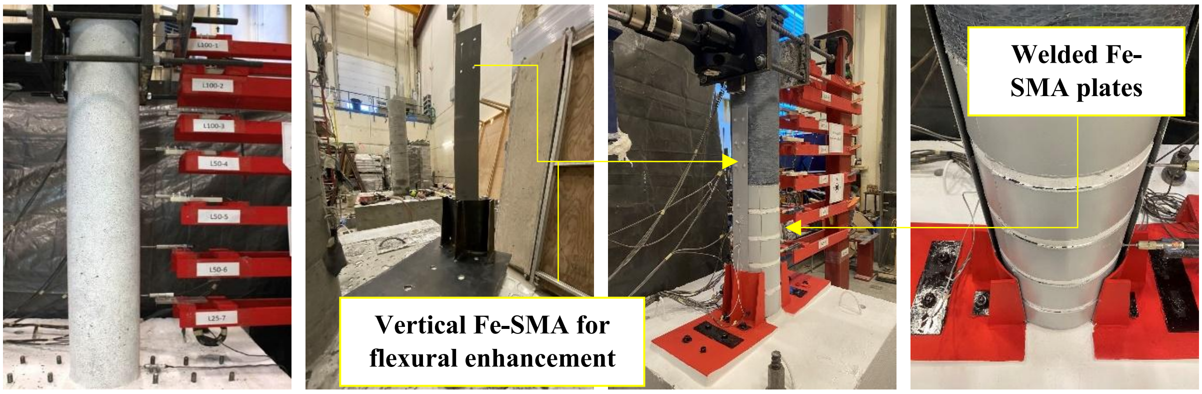

(a) As-built (b) FlexSMA-CSW

Fig. 1. Column testing matrix

These properties stem from a reversible crystallographic transformation between two phases: austenite (A) and martensite (M). Notably, temperature governs this transformation, with the alloy becoming martensitic upon cooling below the martensite start (M_s) and finish (M_f) temperatures and transforming back to austenite when heated above the austenite start (A_s) and finish (A_f) temperatures.

When fully austenitic, SMAs exhibit superelastic behaviour characterized by a flag-shaped stress-strain curve, shown in
Fig. 2, where deformations are fully recoverable upon unloading. In contrast, martensitic SMAs behave similarly to steel under loading but retain significant permanent deformations when unloaded, as presented in
Fig. 2. These deformations, however, can be reversed by heating the alloy above A_f, triggering the shape memory effect (SME). However, if the SMA is restrained during this transformation, it generates significant "recovery stresses," which are crucial for prestressing applications.

Noteworthy, an SMA with a wide thermal hysteresis ($A_s - M_s$) can maintain its recovery stresses even after cooling, making it highly effective for long-term structural use. These distinctive thermo-mechanical behaviours position SMAs as powerful materials in advanced prestressing and seismic strengthening strategies.

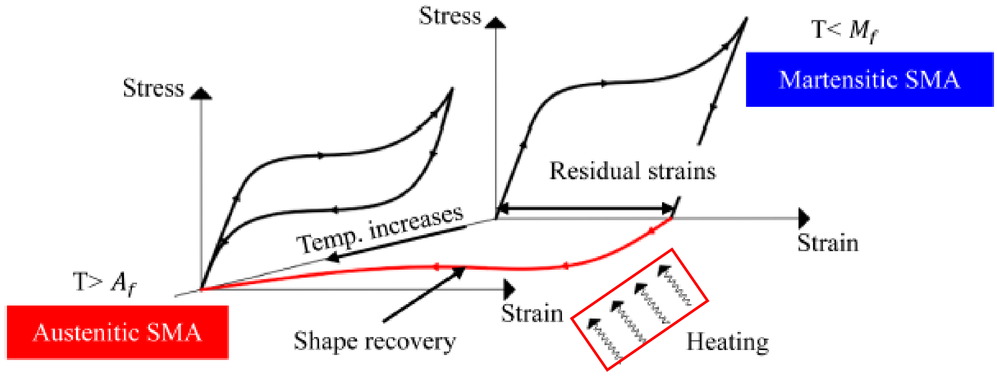

Fig. 2. Mechanical behaviour of SMA under different crystallographic structures

4. Research materials: mechanical characterization

4.1 Concrete

The foundations were cast first, with the columns poured a few months later to replicate a realistic construction timeline. The average compressive strength (f_c') of the columns was measured in accordance with ASTM C39/C39M, yielding values of 44.86 MPa at 28 days and 42.49 MPa at the time of testing. The 28-day strength was determined using 100×200 mm concrete cylinders cured in a humidity-controlled room at 95% humidity, while the strength at the testing age was obtained from uncured cylinders of the same dimensions.

4.2 Steel rebars

In both column specimens, 10M and 20M rebars are used as shear and longitudinal reinforcement, respectively. The 10M bars have a nominal diameter of 11.3 mm, while the 20M bars have a nominal diameter of 19.5 mm. Both types of reinforcement have a specified yield strength of 400 MPa. To determine the actual yield strength, four to six samples of each rebar type were tested under uniaxial tension in accordance with ASTM A370. The average yield strength obtained was 439 MPa for the 10M rebars and 404.4 MPa for the 20M rebars.

4.3 Fe-SMA plates

The Fe-SMA plates used in this study were previously characterized by (Shahverdi, Michels, Czaderski, & Motavalli 2018), who conducted extensive mechanical testing on the same material. Their results, summarized in Table 1, form the basis for this study's material properties. While Shahverdi et al. thoroughly assessed the mechanical behaviour of the Fe-SMA, they did not investigate its use in prestressed flexural or active confinement applications for RC columns, underscoring the novelty of the current research. The Fe-SMA, composed of Fe-17Mn-5Si-10Cr-4Ni-1(V,C) by mass, was supplied in plate form (1.5 mm thick, 120 mm wide) and pre-strained to 2% at room temperature, retaining 1.25% residual strain after unloading. Its transformation temperatures, reported by (Lee et al. 2013), are listed in Table 2. Notably, this research adopted the high-precision results from the aforementioned studies since advanced thermal monitoring, controlled heating systems, and Differential Scanning Calorimetry (DSC) were heavily used to ensure reliable and accurate material characterizations.

Table 1. Mechanical properties of the Fe-SMA plate

Austenitic elastic modulus (GPa)	Martensitic elastic modulus (GPa)	Yield strength (MPa)	Ultimate strength (MPa)	Rupture strain (%)	Recovery stress (MPa)	Stress losses (%)
75	160	534.58	981.32	42.92	386.71	9.6

Table 2. Transformation temperatures of the Fe-SMA plate

Martensitic finish temp. (M_f, °C)	Martensitic start temp. (Ms, °C)	Austenitic start temp. (As, °C)	Austenitic finish temp. (A_f, °C)
-64	-60	103	163

4.4 Carbon FRP wraps

Unidirectional CFRP wraps were applied as secondary confinement to the upper portions of the deficient RC column to strengthen specific anchorage regions and to conform with the strengthening confinement requirements of the CSA S6-19 standard. These wraps, identified as SikaWrap Hex-230 C®, have a thickness of 0.38 mm and manufacturer-reported properties of 801 MPa tensile strength, 74.70 GPa elastic modulus, and 1.01% rupture strain ("Sika Canada. SikaWrap Hex-230 C" 2018). Tensile tests conducted on CFRP coupons in accordance with ASTM D3039/D3039M, yielded average values of 710 MPa for tensile strength, 68.9 GPa for elastic modulus, and 1.29% for rupture strain, as tested by (Abdelrahman 2017).

5. Design of column specimens

The two circular RC columns, designed as 1/3-scale bridge piers, were constructed to evaluate the proposed seismic strengthening systems. Each column has a diameter of 300 mm and a clear height of 1600 mm, supported by a 600 mm thick RC foundation. To simulate realistic construction practices, the foundations were cast months before the columns, allowing the columns to be anchored through protruding reinforcement bars without using chemical bonding agents. This setup ensured load transfer occurred solely through mechanical interlock at the column-foundation interface. The cast is shown in Fig. *3*.

Both columns were built with seismic deficiencies, featuring widely spaced transverse reinforcements that were positioned at 150 mm spacing, thereby falling short of the 75 mm maximum spacing required by CSA S6-19 for ductile performance. The reinforcement detailing is presented in Fig. *3* as well. This low confinement level replicates outdated construction practices that have historically contributed to RC column failures during earthquakes. The columns were reinforced with 8-20M longitudinal bars evenly distributed around the perimeter, resulting in longitudinal and transverse reinforcement ratios of 3.40% and 1.16%, respectively. Concrete covers were 30 mm for columns and 50 mm for foundations.

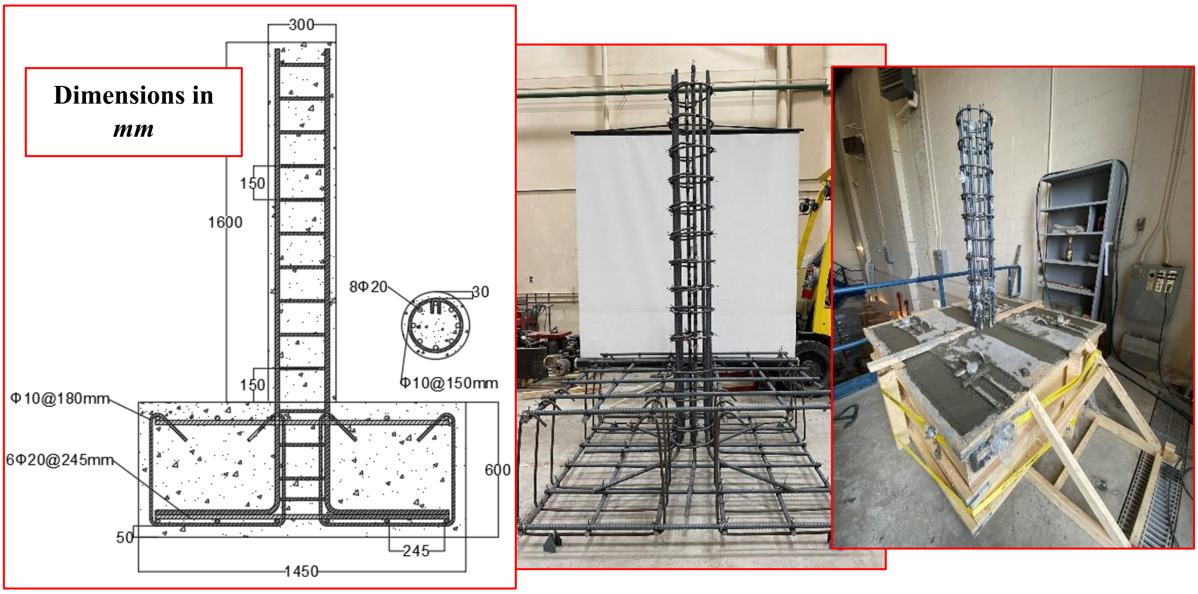

Fig. 3. Reinforcement detailing and columns' casting

6. Description of the lateral cyclic loading regime

Both RC columns were tested under quasi-static lateral cyclic loading applied at their tops using a 250 kN displacement-controlled actuator, with an effective height of 1425 mm, as shown in Fig. 4. The loading protocol, also illustrated in Fig. 4, followed the FEMA testing guidelines to capture key structural responses such as cracking, reinforcement yielding, and strength degradation. A total of 49 pull-push cycles were applied. Initial cycles were conducted at small displacements (0.5–3 mm) with a rate of 0.25 mm/sec. The displacement was then increased in stages − first by 3 mm up to 12 mm, then by 8 mm up to 68 mm, and finally by 15 mm up to 126 mm, with corresponding increases in loading rate, ending at 2 mm/sec. At the aforementioned rate, the columns were left to cycle until failure.

A constant axial load was also applied to simulate gravity effects, as presented in Fig. 4. It ramped from zero to -160 kN before lateral loading began. The axial load was equal to 5% of the column's gross concrete compressive strength, which falls within the axial load limits specified in CSA A23.3-19 for flexure-dominated columns. Consequently, this low axial load level helped isolating the lateral cyclic response of the columns.

7. Strengthening procedure

7.1 Determination of the columns' plastic hinge length (L_p)

The critical plastic hinge length (L_p) of the RC columns was determined using established equations from key studies on plastic hinge behaviour, with values ranging between 0.48h and 0.96h (ChaiI et al. 1991; Corley 1966; Priestley & Park 1987) (h is the column's diameter). However, the CSA S6-19 standard recommends a fixed L_p of $2h$ for such columns. Therefore, to simplify implementation and ensure safety, the authors adopted a conservative estimate of $2h$ (approximately 600 mm) for all specimens. This choice aligns with the code requirements and mirrors similar decisions in other studies (Miralami, Esfahani, & Tavakkolizadeh 2019; Shin & Andrawes 2011) that used L_p values between $1.5h$ and $2h$.

7.2 Utilization of the confining Fe-SMA welded plates

The FlexSMA-CSW column features lateral Fe-SMA plates designed to provide active confinement once activated. These plates are cut, bent, and tightly fastened around the column using hose clamps to eliminate any gaps and ensure a snug fit. The confining Fe-SMA welded plates are installed along the column's 600 mm plastic hinge region. For installation, only the overlap region − set to twice the plate width (2w), or 240 mm − is welded, as shown in Fig. 5.

Following the installation of the confining plates, vertical Fe-SMA plates are added to the FlexSMA-CSW column, following the procedure described subsequently in Section 7.3.

7.3 Utilization of the vertical Fe-SMA plates for prestressed flexural strengthening

In this study, 1100 mm long Fe-SMA plates were vertically installed on opposite sides of the FlexSMA-CSW column, aligned with the direction of the lateral loading. These plates were welded to stiffened steel base plates (Fig. 6a), which were anchored to the column foundations using six cast-in anchors per side (Fig. 6b). The anchors were 16 mm in diameter, Grade 36 steel, and embedded 210 mm deep. While cast-in anchors were used here for ease of testing, real-world applications would employ post-installed wedge anchors or concrete screws capable of withstanding the high tensile demands of the vertical Fe-SMA plates during seismic events.

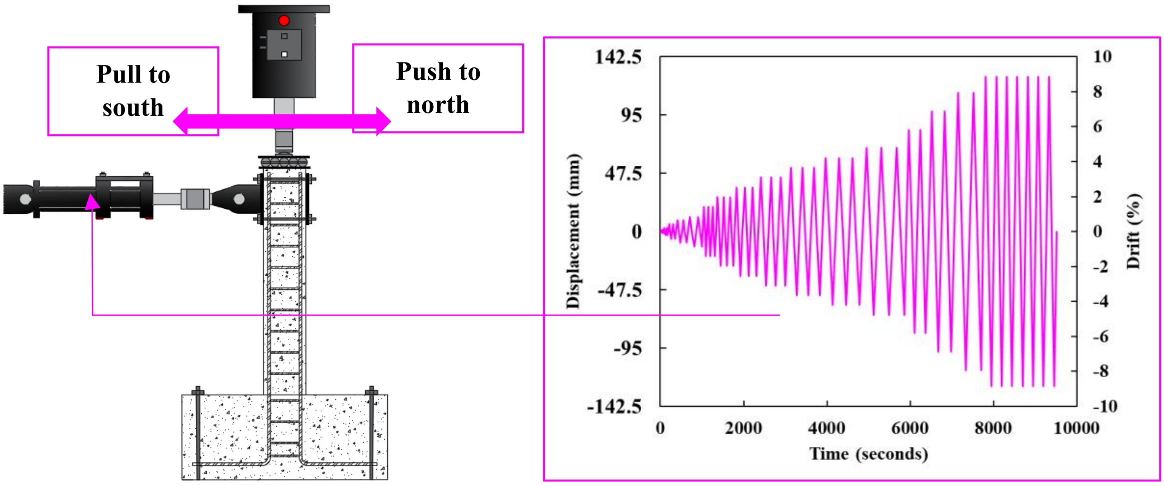

Fig. 4. Testing setup and loading protocol

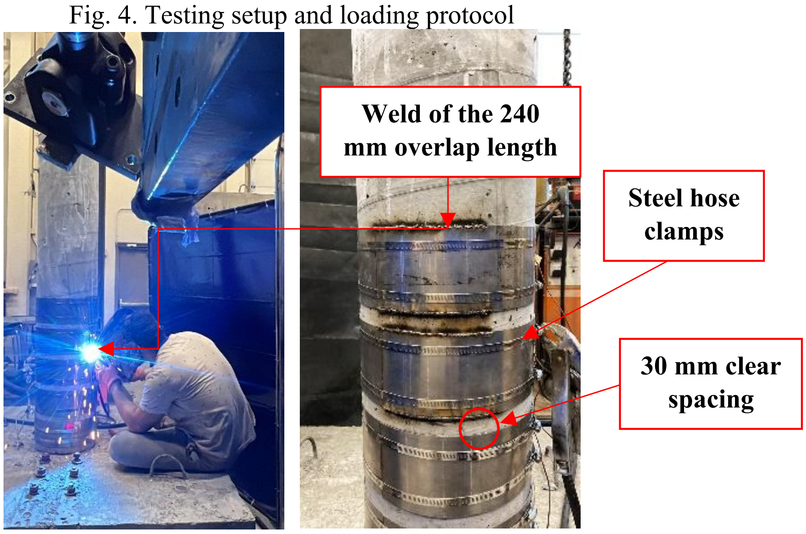

Fig. 5. Welding of the confining Fe-SMA plates

At the top, the plates were fixed to the FlexSMA-CSW column using six post-installed 9.5 mm wedge anchors (Fig. 6c). The effective plate length of the vertical Fe-SMA plates in the FlexSMA-CSW column was 560 mm to match the 600 mm expected plastic hinge length. To prevent anchorage failure in the wedge anchors at the top of the FlexSMA-CSW column due to shallow anchor embedment and moderate concrete strength, two CFRP layers were added (Fig. 6d). A schematic representation of the flexural strengthening system is shown in Fig. 6e.

Though the system may seem complex, it can be simplified for field use by replacing cast-in anchors in the foundation with threaded screw concrete anchors.

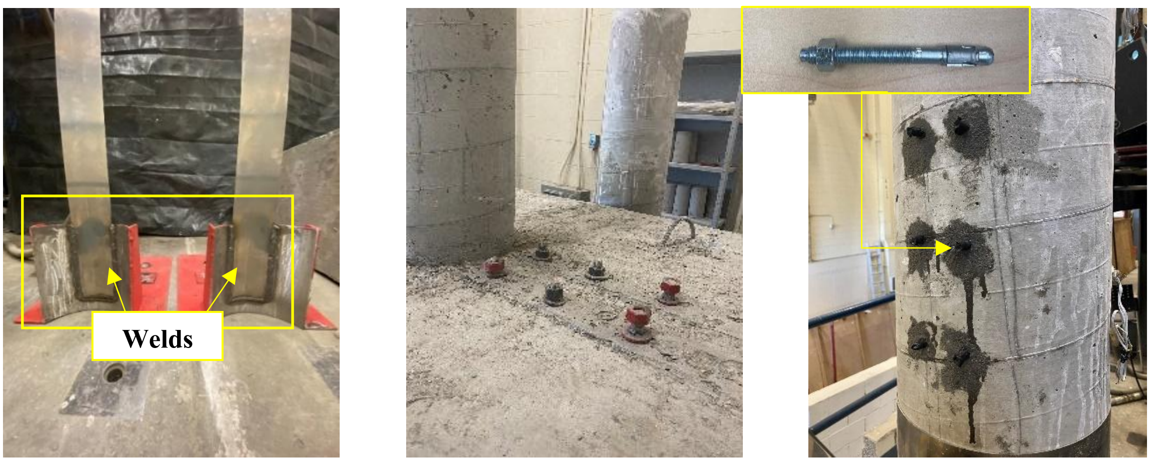

(a) Fe-SMA weld to steel plates (b) Cast-in anchors (c) Post-installed wedge anchors

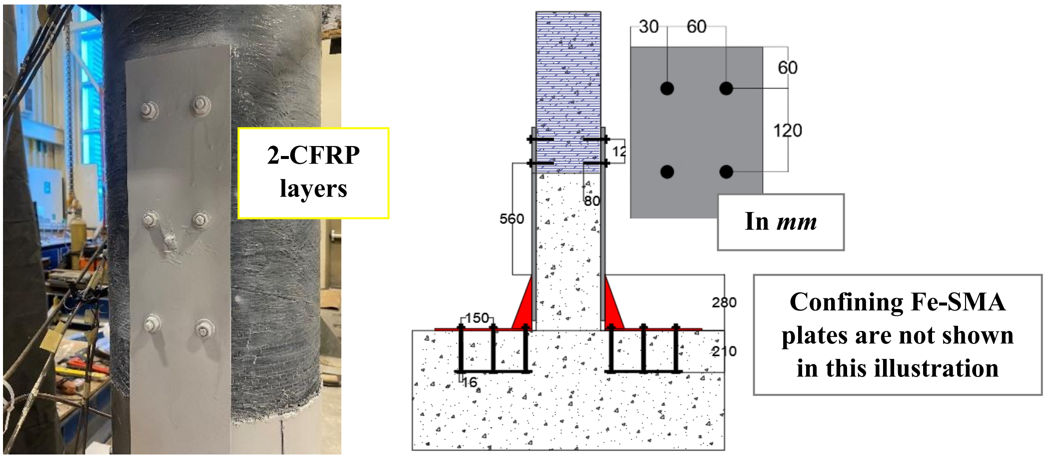

(d) CFRP wrapping (e) Scheme of the flexural system

Fig. 6. Process of the utilization of the vertical Fe-SMA plates in the FlexSMA-CSW column

7.4 Estimation of the Fe-SMA active confinement pressure

The confining Fe-SMA welded plates are designed to achieve a target confinement pressure of 4.05 MPa. This value is determined based on the ductility requirements outlined in the CSA S6-19 standard for FRP-confined systems, specifically from Chapter 16. Other equations from (Mander, Priestley, & Park 1988) were also used to accurately estimate the confinement pressure exerted by the confining Fe-SMA welded plates. Notably, these equations are lengthy and cannot be presented herein for brevity purposes; however, some of the equations are detailed in the author's recent publication (Al Ekkawi & El-Hacha 2025b). As a result, a clear spacing of 30 mm between adjacent Fe-SMA plates was obtained to provide a 4.05 MPa confinement pressure, as shown in Fig. 5.

Additionally, a 50 mm gap is maintained between the lowest Fe-SMA plate and the column base to prevent dislocation and to align with similar spacing requirements found in FRP confinement practices.

Similarly, the two layers of CFRP added at the remaining height (800 mm) of the FlexSMA-CSW column also provide a 4.05 MPa confinement pressure, thus maintaining a uniform confinement pressure along the columns' entire effective height.

7.5 Activation of the Fe-SMA plates

The vertical and confining Fe-SMA plates were heated above 163 °C using a flame torch to activate their shape memory effect (SME), as shown inFig. 7. Since the plates were anchored at both ends, their shape recovery was restrained, inducing vertical prestressing and active confinement in the FlexSMA-CSW column. Two to three thermocouples were attached to each vertical plate to monitor temperatures during heating. An example of temperature results from the FlexSMA-CSW column's south plate is shown inFig. 7, which shows a consistent temperature measured by the two thermocouples, with occasional spikes caused by direct flame contact. Similar temperature behaviour was observed on the other Fe-SMA plates; however, these results are not presented here for brevity.

The peak temperatures reached were 334.9 °C for vertical plates and 500.38 °C for confining plates – which were well above the required activation threshold of 163 °C. This ensured temperatures remained elevated and higher than 163 °C for an average of 12.67 minutes post-heating, thereby enabling a full martensite-to-austenite transformation.

7.6 Estimation of the recovery stresses in the Fe-SMA plates: Brief explanation only

The recovery stress of the Fe-SMA plates was estimated at approximately 450 MPa based on the activation temperature–recovery stress relationship established by (Shahverdi et al. 2018). To evaluate prestress losses, strain gauges (SGs) were attached at the mid-length of the Fe-SMA plates. Using the strain data collected and applying the analytical approach developed by (Al Ekkawi & El-Hacha 2025a) – which allows for accurate estimation of recovery stress from measured strain – the effective recovery stresses were calculated. The results showed that the vertical and confining Fe-SMAs reached an average recovery stress of 264 MPa and 398 MPa, respectively.

8. Results

8.1 Lateral strength

The lateral strength of the tested columns was defined as the peak lateral load attained during the cyclic loading protocol.

Fig. *8* presents the lateral strengths measured in both the push and pull directions for each column.

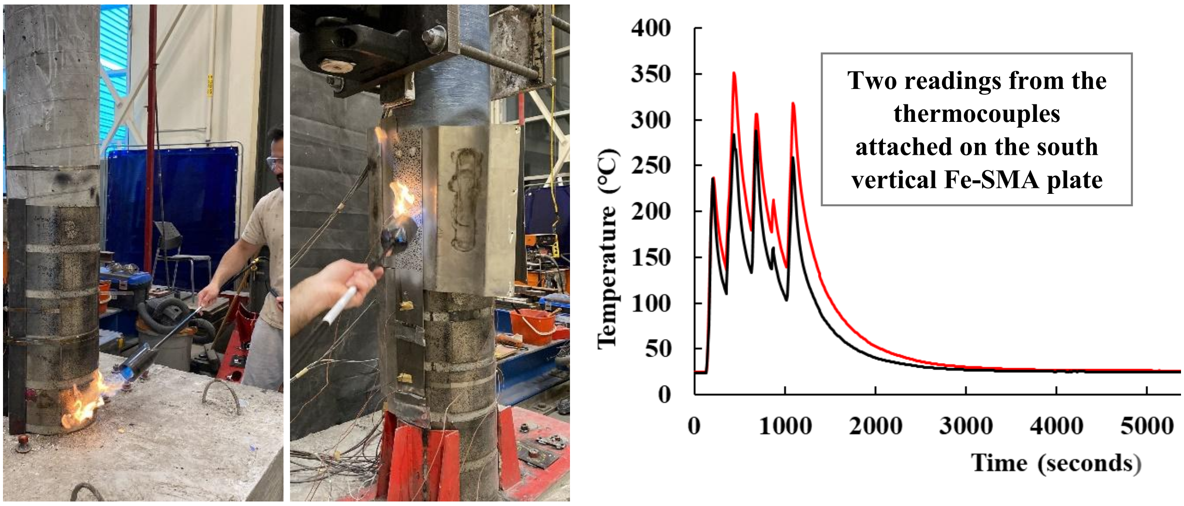

Fig. 7. Activation of the Fe-SMA plates and temperature versus time curves measured by thermocouples

The as-built column exhibited the lowest average lateral strength, reaching 91.53 kN at an average drift of 4.74%. As the drift demand increased beyond this point, a significant decline in strength was observed, driven primarily by severe crushing of the concrete and pronounced buckling of the longitudinal reinforcement. By the end of the test at 8.84% drift, the as-built column experienced a substantial 65.68% reduction in its lateral load capacity after sustaining 42 cycles.

In contrast, the FlexSMA-CSW column, which included both vertical and confining Fe-SMA welded plates, recorded a 35.97% increase in average lateral strength, peaking at 5.55% average drift. Despite the occurrence of a localized rupture in its vertical Fe-SMA plates (

Fig. *8*), the column maintained sufficient strength throughout the test, showing only a 19.69% drop at 8.84% drift and at the 49th cycle. This result illustrates the beneficial role of the vertical and confining Fe-SMA plates in enhancing both lateral resistance and damage resilience of seismically deficient RC columns. However, the authors suggest that adding welded Fe-SMA confinement had limited influence on the column's lateral load capacity, though it may have contributed to improved post-peak behaviour.

8.2 Hysteretic response

The full load-displacement and load-drift responses recorded during the lateral cyclic tests are presented in

Fig. *9*. All columns initially responded elastically until concrete cracking occurred, which was observed at an average lateral load of 12.24 kN and a corresponding drift of approximately 0.12%. As the drift increased, a consistent rise in lateral load was recorded for both specimens up to the point of longitudinal reinforcement yielding.

For the as-built column (

Fig. *9*a), the maximum lateral strength was reached at an average drift of 4.74%. Beyond this point, further increases in drift did not result in a significant gain in lateral capacity. Additionally, the hysteretic loops became increasingly pinched and unstable due to severe crushing of the concrete core and substantial buckling of the longitudinal steel bars. By the 42nd cycle, at 8.84% drift, the column exhibited global instability due to its extensive degradation in its lateral strength in both directions, thereby prompting an early termination of the test to prevent damage to the hydraulic loading system.

The FlexSMA-CSW column (

Fig. *9*c), which combined vertical Fe-SMA plates with confining Fe-SMA welded plates, similarly exhibited a stable and ductile hysteretic behaviour throughout the test. Although a temporary load drop was observed at 4.77% drift in the pull direction during the 34th cycle due to the rupture of the north vertical Fe-SMA plate, the load capacity recovered as the confining plates engaged more fully. Peak lateral strength was achieved at 5.55% average drift, and the column maintained its structural integrity until the onset of flexural cracking at 8.84% drift. The cyclic test was completed after the 49th cycle, with only a modest degradation in load response during the final loading stages.

Overall, the FlexSMA-CSW column maintained a well-defined and wide hysteretic envelope, highlighting the effectiveness of vertical and confining Fe-SMA plates in enhancing damage suppression and displacement capacity of the seismically deficient RC column. The hysteretic responses of the latter remained stable through the entire lateral cyclic test until reaching the maximum drift level of 8.84%. In contrast, the as-built column began to exhibit serious degradation beyond 4.74% drift. These results underscore the critical role of the vertical Fe-SMA plates in improving the displacement capacity, ductility, and cyclic stability of seismically deficient RC columns, particularly under large inelastic deformations. Moreover, the confining Fe-SMA welded plates acted as a second line of defense in enhancing the lateral cyclic response of the FlexSMA-CSW column, right after the rupture of the column's vertical Fe-SMA plates.

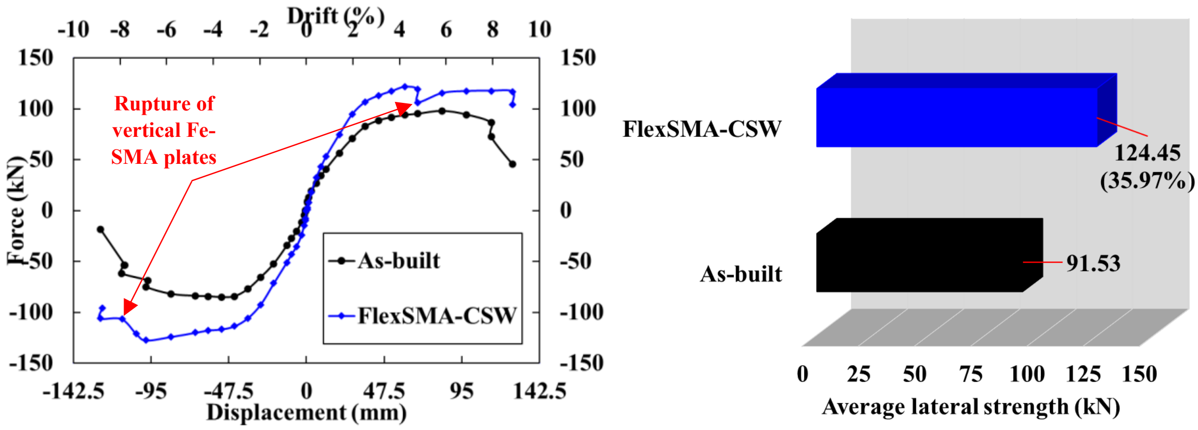

Fig. 8. Backbone curves and illustration of increase in the columns' lateral strength

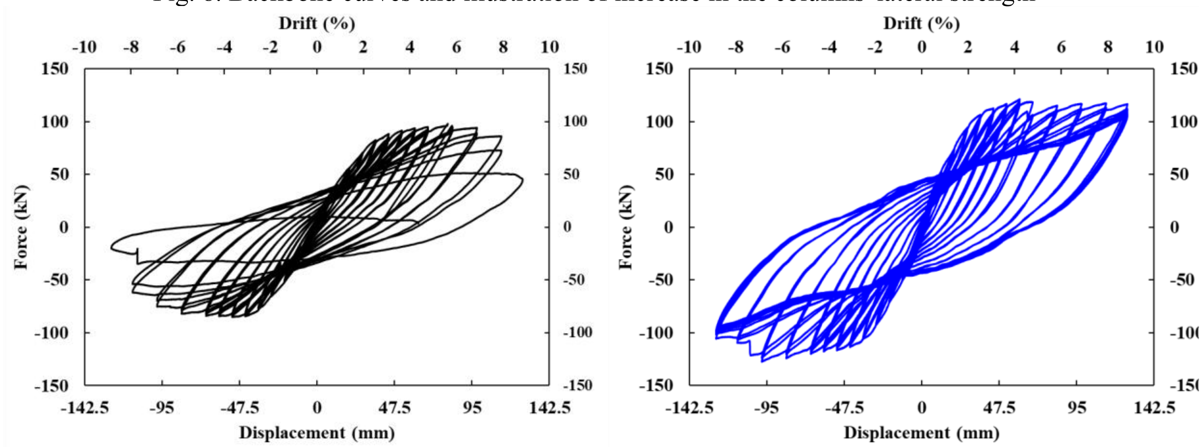

(a) As-built column

(b) FlexSMA-CSW column

Fig. 9. Lateral cyclic hysteretic response of the columns

8.3 Displacement ductility (μ_Δ)

The displacement ductility index (μ_Δ), defined as the ratio between the ultimate drift (Δ_u) and the yield drift (Δ_y), serves as a critical metric for evaluating the capacity of RC columns to undergo inelastic deformations without experiencing rapid strength degradation (Priestley & Park 1987).

In this study, Δ_u is defined as the drift level at which the lateral load declines to 85% of its peak, indicating a 15% loss in lateral strength. On the other hand, Δ_y is identified based on the onset of longitudinal bar yielding, determined from the strain gauge readings attached to the internal reinforcement. The calculated values of Δ_y, Δ_y, and μ_Δ for all tested specimens are summarized in Table 3.

Table 3. Δ_y, Δ_u, and μ_Δ of the tested columns

Column	Average Δ_y (%)	Average Δ_u (%)	Disp. ductility μ_Δ	% increase in μ_Δ
As-built	2.50	7.41	2.96	NA
FlexSMA-CSW	1.93	8.84	4.59	55.16

On the other hand, the FlexSMA-CSW column exhibited a significantly higher μ_Δ value compared to the as-built column, recording an outstanding increase of 55.16%, which corresponds to a value of 4.59. This enhancement is largely attributed to the reduction in the column's yield drift, facilitated by increasing the column's yield stiffness due to the Fe-SMA welded confinement.

As was shown in previous research (Al Ekkawi & El-Hacha 2025a), the utilization of vertical Fe-SMA plates alone did not significantly boost the column's displacement ductility due to absence of confinement. In contrast, the confining Fe-SMA welded plates promoted more uniform stress distribution inside the column's concrete core and delayed damage localization, thereby significantly improving the column's ductile performance.

Moreover, the FlexSMA-CSW column succeeded in surpassing the minimum displacement ductility requirement ($\mu_\Delta \geq 4.0$) stipulated by the CSA S6-19 standard for a single ductile column. This finding demonstrates that the combination of vertical and confining Fe-SMA welded plates offers a promising strategy to meet modern seismic performance standards by effectively improving both deformation capacity and structural resilience.

8.4 Cumulative energy dissipation capacity (E_{cum})

The energy dissipation capacity of the tested columns was evaluated to gain insight into their ability to absorb and dissipate the cyclic input energy through reinforcement yielding and damage mitigation mechanisms. The cumulative energy dissipation, denoted as E_{cum}, was computed by summing the area enclosed within each complete load-displacement hysteresis loop from the beginning of the test until failure, as per the method outlined in (Hwang 1982). The resulting E_{cum} values for all specimens are presented in Fig. 10.

Overall, the FlexSMA-CSW column demonstrated improved energy dissipation capacity compared to the as-built specimen, primarily due to its structural stability that remained up to 8.84% drift, allowing it to undergo more cycles and larger inelastic deformations. The FlexSMA-CSW column showed a significant enhancement in its cumulative energy dissipation − recording a remarkable increase of 107.29% relative to the as-built column. This notable improvement confirms the effectiveness of the hybrid active strengthening system, incorporating prestressed and confining Fe-SMA plates, in facilitating energy absorption and controlling damage progression, making them highly suitable for seismic strengthening applications.

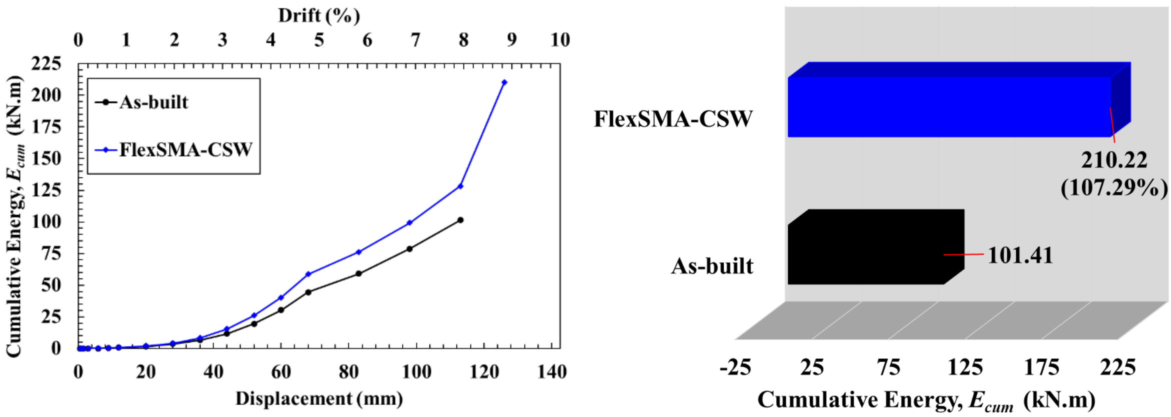

Fig. 10. Increase in columns' energy dissipation capacity with the increase in drift levels

The Fe-SMA welded plates likely provided sustained lateral pressure on the concrete core, thus minimizing premature cracking and enabling the column to retain its structural integrity throughout the inelastic deformation range and absorb further energy. As a result, it is concluded that the confining Fe-SMA welded plates promoted a stable and energy-efficient hysteretic behaviour. Consequently, this finding offer promising potential for advanced seismic retrofit strategies aimed at extending the service life and improving the post-yield performance and energy absorption of vulnerable RC columns.

8.5 Column's recentering ability (Δ_{res})

The elastic deformation capacity of Fe-SMA plates plays a critical role in improving the recentering capability of seismically deficient RC columns. This characteristic helps reduce permanent displacements after significant lateral deformation, thereby enhancing structural resilience under cyclic loading. To evaluate this, the progression of average residual displacements, Δ_{res}, with increasing drift levels, was tracked for all specimens and is illustrated in Fig. 11.

As seen in Fig. 11, both columns maintained relatively low Δ_{res} values up to approximately 2.53% drift, reflecting elastic structural behaviour in the early cycles. Beyond this point, residual displacements began to increase significantly, indicating the transition to an inelastic response and accumulating damage. With continued drift beyond 2.53%, the columns exhibited generally comparable recentering behaviour, as evidenced by similar trends in the average Δ_{res}. However, as the drift levels increased beyond 6.88%, the as-built column began to display a marked rise in residual displacement due to severe internal damage. At 8.84% drift, it reached a peak average residual displacement of 74.55 mm, indicating substantial permanent deformation resulting from concrete crushing and reinforcement buckling.

A greater improvement was observed in the FlexSMA-CSW column, which recorded an average residual displacement of 58.42 mm at 8.84% drift, representing a 21.63% reduction relative to the as-built column. This highlights the effectiveness of vertical Fe-SMA plates in the column's enhancing recentering ability through suppression of damages. Additionally, the notable improvement in recentering performance is also attributed to the active confinement provided by the confining Fe-SMA welded plates, which effectively restrained damage propagation and preserved the integrity of the concrete core throughout the cyclic loading.

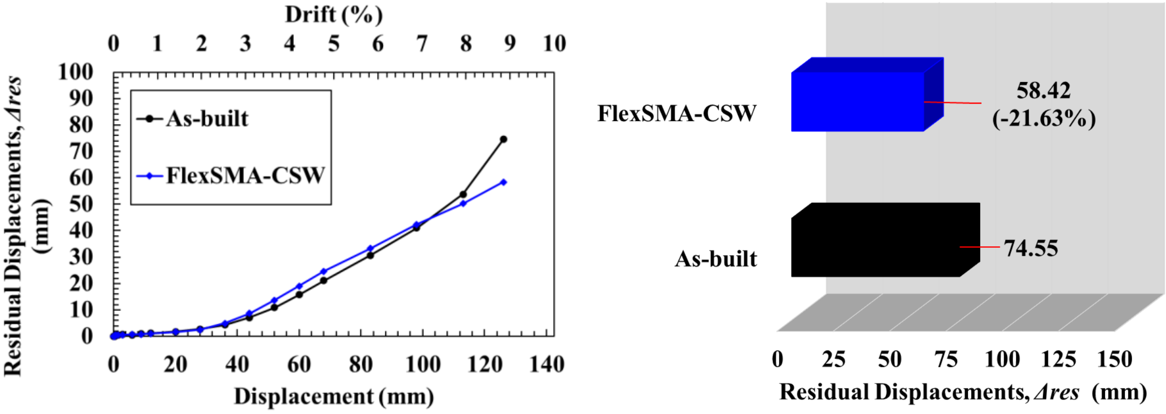

Fig. 11. Increase in columns' residual displacements with the increase in drift levels

Moreover, no abrupt increase in residual displacement was observed despite the rupture of vertical Fe-SMA plates in the FlexSMA-CSW column at 4.77% and 7.93% drift levels in the pull and push directions, respectively (see

Fig. *8*). This further suggests that the primary enhancement in the column's recentering ability was driven by the confining Fe-SMA welded plates as the column approached high drift levels and its ultimate failure, in which the confining plates continued to mitigate damage and maintain column's stability even after the rupture of the vertical Fe-SMA plates.

8.6 Damages accumulated

Among all tested specimens, the as-built column experienced the most severe damage. Concrete crushing initiated at 5.82% drift, and at the maximum applied drift of 8.84%, the column exhibited significant crushing of the concrete core and visible buckling of the longitudinal reinforcements (Fig. 12a). However, no reinforcement rupture occurred by the end of the test.

The FlexSMA-CSW column exhibited much less damage. Both the concrete cover and core remained undisturbed throughout the test, with no reinforcement buckling observed (Fig. 12b). The additional confinement provided by the confining Fe-SMA welded plates further contributed to the column's superior protection, effectively suppressing damage even at high drift levels. Therefore, post-earthquake repair would be limited to replacing the Fe-SMA plates and sealing surface cracks only, making this system particularly attractive for rapid recovery applications.

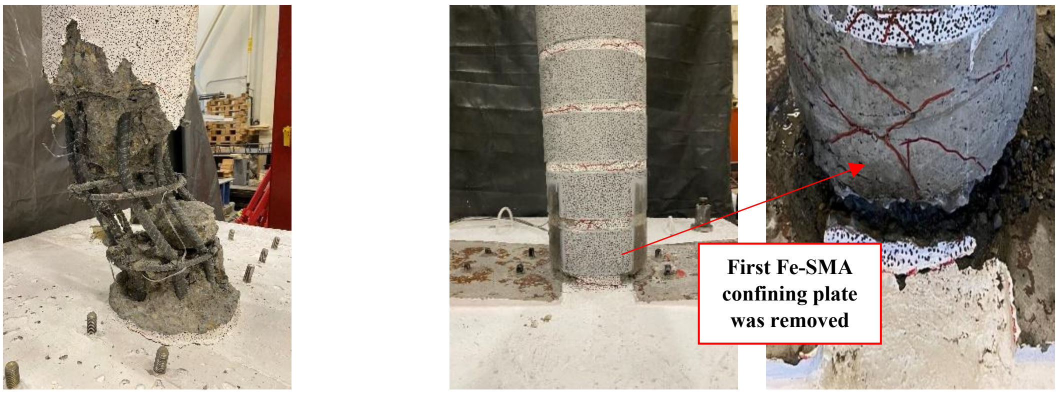

(a) As-built (b) FlexSMA-CSW

Fig. 12. Columns' accumulated damage at the end of the lateral cyclic test

9. Conclusion

This experimental study yielded the following conclusions:

- The as-built column experienced rapid strength degradation, extensive concrete core damage, and reinforcement buckling at large drift levels, indicating limited ductility and poor energy dissipation.
- Strengthening with vertical and confining Fe-SMA plates significantly improved the lateral response, flexural strength, and ductility of the columns. These plates also effectively limited damage to the concrete core and prevented reinforcement buckling.
- Confining Fe-SMA welded plates played a major role in improving column's stability under cyclic loading, increasing energy dissipation, and reducing its residual displacements. This hybrid active system also demonstrated a robust recentering capability and met critical ductility criteria for seismic applications.
- The hybrid active strengthening system provided excellent control over inelastic deformations, allowing the columns to maintain structural integrity under high drift demands.
- Damage in the strengthened column was minimal and localized to the concrete cover. As a result, repairs would be straightforward, primarily involving replacing external strengthening components such as Fe-SMA plates and surface crack sealing.
- The proposed hybrid active system also support rapid post-earthquake repair and reuse, offering practical advantages for resilience-based design and emergency recovery strategies.

In summary, using vertical Fe-SMA plates and confining Fe-SMA welded plates proved to be an effective and reliable method for enhancing the seismic performance of vulnerable RC columns. Noteworthy, the proposed strengthening system can be utilized within a few hours, thereby promoting the system as an effective rehabilitating solution for bridges in emergency situations.

Acknowledgements

The authors acknowledge the financial support of the University of Calgary, the National Sciences and Engineering Research Council of Canada (NSERC), the American Concrete Institute (ACI), and Mitacs. The authors appreciate Re-fer for donating the Fe-SMA plates and Sika for donating the CFRP sheets.

References

Abdelrahman, K. (2017). *Performance of Eccentrically Loaded Reinforced Concrete Columns Confined with Shape Memory Alloy Wires.* (Doctor of Philosophy), University of Calgary, Retrieved from https://prism.ucalgary.ca/items/ba2961a9-ac6b-4339-8080-1913551a0810

Al Ekkawi, A., & El-Hacha, R. (2025a). Experimental comparative study on novel flexural strengthening systems for seismically deficient RC piers: Prestressed Fe-SMA plates vs. externally bonded CFRP sheets. *Engineering Structures, 331*, 119941. doi:https://doi.org/10.1016/j.engstruct.2025.119941

Al Ekkawi, A., & El-Hacha, R. (2025b). Experimental investigation on seismically deficient RC bridge columns strengthened with prestressed vertical Fe-SMA plates and confined with CFRP wraps and UHPFRC jacket. *Engineering Structures, 332*, 120010. doi:https://doi.org/10.1016/j.engstruct.2025.120010

ChaiI, Y. H., Priestley, M. J. N., & Seible, F. (1991). Seismic Retrofit of Circular Bridge Columns for Enhanced Flexural Performance. *ACI Structural Journal, 88*(5), 572-584. doi:https://doi.org/10.14359/2759

Corley, W. G. (1966). Rotational capacity of reinforced concrete beams. *Journal of the Structural Division, 92*(5), 121-146.

ElGawady, M., Endeshaw, M., McLean, D., & Sack, R. (2010). Retrofitting of Rectangular Columns with Deficient Lap Splices. *Journal of Composites for Construction, 14*(1), 22-35. doi:https://doi.org/10.1061/(ASCE)CC.1943-5614.0000047

Hwang, T.-H. (1982). *Effects of variation in load history on cyclic response of concrete flexural members*. Urbana-Champaign: University of Illinois.

Lagoudas, D. C. (2008). *Shape memory alloys: modeling and engineering applications*. New York: Springer.

Lee, W. J., Weber, B., Feltrin, G., Czaderski, C., Motavalli, M., & Leinenbach, C. (2013). Stress recovery behaviour of an Fe–Mn–Si–Cr–Ni–VC shape memory alloy used for prestressing. *Smart Materials and Structures, 22*(12), 1-9. doi:https://doi.org/10.1088/0964-1726/22/12/125037

Mander, J. B., Priestley, M. J., & Park, R. (1988). Theoretical stress-strain model for confined concrete. *Journal of Structural Engineering, 114*(8), 1804-1826.

Miralami, M., Esfahani, M. R., & Tavakkolizadeh, M. (2019). Strengthening of circular RC column-foundation connections with GFRP/SMA bars and CFRP wraps. *Composites Part B: Engineering, 172*(-), 161-172. doi:https://doi.org/10.1016/j.compositesb.2019.05.063

Nesheli, K. N., & Meguro, K. (2006). *Seismic retrofitting of earthquake-damaged concrete columns by lateral pre-tensioning of FRP belts.* Paper presented at the 8th U.S. National Conference of Earthquake Engineering, San Francisco, California.

Priestley, M. J. N., & Park, R. (1987). Strength and Ductility of Concrete Bridge Columns Under Seismic Loading. *ACI Structural Journal, 84*(1), 61-76. doi:https://doi.org/10.14359/2800

Priestley, M. J. N., & Seible, F. (1995). Design of seismic retrofit measures for concrete and masonry structures. *Construction and Building Materials, 9*(6), 365-377. doi:https://doi.org/10.1016/0950-0618(95)00049-6

Saatcioglu, M., & Yalcin, C. (2003). External Prestressing Concrete Columns for Improved Seismic Shear Resistance. *Journal of Structural Engineering, 129*(8), 1057-1070. doi:https://doi.org/doi:10.1061/(ASCE)0733-9445(2003)129:8(1057)

Saeed, Y. M., Aules, W. A., & Rad, F. N. (2022). Flexural strengthening of RC columns with EB-CFRP sheets and NSM-CFRP rods and ropes. *Composite Structures, 301*(-), 1-24. doi:https://doi.org/10.1016/j.compstruct.2022.116236

Sause, R., Harries, K., Walkup, S., Pessiki, S., & Ricles, J. (2004). Flexural behavior of concrete columns retrofitted with carbon fiber-reinforced polymer jackets. *ACI Structural Journal, 101*(5), 708-716. doi:https://doi.org/10.14359/13393

Shahverdi, M., Michels, J., Czaderski, C., & Motavalli, M. (2018). Iron-based shape memory alloy strips for strengthening RC members: Material behavior and characterization. *Construction and Building Materials, 173*(-), 586-599. doi:https://doi.org/10.1016/j.conbuildmat.2018.04.057

Shin, M., & Andrawes, B. (2011). Lateral cyclic behavior of reinforced concrete columns retrofitted with shape memory spirals and FRP wraps. *Journal of Structural Engineering, 137*(11), 1282-1290. doi:https://doi.org/10.1061/(ASCE)ST.1943-541X.0000364

Sika Canada. SikaWrap Hex-230 C. (2018). Retrieved from https://can.sika.com/dam/dms/ca01/f/SikaWrapHex230C_pds.pdf

4th International Civil Engineering & Architecture Conference
17-19 May 2025, Trabzon, Türkiye

The effect of solar power panels on industrial structure's seismic performance

Samet Kılıç*[1], Turgay Çakmak[2]

[1] *Star Yazılım Mühendislik ve Danışmanlık, Ataşehir, Türkiye*
[2] *Protek Proje Tek.Müş.ve Kont. Hizm.Ltd.Şti., Ataşehir, Türkiye*

Abstract. In recent years, the use of solar panels has become quite widespread in our country. In particular, many factories want to meet some of their high electricity consumption with the electricity they produce within themselves. Additionally, solar panels are renewable energy sources. Significant damage was observed in many industrial structures in the Kahramanmaraş earthquake. Some of the damaged and destroyed factories had solar energy panels. Especially the effects of the presence of solar panels on roofs on the earthquake performance of buildings should be carefully examined. It is known that panels, in particular, affect seismic weight by increasing dead weight. In this study, solar panels were added to one of two existing buildings, while the other was left as is. In this way, it is aimed to measure the seismic effect of the panels. SAP2000® software is used for the study. In order to compare the effects of solar panels performance-based assessment is carried out with respect to Turkish Seismic Design Code. While analyzing structures, moving loads of cranes, snow loads, wind loads are also taken into account. Performance levels of structure with/without solar panels, drift ratios, base shear forces, steel elements capacities are checked. The finite element method used in the study is a valid way of seismic performance levels of structures. With this study, the impact of the solar power panels on seismic performance levels and the required precautions can be perceived.

Keywords: Performance based design; Solar energy panels; Seismic design of industrial structures; Retrofit of steel structures; Cranes design

1. Introduction

As businesses embrace renewable energy sources to lower operating costs and carbon footprints, the incorporation of solar panels into industrial buildings has become increasingly popular. Usually mounted on rooftops or other approved mounting locations, solar panel systems pose a special set of engineering difficulties, especially in seismically active areas. Solar energy has long been known to have positive effects on the environment and the economy, but in order to guarantee safety and resilience, a thorough analysis of how solar panel installations affect the seismic performance of industrial facilities is necessary.

Systems with solar panels add heft to the building, which may change how it responds to earthquakes. In addition to raising the dead load, the additional weight may shift the center of gravity of the structure, increasing its vulnerability to seismic forces. According to research, the distribution of mass might increase base shear and overturning moments, which can intensify seismic effects, especially when panels are concentrated in places (ASCE, 2022). Additionally, ill-planned installations may result in unequal loading, which could jeopardize structural integrity due to localized stress concentrations.

The dynamic implications of solar panel systems for the seismic performance of structures are crucial, even beyond static load considerations. Both solar panels and their mounting mechanisms have inherent frequencies. Resonance may arise when these frequencies coincide with the structure's inherent frequencies, intensifying vibrations and raising the risk of structural damage. In order to reduce such dangers, it is crucial to make sure that the dynamic characteristics of the solar panel system are compatible with the host structure, according to studies by Walters et al. (2012).

The seismic performance of industrial buildings is greatly impacted by the way solar panels are fastened to them. Mechanically anchored mounts, which are fixed directly to the structure, and ballasted mounts, which use weight to secure the panels, are examples of common mounting systems. Although ballasted systems are useful for reducing roof penetrations, instability may result from shifting during seismic activity. However, to prevent

*Corresponding author, E-mail: kilicsamet123@gmail.com

https://doi.org/10.31462/icearc2025_ce_eqe_060

water intrusion and guarantee long-term durability, mechanically anchored systems must be carefully designed, even though they offer higher seismic resilience (Baker et al., 2012).

Guidelines for incorporating solar panel systems into industrial facilities are provided by seismic design standards and building codes like ASCE 7 (2022) and Eurocode 8 (2003). With a focus on securing panels to prevent dislodgment and making sure their addition does not jeopardize structure safety; these standards address seismic loading considerations for rooftop solar installations. The new rules in the regulation (ASCE, 2022), provide precise criteria for wind and seismic loads on solar systems, emphasizing the importance of compliance to protect both the panels and the underlying structure (ASCE, 2022).

Retrofitting old industrial facilities with solar panel installations creates new obstacles. Older buildings may be unable to withstand the increased bulk and dynamic forces caused by the panels. Structural assessments are required to determine the building's load-carrying capacity and identify any necessary reinforcements. Advanced approaches, like as finite element modelling (FEM), are increasingly being utilized to predict the seismic performance of retrofitted structures, providing information on potential weaknesses and ideal remedies (Chopra, 2011).

While solar panel installations help to achieve sustainability goals, their impact on seismic resilience must be carefully monitored. Proper planning, material selection, and attention to design requirements can ensure that solar panels improve a structure's energy efficiency while maintaining its earthquake resistance. Innovative technologies, such as lightweight panel materials and vibration-damping systems, present intriguing opportunities for reducing earthquake risk.

The incorporation of solar power panels into industrial facilities represents a significant step toward sustainable energy solutions. However, it brings complications in seismic performance that must be carefully considered during the design, installation, and retrofitting phases. Engineers can ensure that solar panels are structurally safe in seismically prone areas by addressing added mass, dynamic impacts, and correct mounting solutions. Adhering to revised seismic design standards and utilizing advanced technical techniques will be key in attaining this balance and opening the road for safer, more environmentally friendly industrial infrastructure.

In this study, the same structure with and without solar panels were compared by considering the Turkish Regulations (TBDY, 2019; ÇYTHYE, 2016) drift ratios, base shear forces, steel element capacities, and structure performance levels with and without solar panels are examined as described in the relevant studies (Kılıç, 2024; Kılıç et al., 2022; Kılıç et al., 2021).

2. General Information about solar panels usage on roofs of buildings

In the Maraş earthquake in 2023, many residential, commercial and public buildings were destroyed, as well as industrial buildings. In some of the shared images of industrial buildings, as seen in Figure 1, it is noticed that buildings with solar panels were heavily damaged, which are very common today. In recent years, solar power plants have been subsidized by the state due to being a renewable energy source. However, especially when they are installed on existing buildings, their effects on the seismic behavior of the buildings must be examined in detail.

Fig. 1. Damaged Industrial Building with Solar Panels After Maraş Earthquake (Industrial Damage, 2024)

In practice, the static design of these solar panels is usually done by the supplier companies. The structural engineers are provided with layout drawings and distributed load values. Figure 2 shows a finite element model made by a solar energy supplier company. The constructions of solar panels can be manufactured from hot or cold rolled steel profiles as well as aluminium. The dead, live, seismic, snow and wind load of these structures are also made independently. While it is seen that many secondary situations such as the presence of panels or eaves on roofs are examined in the regulations (TS-EN 1991-1-4, 2007; TS-EN 1991-1-3, 2007), there is no special explanation regarding the presence of solar panels. Figure 3 shares a visual of wind analyses performed in the study (Hachem et al., 2024) on solar panels using the computational fluid dynamics method. For these reasons, the effects of newly designed panels with solar panels or panels added to an existing structure on the structural performance were evaluated within the scope of this study.

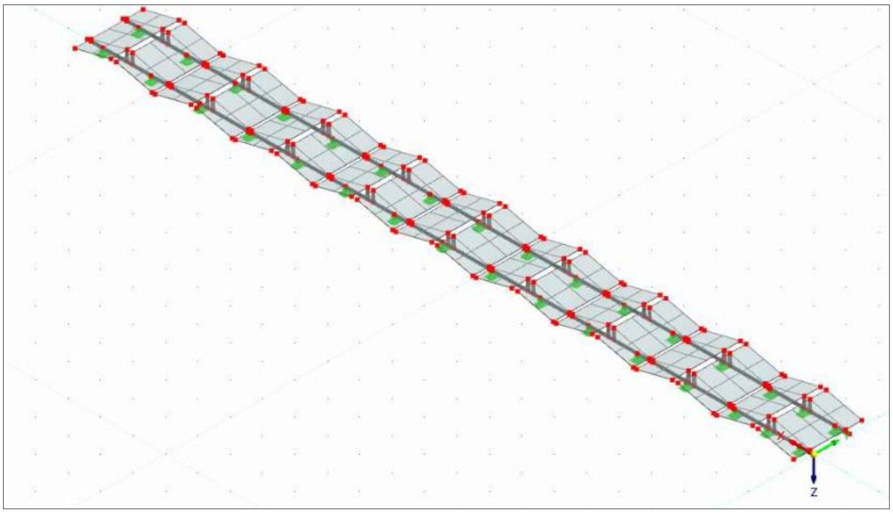

Fig. 2. Independent FEM Solution of Solar Panels (SAP2000, 2021)

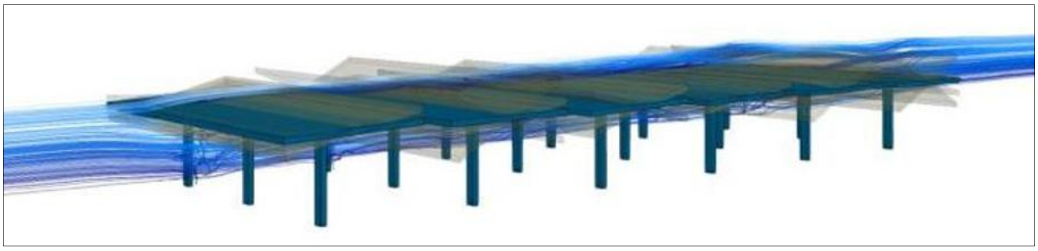

Fig. 3. Wind Loads for Solar Panels (Hachem et al., 2024)

2.1. Linear Models of Industrial Building with/without Solar Panels

In industrial structures consisting of steel trusses pinned on cantilever columns, a performance evaluation request was made due to the increase in crane capacity. In addition, it was planned to place solar panels on the existing structure during this process. For this reason, the seismic evaluation of the relevant structure was made separately for both cases.

Fig. 4. Snow Cleaning Method Views of Solar Panels (Cleaning Methods, 2024; Solar Panels, 2024)

It is very important to keep solar panels constantly clean in practice. Otherwise, electricity production will be interrupted. Therefore, manual and automatic snow cleaning methods are shown in Figure 4. The average loads of solar panels vary between 15-35 kg/m^2. The full snow load considered in this structure is 75 kg/m^2. Sometimes, the fact that snow is constantly cleaned, especially with automatic systems, leads to hesitations about whether the snow load is considered. Considering the coefficients in the loading combinations, it gives the impression that the distributed load of the solar panel is lower than the snow load and that it is on the safer side. However, while the snow load is calculated with a 0.3 live load participation coefficient when calculating the seismic weight, this coefficient is 1 when solar panels are evaluated as dead load. For this reason, seismic evaluation must be done. In addition, during the design, crane loadings as a moving load were renewed and wind and snow loads were revised according to the relevant standards and affected the structure (TS-EN 1991-1-4, 2007; TS-EN 1991-1-3, 2007). In Figure 5, Finite element components are presented. Solely, cantilever columns are for lateral seismic forces. Thus, only columns are evaluated under earthquake loads.

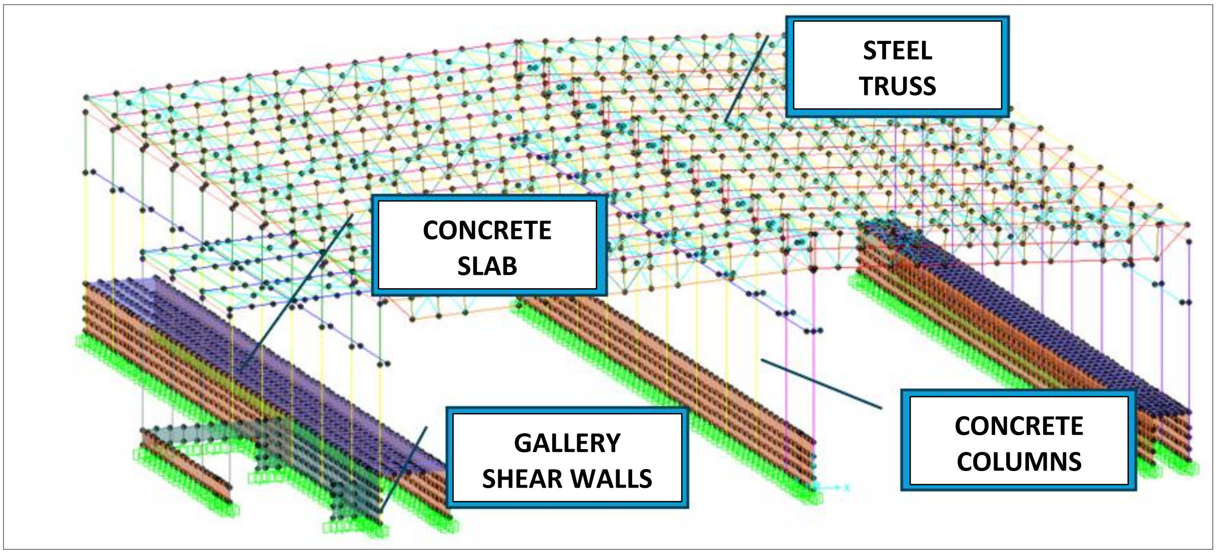

Fig. 5. Finite Element Model of Structure (SAP2000, 2021)

2.2. Result Review of Linear Finite Element Models

Table 1 shows the summary of certain results of the finite element model for two identical buildings with and without solar panels. Here, T_p indicates the dominant period in both directions, and drift indicates the maximum lateral relative displacements. While the addition of solar panels increases the seismic mass of a structure, it causes an increase in the base shear force and also causes a decrease in the base shear force due to the period shift. When Table 1 is examined, it is seen that the dominant period in the x direction does not change much with this addition, while the dominant period in the y direction is extended. For this reason, the base shear force in the x direction has increased, while it has decreased in the y direction. From here, it is expected that there will be very large changes in the base shear forces acting on the columns whose performance levels are important in buildings in which seismic loads are fully resisted by single-story frames with columns hinged at top. The decrease in the base shear force is not very important, but it is predicted that the increase in one direction may worsen the performance level of the elements located especially at the boundaries. When the lateral drift ratios are examined, a striking result emerges. When the base shear forces and dominant periods are close to each other, it is seen that the building with solar panels is shifted to the negative side in lateral drifts. The reason for this is that a very large mass is added to the weight of the roof with solar panels, which causes the upper end of the columns to displace more. This structure was evaluated with this method because it meets the performance analysis criteria with the linear calculation method defined in 15.5.3 of regulation (TBDY, 2019). The most important factor determining the performance of a column in this method is lateral drift. Therefore, due to the two determinations made at the end of this paragraph, in case a solar panel is added to the roof of an existing industrial structure, a performance analysis must be performed and if necessary, retrofit must be made.

Table 1. Summarized Information for Industrial Building’s Model with/without Solar Panels

Solar Panels	$T_p(x)$	$T_p(y)$	Base Shear-X	Base Shear-Y	Drift-X	Drift-Y	Average Steel PMM Ratio
With	0.8165s	0.7173s	5263 kN	5982 kN	1.75%	1.13%	0.44152
Without	0.8165s	0.6952s	5198 kN	6101 kN	1.19%	0.95%	0.42937

Figure 6 shows the Steel PMM Ratios of Roof Elements (SAP2000, 2021). According to the results, all roof elements in both structures meet the strength requirements and do not exceed the deflection limits. However, the 20 kg/m^2 increase in dead load caused small increases in the PMM ratios of many elements. According to Table 1, the average PMM ratio of the structure without solar panels is 0.42937, while the average PMM ratio of the structure with solar panels is 0.44152.

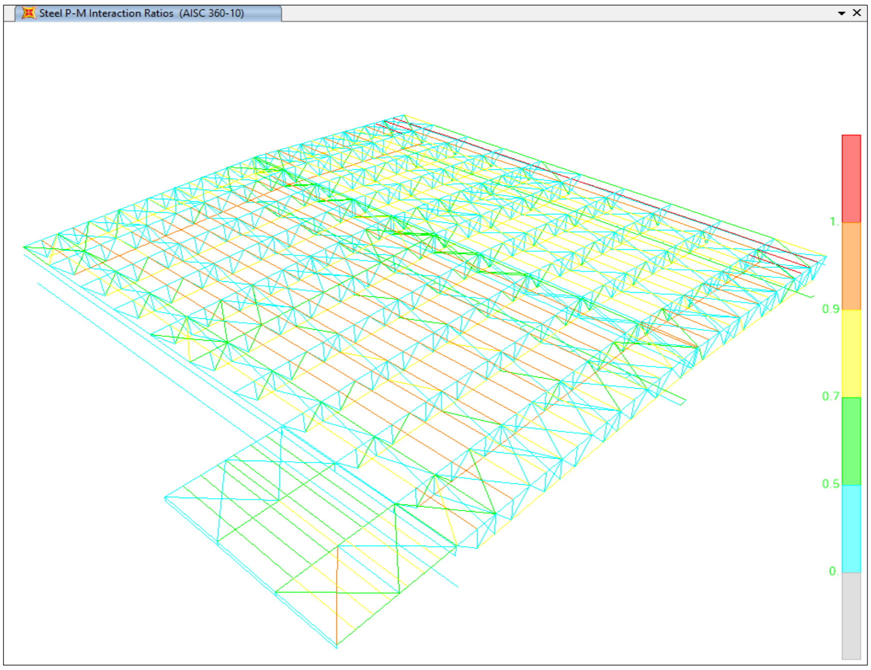

Fig. 6. Steel PMM Ratios of Roof Elements (SAP2000, 2021)

3. Performance based assessment of industrial building with/without solar panels

Since the structure is an existing building, all material research was carried out according to regulation (TBDY, 2019). Enough cores were taken, and the average concrete compressive strength was found to be 40.29 MPa. It was determined that the reinforcement realization rate was 1 with destructive and non-destructive examinations. In addition, it was seen in the stripping that the reinforcement was ribbed. The building's survey was checked, and it was seen that it was exactly compatible with the static project designed in 2014. Comprehensive knowledge level is accepted. Performance analyses of the structure were made by considering all the information.

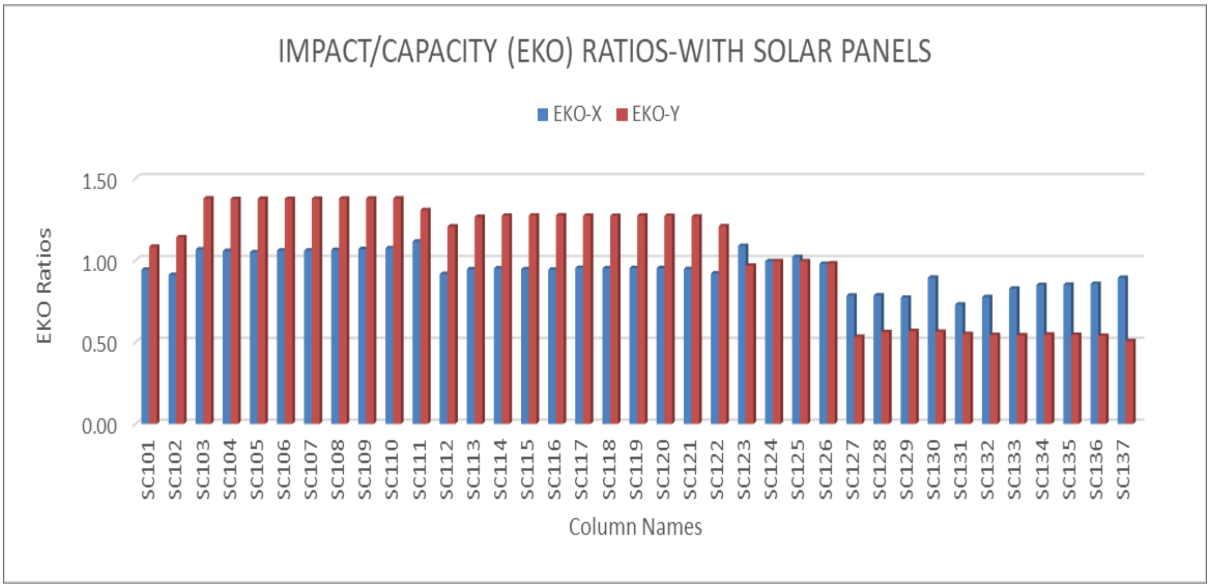

Fig. 7. EKO (Impact/Capacity) Ratios of Column Elements in Model with Solar Panels (Excel 2022)

The impact/capacity ratios, heights, and absence of B3 irregularity of the structures provided the linear performance analysis conditions. When the situation without solar panels was compared with the situation with them, it was seen that both structures provided the controlled damage performance level. In addition, no element was brittle in the shear force control. In this section, the EKO ratios of the elements were compared and presented in Figure 7 and 8 for both structures.

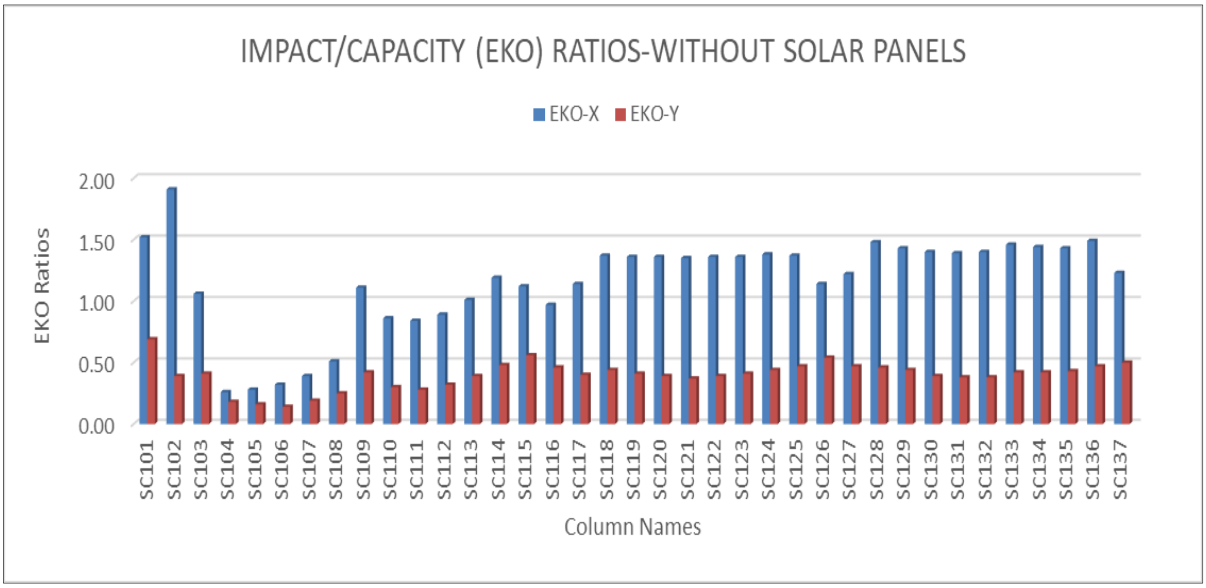

Fig. 8. EKO (Impact/Capacity) Ratios of Column Elements in Model without Solar Panels (Excel 2022)

Table 2 shows the summary of column damage levels where Table 3 illustrates the shear force ratio of columns passing into advanced damage zone to total shear force. In tables IO, LS, CP and CZ refer to immediate occupation, life safety, collapse prevention and collapse damage zones successively. Both structures satisfy the conditions for controlled damages performance level. According to regulation (TBDY, 2019) 15.8.4 (b), the total contribution of vertical elements in the collapse prevention zone to the total shear force carried by the vertical elements on each floor must be less than 20%. In the model without panels, there is no element in this damage zone, but in the model with panels, there are eleven columns in this zone in y direction. So, Table 3 is given below in order to show this limit which is 12.76% lower than 20%. In x direction all elements in both models are in the IO and LS zones.

Table 2. Summary of column damage levels

Solar Panels	Direction	Total Number	IO	LS	CP	CZ	Performance Level
With	X	37	11	26	0	0	Controlled Damage
	Y	37	11	15	11	0	Controlled Damage
Without	X	37	12	25	0	0	Controlled Damage
	Y	37	11	26	0	0	Controlled Damage

Table 3. Shear force ratio of columns passing into advanced damage zone to total shear force

Columns	Direction	V_i (kN)	SV_i (kN)	SV_{It} (kN)	SV_i/SV_{iT}
SC101	Y	533.287	2196.5	17222.0	%12.76
SC102	Y	57.979			
SC103	Y	137.227			
SC104	Y	147.124			
SC105	Y	148.667			
SC106	Y	148.879			
SC107	Y	148.855			
SC108	Y	147.618			
SC109	Y	137.639			
SC110	Y	56.613			
SC111	Y	532.614			

4. Conclusions

With respect to the results obtained from this study, the conclusions are summarized below:

- Average EKO ratios of columns in model without solar panels are 1.16 in the x direction, 0.41 in the y direction; are 0.91 in the x direction, 1.07 in the y direction in model with solar panels. They are lower than 3 which is defined as linear calculation method boundary in regulation (TBDY, 2019) 15.5.3 article. In x direction values are close to each other, however in y direction the values in the model containing solar panels are greater than the other model due to base shear increase as expected.
- When we look at the damage conditions in the columns, it is seen that 11-12 columns in both models in the x direction have IO damage, while the remaining columns remain in LS damage zone. In the y direction, the numbers are the same as in the x direction in the model without panels, while in the y direction with solar panels, it is seen that 11 columns are in IO damage level, 15 columns are in LS zone, and 11 columns are in CP level. Since this building is relatively new, it may have provided controlled damage performance levels, but in structures built in older years with low material quality, the desired performance level could not be achieved, and serious damages could have occurred.
- Changes in EKO values, element damage status obtained from performance analysis, and period, base shear force, drift and average PMM values obtained from linear analysis reveal the fact that structures where solar panels are placed must be subjected to a new seismic assessment. Retrofit work may be required to eliminate deficiencies that may occur after solar panel usage.

References

ASCE. (2022). Minimum Design Loads for Buildings and Other Structures (ASCE/SEI 7-22). American Society of Civil Engineers

Baker, J.W., Walters, J.P., & Malhotra, P. (2012). Seismic considerations for rooftop photovoltaic systems. SEAOC Convention Proceedings

Chopra, A.K. (2011). Dynamics of Structures: Theory and Applications to Earthquake Engineering. Pearson Education

Cleaning Methods. (2024, May 05). Retrieved from https://keremcilli.com/gunes-paneli-temizleme-robotu-robsys/.

ÇYTHYE. (2016). Çelik Yapıların Tasarım, Hesap ve Yapım Esaslarına Dair Yönetmelik (RG no. 29614). Ankara

Excel. (2022). Microsoft, USA (In Turkish).

Eurocode 8. (2003). Design of structures for earthquake resistance. European Committee for Standardization

Hachem, E. et al. (2024). Optimizing Solar Panel Angles Using Machine Learning for Wind Protection. Physics of Fluids, AIP Publishing

Industrial Damage. (2024, May 21). Retrieved from https://www.ntv.com.tr/galeri/turkiye/kahramanmarastaki-buyuk-yikim-havadan-goruntulendi,hbVxKM8gWUmI9UkrROiXHQ.

Kılıç, S. (2015). The Investigation of the 25 Percent Rule in Concentrically Brace Frame Dual System with Special Moment Frame. M.Sc. Dissertation, İstanbul Technical University, İstanbul

Kılıç, S. (2024). Deprem Yalıtımlı tank tasarımında yönetmeliklerin doğrusal olmayan analiz prensiplerinin irdelenmesi. *Karadeniz Fen Bilimleri Dergisi. 14(2):551-575*. https://doi.org/10.31466/kfbd.1385764 (In Turkish)

Kılıç, S., Akbaş, & Zülfikar, A.C. (2021). The evaluation of Seismic Behavior of Broad Tanks Subject to Strong Ground Motions Scaled with Different Approaches., 6th International Conference on Earthquake Engineering and Seismology, Gebze Technical University, Gebze, Kocaeli, Türkiye, October.

Kılıç, S., Akbaş, B., Paolacci, F., & Shen, J. (2022). Seismic behavior of liquid storage tanks with 2D and 3D base isolation systems. *Structural Engineering and Mechanics, 83 (5): 627-644*. Doi 10.12989/sem.2022.83.5.627.

Kılıç, S., Akbaş, B., Uçkan, E., & Çakır, F. (2021). Endüstriyel Yapılarda Yatay Geniş Tanklar ile Dikey Narin Tankların Deprem Esnasındaki Davranışlarının ve Farklı Sismik Yalıtım Sistemleriyle Tasarımlarının İrdelenmesi. 9. Ulusal Deprem Mühendisliği Konferansı, İstanbul, Türkiye, June (In Turkish).

SAP2000. (2021). Structural Analysis Program. CSI., Berkeley, California.

Solar Panels. (2024, May 11). Retrieved from https://futureflow.life/gunes-enerjisi-ureten-kar-citleri-yeni-bir-teknoloji/ (In Turkish)

TBDY. (2019). Türkiye Bina Deprem Yönetmeliği. Türkiye Cumhuriyeti Başbakanlık Afet ve Acil Durum Yönetimi Başkanlığı, Ankara, Türkiye (In Turkish)

TS 498. (2021). Yapı Elemanlarının Boyutlandırılmasında Alınacak Yüklerin Hesap Değerleri. Ankara (In Turkish)

TS500. (2000). Betonarme Yapıların Tasarım ve Yapım Kuralları, Türk Standartları Enstitüsü, Türkiye (In Turkish)

TS-EN 1991-1-3. (2007). Yapılar Üzerindeki etkiler Kar Yükleri. Ankara (In Turkish)

TS-EN 1991-1-4. (2007). Yapılar Üzerindeki etkiler Rüzgâr Yükleri. Ankara (In Turkish)

Walters, J.P., & Malhotra, P. (2012). Dynamic behavior of rooftop photovoltaic systems. Structural Engineering Association of California (SEAOC)

Critical evaluation of empirical and analytical models for predicting the behaviour of FRP-confined concrete

Nisreen Salameh[1], Raafat El-Hacha*[1]

[1] *University of Calgary, Department of Civil Engineering, 2500 University Drive NW, Calgary, Alberta, Canada*

Abstract. This paper presents a comprehensive evaluation of empirical and analytical models used to predict the compressive behaviour of Fibre Reinforced Polymer (FRP)-confined concrete cylinders subjected to uniaxial compression. The study compares theoretical predictions with experimental data, with particular emphasis on ultimate axial strength, ultimate axial strain, and the overall stress–strain behaviour of confined concrete. Seven widely recognized FRP confinement models are investigated, including the empirical models proposed by Fardis and Khalili (1982), Toutanji (1999), Lam and Teng (2003), Berthet et al. (2005), and Fahmy and Wu (2010), as well as the analytical models developed by Spoelstra and Monti (1999) and Teng et al. (2007). The findings reveal notable disparities in predictive accuracy across models, underscoring the importance of selecting confinement models that align with the specific material properties and confinement configurations in question. By identifying the strengths and limitations of each model, this study offers valuable guidance for their practical application in structural design and contributes to the broader understanding of the mechanical behaviour of FRP-confined concrete.

Keywords: FRP-confined concrete; Compressive behaviour; Empirical and analytical models; Ultimate axial strength; Ultimate axial strain

---

1. Introduction

The application of Fiber Reinforced Polymer (FRP) composites for the confinement of concrete has received considerable attention due to the significant improvements in compressive strength and ductility that it offers. Over the past few decades, various empirical and analytical models have been developed to predict the behaviour of FRP-confined concrete. These models aim to capture the complex interaction between the FRP jacket and the concrete core under axial loading, providing critical insights for structural design and analysis.

Empirical models, such as those developed by Fardis and Khalili (1982), Toutanji (1999), and Lam and Teng (2003), derive their predictive expressions from experimental data specific to their respective studies. On the other hand, analytical models, including those by Spoelstra and Monti (1999) and Teng, Yu and Wong (2007), incorporate theoretical frameworks to simulate the confinement effects. Despite their contributions, these models often exhibit varying degrees of accuracy, particularly when predicting the ultimate axial strength and strain of FRP-confined concrete.

This study focuses on evaluating the performance of these existing models by critically comparing their theoretical predictions against experimental results obtained from 12 sets of concrete cylinders confined with Carbon Fiber-Reinforced Polymer (CFRP) and Steel Fiber-Reinforced Polymer (SFRP). The analysis examines the ultimate axial strength, ultimate axial strain, and overall stress-strain response, aiming to identify the limitations of the current models and provide recommendations for their application in structural design.

2. Methodology

2.1. Review of existing confinement models

The performance of various empirical/analytical confinement models are analyzed in this section to assess their accuracy in predicting the ultimate axial strength, ultimate axial strain and the stress-strain behaviour of CFRP- and SFRP-confined concrete cylinders. The confinement models under consideration are summarized in Table 1. Each model is assigned a unique designation ID, as shown in the second column of Table 1 and will be used hereafter when referring to these models in any discussion that follows. The confinement effectiveness coefficient, k_l, adopted by each model is summarized in Table 2.

---

*Corresponding author, E-mail: relhacha@ucalgary.ca

https://doi.org/10.31462/icearc2025_ce_eqe_087

golden light publishing

Table 1. Summary of empirical/ analytical confinement models

Models	Model Designation	Theoretical f'_{cu}	Theoretical ε_{cu}
Fardis and Khalili (1982),	FK-R	$f'_{cu} = f'_{co}\left[1 + 4.1\frac{f_{lu}}{f'_{co}}\right]$	$\varepsilon_{cu} = 0.002 + 0.001\frac{E_{frp}t_{frp}}{Df'_{co}}$
Fardis and Khalili (1982),	FK-N	$f'_{cu} = f'_{co}\left[1 + 3.7\left[\frac{f_{lu}}{f'_{co}}\right]^{0.86}\right]$	$\varepsilon_{cu} = 0.002 + 0.001\frac{E_{frp}t_{frp}}{Df'_{co}}$
Toutanji (1999)	TTJ	$f'_{cu} = f'_{co}\left[1 + 3.5\left(\frac{f_{lu}}{f'_{co}}\right)^{0.85}\right]$	$\varepsilon_{cu} = \varepsilon_{co}\left[1 + (310.57\varepsilon_{frp} + 1.9)\left(\frac{f'_{cu}}{f'_{co}} - 1\right)\right]$
Lam and Teng (2003)	LT	$\frac{f'_{cu}}{f'_{co}} = 1 + 3.3\frac{f_{lu,a}}{f'_{co}}$	$\frac{\varepsilon_{cu}}{\varepsilon_{co}} = 1.75 + 12\left[\frac{f_{lu,a}}{f'_{co}}\right]\left[\frac{\varepsilon_{frp,a}}{\varepsilon_{co}}\right]^{0.45}$
Berthet et al. (2005)	BFH	$f'_{cu} = f'_{co} + k_l f_{lu}$ $k_l = 3.45, 20 \le f'_{co} \le 50\ MPa$ $k_l = \frac{9.5}{(f'_{co})^{1/4}}, 50 \le f'_{co} \le 200\ MPa$	$\varepsilon_{cu} = \varepsilon_{co} + \frac{(\varepsilon_{frp} - v_c\varepsilon_{co})}{\gamma}$
Fahmy and Wu (2010)	FW	$f'_{cu} = f'_{co} + k_l f_{lu}$ $k_l = 4.5{f_{lu}}^{-0.3}, f'_{co} \le 40MPa$ $k_l = 3.75{f_{lu}}^{-0.3}, f'_{co} > 40MPa$	$\varepsilon_{cu} = \frac{f'_{co} - f_o}{E_2}$ $E_2 = m_2(245.61{f'_{co}}^{m_1} + 0.6728E_l)$ $m_1 = 0.5, m_2 = 0.83\ if\ f'_{co} \le 40\ MPa$ $m_1 = 0.2, m_2 = 1.73\ if\ f'_{co} > 40\ MPa$
Spoelstra and Monti, Exact (1999)	SM-E	$f'_{cu} = E_{sec,u}\varepsilon_{cu}$	$\varepsilon_{cu} = \varepsilon_{cc}\left[\frac{E_{sec}[E_{co} - E_{sec,u}]}{E_{sec,u}[E_{co} - E_{sec}]}\right]^{1-\frac{E_{sec}}{E_{co}}}$
Spoelstra and Monti, Approx. (1999)	SM-A	$\frac{f'_{cu}}{f'_{co}} = 0.2 + 3.0\left(\frac{f_{lu}}{f'_{co}}\right)^{0.5}$	$\frac{\varepsilon_{cuc}}{\varepsilon_{co}} = 2 + 1.25\frac{E_c}{f'_{co}}\left(\frac{f_{lu}}{f'_{co}}\right)\varepsilon_{lu}^{\ 0.5}$
Teng et al. (2007)	THY	$\frac{f'_{cuc}}{f'_{co}} = 1 + 3.5\frac{f_l}{f'_{co}}$	$\frac{\varepsilon_{cuc}}{\varepsilon_{co}} = 1 + 17.5\frac{f_l}{f'_{co}}$
CAN/CSA S806-12		$f'_{cu} = 0.85f'_{co} + k_l k_c f_{lu}$ $k_l = 6.7(k_c f_{lu})^{-0.17}$ $f_{lu} = \frac{2t_{frp}\phi_{frp}f_{frp}}{D} \le \frac{2t_{frp}0.006E_{frp}}{D}$	-
CAN/CSA S6-14		$f'_{cu} = f'_{co} + 2f_{lu}$ $f_{lu} = \frac{2\phi_{frp}t_{frp}f_{frp}}{D}$	-

For clarity and consistency in the notation and symbols used in this table, readers are encouraged to consult the original work, as referenced herein, for comprehensive definitions and context.

All the aforementioned confinement models, except SM and THY, are empirical models in which the ultimate axial strength and ultimate axial strain prediction expressions were derived based on their author's own experimental data sets. Furthermore, only four of these models have expressions to predict the entire axial stress-axial and lateral strain curve. These four models are TTJ, BFH, SM and THY models. The rest propose expressions for the axial stress-axial strain curve only.

The two models of FK are the only models, out of the nine, which was developed based on models developed for steel-confined concrete. SM and THY models were based on an actively-confined concrete model by Popovics.

TTJ and BFH utilized a model originally developed by Sargin and modified by Ahmad and Shah for concrete confined by steel spiral, while LT based their model on the four parameter curve by Richard and Abbot (1975).
Of the nine confinement models reviewed in this section, five models, namely, FK-R, LT, BFH, FW, and THY models, have an ultimate strength expression that is based on an expression originally proposed by Richart, Brandtzaeg, and Brown (1928). The strength enhancement coefficients,k_l ,used in the models are summarized in Table 2. The last two FRP confinement models in the table are adopted by the Canadian building code (CSA S806-12) and bridge code (CSA S6-14). Both models are based on a model originally developed by Richart, Brandtzaeg, and Brown (1928), however, CAN/CSA S806-12 adopts a modified version of the model that was proposed by Saatcioglu and Razvi (1992). Neither code has yet adopted any model for ultimate axial strain prediction.

Table 2. Strength enhancement coefficient, k_l, for FRP-confined concrete

Model	Confinement Effectiveness Coefficient k_l
Fardis and khalili (1982), (Richart)	4.1
Farids and Khalili (1982), (Newman)	$3.7\left(\frac{f_{lu}}{f'_{co}}\right)^{-0.14}$
Toutanji (1999)	$3.5\left(\frac{f_l}{f'_{co}}\right)^{-0.15}$
Lam and Teng (2003)	3.3
Berthet et al. (2005)	$k_l = 3.45, 20 \leq f'_{co} \leq 50\ MPa$ $k_l = \frac{9.5}{(f'_{co})^{1/4}}, 50 \leq f'_{co} \leq 200\ MPa$
Fahmy and Wu (2010)	$k_l = 4.5{f_{lu}}^{-0.3}, f'_{co} \leq 40MPa$ $k_l = 3.75{f_{lu}}^{-0.3}, f'_{co} > 40MPa$
Teng et al. (2007)	3.5

3. Results and discussions

3.1. Performance analysis of confinement models

The experimental results versus the theoretical predictions of the various confinement models are first summarized and tabulated for each confinement configuration. The performance of each of these models is then evaluated graphically by plotting the experimental results versus the corresponding theoretical values, with the 45˚ reference line representing the exact match between experiment and theory is also plotted for comparison. Points falling above the 45˚ line imply that the theoretical predictions are lower than the experimental values and, hence, indicate conservative predictions while points falling below the line imply that the theoretical predictions are higher than the experimental values and hence indicate unconservative predictions.

3.1.1. Models' performance in prediction of f'_{cu}

The experimental results versus the theoretical predictions of the ultimate axial strength, f'_{cu} for empirical and analytical confinement models are reported respectively in Table 3 and Table 4. The experimental results versus the theoretical predictions of the ultimate axial strength, f'_{cu} for building and bridge Canadian design codes are reported in Table 5.

Table 3. Empirical models prediction of f'_{cu}

Confinement Designation	Exp. (avg.) (MPa)	FK-R f'_{cu} (MPa)	FK-N f'_{cu} (MPa)	TTJ f'_{cu} (MPa)	LT f'_{cu} (MPa)	BHF f'_{cu} (MPa)	FW f'_{cu} (MPa)
C37.3-CFRP1	51.4	55.4	59.3	58.6	51.9	52.5	50.0
C37.3-CFRP2	69.5	73.5	77.3	75.7	66.5	67.8	58.0
C37.3-CFRP3	92.4	91.7	94.0	91.5	81.0	83.0	64.8
C37.3-SFRP1	94.5	102.3	103.5	100.4	89.7	92.0	68.5
C37.3-SFRP2	146.8	167.4	157.4	151.1	142.0	146.8	87.9
C37.3-SFRP3	194.6	232.4	207.5	197.9	194.4	201.5	104.5
C42.4-CFRP1	59.6	60.5	64.8	64.1	57.0	57.6	53.0
C42.4-CFRP2	75.8	78.6	83.1	81.5	71.6	72.9	59.6
C42.4-CFRP3	94.6	96.8	100.1	97.6	86.1	88.1	65.3
C42.4-SFRP1	98.8	107.4	109.8	106.7	94.8	97.1	68.4
C42.4-SFRP2	153.9	172.5	164.7	158.4	147.1	151.9	84.6
C42.4-SFRP3	200.4	237.5	215.7	206.1	199.5	206.6	98.4

Table 4. Analytical models prediction of f'_{cu}

Confinement Designation	Exp. (avg.) (MPa)	SM-E f'_{cu} (MPa)	SM-A f'_{cu} (MPa)	THY f'_{cu} (MPa)
C37.3-CFRP1	51.4	57.7	46.0	49.0
C37.3-CFRP2	69.5	75.8	61.9	65.9
C37.3-CFRP3	92.4	89.1	74.2	81.8
C37.3-SFRP1	94.5	94.8	80.4	90.4
C37.3-SFRP2	146.8	121.7	110.7	145.8
C37.3-SFRP3	194.6	136.5	133.9	201.0
C42.4-CFRP1	59.6	64.3	49.5	50.1
C42.4-CFRP2	75.8	83.7	66.6	68.5
C42.4-CFRP3	94.6	98.0	79.6	84.8
C42.4-SFRP1	98.8	104.5	86.3	93.2
C42.4-SFRP2	153.9	134.6	118.5	148.6
C42.4-SFRP3	200.4	152.2	143.2	203.5

Table 5. Analytical models prediction of f'_{cu}

Confinement Designation	Exp. (avg.) (MPa)	CAN/CSA S806-12 f'_{cu} (MPa)	CAN/CSA S6-14 f'_{cu} (MPa)
C37.3-CFRP1	51.4	43.6	44.4
C37.3-CFRP2	69.5	52.8	51.4
C37.3-CFRP3	92.4	61.3	58.5
C37.3-SFRP1	94.5	62.8	*
C37.3-SFRP2	146.8	86.9	*
C37.3-SFRP3	194.6	109.0	*
C42.4-CFRP1	59.6	47.9	49.5
C42.4-CFRP2	75.8	57.2	56.5
C42.4-CFRP3	94.6	65.6	63.6
C42.4-SFRP1	98.8	67.1	*
C42.4-SFRP2	153.9	91.2	*
C42.4-SFRP3	200.4	113.3	*

The experimental and theoretical ultimate axial strength are normalized by being divided by their respective cylinders unconfined concrete strength values and are compared respectively for empirical and analytical models in Figure 1 and Figure 2 and for design codes confinement models in Figure 3.

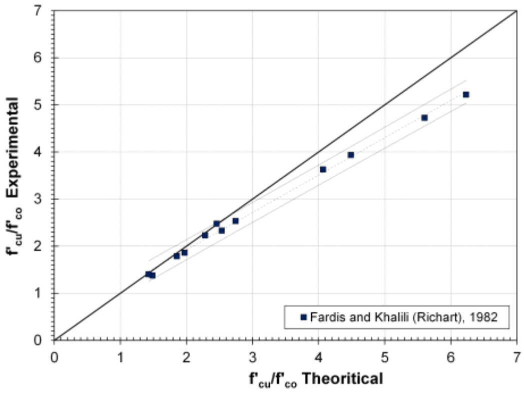

Fardis and Khalili, 1982 (Richart)

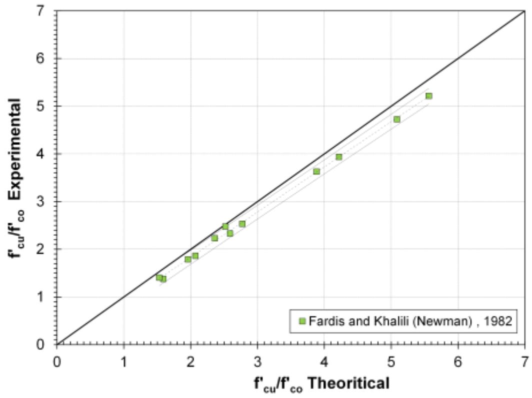

Fardis and Khalili, 1982 (Newman)

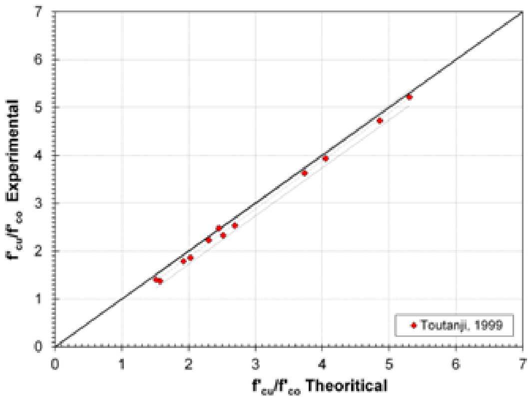

Toutanji, 1999

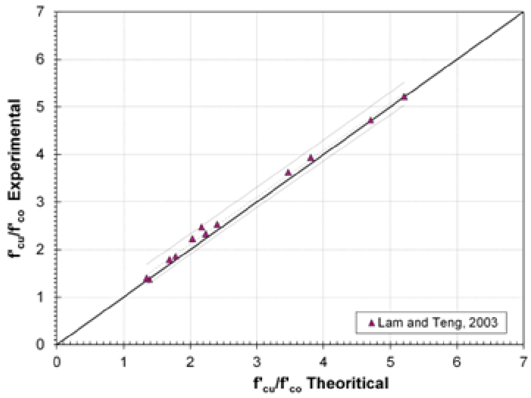

Lam and Teng, 2003

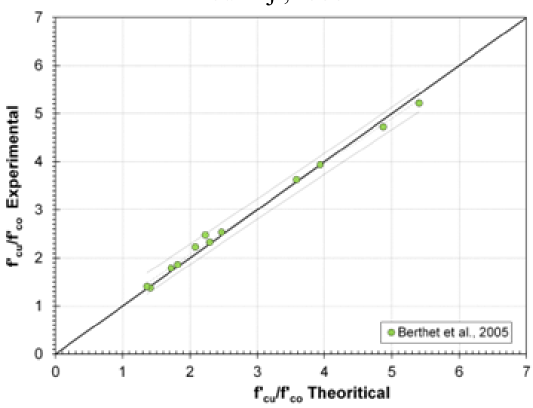

Berthet et al., 2005

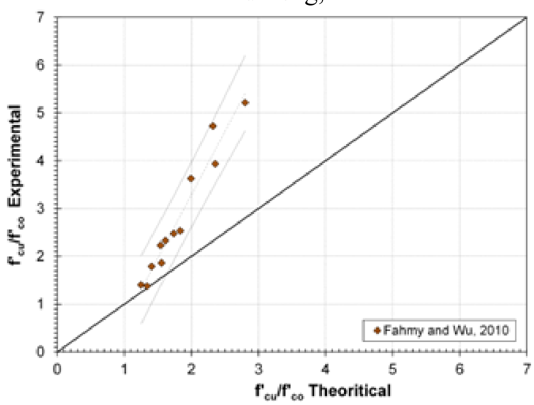

Fahmy and Wu, 2010

Fig. 1. Empirical models' performance in predictingf'_{cu}/f'_{co}

The FK models generally overestimate the ultimate axial strength of FRP-confined concrete, with FK-R showing particularly poor accuracy for cylinders with higher lateral confinement pressure ratios due to its use of a high confinement effectiveness ratio more suited for actively confined concrete. In contrast, FK-N offers better predictions. Models such as TTJ, LT, BFH, and THY provide accurate predictions across different confinement levels, whereas FW and SM-A models significantly underestimate the ultimate axial strength. The SM-E model performs well for weakly and moderately confined cylinders but shows high prediction errors for highly confined ones, unlike the THY model, which accurately predicts the strength of highly confined cylinders but slightly overestimates it for weaker confinement levels.

The overall accuracy of the empirical, analytical and design codes confinement models in predicting the ultimate axial strength is summarized in Table 6 and plotted in Figure 4. The average, standard deviation (SD) and coefficient of variation (COV) of the absolute average error in the prediction are shown for the whole experimental set and for the two distinctive sets of CFRP- and SFRP-confined concrete cylinders, providing insights into the models' predictive performance across different confinement configurations.

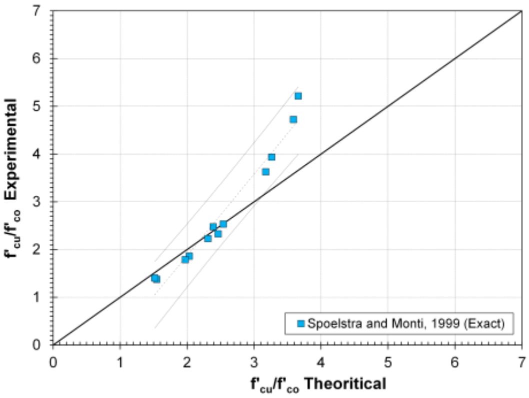

Spoelstra and Monti, 1999 (Exact)

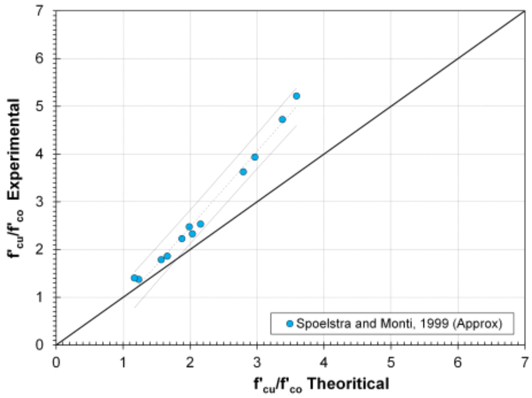

Spoelstra and Monti, 1999 (Approx.)

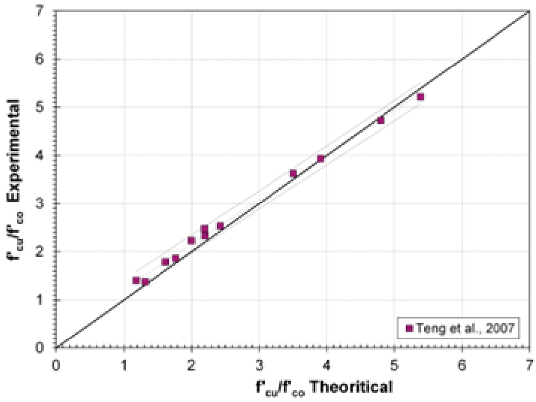

Teng et al., 2007

Fig. 2. Analytical models' performance in predicting f'_{cu}/f'_{co}

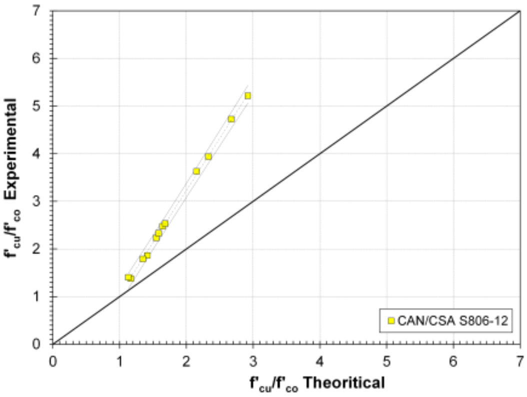

CAN/CSA S806-12

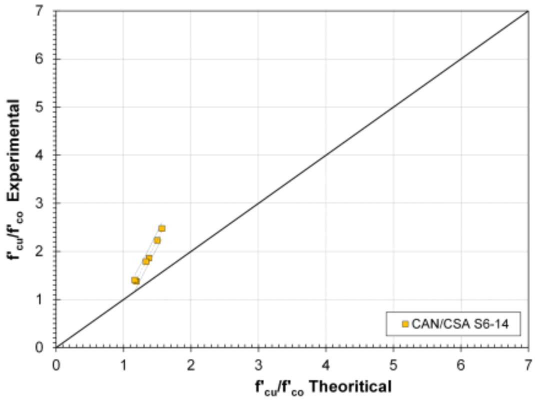

CAN/CSA S6-14

Fig. 3. Canadian codes confinement Models' performance in predicting f'_{cu}/f'_{co}

Figures 4(a) and (b) illustrate the accuracy of various confinement models in predicting the ultimate axial strength of FRP-confined concrete cylinders. The models by BFH, LT, and TTJ demonstrate the highest accuracy for the whole set, with average absolute errors of 3.4%, 4.5%, and 5.6%, respectively. Notably, BFH, LT, TTJ, and THY models perform better for SFRP-confined cylinders, while FK-R, SM-E, SM-A, and FW excel in predicting CFRP-confined cylinders, highlighting the influence of lateral confinement ratio sensitivity. Both Canadian design codes, CAN/CSA S6-14 and CAN/CSA S806-12, underestimate the ultimate axial strength, with S6-14 slightly outperforming S806-12. However, S6-14 lacks provisions for SFRP sheets, limiting its applicability. The higher errors for SFRP-confined cylinders in S806-12 are attributed to its calibration based on CFRP, GFRP, and AFRP data. These findings emphasize the need for refinement in both codes to improve predictions for SFRP-confined concrete.

Table 6. Confinement models accuracy in the prediction of f'_{cu}

Confinement Model	Predictions of f'_{cu} (whole set)			Predictions of f'_{cu} (CFRP)			Predictions of f'_{cu} (SFRP)		
	Avg. (%)	SD (%)	COV (%)	Avg. (%)	SD (%)	COV (%)	Avg. (%)	SD (%)	COV (%)
FK-R	8.6	6.2	72.4	3.7	2.8	76.4	13.5	4.3	32.1
FK-N	8.5	3.2	38.1	8.8	4.3	48.5	8.2	1.6	19.4
TTJ	5.6	3.9	69.6	7.1	4.7	66.1	4.1	2.2	54.4
LT	4.5	3.5	78,4	6.1	4.1	68.0	2.9	1.9	66.9
BFH	3.4	3.8	111.7	4.8	3.8	80.2	2.1	2.4	115.5
FW	29.4	14.1	48.1	18.7	10.0	53.7	40.1	8.4	20.9
SM-E	11.4	13.7	120.8	7.8	5.3	67.0	14.9	12.6	84.4
SM-A	18.4	6.7	36.5	14.3	3.4	23.6	22.5	6.7	29.9
THY	6.3	5.3	84.3	9.5	3.8	40.6	3.2	3.2	102.0
CAN/CSA S806-12	31.8	9.1	28.6	24.6	6.2	25.4	39.1	4.6	11.8
CAN/CSA S6-14	25.2	8.1	32.0	25.2	8.1	32.0	*	*	*

* Resistance reduction factor for SFRP sheet is not provided by code

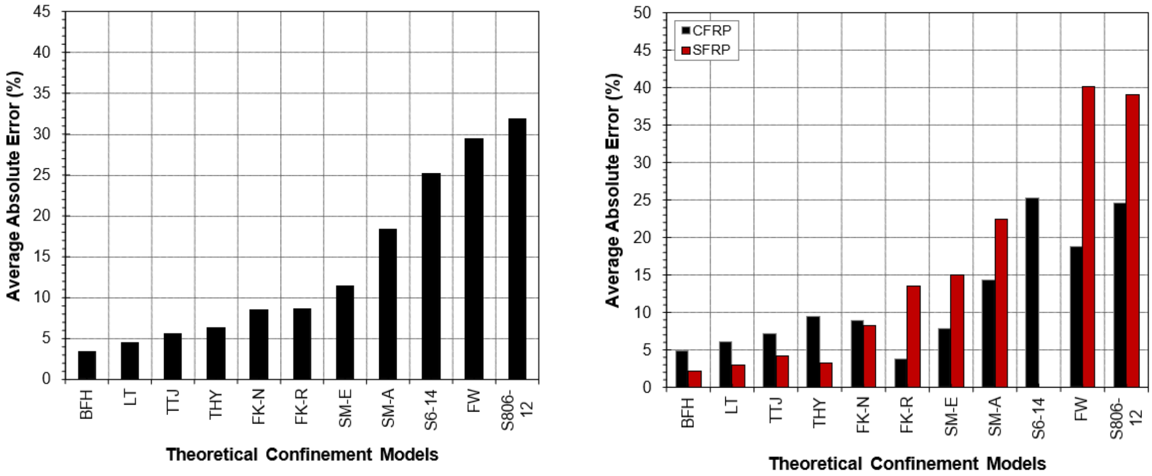

(a) (b)

Fig. 4. Confinement models accuracy in f'_{cu} predictions for: (a) the whole experimental set (b) CFRP and SFRP experimental sets

3.1.2. Models' Performance in Prediction of ε_{cu}

The experimental results versus the theoretical predictions of the ultimate axial strain, ε_{cu} for empirical and analytical confinement models are reported respectively in Table 7 and Table 8.

The experimental and theoretical ultimate axial strain are normalized by dividing them by the unconfined concrete strain at peak values and compared the results for various empirical and analytical models in Figure 5 and Figure 6, respectively. The analysis revealed that prediction errors for ultimate axial strain, ε_{cu} are significantly larger than those for ultimate axial strength, f'_{cu}, consistent with previous research. Among the nine models evaluated, the SM-E and THY models performed well for weakly and moderately confined concrete, with SM-E underestimating and THY overestimating the strain for highly confined cylinders. The TTJ model excelled for highly confined cylinders but underestimated strain for weaker confinement. Other models generally performed poorly, often underestimating the strain.

The overall accuracy of the models in predicting ultimate axial strain is summarized in Table 9, and shown in Figure 7 with the metrics including the average, SD, and COV of the absolute average error for both CFRP- and SFRP-confined concrete cylinders.

It can be concluded that the models that exhibit superior performance when it comes to ε_{cu} prediction are SM-E, TTJ and SM-A, which have average absolute errors respectively of 15.6%, 18.8% and 34%. All models seem to fail in predicting the ultimate axial strain with reasonable accuracy.

Table 7. Empirical models prediction of ε_{cu}

Confinement Designation	Exp. (avg.)	FK-R ε_{cu}	FK-N ε_{cu}	TTJ ε_{cu}	LT ε_{cu}	BHF ε_{cu}	FW ε_{cu}
C37.3-CFRP1	0.0147	0.0065	0.0065	0.0089	0.0066	0.0090	0.0089
C37.3-CFRP2	0.0193	0.0109	0.0109	0.0144	0.0096	0.0131	0.0128
C37.3-CFRP3	0.0254	0.0154	0.0154	0.0195	0.0127	0.0166	0.0152
C37.3-SFRP1	0.0321	0.0162	0.0162	0.0242	0.0151	0.0192	0.0170
C37.3-SFRP2	0.0437	0.0304	0.0304	0.0420	0.0268	0.0293	0.0209
C37.3-SFRP3	0.0545	0.0445	0.0445	0.0585	0.0384	0.0378	0.0223
C42.4-CFRP1	0.0107	0.0059	0.0059	0.0072	0.0056	0.0077	0.0083
C42.4-CFRP2	0.0115	0.0098	0.0098	0.0115	0.0081	0.0112	0.0103
C42.4-CFRP3	0.0155	0.0138	0.0138	0.0155	0.0106	0.0141	0.0111
C42.4-SFRP1	0.0270	0.0145	0.0145	0.0192	0.0126	0.0163	0.0122
C42.4-SFRP2	0.0332	0.0269	0.0269	0.0331	0.0221	0.0248	0.0125
C42.4-SFRP3	0.0474	0.0394	0.0394	0.0460	0.0316	0.0320	0.0122

Table 8. Analytical models prediction of ε_{cu}

Confinement Designation	Exp. (avg.)	SM-E ε_{cu}	SA ε_{cu}	THY ε_{cu}
C37.3-CFRP1	0.0147	0.0167	0.0093	0.0116
C37.3-CFRP2	0.0193	0.0219	0.0130	0.0172
C37.3-CFRP3	0.0254	0.0258	0.0158	0.0229
C37.3-SFRP1	0.0321	0.0305	0.0194	0.0281
C37.3-SFRP2	0.0437	0.0392	0.0273	0.0498
C37.3-SFRP3	0.0545	0.0439	0.0333	0.0716
C42.4-CFRP1	0.0107	0.0108	0.0072	0.0103
C42.4-CFRP2	0.0115	0.0141	0.0100	0.0150
C42.4-CFRP3	0.0155	0.0165	0.0122	0.0197
C42.4-SFRP1	0.0270	0.0194	0.0150	0.0242
C42.4-SFRP2	0.0332	0.0250	0.0211	0.0423
C42.4-SFRP3	0.0474	0.0282	0.0257	0.0604

Table 9. Confinement models accuracy in the prediction of ε_{cu}

Confinement Model	Predictions of ε_{cu} (whole set)			Predictions of ε_{cu} (CFRP)			Predictions of ε_{cu} (SFRP)		
	Avg. (%)	SD (%)	COV (%)	Avg. (%)	SD (%)	COV (%)	Avg. (%)	SD (%)	COV (%)
FK-R	32.5	15.2	46.7	34.9	16.3	46.8	30.1	13.5	44.8
FK-N	32.5	15.2	46.7	34.9	16.3	46.8	30.1	13.5	44.8
TTJ	15.7	15.3	97.3	20.1	15.1	75.1	11.3	13.2	117.4
LT	42.1	9.8	23.3	44.0	9.7	22.1	40.2	9.5	23.7
BFH	28.8	11.2	38.8	24.1	13.4	55.5	33.5	5.2	15.4
FW	43.7	17.5	40.0	29.0	10.3	35.6	58.3	8.6	14.8
SM-E	15.6	18.5	118.2	9.9	7.6	77.1	21.3	11.6	54.6
SM-A	34.7	8.9	25.8	28.9	9.0	31.2	40.4	3.4	8.5
THY	18.8	19.6	104.2	17.1	19.6	114.8	20.5	18.0	87.8

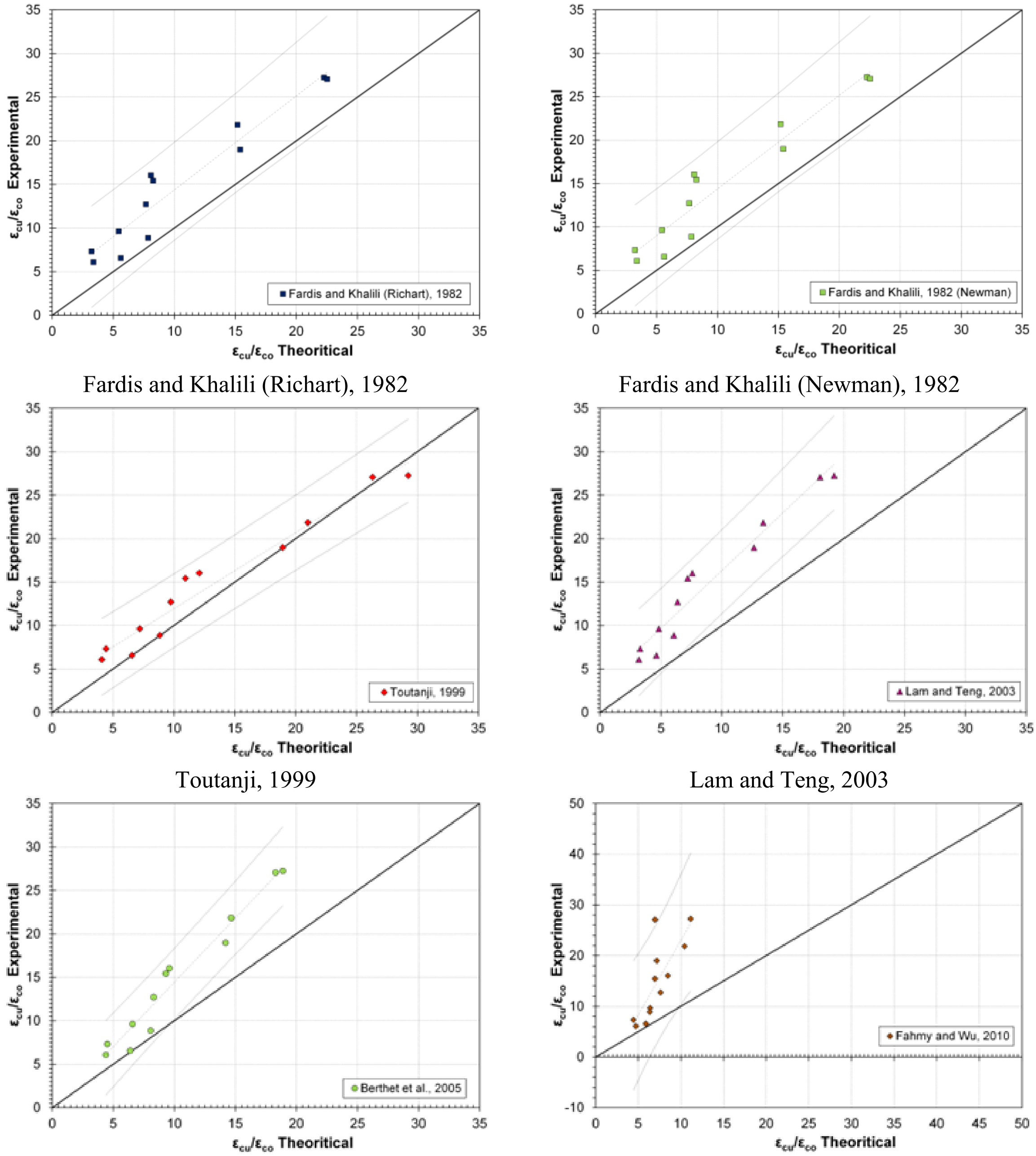

Fardis and Khalili (Richart), 1982 | Fardis and Khalili (Newman), 1982

Toutanji, 1999 | Lam and Teng, 2003

Berthet et al., 2005 | Fahmy and Wu, 2010

Figure 5. Empirical models' performance in predicting of $\varepsilon_{cu}/\varepsilon_{co}$

3.1.3 Axial stress-strain behaviour prediction

The performance of two empirical models, TTJ and BFH, and two analytical models, SM-E and THY, was assessed to predict the stress-strain behaviour of FRP-confined concrete cylinders. These four models were selected as they uniquely provide predictions for the entire axial stress-axial strain and axial stress-lateral strain responses. Other models under consideration were excluded from this evaluation as they only provide partial predictions.

The TTJ model, shown in Figure 8(a), demonstrated notable accuracy in predicting the transition point of the axial stress-lateral strain behaviour, particularly in terms of stress level and the radius of curvature at the transition. However, it exhibited significant limitations in predicting the axial stress-axial strain response. Specifically, it overestimated the radius of curvature at the kinking point and underestimated the ultimate axial strain, leading to inaccuracies in the overall response.

The BFH model, shown in Figure 8(b), effectively captured the experimentally observed upward-shift of the transition point as FRP lateral stiffness increased. Despite this, it tended to overestimate the axial stress-axial strain behaviour, particularly in highly confined cylinders, due to an overestimation of the stress at the transition point. Additionally, the model predicted the smallest radius of curvature at the kinking point, which aligned well with experimental data for weakly to moderately confined cylinders but was less accurate for highly confined cases.

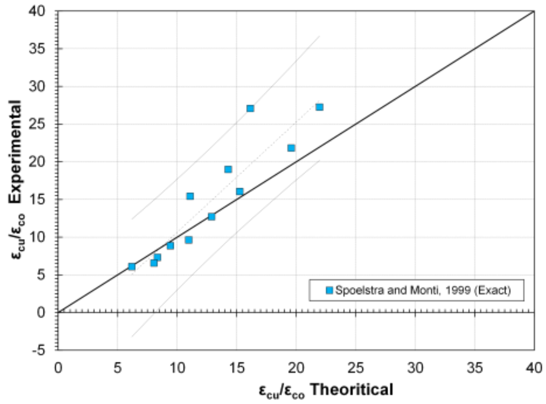

Spoelstra and Monti, 1999 (Exact)

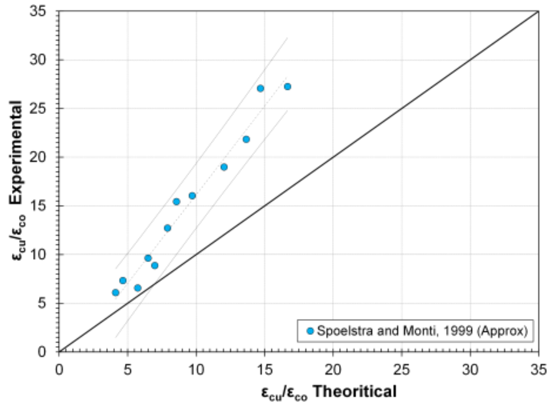

Spoelstra and Monti, 1999 (Approx.)

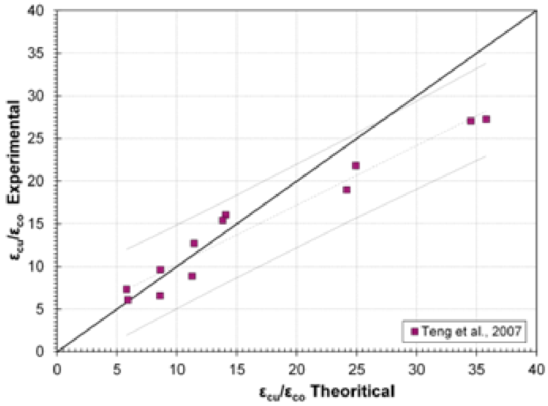

Teng et al., 2007

Fig. 6. Empirical models' performance in predicting of $\boldsymbol{\varepsilon_{cu}/\varepsilon_{co}}$

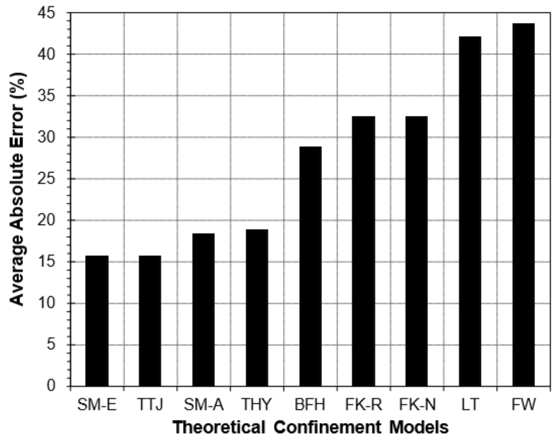

(a)

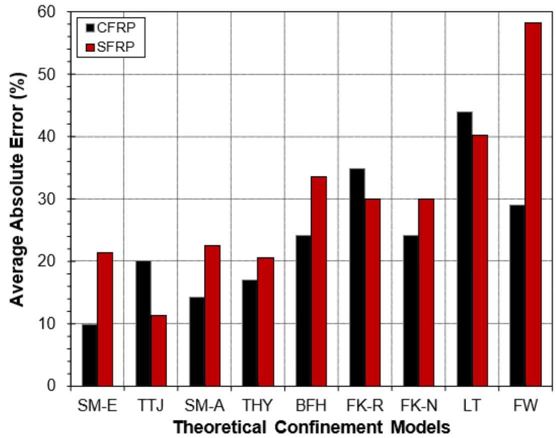

(b)

Fig. 7. Confinement models accuracy in εcu predictions for: (a) the whole experimental set (b) CFRP and SFRP experimental sets

Among the models evaluated, the SM-E model, shown in Figure 8(c), provided the most accurate predictions for weakly and moderately confined cylinders. It successfully captured key aspects of the stress-strain response, including the transition point, initial and final slopes, and ultimate stress and strain. However, the model significantly underestimated the overall stress-strain behaviour of highly confined concrete, highlighting its limitations under extreme confinement conditions.

The THY model, shown in Figure 8(d), while reasonably accurate overall, failed to capture the upward-shift of the transition point with increasing FRP jacket stiffness. It assumed the transition point occurred at stress levels close to unconfined concrete, which deviates from experimental observations. Nonetheless, the model accurately predicted the increase in the radius of curvature at the kinking point as lateral stiffness increased, contributing to its reasonable performance in predicting the overall stress-strain response.

This analysis underscores the variability in the predictive capabilities of empirical and analytical models across different confinement levels. While some models excel under specific conditions, others require refinement to improve their accuracy, particularly for highly confined concrete.

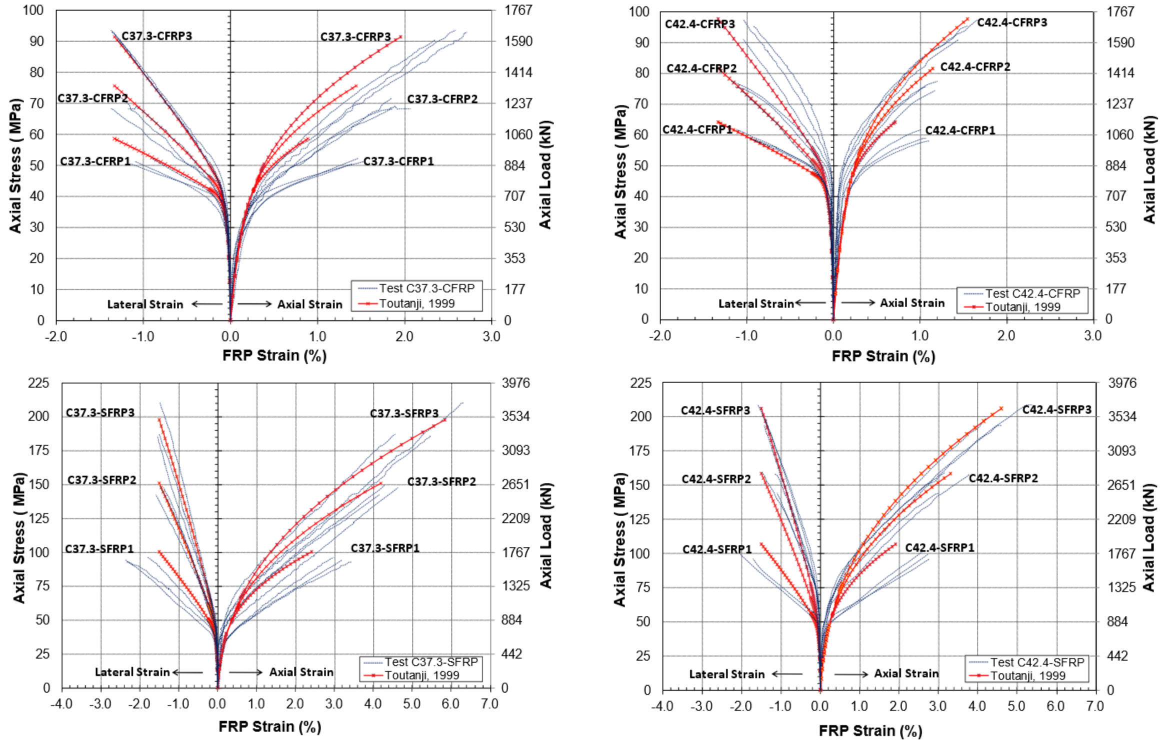

(a)

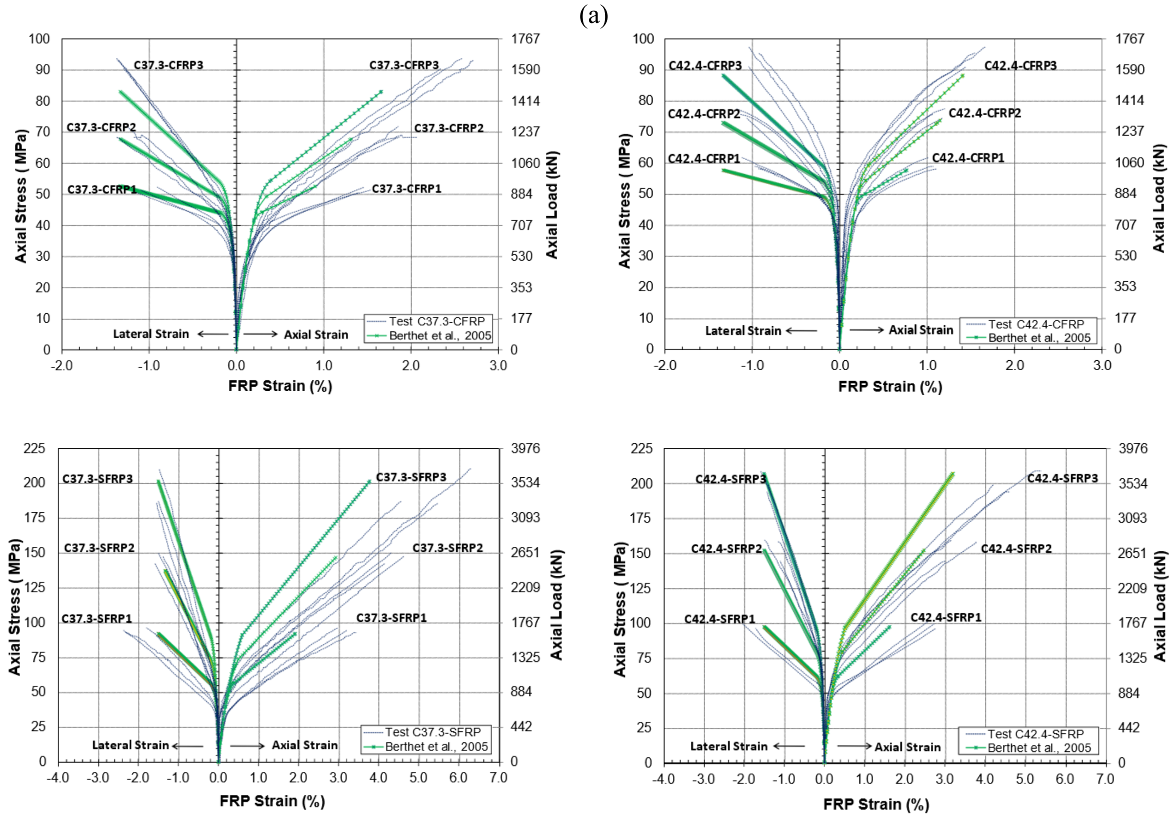

(b)

Fig. 8. Empirical and Analytical models' performance in the prediction of stress-strain behaviour (a) TTJ (b) BFH (c) SM-E (d) THY

Figure 8 Continued

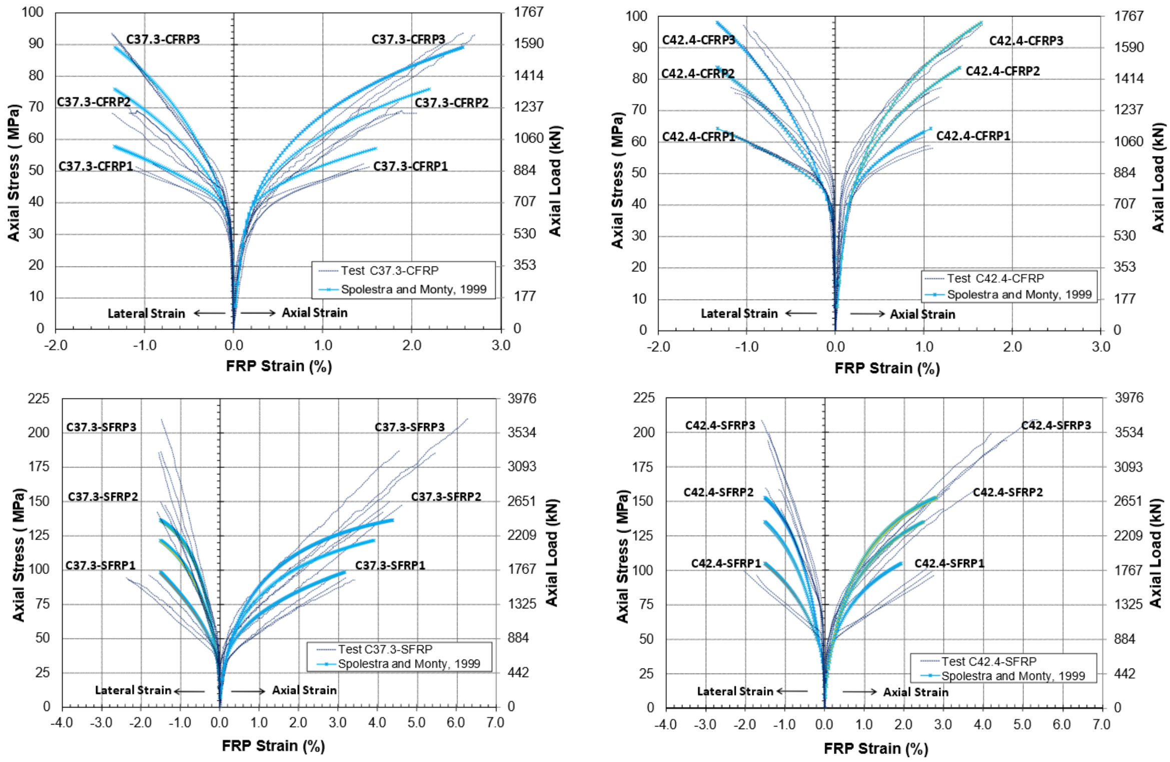

(c)

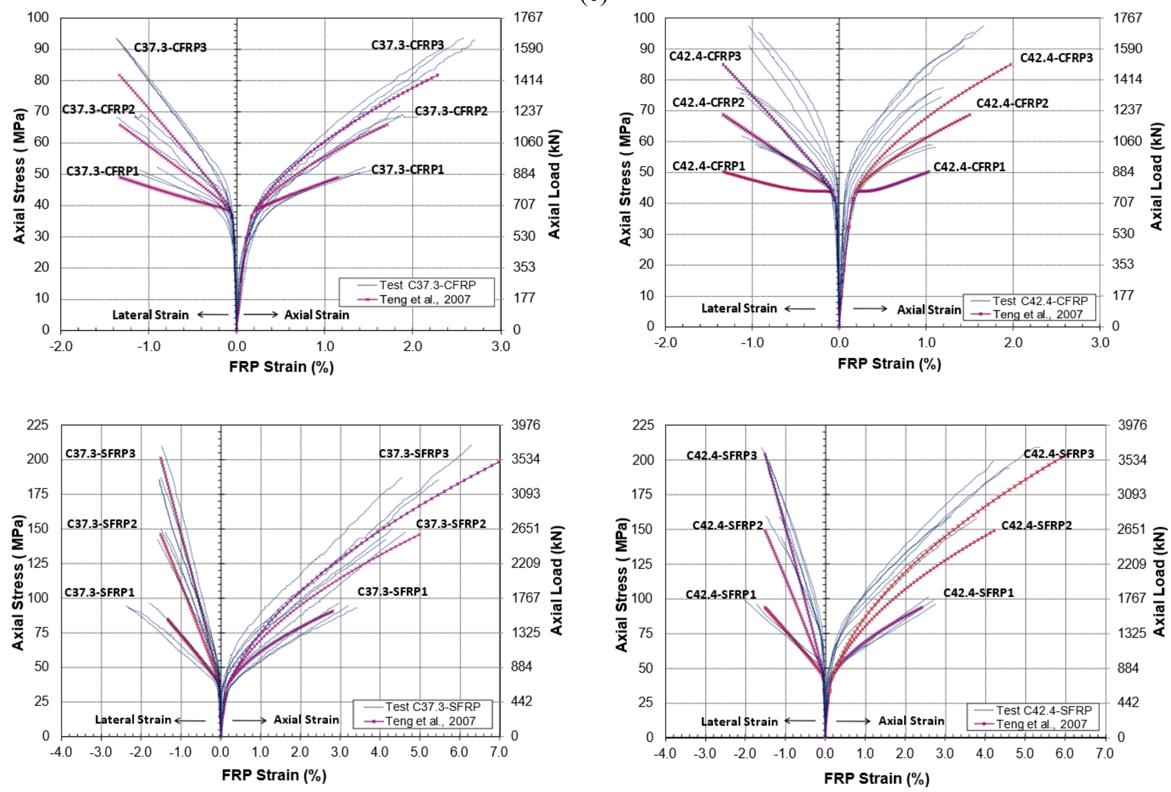

(d)

4. Conclusions

This study performed a comprehensive evaluation of widely used empirical and analytical models for predicting the compressive behaviour of FRP-confined concrete, including both CFRP and SFRP confinement systems. The models were assessed based on their ability to predict ultimate axial strength, axial strain, and full stress–strain behaviour. Comparative analysis with experimental data revealed significant variation in predictive accuracy among models and identified areas requiring refinement. The key conclusions are:

- Empirical models such as BFH, LT, and TTJ demonstrated the highest overall accuracy in predicting ultimate axial strength, with average absolute errors of 3.4%, 4.5%, and 5.6%, respectively.
- The TTJ and THY models provided reliable predictions across a range of confinement levels, particularly for SFRP-confined concrete, while FK-R and SM-A tended to over- or underestimate strength values significantly.
- The Canadian design codes (CAN/CSA S806-12 and S6-14) consistently underestimated ultimate axial strength, especially for SFRP-confined cylinders, due to a lack of calibration with SFRP data.
- Strain predictions showed higher variability than strength predictions across all models. While the SM-E and TTJ models achieved relatively lower average error (~15%), most models—including BFH and FW—underperformed for strain predictions, particularly under high confinement.
- Analytical models SM-E and THY showed better performance for moderately confined cylinders, but exhibited limitations in predicting the behaviour of highly confined concrete, especially in axial strain capacity.
- The TTJ and BFH models offered the best approximations for the stress–strain response of confined concrete, although each had limitations in capturing specific behaviours like curvature or transition points under high confinement.
- No single model demonstrated consistent accuracy across all performance metrics and confinement levels, reinforcing the need for model selection based on the specific type and level of confinement and for further refinement of existing models.
- This study highlights the necessity of refining design code provisions, particularly for SFRP confinement, and encourages the development of hybrid or adaptive models that can improve prediction accuracy for a broader range of FRP systems and concrete strengths.

Acknowledgments
The author gratefully acknowledges SIKA Canada for generously donating the CFRP sheets and epoxy adhesive and Hardwire LLC for providing the SFRP sheets. Appreciation is also extended to the University of Calgary for its partial funding and support of this research.

References

Berthet, J. F., Ferrier, E., & Hamelin, P. (2005). Compressive behaviour of concrete externally confined by composite jackets. Part A: Experimental study. *Construction and Building Materials, 19*(3), 223–232.

CAN/CSA S6-14. (2014). *Canadian highway bridge design code*. Canadian Standards Association.

CAN/CSA S806-12. (2012). *Design and construction of building components with fibre-reinforced polymers*. Canadian Standards Association.

Fahmy, M., & Wu, Z. (2010). Evaluating and proposing models of circular concrete columns confined with different FRP composites. *Journal of Composites for Construction, 14*(4), 451–461.

Fardis, M. N., & Khalili, H. (1982). Concrete encased in fibreglass-reinforced plastic. *Journal of the American Concrete Institute, 79*(6), 471–478.

Lam, L., & Teng, J. G. (2003). Design-oriented stress–strain model for FRP-confined concrete. *Construction and Building Materials, 17*(6–7), 471–489.

Richard, R. M., & Abbott, B. J. (1975). Versatile elastic–plastic stress–strain formula. *Journal of the Engineering Mechanics Division, 101*(4), 511–515.

Richart, F. E., Brandtzaeg, A., & Brown, R. L. (1928). *A study of the failure of concrete under combined compressive stresses* (Bulletin No. 185). University of Illinois Engineering Experiment Station.

Saatcioglu, M., & Razvi, S. R. (1992). Strength and ductility of confined concrete. *Journal of Structural Engineering, 118*(6), 1590–1607.

Spoelstra, M. R., & Monti, G. (1999). FRP-confined concrete model. *Journal of Composites for Construction, 3*(3), 143–150.

Teng, J. G., Yu, T., & Wong, Y. L. (2007). Behavior of GFRP-confined concrete in axial compression. *Journal of Composites for Construction, 11*(3), 263–273.

Toutanji, H. (1999). Stress–strain characteristics of concrete columns externally confined with advanced fiber composite sheets. *Composite Structures, 44*(1), 63–72.

Assessment of the effect of strengthening measures on seismic fragility curves in reinforced concrete structures

Yagmur Aras*[1], Rafet Sisman[1]

[1] *Yildiz Technical University, Department of Civil Engineering, 34420 Istanbul, Türkiye.*

Abstract. Earthquakes are among the most devastating natural disasters, causing substantial destruction to human life and the built environment. In recent years, the increasing frequency and intensity of seismic events worldwide have made it imperative to re-evaluate the seismic performance of existing building stock and to implement appropriate retrofitting measures where necessary. Structures located in high seismic risk zones are often found to be inadequate in terms of strength and ductility, particularly those constructed according to outdated design standards. In this context, performance-based seismic assessment methods play a vital role in ensuring life safety and minimizing economic losses in the event of an earthquake. This study investigates the seismic performance of an existing three-story reinforced concrete (RC) building using a two-dimensional (2D) frame model developed in SAP2000 software. The building's response to lateral loads was evaluated through a nonlinear static pushover analysis. Analysis results revealed that the original structure exhibited insufficient load-bearing capacity and deformation ability. To address these deficiencies, a retrofitting strategy involving column jacketing was proposed and implemented. Separate models were created for both the original and the retrofitted structure, and pushover analyses were conducted for each. Additionally, seismic fragility curves were developed to quantify the probability of damage at various limit states. The findings demonstrate a notable improvement in the seismic capacity of the retrofitted structure, with a significant reduction in damage probabilities, particularly at extensive and collapse-level damage states. This study highlights the effectiveness of column jacketing as a practical and efficient retrofitting technique for improving the seismic resilience of existing RC buildings.

Keywords: Seismic retrofit, Seismic vulnerability, Pushover analysis, Fragility curves, Seismic resilience.

1. Introduction

Earthquakes are among the most devastating natural disasters, causing sudden and widespread destruction. Due to its geographical location, Türkiye is situated on active fault lines and frequently experiences destructive earthquakes. Recent major events, such as the 2023 Kahramanmaraş earthquakes, have once again revealed the vulnerability of the country's existing building stock. The severe loss of life and property has underscored the critical importance of evaluating and improving the seismic safety of structures.

A significant portion of Turkey's building stock was constructed according to outdated seismic codes and often without adequate engineering supervision. Many of these structures exhibit poor construction quality, insufficient detailing, and inadequate material properties, making them highly susceptible to seismic damage. Particularly for older buildings, continuous evaluation is necessary due to factors such as the deterioration of material properties over time, exposure to environmental effects, engineering errors during design, deficiencies in inspection and control mechanisms, and evolving engineering standards (Avcı, 2025). Therefore, assessing the current performance of these buildings and implementing appropriate strengthening measures when necessary is of utmost importance for public safety.

One of the widely used methods for evaluating the seismic performance of existing structures is the pushover (static nonlinear) analysis. This method simulates the progressive nonlinear behavior of a structure under increasing lateral loads, revealing plastic hinge formations and performance levels. Based on the results of pushover analysis, fragility curves can be developed to estimate the probability of reaching various damage states under different levels of seismic intensity. This approach not only enables a detailed assessment of the current performance but also allows for evaluating the effectiveness of proposed strengthening strategies.

In this study, the seismic performance of a three-story reinforced concrete building with a two-dimensional frame system was analyzed using the SAP2000 software, and fragility curves were developed based on the obtained data. Subsequently, a strengthening strategy involving jacketing of columns was proposed, and the

* Corresponding author, E-mail: ygmurars@gmail.com

https://doi.org/10.31462/icearc2025_ce_eqe_090

building's performance was re-evaluated after the strengthening. Both conditions, before and after retrofitting, were compared to assess the improvements. The aim of this study is to contribute to the enhancement of seismic resilience in existing structures by proposing and evaluating practical strengthening methods.

This study seeks to contribute to the analytical evaluation of the seismic performance of existing buildings through the development of fragility curves. By comparing the structural behavior before and after retrofitting, it aims to provide objective data on the effectiveness of strengthening strategies. Thus, the study aspires to establish a scientific basis for improving the earthquake resilience of reinforced concrete structures and for mitigating potential seismic risks.

2. Materials and methods

In this study, the performance analysis of a 3-story reinforced concrete frame structure with a two-dimensional configuration is conducted using static pushover analysis. The analysis is performed using SAP2000, a widely used structural analysis software. The primary objective of this study is to investigate the behavior of the structure under lateral loads and to develop fragility curves for both pre- and post-strengthening conditions. The strengthening strategy involves the application of external insulation to the columns to improve the overall structural performance. All necessary models for the existing and strengthened conditions have been created and analyzed in SAP2000. Additionally, fragility curves have been developed to assess the structure's sensitivity under various loading conditions. The results obtained from these analyses will be compared to evaluate the effectiveness of the proposed strengthening method and to assess the extent to which the capacity of the existing structure can be increased.

2.1. Existing structure characteristics

In this section, the material properties and cross-sectional specifications of the modeled existing building are detailed. A three-story reinforced concrete structure with a two-dimensional frame system was modeled for the purposes of this study. Each story has a height of 3 meters, resulting in a total building height of 18 meters. The structure consists of three spans, with each span having a 6-meter bay width. The cross-sectional layout are presented in Fig. 1.

Given that the building is assumed to be an older structure, the material strengths and section dimensions were defined to reflect this condition. The concrete class was taken as C16/20. The material properties assigned to this concrete class are detailed in Table 1. The columns were modeled with cross-sectional dimensions of 30 cm × 30 cm, designed deliberately with a reinforcement ratio below the minimum code requirements to represent the deficiencies typical of aging structures. S220 grade reinforcing steel was used, with 6Ø12 mm longitudinal bars placed in each column. The stress-strain characteristics of concrete and reinforcing steel, intended for use in the structural behavior model, were obtained by modeling the beam and column cross-sections through the "Section Designer" tool in the SAP2000 (Computers and Structures, Inc., 2023) software. The cross-sectional and material properties of the columns are illustrated in Fig. 2 and Fig. 3. Additionally, the stress strain curve for C16/20 concrete is presented in Fig. 4.

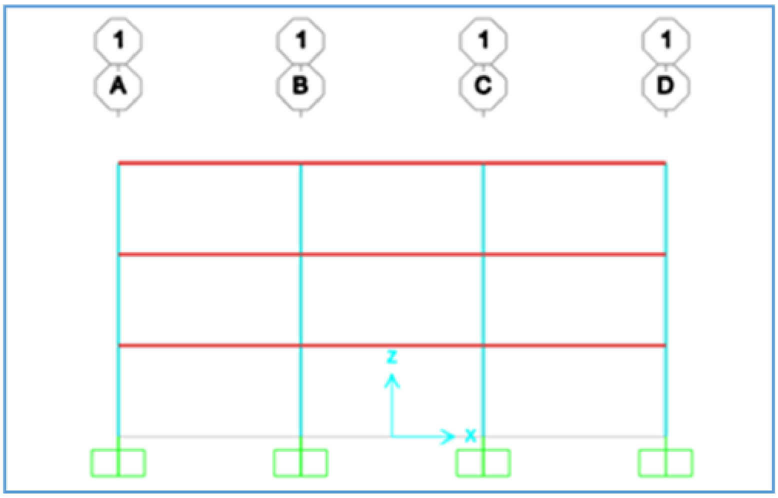

Fig. 1. The cross-sectional layout of the structure

Table 1. The material properties corresponding to C16/20 concrete and S220 reinforcement steel

Material	Parameter	Value
C16/20	Concrete Compressive Strength (f'$_c$)	16 Mpa
	Modulus of Elasticity	27000Mpa
S220	Minimum Yield Stress (F_y)	220 Mpa
	Minimum Tensile Stress (F_u)	340 Mpa

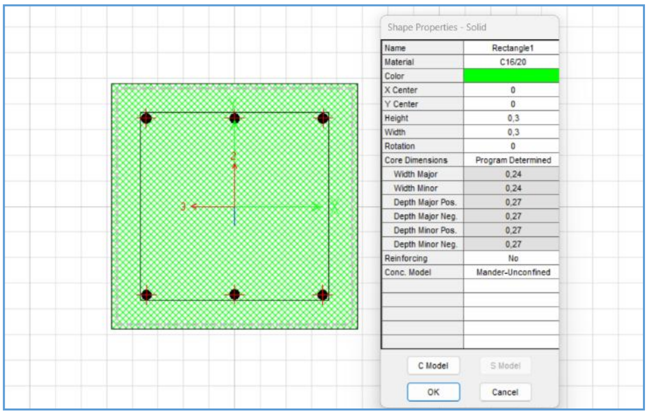

Fig. 2. Cross-sectional properties of the column

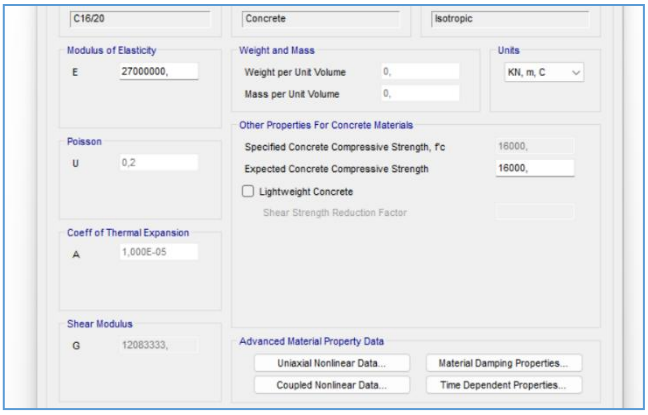

Fig. 3. Material properties of the column

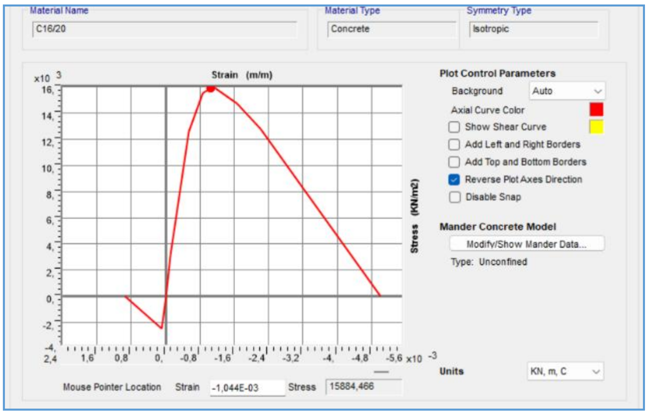

Fig. 4. The stress strain curve for C16/20

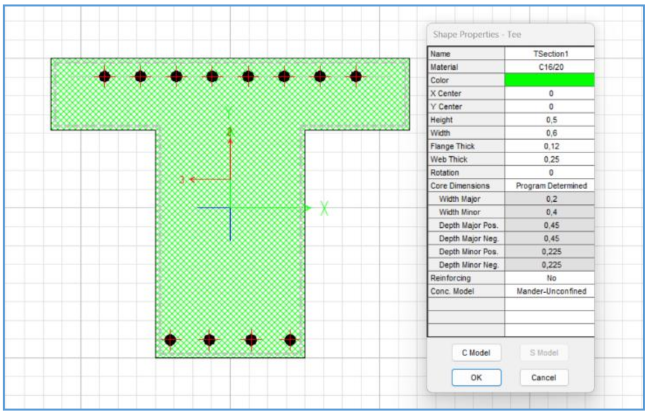

Fig. 5. Cross-sectional properties of the column

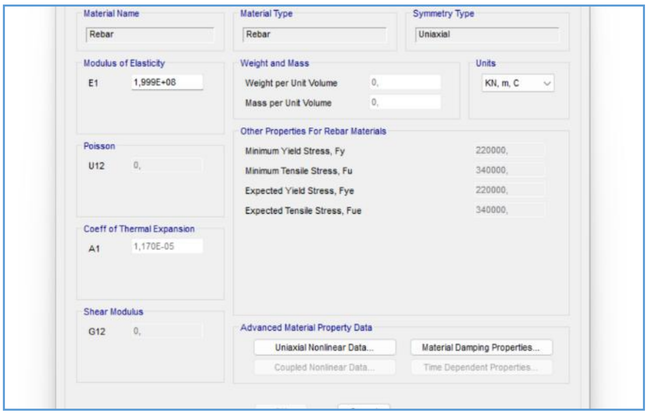

Fig. 6. Material properties of S220 stell

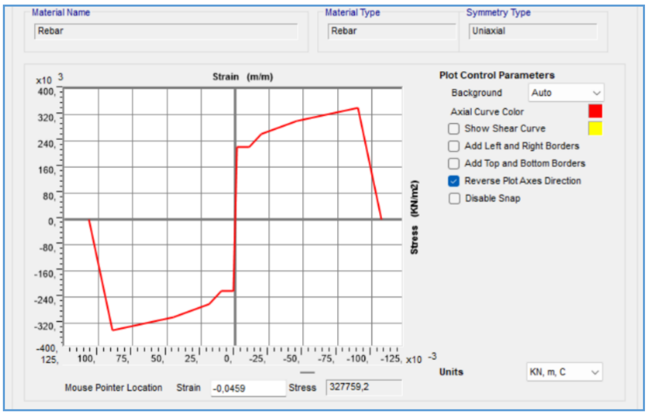

Fig. 7. The stress strain curve for S220

In the beam design, care was taken to ensure that the reinforcement ratio exceeded the minimum requirements. The beams were modeled as T-shaped sections, with an overall depth of 50 cm. The flange width was defined as 60 cm, and the web width as 25 cm. Similar to the columns, S220 grade steel was used for beam reinforcement, with twelve Ø18 mm longitudinal bars provided. Special attention was paid to avoiding a strong-beam weak-column configuration, and the beams were modeled accordingly. Furthermore, based on the assumption that each story carries an approximate total load of 360 kN, a uniformly distributed load of approximately 20 kN/m was applied to each beam element. The detailed cross-sectional and material properties of the beams are provided in Fig. 5. In addition, the material properties and the stress-strain curve for the S220 steel used as reinforcement are presented in Fig. 6 and Fig. 7, respectively.

2.2. Analysis of the existing structure

The existing structure was modeled in SAP2000 based on the properties described above, and its seismic behavior was assessed through a nonlinear pushover analysis. Furthermore, to simulate the nonlinear behavior of structural elements and to evaluate their responses when exceeding load-carrying capacities, plastic hinges were assigned to the load-bearing members. Since only flexural effects were considered in the beams, plasticity was assumed to occur solely around the bending moment axis (M3). In contrast, due to the combined effects of axial force and bending moments in the columns, P-M2-M3 plastic hinges were defined (Kırat, 2025). Considering these parameters, plastic hinges were assigned to the columns and beams in the SAP2000 program to model the plastic behavior of structural elements. The details of the hinge assignments are presented in Fig. 8 and Fig. 9.

After assigning hinges to the relevant sections, the necessary loadings for the pushover analysis have been established. For the nonlinear pushover analysis, a horizontal loading is applied in the X direction (PUSHX). In the first step, the pushover target was set to approximately 5% of the building's height. However, the pushover analysis was not completed up to this value. In such cases, as the value can be reduced to continue the analysis (Ekmen, 2005). In the pushover analysis, the target displacement was defined as approximately 0.45 m, corresponding to 5% of the total building height. However, the analysis terminated at a displacement level of approximately 0.20 m, indicating that the structure could not be pushed further due to numerical instability. This suggests that the structural system reached its collapse mechanism and lacked additional lateral load capacity. The pushover curve reveals a distinct peak followed by a sharp decline in base shear, demonstrating a significant reduction in lateral strength. This behavior is indicative of widespread plastic hinge formation and a subsequent loss of structural stability. The results clearly demonstrate the necessity for structural strengthening. Based on the analysis results, the necessity for structural strengthening was established. Additionally, the pushover curve obtained from the pushover analysis is presented in Fig. 10.

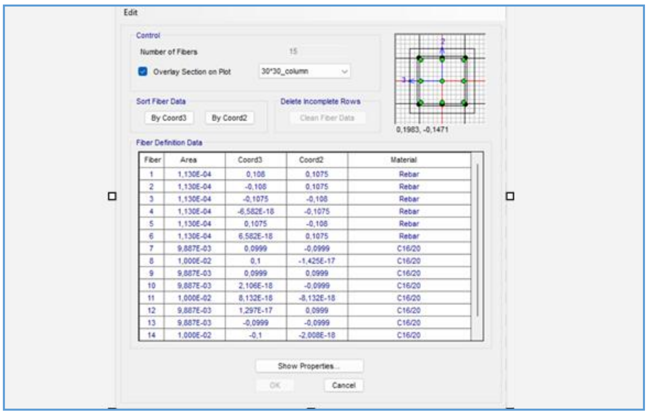

Fig. 8. Column hinge detail

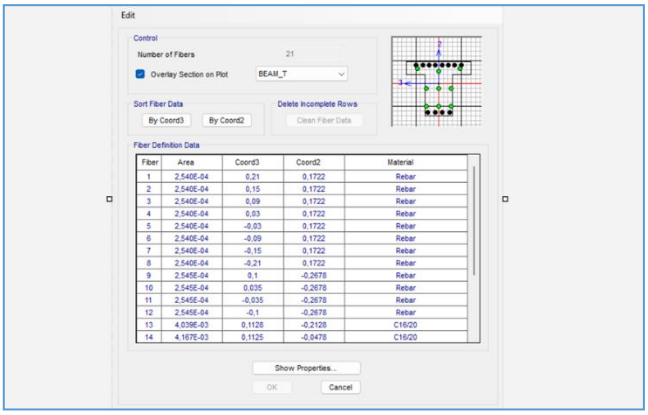

Fig. 9. Beam hinge detail

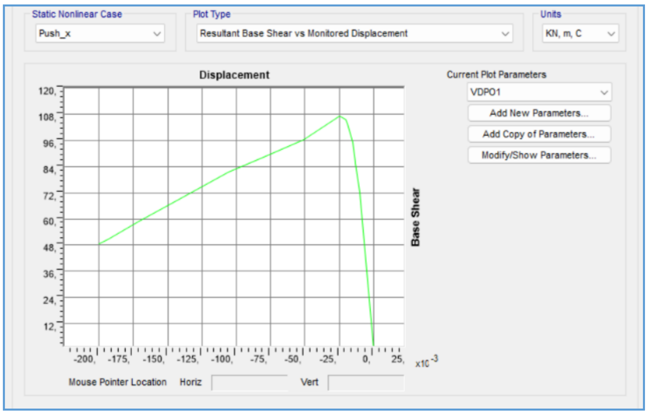

Fig. 10. Pushover curve of existing structure

2.3. Properties of the retrofitted structure

In recent years, column jacketing has become a widely used strengthening technique for reinforced concrete buildings, especially those that do not meet current seismic design requirements. This method enhances both the axial and shear capacity of columns by increasing their cross-sectional area and improving confinement. According to studies in the literature, jacketed columns show significant improvements in ductility and energy dissipation capacity under seismic loading (Altun & Anıl, 2007; Sezen & Moehle, 2004). In this study, the retrofitting strategy involves reinforced concrete jacketing of the existing columns, aiming to improve the structural performance and ensure compliance with current code requirements.

According to the Turkish Earthquake Building Code (TBDY, 2018), the minimum confinement thickness for reinforced concrete columns should be 10 mm. All reinforced concrete column elements were jacketed with a 15 cm layer on all four sides. During the jacketing process, the plaster on the surface of the existing columns was removed and the surface was roughened to eliminate any remaining plaster residues. The surface was then cleaned using pressurized air to remove dust particles, and a bonding agent was applied between the existing and new concrete layers in order to enhance adherence. This procedure ensures monolithic behavior between the old and new concrete.

The retrofitted column model was developed using Section Designer. In older structures, the reinforcement in structural elements is often subjected to corrosion, leading to a reduction in cross-sectional area. Therefore, in strengthening calculations, the existing reinforcement in columns is typically not included in the analytical models. It is generally assumed that these reinforcements have lost their structural effectiveness (Karabacak, 2020). In this study, the existing column reinforcements were not included in the model, and C30/37 grade concrete was used for the jacketing. In addition, S420 grade reinforcing steel was utilized. The properties of these materials are summarized in Table 2. The columns, originally with cross-sectional dimensions of 30 cm × 30 cm, were enlarged to 60 cm × 60 cm through jacketing. Since no deficiencies were identified in the beam elements, no strengthening was deemed necessary. Therefore, the beams were modeled as shown in Fig. 5. In the retrofitted column elements, 32 reinforcing bars with a diameter of 16 mm were used. Furthermore, the cross-sectional and material properties of the retrofitted column is presented in Fig. 11 and Fig. 12. Additionally, the stress strain curve for C30/37 concrete is presented in Fig. 13.

Table 2. The material properties corresponding to C30/37 concrete and S420 reinforcement steel

Material	Parameter	Value
C30/37	Concrete Compressive Strength (f'_c)	30 Mpa
	Modulus of Elasticity	33000 Mpa
S420	Minimum Yield Stress (F_y)	420 Mpa
	Minimum Tensile Stress (F_u)	540 Mpa

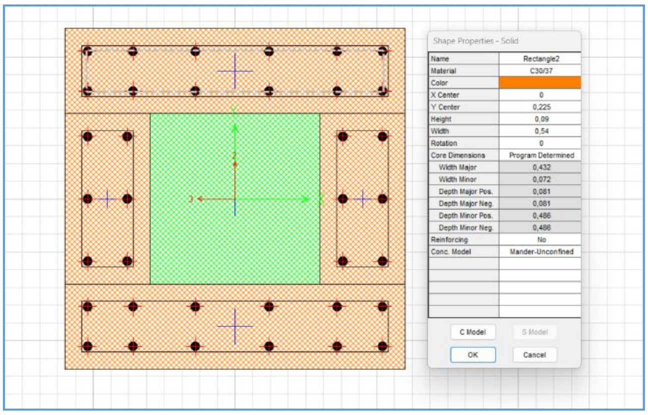

Fig. 11. Cross-sectional properties of retrofitted column

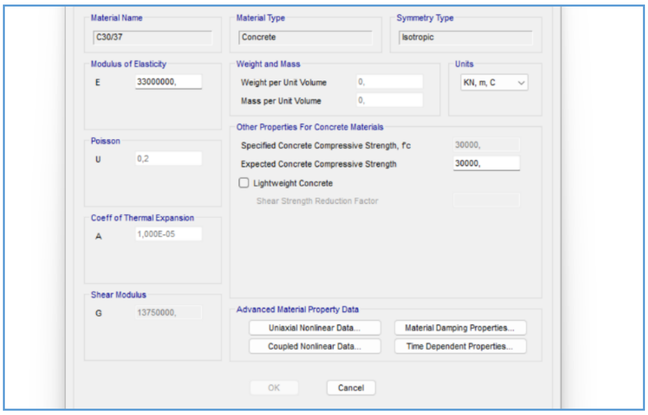

Fig. 12. Material properties of the column

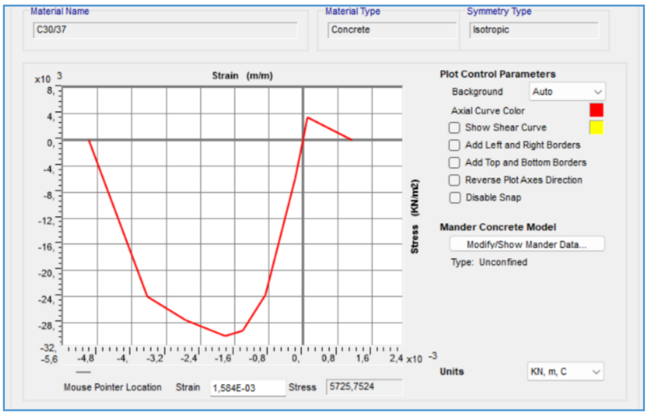

Fig. 13. The stress strain curve for C30/37

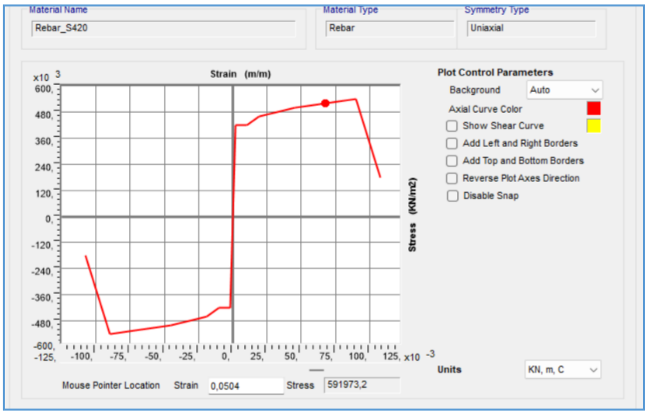

Fig. 14. The stress strain curve for S420

2.4 Analysis of the retrofitted structure

In this section, the nonlinear pushover analysis of the retrofitted building was conducted and the results were evaluated. The retrofitted structural model was created by assigning the previously mentioned material properties to the relevant cross-sections. To simulate the nonlinear behavior of structural elements, plastic hinges were assigned to columns and beams. The details of the hinge assignments are presented in Fig. 15 and Fig. 16. As in the analysis of the existing structure, a lateral load was applied in the X-direction, and the analysis was completed. The resulting pushover curve is presented in Figure 17.

Fig. 15. Retrofitted column hinge detail

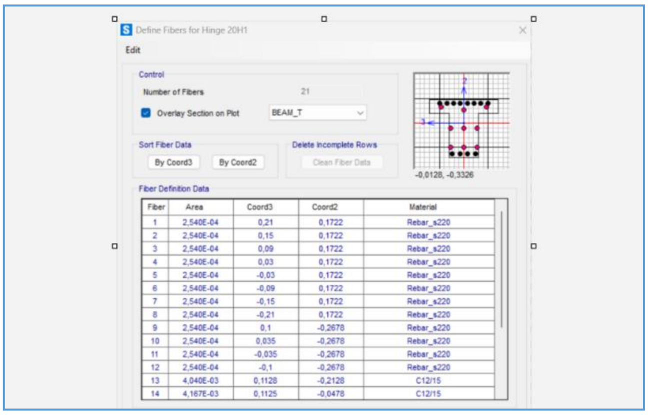

Fig. 16. Beam hinge detail

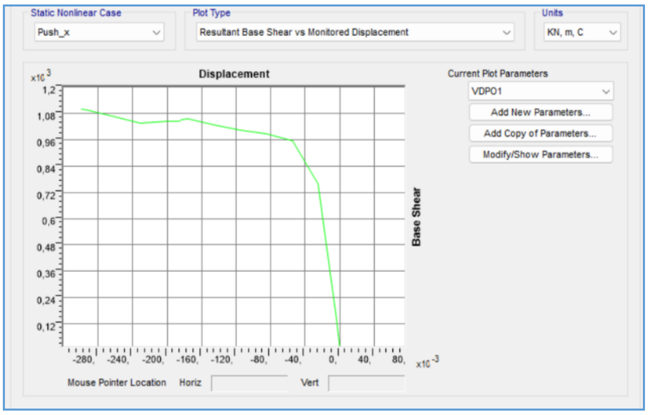

Fig. 17. Pushover curve of retrofitted structure

As illustrated in the pushover curve, the retrofitted structure demonstrates a significant increase in base shear capacity, indicating improved lateral load resistance. Furthermore, the structure exhibits enhanced deformation capacity, reflecting an increase in overall ductility. These results confirm that the applied strengthening strategy effectively improves the seismic performance of the building.

3. Comparison of fragility curves for existing and retrofitted structures

Fragility curves are widely used in seismic risk assessment to represent the probability of a structure reaching or exceeding a specific damage state under varying levels of ground motion intensity. These curves provide a quantitative basis for evaluating the vulnerability of structures and comparing the seismic performance of different structural configurations (Cornell et al., 2002; FEMA, 2009). In this study, fragility curves were developed for both the existing and the retrofitted building models using pushover analysis results. The comparison aims to highlight the improvements in seismic resilience achieved through the column jacketing technique.

3.1. Development of fragility curve for the existing structure

In this section, the process of deriving the fragility curves of the existing structure based on the results of the pushover analysis is explained. The roof displacements corresponding to the yield and ultimate points of the structure were obtained from the SAP2000 model and converted into spectral displacements as yielding displacement D_y and ultimate displacement D_u using Equation (1). For the determination of the fragility curves, four distinct damage states have been considered: slight damage, moderate damage, extensive damage, and complete damage. The standard deviations of the Sd values for these damage states, categorized by building height, have been determined (HAZUS, 2003). Using these values, the mean of the Sd values is obtained. All of these data are summarized in Table 2 and 3. The obtained spectral displacement values are substituted into Equation (2), thereby creating the fragility curves for the structure and the fragility curves for different damage states are illustrated in Fig. 18.

$$S_d = \frac{Roof\ displacement\ in\ first\ mode}{1st\ mode\ participation\ factor\ x\ 1st\ modemodal\ displacement\ roof} \tag{1}$$

$$P\left(\frac{DS}{Sd}\right) = \emptyset\left(\frac{Ln(Sd)-Ln(\lambda)}{\beta}\right) \tag{2}$$

Table 2. Values of the D_y and D_u

	Roof Displacement (m)	D
Yield point	0,0164	0,020676
Ultimate Point	0,2	0,054007

Table 3. Values of the spectral displacement of existing structure

Number	Damage State	Displacement	Mean of S_d (in)	Standart Deviation of S_d (in)
1	Slight	$0.7D_y$	0.569811024	0.81
2	Moderate	D_y	0.814015748	0.84
3	Extensive	$D_y + 0.25\ (D_u - D_y)$	1.142076772	0.86
4	Complete	D_u	2.126259843	0.81

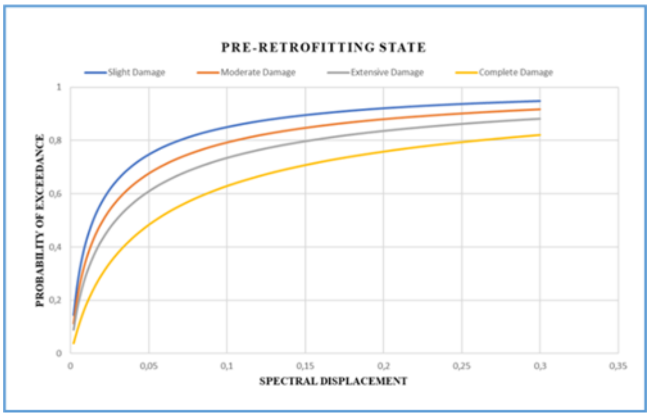

Fig. 18. Fragility curve of existing structure

3.2. Development of fragility curve for the retrofitted structure
In this section, the fragility curves for the strengthened structure have been derived using Equation (1) and Equation (2). The procedures for obtaining these curves are the same as those described in the previous section. Since the yield and ultimate displacements change after strengthening, the spectral displacements have been recalculated. The calculated displacement values are summarized in Table 4 and 5. The obtained spectral displacement values are substituted into Equation (2), thereby creating the fragility curves for the structure and the fragility curves for different damage states are illustrated in Fig 19.

Table 4. Values of the D_y and D_u

	Roof Displacement (m)	D
Yield point	0.0215	0.034858
Ultimate Point	0.041	0.210092

Table 5. Values of the D_y and D_u

Number	Damage State	Displacement	Mean of S_d (in)	Standart Deviation of S_d (in)
1	Slight	$0.7D_y$	0.960653543	0.81
2	Moderate	D_y	1.372362205	0.84
3	Extensive	$D_y + 0.25\ (D_u - D_y)$	3.097106299	0.86
4	Complete	D_u	8.271338583	0.81

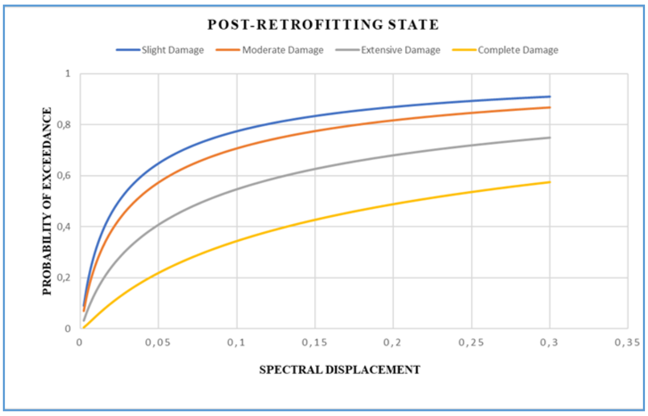

Fig. 19. Fragility curve of retrofitted structure

4. Conclusion

This study aimed to evaluate the impact of retrofitting interventions on the seismic fragility of a reinforced concrete frame structure. A comparative analysis was conducted by comparing the fragility curves of the structure before and after retrofitting. As an illustrative example, the spectral displacement level of 0.15 m was selected to observe how the probability of exceeding various damage states changed due to retrofitting. The results regarding the damage probabilities at this displacement level are as follows:

- The probability of exceeding the slight damage state was approximately 90% before retrofitting and reduced to around 85% after retrofitting. This minor decrease suggests that the retrofitting intervention had limited influence on mitigating low-level damage.
- For the moderate damage state, the probability of exceedance decreased from about 85% in the pre-retrofitting condition to approximately 78% post-retrofitting. This result indicates a modest improvement, implying that the retrofitting provided some level of reduction in the likelihood of moderate damage.
- In the case of extensive damage, a more noticeable change was observed, as the exceedance probability dropped from nearly 80% before retrofitting to around 65% after retrofitting. This reflects the effectiveness of the intervention in significantly reducing the probability of severe structural damage.
- The most significant improvement was observed in the complete (collapse) damage state, where the probability of exceedance at 0.15 m spectral displacement fell from approximately 70% before retrofitting to about 45% afterward. This substantial reduction demonstrates the critical role of retrofitting in enhancing the structural resilience and minimizing the risk of collapse under seismic excitation.
- Overall, these results demonstrate that retrofitting, applied via jacketing, significantly reduces the likelihood of severe damage and collapse, thereby greatly improving the seismic performance and durability of the structure.

References

Altun, F., & Anıl, Ö. (2007). An experimental study on the behavior of reinforced concrete columns strengthened with ferrocement jackets. *Cement and Concrete Composites, 29*(7), 515–521.

Avcı, O. İ. (2025). *The performance analyses of existing and retrofitting reinforced concrete structures by different design software* [Unpublished master's thesis]. Niğde Ömer Halisdemir University, Graduate School of Natural and Applied Sciences, Niğde, Turkey.

Computers and Structures, Inc. (2023). *SAP2000 integrated software for structural analysis and design* (Version 26) [Computer software]. https://www.csiamerica.com/products/sap2000

Cornell, C. A., Jalayer, F., & Hamburger, R. O. (2002). Probabilistic basis for 2000 SAC Federal Emergency Management Agency steel moment frame guidelines. *Journal of Structural Engineering, 128*(4), 526–533.

Ekmen, T. (2025). *Evaluation and strengthening of a school building by using pushover analysis method* [Unpublished master's thesis]. Istanbul Technical University, Science Engineering and Technology Institute, Istanbul, Turkey.

FEMA. (2009). *Quantification of building seismic performance factors (FEMA P-695)*. Federal Emergency Management Agency.

Karabacak, S. (2020). *Comparison of traditional strengthening and base isolation method in a reinforced concrete building* [Unpublished master's thesis]. Istanbul Technical University, Science Engineering and Technology Institute, Istanbul, Turkey.

Kırat, M. (2025). *Performance evaluation of an existing reinforced concrete structure under different Mander material models using incremental pushover analysis* [Unpublished master's thesis]. Ondokuz Mayıs University, Institute of Graduate Studies, Samsun, Turkey.

Ministry of Environment and Urbanization. (2018). *Turkish Earthquake Building Code (TBDY)*.

Sezen, H., & Moehle, J. P. (2004). Shear strength model for lightly reinforced concrete columns. *Journal of Structural Engineering, 130*(11), 1692–1703.

4th International Civil Engineering & Architecture Conference
17-19 May 2025, Trabzon, Türkiye

Investigation of the non-linear design parameters of steel moment frames at different seismic sites in Turkey

Salah Eddine Hamadi *[1], Serkan Bekiroğlu [1]

[1] Yıldız Technical University, Department of Civil Engineering, İstanbul, Türkiye

Abstract. Turkey has a high seismicity and a considerable number of densely populated cities that are located along active faults. This paper investigates the nonlinear design parameters of steel moment frames at different sites in Turkey to evaluate the proportionality between the design parameters of the structure and those of the spectrum with the aim of enhancing the building design. For this purpose, steel moment frames are modeled using SAP2000; all the systems have the same characteristics except the span to height ratio. Then, the capacity spectrum method based on the ATC-40 procedure is performed to calculate the nonlinear behavior parameters for each system, including the effective damping ratio, stiffness ratio, ductility and reduction factor. Additionally, four different demand spectra that include different elastic design spectrum characteristics are used, precisely, the horizontal elastic design acceleration spectrum corner period T_B and the peak ground acceleration (PGA). Afterward, the comparison of the results yields substantial findings regarding the nonlinear behavior of the steel moment frame and the overall building design. This paper provides significant information to the designers about the structural behavior in terms of design parameters. In addition, it offers very important recommendations for researchers to conduct more relevant studies to develop new practical approaches to optimize the building design.

Keywords: Nonlinear behavior parameters; Steel moment frame; Design spectrum parameters; Capacity spectrum method; Reduction factor

1. Introduction

Turkey has a high seismicity rate and a considerable number of densely populated cities that are located along active faults. On February 6, 2023, a series of earthquakes occurred in the Eastern Anatolia region, resulting in varying degrees of damage to various types of buildings and significant human victims. It is worth noticing that the Northwestern region of Turkey is particularly vulnerable to large-scale seismic events(Vuran et al., 2024; Aydin et al., 2025). In this regard, enhancing the design process of the building is imperative to avoid the undesirable drawbacks from both the life safety and economic perspectives.

There are several methods of analyzing the building for the purpose of design. Among them, nonlinear time history analysis has been demonstrated to produce the most accurate results. However, conducting this type of analysis takes a long time and requires precise modeling and interpretation of results, which can present challenges in practical design(Izadinia et al., 2012; Loulelis et al., 2018). In response to these challenges, various simplified methods are used in the codes to design buildings through linear analysis, where the nonlinear behavior of the building is taken in consideration through constant value known as the reduction factor (Loulelis et al., 2018; Boussa et al., 2022). The reduction factor reduces the elastic design spectrum to inelastic design spectrum, in other words, reducing the base shear in the building (Loulelis et al., 2018; Hassan, 2022). In general, the value of the reduction factor is determined based on the resistant system type and certain code specifications (Hassan, 2022; Loulelis et al., 2018). In reality, the value of the reduction factor is proportional to several conditions, making its determination a significant challenge(Boussa et al., 2022). Since the 1960s, a substantial volume of experimental and numerical studies has been conducted to ascertain the values of the reduction factor employed in the design. These studies have considered the site conditions, the level of ground motion, the characteristics of structural systems (Hassan, 2022).

The structure has several types of resisting systems used to withstand seismic forces. The steel moment frames are widely used due to the advantages of the high ductility capacity, their architectural flexibility, and simple applied construction (Özkula, 2023; Yılmaz & Bekiroğlu, 2023). However, the steel moment frames can be exposed to significant damage in cases of severe earthquakes, as was observed in the 1994 Northridge and 1995 Kobe earthquakes (Miller, 1998; Mahin, 1998; Nakashima et al., 1998; Watanabe et al., 1998). This event

* Corresponding author, E-mail: salah.hamadi@std.yildiz.edu.tr

https://doi.org/10.31462/icearc2025_ce_eqe_122

encourages a rigorous investigation of the behavior of steel moment frames. The seismic resistant steel frame has been studied by several researchers, Özhendekci et Özhendekci, 2012 mentioned that the span to height approximately 2 is suitable for both the steel moment frames capacity and economy considerations, On the other hand, using a long span to height greater than 2.5 can lead to damage in the lower stories (Özhendekci & Özhendekci, 2012). In addition, the performance of the steel moment frame can be evaluated through the reduction factor value. Ferraioli et al., 2012 concluded that the average of the reduction factor for irregular steel moment frames is 5.2 and 6.5 for regular steel moment system(Ferraioli et al., 2012). Other studies reported that the reduction factor reduces as number of stories or span length increases and discussed that the effect of number of spans on the reduction factor is related to the number of stories(Hassan, 2022). In most seismic codes, the reduction factor for steel moment frames is specified based on the level of ductility or the type of steel moment frame. In Turkish Building Seismic Code (Code, 2018), the reduction factor (R) value is 8 for steel moment frame with high ductility level, and 4 for the steel moment frame with limited ductility level. Based on previous research, this constant value can be overestimated or underestimated, which significantly affects the design of buildings.

This paper investigates the nonlinear design parameters of steel moment frames at different sites in Turkey to evaluate the proportionality between the design parameters of the structure and those of the spectrum with the aim of enhancing the building design. For this purpose, steel moment frames are modelled using SAP2000; all the systems have the same characteristics except the span to height ratio. Then, the capacity spectrum method based on the ATC-40 procedure is performed to calculate the nonlinear behavior parameters for each system, including the effective damping ratio, stiffness ratio, ductility and reduction factor. Additionally, four different demand spectra that include different elastic design spectrum characteristics are used, precisely, the horizontal elastic design acceleration spectrum corner period T_B and the peak ground acceleration PGA. Afterward, the comparison of the results yields substantial findings regarding the nonlinear behavior of the steel moment frame and the overall building design.

2. Methodology

2.1. Analysis of the nonlinear behavior of steel moment frame using the capacity spectrum method

Fig.1 illustrates the steps to analyze the nonlinear behavior of structures using the Capacity Spectrum Method. A nonlinear static procedure, known as the Capacity Spectrum Method, is employed based on the ATC-40 procedure(Council, 1996) to analyze the nonlinear behavior of the steel moment frame.

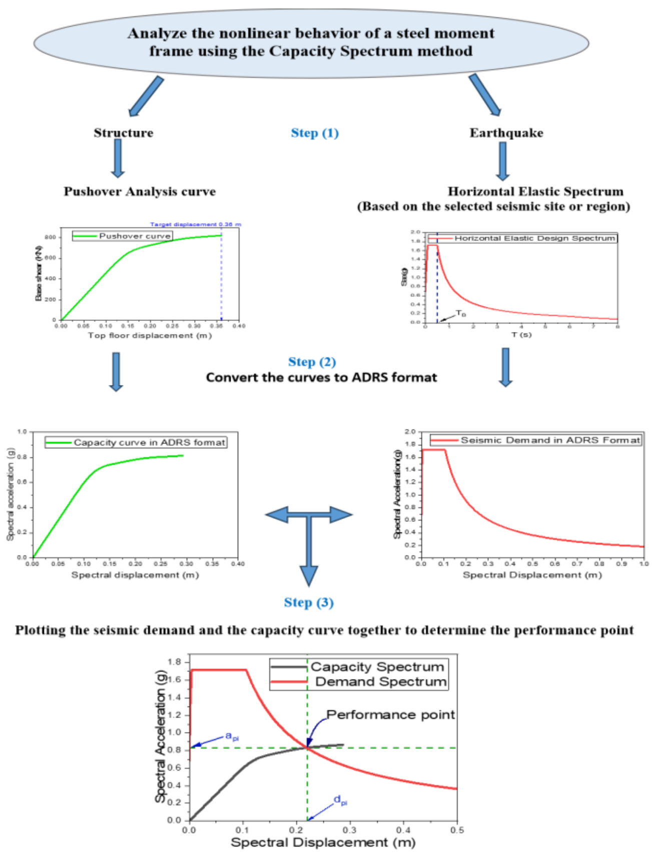

Fig. 1. Steps of the capacity spectrum procedure used to analyze the nonlinear behavior of steel moment frames

The system is pushed according to the first mode pattern up to the target displacement of 0.36 m (4% of the total height of the structure) to obtain the inelastic capacity curve, also known as the pushover curve. It should be noted that this pushover curve characterises the performance of the structure independently of any specific seismic demand (Council, 1996). In this regard, to evaluate the system's performance based on seismic demand, the capacity curve and the specified horizontal elastic design spectrum are transformed into the spectral acceleration–displacement domain (ADRS format). In this way, the capacity curve and the demand curve in spectral acceleration displacement can be plotted together. The intersection of these curves is the performance point of the structure that represents the maximum displacement demand from the system for a specified earthquake. The procedure described in Fig.1 is performed in this study using the SAP2000 software (*Computers and Structures Inc. SAP2000 Basic Analysis Reference Manual*, n.d.).

2.2. Estimating the nonlinear behavior parameters of a steel moment frame

In this study, the following nonlinear parameters are investigated:

- Effective damping ratio; serves as an index of the amount of energy dissipated by the system.
- Stiffness ratio; representing the degradation in the system's strength.
- Ductility; defined as the capacity of a structure to undergo plastic deformation without collapsing.
- Reduction factor; a critical parameter used to reduce the elastic design spectrum to account for the inelastic behavior of the system in the design process.

The bilinear representation has been used to facilitate the calculation of nonlinear parameters of interest in a simplified manner. To achieve this, the capacity curve extended up to the performance point is approximated by a bilinear representation. Based on Chapter 8 of the ATC-40 document (Council, 1996), the flowchart in Fig. 2 illustrates the procedure for converting the nonlinear capacity curve into a bilinear curve, along with the equations used to estimate the aforementioned parameters. It should be noted that, according to the Turkish Building Seismic Code (Code, 2018), the overstrength factor D is taken as 3 (used in this study) for steel moment frames with high ductility and 2.5 for those with limited ductility.

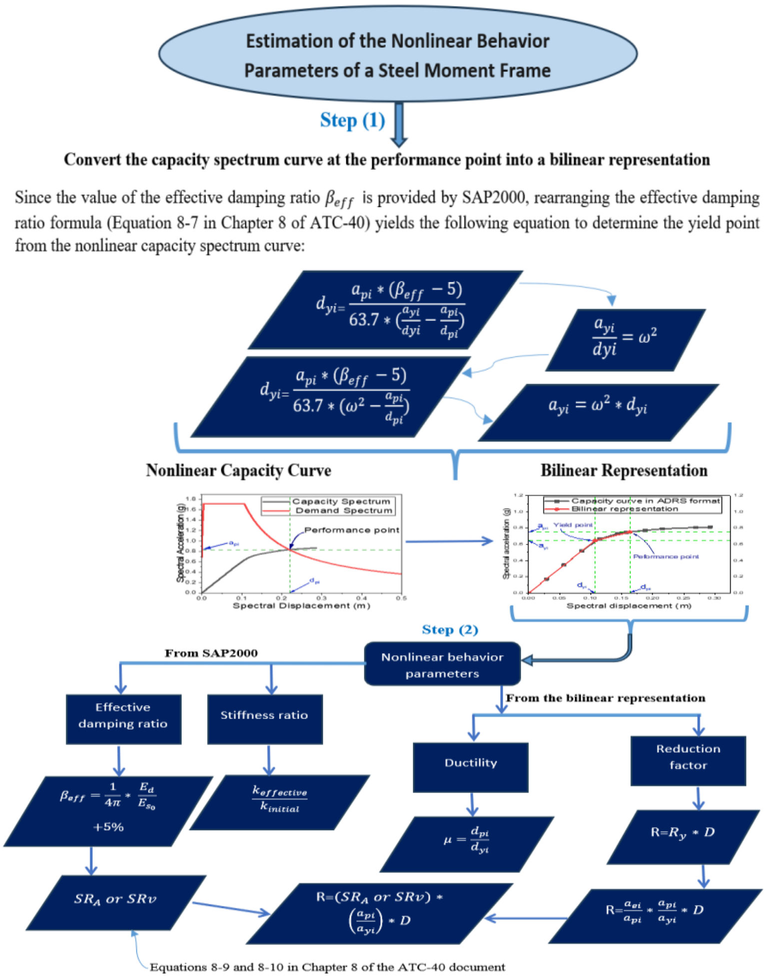

Fig. 2. Flowchart illustrating the calculation of nonlinear behavior parameters

2.3. Numerical study

2.3.1 Benchmark model

A steel moment frame is modeled using SAP2000 (*Computers and Structures Inc. SAP2000 Basic Analysis Reference Manual*, n.d.) and is taken as the benchmark for this study (Fig. 3). The system consists of three spans and three stories, with HE240B columns and IPE300O beams with each section meshed into eight parts. To achieve the objectives of the study, 15 frames are modeled based on this benchmark. The span length of these frames is incrementally increased by 0.3 meters, starting from 3.3 meters and extending to 7.5 meters. This procedure results in a series of steel moment frames that are identical in all properties except for the span-to-height ratio.

Table 1. Presentation of additional characteristics of the steel moment frames

Characteristics	Dead load(kN/m)	Live load(kN/m)	Hinges	Material type
For all systems	13.2	9	Fiber model	Steel material

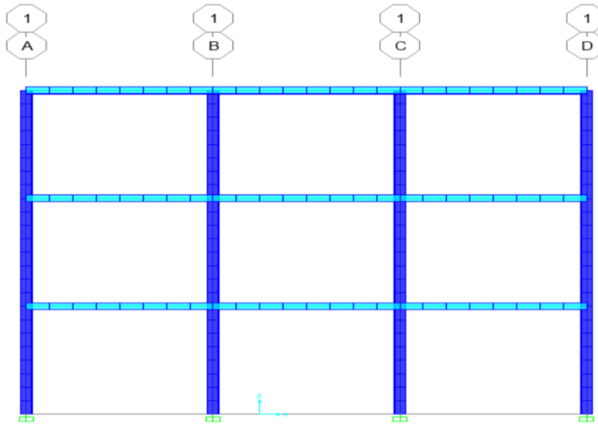

Fig. 3. Two-dimensional model of the steel moment frame

2.3.2 Seismic demands

As illustrated in Fig. 4, the four seismic demands have been selected to represent earthquake loads. The selected horizontal elastic design spectra are obtained from the AFAD seismic hazard map for different seismic regions in Turkey (Database. & Https://deprem.afad.gov.tr/, n.d.). The demand spectra used correspond to an earthquake ground motion level with a 10% probability of exceedance in 50 years (recurrence period of 475 years), specifically Earthquake Ground Motion Level DD-2. The spectra are defined by a variety of characteristics, including peak ground acceleration (PGA), the corner period of the horizontal elastic design spectrum(T_B), and the soil type. It is evident that the seismic demands exhibit variation with respect to high spectral acceleration and earthquake duration. These distinctions enable the investigation of the effect of the external loads on the nonlinear behavior parameters of the system.

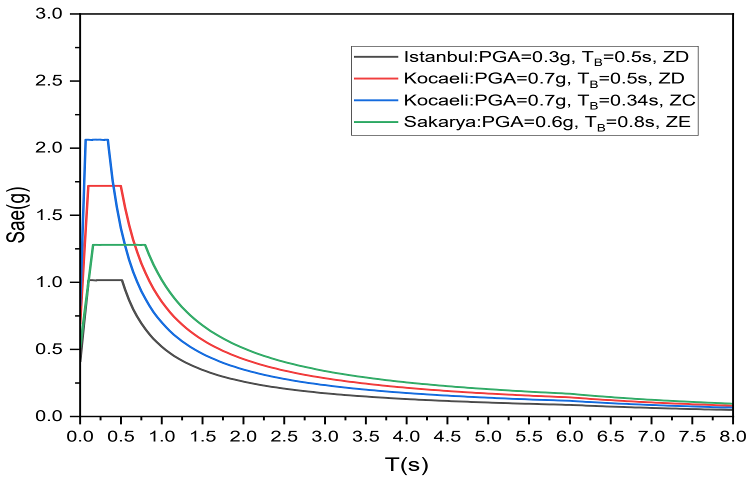

Fig. 4. Horizontal elastic design spectra for different seismic regions in Turkey

3. Results and discussion

3.1. Effect of the span to height ratio on the nonlinear behavior of steel moment frames under different seismic demands

The effective damping ratio values of the different steel moment frames subjected to four seismic demands are illustrated in Fig. 5. Then, it's clear that the increase in span to height ratio increases the initial period of the system, in this manner, the effective damping ratio is getting higher. In addition, the increment degree of the effective damping ratio is affected by the characteristics of seismic demand, more precisely, when we compare the cases of Kocaeli (ZD), Kocaeli (ZC) that have the same PGA and different T_B, it's observed that the systems have high damping when T_B is longer and significantly with large span to height ratio. On the other side, in the Istanbul and Kocaeli ZD cases, we observe that for the same T_B period (Same soil type) and different PGA, the systems have high damping level with the high PGA. Moreover, for the span to height ratio less or equal 1.9, there are no observations of plastic hinges in the columns in all the cases. On the other hand, when the span to height ratio exceeds the value 1.9, the plastic hinges are observed in the columns in the Sakarya case. It is worth noticing that in the Sakarya case, the increment in the effective damping ratio is dramatically compared to other cases. From periods insight, in the Sakarya case, the initial period of the system is less then T_B, the increase of the span to height ratio results to increase in the initial period, in this manner, the initial period of the structure goes more close to T_B of seismic demand, that results to high effective damping ratio due to long vibration term with the formation of the plastic hinges in columns, this is the crucial case where the column sway mechanism can be happen. In other cases, most of the initial periods are greater than T_B, the increase of the span to height ratio increases the initial period, that makes the later far from T_B and provide more effective damping without observation of plastic hinges in the columns.

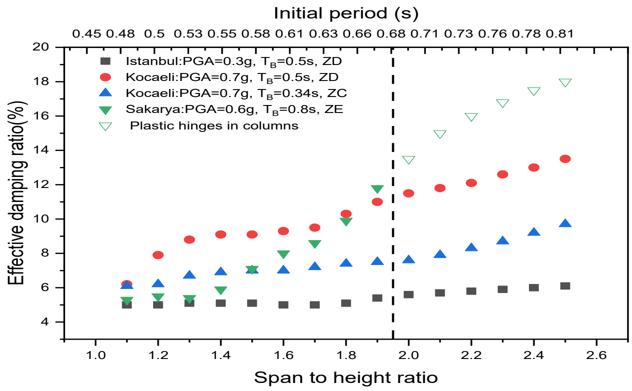

Fig. 5. Effective damping ratio with respect to the span to height ratio and initial period of steel moment frames under different seismic demand cases

Fig. 6 presents the stiffness ratio of the systems in terms of span to height ratio and initial period under different seismic demands. The degradation of the stiffness is increased with the increase of the span to height ratio and initial period, significantly, when T_B and PGA of seismic demand are larger. Furthermore, the degradation of the stiffness is significant and dramatic in the Sakarya case compared to other cases, where after the span to height ratio 1.9, the degradation of stiffness exceeds 15% with the formation of the plastic hinges in the columns, this is due to the increase of the initial period of the structure results from the increase of the span ratio make it close to T_B. In contrast, the plastic hinges in columns are not observed in the other cases. This due to the increase of span to height ratio that increases the initial period, but makes it more greater than T_B, this makes the system in safe zone and reduce the external load effect, the comparison of the Kocaeli cases confirm that, we observed for same PGA and initial period, the degradation of the stiffness of Kocaeli ZD ($T_B = 0.5s$) is greater than the case of Kocaeli ZC($T_B = 0.34s$); the initial period is more closer to T_B. In general, the results of the stiffness ratio confirm the comments of the effective damping ratio.

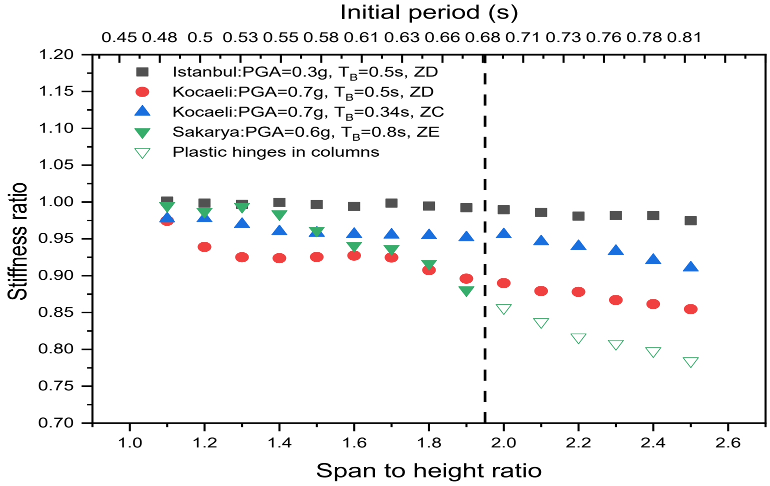

Fig. 6. Stiffness ratio with respect to the span to height ratio and initial period of the steel moment frames under different seismic sites

The ductility of the studied systems presented in Fig. 7 in terms of span to height ratio and initial period of the systems for four seismic regions. The trend of change of the ductility with the variation of the studied parameters is not so clear in this curve; however, in general, it's observed that the ductility value is changed with the variation of the span to height ratio, initial period, and the seismic demand type. The ductility value varies approximately from 1.2 to 2 for the systems that experienced nonlinear behavior, perhaps, we can classified the systems in the same level, but from other insight, if we compare the results of ductility with effective damping ratio and stiffness, we observe that small variation in ductility value has significant effect in the amount of energy dissipation of the systems and also the plastic hinges at the column can be occurred despite the systems have so close ductility level. This observation suggests that the concept of ductility deserves a more precise classification.

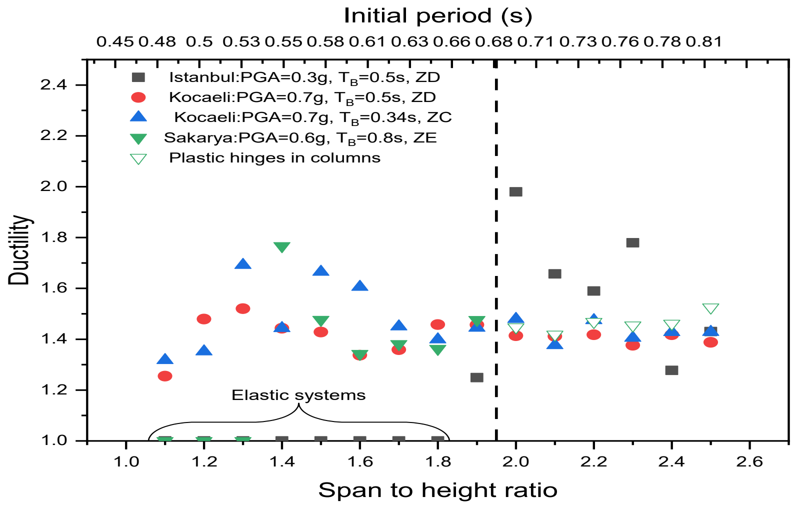

Fig. 7. Ductility with respect to the span to height ratio and initial period of steel moment frames under different seismic demand cases

Fig. 8 illustrates the modal participation mass ratio with respect to the span to height ratio and the initial period of the first mode of the different steel moment frames under four seismic demands. It's visible that the modal participation mass ratio is decreased with the increase of the span to height ratio and the initial period. The use of the long span increases initial period of the system and significantly leads to the occurrence of the plastic hinges in columns in earthquakes with long duration, this is clear in the case of Sakarya ($T_B = 0.8s$) after the span to height ratio exceeds 1.9.

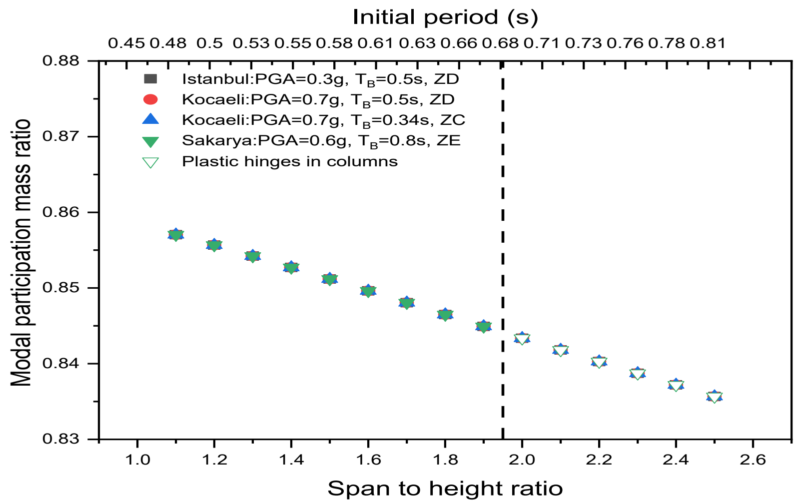

Fig. 8. Modal participation mass ratio of the first mode of the systems with respect to the span to height ratio and initial period of the different seismic cases

The effective damping ratio with respect to ductility of the steel moment frames considered in this study is shown in Fig. 9. It's visible that the effective damping ratio is changed significantly under short range of ductility values. Furthermore, it's clear that the high effective damping ratio can be result from the plastic hinges in the columns. The results of Fig. 9 indicate that the same system type can provide significantly different level of effective damping ratio although there is a small variation in the ductility value. In addition, the high effective damping ratio can not be always acceptable, since it can be provided through the formation of the plastic hinges in the columns.

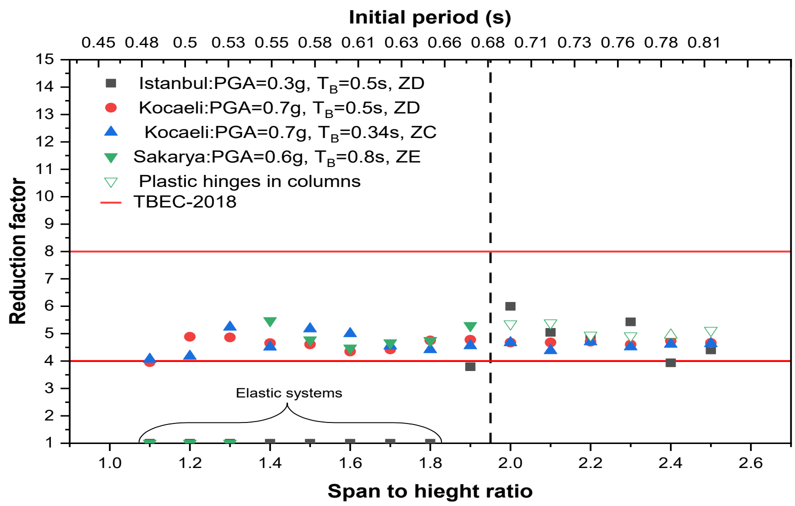

Fig. 9. Effective damping ratio with respect to ductility of the systems in different seismic sites

3.2. Assessment over the reduction factor value within the design with TBEC-2018

Fig. 10 shows the reduction factor of the steel moment frames studied in this paper in terms of the span to height ratio and the initial period. The results in Fig. 10 show that the reduction factor of the studied cases varied in range from approximately 4 to 6. The reduction factor is influenced by the span to height ratio and initial period of structure, additionally, the seismic region. In contrast, TBEC-2018 considers the reduction factor for the steel moment frame type as constants values based on ductility level, the results of Fig. 10 indicate that the reduction factor can take different values for the same system type based on several conditions.

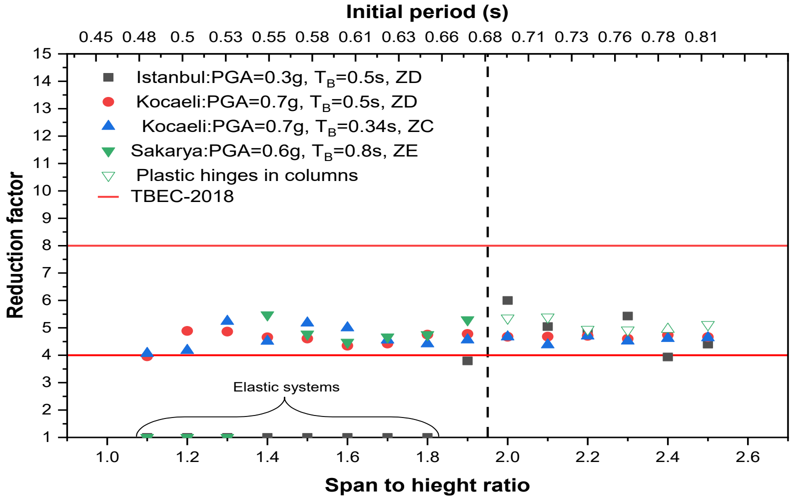

Fig. 10. Reduction factor values with respect to span to height ratio and initial period of the steel moment frames under different seismic demands

The reduction factor values with respect to the period ratio (T_B/T_i) of the different cases of the steel moment frames are illustrated in Fig. 11. In the range where the period ratio (T_B/T_i) is greater than one, the reduction factor value varies with both the span to height ratio and the period ratio (T_B/T_i). It ranges approximately from a minimum value of 4 to a maximum of 5.5. In addition, the plastic hinges are observed in the columns when the long span to height ratios are used, as mentioned earlier, this is the crucial case that's observed in this study, in fact, this case represents the column sway mechanism in real world scenario and can lead to the total collapse of the building. In the other range, the reduction factor value varied between approximately 4 to 6, without any observation of plastic hinges in the columns. Further, we observe some systems have the same period ratio (T_B/T_i) but different reduction factor, it should be mentioned that those cases have different span to height ratio, most straightforward, the span to height ratio increases the initial period T_i and with the change of T_B, we obtained some system with the same period ratio (T_B/T_i) and different span to height ratio. Overall, when we compare the cases with the same period ratio (T_B/T_i) and different span to height ratio as highlighted in Fig. 11, the reduction factor is affected by the span to height ratio.

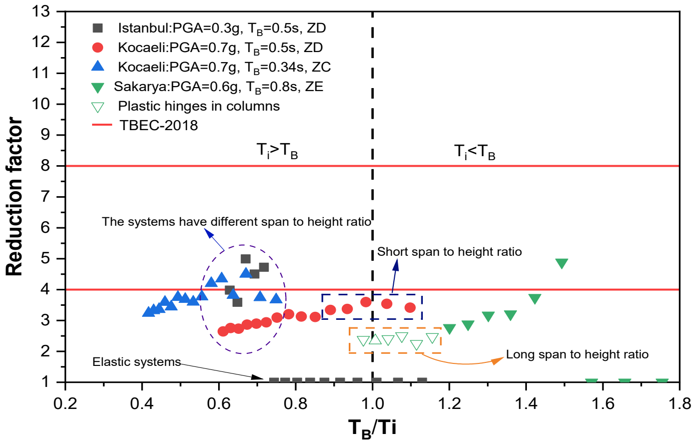

Fig. 11. Reduction factor with respect to the period ratio(T_B/T_i) of the systems in different seismic regions

4. Conclusions

This paper investigates the nonlinear behavior of the steel moment frames that have the same characteristics and different span to height ratios subjected to four different seismic demands. For this purpose, the capacity spectrum method was used to obtain the nonlinear parameters of the systems. The comparisons and the investigations of the results can reach to the following points:

- The long T_B period value of the soil demands a large damping from the system, the later can lead to the formation of the plastic hinges in columns when the long span to height ratio is used, consequently, the structure can collapse due to the column sway mechanism.

- The nonlinear behavior of the steel moment frame is so proportional with the span to height ratio, in addition, the span to height ratio changes the distribution of the plastic hinges, in this regard, the span to height ratio should be optimized to reach high performance of the steel moment frame.
- Increasing the span to height ratio increases high deformation of base floor in the first mode. This is because the plastic hinges can occur in the columns in long period earthquakes when the span to height ratio is more than 1.9 for steel moment frames.
- The reduction factor value is affected by the span to height ratio and the period ratio (T_B/T_i). The variation of those parameters can change the reduction factor value.
- For the same system type and similar level of ductility, the reduction factor value can be significantly different, as a result, assuming a constant value of the reduction factor base on the system type and level of ductility in TBEC-2018 (Code, 2018) can be overestimated or underestimated, which significantly affect the design. In response to these challenges, the reduction factor value should be checked at the end of the design process.

This paper provides significant information to the designers about the structural behavior in terms of design parameters. In addition, it offers very important recommendations for researchers to conduct more relevant studies to develop new practical approaches to optimize the building design.

Acknowledgments
The author(s) declared no potential conflicts of interest with respect to the research, authorship, and/or publication of this article.

References

Aydin, M. F., Altindal, A., Erberik, M. A., & Askan, A. (2025). Extreme Characteristics of the Ground Motions Recorded During the 2023 Kahramanmaras Turkiye Earthquakes and Their Effect on Inelastic Seismic Response of RC Frame Buildings. *Journal of Earthquake Engineering*, 1–19.

Boussa, L., Chemrouk, M., Si Salem, A., & Nekmouche, A. (2022). Seismic reduction factor of reinforced concrete framed structures. *Asian Journal of Civil Engineering*, *23*(2), 153–171.

Code, T. B. E. (2018). Disaster and emergency management presidency. *Ministry of Interior, Ankara, Turkey*.

Computers and Structures Inc. SAP2000 Basic Analysis Reference Manual (Version 25). (n.d.).

Council, A. T. (1996). Seismic evaluation and retrofit of concrete buildings. *Report No. SSC 96-01: ATC-40*, *1*.

Database., A. (n. d.). D. and E. M. P. of T. (AFAD) E., & Https://deprem.afad.gov.tr/, R. from. (n.d.). *No Title*.

Ferraioli, M., Lavino, A., & Mandara, A. (2012). Behaviour Factor for seismic design of moment-resisting steel frames. *15th World Conference on Earthquake Engineering. Lisbon, Portugal*.

Hassan, M. M. (2022). State-of-the-art review: Reduction factor of traditional steel moment resisting, braced or eccentrically braced systems. *Structures*, *35*, 734–747.

Izadinia, M., Rahgozar, M. A., & Mohammadrezaei, O. (2012). Response modification factor for steel moment-resisting frames by different pushover analysis methods. *Journal of Constructional Steel Research*, *79*, 83–90.

Loulelis, D. G., Papagiannopoulos, G. A., & Beskos, D. E. (2018). Modal strength reduction factors for seismic design of steel moment resisting frames. *Engineering Structures*, *154*, 23–37.

Mahin, S. A. (1998). Lessons from damage to steel buildings during the Northridge earthquake. *Engineering Structures*, *20*(4–6), 261–270.

Miller, D. K. (1998). Lessons learned from the Northridge earthquake. *Engineering Structures*, *20*(4–6), 249–260.

Nakashima, M., Inoue, K., & Tada, M. (1998). Classification of damage to steel buildings observed in the 1995 Hyogoken-Nanbu earthquake. *Engineering Structures*, *20*(4–6), 271–281.

Özhendekci, D., & Özhendekci, N. (2012). Seismic performance of steel special moment resisting frames with different span arrangements. *Journal of Constructional Steel Research*, *72*, 51–60.

Özkula, G. (2023). Key Factors that Affect the Behavior of Steel Beams and Columns in Special Moment Frames. *Dicle Üniversitesi Mühendislik Fakültesi Mühendislik Dergisi*, *14*(2), 361–375.

Vuran, E., Serhatoğlu, C., Timurağaoğlu, M. Ö., Smyrou, E., Bal, İ. E., & Livaoğlu, R. (2024). Damage observations of RC buildings from 2023 Kahramanmaraş earthquake sequence and discussion on the seismic code regulations. *Bulletin of Earthquake Engineering*, 1–30.

Watanabe, E., Sugiura, K., Nagata, K., & Kitane, Y. (1998). Performances and damages to steel structures during the 1995 Hyogoken-Nanbu earthquake. *Engineering Structures*, *20*(4–6), 282–290.

Yılmaz, O., & Bekiroğlu, S. (2023). *The frictional and elastomeric seismic joint apparatus and its usage as a steel beam-to-column connection*.

4th International Civil Engineering & Architecture Conference
17-19 May 2025, Trabzon, Türkiye

Numerical Analysis of Historical Masonry Nebi Mosque Minaret Using Finite Element Method

Ömer F. Taş*[1], Ozan İnce[1], Burak Çakıl[1], Ömer F. Osmanlı[1], Muhammet Karaton[1], Erkut Sayın[1], Mesut Gör[1]

[1] *Fırat University, Department of Civil Engineering, 23119 Elazığ, Türkiye*

Abstract. Earthquakes have been one of the greatest threats in human history due to the devastating effects of movements in the Earth's crust. The Kahramanmaraş earthquakes that occurred in 2023, with their large scale and destructiveness, have led us to question the seismic performance of not only modern structures but also historical artifacts. Such disasters have once again revealed the importance of protecting our cultural heritage as well as increasing the resistance of structures to earthquakes. Historical structures require a special approach in terms of engineering as well as their architectural and aesthetic values. Slender and tall structures such as minarets are more vulnerable to earthquakes; therefore, a detailed evaluation of their seismic performance is necessary. Analyses performed for historical masonry structures provide critical information in terms of understanding the current durability of structures and developing the right reinforcement solutions. Ensuring the safety of minarets is not only an engineering problem, but also a necessity for carrying cultural heritage into the future. This study aims to determine the seismic assessment of the historical minaret of Nebi Mosque. For this purpose, a finite element model and seismic analysis of the minaret were carried out using the ANSYS finite element software with the macro modeling technique. The nonlinear analysis method in the time history was applied to the minaret using the of the February 6, 2023 Pazarcık-Kahramanmaraş earthquake (M_w = 7.7). The dynamic response of the minaret was evaluated. The maximum tensile and compressive stresses in the minaret were determined, and the possible locations of the first damage were investigated.

Keywords: Masonry structure; Minaret; Numerical analysis; Finite Element Method

1. Introduction

On 6 February 2023, two major earthquakes with M_w = 7.7 and M_w = 7.6 struck the Pazarcık and Elbistan districts of Kahramanmaraş, Türkiye, causing widespread damage in eleven cities and affecting approximately 15 million people. The earthquakes severely damaged more than 230,000 buildings, including historical structures (Özmen et al., 2024; İnce, 2024; Atar et al., 2024). Mosques are particularly vulnerable to earthquakes due to their structural characteristics, such as slender minarets and massive masonry walls (Eronat et al., 2024). Protecting these unique and irreplaceable buildings and other structures for future generations is a key responsibility. In this context, numerical studies play an important role in the preservation, maintenance, and rehabilitation of historical structures.

Historical mosques are among the most important religious monuments in the world's cultural and architectural heritage. Over time, these structures are subject to various forms of deterioration due to natural disasters, strong ground movements, aging of materials, and adverse environmental conditions. These factors often lead to structural deficiencies that eventually cause partial or total collapse. Protecting these unique and irreplaceable buildings for future generations is a key responsibility. In this context, numerical studies play an important role in preserving, maintaining, and rehabilitating historical structures (Bayraktar et al. 2018). Türkiye is home to many historic mosques, many of which are located in seismically active regions. These structures typically consist of massive masonry walls, central domes, semi-domes, and slender minarets that form an integrated architectural system. The domes are typically constructed of materials such as brick, timber, or stone bonded with mortar, and the minarets - tall and slender masonry towers - are particularly vulnerable during seismic events due to their geometric slenderness and height. One of the primary objectives of structural engineering is to understand and evaluate the behavior of historic mosques under different loading conditions. There has been a growing interest in such structures conservation and seismic assessment in recent years, with numerous numerical studies focusing on

*Corresponding author, E-mail: oftas@firat.edu.tr

https://doi.org/10.31462/icearc2025_ce_eqe_137

their dynamic characteristics and potential vulnerabilities. The literature provides various examples of structural assessments of historic mosques and their minarets, emphasizing the importance of preserving these heritage assets architectural and structural integrity (Lourenço et al., 1995; Mangia et al., 2016; Karaton & Aksoy, 2018). Sezen et al. After the 1999 earthquakes in Düzce and Kocaeli, the damage and vulnerability of 64 reinforced concrete and masonry minarets were assessed (Sezen et al. 2008). Altunışık investigated the dynamic behaviour of a masonry minaret before and after strengthening with FRP (fibre reinforced polymer) composite. For this aim, the 1992 Erzincan earthquake was used to analyse and investigate the analytical model of the minaret. (Altunışık 2011). Yurdakul et al. conducted a study to investigate the seismic performance of a historic minaret in Bayburt, Türkiye. Three acceleration records (1992 Erzincan, 1999 Kocaeli-Duzce and 2011 Van-Ercis) were used to evaluate the seismic behaviour of the historic minaret (Yurdakul et al. 2021). Çubuk et al. focus on the seismic evaluation of the historical Murat Bey Bridge in Kütahya, which was built in 1460. The bridge was evaluated using numerical methods and time-history analysis. The highest displacement and stress values were obtained from the acceleration records of the 2011 Van earthquake, which were used to evaluate the dynamic behaviour of the bridge (Çubuk et al.2022). Taş et al. aimed to determine the seismic assessment of the historical Nebi Mosque (Taş et al., 2024).

This research aims to evaluate the seismic characterization of the historic minaret of the Nebi Mosque. In order to achieve this objective, a finite element model and seismic analysis of the minaret were carried out using ANSYS finite element software with macro modeling methodology. The nonlinear time history analysis technique was applied to the minaret using the recordings of the 2023 Pazarcık-Kahramanmaraş earthquake (M_w = 7.7). The dynamic behavior of the minaret was evaluated. The maximum tensile and compressive stresses within the minaret were identified, and the potential location of initial damage was investigated.

2. The minaret of the Nebi Mosque

The Nebi Mosque is one of the oldest and most remarkable mosques in the Mesopotamian region still in active use in Diyarbakır, a city in southeastern Türkiye (Fig. 1). Constructed during the Akkoyunlu period in the early 15th century, the architect of the mosque remains unknown (Diyarbakır Provincial Directorate of Culture and Tourism, 2025). The minaret of the Nebi Mosque is located in the northeastern part of the structure.

Fig. 1. Location map of Nebi Mosque and minaret location map of Nebi Mosque and minaret (Google Maps)

The historic minaret and mosque were built using basalt stone and mortar for the walls, while the vault, dome, and arches of the Nebi Mosque were built using stone and brick. Stone was used as the primary building material in the construction of the Nebi Mosque. The properties of the structural masonry and mortar used in the mosque were evaluated. The mechanical properties of these materials, such as Young's modulus (E=25000 MPa), Poisson's ratio (v=0.2), and material density (p=1600 kg/m^3), were taken into account for the seismic analyses. The north and south views of the mosque are shown in Fig. 2 and Fig. 3, respectively. A plan view of the mosque is also shown in Fig. 4. The minaret has a square prismatic shaft, which is alternately clad with black and white basalt stones up to the balcony. Above the balcony, a cylindrical shaft has been added.

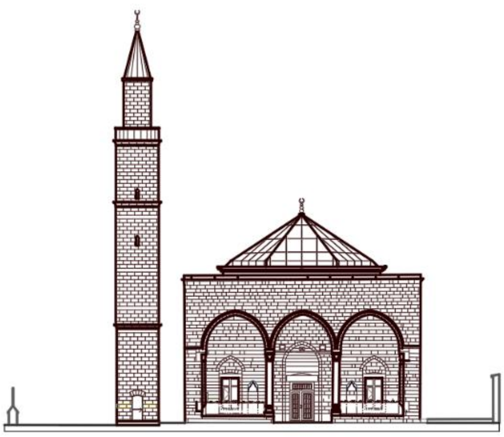

Fig. 2. North view of Nebi Mosque and Minaret

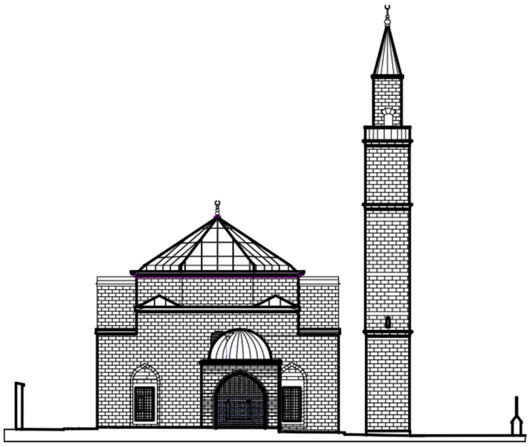

Fig. 3. South view of Nebi Mosque and Minaret

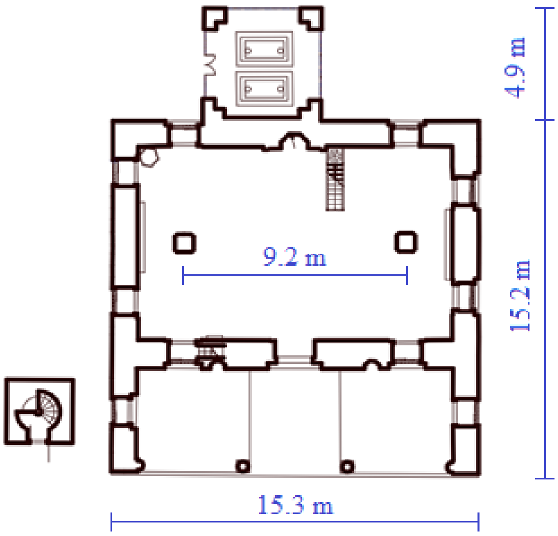

Fig. 4. Plan view of Nebi Mosque and Minaret (Taş et al., 2024)

3. Finite element modelling and analysis

Studying the structural behavior of historical structures using analytical methods requires many assumptions and methods. There are three primary modeling techniques for masonry structures: micro modeling, simplified micro modeling, and macro modeling. The detailed micro-modeling approach represents brick and mortar as separate materials. For the finite element modeling of the mosque minaret, the SOLID65 element, a three-dimensional solid element available in the ANSYS software (Fig. 5), was used (ANSYS, 2015). The SOLID65 element consists of eight nodes with three degrees of translational freedom. This element can be used for linear and non-linear static and dynamic structural analyses. The three-dimensional (3D) solid model of the minaret is shown in Fig. 6.

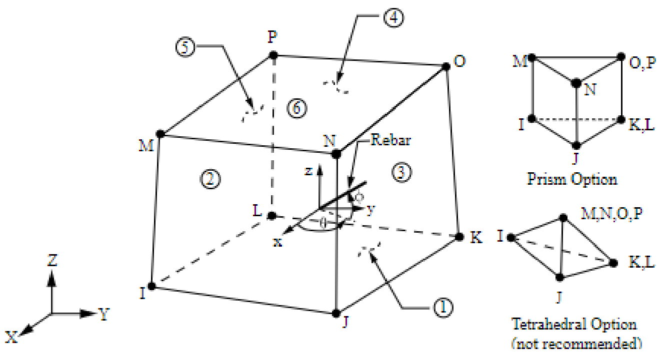

Fig. 5. Geometry of SOLID65 element (ANSYS, 2015)

Fig. 6. a) Three-dimensional geometric representation, b) finite element mesh, and c) internal staircase model of the Nebi Mosque Minaret

According to the literature review, the macro modeling technique is more advantageous for large-scale structural models because of the results' low computational effort and accuracy. It has been used in many studies (Carpinteri, Invernizzi, & Lacidogna, 2005; Sayın, 2016; Erdil, Tapan, Akkaya, & Korkut, 2018). In this study, the macro modeling technique was selected to model the historical minaret. Three-dimensional geometric representation, finite element mesh, and internal staircase model of the Nebi Mosque Minaret are shown in Fig. 6. A 3D finite element model of the minaret was created using the ANSYS finite element software, which included 81,949 nodes and 449,845 elements. All degrees of freedom were also assumed to be fixed at the foundation level.

4. Modal analysis

A modal analysis was conducted to comprehensively understand the dynamic behavior of the minaret and to identify its principal vibration modes, the corresponding mass participation ratios, and the associated periods. This study selected the macro modeling technique to model the minaret. Modal analysis of the minaret's first three mode shapes and their frequencies is shown in Figure 7. The first 20 frequencies of the minaret of the Nebi Mosque are shown in Table 1. A 3D finite element model of the mosque was created using the ANSYS finite element software, which included 26680 nodes and 116445 elements in the three-dimensional finite element model of the Nebi Mosque. All degrees of freedom were also assumed to be fixed at the foundation level.

Table 1. Modes and frequencies of the Nebi Mosque Minaret

Mode no	Frequency (Hz)	Mode no	Frequency (Hz)
1	1.62	11	28.25
2	1.65	12	33.44
3	7.90	13	38.26
4	7.94	14	38.58
5	9.56	15	44.13
6	13.16	16	45.20
7	13.26	17	46.50
8	16.02	18	47.55
9	23.43	19	47.72
10	24.04	20	50.45

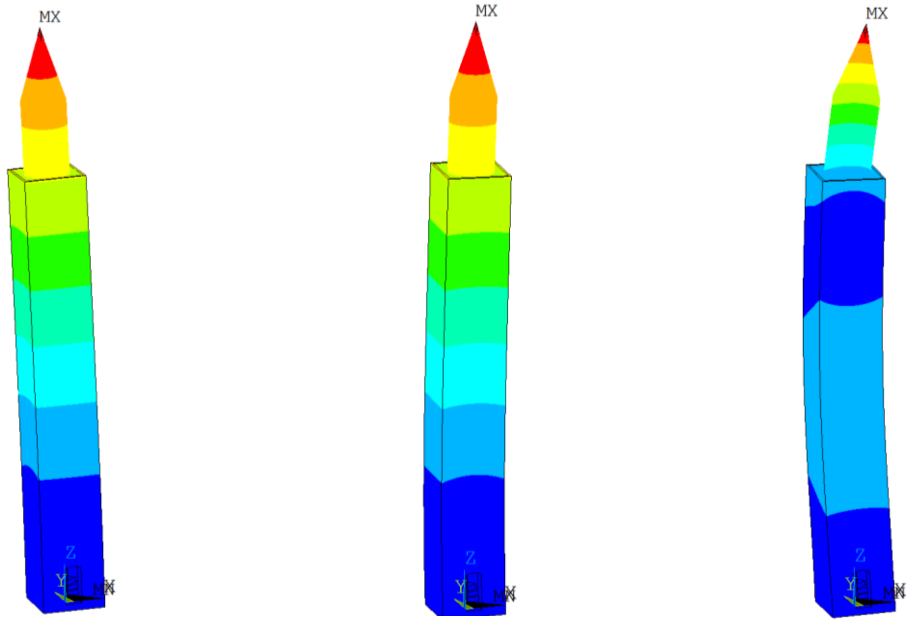

a) Mode 1 (f_1= 1.62 Hz) b) Mode 2 (f_2= 1.65 Hz) c) Mode 3 (f_3= 7.90 Hz)

Fig.7. Modal analysis of the Nebi Mosque Minaret: First three mode shapes and their frequencies

5. Linear dynamic time history analysis

In this study, the acceleration records of the 6 February 2023 Pazarcık-Kahramanmaraş earthquake (Mw=7.7) were used for dynamic analyses to evaluate the seismic performance of the minaret. The most effective 20 seconds of the earthquake were used for time-history analyses of the minaret (Fig. 8 - Fig. 9). In the dynamic analyses, the north-south (N-S) and east-west (E-W) acceleration records of the earthquake were applied to the x and y directions of the minaret, respectively. The principal tensile and principal compressive stresses obtained from the time history analyses are shown in Fig. 10. The time-displacement graphs of the top point of the minaret are also presented in Fig. 11 and Fig. 12.

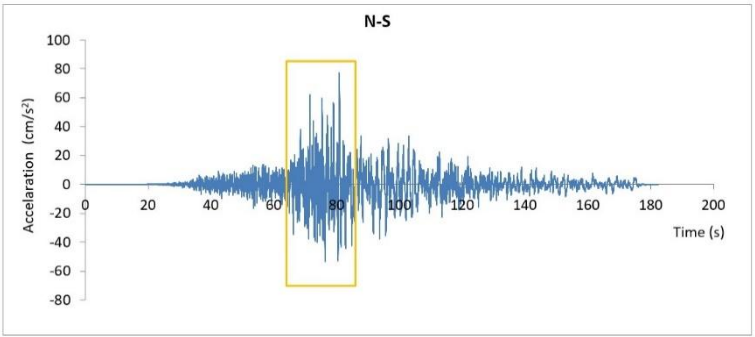

Fig. 8. Pazarcık-Kahramanmaraş North-South component (acceleration station 2101)

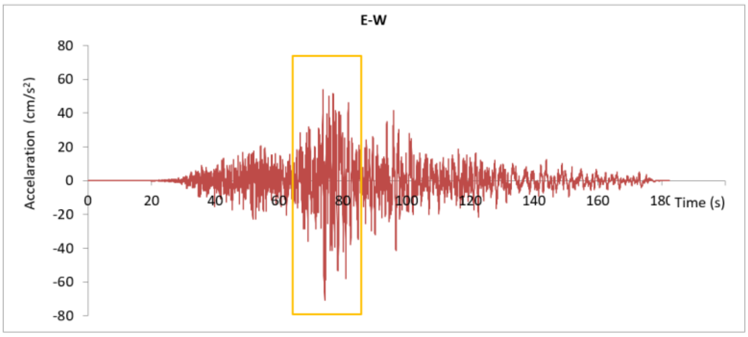

Fig. 9. Pazarcık-Kahramanmaraş North-South component (acceleration station 2101)

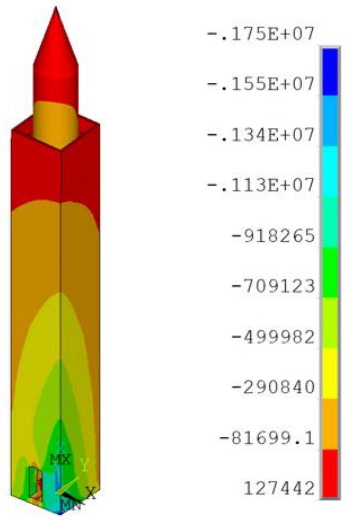

a) Principal compressive stresses (kg/m^2)

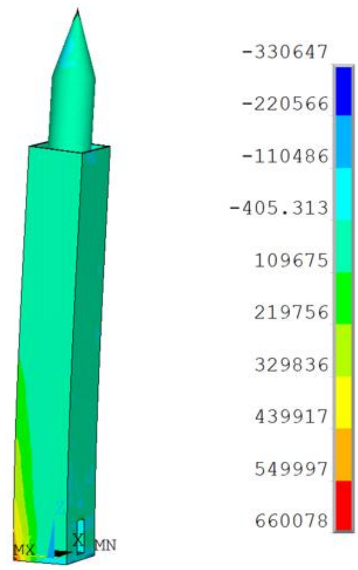

b) Principal tensile stresses (kg/m^2)

Fig. 10. Principal tensile stresses and principal compressive stresses (kg/m^2)

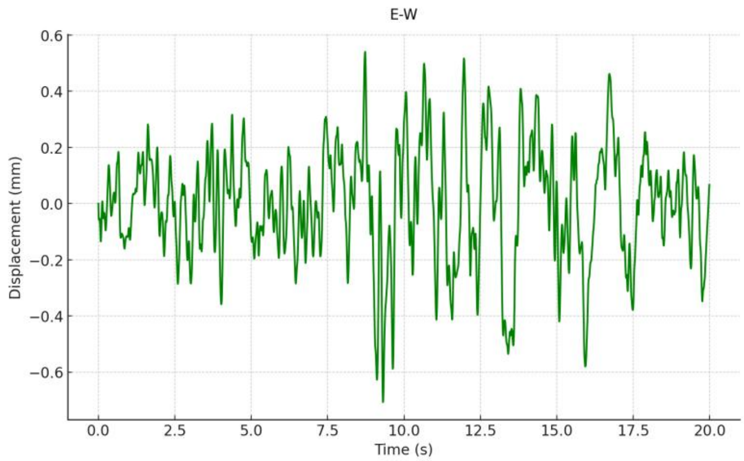

Fig. 11. Time-displacement graphs of the top point of the Nebi Mosque Minaret for E-W direction

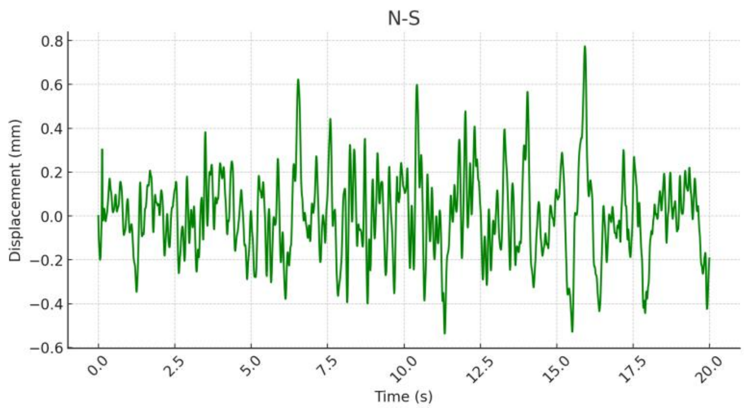

Fig. 12. Time-displacement graphs of the top point of the Nebi Mosque Minaret for N-S direction

Conclusions

This study aims to determine the seismic assessment of the historical minaret of Nebi Mosque. For this objective, a finite element model and seismic analysis of the minaret were executed utilizing the ANSYS finite element software with macro modeling methodology. A linear time history analysis method was employed for the minaret, and the 2023 Pazarcık-Kahramanmaraş earthquake records (M_w = 7.7) were selected. The dynamic response of the minaret was evaluated. The maximum tensile and compressive stresses that developed in the structure were assessed, and potential areas for initial damage were investigated.

- When the analysis results are examined, it is observed that compressive and tensile stresses are concentrated in the bottom parts of the minaret.
- Although the structural system of the minaret is predominantly subjected to compressive forces, the base regions where tensile stresses occur are critical in terms of structural damage risk.
- It is planned to make experimental measurements of the minaret in future studies. Experimental and numerical results will be compared.
- In this study, linear analysis of the minaret was performed. In future studies, it is aimed to determine the damage formation and progression with non-linear analysis.

References

Altunışık, A. C. (2011). Dynamic response of masonry minarets strengthened with fiber reinforced polymer (FRP) composites. *Natural Hazards and Earth System Sciences, 11*(7), 2011–2019.

ANSYS Finite Element Software. (2015). *Swanson Analysis Systems Inc.* https://www.ansys.com/

Atar, M., İnce, O., Taş, Ö. F., Özmen, A., & Sayın, E. (2024). 6 Şubat 2023 Kahramanmaraş depremleri sonrası Malatya ilinde bulunan betonarme binaların ve çelik yapıların hasar durumlarının incelenmesi. *Türk Deprem Araştırma Dergisi, 6*(1), 60–80. https://doi.org/10.46464/tdad.1394039

Bayraktar, A., Hökelekli, E., Türker, T., Çalık, I., Ashour, A., & Mosallam, A. (2018). Window opening effects on structural behavior of historical masonry Fatih Mosque. *International Journal of Architectural Heritage, 13*(4), 585–599. https://doi.org/10.1080/15583058.2018.1447617

Carpinteri, A., Invernizzi, S., & Lacidogna, G. (2005). In situ damage assessment and nonlinear modelling of a historical masonry tower. *Engineering Structures, 27*(3), 387–395. https://doi.org/10.1016/j.engstruct.2004.11.001

Çubuk, E. G., Sayın, E., & Özmen, A. (2022). Dynamic analysis of historical masonry arch bridges under different earthquakes: The case of Murat Bey Bridge. *Turkish Journal of Science and Technology, 17*, 461–473. https://doi.org/10.55525/tjst.1105998

Diyarbakır Provincial Directorate of Culture and Tourism of Republic of Turkey Ministry of Culture and Tourism. (2024). *Nebi Cami*. https://www.diyarbakirkulturturizm.org/Yapit/Details/CAMILER/16/Nebi-Cami/155

Erdil, B., Tapan, M., Akkaya, İ., & Korkut, F. (2018). Effects of structural parameters on seismic behaviour of historical masonry minaret. *Periodica Polytechnica Civil Engineering, 62*(1), 148–161. https://doi.org/10.3311/PPci.10687

Eronat, Ş. S., Sayın, E., & Özmen, A. (2024). Seismic assessment of masonry minarets under different earthquakes. *Turkish Journal of Science and Technology, 19*(2), 427–442. https://doi.org/10.55525/tjst.1466307

Google. (n.d.). *Nebi Mosque and Minaret location map*. Google Maps. Retrieved April 25, 2025, from https://www.google.com/maps

İnce, O. (2024). Structural damage assessment of reinforced concrete buildings in Adıyaman after Kahramanmaraş (Türkiye) earthquakes on 6 February 2023. *Engineering Failure Analysis, 156*, 107799. https://doi.org/10.1016/j.engfailanal.2023.107799

Karaton, M., & Aksoy, H. S. (2018). Seismic damage assessment of an 891 years old historic masonry mosque. *Periodica Polytechnica Civil Engineering, 62*(1), 126–135. https://doi.org/10.3311/PPci.10270

Lourenço, P. B., Rots, J. G., & Blaauwendraad, J. (1995). Two approaches for the analysis of masonry structures: Micro and macro-modeling. *Heron, 40*(4), 313–340.

Mangia, L., Ghiassi, B., Sayın, E., Onat, O., & Lourenço, P. B. (2016). Pushover analysis of historical Elti Hatun mosque. In *Proceedings of the 12th International Conference on Advances in Civil Engineering (ACE)* (pp. 21–23). Sivas, Turkey.

Özmen, A., İnce, O., Taş, Ö. F., Atar, M., Ozbulut, O. E., & Sayın, E. (2024). Seismic performance assessment of structures in Malatya Province after 6 February 2023 Turkey earthquake sequences. *Natural Hazards*, 1–34. https://doi.org/10.1007/s11069-024-07017-x

Sayın, E. (2016). Nonlinear seismic response of a masonry arch bridge. *Earthquakes and Structures, 10*(2), 483–494. https://doi.org/10.12989/eas.2016.10.2.483

Sezen, H., Acar, R., Doğangün, A., & Livaoğlu, R. (2008). Dynamic analysis and seismic performance of reinforced concrete minarets. *Engineering Structures, 30*(8), 2253–2264. https://doi.org/10.1016/j.engstruct.2007.09.004

Taş, Ö. F., İnce, O., & Sayın, E. (2024). Seismic assessment of the historical Nebi Mosque. In *Proceedings of the 5th International Conference on Innovative Academic Studies (ICIAs)* (pp. 359–366).

Yurdakul, M., Yılmaz, F., Artar, M., Can, Ö., Öner, E., & Daloğlu, A. T. (2021). Investigation of time-history response of a historical masonry minaret under seismic loads. *Structures, 30*, 265–276. https://doi.org/10.1016/j.istruc.2020.11.037

Dynamic vibration control through tuned liquid damper under different excitation angle: shaking table tests study

Brahım A. Idriss*[1], Murat Günaydın[1], Fezayil Sunca[1], Fatih Y. Okur[1], Cihat Şahin [1], Algıhan K. Karahasan [2], Ahmet C. Altunışık[1], Yunus E. Akbulut[1]

[1] Istanbul Technical University, Graduate School, Civil Engineering Department, 34469, Istanbul, Turkiye
[2] Avrasya University, Department of Civil Engineering, 61080 Trabzon, Türkiye

Abstract. This study investigates the performance of a building model equipped with a tuned liquid damper through a series of shaking table tests under varying excitation directions. To assess directional effects, the model was rotated in 15-degree increments from 0° to 180°, while the excitation direction remained fixed. Acceleration and displacement time histories were recorded for each orientation to evaluate the damper's effectiveness. The results demonstrate that the TLD effectively reduced both accelerations and displacements of the structure. However, its efficiency declined progressively as the excitation angle increased from 0° to 90°.

Keywords: Different excitation direction; Shake table test; Tuned liquid damper; Vibration control

1. Introduction

Tuned Liquid Dampers (TLDs) are passive control devices widely used in structural and mechanical engineering to mitigate vibrations and enhance the dynamic performance of structures. These systems typically consist of a fluid-filled container and a tuned mass connected to the structure through a spring mechanism. The fluid provides damping through motion or viscosity, while the mass-spring assembly introduces stiffness, allowing the system to be tuned to specific frequencies. By carefully adjusting these parameters, TLDs can effectively reduce structural responses to dynamic loads such as wind or seismic activity. Two primary types of TLDs are commonly employed in buildings: sloshing TLDs, which dissipate energy through fluid motion, and viscous TLDs, which rely on the fluid's viscosity for damping. Depending on design considerations such as fluid depth, container geometry, and function, TLD systems are further categorized into Tuned Liquid Dampers (TLD or TSD-rectangular section), Tuned Liquid Column Dampers (TLCD), Hybrid TLCDs (HTLCD), and Double TLCDs (DTLCD), each offering unique performance characteristics for vibration control.

TLDs offer several notable advantages over other passive damping systems, making them an attractive solution for structural vibration control. Their design is inherently simple, involving no complex mechanical components, which contributes to lower installation and maintenance costs. Furthermore, TLDs are highly adaptable and can be tuned to target a broad spectrum of frequencies, allowing them to perform effectively under various dynamic loading conditions. This versatility makes them suitable for a wide range of applications, including tall buildings, long-span bridges, and offshore structures exposed to wind, wave, or seismic forces. Despite these strengths, the performance of TLDs can be limited in environments characterized by extremely large-amplitude vibrations, where nonlinear effects may reduce damping efficiency. Additionally, in regions with low seismic or dynamic excitation, the benefits of TLDs may be marginal, potentially making them less justifiable compared to other control systems. Nonetheless, their cost-effectiveness, simplicity, and adaptability continue to make TLDs a valuable option in modern structural engineering.

The concept of using fluid-based systems for structural vibration control dates back to the mid-20th century. One of the earliest theoretical foundations was laid by Housner (1954), who explored the influence of earthquake incidence angles on structural seismic response-paving the way for passive control systems such as TLDs. During the late 1950s to early 1970s, researchers began to systematically investigate the use of liquid-filled containers as damping devices to mitigate vibrations in buildings and other structures. Significant advancements occurred in the late 1980s (Miyata et al.,1989; Sakai & Takeda 1989; Sakai et al., 1989; Sun et al.,1989). In the mid-1990s, numerical analysis became prominent (Zhao & Fujino, 1993; Balendra et al.,1995). Subsequent studies further explored adjustable and tunable fluid damping systems. Researchers such as Sun et al.,1992; Gao et al., 1997; and others (Reed et al., 1998; Kanok-Nukulchai & Tam, 1999; Yamamoto & Kawahara, 1999; Yu et al., 1999; Jin et

*Corresponding author, E-mail: idrissfils88@yahoo.fr

https://doi.org/10.31462/icearc2025_ce_eqe_164

al., 2007; Tait, 2008; Colwell & Base, 2009; Tait & Deng, 2010; Behbahani et al., 2016; Sonmez, 2016; Altunışık et al., 2018) expanded the application scope and refined the analytical models of fluid-based dampers. Konar & (Dey) Ghosh (2023) have contributed significantly to the field of structural vibration control by reviewing the performance and development of TLDs. Their studies emphasize the dynamic behavior of TLDs under various excitations, such as wind and seismic loads, and critically analyze the evolution of TLD design, including sloshing mechanisms, hybrid configurations, and optimization techniques for improved efficiency. Similarly, Greciano et. al., (2024) have conducted an in-depth review focused on the integration of passive control systems like TLDs in civil structures. Their work highlights recent experimental advances, modeling techniques, and practical implementation in tall buildings and bridges, with special attention to sustainability and adaptive damping strategies. Collectively, these authors offer a valuable synthesis of current trends and future challenges in the application of TLDs for structural vibration mitigation.

Although extensive research has been conducted on TLDs for mitigating structural vibrations under dynamic loads, studies focusing on their performance under seismic excitations occurring at varying angles of incidence remain limited. Most existing works consider idealized or unidirectional loading conditions, which may not accurately reflect the complex nature of real earthquake events. To address this gap, the present study experimentally investigates the effectiveness of TLDs in controlling structural responses when buildings are subjected to earthquakes impacting from different directions. The findings aim to enhance the understanding of TLD behavior under multi-directional seismic inputs and contribute valuable insights to the existing body of literature on passive vibration control.

2. Building model and design of TLD

A single span three-story steel building model (0.90 x0.90 x 3.0 m, width x depth x height) was built in the laboratory to simulate a dynamic response of a building (Fig. 1). The wight of the model was 172 kg. The model building is designed to represent the behaviour of a mid-rise or relatively high-rise building. This was effective in selecting the dimensions of the carrier elements. The model structure includes columns with dimensions of 20 × 20 × 1.5 mm, beams with a diameter of 8 mm (Ø8). The floor slab and base slab was constructed with 900 × 900 × 25 mm steel plate. To simulate the effect of an earthquake from different angles, the model was mounted on a steel plate with holes drilled at 15-degree intervals. The model was also fixed to uniaxial shaking table using these holes (Fig. 2). In this way, the building was rotated to angles of 0°, 15°, 30°, 45°, 60°, 75°, 90°, 105°, 120°, 135°, 150°, and 165°.

Fig. 1. Building model constructed in the laboratory

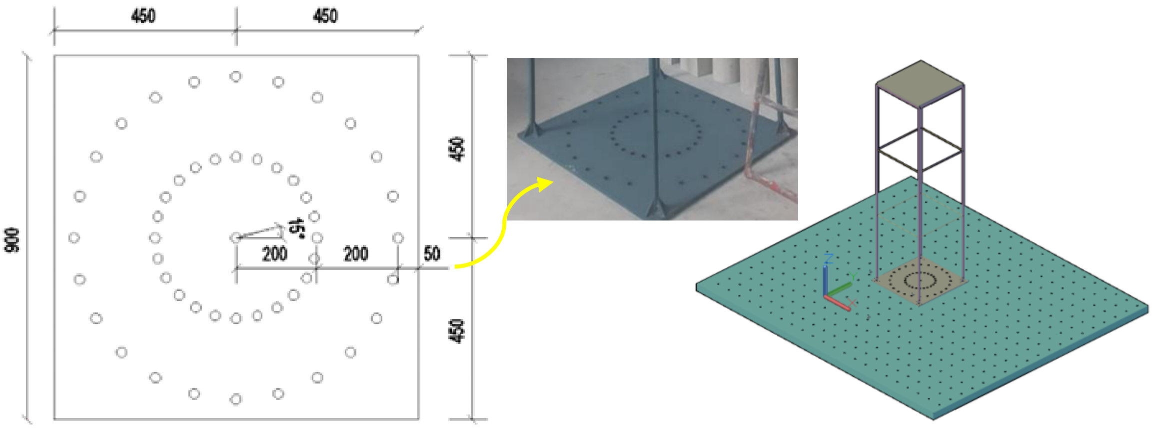

Fig. 2. Base plate with holes drilled at 15-degree intervals and a representative photo of the model on the shaking table

The dynamic characteristics of the building (mode shapes and natural frequencies) were obtained both numerical and experimental. A Finite Element (FE) model of the building was constituted using SAP2000 software (SAP2000, 2015). The experimental dynamic characteristics was detailed using ambient vibration test method. During the test, a B&K 3560 data acquisition system with 17 channels and B&K 4506 type, 9 uni-axial accelerometers having 0.5V/g sensitivity, uni-axial signal cables, PULSE and OMA software were used as the test equipment. Enhanced Frequency Domain Decomposition (EFDD) was employed to extract the dynamic characteristics Fig. 3 shows FE model, the accelerometer layout on the OMA model of the building and Singular Values of Spectral Density Matrices (SVSDM) of the dataset. Fig. 4 present the numerical and experimental mode shapes and corresponding natural frequency values. The mode shapes obtained for both cases included translational and torsional modes. The first three natural frequencies were calculated as 0.59 Hz, 0.59 Hz, and 1.41 Hz for the numerical model, and 0.52 Hz, 0.54 Hz, and 1.35 Hz for the experimental model. These results indicate that the natural frequencies of the numerical and experimental models are in close agreement. It should be noted that the first natural frequency of the building was used in the design of the TLD.

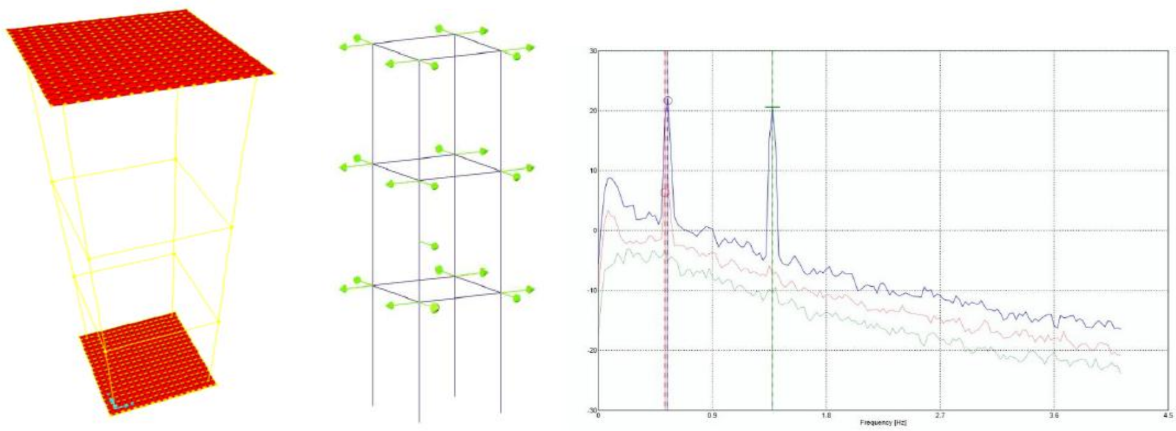

Fig. 3. FE model and OMA model of the building with the SVSDM of the dataset

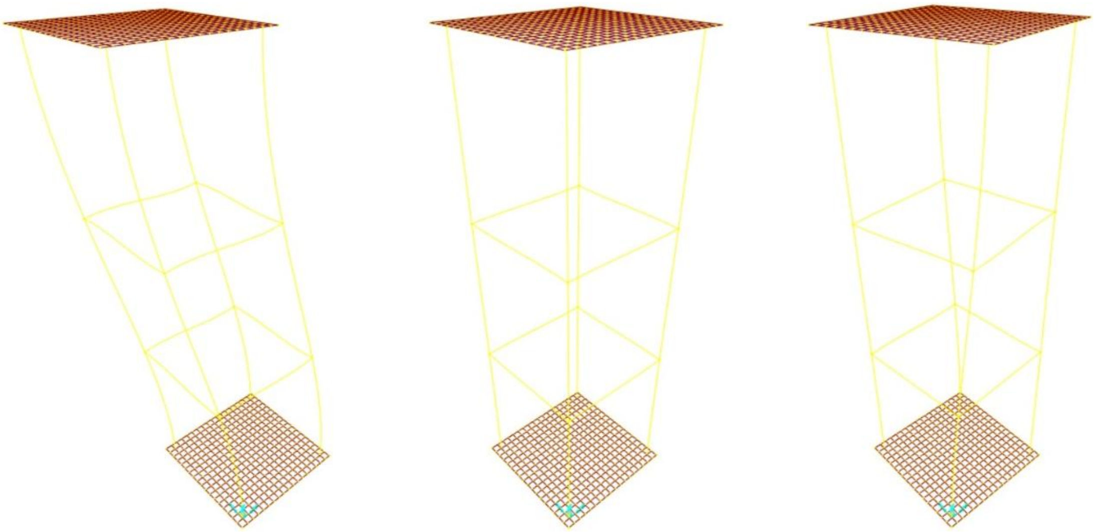

f_1=0.59Hz f_2=0.59Hz f_3=1.41Hz

(a)

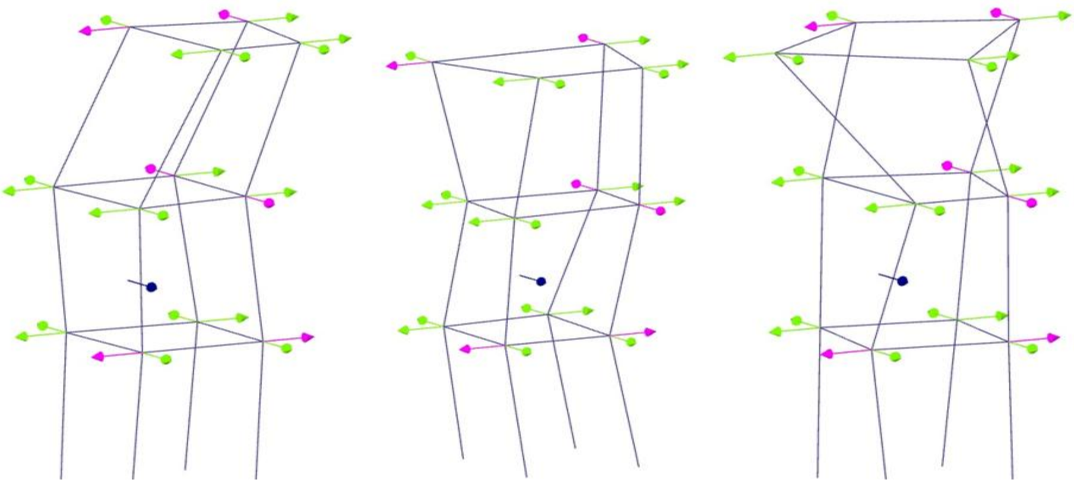

f_1=0.52Hz f_2=0.54Hz f_3=1.35Hz

(b)

Fig. 4. Numerical (a) and experimental (b) mode shapes and corresponding natural frequencies

According to linear wave theory (Lamb, 1932), the fundamental natural frequency of liquid sloshing motion, f_w is given by:

$$f_w = \frac{1}{2\pi}\sqrt{\frac{\pi \times g}{L} tanh(\frac{\pi \times h}{L})} \tag{1}$$

where g is the acceleration due to gravity, L is the length of the tank, h is the depth of the liquid.

During the TLD design process, the sloshing frequency *fw* (sloshing frequency was set equal to the first natural frequency of the building.

$$f_w = \frac{1}{2\pi}\sqrt{\frac{\pi \times g}{L} tanh(\frac{\pi \times h}{L})} = 0{,}59 = f_s \tag{2}$$

In the TLD design, the ratio of water depth to tank length (h/L was taken as 0.1, which is within the typical range of 0.1 to 5 for TLD applications. Based on this ratio and a tank length (L) of 0.67m, and the water depth (h) was calculated as 0.067m (Fig.5). The required liquid mass was calculated as 13.47 kg, based on an 8% mass ratio (range between 1% and 10%) relative to the total structural mass. The tank was constructed using 2.0mm thick plexiglass sheets (Fig. 6).

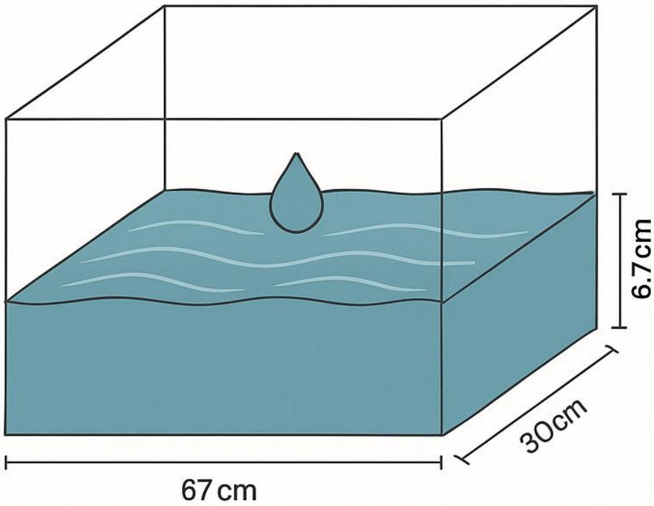

Fig. 5. Dimension of the TLD tank for the building

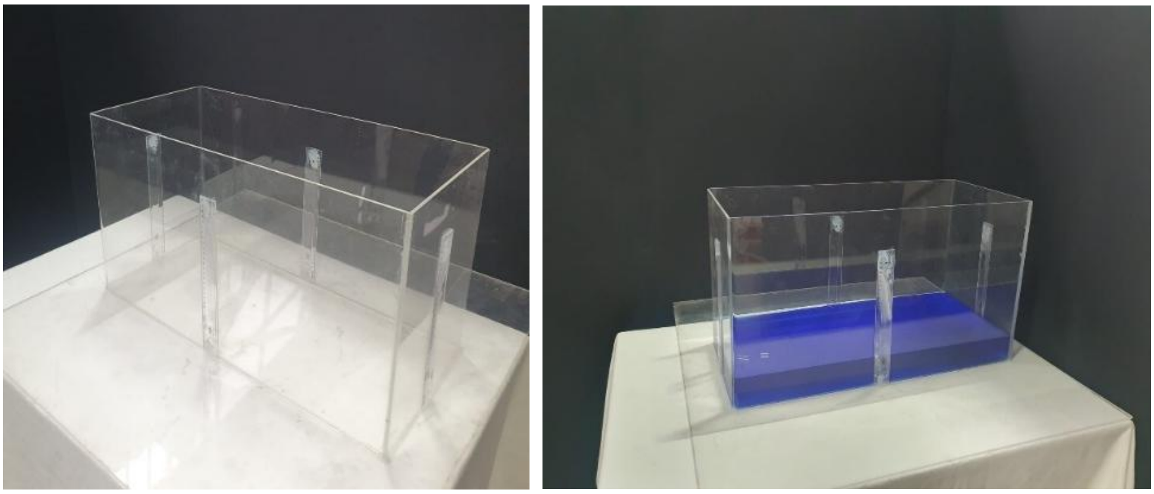

Fig. 6. Views of the TLD constructed using plexiglass.

3. Shaking table tests

A uniaxial shaking table (4.0m by 4.0m, 30tons capacity with accelerations up to 2g) was used to obtain seismic excitations. Three sinusoidal waves with amplitudes of 3mm, 6mm and 9mm each consisting of 5 cycles (Fig. 7), were selected as seismic excitations. During the shaking table tests (Fig. 8), the building was instrumented with four accelerometers in both the X and Y directions-two placed at the base and two at the top of the structure-to measure its dynamic response. To assess the effectiveness of the TLD at various orientations, the model structure was rotated to angles of 0°, 15°, 30°, 45°, 60°, 75°, 90°, 105°, 120°, 135°, 150°, and 165°, and tested on a shake table under three different dynamic excitation scenarios. For each configuration, acceleration responses were recorded at both the base and the top of the building. To analyze the structural response under varying seismic orientations, the acceleration input for each test was resolved into components along the X and Y axes using trigonometric transformations. At each rotation angle of the structure (ranging from 0° to 165° at 15° intervals), the effective acceleration in the direction of shaking was computed using the formula, as can be seen in Fig. 9.

Fig. 7. Shaking table tests of building with and without of TLD

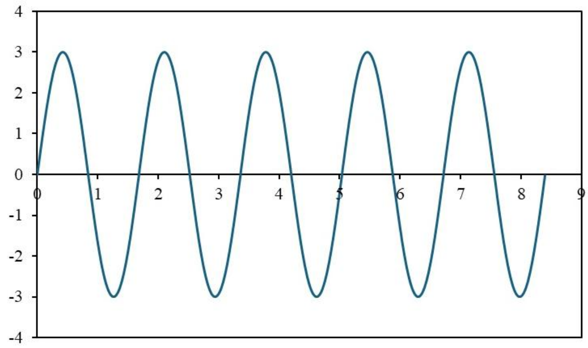

(a)

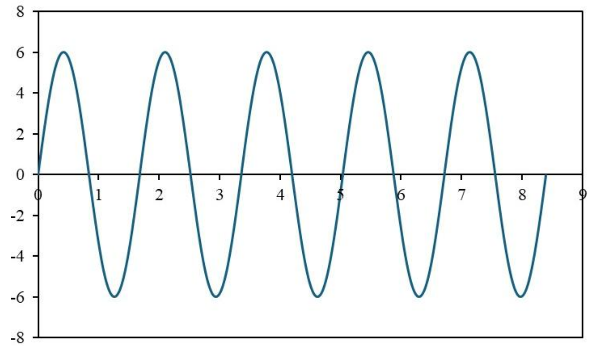

(b)

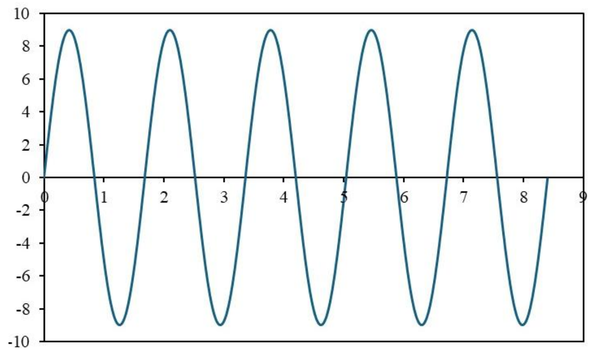

(c)

Fig. 8. Excitations for shaking table tests: (a) 3mm amplitude, (b) 6mm amplitude and (c) 9mm amplitude

golden light publishing®

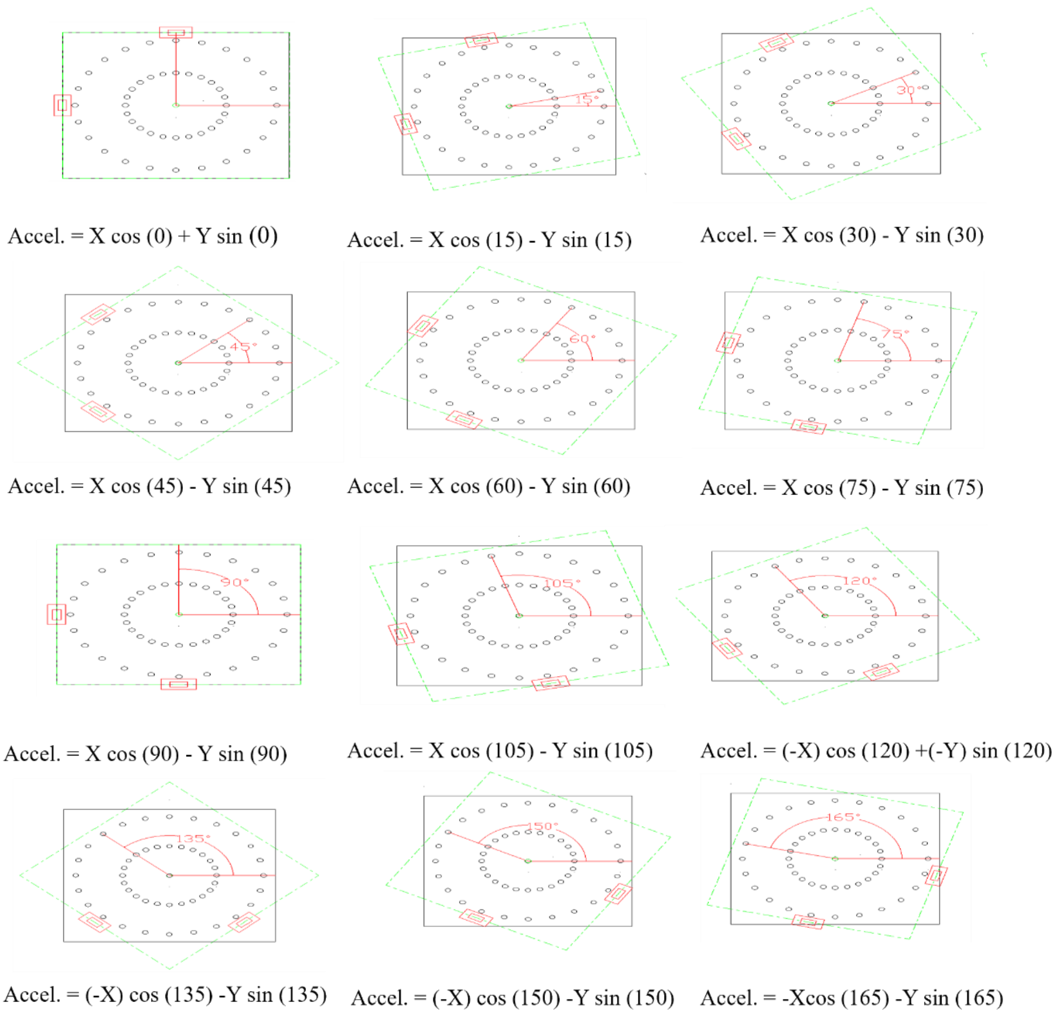

Fig. 9. Acceleration transformation for different structure orientations at 15° intervals.

4. Results and discussion

This section presents the acceleration values measured at the top of the building, both with and without the TLD system, for each excitation angle. The acceleration time histories recorded at the top of the structure under various excitation angles (ranging from 0° to 165° at 15° intervals) are presented for three different dynamic input scenarios (Fig.10). It should be noted that when the TLD is positioned at 0 degrees, the direction of earthquake excitation aligns with the natural sloshing direction of the water. In each case, comparisons are made between the responses of the building with and without the TLD system. It is evident from the graphs that the presence of the TLD leads to a noticeable reduction in peak acceleration amplitudes and a faster decay in oscillation amplitude over time. This damping effect is particularly prominent during the initial response period and remains consistent across all orientation angles. The results demonstrate that the TLD is effective in mitigating structural vibrations regardless of the direction of seismic input, confirming its contribution to enhanced dynamic performance and energy dissipation. The effectiveness is more distinguishable in excitation cases with stronger input amplitudes, where the gap between the with-TLD and without-TLD curves becomes more pronounced. In addition, it can be concluded that the TLD remains effective across all excitation angles. However, its efficiency slightly decreases as the excitation angle increases from 0° to 90°, and then gradually improves from 90° to 180°. This behaviour is also illustrated in Fig. 11. As can be seen in Fig. 11a, the displacement responses remain relatively high and consistent across all angles, showing limited variation with changing direction of excitation. Fig. 11b demonstrates that the structure equipped with a TLD exhibits a direction-dependent displacement response. The damping effectiveness decreases as the excitation angle approaches 90°, where the motion is perpendicular to the sloshing direction, and improves again as it approaches 180°. This pattern confirms that the TLD provides maximum efficiency when aligned with the excitation direction, effectively reducing structural displacement through directional energy dissipation.

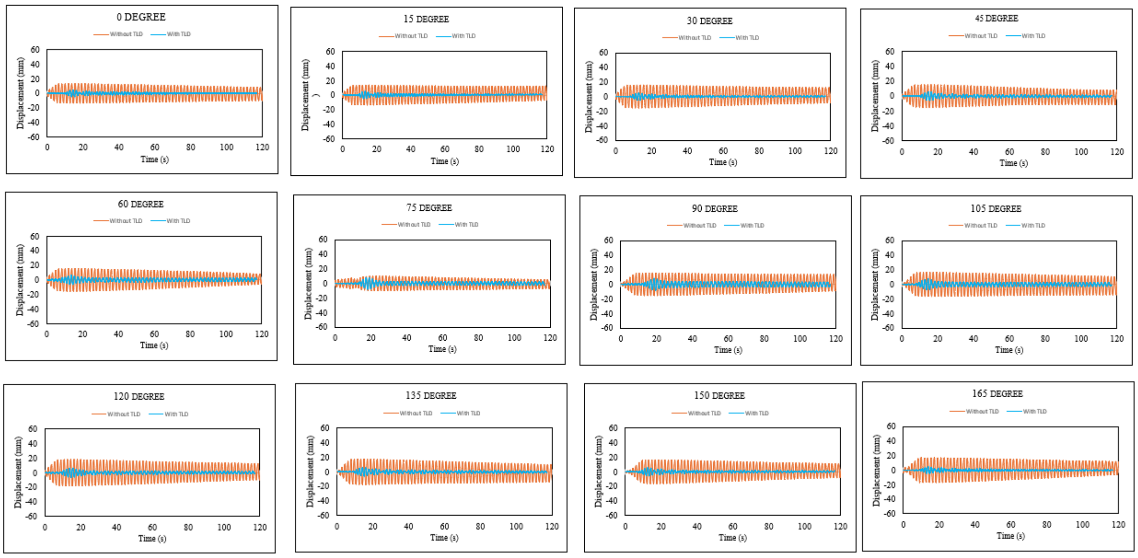

(a)

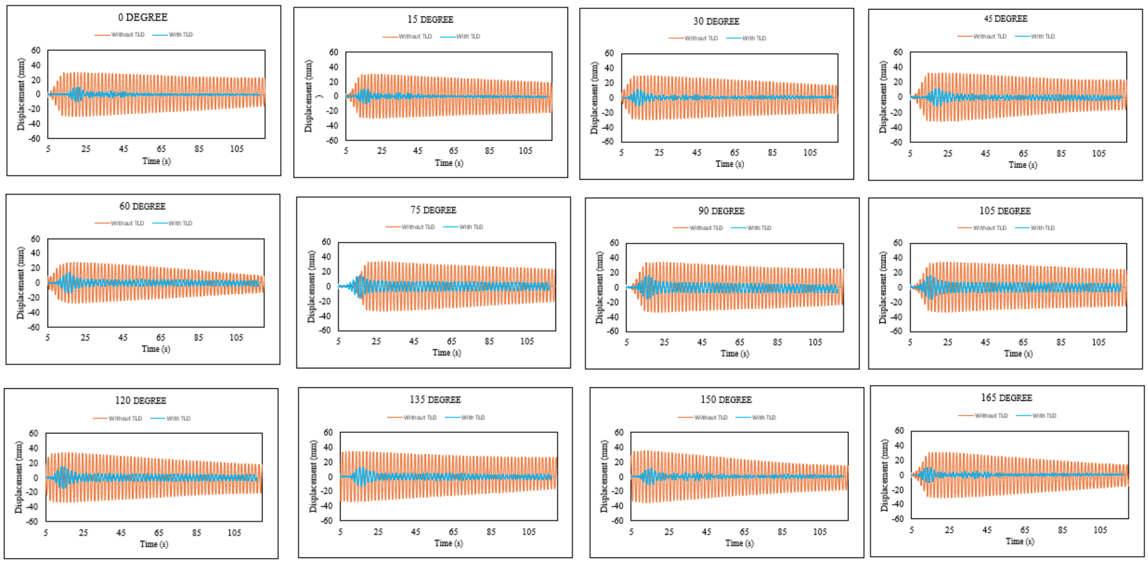

(b)

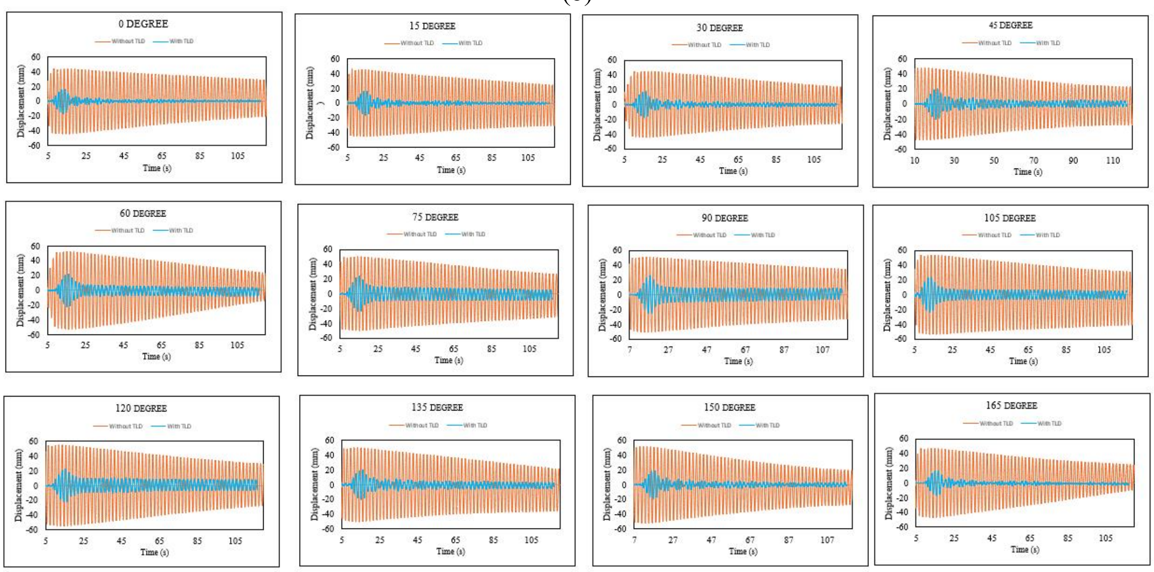

(c)

Fig. 10. Top-story acceleration responses with and without TLD at different excitation angles: (a) 3mm amplitude, (b) 6mm amplitude and (c) 9mm amplitude

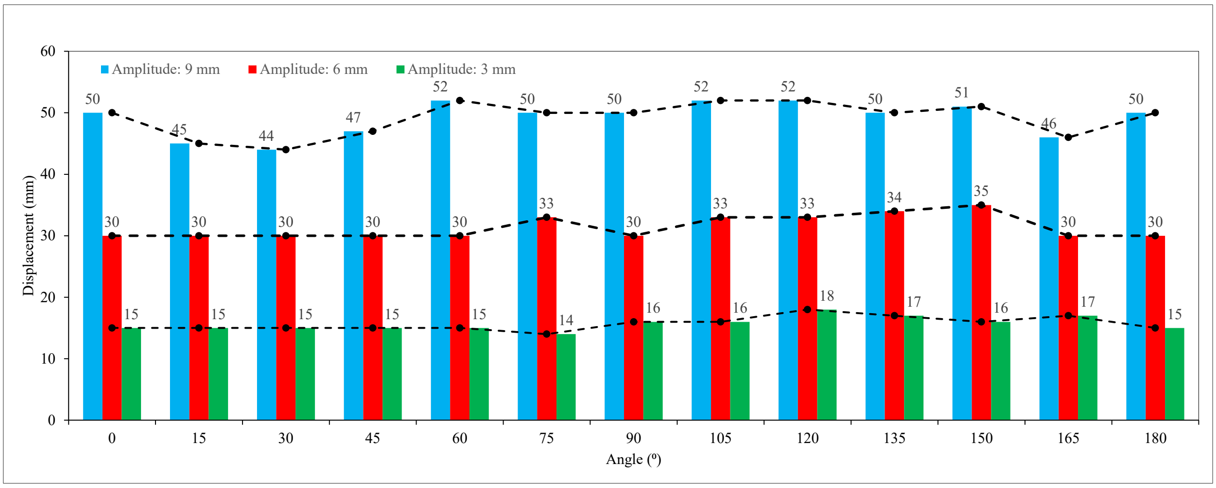

(a)

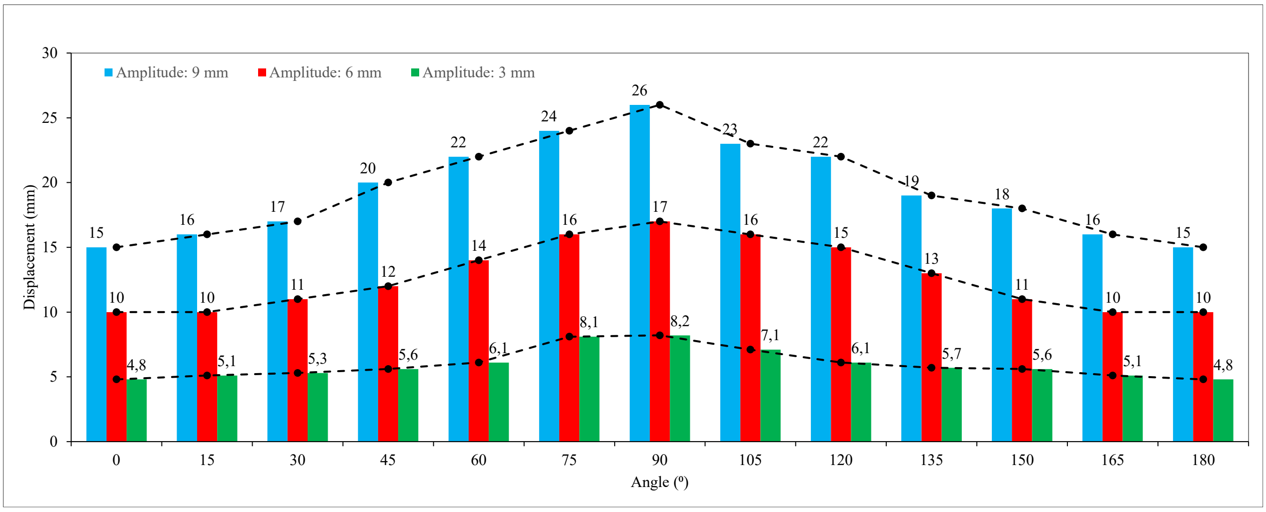

(b)

Fig. 11. Comparison of peak displacement responses of the building: (a) without TLD and (b) with TLD under varying excitation angles and input amplitudes.

5. Conclusion

This study investigated the effectiveness of a Tuned Liquid Damper (TLD) in reducing structural responses under varying excitation angles using shake table experiments. A scaled model structure was tested with and without the TLD at twelve different orientations ranging from 0° to 180°, under three levels of dynamic excitation. Acceleration responses were recorded at both the base and the top of the structure, allowing for a detailed comparison across configurations.

The results clearly demonstrate that the TLD significantly reduces acceleration responses, particularly when the excitation direction aligns with the natural sloshing direction of the liquid (0° and 180°). While the damping performance marginally decreased as the excitation angle approached 90°, it improved again beyond that, confirming the directional dependency of the TLD system. This behavior was consistently observed across different excitation amplitudes and was especially evident in the peak displacement data, where directional effectiveness was most pronounced.

Overall, the findings highlight that even under varying seismic input directions, the TLD maintains its capacity to mitigate structural vibrations, with optimal performance achieved when aligned with the excitation axis. These results affirm the potential of TLDs as a practical and efficient passive control solution for enhancing the seismic resilience of structures.

As a recommendation for future work, the study can be expanded by investigating the performance of alternative TLD configurations, such as multiple tanks with varying orientations or dimensions. Incorporating additional TLDs positioned along different axes may improve damping efficiency across a wider range of excitation angles, thereby enhancing the overall seismic performance of the structure.

Acknowledgments
This study is carried out using a measurement system provided by projects from TUBITAK and Karadeniz Technical University under Research Grant Nos. 106M038, 2005.112.001.1 and 2006.112.001.1, respectively. Shaking table tests carried out using a shake-table provided projects from Karadeniz Technical University under Research Grant No: FAY-2018-7715. Also, the research described in this paper was financially supported by the Karadeniz Technical University under the grant number FBA-2023-11001.

References
Altunışık, A.C., Yetişken, A., Kahya V. (2018) Experimental Study on Control Performance of Tuned Liquid Column Dampers Considering Different Excitation Direction. *Mechanical Systems and Signal Processing* 102:59-71.

Balendra, T., Wang C.M., Cheong H.F. (1995) Effectiveness of Tuned Liquid Column Dampers for Vibration Control of Tower. *Engineering Structure,* 17(9):668-675.

Behbahani, H.P., Adnan, A.bin., Vafaei, M., Shad, H., Pheng, O.P. (2016). Vibration Mitigation of Structures through TLCD with Embedded Baffles, *Exp Tech.,* 41:139–151

Colwell, S., & Basu, B. (2009) Tuned Liquid Column Dampers in Offshore Wind Turbines for Structural Control. *Engineering Structures,* 31(2):358-368

Gao, H., Kwok, K.C.S, & Samali, B. (1997). Optimization of Tuned Liquid Column Dampers. *Engineering Structures* 19(6):476-486.

Housner, G.W (1954). Earthquake Pressures on Fluid Containers. Eight Technical Report under Office of Naval Research, California U.S.A.

Jin, Q., Li, X., Sun, N., Zhou, J., Guan, J. (2007). Experimental and Numerical Study on Tuned Liquid Dampers for Controlling Earthquake Response of Jacket Offshore Platform. *Marine Structures,* 20:238-254.

Kanok-Nukulchai, W., & Tam, B.T. (1999). Structure-Fluid Interaction Model of Tuned Liquid Dampers. *International Journal for Numerical Methods in Engineering*, 46:1541-1558.

Konar, T., & Ghosh, A. (2023). A Review on Various Configurations of the Passive Tuned Liquid Damper. *Journal of Vibration and Control*, 29,9-10, 1945-1980.

Lamb, H. (1932) Hydrodynamics. Cambridge University Press, Cambridge.

Miyata, T., Yamada, H., Saito, Y. (1989). Feasibility Study of the Sloshing Damper System Using Rectangular Containers. *Journal of Structural Engineering*, 35(A):553-560.

OMA (2006). Operational Modal Analysis, Release 4.0. Structural Vibration Solutions A/S, Denmark.

PULSE (2006). Analyzers and Solutions”, Release 11.2. Bruel and Kjaer, Sound and Vibration Measurement A/S, Denmark.

Reed, D., Yu, J., Yeh, H., Gardarsson, S. (1998). Investigation of Tuned Liquid Dampers under Large Amplitude Excitation. *Journal of Engineering Mechanics*, 124(4):405-413.

SAP2000 (2015). Structural Analysis Program, Computers and Structures Inc., Version: 17.1.1, Berkeley, California, USA.

Sakai, F., Takeda, S. (1989). Tuned Liquid Column Damper-New Type Device for Suppression of Building Vibrations. In: Proceedings of international conference on high rise buildings. Nanjing, China.

Sakai, F., Takaeda, S., Tamaki, T. (1989). Tuned Liquid Column Damper-New Type Device for Suppression of Building Vibrations. Proceedings of Internal Conference on Highrise Buildings, Nanjing, China, 926-931.

Sonmez, E., Nagarajaiah, S., Sun, C., Basu, B. (2016). A Study on Semi-Active Tuned Liquid Column Dampers (TLCDS) for Structural Response Reduction Under Random Excitations. *Journal of Sound Vibration*, 362:1-15.

Sun L.M, Fujino, Y., Pacheco BM, Isobe (1989). Nonlinear Waves and Dynamic Pressures in Rectangular Tuned Liquid Damper (TLD) Simulation and Experimental Verification. Structural Engineering/Earthquake Engineering 6(2):251-262.

Sun LM, Fujino Y, Pacheco BM, Chaiseri P (1992) Modeling of Tuned Liquid Damper (TLD). *Journal of Wind Engineering and Industrial Aerodynamics*, 41(44):1883-1894.

Tait, M.J (2008). Modelling and Preliminary Design of a Structure-TLD System. *Engineering Structures,* 30(10):2644-55.

Tait, M.J., Deng, X. (2010). The Performance of Structure Tuned Liquid Damper Systems with Different Tank Geometries. *Structural Control and Health Monitoring*, 17(3):254-77.

Greciano, A.V., López, A.A., Buratti, N., Ortiz Herrera, J.M. (2024). Magnetic Fields to Enhance Tuned Liquid Damper Performance for Vibration Control: A Revie, *Archives of Computational Methods in Engineering*, 31:25–45.

Recent Developments and Applications of Passive Control Systems in Civil Structures: A State-of-the-Art Review. *Archives of Computational Methods in Engineering*, **30**:1003–1044.

Yammamoto, K., & Kawahara, M. (1999). Structural Oscillation Control Using Tuned Liquid Damper. *Computers and Structures,* 71:435-446.

Yu, J.K., Wakahara, T., Reed, D.A (1999). A Non-Linear Numerical Model of the Tuned Liquid Damper. *Earthquake Engineering and Structural Dynamics,* 28:671-686.

Zhao, Z., & Fujino, Y. (1993) Numerical Simulation and Experimental Study of Deeper-Water TLD in The Presence of Screens. *Journal of Structural Engineering*, 39(A):699-711.

4th International Civil Engineering & Architecture Conference
17-19 May 2025, Trabzon, Türkiye

Structural health monitoring in Yusufeli Arch Dam

Ebru Kalkan Okur[*1,2], Fatih Y. Okur[2,3], Ahmet C. Altunışık[2,3]

[1] Karadeniz Technical University, Of Faculty of Technology, Department of Civil Engineering, Trabzon, Türkiye
[2] Earthquake and Structural Health Monitoring Research Center, Karadeniz Technical University, Trabzon 61080, Türkiye
[3] Karadeniz Technical University, Department of Civil Engineering, 61080 Trabzon, Türkiye

Abstract. Arch dams, due to their complex geometry and interaction with reservoir water, are highly sensitive to dynamic effects and long-term environmental influences. The Yusufeli Arch Dam, one of the highest dams in Turkey, are equipped with Structural Health Monitoring (SHM) systems to assess their dynamic behavior and ensure operational safety. Yusufeli Dam, with a height of 275 meters, was recently completed and began reservoir impoundment. Its SHM system includes high-sensitivity accelerometers, temperature sensors, and displacement measurement instruments to track changes in modal characteristics as the water level rises. These data are crucial for understanding how hydrostatic pressure, temperature fluctuations, and external loads affect the dam's stability. The SHM system deployed on the dam provides long-term records of seismic response, structural displacements, and potential material degradation. Previous studies indicate that reservoir filling leads to a decrease in the natural frequencies of the dam, confirming the influence of the added mass effect and changing boundary conditions. Monitoring dam over time offers valuable insights into the structural integrity of high arch dams under real environmental conditions. The collected data contribute to the development of numerical models that improve the reliability of dam safety assessments. These case studies highlight the necessity of integrating SHM techniques into large-scale infrastructure projects to mitigate risks associated with environmental and operational factors.

Keywords: Arch dam; Operational modal analysis; Structural health monitoring; Yusufeli arch dam

1. Introduction

Archaeological discoveries and prehistoric engineering studies show that dam construction dates back to the early periods of human history. The Jawa Dam in Jordan, built around 3000 BCE, is recorded as the oldest known dam. In Ancient Egypt, the Sadd el-Kafara Dam (Dam of the Infidels), built around 2650 BCE on the northern banks of the Nile River, and the Hittite Dam (Alaca Höyük) in Anatolia, still functional and dating back approximately 3,200 years, are testaments to the ancient human effort to control and manage water (Üzen & Çetin, 2012). These structures represent a significant milestone in the storage and management of water, enhancing humanity's ability to intervene in the natural water cycle. The evolutionary journey of dams throughout history has led to an increased appreciation of water's value and more efficient use of water resources.

Over time, the design and functionality of dams have significantly improved. In the Middle Ages, the use of water power increased in Europe, leading to the widespread construction of dams. Notably, the arch dam, discovered by the Mongols in the 13th century, made it possible to build stronger dams with less material (Matthew, 2005). With the evolution of dam construction technology in the early 20th century, dams became more complex structures and an important resource for hydroelectric power generation. The use of materials such as concrete and steel enabled the construction of larger and more robust dams. Structures like the Hoover Dam and Aswan Dam, built during this period, are regarded as significant milestones in the field of engineering (Novokshchenov, 1997; Scott & Molyneux, 2001; Giroux, 2010).

The type and design of a dam to be constructed are determined by various factors such as geographical location, geological conditions, the intended use of water, and environmental impacts. Each type of dam offers specific advantages tailored to particular geological and environmental conditions. Arch dams are water retention structures that effectively utilize the strength of concrete with their curved design. The primary working principle of these dams is to transfer the hydrostatic pressure created by the water to the abutments and foundation through their curved shape. Therefore, the bearing capacity of the foundation and abutments where the dam will be located must be high. These characteristics make arch dams particularly preferred in narrow and steep valleys, providing a more effective and economical solution compared to other dam types in such geographical conditions.

[*] Corresponding author, E-mail: ebrukalkan@ktu.edu.tr

https://doi.org/10.31462/icearc2025_ce_eqe_176

Today, the role of dams is not limited to water storage and energy production; they also serve various purposes such as recreational use, water sports, and wildlife conservation. However, the environmental impacts and social consequences of dams are also heavily debated. These discussions have made it necessary to integrate sustainability and environmental protection measures into the design and operation of dams. Considering that structures storing such large volumes of water could lose functionality if damaged, causing harm to the national economy, and in the event of more significant damage, the collapse of a dam could result in the loss of many lives, accurately determining the static and dynamic behavior of these structures during the design and planning stages is of utmost importance.

The natural frequencies, mode shapes, and damping ratios, which describe the current structural condition of arch dams and all other structures, are referred to as dynamic characteristics and are directly influential in determining static and dynamic effects. The dynamic characteristics of such structures can be determined through numerical and experimental methods. Experimental methods take into account factors directly affecting the structures and test the accuracy of the data obtained from numerical methods, providing a realistic structural assessment. Today, the Experimental Modal Analysis Method is used to experimentally determine the dynamic characteristics of structures, such as their natural frequencies, mode shapes, and damping ratios, by placing sensitive accelerometers at various points on the structure. Since the vibration signals collected via accelerometers include signals from both the structure and the surrounding environment, they are separated using filtering techniques, and the signals belonging to the structure are processed to determine the experimental dynamic characteristics of the structures (Freyman et al., 1996).

Dams are critical infrastructure that serve various functions, such as water storage, energy production, and flood control. As such, maintaining the safety and functionality of these structures is paramount. Structural Health Monitoring (SHM) plays an essential role in ensuring the integrity of dams over time, enabling early detection of potential issues before they evolve into critical failures. By continuously monitoring key parameters such as vibrations, deformations, and crack growth, SHM systems facilitate the assessment of a dam's static and dynamic behavior. This data is invaluable in identifying early signs of damage, deterioration, or unexpected behavior, which might otherwise go unnoticed until they pose significant risks. Moreover, the use of advanced SHM technologies allows for the remote monitoring of dams in real-time, providing a cost-effective alternative to traditional manual inspections. The monitoring of dynamic characteristics, including natural frequencies and damping ratios, allows engineers to evaluate how the dam responds to environmental factors such as water level changes, temperature fluctuations, and seismic activity. Understanding these responses is crucial for predicting the dam's performance under various loading conditions and ensuring its continued safety and functionality. The implementation of SHM systems also aligns with modern engineering practices focused on sustainability, as it minimizes the need for inspections and repairs, reducing both operational costs and environmental impact. SHM represents an essential component of modern dam management, providing vital insights into the health and safety of these critical structures. For this purpose, within the scope of the literature, researchers carry out studies on dams, including operational and laboratory experiments (Darbre et al., 2000; Okuma et al., 2008; Sevim et al., 2012; Lew & Loh, 2013; Oliveira & Alegre, 2022; Hassan et al., 2024)

Within the scope of this study, long-term Structural Health Monitoring (SHM) efforts are aimed at determining the structural behavior of the Yusufeli Arch Dam, which has a height of 275 meters, through experimental methods, considering the effects of reservoir water and changing ambient temperatures. Sensitive accelerometers installed on the dam, whose construction was completed in 2022, have been used to obtain long-term signal data, including the condition where the reservoir is empty. This study is significant in terms of determining the changing dynamic characteristics of a 275-meter-high arch dam as the reservoir begins to fill with water.

2. Yusufeli arch dam

The Yusufeli Dam, situated on the Çoruh River in the Yusufeli district of Artvin, Turkey, stands as a remarkable feat of modern engineering. Construction began in 2013, and the dam was officially completed in 2022, with the reservoir impoundment commencing in November 2022. By November 2023, the dam's power generation activities were underway, and the water level reached a height of +701 meters, with the crest elevation at +715 meters. With a total height of 275 meters, it is the tallest dam in Turkey and ranks as the third-tallest double-curvature concrete arch dam type worldwide.

Boasting an installed capacity of 540 MW, the Yusufeli Dam contributes significantly, with an annual energy output of 1.8 billion kWh. In addition to its energy-generating capabilities, the dam plays a vital role in irrigation, water storage, and flood mitigation, with a reservoir that can hold up to 270 million cubic meters of water. The Yusufeli Dam, through its sophisticated engineering design and technological advancements, delivers long-term benefits, including energy production, environmental conservation, and disaster management. Some images of the dam are shown in Fig. 1.

Fig. 1. Views of Yusufeli Dam

2.1. Sensor installed and operational tests in the Yusufeli dam

Since environmental conditions can lead to structural changes over time in large engineering projects, it is crucial to monitor these changes. To monitor these changes and assess the dynamic characteristics of the dam, ambient vibration tests are employed. These tests use accelerometers placed at strategic points on the dam to capture natural vibrations caused by factors such as water level changes, wind, ground motions, and the passage of heavy vehicles.

Upon the completion of the Yusufeli Dam in 2022, ambient vibration tests were conducted to assess the dam's modal behavior with the reservoir empty. Seven accelerometers were used for each reference measurement along the dam crest to capture vibration data, which was then processed using the OMA (2023) software to determine the dam's dynamic characteristics (Fig. 2). The tests employed Sara SL06 three-axis accelerometers, which have a dynamic range of 156 dB and a frequency range from 0 to 1500 Hz. These accelerometers were positioned along the upstream-downstream axis of the dam crest to measure vibrations during the test. The results showed the first six natural frequency values ranging from 1.881 Hz to 5.191 Hz, with corresponding mode shapes provided.

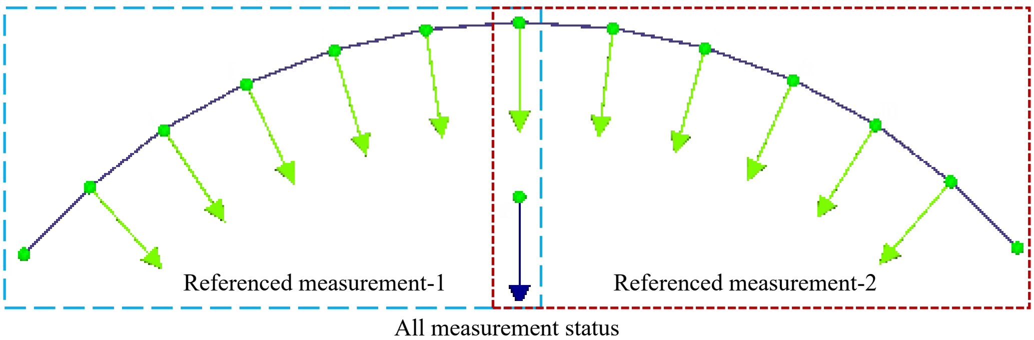

Fig. 2. Accelerometer placement for reference measurements at Yusufeli dam

In Fig. 3, the frequency values of the first six modes are given for the case when the dam reservoir is empty, and the mode shapes corresponding to these modes are given.

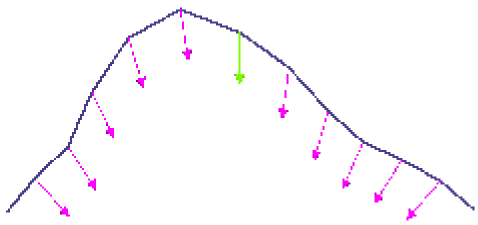

a) 1^{st} mode (1.881 Hz)

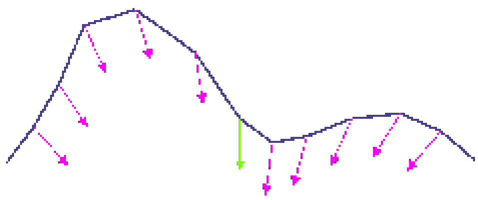

b) 2^{nd} mode (2.095 Hz)

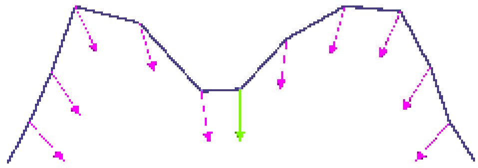

c) 3^{rd} mode (3.105 Hz)

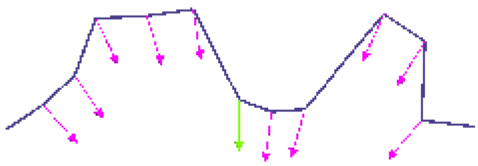

d) 4^{th} mode (3.584 Hz)

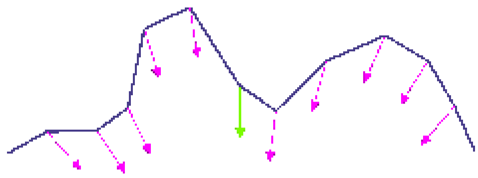

e) 5^{th} mode (3.936 Hz)

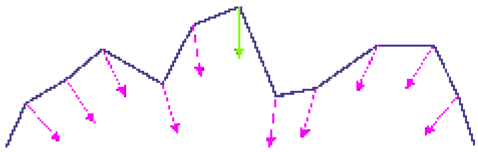

f) 6^{th} mode (5.191 Hz)

Fig. 3. The first six mode shapes and corresponding natural frequencies

As the water level began to rise in the reservoir, the monitoring process continued with three accelerometers installed on the dam crest for long-term monitoring (Fig. 4). These accelerometers provided valuable data on the dam's dynamic behavior at different water levels, using the baseline measurements taken with the seven accelerometers as reference. The data from the three accelerometers, while sufficient for determining frequency values, were not enough to fully characterize the mode shapes. Therefore, the initial detailed data set, obtained when the reservoir was empty, was used to enhance the accuracy of ongoing measurements.

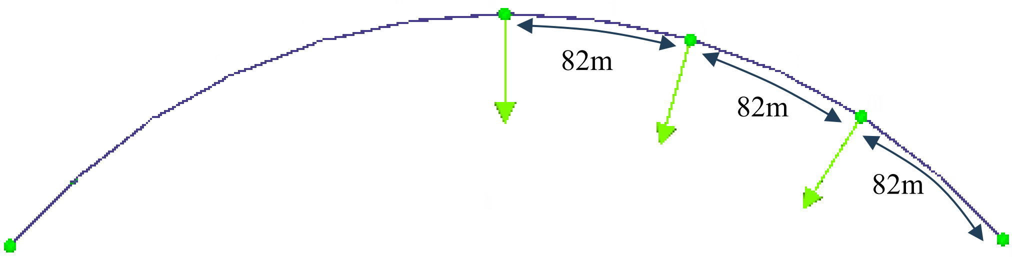

Fig. 4. Accelerometers layout plan

For continuous monitoring, a sensor setup was designed with three accelerometers spaced at equal intervals along the dam crest. These accelerometers were integrated into a system with an industrial modem for real-time online data transmission. The accelerometers were powered by an uninterrupted power supply and equipped with a signal management kit for periodic activation. This setup ensures reliable data collection and monitoring of the dam's dynamic properties, contributing to the long-term assessment of its structural health. Figure 5 shows visuals of the accelerometer installation at the dam crest for continuous monitoring.

Fig. 5. Accelerometers Instrumentation for continuous monitoring

2.2. Structural health monitoring in the Yusufeli dam

A comprehensive Structural Health Monitoring (SHM) study was carried out to evaluate the condition of the Yusufeli Dam, a towering structure, during the process of filling the reservoir and under varying seasonal conditions. The data collected from three accelerometers mounted on the dam were transmitted through an internet connection to an online SHM system developed by Okur (2023) as part of a thesis. An image of the system's interface, customized for Yusufeli Dam, is shown in Fig. 6. This web-based SHM system, together with its integrated software, automatically processes the raw data from the accelerometers and computes the frequency values corresponding to the identified modes. Additionally, the system can access regional air temperature data in real-time. Time-dependent frequency variations for the first six modes, stored in the system's database, are shown in Fig. 7. When Figure 7 is examined, the trends of frequency values belonging to all modes are similar. It first decreases in approximately the same date ranges, then increases, reaches the peak level and then decreases again. In order to observe the effect of environmental parameters on this change, the frequency change of the 1st mode is given in Fig. 8 together with the changes in reservoir water level and ambient temperature.

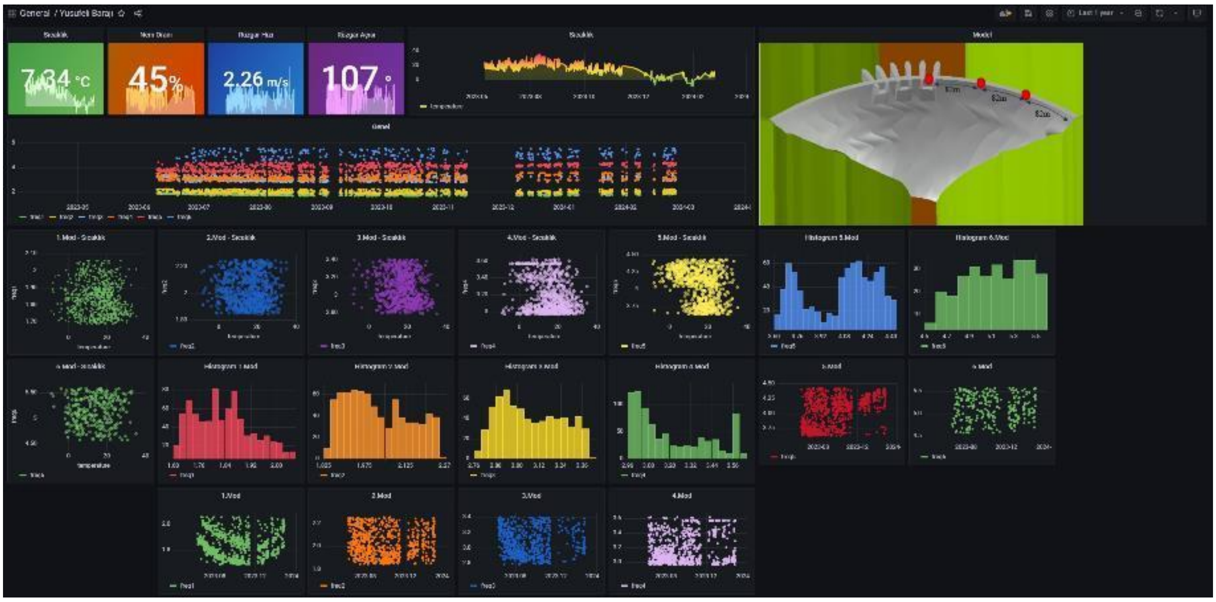

Fig. 6. Web-based structural health monitoring platform

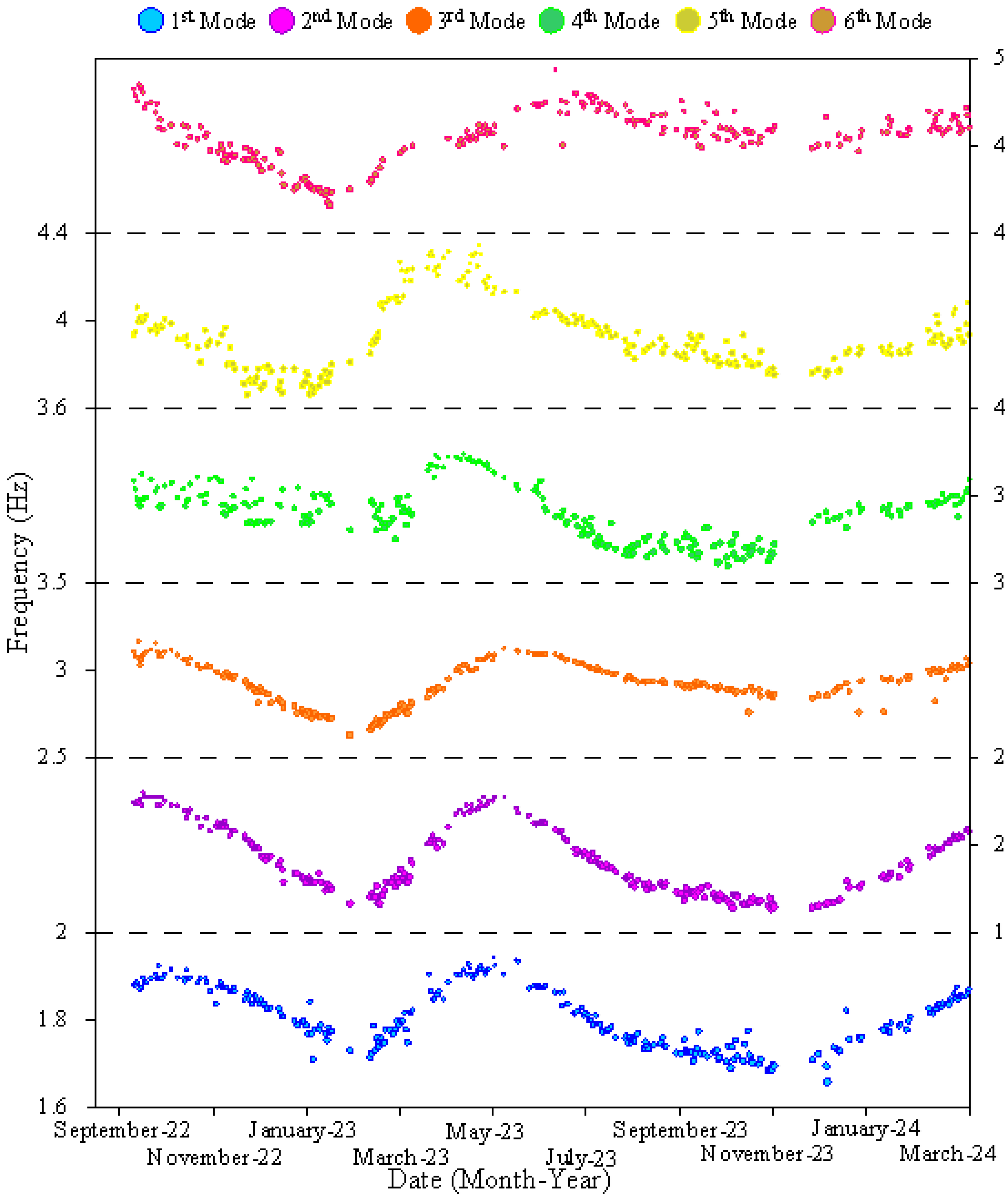

Fig. 7. First six frequency changes during the SHM

As depicted in Fig. 8, temperature data exhibited periodic fluctuations, while the water level steadily increased due to the dam's ongoing water retention process. A direct comparison of frequencies and temperature is challenging, as the thermal conditions change continuously over time with the fluctuation in water level. It is clear that the primary factor influencing the frequency changes is the amount of water in the reservoir. However, other contributing factors also influence the frequency variations over time. One of these factors is the dam's curved structure and daily temperature variations. The dam's vertical construction joints are well known, and these joints can open or close under loading. Literature commonly supports the idea that when the joints open, the dam's stiffness decreases, which in turn reduces the frequency. Conversely, as the joints compress and close, the stiffness increases, leading to higher frequency values.

Frequency values generally decreased until March, after which an upward trend began, continuing through June. This increase in frequency values, despite the rising water levels, is likely attributed to the compression and closing of the contraction joints, which enhances the stiffness of the dam. In March, the water level was at 68 meters, and by June, it had risen to 150 meters. This suggests that the compression of the joints in the double-curved dam body, caused by the increasing water level between 68 and 150 meters, contributed to the rise in stiffness. Beyond 150 meters, as the water level continued to increase, the frequency values began to decrease, which is consistent with the expected trend. It's also worth noting that the rise in water levels in January was much slower and almost stable, so the subsequent increase in frequency after this period may have been influenced by the drop in temperature.

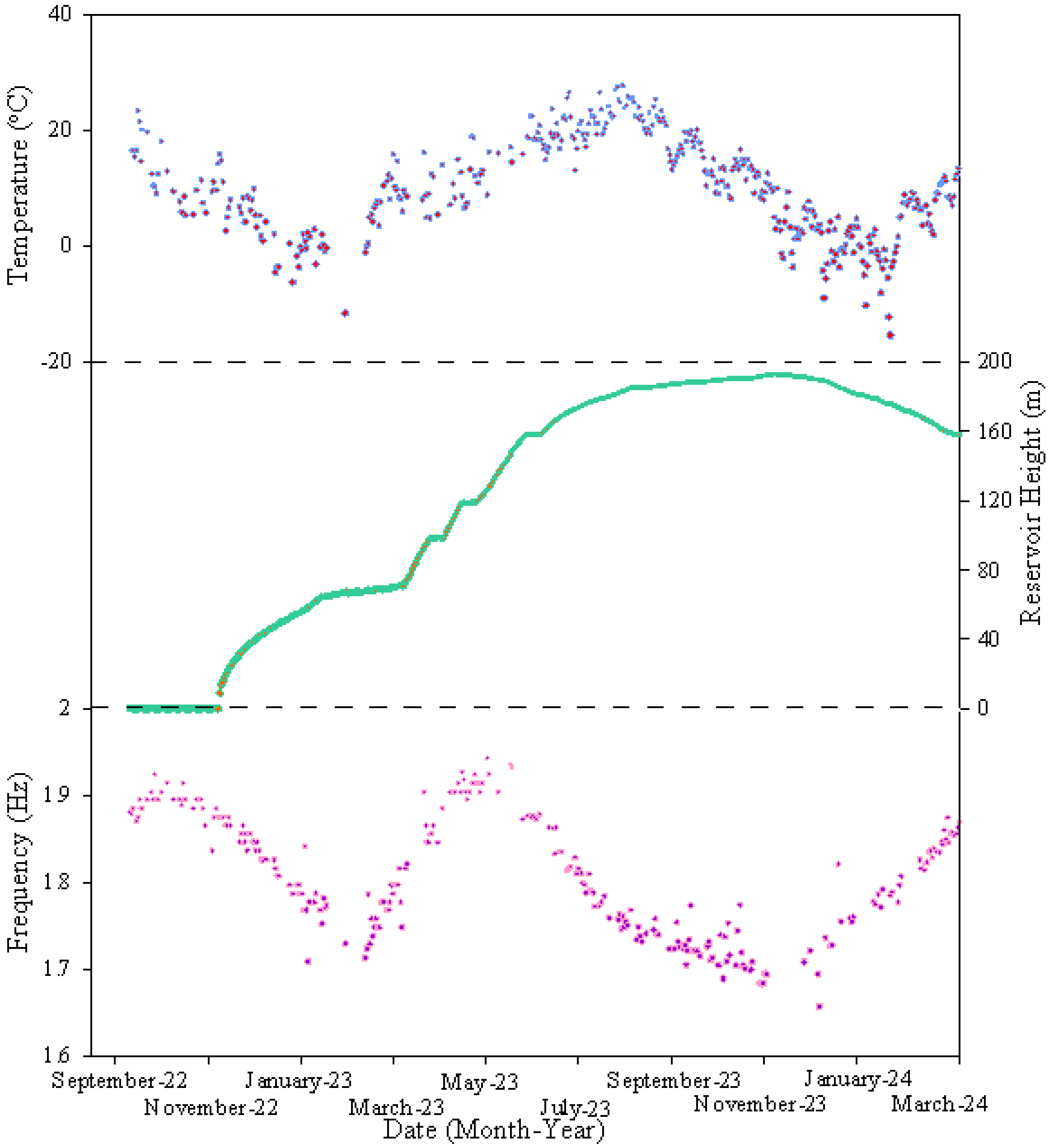

Fig. 8. Changes in ambient temperature, water height and frequency values obtained from the long-term Structural Health Monitoring of Yusufeli Dam

3. Conclusions

This study presents a comprehensive Structural Health Monitoring (SHM) approach to assess the dynamic characteristics and structural integrity of the Yusufeli Arch Dam, which stands as one of the tallest dams in Turkey. The SHM system implemented on the dam includes high-sensitivity accelerometers measurement sensors, providing crucial data on the dam's behavior as the reservoir fills and under varying seasonal conditions. The results obtained within the scope of the study can be listed as;

- The frequency values obtained when the empty reservoir indicated that the dam's initial natural frequencies ranged between 1.881 Hz and 5.191 Hz.
- The natural frequencies of the dam decrease as the reservoir fills, mainly due to the added mass of water.

- Additional factors, such as the dam's curved shape and daily temperature fluctuations, also affect frequency changes.
- The increase in frequency, despite the increase in water level, is due to the increase in hardness of the dam as a result of the compression and closure of the contraction joints.

Overall, the SHM system provides valuable insights into the dam's dynamic properties and allows for real-time monitoring, contributing to the development of more accurate numerical models. These models, in turn, enhance the reliability of dam safety assessments, ensuring the long-term stability and functionality of the structure. This case study underscores the importance of integrating SHM systems into large-scale infrastructure projects, not only for structural assessment but also for mitigating risks associated with environmental and operational factors.

Acknowledgments
The authors would like to extend their sincere gratitude to the General Directorate of State Hydraulic Works for granting the necessary permits for field studies at the Yusufeli Dam. Special thanks are also due to the 26th Regional DSI Branch Directorate for their invaluable support and assistance throughout the experimental studies.

This work was supported by the Karadeniz Technical University Scientific Research Project titled "Establishment of a Structural Health Monitoring Network and Development of Innovative Methods for Engineering Structures of Strategic Importance in the Eastern Black Sea Region" (Project No. FAY-2021-9635). The authors extend their thanks to Karadeniz Technical University for their invaluable support.

References
Darbre, G. R., Smet, C. A. M., & Kraemer, C. (2000). Natural frequencies measured from ambient vibration response of the arch dam of Mauvoisin. *Earthquake Engineering and Structural Dynamics, 29*, 577–586.

Freymann, R., Honsberg, W., Winter, F., & Steinbichler, H. (1996). Holographie modal analysis. In *Laser in research and engineering* (pp. 530–542). Springer. https://doi.org/10.1007/978-3-642-61075-5_61

Giroux, R. (2010). Building Hoover Dam (Men, Machines, and Methods), 360–410. https://doi.org/10.1061/41141(390)20

Hassan, N. H., Zawawi, M. H., Mazlan, A. Z. A., Abas, M. A., Zainol, M. R. R. M. A., Radzi, M. R. M., & Kamaruddin, M. A. (2024). Experimental modal analysis and operational deflection shape analysis for Kenyir Dam spillway physical model. In *Proceedings of AWAM International Conference on Civil Engineering* (Vol. 3). Springer, Singapore.

Lew, J. S., & Loh, C. H. (2013). Modeling of an arch dam long-term static deformation for structural health monitoring. In *54th AIAA/ASME/ASCE/AHS/ASC Structures, Structural Dynamics, and Materials Conference*, Boston, Massachusetts.

Matthew, R. (2005). Dams and development: Transnational struggles for water and power (Review). *Global Environmental Politics, 5*, 131–133.

Novokshchenov, V. (1997). Old Aswan Dam: Standing the test of time. *Civil Engineering, 67*.

Okuma, N., Etou, Y., Kanazawa, K., & Hirata, K. (2008). Dynamic properties of a large arch dam after forty-four years of completion. Paper presented at the *14th World Conference on Earthquake Engineering*, Beijing, China.

Okur, F. Y. (2023). *Development of engineering softwares for damage detection and long-term structural health monitoring of engineering structures* (PhD thesis). Karadeniz Technical University, Institute of Science, Trabzon, Türkiye.

Oliveira, S., & Alegre, A. (2022). A study on the influence of the horizontal cracking on the modal parameters of Cabril Dam: Experimental and numerical results. In *8th World Conference on Structural Control and Monitoring*, Orlando, Florida, USA.

OMA. (2023). *Operational modal analysis* (Release 4.0). Structural Vibration Solution A/S, Denmark.

Scott, C., & Molyneux, J. (2001). Britain's concrete dams: The final 50 years? *Civil Engineering, 144*, 170–180.

Sevim, B., Altunışık, A. C., & Bayraktar, A. (2012). Experimental evaluation of crack effects on the dynamic characteristics of a prototype arch dam using ambient vibration tests. *Computers and Concrete, 10*(3), 277–294.

Üzen, N., & Çetin, Ö. (2012). Water and irrigation management from the past to today. *Journal of Life Sciences, 1*(2), 281–290.

4th International Civil Engineering & Architecture Conference
17-19 May 2025, Trabzon, Türkiye

Performance of reinforced concrete buildings built in Tunceli during the period when the Türkiye Building Earthquake Code 1975 was in force: A case study

Burak Yön*[1], Merve Şahin Yön[1], Mehmet Karataş[1], Abdullah İçen[1], Selim Cemalgil[1]

[1]Munzur University, Department of Civil Engineering, 62000 Tunceli, Türkiye

Abstract. This article focuses on the seismic performance analyzes of 5 reinforced concrete buildings located in different districts of Tunceli province and built during the period when the Türkiye Building Earthquake Code 1975 (TBEC, 1975) was in force. For the numerical study, core samples were taken from the buildings whose plans were prepared and the reinforcement in the structural elements were determined. Ground survey reports were used to determine the ground conditions of the buildings. According to the samples taken from the buildings, it was determined that the concrete strength of all buildings was below 10 MPa. In addition, it was determined that the reinforcements in the structural elements had smooth surfaces and the stirrup spacing was more than 250 mm. In the light of the data obtained, performance evaluation was made by performing nonlinear static pushover analyzes of the buildings. According to the analysis results, it was determined that no building met the adequate performance conditions defined in Türkiye Building Earthquake Code 2018 (TBEC, 2018).

Keywords: RC buildings; Seismic performance; Concrete strenght; Türkiye Building Earthquake Code 1975; Ground servey

1. Introduction

In countries situated on active tectonic faults, such as Türkiye, it is crucial that both new and existing structures are capable of withstanding potential earthquakes at the requisite performance level. However, the loss of life and property resulting from the earthquakes has been an indication that the earthquake performance is inadequate. Research conducted post-earthquakes identified the primary causes of damage in reinforced concrete structures as soil effects, inadequate material strength, irregular design, errors in architectural planning, and non-compliance of reinforcement with seismic codes. (Bayraktar et al., 2013; Demirel et al., 2022; Ertürk et al., 2022; Ivanov and Chow, 2023; Kocakaplan Sezgin et al., 2024; Onat et al., 2022; Sayın et al., 2021; Yön et al., 2024). Damages and losses of life occurring in earthquakes show the importance of earthquake-resistant and adequately safe building design. To do this, it is possible to accurately determine the nonlinear behavior of building systems during earthquakes with selection of accurate method. Reinforced concrete is a building material that is heterogeneous and its behavior is inelastic. However, the change in behavior depending on time and load invalidates the calculation methods developed with the assumption of ideal material in determining the behavior of this material. It uses various models and analysis methods to determine nonlinear behavior.

The static pushover analysis method is an effective approach that facilitates the assessment of existing buildings, the design of retrofitted structures, and offers insights to engineers in the design of new edifices (Hassan and Reyes, 2020; Kimeze and Kyakula, 2023; Kuria and Kegyes-Brassai, 2023; Pierre and Hidayat, 2020; Zebua and Koespiadi, 2022). Analysis: It is an estimated approach for exposing the structure to lateral forces that incrementally grow with a uniform height distribution until the desired displacement is achieved. In nonlinear static pushover analysis, structural systems are depicted using two- or three-dimensional analytical models. This method the horizontal load-peak displacement relationship, which signifies the structural strength under earthquake loads, in accordance with nonlinear theory concerning material and geometric alterations. In this method, the structure is subjected to horizontal loads at the floor levels to simulate dynamic inertia forces. While horizontal loads are applied, vertical loads concurrently exist within the structure. Static horizontal loads are incrementally raised at each stage, maintaining a consistent ratio, until the structure attains a specific displacement or collapse condition, so establishing the link between horizontal load and peak displacement of the structure. With the effect of increased horizontal loads, one or more of the sections reach their carrying capacity and plastic hinges

*Corresponding author, E-mail: burakyon@munzur.edu.tr

https://doi.org/10.31462/icearc2025_ce_eqe_189

form in these sections. Sections formed by plastic hinges continue to rotate without any change in their bearing capacity. The system behaves linearly-elastic between plastic hinges. By continuing to increase the horizontal loads, the collapse load (limit load) is reached, which turns part or all of the structure into a mechanism. By evaluating the plastic hinge distribution under this load and displacement, the damage status of the building and whether the performance target is met are determined.

In this study, seismic performance analyzes of 5 reinforced concrete buildings located in different districts of Tunceli province and built during the period when the TBEC 1975 was in force were performed using the static pushover analysis method. For the numerical study, core samples were taken from the buildings and the reinforcement in the building elements were determined. Ground survey reports were used to determine the ground condition. In the light of the data obtained, non-linear analyzes of the buildings were solved in the STA4CAD building analysis program and performance evaluation was made.

2. Materials and method

The locations of the buildings used in the numerical analysis are shown in Fig. 1. Looking at the location of the buildings, it can be seen that they are very close to the faults. In addition, three-dimensional views of the buildings and destructive tests performed on the buildings are presented in Figs. 2-6, respectively. When the structures are examined, it is seen that the buildings were built with a reinforced concrete frame system and there are few or no reinforced concrete shear walls.

Also, building information, materials properties, horizontal and vertical elastic spectrum of buildings are given in Table 1 and Fig. 7, respecitvely. In this table, B, PB and GF define the Basement, Partial Basement and Ground Floor, respectively. Also, the rightmost number shows the normal floor number. Upon this table was investigated, it can be seen the compressive concrete strength of buildings under the 10 MPa. This value does not meet the TBEC 2018 nor does it meet the TBEC 1975 in which the lowest concrete compressive strength is B225 (C18). Also, transverse reinforcement spacings are well above the Code requirements. Upon Fig. 7 was investigated, it can be seen the Model 5 has the largest spectral acceleration. However, the others models are unders effective ground movements, too.

Fig. 1. Locations of the examined buildings according to the active fault map (MREGD, 2021)

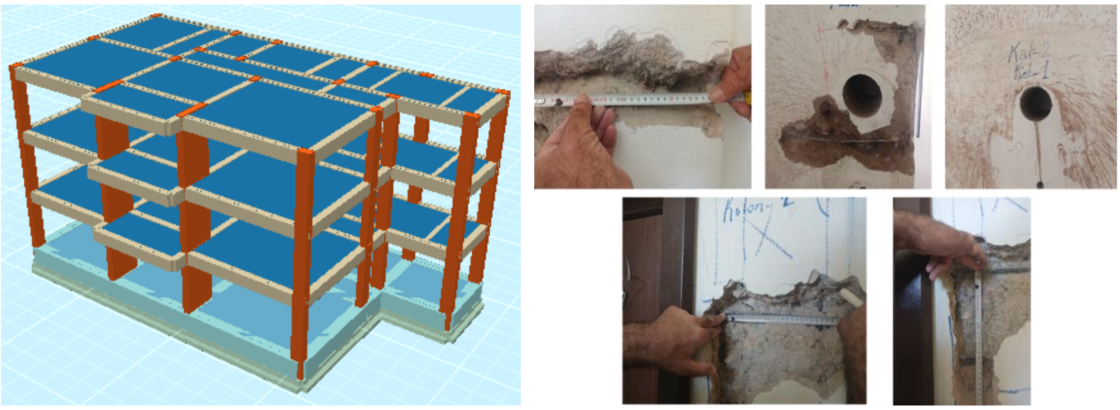

Fig. 2. Three-dimensional view of the Model 1 and destructive experiments in the building (39.1069705; 39.2188764)

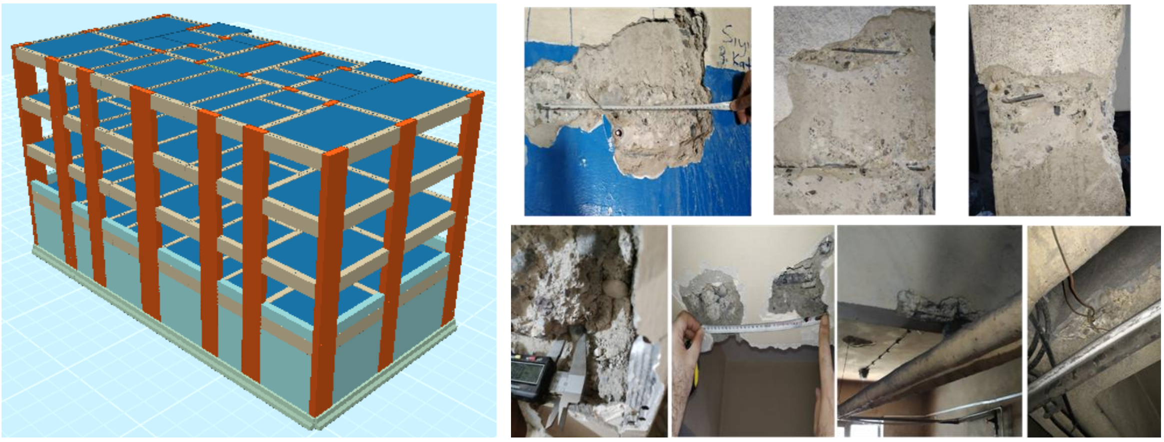

Fig. 3. Three-dimensional view of the Model 2 and destructive experiments in the building (39.0184334; 39.6034958)

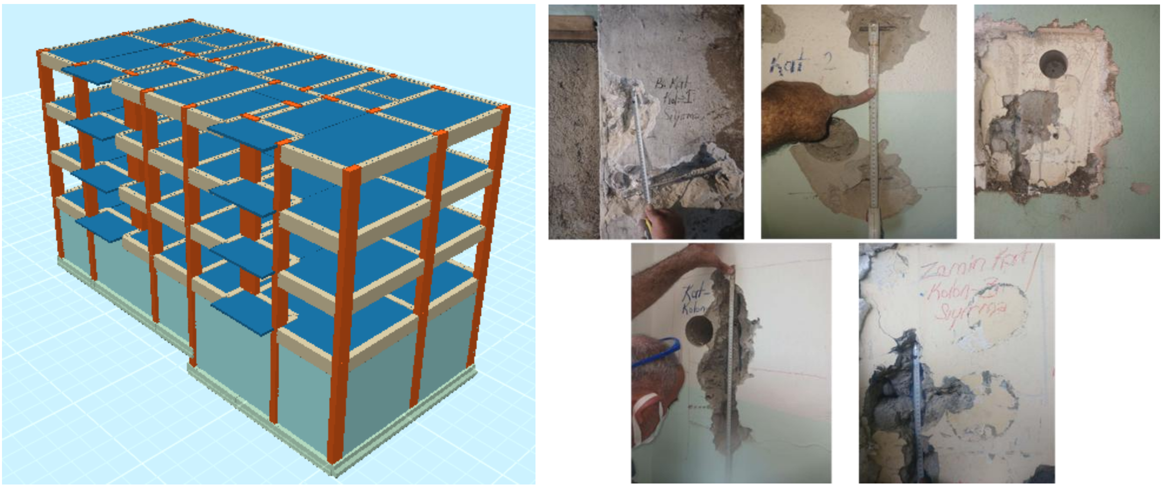

Fig. 4. Three-dimensional view of the Model 3 and destructive experiments in the building (39.1813261; 39.8286052)

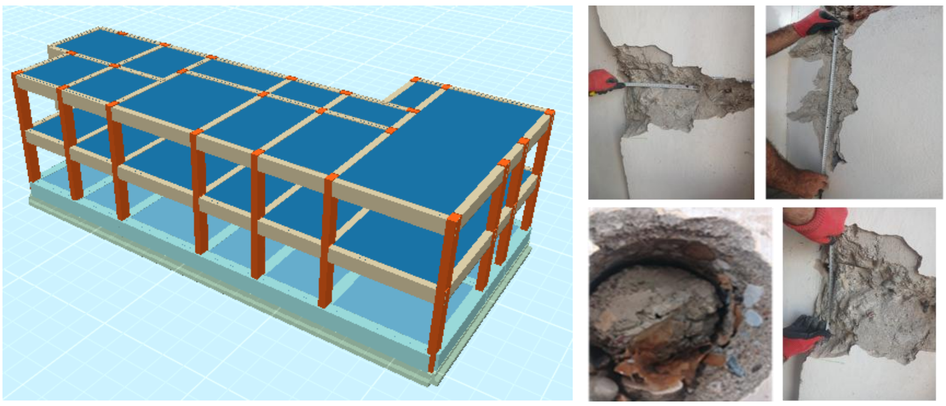

Fig. 5. Three-dimensional view of the Model 4 and destructive experiments in the building (39.3592767; 39.2143010)

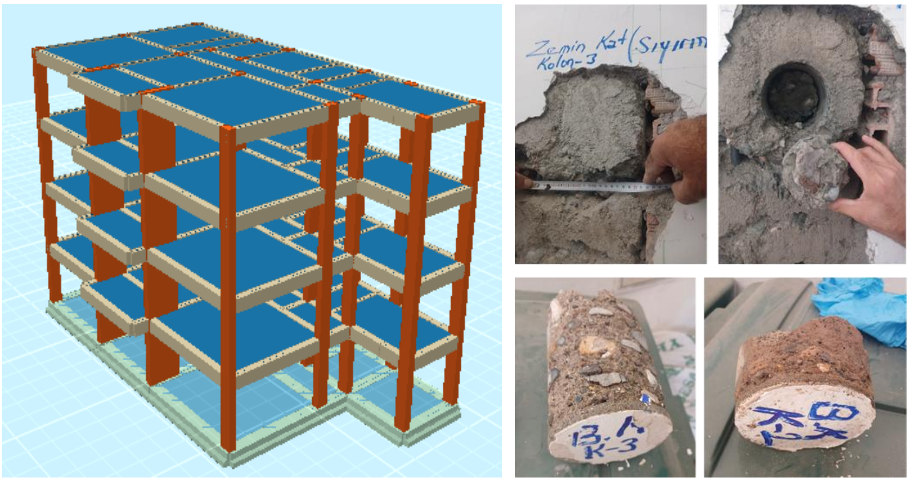

Fig. 6. Three-dimensional view of the Model 5 and destructive experiments in the building (39.4851259; 39.8974192)

Table 1. Materials properties of the buildings

Building Name	Number of Story	Soil Class	Concrete Strength (MPa)	Rebar	Diameter of longitudiunal reinforcement (mm)		Stirrup spacing (mm)		TBEC 1975 Requirements for Stirrup spacing (mm)	
					Column	Beam	Column	Beam	Column	Beam
Model-1	GF+2	ZC	9.45	S220	14	12	250	250	100	d/4
Model-2	B+GF+2	ZD	7.68				250	300		(d:beam
Model-3	B+GF+2	ZD	7.16				300	300		useful
Model-4	GF+1	ZD	9.18				300	300		height)
Model-5	PB+GF+2	ZD	4.34				250	250		

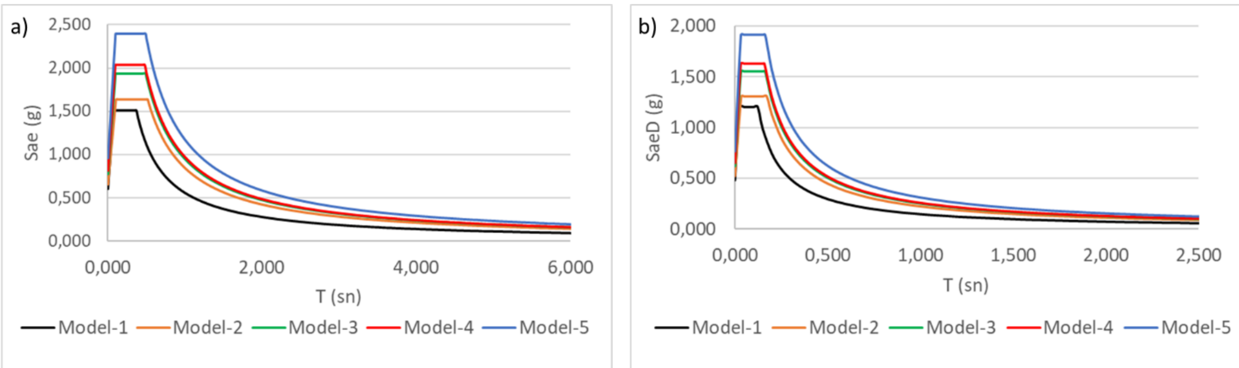

Fig. 7. a) Horizontal Elastic Design Spectrum; b) Vertical Elastic Design Spectrum

3. Results

Structural performances of the models were determined by performing nonlinear static pushover analyses. The capacity spectra and performance results obtained for the x and y directions are presented in Figs. 8-12, respectively. Upon these results were examined, it was determined that all buildings could not provide the desired performance level and collapsed because the capacity spectrum of the buildings was well below the demand spectrum. The lack of reinforced concrete walls in buildings, very low concrete strength, and insufficient transverse reinforcement spacing are the most important reasons for the decrease in the performance of these structures. In addition, the proximity of the structures to active faults caused the structures to experience large earthquake accelerations.

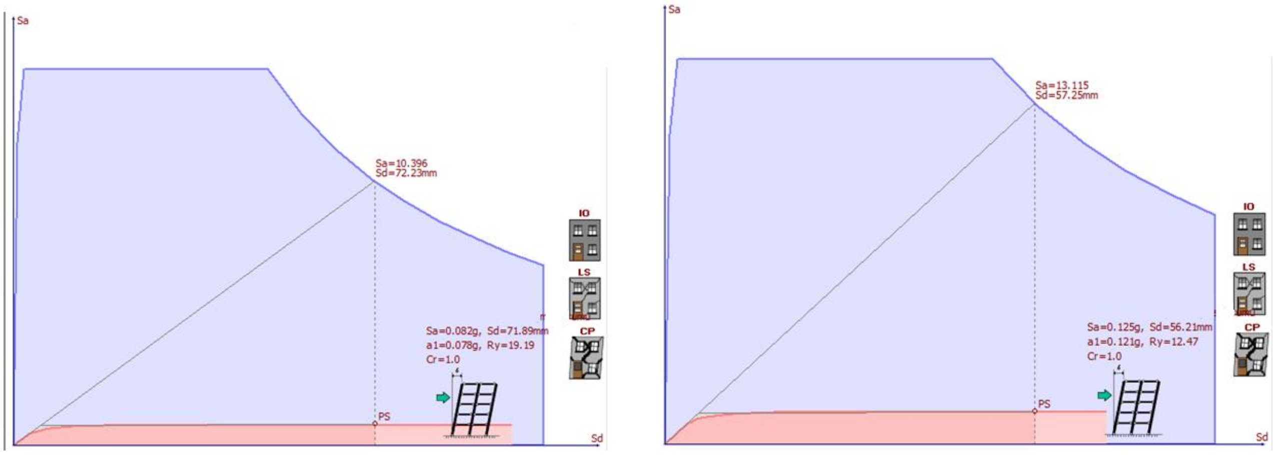

Fig. 8. Performance evaluation for X and Y directions of Model 1

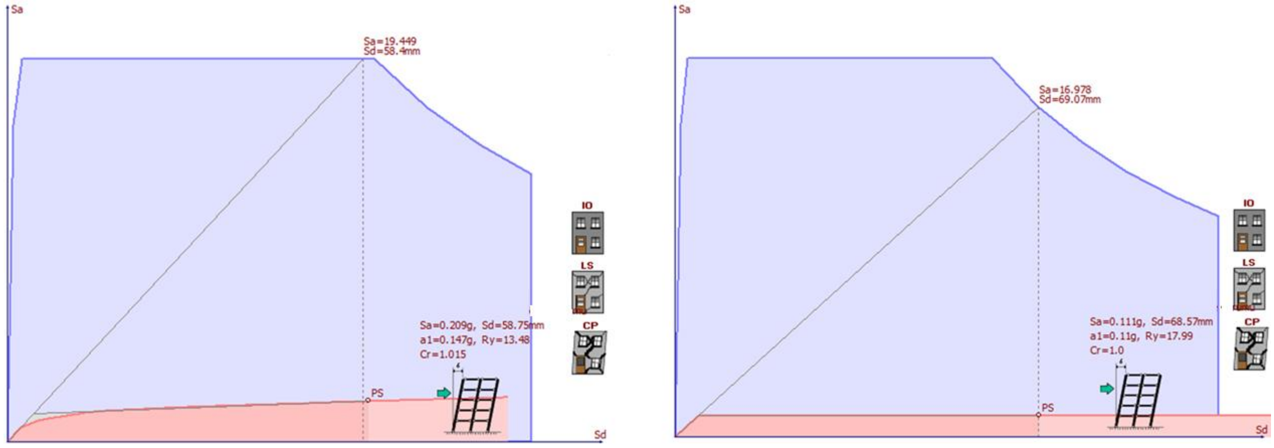

Fig. 9. Performance evaluation for X and Y directions of Model 2

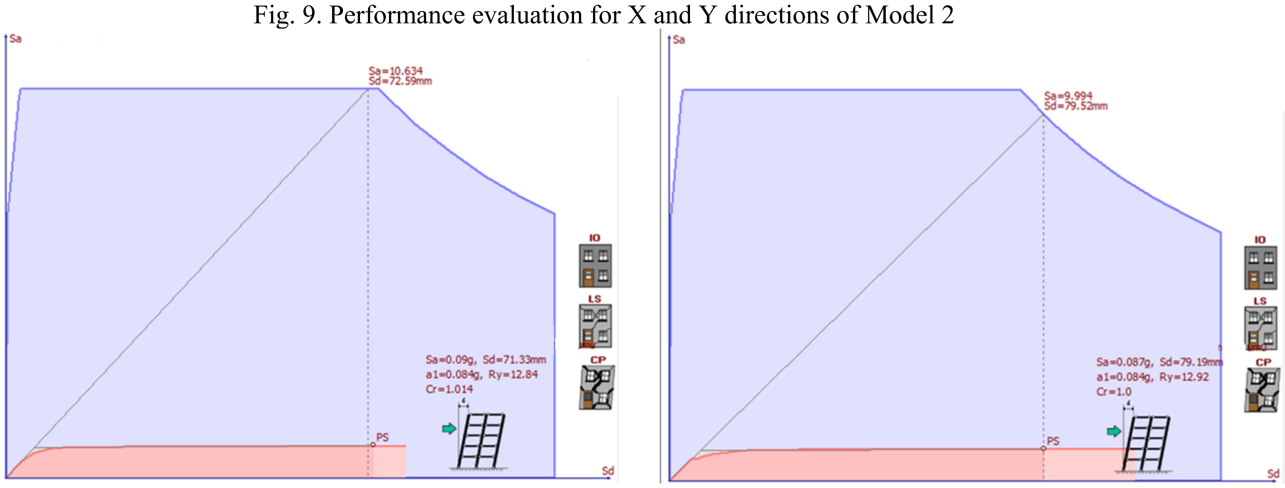

Fig. 10. Performance evaluation for X and Y directions of Model 3

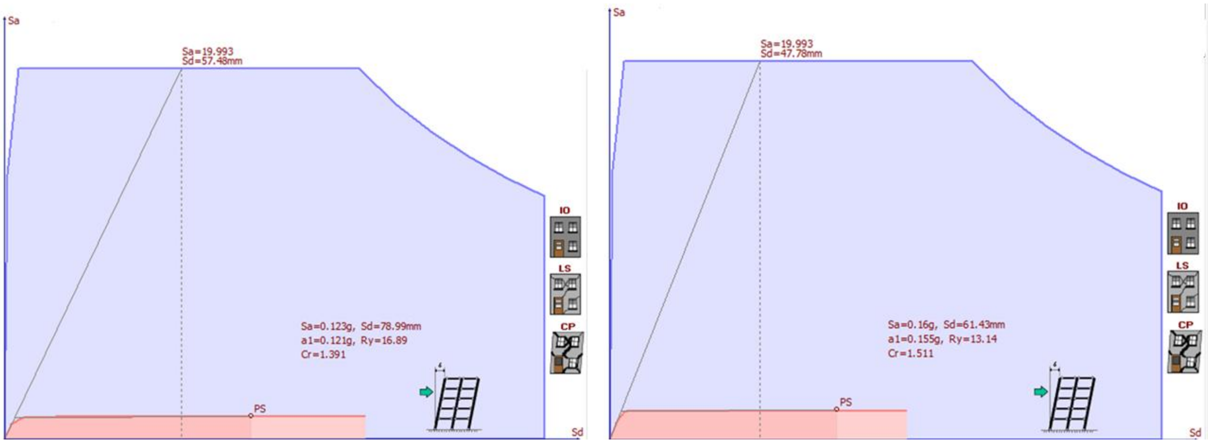

Fig. 11. Performance evaluation for X and Y directions of Model 4

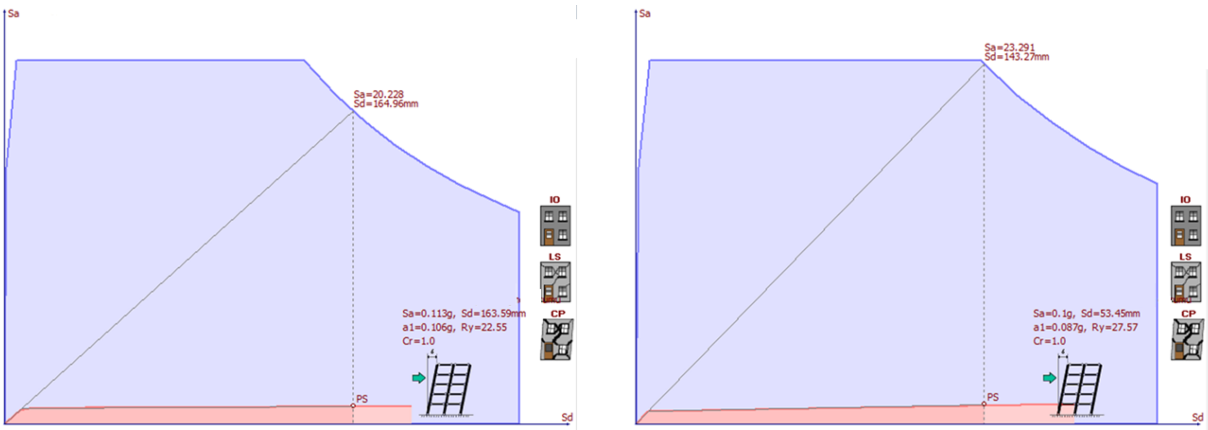

Fig. 12. Performance evaluation for X and Y directions of Model 5

4. Conclusions

In this study, 5 different reinforced concrete buildings built in Tunceli during the period when the TBEC 1975 was in force were examined and the condition of the building stock of this period in Tunceli was evaluated. Core samples were taken from 5 buildings selected for the numerical study and the reinforcement in the building elements was determined. In addition, since there were no plans of the buildings, survey studies were carried out and ground conditions were determined by ground surveys. Then, the buildings were modeled with the STA4CAD building analysis program and nonlinear static pushover analyzes were performed. The results obtained from the study are written below.

- The buildings examined do not even meet the requirements of the TBEC 1975.
- There are not enough reinforced concrete walls in buildings to restrict horizontal drift.
- One of the most important reasons for low structural performance is low concrete strength. Since ready-mixed concrete was not used in the construction of the buildings, casting was done by hand. In the concrete samples examined, river aggregate was used instead of crushed stone as aggregate and not enough cement was used, which caused the concrete strength to be low.
- In the examination carried out in terms of reinforcement, it was determined that smooth surface reinforcement was used in the structural elements. In addition, the large stirrup spacing caused the shear stress resistance of these elements to decrease.

As a result, it is thought that the performance of similar buildings in Tunceli will not be sufficient in the evaluation made on these buildings. In order to prevent loss of life and destruction, performance inspections of buildings with inadequate engineering control and low concrete strength must be carried out. As a result of the evaluation, it is recommended that the relevant buildings be strengthened or demolished and rebuilt.

References

Bayraktar, A., Altunişik, A.C., & Pehlivan, M. (2013). Performance and damages of reinforced concrete buildings during the October 23 and November 9, 2011 Van, Turkey, earthquakes. *Soil Dynamics and Earthquake Engineering*, *53*, 49-72

Demirel, I.O., Yakut, A., & Binici, B., (2022). Seismic performance of mid-rise reinforced concrete buildings in Izmir Bayrakli after the 2020 Samos earthquake. *Engineering Failure Analysis*, *137*, 106277. https://doi.org/10.1016/j.engfailanal.2022.106277

Ertürk, E., Aykanat, B., Altunışık, A.C., & Arslan, M.E. (2022). Seismic damage assessment based on site observation following the Düzce (Gölyaka) earthquake (Mw= 5.9, November 23, 2022). *Journal of Structural Engineering & Applied Mechanics*, *5*(4), 197-221

Hassan, W.M., & Reyes, J.C. (2020). Assessment of modal pushover analysis for mid-rise concrete buildings with and without viscous dampers. *Journal of Building Engineering*, *29*, 101103. https://doi.org/10.1016/j.jobe.2019.101103

Ivanov, M.L., & Chow, W.K. (2023). Structural damage observed in reinforced concrete buildings in Adiyaman during the 2023 Turkiye Kahramanmaras Earthquakes. *Structures, 58,* 105578. https://doi.org/10.1016/j.istruc.2023.105578

Kimeze, H., & Kyakula, M. (2023). A comparative analysis of existing models and a new pushover analysis model of reinforced concrete sections. *Engineering Structures*, *274*, 115073. https://doi.org/10.1016/j.engstruct.2022.115073

Kocakaplan Sezgin, S., Sakcalı, G.B., Özen, S., Yıldırım, E., Avcı, E., Bayhan, B., & Çağlar, N. (2024). Reconnaissance report on damage caused by the February 6, 2023, Kahramanmaraş Earthquakes in reinforced-concrete structures. *Journal of Building Engineering*, *89*, 109200

Kuria, K.K., & Kegyes-Brassai, O.K. (2023). Nonlinear static analysis for seismic evaluation of existing RC Hospital Building. *Applied Sciences*, *13*(21), 11626

Mineral Research and Exploration General Directorate (2021). *GeoScience map viewer.* Retrieved from https://yerbilimleri.mta.gov.tr/anasayfa.aspx.

Onat, O., Yön, B., Öncü, M.E., Varolgüneş, S., Karaşin, A., & Cemalgil, S. (2022). Field reconnaissance and structural assessment of the October 30, 2020, Samos, Aegean Sea earthquake: an example of severe damage due to the basin effect. *Natural Hazards*, *112*(1), 75-117. https://doi.org/10.1007/s11069-021-05173-y

Pierre, A.J., & Hidayat, I. (2020). Seismic performance of reinforced concrete structures with pushover analysis. *IOP Conference Series: Earth and Environmental Science*, *426*(1), pp. 012045

Sayın, E., Yön, B., Onat, O., Gör, M., Öncü, M.E., Tuğrul Tunç, E., Bakır, D., Karaton, M., & Calayır, Y. (2021). 24 January 2020 Sivrice-Elazığ, Turkey earthquake: geotechnical evaluation and performance of structures. *Bulletin of Earthquake Engineering*, *19*, 657-684. https://doi.org/10.1007/s10518-020-01018-4

TBEC. (1975). Afet Bölgelerinde Yapılacak Yapılar Hakkında Yönetmelik. Bayındırlık ve İskan Bakanlığı, Ankara (in Turkish).

TBEC. (2018). Türkiye Bina Deprem Yönetmeliği. Afet ve Acil Durum Yönetimi Başkanlığı, Ankara (in Turkish).

Yön, B., Dedeoğlu, İ.Ö., Yetkin, M., Erkek, H., & Calayır, Y. (2024). Evaluation of the seismic response of reinforced concrete buildings in the light of lessons learned from the February 6, 2023, Kahramanmaraş, Türkiye earthquake sequences. *Natural Hazards*, *121*(1), 873-909

Zebua, D., & Koespiadi (2022). Performance evaluation of highrise building structure based on pushover analysis with ATC-40 method. *Applied Research on Civil Engineering and Environment (ARCEE)*, *3*(02), 54-63

Influence of location of tuned mass damper in reducing vibrations of a building subjected to ground motions

Onur Araz*[1], Mohammed M. A. Saif[1]

[1] *Gumushane University, Department of Civil Engineering, 29100 Gumushane, Türkiye*

Abstract. The loss of life and property caused by earthquakes has led researchers to work more intensively on earthquake-resistant building design. One of the most effective methods used to reduce vibrations in structures subjected to earthquake excitations is the tuned mass damper (TMD). The TMD is a single degree of freedom (SDOF) system consisting of a mass, a stiffness, and a damping element. In order for the TMD to provide adequate control performance, its mechanical properties must be properly determined. Therefore, the majority of studies conducted on TMD are aimed at determining the optimum values of its mechanical properties. Another factor that affects the effectiveness of TMD is the location of TMD. TMD is generally placed on the top floor of buildings under dynamic loads (i.e., wind and seismic loads). Thus, the effect of TMD's location on the effectiveness and optimum design of TMD is investigated in this study. For this purpose, TMD is placed on three different floors (i.e., 1st floor, 2nd floor, and 3rd floor) in a 3-story shear building. The optimum parameters of TMD (i.e., the optimum frequency ratio and damping ratio) are obtained using the genetic algortihm (GA). The optimum parameters obtained in the frequency domain are then tested using twelve earthquake records in time domain analyses. Numerical results show that TMD's location is important in reducing displacement and acceleration responses of the structure affected by ground motions.

Keywords: Earthquake; Seismic response; Tuned mass damper; Vibration control

1. Introduction

Globally, over one million seismic events occur annually. Earthquakes in urban areas can cause structural shaking, deformations, and harm to people (Ras, 2014). High levels of such vibrations may lead to discomfort for individuals or disrupt certain systems. To address these dynamic effects on civil engineering structures, mitigation measures are essential. Researchers have explored various damping systems, including active, semi-active, and passive types (Kahya & Araz, 2019). Active and semi-active systems require external energy to function (Kaveh et al., 2015), unlike passive systems. Among passive devices used in practice, the Tuned Mass Damper (TMD) stands out (Fahimi Farzam et al., 2020).

The primary goal of integrating a TMD into a structure, like other passive systems, is to reduce the structural elements' demand by dissipating part of the input energy (Araz & Kahya, 2021). This is achieved by transferring vibrational energy from the structure to the damper. The concept of the TMD in contemporary applications traces back to dynamic vibration absorbers studied by Frahm in 1909 (Araz, 2021a). In its simplest configuration, a TMD comprises a solid mass and a spring connected to the structure (Araz, 2021b), as shown in Fig. 1. While proposed for seismic design, TMDs have primarily been applied to mitigate wind-induced vibrations.

Several review papers discuss their practical applications, as well as linear and nonlinear theories (Mariantonieta & Hojjat, 2013; Rahimi et al., 2020; Sgobba & Marano, 2010). Numerous studies have analyzed the performance of these systems (Garcí et al., 2021; Takeshi et al., 2019), while others have focused on their enhancement (Khatibinia et al., 2018; Lavan, 2017). Some research has proposed mathematical algorithms to improve structural responses to seismic and wind loads (Gino & Marcus, 2019; Mohtasham et al., 2013). Kaveh and Ardebili (2021) performed a comparative analysis of an optimal tuned mass damper for tall structures, accounting for soil-structure interaction. The effect of different support conditions on the effectiveness of TMD also has been addressed by many researchers (Zhao et al., 2019; Zhao et al., 2024; De Domenico et al., 2018; Araz & Elias, 2024; Araz, 2024, Araz, 2025; Araz et al., 2023).

In this study, the effect of TMD in reducing the dynamic effects of a 3-storey building under earthquake effect will be investigated. In this context, TMD will be placed on the 1st, 2nd and 3rd floors respectively. The dynamic

* Corresponding author, E-mail: onuraraz29@hotmail.com

https://doi.org/10.31462/icearc2025_ce_eqe_217

responses obtained for each case will be compared with the dynamic responses in the uncontrolled case. Finally, the control performance of TMD is compared for different situations.

2. Governing equations of motion

The structural model of a 3-story shear building with TMD is shown in Fig. 1. With the addition of TMD, the degrees of freedom of the building increases from 3 to 4. Here, TMD is placed on the 1st, 2nd and 3rd floors of the building, respectively. In the study, these are named as Case-1, Case2, and Case-3, respectively.

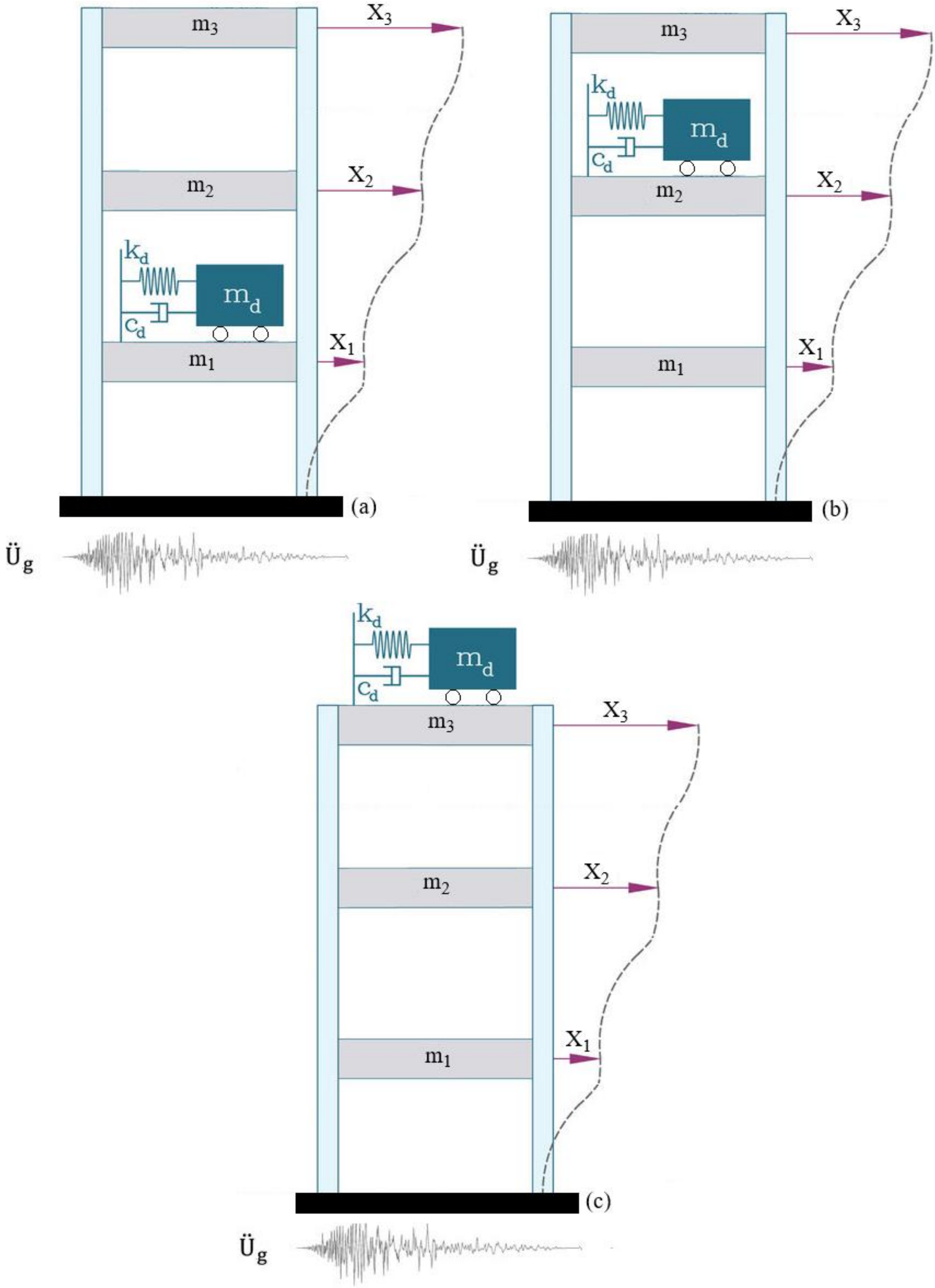

Fig. 1. 3-story building equipped with TMD. a) TMD added to the 1st floor (i.e., Case-1); b) TMD added to the 2nd floor (i.e., Case-2); c) TMD added to the 3rd floor (i.e., Case-3), respectively

The equations governing the motion of the building model with a TMD (i.e., Case-3) are represented by

$$\mathbf{M}\ddot{\mathbf{x}}(t)+\mathbf{C}\dot{\mathbf{x}}(t)+\mathbf{K}\mathbf{x}(t)=-Z\ddot{\mathbf{U}}_g(t) \tag{1}$$

Here, **M**, **C** and **K** are the (*4*×*4*) mass, damping and stiffness matrices, respectively. x denotes the (4×1) horizontal displacement vector. The equations of motion for Case-1 and Case-2 can be derived by taking into account the location of the TMD.

$$\mathbf{M}=\begin{bmatrix} m_1 & & & \\ & m_2 & & \\ & & m_3 & \\ & & & m_d \end{bmatrix} \tag{2}$$

$$\mathbf{C}=\begin{bmatrix} c_1+c_2 & -c_2 & & \\ -c_2 & c_2+c_3 & -c_3 & \\ & -c_3 & c_3+c_d & -c_d \\ & & -c_d & c_d \end{bmatrix} \tag{3}$$

$$\mathbf{K}=\begin{bmatrix} k_1+k_2 & -k_2 & & \\ -k_2 & k_2+k_3 & -k_3 & \\ & -k_3 & k_3+k_d & -k_d \\ & & -k_d & k_d \end{bmatrix} \tag{4}$$

$$\boldsymbol{Z}=\begin{bmatrix} m_1 & m_2 & m_3 & m_d \end{bmatrix}^T \tag{5}$$

$$x(t)=\begin{bmatrix} x_1 & x_2 & x_3 & x_d \end{bmatrix}^T \tag{6}$$

The floor masses, stiffness and damping values are represented as m_i, k_i, and c_i, respectively. m_d, k_d, and c_d are the TMD mass, stiffness, damping coefficients, respectively.

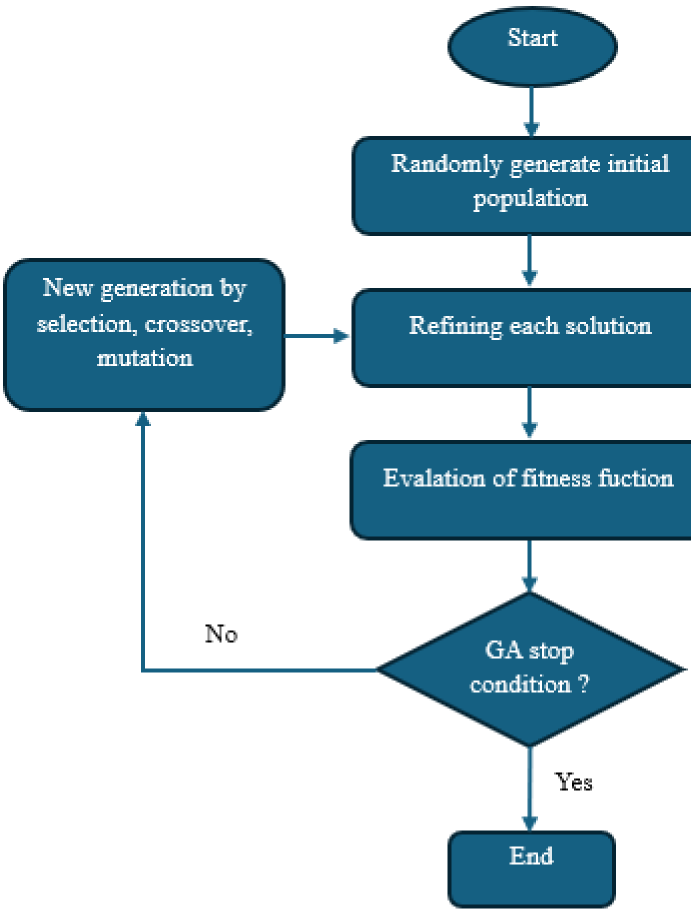

Fig. 2. Flowchart of GA

The design parameters of TMD are obtained by using genetic algorithm (GA) in frequency domain. GA is powerful optimization techniques inspired by the principles of natural selection and evolution, widely applied in engineering to solve complex, non-linear problems. By iteratively evolving a population of candidate solutions through selection, crossover, and mutation operations, GA efficiently explore large search spaces to identify optimal or near-optimal solutions. Their robustness and adaptability make them suitable for diverse applications, including structural design, control systems, and scheduling, where traditional methods may struggle. The aim of the optimization is to minimize the amplitude value of the displacement at the top floor of the building. The flow chart for the genetic algorithm is shown in Fig. 2.

The design parameters of TMD are expressed as follows

$$\xi_d = \frac{c_d}{2m_d\omega_d}; \quad \gamma = \frac{\omega_d}{\omega_1}; \quad \mu = \frac{m_d}{m_1 + m_2 + m_3} \tag{7}$$

Here, ξ_d, γ, and μ are the damping ratio, frequency ratio, and mass ratio of the TMD, respectively. Assuming that the mass ratio of the TMD is known at the beginning, the optimum values of ξ_d and γ are investigated.

3. Numerical study

The proporties of the three-story building considered in the study are given in Table 1. The natural frequencies corresponding to the first three modes of the building are given in Table 2. As can be seen, the obtained values are in agreement with the literature.

The optimum values of TMD for each case considered are summarized in Table 3. In obtaining these values, the mass ratio (μ) is taken as 0.05. As can be seen, from Case-1 to Case-3, the damping values increase while the stiffness values decrease. This situation causes a decrease in frequency ratio (γ) and an increase in the damping ratio (ξ_d). Optimization results obtained for each case are also presented in Fig. 3.

Table 1. Properties of 3-story building

Floor number	Mass (t)	Stiffness (MN/m)	Damping (kNs/m)
1	20	3.5	21.98
2	15	2.5	15.67
3	10	1.0	6.28

Table 2. Natural frequencies (ω_i) of 3-story building (rad/s)

Mode	Present	Marian and Giaralis (2014)
1	6.38	6.37
2	13.02	13.02
3	20.57	20.57

Table 3. Optimum values of the TMD

Case	m_d (kg)	k_d (N/m)	c_d (kNs/m)
Case-1	2250	88.736	1.913
Case-2	2250	81.502	3.719
Case-3	2250	66.935	5.552

In order to examine in detail the changes that occur on the dynamic responses of the building when the TMD is placed on different floors, 90 earthquake records are taken into account in the time history analysis. The features of the selected earthquakes are given in Fig. 4.

Figs. 5 and 6 show the maximum displacements and accelerations obtained at the top floor of the building, respectively. From these figures, it is seen that the responses in the uncontrolled condition are lower than the responses in the controlled condition. When compared to Case-1 and Case-2, it is observed that the responses obtained for Case-3 are lower.

The reductions obtained in displacement and acceleration reactions for the controlled cases are shown in Figs. 7 and 8, respectively. From these figures, it is seen that TMD is ineffective under some ground motions and even causes an increase in dynamic responses. However, the number of these earthquakes is quite low. This is due to the fact that the optimum parameters of TMD are obtained independently from earthquake records.

The average reduction ratios obtained for the displacement and acceleration responses are shown in Fig. 9. It can be seen that the highest control performance is obtained for Case-3, Case-2, and Case-1, respectively. Also, it is seen that TMD is more effective in reducing the displacement responses. This is because the goal of the optimization is to reduce the displacements at the top floor.

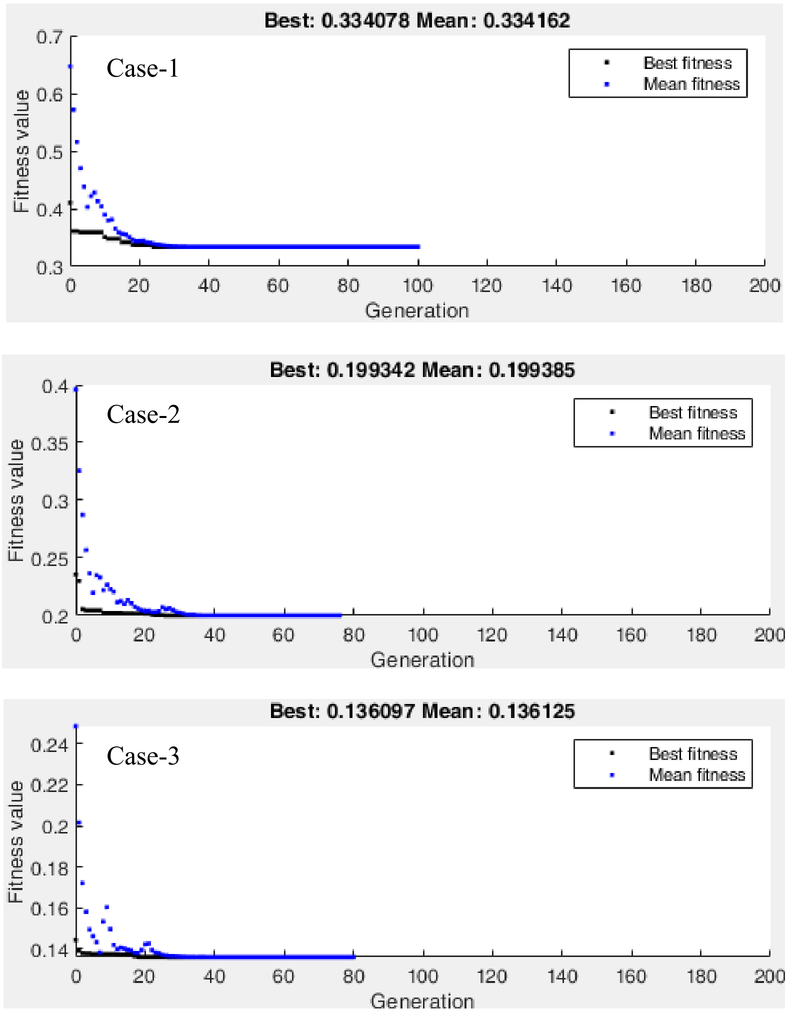

Fig. 3. Optimization results obtained for each case

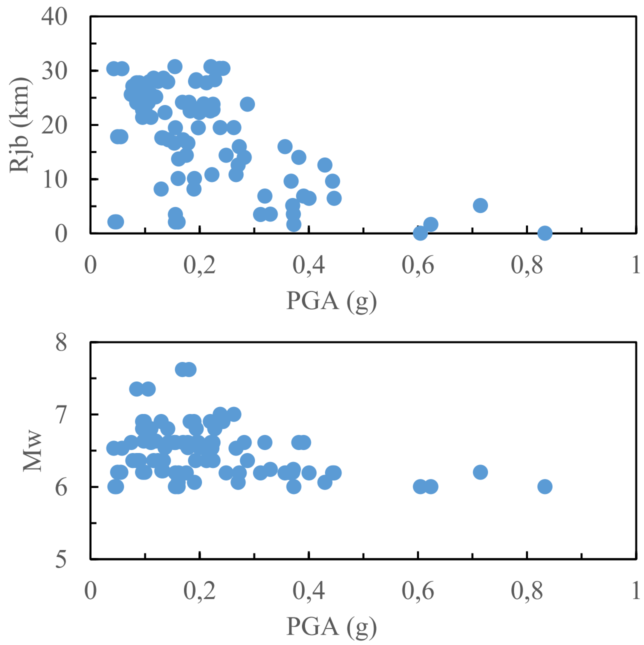

Fig. 4. Optimization results obtained for each case

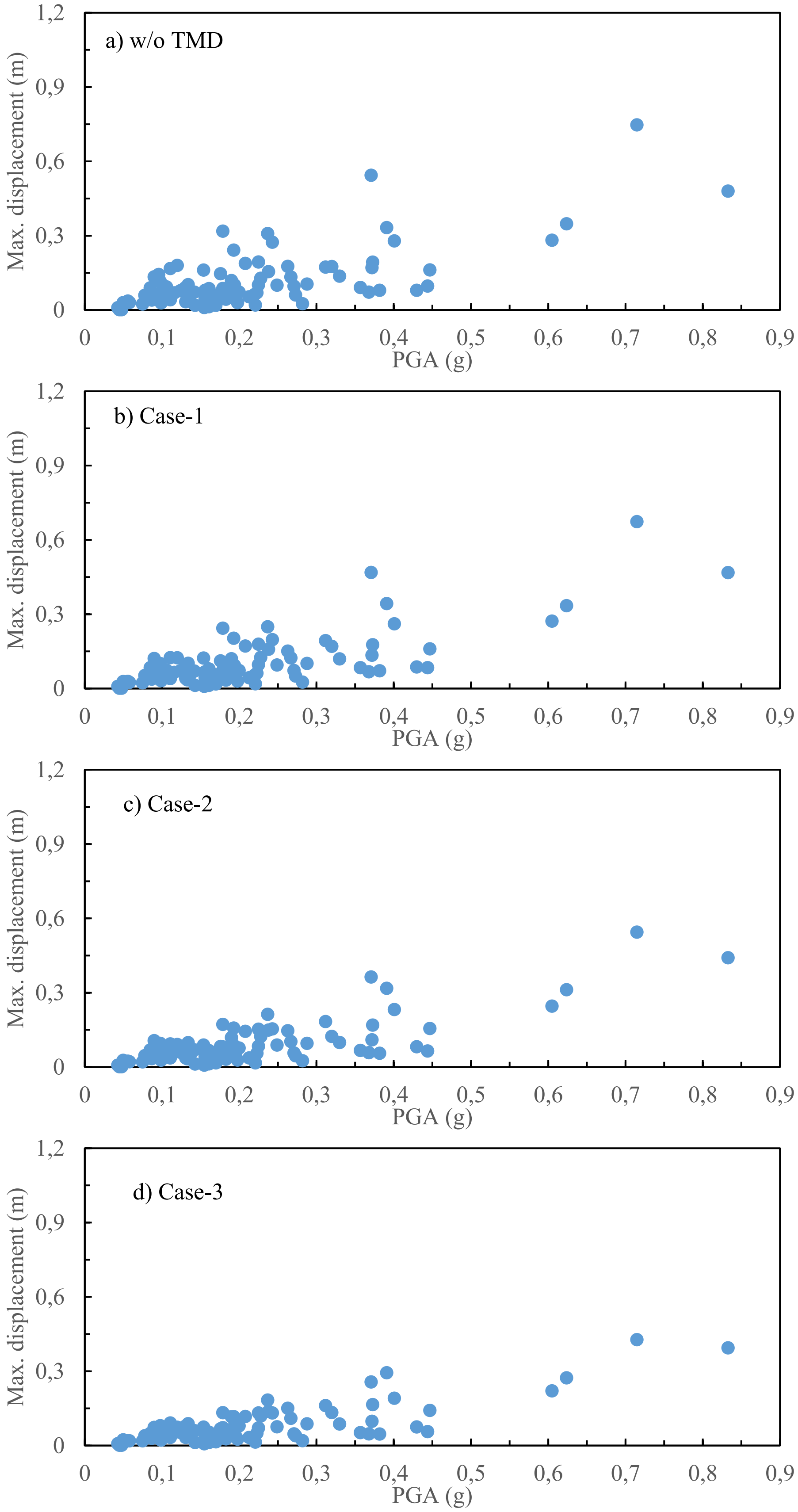

Fig. 5. Maximum displacemet responses of the building at the top story

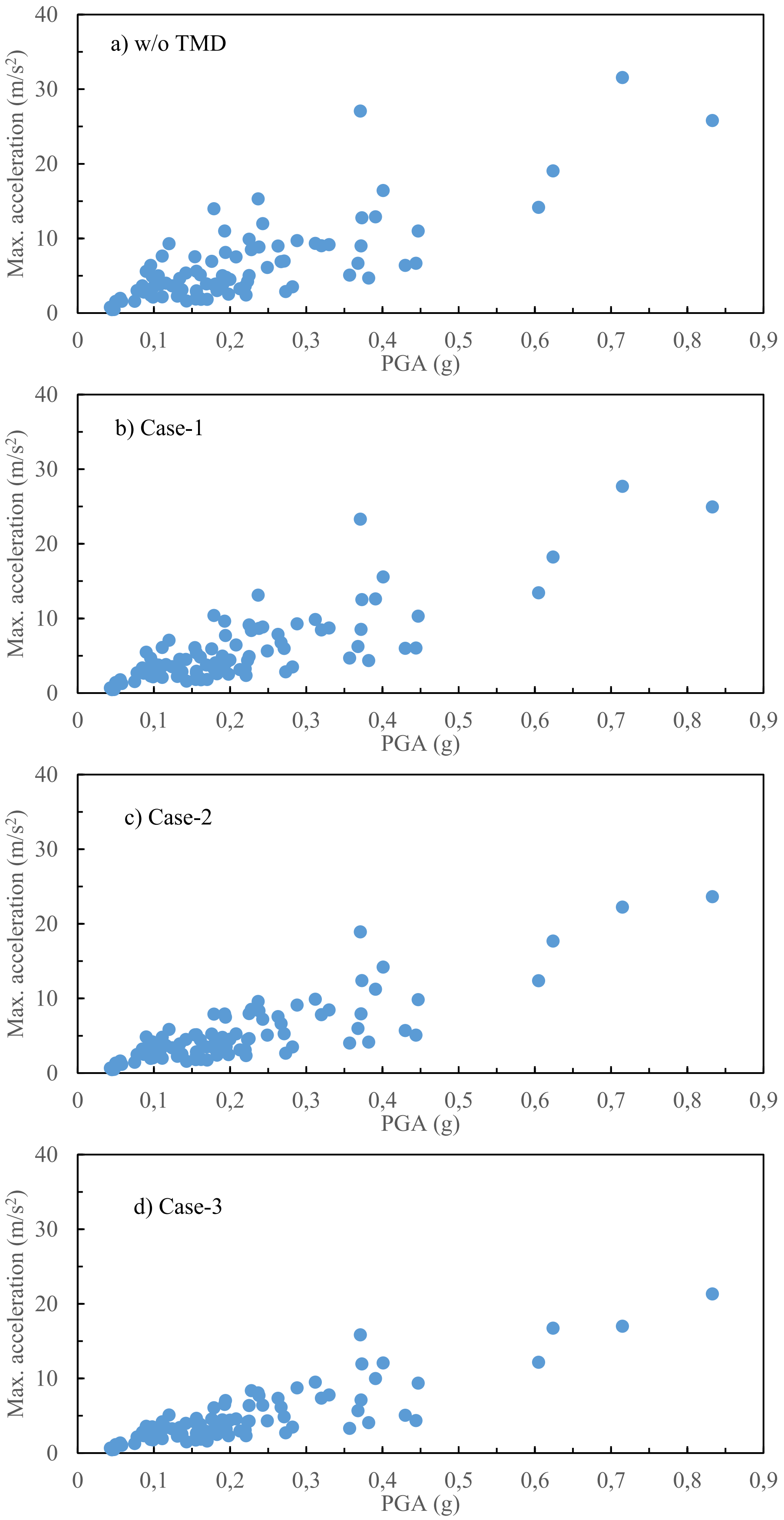

Fig. 6. Maximum acceleration responses of the building at the top story

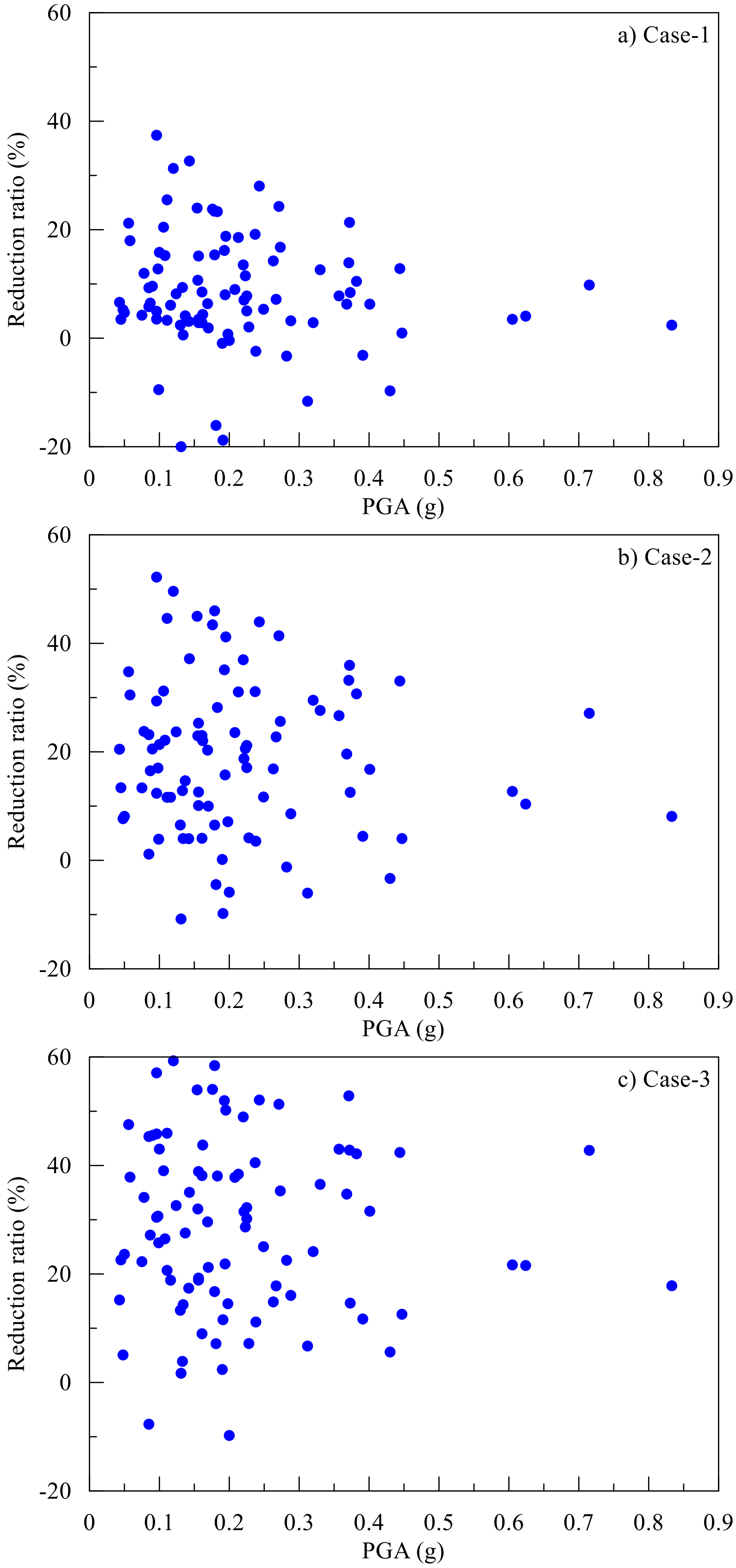

Fig. 7. Reduction ratios of the maximum displacement responses

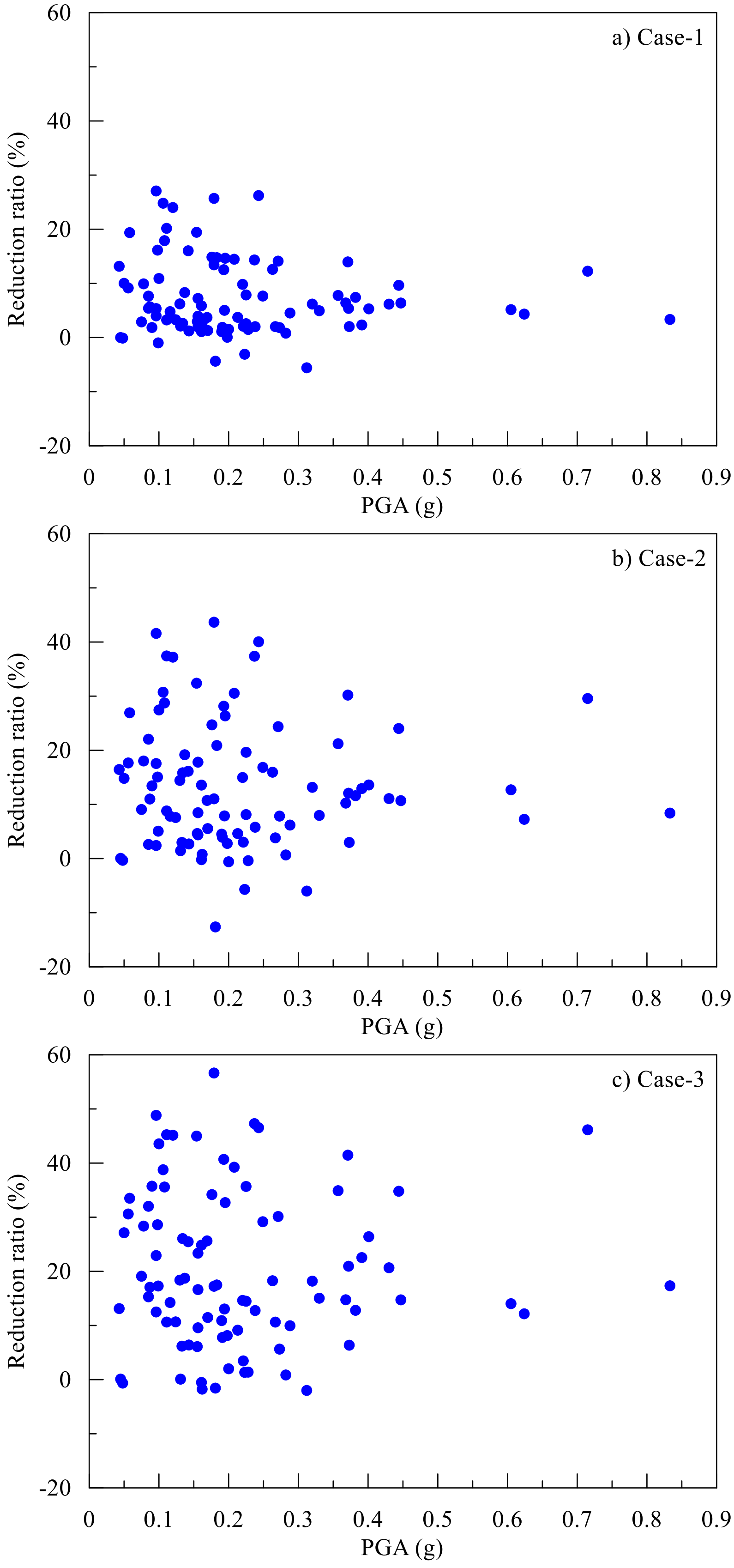

Fig. 8. Reduction ratios of the maximum acceleration responses

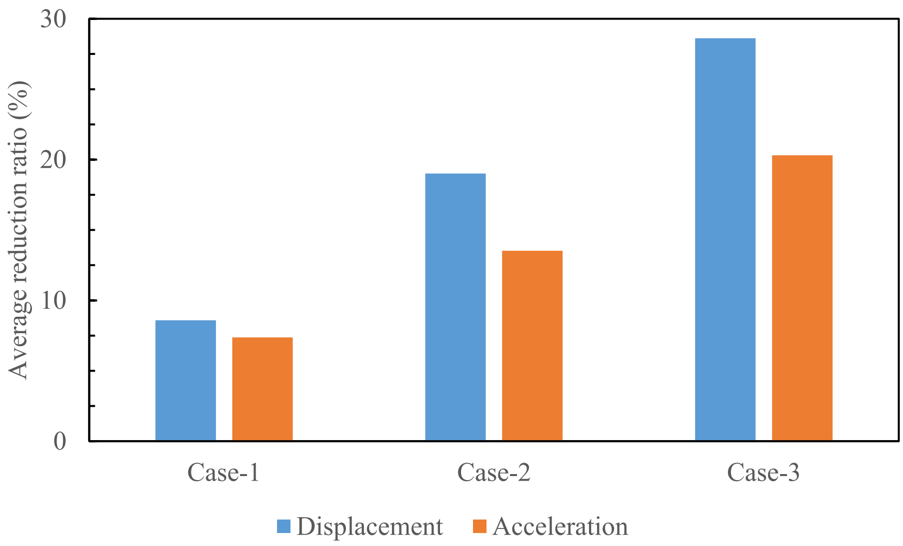

Fig. 9. Average reduction ratios of the maximum dynamic responses

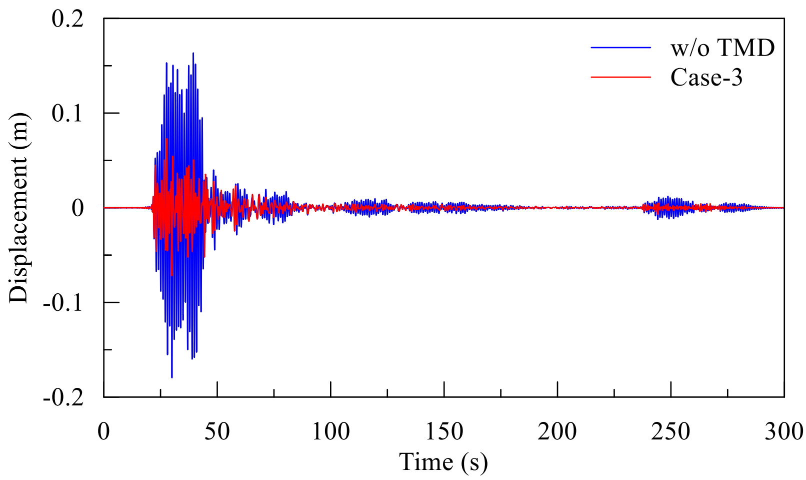

Fig. 10. Displacement time history of the building at the top story

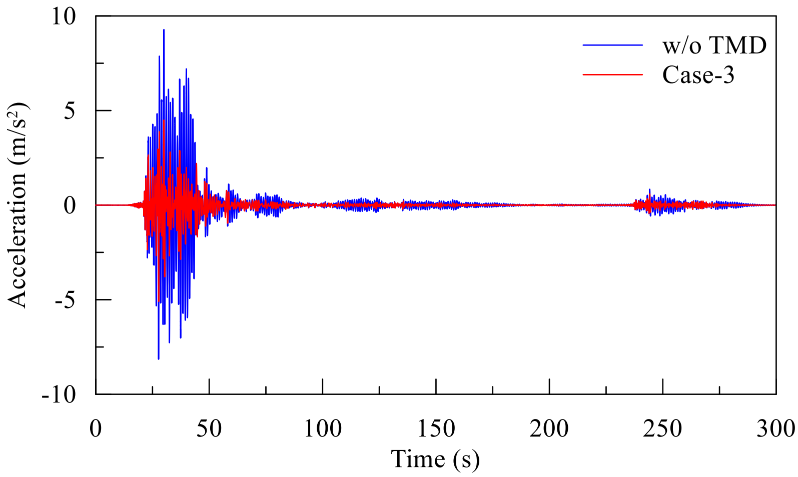

Fig. 11. Acceleration time history of the building at the top story

Figs. 10 and 11 show the time-dependent variation of displacement and acceleration at the top floor of the building under a benchmark earthquake record (i.e., $M_w = 6.63$, $R_{jb} = 25.14$ km, and PGA = 0.12g), respectively. The peak displacement and acceleration are reduced by 59.29% and 45.14%, respectively.

4. Conclusions

In this study, TMD was placed on the 1st, 2nd and 3rd floors of a 3-storey building, respectively, and the optimum values of TMD for these locations are obtained. Then, the accuracy of the obtained optimum parameters is investigated using 90 ground motions in the time domain. The main findings of the study are summarized below.

- Placing the TMD on different floors of the building causes significant changes in the design parameters of the TMD. The highest stiffness value is obtained when the TMD is placed on the 1st floor (i.e., Case-1), while the highest damping value is obtained for the 3rd floor (i.e., Case-3).
- The control performance of the TMD is significantly affected by the placement of the TMD on different floors. The largest reduction ratio in dynamic response values is obtained when the TMD is placed on the third floor (i.e., Case-3).
- When the TMD is placed on the 3rd floor of the building, the displacement and acceleration responses are reduced by approximately 30% and 20%, respectively.

References

Araz, O. (2021a). Optimum three-element tuned mass damper for damped main structures under ground acceleration. *El-Cezeri Journal of Science and Engineering*, 8(3), 1264-1271.

Araz, O. (2021b). Optimum passive tuned mass damper systems for main structures under harmonic excitation. *Mühendislik Bilimleri ve Tasarım Dergisi*, 9(4), 1062-1071.

Araz, O. (2024). Effect of PGV/PGA ratio on seismic-induced vibrations of structures equipped with parallel tuned mass dampers considering SSI. *Structures*, 68, 107188.

Araz, O. (2025). Effect of basic parameters defining principal soil-structure interaction on seismic control of structures equipped with optimum tuned mass damper. *Soil Dynamics and Earthquake Engineering*, 189, 109085.

Araz, O., & Elias S. (2024). Performance of differently arranged double-tuned mass dampers for structural seismic response control including soil-structure interaction. *Engineering Structures*, 319, 118841.

Araz, O, Cakir, T., Ozturk, K.F., & Kaya, D. (2023). Effect of foundation embedment ratio in suppressing seismic-induced vibrations using optimum tuned mass damper. *Soil Dynamics and Earthquake Engineering*, 171, 107981.

Araz, O., & Kahya, V. (2021). Optimization of non-traditional tuned mass damper for damped structures under harmonic excitation. *Uludağ Üniversitesi Mühendislik Fakültesi Dergisi*, 26(3), 1021-1034.

De Domenico, D., Impollonia, N., & Ricciardi, G. (2018). Soil-dependent optimum design of a new passive vibration control system combining seismic base isolation with tuned inerter damper. *Soil Dynamics and Earthquake Engineering*, 105, 37-53.

Fahimi Farzam, M., Kaveh, A., Jalali, H. H., & Maroofiazar, R. (2020). Robust optimum design of tuned mass damper inerter. *Acta Mechanica*, 231, 3871-3896.

Garci, V. J., Duque, E. P., Inaudi, J. A., Marquez, C. O., Mera, J. D., & Rios, A. C. (2021). Pendulum tuned mass damper: optimization and performance assessment in structures with elastoplastic behaviour. *Heliyon*, 7, 114-132.

Gino, C., & Marcus, M. (2019). Optimal pendulum tuned mass damper design applied to high towers using genetic algorithms: two-dof modeling. *Intentional Journal of Structural Stability and Dynamics*, 19, 10.

Kahya, V., & Araz, O. (2019). A sequential approach based design of multiple tuned mass dampers under harmonic excitation. *Sigma*, 37(1), 225-39.

Kaveh, A., & Ardebili, S.R. (2021). A comparative study of the optimum tuned mass damper for high-rise structures considering soil-structure interaction. *Periodica Polytechnica Civil Engineering*, 65(4), 1036-1049.

Khatibinia, M., Gholami, H., & Kamgar, R. (2018). Optimal design of tuned mass dampers subjected to continuous stationary critical excitation. *International Journal of Dynamic Control*, 6(3), 1094-1104.

Kaveh, A., Pirgholizadeh, S., & Khadem Hosseini, O. (2015). Semiactive tuned mass damper performance with optimized fuzzy controller using CSS algorithm. *Asian Journal of Civil Engineering*, 5(16), 587-606.

Lavan, O. (2017). Multi-objective optimal design of tuned mass dampers. *Structural Control Health Monitoring Journal*, 24, e2008.

Marian, L., & Giaralis, A. (2014). Optimal design of a novel tuned mass-damper–inerter (TMDI) passive vibration control configuration for stochastically support-excited structural systems. *Probabilistic Engineering Mechanics*, 38, 156-164.

Mariantonieta, G. S., & Hojjat, A. (2013). Tuned mass dampers. *Archives of Computational Methods in Engineering*, 20, 419-431.

Mohtasham, M., Kazem, S., Ghambarpour, Y. G., & Majzoub, H. (2013). Designing optimal multiple tuned mass dampers using genetic algorithms (GAs) for mitigating the seismic response of structures. *Journal of Vibration and Control*, 19(4), 605-625.
Rahimi, F., Aghayari, R., & Samali, B. (2020). Application of tuned mass dampers for structural vibration control: A state-of-the-art review. *Civil Engineering Journal*, 6(8), 1622-1652.
Ras, A., & Boumechra, N. (2014). Study of nonlinear fluid viscous dampers behaviour in seismic steel structures design. *Arabian Journal for Science and Engineering*, 39(12), 8635-8648.
Sgobba, S., & Marano, G. C. (2010). Optimum design of linear tuned mass dampers for structures with nonlinear behaviour. *Mechanical Systems and Signal Processing*, 24, 1739-1755.
Takeshi, N., Haruhiko, K., Tomoki, Y., & Naoki, K. (2019). Control effect of large tuned mass damper used for seismic retrofitting of existing high-rise building. *Japan Architectural Review*, 2(3), 269-286.
Zhao, Z., Chen, Q., Zhang, R., Pan, C., & Jiang, Y. (2019). Optimal design of an inerter isolation system considering the soil condition. *Engineering Structures*,196, 109324.
Zhao, Z., Hu, X., Zhang, R., Xie, M., & Liu, S. (2024). Advantages and design of inerters for isolated storage tanks incorporating soil conditions. *Thin-Walled Structures*, 195, 111356.

4th International Civil Engineering & Architecture Conference
17-19 May 2025, Trabzon, Türkiye

The effect of material properties on the seismic behavior of historical masonry mosques

İrfan Kocaman*[1], Ömer Mercimek[2], Muhammed Gürbüz[1], Yaşar Erbaş[3], Özgür Anıl[4]

[1] Erzurum Technical Universtiy, Departmen of Civil Engineering, 25100 Erzurum, Türkiye
[2] Ankara University, Department of Civil Engineering, 0600 Ankara, Türkiye
[3] Bartın Universtiy, Departmen of Civil Engineering, 74110 Bartın, Türkiye
[4] Gazi University, Department of Civil Engineering, 0600 Ankara, Türkiye

Abstract. Finite element methods are widely recognized as reliable tools for evaluating the seismic performance of historical structures. However, the accurate definition of parameters such as material properties, which often involve significant uncertainties, is crucial for the validity of these analyses. In this study, the seismic behavior of Malatya Yeni Mosque, which completely collapsed during the 2023 Kahramanmaraş earthquakes, was investigated by examining the impact of different material properties. A finite element model of the mosque was developed, and two distinct sets of material properties recommended in the literature were assigned to the model. The first model (Model-1) utilized material properties derived from previous studies on the structure. The second model (Model-2) incorporated general material properties proposed in the literature for historical masonry mosques. Both models were subjected to dynamic analyses using a ground motion record obtained in Malatya during the Kahramanmaraş earthquakes. The results of the dynamic analyses revealed that material properties significantly influence the seismic performance of the structure. In Model-1, the structure exhibited no signs of damage. However, in Model-2, considerable damage was observed in structural elements, closely resembling the actual collapse mechanisms of the mosque during the earthquake. These findings highlight the critical importance of accurately defining material properties in the seismic performance assessment of historical structures to predict their behavior under seismic loading. Moreover, the study offers valuable insights into the calibration of analyses and the planning of effective retrofitting strategies for such structures.

Keywords: Collapse mechanism; Malatya Yeni Mosque; Material properties effect; Time-history analyses

1. Introduction

In recent years, devastating earthquakes have made the preservation of cultural heritage structures a priority research topic (Kocaman, 2023a; Mercimek, 2023; Yilmaz et al., 2024; Atmaca et al., 2024). These structures, which reflect the craftsmanship, technical knowledge, and cultural fabric of past generations, hold critical importance not only for their architectural and aesthetic value but also for preserving the collective memory of societies. Turkey, with its rich cultural diversity and heritage from various historical periods, stands out as a prominent representative of this legacy. According to data from the Turkish Ministry of Culture and Tourism, approximately 120,000 immovable cultural assets with diverse functions have been registered. Of these, around 9% consist of historical mosques and churches. Furthermore, 19 sites in Turkey are listed as UNESCO World Heritage Sites, with an additional 84 sites on the tentative list (KVMGM, 2005).

Turkey's location within the Alpine-Himalayan seismic belt presents a significant challenge to the preservation of its cultural heritage. Historical masonry mosques are particularly vulnerable to seismic events due to factors such as low tensile strength, limited energy dissipation capacity, weak connections between structural elements, insufficient out-of-plane resistance, and material deterioration (Kocaman & Kazaz, 2023; Aşıkoğlu et al., 2019). In this context, seismic performance assessments of historical structures have become increasingly important for developing effective retrofitting strategies to enhance their earthquake resilience (Şentürk et al., 2022).

Finite element modeling, commonly used to investigate the seismic behavior of historical masonry structures, employs micro- and macro-modeling techniques depending on the desired level of accuracy and the scale of the structure. These methods provide valuable insights into potential collapse mechanisms and help improve the earthquake resistance of such structures (Valente, 2023; Valente & Milani, 2018; Aghabeigi & Farahmand-Tabar,

* Corresponding author, E-mail: irfan.kocaman@erzurum.edu.tr

https://doi.org/10.31462/icearc2025_ce_eqe_241

2021). These analyses contribute to the development of scientifically grounded strategies for preserving cultural heritage.

In structural modeling studies, one of the most critical steps in the finite element method is the accurate characterization of material properties. The non-homogeneous behavior of stone units, their prolonged exposure to environmental effects, and the influence of stone dimensions on the mechanical properties of entire walls present various challenges in this process. National and international codes propose different mechanical properties for stone masonry walls; however, the literature reveals a wide range of compressive strength (fc), tensile strength (ft), and modulus of elasticity (E) values. This wide variability complicates the determination of realistic parameters.

This study presents analyses conducted on Malatya Yeni Mosque, which completely collapsed during the 2023 Kahramanmaraş earthquakes. The mosque had sustained significant damage during the 2020 Elazığ-Sivrice earthquake and subsequently underwent extensive retrofitting and restoration efforts to repair the damage. During the restoration, material properties were determined from samples taken from the mosque and incorporated into finite element models. Two distinct models were utilized in the study: Model-1 employed mosque-specific material properties proposed in previous studies, while Model-2 utilized generic material parameters for masonry stone walls recommended in the literature and codes.

Nonlinear dynamic analyses were performed on both models using ground motion records from the 2023 Kahramanmaraş earthquakes observed in Malatya. The analysis results indicated that Model-1 experienced minimal damage, whereas Model-2 sustained significant damage and eventually collapsed. Additionally, the observed damage mechanisms in Model-2 closely aligned with those identified in post-earthquake field studies. These findings underscore the critical importance of accurately defining material properties for the seismic performance of historical masonry structures.

2. Determining material properties in historical structures

Determining the material properties of historical masonry structures requires more complex and specialized approaches compared to modern construction materials. The properties of the stones and mortars used in masonry structures vary significantly from one building to another, making it difficult to accurately define material parameters (Lourenço, 2002). One of the main challenges is the heterogeneous nature of the structures. The types of stones used, the mortar compositions, and environmental effects directly influence the mechanical properties of the material. Additionally, the limitations in testing historical structures significantly restrict sampling processes and the reliability of these samples. In particular, samples taken from deteriorated or damaged areas may not provide representative information about the overall structure.

Different methods for determining material properties are proposed in the literature and regulations. These methods are generally divided into two categories: non-destructive methods and destructive methods. Non-destructive methods allow for determining material properties while preserving the integrity of the structure. Techniques such as ultrasonic velocity measurements, surface hardness tests, and vibration analysis are among these methods. However, these methods may be insufficient for determining the exact mechanical properties of the material (Pantò et al., 2024). Destructive methods usually require sample collection and laboratory testing. These methods are used to measure compressive strength, tensile strength, and elasticity modulus (Banjo et al., 2024). However, the limitations in the sampling process and the risk of damaging the structure restrict the use of these methods.

Researchers often refer to national and international regulations when determining material properties. These regulations include parameters such as compressive strength (fc), tensile strength (ft), elasticity modulus (E), density (γ), and Poisson's ratio (v) (GERMHS, 2017; TEC-07, 2007; TBEC, 2018; FEMA 356, 2000; Eurocode-6, 2005). However, since historical structures are generally built with local materials, it is more appropriate to rely on national regulations. Nonetheless, the diversity of regulations and uncertainties in the properties of local materials create additional challenges in seismic performance analysis.

Differences between regulations become particularly evident when parameterizing material properties. For example, the GERMHS (2017) regulation defines the relationship between fc and E as 460fc, while TEC-07 (2007) specifies it as 200fc. TBEC-18 (2018) suggests 750fc, FEMA356 (2000) proposes 550fc, and Eurocode-6 (2005) recommends 1000fc. This wide range highlights the lack of standardization in determining material properties and the variability of results in analyses based on regulations.

To overcome these challenges, researchers utilize studies and recommendations found in the literature. Similar building types, wall typologies, and construction techniques provide important references for evaluating material properties. For instance, if buildings constructed in the same region contain similar stone and mortar types, the test results from these structures can serve as guidance for other similar buildings. The impact of construction techniques, stone types, and mortar compositions on material properties is considered to determine parameters that are consistent with local building practices (Kocaman, 2024).

In the literature, material properties used in historical masonry structures are presented over a broad range. For example, compressive strength may vary between 2 MPa and 27 MPa, and elasticity modulus may range from 600

MPa to 5000 MPa. This diversity depends on the geographical location of the structures, the types of materials used, and environmental effects. Therefore, to accurately determine material properties, tests on similar structures and recommendations from the literature are carefully evaluated.

Table 1 summarizes the material properties accepted in the literature for historical masonry structures. This table can serve as a guide for determining material parameters based on the uniqueness of the structures and local conditions. This diversity allows for the accurate analysis of a structure's seismic resilience and the achievement of reliable results.

Table 1. Material properties for historical masonry Structures - recommendations from various studies

Study	Material Properties					Structure type
	Masonry wall				Dome	
	γ (kg/m³)	f_c (MPa)	E (MPa)	v	E (MPa)	
Apostolopoulos & Sotiropoulos (2008)	2000	-	2750	0.20	-	Church
Betti & Vignoli (2008)	2200	4.00	2000	0.25	-	Church
Şeker (2011)	2650	-	8370	0.17	2510	Mosque
Bağbancı (2013)	2400	-	10326	0.17	-	Bulding
Ercan & Nuhoğlu (2014)	2100	10.49	871	0.17	-	Aqueduct
Gentile et al. (2015)	1700	-	2970	0.15	-	Tower
Nohutçu et al. (2015)	2200	7.42	1210	0.17	-	Mosque
Altunışık et al. (2016)	2000	2.40	1600	0.20	1200	Mosque
Torres et al. (2017)	2400	-	1560	-	-	Cathedral
Kazaz et al. (2021)	2790	5.21	3911	0.20	-	Tower
Onat et al. (2024)	2370	2.3	1030	0.23	1000	Mosque
Kocaman et al. (2024a)	2500	7.24	1200	0.18	500	Cupola
	2500	3	750	0.18		
Kocaman & Gürbüz (2024)	2500	3	1000	0.18	500	Mosque
Gürbüz & Kocaman (2024)	2500	3	2000	0.18	1000	Church
Kahya et al. (2024)	2300	2	2400	0.15	-	Building
Vitorino et al. (2024)	2690	27.06	-	0.20	-	Cathedral

2.1. Malatya Yeni Mosque

Malatya Yeni Mosque, also known by the public as "Teze Mosque" and "Ulu Mosque," is a significant structure located in the city center of Malatya. Initially built in 1843 by Hacı Yusuf, this mosque was rendered unusable after fires in 1889 and 1890. Following these fires, no restoration work was carried out, and the mosque was completely destroyed in the 7.1 magnitude earthquake that struck the region in 1893 (Selahattin, 2016). The mosque was rebuilt in 1913 at the same location, retaining its original design; however, only one minaret from the original structure has survived to this day.

The Malatya Yeni Mosque, which was damaged in the 2020 Elazığ-Sivrice Earthquake (Mw 6.8), underwent a comprehensive restoration process and was reopened for prayer in 2022. However, the earthquake centered in Kahramanmaraş on February 6, 2023, caused the complete destruction of the mosque.

Designed with a square plan and a central dome, Malatya Yeni Mosque reflects the characteristics of the late Ottoman architecture. The mosque is approximately 26 meters by 29 meters in size, with wall thickness around 1.2 meters. The load-bearing walls are constructed in a three-leaf arrangement, and there are two minarets located at the northeast and northwest corners of the structure. Between these minarets, the prayer hall is surrounded by five small domes.

The central dome is supported by four octagonal supporting columns (pendentives), which are connected to the walls with an arch system. The diameter of the central dome is approximately 11 meters, and its height has been measured as 21 meters. The appearance and details of the mosque before its destruction are shown in Fig. 1. For more detailed information about Malatya Yeni Mosque, see (Kocaman et al., 2024b).

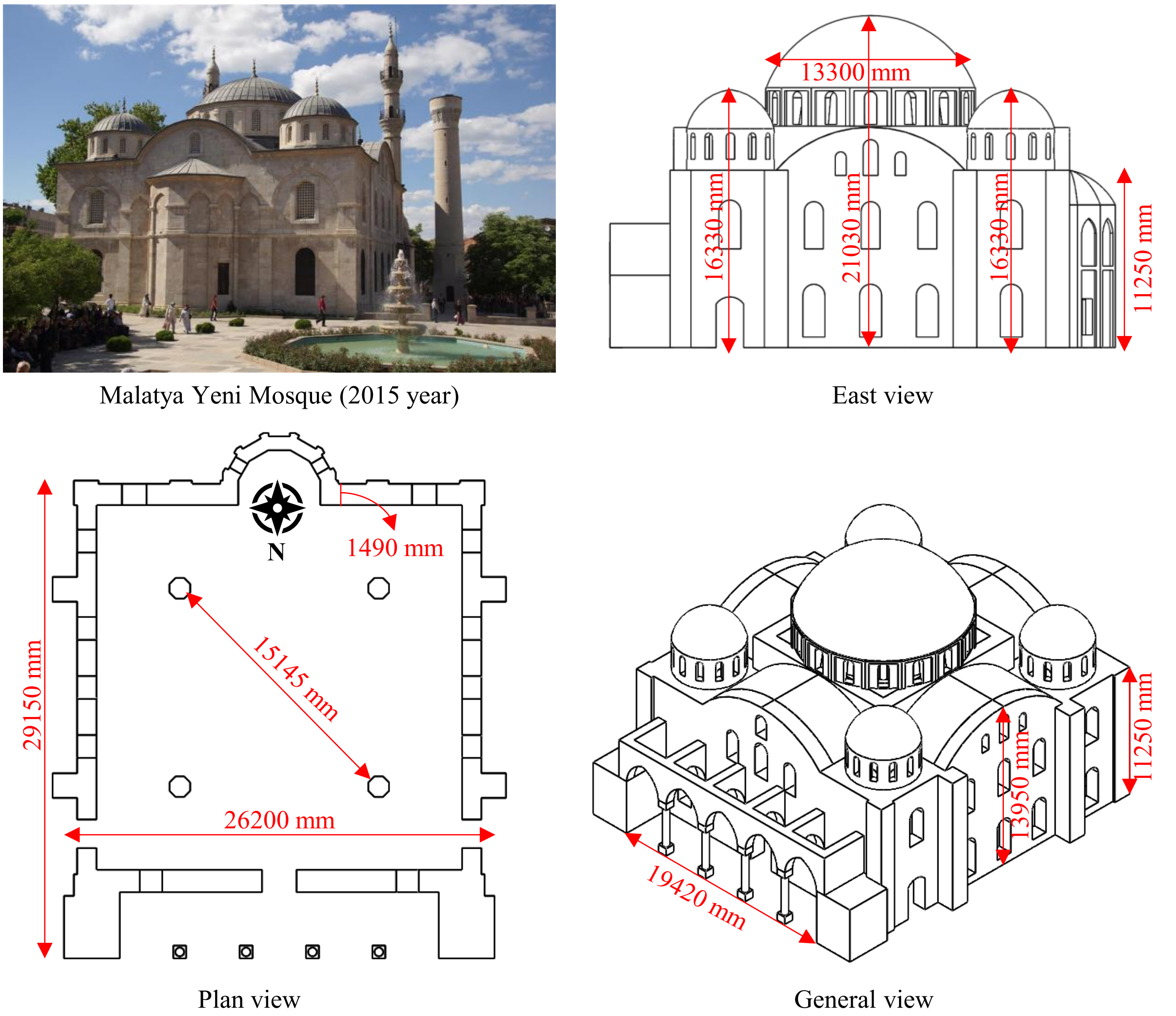

Fig. 1. Historical Malatya Yeni Mosque (Kocaman et al., 2024b)

2.2 Finite element model

The Finite Element Method (FEM) is a commonly used tool for examining the seismic performance of historical masonry mosques. Micro and macro modeling approaches are preferred based on model accuracy and computational efficiency. Micro modeling focuses on the behavior of individual units and mortar, while macro modeling treats the structure as a homogeneous entity, making it more suitable for the analysis of large structures (Valente, 2021). This study uses macro modeling and nonlinear dynamic analysis to understand the seismic behavior of the mosque's walls.

The three-dimensional model of the mosque was created using SolidWorks and transferred to ANSYS APDL for analysis. In the analyses, the SOLID65 element was preferred. This element is particularly notable for its ability to model nonlinear material behavior in masonry structures. The cracking conditions at each integration point and the corresponding material properties were modeled using SOLID65. However, factors such as element mesh density and skewness values are important. In the study, a mesh structure consisting of 286305 elements and 67687 nodes was used, with the element skewness value calculated as 0.16.

The masonry material behavior was analyzed using the Willam-Warnke material model. This model comprehensively defines the failure behavior of masonry materials by considering key parameters such as tensile and compressive strengths. In the analyses, shear transfer coefficients for tensile and compressive strengths were assigned as 0.05 and 0.8, respectively (Kocaman, 2023a).

Structural analysis of historical mosques is influenced by factors such as boundary conditions, material uncertainties, and geometric complexities. These factors require the use of advanced and reliable methods in the analyses. In this study, the mosque's foundational supports were assumed to be fixed, and soil-structure interaction was not considered due to a lack of soil information. Fig. 2 shows the finite element model of the mosque.

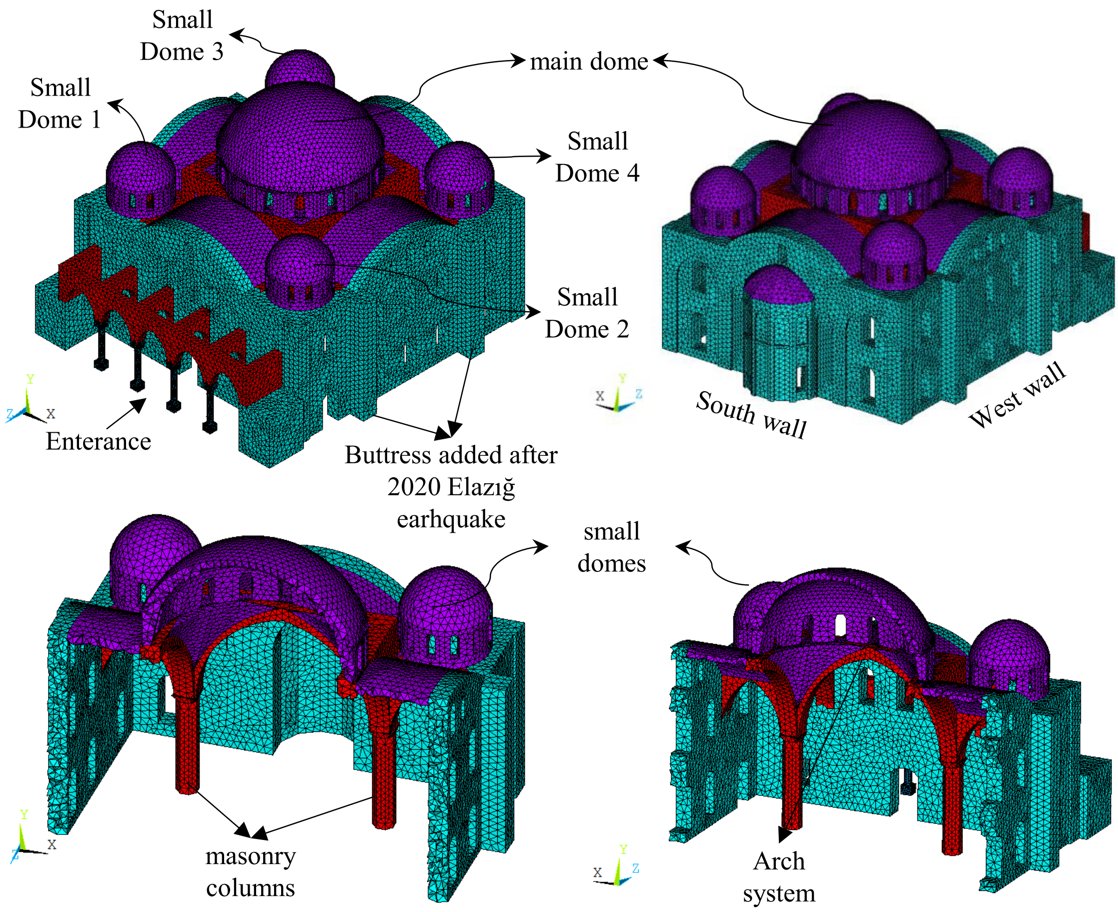

Fig. 2. Finite element model of Malatya Yeni Mosque (Kocaman et al., 2024b)

2.3 Material properties

Historical mosques present significant challenges in determining material properties due to their complex structures and the environmental impacts they have been exposed to over the years. In the literature, destructive and non-destructive tests have been conducted on both damaged and undamaged samples to understand the material properties of these structures. The unique characteristics of natural stones, in particular, reveal a distinctive structural profile for each mosque.

In this study, material properties were first determined through literature and regulatory recommendations. These material properties are used in Model-2 (M2). Demir (2012) conducted comprehensive compression tests on three-leaf walls. The study revealed an average compression strength of 3 MPa. Similarly, various studies in the literature have examined mosques with similar architecture in the region. Aşıkoğlu et al. (2019) used non-destructive methods to determine the material properties of Kurşunlu Mosque and recommended a compression strength of 2.1 MPa for the walls. Additionally, Kocaman and Gürbüz (2023b) performed finite element analyses to identify the collapse mechanisms of the narthex sections in mosques. In their models, they suggested a compression strength of 5.5 MPa for arches and 10 MPa for stone columns. Regarding compression strength values, the Italian Code (2009) recommends a range of 2.6-3.8 MPa for cut stone masonry. Therefore, for this study, the compression strength of the walls was accepted as 3 MPa. It is noteworthy that historical structures have low compression stresses and very low tensile strength. Experimental and analytical studies on historical mosques (Kocaman & Gürbüz, 2024; Gürbüz & Kocaman, 2024) have observed that the tensile strength is approximately 10% of the compression strength, and the Poisson's ratio varies between 0.17 and 0.2.

The second approach involves using material properties determined during restoration and strengthening works carried out after the 2020 Elazığ-Sivrice earthquake. These material properties are used in Model-1 (M1). In a study by Fırat et al. (2022), compression strengths of stone samples taken from the mosque were determined. The average compression strength of three samples was found to be 75.69 MPa, and their densities were 2458.4 kg/m³. The compression strength of the building's walls was calculated using the formula specified in TS EN 1996-1-1 (2005), under the heading "Characteristic compression strength of unreinforced masonry buildings made with general-purpose mortar."

$$f_k = K f_b^{0.65} f_m^{0.25} \tag{1}$$

In this context, fk represents the characteristic compression strength of the wall, fb is the compression strength of the stone, and fm is the compression strength of the mortar. K is a coefficient specified in the relevant regulations (TS EN 1996-1-1, 2005). In this case, the value of K has been determined as 0.40. The formula does not provide a value for the compression strength of the mortar. The compression strength of the mortar has been considered as 1 MPa. Accordingly, the characteristic compression strength of the building's wall body is approximately 6.65 MPa. In the literature, the tensile strength of such materials is approximately 1/10th of the compression strength. Therefore, the tensile strength of the building's wall body has been estimated to be approximately 0.66 MPa. The authors have assumed the value of the modulus of elasticity using the approach 1000fc, resulting in an elasticity modulus of 6650 MPa. Details of the material properties obtained with both approaches are provided in Table 2.

Table 2. Mechanical properties of the materials for M1 and M2

Mosque Part	Tensile strength f_t (MPa)		Compressive strength f_c (MPa)		Specific weight γ (kN/m^3)		Poisson ratio		Modulus of elasticity E (MPa)	
	M1	*M2*	*M1*	*M2*	*M1*	*M2*	*M1*	*M2*	*M1*	*M2*
Walls	0.30	0.66	3.00	6.65	24.5	24.5	0.18	0.30	600	6650
Dome and vaults	0.30	0.66	3.00	3.00	24.5	24.5	0.18	0.30	500	3375
Columns and Arches	0.55	0.66	5.50	6.65	24.5	24.5	0.18	0.30	1100	6650
Stone columns	1.00	1.00	10.00	10.00	29.0	29.0	0.20	0.30	10000	10000

3. Numerical analyses and results

The numerical analyses were conducted using two different models. The first model (Model-1) uses material properties determined based on literature recommendations, while the second model (Model-2) employs material properties obtained from samples taken from the structure and different approaches.

3.1 Modal analyses

In both finite element models of Malatya Yeni Mosque, vibration frequencies and mass participation ratios were determined using the modal analysis method. The analysis focused primarily on the first three modes, with a total of 20 modes evaluated. Table 3 provides the frequency values and mass participation ratios for these modes, offering significant data regarding the horizontal and vertical dynamic behavior of the mosque. In both models, the first mode represents movement in the north-south plane (Z direction), the second mode represents movement in the east-west plane (X direction), and the third mode represents torsional motion (rotation in the Y direction).

Fig. 3 presents graphical representations of the first three mode shapes obtained from both models. These visuals detail how the structure responds to different vibration modes and reveal its modal behavior. In both models, the total mass of the structure was calculated to be approximately 6080 tons. This mass is a key parameter that significantly affects the dynamic behavior of the mosque.

The modal analysis results provide a comprehensive overview of the fundamental vibration characteristics of Malatya Yeni Mosque and lay the groundwork for evaluating its structural performance and potential improvements. The differences between Model-1 and Model-2, particularly regarding changes in material properties, show that the frequency values were affected as expected. However, no significant changes were observed in the mode shapes or mass participation ratios.

Table 3. Frequencies and mass participation ratios (MPR) for the Model-1 and Model-2

Mod	Frequency (Hz)		MPR (X dir. vertical)		MPR (Z dir. vertical)		MPR (Y torsional)	
	M1	M2	M1	M2	M1	M2	M1	M2
1	2.11	6.28	0.66	0.62	0.21E-03	0.61E-04	0.46E-03	0.51E-03
2	2.13	6.37	0.20E-03	0.58E-04	0.70	0.67	0.16E-02	0.15E-02
3	2.66	6.97	0.27E-06	0.97E-06	0.16E-02	0.12E-02	0.32	0.30

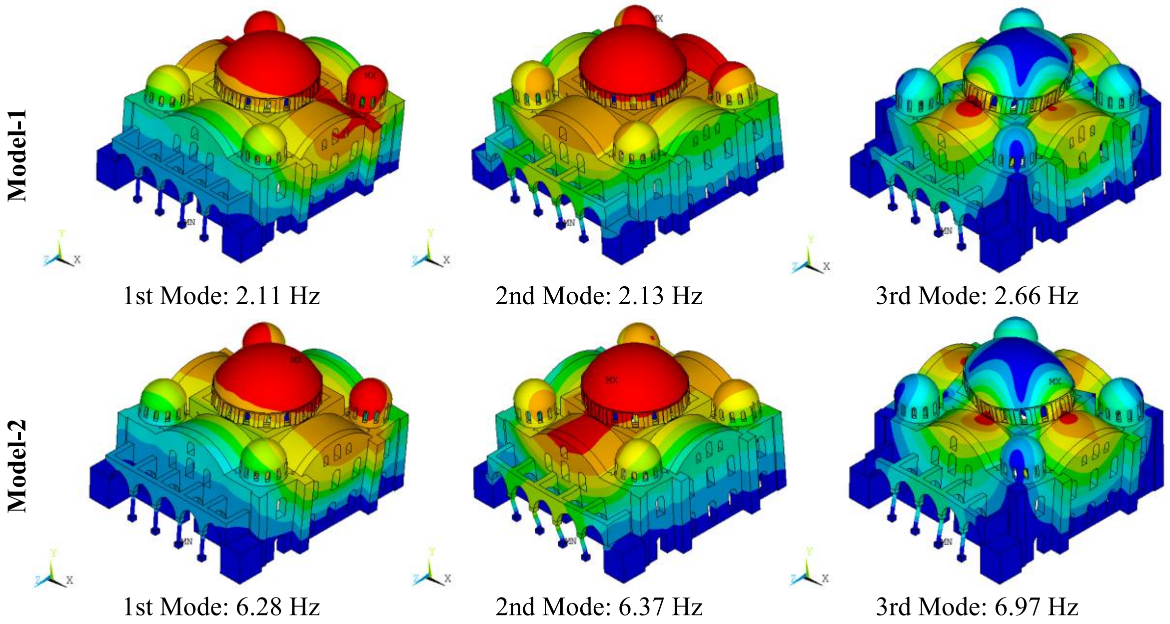

Fig. 3. Model-1 and Model-2 modal shapes of the first three modes

Material property changes result in significant differences in frequency values. Çalık et al. (2020) propose Equation 2 for the frequency value of the first mode of masonry domed mosques.

$$f_1 = 25.230 - 0.715E + 0.518B - 1.706S - 17.690D - 0.447H + 10.554KK + 0.352TA \quad (2)$$

In this equation, f1 represents the frequency value of the first mode (Hz), E is the mosque's short side length, B is the mosque's long side length, S is the length of the vestibule, D is the wall thickness, H is the wall height, KK is the dome thickness, and Ta is the footprint area of all the walls. When these values for Malatya Yeni Mosque are substituted into Equation 2, the frequency value of the first mode is determined to be 2.40 Hz. This result is clearly more suitable when compared to the frequency value of the first mode obtained from Model-1.

3.2. Nonlinear time-history analyses

The dynamic analysis of the mosque in the time domain involved applying the two horizontal components of the selected acceleration record in two orthogonal directions (X-Z). The vertical component was ignored in this analysis. Fig. 4 shows the acceleration-time graphs of the earthquake recorded in the Malatya city center during the Pazarcık-Kahramanmaraş earthquake (04:17 GMT+3, Mw 7.7) on February 6, 2023. Additionally, Fig. 4 presents the response spectra for the East-West (E-W) and North-South (N-S) components. The ground motion data were obtained from the Disaster and Emergency Management Authority (AFAD) database of Turkey (AFAD, 2023), and the dynamic analysis of the mosque was conducted using this recorded ground motion. This analysis allows for the evaluation of how the mosque responds to specific seismic forces produced by the earthquake.

Çalık et al. (2020) conducted experimental modal analysis tests on several historical masonry mosques, revealing damping ratios ranging from 1% to 4%. Additionally, in the literature (Kocaman & Gürbüz, 2024; Gürbüz & Kocaman, 2024; Kocaman, 2023b), a damping ratio of 3% has been proposed by researchers for nonlinear time-history analyses of historical masonry mosques.

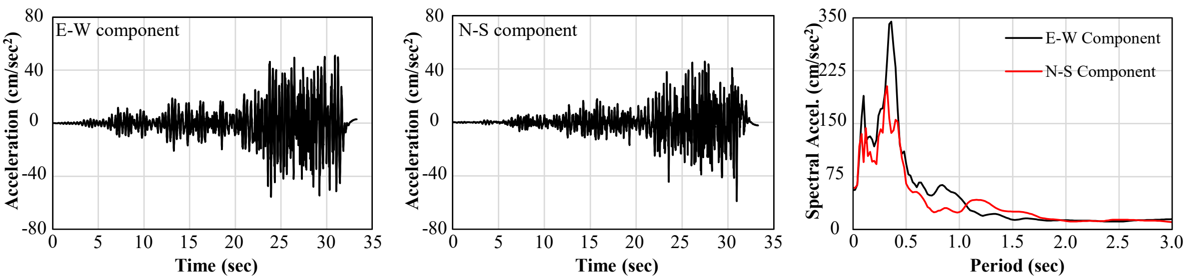

Fig. 4. Malatya city center (station 4414) record of the Pazarcık-Kahramanmaraş earthquake

Fig. 5 shows the peak displacement-time graph obtained from dynamic analyses for two different structural models (Model-1 and Model-2) of the Malatya Yeni Mosque, modeled with different material properties. This analysis, conducted by considering the top of the main dome, compares how the displacement values change over time and the behavior of the structure under dynamic loads. It was observed that Model-2 exhibited limited displacement, around ±5 mm, and remained within elastic limits throughout the analysis. This indicates that the material properties used in Model-2 are consistent with the structure having a high elasticity modulus and compressive strength.

On the other hand, in Model-1, the displacement values exceeded the ±50 mm limit starting from the 16th second and exhibited a sudden collapse behavior by going beyond the elastic limits. This shows that the material properties used in Model-1 represent a structure with a low elasticity modulus and weaker mechanical properties. Once the elastic limits were exceeded, local collapse mechanisms were triggered, and the load-bearing capacity of the main dome's supporting system rapidly decreased. This difference clearly highlights the critical role of material parameters in structural behavior.

The graphical presentation of Fig. 5 emphasizes both the elastic and plastic deformation stages, visualizing the impact of displacement trends on damage mechanisms. Particularly in Model-1, a rapid and uncontrolled displacement process was observed after exceeding the elastic limits, leading to the loss of the structure's overall stability. The analysis results once again emphasize the critical importance of accurately determining the material parameters of historical masonry structures in structural safety assessments and seismic resilience analyses.

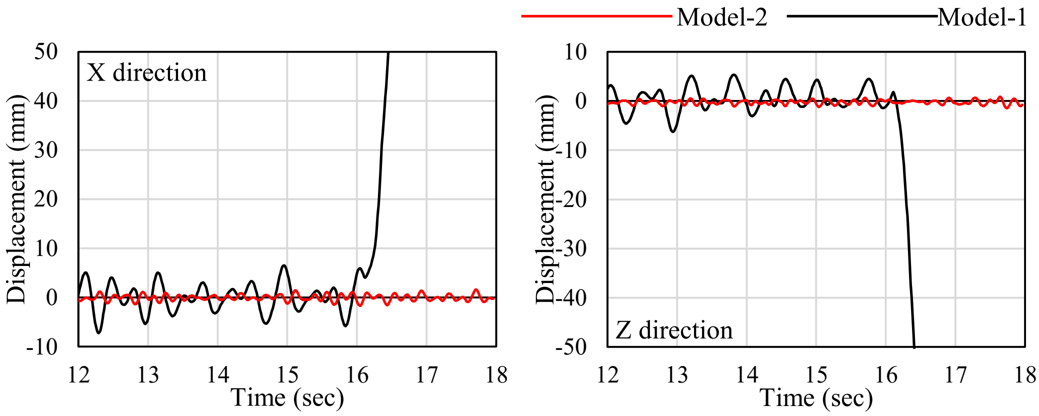

Fig. 5. Displacement-time graphs obtained from Model-1 and Model-2 dynamic analyses

Fig. 6 shows the force-displacement curves obtained from nonlinear dynamic analyses for Model-1 and Model-2 of the Malatya Yeni Mosque. These graphs provide a detailed analysis of the behavior exhibited by the structural components during the elastic and plastic deformation phases. Model-2 demonstrated limited deformation without exceeding the elastic limits under horizontal forces and was observed to have a lateral load-bearing capacity of approximately 5000 kN. This confirms the strength and rigidity provided by the material parameters defined in Model-2. The fact that the elastic limits were not exceeded suggests that no significant damage would occur in the structure and that it could maintain its stability.

The force-displacement curves obtained for Model-1, on the other hand, exhibited a different behavior. In Model-1, the elastic limits were clearly exceeded, and it was observed that the load-bearing capacity of the structure gradually decreased, ultimately resulting in collapse. The loops in the curves indicate that the structure lost its capacity to dissipate energy and that plastic deformations progressed in the structural elements. Particularly, the rapid reduction in the structural capacity was influenced by the damage at the arch-column joints. This collapse behavior is associated with the low strength and rigidity parameters of the materials used in Model-1.

A detailed analysis of the graphs clearly demonstrates how the material differences between the two models affect structural performance. In Model-1, after exceeding the elastic limits, the load-bearing capacity rapidly decreased, indicating that damage progressed quickly. In contrast, the curve for Model-2 shows that the material parameters provided higher strength and allowed the structure to maintain its stability under lateral loads. This analysis once again highlights the critical importance of the accuracy and calibration of material parameters in seismic performance evaluations.

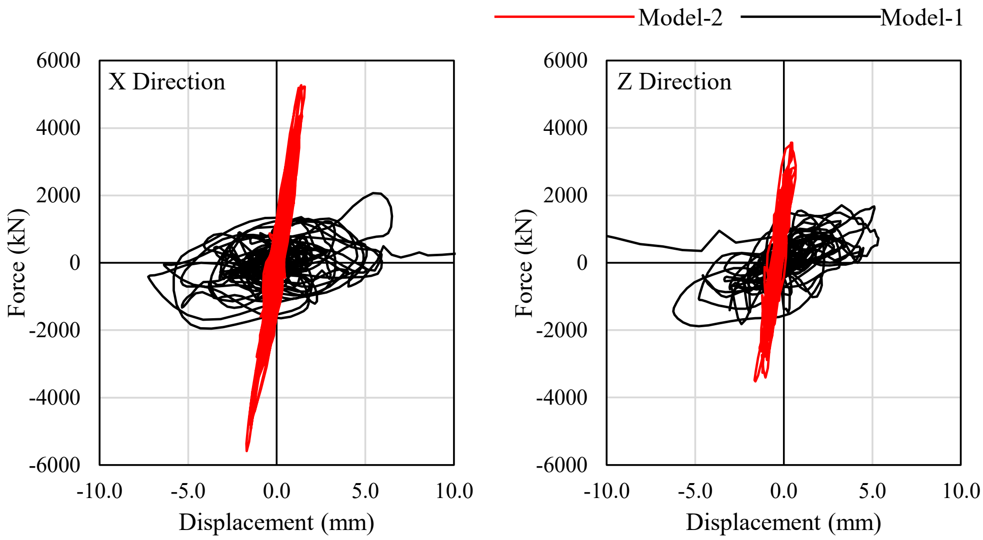

Fig. 6. Force-displacement graphs obtained from Model-1 and Model-2 dynamic analyses

Fig. 7 compares the damage distributions and mechanisms obtained from the finite element analyses of Model-1 and Model-2 of the Malatya Yeni Mosque. In Model-2, the cracks formed in the mosque's domes and some critical areas remained limited to a width of 1-1.5 mm, indicating light damage levels that did not exceed the elastic limits. It was observed that the dome and arch elements maintained their load-bearing capacities, and no collapse mechanism occurred. The high elasticity modulus and strength provided by the material properties of Model-2 helped the structure maintain its integrity under dynamic loads and minimized damage formation.

In contrast, a completely different damage scenario was observed in Model-1. A global collapse mechanism developed in the structure, particularly with severe damage to the arch and column elements that support the main dome. The damage spread from the feet of the arches along the arch system, ultimately leading to the collapse of the main dome. During this collapse, significant damage was also observed in the wall elements. The damage distribution is directly related to the inability of the structural elements in Model-1 to provide adequate rigidity and strength due to the low-pressure strength and elasticity modulus.

The damage distribution in Fig. 7 clearly demonstrates the critical effect of the material properties of both models on the seismic performance of the structure. The damage mechanism observed in Model-1 aligns closely with the actual damage mechanisms identified in field studies. This suggests that the material parameters used in Model-1 better reflect the actual behavior of the structure. Model-2, on the other hand, presents a scenario where the structure is more resistant to earthquakes, based on high strength parameters derived from literature recommendations. However, these parameters did not represent a realistic damage mechanism. These results once again emphasize the importance of carefully calibrating material properties and comparing them with field data.

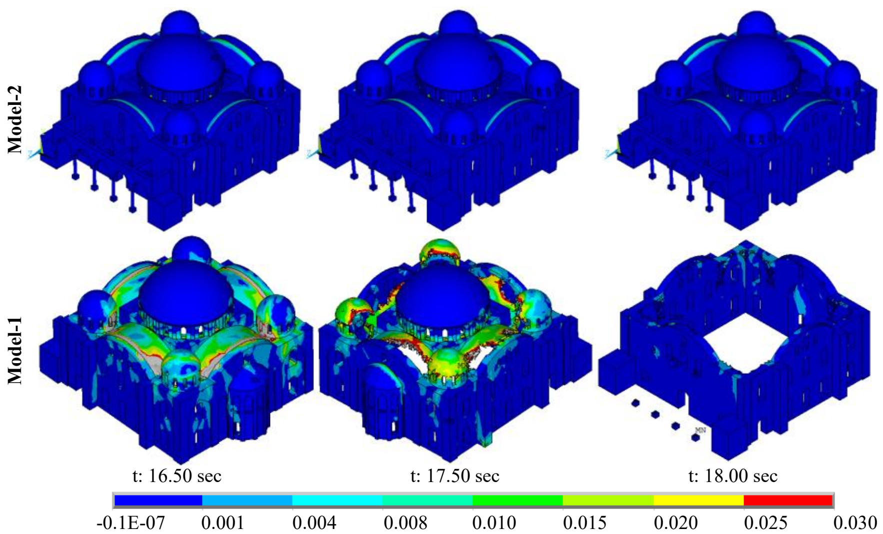

Fig. 7. Damage mechanisms obtained from Model-1 and Model-2 dynamic analyses

Fig. 8 compares the damage distributions obtained from Model-1 and Model-2 with the field observations conducted at Malatya Yeni Mosque following the 2023 Kahramanmaraş earthquakes. The field observations revealed that the structure, particularly the arch-column system, piers, and domes, sustained significant damage, with the collapse mechanism originating from these areas. It was determined that the main dome and side domes had collapsed, and significant cracks had formed in the walls during dynamic loading. The field observations in Fig. 8 show a high degree of agreement with the results from Model-1, while the results from Model-2 present a more optimistic scenario compared to the field damage.

In Model-1, similar damage mechanisms emerged due to the material parameters reflecting low strength and rigidity characteristics. Notably, the loss of stability in the piers supporting the main dome initiated a cascading damage process in the load transfer system. The loss of the arch's load-bearing capacity led to the collapse of the domes and the formation of large cracks in the walls. This analysis, which aligns with the field observations, demonstrates that the literature-based parameters represent the structure's real behavior more accurately.

In Model-2, only minor cracks were observed throughout the structure, with no collapse occurring in critical elements. The limited damage mechanism in Model-2 can be attributed to the high strength and elasticity modulus values used in the model. However, this does not align with the field observations and indicates that the material properties calculated based on literature recommendations fail to reflect the actual structural behavior.

Fig. 8 plays a critical role in the comparison of field observations and analysis results. The visuals demonstrate that Model-1 is more consistent with the field data, while Model-2 underrepresents the severity of the damage mechanisms. These analyses further emphasize the importance of calibration based on local material properties to accurately predict the seismic behavior of historic structures. Additionally, they highlight the necessity of constructing the geometric and material models in a manner consistent with field realities to obtain reliable results in finite element analyses.

Southwest view | Inside view

Southeast view | General view

Fig. 8. Damage mechanisms of Malatya Yeni Mosque obtained field study

4. Conclusions

This study was conducted to understand the seismic behavior and damage mechanisms of Malatya Yeni Mosque, which completely collapsed during the 6th February 2023 Kahramanmaraş earthquakes. Considering the challenges in determining material parameters specific to historical masonry structures, two different finite element models of the mosque (Model-1 and Model-2) were created. In Model-1, material parameters based on literature recommendations were used, while in Model-2, parameters derived from field samples and general parameters from regulations were adopted. Both models underwent nonlinear dynamic analyses using the actual earthquake acceleration-time records recorded in Malatya, and the modal properties and seismic performance of the structure were thoroughly investigated. The following key findings were obtained from the analyses:

- Significant differences were observed in the fundamental frequency values between Model-1 and Model-2. Due to Model-1's low elasticity modulus and compressive strength, its natural frequency was lower, while Model-2 exhibited a more rigid structural behavior, reaching higher frequency values. This difference highlights the critical impact of material properties on structural dynamics.
- It was observed that Model-1 exhibited a severe collapse behavior beyond the elastic limit, while Model-2 remained within elastic limits, maintaining the stability of the structure. However, comparisons with field observations revealed that the damage mechanisms in Model-1 better reflected the actual situation, while Model-2 represented the real damage less severely.
- In Model-1, damage resulted in a global collapse that spread from the piers and arch system to the main dome and load-bearing walls. This mechanism closely matched the field observations. In contrast, in Model-2, only minor cracks were observed, which presented a result that was far from a realistic damage representation. This suggests that the material parameters used in Model-2 did not adequately reflect the structural behavior.
- The accuracy of material properties is one of the most critical parameters in seismic performance analysis of historical masonry structures. The Model-1 analysis, based on field observation-derived parameters, was found to more successfully reflect the actual behavior of the structure. On the other hand, Model-2, created using general parameters from literature or regulatory recommendations, was insufficient in representing real damage mechanisms due to its high strength and rigidity values.
- In conclusion, this study emphasizes once again the importance of calibration based on local material properties in seismic performance analysis of historical structures. To understand the dynamic behavior of historical structures and obtain reliable results, it is necessary to combine field data, literature recommendations, and regulatory guidelines. Additionally, using modal analysis results to verify the accuracy of material properties is an important approach that enhances the reliability of analyses. These findings make significant contributions to engineering studies planned for the preservation and strengthening of historical structures.
- Suggestions for future studies may focus on detailing field observations, applying a broader range of material testing, and comparing the results of different analysis methods. This will allow for a more accurate assessment of the seismic performance of historical structures and the development of effective strengthening strategies.

Acknowledgments
The authors received no specific funding for this research.

References

AFAD. (2023, July 03). *Last Earthquakes*. Retrieved from https://deprem.afad.gov.tr/last-earthquakes.html

Aghabeigi, P., & Farahmand-Tabar, S. (2021). Seismic vulnerability assessment and retrofitting of historic masonry building of Malek Timche in Tabriz Grand Bazaar. *Engineering Structures*, 240, 112418. https://doi.org/10.1016/j.engstruct.2021.112418

Altunisik, A. C., Bayraktar, A., & Genc, A. F. (2016). A study on seismic behaviour of masonry mosques after restoration. *Earthquakes and Structures*, 10(6), 1331–1346. https://doi.org/10.12989/eas.2016.10.6.1331

Apostolopoulos, C., & Sotiropoulos, P. (2008). Venetian churches of Lefkada, Greece: Construction documentation and seismic behaviour of "Virgin Mary of the Strangers." *Construction and Building Materials*, 22(4), 434–443. https://doi.org/10.1016/j.conbuildmat.2006.10.016

Aşıkoğlu, A., Avşar, Ö., Lourenço, P. B., & Silva, L. C. (2019). Effectiveness of seismic retrofitting of a historical masonry structure: Kütahya Kurşunlu Mosque, Turkey. *Bulletin of Earthquake Engineering*, 17, 3365–3395. https://doi.org/10.1007/s10518-019-00603-6

Atmaca, B., Ertürk Atmaca, E., Roudane, B., Güleş, O., Demirkaya, E., Aykanat, B., ... & Akgül, T. (2024). Field observations and numerical investigations on seismic damage assessment of RC and masonry minarets during the February 6th, 2023, Kahramanmaraş (Mw 7.7 Pazarcık and Mw 7.6 Elbistan) earthquakes in Türkiye. *International Journal of Architectural Heritage*, 1-26. https://doi.org/10.1080/15583058.2024.2337651

Bağbancı, M. B. (2013). Examination of the failures and determination of intervention methods for historical Ottoman traditional timber houses in the Cumalıkızık Village, Bursa, Turkey. *Engineering Failure Analysis*, 35, 470–479. https://doi.org/10.1016/j.engfailanal.2013.05.012

Bajno, D., Schabowicz, K., & Grzybowska, A. (2024). Material testing of historic bricks and mortars in degraded masonry structures. *Materials*, 17(13), 3192. https://doi.org/10.3390/ma17133192

Betti, M., & Vignoli, A. (2008). Assessment of seismic resistance of a basilica-type church under earthquake loading: Modelling and analysis. *Advances in Engineering Software*, 39(4), 258–283. https://doi.org/10.1016/j.advengsoft.2007.01.004

Calik, İ., Bayraktar, A., Türker, T., & Akköse, M. (2020). Empirical formulation for estimating the fundamental frequency of historical stone mosques with masonry domes. *The Structural Design of Tall and Special Buildings*, 29(9), e1732. https://doi.org/10.1002/tal.1732

Demir, C. (2012). Seismic behaviour of historical stone masonry multi-leaf walls (PhD thesis). İstanbul Technical University.

Eurocode-6 (2005). Design of masonry structures - Part 1–1: General rules for reinforced and unreinforced masonry structures.

Ercan, E., & Nuhoglu, A. (2014). Identification of historical veziragasi aqueduct using operational modal analysis. *The Scientific World Journal*, 2014(1), 518608. https://doi.org/10.1155/2014/518608

FEMA 356. (2000). Pre-standard and commentary for the seismic rehabilitation of buildings. Federal Emergency Management Agency.

Firat, F. K., Ural, A., & Kara, M. E. (2022). January 24, 2020 Sivrice Earthquake and the response of the masonry Haci Yusuf Tas (New) mosque. *Earthquakes and Structures*, 22(4), 331-343. https://doi.org/10.12989/eas.2022.22.4.331

Gentile, C., Saisi, A., & Cabboi, A. (2015). Structural identification of a masonry tower based on operational modal analysis. *International Journal of Architectural Heritage*, 9(2), 98–110. https://doi.org/10.1080/15583058.2014.951792

GERMHS. (2017). A guideline for earthquake risk management of historical structures. General Directorate of Foundations Türkiye.

Gürbüz, M., & Kocaman, İ. (2024). Enhancing seismic resilience: A proposed reinforcement technique for historical minarets. *Engineering Failure Analysis*, 156, 107832. https://doi.org/10.1016/j.engfailanal.2023.107832

Italian Code C. (2009). Technical standards for constructions. Italy.

Kahya, V., Genç, A. F., Sunca, F., Roudane, B., Altunişik, A. C., Yilmaz, S., ... & Akgül, T. (2024). Evaluation of earthquake-related damages on masonry structures due to the 6 February 2023 Kahramanmaraş-Türkiye earthquakes: A case study for Hatay Governorship Building. *Engineering Failure Analysis*, 156, 107855. https://doi.org/10.1016/j.engfailanal.2023.107855

Kazaz, İ., Gülkan, P., & Kazaz, E. (2021). Numerical assessment of cracks on a freestanding masonry minaret. *International Journal of Architectural Heritage*, 15(4), 526-547. https://doi.org/10.1080/15583058.2019.1629046

Kocaman, İ. (2023a). The effect of the Kahramanmaraş earthquakes (Mw 7.7 and Mw 7.6) on historical masonry mosques and minarets. *Engineering Failure Analysis*, 149, 107225. https://doi.org/10.1016/j.engfailanal.2023.107225

Kocaman, İ. (2023b). Effect of restoration interventions on the seismic behavior of historical masonry buildings: The case of Molla Siyah mosque. *Engineering Failure Analysis*, 148, 107206. https://doi.org/10.1016/j.engfailanal.2023.107206

Kocaman, İ. (2024). Examination of the damage limits and collapse mechanism of Adıyaman Ulu Mosque with finite element model. *Structures*, 70, 107787. https://doi.org/10.1016/j.istruc.2024.107787

Kocaman, İ., & Gürbüz, M. (2023). Collapse mechanism of narthex part of historical masonry mosques. *Engineering Failure Analysis*, 151, 107387. https://doi.org/10.1016/j.engfailanal.2023.107387

Kocaman, İ., & Gürbüz, M. (2024). Enhancing seismic performance of historic mosques through retrofitting measures. *Engineering Structures*, 301, 117245. https://doi.org/10.1016/j.engstruct.2023.117245

Kocaman, İ., & Kazaz, İ. (2023). Collapse mechanism of historical masonry mosques under strong ground motions. *Engineering Failure Analysis*, 144, 106983. https://doi.org/10.1016/j.engfailanal.2022.106983

Kocaman, İ., Gedik, Y., & Okuyucu, D. (2024a). Assessment of seismic behavior of historical masonry cupolas: Case of Emir Saltuk Cupola. *Journal of Building Engineering*, 82, 108275. https://doi.org/10.1016/j.jobe.2023.108275

Kocaman, İ., Mercimek, Ö., Gürbüz, M., Erbaş, Y., & Anıl, Ö. (2024b). The effect of Kahramanmaraş earthquakes on historical Malatya Yeni Mosque. *Engineering Failure Analysis*, 161, 108310. https://doi.org/10.1016/j.engfailanal.2024.108310

KVMGM. (2025, January 23). *Dünya Miras Geçici Listesi*. Retrieved from https://kvmgm.ktb.gov.tr/tr-44395/dunya-miras-gecici-listesi.html

Lourenço, P. B. (2002). Computation of historical masonry structures. *Progress in Structural Engineering and Materials*, 4(3), 301–319. https://doi.org/10.1002/pse.120

Mercimek, Ö. (2023). Seismic failure modes of masonry structures exposed to Kahramanmaraş earthquakes (Mw 7.7 and 7.6) on February 6, 2023. *Engineering Failure Analysis*, 151, 107422. https://doi.org/10.1016/j.engfailanal.2023.107422

Nohutcu, H., Demir, A., Ercan, E., Hokelekli, E., & Altintas, G. (2015). Investigation of a historic masonry structure by numerical and operational modal analyses. *The Structural Design of Tall and Special Buildings*, 24(13), 821–834. https://doi.org/10.1002/tal.1213

Onat, O., Özmen, A., Özdemir, E., & Sayın, E. (2024). Damage propagation and failure mechanism of single dome historical masonry mosque after February 6, 2023, Kahramanmaraş earthquake doublets (Mw= 7.7 and Mw= 7.6). *Structures*, 69, 107288. https://doi.org/10.1016/j.istruc.2024.107288

Pantò, B., Ortega, J., Grosman, S., Oliveira, D. V., Lourenço, P. B., Macorini, L., & Izzuddin, B. A. (2024). Advanced calibration of a 3D masonry arch bridge model using non-destructive testing and numerical optimisation. *Construction and Building Materials*, 438, 137131. https://doi.org/10.1016/j.conbuildmat.2024.137131

Selahattin, S. (2016). 1893 Malatya Depremi ve afet yönetimi. *OTAM-Ankara*, 39, 137–177. https://doi.org/10.1501/otam_0000000687

Şeker, B. Ş. (2011). Mimar Sinan camilerinin statik ve dinamik yükler etkisinde davranışlarının incelenmesi (Doktora tezi). Fen Bilimleri Enstitüsü, Karadeniz Teknik Üniversitesi, Trabzon.

Şentürk, İ., Ergün, M., & Artar, M. (2022). Seismic behavior assessment of historical Alaeddin Bey Mosque and strengthening suggestions by CFRP fabric and steel plate. *Engineering Failure Analysis*, 137, 106242. https://doi.org/10.1016/j.engfailanal.2022.106242

TBEC. (2018). Turkish earthquake code: Specifications for building design under earthquake effects. Ankara.

TEC-07. (2007). Code on structures to build in earthquake regions. General Directorate of Disaster Affairs.

Torres, W., Almazán, J. L., Sandoval, C., & Boroschek, R. (2017). Operational modal analysis of a historical stone building and comparison of natural frequencies with analytical results. *Journal of Vibration and Acoustics*, 139(6), 061009. https://doi.org/10.1115/1.4035798

TS EN 1996-1-1. (2005). Design of masonry structures-Part 1-1: General rules for buildings-rules for reinforced and unreinforced masonry. Ankara (Turkey): Turkish Standard.

Valente, M. (2021). Seismic vulnerability assessment and earthquake response of slender historical masonry bell towers in South-East Lombardia. *Engineering Failure Analysis*, 129, 105656. https://doi.org/10.1016/j.engfailanal.2021.105656

Valente, M. (2023). Earthquake response and damage patterns assessment of two historical masonry churches with bell tower. *Engineering Failure Analysis*, 151, 107418. https://doi.org/10.1016/j.engfailanal.2023.107418

Valente, M., & Milani, G. (2018). Seismic response and damage patterns of masonry churches: Seven case studies in Ferrara, Italy. *Engineering Structures*, 177, 809–835. https://doi.org/10.1016/j.engstruct.2018.08.071

Vitorino, S., Corazzi, R., & Doz, G. (2024). Seismic performance assessment of the historical Cathedral of Santa Maria del Fiore Dome by numerical analysis. *Engineering Failure Analysis*, 165, 108734. https://doi.org/10.1016/j.engfailanal.2024.108734

Yilmaz, Z., Altunişik, A. C., Taciroglu, E., Günaydin, M., Okur, F. Y., Sunca, F., ... & Sezdirmez, T. (2024). Regional building damage survey data on the 2023 Kahramanmaraş, Türkiye, earthquakes. *ASCE OPEN: Multidisciplinary Journal of Civil Engineering*, 2(1), 04024009. https://doi.org/10.1061/AOMJAH.AOENG-0041

4th International Civil Engineering & Architecture Conference
17-19 May 2025, Trabzon, Türkiye

Investigation of the effects of direct integration methods and their parameters on pounding in different impact models

Birkan Dag*[1], Muzaffer Borekci[1]

[1] *Yildiz Technical University, Department of Civil Engineering, 34220 İstanbul, Türkiye*

Abstract. The pounding of adjacent buildings during earthquakes is a significant concern, particularly in densely populated metropolitan areas where maximizing land use is crucial. Insufficient spacing between adjacent buildings often leads to repeated pounding impacts during seismic events which can result in severe damages, even collapse. Therefore, an accurate modeling to predict the pounding phenomena is highly important. Notably, pounding remains a challenging problem characterized by uncertainties and complexities that are difficult to capture in analytical models. This study investigates the pounding effect by comparing different impact models and direct integration methods available in the literature. For this purpose, two adjacent single-degree-of-freedom systems with different natural periods and inadequate gap distances were modeled analytically in SAP2000. Pounding was represented using link elements defined by linear and Hertz models without damping, employing the distinct elements available in SAP2000. Additionally, nonlinear time-history analyses were conducted using various direct integration methods provided in SAP2000, with carefully selected parameters for each method. The study evaluates the effects of the chosen impact models and integration methods, along with their solution parameters, on the estimated pounding forces. This ensures a consistent and precise simulation of the pounding effect and its impact on structural behavior.

Keywords: Pounding; Impact problem; Nonlinear time history analysis; Time integration methods; Single-degree-of-freedom systems

1. Introduction

Reinforced concrete (RC) buildings are generally designed without considering the pounding effect even when they are adjacent to other buildings with insufficient separation gaps. The pounding effect is a critical problem, particularly in metropolitan areas, where limited space leads to closely spaced structures and damage due to pounding is more pronounced in buildings with different vibration periods. In all circumstances, it would be unconservative to design a building without accounting for pounding and numerous studies in the literature have proved this outcome (Rosenblueth and Meli, 1986; Kasai and Maison, 1991; Karayannis and Favvata, 2005).

There are two types of pounding described in the literature: floor-to-floor (story-to-story) pounding and floor-to-column (inter-story) pounding. If the story levels of adjacent buildings are equal, the pounding scenario is classified as floor-to-floor; otherwise, it is floor-to-column. The literature suggests that floor-to-column pounding causes more damage to buildings than floor-to-floor pounding because it generates significant shear forces in the pounded columns due to the impact from adjacent building slabs (Brown and Elshaer, 2022).

A study conducted by Anagnostopoulos (1988) investigated the effects of seismic pounding on single and multi-degree-of-freedom systems. Their findings revealed that variations in mass, stiffness, and period of the modeled buildings lead to notable differences in pounding effects, significantly affecting relative story displacements, shear forces, and dynamic properties. Favvata et al. (2013) analyzed the impact of adjacent buildings on steel and RC structures. Their study found that in RC buildings, upper-story columns are more affected by bending and ductility demands, while lower-story columns are primarily influenced by shear and ductility demands. Conversely, in steel buildings, upper-story columns experience higher shear and ductility demands, whereas lower-story columns are more affected by bending and ductility. Akköse and Sunca (2016) modeled adjacent buildings of equal height but with different dynamic characteristics. They performed nonlinear time-history analyses (NLTHA) using both near-fault and far-fault earthquake records. The results showed that pounding forces under near-fault ground motion are higher than those under far-fault motion, indicating that the gap requirements are insufficient. Raheem et al. (2019) studied the impact of eccentric seismic pounding on

*Corresponding author, E-mail: bdag@yildiz.edu.tr

https://doi.org/10.31462/icearc2025_ce_eqe_259

adjacent symmetric buildings, finding that pounding severity depends on building vibrations and ground motion characteristics. Their analysis showed that pounding increases acceleration and shear force demands, with torsional oscillations playing a significant role in the buildings' seismic response. Mavronicola et al. (2020) analyzed seismic pounding in base-isolated buildings using NLTHA, assessing impacts with adjacent structures. Key factors included seismic directionality, clearance, neighboring structures, and accidental torsion effects. Jiang et al. (2022) conducted experimental shaking table tests on scaled multi-story buildings to investigate seismic pounding, including story-to-story, inter-story, and eccentric pounding. A validated 3D finite element model was used to analyze mass eccentricity effects. The results showed that pounding increases structural response frequencies, with larger impact forces in story-to-story cases. Additionally, mass eccentricity significantly influences base shear and displacement. Taleshian et al. (2022) studied the effectiveness of viscoelastic links in mitigating seismic pounding between adjacent asymmetric-plan buildings. Using white-noise analysis and earthquake simulations, they found that plan asymmetries do not necessarily increase seismic responses. Viscoelastic links significantly reduce relative displacements, with damping effects improving as link stiffness decreases. The results showed up to an 80% reduction in displacement, with a dominant modal damping ratio twice as high in certain eccentric configurations. Miari and Jankowski (2022a) investigated seismic pounding effects between buildings on different soil types. Analyzing 3D models with varying heights, they found that pounding increases peak accelerations and shear forces, while its effect on displacements varies. Buildings on soft clay soil experience the highest displacements and forces, whereas those on rock and hard rock have the lowest. They (2022b) also analyzed floor-to-column pounding effects on buildings with different soil types during earthquakes. Studying various pounding scenarios, they found that pounding significantly increases shear demands, exceeding shear strength in all cases. The highest shear demands occur on soft clay soil, decreasing progressively for stiffer soils, with the lowest on rock and hard rock. Flenga and Favvata (2023) introduced a risk-targeted decision model to assess the seismic performance of RC structures against pounding and determine the minimum required separation gap distance. Using probabilistic seismic demand models and engineering demand parameter (EDP) hazard curves, they defined new performance objectives for pounding risk. The model was demonstrated through a case study, revealing a critical separation gap distance linked to structural pounding risk. Their findings suggest that while pounding risk increases, the required separation gap can be reduced with careful consideration of the pounding risk level. They (2021) also assessed various methodologies for developing fragility curves, concluding that the choice of methodology has minimal effect on risk assessments for highly vulnerable structures. Özer (2024) evaluated pounding effects in fixed-base models considering torsional irregularity, using 3D 5- and 9-story adjacent building combinations. NLTHAs were performed on 176 scenarios with spectrum-compatible ground motions. Results showed that pounding and torsion generally increase displacement demand, interstory drift, damage ratios, and torsional irregularity. The most critical values were found in irregular structures with building eccentricity in the same direction. The large standard deviation across ground motion records highlighted the importance of selecting an appropriate number of records. Börekçi et al. (2024) investigated the seismic behavior of buildings subjected to inter-story pounding, focusing on buildings with different story heights and adjacent on one or both sides. Using NLTHA, they assessed plastic rotations and shear forces in 3-, 6-, and 10-story buildings. The study found that inter-story pounding has a negligible effect on plastic rotations. However, the impacted columns experience increased shear forces, potentially leading to shear failure, particularly when adjacent on both sides. Manoukas and Karayannis (2025) examined floor-to-column pounding between multi-story RC buildings, focusing on the impact point location and gap width. They found that while the impact point affects external columns, the overall building behavior is less influenced. Inadequate seismic joints were found to be more detrimental than no separation, highlighting the importance of adhering to code provisions. They also confirmed that damage to external columns from pounding is usually limited to a small area (about 1 meter).

Accurate modeling of the pounding phenomenon is critical, as significant challenges arise due to inherent uncertainties and complexities that are difficult to fully capture in analytical models. Additionally, the direct integration methods used are of utmost importance for the accurate estimation of responses in pounded structures. This study evaluates different impact models and direct integration methods to predict the pounding effect in adjacent single-degree-of-freedom (SDOF) systems with varying natural periods and insufficient gap distances. The aim is to estimate the effects of different direct integration methods on various impact models and to evaluate the relationships between the considered parameters. Different SDOF systems modelled in SAP2000 with linear and Hertz contact models, and NLTHAs were conducted using 11 pairs of earthquake records with various integration methods. The effects of model choice, direct integration methods, and their parameters on pounding force estimates were assessed.

2. Materials and methodology

2.1. Impact models

Impact models are typically classified as stereomechanical or force-based (Miari et al.,2019). The stereomechanical approach derives pounding forces from momentum and energy laws, while the force-based (penalty) model uses impact stiffness-representing springs. This study adopts the force-based approach due to its modeling clarity and compatibility with the analysis software.

The force-based approach defines impact elements using linear spring, Kelvin-Voigt (linear viscoelastic), Hertz, and Hertz damp (nonlinear viscoelastic) models. Fig. 1 illustrates these models, where m_1 and m_2 are the colliding masses, k and K represent stiffness for linear and nonlinear models, c is the damping coefficient, and d is the gap distance. In this study, linear and Hertz models were used as impact models in the representation of the pounding of adjacent SDOF systems.

2.2. Adjacent SDOF systems

In this study, three different SDOF systems were considered which are equivalent to hypothetical buildings with 5, 8, and 10 stories. Two distinct pounding scenarios were investigated within the scope of this study as pounding between 5 story-10 story buildings and 8 story-10 story buildings. As illustrated in Fig. 2, both pounding scenarios were modeled under the assumption of a 2 cm separation gap between the structures. The impact effect is represented by link elements available in SAP2000.

In these equations, ω is the angular frequency, T is the structural period, m is the mass of the building and k is the stiffness.

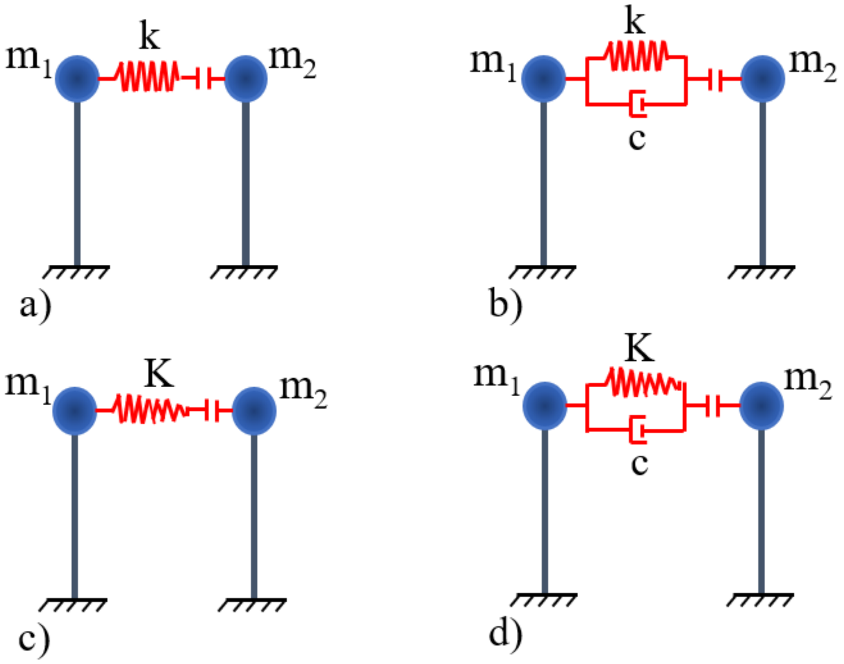

Fig 1. Impact models for pounding: a) Linear, b) Kelvin-Voigt (viscoelastic), c) Hertz, d) Hertz damped (Borekci et al, 2024).

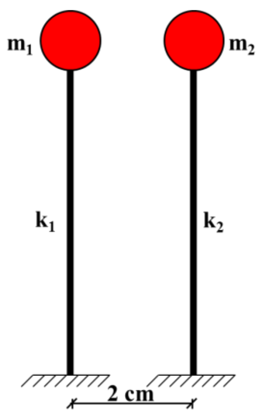

Fig. 2. Reprerantation of two adjacent SDOF systems with different natural period.

Given the known masses and estimated periods of the hypothetical buildings, their stiffness values were calculated using Equation (1–3) to match the target periods. The structural period of a 5-story building is assumed to be 0.5 seconds, the structural period of an 8-story building is assumed to be 0.8 seconds, and the structural period of a 10-story building is assumed to be 1 second. The mass and stiffness values of the corresponding SDOF systems are presented in Table 1.

$$\omega = \frac{2\pi}{T} \tag{1}$$

$$T = 2\pi\sqrt{\frac{m}{k}} \tag{2}$$

$$k = \frac{4\pi^2 m}{T^2} \tag{3}$$

A gap element was used as a linear impact model and multilinear plastic element was used as Hertz impact model. The study utilized impact stiffness values recommended in literature. An impact stiffness of $k=10^9$ N/m was used for the linear spring model, as recommended by Farahani et al. (2019). For the Hertz model, the impact stiffness of $K=1.13\times10^9$ $N/m^{3/2}$ was adopted, following the suggestion given in the study of Jankowski (2005).

2.3. Ground motions

In this study, 11 ground motion record pairs were selected from the Pacific Earthquake Engineering Research Center (PEER) database following the criteria defined in Turkish Seismic Code for Buildings (TSCB) 2018. These criteria consider factors such as soil class, faulting mechanism, magnitude, and distance to rupture. The records used in this study correspond to the ZC soil class, with shear-wave velocities ($V_{s,30}$) ranging from 360–760 m/s at a 30-meter depth. The fault type is strike-slip, with magnitudes ranging from 6.19 to 7.68. Detailed characteristics of the records are listed in Table 2.

The horizontal components of all ground motion records were scaled using the Spectral Matching Method in SeismoMatch to match the 5%-damped design earthquake spectrum from TSCB 2018. Fig. 3 shows the scaled pseudo-acceleration spectra and their average.

Table 1. Properties of SDOF systems.

	5-10 Story Pounding	8-10 Story Pounding
m_1 (kN.s^2/m)	1250	2000
m_2 (kN.s^2/m)	2500	2500
k_1 (kN/m)	197392	123370
k_2 (kN/m)	98696	98696

Table 2. Ground motion characteristics.

NGA#	Earthquake	Year	Station	Mag.	R_{jb} (km)	R_{rup} (km)	$V_{s,30}$ (m/s)
552	Chalfant Valley-02	1986	Lake Crowley - Shehorn Res.	6.19	22.08	24.47	456.83
838	Landers	1992	Barstow	7.28	34.86	34.86	370.08
897	Landers	1992	Twentynine Palms	7.28	41.43	41.43	635.01
1162	Kocaeli, Turkey	1999	Goynuk	7.51	31.7	31.7	424.8
1164	Kocaeli, Turkey	1999	Istanbul	7.51	49.66	51.95	595.2
1166	Kocaeli, Turkey	1999	Iznik	7.51	30.73	30.73	476.62
910	Big Bear-01	1992	Joshua Tree	6.46	40.99	41.87	379.32
1762	Hector Mine	1999	Amboy	7.13	41.81	43.05	382.93
3757	Landers	1992	North Palm Springs Fire Sta	7.28	26.95	26.95	367.84
1626	Sitka, Alaska	1972	Sitka Observatory	7.68	34.61	34.61	649.67
5830	El Mayor-Cucapah, Mexico	2010	Rancho San Luıs	7.2	43.64	45.47	523.99

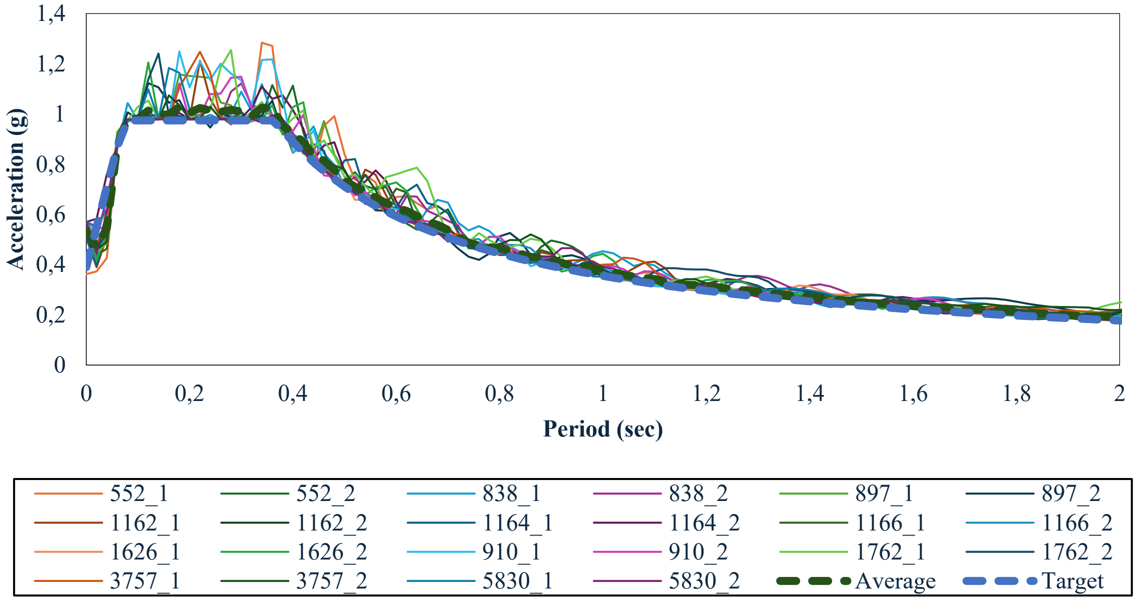

Fig. 3. The scaled pseudo-acceleration spectra and their average.

2.4. Direct integration methods

Direct integration methods are widely used and effective for solving equations of motion in structural dynamics. These methods compute a system's time-dependent response by directly integrating the equations of motion. By advancing through discrete time steps, they can be applied to both linear and nonlinear systems. In this study, direct integration methods available in SAP2000 will be evaluated to estimate the effects of different integration methods on the pounding analyses.

The Newmark (1959) method is a popular time-stepping integration technique that offers a balance between accuracy and stability. It utilizes two parameters, β and γ, to approximate displacement and velocity at each time step. When $\beta = 0.25$ and $\gamma = 0.5$, the method is unconditionally stable and is known as the constant average acceleration method. The linear acceleration method ($\beta = 1/6$, $\gamma = 0.5$) provides higher accuracy but exhibits conditional stability.

The Wilson (1972) method builds upon the Newmark (1959) method, providing enhanced accuracy and a wider stability range. This approach predicts the solution by extending it forward in time. The stability of the method is governed by the parameter θ, which is commonly set to 1.4. Being unconditionally stable, the Wilson (1972) method is especially well-suited for dynamic analyses that involve high-frequency responses.

The method developed by Hilber et al. (1978) builds upon the Newmark (1959) approach, aiming to improve accuracy in low-frequency modes while enhancing the damping of high-frequency modes. The parameter α governs the level of numerical damping and is typically selected within the range of $-1/3$ to 0. This method offers unconditional stability and remains effective even when large time steps are used.

Collocation-based direct integration is a numerical method used to solve equations of motion (Hilber and Hughes, 1978). Unlike traditional direct integration techniques, it seeks to express the solution as a continuous function of time. This approach enhances accuracy, especially in the dynamic analysis of complex structures.

The method developed by Chung and Hulbert (1993) serves as the basis for the widely adopted Generalized Alpha method used in direct integration for structural dynamics. It aims to minimize undesired numerical oscillations in high-frequency modes while providing accurate results in low-frequency modes. Viewed as a generalized version of the classic Newmark (1959) method, the Chung-Hulbert (1993) method is unconditionally stable with proper parameter selection and can be effectively used with large time steps.

The parameters of considered direct integration methods are represented in Table 3. These integration methods are, respectively, Newmark constant acceleration, Newmark average acceleration, Wilson, Hilber-Hughes-Taylor, Collocation, and Chung and Hulbert. The analyses conducted using these direct integration methods are named Case A, Case B, Case C, Case D, Case E, and Case F, respectively.

3. Analysis results

The forces generated in both impact elements, as a result of the pounding of SDOF systems representing 5- and 10-story and 8- and 10-story buildings, are shown in Fig. 4.

Table 3. Different direct integration methods and their relevant parameters.

	Newmark-Constant	Newmark-Average	Wilson	Hilber-Hughes-Taylor	Collocation	Chung and Hulbert
Gamma	0.5	0.5	-	0.83	0.5	0.82
Beta	0.25	0.17	-	0.44	0.17	0.44
Theta	-	-	1.4	-0.33	1	-
Alpha	-	-	-	-	-	-0.33
Alpha-m	-	-	-	-	-	0.5

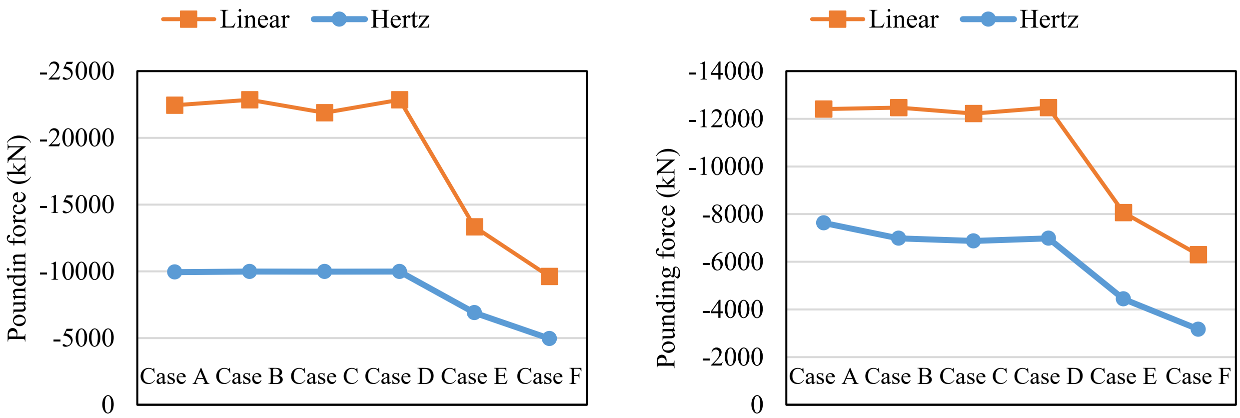

a) Pounding between 5-and 10- story

b) Pounding between 8-and 10- story

Fig. 4. Peak average pounding force of the systems with linear and Hertz impact models over the time history duration.

As seen in Fig. 4, the pounding forces obtained vary depending on the direct integration method and the impact model used. When the Hertz model is selected as the impact model, the resulting pounding forces are consistently smaller compared to the linear model. Regardless of the impact model, the highest force is obtained from Case A, while the lowest force comes from Case F. However, it should be noted that the acceleration records of the earthquakes used do not have the same time step. Some earthquake records have a time step of 0.005 seconds, others 0.01 seconds, and some 0.02 seconds. Authors anticipate that the time step might influence the effects of direct integration methods on the estimated response. Table 4 presents the time steps for the corresponding earthquakes.

Figs. 5 and 6 illustrate the pounding force for the 5- and 10-story buildings and the 8- and 10-story buildings, respectively, considering earthquakes analyzed with different time steps separately. These graphs represent the ratio of the average pounding force obtained for each direct integration method, considering earthquakes with the same time step, to the average pounding force from Case A for both the linear and Hertz impact models.

Table 4. Time intervals (step) of eathquakes.

NGA#	Earthquake	Time Step (s)
552	Chalfant Valley-02	0.005
838	Landers	0.02
897	Landers	0.02
1162	Kocaeli, Turkey	0.005
1164	Kocaeli, Turkey	0.01
1166	Kocaeli, Turkey	0.005
910	Big Bear-01	0.02
1762	Hector Mine	0.02
3757	Landers	0.02
1626	Sitka, Alaska	0.005
5830	El Mayor-Cucapah, Mexico	0.02

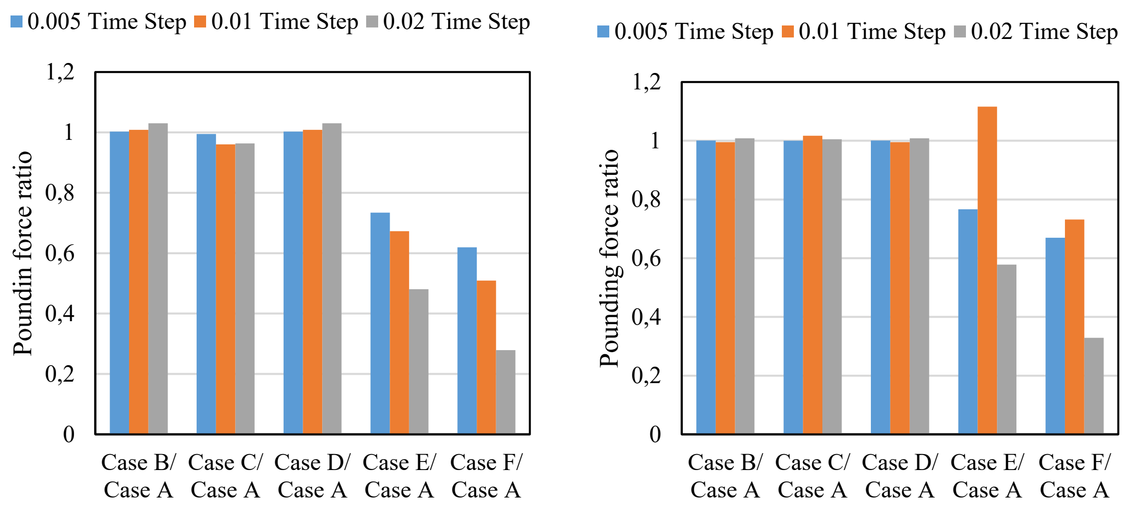

a) Linear model b) Hertz model

Fig. 5. The ratio of avarage pounding forces of each direct integration method to the average of Case A with respect to time step for 5- and 10- story building collision.

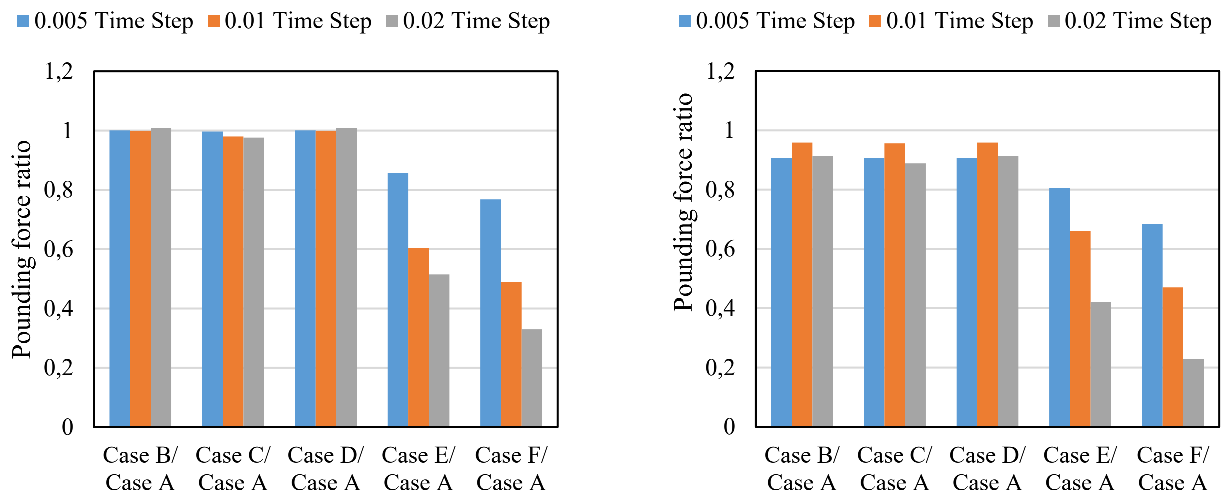

a) Linear model b) Hertz model

Fig. 6. The ratio of avarage pounding forces of each direct integration method to the average of Case A with respect to time step for 8- and 10- story building collision.

4. Conclusions

The study shows that the pounding forces vary depending on the integration method and impact model. The Hertz model consistently yields lower forces than the linear model, with the Newmark constant acceleration method producing the highest forces and the Chung and Hulbert method yielding the lowest. Additionally, the Collocation and Chung and Hulbert integration methods are highly sensitive to the time step of the earthquake's acceleration record. As the time step decreases, the results converge with those from other direct integration methods. To accurately analyze the impact effect, the time step of the earthquake acceleration recordings should either be chosen according to the integration method used or the most optimal integration method should be preferred when using an acceleration recording with a known time step.

References

Akköse, M., & Sunca, F. (2016, May 9–10). Aynı yüksekliğe farklı dinamik özelliklere sahip betonarme binaların arasında bırakılması gereken boşluk miktarının irdelenmesi. Prof. Dr. M. Hasan BODUROĞLU Sempozyumu, İstanbul, Turkey.

Anagnostopoulos, S. A. (1988). Pounding of buildings in series during earthquakes. *Earthquake engineering & structural dynamics*, *16*(3), 443-456.

Borekci, M., Dag, B., & Eroglu, A. (2024). Seismic behaviour of reinforced concrete buildings: Impact of inter-story pounding with adjacent structures on one and both sides. In *Structures* (Vol. 70, p. 107815). Elsevier.

Brown, T., & Elshaer, A. (2022). Pounding of structures at proximity: A state-of-the-art review. *Journal of Building Engineering*, *48*, 103991.

Chung, J., & Hulbert, G. (1993). A time integration algorithm for structural dynamics with improved numerical dissipation: the generalized-α method.

Computers and Structures Inc. (CSI). (n.d.). SAP2000 (Software). Berkeley, CA, USA.

Farahani, D., Behnamfar, F., & Sayyadpour, H. (2019). Effect of pounding on nonlinear seismic response of torsionally coupled steel structures resting on flexible soil. *Engineering Structures*, *195*, 243-262.

Favvata, M. J., Naoum, M. C., & Karayannis, C. G. (2013). Earthquake induced interaction between RC frame and steel frame structures. *WIT Transactions on the Built Environment*, *134*, 839-851.

Flenga, M. G., & Favvata, M. J. (2021). Fragility curves and probabilistic seismic demand models on the seismic assessment of RC frames subjected to structural pounding. *Applied Sciences*, *11*(17), 8253.

Flenga, M. G., & Favvata, M. J. (2023). A risk-targeted decision model for the verification of the seismic performance of RC structures against structural pounding. *Soil Dynamics and Earthquake Engineering*, 175, 108229.

Hilber, H. M., & Hughes, T. J. (1978). Collocation, dissipation and [overshoot] for time integration schemes in structural dynamics. *Earthquake Engineering & Structural Dynamics*, *6*(1), 99-117.

Hilber, H. M., Hughes, T. J., & Taylor, R. L. (1977). Improved numerical dissipation for time integration algorithms in structural dynamics. *Earthquake Engineering & Structural Dynamics*, *5*(3), 283-292.

Jankowski, R. (2005). Non-linear viscoelastic modelling of earthquake-induced structural pounding. *Earthquake engineering & structural dynamics*, *34*(6), 595-611.

Jiang, S., Zhai, C., & Liu, Y. (2022, December). Experimental and numerical studies of seismic induced story-to-story and inter-story pounding. In *Structures* (Vol. 46, pp. 555-569). Elsevier.

Karayannis, C. G., & Favvata, M. J. (2005). Earthquake-induced interaction between adjacent reinforced concrete structures with non-equal heights. *Earthquake engineering & structural dynamics*, *34*(1), 1-20.

Kasai, K., & Maison, B. F. (1991). Observation of structural pounding damage from 1989 Loma Prieta earthquake. In *Proceeding of 6th Canadian Conference of Earthquake Engineering* (pp. 735-742).

Manoukas, G., & Karayannis, C. (2025). Slab-to-Column Seismic Pounding Between Multistorey Buildings: Influence of the Impact Point Location and the Pre-Existing Gap Size. *Buildings*, *15*(4), 581.

Mavronicola, E. A., Polycarpou, P. C., & Komodromos, P. (2020). Effect of ground motion directionality on the seismic response of base isolated buildings pounding against adjacent structures. *Engineering Structures*, *207*, 110202.

Miari, M., & Jankowski, R. (2022). Analysis of floor-to-column pounding of buildings founded on different soil types. *Bulletin of Earthquake Engineering*, *20*(13), 7241-7262.

Miari, M., & Jankowski, R. (2022). Analysis of pounding between adjacent buildings founded on different soil types. *Soil Dynamics and Earthquake Engineering*, *154*, 107156.

Miari, M., Choong, K. K., & Jankowski, R. (2019). Seismic pounding between adjacent buildings: Identification of parameters, soil interaction issues and mitigation measures. *Soil Dynamics and Earthquake Engineering*, *121*, 135-150.

Newmark, N. M. (1959). A method of computation for structural dynamics. *Journal of the engineering mechanics division*, *85*(3), 67-94.

Ozer, E. (2024). Seismic pounding of adjacent buildings considering torsional effects. *Bulletin of Earthquake Engineering*, *22*(4), 2139-2171.

Pacific Earthquake Engineering Research Center (PEER). (n.d.). PEER strong motion database. Available from http://ngawest2.berkeley.edu

Raheem, S. E. A., Fooly, M. Y., Omar, M., & Zaher, A. K. A. (2019). Seismic pounding effects on the adjacent symmetric buildings with eccentric alignment. *Earthq Struct*, *16*(6), 715-726.

Rosenblueth, E., & Meli, R. (1986). The 1985 mexico earthquake. *Concrete international*, *8*(5), 23-34.

SeismoSoft. (2019). SeismoMatch: Earthquake software for response spectrum matching.

Taleshian, H. A., Roshan, A. M., & Amiri, J. V. (2022, February). Seismic pounding mitigation of asymmetric-plan buildings by using viscoelastic links. In *Structures* (Vol. 36, pp. 189-214). Elsevier.

Turkish Seismic Code for Buildings (TSCB). (2018). Ankara, Turkey.

Wilson, E. L., Farhoomand, I., & Bathe, K. J. (1972). Nonlinear dynamic analysis of complex structures. *Earthquake Engineering & Structural Dynamics*, *1*(3), 241-252.

4th International Civil Engineering & Architecture Conference
17-19 May 2025, Trabzon, Türkiye

Evaluating strong-column / weak-beam behavior in reinforced concrete structures: Insights from the 2023 Kahramanmaraş earthquakes

Muhammet Yılmaz*[1], Özkan Hakan[1,2], Ali Haydar Bayram[2], Ramazan Livaoğlu[1,2]

[1] Bursa Uludağ University/Civil Engineering Department, Görükle Campus 16059, Nilüfer, Bursa, Türkiye
[2] RL ProjeDestek Consulting Company. Ulutek Technopark, Görükle, Bursa, Türkiye.

Abstract. In the aftermath of major seismic events, performance-based design principles have exerted a substantial influence on the development of seismic design codes, culminating in the integration of capacity design concepts. A pivotal consideration in the evolution of seismic design over the past five decades has been the necessity of ensuring that vertical load-bearing elements, such as columns, exhibit greater strength compared to beams. This approach has been incorporated into various codes employing distinct criteria, with the objective of enhancing the seismic performance of structures. By prioritising the strong-column/weak-beam behaviour, the overall seismic response of structures is significantly improved, thereby reducing the likelihood of premature collapse due to insufficient ductility.This study examines a reinforced concrete structure affected by the Kahramanmaraş-centred earthquakes on 6 February 2023 in Turkey. Field observations revealed cases where the intended strong-column/weak-beam mechanism was not achieved, leading to damage in vertical load-bearing elements despite the design appearing to be compliant. The present study provides an in-depth examination of the theoretical underpinnings of the observed failures and their impact on the energy dissipation mechanisms of structures subjected to seismic loads. Furthermore, it offers a comparative analysis of the anticipated damage mechanisms, as outlined by capacity-design principles, with the observed damage, thereby providing valuable insights into the effects of compromised energy dissipation capacity. This research endeavors to enhance the comprehension of how deviations from capacity-based principles affect structural performance, thereby offering valuable insights for the enhancement of seismic resilience in future designs.

Keywords: Strong-colum/weak-beam; Frame damage mechanisms; Performance analysis; Energy dissipation

1.Introduction

In recent years, performance-based design approaches have gained prominence as a more accurate means of predicting the seismic behavior of structures and enhancing their safety during earthquakes. These approaches aim not only to ensure the structural strength of buildings but also to prevent collapse mechanisms by enabling controlled dissipation of the energy generated during seismic events. A cornerstone of performance-based seismic design is the capacity design principle, which prescribes that inelastic deformations and damage should be concentrated in the horizontal load-bearing elements namely beams while preserving the integrity of vertical elements such as columns. This concept, widely known as the strong column–weak beam principle, is explicitly defined in numerous international codes and standards, including the Turkish Building Earthquake Code (TBEC-2018). By ensuring that plastic hinges form preferentially in beams rather than columns, this principle facilitates a more ductile response, enhances energy dissipation capacity, and promotes life safety. Equation (1) provides the quantitative criterion used to assess compliance with this principle.

$$(M_{ra} + M_{r\ddot{u}}) \geq 1.2\ (M_{ri} + M_{rj}) \qquad (1)$$

However, field observations have revealed that the seismic behavior anticipated in theoretical design is not always realized in practice. A representative example, examined in detail in this study, was observed following the devastating earthquakes that struck the Southeastern Anatolia Region on February 6, 2023, with epicenters near Kahramanmaraş. While numerous buildings appeared to conform to seismic design principles, including the strong-column/weak-beam concept, significant damage and even total collapse were observed foften attributable to shortcomings in the overall lateral load-resisting system rather than isolated component failure.

* Corresponding author, E-mail: muhammetyilmaz061@gmail.com

https://doi.org/10.31462/icearc2025_ce_eqe_263

Post-earthquake site investigations identified recurring issues, particularly associated with vertical irregularities and discontinuities in structural stiffness. In many cases, shear walls were concentrated in lower-story configurations (such as basements), but were abruptly discontinued in the upper stories, leading to a sudden reduction in lateral stiffness and strength. This configuration resulted in excessive inter-story drift demands, ultimately compromising the structural system's ability to dissipate energy and maintain lateral stability even though the well-known strength ratio equation for achieving the strong-column/weak-beam condition at the beam-column joints was satisfied. These failures highlight the importance of continuous and well-distributed lateral support throughout the height of the structure. Moreover, such damage cannot be attributed solely to construction quality or detailing errors but also stems from insufficient evaluation of global structural behavior during the analysis and design process. For example, as noted in experimental studies by Ning et al. (2016), the contribution of floor slabs to beam stiffness can significantly influence the distribution of internal forces and the location of plastic hinge formations. In systems with discontinuous lateral resistance, this can exacerbate unexpected failure mechanisms, undermining the intended performance goals of modern seismic design.

Another critical factor influencing seismic performance is the axial load acting on columns. While moderate axial loads can enhance a column's load-bearing capacity by increasing compressive strength, excessive axial loading is well known to reduce ductility an essential attribute for energy dissipation during earthquakes. Türker and Gültekin (2023) emphasized that such ductility loss significantly limits the plastic rotational capacity of columns. When axial forces increase unexpectedly, columns may behave in a brittle manner and fail before the beams, resulting in a premature and uncontrolled collapse mechanism that contradicts the strong-column/weak-beam design objective.

According to the Turkish Building Earthquake Code (TBEC-2018), if the axial load acting on a column is less than 10% of the product of its gross cross-sectional area and the characteristic compressive strength of concrete (Equation 2), the strong-column/weak-beam strength verification (Equation 1) is not required. However, if this limit is exceeded under any load combination that includes the effects of dead, live, and earthquake loads, the verification becomes mandatory. TBEC-2018 permits axial loads on columns up to 40% of the gross section capacity under such combinations still below the critical threshold of approximately 60%, beyond which a sharp decline in ductility is typically observed in experimental studies.

$$N_d \leq 0.10 \times Ac \; x \; fck \tag{2}$$

It is also important to highlight that during the February 6, 2023 Kahramanmaraş earthquakes, unusually high vertical ground motion components were recorded in several regions. These vertical accelerations may have temporarily increased axial loads beyond their design values, even in buildings nominally within code compliance. Such transient but severe vertical loading could have triggered brittle column failures in some structures, underscoring the need to more thoroughly account for vertical seismic effects particularly in regions susceptible to pulse-like or near-fault ground motions.

While numerous structures conceptualised in accordance with the strong column–weak beam principle formally almost comply with stipulated code requirements, the seismic events centred in Kahramanmaraş on 6 February 2023 exposed substantial discrepancies between anticipated and observed performance outcomes. In particular, buildings where nonlinear behaviour was accounted for solely through the use of a high seismic reduction factor (R = 8) as selected by practitioners while employing only linear analysis methods, exhibited damage mechanisms inconsistent with this principle. This discrepancy was especially pronounced in workshop-type structures, which are typically characterised by a small number of stories, basements enclosed by rigid shear wall elements, ground floors with greater story heights than upper floors, long structural spans, and heavily reinforced beams designed primarily for gravity loads.

The primary objective of this study is to perform a detailed structural analysis of a reinforced concrete building that experienced damage inconsistent with the strong column–weak beam philosophy during the February 6, 2023 Kahramanmaraş earthquakes. The analysis is conducted in accordance with the deformation-controlled design approach stipulated in the Turkish Building Earthquake Code (TBDY-2018). Moreover, the objective of the present study is twofold: firstly, to identify and evaluate the underlying causes of the observed damage, and secondly, to establish a methodology for the future prevention of such occurrences. The condition of the building, as documented during post-earthquake field investigations, is illustrated in Fig. 1.

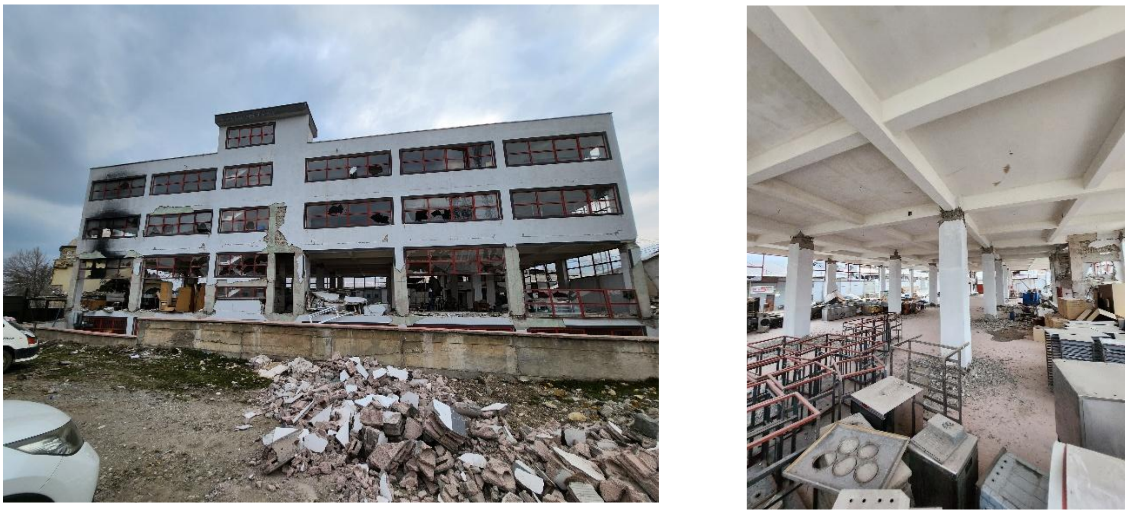

(a) (b)

Fig. 1. (a) General view of the building and (b) Columns damages

2. Numerical modeling

In this study, a structural analysis was conducted by developing a representative model of a four-story reinforced concrete building that was identified, based on field investigations, as having sustained damage during the Kahramanmaraş-centered earthquakes on February 6, 2023. The model was designed to approximately reflect the actual structural characteristics of the original building, including its overall geometry and load-bearing elements (Fig. 2).

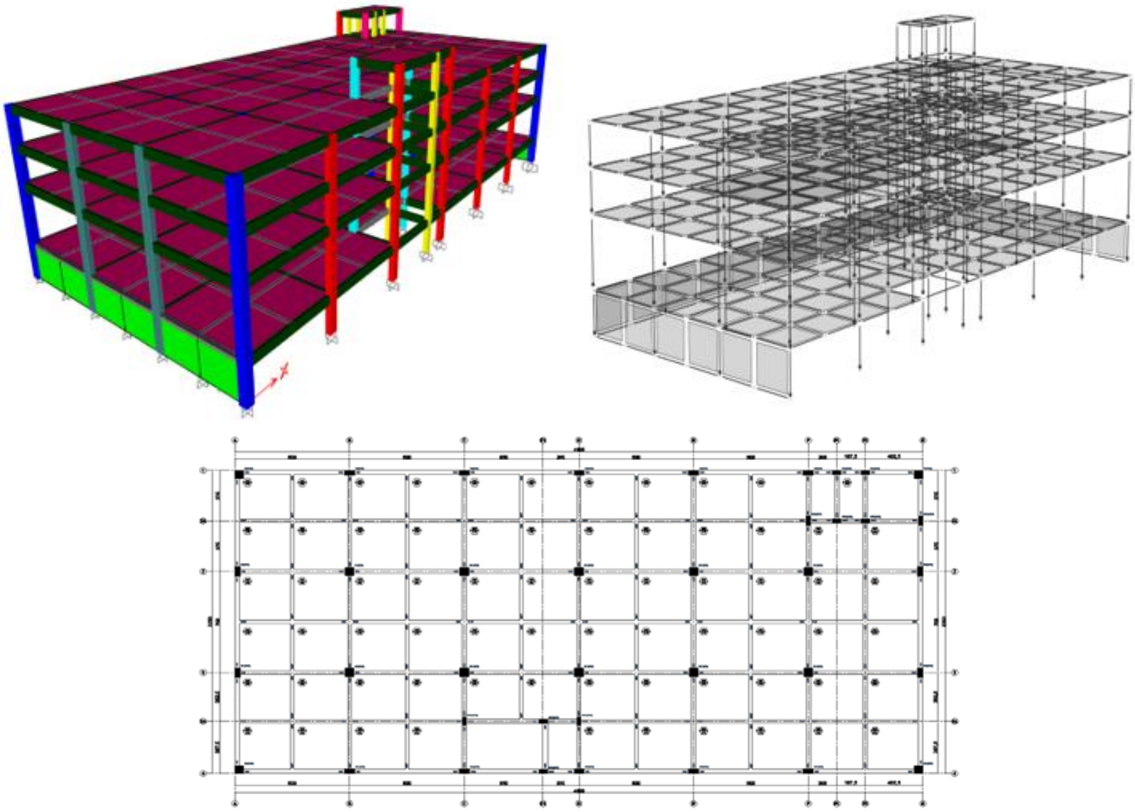

Fig. 2. Generated 3D soil model, formwork

Regarding material properties, the characteristic compressive strength of the concrete used in the reinforced concrete elements was defined as C25 (fck = 25 MPa), while the reinforcement steel was specified as S420 with a yield strength of 420 MPa. For loading conditions, the floor slabs in the basement and typical floors were subjected to a finishing dead load of 2.50 kN/m² and a live load of 3.50 kN/m², while for the roof slab, the finishing dead load and live load were taken as 1.00 kN/m² each).

The nonlinear behavior of the column and beam elements was incorporated into the analysis model using a distributed (fiber) plasticity model. The fiber modeling approach was implemented in accordance with the modeling guidelines specified by NIST (2017), along with the methodology presented by Padalu and Surana (2024) (Fig. 3). To represent the nonlinear material behavior, the material models for concrete and reinforcing steel were defined as shown in Figure 4.

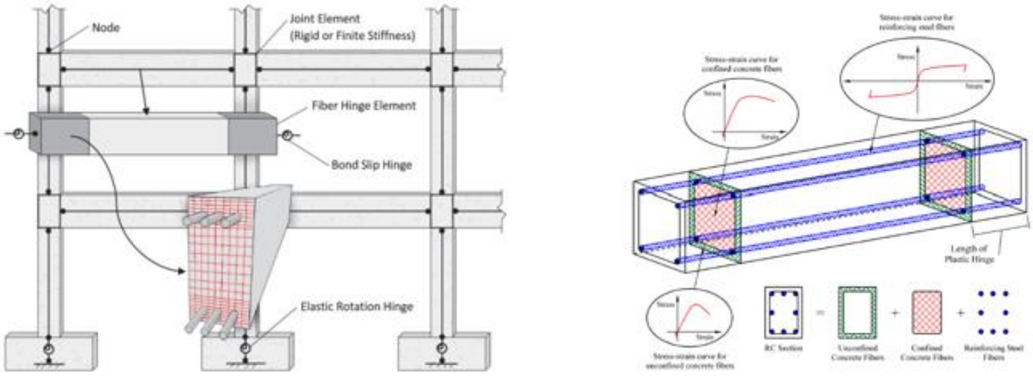

Fig. 3. Schematic representation of the definition of the distributed (fiber) plasticity behavior model

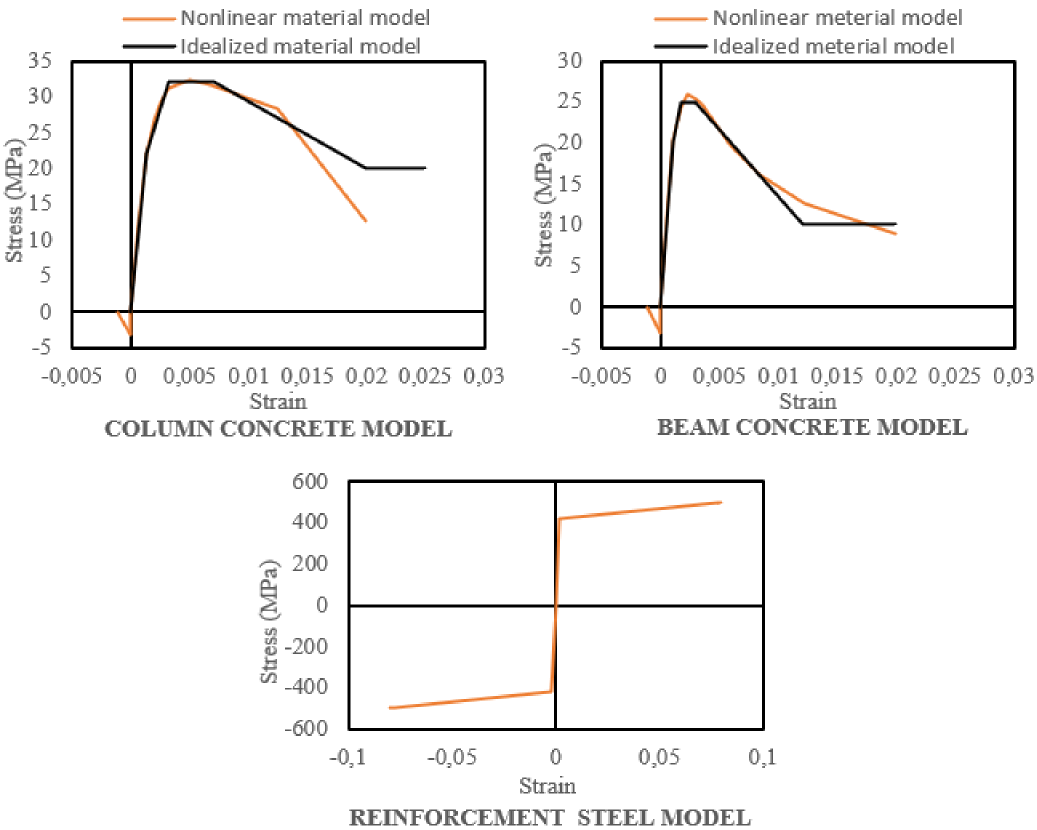

Fig. 4. Nonlinear material models

3. Selection of earthquake ground motion

In accordance with the provisions of the Turkish Building Earthquake Code (TBEC, 2018) and based on the local site-specific conditions, the earthquake that occurred on February 6, 2023 with a moment magnitude of Mw = 7.7 and an epicenter located in Kahramanmaraş was selected to represent the Design Earthquake Level 2 (DD-2) ground motion for the structural analyses. This selection was made using the geographical coordinates of the building under study to ensure consistency with seismic hazard mapping criteria defined in TBEC-2018.

For the analyses, ground motion records in the East–West and North–South directions were obtained from the nearest strong motion station to the damaged structure, identified as Station No. 4625. These records were used to simulate realistic seismic excitation corresponding to the structural location. Additionally, in order to assess the potential impact of regional variation in seismic demand, a second set of ground motion data was incorporated from Strong Motion Station No. 3129, located in Hatay one of the cities severely affected by the same earthquake sequence (Fig. 5). This comparative assessment aims to explore how different local site effects and ground motion intensities may influence structural response.

The selected acceleration records were applied simultaneously in the two horizontal directions (East–West and North–South) during the time history analyses to accurately capture bidirectional seismic effects. The acceleration time histories obtained from both recording stations are shown in Fig. 5. Furthermore, to evaluate the compatibility and intensity of these records, their corresponding response spectra were computed and compared against the elastic DD-2 design spectrum specified in TBEC-2018 for each respective location. These comparisons are presented in Fig. 6, illustrating how the recorded motions relate to code-defined expectations and providing insight into the severity of the ground shaking experienced during the Kahramanmaraş earthquakes.

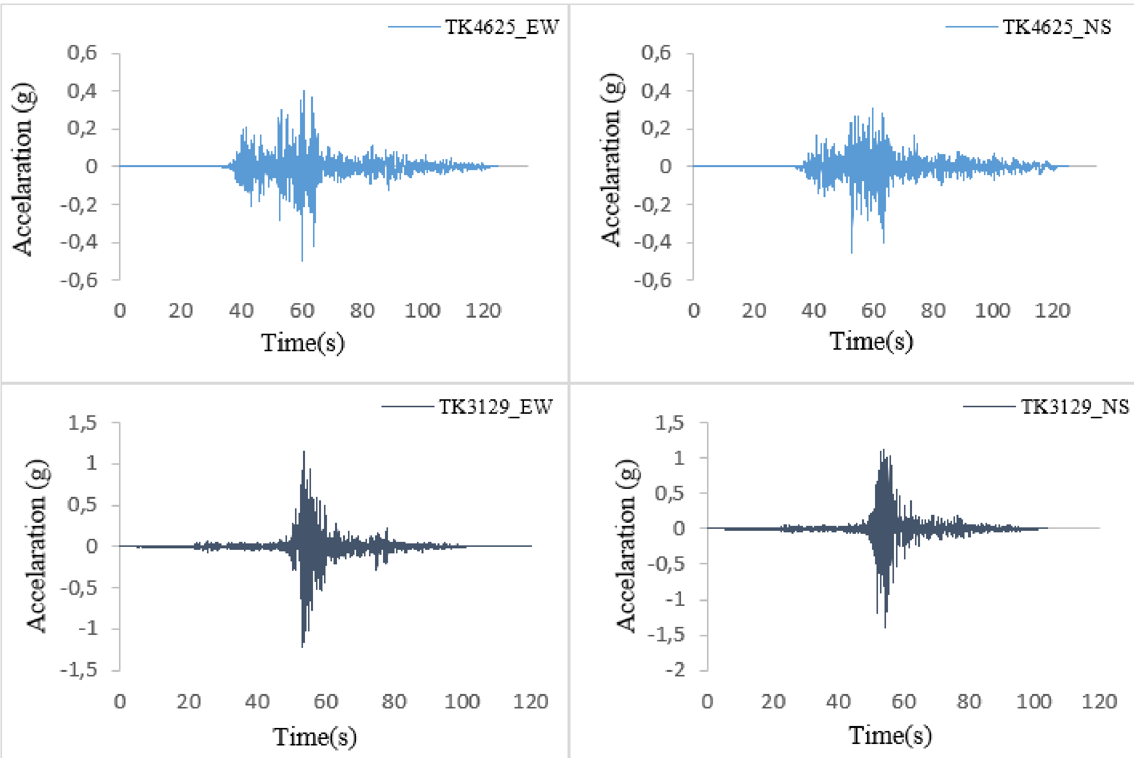

Fig. 5. Acceleration time histories of used earthquake data

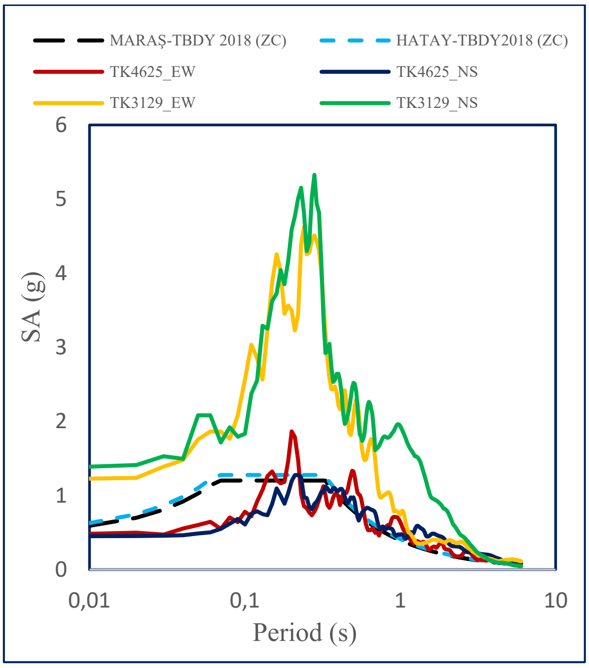

Fig. 6. Response Spectrum of considered records and elastic spekctrum fiven in TBEC-2018 for the site of recods.

4. Analysis and results

The structure assessed in this study was first documented during detailed post-earthquake field investigations. These observations served as the foundation for the development of a numerical model, which accurately incorporated the original geometric characteristics and the longitudinal reinforcement detailing of the building. The reinforcement quantities and layout derived from linear analysis were found to be largely consistent with those observed in the field, lending credibility to the assumptions made in the modeling phase. However, a key discrepancy was noted in the beam–column joint detailing. While the numerical model was constructed in accordance with TBEC-2018 provisions assuming compliant joint confinement and detailing the actual implementation in the field did not fully meet these code requirements. As a result, the model likely overestimates the real structural capacity and ductility, particularly at the critical connections. To evaluate the building's performance under realistic seismic loading, nonlinear time-history analyses were conducted. Material-specific strain limits corresponding to the collapse prevention (CP) performance level were adopted, with values of 0.013 for reinforced concrete column elements, 0.0065 for beams, and 0.032 for reinforcing steel. The analytical results closely matched the damage patterns observed during on-site inspections particularly the premature failure of second-story columns providing strong validation of the model and confirming the inadequacy of relying solely on linear analysis in such cases.

To further illustrate the damage progression captured in the nonlinear time-history analysis, Fig. 6 presents the distribution of plastic hinge formation in the column elements at the instance when yielding is first initiated. As shown, plastic deformation initially localizes in the second-story columns, indicating the onset of nonlinear behavior in vertical load-bearing elements. This finding aligns with field observations, where early signs of cracking and distress were also concentrated in the same story.

Subsequently, as the seismic excitation intensifies, additional plastic rotation demands accumulate, particularly in the same second-story columns. Fig. 7 shows the damage state of the structure when the strain values in these columns exceed the Collapse Prevention (CP) threshold. At this stage, the analytical results indicate that the columns have experienced severe nonlinear deformations beyond acceptable performance limits, while the adjacent beam elements remain in a comparatively lower damage state. This confirms that the failure mechanism is governed by column failure, rather than the intended strong column–weak beam behavior. These visualizations emphasize the critical role of column detailing and system-level stiffness discontinuities in driving collapse mechanisms during strong ground motion.

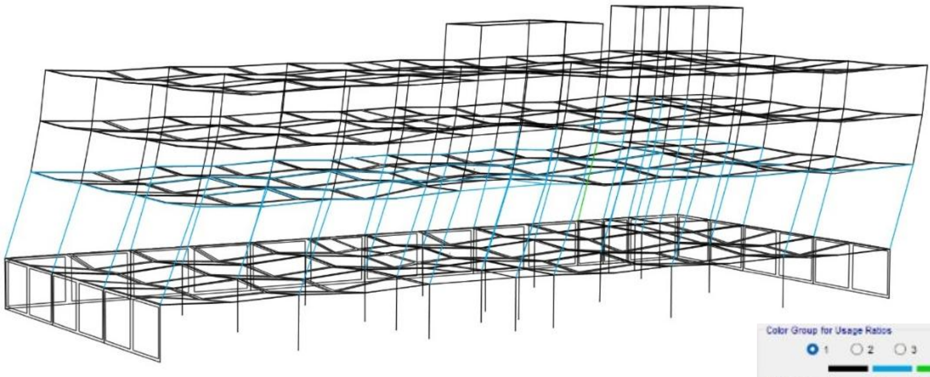

(a) t=52.95 s first yielding

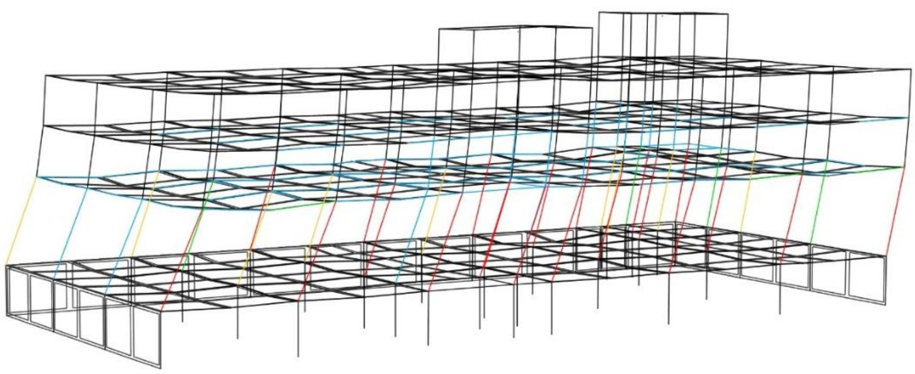

(b) t=53.08 s most of columns pass the CP level (red)

Figure 7. Development of plastic hinges in column elements at two critical time steps during the seismic response of Kahramanmaraş records.

To further demonstrate the damage progression observed in the nonlinear time-history analysis, Fig. 7 illustrates the development of plastic hinges in column elements at two critical time steps during the seismic response. Fig. 7(a) shows the state of the structure at t = 52.95 s, corresponding to the onset of yielding in the second-story columns. At this stage, plastic deformations begin to develop in the vertical elements, marking the initiation of nonlinear behavior. This early yielding in the columns is consistent with the localized damage observed during field investigations and highlights a deviation from the expected strong column–weak beam mechanism.

Fig. 7(b) presents the structural response at t = 53.08 s, where a significant portion of the second-story columns exceed the Collapse Prevention (CP) strain threshold. The accumulation of plastic demands in a short time interval leads to severe damage in the column elements, while the beam elements remain below critical damage levels. This condition indicates the emergence of a soft-story mechanism and confirms that the collapse potential was primarily governed by column failure.

An in-depth evaluation of the nonlinear time-history analysis results under the Maraş (TK4625) and Hatay (TK3129) earthquake records reveals clear differences in the structural response and damage distribution across the building's floors (Table 1 and Table 2). For the Maraş ground motion, all column elements on the second story exceeded the Collapse Prevention (CP) performance level, while no such exceedance was recorded in beams. Most beams remained within the Immediate Occupancy (IO) range, with a few on the second floor reaching up to the IO–Life Safety (LS) transition range. The first, third, and fourth floors exhibited predominantly elastic behavior in both beams and columns, with all elements remaining below the IO threshold except for moderate IO–LS level damage in some third-story columns.

In contrast, under the Hatay ground motion, the demand on structural elements was more severe and widespread. Again, all columns on the second story surpassed the CP level, similar to the Maraş case. However, unlike the previous scenario, beam elements on the second floor also exhibited more advanced damage, with 18 beams exceeding the CP limit, 12 in the IO–LS range, and 31 remaining below IO. This suggests that the Hatay record induced higher energy input into the structural system, pushing some beams beyond critical damage states. Still, beam and column elements on the first, third, and fourth stories mostly stayed within elastic limits, apart from a few minor exceedances in the IO–LS range.

Table 1. Damage levels of load-bearing elements

	MARAŞ-TK4625				
	Story	<IO	IO to LS	LS to CP	>CP
BEAM	1(Basement)	45	-	-	-
	2	28	30	3	-
	3	61	-	-	-
	4	61	-	-	-
COLUMN	1 (Basement)	38	-	-	-
	2	-	-	-	38
	3	27	11	-	-
	4	38	-	-	-

Table 2. Damage levels of load-bearing elements

	HATAY-TK3129				
	Story	<IO	IO to LS	LS to CP	>CP
BEAM	1(Basement)	45	-	-	-
	2	31	12	-	18
	3	55	6	-	-
	4	60	1	-	-
COLUMN	1(Basement)	38	-	-	-
	2	-	-	-	38
	3	27	11	-	-
	4	38	-	-	-

These findings underscore two significant points. First, the second floor consistently emerged as the most vulnerable story, reflecting a concentration of seismic demands and potential soft-story behavior due to stiffness discontinuity or inadequate lateral resistance. Second, the choice of ground motion record significantly influenced the structural performance, with the Hatay earthquake inducing higher damage levels in beam elements compared to the Maraş earthquake. This variability demonstrates the importance of selecting multiple representative ground motions in nonlinear performance-based evaluations to fully capture potential collapse mechanisms and inform retrofitting or design decisions accordingly.

The maximum interstory drift values obtained from the nonlinear time-history analyses were evaluated for both earthquake records to assess the overall deformation demand imposed on the structure. The results indicate that the maximum interstory drift reached approximately 2.92% for the Maraş (TK4625) record, whereas it escalated to 10.06% under the Hatay (TK3129) record (Fig. 8) . According to the deformation-based design limitations prescribed by TBEC-2018, the drift demand under the Maraş record slightly not exceeds the allowable threshold for collapse prevention performance but could still be considered marginally tolerable in practical terms, suggesting the possibility that the structure might survive this level of seismic excitation albeit with severe damage and residual deformations.

In contrast, the extreme drift value induced by the Hatay record far exceeds the permissible limits, pushing the structure into a state of global instability. Despite both records leading to collapse-level damage in the second-story columns, a key distinction lies in the damage progression of the beam elements, as well as the significantly different demand-to-capacity (D/C) ratios, which indicate a more severe overstress condition in the case of the Hatay record. The Hatay excitation not only triggers excessive deformation but also initiates widespread failure mechanisms that are incompatible with the structural system's ductility capacity.

Therefore, while collapse may be avoidable under the Maraş record, the structural response observed under the Hatay record clearly indicates that collapse is inevitable due to the compounded effects of drift exceedance, loss of stiffness in critical elements, and a failure to maintain structural integrity under large lateral displacement demands.

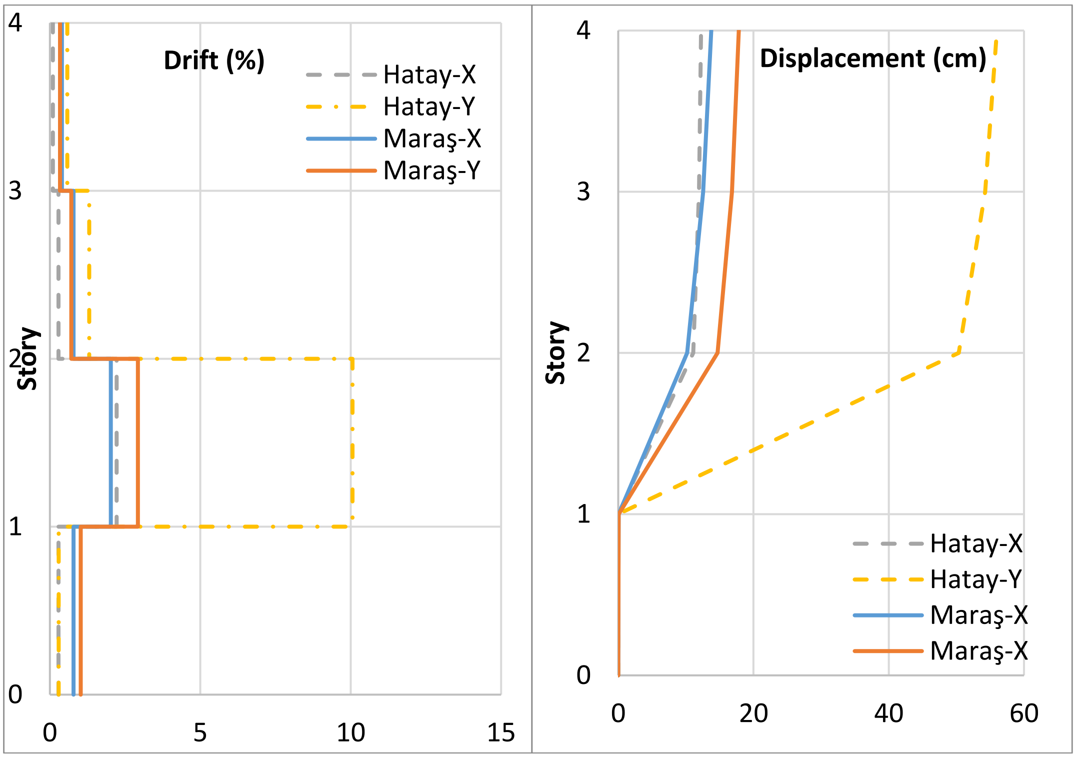

Fig. 8. Calculated displacement and drift variation with height.

The standard check for verifying the strong column–weak beam (SCWB) condition, as illustrated in Fig. 9, is based on the requirement that the inequality defined in Equation 1 must be satisfied for beam moments acting in both directions within the vertical plane of the frame. This check implicitly assumes that the flexural demands on the beams and columns connected to a joint develop in the same direction under lateral loading. This fundamental assumption underpins the moment capacity ratio control prescribed in seismic design codes, including TBEC-2018, and forms the basis of the conventional capacity design approach.

However, field observations from recent earthquakes—particularly the February 6, 2023 Kahramanmaraş events—have demonstrated that this assumption does not hold in many real-world structures. Specifically, in buildings where lower stories are rigidly confined with shear walls (e.g., basement levels), and upper stories consist of moment-resisting frames, the actual behavior deviates significantly from the idealized model. In such cases, columns connected to the beam–column joints being evaluated often develop opposing moments, effectively balancing each other out, resulting in a very low residual moment at the joint. This undermines the intended premise of the SCWB check, which assumes an unbalanced condition favoring beam yielding.

Additionally, analytical results indicate that in buildings with long-span beams subjected to high dead and live loads, the internal moments in these beams—governed primarily by gravity loading—do not significantly change during seismic excitation. As a result, these elements retain large internal moments regardless of lateral load reversals, and the assumption that beam moments will increase significantly under earthquake effects becomes invalid. Consequently, the practical relevance of the SCWB check—as traditionally formulated—diminishes in such systems, and its enforcement does not guarantee the intended energy dissipation mechanism. In such cases, the conventional SCWB verification loses meaning, and a more realistic approach to seismic design and detailing is required—one that considers actual deformation demands and stiffness irregularities in the vertical direction.

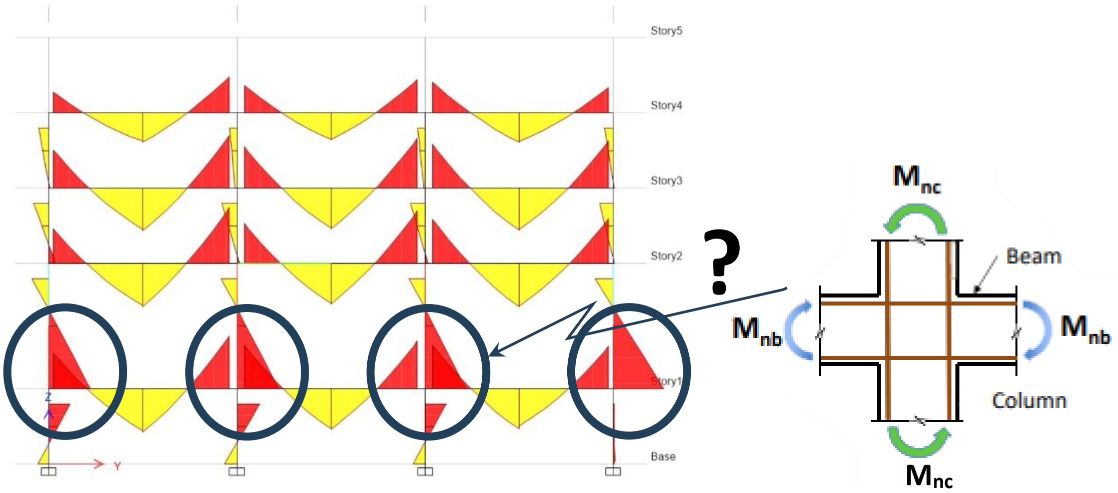

Fig. 9. Typical column moment diagram for investigated structure and assumption for the strong colum weak beam

In such configurations, the building's global behavior deviates from a typical shear-frame mechanism, especially just in the rigid basement level, and instead develops an alternative moment distribution pattern. In these cases, the actual seismic demands on the columns significantly exceed those on the beams, particularly at the interface between the rigid lower stories and the more flexible upper frames. This mismatch leads to concentration of inelastic demands in the columns, initiating damage mechanisms that violate the intended SCWB philosophy and often trigger premature failure at these critical story levels.

As a result, and in light of the preceding discussion, it becomes evident that relying solely on a high behavior factor such as R = 8, which is commonly adopted in design practice, is inadequate for ensuring seismic safety in structural systems exhibiting vertical irregularities. In such configurations—characterized by stiffness discontinuities, unbalanced deformation demands, and concentrated damage zones—the global energy dissipation capacity is significantly reduced, and the assumptions underlying the use of high R-factors are no longer valid. When more realistic values are adopted for ductility, the effective behavior factors must be considerably lower to reflect the actual deformation and failure mechanisms. For example, by adjusting for the material coefficients typically used in design, the effective R-factor can be approximated as R = 3.5 (≈1.5 × 2.38) for the Hatay ground motion and R = 4.0 (≈1.5 × 2.8) for the Maraş ground motion. These adjusted values provide a more accurate representation of the structure's true performance capacity and the level of seismic demand it can safely sustain.

Ultimately, adjusted R-values can provide a rough estimate of the reduced capacity, these values do not fully capture the complex nonlinear behavior of such irregular systems. Therefore, a deformation-based analysis approach is essential to realistically assess the structural response and to provide engineers with a more reliable understanding of how the building will perform under strong ground motion. Only through such advanced analysis techniques can the true inelastic demands, potential damage mechanisms, and collapse risks be identified, allowing for safer and more informed seismic design decisions—especially in structures with pronounced vertical irregularities.and long span only with such revised assumptions and a more performance-consistent evaluation of behavior factors can a realistic and reliable seismic design be achieved—particularly for buildings with significant vertical stiffness irregularities, where conventional code-based simplifications may lead to unsafe design outcomes.

5. Conclusions

This study critically examined the seismic behavior of a reinforced concrete building that suffered significant damage during the February 6, 2023 Kahramanmaraş earthquakes, with a particular focus on the applicability of the strong column–weak beam (SCWB) design principle. The building, which exhibited a vertically irregular configuration characterized by a rigid basement with shear walls supporting a flexible frame system above, was found to deviate substantially from the expected frame behavior under strong ground motions.

Field observations, reinforced by detailed nonlinear time-history analyses, revealed that all second-story columns exceeded the Collapse Prevention (CP) limit under both the Maraş and Hatay earthquake records. Although linear analysis indicated compliance with SCWB criteria, nonlinear analysis uncovered failure mechanisms that contradicted the intended ductile hierarchy. In particular, high demands were concentrated in the second-story columns—primarily due to vertical stiffness discontinuities—which undermined the SCWB mechanism and triggered premature column failure. These results underscore the critical limitations of relying solely on linear analysis and prescriptive R-factors, especially in irregular structures.

The study further highlighted the limitations of the standard SCWB verification method, which assumes that beam and column moments act in the same direction. In the examined case, and many similar configurations observed in earthquake-prone regions, columns connected to the beam-column joints often developed opposing moment demands, reducing residual joint moments and invalidating the assumptions behind the capacity design check. Moreover, long-span beams carrying substantial gravity loads retained large internal moments even during lateral loading, resulting in minimal seismic contribution and rendering the traditional SCWB control ineffective. In this context, nonlinear analysis methods proved essential for realistically evaluating the inelastic demand distribution and accurately capturing the failure mechanisms—particularly in columns situated between stiff and flexible regions. Linear methods, by contrast, failed to predict these critical behaviors, highlighting the risk of underestimating vulnerabilities when such approaches are used exclusively in design. In conclusion, accurate seismic performance assessment of irregular buildings demands an integrated approach—combining detailed nonlinear analysis with realistic design coefficients—to ensure safety, robustness, and code compliance. By adopting such strategies, engineers can deliver more resilient structures capable of withstanding severe seismic demands while minimizing the risk of unexpected failure.

References

Computers and Structures, Inc. (2024). *ETABS* (Version 21.2.0) [Computer software].

Computers and Structures, Inc. (2025). *Perform3D* (Version 10.1.0) [Computer software].

Ning, N., Qu, W., & Mad, Z. J. (2016). Design recommendations for achieving ‘‘strong column-weak beam” in RC frames. *Engineering Structures*. https://doi.org/10.1016/j.engstruct.2016.07.053

NIST. (2017). *Guidelines for nonlinear structural analysis for design of buildings; Part IIb – Reinforced concrete moment frames* (NIST GCR 17-917-46v3).

Padalu, P. K. V. R., & Surana, M. (2024). An overview of performance-based seismic design framework for reinforced concrete frame buildings. *Iranian Journal of Science and Technology, Transactions of Civil Engineering, 48*, 635–667. https://doi.org/10.1007/s40996-023-01217-4

Paulay, T. (1983). Deterministic seismic design procedures for reinforced concrete buildings. *Engineering Structures, 5*(1), 1–8. https://doi.org/10.1016/0141-0296(83)90044-5

TBSC. (2018). *Principles for the design of buildings under the impact of earthquakes* (in Turkish). Ministry of Interior, Disaster and Emergency Management Presidency, Ankara, Turkey.

Türker, K., & Gültekin, C. (2023). Türkiye Bina Deprem Yönetmeliğindeki Performans Düzeylerinin Betonarme Kolonlar için Karşılaştırmalı Değerlendirilmesi. *Turkish Journal of Civil Engineering, 34*(3), 163–190. https://doi.org/10.18400/tjce.1285845

Effect of vertical earthquake components on the base displacement response of seismically isolated buildings

Başak Toprak[1], Seda Öncü Davas*[1]

[1] *Istanbul University-Cerrahpasa, Faculty of Engineering, Department of Civil Engineering, İstanbul, Türkiye*

Abstract. Seismic isolation is a widely implemented strategy for mitigating earthquake-induced demands on structures by incorporating isolator units at the foundation or other appropriate substructure levels. This approach effectively lengthens the natural period of the structure through horizontally flexible isolation elements, allowing the superstructure to respond in a near-rigid-body manner relative to the ground. As a result, interstory drift ratios and floor accelerations are significantly reduced, thereby preserving structural integrity and minimizing damage to non-structural components. Nevertheless, the performance of seismic isolation systems can be adversely affected under near-fault ground motions, which are characterized by high-amplitude velocity pulses and significant vertical ground motion components. These characteristics can notably increase seismic demands on the isolation system, necessitating a detailed evaluation of their effects. Prior studies have emphasized the critical role of such components in the seismic behavior of base-isolated structures. In this study, three-story and six-story three-dimensional reinforced concrete moment-resisting frame structures equipped with lead-rubber bearings (LRBs) were modeled using SAP2000. Two pulse-like ground motion records containing both horizontal and vertical components were selected in accordance with the Turkish Building Earthquake Code (TBEC-2018) and scaled to match the target design spectra for the relevant site classes. Nonlinear time history analyses were conducted under two excitation scenarios: (i) horizontal components only, and (ii) combined horizontal and vertical components. The seismic response was assessed with particular focus on isolator performance, specifically evaluating both horizontal and vertical displacement demands of the isolation units. The findings indicate that the inclusion of the vertical ground motion component increased vertical displacement demands under compressive effects in all isolators of the three-story building, while in the six-story building, it slightly reduced the displacement demands in isolators subjected to tensile effects and slightly increased those in isolators under compressive effects.

Keywords: Seismically isolated building; Vertical components of earthquakes; Horizontal-vertical coupling effects

1. Introduction

Seismic base isolation primarily aims to decouple the superstructure from the foundation, thereby increasing the natural period of the structure and reducing the seismic demands transmitted to it. By extending the period, isolation systems shift the structure's response to a region of the response spectrum associated with lower accelerations. In addition, the supplemental damping provided by the isolators effectively dissipates seismic energy, which leads to a significant reduction in both inter-story drifts and floor accelerations. As a result, seismic isolation minimizes the lateral forces transmitted to the superstructure, contributing to the preservation of both structural integrity and the safety of non-structural components (Naeim & Kelly, 1999).

However, the performance of base isolation systems may be challenged under seismic scenarios dominated by near-fault effects. In this context, two major challenges are commonly identified. The first is the occurrence of long-period, high-amplitude velocity pulses, which are frequently observed in near-fault ground motions. The second involves the vertical ground motion component, which can exceed conventional levels in such events (Bray & Marek, 2004). When the period of the velocity pulse is close to the natural period of the isolation system, a resonance-like interaction may develop, leading to significant increases in isolator displacement demands (Hall, 1998; Alhan & Öncü-Davas, 2016). If these dynamic effects are not adequately addressed during the design process, isolators may exceed their capacity, resulting in potential structural failures such as tearing or buckling.

Although the vertical component of ground motion is typically lower in amplitude than the horizontal component and gravitational acceleration, studies have shown that in near-fault regions it can reach unusually high

* Corresponding author, E-mail: seda.oncu@iuc.edu.tr

https://doi.org/10.31462/icearc2025_ce_eqe_277

golden light publishing

levels and have significant influence on structural response (Bozorgnia & Campbell, 2004). While it is widely accepted that horizontal ground motions generally exhibit higher amplitudes and that vertical components attenuate more rapidly in the far field (Campbell, 1997), recent research demonstrates that vertical ground motions may also play a critical role in the dynamic performance of structures located near active faults (Bozorgnia and Campbell, 2004). Observations from the 2023 Kahramanmaraş earthquakes are consistent with these findings, with peak ground velocity values in the vertical direction reaching up to 100 cm/s at certain stations (Ertuncay & Costa, 2025).

TBEC-2018 does not provide comprehensive provisions regarding the effects of vertical ground motion or the increased seismic demands that may arise under near-fault conditions in the design of base-isolated systems. However, such ground motions often lead to elevated vertical-to-horizontal peak acceleration ratios, which in turn generate significant dynamic demands on structural elements. Base isolation components such as high-damping lead-rubber bearings and frictional bearings may be subjected to substantial tensile forces and uplift effects under these conditions (Kasalanati & Constantinou, 2005). In this context, experimental studies conducted by Kumar et al. (2015) at the University at Buffalo investigated the tensile behavior of rubber isolators and identified cavitation as a potential failure mechanism that may occur under large tensile demands during major seismic events.

To investigate the effect of vertical ground motion on base-isolated structures, three-story and six-story reinforced concrete moment-resisting frame buildings equipped with Lead Rubber Bearings (LRBs) were modeled using SAP2000 (CSI, 2023). The isolation systems were designed for Soil Class ZD in accordance with the DD-1 seismic hazard level, which corresponds to a 2% probability of exceedance in 50 years. Ground motion records containing horizontal and vertical components were selected and scaled in accordance with TBEC-2018 to match the design spectra for each soil classification. Nonlinear time history analyses were carried out considering both horizontal-only excitations and combined horizontal–vertical excitations. The structural response was evaluated based on peak base displacements and vertical displacements in the isolators.

2. Methodology

2.1.Benchmark building model

For comparative analysis, two three-dimensional reinforced concrete moment-resisting frame building models were developed: a three-story and a six-story building. Both models were equipped with lead rubber bearing (LRB) systems designed in accordance with the DD-1 seismic hazard level, which corresponds to a 2% probability of exceedance in 50 years, for Soil Class ZD. As illustrated in the 3D and plan views in Fig. 1, the buildings have a regular plan layout consisting of five bays in the X-direction and three bays in the Y-direction. Each story has a uniform height of 3.5 meters. All columns were designed with cross-sectional dimensions of 50×50 cm, while the beams have cross sections of 30×60 cm. At each floor level, dead and live loads of 2000 N/m² are uniformly assigned to the 20 cm thick slabs.

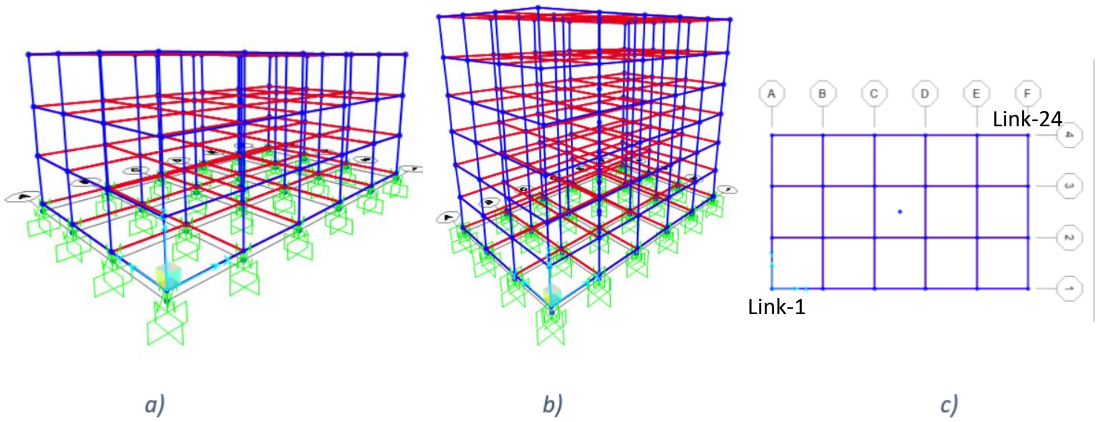

Fig. 1. 3D views of the seismically isolated buildings: (a) three-story model, (b) six-story model, and (c) plan view.

The LRB devices exhibit highly nonlinear hysteretic behavior, which can be effectively modeled using a bilinear force–deformation relationship. The cyclic response of these isolators is represented using the Bouc–Wen model formulation (Bouc, 1967; Wen, 1976), which captures both the pre-yield stiffness and post-yield energy dissipation. The fundamental mechanical parameters that govern the behavior of the Lead Rubber Bearing (LRB) system are derived based on a bilinear idealization of its force–displacement response. These parameters are calculated using a series of interrelated expressions as follows:

Post-yield stiffness (k_2) is determined using the following dynamic relation involving the total weight (W) of the structure and the characteristic period (T_0) of the isolation system:

$$k_2 = 4\pi^2(\frac{W}{g})/\,T_0{}^2 \tag{1}$$

Characteristic strength (F_Q), representing the force at the transition point between pre- and post-yield behavior, is calculated as:

$$F_Q = (k_1 - k_2)D_y \tag{2}$$

Pre-yield stiffness (k_1) is expressed in terms of post-yield stiffness and characteristic strength as:

$$k_1 = k_2 + F_Q/D_y \tag{3}$$

The ratio of post-yield to initial stiffness (α), is given by:

$$\alpha = k_2/k_1 \tag{4}$$

Finally, the yield force (F_y), which represents the onset of nonlinear behavior, is expressed as a function of pre-yield stiffness and yield displacement:

$$F_y = k_1 D_y \tag{5}$$

These equations are consistent with those proposed in the literature (e.g., Naeim & Kelly, 1999; Matsagar & Jangid, 2004), and they form the basis for characterizing the equivalent bilinear representation of LRB isolators in structural analysis.

In this study, the mechanical parameters defining the seismic isolation system were determined through an iterative procedure based on the methodology proposed by Constantinou et al. (2007), in compliance with the requirements of the Turkish Building Earthquake Code (TBEC-2018). In this context, a representative site located at coordinates (41.005427°, 28.940647°) was considered, assuming a ZD soil classification. The design spectral acceleration coefficients corresponding to the DD-1 earthquake level were taken as S_{DS} = 1.757 and S_{D1} = 0.891 for ZD soil. These coefficients were used to construct the design acceleration spectrum and to derive the spectral acceleration values (S_{ae}) required for the dynamic evaluation of the isolation system.

In this study, the mechanical characterization of the lead-rubber bearing (LRB) isolators was carried out through an iterative design process. The initial assumptions included a post-yield to pre-yield stiffness ratio (a) and a characteristic strength ratio (F_Q/W), both taken as 0.1. The shear yield stress of the lead core was assumed as τ_{yp} = 10 MPa, which plays a critical role in defining the isolator's hysteretic energy dissipation capacity. The elastomeric portion of the isolator consists of multiple bonded layers. Each individual layer has a thickness of t = 9 mm, resulting in a total elastomer thickness of T_t = 380 mm. The rubber material properties, specifically the shear modulus (G_v = 0.4 MPa) and the bulk modulus (K = 2000 MPa), were also taken into account, as they significantly influence the horizontal stiffness and volumetric deformation response of the isolator. According to TBEC-2018, when the hardness of the rubber material is assumed to be 60, the empirical constant k is taken as 0.6. For the three-story building model, all isolators are identical, with an elastomer diameter of 500 mm and a lead core diameter of 100 mm. For the six-story building, these dimensions are increased to 600 mm and 120 mm, respectively. Utilizing the aforementioned key parameters, the fundamental properties of the isolation system, including the effective stiffness (K_{eff}), effective period (T_{eff}), effective damping ratio (β_{eff}), and maximum base displacement (D), were calculated in accordance with the formulations provided in Equations 6 to 10.

$$K_{eff} = k_2 + F_Q/D_y \tag{6}$$

$$T_{eff} = 2\pi\sqrt{M/K_{eff}} \tag{7}$$

$$\beta_{eff} = 4Q(D - D_y)/(2\pi K_{eff} D^2) \tag{8}$$

$$\eta = \sqrt{10/(5 + \beta_{eff})} \tag{9}$$

$$D = 1.3T_{eff}^2\eta S_{ae}(T_{eff})g/(4\pi^2\,) \tag{10}$$

In this context, D_y denotes the yield displacement of the isolation bearings. To estimate the maximum displacement at the isolation level (D), it is essential to determine the spectral acceleration (S_{ae}) and the corresponding damping modification factor (η), which is derived based on the effective damping ratio (β_{eff}) of the isolation system. Assuming linear elastic behavior, the spectral acceleration corresponding to the effective period (T_{eff}) is obtained from the design response spectrum. The iterative process terminates once convergence is achieved, specifically when the difference between successive values of D becomes negligible. After the overall dynamic properties of the isolation system are determined using Equations (1)–(10), the mechanical parameters for each isolator are calculated by dividing the total system values by the number of isolation units implemented in the model. These parameters are presented in Table 1.

Table 1. Mechanical LRB parameters of two structures for earthquake level DD-1

	F_Q (kN)	k_2 (kN/m)	k_v (kN/mm)	α	D_y (m)	F_y (kN)	D (m)	K_{eff} (N/mm)	β_{eff} (%)	T_{eff} (s)
3-Story	682.95	152	145	0.1	0.034	52	0.65	224	19	3.51
6-Story	1057.25	386	283	0.1	0.039	75	0.69	316	19	3.4

In this study, the nonlinear behavior of Lead Rubber Bearings (LRBs) was modeled using multilinear plastic link elements to accurately represent their complex force–displacement relationships in both the vertical and horizontal directions under dynamic loading conditions. The fundamental periods of the structure in the horizontal and vertical directions were determined based on the mode shapes that achieve 95% mass participation, as specified in TBEC-2018, and are presented in Table 2. The load combinations to be considered in evaluating the forces acting on the elements located beneath and at the isolation interface are defined in Section 14 of TBEC-2018.

Table 2. Horizontal and vertical fundamental periods and mass participation ratios

3-story					6-story				
Mode	Period	UX	UY	UZ	Mode	Period	UX	UY	UZ
1	3.530321	1.957E-13	1	4.801E-20	1	3.445166	7.999E-14	1	0
2	3.52757	1	1	5.091E-20	2	3.436865	1	1	6.166E-19
3	3.170785	1	1	5.108E-20	3	3.057018	1	1	3.896E-17
13	0.10103	1	1	0.95	11	0.0893	1	1	0.95

2.2. Near-fault earthquakes and basic scaling

Near-fault ground motions, defined as strong ground motions recorded within approximately 15 km of the fault rupture, are characterized by high-amplitude, long-period velocity pulses, which distinguish them significantly from far-field ground motions. In addition to their well-known horizontal effects, recent studies have shown that the vertical component of near-fault ground motions can also attain unusually high amplitudes, particularly in proximity to the fault rupture. This phenomenon has been observed in several destructive earthquakes and is of particular concern for base-isolated structures, where vertical excitation may induce additional demands on isolation systems.

In this study, the influence of vertical ground motion components on the seismic response of base-isolated buildings employing lead-rubber bearings (LRBs) is investigated. To this end, two representative near-fault ground motion records were selected from the PEER Ground Motion Database (2025). The selection and scaling procedures were carried out in accordance with the design response spectrum corresponding to the DD-1 seismic hazard level, which represents a 2% probability of exceedance in 50 years. In addition to matching the target spectrum, several key ground motion parameters were considered during the selection process, including fault rupture distance, moment magnitude (M_w), average shear-wave velocity (V_{s30}), and faulting mechanism.

Following the selection of ground motion records, amplitude scaling was conducted to ensure that the average response spectrum within the period range of $0.5T_{eff}$ to $1.25T_{eff}$ did not fall below 30% of the corresponding design spectrum over the same interval. To account for the influence of near-fault ground motions, the design spectrum was modified in accordance with the methodology proposed by Caltrans (2019) (Eq. 11). The coefficients employed in this spectral adjustment were defined by Equations 12 and 13. The scaling procedure was implemented based on the DD-1 seismic hazard level and site conditions corresponding to Soil Class ZD. Table 3 summarizes the principal parameters of the selected near-fault ground motions, including moment magnitudes (M_w), Joyner–Boore distances (R_{jb}), pulse periods (T_p), and applied scaling factors. Consistent with the definition of Soil Class ZD, the shear wave velocity in the upper 30 meters (V_{s30}) was assumed to be within the range of 180–360 m/s. In order to more accurately represent the seismic behavior of structures located in proximity to active faults, ground motion records classified as pulse-like in the literature and exhibiting pronounced directivity effects were specifically selected. These records were prioritized due to their significant impact on structural response, particularly in scenarios where near-fault effects are predominant. Figure 2 presents the acceleration response spectra of the scaled near-fault ground motion records, considering the horizontal and vertical elastic design spectra defined for the DD-1 earthquake level.

$$S_{a,modified}(T) = S_a(T)N_f \tag{11}$$

$$N_f = 1.2 \quad L_f(km) \le 15km \tag{12}$$

$$N_f = 1.2 - 0.02(L_f - 15) \quad 15km \le L_f(km) \le 25km \tag{13}$$

Table 3. The historical pulse-like earthquake records and their details

RSN	Earthquake	Station	M_w	R_{jb} (km)	T_p (s)	Scale Factor			
						3-story		6-story	
						Horizontal	Vertical	Horizontal	Vertical
1176	"Kocaeli_ Turkey"	"Yarimca"	7.51	1.38	4.949	1.87	0.73	1.86	0.72
6906	"Darfield_ New Zealand"	"GDLC"	7	1.22	6.23	1.10	0.35	1.09	0.35

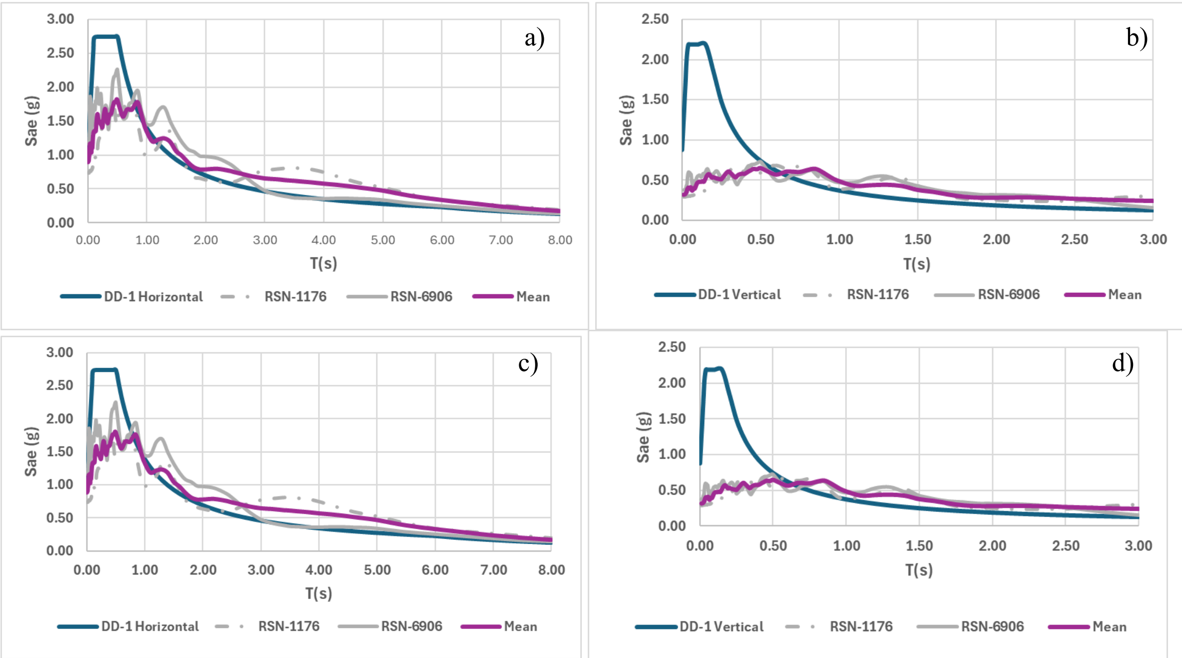

Fig. 2. Spectral acceleration responses of the scaled ground motions for each building model: (a) horizontal and (b) vertical components for the three-story building; (c) horizontal and (d) vertical components for the six-story building.

Based on the effective damping ratio of 19% and the effective isolation period of 3.4 s for the six-story base-isolated building, as provided in Table 2, the spectral displacement values for the x- and y-components of the RSN1776 ground motion were obtained as approximately 101 cm and 93 cm, respectively (see Fig. 3a and 3b). Similarly, for the RSN6906 ground motion, the spectral displacement values were approximately 55 cm and 71 cm for the x- and y-components, respectively (see Fig. 3c and 3d).

3. Results and discussion

For the three-story and six-story base-isolated buildings, scaled near-fault ground motion records were configured into four distinct combinations by rotating the horizontal components by 90 degrees and by including or excluding the vertical ground motion component. Fast nonlinear time history analyses were conducted using these combinations. The results were examined in terms of the horizontal and vertical displacement demands of the isolators for two cases: (i) application of horizontal components only, and (ii) combined application of horizontal and vertical components.

Figure 4 (a) and (b) present the maximum vertical displacement demands of all isolators in the three-story building under the RSN1776 near-fault ground motion record, corresponding to the cases with combined horizontal and vertical components and horizontal components only, respectively. Similarly, Figure 4 (c) and (d) illustrate the results obtained for the RSN9606 near-fault earthquake record. In a comparable manner, Figure 5 presents the results obtained for the six-story building under the same ground motion scenarios, in order to observe the effect of increased number of stories on the vertical displacement response.

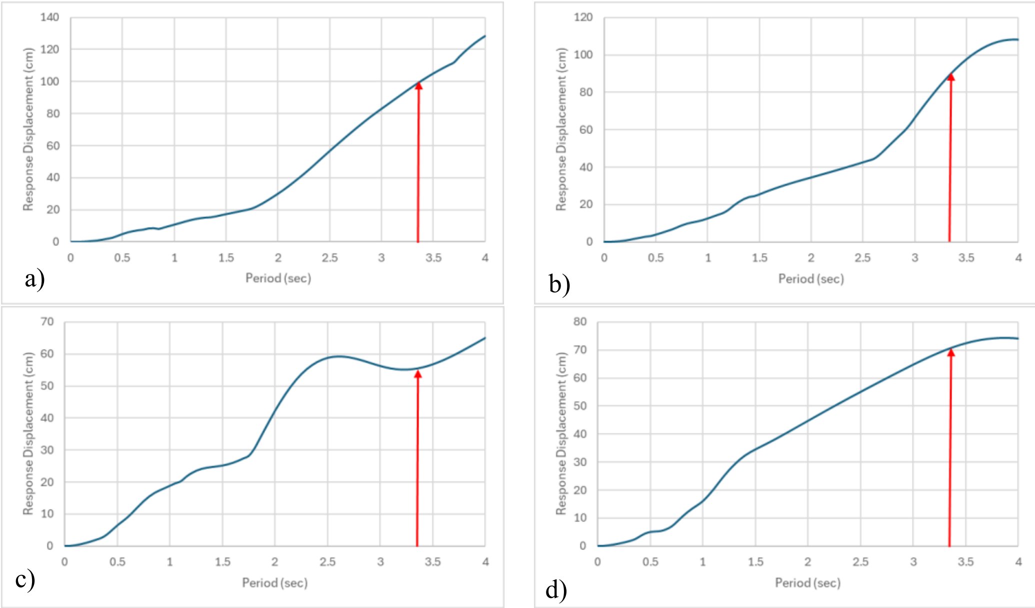

Fig. 3. Isolator damping ratio (19%) displacement spectrum in horizontal x (a) and y (b) directions of RSN 1776 earthquake, horizontal x (c) and y (d) directions of RSN 6906 earthquake at 6-story building

In these graphs, the orange-colored markers represent vertical displacement demands under compressive effects, while the green ones indicate displacements under tensile effects. As observed in Fig. 4, only compressive vertical displacements occurred in the three-story base-isolated building. Moreover, the inclusion of the vertical component (a and c) resulted in slight increases in compressive displacements for some isolators, while causing reductions in others, when compared to the cases with horizontal components only (b and d). Nevertheless, no tensile (uplift) response was observed in any scenario, indicating that the vertical dynamic demands on the isolators remained entirely within the compressive response range throughout the analyses.

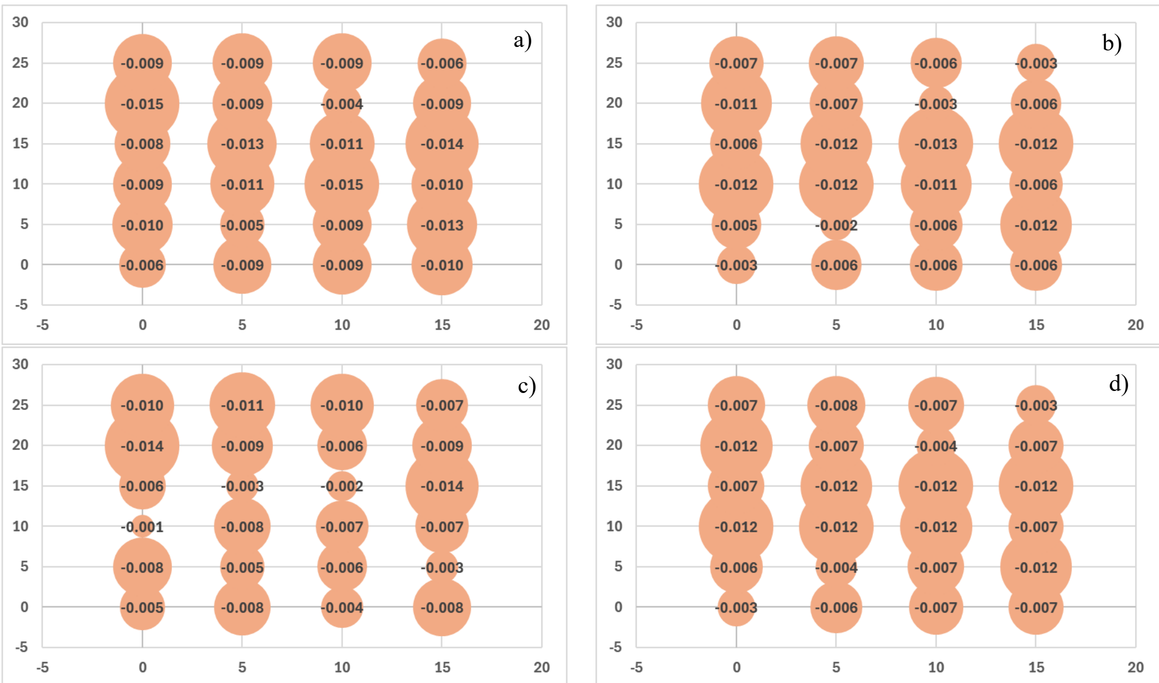

Fig. 4. Maximum vertical displacements (mm) of isolators in three-story base-isolated structure under RSN1176 (a, b) and RSN6906 (c, d) near-fault ground motions: (a, c) with vertical ground motion component, (b, d) without vertical component.

In contrast to the three-story structure, the six-story base-isolated building exhibited both compressive and tensile vertical displacement demands in the isolators, as shown in Fig. 5. The presence of green-colored markers in all four subfigures (a–d) clearly indicates the occurrence of uplift (tensile) responses, particularly in isolators located closer to the building edges. Moreover, the inclusion of the vertical ground motion component (Fig. 5a and 5c) appears to reduce the amplitude of tensile displacement demands in the isolators compared to the scenarios with horizontal components only (Fig. 5b and 5d).

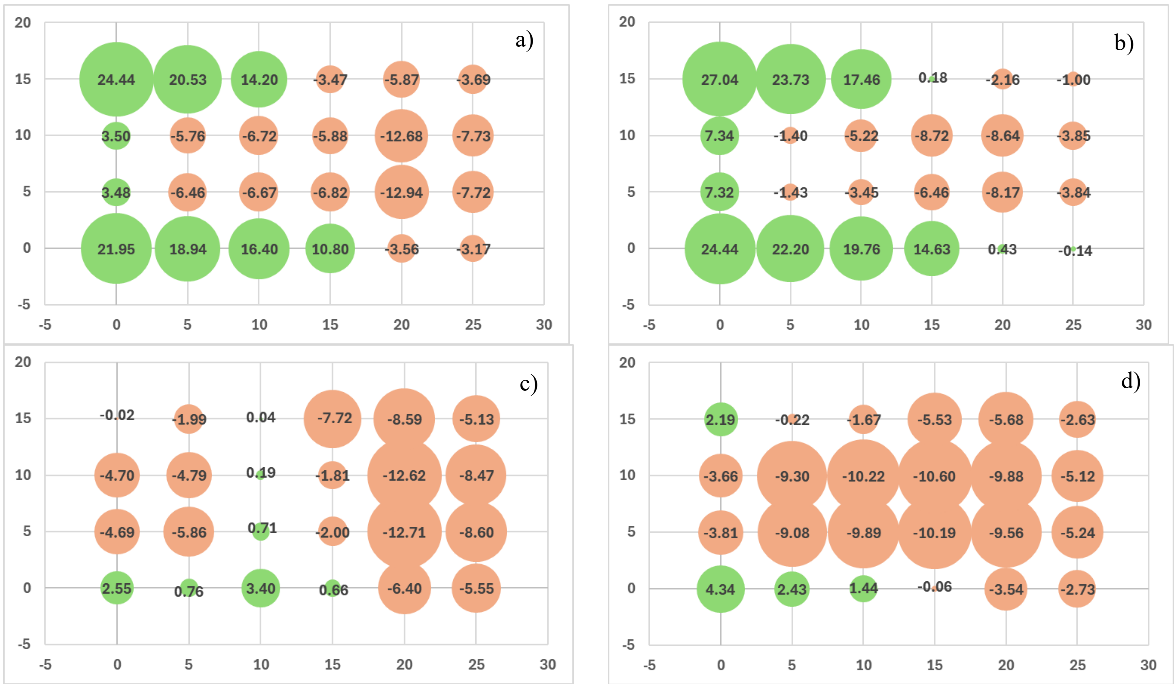

Fig. 5. Maximum vertical displacements (mm) of isolators in six-story base-isolated structure under RSN1176 (a, b) and RSN6906 (c, d) near-fault ground motions: (a, c) with vertical ground motion component, (b, d) without vertical component.

Figures 6 and 7 illustrate the vertical and horizontal displacement demands of the Link-1 and Link-24 isolators (identified in Fig. 1), located at diagonally opposite corners of the six-story base-isolated building, where the influence of vertical ground motion is most pronounced. Based on the combinations selected for maximum displacement demands, Figure 6 corresponds to the RSN1776 near-fault ground motion, while Figure 7 corresponds to the RSN9606 record. As observed in Figs. 6a–b and 7a–b, the Link-24 isolator exhibited its maximum vertical displacement under compressive action, whereas the Link-1 isolator reached its maximum vertical displacement demands under tensile effects. Notably, this tensile peak in Link-1 occurred during the RSN1776 excitation. Comparing the cases with and without vertical ground motion, it is evident that the tensile displacement in the case including vertical excitation (Fig. 6a) is slightly lower than that without vertical excitation (Fig. 6b). A similar trend is observed for the RSN9606 record, as shown in Figs. 7a–b. The peak horizontal base displacements presented in Figs. 6c–f for RSN1776 are consistent with the spectral displacement values in Figs. 3a–b, approximately 101 cm and 93 cm. Likewise, for the RSN9606 excitation, the peak horizontal displacements shown in Figs. 7c–f correspond well with the spectral displacements in Figs. 3c–d, approximately 55 cm and 71 cm. Furthermore, the tensile vertical displacements occurred simultaneously with the peak horizontal displacements for both ground motion records (Figs. 6c–f and 7c–f), indicating that the building model is susceptible to uplift effects under the given seismic excitations.

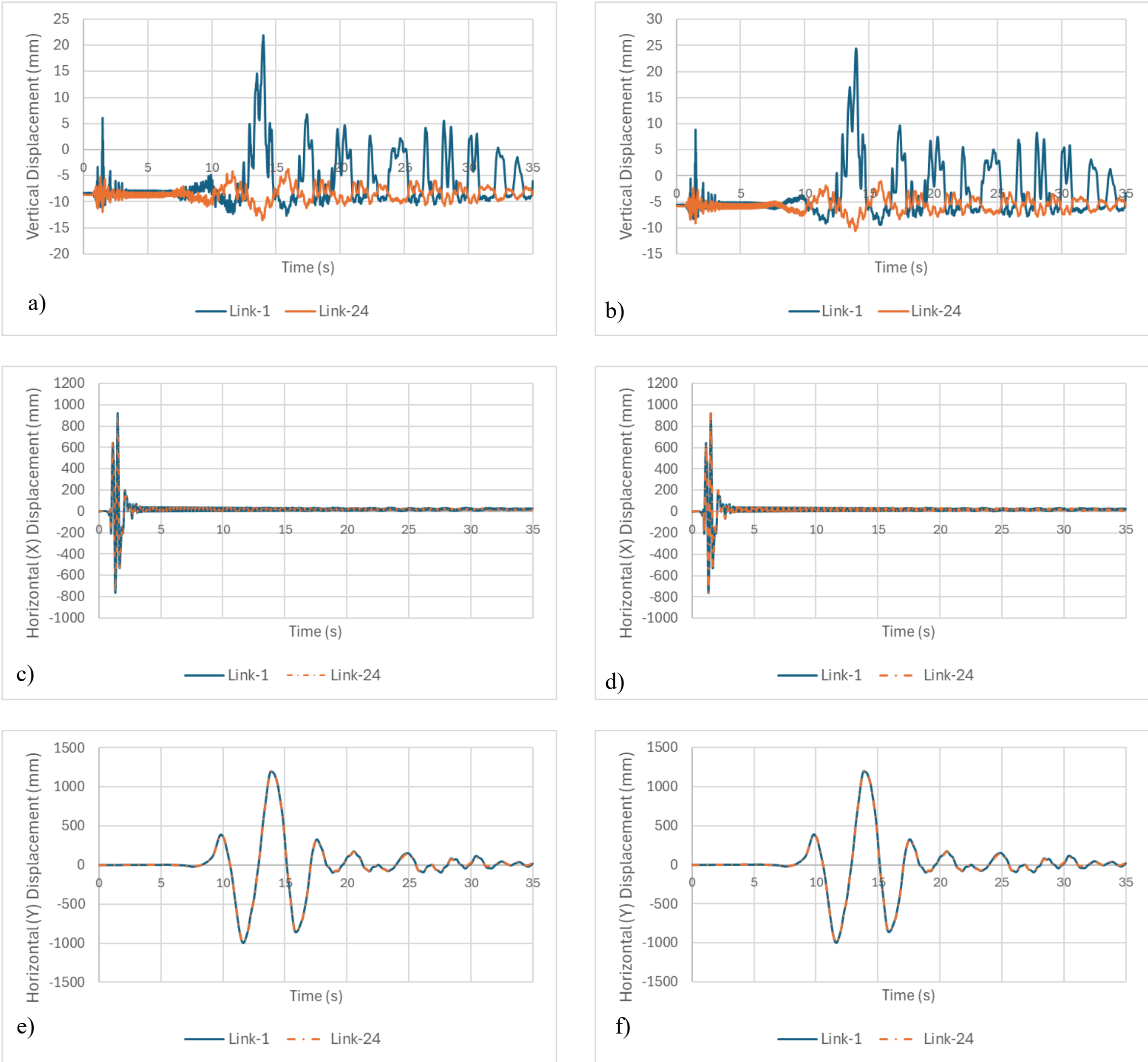

Fig. 6. Vertical (a–b), horizontal-x (c–d), and horizontal-y (e–f) displacement responses of isolators in the six-story building under the RSN1176 record, with (a,c,e) and without the vertical earthquake component (b,d,f).

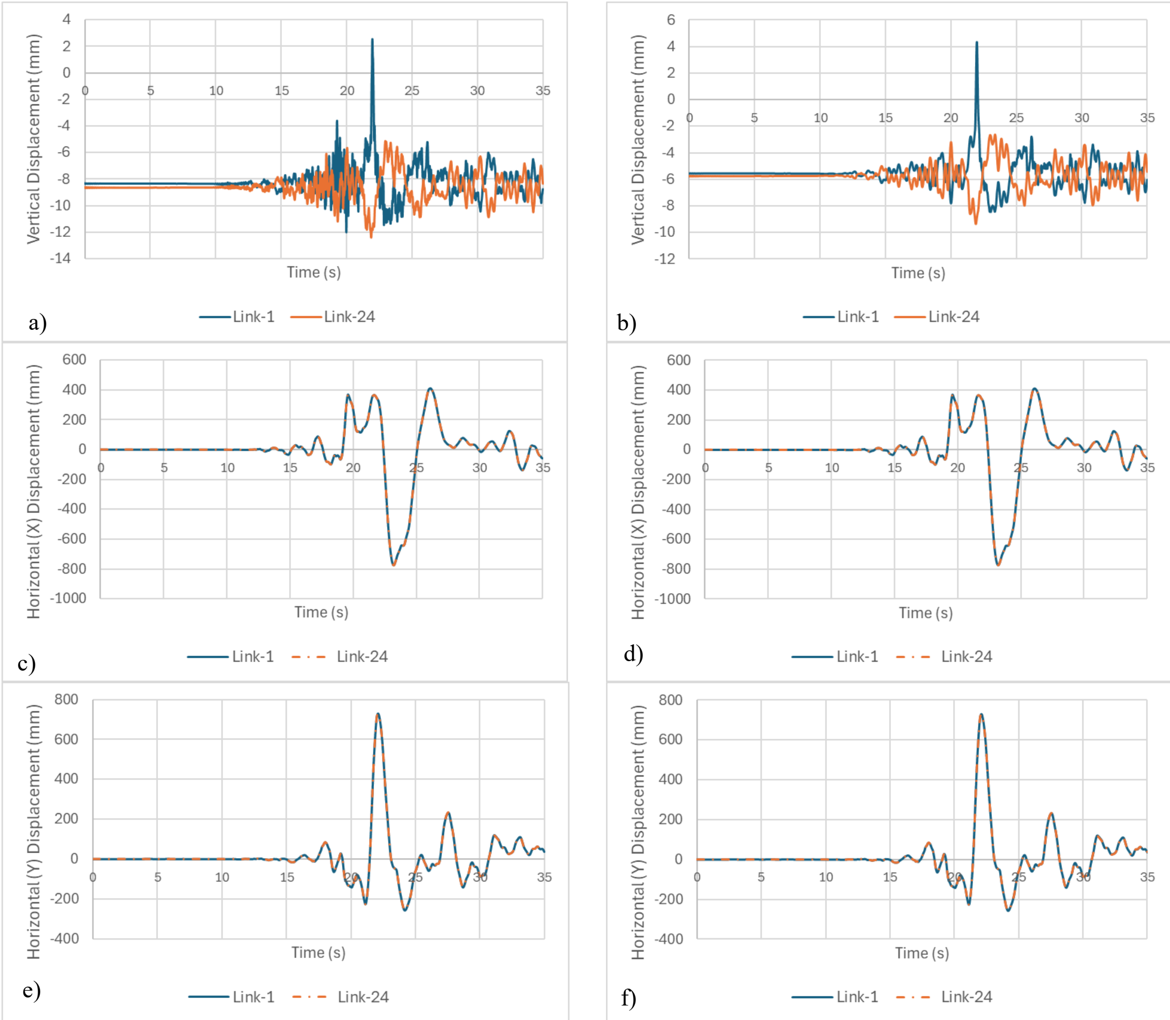

Fig. 7. Vertical (a–b), horizontal-x (c–d), and horizontal-y (e–f) displacement responses of isolators in the six-story building under the RSN9606 record, with (a,c,e) and without the vertical earthquake component (b,d,f).

4. Conclusions

This study examined the influence of near-fault ground motions, including the vertical component, on the seismic performance of three- and six-story base-isolated buildings. Nonlinear time history analyses were conducted using selected ground motion records (RSN1776 and RSN9606) under four different excitation scenarios, which involved rotating the horizontal components by 90° and either including or excluding the vertical component. The displacement responses of the isolators in both horizontal and vertical directions were evaluated, and the following conclusions were drawn:

- In the three-story base-isolated building, all isolators experienced only compressive vertical displacements, even when the vertical ground motion component was included. The inclusion of the vertical component resulted in a slight increase in compressive displacements in some isolators, indicating that the vertical seismic demand remained entirely within the compressive regime for this configuration.
- In contrast, the six-story building exhibited both compressive and tensile vertical displacements. Uplift effects were particularly pronounced in isolators located near the building corners.
- The maximum tensile vertical displacement observed in a corner isolator occurred simultaneously with the peak horizontal displacements. This simultaneity, observed under both RSN1776 and RSN9606 records, indicates a potential structural vulnerability to uplift. However, in certain cases, the inclusion of the vertical ground motion component slightly reduced the tensile response induced solely by horizontal excitation, suggesting that vertical excitation may partially mitigate uplift effects under specific dynamic conditions.

References

Alhan, C., & Öncü-Davas, S. (2016). Performance limits of seismically isolated buildings under near-field earthquakes. *Engineering Structures, 116*, 83–94.

Bouc, R. (1967). Forced vibration of mechanical systems with hysteresis. *Proceedings of the Fourth Conference on Non-linear Oscillation*, Prague, Czechoslovakia.

Bozorgnia, Y., & Campbell, K. W. (2004). The vertical-to-horizontal response spectral ratio and tentative procedures for developing simplified V/H and vertical design spectra. *Journal of Earthquake Engineering, 8*(2), 175–207.

Bray, J. D., & Rodriguez-Marek, A. (2004). Characterization of forward-directivity ground motions in the near-fault region. *Soil Dynamics and Earthquake Engineering, 24*(11), 815–828.

California Department of Transportation (CALTRANS). (2019). *Caltrans seismic design criteria* (Version 2.0). Sacramento, CA.

Campbell, K. W. (1997). Empirical near-source attenuation relationships for horizontal and vertical components of peak ground acceleration, peak ground velocity, and pseudo-absolute acceleration response spectra. *Seismological Research Letters, 68*(1), 154–179. https://doi.org/10.1785/gssrl.68.1.154

Computers and Structures Inc. (CSI). (2023). *SAP2000: Integrated software for structural analysis and design* (Version 2023). Berkeley, USA.

Ertuncay, D., & Costa, G. (2025). Analysis of impulsive ground motions from February 2023 Kahramanmaraş earthquake sequence. *Bulletin of Earthquake Engineering, 23*(3), 965–999.

Hall, J. F. (1998). Seismic response of steel frame buildings to near-source ground motions. *Earthquake Engineering & Structural Dynamics, 27*(12), 1445–1464.

Kasalanati, A., & Constantinou, M. C. (2005). Testing and modeling of prestressed isolators. *Journal of Structural Engineering, 131*(6), 857–866.

Kumar, M., Whittaker, A. & Constantiou, M.C. (2015). Experimental Investigation of Cavitation in Elastomeric Seismic Isolation Bearings. *Engineering Structures*, 101, 290–305.

Matsagar, V. A., & Jangid, R. S. (2004). Influence of isolator characteristics on the response of base-isolated structures. *Engineering Structures, 26*(12), 1735–1749.

Naeim, F., & Kelly, J. M. (1999). *Design of seismic isolated structures*. John Wiley & Sons.

Pacific Earthquake Engineering Research Center (PEER). (2025). *Ground motion database*. http://ngawest2.berkeley.edu/

T.C. Çevre ve Şehircilik Bakanlığı. (2018). *Türkiye Bina Deprem Yönetmeliği (TBEC-2018)*. Resmî Gazete, 30364 (Mükerrer), 18 Mart 2018.

Wen, Y. K. (1976). Method for random vibration of hysteretic systems. *Journal of the Engineering Mechanics Division, 102*(2), 249–263.

4th International Civil Engineering & Architecture Conference
17-19 May 2025, Trabzon, Türkiye

Multiple earthquake effect on seismic behavior of 3D steel moment-resisting frames

Arezou Behrouz[1], Kadir Ozakgul*[2]

[1] Istanbul Technical University, Graduate School, 34469, Istanbul, Türkiye
[2] Istanbul Technical University, Department of Civil Engineering, 34469 Istanbul, Türkiye

Abstract. As aftershocks are an inevitable phenomenon following a mainshock, their impact on the structural behavior of buildings is crucial. However, the consideration of aftershock effects is absent in current seismic design codes, leaving a critical gap in seismic performance evaluation. To address this issue, this study investigate the effect of mainshock-aftershock (MS-AS) sequences on steel moment resisting frames. In this context, 3-, 9- and 20-story steel moment-resisting frames, which were originally developed as part of the SAC steel project are utilized to evaluate their realistic seismic behavior under sequential earthquakes. The nonlinear time history analysis is performed using real sets of successive earthquakes. In analysis near-field and far-fault ground motions are included to provide comprehensive investigation of seismic demands of steel frames. Following the nonlinear analysis, several fundamental variables such as residual interstory drift, maximum displacement, and plastic hinge formation are evaluated to examine the cumulative damage caused by aftershocks. The findings of these analyses depicted the significant role of aftershocks in exacerbating of plastic deformations, distribution of damage, and overall structural strength of steel moment-resisting frames. Subsequently, to mitigate cumulative damage on steel frames, retrofitting strategies such as bracing systems are implemented on the structures. The results of improved systems were compared to the initial findings showed the improvement of seismic behavior of structures under mainshock-aftershock (MS-AS) events. This study highlights the inadequacy of assessment of the seismic performance of steel structures under a single earthquake as well as emphasizes the importance of consideration of multiple earthquake effects. Furthermore, it provides new insights into mitigating further damages by retrofitting existing structures under multiple earthquakes.

Keywords: Steel moment-resisting frames; Mainshock-aftershock effect; Nonlinear time history analysis; Plastic deformations; Retrofitting

---

1. Introduction

Earthquakes are among the most destructive natural phenomena, which may cause major damage to structures and infrastructure, eventually leading to significant human casualties and economic loss. Even though, through the years, understanding the behavior of structures under earthquakes has advanced. There is a critical in assessing the real behavior of structures during earthquakes. Conventional seismic design analysis evaluates structures under a single earthquake; however, in real life buildings are subjected to a mainshock and one or more large aftershocks. The aftershocks impose cumulative damage on structures, especially for those that are already damaged from the mainshock, sometimes rendering the structures unrepairable or resulting in the collapse of them.

Fortunately, there are numerous studies that widely investigated the aftershock effects on the seismic behavior of steel structures. The preceding studies, such as Amadio et al. (2003) and Li and Ellingwood (2007), indicated that repeated aftershocks significantly increase structural damage by reducing the energy dissipation capacity and substantial residual drift compared to a single earthquake. Their findings constituted the foundation for understanding how aftershocks affect structural performance during an earthquake. Following studies expanded on this by evaluating various influencing parameters. Hatzigeorgiou (2010) and Hatzigeorgiou and Beskos (2009) investigated how ground motion characteristics, such as soil types and proximity to the fault, influence displacement and ductility demands. They concluded that sequential ground motions resulted in significantly higher deformation levels. Ruiz-García and Negrete-Manriquez (2011) depicted that near-fault aftershocks increase residual drift in steel moment-resisting frames compared to far-fault ground motions.

Further studies focused on more specific structural configurations. Parekar and Datta (2020) examined the stiffness irregularities and their effect on inter-story drift distribution. It is found that irregularities, especially in

* Corresponding author, E-mail: ozakgulk@itu.edu.tr

https://doi.org/10.31462/icearc2025_ce_eqe_278

lower stories, escalate damage under repeated earthquakes. Torfehnejad and Sensoy (2023) introduced the different collapse behavior in low- to mid-rise and high-rise special moment frames under recorded sequential seismic events. With regard to retrofitted or specialized systems, Mohsenian et al. (2021) evaluated the seismic stability of the eccentrically braced steel frames with vertical energy-dissipating links under mainshock-aftershock(MS-AS) sequences. They concluded that while vertical energy-dissipating links absorb the seismic energy, it helps other structural elements remain elastic. It is also found that EBFs have stronger performance and reliability under design-level earthquakes. Even though there are many studies that have already evaluated the seismic performance of steel structures under single-event and mainshock-aftershock sequences, there are limited investigations that compare the behavior of steel moment-resisting frames with their retrofitted counterparts. Also, it is necessary to evaluate cumulative damage in terms of residual inter-story drift, maximum displacement, and plastic hinge distribution for representative SAC buildings prior to and following retrofitting.

This study bridges the gap by examining and comparing the seismic behavior of steel moment-resisting frames without and with bracing systems. Through nonlinear time-history analysis under successive earthquakes, this research seeks to provide insightful information on how braces improve seismic performance, especially in terms of residual drift, maximum displacement, and plastic hinge distribution.

2. Structural models and seismic inputs

2.1. Structural models

Three standard 3-, 9-, and 20-story steel moment-resisting frames are selected as studied structures for this study. These structures originally developed as part of the SAC joint venture project. This project is designed to represent typical commercial office buildings in accordance with pre-Northridge seismic standards in Los Angeles, California (Gupta & Krawinkler, 1999). These buildings are used as standard models to evaluate the seismic behavior of structures with varying height and layout. Fig. 1 displays the three-dimensional (3D) finite element (FE) models of SAC buildings considered.

Each building has a regular, symmetric floor plan with exterior steel moment-resisting and interior gravity frames. While perimeter moment-resisting frames function as the primary lateral force-resisting frames, interior gravity frames resist vertical loads. The columns of the 3-story structure are modeled as fixed at the base. On the contrary, 9-story and 20-story buildings have pinned supports as well as one and two basement levels, respectively. The applied loads, including gravity, wind, and seismic loading of the steel frames, are consistent with the original SAC report (Gupta & Krawinkler, 1999). The utilized material for modeling beams is A36, and for columns it is A50 steel. In the original SAC Joint Venture study, all the necessary information about the structural members cross-section, the plans, and the loading are given in detail.

Fig. 2 shows the floor plans of steel moment-resisting frames. All three buildings are symmetric in plan, and the moment-resisting frames are shown in bold color. In Fig. 3 the elevation of frames is illustrated. The structures have uniform bay spacing and story height: 9- and 20-story structures incorporating basement levels.

The fundamental period and mass participation factor for the first three modes are compared for the steel frames.

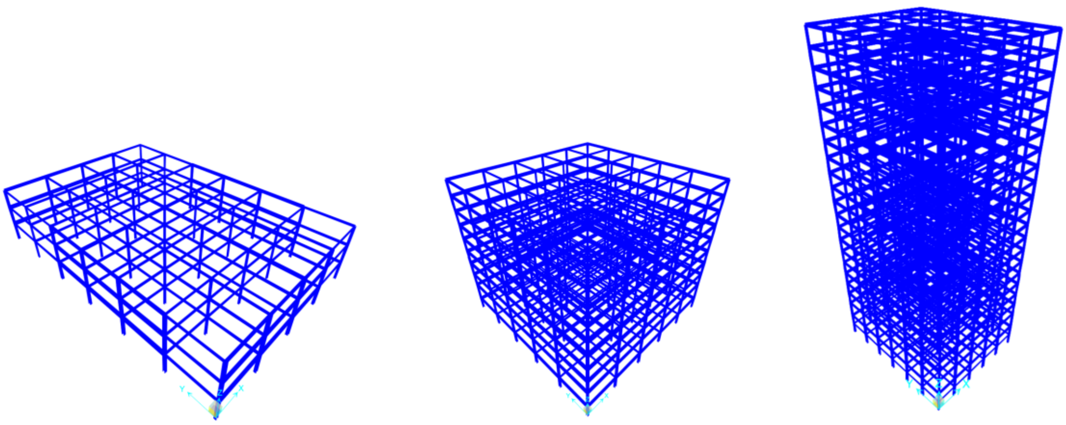

Fig. 1. 3D FE model views of 3, 9 and 20-story SAC buildings

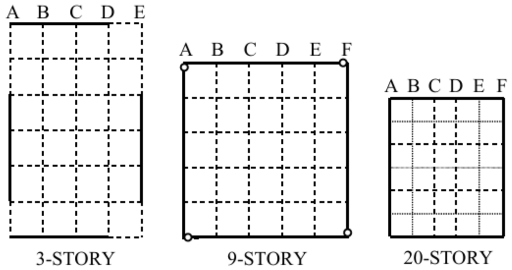

Fig. 2. Floor plans of 3, 9 and 20-story buildings (Gupta and Krawinkler, 1999)

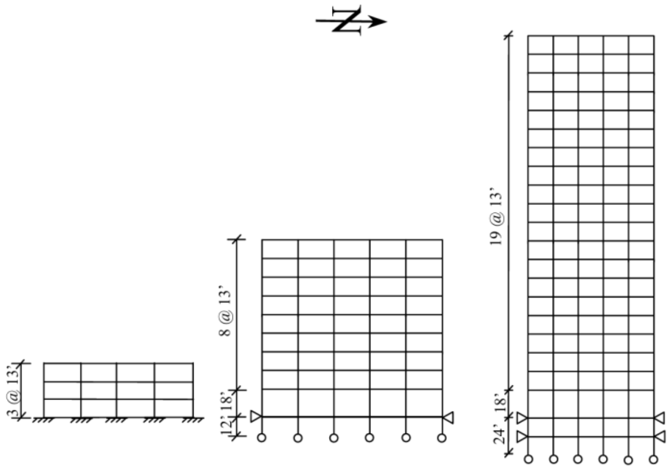

Fig. 3. Elevation for 3-, 9- and 20-story buildings (Gupta and Krawinkler, 1999)

Table. 1. Comparison of FE analysis results with those reported by Gupta and Krawinkler (1999)

No of story	Fundamental Periods (sec)					
	T1 obtained by FE analysis	T1 from the report	T2 obtained by FE analysis	T2 from the report	T3 obtained by FE analysis	T3 from the report
3	1.025	1.03	0.339	0.33	0.185	0.17
9	2.46	2.34	0.929	0.88	0.548	0.50
20	4.15	3.98	1.47	1.36	0.869	0.79

To ensure the accuracy of the developed models, the fundamental periods of the 3-, 9-, and 20-story buildings are compared with those reported in the SAC Joint Venture Project (FEMA 355C, 2000). Table 1 shows the comparison of the fundamental periods of structures. The periods obtained from modal analysis confirm the validation of the analyzed models with the reference structures.

2.2. Description of ground motion

In this study, a set of real mainshock-aftershock (MS-AS) ground motion sequences was considered to assess the seismic behavior of steel moment frame structures under multiple earthquakes. Mainshock-aftershock sequences can be constructed either artificial, repeated or as recorded real ground motions. However, Zhang et al. (2017) outlined that artificial sequences often result in scenario-specific seismic responses due to their inaccurate frequency characteristics. Furthermore, as repeated ground motion approaches assume the identical spectral content for mainshock and aftershock, they oversimplify the actual structural behavior. Therefore, to avoid these limitations as well as obtain realistic dynamic interaction, real recorded earthquakes were used in this study, following Basim et al. (2022), Mohsenian et al. (2021), and Hatzigeorgiou and Beskos (2009).

The selected ground motions include the Chi-Chi (Taiwan), Coalinga, Imperial Valley, Mammoth Lakes, Northridge, and Friuli earthquakes. The selection of these earthquakes was based on criteria such as large magnitudes ($M > 6.0$ for mainshock and $M > 5.0$ for aftershocks) and also the availability of free-field stations to avoid soil-structure interaction effects. Although each earthquake record consists of three components (two horizontal and one vertical), only horizontal components were included in nonlinear time history analysis to focus on the in-plane lateral response of the structures. In mainshock-aftershock sequences, a time gap of 10 seconds was inserted between the mainshock and aftershock to bring the structure to rest and ensure the decay of dynamic response from the mainshock before applying the aftershock.

This study included both near-fault and far-field ground motions to reflect the variability of expected seismic demands. While near-fault earthuqakes occur within a general distance of perhaps 15 to 20 km from the fault rupture, far-fault motions originate from greater distances and typically lack distinct directivity effects (Yang et al., 2015; Alavi & Krawinkler, 2004). All selected seismic records are scaled in accordance with ASCE/SEI 41-13 (2014), which requires the 5% damping ratio for ground motions to ensure the matched or exceeded target spectrum over the defined period range. This defined period ranges typically between 0.2T to 1.5T, where T is the fundamental period of the structure. In this study, a uniform scale factor is applied for the entire acceleration record. The scaling process was performed with emphasis on the period range of the first two fundamental modes, as these two modes predominantly affect the structural response under seismic loading. Table 2 shows the properties of selected earthquakes. It can be seen that these records cover a range of different site classes. This variety allows us to evaluate the seismic behavior of structures under diverse ground conditions and provide a comprehensive understanding of structural performance.

Fig. 4 presents only one horizontal component of the unscaled acceleration time histories of selected MS-AS sequences to provide a clear visual comparison.

Table. 2. The properties of selected ground motions

Result ID	RSN	Earthquake Name	Year	Station Name	Magnitude	Mechanism	Rjb (km)	Vs30 (m/sec)
1	1227	"Chi-Chi_ Taiwan"	1999	"CHY074"	7.62	Reverse Oblique	0.7	553.43
2	2490	"Chi-Chi_ Taiwan-03"	1999	"CHY074"	6.2	Reverse	27.84	553.43
3	122	"Friuli_ Italy-01"	1976	"Codroipo"	6.5	Reverse	33.32	249.28
4	131	"Friuli (aftershock 1)_ Italy"	1976	"Codroipo"	5.91	Reverse	41.37	249.28
5	181	"Imperial Valley-06"	1979	"El Centro Array #6"	6.53	strike slip	0	203.22
6	204	"Imperial Valley-07"	1979	"El Centro Array #6"	5.01	strike slip	7.4	203.22
7	230	"Mammoth Lakes-01"	1980	"Convict Creek"	6.06	Normal Oblique	1.1	382.12
8	248	"Mammoth Lakes-06"	1980	"Convict Creek"	5.94	strike slip	6.44	382.12
9	959	"Northridge-01"	1994	"Canoga Park - Topanga Can"	6.69	Reverse	0	267.49
10	3775	"Northridge-06"	1994	"Canoga Park - Topanga Can"	5.28	Reverse	8.98	267.49
11	368	"Coalinga-01"	1983	"Pleasant Valley P.P. - yard"	6.36	Reverse	7.69	257.38
12	383	"Coalinga-02"	1983	"Pleasant Valley P.P. - yard"	5.09	Reverse	6.51	257.38

3. Analysis methodology

The nonlinear time-history analyses were performed to evaluate the seismic behavior of 3-, 9- and 20-story structures subjected to mainshock-aftershock(MS-AS) sequences. All buildings were modeled in SAP2000, and structural design were defined based on the SAC Joint Venture guidelines (FEMA355C, 2000). While the original models were generated with the as-designed conditions, the retrofitted (RT) structures were created using X-braces to improve lateral stiffness and energy dissipation. Fig. 5 shows the location of X braces for 3-, 9-, and 20-story steel frames.

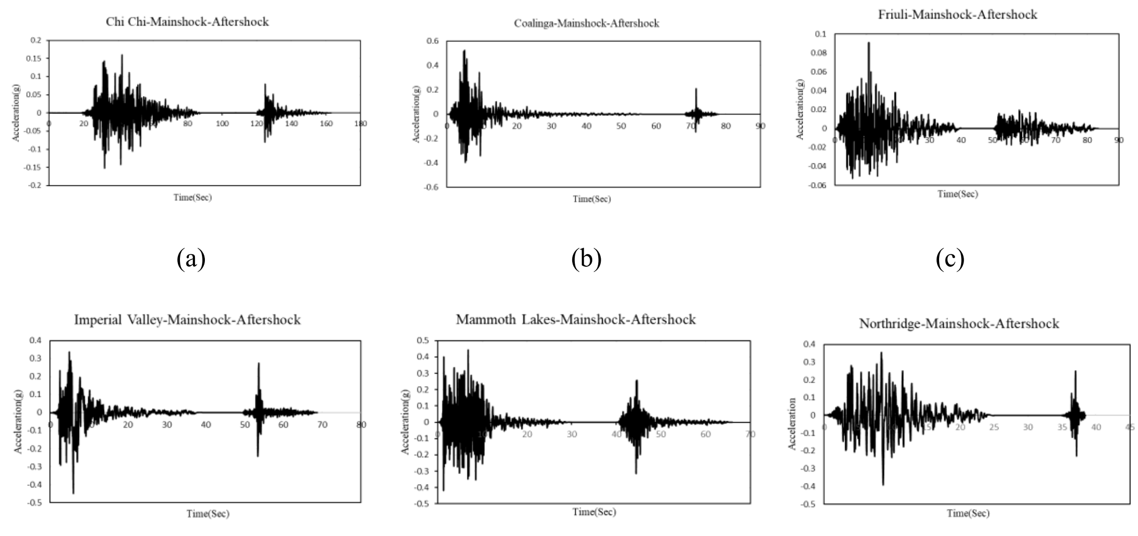

(a) (b) (c)

(d) (e) (f)

Fig. 4. Acceleration time history for selected earthquakes

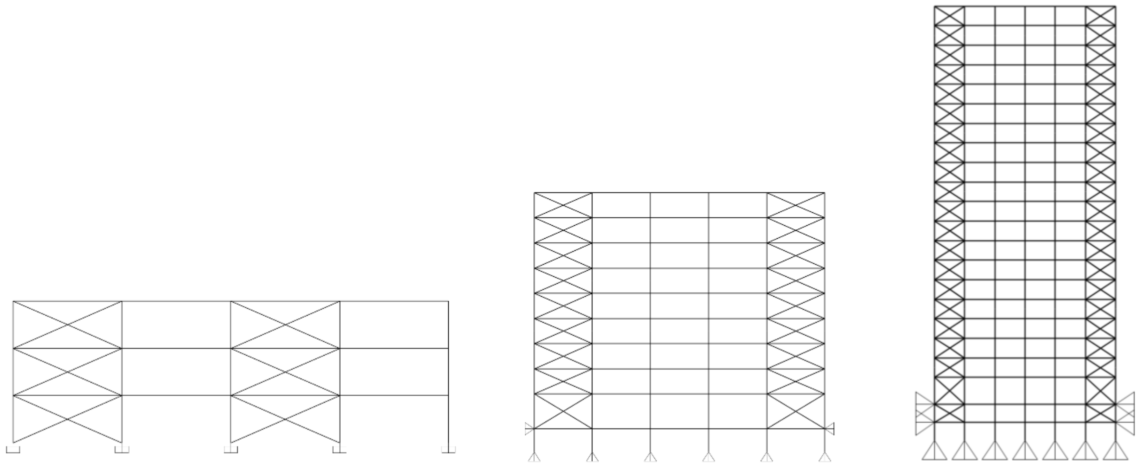

Fig. 5. Retrofitted SAC buildings

Nonlinear behavior of steel frames was simulated by assigning plastic hinges at both ends of the structural elements, beams and columns, where the inelastic deformations are expected to form during seismic events. For the columns and beams, plastic hinges were defined as P-M2-M3 interaction hinges, and M3 moment hinges according to ASCE/SEI 41-13 (2014), respectively.

4. Results and discussions

This section presents the results of nonlinear time history analysis performed on 3-, 9- and 20-story SAC steel moment-resisting structures under MS-AS sequences. Each building was evaluated in both original state and a retrofitted configuration with X-braces. To assess the aftershock effect and retrofitting effectiveness the seismic behavior of structures was determined in terms of inter-story drift ratio, maximum drift as well as plastic hinge formation.

Fig. 6 shows the inter-story drift ratio of evaluated structures under mainshock-only and mainshock-aftershock sequences. Results proved these structures under sequential earthquakes experience greater displacements. It was observed that as the height of the structure increased the inter-story drift decreased. This is due to the distribution of lateral deformation over more stories. Furthermore, since taller buildings has greater fundamental periods, therefore their spectral acceleration demands reduce.

As a representative example, Fig. 7 displays the plastic hinge formation for Chi-Chi earthquake, which has greater magnitude comparing to other selected earthquakes. Only one moment frame was selected for investigation in each structure. Green and red hinges exhibit the Immediate Occupancy(IO) and Collapse Prevention (CP) performance level, respectively. It is clear that the number of plastic hinges increased under sequential earthquakes which means the structures experienced more plastic deformations under multiple earthquakes. Furthermore, the concentration of plastic deformations are significant in lower floors of higher structures.

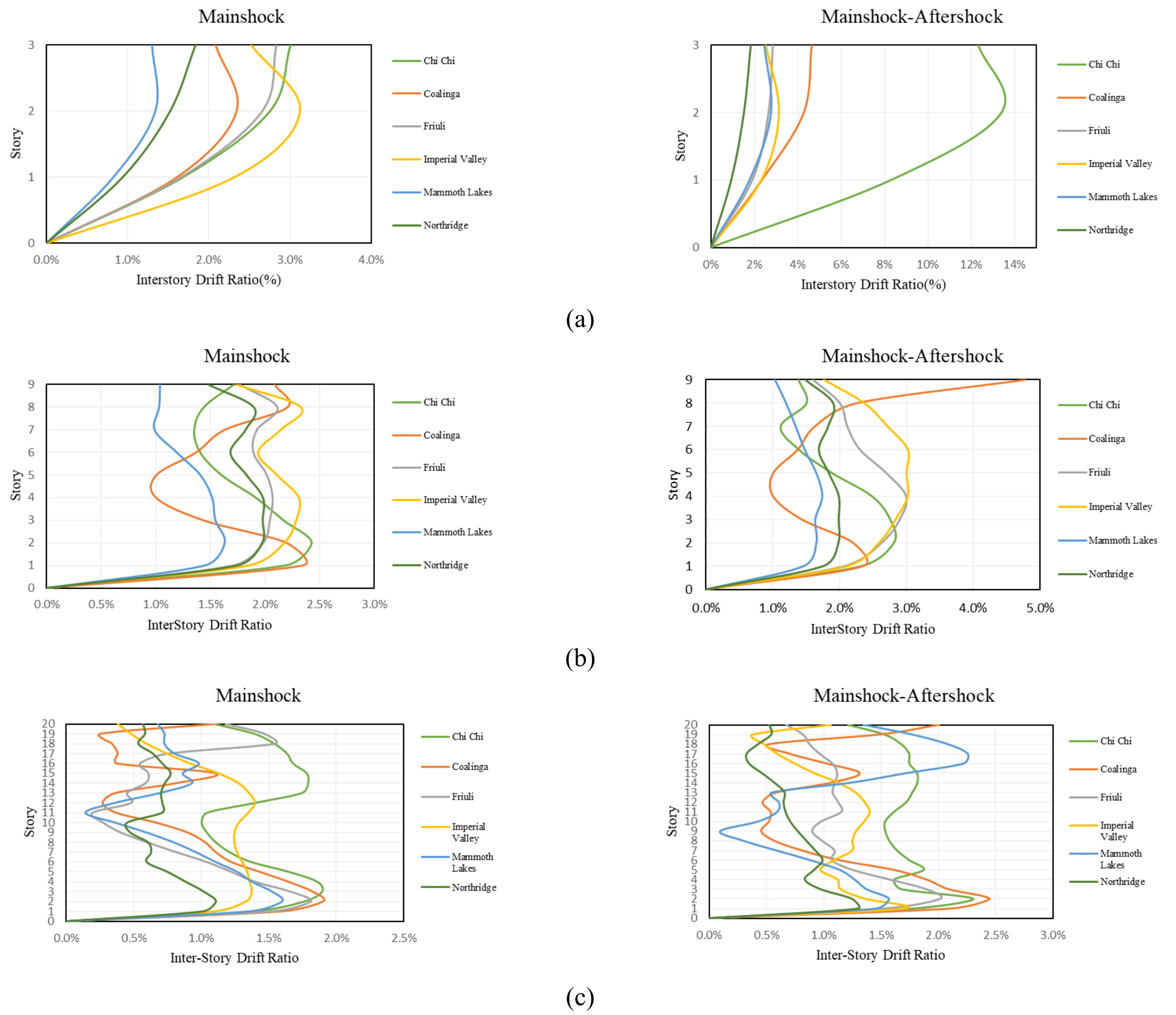

Fig. 6. Comparison of inter-story drift ratio for mainshock (MS)-only and mainshock-aftershock(MS-AS). (a) 3-story building, (b) 9-story building, (c) 20-story building

Fig. 8 displays the result of comparative analysis of the original and retrofitted (RT) structures under MS-AS events. The findings highlight the significant reduction of the residual displacement after retrofitting the steel frames. This reduction emphasizes X braces enhance seismic performance of structures by limiting the deformation and mitigating the cumulative damage under possible seismic sequences. The results also show the importance of the retrofitting after mainshock for damaged structures.

Fig. 9 displays the maximum inter-story drift ratio for all buildings considered. The bar chart shows how drastically the plastic displacement of the frames decreased after retrofitting which proves the importance of X-braces in the resilience of the structure. Moreover, in some earthquakes, such as Friuli, Imperial Valley, and Northridge, drift values were relatively small. This is due to the frequency content of the aftershock as well as the structures' capacity to dissipate seismic energy during the aftershock.

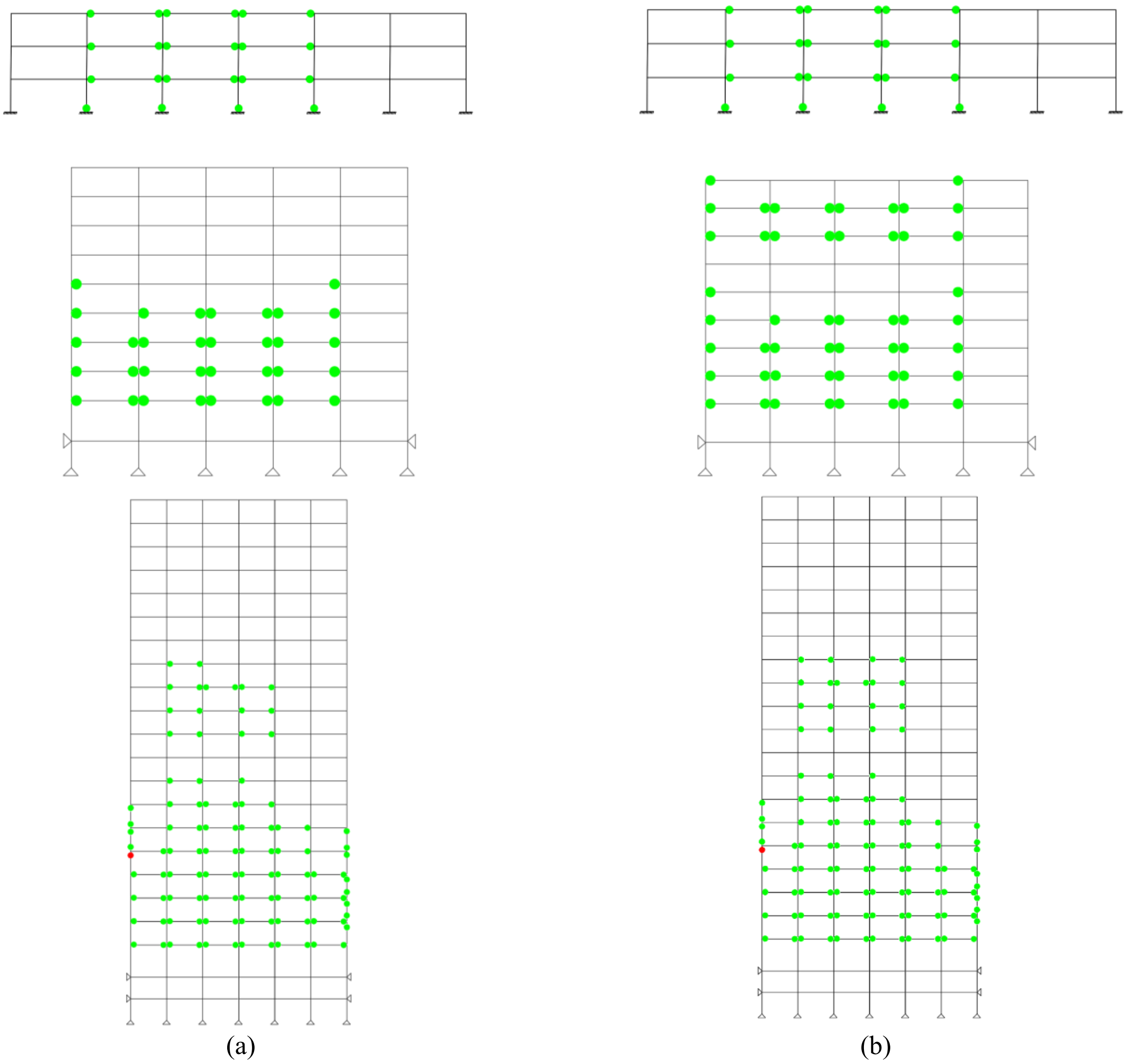

Fig. 7. Plastic hinge formation for 3-, 9-, and 20-story SAC buildings. (a) mainshock-only, (b) MS-AS sequences

4. Conclusions

This study presented the seismic behavior of low-, mid-, and high-rise moment resisting steel structures under successive earthquakes and compared to mainshock-only ground motions. The impact of the X braces in reducing maximum inter-story drift ratios and plastic hinge formation was investigated. The findings exhibited aftershocks significantly increased deformation demands, while retrofitting improved the structural seismic behavior under mainshock-aftershock sequences. The main results are:

- The maximum inter-story drift increased during mainshock-aftershock events compared to mainshock ground motion, which highlighted the cumulative damage effects associated with multiple earthquakes.
- The inclusion of aftershock effect in seismic performance displayed that drift demands decreased with increasing the height of the structure. The 3-story building showed the highest drift ratio among all frames.
- Plastic hinge formations illustrated that considering aftershocks in estimating the cumulative damage was critical. The increased number of plastic hinges proved the importance of the seismic sequence effect on the structures.
- The X-bracing system drastically decreased the inter-story drift ratio, resulting in enhanced seismic performance against mainshock-aftershock sequences.
- In some certain earthquakes, the, the maximum inter-story drift ratio for the mainshock and mainshock-aftershock were relatively close, which is attributed to the characteristics of the aftershock and the energy dissipation of the structures.
- Overall, this study emphasized the importance of considering aftershock effects in seismic design codes and provisions in order to obtain realistic structural behavior and prevent probable cumulative damage.

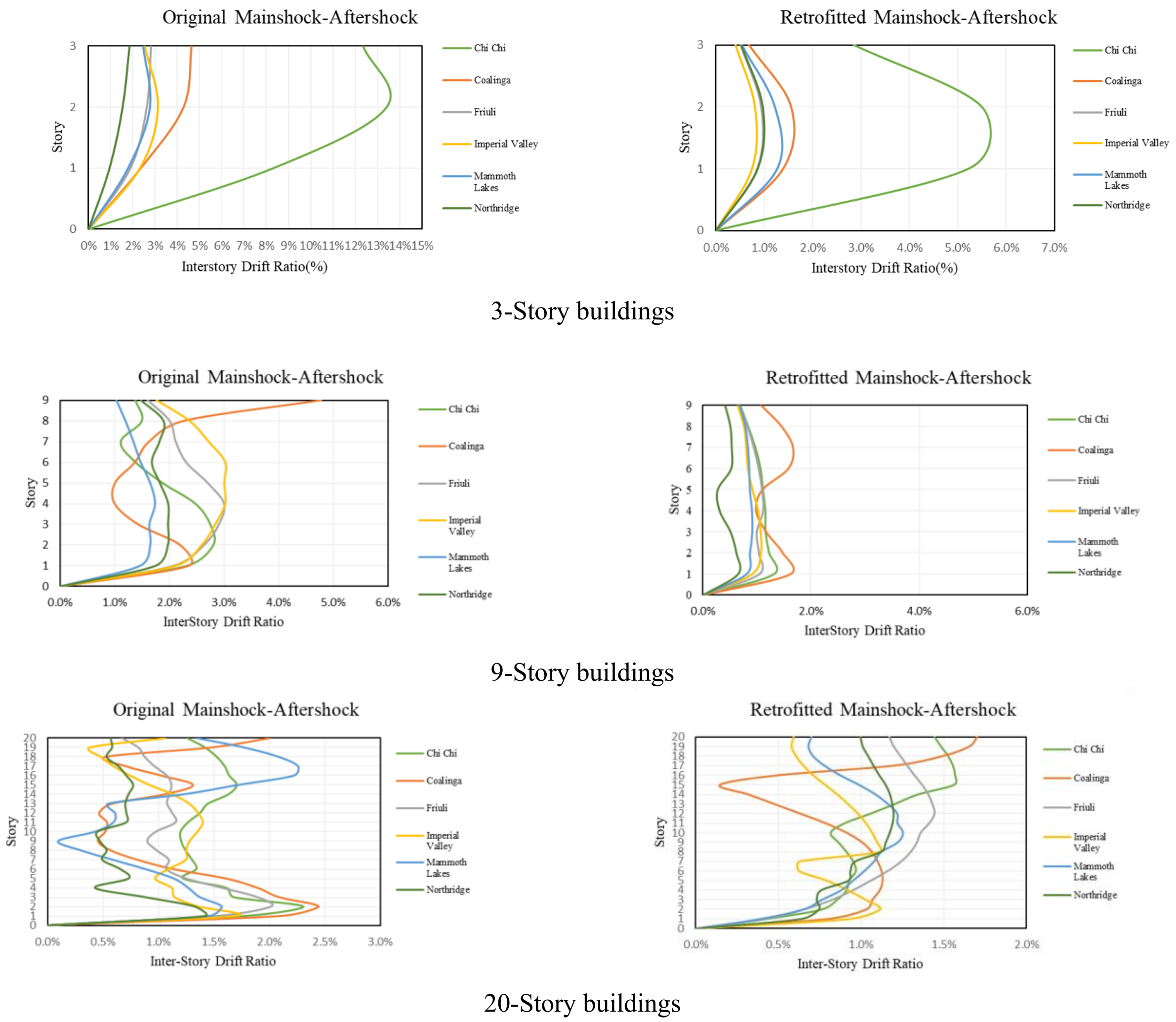

Fig. 8. Comparison of inter-story drift ratio for original and retrofitted structures (RT) under mainshock-aftershock sequences

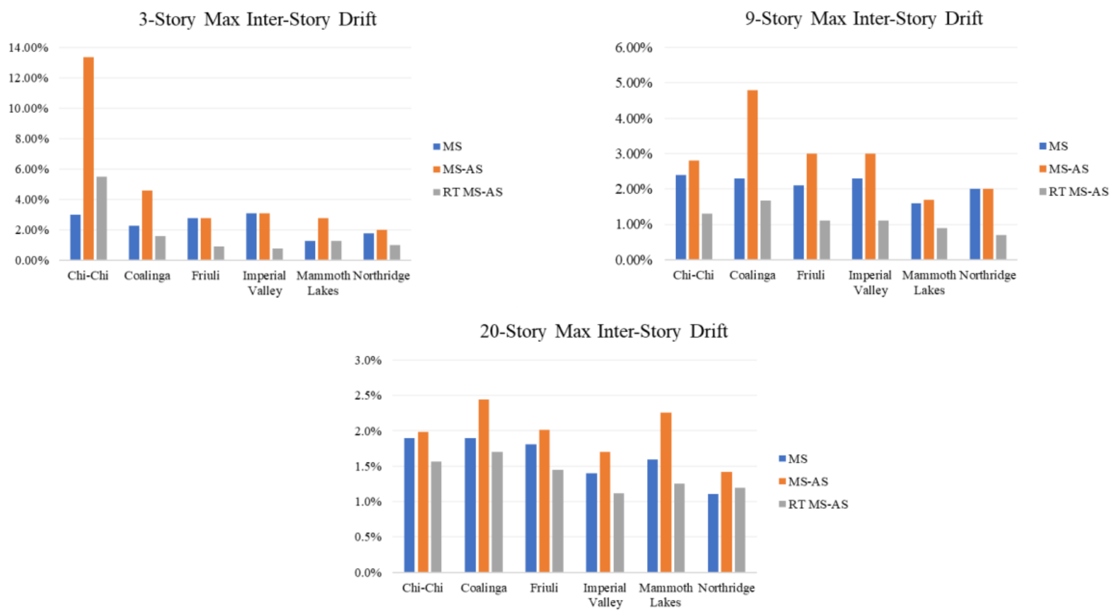

Fig. 9. Maximum inter-story drift ratio for 3-, 9-, and 20-story buildings

References

Alavi, B., & Krawinkler, H. (2004). Behavior of moment-resisting frame structures subjected to near-fault ground motions. *Earthquake Engineering and Structural Dynamics, 33*(6), 687–706. https://doi.org/10.1002/eqe.369

Amadio, C., Fragiacomo, M., & Rajgelj, S. (2003). The effects of repeated earthquake ground motions on the non-linear response of SDOF systems. *Earthquake Engineering & Structural Dynamics*, *32*(2), 291–308. https://doi.org/10.1002/eqe.225

ASCE/SEI 41-13. (2014). Seismic evaluation and retrofit of existing buildings. American Society of Civil Engineers (ASCE), Reston, VA. https://doi.org/10.1061/9780784412855

FEMA 355C. (2000). State of the art report on past performance of steel moment-frame buildings in earthquakes. Federal Emergency Management Agency (FEMA), Washington, DC.

Gupta, A., & Krawinkler, H. (1999*). Seismic demands for performance evaluation of steel moment resisting frame structures (SAC Task 5.4.3*) (Report No. 132). The John A. Blume Earthquake Engineering Center, Stanford University.

Hatzigeorgiou, G. D. (2010). Ductility demand spectra for multiple near- and far-fault earthquakes. *Soil Dynamics and Earthquake Engineering*, 30(4), 170–183. https://doi.org/10.1016/j.soildyn.2009.10.003

Hatzigeorgiou, G. D., & Beskos, D. E. (2009). Inelastic displacement ratios for SDOF structures subjected to repeated earthquakes. *Engineering Structures*, *31*(11), 2744–2755 https://doi.org/10.1016/j.engstruct.2009.07.002

Li, Q., & Ellingwood, B.R. (2007). Performance evaluation and damage assessment of steel frame buildings under main shock–aftershock earthquake sequences. *Earthquake Engineering & Structural Dynamics*, *36*(3), 405–427. https://doi.org/10.1002/eqe.667

Mohsenian, V., Filizadeh, R., Hajirasouliha, I., & Garcia, R. (2021). Seismic performance assessment of eccentrically braced steel frames with energy-absorbing links under sequential earthquakes. *Journal of Building Engineering*, *33*, 101576. https://doi.org/10.1016/j.jobe.2020.101576

Parekar, S.D., & Datta, D. (2020). Seismic behaviour of stiffness irregular steel frames under mainshock–aftershock. *Asian Journal of Civil Engineering*, *21*, 857–870. https://doi.org/10.1007/s42107-020-00245-z

Ruiz-García, J., & Negrete-Manriquez, J.C. (2011). Evaluation of drift demands in existing steel frames under as-recorded far-field and near-fault mainshock–aftershock seismic sequences. *Engineering Structures*, *33*(2), 621–634. https://doi.org/10.1016/j.engstruct.2010.11.021

Torfehnejad, M., & Sensoy, S. (2023). Aftershock collapse capacity assessment of special steel moment frame structures. *Structures*, *56*, 105046. https://doi.org/10.1016/j.istruc.2023.105046

Yang, D., Yang, K., & Chen, G. (2015). Recent advances in engineering characteristics of near-fault ground motions and seismic effects of building structures. *Proceedings of the Second International Conference on Performance-based and Life-cycle Structural Engineering (PLSE 2015),* Brisbane, QLD, Australia.

Zhang, Y., Chen, J., & Sun, C. (2017). Damage-based strength reduction factor for nonlinear structures subjected to sequence-type ground motions. *Soil Dynamics and Earthquake Engineering*, *92*, 298–311. https://doi.org/10.1016/j.soildyn.2016.10.002

4th International Civil Engineering & Architecture Conference
17-19 May 2025, Trabzon, Türkiye

Investigation of soft storey action of a reinforced concrete building by pushover analysis

Mehmet F. Aydıner*[1], Barış Sevim[1], Serkan Bekiroğlu[1], Fatih Alemdar[1], Güray Arslan[1], Yusuf Ayvaz[1]

[1] *Yildiz Technical University, Department of Civil Engineering, 34000 İstanbul, Türkiye*

Abstract. Soft storey action is a common type of vertical stiffness irregularity encountered in earthquake sites. There are different code-defined approaches in terms of determining the presence of soft storey irregularity. Türkiye Building Earthquake regulation (TBDY-2018) requires the stiffness irregularity coefficient determined by the ratio of adjacent storey drift ratios to be greater than 2 to validate this irregularity. As for the American Society of Civil Engineers regulation (ASCE/SEI-7-10), the extreme soft storey is valid if lateral storey stiffness is smaller than 60% of the neighbourhood storey or 70% of the average of the 3 above storeys. As for Japanese regulation, the ratio of the inverse of the drift ratio to the average of the inverse of the drift ratios along all storeys is lower than 0.6. In this work, these stiffness irregularity parameters are calculated and compared with their limit value, both elastic and inelastic behavior of a 3D reinforced concrete frame system with ground storey height greater than other storeys. The variation of the effect of stiffness irregularity while continuing inelastic behavior is investigated by gradually increasing top displacement. The storey drifts, drift ratios, storey shear and stiffness irregularity factors of TBDY-2018, ASCE and Japanese regulations are calculated for all nonlinear pushover steps. The pushover curve and the values of stiffness irregularity factors in terms of top displacement are plotted. As a result of 2% top drift ratio, values of factors of inelastic analysis are obtained as 4-5 times of elastic analysis result.

Keywords: Soft storey; Stiffness irregularity factor; Pushover analysis; Reinforced concrete; Nonlinear modeling

1. Introduction

Soft storey action or interstorey stiffness irregularity is one of the most frequently encountered irregularity problem in earthquake sites, which may result in the collapse of buildings. "*Many failures and collapses can be attributed to the increased deformation demands caused by soft stories*" (Bruneau, 2002). The problem of structural collapse due to soft story irregularity is a phenomenon that can be observed not only in Türkiye. "*Similar damage patterns as a result of soft storey were found in earthquakes in other areas of the world*" (Sharma et al, 2016). As declared in Zhao et al, 2009; "*the data collected in the field shows that most of the reinforced concrete building frames did not perform as intended by the current Chinese code: most failures developed at the columns, either through shear failure or through excessive deformation demands at the ground floor columns in the presence of soft-storey mechanisms, leading to the partial of full collapse of the building structures*" (Zhao et al, 2009). As is known, soft storey action occurs due to interstorey stiffness difference caused by abrupt difference between storey height or unequal degradation of infill walls. That is why this irregularity is frequently encountered in mixed buildings, while the ground floor is used for commercial purposes, the other storeys are used for residential purposes. Another instance that meets this definition from Arlekar et al (1997) is "*Open first storey is a typical feature in the modern multistorey constructions in urban India*". Another example can be given as; "*Soft first storey is a typical feature in the RC buildings in Kathmandu Valley because the first stories of the building have been often used as commercial areas, shops, or car parking*" (Sharma et al, 2016).

As for Türkiye, the field investigations of past earthquakes showed that there is numerous instances of soft storey action. For example, a field investigation study done by Aydıner et al (2023) after recent major Kahramanmaraş earthquakes. In the study, the observed soft storey buildings compared with pre-earthquake state of themselves and the disastrous effect of this irregularity can be seen. The damages caused by earthquake resulted in inelastic behavior of structures. That is why, investigation of soft storey irregularity not only for elastic but also for inelastic behavior of building has own importance.

In the literature, there are studies that examined the impact of soft storey irregularity on the structural behavior of buildings, in reference to code criteria. Yousef et al. (2010) performed nonlinear time history analyses on high

* Corresponding author, E-mail: fatih.aydiner@yildiz.edu.tr

https://doi.org/10.31462/icearc2025_ce_eqe_285

rise ductile buildings composed of both normal and high strength concrete, and compared the results with those from the ELF method. The applicability of the ELF method to buildings with vertical irregularities (in terms of mass, setback, and soft storey) was evaluated. The reliability of soft storey criteria in different seismic codes was assessed. The codes included UBC-97 (IBC-2000), Eurocode 8 (EC-8), Egyptian Codes for Loads (ECL-08), and ESEE-88. It was found that UBC-97 was not suitable for structures with mass or setback irregularities but was sufficiently conservative for soft storey irregularities. ESEE-88 was observed to be generally less conservative than ECL-08. The results indicated that the limit values in UBC-97 and ECL-08 criteria were satisfactory and could be extended by approximately 10%.

Döndüren and Nakipoğlu (2018) interpreted the soft storey criteria and corresponding limit values from DBYBHY-2007 (Türkiye), IS 1893-1-2002 (India), ASCE-7-2002 (USA), and the Japanese seismic design codes based on dynamic analyses conducted in SAP2000. 11 amount of models with varying ground floor heights were analysed. Factors such as the stiffness irregularity coefficient η_{ki}, storey stiffness ratio (k_1/k_2), and R_s values are calculated and compared with the respective limit values in the codes. The results revealed the onset of soft storey behavior and highlighted that the Japanese seismic code provided more reliable and conservative assessments.

Khanal et al. (2019) investigated the effects of varying ground floor heights on 5 amounts of 3D, 5 storey frame models using both linear static and nonlinear time history analyses. The presence of a soft storey was evaluated based on Japanese, Türkiye, and IS seismic codes. It is noted that while the Japanese and Türkiye code evaluations varied with the analysis method, the IS code provided consistent assessments regardless of the method. The Japanese code was found to be more conservative. Moreover, the study emphasised that story drift alone should not be the sole criterion for evaluating structural safety, as many models satisfied the drift requirement despite the presence of soft storey irregularity.

Zavala et al. (2022) explored the effects of stiffness irregularity and P-Δ effects on building response using 9 models of a 20 storey structure: 4 with both geometric nonlinearity and stiffness irregularity, 4 with only stiffness irregularity, and one reference model. Stiffness irregularity was evaluated on each storey according to ASCE-41-13 and nonlinear static pushover analyses were conducted. Results indicated that P-Δ effects became more critical in the presence of storey stiffness irregularity at lower storeys, with reductions in structural stiffness up to 56.3%. Literature studies on buildings with soft storey irregularity predominantly focus on relative displacements, natural periods, member damages, code based irregularity checks, and the quantification of irregularity degrees.

In this study, the code-defined soft storey evaluation methods are examined for both linear and nonlinear case. The code-defined stiffness irregularity factors calculated for each pushover step and compared with each other along with the pushover curve. The magnification effect of nonlinear behavior on soft storey action in a negative way is made visible by drawing graphs. Finally, the graphs drawn were interpreted.

2. Methodology

The examined building is 4 storey 2 bay reinforced concrete frame system with slabs (Fig. 2a, b). While the first storey height is 4.5 m, the others are 2.6 m, and the bay spacing is 3 m. In most cases, this case corresponds architecturally mixed purpose building, while the ground storey is used for commercial purposes, the other storeys are used as residential. Column sizes are determined as 30x25, and beam sizes are 30x40. The columns are placed so that the structure is weaker in the direction of loading (i.e. x axis). There is no infill and shear wall in the structural system. The source of soft storey action stems from the abrupt difference in column length at ground and one upper storey. All structural modeling done in SAP2000 structural analysis software (SAP2000, 2021). The view of structural system and ELF (equivalent lateral force) method loadings are given in Fig. 1a, b and d.

According to Article 28 of the Planned Areas Zoning Regulation of Türkiye, maximum ground floor height is 4.5 m if there is no mezzanine and the ground floor is used for commercial purposes (PAİY, 2017). Also, the minimum internal height of the floor should be higher than 2.6 m (PAİY, 2017). The structural design parameters are given in Table 1.

Table 1. Structural properties of the investigated building

Column section (cm)	30x25	Ground storey height (m)	4.5	Confinement diameters (mm)	12d
Beam section (cm)	30x40	Residential storey heights (m)	2.6	Confinement spacings (cm)	10
Bay width (m)	3	Concrete type	C30	Stiffness modifier of beam	35%
Support Type	Fixed	Reinforcement type	S420	Stiffness modifier of column	70%
Amount of storey	4	Slab type	Shell Thin	Stiffness modifier of slab (bending and membrane)	25%
Amount of bay	2	Column longitudinal rebar diameter (mm)	14d	Beam longitudinal rebar diameter (mm)	12d

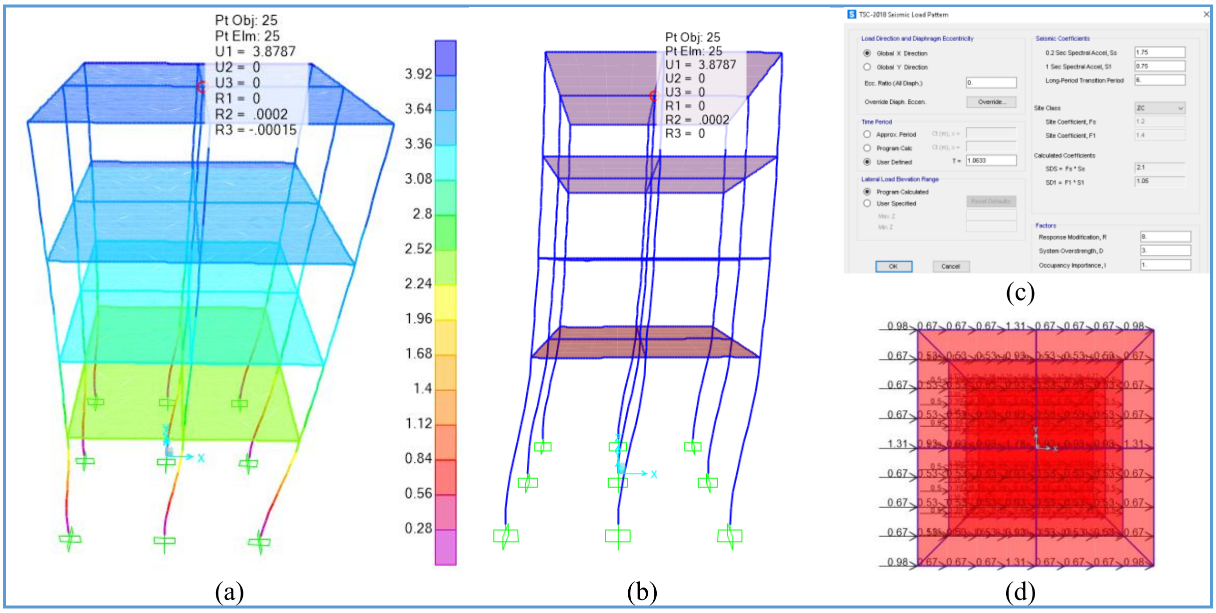

Fig. 1. SAP2000 Model of investigated structure of ELF method (a) displacement contour diagram of +5% eccentricity (b) displacement of zero eccentricity (c) Automatic TBDY-2018 quake loading (d) lateral loads distributed along floors

As indicated at the introduction, there are so many old building having soft ground storey in earthquake sites. As for old regulations like Specification for Structures to be Built in Disaster Areas 1997, size of 25x30 rectangular columns were permitted (ABYYHY, 1997). That was the minimum condition of column section sizes. In this study, the column size was selected in this opinion. For simplicity, all columns are placed at the same direction as the moment of inertia about y axis is weaker. The static loadings for both ELF and pushover acted on the weak direction of the structure, i.e. x direction at Fig. 1. The dead load is taken as $g = 1.5\ kN/m$, and so the live load $q = 2\ \ kN/m$. The mass source of the system is defined by $g + 0.3q$. The load bearing system is moment bearing reinforced concrete frame system which having high structural ductility. The system is assumed to satisfy the capacity and ductile design conditions. The slab thickness is taken as 12 cm and rigid diaphragm definition done at each storey level.

2.1. Soft storey irregularity criteria according to the different codes

In this paper, the soft storey action (i.e. interstorey stiffness irregularity) evaluated based on TBDY-2018 code, ASCE/SEI-7-10 code and BSL code. These codes defines a criterion and a limit value for checking whether the irregularity is valid or not. For Türkiye Building Earthquake Code (TBDY-2018), the criterion is based on whether the division of drift ratios of adjacent storeys is greater than 2. Thus, a stiffness irregularity factor is defined as (1).

$$\eta_{ki} = \frac{\frac{\varDelta_i}{h_i}}{\frac{\varDelta_{i+1}}{h_{i+1}}} > 2 \qquad (1)$$

Here $\varDelta$ denotes storey drift, h denotes storey height, the subindex i denotes related storey number, the ratio of $\varDelta_i/\ h_i$ denotes drift ratio of related storey, and η_{ki} denotes stiffness irregularity factor of related storey. If the inequality given in (1) is satisfied, that means the i th. storey is soft storey. As one can guess, if the ratio of drift ratios at (1) has been taken as upper storey divided by lower, then the inequality would change direction and the limit value would become 0.5.

The American Society of Civil Engineers ASCE/SEI-7-10 code criteria denotes the definition of a soft storey whose stiffness is less than 70% of the upper storey or 80% of the arithmetic mean of the three upper storeys. This criterion is the same one as UBC code. There is also definition of an extreme soft storey, which will be taken into account for this paper since the investigated structure already provides the extreme soft storey condition. The extreme soft storey condition clarified in the code given "*where there is a story in which the lateral stiffness is less than 60% of that in the story above or less than 70% of the average stiffness of the three stories above*" (ASCE/SEI-7, 2010). The condition defined in the text can be defined in an inequality form as $k_i < 0{,}6k_{i+1}$ and $k_i < 0{,}8k_m$, where k_i corresponds to the related storey stiffness, k_{i+1} corresponds to one upper storey stiffness and k_m corresponds mean storey stiffness of three upper storey and defined at (4). As one can guess, if the lateral stiffness of lower storey divided by upper adjacent storey or the mean lateral stiffness of three upper storey divided by the lateral stiffness of related storey, the limit value would became as the inequality given at (2) and (3).

$$\frac{k_{i\pm1}}{k_i} > 1{,}67 \tag{2}$$

$$\frac{k_m}{k_i} > 1{,}25 \tag{3}$$

$$k_m = \frac{k_{i+1} + k_{i+2} + k_{i+3}}{3} \tag{4}$$

As for Building Standard Law of Japan (BSL), the irregularity is investigated by whether the ratio of reciprocal of drift ratio to average reciprocal of drift ratios of all storeys is less than 0.6. In that regard, a factor symbolized as R_s and defined in (5) is calculated.

$$R_{si} = \frac{r_{si}}{\overline{r_s}} < 0{,}6 \tag{5}$$

$$\overline{r_s} = \frac{\sum_{j=1}^{n} r_{sj}}{n} \tag{6}$$

Here while r_{si} is reciprocal of the drift ratio and calculated as h_i/Δ_i, $\overline{r_s}$ is average reciprocal of the drift ratio along all storeys (Aoyama, 1981). In (6), the amount of storey of building symbolized as n.

To sum up, the soft storey action is valif if the value of stiffness irregularity parameters or factors defined in the codes satisfies the corresponding criteria. The criteria defines limit values of those factors. The irregularity is valid if the irregularity factor η_{ki} to be greater than 2 as for TBDY-2018, or if the k_{i+1}/k_i is greater than 1.67 and k_m/k_i is greater than 1.25, or if the factor R_{si} is less than 0.6 limit value. Here one can see that while the inequality direction of TBDY-2018 criteria and ASCE/SEI-7-10 criteria is same, it is inverse for BSL code. In order for them to be compared meaningfully, the inequality direction of (5) changed by taking inverse of the multiplication of each part of the inequality. Thus, the limit value became 1 per 0.6.

$$R_{si}^{-1} = \frac{\overline{r_s}}{r_{si}} > \frac{1}{0.6} = 1.67 \tag{7}$$

As can be understood from the inequality (7), there is soft storey irregularity if R_{si}^{-1} term is greater than 1.67, and that also means R_{si} term to be lower than 0.6. As for calculations, the inequality of (7) will be taken into account. The summary of code-defined stiffness irregularity factor terms and their criteria with limit values that taken into account for this paper given in the Table 2.

Table 2. The conditions of existence of soft storey irregularity of a storey according to investigated codes

The related code	Factor	Definition	Criteria	Limit Value
TBDY-2018[*1]	η_{ki}	$\dfrac{\frac{\Delta_i}{h_i}}{\frac{\Delta_{i+1}}{h_{i+1}}}$	To Be Greater Than	2
ASCE-7-10[*2]	$\dfrac{k_{i+1}}{k_i}$	-	To Be Greater Than	1.67
	$\dfrac{k_m}{k_i}$	$\dfrac{k_{i+1} + k_{i+2} + k_{i+3}}{3k_i}$	To Be Greater Than	1.25
BSL[*3]	R_{si}^{-1}	$\dfrac{\overline{r_s}}{r_{si}}$	To Be Greater Than	1.67

*[1]TBDY-2018: Türkiye Building Eartquake Code - 2018
*[2]ASCE/SEI-7-10: American Society of Civil Engineers/Structural Engineering Istitute 2010
*[3]BSL: Building Standard Law of Japan

2.2. ELF analysis procedure

The linear elastic equilavent lateral force analysis done in order to determine the presence of soft storey irregularity. It is shown that the given structural design has soft story irregularity at the ground storey for all code criteria. The determination whether the irregularity is valid is done using TBDY-2018, ASCE/SEI-7-10 and BSL code criteria defined in (1), (2) and (3), (5) and (7) respectively. ELF procedure has been applied according to TBDY-2018 code. The load bearing system behavior factor is taken as $R = 8$. Site soil condition is taken as ZC. The soil magnification factors corresponding the ZC soil site condition is 1.2 for short period, and 1.4 for 1 second period. In terms of probabilistic seismic hazard assessment, the earthquake hazard level is taken as the earthquake having 2475 year recurrence period defined by TBDY-2018. While spectral acceleration for short period is taken $S_{ds} = 1.75\ g$, it is taken $S_{d1} = 0.75\ g$ as for 1 second period as can be seen from Fig. 1c. The deflected shape of structural system and top displacement can be seen from Fig. 1a, b. Lateral loading direction is taken as x axis and the distributed lateral loads along storey slabs can be seen from Fig. 1d. As can be seen from Fig. 1c, TBDY-2018 load pattern option at SAP2000 used for loading pattern. For both ELF and pushover method, the initial stiffness has been defined from $g + 0.3q$ loading. The calculated values of code-defined factors of ground storey according to linear elastic static analysis results given in the Table 3.

Table 3. The code-defined irregularity factors calculated from the ELF analysis results

$\Delta_1\ (mm)$	$\Delta_2\ (mm)$	$\Delta_3\ (mm)$	$\Delta_4\ (mm)$	$V_t\ (kN)$	$\Delta_1\ (kN)$
24.41	6.85	4.77	2.75	161.53	145.31
$V_3\ (kN)$	$V_4\ (kN)$	η_{k1}	k_2/k_1	k_m/k_1	R_{s1}^{-1}
115.04	72.30	2.059	3.206	3.607	2.786

Here in the Table 3; Δ_i corresponds relative storey drift, Δ_i corresponds storey shear, η_{k1} corresponds TBDY-2018 defined irregularity factor for ground storey, k_2/k_1. k_m/k_1 corresponds ASCE/SEI-7-10 defined criteria parameters for irregularity of ground storey and, R_{s1} is BSL defined factor calculated for ground storey. As for η_{k1}, the criterion is defined as (1), as for k_2/k_1 and k_m/k_1, the criterion is given at (2) and (3) respectively, and for R_{s1}^{-1}, the corresponding criterion is given in the inequality (7). These criteria are summarized at Table 2. One can see that the ground storey has stiffness irregularity for these three codes after comparing the irregularity factor results (Table 3), with their code-defined limit values (Table 2). Note that the storey shear of ground storey, V_1 corresponds to the base shear value.

2.3. Nonlinear static analysis procedure

As a nonlinear static analysis, displacement controlled nonlinear pushover analysis done up to the monitored top displacement of 24.6 cm, which corresponds to the 2% top drift ratio. The pushover load pattern is taken as the same one with equivalent lateral load pattern (Fig. 1.c) with zero eccentricity. The PΔ effects and large displacement taken into consideration, and the nonlinear static analysis began from the end of $g + 0.3q$ loading. The pushover curve is given in Fig. 2a.

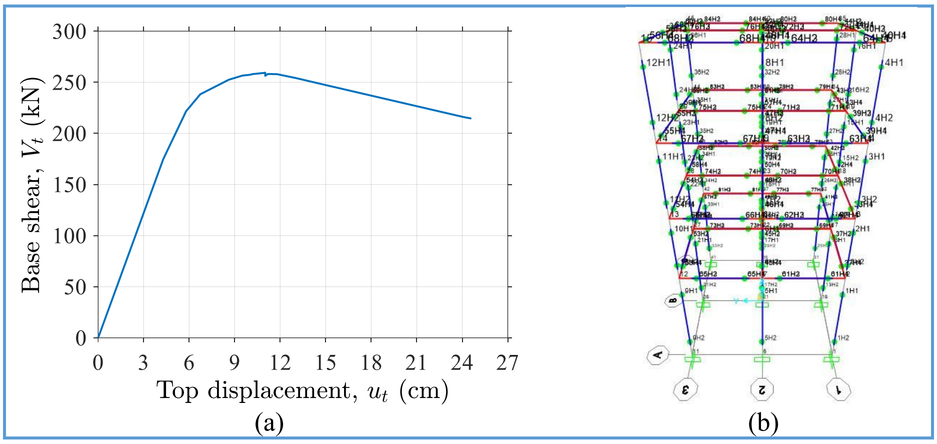

Fig. 2. Nonlinear static analysis case (a) Pushover curve of structure (b) assigned plastic auto hinges

The lumped plastic PMM hinges are defined using the idealised flexural hinge of the auto-hinge option of SAP2000. The assigned plastic hinges can be seen from Fig. 2b. The Plastic hinge length of the column has been calculated as half of the section width and assigned at the middle of the plastic hinge length. In that regard, while the plastic hinge length of columns is 15 cm, it is 20 cm for beams. Plastic hinge absolute distances are defined as 20 cm for columns and 25 cm for beams in x direction and 22.5 cm for beams in y direction, starting from the intersection point of the column and beam member axes.

3. Analysis results

In this paper, the values of code-defined stiffness irregularity factors through inelastic behavior of a reinforced soft storey structure are investigated and graphed along with incrementing top displacement. As can be understood from Table 2, relative storey drift values and storey stiffness values are needed to compute code-defined factors. The storey shear and drift values for all pushover steps are obtained from the SAP2000 analysis. The lateral storey stiffness, k_i calculated by dividing the storey shear, V_i into the relative storey drift, Δ_i. From the obtained results, values of code-defined factors are calculated for each pushover step. Nonlinear pushover analysis and irregularity factor results with the pushover step number given in the Table 4.

In Table 4, the values of irregularity factors are computed. They calculated using corresponding storey drifts and storey stiffnesses calculated from storey shear and storey drifts. The given analysis results are calculated only for the soft ground storey. In Table 4, step number corresponds the pushover step, u_{top} corresponds lateral top displacement for given pushover step, Δ_1, V_1 and Δ_2, V_1 corresponds storey drift and shear of ground and one above storeys and η_{k1}, k_2/k_1, k_m/k_1, R_{s1} are code-defined factors calculated for ground storey corresponding to given top displacement.

Table 4. The nonlinear pushover analysis results

Step No	u_{top} (cm)	Δ_1 (cm)	Δ_2 (cm)	V_1 (kN)	V_2 (kN)	η_{k1}	k_2/k_1	k_m/k_1	R_{s1}	R_{s1}^{-1}
1	1.23	0.77	0.22	50.02	45.08	2.06	3.21	3.63	0.359	2.79
2	2.46	1.55	0.43	100.13	90.19	2.06	3.21	3.62	0.359	2.79
3	3.69	2.32	0.65	150.32	135.33	2.06	3.21	3.62	0.359	2.79
4	4.29	2.70	0.76	174.76	157.34	2.06	3.21	3.62	0.359	2.79
5	5.80	3.66	1.08	221.71	199.75	1.97	3.06	3.74	0.346	2.89
6	6.73	4.34	1.24	238.27	215.01	2.02	3.16	4.04	0.321	3.11
7	8.61	5.87	1.51	252.53	228.84	2.25	3.52	4.95	0.264	3.78
8	9.52	6.67	1.60	256.58	231.51	2.41	3.77	5.46	0.239	4.18
9	10.02	7.14	1.63	257.39	232.25	2.54	3.96	5.80	0.226	4.43
10	10.17	7.27	1.64	257.99	232.78	2.57	4.01	5.89	0.222	4.49
11	10.63	7.69	1.66	258.70	233.41	2.67	4.17	6.19	0.212	4.72
12	10.96	8.00	1.68	259.20	233.86	2.74	4.28	6.40	0.205	4.87
13	11.02	8.04	1.69	259.34	234.61	2.75	4.30	6.43	0.205	4.89
14	11.02	8.08	1.66	256.42	231.29	2.81	4.38	6.49	0.202	4.94
17	11.19	8.22	1.68	258.13	232.62	2.83	4.42	6.55	0.200	5.00
18	11.80	8.82	1.70	257.92	232.85	3.00	4.69	7.01	0.188	5.32
19	13.03	10.08	1.68	254.13	229.48	3.46	5.40	8.11	0.163	6.12
20	14.26	11.34	1.67	249.84	225.73	3.93	6.14	9.27	0.144	6.96
21	15.49	12.61	1.65	245.59	222.10	4.40	6.89	10.45	0.128	7.81
22	16.72	13.87	1.64	241.35	218.47	4.89	7.66	11.68	0.115	8.69
23	17.95	15.13	1.63	237.11	214.83	5.38	8.44	12.94	0.104	9.60
24	19.18	16.40	1.61	232.87	211.20	5.88	9.23	14.23	0.095	10.54
25	20.41	17.66	1.60	228.63	207.57	6.39	10.04	15.58	0.087	11.50
26	21.64	18.92	1.58	224.40	203.94	6.91	10.87	16.96	0.080	12.50
27	22.87	20.19	1.57	220.16	200.30	7.44	11.72	18.39	0.074	13.53
28	24.10	21.45	1.55	215.93	196.67	7.98	12.58	19.87	0.069	14.59
29	24.60	21.96	1.55	214.54	194.94	8.21	12.91	20.45	0.066	15.05

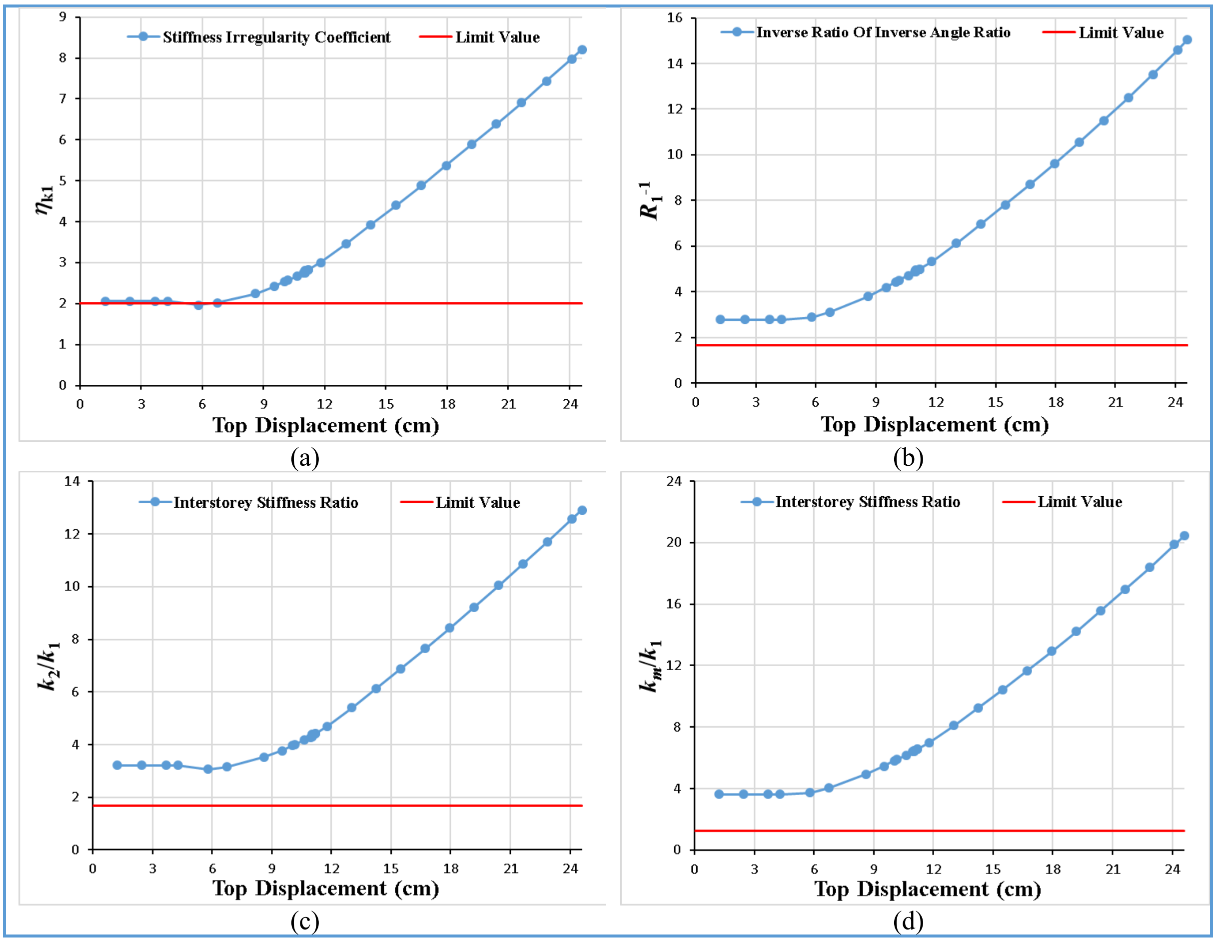

Fig. 3. Code-defined irregularity factor plots (a) TBDY-2018 (b) BSL (c) and (d) ASCE/SEI-7-10 codes

The pushover steps number 15 and 16 are repeated steps. That is why they were erased from Table 4. Storey shear is the sum of the shear force of the bottom section of columns at a storey, and the sum of the bottom section shear force of the ground storey corresponds to the base shear force. Storey stiffness, k_i obtained by the ratio of V_i to Δ_i. In order to observe the changing pattern of the factors of η_{k1}, k_2/k_1, k_m/k_1, R_{s1}^{-1} along with the inelastic behavior of the structure (Fig. 2a), the calculated values of factors are plotted according to the corresponding top displacement values obtained from SAP2000 and given in the Table 4. The plotted graphs are given in Fig. 3a, b, c and d.

In Fig. 3a, b, c and d, the red constant lines define corresponding code-defined limit values of criteria (1), (7), (2) and (3), respectively. The limit values for those inequality criteria are equal to 2 for Fig. 3a, 1.67 for Fig. 3b and Fig. 3c, and 1.25 for Fig. 3d. One can see that all irregularity factors tend to increase in the same manner, except slight decrease at 6 cm top displacement for Fig. 3a and Fig. 3c.

If one looks at all four graphs, one listed under the other, it can be understood that their patterns look identical. They become strictly increasing at the same top displacement, which is approximately 6 cm and corresponds to the governing of plastic hinges at columns. The structural stiffness is changing at the top displacement value approximately 6 cm and 11 cm drastically, as it can be seen from the pushover curve in Fig. 2. Both the slope of the elastic region and the post-strength slope is constant. In Fig. 3a, b, c and d, the corresponding slopes are nearly constant as well. While the increasing inelastic behavior of the structure, the irregularity factors also increased; on the other hand, if the structure remains elastic region, the irregularity factors remain unchanged. Also, it is seen that the pushover analysis results obtained when the frame behaves linearly elastic (the first four rows of Table 4), and the Table 3 results of irregularity factors obtained with the ELF method overlap with each other. This is valid until pushover step 5. This is not unpredictable since the pushover load pattern is taken as the same pattern defined at the ELF method and same stiffness modifiers are used. The first four pushover steps correspond to linear elastic analysis (until 4.3 cm top displacement) where no plastic hinge occurs. This can be seen from the pushover curve Fig. 2a as well.

Due to soft storey action, plastic hinges tend to occur at soft storey column ends before all beam end sections reach plastic moment capacity, resulting in less ductile behavior. But before reaching the ground storey mechanism, the governing of plastic hinges at ground storey beams could be the reason for the slight decrease in η_{k1} and k_2/k_1. The same slight decrease is not seen in Fig. 3b and d. Further investigation is needed to determine the exact reason.

The values of irregularity factors depend on the top displacement value for the inelastic region, and constant for elastic region of the building. That is why, instead of using the linear elastic ELF method to calculate irregularity factors and determine the presence of soft storey irregularity, the determination of soft storey can be evaluated for the top displacement of the inelastic displacement demand of the design earthquake as well.

4. Conclusions

Along with the nonlinear pushover analysis case, the inelastic behavior of the structure accounted for the calculation of each stiffness irregularity factor. Thus, the negative increase in soft story behavior is investigated for each code-defined criterion considered. From the analysis results and obtained graphs, the following can be said.

- The values of irregularity factors are constant for the elastic behavior of the structure. But if the structure crosses post-elastic region, the value of the irregularity factors increases with increasing top displacement for soft storey building. The considered codes have made a similar assessment in terms of the negative aggravation of the soft storey behavior throughout the inelastic behavior of the structure.
- The inequality direction of R_{s1} defined in the BSL code has been made the same inequality direction as TBDY-2018 and ASCE/SEI-7-10 criteria by taking into account of R_{s1}^{-1} using inequality (7) to be able to compare the code criteria in the same way. Thus, both elastic and inelastic behavior patterns of all four irregularity factors due to incrementing top displacement become similar.
- At 2% top drift ratio, the values of irregularity factors η_{k1}, k_2/k_1, k_m/k_1, R_{s1}^{-1} rose by 4, 4, 5.7 and 5.4 times respectively. The significant increase in code-defined stiffness irregularity factors begin by 6 cm top displacement where plastic hinges at ground storey columns occur and the factors increases up to 24.6 cm top displacement, which corresponds to 2% top drift ratio.
- The conservability of codes can be seen from how the elastic analysis results are far from the code-defined limit value. The ASCE/SEI-7-10 is the most conservative code, followed by the BSL code. As for investigated codes, the less conservative one is TBDY-2018. This result is consistent with literatüre review. Khanal et al (2019) was described Japanese code as more conservative than Türkiye code. Also Yousef et al (2020) denoted that UBC code is sufficiently conservative. This result is also consistent with the analysis done in this study since the ASCE and UBC criteria are same.

Acknowledgments
The research described in this paper was financially supported by the Yildiz Technical University Scientific Research Projects Coordination Unit (BAP) under the grant number FBA-2024-6065.

References

ABYYHY (1997). Regulation about the buildings constructed in the disaster regions, *Turkish Ministry of Public Works and Settlement*, Ankara

Aoyama, H. (1981). Outline of earthquake provisions in the recently revised Japanese building code, *Bulletin of the New Zealand National Society for Earthquake Engineering, 14*(2)

ASCE/SEI-7 (2010). Minimum design loads for buildings and other structures, *American Society of Civil Engineers/Structural Engineering Institute*

Arlekar, J.N., Jain, S.K., Murty, C.V.R. (1997). Seismic response of RC frame buildings with soft first storeys, *Golden Jubilee Conference on Natural Hazards in Urban Habitat*

Aydıner, M.F., Sevim, B., Uzun, S., Ayvaz, Y., Ari, A., Akbulut S. (2023). Seismic performance and reason of failure evaluation of reinforced concrete structures based on field investigation after Kahramanmaras earthquakes, *Proceedings of the 3rd international civil engineering & architecture conference,* 889-898

Bruneau, M. (2002). Building damage from the Marmara, Turkey earthquake of August 17, 1999, *Journal of Seismology, 6*, 357-377

BSL (1980). Ministry of Construction, Housing Bureau and Building Research Institute, Commentary on the structural calculation based on the revised enforcement order, Building standard law, *Building Center of Japan*

Döndüren, M.S., Nakipoğlu, A. (2018). Comparison of R/C buildings with a soft-storey irregularity with respect to various national building codes, *Materials and Technology, 52*(5), 575-581

Khanal, N., Singh, S.K., Wagley, S. (2019). Seismic consideration of soft story in RC frame buildings using various national codes, *International Journal of Civil Engineering and Technology (IJCIET), 10*(9), 343-352

PAİY (2017). Türkiye Planned Areas Zoning Regulation, *Republic of Türkiye Ministry of Environment, Urbanization and Climate Change,* Ankara

SAP2000 (2021). Integrated Finite Element Analysis and Design of Structures, *Computers and Structures Inc., Version 23.3.0*, Berkeley, CA

Seyed, B. (2010). Structural irregularities and the building codes, *Proceedings of the 9th U.S. National and 10th Canadian Conference on Earthquake Engineering*

Sharma, K., Deng, L., Nogues, C.C. (2016). Field investigation on the performance of building structures during the April 25, 2015, Gorkha earthquake in Nepal, *Engineering Structures, 121*, 61-74

TBDY (2018). Türkiye building earthquake code, *Disaster and Emergency Management Presidency*

Yousef, A.M., El-Metwaaly, E., El-Mandouh, M.A. (2010). Seismic response of vertically irregular HSC moment-resisting building frames, *Journal of Engineering and Applied Science, 57*(5), 409-430

Zavala, D.J., Torres, C.J., Moreno, J.D. (2022). Influence of the P-Δ effect and stiffness irregularity on the structural behavior of reinforced concrete buildings, *Journal of Physics: Conference Series*

Zhao, B., Taucer, F., Rossetto, T. (2009). Field investigation on the performance of building structures during the 12 May 2008 Wenchuan earthquake in China, *Engineering Structures, 31*, 1707-1723

Design of a seismic resilient CLT multistorey building complying with Eurocode 8 using RSFJ joints: a case study

Loris Douare[1], Chaimaa Jaafari*[1], Rostand M. Pitti[1], Ashkan Hashemi[2], Pierre Quenneville[2]

[1] *INP Clermont Auvergne, CNRS, Institut Pascal, F-63000 Clermont-Ferrand, France*
[2] *Department of Civil and Environmental Engineering, University of Auckland, New Zealand*

Abstract. Cross-Laminated Timber (CLT) shear walls and timber braced frames have emerged as efficient and sustainable systems for seismic areas, offering an alternative to traditional concrete core walls and steel braced frames. Resilient Slip Friction Joints (RSFJ) commercialized by Tectonus, enable low-damage structural performance through energy dissipation and self-centering behavior. These joints have been successfully implemented in projects across Canada and New Zealand, gaining regulatory approval for seismic applications in both countries. This paper explores the applicability of RSFJ connections in European seismic zones, focusing on compliance with Eurocode 8 requirements. A case study was conducted on a 10-story mass timber building, made of CLT shear walls, timber braces, and RSFJ joints. Seismic design analyses, including lateral force analysis, pushover, and nonlinear time history analysis, were performed assuming the building's location in Ljubljana, Slovenia. The results confirm the feasibility of using RSFJ connections in European multi-story timber structures and provide a design methodology for integrating these devices into low-damage construction aligned with Eurocode 8 standards.

Keywords: CLT; RSFJ; Earthquake; Eudocode 8; Resilient; Low damage

1. Introduction

Current environmental concerns are leading to new construction methods, new materials and a different approach to project design. In this context, timber is integrated more and more in the field of construction, even in high seismic areas (Shen et al., 2023). New designed buildings for seismic zones are often hybrid structures that implement timber as part of the overall structural system. In such structures, timber is combined with other materials such as steel or concrete to comply with seismic requirements. Indeed, wood, although having many advantages, such as its easy installation, its low weight, its high strength, its low environmental impact, has a low ductility, which does not allow a correct design in earthquake areas. Therefore, in newly designed hybrid structures, timber is used to support gravity loads, whereas steel or concrete are used to support lateral loads (earthquake, wind). To have structures that are fully made of timber, there is a need to find new ways that enable resisting to earthquakes without relying on steel or concrete structural components. To achieve that, it is for instance possible to use Resilient Slip Friction Joints (RSFJ) as the ones developed by the Tectonus company (Tectonus, 2022). Using such devices, it is possible to come up with assemblies having a high capacity to dissipate seismic energy and to resist several cycles of seismic loading. In addition, these systems are self-centring, which allows the structure to return to its original position after an earthquake without any residual damage. Such property allows extending the life of the structure without a necessity for intervention or maintenance, making the structure more resilient. The Keith Drive building is a 10 storey building under construction in Canada made of CLT shear walls and timber braced frames (Dickof et al., 2023). It was designed in a way to dissipate seismic energy through the use of resilient dissipative RSFJ joints based on the Canadian builing codes. This same building is considered in the present paper (in terms of geometry, *etc*). For the case study, it is supposed to be localized in Ljubliana in Slovania, which is a highly seismic European area. The characteristics of this area are considered (climatic loadings, pic ground acceleration, *etc*) and the building is designed to comply with Eurocode requirements. This article provides the methodology that could be used by practitioners in order to design a resilient fully timber building using RSFJ joints based on current Eurocode requirements (Standard B., 2005). It aims to show the efficiency of the RSFJ joints resilient technology in a European context.

*Corresponding author, E-mail: chaimaa.jaafari@uca.fr

https://doi.org/10.31462/icearc2025_ce_eqe_290

golden light publishing

This article will be composed of 4 sections: in a first section, the lateral force method is applied to the structure in order to design the RSFJ joints. Then, a non-linear pushover analysis is performed on the structure in a second section. The third section presents results obtained when performing a non linear analysis on the office building under study. Last, a conclusion recalls the main findings of the article.

2. Lateral force analysis and design of the RSFJ joints

2.1. Geometry, materials and static design

The building under study is a 10 storey office timber building. It has a total height of 40 meters. Its plan view is shown in Fig. 1. The first 9 storeys have a similar layout wheas the last one is smaller as shown in Fig. 2 (ETAB model of the building). The building is made of CLT floors supported by steel beams. The structure is mainly made of timber seismic resisting systems: timber braces (as shown in blue in Fig. 2) and CLT shear walls (in red in Fig. 2). The thickeness of the shearwalls being equal to 320 mm. In addition, connections are made of resilient slip friction joints (RSFJ). The different structural elements of the builing were designed to comply with Eurocodes requirements: Eurocode 3 for steel (Standard B., 1993) and Eurocode 5 (Porteous & Kermani, 2008) for timber based on loadings presented in Table 1 (taken from Eurocode 1 based on the grographical location of the building).

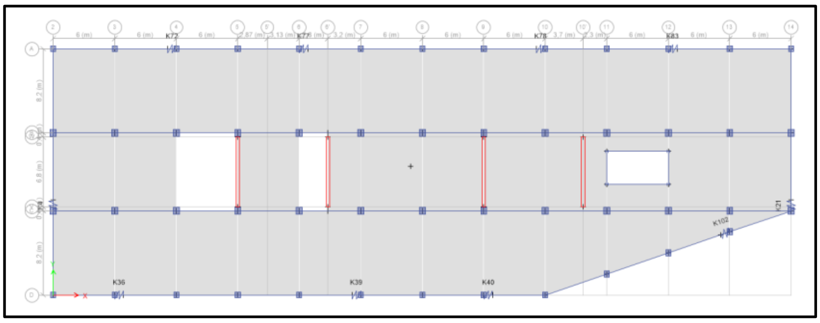

Fig. 1. Plan view of the structure

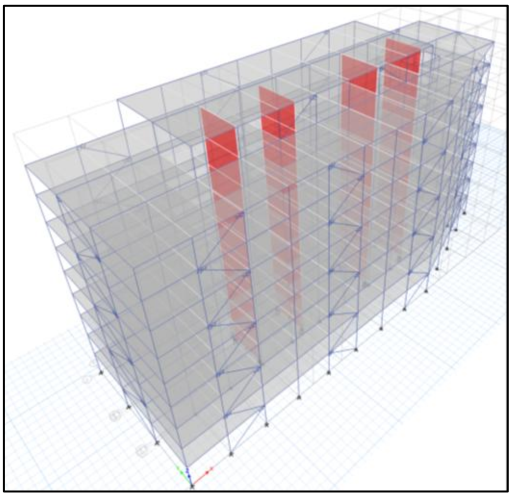

Fig. 2. 3D view of the structure

Table 1. Loads considered in the project

Floor	Areas	DL (kN/m^2)	SDL (kN/m^2)	LL (kN/m^2)	SL (kN/m^2)	WL
1st	All	1.3	1.40	4.80	-	-
2nd to 9th	Office area	1.3	2.50	2.50	-	-
	Exit corridors	1.3	2.50	4.00	-	-
10th	Pink area	1.3	4.90	2.40	-	-
	Blue area	1.3	4.00	4.80	1.51	-
	Snow accumulation	-	-	-	5.60	-
Roof	All	1.3	2.60	1.50	1.51	-

Glulam components are of grade GL28h whereas CLT members have a grade of C24.

Tables 2 and 3 summarize the types of verifications performed for the different timber and steel components. They also show sections chosen for the Etabs model.

Table 2. Verifications according to Eurocode 5 of Wood Sections

Name	Glulam Section GL28h	Verifications Eurocode 5
WC1	535x580	Axial compression and buckling
WC2	430x530	Axial compression and buckling
WC3	530x570	Axial compression and buckling
WB1	400x530	Bending, lateral buckling, shear force and deflection criteria
WB2	175x530	Bending, lateral buckling, shear force and deflection criteria
WB3	365x530	Bending, lateral buckling, shear force and deflection criteria

Table 3. Verifications according to Eurocode 3 of Steel Sections

Name	Steel Section S355	Verifications Eurocode 3
SB1	IPE 500	Section, lateral buckling and deflection criteria
SB2	IPE 300	Section, lateral buckling and deflection criteria
SB3	IPE 300	Section, lateral buckling and deflection criteria
SB5	IPE 550	Section, lateral buckling and deflection criteria
SB7	Hollow square tube 254x254x16	Section, lateral buckling and deflection criteria
SC2	HEA 240	Axial compression and buckling
SC3	HEA 100	Axial compression and buckling

CLT members were designed using the "European Technical Assessment CLT" (European Technical Assessment – CLT, 2023) and the Swedish CLT Handbook (The CLT Handbook, 2025). 320 mm thick CLT floors were chosen for all the storeys and a 260 mm thick CLT was chosen for the roof. For the CLT shearwalls, a thickness of CLT equal to 320 mm was chosen.

2.2. Lateral force method (Eurocode 8)

For this case study, the regularity in plan is not met, because of the slenderness of the building (λ=5>4) but the regularity in elevation is met, the structural elements are continuous from the bottom to the top and there are no significant setbacks. A linear-elastic analysis using the lateral force method could be used for the study. To apply the lateral force method, it is necessary to make many seismic assumptions based on the localisation of the structure (Ljubjana in this case). Table 4 summarizes such properties. Since the structure under study is an office building, it has an importance factor of III. A coefficient q equal to 3 is used which is the value defined for timber for this kind of structure. An assumption of a soil type A (Table 5) was taken into account for the analysis of the structure. Referring to Table 5 in Eurocode 8, a soil type A corresponds to a Rock or other rock-like geological formation, including at most 5 m of weaker material at the surface.

Table 4. Seismic properties of Ljubljana

City	Ljubjana	
$a_{gR}\ (\frac{m}{s^2})$	2.698	T_{NCR} = 475 years
Soil type	IPE 300	*Table 3.1
Spectrum type	IPE 300	*Note 3.2.2.2 (2)
Ductility class	IPE 550	*Table 8.1
Coefficient q	Hollow square tube 254x254x16	*Table 8.1
Importance factor γ_l	HEA 240	*Table 4.3
Peak ground acceleration	HEA 100	T_{NCR} = 475 years
a_g calculation	0.330 g	

Table 5. Calculation values for LFM, ULS

Parameters	Value
Soil Type	A
S	1.0
T_B	0.15
T_C	0.40
T_D	2.0
Time Period (s)	0.795
Seismic weight (kN)	110200
Horizontal Design Spectrum $S_d(T)$	0.138
Base Shear (kN)	12910
Damping correction factor η	1.0

Using the properties described previously, it is possible to get the lateral force on each storey as shown in Table 6. These values enable getting the lateral force required for the ultimate limit state (ULS) as summarized in Table 6.

Table 6. ULS Values using the Lateral Force Method

	Mass (kN)	Height (m)	z_i(m)	F_i(kN)
Story 10	5000	4	40	1090
Story 9	16400	4	36	3210
Story 8	11100	4	32	1930
Story 7	11100	4	28	1690
Story 6	11100	4	24	1450
Story 5	11100	4	20	1210
Story 4	11100	4	16	970
Story 3	11100	4	12	730
Story 2	11100	4	8	490
Story 1	11100	4	4	250
Total	110200	40		

Then, to get the lateral force for the serviceability limit state (SLS), the coefficient v is used to multiply the peak ground acceleration for the calculation. All parameters and values of calculation are summarized in Tables 7 and 8.

Table 7. Calculation values for LFM, SLS

Designation	Value
ag calculation (g)	0.132
Time Period (s)	0.795
Seismic weight (kN)	110200
Horizontal Design Spectrum	0.055
Base Shear (kN)	5165

Table 8. SLS values using the Lateral Force Method

	Mass (kN)	Height (m)	z_i(m)	F_i(kN)
Story 10	5000	4	40	440
Story 9	16400	4	36	1290
Story 8	11100	4	32	780
Story 7	11100	4	28	680
Story 6	11100	4	24	580
Story 5	11100	4	20	490
Story 4	11100	4	16	390
Story 3	11100	4	12	290
Story 2	11100	4	8	200
Story 1	11100	4	4	10à
Total	110200	40		

In reality, thanks to the use of the RSFJs, the damping of the structure is higher than 5% and therefore the damping correction factor should be lower than 1. This allows the reduction of the base shear of the structure and to save cost and materials for the construction. In the following subsection, the determination of the RSFJ will enable the determination of the correct damping factor of the structure.

2.3 Design of the RSFJ

The behaviour of RSFJ is defined by the curve shown in Fig. 3. The parameters depend on the design and the composition of the RSFJ such as the number of bolts, the precompression needed or the number of discs.

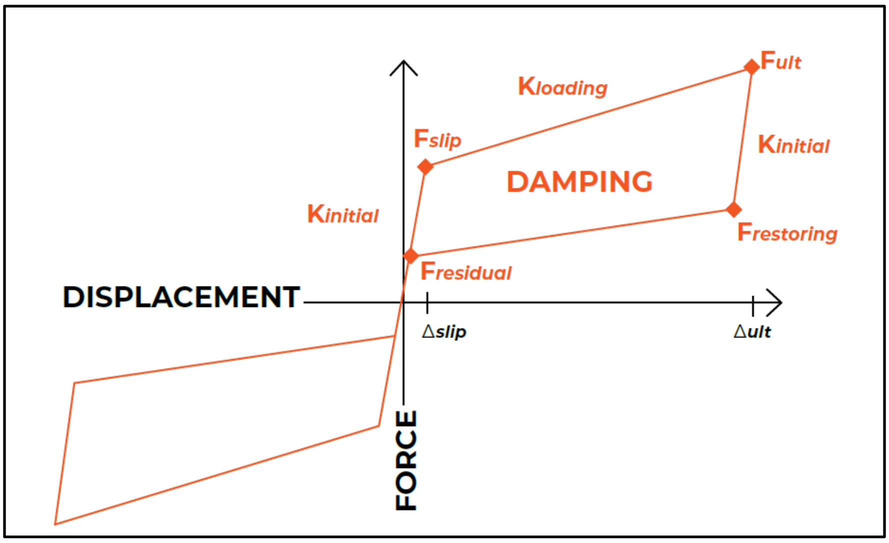

Fig. 3. Shape behaviour of RSFJ (Tectonus, 2022)

As shown in Fig. 3, the RSFJ is defined by 6 parameters: Fult, Fslip, Frestoring, Fresidual, Δslip, Δult. To make the analysis, it is necessary to define these parameters in order to model links in Etabs using appropriate values. Fult: Proceed of the lateral force method with ULS values. It means a no-collapse state for the building. It is determined by the maximum forces in the braces and in the base of the shearwalls. Fslip: Damage limit state. Δult: Defined by the geometry of the bracing and shearwall using the target displacement of the building demand. For this case study, the target displacement was taken equal to 1.5%. Δslip: This parameter is set equal to 2mm. This value is obtained from research and test on RSFJs. Frestoring: Approximatively equal to 30% of the Fult which is an approximation determined from testing of the RSFJs. Fresidual: Taken as 15% of the Fult value which is also an approximation determined from testing of the RSFJs. To define the RSFJ, it is necessary to know the force in the braces and the shearwalls in order to define the Fult of the device. These forces are obtained from the structural model analysis using the lateral force method described in part 2.2. of Eurocode 8. A linear analysis is first carried out to determine the Fult. In order to define correctly the RSFJ with the right damping ratio, it is necessary to make few iterations with the lateral force method, modifying the coefficient η at every iteration. The coefficient η enables one to take into account the damping of the building. Usually estimated to be equal to 5%, it will be greater than this value as a result of using dampers in the structure. The coefficient η is defined by the following formula (1):

$$\eta = \sqrt{\frac{10}{(5+\zeta)}} \geq 0.55 \quad (1)$$

The coefficient ζ corresponds to the damping of the structure and the damping of the RSFJ. The damping of the structure is usually between 2 and 3. 2.5 was the value fixed for the case study.

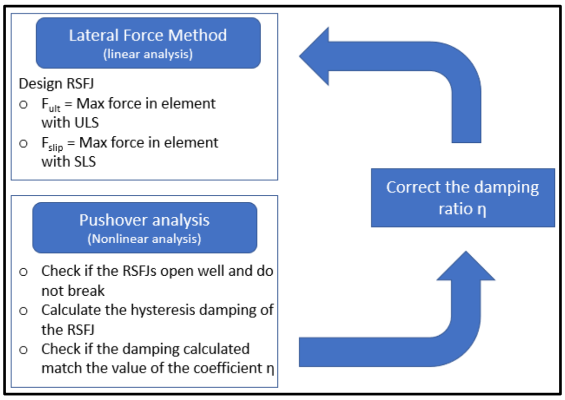

Fig. 4. Method to define RSFJ

The damping ratio is determined using the resulting pushover curve shown in Fig. 5. The “push” and “pull” curve is needed in order to determine the damping hysteresis of the RSFJ. The damping is calculated with the following formula (2):

$$\xi_{hyst} = \frac{2 * A_1}{\pi * A_2} \tag{2}$$

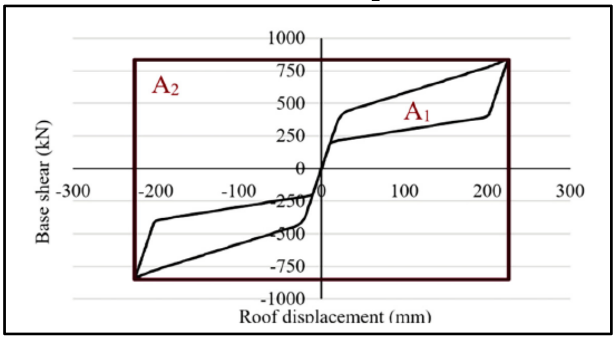

Fig. 5. Flah shape of the hysteresis of the RSFJ (Tectonus, 2022)

For the study, after 2 iterations, the damping of RSFJ was determined as equal to 10% in the y direction and as equal to 11.5% in x the direction and the graph obtained is shown in Fig. 6. X direction being the direction where there are only timber braces to withstand the lateral force and the Y direction is the one with shearwall and bracing system.

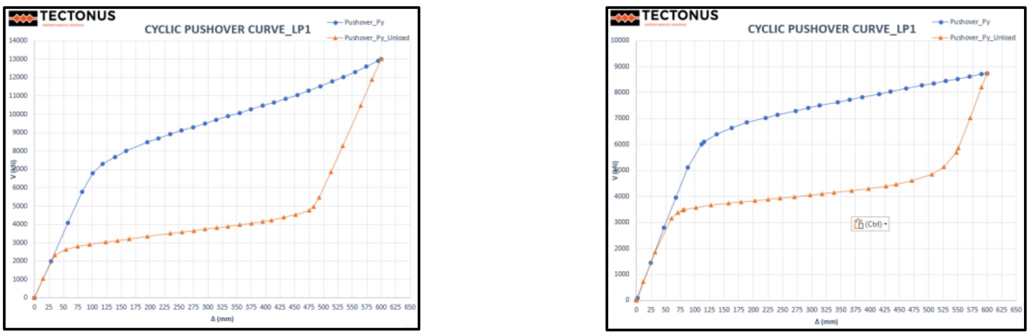

(a) (b)

Fig. 6. Hysteresis damping for (a) x and (b) y directions

Finally the value of the coefficient η is summarize in Table 9. Table 10 shows the different properties of the RSFJ designed to comply with self centering and ductility in the case study.

Table 9. Values for the damping correction factor

Direction	ζelastic	ζhysteresis	coefficient η
X	2.5	11.5	0.73
Y	2.5	10	0.76

Table 10. Properties of the different RSFJs of the structure under study

	Shearwall	A (grey)	B (Green)	C (Orange)	D (Blue)	E (Brown)	F (Red)	G (Purple)
Fult (kN)	3200	1800	1550	1150	1250	700	1400	300
Fslip (kN)	2240	1260	930	690	875	420	980	180
Frestoring (kN)	960	540	465	345	375	210	420	90
Fresidual (kN)	480	270	232.5	172.5	187.5	105	210	45
Delta slip (mm)	2	2	2	2	2	2	2	2
Delta ult (mm)	105	50	50	50	50	50	50	50

3. Pushover Analysis of the structure

After defining correctly the RSFJs of the building, a pushover analysis was performed to determine the non linear behavior of the structure (mainly bilenear thanks to the use of the RSFJs) as illustrated in Fig. 7. The acceleration displacement response spectrum (ADRS) curves for both x and y directions are shown in Fig. 7. The bilinear behaviour of the structure was obtained thanks to the RSFJ devices. The first part of the curves corresponds to the case when the force in the braces is still below the value of Fslip. The second part shows the damping of the structure possible thanks to the RSFJs. The graph presented in Fig. 7 shows also the ULS and SLS spectrums.

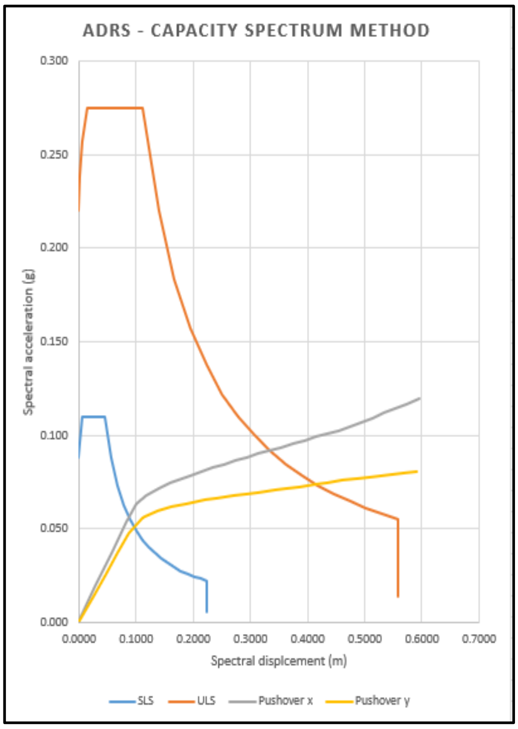

Fig. 7. ADRS Capacity Spectrum Method

Fig. 7 shows that the pushover curve starts its bilinear behaviour just after the blue curve, which is the SLS spectrum. It means that the RSFJs start to open after the SLS, which is the requirement for this kind of devices. In addition, with a graphical method, the intersection point between the pushover curve and the ULS spectrum gives the “performance point”. This point gives an idea about the value of the base shear of the structure. This value should be close to the value found with the lateral force method. For this study, the performance point in the x direction was 10 082kN and in the y direction it was 8 040kN. These values give an idea about the value of the base shear that should be obtained using a nonlinear time history analysis (NLTHA).

4. Nonlinear time history analysis

4.1. Seismic records

The purpose of this analysis is to show the behaviour of the RSFJs and the structure using records of real earthquakes. It allows to verify the design of the RSFJs for the ultimate level state and the Most Considered Earthquake (MCE) level. Even though the Eurocodes do not clearly specify the MCE case to consider, it's important to verify the structure for this case (in addition to the ultimate limite state). The MCE case used is the one given by the ASCE recommandations. Under the different loading scenarios (Ultimate limite state and MCE), the objective is to make sure that the RSFJs stay undamaged . The analysis was proceeded using 9 ground motion records as shown in Table 11. The Eurocodes recommend the use of at least seven records, but nine records were used to get significant results. Each ground motion is composed of two horizontal acceleration records. Each record was scaled. The base shear obtained was compared to the initial base shear found using the lateral method. Moreover, the story drift, the maximum displacement, the residual drift and the behaviour of the RSFJ (displacement and forces) were also analysed and verified. After that, a second series of Non linear analysis were performed using the records scaled to 150% of the design earthquakes (MCE load case).

Table 11.Records information used for the nonlinear time history analysis

RSN	**Name**	**Fault type**	**Region**	**Magnitude**
125	Friuli Italy-01	Reverse	Italy	6.5
169	Imperial Valley-06	Strike Slip	California	6.5
721	Superstition Hills	Strike Slip	California	6.5
828	Cape Mendocino	Reverse	Nothern California	7.0
953	Beverly hills, Mulhol	Reverse	Southern California	6.7
960	Northridge- 01	Reverse	Southern California	6.7
1116	Kobe, Japan	Strike Slip	Japan	6.9
1485	ChiChi, Taiwan	Reverse oblique	Taiwan	7.6
1602	Duwce, Turkey	Strike Slip	Turkey	7.1

In Etabs, the records are imported thanks to the time history function. The shape of the records is presented in Fig. 8.

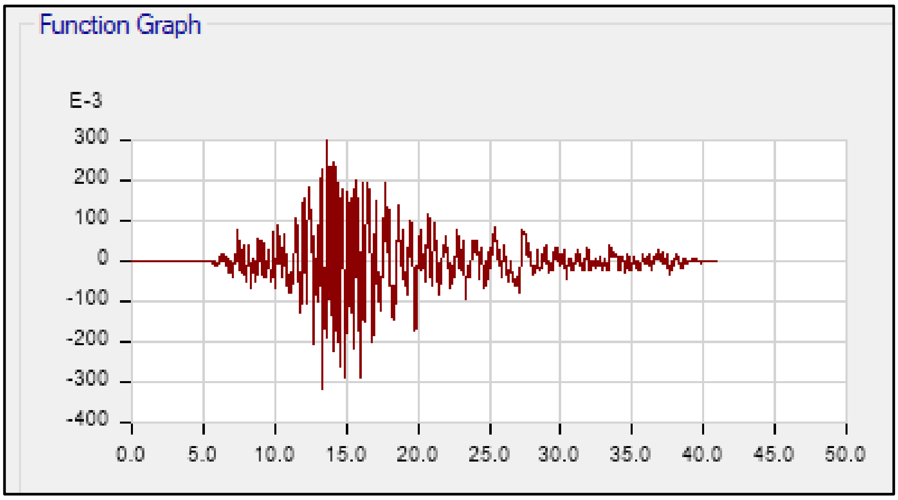

Fig. 8. Shape of the records for NLTHA in Etabs

4.2. Analysis and discussions

First things to compare are the base values of the base shears of the structure. To do that, the NLTHA with the ULS and the MCE were proceeded on the model. The base shear should be close to the base shear obtained with the lateral force method in section 2, which is 9,370kN for x direction and 9,700kN for y direction.

The average base shear showed in Fig. 9 for the x direction is 8,540kN which is below the value of 9,370kN. A similar observation can be done when considering the y direction. These values make sense and confirm that the model is correct. The same procedure was followed with the most considered earthquake (MCE).

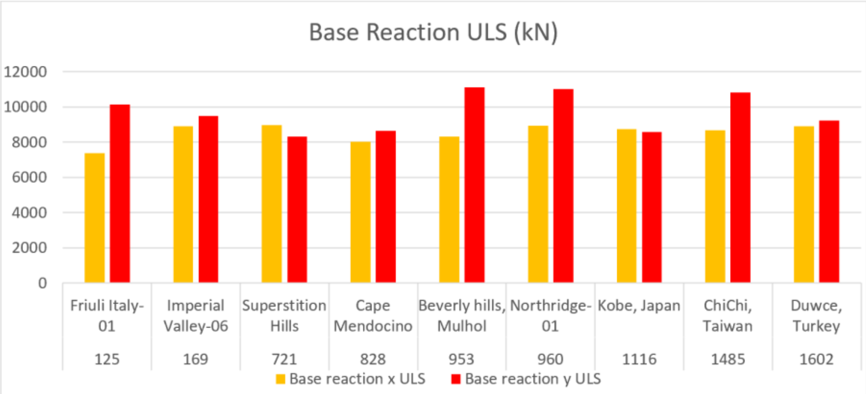

Fig. 9. ULS Base shear

The average value for the x direction is 11,220kN and for the y direction is 13,500kN. These two values are close to the design values, which is desired and correct. Indeed these values are approximately greater than 40% which is acceptable as long as it is not greater than 1.5 of the design value. Second, the displacement of the structure is controlled and verified. Both ULS and MCE cases are presented in Fig. 10.

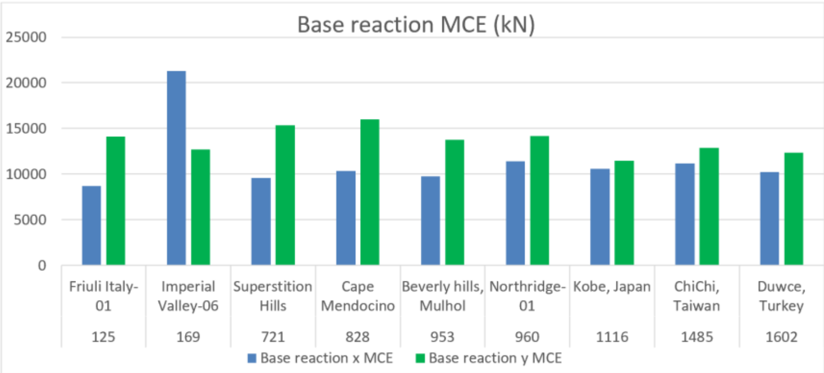

Fig. 10. MCE Base shear

The maximum displacement is 2.50% under the MCE case and there are only 3 values greater than 2.0%. These are really good results and the efficiency of the timber structure in this situation is confirmed. In addition, the average maximum displacement for ULS in x direction is 0.70% and in y direction is 0.75%. This is really close and really good for such a structure. For the MCE, an average of 1.05% and 1.20% were obtained for respectively the x and y directions.

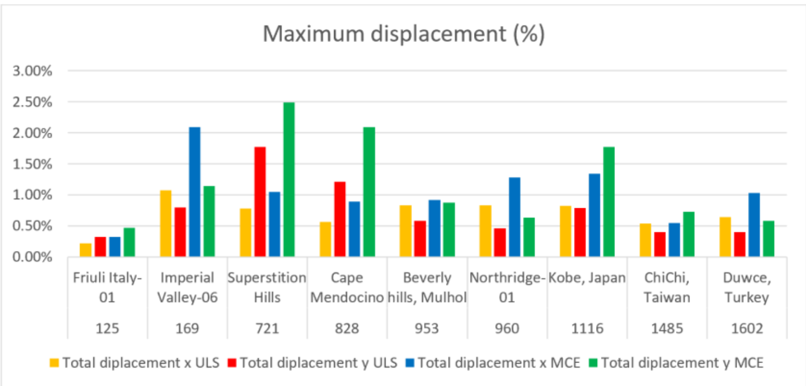

Fig. 11. MCE and ULS maximum displacement

The RSFJs were then checked to see if they don't break and how efficient they are. The properties of the designed RSFJs given in Tables 12 and 13, show that the maximum allowable displacement for the RSFJs in the braces is 50mm and for the shearwalls it is 105mm.

Table 12. RSFJ displacement under ULS

Ultimate Limit State	Max displacement (mm)	Δult (mm)
Brace	41	50
Shearwall	81	105

Table 13. RSFJ displacement under MCE

Most Considered Earthquake	Max displacement (mm)	Δult (mm)
Brace	54	50
Shearwall	109	105

The NLTHA show that the maximum displacement of the RSFJs is a little bit greater than the delta ult under the MCE load case. The delta ult of the RSFJs should be increased in order not to break and to guarantee the security of the building. At the stage of this study, obtained displacement values are considered acceptable. It is interesting to show the other main characteristic of the RSFJ: the self-centring behaviour. Fig. 12 shows the behaviour of one RSFJ (found in the braces) obtained thanks to the NLTHA.

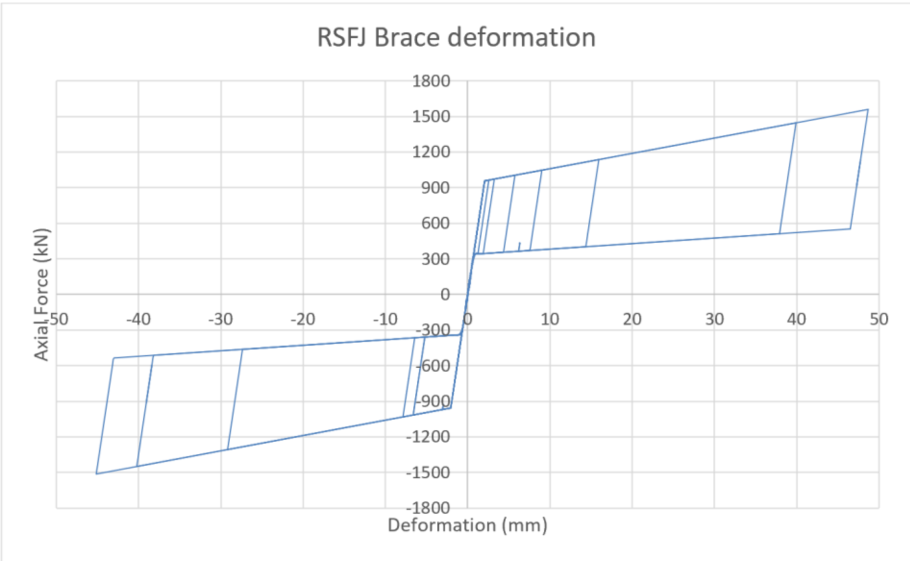

Fig. 12 - Flag shape behaviour of the RSFJ

Fig. 12 shows that the constitutive law of the RSFJ is an hysteresis curve. This corresponds to the flag shape previously described. Indeed, the RSFJ open well when the value of Fslip is reached, then damps to reach the Fult. When the force in the RSFJ decreases, the RSFJ comes back to its initial position. Even after many cycles, the RSFJ is still self-centring and does not show any sign of rupture. Now, that the self-centring behavior of the RSFJ was described, it's important to check the impact of these properties on the structure, especially the residual drift, which should be close to 0% with the RSFJ properties. Results are presented in Fig.s 13 and 14.

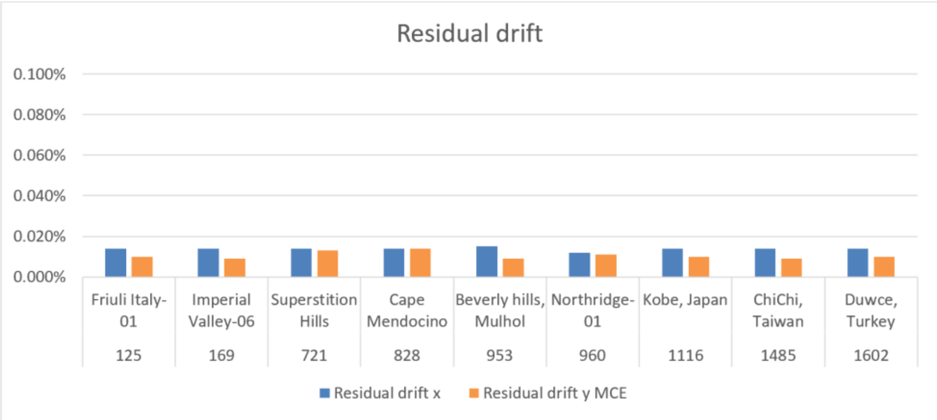

Fig. 13. Residual drift results under MCE records

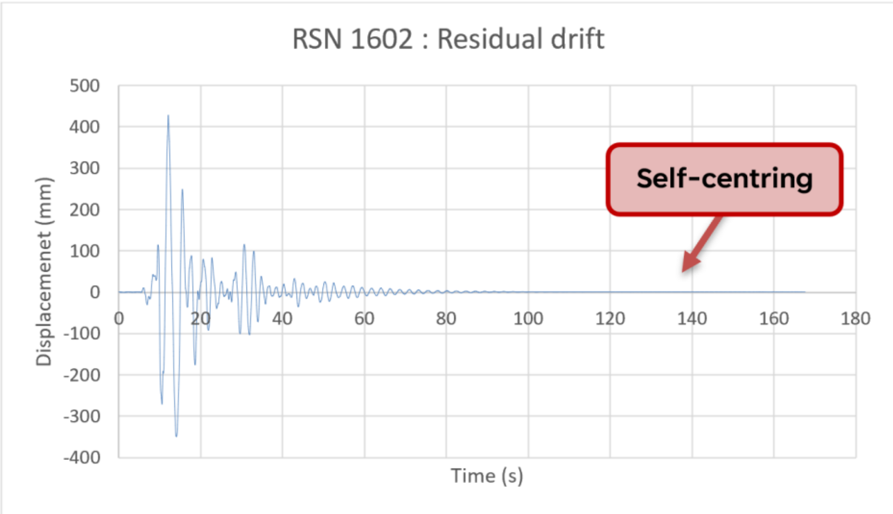

Fig. 14. Displacement of the structure vs time (example record 1602)

As expected, the residual drift of the structure is approximatively equal to 0%. Indeed, the maximum values obtained from the NLTHA are less than 0.020% with MCE configuration which is a really good result. In addition Fig. 43 shows clearly the self-centring properties of the structure obtained using the RSFJs, since after the earthquake event, the building comes back to its initial position on its own.

Another series of NLTHA were run on the same structure without considering any RSFJs or resilient devices. The objective is to show the benefits of the use of such devices in the reduction of the cross sections of the different elements of the structure (Table 14).

Table 14. Brace section comparison

	With RSFJ		Without RSFJ	
	Force demand (kN)	Section (mm^2)	Force demand (kN)	Section (mm^2)
Brace1	2250	450x450	8200	950x950
Brace2	1400	350x350	5500	760x760
Brace3	800	300x300	3000	550x550

Thus, thanks to the RSFJs, the size of the required sections is almost divided by 2, which is huge. The weight of the structure is also significantly reduced thanks to such devices which enables to save of a lot of money. In addition, making connections using RSFJs is less complicated and requires less materials than conventional ones.

Moreover, the force present in the braces is divided by up to 4 times thanks to the RSFJs, which also influences the total base shear of the structure. Therefore, the cost of foundation will decrease significantly with the use of the RSFJs (smaller foundation required necessitating less construction time).

Table 15. Determination of the behaviour factor q

	Base Shear ULS	Behaviour factor q
Both directions	38900	1
x-direction with RSFJ	8540	4.55
y-direction with RSFJ	9370	4.15

Table 15 shows the calculated behaviour factor q of the structure thanks to the use of the RSFJs. Its value is more important than the value 3 typically used for timber structures.

5. Conclusion

To conclude, this research article has explored the potential of integrating a sustainable and resilient technology in timber structures in Europe: The Resilient Slip Friction Joint (RSFJ), which is a New Zealand product.

The findings of this article show that the RSFJs, can be implemented in European timber projects. The various analysis proceeded: the lateral force method (LFM), a pushover analysis and the NLTHA show the very positive impact of such devices on timber structures. Thanks to the RSFJs properties such as their self-centring behaviour, their zero post event damage, the model achieves a high level of performance and an important and efficient energy dissipation. The use of RSFJs also implies on site to have to deal with less complicated connections and allows major savings (smaller cross sections needed, lighter structures). All in all, this article clearly gives the methodology that should be used by practitioners in order to design resilient timber structures using the Eurocodes thanks to the RSFJs.

References

Dickof, C., Jackson, R., Kim, J., & Hashemi, A. (2023). CASE STUDY: A 10 Storey timber braced frame and CLT structure in Vancouver. In BC Proceedings of the 13th World Conference on Timber Engineering, Oslo, Norway.

European Technical Assessment – CLT. (2023, April 20). Retrieved from https://www.cltcz.info/wp-content/uploads/CLT_ETA-14-0349_en.pdf

Porteous, J., & Kermani, A. (2008). Structural timber design to Eurocode 5. John Wiley & Sons.

Shen, Y., Huang, Z., Daneshvar, H., Chui, Y. H., & Huang, D. (2023). Experimental study of CLT panels under combined out-of-plane bending and compression. Engineering Structures, 275, 115262.

Standard, B. (1993). Eurocode 3—Design of steel structures—. BS EN, 1(1), 2005.

Standard, B. (2005). Eurocode 8: Design of structures for earthquake resistance. Part, 1, 1998-1.

Tectonus – Product guide. (2022, December 11). Retrieved from https://www.tectonus.com/resources/design-support

The CLT Handbook. (2025, April 30). Retrieved from http://www.swedishwood.com/publications/list_of_swedish_woods_publications/the-clt-handbook/

4th International Civil Engineering & Architecture Conference
17-19 May 2025, Trabzon, Türkiye

Assessment of sequential earthquake response of the historic Karahan Mosque minaret

Adem Doğangün*[1], Muneeb Jadallah[1]

[1] *Bursa Uludağ University, Faculty of Engineering, Department of Civil Engineering, Turkey*

Abstract. On February 6, 2023, a devastating series of earthquakes struck Turkey, severely affecting historical structures, including the Karahan Mosque minaret in Malatya. This minaret, characterized by its stone base and masonry brick upper sections, exhibited extensive cracking, highlighting critical concerns about its structural integrity and preservation. This study investigates the seismic performance of the minaret under sequential earthquake loading, emphasizing its behavior during repeated seismic events. Nonlinear dynamic analyses, specifically time history simulations, were conducted using the Applied Element Method (AEM) in ELS software to model the structural response of the minaret under sequential seismic forces. Findings reveal that while the minaret exhibited resilience during a single earthquake, it suffered complete structural collapse when subjected to a series of identical seismic events. Key results demonstrated a notable reduction in the minaret's seismic capacity during sequential loading. The lateral displacement at the top of the minaret, measured at 167.8 mm after a single earthquake, increased significantly under sequential events, leading to instability. Furthermore, the maximum principal stress reached 10 MPa, surpassing the material's acceptable limits. After two identical earthquakes, the minaret failed to maintain structural stability and experienced total collapse. These results underscore the vulnerability of historical masonry structures to sequential earthquakes, emphasizing the need for enhanced retrofitting strategies. The study contributes valuable insights into the behavior of heritage structures under repeated seismic loading, guiding preservation efforts and structural reinforcement techniques for similar at-risk buildings.

Keywords: Sequential earthquakes; Karahan Mosque minaret; Nonlinear dynamic analysis; Applied Element Method (AEM); Structural collapse

1. Introduction

The February 6, 2023, Kahramanmaraş earthquakes (Mw 7.7 and Mw 7.6) caused catastrophic damage across southern Turkey, particularly affecting historical masonry structures, including mosques and minarets (Atmaca et al., 2024; Kocaman et al., 2024). These events underscored the vulnerability of heritage buildings to sequential seismic loading, raising critical concerns about their structural resilience and preservation. Previous studies have extensively examined the seismic behavior of historical minarets, revealing their susceptibility to dynamic forces due to their slender geometry and material degradation (Türkeli et al., 2015; Aymelek et al., 2023). However, the impact of repeated earthquakes on such structures remains insufficiently explored, despite evidence that sequential ground motions can exacerbate damage and lead to progressive collapse (Jadallah et al., 2025; Erkek & Yetkin, 2025). Recent research has focused on both the assessment and retrofitting of historical masonry minarets. Studies such as those by Kocaman & Gürbüz (2023) and Gürbüz & Kocaman (2024), and Jadallah et al. (2025) have analyzed collapse mechanisms and proposed reinforcement techniques, including Fiber Reinforced Cementitious Matrix (FRCM) and Fiber Reinforced Polymer (FRP) composites. Similarly, Cosgun et al. (2023) and Şentürk et al. (2022) have investigated post-restoration seismic performance and strengthening methods for historical mosques, emphasizing the need for advanced numerical modeling approaches. The Applied Element Method (AEM) has emerged as a reliable tool for simulating nonlinear dynamic behavior, as demonstrated by Trešnjo et al. (2023) and Onat et al. (2023), offering insights into structural responses under seismic excitation.

* Corresponding author, E-mail: adogangun@uludag.edu.tr

https://doi.org/10.31462/icearc2025_ce_eqe_298

This study examines the seismic performance of the Karahan Mosque minaret in Malatya, which suffered extensive cracking during the 2023 earthquakes. Unlike previous research focusing on single-event analyses, this work investigates the minaret's behavior under sequential earthquake loading, addressing a critical gap in the literature. Using AEM -based nonlinear time-history analysis, the study evaluates displacement patterns, stress distribution, and collapse mechanisms under repeated seismic events. The findings contribute to a deeper understanding of cumulative damage effects in historical masonry.

By integrating field observations with advanced numerical simulations, this research provides valuable insights into the progressive failure of heritage minarets under sequential earthquakes. The results emphasize the necessity of improved reinforcement techniques to mitigate seismic risks, supporting ongoing preservation efforts for vulnerable historical structures in seismically active regions.

2. Description of minaret architectural and material properties

The Karahan Mosque minaret in Malatya, shown in Fig. 1, is a representative example of traditional Ottoman-era masonry architecture, characterized by its slender cylindrical form and distinctive structural elements. The naming of the structural parts of a typical historical masonry minaret is shown in Fig. 2.

Fig. 1. The Minaret of The Karhan Mosque (RESTAŞ, 2024)

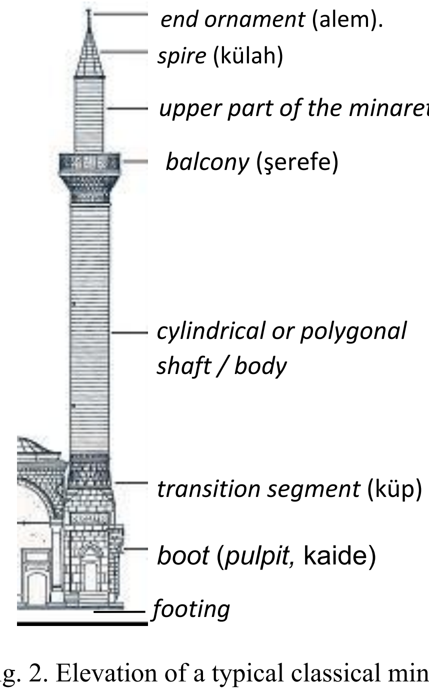

Fig. 2. Elevation of a typical classical minaret (Tuncer, 1996)

The minaret rises from a square stone base and transitions into a circular brick shaft, which terminates in a conical balcony and a pointed spire (külah) at the top. Standing at 19.25 meters in height, the structure was constructed using locally sourced stone for the base and masonry materials for the upper sections, following traditional building techniques. An internal spiral staircase extends up to the balcony level. On February 6, 2023, the mosque was severely affected by a major earthquake, with the minaret sustaining significant damage, including the formation of multiple visible cracks (Fig. 3).

Fig. 3. Horizontal cracks in the minaret

Architectural features:

- Base Section: Constructed from locally sourced cut stone, the height of the base is 3.2m
- Shaft: The main body consists of brick masonry laid in lime mortar, the shaft/body with a height of 7m and the upper shaft with a height of 2.8m.
- Balcony (*Şerefe*): A projecting balcony supported by decorative corbelling marks the transition to the upper section.
- Spire (*Külah*): The pinnacle is built with lightweight timber framing, often clad in lead for weather protection.

Material properties:

- Stone Base: Composed of andesite, exhibiting high compressive strength but limited tensile capacity.
- Brick Masonry: Clay bricks with varying dimensions, bonded with low-strength lime mortar, resulting in anisotropic behavior under seismic loads.
- Mortar: Traditional lime-based mortar, prone to degradation over time, reducing cohesion between bricks.

Material testing and historical records indicate average compressive strengths of 7 MPa for brick masonry and 15 MPa for stone, with negligible flexural resistance. The mortar's weak adhesion exacerbates vulnerability to shear and tensile stresses during earthquakes.

3. Modeling of buildings

This study employs the Applied Element Method (AEM) ASI (2004), a nonlinear analysis technique used to evaluate the seismic behavior of the minaret. AEM is particularly well-suited for analyzing historical masonry structures, as it enables the simulation of structural response from the onset of loading through to complete failure. The method effectively bridges the capabilities of both the Finite Element Method (FEM) and the Discrete Element Method (DEM). While FEM is commonly used to simulate structural behavior up to the point of element separation, DEM is applied to model post-separation behavior. AEM integrates both approaches by representing structural components as an assembly of small discrete elements interconnected by a series of normal and shear springs, as illustrated in Fig. 4. These springs simulate the transfer of stresses and strains across element interfaces. Under extreme loading conditions, these springs may fail, allowing the elements to separate and thus capturing progressive collapse mechanisms. Each element possesses six degrees of freedom—three translational and three rotational—which enables detailed modeling of structural motion, as shown in Fig. 5.

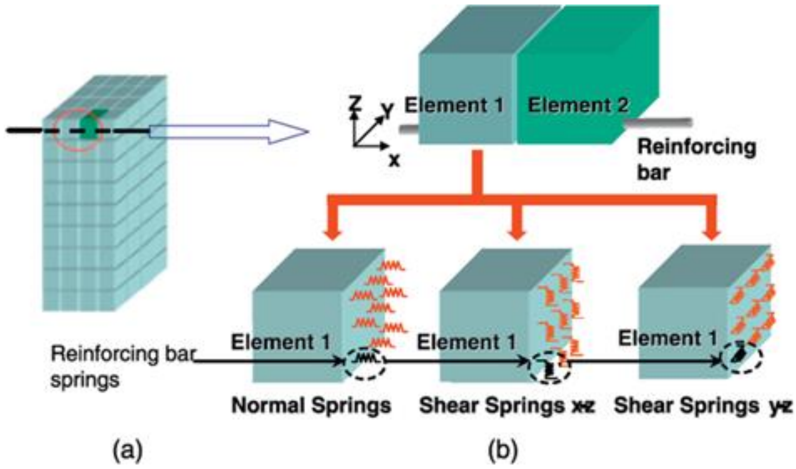

Fig.4. Element of a structure modeled by AEM (ELS website) ASI (2004)

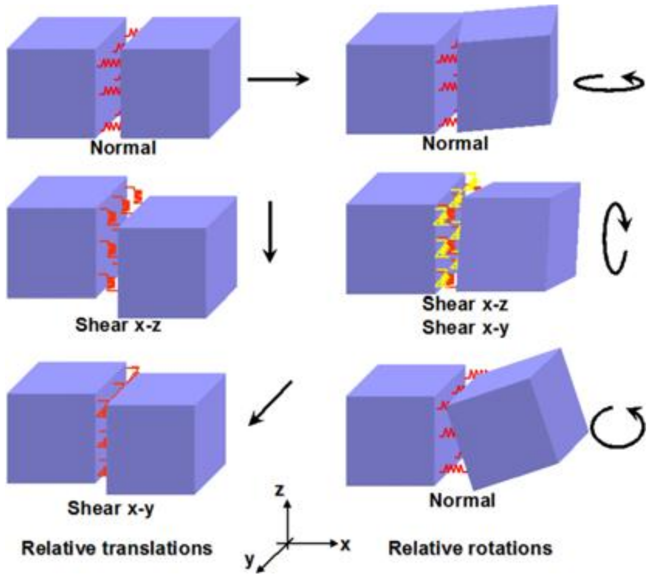

Fig. 5. Element degrees of freedom (ASI website) ASI (2004)

4. Description of the minaret model

The three-dimensional model of the Karahan Mosque's minaret was developed using ELS software Version 10, as illustrated in Fig. 6. The internal spiral stone staircase was also included in the model, extending from the base of the minaret up to the upper balcony.

5. Non-linear time history analysis

A nonlinear analysis was conducted using the earthquake records from the seismic event that occurred on February 6, 2023. The peak ground acceleration (PGA) in Gaziantep, where the Karahan Mosque is located, was recorded at 0.35g, as shown in Fig. 7.

Non-linear time history analysis is a critical method for assessing the seismic performance of structures, particularly historical masonry buildings like the Karahan Mosque minaret. This technique applies a series of ground motion records to a detailed structural model, simulating actual earthquake events to evaluate the structure's behavior under dynamic, non-linear conditions.

Two nonlinear dynamic analyses were performed on the Karahan Mosque minaret using earthquake records to assess its seismic performance. The first scenario, illustrated in Fig. 8, simulates the minaret's response to a single earthquake event. The second scenario, shown in Fig. 9, involves two identical successive earthquakes: the minaret is first subjected to an initial seismic event, and then (without repairing the damage) it experiences a second identical earthquake. This approach allows for evaluating the cumulative damage and the structure's residual capacity under sequential loading. The two considered scenarios are (1) a single-earthquake event using the record in Fig. 8 and (2) a twin-earthquake event using the record in Fig. 9. These analyses aim to examine the minaret's resilience under repeated high-intensity seismic events, which is especially relevant in regions prone to aftershocks.

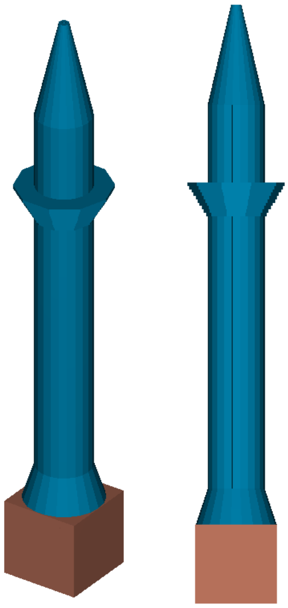

Fig 6. 3D model of minaret (ELS software)

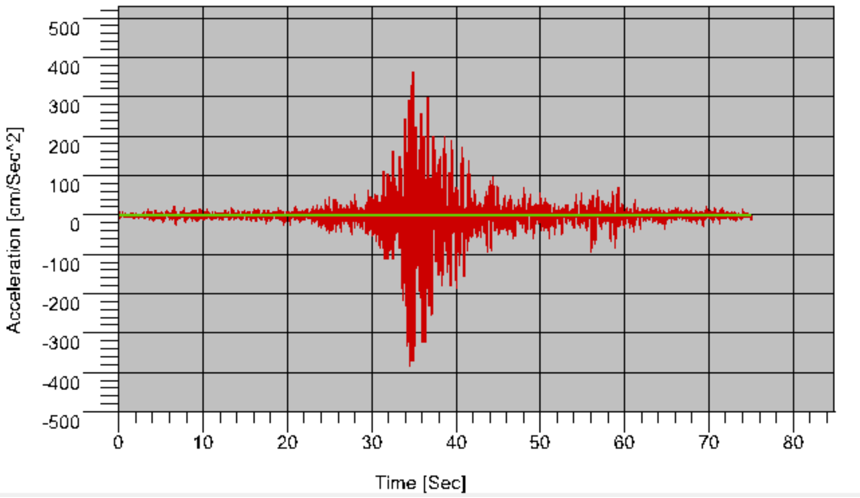

Fig.7. Accelerogram in the X direction.

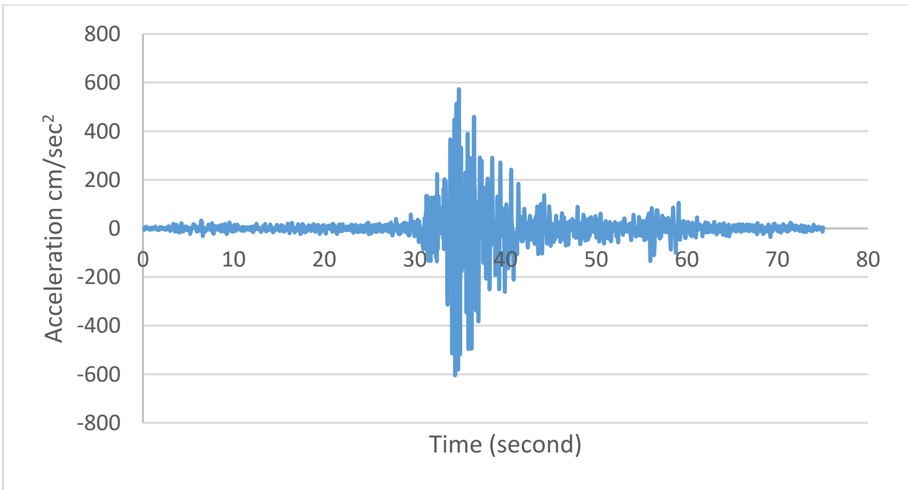

Fig. 8. Accelerogram in the X direction. (AFAD record 2023).

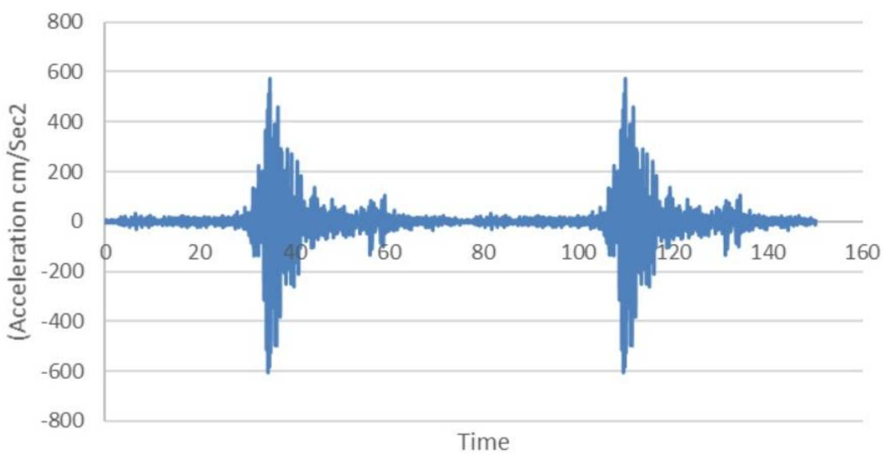

Fig. 9. Twin accelerograms in the X direction. (AFAD record 2023).

6. Results and discussion

6.1. Single seismic event

Under the single earthquake scenario, the analysis revealed that the minaret remained standing without collapsing. However, the structure exhibited a maximum lateral displacement of 167.8 mm, indicating a high susceptibility to seismic forces and a considerable risk of structural damage, as shown in Fig. 10 (a). Significant cracking developed along the shaft due to excessive lateral drift during the seismic event. The maximum compressive stress in the minaret was recorded at 10 MPa, Fig. 10 (b, c), exceeding the compressive strength of the brick masonry, which was limited to 7.0 MPa. This overstressing contributed to the formation of cracks, particularly in the shaft region, as illustrated in Fig. 11. Although the analysis identified localized element separations and masonry crushing under lateral loading, these damages were not extensive enough to compromise the overall structural stability of the minaret.

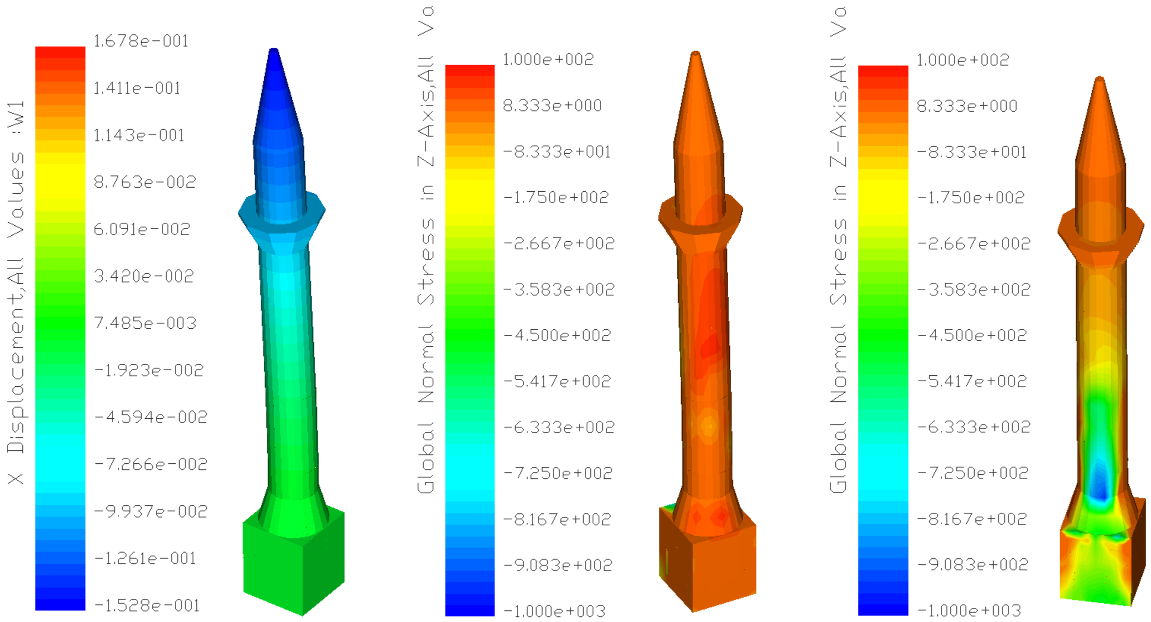

a) Displacement(m) b) Normal stresses (t/m^2) c) Normal stresses (t/m^2)

Fig. 10. a) Maximum displacement in the X direction (m). b) Maximum Normal stresses (tonf/m^2).

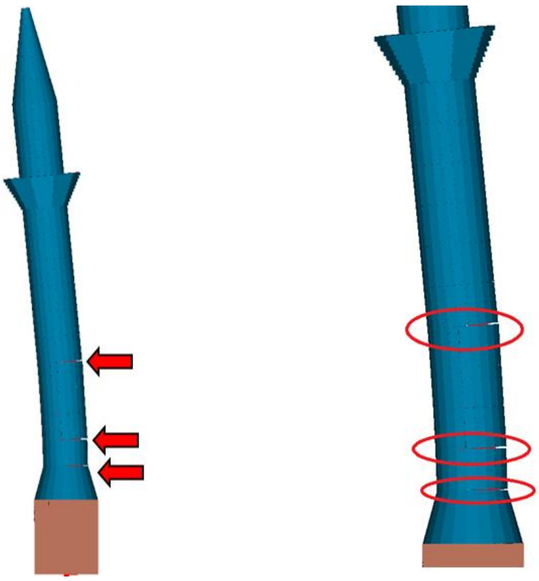

Fig.11. Cracks in the minaret obtained from the single seismic analysis of the minaret (ELS)

6.2. Repeated seismic event

As previously noted, the analysis incorporates the acceleration records shown in Fig. 9, which represent a scenario where the Karahan Mosque minaret is subjected to two identical consecutive earthquakes regardless of whether the structure sustained damage during the first event. The nonlinear analysis results indicate that, in its existing unreinforced condition, the minaret collapsed during the second seismic event. This outcome, illustrated in Fig. 12, highlights the structure's inability to endure repeated seismic loading and underscores its vulnerability to sequential earthquake scenarios.

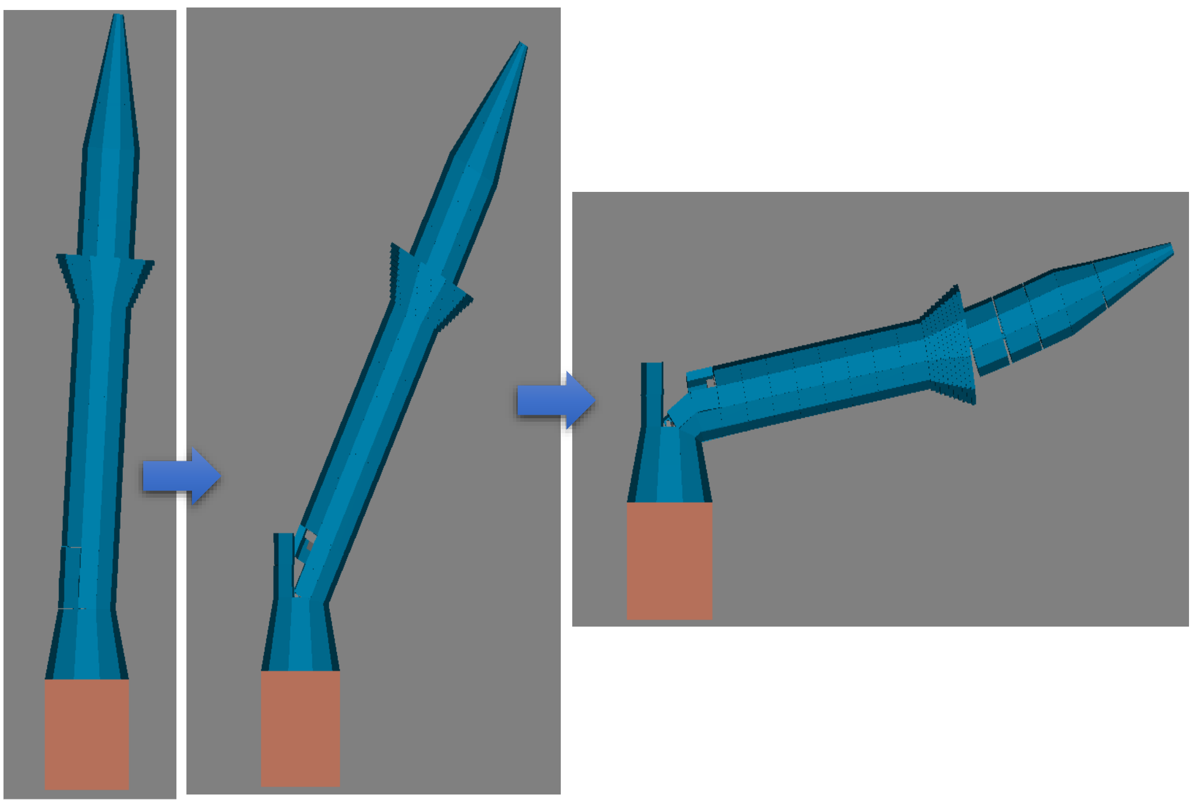

@t= 117s @t= 120s @t= 121.4

Fig.12. Collapse steps of minaret during the second earthquake

7. Conclusion

The devastating earthquake that struck Turkey on February 6, 2023, had a significant impact on the province of Gaziantep. Among the historical structures affected, the Karahan Mosque's minaret experienced noticeable damage. Although the main mosque remained standing and the minaret did not collapse during the initial seismic event, visible cracks developed in the minaret's shaft. However, nonlinear analysis shows that if the same earthquake were to strike twice in succession, mimicking a sequence of strong mainshock-aftershock events, the minaret would not be able to withstand the cumulative damage and would collapse. This highlights the urgent need for structural assessment and retrofitting of such historical structures.

- Under the effect of a single earthquake record, the minaret remained standing, but significant cracks formed in the shaft due to excessive lateral drifts of 167.8mm. The analysis showed that the compressive stresses in some areas exceeded the capacity of the brick masonry, indicating high vulnerability to seismic loading.
- When subjected to two identical consecutive earthquakes representing a more realistic seismic sequence scenario, the minaret collapsed during the second event. This was primarily due to the residual damage from the first shock, which weakened the structure and reduced its capacity to withstand further loading.
- To preserve the historical and architectural integrity of the minaret while enhancing its structural resilience, suitable retrofitting measures are needed. Strengthening solutions should increase both the shear and bending capacity, ideally using minimally invasive methods.

Acknowledgments

We gratefully acknowledge the support provided by the Bursa Uludağ University's BAP project number FDK-2025-2169 in the preparation of this article. In the preparation of this article, RESTAŞ information and files for the project were used. We express our deep appreciation to Applied Science International, LLC (ASI) for their valuable contributions.

References

Atmaca, B., Ertürk Atmaca, E., Roudane, B., Güleş, O., Demirkaya, E., Aykanat, B., ... & Akgül, T. (2024). Field observations and numerical investigations on seismic damage assessment of RC and masonry minarets during the February 6th, 2023, Kahramanmaraş (Mw 7.7 Pazarcık and Mw 7.6 Elbistan) earthquakes in Türkiye. *International Journal of Architectural Heritage*, 1–26. https://doi.org/...

Gürbüz, M., & Kocaman, İ. (2024). Enhancing seismic resilience: A proposed reinforcement technique for historical minarets. *Engineering Failure Analysis*, 156, 107832. https://doi.org/...

Türkeli, E., Livaoğlu, R., & Doğangün, A. (2015). Dynamic response of traditional land buttressed reinforced concrete minarets. *Engineering Failure Analysis*, 49, 31–48.

Aymelek, A., Yanik, Y., Demirtaş, B., Yildirim, Ö., Çalik, İ., & Türker, T. (2023, September). Full-scale structural evaluations of İskenderpaşa minaret. *Structures*, 55, 1028–1044.

Jadallah, M., Almustafa, M. K., Doğangün, A., & Nehdi, M. L. (2025). Nonlinear analysis of historical Toptaş minaret and FRP strengthening for sequence earthquake events. *Journal of Building Pathology and Rehabilitation*, 10(1), 1–19.

Erkek, H., & Yetkin, M. (2023, December). Assessment of the performance of a historic minaret during the Kahramanmaraş earthquakes (Mw 7.7 and Mw 7.6). *Structures*, 58, 105620.

Kocaman, İ., & Gürbüz, M. (2023). Collapse mechanism of narthex part of historical masonry mosques. *Engineering Failure Analysis*, 151, 107387.

Coşgun, T., Akan, A. E., Uzdil, O., Er, A., Örmecioğlu, H. T., & Sayın, B. (2023). Post-restoration seismic performance assessment of a historic hypostyle mosque in Anatolia (13th century AD). *Case Studies in Construction Materials*, 18, e01849.

Şentürk, İ., Ergün, M., & Artar, M. (2022). Seismic behavior assessment of historical Alaeddin Bey Mosque and strengthening suggestions by CFRP fabric and steel plate. *Engineering Failure Analysis*, 137, 106242.

Trešnjo, F., Humo, M., Casarin, F., & Ademović, N. (2023). Experimental investigations and seismic assessment of a historical stone minaret in Mostar. *Buildings*, 13(2), 536.

Onat, O., Toy, A. T., & Özdemir, E. (2023). Block masonry equation-based model updating of a masonry minaret and seismic performance evaluation. *Journal of Civil Structural Health Monitoring*, 13(6), 1221–1241.

RESTAŞ. (2024). *Restoration Contracting Construction Industry and Trade Inc.* Kızılırmak MH. 1443 St. 1071 Plaza B Block flat No: 25B/100, Çankaya, Ankara.

ASI. (2004). *Extreme Loading for Structures, Validation Book*. Applied Science International, LLC, Durham, NC.

Tuncer, O. C. (1996). *Diyarbakır Mosques*. Municipality of Diyarbakır, Cultural and Art Publications, Ankara. (In Turkish)

Autoencoder based damage detection in masonry structures

Tunahan Aslan[1], Kemal Hacıefendioğlu [*1], Ayşecan Bostan[1], Cemile Duman[2]

[1] Karadeniz Technical University, Department of Civil Engineering, 61080 Trabzon, Türkiye
[2] Gazi University, Department of Civil Engineering, 06570 Ankara, Türkiye

Abstract. This study aims to detect and evaluate damage in masonry structures using a contactless structural health monitoring method integrated with an Autoencoder deep learning model. Video recordings of a scaled minaret model constructed in a laboratory environment were taken at specific intervals using an industrial camera-based monitoring system. Subsequently, controlled damage was incrementally applied to the minaret model, and new video recordings were captured. Time-dependent displacement data from four different elevations of the scaled minaret model were extracted using a custom Python® script. A separate code based on an Autoencoder deep learning model was employed to calculate the damage index of the minaret model using the displacement data. Analyses conducted in the undamaged state revealed a stable damage index below 5%. However, analyses performed after the controlled damage steps showed that the damage index exceeded 5%. This study introduces a practical and rapid method for damage detection in masonry and similar engineering structures, facilitating faster diagnostic and decision-making processes in the field of structural health monitoring.

Keywords: Damage detection; Structural health monitoring; Masonry structures; Deep learning; Autoencoder

1. Introduction

Masonry structures represent a significant portion of the world's architectural heritage and are commonly found in both historical and modern constructions due to their durability, low cost, and ease of use. Despite these advantages, masonry buildings are highly vulnerable to various forms of damage, particularly under dynamic loads such as earthquakes. Given their widespread use and cultural importance, ensuring the structural integrity of masonry structures through effective damage detection and monitoring techniques is of utmost importance.

Structural health monitoring (SHM) is critical for ensuring the safety and longevity of civil infrastructure (Anjum et al., 2024; Avci et al., 2022). Machine learning (ML) techniques have emerged as powerful tools for detecting structural damage, with autoencoder-based methods gaining prominence due to their ability to handle unsupervised learning and dimensionality reduction. This response compares autoencoder-based methods with other ML techniques, highlighting their strengths, weaknesses, and applications in civil engineering (Gil Bravo et al., 2024; Mghazli et al., 2024).

Autoencoders, particularly variational autoencoders (VAEs), have shown promise in SHM by learning latent representations of structural data. These models are effective in unsupervised anomaly detection, requiring only normal (undamaged) data for training. For instance, VAEs combined with Hotelling's T2 statistical tool have demonstrated superior performance in identifying and quantifying structural changes in civil structures (Spínola Neto et al., 2024). Similarly, convolutional autoencoders have been successfully applied to detect damage locations in mechanical systems by analyzing changes in stiffness (Bono et al., 2023).

The integration of autoencoders with other techniques, such as mechanics-informed models, has further enhanced their capabilities. For example, a mechanics-informed autoencoder can detect and localize unforeseen damage with minimal training data, achieving up to 35% better performance than standard autoencoders (Li et al., 2024). Additionally, multi-objective VAEs have been used to fuse multi-sensor data for damage detection and localization, outperforming state-of-the-art methods (Anaissi et al., 2023).

Traditional ML techniques, such as K-nearest neighbors (KNN), Gaussian mixture models (GMMs), and one-class support vector machines (OCSVMs), have been widely used for structural damage detection. These methods rely on feature engineering and supervised or semi-supervised learning paradigms. While they are effective in specific scenarios, they often struggle with high-dimensional data and require labeled datasets, which can be challenging to obtain in real-world applications (Che & Tian, 2024; Wang & Cha, 2025).
In contrast, autoencoder-based methods excel in unsupervised settings and can automatically learn features from raw data, reducing the need for manual feature engineering. For example, a comparative study on a laboratory-

[*] Corresponding author, E-mail: kemalhaciefendioglu@ktu.edu.tr

https://doi.org/10.31462/icearc2025_ce_eqe_315

scale steel bridge demonstrated that autoencoders outperformed KNN and GMMs in detecting loosened bolts, highlighting their robustness in unsupervised damage detection (Wang & Cha, 2025).

Deep learning techniques, such as convolutional neural networks (CNNs) and recurrent neural networks (RNNs), have also been applied to SHM. These methods are particularly effective in processing time-series data and capturing temporal patterns. For instance, a deep residual network (DRN) optimized with Bayesian methods has shown superior performance in detecting, localizing, and quantifying structural damage compared to traditional ML methods (Alazzawi & Wang, 2022; Atia et al., 2024; Fernandez-Navamuel et al., 2024).

Moreover, hybrid models combining autoencoders with other deep learning architectures, such as long short-term memory (LSTM) networks, have been developed to enhance damage diagnosis. A multi-head self-attention LSTM autoencoder has demonstrated superior performance in detecting minor damage and localizing multiple damage locations on a full-scale bridge (Ghazimoghadam & Hosseinzadeh, 2024).

component of ML-based damage detection. Traditional methods often rely on handcrafted features, such as modal parameters and frequency-domain metrics, which can be time-consuming and require domain expertise. Autoencoders, on the other hand, can automatically learn damage-sensitive features from raw data, such as acceleration responses and vibration signals (Bono et al., 2023; Spínola Neto et al., 2024).

The effectiveness of autoencoders in feature extraction is further enhanced by their ability to handle multi-sensor data. For example, a multi-objective VAE has been used to fuse data from multiple sensors, capturing correlations and improving damage detection accuracy (Anaissi et al., 2023). Similarly, a deep convolutional variational autoencoder (DCVAE) has been shown to effectively extract features from multisensor data, outperforming traditional methods like principal component analysis (PCA) (Wan et al., 2025).

Autoencoder-based methods are computationally efficient and can be deployed in real-time SHM systems. For instance, a mechanics-informed autoencoder can learn from just 3 hours of data and autonomously detect and localize damage, reducing the need for human intervention (Li et al., 2024). Additionally, autoencoders can be trained on non-standardized time-series data, making them suitable for unsupervised damage localization without requiring extensive preprocessing (Römgens et al., 2023, 2024).

However, the performance of autoencoders can be influenced by the quality and quantity of training data. While they excel in unsupervised settings, their accuracy may degrade in the presence of noisy or incomplete data. Addressing these challenges requires careful data preprocessing and the integration of domain knowledge into the model architecture (Li et al., 2024; Wan et al., 2025).

This study presents a novel application of an Autoencoder-based deep learning approach integrated with a non-contact monitoring system to detect and evaluate damage in masonry structures. A scaled minaret model was constructed and subjected to a series of controlled damage scenarios in a laboratory setting. Displacement data were extracted from video recordings using a custom Python® script, and the damage index was calculated based on the Autoencoder's performance. The findings demonstrate that the proposed method can effectively distinguish between undamaged and damaged states, offering a practical and efficient alternative for structural diagnostics in masonry and similar engineering structures. Autoencoder-based methods have emerged as powerful tools in structural damage detection due to their advantages in unsupervised learning, automatic feature extraction, and ability to handle high-dimensional, multi-sensor data. Building upon these strengths, this study contributes to the advancement of SHM technologies by demonstrating a robust, data-driven approach that can be applied in real-world scenarios, while also highlighting the potential of hybrid models and domain-informed architectures for future research.

2. Materials and methods

Within the scope of this study, a scaled model of a historical masonry minaret was constructed at the Structural Health Monitoring Laboratory of Karadeniz Technical University. This model consists of four main sections: the podium, transition zone, body, and upper body, all designed to align with the architectural elements of minarets. These structural sections were meticulously designed to analyze the real behavior of the minaret through the scaled model. The model, with a total height of 3.85 meters, is supported from the inside by wooden staircase steps. Fig. 1 shows images of the miniature minaret model. After the completion of the model, a curing period of one month was expected. During this period, measurements were taken at regular intervals to observe the behavior of the structure. The aim is to obtain the horizontal and vertical displacements of the structure without subjecting it to any dynamic load through the measurements taken. Using these displacement values, damage detection can be performed through an Autoencoder-based method.

Fig. 1. Construction phase of the miniature minaret model

These measurements were carried out using a system built with high-speed industrial cameras. The most critical aspect of the video camera-based monitoring system is the hardware system created to record video footage. With this system, video recordings can be taken both in the laboratory environment and outdoors. The system consists of four industrial cameras, a camera lens for each of these cameras, a recording device to capture the images, a computer for connecting the CoaExpress recording device and CoreView software, and cables. The technical specifications of each component of the hardware system are provided in Table 1.

The Victorem™ CoaXPress series is a wide range of compact industrial video cameras featuring high-performance Sony CMOS image sensors and high-bandwidth CoaXPress video output. There are various models with different sensors available, allowing the selection of the appropriate Victorem camera for each application. These powerful cameras, with resolutions ranging from 0.4 MP to 26.2 MP and frame rates up to several hundred frames per second, are ideal for performance-oriented applications such as volumetric video capture, machine vision, and automatic optical inspection. When sensors generate hundreds or even thousands of megabytes of video data per second, systems using Victorem™ CoaXPress cameras need ways to access this data stream. The CoaXPress video interface is a perfect match for the bandwidth of these sensors and can support the full resolution and bit depth rate of each sensor without limitations. Other interfaces, such as GigE Vision or USB3 Vision, offer lower bandwidth than CoaXPress, requiring either fewer frames per second or lower bit depth. The CoaXPress protocol is standardized and widely adopted, allowing the use of low-cost, flexible coaxial cables over long distances of more than 100 meters. The CMOS sensors used in Victorem™ CoaXPress cameras offer state-of-the-art features, such as high resolution, low noise, excellent dynamic range, and color accuracy (URL-1, 2024). The cameras are equipped with adjustable exposure settings and image correction tables for gamma or contrast enhancement. They can be used either manually or automatically. Some lenses feature an in-camera correction algorithm to correct for vignetting effects and can be adjusted for flat-field homogeneity. For fast-moving objects, adjustable window settings allow the sensor's smaller areas to output at higher frame rates. The schematic of the created hardware system is provided in Fig. 2.

Table 1. Hardware components technical specifications

Components	Model	Technical Specifications
Video Camera-1	IO Industries CoaxPress VICTOREM 16B276MCX	Maximum Resolution: 1456×1088 Number of Frames: 276 FPS Pixel size: 3,45×3,45 µm²
Video Camera-2	IO Industries CoaxPress VICTOREM 32B216MCX	Maximum Resolution: 2064 x 1544 Number of Frames: 216 FPS Pixel size: 3,45×3,45 µm²
Video Recorder	IO Industries DVR Express Core 2 CoaXPress	Video Format: 8/10/12/14/16-bit Monochrome 24-bit RGB
Computer	HP Victus 16d1006nt	12th Gen Intel(R) Core (TM) i5-12500H 2.50 GHz

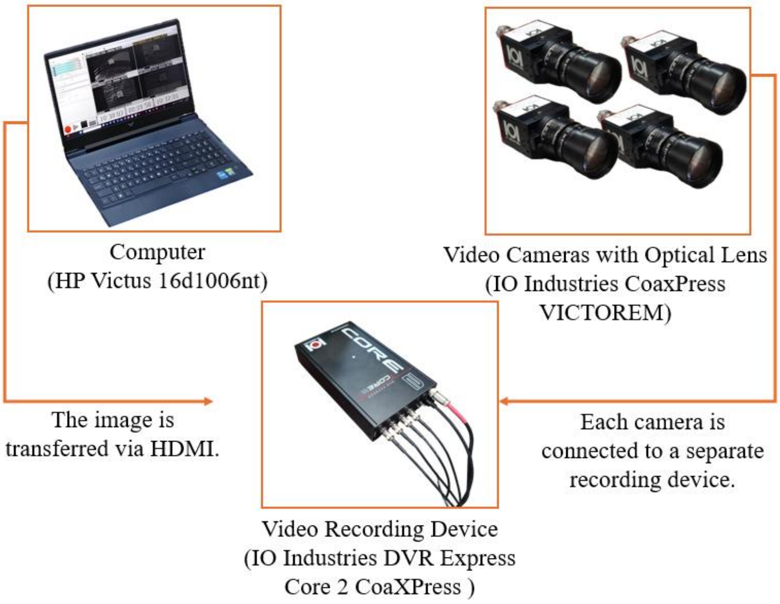

Fig. 2. Monitoring System Hardware Schematic

2.1. Obtaining displacements

A system utilizing template-matching-based displacement sensors has been developed for video camera-based monitoring of objects. Tested on a miniature minaret model in the laboratory environment using templates such as QR codes, the system operates on selected regions of interest (ROIs) on the minaret surface during field measurements. By determining the positions in the initial and final frames, object tracking is performed, and with the use of high-speed industrial cameras, better results are aimed to be achieved compared to conventional methods. The main objective of the study is to evaluate the performance of this system in capturing structural vibrations. Displacement values were obtained from pixel coordinates by applying a scaling factor (Hacıefendioğlu et al., 2024).

The optical flow method differentiates itself from other techniques in computer vision by focusing on object motion tracking. This method is more effective than traditional methods for detecting displacements in video images, as it tracks object movements through image sequences and calculates displacements. Although various methods have been developed to calculate optical flow, the Lucas-Kanade method, which is important for structural health monitoring in this study, has been employed (Lucas & Kanade, 1981). Developed by Bruce D. Lucas and Takeo Kanade, this method assumes that pixel intensity does not change significantly between consecutive frames and predicts pixel displacements by solving a linear system of equations for each point.

The Lucas-Kanade optical flow algorithm may exhibit performance degradation in the presence of large displacements and varying brightness conditions. To overcome these limitations, the Pyramidal Lucas-Kanade Optical Flow technique has been developed.

The Lucas-Kanade method calculates velocity by using the spatial and temporal derivatives of image intensity, and this process is expressed by Equation (1):

$$I(x,t) = I(x+\delta x, t+\delta t) \quad (1)$$

This equation explains the basic assumption of the optical flow method, known as the brightness conservation principle. The intensity of a pixel at position x and time t remains constant after a small time interval δt and a small displacement δx .

This assumption can be expressed in Equation (2) as follows:

$$\nabla I_t(x,t)u + I_t(x,t) = 0 \quad (2)$$

Here, $\nabla I(x,t)$ represents the spatial derivatives across the image, and $I_t(x,t)$ represents the temporal derivatives. u denotes the two-dimensional optical flow vector.

To determine the displacement vector, the least squares approach is applied, and this approach is expressed in Equation (3):

$$E(u) = \sum \left[\nabla I(x,t)u + I_t(x,t) \right]^2 \quad (3)$$

The minaret model has been placed on the shaking table and fixed to the table using anchors. Subsequently, the monitoring system has been positioned perpendicular to the templates. Fig. 3 shows the positioning of the minaret on the shaking table and the monitoring system.

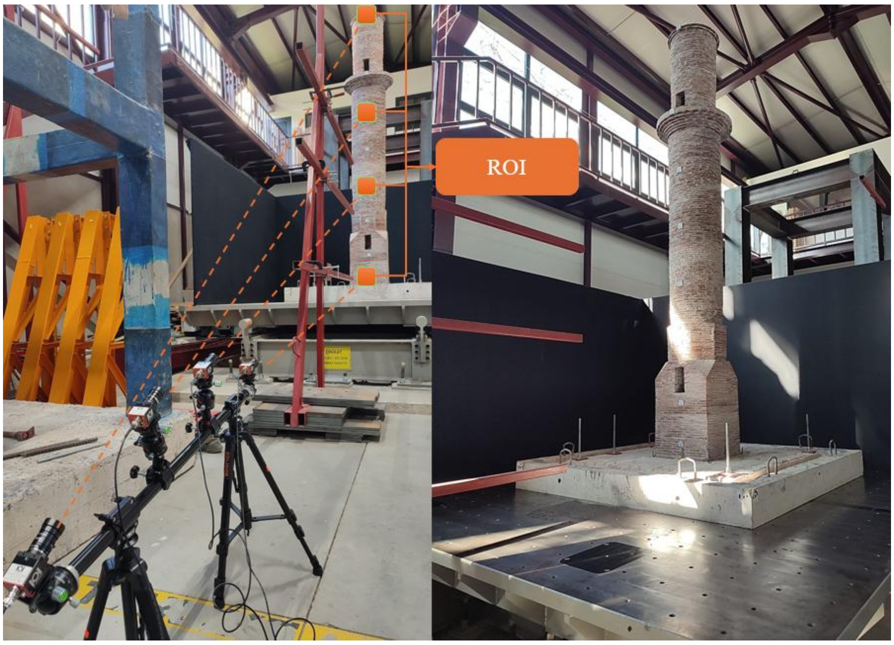

Fig. 3. Monitoring system positioning and shaking table

The miniature minaret model, along with the reinforced concrete block on which it was built, has been fixed to the shaking table with a total of six 50 cm long anchors. As shown in Fig. 3, the front camera is focused on the template located at the bottom of the minaret model, while the rear camera is focused on the template at the top. Four cameras have been mounted on a steel pipe with a 30 cm interval, and the system has been completed with two tripods. This arrangement has completely restricted the movement of the cameras, preventing deviations in the results. A three-stage test was performed on the unidirectional shaking table. The dynamic load was gradually increased, applying a sinusoidal wave to the minaret with the following parameters: 1 Hz frequency, 10 mm amplitude, and 5 cycles; 1 Hz frequency, 20 mm amplitude, and 5 cycles; and 1 Hz frequency, 30 mm amplitude, and 5 cycles. During the final loading, a fracture was observed on the body 30 cm above the transition zone, which was recorded via video. After the tests, an inspection revealed a crack in this region.
The horizontal displacement graphs obtained are shown in Fig. 4. Each graph represents the displacements at the level of the templates tracked by the cameras. These displacements, which are too small to be visible to the naked eye, show a decrease in values when moving from the top to the bottom. These graphs were obtained as a result of analyses performed before and after the shaking table tests. In this way, the data can be compared in the autoencoder-based damage detection system to determine the percentage of damage.

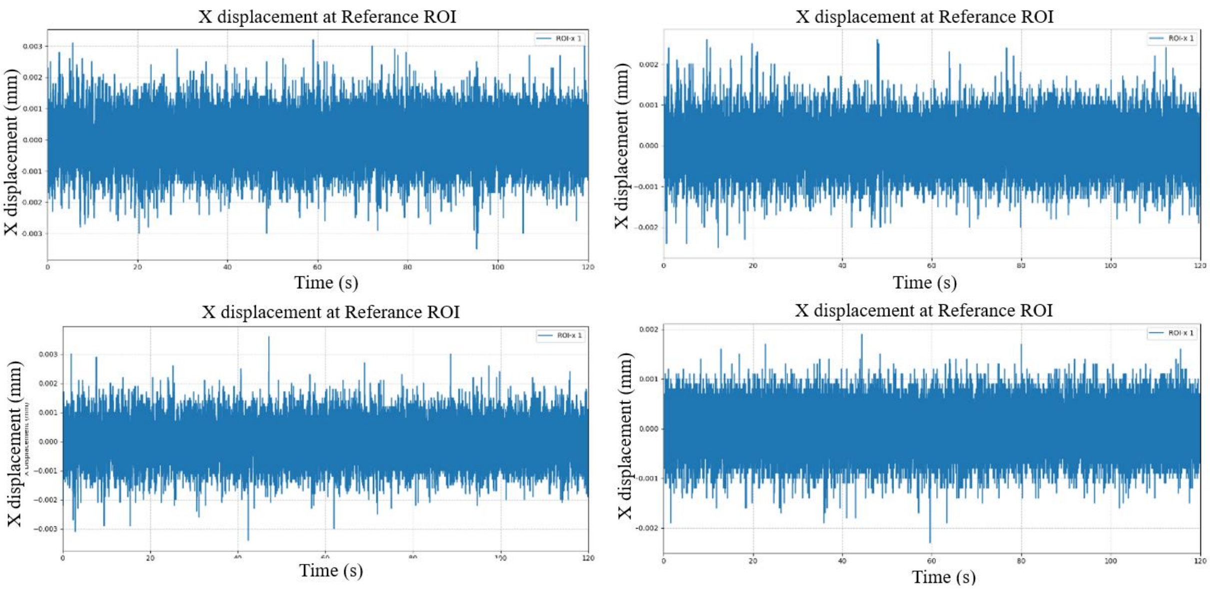

Fig. 4. Horizontal displacements of the miniature minaret model

This study presents a machine learning-based analysis method for structural damage detection using sensor data. The process of separately processing and comparing healthy and damaged data for each sensor enabled the determination of the damage percentage for each sensor. The model predicts reconstructions of the healthy and damaged data, and the reconstruction errors are calculated. The damage percentage is then determined by comparing the errors of the damaged data with a threshold derived from the healthy data. The results are visualized using bar charts, where the sensors with a damage percentage exceeding the threshold are marked. This approach allows for an effective detection of damaged sensors, and the average damage percentage across all sensors is calculated, providing an overall assessment of the structural health. The graphs presented in Fig. 5 were calculated separately for the 30 healthy days. Measurements taken during healthy days revealed that the damage index remained below 5%. After the damage was introduced, the same analyses were performed, and it was observed that the damage percentage exceeded 5%. The damage index graph obtained for both healthy and damaged states is shown in Fig. 6.

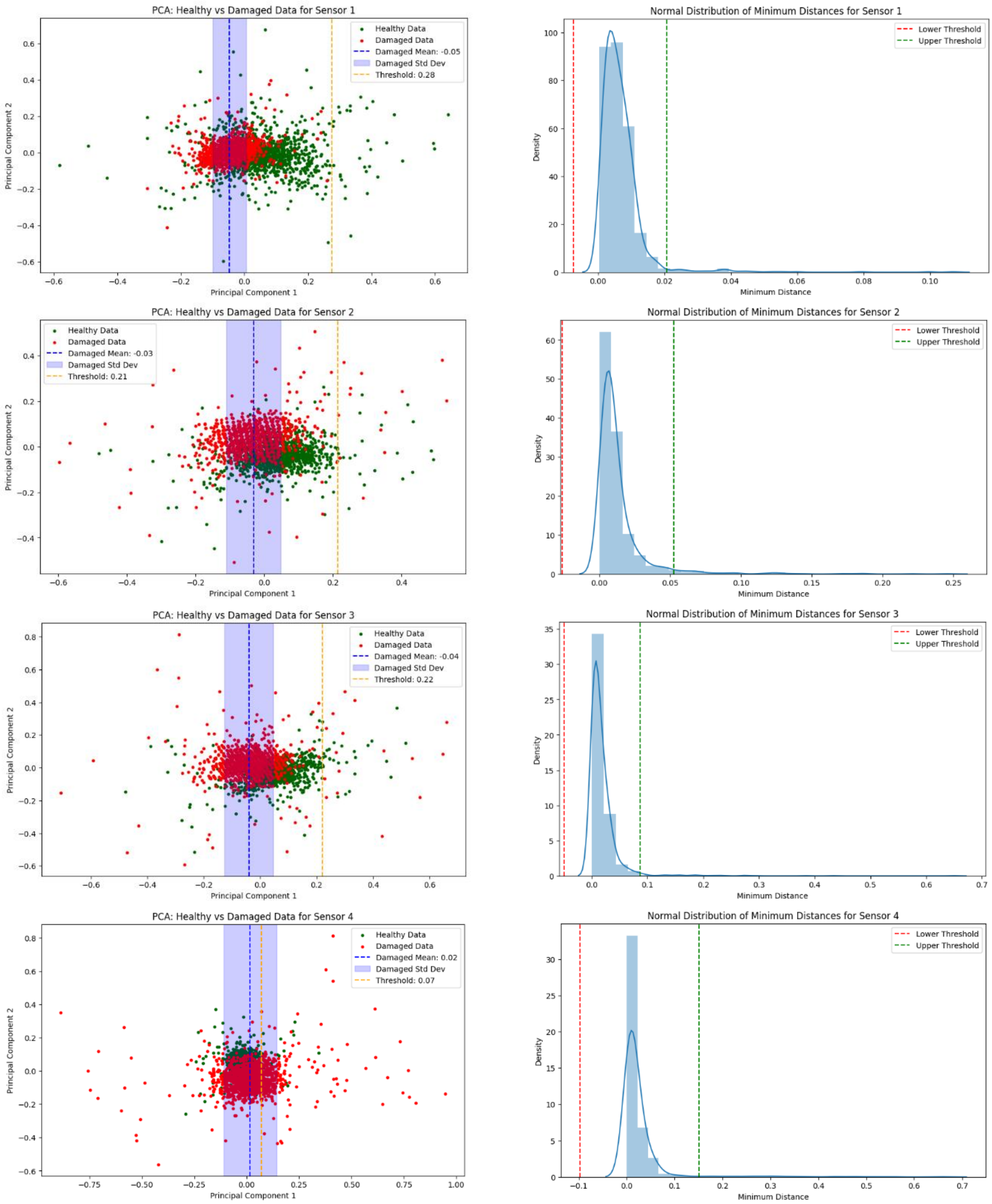

Fig. 5. Calculation of damage index values using the autoencoder model

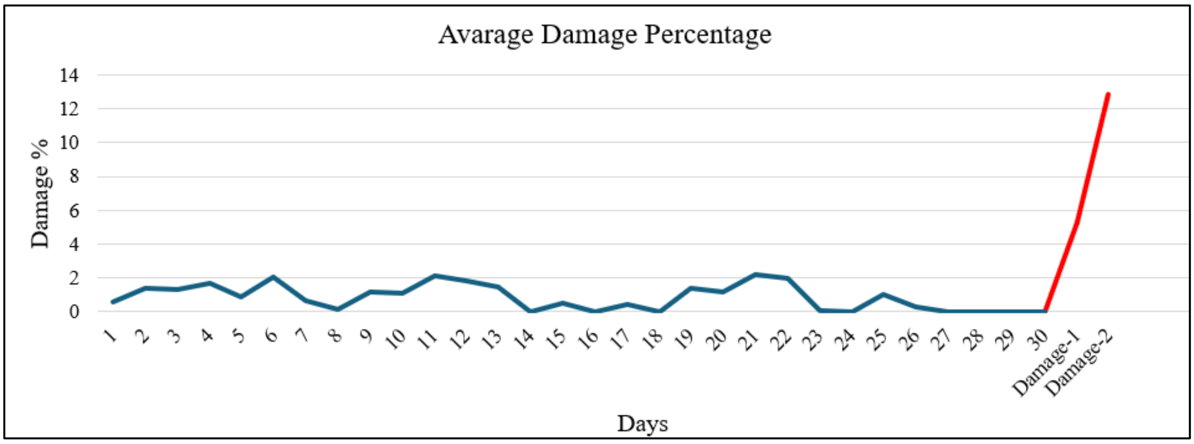

Fig. 6. Average damage percantage

The methodology includes the calculation of reconstruction errors for each sensor and the use of a Z-score-based adaptive threshold for damage detection. This innovative approach enhances the sensitivity of the damage detection process by employing statistical measures to account for variability in the reconstruction errors. A threshold is set based on the standard deviation of healthy reconstruction errors, and the damage percentage is computed by evaluating the reconstructed data of the damaged set against this threshold. The results are presented visually using aesthetically enhanced bar graphs, which also highlight the sensors likely to be damaged. This method, with its detailed and robust analysis, offers a reliable approach for assessing structural health using sensor data and machine learning techniques.

3. Conclusions

This study presents a novel and effective approach to structural health monitoring (SHM) for masonry structures using a non-contact method integrated with an Autoencoder-based deep learning model. The proposed methodology, applied to a scaled minaret model in a controlled laboratory setting, demonstrates the potential of combining advanced machine learning techniques with optical flow-based displacement measurement for the detection and evaluation of damage in masonry structures.

- The results highlight that the Autoencoder-based approach can successfully differentiate between undamaged and damaged states of the structure by calculating a damage index derived from displacement data. The key advantage of this approach lies in its ability to work in an unsupervised manner, relying solely on healthy state data for training, thus eliminating the need for labeled data. This is particularly significant as it reduces the complexity and time-consuming nature of traditional damage detection methods, which often require extensive data labeling and feature engineering
- The laboratory-scale experiments, which involved incremental damage applied to the minaret model, provide compelling evidence that the proposed method can detect even subtle damage changes. In the healthy state, the damage index remained below 5%, but after controlled damage was introduced, the index consistently exceeded 5%, clearly indicating the presence of structural degradation. This threshold-based detection method, enhanced with Z-score adaptive thresholds, allows for a more sensitive and precise assessment of the structural condition, making it a reliable tool for real-time SHM applications.
- One of the critical aspects of this study is the integration of video camera-based monitoring systems and optical flow methods to obtain precise displacement data, which is crucial for accurate damage assessment. The use of industrial-grade cameras and advanced image processing algorithms ensures that the displacement measurements are both accurate and reliable, even under dynamic loading conditions. Moreover, the ability to track displacements at multiple elevations and across different sections of the minaret model further strengthens the robustness of the proposed methodology.
- The application of Autoencoder models, particularly in damage detection tasks, provides several benefits over traditional machine learning methods. By automatically extracting features from raw data and reducing the dimensionality of the input data, Autoencoders are able to identify patterns and anomalies that might not be apparent using conventional methods. Additionally, the ability of these models to handle multi-sensor data and high-dimensional inputs allows for comprehensive damage detection across large-scale structures, such as full-sized masonry buildings or bridges.
- While the current study focused on a scaled model of a masonry minaret, the methodology is highly transferable to other masonry or similar engineering structures, such as historic buildings and infrastructure. The ability to monitor these structures with minimal human intervention, using automated damage detection systems, offers significant advantages in terms of efficiency and cost-effectiveness. Furthermore, this study

contributes to the broader field of SHM by demonstrating how machine learning techniques, particularly Autoencoders, can be seamlessly integrated with modern sensor systems for real-time structural diagnostics.

- Looking forward, future research can explore the enhancement of the current model by incorporating hybrid techniques, such as the combination of Autoencoders with other deep learning architectures, like convolutional neural networks (CNNs) or recurrent neural networks (RNNs). Additionally, expanding the dataset to include a wider variety of damage scenarios, as well as implementing the method on full-scale structures, could further validate and refine the model's performance in real-world applications.

In conclusion, this study not only presents a robust and efficient method for damage detection in masonry structures but also sets the stage for further advancements in SHM through the integration of machine learning techniques. The promising results of this approach suggest that Autoencoder-based models can play a crucial role in the future of structural health monitoring, enabling faster, more accurate, and less resource-intensive damage detection in civil engineering applications.

Acknowledgments

This study is a product of the research project supported within the scope of the TUBITAK 1001 - Scientific and Technological Research Projects Support Program, titled 'Development of Video Camera-Based Structural Health Monitoring for Historical Masonry Minarets and Long-Term Decision-Making Model Based on Deep Learning (Project No: 222M140).

We would like to thank the General and Regional Directorate of Foundations for their support.

References

Alazzawi, O., & Wang, D. (2022). A novel structural damage identification method based on the acceleration responses under ambient vibration and an optimized deep residual algorithm. *Structural Health Monitoring*, *21*(6), 2587–2617. Retrieved from https://doi.org/10.1177/14759217211065009

Anaissi, A., Zandavi, S. M., Suleiman, B., Naji, M., & Braytee, A. (2023). Multi-objective variational autoencoder: an application for smart infrastructure maintenance. *Applied Intelligence*, *53*(10), 12047–12062. Retrieved from https://doi.org/10.1007/s10489-022-04163-2

Anjum, A., Hrairi, M., Aabid, A., Yatim, N., & Ali, M. (2024). Civil structural health monitoring and machine learning: a comprehensive review. *Fracture and Structural Integrity*, *18*(69), 43–59. Retrieved from https://doi.org/10.3221/IGF-ESIS.69.04

Atia, A. E. S. M., Vafaei, M., Tee, K. F., & Aliah, S. C. (2024). A systematic review of structural health monitoring using artificial neural networks: From traditional neural networks to deep learning algorithms. *Preprint.* Retrieved from https://doi.org/10.21203/RS.3.RS-5697583/V1

Avci, O., Abdeljaber, O., & Kiranyaz, S. (2022). Structural damage detection in civil engineering with machine learning: Current state of the art. *Conference Proceedings of the Society for Experimental Mechanics Series, 223–229*. Retrieved from https://doi.org/10.1007/978-3-030-75988-9_17

Bono, F. M., Radicioni, L., Bombaci, G., Somaschini, C., & Cinquemani, S. (2023). An approach based on convolutional autoencoder for detecting damage location in a mechanical system, *Proceedings of SPIE, NDE 4.0, Predictive Maintenance, Communication, and Energy Systems: The Digital Transformation of NDE 12489*, 93–100. Retrieved from https://doi.org/10.1117/12.2657974

Che, C., & Tian, J. (2024). Methods comparison for neural network-based structural damage recognition and classification. *Advances in Operation Research and Production Management*, 3*(1),* 20–26. Retrieved from https://doi.org/10.54254/3029-0880/3/2024022

Fernandez-Navamuel, A., Pardo, D., Magalhães, F., Zamora-Sánchez, D., Omella, Á. J., & Garcia-Sanchez, D. (2024). Deep neural network for damage detection in Infante Dom Henrique bridge using multi-sensor data. *Structural Health Monitoring 24(1),* 372-401. Retrieved from https://doi.org/10.1177/14759217241227455

Ghazimoghadam, S., & Hosseinzadeh, S. A. A. (2024). A novel unsupervised deep learning approach for vibration-based damage diagnosis using a multi-head self-attention LSTM autoencoder. *Measurement*, *229*, 114410. Retrieved from https://doi.org/10.1016/J.MEASUREMENT.2024.114410

Gil Bravo, A., Cardarilli, G. C., Alemu, Y. L., Lahmer, T., & Walther, C. (2024). Damage detection with data-driven machine learning models on an experimental structure. *Eng 2024, 5(2),* 629–656. Retrieved from https://doi.org/10.3390/ENG5020036

Hacıefendioğlu, K., Kahya, V., Limongelli, M. G., Okur, F. Y., Altunışık, A. C., Aslan, T., Pembeoğlu, S., Duman, C., Bostan, A., & Aleit, H. (2024). Applications of optical flow methods and computer vision in structural health monitoring for enhanced modal identification. *Structures*, *69*, 107414. Retrieved from https://doi.org/10.1016/J.ISTRUC.2024.107414

Li, X., Bolandi, H., Masmoudi, M., Salem, T., Jha, A., Lajnef, N., & Boddeti, V. N. (2024). Mechanics-informed autoencoder enables automated detection and localization of unforeseen structural damage. *Nature Communications 2024 15:1*, *15*(1), 1–13. Retrieved from https://doi.org/10.1038/s41467-024-52501-4

Lucas, B. D., & Kanade, T. (1981). An Iterative Image Registration Technique with an Application to Stereo Vision (IJCAI). *Proceedings of the 7th Joint Conference on Artificial Intelligence*, 674–679.
Mghazli, M. O., Zoubir, Z., Rallu, A., Lamdouar, N., & Elmankibi, M. (2024). Experimental machine learning approach for building structural health monitoring application. *Journal of Physics: Conference Series*, *2647*(18), 182031. Retrieved from https://doi.org/10.1088/1742-6596/2647/18/182031
Römgens, N., Abbassi, A., Jonscher, C., Grießmann, T., & Rolfes, R. (2023). Unsupervised Damage Localization Using Autoencoders with Time-Series Data. *Lecture Notes in Civil Engineering*, *433 LNCE*, 511–519. Retrieved from https://doi.org/10.1007/978-3-031-39117-0_52
Römgens, N., Abbassi, A., Jonscher, C., Grießmann, T., & Rolfes, R. (2024). On using autoencoders with non-standardized time series data for damage localization. *Engineering Structures*, *303*, 117570. Retrieved from https://doi.org/10.1016/J.ENGSTRUCT.2024.117570
Spínola Neto, M., Finotti, R., Barbosa, F., & Cury, A. (2024). Structural damage identification using autoencoders: a comparative study. *Buildings 2024, 14*(7), 2014. Retrieved from https://doi.org/10.3390/BUILDINGS14072014
URL-1. (2024, April 25). *Victorem Camera Specification*. Retrieved from https://www.ioindustries.com/victorem-features
Wan, H. P., Zhu, Y. K., Luo, Y., & Todd, M. D. (2025). Unsupervised deep learning approach for structural anomaly detection using probabilistic features. *Structural Health Monitoring*. Retrieved from https://doi.org/10.1177/14759217241226804
Wang, Z., & Cha, Y.-J. (2025). Unsupervised machine and deep learning methods for structural damage detection: A comparative study. *Engineering Reports*, *7*(1), e12551. Retrieved from https://doi.org/10.1002/ENG2.12551

Prediction of newmark displacement via gene expression programming

Arman Atasoy*[1], Adil Yiğit[1], Fatih Çıbuk[1], İbrahim Yüksel[1]

[1] Istanbul Rumeli University, Department of Civil Engineering, Istanbul, Türkiye

Abstract. One of the most important effects of an earthquake is the permanent ground deformation (PGD) that it can cause in the ground, especially on slopes. Estimation of permanent ground displacements is important for both superstructures and infrastructures, and various methods have been developed to calculate this amount of ground movement. Newmark Sliding Block Model is one of these methods. There are many regression equations derived based on this method in the literature. Within the scope of this study, a new equation has been produced by processing strong ground motion records of 28 earthquakes of world-wide importance. The correlation generation process has been carried out with the Gene Expression Programming (GEP), one of the machine learning algorithms that has been widely used in recent years. Newmark Ground Displacement (δ) has been obtained by using the input parameters Arias Intensity (Ia), maximum acceleration (amax) and critical acceleration (a_c) in deriving the equation. The obtained equation results have been compared statistically with the results of the equations suggested by different researchers in the literature. As a result of the evaluation, it has been determined that the correlation obtained using GEP in this study gave the most appropriate output.

Keywords: Newmark sliding block model; Gene expression programming; Ground displacement; Arias intensity; Earthquake

1. Introduction

Newmark (1965) has been devoloped a unique method to predict of any slope during an earthquake. Depending on Newmark suggestion, earthquake induced movement of any slope can be calculated from this record of the earthquake and critical acceleration of the slope. In that approximation, ground is accepted as a sliding block that moves due to the earthquake acceleration values above the critical acceleration value of the slope (Fig.1).

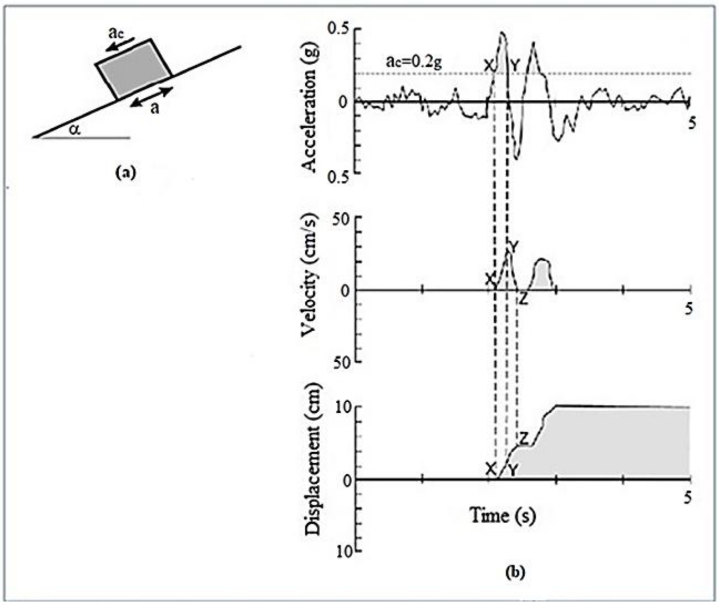

Fig. 1. Newmark approximation (Yigit, 2021)

* Corresponding author, E-mail: arman.atasoy@rumeli.edu.tr

https://doi.org/10.31462/icearc2025_ce_eqe_334

With the developing technology, machine learning programs come to the fore in deriving correlations. Today, algorithms such as Artificial Neural Networks (ANN), Backpropagation Neural Network (BPNN), Genetic Algorithm (GA), Gradient Boosting Trees (GTB), Random Forests (RF), Support Vector Machines (SVM), Decision Trees (DT), Radial Basis Function Neural Networks (RBFNN), Gaussian Process Regression (GPR) and Multiple Linear Regression (MLR) are among the promising methods in artificial intelligence-based analysis. The main purpose of these algorithms is to learn the relationships between the input and output parameters in the data set and to model these relationships. The mentioned methods learn by analyzing the patterns in the data set; then, using these learned patterns, they predict the outputs corresponding to new data. Basically, a machine learning algorithm tries to predict the correct output or response to a new observation with the information it obtains from past data which are obtained by Hou, C., & Zhou, X. G. (2022). In this study, a new relationship was derived using the Gene Expression Programming (GEP) technique and compared with the existing relationships in the literature with the help of statistical parameters.

2. Summary of experimental data

In this study, a new equation was produced by processing the strong ground motion records of 28 earthquakes of worldwide importance.

Table 1. Strong ground motion recodrs used in this study

No	Year	Earthquakes	M_w	No	Year	Earthquakes	M_w
1	1952	Kern County-USA	7,4	15	1992	Cape Mendocino-USA	7,0
2	1971	San Fernando-USA	6,6	16	1992	Landers-USA	7,3
3	1976	Friuli-Italy	6,5	17	1994	Northridge-USA	6,7
4	1978	Tabas-Iran	7,4	18	1995	Afyon-Turkey	6,4
5	1979	Imperial Valley-USA	6,5	19	1995	Kobe-Japan	6,9
6	1980	Mammoth Lakes-USA	6,1	20	1999	Duzce-Turkey	7,1
7	1983	Erzurum-Turkey	6,6	21	1999	Kocaeli-Turkey	7,6
8	1983	Coalinga-USA	6,4	22	1999	Chi-Chi-Taiwan	7,6
9	1984	Morgan Hill-USA	6,1	23	2002	Afyon-Turkey	6,5
10	1985	Nahanni-Canada	6,8	24	2003	Bingol-Turkey	6,3
11	1986	North Palm Springs-USA	6,1	25	2004	Niigata Ken Chuetsu-Japan	6,6
12	1987	Superstition Hills-USA	6,5	26	2011	Van-Turkey	7,0
13	1989	Loma Prieta-USA	6,9	27	2023	Kahramanmaraş (Elbistan)-Türkiye	7,6
14	1992	Erzincan-Turkey	6,6	28	2023	Kahramanmaraş (Pazarcık)-Türkiye	7,7

3. Review of existing formulations for newmark method

According to time-acceleration record (Fig. 1), values of acceleration before X point are less than the sample value of critical acceleration of the slpoe (a_c=0.2g). Therefore, any ground movement doesn't occur. Between X and Y points, acceleration data are above the ciritical acceleration value and integrating this part of the acceleartion-time diagram, velocity-time graph can be obtained as a rising curve. Due to the inertia of the block, movement goes on to Z point. Reverse displacement and friction force cause to stop of the block at this point. Total displacement of the block can be calculated by integrating the velocity-time diagram when the same process continuous at the points that the acceleration values exceed the critical acceleration.

Siyahi et al. (2003) has suggested below equation to calculate the critical acceleration for any slope,

$$a_c = g\left[\frac{c}{\gamma h} + \cos\alpha\tan\phi - \sin\alpha\right] \tag{1}$$

Where, g is the gravitational acceleration, α is the angle of the plane of sliding block with horizontal, Ø is the friction angle of soil, c is the soil cohesion, γ is the unit weight of soil and h is the slope thickness.

Depending on this approximation Ambraseys and Menu (1988), Jibson et al. (1998), Jibson (2007), Hsieh and Chyi-Tyi (2011) and Yigit (2020) have devoleped equations 2-5 respectiveley.

$$\log\delta = 0.90 + \log\left[\left(1-\frac{a_c}{a_{max}}\right)^{2.53}\left(\frac{a_c}{a_{max}}\right)^{-1.09}\right] \tag{2}$$

$$\log\delta = 1.521\log I_a - 1.993\log a_c - 1.546 \tag{3}$$

$$\log\delta = 0.847\log I_a - 10.62a_c + 6.587a_c\log I_a + 1.84 \tag{4}$$

$$\log\delta = 1.2185\log I_a - 1.3669\log a_c + 1.5811\log\left(1-\frac{a_c}{a_{max}}\right) - 0.5532 \tag{5}$$

In these equations, ac is the critical acceleration in g and amax is the maximum acceleration in g, δ is displacement in cm, Ia (m/s) is Arias intensity described as follows by Arias (1970):

$$I_a = \frac{\pi}{2g}\int_0^{T_d}[a(t)]^2 dt \tag{6}$$

Depending on moment magnitude (M) and the earthquake source distance (R, km) Wilson and Keefer (1983) have suggested the Eq.7 to calculate Arias Intensity.

$$\log I_a = M - 2\log R - 4.1 \tag{7}$$

3.1. Gene Expression Programming (GEP)

Machine learning (ML) is one of the promising artificial methods increasingly used in engineering applications because it enables the extraction of meaningful information from large datasets and the optimization of processes. Gene expression programming (GEP) is a machine learning algorithm that learns the relationships between variables within datasets and creates models that explain these relationships. The model creation process with gene expression programming (GEP) begins with the random generation of chromosomes from the population within the defined dataset. These random chromosomes are evaluated for fitness and modified to create generations that acquire new characteristics. The chromosomes in these new generations undergo a similar development process, and this process is repeated until a suitable solution is reached. Thanks to the multiplication of chromosomes, genes are transferred to the next generation, and diversity is fostered through genetic operators. In deriving relationships with GEP, overly narrowing the application range of genetic operators can hinder the achievement of the correct solution by slowing the evolution rate of the population. Conversely, Ferreira, C. (2001 & 2002) showed that excessive expansion of the application range results in the emergence of numerous solutions that are far from optimal. In this study, model estimation was conducted using the GeneXproTools 5.0 program (GeneXproTools, 2023).

$$N_{GEP} = N_1 + N_2 + N_3 + N_4 + N_5 + N_6 \tag{8}$$

$$N_1 = \frac{\sin(-6{,}57766 * d_3) * (d_2 + \frac{d_0}{-6{,}57766})}{-(d_1 + 2{,}3284)} \tag{8a}$$

$$N_2 = \frac{d_3 * d_0}{\frac{d_0}{d_2} + (12{,}10504 - d_0)} \tag{8b}$$

$$N_3 = \frac{\sin(1{,}22610 * d_0) - d_3}{1 - \frac{6{,}12414}{d_1}} + d_0 \tag{8c}$$

$$N_4 = -\frac{d_3 - d_0 + \frac{1}{d_3}}{134{,}49739 * d_1} \tag{8d}$$

$$N_5 = \sin(\sin(d_3)) * (\sin(2d_1 - d_0 - d_2))^2 \tag{8e}$$

$$N_6 = e^{(\sin(d_0 * d_2) + d_1)} * (-1{,}20253 - d_3) \tag{8f}$$

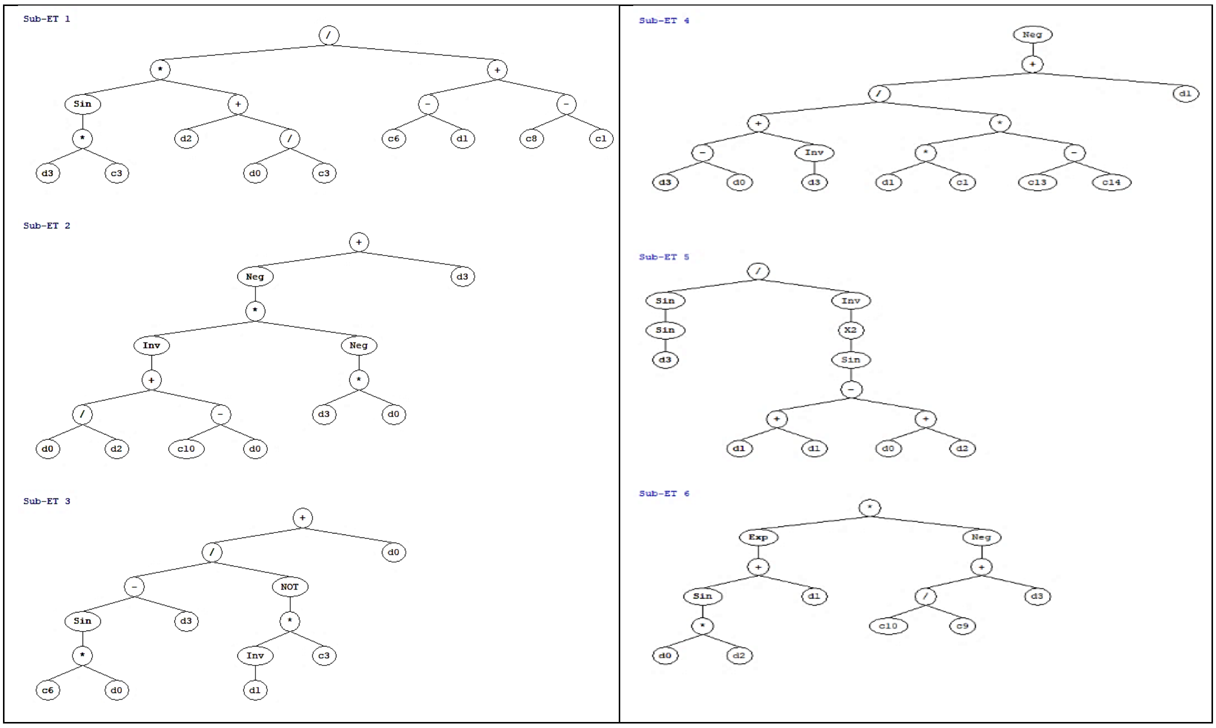

Fig. 2. GENE expression flowchart

To obtain the best fit result, the effects of linkage type, chromosome number, head and gene numbers, and selected mathematical functions on the relationship were explored through trial and error. The gene correlation equations that yielded the best fit results are presented below and displayed in the expression flowchart in Fig. 2.

Table 2. Optimal hyperparameters for ML models

Model	Details of Hyperparameters	
GEP	Input parameters	$\log I_A$, $\log A_C$, $\log(A_C/A_{max})$, $\log(1-A_C/A_{max})$
	Output parameter	$\log d$
	Training records (%75)	3790
	Testing records (%25)	1263
	Chromosomes	100
	Head Size	10
	Genes	6
	Linking function between ETs	Addition
	Function set	$+.-.\times.\div.x^2$.sin.
	Mutation	0.00138
	Inversion rate	0.00546
	One-Point Recombination	0.3
	Two-Point Recombination	0.3
	Gene Recombination	0.1

4. Rerults and discussion

4.1. Model performance evaluation

In this study, the existing relations and the estimation results of the GEP Model were made based on statistical measures such as coefficient of determination (R^2), mean value (M), coefficient of variation (Cov), standard deviation (SD), mean absolute percentage error ($MAPE$) and root mean square error ($RMSE$).

Table 3.Statistical criteria

Statistical criteria	Formulation
Mean absolute percentage error	$MAPE = \frac{100}{n}\sum_{i=1}^{n}\left\lvert\frac{exp - model}{exp}\right\rvert$
Root mean square error	$RMSE = \sqrt{\frac{\sum_{i=1}^{n}(exp - model)^2}{n}}$
Coefficient of determination	$R^2 = \sqrt{\frac{\left[\sum_{i=1}^{n}(exp - \overline{exp})(model - \overline{model})\right]}{\sum_{i=1}^{n}(exp - \overline{exp})\sum_{i=1}^{n}(model - \overline{model})}}$
Coefficient of variation	$Cov = \frac{SD}{M} = \frac{\sqrt{\frac{\sum_{i=1}^{n}(\frac{exp}{model} - M)^2}{n-1}}}{\frac{\sum_{i=1}^{n}\frac{exp}{model}}{n}}$

4.2. Model comparison

The results of statistical comparisons using 3790 training and 1263 testing experiment data collected from the literature are compared in Table 4 for detailed analysis and visually in Fig. 3.

As a result of the comparisons, it was seen that the most reliable estimation result was obtained from the GEP Model. In the comparisons made with the help of statistical parameters, the GEP Model gave the closest results to the real results with the values of R^2=0.860, M=0.906 and RMSE=0.375.

Table 4. Comparisons of different statistical researchers' models

Researcher	$\boldsymbol{R^2}$	$\boldsymbol{COV}$	$\boldsymbol{M}$	$\boldsymbol{SD}$	$\boldsymbol{MAPE}$	$\boldsymbol{RMSE}$
GEP Model	0.860	1.502	0.906	1.361	63.328	0.375
Yiğit (2020)	0.842	1.494	0.826	1.233	61.598	0.401
Hasieh and Chyi-Tyi (2011)	0.691	3.430	0.678	2.325	117.021	0.653
Jibson98 (1998)	0.773	1.798	0.727	1.306	67.857	0.496
Anbraseys ve Menu (1988)	0.687	4.361	0.756	3.297	157.933	0.737

Fig. 3 shows the comparison of the researcher's relations with the measurement results. There is a line with a slope of y=x in the graph. If the experimental and relation results are equal, the points are on the line. If there is a separation in the experimental and relation results, the points move away from the line.

When Table 4 and Fig. 3 are examined, they show a comparison of models from different researchers based on statistical performance criteria. Overall, the GEP Model delivers the best results when all metrics are considered. With an R^2 value of 0.860, it stands out as the model with the highest explanatory power, while the lowest RMSE and MAPE values indicate that this model has very low error rates. This also shows that GEP best captures the relationships among the data and has the least deviation in its predictions.

When looking at the Yiğit (2020) model, the R^2 value is quite high at 0.842 and shows a success that is quite close to the GEP model. When looking at the MAPE value, the Yiğit model offers the lowest percentage error and leaves GEP behind in this metric. This indicates how successful the model is in making predictions, especially proportionally. However, since it makes slightly more errors than the GEP model in the RMSE value, it ranks second in overall accuracy.

One of the older models, Jibson (1993), shows a moderate success in terms of R^2 value, while both MAPE and RMSE values are higher than the GEP and Yiğit models. This shows that although the model provides acceptable accuracy, it falls short of newer methods.

The Hasieh and Chyi-Tyi (2011) model has a very high error rate and a low R^2 value. The model has limited explanatory power for the data and its estimation errors are significantly high. Similarly, the Ambraseys and Menu (1988) model also has low performance. This model is at the bottom of the list with both the lowest R^2 value and the highest MAPE and RMSE values, and is inadequate to meet today's modeling needs.

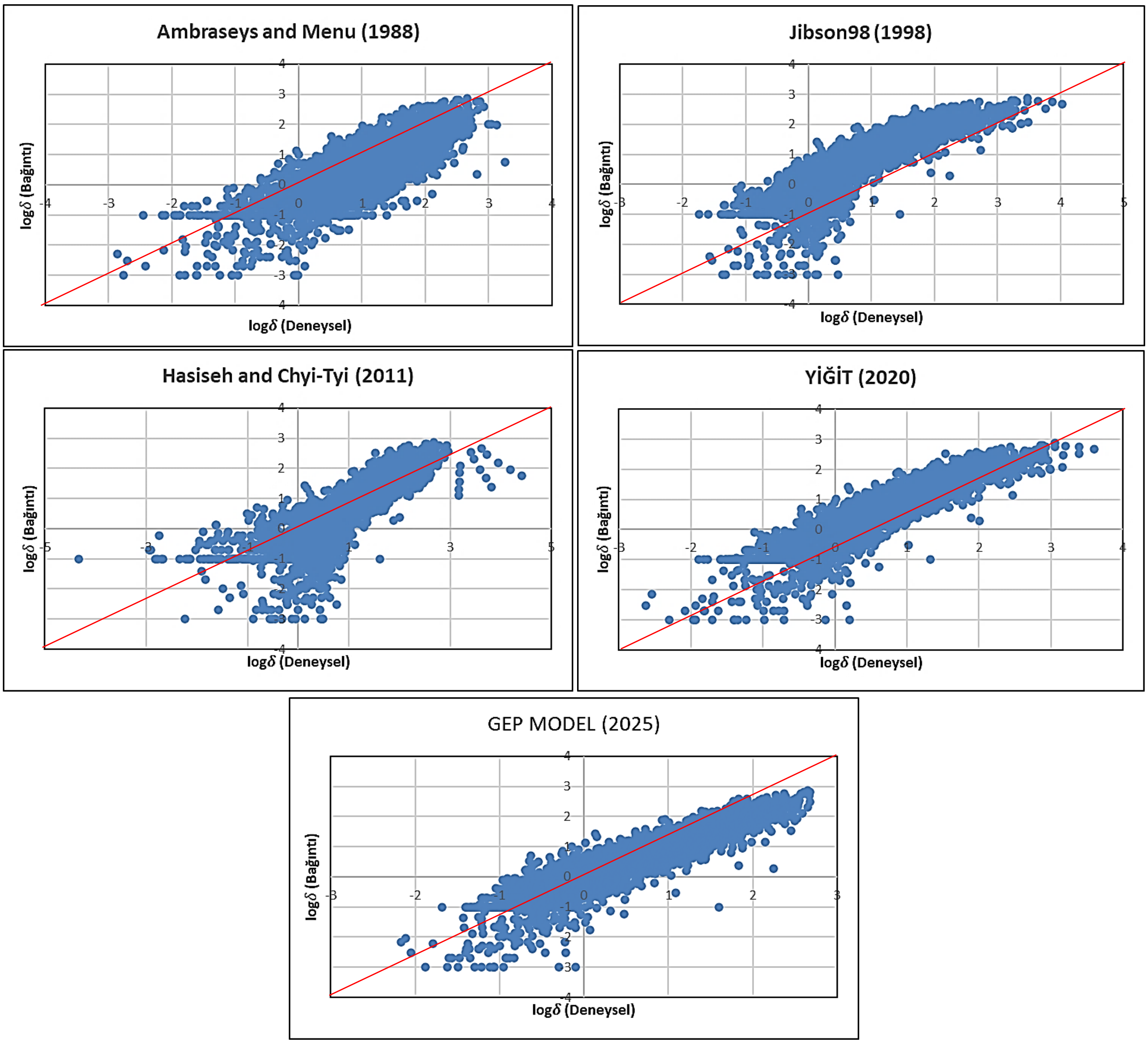

Fig. 3. A comparison of statistical models created by different researchers

5. Conclusions

In this study, Gene Expression Programming (GEP) was used to estimate the ground displacement according to the Newmark Method. These predictions were made using 28 earthquake acceleration records collected from the literature. The prediction results of the GEP Model were compared statistically with the prediction results of the existing correlations obtained from the earthquake acceleration records. The results obtained within the scope of this study are summarized below.

- As a result, when we evaluate the table in general, it shows that the GEP and Yiğit models fit the data better and provide more reliable results. In particular, the GEP Model stands out as the most successful model by exhibiting a balanced and superior performance in all metrics. It is clearly seen that the old models cannot reach the high accuracy and low error levels obtained with current methods.

References

Ambraseys, N.N., & Menu, J.A.M. (1988). Earthquake-induced ground displacements. *Earthquake Engineering & Structural Dynamics, 16*(7), 985-1006

Arias, A. (1970). A measure of earthquake intensity. *Seismic Design for Nuclear Plants*, 438-483

Ferreira, C. (2001). Gene expression programming: a new adaptive algorithm for solving problems. arXiv preprint cs/0102027.

Ferreira, C. (2002). Gene expression programming in problem solving. In Soft computing and industry: recent applications (pp. 635-653). London: Springer London.

GeneXproTools, (2023). Gepsoft GeneXproTools-Veri Modelleme ve Analiz Yazılımı. Available: https://www.gepsoft.com/

Hou, C., & Zhou, X.G. (2022). Strength prediction of circular CFST columns through advanced machine learning methods. *Journal of Building Engineering, 51*, 104289

Hsieh, S.Y., & Lee, C.T. (2011). Empirical estimation of the Newmark displacement from the Arias intensity and critical acceleration. *Engineering Geology, 122*(1-2), 34-42

Jibson R.W. (1993). Predicting earthquake-induced landslide displacements using Newmark's sliding block analysis. *Transportation Research Record, 1411*, 9–1

Jibson, R.W., Harp, E.L., & Michael, J.A. (1998). A method for producing digital probabilistic seismic landslide hazard maps: an example from the Los Angeles, California, area (pp. 98-113). Washington, DC, USA: US Department of the Interior, US Geological Survey.

Jibson, R.W. (2007). Regression models for estimating coseismic landslide displacement. *Engineering Geology, 91*(2-4), 209-218

Newmark, N. M. (1965). Effects of earthquakes on dams and embankments. *Geotechnique, 15*(2), 139-160

Siyahi, B., Erdik, M., Şeşetyan, K., Demircioğlu, M.B., & Akman, H. (2003). Sıvılaşma ve şev stabilitesi hassaslığı ve potansiyeli haritaları: İstanbul örneği. 5. Ulusal Deprem Mühendisliği Konferansı, 26-30 (in Turkish)

Wilson, R.C., & Keefer, D.K. (1983). Dynamic analysis of a slope failure from the 6 August 1979 Coyote Lake, California, earthquake. *Bulletin of the Seismological Society of America, 73*(3), 863-877

Yiğit, A. (2020). Prediction of amount of earthquake-induced slope displacement by using Newmark method. *Engineering Geology*, *264*, 105385

Yiğit, A. (2021). Newmark yöntemine göre zemin deplasmanının tahmin edilmesi. *Politeknik Dergisi*, *24*(3), 943-952

4th International Civil Engineering & Architecture Conference
17-19 May 2025, Trabzon, Türkiye

High temperature and freeze-thaw performance of geopolymers with glass fiber and natural zeolite

Gamze Üçdemir*[1], Fahreddin Melih Dursun[1], Ali Öz[1], Gökhan Kaplan[1]

[1] *Atatürk University, Department of Civil Engineering, 25240 Erzurum, Türkiye*

Abstract. Cement used in concrete production contributes to environmental problems and global warming due to high energy consumption, carbon footprint, and excessive use of natural resources. In this direction, research into sustainable binders is increasing. Geopolymer concrete, which has superior mechanical and durability properties, stands out as an environmentally friendly alternative due to its potential to use industrial waste as a raw material. In this study, the effect of 15% substitution of ground blast furnace slag (GBFS) with natural zeolite (NZ) and 0.3% and 0.6% by volume of glass fiber (GF) on the physical and mechanical properties of concrete in geopolymer composite based on GBFS, an industrial by-product, was investigated. The conclusion display that adding GF and NZ reduces the geopolymer composite's porosity and water absorption percentage. As a result of the reduction in porosity, an increase in flexural and compressive strength was noted in the specimens containing GF and NZ. When compressive strength and mass loss were evaluated by exposing the samples to temperatures of 200°C, 400°C and 600°C, the strength increased with increasing gel formation at 200°C. In comparison, a decrease was observed at 400°C and 600°C. However, increasing fiber content and zeolite addition positively affected high-temperature strength. It was also found that adding NZ and GF reduced the loss of compressive strength in specimens subjected to 18 freeze-thaw cycles. In general, 15% zeolite substitution and 0.3-0.6% GF were found to improve the performance of geopolymer composite.

Keywords: Geopolymer; Zeolite; GBFS; Glass fiber; Durability

1. Introduction

Cement production, the raw material for concrete, the most widely used building material in the construction industry, involves much energy consumption and CO2 gas emissions (rashadll et al., 2016; Rashad et al., 2023). At the same time, the need for natural raw materials in cement production leads to the over-exploitation of natural resource reserves, which causes serious environmental problems in the concrete industry (Summerbell et al., 2016). There has been a search for sustainable materials with low energy consumption and carbon footprint to address these issues. Geopolymer, developed as an alternative to cement and first introduced by J. Davidovits in the 1970s, is a result of this search. Geopolymer is an inorganic polymeric building material formed by the reaction of alumina and silicate-rich materials such as metakaolin, GBFS with strong alkalis such as Na2SiO3, KOH under appropriate curing conditions (Davidovits, 1999). Geopolymers have properties such as high early strength, good thermal resistance, fire resistance, high resistance to sulphate and acid attack, low shrinkage, and disposal of industrial wastes such as blast-furnace slag (BFS) and fly ash (Das & Rout, 2021).

Precursor materials, the raw materials used in geopolymer production, can be natural materials such as zeolite, kaolin and fly ash, or industrial wastes such as metakaolin, BFS and fly ash, which are commonly used in geopolymer production (Nikolov et al., 2017). Among these materials, GBFS, which has pozzolanic and cementitious properties, is an industrial by-product of steel production (Feng et al., 2024). The main product formed by the reaction between high calcium slag and alkaline activator is aluminium (Al) and calcium silicate hydrate with a structure known as C-A-S-H (Das & Rout, 2021). The main problem with GBFS-based geopolymers is their poor workability and rapid setting (Das & Rout, 2021). Each of these precursors has some limitations and good properties. For this reason, many studies aim to obtain geopolymer concrete with better properties by combining different precursor materials. Apart from these, natural pozzolans are also used as geopolymer precursors. For example, the inexpensive and widely available zeolite is a microporous volcanic mineral composed of hydrated aluminosilicate minerals. Due to its microporosity, it reduces workability and increases water requirements. Still, its fine particles can help fill microvoids in the concrete matrix, increasing strength and reducing permeability (Shoaei et al., 2024). However, in some studies where cement and zeolite were used

* Corresponding author, E-mail: gamzeucdemir@atauni.edu.tr

https://doi.org/10.31462/icearc2025_ce_eqe_337

together, a decrease in strength was observed due to increased zeolite (Milović et al., 2022; Karakurt & Topçu, 2011).

Huseien et al. (2018) researched the properties of geopolymer mortars obtained using metakaolin instead of 0-15% GBFS. The mechanical properties of geopolymer mortars were also compared with those of mortars made with Portland cement. According to the results obtained, it was observed that as the metakaolin ratio increased, the setting time increased and the workability of the mortar decreased. In addition, it was found that the flexural and tensile strength of geopolymer mortars reached higher values compared to Portland cement mortars. In another study, the effect of zeolites on geopolymers was studied. It was found that the properties of the hybrid materials formed this way are superior to the raw materials that create them. While the hybrid material formed in this study has high strength due to the geopolymer, the zeolite gives the hybrid material a high surface area and adsorption capacity (Rożek et al., 2019). In the study conducted by Wongsa et al. (2020), the fire behaviour of geopolymer mortar obtained by replacing high calcium fly ash with zeolite and mullite at 10%, 20% and 30% by weight was investigated. According to the results, the fire resistance of the geopolymer mortar obtained using zeolite and mullite alone and together increased. Das and Rout (2021) investigated the properties of fly ash and GBFS based geopolymer materials. As a result of the study, it was found that the strength of fly ash based geopolymer increased due to the formation of N-A-S-H and C-A-S-H gel with the addition of GBFS. Zhang et al. (2023) investigated the effect of silica fume on the drying shrinkage behaviour of FA and GBFS based geopolymer pastes. It was observed that adding silica fume delayed the hydration of calcium silica in the geopolymer and reduced the early strength of the geopolymer. In addition, an improvement in the 28-day compressive strength and a decrease in the drying shrinkage stress were observed due to the reduction of pores in the geopolymer when the silica fume content reached 20%. Amari et al. (2024) studied the properties of zeolite-based geopolymer materials containing different amounts of blast-furnace slag. The study found that geopolymer concrete significantly reduced CO2 emissions compared to conventional cement concrete and showed that the compressive strength did not always increase in direct proportion to the amount of slag, but increased the rate of initial setting. It was also found that the geopolymers produced were resistant to temperatures of up to 800°C.

Chemical fibers such as carbon, steel, and glass fibers are widely used in composites to improve mechanical properties such as flexural strength and control micro-cracks in the material. In addition, depending on the type of fiber, it can be used for various purposes such as increasing electrical conductivity and fire resistance. Although artificial fibers are not sustainable, they are generally more reproducible than natural fibers due to their higher strength (Růžek et al., 2023). Noushini et al. (2018) investigated the effect of different sizes of polypropylene and polyolefin synthetic fibers on the mechanical performance of fly ash-based geopolymer concrete. Due to the low strength of the fibers reinforced in the geopolymer concrete, a decrease in compressive strength was observed compared to concrete without fiber addition. However, an increase in flexural toughness and fracture energy was observed. Alves et al. (2021) examined the effect of adding glass fibers at different ratios to a geopolymer whose precursor is blast-furnace slag on the geopolymer. According to the study results, while the composite's machinability decreases with increasing fiber content, shrinkage cracks are under control thanks to the fibers. The mechanical properties of the geopolymer increase in direct proportion with increasing fiber content up to 0.75% fiber content. On the other hand, the mechanical properties and durability of the geopolymer were negatively affected as the composite obtained by adding 1% fibers was not homogeneous. The study by Hussain et al. (2024) investigated the changes in the mechanical properties of concrete by adding different proportions of steel and polyvinyl alcohol fibers to geopolymer concrete prepared using fly ash, silica fume and slag precursors. The study reported that the fibers limited the shrinkage due to rapid gelation in slag concrete. In addition, the strength of the geopolymer with steel fibers increased more than that of the concrete with polyvinyl alcohol fibers. Still, after exposing the concrete specimens to acid attack, it was observed that the strength of these concretes decreased less than that of those with steel fibers due to the corrosion resistance of the polyvinyl alcohol fibers. Hamdi and Farhan (2025) investigated the effect of glass fibers and ground glass fibers, a by-product of glass fibers, on slag based geopolymer concrete. The workability of the mixes changed depending on the fiber content and length. While the workability decreased with the use of glass fibers and increased fiber length, it was observed that the workability increased with the use of ground glass fibers by up to 10%. Similarly, increased compressive strength was observed with ground glass fiber up to 10%, while increased fiber content decreased strength. An increase in compressive strength was observed with the use of 5% and 10% ground fibers at 150 and 300˚C compared to concrete without fibers, but at 600 and 800˚C concrete specimens with fibers exhibited lower compressive strength than those without fibers.

Many studies in the literature determine the mechanical and durability properties of geopolymer mortars produced using artificial or natural precursors. This study investigated the effect of substituting 15% of GBFS with zeolite and adding glass fiber in different proportions on the properties of concrete in GBFS-based geopolymer concrete mixes. The mechanical properties of the prepared geopolymer specimens were determined, and their resistance performances, such as those of fire and chemical attacks, were evaluated. The effects of zeolite and glass fiber admixtures on GBFS-based geopolymer concrete were comprehensively investigated.

2. Materials and methods

2.1. Raw materials

This study used GBFS and natural zeolite (NZ) as binder materials to produce geopolymer blends. GBFS's specific gravity is 2.84, and its surface area (Blaine method) is 5200 cm2/g. NZ's specific gravity is 2.34, and its surface area is 3200 cm2/g. Table 1 presents the chemical characterisation of GBFS and NZ.

Pumice aggregate with a specific gravity of 1.82 and a water absorption rate of 10.3% was used to prepare geopolymer mixtures. The particle distribution of pumice aggregate with 0-4 mm sieve opening according to ASTM C33 standard is given in Fig. 1. The technical properties of the 12 mm long glass fibre (GF) used in the production of the blends are shown in Table 2.

In this study, sodium hydroxide (NaOH, 12M) and sodium silicate (Na_2SiO_3, liquid) were used as alkali activators in the production of geopolymer mix. Each of these materials plays a critical role in the alkali activation process and ensures the formation of the geopolymer matrix. Sodium hydroxide is a potent alkaline compound that provides a highly alkaline environment. This solution's concentration determines NaOH's effectiveness in initiating solubility and alkali activation reactions. This study used a 12 molar (12M) sodium hydroxide solution. Sodium hydroxide dissolves silicate-based materials (e.g. GBFS, fly ash) in an alkaline environment, breaking the bonds between silica and alumina and promoting the initiation of the geopolymerisation reaction. The NaOH solution was prepared 24 hours before casting. Sodium silicate (Na_2SiO_3) is an alkali metal compound with a silicate structure and is used as an essential activator, especially in alkali activation systems such as geopolymers. The specific gravity of Na_2SiO_3 solution is 1.42 and the silica modulus is 2 (Na_2O=:15.9%, SiO_2: 31.4%).

Table 1. Chemical characterisation of GBFS and NZ

	CaO	SiO_2	Al_2O_3	Fe_2O_3	MgO	Na_2O	K_2O	SO_3	LOI*
GBFS	41.1	33.1	9.8	1.3	13.4	0.3	0.5	0.1	0.3
NZ	1.8	67.7	8.9	1.8	0.2	0.8	1.9	0.1	16.7

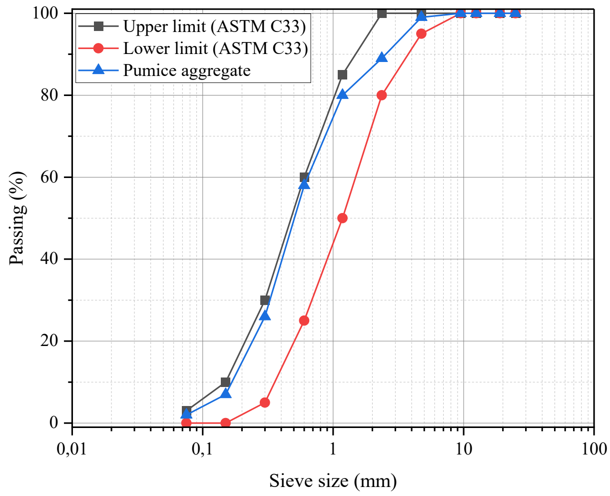

Fig. 1. Particle size distribution of pumice aggregate

Table 2. Technical specifications of the GF

Length (mm)	Diameter (μm)	Tensile strength (MPa)	Modulus of Elasticity (GPa)	Elongation (%)	Density	Color
12	19	1700	72	3.8	2.60	White

2.2. Mix design

GBFS and NZ were used as the main binder in preparing geopolymer mixtures at a 750 kg/m3 dosage. NZ has been replaced by GBFS by 15 per cent by weight. GF added to the mixtures were 0.3% and 0.6% by volume. Alkaline solution consisting of NaOH and Na_2SiO_3 was used at 98% of the binder amount. Due to the high water absorption rate of pumice aggregate and the use of fibre in the mixtures, the amount of alkaline solution was selected high. This way was chosen to reduce the workability losses caused by these two components. The ratio of Na_2SiO_3 and NaOH is 2.5 in all mixtures. Material quantities and mixing ratios of geopolymer blends are given in Table 3.

Table 3. Material quantities and mixing ratios of geopolymer blends

kg/m^3	0GFZ0	3GFZ0	6GFZ0	0GFZ15	3GFZ15	6GFZ15
GBFS	750	750	750	637,5	637,5	637,5
NZ	0	0	0	112,5	112,5	112,5
NaOH	210	210	210	210	210	210
Na_2SiO_3	525	525	525	525	525	525
GF	0	8	16	0	8	16
Pumice aggregate	393	387	380	371	364	358

2.3. Mixing, casting and curing

Mixing was started by mixing GBFS and NZ at low speed for 1 minute. Afterwards, the alkali Solutions were added to the dry mixture and the wet mixture (paste) was obtained by mixing at low speed for 1 minute and at high speed for 2 minutes. In the third step, pumice aggregate was added to the mixture and the mortar mixture was obtained by mixing at low speed for 1 minute and high speed for 2 minutes. In the last step, GF was added to the mortar mixture and mixed at low speed for 1 minute and at high speed for 3 minutes (until homogeneity was obtained). The fiber reinforced geopolymer mixture was then placed in the moulds, covered with cling film and immediately placed in the oven. In the oven with a heating rate of 5 ºC/min, all samples were cured at 70 ºC for 16 hours. The specimens were cooled in the oven at the end of thermal curing. After approximately 1 day (including cooling in the oven), the specimens were removed from the moulds and immediately subjected to physical, mechanical and durability tests.

2.4. Experimental setup

Physical properties of the samples such as water absorption, apparent porosity and dry density were measured. Water absorption and apparent porosity tests were started 24 hours after casting. For this aim, 50x50x50 mm cube specimens were produced following ASTM C642 standard. TS EN 1015-18 standard was used for capillary water absorption test. In this context, 24 50x50x50 mm cube specimens were produced and the amount of water absorbed by capillary at the end of 24 hours was measured. The compressive strength of the specimens was determined approximately 1 day after casting. For this purpose, flexural strength (three-point) was determined by ASTM C348 standard. For flexural strength, 40x40x160 mm specimens were produced. Compressive strength was measured per ASTM C349 standard for specimens broken in half in the flexural test. A muffle furnace was used to determine the high temperature resistance of the samples at 200, 400, and 600 oC. The heating rate of the muffle furnace is 10 ºC/min. The samples were kept for 2 hours after reaching the target temperature and then cooled under laboratory conditions (removed from the muffle furnace). After obtaining constant weight values, weight losses of the samples were determined and compressive strengths were measured. In addition, 20 freeze-thaw cycles (F-T) were applied to the samples to assess the freeze-thaw durability. F-T resistance was performed according to ASTM C666 standard. The samples were kept at -20 ºC for 7 hours and at +4 ºC for 5 hours, and 2 cycles per day were completed. As a result of the cycles, the specimens' weight loss and compressive strength were determined. 50x50x50 mm cube specimens were used to determine the high temperature and freeze-thaw resistance.

3. Results and discussion

This research focused on determining the effect of 15% NZ substitution and different amounts of GF on the physical and mechanical properties of GBFS-based geopolymer blend. The results of the experiments are presented in detail in the following sections.

3.1. Physical properties

The apparent porosity and oven dry density values of the geopolymer blends are shown in Fig. 2. As shown in Fig. 2, the apparent porosity decreases from 2.6 to 8% as the GF content increases. Similarly, the oven dry density increases from 1.6 to 4.2% as the GF content increases. It can be concluded that the GF used in the mixes acted as a micro-aggregate and thus the apparent voids were relatively reduced. In the study by Öz et al. (2023), it was shown that in hot cured GBFS-metakaolin based geopolymer blends, as the amount of polyvinyl alcohol fibers increased, the apparent porosity decreased as a result of the fibers exhibiting microaggregate properties. In addition, Xie et al. (2022) found that using fibers reduced porosity and water absorption because fibers break the connection between pores in the matrix and fill some pores.

A decrease in the apparent porosity value was generally observed by adding NZ. This may be due to the zeolite acting as a micro-filler in the matrix and reducing the porosity of the mortar (Wang et al., 2024). In the mixes where NZ was used, there was a 4.7% decrease in the apparent porosity value of the no GF mix, a 1.6% decrease in the 0.6% vol. GF mix and a 1% increase in the 0.3% vol. GF mix. Thus, the NZ contributed more to the reduction in apparent porosity in the no GF mix. In contrast to porosity, oven dry weight decreased by 4.2 to 4.7% using NZ. The lower specific gravity of zeolite can explain this compared to GBFS (Efe et al., 2024).

Fig. 3 shows geopolymer blends' percentage of submerged and capillary water absorption. The graph shows that increasing GF content decreases the submerged and capillary water absorption rate. This is due to the hydrophilic properties of the GF, which creates a tight adhesion between the matrix and the GF, reducing the porosity and decreasing the sample's water absorption (Mohseni et al., 2016; Yuan & Jia, 2021). With the use of NZ, the percentage of submerged water absorption was obtained in parallel with the porosity, as expected, and there was a decrease ranging from 1.9 to 6.6% among the blends. Hosseinzadehfard and Mobaraki (2024) focused on determining the impact of microsilica and natural pozzolan on the strength and durability of concrete. Similar results were obtained in the study by Sharbaf et al. (2022). However, using NZ increased the capillary water absorption of the mixes by between 5.7 and 24.5%. Similarly, in the study by Sharbaf et al. (2022), there was a decrease in the percentage of water absorption as the amount of pozzolan increased, while the rate of capillary water absorption increased. This shows that despite reducing the amount of voids, the interconnection between the voids increases.

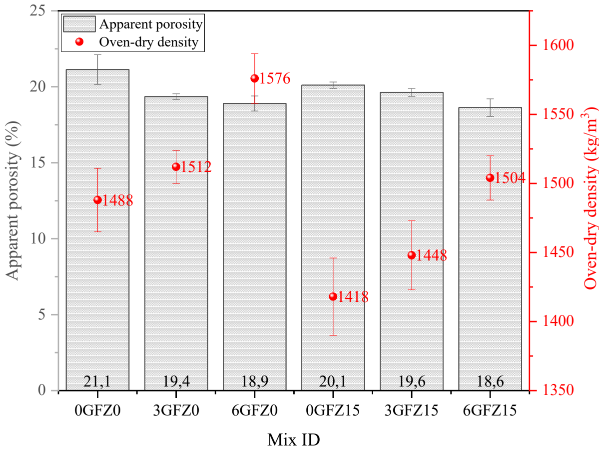

Fig. 2. Apparent porosity and oven-dry density of geopolymer mixes

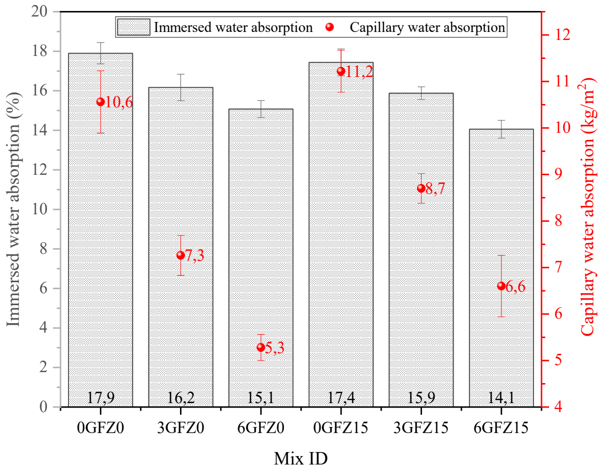

Fig. 3. Immersed water absorption and capillary water absorption of geopolymer mixes

3.2. Mechanical properties

In this part of the work, the impact of NZ and GF on the mechanical properties of GBFS based geopolymer blend was investigated. Fig. 4 shows the test results for flexural and compressive strength of the geopolymer mixes. Fig. 4 shows an increase in compressive strength ranging from 7.4 to 19% depending on the rise in GF ratio. Moreover, a higher GF ratio led to a rise in flexural strength ranging from 22 to 30%. In the previous section, the porosity of concrete is reduced due to the GF used in the mixes acting as a micro-aggregate. The results obtained here support the increase in compressive strength. As mentioned earlier, using fiber has resulted in a more compact concrete by exhibiting micro-aggregate properties. Therefore, the compressive strength of concrete with fewer voids is also higher (Ganesh & Muthukannan, 2021; Yuan & Jia, 2021; Akarken & Cengiz, 2023; Çelik & Özkiliç, 2024). The flexural strength of concrete was increased because the GF used limited cracking (Alves et al., 2021; Akarken & Cengiz, 2023; Çelik & Özkiliç, 2024). In addition, the flexural and compressive strength increased due to the increased amount of zeolite, as zeolite acts as a microfiller and reduces the amount of voids (Andrejkovičová et al., 2016).

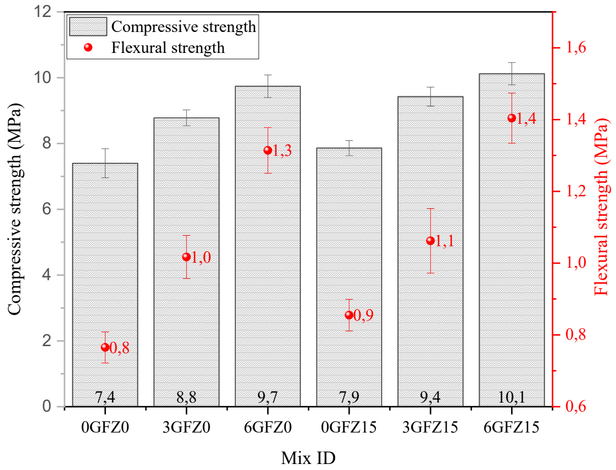

Fig. 4. Compressive strength and flexural strength of geopolymer mixes

3.3. High-temperature resistance

The prepared geopolymer mixes were exposed to 200, 400 and 600˚C for 2 hours to test their high-temperature resistance. Fig. 5 shows the compressive strength of the specimens exposed to high temperature. With the use of GF, the compressive strength of the specimens exposed to 200˚C increased from 33.8% to 57.4%, while 400 and 600˚C temperatures were detrimental to the internal structure of the specimens and reduced the strength. The decrease in compressive strength of concrete specimens exposed to 400˚C temperature varies between 1.3-16%, while the decline at 600˚C temperature varies between 13-23%. As the temperature increases, the gel structure in the matrix degrades more, accelerating the increase in strength loss. In addition, Fig. 5 shows an increase in strength with the rise in GF content between the mixtures with and without NZ. In general, the rise in compressive strength of the samples without NZ at 200˚C is 41.4% on average, whereas the rate of rise in the samples with NZ is 52.4%. As can be seen, the rise in compressive strength is higher for the specimens with NZ. At a temperature of 400˚C, the loss rate of compressive strength in specimens without NZ is 9.2% on average, while this rate is 7.5% in specimens with NZ. A similar situation was observed for specimens exposed to 600˚C. At 600˚C, the average rate of strength loss in the mixtures without NZ is 19.4%, while this rate is 14% in the mixtures with NZ. As seen from this, the loss of compressive strength is reduced using NZ in specimens exposed to high temperatures. In addition, there is an rise in strength with increasing GF content between the mixes with and without NZ. It should also be noted that the most significant decrease in strength at both 400 and 600˚C occurred in the specimen without NZ and with 0.3% GF by volume. Furthermore, as mentioned in section 3.3, increasing the amount of NZ and GF positively affected the strength. Degirmenci (2018) investigated the freeze-thaw and high temperature resistance of pozzolan-based geopolymeric mortars. The strength and mass loss results of GBFS and GBFS+zeolite-based geopolymer mortars exposed to temperatures 300, 600 and 900˚C were evaluated. The results show that using NZ increases the compressive strength of the mortar after high temperature and reduces the mass loss.

The mass loss values of the samples exposed to high temperature are shown in Fig. 6. As can be seen from the figure, the mass loss increases as expected with increasing temperature. The main reason for this is the evaporation of the water contained in the alkaline activators from the matrix in the geopolymer samples exposed to high temperature and the consequent dehydration of the mortar sample. In addition, capillary and microcracks formed in the samples under the influence of high temperature expand over time and turn into macrocracks. This process results in the development of voids in the microstructure of the samples (Guler & Akbulut, 2022). In addition, the mass loss decreases with increasing GF content. In addition, while the mass loss rate of the samples without NZ at 200˚C is 6.3% on average, this rate is 5.8% for the samples with NZ. At 400 and 600˚C the mass loss rate of the samples without NZ is 15.4% and 17.6% respectively, while the mass loss rate of the samples with NZ is 13.9% and 16.7% respectively. It is evident that the mass loss decreases with the addition of NZ in concrete specimens exposed to high temperatures.

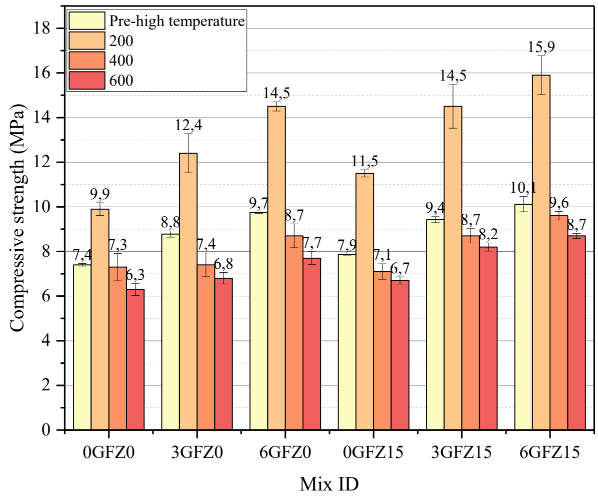

Fig. 5. Compressive strength of geopolymer mixtures exposed to high temperature

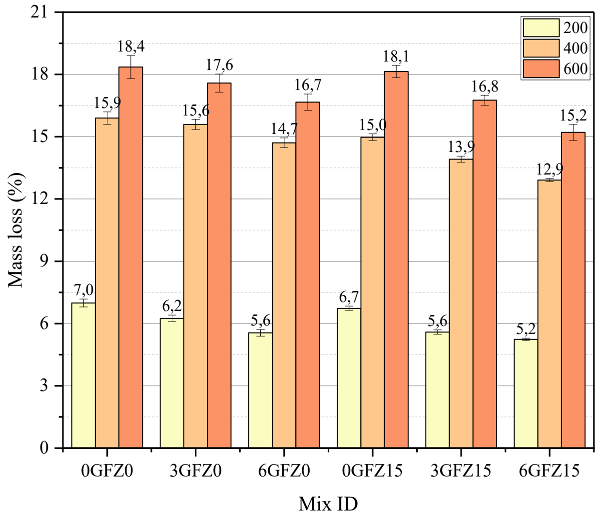

Fig. 6. Loss of mass in geopolymeric mortar samples exposed to high temperatures

3.4. Freeze and thaw resistance

A total of 20 cycles of freeze-thaw testing were performed (Fig. 7). The compressive strength and mass loss values obtained as a result of the test are shown in Fig. 8. While the average loss in compressive strength was 17.4% for the samples without NZ, this was reduced to 10.2% for the mixtures containing NZ. When the glass fibre contribution was examined, the loss in strength was found to be 9.95% in the samples containing 0.3% glass fibre and 5% in the samples containing 0.6% glass fibre. The results show that the strength loss decreases as the fibre content increases.

When evaluated in terms of mass loss, the highest loss was observed in the mixtures without NZ and fibre (Fig. 8). While the average mass loss in the NZ-free samples was 7.9%, this was reduced to 5.5% in the NZ-added samples. When the effect of glass fibre was examined, the average mass loss was 6.1% in samples containing 0.3% glass fibre and 3.7% in samples containing 0.6% glass fibre. The results show that the mass loss decreases with increasing glass fibre content. The results show that using glass fibre and NZ significantly reduces freeze-thaw damage in geopolymer samples.

Fig. 7. Appearance of geopolymer mortar specimens subjected to freeze-thaw cycles

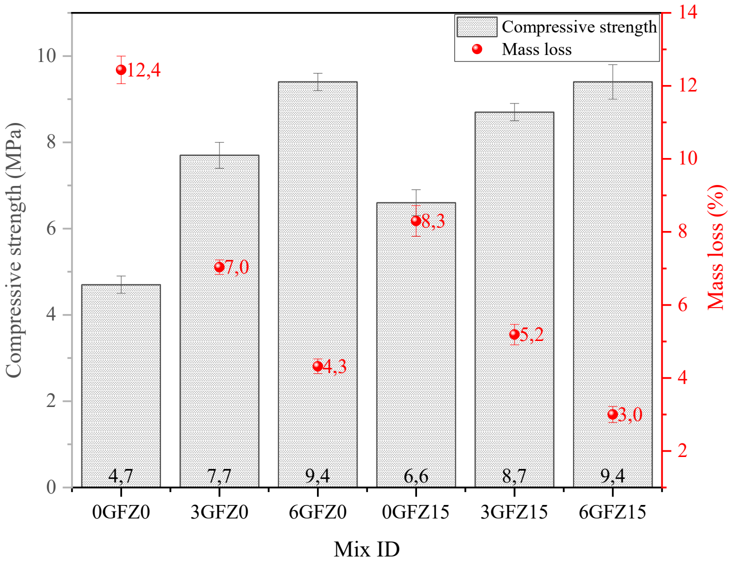

Fig. 8. Compressive strength and mass loss values of geopolymer mortar specimens subjected to freeze-thaw cycles

No study in the literature examines the F-T resistance of NZ-containing geopolymers in detail. The freeze-thaw resistance of NZ is mainly investigated in cement-based composites. The freeze-thaw resistance of the zeolite-based geopolymer mortars is lower than that of those based on fly ash and GBFS, with the residual compressive strength after 25 freeze-thaw cycles dropping to around 74%, indicating a reduction in durability (Degirmenci, 2018). The freeze-thaw resistance of zeolite-containing geopolymers is enhanced by the moist environment during curing, which promotes continuous slag activation and strength development, resulting in improved freeze-thaw durability, particularly in low cycle applications (Aygörmez, 2021). The freeze-thaw resistance of geopolymer-zeolite cementitious composites (GZCC) is poor. All samples fractured after 2 to 20 cycles due to increased open porosity caused by zeolitic crystal formation, allowing easy water ingress during freeze-thaw exposure (Khalid, 2023).

4. Conclusions

Many studies are currently being conducted to develop alternative binders to cement, the main concrete component widely used in buildings due to the high CO_2 emissions and energy consumption required in production. Recently, geopolymer blends obtained by alkaline activation of alumino-silicate compounds have been investigated intensively because they are more environmentally friendly and offer higher strength and durability than cement-based concretes. The present study, the effect of partial replacement of GBFS with zeolite at a rate of 15% and the use of GF at rates of 0.3% and 0.6% on the physical and mechanical properties of GBFS-based geopolymeric mortars was investigated and the results are presented below.

- The GF used in the mixes acts as a micro-aggregate and reduces the apparent porosity of the matrix. As the void content of the blends obtained decreases, the oven dry density rises as the GF content increases. As a result of the zeolite acting as a micro-filler in the matrix, the apparent porosity value generally decreased. However, the specific gravity decreased when zeolite, which has a lower specific gravity than GBFS, was used in the mortar.
- As the porosity decreased with the use of GF, the mortar's water absorption and capillary water absorption percentages decreased. However, when zeolite was added to the mixture, the water absorption percentage decreased as the number of voids decreased. In contrast, the capillary water absorption percentage increased as the connection between voids increased.
- When the mechanical properties of geopolymer mortars were investigated, it was found that GF and NZ made a positive contribution. The mortars' compressive and flexural strength increased with GF and NZ.
- When the resistance of the mortars to 200, 400, and 600˚C temperatures is examined, there is an increase in strength and a decrease in mass loss due to the rise in NZ and GF. Here, as gel formation increased in the matrix structure of the mixes exposed to 200˚C temperature, the strength showed an increase relative to the control mix. However, at 400 and 600˚C the gel structures in the matrix deteriorated and therefore the strength decreased.
- Similar results were observed in mortars subjected to 20 cycles of freeze-thaw. Increasing the amount of zeolite and glass fibre increased the compressive strength and reduced the mass loss. Accordingly, substituting GBFS with 15% NZ and using 0.3% and 0.6% GF improved the mechanical properties of the mortars and had no adverse effect after high temperature and freeze-thaw damage.

Acknowledgments

This research received no specific grant from funding agencies in the public, commercial, or not-for-profit sectors.

References

Akarken, G., & Cengiz, U. (2023). Fabrication and characterization of metakaolin-based fiber reinforced fire resistant geopolymer. *Applied Clay Science*, *232*, 106786.

Alves, L., Leklou, N., de Souza, F., & De Barros, S. (2021). Assessment of the effect of fiber percentage in glass fiber reinforced slag-based geopolymer. *Journal of Asian Ceramic Societies*, *9*(3), 1265-1274.

Amari, S., Darestani, M., Millar, G. J., Samali, B., & Strounina, E. (2024). Engineering and life cycle assessment (LCA) of sustainable zeolite-based geopolymer incorporating blast furnace slag. *Sustainability*, *16*(1), 440.

Andrejkovičová, S., Sudagar, A., Rocha, J., Patinha, C., Hajjaji, W., da Silva, E. F., & Rocha, F. (2016). The effect of natural zeolite on microstructure, mechanical and heavy metals adsorption properties of metakaolin based geopolymers. *Applied Clay Science*, *126*, 141-152.

Aygörmez, Y. (2021). Performance of ambient and freezing-thawing cured metazeolite and slag based geopolymer composites against elevated temperatures. *Revista de la construcción*, *20*(1), 145-162.

CEN, T. (2011). TR 15177. Testing the freeze-thaw resistance of concrete: Internal structural damage.

Çelik, A. İ., & Ozkilic, Y. O. (2024). Lightweight geopolymer concrete using pumice and glass fiber. *Computers and Concrete*, *34*(5), 577-589.

Das, D., & Rout, P. K. (2021). Synthesis and characterization of fly ash and GBFS based geopolymer material. *Biointerface Research in Applied Chemistry*, *11*, 14506-14519.

Davidovits, J. (1999). Chemistry of geopolymeric systems, terminology. In J. Davidovits, R. Davidovits, & C. James (Eds.), *Proceedings of 99 international conference*. France.

Degirmenci, F. N. (2018). Freeze-thaw and fire resistance of geopolymer mortar based on natural and waste pozzolans. *Ceramics-Silikáty*, *62*, 41-49. https://doi.org/10.13168/cs.2017.0043124

Efe, M., Öz, A., Bayrak, B., Kaplan, G., & Aydın, A. C. (2024). Effect of Na2SiO3/NaOH rate and natural zeolite content on basalt fiber reinforced eco-efficient slag-based geopolymer mortar synthesis. *Archives of Civil and Mechanical Engineering*, *24*(4), 215.

Feng, B., Lu, Z., Zhang, Y., Zhang, X., He, L., & Li, Y. (2024). Physical, mechanical properties and microstructure of waste GBFS-based geopolymer incorporated with metakaolin and SiC whiskers (SiCw). *Journal of Building Engineering*, *91*, 109653.

Ganesh, A. C., & Muthukannan, M. (2021). Development of high performance sustainable optimized fiber reinforced geopolymer concrete and prediction of compressive strength. *Journal of Cleaner Production*, 282, 124543.

Guler, S., & Akbulut, Z. F. (2022). Effect of high-temperature on the behavior of single and hybrid glass and basalt fiber added geopolymer cement mortars. *Journal of Building Engineering*, 57, 104809.

Hamdi, A., & Farhan, K. Z. (2025). Influence of glass fiber and waste ground glass fiber powder on thermal resistance properties of alkali activated composites. *Innovative Infrastructure Solutions*, 10(3), 94.

Hosseinzadehfard, E., & Mobaraki, B. (2024). Investigating concrete durability: The impact of natural pozzolan as a partial substitute for microsilica in concrete mixtures. *Construction and Building Materials*, 419, 135491.

Huseien, G. F., Mirza, J., Ismail, M., Ghoshal, S. K., & Ariffin, M. A. M. (2018). Effect of metakaolin replaced granulated blast furnace slag on fresh and early strength properties of geopolymer mortar. *Ain Shams Engineering Journal*, 9(4), 1557-1566.

Hussain, S., Matthews, J., Amritphale, S., Edwards, R., Matthews, E., Paul, N., & Kraft, J. (2024). Influence of steel and poly vinyl alcohol fibers on the development of high-strength geopolymer concrete. *Minerals*, 14(10), 1007.

Karakurt, C., & Topçu, İ. B. (2012). Effect of blended cements with natural zeolite and industrial by-products on rebar corrosion and high temperature resistance of concrete. *Construction and Building Materials*, 35, 906–911.

Khalid, H. R. (2023). Carbonation and freeze-thaw resistance of geopolymer-zeolite cementitious composites. *Materials Today: Proceedings*.

Milović, T., Šupić, S., Malešev, M., & Radonjanin, V. (2022). The effects of natural zeolite as fly ash alternative on frost resistance and shrinkage of blended cement mortars. *Sustainability*, 14(5), 2736.

Mohseni, E., Khotbehsara, M. M., Naseri, F., Monazami, M., & Sarker, P. (2016). RETRACTED: Polypropylene fiber reinforced cement mortars containing rice husk ash and nano-alumina.

Nikolov, A., Rostovsky, I., & Nugteren, H. (2017). Geopolymer materials based on natural zeolite. *Case Studies in Construction Materials*, 6, 198-205.

Noushini, A., Hastings, M., Castel, A., & Aslani, F. (2018). Mechanical and flexural performance of synthetic fiber reinforced geopolymer concrete. *Construction and Building Materials*, 186, 454-475.

Nuaklong, P., Sata, V., & Chindaprasirt, P. (2018). Properties of metakaolin-high calcium fly ash geopolymer concrete containing recycled aggregate from crushed concrete specimens. *Construction and Building Materials*, 161, 365–373. https://doi.org/10.1016/j.conbuildmat.2017.11.152.

Öz, A., Bayrak, B., Kaplan, G., & Aydın, A. C. (2023). Effect of waste colemanite and PVA fibers on GBFS-Metakaolin based high early strength geopolymer composites (HESGC). *Construction and Building Materials*, 377, 131064.

Rashad, A. M., Eessaa, A. K., Khalil, M. H., & Mohamed, O. A. (2023). An initial study on the effect of nano-zirconium on the behavior of alkali-activated slag cement subjected to seawater attack. *Construction and Building Materials*, 370, 130659.

Rożek, P., Król, M., & Mozgawa, W. (2019). Geopolymer-zeolite composites: A review. *Journal of Cleaner Production*, 230, 557-579.

Růžek, V., Dostayeva, A. M., Walter, J., Grab, T., & Korniejenko, K. (2023). Carbon fiber-reinforced geopolymer composites: A review. *Fibers*, 11(2), 17.

Sharbaf, M., Najimi, M., & Ghafoori, N. (2022). A comparative study of natural pozzolan and fly ash: Investigation on abrasion resistance and transport properties of self-consolidating concrete. *Construction and Building Materials*, 346, 128330.

Shoaei, P., Momenzadeh, A., Hosseini, H., Rajaei, S., Ameri, F., & Pilehvar, S. (2024). One-part slag/zeolite geopolymer mortars under ambient and heat curing conditions. *Case Studies in Construction Materials*, 20, e02677.

Summerbell, D. L., Barlow, C. Y., & Cullen, J. M. (2016). Potential reduction of carbon emissions by performance improvement: A cement industry case study. *Journal of Cleaner Production*, 135, 1327-1339.

Wang, T., Fan, X., & Gao, C. (2024, November). Strength, pore characteristics, and characterization of fly ash-slag-based geopolymer mortar modified with silica fume. In *Structures* (Vol. 69, p. 107525). Elsevier.

Wongsa, A., Wongkvanklom, A., Tanangteerapong, D., & Chindaprasirt, P. (2020). Comparative study of fire-resistant behaviors of high-calcium fly ash geopolymer mortar containing zeolite and mullite. *Journal of Sustainable Cement-Based Materials*, 9(5), 307-321.

Xie, L., Zhou, Y., Xiao, S., Miao, X., Murzataev, A., Kong, D., & Wang, L. (2022). Research on basalt fiber reinforced phosphogypsum-based composites based on single factor and RSM tests. *Construction and Building Materials*, 316, 126084.

Yuan, Z., & Jia, Y. (2021). Mechanical properties and microstructure of glass fiber and polypropylene fiber reinforced concrete: An experimental study. *Construction and Building Materials*, 266, 121048.

Zhang, Y., Liu, H., Ma, T., Gu, G., Chen, C., & Hu, J. (2023). Understanding the changes in engineering behaviors and microstructure of FA-GBFS based geopolymer paste with addition of silica fume. *Journal of Building Engineering*, 70, 106450.

4th International Civil Engineering & Architecture Conference
17-19 May 2025, Trabzon, Türkiye

Fragility curves of 100 m³-elevated water tank stock based on operating level

Ali H. Bayram*[1], Özkan Hakan[1,2], Ramazan Livaoğlu[1,2]

[1] RL ProjeDestek Consulting Company. Ulutek Technopark, Görükle, Bursa, Türkiye.
[2] Bursa Uludağ University/Civil Engineering Department, Görükle Campus 16059, Nilüfer, Bursa, Türkiye

Abstract. The aim of this study is to evaluate the seismic performance and risk estimation of 100 m³ capacity elevated water tanks commonly constructed in Turkey. Although elevated water tanks were widely used in the past, their use has significantly decreased with the technological progress. However, elevated water tanks that are partially operational or idle, especially in agricultural and industrial facilities, may pose significant risks during potential earthquakes due to factors such as material strength degradation over time and lack of maintenance. These structures pose risks that could threaten human life and economic activities in both residential and industrial areas. Considering the low concrete strength and inadequate confinement effects observed in the current stock of elevated water tanks, it is essential to conduct a detailed evaluation of their structural condition and potential seismic performance. In this study, an elevated water tank with low concrete strength (C10), no confinement effect, and S220 reinforcing steel was analyzed. The tank levels (empty, half-full, and full) were considered as parameters. A total of 150 earthquake records, scaled according to $S_a(g)(T=1s)$, were generated: 15 records within the 0.1g–0.4g range and 15 within the 0.5g–1g range for both directions. Time-history analyses were performed, and the effects of tank filling on the fragility of elevated water tanks were investigated based on the results. The findings indicate that under poor material quality and unfavorable conditions, changes in water levels have no significant mitigating effect on structural response.

Keywords: Elevated tanks; Fragility curves;Performance evaluation

1. Introduction

Water is one of the fundamental resources for life, and its procurement and storage have a history as old as humanity itself. In the early periods, settlements were established around water sources, initiating a process that evolved over time with the development of various applications for water transportation and storage. Different designs have been created for water storage, among which elevated water tanks gained widespread use in the 19th century. Following the May 1960 Chile earthquake, investigations into damaged elevated water tanks revealed the necessity of considering the movement of water relative to the tank. In this context, Housner (1963) developed a mass-spring model by identifying that, in the presence of a free water surface, the system comprises two distinct masses. After this study, the use of elevated water tanks became more prevalent, leading to various research efforts focused on their design. Notable studies include those by Veletsos (1974), Dieterman (1988), Dutta et al. (2000), and Livaoğlu (2005).

In recent years, advancements in technology and improvements in the quality of construction materials have led to significant changes in water supply methods. Today, pressurizing and transmitting water directly from the main source using specialized equipment has become a common practice, enabling instant access to water. The widespread adoption of this new system has resulted in a noticeable decline in the number of elevated water tanks, which were frequently used in the past. However, elevated water tanks are still utilized in areas where continuous access to water is of critical importance, such as industrial facilities and regions with intensive agricultural activities. Historically, these structures were constructed in compliance with both national and international standards for water storage. However, over time, environmental factors have led to their deterioration, significantly compromising their structural integrity. Today, these aging elevated water tanks pose serious risks, particularly in the event of natural disasters such as earthquakes. Therefore, considering the existing structural degradation, a comprehensive assessment is essential, taking into account regional seismic hazard levels and the dynamic characteristics of these structures (Livaoğlu & Doğangün, 2003).

* Corresponding author, E-mail: a.haydar.bayram@gmail.com

https://doi.org/10.31462/icearc2025_ce_eqe_349

Fragility curves are fundamental analytical tools widely used to assess the seismic performance of various structural types and components. These curves enable the determination of structural fragility levels by accounting for uncertainty factors such as seismic hazard estimation, structural characteristics, soil-structure interaction, and site conditions. The development of fragility curves can be based on experimental, observational, expert judgment-based, and analytical methods. However, due to data limitations, experimental and expert judgment-based approaches may not always be feasible. Therefore, analytical methods provide a significant alternative for deriving fragility curves (Shinozuka et al., 2000).

The creation of fragility curves using analytical methods involves various numerical techniques, such as static pushover analysis, nonlinear time-history analysis, and incremental dynamic analysis. Particularly with advancements in technology and the increased computational capacity of computers, the use of nonlinear time-history analyses has become more widespread, leading to more accurate results. The obtained results are processed using appropriate fragility functions, providing an effective method for predicting the behavior of structures under potential earthquake scenarios. This process offers a crucial tool for evaluating the seismic performance of structures and determining possible damage levels.

For this study, the nonlinear dynamic analysis method in the time domain was chosen as the structural analysis technique. Selecting the necessary earthquake records plays a significant role in conducting these analyses. To ensure that scaling factors do not reach exaggerated values and deviate from accuracy, 15 different earthquake records scaled between 0.1g and 0.4g, and 15 different earthquake records scaled between 0.5g and 1g were selected, resulting in a total of 30 earthquake records. To obtain fragility curves for elevated water tanks, 150 dynamic analyses were performed for each of the three models with weak resistance (C10), representing fully filled, partially filled, and empty states. Fragility curves were derived based on the damage limit for the load-bearing elements, such as columns, using the concrete and reinforcement unit displacement limits.

2. Materials and methods

The creation of fragility curves to determine the seismic performance of structures is a critical area of research in earthquake engineering. However, limitations in obtaining experimental data and the subjective nature of expert judgment-based approaches make it necessary to develop these curves using analytical methods.

The role of analytical methods in the development of fragility curves is becoming increasingly important. To produce reliable results, it is essential to create a finite element model that accurately represents the physical and mechanical properties of the structural system. This model must reflect the geometry, material properties, and boundary conditions of the structure as closely as possible and should be capable of accurately predicting its behavior under seismic effects.

The accuracy of the finite element model directly impacts the reliability of the fragility curves. Therefore, analytical approaches should be applied meticulously during the calibration process of the fragility curves, and high precision must be maintained in the modeling procedures. In this study, a fiber model, which considers distributed plastic behavior, has been chosen to accurately represent the mechanical behavior of the load-bearing elements. Material assumptions were made considering the absence of confinement effects on the load-bearing elements. The damage limits were formulated based on the unit elongation and shortening of the concrete and reinforcement materials.

To evaluate the structural performance under seismic events, the aim is to generate fragility curves using the widely used Multiple Stripe Analysis (MSA) technique in earthquake engineering. This method includes structural analyses conducted at different intensity measure (IM) levels, with different ground motion records being used for each IM level. IM is a measure that expresses the intensity of ground shaking through spectral acceleration (Sa), peak ground acceleration (PGA), or other parameters.

One of the key reasons for selecting Multiple Stripe Analysis (MSA) over other methods (e.g., IDA, TIDA) is that it involves using independent ground motion records for each IM level, rather than scaling a single ground motion record to various intensity levels. This approach allows for a more realistic evaluation of structural behavior at different seismic intensity levels. Moreover, the accuracy and reliability of the method are enhanced through the use of conditional spectra or other advanced techniques when selecting appropriate ground motions for a specific region and IM level.

The purpose of Multiple Stripe Analysis is to comprehensively understand the performance of structures at different seismic levels. By analyzing how the structure responds to multiple ground motion records at various intensity levels, engineers can assess the performance of the structures, identify potential weak points, and determine areas that require design improvements. The analysis results provide critical data, such as fragility curves and capacity-demand diagrams, offering essential information for earthquake risk assessment and seismic structural design (Jack Baker, 2015).

A lognormal cumulative distribution function is often used to define a fragility function:

$$P(C|IM = x) = \Phi\left(\frac{\ln(x/\theta)}{\beta}\right) \tag{1}$$

P(C|IM = x) represents the probability of a ground motion with IM = x causing the collapse of the structure. Φ() stands for the standard normal cumulative distribution function. θ is the median of the fragility function (the IM level with a 50% collapse probability), and β is the standard deviation of ln IM (sometimes referred to as IM dispersion). Equation 1 implies that the IM values of ground motions causing the collapse of a specific structure follow a log-normal distribution; this is a widely accepted assumption in many cases Ibarra and Krawinkler (2005).

Structural analyses, for each intensity measure level IM = xj, generate a certain number of collapses from the total count of ground motions. Assuming that the observation of either collapse or non-collapse for each ground motion is independent of observations for other ground motions, the probability of observing zj collapses out of nj ground motions with IM = xj is given by the binomial distribution.

P(z_j collapses in n_j ground motions) :

$$\binom{n_j}{z_j} p_j^{zj}\left(1-p_j\right)^{nj-zj} \tag{2}$$

Here, pj represents the probability of a ground motion with IM = xj causing the collapse of the structure. Our objective is to determine the fragility function that predicts pj and the maximum likelihood approach identifies the fragility function that maximizes the probability of observing the collapse data obtained from structural analysis. When analysis data is obtained at multiple IM levels, the likelihood for the entire dataset is obtained by multiplying the binomial probabilities at each IM level (from Equation 2). Likelihood can be obtained as below.

$$\prod_{j=1}^{m}\binom{n_j}{z_j} p_j^{z_j}\left(1-p_j\right)^{n_j-z_j} \tag{3}$$

Here, m represents the number of IM levels, and Π is a product that goes over all levels. Subsequently, we substitute Equation 1 for pj, allowing the fragility parameters to be explicitly present in the likelihood function.

$$Likelihood=\prod_{j=1}^{m}\binom{n_j}{z_j}\Phi\left(\frac{\ln\left(x_j/\theta\right)}{\beta}\right)^{z_j}\left[1-\Phi\left(\frac{\ln\left(x_j/\theta\right)}{\beta}\right)\right]^{n_j-z_j} \tag{4}$$

The estimates of fragility function parameters are obtained by maximizing this likelihood function. To achieve the same outcome and facilitate numerical calculations, it is equivalent to maximizing the logarithm of the likelihood function. Therefore, it can perform this transformation as below:

$$\{\theta,\beta\}=\operatorname{argmax}\sum_{j=1}^{m}\left\{\ln\left(\binom{n_j}{z_j}+z_j ln\Phi\left(\frac{\ln\left(\frac{x_j}{\theta}\right)}{\beta}\right)+\left(n_j-z_j\right)ln\left(1-\Phi\left(\frac{\ln\left(\frac{x_j}{\theta}\right)}{\beta}\right)\right)\right\} \tag{5}$$

3. Modeling and analysis

Given that elevated water tanks in older building stock are known to be vulnerable to seismic effects due to low concrete strength and inadequate reinforcement arrangements, a typical elevated water tank with a 100 m³ storage capacity, designed by the General Directorate of Highways, Water, and Electricity (YSE) of the Republic of Turkey, was selected for this study. Considering the observed low concrete strength and reinforcement characteristics in these tanks, a seismic fragility analysis of this type of building stock has been conducted.

3.1. Selection and scaling of earthquakes

In order to perform seismic fragility analyses reliably, it is necessary to select and scale appropriate earthquake records. In this context, 30 earthquakes were selected, including 15 earthquakes scaled between 0.1g-0.4g and 15 earthquakes scaled between 0.5g-1g, taking into account factors such as site conditions, distance to the fault, and scaling coefficients. The station information, earthquake magnitudes, distance to the fault, and fault mechanisms for the selected earthquakes are presented in Table 1.

During the scaling process, the commonly accepted maximum scaling factor of 4 and minimum factor of 0.25, as found in the literature, were used to determine the earthquake scaling coefficients. These limits were applied to ensure that the changes in the frequency content of the earthquake records remained within acceptable levels and to guarantee the realistic scaling of the selected data set. In this study, analyses were performed using both the east-west and north-south components of each earthquake record. This approach aims to better reflect the multi-directional response of the structure to seismic effects.

During the earthquake data scaling process, the geometric average of the acceleration values corresponding to a 1-second period in both directions was calculated. Using these averages, a weighted acceleration value was determined. This method aims to represent the effects of earthquake records in different directions in a balanced manner. Table 2 presents the acceleration spectral values for the east-west and north-south directions of the selected 30 earthquakes, along with their geometric averages. After determining the spectral acceleration (Sa, g) values corresponding to the geometric averages, the earthquake records were either reduced or amplified using the necessary scaling coefficients. This process ensured that the intensity measure (IM) used in the analyses was obtained at the desired level.

Table 1. Selected earthquake records

RSN	Earthquake Name	Year	Station Name	Magnitude	Mechanism	Rrup (km)	Vs30 (m/sec)
1004	Northridge-01	1994	LA - Sepulveda VA	6.69	Reverse Fault	8.44	380
1011	Northridge-01	1994	LA - Wonderland Ave	6.69	Reverse Fault	20.29	1223
1013	Northridge-01	1994	LA Dam	6.69	Reverse Fault	5.92	629
1091	Northridge-01	1994	Vasquez Rocks Park	6.69	Reverse Fault	23.64	996
1108	Kobe_Japan	1995	Kobe University	6.9	Strike-Slip	0.92	1043
1119	Kobe_Japan	1995	Takarazuka	6.9	Strike-Slip	0.27	312
1161	Kocaeli_Turkey	1999	Gebze	7.51	Strike-Slip	10.92	792
1184	Chi-Chi_Taiwan	1999	CHY010	7.62	Reverse Oblique	19.96	539
143	Tabas_Iran	1978	Tabas	7.35	Reverse Fault	2.05	767
1492	Chi-Chi_Taiwan	1999	TCU052	7.62	Reverse Oblique	0.66	579
1602	Duzce_Turkey	1999	Bolu	7.14	Strike-Slip	12.04	294
161	ImperialValley-06	1979	Brawley Airport	6.53	Strike-Slip	10.42	209
175	ImperialValley-06	1979	El Centro Array #12	6.53	Strike-Slip	17.94	197
231	MammothLakes-01	1980	Long Valley Dam	6.06	Normal Oblique	15.46	537
297	Irpinia_Italy-02	1980	Bisaccia	6.9	Normal Fault	14.74	496
30	Parkfield	1966	Cholame - Shandon Array	6.19	Strike-Slip	9.58	290
3548	LomaPrieta	1989	Dam	6.93	Reverse Oblique	5.02	1070
457	MorganHill	1984	Gilroy Array #3	6.19	Strike Slip	13.02	350
495	Nahanni_Canada	1985	Site 1	6.76	Reverse Fault	9.6	605
5618	Iwate_Japan	2008	IWT010	6.9	Reverse Fault	16.27	826
564	Kalamata_Greece-01	1986	Kalamata (bsmt)	6.2	Normal Fault	6.45	382
68	SanFernando	1971	LA - Hollywood Stor FF	6.61	Reverse Fault	22.77	316
811	LomaPrieta	1989	WAHO	6.93	Reverse Oblique	17.47	388
8165	Duzce_Turkey	1999	IRIGM 496	7.14	Strike-Slip	4.21	760
827	CapeMendocino	1992	Fortuna - Fortuna Blvd	7.01	Reverse Fault	19.95	457
879	Landers	1992	Lucerne	7.28	Strike-Slip	2.19	1369
3126	Pazarcık-Kahramanmaraş	2023	Antakya	7.7	Strike-Slip	143.54	350
3129	Pazarcık-Kahramanmaraş	2023	Defne	7.7	Strike-Slip	146.39	447
3141	Pazarcık-Kahramanmaraş	2023	Antakya	7.7	Strike-Slip	125.42	338
4612	Elbistan-Kahramanmaraş	2023	Göksun	7.6	Strike-Slip	66.68	246

Table 2. Spectral acceleration values at T=1s for both directions of earthquakes

Earthquake Name	East-West S_a(T=1s) (g)	North-South S_a(T=1s) (g)	Geomean S_a(T=1s) (g)	Earthquake Name	East-West S_a(T=1s) (g)	North-South S_a(T=1s) (g)	Geomean S_a(T=1s) (g)
RSN1011-NORTHR	0.09	0.17	0.13	RSN1004-NORTHR	1.14	0.63	0.85
RSN1091-NORTHR	0.19	0.20	0.20	RSN1013-NORTHR	0.72	0.55	0.63
RSN1161-KOCAELI	0.25	0.17	0.21	RSN1108-KOBE	0.58	0.40	0.49
RSN1184-CHICHI	0.18	0.20	0.19	RSN1119-KOBE	0.90	0.77	0.84
RSN161-IMPVALL.H	0.21	0.29	0.25	RSN143-TABAS	0.71	0.68	0.70
RSN175-IMPVALL.H	0.19	0.16	0.17	RSN1492-CHICHI	0.94	1.11	1.02
RSN231-MAMMOTH.I	0.21	0.16	0.18	RSN1602-DUZCE	0.76	1.14	0.93
RSN297-ITALY	0.18	0.20	0.19	RSN3548-LOMAP	1.23	1.11	1.17
RSN30-PARKF	0.18	0.15	0.17	RSN495-NAHANNI	0.42	0.49	0.45
RSN457-MORGAN	0.17	0.17	0.17	RSN811-LOMAP	0.54	0.58	0.56
RSN5618-IWATE	0.28	0.24	0.26	RSN879-LANDERS	0.48	0.30	0.38
RSN564-GREECE	0.23	0.25	0.24	3126-HATAY ANTAKYA	1.07	0.93	1.00
RSN68-SFERN	0.25	0.16	0.20	3129-HATAY DEFNE	0.75	1.95	1.21
RSN8165-DUZCE	0.22	0.23	0.23	3141-HATAY ANTAKYA	0.82	0.97	0.89
RSN827-CAPEMEND	0.18	0.19	0.18	4612-MARAS GOKSUN	0.53	0.72	0.62

The spectra obtained for both components of the selected 30 earthquakes were calculated, and then the scaled earthquake spectra based on the selected earthquake spectra and IM (intensity measure) values were presented. The scaled spectra for the 0.1g-0.4g range are shown in Fig. 1, and the scaled spectra for the 0.5g-1g range are shown in Fig. 2.

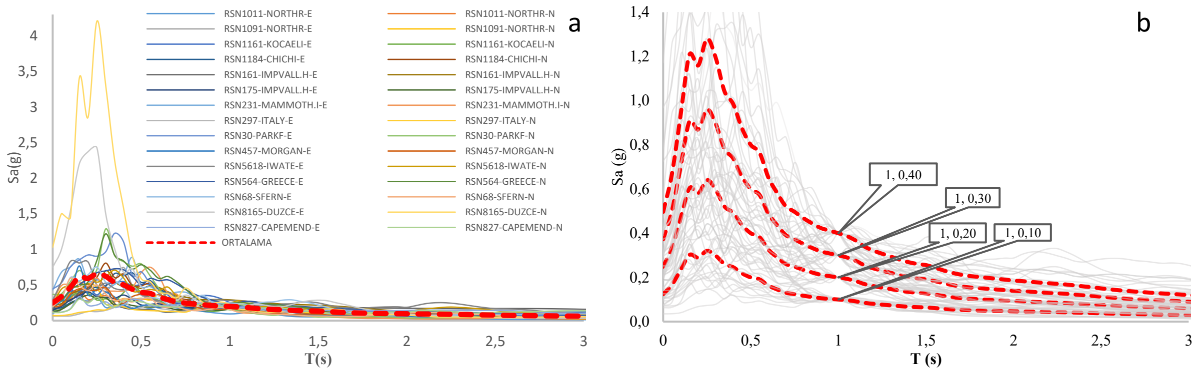

Fig. 1. Selected Spectra for 0.1g-0.4g IM Level (a), Scaled Spectra for 0.1g-0.4g IM Level (b)

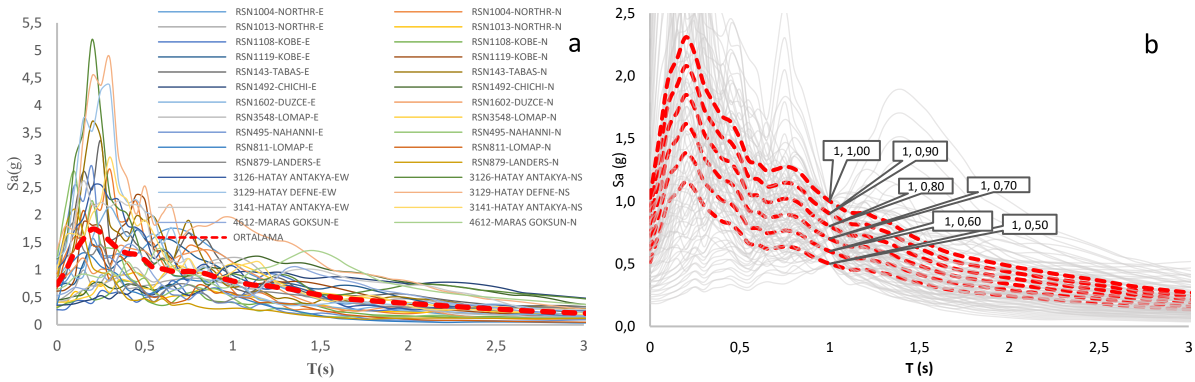

Fig. 2. Spectra selected for 0.5g-1g IM level (a), Scaled spectra for 0.5g-1g IM level (b)

3.2. Modeling of structural elements

As previously mentioned, the elevated water tank was modeled based on the 100 m³ capacity elevated water tank projects prepared by the General Directorate of Roads, Water, and Electricity (YSE) of the Ministry of Rural Affairs of the Republic of Turkey in 1976. The structure consists of a total of 6 floors, with a height of 5 meters per floor, making the total building height approximately 36 meters, including the tank length. Fig. 3 shows the schematic and ETABS model representation of the 100 m³ elevated water tank with a frame system.

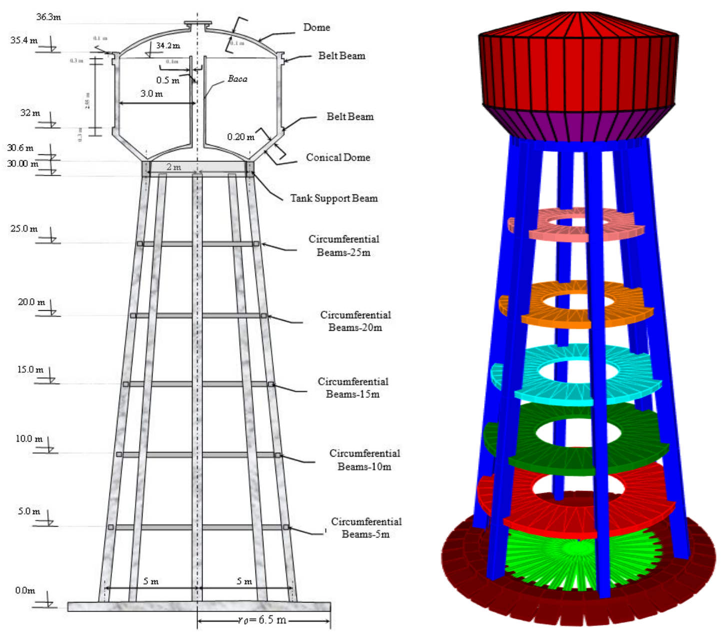

Fig. 3. The 100m³ elevated water tank with a frame system used in the study

The column cross-section between the 0-5 m levels of the elevated water tank is shown in Fig. 4(a), the column cross-section between the 5-30 m levels is shown in Fig. 4(b), and the beam-slab cross-sections from the 5 m level to the 30 m level are shown in Fig. 4(c). The foundation cross-section is presented in Fig. 4(d). Additionally, the floor plan of the elevated water tank is provided in Fig. 4(e).

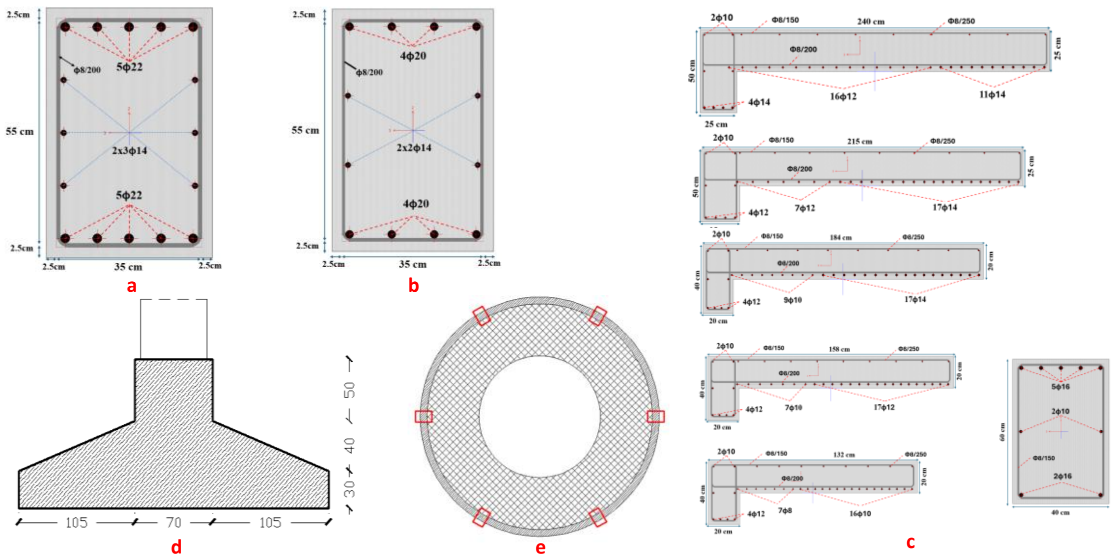

Fig. 4. Load-bearing elements of the 100m³ elevated water tank

3.2.1 Modeling of columns and beams

Although there are different approaches to deformation-based structural modeling in the literature, the modeling of inelastic elements is generally examined under three main categories. These categories are classified based on how the post-elastic behavior is modeled:

1- Concentrate Plastic Model (Macro Model): It is assumed that the post-elastic behavior will accumulate at specific points.

2-Fiber Model (Meso Model): It is assumed that plastic deformation will spread over a certain region.

3-Finite Element Model (Micro Model): It is assumed that plastic behavior will spread throughout the entire section.

Additionally, within the scope of the piled plastic behavior model specified in Article 5.3.1 of TBDY2018, auto M3 plastic hinges are defined in the ETABS software for the body beam elements in accordance with ASCE 41-13. The schematic representation of the piled plastic behavior model is shown in Fig. 5(a), while the plastic hinges defined for the beams in the structure are shown in Fig. 5(b). For the sections where the plastic hinge is not defined, the effective section stiffness factors (0.35) of reinforced concrete structural elements specified in Table 4.2 of the Turkish Building Earthquake Code 2018 (TBDY2018) were used.

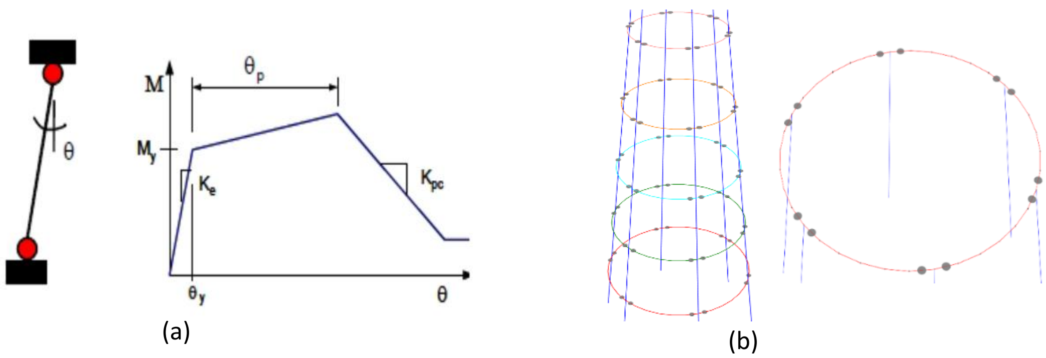

Fig. 5. Beam plastic hinge model and plastic hinge regions

For the columns, the distributed plastic behavior model specified in Article 5.3.2 of TBDY 2018 was used to model the column cross-sections. In Fig. 6(a), the column element cross-sections between the 0-5 m and 5-30 m levels are shown in their divided fiber form, with each red dot indicating the position of a fiber.

It is assumed that there is no confinement effect in the column elements, and the analyses were carried out based on this assumption. In Fig. 6(b), the schematic representation of how the column elements were modeled in the Perform3D program is provided. Here, the stiffness of the column-beam joint regions is defined using the "End Zone" concept, while the stiffness reduction factors specified in the code are applied for the elastic regions. To model the inelastic behavior, fiber cross-sections were defined, adopting a more realistic approach to the analysis.

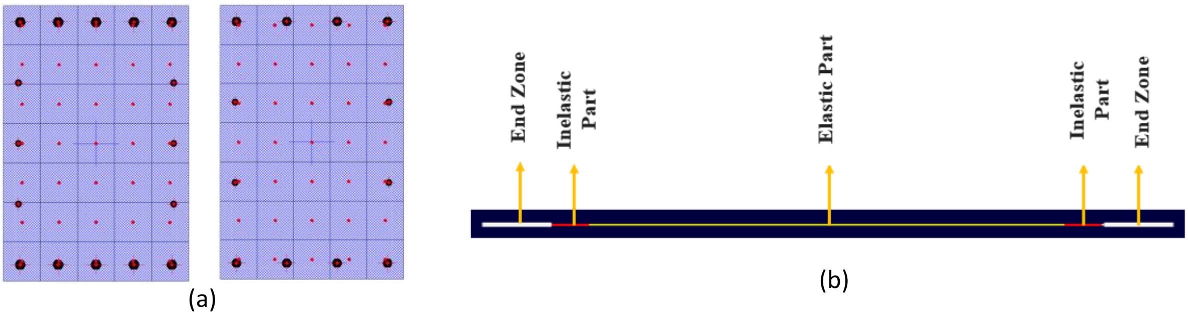

Fig. 6. Column distributed fiber model

3.3. Material and damage limits

In this study, it was assumed that the existing building stock is aged and has weak material properties, and material selections were made accordingly. In this context, the concrete class was determined as C10, and the reinforcement material used was ribbed S220 steel. This selection, which represents the low concrete strength and inadequate reinforcement properties commonly encountered in the older building stock, aims to model the behavior of structures under seismic effects more realistically.

3.3.1. Reinforcement steel

In this study, nonlinear time-history analyses based on displacement were performed. For the analyses, S220 reinforcement steel was used in accordance with TBDY2018 (Article 5A.2). The modulus of elasticity of the reinforcement steel was taken as $E_s = 2\times10^5$ MPa, nd the necessary general information about the steel material used is provided in Table 3.

Table 3. Information on Reinforcement Steel

Quality	f_{sy}*(Mpa)*	ε_{sy}	ε_{sh}	ε_{su}	f_{su}/f_{sy}
S220	220	0.0011	0.011	0.12	1.2

In Article 5.8.1.1 (b) of TBDY2018, the limit for the failure prevention performance level of reinforcement steel is defined in terms of unit strain ε_{su} (unit elongation corresponding to tensile strength) by Equation 6. Using this equation, the failure damage limit value for the reinforcement is determined as ($\varepsilon_s^{(CP)}$) 0.048.

$$\varepsilon_s^{(CP)} = 0.4\,\varepsilon_{su} \tag{6}$$

It is assumed that the reinforcement steel exhibits ideal elastic-perfectly plastic (EPP) behavior, and it has been idealized accordingly, as shown in Fig. 7.

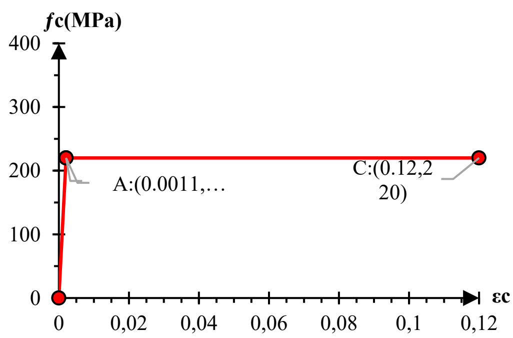

Fig. 7. Idealized reinforcement material model

3.3.2. Unconfined concrete material

In this study, a model without confining reinforcement has been chosen to represent the case where the concrete does not exhibit the effects of confinement due to the absence of confining reinforcement or significant corrosion in the confining reinforcement caused by environmental factors.

$$E_c \cong 5000\sqrt{f_{co}} \quad (MPa) \tag{7}$$

In this study, concrete grade C10 (fc = 10 MPa) has been assumed, and the elasticity modulus of concrete has been calculated as 15,811 MPa using Equation 7 provided in Annex 5A.1 of TBDY 2018. The mechanical properties of concrete play a crucial role in determining the material's load-bearing capacity and deformation behavior. In this context, the behavior of unconfined concrete has been evaluated based on the model defined in the relevant regulation (see Fig. 8a). Additionally, the damage limit for unconfined concrete, corresponding to a strain of 0.0035, along with its idealized form, is presented in Fig. 8.

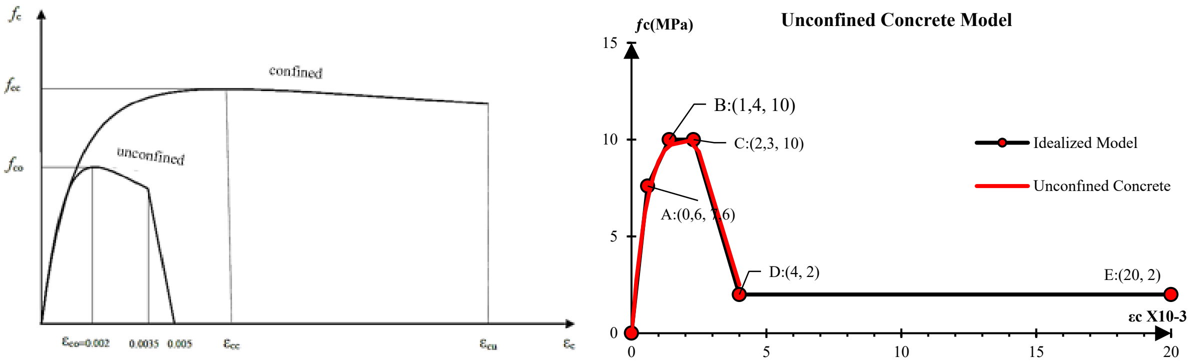

(a) (b)

Fig. 8. TBDY2018 unconfined concrete model and idealized concrete model

3.4. The Modeling of Fluid-Structure Interaction

Various methods have been developed to model the dynamic behavior of the fluid in elevated water tanks. These methods are primarily classified into single-mass and multi-mass systems. Under dynamic loads, tank-fluid systems exhibit two main types of motion. The first is the impulsive mass, where the fluid moves together with the tank. The second is the oscillatory mass, where the fluid oscillates independently of the tank with a certain period (Livaoğlu, 2005).

The mechanical model developed by Housner, which treats the fluid in the tank as two separate masses, is also used as the foundation for this study. This model is shown in Fig. 9 (Housner, 1963). Later, Epstein reformulated the equations of Housner's two-mass model to provide an alternative mathematical formulation (Epstein, 1976).

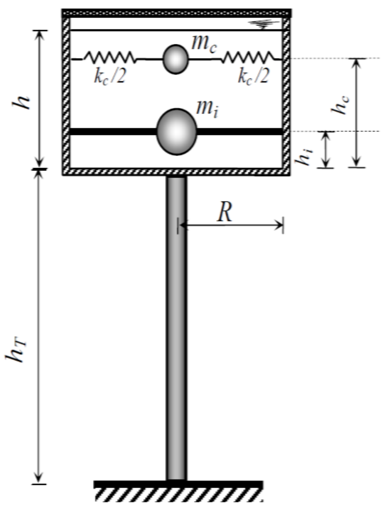

$$\omega^2 = \frac{g}{R} 1.84 \tanh\left(1.84\ \frac{h}{R}\right)$$

$$k_c = m_c \frac{g}{R} 1.84 \tanh\left(1.84\ \frac{h}{R}\right)$$

$$m_c = m_w 0.318 \frac{R}{h} \tanh\left(1.84\ \frac{h}{R}\right)$$

$$m_i = m_w \frac{tanh\left(1.74\frac{R}{h}\right)}{\left(1.74\frac{R}{h}\right)}$$

$$h_c = \left[1 - \frac{cosh(1.84^{h}/_{R})-1}{1.84\frac{h}{R}\, sinh(1.84^{h}/_{R})}\right] h$$

$$h_i = \frac{3}{8} h$$

Fig. 9. Mechanical model of elevated tank-liquid system (Livaoğlu,2005)

In the given equations, k_c denotes the rigidity of the oscillating mass, m_c is the oscillating mass, m_i is the impulse mass, h_c describes the height of the oscillating mass, and h_i describes the height of the impulse mass.

Table 4. Two-mass system approach data

	Liquid Mass (m_w) (kg)	Oscillating Mass (m_c) (kg)	Impulse Mass (m_i) (kg)	Oscillating Mass Stiffness (k_c) (N/m)	Oscillating Mass Height (h_c) (m)	Impulse Mass Height (h_i) (m)
FULL	102403	24065	67720	142703	2.63	1.5
HALF	50644	19754	20093	102126	1.2	0.8

In this study, the gap-hook model was used for modeling the water in the Perform3D program. Models were created based on the mathematical formulations provided above and the data given in Table 4. Fig. 10 shows the model images of the elevated water tanks with the water in the tank section in the following conditions: full (10a), half-full (10b), and empty (10c).

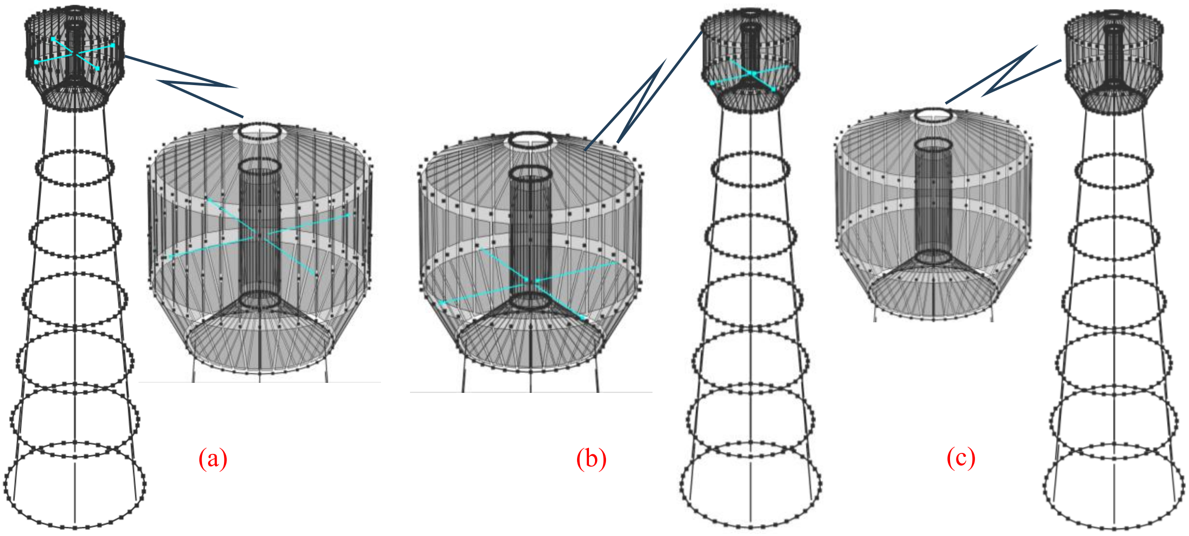

Fig. 10. Perform3D Tank Capacity Fully Filled (a), Half Filled (b), Empty (c) Models

The oscillation periods of the water calculated using the two-mass model proposed by Housner (1963) were compared with the oscillation periods obtained in the Perform3D software. As a result of the analyses, the difference between the two methods was determined to be 2.86% when the tank was completely full, and 1.91% when the tank was half-full. The obtained period values and differences are presented in Table 5.

Table 5. Fluid-structure interaction

Model Feature	Perform 3D Oscillation Period T(s)	Housner Model Oscillation Period T(s)	(%)
C10-S220-FULL	2.65	2.58	2.86
C10-S220-HALF	2.82	2.76	1.91

3.5. Modal information

The elevated water tank, being an axis-symmetric structure, exhibits equal modes in the x and y directions. For the three different models, structural modes other than the water oscillation mode were examined, and the dominant x-y modes resulting from axis-symmetry are presented in three modes (1), (2), and (3) along with their mass participation in Table 6.

Table 6. Structural Modes

Model Description	(1) x-y T(s)	z T(s)	(2) x-y T(s)	z T(s)	(3) x-y T(s)	Mass Participation Ratio (1)	Mass Participation Ratio (2)	Mass Participation Ratio (3)
C10-S220-FULL	1.542	1.319	0.682	0.557	0.347	0.683	0.090	0.046
C10-S220-HALF	1.396	1.024	0.644	0.492	0.337	0.728	0.089	0.056
C10-S220-EMPTY	1.346	1.021	0.620	0.491	0.329	0.805	0.090	0.057

The mode shapes corresponding to the five different mode values presented in Table 6 were examined to better understand the structural behavior. In this regard, as an example, the dynamic behavior of the elevated water tank when the tank is fully filled was analyzed, and the effects of the mode shapes on the general vibration characteristics of the structure were visualized and presented in detail in Fig. 11.

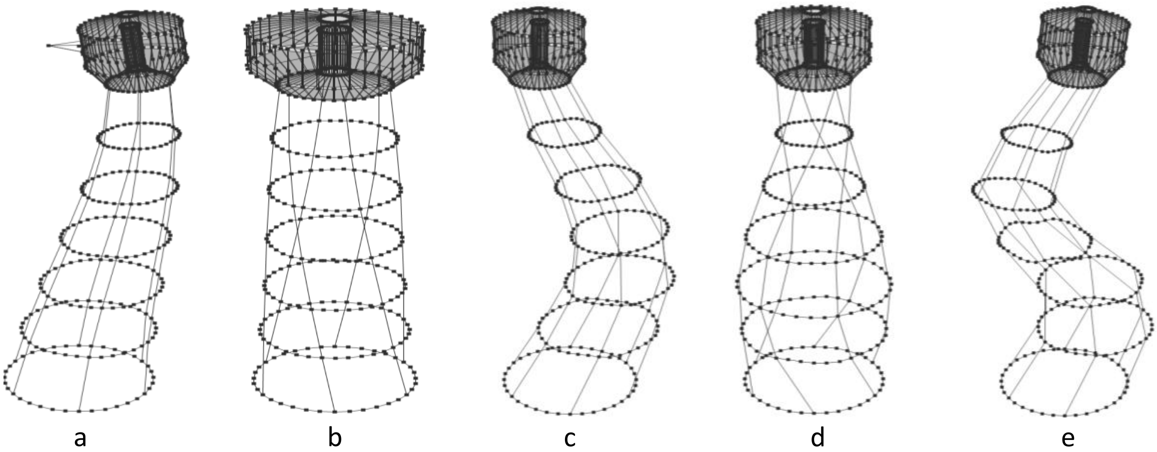

Fig. 11. The mode shapes corresponding to the modes given in Table 6 are presented in the x-y direction (a-c-e) and the z direction (b-d).

3.6. Fragility curves

In this study, fragility curves for the elevated water tank with a frame system were obtained using Multi-Stripe Analysis for three different tank filling levels. In the creation of the fragility curves, the Collapse Prevention (CP) limit states for both the concrete and reinforcement materials were determined for damage definition, and fragility curves were derived based on these values. Since an element-based evaluation was conducted, the fragility curves were created based on the condition where the six column elements on each floor simultaneously exceed their respective limit states.

Initially, the six elements on the first floor were examined, and if all elements exceeded their material damage limits for a specific earthquake, it was assumed that the elevated water tank had reached the Collapse Prevention (CP) state. If not all elements on the first floor were damaged, the elements on the upper floors were examined, and this process continued until the top floor. These values were then solved to generate the fragility curves. Fig. 12 presents the fragility curves of the elevated water tank for three different filling levels, based on both the Collapse Prevention (CP) and Life Safety (LS) limit states..

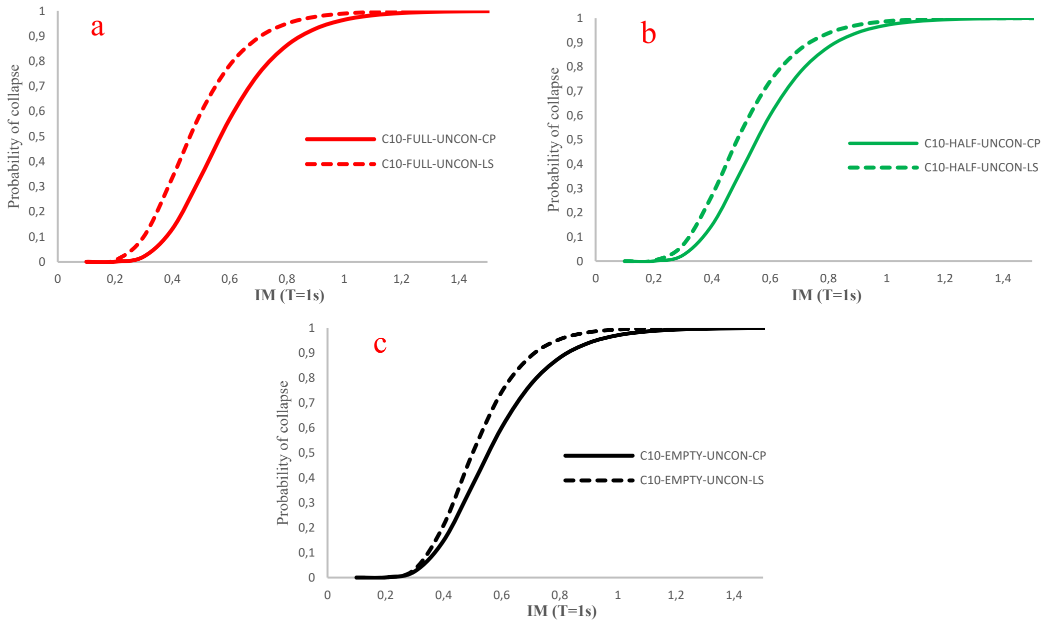

Fig. 12. Fragility curves for three different conditions (full-half-empty) according to CP and LS limit states.

In the case where the tank capacity is full, based on the Collapse Prevention (CP) limit state, the fragility curve representing the scenario where all elements on each floor reach the collapse state (C10-FULL-UNCON-CP) results in an acceleration value of 0.570g for a 50% exceedance probability at T=1s. For the Life Safety (LS) state in the full condition, the corresponding acceleration value for this exceedance probability is determined to be 0.463g, as shown in Fig. 12(a). The fragility curves for the Half and Empty tank capacity conditions are shown in Fig. 12(b) and Fig. 12(c), respectively. The acceleration values corresponding to a 50% exceedance probability at T=1s for all conditions are provided in Table 7.

Table 7. Acceleration values corresponding to a 50% exceedance probability in the elevated water tank.

	CP	LS
C10-FULL-UNCON	0.570	0.463
C10-HALF-UNCON	0.556	0.488
C10-EMPTY-UNCON	0.556	0.500

In the case where the material quality is low and there is no confinement effect in the structural elements, it is observed that for the Collapse Prevention (CP) limit state, the full tank capacity condition is safer compared to the other conditions, while for the Life Safety (LS) limit state, the fragility results indicate a more critical situation. For the Collapse Prevention limit state, the fragilities obtained for the half-full and empty tank conditions are found to have the same values corresponding to the 50% exceedance probability. Furthermore, as shown in Table 7, the acceleration value corresponding to the 50% exceedance probability for the LS condition is determined to be 0.5g for empty tank , while this value decreases to 0.463g for the full tank condition. This indicates that the critical situation in the elevated water tank increases as the tank transitions from empty to full.

When investigating the reason for this situation, it is found that in high-intensity earthquakes, almost all floors suffer damage, while in low-intensity earthquakes, the damage tends to be concentrated on the upper floors. This is due to the additional liquid mass in the tank, which causes more damage to the columns of the top floor supporting the tank. When evaluated from the CP limit state, fragility arises due to damage in the lower floors, as not all elements on the top floor are damaged. However, when considering the LS limit state, it becomes clear that the top floor plays a more critical role in determining the boundary scenario.

As mentioned in Section 3.1, the selected earthquakes were scaled based on acceleration values corresponding to the geometric average for T = 1s. This scaling method provides a rapid fragility assessment using the design spectral acceleration coefficient for a 1.0-second period, as specified in TBDY2018 for SD1. Fig. 13 presents the fragility curves for three different tank capacities, evaluated according to two distinct damage limit states.

The vertical lines in this graph indicate the expected earthquake levels for the design and maximum considered earthquakes for ZC and ZD soil classes, with a point of an example location in the Antakya district of Hatay province. These lines represent the spectral ordinate for T = 1s, obtained from AFAD, corresponding to the city center location's design earthquake (DD2: 10% exceedance probability, 50-year return period, 475-year return period) and maximum considered earthquake (DD1: 2% exceedance probability, 50-year return period, 2475-year return period).

Importantly, these fragility curves show that under such poor initial tank conditions, the structural response becomes highly critical. The predicted acceleration values serve as a strong indicator of the potential risk. Considering the observed accelerations during the Maraş earthquakes and the typical soil characteristics of agricultural areas where these tanks are often constructed, the actual acceleration response is easiliy estimated that it was even higher. In addition, the soils in these areas tend to be softer than the class C soils defined in TBDY2018, exacerbating the vulnerability of the structures.

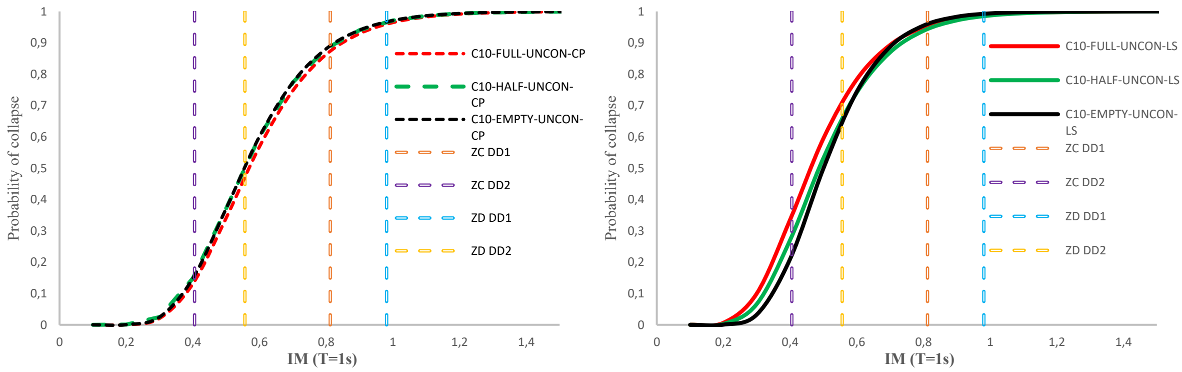

Fig. 13. Fragility curves according to CP and LS damage limits.

Table 8. Acceleration values of earthquake ground motion levels based on local soil classes.

ZC DD2 (g)	ZD DD2 (g)	ZC DD1 (g)	ZD DD1 (g)
0.405	0.556	0.812	0.981

For the examined elevated water tank located in the selected region, in the scenario where the soil class is ZC, and an earthquake with a 2475-year return period occurs, the material grade used in the study is found to be inadequate, and the confinement effect can be neglected. In this case, the exceedance probabilities for the tank being FULL, HALF and EMPTY are observed to be as high as 87.1% and 88.8%, respectively. This situation results in much higher levels for the Life Safety (LS) damage limit state, and these results are presented in Table 9. For the DD2 earthquake, expected to occur with a 475-year return period, in a scenario where the soil class is worse, the values corresponding to the LS damage limit are determined to be 48.1% for the full tank condition, 41.7% for the half-full condition, and 37.2% for the empty tank condition.

Table 9. Exceedance probabilities corresponding to SD1 values in elevated water tanks

	FULL		HALF		EMPTY	
	CP	LS	CP	LS	CP	LS
ZC DD1	87.1%	95.3%	88.8%	94.2%	88.8%	95.8%
ZC DD2	14.1%	34.9%	16.0%	28.4%	16.0%	22.5%
ZD DD1	95.8%	98.7%	96.5%	98.4%	96.5%	99.2%
ZD DD2	24.9%	48.1%	27.3%	41.7%	27.3%	37.2%

4. Conclusions

This study aims to develop fragility curves to assess the seismic vulnerability of a six-story elevated water tank with a capacity of 100 m^3. In this context, different filling ratios have been analyzed under scenarios where there is no confinement effect and material strength is low.

The findings indicate that under severely deteriorated conditions, variations in the water level have no significant mitigating effect on the structural response. While the presence of water slightly reduces the likelihood of exceeding the Collapse Prevention (CP) limit, this effect is minimal and does not improve overall safety. In contrast, for the Life Safety (LS) limit, the additional effects of water significantly increase the exceedance probability, exacerbating the vulnerability of the structure.

Moreover, the fragility assessments emphasize that in regions with poor soil conditions—such as agricultural areas where these tanks are commonly built—the observed acceleration response can be significantly higher than anticipated. Lessons from recent earthquakes, including the Maraş earthquake, highlight that these structures face an even greater risk due to softer soil conditions than the C-class category defined in TBDY2018. The fragility curves, along with spectral acceleration predictions, provide an urgent warning of potential structural failure in such cases.

To ensure the safety of these structures and proactively mitigate risks, a robust evaluation and decision-making mechanism must be established based on the seismic hazard level of the region. A nationwide database should be developed to assess the current condition of these tanks, whether in use or idle, through systematic field studies. By identifying high-risk structures and implementing necessary reinforcements or replacements, earthquake-related hazards can be significantly reduced, contributing to overall structural resilience.

References

Baker, J. W. (2015). Efficient analytical fragility function fitting using dynamic structural analysis. *Earthquake Spectra, 31*(1), 579–599.

CSI. (2023). *ETABS* (Version 24.2.0) [Computer software]. Computers and Structures, Inc.

CSI. (2023). *PERFORM-3D* (Version 9.0.0) [Computer software]. Computers and Structures, Inc.

Dieterman, H. A. (1988). *Dynamics of tower, liquid-structure-foundation interaction* (PhD thesis). Delft University of Technology. http://resolver.tudelft.nl/uuid:8e7437ec-3684-4b1f-9084-32b59065cf6e

Dutta, S. C., Jain, S. K., & Murty, C. V. R. (2000). Assessing the seismic torsional vulnerability of elevated tanks with RC frame-type staging. *Soil Dynamics and Earthquake Engineering, 19*(3), 183–197.

Haroun, M. A., & Temraz, M. K. (1992). Effects of soil-structure interaction on seismic response of elevated tanks. *Soil Dynamics and Earthquake Engineering, 11*(2), 73–86.

Housner, G. W. (1963). The dynamic behavior of water tanks. *Bulletin of the Seismological Society of America, 53*(2), 381–387.

Ibarra, L. F., & Krawinkler, H. (2005). Global collapse of frame structures under seismic excitations. *John A. Blume Earthquake Engineering Center, Stanford University*. https://stacks.stanford.edu/file/druid%3Adj885ym2486/TR152_Ibarra.pdf

Livaoğlu, R. (2005). *Investigation of the earthquake behavior of elevated tanks considering fluid-structure-soil interactions* (PhD thesis). Karadeniz Technical University, Institute of Science, Department of Civil Engineering.

Livaoğlu, R., & Doğangün, A. (2003). Farklı taşıyıcı sisteme sahip ayaklı depoların zemin sınıflarına göre dinamik davranışlarının irdelenmesi. *SAUJS, 7*(2), 70–77. (In Turkish)

TBSC. (2018). *Türkiye Building Seismic Code*. Disaster and Emergency Management Presidency, Ankara, Turkey. (In Turkish)

Veletsos, A. S. (1974). Seismic effects in flexible liquid storage tanks. In *Proceedings of the International Association for Earthquake Engineering Fifth World Conference* (pp. 630–639). Rome.

ICEARC'25
4th International Civil Engineering & Architecture Conference
17-19 May 2025, Trabzon, Türkiye

Performance-based assessment with numerical modeling and strengthening of an masonry historical building

Fatih Y. Okur*[1,2]

[1] Karadeniz Technical University, Department of Civil Engineering, 61080 Trabzon, Türkiye
[2] Earthquake and Structural Health Monitoring Research Center, Karadeniz Technical University, Trabzon 61080, Türkiye

Abstract. Historical masonry buildings are essential components of cultural heritage, yet their structural vulnerability-particularly under seismic actions-necessitates comprehensive evaluation and strengthening strategies. This study presents a structural assessment and retrofitting design for a two-story masonry school building located in Tbilisi, Georgia. The building, characterized by load-bearing stone masonry walls and timber flooring systems, was evaluated to determine its structural performance under both vertical and seismic loading conditions. A detailed three-dimensional finite element model was developed using SAP2000, incorporating all architectural openings and material properties. Structural analyses were conducted separately for gravity loads and lateral earthquake effects in accordance with TS EN 1995-1-1 and the Turkish Building Earthquake Code (TBEC, 2018). Material parameters for masonry and timber elements were defined based on international standards and national guidelines for historical structures. Initial analyses revealed that the existing timber floor system exhibited inadequate shear and bending capacity, as well as excessive deflection under serviceability conditions. Additionally, the unreinforced masonry walls displayed critical tensile and compressive stress concentrations under seismic loading. In response, a strengthening solution was developed, consisting of new steel beams (HEA140 and UPN140) integrated into the floor structure and the application of 2 cm thick fiber-reinforced cement-based repair mortar on the interior surfaces of the masonry walls, combined with 100 kN/m geogrid mesh reinforcement. Post-strengthening analysis results demonstrated that the proposed interventions significantly improved the overall behavior of the structure, reducing stress concentrations and displacement demands to acceptable levels. The strengthened system meets the Life Safety performance level under the DD-3 seismic design scenario. The study underscores the importance of combining traditional conservation with modern engineering tools to ensure the structural integrity of historical buildings without compromising their heritage value..

Keywords: Cultural heritage; Finite element model; Life safety performance; Masonry building

1. Introduction

Masonry structures represent one of the oldest and most widespread forms of construction throughout history, particularly in educational, religious, and residential architecture. These buildings, often composed of natural stone or fired brick bonded with lime or cement mortar, are known for their durability, thermal comfort, and cultural significance. In many regions, such as the Caucasus and Anatolia, masonry buildings constitute a substantial portion of the architectural heritage and serve as living witnesses of local identity and historical continuity.

Despite their historical and architectural value, unreinforced masonry structures are particularly vulnerable to seismic loads due to their brittle behavior, lack of ductility, and limited tensile strength. Earthquakes in recent decades have repeatedly demonstrated the susceptibility of such structures to partial or total collapse, especially in the absence of horizontal diaphragm action and proper wall-to-wall and wall-to-roof connections (Tomazevic, 1999; Lourenço, 2002). The seismic fragility of these buildings poses not only a risk to public safety but also threatens the irreversible loss of cultural heritage.

In parallel with the growing awareness of the need for seismic safety, there has been an increasing focus on conservation-compatible strengthening strategies. Interventions in heritage buildings must balance structural requirements with architectural and historical integrity. The ICOMOS guidelines (ICOMOS, 2003) emphasize the use of minimal intervention, reversibility, and compatibility as core principles in structural retrofitting of historic buildings. Several studies have proposed retrofit techniques ranging from external steel bracing, grout injection, and reinforced shotcrete to more reversible and less invasive solutions such as fiber-reinforced composites or

* Corresponding author, E-mail: yeseviokur@ktu.edu.tr

https://doi.org/10.31462/icearc2025_ce_eqe_382

golden light publishing

geogrid-reinforced mortars (Taghdi, 2000; Abrams & Lynch 2001; ElGawady et al. 2004; Corradi et al., 2008; Binda & Saisi, 2005). These methods are innovative methods that aim to improve performance without compromising originality, and are quite successful in increasing structural strength.

Although numerous experimental and numerical studies have addressed the mechanical characterization of masonry units and traditional mortars (Valluzzi et al., 2004; Lagomarsino & Cattari, 2015), there remains a gap in the literature regarding the performance verification of these materials when applied in real heritage structures using full-scale engineering simulations.

This study addresses this challenge through a case study involving a four-story historical masonry school building located in Tbilisi, Georgia. The building comprises load-bearing stone masonry walls and timber floor systems and has suffered from material deterioration and structural deficiencies. Using a performance-based engineering approach, the study presents the development of a three-dimensional finite element model, assesses the existing condition of the building, and proposes a strengthening solution that combines traditional materials with modern reinforcement techniques. The seismic behavior of the structure before and after retrofitting is evaluated in accordance with the Turkish Building Earthquake Code (TBEC, 2018), offering a quantitative assessment of the intervention's effectiveness and safety.

The findings contribute to the ongoing discourse on the preservation of heritage buildings, demonstrating how structural engineering tools can be harmonized with conservation ethics to ensure the long-term resilience and cultural continuity of historical masonry assets.

2. Architectural and structural characteristics of the building

The case study building is a four-story historical masonry school structure located in Tbilisi, Georgia. According to the architectural documentation and on-site inspections, the building was constructed using traditional stone masonry techniques and timber-based floor systems. The building has a rectangular plan geometry and is composed of thick load-bearing masonry walls constructed from irregular stone units bonded with lime-based mortar. The ground floor houses large corridor spaces and classroom areas, while the upper floor continues with similar functional zoning. The interior partitions are also masonry, contributing to the overall stiffness of the structure. Large openings for windows and doors are symmetrically arranged along the façades, which, while architecturally significant, result in stress concentrations in seismic conditions.

Floor systems consist of timber beams spaced approximately 50 to 60 cm apart, supporting wooden floorboards that span between masonry walls. The roof system is also timber-based, constructed with inclined rafters and covered with lightweight roofing material. However, structural inspections revealed that the timber components, particularly those supporting the floor, have experienced degradation and loss of stiffness over time.

The foundation system was originally constructed with stone footings, without continuous reinforced concrete beams. As a result, differential settlements and minor cracking were observed in several load-bearing walls, particularly near door and window openings.

The architectural configuration includes long corridor spans, which presented challenges in lateral load distribution due to the lack of diaphragm action. Furthermore, the floor-to-wall connections were found to be insufficient to transfer seismic forces effectively, necessitating the design of additional structural measures to ensure integrity and stability during earthquake events.

Figs. 1 and 2 present architectural drawings of the building and some images of the on-site inspection. The combination of thick masonry walls, aged timber elements, and discontinuous connections between horizontal and vertical systems illustrates the complex nature of seismic vulnerability in such heritage buildings. These characteristics were carefully incorporated into the finite element model to ensure realistic simulation of the building's behavior under various load cases.

3. Finite element modeling approach

A three-dimensional finite element model of the historical masonry-timber school building was developed using SAP2000 software to simulate the structural behavior under gravity and seismic loading conditions. The modeling approach adhered to the guidelines outlined in TS EN 1996-1-1 for masonry structures and TBEC (2018) for seismic assessment of existing buildings.

3.1 Model geometry and element types

The building geometry was modeled based on architectural plans and verified with site inspection data. Load-bearing masonry walls were modeled using four-node shell (area) elements to accurately capture in-plane and out-of-plane behavior. Timber beams were modeled using frame (bar) elements with linear elastic properties. All architectural openings, including doors and windows, were explicitly defined in the model to reflect local stress concentrations. Images of the finite element model are given in Figure 3.

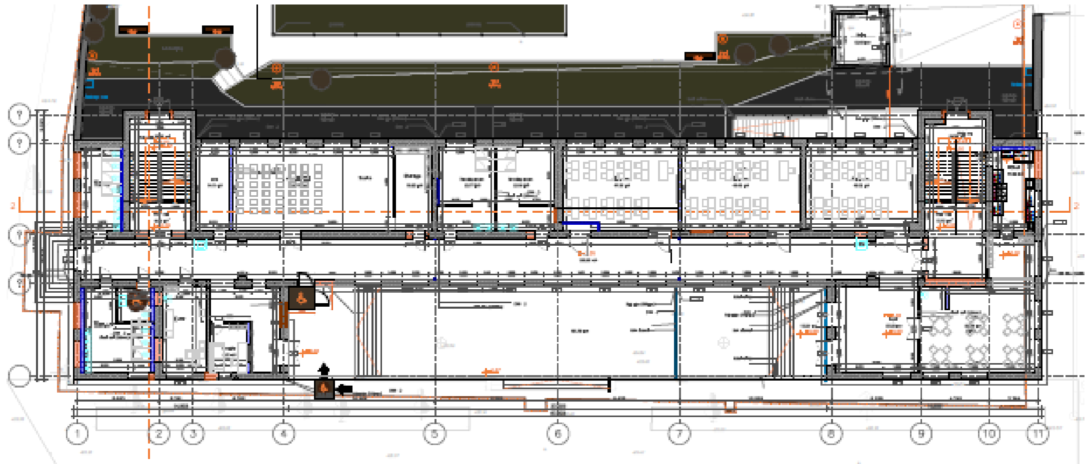

a) Ground floor plan

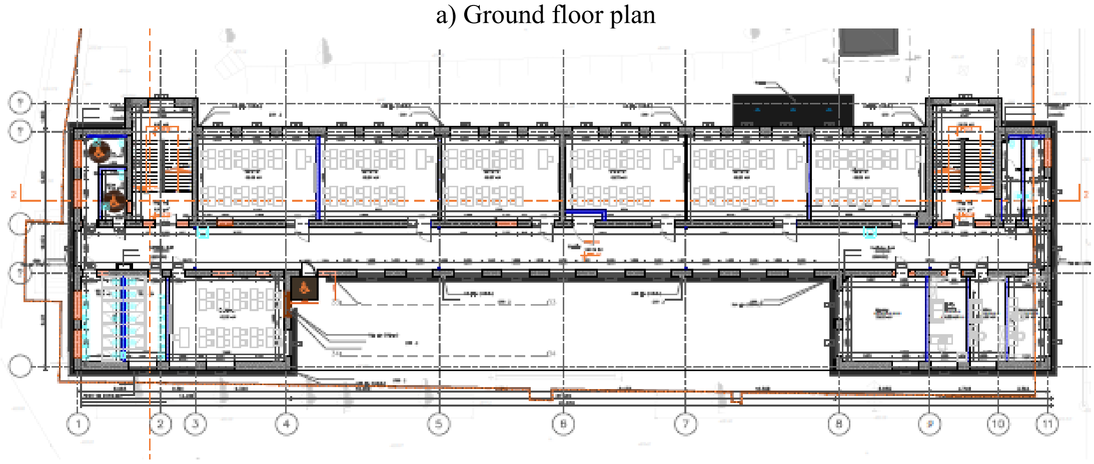

b) Plans for floors 1-3

Fig. 1. Architectural drawings of the building

Fig. 2. Some images of the on-site inspection of the building

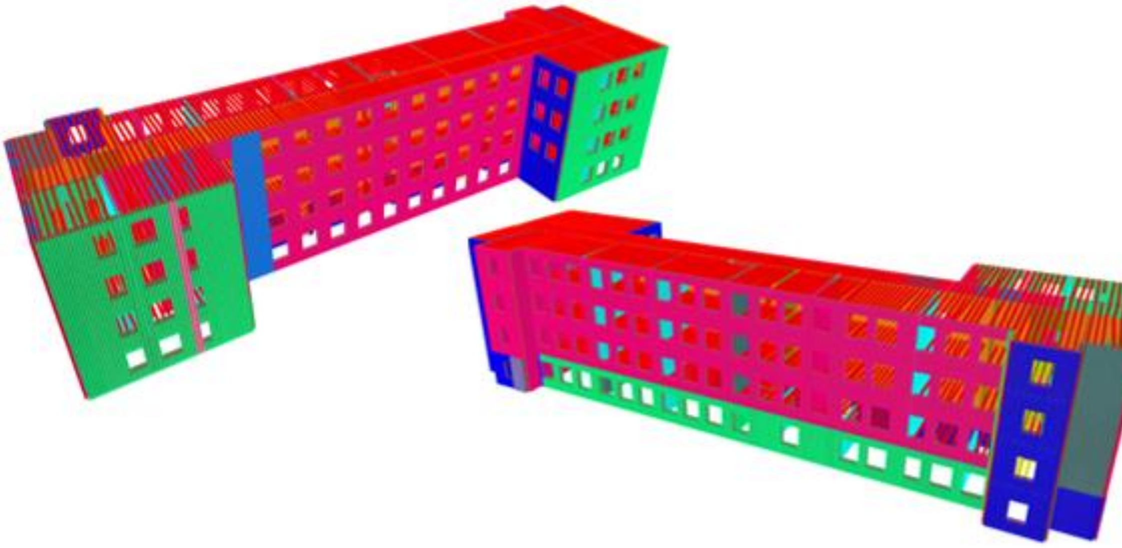

Fig. 3. Finite element model of the building

3.2. Metarial properties

Within the scope of the analysis, the strength classes and material properties of structural timber elements were determined in accordance with the specifications outlined in TS EN 1995-1-1 (Eurocode 5). This standard classifies structural timber into two main groups and twenty distinct strength classes based on their mechanical performance. The classification is derived from a series of mechanical criteria, including bending strength, tensile strength parallel and perpendicular to the grain, compressive strength parallel and perpendicular to the grain, shear strength, modulus of elasticity parallel and perpendicular to the grain, shear modulus, and density.

For the purposes of this study, timber elements were modeled using the mechanical properties corresponding to the C22 strength class. In SAP2000, these properties were assigned as an orthotropic material model to accurately simulate the anisotropic behavior of timber. All timber members in the finite element model were assigned this C22 orthotropic material definition. In accordance with TS EN 1995-1-1, two primary limit states were considered in the structural design and evaluation process:

- Ultimate Limit State (ULS): Ensuring structural safety against collapse under maximum design loads.
- Serviceability Limit State (SLS): Verifying usability and limiting deformations under normal service loads.

Material properties were calculated separately for both limit states, and finite element analyses were conducted accordingly. Table 1 summarizes the material parameters used in the model under ULS and SLS design conditions.

Table 1. The material parameters for the model under ULS and SLS design conditions

Limit State	Design Elasticity Modulus (kN/mm^2)		Design Shear Modulus
	$E_{d//}$ (Parallel)	$E_{d\perp}$ (Perpendicular)	(G_d)
Ultimate	7.69	0.25	0.48
Serviceability	3.33	0.11	0.21

In the determination of the mechanical properties of masonry stone elements, the "Earthquake Risk Management Guide for Historical Structures" published by the Turkish Directorate General of Foundations has been taken into account. This guideline provides appropriate approaches for assessing the material properties of registered historical buildings and aims to ensure realistic modeling of their structural behavior. The masonry stone material parameters used in the analyses within the scope of this study are presented in Fig. 4.

3.2. Determination of loads

The determination of structural loads was carried out in accordance with the load calculation provisions of TS EN 1995-1-1, which governs the design of timber structures, and the EN 1991 series, which addresses environmental actions. According to TS EN 1995-1-1, in order to carry out structural design and verification for timber structures, the loads must be determined in accordance with the following standards:

- TS498: Densities, self-weight, and imposed loads on structures
- •Seismic loads, on the other hand, were determined according to the national standard TBEC (2018).

Wall Type	Compressive Strength (f_m) (MPa)	Shear Strength (τ_0) (kPa)	Elastic Modulus (E) (MPa)	Shear Modulus (G) (MPa)	Unit Weight (w) (kN/m³)
Rubble stone masonry wall	0.6–0.90	20–32	690–1050	115–175	19
Rough stone masonry wall	1.1–1.6	35–51	1020–1440	170–240	20
Well-connected cut stone masonry wall	1.5–2.0	56–74	1500–1980	250–330	21
Soft stone (limestone, tuff) masonry wall	0.8–1.2	28–42	900–1260	150–210	16
Smooth cut stone, plastered masonry wall	1.8–2.8	78–98	2340–2820	390–470	22
Lime mortar brick masonry wall	1.8–2.8	60–92	1800–2400	300–400	18
Cement mortar perforated brick masonry wall	3.8–5.0	240–320	2800–3600	560–720	15
Brick masonry wall with <45% void ratio	4.6–6.0	300–400	3400–4400	680–880	12
Mortarless brick masonry wall with <45% void ratio and vertical joints	3.0–4.0	100–130	2580–3300	430–550	11
Concrete block masonry wall with 45–65% void ratio	1.5–2.0	95–125	2200–2800	440–560	12
Grouted concrete block masonry wall	3.0–4.4	180–240	2700–3500	540–700	14

Fig. 4. Material properties of masonry elements in FEM

The floor loads considered in the structural analysis were defined in accordance with the relevant usage areas within the school building. A uniform dead load of 50 kg/m² was applied to represent the weight of non-structural floor finishes and coverings. The self-weight of the structural system (including beams, slabs, and walls) was automatically calculated by the analysis software. Regarding live loads, 350 kg/m² was assigned to the classroom areas, and 500 kg/m² was applied to the school corridors, in line with typical usage requirements. The roof slab was considered inaccessible, and therefore no live load was applied to this area during the analysis. For the calculation of earthquake loads, the Turkish Building Earthquake Code 2018 (TBEC, 2018) was followed. In the corresponding design spectrum, the site was classified as soil type ZD, which represents medium dense to dense sand, gravel, or very stiff clay layers. The spectrum characteristic parameters for the building site were obtained via the Turkish Earthquake Hazard Maps Interactive Web Application. The values obtained for Erzincan Province which have similar seismic characteristics in Tbilisi, Central District are summarized in Fig. 5. The response spectrum generated based on the parameters obtained from Fig. 5 is presented in Fig. 6. In accordance with the Turkish Building Earthquake Code (TBEC, 2018), the structural classification parameters for the timber building were determined as follows: the Building Height Class (BYS) was selected as 8, the Building Occupancy Class (BKS) as 1, the Earthquake Design Class (DTS) as 2a, and the Importance Factor (I) as 1.5. Although the structural system of the building is not explicitly listed under the predefined categories in Table 4.1 of Article 4.3.2, appropriate seismic design parameters were selected based on the overall configuration and behavior of the load-bearing system. Accordingly, the Structural System Behavior Coefficient was taken as Rx = Ry = 3, and the Overstrength Factor was assumed as D = 1. The loads and load combinations considered in the structural analysis of the building were defined in accordance with relevant codes and implemented in the SAP2000 model.

Input / Output	Value
Seismic Design Level	DD-3 (50% probability of exceedance in 72 years)
Soil Class	ZD
Latitude	39.745615°
Longitude	39.493201°
Short-period Spectral Acceleration Coefficient (SS)	0.497
1.0-second Period Spectral Acceleration Coefficient (S1)	0.133
Design Spectral Acceleration Coefficient (SDS)	0.697
Design Spectral Acceleration Coefficient at 1.0s (SD1)	0.310

Fig. 5. Spectrum characteristic values for Erzincan Central District (TBEC, 2018)

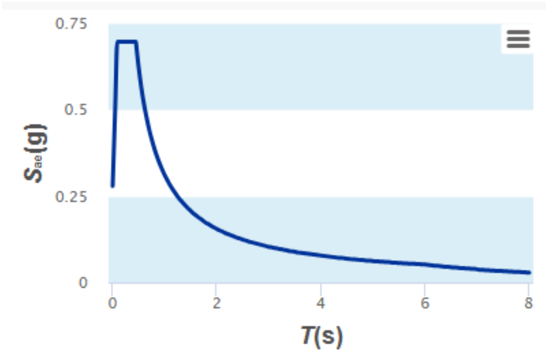

Fig. 6. Response spectrum derived from the seismic parameters in Fig. 5

4. Finite element analysis

4.1. Evaluation of timber floor system
Within the scope of the study, the structural adequacy of the existing timber floor beams is evaluated through detailed calculations. The assessment included the verification of cross-sectional resistance, deformation under service loads, shear capacity, and compatibility with deflection and vibration criteria. The verification process is based on both ultimate limit state (ULS) and serviceability limit state (SLS) requirements.

According to the ULS analysis results, the stresses obtained from the moments and shear forces derived from the finite element model indicate that the bending performance of the timber beams remains within the acceptable limits. However, deficiencies were observed under the effect of shear forces, suggesting that the current configuration may not fully satisfy the shear capacity requirements in its existing state.

Upon examining the SLS analysis results, it is observed that the deflections of the flooring in the classrooms do not fall within permissible limits (Fig. 7). In structural elements with a timber beam load-bearing system, due to inadequacies in both shear verification and deflection, it has been decided to use a steel floor instead of a timber floor.

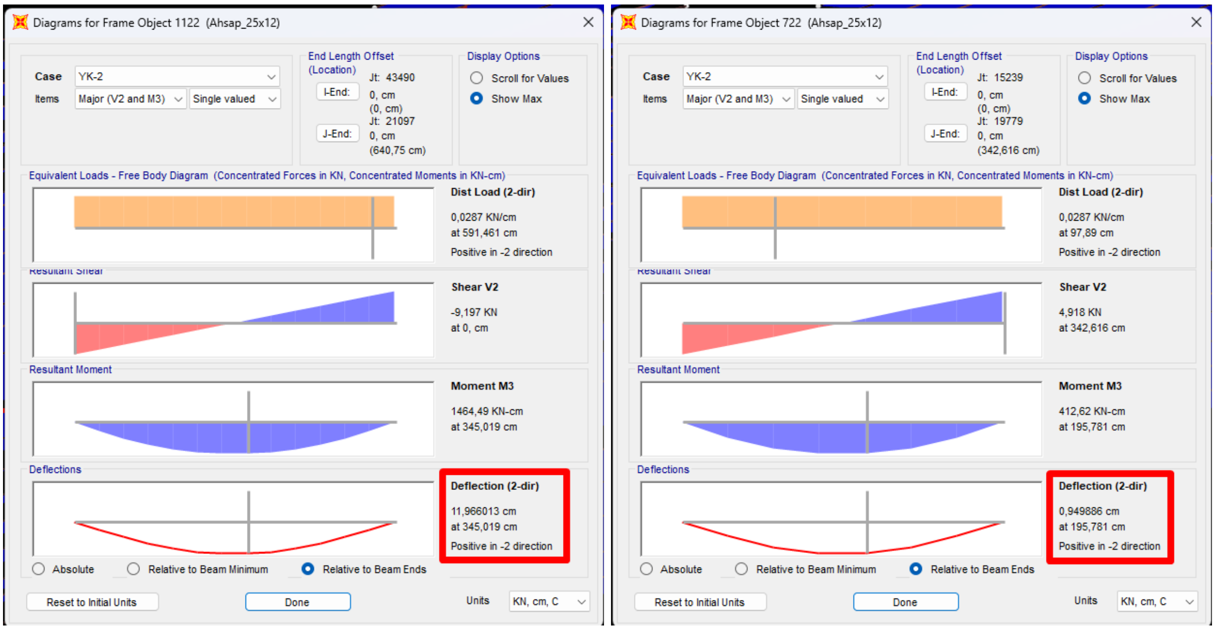

Classrooms: 11.96cm > 2.1 cm ❌ General Corridors: 0.94cm < 1.14 cm ✅

Fig. 7. SLS analysis results of timber floor system

To address these deficiencies, a revised structural analysis was carried out within the scope of this study using steel profile reinforcements as an strengthening method. Based on the results obtained from the finite element analysis:

- In classroom areas, where the design live load was defined as 350 kg/m², it was determined that HEA140 steel profiles provided sufficient flexural and shear resistance.
- In corridor areas, which were subject to a higher live load of 500 kg/m², UPN140 profiles were found to satisfy the structural requirements, particularly due to their adequate performance in shear.

For the roof floor, no significant live load is considered in the design due to its inaccessible nature. Therefore, only the self-weight of the slab was taken into account, and the structural analysis indicated that this dead load could be safely carried by the existing slab configuration without the need for additional strengthening. Strengthening proposal is given in Fig. 8.

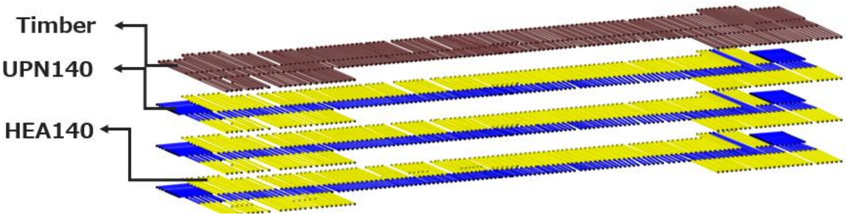

Fig. 8. Proposed alternative strengthening

In timber check results, according to the ULS and SLS analysis results, the stresses obtained from the moments and shear forces derived from the finite element model indicate that the bending effect, shear force and displacement ratio remains within the specified limits (Fig. 9).

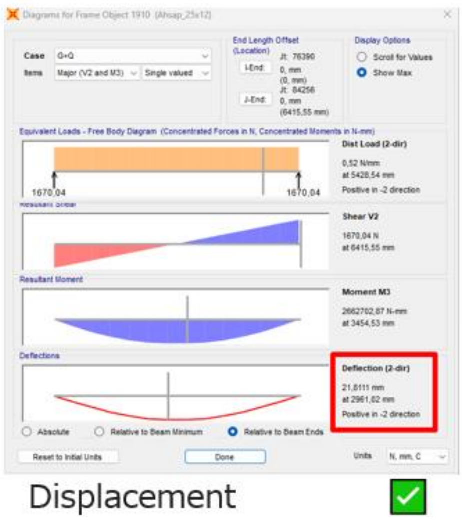

Eleman No	Mesafe (mm)	Kombinasyon	M2_Gerilme (MPA)	M3_Gerilme (MPA)	Ce	Denklem 4.3	Denklem 4.4	Kontrol
931	5.90431	Zarf	0.000	0.228	0.700	0.026	0.018	✓
1278	5.90431	Zarf	0.000	0.228	0.700	0.026	0.018	✓
1625	5.90431	Zarf	0.000	0.228	0.700	0.026	0.018	✓
930	5.90343	Zarf	0.000	0.228	0.700	0.026	0.018	✓
1277	5.90343	Zarf	0.000	0.228	0.700	0.026	0.018	✓
1624	5.90343	Zarf	0.000	0.228	0.700	0.026	0.018	✓
1625	6.39633	Zarf	0.000	0.226	0.700	0.026	0.018	✓
1278	6.39633	Zarf	0.000	0.226	0.700	0.026	0.018	✓
931	6.39633	Zarf	0.000	0.226	0.700	0.026	0.018	✓
931	5.41228	Zarf	0.000	0.226	0.700	0.026	0.018	✓
1278	5.41228	Zarf	0.000	0.226	0.700	0.026	0.018	✓
1625	5.41228	Zarf	0.000	0.226	0.700	0.026	0.018	✓
1624	6.39538	Zarf	0.000	0.226	0.700	0.026	0.018	✓
1277	6.39538	Zarf	0.000	0.226	0.700	0.026	0.018	✓
930	6.39538	Zarf	0.000	0.226	0.700	0.026	0.018	✓
930	5.41148	Zarf	0.000	0.226	0.700	0.026	0.018	✓
1277	5.41148	Zarf	0.000	0.226	0.700	0.026	0.018	✓
1624	5.41148	Zarf	0.000	0.226	0.700	0.026	0.018	✓
1625	6.88836	Zarf	0.000	0.221	0.700	0.026	0.018	✓
1278	6.88836	Zarf	0.000	0.221	0.700	0.026	0.018	✓
931	6.88836	Zarf	0.000	0.221	0.700	0.026	0.018	✓
931	4.92026	Zarf	0.000	0.221	0.700	0.026	0.018	✓

Eleman No	Mesafe (mm)	Kombinasyon	σ_V2 (MPa)	σ_V3 (MPa)		Sınır Değer (MPa)	Oran(%)	Kontrol
1699	8399.04	1.35G+1.5Q	3.54E-01	4.08E-04	<	1.49	23.7202	✓
1692	8398.71	1.35G+1.5Q	3.54E-01	4.39E-04	<	1.49	23.7193	✓
1691	8398.51	1.35G+1.5Q	3.54E-01	4.96E-04	<	1.49	23.7187	✓
1703	8387.49	1.35G+1.5Q	3.53E-01	3.75E-04	<	1.49	23.6876	✓
1702	8376.37	1.35G+1.5Q	3.53E-01	3.45E-04	<	1.49	23.6562	✓
1705	8371.08	1.35G+1.5Q	3.52E-01	3.39E-04	<	1.49	23.6413	✓
1710	8370.82	1.35G+1.5Q	3.52E-01	3.23E-04	<	1.49	23.6405	✓
1711	8370.69	1.35G+1.5Q	3.52E-01	2.79E-04	<	1.49	23.6402	✓
1963	8366.45	1.35G+1.5Q	3.52E-01	6.86E-04	<	1.49	23.6282	✓
1964	8358.09	1.35G+1.5Q	3.52E-01	8.50E-04	<	1.49	23.6046	✓
1965	8349.84	1.35G+1.5Q	3.52E-01	9.45E-04	<	1.49	23.5813	✓
1974	8325.5	1.35G+1.5Q	3.51E-01	1.01E-03	<	1.49	23.5125	✓
1976	8314.13	1.35G+1.5Q	3.50E-01	9.99E-04	<	1.49	23.4804	✓
1980	8303.82	1.35G+1.5Q	3.50E-01	9.72E-04	<	1.49	23.4513	✓
1979	8294.54	1.35G+1.5Q	3.49E-01	9.14E-04	<	1.49	23.4251	✓
1699	7904.98	1.35G+1.5Q	3.12E-01	4.08E-04	<	1.49	20.9296	✓
1692	7904.67	1.35G+1.5Q	3.12E-01	4.39E-04	<	1.49	20.9288	✓
1691	7904.48	1.35G+1.5Q	3.12E-01	4.96E-04	<	1.49	20.9283	✓
1703	7894.11	1.35G+1.5Q	3.12E-01	3.75E-04	<	1.49	20.9008	✓
1702	7883.64	1.35G+1.5Q	3.11E-01	3.45E-04	<	1.49	20.8731	✓
1705	7878.66	1.35G+1.5Q	3.11E-01	3.39E-04	<	1.49	20.8599	✓

Bending Results Check ✓ Shear Results Check ✓

Figure 9. Check timber results in proposed system

4.1. Evaluation of masonry system

The DD-3 earthquake level, as defined in the Turkish Building Earthquake Code (TBEC,, 2018), corresponds to a seismic event with a 50% probability of exceedance in 50 years, which equates to a return period of approximately 72 years. This level of ground motion represents a design earthquake scenario used for evaluating the expected performance of existing structures under moderate seismic demand. Taking into account the nature of the structure and its occupancy classification, the performance assessment of the building was conducted based on the “Life Safety” (Fig. 10) performance level defined in TBEC (2018). This performance objective aims to ensure that the structure retains its overall stability and prevents partial or total collapse under the DD-3 level seismic event, thereby protecting life safety even in the event of moderate damage.

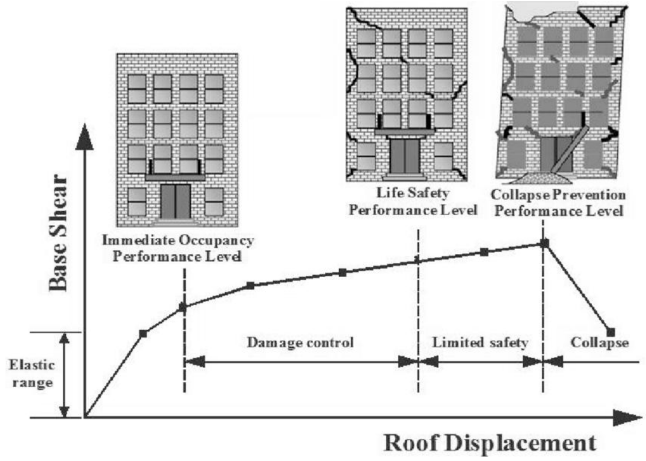

Fig. 10. Performance levels for structural assessment

In line with the Life Safety Performance Objective defined in TBEC (2018), a detailed structural assessment of the building was carried out under the DD-3 level earthquake scenario using finite element analysis. The objective was to evaluate whether the structural system could maintain overall stability and protect human life during a moderate seismic event. The analysis results, including stress distributions, deformation diagrams, and critical regions of failure, are presented in Fig. 11.

When the analysis results were evaluated with respect to the material properties and permissible limits, it was observed that the compressive stresses exceeded the allowable values in several areas, particularly on the first and second floors. These findings indicate insufficient vertical load-carrying capacity in certain masonry wall sections.

In addition, the shear stress distribution revealed more widespread deficiencies. Shear-related weaknesses were identified across all floors, especially concentrated around the wall-to-wall connections, wall-to-floor joints, and window openings. These regions exhibited localized overstressing, suggesting a lack of ductility and inadequate energy dissipation capacity in the existing structural configuration.

Some representative images from the analysis outputs have been provided to illustrate the most critical failure mechanisms and overstressed zones.

Based on these findings, it has been conclusively determined that the existing structural system does not meet the life safety requirements, and that the school building requires retrofitting to address the identified weaknesses. Strengthening interventions should particularly target shear-critical regions and compressive overstress areas to improve the building’s seismic resilience and ensure compliance with performance-based design objectives.

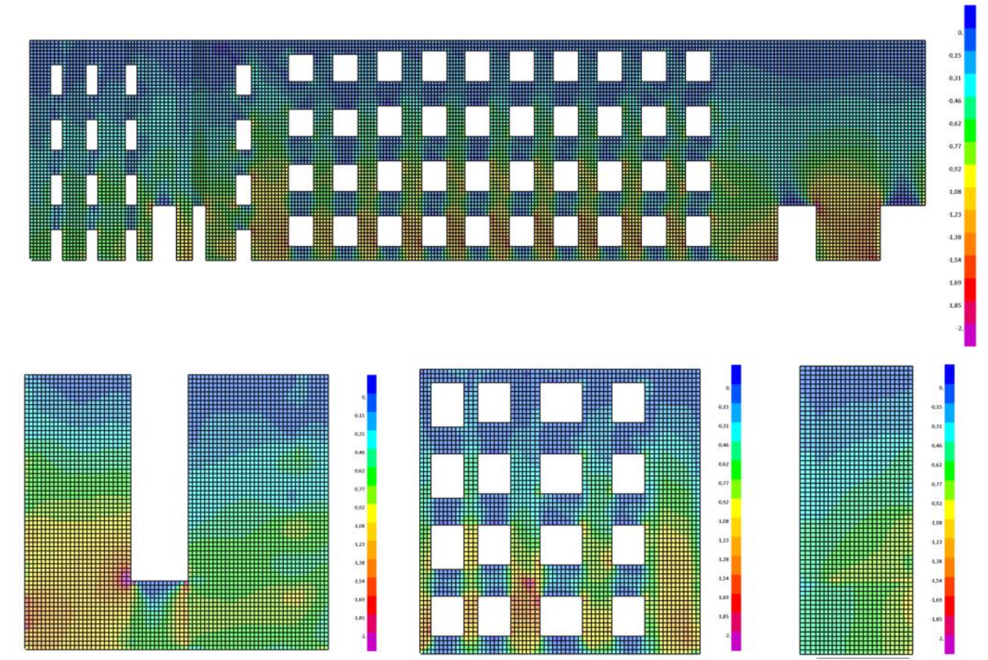

a) Distribution of Principal Compression Stress (G+Q+Ex+0.3Ey+0.3Ez , Units: MPa)

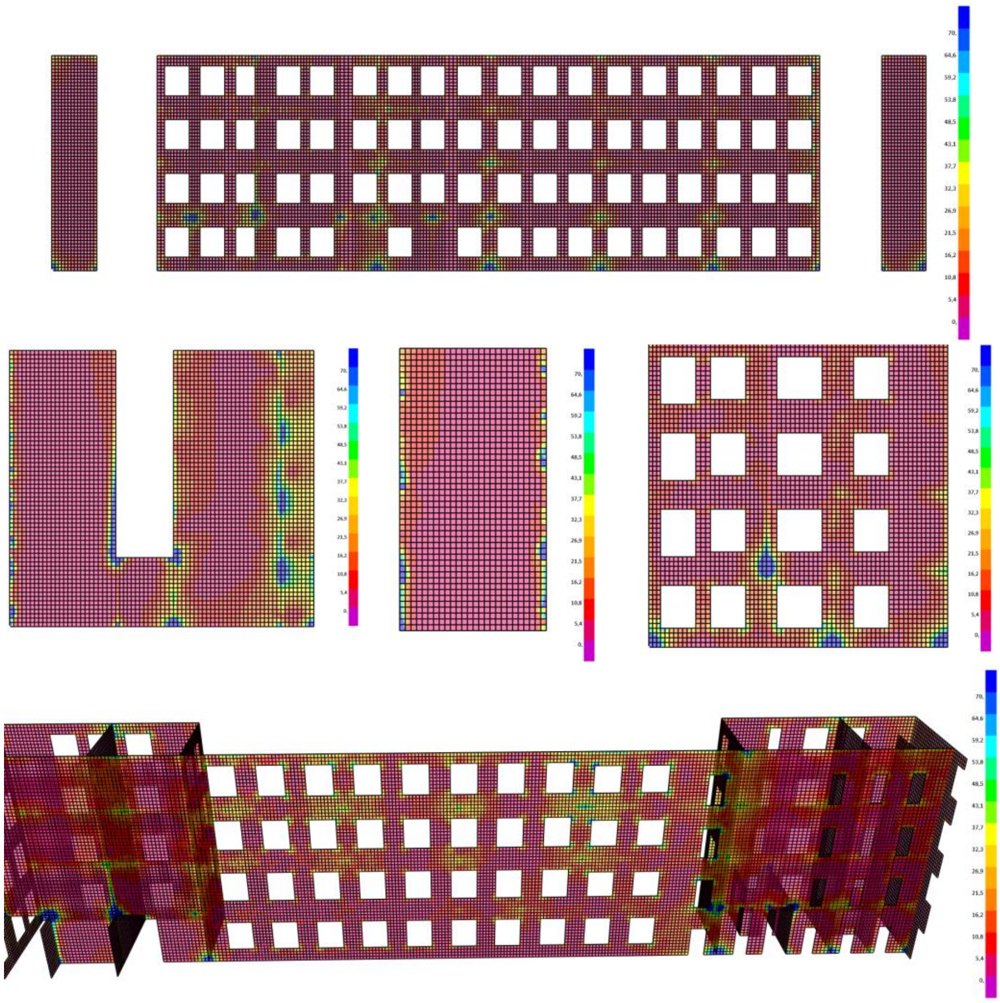

b) Distribution of Principal Principal Shear Stress (G+Q+Ex+0.3Ey+0.3Ez , Units: MPa)

Fig. 11. Some of figures for evaluation structural system results

In response to the widespread deficiencies observed in both compressive and shear stress capacities throughout the structural walls, a practical and structurally effective retrofitting strategy has been suggested. Instead of using shotcrete, the proposed method involves applying a cement-based thick repair mortar to all structural walls. This approach was selected not only for its mechanical effectiveness, but also for its ease of application, compatibility with existing masonry materials, and minimal intrusion on the building's original architectural features.

In the strengthened model, a 2 cm thick layer of cement-based repair mortar will be applied to both faces of each wall, thereby enhancing cross-sectional stiffness, ductility, and energy dissipation capacity under seismic loading. To further improve the tensile behavior and control potential cracking, fiber reinforcement will be incorporated within the repair mortar. The use of fiber-reinforced mortar eliminates the need for traditional rebar cages, reducing the complexity of construction while providing multidirectional stress distribution capacity.

For the exterior walls, the repair mortar will only be applied to the interior face in order to preserve the historical appearance of the facade. Additionally, reinforced bond beams are proposed around window and door openings, where stress concentrations were clearly identified in the analysis. These localized enhancements aim to improve continuity, reduce deformation, and prevent failure in regions susceptible to in-plane and out-of-plane forces.

Post-retrofit finite element analyses confirm that this strengthening configuration significantly reduces stress demands throughout the structure, allowing both compressive and shear stresses to remain within acceptable performance limits. As a result, the building is expected to meet the Life Safety Performance Level under the DD-3 earthquake scenario as defined in TBEC (2018).

The material properties of the cement-based repair mortar and fiber mesh reinforcement (KBT – Basalt Georid 100 kN 40x40mm) used in the strengthening analysis are presented in Figs. 12 and 13, including relevant mechanical parameters such as compressive strength, tensile strength, modulus of elasticity, and unit weight. These values were used in the finite element model to accurately simulate the contribution of the repair layer to the overall stiffness and strength of the structural system.

Property	Value
Appearance	Gray
Shelf Life	12 months in original sealed packaging under dry conditions
Packaging	25 kg kraft bag
Application Temperature	(+5°C) – (+35°C)
Mixing Ratio	3.5 – 4.5 L water / 25 kg powder
Pot Life	Minimum 30 minutes
Open Time	1 day
Application Thickness	10 – 40 mm (in a single layer)
Flexural Strength (EN 12190)	≥ 7.0 N/mm^2
Bond Strength to Concrete (EN 1542)	≥ 2.0 N/mm^2
Compressive Strength (EN 12190)	≥ 45 N/mm^2
Elastic Modulus (EN 13412)	> 20 GPa
Limited Shrinkage (EN 12617-4)	≥ 2 N/mm^2
Capillary Water Absorption (EN 13057)	≤ 0.5 kg/m^{2}h$^{0.5}$
Limited Expansion (EN 12617-4)	≥ 2 N/mm^2
Service Temperature	(-30°C) – (+400°C)
Fire Reaction Class	A1
Hazardous Substances	Refer to the safety data sheet

Fig. 12. Mechanical properties of cement-based repair mortar

Property	Value
Product Name	KBT – Basalt Geogrid 100 kN 40x40 mm
Unit Weight	460 g/m^2
Grid Spacing	40 mm × 40 mm
Elastic Modulus of Fibers	85 ± 98 GPa
Tensile Strength	3200 ± 4840 MPa
Ultimate Strain	1.9 ± 3.2 %

Fig. 13. Mechanical properties of KBT basalt geogrid 100kN 40x40 (4690 g/m^2)

Additionally, Fig 14 presents selected visual outputs from the analysis results, illustrating the stress distributions, deformation patterns, and critical regions before and after the application of the strengthening layer. These visualizations clearly demonstrate the effectiveness of the proposed intervention in reducing both compressive and shear demands on the structural walls.

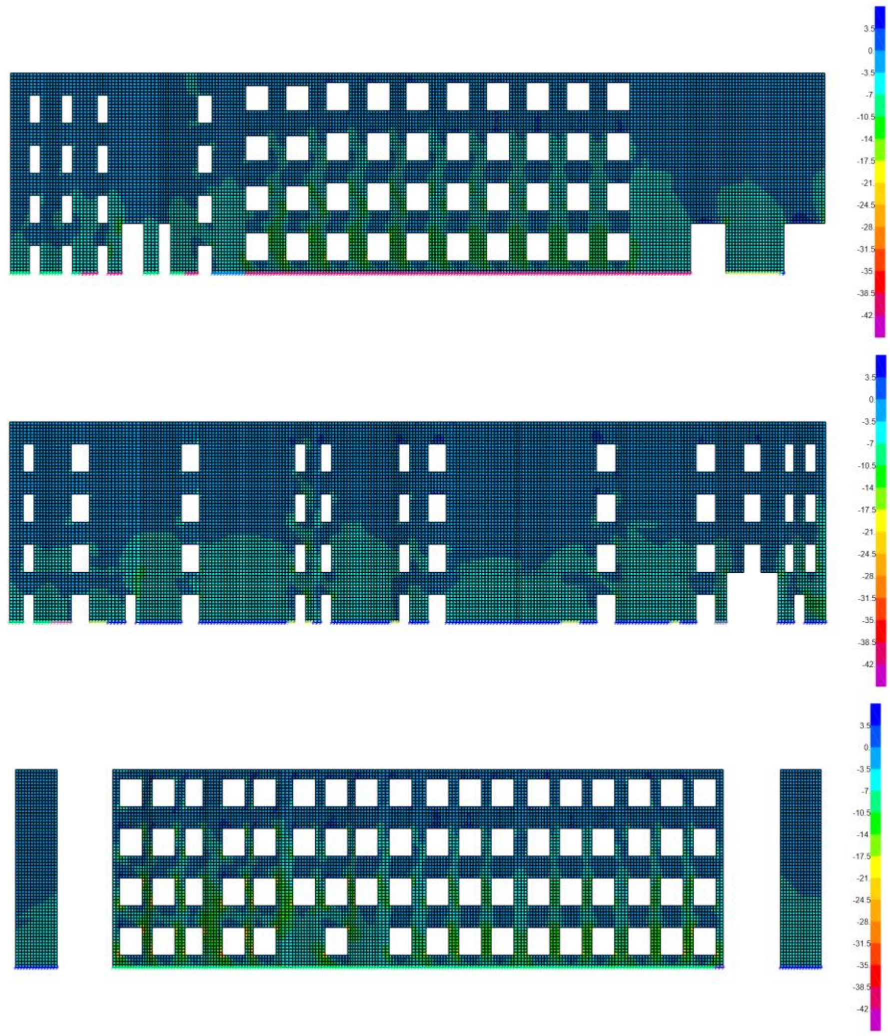

a) Distribution of Principal Compression Stress (G+Q+Ex+0.3Ey+0.3Ez , Units: MPa)

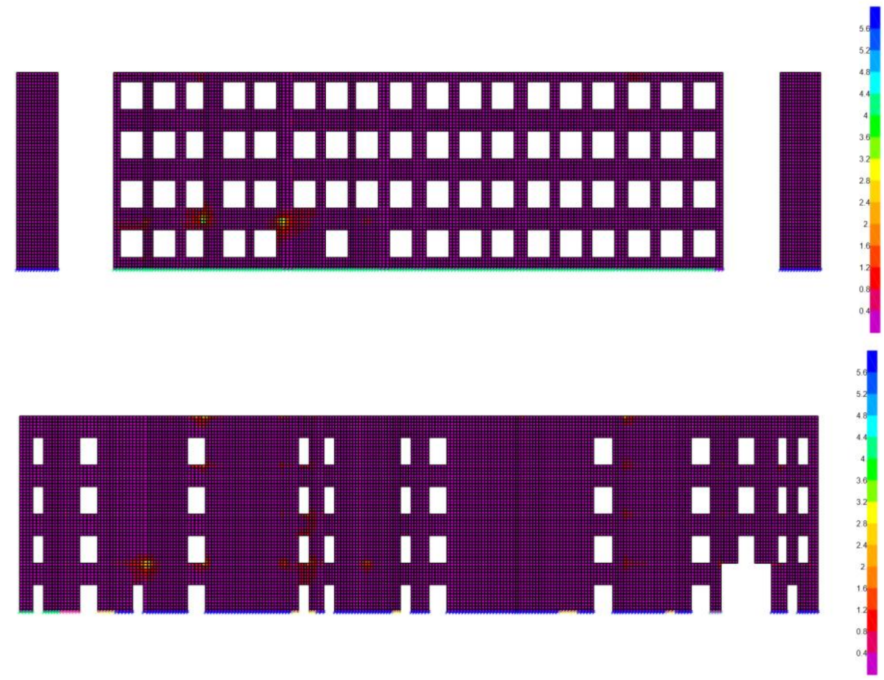

b) Distribution of Principal Shear Stress (G+Q+Ex+0.3Ey+0.3Ez , Units: MPa)

Fig. 14. Some of figures for evaluation reinforced system results

3. Conclusions

This study presented a performance-based structural evaluation and retrofitting proposal for a four-story historical masonry-timber school building located in Tbilisi, Georgia. The assessment process was carried out using a detailed finite element model developed in SAP2000, incorporating the architectural and structural features of the building, as well as material properties and loading conditions compliant with TS EN and TBEC (2018) standards.

The initial analyses revealed that the existing structural system was inadequate to meet safety and serviceability requirements under both gravity and seismic loads. In particular, the timber floor systems exhibited excessive deflection and insufficient diaphragm action, while the unreinforced masonry walls were prone to tensile cracking and shear failure under earthquake loading. To address these vulnerabilities, a dual-stage strengthening solution was proposed. This included the addition of HEA140 and UPN140 steel profiles combined with a reinforced concrete slab to improve the horizontal diaphragm, and the application of a geogrid-reinforced fiber mortar layer on masonry walls to enhance in-plane and out-of-plane performance. The retrofitted model demonstrated significant improvements in stiffness, stress distribution, and displacement control.

- Post-retrofit analyses confirmed that the building met the Life Safety (LS) performance objective under the DD-3 earthquake level, as defined for locally significant heritage buildings.
- The interventions successfully brought all critical stress zones within permissible limits and ensured sufficient seismic resilience.

Overall, this study underscores the value of combining modern structural engineering tools with conservation-sensitive retrofitting techniques. The adopted methodology provides a replicable framework for the assessment and strengthening of similar historical masonry buildings, ensuring both their structural safety and cultural continuity for future generations.

References

Abrams, D. P., & Lynch, J. M. (2001, October). Flexural behavior of retrofitted masonry piers. *KEERC-MAE Joint Seminar on Risk Mitigation for Regions of Moderate Seismicity*, Illinois, USA.

Altunışık, A. C., Adanur, S., Genç, A. F., Günaydın, M., & Okur, F. Y. (2017). An investigation of the seismic behaviour of an ancient masonry bastion using non-destructive and numerical methods. *Experimental Mechanics, 57*, 245–259. https://doi.org/10.1007/s11340-016-0239-x

Binda, L., & Saisi, A. (2005). Research on historic structures in seismic areas in Italy. *Progress in Structural Engineering and Materials*, 7(2), 71–85. https://doi.org/10.1002/pse.204

Corradi, M., Borri, A., & Vignoli, A. (2008). Strengthening techniques tested on masonry structures struck by the Umbria–Marche earthquake of 1997–1998. *Construction and Building Materials*, 16(4), 229–239. https://doi.org/10.1016/S0950-0618(02)00014-4

ElGawady, M., Lestuzzi, P., & Badoux, M. (2004). A review of retrofitting of URM walls using composites. *4th International Conference on Advanced Composite Materials in Bridges and Structures*, Calgary, Canada.

Genç, A. F., Ergün, M., Günaydın, M., Altunışık, A. C., Ateş, Ş., Okur, F. Y., & Mosallam, A. S. (2019). Dynamic analyses of experimentally-updated FE model of historical masonry clock towers using site-specific seismic characteristics and scaling parameters according to the 2018 Turkey building earthquake code. *Engineering Failure Analysis, 105*, 402–426. https://doi.org/10.1016/j.engfailanal.2019.06.054

ICOMOS. (2003). *Principles for the analysis, conservation and structural restoration of architectural heritage*. International Scientific Committee for Analysis and Restoration of Structures of Architectural Heritage (ISCARSAH).

Kaya, A., Adanur, S., Bello, R. A., Genç, A. F., Okur, F. Y., Sunca, F., Günaydın, M., Altunışık, A. C., & Sevim, B. (2023). Post-earthquake damage assessments of unreinforced masonry (URM) buildings by shake table test and numerical visualization. *Engineering Failure Analysis, 143*, 106858. https://doi.org/10.1016/j.engfailanal.2022.106858

Lagomarsino, S., & Cattari, S. (2015). PERPETUATE guidelines for seismic performance-based assessment of cultural heritage masonry structures. *Bulletin of Earthquake Engineering, 13*(1), 13–47. https://doi.org/10.1007/s10518-014-9674-1

Lourenço, P. B. (2002). Computations on historic masonry structures. *Progress in Structural Engineering and Materials*, 4(3), 301–319. https://doi.org/10.1002/pse.120

Taghdi, M. (2000). *Seismic retrofit of low-rise masonry and concrete walls by steel strips* (Doctoral dissertation, University of Ottawa, Department of Civil Engineering, Ottawa, Canada).

Tomazevic, M. (1999). *Earthquake-resistant design of masonry buildings*. London: Imperial College Press.

Turkish Building Earthquake Code (TBEC 2018). *Ministry of Environment and Urbanization.* Ankara, Turkey: Republic of Turkey Official Gazette.

Valluzzi, M. R., Binda, L., & Modena, C. (2005). Mechanical behavior of historic masonry structures strengthened by bed joints structural repointing. *Construction and Building Materials, 19*(1), 63–73. https://doi.org/10.1016/j.conbuildmat.2004.04.036

Ground motion parameters importance in machine learning-based damage prediction

Yasin Fahjan[1], Bilal Ein Larouzi*[1]

[1] Istanbul Technical University, Department of Civil Engineering, 33469 Istanbul, Türkiye

Abstract: Post-earthquake damage assessment is a crucial process for effective disaster management, requiring rapid and accurate evaluation to prioritize response efforts. This study proposes a machine learning-based approach to predict building damage levels by analyzing ground motion parameters and building footprint data. A case study was conducted in the Izmir region, which experienced a devastating earthquake in 2020. The dataset utilized combines real field-collected data with existing datasets containing building footprint geometry. A Random Forest algorithm was employed to develop a predictive model that classifies buildings into three damage levels. Key ground motion parameters—Peak Ground Acceleration (PGA), Peak Ground Velocity (PGV), and Intensity—were tested to determine their importance. Results indicate that PGA is the most critical parameter, achieving an accuracy of 84%, followed by PGV (80%) and Intensity (77%). However, combining all three ground motion parameters yielded the highest model performance, with an accuracy of 90% and an F1 score of 0.90. The study also highlights the importance of incorporating building footprint area as an additional feature for improved predictions. These findings demonstrate the potential of using machine learning models to enhance post-earthquake damage assessment by integrating multiple ground motion parameters and building characteristics. The proposed approach provides a scalable and efficient solution for rapid damage evaluation in seismic-prone regions, supporting effective disaster response strategies.

Keywords: Post-earthquake damage assessment; Machine learning; Ground motion parameters; Random Forest algorithm.

---

1. Intorduction:

Earthquakes are among the most significant natural disasters, impacting human lives and causing substantial economic losses. These impacts arise not only from the immense energy released due to ruptures in the Earth's crust but also from the inherent unpredictability of such events. Consequently, post-earthquake damage assessment and disaster management are critical areas of research that play a crucial role in mitigating loss of life and minimizing economic repercussions following seismic events. One of the traditional methods employed for earthquake risk assessment is the fragility curve. This probabilistic tool compares the seismic capacity of structures with seismic demand, thereby estimating the probability of exceeding predefined damage limit states. The seismic demand is typically represented by ground motion parameters such as Peak Ground Acceleration (PGA), Peak Ground Velocity (PGV), or intensity.

The selection of an appropriate ground motion parameter for describing seismic demand in fragility analyses has been a significant topic of research. Meral (2024) stated that parameters within the velocity and acceleration groups exhibit stronger correlations compared to those in the frequency and displacement groups. However, it should be noted that frequency- and displacement-related parameters tend to have lower correlation values. Acceleration-related parameters demonstrate superior correlation performance for short-period structures, such as four-story buildings, whereas velocity-related parameters are more effective for medium-period structures, including seven-story buildings. Pellissetti et al. (2023) suggested that uncertainties associated with structural capacity, when assessed solely in terms of PGA, can be reduced by developing a vector-valued fragility surface that incorporates both PGA and the PGA/PGV ratio. Furthermore, Massumi et al. (2016) observed that as a structure's natural period increases, the influence of acceleration-related parameters on damage assessment decreases, whereas velocity-related parameters become more significant.

Machine learning (ML), a subfield of artificial intelligence, has been increasingly utilized in generating models capable of classification and prediction based on historical data collected from real-world observations or

* Corresponding author, E-mail: Larouzi20@itu.edu.tr

https://doi.org/10.31462/icearc2025_ce_eqe_392

generated through simulations. In recent decades, ML has been effectively applied in post-earthquake damage assessment, demonstrating its predictive capabilities. For instance, Zhang et al. (2022) introduced a rapid damage assessment model for reinforced concrete frames using machine learning techniques. Similarly, Tang et al. (2021) developed a machine learning model for rapid seismic risk assessment, utilizing datasets generated for various regions in China and comparing the performance of different machine learning algorithms. Additionally, Cosgun (2023) presented a machine learning model for evaluating existing buildings in the Istanbul region of Türkiye. The study revealed that the model, employing the Random Forest algorithm, exhibited high accuracy when compared to simulated results, and it also highlighted the significant impact of building age on the assessment outcomes.

This study aims to conduct a comparative analysis to identify the most influential ground motion parameters used in post-earthquake damage assessment models based on machine learning algorithms.

2. Fragility curve:

Fragility curves are probabilistic tools that quantify the likelihood of a structure exceeding specified damage thresholds under varying seismic intensities. Formulated as cumulative distribution functions, these curves correlate ground motion parameters—such as peak ground acceleration (PGA), peak ground velocity (PGV), or spectral acceleration—with discrete damage states, serving as foundational instruments in performance-based earthquake engineering (PBEE) for evaluating potential structural and socioeconomic losses.

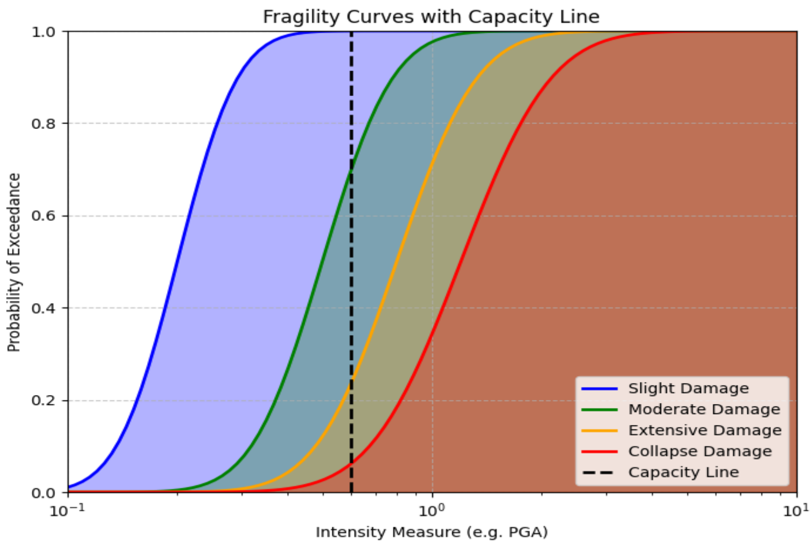

Fig. 1. Seismic fragility curve illustration for 4 damage limit state

3. Machine learning for estimating earthquake damage:

Over the past decade, numerous methodologies and models leveraging artificial intelligence (AI) and machine learning (ML) have been proposed for seismic damage estimation. Unlike fragility curves, which provide probabilistic assessments of damage exceedance, ML models inherently predict discrete damage states for structures subjected to earthquake excitation, offering deterministic outputs aligned with observed or simulated structural responses. The development of ML models for seismic damage estimation entails a systematic workflow:

1. Data collection:

Data collection poses significant challenges due to the difficulty of obtaining representative datasets that accurately reflect real-world conditions. Three primary approaches are employed:

- Structural Simulation: Models are often constructed using synthetic datasets generated from Finite Element Method (FEM)-based simulations of code-compliant structures. These simulations employ nonlinear static (pushover) or dynamic (time-history) analyses to evaluate structural responses under seismic loading. Input features typically include geometric properties (e.g., height, shear area), material characteristics (e.g., concrete strength, steel ductility), and mass distributions, with damage states classified using metrics such as the inner story drift ratio (IDR).
- Real-Building Simulation: Some studies utilize FEM models of existing structures, incorporating material properties derived from laboratory testing of samples extracted from actual buildings. These models undergo nonlinear static or dynamic analyses to estimate damage levels under seismic excitation.

- Field Data Collection: Empirical datasets are compiled from post-earthquake surveys and engineering assessments, correlating observed damage states with structural attributes and ground motion parameters. This approach captures real-world variability but relies on subjective engineer evaluations for damage classification.

2. Building the model:

After the data is collected, the next step is to create the ML model:

- Preparing the Data: Clean the data by fixing errors or removing incomplete information. Adjust the data so all values are on a similar scale, making it easier for the model to learn. Handle missing or noisy data to ensure accuracy.
- Choosing the Algorithm: Selecting an ML algorithm that fits the problem and dataset. Common choices include decision trees, support vector machines (SVMs), and random forests. Simpler problems use basic algorithms, while more complex ones need advanced methods.
- Training the Model: Training the model using the prepared data. During training, the model learns patterns to make accurate predictions.

3. Testing the Model:

Ensuring the model performs well using part of the training data. Metrics like accuracy are used to evaluate its performance. This step ensures the model can handle new data and isn't just memorizing the training examples. It also confirms the model's reliability in real-world scenarios.

4. Random forest:

Random Forest, an ensemble learning method, leverages the power of multiple decision trees to enhance predictive accuracy and robustness. The algorithm constructs a multitude of decision trees during the training phase, each trained on a bootstrapped sample of the original dataset and a random subset of features. This process, known as bagging, introduces diversity among the individual trees, mitigating the risk of overfitting and improving generalization performance.

For classification tasks, Random Forest employs a majority voting scheme, assigning the observation to the class with the most votes across all trees. In regression scenarios, the algorithm averages the predictions of the individual trees to produce a final estimate. Furthermore, Random Forest provides a measure of feature importance, offering insights into the relative contribution of each feature to the model's predictive power. Its ability to handle high-dimensional data, coupled with its inherent robustness and ease of implementation, has led to its widespread adoption.

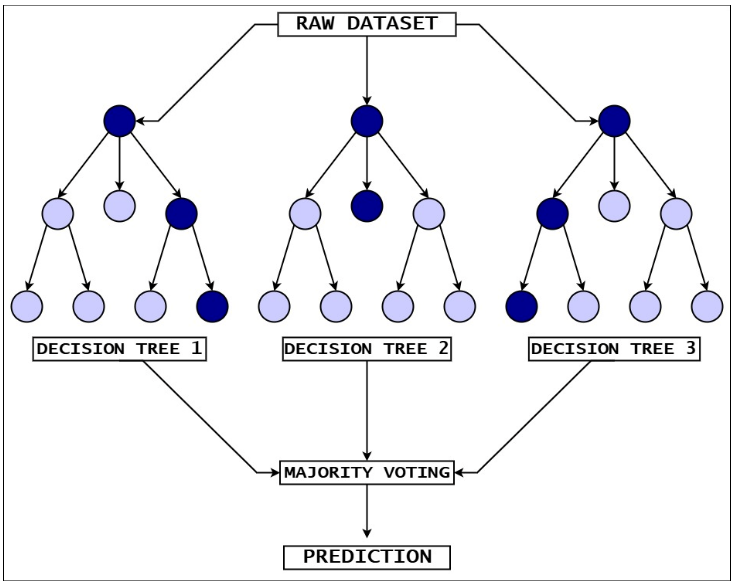

Fig. 2. Random Forest alogrithm

5. Study case:

This paper presents a study case for the data has been collected from field after earthquake stroke the Izmir region in western region of Turkiye in 2020. The dataset is consisting to nearly to 500 data points. The methodology and process of this study is consisting of main steps:

5.1. Data collection:

The data for this study case has been collected and generated from three main sources:

- Observation from field: The data has been collected from the field consisting of damage level and the location of the building after the seismic event.
- Generating ground motion parameters: Using these locations, the ground motion parameters is collected using REDAS software applying the scenario that simulated the seismic event.
- Footprint and elevation: Using the locations and OpenStreetMap the footprint of the region has been generated and using QGIS software the area for each building has been calculated. Using the location coordinate and Open Elevation API the elevation of each coordinate point has been collected.

5.2. Machine learning model creation:
The creation of machine learning model is created and consisted of main steps:
- Preparing Dataset: After collecting the data the dataset has been created by clearing the noises and damage data points, normalizing the features, grouping and classifying some features.
- Model creation and training: The Random Forest algorithm has been used aiming to use the features to predict the damage level. The dataset has been splinted by 80% and 20% as training and testing sets respectively.
- Model performance evaluation: In order to evaluate the model, the confusion matrices has been generated then the accuracy and F1 score have been calculated.

5.3. Damage classification:
The damage level has been classified into three categories based on the observation from field as following:
- Highly Damaged (HD): This class represents collapsed, need to be demolished, and severely damaged buildings
- Moderately Damaged (MD): This class contain the moderate damage and low damage building that need further investigation but that not dangerous for occupation.
- Non-Damaged (ND): This class represents the building that not get damaged in the seismic event.

5.4. The datasets:
As aiming to catch the most critical ground motion parameter seven datasets is prepared. For each dataset the ground motion parameter has been examined separately. Also, the area of the building has been examined to determine the importance of the building area features. The Dataset is shown below by case number:
- Case 1: The dataset is consisting of 7 features as following: The Age of the building, The Number of stories of the building, The elevation of the base of the building from the sea level, The Rupture distance (Rrup), The VS30, Peak Ground Acceleration (PGA) and the damage level.
- Case 2: Same of the case 1 but the ground motion parameter is represented by Peak Ground Velocity (PGV) instead of (PGA).
- Case 3: Same of the case 1 but the ground motion parameter is represented by intensity instead of (PGA).
- Case 4: Same as the case 1 and the footprint area of the building is taking into consideration.
- Case 5: Same as the case 2 and the footprint area of the building is taking into consideration.
- Case 6: Same as the case 3 and the footprint area of the building is taking into consideration.
- Case 7: In this case study the ground motion has been represented by PGA, PGV, and intensity together and the footprint area of the building took into consideration.

5.5 Results:
In order to be able to evaluate the results the confusion matrices, accuracy and F1 score has been calculated for each case.
- Case 1: The confusion matrix shows the model are able to predict the HD by 80% accuracy and there is no confusion between HD and ND classes. The ND class has high accuracy to be predicted correctly in this model as shown in Fig.4 (A).
- Case 2: The confusion matrix shows the model are able to predict the HD by 75% accuracy and there is some confusion to predict HD class as ND, The ND class still have high probability to be predicted correctly as shown in Fig.4 (B).
- Case 3: The confusion matrix shows the model are able to predict the HD by 65% accuracy and there is chance by 35% to predict HD class as MD or ND, The ND class still have high probability to be predicted correctly However, still lower than case1 and case2 as shown in Fig.5 (A).
- Case 4: The confusion matrix shows the model are able to predict the HD by 100% accuracy and there is no confusion between HD and other classes. However, the MD class has high confusion to be predicted as ND as shown in Fig.5 (B).

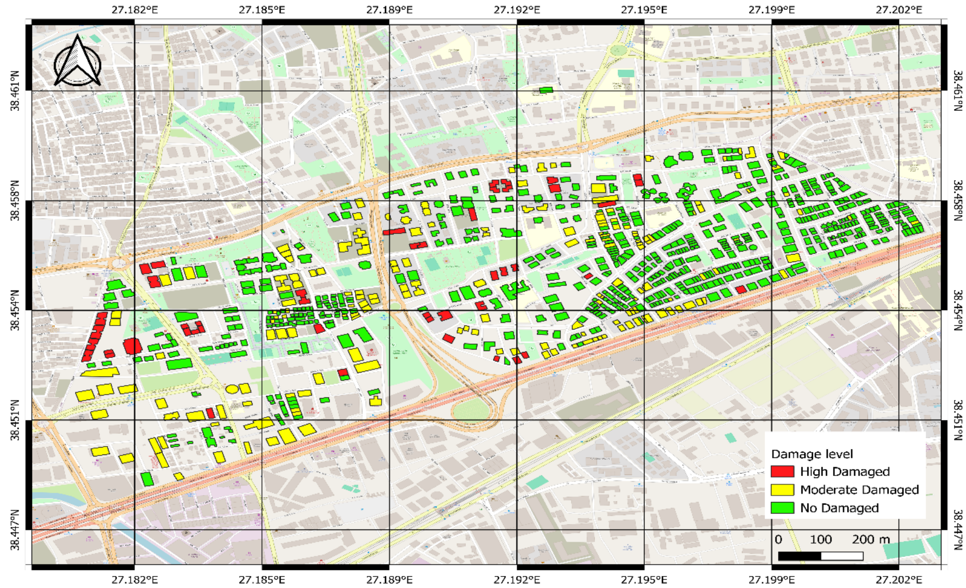

Fig. 3. Building footprint of the area of the studycase classified by damage class

- Case 5: The confusion matrix shows the model are able to predict the HD by 80% accuracy and there is a confusion between HD and MD class. However, the MD class has some confusion to be predicted as ND as shown in Fig.6 (A).
- Case 6: The confusion matrix shows the model are able to predict the HD by 75% accuracy and there is a confusion between HD to be predicted as MD or ND classes. However, the MD class has 35% probability to be predicted incorrectly as shown in Fig.6 (B).
- Case 7: The confusion matrix shows the model are able to predict the HD by 100% accuracy. The MD class has 27% probability to be predicted incorrectly as shown in Fig.7.
- Accuracies and F1-Scores: The accuracy and F1 score represent the performace of the model. The results show that the PGA is most accurate ground motion parameter with 82% accuracy when the area of the building not taken into consideration followed by PGV 78% then the Intensity 76%. However, the area of the building feature could improve the accuracy by 2% reaching 0.83 as F1-score for Case 4, 0.81 for case 5 and 0.77 for case 6. For case 7 the accuracy and F1 score reach 89.7% and 0.89 respectively shows that taking multi ground motion parameters may improve the accuracy of the prediction significantly as shown in Fig.8 and Fig.9 respecivly.

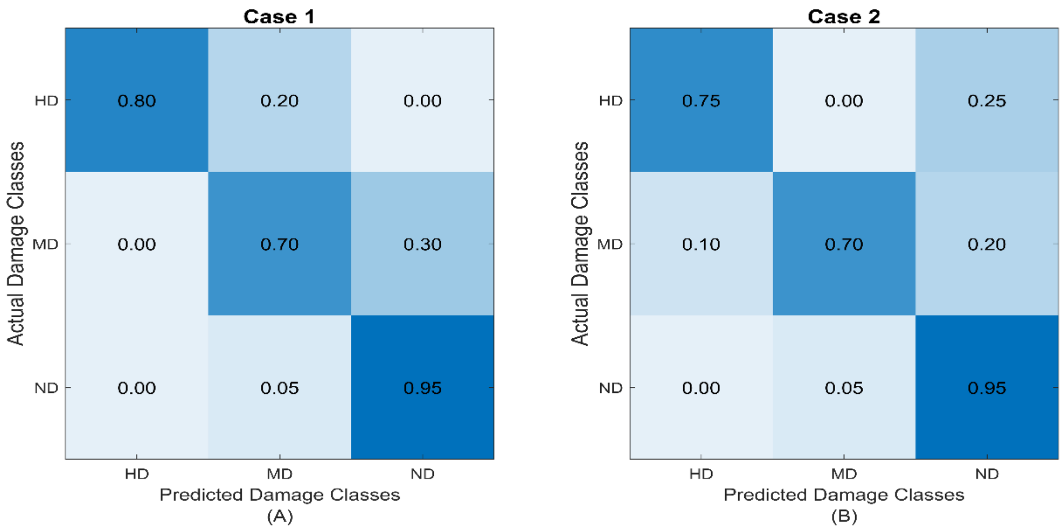

Fig. 4. Confusion matrices (A) Case 1 (B) Case 2

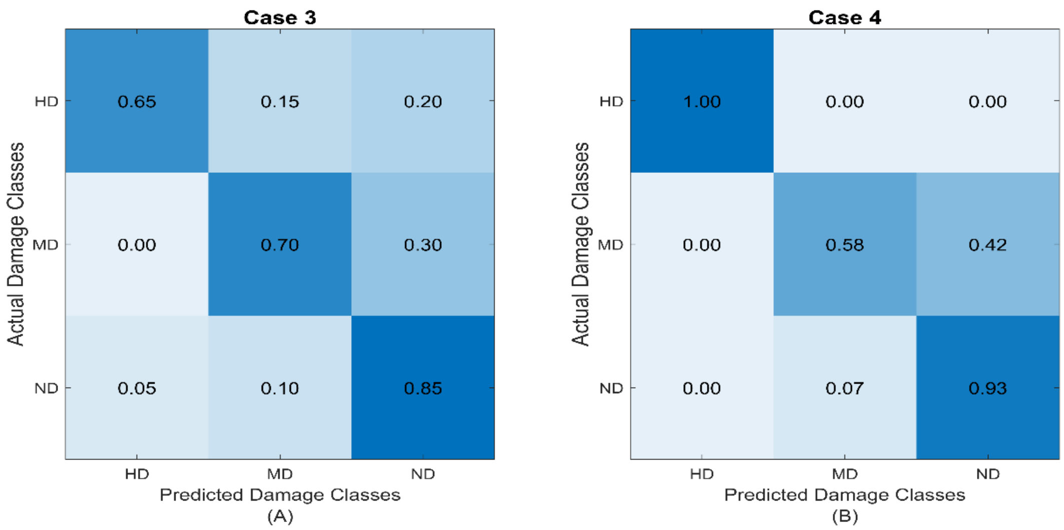

Fig. 5. Confusion matrices (A) Case 3 (B) Case 4

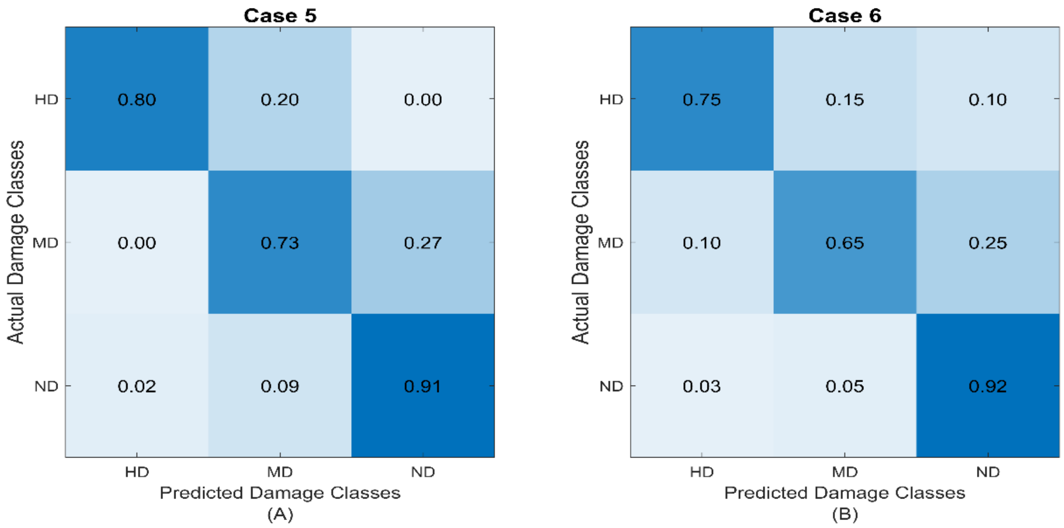

Fig. 6. Confusion matrices (A) Case 5 (B) Case 6

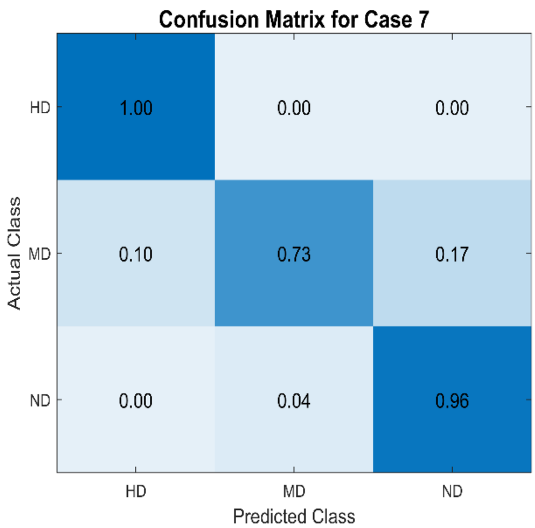

Fig. 7. Confusion matrix for Case 7

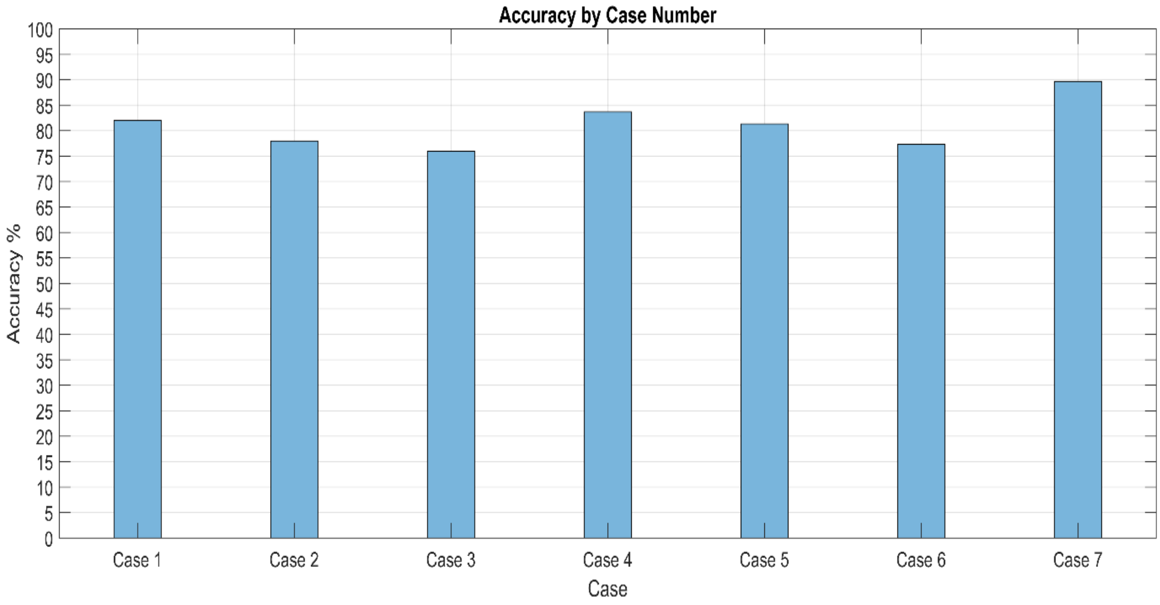

Fig. 8. Accuracy value by case number

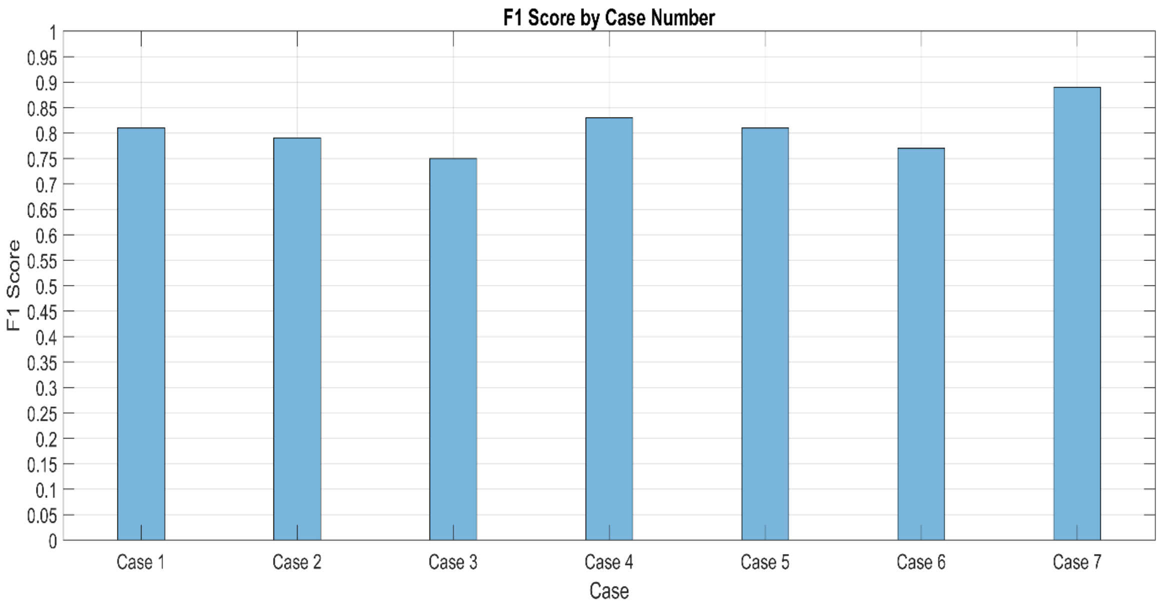

Fig. 9. F1-Score by case number

6. Conclusion:

In summary, this study provides compelling evidence of the efficacy of machine learning techniques—specifically the Random Forest algorithm—in conducting post-earthquake damage assessments. The analysis of various ground motion parameters indicates that Peak Ground Acceleration (PGA) is the most significant individual predictor of building damage, followed by Peak Ground Velocity (PGV) and Intensity. Moreover, the integration of building footprint area as an additional feature further refines the model's accuracy.

The optimal performance was attained by combining all three ground motion parameters with the building footprint area, yielding an accuracy of 90% and an F1 score of 0.90. These results underscore the potential of machine learning to facilitate rapid and precise damage assessments, which are vital for effective disaster response and management in seismically active regions. Overall, the proposed methodology presents a scalable and efficient framework for incorporating multiple ground motion parameters and building characteristics, thereby enhancing the reliability of damage predictions and supporting more informed decision-making in post-earthquake scenarios.

References

Breiman, L. (2001). Random forests. *Machine Learning*, 45(1), 5–32. https://doi.org/10.1023/a:1010933404324

Cosgun, C. (2023). Machine learning for the prediction of evaluation of existing reinforced concrete structures performance against earthquakes. *Structures*, 50, 1994–2003. https://doi.org/10.1016/j.istruc.2023.02.127
Erberik, M. A. (2015). Seismic fragility analysis. In *Encyclopedia of Earthquake Engineering* (pp. 1–10). Springer. https://doi.org/10.1007/978-3-642-36197-5_387-1
FEMA, Applied Technology Council, Hamburger, R. O., Holmes, W. T., Roeder, C., Scawthorn, C., Ellingwood, B., Kennedy, R. P., Mahin, S., Anagnos, T., Bendimerad, F. M., Baker, J., Bonneville, D., & Seligson, H. (2012). *Seismic Performance Assessment of Buildings: Volume 1 – Methodology*. Federal Emergency Management Agency.
Gehl, P., Seyedi, D. M., & Douglas, J. (2013). Vector-valued fragility functions for seismic risk evaluation. *Bulletin of Earthquake Engineering*, 11(2), 365–384. https://doi.org/10.1007/s10518-012-9402-7
Massumi, A., & Gholami, F. (2016). The influence of seismic intensity parameters on structural damage of RC buildings using principal components analysis. *Applied Mathematical Modelling*, 40(3), 2161–2176. https://doi.org/10.1016/j.apm.2015.09.043
Meral, E. (2024). Relationships between ground motion parameters and energy demands for regular low-rise RC frame buildings. *Bulletin of Earthquake Engineering*, 22(6), 2829–2865. https://doi.org/10.1007/s10518-024-01885-1
Tang, Q., Dang, J., Cui, Y., Wang, X., & Jia, J. (2022). Machine learning-based fast seismic risk assessment of building structures. *Journal of Earthquake Engineering*, 26(15), 8041–8062. https://doi.org/10.1080/13632469.2021.1987354
Zhang, H., Cheng, X., Li, Y., He, D., & Du, X. (2022). Rapid seismic damage state assessment of RC frames using machine learning methods. *Journal of Building Engineering*, 65, 105797. https://doi.org/10.1016/j.jobe.2022.105797

4th International Civil Engineering & Architecture Conference
17-19 May 2025, Trabzon, Türkiye

NARS-Z: Earthquake robot

Sedra F. Qutait*[1], Nael M. Karouni[1], Zainab W. Salih[1], Gökhan Gelişen[1], Rania M. Kouchchad[2], Abdul Aziz H. Bou Ali[2], Beste Bahçeci[2]

[1] Bahçeşehir University, Department of Civil Engineering, 34353 Beşiktaş, Istanbul, Türkiye
[2] Bahçeşehir University, Department of Mechatronics Engineering, 34353 Beşiktaş, Istanbul, Türkiye

Abstract. Istanbul is confronted with a considerable seismic hazard, since analysts anticipate the likelihood of a substantial earthquake occurring within this century. The precise time of this event is indeterminate; however, its potential severity necessitates immediate preparedness to mitigate loss of life and infrastructural damage. This research examines the creation of an earthquake reaction robot, a notion currently implemented in nations such as Japan to improve rescue operations during seismic occurrences. The proposed robot is engineered to execute many essential tasks, such as locating survivors ensnared in debris and evaluating the structural stability of edifices. Furnished with sophisticated sensors, high-definition cameras, and autonomous navigation systems, it can traverse debris, identify humans requiring rescue, and assess the safety or peril of structures. This robot utilizes advanced technology to enhance the speed and effectiveness of emergency responses in disaster-affected regions, thereby saving lives and mitigating the effects of earthquakes. The robot's design integrates fundamental ideas of civil engineering and disaster management, enabling effective operation in hazardous and complex conditions. This paper presents a novel and pragmatic answer to the rising global incidence of earthquakes, with the capacity to revolutionize disaster response operations and improve public safety.

Keywords: Seismic hazard; Earthquake; Earthquake response robot; Emergency response

1. Integrated system architecture and communication framework

The earthquake response robot system is designed to integrate advanced mechatronic and civil engineering principles for use in high-risk disaster environments. It provides rapid autonomous inspection, real-time communication, and decision-making capabilities essential for search and rescue operations. This section outlines the system-level architecture, communication technologies, and integration strategies that enable the robot to function reliably in post-earthquake scenarios (Kottege et al., 2019).

Wireless communication enables seamless data exchange between the robot and external control systems, allowing for remote operation and continuous monitoring. Infrared (IR) is employed for short-range communication where line-of-sight conditions are available, though it can be affected by environmental factors such as sunlight (Li et al., 2018). Wi-Fi technology, based on IEEE 802.11 protocols, allows for fast data transmission but is generally limited in range and effectiveness in obstructed disaster zones (Li et al., 2018). Satellite communication, utilizing GPS signals, provides global connectivity and is crucial when traditional networks are compromised (Lin et al., 2021). Cellular networks enhance geographic coverage and facilitate communication across large disaster zones by connecting the robot to base stations (Li et al., 2018).

The robot's sensor integration plays a vital role in situational awareness. A fusion of RGB-D cameras, LiDAR, and inertial measurement units (IMUs) provides comprehensive perception capabilities. By merging sensor inputs, the robot enhances accuracy in obstacle avoidance, localization, and structural assessment (Wang et al., 2021). These data inputs are processed in real-time by onboard computing systems, enabling immediate autonomous responses and reducing reliance on remote operators.

Control system integration is also essential. The robot incorporates actuators and control algorithms that process sensory data to execute precise movements and manipulations. This integration ensures that environmental inputs are translated into responsive action during navigation and interaction with objects or survivors (Sahashi et al., 2013). Advanced machine learning algorithms, particularly convolutional neural networks, support crack detection, object recognition, and survivor identification using visual and thermal data (Kabilan et al., 2021).

* Corresponding author, E-mail: sedra2002sooos@hotmail.com

https://doi.org/10.31462/icearc2025_ce_eqe_420

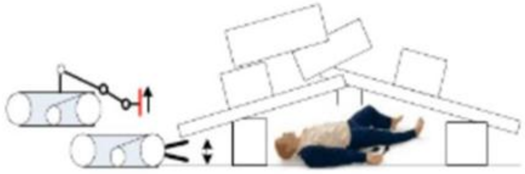

Fig. 1. Working scenario of Earthquakes robots

To facilitate human-robot interaction (HRI), multiple interface options are implemented. These include voice commands, touchscreen inputs, and wireless controls. HRI ensures that the robot can communicate feedback and receive high-level instructions from operators during collaborative missions (Bonarini, 2020; Pajaziti et al., 2021). Integration of user-friendly control devices such as joysticks and mobile platforms further enhances operational flexibility.

SOLIDWORKS is used to develop a detailed mechanical design of the robot, ensuring optimized placement and integration of sensors, actuators, and power modules. This modeling phase is crucial for testing mobility systems, simulating structural responses, and validating the feasibility of deployment in collapsed environments (Kottege et al., 2019).

Communication redundancy is another key feature. The robot is equipped with backup systems such as ad-hoc mesh networks and satellite links to ensure continued operation even if the primary network is disrupted (Lin et al., 2021). This layered communication strategy significantly improves operational resilience and ensures data availability in real time during rescue missions.

In summary, the integrated architecture of the earthquake response robot is designed to meet the demands of harsh disaster environments by combining robust hardware, intelligent software, and multi-layered communication systems. These features collectively enhance the robot's ability to assist human responders, assess structural damage, and save lives.

2. Subsystem: Structural analysis and civil engineering integration

2.1. Emergency communication and response integration system (ECRIS)

Earthquakes as natural hazards have caused substantial economic losses and significant human fatalities worldwide. This project introduces a novel integration system capable of conducting automated inspections and delivering emergency responses following seismic events. This system highlights the critical role of earthquake response robots in modern disaster management strategies (Kottege, Nannapaneni, & Peiris, 2019; Aracil et al., 2020).

The sub-team dedicated to this subsystem was tasked with developing capabilities for human and animal detection, fracture recognition, and prioritization of collected information for effective resource deployment. The integration of intelligent algorithms and advanced sensors enhances the robot's operational efficiency in post-earthquake scenarios

Fig. 2. Four-wheel-type robot designed for rough terrain navigation

Table 1. Comparison of sensing & perception systems

Criteria	Concept A (RoboBees)	Concept B (Sensor Technologies)	Concept C (Performance Evaluation)
Cost	Moderate	Low	-
Complexity	Low	Moderate	-
Performance	Versatile	Accurate	Comprehensive
Features	Aerial Drones	Various Sensors	Visual Evaluation Method
Other Considerations	Environmental Monitoring	Human Detection	Performance Ranking

Table 2. Emergency response assistance capabilities

Criteria	Concept A (Self-Propelled Robot)	Concept B (Robotic Arms)	Concept C (Aid Delivery System)
Cost	Low	Moderate	Moderate
Complexity	Low	Moderate	Low
Performance	Mobile	Precise	Efficient
Features	Self-Propelled Mobility	Robotic Arms	Supply Delivery Capability
Other Considerations	-	Medical Aid Delivery	-

2.2. Requirements

The primary requirements for the subsystem include reliable communication, accurate detection capabilities, rapid response, terrain adaptability, integration with other systems, and robustness and scalability (Wang et al., 2021). Centralized emergency communication centers play a key role in facilitating coordination between human operators and deployed robots, utilizing satellite, wireless, mesh networks, and sensor-based systems to ensure data transmission under emergency conditions (Lin, Huang, & Putranto, 2021). The robot must possess mobility features that enable it to adapt to complex terrain, avoid obstacles, and remain operable remotely in earthquake-affected environments (Sahashi et al., 2013; Kabilan et al., 2021). For inspection tasks, it is equipped with LiDAR and ultrasonic sensors to autonomously assess environments and detect structural anomalies (Li et al., 2018; Lin et al., 2021). Structural assessment is performed using RGB-D cameras, microphones, and accelerometers, while collaborations with industry professionals enhance data precision and improve the training of artificial intelligence algorithms (Wang et al., 2021; Sahashi et al., 2013).

Localization and mapping are facilitated by onboard sensors that create accurate environmental maps, supporting navigation and obstacle avoidance. The robot’s autonomous navigation system uses these maps to safely traverse uneven terrain and access restricted areas (Aracil et al., 2020). Object detection and recognition algorithms continuously scan the environment to identify human and animal forms, aiding in victim search and classification. Once victims are located, the robot uses visual and video data to evaluate their condition and determine the most appropriate course of action. All collected information is transmitted to command centers in real time, while the robot simultaneously enables direct communication with victims when necessary. It also collaborates with human rescuers by guiding them to the exact location of trapped individuals and delivering logistical support throughout the mission.

The robot is capable of continuous operation and environmental monitoring to ensure uninterrupted area coverage, which increases the likelihood of successful rescues. Its multilingual communication system allows it to interact with survivors from diverse linguistic backgrounds, offering verbal guidance and support (Pajaziti et al., 2021; Pajaziti, Bajrami, & Pula, 2021). For emergency response assistance, the robot performs a wide range of functions including debris removal, delivery of supplies, communication relay, and hazard detection (Lin et al., 2021). It is also equipped to handle hazardous materials remotely using appropriate sensing and containment technologies. Human-machine interaction is made possible through intuitive interfaces that enable operators to issue commands and receive feedback in real time (Bonarini, 2020). The entire subsystem is designed for durability and reliability, ensuring it can withstand the harsh physical and environmental stress typical of post-earthquake settings. Finally, its power-efficient architecture ensures prolonged deployment capabilities without requiring frequent recharging, making it suitable for extended rescue operations in critical zones.

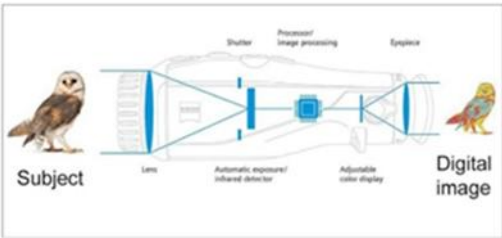

Fig. 3. Thermal imaging and analysis system for detecting survivors

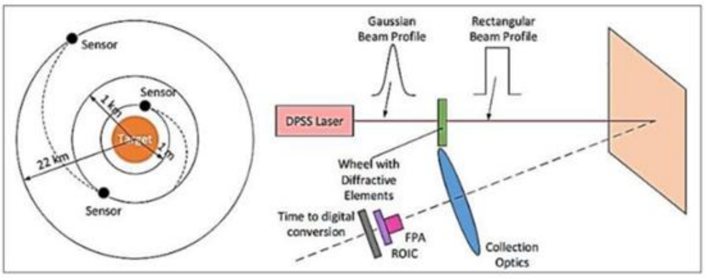

Fig. 4. LIDAR system schematic for environmental scanning and mapping

2.3. Technologies and methods

Historical cases highlight human-robot applications in disasters. Robots were used during Hurricane Wilma (2005), the Great Eastern Japan Earthquake (2011), and Italian earthquakes in 2012. Technologies such as Kinect-based 3D modeling and convolutional neural networks supported human motion analysis (Aracil et al., 2020) (Aracil et al., 2020).

Fall detection was studied using vision-based approaches involving silhouette extraction and motion analysis, achieving high accuracy compared to other sensing methods (Wang et al., 2021) (Wang et al., 2021).

2.4. Conceptualization

Three concepts were considered: (1) wheeled robot with LiDAR, (2) legged robot with RGB-D, and (3) wheeled robot with both RGB-D and LiDAR. The third concept offered the best balance of mobility, mapping, and localization capabilities.

Table 3. Conceptual design comparison

Component	Concept 1 (Wheeled Robot with Lidar)	Concept 2 (Legged Robot with RGB-D)	Concept 3 (Wheel Robot with RGB-D and Lidar)
Motor System	High-torque motor system	Specialized leg mechanisms	High-torque motor system
Image Processing	Powerful onboard computer	High-performance onboard Computer	High-performance onboard computer
Control Algorithm	SLAM techniques	Advanced computer vision techniques	Advanced computer vision techniques
Mobility	Good maneuverability on flat surfaces	Superior mobility over rough terrain	Good maneuverability on flat surfaces
Mapping Capabilities	Efficient mapping capabilities	Limited mapping capabilities compared to Lidar	Efficient mapping capabilities
Complexity	Moderate complexity	Higher complexity	Higher complexity
Cost	Moderate cost	Potentially higher cost	Highest cost

2.4.1. Physical architecture

The robot consists of a wheeled base, RGB-D cameras, microphones, LiDAR, a motor controller, and an onboard computing system. It integrates power management and communication interfaces.

2.4.2. Robot operation

Upon earthquake alerts, the robot initiates inspection using real-time imaging and autonomous navigation. Scenario-based simulations demonstrate its ability to assess injury levels, interact with victims, and direct rescuers.

In diverse building simulations, the robot differentiated between critical and non-critical cases and communicated multilingual guidance. It avoided high-risk zones when information was unclear, and prioritized high-value interventions based on available data.

2.5. Materialization

System materialization included selecting components aligned with functional needs and assembling them in a mechanical and electronic framework. Communication modules such as Wi-Fi, Bluetooth, and cellular were integrated with software protocols to ensure reliable data exchange. Workshops and iterative testing refined subsystem performance.

2.6. Evaluation

Evaluation included comparing conceptual solutions and validating the chosen system's ability to navigate debris, perform rescue tasks, and coordinate with human operators. The wheeled robot with RGB-D and LiDAR was found to be the most efficient in meeting operational goals under real-world constraints.

Rigorous testing confirmed the subsystem's reliability and relevance for disaster response, offering insights into system adaptability and future improvements.

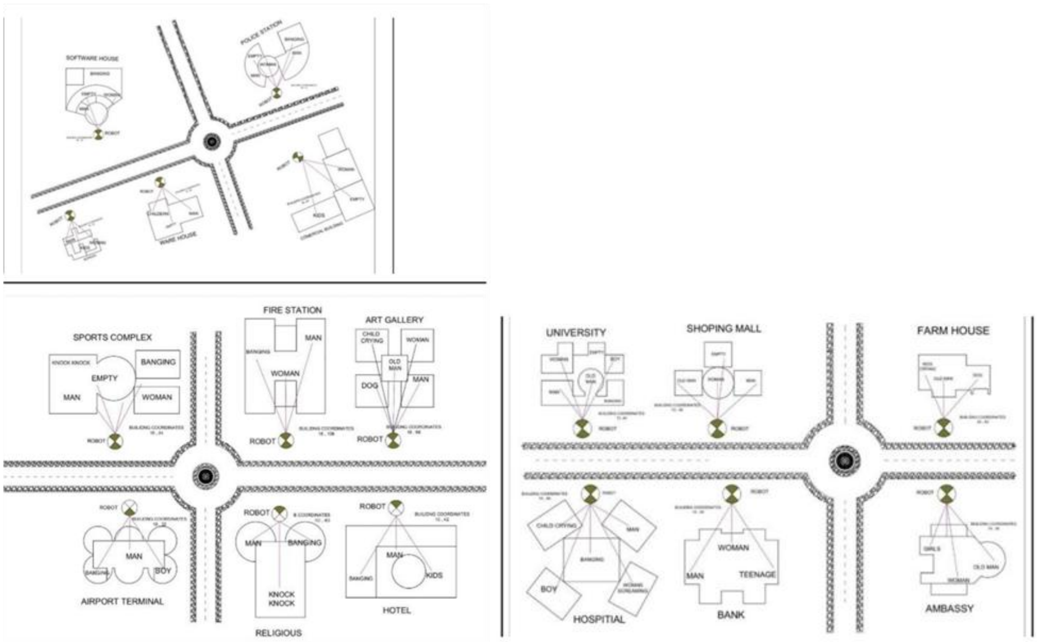

Fig. 5. Evaluation of robot performance across building case studies

3. Subsystem: Mechatronic control and sensory integration architecture

3.1. System overview and functional capabilities

This project is focused on the development of an earthquake response robot aimed at improving post-earthquake rescue operations. The robot's core functionalities include evaluating structural damage, navigating through hazardous environments, and transmitting real-time data to support rescue teams. It is specifically designed to assist in locating and rescuing individuals trapped under debris by providing essential supplies, such as water or blankets, especially in situations involving cold weather.

A key aspect of the robot's design is its ability to prioritize rescue efforts based on real-time assessments of building safety. This is achieved through an advanced voice recognition system that can distinguish between individuals' voices, such as children, the elderly, and animals, within each building. In addition, the robot employs machine learning techniques to assess building safety. The algorithm is trained using a large dataset of images showcasing both safe and damaged buildings, which enables the robot to identify and differentiate between structurally stable and unstable structures based on parameters such as cracks, deformations, and overall stability.

The robot's machine learning model allows for real-time decision-making, enabling it to evaluate the safety of buildings and determine which structures are suitable for entry. This prioritization ensures that rescue efforts are executed efficiently, reducing risk to both the rescuers and the individuals being rescued. The integration of advanced sensor technologies, machine learning, and autonomous decision-making represents a significant advancement in robotics for disaster response.

3.1. Communication and integration subsystem

The communication and integration subsystem is essential for the earthquake response robot, enabling seamless interaction between hardware and software components. It facilitates autonomous operation, real-time decision-making, and effective coordination with external systems. Key features include networking, remote control, fault detection, data logging, and sensor fusion, which enhance the robot's performance in complex disaster scenarios. Additionally, control system integration and human-robot interaction ensure efficient collaboration with human operators, improving the robot's adaptability and reliability during rescue operations.

This subsystem enables the robot to connect with external networks for remote control and monitoring. Key functions include fault detection, data logging, and telemetry. It also integrates multiple subsystems (locomotion, perception, manipulation) and incorporates sensor fusion from cameras, LiDAR, and IMUs. Human-robot interaction through voice, gestures, and wireless communication ensures collaboration with operators in high-risk environments.

3.1.1. Requirements for the earthquake response robot

The robot must fulfil critical performance requirements including survivability, mobility, accurate detection, and reliable communication. The design employs SOLIDWORKS and includes an experimental setup for real-world readiness. Ethical considerations emphasize transparency about the robot’s capabilities.

System integration requirements include real-time communication, sensor fusion, onboard data processing, integrated control systems, user interface support, and power efficiency. These ensure autonomous execution of search, rescue, reconnaissance, and sensing tasks.

3.1.2. Technologies and methods

The robot uses wireless communication, IR, Wi-Fi, satellite, and cellular networks to ensure flexibility and redundancy. Sensor fusion from cameras, LiDAR, and IMUs supports decision-making. SOLIDWORKS aids subsystem integration. Human-robot interaction includes voice and gesture recognition. Redundant systems like mesh networks ensure connectivity during failures.

3.1.3. Conceptualization of the earthquake response robot subsystem

The subsystem must enable seamless communication, coordination, and decision-making. This includes:

- *Integration and Communication:* Coordination between subsystems and external systems with real-time feedback.
- *System Architecture:* Managing data flow and subsystem interaction.
- *Communication Protocols:* Ensuring compatibility and reliability.
- *Redundancy:* Including backup communication mechanisms.
- *Localization:* Using GPS, inertial navigation, and synchronization.
- *Decision Support:* Fusing sensor data for informed action.
- Data acquisition involves high-resolution sensors with real-time processing. Error handling includes self-diagnostics, error-detection codes, and noise filtering.
- Future enhancements include hyperspectral imaging, advanced acoustic sensors, and 3D LiDAR. AI applications such as deep learning, NLP, and predictive analytics improve decision-making.

3.1.4. Physical architecture

The architecture supports autonomous or assisted operation, integrating sensors, actuators, and communication tools. It employs SLAM for navigation and deep learning for victim assessment. Sensors include depth cameras, LiDAR, and acoustic sensors. Actuators and embedded computing enable mobility and processing.

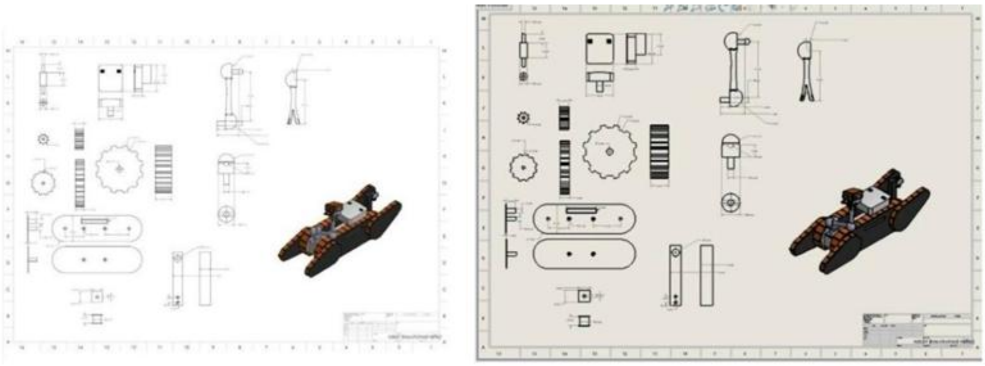

Fig. 6. Technical drawing sheets and 3D assembly view of the earthquake response robot developed using SOLIDWORKS, illustrating the mechanical components and structural integration

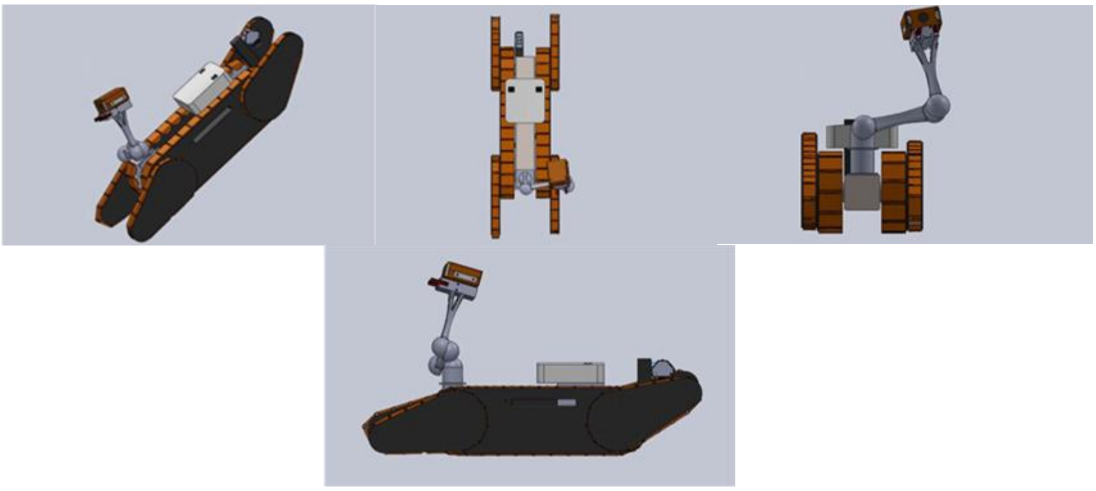

Fig. 7. Multiple perspective views of the earthquake response robot, including front, side, top, and isometric orientations, illustrating its mechanical structure and sensor-arm articulation

4. Conclusions

The earthquake response robot represents a significant advancement in the application of artificial intelligence and modern technologies to the field of disaster management. By integrating intelligent sensing systems, such as LiDAR and infrared imaging, with real-time data analysis and seismic monitoring, the robot enhances both the speed and effectiveness of post-earthquake operations. One of its primary functions is to improve safety in earthquake-prone regions through the early detection of seismic activity and the systematic exploration of affected areas. Furthermore, its ability to provide critical situational data to emergency response teams facilitates more informed and timely decision-making during rescue missions.

The development and deployment of this robotic system mark a transformative step in the management of natural disasters, particularly in high-risk regions like Turkey. Continued investment in such technologies is essential, as it not only improves immediate response capabilities but also contributes to long-term public safety, infrastructure resilience, and national disaster preparedness strategies:

- Effective structural damage assessment
- Survivor detection via sound and heat
- Autonomous navigation in complex terrain
- Real-time data transmission
- AI-powered prioritization of rescue areas
- Low-cost and scalable prototype
- Collaborative data training with real-world inputs
- Reliable power and processing architecture
- Durability and environmental resistance
- Multi-role capability

Acknowledgments

The authors would like to express their deepest gratitude to Prof. Gökhan Gelişen and Prof. Beste Bahçeci for their exceptional mentorship, continuous encouragement, and unwavering support throughout every phase of this project. Their expertise, constructive feedback, and dedication not only enriched our technical development but also inspired us to strive for excellence.

We would also like to sincerely thank our fellow teammates and colleagues for their hard work, collaboration, and perseverance during the development of this project. Their commitment and team spirit played a vital role in overcoming the many challenges we encountered.

A heartfelt thanks goes to our families and friends, whose endless support, understanding, and motivation gave us the strength to remain focused and determined. Their patience during long working hours, and their encouragement through stressful moments, were truly invaluable. This achievement would not have been possible without their love and belief in us.

References

Aracil, R., Carreras, M., Martínez, F., Sagues, C., & Garrell, A. (2020). Swarm robotics in urban search and rescue: Coordination strategies and applications. *Journal of Field Robotics, 37*(6), 1032–1045. https://doi.org/10.1002/rob.21934

Bonarini, A. (2020). Human-robot interaction in emergency response: Communication models and design principles. *International Journal of Human-Robot Interaction, 8*(2), 77–90. https://doi.org/10.1177/1948550920917910

Brooks, D.J., Curtin, D.J., Kuczynski, J., Rodriguez, J., Steinfeld, A., & Yanco, H.A. (2020). Communication paradigms during robot failure: A usability study in search and rescue. *ACM Transactions on Human-Robot Interaction, 9*(4), 1–20. https://doi.org/10.1145/3386361

Kabilan, R., Muthuraman, M., Ranjan, A., & Prasad, S. (2021). Real-time live human detection robots for earthquake scenarios. *IEEE Transactions on Instrumentation and Measurement, 70*, 1–10. https://doi.org/10.1109/TIM.2021.3062987

Kottege, N., Nannapaneni, S., & Peiris, T. (2019). Robotics in disaster management: A review of capabilities, challenges, and technologies. *Disaster Robotics Review, 5*(1), 25–39

Li, L., Meng, X., Ma, Y., & Han, R. (2018). IoT-based earthquake early warning systems: Development and applications. *Sensors, 18*(9), 3045. https://doi.org/10.3390/s18093045

Lin, T.H., Huang, J., & Putranto, A. (2021). Integration of smart robotics with earthquake early warning systems for automated emergency response. *Sensors and Actuators A: Physical, 332*, 113141. https://doi.org/10.1016/j.sna.2021.113141

Pajaziti, A., Bajrami, X., & Pula, G. (2021). Communication and interaction between humanoid robots and humans in rescue missions. *International Journal of Robotics Research, 40*(9), 1174–1192. https://doi.org/10.1177/02783649211030055

Sahashi, T., Okada, T., Tadokoro, S., & Inoue, K. (2013). Development of rescue robots for earthquake disasters: A case study from Japan. *Advanced Robotics, 27*(18), 1431–1445. https://doi.org/10.1080/01691864.2013.812715

Wang, Q., Zhao, Y., Ren, L., Yang, S., & Zhang, Y. (2021). Soft robotic manipulators for debris removal in earthquake-damaged buildings. *IEEE Robotics and Automation Letters, 6*(3), 4872–4879. https://doi.org/10.1109/LRA.2021.3063642

Effect of concrete discharge on tensile strength and fibre distribution of UHPFRC

Marwa M. Ibrahim[1], Raafat El-Hacha[*1]

[1] University of Calgary, Department of Civil Engineering, 2500 University Drive NW, Calgary, Alberta, Canada

Abstract. Ultra High-Performance Fibre Reinforced Concrete (UHPFRC) is a next-generation material known for its exceptional mechanical strength and ductility. In addition to its well-documented compressive strength (>120 MPa), it exhibits a unique post-cracking tensile strength that is UHPFRC-exclusive. Accurately quantifying this tensile performance is critical to fully leverage the material's structural benefits. However, this tensile strength is influenced by fibre content and distribution within the matrix, which are significantly affected by the concrete discharge method during casting. Therefore, this study investigates the effect of the concrete discharge method on the tensile strength of a commercially available UHPFRC mix incorporating steel fibre and carbon nanofibres. Two discharge methods were examined: discharge from one stationary point: one end, and discharge from one stationary point: center. Dog-bone shaped specimens were cast in a single concrete layer and subjected to pure tensile loading. After testing, specimens were transversely cut near the failure location to analyze the fibre distribution within the cross-section. Results indicate that the one stationary point discharge method significantly enhances tensile strength compared to random discharge. Moreover, within the one stationary point category, the one-end location exhibited superior tensile properties over the center location. These findings underscore the critical role of discharge techniques in optimizing fibre distribution and tensile performance. Standardizing placement methods is essential to ensure consistent testing protocols and fair performance comparisons across different UHPFRC compositions. Future research should explore additional variables, like fibre geometry, to refine the application of UHPFRC in construction.

Keywords: Tensile strength; Fibre distribution; Concrete discharge; UHPFRC

1. Introduction

Concrete is the second most consumed material on Earth, after water. Its global usage reaches approximately 30 trillion tonnes per year. In contrast, wood consumption is around 1 trillion tonnes, and steel is about 1.6 trillion tonnes annually (Future Cleantech Architects, 2022). This widespread use is due to concrete's high versatility and energy efficiency. It outperforms many traditional construction materials in cost, durability, and availability. These advantages have driven research into advanced cement-based composites. In the 1980s, the introduction of superplasticizers and pozzolanic materials enabled the development of Ultra-High-Performance Concrete (UHPC), which greatly outperforms conventional concrete. UHPC showed excellent strength and durability, but also exhibited significant brittleness (ACI Committee 239, 2018). To overcome this, fibers were added to improve ductility and fracture resistance. This led to Ultra-High-Performance Fiber-Reinforced Concrete (UHPFRC). During development, some researchers questioned calling it "concrete". However, the term "concrete" was used instead of mortar to highlight the enhanced ductility of UHPC with fibres (Azmee and Shafiq, 2018). Similarly, the term ultra-high performance is selected rather than strength to highlight the wider characteristics of the material, including both mechanical strength and durability performance (Fehling et al., 2014). For context, UHPFRC's compressive strength is more than seven times that of conventional concrete, while its tensile cracking is three times greater (Graybeal, 2009). This combination, accompanied by excellent durability, makes it ideal for a plethora of construction applications, whether structurally demanding, environmentally demanding, or both.

The science behind UHPFRC is simple: removal of coarse aggregates, usage of a low water-to-cementitious materials ratio, utilization of pozzolans and superplasticizers, and optimization of the mix gradations. The preceding results in a 28th-day compressive strength of at least 120 MPa. On the other hand, the incorporation of fibres, mostly high-strength steel fibres at a volumetric ratio of 2%, gives the material an extraordinary post-cracking tensile strength that is steel-like (typically about 5 MPa (Ullah et al., 2022)). Reported UHPRC tensile strengths in the literature are as high as 14.2 MPa (Xu & Wille, 2015). As a result, UHPFRC contributes to the internal tensile load-resisting mechanism in flexural structures, unlike in conventional concretes where this tensile

[*] Corresponding author, E-mail: relhacha@ucalgary.ca

https://doi.org/10.31462/icearc2025_ce_eqe_425

strength is negligible. Recognizing this contribution can offer several advantages. One key benefit is the potential reduction in required longitudinal reinforcement. However, to fully utilise the tensile capacity of UHPFRC, it must be accurately characterised and quantified.

2. Problem definition

The tensile strength of UHPFRC represents a significant advancement in the evolution of concrete technology. This tensile strength must first be accurately quantified to fully exploit the material's attributes. Once established, appropriate subsequent modifications in the design process shall be made to account for this tensile strength and its implications on the member strength and ductility. However, the tensile performance of UHPFRC is influenced, in turn, by various factors, including fibre type and content, specimen or member dimensions, and concrete discharge during casting. This study specifically investigates the influence of the latter on tensile strength and fibre distribution.

3. Experimental testing program

3.1. Materials and mixing

The material utilized in this investigation is a proprietary UHPFRC mix enhanced with Carbon Nanofibres (CNF). Including nanomaterials improves the matrix by bridging nanoscale microcracks, while steel microfibres span larger cracks, enhancing the overall tensile strength. The material is supplied in separate components: bags of steel fibres, a CNF liquid pail, a superplasticizer, and a pre-blended mixture of cementitious and anhydrous materials. The mixing procedure largely mirrors conventional UHPFRC mixing, with an additional step to accommodate the CNF. The shipped CNF pail is first thoroughly mixed to ensure homogeneity before the required quantity is extracted. The CNF is then blended with superplasticizer and water, remixed, and subsequently incorporated into the dry pre-blend. Steel fibres are added gradually, and mixing continues for 10–15 minutes after water addition. Fibre contents are maintained at 2% by concrete volume for steel fibres and 0.75% by binder mass for CNF.

3.2. Companion compressive strength specimens

Three companion compressive cylinders (75 mm × 150 mm) were prepared to evaluate CNF-UHPFRC's compressive strength. Each cylinder was cast in a single layer to preserve the continuity of the fibre network formed during mixing and to avoid creating a potential weak plane at the interface of discrete layers. Following casting, each specimen was manually lightly vibrated to reduce internal voids. Then, the cylinders were immediately covered, demoulded after 24 hours, and then stored in a fog room under standard curing conditions (23 °C and 90% relative humidity) (ASTM, 2021). Prior to testing, the ends of all specimens were ground to ensure uniform axial load distribution. Compressive strength testing was conducted at the 28th-day of curing in accordance with ASTM C39 (ASTM, 2020) and ASTM C1856 (ASTM, 2017). The compressive strength recorded was 139.76, 136.07, and 134.72 MPa for cylinders 1, 2, and 3, respectively, with an average value of 136.86 MPa and a standard deviation of 1.56 MPa.

3.3. Tensile strength specimens

Six dog-bone specimens were fabricated following the guidelines outlined in the Swiss recommendations (Architects, 2016). To ensure continuity in the fibre network, fresh concrete was cast in a single layer, similar to the compressive strength cylinders. However, two distinct concrete discharge types were evaluated: discharge from a fixed point at the end of the mould (labelled "E"), and discharge from a fixed point at the centre (labelled "C"; see Fig. 1 (a)). Specimens were designated based on a two-part naming convention comprising the discharge type (E, C, or R) and a specimen identifier (SP1, SP2, or SP3). After casting, the specimens were also covered with a plastic sheet to prevent moisture loss, demoulded after 24 hours, and cured in a fog room under standard conditions (23 °C and 90% relative humidity).

3.4. Instrumentation and testing

The specimens were tested at the 28-th day of curing. The loading protocol consisted of two displacement-controlled phases: 0.2 mm/min during the elastic and post-cracking hardening stages, and 0.4 mm/min during the softening stage. Initially, a lower rate was used to accurately capture the response during the early loading phases. Due to the challenge of locating a testing machine capable of simultaneously applying axial and lateral hydraulic forces, a custom steel collar was designed and fabricated in-house to laterally restrain the specimen prior to axial loading. The collar enclosed the specimen and included welded transverse plates to prevent out-of-plane displacement, as well as separate aluminum wedges for confinement. Screws were used to engage the wedges and apply lateral pressure. Different wedge configurations—varying in length and angle—were examined in a preliminary phase to optimize the confinement system before initiating the tensile tests (Fig. 2 (a)). During testing, two Linear Variable Displacement Transducers (LVDTs) were mounted on each specimen to measure strain and crack openings. A custom-designed aluminum LVDT holder with a 200-mm gauge length was used to secure the sensors. Fig. 2 (b) illustrates the experimental setup immediately before the application of uniaxial tensile loading.

(a) (b)

Fig. 1. Photographs showing (a) the pouring procedure in a single layer from one stationary point (the center), and (b) cast specimens

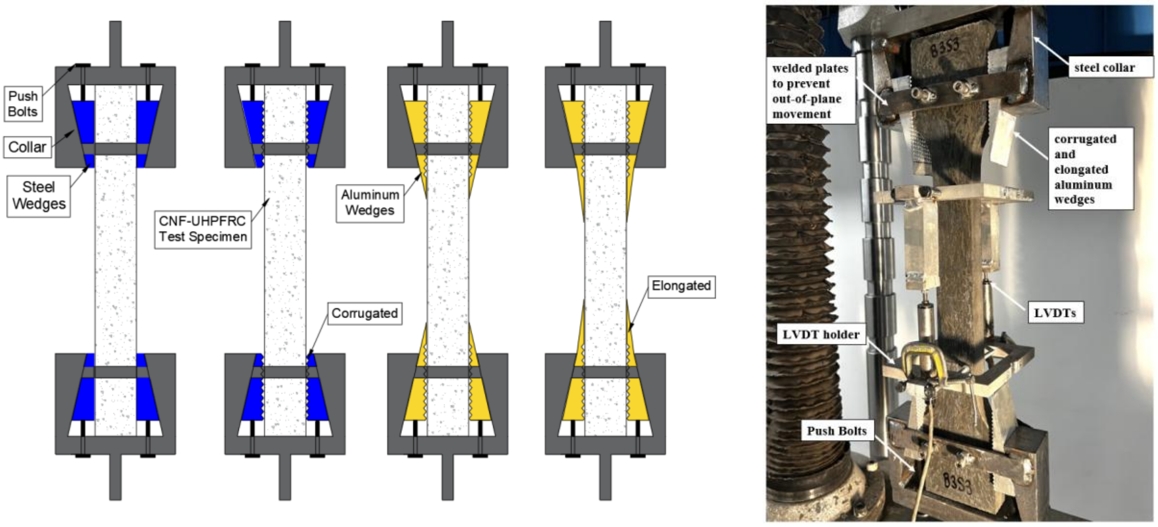

(a) (b)

Fig. 2. Tension Test (a) development of the load-applying collar, and (b) test set-up showing the specimen

4. Results

4.1. Cracking behaviour

UHPFRC is well known for its multi-cracking behaviour under tensile loading (Fig. 3). As such, distributed cracking along the full length of the specimen is typically expected. Table 1 details the acceptance or rejection status of each specimen based on the failure location. Specimens were excluded from further analysis if the localized crack occurred outside the central 200-mm gauge length. Such cases were deemed invalid for the purposes of evaluating tensile behaviour and were accordingly rejected.

Table 1. Summary of the cracking response of the tested dog-bone shaped specimens

Specimen	Visible Cracks	Location of the localizing crack	Condition	Maximum Stress (MPa)
C-SP1	One	within the gage length	Accepted	7.80
C-SP2	One	within the gage length	Accepted	4.93
C-SP3	One	within the gage length	Accepted	6.80
E-SP1	One	Outside the gage length	Rejected	4.06*
E-SP2	Multi-cracking	Outside the gage length	Rejected	9.00
E-SP3	Multi-cracking	Two major cracks within the gage length	Accepted	9.59

*abrupt failure

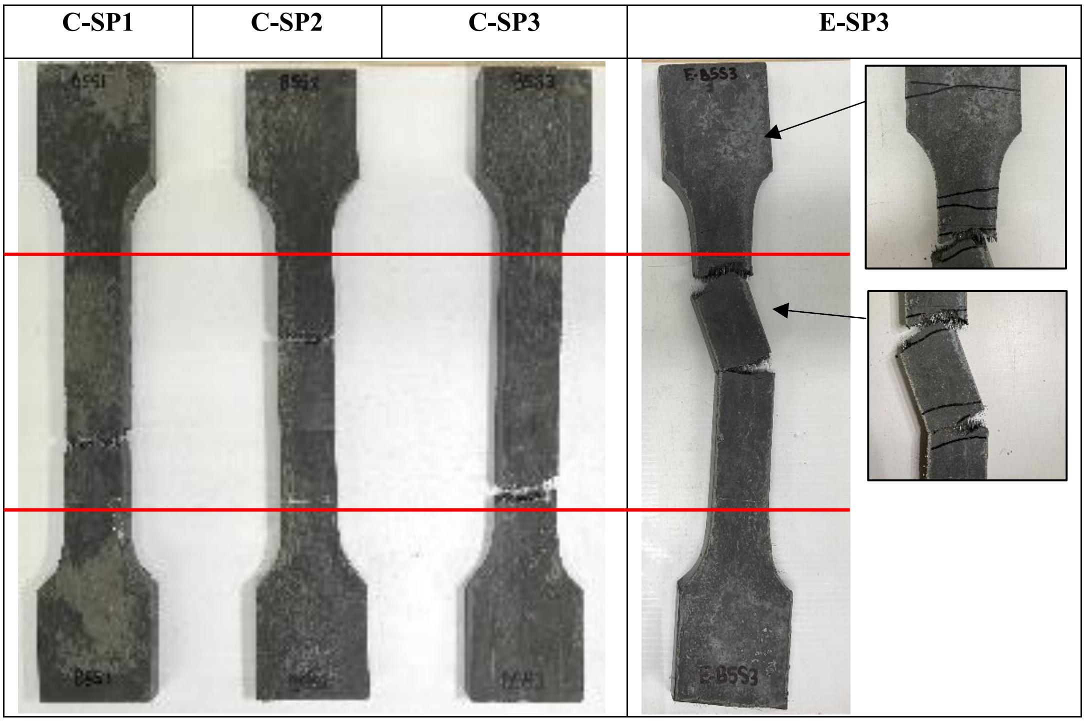

Fig. 3. Photos of accepted specimens: C-SP1, C-SP2, C-SP3, E-SP3 showing multi-cracking behaviour; red lines represent the borders of the instrumented gage length

4.2. Stress-strain response

Fig. 4 shows the full tensile stress-strain behaviour of UHPFRC, with two main cardinal points: cracking and localization. While the cracking onset is common for all concrete types, the post-cracking steel-like behaviour and the accompanying localization onset is UHPFRC inclusive. It is worth noting that the cracking characteristics are matrix-related, while the localization ones are steel fibre related. Therefore, the localization onset refers to the onset of fibre pullout where the fibres can no longer sustain the tensile load. Table 2 summarizes the stress and strain values of these cardinal points for each specimen. It is evident from Fig. 4 that the one end cast specimen showed superior post-cracking behaviour compared to all three centre-cast specimens. This is mainly attributed to the fibre distribution affected by the discharge location, as discussed below.

Table 2. Tabulated Stress-strain results of tested dog-bone shaped specimens under direct tensile load

Specimen	C-SP1	C-SP2	C-SP3	E-SP3
$f_{t,cr}$ *(MPa)*	5.55	4.21	4.22	5.55
$\varepsilon_{t,cr}$ (%)	0.010	0.012	0.017	0.016
$f_{t,loc}$ (MPa)	7.80	4.93	6.80	9.59
$\varepsilon_{t,loc}$ (%)	0.119	0.169	0.228	0.287

$f_{t,cr}$ is the cracking tensile strength; $\varepsilon_{t,cr}$ is the cracking tensile strain; $f_{t,loc}$ is the localization tensile strength; $\varepsilon_{t,loc}$ is the localization tensile strain

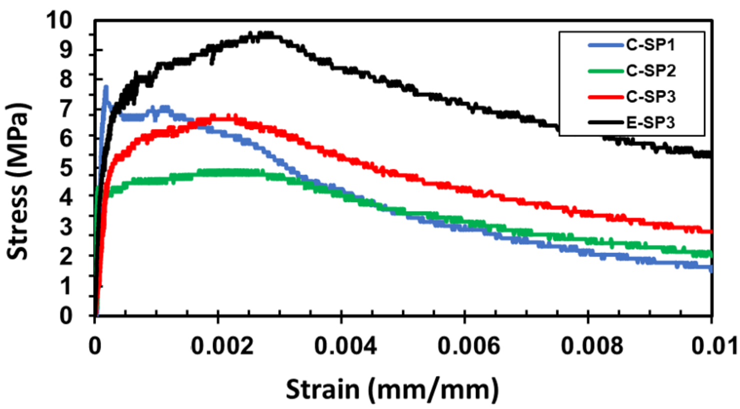

Fig. 4. Stress-strain response of CNF-UHPFRC dog-bone shaped specimens under direct tensile load

4.3. Effect of the discharge type on the tensile strength

While several factors—such as matrix strength, specimen size, and geometry—impact the post-cracking tensile behavior of UHPFRC, the type and volume of fibres at the cracking location are generally the most significant. These fibre-related parameters, however, are influenced by additional factors. The method of concrete discharge determines the fibre distribution along the specimen's length, while the fresh mix flowability governs the distribution of fibres within the cross-section, particularly in terms of potential fibre settlement. Fig. 4 illustrates that specimens cast from one end exhibited the highest tensile strength and strain capacity. Specimen E-SP3 developed multiple cracks, with two dominant ones contributing to enhanced strength and an extended multi-cracking phase. This discharge method preserves the fibre network developed during casting and promotes fibre alignment as fibres orient uniformly along the flow direction. The next observed behaviour corresponds to specimens cast from the centre, where the concrete flow splits into two opposing directions during placement (refer to

Fig. 5). Among these, specimen C-SP1 achieved the highest peak strength in its group but showed an abrupt post-peak strength drop. In contrast, specimens C-SP2 and C-SP3 exhibited more gradual post-peak softening, albeit with reduced peak strengths.

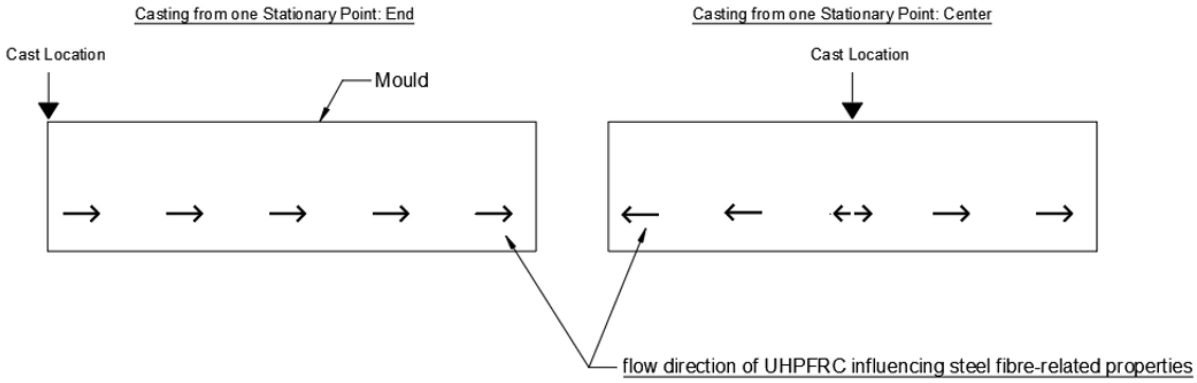

Fig. 5. Schematic demonstrating the influence of the cast direction on the flow properties and steel fibre-related properties of UHPFRC

The Swiss recommendations suggests grinding the surfaces of the hardened CNF-UHPFRC specimen prior to testing to ensure a uniform thickness. However, this practice is likely to introduce microcracks, creating localized weaknesses that can reduce the measured tensile strength and increase variability in test results. Given that the tensile strength of UHPFRC, although superior to that of conventional concrete, remains significantly lower than its compressive strength, such inconsistencies can substantially impact the reliability of test results. As an alternative, applying Tuck Tape to the interior surfaces if the wooden formwork (

Fig. 1 (a)) has proven effective. This, combined with the self-levelling properties of CNF-UHPFRC, yields smooth, uniform and crack-free CNF-UHPFRC surfaces from all sides. In addition, this is also advantageous from a practical point of view.

On the other hand, the application of Tuck Tape to the inner surfaces of the wooden formwork facilitated the visualization of the fibre orientation on the bottom surface of the hardened CNF-UHPFRC specimens. As depicted in

Fig. 6, fibres located near the stationary discharge points —either at the centre or end—exhibited random, non-aligned orientations. However, as the distance from the discharge location increased, fibres demonstrated a tendency to align with the direction of flow. This alignment was particularly evident in end-cast specimens at the critical section (middle cross-section), where fibres traversed a substantial, uninterrupted path, promoting better alignment.

In specimens cast from the centre, fibres are required to traverse distances comparable to those in end-cast specimens to reach the extremities. However, two primary factors often compromise alignment at these terminal regions. Firstly, widening of the cross-section at transition zones induces lateral dispersion of the mix, disrupting fibre orientation. Secondly, the proximity of formwork boundaries at the specimen ends imposes constraints on fibre movement, leading to circular alignment patterns as fibres navigate these spatial limitations (wall effects). This behaviour is consistently observed at end locations across both discharge types. These observations underscore the critical importance of controlled casting procedures to ensure consistent fibre alignment and reliable material behaviour.

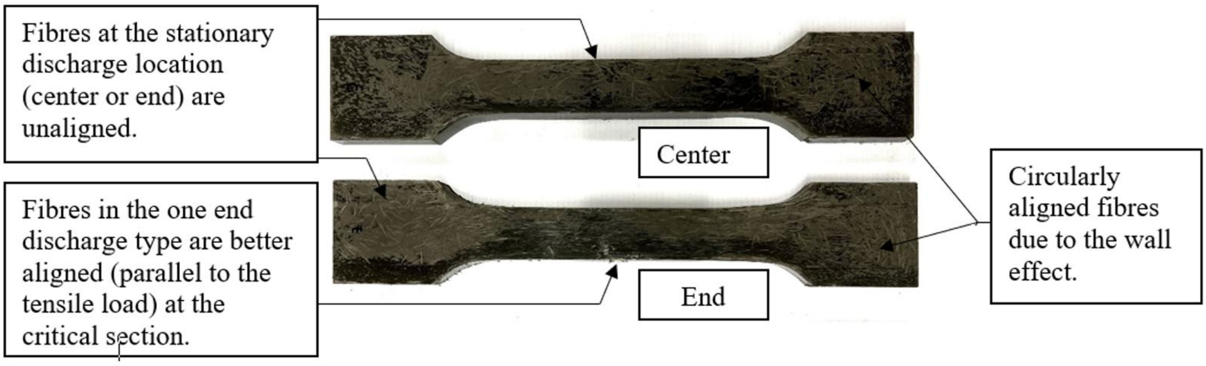

Fig. 6. Behaviour of fibres at the bottom side of the cast specimens

4.4. Effect of the discharge type on the fibre distribution and settlement

The tested dog-bone shaped specimens were transversely cut 10-mm away from the failure location using a wet saw to assess the fibre distribution within the cross-section (

Fig. 7). After conventional post-processing of the captured cross-sectional images, the contrast between the fibres and the surrounding matrix is increased to further differentiate specifically between the grains in the UHPFRC matrix and the fibres. Next, binary images are created, followed by fibre analysis.

Fig. 8 shows that fibres are denser close to the bottom casting side, attributed to potential fibre settlement due to the flowability being on the high end of the acceptable range. It is also evident that specimens cast from a stationary end location generally exhibited a higher fibre density across the cross-section. Conversely, specimens cast from a central stationary point displayed more linear fibre patterns with visible fibre lengths, indicative of less aligned fibres near the failure location. This central casting approach resulted in a lower overall fibre count across the cross-section, compromising the tensile performance of the material.

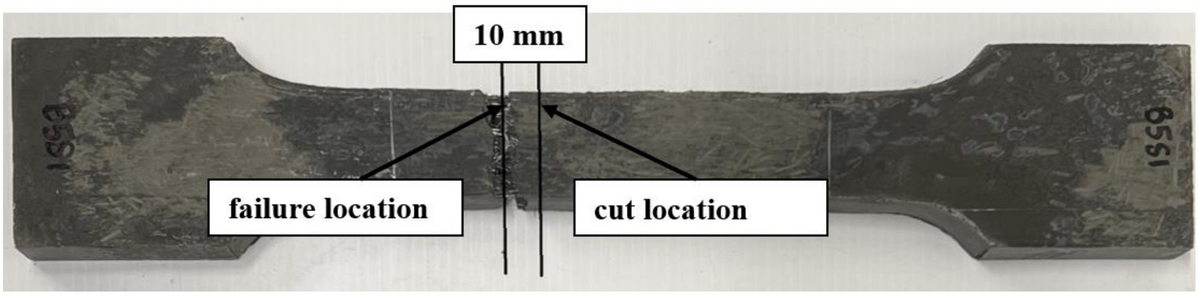

Fig. 7. Cut location of the tested specimen

Table 3 Summarizes the fibre analysis results, including fibre count and average fibre size. These findings align with previous observations: specimen E-SP3, cast from one end, exhibited the highest fibre count and an average fibre size closest to the manufacturer's specified diameter of 0.2 mm, leading to the observed superior tensile strength. The average fibre size within a cross-section serves as an indicator of fibre orientation. When the average fibre size closely matches the actual fibre diameter specified by the manufacturer, it suggests that fibres are predominantly aligned parallel to the applied tensile load and perpendicular to potential crack planes, thereby enhancing crack-bridging effectiveness and tensile resistance. Conversely, a larger average fibre size implies that fibres are oriented parallel to the crack plane, offering minimal resistance to crack propagation and reduced tensile strength. Table 3 also shows that the specimens cast from one stationary point at the centre location (C-SP1, C-SP2, and C-SP3) consistently showed larger average fibre sizes than the one end cast specimen, indicating less aligned fibres due to their proximity to the discharge location.

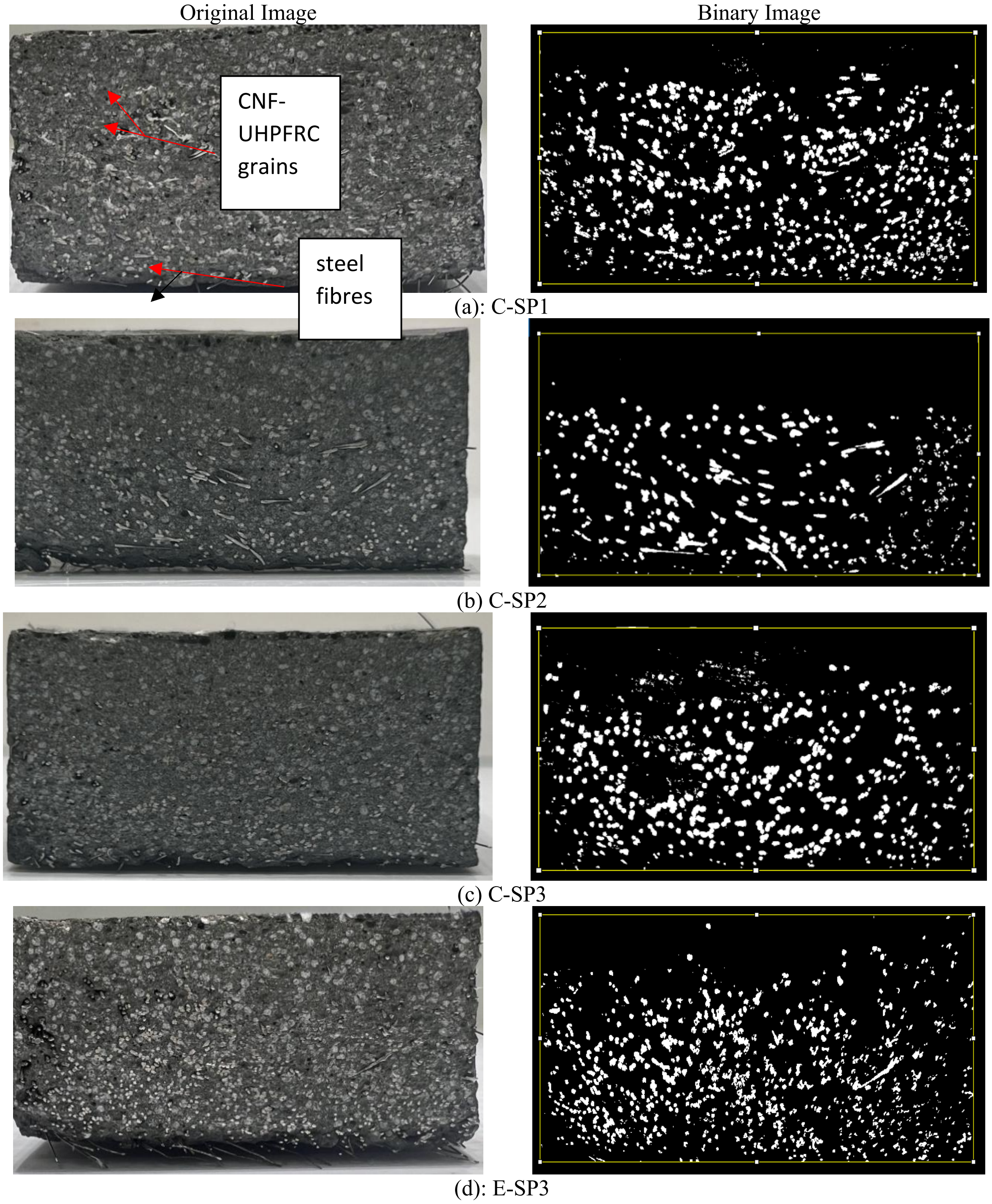

Fig. 8. Original and binary images showing the fibre distribution along the cross-sections of the tested specimens

Table 3. Results of fibre analysis showing the total number and average size of fibres

Specimen	Total number of fibres identified at the cut section	Average fibre size (mm)
C-SP1	505	0.36
C-SP2	300	0.30
C-SP3	410	0.40
E-SP3	555	0.23

The above fibre distribution and tensile strength observations align with the data presented in Fig. 9. Specifically, all centre-cast specimens exhibited a lower fibre count compared to that cast from the end. Notably, specimen C-SP1 had a 9% lower fibre than E-SP1; however, the average fibre size differed significantly (56.52% higher than E-SP1). This variation in fibre size contributed to the 22.94% higher tensile strength observed in E-SP1.

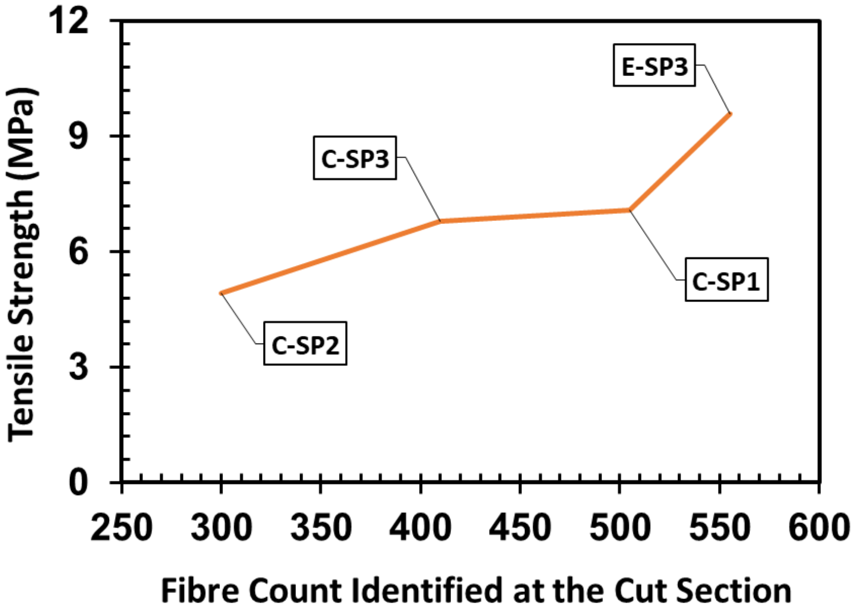

Fig. 9. Relationship between the fibre count identified at the cut section and the maximum tensile strength of each specimen

5. Discussion

The experimental results underscore the critical influence of casting methods on the tensile performance of UHPFRC. Specimens cast from a stationary end position exhibited superior tensile strength and strain capacity, attributed to enhanced fibre alignment along the flow direction, which facilitates effective crack-bridging mechanisms and delays crack propagation. Conversely, specimens cast from a central stationary point showed larger average fibre sizes, indicating less aligned fibres due to their proximity to the discharge location, leading to earlier crack initiation and reduced tensile strength.

These findings highlight two key considerations. First, the stationary discharge type from one end yields the most favourable tensile behaviour. Consequently, implementing this method is strongly recommended for both laboratory characterizations and practical large-scale applications to achieve consistent and optimal material properties. Second, it is important to establish specific protocols for discharge methods in international jurisdictions. This ensures uniformity in tensile strength characterization and compliant characteristics of UHPFRC in practical structural applications.

While specialized devices have been developed to facilitate UHPFRC casting, their practicality in large-scale, on-site applications remains limited. The rapid setting time of UHPFRC necessitates swift casting processes; any delays introduced by such devices can compromise material integrity, particularly under variable environmental conditions. Moreover, employing multiple stationary discharge points may disrupt the fibre network, leading to inconsistent mechanical properties. Therefore, a straightforward casting approach—utilizing a single stationary discharge point from one end—is advocated to maintain the material's structural performance and to streamline the casting process in real-world applications.

Nonetheless, it is essential to recognize that each construction project presents unique challenges and requirements. Engineers must exercise professional judgment to assess and determine the most suitable casting method on a case-by-case basis. Factors such as the volume of UHPFRC to be cast, the dimensions of the structural element (including its depth and length), and the intended function of the member (e.g., structural or non-structural) should be carefully evaluated to select the most appropriate casting strategy. This tailored approach ensures that the casting method supports optimal fibre orientation and distribution, thereby yielding enhanced and consistent UHPFRC performance.

6. Conclusion

Two types of concrete discharge methods were assessed in this study in terms of tensile performance. The findings underscore the importance of selecting appropriate casting techniques to optimize fibre alignment and, consequently, the mechanical properties of UHPFRC elements. Key conclusions drawn from the research include:

- The concrete discharge method significantly affects the tensile strength of UHPFRC. Establishing specific protocols for discharge methods in international jurisdictions is crucial to ensure uniformity in tensile strength characterization and compliance in practical structural applications.
- Discharge from a single stationary point- one end was found to be the most optimal as it promotes better fibre alignment at the critical section. Fibre analysis at the failure location showed that fibres in this specimen had the closest average diameter to the value provided by the manufacturer, leading to superior tensile strength and strain capacity. This method is recommended for practical applications.
- Discharge from a central stationary point results in less aligned fibres at the critical location (discharge location), leading to less effective fibre bridging capabilities and, therefore, a reduced tensile strength.

Further research is needed to develop standardized guidelines for casting procedures, considering factors such as UHPFRC volume, structural element dimensions, and the intended function of the member to ensure optimal fibre orientation and distribution. This way, UHPFRC applications in the construction industry can be advanced, ensuring that the enhanced performance and durability of UHPFRC structural elements are fully realized.

Acknowledgements
This research is funded by NSERC, Mitacs, Alberta Innovates and the University of Calgary. The authors wish to acknowledge the in-kind contribution of ceEntek North America Ltd. and the provided training in the mixing of concrete.

References

ACI Committee 239. (2018). *239R-18 Ultra-High-Performance Concrete: An Emerging Technology Report*. American Concrete Institute.

ASTM C39/C39M-20. (2020). *Standard Test Method for Compressive Strength of Cylindrical Concrete Specimens*. ASTM International.

ASTM C511-21. (2021). *Standard Test Method for Mixing Rooms, Moist Cabinets, Moist Rooms, and Water Storage Tanks Used in the Testing of Hydraulic Cements and Concretes* (Vol. 04.01, p. 3). ASTM International. https://doi.org/10.1520/C0511-21

ASTM C1856/C1856M-17. (2017). *Standard Practice for Fabricating and Testing Specimens of Ultra-High Performance Concrete*. ASTM International.

Azmee, N. M., & Shafiq, N. (2018). Ultra-high performance concrete: From fundamental to applications. *Case Studies in Construction Materials, 9*, e00197. https://doi.org/10.1016/j.cscm.2018.e00197

ceEntek. (n.d.). *UHPC solutions for high-performance construction*. Retrieved June 26, 2024, from https://uhpc2.com

Fehling, E., Baltzer, H., & Janberg, N. (2014). *Ultra-high performance concrete UHPC: Fundamentals, design, examples* (5th ed.). Ernst & Sohn.

Future Cleantech Architects. (2022). *The Basics & The Gap - Cement: Climate Innovation Factsheet Series #2*. https://fcarchitects.org/

Graybeal, B. A. (2009). UHPC making strides. *Public Roads, 72*(4). (FHWA-HRT-09-002).

Swiss Society of Engineers and Architects (SIA). (2016). *SIA 2052: UHPFRC – Materials, Design and Application*. Swiss Standard.

Ullah, R., Qiang, Y., Ahmad, J., Vatin, N. I., & El-Shorbagy, M. A. (2022). Ultra-high-performance concrete (UHPC): A state-of-the-art review. *Materials, 15*(12), 4131. https://doi.org/10.3390/ma15124131

Xu, M., & Wille, K. (2015). Fracture energy of UHP-FRC under direct tensile loading applied at low strain rates. *Composites Part B: Engineering, 80*, 116–125. https://doi.org/10.1016/j.compositesb.2015.05.031

The integrated VS30 maps and soil classification for Sakarya province

Elif Toplu[1], Osman Kırtel*[1]

[1] *Sakarya University of Applied Sciences, Department of Civil Engineering, 54000 Sakarya, Türkiye*

Abstract. This study focuses on the development of an up-to-date and integrated VS30 map for Sakarya province, combining local seismic measurements with raster data provided by the United States Geological Survey (USGS). The USGS employs advanced techniques to generate VS30 maps, which include regression analyses to determine relationships between topographic slope, elevation, and VS30 values. In this research, 2044 seismic data points collected from the region were digitized using QGIS software, followed by interpolation analyses to create density maps. These local seismic data were then integrated with the USGS raster data, resulting in an integrated VS30 map for the province. To validate the map's accuracy, it was calibrated with field measurements, enhancing its reliability. The study's findings include the spatial distribution of the measured VS30 values, the USGS raster data clipped to the boundaries of the province, the integrated VS30 map, and ground classifications in accordance with the TBDY 2018 standards. The integration of local seismic data with global datasets significantly improves the accuracy of geotechnical assessments and enhances the reliability of seismic risk models.

Keywords: VS30 map; QGIS; Geographic information systems; Soil classification; Seismic risk; TBDY 2018.

1. Introduction

Local soil conditions have a significant impact on the magnitude, frequency, and duration of seismic waves. This effect varies depending on the material properties of the ground that seismic waves pass through before reaching the surface (Borcherdt, 1994). Particularly in areas with soft sediments near the surface, significant increases in the intensity of ground shaking may be observed. This phenomenon highlights the importance of the site effect, a factor that directly influences the vulnerability of structures. Vs is used to determine the dynamic response of the soil, liquefaction potential, and soil profile. Vs30, which represents the average shear wave velocity in the upper 30 meters of the soil, is critical for determining dynamic responses (Boore, 2004; Pokhrel et al., 2013; Seed et al., 1983). Vs30 has become a fundamental parameter representing site conditions and is widely used in engineering seismology. Proposed by Borcherdt (1994), this parameter has been made mandatory in the building and seismic design codes of many countries. For example, Eurocode 8 (CEN, 2004), the International Building Code (IBC, 2021), and the Turkish Earthquake Regulation (AFAD, 2018) use this parameter for site classification (Table 1). Additionally, Vs30 values are employed in ground motion prediction equations (GMPEs), playing a direct role in the creation of seismic hazard maps (Abrahamson et al., 2014; Boore & Atkinson, 2008; Bozorgnia et al., 2014; Chiou & Youngs, 2014).

Table 1. Soil Classification (AFAD, 2018)

Soil Classification	ZA	ZB	ZC	ZD	ZE	ZF
Vs30	1500>	760-1500	360-760	180-360	<180	-

However, the direct measurement of Vs30 values is quite costly and time-consuming. Measurements taken using methods such as MASW, SASW, SCPT, and SPT-N involve complex procedures that need to be implemented in the field, making it difficult to perform Vs30 mapping for large areas. As a result, many researchers have developed surrogate parameter-based methods for estimating Vs30. The most prominent of these surrogate parameters is topographic slope. Wald & Allen (2007) established a correlation between slope and Vs30 using data from the Shuttle Radar Topography Mission (SRTM) (Anon n.d.) and demonstrated that this method is applicable in active tectonic regions. Allen & Wald (2009) emphasized that topographic slope-based models yield more successful results when combined with higher-resolution DEM (digital elevation model) data. However, it has also

*Corresponding author, E-mail: okirtel@subu.edu.tr

https://doi.org/10.31462/icearc2025_ce_eqe_432

been noted that these methods achieve limited success in stable tectonic regions (Allen and Wald, 2009). Representing site conditions solely with topographic data can lead to erroneous results in certain regions. In areas with solid bedrock and flat terrain, high Vs30 values are expected, but slope-based models may fail to represent these conditions adequately. Therefore, hybrid models that combine geological data and topographic slope offer a more reliable approach (Thompson et al., 2014; Wills, 2008). Studies by Wills & Clahan (2006), Wills & Gutierrez (2008), and Wills et al. (2015) have shown that approaches that assess both geological units and topography lead to more accurate site classifications. Similarly, Thompson et al. (2010, 2014) and Heath et al. (2020) emphasized the success of hybrid models and enhanced model quality with spatial regression methods like trend kriging. Many Vs30 maps have been developed for various regions in the international literature (Abbasnejadfard et al., 2023; Boyd et al., 2024).

In Turkey, within the framework of studies conducted by AFAD, Vs30 data are collected using seismic methods such as MASW for accelerometer stations and are utilized in applications like ShakeMap (Wald et al., 2022). However, the lack of a detailed Vs30 distribution across the country creates uncertainty, especially in post-earthquake loss estimation and risk analysis. In this context, detailed and up-to-date Vs30 maps, developed using geological maps, digital elevation data, and slope-based surrogate models, are of critical importance in determining site effects. Consequently, to accurately predict the effect of site conditions on ground motions, topographic slope alone is insufficient; hybrid approaches integrating geological knowledge provide more accurate results. This is a fundamental requirement for enhancing the reliability of seismic hazard and risk assessments in countries with active fault zones, such as Turkey (Sahin et al., 2024).

The slope distribution of Sakarya Province not only reflects the topographic and geomorphological segmentation of the region but also illustrates the intensity of deposition and erosion processes and the influence of young tectonics. The study area contains large plains. It is made up of the Samanlı Mountains and Çamdağ elevations, and when examining the settlement patterns of Sakarya Province, it can be observed that the urban centers are widespread in flat areas formed by river-borne sediments and shaped by river influences, characterized by highly fertile land. According to the suitability analysis for settlement, areas with a steep slope (≥ 45%), consisting of magmatic, metamorphic, and sedimentary rocks, which are prone to rockfalls and landslide hazards, as well as alluvial units with marshes, make up the third priority areas for settlement, most of which are located in the southern part of the province. The second priority areas for settlement, which include non-marsh parts of alluvial, alluvial fan, and slope debris areas with slopes up to 10%, contain areas where the groundwater level is close to the surface and consist mostly of alluvial units carried by the Sakarya River, where "liquefaction" is expected during an earthquake. These areas include the city center and the majority of the population. The main morphological units in the newly developed areas in the city center of Adapazarı and to the northwest of the existing city center, which underwent reconstruction after the 1999 earthquakes, are the Kocaeli Peninsula, the KAF Zone (Sapanca Depression), and the Samanlı Mountain Elevation (Sakar, Taga, and Zorlu, 2023).

QGIS, an open-source Geographic Information System (GIS) software, provides capabilities for visualizing, editing, analyzing, and mapping spatial data. With its user-friendly interface and extensive tool support, it is frequently used for spatial analysis and modeling tasks. QGIS software also offers various methods for spatial interpolation. Two main interpolation methods commonly used in QGIS are Inverse Distance Weighting (IDW) and Triangulated Irregular Network (TIN) interpolation. In IDW interpolation, the values of unknown points are estimated based on the distances to surrounding known sample points, with the influence of these points decreasing as the distance increases. This method is effective for cases where the data exhibit spatially continuous variation. The TIN method, on the other hand, involves constructing triangles between sample points to model the surface, but it may lead to sharp transitions and irregular slopes on the surface, creating limitations in representing continuously varying parameters (QGIS, 2022). In this study, the Inverse Distance Weighting (IDW) interpolation method was used to obtain a smoother and more realistic surface for the spatial distribution of Vs30 values.

2. Methodology

In this study, a Geographic Information System (GIS)-based method was employed to determine the spatial distribution of Vs30 (the average shear wave velocity to a depth of 30 meters from the surface) values reflecting local ground conditions within the boundaries of Sakarya Province. In this context, both the globally prepared USGS (United States Geological Survey) Vs30 raster data and the Vs30 point data obtained through on-site measurements at various locations by the Sakarya Metropolitan Municipality (SBB) (Şahvelet, 2022) were utilized.

In the first phase of the study, both datasets were imported into the QGIS software environment. The USGS data was incorporated in raster format, while the SBB Vs30 data, representing point data, was loaded according to the appropriate map coordinate system. The SBB data corresponds to locations that represent different ground properties across the province, providing highly accurate local information.

Subsequently, a continuous Vs30 surface map was created using the "Inverse Distance Weighting" (IDW) interpolation method in QGIS, utilizing the SBB point data. In this process, weighting was applied based on the distance to each measurement point, and Vs30 values in the intermediate areas were estimated. The resulting interpolation map was overlaid with the existing USGS raster data, allowing for the spatial compatibility of the two datasets to be assessed and enhancing the precision of the local map.

3. Data processing and analysis

The map of Vs30 measurements taken within the boundaries of Sakarya Province is presented in Figure 1. Figure 2, on the other hand, shows the USGS Vs30 raster data clipped to the boundaries of Sakarya Province. In Figure 3, an integrated Vs30 map has been generated by combining the measured Vs30 data with the USGS Vs30 data. Additionally, in Figure 5, soil classification has been carried out based on these datasets in accordance with the 2018 Turkish Seismic Design Code (TBEC).

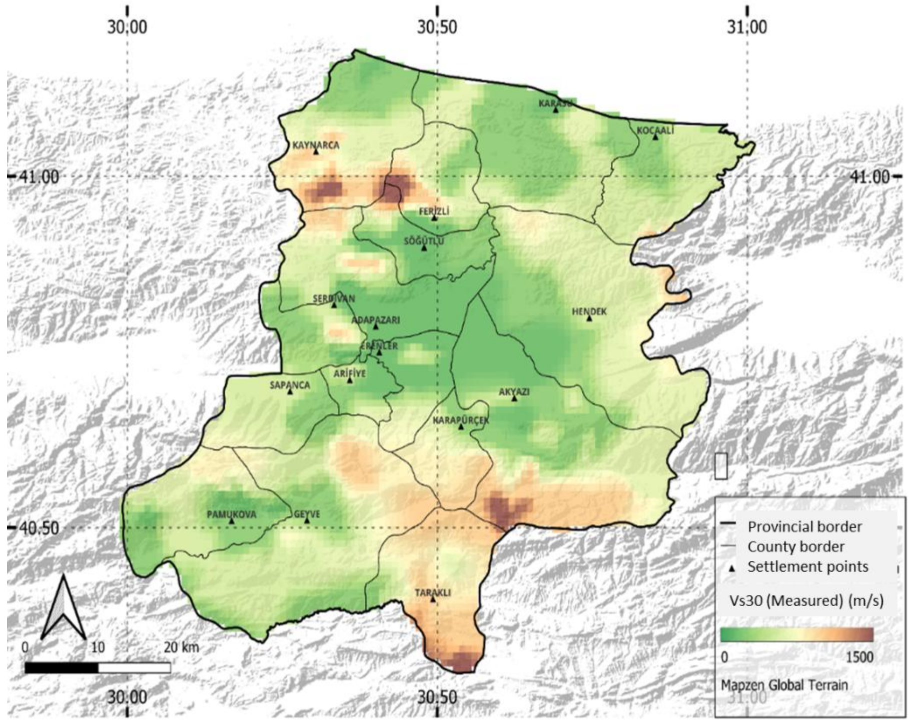

Fig. 1 Measaured Vs30 Map

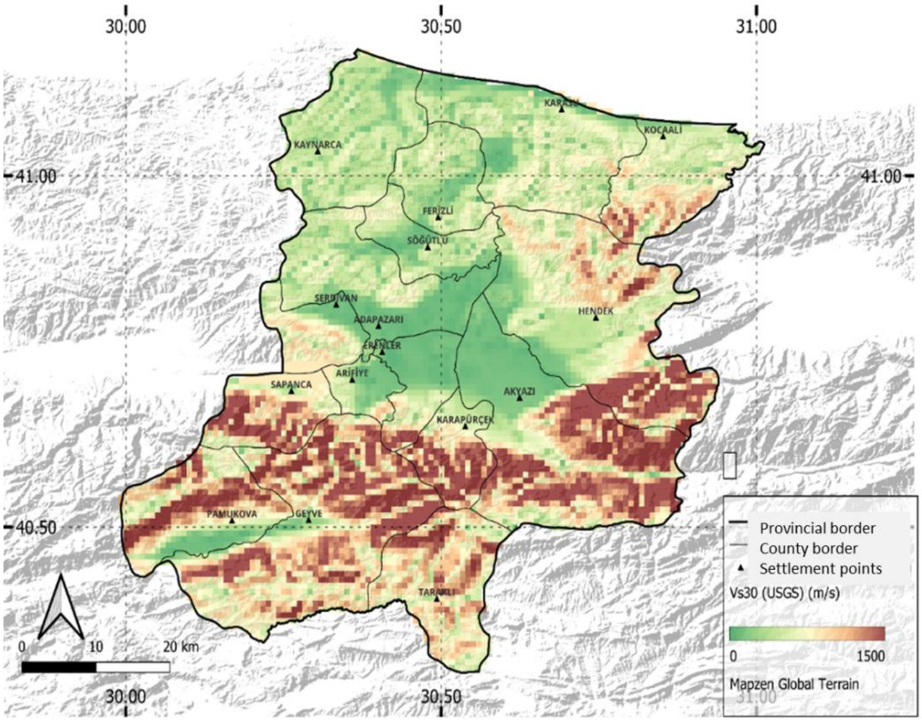

Fig. 2 USGS Vs30 map

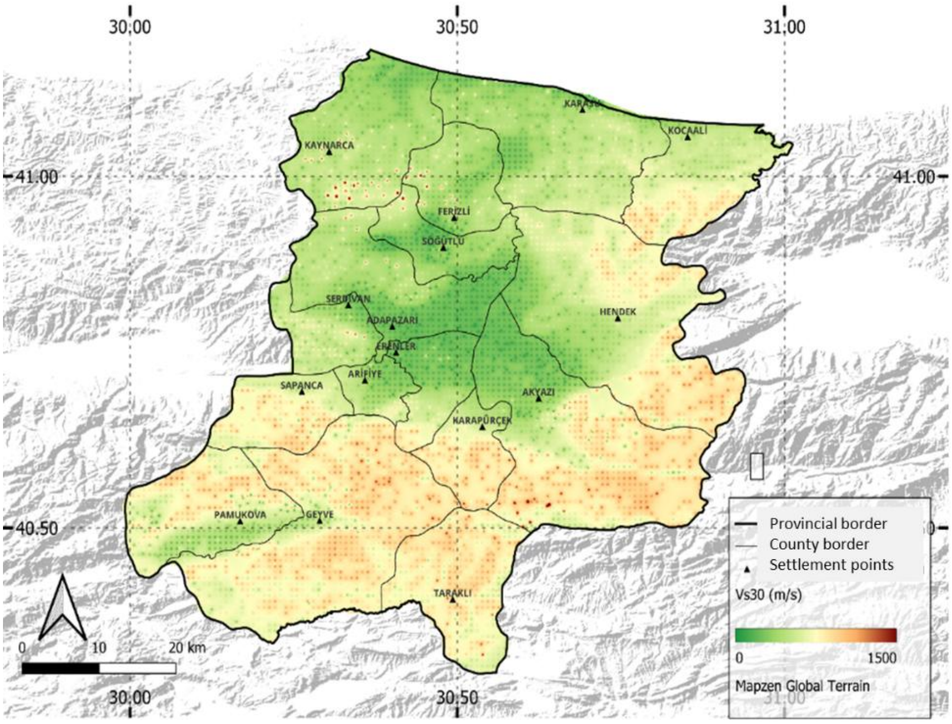

Fig. 3 Integrated Vs30 map

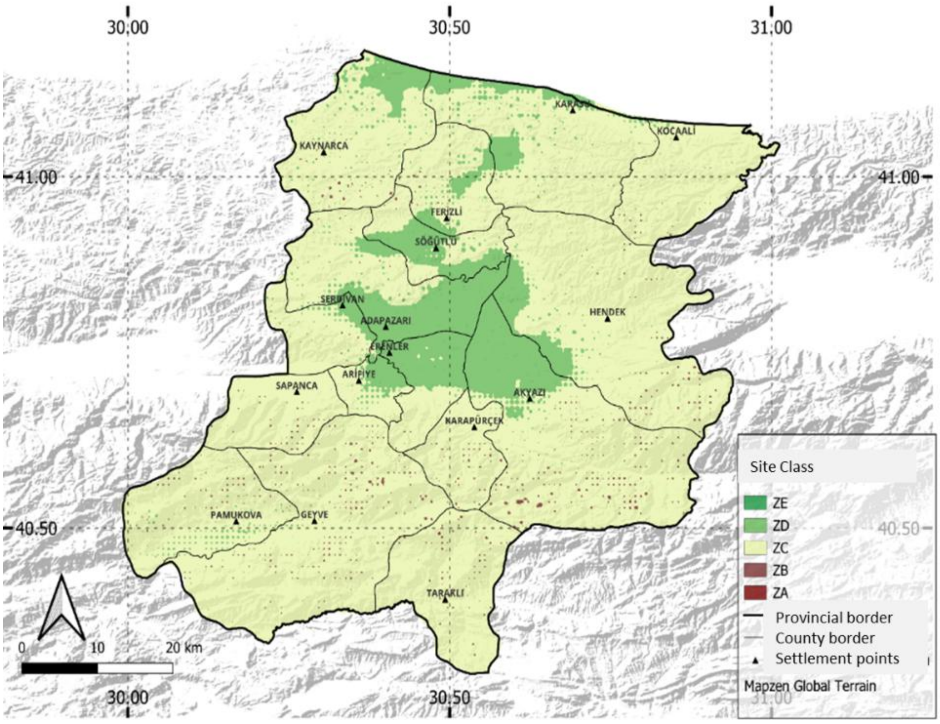

Fig. 4 Site class map

Fig. 3 presents the integrated Vs30 (shear wave velocity) distribution for Sakarya province. The Vs30 value provides information about soil type and stiffness: Low Vs30 values (green tones) are typically associated with soft soils and alluvial units, while high Vs30 values (orange-red tones) are related to firmer, rocky areas. The central and major urban areas of Sakarya (Adapazarı, Serdivan, Erenler, Arifiye) are situated on extensive alluvial plains. These plains, primarily formed by the alluvium deposited by the Sakarya River, are characterized by a high groundwater table, making them susceptible to liquefaction. Areas in the south and southwest of Sakarya (around Pamukova, Geyve, Taraklı) and the western part of Sapanca are represented by orange-red tones. In these regions, the Vs30 values increase (ranging from 1000–1500 m/s), indicating the presence of sloped, rocky terrains.

4. Conclusions

In this study, a spatially continuous Vs30 map has been developed to serve as a foundation for soil classification and seismic risk analyses specific to Sakarya province. The point measurement data provided by the local authority (SBB) were processed in the QGIS environment using interpolation techniques, and the resulting surface was overlaid with USGS data to enhance the map's accuracy. This approach integrated local data with global-scale information, yielding a more reliable soil profile.

As a result, a high-resolution Vs30 distribution map has been generated, which more accurately represents the soil characteristics of the region based on in-situ measurements. This map can be used as a critical data layer for soil classification and for future seismic hazard analysis, damage prediction, and risk assessment studies. In this regard, the study provides a va”luable source of updated, locally supported data that can be used in disaster management planning by local authorities and in engineering applications.

References

Abbasnejadfard, M., Bastami, M., Jafari, M. K., & Azadi, A. (2023). Spatial correlation models of VS30 values: A case study of the Tehran region. *Engineering Geology, 325*, 107300. https://doi.org/10.1016/j.enggeo.2023.107300

Abrahamson, N. A., Silva, W. J., & Kamai, R. (2014). Summary of the ASK14 ground motion relation for active crustal regions. *Earthquake Spectra, 30*(3), 1025–1055. https://doi.org/10.1193/070913EQS198M

AFAD. (2018). *Turkish Buildings Earthquake Code 2018*. Government Gazette, No: 30364. (In Turkish)

Allen, T. I., & Wald, D. J. (2009). On the use of high-resolution topographic data as a proxy for seismic site conditions (VS30). *Bulletin of the Seismological Society of America, 99*(2A), 935–943. https://doi.org/10.1785/0120080255

Boore, D. M. (2004). Estimating VS(30) (or NEHRP site classes) from shallow velocity models (depths < 30 m). *Bulletin of the Seismological Society of America, 94*(2), 591–597. https://doi.org/10.1785/0120030105

Boore, D. M., & Atkinson, G. M. (2008). Ground-motion prediction equations for the average horizontal component of PGA, PGV, and 5%-damped PSA at spectral periods between 0.01 s and 10.0 s. *Earthquake Spectra, 24*(1), 99–138. https://doi.org/10.1193/1.2830434

Borcherdt, R. D. (1994). Estimates of site-dependent response spectra for design (methodology and justification). *Earthquake Spectra, 10*(4), 617–653. https://doi.org/10.1193/1.1585791

Boyd, O. S., Churchwell, D., Moschetti, M. P., Thompson, E. M., Chapman, M. C., Ilhan, O., Pratt, T. L., Ahdi, S. K., & Rezaeian, S. (2024). Sediment thickness map of United States Atlantic and Gulf Coastal Plain strata, and their influence on earthquake ground motions. *Earthquake Spectra, 40*(1), 89–112. https://doi.org/10.1177/87552930231204880

Bozorgnia, Y., Abrahamson, N. A., Al Atik, L., Ancheta, T. D., Atkinson, G. M., Baker, J. W., Baltay, A., et al. (2014). NGA-West2 research project. *Earthquake Spectra, 30*(3), 973–987. https://doi.org/10.1193/072113EQS209M

Chiou, B. S. J., & Youngs, R. R. (2014). Update of the Chiou and Youngs NGA model for the average horizontal component of peak ground motion and response spectra. *Earthquake Spectra, 30*(3), 1117–1153. https://doi.org/10.1193/072813EQS219M

Heath, D. C., Wald, D. J., Worden, C. B., Thompson, E. M., & Smoczyk, G. M. (2020). A global hybrid VS30 map with a topographic slope–based default and regional map insets. *Earthquake Spectra, 36*(3), 1570–1584. https://doi.org/10.1177/8755293020911137

Nedim Şahvelet, M. (2022). *Altyapı sistemlerinin sismik hasar görebilirlik analizi: Sakarya ili örneği* [Master's thesis, Sakarya Üniversitesi]. (In Turkish)

Pokhrel, R. M., Kuwano, J., & Tachibana, S. (2013). A kriging method of interpolation used to map liquefaction potential over alluvial ground. *Engineering Geology, 152*(1), 26–37. https://doi.org/10.1016/j.enggeo.2012.10.003

QGIS. (2022). *QGIS Coğrafi Bilgi Sistemi*. https://www.qgis.org (In Turkish)

Sahin, G., Okalp, K., Kockar, M. K., Yilmaz, M. T., Jalehforouzan, A., Temiz, F. A., Askan, A., Akgun, H., & Erberik, M. A. (2024). Production of GIS-based predicted VS30 maps for Türkiye by combining geological and high-resolution topographical digital maps. In *Springer* (pp. 167–174). https://doi.org/10.1007/978-3-031-57659-1_12

Sakar, S., Taga, H., & Zorlu, F. (2023). Jeolojik ve jeomorfolojik yapının 1999 depremleri sonrası Adapazarı kent dokusunun oluşumundaki etkisi. *Türkiye Jeoloji Bülteni, 66*(3), 421–444. https://doi.org/10.25288/TJB.1289115 (In Turkish)

Seed, H. B., Idriss, I. M., & Arango, I. (1983). Evaluation of liquefaction potential using field performance data. *Journal of Geotechnical Engineering, 109*(3), 458–482. https://doi.org/10.1061/(ASCE)0733-9410(1983)109:3(458)

Shuttle Radar Topography Mission. (n.d.). *NASA's Earth Observing System*. https://eospso.nasa.gov/missions/shuttle-radar-topography-mission

Thompson, E. M., Wald, D. J., & Worden, C. B. (2014). A VS30 map for California with geologic and topographic constraints. *Bulletin of the Seismological Society of America, 104*(5), 2313–2321. https://doi.org/10.1785/0120130312

Wald, D. J., Worden, C. B., Thompson, E. M., & Hearne, M. (2022). ShakeMap operations, policies, and procedures. *Earthquake Spectra, 38*(1), 756–777. https://doi.org/10.1177/87552930211030298

Wills, C. J., Gutierrez, C. I., Perez, F. G., & Branum, D. M. (2015). A next generation VS30 map for California based on geology and topography. *Bulletin of the Seismological Society of America, 105*(6), 3083–3091. https://doi.org/10.1785/0120150105

Wills, C. J. (2008). Investigation of geographic rules for improving site-conditions mapping. https://www.researchgate.net/publication/228797230

Numerical validation of a building model via experimental modal analysis method

Başak Toprak[1], Seda Öncü-Davas*[1], Yener Taşkın[2]

[1] *Istanbul University-Cerrahpasa, Faculty of Engineering, Department of Civil Engineering, İstanbul, Türkiye*
[2] *Istanbul University-Cerrahpasa, Faculty of Engineering, Department of Mechanical Engineering, İstanbul, Türkiye*

Abstract. Understanding the dynamic behavior of structures is crucial, especially for evaluating their performance under seismic dynamic loads. Dynamic characteristics, such as natural frequencies, mode shapes, and damping ratios, define how structures respond to variable loads. Accurately identifying these parameters is essential for assessing seismic performance and ensuring structural safety. Modal analysis methods are widely used to understand and characterize dynamic behavior. This study investigates the dynamic behavior of a building model created using the finite element method (FEM). The goal is to calculate the building's dynamic characteristics through experimental modal analysis (EMA) using displacement data from selected points on one face of the building and validate these results by comparing them with finite element modal analysis outcomes. A dynamic load with sweeping frequency was applied to the base of the building model in order to induce torsional effects and reveal its response at various frequencies. Displacement responses at specific points on each floor were measured over time, providing essential data for understanding the structure's behavior. The displacement data were processed using MATLAB to generate transfer functions, which characterized the building's dynamic behavior and identified its modal parameters. The analysis revealed bending and torsional modal frequencies on the building's front face, and corresponding mode shapes were constructed using amplitude calculations. The results showed strong agreement between the finite element and experimental modal analysis methods, confirming the accuracy and reliability of the proposed approach for determining dynamic characteristics under loading conditions.

Keywords: Experimental modal analysis method; Dynamic behavior; Dynamic characteristics.

1. Introduction

Structures are evaluated based on their dynamic responses to external influences, particularly under seismic loading. One of the fundamental parameters in characterizing these dynamic responses is the natural frequency, which reflects the characteristic oscillatory behavior of engineering structures under free vibration conditions. The natural frequency is determined by the geometric and mechanical properties of the structure, and it serves as a critical indicator of dynamic stability, energy transmission, and resonance behavior. Since this parameter can vary over time due to damage phenomena such as stiffness degradation, it is extensively employed in structural health monitoring and performance assessment (Salawu, 1997). Environmental effects, material aging, and operational conditions can alter structural stiffness over time, thereby inducing variations in the dominant modal periods and mode shapes. Earthquake loadings constitute some of the most critical dynamic actions that structures may encounter during their service life. During such events, energy is dissipated predominantly in regions of reduced stiffness, and the resulting damage in these areas has a direct impact on the global dynamic characteristics of the structure.

Within this framework, structural vibrations are not only a matter of safety but are also critical in terms of serviceability and user comfort. Uncontrolled increases in vibration levels can lead to failures, fatigue damage, or user discomfort in various engineering systems, such as turbine blades, suspension bridges, and high-rise buildings. Therefore, accurate identification of natural frequencies, mode shapes, and damping ratios is essential to ensure that vibration levels remain within acceptable limits during the design phase (Ewins, 2000). Modal analysis techniques, which are used to identify the dynamic parameters of structures, have found widespread application in both analytical and experimental domains. Experimental Modal Analysis (EMA), in conjunction with analytical modeling, is widely used in structural health monitoring, damage detection, and model calibration. However, since

* Corresponding author, E-mail: seda.oncu@iuc.edu.tr

https://doi.org/10.31462/icearc2025_ce_eqe_440

golden light publishing

modal parameters are influenced by environmental and operational factors, the reliability of these techniques requires carefully designed testing protocols and the application of statistical validation methods. For example, the studies conducted by Alampalli et al. (1995) on bridges demonstrated that modal parameters could be employed to identify structural damage, although their localization capabilities may be limited.

Modal analysis defines the vibration modes of a structure through eigenvalue and eigenvector solutions (Zuming, 2018). Modal testing and analysis techniques have rapidly advanced since the 1960s. The development of the Fast Fourier Transform (FFT) algorithm by Cooley and Tukey in 1965 enabled the analysis of experimental data in the frequency domain. Subsequently, the Structural Dynamics Research Laboratory (SDRL) established at the University of Cincinnati played a pioneering role in systematizing experimental modal testing. General-purpose finite element software such as NASTRAN, developed in 1968, standardized modal solutions in engineering analysis. Since the 1980s, modal analysis methods have become applicable to multi-input multi-output (MIMO) systems, and advanced algorithms such as PolyMAX, the HV estimator, and MLMM have provided high accuracy in distinguishing closely spaced modes (Siemens, 2021).

Nevertheless, the evaluation of modal parameters should not be limited to frequency and mode shapes alone. Due to the influence of environmental variability and operational conditions, these parameters must be supported by cross-validation and statistical analysis method (Alampalli, 2000). Moreover, the dynamic behavior of structures can be examined across three frequency regions: low, mid, and high frequencies. At low frequencies, resonance responses are more prominent; as the frequency increases, damping ratios increase, modal density rises, and resonance distinctiveness diminishes. At this point, the resolution capability of conventional modal analysis decreases, necessitating the application of high-resolution techniques such as wavelet transform and time-frequency analysis (Ege et al., 2009).

More recently, Operational Modal Analysis (OMA) has emerged as a significant technique, enabling the identification of modal parameters by utilizing ambient excitations without requiring external input forces. Magalhães and Cunha (2011), for instance, demonstrated the applicability of OMA under field conditions through its implementation on a 280-meter-long concrete arch bridge. Similarly, the vibro-acoustic modal analysis approach proposed by Liu et al. (2022) offers high-accuracy modal parameter estimation using fewer input parameters. Furthermore, studies focusing on the retrofitting of historical structures have diversified methodological approaches in this area. For example, Kocaman et al. (2025) observed, in their analysis of the Kabasakal Mosque in Gaziantep, that reinforced concrete elements added post-construction enhanced structural stiffness but provided limited protection against large-magnitude earthquakes.

In this study, the dynamic characteristics of a four-story reinforced concrete frame system are investigated through a numerically conducted Experimental Modal Analysis (EMA) procedure. Time-dependent displacement data obtained from controlled base angular acceleration excitation were transformed into the frequency domain. The natural frequencies and mode shapes derived from these data were then compared with the eigenvalue solutions obtained via the Finite Element Method (FEM). The results revealed a high level of consistency between both approaches in terms of modal parameters, indicating the reliability of this methodology for model validation purposes. In this context, the study contributes to structural dynamic characterization by integrating EMA principles within a numerical framework and validating them through FEM-based analysis.

2. Material and method

2.1. Benchmark building model

In this study, the structural model was developed using the finite element analysis software SAP2000 (v21.1.0). The model represents a four-story reinforced concrete moment-resisting frame system. In plan view, the structure spans 32 meters in the X-direction and 24 meters in the Y-direction, with equal bay lengths of 8 meters. The story heights were assumed to be 3.5 meters. Figure 1(a) presents the overall structural geometry, while Figure 1(b) illustrates the location and labeling of observation points. The cross-sectional dimensions of structural members were kept constant throughout the height of the structure. Column sections were defined as 60×60 cm, and beam sections as 30×60 cm. The floor system was modeled with the rigid diaphragm assumption, and the foundation system was idealized using fixed support boundary conditions. Dead and live loads were applied as 2000 N/m² on slabs and an additional continuous wall load of 1500 N/m on beams. The material properties used in the model correspond to C35-grade concrete and B420C reinforcing steel.

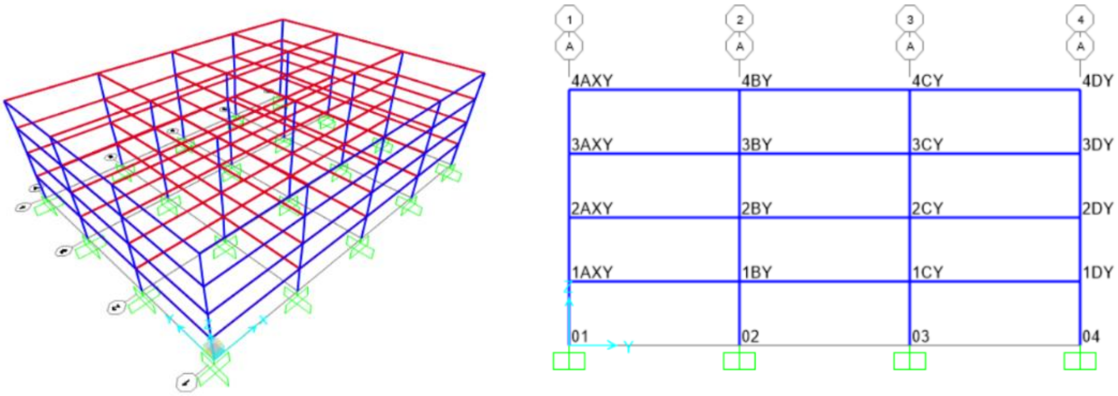

Fig. 1. Structural model: (a) Finite element representation of the building; (b) Observation point layout and labeling scheme

2.2. Dynamic excitation and data acquisition

In the Experimental Modal Analysis (EMA) method, two primary excitation techniques are employed to determine the modal parameters of structural systems: impulse hammer testing and continuous vibrational forcing (shaker test). In this study, the continuous excitation method was selected to identify the natural frequencies and mode shapes of the numerically modeled structural system. A virtual shaker was used to apply a sinusoidal acceleration input at the base of the structure. This excitation was designed to simulate seismic effects originating from the ground and to effectively excite both translational and torsional modes of vibration.

To reveal the torsional modal behavior, an angular acceleration was applied at the base of the structure, generating a moment about the Z-axis (Figure 2). This approach enabled the identification of both translational and torsional components in the structural response. The applied dynamic loading consisted of a sinusoidal acceleration signal with a frequency range increasing from 0.01 Hz to 6 Hz, sustained over a total simulation period of 1000 seconds. The maximum angular acceleration was set to 100 rad/s² (CSI America, 2025), resulting in the acquisition of approximately 1,000,000 data points. These parameters were selected to ensure the excitation of the structural modes within the 0–10 Hz bandwidth.

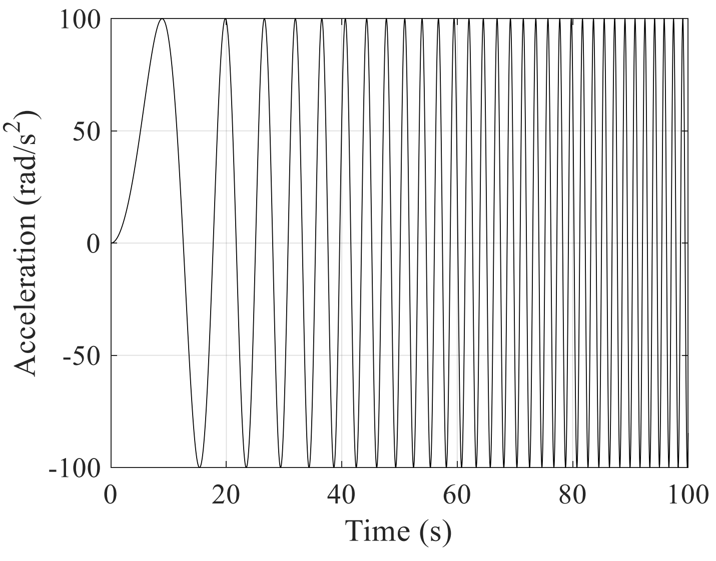

Fig. 2. Applied angular acceleration input used for base excitation

The structural response under forced vibration was analyzed using the direct integration method in the linear time-domain. Time-dependent displacement data were extracted in both the X and Y directions from predefined observation points. These observation points correspond to selected nodal locations in the numerical model, where structural response data were extracted virtually for subsequent modal analysis. These time-series data were subsequently transformed into the frequency domain and processed to identify the modal characteristics of the structural system in accordance with the EMA framework. Frequency analyses were conducted based on the Fast Fourier Transform (FFT), and Frequency Response Functions (FRFs) were generated to characterize the dynamic behavior of the system. The relationship between the input (applied acceleration signal) and the output (obtained displacements) was analyzed, and resonance frequencies were identified by examining amplitude variations along the frequency axis.

A sampling frequency of 1000 Hz was adopted for the analyses. To enhance spectral resolution, the signals were segmented and processed using a windowing technique with 50% overlap. A Hanning window was applied to minimize spectral leakage. Mode shapes corresponding to the identified resonance frequencies were extracted from the frequency response functions, enabling the interpretation of the structure's vibration modes. Furthermore, the system's linearity and time-invariance were evaluated through a consistency analysis. The degree of correlation between the input and output signals across the frequency band served as an indicator for assessing the system's linear behavior. Amplitude and phase characteristics in the frequency domain provided clear insight into the modal properties of the structural system.

All numerical analyses and signal processing steps were conducted within the MATLAB computing environment. The findings demonstrate that both translational and torsional modes of the structure were successfully isolated. Moreover, the modal parameters identified in the frequency domain were rendered suitable for comparison with those obtained through finite element analysis (Avitable, 2000).

3. Results and discussion

Following the application of sinusoidal excitation to the structure, the time-dependent displacement data were transformed into the frequency domain for both directions, and corresponding transfer functions were obtained. Figures 3 and 4 present the computed transfer functions for all observation points in the X and Y directions, respectively. The prominent peaks observed in the amplitude spectra of these plots indicate the resonance frequencies of the structural system and served as primary data for the identification of modal frequencies. The relevant frequency values are summarized in Table 1.

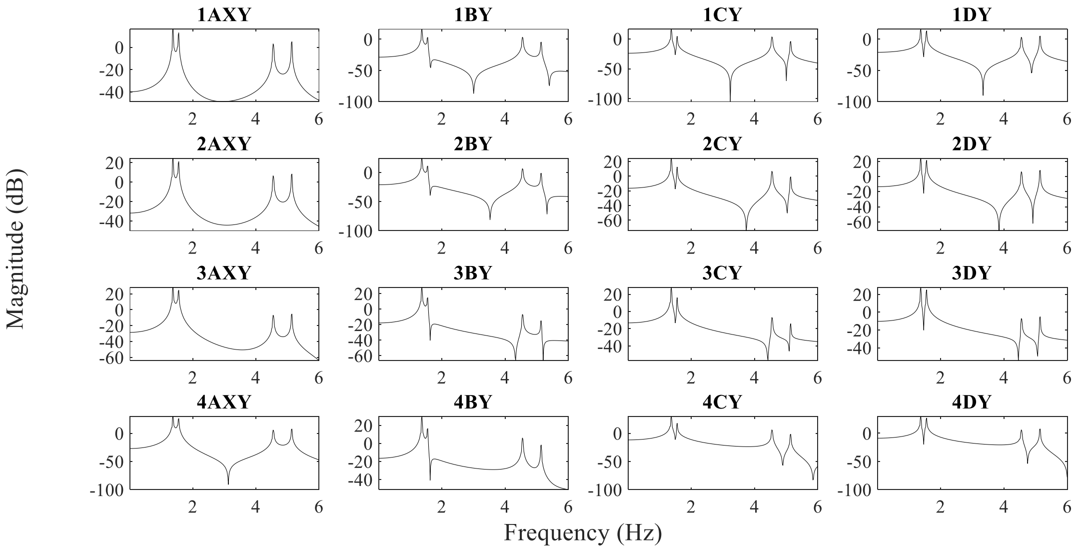

Fig. 3. Frequency response functions (FRFs) in the X-direction obtained from all observation points

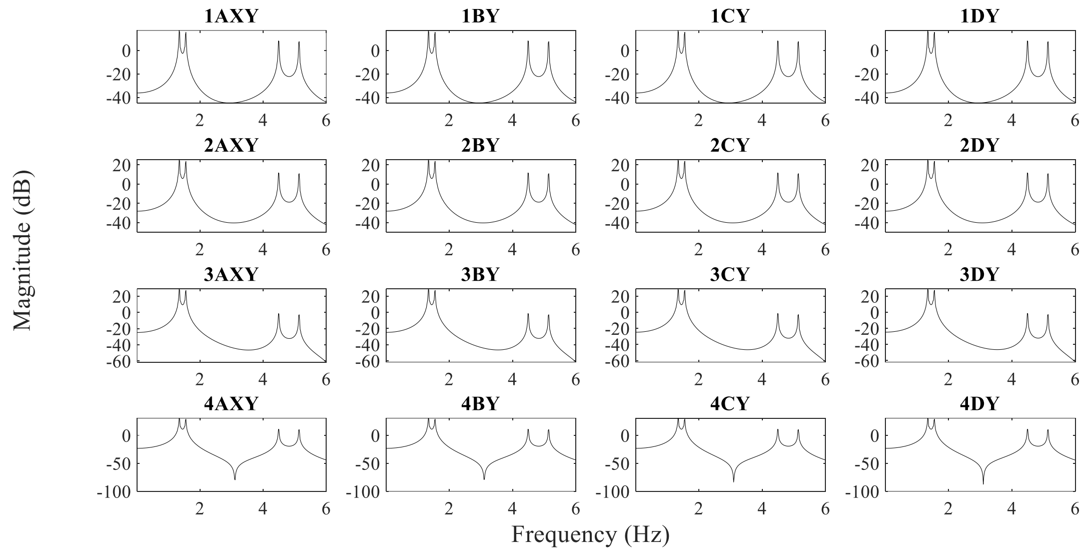

Fig. 4. Frequency response functions (FRFs) in the Y-direction obtained from all observation points

Table 1. Modal frequencies identified from transfer function analysis

Direciton	Frequency			
X	1.3733	1.5546*	4.5471	5.1422**
Y	1.3428	1.5546*	4.4861	5.1422**

* 1st torsional mode and ** 2 nd torsional mode

To assess whether the system exhibits linear and time-invariant behavior, a coherence analysis was conducted between the input (applied dynamic excitation) and the output (measured displacement) signals. Figures 5 and 6 present the calculated coherence spectra in the X and Y directions, respectively. In these plots, the coherence values within the frequency range corresponding to the first six modes of the structure are observed to be very close to 1 (or 100%), indicating strong input-output correlation. This result confirms that the system possesses linear characteristics and that the input-output relationships are represented with high accuracy.

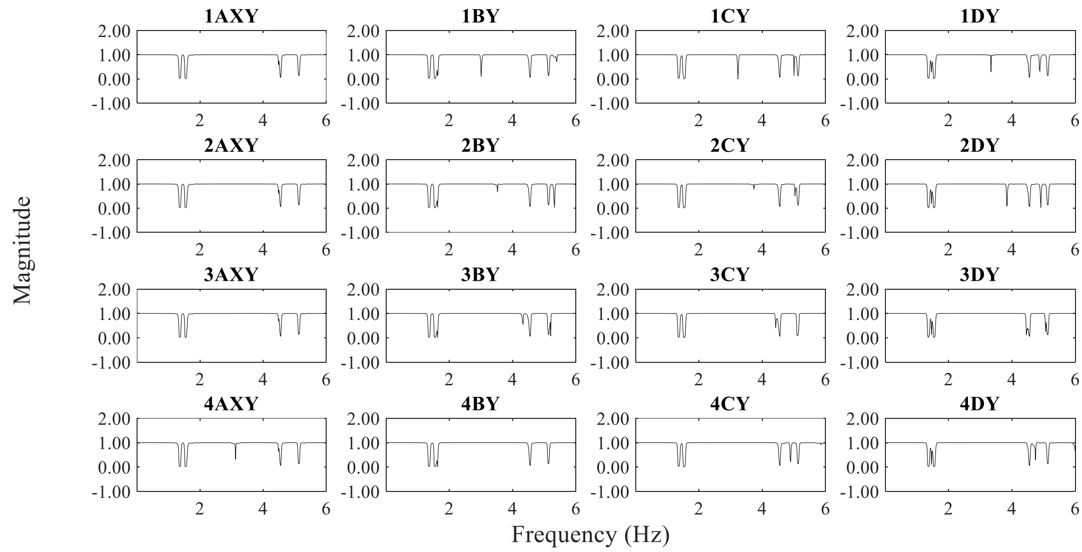

Fig. 5. Coherence function in the X-direction

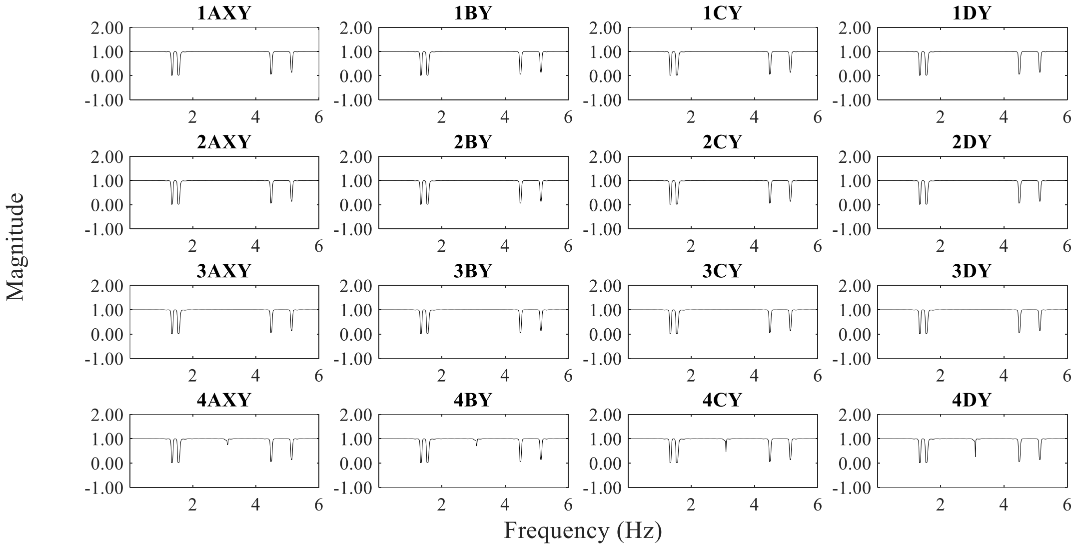

Fig. 6. Coherence function in the Y-direction

The frequencies of 1.549 Hz and 5.137 Hz, identified from the transfer functions presented in Table 1 and observed in both directions, indicate that these modes exhibit torsional characteristics. In contrast, the other frequencies correspond to direction-dependent bending modes. The fact that the lowest frequency was detected in the Y-direction suggests that the flexural stiffness in this direction is lower than that in the X-direction, indicating that the fundamental mode occurs in the Y-direction.

The data used in the computation of the transfer functions are in complex form, and the magnitude profiles corresponding to the mode shapes were derived from the imaginary components of these functions. Figures 7 and 8 present the extracted mode amplitude distributions for the X and Y directions, respectively. The peak points in these graphs correspond to the resonance frequencies listed in Table 1 and identify the characteristic regions of the associated mode shapes.

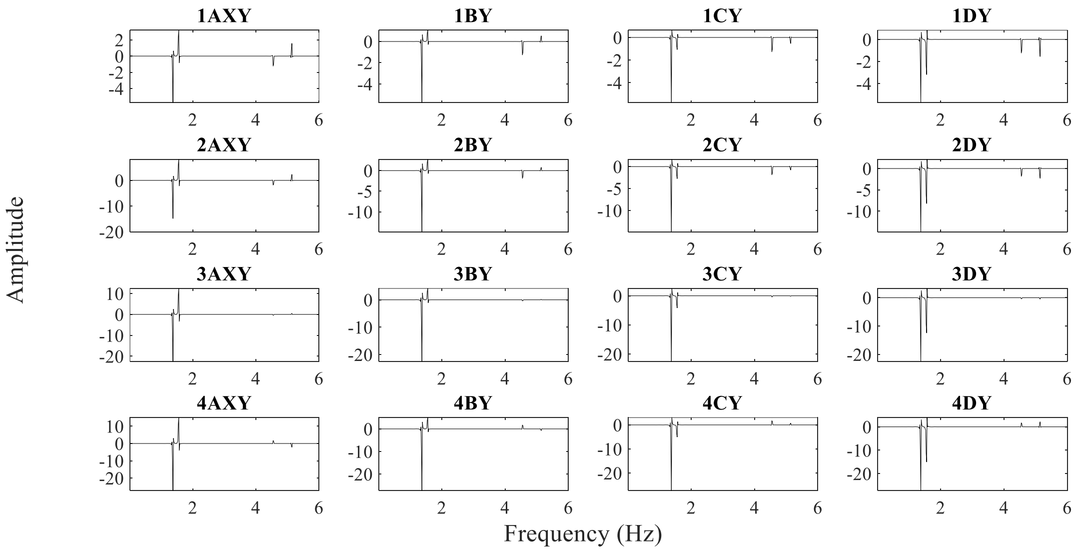

Fig. 7. Frequency-dependent mode shape amplitudes in the X-direction

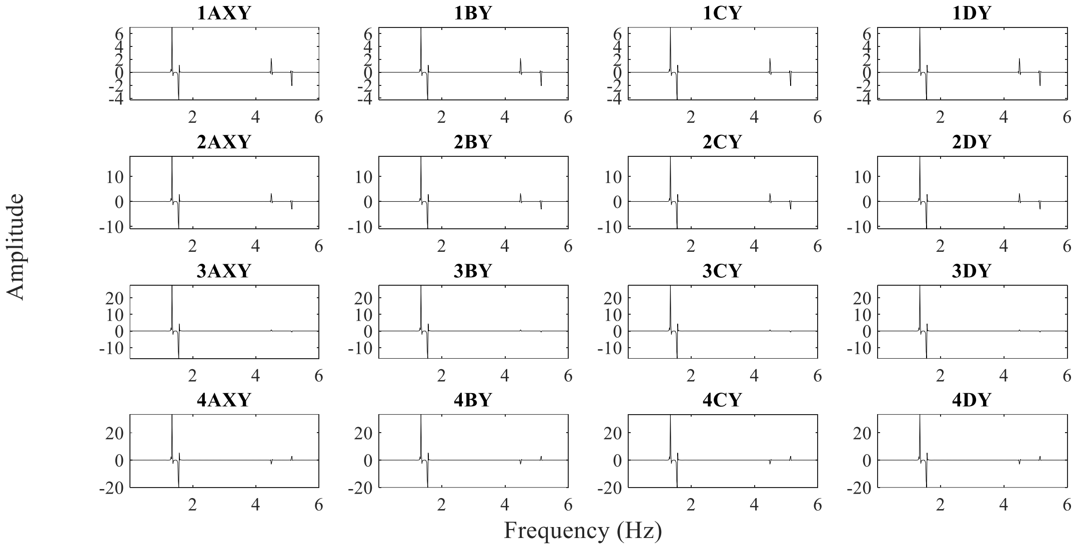

Fig. 8. Frequency-dependent mode shape amplitudes in the Y-direction

The obtained mode amplitudes were normalized with respect to the structural geometry and scaled to more clearly illustrate the relative displacement distribution along the structural axes. Within this scope, a three-dimensional mode shape was graphically constructed based on the amplitude data of the observation points located on the A-axis plane (Figure 9). This visualization provides a spatial representation of the structural system's modal vibration behavior and enables the identification of deformation modes under resonance conditions.

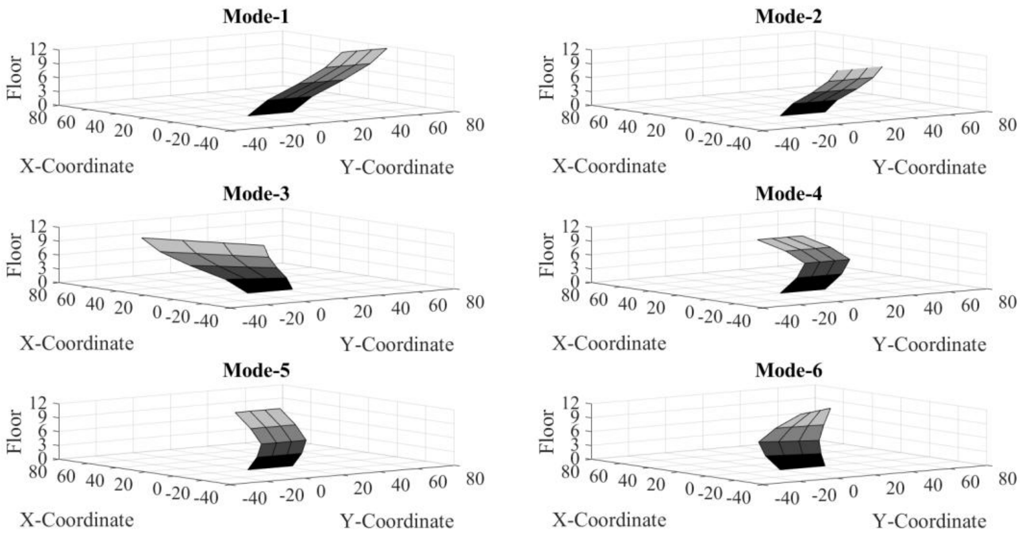

Fig. 8. Three-dimensional representation of mode shapes along the A-axis plane

The modal frequencies obtained through the experimental modal analysis (EMA) procedure conducted on the numerical model were compared with the eigenvalue solutions derived from the finite element analysis (FEA) software. The comparison considered both the modal frequencies and the mass participation ratios in the X and Y directions, as well as about the Z-axis. The corresponding values are presented in Table 2. A high level of agreement was observed between the frequencies identified via EMA simulation and those obtained from FEM results, with the frequency differences for the first six modes remaining below 1%. This outcome supports the applicability of virtual EMA outputs in the model validation process and confirms the reliability of the method.

Table 2. Comparison of modal properties obtained from FEM and EMA results

Mode	Period with FEM	Frequency with FEM	Load Participtaion at X	Load Participation at Y	Load Participation at RZ	Frequency with EMA
1	0.7436	1.3447	0	0.82	0	1.3428
2	0.730537	1.3688	0.82	0	0	1.3733
3	0.645477	1.5492	0	0	0.82	1.5546
4	0.222629	4.4918	0	0.12	0	4.4861
5	0.219598	4.5538	0.12	0	0	4.5471
6	0.194659	5.1372	0	0	0.12	5.1422

4. Conclusions

In this study, the dynamic characteristics of a four-story reinforced concrete frame structure were evaluated through an experimentally simulated modal analysis (EMA) procedure conducted in a numerical environment. By applying a sinusoidal base acceleration with increasing frequency content, both translational and torsional modes were effectively excited. The resulting time-domain displacement data were transformed into the frequency domain to identify the natural frequencies and mode shapes. Analyses based on frequency response functions (FRFs) revealed a high degree of consistency between the modal frequencies obtained through EMA and those calculated via the finite element method (FEM). Additionally, comparisons of the mode shapes demonstrated that both methods were able to identify the same vibration modes.

The findings indicate that the dynamic parameters of structural systems can be estimated through the numerical implementation of experimental modal analysis procedures. Particularly in cases where physical measurement capabilities are limited or inaccessible, such numerical EMA applications may serve as a valuable tool for the preliminary assessment of structural modal properties. The comparison between the extracted modal parameters and FEM results confirmed a consistent level of agreement between the two approaches. In this regard, the numerical EMA framework can be considered a potential engineering tool when in-situ experimental testing is not feasible. However, to enhance the validity of this method, further comprehensive comparison studies supported by physical experimental data on real structures are required.

References

Alampalli, S., 2000, *Effect of Testing, Analysis, Damage and Environment on Modal Parameters*, Mechanical Systems and Signal Processing (2000) 14(1), 63-74, doi:10.1006/mssp.1999.1271.

Alampalli, S., Fu, G., Dillon, E.W., 1995, Measured bridge vibration for detection of structural damage, Research Report 165, Transportation R&D Bureau, NYS DOT, December.

Avitable, P., 2000, *Experimental Modal Analysis (A Simple Non-Mathematical Presentation)*, Modal Analysis and Controls Laboratory, University of Massachusetts Lowell.

Computers and Structures, Inc. (2018). *SAP2000 Integrated Software for Structural Analysis and Design (Version 21)* [Computer software]. Berkeley, California, USA: CSI.

CSI America. (n.d.). *Applying acceleration loads*. CSI America Help. https://help.csiamerica.com/help/sap2000/26/26.0.0/SAP2000/WebHelp/Menus/Define/Load_Cases/Applying_Acceleration_Loads.htmAccessed 20.04.2025.

Ege, K., Boutillon, X., David, B., 2009, High-resolution Modal Analysis, Journal of Sound and Vibration, 325, 852-869.

Ewins, D.J., 2000, Modal Testing: Theory, Practice, and Application. Research Studies Press Ltd, USA.

Kocaman, İ., Eroğlu, E., Ertosun Yıldız, M., Yıldız, M.A., Mercimek, Ö., Çetin, S., 2025, Reinforced concrete interventions on the collapse mechanism of historical masonry structures with detailed finite element analyses: Kabasakal Mosque, Engineering Failure Analysis, 174.

Liu, L., Ripamonti, F., Corradi, R., 2022, *On the experimental vibroacoustic modal analysis of a plate-cavity system,* Mechanical Systems and Signal Processing 180, 109459.

Magalhaes, F., Cunhan, A., 2011, Explaining Operational Modal Analysis with Data from an Arch Bridge, Mechanical Systems and Signal Processing 25(2011)1431–1450.

Salawu, O., 1997, *Detection of Structural Damage Through Changes in Frequency: A Review*, Engineering Structures,19, 718-723.

Siemens, (2021, Feb 13) A Brief History of Modal Testing and Analysis, https://community.sw.siemens.com/s/article/A-Brief-History-of-Modal-Testing-and-Analysis

The MathWorks, Inc. (2023). *MATLAB (Version R2023b)* [Computer software]. Natick, Massachusetts, USA: The MathWorks, Inc.

Zuming, B. (2018). *Finite element analysis application* (Chapter 8). Purdue University Fort Wayne.

The effect of non-uniform scour in transverse direction on seismic behavior of ordinary highway bridges

Serenay Ateş*[1], Özgür Avşar[1]

[1] *Eskisehir Technical University, Department of Civil Engineering, 26555 Eskisehir, Türkiye*

Abstract. The seismic behavior of ordinary highway bridges during earthquakes is significantly influenced by the scour around bridge piles. The process of erosion of the soil surrounding bridge foundations due to water flow causes scour, which becomes particularly critical during seismic events. This study investigates the effect of both uniform (Case-1) and non-uniform scour (Case-2) cases, which take place in transverse direction, on the seismic performance of ordinary highway bridges. Using a combination of analytical models created in the OpenSees program, the effect of scour-induced soil degradation on pile behavior and bridge response during earthquakes was examined by conducting nonlinear response history analyses. Scour depth was supposed to be the same around all piles and varied uniformly in the first scouring type, known as Case-1. In Case-2, two different non-uniform scouring types with linearly varying scour depth around the piles were investigated. In addition, various incidence angles of ground motion pairs were taken into consideration while examining the uncertainty in the excitation direction of the two horizontal components of the earthquake ground motion. The maximum seismic demands of members were assessed for different ground motion incidence angles for each scour cases at the specified scour depth. The results highlight how uniform and non-uniform scour cases can alter the seismic demands in engineering demand parameters such as superstructure displacement, curvature demands of bridge column and shear force demands of piles. The non-uniform scour can increase the shear force demands of pile elements during earthquakes, which can cause a brittle type of shear damage mechanism in the downstream piles.

Keywords: Non-uniform scour; Highway bridges; Incidence angle; Nonlinear response history analysis

1. Introduction

Highway bridges are susceptible to structural damage from a range of external factors, such as scour around bridge supports due to the erosive effects of flowing water. Moreover, the scour effects may come together with the earthquake, and it may lead to increased seismic demands on the bridge elements. The effect of scour around substructure elements on the seismic performance of highway bridges have been the subject of numerous studies in recent years. Bridge-type structures are frequently analyzed under a multi-hazard framework using finite element software and fragility curves was used for seismic vulnerability assessment (Guo & Chen, 2016; He et al., 2020; Prasad & Banerjee, 2013; Wang et al., 2019; Wei et al., 2021). There are several relevant experimental investigations about bridges subjected to earthquake and scour effects in the literature. Shake table tests were conducted by Wang et al. (2015) to examine the seismic behavior of a scouring bridge pier with a pile foundation. The experimental results show that while the demand for the bridge pier decreases as the scour depth increases, the flexural moment and shear demand of the pile increases. This may cause the bridge failure mechanism to shift from the pier to the pile. Zhou et al. (2021) conducted an experimental investigation of the vertical load carrying capacity of reinforced concrete bridge pile group exposed to scouring. Experimental results indicate that corner pile was more vulnerable to seismic damage, because it was the initial location of both the first aboveground and first belowground plastic hinges. Additionally, some studies have been conducted to examine the impacts of an earthquake and scour on existing bridges. Yilmaz et al. (2016) investigated two actual bridges in California in a multi-hazard scenario. For various flood cases, fragility curves and surfaces were obtained. The research results indicate that floods make bridges seismically vulnerable. Avsar et al. (2017) examined the Bahçeli Bridge, which is situated on Lapseki-Biga highway in Türkiye. When comparing the full scour scenario to the no scour case, it was found that the horizontal superstructure displacements under earthquake loads were approximately doubled. There are a few research studies that consider non-uniform scour in bridges. Fioklou and Alipour (2019) calculated the non-uniform scour depth using two different scour scenarios, namely Case 1 and Case 2 corresponding to 25% and 50% more scour in the upstream of bridge's transverse direction, respectively. The results show that, in

* Corresponding author, E-mail: serenayates@ogr.eskisehir.edu.tr

https://doi.org/10.31462/icearc2025_ce_eqe_455

golden light publishing

comparison to the demands derived from non-uniform scour situations, the seismic displacement demand of bridges is underestimated when a uniform variation in scour depth is taken into account. Ateş and Avşar (2024b) used straight and skewed bridge models to perform a series of nonlinear time history analyses while considering non-uniform scour in the transverse direction of the bridge. The outcomes show that in cases of non-uniform scour, shear force demands of piles exceed their shear capacity, resulting in a brittle damage mechanism.

When evaluating the seismic performance of bridges, nonlinear response history analyses are often used. During the analysis, the horizontal components of ground motion are generally applied to the global axis of the structures. However, the exact direction at which an earthquake affects a structure in real life is unknown. Therefore, researchers have been recently concentrating on studies that examine the effects of the earthquake incidence angle on analysis results and bridge performance (Atak et al., 2014; Bhatnagar & Banerjee, 2014; Moschonas & Kappos, 2011; Noori et al., 2019). In the literature, two distinct approaches are used to consider the angle θ, known as the earthquake incidence angle. The first method rotates the horizontal ground motion components while keeping the bridge principal axes constant using linear formation equations, while the second method rotates the bridge's main axes while keeping the horizontal ground motion components constant. According to Ates and Avsar (2024a), seismic demands derived from both approaches give the same outcome. In order to perform a multi-hazard framework, this study uses the first approach to take the earthquake ground motion excitation angle into account.

The objective of this study is to determine the seismic demands of ordinary highway bridges by taking into account two distinct non-uniform scour scenarios in addition to uniform scour. Within the parameters of the study, three distinct scour cases were examined. The scour depth in the first scenario, known as Case-1, was equal across all piles and changed uniformly. On the other hand, a non-uniform scour scenario in the bridge's transverse direction was examined in Case-2 and it was further separated into two distinct categories. In Case 2-1, non-uniform scour occurred in the transverse direction around bridge piles with a scour depth angle of γ=0.6 between upstream and downstream piles. In the second non-uniform scour scenario (Case 2-2), the scour depth angle is γ=1.0. 6 scour depth levels were taken into consideration, ranging from 0 m to 5 m with 1 m increment. During the analysis, horizontal ground motion pairs rotated by using linear transformation equations from 0° to 180° with 15° increments. This study focuses on three engineering demand parameters; superstructure displacement, shear force demand of piles, and curvature demand of bridge pier column.

2. Materials and method

2.1. Bridge model

This study examines a reinforced concrete highway bridge previously analyzed by Atak et al. (2014). The bridge superstructure consists of four spans, each measuring 35 m in length and 12 m in width as seen in Fig. 1. It is composed of 8 prestressed concrete I-section beams supporting a continuous reinforced concrete deck that is 0.22 m thick. Expansion joints are present between the abutments and the bridge deck in both longitudinal and transverse directions. The prestressed beams are made of C40 grade concrete (f_c = 40 MPa), while the remaining RC components have C25 grade concrete (f_c=25 MPa). The steel reinforcement grade is S420 (f_y=420 MPa). The substructure consists of abutments, cap beams, and single-column piers supported by pile foundations. Each column pier features an oblong cross-section with a diameter (D) of 4 m, a width (B_c) of 1.2 m, and a height (H) of 8.7 m. The cap beam has a rectangular cross-section with a width of 1.2 m and a depth of 1.75 m. Each prestressed beam is supported by an elastomeric bearing measuring 450 × 250 × 40 mm, ensuring effective load transfer from the superstructure to the substructure. The bridge superstructure is elastic during an earthquake because of their low lateral stiffness (Caltrans, 2019). Additionally, the pile cap has a rectangular geometry with a width (B_{cap}) of 2.5 m, a length (L_{cap}) of 5 m, and a height (H_{cap}) of 1.5 m. It is supported by six circular piles, each has a diameter (D_{pile}) of 1 m and a height (H_{pile}) of 20 m.

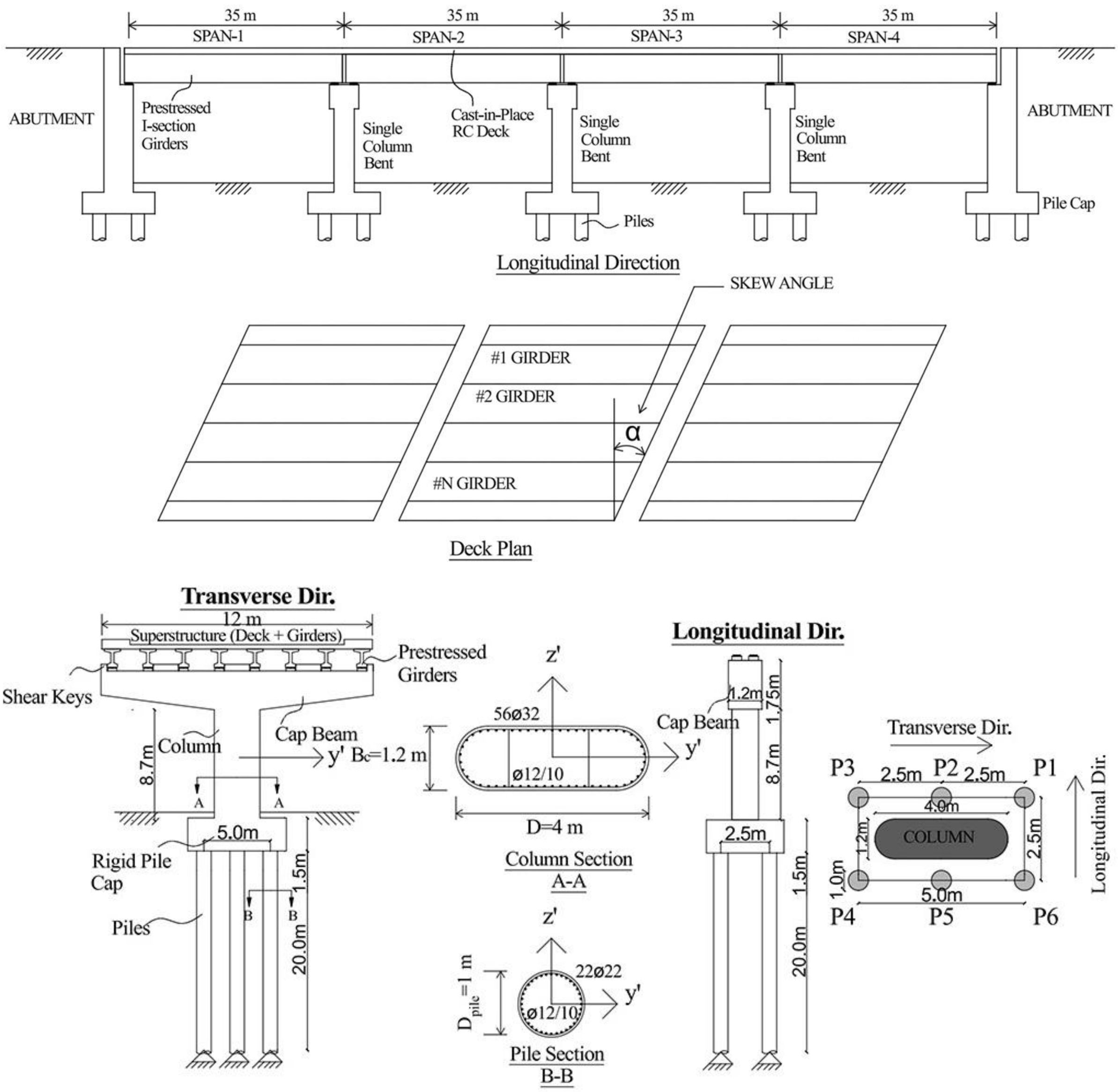

Fig. 1. Properties of bridge members

2.2. Numerical modelling of the bridge

The OpenSees program was adopted to create the three-dimensional numerical model of the reinforced concrete highway bridge in this study as shown in Fig. 2. Superstructure elements are defined as elastic beam column elements because it is expected that the presence of elastomer bearings will keep the bridge superstructure within elastic limits during an earthquake. Moreover, elastic beam column elements are utilized to model cap beams since their load capacity is sufficient to withstand forces of gravity. Nonlinear fiber elements were used to represent the bridge column piers during severe seismic events as they reach their flexural capacity and respond in the inelastic range. Three different material definitions, unconfined concrete, confined concrete, and reinforcement steel were used to model the nonlinear response of columns. At integration points along the length of the column, a distributed plasticity approach was utilized. For unconfined concrete, the crushing strain is ε_{cu} = 0.005, the strain corresponding to peak stress is ε_{co} = 0.002, and the maximum compressive stress is f_{co}= 25 MPa. For confined concrete, the material model presented by Kent and Park (1971) is used. The Concrete 01 material model is used to define confined and unconfined concrete. The S420 reinforcement grade has a 200 GPa modulus of elasticity with a characteristic yield strength of 420 MPa, the ultimate strength of 550 MPa, and the ultimate strain of 0.1. The Steel 01 material model was used to define the reinforcement steel in the OpenSees program. In order to simulate abutment backwall-deck pounding and deck-shear key pounding, nonlinear pounding elements are used in the bridge's longitudinal and transverse directions, respectively. Deck-shear key pounding takes place at the bents as well as the abutments. Between the pounding bridge components, there are 2.5 cm and 5 cm transverse and longitudinal gaps, respectively. Rigid elastic beam column elements were used in OpenSees program to define the pile cap. In the numerical model, piles were defined using elastic beam column elements. It was shown that piles stayed within their elastic limits during the nonlinear response history analyses under various seismic ground motions, based on sensitivity analyses carried out during the construction of numerical modeling of the examined bridges. This is compatible with Caltrans's design specifications (Caltrans, 2019). On the other hand, shear damage may occur when pile elements reach their shear capacity during earthquakes. Therefore, the shear capacity of the pile elements was calculated as 735 kN according to ASCE-ACI 426 (1973) explained in detail in Ateş and Avşar (2024b).

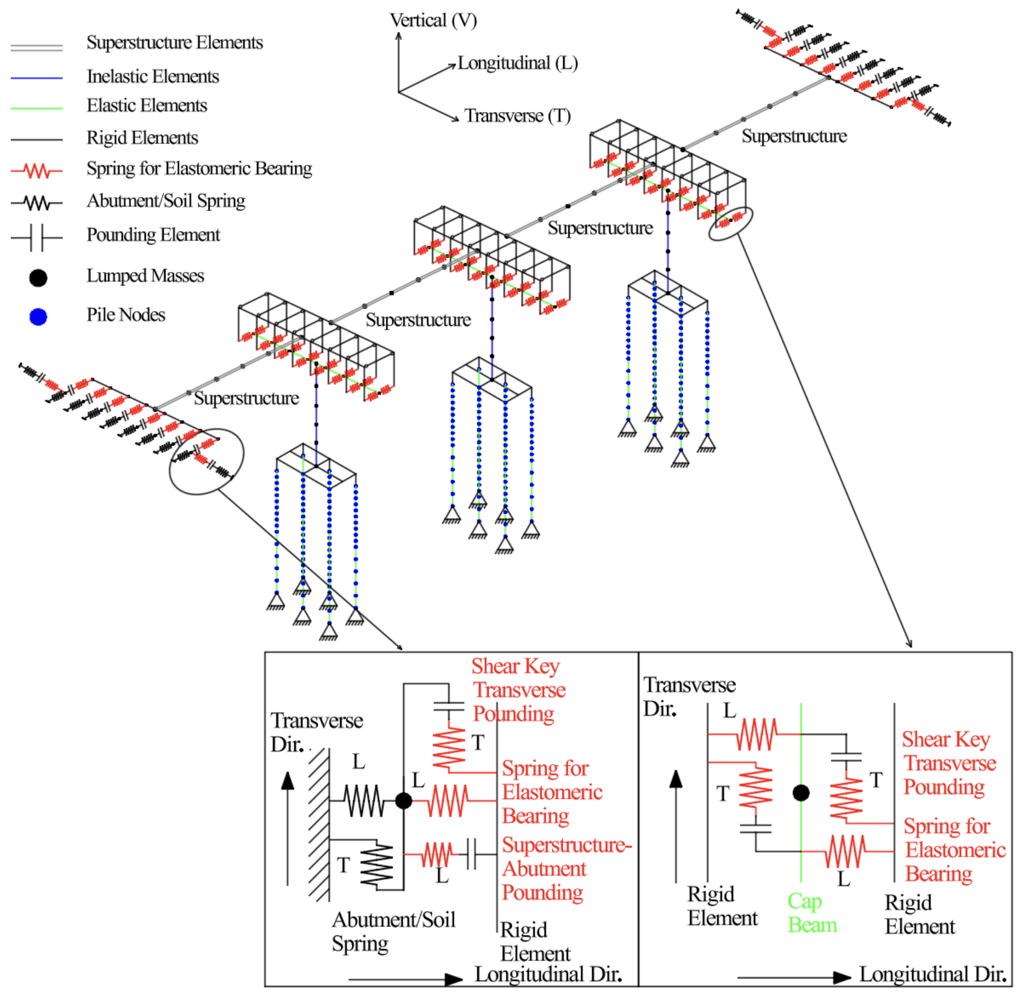

Fig. 2. Numerical bridge model created in OpenSees

The "Py Simple1" material model for lateral soil resistance and the "Tz Simple1" material model for axial resistance were used in the OpenSees program to model the soil structure interaction (SSI) between the piles and the surrounding soil. For the first 10 meters below the pile cap, the pile elements were separated into segments of 0.5 m length, and for the last 10 meters, they were separated into segments of 1 m length. The soil springs were assigned to pile segment nodes. As shown in Fig. 3, t-z springs were formed vertically, whereas p-y springs were defined horizontally (both longitudinally and transversely) along the bridge. Sand, which has an angle of internal friction of 25° and a unit weight of 18 kN/m^3, is the type of soil that has been selected to surround the piles. The calculation of the uniaxial material properties of p-y springs was done in accordance with the American Petroleum Institute (2000). For sand-type soil, the uniaxial material properties of the t-z spring were calculated in compliance with Kulhawy (1991). Finally, the end nodes of the piles were assumed to be restrained by simple support.

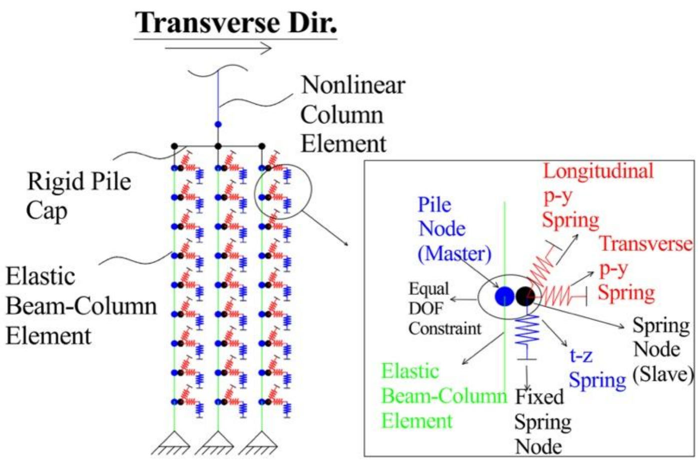

Fig. 3. Properties of the nonlinear soil springs on the piles

2.3. Uniform and non-uniform scour modelling

Seismic effects on the structural elements of water crossing bridges can be increased by scour-induced soil material loss, which reduces the lateral support surrounding the foundation piles. In many previous studies, the impact of scour on bridges was examined by response history analysis by considering uniformly varying scour depth around bridge substructure members. However, the scour depth variation might be non-uniform, resulting in irregularities in the supporting soil surrounding the piles, depending on the riverbed conditions and water flow. The study's objective is to investigate two distinct scour case scenarios for the SSI-modeled bridge with piling base. In the first scenario, shown in Fig. 4 and referred to Case-1, the scour depth is uniformly increased. The uneven scour in the bridge's transverse direction in Case-2 reflects the irregularity in the scour depth variations surrounding the substructure components (Fig. 5). Depending on the flow direction, piles near the upstream are subjected to greater scour than those in the downstream. Additionally, Case-2 is separated into two categories. According to Case-2-1, the scour depth angle (γ) between the upstream and downstream piles is equal to 0.6. In the second subgroup, which is called as Case-2-2, a steeper angle (γ) is taken into consideration by taking γ=1.0. For uniform scour case (Case-1), scour depth is changed starting from 0 m to 5 m with a 1 m increment. Also, for non-uniform scour scenarios, the scour depth for the piles on the downstream side was changed starting from 0 m to 5 m with an increment of 1 m as illustrated in Fig. 5(a) and Fig. 5(b), respectively. OpenSees program was used to create numerical models of non-skewed bridges with uniformly and non-uniformly increasing scour depth. For each scour depth and scenario, nonlinear soil springs were removed from the pile nodes above the scour level. To account for flood-induced soil loss, the nonlinear soil spring parameters were updated at each scour depth.

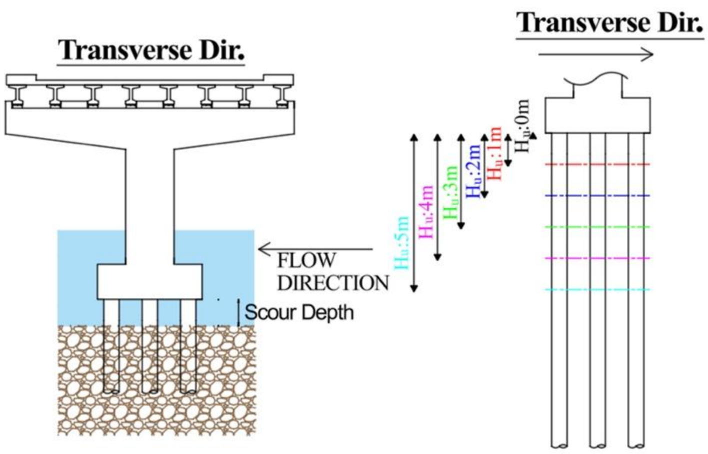

Fig. 4. Representation of uniform scour (Case-1) and the change of scour depth (H_u)

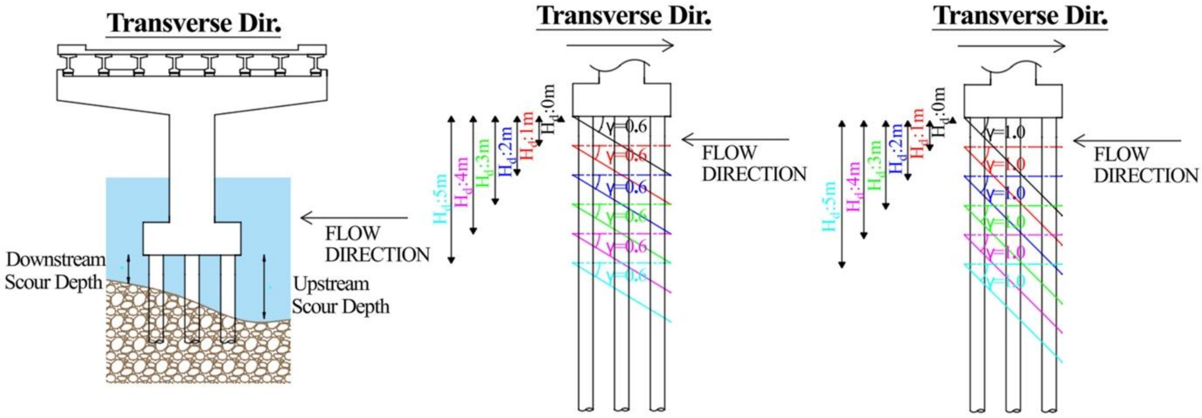

(a) (b)

Fig. 5. Representation of non-uniform scour (Case-2) and the change in scour depth from downstream pile (a) when angle is γ=0.6 (b) when angle is γ=1.0

2.4. Earthquake ground motion data

7 ground motion pairs were chosen from the Pacific Earthquake Engineering Research Center (PEER) database and scaled in compliance with the Principles for the Design of Highway and Railroad Bridges and Viaducts Under the Impact of Earthquakes (2020) in order to perform nonlinear response history analyses. The properties of the horizontal components of the selected ground motion recordings are listed in Table 1. The bridge under examination is assumed in Eskisehir, Turkey, and having the soil type ZD with an average shear wave velocity (V_{s30}) of less than 180 m/s. The Turkish Earthquake Hazard Map (TEHM, n.d.) web interface was used to obtain a target elastic response spectrum for 5% damping ratio as represented in Fig. 6 for the ZD soil class and DD-2 earthquake level (earthquake ground motion level with a 10% probability of exceedance in 50 years) of this location. The SRSS (square root of the sum of the squares) of the spectra of the two horizontal ground motion components is used to determine the response spectrum that results for each chosen ground motion record. The Principles for the Design of Highway and Railroad Bridges and Viaducts Under the Impact of Earthquakes (2020) state that the ratio of the amplitudes of the design acceleration spectrum in the same period range to the average amplitudes of the resultant spectra of all selected records between the period ranges of $0.2xT_p$ and $1.5xT_p$ should not be less than 1.3, where T_p is fundamental period of the bridge. For every given ground motion record, the scale factor of 1.0 satisfies the scaling requirements. The horizontal ground motion component with the largest PGV was applied in the transverse direction of the bridge, whereas the other horizontal component was applied in the longitudinal direction, as the effect of scour is being studied in the transverse direction.

Table 1. Properties of the selected ground motion recordings

No	Event	Station	M_w	Fault type	Component	PGA (g)	PGV (cm/s)	PGD (cm)	Scale factor
1	Coyote Lake, 1979	Gilroy Array #6	5.74	Strike slip	230°	0.42	44.34	12.44	1.0
					320°	0.31	25.39	4.38	
2	Morgan Hill, 1984	Anderson Dam	6.19	Strike slip	250°	0.42	25.40	4.43	1.0
					340°	0.28	27.80	6.43	
3	Imperial Valley, 1979	El Centro Array #4	6.53	Strike slip	140°	0.48	39.64	25.13	1.0
					230°	0.37	80.41	74.26	
4	Landers, 1992	Lucerna	7.28	Strike slip	260°	0.72	133.40	113.92	1.0
					345°	0.78	28.10	25.53	
5	Düzce, 1999	Duzce	7.14	Strike slip	180°	0.40	71.15	49.69	1.0
					270°	0.51	84.23	48.03	
6	Superstition Hills, 1987	El Centro Imp. Co. Cent	6.54	Strike slip	0°	0.35	48.07	19.27	1.0
					90°	0.25	41.79	21.85	
7	Kocaeli, 1999	İzmit	7.51	Strike slip	90°	0.23	38.29	24.29	1.0
					180°	0.16	22.33	11.84	

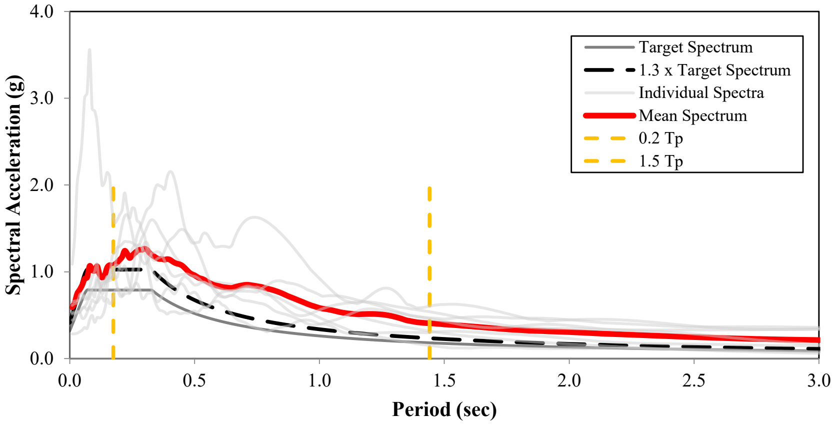

Fig. 6. Elastic response spectra of the selected ground motions with 5% damping ratio

3. Results and discussion

3.1. Superstructure displacement

Superstructure displacement is a significant engineering demand parameter for evaluating the seismic performance of highway bridges. During an earthquake, large superstructure displacements may cause pounding with the abutment backwall in the longitudinal direction or with the shear keys in the transverse direction. The peak displacement demands of the deck midpoint were assessed for each ground motion in both longitudinal and transverse directions. For each scour case and scour depth, the average of the peak displacement demands derived from the response history analysis results of seven ground motions are presented in Fig. 7. The provided graphs show that superstructure displacement demands increase as scour depth increases for all scour scenarios in both longitudinal and transverse directions of bridges, with the transverse direction showing a more noticeable increase. Additionally, a change in non-uniform scour depth has a greater impact on displacement demands than when scour depth varies uniformly.

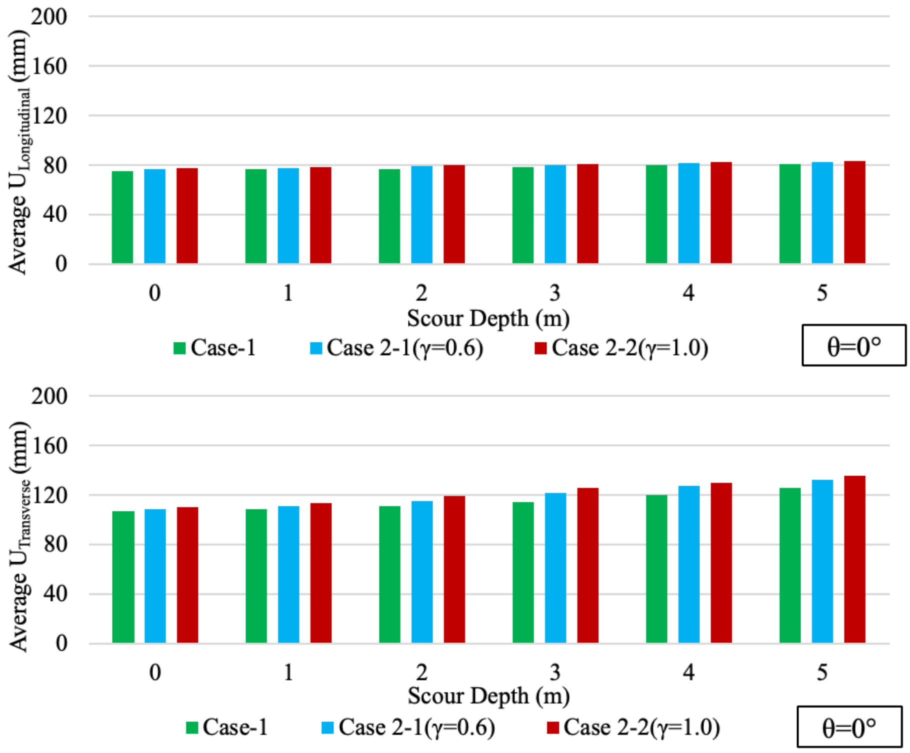

Fig. 7. Average of the peak superstructure displacements for different scour cases and scour depths

In this study, the most critical ground motion incidence angle for bridge-type structures was also examined. OpenSees program was used to assess the ordinary highway bridges by taking Case-1 and Case-2 scour situations into account. Only the analyses results belong to the scour depth of 5 m, which resulted in the largest superstructure displacement demands, were investigated in this part of the study. During the analysis, horizontal ground motion pairs rotated by using linear transformation equations from 0° to 180° with 15° increments. For various scour scenarios and ground motion incidence angles, the average of the peak displacement demands in longitudinal and transverse directions are shown in Fig. 8. According to that, for all scour cases, average displacement demands increase when the ground motion incidence angle shifts from 0° to 90° in the longitudinal direction. On the other hand, the transverse direction of the bridge exhibits the opposite response.

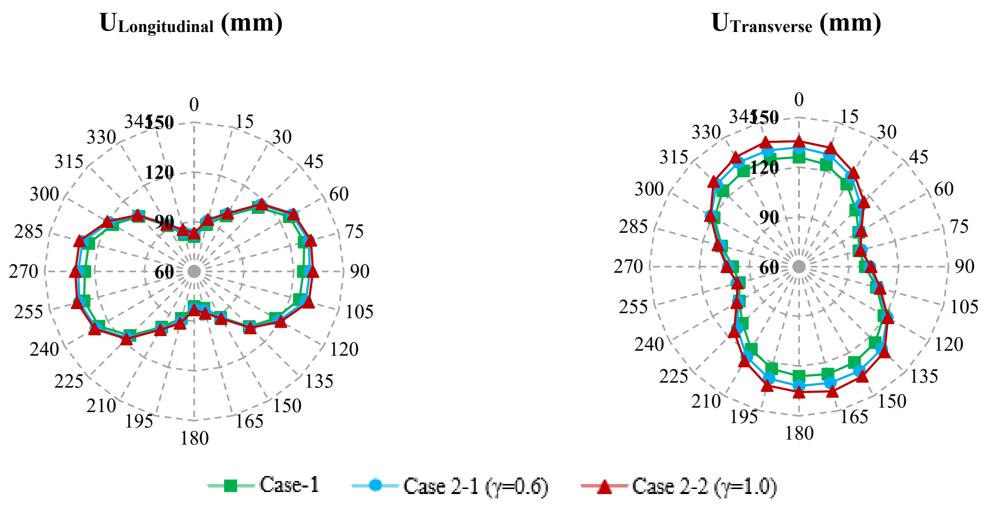

Fig. 8. Average of the peak superstructure displacements for different scour cases and ground motion incidence angles at 5 m scour depth

3.2. Curvature demands of pier column

Although the superstructure, joints, pile shafts, and cap beams of the bridge should all remain to be fundamentally elastic, the pier column is permitted to attain its flexural capacity in compliance with the capacity design principles, according to Caltrans (2019). In order to determine the force and deformation capacity of the bridge column section for both weak and strong axes, section analysis was performed using the XTRACT program. The yield curvature was calculated as $\Phi_{y'}$=0,0033 (1/m) for the weak axis and $\Phi_{z'}$=0,0011 (1/m) for the strong axis of the column section as seen in Fig. 1. Fig. 9 represents the average of the peak curvature demand of the middle bent column's weak and strong axis for each scour scenario and scour depth. Additionally, the graphs included the column yield curvature for each axis as a red dashed line. For each scour scenario and scour depth, the column curvature demands for weak axis are less than the yield curvature. In the strong axis of the column, curvature demands are greater than the yield curvature when scour depth is equal to 0 m (no scour case). For each axis, column curvature demands show a declining trend as the scour depth increases. The substructure, whose lateral stiffness is made up of the stiffness of the piers and piles with supporting soil, has an unsupported clear height that increases as the scour depth increases. As a result, the bridge became more flexible, and the seismic loads placed on the columns were reduced. Additionally, Case-1 (uniform scour) has larger column curvature demands than Case-2 (non-uniform scour). Regardless of the scour depth, Case 2-2 consistently created lower column curvature demands when comparing the demands of the two non-uniform scour scenarios (Case 2-1 and Case 2-2).

Moreover, for different scour scenarios and ground motion incidence angles, Fig. 10 shows the average of the peak curvature demands in the weak and strong axes of the bridge column at 5 m scour depth. For all scour scenarios, the demands on column curvature increase when the ground motion incidence angle shifts from 0° to 120° in both the weak and strong axes of the column. Column curvature demands are lower than their yield capacity in all scour scenarios for a 5 m scour depth as seen in Fig. 9. On the other hand, column curvature demands in the local y' axis can reach its yield curvature when the horizontal ground motion pairs are applied at varied incidence angles. In local z' axis, column curvature demands are below the yield curvature for all incidence angles and scour cases. This result shows the importance of considering various incidence angles in nonlinear response history analyses to achieve the most critical seismic demands for the column deformations.

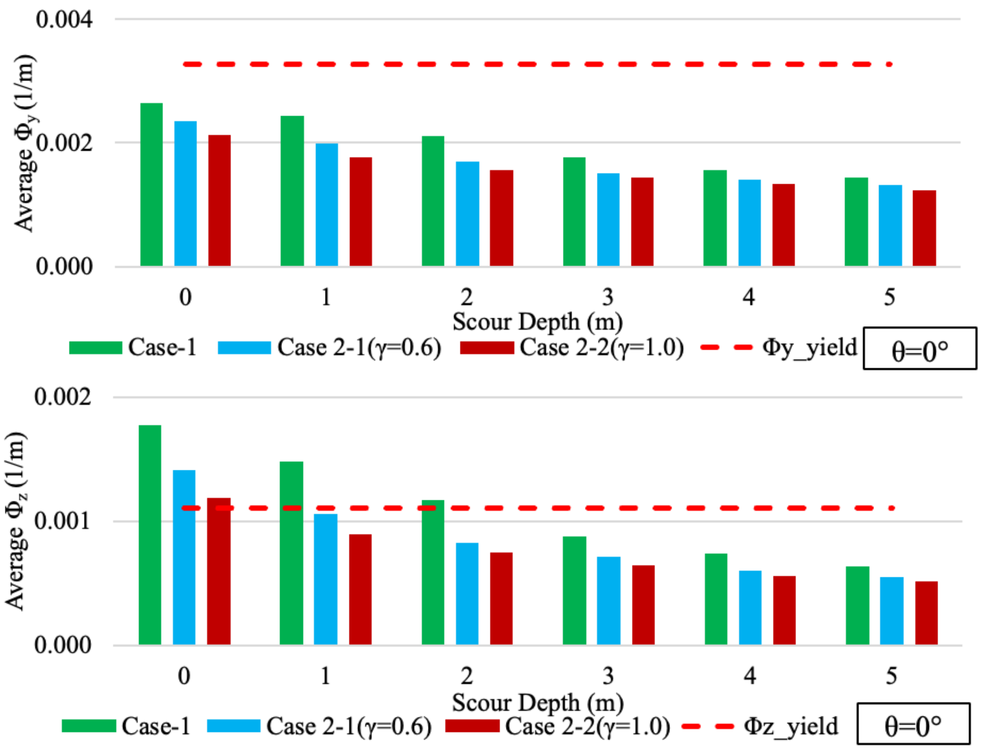

Fig. 9. Average of the peak column curvature demands for different scour cases and scour depths

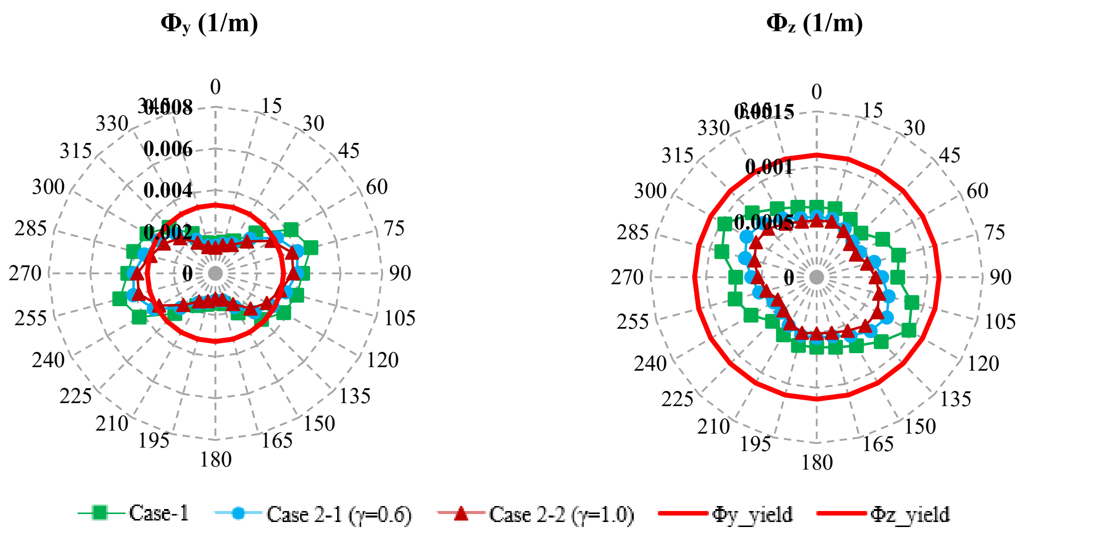

Fig. 10. Average of the peak column curvature demands for different scour cases and ground motion incidence angles at 5 m scour depth

3.2. Shear force demands of piles

Sensitivity analyses were conducted before the response history analyses and pile elements were found to be in their elastic range. However, especially in conditions of scour, it is crucial to verify the shear demands of pile elements. Consequently, the shear force demands of P4 pile, as depicted in Fig. 11 were examined. Similar to pile P3 in the case of non-uniform scour, pile P4 is situated downstream of the bridge and has the lowest clear height. The average of the peak shear force demands obtained from each response history analysis was shown in Fig. 11 for each scour scenario and scour depth. Consequently, when the scour depth increases for each scour situation, the pile P4's shear force demands decrease. The average of the P4 pile's peak shear force in non-uniform scour cases is larger than in uniform scour, when outcomes are compared based on the scour cases. The distribution of shear force demands among the piles is not uniform in the non-uniform scour situation because of the variations in the piles' clear height and, consequently, their stiffness. Higher shear demands are placed on piles with the smallest clear heights than on piles with greater clear heights. The shear capacity of P4 pile was determined as 735 kN using ASCE-ACI 426 (1973), as seen by the red dashed line in Fig. 11. P4 piles were not subjected to any shear damage in the uniform scour scenario when demands and shear capacity were examined. However, P4 had the highest shear demands, particularly in Case 2-2 where the scour depth surrounding the pile was comparatively lower than that of the piles upstream.

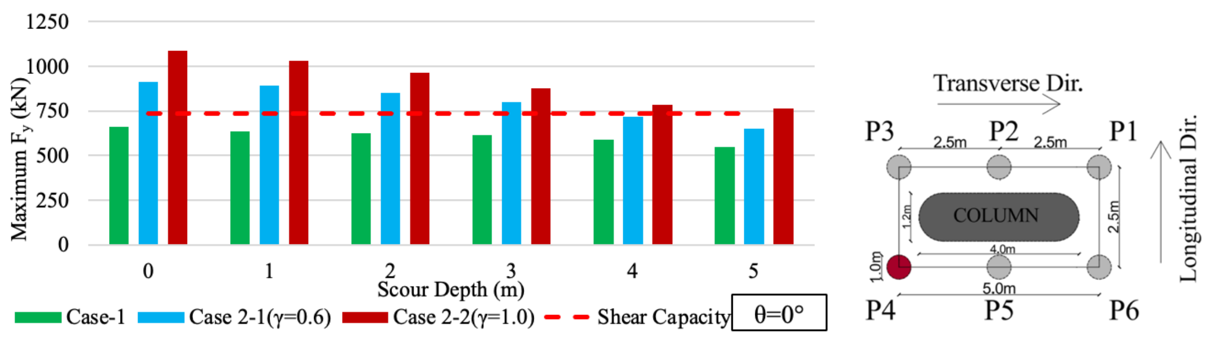

Fig. 11. Average of the peak shear force demands of P4 pile for different scour cases and scour depths

For various scour scenarios and ground motion incidence angles, Fig. 12 shows the average of the peak shear force demands in the local y' axis of the P4 pile for a 5 m scour depth. According to the results, changes in the ground motion incidence angle have an impact on pile shear demands. In contrast to uniform scour case, non-uniform scour cases have higher demands. The P4 pile experiences shear damage when scour is non-uniform and γ=1.0 (Case 2-2), and shear force demands in some incidence angles above the shear capacity of 735 kN.

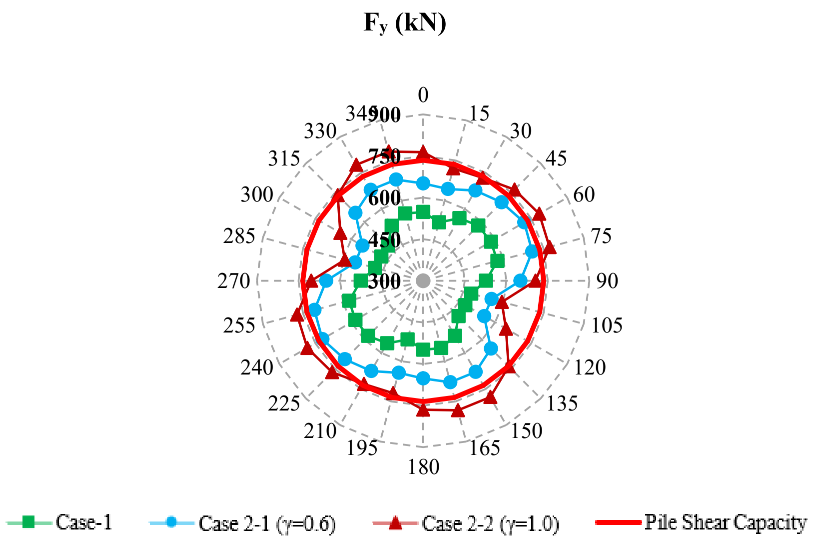

Fig. 12. Average of the peak shear force demands of P4 pile for different scour cases and ground motion incidence angles at 5 m scour depth

4. Conclusions

The safety of lifeline networks depends on the combined impact of earthquakes and flood-induced deterioration on highway bridges. Additionally, one of the key factors affecting a bridge's seismic performance is the ground motion incidence angle. In order to determine the maximum seismic demands of bridge members, a parametric research was carried out, taking into account the uniform or non-uniform scour situation. 7strong ground motion recordings were chosen, and nonlinear response history analyses were performed. The engineering demand parameters for this study are superstructure displacement, shear force demand of piles, and curvature demand of bridge pier columns. The following conclusions can be made in light of the outcomes of the nonlinear response history analyses:

- In all scour scenarios, superstructure demands increase as scour depth increases and this increase is more noticeable in the bridge's transverse direction. Additionally, compared to the case where the scour depth changes uniformly, the displacement demands are more affected by variations in the non-uniform scour depth. For all scour scenarios, displacement demands increase when the ground motion incidence angle shifts from 0° to 90° in the longitudinal direction. On the other hand, the transverse direction of the bridge exhibits an opposite response.
- For each column axis, the curvature demands show a declining trend as the scour depth increases. Additionally, Case-1 (uniform scour) has larger demands than Case-2 (non-uniform scour). In conclusion, the curvature demands of bridge columns are positively impacted by non-uniform scour. For all scour scenarios, curvature demands increase when the ground motion incidence angle shifts from 0° to 120° in both the weak and strong axis of the column. Furthermore, it has been demonstrated that while the column curvature demands are less than the yield curvature at certain incidence angles, the demands are greater at other incidence angles, causing the column to behave nonlinearly during earthquakes.
- As the depth of scour increases, pile P4's shear force demands decrease for all scour cases. The average maximum shear force in non-uniform scour situations is larger than in uniform scour when the results are compared for various scour cases. Additionally, when the scour situation becomes uniform for all depths, pile P4 does not sustain shear damage. However, like in the case of the short column phenomenon, the shear force demands in the case of non-uniform scour exceed the shear capacity and result in a brittle damage mechanism. The variation in the ground motion incidence angle also affects the pile shear demands. When scour is non-uniform and γ=1.0 (Case 2-2), shear damage occurs in the P4 pile because shear force demands in some incidence angles are greater than shear capacity. These findings demonstrate that different earthquake incidence angles should be taken into account in nonlinear response history analysis in order to achieve the most unfavourable seismic demands.

Acknowledgments
The research described in this paper was financially supported by the Turkish Scientific and Technical Research Council (TUBITAK) under the grant number [120M968].

References

API. (2000). Recommended Practice for Planning , Designing and Constructing Fixed Offshore Platforms — Working Stress Design. *Api Recommended Practice*, *24-WSD*(December 2000), 242. http://scholar.google.com/scholar?hl=en&btnG=Search&q=intitle:Recommended+Practice+for+planning,+designing+and+constructing+fixed+Offshore+Platforms+-+Working+stress+design#0

Atak, B., Avşar, Ö., & Yakut, A. (2014). Directional effect of the strong ground motion on the seismic behavior of skewed bridges. *Proceedings of the International Conference on Structural Dynamic , EURODYN*, 1253–1258.

Ateş, S., & Avşar, Ö. (2024a). Representation of Incidence Angle in Seismic Analysis of Skewed Highway Bridges. *Journal of Bridge Engineering*, *29*(2). https://doi.org/10.1061/JBENF2.BEENG-6452

Ateş, S., & Avşar, Ö. (2024b). Seismic performance of skewed bridges with uniform and non-uniform scour. *Soil Dynamics and Earthquake Engineering*, *187*. https://doi.org/10.1016/j.soildyn.2024.108976

Avsar, Ö., Atak, B., & Caner, A. (2017). In-Depth Investigation of Seismic Vulnerability of an Aging River Bridge Exposed to Scour. *Journal of Performance of Constructed Facilities*, *31*(5), 1–13. https://doi.org/10.1061/(ASCE)CF.1943-5509.0001036

Bhatnagar, U. R., & Banerjee, S. (2014). Fragility of skewed bridges under orthogonal seismic ground motions. *Structure and Infrastructure Engineering*, *11*(9), 1113–1130. https://doi.org/10.1080/15732479.2014.936880

Caltrans. (2019). *Seismic Design Criteria, State of California Department of Transportation*.

Fioklou, A., & Alipour, A. (2019). Significance of non-uniform scour on the seismic performance of bridges. *Structure and Infrastructure Engineering*, *15*(6), 822–836. https://doi.org/10.1080/15732479.2019.1584226

Guo, X., & Chen, Z. (2016). Lifecycle multihazard framework for assessing flood scour and earthquake effects on bridge failure. *ASCE-ASME Journal of Risk and Uncertainty in Engineering Systems, Part A: Civil Engineering*, *2*(2), 1–10. https://doi.org/10.1061/AJRUA6.0000844

He, H., Wei, K., Zhang, J., & Qin, S. (2020). Application of endurance time method to seismic fragility evaluation of highway bridges considering scour effect. *Soil Dynamics and Earthquake Engineering*, *136*(111), 106243. https://doi.org/10.1016/j.soildyn.2020.106243

Joint ASCE-ACI Task Committee 426 on Shear and Diagonal Tension of the Committee on Masonry and Reinforced Concrete of the Structural Division. (1973). The Shear Strength of Reinforced Concrete Members. *Journal of the Structural Division*, *99*(6). https://ascelibrary.org/doi/10.1061/JSDEAG.0003532

Kent, D. C., & Park, R. (1971). Flexural Members with Confined Concrete. *Journal of the Structural Division*, *97*, 1969–1990.

Kulhawy, F. H. (1991). Drilled Shaft Foundations. *Foundation Engineering Handbook*, *1991*(c), 537–552. https://doi.org/10.1007/978-1-4757-5271-7_14

Ministry of Transport and Infrastructure of The Republic of Turkey. (2020). *Principles for the Design of Highway and Railroad Bridges and Viaducts Under the Impact of Earthquakes*.

Moschonas, F. I., & Kappos, J. A. (2011). Generalized fragility curves for bearing-supported skew bridges, for arbitrary angle of incidence of the seismic action. *City Research Online*, *37*(9), 1591–1601.

Noori, H. R., Memarpour, M. M., Yakhchalian, M., & Soltanieh, S. (2019). Effects of ground motion directionality on seismic behavior of skewed bridges considering SSI. *Soil Dynamics and Earthquake Engineering*, *127*(July), 105820. https://doi.org/10.1016/j.soildyn.2019.105820

Prasad, G. G., & Banerjee, S. (2013). The impact of flood-induced scour on seismic fragility characteristics of bridges. *Journal of Earthquake Engineering*, *17*(6), 803–828. https://doi.org/10.1080/13632469.2013.771593

TEHM. (n.d.). *Turkish Earthquake Hazard Map*. Retrieved December 6, 2021, from https://tdth.afad.gov.tr

Wang, Shiou-Chun; Liu, Kuang-Yen; Chen, Chia-Han; Chang, K.-C. (2015). Experimental investigation on seismic behaviour of scoured bridge pier with pile foundation. *Earthquake Engineering & Structural Dynamics*, *44*, 849–864. https://doi.org/10.1002/eqe.2489

Wang, X., Ye, A., & Ji, B. (2019). Fragility-based sensitivity analysis on the seismic performance of pile-group-supported bridges in liquefiable ground undergoing scour potentials. *Engineering Structures*, *198*(August), 109427. https://doi.org/10.1016/j.engstruct.2019.109427

Wei, K., He, H., Zhang, J., Yang, C., & Qin, S. (2021). An endurance time method-based fragility analysis framework for cable-stayed bridge systems under scour and earthquake. *Ocean Engineering*, *232*(December 2020), 109128. https://doi.org/10.1016/j.oceaneng.2021.109128

Yilmaz, T., Banerjee, S., & Johnson, P. A. (2016). Performance of Two Real-Life California Bridges under Regional Natural Hazards. *Journal of Bridge Engineering*, *21*(3), 04015063. https://doi.org/10.1061/(asce)be.1943-5592.0000827

Zhou, L., Barbato, M., & Ye, A. (2021). Experimental Investigation of Postearthquake Vertical Load-Carrying Capacity of Scoured Reinforced Concrete Pile Group Bridge Foundations. *Journal of Bridge Engineering*, *26*(12), 1–14. https://doi.org/10.1061/(asce)be.1943-5592.0001799

4th International Civil Engineering & Architecture Conference
17-19 May 2025, Trabzon, Türkiye

Behavior of untopped precast floors in high-seismic applications

Merve Arlı Sönmez*[1], Yüce Yetimoğlu[1], Seyit İ. Ulusoy[1], Ali Koçak[2]

[1] *CEG (Consulting Engineers Group) Türkiye, İstanbul, Türkiye*
[2] *Yıldız Technical University, Department of Civil Engineering, İstanbul, Türkiye*

Abstract. Precast concrete provides a construction method using durable and quickly erectable prefabricated elements to create sustainable and high-quality structures. The seismic behavior of precast buildings is highly dependent on the characteristics of the precast floors. A precast concrete diaphragm is defined as a diaphragm comprising precast concrete components, with the option of incorporating specialized connections along some or all boundaries. Additionally, it may be constructed with or without cast-in-place concrete topping slabs. The most common practice, particularly in the case of the building stock of Türkiye, is to use cast-in-place concrete slabs to provide the diaphragm. Furthermore, according to the seismic code of Türkiye, the use of untopped floors in seismic zones is not permitted. Another commonly employed methodology, particularly within the USA in the context of this study, is the provision of a diaphragm with connections on untopped floors. This is an area that requires further investigation and development in Türkiye. Design requirements were established for untopped diaphragms intended for use in buildings assigned to high seismic zones. In order to satisfy these requirements, it is essential to guarantee that the diaphragms remain elastic throughout the design seismic event, even with the highly conservative diaphragm design forces. The aim of this study is to examine and contrast the behavior of the diaphragm in the building during a seismic event, with particular attention paid to the effects of not having a topping. The design methodology employs a Finite Element Model (FEM) of the subject building to examine the code requirements and the behavior of the floors.

Keywords: Diaphragm; Precast; High-Seismic; Topped floors; Untopped floors; Diaphragm design forces; SAP2000

1.Introduction

Lateral resisting systems are critically important for buildings made of steel, concrete, or precast concrete, regardless of whether they are in a high seismic zone or not. The lateral loads must be transferred to the foundation following the correct load pattern, and diaphragms are the first step in this process. It is essential to understand that diaphragms can behave in three different ways: rigid, semi-rigid, or flexible. Moreover, it should be noted that due to structural irregularities or construction errors, a diaphragm may not behave as expected. Therefore, before starting the design of a building, it is crucial to first determine the diaphragm behavior, as this decision will guide the selection of the appropriate lateral resisting system.

For a common usage, it is mostly preferred to use topped floors for precast buildings. Precast floors could be hollow-core slabs, double-tees, t-slabs and other precast components. After the erection of the floors is completed, cast-in-place concrete is placed on top of them. So, this cast-in-place concrete which is called also topping concrete provides diaphragm behavior. According to the Turkish Seismic Code (2018) a minimum of 7 cm topping concrete is required. Furthermore, the Turkish Seismic Code (2018) does not allow the use of untopped precast floors in any part of Türkiye. So, this study tries to summarize behavior of untopped precast floors at high seismic regions like Türkiye even it is not allowed by the code.

1.1. Behavior of topped floors

It is important to understand the behavior of topped precast systems in relation to the behavior of untopped floors, as both systems can act very similar when special connection details are applied. Figure 1 shows a basic precast system with or without a cast-in-place concrete topping. As seen, the shear walls at the ends of the system act as support against diaphragm forces. In this case, the diaphragm behaves as a deep beam, which is why the diagrams for both systems are similar to a simply supported beam. That is why it is mandatory to take precautions against shear forces, moments, and support connections in order to maintain the rigidity of diaphragm.

* Corresponding author, E-mail: arlimerve6@gmail.com

https://doi.org/10.31462/icearc2025_ce_eqe_481

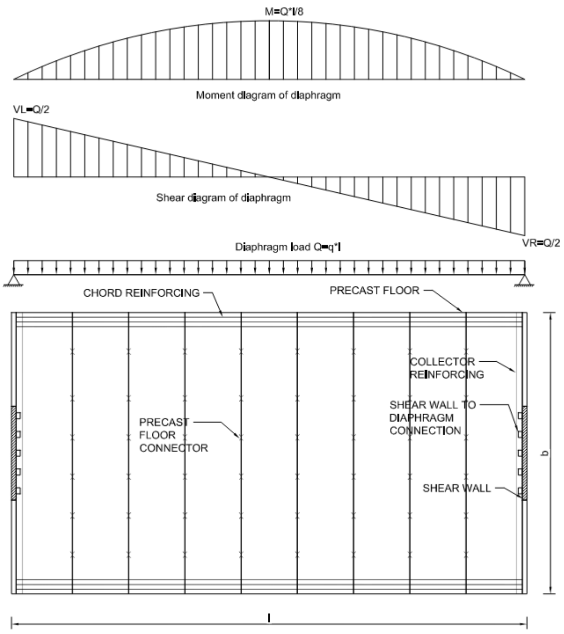

Fig. 1. Topped precast diaphragm system

Fig. 2. Precast slab-to-slab connection (Example of a ceg project application)

As shown in Fig. 1, the first step is to ensure that the precast floors are connected properly to resist shear forces. According to the shear force diagram, shear forces occur between the precast floors. A typical connection type can be seen in Fig. 2. However, when there is a cast-in-place concrete topping, the connection shown in Fig. 2 is necessary only for the erection process. The cast-in-place concrete itself is expected to be capable of resisting all the shear forces and moments.

Given the potential for seismic forces to act in both directions of the diaphragm, it is essential that reinforcement is applied to both sides. Simply, when the moment is divided by the moment arm (denoted as "b" in Fig. 1), it becomes easy to calculate the chord reinforcement. A typical application for chord reinforcement into cast-in-place topping is shown in Figure 3.

As described in Fig. 1, the floor-to-shear wall connections are critical. Since shear walls provide support feature in the diaphragm, it is a matter of designing the connections between the floor and the walls properly. These connections can be as simple as rebar embedded in the topping concrete or more complex welded connections, as shown in Fig. 4. When designing the welded connections, special care must be taken to meet seismic requirements. These connections, which should transfer the diaphragm shear forces to the shear walls, are essential according to the deep beam analogy. Thus, shear walls can transfer lateral loads to foundation with the load path. In most structures, it is not possible to place shear walls along the entire length of the floor. As shown in Fig. 1, shear walls are generally used as partial. In such cases, collector members are used to transferring the residual shear forces to the shear walls. The collector members typically consist of rebars that extend beyond the shear walls in areas without shear walls. The rebars collect the shear forces through their capacity and transfer the forces to the ends of the shear walls.

Fig. 3. Chord reinforcement

Fig. 4. Welded floor connection

1.2. Behavior of untopped floors

Untopped floors demonstrate a comparable behavior to that of topped precast systems. The main advantage of topped systems is that they can act monolithically, which helps to address many construction challenges. However, there may be instances where pouring concrete is not feasible. This can present a particular challenge when the project site is located remotely from a concrete batching plant. In such situations, the use of untopped precast floors can be a key advantage, especially in terms of reducing the amount of on-site work required, which can be crucial for meeting project schedules.

The most significant challenge associated with untopped systems is ensuring the integrity of the floor. In the context of this issue, connection details become very critical. Basically, the primary aim is connecting double-tees to accommodate the lateral shear forces. Regarding this situation, most of the connections are provided by welded connections between double-tee members, as shown in Fig. 5. The connections perform as chord reinforcing. They are standardized products which can be provided by different producers.

Provide chord reinforcement at the ends as shown in Fig. 6. For untopped systems, there are two options for implementing chord connections. The first option is to produce double-tees with recesses at the ends and place the chord reinforcement into the recess with cast-in-place concrete, like the method used in topped systems. The second option is to eliminate all the cast-in-place concrete and use certificated mechanical connections instead, as shown in Fig. 7.

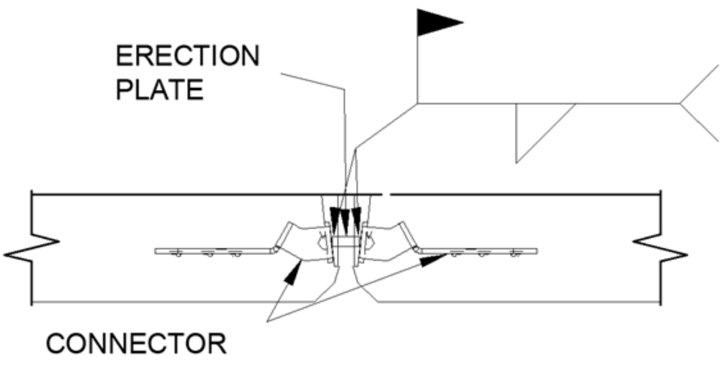

Fig. 5. Welded double tee flange connection (side view)

Fig. 6. DT recess for placing chord and collector reinforcements

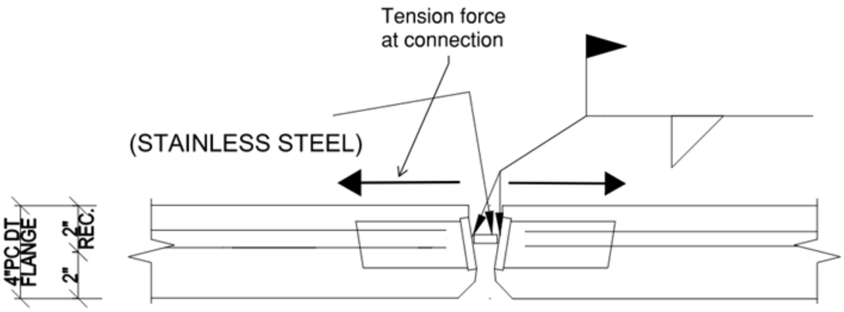

Fig. 7. Chord connection at untopped precast slab (side view)

2. Components and methods

In this research, the diaphragm behavior in the Y direction is observed. In order to examine this behavior, a generic single-storey structure was designed specifically for this study. Information about this structure is summarized in the following section.

2.1. Structure features

The structure has 10 grids in the X direction and 2 grids in the Y direction. The distance between X direction grids is 12ft (~3.66m) and the distance between the Y direction grids is 48ft (~14.6m). The height of the structure is 12ft (~3.66m) and there are 2 shear walls with a section thickness of 1ft (~30.5cm) on the side grids along the Y direction. 4 square columns (2ft~61cm) are located on the middle grids. Beams are extending between the columns and the shear walls. Nine double-tees are positioned from Grid-A to Grid-J. These slabs carrying 1-way loads are connected to each other by connection components.

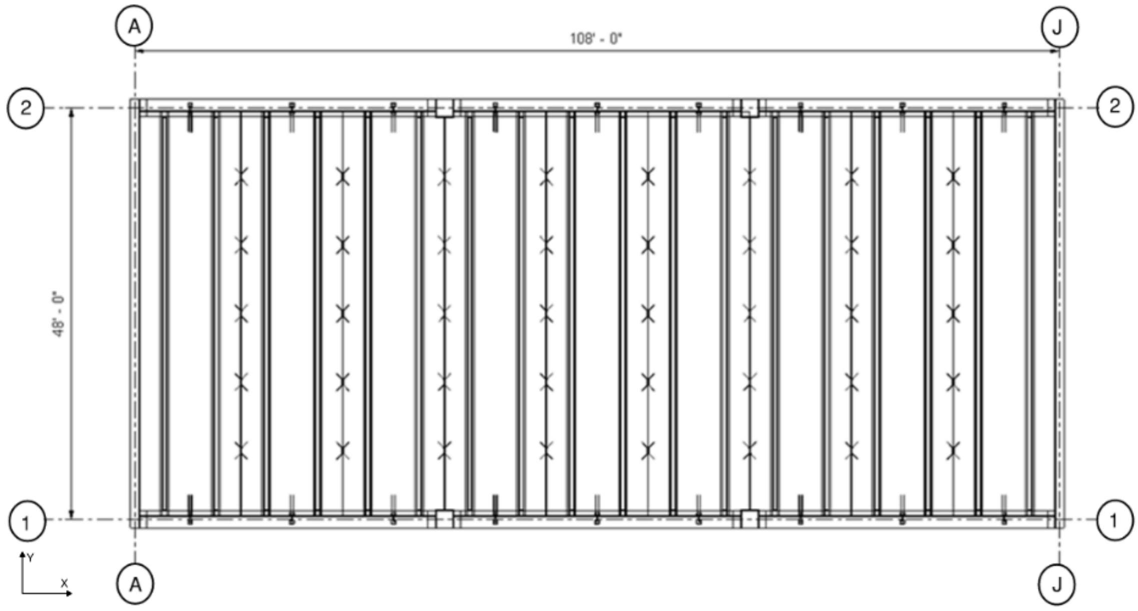

Fig. 8. Typical measured plan

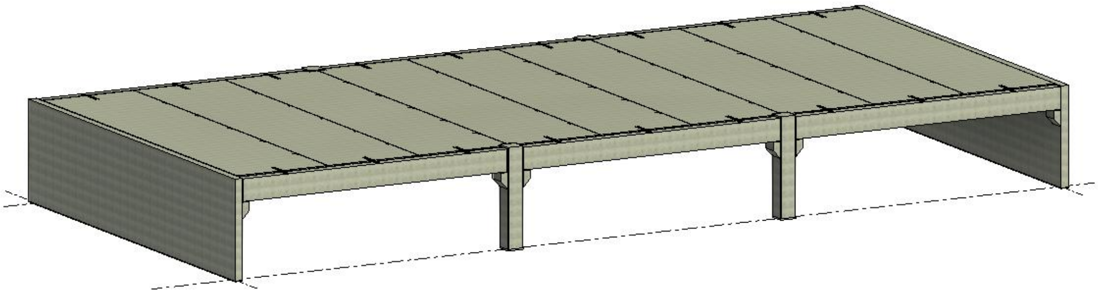

Fig.9. Shaded 3D view

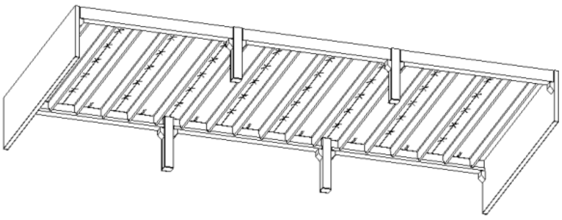

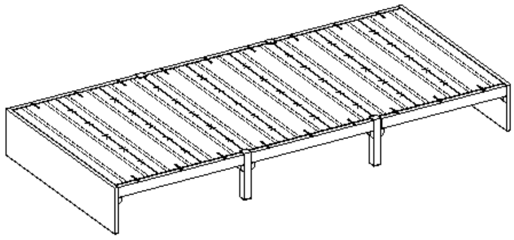

Fig. 10. 3D view from below

Fig. 10a. 3D view from above

The mathematical model was created via SAP2000_V24, and the imperial system was used for units. At this stage, the structure information specified above was used. Release definitions were done at the beam ends. Link components were assigned for the connections. For the link properties, previously researched tables published in PCI Journal were used (Klein and Lindenberg, 2009). Since only the Y-direction diaphragm behavior of the structure was examined in the modeling, only the tensile properties of the link components were used. 5 rows of chord connectors were placed on the sides of the structure and V-shape connectors were placed in the middle part. The mechanical properties of these elements are summarized below. Tensile Capacity and stiffness of diaphragm connections in Table 1.

Table 1. Mechanical properties

Connection Type	Ultimate Capacity [(kips)-(kN)]	Secant Stiffness [(kip/in)-(kN/m)]
V-Shape Connector	(9.7)- (43.1)	(58)-(10157)
Chord Connector (Plate-Edge)	(36.4)-(161.9)	(297)-(52012)

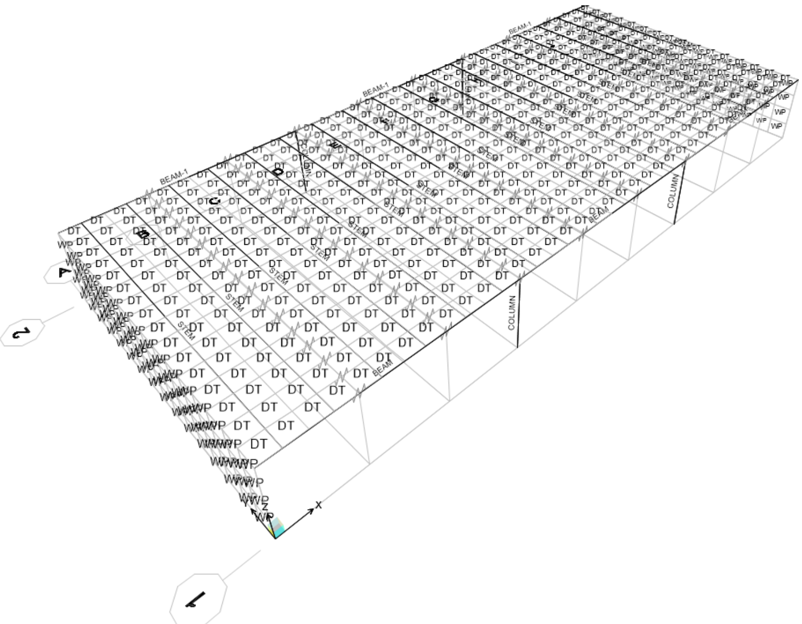

Fig. 11. Frame and area sections

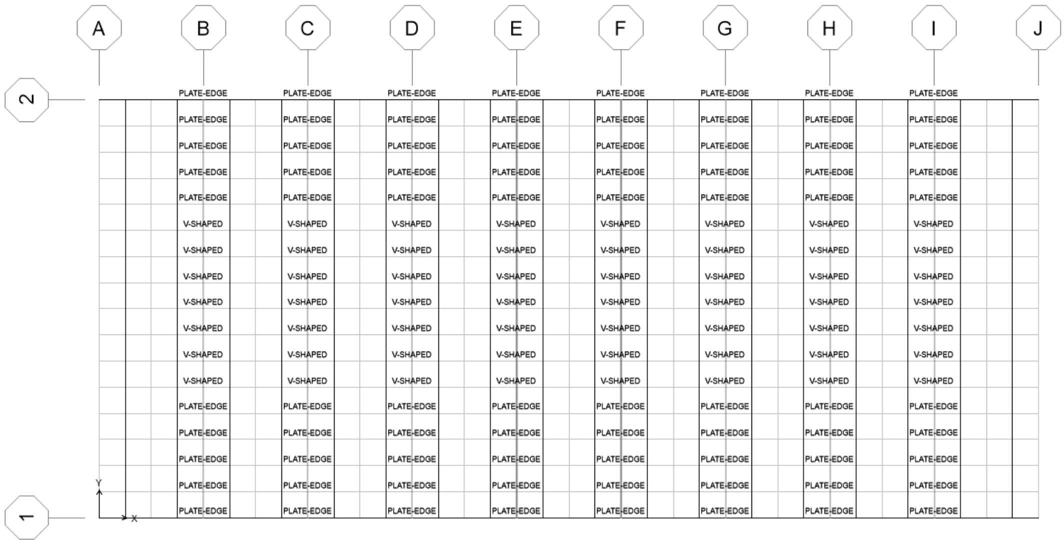

Fig. 12. Defined link properties (SAP2000 V24)

The main structure is created with link components as mentioned above. Link capacities, structure behavior, and incoming forces will be examined through this model. A monolithic model was also created to understand to what extent this modeling represents the diaphragm behavior. There are no connection elements in the monolithic model. It is assumed that a typical topping of concrete is placed. For convenience, the main structure model with the connection elements is named as "MODEL-1" and the model with the topping concrete is named as "MODEL-2".

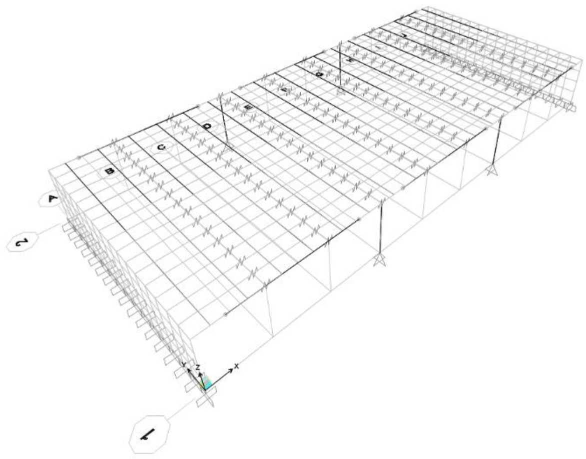

Fig. 13. Model 1-with link components

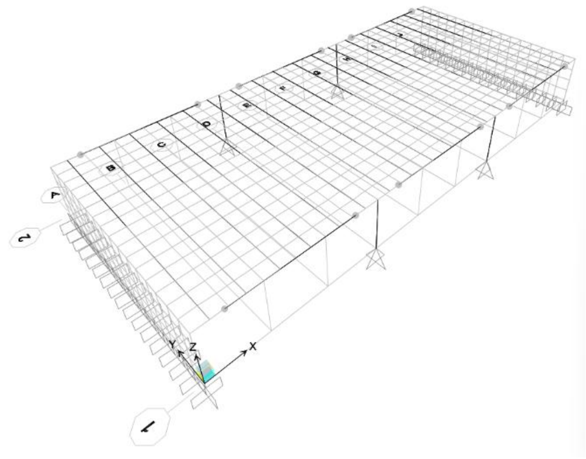

Fig. 13a. Model 2- monolithic

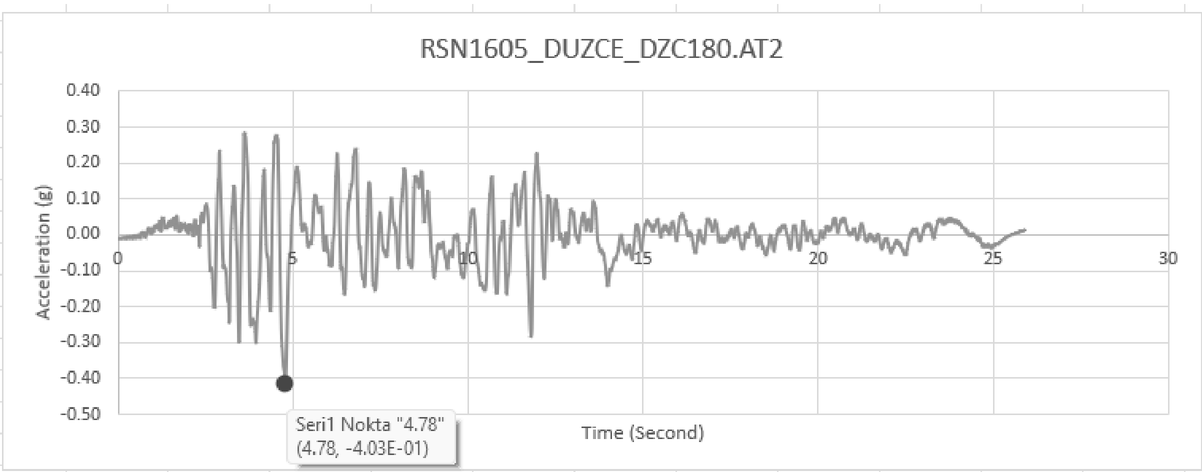

Fig.14. 1999 Düzce earthquake record (PEER)

In order to focus on the horizontal behavior of the diaphragm in the structure, as typical 15 psf (0.71 kN/m2) load definition was assigned for the whole floor as vertical load. This load, which was defined in addition to the loads of the structural components, was taken into account in the earthquake load calculation.

A linear time history analysis was performed for the earthquake loading. For this analysis, the 1999 Düzce Earthquake data was used. The PGA value of this earthquake data, which is preferred in earthquake analyses performed in high seismic regions, is 0.404g.

2.3. Structure seismic results and analysis of the results

As a result of the earthquake analysis, the maximum forces on the link elements in MODEL-1 are given in Fig. 15 below.

It is seen that the link components defined with the information that the tensile capacity of the edge-plate elements (chord connectors) is 36.4k (161.9kN) and the tensile capacity of the V-shaped connector elements is 9.7k (43.1kN) remain under the limit values and can carry the seismic load.

The base shear forces are very close to each other in both models. It is understood that this convergence supports the modeling approaches. The deformed shapes of the monolithic model (MODEL-2) with diaphragm behavior and the linked model (MODEL-1) are compared and these images are given in Fig. 17 above.

The difference in displacements between the two models (MODEL-1 and MODEL-2) is due to the link components being defined as having the ability to move in the direction of the axial load. As a matter of fact, since the maximum displacements are still quite small, it has been observed that they do not create any disadvantages in carrying horizontal loads. Since diaphragm behavior is examined in the structures, the limiting effect of the beams on the movement is also neglected.

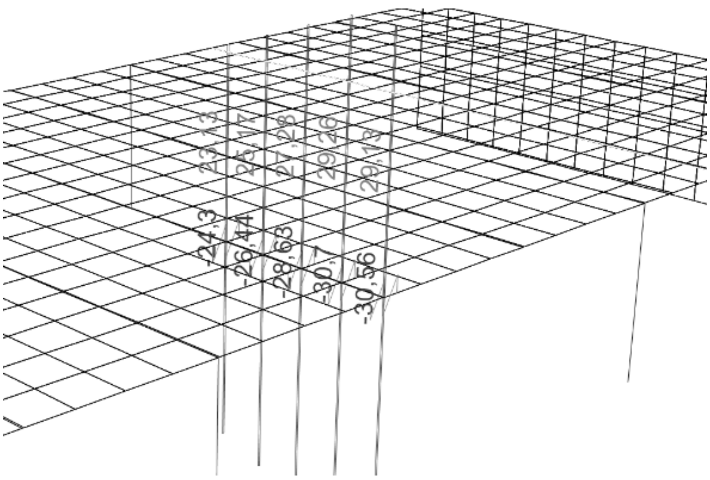

Fig. 15. Maximum link (chord connector) forces

Table 2. Base reactions and displacements

	Base Reactions [(kips)-(kN)]	Maximum Displacement [(in)-(mm)]
MODEL-1	495- 2201.8	0.26- 6.8
MODEL-2	465- 2068.4	0.06- 1.6

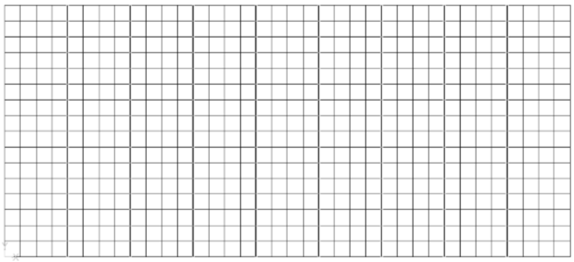

Fig. 16. Undeformed shape for Model-1

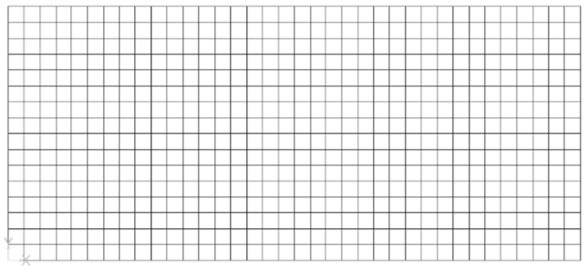

Fig. 16a. Undeformed shape for Model-2

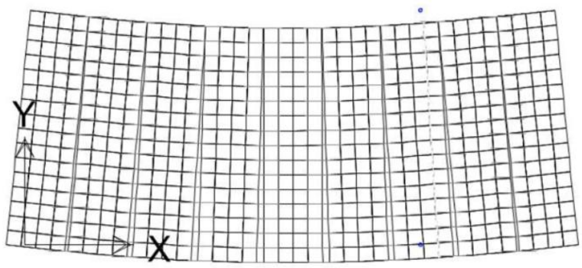

Fig. 17. Deformed shape for Model-1

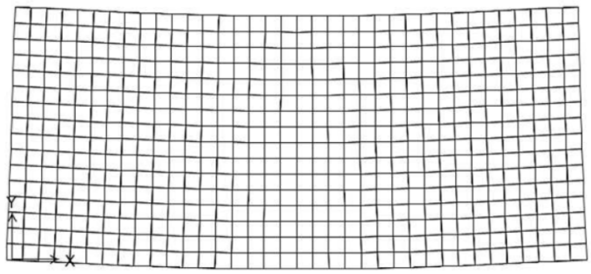

Fig. 17a. Deformed shape for Model-2

3. Conclusions

- Extensive experimental and practical evidence from past studies has demonstrated that adequate diaphragm action in precast structures can be achieved using topping concrete with sufficient thickness.
- Beyond the topping concrete approach, which is currently incorporated into the Turkish Seismic Code (2018), this study indicates that the use of reinforced chord plates—positioned along the sides of precast double-tee slabs, within both tension and compression zones—can perform effectively under high seismic demands, exhibiting structural behavior comparable to that of monolithic systems.
- The findings of this study emphasize the necessity for structure-specific design strategies, including the careful placement of a sufficient number of chord plates with appropriate capacity at strategically critical locations.

- The structural performance afforded by these additional components is highly dependent on the geometric configuration of the building, particularly the width-to-length ratio of the floor diaphragm.
- Given the inherent complexity of seismic ground motion and the variability in fault-specific characteristics, it is evident that further experimental investigations and application-oriented research are essential to validate this method—especially considering its current prohibition in Türkiye.

References

Fleischman, R. B. (2014). *Seismic design methodology document for precast concrete diaphragms*. Charles Pankow Foundation.

Fleischman, R. B., Naito, C. J., Restrepo, J., Sause, R., & Ghosh, S. K. (2005). Seismic design methodology for precast concrete diaphragms Part 1: Design framework. *PCI Journal, 50*(5), 68.

Ghosh, S. K., & Cleland, N. M. (2002). Untopped precast concrete diaphragms in high-seismic applications. *PCI Journal, 47*(6), 94–99.

Ghosh, S. K., Cleland, N. M., & Naito, C. J. (2017). *Seismic design of precast concrete diaphragms* (NEHRP Seismic Design Technical Brief No. 13).

Klein, G. J., & Lindenberg, R. E. (2009). Volume-change response of precast concrete buildings. *PCI Journal, 54*(4).

Pacific Earthquake Engineering Research Center (PEER). (2024). *PEER reports*. University of California, Berkeley.

SAP2000. (2023). *Three dimensional static and dynamic finite element analysis and design of structures: Basic* analysis reference manual (Version 24). Computers and Structures Inc.

T.C. Çevre, Şehircilik ve İklim Değişikliği Bakanlığı. (2018). *Türkiye Bina Deprem Yönetmeliği (TBDY 2018)*. Ankara, Türkiye (in Turkish).

4th International Civil Engineering & Architecture Conference
17-19 May 2025, Trabzon, Türkiye

Structural damage and transportation closure analyses based on earthquake performance

Zeynep Demirel*[1], Seda Selçuk[1]

[1] Çankaya University, Department of Civil Engineering, 06790 Ankara, Türkiye

Abstract. Earthquakes are complex natural disasters with sudden and unpredictable impacts, posing significant threats to human life, structural safety, and transportation networks. Located on active fault lines, Türkiye faces a high earthquake risk, which can lead to multidimensional issues such as structural damage and disruptions in transportation systems in the affected regions. The effects of an earthquake are expected to vary depending on the seismic parameters, soil conditions, and structural characteristics of the affected area. The primary aim of this study is to comprehensively analyse the structural collapses caused by earthquakes, and the resulting road closures. The study examines the effects of an earthquake within the framework of seismic, structural, and geotechnical parameters, it focuses on the determination of the areas covered by collapse of the buildings. In this context, the situations that may lead to potential interruptions in transportation functionality due to the damage that occurred will be available for analysis. In order to determine the level of these potential interruptions, seismic and geotechnical data were analysed to determine road closures due to building collapses within the studied region. This analysis paved the way for reliable predictions regarding the post-earthquake functionality of roads and has the potential to make significant contributions to strategic planning in disaster management processes.

Keywords: Earthquakes parameters; Structural collapses; Road closures; Disaster management; Seismic parameters

1. Introduction

Developing seismology increasingly emphasizes the need to assess the safety of road networks worldwide, especially in countries with high seismic activity. Turkey, one of the countries with high earthquake risk, has been severely affected by the collapse of numerous structures during major earthquakes in the past, and the resulting debris on the road system has seriously affected the functionality of transportation networks and caused widespread congestion (Bakırcı & Aydoğdu, 2023). The dysfunction of transportation systems after earthquakes is a serious problem that disrupts emergency response (McCullough, 1994). Therefore, the accurate assessment of the functionality of transportation networks after earthquakes is necessary for the sound development of emergency response plans and rescue strategies.

Over the years, studies have been conducted to assess the functionality of transportation networks after earthquakes. In these studies, road closures due to building collapse have generally been estimated through probabilistic models; parameters such as seismic intensity, building location, and road typology have been used. Yu and Gardoni (2022) analysed the closure risk in different types of roads by creating fragility curves with a Bayesian approach. Hosseini and Mohammadi (2023) evaluated the opening time of closed roads and the network re-operability of the network with a scenario-based resilience model. In another study conducted in Thessaloniki, the vulnerability of the network was analysed depending on the building location and road geometry; however, in this study, the network closures were evaluated predefined scenarios with fixed plan dimensions and heights for all buildings (Argyroudis et al., 2015). Although these studies provide important contributions in terms of post-earthquake transportation functionality, they are largely based on theoretical assumptions.

Theoretical equations derived to predict debris-covered areas after building collapses are based on probabilistic approaches using Gaussian distribution, which can estimate various collapse scenarios. In this study, using real field data obtained from the regions affected by the February 6, 2023 Kahramanmaraş earthquakes, different scenario estimates of the probabilistic models were compared with the observed data.

Within the scope of the study, the effects of building collapse debris after the February 6, 2023 Kahramanmaraş earthquakes on road closures were analysed using spatial and structural data obtained from the field. Unlike similar studies in the literature, seismic and geotechnical parameters affecting the spread area of collapsed building debris

* Corresponding author, E-mail: c2019017@student.cankaya.edu.tr

https://doi.org/10.31462/icearc2025_ce_eqe_498

were examined comprehensively. In this respect, the study presents an original approach that evaluates expected spread area of the collapsed buildings based on both seismic and geotechnical parameters which would pave the way to assess functionality of transportation networks with much higher precision.

2. Materials and methods

On February 6, 2023, two major earthquakes with magnitudes of Mw = 7.7 and Mw = 7.6 occurred one after the other in Kahramanmaraş, Türkiye. These earthquakes directly affected 10 provinces in the southeast of Türkiye; many structures in these regions were seriously damaged or completely destroyed. In this study, data on the spatial and physical characteristics of the structures affected by these earthquakes were obtained from various sources.

Parameters such as location, number of floors, building plan dimensions (width), proximity of the building to the neighbouring structures and damage status were determined through detailed visual analyses performed on Google Earth (Google, n.d.). In order to evaluate the effect of seismic parameters on the intensity and debris spread area, regional Peak Ground Acceleration (PGA_{475}) and Peak Ground Velocity (PGV_{475}) data of earthquakes with a return period of 475 years, together with the distance to the fault line, were obtained from the AFAD Türkiye Earthquake Hazard Map (TDTH) platform (AFAD, 2019). In addition, in order to analyse the effects of geotechnical parameters; soil class information was obtained from the AFAD Türkiye Acceleration Database and Analysis System (TADAS) (AFAD, n.d.) and data on liquefaction potential were obtained from United States Geological Survey (USGS) sources (United States Geological Survey [USGS], 2023).

2.1. Methods

In this study, the debris spread width (Wd) resulting from building collapse was calculated based on a probability-based model proposed in the literature by Argyroudis et al. (Argyroudis et al., 2015). In this model, Wd is defined under the Gaussian distribution assumption, and the main reason for this assumption is the existence of a correlation between the building geometry and the debris width.

The model indicates that the variability in debris spread for a single building depends on two basic parameters: collapse angle (c) and volume loss rate (kv). These parameters represent the slope of collapse debris and the amount of debris produced, respectively, and are the main sources of uncertainty on the debris spread width. The model allows estimating the probabilities of different debris area scenarios which directly affects level of road functionality.

In addition to these parameters a collapse scenario proposed by Argyroudis et al. was selected for the estimation of debris spread area. The selected scenario is considered more suitable for urban structures constructed in adjacent arrangements and continuous building facade forms (Argyroudis et al., 2015). As shown in Fig. 1, in the Thessaloniki study, building height (Y) was calculated as low, medium and high-rise average values; The building width (W) is assumed as a fixed parameter of 15 m. In addition, the expected value for the volume loss rate is taken as E[kv] = 0.50 and for the collapse angle as E[c] = 45°. The coefficient of variation for both parameters is determined as 30%.

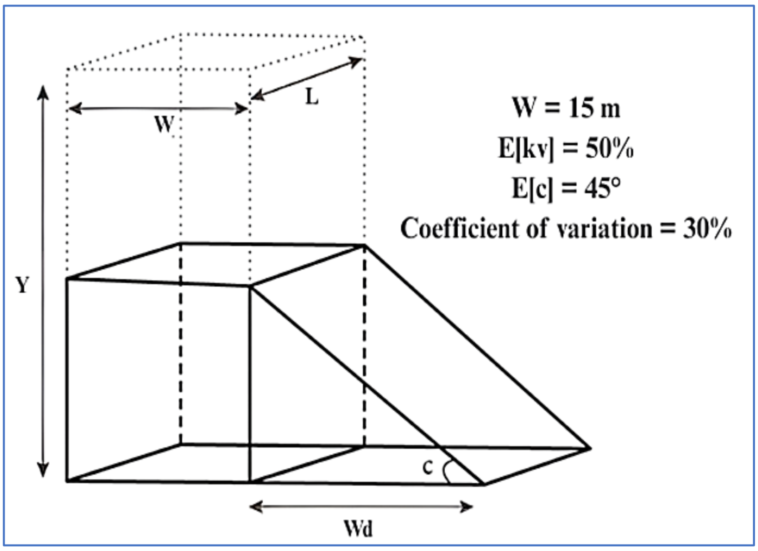

Fig. 1. Selected Scenario and Used Parameters Proposed by Argyroudis et al.

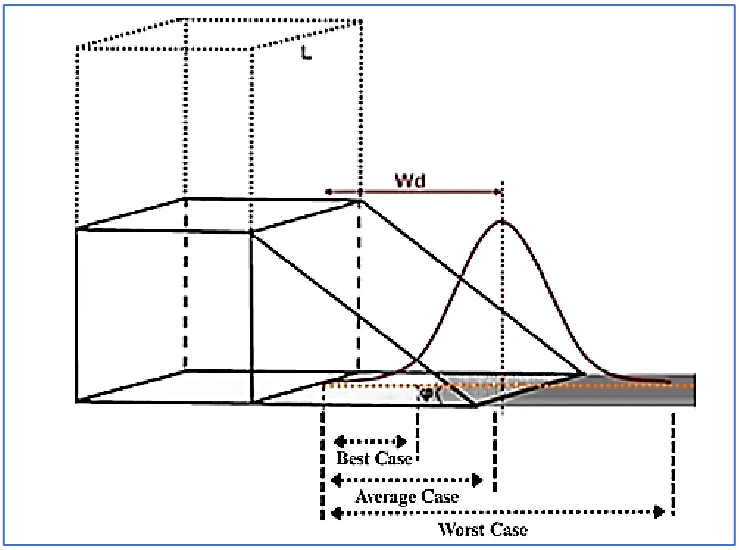

Fig. 2. Different Debris Spreading Cases (Best - Average – Worst) (Argyroudis et al., 2015)

In our study, we modified this approach by assessing building height (Y) and building width (W) separately for each building. The building height was calculated approximately based on the number of floors for each building; while the average floor height was taken as 3 meters, a height of 3.5 meters was used as ground floor height. Thus, the total height of each building was calculated uniquely. Similarly, the building plan geometry was measured for each building via Google to be used in the calculations. Due to the uncertainties inherent in the collapse angle (c) and volume loss ratio (kv) parameters, three different scenarios for the debris spreading width (Wd) are defined based on the variations of these two parameters, as shown in Fig. 2. These scenario parameters allow how the road closure situations may change within the probability distribution according to the collapse type of the buildings and the amount of debris they produce.

- Best Case: The case represents a situation where slope of collapse debris is steeper and the volumetric loss is less. In this case, the structure produces less debris and the road closure level is minimal because the collapse occurs in a narrower area.
- Average Case: The case represents a situation where slope of collapse debris and volumetric loss rate are the mean of the probabilistic distribution . This reflects the amount of road closure most expected to occur if the parameter ranges are following a typical gaussian distribution.
- Worst Case: The case represents a situation where the slope of collapse debris is more horizontal and the volumetric loss is greater. In this scenario, the structure produces more debris and spreads over a wider area, thus the road closure level reaches the maximum level among the three cases.

In each case, the building width and height were taken into account specifically for the building and calculations were performed in accordance with the formula of the relevant model. The obtained theoretical debris spread values were then compared with real data obtained from Google Earth images.

$$Wd = \sqrt{W^2 + \frac{2.kv.W.Y}{tan\ c}} - W \tag{1}$$

In this context, the lateral debris spread (Wd) value for each building was calculated using Equation (1) (Argyroudis et al., 2015). In the equation, the square of the building width (W^2) and the volume loss ratio (kv) multiplied by the building width (W) and the building height (Y) times twice the product divided by the tangent of the collapse angle (tan(c)) are added; the building width (W) is subtracted after the square root of this sum is taken. In addition, the volume loss ratio (kv) and collapse angle (c) parameters used in the model were not kept constant and were determined according to the characteristics of each scenario.

In the Best Case scenario, the minimum road closure was calculated by using a steeper collapse angle and a lower volume loss. The Average Case scenario represented the average values of the probabilistic distribution for volume loss and collapse angle and reflected the expected typical road closure level. In the Worst Case scenario, the maximum road closure level was calculated by using a flatter collapse angle and a higher volume loss.

3. Results and discussion

As can be seen in Fig. 3, the theoretical debris spread widths of the “best”, “average” and “worst” scenarios calculated for each building were compared graphically with the observed (actual) values of these buildings. Following these comparisons, the general distribution percentages showing which scenario is closer to the actual data are presented in Fig. 4. Accordingly, while the debris spread values observed in 75.5% of the 94 buildings examined showed higher compliance with the "worst" scenario, 23.4% gave results closer to the "average" scenario. These findings reveal that our model can be compatible with the conditions specific to the study region and can successfully represent the actual situation in the field.

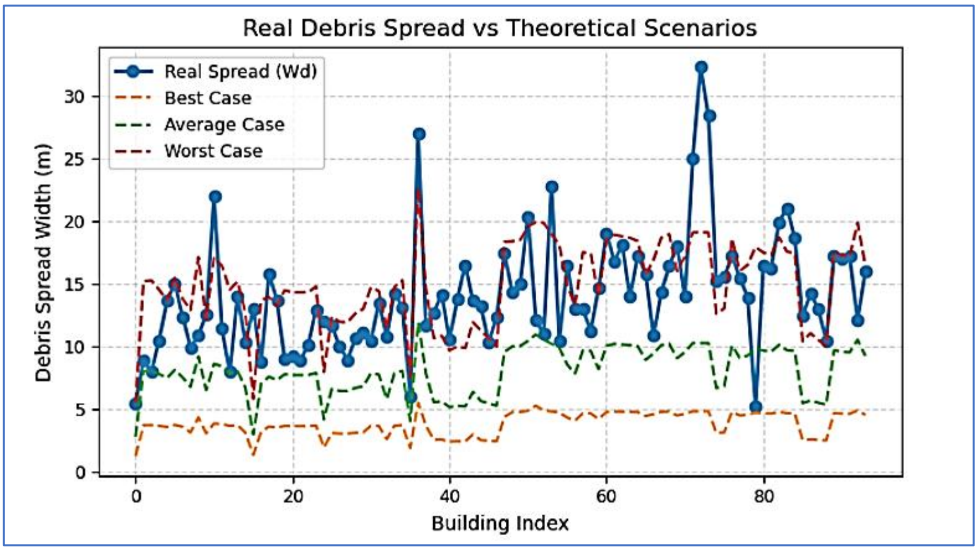

Fig. 3. Comparison of Observed and Model Debris Spread Widths for Each Building

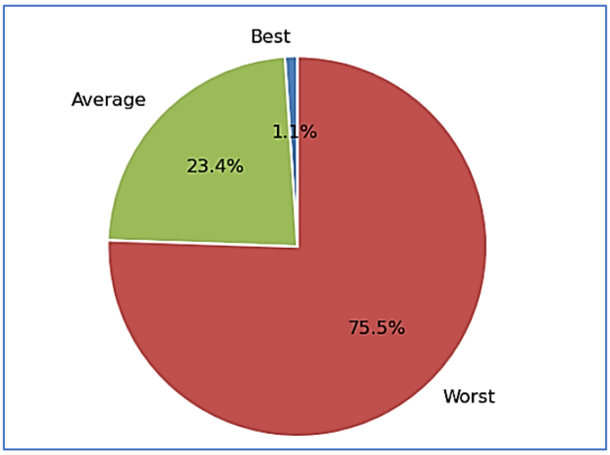

Fig. 4. Percentage of Buildings Closest to Each Collapse Scenario

Approximately 49.3% of the buildings that were compatible with the "worst case", the actual debris spread exceeded the value predicted by the model. The worst value was exceeded by 2.94 meters on average in these buildings. This finding is closely related to the local structural features such as the fact that the examined buildings were mostly built next to each other without space in the form of a continuous facade.

In addition, it has been evaluated that due to the high magnitude and intensity of the earthquake, the debris spread widths may depend not only on structural factors but also on the geotechnical and seismic parameters. Therefore, in order to examine the effects on W_d in more depth, comparative analyses were made according to geotechnical and seismic parameters and the role of these parameters on debris spread was examined.

3.1. Effect of geotechnical parameters on debris dispersion

The binary relationships between debris spreading width (Wd) and geotechnical parameters, namely liquefaction status and soil class, were evaluated separately. Additionally, multiple regression analysis was performed to examine the joint effect of Wd and both parameters. In these analyses, the t-test, one of the basic statistical tests, was used to evaluate whether statistical differences are significant. The t-test is applied to test whether there is a statistically significant difference between the means of two groups. In this evaluation, a criterion called the p-value was used. According to the generally accepted approach, a p-value less than 0.05 indicates that the null hypothesis should be rejected and that the observed difference is very unlikely to have occurred by chance; therefore, the difference is statistically significant. Before applying the t-test, it was checked whether the data used in the study met the necessary conditions to ensure the applicability of this test. These conditions are; the data being in the interval or ratio scale, the data being normally distributed, and the variances between the groups being homogeneous. Since the sample size used in the study was n>30, it was accepted that the distribution of the data was approximately normal within the framework of the Central Limit Theorem (CLT) and thus the assumption of normality was met.

3.1.1. Liquefaction status

The liquefaction status in the soils of the buildings examined in the study was defined as a binary variable as "present" and "absent" and the difference between the average Wd values of these two groups was compared with the independent sample t-test. As a result of the analysis, the t-statistic was found to be -4.8244 and the p-value was found to be 0.000005546. These results show that there is a statistically significant relationship between the liquefaction status and Wd. However, as can be seen in Fig. 5, it was determined that the average Wd values of the buildings located in non-liquefied soils were higher. Contrary to the general expectation, the debris spread was unexpectedly higher in non-liquefied soils. Therefore, this unexpected result may be due to the limited sample size or the fact that the effects of other structural, seismic and geotechnical parameters were not controlled.

3.1.2. Soil class

In the study, since there is only data for ZC and ZD soil classes in the areas where the collapsed buildings are located, the average difference between the soil classes, the Wd averages of these two classes, were also compared with the independent sample t-test. As a result of the analysis, the t-statistic was found to be 4.8244 and the p-value was 0.00001. These results show that there is a statistically significant relationship between the soil class and Wd. However, as can be seen in Fig. 6, it was determined that the average Wd values of the structures in the ZC soil class were higher. This result reflects a situation contrary to expectations; because the ZD class represents a softer soil type and is theoretically expected to cause more debris spread. It is thought that this unexpected difference obtained may be related to the effects of other structural parameters.

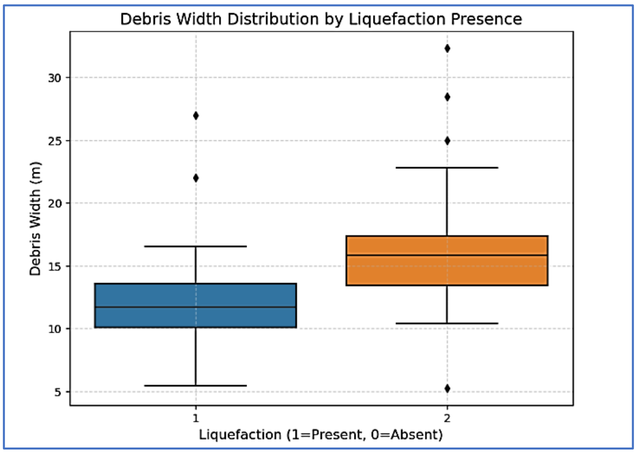

Fig. 5. Effect of Liquefaction Status on Debris Spread (Wd)

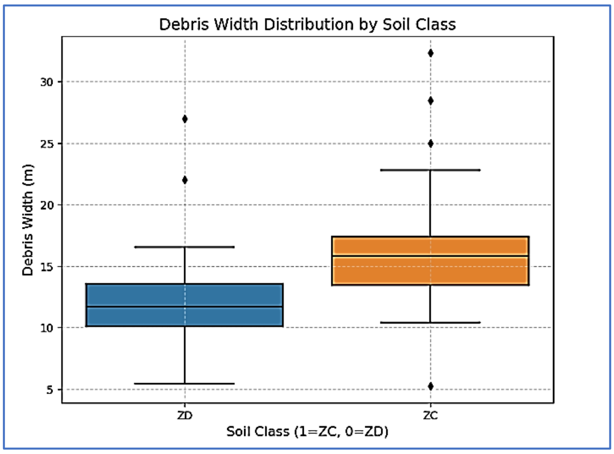

Fig. 6. Effect of Soil Class on Debris Spread (Wd).

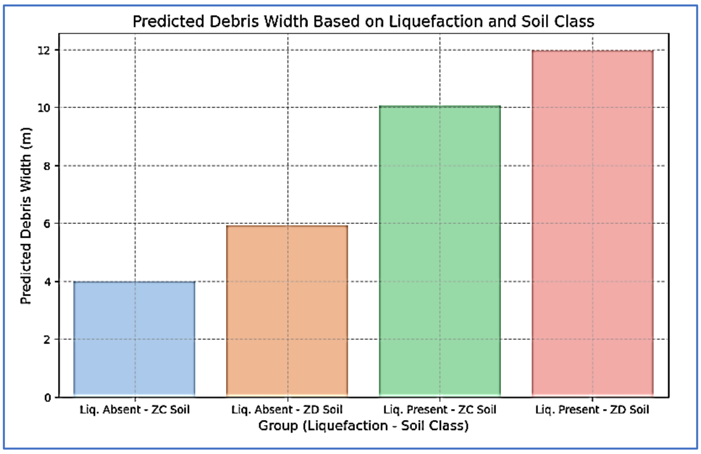

Fig. 7. Combined Debris Spread Effect of Liquefaction Condition and Soil Class on Debris Spread (Wd)

3.1.3. Multiple regression analysis (Liquefaction & Soil Class)

In order to better understand the contradictory findings in the above individual analyses, liquefaction and soil class variables were analysed together with a multiple linear regression model. Multiple regression analysis aims to measure the relationship between the dependent variable and more than one independent variable.

According to the multiple regression results obtained, a significant relationship was found between the presence of liquefaction and the width of the debris spread (Wd) ($p < 0.0001$) and it was determined that liquefaction increased the Wd value by an average of 6.05 meters. Similarly, a significant relationship was found between the soil class variable and Wd ($p = 0.002$) and it was observed that the Wd values of buildings located on ZC class soils were 1.92 meters higher on average compared to ZD class. The overall explanatory power of the model was calculated as $R^2 = 0.202$, indicating that approximately 20% of the change in Wd could be explained by liquefaction and soil class variables.

The results of this analysis allowed a regression equation to be obtained by establishing significant relationships between dependent and independent variables. The graphical comparison of the obtained equation is presented in Fig. 7. According to the graphical results, it was observed that debris spreading was higher under the presence of liquefaction and ZD soil class conditions. This situation reveals that some contradictory findings observed in individual analyses can be explained under the combined effect of the variables.

The multiple regression results generally provide a framework compatible with the literature. In other words, when liquefaction and soil properties are considered together, it is expected that debris will spread over a wider area. However, when individual parameters are examined separately, effects in different directions can be observed, which reveals the importance of evaluating the parameters together.

As a result, the fact that p-values were below 0.05 in all three separate analyses showed that the differences between the variables were statistically significant. However, instead of focusing only on p-values, the context of the analysis, the combined effects of the variables and the explanatory level of the model should also be taken into consideration. Therefore, multiple regression analysis revealed the effects of geotechnical conditions on Wd to be statistically significant but with limited explanatory power, indicating that the contradictory results seen in individual analyses could be explained more by the combined effect of the variables.

3.2. Effect of seismic parameters on debris dispersion

The relationship between debris spread width (Wd) and seismic parameters was investigated using three variables: PGA (Peak Ground Acceleration), PGV (Peak Ground Velocity) and the distance of buildings to the fault. Data characteristics were taken into account in the selection of the statistical test to be used in the evaluation of the relationships. In the preliminary analyses, it was determined that there was no normal distribution and linear relationship between the data. Therefore, the Spearman correlation test was used in the analyses to measure the strength of the sequential (monotonic) relationship between the two variables. In this evaluation, the p-value criterion was used to determine statistical significance. According to the generally accepted approach, if the p-value is less than 0.05, the null hypothesis (H_0) is rejected and it is accepted that the probability of the observed relationship occurring by chance is very low.

3.2.1. Peak ground acceleration (PGA)

PGA refers to the highest acceleration reached by the ground during an earthquake and represents the intensity at which structures are subjected to sudden strain. Since no measurements were made specifically for the buildings in this study, the PGA_{475} value (the regional standard value for the design earthquake expected to occur once in 475 years) was used in all analyses. The relationship between PGA and debris spread width (Wd) was analysed with the Spearman correlation test to measure the monotonic relationship between two continuous variables. As a result of the analysis, Spearman correlation coefficient was found as 0.4150 and p-value was found as 0.0000319.

These results show that there is a moderate positive and statistically significant relationship between PGA and Wd. In other words, as the PGA value increases, debris spread width also increases. This relationship is also visually supported in Fig. 8, where the Debris Width distributions grouped according to the average PGA values are presented.

3.2.2. Peak ground velocity (PGV)

PGV is the highest ground velocity reached during an earthquake and represents the structures subjected to discontinuous deformations. In this study, PGV_{475} value (belonging to the regional design earthquake) was used instead of building-based data. The relationship between PGV and debris spreading width (Wd) was evaluated with the Spearman correlation test. As a result of the analysis, the Spearman correlation coefficient was found to be 0.4245 and the p-value was 0.0000201.

These findings show that there is a moderately positive and statistically significant relationship between PGV and Wd. This relationship is also visually supported in Fig. 9, where Debris Width distributions are presented grouped according to average PGV values.

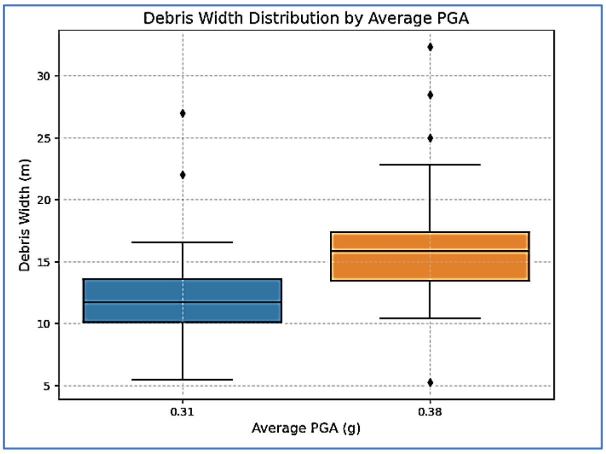

Fig. 8. Relationship Between Average PGA and Debris Spread (Wd)

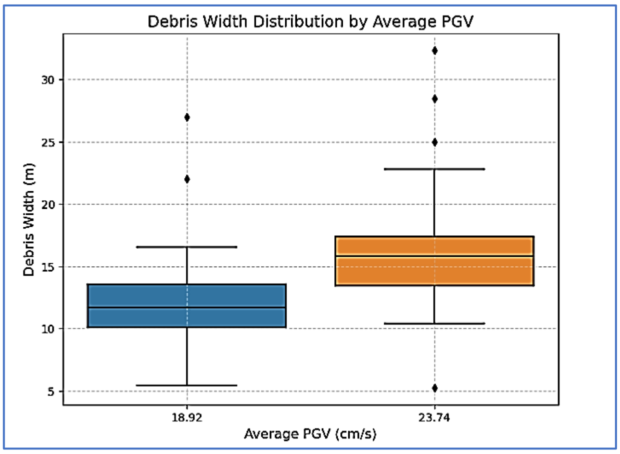

Fig. 9. Relationship Between Average PGV and Debris Spread (Wd)

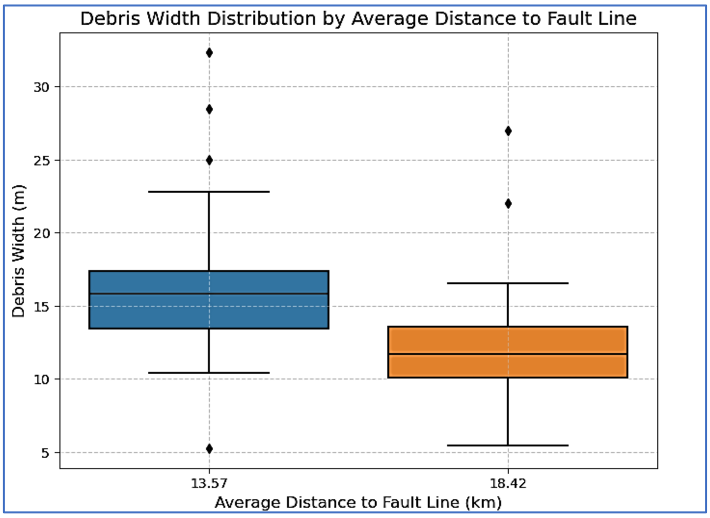

Fig. 10. Effect of average distance to fault line on debris spread (Wd)

3.2.3. Distance to fault line

The relationship between the distance of the structure to the fault line and Wd was also evaluated with the Spearman correlation test. The test result was found to be the correlation coefficient $r = -0.417$ and the p-value 0.00003. These results show that there is a moderately negative and statistically significant relationship between the distance to the fault and Wd. In other words, debris dispersion occurs at a higher level in buildings closer to the fault. This relationship is also visually supported in Fig. 10, where Debris Width distributions are presented grouped according to the average distance to the fault line values.

As a result of the analysis, it was determined that the parameters PGA, PGV and distance to the fault had statistically significant and directional effects on debris dispersion (Wd). As an important limitation, the fact that the PGA and PGV values were not calculated separately for each building but were taken from the standard design data of the region, limited the accuracy of the model, but still provided a sufficient basis for understanding the general trends. Therefore, it was evaluated that seismic effects should definitely be taken into account in the modelling of debris spread from building collapse.

The findings obtained in this study have shown that the debris dispersion (Wd) phenomenon cannot be explained only by structural parameters; more meaningful and realistic results can be achieved when evaluated together with soil properties and seismic effects. A striking finding is that the actual debris dispersion exceeded the theoretical “worst” scenario in approximately 49.3% of the buildings belonging to the worst case scenario. The debris spread width in these buildings was exceeded between a minimum value of 0.07 meters to as much as 13.23 meters.

In the analyses related to geotechnical parameters, when each of the liquefaction and soil class variables were evaluated independently, they yielded statistically significant results that were not consistent with the general expectations. When examined together in the multiple regression model, the effects of these variables were found to be statistically significant but had low explanatory power. These findings reveal that soil behaviour should be evaluated not with single parameters but by considering the soil properties together in interaction. In addition, the fact that both parameters became significant together emphasizes the importance of contextual multivariate approaches in collapse scenarios.

It was observed that seismic parameters have significant effects on debris dispersion (Wd). The statistical analyses revealed that both PGA (Peak Ground Acceleration) and PGV (Peak Ground Velocity) variables are positively correlated with Wd. Especially, the higher explanatory power of PGV suggests that velocity-based ground motion parameters may be more effective in determining the dispersion behaviour compared to acceleration-based parameters. A negative and significant relationship was found between the distance to the fault and Wd. This situation reveals that proximity to the source point is effective on debris dispersion, however, the limited explanatory power of this variable alone shows that debris dispersion is shaped by the combined effect of multiple factors. In this context, evaluating the structure-soil-seismic interaction together will provide a more accurate interpretation of seismic effects.

4. Conclusion

This study aimed to evaluate debris dispersion (Wd) due to building collapses, which is one of the most critical factors causing disruption of transportation infrastructure after an earthquake, from a multidimensional perspective. Analyses based on real field data revealed that debris dispersion should be considered not only through structural features but also together with ground characteristics and seismic effects.

It was observed that probability-based theoretical models were compatible with field observations to a certain extent; however, it was understood that these models should be interpreted flexibly within the framework of local urban morphology, construction patterns and demolition dynamics. Especially in regions with irregular, adjacent and dense building stock, the limitations of theoretical approaches drew attention and the need for recalibration of the model in the local context arose.

It was observed that geotechnical variables can produce meaningful results on debris dispersion when considered in interaction with each other. This finding shows that ground behaviour should be interpreted within the framework of relationships between parameters, not only based on classification in engineering analyses.

When geotechnical variables were evaluated together, they had a statistically significant but limited explanatory effect on debris dispersion. This situation indicates that not only structural damage data but also seismic parameters should be taken into account when assessing post-earthquake transportation risks.

Although structural parameters were evaluated to a limited extent within the scope of the study, the potential effects of these variables on debris distribution are clearly known. Therefore, it is recommended that the subject be examined in more depth with multivariate analyses to be conducted using larger sample groups in the future. In addition, re-conducting the study with larger data sets may provide a more meaningful demonstration of the relationships between the parameters.

In conclusion, this study not only analysed the spatial and physical dimensions of debris dispersion; it also proposed an applicable and holistic method for modelling post-disaster road closure risks, determining intervention priorities and developing urban resilience strategies. The findings provide a multidisciplinary contribution that will guide disaster management and urban planning processes.

Acknowledgements

I would like to thank the organizers of Karadeniz Technical University for providing me with the opportunity to present my work at this conference and all the organizations that contributed. I would like to thank my lecturers from Çankaya University Civil Engineering Department, who did not withhold their support in technical analyses during the project process, and Betül Sultan Şanlı and Salih Emre Savaş from the Software Engineering Department for their contributions.

References

AFAD. (n.d.). *Türkiye Acceleration Database and Analysis System (TADAS)* [Database]. Disaster and Emergency Management Authority of Türkiye. https://tadas.afad.gov.tr/

AFAD. (2019). *Turkey Earthquake Hazard Map (TDTH)* [Web-based application]. Disaster and Emergency Management Authority of Türkiye. https://tdth.afad.gov.tr/TDTH/

Argyroudis, S. A., Selva, J., Gehl, P., & Pitilakis, K. (2015). Systemic seismic risk assessment of road networks considering interactions with the built environment. *Computer-Aided Civil and Infrastructure Engineering*, 30(7), 524–540. https://doi.org/10.1111/mice.12136

Bakırcı, M., & Aydoğdu, M. (2023). Deprem ve Ulaşım: Kahramanmaraş (Pazarcık-Elbistan) depremlerinin ulaşıma ilişkin mekânsal yansımaları. *Türk Coğrafya Dergisi*, (83), 115–129. https://doi.org/10.17211/tcd.1296634

Google. (n.d.). *Google Earth* [Computer software]. https://earth.google.com/web/

Hosseini, Y., & Mohammadi, R. K. (2023). A comprehensive approach in post-earthquake blockage prediction of urban road network and emergency resilience optimization. *Reliability Engineering & System Safety*, 244, 109056. https://doi.org/10.1016/j.ress.2023.109056

McCullough, H. (1994, January 1). *Earthquake damage to transportation systems*. United States Geological Survey. https://pubs.usgs.gov/unnumbered/70114624/report.pdf

United States Geological Survey (USGS). (2023). *M 7.8 - Türkiye-Suriye border region*. U.S. Geological Survey. https://earthquake.usgs.gov/earthquakes/eventpage/us6000jllz/executive

Yu, Y.-C., & Gardoni, P. (2022). Predicting road blockage due to building damage following earthquakes. *Reliability Engineering & System Safety*, 219, 108220. https://doi.org/10.1016/j.ress.2021.108220

4th International Civil Engineering & Architecture Conference
17-19 May 2025, Trabzon, Türkiye

Investigation of Earthquake Performance of Reinforced Concrete Beam Structures Arranged in Different Forms: Flat Beam and Deep Beam Example

Oğuzhan Çelebi*[1], Barış Bayrak[2], Mahmut Kılıç[1], Abdulkadir Cüneyt Aydın[1]

[1] *Atatürk University, Department of Civil Engineering, 25240 Erzurum, Türkiye*
[2] *Kafkas University, Department of Civil Engineering, 36100 Kars, Türkiye*

Abstract. One of the reasons for the damages or collapses observed in reinforced concrete structures in recent earthquakes is due to the different forms of beam arrangement. The aim of this study is to verify the observed damage reasons with numerical analyses. Nonlinear analyses were performed in the time history domain in three different reinforced concrete structures with the same column application plan, normal4 beam arrangement (RC1), flat beam and hollow block slab arrangement (RC2), square column arrangement (RC3) and deep beam arrangement (RC4). In the numerical analyzes, moment-rotation curves and load-displacement curves were taken into account as analysis parameters. At the end of the study, it was determined that collapse prevention (CP) occurred in RC2 and RC4 reinforced concrete models and limited damage levels (IO) occurred in RC1 and RC3 model. It has been suggested that sufficient horizontal stiffness and damping mechanism should be provided in load-bearing elements such as columns and shear walls in order to be able to perform deep beam or flat beam applications.

Keywords: Deep beams; Earthquake behaviour; Flat beams; Nonlinear time history analysis; RC structures

1. Introduction

It is known that structures should have properties such as stiffness, strength, adaptability, stability, damping and ductility in order to be earthquake resistant (ASCE 41-17; FEMA 356). The arrangement of the structural system is of great importance in order to provide the properties stated in the design of structures against earthquakes. Vertical loads coming from slabs and beams under the effect of earthquake should be carried by columns and then safely transferred to the foundation. In the absence of this stable behavior, it is obvious that the earthquake effect will have destructive effects on the structures (Yenidoğan 2023). As a result of the earthquakes experienced in recent years, the design of deep beams has caused heavy damages and even collapses as a result of the formation of strong beams and weak columns (Erdem et al. 2024). In addition, it is known that the arrangement of the structural system in the form of flat beams causes surrounded column irregularity and causes heavy damages. Especially in the February 06, 2023 Maraş earthquakes, it was observed that there were significant heavy damages and collapses in structures with flat beams and hollow slabs and structures with deep beams (Erdem et al. 2024;Yenidoğan 2023). Turkey Building Earthquake Code 2018 and other relevant regulations limit the use of deep beams and hollow slabs (TBEC 2018, FEMA 356). In reinforced concrete building systems with high ductility level, the principle of strong columns and weak beams is adopted. Therefore, the deep beam arrangement is also contrary to the principle of strong columns and weak beams.

Deep beams are defined as beams in which the ratio of shear span to depth is less than 2 (ACI 318-19 2019; CEB-FIP Model Code 1990). In the literature, many experimental and numerical analysis studies have been conducted on the performance evaluation of deep beams (Husem et al. 2022; Saleh et al. 2023). In these studies, shear span/depth ratios are usually given as parameters (Kim et al. 2017). In these studies, load-displacement curves and stress-strain diagrams of the beams were obtained and interpreted (Husem et al. 2022, Chen 2018, Demir 2019). In addition, shear capacities of deep beams were also determined by numerical and experimental studies (Ismail et al. 2024). In order to prevent brittle fracture of deep beams, reinforcements were made with FRP (Fiber Reinforcement Polymer), CFRP (Carbon Fiber Reinforcement Polymer) and basalt fibers (Ahmad et al. 2021; Song et al. 2023). Deep beams were also tested in an experimental environment by changing the longitudinal and transverse donate ratios under different bearing conditions (Hamoda et al. 2024). The experimental studies

* Corresponding author, E-mail: celebioguzhan@atauni.edu.tr

https://doi.org/10.31462/icearc2025_ce_eqe_501

were verified by finite element analysis (Hamoda and Hossain 2019). Similarly, the load-displacement curve of flat beams with weak axis in axial loading has been studied in terms of shear capacity and rotational capacities (Rayan et al. 2021;Feng et al. 2024). An analytical model was developed for the effective width value required to increase the bending capacity of flat beams (Jiang et al. 2023). Garg et al. (2021) conducted a field study on retrofitting methods to prevent collapse in RC beamless slab buildings (Garg et al. 2021). At the end of the study, it was confirmed in static and dynamic analyses that column arrangement and reinforced concrete shear wall placement should be required in such structures.

The current study is aimed at evaluating the effects of deep beam and flat beam arrangement on the seismic behavior of structures separately. The effects of column arrangement in flat beam and hollow slab applications are also investigated. Based on the literature, instead of element-based experimental and numerical studies, the effectiveness of flat beam and deep beam applications in direct buildings is investigated in time domain.

2. Numerical study

In this study, it is evaluated how the seismic behavior of the reinforced concrete structure changes in flat beam and deep beam alignment and some measures to be taken in this case. In this context, nonlinear time domain analysis was applied to 4 different reinforced concrete structural systems. The plan dimensions and storey heights in both directions of the four different reinforced concrete building systems are considered to be the same. Material class C25/30 concrete and B420C reinforcement class were used in the building systems in accordance with the standard (TS498). RC1 model is considered as a beam slab slab type and slab thickness is 15 cm (Fig. 1a). The corner columns were designed as 30x50 cm, the facade columns on the balcony section as 30x90 cm, the other two facade columns as 70x30 cm and the central column as 40x60 cm. Longitudinal and transverse freezes corresponding to these dimensions are designed according to the standard (TS 500; TBEC 2018). Beams were selected in 30x70 cm size. In the RC2 model with the same column and corresponding longitudinal reinforcements, the beams were arranged in a flat form with a size of 70x30 cm (Fig. 1b). In the building system where the hollow slab type is used, the rib beams are 10x30 cm in size and the slab thickness is 7 cm. In RC3 model, only the columns were selected with square cross-section by keeping the flat beam and hollow slab form of RC2 model (Fig. 1c). In RC3 model, the corner columns are designed as 40x40 cm, the facade columns in the middle of the axis are designed as 50x50 cm and the columns in the balcony section are designed as 60x60 cm. In the RC4 model, unlike the RC1 model, a deep beam was applied. The deep beam is arranged in 30x120 cm size (Fig. 1d). The moment of inertia of the deep beam in one direction is greater than the moment of inertia of the column. The finite element model of the reinforced concrete structural systems designed according to TBEC 2018 was created as shown in Fig. 2. The slabs were subjected to 0.212 t/m^2 pavement load and 0.2 t/m^2 live load (TS498). In the walls, 0.625 t/m load was applied.

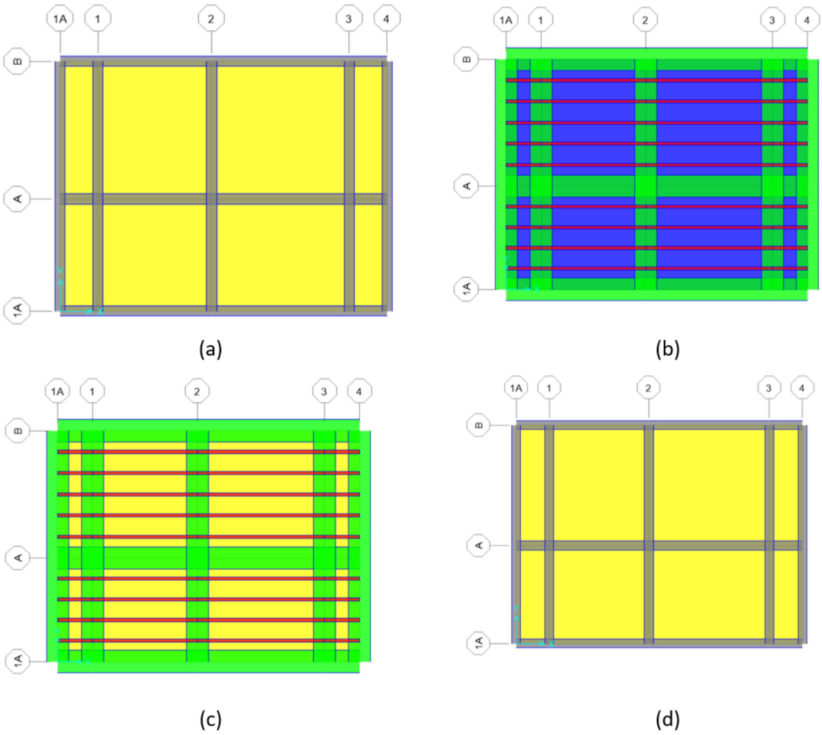

Fig. 1. Slab plans; a) RC1, b) RC2, c) RC3, d) RC4

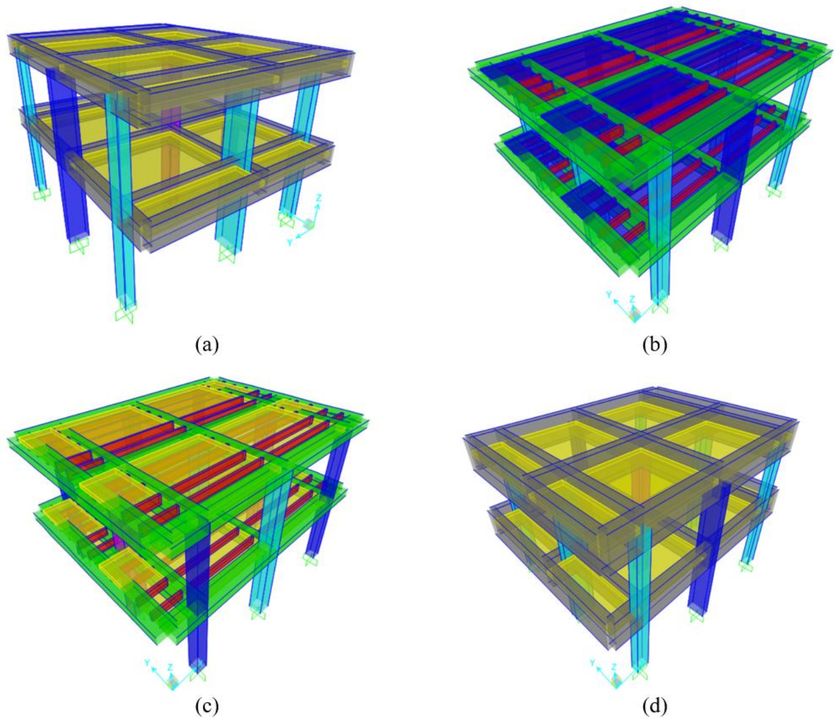

Figure 2. Finite element models; a) RC1, b) RC2, c) RC3, d) RC4

Nonlinear analyses in time domain were applied to reinforced concrete structural systems. In nonlinear analyses, damping ratios of 0.05 are assumed for all modes in reinforced concrete structural systems. Numerical analysis is based on Taylor iteration model. Nonlinear material models are defined in the related structures. For columns, plastic joints (P-M2-M3) including axial compressive force and compound bending are defined at the column end zones. For beams, simple bending (M3) plastic joints are defined in the end zones. The effective stiffnesses of the structural elements are defined in TBEC 2018 (TBEC 2018). For the time domain analyses, the acceleration data of the Elbistan earthquake that occurred on February 6, 2023, centered in Maras, whose characteristics are given in Table 1, were used. The acceleration data of the Elbistan earthquake were scaled as structure-specific within the scope of TBEC 2018 and used in the analysis. Analyses were performed using the horizontal and vertical acceleration components of the Elbistan earthquake. Since it is known that flat beam and deep beam building systems have damages caused by the vertical component of Maraş earthquakes, evaluations were made under the influence of vertical and horizontal acceleration components.

Table 1. Earthquake charecteristics (AFAD 2024)

Earthquake	Date	Latitude	Longitude	Station	Depth (km)	Magnitude (Mw)	PGA (g)-EW*	PGA (g)-UD*
Elbistan (el)	06.02.2023	38.089	37.239	Göksun	7	7,6	0,648	0,501

EW: East-west (horizontal) component of the earthquake*
UD: Vertical component of the earthquake*

Fig. 3 shows the scaled acceleration spectra of the Elbistan earthquake according to TBEC 2018 and the horizontal elastic acceleration spectrum of the structure plotted together for horizontal and vertical components. Fig. 4 shows the scaled and unscaled acceleration-time plots. Spectrally, approximately 1.4 g horizontal acceleration and 0.9 g vertical acceleration were used in the analysis. In addition, 0.5 g horizontal acceleration and 0.45 g vertical acceleration were taken into account in the analysis. The peak ground acceleration value of the structure in question was assumed to be 0.5g according to Turkey Earthquake Hazard Maps (AFAD 2024).

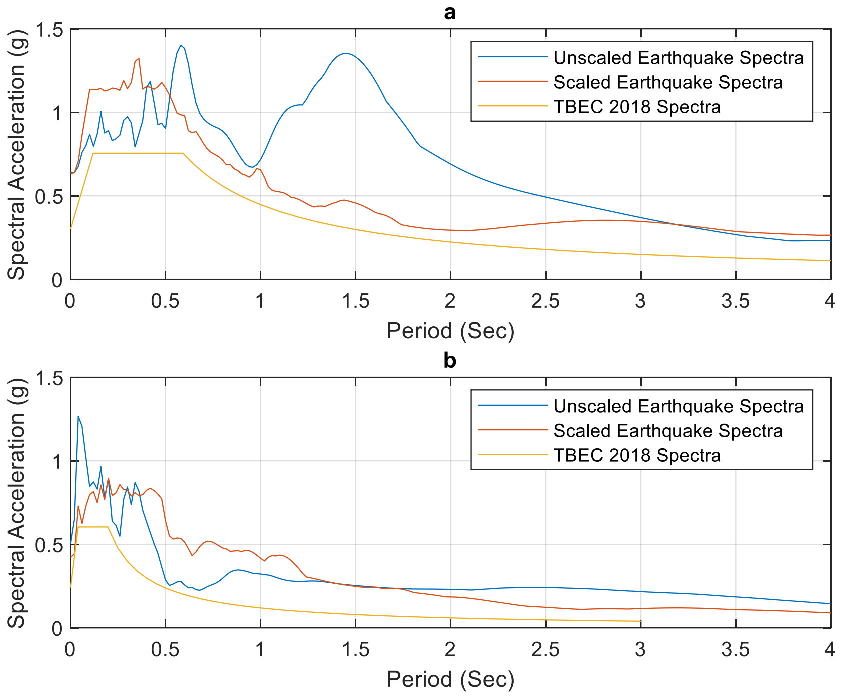

Fig. 3. Earthquake spepectrum acceleration; a) yatay ivme,b) düşey ivme

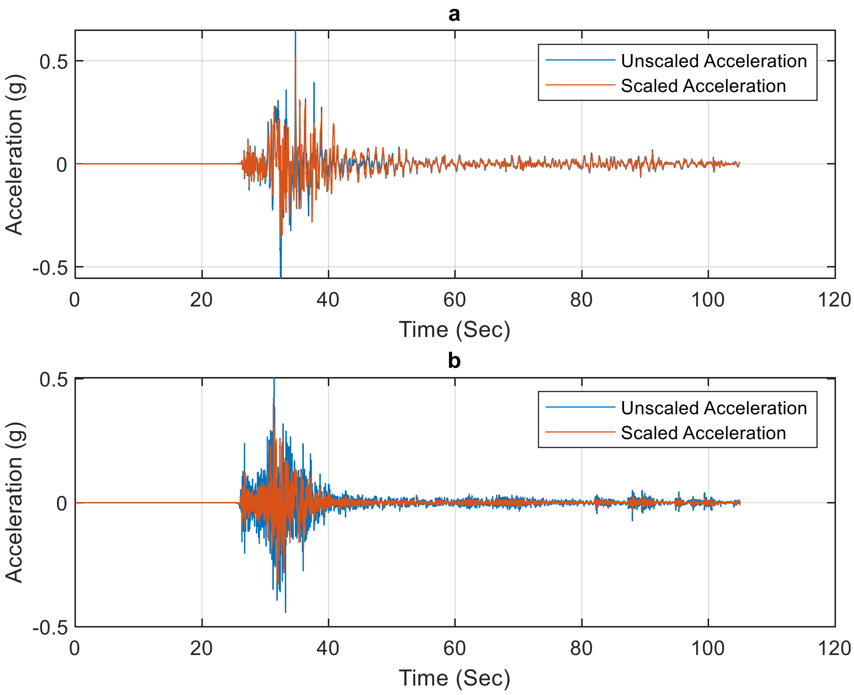

Fig. 4. Acceleration-time graphs; a) yatay ivme,b) düşey ivme

Reinforced concrete structural systems were analyzed in time domain under the influence of Elbistan earthquake acceleration values. The reference points and columns shown in Fig. 5 were taken into consideration in the analysis results. Horizontal displacements, vertical displacements and storey acceleration values were taken at the reference points. Moment-rotation capacities and axial load capacities were evaluated in two columns, one corner and one center. In addition, load-displacement curves were obtained and compared in all building models.

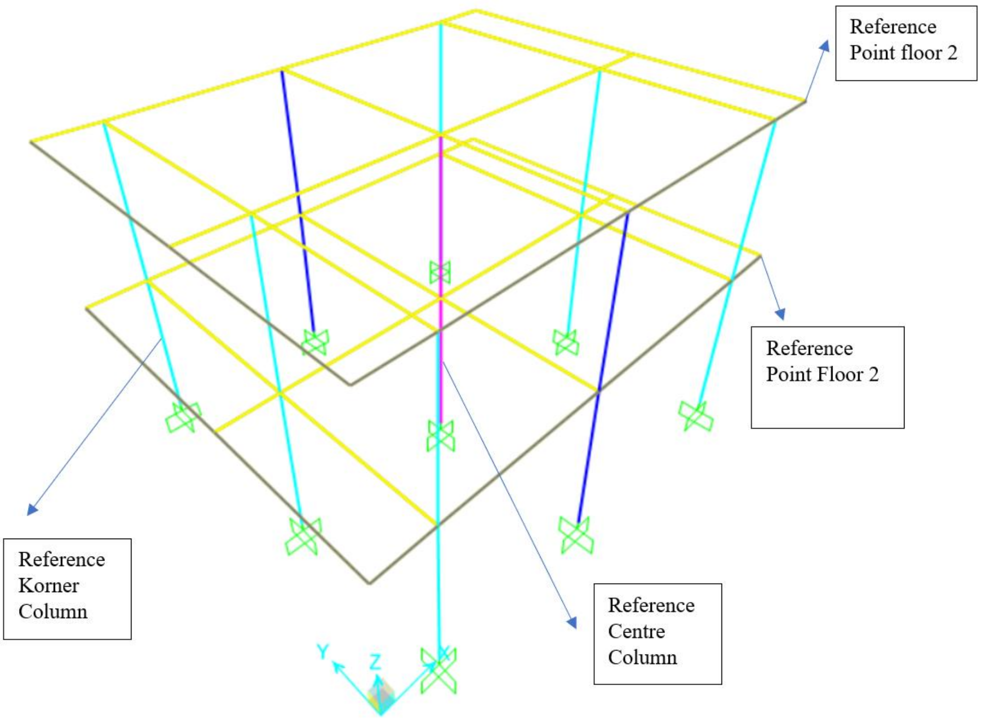

Fig. 5. Points and members taken as reference in the analysis

3. Numerical analysis results

Firstly, the period values (T) and mass participation rates (U) of the structural models were evaluated in the analysis results (Table 2). It was found that the X-direction mass participation ratios (UX) and Y-direction mass participation ratios (UY) were approximately the same in all models. RC2 and RC4 models were found to have higher mass participation ratios (UZ) in torsional mode. It was determined that the dominant mode in all structures was 1st mode. Especially in RC2 model, 1st mode, 2nd mode and 3rd mode period values were found to be close to each other. It is understood from the period values that RC1 model behaves more rigid structurally than the other models. The largest period value was observed in RC2 model.

Table 2. Period values and mass partification ratio

Buildings	T1 (sec)	T2 (sec)	T3 (sec)	UX (%)	UY (%)	UZ (%)
RC1	0.326	0.298	0.251	99.99	100	65.36
RC2	0.391	0.367	0.331	99.99	99.99	72.76
RC3	0.314	0.303	0.294	99.99	99.99	65.61
RC4	0.321	0.288	0.234	99.99	100	66.74

The values of base shear forces, peak displacement and vertical displacement in time domain are obtained and given in Table 3. It was found that the base shear force in RC4 model was 8.47%, 30.39% and 12.40% higher than the base shear forces in RC1, RC2 and RC3 models, respectively. It was determined that the deep beam arrangement increased the base shear force value most effectively. Hollow slab and flat beam arrangement effectively decreased the base shear force. Flat beam and hollow slab arrangement increased the peak displacement, earthquake induced vertical displacement and displacement due to vertical loads by 44.48%, 16.33% and 50% respectively. However, square column arrangement decreased the peak displacement, earthquake induced vertical displacement and displacement due to vertical loads by 15.38%, 18.06% and 30% respectively. The lowest values were observed in RC1 model for peak displacement, RC3 model for earthquake induced vertical displacement and RC4 model for vertical displacement due to vertical loads.

Table 3. Base shear force, roof displacement and vertical displacement values

Buildings	Base Shear Force (kN)	Roof Displacement (m)	Displacement (Z axis) (EQ)(m)	Displacement (Z Axis) (NLoad) (m)
RC1	2096	0.0166	0.000338	0.0005
RC2	1594	0.0299	0.000404	0.001
RC3	2006	0.0253	0.000331	0.0007
RC4	2290	0.0185	0.000349	0.0004

In the analysis results, the acceleration values at the top of the reinforced concrete building models are given in Fig. 6 and the acceleration values at the first floors are given in Fig. 7.

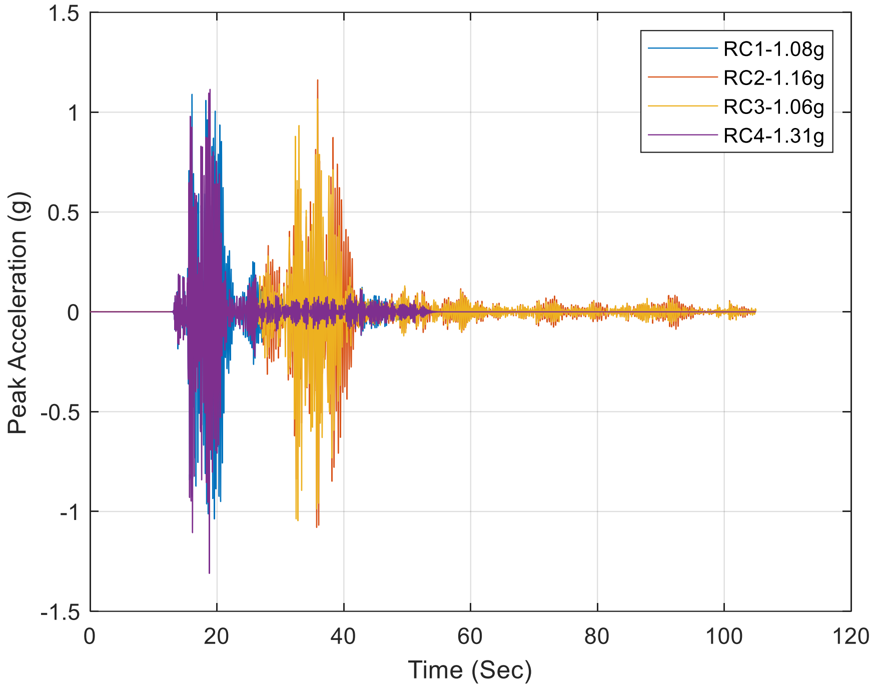

Fig. 6. Peak acceleration values

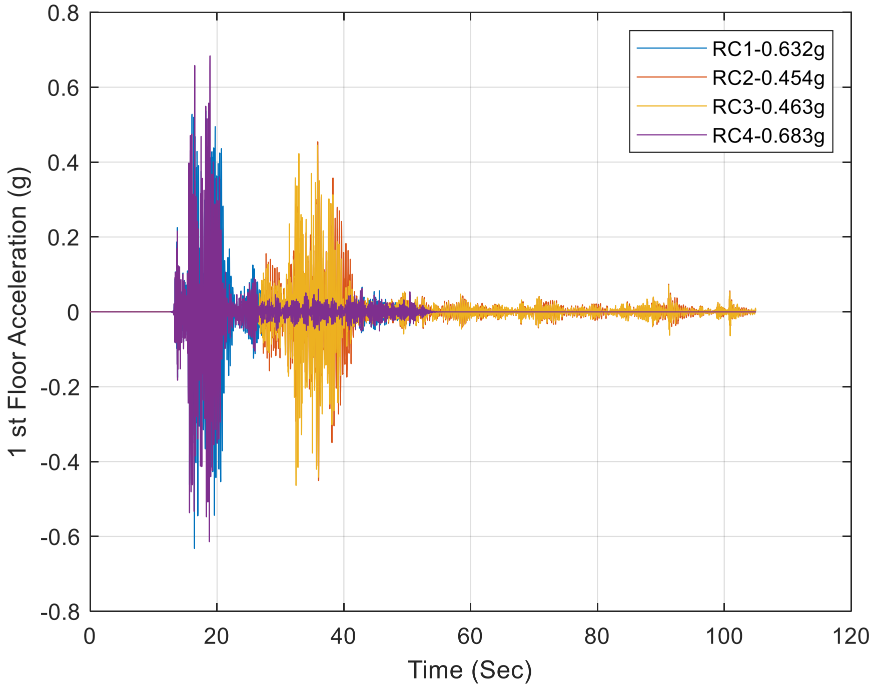

Fig. 7. 1st floor peak acceleration values

The peak and first floor earthquake acceleration values are generally less in the model with square column arrangement (RC3). The peak acceleration values in RC3 model were 1.85%, 8.62% and 19.08% less than the peak acceleration values in RC1, RC2 and RC4 models, respectively. At the first floor, the acceleration values of RC2 model were found to be 1.94% less than RC3 model. It was concluded that the acceleration values of RC3 model at the first floor were 26.74% and 32.21% lower than RC1 and RC4 models, respectively.

Normal stress distributions in the X-Z plane as a result of vertical earthquake loading in time domain are given in Fig. 8. It is observed that RC2 and RC4 models have higher stresses especially at the column beam joints. The square column arrangement was not as effective in reducing the normal stresses as the beamed slab slab. It was determined that the stress values in RC2 model were approximately 47.72% higher.

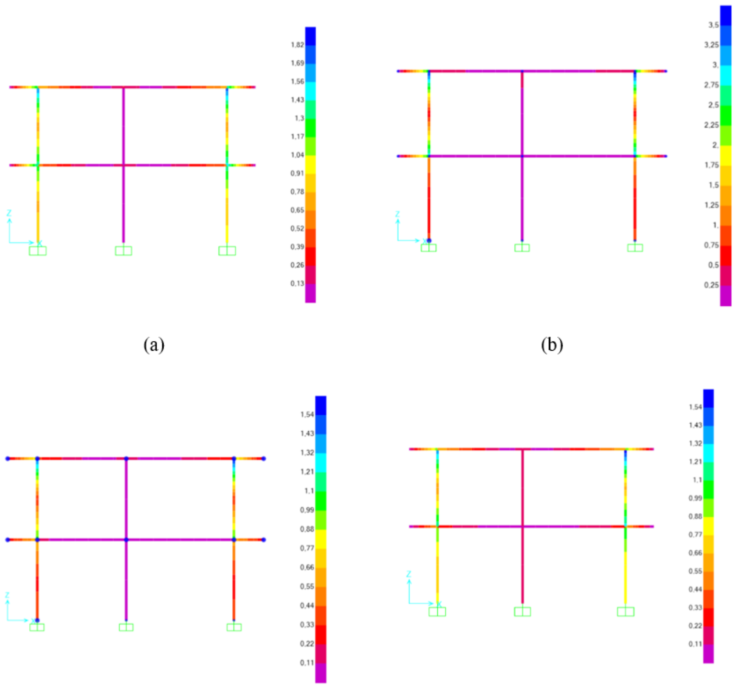

(a) (b)

(c) (d)

Fig. 8. Distributipn of normal stresses

The load-displacement curves obtained at performance acceleration and displacement values in time domain are given in Fig. 9. It is concluded that RC1 model behaves more ductile and RC3 model shows high elasticity. RC4 model was found to have reached the advanced damage level due to the permanent displacements. It was determined that brittle fractures occurred in RC2 model. In RC1 model, it was observed that lower loads occurred and high plastic displacements occurred. It was calculated that 0.0481 m plastic displacement capacity was reached for 488.95 kN shear force in RC1 model, 0.0116 m plastic displacement capacity for 1544.15 kN shear force in RC2 model, 0.0116 m plastic displacement capacity for 1652.47 kN shear force in RC3 model, and 0.0712 m plastic displacement capacity for 500.21 kN shear force in RC4 model. It is determined that higher permanent displacement demands occur for lower load t-values in RC1 and RC4 models. However, RC4 model reached the advanced damage level by making higher permanent deformation. RC2 model could not exhibit sufficiently ductile behavior according to force-displacement values. RC3 model, on the other hand, showed ductile behavior by showing resistance against higher loads and making sufficient permanent displacement.

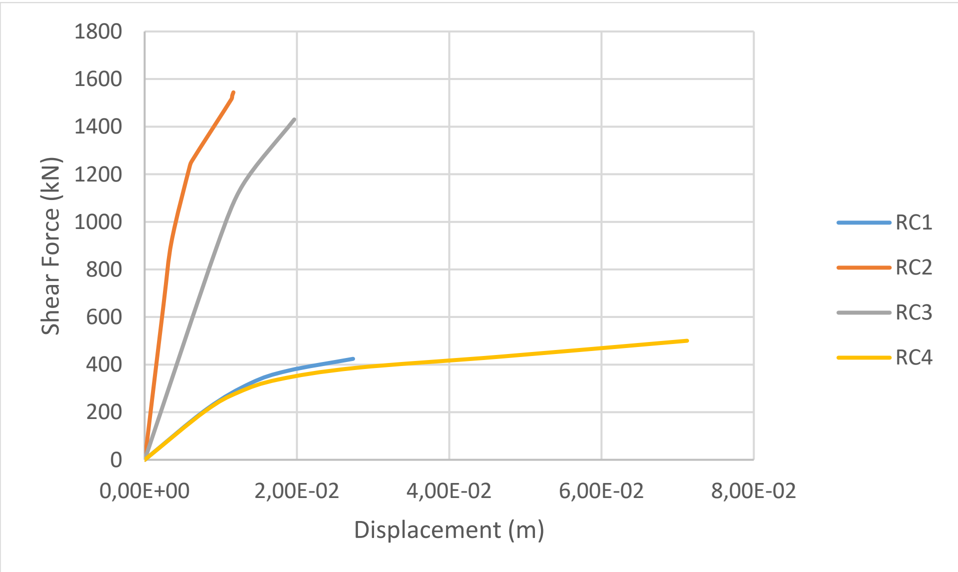

Fig. 9. Load-displacement curves

Fig. 10 shows the moment rotation capacities of the corner columns. It is determined that the moment capacity of RC3 model is 4.89%, 55.29% and 14.47% higher than the moment capacity of RC1, RC2 and RC4 models respectively. Rotation values of RC4 model were calculated to be 81.20%, 91.25% and 95.85% higher than RC1, RC2 and RC3 models, respectively. The RC4 model was at the significant damage level (LS) due to its high rotation value, RC1 model was at the immediate use level (IO) due to its high moment capacity and corresponding rotation, RC2 model was at the collapse prevention damage level (CP) and RC3 model was at the immediate use level (IO). Figure 11 shows the damage types at the joints of the corner column.

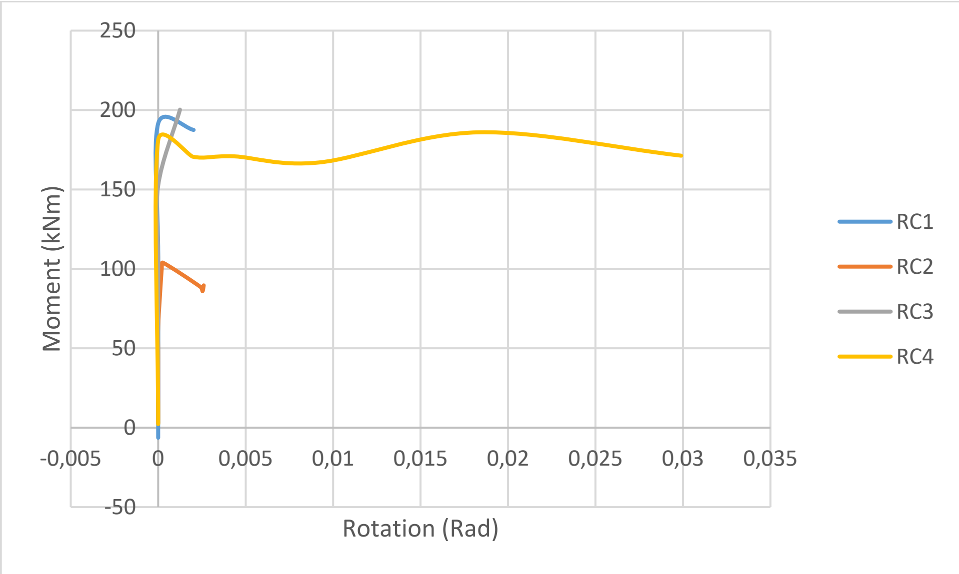

Fig. 10. Moment-rotation values in the corner column

The moment-rotation capacities of the center column taken as reference in the analysis results are given in Fig. 12. It is determined that the moment capacity of RC4 model is 87.42%, 88.89% and 21.88% higher than the moment capacity of RC1, RC2 and RC3 models, respectively. The rotation in RC4 model was calculated to be 79.94% more than RC2 model, while RC1 and RC3 models did not have any rotation. RC4 model entered the collapse zone due to its high rotation value. RC1 and RC3 models remained in immediate use. RC2 model was determined to have entered the collapse zone. Fig. 13 shows the damage types at the joints of the center column.

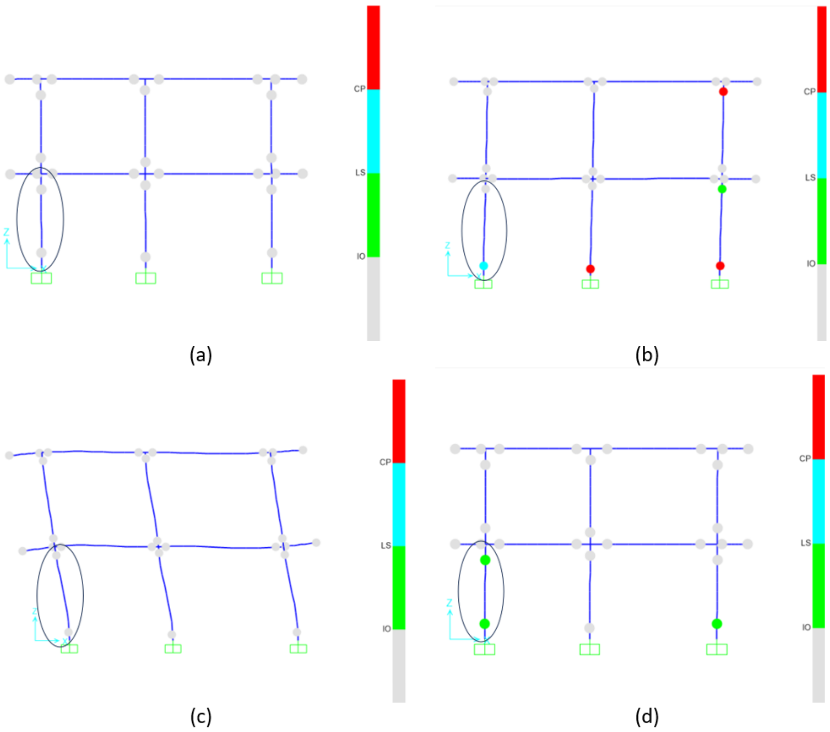

Fig. 11. Hinges in the corner column; a) RC1, b) RC2, c) RC3, d) RC4

As can be shown in Fig. 11, the columns and beams of RC1 and RC3 models remained at immediate use level, some columns of RC2 model collapsed, some columns remained at significant damage level and some columns remained at immediate use level. In the RC4 model, it was observed that some columns were significantly damaged and some columns remained at the immediate use level. It was determined that the beams of RC2 and RC4 models remained at the immediate use level.

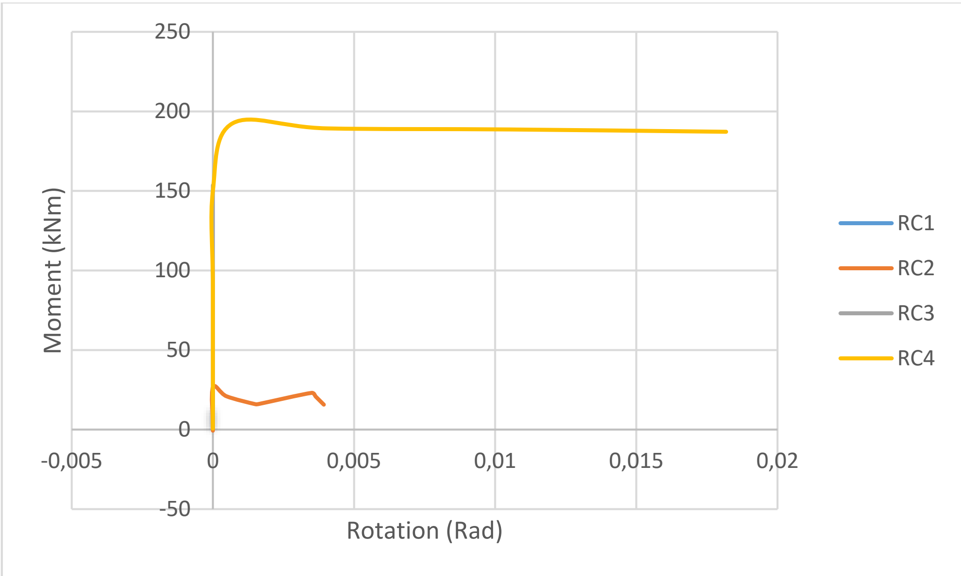

Fig. 12. Moment-rotation values in the center column; a) RC1, b) RC2, c) RC3, d) RC4

As shown in Fig. 13, it is observed that the columns and beams of RC3 model remained at the immediate use level, while some columns of RC1 model reached the significant damage level. Some columns of RC2 model collapsed, some columns remained at significant damage level and some columns remained at immediate use level. In the RC4 model, it was observed that some columns of RC2 and RC4 model were collapsed and some columns remained at the level of significant damage and some columns remained at the level of immediate use. It was determined that the beams of RC2 and RC4 models remained at the immediate use level.

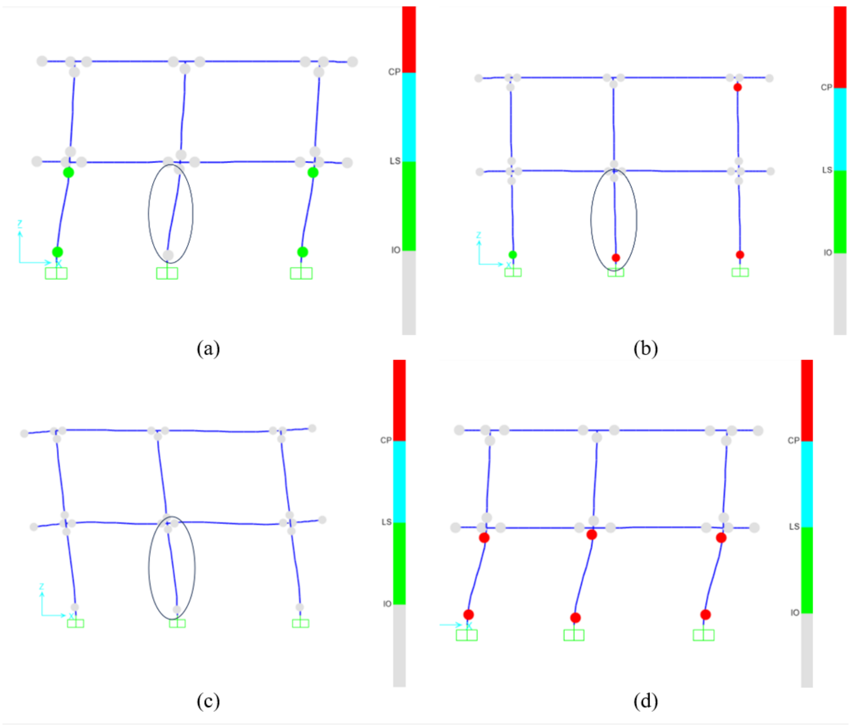

Fig. 13. Hinges in the center column; a) RC1, b) RC2, c) RC3, d) RC4

4. Conclusions

In this paper, the effects of flat beam and deep beam arrangements on the performance of reinforced concrete structural systems are investigated. In four different reinforced concrete structural systems with approximately the same cost, it is emphasized that the brittle fracture problem caused by the flat beam can be eliminated with the square column arrangement and at the same time, instead of deep beams, main beams with a b/d ratio less than 3, which do not create too much weight in the structure, should be used. The results obtained as a result of the analyses applied to reinforced concrete building models in the time domain are briefly summarized below.

- It is concluded that flat and deep beam arrangement increases the dominant period value of the structure and also the mass participation ratio in torsion mode. The square column arrangement decreased the mass participation ratio and the values of the period in torsion mode.
- It was determined that the flat and deep beam arrangement increased the horizontal and vertical displacements due to earthquake and vertical load combinations by approximately 45% and 40%, respectively. It is concluded that the square column arrangement effectively reduces these values in horizontal and vertical.
- Peak acceleration values were found to be the lowest in RC3 model. It was determined that the square column arrangement reduced the peak acceleration values of the system with hollow slab and flat beams by approximately 9%.
- It was observed that the normal stresses due to vertical earthquakes reached the highest values (3.54 MPa) in RC2 model. It was determined that the stress values decreased by approximately 50% with the square column arrangement.
- The results of the nonlinear analysis showed that the use of the deep beam increases the degree of damage due to excessive permanent deformations and the flat beam arrangement increases the risk of brittle fracture.
- It is concluded that RC1 and RC3 models exhibit ductile behavior and have the most ideal moment-rotation capacity.
- RC1 and RC3 were generally found to remain at the immediate use level (IO) and RC2 and RC4 at the collapse prevention performance level (CP).

At the end of this study, it was concluded that the arrangement of the load-bearing columns is very important in order to prevent further damage to the flat beam and hollow slab models under earthquake effects. It is concluded that the column widths and section heights should be chosen close to each other and no weak axis should be created. It is also confirmed that when deep beams should be used, strengthening methods that can reduce permanent deformations should be applied.

References

ACI Committee 318. (2019). *Building code requirements for structural concrete and commentary (ACI 318–19)*. American Concrete Institute.

AFAD. (2024). *Emergency and Disaster Management Presidency*. Ministry of Internal Affairs, Ankara, Türkiye.

Ahmad, S., Elahi, A., Tufail, R. F., Zahid, M., & Tariq, S. B. (2024). Experimental investigation and strength model of RC deep beams externally bonded by CFRP. *Advances in Structural Engineering, 24*(16), 3645–3657. https://doi.org/10.1177/13694332211010583

ASCE. (2017). *Seismic evaluation and retrofit of existing buildings (ASCE/SEI 41-17)*. American Society of Civil Engineers.

CEB-FIP. (1990). *Model code for concrete structures 1990*. fib, Berlin, Germany.

Chen, C. C., Lin, K. T., & Chen, Y. J. (2018). Behavior and shear strength of steel shape reinforced concrete deep beams. *Engineering Structures, 175*, Article 168–179. https://doi.org/10.1016/j.engstruct.2018.08.045

Demir, A., Caglar, N., & Ozturk, H. (2019). Parameters affecting diagonal cracking behavior of reinforced concrete deep beams. *Engineering Structures, 184*, Article 342–352. https://doi.org/10.1016/j.engstruct.2019.01.090

Erdem, B., Çelebi, O., Kılıç, M., Özer, Ç., & Aydın, A. C. (2024). The strong ground motion and structural response analysis of 06 February 2023 Elbistan and Pazarcık earthquakes (Mw 7.7 and 7.6): A case study for Malatya-Türkiye, Eastern Anatolia. *Bulletin of Earthquake Engineering*. https://doi.org/10.21203/rs.3.rs-5079446/v1

FEMA. (2000). *FEMA 356: Prestandard and commentary for the seismic rehabilitation of buildings*. Federal Emergency Management Agency.

Feng, X., Liu, D., Long, X., Duan, K., Zuo, J., Liu, W., & Dong, H. (2024). Flexural capacity of the normal sections of concrete beams strengthened with corrugated steel plates. *Buildings, 14*, Article 1398. https://doi.org/10.3390/buildings14051398

Garg, S., Agrawal, V., & Nagar, N. (2021). Case study on strengthening methods for progressive collapse resistance of RC flat slab buildings. *Structures, 29*, 1709–1722. https://doi.org/10.1016/j.istruc.2020.12.049

Hamoda, A., & Hossain, K. (2019). Numerical assessment of slab–column connection additionally reinforced with steel and CFRP bars. *Arabian Journal for Science and Engineering, 44*, 8181–8204.

Hamoda, A., Yehia, S. A., Ahmed, M., Abadel, A. A., Baktheer, A., & Shanin, R. I. (2024). Experimental and numerical analysis of deep beams with openings strengthened with galvanized corrugated and flat steel sheets. *Case Studies in Construction Materials, 21*, e03522. https://doi.org/10.1016/j.cscm.2024.e03522

Husem, M., Yılmaz, M., & Coşgun, S. I. (2022). Experimental and numerical investigations on reinforcement arrangements in RC deep beams. *Advances in Concrete Construction, 13*(3), 243–254. https://doi.org/10.12989/acc.2022.13.3.243

Ismail, K. S., Mawlood, B. O., Mohammad, A. H., & Guadagnini, M. (2024). Numerical investigation of the shear capacity of reinforced concrete continuous deep beams. *Structural Concrete*, 1–18. https://doi.org/10.1002/suco.202401131

Jiang, Q., Yu, F., Feng, Y., Chong, X., Huang, J., & Zhang, K. (2023). Investigation of flexural performance and effective width of composite wide flat beams. *Engineering Structures, 281*, 115750. https://doi.org/10.1016/j.engstruct.2023.115750

Kim, H. G., Jeong, C. Y., Kim, M. J., Lee, Y. J., Park, J. H., & Kim, K. H. (2017). Prediction of shear strength of reinforced concrete beams without shear reinforcement considering bond action of longitudinal reinforcements. *Advances in Structural Engineering, 21*(1), 30–45. https://doi.org/10.1177/1369433217706778

Rayan, A. A., Khalil, N., Youssef, A., & Eldeib, M. (2021). Flexural behavior of encased beam flat or perforated steel cold formed sections. *International Journal of Steel Structures, 21*(4), 1465–1477. https://doi.org/10.1007/s13296-021-00515-9

Saleh, M., Alhamaydeh, M., & Zakaria, M. (2023). Finite element analysis of reinforced concrete deep beams with square web openings using damage plasticity model. *Engineering Structures, 278*, 115496. https://doi.org/10.1016/j.engstruct.2022.115496

Song, B., Jin, L., Zhang, J., & Du, X. (2023). Size effect tests on shear strength of Basalt FRP-RC deep beams with different shear-span ratios. *Engineering Structures, 294*, 116740. https://doi.org/10.1016/j.engstruct.2023.116740

TBEC. (2018). *Turkish Building Earthquake Code (TBEC 2018)*. Ministry of Environment, Urbanization and Climate Change, Ankara, Türkiye.

Türk Standardları Enstitüsü. (2021). *TS 498: Calculation values of loads to be taken in dimensioning of structural elements*. TSE Standard Preparation Center, Ankara.

Türk Standardları Enstitüsü. (2000). *TS 500: Requirements for design and construction of reinforced concrete structures*. TSE Standard Preparation Center, Ankara.

Yenidoğan, C. (2024). February 6, 2023 earthquakes and preliminary assessment of building damage based on field surveys. *Turkish Journal of Civil Engineering*. https://doi.org/10.18400/tjce.1335742

4th International Civil Engineering & Architecture Conference
17-19 May 2025, Trabzon, Türkiye

Ground motion simulation of the 1859 Erzurum Earthquake

Dursun Burak Özdoğan*[1], Dilek Okuyucu[1], Ayşegül Askan[2]

[1] ErzurumTechnical University, Department of Civil Engineering, 25100 Erzurum, Türkiye
[2] Middle East Technical University, Department of Civil Engineering, 06800 Ankara, Türkiye

Abstract: The earthquake that occurred on June 2, 1859, was recorded as one of the most destructive earthquakes in the history of Erzurum. The magnitude of this earthquake of the pre-instrumental period is evaluated approximately as 6.1, and the intensity value on the MMI scale is IX. Historical documents and publications contain evidence on the fact that the earthquake of June 2, 1859 caused great destruction and loss of life in the residential areas in the center of Erzurum. Understanding the seismicity of the region and reflecting the findings on structural performance is possible with ground acceleration values and spectral acceleration data calculated accordingly. In this context, the importance and necessity of ground motion simulations for pre-instrumental earthquakes become evident. Based on this issue, the presented study aims to produce a synthetic earthquake record of the June 2, 1859 Erzurum earthquake using the stochastic modeling technique. For the acceleration record of the June 2, 1859 Erzurum earthquake simulated at a point of interest in terms of historic stuctures using the stochastic finite fault method, PGA is calculated as 0.19g and PGV as 8.8 cm/sec.

Keywords: Ground motion simulation; Stochastic finite-fault model; Erzurum; 1859 Earthquake.

1. Introduction

Earthquakes affect different fields, from civil engineering to earth sciences and from the economy to health. In the design phase in terms of civil engineering, the main objective is to ensure that the building can survive against possible earthquake loads that the building may be exposed to. The possible earthquake loads must be reliably estimated. Ground motion prediction equations help for this purpose. However, to evaluate the safety and performance of structures, not only the maximum ground motion intensity but also the frequency content of the seismic excitation is of great importance. Therefore, it may be necessary to obtain the full ground motion time series of a past earthquake or a scenario earthquake predicted in the future. In regions where ground motion data are inadequate, recordings from areas with similar seismotectonic characteristics are often used in dynamic analyses, and their averages are calculated. However, in cases where there are no active seismic stations or where historical earthquake records are limited, ground motion simulations are a reliable alternative. Especially in events where instrumental measurement data are not available, such as historical earthquakes, these simulations provide valuable information for earthquake engineering. Ground motion simulation approaches are divided into three main groups: deterministic, stochastic, and hybrid approaches. Deterministic methods are usually based on numerical solutions of the wave equations, and although they offer high accuracy, they are only applicable in certain frequency ranges due to computational costs and physical constraints related to wavelength (e.g.: Frankel 1993,; Frankel et al., 1994; Olsen et al., 1995; Komatitsch et al., 2004). In contrast, stochastic methods provide a lower cost and practical alternative by taking into account the random nature of ground motions (e.g: Boore 1983; Hanks and Boore, 1984; Beresnev and Atkinson, 1997). Hybrid methods combine deterministic and stochastic approaches to produce broadband ground motion simulations. The simulated acceleration records obtained by alternative approaches are validated with active seismic stations or past earthquake records. If there are unrecorded earthquakes, the validation process cannot be performed. In this case, the valdiation of simulations is performed by indirect methods such as earthquake intensity, damage distribution, and empirical ground motion prediction equations (Karimzadeh and Askan, 2018).

Erzurum, which is located in a seismicly hazardous region, has experienced major earthquakes in the history. In extensive literature studies, it has been determined that the city has been exposed to many large earthquakes and substantially damaged at different times (e.g.: Tozlu, 2000; Ambraseys and Finkel, 2006). In particular, the earthquake that occurred on June 2, 1859, was recorded as the most destructive earthquake in the history of Erzurum. The 6.1 magnitude earthquake had a magnitude of IX according to the Mercalli Intensity Measure (MMI) (Özer et al., 2019). The damage caused by the earthquake in the city was frightening. Although the certainty

* Corresponding author, E-mail: bozdoganitu@gmail.com

https://doi.org/10.31462/icearc2025_ce_eqe_520

is not clear, 360 people were reported to have died in the reports written to the capital of that time, Istanbul. In terms of damage, 1462 houses were destroyed, about 3500 houses were severely damaged, 6 mosques were destroyed, and about 20 mosques and masjids were partially destroyed (Tozlu 2000; Sağlam 2021). This study aims to produce a synthetic acceleration record of the 1859 earthquake using a stochastic method.

2. Materials and methods

2.1. Stochastic finite fault methodology

Basically, the complex character of high-frequency ground motion records with frequencies greater than 1 Hz have been inadequate for modeling ground motion simulations. The reason for this inadequacy is the phase inconsistencies resulting from the complex character structures. These phase inconsistencies coupled with computational costs and lack of velocity models for higher frequencies have led to dificulty in analytical or numerical seismic wave equation solutions for modeling simulations of high-frequency ground motions. As a result, the stochastic point source model was developed and used for modeling high frequencies (Boore, 1983). Stochastic techniques are based on the principle of combining an arbitrary phase spectrum with the spectral amplitude of the ground motion. This method has its inherent limitations, as it does not fully reflect the effects of wave propagation, but it is widely used due to its ability to obtain high- and medium-frequency ground motions.However, this point source method is no longer a suitable method to be used in cases where the fault fracture width is larger than the distance between the source and the site because it cannot fully model the near-field effects. In the following years, Beresnev and Atkinson (1998) developed a method to overcome this deficiency in the point source method by modeling the fault as a rectangle and dividing this large fault into small fault segments and considering each segment as a point fault. They called this method the stochastic finite fault element method. These small faults are considered as point sources with an ω-2 spectrum. In this method, an earthquake hypocenter is placed on any of the sub-faults, and waves start to propagate from this hypocenter at a constant speed. While propagating, the waves move similar to rupture motion, and the waves propagating from each fault trigger the other fault. In time, the rupture motions on the sub-faults affect the main fault, and all these effects are summed up. The total acceleration from the fault is obtained as follows:

$$A(t) = \sum_{i=1}^{nl} \sum_{i=1}^{nw} Aij(t + \Delta tj) \tag{1}$$

A(t) is the acceleration record obtained from the whole fault, Aij is the acceleration contribution of the ijth subfault, nl and nw are the number of subfaults along the length and width of the fault, Δtij is the delay time calculated for each subfault. This time is the sum of the time for the rupture surface to reach each subfault and the time for the wave to reach the observation point as shown in Fig. 1. (e.g.: Ünal and Askan 2015; Askan and Karimzadeh 2019).

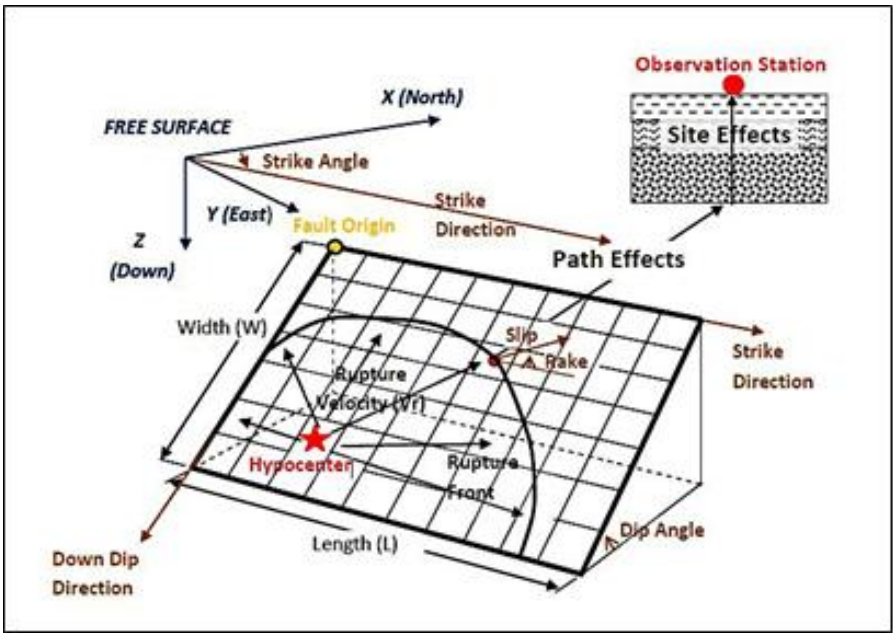

Fig. 1. Stochastic Finite Fault Method (adopted from Uğurhan 2010)

This model had some issues due to the limitation on the total number of subfaults and the direct dependence of the energy in the fault on the subfault dimensions. This limitation was overcome by Motazedian and Atkinson (2005) with a new approach called dynamic corner frequency model, the total energy is no longer dependent on the sub-fault size.

With this update in the stochastic finite fault method, this method is based on the concepts of deterministic spectrum for subfaults, and stochastic phase angles. For any subfault ij, the spectral acceleration relation at frequency f is given as follows:

$$A_{ij}(f) = CM_{0ij}H_{ij}\frac{(2\pi f)^2}{\left[1+\left(\frac{f}{f_{cij}}\right)^2\right]}e^{-\frac{\pi f R_{ij}}{Q(f)\beta}}G\left(R_{ij}\right)A\left(f\right)e^{-\pi kf} \tag{2}$$

$C = \Re^{\theta\varphi}\sqrt{2}\big/4\pi\rho\beta^3$ is the scaling coefficient expressed by the relation., $\Re^{\theta\varphi}$, radiation cover, ρ density, β S wave velocity, $M_{0ij}=\frac{M_0 S_{ij}}{\sum_{k=1}^{nl}\sum_{l=1}^{mw}S_{kl}}$ is theseismic moment of the sub fault, S_{ij} relative shear weights,

$f_{cji}\left(t\right) = N_R\left(t\right)^{-1/3} 4.9x10^6\beta\left(\frac{\Delta_\sigma}{M_{0ave}}\right)$ is the dynamic corner frequency of the sub fault. $\Delta\sigma$ stress drop, N_R (t) is nthe total number of sub-fractures that have broken at any time t ve $M_{0ave} = M_0\big/N$ is the average seismic moment of the sub-faults. Rij distance from observation point, Q(f) is the quality factor, $G(R_{ij})$ is the geometric spreading factor, $A(f)$ is the site amplification factor, $e^{-\pi kf}$ is a high-cut filter to include the spectral decayat high frequencies described with eden Kappa factor of soils (Anderson and Hough, 1984). Hij is the high frequency filter and is expressed as:

$$H_{ij} = \left\{N\frac{\sum\left[\frac{f^2}{1+f_c^2}\right]}{\sum\left[\frac{f^2}{1+f_{ij}^2}\right]}\right\}^{1/2} \tag{3}$$

2.2. June 2, 1859 Erzurum earthquake

The June 2, 1859 earthquake is stated to be the most severe in Erzurum's history. It was the last and most destructive event in a sequence of earthquakes that began at midnight on June 1. Although the initial tremor was not severe and was felt in the western part of the city, it was followed by a series of 12 successive earthquakes that culminated in a major quake around 4:00 a.m. on June 2, impacting the northern and southern parts of the city. A second powerful earthquake struck 15 minutes later, effectively leveling the city. Despite lasting only about 15 seconds, the earthquake had a devastating impact due to its intensity (Tozlu,2000) The magnitude of the earthquake is reported in sources as Mw = 6.1 to the Modified Mercalli Intensity (MMI) scale, the intensity level was IX (Özer et al., 2019).

There are different opinions regarding the affected area of the earthquake. The most well-known of these is the report by German geologist Hermann von Abich (1896), a member of the Russian Academy of Sciences. According to Abich’s report, the epicenter of the earthquake was located somewhere between Palandöken and Eğerlidağ. Waves were especially intense on the northern and eastern slopes of Mount Palandöken, which lies to the south of Erzurum’s city center. The seismic waves did not reach Pasinler to the east of the city or its western parts, and the earthquake was not felt beyond a 60 km radius. Muffled sounds were reportedly heard during the quake (Küçükuğurlu, 2024). The earthquake caused varying degrees of damage across different parts of the city. According to Abich, the southern section of the city, where Erzurum Castle is located, and the Turkish neighborhoods to the east of the castle suffered the most damage. One-third of the city was destroyed. The fact that the damage was more severe in some parts of the city is attributed to differing soil characteristics across the region. In reports sent to the capital, Istanbul—though not entirely verified—it was stated that 360 people died (Tozlu, 2000; Sağlam, 2011). In the 1859 earthquake, 1,462 houses were completely destroyed, around 3,500 were severely damaged, six mosques were entirely demolished, and approximately 20 other mosques and prayer halls were also damaged.(Özdoğan,2024). The location of the 1859 earthquake and the Erzurum fault lines are shown in Fig. 2.

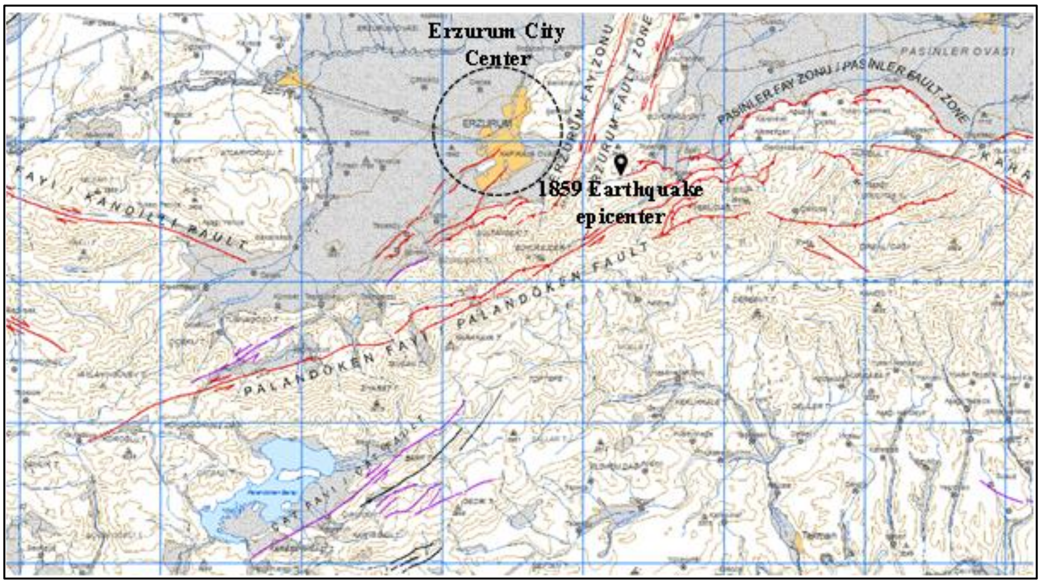

Fig 2. Erzurum faults and 1859 Earthquake center (MTA, 2021).

3. Simulation of June 2, 1859 Erzurum earthquake

Simulation of earthquake records is primarily driven by event-specific parameters, which are crucial in simulating ground motion. In this study, synthetic records for the June 2, 1859 Erzurum earthquake were created using the EXSIM open source code (Motazedian and Atkinson,2005). EXSIM allows users to simulate ground motion by inputting key seismic characteristics (Özdoğan,2024).

Main parameters involved in simulating records include earthquake magnitude, fault coordinates, rupture width, stress drop, faulting mechanism, fault dimensions and depth, wave propagation geometry, crustal density, rupture velocity, shear wave velocity of the crust, the size and number of sub-faults, the earthquake's geographic location, and the local kappa factor. A major challenge in generating synthetic acceleration records for thesimulating the 1859 Erzurum earthquake is the scarcity of historical data, as the event occurred before instrumental recording began. As a result, some parameters could not be directly observed and were instead sourced from prior research. Based on existing literature, the moment magnitude (Mw) of the 1859 earthquake is estimated at 6.1 (BOUN, 2023), and the event is assumed to have occurred near the Erzurum Fault.

The upper edge of the fault coordinates used were 39°94'N and 41°397'E, as reported in the literature. The fault is characterized as a left-lateral strike-slip fault, spanning approximately 38 km in length and 23 km in width, located between the eastern and northern areas of Erzurum. Although direct data on the rupture dimensions are unavailable due to the earthquake's historical nature, studies suggest the Erzurum Fault could extend up to 35 km eastward. For this study, the rupture was assumed to cover a 15 km segment.

Given the earthquake magnitude and fault type, the rupture width was calculated using Equation 3:

$$log(RW) = a + b \times M \tag{3}$$

Where M is the magnitude, and empirical constants a and b are -0.76 and 0.14, respectively, for a left-lateral strike-slip fault (Wells and Coppersmith, 1994). This resulted in a rupture width of 7.5 km, which was input into EXSIM.The dip angle was approximated at 25°, based on the fault's length and calculated width. Since this fault type typically has a vertical dip, a dip angle of 90° was ultimately adopted in the code.

In the stochastic finite-fault model, sub-faults of 1.5 km × 1.5 km were defined. One sub-fault, identified as (5, 3) in the (i, j) grid system, was designated as the earthquake's hypocenter. The stress drop (Δσ) was estimated using Equation 4:

$$\Delta\sigma\left(SS\right) = 8.9xW^{0.8} \tag{4}$$

where W is the fault width (Mohammediun and Serva,2001). Substituting the 7.5 km width into the equation yielded a stress drop of approximately 45 bar. The absence of exact numerical data meant some input parameters were constrained and supplemented using findings from previous studies. To fill data gaps, results from earlier simulations of earthquakes in Erzincan were referenced (Uğurhan,2010; Karimzadeh et al, 2018). Based on these sources, the focal depth of the 1859 Erzurum earthquake was set at 3 km. The quality factor for anelastic attenuation (Q*f*) was defined using the equation:

$$Q = 122xf^{0.68} \tag{5}$$

Geometrical spreading was modeled using:

- R^{-1} for R ≤ 25 km (6a)
- $R^{-0.5}$ for R > 25 km (6b)

The time duration model was expressed as:

$$T = T_0 + 0.05R \tag{7}$$

where T is the total duration, T_0 is the source duration, and R is the hypocentral distance. These values were incorporated into the simulation.

To classify the local site conditions, Vs30 shear wave velocity values were used. According to Turkish seismic code (TBDY, 2018) central Erzurum has Vs30 values between 200–240 m/s, corresponding to local soil class ZD (NEHRP-D site class). This classification and corresponding amplification factors were used in EXSIM. The kappa factor (κ_0), which accounts for local site effects, was also adjusted. The minimum recommended κ_0 for ZD-class soils in eastern Turkey is 0.0365. Previous simulations used values of 0.045 and 0.066 for the 1992 and 1939 Erzincan earthquakes, respectively. In initial simulations for the 1859 event, a κ_0 of 0.040 was used, but this did not yield the expected damage levels for mosques. To address this, the value was gradually lowered. Ultimately, based on the recommendation by Altındal and Askan (2022) and considering the rugged topography of the region, a κ_0 value of 0.025 was adopted using a kappa value corresponding to mean minus one standard deviation. This adjusted value was used to generate the final synthetic acceleration record. The values of 3600 m/s for crustal shear wave velocity and 2800 kg/m³ for crustal density were employed. Once all parameter inputs were finalized, the target location for applying the simulated record was obtained. The parameters of the simulation are shown in Table 1.

Table 1. Simulation parameters of the 1859 earthquake

Parameter	Values
Fault	Dip angle: 25° Depth angle: 90°
Fault Dimensions	15 x 7.5 km
Earthquake Magnitude	6.1
Fault Depth	3.0 km
Sub-fault Dimensions	1.5 x 1.5 km
Stress Drop	45 bar
Crustal Shear Wave Velocity	3.600 m/s
Crustal Density	2.800 kg/m^3
Slip Area Percentage	% 50
κ_0	0.025
Time Duration Model	0.05*R
Attenuation Factor Q(f)	122 $f^{0.68}$
Geometrical Spreading	$R^{-1.1}$, R≤25 km $R^{-0.5}$, R>25 km
Windowing Function	Saragoni- Hart
Local Site Class	ZD

The simulated ground motion record for the 1859 earthquake has a duration of almost 8 seconds. The calculated hypocentral distance is 17.94 km, while the R_{JB} distance is around 11.48 km. The peak ground acceleration (PGA) of the simulated motion is 190 gal, and the peak ground velocity (PGV) is 8.8 cm/sec. The acceleration and velocity time histories are given in Fig. 3.

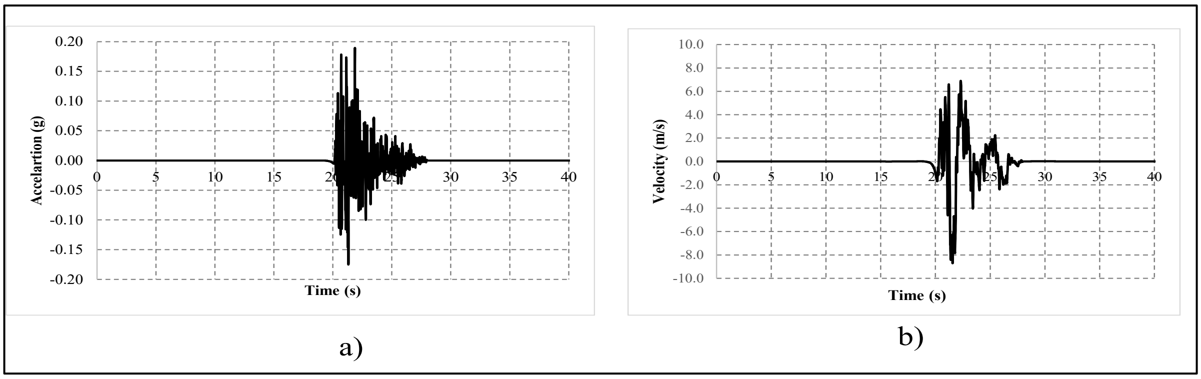

Fig. 3. Simulated a) acceleration, b) velocity graphs generated for the June 2, 1859 Erzurum earthquake.

One of the most crucial steps in generating synthetic earthquake records is the validation phase. For earthquakes that occurred during the instrumental era, the acceleration records simulated using stochastic methods are assessed by comparing them with actual recorded ground motions. Numerous studies in the literature have followed this approach, validating synthetic records of major historical events—such as the 1999 Düzce, 2009 L'Aquila, and 1992 Erzincan earthquakes—by comparing them to the corresponding real acceleration data (Uğurhan, 2010).

The validation process extends beyond the comparison of a single earthquake record at a specific site. It also involves referencing databases that compile records from multiple relevant seismic events in the region. This broader approach allows for adjustments and improvements to the simulated acceleration records as needed (Tsiolou et al., 2019) However, for earthquakes that occurred before the development of seismic instrumentation, direct validation using recorded ground motion data is not possible. In such cases, earthquake intensity has been proposed as an alternative method for validation. Bilal and Askan (2015) stated that when the peak ground acceleration (PGA) is available, the Modified Mercalli Intensity (MMI) can be estimated using Equation 8:

$$MMI = 0.132 + 3.884 \times log(PGA) \tag{8}$$

In this equation, PGA must be provided in units of gal. It is noted that this method has been applied to validate the simulated acceleration record of the 1939 Erzincan Earthquake, which predates instrumental recordings (Karimzadeh and Askan, 2018).

For the June 2, 1859 earthquake, no instrumental acceleration data are available. As a result, the initial validation was carried out by estimating the earthquake intensity based on the simulated record. Historical sources report that the intensity of this earthquake, which affected Erzurum, was level IX on the MMI scale (Özer et al., 2019).Using the PGA value of 190 gal derived from the synthetic record, the calculated intensity from Equation 8 is 9.33. This estimated value aligns closely with the historically reported intensity of IX, supporting the validity of the synthetic data.

A second validation method is to comapre the simulated peaks with those from ampirical ground motion models (GMMS). Among various ground motion models, the models proposed by Akkar and Çağnan (2010) and Kale et al. (2015), which yield results closely matching the recorded data in this region of the country, were selected for analysis. In Table 2 the peak ground acceleration values of the simulated ground motions are compared with the mean predictions and ±1 standard deviation ranges obtained from these models. In these comparisons, the empirical ground motion equations were applied using a moment magnitude (Mw) of 6.1, a Joyner–Boore distance (Rjb) of 11 km, and site conditions corresponding to Vs30 = 240 m/s, consistent with the characteristics of the simulated earthquake

Table 2. Table of Peak Ground Acceleration Values

	Average Peak Ground Acceleration (g) – One Standard Deviation"	Average Peak Ground Acceleration (g)	Average Peak Ground Acceleration (g) + One Standard Deviation"
Akkar and Çağnan (2010)	0.06	0.138	0.317
Kale et al. (2015)	0.07	0.140	0.281
Simulated Peak Ground Acceleration (g)		0.190	

Upon examination of Table 2, it is observed that the peak ground acceleration value obtained from the simulation for the June 2, 1859 earthquake falls within the range of limit acceleration values reported for real earthquakes that occurred under similar conditions. It has been concluded that the peak ground acceleration values corresponding to both the raw and the scaled ground motion records lie within the boundary values specified in both references. Through this study, the peak ground acceleration value obtained from the simulation has been validated.

4. Conclusions

In this study, to enhance the understanding of seismic activity in Erzurum, a strong ground motion record at a point of interest in terms of historic stuctures was simulated and validated for the 2 June 1859 Erzurum earthquake—one of the most devastating events in the region's history—using a stochastic approache. Alongside estimating the earthquake's intensity empirically through the PGA value of the generated record, the reliability of the synthetic data was also assessed by comparing with empirical estimated from groun motion models The following conclusions were drawn from the simulation of this acceleration record:

- For the 1859 Erzurum earthquake, the simulated ground motion record has a peak ground acceleration (PGA) of 0.19g, a peak ground velocity (PGV) of 8.8 cm/s, and a peak ground displacement (PGD) of 2.5 cm. The PGA value is validated against an empirical MMI value obtained from historical damage reports.

- Based on the PGA value, reported shaking experiences, and historical damage data, the earthquake's intensity was classified as IX on the Modified Mercalli Intensity (MMI) scale. Given the nature of Erzurum's building stock at the time, the event was deemed highly destructive.
- Although the PGA value was relatively low, Erzurum experienced substantial damage, which may be attributed more to poor soil conditions and inadequate construction quality rather than to the earthquake's magnitude itself.
- The stochastic modeling technique takes researchers back to the pre-instrument era when earthquake recorders were not available, and allows for the subsequent recording of an earthquake that occurred in the past. Generating records of pre-instrumental earthquakes in our country with this method and validating them against any empirical data with studies similar to this thesis will contribute to a better understanding of the seismicity and earthquake hazard of our country.

References

Abich, H. (1896). *Aus Kaukasischen Ländern. Herausgegeben von dessen Witwe. Zweiter Band: Briefe aus den Jahren 1859–1874 an seine Frau*. Wien.

Akkar, S., & Çağnan, Z. (2010). A local ground-motion predictive model for Turkey, and its comparison with other regional and global ground-motion models. *Bull. Seismol. Soc. Am.*, 100(6), 2978–2995.

Altındal, A., & Askan, A. (2022). Predictive kappa (κ) models for Turkey: Regional effects and uncertainty analysis. *Earthq. Spectra*, 38(4), 2479–2499.

Ambraseys, N. N., & Finkel, C. F. (2003). *Seismic events organized in Türkiye and its neighbors (1500–1800)* (Academic Series 4, p. 252). TUBITAK Publications.

Askan, A., & Karimzadeh, S. (2019). A simulated strong ground motion database for potential earthquake scenarios on North Anatolian Fault Zone. *Turk. J. Earthq. Res.*, 1(1), 76–97.

Beresnev, I. A., & Atkinson, G. M. (1997). Modeling finite-fault radiation from the ω^n spectrum. *Bull. Seismol. Soc. Am.*, 87(1), 67–84.

Beresnev, I. A., & Atkinson, G. M. (1998). Stochastic finite-fault modeling of ground motions from the 1994 Northridge, California earthquake: I. Validation on rock sites. *Bull. Seismol. Soc. Am.*, 88, 1392–1401.

Bilal, M., & Askan, A. (2014). Relationships between felt intensity and recorded ground-motion parameters for Turkey. *Bull. Seismol. Soc. Am.*, 104(1), 484–496.

BOUN. (2023). Boğaziçi University Kandilli Observatory and Earthquake Research Institute. Retrieved from http://www.koeri.boun.edu.tr/sismo/2/deprem-bilgileri/tarihsel-depremler/

Boore, D. M. (1983). Stochastic simulation of high-frequency ground motions based on seismological models of the radiated spectra. *Bull. Seismol. Soc. Am.*, 73(6A), 1865–1894.

Frankel, A. (1993). Three-dimensional simulations of ground motions in the San Bernardino Valley, California, for hypothetical earthquakes on the San Andreas fault. *Bull. Seismol. Soc. Am.*, 83(4), 1020–1041.

Frankel, A., Vidale, J. E., & Borcherdt, R. D. (1994). A three-dimensional simulation of seismic waves in the Santa Clara Valley, California, from an aftershock. In *The Loma Prieta, California, Earthquake of October 17, 1989—Strong Ground Motion* (p. 197). U.S. Geological Survey.

Hanks, T. C., & Boore, D. M. (1984). Moment-magnitude relations in theory and practice. *J. Geophys. Res. Solid Earth*, 89(B7), 6229–6235.

Kale, Ö., Akkar, S., Ansari, A., & Hamzehloo, H. (2015). A ground-motion predictive model for Iran and Turkey for horizontal PGA, PGV, and 5% damped response spectrum: Investigation of possible regional effects. *Bull. Seismol. Soc. Am.*, 105(2A), 963–980.

Karimzadeh, S., Askan, A., Erberik, M. A., & Yakut, A. (2018). Seismic damage assessment based on regional synthetic ground motion dataset: A case study for Erzincan, Turkey. *Nat. Hazards*, 92, 1371–1397. https://doi.org/10.1007/s11069-018-3255-6

Komatitsch, D., Liu, Q., Tromp, J., Süss, P., Stidham, C., & Shaw, J. H. (2004). Simulations of ground motion in the Los Angeles basin based upon the spectral-element method. *Bull. Seismol. Soc. Am.*, 94(1), 187–206.

Kucukugurlu, M. (2024). Eyewitness accounts of 19th century Erzurum earthquakes [Article in Turkish]. *Turcology Research*, 79, 100–110.

Mohammedioun, B., & Serva, L. (2001). Stress drop, slip type, earthquake magnitude, and seismic hazard. *Bull. Seismol. Soc. Am.*, 91(4), 694–707.

MTA. (2021). *General Directorate of Mineral Research and Exploration of Turkey*. Retrieved from https://www.mta.gov.tr/v3.0/sayfalar/hizmetler/doc/diri_fay_haritaları/erzurum.pdf

Olsen, K. B., Archuleta, R. J., & Matarese, J. R. (1995). Three-dimensional simulation of a magnitude 7.75 earthquake on the San Andreas fault. *Science*, 270(5242), 1628–1632.

Özer, Ç., Kocadağıstan, M. E., & Perk, S. (2019). Earthquake monitoring network of Erzurum: ATANET. *Int. J. Sci. Technol. Res.*, 5(8), 35–47.

Özdoğan, D. B. (2024). *Investigation of the dynamic behavior of historical buildings using historical Erzurum earthquake records generated by stochastic modeling method* (PhD thesis). Erzurum Technical University, Institute of Science and Technology.

Sağlam, T. (2021). Formation phases of a street: Erzurum Cumhuriyet Street. *Atatürk Univ. J. Inst. Soc. Sci.*, 25(3), 1171–1199.

TBDY-18. (2018). *Turkey Building Earthquake Regulation*. Disaster and Emergency Management Presidency, Ankara.

Tozlu, S. (2000). Earthquakes in Erzurum history. In *Natural disasters in Anatolia throughout history and earthquake seminar* (pp. 93–117). Istanbul University Faculty of Literature History Research Center.

Tsioulou, A., Taflanidis, A. A., & Galasso, C. (2019). Validation of stochastic ground motion model modification by comparison to seismic demand of recorded ground motions. *Bull. Earthq. Eng.*, 17, 2871–2898.

Uğurhan, B. (2010). *Stochastic strong ground motion simulations on North Anatolian Fault Zone and Central Italy: Validation, limitation and sensitivity analyses* (PhD thesis). Middle East Technical University, The Graduate School of Natural and Applied Sciences.

Unal, B., & Askan, A. (2015). Ground motion simulation for Bursa Region with parameters obtained from local seismic station network. In *3rd Turkish Earthquake Engineering and Seismology Conference*, Dokuz Eylül University, October 14–16, Izmir.

Wells, D. L., & Coppersmith, K. J. (1994). New empirical relationships among magnitude, rupture length, rupture width, rupture area, and surface displacement. *Bull. Seismol. Soc. Am.*, 84(4), 974–1002.

Advanced deep learning models for anomaly detection in masonry structures

Kemal Hacıefendioğlu*[1], Ali Motamedi[1], Tunahan Aslan[1], Cemile Duman[2], Ayşecan Bostan[1]

[1]Karadeniz Technical University, Department of Civil Engineering, 61080 Trabzon, Türkiye
[2] Gazi University, Faculty of Engineering, Department of Civil Engineering, Ankara, Türkiye

Abstract. The detection of structural anomalies is essential for safeguarding the integrity and longevity of buildings with cultural and historical significance, such as masonry minarets. This study explores the use of Convolutional Neural Networks (CNNs) for forecasting vibration responses and identifying patterns indicative of potential structural damage. Vibration data collected from a minaret under both undamaged and controlled damage scenarios are used to train and evaluate a CNN model designed to extract spatial features from time-series signals. The model demonstrates strong performance in distinguishing normal structural behavior from anomalous patterns, offering high accuracy and sensitivity in damage detection. In addition to its predictive capabilities, the CNN approach proves to be computationally efficient and suitable for real-time monitoring applications. The findings highlight the potential of deep learning–based methods, particularly CNNs, to enhance non-contact structural health monitoring strategies, providing a reliable and scalable solution for the preservation of historic structures.

Keywords: Historic masonry structures; Optical flow; Convolutional Neural Networks (CNN); Anomaly detection; Non-contact measurement

1. Introduction

Historic masonry structures, such as minarets, are significant cultural heritage assets that often experience deterioration over time due to aging, environmental conditions, and dynamic forces such as earthquakes (Sabia, Demarie et al., 2022). Maintaining their structural integrity is essential due to their historical and cultural importance. Traditional structural health monitoring (SHM) methods are often invasive and limited by practical challenges and the risk of further damage (Dong and Catbas, 2021). As a result, non-contact and non-intrusive methods, especially video-based SHM, have become increasingly popular for being safe, cost-effective, and efficient (Shariati, Schumacher et al., 2014).

Video-based SHM uses advanced computer vision, image processing, and machine learning (ML) techniques to detect structural damage by analyzing video data. This method provides significant benefits in scalability, accuracy, and safety, allowing continuous monitoring without physical contact (Ghandil, Dabanli et al., 2021; Xiong, 2021). Although video-based SHM has been widely studied, research focused specifically on historic masonry minarets are limited. These structures present unique challenges for monitoring due to their complex geometry, varied materials, and cultural significance.

Recent progress in video-based SHM has highlighted its effectiveness in monitoring structural dynamics and detecting gradual damage in historic buildings. Digital video imaging, in particular, has proven suitable for non-contact dynamic assessment, offering a practical solution for historic masonry structures where traditional sensors are often impractical or pose a risk to the structure (Ghandil, Dabanli et al., 2021). Graph-based video processing techniques have emerged as effective tools for early warning systems in historic masonry structures. By analyzing key deformation patterns, these methods can help predict potential structural failures, offering a means to protect valuable heritage sites from severe damage (Fioriti, Cataldo et al., 2024).

Automated damage detection in masonry using video imaging shortens inspection times and improves safety by removing the need for inspectors to enter hazardous areas (Sangirardi, Altomare et al., 2022). Moreover, advancements in machine learning have greatly enhanced the effectiveness of video-based SHM. Sophisticated algorithms that detect subtle structural changes in video data support long-term monitoring and predictive

*Corresponding author, E-mail: kemalhaciefendioglu@ktu.edu.tr

https://doi.org/10.31462/icearc2025_ce_eqe_529

maintenance, which are especially important for historic masonry buildings exposed to seismic activity and other dynamic forces (Aktürk, Aras et al., 2022; Farrar, Dervilis et al., 2025). Although video-based methods have advanced significantly, their use in monitoring historic masonry minarets has received limited attention. This study aims to bridge that gap by presenting a tailored video-based monitoring framework that considers the unique structural traits and preservation demands of minarets.

This study presents a novel integration of advanced optical flow techniques with deep learning (DL) architectures, specifically CNN model, to capture the distinctive structural behavior of masonry minarets and detect anomalies. The key contributions are: (a) directly addressing the monitoring challenges arising from the complex geometry and material variability of historic masonry minarets, (b) introducing a hybrid Autoencoder-PCA method to efficiently reduce dimensionality and improve anomaly detection by isolating dominant patterns in displacement time-series data, and (c) conducting a detailed analysis of CNN model to evaluate its performance and suitability for video-based monitoring of heritage structures.

2. Theoretical background

2.1. Optical flow methods

Optical flow refers to the apparent motion of objects or surfaces in a scene due to movement between the camera and the environment. In structural health monitoring (SHM), it enables real-time, non-contact tracking of displacements, deformations, and vibrations.

The Lucas-Kanade method is well-suited for tracking small displacements, whereas its extension through the pyramid approach improves reliability in cases involving larger movements (Lucas and Kanade, 1981; Bouguet, 2001; Baker and Matthews, 2004).

2.2. Hybrid autoencoder-PCA

Autoencoders (AEs) are neural networks that use unsupervised learning to extract efficient, lower-dimensional representations of data. They consist of two main parts: an encoder that compresses the input and a decoder that reconstructs it, enabling meaningful features learning from the original data.

2.3. Convolutional neural networks (CNNs)

Convolutional Neural Networks (CNNs) play a pivotal role in deep learning, especially for analyzing visual data such as images and videos. Unlike conventional neural networks that rely on manually selected features, CNNs automatically learn spatial hierarchies of features from raw input, enabling efficient processing of high-dimensional and complex datasets. Their architecture, inspired by the structure of the visual cortex, consists of multiple layers that progressively extract informative patterns relevant to tasks like classification and detection (Fig. 1). The process begins with a convolutional layer that applies learnable filters (kernels) to the input data, extracting features that range from basic edges and textures to more abstract patterns in deeper layers. An activation function—typically the Rectified Linear Unit (ReLU)—is then used to introduce nonlinearity, allowing the network to model complex relationships. Pooling layers follow this step, reducing the spatial dimensions of the feature maps while retaining essential information, which helps lower computational cost and control overfitting. After several convolution and pooling operations, fully connected layers flatten and integrate the extracted features for classification or regression. Each neuron in these layers connects to all neurons in the next layer, enabling high-level reasoning. A SoftMax layer is typically used at the output to convert raw scores into class probabilities, allowing the model to produce interpretable predictions in visual recognition tasks (Simonyan and Zisserman, 2014). CNNs are particularly well-suited for image processing and pattern recognition tasks. Their primary strength lies in their ability to automatically extract hierarchical features from raw data, eliminating the need for manual feature engineering. This makes CNNs highly effective in domains that involve complex visual data.

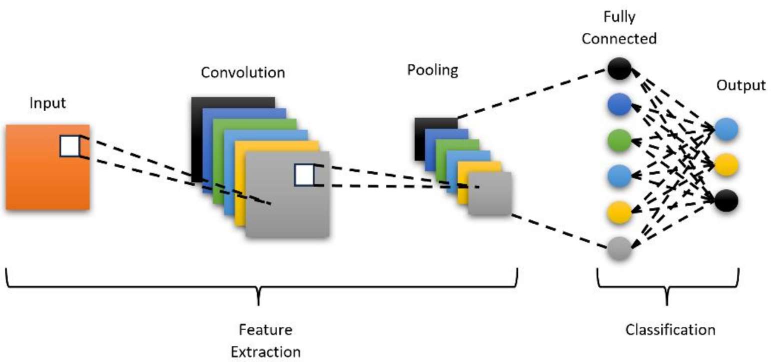

Fig. 1. The structure of a CNN

CNNs have revolutionized many fields, especially those that require the analysis of complex visual data. Their ability to automatically learn features from raw data has made them indispensable in tasks such as image classification, object detection, and medical image analysis. As technology continues to evolve, the applications of CNNs will likely expand even further, playing a critical role in innovations across a wide range of industries. Their effectiveness in understanding complex patterns, coupled with their efficiency, ensures that CNNs will remain a foundational tool in the field of deep learning (Szegedy, Liu et al. 2015).

3. Anomaly assessment methodology

The proposed approach combines advanced image processing with unsupervised learning to evaluate the structural condition of a portable minaret model. Four cameras, positioned at key locations, record high-resolution video of markers placed on the minaret's surface, allowing accurate measurement of both horizontal and vertical displacements under intact and damaged states. Optical flow techniques are used to calculate these displacements, which are then translated from pixel units into real-world values through calibration using known marker dimensions. The resulting displacement time series is used for feature extraction, where a hybrid Autoencoder-PCA model captures the latent patterns of healthy behavior. In parallel CNN architecture leverage both spatial and temporal features to improve anomaly detection. A reconstruction error-based damage index, computed in an unsupervised manner, identifies anomalies by comparing original and reconstructed signals, with detection refined through thresholding and segment-level analysis. This integrated framework enables continuous monitoring and clear visualization of structural damage progression over time.

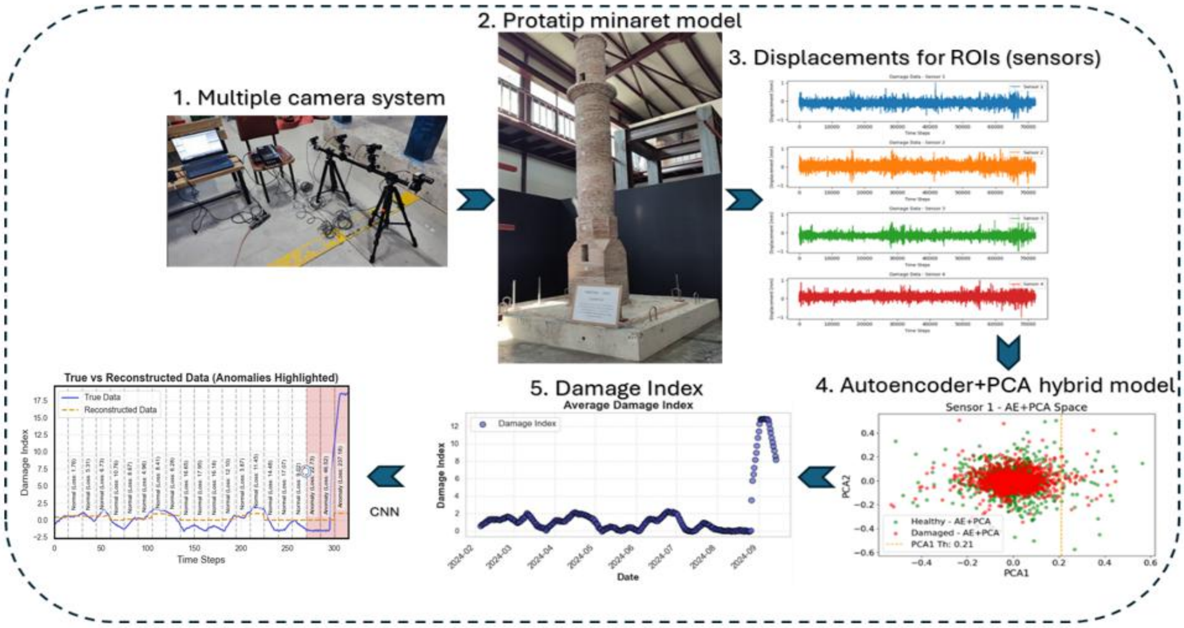

Fig. 2. Steps of proposed damage strategy

Figure 2 illustrates the workflow of the proposed methodology, with each step outlined as follows:

Step 1: Multi-Camera System and Prototype Minaret Model: A portable minaret model was equipped with four cameras positioned strategically to focus on specific markers placed on the surface of the structure. This setup enabled each camera to independently record video data, resulting in four separate and complementary data streams.

Step 2: Displacements for ROI. Each video stream is processed using the optical flow method to compute pixel movements between consecutive frames, capturing horizontal displacements of the minaret. Marker positions and their motion patterns are analysed to distinguish displacements at different locations on the structure. The resulting pixel-based motion vectors are extracted and stored, creating a raw dataset for further analysis.

The pixel-based motion vectors derived from optical flow are then converted into real-world units, such as millimeters or centimeters. This conversion relies on scaling factors determined through the known dimensions of the markers used in the experimental setup, combined with camera calibration parameters to ensure accurate spatial measurements.

These parameters allow for precise conversion of pixel displacements into actual physical distances. The resulting horizontal and vertical displacement values are recorded as time series data for multiple points on the minaret, creating a detailed dataset for subsequent analysis.

Step 3: Feature extraction and model training. To facilitate damage detection, the displacement time series data are transformed into a more compact and informative representation using a hybrid Autoencoder-PCA model. The autoencoder compresses and reconstructs the input signals, capturing their key characteristics. PCA is then applied to further reduce dimensionality and highlight dominant patterns. Importantly, only data from the undamaged (healthy) state are used during training, enabling the model to learn a latent representation that characterizes normal structural behaviour.

Step 4: Unsupervised reconstruction error-based structural damage index. The model is initially trained on the undamaged (reference) dataset of the minaret. Once trained, it is applied to new measurements to calculate a damage index based on reconstruction error. By comparing how well the model reconstructs current data relative to the reference state, deviations indicating potential damage are identified. Tracking these indices over time allows for visualization of damage progression throughout the monitoring period.

DL models are designed to compress input data and reconstruct it with minimal loss. The reconstruction error quantifies how effectively the model can reproduce the input.

4. Experimental implementation

4.1. Controlled damage scenarios

The damage was introduced by selectively removing bricks, a method chosen to observe changes in the structure's dynamic behavior. The targeted damage area was located on the brick wall section aligned with the lowest-level accelerometer, where seven bricks were removed to enable effective 2D displacement measurement. This damage zone was situated roughly 35 cm above the transition section, at a height of 145 cm from the base of the minaret. The procedure used for brick removal is illustrated in Figure 3 and detailed in the following paragraphs:

- Step 1 (Damage-1). The initial damage phase involved the removal of two out of the seven designated bricks, as shown in Figure 3a.
- Step 2 (Damage-2). In the next phase, four additional bricks located next to the initially removed ones were taken out, with two on each side. This resulted in a damaged region measuring approximately 30 cm in width and 3 cm in height, as shown in Figure 3b.
- Step 3 (Damage-3). As in the previous steps, one additional brick was removed from the upper brick layer, bringing the total number of removed bricks to five. Displacement measurements using the camera system were performed after each removal, as shown in Figure 3c.
- Step 4 (Damage-4). In the final stage, three additional bricks were removed from the upper brick layer, resulting in a total of seven bricks being extracted. After each removal, camera-based displacement measurements were repeated, as illustrated in Figure 3d.

Throughout the damage induction process, camera-based measurements were consistently recorded to monitor and evaluate the structural response of the minaret model.

(a) Location of the controlled damage region (Left) and Damage-1 case (Right)

(b) Damage-2 case

(c) Damage-3 case

(d) Damage-4 case

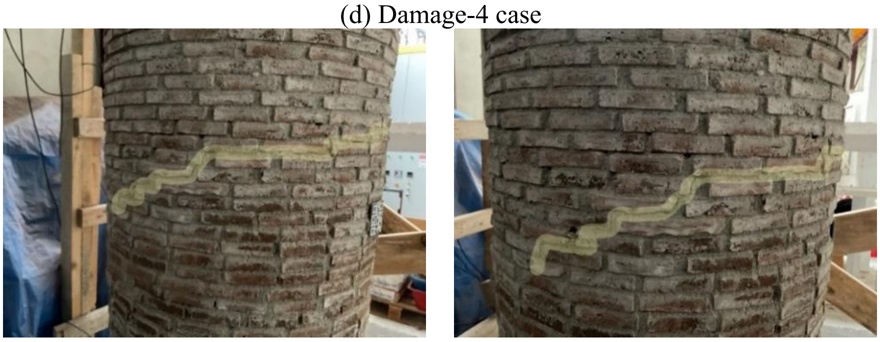

(e) Cracks formed after damage

Fig. 3. Controlled damage scenarios considered in the experimental study

4.2. Data collection and analysis
The monitoring was carried out using predefined regions of interest (ROIs) on the scaled minaret model. A template-matching-based sensing system continuously tracked the motion of selected points to collect displacement data. Measurements were performed using a multi-camera setup, and the data from each camera were analyzed comparatively. Figure 4 illustrates the placement of the template markers and the camera configuration. In this setup, the most distant camera was aimed at the top section of the model, specifically the honeycomb structure, while the other cameras were directed toward the podium, transition zone, and shaft at predefined angles. This arrangement ensured complete high-resolution coverage of all critical regions. The structured positioning allowed each camera to capture motion at different levels, ensuring synchronized and consistent data collection, and enabling accurate analysis of structural behavior and dynamic response.

Fig. 4. Template markers on the minaret and camera layout

During the monitoring process, periodic displacement measurements were analyzed to identify variations in the structure's dynamic behavior. The reference dataset, representing the undamaged state, includes 216,433 data points collected from four distinct measurement locations, as shown in Figure 5. This figure also displays the time-dependent displacement trends for both the training and test sets under undamaged conditions. After introducing controlled damage to the minaret model, measurements were repeated at the same four locations. For instance, the displacement data corresponding to the Damage-4 condition are detailed in Figure 6. These evaluations offer valuable insights into the model's dynamic response following damage and support the assessment of its structural stability.

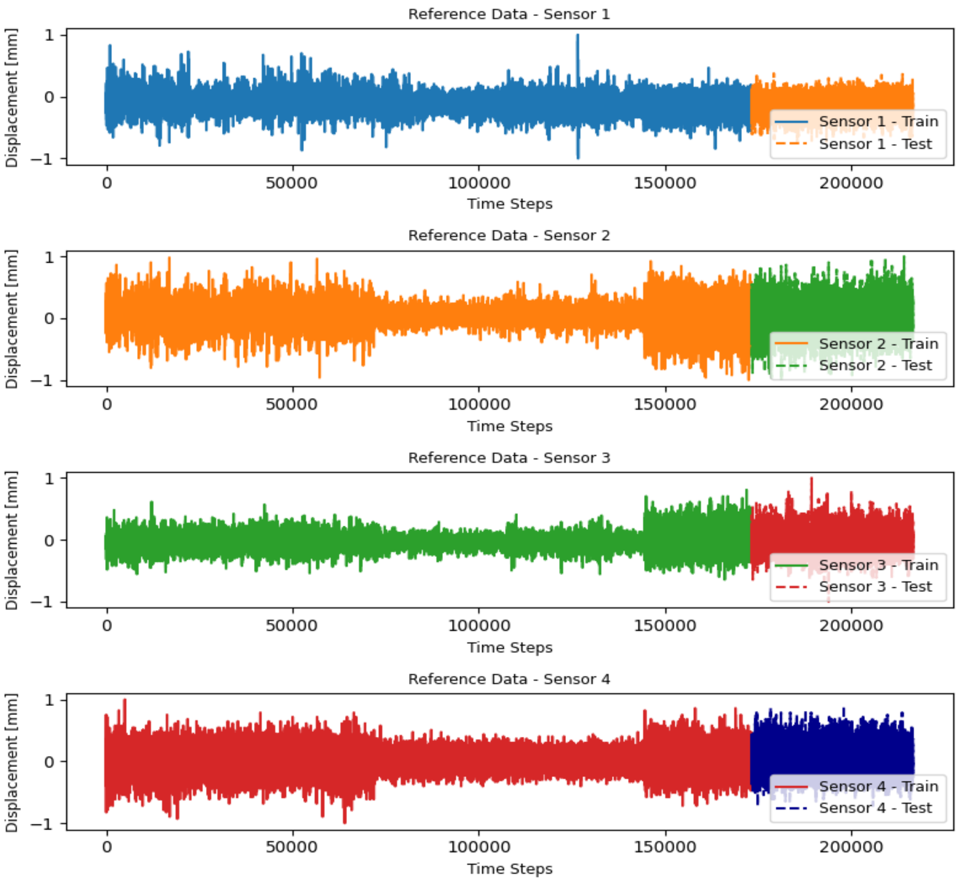

Fig. 5. Displacement-time graphs of the (undamaged) measurements of the first-day a) Sensor-1 horizontal and vertical displacement b) Sensor-2 horizontal and vertical displacement c) Sensor-3 horizontal and vertical displacement d) Sensor-4 horizontal and vertical displacement

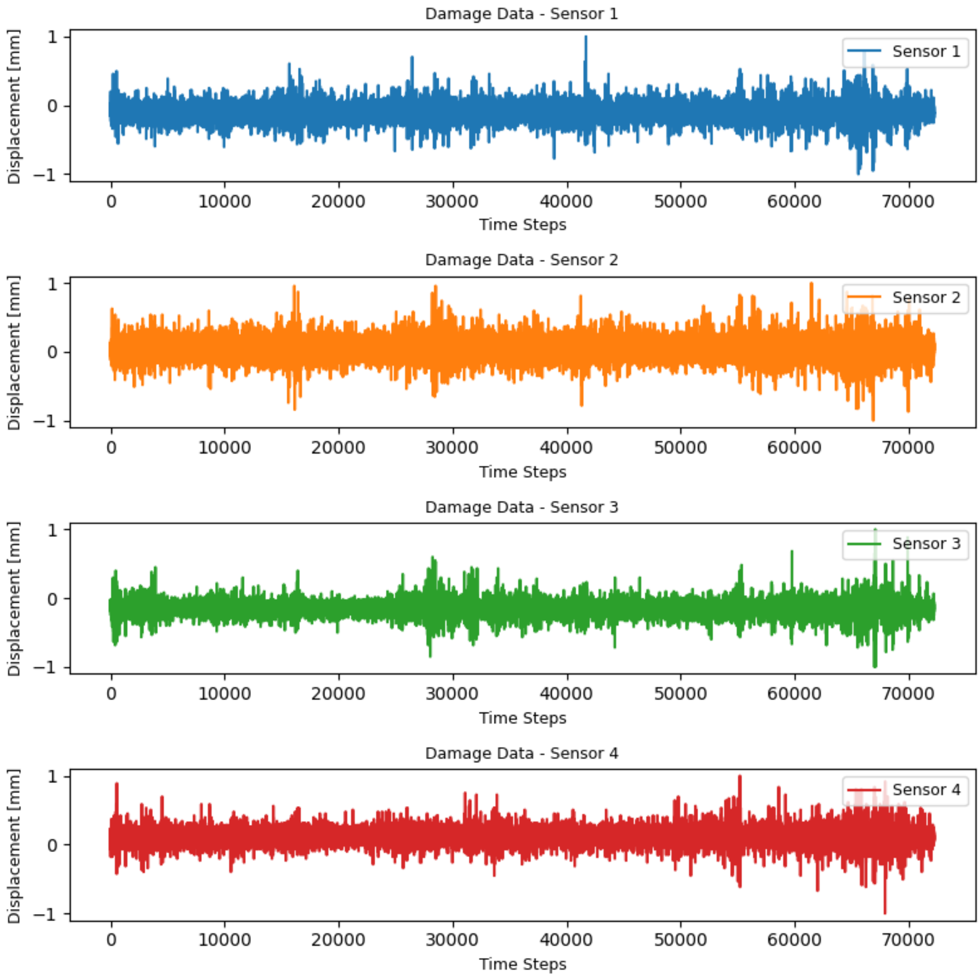

Fig. 6. Displacement-time graphs obtained for Damage-4 after controlled damage a) Sensor-1 horizontal and vertical displacement b) Sensor-2 horizontal and vertical displacement c) Sensor-3 horizontal and vertical displacement d) Sensor-4 horizontal and vertical displacement

5. Results

5.1. CNN model

The CNN model is designed to compress and reconstruct time series data. In the encoder section, sequential 1D convolutional (Conv1D) and max pooling (MaxPooling1D) layers are used to extract and reduce features. The first Conv1D layer applies 64 filters with a kernel size of 3 to capture low-level patterns in the input. This is followed by a MaxPooling1D layer that reduces the temporal resolution by half. The second Conv1D layer uses 128 filters to learn more abstract features, and another pooling layer further compresses the data. By the end of the encoder, the input time series is transformed into a compact latent representation for reconstruction.

The decoder section reconstructs the compressed time series using Conv1DTranspose and UpSampling1D layers. The first transpose convolution layer, with 128 filters, begins expanding the latent representation, followed by an upsampling layer that doubles its size. A second Conv1DTranspose layer with 64 filters further refines the reconstruction, again followed by upsampling. Finally, a third transpose convolution layer with a sigmoid activation restores the time series to its original dimensions, completing the reconstruction process.

The model comprises 99,073 trainable parameters and is optimized using the Mean Absolute Error (MAE) loss function. The Adam optimizer is employed to ensure efficient training. This CNN autoencoder architecture is well-suited for tasks such as feature extraction, anomaly detection, and noise reduction in time series data (Fig. 7). Its structure demonstrates the capability of deep learning models to handle complex temporal patterns, making it a valuable tool for both research and practical applications.

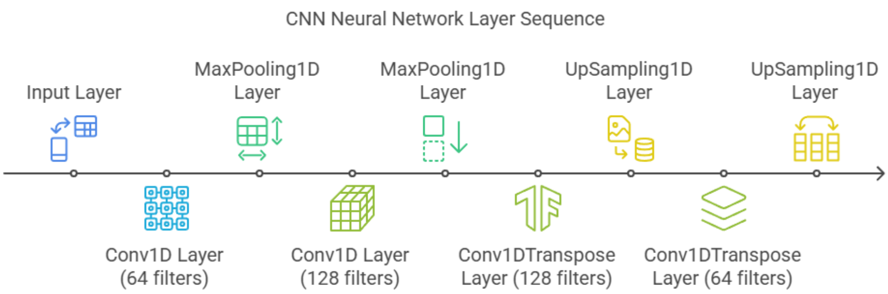

Fig. 7. CNN neural network layer sequence

Fig. 8 shows the training and validation losses of the CNN model. The training loss stabilized at around 0.80, while the validation loss initially decreased from 1.10 to 0.75, then fluctuated between 0.75 and 0.85 during later epochs. The stable training loss suggests that overfitting is not an issue, although the fluctuations in the validation loss might indicate some instability in the model's generalization performance. Overall, the model performs effectively with low loss values. Fig. 9 displays the distribution of MAE losses during training. The losses are predominantly clustered in the 0.4 to 0.6 range, with high loss values being rare. The fact that there are very few samples exceeding the 1.42 threshold indicates that the model performs well on normal data and is effective in anomaly detection. In general, the model has achieved successful learning with low losses. Fig. 10 presents the MAE losses on the CNN model's test data. Most loss values are concentrated below 2, and only a very few samples exceed the threshold of 16.89. This demonstrates that the model successfully reconstructs normal data with low error and is effective in detecting anomalies. Fig. 11 illustrates the CNN model's ability to distinguish between normal and anomalous data. During the time steps 0–250, the model accurately reconstructs normal data with low losses. After the 250th step, it correctly identifies anomalies with high losses (e.g., 46.52 and 237.18). The divergence between the blue and orange lines underscores the model's effective anomaly detection performance.

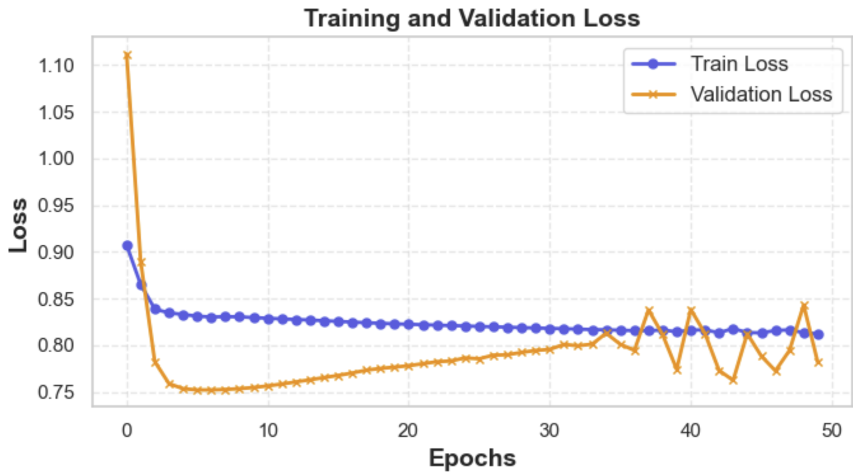

Fig. 8. Training and validation loss graph using CNN model for damage index distribution data

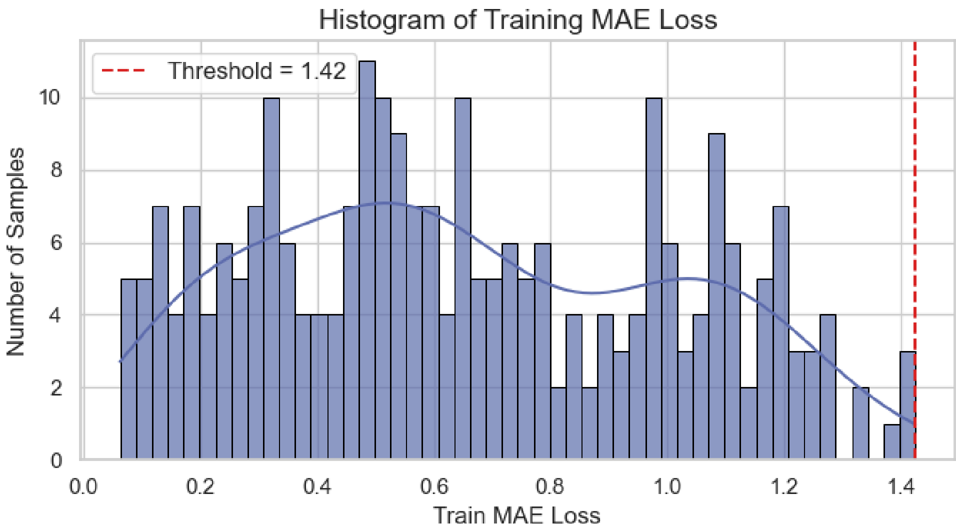

Fig. 9. Histogram of training MAE Loss for CNN model

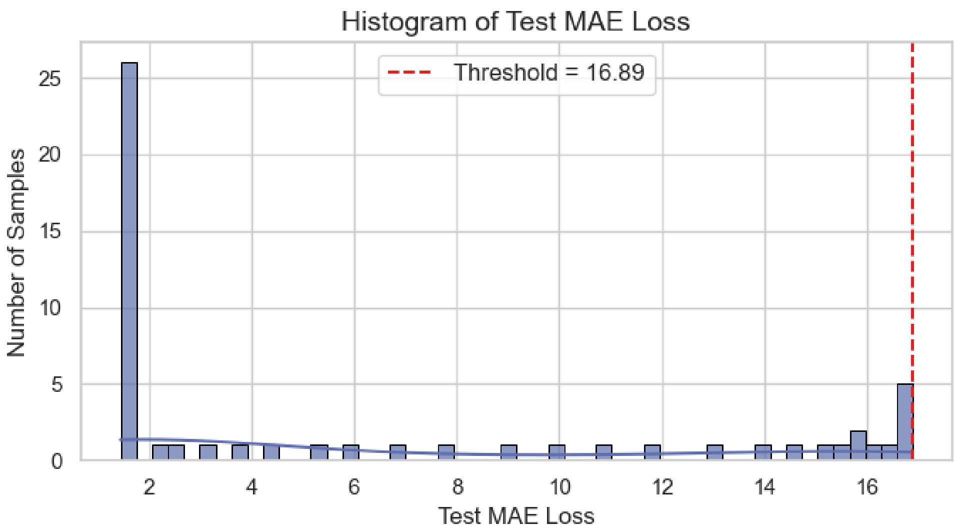

Fig. 10. Histogram of test MAE Loss for CNN model

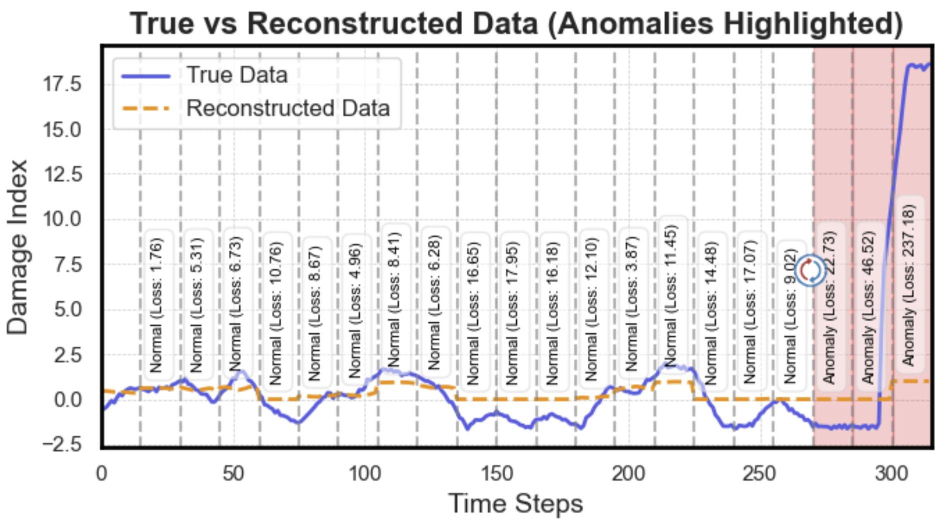

Fig. 11. Anomalies for CNN model

6. Discussion

The proposed video-based structural health monitoring (SHM) system demonstrated considerable promise in assessing the condition of historic masonry minarets through precise, non-contact displacement measurements. By applying advanced optical flow techniques—particularly the pyramidal approach—the system effectively tracked both small and large motions, enabling accurate real-time monitoring of structural dynamics. The conversion of pixel displacements into real-world measurements further confirmed the system's applicability in practical scenarios, especially where traditional sensor-based methods are limited or invasive.

Controlled damage scenarios provided critical insight into the CNN model's performance in anomaly detection. The model exhibited strong spatial feature extraction capabilities, accurately identifying localized damage patterns in the structure. Despite minor fluctuations in validation loss, the CNN maintained stable performance and avoided overfitting, which attests to its reliability for real-world deployment. Its ability to distinguish between normal and anomalous structural conditions underscores the potential of convolutional architectures in video-based SHM applications.

Overall, the findings support the effectiveness of CNNs for spatial anomaly detection in video-based monitoring frameworks. The experimental results validate this approach as a cost-effective, scalable, and non-intrusive tool for continuous structural health assessment, particularly suited for preserving the integrity of historic masonry minarets.

7. Conclusions

This study developed a video-based SHM framework tailored to historic masonry minarets, integrating optical flow techniques with a convolutional neural network (CNN) to achieve accurate, non-invasive anomaly detection. The main findings are as follows:

- Optical flow methods provided reliable, non-contact displacement measurements, enabling structural assessment in areas where direct instrumentation is impractical.
- The CNN model demonstrated strong spatial feature learning capabilities, effectively distinguishing between damaged and undamaged structural states with high accuracy.
- The system's ability to operate under real-time conditions and deliver robust performance under varying damage levels highlights its suitability for long-term structural monitoring.
- The reconstruction-error-based anomaly detection approach enabled the model to generalize from healthy-state data and detect deviations indicative of structural damage.

In conclusion, the proposed video-based SHM system presents a practical and effective approach for monitoring and preserving historic masonry minarets. Its non-invasive nature, combined with the analytical power of CNNs, makes it a valuable contribution to heritage conservation efforts.

Acknowledgments

This study was conducted as part of the research project titled "Video Camera-Based Structural Health Monitoring of Historical Masonry Minarets and Development of a Long-Term Decision-Making Model Based on Deep Learning Method" (Project No: 222M140), supported by the TÜBİTAK 1001 – Scientific and Technological Research Projects Support Program I would like to express my sincere appreciation to the General and Regional Directorates of Foundations for their valuable collaboration and logistical support throughout the research process.

References

Aktürk, F., Aras, F.and Ceribasi, S. (2022). Dynamic response and seismic vulnerabilities of the historic tophane-i amire: dynamic and seismic analysis of a historic masonry building. *J. Comput. Cult. Herit., 15*(3): Article 52.

Baker, S. and Matthews, I. (2004). Lucas-Kanade 20 years on: A unifying framework. *International Journal of* Computer *Vision, 56*, 221-255.

Bouguet, J.-Y. (2001). Pyramidal implementation of the affine lucas kanade feature tracker description of the algorithm. *Intel Corporation, 5*(1-10), 4.

Dong, C.-Z. and Catbas, F. N. (2021). A review of computer vision-based structural health monitoring at local and *global* levels. *Structural Health Monitoring 20*(2): 692-743.

Farrar, C. R., Dervilis, N. and Worden, K. (2025). The Past, Present and Future of Structural Health Monitoring: An *Overview* of Three Ages. *Strain 61*(1): e12495.

Fioriti, V., Cataldo, A., Colucci, A., Ormando, C., Saitta, F.F., Palumbo, D. and Roselli, I. (2024). Innovative graph-based video processing methodology for collapse early warning of historic *masonry* buildings. *Acta IMEKO, 13*(2).

Ghandil, M., Dabanli, O. and Riahi, H.T. (2021). An enhanced indirect video-based measurement procedure for *dynamic* structural system identification applications. *Measurement 182*: 109759.

Lucas, B. D. and T. Kanade (1981). An iterative image registration technique with an application to stereo vision. In: *IJCAI'81: 7th International Joint Conference on Artificial Intelligence.*

Sabia, D., Demarie, G.V. and Quattrone, A. (2022). Structural health monitoring of historic masonry towers: The Case of the Ghirlandina Tower, Modena. *Geotechnical Engineering for the Preservation of Monuments and Historic Sites III*, CRC Press: 191-201.

Sangirardi, M., Altomare, V., De Santis, S.and De Felice, G. (2022). Detecting damage evolution of masonry structures through computer-vision-based monitoring methods. *Buildings 12*(6): 831.

Shariati, A., Schumacher, T. and Ramanna, N. (2014). Exploration of video-based structural health monitoring techniques, Rutgers University. *Center for Advanced Infrastructure & Transportation.*

Simonyan, K. and A. Zisserman (2014). Very deep convolutional networks for large-scale image recognition. *arXiv preprint arXiv*:1409.1556.

Szegedy, C., Liu, W., Jia, W., Sermanet, P., Reed, S., Anguelov, D., Erhan, D., Vanhoucke, V. and Rabinovich, A. (2015). Going deeper with convolutions. In: *Proceedings of the IEEE Conference on Computer Vision and Pattern Recognition*.

Xiong, B. (2021). Video-based vibration analysis for structural health monitoring in civil engineering, Université Rennes 1.

Innovative housing solutions: Integrating ultra-high-performance concrete in modular construction for sustainability and efficiency

Oumaima Awassa [1], Raafat El-Hacha*[1]

[1] University of Calgary, Department of Civil Engineering, 2500 University Drive NW, Calgary, Alberta, Canada

Abstract. The global housing crisis presents an urgent challenge, exacerbated by rapid urbanization, affordability issues, and environmental concerns. Traditional construction methods struggle to meet demand due to high costs, inefficiency, and substantial environmental impact, contributing to over 34% of global energy consumption and nearly 37% of CO_2 emissions. In response, this paper explores the integration of Ultra-High-Performance Concrete (UHPC) in modular construction as a transformative approach to addressing these challenges.
UHPC, recognized for its superior mechanical properties, durability, and sustainability, offers a compelling alternative to conventional construction materials. Its high compressive and tensile strength, combined with its resistance to harsh environmental conditions, makes it an ideal choice for prefabricated modular housing. By leveraging prefabrication techniques, UHPC enables the rapid production of robust and lightweight structural elements, reducing construction timelines, material waste, and overall costs. This study highlights the structural benefits of UHPC sandwich wall panels (SWPs) and waffle slab systems, focusing on their implementation in modular housing. A key aspect of this research is the evaluation of shear connectors used in the SWPs, providing essential data on their mechanical behaviour. The findings contribute to optimizing UHPC modular construction, ensuring efficient load transfer and long-term resilience. Beyond its technical advantages, UHPC modular construction presents a sustainable pathway for urban development. Minimizing embodied carbon, enhancing energy efficiency, and reducing maintenance requirements align with global efforts to achieve net-zero emissions in the built environment. This paper discusses how adopting UHPC in modular housing can significantly enhance construction efficiency while addressing pressing housing shortages in urban and remote regions. The research findings pave the way for a scalable, cost-effective, and environmentally responsible solution to modern housing challenges.

Keywords: Prefabricated modular houses; Sustainability; Ultra high-performance concrete; Sandwich wall panels; Energy efficiency.

---

1. Introduction

Access to safe, affordable, and sustainable housing is foundational to healthy communities and individual well-being. Globally, housing insecurity is reaching critical levels, with 1.6 billion people—roughly 20% of the global population—lacking adequate housing. This includes not only those who are homeless but also millions living in overcrowded, unsafe, or insecure conditions (UN-Habitat, 2024). The housing crisis manifests in various ways across different regions, from urban affordability pressures to post-conflict destruction and climatic extremes As urbanization accelerates—projected to reach 68% of the global population by 2050 (UN-DESA, 2018)—this crisis is poised to deepen unless comprehensive and sustainable strategies are adopted.

In Canada, the housing shortage has intensified, especially in urban centers such as Toronto and Vancouver, where demand consistently outpaces supply. Factors such as rapid immigration-driven population growth, limited land availability, and sluggish construction timelines contribute to surging property and rental prices (Government of Canada, 2023; CBS News, 2023). The Canada Mortgage and Housing Corporation estimates that the country needs an additional 3.5 million housing units by 2030 to restore pre-2004 affordability levels (CMHC, 2024). Although the federal government has committed more than $9 billion since 2013–14 (CHI, 2024), including the $4 billion Housing Accelerator Fund, to streamline approvals and stimulate construction, these measures alone may be insufficient to meet escalating demand (CBS News, 2023).

The Canadian housing crisis also disproportionately impacts remote and northern communities, where geographic remoteness, logistical hurdles, and extreme weather inflate construction costs. In the Northern Territories, where temperatures can drop below -40°C, nearly 26% of households face overcrowding or require

* Corresponding author, E-mail: relhacha@ucalgary.ca

https://doi.org/10.31462/icearc2025_ce_eqe_532

major repairs (CBC News, 2024). The high costs of material transport and the need for specialized, climate-resilient construction exacerbate these issues. A house in northern Canada may cost up to three times more than in southern regions (CMHC, 2024). This national housing crisis reflects a broader global trend. Conflict zones such as Ukraine and Syria have seen catastrophic destruction of residential infrastructure. In Ukraine, nearly 40% of housing in war-affected areas has been damaged or destroyed, displacing millions (IDMC, 2022). Syria, enduring over a decade of civil war, has over 6 million internally displaced citizens, many in inadequate shelters (UNHCR, 2025). These examples underscore the urgent need for rapid, resilient, and adaptable housing solutions.

Climate and environmental pressures add another layer of complexity. Cold-climate regions like Russia and Scandinavia face similar construction and durability challenges. Simultaneously, traditional construction practices significantly contribute to environmental degradation. In 2021, the construction and operation of buildings accounted for 34% of global energy consumption and 37% of CO_2 emissions (IEA, 2022). The embodied carbon in construction materials like cement and steel, alongside lifecycle emissions, intensifies the ecological footprint of the built environment. These environmental concerns have galvanized the construction industry to seek more sustainable alternatives. The World Green Building Council's "Advancing Net-Zero" initiative and other global efforts aim to achieve net-zero carbon buildings by 2050 and reduce embodied carbon by at least 40% by 2030 (WGBC, 2025). McKinsey & Company projects that green construction will represent 60% of new buildings by 2030, and nearly half of the construction firms have already integrated green practices into at least half of their project (McKinsey & Company, 2020).

Innovative technologies such as Ultra-High-Performance Concrete (UHPC) and Carbon Nanofiber-reinforced UHPC (CNF-UHPC) are emerging as promising solutions. These materials offer unparalleled strength, durability, and sustainability. Coupled with modular construction techniques, they present a viable strategy for building resilient, cost-effective, and environmentally conscious housing. Prefabricated modular construction can expedite housing delivery while reducing waste and emissions, making it a compelling alternative to traditional methods. However, to fully assess the viability of modular UHPC-based housing, a life-cycle evaluation is critical to quantify its sustainability benefits relative to conventional construction.

This paper explores the application of UHPC and CNF-UHPC in modular construction as a strategic response to the global housing crisis. It investigates the social, environmental, and economic impacts of these technologies and highlights their role in fostering a more equitable and sustainable future.

2. Modular construction: global perspectives on opportunity and challenges

Modular construction, also known as off-site construction, is rapidly transforming the global construction landscape by providing a compelling alternative to traditional on-site methods. Built-in controlled factory settings using the same materials and regulatory standards as conventional buildings, modular structures can be assembled in significantly shorter timeframes, improving efficiency and sustainability. While the method has demonstrated substantial benefits—including reduced construction time, lower environmental impact, and improved quality—several challenges still hinder its widespread adoption. This integrated overview explores modular construction's advantages, challenges, and real-world applications.

2.1. Distinction between precast and prefabricated construction

Precast construction refers to producing components in reusable molds and transporting them to the site for assembly. Prefabricated construction, however, involves off-site manufacturing of entire building modules—including structural, mechanical, and architectural systems—that are delivered nearly complete. While both methods aim to improve efficiency and quality, modular prefabrication supports faster project delivery and greater environmental and cost savings when implemented at scale (NI, 2025; Quora, 2025; Patyal, 2019; MBI, 2025).

2.2. Key advantages of modular construction

Modular construction offers numerous advantages that span across project performance, sustainability, and user experience:

- Time and Cost Efficiency: Modular projects allow simultaneous off-site fabrication and on-site preparation, resulting in timeline reductions of up to 50% and cost savings of up to 25% (Ferdous et al., 2019; O'Connor et al., 2014; Salama et al., 2017; Becker, 2003; Pan, 2007). Case studies in Melbourne, Australia, demonstrated the construction of high-rise modular buildings—including a 9-story apartment built in 5 days and a 25-story tower completed in 27 weeks—achieved 30% faster completion rates (Ferdous et al., 2019; Gunawardena et al., 2014).
- Sustainability and Environmental Impact: Modular systems can reduce material waste by 65%, CO_2 emissions by 36%, and delivery trips by 70% (Lawson et al., 2012). Other studies report reductions in timber and water usage by 71% and 22%, respectively, along with a 6.6% decrease in human health impacts and 3.5% in ecosystem damage (Cao, 2015).

- Improved Quality Control: Controlled environments facilitate rigorous testing, better tolerance control, and minimized defects. The repetitive nature of factory processes also fosters continuous improvement and reduces variability (Pan, 2007; NRC, 2009).
- Safety: Factory-based production improves worker safety, reducing on-site accidents by up to 80% (Peñaloza, 2017).
- Flexibility and Adaptability: Modular units can be reconfigured, relocated, or expanded easily, making them suitable for evolving demands in housing, healthcare, and disaster relief (Ferdous et al., 2019; Chourasia et al., 2023; Shahzad et al., 2022; Chen et al., 2022).

2.3. Current limitations and implementation challenges

Although modular construction provides substantial benefits—including accelerated project delivery, enhanced quality control, and notable environmental performance—it is not without significant challenges. Despite its growing recognition as a viable approach to meeting the construction industry's evolving demands for efficiency and sustainability, several barriers hinder its broader implementation. These challenges encompass the entire project lifecycle, beginning with the high initial capital investment required to establish prefabrication facilities. Further complexities arise in the logistics of transporting large volumetric modules, as well as in navigating regulatory frameworks that are often tailored to conventional construction methods. Additionally, modular construction is subject to inherent design constraints that may limit architectural flexibility and customization. Market uptake is further constrained by persistent skepticism regarding the structural integrity and long-term performance of modular buildings, underscoring the need for greater public awareness and industry education. The following external factors restrain the widespread adoption of modular construction.

2.3.1. Inadequate design codes and standards

The lack of modular-specific design codes impedes performance prediction and quality assurance. Traditional codes often fail to address unique load paths, connection details, and short-term stresses from transport and lifting. Modular guidelines such as Lawson's *Design in Modular Construction* and region-specific codes like the IRC/IBC/IECC in the U.S. are emerging to bridge this gap (Bogenstätter, 2000; Lacey et al., 2018; Murray-Parkes et al., 2017; Mao et al., 2015; Blagojevich & Whitaker, 2007; Lu et al., 2017 ; Lawson et al., 2014).

2.3.2. Skilled labour shortage

Modular construction requires trained personnel in digital design, precision manufacturing, and hybrid assembly techniques. China and Australia have identified workforce development as a strategic need, prompting collaborations between academia and industry to upskill labour (Lu et al., 2017; Iacovidou et al., 2021).

2.3.3. Transportation and logistics constraints

Large modules are challenging to transport due to size, height, and weight restrictions. Damage during transit and long-distance delivery contribute to delays and cost overruns. To mitigate this, compact module design and factory-site proximity strategies are increasingly employed (Lacey et al., 2018; Godbole et al., 2018; Nester et al., 2003).

2.3.4. High initial investment

Establishing a modular factory demands significant upfront capital, particularly in urban centers with high land values. While long-term gains are evident, the initial barrier discourages small developers. Public incentives and shared investment models are helping reduce this threshold (Rahman, 2014; Chiang et al., 2006; Pan et al., 2012; Ribeiro et al., 2022).

2.3.5. Communication and integration complexity

Successful modular projects demand close collaboration among architects, engineers, manufacturers, and contractors—often working from dispersed locations. Communication lapses can lead to assembly issues, delays, and increased costs. Integrated project delivery (IPD), BIM tools, and regular stakeholder meetings are crucial mitigation strategies (Ribeiro et al., 2022; Ezzeddine & de Soto, 2021; Thurairajah et al., 2023).

Modular construction presents considerable advantages in terms of sustainability, operational efficiency, and cost optimization when executed under appropriate conditions. However, the full realization of these benefits is contingent upon resolving persistent logistical constraints. As the sector advances, developing and implementing long-term, system-level strategies that enhance the logistical infrastructure supporting modular construction is imperative. Such advancements are essential to enable the widespread deployment of modular systems as an efficient, sustainable, and scalable solution to the global housing demand.

2.4. Global Case studies and applications

Modular construction has been applied worldwide in residential towers, emergency hospitals, educational buildings, and military facilities. It is positioned as a strategy to accelerate urban development while aligning with sustainability goals. The COVID-19 pandemic further underscored its utility, with modular hospitals erected in record time (Chen et al., 2022).

Queen Elizabeth University Hospital-Glasgow, Scotland (Multiplex, 2015)

- Queen Elizabeth University Hospital in Glasgow is a state-of-the-art facility, and modular construction was employed to construct certain areas, including plant rooms and support services. The use of prefabricated modular components allowed for faster installation of critical building systems

Mount Sinai Medical Center Expansion – New York City, USA (NK Architects, 2016)

- Mount Sinai Medical Center in New York utilized modular construction techniques for the expansion of certain sections of the hospital. Prefabricated components such as bathroom pods and mechanical systems were manufactured off-site and assembled on-site, allowing for more efficient and less disruptive construction

Dalston Works – London, UK (Waugh Thistleton Architects, 2017)

- Dalston Works is a 10-story modular residential and commercial building in East London. It is constructed entirely from cross-laminated timber, making it one of the tallest timber modular buildings in the world

Clement Canopy – Singapore (dezeen, 2019)

- Clement Canopy is one of the tallest modular buildings in the world, consisting of two 40-story residential towers. The project utilized volumetric modular construction, with each module fully finished and assembled off-site before being stacked on-site

Wuhan Emergency Modular Hospitals – Wuhan, China (Miller, 2020)

- In response to the COVID-19 pandemic, Wuhan built several emergency hospitals using modular construction. One of the most notable examples is the Huoshenshan Hospital, constructed in just 10 days using prefabricated modules. This 1,000-bed hospital was built to treat COVID-19 patients and was one of the fastest examples of healthcare infrastructure being delivered during a crisis

101 George Street – Croydon, London, UK (CTBUH, 2021)

- 101 George Street in Croydon, London, is the tallest modular building in the world, consisting of two towers. The project features 546 units and was developed using volumetric modular construction.

Smith's Garden: 26-Storey Modular Residential Tower–Birmingham, UK (Ongoing) (Goodstone, 2025)

- Smith's Garden is a modular residential development currently under construction in Birmingham, UK. The project includes a 26-story tower constructed using volumetric modular construction techniques. This method enables faster assembly, improved quality control, and reduced environmental impact, offering an efficient solution to meet growing urban housing demands

Horizon North Modular Housing – Various Locations, Canada (ongoing) (Housing Innovation Collaborative, 2025)

- Horizon North is building modular housing units in multiple Canadian cities, including Calgary and Edmonton, as part of a nationwide effort to provide affordable housing.

Fig. 1: Global modular construction projects

3. Ultra-high-performance concrete (UHPC): comparative developments and applications

3.1. Evolution and fundamentals of ultra-high-performance concrete (UHPC)

Ultra-High-Performance Concrete (UHPC) represents a paradigm shift in cementitious composite materials, addressing the limitations of conventional concrete systems by offering superior mechanical performance and exceptional durability under aggressive environmental conditions. Characterized by a water-to-binder ratio ≤ 0.25, compressive strengths exceeding 120 MPa, and post-cracking tensile strengths of at least 5 MPa, UHPC combines optimized granular packing, absence of coarse aggregates, and the inclusion of high-performance pozzolanic admixtures such as silica fume to form a dense, discontinuous pore structure (Ahmed Sbia et al., 2014; Norhasri et al., 2016; Russell & Graybeal, 2013; Al-Osta, 2018; CSA, 2019).

Early advancements in UHPC can be traced to pre-1980s research that emphasized vacuum mixing and thermal curing to densify the matrix and enhance mechanical properties (Roy et al., 1972). Subsequent innovations in the 1980s led to Micro-Defect-Free (MDF) cement and Densified Systems with Ultra-fine Particles (DSP). However, challenges in workability and placement due to the absence of adequate superplasticizers hindered large-scale adoption (Birchall et al., 1981; Bache,1981).

A breakthrough occurred in the 1990s with the development of Reactive Powder Concrete (RPC) by Richard and Cheyrezy, culminating in commercial UHPC products such as Ductal® (Richard & Cheyrezy, 1995). The material was first deployed in the Sherbrooke Pedestrian Bridge in Quebec, Canada, in 1997, showcasing a pioneering use of 3D precast UHPC trusses post-tensioned on-site (Azmee & Shafiq, 2018; Blais & Couture, 1999). Despite the innovation, widespread use remained limited due to RPC's high cost, specialized curing requirements, and the lack of unified design standards.

Post-2000s, the field has witnessed a marked shift toward sustainability and scalability. UHPC formulations now often incorporate supplementary cementitious materials (SCMs) like fly ash, ground granulated blast furnace slag (GGBFS), silica fume, and rice husk ash to reduce environmental impact and energy consumption while enabling ambient curing methods (van Nguyen et al., 2010; Yu et al., 2015). Several design guidelines now offer technical frameworks supporting UHPC's structural applications (CSA, 2019; ACI 239, 2018; PCI (Sim et al., 2020); FHWA (Graybeal & El-Helou 2023); AASHTO, 2024; AFNOR (NF, 2016).

3.2. Mechanical properties and durability characteristics of UHPC

UHPC exhibits a combination of ultra-high compressive strength, enhanced tensile performance, and unparalleled durability, distinguishing it from normal-strength concrete (NSC) and even high-performance concrete (HPC). Typical compressive strengths range from 120 to 150 MPa, with some formulations exceeding 200 MPa depending on curing protocols and mix optimization (Russell & Graybeal, 2013). This exceptional performance is achieved through a highly optimized particle gradation, elimination of coarse aggregates, a very low water-to-binder ratio, and the incorporation of high-range water reducers and silica-based pozzolanic materials (Al-Osta, 2018).

A defining characteristic of UHPC is its post-cracking tensile strength, typically ≥5 MPa, enabled by including steel or synthetic fibres. These fibres enhance the strain-hardening behaviour by bridging micro-cracks and arresting crack propagation, thereby converting a traditionally brittle failure mode into a more ductile response. For example, adding 2% steel fibre volume can lead to tensile strength improvements of up to 228% and flexural strength gains of 180% relative to fibre-free UHPC (El-Abbasy, 2023). This transformation in behaviour is critical in structural applications requiring enhanced energy absorption and impact resistance.

In terms of durability, UHPC's ultra-dense matrix—with minimal capillary porosity and discontinuous pore structure—yields extremely low permeability. Water and chloride ion ingress are significantly curtailed, with the chloride diffusion coefficient up to 50 times lower than that of NSC (Chuang & Huang, 2013). This makes UHPC particularly advantageous for marine and de-icing salt environments where reinforcement corrosion is a major concern.

Carbonation resistance is another critical attribute. While carbonation in conventional concrete reduces alkalinity and depassivates steel reinforcement, UHPC's refined microstructure dramatically retards this process, preserving internal pH and prolonging service life (Li et al., 2020; Andrade & Torres, 2013; Kono et al., 2013; Piérard et al., 2013).

UHPC also demonstrates superior freeze-thaw resistance. The tightly packed microstructure limits internal water movement, mitigating internal stresses induced by freezing cycles. Studies indicate UHPC retains >95% durability factor after 300–600 cycles with negligible mass loss (Li et al., 2020; Zhong & Wille, 2015), and in some cases, performance remains unaffected even after 800 cycles (Wang, 2011). In contrast, NSC commonly suffers deterioration after just 300–400 cycles (ASTM C666, 2008). Furthermore, UHPC's abrasion resistance, fatigue life, and resistance to alkali-silica reaction (ASR) are considerably superior, contributing to its increasingly widespread use in critical infrastructure such as bridges, tunnels, and precast façade systems (van Nguyen et al., 2010; Yu et al., 2015).

3.3. Carbon nanofibre (CNF) innovations in UHPC

Recent advancements in nanotechnology have led to a transformative enhancement in UHPC by incorporating carbon nanofibres (CNFs), ushering in a new generation of high-performance, multifunctional cementitious composites. CNFs are nanoscale carbon-based materials known for their extraordinary tensile strength, elastic modulus, electrical and thermal conductivity, chemical inertness, and low density (Sharon, 2021).

Including CNFs in UHPC matrices has improved fresh and hardened properties. In the fresh state, CNFs act as nucleation sites during the hydration process, facilitating a more uniform and accelerated hydration reaction. Each cubic meter of CNF-UHPC contains approximately 7×10^{19} individual CNFs—equivalent to about eight nanofibres per cement grain—contributing to a more homogeneous internal structure and reduced differential stress during early-age curing. These microstructural refinements offer substantial performance benefits. CNF-reinforced UHPC achieves high early-age compressive strengths—exceeding 80 MPa within 10 hours and surpassing 100 MPa at 24 hours—making it suitable for time-sensitive construction scenarios. The nanofibres also serve as crack arrestors at the micro- and nano-scale, delaying the initiation and growth of tensile cracks and enhancing the modulus of rupture and post-cracking strength. Additionally, CNFs help reduce autogenous shrinkage by forming a nanoscale mesh that counteracts internal tensile stresses. Their presence also densifies the interfacial transition zones (ITZs) between cement paste and aggregates or embedded steel fibres. This densification leads to improved bond strength, particularly the pull-out resistance of steel fibres, thereby enhancing the composite's overall tensile ductility and energy absorption capacity (Sharon, 2021; Yıldırım et al., 2018; Morsy et al., 2010; Patil & Deshpande, 2012; El-Gamal et al., 2017; Shi et al., 2019).

From a sustainability standpoint, CNF-enhanced UHPC (CNF-UHPC) offers a route to reduce the required steel fibre volume while maintaining or improving mechanical performance. This reduction translates into lower embodied energy and carbon emissions. Notably, CNF-UHPC manufactured by ceEntek Pte Ltd achieves compressive strengths up to 160 MPa and tensile strengths near 10 MPa while remaining compatible with standard mixing and placement techniques at precast plants or in-field applications (CeEntek, 2020).

As the industry advances toward low-carbon construction, CNF-UHPC emerges as a robust, resilient, and environmentally conscious alternative to traditional cementitious materials—particularly in regions with extreme weather conditions, seismic risk, or limited infrastructure access.

3.4. Field applications and practical implementation of UHPC

The global deployment of UHPC has grown substantially over the past two decades, driven by its outstanding mechanical performance, durability, and potential for architectural innovation. Initially adopted in bridge construction, UHPC has evolved into a multipurpose material suitable for complex structural and aesthetic applications in precast and cast-in-place formats.

The first landmark application of UHPC occurred in 1997, when the Sherbrooke Pedestrian Bridge was constructed in Quebec, Canada. The bridge comprised six precast UHPC space truss elements post-tensioned on site, marking a turning point in structural precast technology (Corvez, 2011). This innovation was followed by the Mars Hill Bridge in Iowa, USA, completed in 2006, which reinforced UHPC's suitability for accelerated bridge construction and long-span solutions (Azmee & Shafiq, 2018).

In Europe and Asia, UHPC has been employed in pedestrian and vehicular bridges, showcasing slender geometries and extended service life with minimal maintenance. Examples include the Horikoshi C-ramp Bridge in Japan and the Shepherd's Gully Bridge in Australia, where UHPC's high strength-to-weight ratio enabled reduced structural depth and material consumption (Amran et al., 2022).

UHPC's architectural potential has been equally significant. Projects such as the Museum of European and Mediterranean Civilizations (MuCEM) in Marseille (2013), the Fondation Louis Vuitton in Paris (2014), and the roof of the Jean Bouin Stadium illustrate UHPC's capability to form thin, complex geometries with exceptional durability (Azmee & Shafiq, 2018). Similarly, the Olympic Museum in Lausanne employed UHPC to realize elegant, lightweight roofing systems, exemplifying the synergy of form and function (Muttoni et al., 2013). In 2019, the National Museum of Qatar showcased UHPC's versatility by featuring it in its façade design (Azmee & Shafiq, 2018).

In North America, Lafarge Canada, the University of Calgary, and DIALOG Consulting pioneered one of the first ultra-thin UHPC architectural façade systems, used in "The Atrium" project in Victoria, British Columbia. These façade panels, validated through rigorous testing, offered structural integrity and thermal performance. Their success led to subsequent implementations at the Rotman School of Management (Toronto) and Ornan's Infant School in France (Seibert et al. 2012).

The development of standardized design and construction guidelines has also facilitated the practical implementation of UHPC. Organizations such as CSA (2019), ACI 239 (2018), PCI (Sim et al., 2020), FHWA (Graybeal & El-Helou 2023), AASHTO (2024), and AFNOR (NF, 2016) now provide prescriptive guidance for UHPC's structural use, including material characterization, detailing requirements, and durability design. These codified practices are essential to ensuring quality control and broader industry adoption.

Notably, CNF-enhanced UHPC is being investigated for modular construction, seismic retrofitting, and impact-resistant structures. With its extended service life (often exceeding 100 years), reduced section size, and minimal need for passive reinforcement, CNF-UHPC is poised to reshape the landscape of sustainable and resilient infrastructure (CeEntek, 2020).

4. Benefit of integrating UHPC in modular construction

The expected benefits of integrating UHPC into modular housing systems are multi-dimensional:

- Alleviating Housing Shortages: The speed and scalability of modular construction using UHPC systems make them ideal for addressing housing crises in developed and developing regions, especially where onsite construction is impeded by weather, terrain, or socio-political constraints.
- Improved Affordability and Lifecycle Economics: Although the initial material and fabrication costs may be higher than conventional methods, these are offset by savings in construction time, energy consumption, maintenance, and transportation logistics due to lighter elements and faster installation cycles.
- Resilience and Disaster Resistance: UHPC-based modular units exhibit high resistance to impact, freeze-thaw cycles, chloride penetration, and other environmental deteriorations, making them well-suited for disaster-prone and climate-vulnerable areas.
- Architectural and Functional Flexibility: UHPC's rheological properties allow for intricate mouldings and customized finishes without additional treatments, addressing aesthetic considerations while maintaining strength. This opens new avenues in modular design, where standardization and customization often compete.
- Development of Standardized Guidelines: There is a growing need to formalize design frameworks and construction specifications for UHPC modular systems. Establishing comprehensive codes and guidelines will support broader adoption by engineers and practitioners, fostering economic and environmentally conscious practices.

5. Design challenges in UHPC-based modular construction

5.1. Absence of standardized design guidelines

Integrating UHPC into modular construction presents significant challenges due to the lack of standardized design guidelines tailored to UHPC, which is a primary challenge in the structural design of modular housing systems. While UHPC offers substantial benefits such as reduced member thickness, enhanced durability, and lower self-weight, its application in modular systems such as ribbed floor slabs and lightweight roofing panels is constrained by the limited availability of codified methodologies. In particular, although structurally efficient, the slenderness of UHPC floor systems may introduce serviceability concerns related to vibrations, potentially affecting occupant comfort and satisfaction. Studies have highlighted that high-strength slender floor elements can exhibit vibration issues that impact user comfort.

5. 2. Connection detailing and structural continuity

Another significant design consideration involves the performance and detailing of connections. Ensuring effective load transfer across prefabricated components is crucial for structural integrity. However, the behaviour of connections, especially under dynamic and long-term loading conditions, especially for UHPC elements, remains insufficiently documented in existing codes. This lack of information poses reliability concerns during the assembly and service of UHPC elements. UHPC connections require careful detailing to maintain structural continuity and performance.

5.3. Performance under extreme loading conditions

Furthermore, desiginig for structural safety under extreme loading conditions—such as seismic events, wind loads, and fire exposure—remains a design grey area for UHPC applications and is challenging due to the lack of well-established predictive models or design provisions for UHPC in current standards (Graybeal, 2011). This is particularly problematic for modular buildings where structural redundancies are minimized. Studies have emphasized the need for comprehensive guidelines to address UHPC behaviour under such extreme conditions (Jabbar et al., 2022).

5.4. Thermal performance and airtightness

Similarly, thermal performance and airtightness—especially in wall and roof assemblies using thinner UHPC sections—necessitate detailed consideration to meet energy efficiency targets. Thermal performance and airtightness are critical factors, especially in modular construction, where energy efficiency is a priority. Research has shown that UHPC sandwich panels can be designed to improve energy efficiency while maintaining structural performance (Ghazy et al., 2025).

5.5. Foundation systems for lightweight modular construction

Developing foundation systems compatible with lightweight modular construction and adaptable to variable geotechnical conditions is essential. The reduced weight of UHPC elements requires foundations that can accommodate these characteristics without compromising stability. Innovative foundation solutions are needed to support the unique demands of UHPC modular systems.

5.6. Sandwich wall panels (swps) design complexity
Among the most complex components from a structural and thermal design perspective are Sandwich Wall Panels (SWPs). These elements simultaneously serve as load-bearing components and as integral parts of the thermal envelope. Typically composed of two concrete wythes separated by a rigid insulation core, SWPs must achieve adequate shear transfer between layers while minimizing thermal bridging. Careful detailing of connectors and embedment strategies is necessary to balance structural and thermal performance (Ghazy et al., 2025).

6. UHPC in modular housing development at the University of Calgary

6.1 Proposed UHPC modular hourse
Integrating UHPC, particularly CNF-UHPC developed by ceEntek Pte Ltd, into modular construction systems represents a pivotal advancement in modern construction technologies. UHPC is recognized for its exceptional mechanical and durability properties, including ultra-high compressive and tensile strengths, improved fire resistance, and superior resistance to environmental degradation. These characteristics significantly reduce the thickness and weight of structural components, optimizing material use and improving logistics, especially in volumetric modular housing systems.

Prefabricated modular homes, often constructed using volumetric three-dimensional units manufactured off-site, benefit extensively from UHPC's performance. These modules are especially suitable for applications such as multi-unit residential buildings, hotels, dormitories, and single-family housing. The lightweight nature of UHPC structural components allows for more efficient transportation and erection, minimizing on-site construction time and enabling rapid deployment in both urban and remote contexts. This is particularly beneficial in regions facing urgent housing needs due to conflict, natural disasters, or climate-related challenges.

The modular system under development, showcased in ongoing research at the University of Calgary, utilizes insulated CNF-UHPC sandwich wall panels (SWPs), CNF-UHPC waffle floor slabs, and CNF-UHPC roof components (Figure 2). The SWPs incorporate thin inner and outer UHPC wythes (typically 15–50 mm thick), separated by high-performance insulation up to 150 mm in thickness. These wythes are interconnected using non-metallic Glass Fiber Reinforced Polymer (GFRP) shear connectors, chosen for their corrosion resistance, low thermal conductivity, and cost-effectiveness compared to other FRP types. All elements are wet-cast in a controlled factory environment using CNF-UHPC mix designs optimized for flowability and strength retention across interfaces.

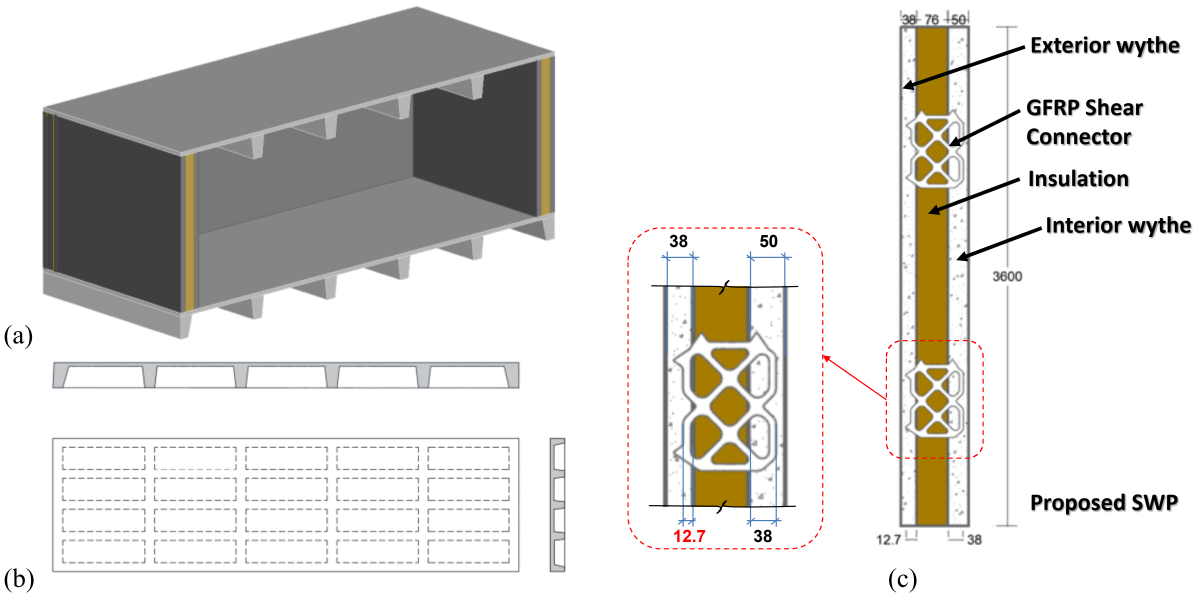

Fig. 2: (a) Prefabricated UHPC modular house, (b) waffle floor/roof element, and (c) proposed insulated sandwich wall panel

The structural system's reduced mass—often under 20 tonnes for an entire modular unit—allows for deployment with smaller cranes and transport vehicles, cutting overall construction and installation costs. Moreover, integrating waffle slabs for floors and roofs enhances load distribution efficiency and system robustness while maintaining minimal weight. The result is a resilient, high-performance building envelope capable of enduring dynamic and static loads, seismic activity, high winds, and fire exposure.

Beyond structural benefits, using CNF-UHPC in modular housing aligns with global sustainability goals. Its high durability and resistance to degradation extend service life and reduce maintenance requirements, thus lowering life cycle costs and environmental impacts. Adopting CNF-UHPC in modular housing promotes sustainable construction practices by reducing material use, minimizing construction waste, and improving energy efficiency. Such systems are especially suited for sustainable development in areas facing logistical or climatic constraints. The thermal efficiency and reduced mass of UHPC panels contribute significantly to reducing heating and cooling loads, constituting the largest share of energy consumption in residential buildings.

A critical element in validating this innovative construction system involves extensive performance evaluations at both the material and structural levels. At the material level, CNF-UHPC's mechanical properties, including tensile ductility, compressive strength, and long-term durability, are being thoroughly investigated. At the structural level, tests on full-scale SWPs, waffle slabs, and roof elements under varying loading conditions are being conducted. Special focus is given to evaluating air-tightness, thermal performance, and lifecycle cost metrics to assess the modular system's competitiveness against conventional alternatives. Testing is ongoing to confirm CNF-UHPC's capacity to deliver superior thermal insulation and airtightness, thereby reducing operational energy consumption and greenhouse gas emissions throughout the building's life cycle.

6.2 Experimental validation of GFRP shear connectors

A comprehensive experimental program was initiated to validate the mechanical performance of UHPC modular elements under realistic conditions. One particular design constraint arose from the need to utilize thinner panel sections, which precluded the use of the manufacturer-recommended minimum embedment length of 1.5 inches for GFRP shear connectors (Figure 2c). Thus, the 1.5 inches minimum embedment length for GFRP shear connectors could not be achieved. Instead, panels were fabricated with a reduced embedment length of 0.5 inches, necessitating experimental verification of their shear transfer capacity.

6.2.1 Double shear test setup and results

A double shear test was conducted to assess the structural performance of the GFRP connectors under these modified conditions (refer to Figure 3). The average shear capacity was determined to be 9.18 kN, closely aligning with the manufacturer's reported capacity of 7.94 kN, despite the latter being based on normal-strength concrete and longer embedment. These findings suggest that the used GFRPshear connectors retain robust mechanical performance even with reduced embedment in UHPC, likely due to the superior bond characteristics and matrix strength of UHPC compared to conventional concrete (Yoo & Yoon, 2017). All specimens showed the same failure mode, indicating rupture of the GFRP shear connectors (Figure 4).

This outcome validates the use of shorter embedment lengths in thin UHPC wall panels and reinforces the feasibility of efficient and structurally sound SWP designs within modular construction frameworks. The improved understanding of connector behaviour under constrained embedment conditions offers valuable flexibility in the geometric and architectural design of UHPC-based modular systems.

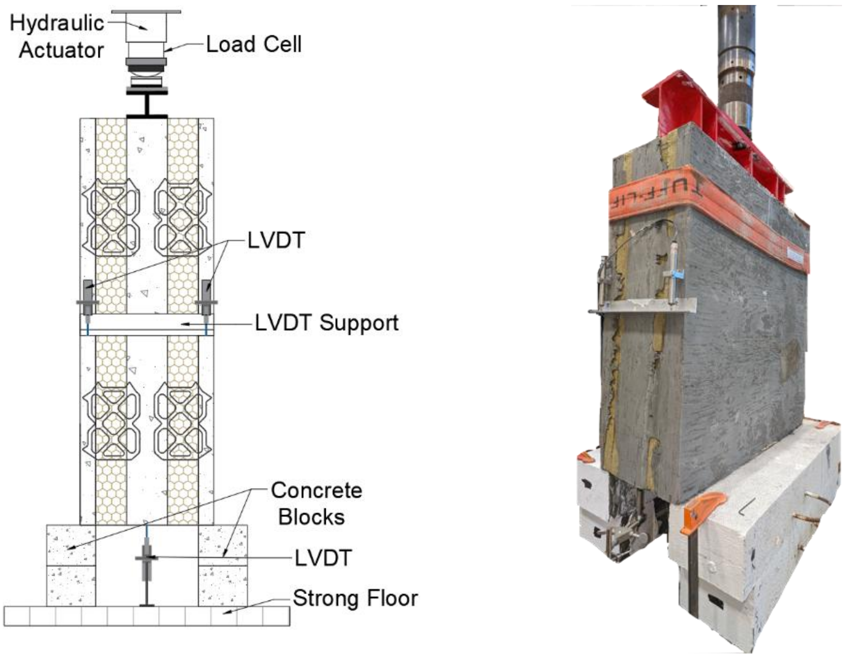

Fig. 3: Double Shear Test Set-up for GFRP Connectors

Fig 4. Failure of the GFRP shear connectors

7. Executive summary and conclusion

Modular construction is no longer a niche approach—it is an innovative paradigm with a proven ability to deliver quality, speed, and sustainability in the built environment. Although challenges remain—particularly in logistics, standards, and labour—the rapid evolution of digital tools, manufacturing technologies, and collaborative project delivery models are paving the way for broader adoption. A coordinated global effort in training, regulation, and innovation is essential to unlocking its full potential as a resilient and adaptable construction methodology for the future.

Incorporating Carbon Nanofiber Ultra-High-Performance Concrete (CNF-UHPC) into modular housing systems presents a significant advancement in pursuing high-performance, durable, sustainable and resilient residential construction. These advanced cementitious materials combine superior mechanical and durability properties with eco-efficient features, enabling the fabrication of thin, lightweight yet high-strength components, resulting in modular units with reduced material consumption and embodied energy while maintaining structural integrity and resilience under extreme conditions, including high wind loads, seismic activity, and aggressive environments. The high mechanical properties of UHPC allow for the creation of thinner elements, which facilitate easier transportation and rapid onsite assembly, thus aligning with the core principles of modular construction.

From a sustainability standpoint, UHPC-based systems significantly minimize construction waste and carbon emissions while offering service lives exceeding 100 years with minimal maintenance and repair interventions, especially in severe environments. These properties address critical demands in contemporary housing, particularly in regions facing shortages, harsh environmental constraints, or rapid urbanization pressures. Furthermore, UHPC modules exhibit enhanced resistance to natural disasters such as floods, high winds, and extreme temperatures, making them highly suitable for deployment in climate-vulnerable and disaster-prone areas. Such longevity reduces lifecycle costs and alleviates the burden on landfills, particularly in regions with limited waste-processing infrastructure. Despite higher initial material and production costs, the long-term economic benefits of UHPC—through reduced maintenance, extended service life, and operational energy savings—render them cost-effective over the building lifecycle. In addition, the aesthetic versatility of UHPC allows for the replication of detailed architectural textures and finishes, expanding the design possibilities for modular housing without compromising structural integrity.

The SWPs utilized in the modular construction comprised two CNF-UHPC wythes with an insulating core. The design aimed to ensure effective load transfer between the layers while minimizing thermal bridging. Experimental results from double shear tests conducted on sandwich wall panels (SWPs) utilizing CNF-UHPC and GFRP shear connectors confirmed that even with reduced embedment lengths, effective shear transfer between the two wythes can be achieved. The successful performance of GFRP shear connectors with reduced embedment lengths supports the feasibility of efficient and structurally sound SWP designs within modular construction frameworks. These findings support the development of lighter and thinner prefabricated modules without compromising mechanical reliability and structural performance, thereby enhancing transportability and onsite assembly. CNF-UHPC further expands the performance envelope of UHPC and, in particular, augments these benefits by incorporating nanofiber reinforcement within its matrix that enhances the ductility, thermal performance, and fracture resistance. The dense microstructure of CNF-UHPC results in lower thermal conductivity, which contributes to decreased energy consumption in extreme climate conditions and improved building envelope efficiency. This contributes significantly to lower operational energy demands, especially in climates requiring intensive heating or cooling. Combined with SWP systems, CNF-UHPC modules have the potential to become net-zero-ready units, aligning with global decarbonization and sustainability goals.

The findings presented herein underscore the importance of continuing efforts to standardize design and construction practices for UHPC-based modular systems. Developing comprehensive design guidelines and construction specifications is necessary to facilitate the wider adoption of CNF-UHPC in modular housing applications, ensuring consistency in performance, safety, and economic viability. As the construction industry seeks innovative solutions for affordable, resilient, and environmentally conscious housing, CNF-UHPC modular technologies are prepared to play a pivotal role in shaping the future of sustainable residential infrastructure. In summary, the convergence of UHPC technologies and modular construction offers a promising pathway toward rapid deployment of next-generation housing solutions that are durable and environmentally responsible. Future work should focus on scaling production methods, optimizing thermal and acoustic insulation of composite panels, and harmonizing international design standards to accelerate the global adoption of UHPC modular housing systems.

In conclusion, the synergy between CNF-UHPC and modular construction presents an innovative path toward rapid, sustainable, and cost-effective housing solutions. The potential for immediate deployment, combined with long-term durability and reduced environmental impact, underscores CNF-UHPC's transformative role in the evolution of prefabricated building systems. As testing and development progress, these systems are poised to become central to addressing the global housing crisis and advancing sustainable infrastructure development.

References

UN-Habitat. (2024). *United Nations Human Settlements Programme*: *World Cities Report 2024*. Retrieved from https://unhabitat.org/wcr

UN-DESA. (2018). *United Nations Department of Economic and Social Affairs: World Urbanization Prospects: The 2018 Revision*. Retrieved from https://population.un.org/wup/Publications/Files/WUP2018-Report.pdf

Government of Canada. (2023). *Housing Plan: Addressing the Housing Crisis in Canada*. Retrieved from https://publications.gc.ca/collections/collection_2023/ccdp-chrc/CH1-44-2023-eng.pdf

CBC News. (2023). *CBC News Interactives*: *Where Can You Afford to Rent? Canada's Rental Housing Crisis*. Retrieved from https://newsinteractives.cbc.ca

CMHC. (2024). *Canada Mortgage and Housing Corporation: Housing Market Outlook: 2024 Forecast*. Retrieved from https://www.cmhc-schl.gc.ca

CHI. (2024). *Canada Housing Infrastructure: Solving the Housing Crisis: Canada's Housing Plan*. Retrieved from https://housing-infrastructure.canada.ca

CBC News. (2024). *CBC News Interactives: Canada's Rental Affordability Crisis: A Nationwide Issue*. Retrieved from https://newsinteractives.cbc.ca/features /2024/rentals-affordability-crisis/

IDMC. (2022). *Internal Displacement Monitoring Centre:* Global Report on Internal Displacement. Retrieved from https://www.internal-displacement.org/global-report/grid2022/

UNHCR (2025). *Syrian Arab Republic*. Retrieved from https://www.unhcr.org/us/countries/syrian-arab-republic

IEA. (2022). *International Energy Agency: World Energy Outlook 2022*. Retrieved from https://www.iea.org/reports/world-energy-outlook-2022

WGBC. (2025). *World Green Building Council: Advancing Net Zero*. Retrieved from https://worldgbc.org/climate-action/embodied-carbon/

McKinsey & Company. (2020). *The Next Normal in Construction: How Disruption is Reshaping the World's Largest Ecosystem*. Retrieved from https://www.mckinsey.com/industries/engineering-construction-and-building-materials/our-insights/the-next-normal-in-construction-how-disruption-is-reshaping-the-worlds-largest-ecosystem

NI. (2025). *Northgate Industries: What is the difference between precast construction and prefabricated construction?* Retrieved from https://www.northgateindustries.com

Quora. (2025). *What is the basic difference between precast and prefabricated structures?*. Retrieved from https://www.quora.com/Design-What-is-the-basic-difference-between-precast-and-prefabricated-structures?topAns=309492622

Patyal, N. (2019, Feb. 21). *Precast and prefabricated components and structures and the connection between them*. Retrieved from https://www.slideshare.net/nishantpatyal

MBI. (2025). *Modular Building Institute. Why Modular?* Retrieved from https://www.modular.org/

Ferdous, W., Bai, Y., Ngo, T. D., Manalo, A., & Mendis, P. (2019). New advancements, challenges and opportunities of multi-storey modular buildings–A state-of-the-art review. *Engineering structures*, *183*, 883-893.

O'Connor, J. T., O'Brien, W. J., & Choi, J. O. (2014). Critical success factors and enablers for optimum and maximum industrial modularization. *Journal of construction engineering and management*, *140*(6), 04014012.

Salama, T., Salah, A., Moselhi, O., & Al-Hussein, M. (2017). Near optimum selection of module configuration for efficient modular construction. *Automation in construction*, *83*, 316-329.

Becker, P., Fullen, M., & Takacs, B. (2003). Safety hazards to workers in modular home construction. Silver Spring. The Center toProtectWorkers' Rights.

Pan, W., Gibb, A. G., & Dainty, A. R. (2007). Perspectives of UK housebuilders on the use of offsite modern methods of construction. *Construction management and Economics*, *25*(2), 183-194

Gunawardena, T., Ngo, T., Mendis, P., Aye, L., & Crawford, R. (2014). Time-efficient post-disaster housing reconstruction with prefabricated modular structures. *Open House International*, *39*(3), 59-69.

Lawson, R. M., Ogden, R. G., & Bergin, R. (2012). Application of modular construction in high-rise buildings. *Journal of architectural engineering*, *18*(2), 148-154.

Cao, X., Li, X., Zhu, Y.,& Zhang, Z. (2015). A comparative study of environmental performance between prefabricated and traditional residential buildings in China. *Journal of Cleaner Production*, *109*, 131-143.

NRC. (2009). National Research Council, Division on Engineering, Physical Sciences, Board on Infrastructure, the Construced Environment, Committee on Advancing the Productivity, & Competitiveness of the US Industry Workshop. *Advancing the competitiveness and efficiency of the US construction industry*. National Academies Press. https://doi.org/10.17226/12717.

Peñaloza, G. A., Formoso, C. T., & Saurin, T. A. (2017). Resilience skills used by front-line workers to assemble precast concrete structures: an exploratory study. *Ambiente Construído*, *17*, 25-43.

Chourasia, A., Singhal, S., & Manivannan. (2023). Prefabricated volumetric modular construction: A review on current systems, challenges, and future prospects. *Practice Periodical on Structural Design and Construction*, *28*(1), 03122009.

Shahzad, W. M., Rajakannu, G., & Kordestani Ghalenoei, N. (2022). Potential of Modular Offsite Construction for Emergency Situations: A New Zealand Study. *Buildings*, *12*, 1970.

Chen, L., Zhai, C., Wang, L., Hu, X., & Huang, X. (2022). Modular structure construction progress scenario: a case study of an emergency hospital to address the COVID-19 PANDEMIC. *Sustainability*, *14*(18), 11243.

Bogenstätter, U. (2000). Prediction and optimization of life-cycle costs in early design. *Building Research & Information*, *28*(5-6), 376-386.

Lacey, A. W., Chen, W., Hao, H., & Bi, K. (2018). Structural response of modular buildings–an overview. *Journal of building engineering*, *16*, 45-56.

Murray-Parkes, J., Bai, Y., Styles, A., & Wang, A. (2017). Handbook for the design of modular structures. *Monash University: Melbourne, Australia*.

Mao, C., Shen, Q., Pan, W., & Ye, K. (2015). Major barriers to off-site construction: The developer's perspective in China. *Journal of management in engineering*, *31*(3), 04014043.

Blagojevich, R. R., & Whitaker, E. E. (2007). Regulation of factory built structures in Illinois.

Lu, Y., Wu, Z., Chang, R., & Li, Y. (2017). Building Information Modeling (BIM) for green buildings: A critical review and future directions. *Automation in Construction*, *83*, 134-148.

Lawson, M., Ogden, R., & Goodier, C. (2014). Design in modular construction (Vol. 476. Boca Raton, FL: CRC press, 2014.

Iacovidou, E., Purnell, P., Tsavdaridis, K. D., & Poologanathan, K. (2021). Digitally enabled modular construction for promoting modular components reuse: A UK view. *Journal of building engineering*, *42*, 102820.

Godbole, S., Lam, N., Mafas, M., Fernando, S., Gad, E., & Hashemi, J. (2018). Dynamic loading on a prefabricated modular unit of a building during road transportation. *Journal of Building Engineering*, *18*, 260-269.

Nester, T. M., Haddow, A. G., Shaw, S. W., Brevick, J. E., & Borowski, V. J. (2003). *Vibration reduction in a variable displacement engine using pendulum absorbers* (No. 2003-01-1484). SAE Technical Paper.

Rahman, M. M. (2014). Barriers of implementing modern methods of construction. *Journal of management in engineering*, *30*(1), 69-77.

Chiang, Y. H., Chan, E. H. W., & Lok, L. K. L. (2006). Prefabrication and barriers to entry—A case study of public housing and institutional buildings in Hong Kong. *Habitat international*, *30*(3), 482-499.

Pan, W., Gibb, A. G., & Dainty, A. R. (2012). Strategies for integrating the use of off-site production technologies in house building. *Journal of construction engineering and management*, *138*(11), 1331-1340.

Ribeiro, A. M., Arantes, A., & Cruz, C. O. (2022). Barriers to the adoption of modular construction in Portugal: An interpretive structural modeling approach. *Buildings*, *12*(10), 1509.

Ezzeddine, A., & de Soto, B. G. (2021). Connecting teams in modular construction projects using game engine technology. *Automation in Construction*, 132, 103887.

Thurairajah, N., Rathnasinghe, A., Ali, M., & Shashwat, S. (2023). Unexpected Challenges in the Modular Construction Implementation: Are UK Contractors Ready? *Sustainability*, *15*(10), 8105.

Multiplex. (2015). *Delivering a world-class hospital complete with state-of-the-art facilities-The Queen Elizabeth University Hospital & The Royal Hospital for Children Glagsgow*. Retrieved from https://www.multiplex.global/projects/the-queen-elizabeth-university-hospital-the-royal-hospital-for-children/

NK Architects (2016). *Mount Sinai Queens New Emergency Department*. Retrieved from https://www.architectmagazine.com/project-gallery/mount-sinai-queens-new-emergency-department

Waugh Thistleton Architects. (2017). *Dalston Works*. Retrieved from https://waughthistleton.com/dalston-works/

dezeen. (2019). *World's Tallest Modular Tower by Bouygues*. Retrieved from https://www.dezeen.com/2019/07/02/clement-canopy-worlds-tallest-modular-tower-bouygues/

Miller. H. (2020). *In pictures: China is builduing two hospitals in less than two weeks to combat coronavirus*. Retrieved from https://www.cnbc.com/2020/01/31/pictures-china-builds-two-hospitals-in-days-to-combat-coronavirus.html
CTBUH. (2021). *Council on Tall Buildings and Urbamn Habitat: Ten Degrees Croydon*. Retrieved from https://www.skyscrapercenter.com/building/ten-degrees-croydon/31572
Goodstone. (2025). *Smith's Garden – Birmingham*. Retrieved from https://www.goodstoneliving.com/smiths-garden-birmingham.html
Housing Innovation Collaborative. (2025). *Horizon North:* Modular *Housing Projects*. Retrieved from https://housinginnovation.co/collaborative/horizonnorth/
Ahmed Sbia. L., Peyvandi, A., Soroushian, P., Lu, J., & Balachandra, A. M. (2014). Enhancement of ultrahigh performance concrete material properties with carbon nanofiber. *Advances in Civil Engineering*, *2014*(1), 854729.
Norhasri, M. M., Hamidah, M. S., Fadzil, A. M., & Megawati, O. (2016). Inclusion of nano metakaolin as additive in ultra high-performance concrete (UHPC). *Construction and Building Materials*, *127*, 167-175.
Russell, H. G., & Graybeal, B. A. (2013). *Ultra-high performance concrete: A state-of-the-art report for the bridge community* (No. FHWA-HRT-13-060). United States. Department of Tranpostation. Federal Highway Administration. Office of Infrastructure Research and Development.
Al-Osta, M.A. (2018).'Exploitation of ultrahigh-performance fibre-reinforced concrete for the strengthening of concrete structural members. *Advances in Civil Engineering*, *2018*(1), 1-12.
CSA. (2019). CSA A23.1-19, Annex U, Materials and Methods for Ultra-High Performance Concrete. CSA Group, Rexdale, ON, Canada, 2019.
Roy, D. M., Gouda, G. R., & Bobrowsky, A. (1972). Very high strength cement pastes prepared by hot pressing and other high pressure techniques. *Cement and Concrete Research*, *2*(3), 349-366.
Birchall, J. D., Howard, A. J., & Kendall, K. (1981). Flexural strength and porosity of cements. *Nature*, *289*(5796), 388-390.
Bache, H. H. (1981). Densified cement ultra-fine particle-based materials.
Richard, P., & Cheyrezy, M. (1995). Composition of reactive powder concretes. *Cement and concrete research, 25*(7), 1501-1511.
Azmee, N. M., & Shafiq, N. (2018). Ultra-high performance concrete: From fundamental to applications. *Case Studies in Construction Materials*, *9*, e00197.
Blais, P. Y., & Couture, M. (1999). Precast, prestressed pedestrian bridge-world's first reactive powder concrete bridge. *PCI journal*, *44*(5).
van Nguyen, T., Ye, G., & van Breugel, K. (2010). The possibility of using rice husk ash to produce ultra high performance concrete. In *8th fib International PhD symposium in civil engineering, Lyngby, Denmark* (pp. 437-442). DTU Byg.
Yu, R., Spiesz, P. H. J. H., & Brouwers, H. J. H. (2015). Development of an eco-friendly Ultra-High Performance Concrete (UHPC) with efficient cement and mineral admixtures uses. *Cement and Concrete Composites*, *55*, 383-394.
ACI 239. (2018). Ultra-High Performance Concrete: An Emerging Technology Report.. American Concrete Institute: Farmington Hills, MI, USA.
Sim, C., Tadros, M., Gee, D., & Asaad, M. (2020). Flexural design of precast, prestressed ultra-high-performance concrete members. *PCI Journal*, *65*(6).
Graybeal, B. A., & El-Helou, R. (2023). *Structural design with ultra-high performance concrete* (No. FHWA-HRT-23-077). United States. Department of Tranpostation. Federal Highway Administration. Office of Infrastructure Research and Development.
AASHTO. (2024). Guide specifications for structural design with ultra-high performance concrete, 1st Editio.
NF, P. (2016). P 18-710 Calcul des structures en béton–Règles spécifiques pour les bétons fibrés à ultra-hautes performances (BFUP). AFNOR, Paris.
El-Abbasy, A. A. (2023). Tensile, flexural, impact strength, and fracture properties of ultra-high-performance fiber-reinforced concrete–A comprehensive review. *Construction and Building Materials*, *408*, 133621.
Chuang, M. L., & Huang, W. H. (2013). Durability analysis testing on reactive powder concrete. *Advanced materials research*, *811*, 244-248.
Li, J., Wu, Z., Shi, C., Yuan, Q., & Zhang, Z. (2020). Durability of ultra-high performance concrete–A review. *Construction and Building Materials*, *255*, 119296.
Andrade, C. & Torres, J. (2013, October). Long term carbonation of UHPC, in *Proceedings of the International Symposium on UHPC, Marseille, France*, (pp. 1-3).
Kono, K., Musha, H., Kawaguchi, T., Eriguchi, A., Tanaka, S., Kobayashi, T., & Ikeda, M. (2013). Durability study of the first PC bridge constructed with ultra high strength fiber reinforced concrete in Japan. In *Proceedings of the RILEM-fib-AFGC International Symposium on Ultra-High-Performance Fibre-Reinforced Concrete* (pp. 239-248).

Piérard, J., Dooms, B., & Cauberg, N. (2013, October). Durability evaluation of different types of UHPC. In *Proceedings of the RILEM-fib-AFGC International Symposium on Ultra-High Performance Fiber-Reinforced Concrete* (pp. 275-284).

Zhong, R., & Wille, K. (2015). Material design and characterization of high performance pervious concrete. *Construction and Building Materials*, *98*, 51-60.

Wang, Z. (2011). Chloride-ion Permeability of Reactive Powder Concrete [Maser Thesis*]. Beijing Jiaotong University*.

ASTM C666. (2008). Standard test method for resistance of concrete to rapid freezing and thawing. American Society for Testing and Materials.

Sharon, M. (2021). “An introduction to carbon nanofiber.” *Carbon Nanofibers: Fundamentals and Applications*, (2021): 1-20.

Yıldırım, G., Sarwary, M. H., Al-Dahawi, A., Öztürk, O., Anıl, Ö., & Şahmaran, M. (2018). Piezoresistive behavior of CF-and CNT-based reinforced concrete beams subjected to static flexural loading: Shear failure investigation. *Construction and Building Materials*, *168*, 266-279.

Morsy, M. S., Alsayed, S. H., & Aqel, M. (2010). Effect of nano-clay on mechanical properties and microstructure of ordinary Portland cement mortar. *International Journal of Civil & Environmental Engineering IJCEE-IJENS, 10*(01), 23-27.

Patil, R., & Deshpande, A. (2012). Use of nanomaterials in cementing applications. in *SPE International Oilfield Nanotechnology Conference and Exhibition* (pp. SPE-155607). SPE.

El-Gamal, S. M. A., Hashem, F. S., & Amin, M. S. (2017). Influence of carbon nanotubes, nanosilica and nanometakaolin on some morphological-mechanical properties of oil well cement pastes subjected to elevated water curing temperature and regular room air curing temperature. *Construction and Building Materials*, *146*, 531-546.

Shi, T., Li, Z., Guo, J., Gong, H., & Gu, C. (2019). Research progress on CNTs/CNFs-modified cement-based composites–a review. *Construction and Building Materials*, *202*, 290-307.

CeEntek. Pte. Ltd. (2020). Ultra-High-Performance Concrete: Manufacturing and Sustainability. Retrieved from https://ceentek.com/technology and https://ceentek.com/sustainability

Corvez, D. (2011). MuCEM, Jean Bouin:«Le passage à l’ère industriel du matériau BFUP». Débat de l’AFGC:«*Nouveaux bétons: Mise en œuvre et propriétés*.

Amran, M., Huang, S. S., Onaizi, A. M., Makul, N., Abdelgader, H. S., & Ozbakkaloglu, T. (2022). Recent trends in ultra-high performance concrete (UHPC): Current status, challenges, and future prospects. *Construction and Building Materials*, *352*, 129029.

Muttoni, A., Brauen, U., Jaquier, J. L., & Moullet, D. (2013, October). A new roof for the olympic museum at Lausanne, Switzerland. In *Proceedings of International Symposium on Ultra-High Performance Fiber-Reinforced Concrete* (pp. 69-76).

Seibert, P., Perry, V., Ghoneim, G., Carson, G., El-Hacha, R., Cariaga, I., & Zakariasen, D. (2012, March). The First Architectural UHPC Façade Application in North America. In *International Symposium on UHPC and Nanotechnology for High Performance Construction Materials*, Kassel.

Graybeal, B. (2011). Ultra-high performance concrete (No. FHWA-HRT-11-038).

Jabbar, A. M., Hamood, M. J., & Mohammed, D. H. (2022). Structural behavior of ultra-high-performance concrete beams under flexural and shear action: a review. *Engineering and Technology Journal, 40*(05), 743-758.

Ghazy, M.F., Abd Elaty, M. A. A., Sakr, M. A. E., & Arafa, E. M. (2025). Thermo-Mechanical Performance of Sustainable Lightweight Sandwich Panels Utilizing Ultra-High-Performance Fiber-Reinforced Concrete. *Buildings, 15*(4), 593.

Yoo, D. Y., & Yoon, Y. S. (2017). Bond ehavior of GFRP and steel bars in ultra-high-performance concrete. *Advanced Composite Mterials, 26*(6), 493-510.

Timber as the sustainable building material of the 21st Century: key advantages and facts

Ahmet Turer*[1]

[1] *Middle East Technical University, Department of Civil Engineering, 06800 Ankara, Türkiye*

Abstract. Timber is a natural and sustainable construction material with several advantages, including its negative carbon footprint, high strength-to-weight ratio comparable to steel, and characteristic bending, compressive, and tensile strength of 15 to 30 MPa. It is also five times lighter than reinforced concrete structures, reducing foundation loads, while offering faster construction and lower costs, making it a highly cost-effective option. Seismic performance is the primary advantage of timber buildings, as earthquake forces are directly correlated to building mass. Lighter structures experience lower seismic forces, and timber's combination of strength and lightweight properties provides a significant advantage over heavy and brittle materials like concrete. Fire safety in timber structures can be significantly enhanced through impregnation technologies and intumescent paints. Additionally, timber's slow-burning characteristics and natural heat insulation allow for 60-90 minutes of fire resistance, making it a viable choice when properly designed. Protective covers would further improve its fire performance. The new Turkish Timber Building Regulation (TABY-2024) introduces key structural design provisions, covering tension, bending, compression, shear, lateral-torsional buckling, and column buckling, along with guidelines for connection design and various member types such as glulam, CLT, and spaced columns. It also includes important considerations for serviceability, vibrations, creep, thermal, water, and sound insulation, as well as fire resistance calculations. As a conclusion, the lightweight properties, superior earthquake resistance, and sustainable production of timber, establishes it as the construction material of the 21st century.

Keywords: Timber; Regulation; Sustainable; Building; Design

1. Introduction

Timber is a renewable and biodegradable material which is dominantly used as the main structural engineering material in USA and Canada, where more than 90% of the houses are built using timber. For countries like Turkey, timber is recently gaining recognition as the sustainable building material of the 21st century. The initiation is largely by the pioneering efforts of TORID (Türkiye Orman İş Adamları Derneği) and UAB (Ulusal Ahşap Birliği), who have strongly advocated for timber's structural use in modern construction. Complementing these institutional efforts, the Department of Civil Engineering at Middle East Technical University has offered a dedicated timber engineering course (CE4008) since 2016, helping educate a new generation of engineers. Similarly, Kocaeli University, Van Yüzüncü Yıl University, and Mimar Sinan Fine Arts University have taught timber design for many years, establishing themselves as academic leaders in timber design in Türkiye.

A critical milestone was achieved in 2020 when the General Directorate of Forestry (OGM) initiated the classification of national coniferous timber species for structural applications, aligning them with international standards (OGM, 2020). Studies conducted in 4 universities, in accordance with TS 1265 (Sawn timber Coniferous - For building construction / Kereste İğne Yapraklı Ağaç Keresteleri - Yapılarda Kullanım için) have enabled classification of Turkish timber in European standards and now listed under TS EN 1912 (Structural timber - Strength classes - Assignment of visual grades and species / Yapı kerestesi - Mukavemet sınıfları - Ağaç türleri ve görsel sınıfların tasnifi). This study provided the strength classification for main tree species produced in Türkiye (Table 1).

The availability of these high-quality native species now enables structural usage of timber in Türkiye, as well as also compete structurally with concrete and steel considering traditional materials. Unlike concrete and steel, timber requires low processing energy, stores carbon, and enables faster and lighter construction. In order to further encourage use of timber in buildings, the Ministry of Environment, Urbanization and Climate Change has founded The Turkish Timber Building Regulation (TABY-2024) for a inter university large executed by Middle East Technical University (METU), Kocaeli University, Van Yüzüncü Yıl University, and Mimar Sinan Fine Arts University which is now in effect since January 1st, 2025; as the product of a three year intense work and provides

* Corresponding author, E-mail: aturer@metu.edu.tr

https://doi.org/10.31462/icearc2025_ce_eqe_551

a modern engineering framework for timber buildings, accelerating its acceptance. The Turkish Timber Building Regulation (TABY-2024) provides detailed provisions for mainly for a) strength-oriented member design (tension, compression, bending, shear, buckling lateral-torsional, column, connection design, glulam, CLT, and similar), b) Serviceability: deflection, vibration, creep, c) Fire design, and d) Insulation design (thermal, moisture, acoustic). Consistency was satisfied with Eurocode 5 was satisfied by building it upon EN 1995 with many improvements such as buckling, rigid vs flexible diaphragm action of slabs, and vibration performance calculations.

Table 1. The strength classification for main tree species

Tree Species	Grade I	Grade II	Grade III
Black Pine (Karaçam)	C35	C24	C18
Fir (Göknar)	C27	C24	C18
Scots Pine (Sarıçam)	C35	C27	C20
Red Pine (Kızılçam)	C35	C24	C18
Cedar (Sedir)	C24	C20	C16
Spruce (Ladin)	C27	C22	C20

2. Earthquake resistance of timber structures

One of timber's most crucial advantages is its seismic performance. Since earthquake forces are proportional to mass, timber having about 1/5th mass of reinforced concrete but having similar characteristic strength significantly reduces seismic demand. For example, native Turkish timbers, such as black pine, scoots pine, and red pine, achieve characteristic strengths up to C35 (i.e., 35 MPa 5% characteristic bending strength per EN 338). This strength to weight ratio is comparable to steel even exceeding mild and ordinary steel (Fig. 1). The relatively low strength of C35 concrete normalized with density can be clearly seen; when the tensile strength of concrete is taken as about 1/10th of compressive strength, the difference is more pronounced. Since normalized strength by density are similar but timber density is more than 15 times lighter than steel, sections have about similar total mass but timber sections are relatively larger mostly eliminating buckling related problems. Lightweight construction using timber also enables smaller and less costly foundations, benefiting weak soil conditions.

In seismic design, flexibility and energy dissipation are the major concerns. Timber structures, especially when connected using nailed systems, can exhibit ductile behavior. Nails have superior energy dissipation properties compared to screws due to their ability to deform plastically under cyclic loads also move in and out of their holes dissipating energy via friction.

Usage of timber especially after earthquakes has additional advantages: aftershocks can adversely affect concrete curing and damage fresh RC elements; whereas, timber structures are prefabricated (dry-assembled) and can be rapidly constructed even in post-disaster areas for rapid housing.

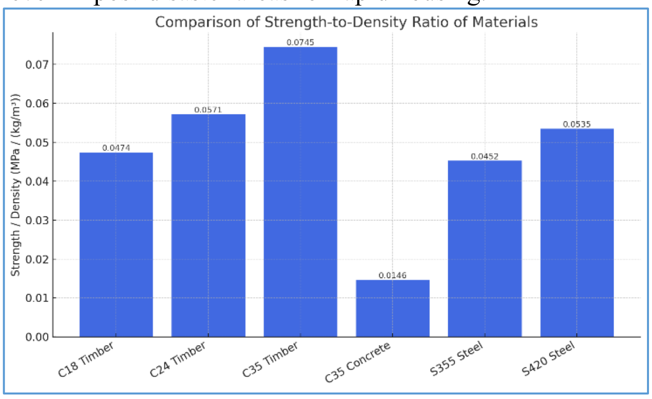

Fig. 1. Comparison of Strength-to-Density Ratio of Construction Materials

3. Environmental benefits

Timber is produced naturally as the trunk of trees which is made by mostly the carbon absorbed as CO_2 from the atmosphere. On average, 1 ton of dry timber uses about 1.7 to 2 tons of CO_2 positively effecting in reduction of CO_2 levels in the atmosphere. In contrast, producing 1 ton of cement emits 0.9 ton CO_2 for 1 ton of cement, 1 m^3 concrete production emits about 0.159 ton CO_2 (typically 10 to 15% of cement), and 1 ton of steel production emits about 1.89 tons CO_2 [2], The production of cement and steel also emits CO_2 during chemical process (Eqn. 1) other than burning fuel.

$$CaCO_3 + heat \rightarrow CaO + CO_2 \tag{1}$$

Timber grows naturally, powered by solar energy, without the need for high-temperature industrial processes used for steel or cement. Furthermore, forests contribute to preventing erosion, maintaining humidity, regulating microclimates, and hosting biodiversity. When sustainably harvested, most pine forests in Turkey takes about 60 to 80 years to regenerate to harvesting size, depending on climate and region. Thus, timber is not only carbon-negative but also contributes to broader ecological balance.

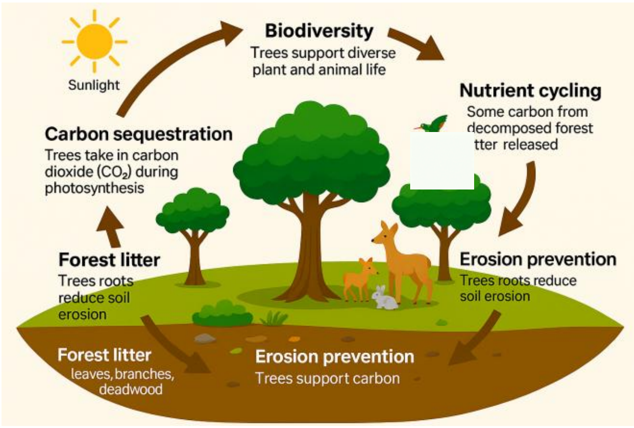

Fig. 2. The role of trees in CO_2 sequestration

4. Economic and constructional advantages

Timber construction offers numerous economic advantages that make it a better alternative to conventional building materials. One of the best known benefits is the speed of construction; prefabricated timber systems enable rapid on-site assembly, significantly reducing project timelines. Floors can be finished in a week's time or less without any requirement to wait strength gain to remove forms or scaffolding. In addition, construction of timber structures requires less labor and equipment, as they eliminate the need for steel reinforcement, formwork, and curing processes typical of reinforced concrete. The lightweight nature of timber also allows for the use of smaller cranes or even manual handling in certain cases, which further lowers construction costs. Transportation expenses are minimized due to the reduced material weight, leading to decreased fuel consumption and associated CO_2 emissions. These factors collectively result in a faster use of the building either by rent or use, as buildings can become operational and income-generating more quickly. The survivors can start using their homes much faster than reinforced concrete buildings, literally in one or two months' time eliminating costly and uncomfortable container homes or tents. In North America, timber buildings have been shown to be up to 13% more economical than reinforced concrete buildings [6]. Moreover, the reduced dead load simplifies seismic design requirements and leads to smaller, more cost-effective foundations. Soil improvement studies such as piles or deep mixing are usually not necessary due to the reduced overall weight of the building.

5. Timber construction techniques

Timber construction has evolved to include a variety of structural systems, many of which developed independently in different parts of the world but are now globally categorized into distinct structural types. Timber-based load-bearing systems are adapted to suit various architectural needs, performance criteria, and levels of prefabrication. One of the most widespread methods is light frame construction (Fig. 3), which is especially common in low to mid-rise residential buildings. In fact, this system has been used for buildings up to ten stories high in the United States. It utilizes small cross-section members, such as studs and joists, arranged in a repiting pattern to form walls. Floors are also similarly constructed with small but frequent beams and again board connecting all beams together. The popularity of light frame construction stems from its cost-efficiency, speed of assembly, and layout flexibility.

Although the term "frame" is used, when the studs are covered with plywood or oriented strand board (OSB), the system behaves like a shear wall, creating a rigid and strong structural element. In this way, the structural behavior resembles that of "tunnel-form reinforced concrete buildings" rather than a typical light frame. These systems are relatively easy to construct, resistant to lateral loads, and the wall cavities can be filled with insulation materials such as glass wool, stone wool, wood wool, or polyurethane expanding foam. Not all walls are load-bearing; some are used mainly for partitioning purposes where gypsum boards can be used, which are not load bearing members.

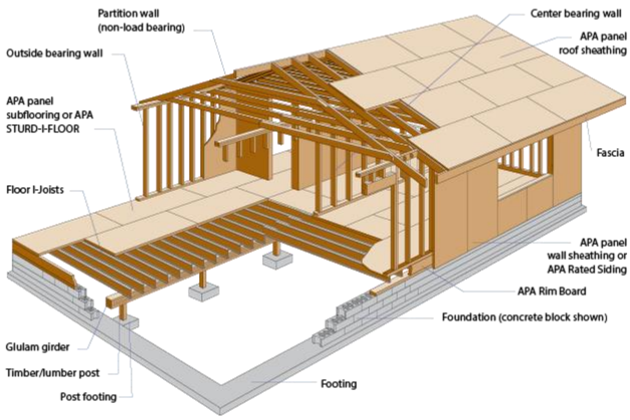

Fig. 3. Light frame construction - Labeled house construction diagram (CleanPNG, 2025).

Another traditionally used method is the “post-and-beam” system, which is quite similar to the reinforced concrete frame structures in Türkiye, as beams and columns form the load-bearing frames. Nevertheless, the connections of beam and columns require special attention and may not be the best solution for seismically active regions. The connections require to transmit bending moment and shear, which may be difficult for 3D beam and column connections. Traditional Japanese connections involve major cutting and grooving which would reduce the cross section and make the members vulnerable at the most critical load transfer location. Although energy dissipation properties and introduced additional flexibility may bring advantages, a frame system has to transfer moment and shear properly. Just like reinforced concrete structures require shear walls, post and beam buildings would require a sound way to transfer inertial forces. Although wooden slabs are relatively much lighter compared to reinforced concrete slabs, the “flexible slab” vs “rigid slab” behavior differences also play an important role for the diaphragm action. Structural designer must be extremely careful when designing post-and beam load carrying system in earthquake prone regions since this system may not be suitable for seismically regions unless shear walls or proper cross-bracing is introduced.

A relatively more modern system is Cross-Laminated Timber (CLT), which involves bonding layers of lumber at right angles to form large, dimensionally stable panels. The number of layers is mostly defined as odd integer numbers and the direction with most fibers are usually used in the vertical direction. These CLT panels may serve as structural walls, floors, and roofs, offering high strength in both directions and excellent seismic and fire performance. CLT enables rapid construction and is increasingly used in mid to high-rise buildings due to its rigidity and mass. Best examples can be found in buildings such as the 86-meter-tall Mjøstårnet in Norway and the Ascent tower in the USA as they illustrate how CLT can be applied at demanding high structures. Nevertheless, the rolling shear of CLT panels is their weakest point. Most of the times, the shear acting perpendicular to the fibers without cutting them causes rolling action and failure. Another weakness of CLT panels may the metal connectors between walls to the ground or slab to slab connections. These connections and connectors must be carefully planned and designed to prevent any premature failures.

Panelized construction offers a fast and high quality “prefabricated” solution, where wall and floor elements are manufactured off-site in the factory and assembled on location using light cranes. This method speeds up construction timelines and ensures better quality control since most of the manufacturing is completed in the factory, while maintaining architectural adaptability. The panels often times have the windows and doors installed on them during pieces are combined on the site. Sandwich panels are also considered as panelized construction since exterior timber plates are combined using foam that sticks to both timber panels, fill the void, and transfer shear force between the exterior panels.

Finally, hybrid systems combine timber with reinforced concrete or steel cores. A common configuration includes a reinforced concrete core to house stairwells and elevators, which attracts almost all of the seismic loads, while the remaining structural framework is composed of timber. The system relies on the lateral load carrying capability of the core(s), which are always preferred to be symmetrically placed and present more than one core. The most critical and important aspect of hybrid system in earthquake prone regions is 1) make sure the connection between slab and core(s) are successfully maintained 2) the timber slabs connecting to cores are a) form a rigid diagram and b) slabs are light weight to minimize the earthquake forces. However, the slabs should not be overly light weight since “serviceability” becomes a major concern for light weight and flexible slabs. Many people may feel uncomfortable if too much and low frequency vibration is present in the slabs. Sometimes, the slab may be constructed unnecessarily stiff and stronger than it should be from a strength point of view. The hybrid systems provide seismic resilience and lightness of timber since timber is already a light weight material and the columns would only carry vertical loads during an earthquake. The rigid cores would be the major horizontal load carrying system. The cores are not only active during earthquakes, but they are also active during high wind conditions especially for taller buildings.

The civil engineer to perform the structural design should be careful to select the most appropriate load carrying system and be very careful with the connections. The members may be very strong and high quality, but the connections play a very important role in the load carrying mechanism during an earthquake. Connections are often times form the weakest link of load resisting chain.

Structural design of a building cannot be complete by only checking “strength” criteria though. Additionally, “serviceability”, “fire safety”, and “humidity, heat insulation, and “sound insulation” are the other key issues in timber building design.

6. Current seismic code limitations and suggestions

As per Turkey's current seismic code (2018), Table 4.1 limits timber buildings to Building Height Classes BYS 7 and 8 (up to 7 m and 10.5 m respectively in high seismic zones). The height limits are increased to 10.5m and 17.5 m respectively for low seismic zones but the performance advantage of timber buildings is the most dominant at earthquake prone regions.

Addition of “hybrid structures” were proposed, which would incorporate symmetrically placed core towers with rigid diaphragm action and proper deck to core connections. In this way, BYS=6 may be introduced to Türkiye, where engineered timber buildings can rise up to 17.5 m, about 5 floors, in highly seismic zones as well. The reduced seismic force due to timber’s low mass would enable safe and economical designs.

7. Fire safety considerations

Contrary to common perceptions, timber can be a fire-safe material when properly designed. One of the key mechanisms that make timber behave reliably in fire is the formation of a char layer on the surface of exposed wood. As the timber burns, a blackened char not only generates a thermal barrier, but also blocks the oxygen significantly to slow down the burning process. This predictable charring process insulates the unburned core and allows timber members to retain their load-bearing capacity for a prolonged time, often sufficient for the fire department to arrive and extinguish the fire. According to Eurocode 5 (EN 1995-1-2), the design charring rate for softwood is typically taken as 0.65 mm/min in standard fire exposure (ISO 834), though 0.8 mm/min is often used as a conservative and practical approximation in preliminary design. This rate implies that a structural timber member with a sacrificial outer layer can survive fire exposure of 60–90 minutes while still supporting its load, which is in line with many code requirements for medium-rise buildings. If the cross sections are selected to be 72 mm thicker in the fire exposed regions considering 0.8 mm/min and 90 mins, the members would be immune to fire for 90 minutes.

Timber's fire resistance can be further enhanced through the use of impregnation treatments and intumescent coatings, which either chemically slow the combustion process or expand to form an insulating black foam-like barrier when exposed to heat. In building practice, massive timber elements such as glulam and CLT panels outperform unprotected steel, which loses its strength rapidly at high temperatures. While steel may reach critical failure temperatures (around 550°C) within minutes, timber’s gradual degradation provides crucial time for evacuation and firefighting efforts.

In modern construction, additional fire protection measures are routinely taken for timber buildings. These include multi-layer gypsum board cladding for internal faces and non-combustible surface finishes like magnesium panels to delay ignition and heat transfer. Other major fire protection technique that must be mentioned is the simple sprinkler systems. Recently, new springers of water mist and/or gas based firefighting strategies are also being used. As a result, timber buildings (especially those designed under contemporary codes and fire engineering principles) can safely meet or exceed the 60–90 minute fire resistance thresholds required for structural elements in most low to mid-rise applications.

8. Conclusions

Timber was not an unfamiliar construction material to Ottomans and Turkish Republic since “yalılar ve konaklar” which can be translated as waterside and inland mansions of Ottoman-Turkish architecture as well as “Hımış”, “Bağdadi”, “Şamdolma” type of construction in Black Sea (Safranbolu specifically) and Anatolia regions are very common. The large Istanbul earthquake occurred on 10 September 1509, often referred to as “The Lesser Judgment Day” (Küçük Kıyamet) in Ottoman chronicles has been the point of dominantly timber usage in buildings since the timber buildings performed well during the earthquake. Timber material in building construction has reemerged as a powerful structural material, offering a compelling combination of sustainability, strength, and seismic resilience. The warm looks and many health benefits has been the major decision making of modern timber buildings. The structural safety, resilience, earthquake performance, being light weight, and economically compelling; timber buildings are dominantly used in North America for low and mid-rise construction.

Timber’s coming back in Türkiye after reinforced concrete structures’ dominance (starting with early 20th century until now) was initiated and accelerated through the efforts of institutions such as TORID, UAB, and leading universities, along with the support of the General Directorate of Forestry and the introduction of the Turkish Timber Building Regulation (TABY-2024) by Urbanization and Climate Change (CSIB). The structural classification of Turkish softwoods in accordance with international standards such as EN 338 and EN 1912 and registration to TS 1265 has made it feasible to use nationally produced structural timber in timber building construction with confidence.

Timber's strength-to-weight ratio, especially in species like black, red, and scots pine, is comparable to or exceeds that of mild steel on a density-normalized basis. Structural timber's lightweight character not only reduces seismic demand, soil requirements, and foundation costs but also enhances constructability and post-earthquake resilience. Timber members can be prefabricated and dry-assembled rapidly, avoiding delays otherwise due to concrete curing or too cold, too hot, rainy weather.

From an environmental and life-cycle perspective, timber stands out as a carbon-negative material, absorbing more CO_2 during its growth than it emits during processing. It helps mitigate the 38% share of global CO_2 emissions attributed to the construction sector, while also contributing positively to the forest ecosystems through erosion control, biodiversity support, and climate regulation. Timber also allows for fast and cost-effective construction, with studies confirming up to 13% cost savings compared to reinforced concrete in mid-rise buildings. The adaptability of timber construction systems, considering light-frame, CLT, post and beam, or hybrid core configurations, ensures architectural and structural flexibility. Fire safety, often misunderstood aspect, can be easily and effectively addressed with proper design, accounting for predictable charring rates, and protective strategies such as intumescent coatings, gypsum cladding, and sprinkler systems. As Türkiye continues to face the dual challenges of seismic risk and climate responsibility, engineered timber stands out as main construction material for the buildings of the 21st century.

Acknowledgments

The author would like to express his sincere appreciation to Assoc. Prof. Dr. Barış Erdil, Asst. Prof. Dr. Erkan Akpınar, and Assoc. Prof. Dr. Mehmet Selim Ökten, along with their dedicated team members, for their valuable contributions to the development of timber engineering in Türkiye. Gratitude is also extended to the General Directorate of Forestry (OGM), the Türkiye Orman İş Adamları Derneği (TORID), the Ulusal Ahşap Birliği (UAB), and the Ministry of Environment, Urbanization and Climate Change (CSIB) mainly Dr. Mustafa Tekin for their ongoing support and leadership in promoting sustainable timber construction.

References

General Directorate of Forestry (OGM). (2020). *Yerli iğne yapraklı ağaç türlerimizden karaçam, göknar, sarıçam, kızılçam, sedir ve ladin ağaç türlerimize uluslararası standart alınması*. https://www.ogm.gov.tr/marmaraarastirma/haberler/yerli-igne-yaprakli-agac-turlerimizden-karacam-goknar-saricam-kizilcam-sedir-ve-ladin-agac-turlerimize-uluslararasi-standart-alinmasi-38

Turkish Ministry of Environment, Urbanization and Climate Change. (2024). *Türkiye Ahşap Bina Yönetmeliği (TABY-2024)*. Official Gazette. https://www.resmigazete.gov.tr/eskiler/2024/03/20240324-1.htm

European Committee for Standardization. (2012). *EN 338: Structural timber – Strength classes*. Brussels, Belgium: CEN.

European Committee for Standardization. (2012). *EN 1912: Structural timber – Strength classes – Assignment of visual grades and species*. Brussels, Belgium: CEN.

Worldsteel Association. (2025, April). *Climate change and the production of iron and steel*. https://worldsteel.org/climate-action/climate-change-and-the-production-of-iron-and-steel/

RSMeans, Atlantic WoodWORKS, & LRI Engineering Inc. (2017). *Wood for mid-rise construction: Cost comparison of building materials in mid-rise residential buildings*. https://atlanticwoodworks.ca/atlantic-mid-rise-wood-case-study/

CleanPNG. (2025). *Labeled house construction diagram*. https://www.cleanpng.com/png-raised-floor-architectural-engineering-framing-joi-3811272/

Numerical and analytical study of the dynamic behaviour of Tokat Clock Tower

Muhammed M. Öztürk[1], Emre Alpaslan[2], Şahin Sözen[*1]

[1] *Tokat Gaziosmanpaşa University, Department of Civil Engineering, 60010 Tokat, Türkiye*
[2] *Ondokuz Mayıs University, Department of Civil Engineering, 55100 Samsun, Türkiye*

Abstract. It is very important to determine the dynamic behavior of historical buildings, which are a part of cultural heritage. The dynamic behavior of structures is obtained depending on parameters such as material properties, boundary conditions, and damage conditions of the existing structure. The modal analysis method is used to solve dynamic problems in many fields, especially in civil engineering. In this method, dynamic parameters such as natural frequency, mode shape and damping ratio of the structure are obtained. Slenderness is a very important problem in tall, thin masonry structures such as towers and minarets which are sensitive to lateral loads. Damages may occur in such engineering structures due to severe earthquakes. In this study, the linear dynamic analysis of the historical masonry Tokat Clock Tower located in the central district of Tokat province was carried out. Built in 1902, the clock tower was replaced and modernised in 1917. Finally, the dimensions of the building, which underwent a restoration process in 2019, were obtained by using the technical drawings in the restoration report. The dynamic characteristics of the historical building in question were obtained numerically and analytically. In the numerical study performed using ANSYS software, response spectrum analysis was performed according to 2007 and 2018 Turkish Earthquake Codes (TEC 2007 and TEC 2018). The results of the analyses according to both regulations are compared. In the analytical study, the fundamental period of the clock tower was determined by using an approach based on the Rayleigh method. At the end of the study, the dominant period of the clock tower obtained by the finite element method was found to be very close to the result obtained by the Rayleigh method. In addition, it was determined that the forces and displacements obtained according to the TEC 2007 have larger values compared to the TEC 2018.

Keywords: Masonry structure; Dynamic behaviour; Finite element method; Rayleigh method.

1. Introduction

The preservation of historical buildings is of paramount importance, as they constitute a significant component of our cultural heritage, and it is imperative to ensure their transmission to future generations. It is an established fact that throughout their existence, historical edifices are susceptible to damage or complete destruction as a result of natural disasters such as earthquakes, floods, wars, and fires. Consequently, a comprehensive investigation into the structural integrity of historical edifices is imperative, followed by the implementation of requisite measures to ensure the preservation of these structures for posterity. In this context, in order to ascertain the current behaviour of historical buildings, it is necessary to determine the properties of the materials used in their construction.

Tall and fragile structures such as clock towers, mosque minarets and bell towers, which are among the historical buildings, exhibit a more sensitive behaviour, especially against seismic effects. Numerous studies have been conducted to ascertain the dynamic behaviour of such structures (El-Attar et al., 2005; Beyan, 2007; Livaoğlu et al., 2016; Gökdemir & Baki, 2024). In the majority of studies, the existing behaviour of structures is modelled using the finite element method (Akan & Özen, 2005; Mortezaei et al., 2012; Sözen, 2022). The finite element method facilitates the development of numerical models of structures and the investigation of their static and dynamic behaviours through analyses conducted on these models.

The dynamic behaviour of structures is represented by parameters such as mode shape, natural frequency and damping ratio. The aforementioned parameters can be obtained either numerically by theoretical modal analysis method or experimentally by operational modal analysis method (Serhatoğlu et al., 2015; Hacıefendioğlu et al., 2016; Altunışık et al., 2023).

[*]Corresponding author, E-mail: sahin.sozen@gop.edu.tr

https://doi.org/10.31462/icearc2025_ce_eqe_569

golden light publishing

In this study, the structural behaviour of the historical Tokat Clock Tower, located in the centre of Tokat province, is investigated by both numerical and analytical methods. The results obtained are intended to make a contribution to the studies on earthquake protection of masonry historical buildings with similar characteristics. The distinguishing feature of this study is that the linear analysis of the Tokat Clock Tower is conducted by taking into account both the 2007 and 2018 Turkish Earthquake Regulations, and the fundamental period of the structure is analytically determined using the Rayleigh method. The accuracy of the analytical approach is evaluated by comparing the results obtained from finite element analysis and Rayleigh method.

2. Architectural and structural features of the Historic Tokat Clock Tower

The Tokat Clock Tower, erected in 1902 in the Behzat neighbourhood in the city centre, was constructed with the intention of being visible from all parts of the city. The tower, constructed from cut stone, features an octagonal design that narrows towards the top from a square base, with a total height of 33 metres. The main entrance of the building is situated on the south side. Current photographs of the building are shown in Fig. 1.

Fig 1. Current photos of the clock tower

In 2019, Seka Architecture was responsible for the technical drawings of the Clock Tower, which had just undergone restoration. The tower is composed of four distinct octagonal sections, which rise from a square base. The 5.8-meter-high pedestal measures 5.6 meters in length and width. The lateral dimensions of the octagonal blocks, which vary in size, range from 1.5 to 2 meters. The stairs within the tower are composed of monolithic cut stone. These stones are supported by a 20-centimeter-thick hollow circular core. The plan view and height of the tower at +20.10 m are illustrated in Fig. 2.

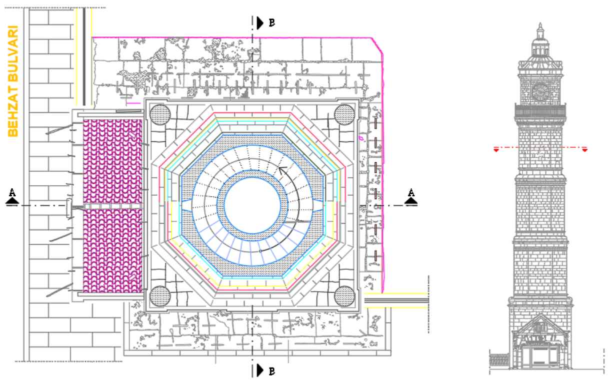

Fig. 2. Plan and height of the clock tower

3. Material and method

The objective of the study was to ascertain the dynamic behavior of the Tokat Clock Tower under earthquake loads. In order to perform the structural analysis, it is necessary to determine the material properties. The materials of historical buildings may deteriorate due to exposure to various environmental conditions over extended periods.

It is important to note that natural stone samples extracted from the same quarry may exhibit different mechanical properties. Consequently, ascertaining the mechanical properties of materials utilized in historical edifices poses a considerable challenge. A plethora of test methods, both destructive and non-destructive, have been documented in the extant literature for the purpose of determining material properties. However, due to the historical nature of the tower, it was not possible to perform a destructive test by taking a material sample. Consequently, the non-destructive test method and the material properties documented in the extant literature were employed to develop the material model for the analysis.

In a study of the Tokat Clock Tower, an N-type Schmidt hammer—a non-destructive testing device—was utilized to ascertain the compressive strength of the cut stone employed in the tower's construction. The mean compressive strength of the stone was found to be 31.67 MPa. Subsequently, the compressive strength and modulus of elasticity of the wall were determined using empirical formulas from the extant literature. The resulting values were 4.52 MPa and 3390 MPa, respectively (Sözen, 2022).

The tensile strength of masonry walls has been observed to range from 5% to 20% of the compressive strength (Gönen & Soyöz, 2021). In this study, the tensile strength of the wall was set at 0.3 MPa.

The unit volume weight and Poisson's ratio employed in the analysis of the tower were 2650 kg/m^3 and 0.2, respectively, in accordance with the values reported in the extant literature (Ertek & Fahjan, 2007; Gönen & Soyöz, 2021; Sözen, 2022).

4. Dynamic Analysis of the Tower

The dynamic analysis of the Tokat Clock Tower was performed according to the widely used mode coupling method, which yields results that are close to those of time domain analysis. ANSYS software was utilized in the analysis. Subsequently, response spectrum analysis was executed in accordance with both TEC 2007 and TEC 2018 regulations. The resulting data were then subjected to comparative analysis.

As indicated by the geotechnical analyses carried out by the Tokat Municipality, the shear wave velocity in the upper 30 meters was determined to be $2(V_s)_{30} = 225\ m/sn$. According to the regulations outlined in TEC 2007 and TEC 2018, the soil class of the building was determined to be Z3 and ZD, respectively.

The parameters employed in the spectrum analysis of the tower, as outlined in the TEC 2007 and TEC 2018 Regulations, are enumerated in Table 1.

Table 1. Parameters for spectral analysis

Regulation	TEC 2007	TEC 2018
Classification of Soil	Z3	ZD
Effective Acceleration Coefficient (A_o)	0.4	-
Structural Importance Factor (I)	1	-
Map Spectral Acceleration Coefficient for Short Period Region (SS)	-	0.749
Map Spectral Acceleration Coefficient for 1.0 Second Period Region (S1)	-	0.258
Peak Ground Acceleration (PGA)	-	0.316
Local Soil Effect Coefficient for Short Period Region (FS)	-	1.2
Local Soil Effect Coefficient for 1.0 Second Period Region (F1)	-	2.1
Design Spectral Acceleration Coefficient for Short Period Region (SDS)	-	0.899
Design Spectral Acceleration Coefficient for 1.0 Second Period Region (SD1)	-	0.542

In the context of the study, the analysis is confined to the horizontal response spectrum, as the effect of the vertical response spectrum is deemed negligible. The elastic design spectra of the TEC 2007 and TEC 2018 earthquake codes are presented in Fig. 3.

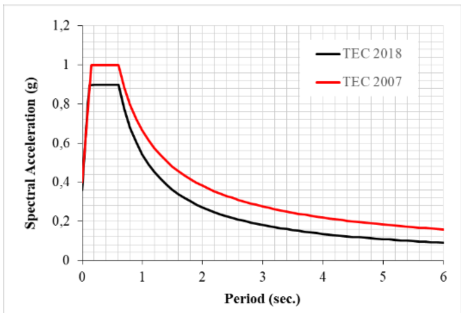

Fig. 3. Elastic design spectrums according to TEC 2007 and TEC 2018

4.1. Finite Element Analysis

In the linear analysis of the tower, all elements of the structure (including the stair treads) were modeled as solid. The SOLID187 element was utilized in the modeling process. The element is defined by 10 nodes having three degrees of freedom at each node: translations in the nodal x, y, and z directions. The element has plasticity, hyperelasticity, creep, stress stiffening, large deflection, and large strain capabilities (Ansys, 2025). The structure was subdivided into a total of 206,446 elements, and the total weight of the structure was calculated as 7,930 kN. As illustrated in Fig. 4, the finite element model and mesh network of the structure are presented.

The mode shape and frequency values, which are dynamic characteristics of the structure, were obtained as a result of performing a modal analysis on the finite element model. The frequency and period values of the first five modes of Tokat Clock Tower are enumerated in Table 2, while the mode shapes are illustrated in Fig. 5.

Spectrum analysis was performed on the tower, with separate analyses conducted for the x and z directions. These analyses were conducted in accordance with the elastic design spectra presented in Fig. 3. The peak displacement, base shear force, and equivalent (von-Mises) stress values obtained as a result of the analysis are given in Table 3.

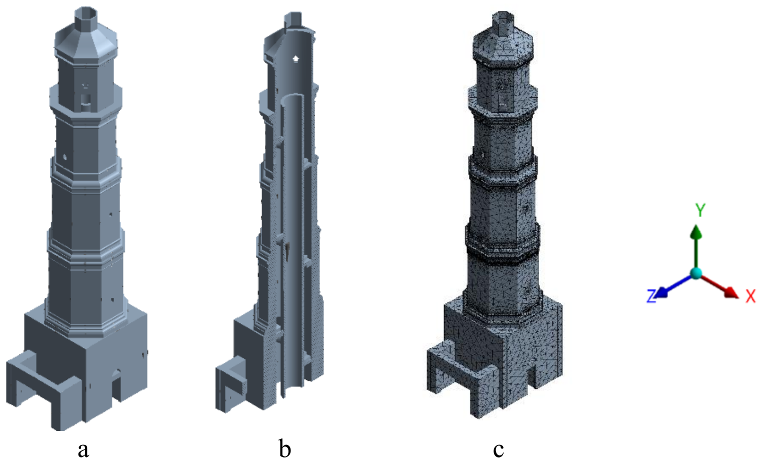

Fig. 4. Finite element model (a-b) and mesh network (c) of Tokat Clock Tower

Table 2. The initial five periods of the Tokat Clock Tower

Mode	Direction	Characteristics	Frequency, *Hz*	Period, *sec.*
1	x	Translational	2.41	0.41
2	z	Translational	2.47	0.40
3	x	Translational	7.89	0.13
4	z	Translational	8.01	0.12
5	-	Torsion	11.2	0.09

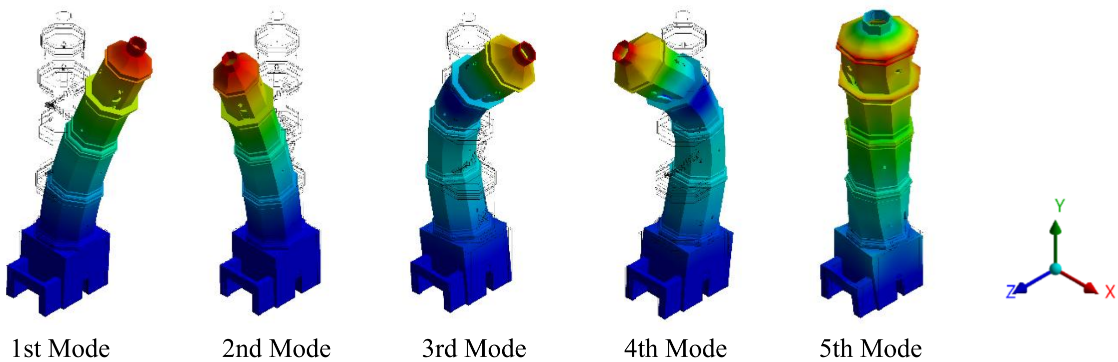

Fig. 5. Mode shapes of Tokat Clock Tower

Table 3. Spectrum analysis results obtained for X and Z direction according to TEC 2007 and TEC 2018 regulations

	X direction		Z direction	
	TEC 2007	TEC 2018	TEC 2007	TEC 2018
Displacement of the top point, *mm*	92	83	88	79
Shear force of the base, *kN*	3420	2970	3370	2910
Equivalent (von-mises) stress, *MPa*	9.02	8.13	8.90	7.99

4.2. Determination of Fundamental Period Using the Rayleigh Method

The Rayleigh method is a mathematical technique used to calculate the dominant period of a tower (Kılıç et al., 2019). This calculation is performed by utilizing equation 1, which is derived from the Rayleigh method. In this instance, the tower is modeled as an equivalent Timoshenko beam, as outlined in the extant literature. In this case, Equation 2-11 can be written as follows (Dym & Williams, 2012):

$$T_1 = \frac{2\pi}{\omega} \tag{1}$$

In this equation, ω denotes angular frequency, which is calculated using the provided Equation 2.

$$\omega^2 = \frac{\omega_e^2 \omega_k^2}{\omega_e^2 + \omega_k^2} \tag{2}$$

Here, ω_e is the angular frequency calculated from pure bending deformations and ω_k is the angular frequency calculated from pure shear deformations and can be calculated by Equations 3 and 4:

$$\omega_e^2 = \frac{\int_0^1 EI(\varepsilon)\left(\frac{d^2 y_e}{d\varepsilon^2}\right)^2}{H^4 \int_0^1 \rho A(\varepsilon)\, {y_e}^2} \tag{1}$$

$$\omega_k^2 = \frac{\int_0^1 kGA(\varepsilon)\left(\frac{dy_k}{d\varepsilon}\right)^2}{H^2 \int_0^1 \rho A(\varepsilon)\, {y_k}^2} \tag{4}$$

Where E is the modulus of elasticity, G is the shear modulus, $I(\varepsilon)$ is the moment of inertia function, $A(\varepsilon)$ is the cross-sectional area and k is the shear deformation factor. The mode 1 shape consisting of pure bending and pure shear deformations y_e and y_k, respectively, can be approximated as in Equations 5 and 6:

$$y_e = 1 - \cos\left(\frac{\pi\varepsilon}{2}\right) \tag{5}$$

$$y_k = \sin\left(\frac{\pi\varepsilon}{2}\right) \tag{6}$$

Here ε is defined by Equation 7:

$$\varepsilon = \frac{z}{H} \tag{7}$$

Where z is the variation along the height of the tower and H is the total height of the tower. In this study, parabolic and cubic variations of moment of inertia and cross-sectional area along the height of the structure are considered and presented in Equations 8-11:

$$I(\varepsilon) = I(O)\left[1 - \left(1 - \frac{I(H)}{I(O)}\right)\varepsilon^2\right] \tag{8}$$

$$A(\varepsilon) = A(O)\left[1 - \left(1 - \frac{A(H)}{A(O)}\right)\varepsilon^2\right] \tag{9}$$

$$I(\varepsilon) = I(O)\left[1 - \left(1 - \frac{I(H)}{I(O)}\right)\varepsilon^3\right] \tag{10}$$

$$A(\varepsilon) = A(O)\left[1 - \left(1 - \frac{A(H)}{A(O)}\right)\varepsilon^3\right] \tag{11}$$

Where $I(O)$ and $A(O)$ are the inertia and cross-sectional area at the base, and $I(H)$ and $A(H)$ are the moment of inertia and cross-sectional area at the peak. The fundamental period values were calculated for parabolic and cubic variation assumptions using Equations 1-11. Uncracked and cracked section fundamental period values for parabolic and cubic variations of moment of inertia and cross-sectional area by Rayleigh method are given in Table 4.

Table 4. Fundamental period obtained using Rayleigh method

Change Acceptance	Parabolic	Cubic
Period, *sec.*	0.35	0.38

5. Conclusions

In this study, the dynamic parameters of the historical clock tower in Tokat Province were determined using ANSYS software. The results obtained by using solid element type in finite element analysis were evaluated. The tower was subjected to an analysis in accordance with TEC 2007 and TEC 2018 using the response spectrum analysis method.

- It was concluded that the peak displacement, base shear force and equivalent stress values obtained as a result of the response spectrum analyses performed in the X and Z directions differ due to the geometry of the structure. In addition, the values obtained in the X direction were found to be larger.
- When the results of 2007 and 2018 earthquake code analyses are compared, it is seen that the values obtained from 2007 earthquake code have higher values.
- The maximum peak displacement obtained was 92 mm, base shear force was 3420 kN and equivalent stress values were 9.02 MPa. These values were obtained as a result of the analysis carried out in the x direction according to TEC 2007 regulations.
- In the context of the study, a methodology is proposed for the practical determination of the fundamental period, employing the Rayleigh method as a means to achieve this objective. The fundamental period value obtained by the proposed approach is found to be in close agreement with the fundamental period value obtained by finite element analysis.

Consequently, the analyses conducted in this study are predicated on linear behavior. To ensure the integrity and safety of the tower in the event of a major seismic event, nonlinear analyses must be conducted to assess its behavior during such an event.

Acknowledgments

The research described in this article was not financially supported by any Foundation/Institute.

References

Akan, A.E., & Özen, Ö. (2005). Bursa Yeşil Türbe'nin sonlu elemanlar yöntemi ile deprem analizi. *Deprem Sempozyumu,* 758-762.

Altunişik, A.C., Öztürk, M.M., Genc, A.F., Günaydin, M., Kaya, A., Akbulut, Y.E., & Sunca, F. (2024). Dynamic characteristics changes of masonry arches exposed to elevated temperature. *Construction and Building Materials,* 418, 135423.

Ansys, (2025, April 29). *Description of the SOLID187 element used in the analysis.* Retrieved from https://ansyshelp.ansys.com/public/account/secured?returnurl=/Views/Secured/corp/v242/en/ans_elem/Hlp_E_SOLID187.html?q=SOLID187

Beyen, K. (17). Ağustos 1999 Kocaeli Depreminde Hasar Alan Fatih Camiinin Dinamik Karakteristiklerinin Tanımlanması. *Altıncı Ulusal Deprem Mühendisliği Konferansı,* 16-20.

Dym, C. L., & Williams, H. E. (2012). Analytical estimates of structural behavior. Londan, NewYork: Crc Press.

El-Attar, A.G., Saleh, A.M., & Zaghw, A.H. (2005). Conservation of a slender historical Mamluk-style minaret by passive control techniques. *Structural Control and Health Monitoring*, 12(2), 157-177.

Ertek, E., & Fahjan, Y. M. (2007). Structural systems of ottoman minarets: classification, modelling and analysis. *Sixth National Conference on Earthquake Engineering,* 413-424.

Gökdemir, A., & Baki, Z. (2024). Structural Analysis of the Historical Sungurlu Clock Tower. *Applied Sciences,* 14(16), 7085.

Gönen, S., & Soyöz, S. (2021). Seismic analysis of a masonry arch bridge using multiple methodologies. *Engineering Structures,* 226, 111354.

Hacıefendioğlu, K., Demir, G., & Alpaslan, E. (2016, March). Determination of modal parameters of historical masonry minarets by using operational modal analysis. *In Proceedings of the World Congress on Civil, Structural, and Environmental Engineering,* (CSEE'16).

Kılıç, İ., Bozdoğan, K.B., Aydın, S., Gök, S.G., & Gündoğan, S. (2019). Determination of dynamic behavior of tower type structures: the case of Kırklareli Hızırbey Mosque minaret. *Journal of Polytechnic*, 23(1), 19-26.

Livaoğlu, R., Baştürk, M.H., Doğangün, A., & Serhatoğlu, C. (2016). Effect of geometric properties on dynamic behavior of historic masonry minaret. *KSCE Journal of Civil Engineering,* 20, 2392-2402.

Mortezaei, A., Kheyroddin, A., & Ronagh, H.R. (2012). Finite element analysis and seismic rehabilitation of a 1000-year-old heritage listed tall masonry mosque. *The Structural Design of Tall and Special Buildings,* 21(5), 334-353.

Serhatoğlu, C., Livaoğlu, R., Bağbancı, B., Aenlle, M.L., Pelayo, F., Canas, F.J.C., & Canteli, A.F. (2015). Dynamic identification of monumental and historical minaret of the sehadet. *6. International Operational Modal Analysis Conference,* 3-11.

Sözen, Ş. (2022). Assessment of Seismic Load Capacity of a Slender Masonry Clock Tower. *Periodica Polytechnica Civil Engineering,* 66(2), 491-501.

Turkish Earthquake Code (TEC) (2007). Specifications for buildings to be built in seismic areas. Ministry of Public Works and Settlement. Ankara, Turkey (in Turkish)

Turkish Earthquake Code (TEC) (2018). Specifications for buildings to be built in seismic areas. Ministry of Public Works and Settlement. Ankara, Turkey (in Turkish)

The design of multi-story steel industrial building with various equipment

Samet Kılıç*[1]

[1] *Star Yazılım Mühendislik ve Danışmanlık, Ataşehir, Türkiye*

Abstract. In industrial facilities, multi-story steel structures contain many non-structural elements; These are components whose design is crucial under earthquake and wind loads. The interaction of these elements with the main structure is critical. Silos, tanks, vessels, mills, filters, pipes, solar panels, monorails and cranes are examples of them. Besides their mass and inertia, the material loads inside the tank; operating frequencies of equipment like mill, crusher etc., should be observed. Fluid dynamics and thermal expansion effects in pipes; brake loads in cranes must be considered. With these technical difficulties, there are problems like lack of clarity of design responsibility, especially with mechanical discipline, the conflict of design codes and the limitations of numerical analysis tools. In this study, the design and detailing of a multi-story steel structure containing various solution methods against these problems, is mentioned. Finite element method is applied with SAP2000® software. In detailing, fiber bolts, slotted holes, special pipe supports, and dampers are used. Thermal insulations and compensators are used for thermal expansions. Possible non-structural elements can be modeled together with the main structure. The building vibration modes are compared with frequencies of equipment causing resonance. Special polymers and isolators are other solutions. Grounding is for electrical effects and cathodic protection is used against corrosion. This study may be helpful for structural engineers at designing steel structures with different instruments and equipment.

Keywords: Multi-story steel structures; Solar energy panels; Seismic design of industrial structures; Cranes and monorail design; Machinery foundations

1. Introduction

A careful balance between structural integrity, operational efficiency, and adaptability is necessary in the intricate and diverse process of designing multi-story industrial buildings. These buildings are being used more and more in urban and space-constrained locations where a variety of industrial operations require vertical development. A comprehensive approach to design that incorporates engineering, architectural, and operational issues is required when integrating different machines and equipment into a multi-story structure. Important design factors of multi-story industrial structures are made to support heavy loads from operational procedures, machinery, and equipment. A mix of static and dynamic loads must be handled by the structural system.

The structure's self-weight is referred to as a dead load, whilst the weights of workers, materials, machinery, and equipment are referred to as live loads. To provide load distribution without overloading any particular structural member, the design must take into account the various weights and positions of the equipment (McCormac & Brown, 2015). Environmental elements including wind and seismic forces, operating loads, and vibrations caused by equipment all contribute to dynamic loading. Under these circumstances, structural performance is analyzed and optimized using sophisticated computer techniques like finite element analysis (FEA) (Chopra, 2011). Multi-story industrial buildings frequently use materials like structural steel and reinforced concrete. Steel is frequently chosen because of its excellent strength-to-weight ratio, high ductility, ease of building, and adaptability when designing open floor layouts to fit huge machinery. Composite materials provide increased structural efficiency by integrating steel and concrete (Chung, 2019).

Effective spatial planning is necessary when integrating different pieces of equipment into a multi-story structure in order to maximize efficiency and save material handling expenses. One of the elements affecting layout design is equipment location. To reduce structural stresses and vibration transmission, heavy machinery is usually positioned on lower floors. To preserve operational efficiency and balance weight distribution, lighter equipment and administrative areas are situated on upper levels. Another parameter is vibration control. Specialized slab systems, calibrated mass dampers, or isolation pads must be installed in order to reduce vibrations in sensitive

*Corresponding author, E-mail: kilicsamet123@gmail.com

https://doi.org/10.31462/icearc2025_ce_eqe_575

equipment. These characteristics prolong the life of machinery and provide steady operations (Den Hartog, 1956). Flexibility for the future is one of the most important issues in industrial design. Flexible floor layouts and modular construction enable flexibility in response to change industry demands. Effective retrofitting and modifications are made possible by this method without seriously interfering with continuing business operations.

To guarantee functionality and safety, multi-story industrial buildings must abide by national and international construction norms and standards (ASCE, 2022; ÇYTHYE, 2016; TBDY, 2019). Important things to think about are codes of structure, fire safety and environmental sustainability. Guidelines for load combinations, structural integrity, and material specifications are provided by standards like the International Building Code (IBC). The building's ability to endure expected operational and environmental stressors is guaranteed by compliance (International Code Council, 2021). To reduce the dangers connected with industrial processes, design includes sprinkler systems, emergency evacuation routes, and fire-resistant materials for fire safety. Maintaining compliance and preparedness requires routine fire safety audits (NFPA, 2020). Energy-efficient systems, such light-emitting diode (LED) lighting and renewable energy sources, lower operating costs and support sustainability objectives. Eco-friendly techniques in industrial construction are promoted by green certifications like LEED (USGBC, 2020).

The main difficulties in constructing multi-story industrial buildings are balancing the interaction of large loads, vibrations, and spatial limitations. These structures' structural capacities have been improved by advancements in building materials, such as high-performance concrete and sophisticated steel materials. Building Information Modeling (BIM) also makes it easier for stakeholders to collaborate, which guarantees accuracy in design and implementation.

Designing multi-story industrial structures with a variety of equipment is a very specialized task that calls for advanced engineering solutions and interdisciplinary collaboration. Designers are able to produce robust and flexible facilities that satisfy the needs of contemporary businesses by taking structural, operational, and regulatory factors into account. The efficiency and utility of these structures will be further improved by upcoming advancements in materials, technologies, and sustainable practices, guaranteeing their continued relevance in an industrial world that is changing quickly.

2. Design of highrise industrial structure with precautions

2.1. Nonstructural design precautions

The most important reason for the construction of high-rise steel industrial structures is the need to place many equipment such as silos, filters, pumps, fans, mills, solar panels, etc. in a way that they will go down from a certain height within the process. For this reason, the presence of equipment in such structures is one of the most important criteria in design. Equipment is not only weight, but also special precautions must be taken in structures according to their characteristics. For example, solar panels have been used in many structures in recent years. These panels increase seismic loads and cause the dominant periods shift of the structure to some extent. In addition, snow cleaning must be done manually or with automation on the roofs so that the solar panels are always in working order. It is very important to have work safety railings on the outer lines for the use of ropes etc. for roof works. Due to the height of the structures, it is important to have warning signs and lighting for unmanned aerial vehicles such as helicopters, drones, etc. Drainage must be designed for rainwater drainage as shown in Figure 1. In order to prevent rainwater from seeping through the roof and electrical equipment from being damaged, the roof cladding and insulation must be proper. It is recommended to use cathodic protection and effective insulation to protect structures from corrosion. In addition, lightning rods are an indispensable part of the design to protect against lightning. Similarly, grounding, which supplies energy-efficient and environmentally sustainable systems, is a priority in electrical design.

It is essential for possible disassembly that the roof elements are not welded. Especially silos and tanks are located at the highest elevations of such structures. It is very important to arrange the steel elements and their connections in such a way that they can be removed from the structure with a tower crane from the top in case of any failure. Also, it is crucial for future expansion. In general, all elements including the railings should be connected with bolts to facilitate the disassembly of the equipment in the entire structure, and field welding should be avoided as much as possible. Monorails or cranes should be designed for easy movement of equipment within the structure. Cranes such as monorail are preferred more than cranes in high-rise structures. In addition, doorways should be left on the facades for exits from many floors. Since the structures are high-rise structures, it is important for them to have fire escape engineering, to have fire escapes and to have elevators for vertical human circulation. It is inevitable to arrange mini platforms to provide access to each equipment. Sufficient thermal insulation of the hot air lines (pipes and pipe supports) passing through the structure will prevent excessive thermal load from passing to the structural elements.

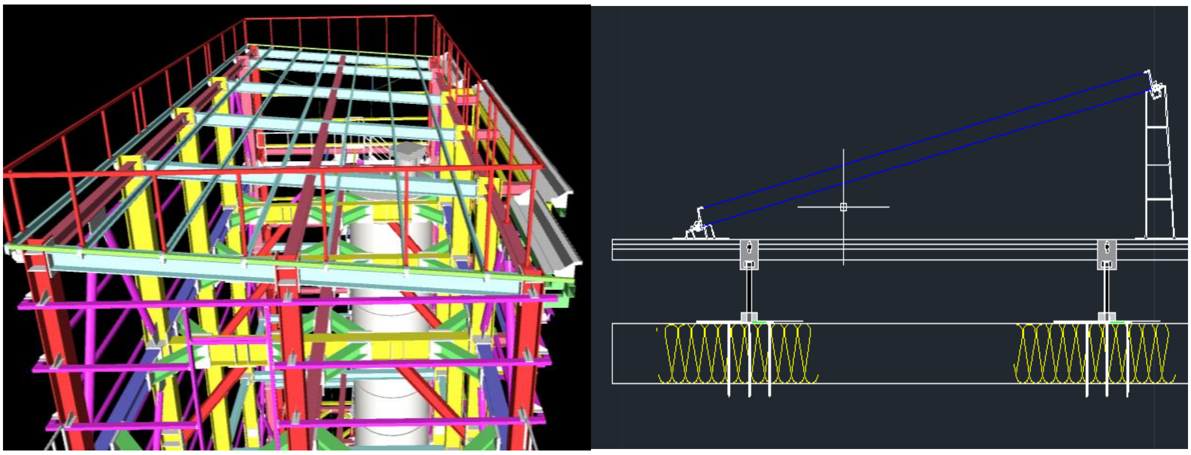

Fig. 1. Solar Panels and Roof Design (Navisworks, 2022)

2.2. Structural design precautions

The most important structural design problem in high-rise buildings compared to hangar-type structures is the limitation of lateral drift. While it is possible to choose a direction moment frame, a direction center or eccentric brace in hangar-type structures, it is not possible for moment frames to solve the displacement problem, especially as the structure rises. For this reason, it is necessary to use dual systems (Kılıç, 2015) where braces are used together with moment frames instead of moment frames. It is also very important to limit lateral drifts caused by wind loads in high-rise structures. The increase in the width of the facade and the height of the structure increases the wind load exposed. A drift limitation is made in a way that does not allow non-linear behavior under wind loads (ASCE, 2022). The analysis of the panels used for solar energy under wind and dead loads should be made by the supplier companies and should be added to the finite element models.

Elements such as silos, tanks or bunkers in high-rise steel structures are generally evaluated under the discipline of mechanical design, therefore only the support loads are affected in structural models. Often, the designs of such non-structural elements are out of scope and their rigidity is neglected in the models. As shown in Figure 2, silos were considered in the finite element model. In addition (BIM) is used in 3D models to prevent any clashing.

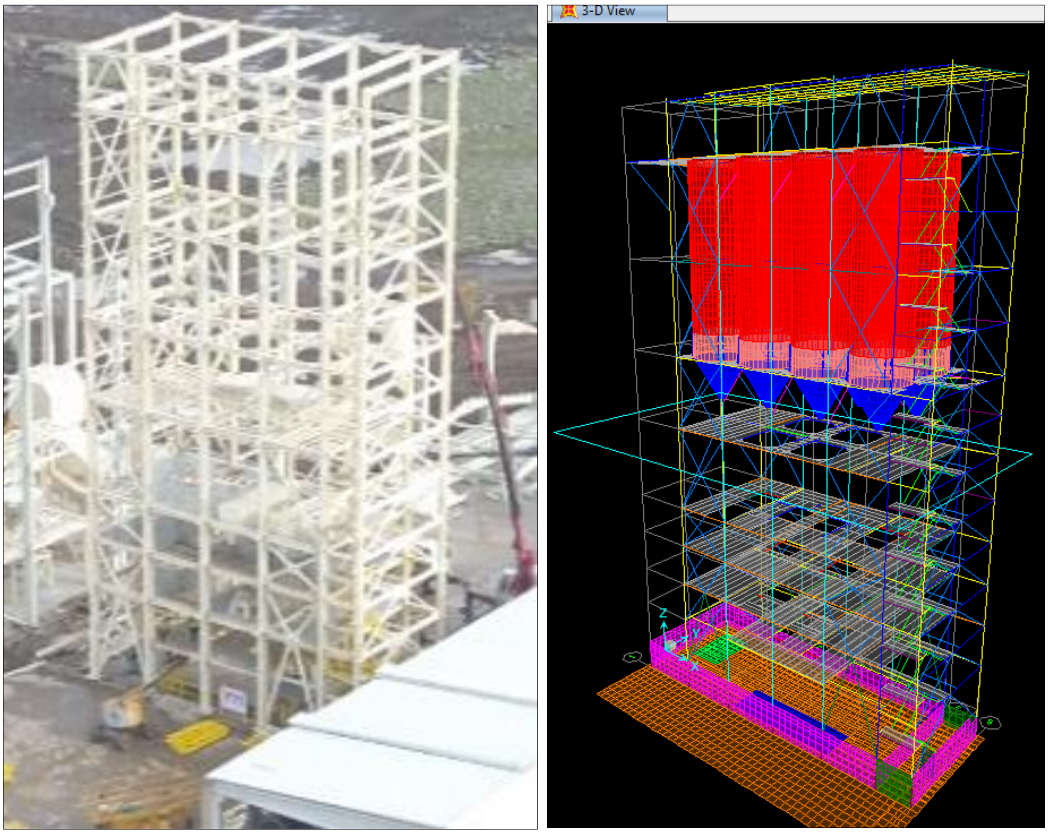

Fig. 2. Real view and FEM Model of Industrial Building (SAP2000, 2021)

In addition, pipes with large diameters and therefore high rigidity located within the structure are only affected as a load on the system. It is possible to model pipes in advanced finite element programs used today. It will be possible to add pipes to the system isostatically with the help of one roller and one fixed support. In addition, even if we cut off the heat transfer of the pipes to the outside with the necessary insulation, it is not possible to prevent thermal extension within them. For this reason, as seen in Figure 3 below, expansion joints with sufficient distance should be used and the extension should be absorbed here. The necessary strength should be provided in piping with pipe stress analyses. Reservoirs such as silos should also be added to the system and additional effects such as overturning moments on the structure should be taken into account. When the models in which such equipment is processed or continued with support reactions without processing are compared, it has been determined that some additional forces are seen especially in steel columns extending towards the top level of the silo due to the movement of the top of the silo. Apart from this, silos, tanks, etc. whether the equipment meets the earthquake loads and material, wall stress under liquid pressures, buckling resistance, lateral displacement limits should be checked externally, and coarse thicknesses from other disciplines should be checked (Kılıç, 2024; Kılıç et al., 2022; Kılıç et al., 2021).

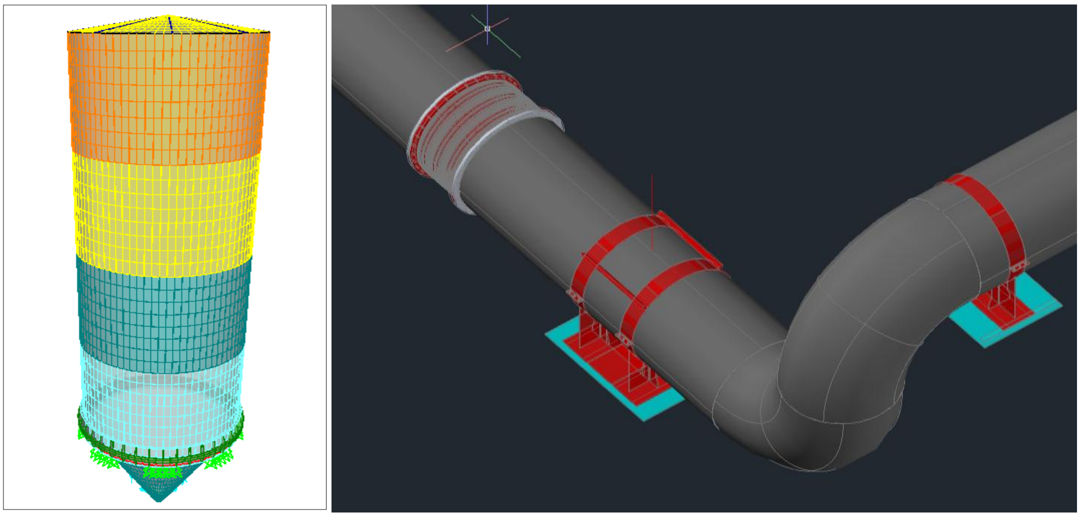

Fig. 3. Independent Solutions for Silos and Pipes (Navisworks, 2022)

In the case of presence of pressure vessels in the structures or equipment with computational fluid dynamics and support reactions, it is very important to continue with the data and loads received from technology companies.

3. Vibration control of structure

3.1 Steady state analysis and vertical modal analysis check

It is very important to provide vibration comfort in all steel structures. As seen in Figure 4 below, it is desired for the frequency to remain within certain vibration limits depending on the acceleration and load in structures such as residences, shopping malls, etc. In steel structures, diamond-patterned sheet metal etc. claddings are made on the floors. It is possible to limit vibration by switching to composite slabs. In high-rise industrial structures, the presence of machines operating at higher vibrations compared to human walking excitation. These machines cause large vibrations in the entire structure. As a result of vibrations, fatigue occurs in the structural elements and various comfort problems occur in the long term. One of the ways to prevent these problems is to find the vibration frequency of the machine and move away from the dominant vibration frequencies of the structure that will cause resonance. Here, the level where the equipment causing vibration is located in the building is very important. Simply, it is important whether it is on the foundation of the building, on the first floor or on higher floors other than the first floor. If it is on the foundation level of the building, the ideal solution is to separate the building foundation from the machinery foundation. Afterwards, a steady state analysis should be performed on the equipment foundation to try to separate the equipment vibration frequency from the fundamental frequency. This process is implemented as described below. Firstly, the steady state function was defined in related software SAP 2000 (SAP2000, 2021) as described in CSI Analysis Reference Manual, chapter "Frequency Domain Analyses", section "Steady-State Analysis". Steady-State function was introduced to software with the equation (1) below. "w" and "f" refer to angular velocity and frequency.

$$w^2 = (2\pi f)^2 \quad (1)$$

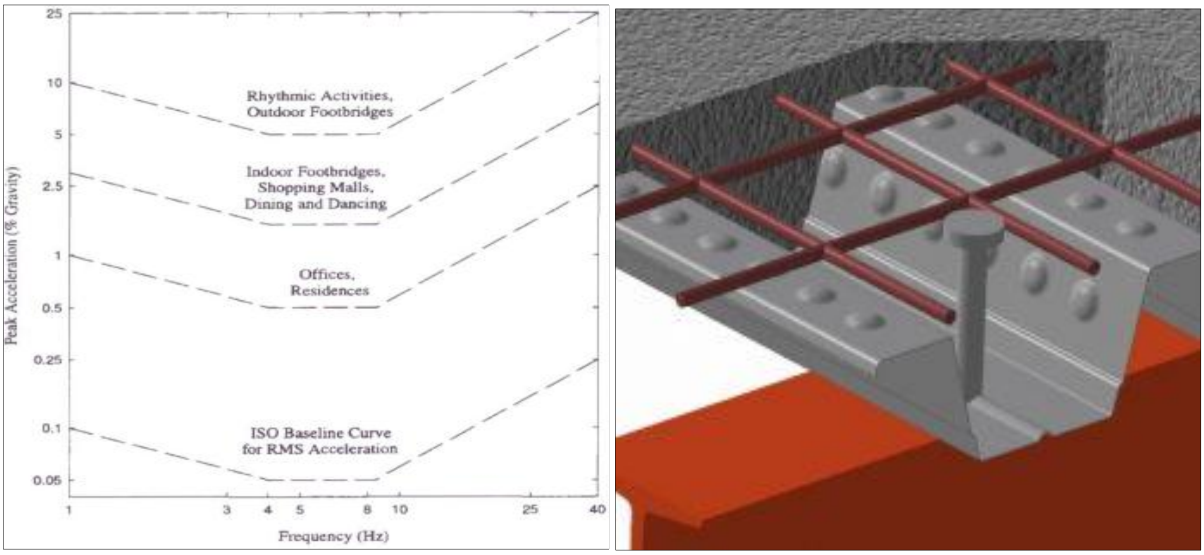

Fig. 4. Walking Excitation and Composite Slab Design (Composite Slab, 2025)

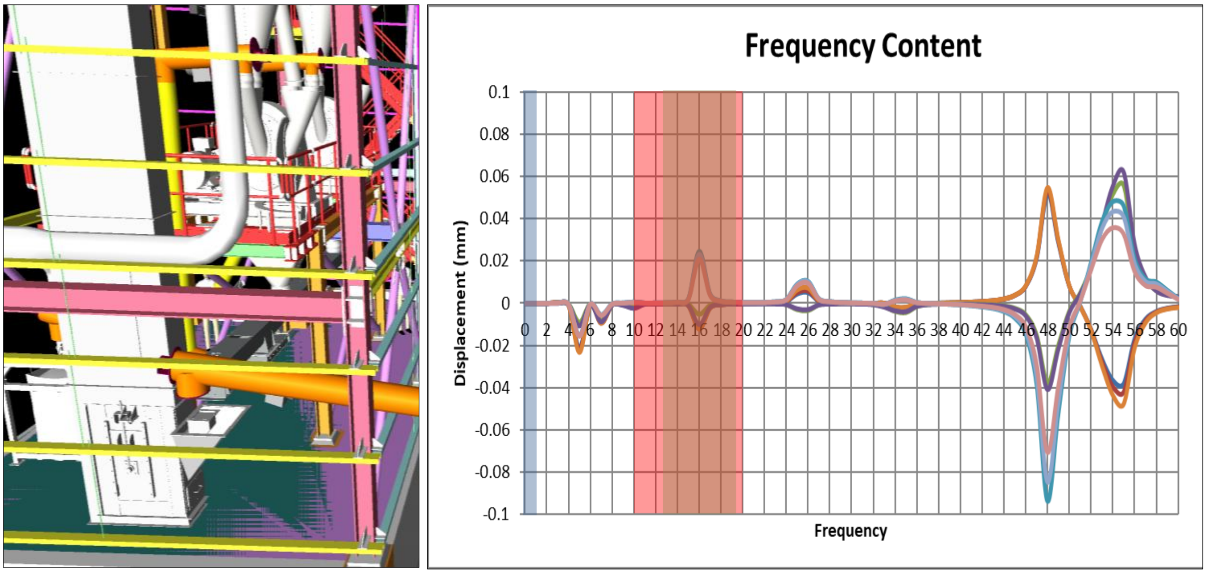

Fig. 5. Different Level of Equipment Platforms and Frequency Content Check (Navisworks, 2022; Excel 2022)

After the steady state analysis, the values and the graph are illustrated above. It is expected that the structure resonates for frequencies of mode which is vertical. After finishing analysis, the frequencies and the maximum displacement places are compared. For this reason, initially the values' unit is converted from rpm to Hz. Then to be on the safe side, the resonance frequency should be different at least %20 percent of operational frequencies (Siyahi, 2012). So, calculated the values of frequencies multiplied coefficients "1, 2" and "0, 8" are shown in Figure 5. It is impossible to show every joint displacement in excel graph. So, only a few of the joints are shown in Figure 5 which is not in the operational frequency borders as indicated. The resonance occurs in the mode where the highest mass participation exists, as expected (Kılıç, 2023).

3.2 Measures against resonance

Despite such measures, it is not possible to eliminate the vibration felt in the structure. There are additional solutions that claim to reduce vibrations by half. An example is sylomer. This unique polymer was added to the system in a bundling manner. Figure 6 shows the force-deflection and damping curves following the application of a particular polymer. Equipment vibrations are absorbed by this unique polymer (Getzner, 2022).

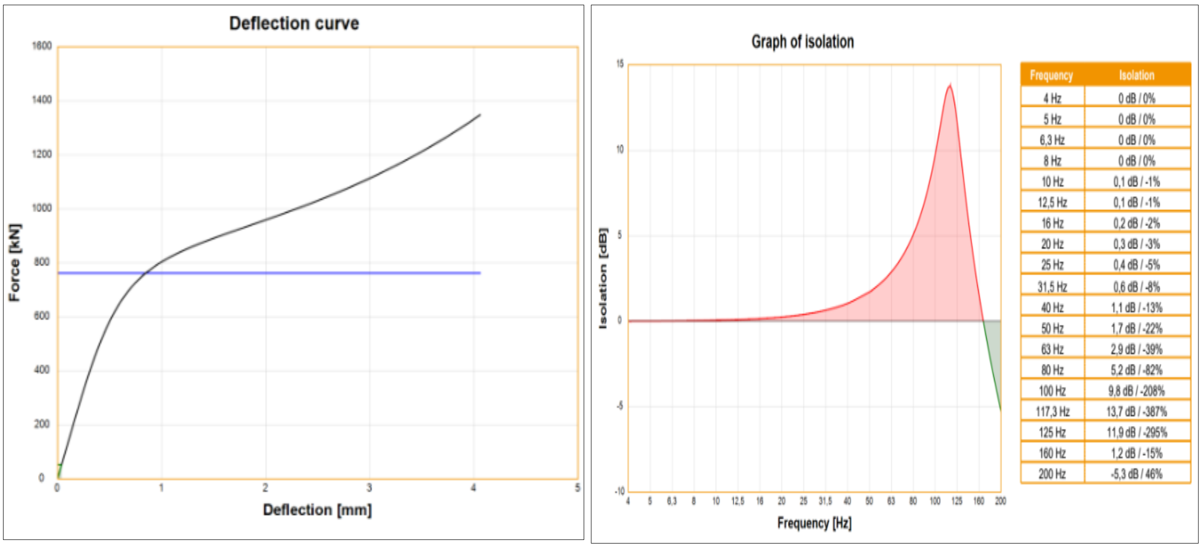

Fig. 6. Force-Deflection and Damping Curves of Sylomer (Getzner, 2022)

Another situation is when the vibrating equipment is on the first floor of the building. In this case, to the extent that the floor heights allow, the first floor is detached from the main building, and it is ensured to work as a separate platform. The most important problem that will be encountered in this case is the formation of soft story irregularity in the building. The way to prevent this is to connect all the frame columns of the building to each other with steel beams in the same way. Since the platform level will be the first-floor level, the platform level has slightly increased. The level of the steel beams is arranged so that they remain below the platform level. In this way, slender columns and different floor heights are prevented, and the system to which the vibrating equipment is connected is detached from the main structure. In the case of the equipment on the upper floors, it is aimed to provide vertical mode participation in a way that prevents resonance. According to the experience gained from steady state analyses, the points where the vibration is the greatest are the periods/frequencies where the highest participation is seen in vertical modes. Based on this experience, by looking at the vertical mode contributions of the building, it is checked whether they are the same as the equipment dominant modes, and if there are overlapping modes, it is tried to get away from these points by trying beams with different stiffnesses if possible. The connections of the beams on which the equipment sits should be designed to resist torsion. In addition, it is very important to support them laterally from several points if possible. In cases where this is not possible, some isolators are used as shown in Figure 7 below. Similarly, slotted holes are used to absorb equipment vibration. Another solution is to choose fiber bolts for connecting the equipment under the control of mechanical discipline to the beams. The energy absorption capacity of these types of bolts is higher than normal bolts.

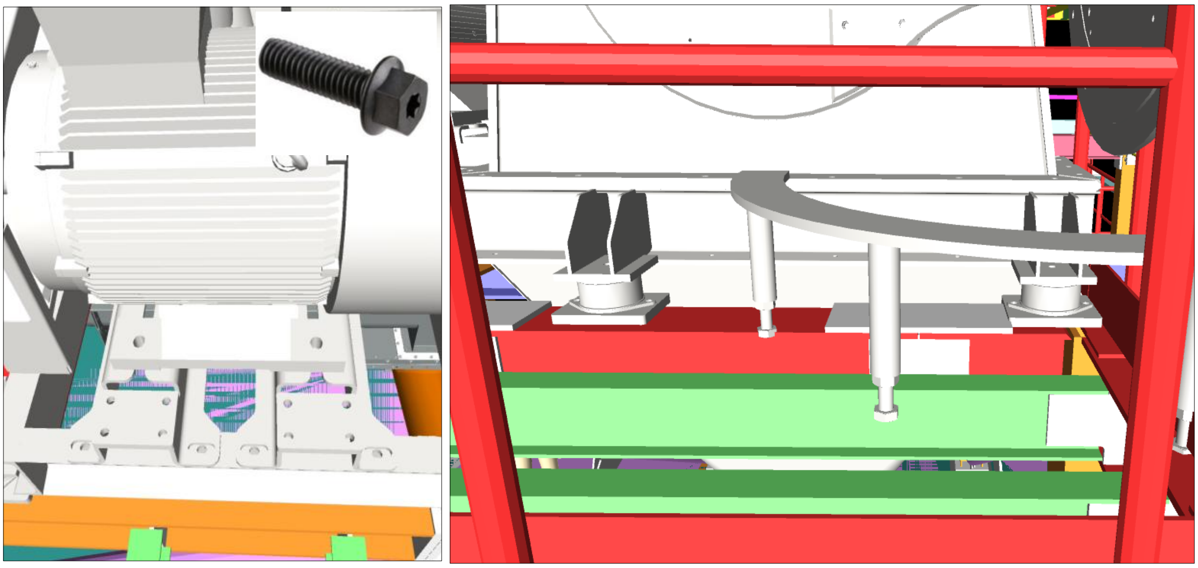

Fig. 7. Fiber Bolts, Slotted Holes and Isolators for Equipment (Navisworks, 2022)

4. Conclusions

According to the results obtained from this study, the conclusions are summarized below:

- Steel structure systems are ideal for high-rise industrial structures. Thanks to its advantages such as lightness, high carrying capacity, fast assembly and large openings, steel is one of the most suitable material options for industrial buildings.
- Heavy and bulky equipment directly affects structural load distribution. Therefore, architectural planning and static calculations should be integrated according to the location and operating principles of the equipment. It is very important to dampen machines that cause high vibration in structures with various methods.
- Engineering methods such as finite element analysis, modal analysis and earthquake calculations, where all possible non-structural elements (tanks, silos, piping, etc.) are integrated, allowing the durability of the structure to be modeled correctly.
- Increasing the fire resistance of steel structures is possible with fire-resistant paint, composite flooring systems and appropriate evacuation plans. At the same time, protection against corrosion is also necessary for long life.
- Solutions such as energy efficiency, natural lighting, grounding, and lightning rod use both reduce operating costs and have an environmental impact. The use of recyclable steel is also an important factor in this context.
- The design process should be carried out with a multidisciplinary approach. Architecture, civil engineering, mechanical-electrical system design and production processes should be considered as a whole, and all stakeholders should be integrated into the project process. The use of BIM in design is of vital importance

References

ASCE. (2022). *Minimum design loads for buildings and other structures (ASCE/SEI 7-22)*. American Society of Civil Engineers.

Chopra, A. K. (2011). *Dynamics of structures: Theory and applications to earthquake engineering*. Pearson Education.

Chung, D. D. L. (2019). *Composite materials: Science and applications*. Springer.

Composite Slab. (2025, February 22). Retrieved from https://www.insaatgundemi.com/kompozit-doseme.html

ÇYTHYE. (2016). *Çelik Yapıların Tasarım, Hesap ve Yapım Esaslarına Dair Yönetmelik (RG No. 29614)*. Ankara (In Turkish).

Den Hartog, J. P. (1956). *Mechanical vibrations*. McGraw-Hill.

Excel. (2022). Microsoft.

Getzner. (2022, May 21). Retrieved from https://www.getzner.com/en/downloads

International Code Council. (2021). *International building code*. ICC.

Kılıç, S. (2015). *The investigation of the 25 percent rule in concentrically brace frame dual system with special moment frame* (M.Sc. Dissertation). İstanbul Technical University, İstanbul.

Kılıç, S. (2023, March). The steady-state analysis of machinery foundation. In *ICE2023 International Conference on Istanbul and Earthquake*, Istanbul Arel University, İstanbul, Türkiye.

Kılıç, S. (2024). Deprem yalıtımlı tank tasarımında yönetmeliklerin doğrusal olmayan analiz prensiplerinin irdelenmesi. *Karadeniz Fen Bilimleri Dergisi, 14*(2), 551–575. https://doi.org/10.31466/kfbd.1385764

Kılıç, S., Akbaş, & Zülfikar, A. C. (2021, October). The evaluation of seismic behavior of broad tanks subject to strong ground motions scaled with different approaches. In *6th International Conference on Earthquake Engineering and Seismology*, Gebze Technical University, Gebze, Kocaeli, Türkiye.

Kılıç, S., Akbaş, B., Paolacci, F., & Shen, J. (2022). Seismic behavior of liquid storage tanks with 2D and 3D base isolation systems. *Structural Engineering and Mechanics, 83*(5), 627–644. https://doi.org/10.12989/sem.2022.83.5.627

Kılıç, S., Akbaş, B., Uçkan, E., & Çakır, F. (2021, June). Endüstriyel yapılarda yatay geniş tanklar ile dikey narin tankların deprem esnasındaki davranışlarının ve farklı sismik yalıtım sistemleriyle tasarımlarının irdelenmesi. In *9. Ulusal Deprem Mühendisliği Konferansı*, İstanbul, Türkiye (In Turkish).

McCormac, J. C., & Brown, R. H. (2015). *Design of reinforced concrete*. Wiley.

National Fire Protection Association (NFPA). (2020). *NFPA 101: Life safety code*. NFPA.

Navisworks. (2022). Autodesk.

SAP2000. (2021). *Structural analysis program*. Computers and Structures, Inc., Berkeley, California.

Siyahi, B. (2012). *Dinamik yüklü temel tasarımı*. TMMOB, İMO İstanbul Şubesi, İstanbul (In Turkish).

TBDY. (2019). *Türkiye Bina Deprem Yönetmeliği*. Türkiye Cumhuriyeti Başbakanlık Afet ve Acil Durum Yönetimi Başkanlığı, Ankara, Türkiye (In Turkish).

U.S. Green Building Council (USGBC). (2020). *Leadership in energy and environmental design (LEED)*. USGBC.

4th International Civil Engineering & Architecture Conference
17-19 May 2025, Trabzon, Türkiye

Nonlinear static pushover analysis for evaluating steel rack systems' seismically optimal down-aisle configuration

Fuad M. AL-gaadi *[1], Fatih Alemdar[1]

[1] *Yildiz Technical University, Department of Civil Engineering, 34220 Istanbul, Türkiye*

Abstract. Bracing in the down-aisle direction of rack systems is restricted due to operating requirements. Additionally. Single-symmetry-axis thin-walled members are generally used in rack systems. As a result, the structure may experience eccentric situations that might negatively impact system stability. As well as these members are particularly subjected to local and torsional buckling due to lateral loadings and gravitational forces. The most widely used methods for assessing the seismic response of any structural system are nonlinear time history analysis (NTHA) and nonlinear static pushover analysis (NSPA). Despite being the most accurate method for predicting seismic demand and assessing performance, NTHA is computationally demanding and requires selecting and using a relevant set of ground excitations. This paper presents a straightforward method for conducting nonlinear static pushover analyses of standard pallet racking structures under progressively increasing lateral forces. It aims to identify the most effective configuration in the down-aisle direction based on their seismic behavior and energy dissipation capacity. Using Ansys Workbench software, finite element models of four three-story full-scale rack systems with different bracing conditions in the down-aisle direction are developed and evaluated under monotonic lateral loading. In this context, it was found that the system's bracings offer it stiffness; nevertheless, in single-modular racking systems, such as the one we investigated, the external bracings result in torsional effects. As a result, the bracing's positive benefits cannot be utilized fully. Results show that bracing members may be employed to improve the rack systems' behavior in the down-aisle direction.

Keywords: Nonlinear pushover analysis; Cold-formed steel; Seismic behaviour; Storage rack systems; Finite element analysis**.**

---

1. Introduction:

Steel storage rack systems are important for the business since they store industrial goods. Rack structures are in high demand because they can store a lot of merchandise with minimal space over multiple levels in a small area. Typically, cold-formed thin-walled members are utilized in the design of standard storage rack systems. Beams have boxed cross sections, whereas uprights have open, thin-walled sections perforated for attaching beam end connector hooks that connect the upright and beam components without bolts or welds (Fig.1). Because most storage racking sections have a single symmetrical axis, different buckling conditions may occur across connections, sections, or the rack system.

Perforated uprights are affected by local deformation events, including multiple buckling modes (local, distortional, and global) and their interactions, which cause various failure modes in storage rack systems due to differences in the directional stiffness and section characteristics of thin-walled structural (Castiglioni, 2016). Storage racking system design becomes difficult. Inadequate storage rack system design, installation, loading, or maintenance can cause them to overturn or collapse during earthquakes, causing economic losses in damaged goods and worker safety risks.

Standard rack systems can be classified into braced and unbraced frames. In rack systems, the longitudinal direction is referred to as the down-aisle direction, and the transverse direction is the cross-aisle direction. The braced system includes bracings in both the cross-aisle and down-aisle directions. Unbraced rack frames contain bracing only in the cross-aisle direction, keeping the down-aisle unbraced. In general, diagonal bracing distributes lateral forces over the cross-aisle direction. However, due to operating considerations, the system's utilization of bracing is restricted in the down-aisle direction, and the bending stiffness of the adjustable beam-upright column connectors and base connections provides rack stability in this direction.

The Rack Manufacturers Institute's specification (RMI, 2012) works as a design guideline in the United States and certain other countries. As a result, pallet rack analysis and design are extremely complicated. Nonlinear

---

* Corresponding author, E-mail: fuadeng5@gmail.com

https://doi.org/10.31462/icearc2025_ce_eqe_578

history analysis (NTHA) is the most effective technique for evaluating seismic structural performance. Nevertheless, this method necessitates the application of an acceptable set of ground motions, as well as an adequate computational tool that conducts the analysis, to provide ready-to-use results within the time restrictions of design companies. Experienced practicing designers prefer the nonlinear static pushover analysis (NSPA), which requires less computational time as an alternative method to time history analysis (NTHA).

Recently, damage and collapse of storage racks caused by earthquakes in regions subject to earthquakes have been investigated by (Bernuzzi & Castiglioni, 2001; Connor, 2012.; Firouzianhaij et al., 2021; Krawinkler et al., 1979). On the other hand, storage racks were excluded from regular design specifications because they were classified as movable equipment. However, in response to earthquake damage, a few countries have offered specifications for storage racks, which include structural component testing by user needs (Fema460, 2005.; Steel Storage Racking, 2012).

Regarding rack system rigidity in the down-aisle direction, beam-to-upright connections and upright thickness are extremely effective (Dai et al., 2018; Galeotti et al., 2021; Gilbert & Rasmussen, 2010). Many studies in the literature evaluate the semi-rigid behavior of the upright-beam connector within the system (Bajoria & Talikoti, 2006). Yin et al. (2016) investigated five distinct beam connectors, including lock fasteners and bolted connections, under both monotonic and cyclical loads. The test findings indicated that bolted connections demonstrate nearly double the load-carrying and energy dissipation capacities compared to locking fastener connections. Prabha et al. (2010) conducted cantilever experiments on 18 samples to figure out the ultimate capacity of hooking connectors, considering upright thickness, number of hooks, and beam height as parameters. Researchers have developed many testing methods to achieve results that more accurately represent actual rack system implementations. Nevertheless, due to the high expenses associated with testing, optimization may be implemented in rack systems through verified numerical studies (Bové et al., 2021; Chulin Chen et al., 2019; Vujanac et al., 2020).

Huang et al. (2021) investigated experimentally how base plate connection thickness, upright thickness, and eccentric anchor bolt conditions affected the flexural behavior of base plate upright connections. The initial stiffness, which was significantly affected by the base plate-upright connection, was found to predict the whole system's behaviour.

Gilbert & Rasmussen (2011) investigated base plate stiffness under various axial loads utilizing a dual-actuator test setup. They figured out that base plate configurations have a significant influence on the total buckling strength and the down-aisle direction lateral resistance of the storage racks.

Avgerinou et al. (2019) conducted pushover testing on rack systems. The test results recommended the use of plane bracings to ensure diaphragm behavior. Furthermore, based on their analytical results, using higher rotational stiffness base plates has been suggested as one of the best techniques for improving rack system capacity. The test results additionally showed distortional buckling developments in the uprights.

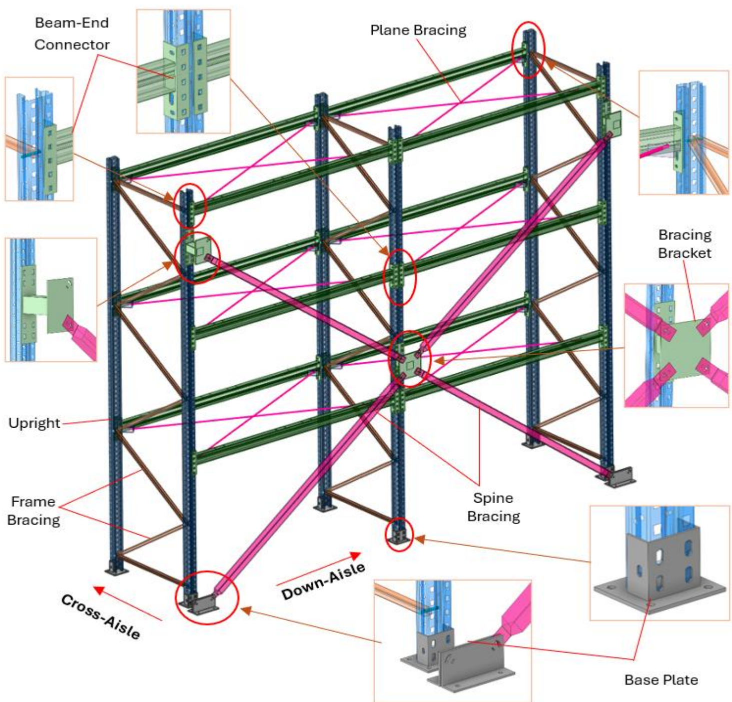

Fig. 1. Components of typical storage rack systems

Kanyilmaz et al. (2016) performed pushover tests on full-scale storage racks to evaluate the key factors affecting the responses and failure modes of different configurations of storage rack systems. In the case of a single bolt that was utilized under different baseplate connection applications, the plasticity variation was extremely limited, with more than half of the drift concentrated on the first level.

Gusella et al. (2022) investigated the failure mode and stiffness of the brace-column connection using joint models. They recommend that experiments using dynamic external forces need to be performed to comprehend the dynamic responses of storage racks. They will also be expected to upgrade the design by considering dynamic external forces, including seismic events.

Petrone et al. (2016) conducted quasi-static tests on the cross-aisle for multiple rack systems to evaluate the seismic performance of these structures after anchoring one side of the storage rack baseplate to the ground using two bolts. The results indicated that the cross-aisle direction is more vulnerable to overturning than the down-aisle direction, and lateral displacement could cause a collapse. The tests showed that the inelastic deformation of the baseplate resulted in stable hysteresis responses due to substantial ductility and energy dissipation.

Andrea et al. (2016) conducted pushover tests on full-scale rack systems, employing different external bracing components that improved system stiffness in the down-aisle direction. The collapse mechanisms for the tension rod prototypes were identified. In their study, they utilized system behavior parameters for estimating the efficiency of the various stability braces and the connection specifications associated with these braces to improve the system's stiffness.

Heo et al. (2023) conducted full-scale shaking table tests to investigate how the base plate-to-ground fixing situations affected the seismic behavior of the rack systems. The experiments were carried out under four different base-to-ground fixing configurations: one bolt, two bolts, four bolts, and fixed conditions. The results demonstrate that a pallet rack with moderate resistance to external forces may resist displacement if it is tightly connected to the ground. According to the results, the damage was severe under the 1-bolt condition, repairable under the 2-bolt and fixing conditions, and fatal under the 4-bolt condition due to cumulative displacement due by permanent external force.

Çelik et al. (2022) evaluated the influence of base-plate types on the down-aisle direction seismic behavior of storage rack systems using pushover testing. The findings indicated that an increase in the rotational stiffness of the base support decreases torsional impacts. Consequently, it can be suggested that in low-rise rack systems, employing high-value stiffness base plates could improve system stability and offer more economical solutions.

Racking designers typically eliminate bracing in the down-aisle direction so that during service, the racks can be accessible from each side of two aisles and goods can be loaded and unloaded easily. However, in active seismic areas, this design can sometimes not be enough for carrying large horizontal loads due to the insufficient lateral stiffness and strength, which is related to the significant second-order effects (Orlando et al., 2017) and the weak rigidity and gaps of the base and beam-to-upright connections (Bonada et al., 2021). As a result, vertical spine braces are commonly used to mitigate the down-aisle's instinctively weak lateral stability; nevertheless, this bracing system is required to be located just at the back, resulting in undesirable global torsional conditions. The literature shows that diagonal bracings in the cross-aisle direction can increase displacement stiffness in rack systems. Down-aisle stability improvement is limited because the system is meant to meet operational goals. This led to applications using tension rods and vertical spine braces. Even while vertical spine bracings provide effective rigidity in back-to-back rack systems, they result in torsional effects. These torsional effects impact the system's collapse mechanism and energy dissipation capacity. Therefore, the safety design of these systems requires investigating methodologies to avoid connection and section torsional behavior.

In this research study, nonlinear static pushover analysis was performed on different configurations of the rack systems to investigate the behaviour of the rack systems in the down-aisle direction under lateral loads. Stability components, such as tension rods and spine vertical bracing systems, were used in the down-aisle direction to increase the stability of such systems in this direction. The FE numerical models were simulated and analyzed using the finite element analysis software ANSYS Workbench. In the finite element analysis, the effect of using the stability components and the base plate to ground fixing conditions on the rack systems' failure mechanisms, energy dissipation, and torsional capacity has been investigated. In addition, in the literature, the perforations on assembling parts of the rack systems are typically neglected in most numerical evaluations. Nevertheless, perforations in the members compound the rack systems and might considerably decrease the critical buckling load of the uprights, based on the local deformations. In this study, the numerical analysis has sufficiently captured all details of the system, including perforations and tabs, to investigate the seismic behavior of the system.

2. Materials and methods:

2.1. Details of the storage rack frame:

This study aims to investigate the global seismic response behavior of down-aisle pallet rack systems. For this purpose, three full-scale rack model systems were designed with different configurations in the down-aisle direction: RK1, RK2, and RK3. RK1 is the configuration that has no vertical or plane bracings, as shown in Fig.4.

To figure out the effects of the bracings that were designed and used in the down-aisle direction on the lateral structural behaviour of the rack system, this model has been selected as the basis for the reference system. The RK2 rack configuration is an upgraded model of the RK1 rack system that is enhanced with plane bracings and a tension rod system, which are commonly used in the down-aisle direction of the rack systems. Console brackets are used in this system as connections for tension rod braces to the rack system. The RK3 rack configuration is a strengthened model of the RK1 rack model in the down-aisle direction that has plane bracings on each level and vertical spine bracings. The RK3 rack system's spine brace sections are much larger than the RK2 rack system's tension rods. In contrast to the tension rod bracing system in RK2, the spine bracing system in RK3 is connected to the rack system and the ground by brace connection plates so that it works as a rigid structure in the down-aisle direction.

In the configurations of braced rack systems, braces are employed just on one side in the down-aisle direction to meet the operational requirements of the rack systems. Consequently, horizontal bracings are employed for connecting upright columns, increasing the distribution of seismic forces from the unbraced vertical plane of the column to the braced vertical plane. Torsional phenomena resulting from global irregularity are effectively minimized. The rack models' geometrical details were chosen based on popular market rack configurations. They match practical applications of conditions concerning weight, unit load specifications, and beam levels. Therefore, all the designed rack models consist of three levels with two spans. The rack's total height is 4300 mm, and the beam length is 2400 mm. The upright section, D-type diagonal braces, and horizontal braces remain constant in all rack models in the cross-aisle direction (Fig. 2).

This study analyzed three different fixing conditions (Table 1) to investigate the impact of base plate-to-ground fixing conditions on the behavior of rack systems in the down-aisle direction: Case 1 (2 bolts), Case 2 (4 bolts), and Case 3 (fixed), as shown in Fig. 5. A nonlinear static pushover FE analysis was performed and evaluated for the three different configurations under lateral loads. The base plate has been connected to the ground using M8.8 bolts.

Fig.3 illustrates details of the upright, beam and brace sections. The beam sections consist of two interconnecting C-lipped channel profiles with dimensions of 100x50x1.5 mm. They have been continuously spot-welded across the beam direction. The uprights are open U-sections with dimensions of 100x70x2 mm. For the diagonal brace in the cross-aisle direction and the spine braces in the down-aisle directions, C 28x28x1.5 mm and SHS 60X60X3 mm profiles were used, respectively.

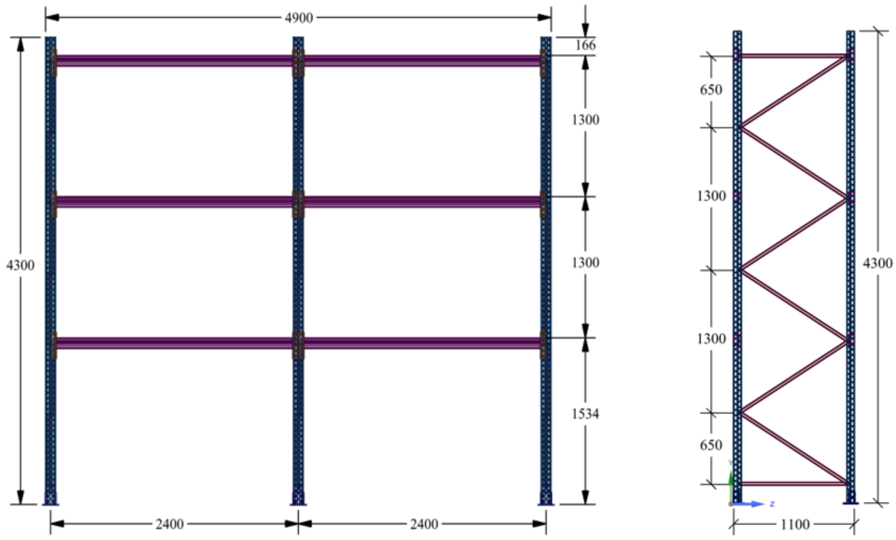

Fig. 2. Dimensions of the rack systems (unit: mm)

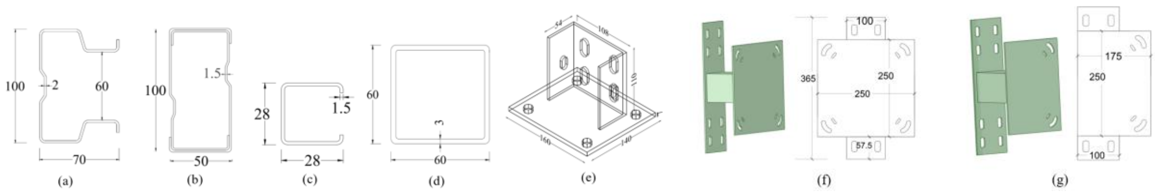

Fig. 3. Section dimensions (unit: mm)

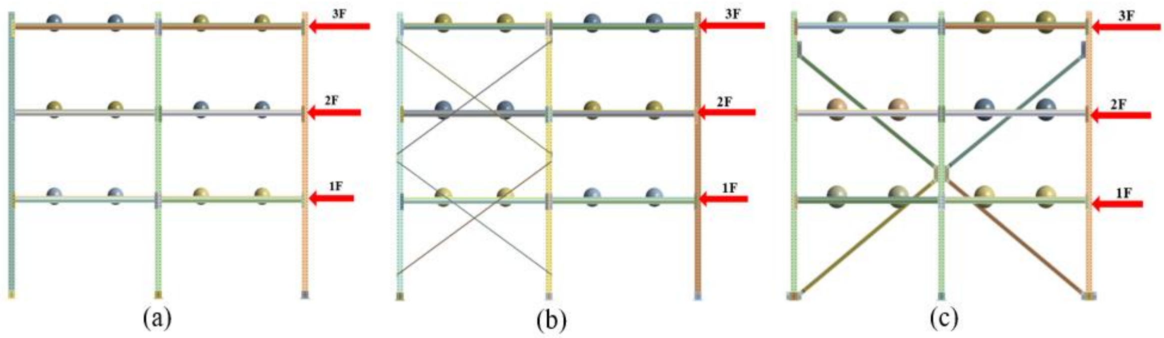

Fig. 4. General views of the configurations of rack systems: a) RK1 model, b) RK2 model and c) RK3 model

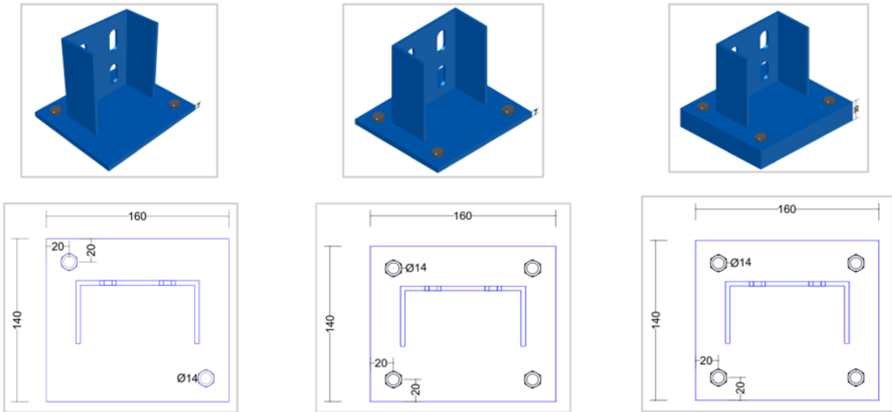

Case 1: 2 bolts   Case 2: 4 bolts   Case 3: Fixed

Fig. 5. Different baseplate fixing conditions (unit: mm)

Table 1. Variable parameters of the finite element models of the studied rack systems

Rack Prototype	Down-aisle configuration			Base-to-ground fixing condition		
	No braces	Tension rod braces	X-spine braces	Case 1 (2 Bolts)	Case 2 (4 Bolts)	Case 3 (Fixed)
RK1.1	✓			✓		
RK1.2	✓				✓	
RK1.3	✓					✓
RK2.1		✓		✓		
RK2.2		✓			✓	
RK2.3		✓				✓
RK3.1			✓	✓		
RK3.2			✓		✓	
RK3.3			✓			✓

2.2. Materials:

To take into account the nonlinear effects of the materials in numerical analysis, the material mechanical properties of the rack sections are presented by (Çelik et al., 2022) were considered as input in the FE analysis. The material properties were determined through three coupon tests conducted on plates used in all the profiles of the rack system. The stress-strain graph for the numerical models is obtained using the average values of the tested coupons. The stress-strain relationship of the materials is shown in Fig. 6.

2.3. FE modeling and mesh

Finite element analyses should take geometrical nonlinearities into account for reliable results. The utilization of shell and solid parts additionally contributed to the study to more accurately capture the buckling conditions. Because of their thin wall thickness, the members that comprise diagonal bracing, the beam, upright, X bracing,

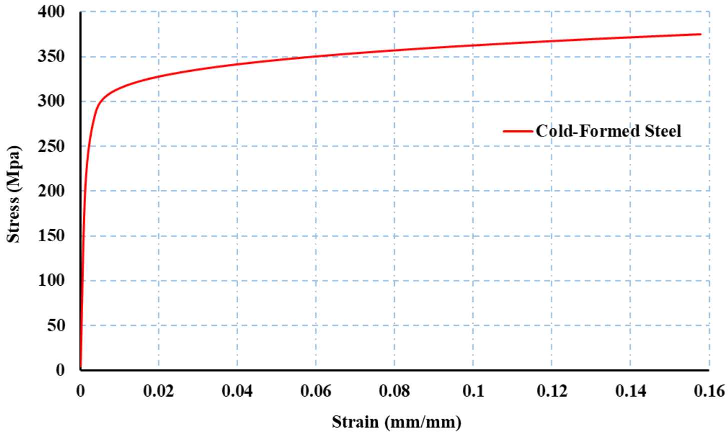

Fig. 6. Stress-strain relationship of the cold-formed steel used in FE analysis (Çelik et al., 2022)

tension rod, upright frame, plane bracing, and connection elements were represented in the numerical models using the Shell 181 element. Shell 181 is the appropriate shell element type for analyzing thin and medium-thick shells structures. It consists of four nodes, each with six degrees of freedom; movements and rotational motions along the X, Y, and Z axes may be taken into account. Pins are employed to connect the uprights to the diagonal bracing and horizontal brace members. A solid 187 elements were utilized to simulate them in the numerical models. The solid 187 elements have the potential for strain hardening, plasticity, and large deflections.

In reality, x-bracing, base plates, tension rods, bracket members, and plane bracing are all bolted together in rack systems. Since the model is very big, the bolts were not simulated in the mathematical models of the rack systems. The beam188 element was utilized to represent the bolts in the numerical models. Linear solutions with large rotations or nonlinear solutions with large strains are appropriate matches for this element. Table 2 shows the details of the elements used for finite element analysis

The elements that compose the upright frames of rack systems are connected by pins. Therefore, the upright frame's vertical, horizontal, and diagonal bracing elements were represented as edge-to-face bonded to a pin. In rack systems, the ends of the beams are joined by welding to the beam-connecting elements. Edge-to-face contact was employed as a bonded interaction between the beam and the beam connection in the numerical models to reflect this condition. The bottom edges of the upright and the base plate surface are connected by edge-to-face contact as a no-separation interaction to represent accurately the upright-base plate connection in the numerical models. Additionally, the uprights are connected to the base plate at their backs using bolts. In the numerical models, the edges of the base plate holes were defined as Ux = Uy = Uz = 0, and the surfaces of the base plates in contact with the ground were defined as Uz = 0.

In the finite element analysis of large rack systems, upright perforations are typically neglected when utilizing shell elements. This study utilizes local meshing at areas of geometric changes, bolt holes, and perforation holes. Furthermore, a convergence evaluation was conducted in all finite element models, finding the appropriate global mesh size of 35 mm. For the RK1, RK2, and RK3 models, the element counts/node counts are 660759/616227, 654013/706529, and 800811/857929, respectively.

Table 2. Details of the elements used for finite element analysis

Part	Element	Description
Upright section, Beam section, Down-aisle bracing	Shell 181	4-noded shell element with six degrees of freedom at each node: translations and rotations in the x, y, and z directions.
Bolts	Beam188	Linear, quadratic, or cubic two-noded solid element with six or seven degrees of freedom at each node: translations and rotations in the x, y, and z directions.
Base plate and Pin	SOLID187	10-noded quadratic solid element with three degrees of freedom at each node: translations in the nodal x, y, and z directions.

2.4. Loading and boundary conditions

A two-step analysis has been developed for the loading conditions in the ANSYS Workbench application. At first, point masses representing the pallets were applied to the beam, as shown in Fig. 4. Point masses were applied as a single point mass on each of the four surfaces on the beam. The finite element analysis neglected the movement of pallets on the beams. At first, considering gravitational force, rack systems were exposed to a vertical load of 72 kN. After that, in the second step of the analysis, lateral loading of the system was applied as shown in Fig. 4 (F force for the first floor level, 2F force for the second floor level, and 3F force for the third floor level). The system has been pushed to its maximum displacement limit, approaching the failure condition. To evaluate their characteristics, such as stiffness, Q-factor, and ductility, the investigated systems were subjected to displacement values exceeding code limitations.

3. Results and discussion:

Thin-walled, cold-formed steel profiles were utilized to design all the considered storage rack systems. The results of the finite element analysis revealed that local deformations in the system's structural components had a significant impact on its performance and capacity. The failure mechanism of the carrier system and its ability to absorb energy are significantly impacted by plastic deformations, particularly at the upright-beam connections, uprights and base plates, and stability and bracket members. In this research, the load-displacement graph was employed to figure out the system's energy dissipation capacity.

Due to the absence of vertical stabilization components in the down-aisle direction within the first specimen, RK1, no torsional impacts have been observed in the pushing direction (Fig.7). Nevertheless, the RK2 and RK3 rack specimens have been enhanced with vertical stability bracings throughout one axis. This situation has induced torsional effects in the whole system and, subsequently, in the uprights as well. Furthermore, the bracket-type assembly of the stability elements led to torsional elastic and post-elastic deformations in these bracket elements. Many researchers used analytical tools to investigate behavioral characteristics. However, the pallet rack has model arrangement challenges, such as the column-beam connection gap, the member connection system utilizing bolts, and the distance between bolts and holes. As a result, it is difficult to determine the specific behavioral characteristics of storage racks using analytical investigations. In this study, to investigate the actual behavioral characteristics of the pallet rack under different baseplate connection conditions, an FE analysis was carried out under the same parameters mentioned in Table 1. The perforations in the uprights and tabs in the traverse-upright connection, material definition, stability bracing system connections, bolts, and pins utilized in base plates, and the diagonals have been simulated to reflect their actual behavior in the created FE numerical models.

The results of Von Misess stress distributions from the finite element model investigation are illustrated in Fig. 7 to 9. In the RK1 model without any bracing in the down-aisle direction, significant stresses are observed at the connections between the beam and the upright, the base plate, and the pushing region in the upright. the base plate and the ground significantly affected the results in comparison to case 1, which used a two-bolt arrangement. The upright sections cannot rotate freely, resulting in increased stress at the base support and the midpoint of the first floor in the RK2 and RK3 configurations.

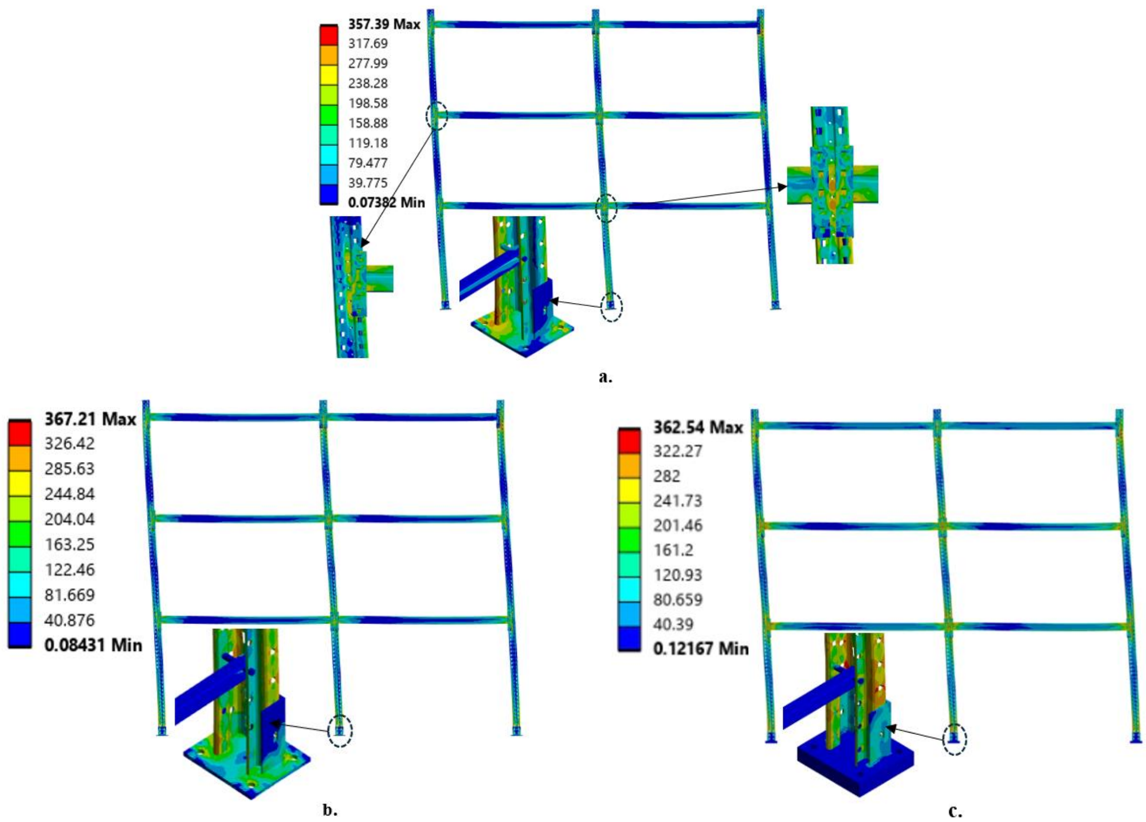

Fig.7. Stress distributions of the numerical models created for: a. RK1.1, b. RK1.2 c. RK1.3

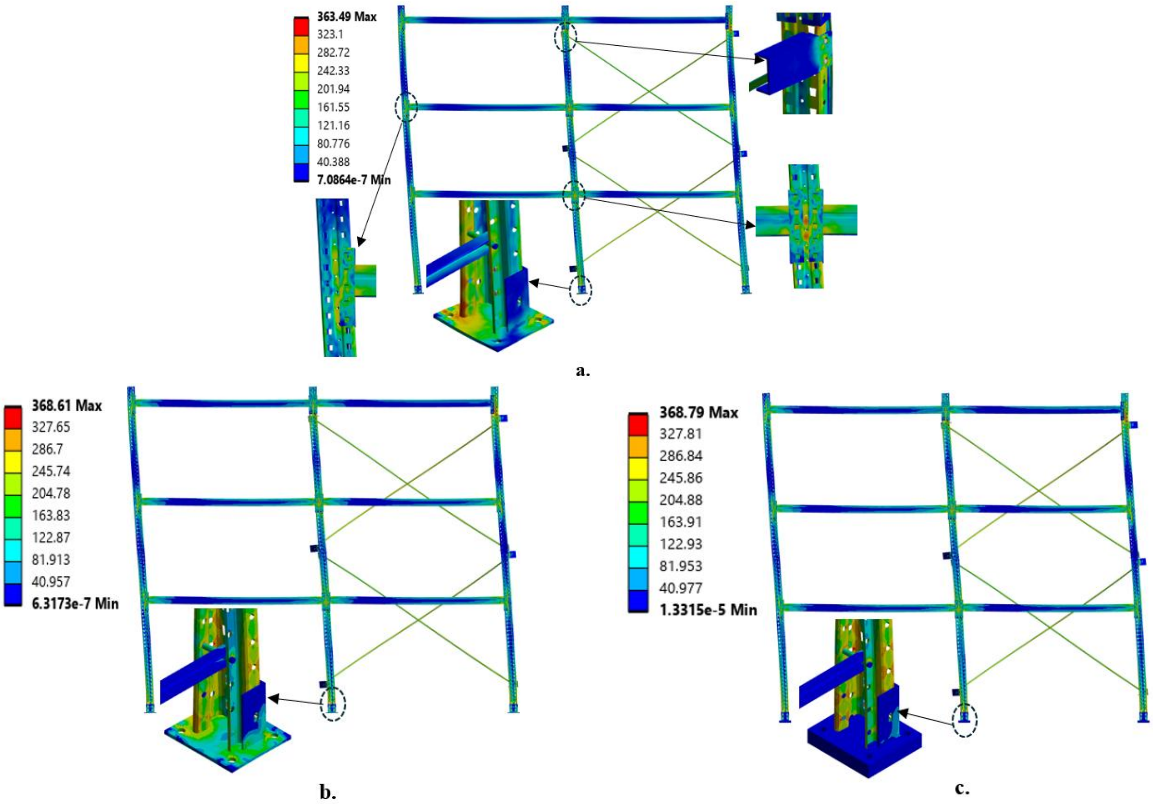

Fig.8. Stress distributions of the numerical models created for: a. RK2.1 b. RK2.2 and c. RK2.3

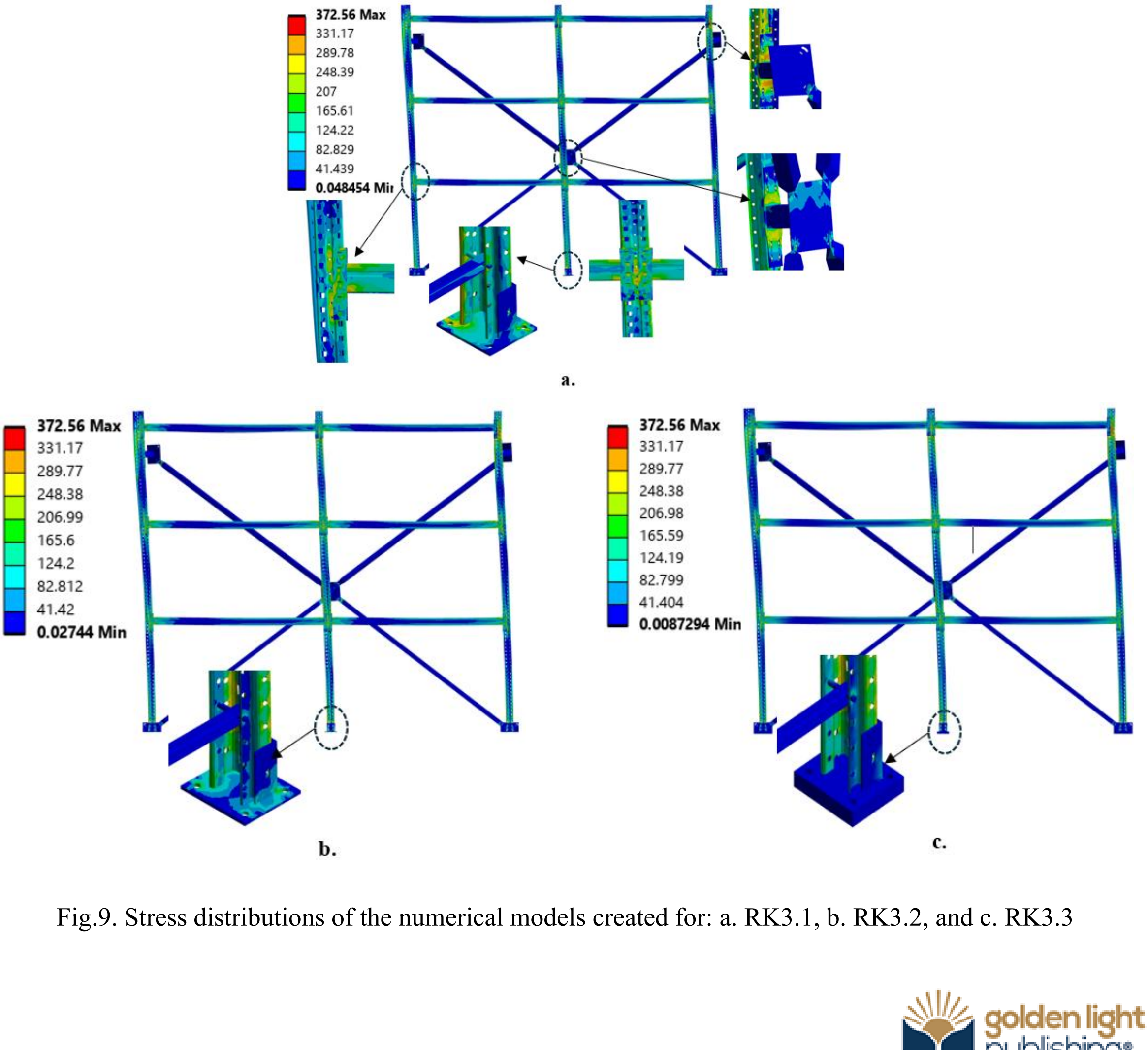

Fig.9. Stress distributions of the numerical models created for: a. RK3.1, b. RK3.2, and c. RK3.3

The RK1 model demonstrates that the beam connector at the first-floor upright-beam connection has exhibited plastic deformation. The evaluation of Von Mises stresses revealed that modifying the fixing conditions between the base plate and the ground significantly affected the results in comparison to case 1, which used a two-bolt arrangement. The upright sections cannot rotate freely, resulting in increased stress at the base support and the midpoint of the first floor in the RK2 and RK3 configurations. Fig. 9 illustrates the deformation of the exterior and planar bracings. The deformation results of the plane bracings' connection components indicate that they effectively mitigate torsional effects.

The analysis of the RK2 model demonstrated plastic deformations in the mid-axis beam-upright connector, the tension rod-to-upright component connection, and the upright component. Other numerical models that have different base plate fixation conditions exhibit stress situations similar to the RK2 model, except in the support regions (Fig. 8). The upright connecting element experienced considerable deformation due to the tension rod component, whose stress type depends on the direction of the push. Furthermore, the upright element developed distortional buckling. The RK2 model exhibited lower displacement stiffness compared to the RK3 model as a result of the tension rod stabilizing bracing. The stability bracing is additionally connected to the side of the upright. This situation resulted mainly in the rotation and buckling of the upright side surface.

Fig. 9 illustrates the deformation of the console members that connect the stability components and the system during the application of load from the RK3 models. As shown in the figure, local buckling was observed at the ends of the X bracing and the upright connecting brackets. This connection works effectively in back-to-back systems due to its central position. In the rack systems investigated in this paper, torsional effects from the upright to the bracing result in torsion-induced buckling and plastic deformations in the connecting plate. RK1 and RK2 were displaced by 200 mm in the displacement-controlled analysis. Nonetheless, local buckling at the X-brace endpoints and upright connection components of the RK3 model affected the results from the finite element study. The connected uprights experience flexural-torsional buckling in specific regions. This situation resulted in the RK3 sample's early failure compared to other models. Consequently, the finite element analysis pushed the RK3 sample to 160 mm. This situation is also reflected in the RK3 model analysis (Fig. 9).

The capacity curves were drawn using the lateral displacement and the base shear force values. Fig.10 presents the capacity curves calculated from the static pushover analysis of all numerical models in a comparative form. The system's stiffness and load-carrying capability are significantly improved when employing a fixed base plate in the ground condition (case 3) compared to the two-bolted or four-bolted arrangements (cases 1 and 2), as shown in Fig.10. This increase was noted in the RK1 system. The capacity curves in Fig. 10 are used for calculating the base shear force values and energy dissipation capacities for the numerical models illustrated in Fig. 12. Consequently, the system's response to the fixing conditions between the base plate and the ground can potentially be evaluated. Fig. 10 illustrates the maximum base shear force and the increase in base shear force of the numerical models.

The RK1 non-braced model exhibits the greatest increases in carrying capacity as a result of the base plate change, as illustrated in Fig. 12a. The condition of a four-bolted base plate with a thickness of 7 mm (case 2) resulted in a 21% increase in carrying capacity in the RK1 model. The fixed 30 mm base plate thickness condition (case 3) resulted in a 79% increase in carrying capacity.

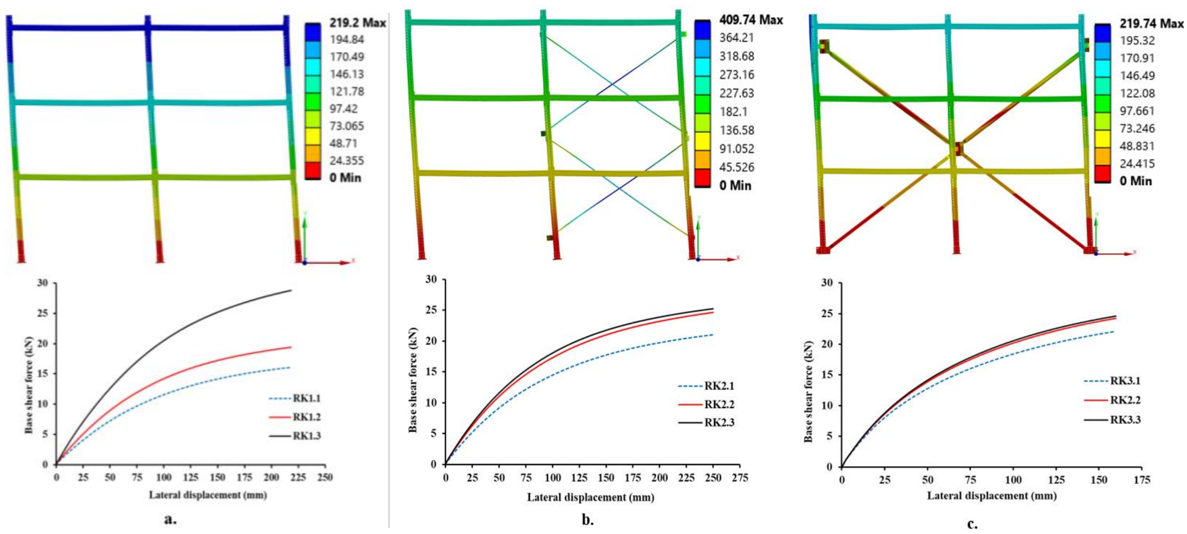

Fig. 10. Comparison of capacity curves of numerical models for: a. RK1, b. RK2, c. RK3

The carrying capacity of the RK2 tension rod model increased by 17.42% when the four-bolted base plate with a thickness of 7 mm (case 2) was used. The fixed 30 mm base plate thickness condition (case 3) resulted in a 20.3% increase in carrying capacity. The condition of a four-bolted base plate with a thickness of 7 mm (case 2) achieved a 9.5% increase in carrying capacity in the RK3 X-bracing model. The carrying capacity increased by 11.2% under the fixed condition of a 30 mm base plate thickness (case 3). Using the two-bolted base plate (case 1) increased the carrying capacity of RK2 and RK3 by 31% and 38%, respectively, in comparison to RK1. On the other hand, when compared to the nonbraced model (RK1), it is demonstrated that the base plate-related changes can be less effective in the models that are employed for the extra stability components (RK2 and RK3). In comparison to the base support fixing conditions, the stability component's response to the displacement develops quicker and is more efficient, which is the primary cause of this issue.

It was found from the research that had been published in the academic literature that capacity curves may be plotted by making use of the global yield shear force and the displacement values that are associated with it. As a result, it is possible to obtain essential information describing the behavior of the rack system, examples of which include system stiffness and ductility. An investigation into the benefits that are associated with base support conditions was carried out in the present study, which focused on brittle failure mechanisms that are generated by torsional effects under different stability conditions.

In this particular development, (Kanyilmaz et al., 2016) implemented the procedure that is described as follows: after obtaining the origin of the F-d curve, the equation E = tgαy is determined.

- Following this, the tangent, which corresponds to one-tenth of the E value, is adjusted so that it intersects both the Fu and du values.
- Both the vertical value, denoted by Vy, and the horizontal value, denoted by dy, are associated with the intersection of these two tangents. System stiffness was obtained using Eq. (1)

$$k = \frac{V_y}{d_y} \tag{1}$$

Where: Vy is the global yield shear force, dy is the yield displacement, E is the elasticity modulus, and dy is the displacement value corresponding to the global yield shear force (Fig. 11).

In terms of operation, the values of the behavior factor q essentially describe the equilibrium that occurs between resistance and the capacity to dissipate energy. The over-strength and the ductility ratio are the two factors that are used to calculate the q-factor. The following equations explain how this value is calculated:

$$\Omega = \frac{V_u}{V_y} \tag{2}$$

$$\mu = \frac{d_u}{d^{'}} \tag{3}$$

$$q = \mu.\Omega \tag{4}$$

Where μ is the ductility ratio,Ω is the over-strength factor, Vy is the global yield base shear, Vu is the ultimate load before collapse, du is the displacement associated with Vu, and d' is the displacement associated with the intersection between the tangent slope and Vu. Table 3 displays the values of the results obtained from the models that were investigated in this study.

Table 3 displays a significant impact of the base plates on the ground fixing conditions used in this study concerning system displacement stiffness and the energy dissipation capacity. The effect for the RK1, RK2, and RK3 models varies between 123–174%, 119–131%, and 102–104%, respectively. The number of bolts and the configuration of the base fixing plate substantially affect the displacement stiffness of the system. This effect is noticeable in models without bracing in the down-aisle direction compared to those that include bracing.

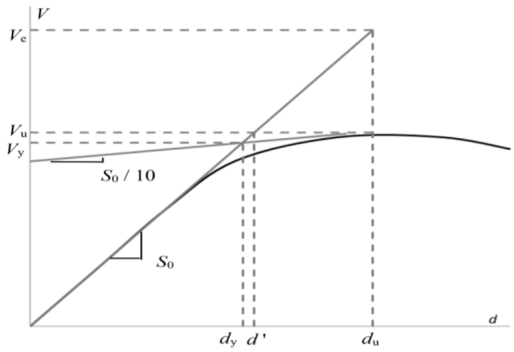

Fig. 11. Bilinear approach of the capacity curve. Yield, elastic and ultimate points (Kanyilmaz et al., 2016)

Table 3. Behaviour factors and energy dissipation capacity of the models

Model	RK1.1	RK1.2	RK1.3	RK2.1	RK2.2	RK2.3	RK3.1	RK3.2	RK3.3
Vu	16.048	19.414	28.797	21.011	24.671	25.274	22.149	24.245	24.64
du	218.140	218.170	218.150	250.170	250.190	250.190	159.740	159.710	159.70
Vy	14.117	16.940	25.424	17.874	20.925	20.903	18.261	20.438	20.757
dy	90.486	88.156	93.634	90.639	89.434	80.764	51.050	55.779	55.663
d'	103.252	101.158	106.116	106.592	105.509	97.907	61.919	66.172	66.067
k	0.156	0.192	0.272	0.197	0.234	0.259	0.358	0.366	0.373
μ	2.113	2.157	2.056	2.347	2.371	2.555	2.580	2.414	2.417
Ὼ	1.141	1.147	1.133	1.176	1.180	1.212	1.213	1.186	1.187
q	2.411	2.475	2.330	2.760	2.797	3.098	3.129	2.863	2.869
Q*	2.270	2.787	4.344	3.669	4.308	4.644	2.413	2.607	2.634

k: Stiffness; μ: Ductility ratio ; Ὼ: Overstrength factor; q: Behaviour factor; Q*: Energy dissipation capacity kN.m

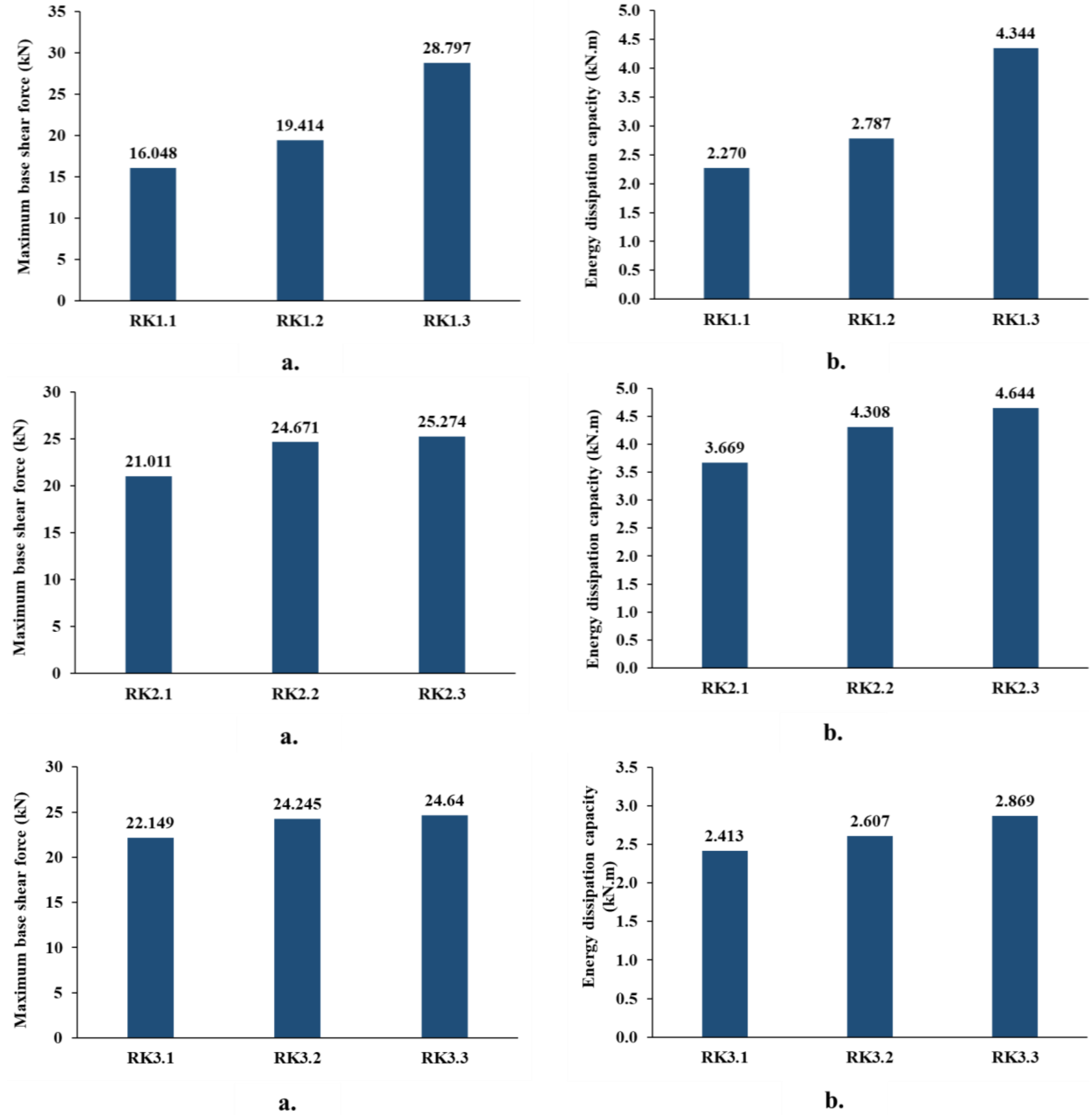

Fig. 12. Maximum base shear forces and energy dissipation capacity for numerical models. a. Comparison of maximum base shear forces. b. Energy dissipation capacity for the numerical models

4. Conclusions

This study investigated the seismic response characteristics of a pallet rack subjected to an external force based on different baseplate fixing conditions via nonlinear static pushover analysis. To determine and evaluate the displacement response resulting from external forces, three different configurations in the down-aisle direction of popular pallet rack systems were analyzed using ANSYS Workbench software under varying baseplate connection fixing conditions. The following are the results and conclusions of this study:

- In the numerical analysis, it was found that the system stiffness increased in case 2 and case 3 base plates in comparison to the base plate used in case 1. The percentage increases were as follows: 123% and 174% for RK1, 119% and 131% for RK2, and 102% and 104% for RK3 (Fig. 12.a).
- The stress concentrations on the uprights have been transferred from the base support region to the level of the floor as a result of the base plate fixing situation that has enhanced rotational stiffness. This has occurred in all three configurations. The fact that this situation occurs demonstrates that the base plates to the ground fixing conditions that were used have had a favorable effect on the upright rotational degrees.
- The results demonstrated that the base plate-fixing changes can be less effective in the models that are employed for braced models (RK2 and RK3) rather than the non-braced model (RK1).
- The FE results proved that the load-carrying capacity was significantly improved when employing a fixed base plate to the ground condition (case 3) compared to the two-bolted or four-bolted fixing conditions (cases 1 and 2) as shown in Fig.12b.
- The results indicated that the pallet rack, which lightly resists external force, is capable of withstanding displacement if it is securely fixed to the ground. Nevertheless, the significant displacement at the top may result in cargo falling. The collapse may occur as a result of the displacement caused by a significant external force due to the baseplate's insufficient resistance if it is bolted to the ground with two bolts for simplicity of installation.
- The results indicated that significant global torsional distortions occurred in the braced rack configurations, wherein the spine braces are only connected to the uprights on one side. These kinds of situations can be avoided by employing plane bracing systems that connect both the uprights and the spine bracing planes, thereby assuring effective load transmission between both of them.

Acknowledgments

It is with great gratitude that the authors express their gratitude to their friends and colleagues from Yildiz Technical University for their assistance in the aforesaid research.

References

Andrea, C., Politecnico, C., Milano, D., Brambilla, G., Paolo, G., Politecnico, C., Bernuzzi, C., & Di Milano, P. (2016). Experimental results of full-scale push over tests of Project SEISRACKS2 (seismic behaviour of steel storage pallet racking systems). In *2nd European Conference on Earthquake Engineering and Seismology (2nd ECEES)*. Istanbul: Curran Associates, Inc.

AS 4084. (2012). *Steel storage racking*. Sydney, Australia: Standards Australia Limited.

Avgerinou, S., Lignos, X., Tsarpalis, D., & Vayas, I. (2019). Full-scale tests on used steel storage racks. *Steel Construction, 12*(3), 231–242.

Bajoria, K. M., & Talikoti, R. S. (2006). Determination of flexibility of beam-to-column connectors used in thin-walled cold-formed steel pallet racking systems. *Thin-Walled Structures, 44*(3), 372–380.

Bernuzzi, C., & Castiglioni, C. A. (2001). Experimental analysis on the cyclic behaviour of beam-to-column joints in steel storage pallet racks. *Thin-Walled Structures, 39*, 841–859.

Bonada, J., Casafont, M., Roure, F., & Pastor, M. M. (2021). Geometrically nonlinear analysis of perforated rack columns under a compression load by means of Generalized Beam Theory. *Thin-Walled Structures, 166*, 1–17.

Bové, O., Ferrer, M., Almansa, L., & Roure, F. (2021). Comparison between two types of seismic tests of racking systems. *Ce/papers, 4*.

Castiglioni, C. A. (2016). *Seismic behavior of steel storage pallet racking systems*. Milano, Italy: Springer.

Çelik, İ. D., Yildiz, İ., Arslan, K. Y., Öztürk, Y., Efe, M. E., & Kocaman, T. B. (2022). Effect of base-plate types on system behaviour in down-aisle pallet rack systems. *Journal of Constructional Steel Research, 198*, 1–15.

Chen, C., Shi, L., Shariati, M., Toghroli, A., Mohamad, E. T., Bui, D. T., & Khorami, M. (2019). Behavior of steel storage pallet racking connection – A review. *Steel and Composite Structures, 30*(5), 457–469.

Connor, I. (2012). Performance of steel storage racks in the Darfield earthquake. *Bulletin of the New Zealand Society for Earthquake Engineering, 45*, 61–70.

Dai, L., Zhao, X., & Rasmussen, K. J. R. (2018). Flexural behaviour of steel storage rack beam-to-upright bolted connections. *Thin-Walled Structures, 124*, 202–217.

FEMA 460. (2005). *Seismic considerations for steel storage racks located in areas accessible to the public*. Federal Emergency Management Agency.

Firouzianhaij, A., Usefi, N., Samali, B., & Mehrabi, P. (2021). Shake table testing of standard cold-formed steel storage rack. *Applied Sciences (Switzerland), 11*(4), 1–20.
Galeotti, C., Gusella, F., Orlando, M., & Spinelli, P. (2021). On the seismic response of steel storage pallet racks with selective addition of bolted joints. *Structures, 34*, 3806–3817.
Gilbert, B. P., & Rasmussen, K. J. R. (2010). Bolted moment connections in drive-in and drive-through steel storage racks. *Journal of Constructional Steel Research, 66*(6), 755–766.
Gilbert, B. P., & Rasmussen, K. J. R. (2011). Determination of the base plate stiffness and strength of steel storage racks. *Journal of Constructional Steel Research, 67*(6), 1031–1041.
Gusella, F., Orlando, M., & Peterman, K. (2022). Stiffness and resistance of brace-to-upright joints with lipped channel braces assembled flange-to-flange. *Journal of Constructional Steel Research, 193*, 1–15.
Heo, G., Ko, B., Seo, Y., & Kim, C. (2023). Analysis of behavioral characteristics according to the fixing condition of pallet rack. *Journal of Constructional Steel Research, 203*, 1–14.
Huang, Z., Wang, Y., Zhao, X., & Sivakumaran, K. S. (2021). Determination of the flexural behavior of steel storage rack baseplate upright connections with eccentric anchor bolts. *Thin-Walled Structures, 160*, 1–13.
Kanyilmaz, A., Brambilla, G., Chiarelli, G. P., & Castiglioni, C. A. (2016). Assessment of the seismic behaviour of braced steel storage racking systems by means of full-scale push over tests. *Thin-Walled Structures, 107*, 138–155.
Kanyilmaz, A., Castiglioni, C. A., Brambilla, G., & Chiarelli, G. P. (2016). Experimental assessment of the seismic behavior of unbraced steel storage pallet racks. *Thin-Walled Structures, 108*, 391–405.
Krawinkler, H., Cofie, N. G., Astiz, M. A., & Kircher, C. A. (1979). Experimental study on the seismic behavior of industrial storage racks. *Report No. 41*, John A. Blume Earthquake Engineering Center, Stanford University.
Maurizio Orlando, G., Lavacchini, G., Ortolani, B., & Spinelli, P. (2017). Experimental capacity of perforated cold-formed steel open sections under compression and bending. *Steel and Composite Structures, 24*(2), 201–211.
Petrone, F., Higgins, P. S., Bissonnette, N. P., & Kanvinde, A. M. (2016). The cross-aisle seismic performance of storage rack base connections. *Journal of Constructional Steel Research, 122*, 520–531.
Prabha, P., Marimuthu, V., Saravanan, M., & Arul Jayachandran, S. (2010). Evaluation of connection flexibility in cold formed steel racks. *Journal of Constructional Steel Research, 66*(7), 863–872.
Rack Manufacturers Institute (R.M.I.). (2012). *Specification for the design, testing and utilization of industrial steel storage racks*. American National Standards Institute (ANSI), Inc.
Vujanac, R., Miloradović, N., Vulović, S., & Pavlović, A. (2020). A comprehensive study into the boltless connections of racking systems. *Metals, 10*(2), 1–17.
Yin, L., Tang, G., Zhang, M., Wang, B., & Feng, B. (2016). Monotonic and cyclic response of speed-lock connections with bolts in storage racks. *Engineering Structures, 116*, 40–55.

4th International Civil Engineering & Architecture Conference
17-19 May 2025, Trabzon, Türkiye

Influence of infilled walls on the seismic vibration period of reinforced concrete structures with shear walls

Ali Koçak*[1], Houssein Aleit[2]

[1] Yıldız Technical University, Department of Civil Engineering, 34220 Istanbul, Türkiye
[2] Yıldız Technical University, Graduate School of Science and Engineering, 34220 Istanbul, Türkiye

Abstract. The fundamental vibration period of reinforced concrete structures is critical for assessing seismic performance. Infilled walls interact with structural frames and significantly influence this period by enhancing rigidity. However, traditional design approaches often simplify their contributions, leading to discrepancies in period estimations. This study investigates the effects of infilled walls on the vibration period of reinforced concrete structures with shear walls. The research evaluates their influence on structural dynamics by systematically varying wall parameters, such as thickness, material elasticity, and wall-to-floor ratios. Shear wall configurations are also analyzed to understand their interaction with infilled walls and their combined impact on rigidity. The study develops an original equation for estimating the vibration period, incorporating infill wall characteristics and shear wall configurations. Results demonstrate that wall elasticity, placement, and thickness are pivotal in determining the vibration period. The proposed equation offers a refined approach, improving the accuracy of seismic design and performance assessments for reinforced concrete systems. This research bridges the gap between empirical simplifications and real-world structural behavior, providing valuable insights for engineers aiming to optimize designs for enhanced seismic resilience.

Keywords: Natural period; Infilled walls; Reinforced concrete; Shear walls; Structural optimization

1. Introduction

The fundamental vibration period of a structure is one of the most influential parameters in seismic design, as it directly governs the magnitude and distribution of lateral forces during an earthquake. Accurate estimating this period is essential for ensuring compliance with seismic codes and evaluating new and existing buildings' structural performance and safety (Goel & Chopra, 1997).

Reinforced concrete (RC) buildings, particularly those with frame systems, often include non-structural Masonry-infilled walls that are primarily intended for the architectural enclosure. However, numerous experimental and analytical studies have demonstrated that these infill panels actively contribute to the lateral stiffness and strength of the structure, especially under seismic loading. Infilled walls reduce lateral deformations and can significantly alter the system's dynamic characteristics, notably by decreasing the fundamental vibration period.

Despite their structural influence, infill walls are often simplified or neglected in many seismic designs (Crowley& Pinho, 2004) codes. Most national and international building regulations estimate the fundamental period using empirical equations that rely on building height and structural type without explicitly accounting for the presence of infilled walls or their mechanical properties. Depending on the case, this simplification may lead to unsafe underestimations of seismic demands or over-conservatism in design.

Researchers have proposed refined methodologies and alternative empirical formulations to address this gap. For example, Goel and Chopra (1997) derived period-height relationships based on extensive observations of moment-resisting frames and shear wall-dominated buildings. Similar efforts by Hong and Hwang (2000) and Zarnic and Tomazevic (1998) emphasized the critical role of infill walls in modifying the natural period. Later studies by Panagiotakos and Fardis (1999) confirmed that variations in stiffness caused by infill placement and distribution could dramatically impact modal behavior.

Further investigations have explored the influence of infill material properties, thickness, and opening ratios. These parameters have been shown to affect stiffness, damping, and overall seismic performance (Koçak et al., 2018) demonstrated, through post-earthquake assessments, that neglecting the contribution of infill walls leads to substantial errors in dynamic analysis. More recent studies have also incorporated soil-structure interaction and

* Corresponding author, E-mail: akocak@yildiz.edu.tr

https://doi.org/10.31462/icearc2025_ce_eqe_580

foundation flexibility to capture better the actual behavior of RC buildings under seismic excitation (Oliveira & Navarro, 2010).

The interaction becomes even more complex in buildings that combine RC frames with structural shear walls. While shear walls are intentionally designed to carry lateral loads, infill walls act as unintended yet influential stiffening elements. The interplay between these two components can either amplify or dampen dynamic responses, depending on their relative stiffness, distribution, and continuity stated by Koçak (2020).

This study aims to systematically investigate the impact of infilled walls on the fundamental vibration period of RC buildings with shear walls. Through comprehensive numerical modeling using SAP2000, various configurations of frame, infill, and shear wall systems are analyzed. Key parameters such as wall thickness, elastic modulus, and shear wall-to-floor area ratio are varied to quantify their individual and combined effects. The ultimate goal is to develop an enhanced empirical expression that accounts for the real stiffness contribution of infill walls in seismic design, thereby narrowing the gap between code-based estimates and actual dynamic behavior (SAP2000, 2024).

2. Methodology and building model

Four representative building models were developed to evaluate the influence of infilled walls on the dynamic behavior of reinforced concrete structures, comprising three, six, nine, and eleven storeys, respectively. All models were designed with uniform storey heights to maintain consistency in vertical geometry. However, the shear wall ratio—the total wall area relative to the floor area—was varied across the different models to capture its effect on lateral stiffness and vibration characteristics.

Fig. 1 illustrates the buildings' architectural layout and structural configuration. It presents a plan view of the sample structure. Table 1 summarizes the detailed geometrical properties of the beams, columns, and shear walls used in the models.

All simulations were conducted using C30-grade reinforced concrete, a commonly adopted material class in modern structural design. The underlying soil condition was modeled as Type Z2, following the classification the Turkish Seismic Code provided, representing medium-stiff soil typically encountered in urban development zones.

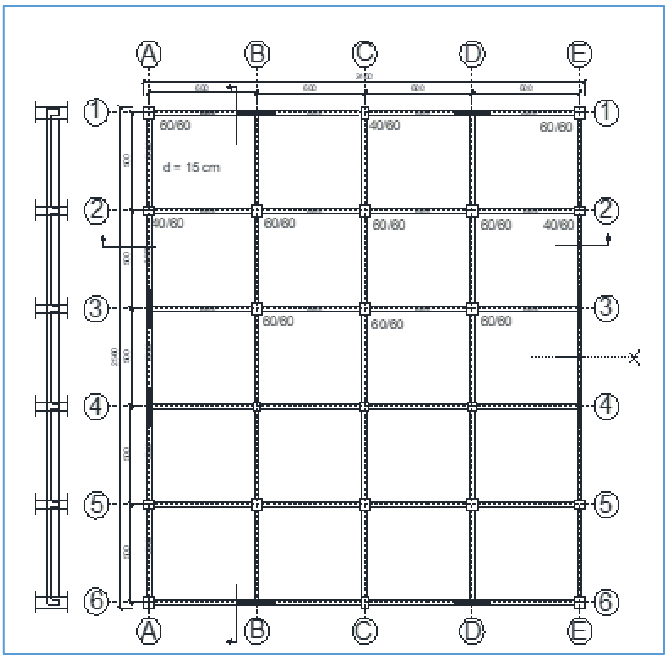

Fig. 1. Plan layout of the representative RC building model used in the analysis

Table 1. Geometrical characteristics of the structural components used in the model

Number of Storeys	Floors	Rectangular Columns (cm x cm)	Square Columns (cm x cm)	Beams
11 STOREY	1. 2. 3.	60 x 60	40 x 60	35 x 60
	4. 5. 6	55 x 55	40 x 55	35 x 55
	7. 8. 9.	50 x 50	40 x 50	35 x 50
	10. 11.	45 x 45	40 x 45	35 x 45
9 STOREY	1. 2. 3.	55 x 55	40 x 55	35 x 55
	4. 5. 6.	55 x 50	40 x 50	35 x 50
	7. 8. 9.	55 x 45	40 x 45	35 x 45
6 STOREY	1. 2.	55 x 55	40 x 55	35 x 55
	3. 4.	55 x 50	40 x 50	35 x 50
	5. 6.	55 x 45	40 x 45	35 x 45
3 STOREY	1. 2.	45 x 45	40 x 45	35 x 40
	3.	40 x 40	40 x 40	35 x 40

The analyses are conducted for the following three conditions: buildings without infill walls, those that contain infill walls for each frame, and buildings with various ratios of infill walls, i.e., percentage of frames with infill walls. For the condition that the infill walls are modeled as diagonal rods (Ersin et al., 1998; Güler et al., 2008), the values suggested by Koçak (2017) are used for the non-axial pressures of the walls manufactured from low endurance bricks. Modulus of elasticity parallel (E_{par}) and perpendicular to the hollow direction (E_{per}) along with their average value (E_{ave}) are listed in Table 2.

Equivalent elastic axial rigidity of the diagonals representing the walls can be represented by Eqn 1:

$$\frac{EA}{L_d} = Et\alpha\beta \tag{1}$$

where:
E: modulus of elasticity (MPa)
t: thickness (mm)
L_d: diagonal length of the wall (mm)
α: coefficient taking the rigidity ratio between the wall and reinforced concrete frame into account
β: coefficient taking the effect of the walls into account

Values provided by Koçak (2017) were used for the coefficients of α and β.

Table 2. Modulus of elasticity of infill walls

Modulus of elasticity (MPa)	E_{per}	E_{par}	E_{ave}
Non-Plastered	2500	4600	3550
Plastered	4200	7800	6000

2.1. Model configuration

Eight structural configurations were analyzed to assess the impact of infilled walls and varying shear wall dimensions on the fundamental vibration period. The first four models (Conditions #1 to #4) represent bare frame structures without infilled walls. In these models, shear walls were incrementally introduced and scaled in size—specifically, 25 cm × 175 cm, 25 cm × 200 cm, 25 cm × 250 cm, and 25 cm × 300 cm, respectively. These variations allowed for systematically examining how increasing shear wall dimensions influence structural stiffness without infill (Kocak et al., 2018).

The second set of configurations (Conditions #5 to #8) mirrored the same shear wall dimensions as the first group but incorporated infilled walls throughout the structural frames. This set, referred to as the "fully infilled" condition, enabled a comparative analysis to isolate and quantify the effect of infilled walls on the overall dynamic behavior of the system. Table 3 summarizes the shear wall dimensions and corresponding area ratios for each building height and configuration.

Table 3. Shear wall area-to-floor area ratios for different building heights

Shear Wall Dimensions (cm x cm)	11 Storey	9 Storey	6 Storey	3 Storey
25 x 175	0.20	0.22	0.22	0.29
25 x 200	0.22	0.25	0.25	0.32
25 x 250	0.26	0.29	0.29	0.37
25 x 300	0.29	0.33	0.33	0.41

3. Numerical evaluation and outcomes

In this study, a series of reinforced concrete frame models were developed to investigate the impact of shear wall dimensions and the presence of infill walls on the fundamental period of multi-story buildings (Koçak, 2013). The analyses were conducted using SAP2000 Version 26, and each building configuration was assessed under fully infilled and bare frame conditions (SAP2000, 2024).

For the first case, Conditions #1 through #4, infill walls were included beneath all frames.

In these configurations, the dimensions of the shear walls were varied incrementally across four levels:

- Condition #1: 25 cm × 175 cm
- Condition #2: 25 cm × 200 cm
- Condition #3: 25 cm × 250 cm
- Condition #4: 25 cm × 300 cm

The second case, represented by Conditions #5 through #8, involved identical structural configurations regarding shear wall dimensions but excluded all infill walls, modeling the buildings as bare frames. These cases ranged from 25 cm × 175 cm to 25 cm × 300 cm shear wall dimensions.

Each structural variant was analyzed at four building heights—3, 6, 9, and 11 stories—to assess how the interaction between shear wall ratio and vertical dimension influences the structure's dynamic behavior (Balkaya et al., 2002). The effect of increasing infill wall ratio on structural stiffness was captured by tracking the reduction in the fundamental period, and the results are presented in Table 3 and visualized in Figs. 2 to 5.

Following Koçak et al. (2013), window openings on external walls and door openings on internal walls were incorporated into the models to reflect realistic boundary and stiffness conditions. The observed reductions in fundamental periods ranged between 10% and 50% for fully infilled models compared to their bare frame counterparts.

An empirical relationship was developed based on the ratio of infill wall area to the total structural system area (sum of column and wall areas). This approach (Hong & Hwang, 2000) provides a rational correlation between infill wall density and structural dynamic response, highlighting the critical contribution of masonry infill in lateral stiffness and seismic performance.

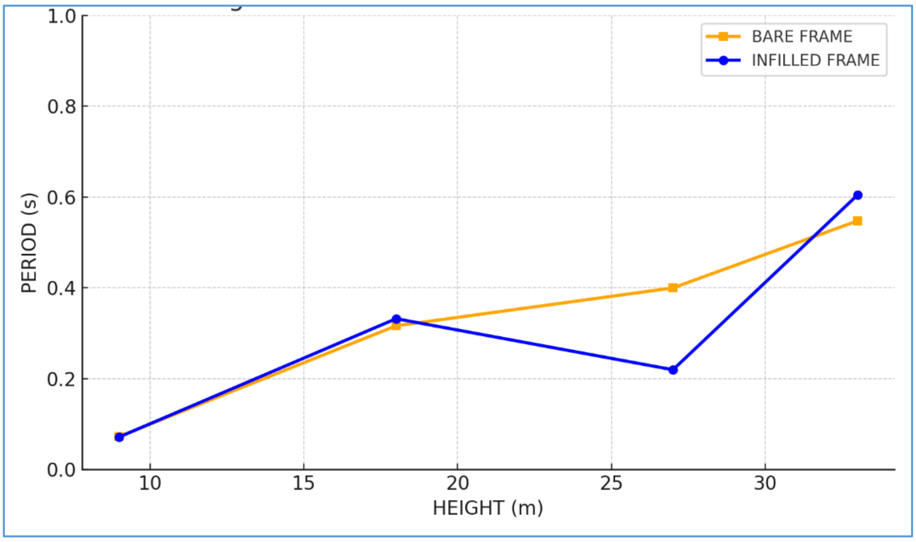

Fig. 2. Shear wall ratio between 0.2 to 0.30

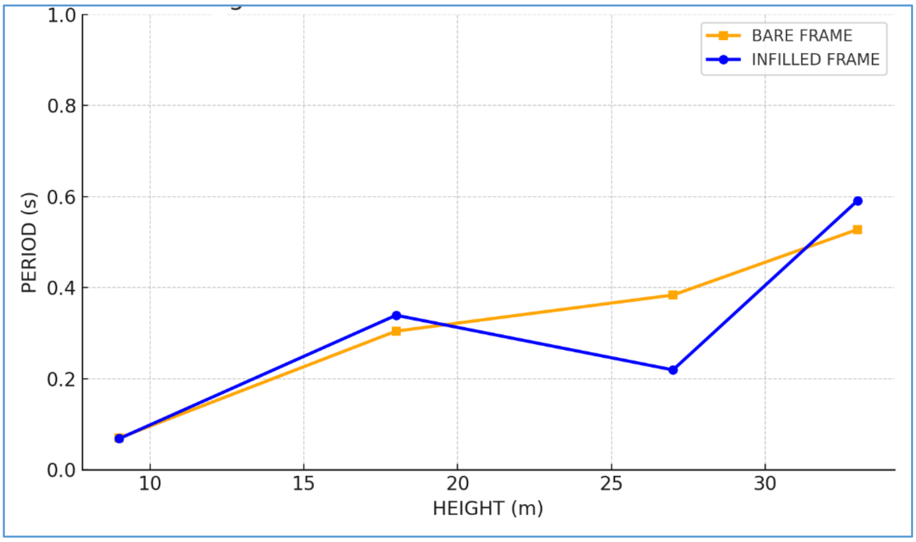

Fig. 3. Shear wall ratio between 0.2 to 0.35

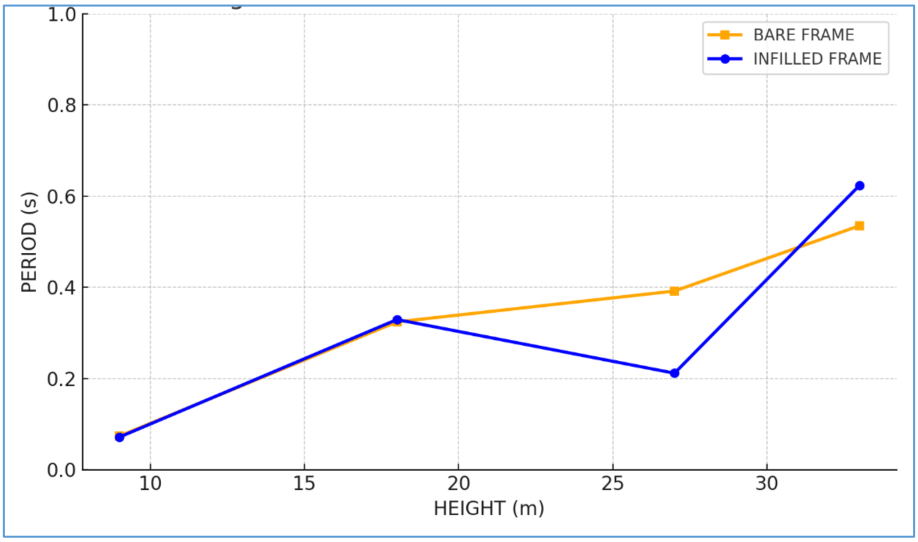

Fig. 4. Shear wall ratio between 0.2 to 0.4

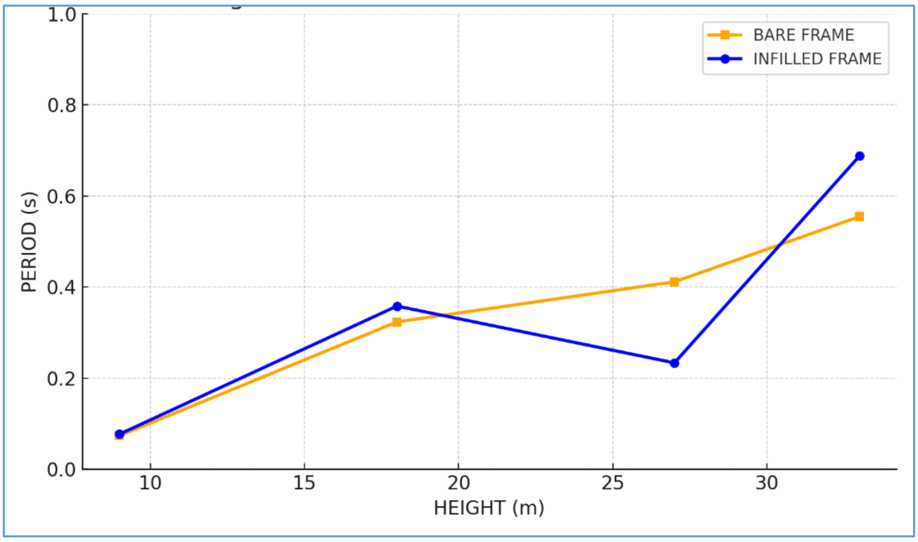

Fig. 5. Shear wall ratio between 0.2 to 0.45

3.1. Estimation of the fundamental period of buildings

The fundamental period of vibration is one of the most critical parameters in structural seismic design and dynamic analysis. Accurate estimating this parameter ensures a realistic prediction of seismic forces and dynamic response (Ozkul et al., 2019). Consequently, various international codes propose empirical formulas based on building height and structural system characteristics.

The Uniform Building Code (UBC, 1997) provides an empirical expression for estimating the fundamental (Goel & Chopra, 1997) period T_d of a building:

$$T_d = C_t (h_N)^{3/4} \tag{2}$$

where:
T_d is the fundamental period (seconds),
h_N is the height of the building measured from the base to the roof level (meters),
C_t is a coefficient that depends on the structural system, with typical values of:

- C_t= 0.0731 for reinforced concrete moment-resisting frames,
- C_t= 0.0488 for all other building types.

The Turkish Seismic Code (1998**)** also adopts a similar empirical form (TSC 1998):

$$T_d = C_t H^{3/4} \tag{3}$$

where:
H denotes the total building height (meters),
C_t values are assigned based on structural typology:

- C_t= 0.07 for reinforced concrete moment-resisting frames and steel eccentrically braced frames,
- C_t= 0.08 for steel frames,
- C_t= 0.05 for other building categories.

Despite the similarity in functional form (both using an exponent of 0.75), the different C_t coefficients lead to variations in the predicted periods between the UBC and Turkish seismic regulations.

Furthermore, Eurocode 8 (EN 1998-1) introduces an analogous formulation for the fundamental period (CEN, 2004):

$$T = C_t H^{3/4} \tag{4}$$

where:
T is the estimated fundamental period (seconds),
C_t is selected according to structural characteristics:

- C_t= 0.05 for reinforced concrete moment-resisting frames,
- C_t= 0.075 for wall-dominated reinforced concrete structures,
- C_t= 0.085 for steel moment-resisting frames.

Unlike UBC 1997 and the Turkish Code, Eurocode 8 explicitly differentiates between frame-dominated and wall-dominated buildings by modifying the coefficient C_t accordingly. This allows a more refined estimation depending on the degree of lateral stiffness contribution from infill walls or shear walls.

This study compares the fundamental periods obtained through detailed numerical modal analyses against the empirical estimations from UBC 1997, the Turkish Seismic Code (1998), and Eurocode 8. The comparison aims to evaluate the conservatism and accuracy of code-based estimations relative to realistic structural behavior.

Table 4 presents a detailed summary of the computed periods for different structural configurations, followed by a discussion of the observed differences. As illustrated in Fig. 6, the estimated periods from this study are consistently lower than those suggested by the seismic codes, particularly for buildings with higher infill wall ratios.

Table 4. Fundamental period evaluation via modal analysis and seismic code formulations

			This Study	Turkish Seismic Code	UBC 1997	Eurocode 8
			T_x (s)	$T_d = C_t H^{3/4}$ (s)	$T_d = C_t (h_N)^{3/4}$ (s)	$T = C_t H^{3/4}$ (s)
11 STOREY	FRAME + SHEAR WALL	CONDITION #1	0.559			
		CONDITION #2	0.511			
		CONDITION #3	0.247			
		CONDITION #4	0.536	0.964	1.006	0.688

Table 4. Continued

	INFILL + SHEAR WALL	CONDITION #5	0.332			
		CONDITION #6	0.249			
		CONDITION #7	0.144			
		CONDITION #8	0.329			
9 STOREY	FRAME + SHEAR WALL	CONDITION #1	0.413	0.829	0.866	0.592
		CONDITION #2	0.386			
		CONDITION #3	0.197			
		CONDITION #4	0.394			
	INFILL + SHEAR WALL	CONDITION #5	0.234			
		CONDITION #6	0.174			
		CONDITION #7	0.123			
		CONDITION #8	0.232			
6 STOREY	FRAME + SHEAR WALL	CONDITION #1	0.323	0.612	0.639	0.437
		CONDITION #2	0.308			
		CONDITION #3	0.272			
		CONDITION #4	0.323			
	INFILL + SHEAR WALL	CONDITION #5	0.139			
		CONDITION #6	0.112			
		CONDITION #7	0.11			
		CONDITION #8	0.364			
3 STOREY	FRAME + SHEAR WALL	CONDITION #1	0.117	0.364	0.38	0.26
		CONDITION #2	0.095			
		CONDITION #3	0.061			
		CONDITION #4	0.059			
	INFILL + SHEAR WALL	CONDITION #5	0.071			
		CONDITION #6	0.058			
		CONDITION #7	0.028			
		CONDITION #8	0.117			

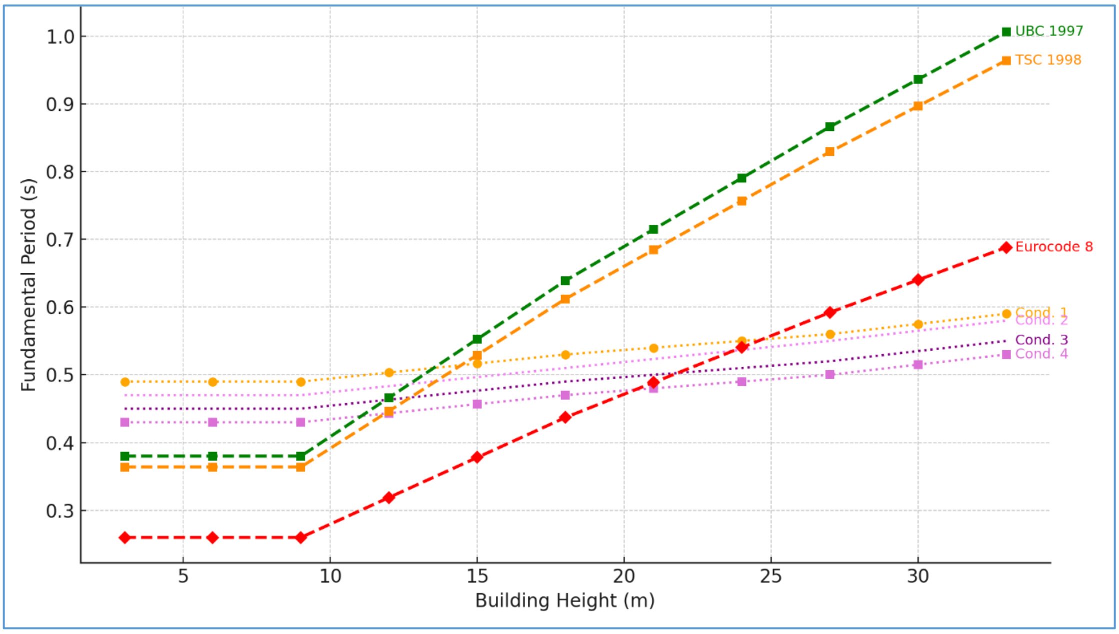

Fig. 6. Comparison of fundamental period–height relationships between this study and code-based formulations

4. Conclusions

In this study, the influence of infill walls on the dynamic behavior of reinforced concrete buildings was systematically investigated through detailed modal analyses. Four building models with varying heights (three, six, nine, and eleven stories) and eleven different infill wall configurations were evaluated to capture a wide range of practical design scenarios.

The results demonstrate that the presence of infill walls considerably enhances the lateral stiffness of buildings, leading to a significant reduction in the fundamental vibration periods (Hatzigeorgiou & Kanapitsas, 2013). It was observed that:

- For nine- to eleven-storey buildings, infill walls reduced the period by approximately 10% to 40% compared to bare frame configurations.
- For low- and mid-rise buildings (three to six stories), the reduction was even greater, ranging between 15% and 45%, emphasizing the proportionally larger contribution of infill walls to the overall stiffness of shorter structures.

The sensitivity of the period to the infill wall area ratio was also analyzed. It was found that:

- For an infill ratio between 0.20 and 0.40, the period reduction ranged from 10% to 25% for taller structures and 14% to 30% for lower ones.
- For higher infill ratios (0.40–0.60), the reduction became more pronounced, reaching 25%–40% in tall buildings and 28%–45% in low- to mid-rise structures.

Notably, an empirical formula was proposed to relate the infill wall area to the expected reduction in the fundamental period. This formula was validated against the results obtained by Yıldırım (2009) and found to closely align with both experimental data and the empirical formulations suggested by Güler et al. (2008).

A comparative evaluation against code-based period estimations revealed notable insights. While the Turkish Seismic Code (1998) and UBC 1997 provide useful baseline estimations, they tend to overpredict the periods for buildings with significant infill wall contribution, especially in the mid-rise range. Eurocode 8, with its more differentiated approach to frame-dominated versus wall-dominated systems, produced period estimates that were closer to the numerical analysis for frame-dominated cases. However, no standard code formula fully captured the reduction trends observed due to varying infill wall ratios (Namata Saidou & Koçak, 2018).

These findings highlight the need for refined empirical formulations that explicitly account for the infill wall contribution in seismic period estimations (Hatzigeorgiou & Kanapitsas,2013). Neglecting the infill effect may lead to conservative period predictions, resulting in misjudgment of seismic forces and inappropriate design decisions. Incorporating realistic stiffness contributions from infill walls can improve the accuracy of seismic demand assessments and the efficiency of structural designs.

Thus, the proposed empirical formula developed in this study offers a practical and more accurate tool for engineers aiming to account for the effects of infill walls during seismic design of reinforced concrete structures.

References

Balkaya, C., & Kalkan, E. (2002). Estimation of fundamental periods of shear-wall dominant building structures. Rensselaer Polytechnic Institute, Troy, NY, USA.

CEN. (2004). *Eurocode 8: Design of structures for earthquake resistance – Part 1: General rules, seismic actions and rules for buildings (EN 1998-1)*. European Committee for Standardization, Brussels.

Crowley, H., & Pinho, R. (2004). Period-height relationship for existing European reinforced concrete buildings. *Journal of Earthquake Engineering*, *8*(S.I.1), 93–119

Ersin, U.D., Yuksel, E., Koçak, A., Hayashi, M., & Karadogan, F. (1998). System identification by means of micro tremor measurements. *Second Japan-Turkey Workshop on Earthquake Engineering*, 633–648

Goel, R.K., & Chopra, A.K. (1997). Period formulas for moment-resisting frame buildings. *Journal of Structural Engineering*, *123*(11), 1454–1461

Güler, K., Yüksel, E., & Koçak, A. (2008). Estimation of the fundamental vibration period of existing RC buildings in Turkey utilizing ambient vibration records. *Journal of Earthquake Engineering*, *12*(S2), 140–150

Hatzigeorgiou, G.D., & Kanapitsas, G. (2013). Evaluation of fundamental period of low-rise and mid-rise reinforced concrete buildings. *Earthquake Engineering and Structural Dynamics*, *42*(11), 1599–1616

Hong, L.L., & Hwang, W.L. (2000). Empirical formula for fundamental vibration periods of reinforced concrete buildings in Taiwan. *Earthquake Engineering and Structural Dynamics*, *29*, 327–337

Koçak, A. (2013). Infill wall effect in seismic behaviour of RC structures. *Sigma Journal of Engineering and Natural Sciences*, *31*(1), 1–10

Koçak, A. (2017). Prediction of the fundamental periods for infilled RC frame structures. *Karaelmas Fen ve Mühendislik Dergisi*, *7*, 381–394

Koçak, A. (2020). The effects of infill walls and basement shear walls on the seismic performance of existing damaged building. *Engineering Failure Analysis*, *118*, 104797

Koçak, A., Börekçi, M., & Zengin, B. (2018). Period formula for RC frame buildings considering infill wall thickness and elasticity modulus. *Scientia Iranica, 25*

Koçak, A., Kalyoncuoğlu, A., & Zengin, B. (2013). Effect of infill wall and wall openings on the fundamental period of RC buildings. In *Proceedings of the 9th International Conference on Earthquake Resistant Engineering Structures* (Vol. 132, pp. 121–131). Coruna, Spain

Namata Saidou, S., & Koçak, A. (2018). Behavior of RC building with and without infill wall under blast loading. *Sigma Journal of Engineering and Natural Sciences*, *36*(4), 993–1008

Oliveira, C.S., & Navarro, M. (2010). Fundamental periods of vibration of RC buildings in Portugal from in-situ experimental and numerical techniques. *Bulletin of Earthquake Engineering*, *8*, 609–642

Ozkul, T.A., Kurtbeyoğlu, A., Börekçi, M., Zengin, B., & Koçak, A. (2019). Effect of shear wall on seismic performance of RC frame buildings. *Engineering Failure Analysis*, *100*, 60–75

Panagiotakos, T.B., & Fardis, M.N. (1999). Deformation-controlled earthquake resistant design of RC buildings. *Journal of Earthquake Engineering*, *3*(4), 495–518

SAP2000. (2024). *SAP2000 integrated software for structural analysis and design* (Version 26). Computers and Structures, Inc., Berkeley, California, USA

TSC. (1998). *Turkish Code for Buildings in Seismic Zones*. Ministry of Public Works and Settlement, Ankara, Turkey

Yıldırım, M.K. (2009). *Determining the period of structure according to the infill wall ratio of RC frame structures* (Master's thesis). Yıldız Technical University, Istanbul, Turkey (in Turkish)

Zarnic, R., & Tomazevic, M. (1998). An experimentally obtained method for evaluation of the behaviour of masonry infilled RC frames. *Proceedings of the 9th World Conference on Earthquake Engineering*, Kyoto

4th International Civil Engineering & Architecture Conference
17-19 May 2025, Trabzon, Türkiye

Seismic evaluation of soil-structure interaction for Bursa Uludağ University Hospital using ambient noise and site response analyses

Seda Özgençli[1], Mustafa Şenkaya*[1,2]

[1]Bursa Uludağ University, Department of Civil Engineering, 16240 Bursa, Türkiye
[2] Earthquake Research and Structural Health Monitoring Laboratory, Bursa Uludağ University, 16240 Bursa, Türkiye

Abstract. This study aims to investigate the soil-structure interaction of the A and B Block building, which includes the Polyclinics section of Bursa Uludağ University Hospital, through seismic parameters. As part of the study, ambient noise recordings were simultaneously conducted on both the hospital building and the underlying soil. Measurements within the hospital were taken near structural elements and around the center of mass on each floor, while ground recordings were collected from four surrounding locations around the building. The findings clearly show that Block A experiences variations in predominant frequencies across its different sides, which may lead to uneven oscillations during an earthquake and potentially generate additional forces, such as torsional effects, within the structure. Conversely, Block B demonstrates relatively consistent predominant frequencies across its corners; however, these frequencies differ significantly from those observed at the ground level. Moreover, the measured frequencies are slightly higher than the values anticipated based on theoretical estimations.

Keywords: 2023 Kahramanmaraş earthquakes; Machine learning; Building damage

1. Introduction

A significant portion of Türkye is situated within an active seismic zone and faces considerable earthquake hazards. the Bursa Plain representing the city center of Bursa is particularly vulnerable due to its proximity to active faults located both within the region and in the northern and southern parts of the Marmara region. Historical and instrumental earthquake records indicate that Bursa has experienced moderate to severe earthquake impacts at least three times per century. The most imminent threat arises from a potential major earthquake expected to occur along the segment of the North Anatolian Fault beneath the Sea of Marmara.

The Quaternary and Miocene–Pliocene-aged geological formations in the Bursa Plain—where Bursa Uludağ University is situated—are known to amplify the surface effects of potentially destructive earthquakes. The Görükle Campus of Bursa Uludağ University serves as a critical hub for regional services and research and development activities, hosting key institutions such as the Faculties of Medicine and Engineering, a technopark, and various research laboratories (Fig. 1). The campus comprises 52 buildings, many of which have high building importance coefficients and are designated for immediate post-earthquake use. Additionally, a significant number of these buildings contain hazardous materials, posing a risk of secondary disasters in the aftermath of a major seismic event.

One of the most critical structures within the campus is the Bursa Uludağ University Faculty of Medicine Hospital. The Faculty of Medicine (BUU-TF) was established in 1970 as an affiliate of Istanbul University and has since expanded through the construction of various buildings over the years. The hospital encompasses a total enclosed area of 165,543.00 m² and comprises five main blocks: A, B, C, D, and E. This study focuses on Block A, the oldest building within the faculty, which houses outpatient clinics, imaging units, and the radiation oncology department. Block B accommodates inpatient clinics, while Block D is dedicated to ophthalmology services. Block E provides care for pediatric hematology and oncology patients.

The aim of this study is to investigate the ground–structure interaction of Block A and B of BUU-TF by analyzing the dominant vibration periods of both the building and the underlying soil. To achieve this, ambient-noise measurements were conducted using a broadband accelerometer at various locations, including different

*Corresponding author, E-mail: mustafasenkaya@uludag.edu.tr

https://doi.org/10.31462/icearc2025_ce_eqe_596

floors of the building, around the center of mass, the corners, and the ground beneath the structure. The collected data were then evaluated using the Horizontal-to-Vertical Spectral Ratio (HVSR) method.

The HVSR method, also referred to as the Nakamura method (Nakamura, 1989), relies on the ratio of horizontal to vertical components of ambient seismic noise. This approach is particularly useful for detecting the natural resonance frequency of soft sediment layers above bedrock, which is closely linked to the stiffness and layering of subsurface materials. Besides offering valuable geotechnical insights, the HVSR method is popular due to its straightforward, cost-effective, and non-invasive nature. Bhandary (2021) investigated the resonance effects on the shaking of tall buildings in the Kathmandu Valley during the 2015 Gorkha earthquake using HVSR analysis. Similarly, Mukai (2022) employed the method to evaluate the seismic behavior of historic masonry buildings following the Nepal earthquake. Gosar and Martínec (2008) conducted HVSR-based studies both within buildings and on the underlying soil to determine site effects. Parolai et al. (2005) utilized ambient noise and HVSR analysis to assess the vibrational characteristics of Holweide Hospital in Cologne, Germany. Galipol et al. (2004)examined the structure, soil–structure interaction, and damage effects using the HVSR method. Additionally, Barani et al. (2014) analyzed the structural response of masonry buildings in the historic center of Genoa, Italy, through HVSR measurements.

2. The study area

The majority of the Görükle district and the Görükle Campus, where the BUU-TF is located, is situated on the Miocene–Pliocene-aged Mudanya Formation and partly on younger Quaternary alluvial deposits (Fig. 2). The Mudanya Formation is extensively distributed across the north–northwestern part of Bursa Province and has an estimated thickness ranging from 50 to 300 meters. It is composed of conglomerate, sandstone, siltstone, claystone, marl, and limestone. These lithologies transition laterally and vertically, typically forming various combinations. While most of the rocks in the formation are considered very weak or weak in terms of strength, the limestone in Mudanya formation could represent strongly cemented character in some areas. The alluvium, on the other hand, covers much of the Bursa Plain. According to DSI (1973), its thickness varies between approximately 140–200 meters in the central and eastern parts, around 100 meters in the north, and up to 150–200 meters in the west and northwest. It consists of unconsolidated gravel- to clay-sized materials. The general geotechnical properties of both soil types are considered prone to amplifying seismic loads and effectively transmitting these loads to overlying structures during a potential earthquake.

The Bursa Plain, where the Görükle Campus is situated, is an east–west-oriented basin enriched by river systems, bounded by the Katırlı Mountains to the north and the Uludağ Mountains to the south. The plain generally lies at an elevation below 200 meters, and its slope ranges between 0° and 2° across most of its extent, excluding the steeper mountain flanks (Öncü, 2021). The region is tectonically active and bordered by several significant fault zones. To the south, the Bursa, Uludağ, Uluabat, Mustafa Kemalpaşa, and Manyas faults are prominent, while the northern boundary is defined by the İznik, Gemlik, Zeytinbağı, and Bandırma faults (Özalp, Emre ve Doğan, 2013). Additionally, the North Anatolian Fault Zone (NAFZ) constitutes a major seismic source for the area, particularly for settlements located on the plain. Both historical and instrumental records indicate that Bursa and its surroundings have been exposed to destructive earthquakes. Notable events include the 1419 Gemlik, 1855 Bursa (two successive events in March and April), 1894 Marmara, 1953 Yenice-Gönen, 1964 Bursa–Karacabey, 1970 Gediz, and 1999 Gölcük earthquakes.

3. Methods and data

The HVSR method requires three-component microtremor recordings, which consist of vibrations of either natural or anthropogenic origin. These microtremors are typically associated with displacements ranging from 10^{-6} to 10^{-2} mm and are predominantly characterized by periods shorter than 1 second (Okada ve Suto, 2003). In recent years, such signals have increasingly been referred to as “ambient noise” in the scientific literature (Maggio, Subašić ve Bean, 2022; Panzera ve diğerleri, 2016), and can be collected using mobile single-station seismometers or through various types of sensors installed at permanent seismic monitoring stations.

In the HVSR method, the horizontal-to-vertical spectral ratio of microtremor recordings obtained at the surface is calculated using Equation (1), which represents the ratio of the horizontal to vertical components of the ground motion spectra. This ratio provides insights into the impedance contrast between the overlying soil layers and the underlying bedrock.

$$A(w)_{H/V} = \frac{\left(H_s(w) / H_b(w) \right)}{\left(V_s(w) / V_b(w) \right)} \tag{1}$$

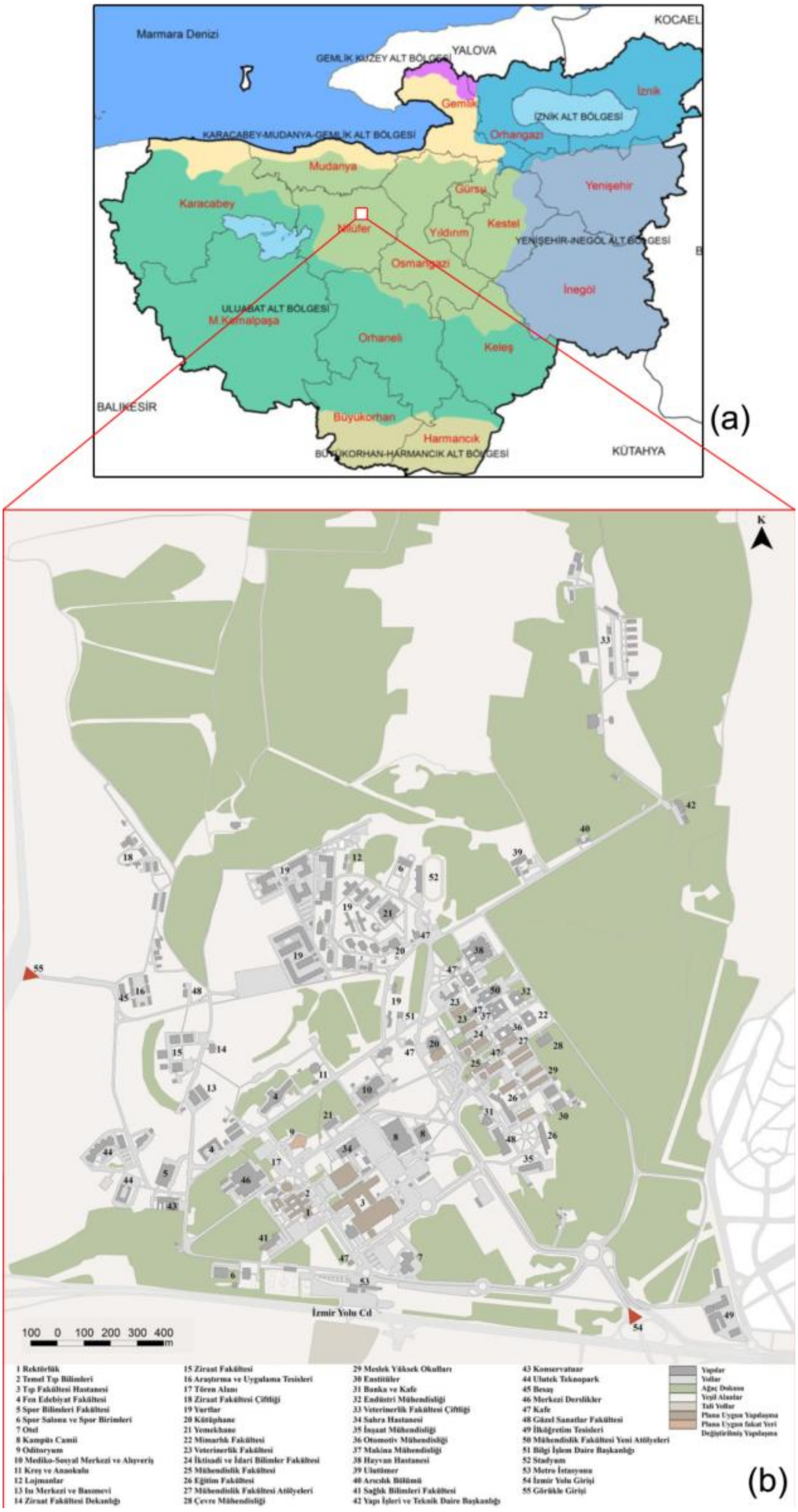

Fig. 1. Location of BUU and distribution of buildings

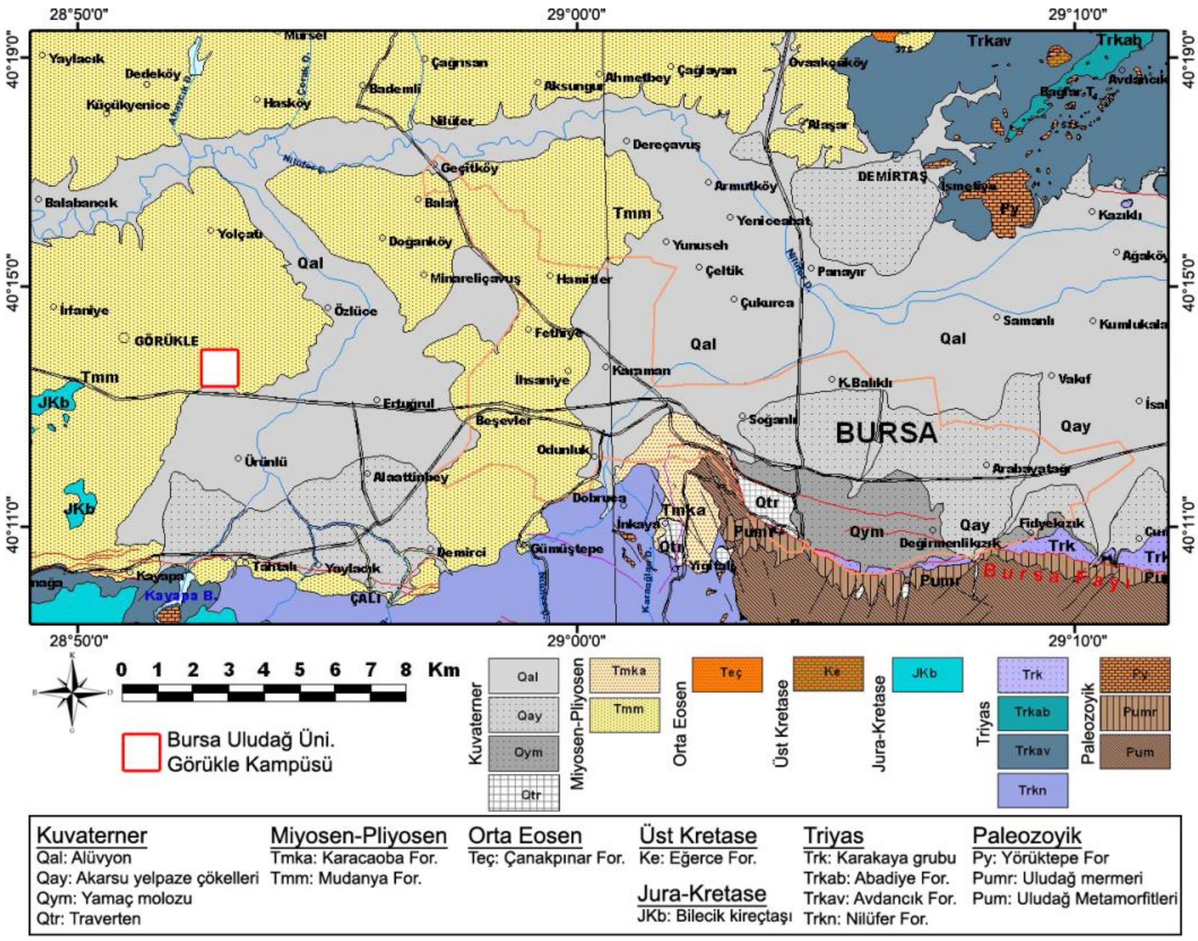

Fig. 2. Geology of Bursa plain. The study are is indicated by red frame.

In this context, Hs and Hb denote the horizontal components of the ground motion spectra at the surface and bedrock, respectively, while Vs and Vb represent the corresponding vertical components. The HVSR method relies on two key assumptions: (i) the spectral ratio of horizontal to vertical motion at the bedrock level is equal to 1 (Hb/Vb = 1), and (ii) the vertical component of microtremor signals is not significantly amplified by the soil layers.

Therefore, the horizontal/vertical spectrum ratio for a microtremor signal recorded at the surface becomes,

$$A(w)_{H/V} = \frac{\left(H_s(w) / H_b(w) \right)}{\left(V_s(w) / V_b(w) \right)} = \frac{H_s(w)}{V_s(w)} \frac{V_b(w)}{H_b(w)} = \frac{H_s(w)}{V_s(w)} \qquad (2)$$

and this ratio is called the HVSR spectral ratio. The HVSR curve is obtained by computing the horizontal-to-vertical spectral ratio across a range of frequencies or periods. The peak of this curve defines the HVSR amplitude, while the corresponding frequency (f_0) or period (T_0) at which the peak occurs indicates the site's fundamental (or dominant) resonance frequency or period.

In recent years, one of the applications of the HVSR method has been the determination of buildings' natural resonance periods under ambient loading conditions (Molnar ve diğerleri, 2022). In these applications, to measure the building's resonance periods in both horizontal directions (transverse and longitudinal), the horizontal components (N-S and E-W) of the broadband seismometer are aligned parallel to the transverse and longitudinal axes of the structure (Gosar ve Martinec, 2008; Parolai ve diğerleri, 2005). Since the target frequency range in these measurements is higher compared to ground-based surveys, the required recording durations can be relatively shorter. When such measurements are carried out simultaneously at each floor of the building as well as at the ground level on which the building stands, the resonance periods and, in particular, the ratios of HVSR amplitudes between floors can reveal the differences in dynamic behavior of the floors and their compatibility or incompatibility with the ground during an earthquake (Bhandary ve diğerleri, 2021; Mukai ve diğerleri, 2022).

Data were collected at nine locations using three-component broadband velocimeters (Fig. 3). One dataset, comprising 30 minutes of recordings, was obtained from a ground-based station to characterize site properties. The remaining eight datasets were acquired from the top floors of Blocks A and B, particularly the 2nd and 6th floors respectively, with each recording lasting a minimum of 15 minutes. Data evaluation was conducted according to SESAME (2004) guidelines, and all results were also assessed against the criteria outlined by SESAME (2024).

4. Results

While the ground measurements indicated a predominant frequency at 0.37 Hz (Fig. 4a), the southwest side of Block A, represented by points 2 and 5 (Fig. 4b and 4c), exhibited a twin-peak response at approximately 0.38 Hz and 4.40 Hz. This condition may give rise to a resonance effect at the site. In contrast, the northeast side, represented by points 4 and 3, showed a predominant frequency at 4.20 Hz, which corresponds well with the building's floor length (Fig. 4d and 4e). This difference in predominant frequencies may cause the northeast and southwest sides of the structure to oscillate differently during an earthquake, potentially inducing additional forces such as torsion within the structure. On the other hand, all corners of Block B exhibited predominant frequencies ranging between 2.20 Hz and 2.61 Hz, which are notably different from the ground's predominant frequency (Fig. 4f to i). However, these frequencies are approximately 1 Hz higher than the expected value estimated by the expression (floor count × 0.1)$^{-1}$.

Fig. 3. Distribution of measurement locations

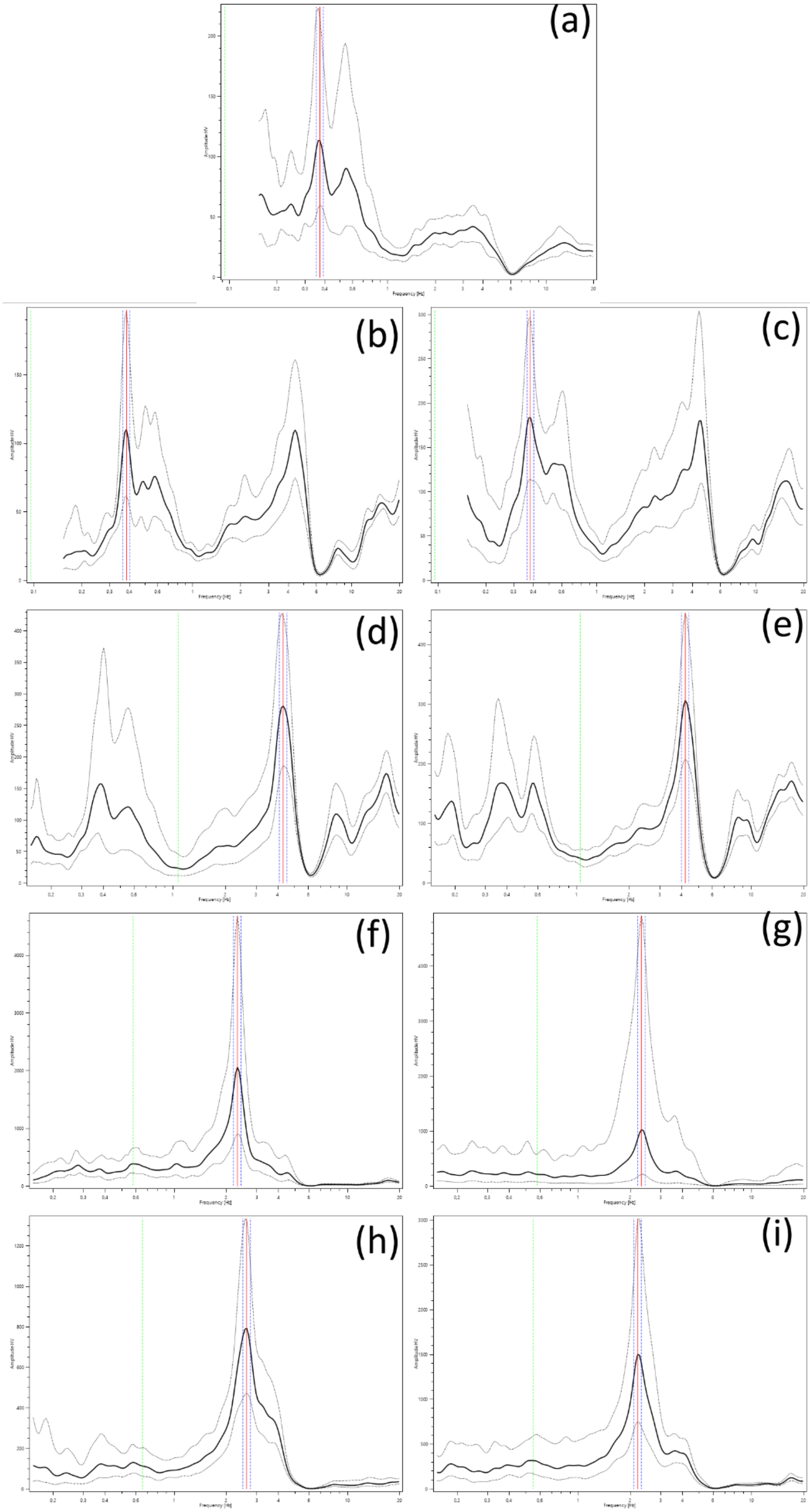

Fig. 4. HVSR result for a) ground, b) 2, c) 5, d) 3, e) 4, f) 6, g) 9, h) 7, i) 8

5. Conclusions

The aim of this study is to investigate the ground–structure interaction of Blocks A (2 floors) and B (7 floors) of BUU-TF by analyzing the dominant vibration periods of both the buildings and the underlying soil. Ambient noise measurements were conducted at eight indoor locations and one location on the ground. The collected data were evaluated using the Horizontal-to-Vertical Spectral Ratio (HVSR) method. The results clearly indicate that Block A exhibits variations in predominant frequencies between different sides, which could cause differential oscillations during an earthquake and potentially induce additional forces such as torsion within the structure. In contrast, Block B displays relatively stable predominant frequencies, although these frequencies are notably different from those of the ground. Nevertheless, the observed values are slightly higher than the expected frequencies.

Acknowledges

This study has been supported by scientific research projects coordinatorship of Bursa Uludağ University, project number FAY-2024-1501

References

Barani, S., Ferrari, R. D., Cattari, S., Eva, C., Lagomarsino, S. ve Pieracci, A. (2014). Structural response of masonry buildings in the historic center of Genoa, Italy (C. Session 2.3, ss. 314-318). GNGTS 2014,

Bhandary, N. P., Paudyal, Y. R. ve Okamura, M. (2021). Resonance effect on shaking of tall buildings in Kathmandu Valley during the 2015 Gorkha earthquake in Nepal. *Environmental Earth Sciences*, *80*(13), 459.

DSİ. (1973). *Bursa ve Çayırköy ovalarının hidrojeolojik etüt raporu*. Ankara.

Gallipoli, M. R., Mucciarelli, M., Castro, R. R., Monachesi, G. ve Contri, P. (2004). Structure, soil–structure response and effects of damage based on observations of horizontal-to-vertical spectral ratios of microtremors. *Soil Dynamics and Earthquake Engineering*, *24*(6), 487-495.

Gosar, A. ve Martinec, M. (2008). Microtremor HVSR Study of Site Effects in the Ilirska Bistrica Town Area (S. Slovenia). *Journal of Earthquake Engineering*, *13*(1), 50-67. doi:10.1080/13632460802212956

Maggio, G., Subašić, S. ve Bean, C. J. (2022). Subsurface characterization using passive seismic in the urban area of Dublin City, Ireland. *Geophysical Prospecting*, *70*(8), 1432-1454.

Molnar, S., Sirohey, A., Assaf, J., Bard, P.-Y., Castellaro, S., Cornou, C., Yong, A. (2022). A review of the microtremor horizontal-to-vertical spectral ratio (MHVSR) method. *Journal of Seismology*, *26*(4), 653-685.

Mukai, Y., Hoshino, H., Yamamoto, N., Masui, M., Miyauchi, A. ve Suwal, R. P. (2022). Investigation of microtremors observed at historic masonry townhouse buildings after Nepal earthquake. *Frontiers in Built Environment*, *8*. https://www.frontiersin.org/articles/10.3389/fbuil.2022.918960 adresinden erişildi.

Nakamura, Y. (1989). A method for dynamic characteristics estimation of subsurface using microtremor on the ground surface. *Railway Technical Research Institute, Quarterly Reports*, *30*(1), 25-33.

Okada, H. ve Suto, K. (2003). *The Microtremor Survey Method*. Geophysical Monograph Series. Society of Exploration Geophysicists.

Öncü, S. (2021). *CBS yöntemiyle Bursa'nin bütünleşik doğal tehlike analizi*. Bursa Uludağ Üniversitesi.

Özalp, S., Emre, Ö. ve Doğan, A. (2013). THe segment structure of southern branch of the north anatolian fault and paleoseismological behaviour of the Gemlik fault, NW Anatolia. *Bulletin of the Mineral Research and Exploration*, *147*(147), 1-17.

Panzera, F., Sicali, S., Lombardo, G., Imposa, S., Gresta, S. ve D'Amico, S. (2016). A microtremor survey to define the subsoil structure in a mud volcanoes area: The case study of Salinelle (Mt. Etna, Italy). *Environmental Earth Sciences*, *75*(15), 1140.

Parolai, S., Fäcke, A., Richwalski, S. M. ve Stempniwski, L. (2005). Assessing the Vibrational Frequencies of the Holweide Hospital in the City of Cologne (Germany) by Means of Ambient Seismic Noise Analysis and FE modelling. *Natural Hazards*, *34*(2), 217-230.

SESAME. (2004). *Guidelines for the implementation of the h/v spectral ratio technique on ambient vibrations measurements, processing and interpretation* (European research project No: WP12 – Deliverable D23.12). European research project.

4th International Civil Engineering & Architecture Conference
17-19 May 2025, Trabzon, Türkiye

An examination of the impact of infill walls on the seismic performance of RC prefabricated structures

Joltai Khonaiv*[1], Mehmet Ö. Timurağaoğlu[1], Özkan Hakan[2], Ramazan Livaoğlu[1,2]

[1] *Bursa Uludağ University, Department of Civil Engineering, 16059 Bursa, Türkiye*
[2] *RL ProjeDestek Consulting Company, Bursa, Türkiye*

Abstract. In conventional design practice, infill walls are typically considered as non-structural elements contributing only to mass and gravity loads. However, it is well established that infill walls can significantly enhance the stiffness, reduce vibration periods, and alter internal force distributions of structures during earthquakes. This study investigates the impact of infill walls on the seismic performance of reinforced concrete (RC) prefabricated structures, commonly used for industrial buildings due to their construction efficiency and cost-effectiveness. A representative prefabricated building model was developed, incorporating realistic connection details and nonlinear material behavior. Infill walls were modeled using an equivalent strut approach with appropriate hysteretic behavior. Nonlinear dynamic analyses were performed based on the Turkish Building Seismic Code (TBSC, 2018) for both the pinned RC prefabricated structure with and without infill walls. A total of 44 analyses were conducted using matched earthquake records derived from site-specific seismic hazard analyses. The seismic performance was evaluated by examining demand-to-capacity (D/C) ratios for critical components, including corbel-to-roof beam connections, purlin-to-roof beam connections, and column bending and shear capacities. The results reveal that infill walls significantly increase lateral stiffness, shorten natural periods, and improve modal energy distribution. Strain- and drift-based D/C ratios confirmed that structures with infill walls exhibit lower seismic demands, reduced deformation, and better overall resilience, whereas structures without infill walls showed higher vulnerability under seismic loads. Additionally, secondary elements such as purlin-to-roof beam and corbel connections remained within acceptable performance limits when infill walls were present.

Keywords: RC prefabricated structures; Infill wall; Nonlinear time history analysis; Performance evaluation

1. Introduction

Reinforced concrete (RC) prefabricated structures are widely adopted in industrial-type buildings due to their numerous advantages, including streamlined manufacturing processes, reduced construction time, minimization of workmanship-related errors, and overall cost efficiency. In these systems, structural elements are prefabricated under controlled factory conditions and rapidly assembled on-site, resulting in significant reductions in labor demand and associated costs (Ersoy, 1997).

The 2023 Kahramanmaraş earthquakes revealed significant vulnerabilities in prefabricated reinforced concrete (RC) industrial buildings. Post-earthquake assessments indicated that the poor detailing at the connections in the affected region contributed to the prevailing damage in prefabricated structures. Furthermore, critical deficiencies were identified in beam-column connection details and anchorage systems. The primary contribution of weak connections between prefabricated components, particularly at joint regions, to structural damage was also emphasized worldwide (Muguruma et al., 1995; Savoia et al., 2017; Sezen & Whittaker, 2006). Notably, damage in these structures was attributed more to displacement demands than to seismic forces. These findings underscore the need to enhance the lateral stiffness of prefabricated industrial systems and to limit the use of hinged connections in order to improve their seismic resilience (Arslan et al., 2024; Kırtel et al., 2024). In typical single-story industrial buildings in Turkey, inadequate roof diaphragms and diaphragm connections allowed large relative lateral displacements of frames, leading to complete structural collapse due to insufficient lateral stiffness.

Additionally, full-height and partial-height unreinforced masonry infills imposed excessive seismic demands on prefabricated concrete columns (Arslan et al., 2006; Saatçioğlu et al., 2001). In most structural designs, infill walls are not considered as load-bearing elements but only as additional mass and load. However, under seismic

*Corresponding author, E-mail: 502226023@ogr.uludag.edu.tr

https://doi.org/10.31462/icearc2025_ce_eqe_597

effects, infill walls contribute significantly to the rigidity of the structure, shorten vibration periods, and significantly affect the distribution of internal forces. Moreover, infill walls make a substantial contribution to damping earthquake energy with their permanent deformations. When infill walls reach their load-bearing capacity, they crack, and their contribution to the rigidity and strength of the structure suddenly ended. The friction that grows at the crack interfaces, due to the structural vibration, increases the damping of the structure. The increase in structural damping reduces the seismic demand on the structure, which means a decrease in the horizontal seismic forces acting on the structure.

The most common approach in considering infill walls in structural analyses is to represent these elements using the compression-only equivalent diagonal strut model. In this method, the structural contribution of the wall is idealized as a uniaxial compression element, taking into account the interaction between the infill wall and the horizontal and vertical elements that make up the frame. In determining the effective width of the equivalent compression strut, the relationship between the diagonal length of the wall (dm) and the effective width (w) is typically utilized. This approach plays a crucial role in defining the effects of infill walls on rigidity and strength, particularly in nonlinear structural analyses. Pioneering studies on this subject have been presented in literature by (Mainstone, 1971; Polyakov, 1960; Smith, 1962).. In prefabricated industrial buildings, it has been observed that infill walls not only increase the lateral rigidity of the structure but also have an effect on displacement demands and base shear forces (Korkmaz & Karahan, 2011).

In this study, the influence of infill wall on the seismic performance of RC prefabricated strutcures are thoroughly scrutinized numerically by modeling connection behavior in details. In accordance with the Turkish Building Seismic Code (TBSC, 2018), nonlinear time history analyses were conducted on a pin-connected RC prefabricated industrial building, both with and without infill walls, using ETABS software (ETABS, 2024). The results were evaluated based on demand-to-capacity (D/C) ratios, considering factors such as the connections between the corbel and roof beam, purlin and roof beam, as well as the bending and shear capacities of the columns.

2. Numerical modeling

In this study, a single-story, single-bay RC prefabricated industrial structure, representative of existing building typologies in Turkey, is analyzed. The structure features columns with a height of 6 meters. It spans 15 meters in the X-direction and 6 meters in the Y-direction, with a total modeled length of 48 meters in the Y-direction, corresponding to eight bays (6 m × 8 = 48 m). The structural layout consists of a single primary axis (A-B) in the X-direction and nine grid lines (1–9) in the Y-direction (Fig. 1).

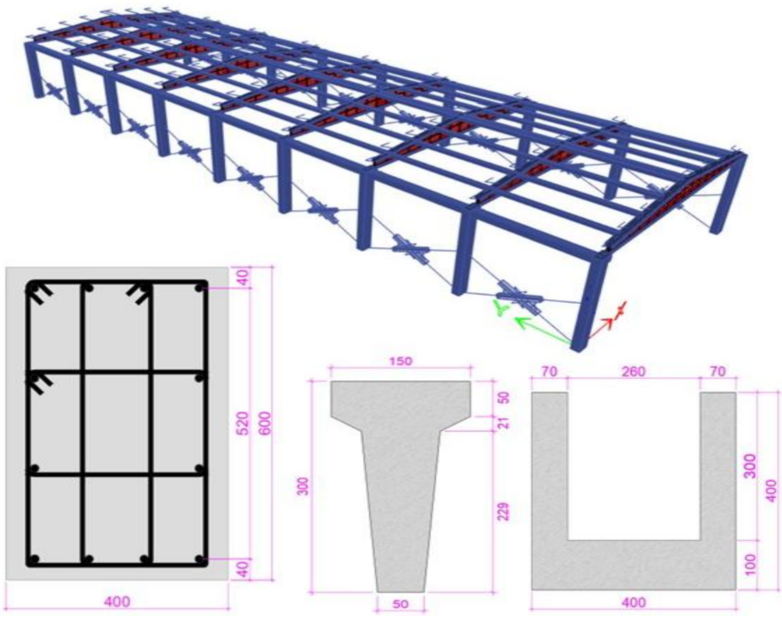

Fig. 1. Generated 3D model view of the single-story structure and cross-sectional details

The vertical load-bearing elements are RC columns with cross-sectional dimensions of 600 × 400 mm. Each column is reinforced with 12 longitudinal bars of 16 mm diameter and transverse reinforcement consisting of 8mm diameter stirrups spaced at 100 mm intervals. Roof trusses are modeled as thin shell elements, with upper chord width of 350 mm, web width of 100 mm, and lower chord width of 250 mm. The prefabricated gutters are represented by U-shaped beam elements with cross-sectional dimensions of 400 × 400 mm. Purlins, which support the roof cladding and act within the truss plane, are modeled with a T-shaped cross-section. Additionally, cantilever (corbel) elements are modeled with a width of 400 mm and a depth of 450 mm.

Figure 1 presents the three-dimensional model of the single-story prefabricated structure, detailing its geometric configuration and principal structural components. The concrete strength class employed is C30 (fck = 30 MPa), while the reinforcement class is S420 (fyk = 420 MPa). The roof cladding is assumed to consist of aluminum sandwich panels. Applied loads include a roof cladding load of 0.12 kN/m², a snow load of 0.75 kN/m², and a façade cladding load of 4.5 kN/m². In accordance with the Turkish Building Seismic Code (TBSC, 2018), mass multiplier factors are taken as 1.0 for gravity loads and 0.3 for snow loads.

2.1. Modeling of connections

The corbel-roof girder connection were modeled to represent nonlinear behavior at the joints. One of the most critical challenges in the seismic design of prefabricated reinforced concrete structures is the proper design of connections, particularly at beam-to-column joints. Prefabricated beam and column elements connected by dowels have been tested under both monotonic and cyclic pure shear loading to understand its seismic behavior. In a study conducted by Psycharis & Mouzakis (2012a), the shear ductility capacity of the connections and the influence of various design parameters on strength were investigated. A formula is proposed for calculating the shear strength of dowel connections that can be used in seismic design.

$$R_u = 1.10 * n * D^2 * \sqrt{f_{ck} * f_{yk}} \qquad \mathrm{d/D} > 6 \tag{1}$$

$$R_u = 1.10 * \left(\frac{0.25d}{D} - 0.50\right) * n * D^2 * \sqrt{f_{ck} * f_{yk}} \qquad 4 \leq \mathrm{d/D} \leq 6 \tag{2}$$

Table 1. Dowel element specifications and material properties for corbel and purlin components

Component	n	D (mm)	d_n (mm)	f_{ck} (MPa)	f_{yk} (MPa)	f_{cd} (MPa)	f_{yd} (MPa)	d/D	C_0	γ_R	R_u (kN)	R_d (kN)
Corbel	2	16	100	30	420	20	365.2	6.25	0.95	1.3	63.2	32.0
Purlin	1	14	60	30	420	20	365.2	4.29	0.95	1.3	13.8	7.0

For the safe design of connections, calculations should be performed considering material safety factors and relevant design parameters. In this context, the coefficient C_0, which depends on the magnitude of rotation at the connection, varies between 0.90 and 1.10. Particularly in systems with flexible columns where large joint rotations may occur, a C_0 value in the range of 0.90–0.95 is recommended. Additionally, a safety factor of γ_R=1.30 is proposed (Psycharis & Mouzakis, 2012b). The maximum shear resistance at the corbel-roof girder connection was calculated as R_u=63.2kN, while the design shear resistance was determined as R_d=32.0kN. Similarly, the maximum and design shear resistances of the purlin-roof girder connection were found to be R_u=13.8kN and R_d=7.0kN, respectively, as given in Table 1.

Based on the calculated shear resistances, nonlinear models were developed to represent the corbel and purlin connections. In these models, dowel connections were represented as link elements. The corbel element was modeled using the degrading hysteresis model by incorporating both force-displacement and moment-rotation relationships, while the purlin element was modeled based solely on its force-displacement behavior. The roof beam–corbel connection was modeled as connection elements based on the commonly used moment-rotation and force-displacement relationships found in the literature based on the experimental studies. On the other hand, the roof beam–purlin connection was defined according to the force-displacement relationship. To accurately represent their dynamic behavior, the roof beams were modeled using shell elements. The calculated moment-rotation and shear force-dispalcement curves are given in Fig. 3. The calculated shear force-displacement relationships at the purlin connections is shown in Fig. 4.

2.1. Infill wall modeling

The initial approach for determining the effective width (w) of the equivalent compression strut is calculated using Equation (2), which represents the diagonal length (d_m) of the infill wall, and various formulas have been proposed in the literature (Abdul-kadir, 1974; Bazan & Meli, 1980; Bertoldi et al., 1993; Cavaleri et al., 2005; Durrani & Luo, 1994; Hendry, 1981; Holmes, 1961; Mainstone, 1971; Paulay & Priestley, 1992; Smith, 1967; Tassios, 1984; TBSC, 2018) on this subject.

$$w = \frac{d_m}{3} \tag{3}$$

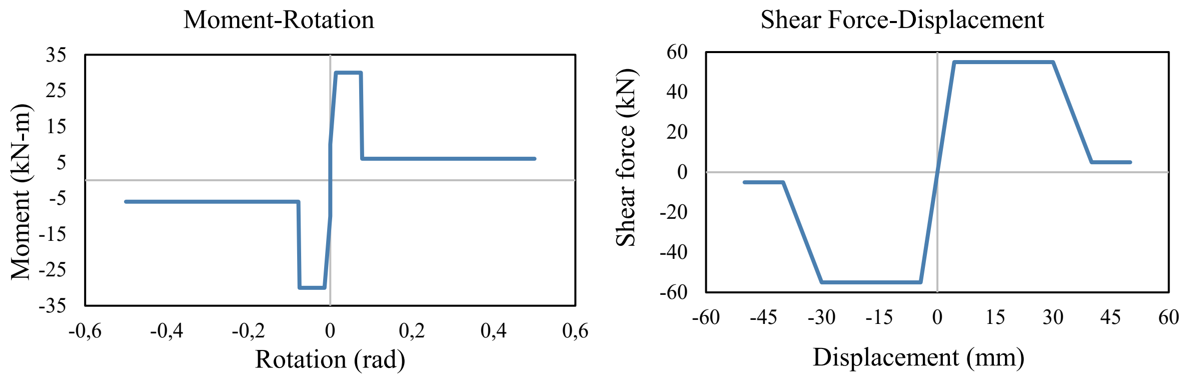

Fig. 3. Nonlinear behavior at the corbel-roof girder connection

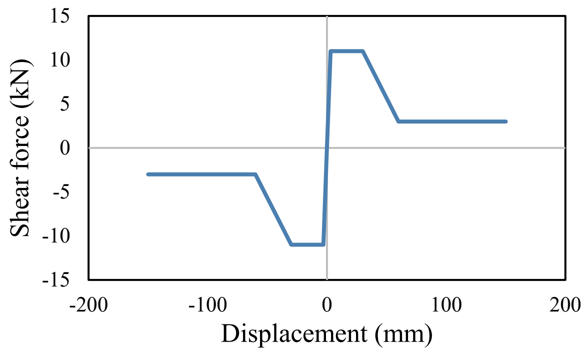

Fig. 4. Nonlinear behavior at the purlin-roof girder connection

Taking all the proposed formulas into account, the effective width (w) of the equivalent compression strut was calculated, and the results are presented in the Fig. 5. The equivalent strut width of the infill wall was calculated based on the proposed formulas, and as a result, the width of the equivalent compression strut was determined to be 1 m. In the model, infill walls were modeled as multilinear plastic link elements using the widely accepted equivalent diagonal strut approach in literature. Based on this representation, the Concrete hysteresis type that is given in ETABS is selected to simulate the cyclic behavior of infill walls under lateral loading. The axial stiffness and force-displacement relationship of the infill wall were calculated, and the resulting nonlinear behavior model is presented in Fig. 6.

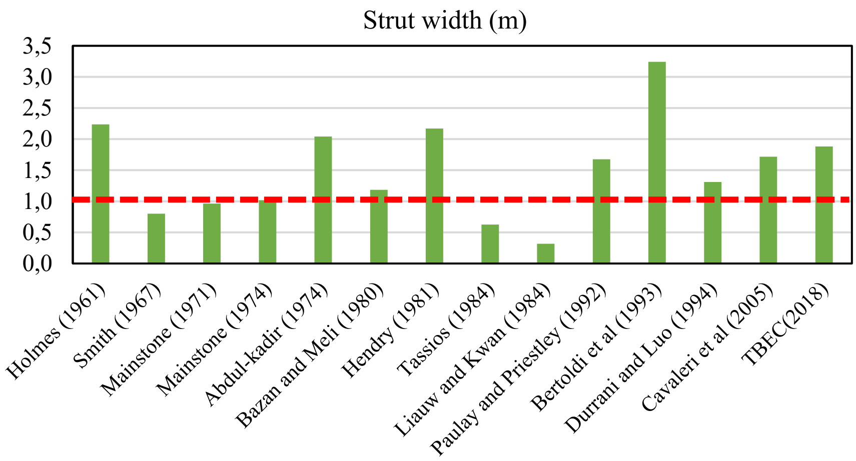

Fig. 5. Calculated effective width of the diagonal strut

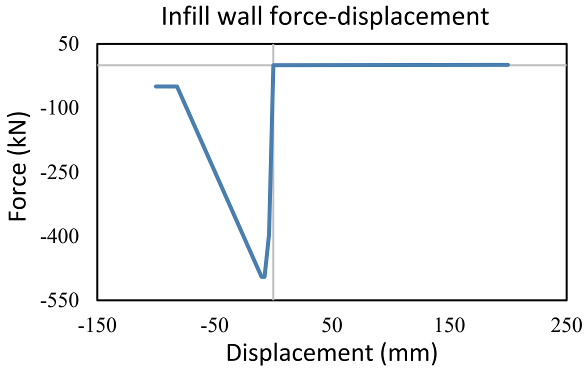

Fig. 6. Nonlinear behavior for infill wall

3. Selection and scaling of earthquakes

According to TBSC (2018), the amplitude of the horizontal component spectra of earthquake records to be used in dynamic analyses must be scaled based on the design spectrum ordinates within the period range between $0.2T_P$ and $1.5T_P$, where T_P represents the fundamental natural vibration period of the structure. This value has been calculated as $T_P = 0.57$ s (1st mode). The design spectra used in the model correspond to the exceedance probabilities for earthquake level DD-1, which is associated with return periods 2475 years.

3.1.1. Scaling of ground motion records

In this study, both horizontal components were multiplied by the same scaling factor during the scaling process. As a result, the original relationship between the horizontal components was preserved after scaling. The number of earthquake records must be at least 11, and the number of record sets from the same earthquake must not exceed three. In the initial stage of scaling the selected records for three-dimensional design, the combined horizontal spectrum should be obtained by taking the square root of the sum of the squares of the spectral ordinates of the two horizontal components of each record set (TBSC, 2018).

3.2 Selection of ground motion records

For each selected horizontal ground motion component, the accepted maximum scaling factor was primarily set in the range of 0.25 to 4.0, and in exceptional cases where this range could not be satisfied, it was allowed up to 5.0. Additionally, the number of records selected from the same earthquake was limited to a maximum of three within the total of eleven records. The spectra of the scaled candidate records were compared with 1.3 times the target spectrum, and 11 suitable records along with their two horizontal components were selected. In light of these criteria, Fig. 7 presents, in terms of acceleration spectrum, the 1.3 times target spectrum for 2475 years according to TBSC (2018), the selected records, and their average. Table 2 lists the selected records along with their corresponding values for Magnitude (M_w), Joyner-Boore distance (R_{JB}), Shear wave velocity (V_{S30}), fault mechanism (FM), and scaling factor (SF). In the FM column, SS denotes strike-slip fault, and RV refers to reverse fault types.

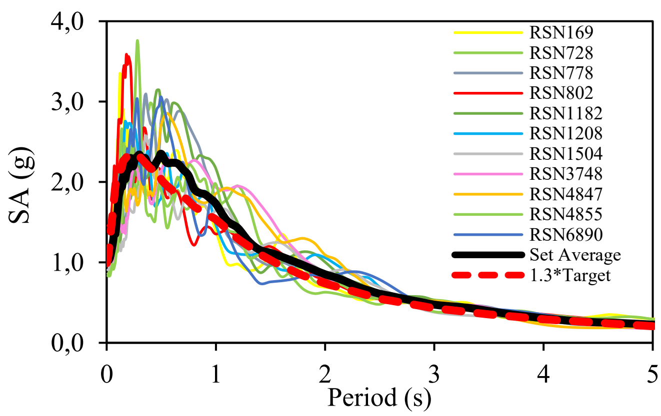

Fig. 7. Target spectrum at DD-1 (2475-year) level, record spectra, and the variation of average spectral acceleration values of the record set with respect to period

Table 2. Earthquake ground motion records and their characteristics

RSN	Earthquake Name	Year	Station Name	Magnitude (M_w)	R_{JB} (km)	V_{S30} (m/s)	FM	SF
1182	Chi-Chi, Taiwan	1999	CHY006	7.62	9.76	438	RV	2.06
1208	Chi-Chi, Taiwan	1999	CHY046	7.62	24.1	442	RV	4.17
1504	Chi-Chi, Taiwan	1999	TCU067	7.62	0.62	434	RV	1.53
169	Imperial Valley-06	1979	Delta	6.53	22.03	242	SS	2.53
3748	Cape Mendocino	1992	Ferndale Fire Station	7.01	16.64	388	RV	2.09
4847	Chuetsu-oki	2007	Joetsu Kakizakiku Kakizaki	6.8	9.43	383	RV	1.97
4855	Chuetsu-oki	2007	Sanjo	6.8	21.4	245	RV	4.79
6890	Darfield, New Zealand	2010	Christchurch Cashmere High School	7	17.64	204	SS	2.93
728	Superstition Hills-02	1987	Westmorland Fire Sta	6.54	13.03	194	SS	3.15
778	Loma Prieta	1989	Hollister Differential Array	6.93	24.52	216	RV	2.71
802	Loma Prieta	1989	Saratoga - Aloha Ave	6.93	7.58	381	RV	2.39

4. Analysis and results (discussion)

To investigate the effects of infill walls on seismic performance of RC prefabricated structures, two structural models—one with infill walls and one without—were subjected to nonlinear time-history analyses using 11 ground motion records, yielding a total of 44 (22x2) analyses. Modal analysis results for the first three modes of both structural models are presented in Table 3. The findings clearly demonstrate the influence of infill walls on the structural stiffness and dynamic behavior of the system. For the system with infill walls, the period of the first mode was determined to be $T_1 = 0.574$s, with 39% modal mass participation in the transverse (UY) direction and 64% in the torsional (RX) direction. In contrast, the system without infill walls exhibited a first mode period of $T_1 = 0.765$s, indicating a more flexible structural behavior. In this mode, the modal mass participation ratios were 87% in the UY direction and 96% in the RX direction, suggesting that a significant portion of the system's vibrational energy is concentrated in the first mode along the horizontal axis (UY).

Overall, it can be stated that the additional stiffness provided by the infill walls results in shorter natural periods, thereby reducing displacements and achieving a more balanced distribution of modal energy. On the other hand, the elongated period observed in the structure without infill wall leads to a notable change in the dynamic response, with higher mode shapes exerting increased influence on the structural behavior.

Table 3. Modal participating Mass Ratio

	Modal Participating Mass Ratio				
	Mode	Period (sec)	UX	UY	RZ
With infill	1	0.574	0	39%	0
	2	0.39	54%	0	0
	3	0.39	0	0	21%
Without infill	1	0.765	0	87%	0%
	2	0.472	0	0	14%
	3	0.428	66%	0	0

As part of this study, the damage levels observed in the columns of a prefabricated industrial structure were evaluated by considering the strain limits of both concrete and reinforcement materials. To accurately capture inelastic deformations, fiber plastic hinges were defined along the columns, and nonlinear time history analyses were performed. In line with material-specific performance criteria, strain limits corresponding to the collapse prevention performance level were adopted, with a threshold of 0.010 for concrete and 0.032 for reinforcement. These limits were based on the strain capacities beyond which damage initiates, potentially affecting the serviceability of the structure.

Following the analyses, strain demands obtained from the plastic hinge regions were used to compute Demand-Capacity (D/C) ratios for both concrete and reinforcement. The given D/C ratios are the average of 22 performed analyses for each model. As illustrated in Fig. 8, significantly lower D/C values were observed in the infilled wall model compared to the model without infill wall, for both materials. This finding highlights the beneficial contribution of infill walls to the overall lateral stiffness of the structure, effectively reducing seismic demands on critical structural elements such as columns. Quantitatively, in the infilled wall system, the average D/C ratio was found to be 0.609 for concrete and 1.1416 for reinforcing steel. In contrast, in the system without infill wall, the corresponding D/C ratios increased to 1.382 for concrete and 2.086 for reinforcing steel. These results underscore the significant role of infill walls in enhancing structural performance by limiting inelastic deformations and mitigating potential damage during seismic events.

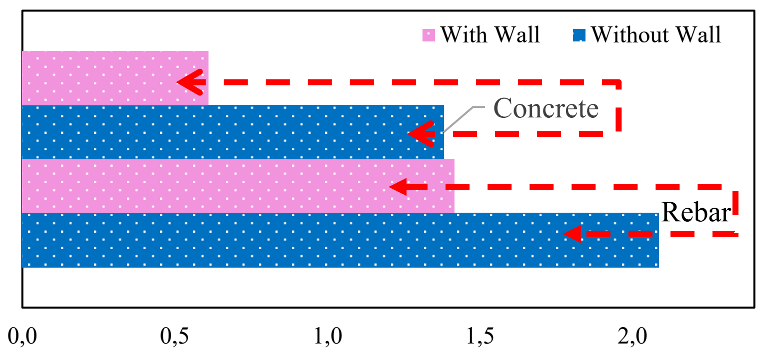

Fig. 8. D/C Ratios in the Column for concrete and Rebar

In addition, D/C ratio based on drift ratios were calculated to assess the lateral displacement capacities of the structures. In these calculations, a drift limit of 3% (0.03) was adopted, in accordance with TBSC (2018). Fig. 9a illustrates the D/C ratios at purlin-roof girder connection for floor drift (calculated as displacement at the top of column divided by column height) and shear force. As presented in the Figure, the systems with and without infill wall, as expected, exhibited similar performance in the UX direction in terms of drift demands (no infill wall available in UX direction). However, in the UY direction, the system without infill wall approached a critical level, with D/C ratio exceeding 1.70. These results clearly demonstrate that the presence of infill walls significantly enhances the lateral stiffness of the structure, thereby reducing drift demands in Y direction under seismic loading.

The nonlinear time history analyses were conducted to evaluate both in-plane and out-of-plane shear demands acting on the purlins. Based on these demands, D/C ratios were calculated, and the results are presented in Fig. 9b. The findings reveal that purlin elements in infilled wall systems experienced notably higher shear demands compared to those without infill for both in plane and out of plane behavior. Nevertheless, these increased demands remained within acceptable limits defined by the CP performance level.

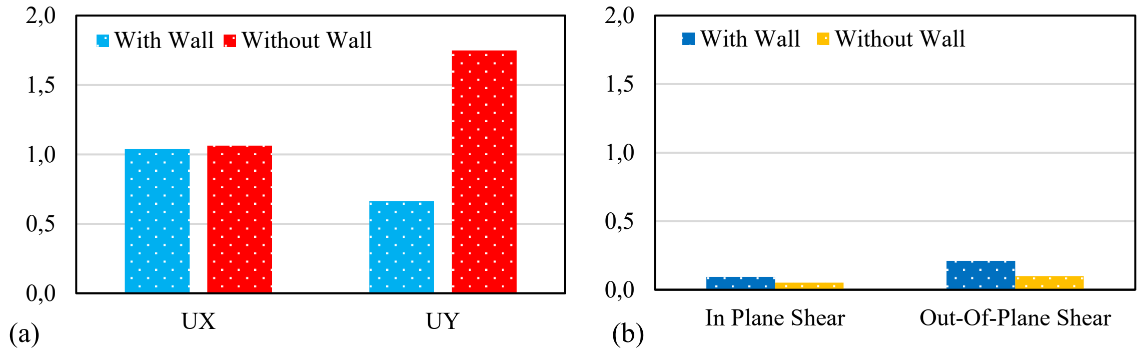

Fig. 9. D/C ratio at purlin-roof girder connection for (a) Floor Drift and (b) Shear Force

Fig. 10 illustrates average D/C ratios for shear force and rotation response at the corbel-roof girder connections. As presented in Fig. 10, several ground motion records (RSN1182XY, RSN1504YX, RSN4847YX, RSN3748YX, RSN802YX) were excluded from the graph due to excessively high out-of-plane rotation demands observed in the infilled wall system. Therefore, the graph was constructed based on the average values of the remaining 17 ground motion records.The analyses revealed that infilled wall systems visibly increases the shear response both in plane and out of plane directions. Additionally, out-of-plane rotation demands on the corbel elements increased significantly although no visible influence of infill wall on in plane rotations is detected.

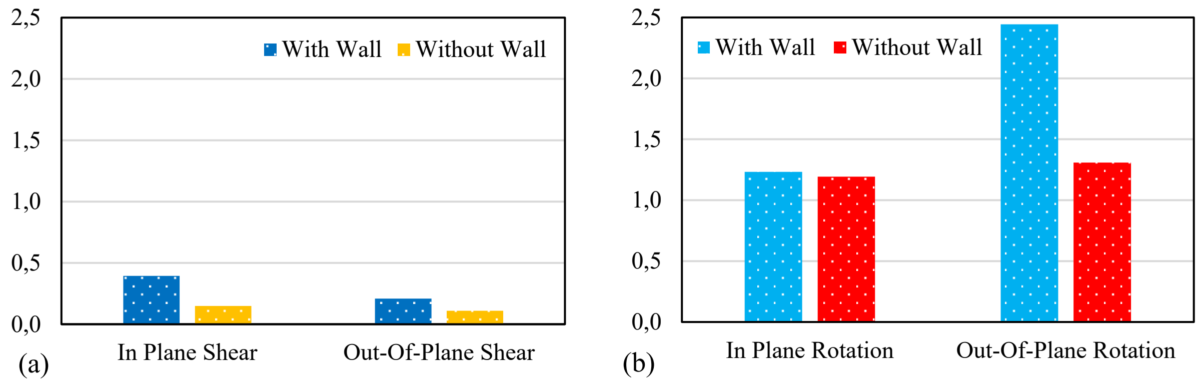

Fig. 10. D/C ratio at Corbel-roof girder connection for (a) Shear force and (b) Rotation

5. Conclusions

This study evaluated the seismic performance of a pin-connected prefabricated industrial building by comparing structures with and without infill walls through nonlinear time-history analyses, in accordance with the Turkish Building Seismic Code (TBSC, 2018). The results showed that infill walls significantly enhance lateral stiffness, shorten natural periods, and improve the distribution of modal energy, particularly influencing the out-of-plane behavior of the system. Strain- and drift-based D/C ratio assessments confirmed that infilled systems experience lower seismic demands and reduced deformation, whereas structures without infill walls are more susceptible to damage. Additionally, secondary elements such as purlin-to-roof beam and corbel connections remained within acceptable performance limits when infill walls were present. Overall, the findings highlight that infill walls substantially improve both the global and local seismic performance of prefabricated structures, supporting their explicit consideration in design and assessment, especially for industrial buildings in high seismic risk regions.

References

Abdul-kadir, M. R. (1974). *The structural behaviour of masonry infill panels in framed structures*. Doctorate dissertation, University of Edingburgh.

Arslan, M. H., Dere, Y., Ecemiş, A. S., Doğan, G., Özturk, M., & Korkmaz, S. Z. (2024). Code-based damage assessment of existing precast industrial buildings following the February 6th, 2023 Kahramanmaraş earthquakes (Pazarcık Mw 7.7 and Elbistan Mw7. 6). *Journal of Building Engineering*, *86*, 108811.

Arslan, M. H., Korkmaz, H. H., & Gulay, F. G. (2006). Damage and failure pattern of prefabricated structures after major earthquakes in Turkey and shortfalls of the Turkish Earthquake code. *Engineering Failure Analysis*, *13*(4), 537–557. https://doi.org/10.1016/j.engfailanal.2005.02.006

Bazan, E., & Meli, R. (1980). Seismic analysis of structures with masonry walls. *Proceedings of 7th WCEE*.

Bertoldi, S. H., Decanini, L. D., & Gavarini, C. (1993). Telai tamponati soggetti ad azioni sismiche, un modello semplificato: confronto sperimentale e numerico. *Atti Del VI Convegno ANIDIS*, 815–824.

Cavaleri, L., Fossetti, M., & Papia, M. (2005). Infilled frames: Developments in the evaluation of cyclic behaviour under lateral loads. *Structural Engineering and Mechanics*, *21*(4), 469–494. https://doi.org/10.12989/sem.2005.21.4.469

Durrani, A. J., & Luo, Y. H. (1994). Seismic retrofit of flat-slab buildings with masonry infills. *Proceedings of the NCEER Workshop on Seismic Response of Masonry Infills*.

Ersoy, U. (1997). *Seismic Behavior of Precast Frame Structures a Critical Look*.

ETABS. (2024). *Documentation and Training Manuals*. Computer and Structures, Inc.(CSI).

Hendry, A. W. (1981). *Structural Brickwork*. MacMillan Press, Ltd., Ed.

Holmes, M. (1961). Steel Frames with Brickwork and Concrete Infilling. *Proceedings of the Institution of Civil Engineers*, *19*(2), 473–478.

Kırtel, O., Aydın, F., Boru, E., Toplu, E., Aydın, E., Sarıbıyık, A., & Ceyhunlu, A. I. (2024). Seismic damage assessment of under-construction industrial buildings: Insights from the february 2023 Türkiye-Syria earthquakes. *Case Studies in Construction Materials*, *21*, e03507.

Korkmaz, K. A., & Karahan, A. E. (2011). Investigation of Seismic Behavior and Infill Wall Effects for Prefabricated Industrial Buildings in Turkey. *Journal of Performance of Constructed Facilities*, *25*(3), 158–171. https://doi.org/10.1061/(asce)cf.1943-5509.0000148

Mainstone, R. J. (1971). On the stiffnesses and strengths of infilled frames. *Proceedings of Institution of Civil Engineers*, *Supplement*, 57–90.

Muguruma, H., Nishiyama, M., & Watanabe, F. (1995). Lessons learned from the Kobe earthquake - a Japanese perspective. *PCI Journal*, *40*(4), 28–42. https://doi.org/10.15554/PCIJ.07011995.28.42

Paulay, T., & Priestley, M. (1992). *Seismic Design of Reinforced Concrete and Masonry Buildings*.

Polyakov, S. V. (1960). On the interaction between masonry filler walls and enclosing frame when loading in the plane of the wall. *Translation in Earthquake Engineering, Earthquake Engineering Research Institute (EERI)*.

Psycharis, I. N., & Mouzakis, H. P. (2012a). Shear resistance of pinned connections of precast members to monotonic and cyclic loading. *Engineering Structures*, *41*, 413–427. https://doi.org/10.1016/j.engstruct.2012.03.051

Psycharis, I. N., & Mouzakis, H. P. (2012b). Shear resistance of pinned connections of precast members to monotonic and cyclic loading. *Engineering Structures*, *41*, 413–427. https://doi.org/10.1016/j.engstruct.2012.03.051

Saatçioğlu, M., Mitchell, D., Tinawi, D., Gardner, N. J., Gillies, A. G., Ghobarah, A., Anderson, D. L., & Lau, D. (2001). The August 17, 1999, Kocaeli (Turkey) earthquake-damage to structures. *Canadian Journal of Civil Engineering*, *28*(4), 715–737.

Savoia, M., Buratti, N., & Vincenzi, L. (2017). Damage and collapses in industrial precast buildings after the 2012 Emilia earthquake. *Engineering Structures*, *137*, 162–180. https://doi.org/10.1016/J.ENGSTRUCT.2017.01.059

Sezen, H., & Whittaker, A. S. (2006). Seismic Performance of Industrial Facilities Affected by the 1999 Turkey Earthquake. *Journal of Performance of Constructed Facilities*, *20*(1), 28–36. https://doi.org/10.1061/ASCE0887-3828200620:128

Smith, B. S. (1962). Lateral stiffness of infilled frames. *Proceedings of the American Society of Civil Engineering, Journal of Structural Division*, *88*(6), 183–199.

Smith, B. S. (1967). Methods for Predicting the Lateral Stiffness and Strength of Multi-Storey Infilled Frames. *Engineering Science*, *2*, 247–257.

Tassios, T. P. (1984). Masonry infill and R/C walls under cyclic actions, (An invited state-of-the-art report). *Proceedings of the 3rd International Symposium on Wall Structures*.

TBSC. (2018). *Principles for the Design of Buildings Under the Impact of Earthquakes (In Turkish)*. Ministry of Interior, Disaster and Emergency Management Presidency, Ankara, Turkey.

4th International Civil Engineering & Architecture Conference
17-19 May 2025, Trabzon, Türkiye

Nonlinear behavior of multi-tiered steel eccentrically braced frames: Effects of lateral support and initial imperfections

Hasim Cayir*[1,2], Cuneyt Vatansever[1]

[1] *Istanbul Technical University, Department of Civil Engineering, 34469 Istanbul, Türkiye*
[2] *Fatih Sultan Mehmet Vakif University, Department of Civil Engineering, 34015 Istanbul, Türkiye*

Abstract. Multi-tiered steel eccentrically braced frames (MT-EBFs) can be utilized as lateral load-resisting systems in tall single-story and multi-story buildings due to their high ductility, energy dissipation capacity, and architectural flexibility. However, the stability of link beams and the influence of initial imperfections on the overall performance of MT-EBFs remain critical design considerations. This study evaluates the effects of lateral support on the lateral-torsional buckling behavior of link beams and examines the impact of initial geometric imperfections on the load-carrying capacity of MT-EBFs. The link beams in MT-EBFs are selected to dissipate seismic-input energy through shear yielding. Nonlinear pushover analyses were conducted using SAP2000 and ABAQUS software to evaluate the lateral performance of MT-EBFs under seismic loading. Additionally, the sensitivity of the capacity of the frame to initial imperfections, such as out-of-straightness and residual stresses, is analyzed. The results reveal that adequate lateral support significantly enhances the stability of intermediate beams, reducing the likelihood of lateral-torsional buckling and increasing load capacity. Furthermore, initial imperfections are shown to reduce the load-carrying capacity of the frame by up to 7%, emphasizing the importance of their consideration in design. A comparative evaluation of the results from SAP2000 and ABAQUS highlights the complementary strengths of different modeling approaches for predicting the behavior of MT-EBFs. This study provides valuable insights into the seismic performance of MT-EBFs and offers recommendations for improving their design to ensure enhanced stability under seismic loading.

Keywords: Multi-tiered eccentrically braced frames; Lateral-torsional buckling; Initial imperfections; Nonlinear pushover analysis; ABAQUS

1. Introduction

Steel structures are fundamental components of modern infrastructure, particularly in regions prone to seismic activity. Designing these structures to withstand earthquake-induced forces requires systems that possess not only adequate strength and stiffness but also significant ductility and energy dissipation capacity. Among various lateral load-resisting systems, Eccentrically Braced Frames (EBFs) have gained prominence due to their ability to combine the stiffness characteristics of concentrically braced frames with the ductility and energy dissipation potential of moment-resisting frames (Popov & Engelhardt, 1988). This is achieved by intentionally designing specific segments, known as links, to yield and absorb seismic energy, thereby protecting other frame members like columns and braces from significant damage.

In applications involving tall single-story buildings (such as convention centers, sports facilities, warehouses, or industrial structures) or certain multi-story configurations, the height necessitates dividing the bracing system into multiple panels along the vertical axis. This leads to the concept of Multi-Tiered Braced Frames (MT-BFs) (Fig. 1). Using a single, long bracing panel in such structures is often impractical and uneconomical due to the required size and slenderness of the bracing members. Multi-tiered configurations allow for shorter, more efficient braces and provide intermediate lateral support points for the columns within the plane of the frame, reducing their effective buckling length (Ashrafi & Imanpour, 2021). While multi-tiered concentrically braced frames (MT-CBFs) have been more commonly studied and implemented, Multi-Tiered Eccentrically Braced Frames (MT-EBFs) offer a potentially advantageous alternative, leveraging the high ductility and stable energy dissipation characteristics inherent in EBF link mechanisms. MT-EBFs consist of multiple braced panels with intermediate links stacked along the frame height, providing architectural versatility alongside their seismic performance benefits.

*Corresponding author, E-mail: hcayir@fsm.edu.tr

https://doi.org/10.31462/icearc2025_ce_eqe_612

Despite these potential advantages, the seismic behavior of MT-EBFs presents unique challenges that are not fully addressed by design provisions developed for conventional, single-story EBFs. The interaction between multiple tiers, the stability of intermediate links located at strut levels between tiers, and the flexural demands placed on the continuous columns are critical aspects requiring specific investigation. The nonlinear behavior and ultimate capacity of MT-EBFs are significantly influenced by factors such as the provision of lateral support to the intermediate links and the presence of initial geometric imperfections in the frame members.

The primary energy dissipation mechanism in EBFs, including MT-EBFs, relies on the inelastic action of the links, typically designed for shear yielding, flexural yielding, or a combination thereof. However, the performance of the entire system depends critically on the stability of these links and the surrounding members. Research, particularly on MT-CBFs, has shown that uneven yielding or buckling of braces across different tiers can lead to a concentration of inelastic deformation in one tier (the "critical tier"), imposing large in-plane bending moments on the columns (Imanpour et al., 2016). This phenomenon raises concerns about potential column instability due to combined axial load and bending. Similar issues are anticipated in MT-EBFs, where sequential or uneven yielding of links across tiers can induce significant in-plane moments in the columns.

A pivotal study by Ashrafi and Imanpour (2021) specifically investigated the seismic response of a two-tiered EBF using nonlinear static analysis with the OpenSees framework. This research underscored that the stability of MT-EBFs is heavily dependent on adequate lateral bracing for intermediate links and that conventional EBF design provisions might be insufficient, potentially leading to premature failure modes. They concluded that the potential for link and column instability necessitates revisiting design standards for MT-EBFs, which were (and often still are) restricted in major design codes due to lack of supporting research data.

The instability observed by Ashrafi and Imanpour (2021) involved out-of-plane buckling. However, link beams, particularly those subjected to high shear and bending moments during seismic events, are also susceptible to Lateral-Torsional Buckling (LTB). LTB is a complex failure mode involving simultaneous out-of-plane bending and twisting, which can significantly degrade the link's capacity and ductility if not properly restrained. The effectiveness of lateral support in preventing LTB is therefore a crucial design consideration. Furthermore, the detailing of connections between braces and beams can influence the rotational restraint provided to the link ends, potentially affecting LTB behavior. For instance, Rezaee and Asghari (2024) noted that different connection configurations (e.g., gusset plates vs. direct welding) can offer varying levels of stiffness against LTB in intermediate beams. Ensuring sufficient lateral and torsional restraint is paramount for achieving the desired stable, ductile shear-yielding mechanism in MT-EBF links.

Beyond the provision of lateral support, the structural response of steel frames is invariably affected by initial imperfections. These imperfections, stemming from manufacturing tolerances, fabrication processes, and erection procedures, include deviations such as member out-of-straightness, column out-of-plumbness, and residual stresses locked in during rolling or welding. While design codes provide tolerance limits, even imperfections within these limits can significantly influence the nonlinear behavior and ultimate capacity of steel structures. Ma and Xu (2020) emphasized that initial imperfections increase deflections and decrease the load-carrying capacity of steel frames, potentially leading to instability. Jin et al. (2014) found that while the ultimate deformation of steel braced frames is proportional to the size of imperfections, even frames with small imperfections behave differently from theoretically perfect frames.

Fig. 1. Multi-tiered eccentrically braced frame (Dusicka et al., 2006)

The presence of imperfection can reduce the lateral stiffness of frames, making them more prone to instability, a factor particularly noted in studies on partially braced frames (Hou & Li, 2008). Accurately capturing the influence of imperfections often requires advanced analysis techniques. Geometrically and materially nonlinear analyses incorporating imperfections, frequently represented as scaled eigenmodes derived from elastic buckling analysis, are increasingly used (Slack et al., 2024), (Shayan et al., 2014). The selection of appropriate buckling modes and scaling factors is critical for reliable predictions (Jindra et al., 2024). While the specific direction of imperfections might have a limited effect on the ultimate load, considering combinations of buckling modes is often necessary to capture the most critical scenarios (Arrayago & Rasmussen, 2022). Furthermore, imperfections can exacerbate the structural response under other demanding conditions, such as sudden column removal scenarios, by increasing demands on remaining members and reducing overall ductility (Mageirou & Lemonis, 2021). Therefore, understanding the sensitivity of MT-EBFs to these inherent imperfections is crucial for robust seismic design.

While the study by Ashrafi and Imanpour (2019) provided valuable insights into the necessity of lateral support and the potential failure modes in MT-EBFs, and various researchers have investigated the general effects of imperfections on steel frames, a focused investigation into the interplay between lateral support effectiveness (specifically concerning LTB prevention in links) and the sensitivity of the overall MT-EBF response to initial geometric imperfections remains warranted. Furthermore, the choice of analytical software can influence the predicted behavior, particularly when complex phenomena like LTB and post-buckling response are involved. Design engineers commonly use structural softwaresi such as SAP2000, while more detailed finite element analyses are often performed using ABAQUS , which allows for sophisticated modeling of shell elements, material nonlinearity, geometric imperfections, and contact interactions. A comparative assessment of these tools for MT-EBF analysis is lacking.

This study aims to address these challenges by comprehensively evaluating the nonlinear behavior of multi-tiered steel eccentrically braced frames, with a specific focus on the effects of lateral support conditions on the lateral-torsional buckling behavior of intermediate link beams and the impact of initial geometric imperfections on the overall frame capacity and stability. Utilizing nonlinear pushover analyses conducted with both SAP2000 and ABAQUS software, this research will:

1. Investigate the effectiveness of lateral support configurations in enhancing the stability of intermediate link beams against lateral-torsional buckling.
2. Analyze the sensitivity of the load-carrying capacity and deformation behavior of MT-EBFs to initial geometric imperfections, including member out-of-straightness.
3. Compare the predictive capabilities and results obtained from SAP2000 and ABAQUS for modeling the complex nonlinear response of MT-EBFs, including link yielding and buckling phenomena.

By examining these aspects, this study seeks to provide valuable insights into the seismic performance of MT-EBFs, contributing to a better understanding of their failure mechanisms and offering recommendations for improved design practices that explicitly account for lateral support requirements and the unavoidable presence of initial imperfections, ultimately ensuring enhanced stability and reliability under seismic loading.

2. Seismic design of multi-tier eccentrically braced frame based on TSCB 2018

The seismic design of the two-tiered eccentrically braced frame was carried out in compliance with the Turkish Seismic Code for Buildings (TSCB) 2018, whose seismic provisions for structural steel buildings are substantially consistent with those of AISC 341-16, as well as with the Turkish Code for Design and Construction of Steel Structures (TCDCSS) 2016, which closely parallels the requirements of AISC 360-16. The design process follows capacity design principles which have been developed for building-type structures with diaphragms, ensuring that the structural system effectively dissipates seismic energy through controlled plastic deformations in designated elements while maintaining the stability of other structural components.

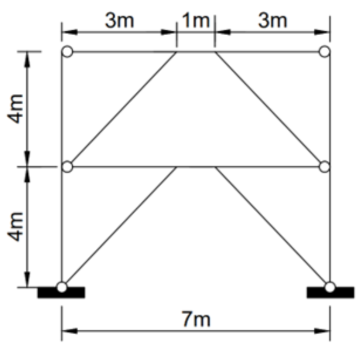

Fig. 2. Geometry of the selected two-tiered EBF

Table 1. Characteristics of steel material

Modulus of elasticity, E [GPa]	200
Poisson's ratio, ν	0.3
Density, ρ [kg/m^3]	7850
Yield strength, F_y [MPa]	275
Ultimate strength, F_u [MPa]	430

Table 2. Cross-section of members

Column	HE220B
Link Beam	HE200B
Beam Outside Link	HE200B
Brace	HE200B

The geometry of the frame, shown in Fig. 2, is a two-tiered eccentrically braced frame with a floor height of 4m each (total height of 8m) and a total span of 7m. The bracing system adopts a multi-tiered eccentrically braced configuration, with a 1-meter-long link beam at each tier. This configuration was selected to optimize the distribution of seismic forces and enhance the overall stability of the frame. The steel grade of S275 was used as the material of the two-tiered eccentrically braced frame. The basic mechanical properties of the steel material were shown in Table 1, while the cross-sectional properties of the structural members were detailed in Table 2.

The design process began with the link beams, which are the primary energy-dissipating elements in the MT-EBF. The link beams were proportioned to yield in shear, ensuring that seismic energy is dissipated through stable plastic deformations. To achieve this, the link length e was selected such that it does not exceed $1.6M_p/V_p$, where M_p and V_p are the nominal plastic moment and plastic shear strength of the link beam, respectively. This ensures that the yielding mechanism is dominated by shear behavior. Additionally, the link deformations were limited to the values specified by the limits provided in TSCB 2018. The selected I-shaped link section satisfies the seismic compactness requirements, ensuring that the width-to-thickness ratios for both the flange and web comply with the highly ductile member criteria specified by TSCB 2018. Once the link beams were sized, the adjacent members, including the outer beam segments, braces, and columns, were designed to remain elastic under the capacity-induced forces from the link beams. All structural members other than the link beam also meet the high ductility limit values specified in TSCB 2018, ensuring compliance with local buckling prevention criteria.

The axial load on each column was assumed to be 20% of its axial yield strength, reflecting realistic loading conditions. Columns were modeled to be pinned at the base, though torsional restraint was provided. The beams were connected to the columns with pinned connections, while the braces were pinned at the beam-column connections and rigidly connected at the link beam ends. This connection configuration ensures proper force transfer and stability while maintaining the intended energy dissipation mechanism in the link beams.

The potential for lateral-torsional buckling (LTB) in the link beams was a critical consideration in the design. The stability of the link beams against LTB was investigated in this study, focusing on the effects of lateral and torsional restraints on their behavior and energy dissipation capacity. The braces, which are rigidly connected to the link beams, act as lateral restraints, reducing the risk of LTB. However, the absence of lateral bracing at intermediate tiers introduces a potential vulnerability that will be analyzed in detail.

By adhering to these design principles and code provisions, the two-tiered MT-EBF was designed to provide a robust and ductile seismic response. The link beams serve as the primary energy-dissipating elements, while the other members remain elastic under the maximum expected seismic loads. This approach ensures the safety and reliability of the structure during seismic events.

3. Finite element (FE) model

The nonlinear behavior of the MT-EBF has been investigated by conducting the nonlinear pushover analyses of finite element models developed by using ABAQUS/Explicit software and SAP2000. The two-tiered steel frame was modeled in three dimensions using ABAQUS software to investigate the effect of lateral bracing on the behavior of the intermediate link beam in multi-tier eccentrically braced frames. The primary objective of this analysis was to evaluate the influence of lateral-torsional buckling (LTB) on the seismic performance of the frame and to determine the effectiveness of lateral bracing in mitigating instability in the link beam.

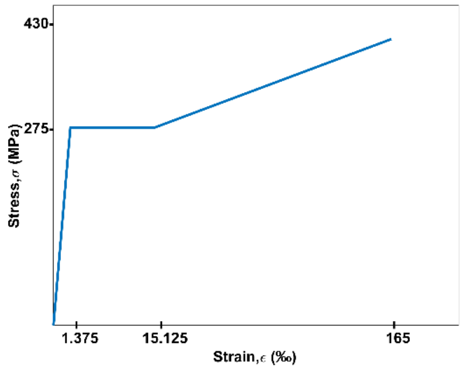

Fig. 3. Stress–strain curve for the steel material of the two-tiered EBF

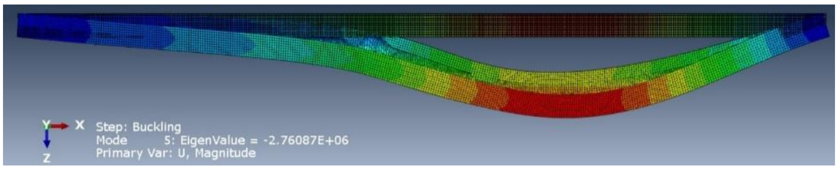

a) Fifth mode shape

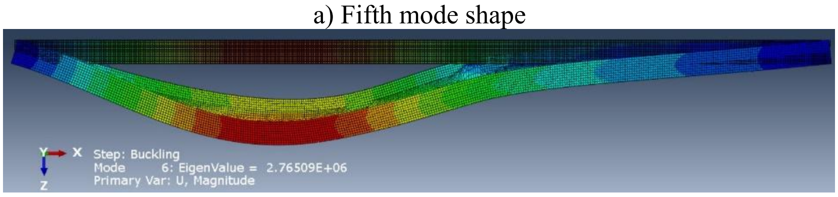

b) Sixth mode shape

Fig. 4. Mode shapes causing lateral-torsional buckling in the lower-story link beam

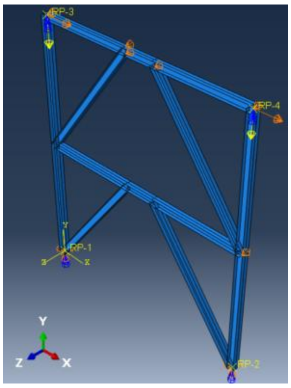

a) Unbraced model

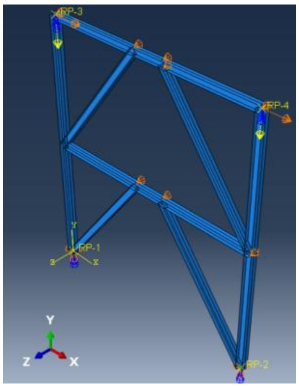

b) Braced model

Fig. 5. Finite Element (FE) models of the two-tiered EBF

The material model proposed by Baei et al. (2012) was adopted to accurately represent the nonlinear behavior of the steel material Strain-hardening behaviour was incorporated into the finite element model, as illustrated in Fig. 3. The strain corresponding to the onset of strain-hardening was defined as $\varepsilon_s = 11\varepsilon_y$, while the ultimate strain was taken as $\varepsilon_u = 120\varepsilon_y$. An isotropic hardening model was employed in the numerical analysis to effectively capture the expansion of the yield surface under multi-dimensional stress conditions.

Initial geometric imperfection and residual stress were incorporated into the model by scaling the lateral-torsional buckling mode shapes to 1/750 times the element length (L/750), as illustrated in Fig. 4. This approach, commonly used in advanced finite element analysis, ensures that the model captured realistic structural behavior under seismic loading, including second-order effect and imperfection. The magnitude of L/750 was selected to represent typical fabrication and erection tolerances found in steel construction practice.

To simulate realistic loading conditions, concentrated vertical loads of 500.5 kN, corresponding to 20% of the column's axial yield strength, were applied to the top ends of the upper-story columns. These loads were intended to replicate the compressive forces typically experienced by columns in multi-tier frames under seismic and gravity loads. The structural members were modeled using four-node "S4R" shell elements, which are well-suited for capturing the nonlinear behavior of thin or thick shell structures. All elements in the frame were merged into a single part, ensuring continuity and eliminating the need for explicit modeling of welds. This approach also simplified the analysis by treating the frame as a single, unified structure (Vatansever & Cayir, 2024).

Analysis was conducted using two distinct models to evaluate the effect of lateral bracing on the link beam. In the first model (Fig. 5a), the out-of-plane displacement of the lower-story link beam was left unrestrained (Unbraced Model), allowing for potential lateral-torsional buckling under seismic loading. In the second model (Fig. 5b), lateral bracing was introduced to restrain the out-of-plane displacement of the link beam (Braced Model). This comparison enables a direct assessment of the impact of lateral bracing on the stability and overall seismic performance of the MT-EBF.

4. Validation of finite element model

The experimental study conducted by Berman and Bruneau (2007) on eccentrically braced steel frame systems was used as the basis for the finite element model validation. While this experiment did not specifically examine MT-EBFs, it provides valuable data on the behavior of link beams in EBFs, which is directly applicable to the current study. The member sizes used in the experiment are shown in Fig. 6. The three-dimensional finite element model was created to replicate the experimental setup and specimen. The cross-sectional components of the elements, including flanges and webs, were modeled using the "S4R" shell element available in the ABAQUS library. All elements in the frame were defined using shell elements aligned along their centerlines, as shown in Fig. 7.

To simplify the model, welds at the connections were excluded, as no plastic deformation was expected in these regions. Instead, all elements were merged in the model, creating a single continuous part. Rigid body constraints were applied to the rigid plates located at the top and bottom ends of the columns. Reference points were defined at the center of gravity of these plates, and the plates were rigidly connected to these points. This setup allowed boundary conditions and loading to be applied directly to the reference points. Additionally, reaction forces and displacements at these points were used in the analysis results.

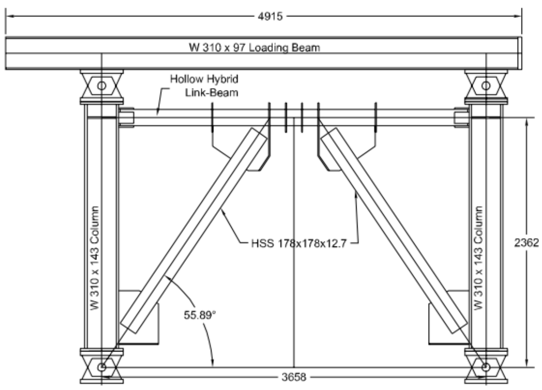

Fig. 6. Test specimen dimensions and member sizes

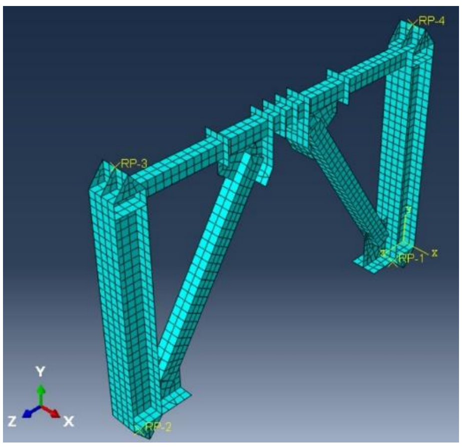

Fig. 7. FE model of the test specimen

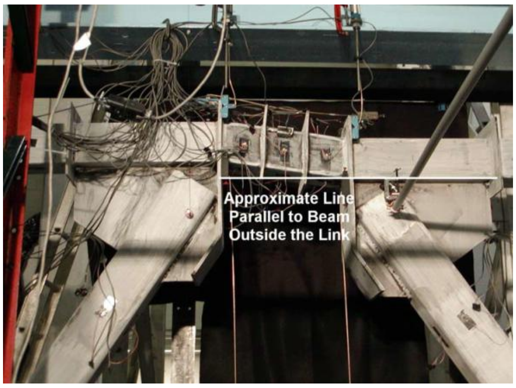

a) result of experiment

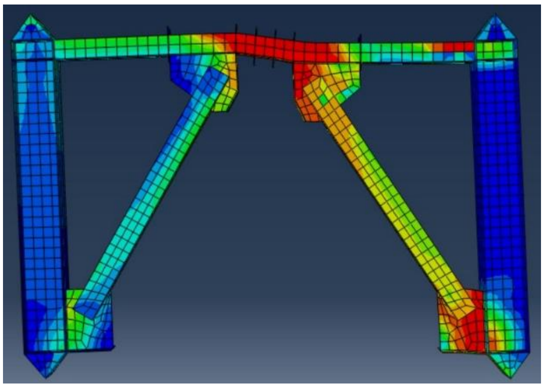
b) result of finite-element model analysis

Fig. 8. Comparison of link deformations

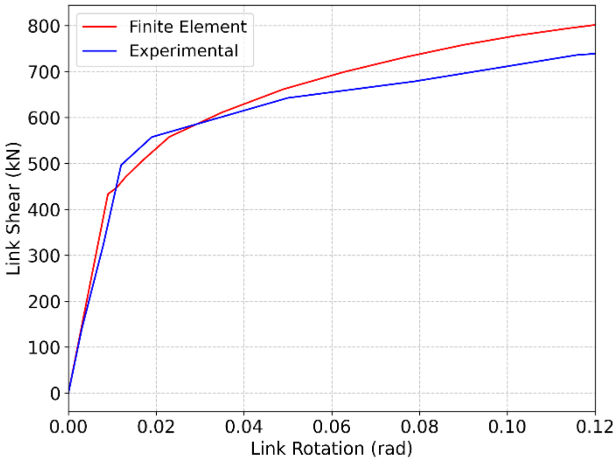

Fig. 9. Comparison of analytical and experimental link shear-rotation curves

To account for second-order effects due to geometric nonlinearity, the "nlgeom" option in ABAQUS was activated. The frame was analyzed using a nonlinear static pushover method. The deformed shape obtained from the analysis was compared with the experimentally observed deformed shape, as shown in Fig. 8. The comparison of the deformed shape of the link beam from the experiment and the finite element analysis (FEA) revealed similar yielding patterns, particularly in the plastic hinge regions. Furthermore, the shear force-rotation curve of the link beam obtained from the experiment was compared with the results from the finite element analysis, as shown in Fig. 9.

The results demonstrated a strong agreement between the experimental and numerical data, with the FEA model accurately capturing both the initial stiffness and post-yield behavior of the link beam. The maximum shear force values from both the experiment and FEA were within 5% of each other, and the rotation capacities showed similar trends. This consistency indicates that the numerical model adequately represents the experimental behavior of the eccentrically braced steel frame system and provides confidence in applying the same modeling approach to the MT-EBF configuration studied in this research.

5. Finite element analysis results

Nonlinear static pushover analyses were performed for both the unbraced and braced models, and the deformed shapes of the frame corresponding to 5% drift ratio were obtained. The deformed shapes for both conditions are shown in Fig. 10. The results revealed that nonlinear deformations in the frame first occurred in the link beam, as expected, confirming the effectiveness of the capacity design approach in concentrating inelastic behavior in the designated energy-dissipating elements.

5.1. Effect of lateral bracing on link beam stability

In the unbraced model, significant out-of-plane deformations were observed in the lower-story link beam due to lateral-torsional buckling. These deformations, shown in Fig. 11a, indicate that the absence of lateral bracing allowed the link beam to become unstable, leading to a reduction in the overall load-carrying capacity of the frame.

The deformation pattern visible in Fig. 11a shows a pronounced twisting of the link beam, with significant out-of-plane displacement. This lateral-torsional buckling mode is particularly concerning as it occurs after the link has already undergone substantial shear yielding, thus compromising the frame's ability to maintain its energy dissipation capacity during continued seismic loading. The buckling pattern indicates that the open-section link beam (I-shaped in this study) does not offer adequate lateral-torsional restraint when the link is subjected to high shear forces.

In contrast, in the braced model (Fig. 11b), the out-of-plane movement of the link beam was effectively restrained, preventing lateral-torsional buckling and maintaining the stability of the frame. The braced model exhibited stable behavior throughout the analysis, with no out-of-plane deformations observed in the link beam even at story drift ratio exceeding 5%. The deformation pattern in this case shows pure in-plane deformation, allowing the link to develop its full shear yielding capacity without premature instability. This highlights the critical role of lateral bracing in enhancing the seismic performance of MT-EBFs.

The capacity curves obtained from the finite element analysis further highlight the critical role of lateral bracing in enhancing the seismic performance of the frame. As shown in Fig. 12, the unbraced model exhibited a significant reduction in lateral load-carrying capacity compared to the braced model. The braced model demonstrated substantially higher capacity that continued to increase throughout the analysis, demonstrating the significant enhancement in structural performance achieved through the provision of lateral bracing.

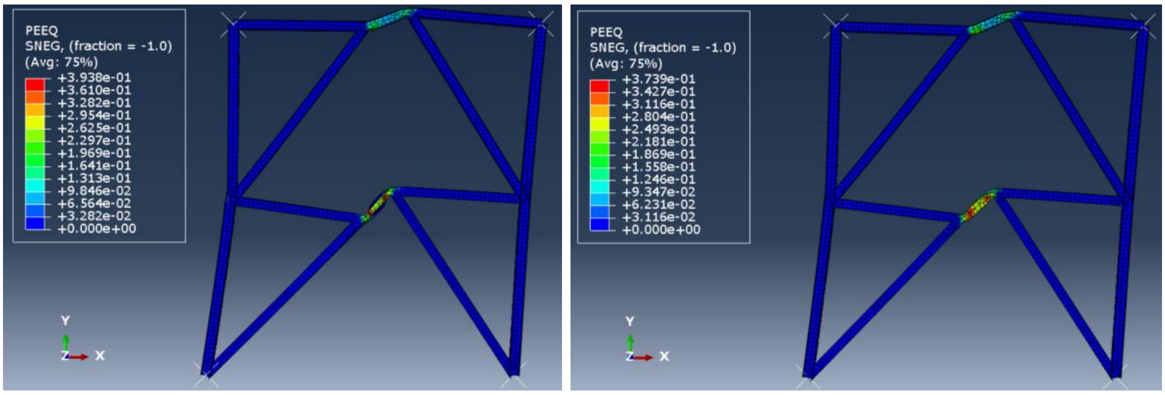

a) Unbraced model

b) Braced model

Fig. 10. Deformed shape corresponding to 5% storey drift

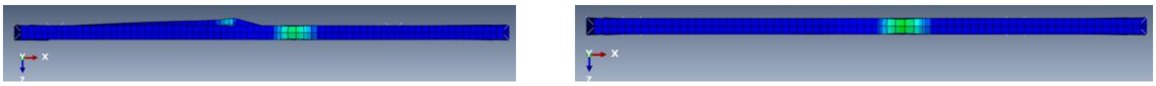

a) Unbraced model

b) Braced model

Fig. 11. Out-of-plane deformation of the lower-story link beam

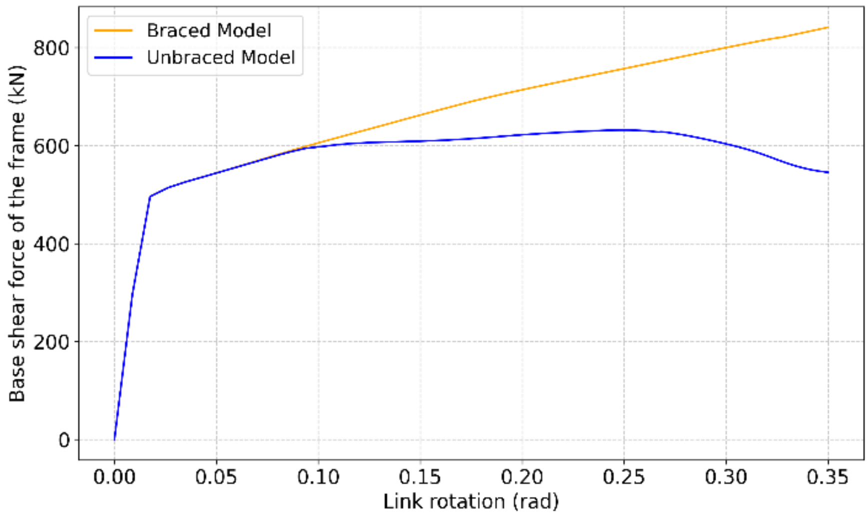

Fig. 12. Pushover curves of the frame to show the lateral bracing

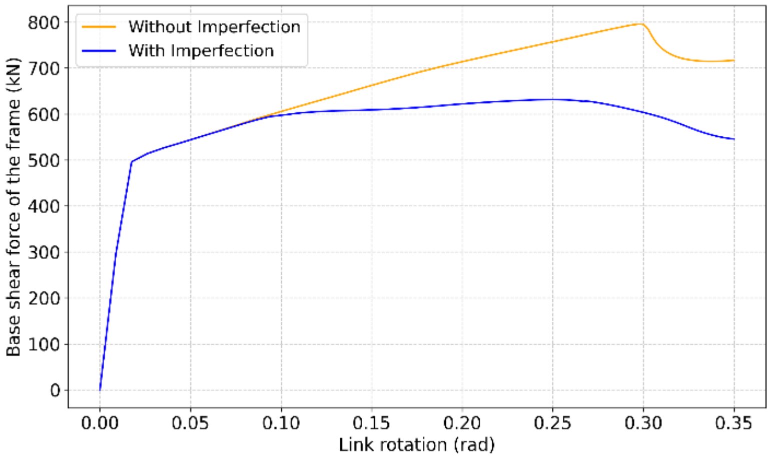

Fig. 13. Pushover curves of the frame to show the effect of the imperfection

The pushover curve in Fig. 12 reveals several important characteristics of the structural behavior. The initial elastic stiffness of both models is identical, as expected, since the lateral bracing does not affect the in-plane stiffness of the frame. The lateral deformations of the frame increase linearly up to 0.25% story drift. At this level, shear yielding of the link beams occurs and nonlinear behavior begins, causing the response curves to diverge. The unbraced model shows limited capacity development and reaches a plateau at higher drift ratios, while the braced model continues to develop increasing resistance. This difference in behavior corresponds with the onset of lateral-torsional buckling observed in the link beam of the unbraced model.

The link rotation measurements indicate that the unbraced model experiences instability at significantly lower rotation demands compared to the braced model. This premature instability in the unbraced model prevents the full development of the link's shear capacity, resulting in reduced overall frame strength and ductility. In contrast, the braced model allows the links to develop their full rotation capacity without instability, leading to superior seismic performance.

5.2. Effect of initial imperfection on link beam stability

The effect of initial imperfection on the behavior of the unbraced model is illustrated in Fig. 13. The pushover curves clearly demonstrate how initial geometric imperfections influence the frame's performance. The model without initial imperfection exhibited a lateral load-carrying capacity approximately 26% higher than the model with initial imperfection. This difference highlights the significant impact of initial imperfection on the overall stability of the frame.

Fig. 13 reveals that both models (with and without imperfections) exhibit identical behavior in the elastic range, with the curves perfectly overlapping until approximately 0.08 radians of link beam rotation. After this point, the curves begin to diverge, indicating that the influence of initial imperfections becomes significant only in the post-yield range. Both models maintain the same stiffness throughout the elastic loading phase, but the model without initial imperfection continues to develop higher capacity in the inelastic range and reaches its peak capacity at a slightly higher story drift ratio. This suggests that initial imperfection primarily affects the post-yield behavior and ultimate capacity rather than the initial elastic response of the frame.

The most significant difference is observed in the post-peak behavior. The model with initial imperfection experiences lateral-torsional buckling at a lower story drift ratio compared to the model without initial imperfection, and the subsequent capacity degradation follows a different pattern. This indicates that initial imperfection serves as triggers for instability, effectively lowering the critical buckling load of the link beam.

The initial imperfection ratio of L/750 used in this study is within typical tolerance limits observed in real structures. Therefore, considering initial imperfection in the design of MT-EBFs is critical for accurately predicting the actual behavior of the frame under seismic loading. The 26% reduction in capacity due to initial imperfections is particularly significant in seismic design, where capacity design principles rely on accurate predictions of member strengths.

5.3. Comparison of SAP2000 and ABAQUS results

The two-tiered eccentrically braced frame was also modeled using SAP2000 software. In this two-dimensional model, a lumped plasticity behavior model was employed for the elements of frame. Plastic hinges were assigned to the midpoints of the link beams and braces, while for the columns and beam outside the link sections, plastic hinges were defined at the ends of the respective members. Since the link beams were designed to yield under shear forces, the plastic hinges in the link beams were modeled as shear hinges. For beam outside the link sections, M3 moment hinges were defined, while for the braces, P axial force hinges were used. In the columns, P-M3 hinges were assigned to account for the combined effects of axial load and strong-axis bending. All plastic hinge properties followed in ASCE 41-13 guidelines.

In the two-dimensional model, the out-of-plane displacements of the link beams were restrained, and a nonlinear static pushover analysis was performed. The deformed shape of the frame at the point of collapse is shown in Fig. 14a. The plastic hinge model used in the analysis is also illustrated in the Fig. 14a, with a strain hardening coefficient of 1.35 taken into account. As the applied lateral load increased, nonlinear deformations were observed primarily in the link beams. Since the shear hinges in the link beams were defined according to ASCE 41-13, collapse occurred when the rotation limit of the link beam was exceeded.

A comparison of the deformed shapes from SAP2000 (Fig. 14a) and ABAQUS (Fig. 14b) reveals interesting differences in how the two software packages represent the collapse mechanism. The SAP2000 model shows concentrated deformations at the predefined hinge locations, with the link beams exhibiting the most significant rotations. The ABAQUS model, on the other hand, shows a more distributed pattern of deformation, with yielding spreading throughout the link beam web and flanges. This difference reflects the fundamental distinction between the lumped plasticity approach in SAP2000 and the distributed plasticity approach in ABAQUS.

Modeling initial geometric imperfection and residual stress in SAP2000 is inherently more challenging compared to ABAQUS. Zhao and Astaneh-Asl (2007) suggested that reducing the elastic modulus can be an effective approach to approximate the effects of initial geometric imperfection and residual stress. In this study, instead of directly modeling these effects in SAP2000, a 5% reduction in the expected yield strength was applied as a calibration method to align the SAP2000 results with those obtained from ABAQUS. This calibration ensured that the SAP2000 pushover curve closely matched the ABAQUS results, effectively accounting for the effects of initial warping, geometric imperfection, and residual stress.

The comparison of base shear versus story drift ratio curves in Fig. 15 shows excellent correlation in the elastic range and good agreement in the post-yield range. Both models predict similar initial stiffness, yield points, and post-yield behavior. The primary difference appears in the ultimate drift capacity, with the SAP2000 model predicting slightly earlier collapse than the ABAQUS model. This difference can be attributed to the distinct methodologies employed in modeling material nonlinearity and failure criteria.

Despite their methodological differences, the close agreement between results validates both approaches for modeling MT-EBF behavior. The ABAQUS model offers more comprehensive capabilities for complex phenomena, such as lateral-torsional buckling and initial imperfections, while the SAP2000 model provides a more accessible approach for routine design work. This comparison suggests that practicing engineers can confidently use either software for MT-EBF analysis with appropriate calibration, selecting based on the specific requirements of their project: SAP2000 for standard design applications and ABAQUS for more detailed investigations of complex instability modes.

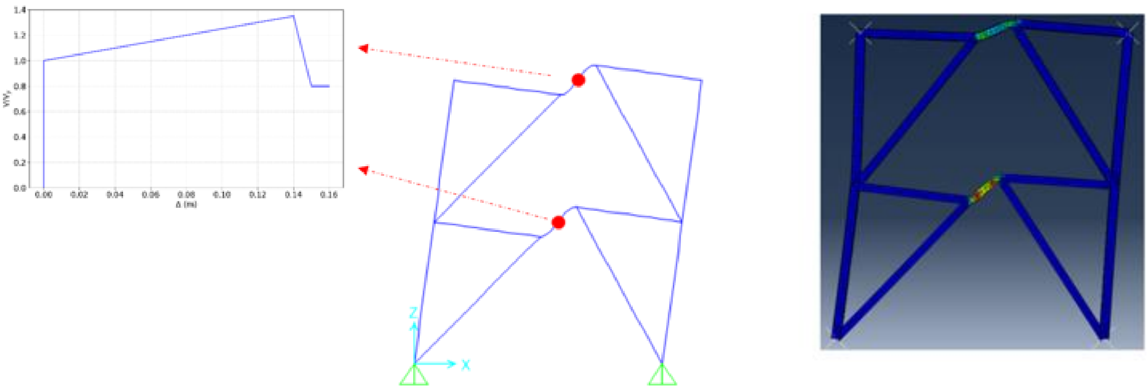

a) SAP2000 Model b) ABAQUS Model

Fig. 14. The deformed shape of the frames at the point of collapse

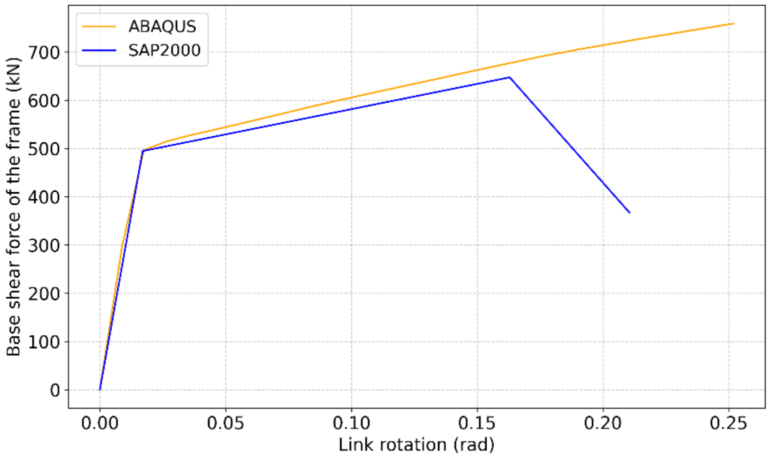

Fig. 15. Pushover curves of the frame to compare two different structural software

6. Conclusions

This study provides valuable insights into the nonlinear behavior of multi-tiered steel eccentrically braced frames (MT-EBFs) under seismic loading. The following conclusions can be drawn from the analysis:

- Lateral bracing significantly enhances the stability of link beams by preventing lateral-torsional buckling. The braced model demonstrated a significant increase in lateral load-carrying capacity compared to the unbraced model, highlighting the critical role of lateral bracing in ensuring the seismic performance of MT-EBFs.
- Initial geometric imperfections, such as member out-of-straightness, reduce the load-carrying capacity of the frame by up to 26%. This emphasizes the importance of considering imperfections in the design process to ensure the reliability of MT-EBFs under seismic loading. The presence of initial imperfections not only reduces the maximum capacity but also affects the post-yield behavior of the frame, leading to earlier onset of lateral-torsional buckling.
- The provision of lateral bracing not only prevents lateral-torsional buckling but also enhances the energy dissipation capacity of the frame, contributing to its overall seismic resilience. By maintaining the stability of the link beams, lateral bracing ensures that they can effectively dissipate seismic energy through the intended shear yielding mechanism. This is particularly important for MT-EBFs, where the link beams are the primary energy-dissipating elements.
- Both SAP2000 and ABAQUS can effectively model the nonlinear behavior of MT-EBFs, with results showing strong agreement despite different modeling approaches. The pushover curves from both software packages show excellent agreement in the elastic range and good agreement in the post-yield range, with the primary difference appearing in the ultimate story drift capacity. This provides confidence in the results and suggests that practicing engineers can use either structural software for the analysis of MT-EBFs, with appropriate calibration.
- For two-tiered eccentrically braced frames, initial geometric imperfection and residual stress can be approximated in SAP2000 by reducing the expected yield strength by 5%. This method, calibrated using ABAQUS results, provides a practical and efficient approach for engineers to account for these effects in their designs.

These findings have important implications for the design and analysis of MT-EBFs in seismic regions. The results emphasize the need for adequate lateral bracing of link beams, particularly at intermediate tiers, to prevent lateral-torsional buckling and ensure stable energy dissipation. Additionally, the consideration of initial imperfections is crucial for accurately predicting the capacity and behavior of MT-EBFs under seismic loading. The comparative analysis of SAP2000 and ABAQUS results provides valuable guidance for practicing engineers on the selection and calibration of analysis tools for MT-EBF design.

References

ABAQUS. 2017. "Getting Started with ABAQUS: Interactive Edition. Hibbit, Karlsson, and Sorenson, Inc, RI, USA."

AISC 360-16. 2016. *Specification for Structural Steel Buildings. American Institute of Steel Construction, Chicago, Illinois, USA.* Chicago, Illinois, USA.

Arrayago, Itsaso, and Kim J.R. Rasmussen. 2022. "Influence of the Imperfection Direction on the Ultimate Response of Steel Frames in Advanced Analysis." *Journal of Constructional Steel Research* 190: 107137. doi:10.1016/j.jcsr.2022.107137.

ASCE 7-22. 2022. *Minimum Design Loads for Buildings and Other Structures. American Society of Civil Engineers, Reston, Virginia, USA.*

ASCE 41-13. 2014. *Seismic Evaluation and Retrofit of Existing Buildings, American Society of Civil Engineers, Reston, Virginia, USA.*

Ashrafi, Abolfazl, and Ali Imanpour. 2021. "Seismic Response of Steel Multi-Tiered Eccentrically Braced Frames." *Journal of Constructional Steel Research 181*: 106600. doi:10.1016/j.jcsr.2021.106600.

Baei, Mahmoud, Mehdi Ghassemieh, and Alireza Goudarzi. 2012. "Numerical Modelling Of End-Plate Moment Connection Subjected To Bending And Axial Forces." *Journal of Mathematics and Computer Science* 04(03): 463–72. doi:10.22436/jmcs.04.03.21.

Berman, Jeffrey W., and Michel Bruneau. 2007. "Experimental and Analytical Investigation of Tubular Links for Eccentrically Braced Frames." *Engineering Structures 29*(8): 1929–38. doi:10.1016/j.engstruct.2006.10.012.

Dusicka, Peter, Ahmad M. Itani, and Ian G. Buckle. 2006. *Built-up Shear Links as Energy Dissipators for Seismic Protection of Bridges*. Reno, Nevada, USA.

Hou, He-tao, and Guo-qiang Li. 2008. "Influence of Initial Geometric Imperfections on Behavior of Partially-Braced Steel Frame Columns." *Engineering Mechanics 25*(3): 85–90.

Imanpour, Ali, Robert Tremblay, Ali Davaran, Christopher Stoakes, and Larry A. Fahnestock. 2016. "Seismic Performance Assessment of Multitiered Steel Concentrically Braced Frames Designed in Accordance with the 2010 AISC Seismic Provisions." *Journal of Structural Engineering 142*(12). doi:10.1061/(ASCE)ST.1943-541X.0001561.

Jin, Lu, Han Si, and Lian Guang Jia. 2014. "Study on Deformation Performances of Steel Braced Frame Structures with Random Imperfections." *Applied Mechanics and Materials* 644–650: 543–46. doi:10.4028/www.scientific.net/AMM.644-650.543.

Jindra, Daniel, Zdeněk Kala, and Jiří Kala. 2024. "Probabilistically Modelled Geometrical Imperfections for Reliability Analysis of Vertically Loaded Steel Frames." *Journal of Constructional Steel Research 217*: 108627. doi:10.1016/j.jcsr.2024.108627.

Ma, Terence, and Lei Xu. 2020. "Effects of Column Imperfections on Capacity of Steel Frames in Variable Loading." *Journal of Constructional Steel Research* 165: 105819. doi:10.1016/j.jcsr.2019.105819.

Mageirou, G.E., and M.E. Lemonis. 2021. "Influence of Imperfections on the Progressive Collapse of Steel Moment Resisting Frames." *Journal of Constructional Steel Research 183*: 106744. doi:10.1016/j.jcsr.2021.106744.

Popov, Egor P., and Michael D. Engelhardt. 1988. "Seismic Eccentrically Braced Frames." *Journal of Constructional Steel Research 10*: 321–54. doi:10.1016/0143-974X(88)90034-X.

Rezaee, Mohammad, and Abazar Asghari. 2024. "Lateral-Torsional Buckling Investigation of Multi-Tiers Eccentrically Braced Frames with Shear Link Beam." *Structures 68*: 107063. doi:10.1016/j.istruc.2024.107063.

SAP2000. 2020. "Integrated Software for Structural Analysis and Design V20.2. Computers and Structures Inc., Berkeley, California, USA."

Shayan, Shabnam, Kim J.R. Rasmussen, and Hao Zhang. 2014. "On the Modelling of Initial Geometric Imperfections of Steel Frames in Advanced Analysis." *Journal of Constructional Steel Research 98*: 167–77. doi:10.1016/j.jcsr.2014.02.016.

Slack, Harry, Fiona Walport, Hou Un Chan, M. Ahmer Wadee, and Leroy Gardner. 2024. "A Consistent Approach to the Definition of Initial Geometric Imperfections for In-Plane Stability Design of Steel Moment Frames." *Structures 65*: 106596. doi:10.1016/j.istruc.2024.106596.

TCDCSS. 2016. *Turkish Code for Design and Construction of Steel Structures 2016. Ministry of Environment and Urbanization, Ankara, Turkey.* Ankara, Turkey.

TSCB. 2018. *Turkish Seismic Code for Buildings. Disaster and Emergency Management Presidency, Ankara, Turkey.* Ankara, Turkey.

Vatansever, Cuneyt, and Hasim Cayir. 2024. "Design and Nonlinear Dynamic Response of a Steel Stack." *Arabian Journal for Science and Engineering*. doi:10.1007/s13369-024-09182-4.

Zhao, Qiuhong, and Abolhassan Astaneh-Asl. 2007. "Seismic Behavior of Composite Shear Wall Systems and Application of Smart Structures Technology." *Steel Structures 7*(1): 69–75.

Seismic design of high-rise building with differe structural configuration

Sule Yıldırım[1], Mehmet F. Yılmaz[*1]

[1] *Ondokuzmayis University, Engineering Faculty, Department of Civil Engineering, 55105, Samsun, Türkiye*

Abstract. The increasing population of humanity causes the need for all kinds of structures to increase, and the need for high-rise buildings to meet this need is also increasing at a parallel rate. Many studies and research are being carried out on various construction techniques for these high-rise buildings to be economical, sustainable, safe, and continue to be done every passing day. At this point, the diagrid construction technique attracts attention because it is theoretically considered more efficient than traditional construction methods. In addition, its aesthetic appearance attracts attention. However, since a significant part of the diagrid structures built are located in areas with relatively low seismicity, more research is needed to examine the behaviour of diagrid structures under earthquake effects. Within the scope of this research, to better understand the earthquake behaviour of diagrid structures, two different steel structures with traditional braces and diagrid braces will be compared under the effect of various ground motions, and a comparison will be made about the earthquake behaviour of diagrid structures.

Keywords: Steel building; High rise building; Diagrid structures; Concentrically braced system

1. Introduction

The demand for tall buildings is increasing day by day due to the growing population, evolving needs, and limited urban space. Building design and calculation methods have continuously developed from the past to the present, and engineering has started to produce innovative solutions to respond to increasingly complex structural needs. In addition to all these, high-rise buildings are designed to be higher than the previous one in order to respond to changing needs. With the increase in height, the solutions for the safe transportation of both horizontal and vertical loads have become more complex. Although central core or braced systems are generally preferred for tall buildings, diagrid systems, one of the innovative structural systems that have existed in the engineering literature for many years but have recently received renewed attention, offer significant advantages, especially in terms of aesthetics and structural efficiency. This study will focus on the earthquake performance of diagrid structures by comparing the behaviour of diagrid systems under earthquake effects with one of the traditional methods, braced systems.

Diagrid systems are a construction technique that can also be applied in building reinforcement, generally in high-rise buildings. Diagrid systems can be defined as systems consisting of a grid of triangles that encircle the exterior of the building along the structure and thus carry both horizontal loads and vertical loads. "It is a particular form of space truss mixed with tubular system, and the perimeter diagonal grids make the structure stable even without any vertical column in the perimeter of the building. Diagrid is suitable for constructing large buildings with both regular and irregular forms. Compared with conventional framed tubular structures without diagonals, diagrid structures are more effective in minimizing shear deformation because they carry shear by axial action of the diagonal members." (Kim & Lee, 2012a). In this construction technique, the diagrid elements on the exterior of the building significantly eliminate the vertical columns on the exterior face. Diagrid building systems generally consist of a main core, diagonal elements with varying angles, peripheral beams connecting the diagonal elements, other beams connecting the slab and core, and nodes connecting the diagonals and beams. Although theoretically, diagrid structures can safely carry vertical and horizontal loads without additional support, when applied in high-rise buildings, a core is added to the structure, and columns are added at the corner points in order to reduce the dimensions of the diagrid elements and to provide an additional measure.

In this construction method, since there are no vertical columns along the outer line, the horizontal and vertical loads are carried by diagrids along the outer line of the structure. These elements act as both diagonals and columns,

[*] Corresponding author, E-mail: mehmetfatih.yilmaz@omu.edu.tr

https://doi.org/10.31462/icearc2025_ce_eqe_616

and the angles of these diagrids are used differently from the angles of the diagonals used in traditional structures. This angle is related to the load on the structure and the height. Theoretically, the angle for diagrids should take a value between 45-70 degrees. The optimal angle is different for each structure according to the aspect ratio, height, and loads on the structure. “The lateral deflection in a building can be conceived as deriving from two sources. One is produced by the overturning moment, and the other by local shear. The lateral deflection patterns of tall buildings with different aspect ratios are rather different. Generally, in a building with a small aspect ratio less than 3, the shear deflection component predominates, while in a building with a moderate aspect ratio approximately between 3 and 5, the bending deflection component becomes non-negligible and may be on equal terms with shear deflection. For a building with a large aspect ratio from more than 5 to 7, the bending rather than the shear may contribute a lot towards lateral deflection. Furthermore, for a building with a larger aspect ratio beyond 7, the overturning moment deflection predominates instead of the shear deflection.” (Zhang et al., 2012). Since the design of the lower diagrids of the building is based on the bending effect and the upper diagrids on the shear effect, there is not always a single angle for the diagrids, and if necessary, changing the diagrid angle at the upper floors allows for optimal solutions.

In a study conducted by (Kim & Lee, 2012a) for a 36-story diagrid structure, they concluded that the lateral stiffness of the structure decreases as the diagrid angle increases and that both vertical and horizontal loads are optimally carried when the diagrid angle is between 60° and 70° degrees. In addition, when the height of the structure is low, narrower diagonal angles are sufficient since the structure is mostly stressed by shear effect, but as the height of the structure increases, wider diagonal angles become optimal since the structure starts to be stressed by bending effect in addition to shear effect.

In a study conducted by Sun (2015), diagrid models were compared with outrigger and frame models for 60-story and 8-story buildings. The results of the study showed that steel diagrids performed better than all other models in limiting the top displacements; however, their effectiveness in limiting top accelerations was found to be low.

Diagonal elements in diagonal construction are theoretically more efficient than conventional diagonal braced systems since they provide rigidity to the system in carrying loads in horizontal and vertical directions. There are no specific rules and constraints for diagrid structural systems in any of the regulations. However, the design of the elements other than the diagrid elements can be dimensioned as in common construction methods, only additional controls are needed to ensure that the dimensioning and angles of the diagrid elements are optimally designed. However, further studies are needed to better understand the seismic performance of diagrid structures, as “Looking through the entire portfolio of completed diagrid structures, there are very few diagrid tall building structures located in the area where seismic forces govern the lateral design” (Sun, 2015)

2. Finite element modelling of buildings

2.1. Description of buildings

Within the scope of this study, in order to better understand the behaviour of diagrid structures under earthquake effects, it will be compared with a steel structure modelled with conventional braces. The ETABS program will be used for the analysis, and the peak displacements, story drifts, and base shear parameters will be evaluated under the influence of the design spectrum taken from the AFAD Earthquake Hazard Map and various selected earthquake records. The location of the buildings in the Istanbul/Ataşehir region is 41.003911° latitude and 29.102972° longitude, and the soil class for this region is ZC.

2.2. Modelling of the structures

2.2.1. Creating models

The models of both structures were created and analysed with ETABS program. For ease of calculation, the models are 25 meters by 25 meters, and the approximate floor plans are nearly identical and symmetrical. Also, to avoid large variations in the earthquake effects acting on the structures, the models are arranged so that the building weights are approximately. Each model has 20 stories (see Fig. 1), and the storey heights are chosen to be 3 meters. In both models, the material class was selected as S355 for each element. In the model using the traditional diagonal system, the angle of the diagonals was modelled as 50 degrees to be close to the optimum angle, while in the diagrid system it was modelled as 67.38 degrees. The imposed loads on the building slabs are taken as 2 kN/m² for both typical floors and the roof floor, while the dead loads are taken as 2.5 kN/m² for typical floors and 4 kN/m² for the roof floor.

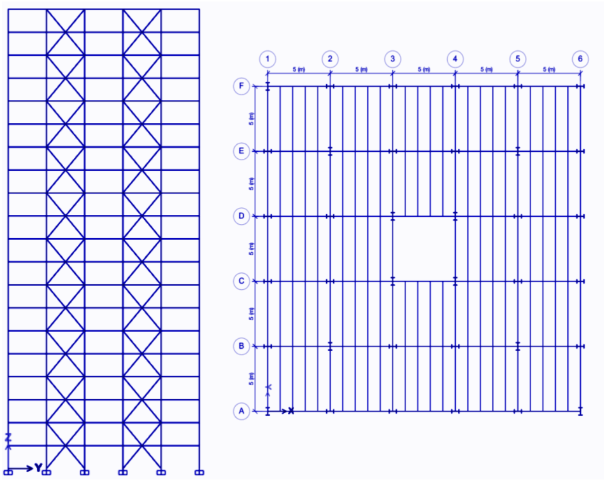

(a)

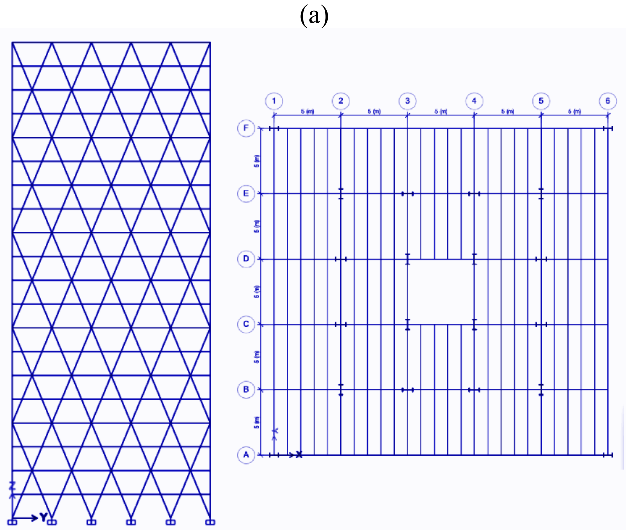

(b)

Fig. 1. Model plan and elevation (a) braced model (b) diagrid model

2.2.2. Comparison of dynamic parameters

As a result of the analysis of two models with the same building weight and floor plans, the period of the model with the Diagrid system was determined as 1.37 seconds, and the period of the model with the Braced system was determined as 4.7 seconds. There is almost a 3.5 times difference between the periods of the two models. Accordingly, it can be said that Diagrid systems are more rigid than Braced systems. The mode shapes of both models are the same, and no significant difference can be observed. The first two modes of the models are lateral translation, and the third mode is torsion.

3. Selection of earthquake records

In this study, 20 unscaled real earthquake records were selected to be used. The magnitudes of the earthquake records are between 5.9 and 7.5 (see Fig. 2), the PGA values are between 0.002 and 0.65, and the depths of the earthquakes are between 1 and 19 kilometres. The earthquake records are defined in the U1 and U2 directions, and no earthquake records in the vertical direction were used in the analysis. The mechanisms of the selected earthquakes are mostly strike-slip, but there are also records of blind thrust and oblique-slip earthquakes.

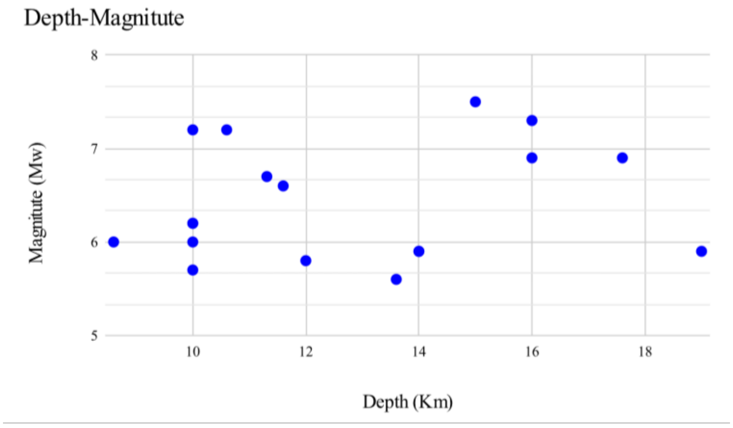

Fig. 2. Earthquake data graph

4. Time history analysis and results

4.1. Comparison of base shear forces
As a result of the analyses conducted using Diagrid and Braced models, it was generally observed that as the peak ground velocity (PGV) increased, the base shear force also increased. Accordingly, a significant relationship was identified between the base shear force and the PGV values of the selected ground motions. When the correlation between PGV and base shear force was examined, the determination coefficients (R^2) were found to be 0.607 for the Braced model and 0.734 for the Diagrid model (see Fig. 3).

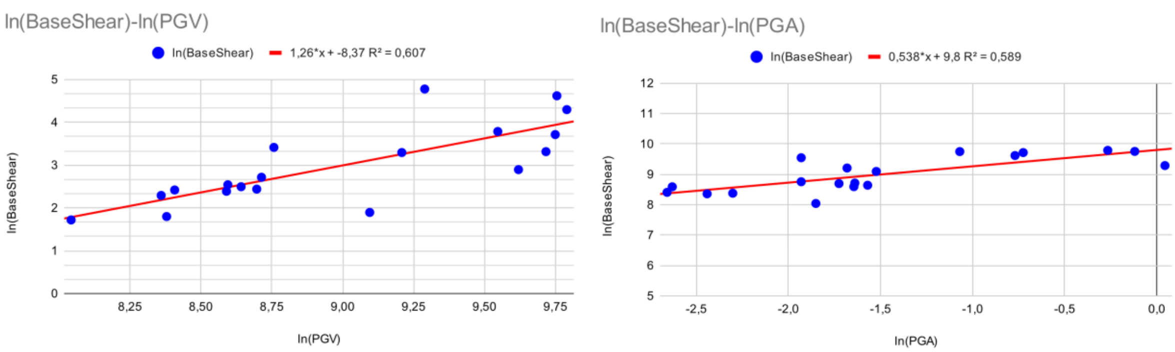

Fig. 3. Braced model base shear-PGV&PGA graph

Similarly, when comparing the peak ground acceleration (PGA) values of the selected ground motions with the base shear forces, it was observed that the base shear force generally increased with increasing PGA values, suggesting a potentially meaningful relationship. The determination coefficients (R^2) between PGA and base shear force were found to be 0.589 for the Braced model and 0.504 for the Diagrid model. Considering all these findings, it was concluded that the correlation between base shear forces and PGV is more pronounced and significant compared to that between base shear forces and PGA (see Fig. 4).

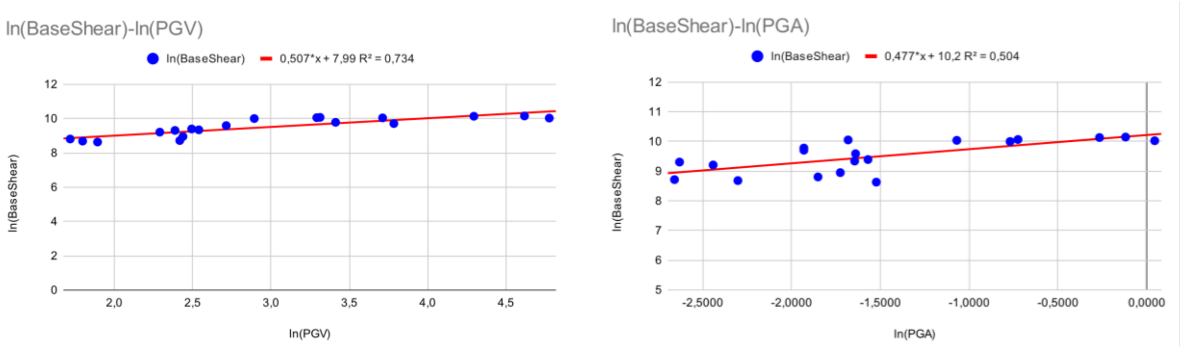

Fig. 4. Diagrid model base shear-PGV&PGA graph

When the maximum base shear forces acting on the Diagrid and Braced models were examined, it was found that in 95% of the analysed ground motions, the base shear values in the Diagrid model were higher compared to those in the Braced model.

4.2. Comparison of top displacements

When the top displacements obtained from the analyses using Diagrid and Braced models were compared with the PGV values of the selected ground motions, no significant correlation was found between these two parameters. The determination coefficients (R^2) for the relationship between PGV and top displacements were found to be 0.224 for the Braced model and 0.17 for the Diagrid model (see Fig. 5). Similarly, when comparing the PGA values of the selected ground motions with the top displacements, no significant relationship was identified between these parameters either, with determination coefficients (R^2) of 0.012 for the Braced model and 0.086 for the Diagrid model.

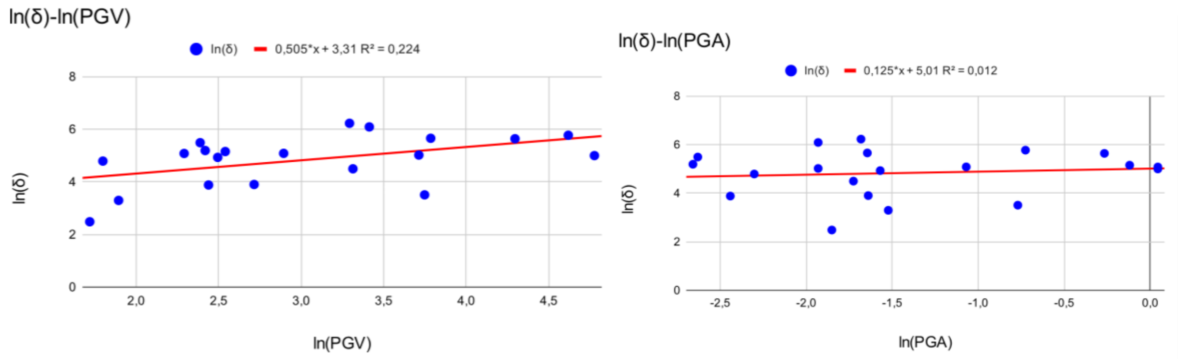

Fig. 5. Brace model top displacement-PGV&PGA graph

As a result, it was observed that both PGA and PGV parameters are not meaningful or sufficient indicators in explaining top displacements (see Fig. 5 and Fig. 6).

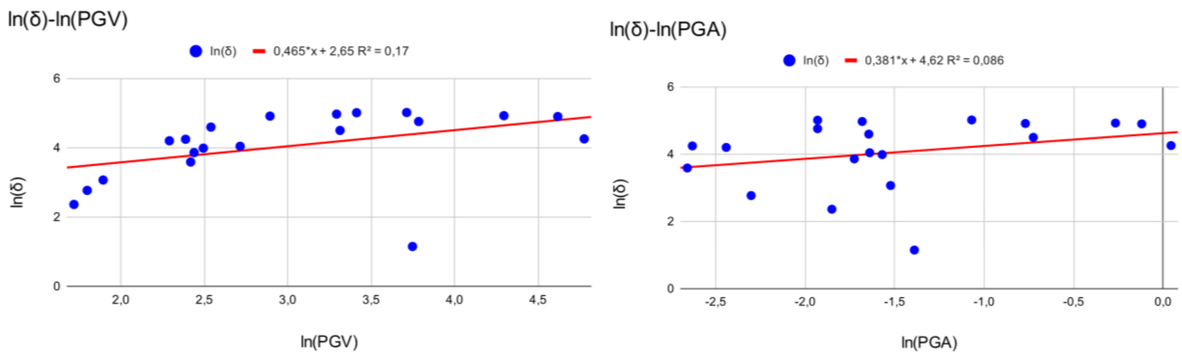

Fig. 6. Diagrid model top displacement-PGV&PGA graph

When the maximum top displacement values of the Diagrid and Braced models were examined, it was found that in 90% of the selected ground motions, the top displacement values of the Diagrid model were significantly lower than those of the Braced model. In cases where the Diagrid model had higher displacement values, the difference did not exceed 13%. Consequently, it was concluded that the Diagrid model performs better than the Braced model in limiting top displacements. This is a result that was anticipated, and similar outcomes have been reported in related studies.

4.3. Comparison of story drift

When the story drift values obtained from the analyses using Diagrid and Braced models were examined, similar to the peak displacements, no significant correlation was found between the story drifts and the PGV and PGA parameters. As a result, both PGV and PGA were determined to be unsuitable parameters for interpreting or predicting story drifts. Analysing the obtained drift values, it was generally observed that the story drift values of the Diagrid model were significantly lower than those of the Braced model (see Figs. 7-10), consistent with the top displacement data.

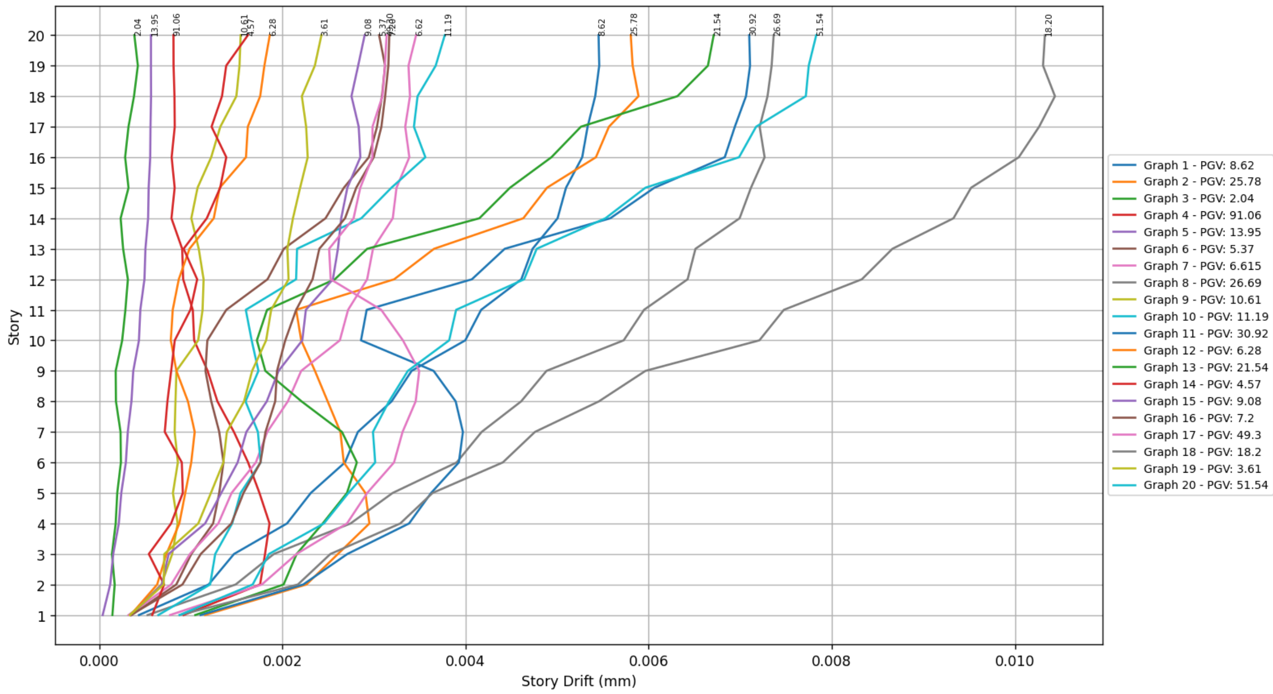

Fig. 7. Braced model story drift X-direction graph

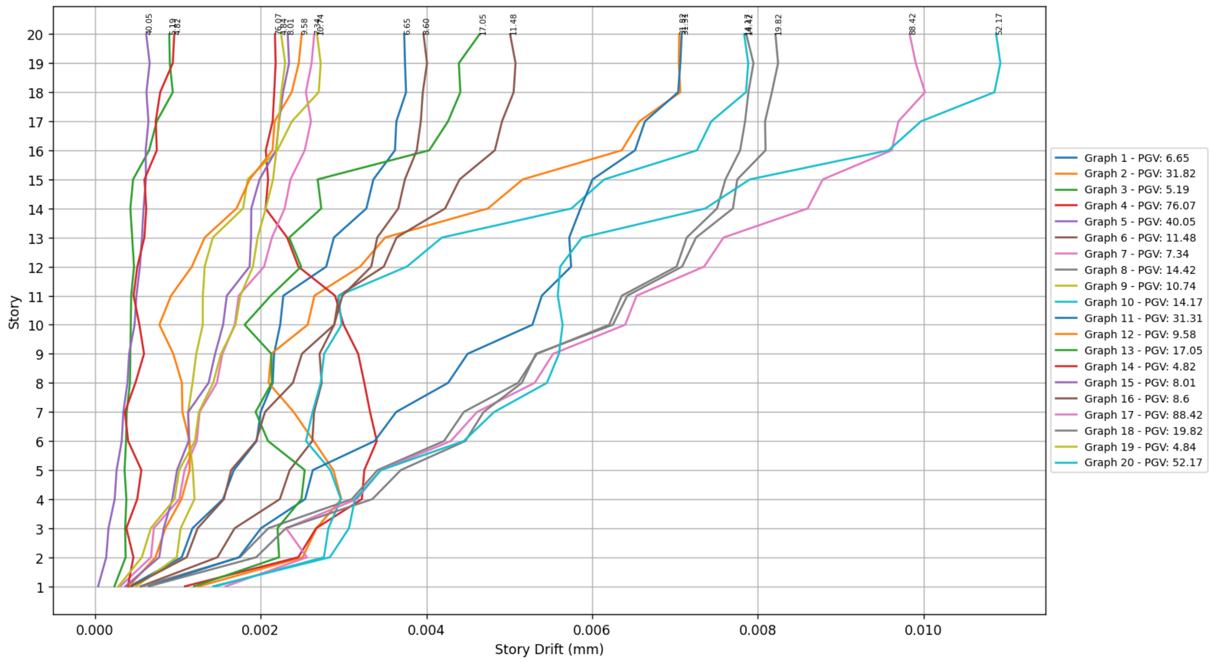

Fig. 8. Braced model story drift Y-direction graph

When the story drifts in the X and Y directions were examined, it was found that the drift values at the first story were quite similar in both models (see Figs. 7-10); however, at the upper stories, the Diagrid model exhibited significantly lower story drifts compared to the Braced model. Additionally, the maximum story drift observed in the Braced model was approximately 3.5 times greater than the maximum drift in the Diagrid model.

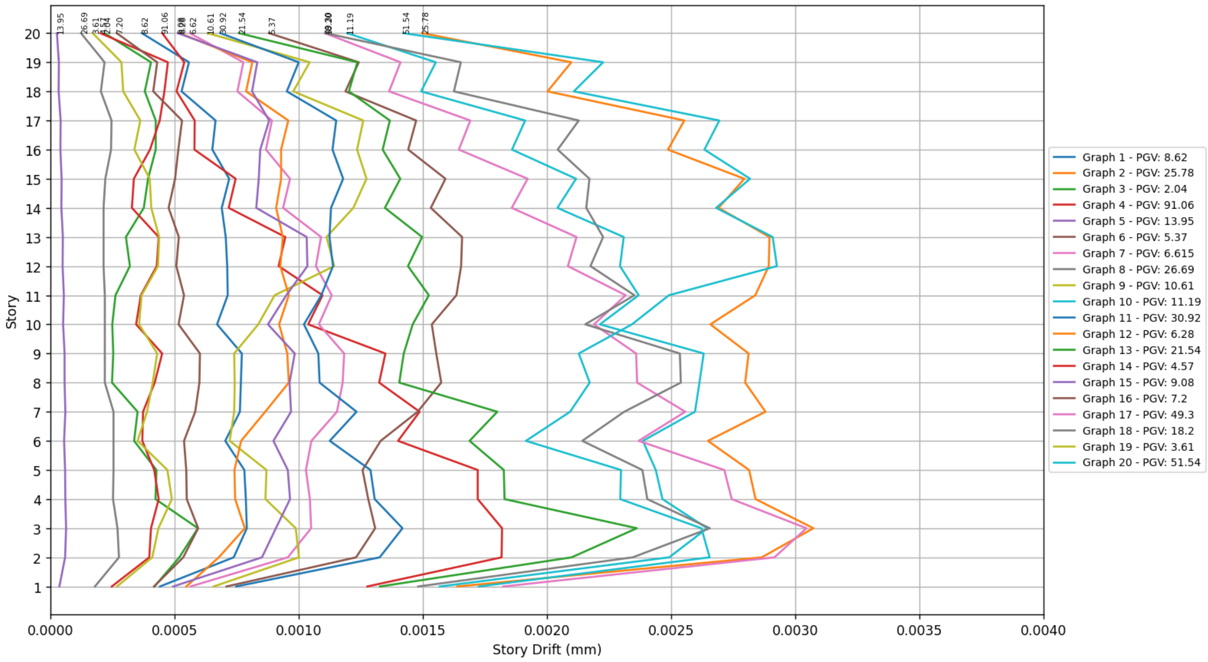

Fig. 9. Diagrid model story drift X-direction graph

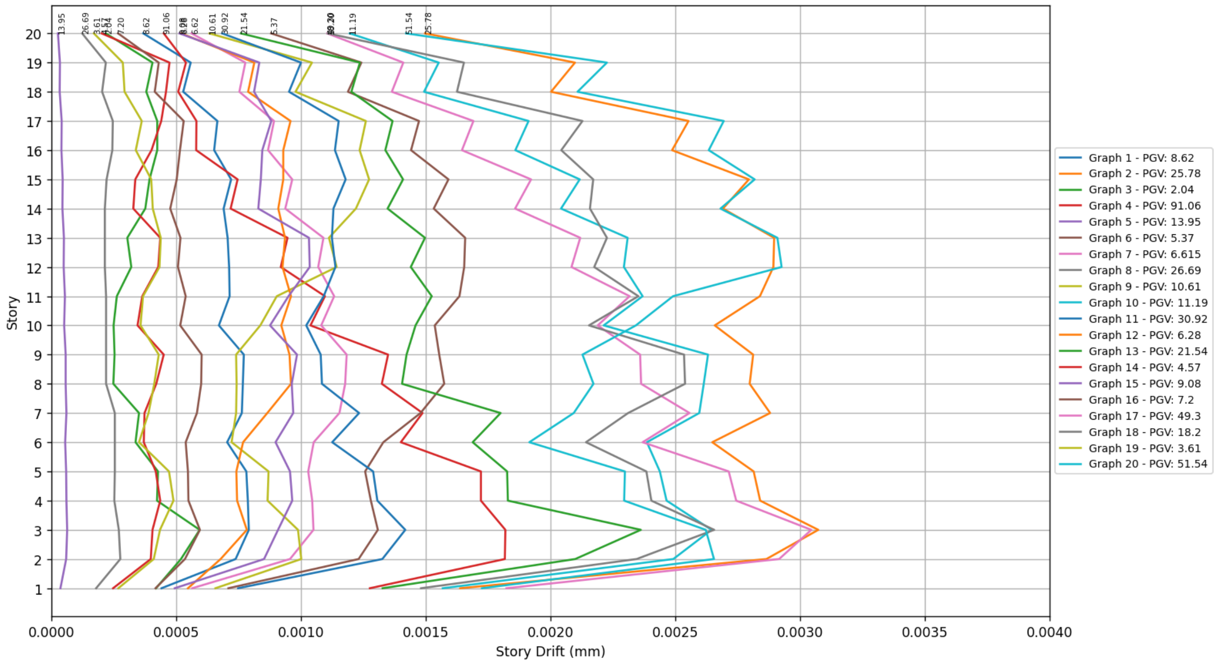

Fig. 10. Diagrid model story drift Y-direction graph

In conclusion, as expected, in addition to its strong performance in limiting top displacements, the Diagrid model also demonstrated generally better performance than the Braced system in limiting story drifts.

5. Conclusions

The growing demand for high-rise buildings in response to modern needs has increased interest in more efficient structural systems. In this study, although not a new system, Diagrid systems, which are gaining popularity but are still relatively uncommon in highly seismic regions, were compared with Braced systems, which can be found almost everywhere, in terms of their seismic performance based on top displacements, base shear forces, and story drifts.

- As a result of the modal analyses, no difference was observed between the mode shapes of the Braced and Diagrid models, which share the same and symmetric floor plans. However, when considering the fundamental periods, the period of the Diagrid model was found to be shorter.
- In the non-linear time history analyses, it was observed that the base shear forces of the Diagrid model were generally higher than those of the Braced model.
- The top displacements obtained from the non-linear time history analyses showed, as expected, that the Diagrid model had significantly lower top displacements compared to the Braced model.
- Similarly, the story drifts obtained from the non-linear time history analyses indicated that the Diagrid model exhibited significantly lower story drifts than the Braced model.

In conclusion, Diagrid systems generally demonstrate stiffer behaviour compared to Braced systems. Moreover, they are considerably more effective than Braced systems in limiting both story drifts and top displacements. However, while these parameters and results provide insight into the seismic performance of the two models, they are not sufficient on their own, and further research and studies are needed.

References

Boake, T.M. (2014). Diagrid structures: systems, connections, details. Walter de Gruyter.

Gerasimidis, S., Pantidis, P., Knickle, B., & Moon, K.S. (2016). Diagrid structural system for high-rise buildings: applications of a simple stiffness-based optimized design. *International Journal of High-Rise Buildings*, *5*(4). https://doi.org/10.21022/ijhrb.2016.5.4.319

Kim, J., & Lee, Y.H. (2012a). Seismic performance evaluation of diagrid system buildings. *Structural Design of Tall and Special Buildings*, *21*(10). https://doi.org/10.1002/tal.643

Kim, J., & Lee, Y.H. (2012b). Seismic performance evaluation of diagrid system buildings. *The Structural Design of Tall and Special Buildings*, *21*(10), 736–749. https://doi.org/https://doi.org/10.1002/tal.643

Kyoung Sun Moon. (2008). Optimal grid geometry of diagrid structures for tall buildings. *Architectural Science Review*, *51*(3)

Montuori, G.M., Mele, E., Brandonisio, G., & De Luca, A. (2014). Geometrical patterns for diagrid buildings: Exploring alternative design strategies from the structural point of view. *Engineering Structures*, *71*, 112–127. https://doi.org/10.1016/J.ENGSTRUCT.2014.04.017

Moon, K.S. (2008). Practical design guidelines for steel diagrid structures. In *Proceedings of the AEI 2008 Conference - AEI 2008: Building Integration Solutions*, *328*. https://doi.org/10.1061/41002(328)34

Moon, K.S. (2012). Optimal configuration of structural systems for tall buildings. In *20th Analysis and Computation Specialty Conference - Proceedings of the Conference*. https://doi.org/10.1061/9780784412374.027

Moon, K.S. (2016). Diagrid systems for structural design of complex-shaped tall buildings. *International Journal of High-Rise Buildings*, *5*(4). https://doi.org/10.21022/ijhrb.2016.5.4.243

Moon, K.S., Connor, J.J., & Fernandez, J.E. (2007). Diagrid structural systems for tall buildings: Characteristics and methodology for preliminary design. *Structural Design of Tall and Special Buildings*, *16*(2). https://doi.org/10.1002/tal.311

Ozakgul, K., Yilmaz, M.F., Yilmaz, F., Caglayan, B.O., & Hajirasouliha, I. (2024). Serviceability fragility assessment of non-seismically designed railway viaducts in Turkey under near-field and far-field earthquakes. *Structures*, *68*, 107102

Sun, M. (2015). *A Comparative Study on the Seismic Performance of Concrete and Steel Diagrid Structures* (Master’s thesis). Massachusetts Institute of Technology. http://dspace.mit.edu/handle/1721.1/7582

Zhang, C., Zhao, F., & Liu, Y. (2012). Diagrid tube structures composed of straight diagonals with gradually varying angles. *Structural Design of Tall and Special Buildings*, *21*(4), 283–295. https://doi.org/10.1002/tal.596

4th International Civil Engineering & Architecture Conference
15-17 May 2025, Trabzon, Türkiye

Retrofitting of single-story RC prefabricated structures with FVD

Özkan Hakan[1,2*], Mehmet Ö. Timurağaoğlu[1], Ramazan Livaoğlu[1,2]

[1] Bursa Uludağ University, Department of Civil Engineering, 16059 Bursa, Türkiye
[2] RL ProjeDestek Consulting Company, Bursa, Türkiye

Abstract. The present study investigates the seismic performance enhancement of single-story reinforced concrete prefabricated (RCP) structures, which are widely used as industrial buildings in Türkiye. Whilst these structures offer certain advantages, such as rapid construction and cost efficiency, they often exhibit vulnerabilities at critical connection points, necessitating additional measures to ensure seismic safety. Given the high seismicity of Türkiye, due to its location on major fault lines, the enhancement of the resilience of such structures is of paramount importance. In this research, viscous dampers were employed to enhance the energy dissipation capacity of a prefabricated structure. The dampers were installed in a symmetrical manner between the upper ends of the columns and the girder beams, aligned parallel to the direction of the beams. Nonlinear dynamic analyses were conducted for high seismicity regions with relatively good soil conditions, utilizing 11 pairs of ground motion records that were compatible with the regional target spectra. The comparative analyses, performed with and without viscous dampers, demonstrated that the inclusion of viscous dampers significantly reduced interstory drifts, improved overall structural stability, and enhanced the nonlinear behavior of prefabricated columns. The findings of this study demonstrate the efficacy of damping-based retrofitting strategies in enhancing the seismic performance of prefabricated industrial structures. The results of this study will contribute to ongoing efforts to increase seismic resilience in earthquake-prone regions, offering practical insights for both design and retrofit applications.

Keywords: Seismic Performance; Fluid viscous dampers (FVD); Prefabricated reinforced concrete, Structures, Structural retrofitting, Nonlinear seismic analysis.

1. Introduction

Single-story reinforced concrete prefabricated (RCP) structures constitute a significant portion of industrial and commercial building stock, particularly in regions with rapidly growing construction demands (Magliulo et al., 2023). While these structures offer notable advantages such as accelerated construction timelines, cost efficiency, and quality control under factory conditions, their seismic performance has raised concerns in past earthquake events. Key vulnerabilities are often associated with insufficient connection detailing, limited lateral stiffness, and inadequate energy dissipation capacity, which can lead to significant damage under strong ground motions (Belleri et al., 2015).

In response to these challenges, retrofitting strategies that enhance energy dissipation without substantially altering the structural configuration have gained increasing attention. Minimizing interventions to the existing structural system is crucial, as excessive alterations can increase project costs, construction time, and operational disruptions, which are often unacceptable for existing facilities. Among the available retrofitting techniques, the application of Fluid Viscous Dampers (FVDs) presents a promising solution by providing effective energy dissipation without introducing undesirable stiffness, while allowing for fast installation and contributing negligible additional mass (Guo et al., 2015). FVDs are capable of absorbing seismic energy efficiently, thereby reducing demand on critical structural components and improving overall seismic resilience. Moreover, their installation can often be accomplished with minimal disruption to existing functionality, making them particularly suitable for retrofitting purposes.

This study aims to improve the seismic performance of single-story RCP structures through retrofitting with Fluid Viscous Dampers (FVDs). Nonlinear dynamic analyses are conducted on representative structural models subjected to selected ground motion records, enabling a comparative assessment between the original and retrofitted configurations. The effectiveness of the proposed retrofitting strategy is evaluated based on reductions in interstory drift demands, connection demands, and ductility demands on prefabricated RC columns. The

*Corresponding author, E-mail: ozkan@rlprojedestek.com

https://doi.org/10.31462/icearc2025_ce_eqe_631

findings are intended to contribute to the development of practical and efficient retrofitting methodologies for enhancing the seismic resilience of existing RCP structures.

2. Viscos dampers and numerical modeling

Fluid Viscous Dampers (FVDs) are passive supplemental energy dissipation devices that generate a resisting force as a function of the relative velocity between their ends, following a nonlinear constitutive relationship. The force-velocity behavior of a typical FVD can be described by the equation:

$$f = c\,|\,\dot{u}\,|\,\mathrm{sgn}(\dot{u}) \tag{1}$$

where f is the damping force, c is the damping coefficient, $\dot{u}$ is the relative velocity across the damper, and α is the velocity exponent, typically ranging from 0.2 to 1.0. Linear damper behavior is obtained when $\alpha = 1$, while most practical FVDs exhibit nonlinear behavior with $\alpha < 1$ (Guo et al., 2015) as illustrated in Figure 1 by the force-velocity and force-displacement relationships for different velocity exponents. In addition to the force-velocity behavior, the internal mechanical configurations of commonly used FVDs are illustrated in Fig. 2a and Fig. 2b to provide a general understanding of their practical application.

The effectiveness of FVDs depends significantly on their placement strategy within the structure. Among the commonly adopted layouts, diagonal and chevron configurations are widely used, wherein damper displacements are directly aligned with interstory drifts, as illustrated in Fig.2c and Fig.2d (Guo et al., 2015). More advanced configurations, such as the toggle and scissor systems, employ linkage mechanisms to amplify damper displacements, thereby increasing the energy dissipation capacity for a given level of story drift, as shown in Fig.2e. and Fig.2f. (Constantinou et al., 2001; Şigaher & Constantinou, 2003).

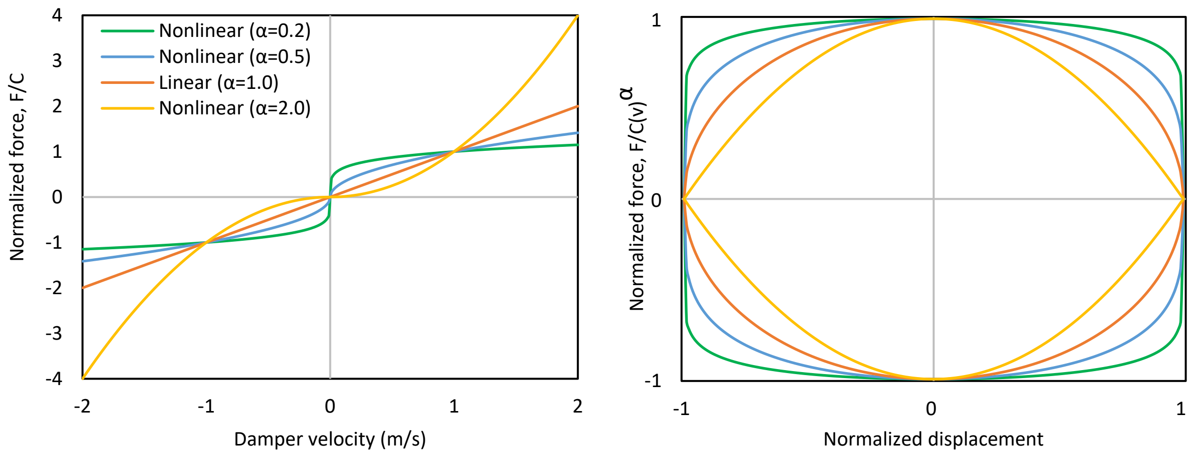

Fig. 1. Force-velocity and force-displacement relationship for FVD under harmonic motion

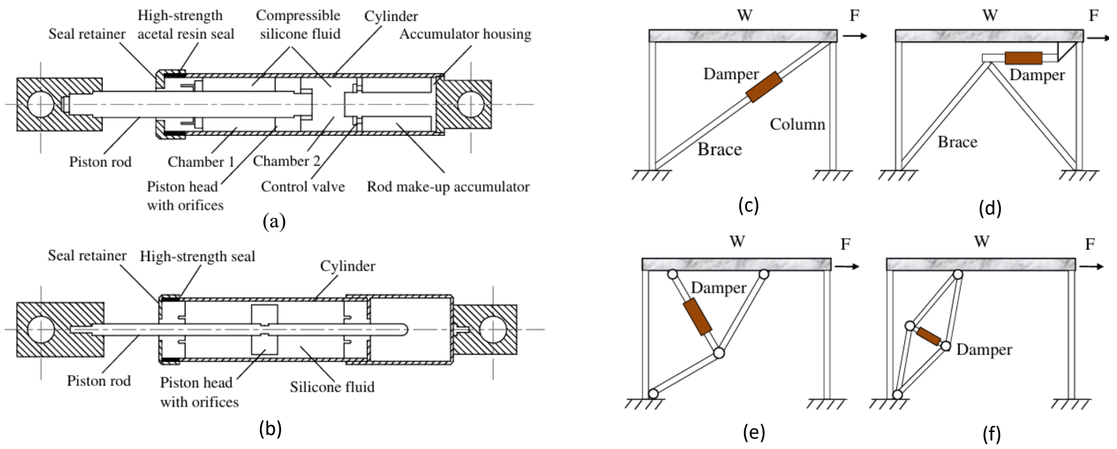

Fig. 2. Configuration of Two Commonly Used FV Dampers and Illustration of a Single-Story Structure with Fluid Viscous Dampers: (a) damper with an accumulator, (b) run-through piston rod, (c) diagonal, (d) chevron, (e) toggle, (f) scissor (Guo et al., 2015)

Inspired by the reverse toggle configuration, this study proposes a novel damper arrangement aimed at further enhancing energy dissipation efficiency while maintaining practical constructability. As illustrated in Fig. 3, the proposed configuration employs an optimized bracing system that magnifies damper deformations under seismic excitation, thereby improving the overall supplemental damping effect.

Two nonlinear time history analysis models were developed for a single-story RCP structure: one without any supplemental damping devices and another retrofitted with two parallelly placed Fluid Viscous Dampers (FVDs). Both models were constructed using Perform-3D. The overall structural configuration is shown in Fig. 4.

In the modeling approach, columns were represented using fiber elements over a length corresponding to the expected plastic hinge regions, allowing for accurate simulation of nonlinear flexural behavior. Beam-to-column and purlin-to-column connections, on the other hand, were modeled based on nonlinear force-displacement relationships derived from the experimental study conducted by Psycharis and Mouzakis (2012), enabling realistic representation of connection nonlinearity observed in prefabricated structures (Psycharis & Mouzakis, 2012).

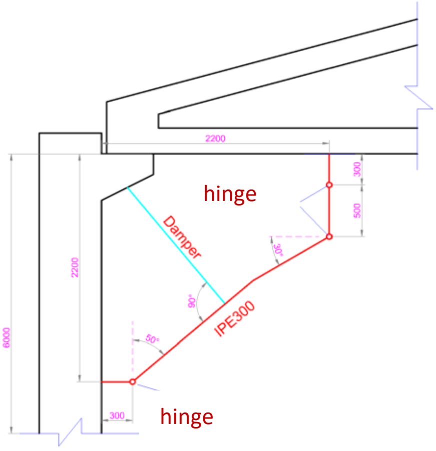

Fig. 3. Schematic diagram of the proposed damper configurations

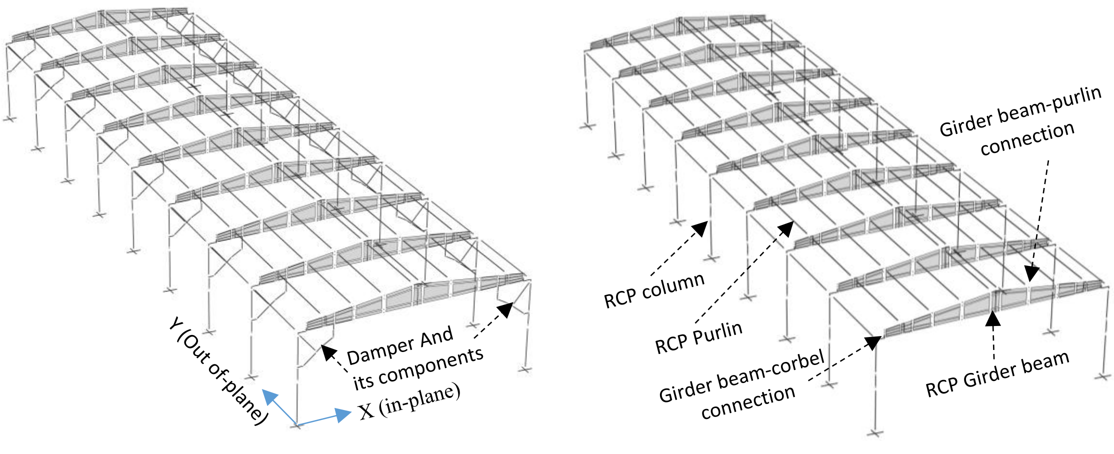

Fig. 4. Generated three-dimensional models of the single-story RCP structure in Perform-3D software

Table 1. Limit values corresponding to the Collapse Prevention (CP) performance level used in the analysis

Limit State	Short Name	CP Limit	unit
Column Rebar Fiber Tension	C-Fbr-T	0.032	strain
Column Concrete Fiber Compression	C-Fbr-C	0.01	strain
Girder Beam-Corbel Connection In-plane Shear Displacement	GBC-In-Sh	20	mm
Girder Beam-Corbel Connection Out-of Plane Shear Displacement	GBC-Out-Sh	20	mm
Girder Beam-Corbel Connection In-plane Rotation	GBC-In-Ro	0.025	radian
Girder Beam-Corbel Connection Out-of Plane Rotation	GBC-Out-Ro	0.025	radian
Purlin-Beam Connection Shear Displacement	PB-Sh	20	mm
Top-of-Column Drift	C-D-	0.03	ratio
Column Shear	C-ShF	2.6	MPa

The structural model represents a single-story RCP structure consisting of eight bays of 6m in the Y direction and a single bay of 15m in the X direction, with a story height of 6m. The columns were modeled as rectangular cross sections with dimensions of 40cm × 60cm, oriented with the longer side parallel to the X axis. Concrete was defined with a characteristic compressive strength of 30 MPa (C30), and reinforcing steel was modeled with a yield strength of 420 MPa (S420). Additionally, low-capacity FVDs with a nominal force of 40 kN (C = 64.83 kN·(s/m)^0.3, α = 0.3) were included in the numerical models.

Based on the nonlinear behavior incorporated into the model, internal force and displacement demands were extracted for critical structural components. Demand-to-capacity ratios (DCRs) were then calculated considering predefined limit states corresponding to the Collapse Prevention (CP) performance level. The limit values adopted for evaluating these ratios are summarized in Table 1.

3. Selection of earthquake ground motion

In accordance with TBDY 2018, eleven ground motion records were selected to represent the DD-1 seismic hazard level based on site-specific conditions. The selected records were scaled and matched to the target spectrum defined for the site. Information regarding the selected ground motions is provided in Table 2, while Fig. 5 illustrates the comparison between the target spectrum and the response spectra of the scaled records.

In the analyses, the selected ground motions were simultaneously applied along the two horizontal directions of the structure. Subsequently, the orientations of the input motions were reversed, and the analyses were repeated to account for directional variability.

Table 2. Properties of selected ground motion records for DD-1 seismic hazard level

Location (City)	Soil class	RSN	Earthquake name	Mw	RJB (km)	Vs30 (m/s)	Fault Mechanism	Scale Factor
BURSA	ZD V_{s30} = 350 m/s	1614	Duzce_Turkey	7.1	11.5	481	S	3.9
		230	Mammoth Lakes-01	6.1	6.6	382	N	1.9
		231	Mammoth Lakes-01	6.1	15.5	537	N	2.6
		232	Mammoth Lakes-01	6.1	4.7	347	N	2.7
		300	Irpinia_Italy-02	6.2	8.8	456	N	2.0
		313	Corinth_Greece	6.6	10.3	361	N	2.3
		564	Kalamata_Greece-01	6.2	6.5	382	N	2.2
		5678	Iwate_Japan	6.9	11.1	399	RV	3.1
		6886	Darfield_New Zealand	7.0	14.5	280	SS	3.0
		6893	Darfield_New Zealand	7.0	11.9	344	SS	1.6
		881	Landers	7.3	17.4	396	SS	2.3

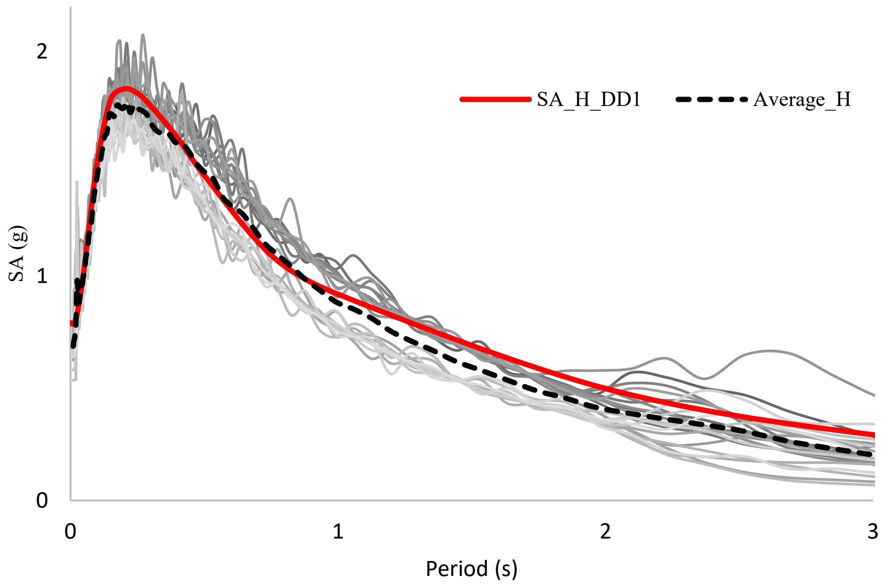

Fig. 5. Comparison of the target spectrum with the response spectra of the selected ground motion records

3. Comparison of analysis results

Based on the capacity limits defined in Table 1, seismic demands were evaluated across the 11 pairs of nonlinear time history analyses. For each analysis, the maximum structural demands, including internal forces and displacement responses, were extracted and subsequently averaged. Demand-to-capacity ratios (DCRs) were calculated by normalizing the averaged demands with respect to the corresponding capacities. Fig. 6 presents the maximum value among the averaged DCRs obtained from all structural components.

The results clearly demonstrate that the implementation of Fluid Viscous Dampers (FVDs) provides a significant improvement in seismic performance by substantially reducing the maximum demand-to-capacity ratios.

To better quantify the improvements achieved through the use of Fluid Viscous Dampers (FVDs), the percentage reductions in the maximum averaged demand-to-capacity ratios (DCRs) were calculated for critical structural components. The differences between the damped and undamped cases were expressed as percentage changes, as summarized in Table 3. This representation allows for a clearer understanding of the extent of the performance enhancement provided by the dampers.

To further evaluate the behavior of the fluid viscous dampers (FVDs), displacement-force and velocity-force relationships for a representative damper were extracted from all ground motion analyses. These hysteretic responses are presented side-by-side in Fig. 7. It is observed that the dampers operated effectively within a maximum stroke of approximately 2 cm, maintaining stable energy dissipation characteristics throughout the seismic excitations.

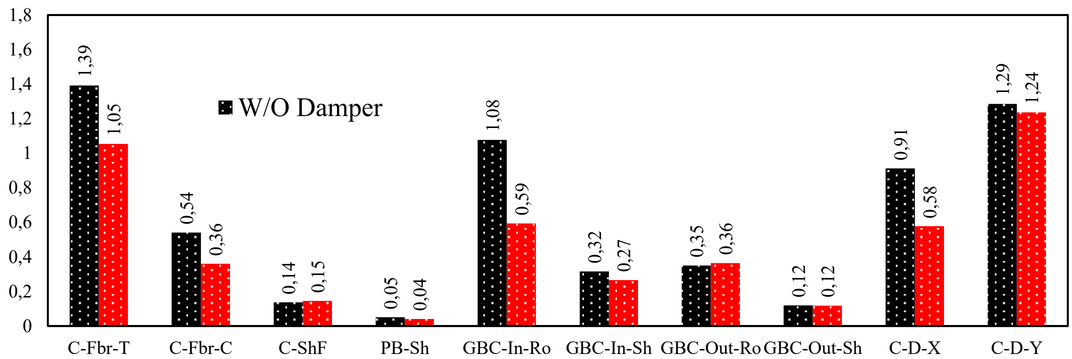

Fig. 6 Maximum averaged demand-to-capacity ratio (DCR) obtained from nonlinear time history analyses

Table 3. Percentage reduction in maximum averaged demand-to-capacity ratios due to fluid viscous damper

		Girder Beam				Columns			Purlin	Drift	
		In- θ[1]	Out-θ[2]	In-Sh[3]	Out-Sh[4]	T	C	Sh	In-Sh[3]	X-X	Y-Y
Bursa ZD	W Damper	-50%	+1%	-5%	0.2%	-34%	-18%	+1%	-1%	-33%	-5%

1 In Plane rotation, 2Out of Plane rotation, 3In plane Shear displacement, 4Out of Plane Shear displacement, T: Tension in Column Fiber C: Compression in Column Fiber, W/O: without, W: with, Sh: shear force

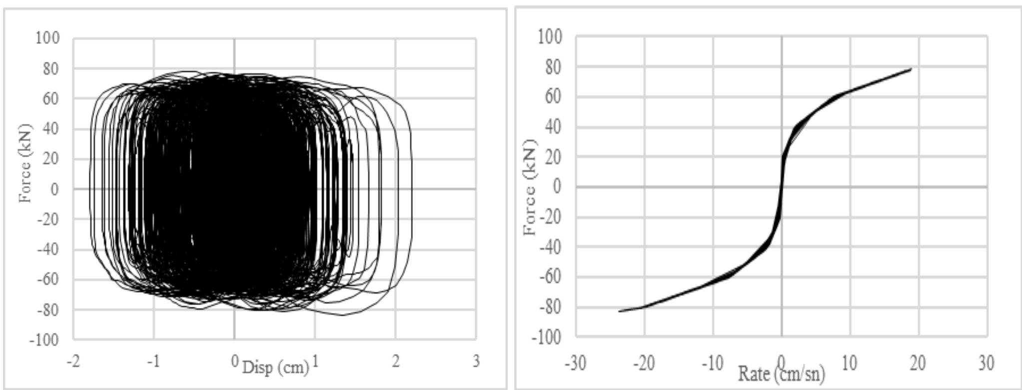

Fig. 7. Displacement–force and velocity–force hysteretic responses of a representative fluid viscous damper under selected ground motion analyses.

4. Conclusions

The present study demonstrates the effectiveness of the proposed small-size, low-capacity viscous damper configuration in enhancing the seismic performance of reinforced concrete prefabricated structures. In contrast to conventional damper systems, such as diagonal, chevron, or toggle configurations, which frequently demonstrate limited efficiency in prefabricated applications, the proposed arrangement attains substantial enhancements in energy dissipation, reduction of inelastic deformations, and enhancement of lateral stability. It is important to note that these benefits are achieved without compromising the structural integrity, architectural considerations, or constructability of the system.

The analysis results confirm that, despite its compact dimensions and reduced force capacity, the proposed damper system effectively mitigates seismic demands. A notable decline in demand-to-capacity (D/C) ratios for columns and roof drift values was observed, thereby demonstrating the system's capacity to regulate critical structural responses and restrict damage incurred during seismic loading. Moreover, the lightweight and space-efficient design of the damper configuration facilitates practical implementation within the dimensional and load constraints commonly associated with prefabricated structures.

The proposed configuration of small-size, low-capacity damper is a promising and practical retrofitting solution for improving the seismic resilience of prefabricated reinforced concrete buildings. It achieves an optimal balance between enhanced performance, cost efficiency, and ease of application.

References

Belleri, A., Brunesi, E., Nascimbene, R., Pagani, M., & Riva, P. (2015). Seismic Performance of Precast Industrial Facilities Following Major Earthquakes in the Italian Territory. *Journal of Performance of Constructed Facilities*, *29*(5). https://doi.org/10.1061/(asce)cf.1943-5509.0000617

Constantinou, M. C., Tsopelas, P., Hammel, W., & Sigaher, A. N. (2001). Toggle-Brace-Damper Seismic Energy Dissipation Systems. *Journal of Structural Engineering*, *127*(2). https://doi.org/10.1061/(asce)0733-9445(2001)127:2(105)

Guo, T., Xu, J., Xu, W., & Di, Z. (2015). Seismic Upgrade of Existing Buildings with Fluid Viscous Dampers: Design Methodologies and Case Study. *Journal of Performance of Constructed Facilities*, *29*(6). https://doi.org/10.1061/(asce)cf.1943-5509.0000671

Magliulo, G., D’Angela, D., Piccolo, V., Di Salvatore, C., & Caterino, N. (2023). Seismic capacity and performance of code-conforming single-story RC precast buildings considering multiple limit states and damage criteria. *Journal of Building Engineering*, *70*. https://doi.org/10.1016/j.jobe.2023.106316

Psycharis, I. N., & Mouzakis, H. P. (2012). Shear resistance of pinned connections of precast members to monotonic and cyclic loading. *Engineering Structures*, *41*. https://doi.org/10.1016/j.engstruct.2012.03.051

Şigaher, A. N., & Constantinou, M. C. (2003). Scissor-jack-damper energy dissipation system. *Earthquake Spectra*, *19*(1). https://doi.org/10.1193/1.1540999

ICEARC'25
4th International Civil Engineering & Architecture Conference
17-19 May 2025, Trabzon, Türkiye

Risk analysis of buildings with earthquake performance index

Kuban Akkaya [*1], Selin Baş[1], Seda Selçuk[1]

[1] *Cankaya University, Department of Civil Engineering, 06815 Ankara, Türkiye*

Abstract. This research proposal aims to evaluate the most commonly used earthquake performance index by analyzing key structural and geotechnical parameters based on the effects of the 2023 Kahramanmaraş Earthquake. The Rapid Building Type Earthquake Impact Evaluation (RBTEIE) method was evaluated to assess buildings seismic resilience in a specified region. The index is calculated based on several critical parameters, to identify potential damage risks and categorize buildings accordingly. The research methodology consists of data collection, and validation. Data was gathered from various official sources, while validation phase involves testing predictive capacity of the index. We evaluated the effect of two improvements to the RBTEIE index: removing the shear wall parameter in order to improve the applicability of the method and increasing the detail of the visual index to improve the quality of information coming from the visual state of the building. The improved index found was highly accurate when high quality data is collected in predicting building performance in the validation stage. The findings of this study can contribute significantly to regional earthquake risk management and inform urban planning and disaster preparedness strategies.

Keywords: Erthquake performance; Structural analysis; Geotechnical parameters; Damage estimation; Building classification

1. Introduction

In recent years, earthquakes occurring particularly in seismically active regions such as Turkey have clearly revealed the inadequate seismic performance of a significant portion of the existing building stock (Yakut, 2004). This alarming situation has highlighted the necessity for rapid and reliable assessment methods to evaluate the seismic vulnerability of buildings, which constitutes a crucial component of effective disaster management strategies. Assessment techniques such as FEMA 154, the Japanese Seismic Index, and various rapid screening methods widely implemented in Turkey have long been utilized to identify potentially vulnerable structures (Sextos et al., 2008). However, these conventional approaches primarily focus on structural attributes, including building type, number of stories, and material quality, often neglecting critical factors such as soil conditions and regional seismic characteristics.

While most existing rapid assessment methods typically focus on limited structural characteristics like building type, number of stories, and material quality, recent research demonstrates that the inclusion of detailed geotechnical parameters and regional seismic data substantially improves the accuracy of seismic performance evaluations (Erberik, 2008, Halder et al., 2020). To address these shortcomings, the Rapid Building Type Earthquake Impact Evaluation (RBTEIE) method offers a standardized and comprehensive framework by integrating both structural and geotechnical parameters, including soil classification and regional seismic hazard characteristics (RBTEIE, 2023). This approach significantly enhances the accuracy and reliability of seismic vulnerability assessments, especially for mid- and high-rise reinforced concrete buildings, and stands out as a valuable tool for strengthening disaster risk reduction strategies.

There are few studies in the literature that attempts to meause the efficiency and accuracy of RBTEIE method (Yakut, 2004). Our study aims to the validate RBTEIE method through the use of real-world damage data to quantify the accuracy of the index on building assessment. Evaluation of the index with actual data can provide valuable insights for the development of effective risk reduction strategies and for enhancing the safety of the existing building stock.

[*] Corresponding author, E-mail: c1819006@student.cankaya.edu.tr

https://doi.org/10.31462/icearc2025_ce_eqe_647

golden light publishing

2. Materials and methods

2.1. Dataset description and parameters

The data utilized in this study were collected from only reinforced concrete (RC) buildings that experienced varying degrees of structural damage during the 2023 Kahramanmaraş earthquakes. Initially, the geographic locations, number of stories, and plan geometries of the buildings were identified through the analysis of Google Earth satellite imagery (Google Earth Pro, 2023). Following this, site-specific seismic hazard parameters, including Peak Ground Acceleration (PGA), Peak Ground Velocity (PGV), and soil classification information, were obtained from the official databases of AFAD (Disaster and Emergency Management Authority of Turkey)

Using these parameters, supplementary seismic hazard indicators such as S_S (Spectral Acceleration at Short Period), S_1 (Spectral Acceleration at 1-second Period), F_1 (Site Coefficient for Short Period), and F_S (Site Coefficient for 1-second Period) were also retrieved from AFAD resources to enhance the accuracy of the seismic hazard characterization (AFAD, 2023). These parameters are essential for estimating the local amplification effects and dynamic characteristics of ground shaking, which vary based on both soil type and seismic input. The compiled dataset comprises a wide range of structural, seismic, and geological parameters, including number of stories, plan geometry, structural irregularities (such as soft stories, short columns, and cantilever extensions), vertical irregularities, regional soil classification, VS30, PGA and PGV values, as well as the distance to the nearest active fault line. In total, 20 parameters were considered in the seismic vulnerability assessment framework, as typically used in the RBTEIE index. All parameters are listed in Table 1.

Table 1. Parameters

Data Source	Collected Parameter(s)
Google Earth	Building conditions Visual assessment Slope Vertical Asymmetry Plan Asymmetry Short Columns Soft Story Cantilever Pounding Effect
AFAD TDTH	PGA and PGV values S_S, S_1, F_1, F_S, S_{DS}, S_{D1}
TKGM	Number of stories Structural type of the building
AFAD TADAS	VS30 Soil class

The Fig. 1. illustrates distribution of buildings according to their number of stories and percent of collapsed buildings for each story group. Notably, while mid-rise buildings (particularly five-story structures) constitute the largest share of the total dataset, the collapse ratio increases significantly for six or more story buildings.

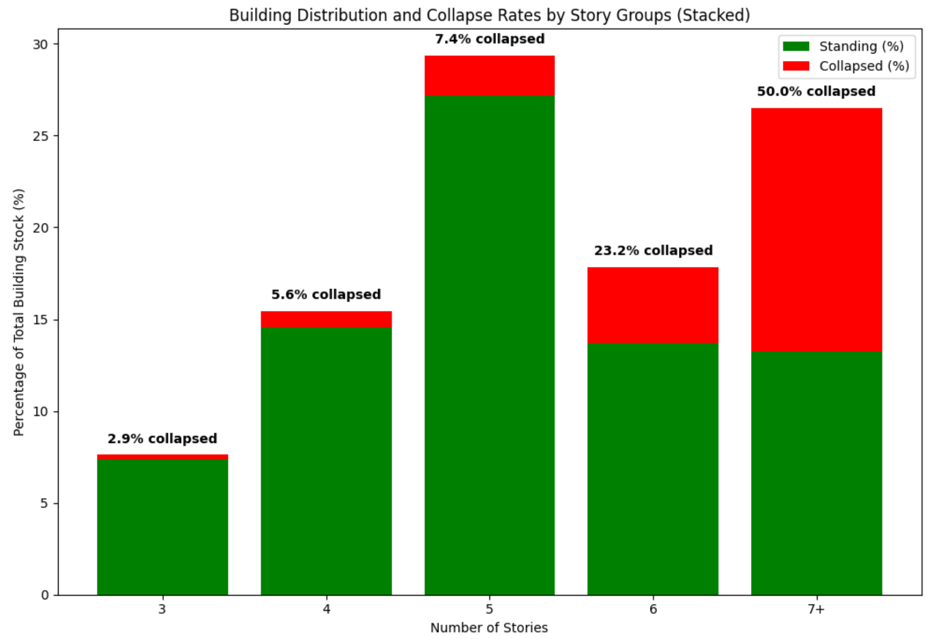

Fig. 1. Distribution of Building Stock and Collapse Rates Across Different Story Groups

The significant increase in collapsed buildings for six or more stories highlights the critical role of story number as a determinant of seismic vulnerability. The collapse rate exceeds 50% in the buildings categorized as seven stories or more, revealing a clear trend of increasing structural vulnerability with greater building height. This pattern suggests the necessity for targeted seismic risk mitigation, especially in taller structures. In Fig. 1., both collapsed buildings and heavily damaged buildings are evaluated together under the category of "failed" structures.

Buildings that were demolished following damage assessment studies conducted after the earthquake were classified as heavily damaged. This approach enables the effective inclusion of not only the buildings that experienced total collapse during the earthquake, but also those that suffered severe structural damage and were subsequently designated for demolition, within the seismic vulnerability assessment framework.

2.2. Seismic vulnerability assessment and performance index (PP) calculation

In this research, the Rapid Building Type Earthquake Impact Evaluation (RBTEIE) methodology was adopted as the core assessment approach to evaluate the seismic vulnerability of buildings (RBTEIE, 2023). The RBTEIE framework allows for the integration of both structural characteristics and geotechnical conditions to provide a holistic risk assessment. The evaluation process involved several key analytical steps, including structural irregularity identification, hazard zone determination, and visual quality assessment. As mentioned earlier, the effect of two improvements to the RBTEIE index, removing the shear wall parameter and increasing the detail of the visual index, was evaluated.

It is important to mention that we assumed all buildings were designed as reinforced concrete frame systems without shear walls. We made this assumption based on our data collection system, which uses Google Street View. It was not possible to detect the presence of shear walls from the street view of the building, so we decided to omit the shear wall parameter used in the RBTEIE method. This assumption can be useful in decreasing data collection duration since it can take a lot of time to evaluate the presence of a shear wall if the structural plans of a building are not available. Removing the shear wall parameter from the RBTEIE method would make the method more practical. Consequently, we also evaluated the effect of the shear wall parameter on the accuracy of the index.

We wanted to increase the detail and quality of data obtained from visual state of the building. Consequently, the visual construction quality of the buildings was classified into four damage levels based on observable indicators: 0 for no visual markings/problems, 1 for slight visual problems, 2 for moderate visual problems, and 3 for severe visual problems. This classification was derived from the presence of white and/or brown stains, surface cracking, concrete spalling, and general deterioration of structural integrity. Brown stains were associated with corrosion-related rust stains, while white stains were interpreted as signs of leaching (efflorescence) due to moisture migration within the concrete.

For each building, individual damage-related parameters were used to determine total score that was used to assign the building to one of the defined quality categories in RBTEIE index. This process provided an objective quantification of visual quality, which was then incorporated into the vulnerability analysis as a numerical parameter.

The Performance Index (PP) (RBTEIE, 2023), representing the seismic vulnerability score of each building, was calculated using the following equation:

$$PP = TP + \sum(Oi \times OPi) + YSP \quad (1)$$

Where, TP (Base Performance Score), reflects the inherent seismic resistance based on the number of stories and the seismic hazard level at the building site.

YSP (Structural System Contribution), accounts for the structural system's effect on overall performance (assuming a bare frame system for all buildings in this study).

$\sum(Oi \times OPi)$, represents the cumulative impact of observed structural irregularities, weighted according to their assigned significance. In this expression, Oi denotes the presence (binary or graded occurrence) of the i-th structural irregularity observed in a building (e.g., soft story, short column, cantilever extension), while OPi corresponds to the predefined penalty score that quantifies the relative importance or severity of that irregularity in terms of its contribution to seismic vulnerability.

3. Results and discussion

The total performance score of each building was determined by summing the base score (TP), the structural system contribution (YSP), and the weighted influence of various structural irregularities. The TP value reflects the inherent seismic resistance based on the number of stories and the seismic hazard level of the building's location, while the YSP component represents the structural system's contribution to overall performance. In the scope of this analysis, all buildings were assumed to have simple reinforced concrete frame system without shear walls.

The effectiveness of this risk classification system was validated through comparative analysis between the computed PP scores and the observed damage states of the buildings. Fig. 2 illustrates the prediction accuracy for identifying safe (undamaged or slightly damaged) and risky (collapsed or heavily damaged) buildings at various PP score thresholds. The horizontal axis represents the applied risk limit, while the vertical axis shows the prediction success rate (%). The results demonstrate that the optimal separation between safe and risky groups occurs within the -20 to 0 score threshold. When this range is applied as the decision boundary, the model achieves an overall prediction accuracy of approximately 80%, indicating a strong classification performance around this threshold interval. Using this information, the calculated PP scores (see Table 2) were categorized into four distinct seismic vulnerability groups based on threshold values derived from empirical data analysis and supported by field observations. The classification thresholds were defined through empirical analyses supported by field observations, allowing for the categorization of buildings into four distinct risk groups: Very High Risk, High Risk, Moderate Risk, and Low Risk.

It is noteworthy that while Yakut (Yakut, 2004), in the context of the 1999 Düzce earthquake, reported a prediction accuracy level of approximately 50% using a rapid seismic performance assessment approach, the method applied in this study achieved an accuracy of around 80% within the defined -20 to 0 PP score threshold. This significant improvement can be attributed to the integration of detailed post-earthquake damage data, particularly the careful consideration of visible structural deficiencies and ground-related parameters, which enhanced the model's capability to differentiate between vulnerable and resilient buildings.

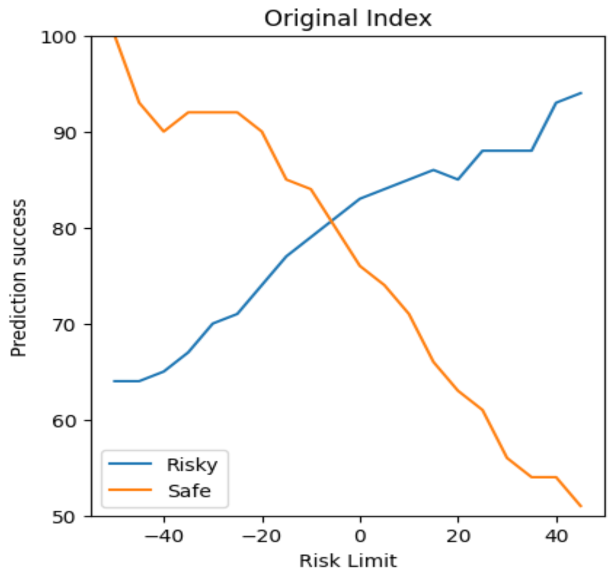

Fig. 2. Prediction Success Rates of Risk Classification Based on Original PP Score Across Various Risk Limits

Table 2. PP score

Risk Category	PP Score Range
Very High Risk	-20 ≤ PP < 0
High Risk	0 ≤ PP < 20
Moderate Risk	PP ≥ 20
Low Risk	-20 ≤ PP < 0

Figure 3 visualizes the distribution of PP scores against the number of stories, with red dots representing collapsed or heavily damaged buildings and green dots representing non-collapsed and non-heavily damaged structures. The plot reveals a general trend where higher-rise buildings exhibit lower PP scores and demonstrate greater damage susceptibility, supporting the validity of the scoring system and the proposed risk classification approach. Moreover, when applying the risk threshold determined through empirical analysis, it is clearly observed that buildings positioned below the PP score of 0 predominantly correspond to the risky group (failed structures), while those above the score of 0 are largely concentrated within the safe group. This distinction reinforces the effectiveness of the selected score interval, where 0 serves as a critical boundary separating high-risk buildings from low-risk or safe structures within the assessment framework. These analytical results indicate that the PP-based classification provides a reliable and effective framework for identifying the seismic vulnerability of buildings. The methodology not only aligns well with observed damage patterns but also reinforces the practical applicability of the RBTEIE method as a rapid assessment tool for earthquake risk mitigation.

Fig. 4 presents the PP-based risk distribution for both collapsed buildings and those that remained standing after the 2023 Kahramanmaraş earthquakes. The left side of the Fig. illustrates the risk categorization of collapsed structures, while the right side depicts the classification of standing buildings. As can be seen from these graphs approximately 75% of the buildings were classified as very high risk and high risk using the improved index. Likewise, approximately 78% of the non-damaged buildings were classified as low risk and moderate risk when we calculated RBTEIE index. These findings confirm that the proposed PP scoring system and its associated risk thresholds are consistent with the actual damage outcomes observed in the field. The dominance of higher-risk scores among collapsed buildings, along with the prevalence of lower-risk scores among standing structures, demonstrates the capability of the RBTEIE index to effectively differentiate between vulnerable and resilient buildings.

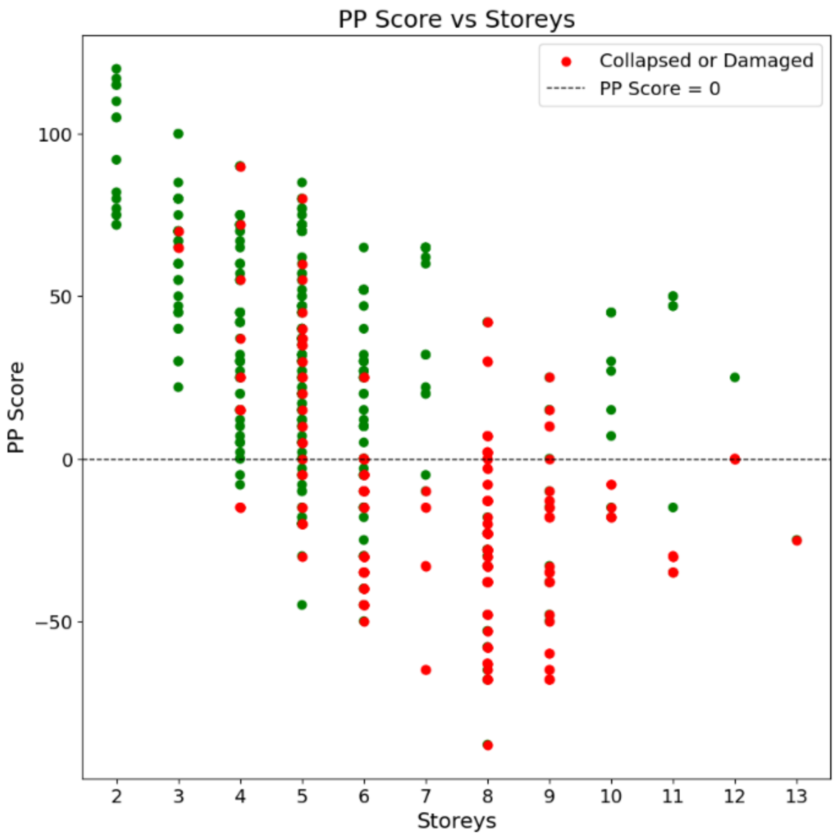

Fig. 3. Distribution of PP Scores by Story Level and Damage Condition

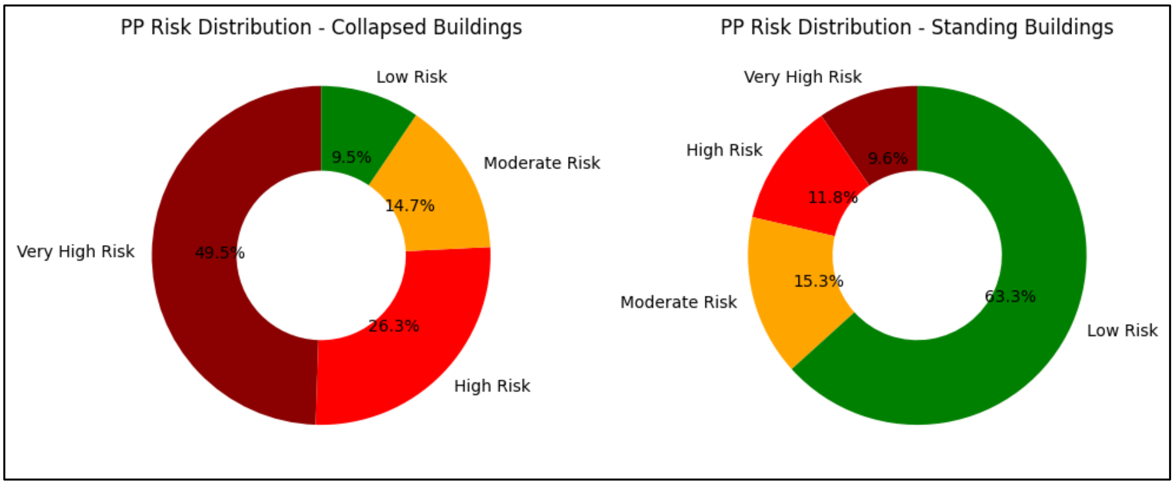

Fig. 4. Distribution of PP categories for all collapsed/non-collapsed buildings

4. Conclusions

This study presented a detailed seismic vulnerability assessment of reinforced concrete buildings affected by the 2023 Kahramanmaraş earthquakes, employing the Rapid Building Type Earthquake Impact Evaluation (RBTEIE) methodology. We proposed two improvements to the RBTEIE method: integrating a more structured and detailed visual assessment parameter and removing the presence of shear wall parameter.

One of the significant outcomes of the study was the achievement of prediction accuracy levels approaching 80%, despite the structural system of all buildings being uniformly assumed as reinforced concrete frame systems due to the lack of specific data on shear wall presence. This high level of accuracy can primarily be attributed to the detailed and systematic evaluation of visible damage parameters, including surface cracking, white markings, concrete spalling, and other observable structural deficiencies. The careful quantification of these visual indicators allowed for a realistic reflection of the actual damage state of the buildings, enhancing the predictive power of the applied vulnerability model. In addition, the risk thresholds were determined by prioritizing the safe region, and the classification boundaries were adjusted accordingly to maintain accuracy within this zone.

The risk classification based on the Performance Index (PP) proved to be effective in distinguishing between damaged and undamaged structures. Collapsed and heavily damaged buildings were predominantly concentrated in the higher-risk categories, while the majority of standing structures were correctly classified within the low-risk group. This consistency between the computed PP scores and the observed damage patterns confirms the validity and reliability of the proposed scoring system. The overall results highlight the effectiveness of the RBTEIE framework as a practical and reliable tool for rapid seismic vulnerability evaluation, especially when supported by real damage data obtained from post-earthquake field observations.

The study also reaffirmed the critical role of number of stories as a dominant vulnerability factor, particularly in conjunction with structural deficiencies such as soft stories, short columns, and plan irregularities. The observed increase in collapse ratios among mid- and high-rise buildings highlights the necessity for targeted mitigation policies focusing on these structural groups.

In summary, this research demonstrates that even without crucial structural system information, when combined with a careful evaluation of visible damage indicators, seismic vulnerability assessments can achieve high levels of predictive accuracy. The results emphasize the value of integrating real life damage data and multi-parameter assessment methodologies, such as RBTEIE, for developing effective disaster risk reduction strategies and improving the resilience of the existing building stock.

Future work is recommended to expand upon these findings by incorporating a wider range of variables and by validating the methodology across different seismic regions and building typologies. Such efforts will contribute to refining vulnerability models and enhancing their applicability in real-world risk management practices.

References

AFAD (Disaster and Emergency Management Authority). (2023). *Turkey earthquake hazard maps and data*. Retrieved from https://en.afad.gov.tr

Albayrak, U., Canbaz, M., & Albayrak, G. (2015). A rapid seismic risk assessment method for existing building stock in urban areas. *Procedia Engineering, 118*, 1242-1249.

Erberik, M. A. (2008). Generation of fragility curves for Turkish masonry buildings considering in-plane failure modes. *Earthquake Engineering and Structural Dynamics, 37*(3), 387-405.

Google Earth Pro. (2023). *Google Earth Satellite Imagery*. Retrieved from https://earth.google.com

Halder, L., Dutta, S. C., & Sharma, R. P. (2020). Damage study and seismic vulnerability assessment of existing masonry buildings in Northeast India. *Journal of Building Engineering, 29*, 101190.

RBTEIE - Rapid Building Type Earthquake Impact Evaluation. (2023). *International Journal of Disaster Risk Reduction, 58*, 102345.

Sextos, A. G., Kappos, A. J., & Stylianidis, K. C. (2008). Computer-aided pre- and post-earthquake assessment of buildings involving database compilation, GIS visualization, and mobile data transmission. *Computer-Aided Civil and Infrastructure Engineering, 23*, 59-73.

USGS (United States Geological Survey). (2023). *Liquefaction susceptibility and ground deformation data*. Retrieved from https://earthquake.usgs.gov

Yakut, A. (2004). Preliminary seismic performance assessment procedure for existing RC buildings. *Engineering Structures, 26*(10), 1447-1461.

Evaluation of seismic pile demands resting on soft soils across seismic hazards

Mehmet Ö. Timurağaoğlu*[1], Özkan Hakan[1], Ramazan Livaoğlu[1,2]

[1] *Bursa Uludağ University, Department of Civil Engineering, 16059 Bursa, Türkiye*
[2] *RL ProjeDestek Consulting Company, Bursa, Türkiye*

Abstract. Soil-pile interaction is a critical aspect of foundation engineering, particularly for structures built on soft or loose soil. The interaction is governed by the transfer of loads from the pile to the soil and the resulting response of both materials. The interaction depends on various factors, including the pile type, soil properties, depth of the pile, and loading conditions. It is important to consider the soil's resistance to penetration, its shear strength, and the frictional forces between the pile and the soil. Modern techniques, such as numerical modeling and advanced analytical methods, allow engineers to better predict pile behavior and optimize foundation design. The study is focuses on kinematic interaction of a soil-pile system investigating the pile response in upper and lower limits of ZD soil class according to Turkish Building Seismic Code (TBSC, 2018). The pile-soil interface is modeled through contact elements that simulate friction and normal forces between the pile and the soil. Additionally, the nonlinear behavior of the soil is incorporated to improve the accuracy of predictions. The absorbent boundary condition is applied at the boundaries of the model and the response of the system is calibrated against one-dimensional site response analysis. The nonlinear time history analyses are carried out under mentioned boundary conditions and structural loadings. The responses of piles in the soil at the lower and upper limits of the ZD soil class are compared in terms of shear force and moment variation throughout the pile length.

Keywords: Kinematic interaction; Soil structure interaction; Soil pile interaction; Dynamic analysis

1. Introduction

The interaction between structures and the supporting soil has long been a critical consideration in the fields of geotechnical , earthquake and structural engineering. Commonly referred to as soil-structure interaction (SSI), this phenomenon becomes especially significant under dynamic loading conditions such as earthquakes, where the assumption of a fixed-base structure fails to capture the realistic behavior of the system (Kramer, 1996; Wolf, 1985). Traditional design practices often neglect SSI effects by fixing the base of the structure. However, this simplification can lead to unsafe or overly conservative designs, particularly in soft or layered soil profiles (Mylonakis & Gazetas, 2000).

Pile foundations are widely used in regions with weak surface soils to transfer structural loads to deeper, more competent layers. The inclusion of piles introduces additional complexity into the SSI problem, resulting in what is commonly referred to as structure-pile-soil interaction (SPSI). In such systems, load transfer mechanisms are governed by both shaft friction and end-bearing, with the piles acting as intermediaries between the superstructure and the underlying soil. The solution of such systems can be approached either directly or using a substructure approach based on the principle of superposition, where the solution is carried out in two stages: kinematic and inertial interaction.

Recent advancements in computational modeling, particularly through the finite element method (FEM), have enabled more accurate simulation of SPSI effects. These method can account for nonlinear soil behavior, interface friction between pile and soil, group effects in pile foundations, and even the degradation of stiffness under cyclic loading. Such comprehensive modeling is essential for understanding the real dynamic response of the structure-foundation-soil system.

Kinematic bending effects at the pile head in homogeneous and layered soils are widely studied and highlighted in literatüre (Chiou & Wei, 2021; de Sanctis et al., 2010; Di Laora et al., 2012; Di Laora & Rovithis, 2015; Luo et al., 2021). In cases where the pile head is embedded in soft or highly compressible soils, the overall load-transfer mechanism and deformation pattern of the pile can be significantly altered. Soft soils at the pile head may lead to

*Corresponding author, E-mail: omertao@uludag.edu.tr

https://doi.org/10.31462/icearc2025_ce_eqe_678

reduced lateral stiffness and increased head displacement under lateral or combined loading, which in turn can amplify bending moments along the pile shaft (Reese & Van Impe, 2011). Additionally, the presence of weak soils in the upper layers can contribute to non-uniform settlement and increased differential displacements across pile groups, potentially compromising the structural performance of the superstructure supported by the pile cap. Therefore, proper characterization of near-surface soil conditions is critical for accurately predicting pile performance and ensuring the integrity of pile-supported systems.

This study aims to investigate the kinematic response of soil-pile system under two separate soil profiles being in the upper and lower levels of ZD soil class under three different earthquake ground motion records. Emphasis will be placed on assessing how soil properties influence the pile response, providing insights for more resilient and optimized foundation design. The results are evaluated by comparing the force and moment responses obtained from both profiles.

2. Soil profile and numerical modeling

Based on the data obtained from borehole drilling, field, and laboratory tests, it has been determined that the soil structure in the project area consists of light brown-colored, locally gravelly layers of low plasticity silty clay/sandy clay/clayey silt near the surface, and beige-colored, high plasticity silty clay/sandy clay/clayey silt units at deeper levels (~120m) as shown in Fig. 1. The idealized profiles are selected based on field and laboratory tests. The identification of geological unit variations and the assessment of shear wave velocity (Vs) as a function of depth were determined based on the results obtained from Multi Channel Analysis of Surface Wave (MASW) method conducted in the field as given in Fig. 1.

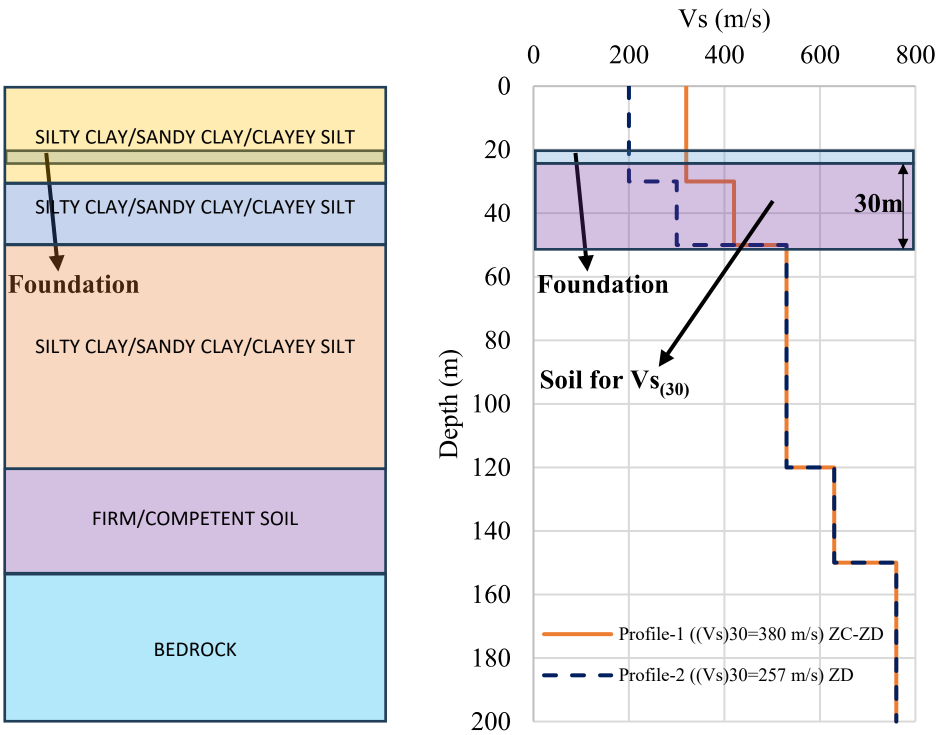

Fig. 1. Soil layers and Vs profiles used in numerical models

The foundation system has a 3m raft thickness with 36 piles with lengths of 32m, 71 piles with lengths of 36m and 66 piles with lengths of 43m. The piles are rectangular shaped barettes with 0.8x2.4m dimensions to resist vertical and horizontal loads. The visual representations associated with the 3D model generated using the Midas GTS NX (2023) finite element program are presented in Fig. 2. It is important to note that smaller element sizes were employed in the region where the building's foundation is to be located, while larger element dimensions were applied towards the model boundaries. To mitigate reflection effects at the lateral boundaries of the model, free-field elements were incorporated to minimize the impact of reflections. These elements utilize the infinite element model proposed by Lysmer and Kuhlemeyer (1969). Within the 3D model, the compliant base feature, available within the software package, was utilized to prevent the reflection of waves reaching the base of the soil domain. In the 3D finite element model, the soil, foundation (raft), and basement walls were modeled using solid elements, while the piles were represented by beam elements. The building foundation, along with the surrounding basement walls up to the ground floor level, was modeled using massless, infinitely rigid elements (Fig. 2) in accordance with TBSC (2018). An appropriate interface has been defined between the pile and the soil. To define these interfaces, it is necessary to determine the ultimate shear force, shear stiffness (K_t), and normal (K_n) stiffness parameters. In this study, the ultimate shear force for the pile-soil interaction was determined using the beta method found available in the literature (Das, 2016). Tip resistance is also defined at the pile bottom to account for the soil resistance at the bottom of piles. The rotation of piles at the Z directions (R_z) is contrained to to prevent torsional behavior. For the 1D analyses, the elastic-half-space option was used in the Deepsoil program (Hashash et al., 2024) at the base to prevent reflections. Three ground motion records were employed for the analysis while one of them (RSN721_X) is used for model dimension calibration in site response analysis. The corresponding record and response spectrum for the earthquakea are shown in Fig. 3.

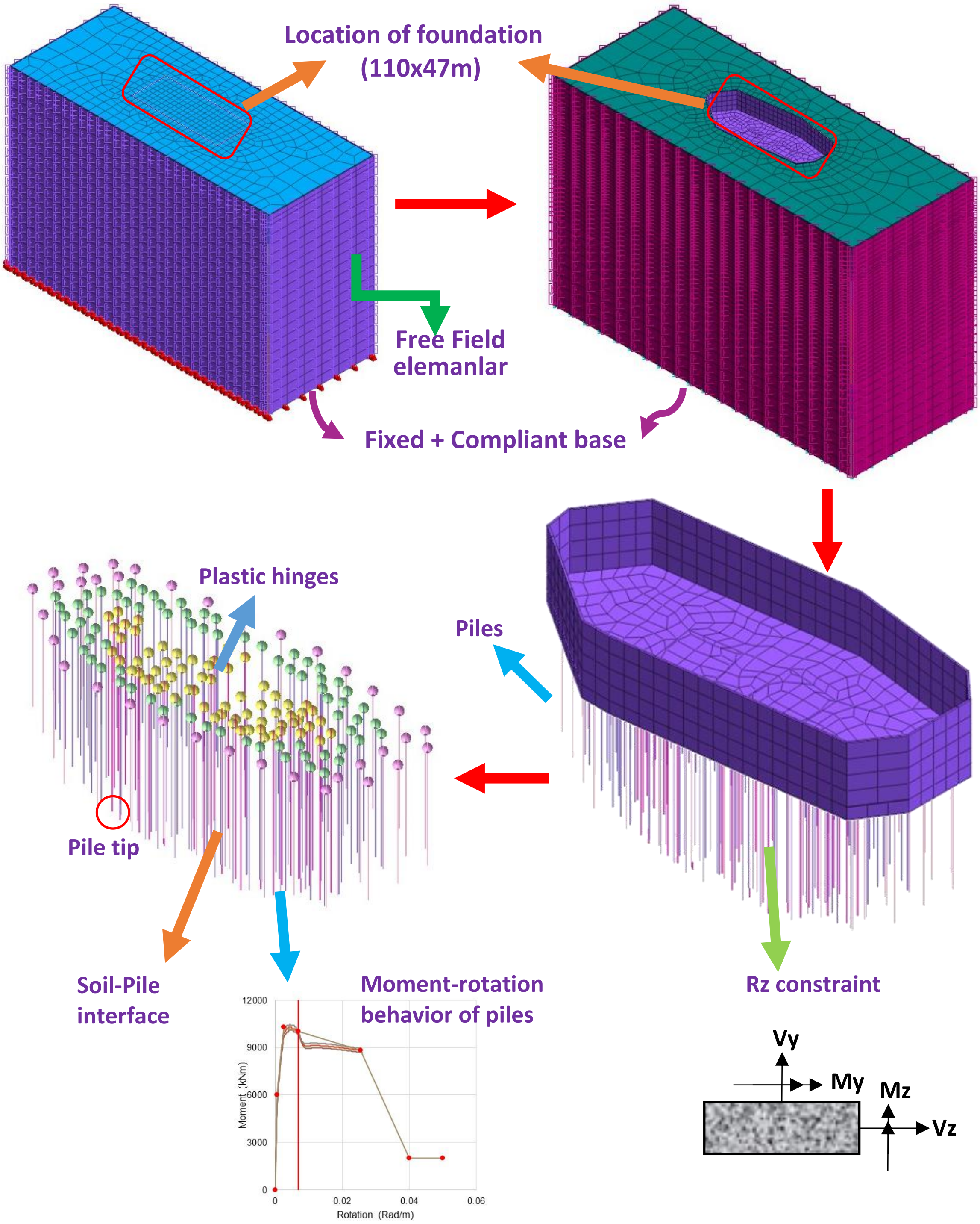

Fig. 2. Generated 3D soil model, foundation and piles

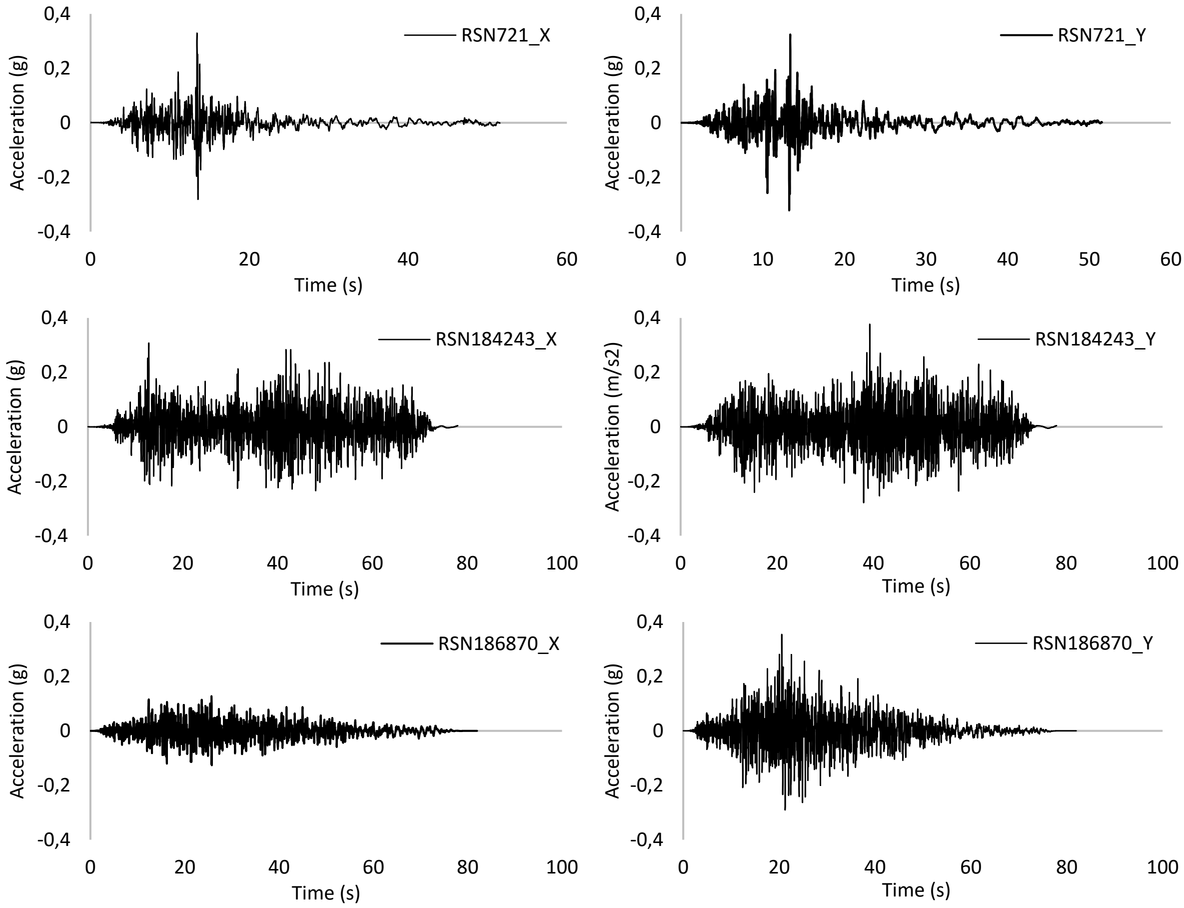

Fig. 3. Time history and response spectrum of the records

3. Soil model parameter calibration

In the present study, the Ramberg & Osgood (1943) material model, which is widely recognized in the literature for representing the nonlinear material properties of soil, has been employed. Initially developed for metals such as aluminum, which exhibit an undefined yield stress, this model was subsequently adapted by Faccioli et al. (1973) to model the shear modulus reduction curves of sands, thus facilitating the representation of soil behavior. The model is implemented in the Midas GTS NX (2023) software package. To characterize soil behavior within the framework of this model, three parameters are required: the initial shear modulus (G_0), the reference strain (γ_r), and the maximum damping value (h_{max}). In light of these parameters, the yield criterion of the model is formulated through simple equations (Midas GTS NX, 2023) in which masing's rule is applied to represent the curves for unloading and reloading behavior. During the calibration process, the reference strain for each layer was determined individually, based on the shear strength (τ_f), cohesion (c), and internal friction angle (ϕ) of each respective layer. The maximum damping value was then established by comparing it with the results presented by Darendeli (2001), as illustrated in Fig. 4, for layer 2. Similar calibration procedure is applied for each layer. In this study, the maximum damping value was set as 20%. Furthormore, an additional 1% Rayleigh damping was introduced into the numerical model to represent damping at small deformations. Additional damping is input in 3D model throuhout Rayleigh damping.

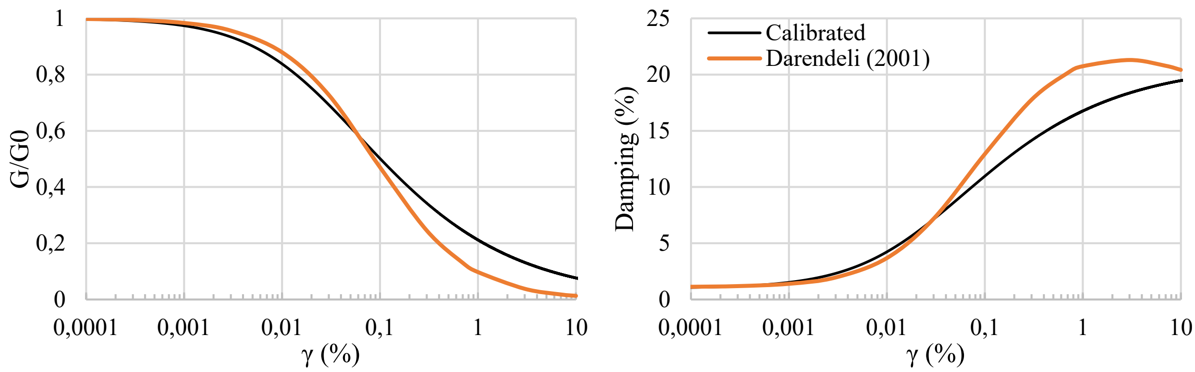

Fig. 4. Shear modulus and damping curves for Layer 2

4. Comparison of analysis results

The analysis are conducted in two phases namely site response analysis and kinematic interaction analysis. In site response analyses, the soil responses occurring at various depths are evaluated in the absence of the superstructure. In contrast, kinematic analyses consider the presence of the pile foundation, allowing for the assessment of responses that develop within both the piles and the foundation. Although the TBSC (2018) suggests dimensions seven times the foundation dimensions (110x47m), a 300x120m soil model has been selected for the 3D model. In this way, a significant analysis burden is mitigated while striving to achieve a behavior that is consistent with the results obtained from the 1D model.

The acceleration response spectrums at the ground surface for both soil profiles under RSN721 earthquake is given in Fig. 5. For both profiles, it is observed that the 1D and 3D analysis results exhibit a high degree of consistency, with comparable response values obtained at both the foundation edges and its center. This indicates that the response in generated 3D model is a reliable model compared with 1D model results. When the results of both profiles are compared, it is observed that in cases where the upper layer consists of weak soil, responses tend to be attenuated at shorter periods (0–0.5 s), whereas relatively larger responses occur at intermediate periods (0.5–2.0 s).

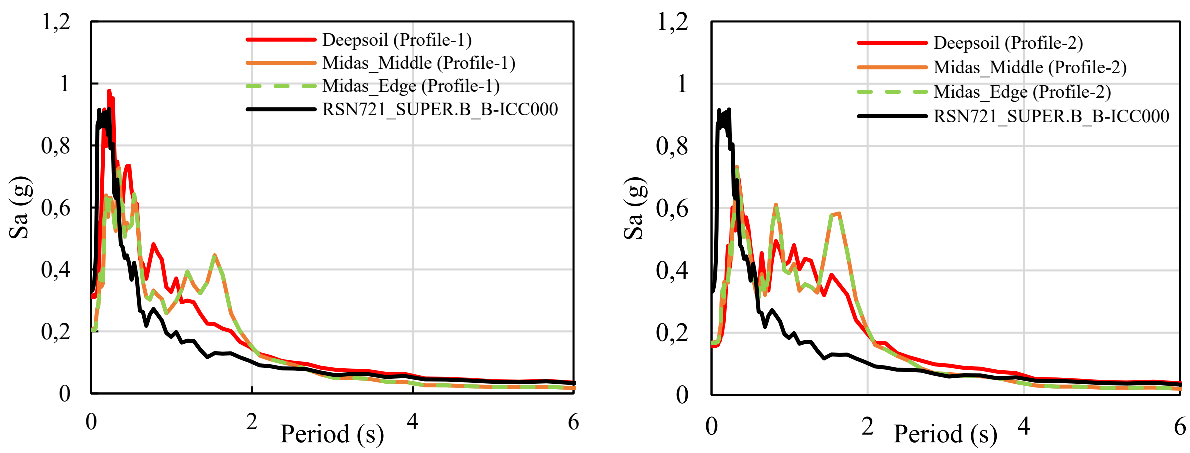

Fig. 5. Comparison of 1D and 3D site response analysis

Evaluations of analysis results were conducted based on the average values of the nonlinear analyses performed in the time domain for three different ground motions. Since the superstructure is positioned at the center of the foundation, longer piles are placed in this area to resist the loads from the superstructure, while the pile lengths decrease towards the edges. The average values of the maximum absolute results obtained from the analyses are presented as the Mz and My versus depth relationships in Fig. 6, and the Vz and Vy versus depth relationships in Fig. 7. In the figures, P1 and P2 defines soil Profile-1 and Profile-2, respectively and explained in Fig.1. The figures show that the moments at the pile head are increased up to 50% in Mz of pile length of 32m for weak soil profile (P2). An examination of both figures in terms of moment and shear force variations indicate that as the pile length increases, the difference between the results for the weak soil condition (Profile-2) and the good soil condition (Profile-1) at the base of the foundation becomes less pronounced. The primary reason for this is that the longer piles are located near the center of the foundation, surrounded by shorter piles, with the shortest piles positioned along the foundation boundaries. AS can be seen from both figures, the observed increases in moment and shear force near the toe regions of the shorter piles located at the foundation edges can also be attributed to this configuration. On the other hand, the largest moment occurs at the pile head of short barrettes (32m) located at the base boundary, while the lowest moments are observed in the longer piles situated in the middle. In the direction where the pile stiffness is relatively low, moments develop along the length of the pile, whereas in the direction of higher stiffness, the moments are high at the pile head and exhibit a decreasing trend towards the pile tip. The opposite responses are observed for shear forces (Fig. 7).

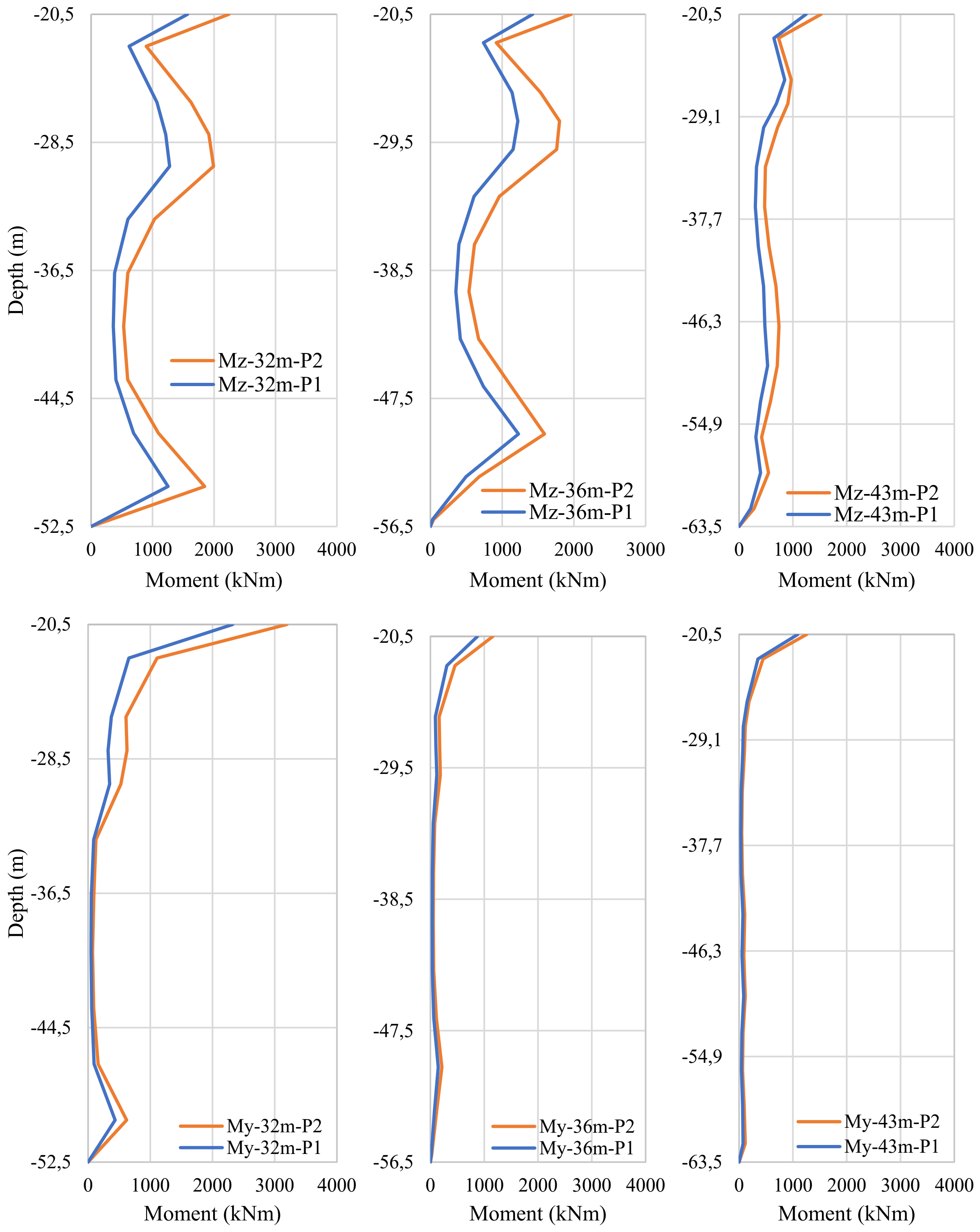

Fig. 6. Comparison of average Mz and My-depth relationship for barette piles

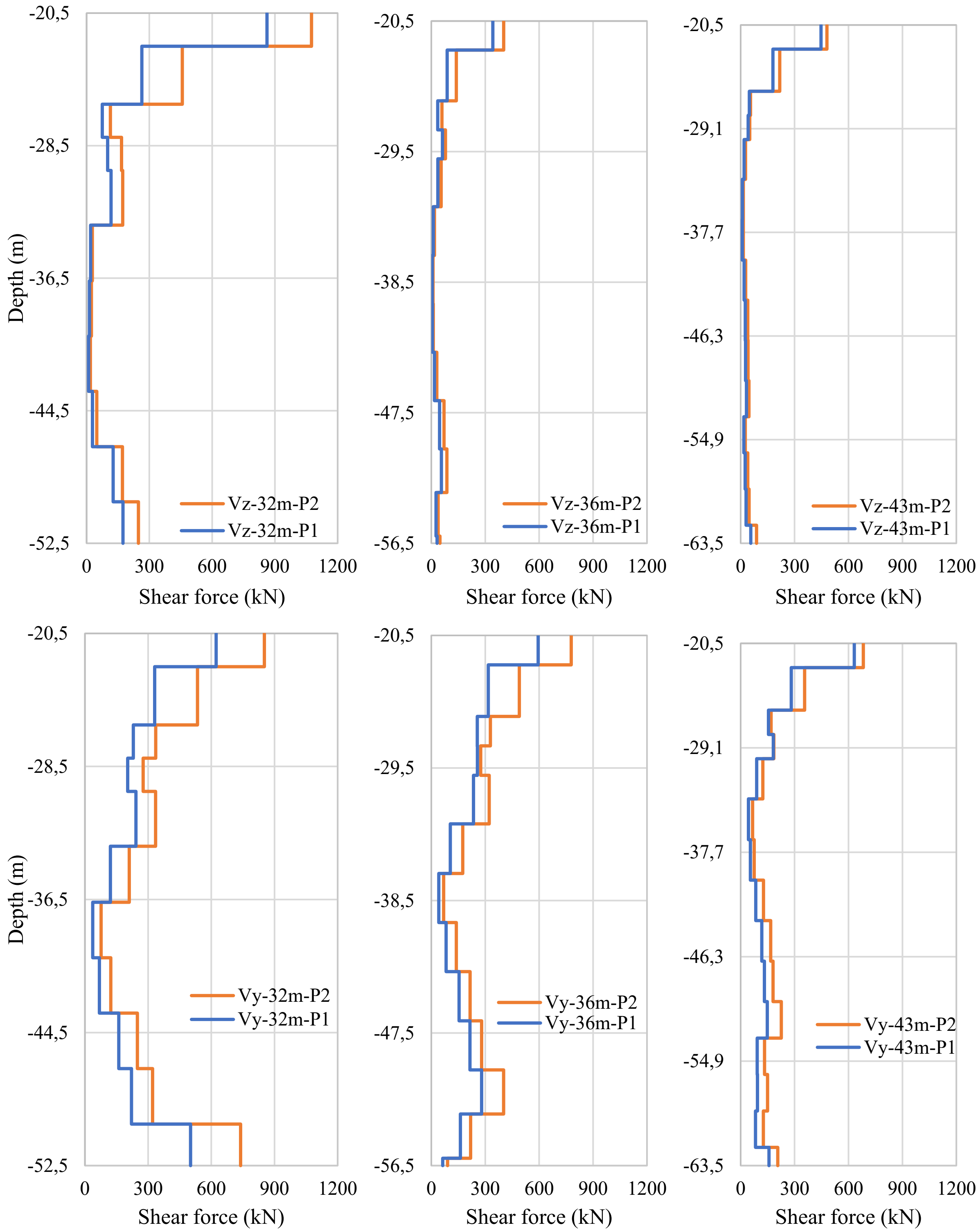

Fig. 7. Comparison of average Vz and Vy-depth relationship for barette piles

One of the key results obtained from the kinematic interaction analyses is the foundation input motions (FIM). Figures 8a and 8b present the response spectra obtained at the foundation level as a result of the conducted analyses, for Profile-1 and Profile-2, respectively. Additionally, the response spectrums for both profiles are compared in Figure 8c, indicates that the response at the foundation having the weak soil profile is slightly higher that the relatively better soil profile. This slight difference in the response spectrum may cause significant alterations in the internal forces generated in piles as indicated above.

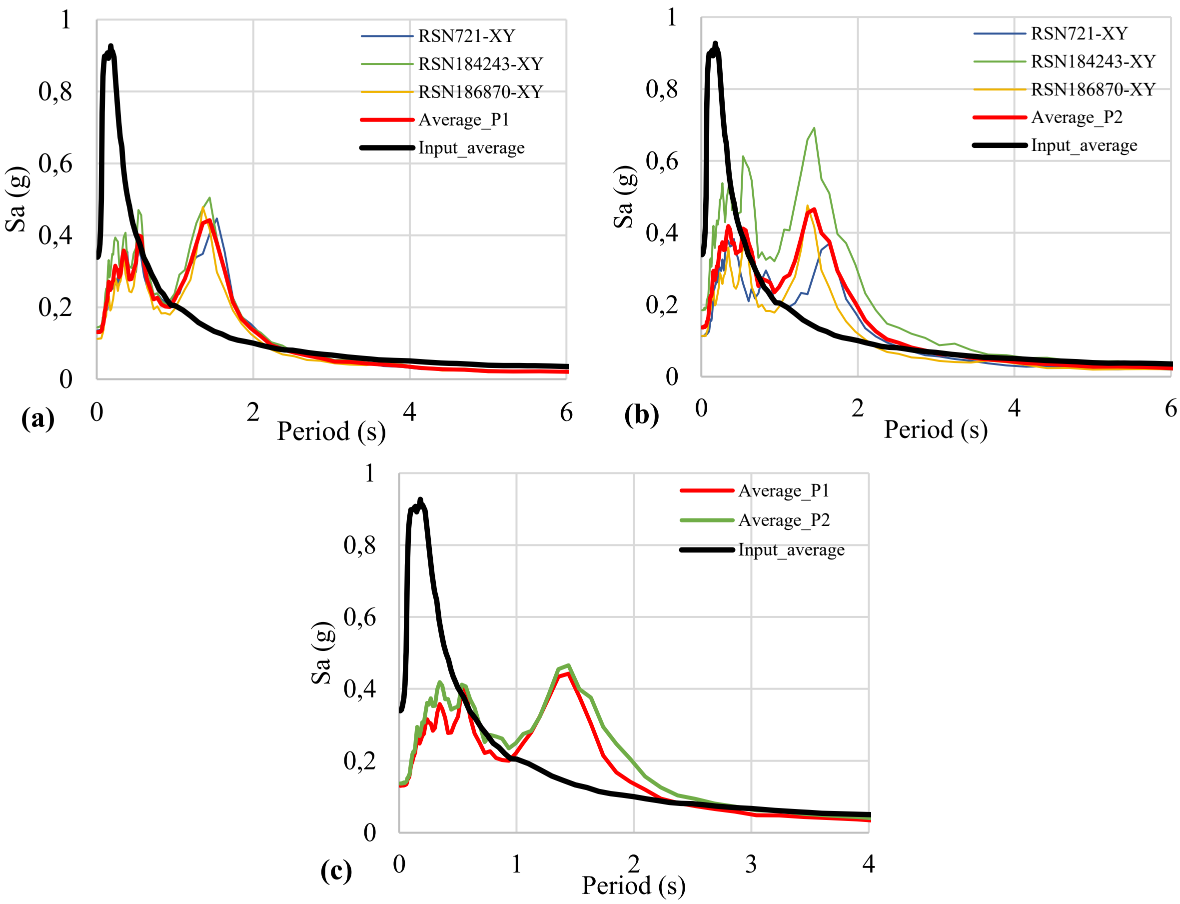

Fig. 8. Comparison of response spectrums at the foundation level for both profiles

5. Conclusions

The study compares the kinematic response of piles in the soils at the lower and upper limits of the ZD soil class in terms of shear force and moment variation throughout the pile length. For this study, a detailed 3D numerical model has been developed to represent the nonlinear behavior of the soil under dynamic loads and the pile-soil interaction.

In conclusion, the conducted site response and kinematic interaction analyses provide valuable insights into the dynamic behavior of pile foundations under seismic loading seated on weak soil profiles. The comparison of the 1D and 3D analysis results demonstrates a high degree of consistency, confirming the reliability of the 3D model in replicating the response behavior observed in the 1D model.

The evaluation of acceleration response spectra reveals that the response characteristics are influenced by the soil profile, with weaker soils leading to more pronounced attenuation at shorter periods and larger responses at intermediate periods.

Furthermore, the results highlight the importance of pile length and distribution in controlling the internal forces within the foundation. Specifically, longer piles, positioned centrally within the foundation, experience reduced variation in internal forces along the pile length, while shorter piles at the foundation edges exhibit higher moments and shear forces. The kinematic interaction analysis results further emphasize the impact of soil conditions on the seismic behavior of the foundation. The comparison of the response spectra for both soil profiles suggests that foundations resting on weaker soils experience slightly higher seismic responses, thereby underscoring the significance of soil-pile-structure interaction in the design and performance of pile foundations.

References

Chiou, J. S., & Wei, W. T. (2021). Numerical investigation of pile-head load effects on the negative skin friction development of a single pile in consolidating ground. *Acta Geotechnica*, *16*(6), 1867–1878. https://doi.org/10.1007/s11440-020-01134-0

Darendeli, M. B. (2001). *Development of a New Family of Normalized Modulus Reduction and Material Damping Curves*. The University of Texas at Austin.

Das, B. M. (2016). *Principles of foundation engineering*. Cengage Learning, Global Engineering.

de Sanctis, L., Maiorano, R. M. S., & Aversa, S. (2010). A method for assessing kinematic bending moments at the pile head. *Earthquake Engineering & Structural Dynamics*, *39*, 1133–1154. https://doi.org/10.1002/eqe.996

Di Laora, R., Mandolini, A., & Mylonakis, G. (2012). Insight on kinematic bending of flexible piles in layered soil. *Soil Dynamics and Earthquake Engineering*, *43*, 309–322. https://doi.org/10.1016/j.soildyn.2012.06.020

Di Laora, R., & Rovithis, E. (2015). Kinematic Bending of Fixed-Head Piles in Nonhomogeneous Soil. *Journal of Geotechnical and Geoenvironmental Engineering*, *141*(4), 1–10. https://doi.org/10.1061/(ASCE)GT.1943-5606.0001270

Faccioli, E., Santayo, V., & Leone, J. (1973). Microzonation criteria and seismic response studies for the city of Managua. *Proceeding of Earthquake Engineering Research Institute Conference*, 271–291.

Hashash, Y. M. A., Musgrove, M. I., Harmon, J. A., Ilhan, O., Groholski, D. R., Philips, C. A., & Park, D. (2024). *DEEPSOIL 7.0, User Manual*.

Kramer, S. L. (1996). *Geotechnical Earthquake Engineering*. Prentice Hall, Englewood Cliffs, New Jersey.

Luo, R., Yang, M., & Li, W. (2021). Assessments of Kinematic Bending Moment at Pile Head in Seismic Area. *Journal of Earthquake Engineering*, *25*(5), 970–991. https://doi.org/10.1080/13632469.2018.1550024

Midas GTS NX. (2023). *Online Manual. MIDAS Information Technology Co.* MIDAS Information Technology Co.

Mylonakis, G., & Gazetas, G. (2000). Seismic soil-structure interaction: Beneficial or detrimental? *Journal of Earthquake Engineering*, *4*(3), 277–301. https://doi.org/10.1080/13632460009350372

Ramberg, W., & Osgood, W. R. (1943). *Description of stress-strain curves by three parameters*.

Reese, L., & Van Impe, W. F. (2011). *Single Piles and Pile Groups Under Lateral Loading* (2nd edition). Crc press.

TBSC. (2018). *Principles for the Design of Buildings Under the Impact of Earthquakes (In Turkish)*. Ministry of Interior, Disaster and Emergency Management Presidency, Ankara, Turkey.

Wolf, J. P. (1985). *Dynamic soil-structure interaction.* Prentice Hall, Englewood Cliffs, New Jersey.

Development of rapid visual screening method for earthquake risk assessment of existing RC buildings using deep learning-based classification

Ömer F. Nemutlu *[1], Hüseyin Üzen[2], Salih T.A. Özçelik[3], Ali Sarı[4]

[1] *Bingol University, Department of Civil Engineering, 12000, Bingöl, Türkiye*
[2] *Bingol University, Department of Computer Engineering, 12000 Bingöl, Türkiye*
[3] *Bingol University, Department of Electrical-Electronics Engineering, 12000 Bingöl, Türkiye*
[4] *Istanbul Technical University, Faculty of Civil Engineering, 34467 Maslak, İstanbul, Türkiye*

Abstract. It is important for existing RC buildings to be prepared for possible earthquakes in the future in order to minimize the damages that may occur after earthquakes. Even if the existing building stocks are considered to have been built in accordance with the seismic codes valid at the time of construction, they may have weaknesses that may cause some negativity during earthquakes. For this reason, existing building stock in a region should be evaluated in order to be minimally affected by earthquakes. In the first stage of the evaluation of the existing building stock, rapid visual screening (RVS) methods are used. With these methods, risk prioritization of buildings is carried out based on the characteristics of the buildings that can be determined by looking at them from the outside. Despite being described as fast, fieldwork has negative aspects in terms of labor and time. Within the scope of this study, it is aimed to use artificial intelligence tools in the evaluation of structures. The images of the buildings were used as training data in deep learning models, and the detection of negativity situations was made through conventional neural network(CNN) methods. The obtained visuals of the buildings were transferred to the digital environment and building performance scores were obtained. The images were evaluated in terms of critical parameters affecting the building condition. In order to classify these parameters, four different advanced deep learning models such as VGG16, DenseNet121, InceptionV3 and ResNet101 were used. Looking at the results; Parameters that stand out for their high accuracy and F1-scores in all models include Heavy Overhang (accuracy over 80%), Soft-Weak Story (accuracy over 75%) and Structural System Type (accuracy over 70%).

Keywords: RVS; Earthquake risk assessment; Existing building stock; CNN; Artificial intelligence

1. Introduction

Turkey is located in active seismic zones, which indicates that the country is facing a significant seismic hazard. In particular, large active fault lines such as the North Anatolian Fault (NAF) and the East Anatolian Fault (EAF) have caused many earthquakes in the historical process. In addition, the West Anatolian Fault is considered as one of the active faults in Turkey. The distribution of active fault lines in Turkey is presented in Figure 1 (Akkar et al., 2018).

In recent years, destructive earthquakes have occurred on active fault lines in Turkey. On January 24, 2020, an earthquake with a magnitude of 6.8 (Mw) occurred in the Sivrice district of Elazig, according to Disaster and Emergency Management Affair(DEMA) data, and this earthquake caused serious structural damage in Malatya and Elazig(AFAD, 2020). As a result of the disaster, 41 people lost their lives and 1607 people were injured. Similarly, on October 30, 2020, an earthquake with a magnitude of 6.9 (Mw) occurred on the West Anatolian Fault, off the Aegean Sea, at 14:51 Turkey time, according to the data of the Kandilli Observatory. In this earthquake, 117 people lost their lives and approximately 1100 people were injured. One of the biggest earthquakes that has occurred in recent years is the February 6, 2023 Kahramanmaraş earthquakes, and these tremors took place on the East Anatolian Fault (DAF) (AFAD, 2023). Two destructive earthquakes, which occurred 9 hours apart, affected a wide geographical area. As a result of the earthquakes with a magnitude of 7.7 (Mw) with the epicenter of Pazarcık at 04.17 local time and 7.6 (Mw) with the epicenter of Elbistan at 13.24, more than 250,000 buildings in 11 provinces became unusable and the death toll from the earthquake exceeded 50,000 (Nemutlu et al., 2023a).

* Corresponding author, E-mail: ofnemutlu@bingol.edu.tr

https://doi.org/10.31462/icearc2025_ce_eqe_694

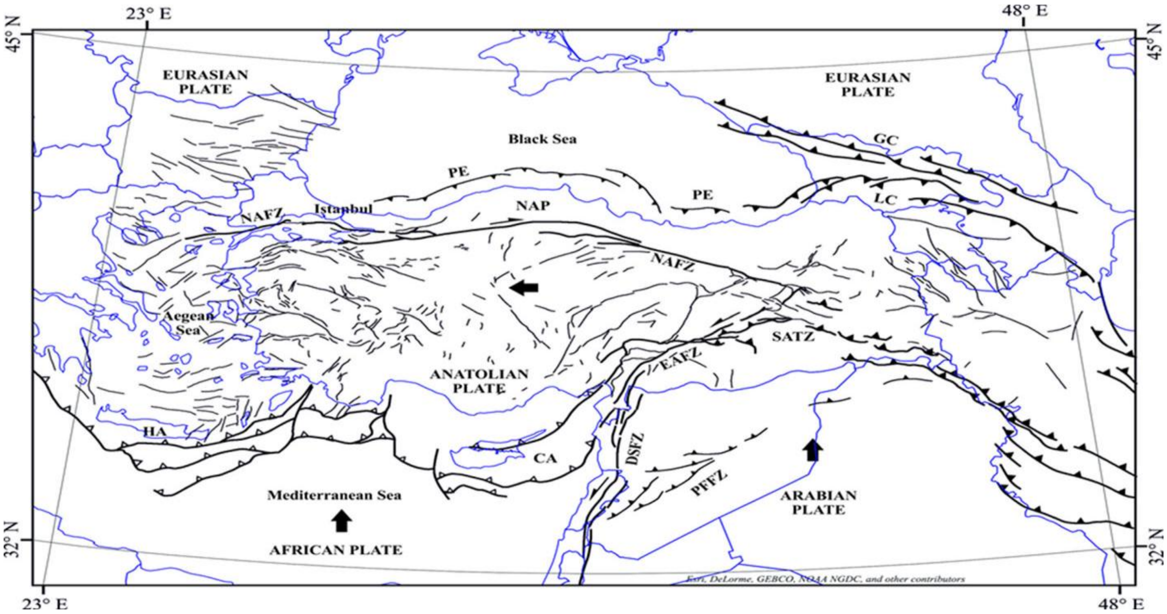

Fig. 1. Active fault of Türkiye

In order to minimize the impact of earthquakes, it is of great importance to evaluate the existing building stock before the earthquake. In this context, studies have been carried out in the literature to evaluate the existing building stock in various regions throughout Turkey(Ay & Erberik, 2008; Çavuş & Akyol, 2015; Işık, 2013a, 2013b; Işık et al., 2016, 2018). In his doctoral study, Işık discussed the probabilistic evaluation of seismic performance for Bitlis province(Işık, 2010). In the study, first of all, seismic hazard analysis was performed, and then first, second and third stage methods were used to determine the existing building inventory. In line with the data obtained, fragility curves were created and the vulnerability of the structures against earthquakes was examined. As a result of the study, an earthquake damage loss model based on different earthquake scenarios was developed and social and economic losses were evaluated in terms of the post-earthquake period. In cooperation with Izmir Metropolitan Municipality, Özçelik et al. carried out building stock inventory studies and earthquake safety assessment in Balçova and Seferihisar districts (Özçelik et al., 2013). In this context, a questionable zoning information system was created, special data of buildings were used and risk assessment was made at the building level. In the study, it was also aimed to identify the buildings that need to be improved, to make cost analysis for reinforcement works and to develop post-disaster response plans. In recent years, street screening methods have come to the fore as an important approach in terms of evaluating the existing building stock. In particular, the February 6, 2023 Kahramanmaraş earthquakes once again revealed the importance of the seismic behavior of structures. Although street scanning methods do not directly identify risky buildings, they help identify risky areas and allow prioritization. In this way, the relevant institutions can prioritize the evaluation of the existing building stock.

In the study carried out by Nemutlu, an analysis was made on the evaluation of the building stock of Bingöl province and a loss model was created based on the post-earthquake vulnerability of the buildings (Nemutlu, 2023). In the study, the prioritization of the buildings was ensured by using the street scanning method and risky areas were identified. Similar street survey studies have been carried out in many cities throughout Turkey, and risk analyzes of the buildings have been carried out in line with the structural performance scores obtained. When we look at the studies in the literature, it is seen that the field survey method is widely used. In the street scans carried out in line with the forms prepared by different regulations and institutions, the structural features are determined by visual inspection of the buildings from the outside. These structural features are scored according to their positive or negative effects, resulting in a total score for each building. Depending on the distribution of the scores obtained, certain levels are established and risk prioritization is made. However, this method requires significant time and labor. In order for the data collection process to be carried out in a healthy way, qualified human resources, sufficient time and technical equipment are needed. In the literature, studies on rapid visual evaluation methods with images obtained using drones are limited. However, there is a variety of research available on the integration of AI tools into rapid visual scanning methods. In the study conducted by Bektaş and Kegyes-Brassai, neural networks were integrated into the traditional street scanning method and the behavior of buildings against earthquakes was estimated with an accuracy rate of 68% using the parameters determined on the basis of the building (building period, spectral acceleration, etc.) (Bektaş & Kegyes-Brassai, 2024). In the research of Yu et al., buildings with soft floor irregularities, which are frequently encountered in earthquake-induced damages, were determined by deep learning-based models. Within the scope of the study, street images were obtained from Google to detect buildings with soft floor irregularities (Yu et al., 2020). In another study, rapid visual scanning methods were carried out with a fuzzy logic-based model. In this study, a fuzzy logic model was created on 40 buildings damaged in the 2019 Albania earthquake. The study reveals that it is possible to integrate artificial intelligence tools into street screening methods (Bektaş & Kegyes-Brassai, 2023). In general, studies in the literature show that artificial intelligence tools can be successfully integrated into street scanning methods. In this direction, it is considered that artificial intelligence-supported approaches can provide a faster and more systematic evaluation opportunity by reducing time and labor costs in field scans.

Within the scope of the project proposal, which forms the main basis of this study, it is aimed to develop original methods for automating the street scanning method. In this direction, problem-specific optimization processes will be carried out using various deep learning models. Although the street scanning method does not directly detect risky buildings, it is a fast and satisfactory method in terms of identifying risky areas and directing. Although it is stated in the literature that the street screening method is a rapid evaluation tool, it is possible to accelerate this process with today's technological possibilities. Images for structural evaluation will be obtained with the street scanning method to be carried out in the study area. Then, the parameters and images obtained by this method will be trained using artificial intelligence architectures and the re-estimation of the parameters will be performed. In this context, the main purpose of the study is to quickly prioritize the earthquake risk of the structures in the determined region with the support of artificial intelligence and to evaluate the applicability of the method. Thus, it is aimed to develop a more efficient and systematic analysis process compared to traditional field scans. The building evaluation process, which is carried out manually by qualified personnel in the field in traditional methods, will be automated with the support of artificial intelligence, thus providing a faster and more systematic analysis

2. Materials and method

It is of great importance to estimate the damages caused by earthquakes before a possible earthquake occurs. If we have detailed information about a possible earthquake in a certain region and up-to-date building inventory data, it may be possible to predict the damages that may occur in line with this data and take the necessary precautions. However, examining the earthquake performance of the buildings in a region in detail on a building basis is a very difficult process in terms of time and cost (Işık, 2013c). For this reason, the street screening method has been developed as a fast and economical method.

When the damages that occurred in past earthquakes are examined, it is known that structural damages vary depending on the building characteristics. Therefore, it is necessary to classify and evaluate the main characteristics of structures. There are many different street screening methods in the literature. Some of these are the street screening method developed by the Federal Emergency Management Agency (FEMA) and the eight-parameter street screening method developed by Haluk Sucuoğlu et al. (2007) (P-155, 2015, s. 155; Sucuoğlu, 2007). In addition, in the regulation of the Ministry of Environment, Urbanization and Climate Change on the Principles for the Detection of Risky Structures, a street screening method that can be applied to buildings between 1 and 7 floors is defined for reinforced concrete and masonry structures (RYTEİY, 2013). It would be an appropriate approach to use this method in order to be compatible with current earthquake regulation data.

The street scanning method to be used within the scope of this study will also be carried out on the basis of the method defined in the relevant regulation. This method calculates building performance scores using specific structural parameters. As stated in the study conducted by Nemutlu et al. (Nemutlu et al., 2023b), the parameters evaluated within the scope of the method in question are; the number of floors of the building, the earthquake hazard of the region where it is located, the characteristics of the structueral system, the soft/weak storey condition, irregularities in the plan and vertical, topographic effects, the visual quality of the building, ground characteristics, short column effect, building order and heavy overhangs. In order to apply the street scanning method, a form containing the parameters given above is prepared digitally and physically and these forms are used in field studies. Afterwards, these forms are transferred to the digital environment and the performance scores are calculated. In the relevant form, in addition to the structural features of the building, information such as visuals, location information, ground features of the building are filled in. According to these forms, the buildings are evaluated and the performance scores of each building are calculated. This score is obtained for each building in the study area. As a result of the performance scores obtained, the score distributions of the buildings in the study area are examined. For the specified threshold level, scores below this score are considered risky, and scores above it are considered risk-free. Thus, the regions where the buildings below the threshold score are concentrated are determined as priority regions and the detailed evaluation of the buildings in these regions is started.

Evaluation of the existing building stock in earthquake-prone areas is of critical importance in terms of earthquake preparedness. Site scans performed by expert engineers are a common method that evaluates the earthquake risk of buildings by analyzing the structural features of these structures with the street scanning method. However, when this process is carried out manually, it is time-consuming and requires high labor. At this point, the integration of artificial intelligence and drone technologies will allow the process to be carried out more quickly and efficiently.

Drone technology offers a number of advantages over traditional methods. Drones have the capacity to scan large areas in a short time and can obtain visual data from higher angles, different perspectives, and more comprehensive than taking photos from the ground. This allows for a more detailed analysis of structural features, especially on the upper floors of buildings. In addition, drones offer the ability to collect data in hard-to-access areas such as narrow streets, increasing both safety and the efficiency of the process.

In addition, artificial intelligence techniques to be used in automation produce numerical data and quantitative results, making the process more objective and accurate. While this automation minimizes human errors, it also allows large amounts of data to be processed quickly. Structural assessments obtained by processing drone images provide an effective and fast method of prioritizing earthquake risks in the region. As a result, a robust and scientifically based evaluation mechanism that can be used in disaster management processes will be established.

The scope of the buildings examined within the scope of the study includes residential type structures. Public institutions, mosques, warehouses, buildings used for commercial purposes, schools, huts will not be considered within the scope of the study. The process of obtaining the images used in the study and evaluating the street scanning method is given in Figure 2.

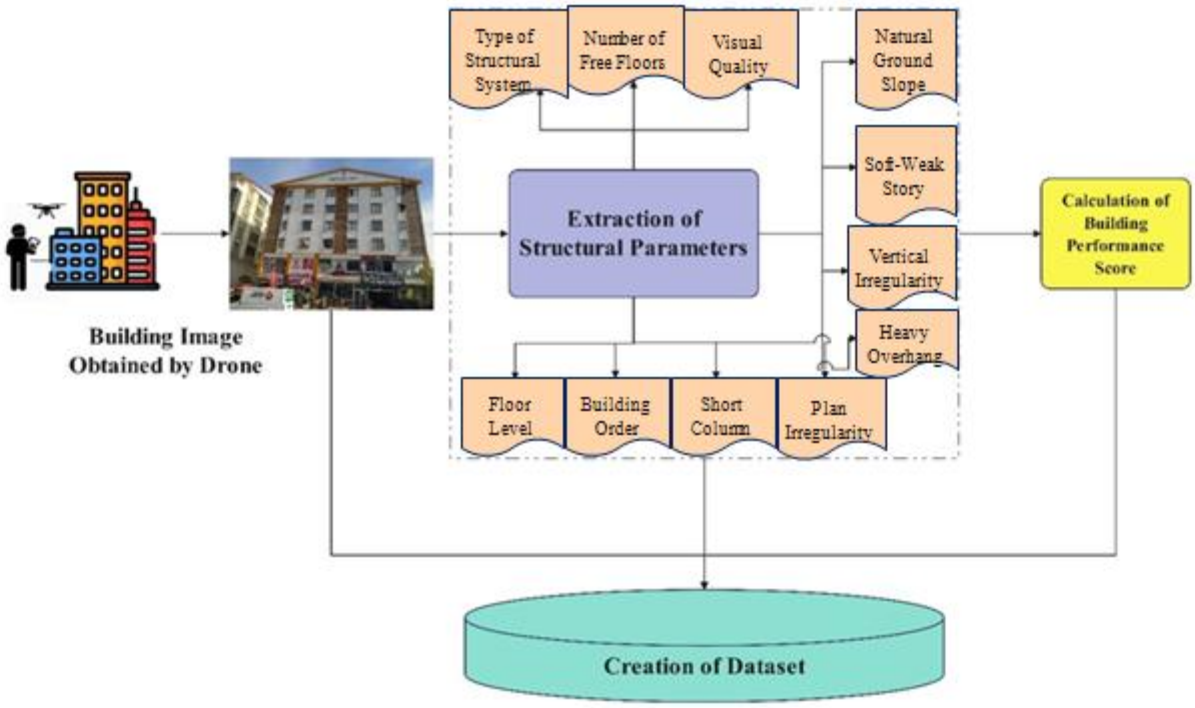

Fig. 2. Preparation of the dataset

Training of the proposed artificial intelligence model is a comprehensive process that aims to automate building performance evaluation and consists of stages such as data collection, labeling, pre-processing, model design and performance evaluation. For the training of the model, first, high-resolution images were obtained from buildings in different regions by means of drones. In order to accurately reflect the structural features of the buildings, images taken from different angles (front and top) were used. Along with the images, labels containing building features will be created based on manual inspections, and the model will be trained with a supervised learning approach. For training the deep learning model, the images will first be resized to match the input size of the model (256x256x3 or 512x512x3 as needed). Deep learning-based Convolutional Neural Networks (CNN) architectures will be used in model design. In particular, special CNNs will be optimized to learn the characteristics of buildings, such as the number of floors, visual quality and structural irregularities. For a faster and more effective learning process, pre-trained models such as DenseNet121(Li et al., 2021), Inceptionv3(Szegedy et al., 2016) and VGG16 will be used with the transfer learning method.

In this regard, in the first step, the images will be classified separately according to the structural parameters given in Figure 2. For example, the case of severe displacement will be trained in two classes as "YES" and "NO". Heavy overhangs will form an important part of the risk analysis, as they can adversely affect the performance of buildings. Similarly, the tile level will be trained in two classes, "SAME" and "DIFFERENT". In addition, a parameter such as the type of structural system is a parameter that specifies the type of load-bearing system of the building, and this parameter will be trained in two classes as "Reinforced Concrete Frame" and "Reinforced Concrete Frame -Shear Wall". In this way, the training of each structural parameter using 11 structural parameters will be carried out separately using the convolutional neural network (CNN) (Alzubaidi et al., 2021; Hüseyin Üzen, 2022; M. Shaha & M. Pawar, 2018; Saida et al., 2023; Xia et al., 2023). The planned framework for the development of the proposed model is given in Figure 3.

During the training of the model, 80% training and 20% test data sets were adjusted by randomly selecting from the images obtained using drone images. This data separation rate aims to increase the generalizability of the model and prevent overfitting. The model will be trained on different building categories and structural features. In order to reduce the error rate in the training process, the cross entropy loss function and the Adam optimization algorithm were used. This method speeds up the model's learning process and improves its accuracy.

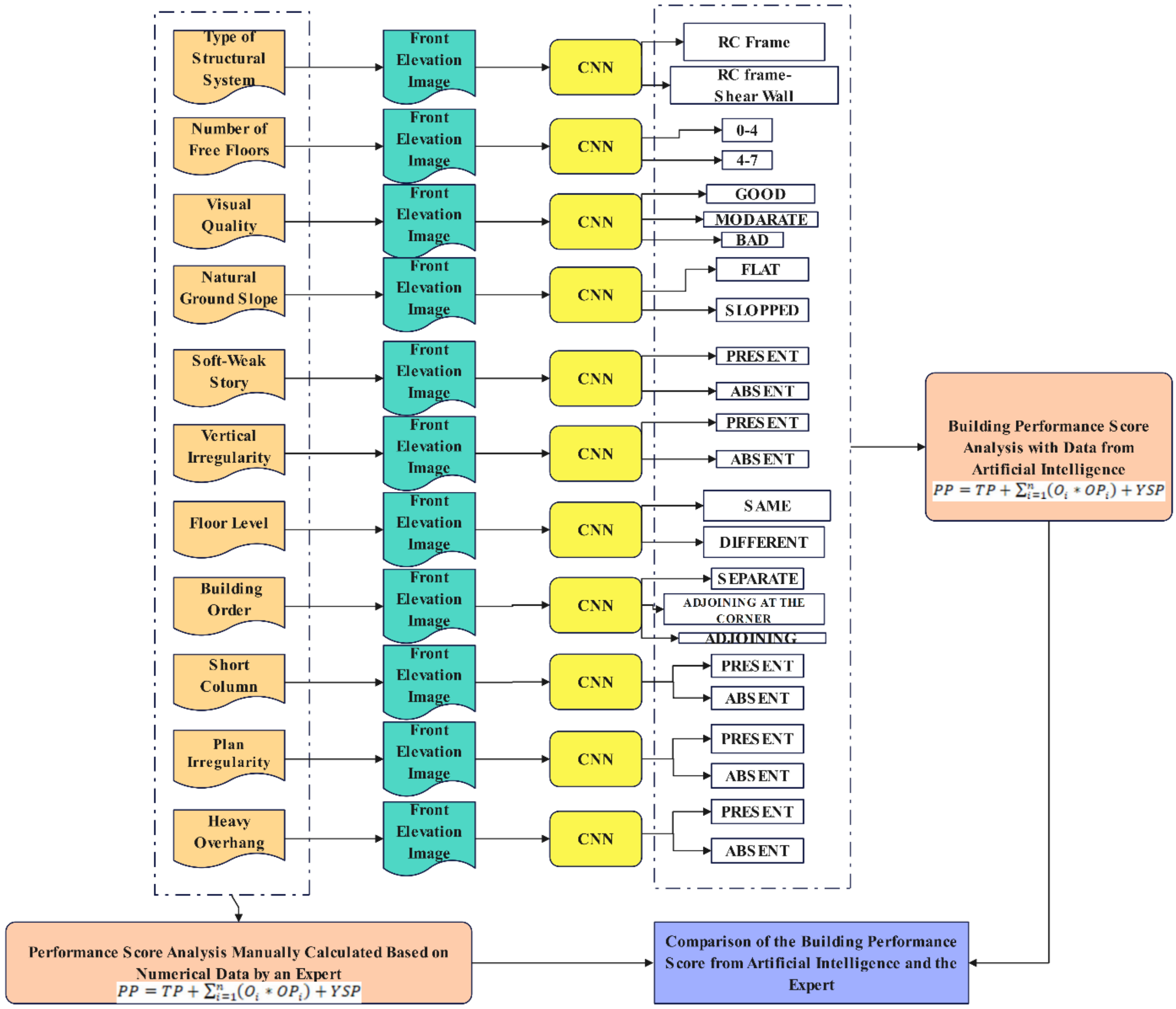

Fig. 3. Implementation of the proposed model

The success of the model will be evaluated with various performance metrics during training. These metrics include accuracy, precision, recall rate, and F1 score. Accuracy is calculated as the ratio of the correct classifications of the model to all predictions; Precision refers to the ratio of the model's correct positive predictions to all positive predictions. The recall rate shows the ratio of true positive predictions to true positive situations, while the F1 score is the harmonic mean of the accuracy and recall rate. These metrics are used to evaluate the overall performance of the model and how it performs, especially on unbalanced data sets (e.g., rare types of damage).

3. Results

In this study, a comprehensive preliminary analysis was carried out to evaluate the feasibility of the planned project. In this analysis, 344 images labeled in detail by expert academics working in the earthquake area(Bingol city center) were used.

The images used consist of buildings in 14 neighborhoods in the city center of Bingöl province. The building images prepared for the preliminary study are the buildings on the main streets of the neighborhoods in the city center. The building stock on the main streets generally reflects the building stock in the neighborhoods. The building visuals obtained for the preliminary study were obtained with the help of street scanning. The obtained visuals and the parameters required for the evaluation of the buildings were transferred to the digital environment after the field work and building performance scores were obtained.

The images were evaluated in terms of critical parameters such as 'Heavy Overhang', 'Floor Level', 'Vertical Irregularity', 'Visual Quality', 'Short Column', 'Irregularity in Plan', 'Number of Free Floors', 'Building Order', 'Structural System Type' and 'Soft-Weak Storey' affecting the building condition. In order to classify these parameters, four different advanced deep learning models such as VGG16, DenseNet121, InceptionV3 and ResNet101 were used. In the experimental study, the dataset was divided into 80% training and 20% testing, and each model was trained to classify the relevant building parameters. After the training process, the models were tested on the test dataset. The results obtained are summarized in Table 1 in order to compare the classification performance of the models. Table 1 contains the macro accuracy (ACC) and macro F1-scores of each model in parameters such as 'Heavy Overhang', 'Floor Level', 'Vertical Irregularity', 'Visual Quality', 'Short Column', 'Irregularity in Plan', 'Number of Free Floors', 'Building Order', 'Structural System Type', 'Soft-Weak Floor' and 'Building Estimated Age' (Alzubaidi et al., 2021; He et al., 2016; Simonyan & Zisserman, 2014; Szegedy et al., 2016).

Table 1. Classification Performance of Deep Learning Models for Building Parameters

Parameter	VGG16 ACC	VGG16 F1-score	DenseNet 121 ACC	DenseNet 121 F1-score	Inception V3 ACC	Inception V3 F1-score	ResNet1 01 ACC	ResNet1 01 F1-score
Heavy Overhang	85.29	82.29	83.82	80.23	85.29	81.11	80.88	74.99
Floor Level	77.94	73.81	75.00	67.30	76.47	67.31	83.82	79.58
Visual Quality	52.94	52.01	57.35	56.20	63.24	63.29	60.29	59.96
Short Column	95.59	48.87	95.59	48.87	95.59	48.87	95.59	48.87
Number of Free Floors	51.47	43.02	47.06	39.15	47.06	35.94	52.94	43.33
Building Order	73.53	56.56	64.71	50.35	55.88	39.20	73.53	57.09
Structural System Type	67.65	66.21	79.41	78.75	82.35	80.68	79.41	77.00
Soft-Weak Floor	73.53	73.32	82.35	82.21	79.41	79.12	82.35	82.29
Irregularity in Plan	69.12	40.87	88.24	46.87	86.76	46.46	86.76	46.46
Vertical Irregularity	Data Insufficient							

The data presented in Table 1 compares the performance of four different deep learning models (VGG16, DenseNet121, InceptionV3, ResNet101) used in the classification of building condition parameters. The performance of the models was evaluated on macro accuracy (ACC) and macro F1-scores. Based on these values, Table 1 reveals several important points. Among the parameters that attract attention with their high accuracy and F1-scores in all models are "Heavy Overhang", "Soft-Weak Floor" and "Structural System Type". In particular, DenseNet121 and InceptionV3 performed better than other models in the "Structural System Type" parameter. On the other hand, in parameters such as "Visual Quality" and "Number of Free Floors", the performance of all models remained low in general. This suggests that these parameters are more difficult to classify and require more data or model optimization. In particular, the decline in F1-scores indicates that the models are struggling to balance these parameters. The sample distributions in the dataset related to these parameters are presented in Table 2.In the sample distribution given in Table 2, the data distributions of "Heavy Overhang", "Soft-Weak Storey" and "Structural System Type" parameters are partially balanced. However, there is a class imbalance in the "Number of Free Floors" parameter. The balance of the dataset in the parameters of "Heavy Overhang", "Soft-Weak Storey" and "Structural System Type" and the low number of subclasses contributed to the high success of deep learning models. However, although a balanced distribution was achieved among the subclasses in the "Visual Quality" parameter, the success was low. The main reason for this is that the "Visual Quality" parameter is labeled with a personal approach, and structurally, the subclasses are similar. Therefore, the deep learning model is insufficient to separate subclasses. To solve this problem, it is necessary to create a more standard dataset and increase the number of samples. In addition, the low number of 7-storey buildings in the "Number of Free Floors" parameter directly affects the success. In addition, it is difficult for the deep learning model to determine the number of floors in buildings with mezzanines. To solve this problem, it is planned to increase the dataset for future studies and to perform analyzes using 3 classes as 0-2, 3-5, and 5+.

Table 2. Distribution of building parameters based on class labels

Heavy Overhang	Count	Soft-Weak Floor	Count	Structural System Type	Count	Visual Quality	Count	Number of Free Floors	Count
PRESENT	240	PRESENT	185	RC Frame and Shear Wall	232	GOOD	130	1	31
ABSENT	104	ABSENT	159	RC Frame	112	MODERATE	126	2	25
						BAD	88	3	33
								4	77
								5	127
								6	42
								7	9

As a result, poor performance in the "Visual Quality" and "Number of Free Floors" parameters indicates difficulties in the classification of these parameters. This indicates that these parameters, with the diversity of the data and their quality deficiencies, require more complex structures. In particular, more data and model optimization is required for the correct classification of parameters such as "Number of Free Floors".

The model-by-model comparison evaluates the classification performance of building condition parameters of four different deep learning models (VGG16, DenseNet121, InceptionV3, and ResNet101) based on the F1-score. The F1-score provides a more accurate measure of performance in the event of an imbalance between classes. The results presented in Table 1 show the performance of each model in terms of F1-scores. The VGG16 performed best in the "Heavy Overhang" parameter, achieving the highest F1-score. DenseNet121 and InceptionV3 achieved results close to VGG16, with VGG16's superiority evident. The ResNet101 has shown a lower performance compared to other models. The ResNet101 achieved the highest F1-score in the "Floor Level" parameter, outperforming the other models. ResNet101 gives better results in this parameter, suggesting that the model may be better suited for this specific classification task. InceptionV3 achieved the highest F1-score in the "Structural System Type" parameter, outperforming the other models. DenseNet121 and ResNet101 have also achieved quite good results, but the superior performance of InceptionV3 is remarkable. VGG16 showed the lowest performance in this parameter. ResNet101 and DenseNet121 achieved the highest F1-scores in the "Soft-Weak Storey" parameter. These two models have shown high performance in this parameter. The InceptionV3 was just behind these two models, while the VGG16 achieved a lower F1-score. Based on the F1-scores, it can be said that each model has strengths and weaknesses in certain parameter classifications. In particular, VGG16 excelled in the "Heavy Overhang" parameter, while ResNet101 achieved the highest success in the "Floor Level" parameter. InceptionV3 gave the best results in the "Structural System Type" parameter, while DenseNet121 and ResNet101 achieved strong results in the "Soft-Weak Storey" parameter. The performance of each model varies according to the difficulty levels of the parameters, which emphasizes that different requirements on a parameter basis should be taken into account when choosing a model. Overall, low F1-scores in some parameters indicate that deep learning models face particular challenges. In the "Visual Quality" parameter, the performance of all models was below average; in particular, the VGG16 performed inferiorly to other models with an F1-score of 52.01. This low achievement indicates that the "Visual Quality" parameter is not able to handle the model's data variance well enough in the classification task, or that the parameter presents challenges in terms of labeling and data diversity. In the "Short Column" parameter, all models achieved similarly low F1-scores; Poor performance on this parameter indicates that the model is not able to perform this specific classification task well enough. A similar low success rate was observed in parameters such as "Number of Free Floors" and "Building Estimated Age", indicating that the models could not provide adequate performance on these tasks and required further data or model optimization on these parameters. Overall, these underperformances reveal that the parameters involved require more complex structures or more data, and that the ability of existing models to deal with these challenges is limited. The complexity matrices of the methods in the "Visual Quality" parameter for Model-Based Comparison are given in Table 3.

In the "Visual Quality" complexity matrices given in Table 3, it is seen that the DenseNet121 and InceptionV3 models exhibit the highest performance in the "Good" class. These models correctly predicted most of the true values in the "Good" class and showed lower numbers in the wrong classifications. VGG16 and ResNet101, on the other hand, performed lower in the "Bad" class, indicating that these models had difficulty correctly predicting the "Bad" class. Performance in the "Moderate" and "Bad" classes reflects the difficulties experienced by each model in transitioning between classes. The main reason for these poor performances is the high similarities between the classes. In addition, the limited dataset causes artificial intelligence systems to have difficulty distinguishing between "Moderate" and "Bad" classes. This means that the collection of a more comprehensive and diverse dataset is expected to improve the quality of model training and provide higher performance.

It is seen that the number of parameters used in the studies carried out in the literature is generally limited. In this study, the evaluation of 14 different parameters reflecting the building characteristics stands out as an important factor that distinguishes the study from the existing literature. On the other hand, existing artificial intelligence models are generally limited to traditional machine learning methods and have deficiencies in developing a problem-specific network architecture.

Table 3. Confusion matrices of deep learning models for visual quality classification

Model	Actual \ Predicted	G	M	B
	G	18	3	4
VGG16	M	5	10	12
	B	1	7	8
	G	20	5	0
DenseNet121	M	6	10	11
	B	1	6	9
	G	17	6	2
InceptionV3	M	4	14	9
	B	1	3	12
	G	18	6	1
ResNet101	M	6	14	7
	B	0	7	9

4. Conclusions

Within the scope of the study, it is aimed to integrate artificial intelligence tools into the street scanning method, which is one of the rapid evaluation methods of existing reinforced concrete buildings. In this context, the data obtained with different deep learning models were evaluated and the performance of parameters and deep learning models among each other was evaluated. The results obtained were evaluated with their justifications.

Performance analysis of deep learning models used in the classification of building condition parameters reveals success differences in various parameters. High macro accuracy (ACC) and macro F1-scores were obtained in parameters such as "Heavy Overhang", "Soft-Weak Storey" and "Structural System Type". In particular, DenseNet121 and InceptionV3 showed high performance in the "Structural System Type" parameter, while VGG16 and ResNet101 gave lower results in this parameter. In other parameters, significant differences were observed in the performance of the models. In general, low successes were achieved in the "Visual Quality" and "Number of Free Floors" parameters. The sample distributions presented in Table 7 show that the parameters of "Heavy Overhang", "Soft-Weak Floor" and "Structural System Type" are evenly distributed in the dataset. However, the class imbalance in the "Number of Free Floors" parameter directly affected the classification performance related to this parameter. In addition, although the data distribution is balanced in the "Visual Quality" parameter, it is seen that the model cannot classify this parameter well enough. It can be concluded that this is due to the diversity of the dataset and the deficiencies in the labeling processes. The imbalances and low-performance parameters in the dataset in the study highlight the importance of improving data diversity and labeling processes to increase analysis success. The follow-up studies will not only evaluate existing deep learning approaches, but also aim for higher accuracy and overall performance using hybrid modeling strategies and data enrichment techniques. By strengthening the role of artificial intelligence in building condition assessment processes, it will provide significant innovations and efficiencies to applications in the sector.

Acknowledgments
This study was supported by Scientific and Technological Research Council of Türkiye (TUBITAK) under Grant Number 224M607. The authors thank TUBITAK for their support.

References
AFAD. (2020). *Afet ve Acil Durum Yönetimi Başkanlığı (AFAD) 24 Ocak 2020 Sivrice (Elazığ) Mw 6.8 depremine ilişkin ön değerlendirme raporu*. Afet ve Acil Durum Yönetimi Başkanlığı (in Turkish).

AFAD. (2023). *06 Şubat 2023 Pazarcık-Elbistan (Kahramanmaraş) Mw: 7.7 – Mw: 7.6 depremleri raporu* (s. 140). Afet ve Acil Durum Yönetimi Başkanlığı (in Turkish).

Akkar, S., Azak, T., Çan, T., Çeken, U., Tümsa, M. B. D., Duman, T. Y., Erdik, M., Ergintav, S., Kadirioğlu, F. T., Kalafat, D., Kale, O., Kartal, R. F., Kekovalı, K., Kılıç, T., Özalp, S., Poyraz, S. A., Şeşetyan, K., Tekin, S., Yakut, A., ... Zülfikar. (2018). Evolution of seismic hazard maps in Turkey. *Bulletin of Earthquake Engineering, 16*(8), 3197–3228. https://doi.org/10.1007/s10518-018-0349-1

Alzubaidi, L., Zhang, J., Humaidi, A. J., Al-Dujaili, A., Duan, Y., Al-Shamma, O., Santamaría, J., Fadhel, M. A., Al-Amidie, M., & Farhan, L. (2021). Review of deep learning: Concepts, CNN architectures, challenges, applications, future directions. *Journal of Big Data, 8*(1), 53. https://doi.org/10.1186/s40537-021-00444-8

Ay, B. Ö., & Erberik, M. A. (2008). Vulnerability of Turkish low-rise and mid-rise reinforced concrete frame structures. *Journal of Earthquake Engineering, 12*(Suppl. 2), 2–11. https://doi.org/10.1080/13632460802012687

Bektaş, N., & Kegyes-Brassai, O. (2023). Development in fuzzy logic-based rapid visual screening method for seismic vulnerability assessment of buildings. *Geosciences, 13*(1). https://doi.org/10.3390/geosciences13010006

Bektaş, N., & Kegyes-Brassai, O. (2024). Enhancing seismic assessment and risk management of buildings: A neural network-based rapid visual screening method development. *Engineering Structures, 304*, 117606. https://doi.org/10.1016/j.engstruct.2024.117606

Çavuş, Ş. U., & Akyol, C. (2015). Burdur deprem riski ve hasar tahmini. *Uluslararası Burdur Deprem ve Çevre Sempozyumu*, Mayıs, 32–40 (in Turkish).

He, K., Zhang, X., Ren, S., & Sun, J. (2016). Deep residual learning for image recognition. In *Proceedings of the IEEE Conference on Computer Vision and Pattern Recognition* (pp. 770–778). https://doi.org/10.1109/CVPR.2016.90

Üzen, H. (2022). *İmalat sistemlerinde derin öğrenme tabanlı doku hata tespiti* [Doktora tezi, İnönü Üniversitesi].

Işık, E. (2010). *Bitlis şehri deprem performans analizi* (in Turkish).

Işık, E. (2013a). Bitlis ili yapı stoğunun birinci kademe (sokak taraması yöntemi ile) değerlendirilmesi. *Süleyman Demirel Üniversitesi, Fen Bilimleri Enstitüsü Dergisi, 17*(1), 173–178 (in Turkish).

Işık, E. (2013b). Bitlis ilinde bulunan yığma yapı stoğunun sokak tarama yöntemi ile değerlendirilmesi. *BEÜ Fen Bilimleri Dergisi, 2*(1), 22–30 (in Turkish).

Işık, E. (2013c). The evaluation of existing buildings in Bitlis Province using a visual screening method. *Suleyman Demirel University Journal of Natural and Applied Science, 17*(1), 173–178.

Işık, E., Bozkurt, N., & Taşkın, V. (2016). Muş ili yapı stoğunun Kanada sismik tarama yöntemi ile incelenmesi ve bölgenin depremselliği. *Süleyman Demirel Üniversitesi, Fen Bilimleri Enstitüsü Dergisi, 20*(2), 1–9. https://doi.org/10.19113/sdufbed (in Turkish).

Işık, E., Sağıroğlu, Ç., Tozlu, Z., & Ustaoğlu, Ü. S. (2018). Farklı deprem senaryolarına göre Kırşehir ili kayıp tahmin analizleri. *Doğal Afetler ve Çevre Dergisi, 90*(434), 80–93. https://doi.org/10.21324/dacd.432592 (in Turkish).

Li, G., Zhang, M., Li, J., Lv, F., & Tong, G. (2021). Efficient densely connected convolutional neural networks. *Pattern Recognition, 109*, 107610. https://doi.org/10.1016/j.patcog.2020.107610

Shaha, M., & Pawar, M. (2018). Transfer learning for image classification. In *2018 Second International Conference on Electronics, Communication and Aerospace Technology (ICECA)* (pp. 656–660). https://doi.org/10.1109/ICECA.2018.8474802

Nemutlu, Ö. F. (2023). *Bingöl ili şehir merkezindeki binalarda deprem performansı, yapısal riskler ve kayıpların incelenmesi* [Yüksek lisans tezi, İstanbul Teknik Üniversitesi]. http://hdl.handle.net/11527/24214 (in Turkish).

Nemutlu, Ö. F., Sari, A., & Balun, B. (2023a). 06 Şubat 2023 Kahramanmaraş depremlerinde (Mw 7.7–Mw 7.6) meydana gelen gerçek can kayıpları ve yapısal hasar değerlerinin tahmin edilen değerler ile karşılaştırılması. *Afyon Kocatepe University Journal of Sciences and Engineering, 23*(5), 1222–1234. https://doi.org/10.35414/akufemubid.1302254 (in Turkish).

Nemutlu, Ö. F., Sari, A., & Balun, B. (2023b). A novel approach to seismic vulnerability assessment of existing residential reinforced concrete buildings stock: A case study for Bingöl, Turkey. *Iranian Journal of Science* *and Technology, Transactions of Civil Engineering, 47*(6), 3609–3625. https://doi.org/10.1007/s40996-023-01206-7

Özçelik, Ö., Mısır, İ. S., Baran, T., Kahraman, S., Saatçi, A., & Girgin, S. C. (2013). Balçova ve Seferihisar ilçelerinde gerçekleştirilen yapı stoğu envanter ve deprem güvenliği ön değerlendirmesi projesi sonuçları. In *2. İzmir Kent Sempozyumu*. https://doi.org/10.13140/2.1.2316.9925 (in Turkish).

Federal Emergency Management Agency. (2015). *FEMA-155: Rapid visual screening of buildings for potential seismic hazards: Supporting documentation*.

Resmî Gazete. (2013). *Riskli yapıların tespit edilmesine ilişkin esaslar (RYTEİY)*. https://www.resmigazete.gov.tr/ (in Turkish).

Saida, T., Rashid, M., Nemoto, Y., Tsukamoto, S., Asai, T., & Nishio, M. (2023). CNN-based segmentation frameworks for structural component and earthquake damage determinations using UAV images. *Earthquake Engineering and Engineering Vibration, 22*(2), 359–369. https://doi.org/10.1007/s11803-023-2174-z

Simonyan, K., & Zisserman, A. (2014). Very deep convolutional networks for large-scale image recognition. *arXiv*. https://arxiv.org/abs/1409.1556

Sucuoğlu, H. (2007). A screening procedure for seismic risk assessment in urban building stocks. In *Altıncı Ulusal Deprem Mühendisliği Konferansı*, İstanbul, October, 267–284.

Szegedy, C., Vanhoucke, V., Ioffe, S., Shlens, J., & Wojna, Z. (2016). Rethinking the inception architecture for computer vision. In *Proceedings of the IEEE Conference on Computer Vision and Pattern Recognition* (pp. 2818–2826). https://doi.org/10.1109/CVPR.2016.308

Xia, H., Wu, J., Yao, J., Zhu, H., Gong, A., Yang, J., Hu, L., & Mo, F. (2023). A deep learning application for building damage assessment using ultra-high-resolution remote sensing imagery in Turkey earthquake. *International Journal of Disaster Risk Science, 14*(6), 947–962. https://doi.org/10.1007/s13753-023-00526-6

Yu, Q., Wang, C., McKenna, F., Yu, S. X., Taciroglu, E., Cetiner, B., & Law, K. H. (2020). Rapid visual screening of soft-story buildings from street view images using deep learning classification. *Earthquake Engineering and Engineering Vibration, 19*(4), 827–838. https://doi.org/10.1007/s11803-020-0598-2

Seismic performance assessment of an existing pre-stressed reinforced concrete bridge

Ömer F. Ertaş*[1], Kadir Güler[1]

[1] Istanbul Technical University, Department of Civil Engineering, Ayazaga Campus 34469 İstanbul, Türkiye

Abstract. The seismic performance evaluation of existing reinforced concrete bridges is important in terms of emergency actions and ensuring continuity of services after an earthquake. Depending on the seismic performance level, the existing bridges may require strengthening; if it is not feasible, it may be required rebuilt. In this study, the seismic performance evaluation of an existing reinforced concrete bridge was accomplished, whose deck consists of precast pre-stressed beams and topping concrete. The existing bridge was built in 1989 in the Merzifon district of Amasya Province. The bridge has four spans, total length of bridge is 73.80m. The bridge deck consisting of prestressed RC beams and topping concrete is connected to the bridge cap with elastomeric bearings. The bridge cap is connected to piers (as piles) of the bridge. CSI Bridge software was used to establish the bridge numerical analysis model. In the numerical model, springs are assigned to the piles (piers of the bridge) to consider the soil-structure interaction. According to the Turkish Earthquake Code for Bridges (2020), the earthquake performance assessment of the bridges is proposed to carry out in two stages. In Stage 1, seismic performance evaluation was made by obtaining the strain method. At this stage, it is aimed to show the Limited Damage performance at the DD-2 Earthquake Level (design earthquake) by using pushover analysis of the piers. In Stage 2, it was checked whether the Collapse Prevention performance level was achieved at the DD-1 Earthquake Level (maximum earthquake) by using the non-linear time history analysis method. Based on the results obtained in both stages, it is decided the necessity of strengthening level and technique of the existing bridge. The numerical results on the seismic performance assessment of the considered bridge are given in tables and graphs, comparatively.

Keywords: Seismic performance; Concrete bridge; Pushover analysis, Pre-stressed concrete

1. Introduction

Bridges and viaducts are among the most important components of today's road and railway transportation networks. While these art structures are so important for transportation, it has become a necessity to determine the seismic performance of existing bridges and viaducts in countries with high seismicity. It is necessary to evaluate whether the bridge will be able to continue its operational activities after a possible earthquake and whether emergency aid will not be able to reach the relevant places. There are lot of studies on the performans assessment of existing bridges (Batbayar, 2008; Elmas, 2008; Şengül, 2018). Design and earthquake performance assessment of a bridge with prestressed concrete girder is studied by Salimee (Salimee, 2019).

In this study, the seismic performance of one of the existing bridge, the Kayadüzü overpass bridge on the Suluova-Amasya state highway, is evaluated by using nonlinear analysis method. According to the numerical results obtained. The numerical results are carried out by using CSI Bridges software. The results are given in figures and tables.

2. Materials and methods

2.1. General information

The bridge examined in this study consists of two identical parallel bridges on the main artery on the Suluova-Amasya road. The location and picture of the bridge are shown in Fig. 1 and Fig. 2. According to the information obtained from the project of the bridge, the construction year is 1989. The bridge has 4 spans in total, each span has 18 m long. The total length of the bridge is 73.8 m and the width is 12 m. As can be seen in Fig. 3, the bridge has a skew of 15°. The center piers of the bridge consist of 4 circular columns joined by a cap beam. These circular columns continue on the soil for 25 m and work as pile-columns that also form the foundation of the bridge(Fig. 4). The pile-columns are friction piles. As shown in Fig. 5, the superstructure of the bridge consists of

*Corresponding author E-mail: ertaso22@itu.edu.tr

https://doi.org/10.31462/icearc2025_ce_eqe_738

7 number of 127.5 cm high precast I-section prestressed reinforced concrete girders and a 22 cm thickness reinforced concrete deck.

Fig. 1. Location of the Kayadüzü bridge

Fig. 2. General view of Kayadüzü bridge

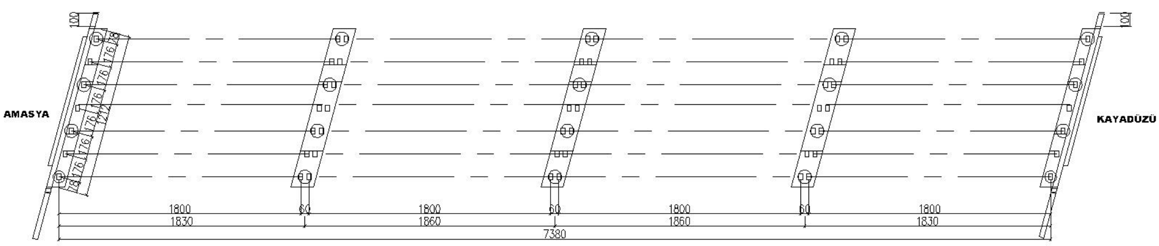

Fig. 3. Bridge plan view

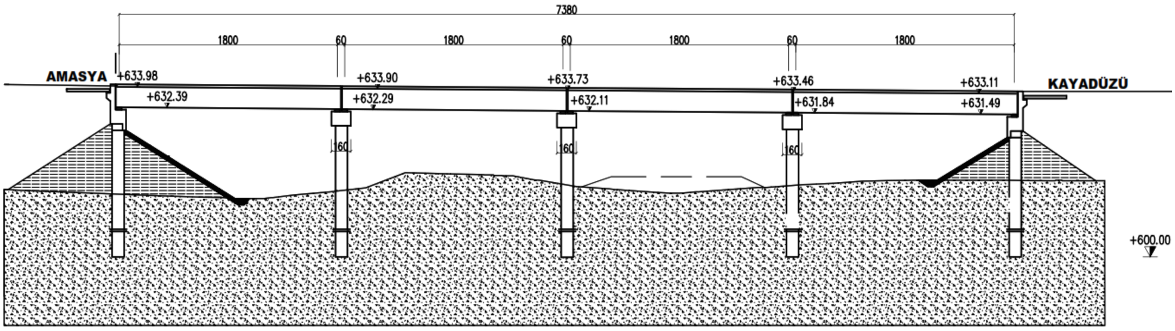

Fig. 4. Bridge longitudinal cross section

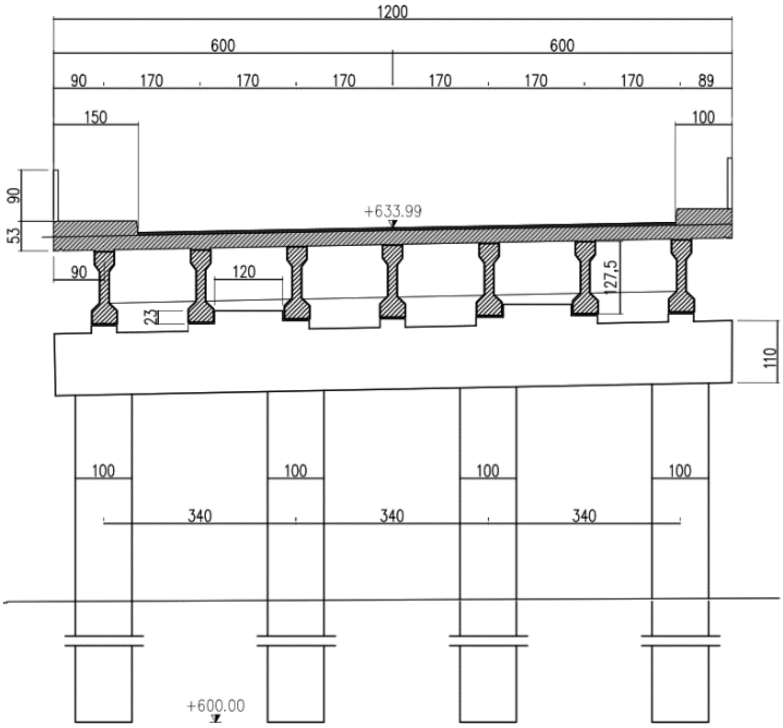

Fig. 5. Bridge cross section

2.2. Calculation principles and modeling of bridge

In the modeling of the bridge, CSIBridge software was used(CSI, 2022). The structural system is modeled with finite frame elements. Damping ratio was assumed to be 5% in the analysis. Elastomeric bearings, between precast prestressed beams and cap beams, are assigned as linear link elements. Fixed elements were used to transfer the loads from the deck and precast beam to the elastomeric bearings. The connections between the elastomer bearings and the cap beam were also modeled with fixed elements. In order to transfer the dead loads such as coating and sidewalk to the system, a load of 27.03 kN/m was applied to the unit length of the bridge deck.

In order to determine the concrete compressive strength of the structural members of the existing bridge, a certain number of core samples were taken from the structural members. based on the compressive test results obtained from the laboratory, the material strengths of the structural elements were found as shown in Table 1.

Table 1. Existing concrete compressive strengths

Structural Element	Core Size	Number of Cores	f_{cm}(N/mm^2)
Pile-Column	h/R=1(100mm)	6	19.01
Cap Beam	h/R=1(100mm)	6	23.08
Pre-Stressed Beam	h/R=1(100mm)	3	53.24
Deck	h/R=1(100mm)	4	37.72

Diameter of pile-columns is 1.00 m. Reinforcement details used in the section are; 12ϕ26 longitudinal rebar and ϕ10/10 spiral ties. The rebar steel in pile-columns is S220 (plain reinforcement) and S420 (deformed reinforcement) in other structural elements. Section details of columns and prestressed beams are given in Fig. 6. Xtract program based on Mander concrete model (Mander et al., 1988) was used to calculate the material properties, cracked section properties and element strengths of the columns (Xtract, 2001). Confined and unconfined concrete models and the material model of the rebar steel are given in Fig. 7. The cracked section stiffnesses for the columns were reduced by the stiffness reduction factors calculated with the data obtained from the moment-curvature relationship according to Eq. 1. Cracked and uncracked section properties of the columns are given in Table 2.

For the interaction of the pile-columns with the soil, springs are defined on the piles. In the part buried in the ground, lateral springs with 2/3 of the vertical spring coefficients are defined. The modulus of subgrade reaction values used in the definition of springs are given in Table 3.

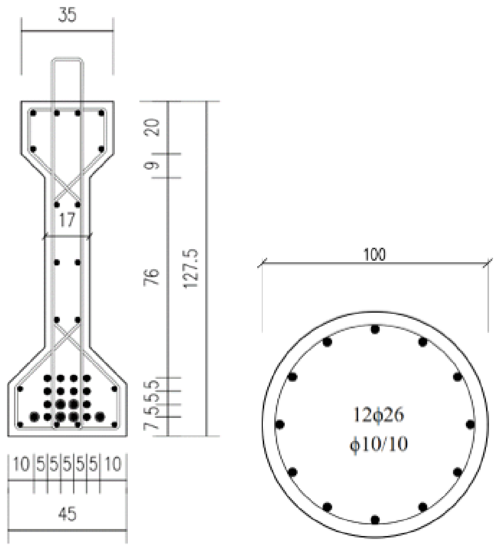

Fig. 6. Prestressed I beam and circular column section

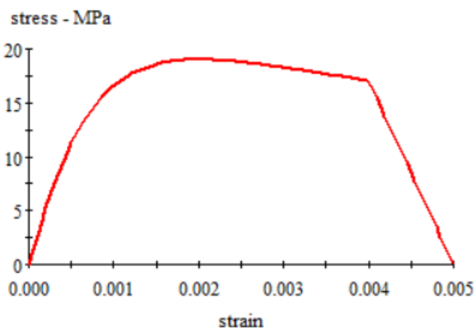

a)Unconfined concrete

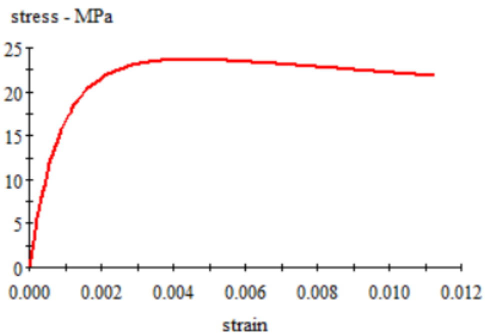

b)Confined concrete

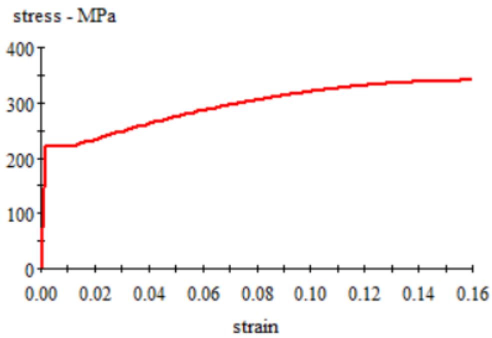

c)S220 Rebar steel

Fig. 7. Column material properties

Table 2. Cracked and uncracked sectional properties of columns

Axial Forces(kN)	E_c(kN/m2)	M_y(kN.m)	ϕ_y(rad)	$I=I_{22}=I_{33}(m^4)$	$I_{eff}(m^4)$	I_{eff}/ I
840	27500000	611	0.0019	0.04908	0.0117	0.238
900	27500000	630	0.00191	0.04908	0.012	0.244
975	27500000	651	0.00193	0.04908	0.0122	0.25
1035	27500000	671	0.00195	0.04908	0.0125	0.255

$$E_c I_{eff} = \frac{M_y}{\phi_y} \quad (1)$$

Table 3. Modulus of subgrade reactions

Depth	$Kh(kN/m^3)$
0-13 m	4000
13-25 m	7000

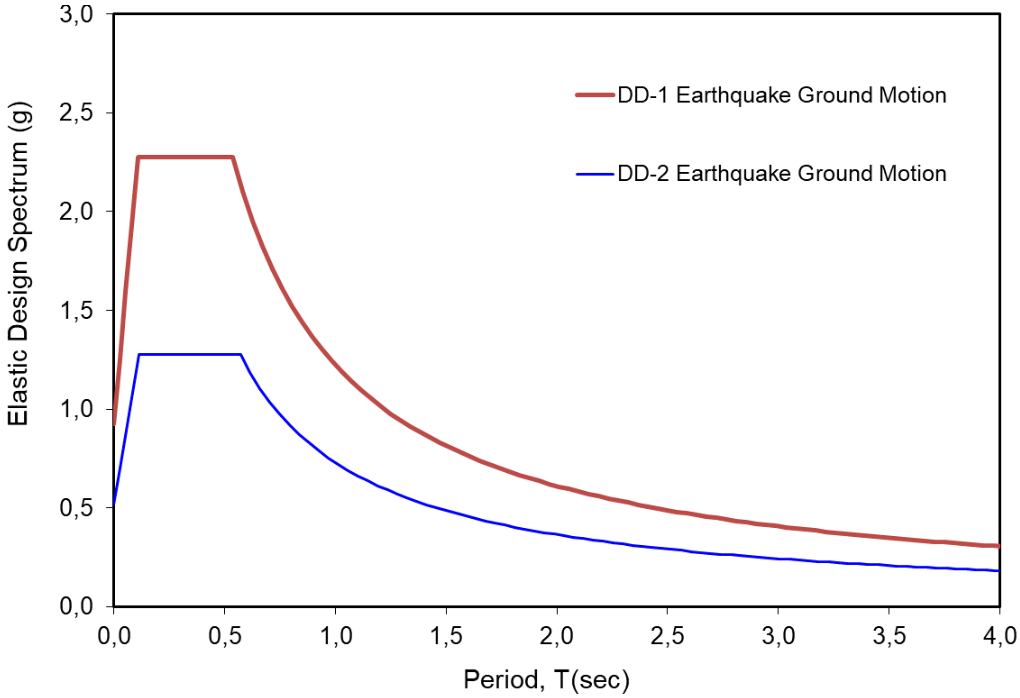

Fig. 8. DD-1 and DD-2 Elastic design spectra

The soil class was assumed as ZD TBSC (2018) with the drilling data included in the bridge project. Along the 25 m length of the pile columns within the ground, it was determined that there were soft clay layers between 0-13 m and solid clay layers between 13-25 m.

Design spectra for DD-1 and DD-2 ground motions to be used in the analysis were obtained from AFAD "Turkish Earthquake Hazard Map" (https://tdth.afad.gov.tr) considering ZD soil class. The spectra obtained are shown in Fig. 8.

2.3. Calculation methods and numerical analyses

Earthquake performance assessment of the bridge will be evaluated in two stages according to the Turkish bridge earthquake code (TKDY, 2020). Stage 1 level evaluation will be based on nonlinear pushover analysis method using DD-2 Earthquake ground motion level. Stage 2 level assesment will be carried out by nonlinear time history analysis method using DD-1 ground motion level. The Stage 1 assesment will aim to provide immediate occupancy performance level and the Stage 2 level earthquake calculation will aim to provide to check the collapse prevention performance level.

3D model of the bridge is shown in Fig. 9. The deck is assigned in the model as a composite section with girders. As it is a reinforced concrete bridge, the damping rate is assumed to be 5%.

The frequency, period and mass participation ratios of the first 12 modes obtained from the modal analysis of the bridge are given in Table 4. The mode shapes of the first 3 modes are shown in Fig. 10. Analyses were performed separately for transverse and longitudinal directions and the results were examined.

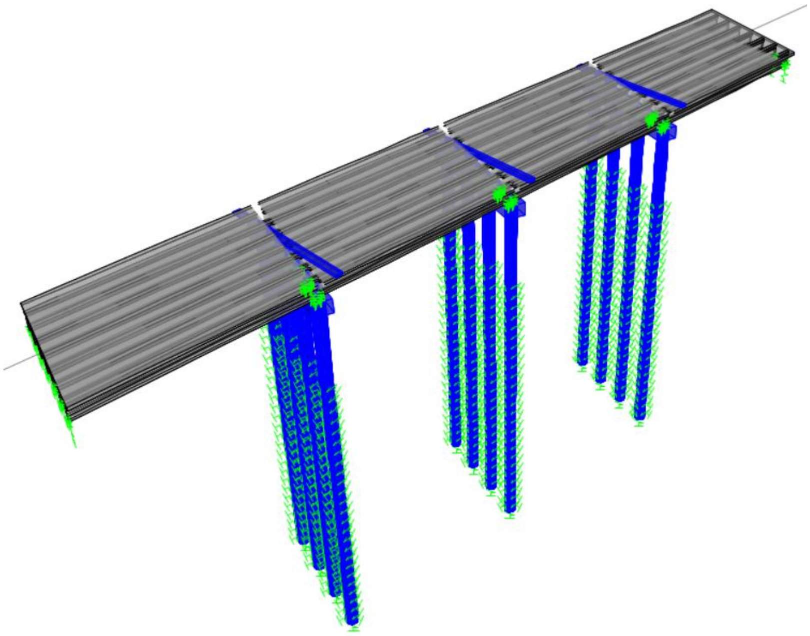

Fig. 9. 3D model of the bridge

Table 4. Modal periods and frequencies

Mode Number	Period (s)	Frequency (Hz)
Mode 1	0.948	1.055
Mode 2	0.539	1.854
Mode 3	0.291	3.439
Mode 4	0.290	3.448
Mode 5	0.269	3.723
Mode 6	0.259	3.855
Mode 7	0.252	3.975
Mode 8	0.251	3.980
Mode 9	0.245	4.074
Mode 10	0.185	5.403
Mode 11	0.183	5.450
Mode 12	0.181	5.533

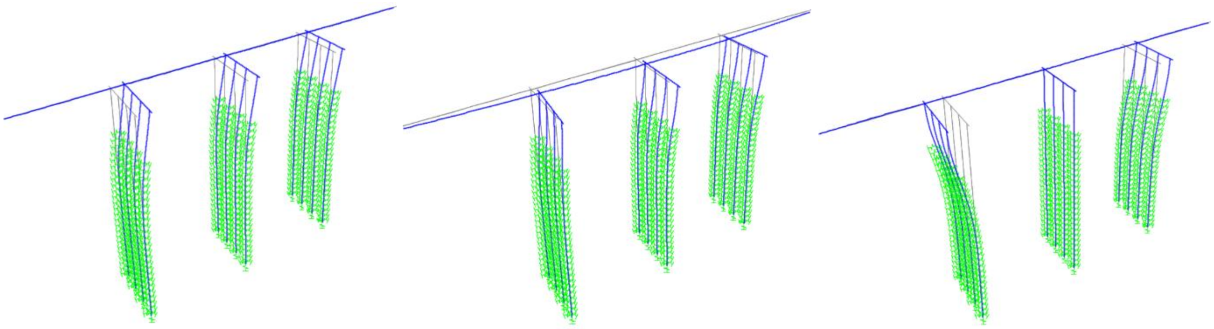

a)1. Mode shape(Longitudinal) b) 2. Mode shape (Transverse) c)3. Mode shape

Fig. 10. Mod shapes of the four span bridge

2.3.1. Nonlinear pushover analysis

In this part, a nonlinear static pushover analysis of the bridge in the transverse and longitudinal directions is performed. Static pushover analysis was performed separately for each pier. First of all, to provide the nonlinearity, a lumped plastic hinge was defined at a distance of Lp/2 from the connection point of the columns with the cap beams and at the points where the moment is maximum in the piles in the soil. PMM hinge was defined since the columns carry both axial force and moment in both axes. Hinge properties were determined by interaction diagram obtained from the normal force transferred to the columns and the sectional properties. Hinge length (Lp) was calculated by Eq. 2 according to Caltrans (2019). In the equation, f_{ye} symbolizes the expected yield strength of the reinforcing steel and d_{b1} symbolizes the nominal diameter of the longitudinal reinforcement of the column. The locations of the hinges are shown in Fig. 11.

In the first step, the static pushover curve of the bridge in the transverse and longitudinal directions, which gives the relationship between base shear force and peak displacement, was obtained. The pushover curves in transverse and longitudinal directions are shown in Fig. 12 and Fig. 13. As it is seen Fig. 12 and Fig. 13, lateral rigidity is stronger in transverse direction as it is anticipated, the reason frame behavior while its lateral rigidity is low in the longitudinal direction due to cantilever behavior.

$$L_p = 0.08L + 0.22f_{ye}d_{b1} \geq 0.044f_{ye}d_{b1} \quad (2)$$

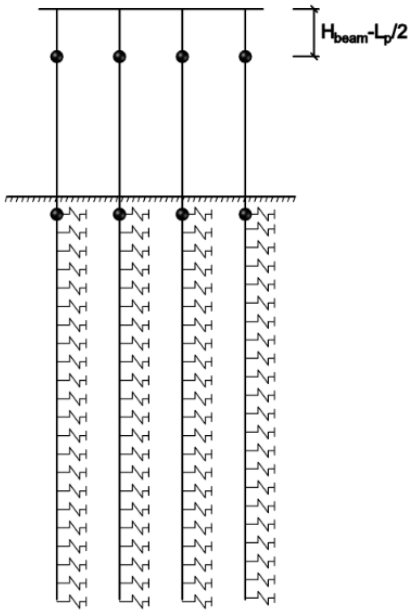

Fig. 11. Plastic hinge layout of pile-columns

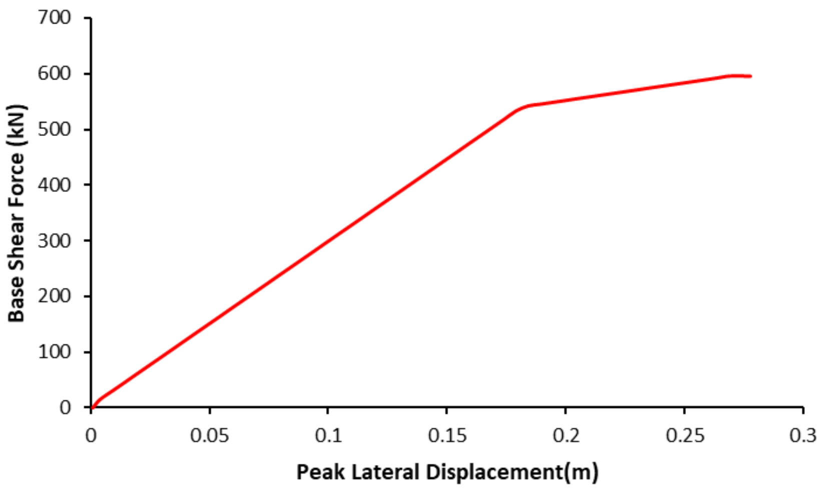

Fig. 12. Pushover curve in longitudinal direction

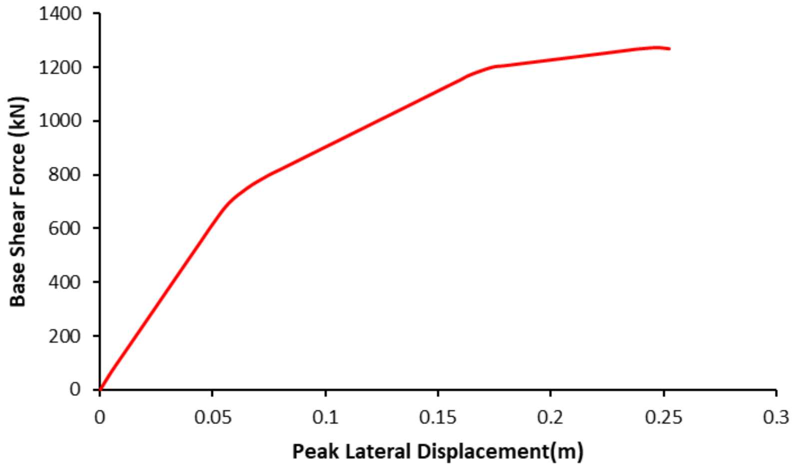

Fig. 13. Pushover curve in transverse direction

At the second step, pushover curves obtained were converted into Sa-Sd capacity curve. In the next step, the horizontal elastic design spectrum obtained for DD-2 Ground Motion level was converted into spectral acceleration-spectral displacement graph. In the last step, the performance points in the transverse and longitudinal directions of the bridge were determined by matching the Sa-Sd spectra obtained from the design spectrum with the demand curve. Accordingly, the performance point of the bridge in the longitudinal direction is 22 cm and the performance point in the transverse direction is 13 cm.

The bridge is pushed transversely and longitudinally to the performance points. The span lengths, pier heights, dimensions and dead loads on each pier are equal to each other. For this reason, the analysis results for only one pier of the bridge were assessed. The performance levels of the other piers will be considered equal to the analyzed pier. As a result of the pushover analysis, the plastic rotations occurring in the plastic hinge joints and the limit values for the performance levels are shown in Table 5. The plastic hinges resulting from the pushing of the bridge in two directions are shown in Figure 14. The hinges in green color represent the plastic deformation and the gray ones represent the hinges that do not show plastic behavior. The life safety and collapse prevention limit values of the plastic hinges are calculated according to Eq. 3 and Eq. 4. Table 5 yields that, the existing bridge structural system both transverse and longitudinal directions satisfies the immediate occupancy performance level under nonlinear pushover analysis.

As a result of the analysis performed at stage 1 level, it is observed that the bridge meets the immadiate occupancy performance level. The target performance level of immadiate occupancy performance level has been satisfied. The bridge structural system is sufficient.

$$\theta_p^{(LS)} = \left(0.5\phi_u - \phi_y\right) L_p \tag{3}$$

$$\theta_p^{(CP)} = \left(0.67\phi_u - \phi_y\right) L_p \tag{4}$$

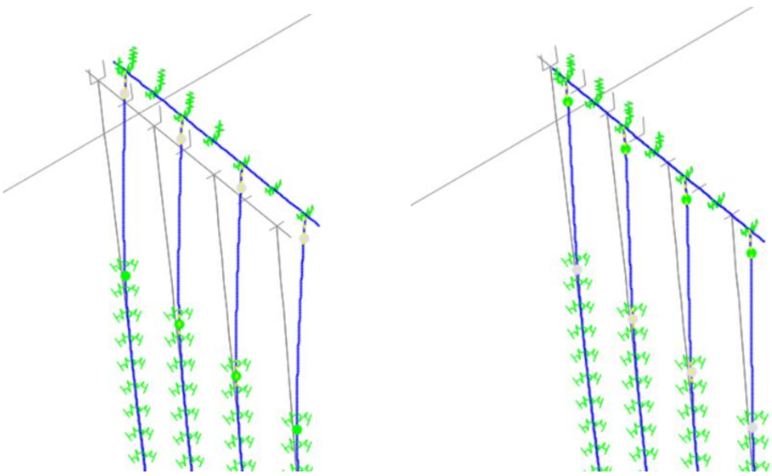

a)Longitudinal (R2) b)Transverse (R3)

Fig. 14. Plastic hinge development

Table 5. Performance limits and plastic rotations of the bridge in transverse and longitudinal directions

Direction	Pier No	θ_p	$\theta_p^{(LS)}$	$\theta_p^{(CP)}$	Performance Level
Transverse (R3)	Pier 1	0.00477	0.0051	0.00734	Immadiate Occupancy
	Pier 2	0.00477	0.0051	0.00734	Immadiate Occupancy
	Pier 3	0.00477	0.0051	0.00734	Immadiate Occupancy
Longitudinal (R2)	Pier 1	0.00453	0.0051	0.00734	Immadiate Occupancy
	Pier 2	0.00453	0.0051	0.00734	Immadiate Occupancy
	Pier 3	0.00453	0.0051	0.00734	Immadiate Occupancy

2.3.2. Nonlinear time history analysis

A total of 10 earthquake records were selected from PEER Strong Motion Database (PEER, 2025) for nonlinear time history analysis. The records were selected based on their distance to the fault and the shear-wave velocity between 180-360 m/s since the soil class of the bridge is ZD. Details of the selected earthquake records are given in Table 6. Direct integration method was selected as the analysis type . This analysis type considers the change of the stiffness matrix with each time interval due to the nonlinear behavior. The coefficients in the Rayleigh proportional damping matrix were determined according to the periods of the first two modes that contribute the most mass participating in the longitudinal and transverse directions of the bridge.

The target spectrum was obtained by scaling the spectra generated by the SRSS method of the selected recordings with the simple scaling method to approximate the DD-1 design spectrum. The scaled spectra, the target spectrum obtained by averaging these spectra and the design spectrum are shown in Fig. 14. For each earthquake, the scaled acceleration records in two perpendicular directions were introduced to the model in transverse and longitudinal directions.

Nonlinear multilinear plastic link elements have been defined in the hinge areas of the piers instead of lumped plastic hinges. These elements are defined to add the energy damped by each element in addition to the energy damped by the bridge as a whole. Takeda model (Takeda et al., 1970) is used as hysteresis type. The translational and rotational stiffnesses used in the definition of multilinear plastic elements were calculated using section properties and plastic hinge length (Table 7 and Table 8). The section properties and force-deformation relationship used in the calculations were obtained from moment curvature graphs under the effect of 4 different axial forces. θp was obtained by Eq. 5, $\theta p1$ by Eq. 6 and $\theta p2$ by Eq. 7 (Priestley et al., 1996). The obtained plastic rotations are shown in Table 9.

Table 6. Selected earthquake records for time history analysis

Earthquake Name	Station	M_w	R_{rup}(km)	V_s30(m/s)	Scaling Factor
Imperial Valley-06	El Centro Array #13	6.53	21.98	249.92	5.55
Superstition Hills-02	Plaster City	6.54	22.25	316.64	5.3
Landers	Desert Hot Springs	7.28	21.78	359	4.62
Kobe, Japan	Shin-Osaka	6.9	19.14	256	3.18
Kocaeli, Turkey	Duzce	7.51	15.37	281.86	1.75
Manjil, Iran	Qazvin	7.37	49.97	302.64	5.03
Hector Mine	Joshua Tree	7.13	31.06	379.32	4.66
Tottori, Japan	SMN001	6.61	14.42	331	4.54
El Mayor-Cucapah, Mexico	El Centro - Imperial & Ross	7.2	20.08	229.25	1.78
Darfield, New Zealand	Styx Mill Transfer Station	7.0	20.86	247.5	2.96

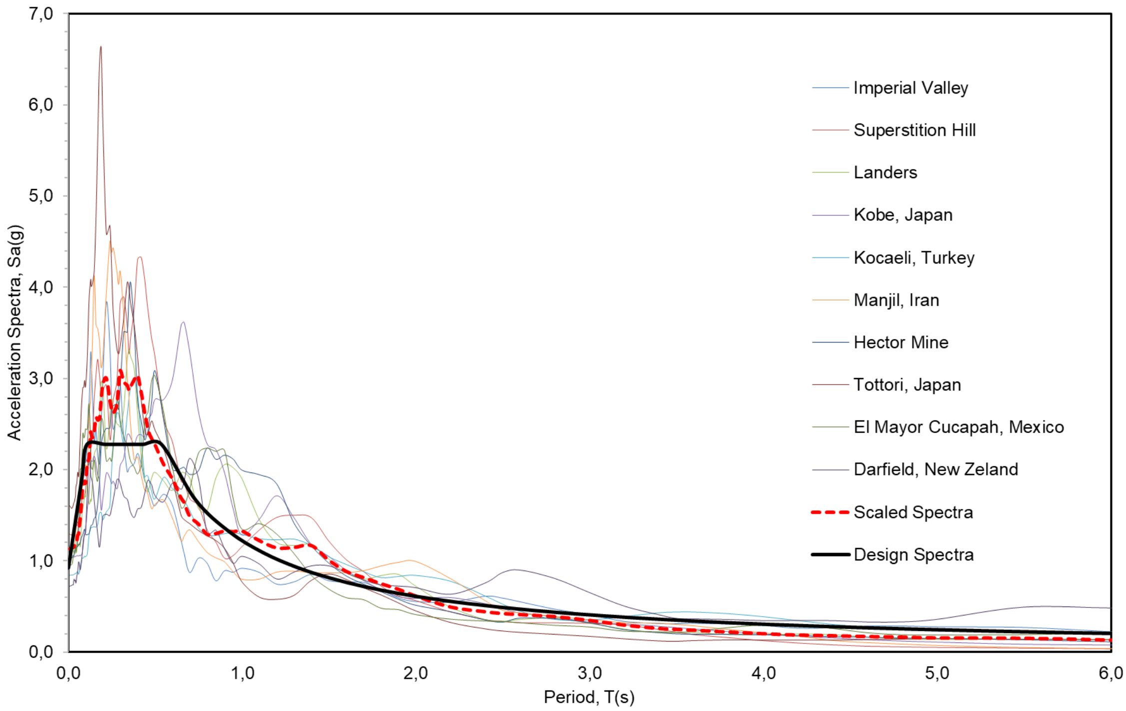

Fig. 15. Scaled acceleration spectra and mean spectra

Table 7. Section properties

$E(kN/m^2)$	G $kN/m^3)$	$I(m^4)$	$J(m^3)$	$A(m^2)$	$L_p(m)$
28166420	0.539	0.291	0.290	0.269	0.726

Table 8. Translational and rotational stiffnesses

k1(kN/m)	k2(kN/m)	k3(kN/m)	R1(kN/m)	R2(kN/m)	R3(kN/m)
30455427	43360678	10840170	1522383	1904531	1904531

Table 9. Rotational deformations in link elements

Axial Forces(kN)	ϕ_u	ϕ_y	ϕ_{yideal}	θ_{p1}	θ_{p2}	M_p (kNm)	M_{max} (kNm)
840	0.0511	0.0019	0.0027	0.03567	0.00195	891.37	920.73
900	0.0498	0.001917	0.00267	0.0347	0.00193	905.95	934.34
975	0.0484	0.00194	0.00265	0.0338	0.00192	923.6	950.97
1035	0.0473	0.00196	0.00265	0.03287	0.00192	943.7	964.3

$$\phi_p = (\phi_u - \phi_y) \tag{5}$$

$$\theta_{p1} = L_p(\phi_u - \phi_y) \tag{6}$$

$$\theta_{p2} = L_p \phi_{y\,ideal} \tag{7}$$

P-y curves were created with the drilling data in the existing project in order to provide the pile-soil interaction of the bridge. As a result of the investigations, since the soil response does not increase linearly with displacement, the displacement-force relationship corresponding to each displacement was obtained and defined to the piles as multilinear elastic link elements separately for different depths in the model.

Two load combinations were defined to obtain the bridge strain demands in the transverse and longitudinal directions by averaging 10 scaled earthquake records separately for the two directions. In each combination, a total of 20 loading cases were averaged to obtain the strain demands.

When the results are considered, the largest R3 deformation occurred in the link element no. 177 and the largest R2 deformation occurred in the link element no. 175. The largest observed rotational deformations are given in Table 10.

Table 10. Maximum Rotational Deformations of Link Elements

Link No	Combination	R1(rad)	R2(rad)	R3(rad)
175	MEAN_Y	2.64 E-07	0.00051	0.003339
175	MEAN_X	9.778E-09	0.005819	0.001751
177	MEAN_Y	1.501E-09	0.00051	0.004704
177	MEAN_X	5.077E-09	0.005737	0.001678

Table 11. Performance limits and plastic rotations

Direction	θ_p	$\theta_p^{(LS)}$	$\theta_p^{(CP)}$
Transverse(R3)	0.00268	0.0051	0.00734
Longitudinal (R2)	0.0038	0.0051	0.00734

Stage 2 evaluation of plastic rotation limits for life safety and collapse prevention performance levels were calculated according to Eq. 3 and Eq. 4. Rotation values obtained from the average of 10 earthquake records in the transverse and longitudinal directions of the bridge were calculated according to Eq. 6.

The calculated performance level limits and the maximum rotations occurring in the link elements are given in Table 11. When the results are compared, it is seen that the bridge achieved the limited damage earthquake performance level in the transverse and longitudinal directions.

As a result of the analysis performed at stage 2 level, it was observed that the performance level of collapse prevention was satisfied. The bridge structural system is sufficient. No strengthening is required.

3. Conclusions

In this study, the earthquake performance of a 4-span reinforced concrete bridge exist on the Suluova-Amasya state highway is examined. The assessment was done in two stages. In the first stage, nonlinear pushover analysis was performed separately for the transverse and longitudinal behavior of the bridge considering DD-2 (design earthquake) ground motion level. Plastic hinges were defined at the piers, the bridge was pushed in two directions up to the performance points and the plastic rotations at the plastic hinges were developed. According to the results obtained from the pushover analysis, the plastic rotational deformations of the 3 piers of the bridge in both directions are between the immediate occupancy and life safety performance level limit values. The performance level of the bridge was determined as immediate occupancy according to the pushover analysis.

In the second stage evaluation, nonlinear earthquake calculation method nonlinear time history analysis was used. 10 earthquake records were selected and scaled according to DD-1 (maximum earthquake) ground motion level and applied to the system in transverse and longitudinal directions. Multilinear link elements were defined at the piers using Takeda model and deformations were observed by averaging 10 records separately in transverse and longitudinal directions. According to the results, plastic rotations in both directions provided immediate occupancy performance level.

The bridge satisfied the first stage evaluation performance target of immediate occupancy and the second stage performance target of collapse prevention according to the code. No retrofitting is required for the bridge pile-columns.

References

AFAD. (2024). *Turkish Earthquake Hazard Map*. https://tdth.afad.gov.tr (Accessed December 10, 2024)

Batbayar, G. (2008). *Köprülerin deprem performansının itme analizi yöntemi ile belirlenmesi ve Bayrampaşa köprüsünün güçlendirilmesi* (Master's thesis, Istanbul Technical University). [In Turkish]

Caltrans. (2019). *Seismic design criteria*. State of California Department of Transportation.

CSIBridge v24.0.0. (2022). *Finite element analysis programs for the bridge analysis* [Computer software]. Computers and Structures Inc., California, USA.

Elmas, Ö. (2008). *Viyadüklerin deprem durumunda caltrans standardına göre incelenmesi ve Hereke Kavşak Viyadüğünün güçlendirilmesi* (Master's thesis, Istanbul Technical University). [In Turkish]

PEER Ground Motion Database. (n.d.). *PEER Center*. https://ngawest2.berkeley.edu/ (Accessed January 14, 2025)

Priestley, M. J. N., Mander, J. B., & Park, R. (1988). Theoretical stress-strain model for confined concrete. *Journal of Structural Engineering, 114*(8), 1804–1826.

Priestley, M. J. N., Seible, F., & Calvi, G. M. S. (1996). *Seismic design and retrofit of bridges*. John Wiley & Sons.

Salimee, M. T. (2019). *Design and earthquake performance assessment of a bridge with prestressed concrete girder* (Master's thesis, Istanbul Technical University).

Şengül, E. (2018). *İstanbul Havalimanındaki bir viyadüğün tasarımı ve sismik performans değerlendirmesi* (Master's thesis, Istanbul Technical University). [In Turkish]

Takeda, T., Sozen, M. A., & Nielsen, N. N. (1970). Reinforced concrete response to simulated earthquakes. *Journal of the Structural Division, 96*(12), 2557–2573.

TBSC. (2018). *Türkiye Building Seismic Code*. Disaster and Emergency Management Presidency, Ankara, Türkiye. [In Turkish]
TKDY. (2020). *Deprem etkisi altında karayolu ve demiryolu köprü ve viyadükleri tasarımı için deprem esasları, Türkiye Köprü Yönetmeliği*. Ankara, Türkiye. [In Turkish]
XTRACT. (2001). *Cross-sectional analysis of components* [Computer software]. Imbsen Software System, Sacramento, USA.

4th International Civil Engineering & Architecture Conference
17-19 May 2025, Trabzon, Türkiye

Predicting displacement demands in SDOF systems using seismic input energy: A machine learning approach

Furkan Çalım*[1], Ahmet Güllü[1], Ercan Yüksel[1]

[1] *Istanbul Technical University, Faculty of Civil Engineering, Istanbul, Türkiye*

Abstract. This study investigates the seismic input energy–displacement demand relationships and establishes a robust correlation between them. A suite of ground motion records is utilized to perform linear and nonlinear time history analyses on SDOF systems with varying dynamic properties. The computed seismic input energy and corresponding displacement demands are analyzed to identify trends and patterns, providing insights into the energy-displacement relationship across different seismic scenarios. Based on this comprehensive numerical investigation, the study further investigates the effectiveness of different machine learning models (i.e., linear models, tree-based models, boosting algorithms, neural networks, and kernel methods) in predicting the relationship between seismic input energy and displacement demands. The performance of these models is assessed regarding their accuracy, robustness, and generalization capability. The results provide valuable insights into the optimal machine learning approach for estimating displacement demands, which are among the essential input parameters for structural performance evaluation and design methodologies. This research contributes to the growing body of knowledge in energy-based seismic engineering and highlights the potential of data-driven approaches in earthquake engineering applications.

Keywords: Machine learning; Earthquake engineering; Seismic input energy; Displacement demands; Nonlinear time history analysis

1. Introduction

In recent years, energy-based approaches have gained traction in seismic design and performance assessment. As they consider crucial parameters like the frequency content, duration, and cumulative damage potential of ground motions, they offer a sought-after alternative to conventional force- and displacement-based methods (Benavent-Climent and Mollaioli, 2021; Varum et al., 2023).

Seismic input energy imparted into the structures by a ground excitation has emerged as a promising metric for evaluating structural demands. Several studies in the literature have highlighted its potential in frame-type reinforced concrete and steel buildings (Fujii and Shioda, 2023; Güllü et al., 2023). However, these methods may prove less effective when the building exhibits complex nonlinear dynamic behavior, which is not fully captured in simplified models.

To address this challenge, machine learning algorithms have gained extra popularity because they can model complex relationships without needing explicit mathematical equations. Machine learning applications in earthquake engineering practice (Xie et al., 2020) have included different topic areas, such as seismic hazard analysis (Tang et al., 2022), system identification and damage detection (Salkhordeh et al., 2023), seismic fragility assessment (Kazemi et al., 2023), and structural control for earthquake mitigation (Chen and Chien, 2020). However, studies specifically focusing on predicting displacement demands based on seismic input energy using machine learning algorithms are still limited.

This study aims to fill the gap by evaluating the predictive performance of various machine learning algorithms, including linear models, tree-based models, boosting algorithms, neural networks, and kernel methods, to estimate the displacement demand of SDOF systems using seismic input energy as the primary input feature. A total of 16 models are trained and tested utilizing the ground acceleration records from the 2023 Kahramanmaraş earthquakes. The goal is to discuss the applicability of machine learning models in energy-based seismic engineering applications and to determine the most effective algorithm in predicting the displacement demand of SDOF systems.

* Corresponding author, E-mail: calimf@itu.edu.tr

https://doi.org/10.31462/icearc2025_ce_eqe_744

2. Materials and methods

A comprehensive machine learning approach was adopted to predict the displacement demands in SDOF systems from the 2023 Kahramanmaraş earthquakes. Several algorithms were evaluated regarding their predictive performance in capturing the relationship between the seismic input energy and structural response. These models were trained and validated on a dataset derived from extensive linear and nonlinear time history analyses. The performance of each algorithm was comparatively assessed based on accuracy metrics, providing insight into their applicability and robustness.

2.1. Ground motion data

The 2023 Kahramanmaraş earthquakes refer to a catastrophic earthquake doublet that struck southeastern Türkiye on February 6, 2023. The first event of the doublet, with a moment magnitude of 7.8, occurred at 04:17 a.m. local time, centered near Pazarcık in Kahramanmaraş province. Around nine hours later, at 01:24 p.m. local time, the second event with a moment magnitude of 7.5 took place near Elbistan county, approximately 90 kilometers north of the first epicenter. The sequence of two large-magnitude earthquakes generated extremely intense and long-duration ground shaking. These characteristics contributed to widespread structural damage across 11 provinces.

In the current study, a seismic demand dataset was generated using the ground motion records from the first event of the doublet. The acceleration records from the 200 nearest stations to the epicenter were utilized in the analyses. The seismic input energy and displacement demands were computed after performing linear and nonlinear time history analyses on a wide range of SDOF systems with varying natural periods (T), damping ratios (ζ), and displacement ductility demands (μ). For the success evaluation of the developed machine learning models, the data for the SDOF systems with a natural period of 1.0 s and a damping ratio of 5% were employed, as displayed in Fig. 1.

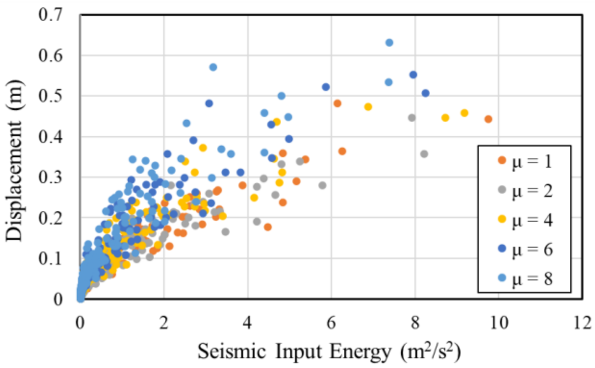

Fig. 1. Seismic input energy and displacement demand dataset

2.2. Machine learning models

Several machine learning models were investigated regarding their effectiveness for predicting the displacement demand of SDOF systems using seismic input energy. This section summarizes the employed machine learning models categorized by their types: linear models, tree-based models, boosting algorithms, neural networks, and kernel methods.

2.2.1. Linear models

Linear models form the foundation of many machine learning approaches. They are commonly used for regression tasks due to their simplicity, efficiency, and interpretability, as they assume a linear relationship between input features and the target variable. In this study, three linear models (i.e., Ridge Regression, ElasticNet, and Bayesian Ridge Regression) were utilized to capture linear trends within the data.

Ridge Regression is a linear model that addresses the multicollinearity issues in linear regression by introducing a penalty term to the loss function. This reduces model complexity and prevents overfitting. However, this method's shortcomings include complicated interpretation and the inability to perform variable selection (Hoerl & Kennard, 1970).

Bayesian Ridge Regression incorporates Bayesian principles into linear regression. In this model, the coefficients are treated as random variables with specified distributions, allowing for the estimation of uncertainties. Even though it is robust to multicollinearity, it is computationally more intensive (MacKay, 1992).

ElasticNet is a hybrid approach that combines the penalty terms of the Ridge and Lasso Regressions. It is effective when working with multiple correlated variables. However, it is a complex and computationally intensive method as it requires tuning two hyperparameters (Zou & Hastie, 2005).

2.2.2. Tree-based models

Tree-based models are popular for regression and classification tasks because of their intuitive structure, interpretability, and capacity to model nonlinear relationships. This study employed three different tree-based models (i.e., Decision Tree, Random Forest, and Extra Trees) to evaluate their displacement demand prediction performance.

Decision Tree is a non-parametric model that splits the feature space into separate regions according to feature values, forming a tree-like decision structure. Each internal node represents a test on a feature, each branch signifies the result of that test, and each leaf depicts a predicted value. While they offer several benefits, such as ease of interpretation and visualization, compatibility with both numerical and categorical data, and minimal data processing requirements, they also have limitations. These include susceptibility to overfitting and sensitivity to minor data fluctuations (Breiman et al., 1984).

Random Forest is an ensemble machine learning method that constructs an assembly of decision trees during the model's training and outputs the mean prediction of individual trees. Its randomness comes from selecting random subsets of features for each tree, enabling the model to reduce overfitting. However, it may be less interpretable and more computationally intensive than individual decision trees (Breiman, 2001).

Extra Trees (i.e., Extremely Randomized Trees) is an ensemble method similar to the Random Forest. However, it introduces more randomness during the splitting process. Later, it chooses the best option among the selected splits for each feature, which further reduces the overfitting. Even though it is faster to train, it may perform worse than Random Forest on certain structured datasets (Geurts et al., 2006).

2.2.3. Boosting algorithms

In the boosting algorithms, the models are sequentially trained to correct the errors, improving their overall predictive performance. They combine weak learners into a strong predictive model, which is effective in capturing nonlinear patterns. This study analyzed four boosting algorithms (i.e., AdaBoost, Gradient Boosting, XGBoost, and LightGBM).

AdaBoost (i.e., Adaptive Boosting) is a boosting algorithm that combines multiple weak learners by reweighting the samples. The purpose is to focus on the misclassified instances in the following iteration. Its advantages include being simple and effective for binary classification tasks, improved model performance, and robustness to overfitting. In contrast, it is sensitive to outliers and might not perform well on high-dimensional datasets (Freund and Schapire, 1997).

Gradient Boosting focuses on improving weak learners step-by-step by correcting the residual errors of the previous one. It provides high predictive accuracy and flexibility through custom loss functions. However, the training task might be relatively slower as it builds models sequentially. In addition, it might be sensitive to outliers and overfitting (Friedman, 2001).

XGBoost is currently one of the most popular machine learning algorithms due to its improved performance in structured datasets. It employs regularization for the penalty terms of the Ridge and Lasso Regressions, which prevents overfitting. In addition to being efficient in terms of training time and scalability, it requires extra care in tuning its hyperparameters (Chen and Guestrin, 2016).

LightGBM uses histogram-based algorithms that require less memory and offer faster training times compared to XGBoost. It can handle large datasets efficiently and supports categorical features natively. However, overfitting may be an issue when working with small datasets (Ke et al., 2017).

2.2.4. Neural networks

Neural networks, which can automatically learn feature representations, are capable of modeling complex and nonlinear relationships. In this study, the Multi-Layer Perceptron (MLP) algorithm was utilized to evaluate its performance in generalizing displacement demands of SDOF systems based on seismic input energy.

MLP is an algorithm capable of modeling complex nonlinear relationships, trained using backpropagation. While it performs well across a wide range of regression tasks, its drawbacks include longer training times, higher computational resource demands, and the necessity for large amounts of data and careful tuning (Rumelhart et al., 1986).

2.2.5. Kernel methods

Kernel-based machine learning models capture nonlinear relationships by projecting input data into higher-dimensional feature spaces, enabling effective learning in complex domains. This study investigated three kernel-based models (i.e., Support Vector Machines (SVM) with a Radial Basis Function (RBF), a linear version of SVM, and Kernel Ridge).

SVM with RBF operates in a higher-dimensional space, adeptly handling complex nonlinear relationships. While it is a powerful algorithm for nonlinear regression, it is also computationally intensive and requires careful tuning (Cortes & Vapnik, 1995).

On the other hand, the linear version of SVM is suitable for datasets with approximately linear relationships between input features and target parameters. Although it is fast and efficient when using linear kernels, its performance declines with complex datasets (Cortes & Vapnik, 1995).

Kernel Ridge operates in a high-dimensional feature space by combining Ridge Regression with the kernel trick to effectively model nonlinear relationships. It is more suitable for small and medium-sized datasets rather than large ones (Saunders et al., 1998).

2.2.6. Other models

This study also evaluated some additional machine learning algorithms that do not strictly fall into the aforementioned categories. These models (i.e., K-Nearest Neighbors and Bagging Regressor) offer ensemble performance capabilities.

K-Nearest Neighbors (KNN) predicts the target variable by averaging the training sample values. Because it does not require a training phase, it is simple to implement and performs well with low-dimensional data. However, when dealing with high-dimensional data, it tends to slow down in making predictions and may encounter performance difficulties (Cover and Hart, 1967).

Bagging Regressor is a collective model that trains multiple decision trees on random subsets of the input data. To reduce the variance and prevent overfitting, the average of their predictions was used as the overall prediction of the model. Even though it is a simple and well-performing algorithm on unstable models, it fails to reduce bias. (Breiman, 1996).

2.3. Training and testing strategy

A Python-based code was utilized to employ the detailedly discussed machine learning models. The dataset, including the features (i.e., seismic input energy and ductility ratio) and the target variable (i.e., displacement demand), was introduced to the model. Later, it was randomly split into training and testing sets with an 80-20 ratio. To improve numerical stability and model performance, data normalization was applied. After initializing each machine learning model with some basic parameters, they are trained and used for the prediction of displacement demands.

```
# Initializing the models with some basic hyperparameters
models = {
    # Linear Models
    "Ridge Regression": Ridge(alpha=1.0),
    "Bayesian Ridge": BayesianRidge(),
    "ElasticNet": ElasticNet(alpha=0.1, l1_ratio=0.5),

    # Tree-based Models
    "Decision Tree": DecisionTreeRegressor(max_depth=5, random_state=42),
    "Random Forest": RandomForestRegressor(n_estimators=100, random_state=42),
    "Extra Trees": ExtraTreesRegressor(n_estimators=100, random_state=42),

    # Boosting Algorithms
    "AdaBoost": AdaBoostRegressor(n_estimators=50, learning_rate=1.0, random_state=42),
    "Gradient Boosting": GradientBoostingRegressor(n_estimators=100, learning_rate=0.1, max_depth=3,
random_state=42),
    "XGBoost": xgb.XGBRegressor(objective="reg:squarederror", n_estimators=100, learning_rate=0.1,
max_depth=6, random_state=42),
    "LightGBM": lgb.LGBMRegressor(n_estimators=100, learning_rate=0.1, max_depth=6, random_state=42),

    # Neural Networks
    "MLP": MLPRegressor(hidden_layer_sizes=(100,50), activation='relu', solver='adam', max_iter=500,
random_state=42),

    # Kernel Methods
    "SVM (RBF)": SVR(kernel='rbf', C=100, gamma=0.1),
    "SVM (Linear)": SVR(kernel='linear', C=100),
    "Kernel Ridge": KernelRidge(alpha=1.0, kernel='rbf', gamma=0.1),

    # Other Models
    "KNN": KNeighborsRegressor(n_neighbors=5),
    "Bagging": BaggingRegressor(n_estimators=10, random_state=42),
}
```

Fig. 2. Python-based code

3. Results and discussions

Each machine learning model was trained using a randomly selected 80% portion of the original dataset, and its performance was subsequently evaluated for the remaining 20%. The predicted displacement demand values were compared with the corresponding actual ones for each model. Given that the total dataset length was 2000, each comparison was made for 400 data points, each representing an individual ground motion record. An evaluation was made regarding the computed R^2 score, which is a statistical measure indicating the wellness of a regression model. It is computed by subtracting the ratio of the sum of squared residuals to the total sum of squares from one.

Fig. 3 displays the predicted versus actual values for the displacement demands for linear models. ElasticNet had the lowest predictive performance among them, with an R^2 value of only 0.5457, indicating its limited effectiveness in estimating SDOF systems' displacement demands. On the other hand, Ridge Regression and Bayesian Ridge models showed moderate prediction accuracy, with predictions clustering around the 45º-line with some visible scattering.

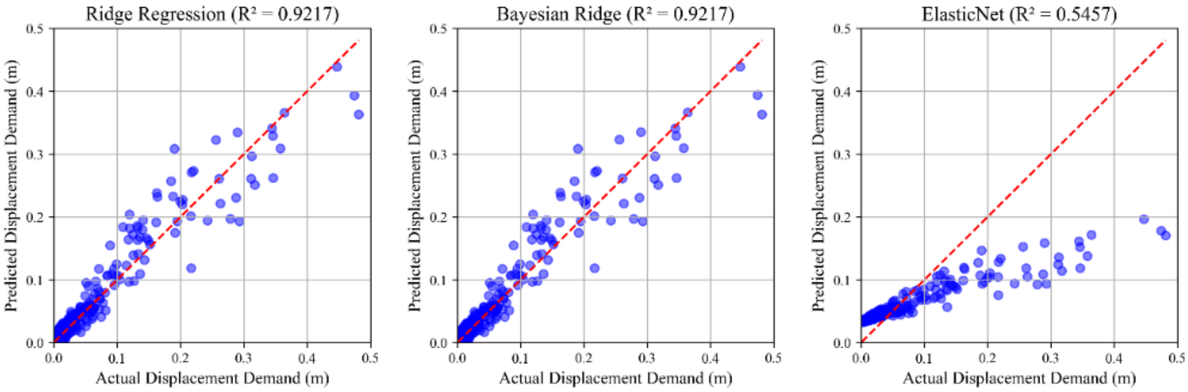

Fig. 3. Predicted versus actual values for the displacement demands using linear models

Fig. 4 presents the predictive success evaluation of tree-based machine learning models. All three models (i.e., Decision Tree, Random Forest, and Extra Trees) displayed improved prediction performance over linear models. In particular, Decision Tree provided the best fit among them with fewer extreme outliers and an R^2 value of 0.9330, suggesting more substantial generalization capabilities.

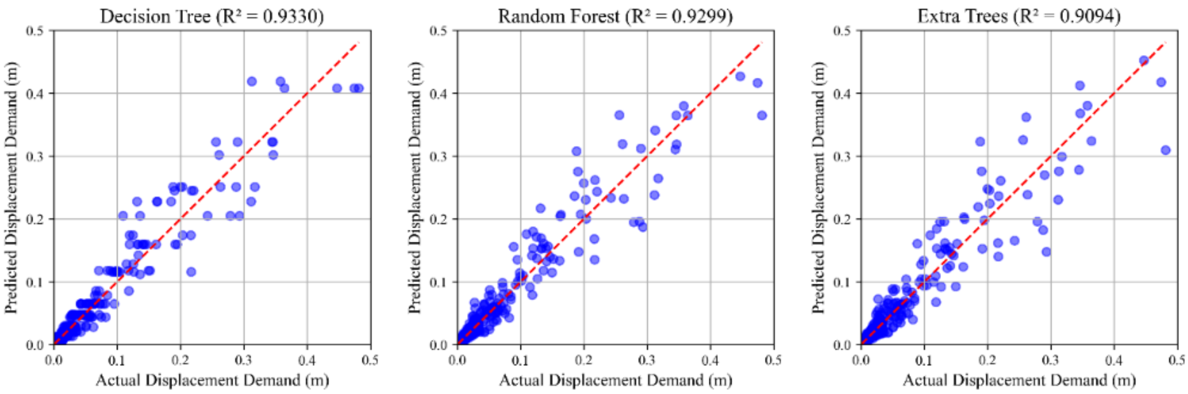

Fig. 4. Predicted versus actual values for the displacement demands using tree-based models

Boosting algorithms (i.e., AdaBoost, Gradient Boosting, XGBoost, and LightGBM) resulted in the most concentrated prediction clusters along the 45º-line and relatively higher R^2 scores, as displayed in Fig. 5. Specifically, Gradient Boosting and LightGBM outperformed the others, with R^2 scores of 0.9413 and 0.9363, respectively.

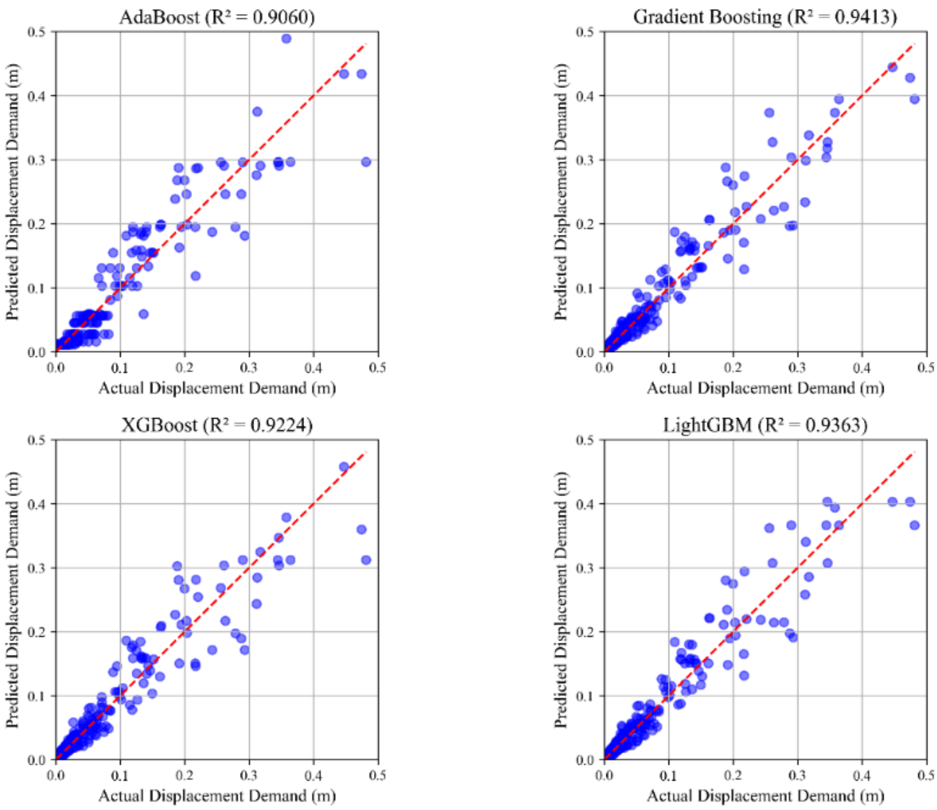

Fig. 5. Predicted versus actual values for the displacement demands using boosting algorithms

The MLP model, which employs a neural network algorithm, showed competitive results by yielding predictions closely matching the actual displacement demand values, as presented in Fig. 6. Its predictions resulted in an R^2 value of 0.9336.

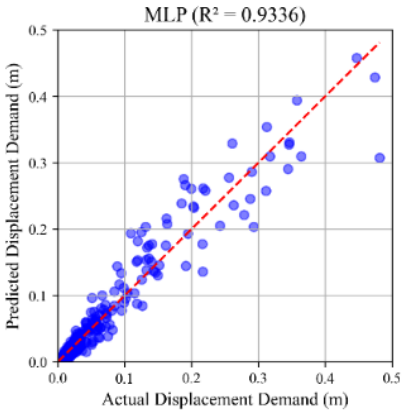

Fig. 6. Predicted versus actual values for the displacement demands using neural networks

Fig. 7 compares the actual displacement demands to those predicted by the kernel methods. The Kernel Ridge model delivered the strongest performance among all the evaluated machine learning models, with an R^2 value of 0.9421. It resulted in smooth and consistent predictions. On the other hand, both linear and RBF-type SVR performed very poorly (i.e., with R^2 values of 0.6500 and 0.1406, respectively), especially for the lower displacement demands.

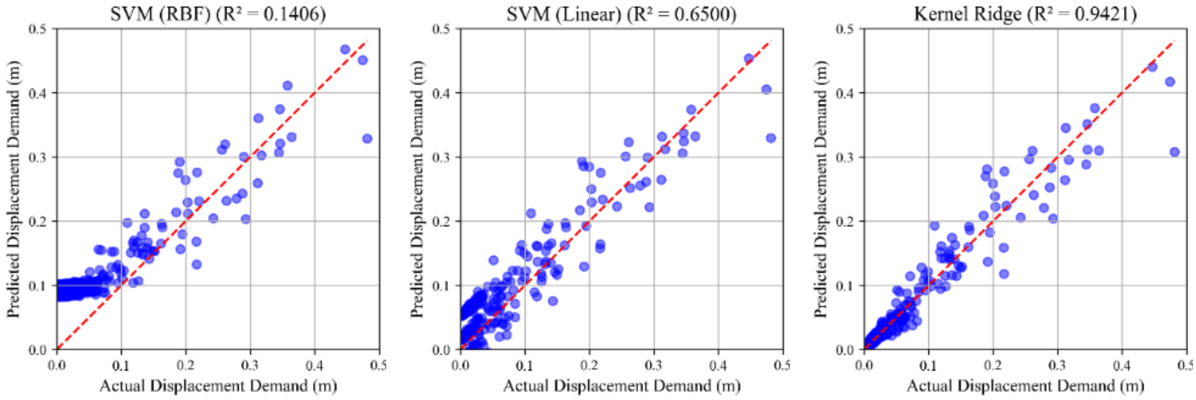

Fig. 7. Predicted versus actual values for the displacement demands using kernel methods

The KNN and Bagging Regressors yielded satisfactory prediction performances, with R^2 values of 0.9339 and 0.9281, respectively, as shown in Fig. 8. While KNN outperformed Bagging Regressor in terms of stability and alignment with actual demand values, a performance degradation was observed in the moderate displacement demand predictions by Bagging Regressor.

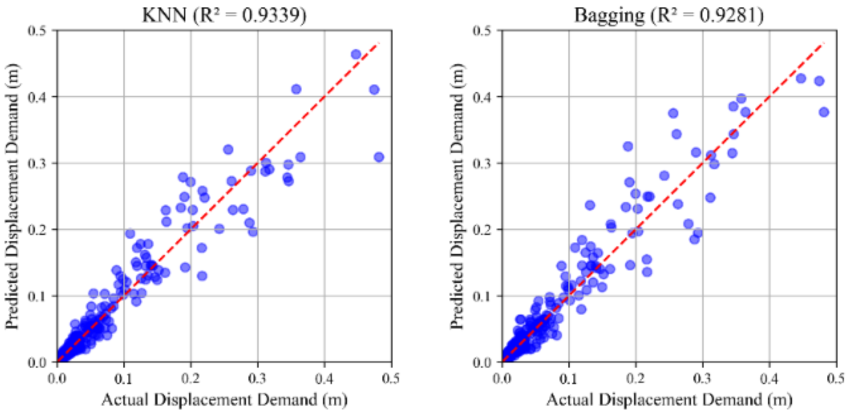

Fig. 8. Predicted versus actual values for the displacement demands using other models

Fig. 9 compares the model performance based on the error metrics. Specifically, root mean squared error (RMSE) and mean absolute error (MAE) values were calculated for each machine learning model to assess their prediction accuracy. RMSE indicates the square root of the average of the squared differences between predicted and actual displacement demand values. In contrast, MAE represents the average of the absolute differences between predicted and actual values. While the SVM (RBF), ElasticNet, and SVM (Linear) models produced the highest error values, the other models resulted in relatively lower and similar RMSE (i.e., approximately 0.02) and MAE (i.e., approximately 0.01) values. In general, the boosting algorithms yielded the best predictive performance. However, particularly, the Kernel Ridge model from the kernel methods became the most successful one among the others, with an RMSE value of 0.0192 and an MAE value of 0.0089.

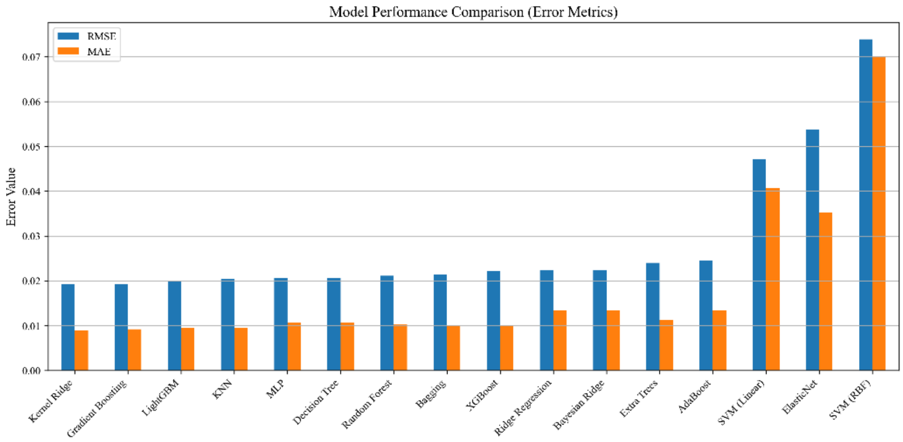

Fig. 9. Model performance comparison

4. Conclusions

This study investigated the use of seismic input energy in predicting displacement demands, utilizing a broad range of machine learning models. The predictive performance of the selected 16 models was compared using data generated from linear and nonlinear time history analyses of the 2023 Kahramanmaraş earthquake's acceleration records. The following conclusions were drawn:

- The boosting algorithms yielded the most reliable displacement demand predictions, whereas the linear models and some kernel methods yielded the least successful ones. Specifically, Support Vector Machines with a Radial Basis Function, ElasticNet, and a linear version of Support Vector Machines achieved the lowest R^2 scores and highest error metrics.
- Among the studied machine learning models, Gradient Boosting, LightGBM, and Kernel Ridge Regression stood out, resulting in R^2 values above 0.94 and RMSE values below 0.02. It indicates their high degree of prediction accuracy and model reliability for the displacement demand estimations.
- The results showed that the seismic input energy is a valuable metric for predicting the structural displacement demands of SDOF systems, especially when integrated into machine learning algorithms.

This study contributes to the growing intersection between earthquake engineering and data science. By augmenting traditional analytical techniques, it demonstrates the potential of machine learning algorithms to improve seismic response predictions. Additionally, the following recommendations are proposed for future studies:

- Some additional intensity measures (e.g., PGA, PGV, Arias intensity) and earthquake metrics (e.g., significant duration, spectral shape indicators) should be introduced as input features to enhance model accuracy.
- The study should be extended to MDOF systems, which would yield a more complex and nonlinear relationship between the seismic input energy and displacement demands.
- Hyperparameter optimization techniques should be applied to further improve the models' prediction performance.
- To assess their applicability and robustness, the trained and tested machine learning models should be validated using experimental data from shaking table tests or real-world instrumented buildings.
- The use of hybrid or ensemble meta-models should be explored to combine the strengths of multiple machine learning algorithms for improved prediction stability.

References

Benavent-Climent, A., & Mollaioli, F. (Eds.). (2021). *Energy-based seismic engineering: Proceedings of IWEBSE 2021* (Vol. 155). Springer Nature.

Breiman, L. (1996). Bagging predictors. *Machine Learning, 24*, 123–140.

Breiman, L. (2001). Random forests. *Machine Learning, 45*, 5–32.

Breiman, L., Friedman, J., Olshen, R. A., & Stone, C. J. (1984). *Classification and regression trees*. Wadsworth International Group.

Chen, P. C., & Chien, K. Y. (2020). Machine-learning based optimal seismic control of structure with active mass damper. *Applied Sciences, 10*(15), 5342.

Chen, T., & Guestrin, C. (2016). XGBoost: A scalable tree boosting system. In *Proceedings of the 22nd ACM SIGKDD International Conference on Knowledge Discovery and Data Mining (KDD'16)* (pp. 785–794).

Cortes, C., & Vapnik, V. (1995). Support-vector networks. *Machine Learning, 20*, 273–297.

Cover, T., & Hart, P. (1967). Nearest neighbor pattern classification. *IEEE Transactions on Information Theory, 13*(1), 21–27.

Freund, Y., & Schapire, R. E. (1997). A decision-theoretic generalization of on-line learning and an application to boosting. *Journal of Computer and System Sciences, 55*(1), 119–139.

Friedman, J. H. (2001). Greedy function approximation: A gradient boosting machine. *Annals of Statistics*, 1189–1232.

Fujii, K., & Shioda, M. (2023). Energy-based prediction of the peak and cumulative response of a reinforced concrete building with steel damper columns. *Buildings, 13*(2), 401.

Geurts, P., Ernst, D., & Wehenkel, L. (2006). Extremely randomized trees. *Machine Learning, 63*, 3–42.

Güllü, A., Çalım, F., & Yüksel, E. (2023). Estimation of the story response parameters through the seismic input energy for moment-resisting frames. *Soil Dynamics and Earthquake Engineering, 164*, 107636.

Hoerl, A. E., & Kennard, R. W. (1970). Ridge regression: Biased estimation for nonorthogonal problems. *Technometrics, 12*(1), 55–67.

Kazemi, F., Asgarkhani, N., & Jankowski, R. (2023). Machine learning-based seismic fragility and seismic vulnerability assessment of reinforced concrete structures. *Soil Dynamics and Earthquake Engineering, 166*, 107761.

Ke, G., Meng, Q., Finley, T., Wang, T., Chen, W., Ma, W., ... & Liu, T. Y. (2017). LightGBM: A highly efficient gradient boosting decision tree. *Advances in Neural Information Processing Systems, 30*.

MacKay, D. J. (1992). Bayesian interpolation. *Neural Computation, 4*(3), 415–447.

Rumelhart, D. E., Hinton, G. E., & Williams, R. J. (1986). Learning representations by back-propagating errors. *Nature, 323*(6088), 533–536.

Salkhordeh, M., Mirtaheri, M., Rabiee, N., Govahi, E., & Soroushian, S. (2023). A rapid machine learning-based damage detection technique for detecting local damages in reinforced concrete bridges. *Journal of Earthquake Engineering, 27*(16), 4705–4738.

Saunders, C., Gammerman, A., & Vovk, V. (1998). Ridge regression learning algorithm in dual variables. In *Proceedings of the 15th International Conference on Machine Learning* (pp. 515–521).

Tang, Q., Dang, J., Cui, Y., Wang, X., & Jia, J. (2022). Machine learning-based fast seismic risk assessment of building structures. *Journal of Earthquake Engineering, 26*(15), 8041–8062.

Varum, H., Benavent-Climent, A., & Mollaioli, F. (Eds.). (2023). *Energy-based seismic engineering: Proceedings of IWEBSE 2023* (Vol. 236). Springer Nature.

Xie, Y., Ebad Sichani, M., Padgett, J. E., & DesRoches, R. (2020). The promise of implementing machine learning in earthquake engineering: A state-of-the-art review. *Earthquake Spectra, 36*(4), 1769–1801.

Zou, H., & Hastie, T. (2005). Regularization and variable selection via the elastic net. *Journal of the Royal Statistical Society: Series B (Statistical Methodology), 67*(2), 301–320.

Calibration of FE models of reinforced concrete specimens using experimental modal analysis

Sena Kapıcıoğlu*[1], Mehmet F. Aydıner[1], Fatih Alemdar[1], Barış Sevim[1], Serkan Bekiroğlu[1], Güray Arslan[1], Yusuf Ayvaz[1]

[1] *Yildiz Technical University, Department of Civil Engineering,34220 İstanbul, Türkiye*

Abstract. In modern engineering practices, finite element models of structures are generated using specialized structural analysis software, and simulations are conducted in computational environments. To ensure that these analyses accurately represent the actual structural behavior and produce realistic results, finite element models are calibrated using dynamic properties obtained from experimental modal analysis. In this study, five small-scale two storey one bay reinforced concrete specimens tested. Theoretical modal analysis results were obtained for these specimens using the SAP2000 software. Concurrently, the reinforced concrete specimens were excited using an impact hammer (modal hammer), and their dynamic responses were recorded using uniaxial accelerometers installed at specific floor levels. The force and acceleration signals collected during the experiments were processed in the frequency domain using dedicated signal processing software to derive transfer functions for the reinforced concrete models subjected to impact excitation. Through these analyses, the dynamic properties of the structures, including mode shapes, natural frequencies, and damping ratios, were determined. Then, the experimental modal analysis results for each reinforced concrete specimen were compared with the theoretical modal analysis results of the SAP2000 finite element model calibrated with the modulus of elasticity variation. Calibrating the analytical model with the experimental modal analysis results increases the reliability of the finite element model. This approach contributes significantly to accurately predicting structural behavior and provides a robust basis for more precise finite element modeling in future structural engineering research.

Keywords: Experimental modal analysis; Modal hammer; Finite element model; RC specimens

1. Introduction

In structural engineering, accurately predicting the behavior of designed systems under various external forces forms the basis of safe and functional designs (Chopra, 2017). In addition to static loads, dynamic loads—such as earthquakes, wind, traffic, or machine vibrations—have been shown to influence the response of structures significantly. These dynamic interactions are directly related to the fundamental properties of structures, such as mass and stiffness, and can lead to undesirable consequences like resonance, excessive oscillation, and structural damage.

At this stage, Modal Analysis is a critical method. This discipline, which involves the determination of a structure's vibratory properties through either experimental investigation or analytical modeling, facilitates the comprehension of structural dynamic behavior by characterizing its natural frequencies, damping ratios, and mode shapes (Ewins, 2000). Knowing these vibration properties is crucial for predicting and improving how structures respond to different dynamic forces.

Modal analysis is a methodology widely applied in various engineering disciplines. It is used in various fields such as civil engineering, automotive engineering, aeronautical engineering, astronautical engineering, electronics, and sports equipment design. The material properties specific to structures in these various engineering branches, combined with the variability of the environmental conditions to which they are exposed, often require various measurement techniques and data processing strategies.

Operational Modal Analysis (OMA) and Experimental Modal Analysis (EMA) represent two primary methodologies for identifying the dynamic properties of structures, which are fundamentally different from these models by the treatment of input excitation. OMA takes advantage of naturally occurring ambient or operational forces acting on a structure, where these input forces are not directly measured; the analysis focuses only on the

*Corresponding author, E-mail: sena.kapicioglu@yildiz.edu.tr

https://doi.org/10.31462/icearc2025_ce_eqe_748

golden light publishing

structural response. In contrast, EMA involves the application of a known and measurable input force to the structure, typically using instruments like modal hammers or shakers, allowing for direct input-output characterization of the system's dynamic behavior. This difference in input force measurement forms the core distinction between these two widely applied techniques in structural dynamics.

The practical difficulties of using impact hammers can make EMA challenging, especially when studying large structures. For this reason, OMA is often a more practical and effective method for understanding the dynamics of large-scale systems (Grosel et al., 2014). However, when analyzing smaller structures, both EMA and OMA have been shown to produce similar and reliable results.

Nowadays, EMA, especially when applied to impact testing, is a frequently used and preferred method for determining the vibration characteristics of structures. EMA has been widely accepted due to its advantages, such as low uncertainty in the applied force, a better understanding of the test conditions, easy applicability, fast results, and economy (Schwarz & Richardson, 1999; Zoltowski & Napieraj, 2017).

In current engineering design processes, finite element (FE) software is common, often relying on certain assumptions. The economic benefits of FE analysis frequently lead to its selection over physical experiments. However, it is important to recognize that real-world structural behavior may differ from theoretical predictions. Therefore, a reliable way to improve the validity and accuracy of FE analysis assumptions is to compare the outcomes of experimental studies with those from FE simulations. Many research projects have assessed the effectiveness of EMA on different structural materials and systems and how well its results align with analytical findings.

Prasad and Seshu (2008) conducted an experimental modal analysis on beams of different materials using an impact hammer. In their study, they compared their experimental results with theoretical analyses and FE software analysis results. Similarly, a study by Walunj et al. (2015) investigated the modal parameters of cantilever beams using the experimental modal analysis method. Sharma (2019) also presented a comparative study of theoretical and experimental modal analysis on beams.

Chandravanshi and Mukhopadhyay (2013) investigated the dynamic characteristics (frequency, mode shape, damping) of a two-story steel structure using experimental modal analysis. They then analyzed the same structure using the finite element method with the ANSYS program and subsequently compared the results obtained from the experimental and numerical approaches.

Bayraktar et al. (2010) experimentally obtained and investigated the dynamic parameters of three reinforced concrete buildings at different construction stages. Altunisik et al. (2013) applied analytical and experimental modal analyses to determine the dynamic characteristics of a scaled bridge model.

Arslan and Durmus (2014) conducted OMA experiments on single-story reinforced concrete frames to investigate the role of infill walls on the dynamic response of structures. These experiments tested both bare frames and frames with brick infill walls. A finite element model was also created and calibrated using the SAP2000 program.

Orlowitz and Brandt (2017) conducted a detailed comparison of EMA and OMA using a laboratory-tested plate. Their study aimed to evaluate the effectiveness and applicability of both methods under controlled conditions. The research examined the accuracy of identified dynamic properties and the practical aspects of each technique. This work provides knowledge of the relative merits of EMA and OMA for structural analysis.

Azmi et al. (2021) conducted an experimental modal analysis on a two-story reinforced concrete frame. In this study, they determined the structure's natural frequencies using impact testing and accelerometers. They compared the experimental results with the results from a finite element model they created using the HYPERWORK program. The findings showed that the natural frequencies measured experimentally were in significant agreement with those obtained through numerical modeling.

Filippoupolitis and Hopkins (2021) conducted a study investigating the dynamic behavior of damaged reinforced concrete beams. In their research, they utilized EMA to understand the effects of structural discontinuities on the vibration characteristics of these beams. Additionally, they employed Finite Element Methods (FEM) to support their experimental findings with numerical modeling.

In a study by Ahmed and Mohammad (2015), the EMA method was employed to understand the dynamic characteristics of reinforced concrete square plates. These researchers determined the plates' natural frequencies and mode shapes through experiments performed in a laboratory setting.

Sevim et al. (2011) collected experimental data on the dynamic properties of two historical arch bridges using ambient vibration tests, and they calibrated the finite element models created in the ANSYS program using this data. Günaydin et al. (2017) initially performed an analytical determination of the modal parameters of the reinforced concrete buildings constructed under laboratory conditions, employing the ANSYS software. Subsequently, they conducted ambient vibration tests to experimentally validate these parameters, utilizing the acquired data to refine the initial finite element models for increased accuracy.

Altunisik et al. (2024) updated the finite element models of the historical Santa Maria Church and its Guesthouse in Trabzon using the dynamic properties obtained from a non-destructive experimental investigation with ambient vibration testing.

Fig. 1. RC specimens

In this study, experimental modal analysis was performed on five reinforced concrete frame structures, as presented in Fig. 1. Using an impact hammer as an exciter, the natural vibration frequencies and corresponding mode shapes, which are the basic dynamic characteristics of the structures, were determined. In addition, the modal analysis of the same structural configurations was carried out analytically using SAP2000 software. A calibration process was applied to ensure the validity and predictive ability of the numerical models. In this process, the parameters of the analytical models were systematically adjusted by comparing them with the data obtained from the experimental modal analyses. The agreement between the analytical and experimental findings supported the overall reliability and validity of the numerical representations developed for the reinforced concrete frame structures.

2. Materials and methods

This study focuses on the experimental modal analysis of small-scale, two-story reinforced concrete structures, each featuring a story height of 20 cm and a span of 20 cm. Five distinct specimens were examined as part of this research. Three of these specimens were constructed with rectangular columns, each having a cross-sectional size of 25x25 mm (Fig. 2a). The remaining two specimens incorporated circular columns, each with a diameter of 20 mm (Fig. 2b).

(a)

(b)

Fig. 2. Two type of specimen having a) Rectangular column cross-section b) Circular column cross-section

At the beginning of this study, finite element (FE) simulations were performed before the experimental modal analysis to find the approximate natural frequency range of the structures. This frequency range obtained from the FE models was important in determining the necessary measurement settings (e.g., sampling frequency, frequency resolution) for the experimental modal analysis.

The reinforced concrete frame structures were stimulated with a calibrated modal impact hammer. The frequency content of the impact applied by the hammer depends on the hardness of the tip used; harder tips affect a wider frequency range. As stated in the literature by Avitabile (2001), selecting the appropriate tip is important to adequately excite all structural modes relevant to modal identification. Therefore, a modal impact hammer is used with appropriate sensitivity and linearity to accurately measure the force applied to concrete structures (Fig. 3a).

We used uniaxial accelerometers to study how structures vibrate (Fig. 3b). These special sensors generate electrical signals directly proportional to the movement of a small mass inside. These signals are converted from analog to digital, allowing us to obtain precise acceleration values at the points where the sensors are placed. In this way, we can comprehensively understand the dynamic behavior of structures.

In the experimental phase of this research, transient vibrational excitations generated in structural systems by the controlled impact forces of the modal hammer were recorded using three uniaxial accelerometers. The roving hammer technique was applied. Under this methodology, accelerometers were placed at strategic points in the structural frames to record linear acceleration components along the x and y horizontal axes.

(a) (b)

Fig. 3. Test setups a) Modal hammer b) Uniaxial accelerometers

The data obtained from the experimental studies was recorded using Dewesoft signal processing software installed on a personal computer. During this process, the force signal from the modal hammer was visualized as a force-time graph in the time domain. In contrast, the vibration response signals from the accelerometers were recorded as acceleration-time graphs. To accurately analyze these time-dependent data, they were transformed into the frequency domain using the Fast Fourier Transform (FFT) algorithm integrated within the software. Subsequently, Frequency Response Functions (FRFs) that characterize the dynamic properties of the structures were calculated.

The Frequency Response Function (FRF) mathematically describes how a structure responds to an applied force. This response is usually measured by acceleration, velocity or displacement. The FRF examines the components of both the applied force and the structure's response at different frequencies. To do this, we convert time-varying signals into the frequency domain using the Fourier Transform method. This allows us to see how much the structure increases or decreases the forces at different frequencies. The FRF is a complex number representing the magnitude ratio and phase difference between the input and output at each frequency. Notably, the specific mathematical points (poles) of the FRF indicate the structure's natural vibrational frequencies. The shape of the FRF around these points indicates the damping characteristics of the structure (how fast it dampens vibrations) (Avitabile, 2001).

In the calculation of the Frequency Response Functions (FRFs) by transforming the obtained time data into the frequency domain, the following fundamental frequency response function formula was used by the software. Here, H(ω) represents the Frequency Response Function; X(ω), the Fourier Transform of the output response; F(ω), the Fourier Transform of the input force; and ω, the Frequency.

$$H(\omega) = \frac{F(\omega)}{X(\omega)} \tag{1}$$

Through this mathematical relationship, the frequency domain response of the structure to the applied force is analyzed in detail, and the structural dynamic properties (natural frequencies, damping ratios, and mode shapes) are determined.

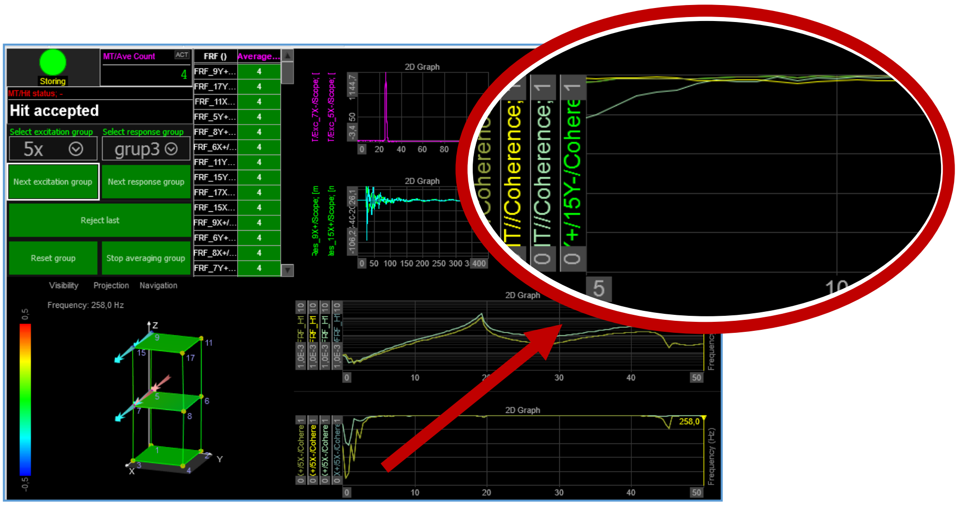

Fig. 4. Measurement screen and detail of coherence

In the experimental studies, various impact application points were used to ensure a comprehensive determination of the structures' dynamic behavior. The structures' corner points were excited in both x and y directions, as impacting the corner points facilitates the excitation of a larger number of modes compared to impacting the center point (Mali & Singru, 2018).

The coherence function was used to evaluate the data quality. This function shows how linearly the measured output is related to the applied input. Inconsistent pulses in the measurement can lead to variations in the resonance values. Therefore, four controlled and consistent pulses were applied to each point for reliable results. If the coherence value of the pulses at a point was between 0.7 and 1, that measurement was accepted (Fig. 4). This process aims to increase the reliability of the Frequency Response Functions (FRF).

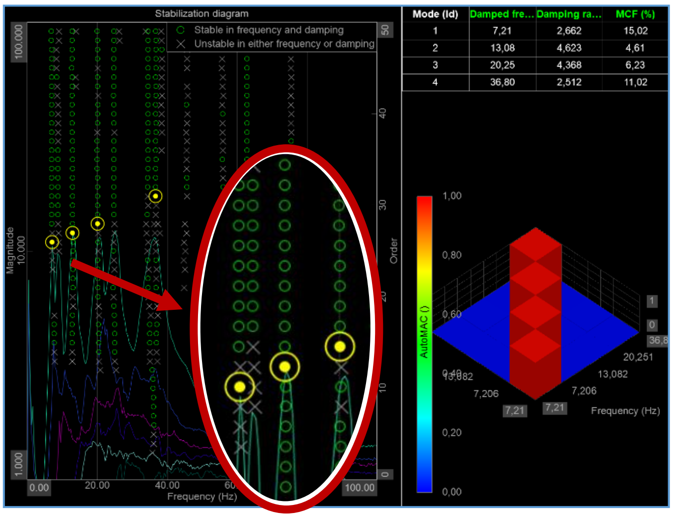

Fig. 5. Stabilization and AutoMAC diagram

The Frequency Response Functions (FRFs) generated from the acquired measurement data were converted into stabilization diagrams using the software (Fig. 5). These diagrams visually illustrate the consistency of the structural vibration frequencies and damping characteristics calculated for different mathematical model complexities (model orders). As the model complexity increases, peak points that do not show a significant change in frequency and damping values, i.e., remain "stable," are marked on this diagram.

These stable peak points represent frequencies more likely to correspond to actual structural modes. Subsequently, these stable frequency values were used to generate the AutoMAC (Automated Modal Assurance Criterion) diagram. The AutoMAC diagram evaluates the similarity and consistency between the vibration patterns at different measurement points. This process helps identify "significant" physically meaningful " vibration modes, thus avoiding misleading results. These stages are crucial for enhancing the accuracy and reliability of the structural dynamic properties obtained from the experimental data (Dewesoft).

The SAP2000 models for samples given in Fig. 2a and Fig. 2b was developed using centroid lines of elements and midplanes for slabs. The models were generated separately for calibration. Calibration was made according to the modulus of elasticity of concrete of samples. The change in modulus of elasticity affects stiffness and also accounts for cracks as well. At first, the supports defined as fixed support and modulus of elasticity of concrete is taken as 24855 MPa, the default value. The effective flexural stiffness multiplier was taken as 0.7 for columns. The system is a flat slab building. The slab type definition is important for calibration, since the modal frequencies are affected by it. While “shell thin” makes column ends more like fixed ends. On the other hand, out of plane bending deformation of the slab does not accounted for the membrane, resulting decrease in the stiffness of columns. The theoretical modal analysis was done using the FE model at SAP2000 by eigenvalue analysis. In Fig. 6, the four mode shapes for different slab type definitions are given.

As can be seen from Fig. 6a and b, the nearly 90° angle of joints and “S” shape of columns can be observed from shell thin defined slab model mode shapes (Fig. 6a). On the other hand, it is more like free end for columns of membrane defined slab model mode shapes (Fig. 6b). This difference in behavior affects structural stiffness and the modal frequencies as well. Therefore, it was studied comparatively. The modal frequencies with automeshed slab models are given in Table 1.

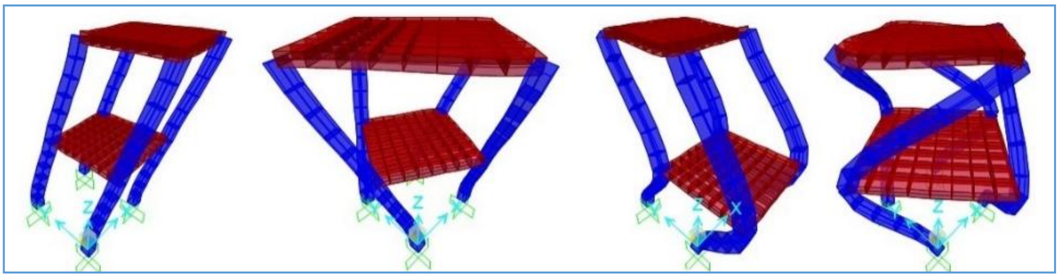

(a)

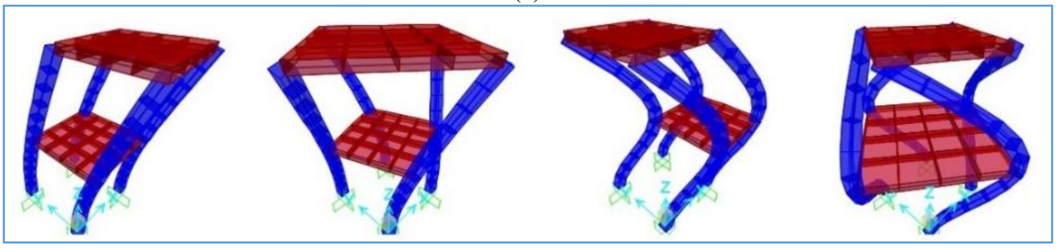

(b)

Fig. 6. SAP2000 theoretical mode shapes a) for slabs defined as shell thin b) for slabs defined as membrane

Table 1. Slab types and corresponding modal frequencies (Hz)

Slab Type	Mod 1	Mod 2	Mod 3	Mod 4
Shell Thin	62.44	86.9	203.43	268.23
Membrane	28.40	43.60	171.48	220.40

The construction of a small-scale low-strength building, like Fig. 2a and b, is a sensitive job. As a result, there are numerous governed cracks at slabs near joints. That is why membrane slab type is selected for model to describe reality. By increasing the mesh number of slab, as for shell thin model, the modal frequency is decreasing to a point. In that manner, the results given in Table 1 are obtained for 20x20 auto meshing of each slab. While gradually increasing the amount of mesh number, as for membrane, the slight change in modal frequency occurs only in torsional modes, the modal frequency for translational modes becomes constant.

Aside from slab type, the support type should defined similar to the reality. The systems have a basement, and the basement sits on a steel I beam, as can be seen from Figs. 2 a and b while the measurements of EMA are taken. The column supports are the basement itself, meaning the boundary condition of bottom of columns provided by deformation of basement. Note that not the entire basement sits on the steel beam. This situation is taken into consideration in the SAP2000 model by adding a basement, dividing it into quads, and assigning pinned supports at the nodes corresponding to the mentioned I beam and basement intersection. The bottom perspective view of the basement can be seen in Fig. 7a. The basement defined by shell thin in order to the flexural behavior of the cantilever part of basement affect the boundary condition of bottom of columns. The mode shapes for Fig. 2a building are given in Fig. 7b, c, d, and e as well.

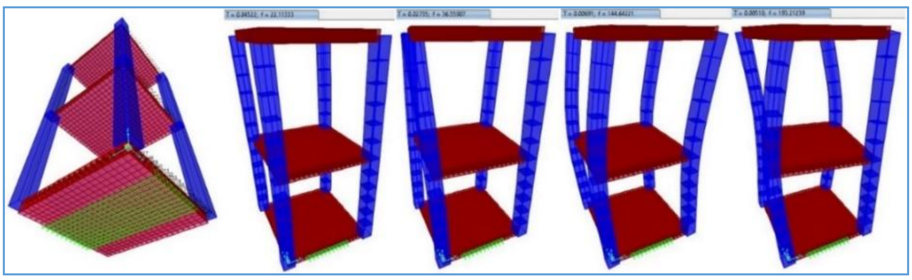

(a) (b) (c) (d) (e)

Fig. 7. SAP2000 model for rectangular column section samples a) realistic basement modeling of measured building and b) Mode 1 c) Mode 2 d) Mode 3 e) Mode 4

If one to compare Table 1 membrane defined model results with fixed support with Fig 7b, c, d, e, then the decrease in modal frequency can be observed. The basement support model provided in Fig 7a has less structural stiffness compared to fixed supported models. That is why, Fig 7 is taken as a more realistic support model and taken into account for the results in Table 2. The same procedure (membrane slab type and realistic support modeling) was done for modeling the samples with circular cross-sectional columns (Fig. 2b) since the only difference between Fig. 2a and Fig. 2b is the columns sections. The mode shapes and corresponding modal frequencies for the samples having circular column sections are given in Fig. 8.

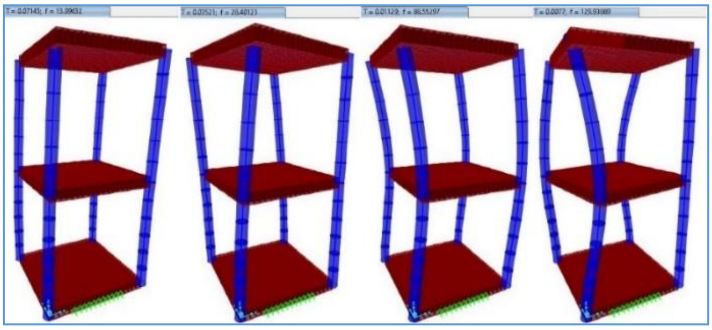

(a) (b) (c) (d)

Fig. 8. SAP2000 model for circular column section samples a) Mode 1 b) Mode 2 c) Mode 3 d) Mode 4

3. Results and discussion

The experimental analyses concluded by identifying four main vibration patterns (modes) for each small reinforced concrete structure we studied. This was done using special software. These fundamental modes, which show how the structures naturally vibrate, were consistently found in all samples.

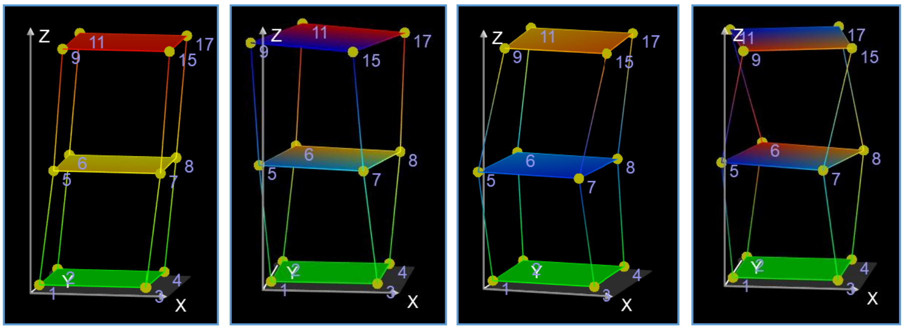

(a) (b) (c) (d)

Fig. 9. Mode shapes (EMA) a) Mode 1 b) Mode 2 c) Mode 3 d) Mode 4

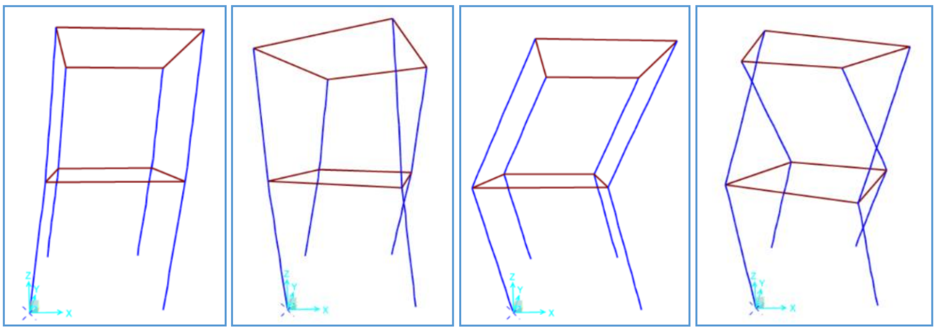

(a) (b) (c) (d)

Fig. 10. Mode shapes (SAP2000) a) Mode 1 b) Mode 2 c) Mode 3 d) Mode 4

The mode shapes obtained from the finite element program SAP2000 are presented in Fig. 10a, b, c and d. Observations indicate a significant overlap between the mode shapes derived from the experimental analyses and analytical results. For experiment and eigenvalue analysis, the first mode corresponds to primary translational mode (Fig. 9a and Fig. 10a), second mode corresponds to primary torsional mode (Fig. 9b and Fig. 10b), third mode corresponds to secondary translational mode (Fig. 9c and Fig. 10c) and forth mode corresponds to the secondary torsional mode (Fig. 9d and Fig. 10d). The order of these modes overlaps as EMA and FE analysis modes. This substantial agreement supports the accuracy of both the experimental methodology and the finite element model in effectively capturing the modal characteristics of the structural behavior. These modes are important for understanding how these reinforced concrete structures might behave when forces are applied to them.

Table 2. Frequency of modes (Hz)

Sample No	Analysis	Mode 1	Mode 2	Mode 3	Mode 4	Error (%)
1	EMA[*1]	19.79	43.75	104.63	176.17	11.72
	SAP2000[*2]	22.11	36.56	144.64	193.21	
2	EMA	18.05	40.87	87.303	136.4	22.49
	SAP2000	22.11	36.56	144.64	193.21	
3	EMA	17.1	33.7	48.1	84.6	29.30
	SAP2000	22.11	36.56	144.64	193.21	
4	EMA	7.21	13.08	20.25	36.80	94.17
	SAP2000	14.00	28.40	88.55	129.94	
5	EMA	5.32	9.19	14.94	30.51	163.16
	SAP2000	14.00	28.40	88.55	129.94	

[*1]EMA: Experimental Modal Analysis
[*2]SAP2000 noncalibrated results with membrane slab definition and more realistic basement modeling

In the comparison conducted, the frequency values obtained from the experimental and finite element analyses are presented in detail in Table 2. The percent error (percentage of relative error) was calculated for the most dominant –first-mode frequencies of FE and EMA analysis. The relative error is calculated by the ratio of absolute error, which is the difference between FE and EMA analysis, to the EMA analysis result (actual value). For the results of the rectangular cross-sectional model (Fig. 2a), the finite element analysis was compared with the experimental modal analysis results. Considering the dimensions of the reinforced concrete frame, its complex behavior, and the proximity of the support assumptions made in the finite element model to the actual structural behavior, these error percentages are evaluated to be within acceptable limits for the samples having rectangular cross-sectional columns.

On the other hand, for circular cross-sectional samples as Samples No. 4 and 5 (Fig. 2b), the percentage of error obtained is quite high. This is understandable due to the poor construction of circular cross-sectional samples relative to rectangular cross-sectional samples due to the constructional hardships of small-scale buildings. The flexibility of Samples 4 and 5 could be observed during the experiment as well.

The modal damping ratios corresponding to the different mode shapes of the two-story reinforced concrete frame obtained from the experimental analyses are presented in Table 3.

Table 3. Damping ratios (%)

Sample No	Mode 1	Mode 2	Mode 3	Mode 4
1	4,833	7,54	2,56	2,01
2	12,83	10,48	6,56	6,53
3	7,09	5,06	6,15	0,62
4	2,66	4,62	4,37	2,51
5	6,22	5,12	4,13	2,87

The calibration for both Fig 2a and Fig 2b buildings was done by changing the elastic modulus of concrete. The manual calibration was done based on mode number 1, the most dominant one. The non-calibrated model (with membrane slab and more realistic basement modeling), the calibrated model, and the obtained EMA results are given in Table 4.

Table 4 shows that while the calibrated FE model and EMA modal frequency of the first mode are nearly the same, the modal frequencies of the other modes differ. The calibration was done manually and for one independent variable, i.e., the elasticity modulus of concrete. However, the factors affecting translational and torsional modes differ. Multivariable calibration might be needed to calibrate modal frequencies more than one.

Table 4. Elastic modulus of uncalibrated and calibrated SAP2000 models and corresponding modal frequencies

Sample No	State	Elastic Modulus (MPa)	Mode 1(Hz)	Mode 2(Hz)	Mode 3(Hz)	Mode 4(Hz)
1	Un-Calibrated*1	24855	22.11	36.56	144.64	193.21
	Calibrated*2	19000	19.76	32.00	126.46	168.93
	Experimental*3	-	19.79	43.75	104.63	176.17
2	Un-Calibrated	24855	22.11	36.56	144.64	193.21
	Calibrated	16500	18.02	29.79	117.85	157.42
	Experimental	-	18.05	40.87	87.30	136.4
3	Un-Calibrated	24855	22.11	36.56	144.64	193.21
	Calibrated	15000	17.18	28.4	112.36	150.10
	Experimental	-	17.10	33.70	48.10	84.60
4	Un-Calibrated	24855	14.00	28.40	88.55	129.94
	Calibrated	6600	7.21	14.64	45.63	66.96
	Experimental	-	7.21	13.08	20.25	36.80
5	Un-Calibrated	24855	14.00	28.40	88.55	129.94
	Calibrated	3600	5.33	10.81	33.70	49.45
	Experimental	-	5.32	9.19	14.94	30.51

*1 Un-Calibrated: SAP2000 noncalibrated results with membrane slab definition and more realistic basement modeling
*2 Calibrated: SAP2000 calibration by changing the modulus of elasticity according to mode 1
*3 Experimental: Experimental modal analysis results

4. Conclusions

Within the scope of this study, the dynamic characteristics of two-story reinforced concrete structures were thoroughly investigated using experimental and analytical methods. In the experimental modal analysis conducted in a laboratory setting, the modal hammer excitation method was employed to determine the natural frequencies and mode shapes of the structures. Simultaneously, a finite element model of the same structures was created using SAP2000 software, and theoretical modal analyses were performed.

For the beamless (flat slab) frame samples, the slab type shows importance in theoretical modal analysis due to a significant change in modal frequencies. Since constructed small-scale buildings have cracks at slabs near joints and systems have defects, the joints are assumed to not be well stiff. In that regard, slabs are modeled as membranes. Even if the shell thin definition is less assuming, the membrane definition describes the real structure more suitably. This resulted in the first mode frequency decrease to %45 of it (decreased by almost half). Also, the bottom of columns is modeled not as fixed support but connected to a basement resting on a beam (with pinned supports at middle nodes). The flexural behavior of the cantilever part of the basement (outside of the steel beam) also results in a slight decrease in modal frequencies. The decrease percentage is %22. This is the pre-state of calibration changing the elastic modulus of concrete.

Manual calibration is done by changing the modulus of elasticity concrete to describe cracks in low-strength concrete. Decreasing the modulus of elasticity affects the stiffness matrix, and modal frequencies decrease as well. The first mode is considered for calibrating FE models, and Table 4 is obtained. The difference between EMA and FE modal frequencies increases with higher mode numbers. The modulus of elasticity the first three samples (rectangular cross-sectional) would be reasonable if the compressive strength of low-strength concrete is approximately 3-5 MPa.

On the other hand, the error obtained was significantly higher for Samples 4 and 5, which are circular column buildings. Due to improper construction and manufacturing difficulty, these two samples obtained way more flexible in reality than encountered in experimental results. There are some advanced calibration methods that are way more realistic. For example, in order to calibrate other modes, other calibration approaches, such as changing joint stiffness, can be evaluated. In addition, the modulus of elasticity samples can be obtained by test equipment and can be used for calibration.

The comparison of the experimental and analytical results shows that the methods used to determine the dynamic behavior of the structures and the assumptions made in the finite element model are generally consistent and reliable. In particular, the overlap in the mode shapes and the calibrated frequency values indicate that both approaches successfully capture the fundamental dynamic characteristics of the structures. Despite potential discrepancies due to the reinforced concrete frame's geometrical complexity and the material properties' idealization, the obtained agreement supports the use of the finite element model as an effective tool for the dynamic analysis of such structures. Future research can expand the knowledge in this area with different structural configurations and advanced modeling techniques.

References

Ahmed, M.S., & Mohammad, F.A. (2015). Experimental modal analysis of reinforced concrete square slabs. *International Journal of Mechanical, Aerospace, Industrial, Mechatronic and Manufacturing Engineering*, *9*(3)

Altunişik, A.C., Bayraktar, A., & Sevim, B. (2013). Analytical and experimental modal analyses of a highway bridge model. *Computers and Concrete, An International Journal*, *12*(6), 803-818

Altunişik, A.C., Günaydin, M., Ertürk Atmaca, E., Genç, A.F., Okur, F.Y., & Sevim, B. (2024). Experimental measurement-based FE model updating and seismic response of Santa Maria Church and its guesthouse building. *Journal of Civil Structural Health Monitoring*, *14*(3), 663-692

Arslan, M.E., & Durmuş, A. (2014). Modal testing and finite element model calibration of in-filled reinforce concrete frames. *Journal of Vibration and Control*, *20*(13), 1946-1959

Avitabile, P. (2001). Modal analysis and testing: Theoretical, experimental and operational. *Sound and Vibration Magazine, 35*(1), 22-29

Azmi, I.F., et al. (2021). Validation of Modal Analysis of Two-Storey Reinforced Concrete Frame. *IOP Conference Series: Materials Science and Engineering, 1062*(1), 012048.

Bayraktar, A., Türker, T., Altunışık, A.C., Sevim, B., Şahin, A., & Özcan, D.M. (2010). Binaların dinamik parametrelerinin operasyonal modal analiz yöntemiyle belirlenmesi. *Teknik Dergi*, *21*(104), 5185-5205

Chandravanshi, M.L., & Mukhopadhyay, A.K. (2013). Modal analysis of structural vibration. In: *ASME International Mechanical Engineering Congress and Exposition* (Vol. 56437, p. V014T15A052). American Society of Mechanical Engineers.

Chopra, A.K. (2017). Dynamics of structures (5th ed.). Pearson Education

Dewesoft (2025). Modal Test and Analysis-Solution User Manual, Version 2025.1

Ewins, D.J. (2000). Modal testing: Theory, practice and application (2nd ed.). Research Studies Press

Filippoupolitis, M., & Hopkins, C. (2021). Experimental validation of finite element models for reinforced concrete beams with discontinuities that form dowel-type joints. *Vibration*, *4*(3), 537-550

Grosel, J., Sawicki, W., & Pakos, W. (2014). Application of classical and operational modal analysis for examination of engineering structures. *Procedia Engineering*, *91*, 136-141

Günaydin, M., Adanur, S., Altunişik, A.C., Sevım, B., & Bayraktar, A. (2017). Finite modeling updating effects on the dynamic response of building models. *Journal of Testing and Evaluation*, *45*(5), 1630-1649

Mali, K.D., & Singru, P.M. (2018). Study on the effect of the impact location and the type of hammer tip on the frequency response function (FRF) in experimental modal analysis of rectangular plates. In: *IOP Conference Series: Materials Science and Engineering* (Vol. 330, No. 1, p. 012102). IOP Publishing

Orlowitz, E., & Brandt, A. (2017). Comparison of experimental and operational modal analysis on a laboratory test plate. *Measurement*, *102*, 121-130

Prasad, D.R., & Seshu, D.R. (2008). A Study on Dynamic Characteristics of Structural Materials using Modal Analsis. *Asian Journal of Civil Engineering (Building and Housing), 9*(2), 141-152

SAP2000 (2021). Integrated Finite Element Analysis and Design of Structures, Computers and Structures Inc., Version 23.3.0, Berkeley, CA.

Schwarz, B.J., & Richardson, M.H. (1999). Experimental modal analysis. *CSI Reliability Week*, *35*(1), 1-12

Sevim, B., Bayraktar, A., Altunişik, A. C., Atamtürktür, S., & Birinci, F. (2011). Finite element model calibration effects on the earthquake response of masonry arch bridges. *Finite elements in analysis and design*, *47*(7), 621-634

Sharma, J.K. (2019). Theoretical and experimental modal analysis of beam. In: *Engineering Vibration, Communication and Information Processing: ICoEVCI 2018, India* (pp. 177-186). Springer Singapore.

Prashant, S.W., Chougule, V.N., & Mitra, A.C. (2015). Investigation on modal parameters of rectangular cantilever beam using experimental modal analysis. *Materials Today: Proceedings*, *2*(4-5), 2121-2130

Żółtowski, M., & Napieraj, K. (2017). Experimental modal analysis in research. *Budownictwo i Architektura*, *16*(3), 005-012

Impact of infill walls and strengthening methods on the seismic behavior of rc buildings: A time-history approach

Özge Onat[1], Pınar Usta Evci*[1]

[1] *Isparta University of Applied Science, Department of Civil Engineering, 32200 Isparta, Türkiye*

Abstract. Time history analyses are a critical tool for understanding the behaviour of structures during earthquakes. Nevertheless, due to modelling challenges, infill walls are often excluded from seismic evaluation processes, which limits the realistic examination of structural behaviour. In regions where such structures are prevalent, a more comprehensive assessment of their impact on seismic performance is imperative. This study utilised the SAP2000 V25 finite element program to model and analyse a five-story reinforced concrete building located in Izmir. The building was evaluated under four different scenarios: without infill walls, with infill walls, strengthened with Fiber Reinforced Polymer (FRP) , and strengthened with a steel frame. The analyses utilised time history records from the Kahramanmaraş Pazarcık (Mw 7.7) and Elbistan (Mw 7.6) earthquakes that occurred on 6 February 2023, and the Izmir earthquake (Mw 6.6) on 30 October 2020. These records were modelled using acceleration-time graphs with peak ground acceleration values of 2178.72 cm/s² (Pazarcık), 635.45 cm/s² (Elbistan), and 179.31 cm/s² (Izmir). The results of the time history analyses were then compared. The effects of infill walls and strengthening techniques on parameters such as period, base shear force, interstory drift ratios, and story shear forces have been evaluated.

Keywords: Reinforced concrete structure; Infill wall; Time history analysis; Fiber reinforced polymer (FRP); Steel frame strengthening

1. Introduction

Türkiye's geographic location within the Alpine-Himalayan seismic belt has rendered it highly susceptible to numerous devastating earthquakes throughout history. Moreover, the country continues to face significant seismic hazards. (Altindal et al., 2021; Karimzadeh et al., 2024). This vulnerability is further compounded by the convergence of the Arabian, Eurasian, and African tectonic plates, in conjunction with the presence of active fault zones, including the North Anatolian, East Anatolian, and West Anatolian Faults (Onat & Evci, 2024; Karimzadeh et al., 2018; Jiang et al., 2023). In particular, the Aegean Region has experienced a notable increase in seismic events, which have the potential to pose significant risks to the region's building stock (Askan et al., 2022; Usta et al., 2023). The substantial economic losses and widespread destruction resulting from past earthquakes have heightened the importance of seismic safety in Türkiye (Şahin & Kılınç, 2016). Given that reinforced concrete (RC) buildings constitute the majority of Türkiye's building inventory, it is imperative to assess their current conditions and seismic performance under strong ground motions (Yüksel, 2008). Conventionally, infill walls have been regarded as non-structural components, contributing solely to dead loads, and their effect on the overall structural behaviour has frequently been disregarded (Tekin et al., 2007; Akyürek et al., 2018). However, both field observations from past earthquakes and extensive academic studies have demonstrated that infill walls significantly enhance the lateral stiffness and load-carrying capacity of RC structures, while the absence of sufficient infill walls at ground floors often leads to severe damage (Uysal, 2023; Onat, 2022; Sancıoğlu et al., 2022). Consequently, realistic modelling of infill walls is imperative for accurate seismic performance evaluation (Onat, 2022). The Turkish Building Earthquake Code (TBDY-2018) advocates the utilisation of the equivalent diagonal strut approach for the modelling of infill walls, while concurrently providing the requisite parameters, including elastic modulus, compressive strength, and shear strength, for a range of infill materials (TBDY, 2018).

This section presents a review of previous studies focusing on the influence of infill walls and retrofitting techniques on the seismic performance of reinforced concrete buildings. Malekkianie (2006) constitutes a comprehensive analysis of the seismic performance of reinforced concrete (RC) frames with infill walls and frames retrofitted using carbon fibre reinforced polymer (CFRP). The research adopted both experimental and numerical approaches. Three full-scale specimens were tested: a bare frame, a frame with masonry infill, and a frame

* Corresponding author, E-mail: pinarusta@isparta.edu.tr

https://doi.org/10.31462/icearc2025_ce_eqe_805

golden light publishing

strengthened using diagonally applied CFRP strips. The specimens were subjected to cyclic lateral displacements in order to simulate earthquake loading. Furthermore, nonlinear finite element analyses were conducted using SAP2000 software to validate the experimental outcomes. The findings of the study demonstrated that the incorporation of infill walls significantly enhanced the lateral stiffness and strength of the RC frames, thereby augmenting the lateral load capacity by approximately fourfold in comparison with the un strengthened frame. The CFRP retrofitting further enhanced the lateral strength by approximately 30%, whilst also promoting a more uniform distribution of damage. This approach mitigated the risk of brittle failure and provided a pragmatic and non-intrusive retrofit solution, enabling strengthening without the necessity of vacating the building. Binici et al. (2007) presents a comprehensive analytical and experimental approach for the strengthening of reinforced concrete frames with hollow clay tile infill walls using fibre-reinforced polymer (FRP) composites. The authors draw attention to the common seismic vulnerability of mid-rise RC buildings in Türkiye, particularly due to insufficient lateral strength and inadequate detailing. In order to address this issue, a proposal has been put forward for an FRP retrofit system. This system has been designed to enhance the in-plane load-carrying capacity of infill walls. It does this by anchoring diagonal FRP ties to the surrounding RC frame. The method is designed to reduce inter-storey drift and enhance seismic performance without the necessity of occupant relocation. A simplified analytical model was developed based on a previously verified nonlinear model, and displacement-based design recommendations were provided. The methodology was validated through a case study on a deficient RC residential building in Istanbul. Pushover analyses revealed that the FRP retrofit approximately doubled the base shear capacity and reduced the number of collapsed columns by half. Furthermore, the retrofitted structure was found to be in accordance with the collapse prevention performance criteria outlined in the Turkish Earthquake Code. The findings indicate the efficacy of FRP systems as a seismic retrofitting solution for deficient RC buildings with masonry infill walls, characterised by their efficiency, minimal invasiveness, and structural effectiveness. Çöğürcü (2007) conducted a study on the enhancement of the seismic resistance of unreinforced masonry structures through the implementation of epoxy-based FRP along the horizontal mortar joints. Two masonry wall specimens were constructed identically, with one unreinforced and one reinforced with FRP sheets applied to the horizontal joints. Both specimens were then subjected to out-of-plane cyclic loading. The unreinforced specimen failed in a brittle manner with limited load capacity, whereas the fibre-reinforced polymer (FRP)-strengthened wall showed a significant improvement, exhibiting up to three times greater resistance to failure. The study emphasised that the utilisation of FRP in the reinforcement of horizontal joints can efficaciously augment the seismic resilience of masonry walls. Viswanath et al. (2010) conducted a study on the seismic behaviour of reinforced concrete (RC) frames retrofitted with steel bracings. A series of structural models were constructed and analysed using STAAD.Pro software, encompassing buildings with four, eight, twelve and sixteen storeys. In order to enhance the lateral load-carrying capacity of existing structures, X-type steel bracing systems were employed. The findings indicated that steel bracings significantly reduced lateral displacements in comparison to unbraced frames, with X-braced systems achieving approximately 74% reduction in drift for four-storey buildings. Furthermore, the integration of steel bracings resulted in a reduction of bending moments and shear forces in the columns, although it induced an increase in axial compression. However, given the inherent strength of RC columns in compression, this was not regarded as a structural issue. The study concluded that X-type steel bracing is an effective method for improving the seismic performance of multi-storey RC buildings. Sivri et al. (2015) conducted a study on the nonlinear seismic behaviour of RC frames with infill walls of varying compressive strengths (2 MPa, 4 MPa, and 6 MPa), as well as those retrofitted with steel bracing systems. In this study, the authors employed ANSYS finite element software to analyse a three-storey, two-bay RC frame under lateral loading conditions. The incorporation of infill walls resulted in a substantial enhancement of lateral stiffness and load-bearing capacity. However, brittle failures were frequently initiated within the masonry. Conversely, frames fortified with steel bracing exhibited a 234% surge in lateral strength while maintaining ductility. The findings of the study demonstrated that the integration of infill walls with steel bracing can lead to a substantial enhancement in seismic resilience without compromising deformation capacity. Parastesh & Saatcioglu (2017) presented a detailed analytical and numerical evaluation of RC frames retrofitted with FRP sheets applied to masonry infill walls. A 10-storey RC building model was analysed using SAP2000 with a nonlinear pushover approach. The infill walls were represented as diagonal struts, and the FRP strengthening was modelled using shell elements. Calibrated against experimental data from prior cyclic tests, the model showed that FRP retrofitting significantly increased lateral load capacity nearly threefold compared to unretrofitted specimens and enhanced overall stiffness. However, the retrofitting did not contribute to ductility improvement, as both masonry and FRP components behaved in a brittle manner. The study concluded that while FRP is effective in increasing elastic strength and stiffness, it may not prevent brittle collapse unless used in conjunction with ductility-enhancing techniques. Yu et al. (2024) examined the effect of fibre-reinforced polymer (FRP) retrofitting on the seismic resilience of low-ductility reinforced concrete (RC) frame structures. The finite element models of RC frames before and after FRP retrofitting were developed using OpenSEES software, and fragility functions were established. The assessment of seismic resilience indicators, encompassing repair costs, repair time, casualties, and carbon emissions, was conducted utilising PACT software in accordance with the FEMA P-58 methodology. The study demonstrated that

FRP retrofitting led to notable improvements, especially at low seismic intensities, reducing average annual repair costs by 5.32%, repair times by 6.90%, and carbon emissions by 7.16%. Furthermore, the implementation of FRP retrofitting measures has been shown to result in a significant reduction in fatalities, with a documented decrease of 57.6% in injury rates. Despite the effectiveness of retrofitting diminishing under very high seismic intensities, the findings emphasised the overall benefits of FRP application in enhancing seismic performance and resilience of low-ductility RC frames.

In this study, the seismic performance of a five-storey reinforced concrete building located in Izmir was investigated using the SAP2000 V25 finite element analysis software. The edifice was subjected to rigorous scrutiny under four distinct modelling configurations: (a) a configuration without infill walls, (b) a configuration with infill walls, (c) a configuration where infill walls were fortified with Fiber Reinforced Polymer (FRP), and (d) a configuration where infill walls were fortified with a steel bracing system. In order to assess the dynamic behaviour of the structure, nonlinear time history analyses were performed using acceleration records from three major earthquakes: the Kahramanmaraş Pazarcık (Mw 7.7) and Elbistan (Mw 7.6) earthquakes that occurred on 6 February 2023, and the Izmir earthquake (Mw 6.6) of 30 October 2020. The records were modelled on the basis of acceleration-time histories, incorporating peak ground acceleration (PGA) values of 2178.72 cm/s² for Pazarcık, 635.45 cm/s² for Elbistan, and 179.31 cm/s² for Izmir.

The structural and modelling specifics for the various configurations are delineated in Section 2. Section 3 focuses on the nonlinear time history analysis methodology employed to evaluate the seismic response of both strengthened and unstrengthened models. The fourth chapter of this study presents the key findings, and provides a comparative assessment of the building's seismic behaviour across the different strengthening strategies.

2. Building geometry and finite element modelling

The present study focuses on a reinforced concrete residential building located in Izmir, a city situated within Türkiye's seismically active Aegean Region. The architectural composition of the structure comprises a ground floor and four upper floors, thus amounting to a total of five storeys. The structure is notable for its absence of a basement, with continuous footings providing the primary means of support. The ground floor, with a story height of 3.65 m, serves commercial and administrative functions, including retail spaces and a janitor's office. The four upper floors, each 2.70 m in height, are residential, housing a total of 16 apartments arranged as four units per floor. The overall height of the building is 14.45 m. The local soil condition has been classified as type ZD in accordance with the Turkish seismic code standards.

The structural system incorporates nine reinforced concrete shear walls per floor, with a thickness of 20 cm. The edifice boasts three distinct column cross-sections, measuring 30x70 cm, 30x80 cm, and 30x90 cm, respectively. These dimensions undergo a systematic reduction of 10 cm from the lower to the upper levels of the structure. Two categories of beams have been incorporated into the design: internal beams measuring 20x50 cm and external beams sized 25x50 cm. The thickness of the slab is contingent upon its function. The dimensions for intermediate floors are 12 cm, 15 cm for other floors, and 20 cm for balconies. Fig. 1 provides a representation of the floor plan of the existing building.

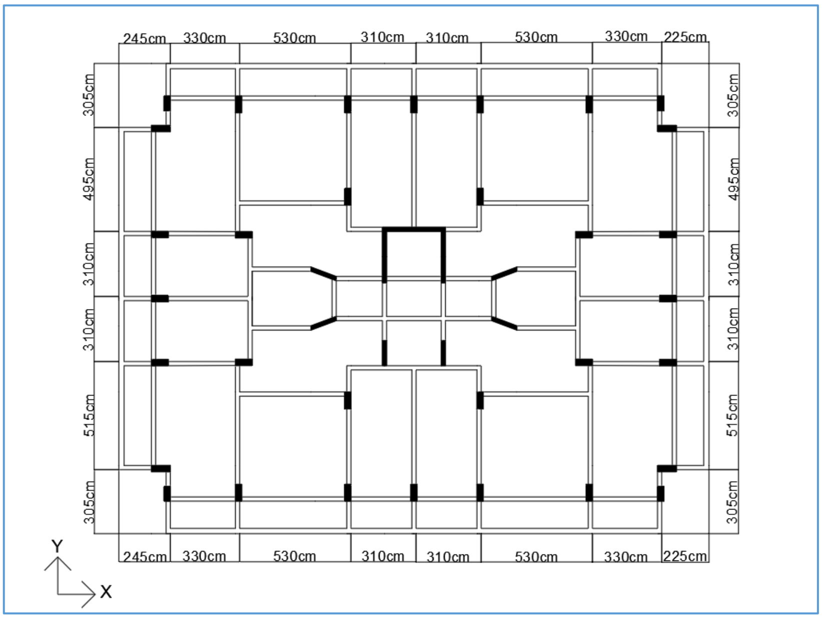

Fig. 1. Structural floor layout (Onat & Evci, 2024)

The material properties used in the model are based on actual structural test results. The compressive strength of concrete is taken as 8.27 MPa (designated as C8.27), and modelled in SAP2000 V25 using the formulation described in Section 5A.1 of the Turkish Building Earthquake Code (TBDY, 2018), which distinguishes between confined and unconfined concrete behaviour. Longitudinal reinforcement consists of deformed steel with a yield strength of 420 MPa, while transverse reinforcement is rated at 220 MPa. The modelling of these steel components was undertaken in accordance with the parameters specified in TBDY (2018), Section 5A.2.

The structural model was developed using SAP2000 V25 finite element software. The beams and columns were defined as frame elements, the shear walls were modelled using shell elements, and the infill walls were represented through link elements based on the equivalent compression strut approach. The 3D structural model incorporates all pertinent geometrical and material characteristics, thereby ensuring a precise reflection of the actual building configuration.

The allocation of dead and live loads was conducted in accordance with the designated utilisation of each floor. The software automatically calculated floor self-weights and applied them as two-way distributed loads. A dead load of 2.0 kN/m² was applied to the intermediate floors, while the roof was assigned a dead load of 2.5 kN/m². The live loads were specified as 2.0 kN/m² for typical floors, 3.5 kN/m² for partitioned residential areas, and 1.5 kN/m² for the rooftop level. Furthermore, non-structural partition walls not included in the concrete frame design were considered as distributed line loads on the beams. The material and thickness of the masonry were taken into consideration in the definition of the load-bearing capacity. The former was categorised as 2.4 kN/m² for masonry 20 cm in thickness, and as 2.0 kN/m² for masonry 10 cm in thickness.

For infill walls, a macro modelling technique was adopted. The equivalent strut method was employed, whereby each infill wall was modelled as a compression-only link element. The stiffness parameters were derived using the empirical formulations provided in Appendix 15C of TBDY (2018), ensuring an accurate representation of their contribution to lateral stiffness.

The edifice was subjected to analysis under four distinct configurations: (1) without infill walls ; (2) with infill walls; (3) nfill walls strengthened with Fiber Reinforced Polymer (FRP); and (4) infill walls strengthened with a steel bracing system. Nonlinear time history analyses were conducted using strong ground motion records from the 6 February 2023 Kahramanmaraş Pazarcık (Mw 7.7) and Elbistan (Mw 7.6) earthquakes, as well as the 30 October 2020 İzmir (Mw 6.6) earthquake. The acceleration-time histories exhibited peak ground accelerations of 2178.72 cm/s² for Pazarcık, 635.45 cm/s² for Elbistan, and 179.31 cm/s² for Izmir. Table 1 presents a compendium of the characteristics of the earthquakes selected for time history analysis.

Table 1. Earthquakes used for time history analysis

Name	Earthquke Code	Date	Magnitude (MW)	Depth (km)	Epicenter	PGA (cm/s^2)	PGV (cm/s)
Izmir	3536	30 October 2020 11:51	6.6	14.9	Ege Denizi 17.26 km Seferihisar (Izmir)	179.31	22.53
Kahramanmaras (Elbistan)	4631	6 February 2023 10:24	7.6	7	Elbistan (Kahramanmaras)	635.45	170.79
Kahramanmaras (Pazarcık)	615	6 February 2023 01:17	7.7	8.6	Pazarcık (Kahramanmaras)	2178.72	212.94

The FRP retrofitting system was defined in the SAP2000 model using a material with a modulus of elasticity of 61 GPa, a Poisson's ratio of 0.22, and a shear modulus of 25 GPa. The strips were modelled as rectangular cross-section link elements with dimensions of 0.3 m in width and 0.0003 m in thickness, placed diagonally across structural bays to simulate the behaviour of externally bonded FRP applications. These elements were assigned compression-only properties in order to reflect the unidirectional behaviour that is typical of composite materials under seismic loads.

The steel bracing configuration was modelled using round cross-section S420-grade steel bars with a diameter of 100 mm. The elements were positioned diagonally between the beam-column joints within the selected bays, thus forming an X-shaped bracing system. The steel braces were defined as tension-compression members, thereby capturing their dual-directional capacity under seismic excitation. This approach facilitated a realistic depiction of the bracing effect on both stiffness and energy dissipation of the structural system under earthquake loading. The structural layouts of the four models (a) without infill walls ; (b) with infill walls; (c) infill walls strengthened with Fiber Reinforced Polymer (FRP); and (d) infill walls strengthened with a steel bracing system are depicted in Fig. 2.

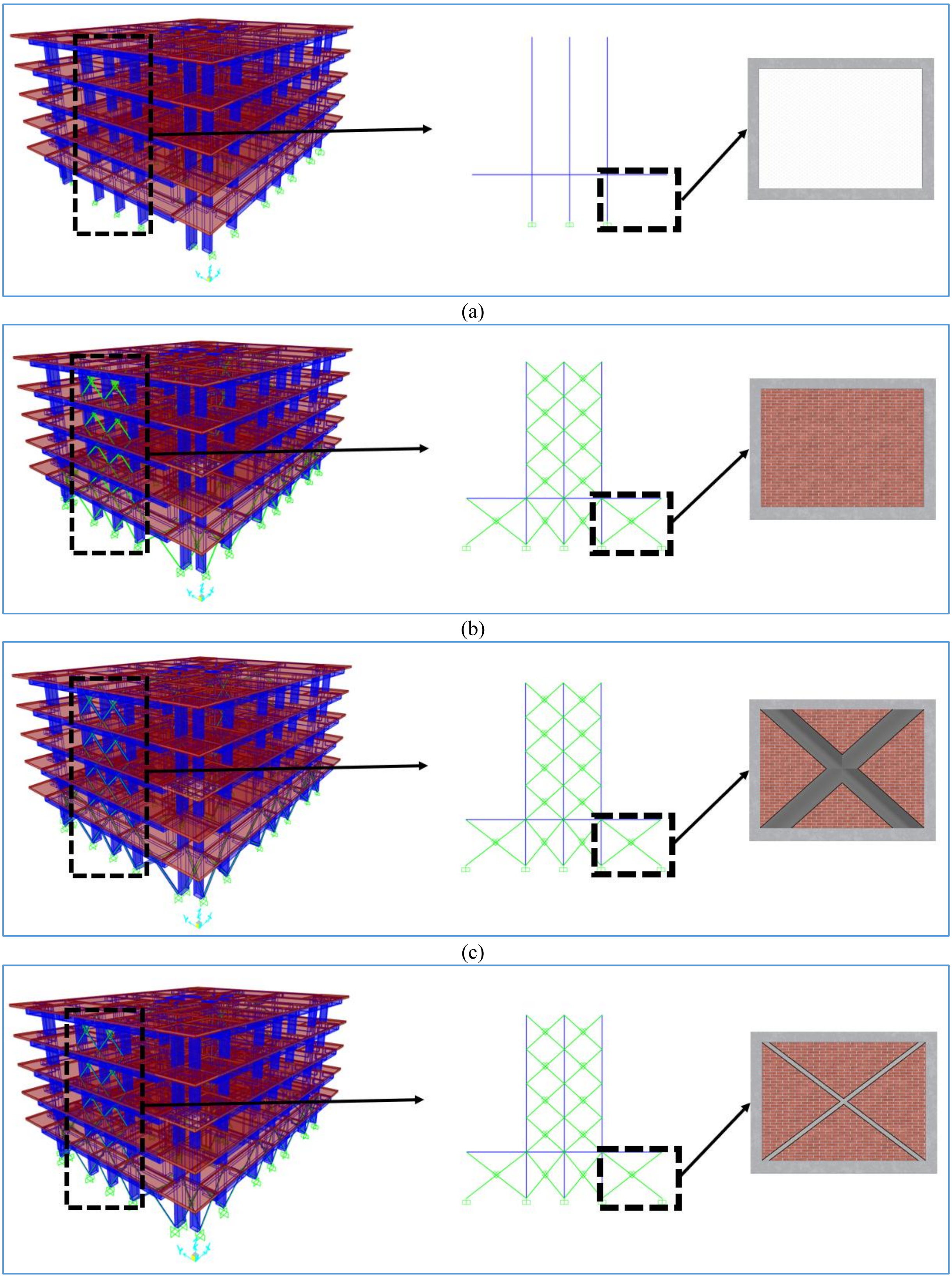

(a)

(b)

(c)

(d)

Fig. 2. Four different models: (a) without infill walls ; (b) with infill walls; (c) nfill walls strengthened with Fiber Reinforced Polymer (FRP); and (d) infill walls strengthened with a steel bracing system.

3. Nonlinear Time History Analysis of Strengthened and Unstrengthened Structures

Prior to conducting the nonlinear time history analysis, a modal analysis was performed to evaluate the dynamic characteristics of the structural models. The period values of the models are presented in Fig. 3.

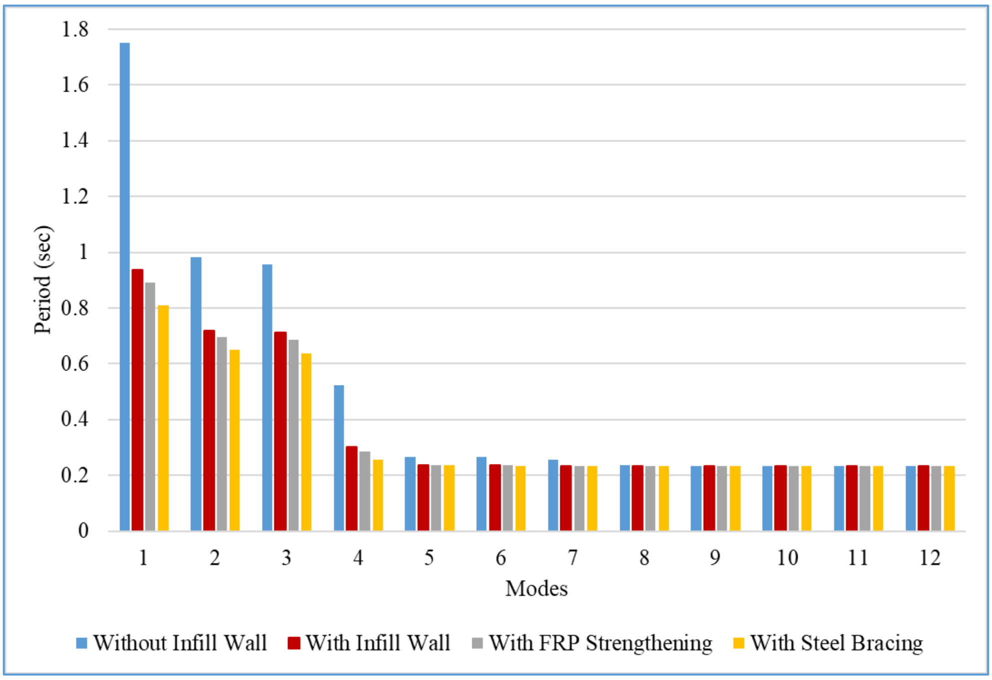

Fig. 3. The period values of the models

As demonstrated in Figure 3, the model without infill walls exhibited the highest period value of 1.75 seconds in the first mode, indicating the lowest lateral stiffness among all configurations.

The incorporation of infill walls resulted in a substantial reduction of the structure's natural period. When infill walls were modelled, the period in the first mode decreased to 0.94 seconds. In the FRP-strengthened model, a further reduction was observed, with the period dropping to 0.89 seconds, demonstrating an additional increase in stiffness through composite retrofitting. The steel-braced model demonstrated the most rigid behaviour, exhibiting a period of 0.81 seconds in the first mode.

Analogous tendencies were discerned in the second and third modes, where the period values underwent a gradual decline across the various strengthening types, from the unadorned frame to the steel bracing.

Nonlinear time history analysis was employed to calculate the total base reactions for each structural model in both the x and y directions. The results are presented in Fig. 4 and Fig. 5.

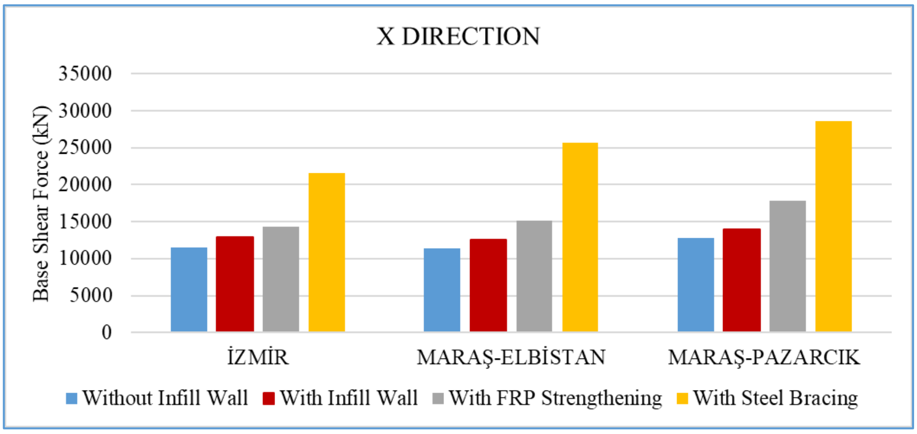

Fig. 4. Base shear forces of models in x-direction

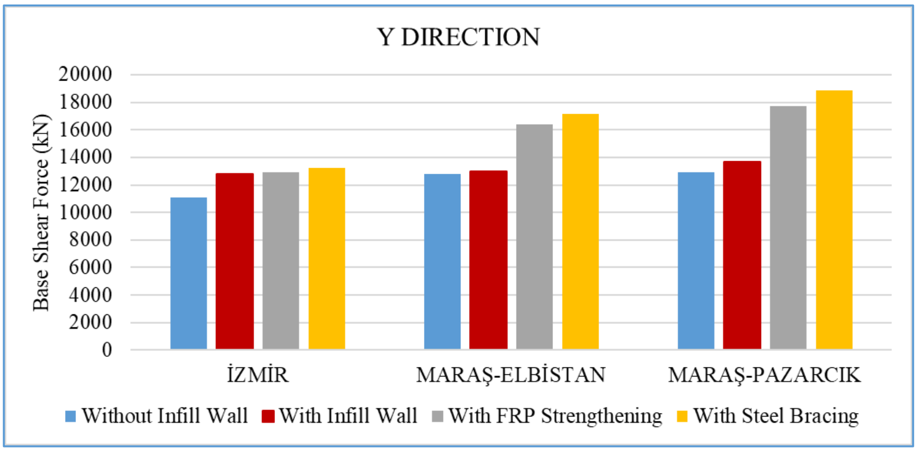

Fig. 5. Base shear forces of models in y-direction

In the x-direction, the highest base reaction was observed in the steel-braced model, particularly under the Kahramanmaraş (Pazarcık) earthquake, reaching 28,630.82 kN. This was followed by the same model under the Maraş-Elbistan record with 25,642.11 kN. The FRP-strengthened models also demonstrated notable performance, especially in the context of the Maraş-Pazarcık earthquake, during which they recorded a peak value of 17,820.58 kN. Models with infill walls exhibited moderate increases in base reactions when compared to bare frames. Conversely, models devoid of infill walls demonstrated consistently minimal base reactions across all earthquake scenarios.

In the y-direction, analogous trends were identified. The steel-braced configuration demonstrated the highest base reaction of 18,875.31 kN during the Maraş-Pazarcık earthquake, closely followed by the model strengthened with fiber reinforced polymer (FRP), which reached 17,727.41 kN.

Subsequent to the nonlinear time history analyses, interstorey drift values were calculated in accordance with the Turkish Building Earthquake Regulation (TDBY, 2018). Fig. 6, Fig. 7, Fig. 8 and Fig. 9 illustrate the variation in interstorey drift responses across different structural configurations and earthquake records. Positive drift values are indicative of displacement in the direction of ground motion, whilst negative values denote displacement in the opposite direction.

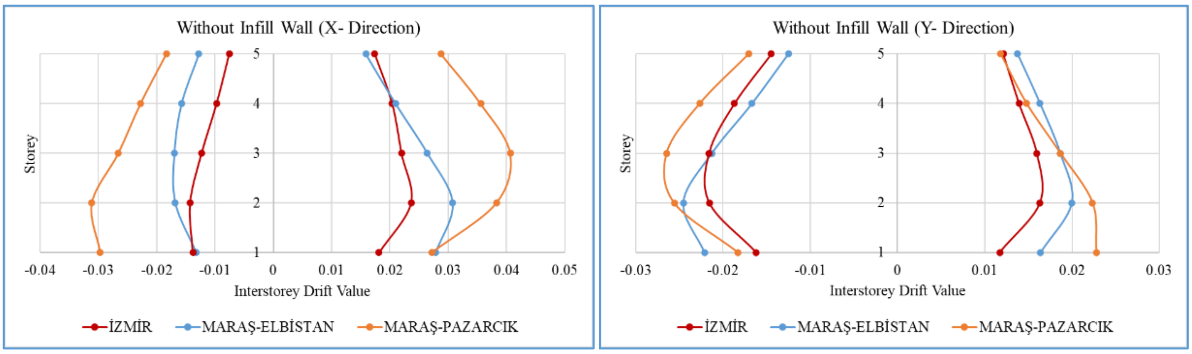

Fig. 6. Interstory shear value of the model without infill wall

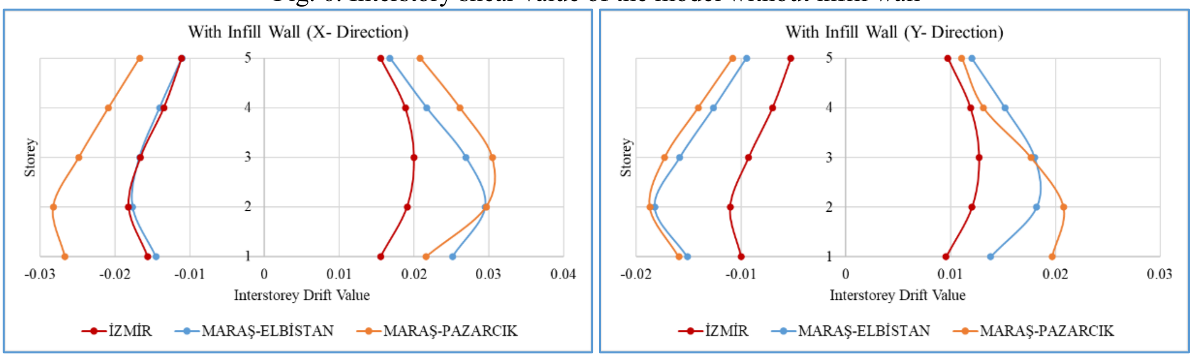

Fig. 7. Interstory shear value of the model with infill wall

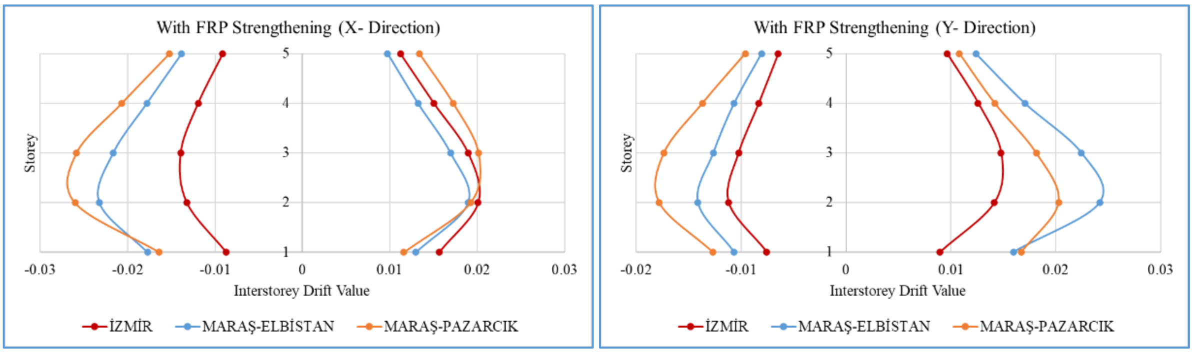

Fig. 8. Interstory shear value of the model with FRP strenghening

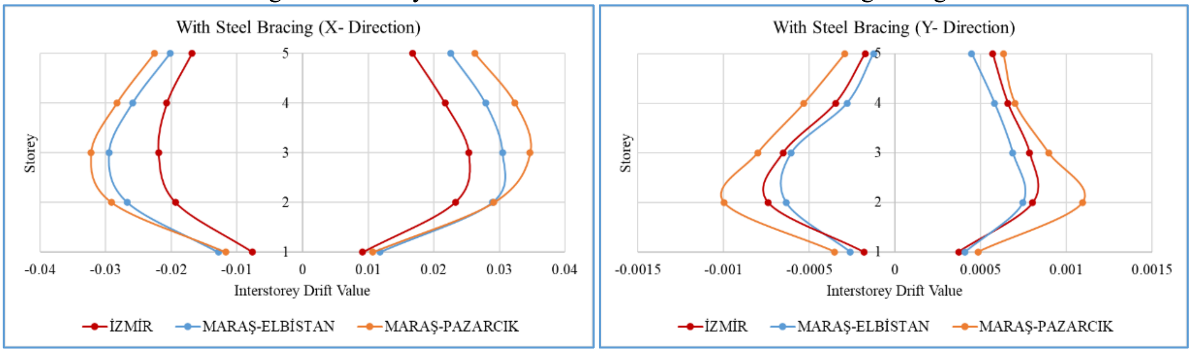

Fig. 9. Interstory shear value of the model with steel bracing

In the X direction, the without infill wall model experienced the highest average interstorey drift, reaching up to 0.03357 under the Maraş-Pazarcık earthquake, which is consistent with its high peak ground acceleration (PGA) of 2178.72 cm/s². Following the incorporation of infill walls, the maximum average drift reduced to 0.0303, indicating enhanced lateral stiffness. The FRP-strengthened model exhibited an enhancement in performance, yielding a maximum average drift of 0.0258, while the steel bracing system demonstrated the most significant performance, achieving a substantially reduced drift of 0.01995 under the same earthquake scenario.

In the Y direction, analogous patterns were identified. The without infill wall model exhibited the poorest performance, with a maximum drift of 0.02926 under the Maraş-Pazarcık motion. The model incorporating infill walls demonstrated a marked enhancement, with drift being constrained to 0.02779. This observation was further refined by the implementation of fiber reinforced polymer (FRP) strengthening, which led to a further reduction in drift to 0.0228. The most effective result was once again observed in the steel bracing system, where the average interstorey drift values were well below the code limit, with the highest recorded value being approximately 0.001096, demonstrating exceptional resistance to lateral displacements.

As stated in TDBY (2018), the maximum allowable interstorey drift for performance-based seismic design is 0.008. The findings unequivocally demonstrate that solely the steel-braced models adhered to the stipulated limit across all earthquake scenarios, while other configurations repeatedly exceeded the permissible threshold.

In accordance with the findings of the nonlinear time history analyses, the total story shear forces for each model were calculated. The shear force distributions for both the x and y directions are illustrated in Fig. 10, Fig. 11, Fig. 12 and Fig. 13.

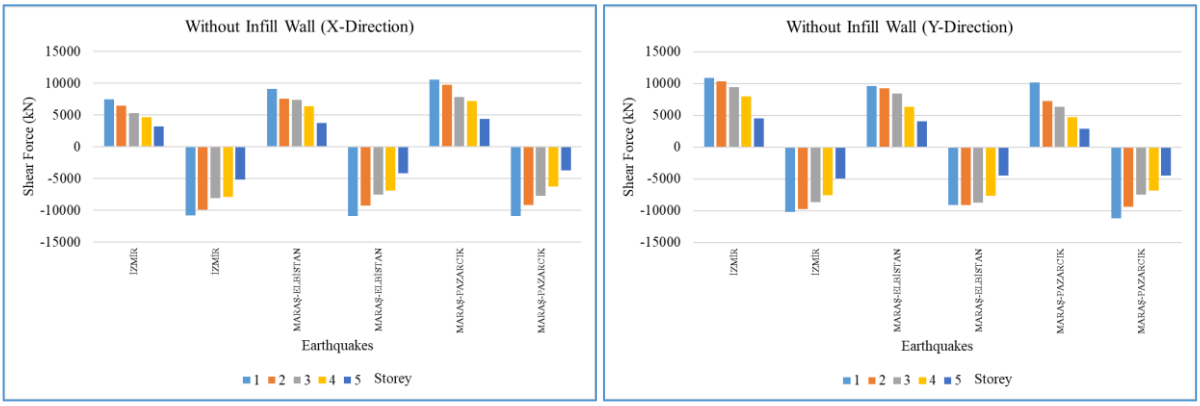

Fig. 10. Storey shear forces of the model without infill wall

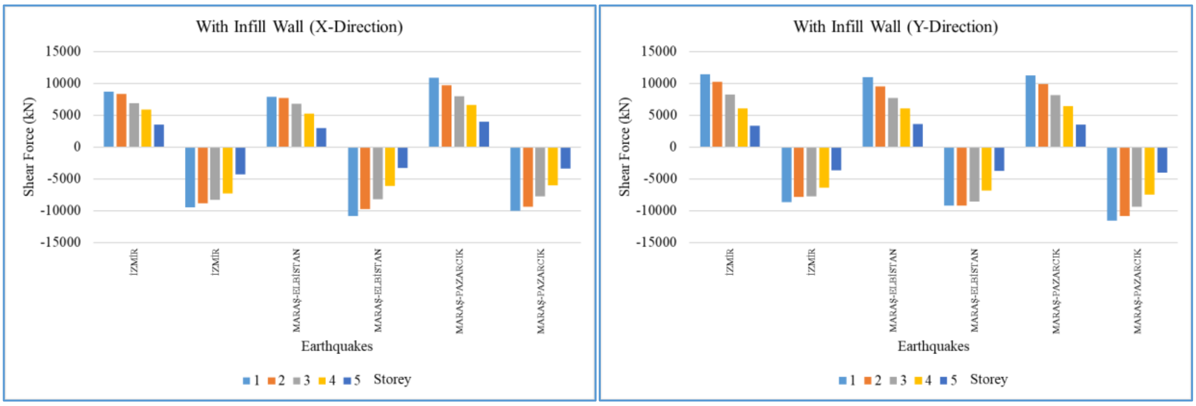

Fig. 11. Storey shear forces of the model with infill wall

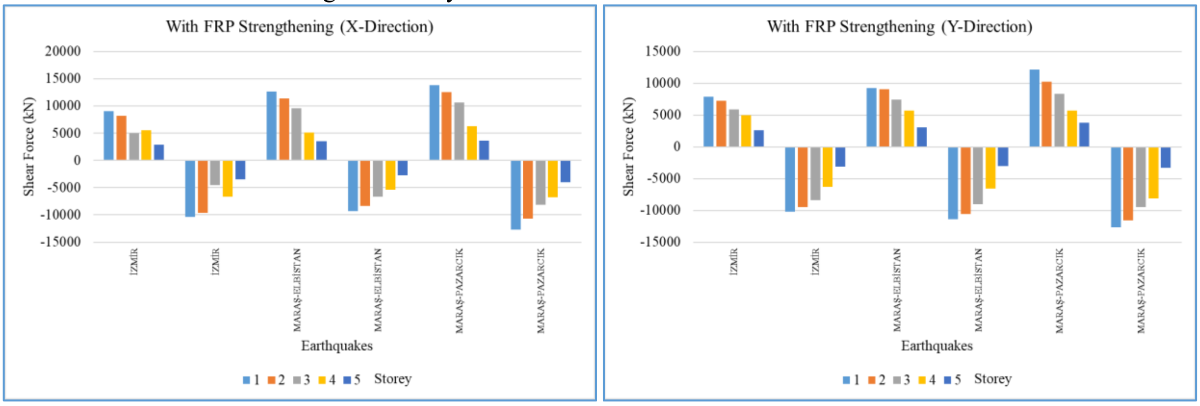

Fig. 12. Storey shear forces of the model with FRP strenghening

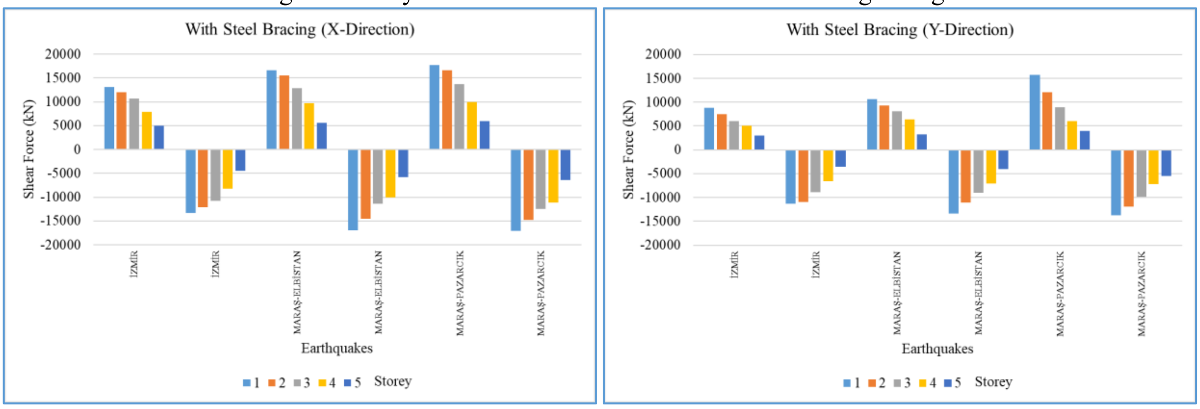

Fig. 13. Storey shear forces of the model with steel bracing

In the x-direction, the model devoid of infill walls exhibited the maximum shear force on the ground floor, measuring 10,534.83 kN, during the seismic event in Kahramanmaraş (Pazarcık). For the model incorporating infill walls, the maximum observed shear force was 10,888.29 kN, also during the Pazarcık earthquake. The model strengthened with fiber reinforced polymer (FRP) experienced a significantly higher shear force, reaching 13,856.30 kN under the same ground motion. The steel bracing model demonstrated the highest value, reaching a maximum of 17,705.75 kN, an outcome attributed to the seismic activity in Pazarcık.The following investigation is concerned with the comparative evaluation of the x-direction ground floor shear forces.The infill wall model exhibited an average increase of 23% in shear strength under Pazarcık compared to other seismic events.The FRP model exhibited a 31% increase in base shear under Pazarcık.The steel bracing model exhibited an average increase of 36%, thereby demonstrating the intensifying effect of the high peak ground acceleration from the Pazarcık earthquake.

In the y-direction, the highest storey shear force in the bare frame model was 10,146.08 kN on the ground floor during the Pazarcık earthquake. For the infill wall model, the corresponding value increased to 11,278.57 kN. In the FRP-strengthened model, the ground floor shear force reached 12,134.47 kN, while the steel bracing model displayed the highest value of all: 15,712.46 kN, again due to the Pazarcık earthquake.The evaluation of y-direction shear forces indicates:The infill wall model demonstrated a 22% increase in ground floor shear after the Pazarcık earthquake.The reinforced concrete structure exhibited an average increase of 29% in strength compared to non-reinforced structures during seismic events.The steel bracing model demonstrated an enhancement in stiffness and energy dissipation, resulting in a 37% increase in ground floor shear force following the Pazarcık event.

4. Conclusions

In this study, a five-storey reinforced concrete building was modelled using SAP2000 software with actual material properties, and nonlinear time history analyses were carried out based on the ground motion records of the 2023 Kahramanmaraş (Pazarcık and Elbistan) and İzmir earthquakes. Four structural configurations were considered in the analysis: (a) without infill walls ; (b) with infill walls; (c) infill walls strengthened with Fiber Reinforced Polymer (FRP); and (d) infill walls strengthened with a steel bracing system.

- The results of the modal analysis indicate that the without infill walls model exhibited the highest fundamental period of 1.75 seconds, suggesting that it possesses the lowest lateral stiffness. The incorporation of infill walls led to a 46% reduction in this value, thereby reducing the period to 0.94 seconds. In the FRP-strengthened model, the period decreased by 49% to 0.89 seconds, while the steel-braced model exhibited the highest stiffness with a 54% reduction to 0.81 seconds. Analogous trends were also observed in the second and third mode shapes, where the periods gradually decreased from the without infill walls configuration towards the steel-braced configuration.
- With regard to base shear reactions, the highest value in the x-direction was observed in the steel-braced model under the Kahramanmaraş (Pazarcık) earthquake, reaching 28,630.82 kN. This figure represents an approximate increase of 149% in comparison with the without infill walls model. The same model recorded 25,642.11 kN under the Elbistan record, corresponding to a 124% increase. The FRP-strengthened model demonstrated a maximum load of 17,820.58 kN under the Pazarcık record, exhibiting an 82% increase in load capacity. Models incorporating infill walls exhibited a mere 3% increase in comparison with the without infill walls. The without infill walls model demonstrated a consistent tendency to exhibit the lowest base reactions across all earthquake scenarios.
- A similar pattern was observed in the y-direction. The highest base shear was measured in the steel-braced model as 18,875.31 kN under the Pazarcık earthquake, representing an 86% increase compared to the without infill walls. The FRP-strengthened model demonstrated a 76% increase, reaching 17,727.41 kN, while the model with solely infill walls exhibited an 11% rise.
- The interstorey drift ratios were calculated in accordance with the Turkish Building Earthquake Code (TBDY, 2018), thereby demonstrating variations among structural configurations and earthquake records. In the x-direction, the without infill walls model exhibited the highest average drift ratio of 0.03357 under the Pazarcık earthquake, a phenomenon attributed to its elevated peak ground acceleration (PGA) of 2178.72 cm/s². The incorporation of infill walls resulted in a decrease to 0.0303 (a 9.7% reduction), and a subsequent further decrease to 0.0258 (a 23% reduction) in the FRP-strengthened model. The steel-braced model demonstrated the most significant enhancement, exhibiting a maximum average drift of 0.01995, which corresponds to a 40.6% reduction.
- In the y-direction, the maximum interstorey drift for the without infill walls model was 0.02926, while it decreased to 0.02779 in the model with infill walls. The FRP-strengthened model demonstrated a further reduction to 0.0228, and the steel-braced model exhibited a substantial limitation of drifts to 0.001096, signifying a reduction of over 95%. This outcome unequivocally substantiates the efficacy of the steel bracing system in constraining seismic displacements.
- TBDY (2018) asserts that the maximum allowable interstorey drift ratio for performance-based seismic design is 0.008. The findings indicate that solely the steel-braced configuration adhered to the stipulated limit across all earthquake scenarios, while the remaining models persistently exceeded the permissible threshold, thereby signifying a probable hazard of structural impairment.

In summary, infill walls contribute to enhanced stiffness by reducing natural periods and limiting displacements. The implementation of fiber reinforced polymer (FRP) strengthening measures has been demonstrated to engender a moderate enhancement in performance metrics. However, it should be noted that the efficacy of this approach is comparatively inferior to that of steel bracing. The utilisation of steel-braced systems has been demonstrated to consistently yield optimal performance in all analyses, thereby substantiating their efficacy as a highly effective solution for seismic safety enhancement.

Consequently, in instances where seismic retrofitting is imperative for extant structures, the implementation of steel bracing systems is emphatically advocated. In addition, subsequent studies should encompass a range of building types, varying story heights and infill wall materials, thereby facilitating more extensive and exhaustive parametric analyses.

References

Akyürek, O., Tekeli, H., & Demir, F. (2018). The effects of infill walls located in plan on buildings performance. *International Journal of Engineering Research and Development, 10*(1), 42–55. https://doi.org/10.29137/umagd.419660

Altindal, A., Karimzadeh, S., Erberik, M. A., Askan, A., Anil, O., Kockar, M. K., & Sahmaran, M. (2021). A case study for probabilistic seismic risk assessment of earthquake-prone old urban centers. *International Journal of Disaster Risk Reduction, 61*, 102376. https://doi.org/10.1016/j.ijdrr.2021.102376

Askan, A., Gülerce, Z., Roumelioti, Z., Sotiriadis, D., Melis, N. S., Altindal, A., ... & Margaris, B. (2022). The Samos Island (Aegean Sea) M7.0 earthquake: Analysis and engineering implications of strong motion data. *Bulletin of Earthquake Engineering, 20*(14), 7737–7762. https://doi.org/10.1007/s10518-021-01251-5

Binici, B., Ozcebe, G., & Ozcelik, R. (2007). Analysis and design of FRP composites for seismic retrofit of infill walls in reinforced concrete frames. *Composites Part B: Engineering, 38*(5–6), 575–583. https://doi.org/10.1016/j.compositesb.2006.08.007

Çöğürcü, M. T. (2007). *Strengthening of masonry structures through horizontal joint reinforcement* (Doctoral dissertation, Selçuk University, Institute of Science and Technology, Konya, Türkiye).

Jiang, X., Song, X., Li, T., & Wu, K. (2023). Moment magnitudes of two large Turkish earthquakes on February 6, 2023, from long-period coda. *Earthquake Science, 36*(2), 169–174. https://doi.org/10.1016/j.eqs.2023.02.008

Karimzadeh, S., Askan, A., Erberik, M. A., & Yakut, A. (2018). Seismic damage assessment based on regional synthetic ground motion dataset: A case study for Erzincan, Türkiye. *Natural Hazards, 92*, 1371–1397. https://doi.org/10.1007/s11069-018-3255-6

Karimzadeh, S., Funari, M. F., Szabó, S., Hussaini, S. S., & Rezaeian, S. (2024). Stochastic simulation of earthquake ground motions for the seismic assessment of monumental masonry structures: Source-based vs site-based approaches. *Earthquake Engineering and Structural Dynamics, 53*(1), 303–330. https://doi.org/10.1002/eqe.4012

Malekkianie, B. (2006). *Strengthening of reinforced concrete frames with infill walls using carbon fibers* (Master's thesis, Istanbul Technical University, Institute of Science and Technology, Department of Earthquake Engineering).

Onat Ö. (2022). *Investigation Of The Effect Of Infill Wall On Damages In Reinforced Concrete Structures Under The Effect Of Earthquake 30 October 2020 İzmir Earthquake Example.* (Master's Thesis, Isparta Applied Sciences Unıversıty, Department Of Civil Engineering).

Onat, Ö., & Evci, P. U. (2024). A parametric study in reinforced concrete frames with different infill wall materials. *Bulletin of Earthquake Engineering*, 1–30. https://doi.org/10.1007/s10518-024-01936-7

Parastesh, H., & Saatcioglu, M. (2017). Analysis of masonry infill panels retrofitted with FRP sheets in R/C frames. *Journal of Structural Engineering and Geo-Techniques, 7*(2), 85–96.

Sancıoğlu, S., Soydoğan, H. F., & Can, H. (2022). The Effect of Different Infill Wall Materials and Their Location in Plan on the Behaviour of a Reinforced Concrete Building. *International Journal of Engineering Research and Development, 14*(2), 457-474. https://doi.org/10.29137/umagd.1028494

SAP2000. (2018). *SAP2000: Structural Analysis User's Manual* (Version 25). Computers and Structures Inc., Berkeley, California.

Sivri, M., Çelik, İ., Fenkli, M., Kımıllı, N., & Ay, Z. (2015). Çelik çaprazla güçlendirilmiş dolgu duvarlı betonarme çerçevelerin doğrusal olmayan davranışı. *Süleyman Demirel Üniversitesi Fen Bilimleri Enstitüsü Dergisi, 19*(1), 63–68.

Şahin, İ., & Kılınç, T. (2016). Economic effects of earthquakes in Türkiye between 1980–2014. *Journal of Economic Innovation, 4*(1), 33–42. https://dergipark.org.tr/en/pub/iy/issue/22662/242031

TBDY. (2018). *Turkish Building Earthquake Regulation*. Ministry of Environment and Urbanization, Ankara.

Tekin, M., Alsancak, E., & Murat, A. Y. (2007). Investigation of the effect of masonry wall on the reinforced concrete frame. *Celal Bayar University Journal of Science, 3*(1), 95–104. https://dergipark.org.tr/en/pub/cbayarfbe/issue/4044/53322

Usta, P., Onat, Ö., & Bozdağ, Ö. (2023). Effect of masonry infill walls on the nonlinear response of reinforced concrete structure: October 30, 2020 İzmir earthquake case. *Engineering Failure Analysis, 146*, 107081. https://doi.org/10.1016/j.engfailanal.2023.107081

Uysal, N. (2023). *Determination of the dynamic behavior of historical masonry public buildings: Isparta registered stone building example* (Master's thesis, Isparta Applied Sciences University, Department of Civil Engineering).

Viswanath, K. G., Prakash, K. B., & Desai, V. A. (2010). Seismic analysis of steel braced reinforced concrete frames. *International Journal of Civil and Structural Engineering, 1*(1), 114–121.

Yu, X., Li, Z., Jiang, Z., & Dai, K. (2024). The effect of FRP retrofitting on the seismic resilience of low-ductility RC frame structures: A case study. *Disaster Prevention and Resilience, 3*(11). https://doi.org/10.20517/dpr.2024.14

Yüksel, İ. (2008). Post-earthquake emergency damage assessments of reinforced concrete buildings. *Erciyes University Journal of Science, 24*(1), 260–276. https://dergipark.org.tr/en/pub/erciyesfen/issue/25577/269794

Finite element model updating of different Cross-Laminated Timber (CLT) panel groups using dynamic tests

Algıhan K. Karahasan[1*], Ahmet C. Altunışık[2,3], Cenk Demirkır[4], Fatih Y. Okur[2,3], Fezayil Sunca[3,5]

[1] *Avrasya University, Department of Construction Technologies, 61000, Trabzon, Türkiye*
[2] *Karadeniz Technical University, Department of Civil Engineering, 61080 Trabzon, Türkiye*
[3] *Karadeniz Technical University, Earthquake and Structural Health Monitoring Research Center, 61080 Trabzon, Türkiye*
[4] *Karadeniz Technical University, Department of Forest Industry Engineering, 61080, Trabzon, Türkiye*
[5] *Karadeniz Technical University, Department of Construction Technologies, 61080 Trabzon, Türkiye*

Abstract. Cross-laminated timber (CLT) has emerged as an innovative construction material, offering advantages such as sustainability, low carbon emissions, and ease of application, making it a strong alternative to conventional building materials. By integrating the natural benefits of wood with advanced engineering techniques, CLT provides an environmentally friendly and structurally efficient solution for modern construction. However, the numerical analysis of CLT structures presents significant challenges due to the absence of standardized constitutive models for connections, the anisotropic behavior of wood, and the limited guidance provided by existing design codes. Consequently, experimental data plays a crucial role in the accurate development and validation of finite element models (FEMs) for such structures. This study investigates the structural behavior of 30 CLT panel groups with varying properties under dynamic loading conditions using experimental methods. The dynamic characteristics of the panels were identified through ambient vibration tests employing the Operational Modal Analysis (OMA) method. The FEM updating process was conducted exclusively based on experimental data obtained from dynamic tests, utilizing SAP2000 software to apply a frequency-based updating approach. The accuracy of the updated models was assessed by analyzing discrepancies between experimental and numerical fundamental natural frequency values. Furthermore, the influence of different material and boundary condition assumptions on model accuracy was examined.

Keywords: Finite element model; Model updating; Cross laminated timber; Operational modal analysis; Dynamic characteristics

1. Introduction

In engineering disciplines, problem-solving has traditionally relied on domain-specific expertise and experiential knowledge. Both experimental and numerical methods have been utilized in addressing complex challenges. Advances in computer technology have significantly enhanced the speed and efficiency of numerical analyses, leading to the development of various computational techniques. Among these, FEM, introduced in the mid-20th century, has emerged as a fundamental computational tool in engineering analysis. FEM provides high accuracy in the numerical modelling of various physical systems, offering comprehensive and reliable insights into the behaviour of structural components and materials (Madenci & Guven, 2015; Altunişik et al., 2018)

FEM is extensively employed in structural engineering applications such as structural analysis, health monitoring, and damage assessment. Despite its widespread use, FEM-based numerical models often fail to capture the full complexity of the physical and geometric characteristics inherent in real-world structures. As a result, discrepancies may arise between simulated outcomes and experimental observations obtained from static or dynamic testing. To minimize such inconsistencies and enhance the predictive capability of the numerical model, finite element model updating becomes essential. This process involves the calibration of model parameters based on experimental data, with the aim of reducing uncertainties and improving the overall accuracy and reliability of the model.

Initial FEMs frequently fall short in accurately reflecting the actual structural performance of a system, largely due to uncertainties inherent in the early modelling stages such as approximations in material characteristics,

[*]Corresponding author, E-mail: algihankasif.karahasan@avrasya.edu.tr

https://doi.org/10.31462/icearc2025_ce_eqe_806

boundary condition definitions, and mesh discretization. To improve the model's predictive capabilities and ensure its consistency with experimental observations, it becomes necessary to update the initial FEM. This calibration process relies on referencing parameters obtained from experimental data, typically through static or dynamic testing, and adjusting uncertain model variables iteratively until a satisfactory level of accuracy is achieved (Günaydin et al., 2022; Butt & Omenzetter, 2014). Two principal methods are used for model updating: a manual approach based on trial-and-error, and an automated approach that leverages specialized computational tools. In the context of this study, the manual updating technique was implemented (Günaydin et al., 2022). Applying such model refinement strategies allows engineers to enhance the correlation between numerical and experimental results, ultimately leading to more precise structural assessments and more efficient detection and management of potential damage (Gurholt & Mikalsen, 2021).

Dynamic characteristics of engineering structures are widely utilized in the updating of FEMs (Brank & Carrera, 2000; Sunca et al., 2021; Altunışık et al., 2023; Oh et al., 2017). In addition, the experimental data employed during the model updating process may include various measurable quantities that can be directly compared with the numerical model. In this context, dynamic responses obtained through experimental studies are considered valuable data sources for enhancing the accuracy and reliability of FEMs.

Alongside the development of numerical modelling methods, the construction industry's interest in and application of timber-based materials has markedly increased. This growing trend is largely attributed to the inherent qualities of wood as an environmentally friendly and renewable resource. The use of timber has expanded in tandem with technological progress in adhesive and manufacturing techniques, as well as improvements in fire resistance strategies. Within the scope of innovative wood products, cross-laminated timber (CLT) has gained significant attention as a leading material (Wieruszewski & Mazela, 2017). Due to its ecological advantages and suitability for rapid construction, CLT represents a compelling alternative to conventional construction materials Öztürk et al., 2020).

CLT was first introduced in Europe during the early 1990s and has since achieved widespread recognition and acceptance within the construction industry (Espinoza et al., 2016). Often referred to as "mass timber," CLT represents a contemporary advancement among engineered wood products, contributing significantly to the evolution of timber usage in structural systems (Younis & Dodoo, 2022). Structurally, CLT panels are typically composed of an odd number of layers commonly three, five, seven, or more with the wood grain in each layer oriented orthogonally to that of adjacent layers (Fig. 1) (Gagnon & Pirvu, 2011). This crosswise configuration enables CLT to exhibit robust load-bearing capacities in both in-plane and out-of-plane directions, classifying it as a semi-rigid composite material in panel form. These mechanical characteristics make CLT a reliable and versatile option for a wide range of structural applications.

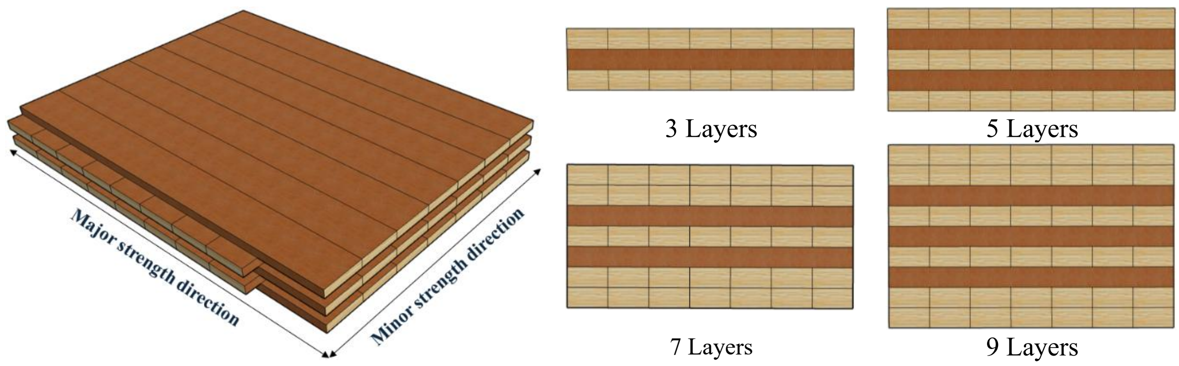

Fig. 1. Typical layer arrangement and fiber direction in CLT panels

FEM updating process plays a vital role in accurately predicting the dynamic responses of CLT structural components. To achieve this, modal tests are conducted on specimens to determine their natural frequencies and mode shapes. The discrepancies between the experimental data and the numerical models of the specimens are then reduced through FEM updating, ensuring the accuracy and reliability of the model (Kurent et al., 2024; Kurent et al., 2023; Aloisio et al., 2020).

2. Operational modal analysis (OMA)

Operational Modal Analysis (OMA) is a non-invasive method used to experimentally identify the dynamic properties of structures, including natural frequencies, mode shapes, and damping ratios, by analyzing their vibration responses. This approach is generally divided into two main types depending on the source of excitement: Ambient Vibration Testing and Forced Vibration Testing. In the present study, system identification was performed using ambient vibrations to determine the dynamic characteristics of the structures.

The equipment used for determining dynamic characteristics is presented below:

- B&K 4506 type three-axial accelerometer (Fig. 2 and Table 1)
- B&K 3560 data acquisition system with 17 channels (Fig. 3)
- PULSE software for signal processing (PULSE, 2006).
- OMA software to extract dynamic characteristics (OMA, 2006).

Fig. 2. B&K 4506 type three-axial accelerometer

Table 1. Properties of the accelerometers

Model	B&K 4506
Sensibility	0.5 V/g
Frequency range	0.3-2000 Hz
Maximum acceleration	±14g
Operating temperature	-54 to +100°C
Dimensions	17 x 17 x 17 mm
Total Mass	18 gr

Fig. 3. B&K 3560 C type 17-channel data acquisition unit

The structural response signals generated by environmental influences can be evaluated using both frequency-domain and time-domain algorithms. To extract modal parameters from these signals, a variety of techniques are available. These include Peak Picking (PP), Frequency Domain Decomposition (FDD), and Enhanced Frequency Domain Decomposition (EFDD) within the frequency domain, and methods such as Random Decrement, Recursive Techniques, and Stochastic Subspace Identification (SSI) within the time domain. In recent years, novel system identification techniques have also been proposed. Frequency-domain approaches focus on analyzing individual measurement points and the relationships between signals, whereas time-domain methods utilize the temporal progression of the signal or fit a mathematical model using correlation functions (Ramos, 2007; Ni & Zhang, 2019; Di Matteo et al., 2021; Russotto et al., 2022). Both categories are widely adopted for determining modal parameters. In the present study, system identification was performed using the EFDD technique, which is based on frequency-domain analysis.

The Enhanced Frequency Domain Decomposition (EFDD) method represents a refined version of the standard FDD technique. It identifies modal parameters by detecting peaks in the singular value decomposition (SVD) of the spectral density matrix. While the original FDD approach is limited in that it does not provide damping ratio information, it is effective in determining natural frequencies and mode shapes. In contrast, the EFDD method not only improves accuracy but also enables the estimation of damping ratios (Jacobsen et al., 2006). The mathematical relationship between the unknown excitation and the measured output within the EFDD framework is defined by Equation (1). Further explanation regarding the formulation and parameters of this equation can be found in previous studies (Brincker et al., 2000; Bendat & Piersol, 2011).

$$G_{yy}(j\omega) = H^{*}(j\omega) G_{xx}(j\omega) H^{T}(j\omega) \tag{1}$$

where the matrix Gxx represents the power spectral density of the input, where r denotes the number of inputs, while Gyy is the power spectral density matrix of the responses, with mmm indicating the number of responses. The matrix H(ω) is the frequency response function matrix, characterized by dimensions m×r.

Fig. 4 presents several images captured during the ambient vibration tests. In each test setup, a total of four accelerometers were employed two positioned at the upper corner locations (points 2 and 4), and the other two placed at the mid-height edge locations (points 1 and 3) of the CLT panels. Data acquisition was conducted over a 15-minute period, with raw signals recorded within the frequency range of 0–400 Hz.

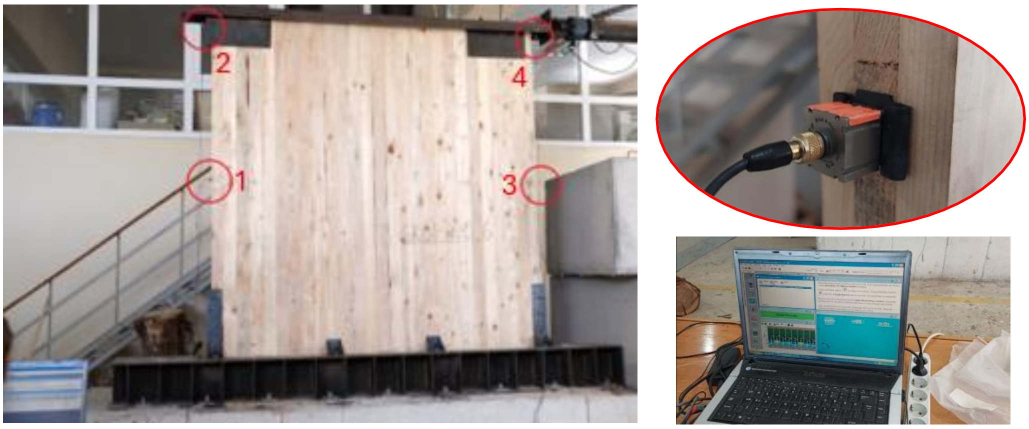

Fig. 4. Some view from the ambient vibration tests

Fig. 5 displays the spectral density matrices derived through the EFDD method. Due to page constraints, instead of presenting graphs for all 30 CLT panels, one representative graph from each material group is shown: spruce (Fig. 5a), alder (Fig. 5b), and hybrid (Fig. 5c). The analysis focused solely on the in-plane modes of the CLT panels, while out-of-plane modes were excluded from the scope of this study. Peak selections were made accordingly. Fig. 6 illustrates the first and second in-plane lateral modes identified from the experimental data. As similar mode shapes were consistently observed across all tests, only a single representative plot is provided. Table 2 summarizes the natural frequencies corresponding to the first two in-plane modes for each CLT panel.

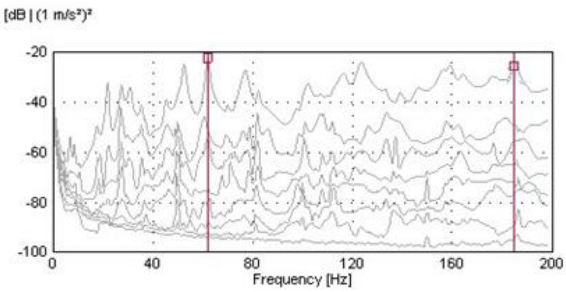

(a) Spruce

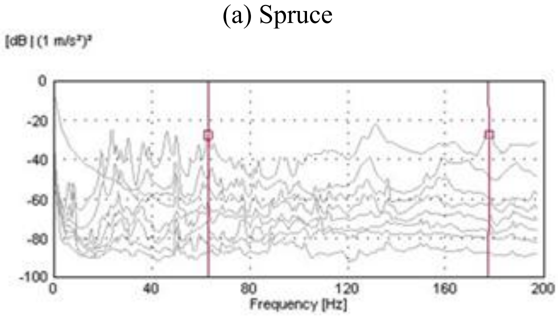

(b) Alder

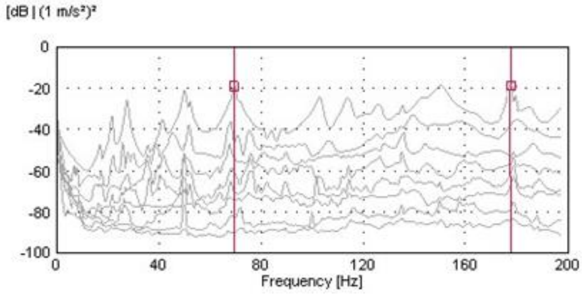

(c) Hybrid

Fig. 5. Spectral density matrices derived via the EFDD method for the undamaged state

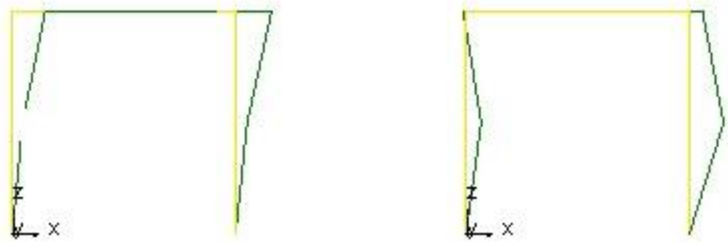

(a) 1st mode (b) 2nd mode

Fig. 6. Experimentally identified first two in-plane modes

Table 2. Experimental identified natural frequencies for each CLT panel

Group Number	Layer Combination	Frequency (Hz)	
		1st Mode	2nd Mode
1	C_{16} - C_{16} - C_{16}	63.03	177.2
2	C_{22} - C_{22} - C_{22}	62.03	177.1
3	C_{30} - C_{30} - C_{30}	62.09	184.7
4	C_{16} - C_{22} - C_{16}	67.91	170.1
5	C_{22} - C_{16} - C_{22}	61.49	169.8
6	C_{16} - C_{30} - C_{16}	64.18	141.3
7	C_{30} - C_{16} - C_{30}	69.04	178.9
8	C_{22} - C_{30} - C_{22}	64.15	174.8
9	C_{30} - C_{22} - C_{30}	63.51	185.8
10	D_{18} - D_{18} - D_{18}	60.81	189.6
11	D_{30} - D_{30} - D_{30}	61.98	189.6
12	D_{40} - D_{40} - D_{40}	59.58	180.4
13	D_{18} - D_{30} - D_{18}	74.03	176.3
14	D_{30} - D_{18} - D_{30}	65.84	175.3
15	D_{18} - D_{40} - D_{18}	73.44	186.5
16	D_{40} - D_{18} - D_{40}	63.07	177.4
17	D_{30} - D_{40} - D_{30}	60.58	177.0
18	D_{40} - D_{30} - D_{40}	74.50	173.7
19	C_{16} - D_{18} - C_{16}	68.23	177.7
20	C_{22} - D_{30} - C_{22}	65.60	176.5
21	C_{30} - D_{40} - C_{30}	43.85	174.0
22	D_{18} - C_{16} - D_{18}	64.44	175.8
23	D_{30} - C_{22} - D_{30}	63.00	192.4
24	D_{40} - C_{30} - D_{40}	66.97	183.0
25	C_{16} - D_{30} - C_{16}	65.62	174.4
26	C_{16} - D_{40} - C_{16}	76.84	157.6
27	C_{22} - D_{40} - C_{22}	54.91	182.0
28	D_{18} - C_{22} - D_{18}	64.03	184.4
29	D_{18} - C_{30} - D_{18}	40.95	174.9
30	D_{30} - C_{30} - D_{30}	42.42	183.8

3. Numerical studies

3.1. FEM of the CLT panels

FEMs of the CLT panels were developed using the SAP2000 software. In the modelling process, area, link, and spring elements were utilized, and a mesh size of 10 cm was selected based on the outcomes of convergence analyses. Each model consisted of 1875 nodes, 1728 area elements, and 1250 link elements. The two-dimensional area elements were employed to represent the CLT panels similarly to shell elements. Link elements were used to simulate the adhesive-like interaction between the individual layers of the panels. For the experimental setup, a steel H-profile was anchored prior to concrete casting in order to support the CLT panels on a reinforced concrete strip foundation constructed in the laboratory. Spring elements modelled the connection between the panels and the rigid foundation. To eliminate out-of-plane movement, a UPN 160 steel profile was installed at the top of the CLT panels, and this structural detail was also incorporated into the FEM. Fig. 7 provides a visual representation of the FEM layout for the CLT panels.

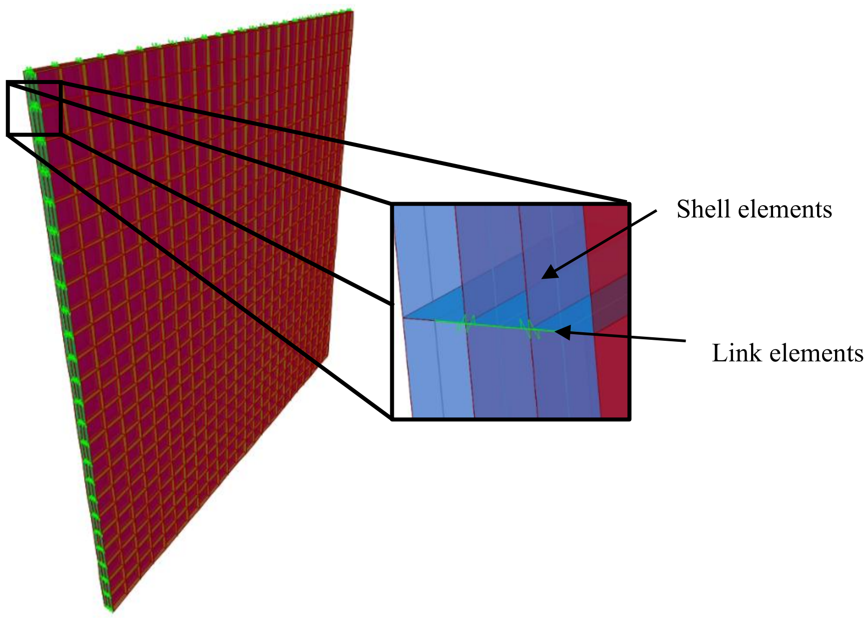

Fig. 7. Representation of the finite element model of CLT panels

A consistent finite element model was used across all cases, with adjustments made to reflect differences in material properties based on wood species, fiber orientations within the layers, and the stiffness of the springs positioned beneath the panels. The mechanical properties of the CLT panels were derived from EN 338 standards and are summarized in Table 3.

Fig. 8 illustrates the first and second in-plane lateral modes obtained through FEM analysis. As the mode shapes showed high similarity across all analyses, only one representative plot is presented. A strong correlation was observed between the experimentally measured and numerically computed first two in-plane modes.

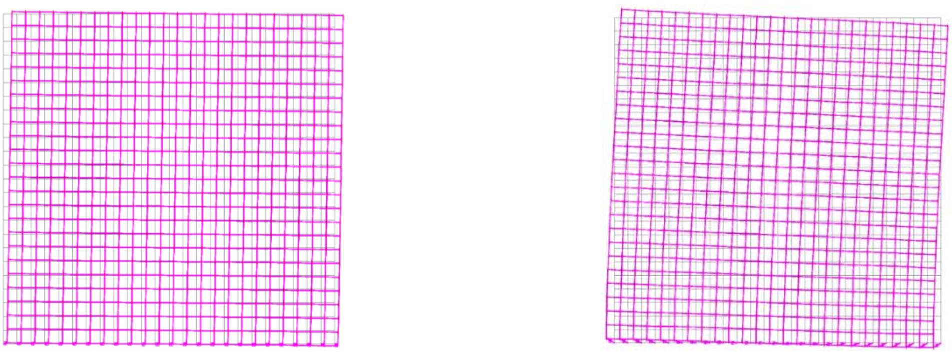

1st mode 2nd mode

Fig. 8. First and second in-plane modes determined through numerical analysis

Table 3. Strength and rigidity properties of wooden material

Wood Class	Strength Properties (N/mm^2)						Stiffness Properties (kN/mm^2)					
	Bending	Tension Parallel	Tension Perpendicular	Compression Parallel	Compression Perpendicular	Shear	Mean Modulus of Elasticity Parallel	5% Modulus of Elasticity	Mean Modulus of Elasticity Perpendicular	Mean Shear Modulus	Characteristic Density (kg/m^3)	Mean Density (kg/m^3)
	$f_{m,k}$	$f_{t,0,k}$	$f_{t,90,k}$	$f_{c,0,k}$	$f_{t,90,k}$	$f_{v,k}$	$E_{0,mean}$	$E_{0.05}$	$E_{90,mean}$	G_{mean}	ρ_k	ρ_{mean}
C14	14	8	0.4	16	2	3	7	4.7	0.23	0.44	290	350
C16	16	10	0.4	17	2.2	3.2	8	5.4	0.27	0.5	310	370
C18	18	11	0.4	18	2.2	3.4	9	6	0.3	0.56	320	380
C20	20	12	0.4	19	2.3	3.6	9.5	6.4	0.32	0.59	330	390
C22	22	13	0.4	20	2.4	3.8	10	6.7	0.33	0.63	340	410
C24	24	14	0.4	21	2.5	4	11	7.4	0.37	0.69	350	420
C27	27	16	0.4	22	2.6	4	11.5	7.7	0.38	0.72	370	450
C30	30	18	0.4	23	2.7	4	12	8	0.4	0.75	380	460
C35	35	21	0.4	25	2.8	4	13	8.7	0.43	0.81	400	480
C40	40	24	0.4	26	2.9	4	14	9.4	0.47	0.88	420	500
C45	45	27	0.4	27	3.1	4	15	10	0.5	0.94	440	520
C50	50	30	0.4	29	3.2	4	16	10.7	0.53	1	460	550
D18	18	11	0.6	18	7.5	3.4	9.5	8	0.63	0.59	475	570
D24	24	14	0.6	21	7.8	4	10	8.5	0.67	0.62	485	580
D30	30	18	0.6	23	8	4	11	9.2	0.73	0.69	530	640
D35	35	21	0.6	25	8.1	4	12	10.1	0.8	0.75	540	650
D40	40	24	0.6	26	8.3	4	13	10.9	0.86	0.81	550	660
D50	50	30	0.6	29	9.3	4	14	11.8	0.93	0.88	620	750
D60	60	36	0.6	32	10.5	4.5	17	14.3	1.13	1.06	700	840
D70	70	42	0.6	34	13.5	5	20	16.8	1.33	1.25	900	1080

Table 4 summarizes the natural frequencies obtained from the initial finite element model (FEM), along with the corresponding experimental results for comparison. When the numerically and experimentally obtained frequency values were compared, significant discrepancies were observed up to 47.96% for the first mode and 79.89% for the second mode. These findings indicate a substantial inconsistency between the frequency responses of the initial FEM and the experimental data. Therefore, model updating was deemed necessary to ensure an accurate representation of the structural behavior through the FEM.

Table 4. Comparison of initial FEM responses with experimental data

Group Number	Natural Frequencies (Hz)					
	1.Mode			2.Mode		
	Initial FEM	Experiment	Dif. (%)	Initial FEM	Experiment	Dif. (%)
1	50.66	63.03	19.63	260.17	177.2	46.82
2	48.57	62.03	21.70	274.53	177.1	55.01
3	46.14	62.09	25.69	282.67	184.7	53.04
4	49.94	67.91	26.46	257.63	170.1	51.46
5	48.26	61.49	21.52	251.17	169.8	47.92
6	47.12	64.18	26.58	254.18	141.3	79.89
7	47.5	69.04	31.20	288.26	178.9	61.13
8	47.72	64.15	25.61	270.95	174.8	55.01
9	46.90	63.51	26.15	286.04	185.8	53.95
10	41.15	60.81	32.33	228.93	189.6	20.74
11	39.03	61.98	37.03	231.62	189.6	22.16
12	38.64	59.58	35.15	247.04	180.4	36.94
13	40.41	74.03	45.41	225.81	176.3	28.08
14	39.70	65.84	39.70	234.54	175.3	33.79

Table 4. Continued

15	40.26	73.44	45.18	226.28	186.5	21.33
16	39.42	63.07	37.50	249.65	177.4	40.73
17	38.90	60.58	35.79	232.12	177.0	31.14
18	38.77	74.50	47.96	246.57	173.7	41.95
19	46.78	68.23	31.44	242.84	177.7	36.66
20	44.65	65.6	31.94	254.72	176.5	44.32
21	43.17	43.85	1.55	266.89	174.0	53.39
22	43.68	64.44	32.22	240.63	175.8	36.88
23	41.55	63.00	34.05	244.42	192.4	27.04
24	40.71	66.97	39.21	258.08	183.0	41.03
25	45.68	65.62	30.39	238.20	174.4	36.58
26	46.46	76.84	39.54	238.45	157.6	51.30
27	44.44	54.91	19.07	254.94	182.0	40.08
28	43.24	64.03	32.47	239.29	184.4	29.77
29	42.65	40.95	4.15	237.12	174.9	35.57
30	41.03	42.42	3.28	242.47	183.8	31.92

3.2. FEM updating using ambient vibration (dynamic) tests results

At this stage, the natural frequencies derived from ambient vibration tests were used as reference values, and the FEMs were updated by adjusting the stiffness of the spring elements at the support locations as the primary variable. Table 5 provides a comparison between the first two experimental natural frequencies and those obtained from the updated FEMs, along with the final values of the spring stiffnesses. Prior to model updating, the discrepancies in natural frequencies were as high as 79.89%, whereas post-update differences were significantly reduced to 7.09% for the first mode and 6.45% for the second mode. These results demonstrate a strong correlation between the experimental and numerical outcomes after the model updating process.

Table 5. The first two experimental natural frequencies with updated frequency-based FEM

Group Number	Modal Analysis						Spring Parameters		
	1st Mode (Hz)			2nd Mode (Hz)					
	Exp.	Dif. (%)	Updated Model	Exp.	Dif. (%)	Updated Model	U_x	U_y	U_z
1	63.03	1.05	62.37	177.2	4.94	182.49	650	650	1500
2	62.03	2.37	60.56	177.1	1.83	180.34	700	700	1500
3	62.09	4.45	59.33	184.7	0.15	184.98	900	900	1500
4	67.91	4.79	64.66	170.1	2.82	174.90	500	500	2200
5	61.49	4.11	58.96	169.8	1.90	173.02	600	600	1800
6	64.18	2.03	62.88	141.3	5.06	148.45	300	300	1800
7	69.04	4.74	65.77	178.9	2.04	182.55	650	650	2300
8	64.15	0.95	63.54	174.8	2.81	179.72	600	600	2150
9	63.51	5.01	60.33	185.8	2.20	189.89	900	900	1500
10	60.81	1.73	61.86	189.6	5.52	179.13	1000	1000	2500
11	61.98	1.58	61.00	189.6	4.15	181.74	1200	1200	2600
12	59.58	0.43	59.32	180.4	0.07	180.27	1200	1200	2400
13	74.03	6.12	69.50	176.3	6.45	187.68	1050	1050	4200
14	65.84	4.98	62.56	175.3	3.71	181.8	850	850	2100
15	73.44	4.62	70.05	186.5	3.49	193.00	1200	1200	4000
16	63.07	3.58	65.33	177.4	1.96	180.87	1000	1000	3500
17	60.58	2.91	58.82	177.0	3.49	170.82	1000	1000	2500
18	74.50	7.09	69.22	173.7	6.29	184.62	900	900	5500
19	68.23	2.80	66.32	177.7	2.21	181.63	700	700	2500
20	65.60	4.25	62.81	176.5	0.98	178.23	900	900	2300
21	43.85	0.50	43.63	174.0	3.90	167.22	900	900	700
22	64.44	4.41	61.60	175.8	2.69	180.53	900	900	2100
23	63.00	1.50	63.96	192.4	0.42	191.60	1200	1200	2500
24	66.97	3.73	64.47	183.0	4.48	191.20	1200	1200	2700

Table 5. Continued

25	65.62	2.38	64.06	174.4	4.11	181.56	800	800	2200
26	76.84	2.97	74.56	157.6	3.71	163.45	550	550	2100
27	54.91	1.78	55.89	182.0	2.04	178.29	900	900	1400
28	64.03	0.03	64.01	184.4	3.91	191.61	1100	1100	2300
29	40.95	4.32	39.18	174.9	1.08	176.79	1100	1100	500
30	42.42	3.25	41.04	183.8	3.29	177.75	1200	1200	650

4. Conclusions

In this study, the dynamic characteristics of 30 CLT panels with different properties were identified through ambient vibration tests, and FEMs were developed based on the experimental data. A frequency-based model updating approach was employed to enhance the accuracy of the numerical models. The analyses conducted yielded the following findings:

When the initial FEMs were compared with the experimental results, the differences in the natural frequencies of the first and second modes were found to reach up to 79.89% and 65.31%, respectively. This clearly demonstrated the necessity of performing model updating.

Following the frequency-based FEM updating, the discrepancies between the numerical and experimental natural frequencies were significantly reduced—down to 7.09% for the first mode and 6.45% for the second mode. These results indicate that the model updating procedure effectively improved the accuracy of the numerical representations.

In conclusion, the frequency-based model updating method contributed to obtaining finite element models that more accurately reflect the dynamic behavior of CLT panels. In this context, careful consideration of parameters such as support conditions, material properties of the panels, and boundary constraints is of critical importance for achieving consistency with experimental results.

References

Altunişik, A.C., Okur, F.Y., Genç, A.F., Gunaydin, M., & Karahasan, O. (2018). Automated model updating effect on the linear and nonlinear dynamic responses of historical masonry structures. *Experimental Techniques, 42*, 605–621

Altunışık, A.C., Sunca, F., & Sevim, B. (2023). Modal parameter identification and seismic assessment of historical timber structures under near-fault and far-fault ground motions. *Structures, 47*, 1624–1651

Aloisio, A., Pasca, D., Tomasi, R., & Fragiacomo, M. (2020). Dynamic identification and model updating of an eight-storey CLT building. *Engineering Structures, 213*, 110593

Bendat, J.S., & Piersol, A.G. (2011). Random data: Analysis and measurement procedures (4th ed.). John Wiley & Sons

Brank, B., & Carrera, E. (2000). Multilayered shell finite element with interlaminar continuous shear stresses: A refinement of the Reissner–Mindlin formulation. *International Journal for Numerical Methods in Engineering, 48*(6), 843–874

Brincker, R., Zhang, L., & Andersen, P. (2000). Modal identification from ambient responses using frequency domain decomposition. In *Proceedings of the 18th International Modal Analysis Conference (IMAC)* (pp. 625–630). San Antonio, Texas, USA

Butt, F., & Omenzetter, P. (2014). Seismic response trends evaluation and finite element model calibration of an instrumented RC building considering soil–structure interaction and non-structural components. *Engineering Structures, 65*, 111–123

Di Matteo, A., Masnata, C., Russotto, S., Bilello, C., & Pirrotta, A. (2021). A novel identification procedure from ambient vibration data. *Meccanica, 56*, 797–812

Espinoza, O., Trujillo, V.R., Mallo, M.F.L., & Buehlmann, U. (2016). Cross-laminated timber: Status and research needs in Europe. *BioResources, 11*(1), 281-295

Gagnon, S., & Pirvu, C. (2011). CLT handbook: Cross-laminated timber. FPInnovations.

Günaydin, M., Sunca, F., Altunişik, A.C., Ergün, M., & Okur, F.Y. (2022). Nondestructive experimental measurement, model updating, and fatigue life assessment of Çarşamba Suspension Bridge. *Journal of Bridge Engineering, 27*(2), 05021017

Jacobsen, N.J., Andersen, P., & Brincker, R. (2006). Using enhanced frequency domain decomposition as a robust technique to harmonic excitation in operational modal analysis. In *Proceedings of ISMA2006: International Conference on Noise & Vibration Engineering*. Katholieke Universiteit Leuven

Kurent, B., Friedman, N., & Brank, B. (2024). Modelling of multi-storey cross-laminated timber buildings for vibration serviceability. *Buildings, 14*(3), 689

Kurent, B., Brank, B., & Ao, W.K. (2023). Model updating of seven-storey cross-laminated timber building designed on frequency-response-functions-based modal testing. *Structure and Infrastructure Engineering, 19*(2), 178–196

Madenci, E., & Guven, I. (2015). The finite element method and applications in engineering using ANSYS®. Springer

Ni, Y.C., & Zhang, F.L. (2019). Fast Bayesian frequency domain modal identification from seismic response data. *Computers & Structures, 212*, 225–235

Oh, B.K., Kim, D., & Park, H.S. (2017). Modal response-based visual system identification and model updating methods for building structures. *Computer-Aided Civil and Infrastructure Engineering, 32*(1), 34–56

OMA, (2006) Release 4.0. Computer Software. Structural Vibration Solution, Aalborg, Denmark

Öztürk, H., Yücesoy, D., & Çolak, S. (2020). Thermal conductivity of cross laminated timber (CLT) with a 45° alternating layer configuration. *Wood Industry and Engineering, 2*(1), 13–16

PULSE. Analyzers and Solutions, Release 11.2. Bruel and Kjaer, Sound and Vibration Measurement A/S, Denmark (2006)

Ramos, L.F. (2007). *Damage identification on masonry structures based on vibration signatures* (Doctoral dissertation). University of Minho.

Russotto, S., Di Matteo, A., & Pirrotta, A. (2022). An innovative structural dynamic identification procedure combining time domain OMA technique and GA. *Buildings, 12*(7), 963

Sunca, F., Ergün, M., Altunişik, A.C., Günaydin, M., & Okur, F.Y. (2021). Modal identification and fatigue behavior of Eynel steel arch highway bridge with calibrated models. *Journal of Civil Structural Health Monitoring, 11*(5), 1337–1354

Wieruszewski, M., & Mazela, B. (2017). Cross laminated timber (CLT) as an alternative form of construction wood. *Wood Industry/Drvna Industrija, 68*(4), 343–348

Younis, A., & Dodoo, A. (2022). Cross-laminated timber for building construction: A life cycle assessment overview. *Journal of Building Engineering, 52*, 104482

ICEARC'25

4th International Civil Engineering & Architecture Conference
17-19 May 2025, Trabzon, Türkiye

The importance of evaluating building needs in retrofitting method selection

Muhammed Can Esen*[1], Kadir GÜLER[2]

[1] *Istanbul Technical University, Department of Civil Engineering, Istanbul, Türkiye*
[2] *Istanbul Technical University, Department of Civil Engineering, Istanbul, Türkiye*

Abstract: The 2023 Kahramanmaraş Earthquakes triggered a short-lived state of panic among residents in high-acceleration regions, particularly in areas specified by the Turkish Seismic Hazard Map 2018 (TDTH 2018). In response, many citizens sought to assess the seismic resistance of their buildings and retrofit them accordingly. In some of the implemented retrofitting projects, it was observed that despite the building having recently experienced an earthquake, the performance exhibited during the previous event was not evaluated. In some cases, expensive methods were chosen over more practical and cost-effective alternatives, while in others, retrofitting was carried out without conducting any static analysis to increase the element ductility (generally only applying FRP wrapping or steel jacketing to the existing reinforced concrete columns).Such practices can result in various negative outcomes, including failure to meet expected performance levels, which posing risks to human safety; over-design, leading to unnecessary expenses; and inefficient resource allocation, with retrofitting efforts focusing on adequate parts of buildings rather than addressing deficiencies. This study underscores the critical importance of selecting the appropriate retrofitting method for a building to prevent the financial and human losses. It demonstrates that retrofitting methods should be chosen based on the specific needs of the building. By evaluating retrofitting strategies within the framework of TBDY-2018 (Turkish Building Earthquake Code 2018), the study examines their outcomes in buildings with different deficiencies in Türkiye. Additionally, it provides recommendations for retrofitting approaches suitable for various structural weaknesses. In conclusion, the study emphasizes that retrofitting methods must be carefully selected based on a thorough evaluation of the reinforced concrete building's deficiencies and specific needs.

Keywords: Retrofitting methods; TBDY-2018; Seismic resistance; Cost-effective retrofitting; Structural weaknesses

1. Introduction

The need for strengthening buildings may be for buildings moderately damaged after an earthquake, or to increase the seismic performance of existing buildings. In 2023, two major earthquakes occurred in Kahramanmaraş in the same day of 6th February, the first measuring 7.7 Mw and the second 7.6 Mw. After the earthquakes, many buildings were evaluated as heavily damaged, while some were classified as moderately damaged. (Altıok, Şevik, & Demir, 2024)

In some of the moderately damaged buildings, the owners opted for demolition and reconstruction, while in others, repair and retrofitting methods were preferred. In some of the buildings where retrofitting was decided, it was observed that the applied methods were chosen without considering the needs of the building, and in some cases, retrofitting was carried out without any structural system analysis (CAEES/ACGPS, 2023)

Such improper practices lead to unnecessary costs, causing financial losses to citizens who are already facing economic difficulties due to the earthquake, and in some cases, they mislead the public, posing risks to life safety. This study emphasizes the importance of evaluating the needs of the building when selecting a retrofitting method and discusses various methods that can be applied for different level of deficiencies.

2. Retrofitting methods

When it comes to strengthening buildings, system and element strengthening should be understood together. However, element strengthening is mostly used and understood in the sense of strengthening the building/structure. This is not true. Because in the existing building stock, in addition to the lack of sufficient wrapping in columns

*Corresponding author, E-mail: esen22@itu.edu.tr

https://doi.org/10.31462/icearc2025_ce_eqe_824

golden light publishing

in buildings, lateral rigidity is also not sufficient. Due to the lack of sufficient wrapping effect in columns (insufficient stirrups, 90-degree hooks and easy opening of these hooks, buckling of column longitudinal reinforcements and crushing of core concrete, severe damage to columns, reaching strength loss), the earthquake behavior of frame system buildings does not occur as expected. In order to repair and strengthen damaged columns and as a structural system strengthening in existing buildings, columns are mostly tried to be wrapped. However, this application means increasing the ductility of the element. In very few cases, element strengthening may include structural system strengthening. Some of the options for element and system level strengthening are given below. This section discusses the various retrofitting methods and their benefits. The methods to be examined include Fiber Reinforced Polymer (FRP) retrofitting, Reinforced Concrete Jacketing, Retrofitting by Adding Shear Walls, Steel Jacketing/Strip Retrofitting, and Retrofitting with Steel Braces (including buckling restrained braces, BRB).

2.1. Retrofitting with fiber-reinforced polymer (FRP)

In the FRP retrofitting method, structural elements are strengthened using materials made from glass, aramid, or carbon fibers by wrapping or strip application. These materials consist of fiber and resin. The mechanical properties of the material vary depending on the type of fiber used.

Glass fibers are recommended for elements where high load-bearing is not crucial and where large deformations are not expected, while carbon fibers are recommended for elements where high load-bearing is essential and significant deformation is expected (İlki, Demir, & Cömert, 2023). Aramid fibers offer high tensile strength but are less commonly used due to higher costs (Jibu & Joseph, 2022).

Retrofitting by FRP can be applied in two ways: wrapping or strip application. The main difference is that wrapping provides a confinement effect due to its continuity, resulting in an increase in the axial load capacity of the element. The main advantages of this method are fast application, minimal reduction in usable space, increased ductility of the element, and significant improvement in shear strength depending on capacity. (Antoniou, Fibre – Reinforced Polymers (FRPs), 2022). Wrapping application is much effective in low strength concrete circular and squared column sections. Strip application of FRP is used to increase the flexural rigidity (at beams and slabs) and shear resistance of columns and beams.

Fig. 1. CFRP strip application to increase the flexural rigidity of slabs (SİKA, 2024)

2.2. Retrofitting with reinforced concrete jacketing

In this strengthening method, it is assumed to increase the bending rigidity and ductility by increasing the sizes of the section from one side to four sides. It is important to fix the longitudinal reinforcements to the foundations in the sheathing and to ensure their continuity at the floor slab levels. To improve the bond between the existing and new jacketing sections, it is important to perform the surface roughness and chemical anchorage of reinforcement between existing and new sections.

As a result, it improves the ductility, axial load, and shear capacity of the element and enhances the overall structural stiffness. However, the drawbacks include reduction in usable space and long, labor-intensive application processes (Sichko & Sezen, 2017).

Fig. 2. RC column jacketing application (Structville, 2023)

2.3. Retrofitting with reinforced concrete shear walls
This method involves adding new shear wall elements in the direction where they do not already exist in the building, enhancing stiffness and enabling the building to resist significant lateral forces. These elements can be added either between frame columns, or by connecting to existing columns independently. In retrofitting buildings with adding shear walls, at least three shear walls should be used and their axis should not intersect at one point. The location of shear walls should not disturb the architectural functions of the building. Continuity of the shear walls between slabs is important.

By adding shear walls, the building's stiffness is significantly improved, and it becomes more capable of resisting shear forces in the direction of the walls located. Although this is a difficult and laborious process, when shear walls are placed within infill walls, they may not reduce usable space. (Antoniou, New Reinforced Concrete Shear Walls, 2022)

Fig. 3. Adding shear walls to existing structural system (Seismosoft, 2022)

2.4. Retrofitting with steel jacketing/straps
In this method, existing structural system elements (columns and beams) are retrofitted using steel members with various mechanical properties, either by jacketing or by attaching strip-shaped steel elements.

Similar to FRP, this method allows relatively easy application. Jacketing increases both axial load and shear force capacity, while strip application mainly improves the shear force capacity. It also enhances the ductility of the column or beam applied.

This method does not significantly reduce usable space and is relatively fast to apply. However, the material and labor costs are high, and corrosion susceptibility depends on the type of steel used. (Chong, ve diğerleri, 2024). It is recommended to perform an economic analysis with that of FRP wrapping for increase in shear capacity.

Fig. 4. Steel jacketing (Kaplan & Yilmaz, 2012)

2.5. Retrofitting with steel bracing (BRB)
In this method, buckling-restrained steel braces are added externally or internally to increase the structural system's stiffness. Similar to adding rc shear walls, this method enhances the stiffness. Although it is costly, it can save time and enable the building to continue to provide service.

To apply this method, the amount of concrete compressive strength of the structural elements is important. In case of low concrete strength, in addition to the need for steel jacketing on columns, jacketing of some beams may also be required to meet in-plane effects. . (Güler, 2022)

Fig. 5. Buckling restrained braces application (Arfenbrb, 2022)

3. Selecting retrofitting methods based on structural needs

In Türkiye, buildings are predominantly constructed according to the seismic codes of 1975, 1997, 2007, and 2018, These codes have evolved over time due to changing conditions, advancements in technology, capacity design principles and practical applications. The requirements on capacity design principles, structural irregularities and reinforcement details are given in 1997 seismic code. Earthquake codes generally include rules regarding the design of structural systems under vertical and lateral loads with a strength-based approach. Rules regarding the seismic performance assessment and strengthening of existing buildings are included in the 2007 and 2018 earthquake codes.

In addition to changes in seismic codes, inspection mechanisms and engineering software have also improved over time, contributing to today's standards. At this point, analyzing the deficiencies and needs of buildings resulting from past mistakes is crucial for proper retrofitting.

Deficiencies in the existing buildings can be classified as element level and system level.

Element level deficiencies include insufficient strength, rigidity and ductility. The most critical system level deficiency in the existing buildings is inadequate lateral stiffness and insufficient confinement for columns. For that reason, only element level strengthening cannot be sufficient, at the same time the system level retrofitting is required to prevent collapse the buildings and save human life.

Below is a table showing the effects of various retrofitting methods for commonly encountered deficiencies.

Table 1. Effectiveness of various retrofitting methods

Retrofitting Method	Cost	Labor & Time	Contribution to Axial Load Strength (Element-Level)	Contribution to Shear Strength (Element-Level)	Contribution to Stiffness (System-Level)	Contribution to Ductility
Retrofitting with FRP	+	+*	+ (only for wrap)	+*	-	+*
Retrofitting with RC Jacketing	+*	-	+	+	+	+
Retrofitting with RC Shear Wall	-	-	~	~	+*	-
Retrofitting with Steel Jacketing/Strips	-	+	- (For strip)	+*	~	+*
Retrofitting with Steel BRB	-*	+	-	-	+*	-

+ good, +* very good, ~ partial contribution, - costly/ineffective, -* very costly
*BRB = buckling restrained brace

4. Importance of selecting retrofitting methods based on needs using a sample building

In this section, the outcomes of a building retrofitted using fiber-reinforced polymer (FRP) were examined.
The building consists of beam and column elements, frame system, and does not contain any reinforced concrete shear walls.

The building has a ground floor and six typical stories. It was constructed using concrete with a compressive strength of 20 MPa and S420 grade deformed reinforcement. Carrying out nonlinear analysis, it was observed that four columns experienced collapse, and FRP retrofitting was decided upon to prevent the failure of the building.

The results obtained after the retrofitting process are as follows:

The ductility capacity, shear and compressive strength of reinforced concrete columns were improved through FRP wrapping. Additionally, in cases where the lap splice length of longitudinal reinforcement at bottom ends of the columns was insufficient, FRP wrapping can enhance the bond strength of the reinforcement.

The displacement capacity of columns was increased with FRP wrapping. Before FRP wrapping, 142 mm displacement is calculated, 83 structural elements showed significant damage level and 4 columns collapsed level. After the wrapping, the number of collapsed elements was reduced to zero, and the structural safety was ensured. In fact, story drifts did not changed, they were in acceptable limits.

The wrapping of the structural system with FRP material, the shear capacity of the structural system elements was increased to the Vmax limit defined by the seismic code 2018. However, in order to classify the building as shear-safe, it was determined that some columns and beams needed to be strengthened by rc jacketing. This is due to the code limitation that the maximum shear capacity of FRP-wrapped members cannot exceed Vmax.

Due to the current building conditions, some columns are weaker than the beams, resulting in the building behaving like a limited ductility system, so earthquake loads are increased and existing lateral rigidity is insufficient. In order to upgrade the system classification to a high-ductility system, jacketing of some columns is required.

While the building initially exhibited collapse performance, with FRP wrapping and the additional jacketing of necessary structural elements, the building achieved the desired Controlled Damage performance level according to TBSC 2018.

Despite these improvements, the FRP wrapping method caused almost no reduction in usable space compared to other retrofitting techniques.

FRP retrofitting remains an active area of research, and codes from different countries impose varying limitations.

For example, in the Turkish Building Earthquake Code 2018 (TBDY-2018):

a) In order to enhance the axial compressive strength of columns via FRP wrapping, the ratio of the longer side to the shorter side of the column cross-section must not exceed 2.5.

b) To improve the ductility of columns using FRP wrapping, the same aspect ratio condition (≤2.5) must also be satisfied.

c) For columns with a cross-section aspect ratio greater than 2 or longitudinal reinforcement with plain bars, confinement is inadequate, and FRP wrapping cannot be used to strengthen the lapped splice regions.

If some elements in the building do not meet the above requirements, another suitable retrofitting method must be selected. This alternative method can be used in combination with other techniques as part of a composite approach.

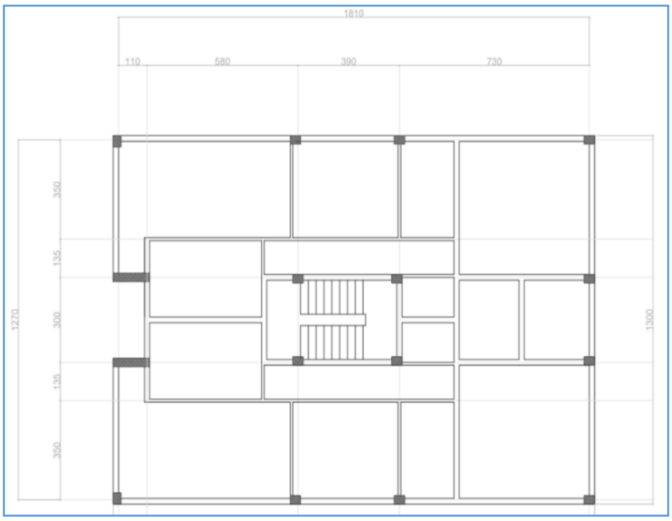

Fig. 6. Floor plan

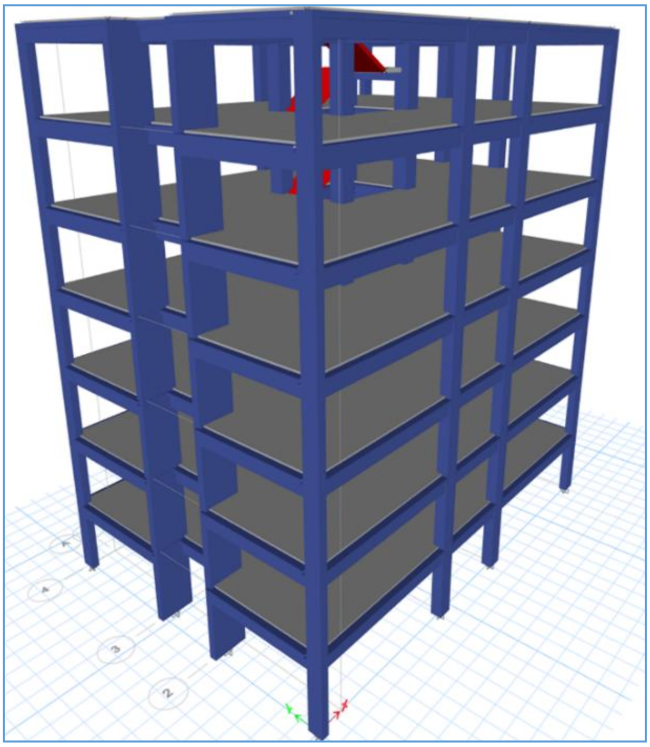

Fig. 7. 3D model of building

Table 2. Evaluation of Retrofitting Methods According to Structural Deficiencies

Structural Deficiency	Retrofitting Method	Contribution of the Method
Inadequate shear strength	FRP wrapping	Increases shear capacity; fast and space-saving
	Steel strip	Increases shear capacity; cost-effective depending on conditions
Inadequate axial load capacity	RC jacketing	Increases shear, axial, and ductility capacities
	RC jacketing	Increases axial and shear strength, improves ductility
	Steel jacketing	Increases axial and shear capacity
	FRP wrapping (full wrapping)	Increases axial capacity through confinement
Inadequate ductility	RC jacketing	Enhances ductility and energy dissipation capacity
	Steel jacketing	Enhances ductility
	FRP wrapping	Enhances ductility
Inadequate structural stiffness	Adding shear walls	Increases stiffness and lateral load capacity
	Steel bracing	Increases stiffness; shorter application time

Damper and base isolation strengthening techniques are not considered in this study.

5. Conclusions

The need for retrofitting is specific in the strengthening of damaged buildings, and the strengthening system can be decided accordingly. However, determining the earthquake performance of the existing buildings and deciding on the strengthening system requires professional experience. A decision should be made on the applicable and economical reinforcement technique according to the reinforcement need on a system level and, if any, on an element level. Each retrofitting method has its own advantages and disadvantages. During retrofitting processes, the negative aspects of the building should be evaluated, and the most effective method for addressing these should be chosen.

There is no obligation to use a single retrofitting method, hybrid methods may be applied. Sometimes, one method may not be sufficient to address all deficiencies, and multiple methods may need to be combined.

For example, after increasing the stiffness of a building by adding new shear walls to the existing structural system, for element level deficiencies can be resolved using FRP wrapping or jacketing of some columns.

- For the elements of columns with insufficient axial load, shear strength, or ductility, if the required capacities defined in the code are met, the use of FRP is recommended. If not, reinforced concrete jacketing is advised.
- If the shear strength of columns needs to be increased within the capacity limits of the element, either FRP or steel strips can be used. The choice between these methods may depend on cost, labor, and retrofitting time.
- For buildings with structural system level deficiencies, new shear walls or steel braces can be used depending on the building's needs, cost, and timeline. To use the steel braces, the concrete compressive strength in the frame system must be sufficient (not less than 15MPa). Both methods require compatibility with the building's slab plan and locations of columns without changing the architectural functions of the building.

References

ABYBHY. (1975). *Afet bölgelerinde yapılacak yapılar hakkında yönetmelik*. İmar ve İskan Bakanlığı. (in Turkish)

ABYBHY. (1997). *Afet bölgelerinde yapılacak yapılar hakkında yönetmelik*. Bayındırlık ve İskan Bakanlığı. (in Turkish)

Altıok, T. Y., Şevik, M., & Demir, A. (2024, August). Seismic performance of retrofitted and non-retrofitted RC school buildings after the February 6th, 2023, Kahramanmaraş earthquakes. *Bulletin of Earthquake Engineering*, 1017–1052. https://doi.org/10.1007/s10518-024-01729-z

Antoniou, S. (2022, January 20). Fibre–Reinforced Polymers (FRPs). Seismosoft. https://seismosoft.com/fibre-reinforced-polymers-frps

Antoniou, S. (2022, March 11). New reinforced concrete shear walls. Seismosoft. https://seismosoft.com/new-reinforced-concrete-shear-walls

Arfenbrb. (2022). *Burkulması önlenmiş çelik çaprazlar - BRB*. Arfenbrb. https://arfenbrb.com/burkulmasi-onlenmis-celik-caprazlar-brb

CAEES/ACGPS (Canadian Association for Earthquake Engineering). (2023). *CAEES/ACGPS reconnaissance report on February 6, 2023 Kahramanmaraş earthquakes in Türkiye*. Canadian Association for Earthquake Engineering.

Chong, X., Liu, H., Xie, L., Zhou, A., Huang, J., & Sha, H. (2024, April). Experimental investigation of retrofitting seismically damaged reinforced-concrete frames using steel jacketing. *Structures*. https://doi.org/10.1016/j.istruc.2024.04.057

DBYBHY. (2007). *Deprem bölgelerinde yapılacak binalar hakkında yönetmelik*. Bayındırlık ve İskan Bakanlığı. (in Turkish)

Esen, M. C., Türk, A. M., & Özdemir, F. E. (2021, June). Betonarme yapılarda güçlendirme. İstanbul, Türkiye. (in Turkish)

Güler, K. (2022). *Yapıların onarım ve güçlendirilmesi*. İTÜ LEE YL Ders Notları, İstanbul, Türkiye. (in Turkish)

İlki, A., Demir, C., & Cömert, M. (2023). *Yapıların LP kompozitler ile güçlendirilmesi ders notu*. İstanbul, Türkiye. (in Turkish)

Jibu, J. M., & Joseph, N. (2022, April). Literature review on FRP wrapping over structural components. *International Research Journal of Engineering and Technology (IRJET)*, 9(4), 486–491.

Kaplan, H., & Yilmaz, S. (2012, February). Seismic strengthening of reinforced concrete buildings. In A. Zingoni (Ed.), *Earthquake-resistant structures – Design, assessment and rehabilitation* (pp. 408–428). IntechOpen. https://doi.org/10.5772/54091

Seismosoft. (2022, March 11). New reinforced concrete shear walls. Seismosoft. https://seismosoft.com/new-reinforced-concrete-shear-walls/

Sichko, A., & Sezen, H. (2017). Evaluation of retrofit methods for reinforced concrete beams. In *SMAR 2017*. Columbus, USA.

SİKA. (2024). *Karbon lifli polimer (CFRP) plakalar*. Sika Türkiye. https://sika.scene7.com/is/image/sika/tr-yapi-guclendirme-03:16-9?wid=1024&hei=576&fit=crop%2C1&fmt=webp-alpha

Structville. (2023, May 16). Jacketing of reinforced concrete (RC) columns. Structville. https://structville.com/jacketing-of-rc-columns

TBDY. (2018). *Türkiye bina deprem yönetmeliği (TBDY)*. Afet ve Acil Durum Yönetimi Başkanlığı. (in Turkish)

Evaluation of strengthening RC building with X steel cross elements

Gürkan Tam*[1], Burak Yön[1]

[1]Munzur University, Department of Civil Engineering, 62000 Tunceli, Türkiye

Abstract. In this study, a building with C12 concrete strength, unchanged column and beam dimensions, S420 reinforcement steel and 250 mm transverse reinforcement spacing was modeled. Then, this building was strengthened with X steel diagonal elements to form a total of two buildings. Nonlinear static and incremental dynamic analyses were performed to evaluate the seismic response of the buildings. 11 different earthquake records were selected for incremental dynamic analyses. These records were applied to the structures with 0.1 increments between 0.1g and 1.0g. As a result of the analyses, the capacity curves of the buildings, interstory drifts and hysteretic curves of some selected columns were obtained. According to the results obtained, it was determined that as a result of the strengthening using X-steel diagonal elements, the interstory drifts and displacements in the columns of the strengthened structure were significantly reduced compared to the existing structure, and the base shear forces that the strengthened structure faced compared to the current situation increased approximately 4.3 times.

Keywords: Retrofitted concrete building; Capacity curve; Interstory drift; Incremental dynamic analysis; X steel cross element, Hysterical curves

1. Introduction

Türkiye is situated in one of the most seismically active regions globally, resulting in a significant earthquake hazard across the nation. Active faults, particularly the North Anatolian Fault Zone, East Anatolian Fault Zone, Bitlis Thrust Zone, and Aegean Depression System, induce significant earthquakes. Numerous lives and properties were lost due to significant disasters, including the 1999 Kocaeli Earthquake, the 2011 Van Earthquakes, the 2020 Elazığ and İzmir Earthquakes, and the 2023 Kahramanmaraş Earthquakes. In Turkey, consistently susceptible to earthquakes, field research conducted post-quake uncovered numerous deficiencies, including the utilization of low-strength concrete in transverse reinforced concrete structures, design flaws, inspection-related issues, and excessive spacing of confinement reinforcement. Reinforced concrete structures with such defects, when subjected to significant ground movements, result in substantial loss of life and property. Consequently, the seismic performance of the current reinforced concrete building inventory at different danger levels must be assessed and fortified employing suitable techniques (Yurdakul et al., 2021; Rizvan et al, 2021).

The objective of seismic design is to avert loss of life by ensuring that structures exhibit appropriate behavior under lateral loads during an earthquake, maintain structural damage within repairable limits and most critically, prevent structural collapse (Gunel & Ilgin, 2007). Nevertheless, older buildings, constructed in accordance with previous design rules and standards, are unable to satisfy the performance criteria established by contemporary regulations (Alkhayyat & Ozay, 2024; Villar et al, 2020; Beiraghi et al, 2022; Sidika et al, 2020; Doğan et al, 2021; Pohoryles et al, 2022). As a result, the imperative to enhance the seismic performance of these structures arises (Tam, 2024). The option of reinforcing with steel cross members is emerging as a cost-effective and efficient method to enhance structural performance and provide stability against lateral loads. These support parts confer stiffness and stability to the structure, particularly in high-rise buildings (Hassan & Al-Wazni, 2023; Patil & Angalekar, 2021). The implementation of cross member systems is an effective strategy to mitigate structural damage, interstorey drifts and storey displacements during seismic events (Ahiwale et al, 2023; Kirruti & Balkıs, 2020).

This numerical study employed static pushover analysis and incremental dynamic analysis to examine the impact of steel cross member reinforcement on the seismic performance of retrofitted concrete structures.

*Corresponding author, E-mail: gtam@munzur.edu.tr

https://doi.org/10.31462/icearc2025_ce_eqe_828

Capacity curves, average interstorey drifts, and hysteretic curves for specific columns were derived for the selected structures.

2. Material and method

The current 5-storey symmetrical reinforced concrete structure was used as the benchmark for the numerical analysis. The height of each floor is designated as 3 meters. The building's total height was established at 15 m, the floor thickness at 12 cm, the concrete grade at C12, and the steel grade at S420. All columns of the reference structure measure 400x400 mm, all beams measure 250x500 mm, and the existing building is modeled with confinement reinforcement spacing of 250 mm for both columns and beams. During the second phase of the project, the existing structure was reinforced by including X steel cross members. A comparison of the seismic performance of the two simulated structures was conducted. The Mander confined concrete model (Mander et al, 1988) was selected for concrete, the Menegotto-Pinto model (Menegotto & Pinto, 1973) for steel, and the SHS 150x8 mm material model (Seismostruct, 2024) for the X steel cross reinforcement element. The SeismoStruct V24 structural analysis software (Seismostruct, 2024) was utilized for the analysis. Fig.s 1-3 present the floor plans and perspectives of the existing and retrofitted structures utilized in the numerical analysis, while Table 1 provides the specifications of the columns and beams.

The static pushover analysis approach was initially employed in the study to assess the nonlinear behavior of both existing and retrofitted structures. Static pushover analysis involves the determination of demand-capacity curves through the estimation of plastic hinges and displacements. The investigation investigates the development of plastic hinges under progressively increasing lateral strains (Ueda & Takewaka, 2007; Rodriguez et al, 2024; Ruggieri & Uva, 2020; Prince et al, 2023). The second technique employed in numerical analysis is the incremental dynamic analysis method. This method involves doing a series of nonlinear time history analyses to assess the structural response to dynamic loads (Prince et al, 2023; Verki & Preciado, 2022). This technique delivers insights into structural demand levels, including damage status in structural components, maximum peak displacement, and interstory drift for earthquake data of varying amplitudes (Karaşin, 2023). The relative storey drifts derived from dynamic analyses were compared with the threshold values established for various performance levels in the HAZUS program, a nationally standardized risk assessment methodology in the United States administered by the FEMA-2000 (Federal Emergency Management Agency) natural disaster risk assessment initiative. The limit values utilized in the investigation are presented in Table 2 for framed constructions.

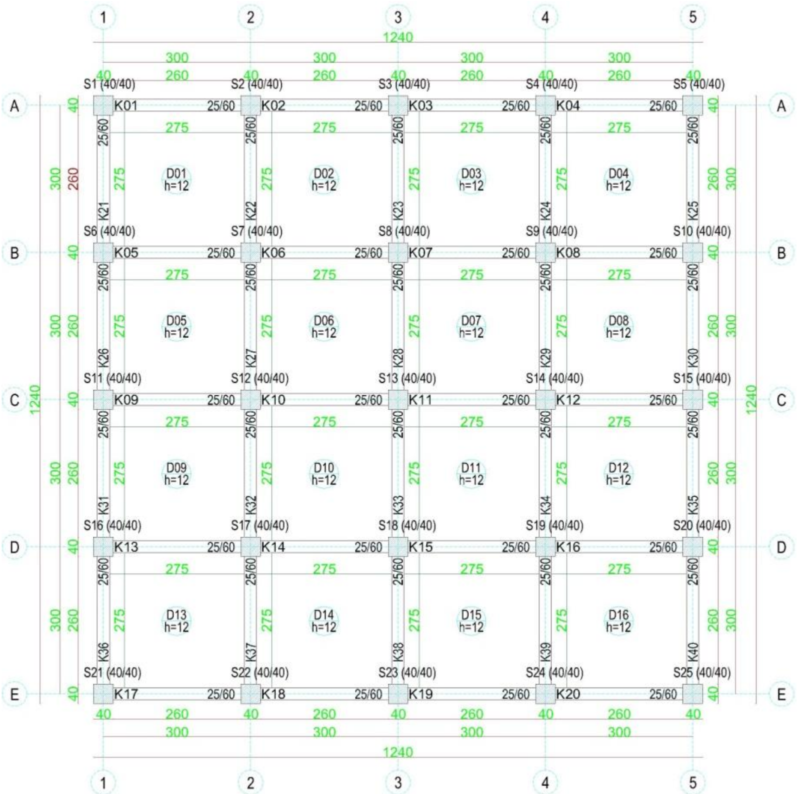

Fig. 1. Normal floor plan of the selected building

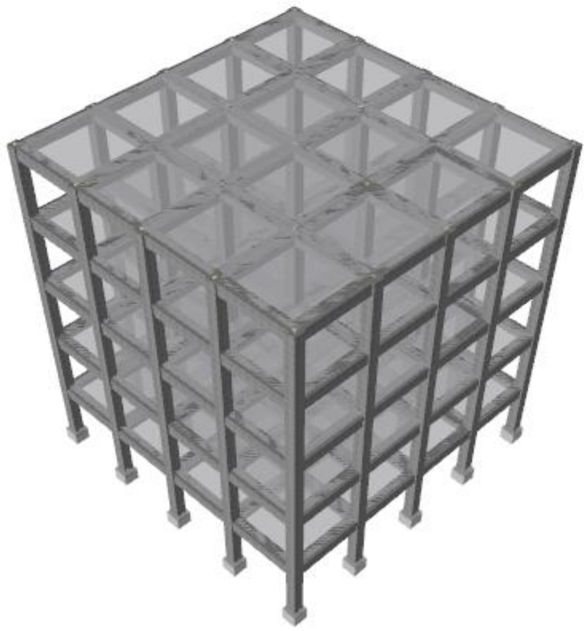

Fig. 2. Appearance of the current model

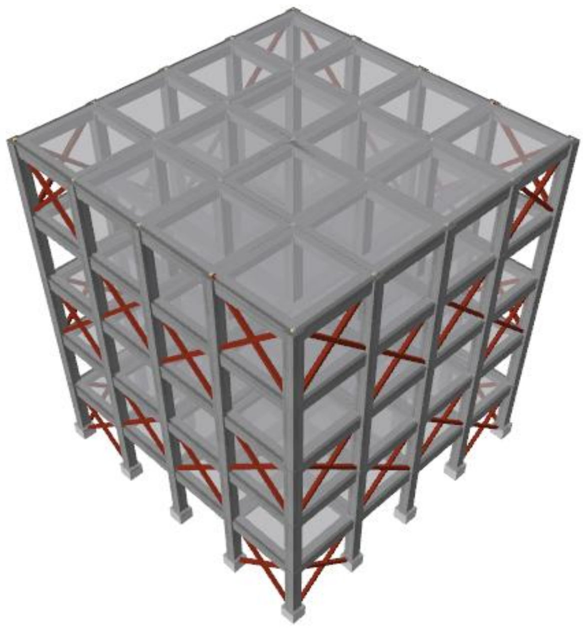

Fig. 3. Appearance of the retrofitted model

Table 1. Dimensions of beams and columns and reinforcement arrangement

Elements	Reinforcement layout	Element Dimensions (mm)	Longitudinial Reinforcement (mm)	Transverse Reinforcement (mm)
Columns	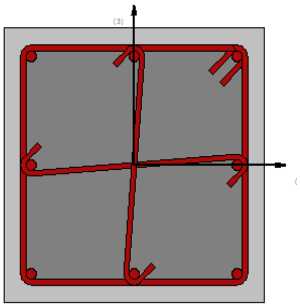	400/400	8ϕ16	ϕ8/250
Beams	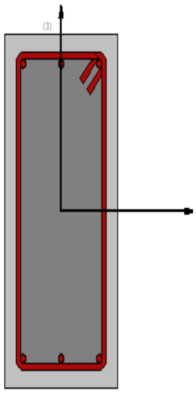	250/500	3ϕ12 3ϕ12	ϕ8/250

Table 2. Interstory drift rates given in HAZUS (HAZUS)

Slight Damage	Moderate Damage	Heavy Damage	Collapse
0.0033	0.0067	0.02	0.053

3. Findings and discussion

This section presents capacity curves derived from the non-linear analysis of the analyzed structures, average interstorey drifts, and hysteresis curves observed in selected columns.

3.1. Capacity Curves

Static pushover analyzes of the selected buildings were carried out according to the DD-2 earthquake level and ZD local soil class criteria, taking into account the earthquake forces and the additional eccentricity effect. Continuously increasing lateral force was applied to the models until the roof displacement reached 3% of the building height. The comparison of the obtained capacity curves between existing and retrofitted buildings is presented in Fig. 4.

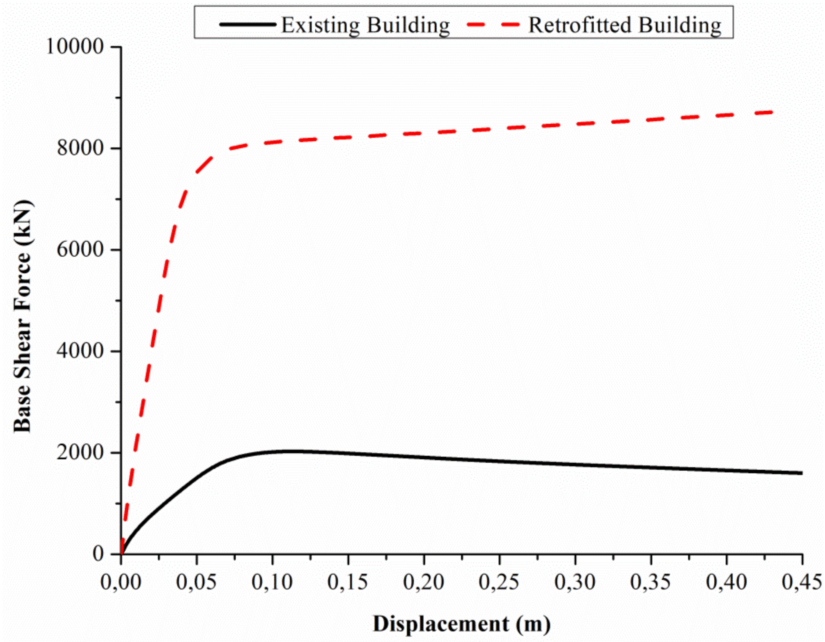

Fig. 4. Comparison of capacity curves

Upon examination of Fig. 4, it is evident that the capacity curve of the retrofitted structure significantly surpasses that of the existing building. The maximum base shear force resisted by the retrofitted building was 8748 kN, while the original building resisted a maximum base shear force of 2028 kN. The capacity values of the building reinforced with X steel cross members rose by over fourfold compared to the capacity value of the existing structure. Furthermore, the horizontal load-bearing capacity of the existing building diminished following a displacement of 0.10 m, but no reduction was noted in the capacity of the retrofitted structure.

3.2. Interstorey drift ratio

The average of the interstorey drift ratios obtained according to the acceleration amplitudes of the two buildings that were numerically analyzed was compared with the limit values specified for different performance levels in the HAZUS program, based on earthquake amplitudes of 0.1g-1.0g (Fig. 5-6).

Fig. 5 presents the average interstory drifts of the existing building based on a total of 11 earthquake records ranging from 0.1g to 1.0g. The relative storey drift ratios of the building were assessed to be between moderate and heavy damage at 0.1g and 0.2g, between heavy damage and collapse at 0.3g, and beyond the collapse threshold at higher acceleration amplitudes.

The average of the interstorey drift ratios of the retrofitted building calculated according to a total of 11 earthquake records between 0.1g-1.0g is given in Fig. 6. Accordingly, for 0.1g acceleration amplitude, the building is below the light damage level, for 0.2g and 0.3g acceleration amplitudes, it is between slight damage and moderete damage level, for 0.4g-0.7g, it is between moderete damage and heavy damage level, for 0.8g, For acceleration amplitudes of 0.9g and 1.0g, it was determined that it remained between the levels of severe damage and collapse.

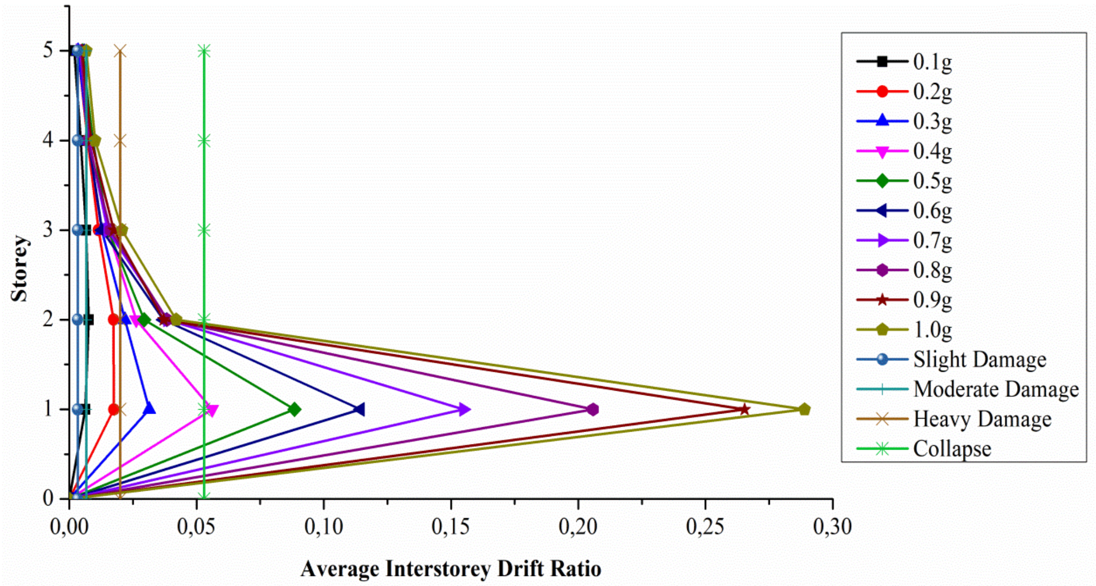

Fig. 5. Average interstorey drift ratios of the existing building under earthquakes with accelerations of 0.1g-1.0g

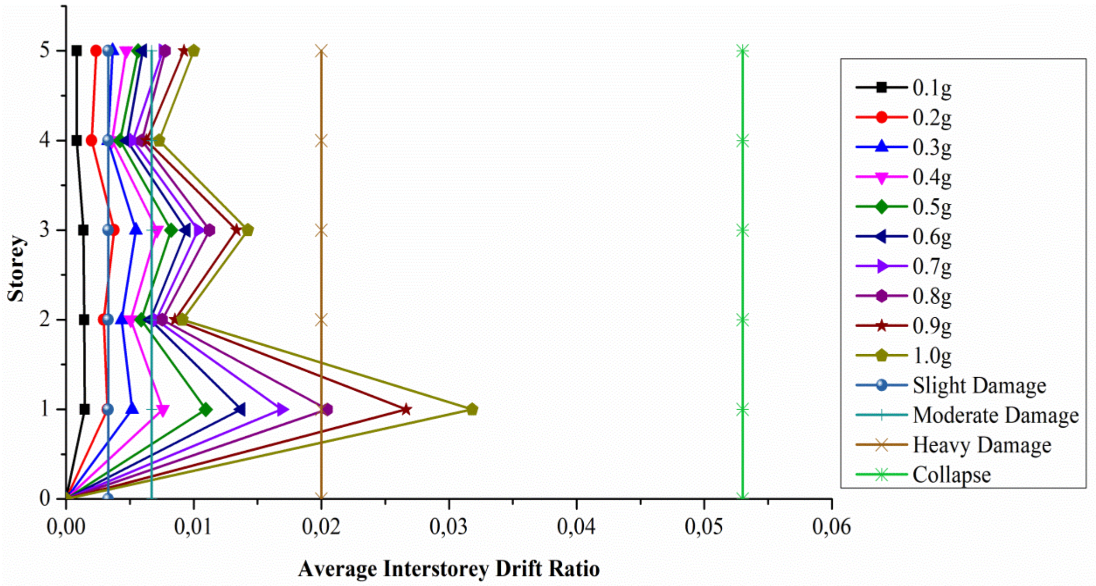

Fig. 6. Average interstorey drift ratios of the retrofitted building under earthquakes with accelerations of 0.1g-1.0g

3.3. Hysteresis curve

The hysteretic curves obtained as a result of nonlinear analyzes using the 0.7g amplitude acceleration record of the Bingöl earthquake for some selected columns in the examined buildings are given in Figs. 7-9.

Upon examining Fig. 7, the maximum displacement value for the ground floor S13 column is 0.024 meters in absolute terms, whereas the maximum lateral shear force is around 1400 kN. Following the fortification of the structure, the peak displacement value for the identical column diminished to 0.0096 meters in absolute terms, although the highest shear force escalated to 5898 kN.

In the first floor S21 column, the current maximum displacement value was 0.042 meters in absolute value and the largest lateral shear force was approximately 1419 kN. After the building was strengthened, the maximum displacement value for the same column decreased to 0.006 meters in absolute value, while the maximum shear force increased to approximately 5900 kN (Fig. 8).

In the S3 column on the second floor, the maximum displacement value is 0.03 meters in absolute terms, and the peak lateral shear force is approximately 1500 kN. Conversely, in the retrofitted structure, the maximum displacement value for the same column is 0.011 meters in absolute terms, with the highest shear force reaching approximately 5900 kN.

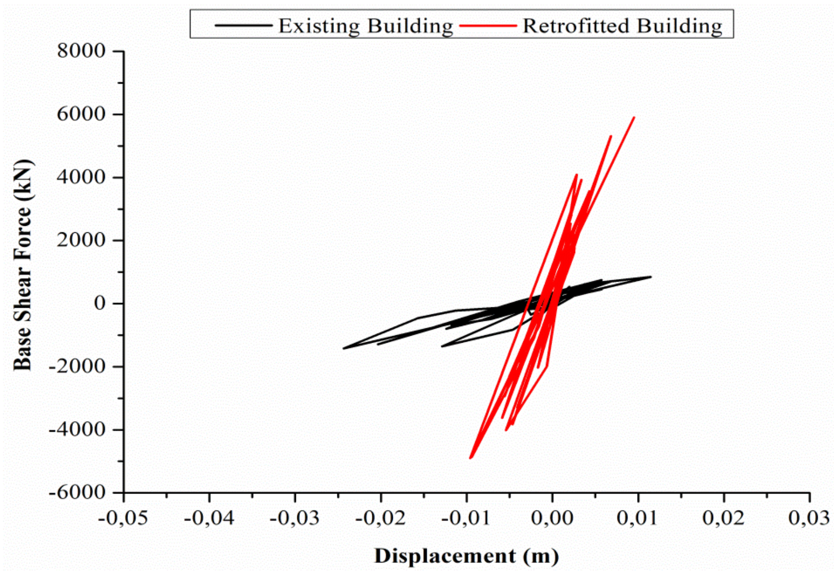

Fig. 7. Hysterical curves formed in the ground floor S13 column of existing and retrofitted buildings

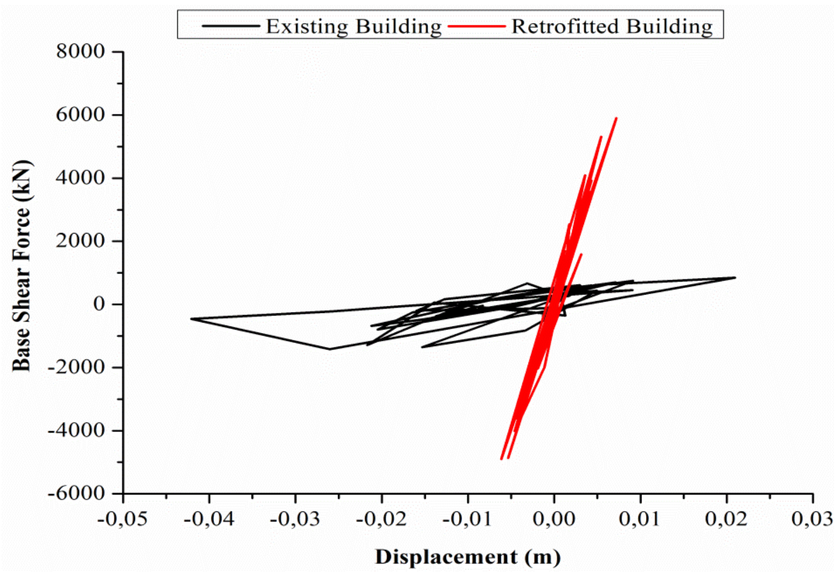

Fig. 8. Hysterical curves formed in the first floor S21 column of existing and retrofitted buildings

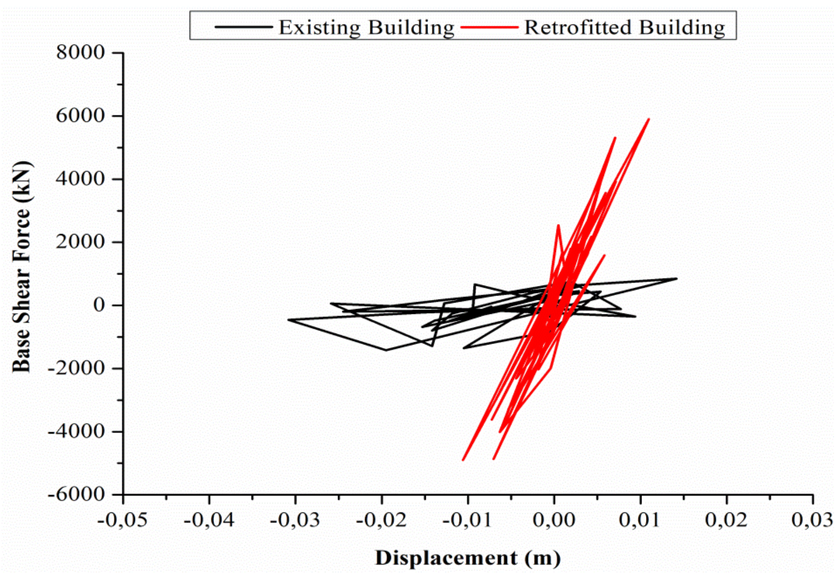

Fig. 9**.** Hysterical curves formed in the second floor S3 column of existing and retrofitted buildings

4. Conclusions

This study conducted static pushover and incremental dynamic analyses of chosen building models to investigate the impact of X steel cross members on the reinforcement of reinforced concrete structures. A structure with a confinement reinforcement spacing of 250 mm and a concrete strength of C12 was modeled for this purpose. This building, subsequently modeled, was reinforced with X steel cross members, resulting in a total of two models. The investigations yielded capacity curves for the modeled buildings, average relative floor drifts, and hysteresis curves for chosen columns. The findings derived from the investigation are presented below.

- The assessment of capacity curves indicates that the lateral load-bearing capacity of the building reinforced with X steel cross members has grown to roughly 4.3 times that of the existing structure. Nevertheless, the horizontal load-carrying capacity of existing structures diminished following a displacement of 0.10 m, although no reduction was noted in the capacity of rtrofitted structures.
- The evaluation of the average interstorey drifts from 11 earthquake records with acceleration amplitudes ranging from 0.1g to 1.0g revealed that the interstorey drift rates for the existing building surpassed the collapse threshold at acceleration amplitudes exceeding 0.3g. The retrofitted structure exhibited average interstorey drifts that fluctuated between severe damage and collapse thresholds for acceleration amplitudes of 0.8g, 0.9g, and 1.0g.
- As a result of examining the 0.7g amplitude Bingöl earthquake data, hysteresis curves were obtained for the specified columns. When these curves were evaluated, it was determined that steel cross members reduced the maximum displacement in the columns by more than two times and increased the shear forces encountered by the columns by four times.

The investigation concluded that the strengthening using X steel diagonal members postponed the performance limit values to high amplitude acceleration levels, significantly reduced column displacements and significantly increased the base shear force resisted by the building.

References

Ahiwale, D. D., Kontoni, D. P. N., & Darekar, P. L. (2023). Seismic performance assessment of reinforced concrete frames with different bracing systems. *Innovative Infrastructure Solutions, 8*(102), 1–18. https://doi.org/10.1007/s41062-023-01071-3

Alkhayyat, E., & Ozay, G. (2024). Retrofitting reinforced concrete buildings by using steel bracing. *Transactions of Civil and Environmental Engineering, 10*(2903), 1–12. https://doi.org/10.61186/crpase.10.29031

Beiraghi, H., Kheyroddi, A., & Nafechi, Z. F. (2022). Behavior of reinforced concrete frames retrofitted by different configurations of concentric steel braces. *Iranian Journal of Science and Technology, Transactions of Civil Engineering, 46*, 2039–2052. https://doi.org/10.1007/s40996-021-00799-1

Doğan, T. P., Kızılkula, T., Mohammadi, M., Erkan, İ. H., Tekeli Kabaş, H., & Arslan, M. H. (2021). A comparative study on the rapid seismic evaluation methods of reinforced concrete buildings. *International Journal of Disaster Risk Reduction, 56*, 102143, 1–17. https://doi.org/10.1016/j.ijdrr.2021.102143

FEMA (Federal Emergency Management Agency). (2000). *Hazus Earthquake Model Technical Manual*. Washington, D.C., USA. https://www.fema.gov/flood-maps/tools-resources/flood-map-products/hazus/user-technical-manuals (Access Date: 30 January 2025).

Günel, M. H., & Ilgin, H. E. (2007). A proposal for the classification of structural systems of tall buildings. *Building and Environment, 42*, 2667–2675. https://doi.org/10.1016/j.buildenv.2006.07.007

Hassan, Z. Q., & Al-Wazni, S. (2023). A review of retrofitting in the structural steel buildings using bracing systems. *IOP Conference Series: Earth and Environmental Science, 1232*(012031), 1–13. https://doi.org/10.1088/1755-1315/1232/1/012031

Karaşin, İ. B. (2023). *Design and a new wall model based on resistance to reinforced concrete separation using seismic fragility analysis* (Master's thesis, Dicle University, Diyarbakır).

Kirruti, P., & Balkıs, A. P. (2020). Seismic performance assessment of steel bracing systems in high-rise reinforced concrete structures. *Journal of Structural Engineering & Applied Mechanics, 3*(2), 110–126. https://doi.org/10.31462/jseam.2020.02110126

Mander, J. B., Priestley, M. J. N., & Park, R. (1988). Theoretical stress-strain model for confined concrete. *Journal of Structural Engineering, 114*(8), 1804–1826.

Menegotto, M., & Pinto, P. E. (1973). Method of analysis for cyclically loaded RC plane frames including changes in geometry and non-elastic behavior of elements under combined normal force and bending. In *Symposium on the Resistance and Ultimate Deformability of Structures Acted on by Well Defined Repeated Loads*, International Association for Bridge and Structural Engineering, Zurich, Switzerland, pp. 15–22.

Patil, S. P., & Angalekar, S. S. (2021). Seismic analysis of concrete structures with and without bracings. *International Research Journal of Engineering and Technology, 8*(8), 722–729.

Pohoryles, D. A., Bournas, D. A., Da Porto, F., Caprino, A., Santarsiero, G., & Triantafillou, T. (2022). Integrated seismic and energy retrofitting of existing buildings: A state-of-the-art review. *Journal of Building Engineering, 61*, 105274, 1–26. https://doi.org/10.1016/j.jobe.2022.105274

Prince, M. B., Mollah, N. I., Chowdhury, R. A., & Sen, D. (2023). Comparison of lateral behavior of an existing RC building under nonlinear static and incremental dynamic loads. *Asian Journal of Civil Engineering, 24*, 2155–2164. https://doi.org/10.1007/s42107-023-00632-2

Rizvan, M., Ahmed, N., & Khan, A. N. (2021). Seismic performance assessment of reinforced concrete moment resisting frame with low strength concrete. *Structures, 30*, 1140–1160. https://doi.org/10.1016/j.istruc.2020.10.038

Rodriguez, C. A., Rodriguez Perez, A. M., Lopez, R., & Caparros Mancera, J. J. (2024). Comparative analysis and evaluation of seismic response in structures: Perspectives from non-linear dynamic analysis to pushover analysis. *Applied Sciences, 14*(2504), 1–15. https://doi.org/10.3390/app14062504

Ruggieri, S., & Uva, G. (2020). Accounting for the spatial variability of seismic motion in the pushover analysis of regular and irregular RC buildings in the new Italian building code. *Buildings, 10*(177), 1–22. https://doi.org/10.3390/buildings10100177

Seismosoft. (2024). *SeismoStruct 2024 – A computer program for static and dynamic nonlinear analysis of framed structures*. Retrieved from https://seismosoft.com

Siddika, A., Al Mamun, A., Ferdous, W., & Alyousef, R. (2020). Performances, challenges and opportunities in strengthening reinforced concrete structures by using FRPs–A state-of-the-art review. *Engineering Failure Analysis, 111*, 104480, 1–29. https://doi.org/10.1016/j.engfailanal.2020.104480

Tam, G. (2024). *Evaluation of seismic behavior of reinforced concrete building reinforced with steel cross members* (Master's thesis, Munzur University, Tunceli).

Ueda, T., & Takewaka, K. (2007). Performance-based standard specifications for maintenance and repair of concrete structures in Japan. *Structural Engineering International, 17*, 359–366. https://doi.org/10.2749/101686607777723919

Verki, A. M., & Preciado, A. (2022). Nonlinear incremental dynamic analysis and fragility curves of tall steel buildings with buckling restrained braces and tuned mass dampers. *Earthquakes and Structures, 22*(2), 169–184. https://doi.org/10.12989/eas.2022.22.2.169

Villar-Salinas, S., Guzman, A., & Carrillo, J. (2020). Performance evaluation of structures with reinforced concrete columns retrofitted with steel jacketing. *Journal of Building Engineering, 33*(101510), 1–14. https://doi.org/10.1016/j.jobe.2020.101510

Yurdakul, Ö., Duran, B., Tunaboyu, O., & Avşar, Ö. (2021). Field reconnaissance on seismic performance of RC buildings after the January 24, 2020 Elazığ Sivrice earthquake. *Natural Hazards, 105*, 859–887. https://doi.org/10.1007/s11069-020-04340-x

4th International Civil Engineering & Architecture Conference
17-19 May 2025, Trabzon, Türkiye

Progressive Collapse and the Turkish Earthquake Code 2018: a review for precast industrial buildings

Samwel Amumpeire*[1], Aydın Demir[2]

[1] Sakarya University, Institute of Applied Sciences, 54050, Sakarya, Türkiye
[2] Sakarya University, Department of Civil Engineering, 54050, Sakarya, Türkiye

Abstract
Progressive collapse represents a severe structural safety issue, particularly for precast reinforced concrete industrial buildings in seismic zones. Observations from the 2023 Kahramanmaraş earthquakes revealed widespread damage with over 60% of Türkiye's precast industrial structures severely affected. This study provides a succinct review of progressive collapse mechanisms, design methodologies, and the relevant provisions of the Turkish Building Earthquake Code 2018 (TEC 2018). While TEC 2018 emphasizes seismic resilience of the structure through ductility and joint integrity, it lacks explicit guidance on progressive collapse mitigation for precast RC buildings. Drawing from international standards, the review identifies significant gaps in the code and highlights advanced design approaches, including Alternate Path and Enhanced Local Resistance methods. The findings emphasize the need for integrated strategies combining seismic and progressive collapse design to ensure structural safety under multi-hazard scenarios. The study proposes a unified framework for updating TEC 2018, informed by recent case studies and international best practices. These recommendations aim to enhance the resilience of Türkiye's industrial infrastructure, mitigating future risks and fostering sustainable development.

Keywords: Progressive collapse; Turkish Earthquake Code; Precast concrete; Industrial buildings; Structural resilience.

1. Introduction

Progressive collapse, such a catastrophic chain reaction that is initiated by a localized structural element's failure, has been a topic of growing concern following serious events such as that of the Ronan Point Apartment, Fig. 1(a), collapse in 1968, the terrorist attack on the World Trade Center in 2001, and the bombing of Alfred P. Murrah – Federal Building, Fig. 1 (b**)**, in 1995. These incidents underscored the disproportionate outcomes of minor failures in structural elements, particularly in precast reinforced concrete systems that rely extensively on the joint integrity and modular connections. Precast RC buildings are considered a preferred choice for industrial applications in Türkiye due to their rapid and construction-effectiveness (Demir & Sezen, 2024). However, their modular nature introduces unique vulnerabilities, particularly under abnormal loading scenarios such as explosions, impacts, and seismic events (Ghaderi et al., 2020; Z. Xu & Huang, 2024).

Progressive collapse can be briefly defined as a situation where the local failure of a key structural element leads to a series of cascading failures, consequently resulting in the collapse of an entire building or a large portion of it (GSA, 2016; UFC 4-023-03, 2009). The UFC (2009) code based on ASCE 7-05 code of practice, further highlights progressive collapse as "the expansion of initial local collapse from an element into another element of the structure which eventually leads to the entire or part of it in a disproportionate way." (UFC 4-023-03, 2009).

In Türkiye, the February 2023 earthquakes devastated the industrial zones, revealing systematic weaknesses in the application of the Turkish Building Earthquake Code (TEC) 2018 to precast reinforced concrete systems. These events demonstrated the need for robust design strategies not only to mitigate the seismic actions but also progressive collapses that might arise in multi-hazard situations. According to a seismic performance study on industrial buildings by Demir & Sezen (2024) following the 2023 Kahramanmaraş Türkiye earthquakes, it is indicated that the highest levels of damage and collapses were reported in precast RC buildings (Demir & Sezen, 2024). Although these buildings were designed as per the seismic code requirements, Xu et al. (2024), highlight that whereas the traditional aseismic and seismic designs focus at enhancing a structure's strength and deformability, allowing a structure to absorb and dissipate part of seismic or impact energy mainly through plastic deformation, their suitability in multi-hazard scenarios is not certain (G. Xu et al., 2024).

*Corresponding author, E-mail: samwel.amumpeire@ogr.sakarya.edu.tr

https://doi.org/10.31462/icearc2025_ce_eqe_863

This means that, if there is no explicit consideration for progressive collapse design, the structures' integrity in such extreme situations remain unpredictable. The latest Turkish Building Earthquake Code, TEC 2018, provide comprehensive design specifications for ductility and deformability in reinforced concrete and precast structures. However, there is not a single specific guideline/ specification provided by this code of practice regarding the explicit design for extreme instances of progressive collapse (Demir, 2022). The code emphasizes the integrity of joints, including the beam-to-column, and column-to-foundation connections. These joint specifications are undoubtedly critical for seismic performance response and can indirectly influence the progressive collapse resistance of a structure. On contrary, with no clear specification and guideline, the performance of these joints in arresting progressive collapse cannot be guaranteed.

In fact, most codes of practice including the Turkish Building Earthquake Code 2018, do not have provisions explicitly considering the design and mitigation criteria for progressive collapse. Only a few like the BS EN 1991-1-7 do highlight some design philosophies that indirectly might mitigate disproportionate collapses by consideration of extra lateral and vertical reinforcing ties. However, the US Department of Defense (DoD)'s GSA(GSA, 2016) and UFC(UFC 4-023-03, 2009) codes have published analysis guidelines with an attempt at addressing the progressive collapses in buildings. The analysis philosophies in the UFC (Unified Facilities Criteria) 4-023-03, include entirely three methods; Tie forces, Alternate path, and Enhanced local resistance methods.

It is however worth noting that the American code of practice, ASCE 7-05,(ASCE, 2006) which also provides guidelines for designing against progressive collapse, encompasses only two general approaches: Direct, and indirect approaches. The direct design approach explicitly considers the building's resistance to progressive collapse during the design stages. This strategy combines the alternate path method (AP) and the Enhanced local resistance (ELR) methods. Whereas the direct design approach achieves the resistance to progressive collapse implicitly through regulation of least levels of resistance, continuity and ductility in frames play a critical role (Delfian & Hassanipour, 2020).

The alternate path (AP) method of progressive analysis stands out to be the commonly employed practice. This is evidenced by its adoption by both the GSA and UFC codes of practice. However, in this analysis technique only single critical element failure is investigated one at a time. Yet, questions continue to arise about the effectiveness of the approach in addressing the far extreme failure scenarios of multi-column failures in a structure, more so its adaptability to precast modular systems.

Fig. 1. Some of critical progressive collapse instances: a) Ronan Point apartment (Juinio, 2018), b) Alfred P. Murrah (FBI, 1995).

Moreover, precast systems in Türkiye are particularly attractive due to their rapid assembly and cost-efficiency yet their performance under multi-hazard scenarios such as seismic and progressive collapse risks, remain a significant concern (Demir & Sezen, 2024). By critically analyzing both local and international design practices, this review seeks to offer a concise understanding of progressive collapse in precast reinforced concrete industrial buildings. Drawing from the recent studies and real-world implementations of the Turkish Building Earthquake

Code (TEC) 2018, the paper provides a succinct overview of the vulnerabilities and mitigation techniques for such structures. It aims to relay future directions for enhancing structural resilience in seismically vulnerable areas by synthesizing current research and recent case studies.

1.1. Mechanisms of progressive collapse

Whereas the continuous disproportionate collapse of a building is generally referred to as progressive collapse, it is important to note that there are differing mechanisms through which this disproportion does occur. The typology of progressive collapse was first brought to attention by Starossek back in 2007 (Starossek, 2007). According to Starossek, in order to lessen the progressive collapse analysis and its related prevention design, it is of great need to first understand the underlying mechanisms through which the catastrophe happens. Thus, the author did summarize these collapse mechanisms into six groupings that is; Pancake-type, Zipper-type, Domino-type, Instability-type, and the Mixed-type as further discussed. All these mechanisms are identified and characterized by features with which they occur.

1.1.1. Pancake-type collapse

Pancake-type collapse, Fig. *2*(a)**,** is one of the most catastrophic forms of structural failure that is characterized by a sequential and vertical progression of collapse. It begins with the failure of critical vertical load-bearing elements such as columns or walls, often triggered by localized damages like fires, impact, or explosions. Then upper sections of the structure then lose support and fall onto the lower sections, converting all the potential energy to kinetic energy. The resulting impact then creates extreme forces far exceeding the structural reserve capacity of the lower levels which results in their collapse. The process continues until the entire structure is compromised with gravity acting as the driving force. A famous example of pancake-type collapse is the collapse of The World Trade Center Towers, where the weight and velocity of falling debris caused catastrophic failure of successive floors (Starossek, 2007).

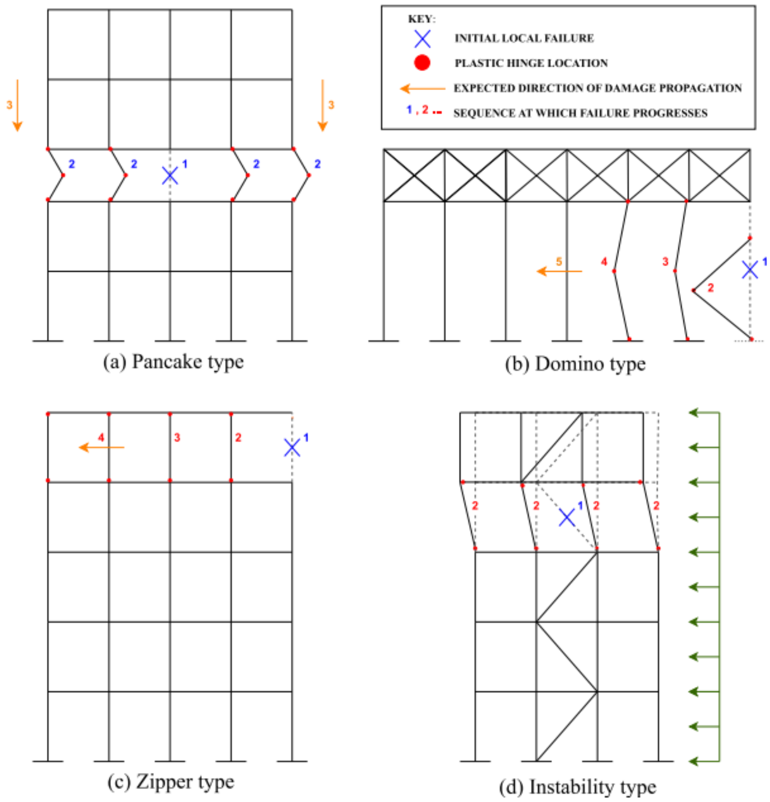

Fig. 2. Different progressive collapse mechanisms (Elkady et al., 2024)

1.1.2. Zipper-type collapse

Except for the initial failure of tension elements, the zipper-type collapse mechanism, Fig. *2*(c), is unconstrained. It is one of the common types of collapse because it can occur in almost any structural arrangement. Zipper-type collapse is usually distinguished by force redistribution into alternate paths, impulsive loading caused by sudden element failure, and static and dynamic force concentration in elements that will fail next. The propagating action caused by the failure of one element is the inverse of the force present prior to failure, acting as an impulsive loading at the point of failure. Unlike the pancake-type, impact forces are rarely encountered (Starossek, 2007).

1.1.3. Instability collapse

Instability-type of collapse mechanism, Fig. *2*(d), arises from the failure of stabilizing elements, leading to instability in load-carrying members. It starts with the loss of bracing or stiffening components, which destabilizes the primary members during compression. Small perturbations such as minor loads or imperfections, can cause destabilized members to collapse. Unlike other collapse mechanisms, instability-type does not always result in a cascading failure. However, in some cases, losing a single critical member, such as a truss leg, can cause immediate global collapse. Truss towers and pipelines are two examples where the failure of bracing elements may result in buckling or large deformations in the main structure. This form of collapse mechanism emphasizes the importance of maintaining stability through proper bracing and stiffness.

1.1.4. Section-type collapse mechanism

Section-type collapse occurs within the cross-section of structural elements such as beams or columns, and is characterized by progressive failure though stress redistribution. When a portion of a cross-section fails, the remaining section experiences an increase in stress which may exceed its reserve capacity, causing further rupture. This process continues until the entire cross-section is compromised. Section-type of collapse is analogous to zipper-type but confined to the scale of a single element. Examples include; weld or splice failures in steel or reinforced concrete components, where localized damage propagates through the section. This mechanism of collapse underscores the importance of uniform stress distribution and robust detailing to prevent localized weaknesses that might otherwise trigger a chain reaction of failure.

1.1.5. Domino-type mechanism

Domino-type of collapse, Fig. *2*(b), occurs when structural elements overturn sequentially, resembling the fall of a row of dominos. This mechanism commences with the overturning of one element, often triggered by horizontal forces such as winds, impact or an explosion. The falling element then strikes an adjacent component, transferring the horizontal forces that may cause it to overturn as well. This sequence continues, propagating a collapse horizontally through the structure. Domino-type collapse is extremely dynamic, this means that it involves the conversion of potential energy into kinetic energy, which magnifies the impact forces. An example of this mode of collapse is the cascading failure of overhead transmission towers, where the tension in connecting cables transmits forces that lead to the sequential toppling of towers. This type of collapse highlights the critical importance of lateral stability and robust connections between structural elements.

1.1.6. Mixed-type collapse

This type of collapse combines the features of multiple collapse mechanisms, creating a system of complex and unpredictable progression patterns. This mechanism often arises in real-world scenarios where structural systems have diverse load paths and interconnected components. For instance, a structure may exhibit features of pancake-type collapse such as vertical progression, alongside domino-type characteristics such as horizontal propagation through horizontal forces. Mixed-type collapse is indeed challenging to analyze due to the interplay of various forces and failure modes. An example is the Murrah Federal Building collapse, Fig. 1(b), where both vertical and horizontal forces contributed to the progressive failure. Mixed-type collapse underscores the need for comprehensive design approaches that account for multiple potential failure modes and their interactions.

1.2. Design philosophies of progressive collapse

Progressive collapse resistance involves designing structures capable of withstanding localized failures without undergoing catastrophic chain reactions. Since progressive failure mechanisms have catastrophic implications, design philosophies for progressive collapse resistance are a focal point of structural engineering research and practice. These philosophies have evolved over the years, shaped by incidents like the Ronan Point collapse (1968) and the World Trade Center attacks (2001).

The Unified Facilities Criteria code (UFC 4-023-03, 2009), alongside other guidelines like the U.S. General Services Administration code (GSA, 2016), provides detailed design philosophies and methodologies aimed at achieving this resilience. The integration of robust alternate path analysis, material optimization, and advanced performance-based methods continue to shape the field, ensuring resilient structural systems in the face of unforeseen disasters. These philosophies are central to structural engineering for mitigating progressive collapse occurrences. Some of the common and emerging progressive collapse resistance design philosophies include;

1.2.1. Alternate path approach

The alternate path method (AP) emphasizes structural redundancy, enabling load redistribution when a critical element is lost. This philosophy is widely applied in modern codes, including UFC 4-023-03 and GSA 2016. The approach involves simulating column removal scenarios, Fig. 4 to evaluate a structure's ability to form alternate load paths. Alternate path method ensures a robust load redistribution mechanism, preventing localized damage from escalating into global failure. In this philosophy, nonlinear dynamic analysis is commonly employed to test alternate path capacities. Several studies show that ductility and connection integrity are important factors that influence alternate path formation (Singh & Mohit Bhandari, 2024).

1.2.2. Enhanced local resistance approach

The enhanced local resistance (ELR) or specific local resistance approach (SLR), focuses at enhancing the resilience of critical elements to prevent initial failure. The UFC 4-023-03 code of practice, specifies reinforcement and detailing requirements for structural components prone to progressive collapse. This philosophy ensures components, such as columns and joints, are overdesigned to withstand abnormal loads. According to a number of studies, materials such as fiber-reinforced polymers (FRP) and high-strength steels are increasingly being used to improve component capacities (Kiakojouri et al., 2022). Furthermore, the numerical studies emphasize that increasing reinforcements in joints regions do facilitate mitigation of the initial failures that could otherwise propagate progressive collapse of a structure (Elkady et al., 2024).

1.2.3. Tie force approach

The Tie Force Method (TF) ensures structural elements are interconnected to maintain integrity under abnormal loads. The UFC 4-023-03 code mandates horizontal and vertical ties to sustain residual capacity after localized failures as shown in Fig. 3. Tie force method relies on developing continuous tension and compression ties through the structure. Studies like those of (Kiakojouri et al., 2022), do highlight the effectiveness of the tie forces approach in arresting the progressive collapse propagation especially in precast concrete structures.

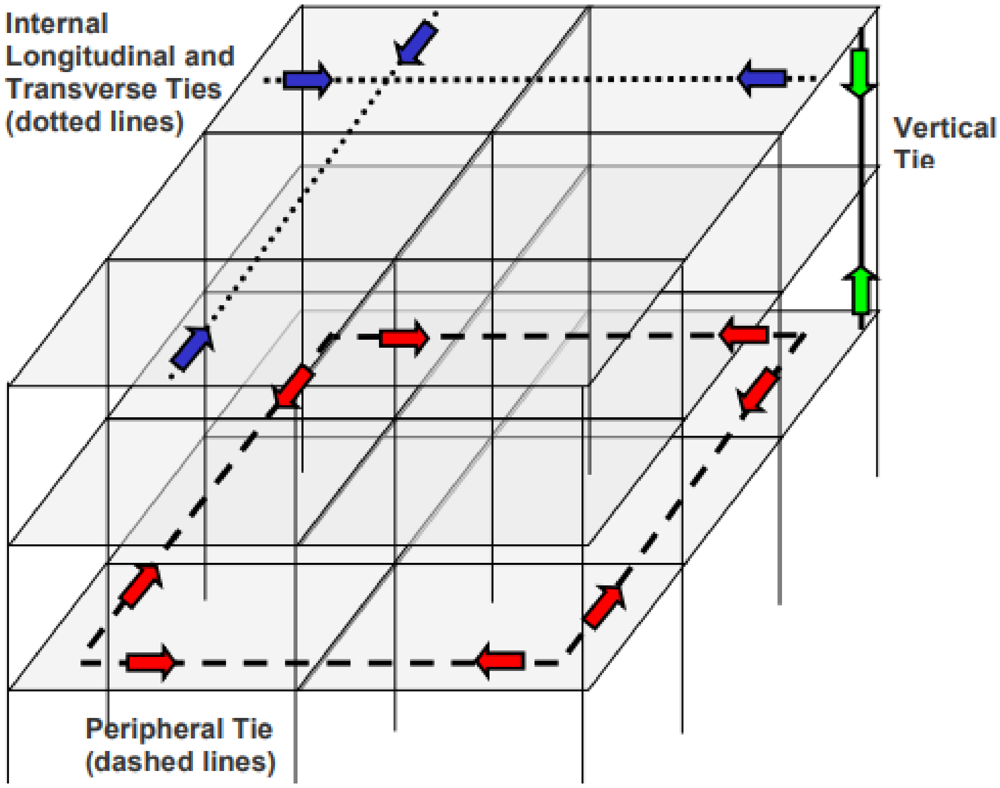

Fig. 3. Tie forces in a frame structure (UFC 4-023-03, 2009).

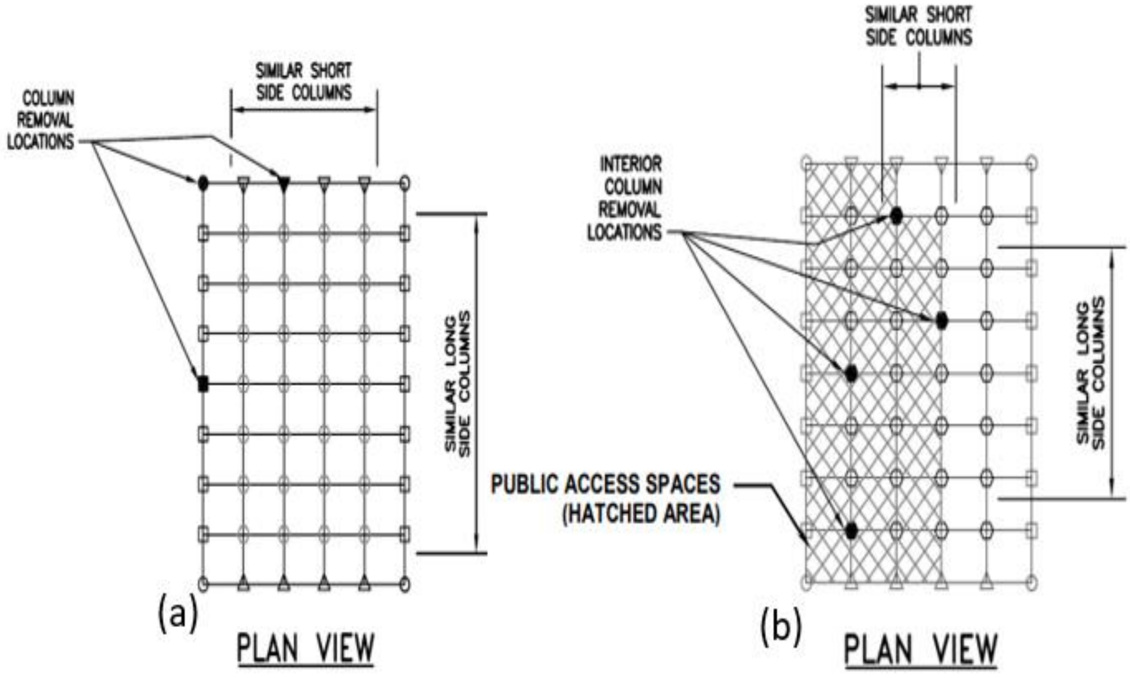

Fig. 4. Critical locations for column removal in AP approach (UFC 4-023-03, 2009).

1.2.4. The mixed design approaches

The Mixed Design Approach combines Alternate Path and Enhanced Load Resistance approaches to address both system-level and component-level vulnerabilities. The UFC 4-023-03 code, highlights the importance of this integrated strategy, particularly for large and complex structures. By addressing redundancy and local resistance simultaneously, the mixed approach ensures robust overall performance. Experimental observations indicate that that hybrid designs (such as those of prestressed joints combined with ductile reinforcements) out performs singular strategies (Singh & Mohit Bhandari, 2024).

1.2.5. Ductility-based design approach

The ductility-based designs aim to enable structures to undergo significant deformations without losing load-bearing capacity. The UFC 4-023-03's specifications emphasize ductility in beam-column joints which are critical for progressive collapse resistance. Studies indicate that connections with high ductility allow energy dissipation during extreme events. Moreover materials such as high-performance concrete (HPC) and shape memory alloys (SMAs) are being used to achieve high ductility in designs (Elkady et al., 2024). Additionally, the dynamic tests indicate that ductile designs significantly delay collapse onsets in structures (Singh & Mohit Bhandari, 2024).

2. The Turkish Earthquake Code (TEC) 2018 provisions for precast systems

The Turkish Earthquake Code (TEC, 2018), is a comprehensive guideline tailored for seismic resilience in building structures. Chapter 8 of this code specifically focuses on precast reinforced concrete (RC) buildings, addressing critical aspects like material properties, joint configurations, and diaphragm behaviors under seismic forces. While progressive collapse resistance isn't explicitly stated, many provisions in Chapter 8 indirectly may enhance a structure's capacity to prevent disproportionate failure after localized damage.

2.1. Precast RC structural elements and connections

The chapter begins with an overview of precast RC components and their connection requirements (section 8.2.1). Precast buildings are made up of factory-produced elements like beams, columns, walls, and slabs that are assembled on-site with mechanical or cast-in-place connections. The code explicitly highlights key provisions for two joint connections.

2.1.1. Moment resisting connections (MAB)

These connections are designed to transfer moments and exhibit ductile behavior under seismic and other extreme loads (Section 8.4.1). This ensures the structure retains its integrity during localized failures. The code specifies that these joints must sustain high moments without degradation ensuring stability under dynamic loads.

2.1.2. Pinned connections (MFB)

Primarily used in non-moment-resisting systems, pinned connections transfer axial and shear forces while minimizing rotations (Section 8.3.1). The friction forces at these connections are neglected, emphasizing the importance of mechanical stability. The shear capacity provided by the code for pinned connections is computed from the equation;

$$V_r = 0.7n\phi^2\sqrt{f_{cd}.f_{yd}} \quad (1)$$

Where V_r: shear capacity, n: number of joints, f_{cd}: compressive strength of concrete, f_{yd}: yield strength of pins, and ϕ: pin diameter.

The design emphasis on robust joint performance and load transfer mechanisms is essential for mitigating progressive collapse. The moment-resisting connections ensure that alternate load paths are maintained after an element failure, while the pinned connections provide stability against shear forces that could otherwise trigger disproportionate collapse.

2.2. Material specification

Section 8.2.3 of TEC 2018 defines the threshold material properties for precast elements and their connections. The C30 concrete quality class is mandated as the minimum grade, ensuring sufficient compressive strength to resist abnormal loads. Moreover, high-strength, non-shrinking grout (grout for connections) is required for joint connections. The code requires that the compressive strength of this grout be at least equal to that of the connected elements.

The code's specification for high-strength materials aims to reduce the risk of brittle failures, particularly at critical joints. By ensuring the grout's strength matches or exceeds that of the precast components, the code minimizes weak points that could compromise structural integrity during extreme events.

2.3. Ductility and redundancy requirements

The chapter emphasizes ductility in structural elements and connections, as describe in sections 8.2.2 and 8.4 of the code. The code highlights two possible ways on how ductility can be achieved in a structure: through detailing and redundancy.

2.3.1. Ductile detailing

The code specifies that columns, beams, and connections must be designed for high or limited ductility, depending on their roles in the structural system (Sections 7.3 and 7.7).

2.3.2. Redundancy

The code provision requires that behavior factors, denoted by (R), be assigned based on the ductility level and connection type to ensure sufficient redundancy in load distribution. Ductile detailing enables elements to deform without losing their load-bearing capacity. This is critical for maintaining alternate load paths after localized damage in a structure. Additionally, redundancy ensures that no single failure leads to a cascading collapse that might give rise to the collapse of the entire structure. The material behavioral factor, R, is generally given by an expression;

$$R = \frac{Q_u}{Q_d} \quad (2)$$

Where Q_u is the ultimate strength parameter, and Q_d is the design strength parameter.

Behavioral factor, R, ensures that structure has an adequate reserve capacity. Table 4.1 of TEC2018 provides a descriptive summary of these behavioral factors for easy application in analysis and design.

2.4. Dynamic and performance-based design

Section 8.2.2.3 of TEC2018 incorporates advanced performance-based analysis and design approaches;

2.4.1. Performance targets

The code requires that structures be evaluated for controlled damage under severe earthquakes (DD-1) and limited damage under moderate earthquakes (DD-3).

2.4.2. Nonlinear dynamic analysis

The code specifies this analysis requirement for critical components, considering load combinations beyond seismic forces.

Generally, the performance-based design evaluates structures for failure scenarios like column removal, aligning with global collapse mitigation standards.

2.5. Diaphragm and load transfer provisions

Section 8.6 of the TEC 2018 provides specific requirements for diaphragms in precast systems. These diaphragms are broadly discussed as composite and reinforcement diaphragms.

2.5.1. Composite diaphragms

The code describes these diaphragms as those that constitute of floor and roof, and must integrate precast and cast-in-place elements to ensure effective lateral force transfer.

2.5.2. Reinforcements

The code provides a specification that requires that, reinforcement ratios be such that they prevent separation or failure under seismic forces. By this specification, the code aims at emphasizing a rigid diaphragm that holds together all the frame elements they by enhancing the frame rigidity and collapse resistance. The general diaphragm shearing force is provided by a relation;

$$V_d = A_s . f_y \tag{3}$$

Where V_d denotes diaphragm shearing forces, A_s denotes the reinforcement area, and f_y denotes the yield strength of the reinforcements.

It is worthy to note that, well-designed diaphragms ensure strong connectivity between structural elements. This is a key factor in redistributing loads in cases of a primary element failure, a critical requirement for progressive collapse mitigation. Moreover, the integration of cast-in-place toppings improve the structural rigidity and continuity in precast structural systems.

3. The state of industrial infrastructure in Türkiye

The industrial infrastructure forms the backbone of the Türkiye's economic activities, encompassing manufacturing plants, warehouses, and logistical hubs. Precast concrete structures have increasingly gained prominence due to their efficiency, durability, and adaptability (Akduman et al., 2024; Arslan et al., 2024). These pre-fabricated systems align with the nation's rapid urbanization and industrialization goals. However, challenges such as seismic risks and adoption limitations continue to hinder their potential.

3.1. Overview of precast structures in Türkiye

Precast concrete structures are prefabricated components manufactured off-site and assembled on location, offering faster construction times and consistent quality. Türkiye has seen a consistent increase in the use of these systems, particularly in industrial projects, driven by their cost-effectiveness and resilience (Gumusburun Ayalp & Ay, 2021). Historical analysis highlights their evolution as a preferred choice for industrial facilities, especially in regions prone to rapid urbanization (Demir & Sezen, 2024). Despite their advantages, the adoption of precast concrete systems remain uneven across the country, often influenced by regional policies and economic factors.

3.2. Seismic resilience of precast structures

Seismic activity poses a significant challenge to Türkiye's industrial infrastructure. The devastating 2023 Kahramanmaraş earthquakes highlighted vulnerabilities in existing precast buildings. Studies reveal that industrial facilities with precast structural frameworks experienced varying levels of severe damage depending on design and construction quality (Arslan et al., 2024; Demir et al., 2024). Adopting advanced materials such as fiber-reinforced concrete and improving connection technologies are among the tremendous efforts that need to be made to improve the seismic performance of precast structures. Additionally, collaborative efforts between academia and industry continue to propose innovative solutions to reduce these risks and ensure structural integrity under seismic loads (Akduman et al., 2024).

Moreover, during the Kahramanmaraş earthquakes, joint failures and inadequate roof connections were frequently observed as reported by field studies (Sagbas et al., 2024). These failures underscore the need for enhanced joint detailing and dynamic performance evaluations in these infrastructures.

3.3. Challenges in adoption of precast structures

The adoption of precast systems in Türkiye faces several barriers. A 2021 study identified key limiting factors, including lack of technical expertise, regulatory constraints, and high initial costs (Gumusburun Ayalp & Ay, 2021). According to the authors, these difficulties are exacerbated by perceptions that prefabrication is a low-quality option, despite evidence to the contrary. In fact, a survey conducted by the authors revealed that 65% of Turkish contractors cite high initial costs as the primary barrier to precast adoption.

However, Government support and strategic policy interventions could address these barriers. For instance, incentives for precast manufacturing facilities and standardized building codes could enhance adoption rates. The available comparative studies from neighboring countries already demonstrate the economic and operational benefits of such policies (Ogaili & Abdulrahman, 2022).

3.4. Innovations and future trends

The recent advancements in precast technology demonstrate a promising revolutionary in the industrial construction sector of Türkiye. The integration of geopolymer concrete, a sustainable alternative to traditional materials, offers environmental and performance advantages (Akduman et al., 2024). Moreso, the incorporation of automation in the prefabrication processes has greatly improved precision and reduced labor dependency (Batalha et al., 2019).

Additionally, the precast systems are also exponentially gaining traction in disaster-resilient construction. Modular designs and demountable systems are being tested for their adaptability to post-disaster scenarios, ensuring continuity of operations in industrial facilities (Sagbas et al., 2024). According to a study by Batalha et al., (2019), advanced automation in precast manufacturing revolutionizes the industry by reducing human error and improving precision. According to the author, robotic assembly techniques have been shown to reduce production times by 25% while ensuring consistent quality (Batalha et al., 2019). These innovations are in a sync with the Türkiye's broader goals for enhancing infrastructure resilience and sustainability.

It is thus critical to note that, Türkiye's industrial infrastructure, supported by precast structures, has enormous potential for modernization and growth. While challenges such as seismic vulnerabilities and adoption barriers persist, ongoing innovations and policy support can transform the sector. By addressing these issues, Türkiye can harness the full benefits of precast systems, ensuring sustainable and resilient industrial development.

4. Conclusion

Progressive collapse remains a critical yet under-addressed vulnerability in Türkiye's precast industrial buildings, as starkly revealed by the 2023 Kahramanmaraş earthquakes. While the Turkish Building Earthquake Code (TEC) 2018 provides robust guidelines for seismic resilience – emphasizing ductility, joint integrity, and material strength, it lacks explicit provisions for mitigating cascading failures triggered by abnormal loads. This gap leaves structures compliant with TEC 2018 susceptible to disproportionate collapse, particularly in multi-hazard scenarios.

Key findings from this review highlight the unique risks posed by precast modular systems, such as their reliance on joint performance and susceptibility to pancake or zipper type collapse mechanisms. Although TEC 2018's focus on redundancy and dynamic analysis indirectly supports progressive collapse resistance, its omission of internationally recognized strategies like the Alternate Path (AP) method or Enhanced Local Resistance (ELR) approaches limits its applicability. Case studies from U.S. standards (UFC 4-023-03, GSA 2016) demonstrate that the hybrid design philosophies – integrating ductility, advanced materials (e.g., fiber-reinforced polymers), and performance-based analysis can significantly enhance resilience.

The implications of these findings are twofold. Theoretically, this work bridges the divide between seismic and progressive collapse engineering, advocating for multi-hazard design frameworks. Practically, updating TEC 2018 to address cascading failures could safeguard Türkiye's industrial infrastructure, reducing economic and human losses in future disasters. However, this study is limited by its reliance on post-earthquake observational data rather than experimental validation, and it does not fully address regional challenges such as barriers or uneven technical expertise in adopting advanced precast systems. To address these gaps and advance the field, the following recommendations are proposed:

- Revise TEC 2018 to incorporate progressive collapse mitigation strategies, including AP and ELR methodologies, with localized adaptations for Türkiye's industrial building typologies.
- Promote hybrid systems combining geopolymer concrete, demountable connections, and automation to enhance sustainability and multi-hazard resilience.
- Invest in empirical research, including large-scale testing of precast joints under combined seismic and abnormal loads, to refine performance-based design criteria.

Conclusively, as Türkiye continues to industrialize, harmonizing seismic and progressive collapse design principles is no longer optional, it is a societal imperative. By integrating global best practices and fostering innovation in modular construction, Türkiye can transform its industrial infrastructure into a model of resilience, ensuring that future seismic events become catalysts for advancement rather than catastrophe.

Acknowledgements

The authors would wish to acknowledge the guidance from the institute of Natural Sciences, Sakarya University, during the preparation stage of this manuscript.

References

Akduman, S., Aktepe, R., Aldemir, A., Ozcelikci, E., Alam, B., & Sahmaran, M. (2024). Opportunities and challenges in constructing a demountable precast building using C&D waste-based geopolymer concrete: A case study in Türkiye. *Journal of Cleaner Production, 434*, 139976.

Arslan, M. H., Dere, Y., Ecemiş, A. S., Doğan, G., Özturk, M., & Korkmaz, S. Z. (2024). Code-based damage assessment of existing precast industrial buildings following the February 6th, 2023 Kahramanmaraş earthquakes (Pazarcık Mw 7.7 and Elbistan Mw7.6). *Journal of Building Engineering, 86*, 108811.

ASCE. (2006). *Minimum Design Loads for Buildings and Other Structures (ASCE Standard ISBN 0-7844-083 1-9)*. American Society of Civil Engineering.

Batalha, N., Rodrigues, H., & Varum, H. (2019). Seismic performance of RC precast industrial buildings—Learning with the past earthquakes. *Innovative Infrastructure Solutions, 4*(1), 4.

Delfian, J., & Hassanipour, A. (2020). A Review on Progressive Collapse Designing Based on UFC Regulation. *Journal of Building Material Science, 1*(2), 9–15.

Demir, A. (2022). Progressive collapse resistance of low and mid-rise RC mercantile buildings subjected to a column failure. *Structural Engineering and Mechanics, 83*(4), 563–576.

Demir, A., Celebi, E., Ozturk, H., Ozcan, Z., Ozocak, A., Bol, E., Sert, S., Sahin, F. Z., Arslan, E., Dere Yaman, Z., Utkucu, M., & Mert, N. (2024). Destructive impact of successive high magnitude earthquakes occurred in Türkiye's Kahramanmaraş on February 6, 2023. *Bulletin of Earthquake Engineering*.

Demir, A., & Sezen, H. (2024). Seismic Performance of Industrial Buildings During the 2023 Kahramanmaras, Turkey Earthquakes. *Journal of Earthquake Engineering*, 1–15.

Elkady, N., Augusthus Nelson, L., Weekes, L., Makoond, N., & Buitrago, M. (2024). Progressive collapse: Past, present, future and beyond. *Structures, 62*, 106131.

FBI. (1995). *Oklahoma City Bombing [Page]*. Federal Bureau of Investigation. https://www.fbi.gov/history/famous-cases/oklahoma-city-bombing

Ghaderi, P., Ferreira, D., Cavaco, E., & Lúcio, V. (2020). Progressive Collapse Prevention Design of Framed RC Structures-Cost–Benefit Analysis. *Journal of Failure Analysis and Prevention, 20*(4), 1244–1257.

GSA. (2016). *Alternate Path Analysis & Design Guidelines For Progressive Collapse Resistance (Standard Code of Practice Revision 1, Jan 28 2016)*. General Services Administration. https://www.gsa.gov/cdnstatic/Progressive_Collapse_2016.pdf

Gumusburun Ayalp, G., & Ay, I. (2021). Model validation of factors limiting the use of prefabricated construction systems in Turkey. *Engineering, Construction and Architectural Management, 28*(9), 2610–2636.

Juinio, M. (2018). *Progressive Collapse of Structures [Blog]*. BSBG Media. https://bsbgroup.com/blog/progressive-collapse-of-structures

Kiakojouri, F., De Biagi, V., Chiaia, B., & Sheidaii, M. R. (2022). Strengthening and retrofitting techniques to mitigate progressive collapse: A critical review and future research agenda. *Engineering Structures, 262*, 114274.

Ogaili, A., & Abdulrahman, S. M. (2022). The impacts of project management and government support on project's economy: A comparative study of precast concrete factories in Iraq [Thesis, YÖK Ulusal Tez Merkezi - İstanbul Gelişim Üniversitesi]. *Yüksek Lisans Tezleri*. https://hdl.handle.net/11363/3689

Sagbas, G., Sheikhi, R., Sarıkaya, K., & Deniz, D. (2024). Field Observations for Industrial Buildings After 2023 Kahramanmaras Earthquakes. In E. Uckan, H. Akgun, E. Gok, & C. Yenidogan (Eds.), *Proceedings of the 7th International Conference on Earthquake Engineering and Seismology* (Vol. 488, pp. 147–156). Springer Nature Switzerland.

Singh, H., & Bhandari, M. (2024). A contemporary review on progressive collapse. *IOP Conference Series: Earth and Environmental Science, 1326*(1), 012027.

Starossek, U. (2007). Typology of progressive collapse. *Engineering Structures, 29*(9), 2302–2307.

TEC. (2018). *Turkish Building Earthquake Code*. Turkish Ministry of Public Works and Housing. http://www.resmigazete.gov.tr/eskiler/2018/03/20180318M1-2-1.pdf

UFC 4-023-03. (2009). *Unified Facilities Criteria: Design of Buildings to Resist Progressive Collapse (Version change 4, 10 June 2024)* [Standard]. U.S. Department of Defence. https://www.wbdg.org/FFC/DOD/UFC/ufc_4_023_03_2009_c4.pdf

Xu, G., Guo, T., Li, A., Zhang, H., Wang, K., Xu, J., & Dang, L. (2024). Seismic resilience enhancement for building structures: A comprehensive review and outlook. *Structures, 59*, 105738.

Xu, Z., & Huang, Y. (2024). Finite element analysis of progressive collapse resistance of precast concrete frame beam-column substructures with UHPC connections. *Journal of Building Engineering, 82*, 108338.

4th International Civil Engineering & Architecture Conference
17-19 May 2025, Trabzon, Türkiye

Seismic performance assessment of a fire-damaged reinforced concrete building according to TBDY-2018

Mert Hacıemiroğlu*[1], Metin Aydoğan[2], Cenk Alhan[3]

[1] Founder, SISDEC CO. LTD. , 34829 Istanbul, Türkiye
[2] Istanbul Technical University, Department of Civil Engineering, 34469 Istanbul, Türkiye
[3] Istanbul University-Cerrahpaşa, Department of Civil Engineering, 34320 Istanbul, Türkiye

Abstract: Fires are catastrophic events that can severely degrade the seismic performance of buildings. High temperatures weaken concrete and steel, reducing their strength. This can lead to premature collapse and increased damage during earthquakes. The duration of the fire, the temperature reached, and the extent of structural damage all influence the seismic performance negatively. Ignoring the fire effects in seismic assessment can severely underestimate the risk and thus jeopardize safety. Unfortunately, some fire-damaged reinforced concrete buildings continue their service life without any repair or strengthening intervention. On the other hand, it is possible for reinforced concrete buildings to be reused safely if properly repaired or strengthened following a fire. Thus, accurate assessment of fire-damaged buildings is crucial to determine their remaining capacity and identify the need for strengthening or demolition. In this study, the seismic performance of a benchmark reinforced concrete building exposed to fire is examined according to the TBDY-2018, Turkish Building Earthquake Code, considering its nonlinear behavior. For this purpose, the structure is modeled considering the parameters defining the relationship of the material with temperature mentioned in TS EN-1992-1-2, structural fire design code, and using the temperature-time curve given in ISO-834, fire resistance tests code. The occurrence of fire on ground floor was considered and nonlinear static pushover analyses were performed considering the capacity losses of the structural elements under the influence of a typical 120 minute duration. The results of the seismic performance assessment are presented in comparison with the building condition that is not exposed to fire.

Keywords: Reinforced concrete building, Fire, Nonlinear structural analysis, Seismic performance assessment

---

1. Introduction

Reinforced concrete structures, like all other building types, have the potential to cause significant loss of life and property in the event of disasters if adequate fire safety precautions are not taken. Compared to the earthquake disaster, the phenomenon of fire is considered to have a higher probability of occurrence than earthquakes in terms of frequency. This is because the timing, intensity, and recurrence intervals of earthquakes, which are natural events, are less predictable compared to fires. In developed countries, the fire resistance of structures is mandated through building codes, similar to seismic resistance. This approach is considered an integral part of structural safety. Notably, in the aftermath of fires occurring in residential buildings, sometimes damaged structural elements are continued to be used without employing any repair or strengthening procedures. Such structural deficiencies can negatively impact the performance these buildings would exhibit during an earthquake.

Reinforced concrete structures demonstrate superior performance against fire compared to steel structures. The duration of this resistance, assuming the concrete has been properly cast, is directly related to the concrete cover thickness over the reinforcement. The primary reason for this is that steel material experiences sudden and significant losses in strength at critical temperatures. In this context, having sufficient concrete cover is critically important for assuring the fire safety of reinforced concrete structures. The methodology in this study is mainly adopted from Hacıemiroğlu (2014) with the primary exception that the seismic performance evaluations are made according to the current seismic building code, namely Turkish Building Earthquake Code, TBDY (2018).

* Corresponding author, E-mail: mhaciemiroglu@sisdec.com.tr

https://doi.org/10.31462/icearc2025_ce_eqe_867

2. Structural Modelling

2.1. Building geometry

In this study, a fire model for a structure (Figure 1) is developed, featuring four bays in both directions (6 meters between each axis) and a storey height of 4 meters. In this model, assuming a 120-minute fire occurred on the ground floor, the strength losses in the cross-sections were determined using the finite element method. The structure has a symmetric configuration with respect to both the X and Y axes. The column and beam elements have the same dimensions on each floor; the column dimensions are set as 50 cm x 50 cm and the beam dimensions as 40 cm x 50 cm. The concrete class is C25 (f_{ck}=25 MPa) and reinforcement steel class is S420b.

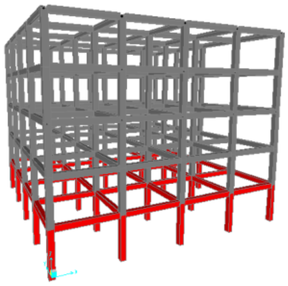

Fig. 1. 3D view of the benchmark building with ground floor affected by fire.

2.2. Fire scenario

The structural design of the existing building was performed assuming a concrete cover thickness of 2 cm for columns and beams. The seismic performance of the existing condition was compared with the seismic performance after a 120-minute fire resistance period. Nonlinear static pushover analyses were employed. The details regarding the scenarios considered are provided in Table 1.

Table 1. Details of the fire scenarios

Scenario#	Scenario Name	Fire Effect #	Cover for Column	Cover for Beam	Fire Duration (min)
1	With Fire	Ground Floor	2 cm	2 cm	120
2	Without Fire	-	2 cm	2 cm	-

2.3. Earthquake design parameters

The earthquake design parameters used in the design of the structural system designed according to TBDY-2018 are given in Table 2 where DD2 is the 475 year return period design earthquake level and F_s and F_1 are the soil influence parameters for local soil class ZC.

Table 2. Earthquake design parameters of the benchmark building

Building Use Class (BKS)	BKS = 3 – TBDY-2018, Table 3.1
Building Importance Factor (I)	I = 1.00 – TBDY-2018, Table 3.1
Spectral Acceleration Coefficients for DD2	$S_s = 1.223$ and $S_1 = 0.337$
Design Spectral Acceleration Coefficients for DD2	$S_{DS} = S_s \times F_s = 1.223 \times 1.2 = 1.468$ $S_{D1} = S_1 \times F_1 = 0.337 \times 1.5 = 0.506$
Earthquake Design Class (DTS)	for $S_{DS} = 1.468 > 0.75$ and BKS = 3 DTS = 1 – TBDY-2018, Table 3.2
Building Height Class (BYS)	for 17.5m < $H_N \leq 28$ m and DTS=1 BYS = 5 – TBDY-2018, Table 3.3

2.4. Loading details

The load per unit area of the external walls (20 cm thick and plastered) is calculated as 3.8 kN/m². This value for the internal walls (10 cm thick and plastered) is 2.5 kN/m². The additional load created by the plaster and coating layers on the surface of the structure is calculated as 1.5 kN/m². The live load is assumed as 5 kN/m² and the snow load that the structure may be exposed to is calculated as 0.75 kN/m². In addition to these loads, the self-loads from the self-weight of the elements are taken into account during the analysis. The reinforced concrete unit volume weight is accepted as ρ=25 kN/m³.

2.5. Change of material properties with high temperature

2.5.1. Change of concrete material properties with temperature
In order to reliably assess the behavior of structures under fire conditions, it is necessary to accurately determine the temperatures to which the constituent materials of structural elements are exposed during a fire and their material properties at these temperatures. Although concrete is classified as A1 class ('non-combustible') in terms of flammability, the high temperatures encountered during a fire and the duration of exposure to these temperatures may still cause significant changes in the mechanical, physical, and thermophysical properties of concrete. These effects become particularly pronounced at temperatures of 600°C and above. Currently, the effect of high temperatures on the reduction in compressive strength of normal and high-strength concrete is included in standards covering structural fire design principles. In these standards, the stress-strain relationships, physical, and thermal properties of normal strength concrete under high temperatures are expressed with different values and empirical relationships depending on the type of aggregate used (Yüzer & Özçiftçi, 2006). Furthermore, it is stated that the thermal properties defined for normal strength concrete can also be used for high-strength concrete. These standards, available for use by designers, also provide temperature distributions (temperature profiles) within structural elements depending on the exposure temperature and duration (Bingöl & Gül, 2009).

2.5.2. Change in concrete stress-strain curve
The change in the concrete stress-strain curve with temperature must be known to determine the load-bearing capacity of a structure after fire exposure and its behavior during an earthquake. The strength and deformation properties of concrete subjected to uniaxial compression at high temperatures are given in EN 1992-1-2:2023 as the stress-strain relationship for concrete made with siliceous aggregate. The stress-strain relationship of concrete is expressed with two parameters: the compressive strength $f_{c,\theta}$ and the corresponding strain, $\varepsilon_{c1,\theta}$. Linear interpolation is applied for intermediate temperature values. The stress-strain relationship for concrete subjected to compression at high temperatures is given in EN 1992-1-2:2023, Table 5.1. In the internal regions of fire-damaged elements, where the temperature has not changed, the material properties of concrete at normal temperature (20 °C) are taken as the values given for normal temperature design in EN 1992-1-1, Eurocode 2: Design of concrete structures. The change in the modulus of elasticity of concrete with temperature is obtained using the relationships regarding the change in the modulus of elasticity of concrete with temperature provided in EN 1992-1-2 (Eren & Gençoğlu, 2012).

2.5.3. Change of reinforcement steel properties with temperature
As a result of a research study in which the yield strength of reinforcement steel was tested, the yield strength loss curve showing the temperature-dependent change in yield strength, along with the condition of uninsulated reinforcement used in the high-temperature test before being exposed to high temperatures, have been shared. It is observed in the study that the yield strength losses of the steel material start to decrease after 300 °C, and this decrease is much more rapid in the uninsulated specimen (Ünlüoğlu, Topçu & Yalaman, 2007). Within the scope of this study, while utilizing the test results, the strength of the reinforcement steel in a non-corroded state were taken into consideration. The reason for this is that when calculating the temperature reached by the reinforcement of column and beam elements subjected to section analysis, the extent to which the ambient temperature raised the temperature of the reinforcement within the section over time was calculated.

2.5.4. Change of mechanical properties of reinforcement steel with temperature
Reinforcement steel temperature has been assumed to be equal to the concrete temperature at the depth of the reinforcement. The temperature values of the flexural reinforcement and stirrup reinforcement were calculated separately depending on the concrete cover thickness and the duration of fire exposure. It can be assumed that the density of the reinforcement steel, ρ_s=7850 kg/m^3, does not change at high temperatures (EN 1992-1-2:2023). The coefficient of thermal expansion of steel, α_s, has been calculated according to the equations given in EN 1992-1-2:2023 (Öztürk & Yavuz, 1995). The high-temperature value for the parameters related to hot-rolled and cold-worked reinforcing steel is given in EN 1992-1-2:2023. Within the scope of this study, parameters for cold-worked steel, which is widely used in Turkey, are included. The high-temperature steel strength and deformation properties are given as stress-strain relationships in EN 1992-1-2:2023, Table 5.2 and Table 5.3. The strain corresponding to the proportional limit $f_{sp,\theta}$ is expressed as $\varepsilon_{sp,\theta}$, the strain corresponding to the maximum stress level $f_{sy,\theta}$ is expressed as $\varepsilon_{sy,\theta}$ and the slope of the linear elastic part is expressed as $E_{s,\theta}$.

3. Material properties after fire effect
The temperature values reached by each 1 cm layer of concrete cover from the outermost layer inwards for column and beam elements exposed to fire effect were calculated using the software SAFIR and DIAMOND. When creating the finite element model in SAFIR (Gernay & Franssen, 2011), silica aggregate concrete with a compressive strength of 25 MPa and 3% water content was used. The density of concrete at normal temperature

was taken as 2500 kg/m³. In Figure 2, images showing the fire direction and temperature distribution for the column and beam cross-sections used for thermal analysis are shared, along with images demonstrating the layer-by-layer cross-section definition in SAP2000 and XTRACT software.

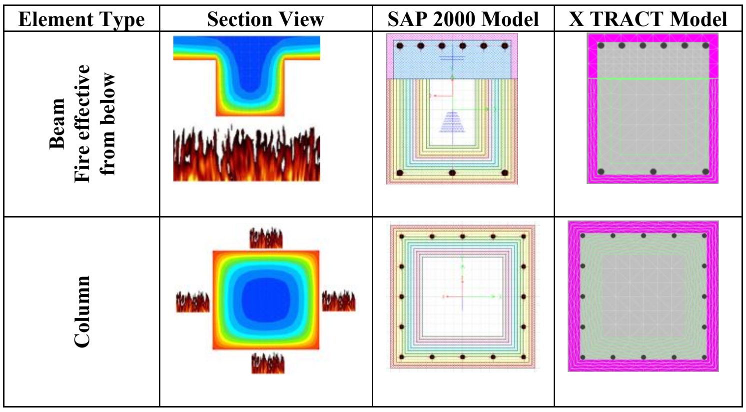

Fig. 2. Sample column and beam section fire model.

The column section with dimensions of 50 cm x 50 cm was defined in SAFIR with quarter symmetry. The time-dependent temperature change in the diagonal direction from the corner of the column is given in Figure 3.

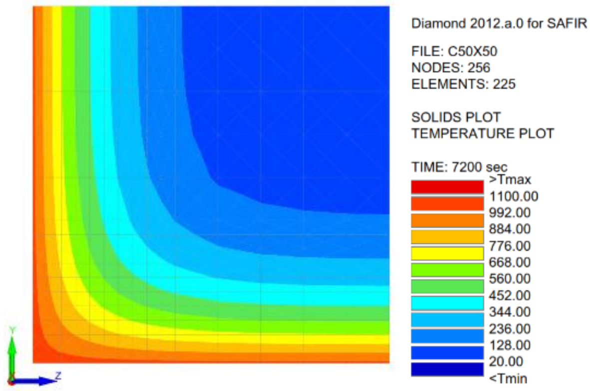

Fig. 3. Temperature change with time for a 50cm x 50cm column under fire effect for 120 minutes.

In order to calculate the confined concrete model of the elements exposed to fire, the concrete temperature was obtained from the outermost to the innermost. Depending on these temperature values, material properties were calculated for 1 cm layers. The values used for the columns are given in Tables 3 and 4.

Table 3. Temperature reached by each 1 cm concrete layer of a 50 cm x 50 cm column after a 120-minute fire and corresponding concrete mechanical properties.

Distance to Fire	Temperature		Siliceous Aggregates	Concrete Strength		Density	Modulus of Elasticity
(cm)	(°C)	$f_{c,\theta} / f_{ck}$	$\varepsilon_{c1,\theta}$	$\varepsilon_{cu1,\theta}$	$f_{c,\theta}$ (MPa)	ρ_c (kg/m^3)	E_c (MPa)
1	1048 °C	0.0256	0.0250	0.0462	0.64	2233	310
2	880 °C	0.0940	0.0250	0.0420	2.35	2270	620
3	668 °C	0.3480	0.0250	0.0367	8.70	2316	1984
4	542 °C	0.5370	0.0192	0.0336	13.43	2344	9796
5	500 °C	0.5985	0.0151	0.0325	14.96	2353	12400
6	415 °C	0.7275	0.0108	0.0304	18.19	2371	17670
7	352 °C	0.7980	0.0086	0.0288	19.95	2393	21576
8	289 °C	0.8610	0.0068	0.0272	21.53	2416	25482
9	225 °C	0.9250	0.0059	0.0256	23.13	2440	29450
10	36°C	1.0000	0.0028	0.0205	25.00	2500	31000

Table 4. Stress and strain parameters corresponding to the temperatures reached by the column stirrup and bending reinforcement steel.

Scenario	Cover	Reinforcement Type	Distance to Fire	Fire Duration	Tmp °C	$f_{sp,\theta}$ Mpa	$f_{sy,\theta}$ Mpa	$E_{s,\theta}$ Mpa	$\varepsilon_{sp,\theta}$	$\varepsilon_{sy,\theta}$	$\varepsilon_{st,\theta}$	$\varepsilon_{su,\theta}$
1	2 cm	Stirrup	2 cm	2 hours	668	44.2	128.9	37520	0.0012	0.02	0.05	0.10
1	2 cm	Longitudinal	3 cm	2 hours	542	119.4	272.9	95640	0.0012	0.02	0.05	0.10

The 40 cm x 50 cm beam cross-section was modeled in SAFIR together with a slab thickness of 15 cm. Figure 4 shows the time-dependent temperature change diagonally from the bottom corner of the beam. Beam elements are exposed to fire from the bottom according to the Scenario 1. The mechanical properties of the materials are given in Tables 5 and 6.

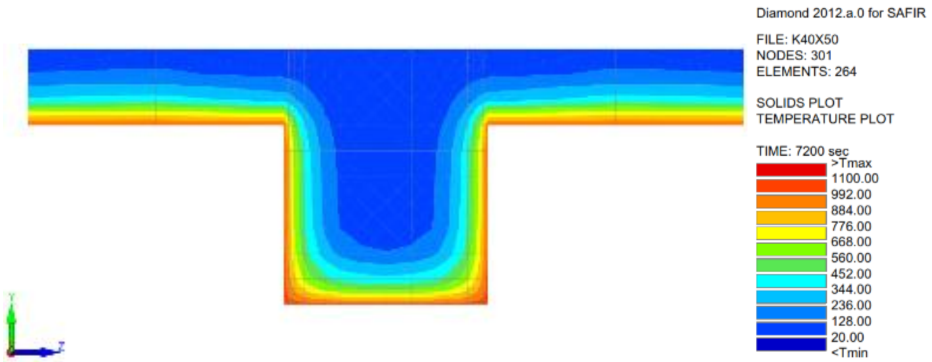

Fig. 4. Temperature change with time for a 40cm x 50cm beam for 120 minutes. Fire is affected from the bottom face only.

Table 5. Temperature reached by each 1 cm concrete layer of a 40cm x 50cm beam after a 120-minute fire and corresponding concrete mechanical properties. The fire is affected from the bottom face only.

Distance to Fire (cm)	Temperature (°C)	Siliceous Aggregates $f_{c,\theta}/f_{ck}$	$\varepsilon_{c1,\theta}$	$\varepsilon_{cu1,\theta}$	Concrete Strength $f_{c,\theta}$ (MPa)	Density ρ_c *(kg/m³)*	Modulus of Elasticity E_c (MPa)
1	1048 °C	0.0256	0.0250	0.0462	0.64	2233	310
2	877 °C	0.0961	0.0250	0.0419	2.40	2271	3875
3	706 °C	0.2910	0.0250	0.0377	7.28	2308	6076
4	536 °C	0.5460	0.0186	0.0334	13.65	2345	10168
5	451 °C	0.6735	0.0126	0.0313	16.84	2364	15438
6	365 °C	0.7850	0.0090	0.0291	19.63	2388	20770
7	365 °C	0.7850	0.0090	0.0291	19.63	2388	20770
8	280°C	0.8700	0.0067	0.0270	21.75	2420	26040
9	280°C	0.8700	0.0067	0.0270	21.75	2420	26040
10	110°C	0.9950	0.0042	0.0228	24.88	2500	31000

Table 6. Stress and strain parameters corresponding to the temperatures reached by the beam stirrup and bending reinforcement steel. Fire is affected from the lower face only.

Scenario	Cover	Reinforcement Type	Distance to Fire	Fire Duration	Temp	$f_{sp,\theta}$ Mpa	$f_{sy,\theta}$ Mpa	$E_{s,\theta}$ Mpa	$\varepsilon_{sp,\theta}$	$\varepsilon_{sy,\theta}$	$\varepsilon_{st,\theta}$	$\varepsilon_{su,\theta}$
1	2 cm	Stirrup	2 cm	2 hours	706	28.9	93.6	25520	0.0011	0.02	0.05	0.10
1	2 cm	Longitudinal	3 cm	2 hours	536	124.0	280.7	99120	0.0012	0.02	0.05	0.10

4. Analysis

XTRACT v3.0.8 software (Chadwell, 2002) was used to calculate the plastic hinge properties of columns and beams required for nonlinear static pushover analysis.

4.1. Column section analysis

In the existing structural system, all column sections contain 16Φ16 longitudinal reinforcement and Φ10/10/20 four-legged stirrups. The hooks of the stirrups are arranged with a 135° bend as special seismic stirrups defined in TBDY-2018. Therefore, confinement effect is present in the columns. For use in nonlinear elastic analyses, yield surfaces under biaxial bending and axial force effects for column sections were obtained using XTRACT . After obtaining the yield surfaces for the columns, these values were defined in the axial load and biaxial bending hinges created in SAP2000 where, the yield surfaces were defined at 0 and 45 degree angles; 0 and 90 degrees are symmetrical. When assigning hinge properties in SAP2000, the axial load-moment interaction surfaces were defined as convex. After obtaining the yield surfaces for the columns, the demands obtained from the nonlinear analyses were compared with the strain capacities provided for each damage limit. Axial load-curvature diagrams were created to determine the performance of the structural system at the cross-sectional level. Using the considered strain capacities, axial force – total curvature diagrams were generated. The plastic hinge lengths of the columns were used in the analyses as half of the section depth in the direction of action, as defined in TBDY-2018. The plastic hinges were defined at the ends of the clear spans of the columns. The sample compressive strength – strain diagrams under different temperature effects for the confined and unconfined concrete models used in the column section analyses are presented in Figure 5. The plot showing the change in reinforcement steel property with temperature is given in Fig. 6.

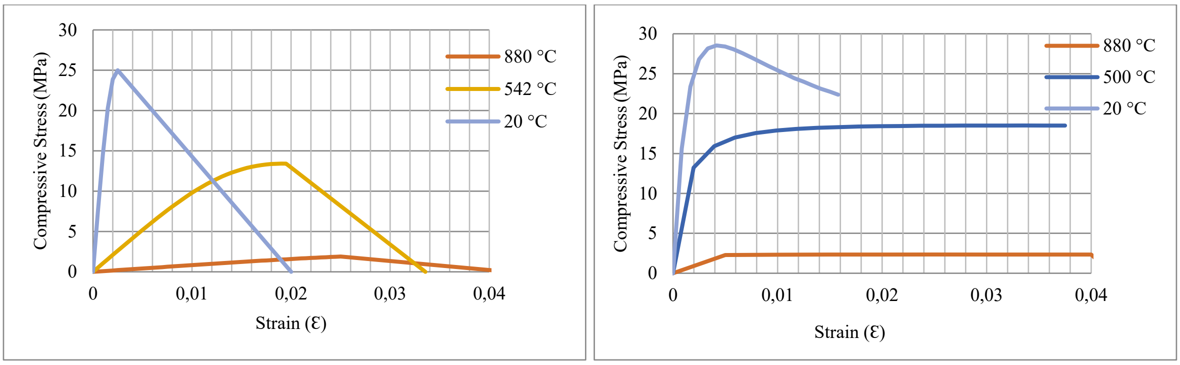

Fig. 5. (a) Unconfined concrete stress-strain plot for 50 cm x 50 cm column section (b) Confined concrete stress-strain plot for 50 cm x 50 cm column section

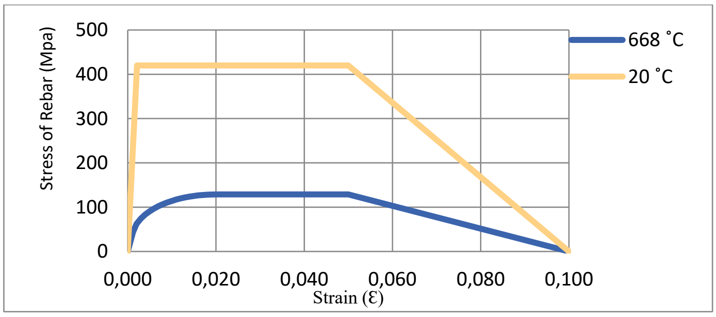

Fig. 6. Temperature-dependent stress-strain plot of reinforcement steel for a 50 cm x 50 cm column section

4.2 Beam section analysis

In the structural system of the building, all beams have dimensions of 40x50 cm but the reinforcement layout varies according to the beam types. The beam stirrups are specified as Φ10/10 for all beams and are designed as two-legged stirrups. It is assumed that the stirrup hooks are bent at 135° and are arranged as special seismic stirrups as defined in TBDY-2018. Therefore, capacity calculations have been performed assuming the presence of confinement effect in the beams. Moment-curvature relationships for the beam sections were obtained using XTRACT . The calculated moment-curvature analysis results were idealized and transferred to the SAP2000. The plastic hinge lengths of the beams were considered in the analyses as half of the effective section depth, as defined in TBDY-2018. Plastic hinges were defined at the ends of the clear spans of the beams. From the plastic rotation demands obtained in the final step of the pushover analysis, total curvature demands were calculated. From the moment-curvature relationship, the strain demands corresponding to the total curvature demand were found, and these values were compared with the strain capacities defined for each damage limit to determine the section damage level. For the confined and unconfined concrete models used in the beam section analyses, several different stress – strain plots under temperature effects for unconfined concrete are presented in Fig. 7(a). The plot showing the variation of reinforcement steel property with temperature is presented in Fig. 7(b).

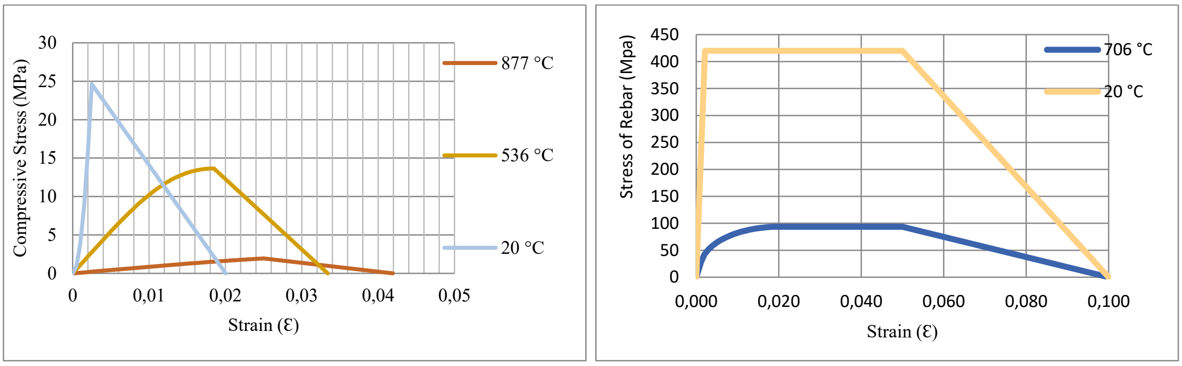

Fig. 7. (a) Unconfined concrete stress-strain plot of a beam section with dimensions 40cm x 50cm (b) Temperature-dependent stress-strain plot of shear reinforcement in a 40cm x 50cm beam

4.3. Nonlinear static pushover analysis

The definition of pushover analysis in TBDY-2018 is the performance under the effect of equivalent seismic loads that are monotonically increased step-by-step, proportional to the first (dominant mode) vibration mode shape, up to the seismic demand limit. In each step of the pushover analysis following the vertical load analysis, the displacements, plastic deformations, and internal force increments occurring in the structural system, as well as their cumulative values and the maximum values corresponding to the seismic demand in the final step, are calculated. To perform pushover analysis, it is first necessary to determine the lateral load distribution, i.e., the equivalent seismic loads, which will be gradually increased in the analysis. In SAP 2000, the distribution of equivalent loads at each story level was achieved by selecting modal analysis as the initial condition (Celep, 2007). The distribution of these loads is determined using the dominant mode shape amplitudes in the analysis direction of the building and the story masses. Changes occur in the dominant mode shape of the building due to the plastic sections formed during the pushover analysis. In this case, the load distribution is defined to be proportional to the value obtained by multiplying the mass associated with the first (dominant mode) natural vibration mode shape amplitude, calculated for linear elastic behavior at the beginning of the analysis. In buildings where floor slabs are idealized as rigid diaphragms, the amplitudes of the first natural vibration mode shape are considered as the two orthogonal horizontal translations at the center of mass of each story and the rotation about the vertical axis passing through the center of mass. According to TBDY-2018, there are conditions that must be met for the Incremental Equivalent Seismic Load Method to be used in pushover analysis. The buildings examined in this study are symmetric in plan in terms of both stiffness and mass. Therefore, torsional effects do not occur. The effective mass ratio of the first (dominant) vibration mode, calculated based on linear elastic behavior in the considered earthquake direction, to the total building mass must be at least 0.70. In analyzed scenarios, this ratio is in the order of 0.85.

4.4. Determination of effective bending stiffness ratios

The effective cross-sectional stiffness of columns and beams modeled according to lumped plasticity behavior were calculated according to TBDY-2018 as defined by Equations (1) and (2). These equations are calculated in relation to the effective yield moments of the plastic hinges at the member ends. M_y and θ_y represent the average of the effective yield moments and yield rotations of the plastic hinges at the ends of the bar element. L_s indicates the shear span, h indicates the section depth, Φ_y indicates the effective yield curvature at the plastic hinge section, d_b indicates the average diameter of the reinforcing steel anchored to the support, and f_{ce} and f_{ye} indicate the average compressive strength of concrete and yield strength of steel, respectively. According to TBDY-2018, η is taken as 1 in beams and columns. $(EI)_e$ is the effective section stiffness of columns and beams modeled according to plastic behavior and $(EI)_g$ is the gross section stiffness of columns and beams.

$$(EI)_e = \frac{M_Y}{\theta_Y}\frac{L_S}{3} \tag{1}$$

$$\theta_y = \frac{\Phi_y L_S}{3} + 0.0015\eta\left(1 + 1.5\frac{h}{L_S}\right) + \frac{\Phi_y d_b f_{ye}}{8\sqrt{f_{ce}}} \tag{2}$$

Table 7. Effective stiffness values of structural elements

	Element	Width m	Depth m	L_{net} m	L_s m	M_y kN.m	Φ_y 1/m	$(EI)_e/(EI)_g$
Ground Floor	Column	0.5	0.5	3.5	1.75	405	0.00765	0.19
First Floor	Column	0.5	0.5	3.5	1.75	376	0.00765	0.18
Second Floor	Column	0.5	0.5	3.5	1.75	321	0.00765	0.15
Third Floor	Column	0.5	0.5	3.5	1.75	279	0.00765	0.13
Fourth Floor	Column	0.5	0.5	3.5	1.75	211	0.00765	0.10
Type-1	Beam	0.4	0.5	5.5	2.75	241	0.00678	0.19
Type-2	Beam	0.4	0.5	5.5	2.75	241	0.00678	0.19
Type -3	Beam	0.4	0.5	5.5	2.75	194	0.00678	0.15
Type -4	Beam	0.4	0.5	5.5	2.75	150	0.00678	0.12
Type -5	Beam	0.4	0.5	5.5	2.75	108	0.00678	0.08

Note: The effective section stiffnesses of the beams with the same section size but five different reinforcement configurations.

4.5. Determination of target displacement

Performance points for the scenarios were determined based on the peak displacement - base shear force curves (pushover curve, capacity curve). The procedure for the determination of the building performance point that is explained in detail in TBDY-2018 is followed. For the Design Earthquake level with a 10% probability of exceedance in 50 years (DD2), the peak displacement demand was calculated. As a result of the structure being a frame system and the stiffnesses being significantly reduced, the dominant periods in the scenarios are calculated to be larger than that considered normal for a 5-story building. Given that the dominant periods are larger than the characteristic period of the earthquake, the equal displacement rule is valid. This allows the nonlinear spectral displacement to be taken as equal to the linear elastic displacement. Table 8 presents the calculated peak displacement values for the scenarios. The periods and consequently the peak displacement demands of the models analyzed based on the material properties of the elements exposed to fire effects show differences. T_x represents the natural vibration period of the first mode, Φ_{Nx1} represents the amplitude in the x direction of the variable mode shape, which is updated with free vibration analysis at each pushover step at the N^{th} story, Γ_{x1} represents the modal participation factor calculated based on the fixed mode shape determined in the first pushover step for the earthquake direction and not changed throughout the pushover analysis, M represents the mass, C_r represents the spectral displacement ratio, and u_{Nx1} represents the displacement calculated at the top of the building in the x-axis direction at the pushover step for the earthquake direction.

Table 8. Target displacement calculation table for scenarios.

#	Scenario Name	T_x sec.	Φ_{Nx1}	Γ_{x1}	Ɣx %	$\sum M$	Cr	u_{Nx1} m	$V^{(i)}_{x1}$ kN
1	With Fire	2.790	0.0221	58.85	0.884	4023	1	0.349	3415.9
2	Without Fire	2.795	0.0233	58.85	0.885	4023	1	0.311	4093.0

The obtained nonlinear spectral displacement values are equal to the modal displacement demand. The modal displacement demands calculated for the equivalent single degree of freedom system are converted to the peak displacement demand of the multiple degree of freedom system through appropriate coordinate transformation. The peak displacement demands for the X-direction of the building are given in Table 8. These obtained values were transferred to SAP2000, and each scenario's analytical model was pushed up to the calculated displacement demand. In the final step, some results pertaining to all demand magnitudes obtained at the last step were examined.

5. Results

The results of the analyses presented in this section have been evaluated under two main headings. Firstly, the general results were examined, covering the findings for two scenarios and a comparison of these findings. Secondly, the focus was on element-level results, and within this scope, a comparison was made between the internal forces developed in beams and columns and the capacities specified in TBDY-2018. These results, obtained using the nonlinear incremental pushover method, are presented for the current state of the structure and the defined scenarios. The obtained data were compared in Figure 8 through base shear force-roof displacement relationships and modal capacity curves.

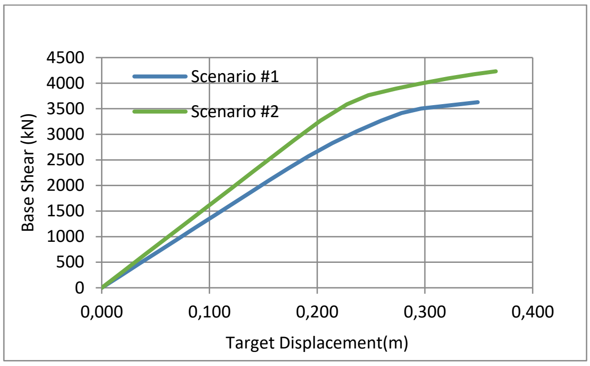

Fig. 8. Base shear force-peak displacement curves of scenarios

In the plots above, the base shear forces at the final stage of the static pushover analysis are compared for the existing condition and the fire condition. In cases affected by fire, the decrease in structural stiffness can be explained as a corresponding decrease in the lateral load-carrying capacity of the system. The reason for this reduction is the loss of material strength due to the effect of fire, and consequently, the formation of plastic hinges at lower deformations compared to the existing condition. On the other hand, the decrease in the stiffness of structural elements due to the fire effect increased the target displacement value by approximately 12% compared to the existing condition.

Based on the conducted analyses, the plastic strain demands on column elements were compared with the defined deformation capacities for various damage limits. According to the results of the uniaxial pushover analysis, almost all columns on all floors of the building are in the Limited Damage (LD) range for original state, i.e. Scenario 2. In Scenario 1, representing a fire on the ground floor, it is observed that all columns transition from the Limited Damage to the Controlled Damage (CD) range.

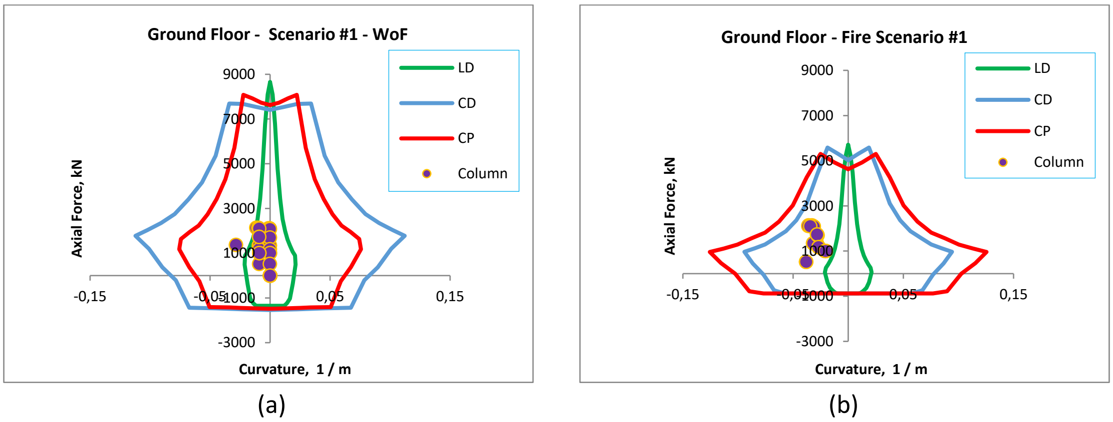

Fig. 9. (a) Ground Floor Column Results Scenario #2 (b) Ground Floor Column Results Scenario #1 (Note: LD-Limited Damage, CD-Controlled Damage, and CP-Collapse Prevention).

6. Conclusions

The analysis results presented in this section were obtained using the nonlinear static pushover method and compare the effects of different fire scenarios on the global and structural element behavior of an existing structure with the capacities specified in TBDY-2018. The overall results indicate that a fire occurring on the ground floor causes significant reductions in base shear force and a decrease in structural stiffness, thereby reducing the lateral load bearing capacity. At the component level, it was concluded that columns which were initially in the limited damage zone were transitioned to the controlled damage zone as a result of the ground floor fire.

In light of the results obtained from this study, further studies will be conducted considering fire conditions on different floors, different concrete cover, and different fire durations.

References

Afet ve Acil Durum Yönetimi Başkanlığı. (2018). *Türkiye Bina Deprem Yönetmeliği*. Ankara. (In Turkish)

Bingöl, A. F., & Gül, R. (2009). Donatı-beton aderansı, yüksek sıcaklıkların beton dayanımına ve aderansa etkileri konusunda bir derleme. *Atatürk Üniversitesi, Mühendislik Fakültesi, İnşaat Mühendisliği Bölümü*, Erzurum. (In Turkish)

Celep, Z. (2007). *Betonarme taşıyıcı sistemlerde doğrusal olmayan davranış ve çözümleme*. Beta Yayıncılık. (In Turkish)

Chadwell, C. B. (2007). *XTRACT: Cross section analysis software for structural and earthquake engineering*. Imbsen & Associates.
Computers and Structures Inc. (2025). *SAP2000 Advanced: Structural analysis program*. Berkeley, California.
DIAMOND. (2013). *A thermal/structural program showing the evolution of various results under fire*. (n.d.).
Eren, İ., & Gençoğlu, M. (2012). *Yapısal yangın güvenliği ders notları*. İ.T.Ü. İnşaat Fakültesi, İstanbul. (In Turkish)
Fédération Internationale du Béton (FIB). (2008). *Fire design of concrete structures – Structural behaviour and assessment (Fib Bulletin 46)*. Lausanne, Switzerland.
Gernay, T., & Franssen, J. M. (2011). *SAFIR manual*. Faculté des Sciences Appliquées, Département d'Architecture, Géologie, Environnement & Constructions, Belgique.
Hacıemiroğlu, M. (2014). *Yangın geçirmiş betonarme bir yapının deprem performansının değerlendirilmesi* (Master's thesis). İstanbul Teknik Üniversitesi. (In Turkish)
Imbsen Software Systems. (2004). *XTRACT: Cross section analysis program of structural engineers*.
Khoury, G. A. (2000). Effect of fire on concrete and concrete structures. *Progress in Structural Engineering and Materials, 2*, 429–447.
Öztürk, A., & Yavuz, H. (1995). *Uygulamalarla ısı geçişi: Taşınım ve ışınım*. Çağlayan Basımevi, İstanbul. (In Turkish)
SAFIR. (n.d.). *A thermal/structural program modeling structures under fire*.
Türk Standardları Enstitüsü. (2000). *Betonarme yapıların tasarım ve yapım kuralları (TS 500)*. Ankara. (In Turkish)
Türk Standardları Enstitüsü. (2023). *Betonarme yapıların tasarımı - Bölüm 1-2: Genel kurallar - Yapısal yangın tasarımı (Eurocode 2) (TS EN 1992-1-2)*. Ankara. (In Turkish)
Ünlüoğlu, E., Topçu, İ. B., & Yalaman, B. (2007). Yüksek sıcaklıkta kalmış yapılarda pas payının betonarme çelik donatı özeliklerine etkisi. *İMO Teknik Dergi*, (Yazı 273), 4145–4155. Eskişehir. (In Turkish)
Yüzer, N., & Özçiftçi, N. (2006). Yüksek sıcaklık etkisinde beton davranışı. *Yıldız Teknik Üniversitesi*, İstanbul. (In Turkish)

Investigation of the effect of different wall layouts on B1 irregularity in buildings

Abdulkadir Solak[*1], Amissou M. Pamom[1], Mehmet Kamanlı[1]

[1] *Konya Technical University, Department of Civil Engineering, 42250, Konya, Türkiye*

Abstract. Infill walls can be partially or completely removed at different floor levels of reinforced concrete framed structures for a variety of reasons, including architectural requirements. However, this can have a substantial impact on the seismic behaviour of the structure, potentially leading to irregularities in the stiffness distribution (B1 type). The present study was conducted with the objective of quantitatively evaluating the effects of different infill wall arrangements on the structural performance, with a particular focus on analysing the risk of soft story irregularities. In this study, an 11-storey reinforced concrete frame structure is modelled in accordance with the TS500 and TBEC-2019 standards. A total of eight distinct configurations were analysed in this study, representing partial or complete removal of infill walls. These configurations were analysed using ETABS v22, a software program designed for structural analysis and design. The structural parameters analysed in this study included foundation period, base shear, displacement and soft story irregularity coefficient (ηki). The findings indicated that the implementation of infill walls resulted in an augmentation of structural stiffness, consequently diminishing the necessity for foundation periods and, in certain instances, precipitating an escalation in roof displacements. The findings emphasise the importance of incorporating infill walls into the design process and suggest that additional measures should be implemented when infill walls are removed in successive storeys.

Keywords: Infill wall; Reinforced concrete structures; ETABS; B1 irregularity; Soft story

1. Introduction

Advances in construction technology, innovations in material science and accumulated experience in engineering-architecture disciplines have resulted in structural system designs and structural planning solutions which are becoming increasingly diversified. In buildings of differing architectural design and constructed for different purposes, non-bearing infill walls are not applied at different floor levels due to architectural requirements. It is a common occurrence to observe the presence of commercial units situated on the ground floors of various buildings within the built environment (Fig. 1).

In addition to these cases, there are many structures in which the infill walls of the structure are damaged even if the structural system is not severely damaged by the earthquake effect. (Fig. 2) In case of damage to the infill walls, the infill walls will be dysfunctional in load transfer in new earthquake conditions that will affect the structure.

In engineering design, the contribution of infill walls to the stiffness of reinforced concrete framed buildings is often overlooked. The primary factors contributing to this oversight can be attributed to the intricacy and challenge inherent in the development of calculation models that encompass the contribution of infill walls. This complexity arises from the absence of standardised calculation methodologies to evaluate this contribution at the project design stage. Additionally, the exclusion of the infill wall effect from calculations is driven by a desire to maintain a cautious approach, thereby ensuring safety (Sayın, 2003). However, infill walls are widely used in both interior and exterior sections of reinforced concrete structures. These walls are important structural elements that separate the building from the external environment and provide the creation of architecturally different spaces (Luo et al., 2024). Despite their classification as non-structural elements, they contribute to the structure's energy absorption capacity and stiffness by working in conjunction with the frame under earthquake loads.

* Corresponding author, E-mail: abdulkadirsolak@ktun.edu.tr

https://doi.org/10.31462/icearc2025_ce_eqe_868

Fig. 1. Designs without infill walls at different floor levels

The effect of infill walls makes it necessary to produce solutions that will both meet architectural requirements and comply with engineering design principles. In the literature, there are many theoretical and experimental studies investigating the effect of infill walls on structural behaviour (Korkmaz and Ucar, 2006; Tekin et al., 2007; Balık, 2012). Mainstone (1974) proposed the method of equivalent pressure bars to facilitate the analysis of frames with infill walls and developed various formulations to calculate the widths of these bars. Sivri (2003) showed that infill walls increase the stiffness of the structure and reduce the structural period and lateral displacements. Smith (1962) showed that the lateral stiffness and strength of frames with infill walls depend on the wall dimensions, physical properties and contact length with the column. Similarly, Beklen (2009) stated that infill walls have significant effects on parameters such as stiffness, period, horizontal displacement and base shear force and directly affect building behaviour.

This study was carried out to investigate the effect of infill walls on building behaviour in more detail. An 11-storey framed building with sections dimensioned in accordance with TS500 and Turkish Building Earthquake Code (TBEC-2019) is modelled in ETABS v22 analysis software. These analyses were carried out in order to understand the contribution of infill walls to building performance and to make more informed decisions in design processes.

Fig. 2. Collapse of infill walls on some floors under earthquake effect (Kamanli et al., 2023)

2. Materials and methods

In this study, a reinforced concrete frame structure with ground + 11 normal storeys is analysed. The characteristics of each analysed building model are given in Table 1. The structure and structural system elements are dimensioned in accordance with TS500 and Turkish Building Earthquake Code (TBEC-2019). C25 concrete class and S420 reinforcement class were used in material definitions. The soil class was determined as ZC. As a result of the equivalent earthquake analysis, the elastic first mode natural vibration period of the 11-storey solid frame was calculated as T1=1.309 s.

In the design and modelling, all storey heights were taken as 3.00 m, except for the ground floor with a height of 3.5 m, for the structures whose section plans are given in Figure 1 (a-h). Slab thickness is 12 cm, beam dimensions are 25x40 cm and column dimensions are 30x45 cm. Table 1 shows the different building models (Types) and Figure 3 shows the geometry of the structure in plan.

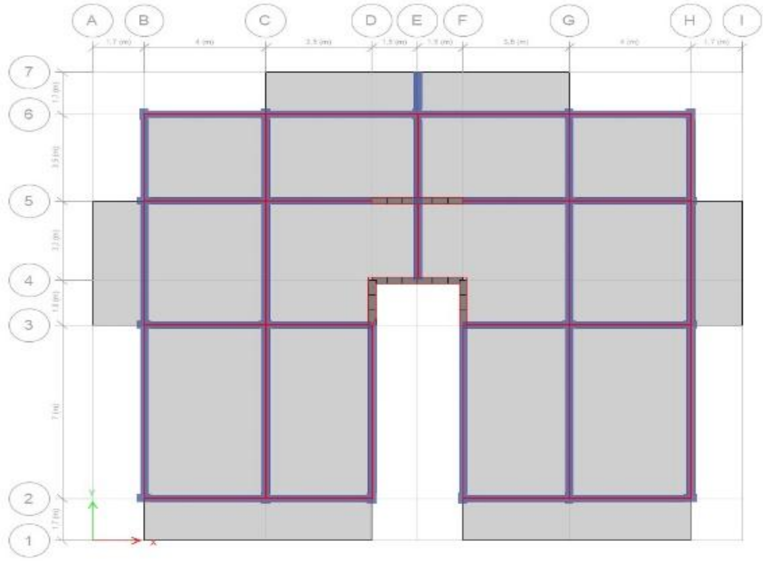

Fig. 3. Plan of the building

The frame system has been designed to exhibit a high level of ductility, with the behaviour coefficient of the structural system set at R=8 for bond beam shear walls in the Y direction and R=7.5 for hollow walls in the X direction. In the process of dimensional analysis, the live load of 2 kN/m² was applied to slabs and 5 kN/m² to balconies. These values were derived from the live load table, which is specified in TS498 [ts498] and is based on the intended use of the building. Panels with a thickness of 20 centimetres were modelled to represent the infill wall, whereas 20 centimetres was taken for both interior and exterior walls.

In the study, parameters such as periods, earthquake shear forces, displacements, relative storey drifts and soft storey irregularities of the structures under the same earthquake effect, by removing the infill walls at different floors, were evaluated separately for each case.

3. Results and discussion

3.1 Investigation of period changes

The analysis results indicate that the configuration of infill walls exerts a substantial influence on the structural period. The fully infilled system (Type 1) demonstrates the most rigid behaviour, exhibiting a period of 1.309 s. In contrast, the completely wallless configuration (Type 8) exhibits a period value of 2.134 s, which is the highest observed. These findings are consistent with the fundamental period formula relationship expressed in Hooke's Law (Westergaard, 1952). In cases involving the removal of walls in a single floor (Type 2, Type 4, Type 6), the observed period increase remained within the range of 7-12%. In contrast, the configuration involving three consecutive floors without walls (Type 3) resulted in a substantial period increase of 34.5%. The elimination of all barriers (Type8) resulted in a significant surge of 63% (Table 2).

Table 1. Structure models

Model	Configuration Image	Description	Model	Configuration Image	Description
Type 1	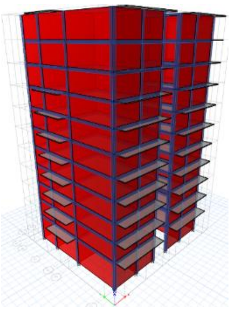	Full infill: All stories have infill walls	Type 5	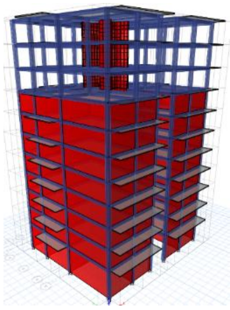	8th-11th stories infills removed
Type 2	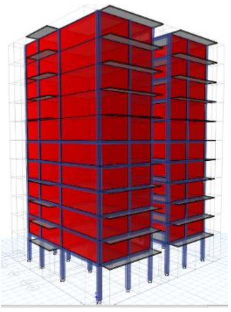	Ground story infills removed	Type 6	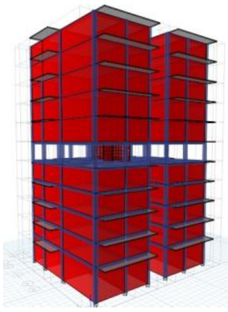	6th story infills removed
Type 3	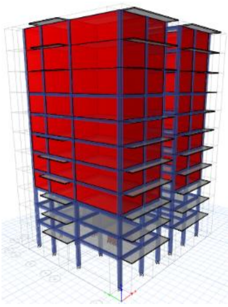	Ground + first 2 stories infills removed	Type 7	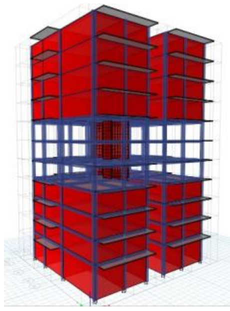	4th-7th stories infills removed
Type 4	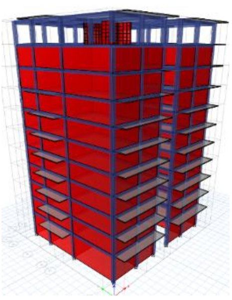	11th story infills removed	Type 8	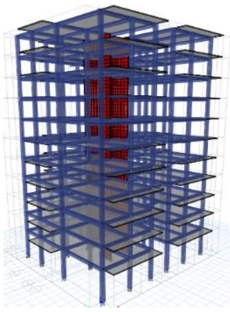	Bare frame: All infills removed

Table 2. Period values and rates of change

Model Type	Periyot (s)	Change (%)
Type1	1.309	Reference
Type2	1.459	+11.5
Type3	1.760	+34.5
Type4	1.400	+7.0
Type5	1.440	+10.0
Type6	1.463	+11.8
Type7	1.617	+23.5
Type8	2.134	+63.0

3.2. Distribution of base shear forces

An analysis of the base shear forces acting on the structure revealed that the fully filled system (Type 1) yielded a maximum shear force of 1534.15 kN, while the wallless configuration (Type 8) generated a 6% lower shear force of 1445.18 kN. In alternative wall configurations, it was observed that the distribution of the base shear forces occurring in the structure was at a lower level (Table 3).

Tablo 3. The maximum earthquake shear forces

Model Type	Shear Force (kN)	Change (%)
Type1	1534.15	Reference
Type2	1512.82	-1.4
Type3	1499.31	-2.3
Type4	1511.72	-1.5
Type5	1498.82	-2.3
Type6	1512.96	-1.4
Type7	1499.21	-2.3
Type8	1445.18	-5.8

3.3. Total deformation

According to the peak displacements of the structure, the maximum displacement, which was 57.31 mm in the reference system, reached 117.24 mm (104.7% increase) in the configuration without walls. The variation in floor levels where the walls are not present has been shown to significantly affect the peak displacement value. For instance, the wall-less configuration near the ground floor (Type 2) resulted in an 11.8% increase in displacement, the wall-less configuration in the middle floors (Type 6) resulted in an 8.0% increase in displacement, and the wall-less configuration in the upper floors resulted in a 4.9% increase in peak displacement (Type 4). The findings of this study demonstrate that the storey level of the wallless floors exerts an influence on the deformation behaviour of the structure (Table 4).

Table 4. Maximum displacement values

Model Type	Max. Displacement (mm)	Change (%)
Type1	57.31	Reference
Type2	64.07	+11.8
Type3	75.38	+31.6
Type4	60.10	+4.9
Type5	66.00	+15.2
Type6	61.90	+8.0
Type7	72.70	+26.9
Type8	117.24	+104.7

3.4. Soft storey irregularity analysis

Although the Type B2 Coefficient of Irregularity (Soft Storey) specified as

$$\mathrm{\eta ki} = (\Delta \mathrm{i}(X)/\mathrm{hi})\mathrm{ort}/(\Delta \mathrm{i} + 1(X)/\mathrm{hi} + 1)\mathrm{ort} > 2.0 \tag{1}$$

$$\mathrm{\eta ki} = (\Delta \mathrm{i}(X)/\mathrm{hi})\mathrm{ort}/ (\Delta \mathrm{i} - 1(X)/\mathrm{hi} - 1)\mathrm{ort} > 2.0 \tag{2}$$

in TBEC-2019 was achieved in all models, the models with wallless configuration in the middle floors (Type6-Type7) gave the closest results to the limit value with ηki = 1.279-1.450. In the ground floor wallless case (Type2), ηki = 1.185. These findings indicate that the risk of soft storey formation should be carefully evaluated, especially in wall removal operations in the middle floors (Table 5).

Table 5. Soft story irregularity coefficients

Model Type	ηki
Type1	1.204
Type2	1.185
Type3	1.186
Type4	1.102
Type5	1.187
Type6	1.279
Type7	1.450
Type8	1.195

The findings of this study provide quantitative evidence for the critical effect of infill walls on structural behaviour. The findings of the present study demonstrate that the presence of walls exerts a direct influence on the stiffness of the structure. It has been observed that the effect of wall configuration on shear force distribution is limited. With regard to displacement behaviour, it is understood that the location of the wall-less floors is decisive on the structural performance. It is imperative that the soft storey irregularity coefficient is subjected to meticulous analysis, with particular emphasis on its manifestation in the middle storeys of wallless configurations. The results of all analyses obtained from this study are presented in Table 6.

Table 6. Comparative analysis results for all models

Model Type	Period (s)	Shear Force (kN)	Max. Displacement (mm)	ηki
Type1	1.309	1534.15	57.31	1.204
Type2	1.459	1512.82	64.07	1.185
Type3	1.760	1499.31	75.38	1.186
Type4	1.400	1511.72	60.10	1.102
Type5	1.440	1498.82	66.00	1.187
Type6	1.463	1512.96	61.90	1.279
Type7	1.617	1499.21	72.70	1.450
Type8	2.134	1445.18	117.24	1.195

4. Conclusions

All papers must include a Conclusions section. The main findings of the study must be given there. Bullets must In this study, the effects of different infill wall configurations on the structural behaviour of an 11-storey reinforced concrete frame structure are evaluated. The results of the analyses can be summarised as follows:

- Inclusion of infill walls in the structure causes a significant decrease in the structural periods. Especially in completely unfilled systems, longer period values occur compared to fully filled systems.
- The absence of infill walls in more than one consecutive storeys has more adverse effects than the wallless configurations in single storeys and significantly reduces the stiffness of the structure.
- The storey level at which the wall-less configuration is located influences the dynamic characteristics of the structure. Wall-less configurations at upper storeys show more limited effects compared to lower storeys.
- Infill walls have a limited effect on the shear force distribution of the structural system.
- The absence of infill walls increases the horizontal displacements in the structure. Especially the configurations without walls in the lower storeys cause larger displacements than the upper storeys.
- In terms of soft storey irregularity, all configurations are within acceptable limits, but especially the wallless configurations in the middle storeys are found to reach values closer to these limits.

The findings indicate that the impact of infill walls on the structural system should not be disregarded. It is imperative to note that the absence of walls, particularly in lower and consecutive floors, has the potential to adversely impact the seismic performance of the structure. Consequently, the implementation of supplementary engineering measures is crucial in designs involving such configurations. Moreover, it is imperative to enhance the prevailing analysis methodologies so as to more accurately depict the behaviour of infill walls in structural analyses, with a view to ensuring structural safety.

References

Balık, F. S. (2012). *Betonarme dolgu duvarla güçlendirilmiş deprem davranışı yetersiz betonarme çerçevelerin davranışına pencere boşluklarının etkisi* (Doctoral thesis). Selçuk Üniversitesi, Fen Bilimleri Enstitüsü. (In Turkish).

Beklen, C. (2009). *Binalarda dolgu duvar etkisinin incelenmesi* (Master's thesis). Çukurova Üniversitesi, Fen Bilimleri Enstitüsü. (In Turkish).

Kamanli, M., Donduren, M. S., Cogurcu, M. T., Kekec, B., & A. (2023). *February 6 2023 Kahramanmaraş earthquakes: Hatay*. Eğitim Yayınevi. (In Turkish).

Korkmaz, A., & Uçar, T. (2006). Betonarme binaların deprem davranışında dolgu duvar etkisinin incelenmesi. *Dokuz Eylül Üniversitesi Mühendislik Fakültesi Fen ve Mühendislik Dergisi, 8*(1), 101–108. (In Turkish).

Luo, R., Guo, X., Wang, B., Dong, X., Zhang, Q., & Ouyang, Z. (2024, January). The impact of infill wall distribution on the mechanical behavior and failure patterns of multi-story RC frame structures: An acceleration–strain coupled testing approach. *Structures, 59*, 105737. https://doi.org/10.1016/j.istruc.2023.105737

Mainstone, R. J. (1974). Supplementary note on the stiffness and strengths of infilled frames. *Building Research Station*, UK, Current Paper 13/74.

Sayın, B. (2003). *Mevcut betonarme yapıların yeni deprem projelendirilmesi yönetmeliğine ve göre güçlendirilmesi teknikleri* (Master's thesis). İstanbul Üniversitesi, Fen Bilimleri Enstitüsü. (In Turkish).

Sivri, M. (2003). *Dolgulu çerçevelerin deprem davranışı* (Master's thesis). Süleyman Demirel Üniversitesi, Fen Bilimleri Enstitüsü, Isparta. (In Turkish).

Smith, B. S. (1962). Lateral stiffness of infilled frames. *ASCE Structural Division Journal*, 183–199.

TBEC. (2019). *Türkiye Bina Deprem Yönetmeliği*. Afet ve Acil Durum Yönetimi Başkanlığı, Ankara, Türkiye. (In Turkish).

Tekin, M., Alsancak, E., & Ay, M. (2007). Betonarme çerçevelerde dolgu duvar etkisinin incelenmesi. *Celal Bayar University Journal of Science, 3*(1), 95–104. (In Turkish).

Türk Standardları Enstitüsü. (2021). *TS 498: Yapı elemanlarının boyutlandırılmasında alınacak yüklerin hesap değerleri*. Ankara, Türkiye. (In Turkish).

Türk Standardları Enstitüsü. (2000). *TS 500: Betonarme yapıların tasarım ve yapım kuralları*. Ankara, Türkiye. (In Turkish).

Westergaard, H. M. (1952). *Theory of elasticity and plasticity*. Harvard University Press.

4th International Civil Engineering & Architecture Conference
17-19 May 2025, Trabzon, Türkiye

Effects of seismic isolators on the structural behavior of reinforced concrete buildings

Hacer Tülen*[1], Hakan Öztürk[2], Hilal Meydanlı Atalay[1]

[1] Kocaeli University, Department of Civil Engineering, 41001 Kocaeli, Türkiye
[2] Sakarya University, Department of Civil Engineering, 54050 Sakarya, Türkiye

Abstract. Seismic force is a critical parameter in the design and performance evaluation of buildings. In the field of earthquake engineering, seismic isolators, which are developed to reduce structural damage and enhance the seismic performance of buildings, are increasingly used in modern building systems. The primary function of seismic isolators is to reduce the seismic forces acting on a building by increasing its natural period of the building. In this study, it is aimed to investigate the effect of the use of seismic isolators on the structural behavior of reinforced concrete buildings with varying period. For this purpose, five-storey, seven-storey and nine-storey reinforced concrete frame systems without irregularities, selected to change the mass, were designed in accordance with the 2018 Turkish Building Earthquake Code (TBEC-2018). Six models were established to evaluate the seismic performance of buildings under different support conditions. Structural analyses were performed using the linear time history analysis method and 11 different ground motion records were selected to compare the effects of different scaling methods on the structural response. Simple and geometric scaling methods were used to scale these records in accordance with the spectral matching criteria specified in TBEC-2018. Both horizontal components (X and Y directions) of each scaled earthquake record were applied to the structural models and linear time history analyses were performed. The results of the analyses were compared in terms of building period, roof displacement ratio and story acceleration. The results show that the use of seismic isolators positively affects the seismic behavior of buildings and significantly reduces the story acceleration.

Keywords: Seismic isolators; Reinforced concrete buildings; Scaling method; Time history analysis; Seismic performance.

1. Introduction

Earthquakes in the past years have caused loss of life and economic losses. This situation has given rise to the concept of earthquake-resistant structural design.There are two approaches to earthquake-resistant structural design. The traditional method aims to reduce structural damage and to have the damage occur in the predicted places.The implementation of seismic isolation aims to increase the structural period and improve the overall seismic performance of the structure. Rubber isolators and friction surface isolators are frequently used in seismic isolation systems (Meral,2021). The effects of seismic isolation systems on structures behavior have been addressed by many researchers for various parameters. The effect of the use of isolation systems in regular and irregular buildings on the structural behavior was examined by Özer (2022), Öztürk (2022) and Meral (2021). Türk (2019) investigated the effects of different isolator types and number of stories on the behavior and stated that structures with seismic isolators become safe. Özkan et al. (2023) investigated reinforced concrete buildings with varying ground storey heights and number of stories, and reported that interstory drifts were significantly reduced in seismically isolated structures.

Codes recommend that analyses of structures with isolators be performed in the time history. There are various criteria in determining the earthquake records to be used. In TBEC-2018, regarding scaling, the condition that the average of the resultant horizontal spectrum values of the earthquake record should be greater than 1.3 times the design spectrum in the specified period range is included. No details are given regarding the method to be used in scaling the earthquake records. The effect of the scaling method on the structures behavior has been studied by many researchers. Shome et al. (1998) adopted the concept of scaling ground motions by matching the spectral acceleration of the structure's target spectrum. However, there are many parameters affecting the structures period, a scaling method has been developed within a specific period range. Stewart et al. (2001) and Huang (2008) used

*Corresponding author, E-mail: hacer.tulen@kocaeli.edu.tr

https://doi.org/10.31462/icearc2025_ce_eqe_883

the geometric mean scaling method in their studies.When determining appropriate scaling factors for earthquake records, it is recommended that the scale factor not be greater than 4. In the literature, studies related to scaling often consider structures with fixed-base supports. However, studies conducted for isolator structures are limited. When examining the effect of changing the number of stories on the behavior of the structure in isolator structures, a single scaling method is often used. In this study, building models with 5, 7 and 9 storeys fixed supports and lead core rubber isolators were subjected to linear analysis in the time history using earthquake records scaled with two different methods. As a result of the analysis, structures periods, roof displacements ratio and story acceleration values changes were examined.

2. Material and methods

In this study, the changes in the behavior of reinforced concrete structures with a fixed and isolated base depending on the story height and the earthquake record scaling method were investigated. The buildings were modeled as 5, 7 and 9 storeys and the floor heights were determined as 3 m. The plan area was kept the same for all buildings. The buildings were designed in accordance with the design principles in TBEC-2018. Building models consist of a typical column-beam system. The bay spacing in the X and Y directions were chosen as 4 m. In the load-bearing system, all column sections are 45x45 cm, beam sections are 25x50 cm, and the floor thickness is 15 cm. The plan used in all buildings is given in Figure 1 and the 3D view of the 7-storey building is given in Figure 2. In all structures, the concrete compressive strength is defined as 25 Mpa (C25) and the yield strength of the reinforcement is defined as 420 Mpa. A rigid diaphragm was defined at every story in all models. The dead and live loads on the slabs were considered as 3.75 kN/m^2 and 2.0 kN/m^2 (1.5 kN/m^2 on the upper floors), respectively. A load of 4.5 kN/m was applied to the beams as infill wall load, except for the beams located on the roof floor. SAP2000 that is a structural analysis program was used in modeling and time history analysis of buildings.

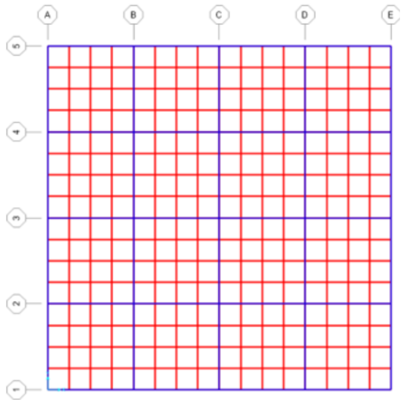

Fig. 1. Plan for all buildings

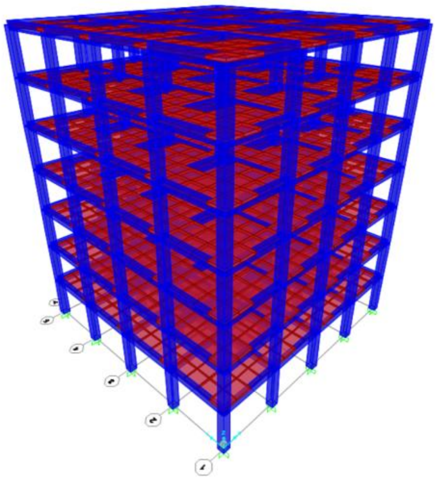

Fig. 2. 3D model of 7-storey building

2.1. Lead rubber bearings

Lead-core rubber bearings are commonly used to improve structural behavior. These isolators are created by combining rubber and steel plates. İn addition to, there is one or more lead cores in its center. The lead core provides the necessary damping (Komodromos, 2000). A representative image of the isolator and the force-displacement relationship are given in Figure 3. The design parameters used for the isolated building models are given in Table 1.

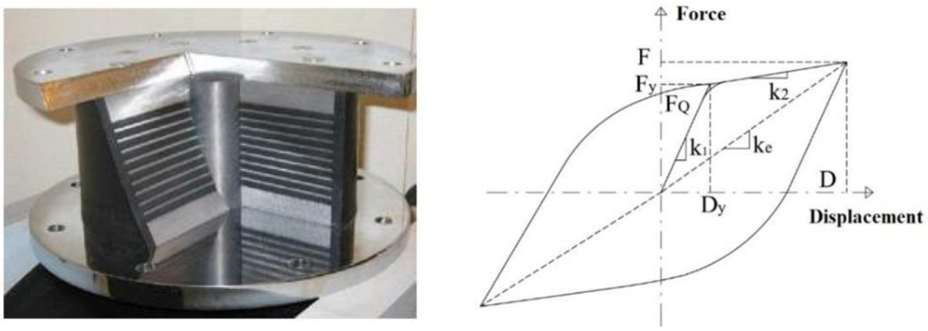

(a) (b)

Fig. 3. (a) Lead rubber bearing (Özpalanlar, 2004), (b) Force-displacement relationship (TBEC,2018).

Table 1. Design parameters of models with isolators

Parameters	5 storey	7 storey	9 storey
Shear modulus (Mpa)	0.5	0.5	0.5
Lead core diameter (mm)	140	160	175
Rubber diameter (mm)	850	950	1000
Total rubber layer thickness (mm)	336	336	312
Post-yield stiffness (kN/m)	821	1024	1220
Post-yield stiffness / Elastic stiffness	0.1	0.1	0.1
Effective yield strength (kN)	154	201	240
Elastic stiffness (kN/m)	1083	1350	1573

2.2 Scaling of earthquake ground motions

In the study, the reinforced concrete building models were subjected to linear time history analysis. It was assumed that the buildings were located in Kocaeli and the soil class was determined as ZC. In selecting the earthquake records in determining, a moment magnitude (M_w) of the earthquake records was chosen between 6.5 and 7.6, a distance to the fault rupture(R) between 0 and 20 km, and a shear wave velocity in the top 30 meters of soil between 180 and 360 m/s were considered. These parameters affect the analysis sensitivity. Eleven earthquake record sets in the analyses were selected through the Pacific Earthquake Engineering Research Center (PEER) database. Selected records are given in Table 2.

In the study, the resultant horizontal spectrum was determined by taking the Square Root of the Sum of the Squares of the two horizontal components (SRSS) of each earthquake. The method in which the scale coefficient is determined according to the design spectrum is determined as the first method. As the second method, the geometric mean scaling method developed by Huang et al. (2008) was used. It was investigated how the scaling method affects the behavior of isolator structures with different number of floors. In the first method, the horizontal components of each earthquake are determined. The horizontal spectrum is obtained by taking the square root of the sum of the squares of the horizontal components. The average of the combined horizontal spectra of all records is taken. The scale factor is determined by harmonizing the obtained combined spectrum with the horizontal design spectrum. In the geometric mean scaling method, first the horizontal components of the selected records are determined and the resultant horizontal spectrum is created by taking the geometric mean. In order to minimize the difference between each resultant horizontal spectrum and the design spectrum, the amount of error is calculated and the first scale factor is determined. In the next stage, the horizontal spectrum is obtained by averaging the root mean square sum (SRSS) of the spectrum curves scaled by the first scale factor. The compatibility between the design spectrum and the resultant spectrum is examined, and the second scale factor is determined. The final scale factor is determined by multiplying the two scale factors. For scaling, DD-1 earthquake ground motion was taken into account. Scaling coefficients were calculated for a 3 s period in the range of $0.5T_m$-$1.5T_m$. The scaling of both horizontal components is used with the same scale coefficients.

Table 2. Information and scaling coefficients of earthquake records

Earthquake No	Earthquake Name	Station	M_w	R (km)	Component	ScaleFactor M1	ScaleFactor M2
1	Imperial Valley	El Centro Array #4	6.5	7.1	230 140		3.36
2	Imperial Valley	El Centro Array #6	6.5	1.4	230 140		2.1
3	Chi-Chi	CHY101	7.6	9.94	E N		2.3
4	Chi-Chi	TCU110	7.6	11.6	E N		2.07
5	Chi-Chi	TCU065	7.6	0.6	E N		1.58
6	Kobe	Takatori	6.9	1.5	000 090	1.6	1.08
7	Kobe	Port Island	6.9	3.31	000 090		2.08
8	Kocaeli	Duzce	7.5	15.4	180 270		2.75
9	Kocaeli	Yarimca	7.5	4.8	60 150		2.69
10	Duzce	Duzce	7.1	6.6	180 270		2.82
11	Erzincan	Erzincan	6.7	4.4	NS EW		2.25

3. Analysis Results

The period values of the structures, roof displacement ratios, and story accelerations obtained from the linear time history analyses were evaluated for 11 different earthquake records and two scaling methods.

3.1 Comparison of the Natural Vibration Periods of the Structures

The natural vibration periods obtained as a result of the analysis of the building models with fixed supports and isolators are given in Table 3. The difference in scaling coefficients don't cause a any change in the structural periods. The periods of structures modeled with isolators are larger than the periods of fixed-supported structures.

Tablo 3. Structural periods

Number of Floors	Mod	T_{fixed}(sn)	$T_{isolator}$(sn)
5	1	0.6	1.71
7	1	0.86	1.89
9	1	1.12	2.08

3.2 Comparison of Roof Displacement Demands

As a result of the analysis, the roof displacement ratios obtained are presented in Figure 4 for 11 earthquake records and 2 different scaling methods. Roof displacements were normalized by dividing by the building heights. In the figure; FIXED indicates fixed supported structures, ISO indicates isolated structures, 1 and 2 indicate the scaling method, and the numbers indicate the number of floors. Since the comparison was made with the fixed supported models, the roof displacements were determined by subtracting the isolator displacements in the isolated structures. When the average of maximum roof displacement rates of 11 earthquake records was examined, it was seen that the displacement demand decreased in isolated structures.

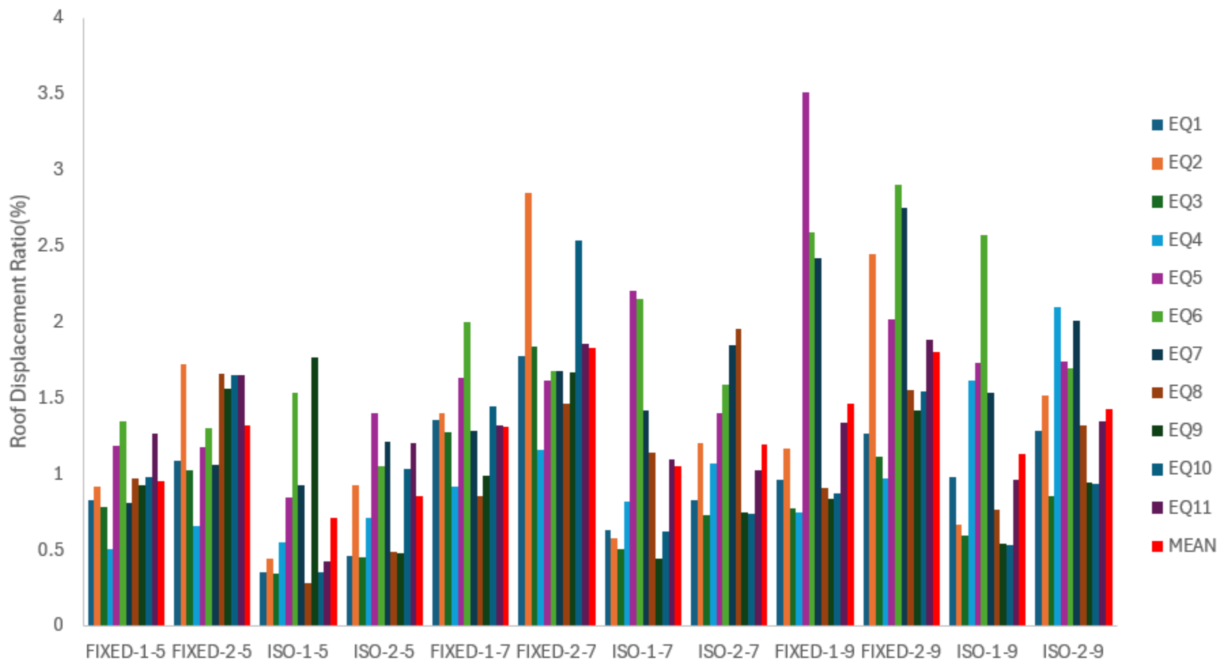

Fig 4. Roof displacement ratios

3.3 Story accelerations

The average maximum acceleration values obtained as a result of the analyses are shown in Figure 5 for 5-storey, 7-storey and 9-storey buildings. When the graphs were examined, it was seen that were greater the story accelerations in the buildings with fixed support. Additionally, there is less acceleration difference between floors in isolated structures. When compared in terms of scaling methods, it was observed that the floor accelerations were greater in the analyses made using the second method.

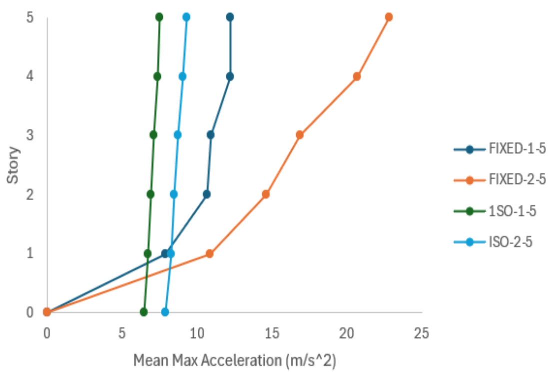

(a)

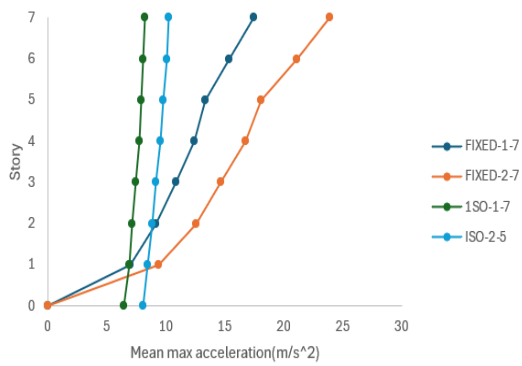

(b)

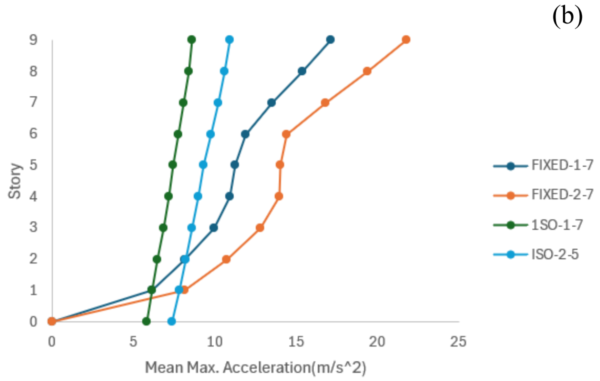

(c)

Fig 5. Maximum floor accelerations, (a) 5 story , (b) 7 story , (c) 9 story

4. Conclusions

In the study, building models with different number of stories, incorporating fixed-support and lead-core rubber isolators, were subjected to linear time history analysis using 11 earthquake records. The records used in the analysis were scaled using two different methods. As a result of the analysis, structural periods, roof displacement rates and changes in floor accelerations were examined.

- When examining the structural periods, it was observed that the periods of the isolated structures increased. However, the scaling method has no effect on the period of structural.
- In terms of the mean maximum roof displacement ratios, it was found that the roof displacements of isolated buildings were smaller than fixed-supported buildings. Comparing the scaling methods, it it was observed that the geometric scaling method resulted in greater roof displacements in both fixed support and isolated buildings.
- The story acceleration values were lower in isolated structures compared to fixed support buildings. In fixed supported buildings, floor acceleration values increased as the number of stories increased. It is observed that the acceleration values on the floors in isolated buildings are closer to each other. This shows that a significant section of the earthquake demands are damped at the isolator interface.

The use of isolators in structures leads to an increase in structural periods and a reduction in seismic demands. The application of two different scaling methods resulted in differences in roof displacement ratios and story accelerations. Therefore, careful consideration should be given to the selection of the scaling method for earthquake records and its application to the building.

References

American Society of Civil Engineers/Structural Engineering Institute. (2016). *Minimum design loads for buildings and other structures (ASCE/SEI 7-16)*. Reston, VA.

Computers and Structures, Inc. (CSI). (2018). *SAP2000: Integrated finite element analysis and design of structures basic analysis reference manual*. Berkeley, CA: CSI.

European Committee for Standardization. (2004). *Eurocode 8: Design of structures for earthquake resistance—Part 1: General rules, seismic actions and rules for buildings (EN 1998-1)*.

Huang, Y. N., Whittaker, A. S., & Luco, N. (2008). *Performance assessment of conventional and base-isolated nuclear power plants for earthquake and blast loadings* (Technical Report No. MCEER-08). State University of New York at Buffalo, Volume 19.

Komodromos, P. (2000). *Seismic isolation for earthquake resistant structures*. WIT Press.

Meral, E. (2021). Determination of seismic isolation effects on irregular RC buildings using friction pendulums. *Structures, 34*, 3436–3452. https://doi.org/10.1016/j.istruc.2021.09.062

Özer, E. (2022). *Geleneksel ve taban izolatörlü betonarme binaların sismik davranışlarının karşılaştırılması* (Doctoral thesis). Pamukkale University, Denizli, Türkiye. (In Turkish)

Özpalanlar, C. G. (2004). *Depreme dayanıklı yapı tasarımında sismik izolasyon ve enerji sönümleyici sistemler* (Master's thesis). İstanbul Teknik University, İstanbul, Türkiye. (In Turkish)

Öztürk, H. (2022). Effects of lead core heating on the response of isolated-base and fixed-base regular and irregular reinforced concrete structures. *Buildings, 12*, 1087. https://doi.org/10.3390/buildings12081087

Pacific Earthquake Engineering Research Center (PEER). (2010). *PEER Ground Motion Database* [Web application]. https://ngawest2.berkeley.edu/

Shome, N., Cornell, C. A., Bazzurro, P., & Carballo, J. E. (1998). Earthquakes, records, and nonlinear responses. *Earthquake Spectra, 14*, 469–500.

Stewart, J. P., Chiou, S. J., Bray, J. D., Graves, R. W., Somerville, P. G., & Abrahamson, N. A. (2001). *Ground motion evaluation procedures for performance-based design* (PEER Report 2001/09). Pacific Earthquake Engineering Research Center, University of California, Berkeley.

Türk, H. A. (2019). *Çok katlı betonarme yapılarda farklı sismik izolatör sistemlerin ve kat adedinin deprem davranışına etkisi* (Master's thesis). Konya Teknik University, Konya, Türkiye. (In Turkish)

Turkish Building Earthquake Code (TBEC). (2018). *Principles for the design of buildings under earthquake*. Ankara, Türkiye.P

4th International Civil Engineering & Architecture Conference
17-19 May 2025, Trabzon, Türkiye

Investigation of progressive collapse behavior in seismically and non-seismically detailed RC frames under middle column removal scenario

Bedirhan Keçeci*[1], Sameer Alabsi[1], Fezayil Sunca[2,3], Ahmet C. Altunışık[1,3]

[1] *Karadeniz Technical University, Department of Civil Engineering, 61080 Trabzon, Türkiye*
[2] *Karadeniz Technical University, Department of Construction Technologies, 61080 Trabzon, Türkiye*
[3] *Karadeniz Technical University, Earthquake and Structural Health Monitoring Research Center, 61080 Trabzon, Türkiye*

Abstract. Progressive collapse is a process initiated by the sudden loss of load-carrying capacity of a local structural element, leading to the propagation of damage to other elements and resulting in significant structural damage or collapse. In this study, the progressive collapse behavior of reinforced concrete frames under middle column removal scenarios was investigated. Within the scope of the study, two different types of frames are evaluated: a frame designed according to the Turkish Building Earthquake Code 2018 (seismically detailed) and a frame with low concrete strength, smooth reinforcing bars and insufficient transverse reinforcement (lacking seismic detailing). The main objective of the study is to examine the development of progressive collapse mechanisms in these frames and compare their structural responses. For this purpose, the progressive collapse behavior of reinforced concrete frames was simulated using finite element modeling in ABAQUS software. As a result of the analyses, the resistance capacities of the frames against progressive collapse were obtained. In addition, changes in axial forces at the ends of the beam were determined to gain a better understanding of the load transfer mechanisms. Furthermore, the effects of concrete strength and variations in stirrup spacing on the load-carrying capacity were examined in detail through numerical models.

Keywords: Progressive collapse; RC frames; Seismic detailing; Finite element analysis

1. Introduction

Progressive collapse is a failure mechanism initiated by the sudden damage of a local structural element, which subsequently propagates to other elements, potentially resulting in the partial or total collapse of the entire structure (GSA, 2016). This type of collapse first drew attention with the failure of the 22-story Ronan Point apartment building in London in 1968, and later gained global prominence following the tragic collapse of the World Trade Center in 2001 (Elkady et al. 2024). In the aftermath of these events, various design methods and guidelines have been developed to enhance structural resistance against progressive collapse. The United States General Services Administration (GSA, 2016) published practical design guidelines for federal buildings, while the U.S. Department of Defense (DoD, 2024) issued a comprehensive manual outlining design criteria aimed at preventing progressive collapse.

In addition to the development of such guidelines, extensive experimental and numerical studies have been conducted to better understand the underlying mechanisms of progressive collapse. These investigations have primarily been carried out on scaled models such as beam-column frames or beam-slab subassemblies, often under column removal scenarios that simulate the sudden loss of a vertical load-carrying element. In reinforced concrete (RC) structures, progressive collapse is typically triggered by the loss of a column, and in such cases, the prevention of collapse progression depends on the effective redistribution of loads to adjacent members and the formation of alternative load paths (Adam et al., 2018). To examine the contribution of alternative load paths to mitigating collapse, various experimental tests have been performed (Yu et al., 2013; Yi et al., 2008; Xiao et al., 2015). Several studies have also investigated the force transfer mechanisms at beam-column connections, particularly in beams with axial restraints (Forquin and Chen, 2017; Lim et al., 2017). Moreover, the influence of parameters such as transverse reinforcement ratio, seismic detailing level, and span-to-depth ratio of beams on progressive collapse behavior has been explored through both experimental and numerical approaches (Qian & Li, 2013; Kang & Tan, 2015; Yap & Li, 2011; Choi & Kim, 2011; Yu & Tan, 2013).

* Corresponding author, E-mail: bedirhankececi@ktu.edu.tr

https://doi.org/10.31462/icearc2025_ce_eqe_884

This study investigates the progressive collapse behavior of reinforced concrete frames with and without seismic detailing through numerical modeling. In this context, frames with identical geometries but different reinforcement details were modeled using the ABAQUS software. The models were analyzed under middle column removal scenarios to determine their force transfer mechanisms, which were then compared. The comparison revealed the effect of seismic detailing on the progressive collapse resistance of RC frames.

2. Numerical modeling of reinforced concrete frames

In this section, the progressive collapse behavior of reinforced concrete (RC) frames under middle column removal scenarios was investigated through numerical analyses using the ABAQUS software. Within the scope of the analysis, the influence of seismic and non-seismic detailing on the structural response was evaluated. Based on widely adopted approaches in the literature, a prototype building was first designed, and subsequently, a representative frame from this building was selected and modeled at scale.

The prototype building features a span length of 4500 mm in both directions and a story height of 3000 mm (Fig 1). The critical frame used in the progressive collapse analysis was extracted from this prototype building and modeled in detail. To ensure computational efficiency and representativeness in the numerical simulations, 1/3 scale models were employed.

The RC frames were designated as RCF-1, RCF-2, RCF-3, and RCF-4. The geometric properties of the prototype building and frames are provided in Table 1. In the prototype building, columns measure 600×600 mm and beams measure 450×600 mm, whereas in the scaled frames, columns are 200×200 mm and beams are 150×200 mm.

The four frames used in this study share the same geometric characteristics but differ in concrete strength class and stirrup spacing. Material properties and reinforcement details of the RC frames are given in Table 2. Specifically, RCF-1 and RCF-2 frames utilize C30 (concrete with characteristic cylinder compressive strength 30MPa) concrete, while RCF-3 and RCF-4 employ C14 (concrete with characteristic cylinder compressive strength 14MPa) concrete. Additionally, 8 mm diameter stirrups spaced at 50 mm were used in the RCF-1 and RCF-3 frames, while 8 mm diameter stirrups spaced at 200 mm were used in the RCF-2 and RCF-4 frames. In all frames, column longitudinal rebar consists of 4⌀12 bars, and beam longitudinal rebar consists of 2⌀10 bars at both the top and bottom, with B420C (rebar with yield strength of 420 MPa) rebar grade employed. The reinforcement details of the frames are presented in Fig. 2, where the reinforcement layouts of the frames with 50 mm and 200 mm stirrup spacing are shown in detail.

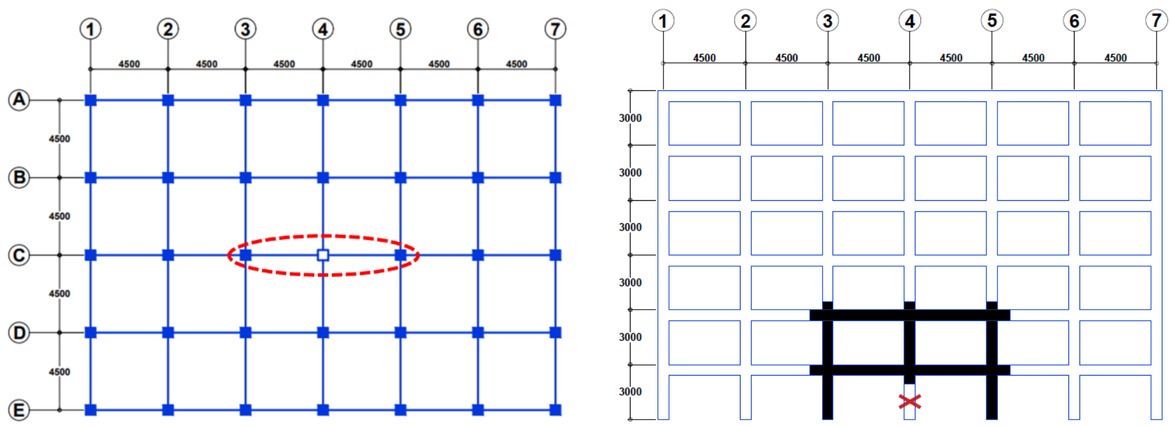

(a) Plan view (b) Elevation view

Fig. 1. Views of the prototype building

Table 1. Geometric properties of prototype building and RC frames

Property	Column section (mm)	Beam section (mm)	Story height (mm)	Span (mm)
Prototype building	600×600	450×600	3000	4500
RCF-1 RCF-2 RCF-3 RCF-4	200×200	150×200	1000	1500

Table 2. Material properties and reinforcement details of the RC frames

Frame ID	Concrete grade	Stirrup diameter (mm)	Stirrup spacing (mm)	Column longitudinal rebar	Beam longitudinal rebar
RCF-1	C30	8	50	4ø12	2ø10 (top and bottom)
RCF-2	C30	8	200	4ø12	2ø10 (top and bottom)
RCF-3	C14	8	50	4ø12	2ø10 (top and bottom)
RCF-4	C14	8	200	4ø12	2ø10 (top and bottom)

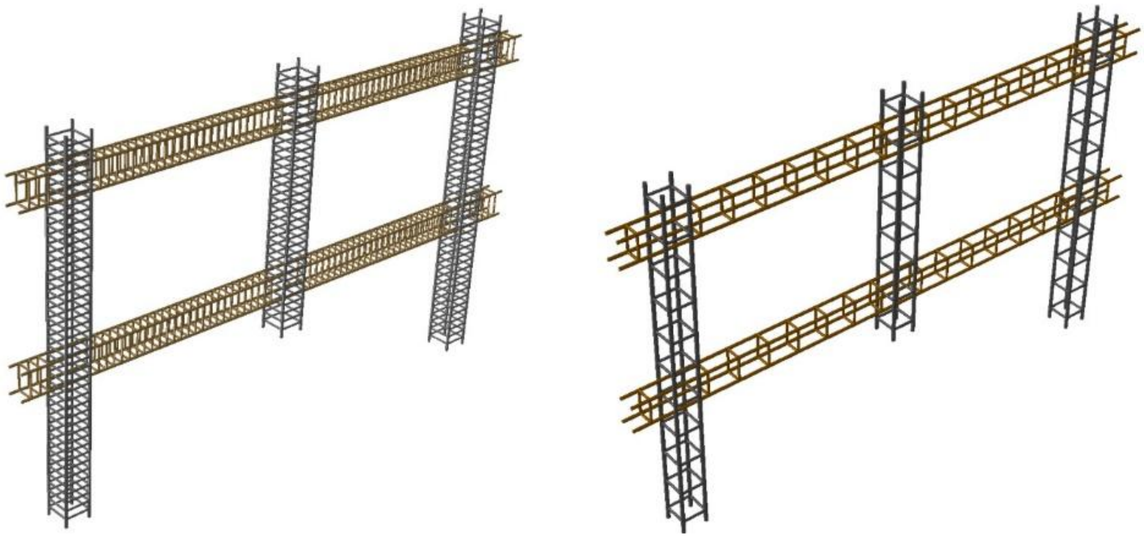

(a) Frame with 5cm stirrup spacing (b) Frame with 20cm stirrup spacing

Fig. 2. Reinforcement detailing of RC frames

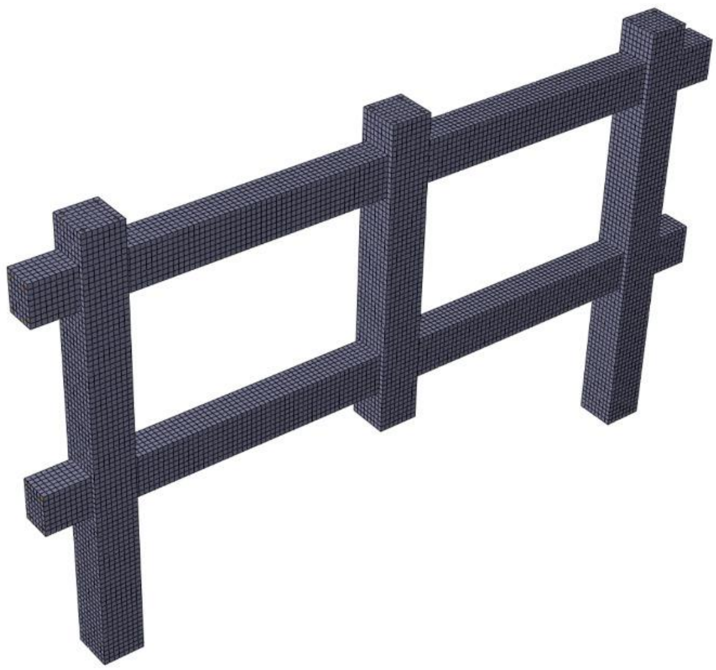

Fig. 3. Abaqus model of RC frames

In the ABAQUS software, the columns and beams were modeled using three-dimensional solid elements, while the reinforcements were represented as wire elements. To ensure a high level of analysis precision, the mesh size was set to 25 mm (Fig. 3). The other parameters of the ABAQUS model were selected based on the study by Qingfu (2020). An axial force of 240 kN, corresponding to 20% of the axial load-carrying capacity of the columns, was applied on top of the edge columns and kept constant throughout the analyses. The frames are supported at the ends of the beams on either side of each span and only rotations are allowed at these points. These boundary and loading conditions were established to realistically capture the progressive collapse mechanisms that may occur under the middle column removal scenario. Subsequently, a displacement-controlled axial force was applied incrementally on the middle column, starting from zero. To monitor the development of progressive collapse behavior and to assess the damage in the beam–column joint regions, the Simplified Damage Plasticity (SCDP) equation proposed by Hafezolghorani et al. (2017) was employed. This numerical approach enabled the evaluation of the progressive collapse behavior of RC frames and the investigation of the effects of various design parameters on the collapse mechanisms.

3. Results and discussion

This study has revealed the progressive collapse behavior of four different reinforced concrete frames (RCF-1, RCF-2, RCF-3, RCF-4) under middle column removal scenario. The load-carrying and deformation capacities of the frames were evaluated using load–displacement and horizontal reaction force graphs (Fig. 4–7), while the damage mechanisms that developed during this behavior were illustrated through damage distribution visualizations (Fig. 8–11).

Fig. 4 and 5 present the vertical load–displacement relationships, highlighting the effects of concrete strength and stirrup spacing on load-carrying capacity and ductility. Among the C30 concrete frames (RCF-1, RCF-2), the RCF-1 frame with 50 mm stirrup spacing exhibited a notably higher load-carrying capacity compared to RCF-2. In RCF-1, following the initial flexural action stage, a maximum load of 183 kN was recorded, after which the frame exhibited pronounced ductile behavior during the development of compressive arch and catenary action stages, dissipating a significant amount of energy prior to collapse. In contrast, the RCF-2 frame displayed no substantial difference in maximum load during the initial flexural action stage compared to RCF-1; however, due to the 200 mm stirrup spacing, ductility and energy dissipation capacity were reduced during the compressive arch and catenary action stages, leading to an earlier onset of collapse.

A similar trend was observed in the C14 concrete frames: RCF-3 (50 mm stirrup) demonstrated superior load-carrying and deformation capacity relative to RCF-4 (200 mm stirrup). The concrete class comparisons in Figure 5 clearly show that the frames with C30 concrete grade are superior to the frames with C14 concrete grade in terms of both load-carrying and ductility. Fig. 6 and 7 present the axial force variations in the edge beams of the frames, as derived from the horizontal reaction force–displacement graphs. During the initial loading phase, significant axial compressive forces developed only in the first-floor beams, while the second-floor beams experienced only limited compression. Furthermore, as the vertical displacement increased, the axial forces in the first-floor beams transitioned from compression to tension, indicating the formation of the catenary action stage in the beams.

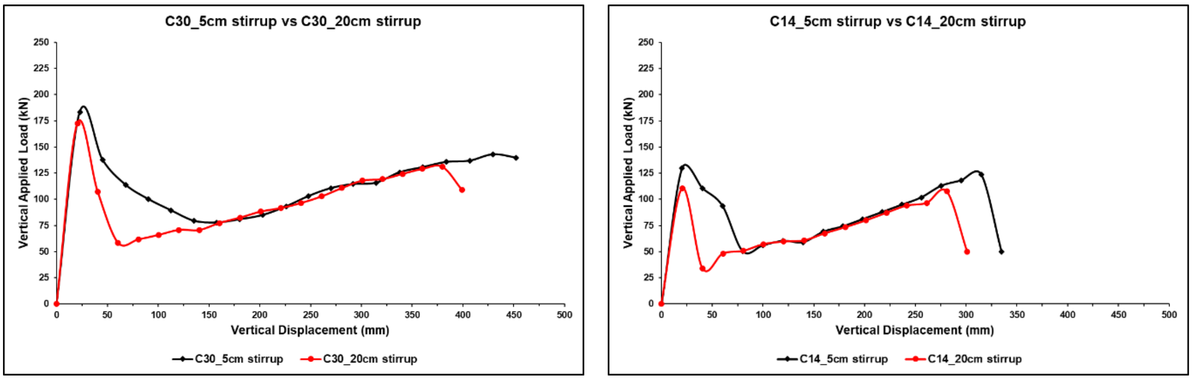

(a) Vertical load–displacement curve for RCF-1 and RCF-2 (C30 concrete frames)

(b) Vertical load–displacement curve for RCF-3 and RCF-4 (C14 concrete frames)

Fig. 4. Vertical load–displacement relationships of RC frames under middle column removal scenario

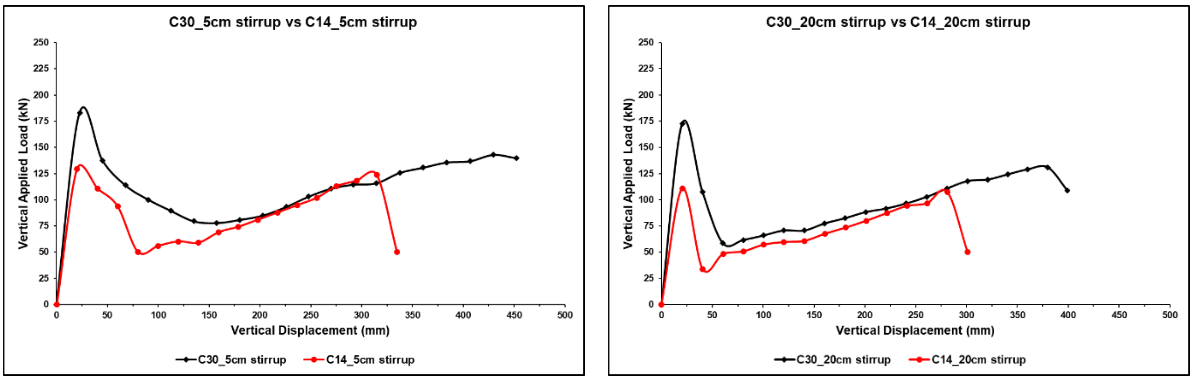

(a) Vertical load–displacement curve comparing C30 and C14 concrete for 50 mm stirrup spacing

(b) Vertical load–displacement curve comparing C30 and C14 concrete for 200 mm stirrup spacing

Fig. 5. Effect of concrete strength on vertical load–displacement behavior of RC frames

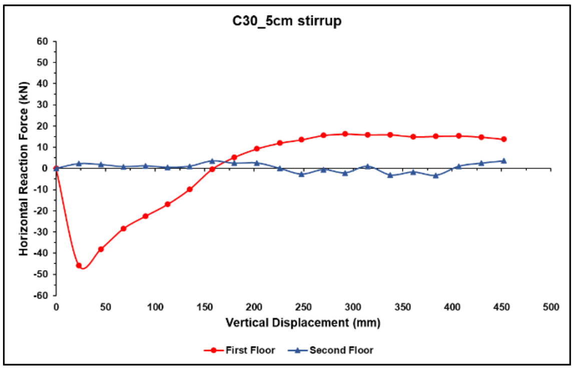

(a) Horizontal reaction force–displacement curve for RCF-1 frame

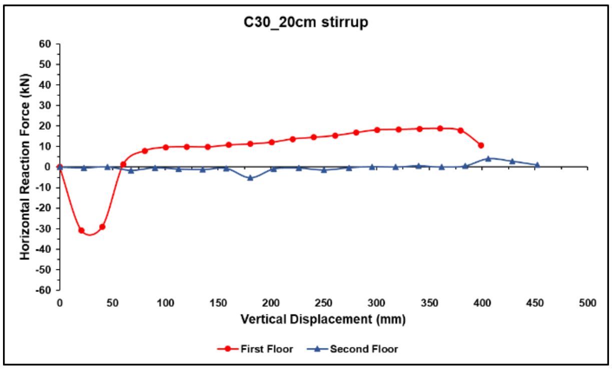

(b) Horizontal reaction force–displacement curve for RCF-2 frame

Fig. 6. Horizontal reaction force-displacement relationships at beam ends of reinforced concrete frames with concrete grade C30

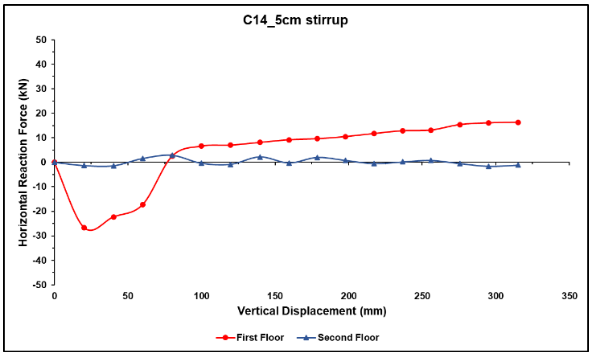

(a) Horizontal reaction force–displacement curve for RCF-3 frame

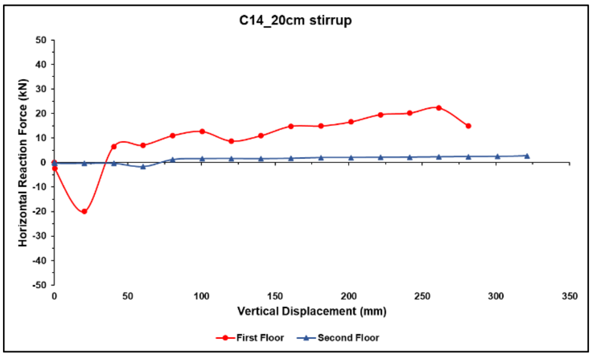

(b) Horizontal reaction force–displacement curve for RCF-4 frame

Fig. 7. Horizontal reaction force-displacement relationships at beam ends of reinforced concrete frames with concrete grade C14

The load-carrying and deformation behaviors obtained from the vertical load–displacement and horizontal reaction force graphs of the RC frames were directly correlated with the damage distribution visualizations (Figures 8–11). In the RCF-1 frame (C30, 50 mm stirrup spacing), concrete damage was observed at the beam–column joints at a displacement of 158 mm, followed by the initiation of the catenary action stage, and ultimately, at the maximum displacement of 452 mm, extensive damage occurred at the joints. The confinement effect provided by the closely spaced stirrups delayed the formation of plastic hinges and enhanced the ductility of the system. In contrast, in the RCF-2 frame (C30, 200 mm stirrup spacing), damage at the beam–column joints began to appear at 60 mm displacement, while at 399 mm, pronounced plastic deformations, core concrete crushing, and local failures at the joints were observed.

In the C14 concrete frames, the RCF-3 frame with 50 mm stirrup spacing exhibited joint concrete damage at 80 mm displacement, and severe damage was noted at 315 mm. Despite the lower concrete strength, the use of closely spaced stirrups delayed the progression to collapse. In the RCF-4 frame (C14, 200 mm stirrup spacing), the earliest collapse behavior was observed; concrete damage at the joints initiated at 40 mm displacement, and severe joint damage developed at 281 mm. The damage distribution visualizations clearly revealed the underlying mechanisms responsible for the behaviors observed in the load–displacement and horizontal reaction force graphs.

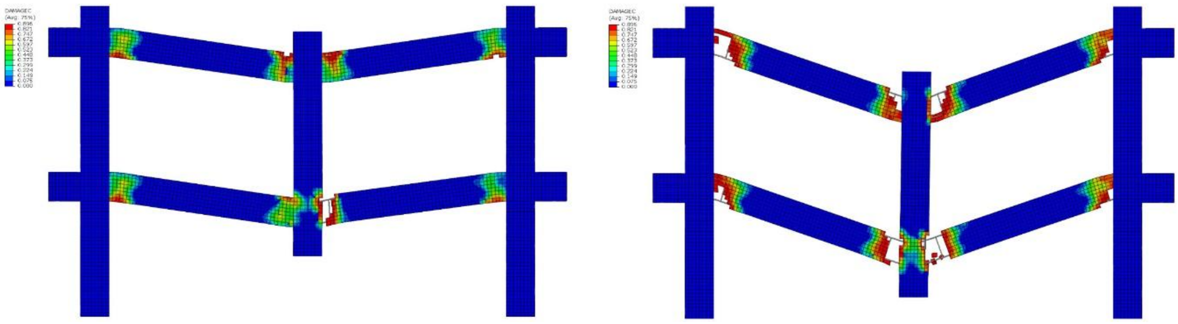

(a) 158 mm (b) 452 mm

Fig. 8. Damage distribution in RCF-1 (C30, 50 mm stirrup) at different displacement levels

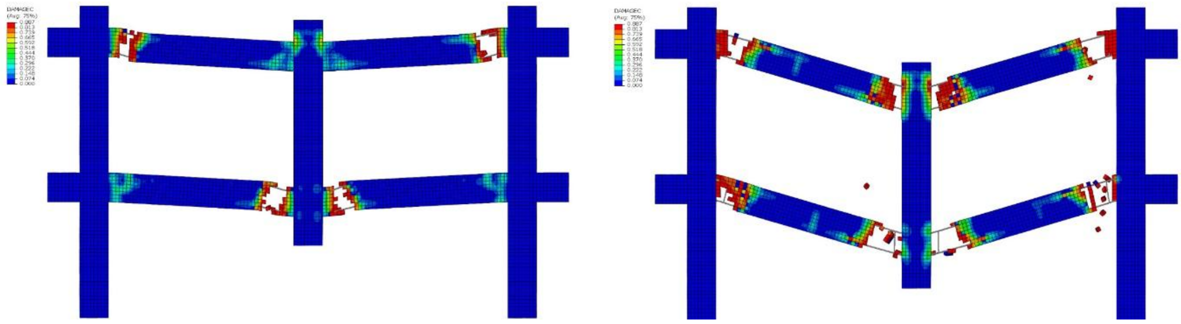

(a) 60 mm (b) 399 mm

Fig. 9. Damage distribution in RCF-2 (C30, 200 mm stirrup) at different displacement levels

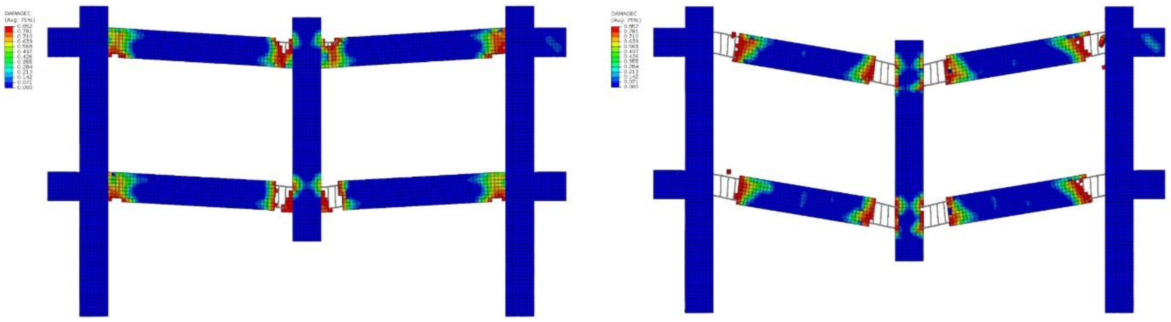

(a) 80 mm (b) 315 mm

Fig. 10. Damage distribution in RCF-3 (C14, 50 mm stirrup) at different displacement levels

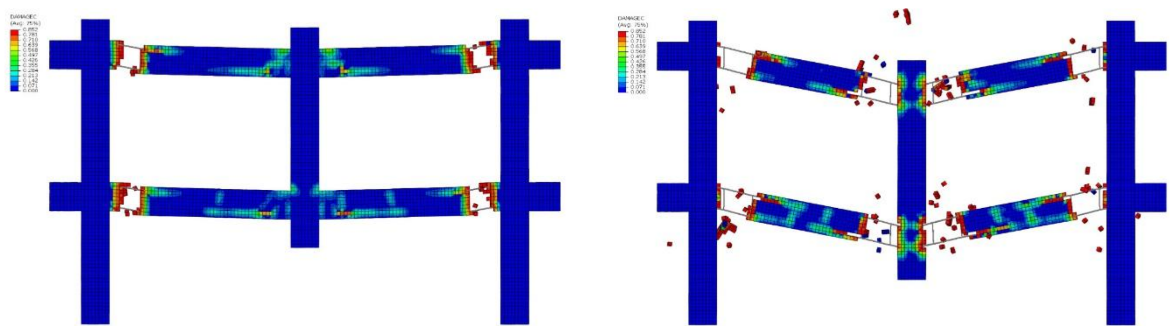

(a) 40 mm (b) 281 mm

Fig. 11. Damage distribution in RCF-4 (C14, 200 mm stirrup) at different displacement levels

4. Conclusions

This study investigated the progressive collapse behavior of seismically and non-seismically detailed reinforced concrete (RC) frames under middle column removal scenario through numerical analyses. Based on the results obtained, the following key conclusions can be drawn:

- Seismically detailed RC frames (C30 concrete, 50 mm stirrup spacing) exhibited significantly higher load-carrying capacity, ductility, and energy dissipation performance compared to non-seismically detailed frames (C30 concrete, 200 mm stirrup spacing).
- Although low-strength concrete (C14) frames showed weaker performance compared to high-strength concrete (C30) frames, the use of closely spaced stirrups still improved progressive collapse resistance by delaying the onset of catenary action and ultimate collapse.
- Axial force redistribution was primarily observed in the first-floor beams; as displacement increased, compressive forces in the beams transitioned to tensile forces, indicating the activation of compressive arching and catenary mechanisms that are critical for maintaining structural integrity following column removal.
- The numerical results highlight the importance of proper seismic detailing, particularly in terms of stirrup spacing and concrete strength, in enhancing the strength and robustness of RC frames against progressive collapse.

Acknowledgments

The study in this paper is supported by Karadeniz Technical University, Scientific Research Projects Unit within the scope of Research Universities Support Program Project. Project no: FBA-2024-11059.

References

GSA (General Services Administration). (2016). Alternate path analysis & design guidelines for progressive collapse resistance. General Services Administration.

Elkady, N., Nelson, L. A., Weekes, L., Makoond, N., & Buitrago, M. (2024). Progressive collapse: Past, present, future and beyond. In Structures (Vol. 62, p. 106131). Elsevier.

DoD, U. (2024). Unified facilities criteria: design of buildings to resist progressive collapse. UFC 4-023-03. United States Department of Defense.

Adam, J. M., Parisi, F., Sagaseta, J., & Lu, X. (2018). Research and practice on progressive collapse and robustness of building structures in the 21st century. Engineering Structures, 173, 122-149.

Yu, J., & Tan, K. H. (2013). Structural behavior of RC beam-column subassemblages under a middle column removal scenario. *Journal of Structural Engineering*, *139*(2), 233-250.

Yi, W. J., He, Q. F., Xiao, Y., & Kunnath, S. K. (2008). Experimental study on progressive collapse-resistant behavior of reinforced concrete frame structures. *ACI Structural Journal*, *105*(4), 433.

Xiao, Y., Kunnath, S., Li, F. W., Zhao, Y. B., Lew, H. S., & Bao, Y. (2015). Collapse test of three-story half-scale reinforced concrete frame building. *ACI Structural journal*, *112*(4), 429.

Forquin, P., & Chen, W. (2017). An experimental investigation of the progressive collapse resistance of beam-column RC sub-assemblages. *Construction and Building Materials*, *152*, 1068-1084.

Lim, N. S., Tan, K. H., & Lee, C. K. (2017). Effects of rotational capacity and horizontal restraint on development of catenary action in 2-D RC frames. *Engineering Structures*, *153*, 613-627.

Qian, K., & Li, B. (2013). Performance of three-dimensional reinforced concrete beam-column substructures under loss of a corner column scenario. *Journal of Structural Engineering*, *139*(4), 584-594.

Kang, S. B., & Tan, K. H. (2015). Behaviour of precast concrete beam–column sub-assemblages subject to column removal. *Engineering Structures*, *93*, 85-96.

Li, B., & Yap, S. L. (2011). Experimental investigation of reinforced concrete exterior beam-column subassemblages for progressive collapse.

Choi, H., & Kim, J. (2011). Progressive collapse-resisting capacity of RC beam–column sub-assemblage. *Magazine of concrete research*, *63*(4), 297-310.

Yu, J., & Tan, K. H. (2013). Experimental and numerical investigation on progressive collapse resistance of reinforced concrete beam column sub-assemblages. *Engineering Structures*, *55*, 90-106.

Qingfu, L., Wei, G., & Yihang, K. (2020, March). Parameter calculation and verification of concrete plastic damage model of ABAQUS. In *IOP conference series: Materials science and engineering* (Vol. 794, No. 1, p. 012036). IOP Publishing.

Hafezolghorani, M., Hejazi, F., Vaghei, R., Jaafar, M. S. B., & Karimzade, K. (2017). Simplified damage plasticity model for concrete. *Structural engineering international*, *27*(1), 68-78.

Comparative analysis of Kahramanmaraş Earthquakes for old and new buildings

Kevser Damlar[1], Hakkı C. Demir[1], Mehmet Palanci[*1], Rojda Orman Subaşı[1]

[1] *Istanbul Arel University, Department of Civil Engineering, 34537 Istanbul, Türkiye*

Abstract. In this study, acceleration and displacement response spectra were calculated using earthquake simulations using earthquake records recorded in the Kahramanmaraş and Hatay regions during the Kahramanmaraş earthquake sequences. Considering the general topology of the regions, low- and mid-rise reinforced concrete buildings were analyzed. Using these general structural characteristics of these buildings, earthquake loads affecting these buildings due to recorded earthquakes were calculated. For the comparison, the former Turkish Earthquake Code (TEC) 2007 and recent Turkish Building Earthquake Code (TBEC) 2018 were considered, and code-based elastic forces and displacement were computed. During the comparisons, the earthquake loads affecting these buildings were compared using the earthquakes codes, such as 2007 and 2018 regulations. Thus, a force-based evaluation of the buildings was performed. Following the force-based evaluation, displacement spectra were used to determine the ductility demands in the buildings, and the ductility demands demanded from the buildings were evaluated. The force-displacement damage relationship was evaluated by comparing the obtained data with the post-earthquake damages.

Keywords: Kahramanmaraş earthquakes; Force-based evaluation; Seismic codes

1. Introduction

Many natural disasters, such as earthquakes, floods, and storms, cause loss of life and property, as well as major destruction both around the world and in our country. In the last 100 years, Türkiye has experienced 20 earthquakes with a magnitude of 7 and above, highlighting that Türkiye is an active, earthquake-prone country. On February 6, 2023, two earthquakes with magnitudes of Mw7.7 and Mw7.6 occurred in our country, with epicenters located in the Pazarcık and Elbistan districts of Kahramanmaraş. These earthquakes directly influenced the 11 provinces, resulting in significant loss of life and property. Additionally, the cost of the destruction and the severely damaged energy and communication infrastructure to our country was 103.6 billion dollars. This situation reveals that Turkey is one of the countries most severely affected by earthquakes (Presidency of the Republic of Türkiye Strategy and Budget Presidency, 2023).

From an earthquake engineering perspective, the intensity of the earthquake, the examination of structures under the influence of earthquakes with experimental and theoretical methods, and the interpretation of the obtained data from these empirical models are among the important topics of study. These topics allow us to focus on the development of the design of earthquake-resistant structures and the strengthening of existing structures against earthquake effects. In addition, the characteristics of ground motion records are an effective parameter in examining the behavior of structures under the earthquake excitations. Ground motion records vary depending on various parameters such as the magnitude of the earthquake, the duration of the earthquake, local soil conditions, the type of faulting, and the distance between the epicenter and the recording station. Therefore, the ground motion record to be used in the analyses will directly determine the design or performance evaluation to be made, as it will affect the analysis results to be obtained (Demir, 2015).

With the performance-based design approach, realistic results can be obtained regarding the amount of deformation that a new or existing building will undergo under the effect of an earthquake, the type and condition of damage it will receive, and the general performance of the structure. Although different methods are applied in many codes in the world, a common perspective is based on the performance-based design principle. In this design approach, the deformation demands of the structural elements must be determined first. To obtain these demands, the analysis of structures or systems in the time history domain is widely adopted. There are many studies in the literature using these methods.

[*] Corresponding author, E-mail: mehmetpalanci@arel.edu.tr

https://doi.org/10.31462/icearc2025_ce_eqe_890

Ruiz-García & Miranda, (2006) comprehensively investigated the magnitude and distribution of the permanent drift demand of a 12-story, single-span frame system. Nonlinear analysis was performed using 40 scaled acceleration records for the analysis. As a result of the study, the effects of parameters such as ground motion intensity, vibration period, number of floors, and system strength on the permanent drift behavior were statistically examined. It was explained that the permanent relative drift demand should also be taken into consideration in the performance evaluation.

Fahjan et al., (2011) performed linear and nonlinear analysis of a 12-story reinforced concrete building using 10 scaled real earthquake records. It was emphasized that at least 7 earthquake records should be used, and the average of the obtained results should be taken as a basis to obtain reliable results.

İnel et al., (2011) compared the three-dimensional models of 2-, 4-, and 7-story reinforced concrete buildings representing the existing building stock in Türkiye, considering the single degree of freedom (SDOF) models. 19 real acceleration records were used in the nonlinear elastic analyses. It was stated that the roof drift demands of the SDOF models were higher than the three-dimensional models. Hamsici (2019) investigated the effects of earthquake ground motion spectra calculated within the scope of TEC 2007 (TEC, 2007) and TBEC 2018 (TBEC, 2018) codes on base shear force and maximum relative story drifts. Seismic analysis of 4-, 7-, and 10-story structures under 4 different soil types located in different earthquake zones was performed using the FEM program according to principles of both codes. The analysis results showed that as the number of stories increased, the base shear force values calculated according to TBEC 2018 decreased compared to TEC 2007. On the other hand, the maximum effective story drift values increased significantly compared to the former code.

Çoruh, (2024) compared the earthquake design spectra of a school building according to different earthquake codes. The contents of the codes, soil classes, and horizontal elastic design spectra were examined, and graphical comparisons were made for different soil types. As a result, it was stated that there were similarities between the codes as well as significant differences and deficiencies, especially regarding the consideration of soil conditions. Keyik (2019) investigated the different parameters adopted by TBEC 2018 and ASCE 41-17 (ASCE/SEI 41-17, 2017) codes when making performance-based evaluations. It was explained that while TBEC 2018 strain values play an important role in determining performance levels. Meral (2021) compared the seismic demands of 3, 6, and 9-story reinforced concrete buildings, obtained as a result of linear elastic and linear inelastic time history analyses using 12 earthquake records. It was observed that base shear force demands are prominent in linear analyses, while displacement demands are prominent in nonlinear analyses.

In this study, the acceleration and displacement response spectra of low and medium-rise (3, 5, and 7-story) reinforced concrete residential buildings were compared with the records of the Kahramanmaraş earthquake sequences (Kahramanmaraş and Hatay) by the TEC 2007 and TBEC 2018 codes. Then, the ductility demands and the force-displacement relationship obtained from the displacement spectra were examined.

2. Typical building models

In this study, three different residential buildings with 3, 5, and 7 stories were considered, and it was assumed that these buildings were designed according to TEC 2007, which uses capacity design principles. The height of the first floor was 3.5 m, and the height of the other floors were taken as 3 m. The concrete quality was taken as C25, and the reinforcement quality was assumed as S420. In 3- and 5-story buildings, the cross-sectional dimensions of beams and columns were taken as 30x60cm, while in the 7-story building, columns were 40x70cm and beams were 30x60cm. It was assumed that the reinforced concrete buildings are located in the first degree earthquake zone and on Z3 class soil, according to TEC 2007. Buildings were designed as high ductile buildings with beam-column frame systems. Typical representation and designed residential buildings are plotted in Fig. 1.

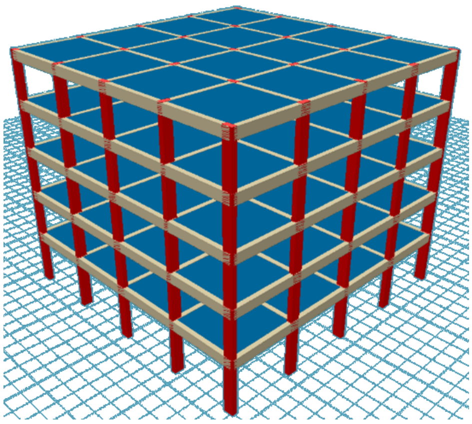

Fig. 1. Three dimensional representation of typical buildings considered

Buildings were considered as regular in plan and height. The buildings have five axis and four bays in plan, and the width of the bays were taken constant as 4.50 m. As a result of the modal analysis, the periods of the 3-, 5-, and 7-story buildings were found to be 0.538 s, 0.839 s, and 0.938 s, respectively. Using these period values, the elastic earthquake forces and displacement demands acting on the buildings are analyzed, assuming that the buildings are located in the Hatay and Maraş regions. To consider Kahramanmaraş sequences, the location of accelerometer 3129 in Hatay was taken into consideration since the maximum accelerations were recorded in Hatay province for a magnitude of Mw=7.7, and the location of accelerometer 4612 in Kahramanmaraş was taken into consideration since the maximum accelerations measured were in Maraş province for the earthquake with a magnitude of Mw=7.6.

2.1. Calculation of target elastic acceleration spectra for Hatay and Kahramanmaraş regions

The comparison of the target spectra calculated according to the TEC2007 and TBEC2018 codes for Hatay and Maraş provinces and the earthquake spectra obtained from corresponding stations (i.e., 3129 and 4612 stations) are shown in Fig. 2.

The location of the 3129 station is in Hatay-Antakya, and this location is in the 1st degree earthquake zone according to TEC-2007. Therefore, the effective ground acceleration coefficient (A_0) is taken as 0.40. In addition, the location of 4612 station is in Maraş-Göksun, and this location is in the 3rd degree earthquake zone according to TEC-2007, and so, effective ground acceleration coefficient (A_0) is considered as 0.20 for TEC-2007. For the elastic target spectrum, similar analyses were also made for TBEC 2018, and based on the location of stations, local soil class (according to NEHRP site classification), local soil coefficients (F_S and F_1), and response acceleration parameters (S_S, S_1, S_{DS}, S_{D1}) were calculated. The parameters during the calculation of the target spectra for both seismic codes are provided in Table 1. It is worth noting that target elastic spectral accelerations were computed for a design earthquake that has a return period of 475 years, which corresponds to the 10% probability of exceedance in 50 years.

In addition to target spectra determined from the seismic codes, the spectral acceleration spectrum of recorded ground motions recorded at the 3129 and 4612 stations for both components, such as east-west (EW) and north-south (NS), were considered. These spectral accelerations are plotted in Fig. 2 to make a comparison of target and recorded real ground motions. It can be seen from the figure that spectral accelerations of TBEC are higher than TEC at low periods ($T < 0.6$ s), and spectral accelerations tend to get similar with increasing periods. Spectral acceleration of TBEC is slightly lower than TEC in Hatay when $T > 0.6$ s. Figure also clearly demonstrates that spectral acceleration of record motion in NS and EW components is higher than both seismic codes. Especially recorded motions in Hatay are highly observatory for periods ($T < 1.2$ s). When the recorded motion in Kahramanmaraş is observed, it can be said that spectral acceleration of TBEC and recorded motions are very close when $T < 1.0$ s. On the other hand, spectral acceleration is greatly diverged from the seismic codes when $T > 1.2$ s. For periods of considered residential buildings, it can be said spectral acceleration of record motion at these periods are generally higher, which will cause higher lateral shear forces.

Table 1. The parameters for the calculation of elastic target spectrum for TEC-2007 and TBEC-2018

Parameters		Soil type	A_0	I	T_A	T_B
TEC-2007	Hatay	Z2	0.4	1.0	0.15	0.4
	Kahramanmaraş	Z3	0.2	1.0	0.15	0.6
Parameters		Soil type	S_s	S_1	T_A	T_B
TBEC 2018	Hatay	ZC	1.064	0.276	0.065	0.324
	Kahramanmaraş	ZD	0.688	0.178	0.093	0.464

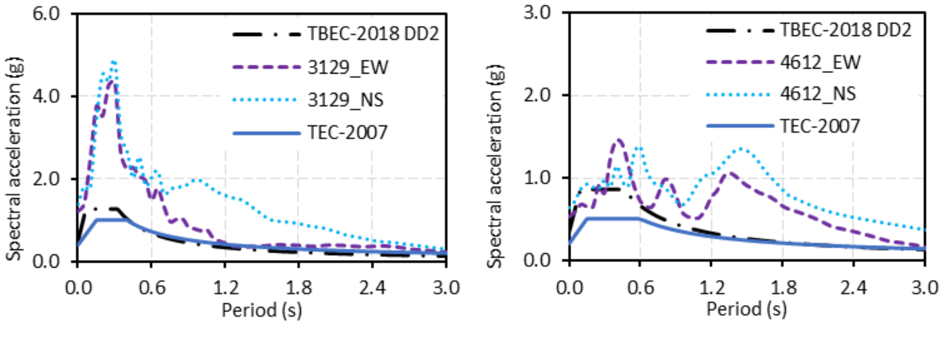

Fig. 2. Comparison of spectral accelerations computed for seismic codes and recorded real ground motions in the stations (Left: Hatay, Right: Maraş)

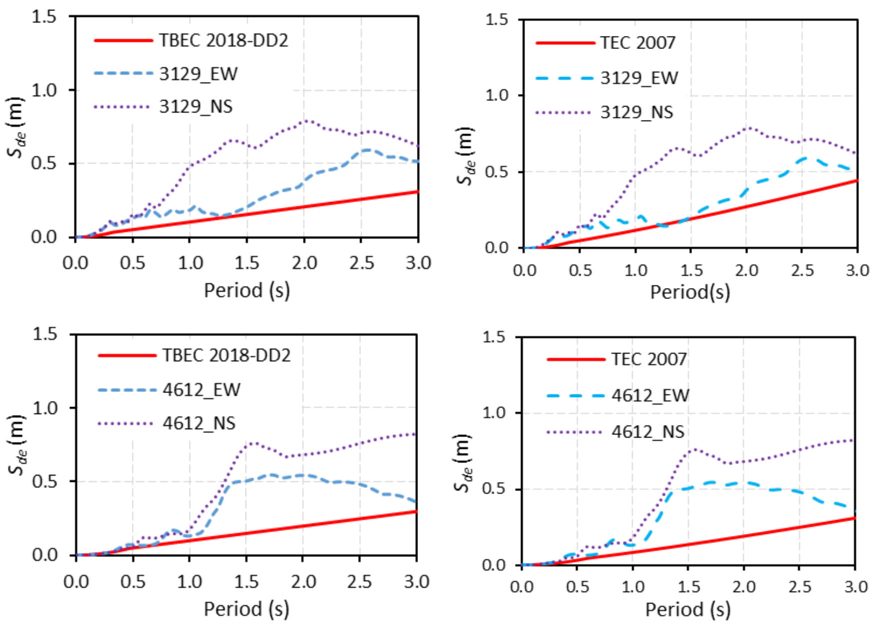

Fig. 3. Displacement spectrum of seismic codes and recorded ground motion in Hatay (up) and Kahramanmaraş (bottom)

2.1. Calculation of displacement spectra for Hatay and Kahramanmaraş regions

To make displacement-based comparison, displacement spectra of seismic codes and recorded ground motions were made. The determination of displacement spectra will allow to make displacement-based evaluation of demands for the considered buildings. In this way, displacement based and force based comparisons will be made for considered building topologies.

Since spectral acceleration of seismic codes are computed, these accelerations can be converted to spectral displacement based on Equation 1. Linear time history analysis were made to compute spectral displacement of recorded ground motions. A comparsion of the spectral displacement of recorded motion considering both components and seismic codes are plotted in Fig. 3. This clearly demonstrates that not only spectral acceleration but also displacement demands determined from recorded motions are higher than seismic codes. Numerical comparisons will also be made to make a comparative assessment between shear forces and displacement demands.

$$S_{de}(T) = \left(\frac{T^2}{4\pi^2}\right) S_{ae}(T) \tag{1}$$

3. Analysis results

3.1. Force-based assessment using seismic codes

In order to make force-based comparisons, base shear demands are determined from the target spectral acceleration for each seismic code. An example calculation is given in Table 2 for TEC-2007 and Table 3 for TBEC-2018, considering Hatay and Kahramanmaraş (Maraş) city.

Table 2. Calculations of base shear force according to TEC-2007 for 3-story building

Building	Parameters		Hatay	Maraş
	Effective ground acc.	A_0	0.4	0.2
	Period	T_1 (s)	0.538	
	Soil type		Z2	Z3
	Importance factor (I)		1	
3 story	Ductility	R_a	8	
	Building weight	W (t)	2258.36	
	Spectral coefficient	S(T)	1.97	2.50
	Elastic spectral acc	S_{ae}(T) (g)	0.79	0.50
	Base Shear Force	V_{te} (t)	222.70	141.15

Table 3. Calculations of base shear force according to TBEC-2018 for 3-story building

Building	Parameters		Hatay	Maraş
3 story	Map spectral coefficients	$S_S;S_1$	1.064;0.276	0.688;0.178
	Period	T_1 (s)	0.538	
	Soil type		ZC	ZD
	Importance factor (I)		1	
	Ductility	R	8	
	Building weight	W (t)	2258.36	
	Horizontal spectral acc.	$S_{ae}(T)$ (g)	0.77	0.74
	Reduced hor. spectral acc.	$S_{aR}(T)$ (g)	0.096	0.093
	Base Shear Force	V_{te} (t)	217.37	209.36

Using the similar procedure given in Table 2 and Table 3, base shear force (V_{te}) acting on all 3, 5 and 7 story residential buildings is calculated considering TEC2007 and TBEC2018 regulations, and results are given in Table 4. It can be seen from the table that base shear force demands obtained from TEC-2007 are higher than TBEC-2018 in Hatay, whereas TBEC-2018 is higher than TEC-2007 for Maraş city.

Table 4. Comparison of base shear forces for 3-, 5- and 7-story building according to TEC-2007 and TBEC-2018

Number of story	Hatay		Maraş	
	TEC-2007 (t)	TBEC 2018 (t)	TEC-2007 (t)	TBEC 2018 (t)
3	222.70	217.37	141.15	209.36
5	267.92	239.11	185.29	230.45
7	358.70	313.07	248.07	301.73

3.2. Force-based assessment using recorded ground motions

In order to make force-based comparison between seismic codes and recorded motions, base shear demands must also be determined from the recorded motions. For this purpose, building periods corresponding to spectral acceleration ($S_{ae}(T)_{EQ}$) of recorded ground motions are obtained. An example calculation for the determination of $S_{ae}(T)_{EQ}$ is sketched in Fig. 4. The example is plotted for 5-story building, which T=0.839 s, and spectral acceleration at this period for NS and EW directions were obtained as 1.80g and 1.04g, respectively. Based on these spectral accelerations, base shear demand for these components were calculated 503.28 t and 871.23 t (see Table 5) for NS and EW directions in Hatay, respectively. Similar computations were also made for other buildings and Maraş city.

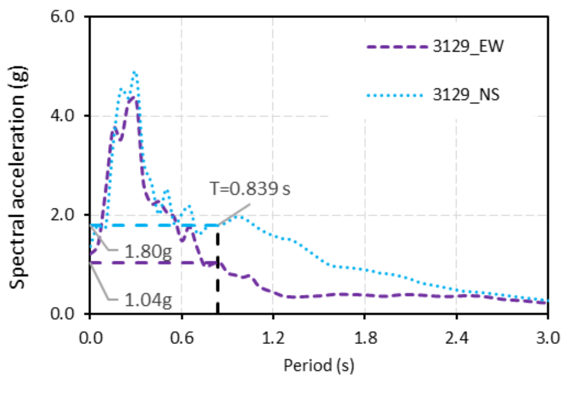

Fig. 4. Calculation of $S_{ae}(T)_{EQ}$ for sample building considered for Hatay city

Table 5. Calculation of base shear force from recorded motions for 5-story building considering Hatay city

Building	Parameters		EW	NS
5 story	Period	T_1 (s)	0.839	
	Soil type		ZC	
	Importance factor (I)		1	
	Ductility	R	8	
	Building weight	W (t)	3876.62	
	Horizontal spectral acc.	$S_{ae}(T)_{EQ}$ (g)	1.04	1.80
	Reduced hor. spectral acc.	$S_{aR}(T)_{EQ}$ (g)	0.130	0.225
	Base Shear Force	V_{te} (t)	503.28	871.23

3.3. Comparison of elastic force-based results

Using this base shear force demand obtained in Section 3.2 and Section 3.1, code-based and earthquake based shear demands for 3.5 and 7-story buildings are compared in Table 6. Comparisons are made in terms of ratios. For example, base forces of seismic codes are found to make code based assessments in terms of ratios. Similar ratios were also computed for both components. In addition, base shear demands are divided to code based shear forces to understand shear demanded by the recorded motion in corresponding stations.

It can be seen from Table 6 that base shear demand ratios for seismic codes change depending on the region considered. For example, the ratio of TBEC 2018 to TEC 2007 is lower than 1.0 and it is found 0.98, 0.89 and 0.87 for 3-, 5- and 7- story buildings, respectively. On the other hand, these ratios are higher than 1.0 such as 1.48, 1.24 and 1.22 for 3-, 5- and 7- story buildings, respectively, indicating that TBEC shear demands are higher than TEC 2007.

Since the Turkish Building Earthquake Code is currently in practice, earthquake demands are proportioned by taking this code into account, and base shear demands determined from the recorded motions are divided to TBEC based base shear forces. It can be observed from Table 6 that code based shear demands are lower than those of record motions, the lowest ratio is 1.29 and the highest ratio is obtained as 4.39. The lower ratios are obtained from Kahramanmaraş city for a 3-story building when considering the east-west direction of recorded motion, but when the NS component is considered, this ratio increases to 1.63.

When the obtained results are investigated for Hatay city, it can be said that a higher ratio (see Table 6, i.e., 4.39) is obtained from Hatay city for a 7-story building when considering the north-south direction of recorded motion, but when the EW component is considered, this ratio decreases to 1.83. Based on the above results, it can be said that code based forces are lower than recorded motions, indicating that designed buildings may undergo elastic displacement, and hence nonlinear deformation may be needed.

One may also think that buildings may be inadequate when only shear forces are considered. On the other hand, it is worth keeping in mind that code-based design allows buildings to behave in a nonlinear phase since code-based spectral accelerations are obtained under uncertainties involved in seismic hazard analysis. Accordingly, obtained results clearly indicate that buildings should have certain ductility when shear forces are exceeded to ensure their performance level, which is Life Safety for ordinary buildings.

3.4. Comparison of elastic displacement-based results

In the earlier section (section 2.1), elastic spectral displacement versus periods were computed for both seismic codes and recorded ground motions. Based on the results, elastic spectral displacement demands corresponding to buildings periods were obtained. Using these elastic displacement values, the ratio of displacement demands were calculated and results are provided in Table 7.

It can be seen from Table 7 that as calculated displacement ratios are identical with force-based ratios, the calculations behind displacement for the seismic code is based on Eq. 1. Accordingly, displacement demands are proportional to spectral accelerations and hence, displacement ratios are the same as ratios obtained from accelerations. When displacement ratios determined from the real earthquakes are compared, it can be said that ratios differ.

Table 6. Comparison of code- and recorded earthquake- based base shear demands for buildings considering Hatay and Kahramanmaraş cities

Building Story	TBEC 2018/ TEC 2007 Hatay	TBEC 2018/ TEC 2007 Maraş	3129EW/ TBEC 2018	3129NS/ TBEC 2018	4612EW/ TBEC 2018	4612NS/ TBEC 2018
3	0.98	1.48	2.58	2.60	1.29	1.63
5	0.89	1.24	2.10	3.64	2.01	1.75
7	0.87	1.22	1.83	4.39	1.51	1.60

Table 7. Comparison of code- and recorded earthquake- based ratio of horizontal elastic design displacement for DD2 level considering Hatay and Kahramanmaraş cities

Building Story	TBEC 2018/ TEC 2007 Hatay	TBEC 2018/ TEC 2007 Maraş	3129EW/ TBEC 2018	3129NS/ TBEC 2018	4612EW/ TBEC 2018	4612NS/ TBEC 2018
3	0.98	1.48	2.56	2.55	1.28	1.65
5	0.89	1.24	2.10	3.72	2.00	1.75
7	0.87	1.22	1.81	4.54	1.50	1.61

It can be observed from the Table 7 that code based displacement demands are lower than those of record motions and lower ratio is 1.28 and the highest ratio is obtained as 4.54. The lower ratios are obtained from Kahramanmaraş city for 3-story building for the east-west direction, but when the NS component is considered, this ratio increases to 1.65.

The obtained results from Hatay city indicate that the highest ratio is 4.54 for a 7-story building when considering the north-south direction of recorded motion. For the same station, this ratio decreases to 1.81 for the EW component. Based on the above displacement results, it can be said that code based displacement demands, once again, are lower than recorded motions.

When displacement based results are compared with force-based results, it can be said that buildings are expected to undergo beyond the elastic phases. One may bear in mind, that the nonlinear behavior of these buildings are not investigated, even in the elastic phase, even for displacement and acceleration based results. In addition, obtained results revealed that not only force-based but also displacement based evaluations must not be overlooked by practicing engineers, and displacement based evaluation is needed and as important as elastic spectral acceleration to understand building behaviour.

3.5. Nonlinear displacement based evaluation

Based on the elastic-based analysis results, nonlinear dynamic analysis is performed. For this purpose, simple structures idealized as single-degree of freedom (SDOF) buildings are considered to consider the real building characteristics. SDOF structures are identified by stiffness (k), damping (c), mass (m), and strength (Fy). In this study, four T values with increments of 0.2 s (e.g., 0.4, 0.6, 0.8, and 1.0) were considered. It is worth noting that these values also cover the period values corresponding to 3-, 5-, and 7-story buildings used in this study and mainly represent low- to mid-rise buildings.

SDOF systems were represented by Fy/W, and they were taken as 0.1, 0.2, and 0.3 according to consideration of various studies (Akkar et al., (2005); Ucar et al., (2015); Palanci et al., (2021)). Low strength ratios (i.e., 0.1) can be attributed to structures that do not have sufficient stiffness and strength according to modern seismic codes. Finally, elastic-perfectly plastic (EPP) model is used to represent structural behavior. Typical presentation of the SDOF system is shown in Fig. 5. The general equation of motion of an inelastic SDOF system subjected to an earthquake excitation can be solved by Equation 2.

$$m\ddot{x}(t) + c\dot{x}(t) + kx(t) = -m\ddot{x}_g(t) \tag{2}$$

To make code-based comparison, the maximum displacement demands of each SDOF system were obtained using acceleration records obtained from 3129 stations in Hatay and 4612 stations in Maraş. Later, acceleration records were obtained for each station according to TBEC 2018 (11 acceleration records) and TEC 2007 (7 acceleration records), and using these records, the average maximum displacement demands were obtained for relevant seismic code. For code-based record selection, a stochastic optimization software developed by Kayhan et al., (2022) and later improved by Demir et al., (2025) is used. Details about the selected records are not discussed here, readers are suggested to see relevant studies for more information. Finally, the maximum displacement demands obtained from the stations were compared with the average maximum displacement demands obtained from the selected ground motions based on the target spectral shape of relevant seismic codes.

The maximum displacement demands of SDOF systems obtained from 3129 and 4612 stations are plotted in Fig. 6. It can be seen from the figure that nonlinear displacement values determined from 3129-NS is dramatically higher than 3129-EW values. In general, nonlinear displacement values are higher than 40 cm. Note that nonlinear displacement values are also dramatically higher than displacement values determined from elastic displacement curves. For Kahramanmaraş city (4612 station), maximum displacement values determined from 4612-NS is higher than 4612-EW component.

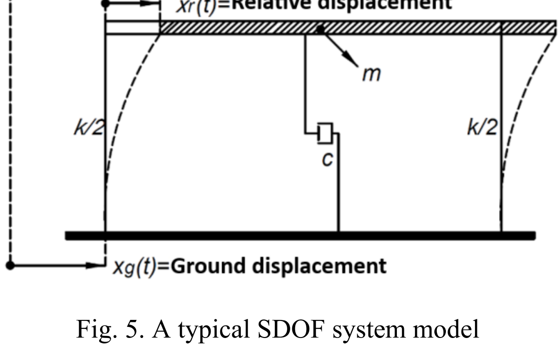

Fig. 5. A typical SDOF system model

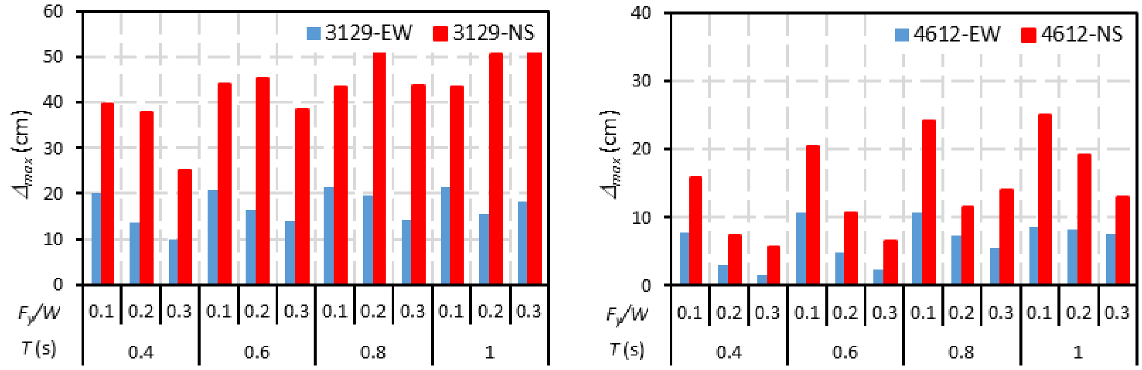

Fig. 6. Maximum nonlinear displacement values calculated for left: 3129 (Hatay) and right: 4612 (Maraş) and stations

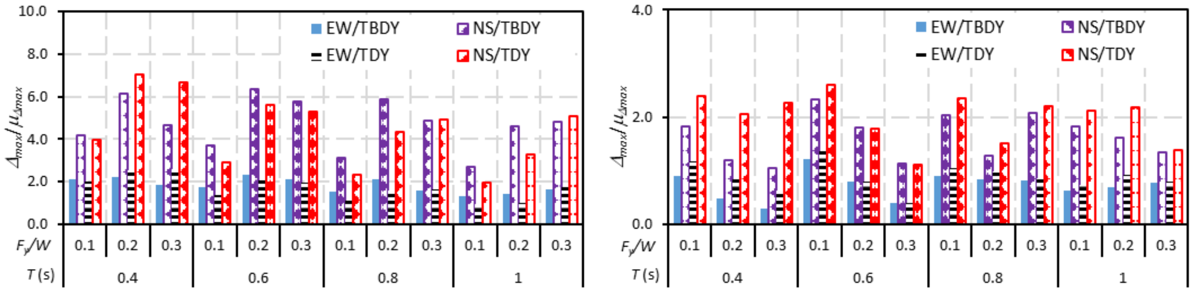

Fig. 7. Ratios of maximum displacements (Δ_{max}) of recorded earthquake motions (Left: 3129 and right: 4612) to average displacement ratios ($\mu_{\Delta max}$) determined according to code-based record selection for Hatay (left) and Maraş (right) cities

The displacement ratios of recorded earthquake motions (D_{max}) to average displacement ratios (m_{Dmax}) determined according to code-compatible record selection for Hatay and Maraş cities are obtained from nonlinear dynamic analysis using different lateral strength ratios and periods, and results are plotted in Fig. 7. It can be seen from the figure that the ratios may up to 7 times (mainly higher than 4.0) when nonlinear responses are considered, especially for buildings with lateral strength ratios higher than 0.2 in Hatay city for NS direction of the 3129 station. Meanwhile, figures implies that ratios may be up to 2.5 times in Hatay city for the EW direction of the 3129 station.

When the ratios for the Kahramanmaraş case (right side in Fig. 7) are investigated, it can be said that the ratios mainly range between 1.06 and 2.61 depending on the lateral strength ratio and building period. Nevertheless, it can be said that nonlinear displacements determined from the Maraş earthquakes are still higher than code-based nonlinear displacements. This situation highlighted that majority of buildings are subjected to high displacement ratios rather than shear forces when the nonlinear behavior of buildings is considered.

4. Damage measures and implications from the Kahramanmaraş sequences

Analysis results have shown that building damages is not only attributed to shear forces but also displacement demands mostly dominate the behavior. To overcome displacement demands, buildings must dissipate energy and energy demand, and hence displacement can be overcome considering capacity-design principles such as strong column-weak beam and ductility concepts. Ductility of members can be increased by application of appropriate details dictated by seismic codes (i.e., TBEC-2018 currently in force), and practitioners must comply with the rules such as the length of the confinement regions, confinement reinforcement with sufficient wrapping including stirrups and crossties, and appropriate reinforcement arrangements like 135-degree hooks. These details and concepts are necessary to ensure ductility demands, which are required to meet earthquake demands.

Analysis results also demonstrated that if common mistakes are made, it is natural to obtain such damages resulting from mistakes made during the design or in the construction process. Many field reconnaissance studies also confirm the results obtained in this study, and these studies revealed that existing reinforced concrete structures still suffer from common mistakes given above (İnce, (2024); Ivanov & Chow, (2023); Vuran et al., (2025); Avcil et al., (2024)) and the majority of buildings suffer from deficiencies resulting from inadequate ductility and bad applications in Türkiye.

In Fig. 8 and Fig. 9, some bad applications and engineering practices are demonstrated. These examples are taken from various studies after Kahramanmaraş earthquake sequences (Ince, (2024); Ivanov and Chow, (2023); Vuran et al., (2025); Avcil et al., (2024)). The picture in Fig. 8 (left) shows insufficient transverse reinforcement, which can be seen in common in field observations (Ince, 2024), and the picture on the right side shows the differences in structural behaviour between the adjacent buildings due to the impact of engineering practices and quality. It can be seen that buildings are in the same location, and so they undergo the same seismic, but they have distinct responses and damages (Ivanov and Chow, (2023)).

In Fig. 9 (left) collapsed post-2000 building is observed by Vuran et al., (2025). It was mentioned that buildings presumably stem from bond-slip failure, which may have possibly resulted from a lack of adequate length of the confinement regions, which implies bad construction practice. The other damage failure observed in the field is shown in Fig. 9 (right) and the main reason for this damage was mentioned by lateral collapse mechanism as a result of the formation of plastic hinges in the columns due to construction of strong beams, weak columns, not paying attention to the confinement of stirrups, and poor concrete quality by Avcil et al., (2024).

Despite the bad application and construction practices, one could observe the good practices that performed well after Kahramanmaraş earthquake sequences, as seen in Fig. 10 (Erbaş et al., (2025)), which highlight the importance of the capacity-design principles and ductility concepts.

Fig. 8. Some bad applications and engineering practices (Left: Insufficient transverse reinforcement (Ince, (2024)); Right: Two buildings in the same location (Ivanov and Chow, (2023))

Fig. 9. Some collapsed buildings stemming from formation of plastic hinges primarily in the columns, insufficient reinforcement, low-strength material, and RC frame insufficiency stemming from bad construction practices (Left: presumably bond-slip failure due to lack of adequate length of the confinement regions (Vuran et al., (2025)); Right: Lateral collapse (accordion) damages (Avcil et. al., (2024))

Fig. 10. Some well performed buildings examples (Erbaş et. al., (2024))

4. Conclusions

In this study, the displacement response spectra of residential buildings with varying floor heights, presumed to be located in Hatay and Kahramanmaraş provinces, were derived according to TEC 2007 and TBEC 2018 codes and compared with earthquake records obtained from Kahramanmaraş and Hatay. The results can be summarized as follows:

- In Hatay, the base shear force acting on 3, 5, and 7-story residential buildings of the TEC 2007 is higher than that of the TBEC 2018. However, in Kahramanmaraş, the base shear forces calculated according to the TEC 2007 were lower than those of the TBEC 2018.
- When force-based comparisons are made, the base shear force demands obtained from earthquake records are higher than the base shear forces calculated according to the 2007 and 2018 codes.
- It was seen that all buildings exceeded the elastic displacement limits and required inelastic deformation. Thus, emphasizing that not only force-based but also displacement-based approaches should be considered during the evaluation of structures.
- It can be said that nonlinear displacements determined from Maraş earthquakes are still higher than code-based nonlinear displacements.
- Kahramanmaraş earthquake sequences illustrated that distinct damage could be observed for the buildings at the same location even if they were exposed to the same seismic effects. The reasons behind this situation was observed as bad application and construction practices, such as poor concrete quality, not paying attention to the confinement of stirrups, weak columns, etc.

Acknowledgments

The authors express their thanks to Dr. Ahmet Demir for providing seismic code compatible real ground motion records.

References

Akkar, S., Sucuoğlu, H., & Yakut, A. (2005). Displacement-Based Fragility Functions for Low- and Mid-rise Ordinary Concrete Buildings. *Earthquake Spectra*, *21*(4), 901–927. https://doi.org/10.1193/1.2084232

ASCE/SEI 41-17. (2017). *Seismic Evaluation and Retrofit of Existing Buildings*. American Society of Civil Engineers. https://doi.org/10.1061/9780784414859

Avcil, F., Işık, E., İzol, R., Büyüksaraç, A., Arkan, E., Arslan, M.H., Aksoylu, C., Eyisüren, O., & Harirchian, E. (2024). Effects of the February 6, 2023, Kahramanmaraş earthquake on structures in Kahramanmaraş city. *Natural Hazards*, *120*(3), 2953–2991. https://doi.org/10.1007/s11069-023-06314-1

Çoruh, R. (2024). *Examination of earthquake design spectrums in different earthquake regulations* (Master's thesis). Kocaeli University (in Turkish).

Demir, A. (2015). *Statistical evaluation of nonlinear dynamic displacement demands using code compatible ground motion record sets* (Master's thesis). Pamukkale Üniversitesi (in Turkish).

Demir, A., Palanci, M., & Kayhan, A. H. (2025). Enhanced conditional ground motion selection model considering spectral compatibility and variability of three components for multi-directional analysis. *Applied Sciences*, *15*(8), 4135. https://doi.org/10.3390/app15084135

Erbaş, Y., Mercimek, Ö., Anıl, Ö., Çelik, A., Akkaya, S.T., Kocaman, İ., & Gürbüz, M. (2025). Design deficiencies, failure modes and recommendations for strengthening in reinforced concrete structures exposed to the February 6, 2023 Kahramanmaraş Earthquakes (Mw 7.7 and Mw 7.6). *Natural Hazards*, *121*(3), 3153–3194. https://doi.org/10.1007/s11069-024-06925-2

Fahjan, Y.M., Vatansever, S., & Özdemir, Z. (2011). Ölçeklenmiş gerçek deprem kayıtları ile yapıların doğrusal ve doğrusal olmayan dinamik analizleri. *1. Türkiye Deprem Mühendisliği ve Sismoloji Konferansı*, 11–14. Ankara, Türkiye.

Hamsici, M. (2019). *Multi-storey reinforced concrete buildings investigation of the effect of the 2018 earthquake regulations as defined by the spectrum curves* (Master's thesis). Sakarya Uygulamalı Bilimler Üniversitesi (in Turkish).

İnce, O. (2024). Structural damage assessment of reinforced concrete buildings in Adıyaman after Kahramanmaraş (Türkiye) Earthquakes on 6 February 2023. *Engineering Failure Analysis*, *156*, 107799. https://doi.org/10.1016/j.engfailanal.2023.107799

İnel, M., Çelik, S., Özmen, H.B., & Önür, Ö. (2011). Betonarme binaların deplasman taleplerinin 3-B doğrusal elastik olmayan dinamik analizle değerlendirilmesi. *1. Türkiye Deprem Mühendisliği ve Sismoloji Konferansı*, 11–14. Ankara, Türkiye.

Ivanov, M.L., & Chow, W.K. (2023). Structural damage observed in reinforced concrete buildings in Adiyaman during the 2023 Turkiye Kahramanmaras Earthquakes. *Structures*, *58*, 105578. https://doi.org/10.1016/j.istruc.2023.105578

Kayhan, A.H., Demir, A., & Palanci, M. (2022). Multi-functional solution model for spectrum compatible ground motion record selection using stochastic harmony search algorithm. *Bulletin of Earthquake Engineering*, *20*(12), 6407–6440. https://doi.org/10.1007/s10518-022-01450-8

Keyik, T.Z. (2019). *Siesmic performance assessment of an existing reinforced concrete structure using ASCE 41-17 and Turkish earthquake code and comparison of results* (Master's thesis). Dokuz Eylul Universitesi (in Turkish).

Meral, E. (2021). Betonarme binaların doğrusal elastik ve doğrusal elastik olmayan zaman tanım alanında analizlerinden elde edilen sismik taleplerin karşılaştırılması. *Avrupa Bilim ve Teknoloji Dergisi*, *32*, 183–190

Palanci, M., Demir, A., & Kayhan, A.H. (2021). The investigation of displacement demands of single degree of freedom models using real earthquake records compatible with TBEC-2018. *Pamukkale University Journal of Engineering Sciences*, *27*(3), 251–263. https://doi.org/10.5505/pajes.2020.47936

Presidency of the Republic of Türkiye Strategy and Budget Presidency. (2023). 2023 Kahramanmaraş ve Hatay Depremleri Raporu. *Erişim Adresi: https://www.sbb.gov.tr/2023-kahramanmaras-ve-hatay-depremleri-raporu/*

Ruiz-García, J., & Miranda, E. (2006). Residual displacement ratios for assessment of existing structures. *Earthquake Engineering & Structural Dynamics*, *35*(3), 315–336

TBEC. (2018). *Türkiye Building Earthquake Code:TBEC 2018. Disaster and Emergency Management Presidency (AFAD), Ministry of Public Works and Settlement, Ankara, Türkiye*.

TEC. (2007). *Specification for Structures to Be Built in Disaster Areas: TEC2007. Ministry of Public Works and Settlement, Ankara,Türkiye*.

Ucar, T., Merter, O., & Duzgun, M. (2015). Determination of lateral strength and ductility characteristics of existing mid-rise RC buildings in Turkey. *Computers and Concrete*, *16*(3), 467–485. https://doi.org/10.12989/cac.2015.16.3.467

Vuran, E., Serhatoğlu, C., Timurağaoğlu, M.Ö., Smyrou, E., Bal, İ.E., & Livaoğlu, R. (2025). Damage observations of RC buildings from 2023 Kahramanmaraş earthquake sequence and discussion on the seismic code regulations. *Bulletin of Earthquake Engineering*, *23*(3), 1153–1182. https://doi.org/10.1007/s10518-023-01843-3

4th International Civil Engineering & Architecture Conference
17-19 May 2025, Trabzon, Türkiye

Development of a cloud-based website for structural health monitoring in engineering structures

Fatih Y. Okur*[1,2], Ahmet C. Altunışık[1,2], Ebru Kalkan Okur[2,3]

[1] *Karadeniz Technical University, Department of Civil Engineering, 61080 Trabzon, Türkiye*
[2] *Earthquake and Structural Health Monitoring Research Center, Karadeniz Technical University, Trabzon 61080, Türkiye*
[3] *Karadeniz Technical University, Of Faculty of Technology, Department of Civil Engineering, Trabzon, Türkiye*

Abstract. Structural Health Monitoring (SHM) plays a critical role in ensuring the safety and long-term performance of engineering structures by continuously assessing their dynamic behavior and detecting potential anomalies. With advancements in cloud computing and web technologies, the integration of SHM systems into cloud-based platforms has become increasingly feasible, allowing for real-time data processing, remote access, and improved decision-making. This study presents the development of a cloud-based website designed for monitoring the structural health of engineering structures. The platform is designed to collect, process, visualize, and analyze real-time sensor data from various SHM systems installed on structures such as bridges, dams, and high-rise buildings. Key features of the system include real-time data streaming, automated anomaly detection using machine learning algorithms, and an intuitive user interface for remote monitoring. The cloud-based infrastructure enables scalable data storage and computational efficiency, ensuring seamless access for engineers and decision-makers. The proposed platform is tested using sensor data from case studies involving large-scale civil infrastructure, demonstrating its effectiveness in identifying changes in modal parameters and potential structural anomalies. The results indicate that cloud integration significantly enhances the accessibility and efficiency of SHM systems while reducing on-site computational demands. This study highlights the potential of cloud-based SHM platforms in transforming traditional structural monitoring approaches by providing real-time insights and predictive maintenance capabilities. Future developments will focus on enhancing the system's AI-based diagnostics and expanding its application to a broader range of engineering structures.

Keywords: Arch dam; Cloud-based website; Operational modal analysis; Structural health monitoring

1. Introduction

In the field of civil engineering, the design and analysis of structures are increasingly relying on computer-aided methods, facilitating the process of creating efficient and reliable structural systems. However, during the design phase, it is often challenging to perform analytical solutions, especially for complex structures, due to the computational effort required. To mitigate this challenge, numerical methods such as Finite Element Method (FEM) and Finite Difference Method (FDM) are employed to assess structural behavior, including modal, static, dynamic, linear, and nonlinear responses. Despite these advanced techniques, the assumptions made during the design phase may not always align with the actual conditions encountered during construction or over time, due to factors such as cracks, fatigue, foundation settlement, or other external influences. This divergence can lead to discrepancies between the expected and actual performance of the structure.

To address these uncertainties and ensure the continued safety and functionality of engineering structures, Structural Health Monitoring (SHM) systems play a critical role in providing real-time data on structural conditions. SHM systems enable the continuous assessment of structural health by monitoring key parameters, such as displacement, deformation, and strain, through the use of various sensors. These systems can detect potential damage and predict future issues, thus preventing significant losses in both human lives and property.

In the last twenty years, Structural Health Monitoring (SHM) has significantly grown with the advancement of sensor technologies, important progress in computing, and the inclusion of structural control approaches (Basu et al., 2014; Aydın et al., 2020). The SHM system generally consists of three main components: sensors, a data processing unit, and a data interpretation system (Amezquita and Adeli, 2016). SHM involves collecting data from precise sensors placed at predetermined points of the structure, storing and processing these data within a system,

* Corresponding author, E-mail: yesevi@ktu.edu.tr

https://doi.org/10.31462/icearc2025_ce_eqe_893

and interpreting them to identify potential damages in the structure. In SHM, both local and global methods are used for damage detection or structural condition assessment (Doebling, 1998). Local methods help in identifying or monitoring regional damage in structural elements (Shih, 2009). The most commonly used local methods include ultrasonic testing, eddy current, liquid penetrant testing, radiography, acoustic emission, visual inspection, etc. Global methods provide information about the overall condition of the structure and are used to detect the presence of damage. Various global methods, such as optical inspection, optoelectronic scanning, 3D laser scanning, and vibration-based methods, are used. Vibration-based methods are among the most widely used because they are greatly influenced by changes resulting from behavioral differences in the structure, regardless of its complexity (Boscato, 2019). Vibration-based methods are divided into Ambient Vibration Testing (AVT) and Forced Vibration Testing. The most commonly used method is Ambient Vibration Testing (AVT). In AVT, algorithms are used in the frequency and time domain for data processing to obtain dynamic characteristics of the structure. Many studies in the literature aim to interpret the data obtained from long-term monitoring of the dynamic characteristics of the structure through sensors (Rageh et al., 2018; Ono et al., 2019; Huseyno et al., 2020; Jayasundara et al., 2020; Vega & Yu, 2022; Zhang et al., 2022). These valuable studies are important for the development of SHM systems.

Given the increasing size and complexity of infrastructure projects, there is a growing need for scalable and efficient systems to manage and interpret the vast amounts of data generated by SHM systems. Cloud computing and web-based platforms have emerged as promising solutions, providing a centralized, accessible framework for real-time monitoring and data analysis. These platforms enable remote access, enhanced decision-making, and the integration of AI-driven diagnostics to improve the overall performance and maintenance of engineering structures.

This study presents the development of a cloud-based SHM platform designed to monitor and assess the structural health of various engineering structures. A web-based software has been developed, which can store raw signals and generate time-dependent visual graphs, provide alerts when signals reach predefined threshold levels, automatically track frequencies for obtaining dynamic characteristics, determine the confidence interval of uncertainties arising from changing environmental conditions using Bayesian Neural Networks, and perform anomaly detection through a deep learning-based methodology with an autoencoder. The platform utilizes real-time sensor data to detect anomalies and provide valuable insights for decision-makers. By integrating these developed algorithms, the SHM system aims to transform traditional SHM approaches and provide a more efficient and proactive solution for ensuring the safety and longevity of critical infrastructure.

2. Cloud-based structural health monitoring system

The online monitoring of signals that represent the current state of engineering structures, which can vary depending on various environmental factors such as ambient temperature, humidity, and wind speed, is facilitated through a web-based Structural Health Monitoring Platform. This platform enables the processing, interpretation, graphing, reporting of data, and easy access to data from any desired date. Deep learning-based methodologies have been developed for the automatic processing of dynamic characteristic data and for anomaly detection in the continuously obtained signals. Additionally, a study has been conducted to determine the confidence interval using Bayesian Neural Networks under uncertainties caused by changing environmental conditions, and this has been integrated into the platform. ASP.NET MVC, C#, Python, Grafana, and PostgreSQL were used in the development of the platform and its database.

With the Structural Health Monitoring platform, in addition to having 24/7 access to all data related to ongoing work and obtaining information about the structure at any desired time, the following can also be achieved:

- Continuous monitoring can be provided through sensors placed on the structure.
- Signals from the structures can be transferred to the main server, stored, and processed for evaluation.
- Processed data can be displayed systematically with date and time, and comparisons can be made with new data received during the monitoring process.
- Data processing algorithms can be applied during the monitoring process.
- Changes in structural behavior can be presented in real-time, and emergency intervention can be facilitated in extreme situations.
- Site members can access their structures at any time of the day with their personalized passwords, and emergency alerts can be sent via email.

The main entry screen of the Cloud-Based Structural Health Monitoring Platform developed in this study is shown in Fig. 1. This platform includes a dedicated page for each monitored structure. Authorized individuals, as defined by the requesting party, can access the structure's page using the designated password (Fig. 2). On this page, graphs of signals received 24/7 from sensors placed on the structure, as well as information about the current condition of the structure and reports, can be accessed (Fig. 3).

Fig. 1. Visual of the Cloud-Based Structural Health Monitoring Platform login screen

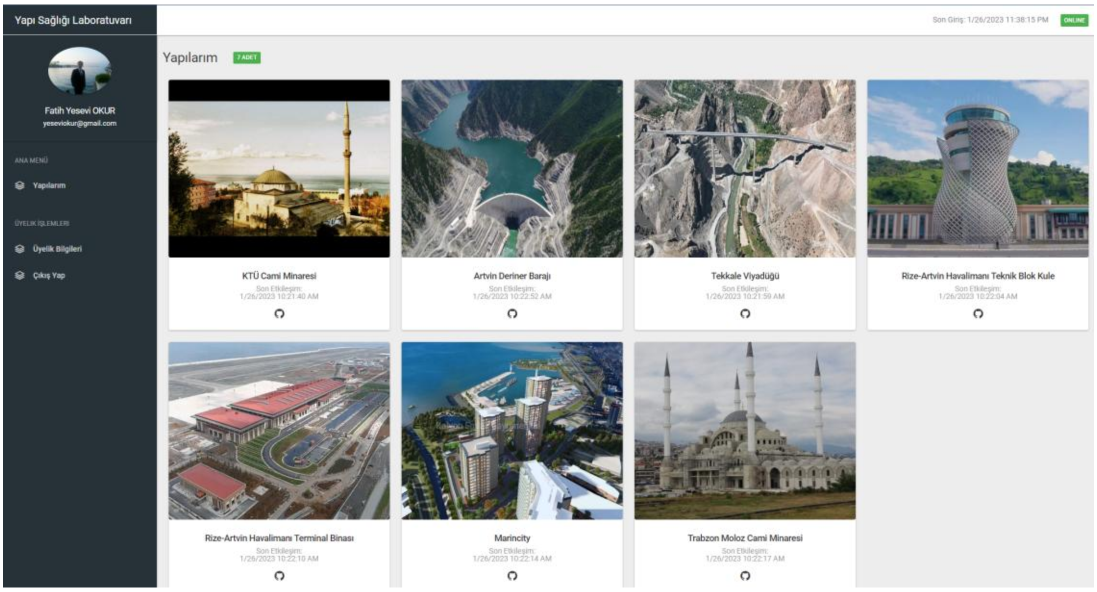

Fig. 2. Visual of buildings monitored on the Cloud-Based Structural Health Monitoring Platform

Fig. 3. A page of an example structure from the Cloud-Based Structural Health Monitoring Platform

2.1. Structural health monitoring in multi-storey reinforced concrete building

Within the scope of long-term structural health monitoring study in a multi-storey reinforced concrete building located in Yomra District of Trabzon Province, sensor installations were carried out and data transfer was provided to the web-based site. The building consists of a ground floor and 20 additional floors, with a net floor height of 2.95 meters for each floor. The total height of the building, starting from the ground floor, is approximately 65 meters. For vibration-based Structural Health Monitoring in the multi-story reinforced concrete building, two three-axis accelerometer sensors have been placed at the north-west and south-west corner points of the top floor. The data has been integrated into the Cloud-Based Structural Health Monitoring Platform. The SARA SL06 model has been used as the three-axis accelerometer sensor. FiG. 4 shows the placement and installation visuals of the accelerometer sensors. Fig. 5 shows the main visual screen of the data obtained from the web-based structural health monitoring platform. Fig. 6 shows the change of automatically obtained frequencies with respect to time.

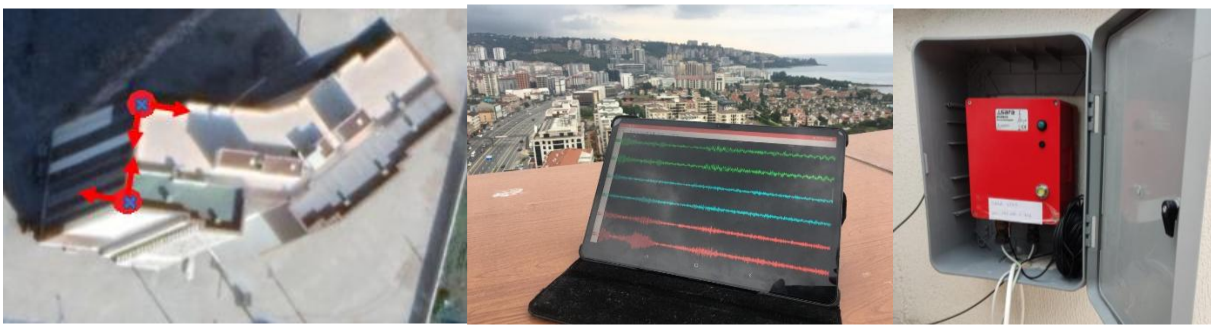

Fig. 4. Visual of the accelerometer sensor placement and sensor installations of the structure

Fig. 5. Main visual screen of the structure on the cloud-based structural health monitoring platform

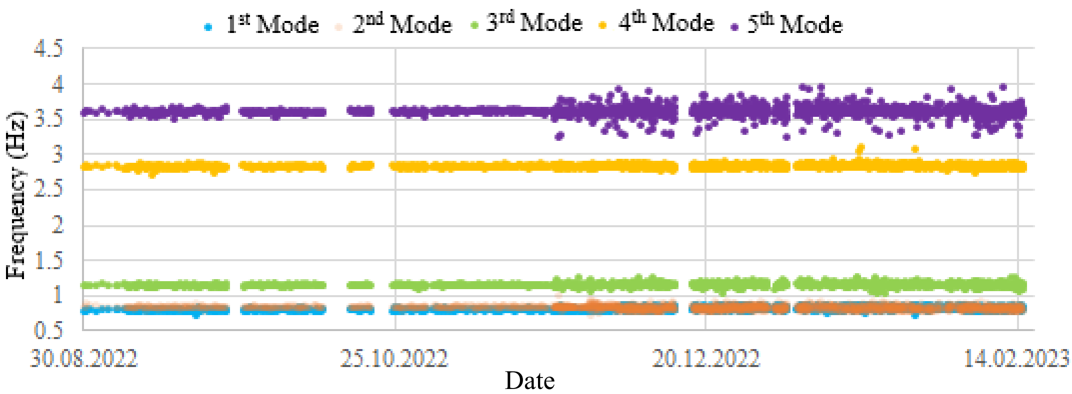

Fig. 6. Change of frequencies obtained automatically within the scope of the developed platform according to time

2.2. Structural health monitoring in Tekkale Viaduct

Within the scope of long-term structural health monitoring study in Tekkale Viaduct located in Yusufeli District of Artvin Province, sensor installations were carried out and data transfer was provided to the web-based site. The bridge was constructed with the balanced cantilever technique and consists of 5 spans with span distances ranging from 53 to 175 m. The total length of the bridge is 628 m. The superstructure width and the highest pier length of the bridge are 14.5 m and 144 m, respectively. A total of three sensors were placed in the middle of the main span, one in four and one on the column, in the section where the structural health monitoring based on vibration of the Tekkale Viaduct is the largest. The data has been integrated into the Cloud-Based Structural Health Monitoring Platform. The SARA SL06 model has been used as the three-axis accelerometer sensor. Fig. 7 shows the placement and installation visuals of the accelerometer sensors. Fig. 8 shows the main visual screen of the data obtained from the web-based structural health monitoring platform. Fig. 9 shows the change of automatically obtained frequencies with respect to time.

Fig. 7. Visual of the accelerometer sensor placement and sensor installations of the structure

Fig. 8. Main visual screen of the structure on the cloud-based structural health monitoring platform

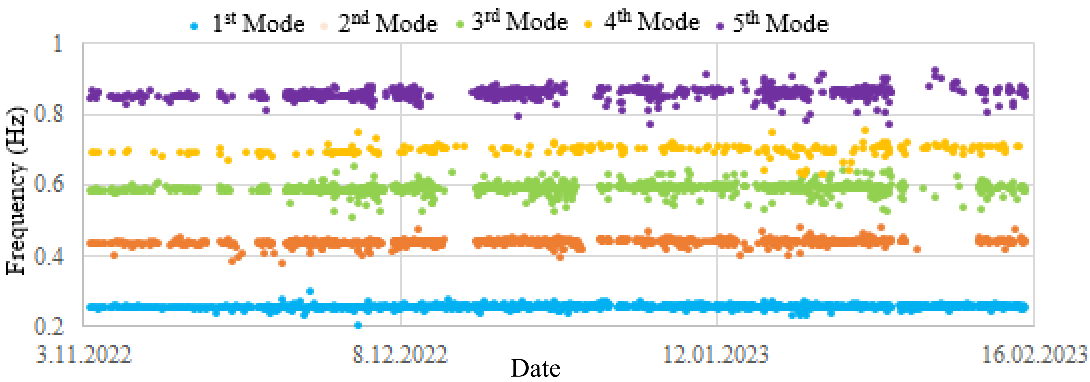

Fig. 9. Change of frequencies obtained automatically within the scope of the developed platform according to time

2.3. Structural health monitoring in Rize-Artvin Airport technical block tower building

Within the scope of long-term structural health monitoring study in Tekkale Viaduct located in Pazar District of Rize Province, sensor installations were carried out and data transfer was provided to the web-based site. The Technical Block Tower Building has a core reinforced concrete shear wall structural system designed with concentric walls, and it has a height of approximately 30.5 meters from the foundation level. The thicknesses of the outer and inner shear walls are 40 cm and 30 cm, respectively, while their diameters are 7.10 meters and 3.50 meters, respectively. The building features a reinforced concrete staircase that connects the two cores and spirals upwards along the height of the core. The tower building consists of a total of 8 floors, including the ground floor and 7 additional floors. In the Technical Block Tower Building, a total of 7 three-axis accelerometer sensors are installed: one on the ground floor, and two on the 2nd, 4th, and 7th floors. The three-axis accelerometer sensor used is the SENSEBOX 7043-D model. Additionally, a meteorological data measuring sensor is installed on the rooftop. Fig. 10 shows the placement and installation visuals of sensors. Fig. 11 shows the main visual screen of the data obtained from the web-based structural health monitoring platform. Fig. 12 shows the change of automatically obtained frequencies with respect to time.

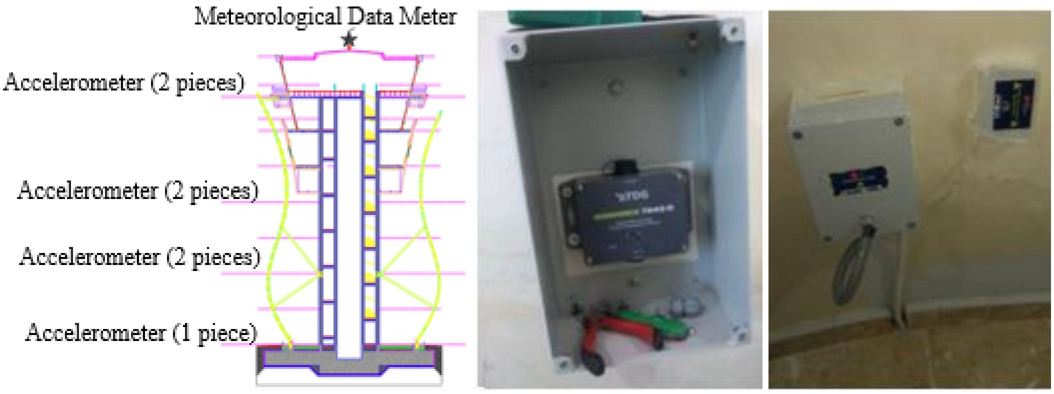

Fig. 10. Visual of the accelerometer sensor placement and sensor installations of the structure

Fig. 11. Main visual screen of the structure on the cloud-based structural health monitoring platform

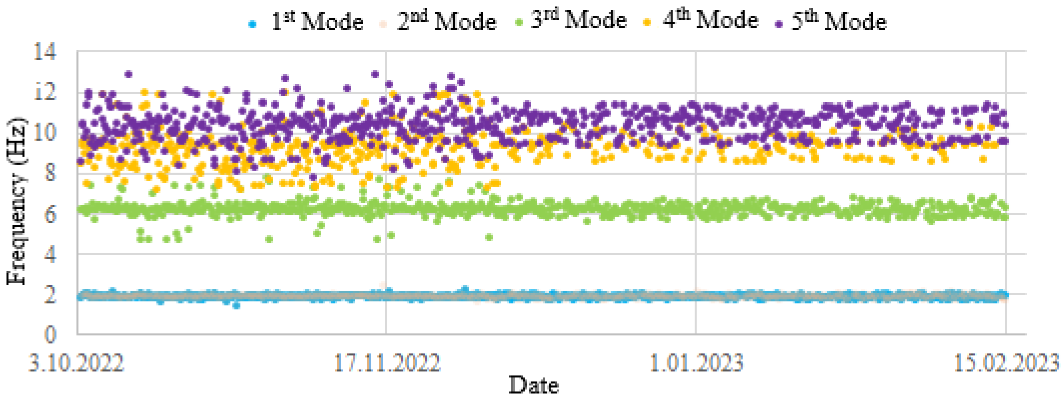

Fig. 12. Change of frequencies obtained automatically within the scope of the developed platform according to time

3. Conclusions

This study presents the development and implementation of a cloud-based Structural Health Monitoring (SHM) platform designed to monitor the dynamic behavior and structural integrity of engineering structures. By leveraging advanced technologies in cloud computing, web-based platforms, and deep learning methodologies, the system provides a comprehensive solution for real-time monitoring, data processing, and anomaly detection. The key findings of this study include:

- The platform facilitates continuous monitoring of engineering structures through the integration of various sensors, enabling real-time data acquisition.
- The collected sensor data is transferred, stored, and processed in a centralized cloud environment, providing easy access to engineers and decision-makers.
- The system incorporates deep learning techniques for automatic anomaly detection, ensuring early identification of potential structural issues.
- Bayesian Neural Networks are utilized to determine confidence intervals, taking into account uncertainties arising from environmental changes, enhancing the reliability of the data.
- The platform's user-friendly interface allows for seamless visualization of structural data, historical comparisons, and the ability to respond to emergency alerts promptly.

In conclusion, the developed cloud-based SHM platform significantly enhances the accessibility, efficiency, and accuracy of structural health monitoring systems. It represents a shift toward more proactive, data-driven decision-making in the maintenance and safety of critical infrastructure. Future work will focus on expanding the system's capabilities to include more advanced AI-driven diagnostics and its application to a broader range of engineering structures, ensuring its scalability and adaptability to evolving industry needs.

Acknowledgments

This work was supported by the Karadeniz Technical University Scientific Research Project titled “Establishment of a Structural Health Monitoring Network and Development of Innovative Methods for Engineering Structures of Strategic Importance in the Eastern Black Sea Region” (Project No. FAY-2021-9635). The authors extend their thanks to Karadeniz Technical University for their invaluable support.

References

Amezquita-Sanchez, J. P., & Adeli, H. (2016). Signal processing techniques for vibration-based health monitoring of smart structures. *Archives of Computational Methods in Engineering, 23*(1), 1–15.

Aydın, E., Ozturk, B., Farsangi, E. N., & Bogdanovic, A. (2020). Editorial: New trends and developments on structural control & health monitoring. *Frontiers in Built Environment, 6*, 53.

Basu, B., Bursi, O. S., Casciati, F., Casciati, S., Del Grosso, A. E., & Domaneschi, M. (2014). A European Association for the Control of Structures joint perspective: Recent studies in civil structural control across Europe. *Structural Control and Health Monitoring, 21*(12), 1414–1436.

Boscato, G., Fragonara, L. Z., Cecchi, A., Reccia, E., & Baraldi, D. (2019). Structural health monitoring through vibration-based approaches. *Shock and Vibration, 2019*, 2380616.

Doebling, S. W., Farrar, C. R., & Prime, M. B. (1998). A summary review of vibration-based damage identification methods. *Shock and Vibration, 30*(2), 91–105.

Huseynov, F., Kim, C., O’Brien, E., Brownjohn, J., Hester, D., & Chang, K. (2020). Bridge damage detection using rotation measurements – Experimental validation. *Mechanical Systems and Signal Processing, 135*, 106380.

Jayasundara, N., Thambiratnam, D., Chan, T., & Nguyen, A. (2020). Damage detection and quantification in deck-type arch bridges using vibration-based methods and artificial neural networks. *Engineering Failure Analysis, 109*, 104265.

Ono, R., Ha, T. M., & Fukada, S. (2019). Analytical study on damage detection method using displacement influence lines of road bridge slab. *Journal of Civil Structural Health Monitoring, 9*(4), 565–577.

Rageh, A., Linzell, D. G., & Azam, S. E. (2018). Automated, strain-based, output-only bridge damage detection. *Journal of Civil Structural Health Monitoring, 8*(5), 833–846.

Shih, H. W. (2009). *Damage assessment in structures using vibration characteristics* (Doctoral dissertation, Queensland University of Technology, Brisbane).

Vega, F., & Yu, W. (2022). Smartphone-based structural health monitoring using deep neural networks. *Sensors and Actuators A: Physical, 346*, 113820.

Zhang, Y., Tang, Z., & Yang, R. (2022). Data anomaly detection for structural health monitoring by multi-view representation based on local binary patterns. *Measurement, 202*, 111804.

4th International Civil Engineering & Architecture Conference
17-19 May 2025, Trabzon, Türkiye

Hysteretic behaviour of aluminium foam filled double-skin steel sections

Gulshen Shukurova[1], Emre Ozyurt*[2]

[1] Gümüşhane University, Graduate Education Institute, Gümüşhane, Türkiye
[2] Gümüşhane University, Faculty of Engineering and Natural Science, Department of Civil Engineering, Gümüşhane, Türkiye

Abstract. This study uses the non-linear finite element method to evaluate the hysteretic behaviours, energy absorbation capacities, and ductility ratios of corrugated and non-corrugated double-skin sections under cyclic loads. The double-skin sections consist of layers (inner and outer skins) in different combinations of aluminium foam filling. Also, the concrete-filled columns are modelled as a reference column. The investigated sections include configurations where both inner and outer skins are flat (without corrugations), only the inner skin is corrugated and the outer skin is flat, or only the outer skin is corrugated and the inner skin is flat. In the parametric analyses using the validated Finite Element (FE) models, the hysteretic behavior, energy dissipation capacity, plastic strain distributions, and ductility ratios of the composite columns are evaluated. The results revealed that increasing the wall thickness of the concrete-filled columns increased the strength and the ductility. In addition, the configurations with outer surface corrugated generally exhibited better cyclic performance for each fi. As for the aluminium foam-filled columns, their load-bearing capacity was less than their corresponding concrete-filled specimens, but they had higher energy dissipation capacity and ductility ratios. It may be possible to use aluminium foam-filled corrugated members in seismic regions because of their high energy dissipation capacity and the advantage of lightweight.

Keywords: Aluminium foam; Concrete filled; Corrugated; Energy absorbation capacity; Hysteretic behaviour.

1. Introduction

In recent years, the demand for lightweight yet high-performance structural materials has significantly increased in the field of civil engineering. Structural efficiency, cost-effectiveness, and material sustainability have become critical factors in the selection of construction materials. Corrugated structures, known for their superior strength-to-weight ratio, have been widely used in various applications, including aerospace, automotive, and civil engineering. These structures offer enhanced mechanical properties due to their unique geometry, which provides excellent load-bearing capacity and energy absorption characteristics. However, while numerous studies have been conducted on concrete-filled corrugated panels, limited research has been devoted to exploring the potential of foam-filled configurations, particularly under cyclic loading conditions.

Foam-filled structures present a promising alternative to traditional concrete-filled systems by offering significant weight reduction while maintaining structural integrity. The integration of foam as a filling material has the potential to improve energy dissipation, stiffness, and overall durability, making them suitable for seismic and impact-resistant applications. However, the structural response of foam-filled corrugated systems under cyclic loading remains largely unexplored. Understanding the mechanical behaviour of these systems is crucial for assessing their viability in real-world engineering applications.

The behavior of concrete filled double skin steel tube (CFDSST) members under cyclic loading has become a subject of significant interest in recent years. The researchers have explored various aspects of these structures, including their mechanical properties, failure mechanisms, and potential applications in structural engineering. Fan et al. (2024) evaluated the failure mechanism under cyclic loads by performing low-cycle fatigue tests of CFDSST specimens under different loading conditions and evaluated the effects of parameters such as clearance, slenderness and shear rate, revealing that low fatigue life is related to defects and stress levels. Zhou et al. (2022); (2016) studied the failure mechanism of CFDSST beam-columns under cyclic bending loading, evaluated the

*Corresponding author, E-mail: emre.ozyurt@gumushane.edu.tr

https://doi.org/10.31462/icearc2025_ce_eqe_896

effects of design parameters on ductility, energy dissipation capacity and ultimate moment capacity, verified the accuracy of existing design methods and showed that the strain hardening of stainless steel and the limiting effect of tubes on concrete should be taken into account in the design. Lu et al. (2022) assessed the effects of various parameters on the torsional capacity of CFDSST columns and suggested accurate design formulas to predict the torsional capacity. Wang et al. (2024) analyzed the effects of different parameters (void ratios, axial compression ratios, infill material types) on the hysteretic performance of CFDSST columns with non-standard D/t ratios, and proposed a moment resistance model that takes into account the tensile strength of ECC.

Additionally, the innovative form of concrete filled corrugated steel tube (CFCST) members have been studied. Zou et al. (2023) proposed a new formulas to predict the ultimate axial strength of CFCST columns, investigated the confinement mechanism of multicellular steel tube columns by axial compression tests and 3D finite element modeling. Fang et al. (2024) examined the torsional hysteretic behavior in detail by testing nine specimens under cyclic torsional loads. Tong et al. (2024) performed axial compression tests of 20 CFCST columns, proposed a theoretical formula for the axial bearing capacity of CFCST columns. Fang et al. (2021) examined the failure modes, axial load-axial strain curves, plastic strains and stress failures in detail by performing monotonic and cyclic axial compression tests on CFCST specimens with large helical angles. Farahi et al. (2016) further analyzed the compressive behavior of concrete-filled double-skin sections consisting of corrugated plates, emphasizing their mechanical efficiency.

Furthermore, several studies have focused on the behavior of aluminium foam filled steel tube (AFST) members under various loading conditions. Duarte et al. (2018); (2015) investigated the static and dynamic axial crush performance of in-situ AFST, demonstrating the potential of these structures for energy absorption applications. Yanjun et al. (2023) and Li et al. (2018) conducted experimental and numerical studies AFST, analyzing their mechanical behaviors and crashworthiness properties. Moreover, Seitzberger et al. (1997) investigated the crushing behavior of axially compressed AFST, contributing to the understanding of impact resistance.

This study aims to investigate the cyclic behavior of double-walled corrugated structures reinforced with foam filling. The primary objectives include analyzing the stiffness, energy dissipation capacity, and load-bearing performance of foam-filled panels and comparing their behavior with conventional concrete-filled structures. Hence, this study evaluates whether foam-filled members can be applicable as a viable alternative to heavier and more rigid concrete-filled designs.

2. Verification of numerical model

In this study, the numerical modeling of the compressive behaviour of double-skin steel sections with concrete filling was validated. The results of the experimental studies conducted by Farahi et al. (2016) were used for validation study. A nonlinear finite element (FE) method was used, for simulating the experimental study. In double-skin steel sections, the interaction between the steel surface and the concrete filling significantly affects the overall behaviour of the composite member. Therefore, the interaction definitions was one of the most important issues of the numerical modeling. In addition, the appropriate material models were selected to represent the actual behaviour of steel and concrete materials.

The numerical stability of the FE simulations is another important issue to be considered, especially during loading step. Events such as the onset of local buckling in steel walls, crushing and contact interactions in concrete can cause sudden strength decreases and local instabilities. In such cases, it may be necessary to use dynamic analysis methods instead of static analysis methods. In this study, ABAQUS/Explicit dynamic analysis method was used to model the compressive behavior of CFDST columns accurately.

2.1. Detail of numerical model

Fig. 1 illustarates geometrical configurations of CFDST columns of Farahi et al. (2016). A constant length and steel wall thickness of 1000 mm and 3 mm were used in their test, respectively. The outer and inner widths of the columns are also presented in Fig. 1. Table 1 summarizses the geometrical parametes of the corrugated steel plates. Accordingly, the columns are categorised into two types, namely IC1 and OC1, based on positioning of the corrugations on the inner or outer surface. Fig. 2 illustrates the typical geometry of the cross-section of a corrugated steel plate. The geometry consists of alternating inclined and flat segments, forming a repetitive zig-zag pattern. Key geometrical parameters include the inclined length *(l)*, horizontal length *(a)*, vertical depth *(b)*, plate thickness *(t)*, and angle of inclination *(α)*.

The boundary conditions were defined to ensure that the numerical model accurately replicated the experimental setup. The bottom of the column was rigidly fixed in all directions to prevent any translational or rotational movements. The top of the column, on the other hand, was allowed to move along the vertical direction, providing the necessary freedom for axial deformation under the applied loads.

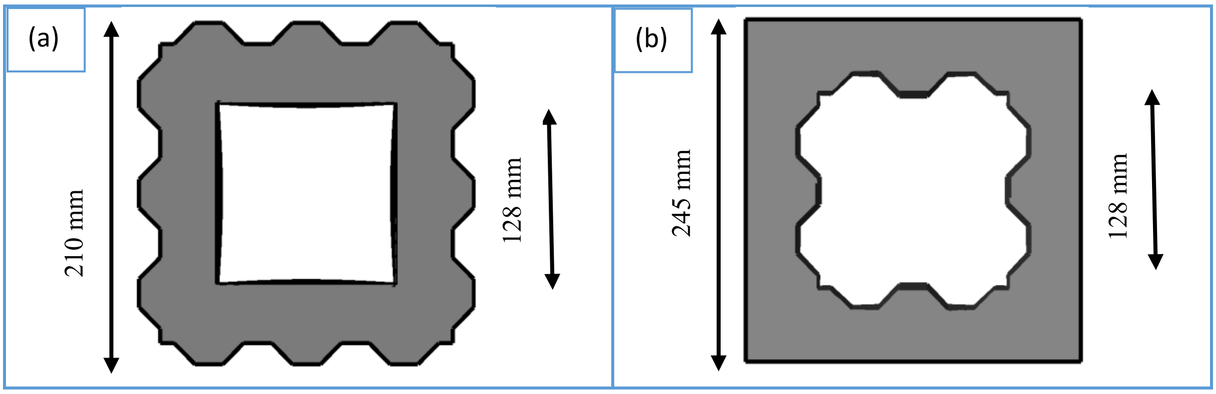

Fig. 1. Geometrical configurations; (a) OC1 from the test of Farahi et al. (2016), (b) IC1 – from the test of Farahi et al. (2016)

Table 1. Geometrical parameters of the corrugated steel plate

	α (°)	a	h	t	l	d	c	b
Type1	45	20.00	15.00	3.00	70.00	15.00	21.21	210.00

2.2. Material models

In this study, the Concrete Damaged Plasticity (CDP) model in Abaqus software was used to model the behaviour of concrete. This model allows us to define the behaviour of concrete under compression and tension separately. In the model, the rules of increasing the strength (hardening) and decreasing the strength (softening) of the concrete and the development of the scalar damage variable in compression and tension were developed based on the model of Han et al. (2001). Both the increase/decrease in strength and the development of the damage variable were defined depending on the plastic deformations (crushing and cracking strain) of the concrete after crushing and cracking, respectively. The ultimate compressive strength, Young's modulus and Poisson's ratio of the concrete were 40 MPa, 31350 MPa and 0.2, respectively.

Table 2. CDP model parameters

Dilation angle	Eccentricity	f_{b0}/f_c*	K	Viscosity Parameter
10	0.1	1.137	0.87	0.008

*f_{b0}/f_c: Ratio of the compressive strength under biaxial loading to uniaxial compressive strength

*K: Ratio of the second stress invariant on the tensile meridian to that on the compressive meridian

For steel material, 250 mild-steel flat plates were used in the specimens of Farahi et al. (2016). The steel material properties used in the numerical model are adapted as follows: The proof stress, tensile strength and strain conrresponding to the tensile strength were assumed to be 280 MPa, 410 MPa and 23%, while Young's modulus and Poisson's ratio of the concrete were 200000 MPa and 0.3, respectively.

2.3. Contact and element details

The rigid plates were attached to the both ends of the columns using tie function in Abaqus. Reference points were also defined at the centre of the rigid plates to apply loading and boundary conditions. Furthermore, the interaction between the steel plates and the concrete core was modeled using contact elements, which were carefully defined to represent the real bonding conditions between the two materials. In the numerical simulations, surface-surface contact was defined to model the interaction between the concrete core and the steel tube. Coulomb friction model with a friction coefficient of 0.25 was used for the tangential behavior of the contact interaction. This value represents the shear resistance between the concrete and the steel. The normal behavior was defined as 'hard contact'. This prevents the contact surfaces from penetrating each other and allows the transfer of pressure forces. In defining the contact interaction, the node-surface formulation of the surfaces was used.

Fig. 2 presents the finite element mesh details applied to the reference samples IC1 and OC1 columns. In the modeling of the steel plates, four-node, reduced integration shell elements (S4R) were used. The infill concrete was represented by eight-node, reduced integration linear brick elements (C3D8R). As a result of the mesh sensitivity analyses performed, the maximum mesh element size for the column models used in the simulations was determined as 10 mm.

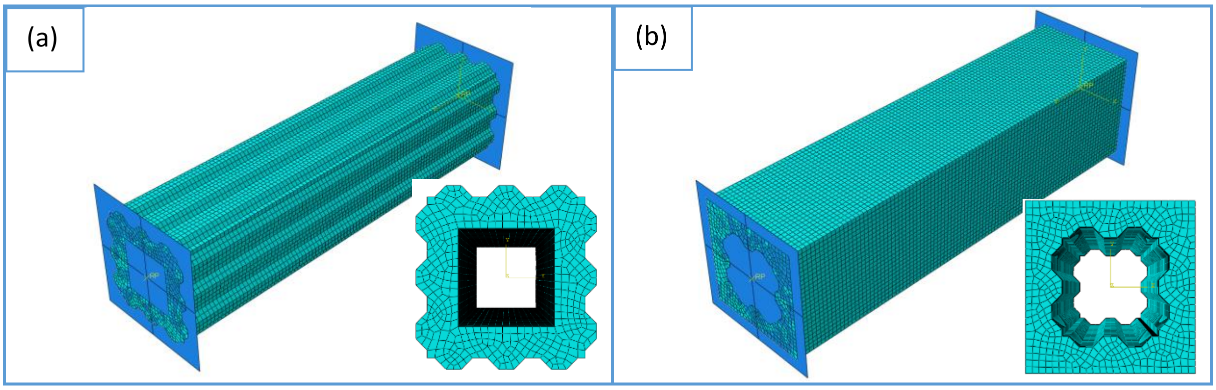

Fig. 2. Mesh layouts; (a) OC1, (b) IC1

2.4. Verification results

After the completion of the numerical modeling procedure, experimental results for reference specimens IC1 and OC1 were used to verify the accuracy of the developed finite element models. Comparison of the failure modes of OC1 and IC1 presented in Fig. 3 reveals that the numerical models show a high level of similarity with the experimental observations. Furthermore, examination of the load-nominal axial strain curves in Fig. 4 shows that all numerical models can predict the elastic behavior of the column specimens with considerable accuracy. The ultimate strength values obtained from the numerical simulations also show good agreement with the values obtained from the experimental studies. It is anticipated that the approach used in this validation study may also provide reliable results in the parametric studies of composite steel columns, both with concrete fill and aluminum foam fill.

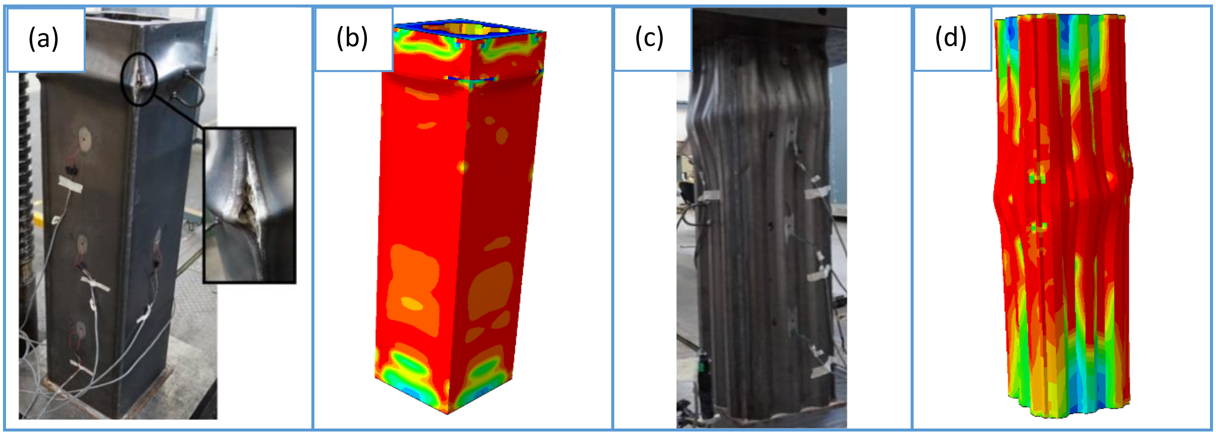

Fig. 3. Comparison of the failure modes; (a) IC1 – Test results of Farahi et al. (2016), (b) IC1 – FE results, (c) OC1 – Test results of Farahi et al. (2016), (d) OC1 – FE results

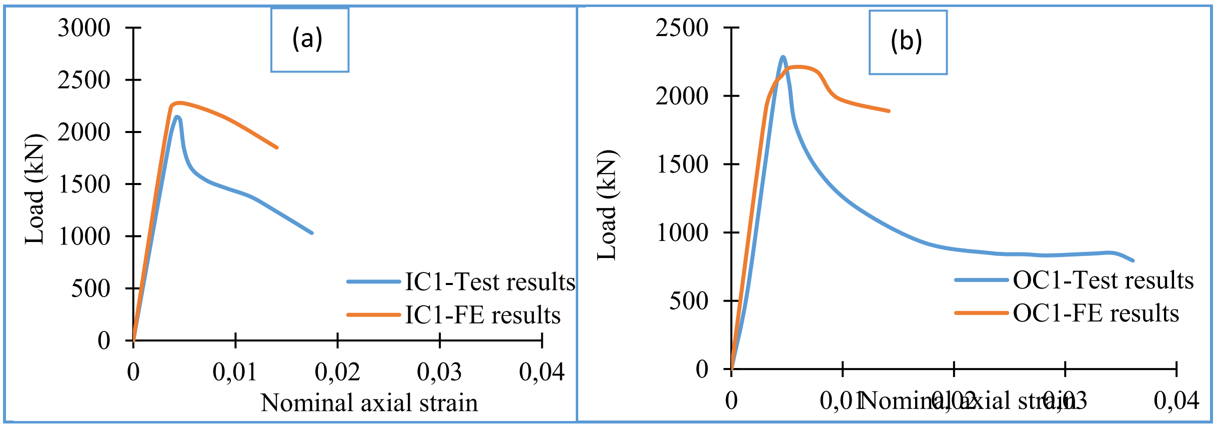

Fig. 4. Comparison of the nominal axial strain-load curves; (a) IC1, (b) OC1

3. Parametric study

In this study, the behavior of double-skin steel corrugated columns under cyclic loads was investigated with a parametric approach. In the numerical analyses, the effects of parameters such as the positioning of the corrugations on the inner or outer surface, the wall thickness of the steel walls and the type of filling material (concrete or aluminum foam) on the structural behavior were evaluated comprehensively. In the parametric analyses, the wall thicknesses of the steel walls were taken into account in three different values as 3 mm, 5 mm and 7 mm.

The effects of those parameters on energy absorption capacities, ductility ratios and damage mechanisms of concrete-filled columns or aluminum foam-filled columns were compared. Each column specimen examined in the parametric study was numbered with a unique code indicating the position of the corrugated plate ('O' outer, 'I' inner surface), the infill material ('C' concrete, 'A' aluminium foam) and the steel wall thickness in mm; for example, 'OC1-3' refers a column with corrugated outer surface, concrete infill and 3 mm wall thickness, and 'IA1-5mm' is a column with corrugated inner surface, aluminium foam infill and 5 mm wall thickness.

3.1 Definition of loading protocol

The loading protocol used in the parametric study was designed in two stages in order to reflect the realistic behaviour of the structural members. In the first stage, the axial load carrying capacity (P_u) of each finite element model was determined. This capacity represents the maximum strength of the composite columns under axial loads. In the second stage, a constant axial load was applied to the column. This axial load was set as 20% of the determined P_u value.

Under the constant axial load, the columns were subjected to lateral cyclic loading. The details of the applied cyclic loading are shown in Fig. 5. Based on the yield displacement (Δ_y) estimated by FE analysis, it was applied at $0.25\Delta_y$, $0.5\Delta_y$ and $0.75\Delta_y$ levels. After the yield strength was reached, the displacements were increased to Δy, $1.5\Delta_y$, $2\Delta_y$, $2.5\Delta_y$, $3\Delta_y$, $5\Delta_y$ and $7\Delta_y$ levels. One cycle was applied at each displacement level. The smilar cycling loading proccess was also used by previous researchers (Mashaly et al., 2011; Ozyurt & Gunaydin, 2024; Seitzberger et al., 1997; Xia et al., 2017).

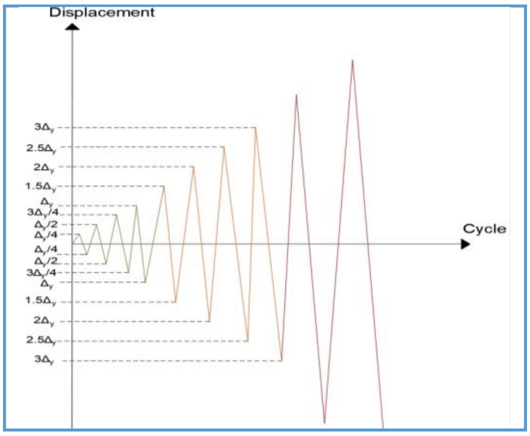

Fig. 5. Horizontal loading protocol

3.2 Hysteretic behavior

The loading protocol used in the parametric study was designed in two stages in order to reflect the realistic behaviour of the structural members. In the first stage, the axial load carrying capacity (P_u) of each finite element model was determined. This capacity represents the maximum strength of the composite columns under axial loads. In the second stage, a constant axial load was applied to the column. This axial load was set as 20% of the determined P_u value. Fig. 6 comparatively illustrates the hysteretic behavior of columns with corrugated plates on the outer (O) or inner (I) surfaces, filled with concrete (C) or aluminum foam (A) and with different wall thicknesses (3, 5, 7 mm).

Fig. 6(a) presents the hysteretic curves of the OC1-3) and IC1-3 columns, both concrete filled and 3 mm wall thickness. It is understood that the IC1-3 column exhibits wider hysteretic loops and therefore can dissipate more energy. In addition, the maximum load level reached by the IC1-3 column is higher than that of the OC1-3 column. Increasing the wall thickness in the concrete-filled composite columns significantly exhibited the wider hysteretic loops, indicating a more stable behavior under cyclic loading, while columns with internal corrugated surfaces tend to offer higher strength and energy dissipation capacity compared to those with external corrugated surfaces at the same wall thickness.

Fig. 6(d) compares the hysteretic curves of the OA1-7 and IA1-7 columns with aluminum foam filling instead of concrete filling and having a wall thickness of 7 mm. It is observed that the hysteretic loops of the aluminum foam filled columns are narrower and the maximum load levels they reach are significantly lower compared to the concrete filled columns. However, it is observed that the IA1-7 column has a slightly better energy dissipation capacity and can carry higher loads than the OA1-7 column.

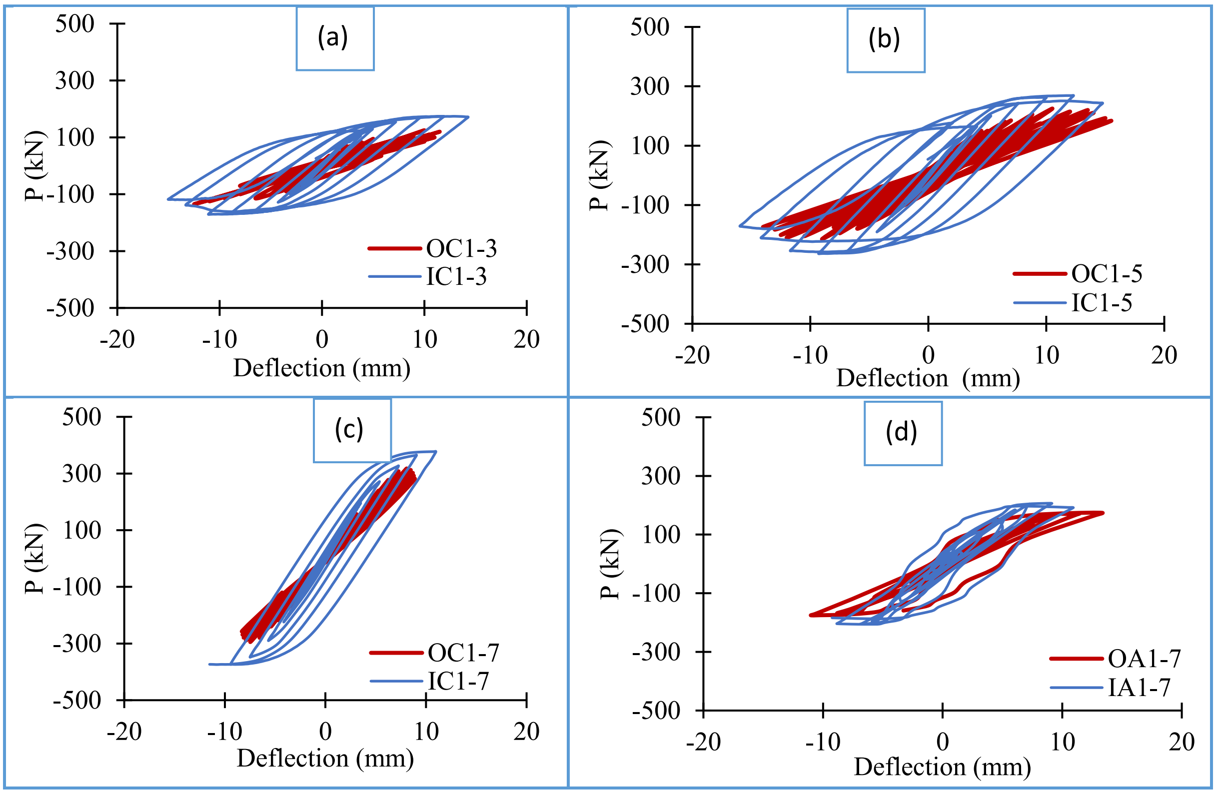

Fig. 6. Hysteretic curves of composite columns; (a) OC1-3&IC1-3, (b) OC1-5&IC1-5, (c) OC1-7&IC1-7, (d) OA1-7&IA1-7

3.3 Energy dissipation capacity

In this section, the normalised energy dissipation capacities (E/E_y) of composite columns with different configurations under cyclic loads are assessed. Fig. 7 show the change in the energy dissipation capabilities of the columns as the number of cycles progresses. Here, E represents the energy dissipated in each cycle and E_y represents the energy dissipation capacity at the initial yield stress. The energy dissipation capacity of composite columns are evaluated using the area under the load-displacement hysteretic curves.

The columns with corrugated inner surfaces and especially aluminum foam filled columns can reach much higher energy absorption capacities according to the normalised energy dissipation. In the concrete filled columns, increasing the wall thickness and positioning the corrugated plate on the outer surface positively affect the energy absorption capacity. The high energy absorption potential of the aluminum foam filled columns indicates that such lightweight composite structural elements can be a promising alternative to increase the performance of structural systems under dynamic loads.

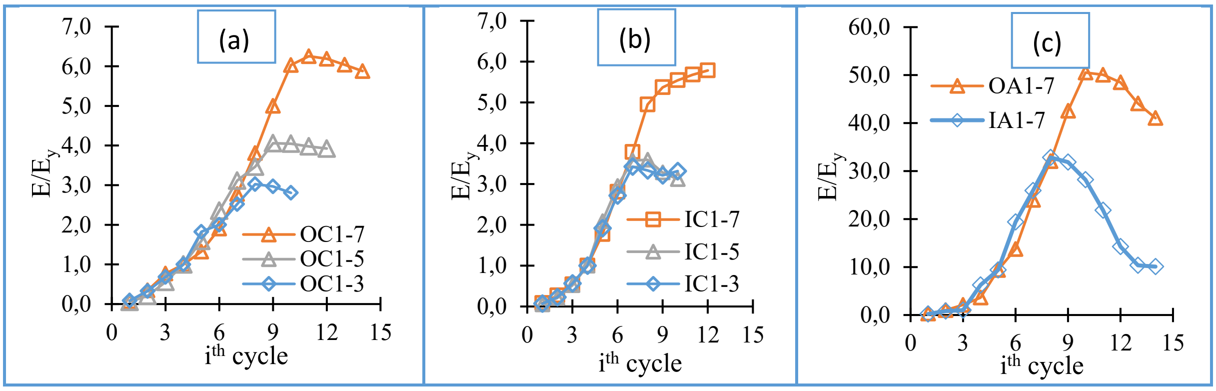

Fig. 7. Comparison of normalised energy dissipation capacity of composite columns; (a) OC1, (b) IC1, (c) OA1&IA1

Fig. 8 presents the plastic equivalent strain (PEMAG) distributions of the FE results of composite columns with aluminum foam filling and 7 mm wall thickness, with corrugated outer and inner surfaces. It can be seen that the position of the corrugated plate has a significant effect on the plastic deformation mechanism and distribution. While the plastic deformation in the IA1-7 column with the corrugated inner surface remains more localised and at lower levels, the plastic deformation in the OA1-7 column with the corrugated outer surface is more widespread and severe. The reason for that the presence of the corrugated plate on the outer surface may increase the yielding area of the column by dissipating higher energy with the aluminum foam filling.

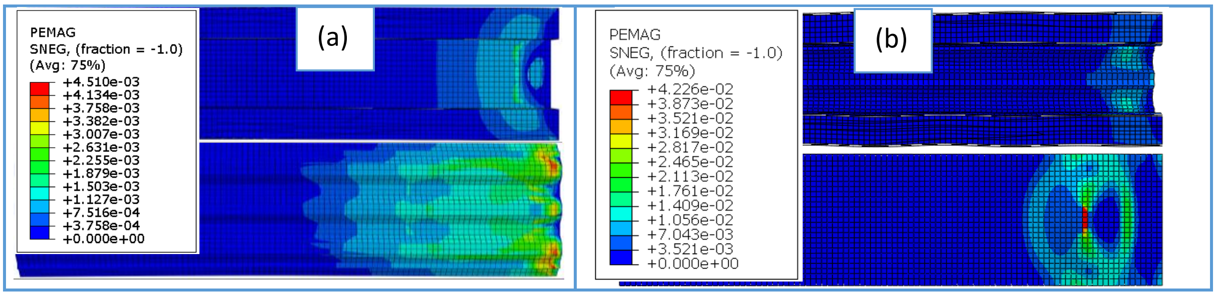

Fig. 8. Comparison of plastic equivalent magnitude of composite columns; (a) OA1-7, (b) IA1-7

3.4 Ductility

The effects of the steel wall thicknesses and infill materials on the ductility ratios (μ) of the composite columns are examined. The ductility ratio is the displacement at failure (δ_u) to the displacement at yielding (δ_y) ($\mu = \delta_u/\delta_y$). Fig. 8 compares the ductility performances of the composite columns with outer surface corrugated (O1) and inner surface corrugated (I1) configurations for the concrete filled (CF) and aluminum foam filled (AF) columns at different steel wall thicknesses.

It can be noted from Fig. 8 that there is an increasing tendency in the ductility ratios of O1 and I1 columns with increasing in the steel wall thickness. In addition, the O1 column provides a better ductility performance than the corresponding I1 column because of larger yielding areas. As for the AF columns, they exhibit significantly higher ductility ratios compared to the corresponding concrete filled columns. In particular, the ductility ratio of the O1 aluminum foam filled column is the highest. Moreover, the I1 AF column also exhibits significantly higher ductility than its CF counterparts.

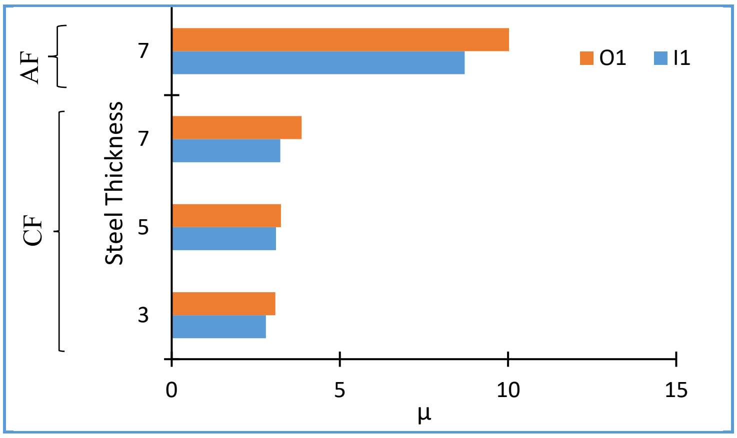

Fig. 8. Comparison of ductility ratios of composite columns with various steel thicknesses and fillings

4. Conclusions

This study comprehensively examines the structural behavior of double-walled corrugated composite columns under cyclic loads by the numerical methods. The obtained hysteretic curves showed that the energy dissipation capacities and ductility ratios, the location of the corrugated plate, the steel wall thickness and the type of infill material (concrete or aluminum foam) have significant effects on the performance of the composite columns. In the concrete-filled columns, increasing wall thickness generally increases the load-carrying capacity and energy dissipation, while the configurations with external corrugated surfaces exhibited superior cyclic behavior compared to those with internal corrugated surfaces. In terms of ductility, while increasing wall thickness in concrete-filled columns tended to cause an increase in ductility ratios, the columns with external corrugated surfaces provided better performance than those with internal corrugated surfaces. Although aluminum foam-filled columns had significantly lower load-carrying capacities compared to concrete-filled columns with the same wall thickness, they showed significantly superior performance in terms of energy dissipation capacities and especially ductility ratios. In particular, the columns with corrugated aluminum foam filler on the outer surface reached the highest ductility values. Plastic deformation analyses revealed that the location of the corrugated plate significantly affects the damage mechanisms and deformation distribution. In conclusion, this study emphasizes the critical role of material selection and geometric configuration in the design of lightweight and high-performance composite structural elements. In particular, the high energy dissipation and ductility potential of aluminum foam filled corrugated columns offers a promising alternative for seismic and impact resistant applications.

References

Duarte, I., Krstulović-Opara, L., & Vesenjak, M. (2018). Axial crush behaviour of the aluminium alloy in-situ foam filled tubes with very low wall thickness. *Composite Structures, 192*, 184-192.

Duarte, I., Vesenjak, M., Krstulović-Opara, L., & Ren, Z. (2015). Static and dynamic axial crush performance of in-situ foam-filled tubes. *Composite Structures, 124*, 128-139.

Fan, J.-H., Wang, W.-D., Shi, Y.-L., & Zheng, L. (2024). Low-cycle fatigue behaviour of concrete-filled double skin steel tubular (CFDST) members for wind turbine towers. *Thin-Walled Structures, 205*, 112384.

Fang, Y., Wang, Y., Elchalakani, M., & Yang, H. (2021). Experimental investigation on concrete-filled corrugated steel tubular column under constant axial load and cyclic load. *Engineering Structures, 248*, 113245.

Fang, Y., Yang, H., Chan, T., & Wang, Y. (2024). Experimental investigation on seismic behaviour of concrete-filled corrugated steel tubes under cyclic torsional loads. *Engineering Structures, 309*, 118062.

Farahi, M., Heidarpour, A., Zhao, X.-L., & Al-Mahaidi, R. (2016). Compressive behaviour of concrete-filled double-skin sections consisting of corrugated plates. *Engineering Structures, 111*, 467-477.

Han, L.-H., Zhao, X.-L., & Tao, Z. (2001). Tests and mechanics model for concrete-filled SHS stub columns, columns and beam-columns. *Steel and Composite Structures, An International Journal, 1*(1), 51-74.

Li, Z., Chen, R., & Lu, F. (2018). Comparative analysis of crashworthiness of empty and foam-filled thin-walled tubes. *Thin-Walled Structures, 124*, 343-349.

Lu, G.-B., Zhou, X.-H., Wang, Y.-H., Deng, X.-W., Bai, Y.-T., & Zhu, R.-H. (2022). *Numerical investigation on circular concrete-filled double skin steel tube columns under torsion.* Paper presented at the Structures.

Mashaly, E., El-Heweity, M., Abou-Elfath, H., & Osman, M. (2011). Finite element analysis of beam-to-column joints in steel frames under cyclic loading. *Alexandria Engineering Journal, 50*(1), 91-104.

Ozyurt, E., & Gunaydin, M. (2024). Hysteretic behaviour of square-hollow-section T-and X-joints with in-plane bending moment. *Journal of Constructional Steel Research, 220*, 108813.

Seitzberger, M., Rammerstorfer, F. G., Degischer, H. P., & Gradinger, R. (1997). Crushing of axially compressed steel tubes filled with aluminium foam. *Acta Mechanica, 125*, 93-105.

Tong, J.-Z., Zhang, J.-M., Yu, C.-Q., Wu, R.-M., Tong, G.-S., Chen, M., & Gao, W. (2024). Experimental study on axial compressive behavior of concrete-filled corrugated steel tubular columns. *Engineering Structures, 313*, 118267.

Wang, J.-T., Sun, Q., Li, Y.-W., & Liu, X.-H. (2024). Hysteretic performance of circular high-strength concrete-filled double skin steel tubular columns: Experiment. *Marine Structures, 93*, 103519.

Xia, J., Chang, H., Goldsworthy, H., Bu, Y., & Lu, Y. (2017). Axial hysteretic behavior of doubler-plate reinforced square hollow section tubular T-joints. *Marine Structures, 55*, 162-181.

Yanjun, Z., Yunfei, C., Liuyang, L., Jingrui, Z., & Xiukang, C. (2023). Experimental and finite element simulation study of the mechanical behaviors of aluminum foam-filled single/double tubes. *Materials Research Express, 10*(4), 046506.

Zhou, F., Li, Y., & Dong, B. (2022). Experimental investigation of concrete-filled double-skin stainless steel tubular beam-columns. *Journal of Constructional Steel Research, 196*, 107406.

Zhou, F., & Xu, W. (2016). Cyclic loading tests on concrete-filled double-skin (SHS outer and CHS inner) stainless steel tubular beam-columns. *Engineering Structures, 127*, 304-318.

Zou, Y., Wang, L., Sun, Z., Pan, J., Chen, M., & Wu, Y. (2023). Experimental and numerical studies of concrete-filled corrugated steel tubular column under axial compression. *Engineering Structures, 276*, 114813.

4th International Civil Engineering & Architecture Conference
17-19 May 2025, Trabzon, Türkiye

A comprehensive assessment of the as-built projects of severely damaged or collapsed residence in Malatya after Feb 6, 2023, Kahramanmaraş earthquakes

Onur Onat*[1], Şenol Albayrak[1]

[1] *Inonu University, Department of Civil Engineering, 44280, Malatya, Türkiye*

Abstract. The basic purpose of this study is to evaluate design parameters of as-built blueprint residence project in Malatya. This study includes theoretical investigation on the base of as-built projects. For this aim, 41 projects were investigated in detail and then selected features were presented with suitable graphs. These selected features were construction year, earthquake regulations in force in the year the structure was built, target concrete compressive strength, target steel grade, thickness of foundation and deep foundation level (excavation from ground surface), total height and settlement area of residences, numbers of column in transvversal and longitudinal directions of the plan, minimum distance of shear reinforcement in column and beam, minimum tension reinforcement in beam and minimum reinforcement in colum section was evaluated.

Keywords: Kahramanmaraş earthquakes; Building stock of Malatya; Design evaluation; Blueprint project

1. Introduction

On February 6, 2023, a pair of earthquakes with magnitudes Mw 7.7 and Mw 7.6 struck the Eastern Anatolian Fault Zone, centered in the Pazarcık and Elbistan districts of Kahramanmaraş Province, an event which was later described as the "Disaster of the Century." These two powerful earthquakes, occurring 9 hours apart, affected 11 provinces in Eastern and Southeastern Anatolia, resulting in 50,783 fatalities, 107,204 injuries, and causing an economic loss of 178 billion USD. Despite being located 165 km from the epicenter of the Pazarcık-centered earthquake and 100 km from the Elbistan-centered earthquake, the province of Malatya was the third most affected, with 6,444 injuries and 1,237 fatalities. Although the loss of life was not as severe, Malatya experienced extensive damage, including heavy structural damage to 44,000 buildings. Therefore, significant destruction occurred in Malatya, with a large number of reinforced concrete buildings being either destroyed or severely damaged. The first of them occurred at 04:17 local time at Kahramanmaraş-Pazarcık. Nine hours later, at 13:24 local time, Kahramanmaraş-Elbistan triggered another earthquake. The measured PGA of the first earthquake was reached to 2.05 g (Onat et al. 2024). The earthquake exceeded the highest design level, which defied the Turkish Building Earthquake Code 2018 (TBEC, 2018). The two shocks inflicted significant damage, leading to a total of 53537 casualties. 39441 structural systems completely collapsed, while 206907 structural systems suffered heavy damage. The heavy damage distribution of old and new building stock from the epicenter to 165 km away from the Elbistan earthquake is mystery. This study given an emphasis to a different perspective of heavy damage distribution of building stock in Malatya in terms of code based design requirements. In the content of this manuscript, the statistical evaluation of heavily damaged and destroyed buildings has been conducted based on various parameters. Subsequently, using selected parameters from 41 different projects with varying construction years, a statistical analysis was performed to assess whether there were deviations from the design standards. Architectural conditions and minimum requirements in the relevant regulations were taken into account when determining the design parameters. The goal is to investigate and propose new inter-floor displacement limits for existing buildings.

2. Literature review of Kahramanmaraş Earthquakes

On February 6, 2023, the Kahramanmaraş earthquakes were extraordinarily strong ground motions that gave emphasis to the design of the earthquake level, whose return period is 2475 years and effected eleven cities, 124 town and 6929 villages as presented in Fig. 1.

*Corresponding author, E-mail: onur.onat@inonu.edu.tr

https://doi.org/10.31462/icearc2025_ce_eqe_898

Fig. 1. Earthquake effected cities during Feb 6, 2023

These earthquakes did not make up for the lack of knowledge in design and basic theory in far-fault territories, including classic and non-engineered structures. For this reason, after field observations in different cities, different results were registered in the literature. For instance, Vuran et al. (2024) investigated structural damages into two categories pre 2000 and post 2000. They emphasized that pre-2000 buildings could not satisfy the ductility requirements and updated basic calculations. İnce (2024) emphasized that the effective use of reinforcement, the hammer effect, and the discontinuous frame that resulted in damages and collapse in Adyaman. Kazaz et al. (2024) underlined the failure reasons as followed: i) production of shear wall system, ii) wall position, and iii) insufficient seismic detailing of new RC residences that resulted in total collapse of new buildings in Hatay. Tura et al. (2024) reported that missing confinement detail on site, mis bending of crossties, unexpected and early loss of moment capacity resulted in a severe damage beyond collapse prevention damage levels. Ozdemir (2024) prepared a list for an evaluation of the post-earthquake damages of 2790 buildings in the Antakya stock. They underlined that the construction year, building typologies, number of floors, ground level, and load-bearing systems as the primary factors contributing to damage. Sezgin et al. (2024) performed field observations in İskenderun to identify main reasons for damage and failure. The basic problem is identified as liquefaction in İskenderun and Hatay, problems with material quality, aggregate and gradation, the effect of humidity on concrete and reinforcement, problems with design and application, loose detailing of main bearing elements, stairs that don't have enough bearing capacity, and finally not following the rules about irregularities that aren't allowed in seismic codes. Sevim et al. (2024), Erbaş et al. (2024) and Yön et al. (2025) highlighted the conventional damages that occurred, particularly in old building stock constructed during the out-of-date seismic codes. After these valuable field observations and numerical studies, there is a question: What is the problem related to accepted projects from the local municipality? This study is devoted to clarify this questions on the base of design parameters.

3. Materials and method

In the current study, the parameters that were considered for the evaluation of the examined structures according to their blueprint projects are as follows:

a) The project regulations for the structure and the site boundaries,
b) Foundation and soil characteristics,
c) Material properties,
d) Architectural features,
e) Structural load-bearing system.

The evaluation was carried out based on these headings. Subsequently, the parameters evaluated have been explained in detail. Additionally, the subheadings under the specified main headings are as follows: reinforced concrete damage states of the structures; location, municipal regulations, construction year, number of floors, concrete class, steel class, total building height (m), settlement area (m²), soil type, foundation type, foundation thickness (cm), existence of a basement, foundation excavation depth, ground floor height, short shear wall ratio, long shear wall ratio, short column count, long column count, smallest column dimensions, beam dimensions, plan irregularity, vertical irregularity, presence of mezzanine, number of cantilever beams, column reinforcement ratio, shear wall reinforcement ratio, minimum beam reinforcement, beam ratio in tension zones, beam reinforcement ratio, column stirrup spacing (cm), beam stirrup spacing, and other similar mechanisms have been examined.

4. Results and discussion

4.1. The earthquake regulations in force and the administrative boundaries at the time the structure was designed
In this subsection, the regulations in force during the years when the structures were initially designed have been identified, with the specific regulations being the 1968, 1975, 1998, 2007, and 2018 codes. A total of 41 projects were examined according to these regulations, with the number of structures analyzed for each regulation being 3, 10, 8, 14, and 6, respectively, thus generating quantitative data as seen in Fig. 2.

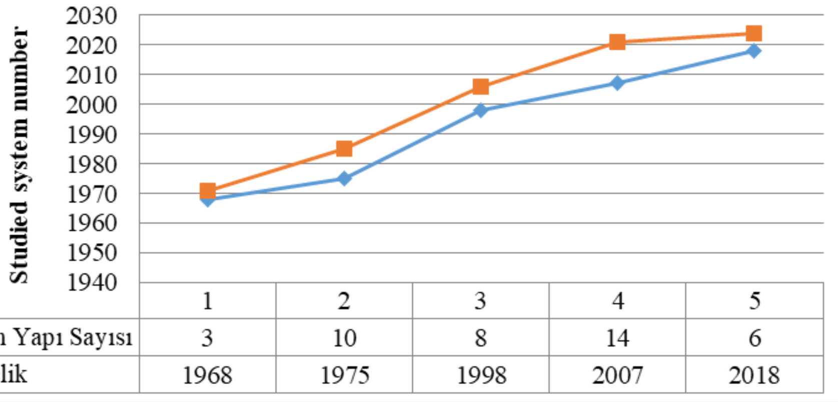

Fig. 2. The regulations under which the examined structures were designed and the number of structures analyzed

Under the aforementioned regulations, the construction years of the examined structures are as follows: For structures designed according to the 1968 regulation, the construction years range from 1971 to 1974. Structures designed under the 1975 regulation were built between 1976 and 1997. Buildings designed according to the 1998 regulation were constructed between 1998 and 2000. Structures designed under the 2007 regulation were built between 2015 and 2018. Lastly, buildings constructed according to the 2018 regulation were built between 2018 and 2021. Regarding the administrative boundaries, Malatya gained metropolitan status in 2012 with the Municipal Law, and it remained as Malatya province under the 1968, 1975, 1998, and 2007 regulations. However, when the 2018 regulation was enacted, Malatya province was divided into two districts: Yeşilyurt and Battalgazi. Our study focused on the structures within the boundaries of Yeşilyurt, where the seismic impact is the most destructive.

4.2. Foundation and soil characteristics
In this subsection, the foundation and soil characteristics of the structures designed under the regulations in force during their construction years are evaluated. It was found that the buildings designed according to the 1968 and 1975 regulations were of lower height, while those designed according to the 1998, 2007, and 2018 regulations were taller. Additionally, there were no basements in buildings designed under the 1968 regulation, whereas basements began to be constructed starting from the years following the 1975 regulation. The foundation thicknesses have gradually increased over time, as the regulations required thicker foundations for enhanced structural integrity. In terms of foundation types, buildings designed under the 1968 regulation generally used individual (single) foundations, while those under the 1975 and 1998 regulations employed continuous (slab) foundations. In contrast, buildings designed according to the 2007 and 2018 regulations were found to predominantly use raft foundations. The temporal changes in these parameters can be attributed to the increasing need for safer and more robust structures as buildings became taller, leading to a growth in the physical dimensions of the buildings.

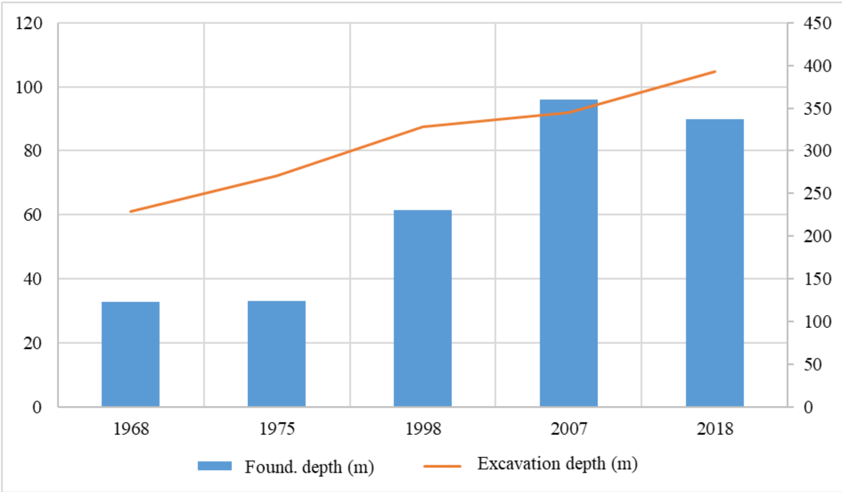

Fig. 3. The foundation excavation depth and foundation thickness of structures under the regulations

4.3. Material properties

In this evaluation step, it was observed that as the physical dimensions of the structures examined increased within the framework of the mentioned regulations, there has been a consistent increase in concrete and steel grades over time. This trend can be attributed to the fact that, in an effort to save costs, people began to build taller structures by coming together, which in turn necessitated improvements in the quality of concrete and steel grades. This conclusion is supported by the numerical data obtained from the analysis.

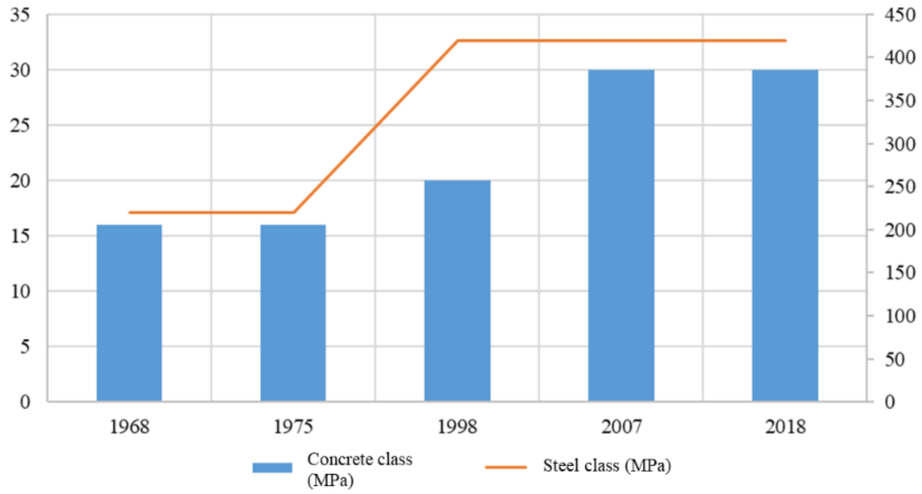

Fig. 4. Changes in concrete grade and steel grade according to the regulations

4.4. Architectural features

In terms of architectural features, when evaluating the structures based on the regulations for each respective construction year, it was observed that the footprint areas, total building heights, and the number of floors of buildings designed from the 1968 regulation to the 2018 regulation have progressively increased. In this context, it was also assessed that the increasing living standards of people have led to a growing need for higher buildings and more floors, reflecting the changes in the coefficients and total heights of the buildings over time.

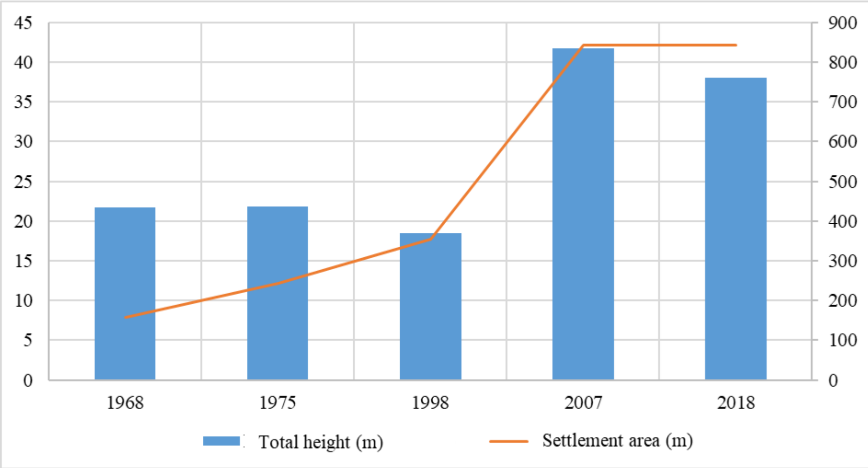

Fig. 5. The relationship between the construction area in m^2 area and total building height according to the regulations

When considering the physical dimensions of buildings designed under the 1968 regulation, it was observed that the number of tie beams was low, and mezzanines were not constructed. In contrast, for buildings designed according to later regulations, the number of tie beams increased, and mezzanines were built until the 2007 regulation. However, no mezzanines were included in buildings designed according to the 2018 regulation. Additionally, it was found that there were no vertical or plan irregularities in structures designed under the 1968 regulation. In buildings designed according to the 1975 and 1998 regulations, soft-story irregularities were observed. For buildings designed under the 2018 regulation, there were no mezzanines or vertical and plan irregularities. Furthermore, the ground floor heights have also increased over time, in accordance with the physical dimensions of the buildings, reflecting the changes in the regulations from the past to the present.

4.5. Main bearing structural system
According to the average project data based on the relevant regulations, the smallest beam size is 20x60 cm, and the smallest column size is 25x60 cm. The number of columns in both the long and short directions has increased with the regulations, which can be attributed to the increased footprint area of the buildings. The wall ratio in the long and short directions was found to be nonexistent in buildings designed under the 1968, 1975, and 1998 regulations. However, for buildings designed according to the 2007 and 2018 regulations, the average wall ratios were calculated as 0.26 and 0.0085, respectively. In structures designed under the 1968 regulation, the number of columns in both the short and long directions was lower compared to those designed under later regulations. Between the 1975 and 1998 regulations, the number of columns in the long direction remained stable, but it increased again in buildings designed according to the 1998, 2007, and 2018 regulations. The number of columns in the short direction, however, increased from the 1968 regulation until the 2007 regulation, with a subsequent decrease under the 2018 regulation.

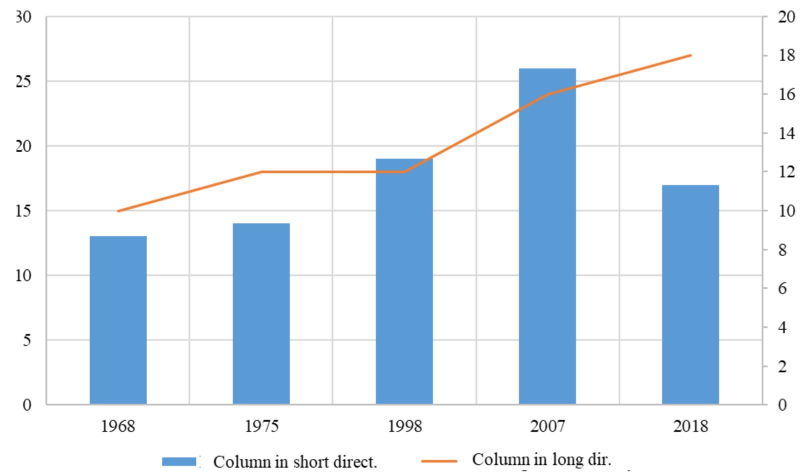

Fig. 6. The relationship between the number of columns in the short direction and the number of columns in the long direction for structures designed according to the regulations

It was observed that in the 1968 and 1975 regulations, there was no increase in the spacing of beams, columns, and stirrups. However, in structures built under subsequent regulations, the spacing was adjusted according to the regulations. This indicates that the concept of ductility was incorporated into the seismic behavior of buildings through the regulations.

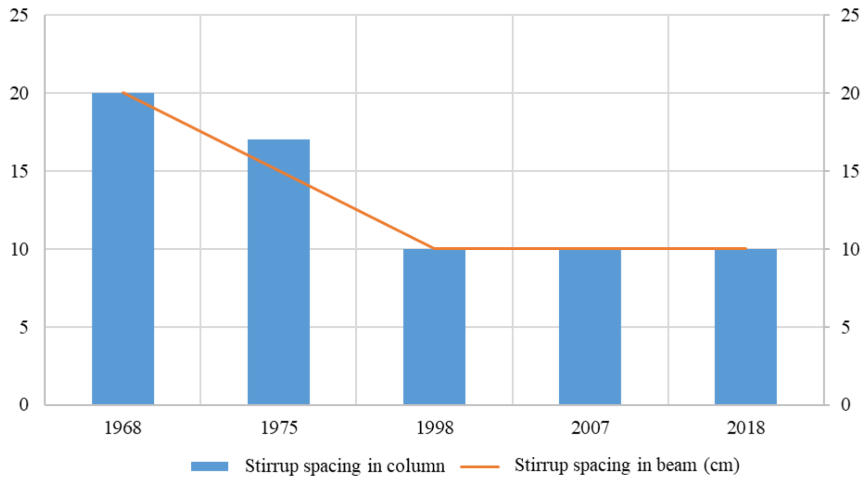

Fig. 7. Changes in the beam stirrup spacing and column stirrup spacing for structures designed according to the regulations

It was also observed that the beam stirrup spacing decreased from 20 cm to 10 cm according to the regulations. The same situation applies to the columns, where the spacing also decreased from 20 cm to 10 cm. When analyzing the reinforcement ratio in beams, it was found that the regulations set a minimum limit for the reinforcement in the tension zone. These values changed from the minimum value prescribed by the regulations to a value of 0.0062.

In terms of column reinforcement ratio, according to the TBDY 2018 regulations, the longitudinal reinforcement area in columns should not be less than 1% and should not exceed 4% of the gross cross-sectional area. It was observed that the average column reinforcement ratio remained around 0.875% for buildings designed according to the 1968 and 1975 regulations, while it increased slightly above 1% after the 1998 regulation.

The dimensions of both columns and beams increased as a result of the physical dimensions of the structures. The number of columns increased according to the long and short directions of the building. The beam reinforcement ratio, tension region beam ratio, and minimum beam reinforcement values were at their minimum level under the 1968 regulation, whereas in later regulations, the values remained within the limits prescribed by the regulations.

Regarding the wall reinforcement ratio, it was found that there were no walls in structures designed according to the 1968, 1975, and 1998 regulations. However, in buildings designed according to the 2007 and 2018 regulations, the numerical values of the wall reinforcement ratio met the minimum conditions prescribed by the regulations.

5. Conclusions

Although many field studies and reports have been conducted regarding the earthquakes centered in Pazarcık-Elbistan, Kahramanmaraş on February 6, 2023, there have been no studies where criteria were set based on project data. However, this seminar aimed to address this gap, focusing solely on the province of Malatya. In this context, selected buildings were specifically studied and examined at the provincial level.

In this regard, in order to investigate the deficiencies in the design of reinforced concrete structures, a study of 41 building projects was conducted. The findings revealed that for structures built according to newer regulations, design errors related to vertical load-bearing were rarely observed. However, the presence of tie beams and non-continuous elements that did not form frames was noteworthy. It was also concluded that nonlinear analyses based solely on vertical loads and equivalent seismic loads were insufficient for buildings taller than 30 meters, and that performance-based design had become a necessity. Alongside design, factors such as unqualified workmanship, the use of unsuitable materials, and flaws in inspection mechanisms were emphasized as influential elements in this study.

References

Erbaş, Y., Mercimek, Ö., Anıl, Ö., Çelik, A., Akkaya, S.T., Kocaman, İ., & Gürbüz, M. (2024). Design deficiencies, failure modes and recommendations for strengthening in reinforced concrete structures exposed to the February 6, 2023 Kahramanmaraş Earthquakes (Mw 7.7 and Mw 7.6). *Natural Hazards*, 1-42

İnce, O. (2024). Structural damage assessment of reinforced concrete buildings in Adıyaman after Kahramanmaraş (Türkiye) Earthquakes on 6 February 2023. *Engineering Failure Analysis, 156*, 107799

Kazaz, İ., Bilge, İ.H., & Gürbüz, M. (2024). Near-fault ground motion characteristics and its effects on a collapsed reinforced concrete structure in Hatay during the February 6, 2023 Mw7. 8 Kahramanmaraş earthquake. *Engineering Structures*, *298*, 117067

Onat, O., Yön, B., Uslu, A., Öncü, M.E., Varolgüneş, S., Karaşin, İ.B., & Gör, M. (2024). Seismic resistance and performance evaluation of masonry dwellings after the February 6, 2023, Kahramanmaraş Earthquake sequence in Türkiye. *Journal of Earthquake and Tsunami*, *18*(04), 2450013

Ozdemir, A. (2024). Examining the effect of structural characteristics of Antakya building stock on the damage level after the Kahramanmaraş earthquakes. *Journal of Earthquake Engineering*, 1-30

Sevim, B., Ayvaz, Y., Akbulut, S., Aydıner, M.F., Uzun, S., & Ari, A. (2024). Seismic performance and damage evaluation of reinforced concrete structures based on field investigation made after February 6, 2023, Kahramanmaraş earthquakes. *Journal of Earthquake and Tsunami*, *18*(01), 2350032

Sezgin, S.K., Sakcalı, G.B., Özen, S., Yıldırım, E., Avcı, E., Bayhan, B., & Çağlar, N. (2024). Reconnaissance report on damage caused by the February 6, 2023, Kahramanmaraş Earthquakes in reinforced-concrete structures. *Journal of Building Engineering*, *89*, 109200

TBEC2018. (2018). Turkish Building Earthquake Code, Ministry of Environment, Urbanization and Climate Change.

Tura, C., Orakcal, K., Kusunoki, K., & Ilki, A. (2024). Seismic response simulation of a reinforced concrete wall-frame building that collapsed during the February 2023 Kahramanmaras Earthquake. *Journal of Earthquake Engineering*, 1-25

Vuran, E., Serhatoğlu, C., Timurağaoğlu, M.Ö., Smyrou, E., Bal, İ.E., & Livaoğlu, R. (2025). Damage observations of RC buildings from 2023 Kahramanmaraş earthquake sequence and discussion on the seismic code regulations. *Bulletin of Earthquake Engineering*, *23*(3), 1153-1182

Yön, B., Dedeoğlu, İ.Ö., Yetkin, M., Erkek, H., & Calayır, Y. (2025). Evaluation of the seismic response of reinforced concrete buildings in the light of lessons learned from the February 6, 2023, Kahramanmaraş, Türkiye earthquake sequences. *Natural Hazards*, *121*(1), 873-909

4th International Civil Engineering & Architecture Conference
17-19 May 2025, Trabzon, Türkiye

Compressive behaviour of CFRP- and SFRP-confined concrete: A performance assessment

Biçimlendirilmiş: Aralık Önce: 24 nk, Sonra: 12 nk

Nisreen Salameh[1], Raafat El-Hacha*[1]

[1] *University of Calgary, Department of Civil Engineering, 2500 University Drive NW, Calgary, Alberta, Canada*

Abstract. This study presents a comparative assessment of the compressive behaviour of concrete cylinders confined with Carbon Fibre-Reinforced Polymer (CFRP) and Steel Fibre-Reinforced Polymer (SFRP) jackets. While the differences in compressive behaviour between CFRP- and SFRP-confined cylinders have been extensively explored in terms of ultimate axial strength, ultimate axial strain, and load-deformation behaviour, this research shifts focus to other critical performance metrics. These include dilation behaviour, CFRP and SFRP confinement effectiveness coefficient, strain ductility index, and energy ductility index. Forty-two cylinders were tested under uniaxial compression with varying concrete strengths, FRP types, and jacket thicknesses.
Experimental results reveal significant distinctions in the performance of CFRP and SFRP confinement systems. CFRP demonstrates superior confinement effectiveness due to its high stiffness and strength, significantly enhancing compressive strength and controlling dilation. In contrast, SFRP exhibits distinct advantages in strain and energy ductility, attributed to its metallic properties that enable greater deformation capacity and energy absorption. The study also provides insights into the interaction between the confining jacket and the concrete core, focusing on dilation behaviour as a key factor in confinement mechanics.
The findings underscore the importance of balancing strength and ductility in designing FRP-confined concrete systems. A comparative framework highlights the unique benefits of CFRP and SFRP, offering guidelines for optimizing material selection based on specific structural requirements. This research contributes to advancing the understanding of FRP-confinement mechanics and offers practical recommendations for enhancing the performance of confined concrete under axial loads.

Keywords: FRP-confined concrete; Compressive behaviour; Ultimate axial strength, Ultimate axial strain, Stress-strain behaviour

1. Introduction

The use of Fiber Reinforced Polymer (FRP) composites for strengthening and retrofitting concrete structures has seen significant advancements since their introduction in the late 1980s. Initially developed in Europe and Japan and later adopted in North America, FRP composites, including Carbon Fiber-Reinforced Polymer (CFRP) and Steel Fiber-Reinforced Polymer (SFRP), have become key materials for addressing structural deficiencies in civil infrastructure, particularly in seismic zones (Bank, 2006). The appeal of FRP composites lies in their high strength-to-weight ratios, corrosion resistance, and ease of installation compared to traditional methods like concrete and steel jacketing.

While traditional methods such as concrete and steel jacketing effectively enhance structural performance, they are often associated with significant drawbacks. Concrete jacketing increases the weight and cross-sectional area of structural members, while steel jacketing, though robust, is labour-intensive, costly, and prone to corrosion. In contrast, FRP composites provide an efficient solution, delivering enhanced structural performance with minimal weight addition, superior durability, and adaptable installation techniques. These advantages have driven extensive research into their use for concrete confinement (Fahmy & Wu, 2010).

*Corresponding author~~, Professor~~, E-mail: relhacha@ucalgary.ca

Biçimlendirdi: Altı Çizili

https://doi.org/10.31462/icearc2025_ce_eqe_910

Among FRP systems, CFRP has been widely studied, with its high stiffness and tensile strength enabling significant improvements in the compressive strength and ductility of confined concrete. The effectiveness of CFRP confinement has been well-documented, highlighting its ability to enhance ultimate axial strength, axial strain, and overall load-deformation behaviour (Lam & Teng, 2003; Li, 2006; Xiao & Wu, 2000). SFRP, on the other hand, offers unique advantages, combining the tensile strength of steel fibres with the lightweight and corrosion-resistant properties of polymer matrices. Recent studies, such as those by Mashrik (2011) and Abdelrahman (2011), have demonstrated the inherent ductility and cost-effectiveness of SFRP, although its application in concrete confinement remains underexplored.

Despite the significant body of research on the axial strength and strain capacity of FRP-confined concrete, certain key performance metrics have received comparatively less attention. Metrics such as dilation behaviour, strain efficiency, confinement effectiveness, and ductility indices are crucial for understanding the mechanics of FRP-confinement systems (Chen, 1982). Additionally, parameters such as FRP jacket thickness, type, and compressive strength of unconfined concrete significantly influence the performance of confined concrete.

This study addresses these gaps by providing a detailed comparative analysis of CFRP and SFRP-confined concrete under uniaxial compression. By focusing on metrics like dilation behaviour, strain efficiency, and ductility indices, this research aims to advance the understanding of FRP-confinement mechanics and inform the optimization of material selection based on specific structural requirements.

2. Methodology

2.1 Experimental program overview

The experimental program was designed to investigate the compressive behaviour of concrete cylinders confined with Carbon Fiber-Reinforced Polymer (CFRP) and Steel Fiber-Reinforced Polymer (SFRP) under monotonic uniaxial compression. The study variables included the concrete compressive strength and the type and thickness of the FRP jacket. The concrete cylinders were divided into two groups based on target unconfined concrete compressive strengths of 35.0 MPa and 45.0 MPa. Each group included three unwrapped control cylinders as benchmarks, alongside various CFRP and SFRP confinement configurations.

In total, 42 circular small-scale unreinforced concrete cylinders were prepared and tested, consisting of 18 specimens wrapped with SFRP, 18 specimens wrapped with CFRP, and 6 unwrapped control specimens. All cylinders had an outer diameter of 150 mm and a height of 300 mm. The specimens were cast in two batches with different concrete mix designs to achieve the desired compressive strengths. A summary of the experimental program and cylinder configurations is detailed in Table 1.

The designation system assigned to cylinders referred to hereafter in all subsequent discussions and graphical plots, is presented next. The designation system adopted takes the following general form:

C(F)-FBR(N)

where;

C = Cylinder;

F = Concrete 28-day specified compressive strength;

FBR = Fibre type;

N = Number of plies;

It should be noted that when N=0, when the specimen is unwrapped, the notation FBR(N) will be simply replaced by UW notation.

Table 1. Summary of test cylinders

Cylinder ID	No.	Confinement Configuration			Cylinder ID	No.	Confinement Configuration		
		f_c' (MPa)	Fibre Type	No. of FRP Layers			f_c' (MPa)	Fibre Type	No. of FRP Layers
C37.3-UW	3	37.3	-	-	C42.4-UW	3	42.4	-	-
C37.3-SFRP1	3		SFRP	1	C42.4-SFRP1	3		SFRP	1
C37.3-SFRP2	3			2	C42.4-SFRP2	3			2
C37.3-SFRP3	3			3	C42.4-SFRP3	3			3
C37.3-CFRP1	3	37.3	CFRP	1	C42.4-CFRP1	3	42.4	CFRP	1
C37.3-CFRP2	3			2	C42.4-CFRP2	3			2
C37.3-CFRP3	3			3	C42.4-CFRP3	3			3

2.2 Material properties

2.2.1 Concrete

Normal-strength concrete was used for all specimens. The mix design for both batches are summarized in Table 2.

2.2.2 SFRP sheets

The SFRP sheets used were 3×2-20-12, manufactured by Hardwire LLC. The typical properties of SFRP composite are detailed in Table 3.

2.2.3 CFRP sheets

The CFRP sheets used were SikaWrap® Hex 230C, manufactured by Sika Canada Inc. The typical properties of carbon cured laminate with Sikadure 330 Epoxy are presented in Table 4.

Table 2. Summary of concrete mix design

Mix Design	Units	Batch	
		1	2
w/c	ratio	0.59	0.38
Portland Cement	kg/m^3	315	545
Water	kg/m^3	186	207
Coarse Aggregate	kg/m^3	1085	1035
Fine Aggregate	kg/m^3	870	516

Table 3. Typical properties of SFRP composite system, HARDWIRE (2014)

Properties	3×2-20
Laminate Density (kg/m3)	3110
Laminate thickness (mm)	1.2
Ultimate Tensile stress (MPa)	985
Effective Modulus (GPa)	66.1

Table 4. Typical properties of carbon-cured laminate, SikaWrap® Hex 230C (2014)

Properties	Value		ASTM Method Test
	Average	Design	
Tensile Strength (MPa)	894	715	D-3039
Tensile Modulus (GPa)	65.402	61.012	D-3039
Tensile Elongation (%)	1.33	1.09	D-3039
Compressive Strength (MPa)	779	668	D-695
Compressive Modulus (GPa)	67.003	63.597	D-695
Shear Strength (MPa)	63	56	D-3518
Shear Modulus (GPa)	2.902	2.8	D-3518
Laminate Thickness (mm)	0.381	0.381	-

2.3 Instrumentation

2.3.1 Strain gauges

Conventional foil strain gauges with a resistance of 120 Ω and a gauge length of 6.35 mm were employed. Unwrapped specimens were equipped with four strain gauges (two vertical and two radial), while wrapped specimens were equipped with two strain gauges (one vertical and one radial).

2.3.2 Linear strain converters (LSCs)

Wenglor high-performance distance sensors were utilized to measure axial and lateral displacements.

2.3.3 Digital image correlation (DIC)

High-resolution cameras were used to capture strain behaviour along the entire height of the cylinders. Images were taken every 5 seconds during testing and processed with GeoPIV software via Matlab.

2.4 Test setup and loading

The test setup involved positioning the cylinders within a 9 MN loading frame, equipped with high-resolution cameras and work lights to ensure a well-lit environment. Axial compressive loading was applied using a load control mechanism at a rate of 0.15 MPa/s to 0.35 MPa/s until complete failure. This testing protocol ensures precise and reliable measurement of the compressive behaviour of FRP-confined concrete cylinders, offering valuable insights into the performance variations between different FRP confinement configurations.

3. Results

3.1 Ultimate axial strength

The average ultimate axial strength for the tested cylinders is presented in Table 5, showing significant improvements for both CFRP- and SFRP-confined concrete compared to unconfined concrete. SFRP-confined cylinders outperform CFRP-confined ones, with C37.3-SFRP3 achieving a 421% strength increase compared to 147% for C37.3-CFRP3. For higher-strength concrete (C42.4), SFRP3 achieves a 373% increase, while CFRP3 reaches 123%. These results highlight the superior confinement effectiveness of SFRP, particularly with additional layers, though the relative strength gains are reduced for higher-strength concrete.

Table 5. Ultimate axial strength of CFRP- and SFRP-confined concrete cylinders

	Ultimate Axial Strength				Ultimate Axial Strength		
Confinement Configuration	Avg. (Mpa)	f'_{cu}/f'_{co}	Strength Increase (%)	Confinement Configuration	Avg. (MPa)	f'_{cu}/f'_{co}	Strength Increase (%)
C37.3-CFRP1	51.4	1.4	38	C42.4-CFRP1	59.6	1.4	40
C37.3-CFRP2	69.5	1.9	86	C42.4-CFRP2	75.8	1.8	79
C37.3-CFRP3	92.4	2.5	147	C42.4-CFRP3	94.6	2.2	123
C37.3-SFRP1	94.5	2.5	153	C42.4-SFRP1	98.8	2.3	133
C37.3-SFRP2	146.8	3.9	293	C42.4-SFRP2	153.9	3.6	263
C37.3-SFRP3	194.6	5.2	421	C42.4-SFRP3	200.4	4.7	373

3.2 Ultimate axial strain

The average ultimate axial strain, measured from strain gauges at the mid-height of the cylinders for each of the three nominally identical tested cylinders, is presented in Table 6. The results demonstrate a substantial increase in ultimate axial strain across all 18 cylinders compared to the axial strain of unconfined concrete. Notably, SFRP-confined cylinders exhibit superior strain capacity compared to CFRP-confined cylinders. For example, the strain increase for C37.3-SFRP3 reaches 2682%, significantly exceeding the 1199% observed for C37.3-CFRP3. Increasing the number of FRP layers enhances confinement effectiveness for both CFRP and SFRP systems. However, for higher-strength concrete C42.4, the ultimate strain values are consistently lower than those for C37.3, suggesting that FRP confinement is less effective in improving strain capacity for higher-strength concrete, which inherently has lower ductility.

Table 6. Ultimate axial strain of CFRP- and SFRP-confined concrete cylinders

	Ultimate Axial Strain				Ultimate Axial Strain		
Confinement Configuration	Avg. (με)	$\varepsilon_{cu}/\varepsilon_{co}$	Strain Increase (%)	Confinement Configuration	Avg. (με)	$\varepsilon_{cu}/\varepsilon_{co}$	Strain Increase (%)
C37.3-CFRP1	14652	7.5	648	C42.4-CFRP1	10659	6.1	507
C37.3-CFRP2	19265	9.8	884	C42.4-CFRP2	11491	6.5	554
C37.3-CFRP3	25440	13.0	1199	C42.4-CFRP3	15525	8.8	784
C37.3-SFRP1	32088	16.4	1538	C42.4-SFRP1	27007	15.4	1437
C37.3-SFRP2	43674	22.3	2130	C42.4-SFRP2	33227	18.9	1791
C37.3-SFRP3	54495	27.8	2682	C42.4-SFRP3	47361	27.0	2596

3.3. Ultimate lateral strain

Table 7 shows the ultimate lateral strain results, indicating that SFRP-confined cylinders achieve significantly higher lateral strain values compared to CFRP-confined ones. For example, C37.3-SFRP1 reaches 1478%, far exceeding the 664% observed for C37.3-CFRP1, demonstrating the superior strain capacity of SFRP. However, the lateral strain values decrease for higher-strength concrete C42.4, highlighting the reduced effectiveness of confinement in enhancing lateral strain for stiffer concrete cores.

Table 7. Ultimate lateral strain of CFRP- and SFRP-confined concrete cylinders

Confinement Configuration	Ultimate Lateral Strain			Confinement Configuration	Ultimate Lateral Strain		
	Avg. (με)	$\varepsilon_l/\varepsilon_{co}$	Strain Increase (%)		Avg. (με)	$\varepsilon_l/\varepsilon_{co}$	Strain Increase (%)
C37.3-CFRP1	-10491	7.6	664	C42.4-CFRP1	-10024	9.0	801
C37.3-CFRP2	-12632	9.2	820	C42.4-CFRP2	-11268	10.1	913
C37.3-CFRP3	-13419	9.8	878	C42.4-CFRP3	-10009	9.0	800
C37.3-SFRP1	-21655	15.8	1478	C42.4-SFRP1	-18714	16.8	1583
C37.3-SFRP2	-14896	10.9	985	C42.4-SFRP2	-12491	11.2	1023
C37.3-SFRP3	-15085	11.0	999	C42.4-SFRP3	-14722	13.2	1224

3.4 Load-deformation behaviour

Stress-strain curves for CFRP- and SFRP-confined concrete cylinders for each confinement configuration are plotted in Figure 1, respectively. For comparison, the stress-strain curves of the corresponding unconfined concrete are also included. As depicted in the figures, all FRP-wrapped cylinders exhibit a bilinear ascending stress-strain behaviour up to the point of FRP failure.

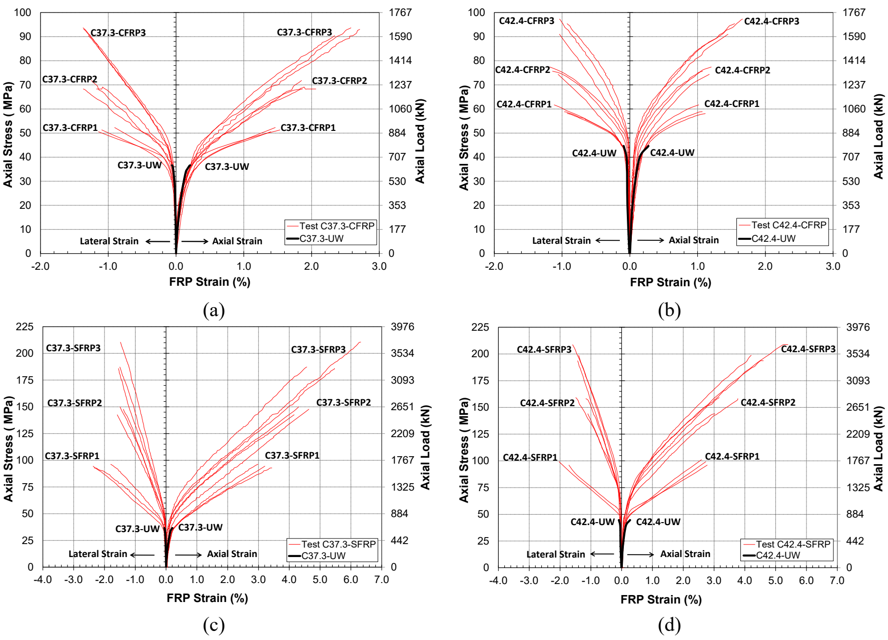

Fig. 1. Stress-strain curves for (a) C37.3-CFRP (b) C42.4-CFRP (c) C37.3-SFRP (d) C42.4-SFRP

3.5 Dilation behaviour

Axial stress data, used for plotting axial stress-volumetric strain curves shown in Figure 2, were calculated by dividing the loads obtained from the data acquisition system by the cylinder's cross-section area. Volumetric strain,

ε_v, which is defined as the volume change per unit volume [8], is calculated from Equation 1 using axial strain, ε_c, and lateral strain, ε_l, both obtained from the foil strain gauges installed at the mid-height of each cylinder.

$$\varepsilon_v = \frac{\Delta V}{V} = \varepsilon_c + 2\varepsilon_l \tag{1}$$

—where ΔV is the change of volume, and V is the original volume.

Biçimlendirilmiş: Girinti: İlk satır: 0,32 cm

The plots highlight distinct dilation and compaction behaviours for CFRP and SFRP-confined concrete, illustrating the influence of confinement type and concrete strength on volumetric response under axial loading.

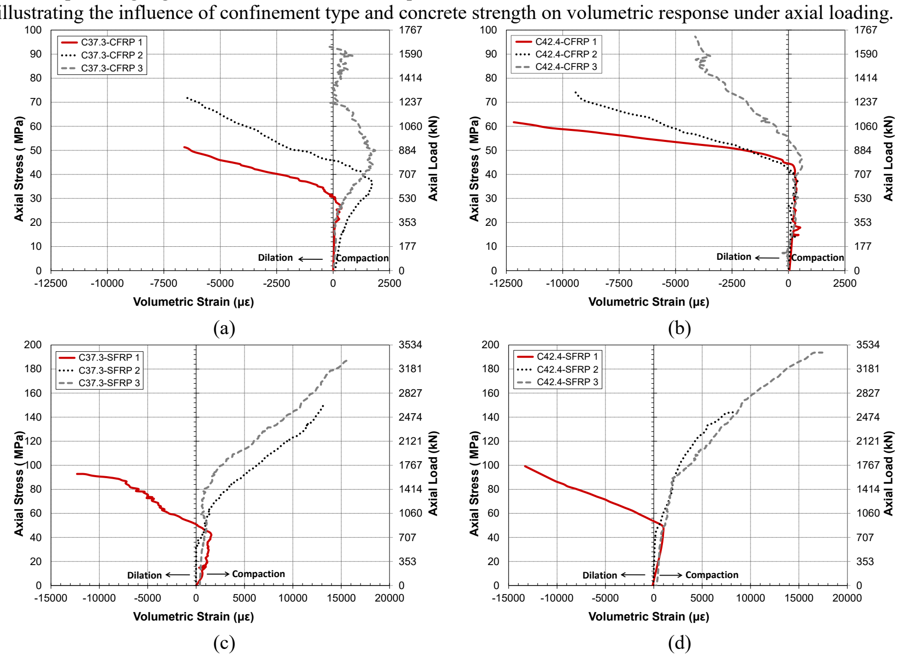

Fig. 2. Dilation behaviour for (a) C37.3-CFRP (b) C42.4-CFRP (c) C37.3-SFRP (d) C42.4-SFRP

Biçimlendirilmiş: Aralık Önce: 0 nk, Satır aralığı: tek

4. Performance ~~Comparison~~ comparison between CFRP- and SFRP-~~Confined~~ confined ~~Cylinders~~cylinders

The performance of CFRP- and SFRP-confined concrete was compared by examining the confinement effectiveness coefficient, strain ductility indices, and energy ductility indices.

The experimental confinement effectiveness coefficient, k_l, is calculated utilizing the formula originally developed by Richart et al. (1928), as shown below:

$$k_l = \frac{(f'_{cu} - f'_{co})}{f_{lu}} \tag{2}$$

The strain ductility factor, μ_{cu}, measures the ability of a structural member to undergo large inelastic deformation without significant loss in strength. It is defined as the ratio of the FRP ultimate axial strain at rupture, ε_{cu} over the axial strain corresponding to unconfined concrete at peak, ε_{co}. It is calculated as per the following equation:

$$\mu_{cu} = \frac{\varepsilon_{cu}}{\varepsilon_{co}} \tag{3}$$

The energy ductility index, ω_{cu}, is defined as the area under the stress-strain curve up to the failure of the FRP jacket over the area under the stress-strain curve corresponding to the unconfined state. It expresses the ability of the structural member to dissipate energy during inelastic deformation.

$$\omega_{cu} = \frac{Area_1}{Area_2} \tag{4}$$

Different parameters of ductility indices for bilinear stress-strain response are illustrated in Figure 3.

Table 8 compares the confinement effectiveness coefficient, kl, and ductility indices, μ_{cu} and ω_{cu}, for different confinement configurations of CFRP- and SFRP-confined cylinders. The results show that SFRP-confined cylinders achieve higher ductility indices compared to CFRP-confined cylinders. For instance, C37.3-SFRP3 achieves a strain ductility index, μ_{cu}, of 27.8 and an energy ductility index, ω_{cu}, of 107.9, significantly outperforming C37.3-CFRP3, which has values of 13.3 and 26.0, respectively. This highlights SFRP's superior deformation and energy absorption capacity due to its metallic properties. However, the confinement effectiveness coefficient (k_l) is slightly higher for CFRP-confined cylinders (up to 4.08) compared to SFRP systems (ranging from 3.33 to 3.63), reflecting CFRP's higher stiffness. Overall, while CFRP provides better confinement effectiveness, SFRP excels in enhancing strain and energy ductility, making it more suitable for applications requiring greater deformability.

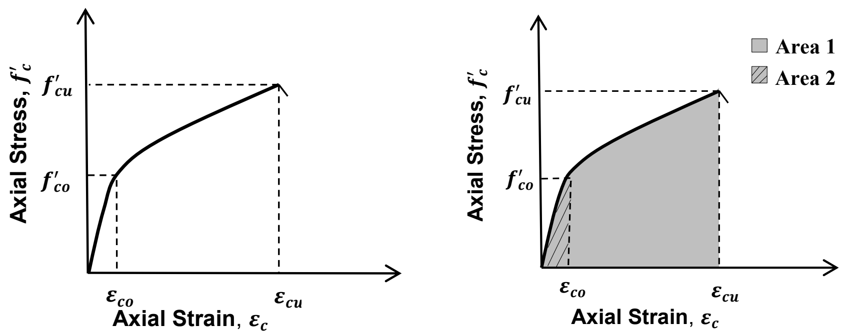

(a) Strain ductility index (b) Energy ductility index

Fig. 3: Definition of ductility indices: (a) Stain ductility index (b) Energy ductility index

Table 8. Confinement effectiveness and ductility indices for CFRP and SFRP-confined concrete

Configuration Designation	Lateral Confinement Parameters					Ductility Indices	
	Lateral Conf. Pressure	Conf. Ratio	Lateral Stiffness (MPa)	Lateral Stiffness Ratio	Confinement Effectiveness Coefficient	Strain Ductility Index	Energy Ductility Index
	f_{lu}	f_{lu}/f'_{co}	$(2Et/D)$	$(2Et/Df'_{co})$	k_l	μ_{cu}	ω_{cu}
C37.3-CFRP1	4.54	0.12	332	8.9	3.10	7.5	9.6
C37.3-CFRP2	9.08	0.24	664	17.8	3.54	9.8	15.8
C37.3-CFRP3	13.62	0.37	997	26.7	4.04	13.0	26.0
C42.4-CFRP1	4.54	0.11	332	7.8	3.40	6.1	11.0
C42.4-CFRP2	9.08	0.21	664	15.7	3.68	6.5	14.3
C42.4-CFRP3	13.62	0.32	997	23.5	3.83	8.8	24.2
C37.3-SFRP1	15.78	0.42	1058	28.4	3.63	16.4	32.8
C37.3-SFRP2	31.55	0.85	2115	56.7	3.47	22.3	66.6
C37.3-SFRP3	47.33	1.27	3173	85.1	3.33	27.8	107.9
C42.4-SFRP1	15.78	0.37	1058	24.9	3.57	15.4	40.6
C42.4-SFRP2	31.55	0.74	2115	49.9	3.53	18.9	77.7
C42.4-SFRP3	47.33	1.12	3173	74.8	3.34	27.0	139.0

5. Conclusions

This study conducted a detailed experimental assessment of the compressive performance of concrete cylinders confined with Carbon Fibre-Reinforced Polymer (CFRP) and Steel Fibre-Reinforced Polymer (SFRP) jackets. Beyond conventional strength metrics, the research explored critical performance indicators, including dilation behaviour, confinement effectiveness, and ductility indices. The findings offer valuable insights into how different FRP systems influence the axial behaviour of confined concrete and provide a comparative foundation for material selection in structural applications. The main conclusions drawn from the study are as follows:

Biçimlendirilmiş: Aralık Önce: 0 nk, Satır aralığı: tek

Biçimlendirilmiş: Satır aralığı: tek

- CFRP confinement provides superior strength enhancement, with a higher confinement effectiveness coefficient (up to 4.08), attributed to its high tensile strength and stiffness. It is especially suitable for applications requiring high axial strength and stiffness under compressive loads.
- SFRP confinement significantly outperforms CFRP in strain and energy ductility, achieving up to 27.8 in strain ductility index and 139.0 in energy ductility index. These results underscore SFRP's ability to undergo larger deformations and absorb more energy due to its metallic fibre composition.
- Increasing the number of FRP layers enhances overall confinement performance for both CFRP and SFRP. However, the rate of improvement is more pronounced in SFRP-confined specimens, especially for strain-related metrics.
- Higher-strength concrete exhibits diminished confinement benefits, both in terms of strength and ductility enhancements, compared to lower-strength concrete due to its inherently lower ductility and stiffer core.
- Dilation behaviour analysis reveals distinct confinement mechanisms: CFRP effectively restricts dilation due to its stiffness, while SFRP accommodates greater volumetric strain, contributing to its enhanced energy dissipation capacity.
- From a performance efficiency standpoint, SFRP-confined systems offer a favourable balance between strength gain and enhanced ductility, making them more suitable for seismic or energy-dissipative applications, whereas CFRP remains optimal for stiffness-critical strengthening.

Acknowledgments
The author gratefully acknowledges SIKA Canada for generously donating the CFRP sheets and epoxy adhesive and Hardwire LLC for providing the SFRP sheets. Appreciation is also extended to the University of Calgary for its partial funding and support of this research.

References
Abdelrahman, A. A. (2011). *Behavior of concrete confined with steel fiber-reinforced polymer composites* [PhD thesis, University of Manitoba].
Bank, L. C. (2006). *Composites for construction: Structural design with FRP materials*. John Wiley & Sons.
Chen, W. F. (1982). *Plasticity in reinforced concrete*. McGraw-Hill.
Fahmy, M. F., & Wu, Z. S. (2010). Post-peak behavior of concrete cylinders confined with FRP composites. *Construction and Building Materials, 24*(9), 1658–1669. https://doi.org/10.1016/j.conbuildmat.2010.02.014
Lam, L., & Teng, J. G. (2003). Design-oriented stress–strain model for FRP-confined concrete. *Construction and Building Materials, 17*(6–7), 471–489. https://doi.org/10.1016/S0950-0618(03)00045-X
Li, Y. (2006). Behavior of concrete cylinders confined with FRP composites. *Journal of Composites for Construction, 10*(6), 552–559. https://doi.org/10.1061/(ASCE)1090-0268(2006)10:6(552)
Mashrik, M. (2011). *Behavior of FRP-confined concrete columns* [PhD thesis, University of Calgary].
Xiao, Y., & Wu, H. (2000). Compressive behavior of concrete confined by various types of FRP composite jackets. *Journal of Reinforced Plastics and Composites, 19*(10), 838–850. https://doi.org/10.1177/073

Cost-effective seismic retrofitting of deficient RC structures using shape memory alloy bars

Yunus Demirtaş[*1,2], Özgür Yurdakul[3], Özgür Avşar[1]

[1] *Eskişehir Technical University, Department of Civil Engineering, Eskişehir, Türkiye*
[2] *Uşak University, Department of Civil Engineering, Uşak, Türkiye*
[3] *University of Pardubice, Department of Transport Structures, Pardubice, Czech Republic*

Abstract. Enhancing the seismic performance of deficient reinforced concrete (RC) buildings through retrofitting significantly reduces potential of severe structural damage during earthquakes. With the increasing adoption of retrofitting techniques, shape memory alloy (SMA) bars have emerged as a promising alternative to traditional steel reinforcement in critical structural elements. SMAs with inherent superelastic behavior enable to regain the original shape after undergoing plastic deformations within specific strain limits. Therefore, residual displacements following seismic events can be minimized by incorporating SMA rebars. However, the high cost of SMA materials remains a challenge for their widespread application in retrofitting projects. A parametric study was conducted on SMA rebar with different configurations in the critical sections of first-story columns of a previously tested substandard RC frame. Using the lattice modeling technique in the OpenSees platform, the concrete and reinforcement elements of critical sections in RC frames were represented as truss elements with their corresponding material properties. Nonlinear time history analyses were performed on generated numerical models with different SMA rebar configurations,previously validated using pseudo-dynamic tests. The study compared peak and residual drifts at the first story, which has severely damaged columns and beam-column joints (BCJs), for each SMA rebar arrangement. Optimization analysis revealed that specific SMA rebar configuration in RC section effectively reduced both peak and residual drifts. The optimal SMA rebar layout provides a strategic balance between cost-effectiveness and enhanced seismic resilience in retrofitted RC structures.

Keywords: Smart material; Shape Memory Alloy; Retrofitting; Lattice modelling

1. Introduction

Local deficiencies, including the utilization of low-strength concrete, plain round bars, inadequate detailing in RC components, and unverified construction practices, negatively impact the seismic performance of structures within the current inventory of RC buildings (Yurdakul et al., 2021). Demolition and reconstruction of all these vulnerable structures is not feasible due to constraints related to time, cost, and application. Upgrading processes are essential for enhancing the structural performance of inadequate structures and mitigating the seismic risk in urban areas (Duran et al., 2019). Traditionally, upgrading procedures have depended on established methods (Yurdakul et al., 2023). A prevalent method is the application of local strengthening techniques to improve the load-bearing capacity of particular structural elements (Ciro et al., 2014; Yurdakul & Avşar, 2016; Del Zoppo et al., 2017; Lee et al., 2017; Teresa et al., 2020; Yurdakul et al., 2020, 2024). Alternatively, the implementation of supplementary support systems, structural walls, or other advanced mechanisms represents various approaches to enhance the overall performance of structures (Maheri et al., 2003; Elias et al., 2014; Cao et al., 2022; Cerè et al., 2022; Joseph et al., 2022).

In recent years, the concept of performance-based seismic design and assessment has gained traction and integrated into seismic design codes. In addition to prioritizing life safety, these codes place a growing emphasis on performance criteria that limit structural damage, even for severe earthquakes. The objective is to preserve building functionality while reducing both imposed and residual drifts. The increasing focus on enhanced structural performance has attracted significant attention in earthquake engineering research related to smart materials. SMAs are distinguished within the category of smart materials due to their exceptional characteristics, including superelasticity (SE) and the shape memory effect (SME). The inherent attributes of SMAs, such as their capacity to "remember" their original shape and geometry following deformation due to solid-to-solid phase

[*] Corresponding author, E-mail: yunus_demirtas@eskisehir.edu.tr

https://doi.org/10.31462/icearc2025_ce_eqe_911

golden light publishing

transformations, enable them to revert to their original shapes with minimal residual deformations once the load is removed (Desroches & Smith, 2004; Song et al., 2006).

The success of SMAs in enhancing the seismic performance of structures has been adequately demonstrated (Duran et al., 2019; Yurdakul et al., 2018; Ozbulut et al., 2011). SMAs have been utilized as an alternative to traditional materials for seismic retrofitting applications for the past twenty years. SMAs are applicable for retrofitting RC components using several techniques. These include internal reinforcement within RC structural members, near-surface mounted (NSM) reinforcement, embedded reinforcement within a shotcrete layer, and externally anchored reinforcement (Raza et al., 2022). Superelastic Nickel-Titanium (Ni-Ti) and Copper-based shape memory alloys (SMA) have been utilized as internal reinforcements in beams (Saiid et al., 2007; Abdulridha et al., 2013; Shrestha et al., 2013; Pareek et al., 2018; Azadpour & Maghsoudi, 2020), columns (Saiidi & Wang, 2006; Shin & Andrawes, 2011; Cruz Noguez & Saiidi, 2012; Hosseini et al., 2015; Tazarv & Saiid Saiidi, 2016), and BCJs (Youssef et al., 2008; Nehdi et al., 2010, 2011; Oudah & El-Hacha, 2017, 2018).

SMAs demonstrate potential as reinforcements for NSMs in existing RC structures, specifically in improving flexural strength and reducing post-inelastic displacements through their re-centering capabilities. Initially, grooves are created in the concrete cover. Following that, SMA rebars are installed within these grooves, which are then filled with either epoxy or cement mortar. Remarkable research has shown how well this method works to strengthen RC beams (Shahverdi et al., 2016; Rojob & El-Hacha, 2017, 2018; El-Hacha & Rojob, 2018; Hong et al., 2018). This method is effective for enhancing strength, helping crack healing, and minimizing residual displacements (Raza et al., 2022).

Based on the literature survey conducted, it is observed that while SMA bars have been employed to strengthen RC components in previous studies, there has been no optimization analysis utilizing numerical methods focused on the configuration of SMA rebars in RC components to reduce their quantity. Various approaches have been proposed in the literature for modeling substandard RC components. This study adopts the lattice modeling approach. The evaluation of the lattice modeling approach focuses on beam members's capacity to precisely reproduce the behavior of different RC components (Bowers, 2014; Lu & Panagiotou, 2014; Lu et al., 2016; Xing et al., 2018; Alvarez et al., 2019; Deng et al., 2021; Aydin et al., 2022; Demirtas et al., 2023). A numerical study was conducted together with an optimization strategy to evaluate the effectiveness of retrofitting techniques utilizing various SMA rebar configurations in the structural components of a sub-standard RC frame. One of the evaluated substandard RC frames exhibits a strong beam-weak column phenomenon along with inadequate BCJs. Additionally, the structure is composed of low-strength concrete and incorporates non-seismic transverse reinforcement details. Consequently, structural damage is primarily concentrated at the column ends and BCJs of the evaluated frame.

SMA bars presently exhibit a higher cost compared to conventional steel reinforcement bars. Due to the capacity of SMA materials to return to their original shape, they carry the potential to improve the seismic performance of structural systems when applied appropriately (Wilson & Wesolowsky, 2005). It is essential to establish the optimal quantity of SMA rebars required for retrofitting purposes. A study was conducted to address this issue within the scope of this research. A ½-scale, 3-story, 3-span substandard RC frame was subjected to laboratory testing under pseudo-dynamic conditions. The structure was modeled using the lattice modeling approach within the OpenSees platform (McKenna et al., 2016). Subsequent to this, nonlinear time history analyses were performed on both the retrofitted and reference RC frames, utilizing the ground motion recordings that were applied during the tests. The SMA rebar layout is subsequently optimized to identify the most efficient sections.

This study's originality exists in the identification of the optimal configuration of SMA rebars, aimed at enhancing the seismic response of the tested RC frame. NiTi and CuAlMn shape memory alloy rebars were utilized in various configurations exclusively within the column sections of the plastic hinge regions located in the first story. This method focused on reducing residual drifts while employing the minimum amount of SMA rebars necessary.

2. Test frame SP3

The lattice modeling approach was first confirmed using the results of pseudo-dynamic testing done by Mutlu (2012) on an RC frame called SP3. The nonlinear time history analyses were conducted utilizing the OpenSees program (McKenna et al., 2016). The specimen was constructed with minimal reinforcement features and constructed from plain round bars and low-strength concrete to illustrate the typical defects found in Turkish building stock. Table 1 and Fig. 1 present the primary characteristics of the SP3 specimen, along with the reinforcing details. Fig. 1 illustrates the geometric details and the dimensions of the cross-section. The cross-sections of all columns are aligned to work in their strong axes in accordance with the in-plane loading direction of the test frame. Column and beam sections utilized plain rebars with diameters of 8 mm and 10 mm, respectively. The yield strength of steel reinforcing bars with diameters of 8 mm and 10 mm is measured at 320 MPa and 355 MPa, respectively. The strains of the reinforcing steel are derived from TBEC (2018) The initial strain at the beginning of strain hardening is 0.008 mm/mm, whereas the strain associated with ultimate strength is 0.08 mm/mm. The elasticity modulus of reinforcing steel is estimated at 200 GPa in a average sense. The specimen consists of low-strength concrete, exhibiting an average compressive strength of 11.9 MPa. The axial load at the ground story is determined to be $0.23A_cf_c$ for the inner columns and $0.13A_cf_c$ for the outer columns, as a result of the vertical loads from the additional weights illustrated in Fig. 1. Additional information regarding the specimen is available in Sucuoglu et al. (2014).

Table 1. Main properties of the test specimen

Property	Value	
f_c (MPa)	11.9	
f_y (MPa)	320	
Type of longitudinal reinforcement	Plain	
Beam cross-section	175 x 150 mm	
Column cross-section	200 x 150 mm	
Beam longitudinal reinforcement ratio	Support region	Span region
	1.8%	1.1%
Column longitudinal reinforcement ratio	2%	
Transverse reinforcement in BCJ	N.A.	
Spacing of transverse reinforcement in column (mm)	Ø4/100	
Spacing of transverse reinforcement in beam (mm)	Support region	Span region
	Ø4/50	Ø4/80
Column axial load ratio, N_d/f_cA_c	Inner columns	Outer columns
	0.23	0.13
Application of displacement	At the floor level	
Loading type	Pseudo-Dynamic	
Failure mode	Damages at the member ends and BCJs	

Table 2 shows the ground motions employed for continuous pseudo-dynamic testing. The motions align with the earthquake design spectrum created for the specific location, taking into account various soil types, each presenting distinct probabilities of surpassing certain limits. Three acceleration time series, designated as D1, D2, and D3, were utilized in the pseudo-dynamic testing (Sucuoglu et al., 2014).

Fig. 2 illustrates the acceleration time series, their application sequence, and the response spectra of the associated ground motions. The damage mechanism of the reference test frame is primarily influenced by deformations and damages that occur at the column ends and BCJ regions, as indicated by experimental results and observations (Fig. 3). Structural damage is primarily observed at the ends of the columns, characterized by concrete crushing and significant cracking resulting from flexural demands (Fig. 3a). Shear cracks have been detected in the BCJ panel zone (refer to Fig. 3b).

Table 2. Ground motion properties used for the SP3 specimen

Earthquake	Exceedance Probability in 50 Years	Soil Type	PGA (g)
D1	50 %	Rock	0.254
D2	10 %	Rock	0.545
D3	10 %	Soft	0.604

3. Lattice modelling of the test frame

A numerical model of the test frame has been developed using the OpenSees platform (McKenna et al., 2016) to reproduce the results obtained from experiments. Factors such as computational effort, capabilities, and analysis time must be considered when evaluating various nonlinear modeling techniques available in the literature, which include lumped-parameter models and detailed finite-element models. The lattice modeling approach, combined with fiber-based distributed plasticity modeling, is identified as an appropriate selection for the designated test frame (Demirtas et al., 2023). The lattice modeling approach represents concrete, reinforcing steel, and bar slip elements of RC BCJs, along with certain sections of beam and column ends, as truss elements characterized by uniaxial material properties. The test frame is accurately modeled using the lattice modeling approach, which requires minimal computing efforts in comparison to more advanced modeling methods like finite element modeling. This study employs the diagonal, vertical, and horizontal components of the tension/compressive strut force transfer mechanisms to develop a nonlinear lattice structure. The springs characterized by zero-length sections connected to concrete and steel components illustrate the relationship between reinforcement bar slip. The nonlinear characteristics of concrete truss elements are described through a nonlinear concrete constitutive stress-strain model. In contrast, the behavior of steel truss elements is characterized by uniaxial stress-strain behavior specific to reinforcing steel.

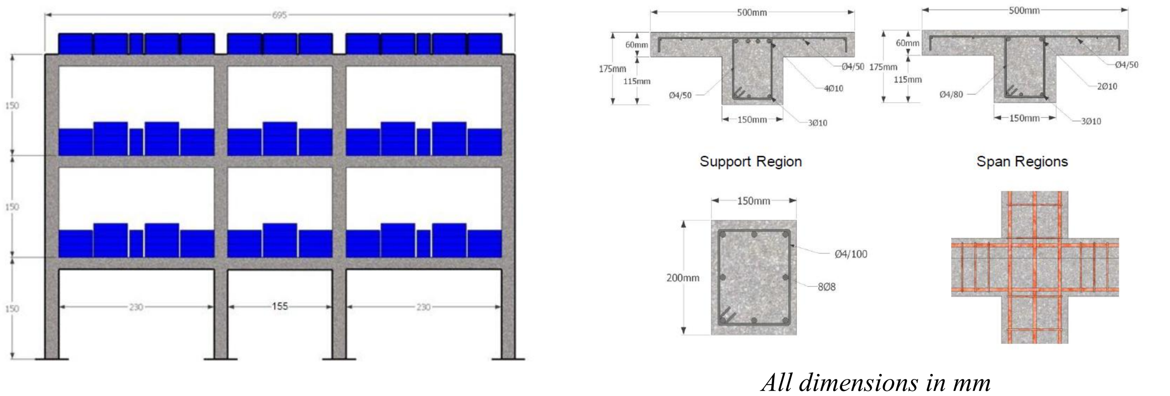

Fig. 1. Details of SP3 test specimen and elevation view (Sucuoglu et al., 2014)

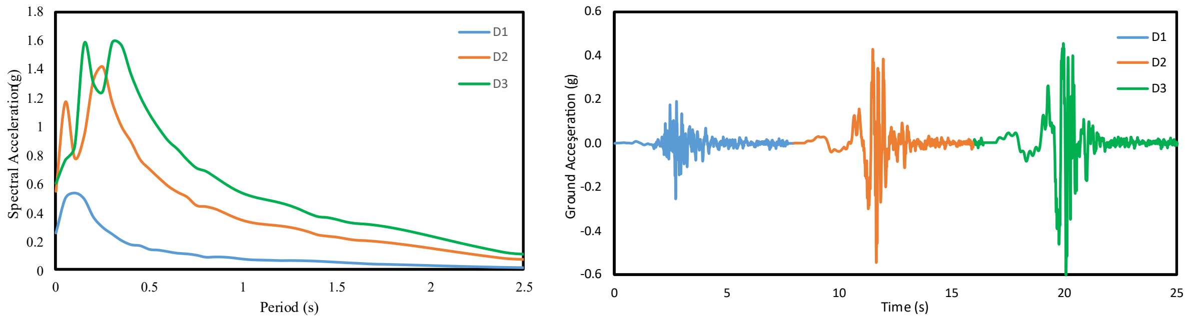

Fig. 2. Response spectra and acceleration time series of the ground motions (Sucuoglu et al., 2014)

(a)

(b)

Fig. 3. Structural damage observed in the first story of SP3 (a) column ends and (b) BCJs (Mutlu, 2012)

Fig. 4 illustrates the comprehensive configuration of the lattice model for RC beam-column joints, along with specific segments of the beam and column end sections. The model consists of concrete, reinforcement, bar slip, and rigid elements. A cell structure consists of vertical and horizontal concrete elements. The mesh size of the model is defined by the dimensions of each cell, which includes diagonal concrete struts. The diagonal elements serve the primary function of providing shear resistance, whereas the vertical and horizontal concrete elements, combined with reinforcing steel, enhance flexural resistance. Nonlinear zero-length springs that link the concrete and steel components illustrate the bar slip behavior.

Fig. 5 presents the cross-sectional areas of the concrete truss members. The calculation of the cross-sectional areas for the vertical and horizontal concrete truss members is carried out by multiplying the out-of-plane thickness by half of the tributary width, represented as *b/2*. The effective width of the diagonal concrete members is calculated using Equation (1), as proposed by Xing (2019). The calculation of the cross-sectional areas for diagonal members is carried out by multiplying the out-of-plane thickness by half of the effective width, represented as *b/2*. The use of half-width for all concrete truss members is attributed to the overlapping of their tributary widths (Demirtas, 2022; Salinas et al., 2022).

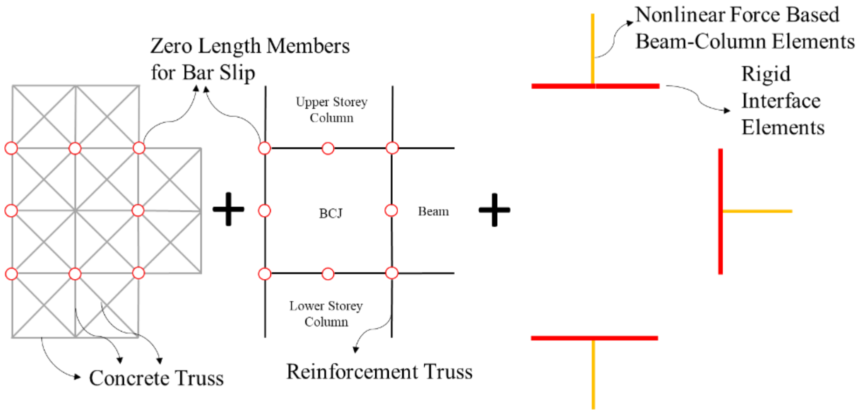

Fig. 4. Layout of the lattice model for BCJ (Demirtas et al., 2023)

(a) Tributary widths of the horizontal and vertical concrete truss members

(b) Tributary width of the diagonal concrete truss members

Fig. 5. Details of the cross-sectional areas of the concrete truss members (Demirtas, 2022)

$$b_{eff} = \frac{a \times b}{\sqrt{a^2+b^2}} \quad (1)$$

The amount of reinforcing steel in the model determines the cross-sectional areas of the reinforcement truss members, which are positioned at the edges of the sections. A rigid beam-column element is utilized to model the interaction between the BCJ and the neighboring beam or column. This guarantees that the cross-sections of beams and columns maintain their plane and perpendicular orientation relative to the deformed center of the frame member. Nodes at the truss members and rigid beam-column components are interconnected through EqualDof constraints in the x and y directions for the translational degree of freedom, thereby ensuring structural integrity at these locations.

3.1. Concrete model

The ConcretewBeta Material model, as presented in OpenSees (McKenna et al., 2016), is utilized to establish the constitutive model for both the compressive and tensile behavior of concrete. The specific characteristics of the trusses are established utilizing the constitutive model developed by Lu & Panagiotou (2014) within the OpenSees.

Fig. 6 shows the uniaxial stress-strain relationship for concrete. In this model, f_c represents the maximum compressive strength of concrete at a strain of ε_0, whereas ε_u indicates the ultimate strain of unconfined concrete. The parameters of the model are determined using the concrete's compressive strength. In this model, the value of ε_0 was set to 0.002. The ultimate strain ε_u of concrete is adjusted to incorporate mesh-size effects as outlined by

Demirtas et al., (2023). The ultimate tension strain of concrete is characterized by a significantly high value, for instance, 1.0, as demonstrated in Fig. 6, to prevent tensile failure of concrete and ensure computational stability.

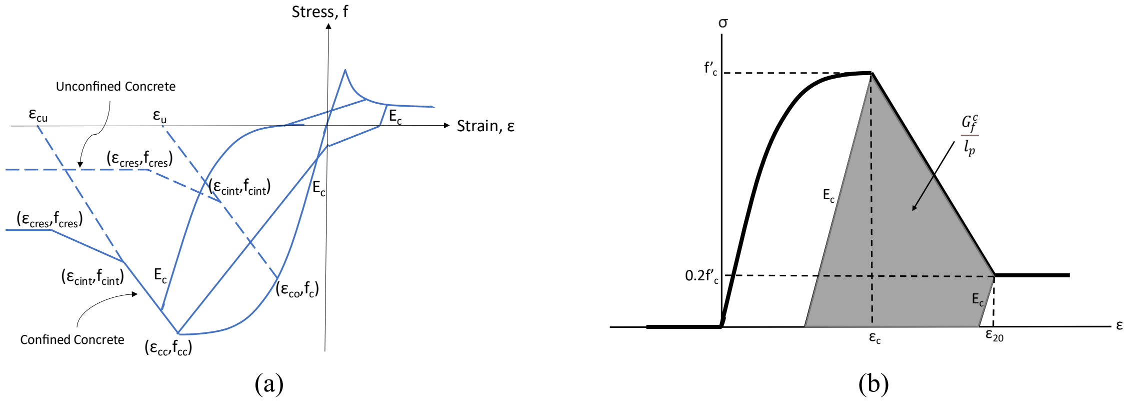

Fig. 6. (a) Uniaxial stress-strain relationship of concrete (Lu & Panagiotou, 2014) (b) Kent–Park concrete stress-strain model with fracture energy G_f^c in compression as shaded area (Scott & Fenves, 2006)

3.2. Reinforcement model

OpenSees' Reinforcing Steel material model, which is based on Chang and Mander (1994) uniaxial steel model, is used. Fig. 7 demonstrates the stress-strain behavior of the reinforcing bar, represented by the backbone curve. The initial strain at the beginning of strain hardening is defined as 0.008 mm/mm, while the strain associated with ultimate strength is established at 0.08 mm/mm.

The relationship between reinforcing bar slip is represented by zero-length springs that are connected to concrete and steel bars through the uniaxial material model BarSlip, which is available in OpenSees (Fig. 8). S_{lim}^C and S_{lim}^T represent the compression and tension slip limits, respectively. F_{lim}^C and F_{lim}^T denote the force limits for compression and tension, respectively. In OpenSees, the BarSlip material model is categorized as a uniaxial material model. It is defined utilizing the Pinching4 material model, which takes into account various parameters including the compressive strength of the concrete, the modulus of elasticity, the yield strength, and the ultimate strength of the reinforcing steel. Additionally, the diameter and quantity of reinforcing bars are considered to compute the backbone curve.

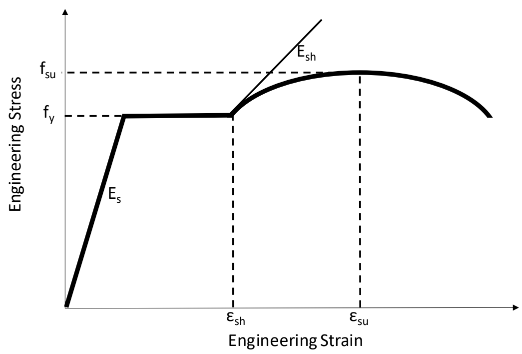

Fig. 7. Backbone curve of the Reinforcing Steel material (Chang & Mander, 1994)

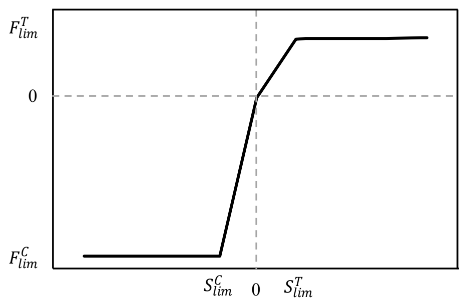

Fig. 8. Backbone curve of the BarSlip material (Demirtas, 2022)

3.3. Lattice model of the SP3 specimen

A lattice model featuring a grid size of 0.1 x 0.0875 m is implemented in OpenSees to simulate the essential components of the SP3 specimen. In addition to the BCJs, the columns experienced damage during the pseudo-dynamic testing process. The lattice structure is extended to the edges of the columns for a specified length to accurately capture the damage at the boundaries of the plastic hinge zone of the columns. Fig. 9 shows the overall configuration of the models incorporating a lattice structure alongside nonlinear force-based beam-column elements. The supplementary masses are allocated to the edges of the beams to accurately represent the masses and their correct positioning during dynamic analysis.

4. Retrofit study

SMAs are classified as metallic smart materials characterized by their ability to recover from significant deformations, attributed to their inherent shape-changing properties. In the past two decades, SMAs have emerged as an alternative to conventional materials for applications related to seismic strengthening. The effective use of SMAs in enhancing structural seismic performance has been successfully established (Yurdakul et al., 2018; Duran et al., 2019). SMA bars may be utilized as internal reinforcement within RC structural members for new constructions. SMA bars and plates are applicable in multiple techniques, including NSM reinforcement, embedded reinforcement within a shotcrete layer, and externally anchored reinforcement, for the rehabilitation and strengthening of existing structures (Fig. 10). This study employs a method similar to the NSM technique for the retrofitting of the SP3 specimen. Fig. 11 illustrates the replacement of steel reinforcement with SMA rebars in the plastic hinge region at the ends of the columns. The SMA replacement was not implemented in the reinforcements of the BCJ, which is susceptible to seismic damage primarily due to insufficient transverse reinforcement in the BCJ panel. Furthermore, within the current 3D structures, the existence of out-of-plane beams inhibits the replacement of longitudinal bars in the BCJ panel. SMA rebars and steel rebars are presumed to be interconnected via couplers within the plastic hinge region at the ends of the columns, consistent with the practical applications observed in the research conducted by Pareek et al. (2018).

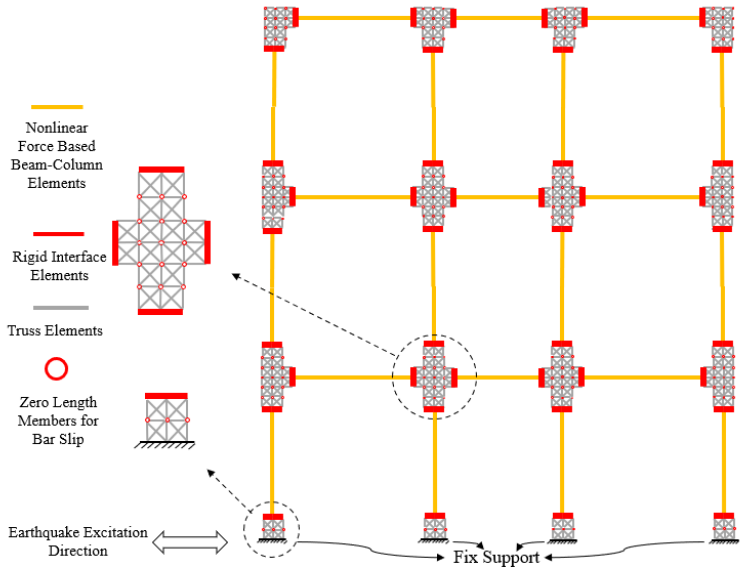

Fig. 9. General layout of the lattice model of SP3

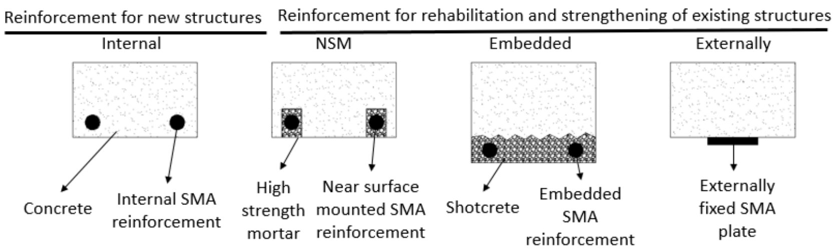

Fig. 10. Retrofitting techniques by SMA rebars (Raza et al., 2022)

Two categories of SMA materials, specifically CuAlMn and NiTi, are utilized as reinforcement materials across various cross-section configurations. In every configuration of the RC column section, the current steel rebars are replaced with the chosen SMA rebars within the plastic hinge region, as illustrated in Fig. 11. The SelfCentering material model implemented in OpenSees was utilized as the material model for the SMA rebars (Fig. 12). This model is predicated on the assumption that the SMA material exhibits an ideal re-centering capability. The numerical values for the modeling parameters of CuAlMn and NiTi materials, as illustrated in Fig. 12, are detailed in Table 3. The cost of SMA materials is still greater than that of traditional steel materials, even if their use in retrofitting existing buildings is growing (Molod et al., 2022). Therefore, optimizing the quantity of SMA material is crucial for attaining a cost-effective retrofitting solution. As illustrated in Fig. 13, SMA materials are implemented in various configurations specifically within the critical cross-sections of the first story columns, which experienced significant flexural damage during the pseudo-dynamic testing (Fig. 3a). In these cross-section configurations, variations are observed in both the quantity of SMA bars and their positioning. The longitudinal rebar layout remains consistent across all configurations (Fig. 13). Steel transverse reinforcement is utilized with consistent spacing and detailing across all reinforced concrete sections.

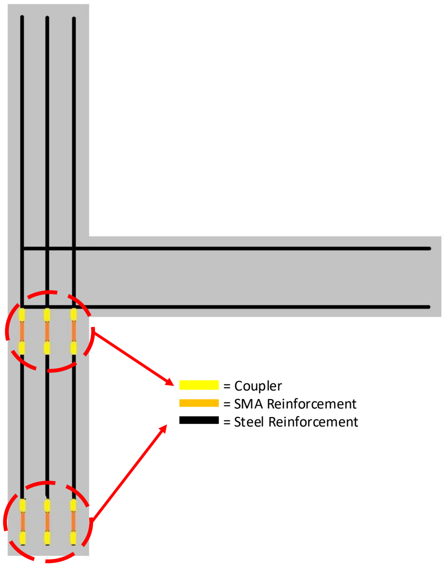

Fig. 11. Connection of SMA rebars to the existing steel rebars

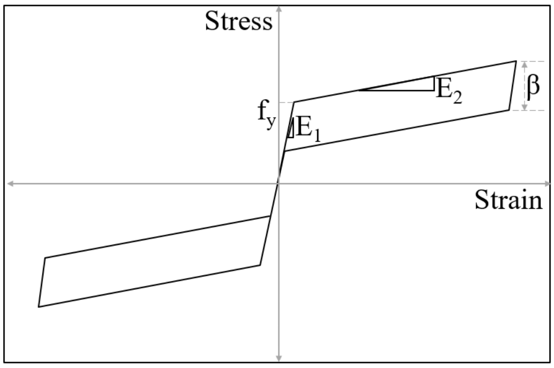

Fig. 12. Backbone curve of the SelfCentering material (McKenna et al., 2016)

Table 3. Main properties of the SMA materials

	CuAlMn (Pareek et al., 2018)	NiTi (Duran, 2018)
E_1 (MPa)	25000	64500
E_2 (MPa)	5	372
f_y (MPa)	179.3	365
Beta (%)	10	59

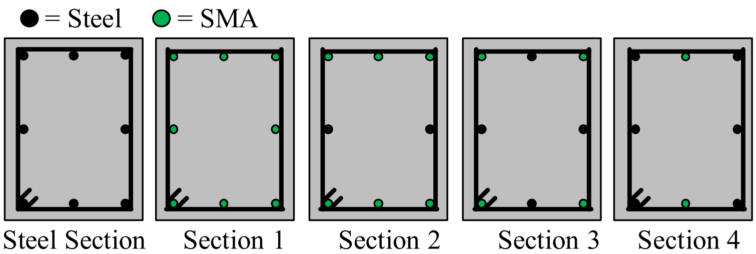

Fig. 13. Cross-section configurations

4.1. Results of nonlinear time history analyses

The SP3 specimen, with parameters detailed in Section 2, performed ground motion records during the pseudo-dynamic testing process. The interstory drift ratio and the residual displacement demands serve as critical metrics for assessing the seismic damage levels of structural and nonstructural components. The hysteretic behavior related to the first story shear force and interstory drift ratio for various column section configurations is illustrated in Fig. 14, as structural damage mostly exhibited in the first story of the tested frame. The reference section, which is fully reinforced with reinforcing steel, provided an accurate estimation of the peak story shear force and residual displacement derived from the experimental results. The first-story shear force is consistent across the configurations of CuAlMn and NiTi SMAs in both Section 3 and Section 4. However, compared to the steel reinforced section, the peak interstory drift ratio was much greater when SMA reinforcement was used throughout Section 1. However, the peak interstory drift ratios are more consistent with the steel reinforced section observed in Sections 2 and 4. Additionally, the residual displacements observed in Sections 1 and 2 are significantly lower than those recorded in the steel-reinforced section. In contrast, Sections 3 and 4 exhibit residual displacements that are comparable to or exceed those in the steel reinforced section. The steel reinforcement rebars in Sections 3 and

4 are the primary contributors to the structural response. The addition of SMA bars in these sections demonstrates reduced effectiveness compared to Sections 1 and 2 regarding residual displacements.

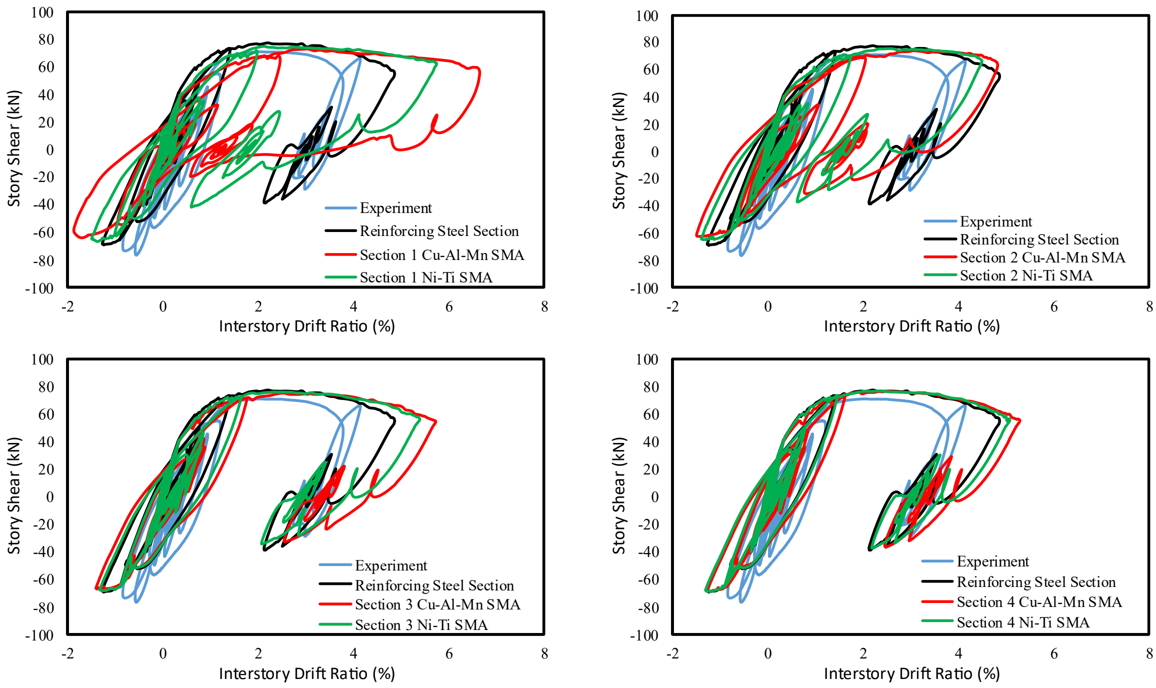

Fig. 14. Comparison of first story shear force versus interstory drift ratio between the experimental, steel, CuAlMn and NiTi lattice model results

The calculated peak values of the drift ratio and the residual drift at the first story are compared for the investigated cross-section configurations with the experimental response. The lattice model incorporating NiTi SMA reinforced column sections demonstrates a reduced peak interstory drift ratio compared to the lattice model utilizing CuAlMn SMA reinforced sections (Fig. 15). The same trend is observed for the residual drift ratio, with the exception of Section 1. Section 1 indicates that the peak drift ratio for the NiTi SMA reinforced model is 5.5%, whereas the peak drift ratio for the CuAlMn SMA reinforced section is 7.5%. The residual drift ratio of Section 1 is comparable for both SMA materials. The peak interstory drift ratio and residual drift ratio in Sections 3 and 4 exhibit similarities to those observed in the steel reinforced reference section. The peak drift ratio demands for Section 2, which includes both NiTi SMA reinforced and CuAlMn SMA reinforced sections, are identified as the lowest values within the analyzed sections, ranging from 4.5% to 5.0%. The residual drift ratio in Section 2 is calculated as 1.5%, which is significantly lower than that of the other sections, with the exception of Section 1. Upon comparison of Sections 1 and 2 regarding residual displacements, the negligible difference observed suggests that the implementation of SMA rebars throughout the entire longitudinal rebar configuration is unnecessary. An optimal layout for SMA rebar must be determined to ensure the most advantageous structural response regarding peak and residual displacements, while also reducing the quantity of SMA material utilized.

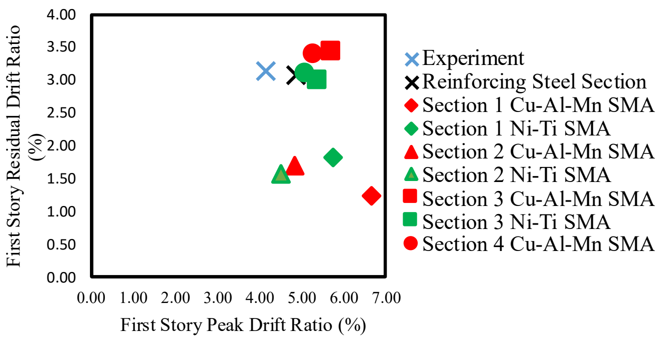

Fig. 15. Comparison of first story peak drift ratio versus residual drift ratio between the experimental at the end of the loading history D3, steel, CuAlMn and NiTi lattice model results

5. Conclusions

SMAs are increasingly utilized in the retrofitting of sub-standard RC buildings, owing to their essential superelastic properties, which enable them to revert to their original shape upon the removal of applied loads. Given that SMAs are not cost-effective materials, it is essential to utilize them in quantities that produce the best structural performance. This study employs NiTi and CuAlMn SMA rebars arranged in various layout configurations within the plastic hinge region of the first story columns of a three-story, three-span RC frame characterized by non-seismic detailing and substandard structural configuration. The response of the RC frame, which was subjected to experimental testing, was replicated in the OpenSees platform utilizing the lattice modeling approach. This technique involves modeling concrete and reinforcement elements located in the critical position of the RC frame as truss elements, utilizing their respective material properties. The developed models were subjected to nonlinear time history analysis utilizing the sequential ground motion records applied during the pseudo-dynamic testing. The analysis focused on the peak drift ratio and residual drift ratio of the first story across each developed numerical model, which evaluates the optimal configuration of SMA bars for improving seismic performance.
For the identical section configuration utilizing various SMA rebars, sections incorporating CuAlMn rebars exhibited a greater peak drift ratio compared to those with NiTi rebars. Because CuAlMn has a lower yield strength and post-yield behavior than NiTi, sections containing CuAlMn rebars may need more displacement, which might result in a greater dissipation of seismic energy.

- With the exception of Section 1, which utilizes a uniform rebar material for all longitudinal bars, sections incorporating CuAlMn rebar have demonstrated reduced residual displacements in comparison to those utilizing NiTi rebar. The variation in residual displacements between the two distinct SMA materials is less pronounced compared to the variation observed in peak displacements.
- Sections 1 and 2 achieve the smallest residual displacement demands. The use of SMA material for all longitudinal bars in the critical cross-section is unnecessary. Consequently, it is essential to identify an optimal layout for SMA rebar to attain the most advantageous structural response, characterized by peak and residual displacements, while also reducing the quantity of SMA material utilized.
- The inclusion of steel longitudinal rebars in both the top and bottom bar layers significantly influences the behavior of the cross-section. The SMA rebars exhibit inefficiency in Sections 3 and 4, leading to comparable residual displacements when compared to the original steel rebar configuration. In order to attain the required seismic response, it is essential to evaluate the performance of the cross-section to identify a cost-effective retrofit solution utilizing SMA materials as longitudinal reinforcing bars.

References

Abdulridha, A., Palermo, D., Foo, S., & Vecchio, F.J. (2013). Behavior and modeling of superelastic shape memory alloy reinforced concrete beams. *Engineering Structures*, *49*, 893–904

Alvarez, R., Restrepo, J.I., Panagiotou, M., & Santhakumar, A.R. (2019). Nonlinear cyclic truss model for analysis of reinforced concrete coupled structural walls. *Bulletin of Earthquake Engineering*, *17*, 6419–6436

Aydin, B.B., Binici, B., Hendriks, M.A.N., & Tuncay, K. (2022). Lattice modeling and testing of aerated autoclaved concrete infilled frames. *Engineering Structures*, *251*, 113467

Azadpour, F., & Maghsoudi, A.A. (2020). Experimental and analytical investigation of continuous RC beams strengthened by SMA strands under cyclic loading. *Construction and Building Materials*, *239*, 117730

Bowers, J.T. (2014). *Nonlinear cyclic truss model for beam-column joints of non-ductile RC frame* (Master's thesis). Virginia Polytechnic and State University.

Cao, X.-Y., Shen, D., Feng, D.-C., Wang, C.-L., Qu, Z., & Wu, G. (2022). Seismic retrofitting of existing frame buildings through externally attached sub-structures: State of the art review and future perspectives. *Journal of Building Engineering*, *57*, 104904

Cerè, G., Rezgui, Y., Zhao, W., & Petri, I. (2022). Shear walls optimization in a reinforced concrete framed building for seismic risk reduction. *Journal of Building Engineering*, *54*, 104620

Chang, G.A., & Mander, J.B. (1994). *Seismic Energy Based Fatigue Damage Analysis of bridge Columns: Part 1 - Evaluation of Seismic Capacity*.

Ciro, D.V., Marco, D.L., Alberto, B., Andrea, P., Gaetano, M., & Mauro, D. (2014). Experimental investigation of exterior RC beam-column joints retrofitted with FRP systems. *Journal of Composites for Construction*, *18*(4), 4014002

Cruz Noguez, C.A., & Saiidi, M.S. (2012). Shake-table studies of a four-span bridge model with advanced materials. *Journal of Structural Engineering*, *138*(2), 183–192

Del Zoppo, M., Di Ludovico, M., Balsamo, A., Prota, A., & Manfredi, G. (2017). FRP for seismic strengthening of shear controlled RC columns: Experience from earthquakes and experimental analysis. *Composites Part B: Engineering*, *129*, 47–57

Demirtas, Y. (2022). *Lattice modelling of sub-standard reinforced concrete beam-column joints* (Master's thesis). Eskişehir Technical University, Eskişehir, Türkiye.

Demirtas, Y., Yurdakul, Ö., & Avşar, Ö. (2023). *Lattice modelling of substandard RC beam-column joints considering localization issues*. *47*(January), 2515–2530

Deng, X., Koutromanos, I., Murcia-Delso, J., & Panagiotou, M. (2021). Nonlinear truss models for strain-based seismic evaluation of planar RC walls. *Earthquake Engineering and Structural Dynamics*, *50*, 2939–2960

Desroches, R., & Smith, B. (2004). Shape memory alloys in seismic resistant design and retrofit: A critical review of their potential and limitations. *Journal of Earthquake Engineering*, *8*(3), 415–429

Duran, B. (2018). *Seismic performance upgrading of reinforced concrete frames using shape memory alloy bars* (Master's thesis). Anadolu University, Eskişehir, Türkiye.

Duran, B., Tunaboyu, O., Atli, K.C., & Avsar, Ö. (2019). Seismic performance upgrading of substandard RC frames using shape memory alloy bars. *Smart Materials and Structures*, *28*

El-Hacha, R., & Rojob, H. (2018). Flexural strengthening of large-scale reinforced concrete beams using near-surface-mounted self-prestressed iron-based shape-memory alloy strips. *PCI J*, *63*(6), 51–62

Elias, S., Xenophon, P., Stathis, N.B., & Michael, N.F. (2014). Experimental investigation of concrete frames infilled with RC for seismic rehabilitation. *Journal of Structural Engineering*, *140*(1), 4013033

Hong, K., Lee, S., Yeon, Y., & Jung, K. (2018). Flexural response of reinforced concrete beams strengthened with near-surface-mounted fe-based shape-memory alloy strips. *International Journal of Concrete Structures and Materials*, *12*(1), 1–13

Hosseini, F., Gencturk, B., Lahpour, S., & Gil, D.I. (2015). An experimental investigation of innovative bridge columns with engineered cementitious composites and Cu-Al-Mn super-elastic alloys. *Smart Materials and Structures*, *24*(8), 85029

Joseph, R., Mwafy, A., & Alam, M.S. (2022). Seismic performance upgrade of substandard RC buildings with different structural systems using advanced retrofit techniques. *Journal of Building Engineering*, *59*, 105155

Lee, D.H., Han, S.-J., Kim, K.S., & LaFave, J.M. (2017). Shear strength of reinforced concrete beams strengthened in shear using externally-bonded FRP composites. *Composite Structures*, *173*, 177–187

Lu, Y., & Panagiotou, M. (2014). Three-dimensional cyclic beam-truss model for nonplanar reinforced concrete walls. *Journal of Structural Engineering*, *140*, 04013071

Lu, Y., Panagiotou, M., & Koutromanos, I. (2016). Three-dimensional beam-truss model for reinforced concrete walls and slabs – part 1: Modeling approach, validation, and parametric study for individual reinforced concrete walls. *Earthquake Engineering & Structural Dynamics*, *45*, 1495–1513

Maheri, M.R., Kousari, R., & Razazan, M. (2003). Pushover tests on steel X-braced and knee-braced RC frames. *Engineering Structures*, *25*(13), 1697–1705

McKenna, F., Fenves, G.L., Scott, M.H., & Jeremic, B. (2016). *OpenSees: Open system for earthquake engineering simulation.* http://opensees.berkeley.edu.

Molod, M.A., Spyridis, P., & Barthold, F.J. (2022). Applications of shape memory alloys in structural engineering with a focus on concrete construction – A comprehensive review. In *Construction and Building Materials* (Vol. 337). Elsevier Ltd.

Mutlu, M.B. (2012). *Numerical simulations of reinforced concrete frames tested using pseudo-dynamic method* (Master's thesis). Middle East Technical University, Ankara, Türkiye.

Nehdi, M., Alam, M.S., & Youssef, M.A. (2010). Development of corrosion-free concrete beam–column joint with adequate seismic energy dissipation. *Engineering Structures*, *32*(9), 2518–2528

Nehdi, M., Alam, M.S., & Youssef, M.A. (2011). Seismic behaviour of repaired superelastic shape memory alloy reinforced concrete beam-column joint. *Smart Structures and Systems*, *7*(5), 329–348

Oudah, F., & El-Hacha, R. (2017). Joint performance in concrete beam-column connections reinforced using SMA smart material. *Engineering Structures*, *151*, 745–760

Oudah, F., & El-Hacha, R. (2018). Innovative self-centering concrete beam-column connection reinforced using shape memory alloy. *Structural Journal*, *115*(3), 607–620

Ozbulut, O.E., Hurlebaus, S., & Desroches, R. (2011). Seismic response control using shape memory alloys: A review. *Journal of Intelligent Material Systems and Structures*, *22*(14), 1531–1549

Pareek, S., Suzuki, Y., Araki, Y., Youssef, M.A., & Meshaly, M. (2018). Plastic hinge relocation in reinforced concrete beams using Cu-Al-Mn SMA bars. *Engineering Structures*, *175*(August), 765–775

Raza, S., Shafei, B., Saiid Saiidi, M., Motavalli, M., & Shahverdi, M. (2022). Shape memory alloy reinforcement for strengthening and self-centering of concrete structures—State of the art. *Construction and Building Materials*, *324*, 126628

Rojob, H., & El-Hacha, R. (2017). Self-prestressing using iron-based shape memory alloy for flexural strengthening of reinforced concrete beams. *Structural Journal*, *114*(2), 523–532

Rojob, H., & El-Hacha, R. (2018). Fatigue performance of RC beams strengthened with self-prestressed iron-based shape memory alloys. *Engineering Structures*, *168*, 35–43

Saiid, S.M., Mahmoud, S.-Z., Chadi, A., & Ahmad, I. (2007). Pilot study of behavior of concrete beams reinforced with shape memory alloys. *Journal of Materials in Civil Engineering*, *19*(6), 454–461

Saiidi, M.S., & Wang, H. (2006). Exploratory study of seismic response of concrete columns with shape memory alloys reinforcement. *ACI Structural Journal*, *103*(3), 436–443

Salinas, D., Koutromanos, I., & Leon, R.T. (2022). Nonlinear truss modeling method for masonry-infilled reinforced concrete frames. *Engineering Structures*, *262*(2022), 114329

Scott, M.H., & Fenves, G.L. (2006). Plastic hinge integration methods for force-based beam–Column elements. *Journal of Structural Engineering*, *132*(2), 244–252

Shahverdi, M., Czaderski, C., & Motavalli, M. (2016). Iron-based shape memory alloys for prestressed near-surface mounted strengthening of reinforced concrete beams. *Construction and Building Materials*, *112*, 28–38

Shin, M., & Andrawes, B. (2011). Emergency repair of severely damaged reinforced concrete columns using active confinement with shape memory alloys. *Smart Materials and Structures*, *20*(6)

Shrestha, K.C., Araki, Y., Nagae, T., Koetaka, Y., Suzuki, Y., Omori, T., Sutou, Y., Kainuma, R., & Ishida, K. (2013). Feasibility of Cu-Al-Mn superelastic alloy bars as reinforcement elements in concrete beams. *Smart Materials and Structures*, *22*

Song, G., Ma, N., & Li, H.N. (2006). Applications of shape memory alloys in civil structures. *Engineering Structures*, *28*(9), 1266–1274

Sucuoglu, H., Lin, W.W.C., Binici, B., & Ezzatfar, P. (2014). Pseudo-dynamic testing, performance assessment, and modeling of deficient reinforced concrete frames. *ACI Structural Journal*, *111*(5), 1203–1212

Tazarv, M., & Saiid Saiidi, M. (2016). Low-damage precast columns for accelerated bridge construction in high seismic zones. *Journal of Bridge Engineering*, *21*(3), 04015056

TBEC. (2018). Turkish Building Earthquake Code. *Disaster and Emergency Management Presidency*, 416.

Teresa, D.R.M., Ciro, D.V., Paolo, R., Marco, D.L., Andrea, P., & Mario, V.G. (2020). Light FRP strengthening of poorly detailed reinforced concrete exterior beam–Column joints. *Journal of Composites for Construction*, *24*(3), 4020014

Wilson, J.C., & Wesolowsky, M.J. (2005). Shape memory alloys for seismic response modification: A state-of-the-art review. *Earthquake Spectra*, *21*(2), 569–601

Xing, C. (2019). *An analytical study on the behavior of reinforced concrete interior beam-column joints* (Doctoral dissertation). Virginia Polytechnic Institute and State University.

Xing, C., Koutromanos, I., Leon, R., & Moharrami, M. (2018). Computational simulation of RC beam-to-column connections under earthquake loading. In *11th National Conference on Earthquake Engineering 2018, NCEE 2018: Integrating Science, Engineering, and Policy*.

Youssef, M.A., Alam, M.S., & Nehdi, M. (2008). Experimental investigation on the seismic behavior of beam-column joints reinforced with superelastic shape memory alloys. *Journal of Earthquake Engineering*, *12*(7), 1205–1222

Yurdakul, Ö., & Avşar, Ö. (2016). Strengthening of substandard reinforced concrete beam-column joints by external post-tension rods. *Engineering Structures*, *107*, 9–22

Yurdakul, Ö., Del Vecchio, C., Di Ludovico, M., Avşar, Ö., & Prota, A. (2023). Fragility functions for fiber-reinforced polymers strengthened reinforced concrete beam-column joints. *Engineering Structures*, *279*, 115570

Yurdakul, Ö., Duran, B., Tunaboyu, O., & Avşar, Ö. (2021). Field reconnaissance on seismic performance of RC buildings after the January 24, 2020 Elazığ-Sivrice earthquake. *Natural Hazards*, *105*(1), 859–887

Yurdakul, Ö., Tunaboyu, O., & Avşar, Ö. (2018). Retrofit of non-seismically designed beam-column joints by post-tensioned superelastic shape memory alloy bars. *Bulletin of Earthquake Engineering*, *16*, 5279–5307

Yurdakul, Ö., Tunaboyu, O., Routil, L., & Avşar, Ö. (2020). Parameter sensitivity of CFRP retrofitted substandard joints by stochastic computational mechanics. *Composite Structures*, *238*, 112003

Yurdakul, Ö., Vnenk, P., Routil, L., Culek, B., & Avşar, Ö. (2024). Post-damage recovery of substandard RC columns by CFRPs. *Engineering Structures*, *306*, 117806

4th International Civil Engineering & Architecture Conference
17-19 May 2025, Trabzon, Türkiye

Pounding-induced seismic response of base-isolated and fixed-base buildings: Effect of separation distance

Furkan Şen*[1], Fezayil Sunca[2], Ahmet C. Altunışık[3,4]

[1] Giresun University, Department of Civil Engineering, 28200 Giresun, Türkiye
[2] Karadeniz Technical University, Department of Construction Technologies, 61080 Trabzon, Türkiye
[3] Karadeniz Technical University, Department of Civil Engineering, 61080 Trabzon, Türkiye
[4] Karadeniz Technical University, Earthquake and Structural Health Monitoring Research Center, 61080 Trabzon, Türkiye

Abstract. In densely populated metropolitan areas, buildings are often constructed with insufficient gaps between them, increasing the risk of poundings during seismic events, which can cause damage to structural elements. Therefore, evaluating the seismic behavior of buildings subjected to the pounding effect is essential. This study investigates the structural pounding effects between a base-isolated and a fixed-base reinforced concrete building under seismic excitation. Both buildings were designed as four-story structures in accordance with the Türkiye Building Earthquake Code. Finite element models of the buildings were developed using the SAP2000 software. The interaction between these two structures was examined through nonlinear time-history analyses using eleven pairs of ground motion records. The separation distances between the base-isolated and fixed-base buildings are set at four different levels: 25%, 50%, 75%, and 100% of the total design displacement of isolators. The interaction and transfer of pounding forces between adjacent structures were simulated using nonlinear elastic spring model, specifically the Hertz contact model. The seismic behavior of both base-isolated and fixed-base buildings under the influence of pounding effects were evaluated by analyzing the structural response in terms of story accelerations, plastic rotations, and shear force demands. Story accelerations were analyzed to assess the amplification of inertial forces due to pounding. Impact forces generated during poundings were examined to determine their magnitude and effect on structural components. Plastic hinge rotations were evaluated to identify potential locations of excessive deformation and damage concentration, providing insights into the structural performance under repeated impact loading. The results demonstrate that reduced separation distances significantly amplify seismic demands. At 25% separation, plastic rotations in column elements—especially in the fixed-base building—frequently exceed the Collapse Prevention performance level. Conversely, at 100% separation, pounding is effectively mitigated, and structural responses are substantially reduced. It is observed that the highest pounding forces typically occur at the isolation level and upper stories, with non-uniform distribution along the height. Base-isolated buildings exhibit consistently lower plastic hinge demands compared to fixed-base buildings under identical conditions, particularly in columns. Moreover, beams located at the isolation level remain largely within elastic limits across all scenarios. Directional analyses reveal that structural elements aligned with the pounding direction experience significantly higher demands than those in the orthogonal direction. The findings confirm that inadequate separation distances severely compromise the efficiency of seismic isolation systems by increasing acceleration demands and structural deformations. Thus, ensuring sufficient clearance is critical for the optimal performance of base-isolated buildings during strong ground motions.

Keywords: Reinforced concrete building; Base isolation; Pounding; Separation distance; Damage evaluation

1. Introduction

Base isolation systems have been widely adopted as an effective strategy for enhancing the seismic resilience of structures by significantly reducing inertial demands transmitted to the superstructure (Komodromos et al., 2007; Domadzra et al., 2024). Despite their effectiveness, base-isolated structures are susceptible to large lateral displacements during seismic events, which can lead to pounding between adjacent buildings or between the superstructure and the surrounding moat wall (Pant & Wijeyewickrema, 2012). Seismic design codes prescribe minimum separation distances to avoid such poundings. However, several studies have shown that these provisions

* Corresponding author, E-mail: furkan.sen@giresun.edu.tr

https://doi.org/10.31462/icearc2025_ce_eqe_915

may not always be sufficient under certain structural configurations or when subjected to extreme or near-fault ground motions (Rajaram & Kumar, 2012; Kamal & Inel, 2022; Altunışık et al., 2023).

While the literature has extensively examined the pounding between base-isolated buildings and moat walls (Komodromos, 2008; Masroor et al., 2012; Liu et al., 2014; Mavronicola et al., 2017), limited attention has been paid to pounding scenarios involving base-isolated and adjacent fixed-base buildings. These interactions can occur at the isolation level or story-to-story depending on the height and dynamic characteristics of the structures involved (Mavronicola et al., 2020; Sadeghi-Movahhed et al., 2024). Earlier numerical studies demonstrated that pounding-induced responses are sensitive to the base type, stiffness contrast, and separation distance (Mahmoud & Jankowski, 2010; Naderpour et al., 2019). Moreover, inadequate separation can significantly amplify seismic demands in both structures, sometimes resulting in localized damage or even collapse.

Another important aspect insufficiently addressed in prior studies is the effect of ground motion characteristics on pounding behavior. Most investigations rely on a limited number of records and often neglect the distinctions between near-fault and far-field ground motions. In particular, near-fault motions are known to contain velocity pulses, which can significantly increase displacement demands and consequently elevate the risk and severity of pounding (Kazemi et al., 2021; Ebrahimiyan et al., 2022).

In this context, the present study aims to investigate the seismic performance and behaviour of base-isolated and fixed-base reinforced concrete building subjected to pounding. For this purpose, four separation distances are analyzed, corresponding to 25%, 50%, 75%, and 100% of the total design displacement of the isolation system. Nonlinear time-history analyses are performed to comprehensively assess the influence of both separation on pounding-induced demands such as plastic hinge rotations, pounding forces, and story accelerations.

2. Modeling and design

2.1. Superstructure and pounding configuration

This study focuses on evaluating the influence of seismic pounding-occurring between base-isolated buildings and adjacent fixed-base buildings-on the plastic hinge rotations, pounding forces, and maximum story accelerations. To evaluate the influence of separation distance, the base-isolated building is assumed to be separated from the adjacent fixed-base building by varying clearance distances, denoted as d_g. The ratios of separation distance to the total maximum design displacement, $d_g/D_{T,max}$ are taken as 25%, 50%, 75%, and 100%. A four-story, four-bay by four-bay reinforced concrete structure is adopted as the representative fixed-base and base-isolated buildings. Each bay measures 6.0 meters in both longitudinal and transverse directions, with a uniform story height of 3.2 meters. Both the base-isolated and fixed-base buildings are assumed to be regular in plan and exhibit no vertical irregularities. The investigated pounding configuration is illustrated in Fig. 1.

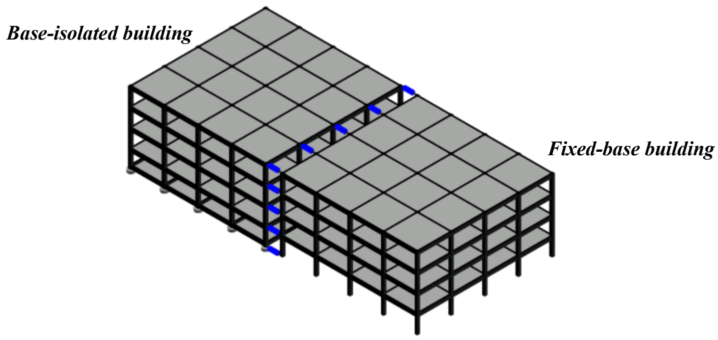

Fig. 1. The considered pounding configuration.

In the base-isolated building, column and beam cross-sections are 50×50 cm and 30×60 cm, respectively, while in the fixed-base building, columns are 60×60 cm with identical beam dimensions. Slab thickness is 15 cm in both buildings, except at the isolation interface where it is increased to 25 cm to ensure diaphragm effect. The concrete is C30 (f_{ck} = 30 MPa) and reinforcement is B420C (f_{yk} = 420 MPa). Nonlinear behavior of confined and unconfined concrete is modeled using the Mander model (Mander et al., 1988). The modulus of elasticity, Poisson's ratio, and unit weight of concrete are 31000 MPa, 0.2, and 25 kN/m³, respectively. For reinforcement, these values are 200000 MPa and 76.97 kN/m³. Fig. 2a presents the elastic design spectra corresponding to the Design Basis Earthquake (DBE) and Maximum Considered Earthquake (MCE), as defined in the Türkiye Seismic Hazard Map (TSHM, 2018). Finite Element (FE) models were developed using SAP2000 (2020). To represent nonlinear behavior in the superstructure, a concentrated plastic hinge model was adopted, with linear behavior assumed between hinge locations. These hinges were generated using SAP2000's default auto hinge properties in compliance with ASCE 41-17. The typical force–deformation behavior of plastic hinges is illustrated in Fig. 2b.

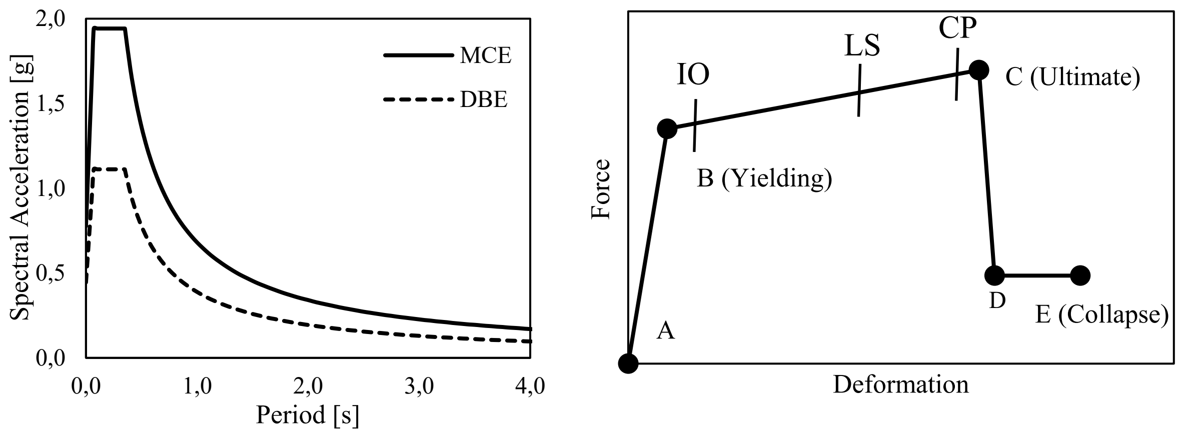

(a) (b)

Fig. 2. (a) Elastic design spectrum of selected location for DBE and MCE level (b) Force–deformation relationship for a typical plastic hinge

2.1. Superstructure and pounding configuration

Lead-Rubber Bearings (LRBs) were selected for the seismic isolation of the superstructure. To improve their energy dissipation capabilities, each was equipped with a lead plug at its core. This design feature notably enhances the efficiency of LRBs in absorbing energy, making them highly effective base isolation devices, as demonstrated by Kelly et al., (2010). The typical force-displacement behavior of LRBs is illustrated graphically in Fig. 3b. Plasticity model is based on hysteretic behavior introduced by Wen (1976); Park et al., (1986) and recommended for base-isolation analysis by Nagarajaiah et al., (1991). Several key parameters influence the force-displacement relationship, and the formulas for these parameters can be found in numerous codes (UBC, 1997; ACSE-41-17, 2017; TBEC, 2018) or publications (Naeim and Kelly, 1999). Fig. 3a presents the geometrical dimensions of the LRBs designed within the scope of Türkiye Building Earthquake Code (TBEC, 2018). The lower and upper bound properties of isolators are determined using property modification factors. Instead of using the post-yield stiffness k_2 and characteristic strength F_Q directly, lower bound values are obtained as $k_2\lambda_{low,k_2}$ and $F_Q\lambda_{low,F_Q}$, while upper bound values are calculated as $k_2\lambda_{up,k_2}$ and $F_Q\lambda_{up,F_Q}$ (TBEC, 2018). Design and performance checks are conducted using nominal, lower bound, and upper bound properties. For instance, maximum isolator displacement is checked using MCE and lower bound properties; the substructure is designed with MCE and upper bound properties; story accelerations are evaluated using DBE and nominal properties; and the superstructure design is based on DBE and upper bound properties (TBEC, 2018).

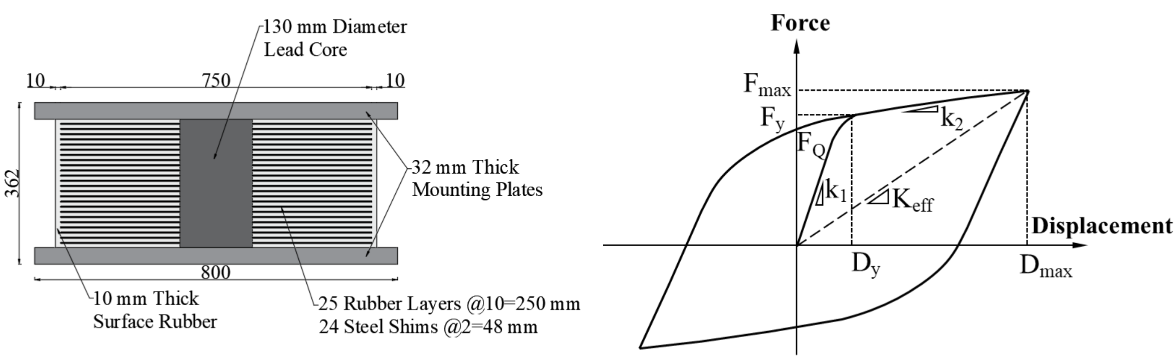

(a) (b)

Fig. 3. (a) The geometry and (b) horizontal force-displacement relationship of LRBs

The total design displacement of the isolation interface, $D_{T,max}$, is determined by adding torsional displacements from the superstructure and isolation system to the design displacement. Instead of using values from Eq. (1) alone, the greater of the calculated displacement and $1.1D_{max}$ is considered (TBEC, 2018). Eq. (1) accounts for eccentricity effects, where seismic force $K_{eff}D_{max}$ acts at the center of mass, offset by eccentricity from the center of stiffness. Table 1 presents the nominal, lower, and upper bound properties of the LRBs for both DBE and MCE levels.

$$D_{T,max} = D_{max}\left[1 + y\frac{12e}{b^2 + d^2}\right] \tag{1}$$

Table 1. The design parameters of LRBs

Parameter	Unit	Lower bound		Nominal		Upper bound	
		DBE	MCE	DBE	MCE	DBE	MCE
k_v	[kN/m]	975790.54					
k_2	[kN/m]	655.63		857.03		1569.54	
k_1	[kN/m]	6556.25		8570.26		15695.37	
F_Q	[kN]	78.98		132.73		213.32	
D_y	[mm]	13.38		17.21		15.10	
F_y	[kN]	87.75		147.48		237.02	
β_e	[%]	25.69	13.96	32.77	21.69	34.72	25.47
K_{eff}	[kN/m]	1074.39	821.20	1839.47	1263.99	3848.02	2556.11
D_{max}	[cm]	16.76	42.40	12.01	28.99	8.32	19.22
$D_{T,max}$	[cm]	18.44	46.64	13.21	31.89	9.15	21.41
η	[-]	0.571	0.726	0.535	0.612	0.535	0.573
T	[s]	2.328	2.663	1.779	2.146	1.230	1.509

Many codes (e.g., UBC, 1997; TBEC, 2018) recommend providing a gap at the isolation interface at least equal to the total design displacement calculated using MCE and the lower bound properties of isolators, as this yields the maximum displacement. Accordingly, to assess potential pounding between base-isolated buildings, nonlinear time-history analyses were conducted using MCE and lower bound isolator properties.

The interaction and transmission of pounding forces between neighboring structures was simulated using a nonlinear elastic spring model, specifically the Hertz model, which is widely referenced in the literature (Wang et al., 2009; Miari et al., 2019; Borekci et al., 2024). The nonlinear impact stiffness k_G, was set at 1.13×10^6 kN/m$^{3/2}$ for concrete-concrete interactions, as indicated by Jankowski (2005).

3. Ground motion selection

To investigate the effects of structural pounding between fixed-base and base-isolated buildings, a set of 11 near-fault ground motion records was employed. The selection and scaling procedures for these records were carried out in accordance with the provisions of the TBEC (2018). For each record, a resultant horizontal response spectrum was computed by taking the square root of the sum of the squares (SRSS) of the two orthogonal horizontal components. All ground motions were scaled such that the average resultant spectra complied with the spectral matching criteria prescribed by the code over the relevant period intervals.

For fixed-base structures, the response spectra were selected and scaled to ensure that the mean spectral amplitudes within the period range of $0.2T_P$ to $1.5T_P$ —where T_P denotes the fundamental period of the fixed-base building—were not less than 1.3 times the corresponding segment of the code-defined design spectrum.

In the case of base-isolated structures, the period range was adjusted in line with isolation-specific requirements defined in the TBEC. Accordingly, the average spectral amplitudes were scaled within the range of $0.5T_M$ (T_M is the effective period of vibration calculated based on the upper-bound values of the base-isolated building under the maximum displacement of the isolation system) to $1.25T_M$ (T_M is the effective period of vibration calculated based on the lower-bound values of the base-isolated building under the maximum displacement of the isolation system). As with the fixed-base case, the applied scale factor was uniformly used for both horizontal components of each record to preserve directional consistency and spectral shape.

Furthermore, in accordance with the same code, fixed-base residential buildings are intended to meet the performance objectives associated with the DBE. Therefore, the records employed for fixed-base models were scaled to match the DBE-level target spectrum within the specified period range. In contrast, the design of base-isolation systems is governed by the MCE level, and consequently, the corresponding records were scaled to match the MCE level target spectrum over the isolation-specific period range. This methodology ensures that the scaled ground motions appropriately reflect the seismic demand levels corresponding to the structural system type and its associated performance objectives. These ground motions were obtained from the Pacific Earthquake Engineering Research Center Ground Motion Database (PEER, 2019), and the acceleration response spectra for 5% damping ratio are presented in Fig. 4. Also, the properties of the selected ground motions were listed in Tables 2.

Table 2. Selected near-field ground motion records

NGA Record Number	Event Name	Station Name	Year	PGA (g)	M_w	R_{rup} (km)	V_{S30} (m/s)
126	Gazli, USSR	Karakyr	1976	0.864	6.80	5.46	259.59
160	Imperial Valley-06	Bonds Corner	1979	0.777	6.53	2.66	223.03
181	Imperial Valley-06	El Centro Array #6	1979	0.447	6.53	1.35	203.22
182	Imperial Valley-06	El Centro Array #7	1979	0.469	6.53	0.56	210.51
292	Irpinia, Italy-01	Sturno (STN)	1980	0.321	6.90	10.84	382.00
723	Superstition Hills-02	Parachute Test Site	1987	0.384	6.54	0.95	348.69
825	Cape Mendocino	Cape Mendocino	1992	1.494	7.01	6.96	567.78
828	Cape Mendocino	Petrolia	1992	0.472	7.01	8.18	422.17
1086	Northridge-01	Sylmar-Olive View Med FF	1994	0.230	6.69	5.30	440.54
1503	Chi-Chi, Taiwan	TCU065	1999	0.790	7.62	0.57	305.85

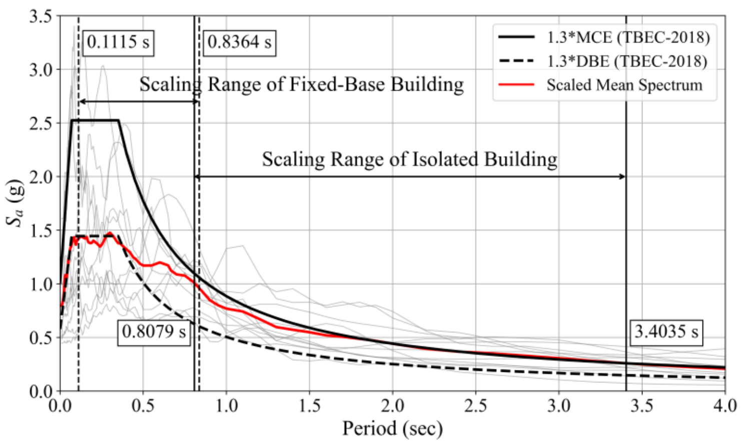

Fig. 4. The acceleration response spectra of selected ground motions for 5% damping ratio

4. Result and discussion

The nonlinear time-history analyses were conducted to evaluate the seismic pounding behavior between two adjacent buildings-one fixed-base and the other base-isolated-under various separation distances. The effects of separation distance on plastic hinge rotations were evaluated in detail. In addition to local member responses, inter-building maximum pounding forces and story accelerations were also assessed to evaluate dynamic interaction and the amplification of seismic demand due to pounding. Four separation scenarios were considered (25%, 50%, 75%, and 100% of the total design displacement of seismic isolators), and the resulting plastic rotations in columns and beams were compared against three performance levels: (i) Collapse Prevention (CP), (ii) Life Safety (LS), and (iii) Immediate Occupancy (IO). Box plots were employed to illustrate the distribution of plastic hinge rotations under 11 ground motion records for each separation distance. Special emphasis was placed on the directional response differences between the pounding direction (R3) and the orthogonal direction (R2). The results offer a comparative assessment of seismic responses in both buildings and directions and highlight the effectiveness of base isolation in mitigating pounding-induced damage.

Plastic hinge rotations for all structural members-beams and columns-are presented separately for each building (fixed-base and base-isolated) and for both directions (R3 and R2) in Fig. 5, under considered separation distances. The pounding analysis results indicate that decreasing the separation distance between the two buildings significantly amplifies plastic hinge rotations. At the smallest separation distance (25%), plastic rotations in both columns and beams reach their highest levels. Specifically, in the fixed-base building, the median plastic rotation in columns along the pounding direction (R3) is approximately 0.0157 radians, already exceeding the CP performance level, while the maximum value reaches about 0.027 radians—nearly twice this limit. At a 50% separation distance, the median plastic rotation reduces to approximately 0.0118 radians, falling below the CP threshold but slightly surpassing the LS threshold of 0.0109 radians. Although the damage potential is lower compared to the 25% case, plastic rotations remain considerably high, with maximum values reaching 0.018 radians, still above the CP performans level. At wider separations (75% and 100%), plastic hinge rotations are significantly reduced, with median values decreasing to around 0.0106 radians. Although occasional exceedances of the LS threshold persist, their frequency diminishes considerably. Similarly, increasing the seperation distance reduces plastic demands in beam elements. Particularly in the fixed-base building, where pounding occurs, the median beam plastic rotation at 25% separation is around 0.0158 radians, while at 100% separation it decreases to approximately 0.0107 radians. These findings confirm that insufficient separation increases plastic hinge demands and raises damage levels in structural elements, whereas adequate separation distances mitigate rotations and help maintain elements near their elastic limits.

A comparison between the fixed-base and base-isolated building elements reveal that columns and beams exhibit different behaviors during pounding. Overall, plastic hinge rotations in the base-isolated building elements are lower compared to those in the fixed-base building under the identical separation conditions. The influence of isolation is particularly evident in columns: in the base-isolated building, the median rotation at 25% separation distance remains around 0.0105 radians, with the majority of the values remaining below the LS performance level of 0.0115 radians. In contrast, in the fixed-base building under the same conditions, the median column rotation is approximately 0.0157 radians, with a significant portion of the columns exceeding the CP performance level. These observations suggest that base isolation can significantly reduce pounding effects and limit damage in column elements. A similar trend is observed for beams; however, the distinction is slightly less pronounced compared to columns. In the fixed-base building, beams exhibited a median plastic rotation of approximately 0.0155 radians at 25% seperation distance, and some cases exceeded the CP performance level of 0.0138 radians. Conversely, in the base-isolated building, the median beam rotation at the same separation is around 0.0115 radians—above the LS threshold of 0.0104 radians but generally remaining below the CP performance level. In both building types, the plastic rotations of beams were generally lower than those of columns. This difference is attributed to the structural role of columns, which play a more critical role in the load-bearing system of the frame and are subjected to greater demands during poundings. The isolation system effectively reduces the transmission of acceleration and shear forces to the superstructure, resulting in lower plastic demands in both beams and columns of the isolated building. At moderate to large separations, plastic hinge formation in the isolated building is substantially limited, and plastic rotations remain within elastic bounds. Moreover, no significant damage was observed in the beams located at the isolation level under any earthquake scenario, and maximum plastic rotations remained below the LS performance limit across all separation distances. However, in the fixed-base building, noticeable plastic rotation demands persist in certain elements even at these larger separations.

When plastic hinge rotations in the R3 and R2 directions are evaluated separately for column elements, the results demonstrate a clear directional disparity. Damage accumulation is significantly more pronounced in the R3 direction, while plastic demands in the R2 direction are relatively limited. For example, at 25% separation, columns in both the fixed-base and base-isolated buildings exhibit plastic rotations nearing or surpassing their deformation capacities in the R3 direction. In contrast, due to the absence of direct contact in the R2 direction, plastic rotations are markedly lower. In the fixed-base building, the median column rotation at 25% separation is approximately 0.0157 radians in R3, while it is only about 0.0083 radians in R2. Similarly, the base-isolated building shows a median column plastic rotation of approximately 0.0105 radians in R3, compared to about 0.003 radians in R2, which remains below the LS performance level, highlighting the directional dependence of damage due to seismic pounding and the effectiveness of base isolation in limiting out-of-pounding direction plastic demands.

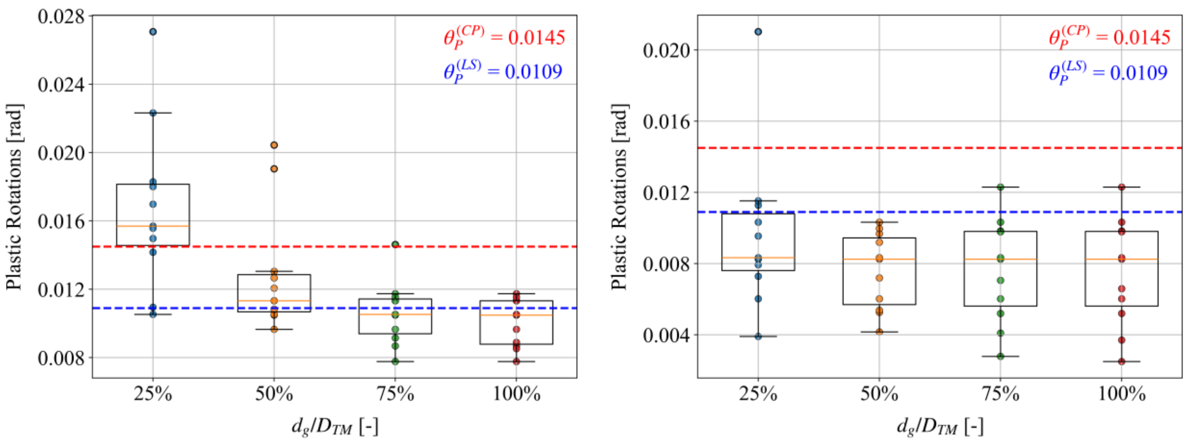

(a) Columns of Fixed-Based Building (R3)

(b) Columns of Fixed-Based Building (R2)

Fig. 5. Plastic hinge rotations of structural elements in fixed-base and base-isolated buildings evaluated along R2 and R3 directions

Fig. 5. Continued

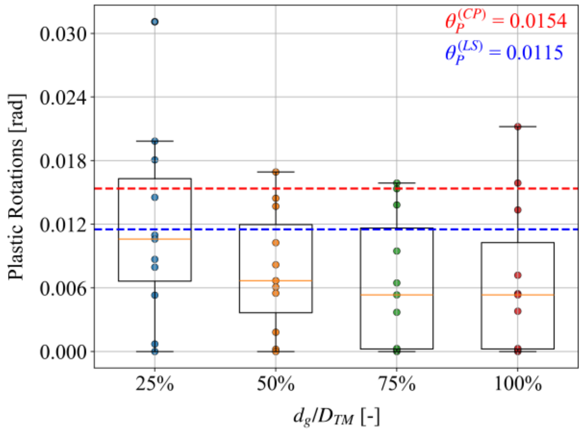

(c) Columns of Base-Isolated Building (R3)

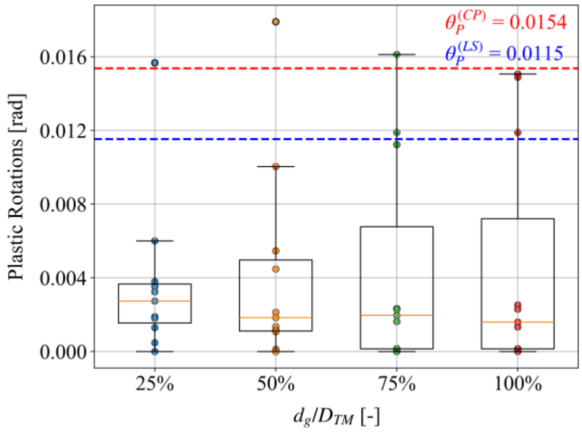

(d) Columns of Base-Isolated Building (R2)

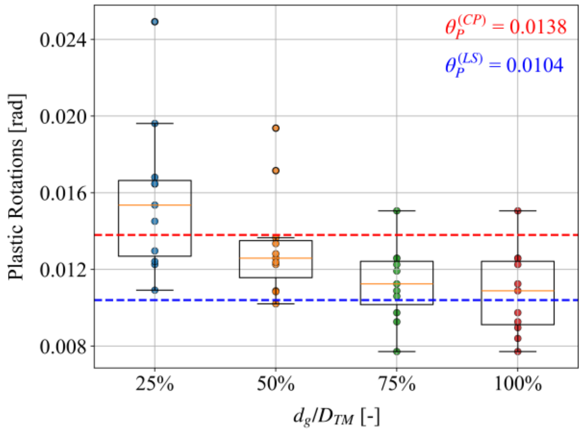

(e) Beams of Fixed-Based Building (R3)

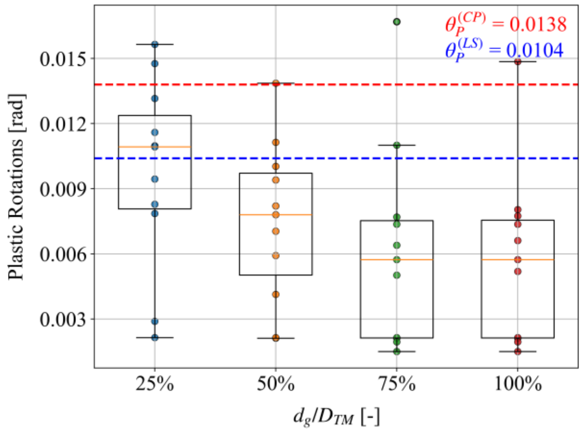

(f) Beams of Base-Isolated Building (R3)

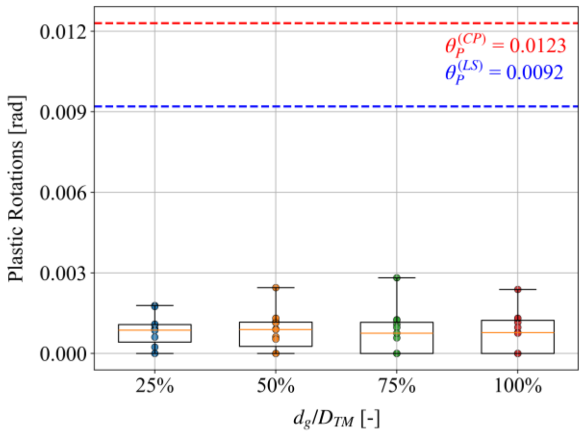

(g) Beams of Base-Isolated Building_IL (R3)

The analysis of inter-story pounding forces between the fixed-base and base-isolated buildings, as illustrated in Fig. 6, reveals substantial variations depending on both the separation distance and the story level. The findings are evaluated considering the magnitude and distribution of pounding forces under 11 different ground motion records and four separation distances. A clear inverse relationship is observed between the separation distance and the magnitude of pounding forces. At 25% of the design separation distance, most of the earthquake records resulted in pounding forces exceeding 20,000 kN—with maximum values such as 25,902 kN (EQ ID: 825), 24,067 kN (EQ ID: 1086), and 22,208 kN (EQ ID: 828). As the separation distance increases, a consistent reduction in pounding intensity is evident. At 50% separation, forces at the isolation story drop to around 10,000–15,000 kN, and at 75%, they are generally below 5,000 kN. At 100% separation, pounding forces are effectively eliminated across all stories, confirming the adequacy of this clearance in preventing poundings. Nevertheless, for one ground motion record (EQ ID: 723), pounding still occurs at the 3rd and 4th story levels, indicating that while the total design displacement is effective at the isolation interface, upper-story interactions may still arise under certain excitation characteristics.

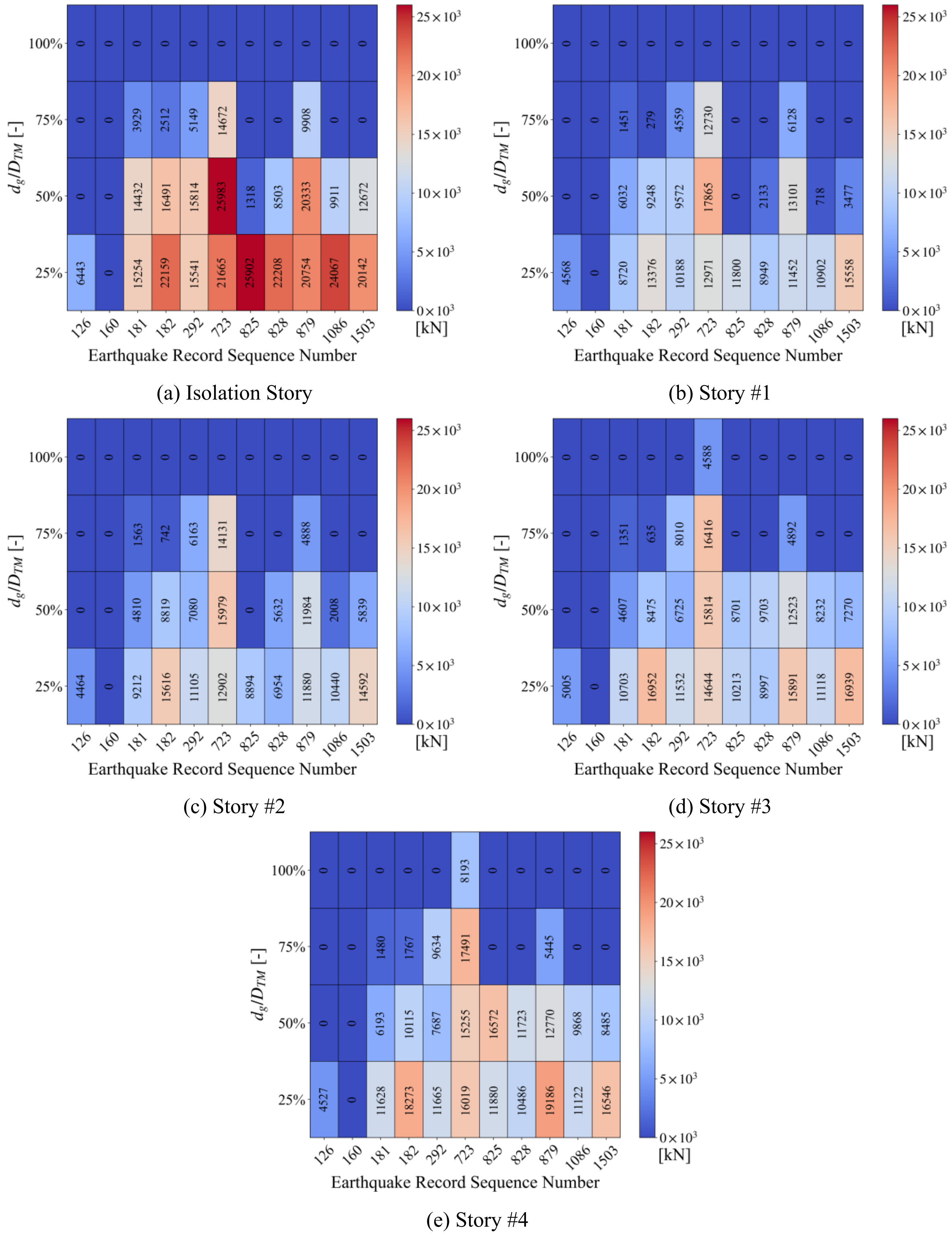

Fig. 6. Inter-story pounding forces at different separation distances for each story under multiple earthquake records

Among the upper stories, 1st and 2nd stories exhibit relatively lower average pounding forces (9,862 kN and 9,642 kN, respectively) when compared to the isolation story for the 25% seperation distance. In contrast, 3rd and 4th stories experience higher average forces, evaluated as 11,090 kN and 11,939 kN, respectively. Although these values are still lower than the maximum average force observed at the isolation story (17,648 kN), they clearly indicate that the pounding demand does not monotonically decrease with height. Instead, 3rd and 4th stories are subjected to greater average pounding forces than 1st and 2nd stories, highlighting that upper stories may also be critically affected by pounding, depending on structural and dynamic characteristics. Furthermore, in some earthquake records (e.g., EQ ID 723 and 825), pounding occurred in the upper stories while no impact was observed in the lower stories. This pounding pattern indicates that the relative motion between buildings during seismic excitation is not uniformly distributed across the height of the structure.

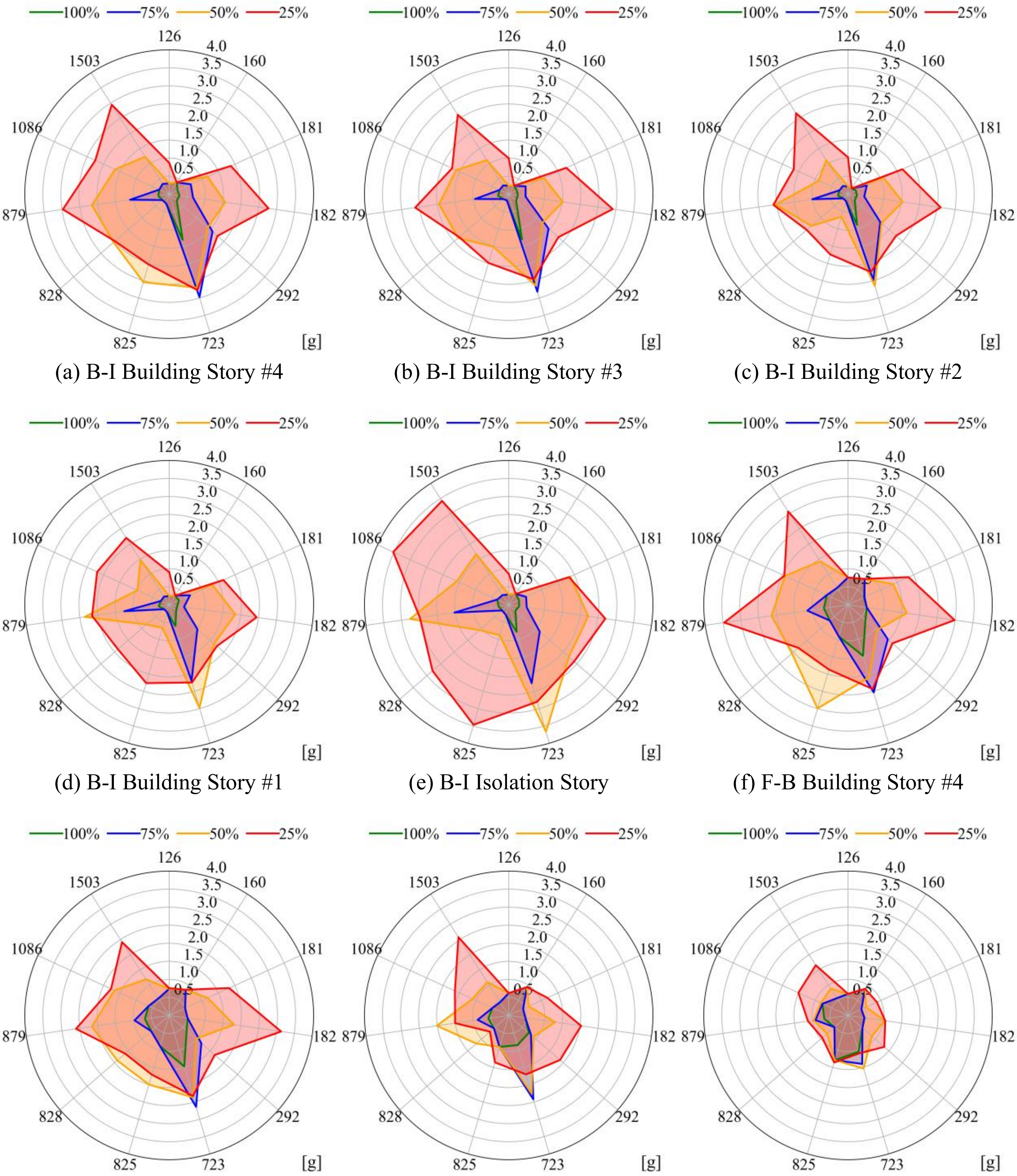

(a) B-I Building Story #4 (b) B-I Building Story #3 (c) B-I Building Story #2

(d) B-I Building Story #1 (e) B-I Isolation Story (f) F-B Building Story #4

(g) F-B Building Story #3 (h) F-B Building Story #2 (i) F-B Building Story #1

Fig. 7. Radar charts of maximum story accelerations for each story of the base-isolated and fixed-base buildings

The analysis indicates that as the separation distance between the base-isolated (B-I) and fixed-base (F-B) buildings decreases, story accelerations in the both buildings increase markedly. When a 100% separation is provided, the isolation system demonstrates effective performance by substantially reducing story accelerations, with an maximum value of 0.391g. In contrast, the fixed-base building experiences significantly higher accelerations under the same separation condition, reaching an maximum of 0.745g, thereby confirming the critical role of adequate clearance in maximizing the efficiency of seismic isolation systems. As the separation distance is reduced to 75%, story accelerations in the base-isolated building increase moderately, reaching a maximum of 0.803g, yet remain lower than those observed in the fixed-base building, which records a peak of 0.960g. Notably, even at this reduced separation distance, the maximum story acceleration observed in the base-isolated building exceeds that of the fixed-base building at 100% separation, highlighting the adverse impact of insufficient clearance on the effectiveness of the isolation system. However, the disparity between the two buildings diminishes substantially at 50% separation, where accelerations in the base-isolated building surge to 1.690g, nearly equaling those in the fixed-base building, which reach 1.667g. At 25% separation, the displacement capacity of seismic isolators becomes critically constrained, and the accelerations in the base-isolated building escalate further, reaching up to 2.430g. The fixed-base building also shows high value of 2.062g, at this level of separation, the accelerations in the base-isolated system not only approach but even exceed those observed in the fixed-base building (Fig. 7). This finding confirms that the isolation system's effectiveness strongly depends on maintaining sufficient separation, and when that condition is compromised, impact effects and restrained isolator movement significantly amplify the dynamic response.

4. Conclusions

This study investigated the seismic pounding behavior between a fixed-base and a base-isolated building using nonlinear time-history analyses under 11 ground motions and four different separation distances (25%, 50%, 75%, and 100% of the total design displacement od isolators). Plastic hinge rotations, inter-story pounding forces, and story accelerations were comprehensively assessed. The analysis aimed to evaluate the influence of separation distance on the severity and distribution of seismic demands.

- Insufficient separation distance causes excessive plastic hinge rotations in both buildings, especially in columns along the pounding direction, frequently exceeding CP performance level.
- Adequate separation ensures the effectiveness of the isolation system by minimizing both accelerations and plastic deformations.
- The directional assessment of plastic rotations reveals that structural elements aligned with the pounding direction (R3) are subjected to considerably higher deformation demands than those in the orthogonal direction (R2), highlighting the directionality of damage mechanisms in pounding scenarios.
- At reduced separation distances, plastic hinge rotations in columns consistently exceeded those in beams, highlighting the greater susceptibility of columns to pounding-induced demands.
- Inter-story pounding forces reach critical levels at 25% separation, especially at the isolation and upper stories. These forces decrease markedly as separation increases and are eliminated at 100%, except for rare upper-story interactions.
- The pounding forces are highest at the isolation story; however, upper storys—particularly the third and fourth stories—tend to experience greater average forces than the lower storys, indicating a non-monotonic distribution of pounding demands along the building height.
- Story accelerations increase significantly in both base-isolated and fixed-base buildings as the separation distance between them decreases.
- Even 75% under separation distance, the maximum story acceleration in the base-isolated building surpasses the peak acceleration observed in the fixed-base building at full (100%) separation, clearly demonstrating how inadequate clearance can significantly impair the performance of the isolation system.
- Story accelerations in the base-isolated building dramatically increase under reduced separation. At 25%, isolator efficiency is severely compromised, with accelerations exceeding those of the fixed-base building, indicating the critical importance of maintaining adequate clearance for isolation systems to function properly.
- No significant damage was observed in beams located at the isolation level of the base-isolated building for any earthquake scenario, with all plastic hinge rotations remaining below the LS threshold, suggesting that isolation floor beams are less vulnerable under proper design conditions.

References

Altunisik, A. C., Arslan, M. E., Kahya, V., Aslan, B., Sezdirmez, T., Dok, G., ... & Sunca, F. (2023). Field observations and damage evaluation in reinforced concrete buildings after the february 6th, 2023, Kahramanmaras-Turkiye earthquakes. *Journal of Earthquake and Tsunami, 17(6).*

ASCE 41-17 (2017). Minimum Design Loads and Associated Criteria for Buildings and Other Structures. ASCE/SEI 7-16. American Society of Civil Engineers.

Borekci, M., Dag, B., & Eroglu, A. (2024, December). Seismic behaviour of reinforced concrete buildings: Impact of inter-story pounding with adjacent structures on one and both sides. In *Structures* (Vol. 70, p. 107815). Elsevier.

Domadzra, Y., Bhandari, M., & Hasan, M. (2024). Seismic response of base-isolated buildings: exploring isolator properties. *Asian Journal of Civil Engineering*, 1-13.

Ebrahimiyan, F., Hadianfard, M. A., Naderpour, H., & Jankowski, R. (2022). Fragility analysis of structural pounding between adjacent structures arranged in series with various alignment configurations under near-field earthquakes. *Bulletin of Earthquake Engineering, 20(13),* 7215-7240.

Jankowski, R. (2005). Non-linear viscoelastic modelling of earthquake-induced structural pounding. *Earthquake Engineering & Structural Dynamics, 34(6)*, 595-611.

Kamal, M., & Inel, M. (2022). Simplified approaches for estimation of required seismic separation distance between adjacent reinforced concrete buildings. *Engineering Structures*, 252, 113610.

Kazemi, F., Miari, M., & Jankowski, R. (2021). Investigating the effects of structural pounding on the seismic performance of adjacent RC and steel MRFs. *Bulletin of Earthquake Engineering, 19(1)*, 317-343.

Kelly, T. E., R. I. Skinner, and W. H. Robinson. (2010). Seismic isolation for designers and structural engineers. Kanpur, India: Indian Institute of Technology.

Komodromos, P. (2008). Simulation of the earthquake-induced pounding of seismically isolated buildings. *Computers & Structures, 86(7-8)*, 618-626.

Komodromos, P., Polycarpou, P. C., Papaloizou, L., & Phocas, M. C. (2007). Response of seismically isolated buildings considering poundings. *Earthquake Engineering & Structural Dynamics, 36(12)*, 1605-1622.

Liu, Y., Liu, W. G., Wang, X., He, W. F., & Yang, Q. R. (2014). New equivalent linear impact model for simulation of seismic isolated structure pounding against moat wall. *Shock and Vibration, 2014(1)*, 151237.

Mahmoud, S., & Jankowski, R. (2010). Pounding-involved response of isolated and non-isolated buildings under earthquake excitation. *Earthquake and Structures, 1(3)*, 231-252.

Mander, J. B., Priestley, M. J., & Park, R. (1988). Theoretical stress-strain model for confined concrete. *Journal of structural engineering, 114(8)*, 1804-1826.

Masroor, A., & Mosqueda, G. (2012). Experimental simulation of base-isolated buildings pounding against moat wall and effects on superstructure response. Earthquake Engineering & Structural Dynamics, 41(14), 2093-2109.

Mavronicola, E. A., Polycarpou, P. C., & Komodromos, P. (2017). Spatial seismic modeling of base-isolated buildings pounding against moat walls: effects of ground motion directionality and mass eccentricity. *Earthquake Engineering & Structural Dynamics, 46(7)*, 1161-1179.

Mavronicola, E. A., Polycarpou, P. C., & Komodromos, P. (2020). Effect of ground motion directionality on the seismic response of base isolated buildings pounding against adjacent structures. *Engineering Structures, 207*, 110202.

Miari, M., Choong, K. K., & Jankowski, R. (2019). Seismic pounding between adjacent buildings: Identification of parameters, soil interaction issues and mitigation measures. *Soil Dynamics and Earthquake Engineering, 121*, 135-150.

Naderpour, H., Danaeifard, P., Burkacki, D., & Jankowski, R. (2019). Earthquake-Induced pounding of medium-to-high-rise base-isolated buildings. *Applied Sciences, 9(21)*, 4681.

Naeim, F., and Kelly, J. M. (1999). Design of seismic isolated structures: From theory to practice. New York: Wiley.

Nagarajaiah, S., Reinhorn, A. M., & Constantinou, M. C. (1991). Nonlinear dynamic analysis of 3-D-base-isolated structures. *Journal of Structural Engineering, 117(7)*, 2035-2054.

Pant, D. R., & Wijeyewickrema, A. C. (2012). Structural performance of a base-isolated reinforced concrete building subjected to seismic pounding. *Earthquake Engineering & Structural Dynamics, 41(12)*, 1709-1716.

Park, Y. J., Wen, Y. K., & Ang, A. H. S. (1986). Random vibration of hysteretic systems under bi-directional ground motions. *Earthquake engineering & structural dynamics, 14(4)*, 543-557.

PEER (2019). Pacific Earthquake Engineering Research Center. University of California, Berkeley, CA, USA.

Rajaram, C., & Kumar, R. P. (2012). Three dimensional modeling of pounding between adjacent buildings. In *Fourth international conference on structural stability and dynamics (ICSSD 2012), Malaviya National Institute of Technology, Jaipur & Texas A&M University, USA* (pp. 4-6).

Sadeghi-Movahhed, A., De Domenico, D., & Majdi, A. (2024). Structural flexibility impact on pounding severity and seismic performance of adjacent isolated buildings. *Soil Dynamics and Earthquake Engineering*, 181, 108667.

SAP2000 CSI (2020). Structural Analysis Program, Computers and Structures Inc., Berkeley, California, USA.

TBEC (2018). Specification for buildings to be built in seismic zones, Disaster and Emergency Presidency of Türkiye, TBEC Türkiye Building Earthquake Code, Ankara, Turkey.

TSHM (2018). Turkish Seismic Hazard Map. Republic of Türkiye Prime Ministry Disaster and Emergency Management Authory Presidential of Earthquake Department. Ankara, Türkiye.

UBC (1997). International building code. *International Code Council, USA*.
Wang, L. X., Chau, K. T., & Wei, X. X. (2009). Numerical simulations of nonlinear seismic torsional pounding between two single-story structures. *Advances in Structural Engineering, 12(1)*, 87-101.
Wen, Y. K. (1976). Method for random vibration of hysteretic systems. *Journal of the Engineering Mechanics Division, 102(2)*, 249-263.

4th International Civil Engineering & Architecture Conference
17-19 May 2025, Trabzon, Türkiye

Semi-automatic detection of unusable roads after an earthquake

Ömer Canözü[1], Hayrettin Acar*[2]

[1] Sivas Technical Sciences Vocational School, Cartography and Cadastre, Architecture and Urban Planning, Sivas, Turkey
[2] Karadeniz Technical University, Department of Geomatics, 61080 Trabzon, Türkiye

Abstract. After an earthquake, there is often significant loss of life and property. To minimize the loss of life, it is crucial to quickly reach the affected buildings and individuals. The planning of search and rescue operations or the transit times of aid convoys can vary depending on the condition of the roads after the earthquake. In city centers, where major destruction may occur, it is especially important to rapidly determine which roads are usable after the earthquake. Roads often become unusable due to cracks or collapses in areas intersecting fault lines or debris from collapsed buildings blocking the road. In this study, roads blocked and unusable by building debris after an earthquake were identified using a semi-automatic method. Since it is impossible to predict where and when earthquakes will occur, obtaining precise 3D data for all areas prior to an earthquake is not feasible. In this study, single-period point cloud data obtained from unmanned aerial vehicles were combined with building vector data from cadastral maps. The vectorial road data from cadastral maps were adapted for 3D analysis through algorithms developed. Thus, without the need for two-period LiDAR data, unusable roads after an earthquake were identified using single-period point cloud data and cadastral maps through 3D analyses.

Keywords: Earthquake; Unusable roads; Point Cloud

1. Introduction

Earthquakes are unpredictable natural disasters that can cause severe destruction, particularly in regions with unplanned urban development. In such areas, the extent of damage is significantly greater, adversely affecting both human life and emergency response efforts. The damage caused by earthquakes is not limited to the collapse of buildings; debris from ruined structures often blocks roads, impeding access and delaying the arrival of search and rescue teams. For post-disaster response operations to be conducted effectively, it is essential to rapidly and accurately identify damaged infrastructure. In this context, information regarding whether roads are open or blocked plays a critical role in the planning and coordination of search and rescue missions. Remote sensing technologies have emerged as vital tools in disaster management, particularly for damage assessment following earthquakes. Commonly used data sources include satellite imagery, aerial photographs, orthophotos, SAR data, thermal imagery, LiDAR, and 3D point clouds. While multi-temporal analyses are prevalent in the literature, studies utilizing only single-epoch data for road blockage and damage detection remain limited. This gap underscores the necessity for the development of rapid and (semi-)automated systems, particularly in scenarios requiring urgent intervention.

This study focuses on the semi-automatic detection of earthquake-induced road blockages caused by collapsed building debris using single-epoch three-dimensional (3D) point cloud data. The proposed method aims to support the effective and timely deployment of search and rescue teams by facilitating the strategic planning of intervention routes. The literature demonstrates the widespread application of various technologies in identifying post-earthquake road blockages. These include deep learning, machine learning, image processing, LiDAR, radar, photogrammetry, and satellite imaging—all of which play significant roles in decision-making processes within disaster management. Notably, Hosseini et al. (2024) proposed a probabilistic model based on seismic parameters to assess road blockage and clearance time, while Muhammad et al. (2023) provided a comprehensive review of technologies used for detecting road obstacles post-disaster. Yu et al. (2022) introduced a Bayesian approach using data from the Haiti earthquake to estimate conditional probabilities of accessibility. Earthquake events critically reduce the functionality of urban road networks due to building collapses and infrastructure damage. Costa et al. (2020) analyzed pre-disaster road densities and post-disaster traffic impacts, emphasizing the importance of

* Corresponding author, E-mail: h_acar@ktu.edu.tr

https://doi.org/10.31462/icearc2025_ce_eqe_916

promptly clearing critical routes. Argyroudis et al. (2015) evaluated the systemic risk posed by building and bridge collapses on road infrastructure. Similarly, Moya et al. (2020) statistically analyzed factors affecting debris spread and its correlation with road blockages. In their study, LiDAR and aerial imagery were utilized to assess obstructed roads. LiDAR data, in particular, has proven to be a valuable resource for conducting 3D analyses of post-collapse road blockages. Seydi et al. (2019) employed CNN and multilayer perceptron (MLP) models to detect debris areas from LiDAR point clouds, enabling precise identification of structural damage on road networks.

High-resolution satellite imagery has become prominent in deep learning-based automatic damage assessment. For instance, Zhang et al. (2024) achieved a 76.09% F1 score using their segmentation network, RDSeg, which outperformed CNN and transformer models. ViT-B and ResNet-18 integration allowed for pixel-based road damage detection. Doğan et al. (2022) proposed a CNN-based model for detecting road cracks on the Crack500 dataset, while Cheng et al. (2019) attained 94.89% accuracy using a CNN with the Gai-ReLU activation function. The integration of satellite imagery with vector data has also proven to be an effective strategy for detecting road damage. For example, Rastiveis et al. (2015) generated damage maps using WorldView II imagery and vector maps, and Zhao et al. (2022) applied the TLD algorithm for identifying damaged roads from remote sensing images. Chen et al. (2018) overlaid UAV images with vector roads, extracted buffered road zones, and applied object-based classification.

The use of autonomous systems and Edge AI technologies for real-time, automated road damage detection is becoming increasingly widespread. Bibi et al. (2021) developed a system for autonomous vehicles to detect and share road anomalies such as potholes, cracks, and speed bumps, achieving over 99% classification accuracy using ResNet-18 and VGG-11. Kizdarbekova et al. (2015) proposed a CNN-based method capable of detecting road damage under varying environmental conditions, highlighting the limitations of vision-only systems due to spectral variability and time constraints. Hence, the inclusion of sensor data such as LiDAR is suggested to enhance accuracy.

Deep learning and machine learning algorithms have achieved high accuracy in classifying road cracks. Reis et al. (2024) used ResNet152 for feature extraction from post-earthquake images, reaching 98.68% accuracy with SVM and EL classifiers. Alqethami et al. (2020) introduced the RoadNet CNN model, achieving 98.6% accuracy and outperforming AlexNet, VGG-16, and ResNet-34, although the study highlighted generalizability issues due to limited datasets. Optimized image processing and machine learning methods are employed to distinguish and classify different types of road cracks. Hoang et al. (2022) classified asphalt surface cracks with 91.33% and 92.83% accuracy using the Salp Swarm Algorithm and multi-class SVM. Fang et al. (2023) generated crack density maps using NSCT and classified them with SVM, achieving an F1 score above 85%. However, the cost and computational demands of high-resolution imagery were noted as challenges. The success of deep learning methods is highly dependent on data quality and accurate labeling. Rill-García et al. (2022) emphasized the impact of annotation errors on F1 scores and proposed the Syncrack dataset to address this issue. The U-VGG19 model highlighted the benefits of self-supervised learning and 5-neighbor voting techniques. In addition to AI systems, IoT sensors have also demonstrated efficacy in detecting road cracks post-earthquake. Ma et al. (2023) analyzed low-frequency vibration signals generated by vehicles, achieving 93.3%–96.7% accuracy using LR, SVM, and RFC classifiers.

Several studies have focused solely on detecting road damage using image data. These approaches aim to establish continuous monitoring mechanisms by identifying surface irregularities. However, their accuracy often varies depending on the study area, time frame, and data type. Image-based, deep learning approaches typically require extensive datasets, which makes training time-consuming for each new area of study.

In the proposed study, a novel approach focusing on 3D geometric deformations is introduced for detecting roads rendered unusable by earthquakes. By integrating cadastral data of collapsed buildings, a semi-automatic method has been developed to accurately identify roads affected by debris. The method relies on pre-disaster base maps and post-disaster 3D point cloud data, which can be rapidly acquired using UAV technologies. Through joint analysis of post-collapse 3D point clouds with vector data of roads and buildings, the extent and direction of debris spread are calculated, and obstructed road segments are identified. The resulting road damage map enables search and rescue teams to plan optimal intervention routes, shortening response times and enhancing the effectiveness of rescue operations. This method not only provides significant time and resource savings but also aims to reduce casualties, facilitate logistics, and improve coordination during crises. Moreover, it contributes to post-disaster urban planning, environmental impact assessments, and efforts to strengthen community resilience.

2. Materials and methods

In the proposed method, a semi-automatic approach is employed to determine whether debris from collapsed buildings after an earthquake has blocked the roads. To implement this method, cadastral polygon data of collapsed buildings, road network data, and a post-earthquake three-dimensional photogrammetric point cloud are required. The study area is selected as Antakya, a district of Hatay province in Turkey, which was severely affected by the major earthquake on February 6, 2023, and is visually presented in Fig. 1. The historical texture of Antakya and its dense, adjacent construction style have led to the prevalence of narrow streets. This condition significantly increases the risk of road blockage due to falling debris during the earthquake.

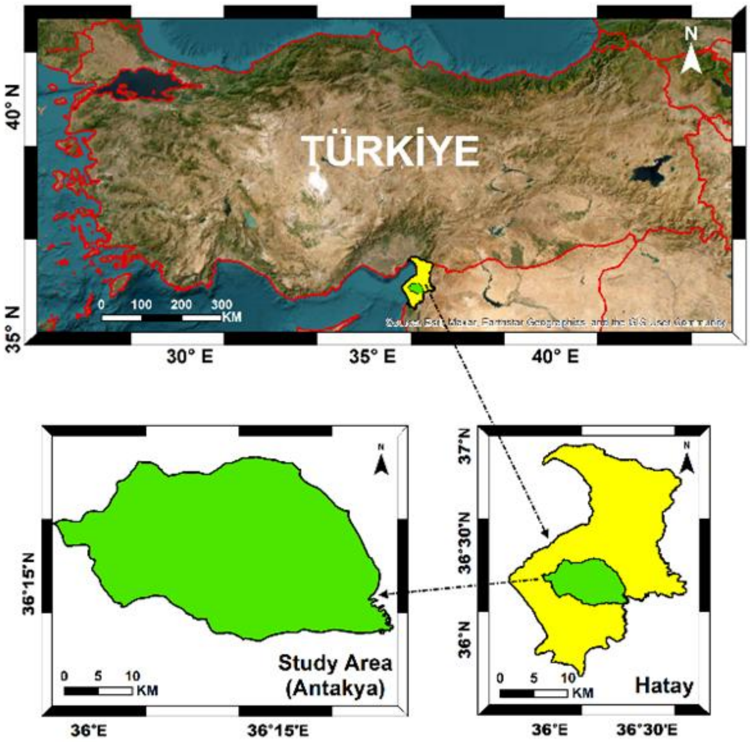

Fig. 1. Study area

The study area covers a 64-hectare region that includes roads of varying widths. This area contains a three-dimensional photogrammetric point cloud obtained via an unmanned aerial vehicle (UAV), with an average density of 8 points/m². Additionally, up-to-date vector road data for the earthquake-affected region were acquired from OpenStreetMap (OSM). Furthermore, cadastral polygon data of collapsed buildings are also available. Fig. 2 illustrates the orthophoto generated from UAV imagery of the test site, overlaid with the collapsed building polygons and vector road data.

Fig. 2. Visualization of collapsed building polygons and cadastral road data on the orthophoto

The effective management of post-earthquake disaster response processes depends on the rapid and accurate assessment of the extent of destruction. In particular, the condition of transportation infrastructure is critically important for the coordination of search, rescue, and relief operations. In this context, debris originating from collapsed buildings may scatter unpredictably depending on the direction of collapse, leading to road blockages and hindering emergency response efforts.

The main objective of this study is to identify roads blocked by debris by estimating both the amount and direction of debris generated by collapsed buildings. To this end, the amount of debris produced by a collapsed building was first determined. Simultaneously, the direction in which the debris was distributed and the spread width were also identified. Costa et al. (2020) developed a manually applied method to estimate how much debris a building could produce and the approximate extent of its spread. In this method, the debris spread width is calculated manually based solely on the total amount of debris a building could generate, without considering how many floors have collapsed.

In the proposed method, the varying collapse heights of individual buildings are taken into account. The corresponding values in the developed formula were automatically detected using software implemented in the MATLAB environment. The newly developed formula is presented in Equation (1).

$$\mathrm{Wd} = \sqrt{\bar{\mathrm{W}} - \frac{2*\mathrm{k_v}*\mathrm{Zh}}{\cot(\mathrm{c})}} - \bar{\mathrm{W}} \tag{1}$$

Wd = Debris spread width
Zh=Collapse height of the building
Zh=Collapse height of the building
$\bar{W}$=(W+L)/2
k_v=Collapsed volume ratio
c=Debris slope angle

The height loss (Zh) of each collapsed building was calculated by comparing the 3D building models derived from pre-earthquake cadastral data with post-earthquake point cloud data. The developed formula provided more accurate results by considering varying degrees of collapse for each building. The inclusion of Zh (collapse height) allowed for a more accurate calculation of the debris spread width by incorporating the collapsed portion rather than just the total building height. Additionally, the use of cot(c) models the debris spread width more realistically by taking the slope angle into account. As a result, Wd (debris spread width) was calculated to produce results that are consistent with physically meaningful field data. The final condition of a road completely blocked by debris from the collapse of two floors of a four-story building is shown in Fig. 3.

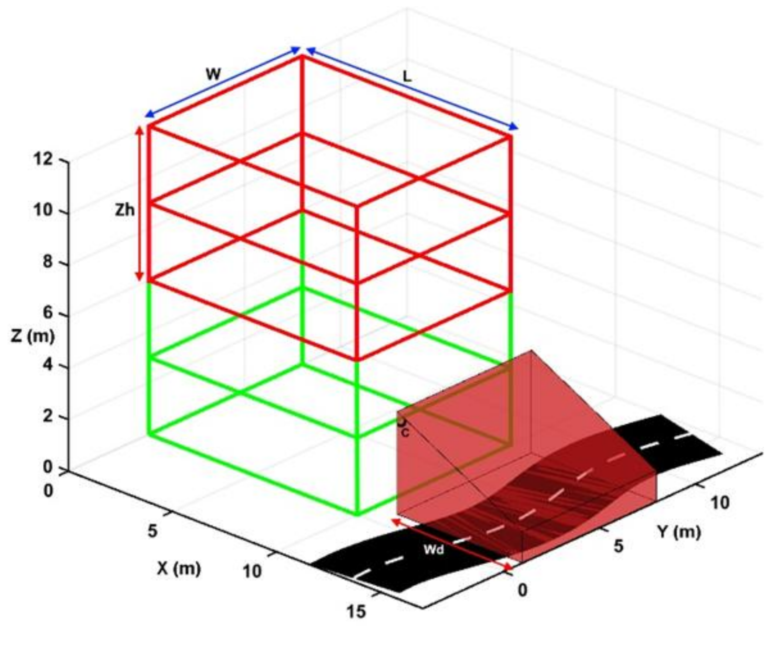

Fig. 3. Visualization of the debris spread width (Wd) of a building on the figure

Using the developed formula, the debris spread widths for each collapsed building in the study area were automatically calculated. This information is essential for detecting the direction of debris distribution and identifying the roads blocked by the debris. To determine the direction of debris distribution, three-dimensional buffer areas encompassing the polygon boundaries of the buildings were created. The 3D polygon buffer generated around a building's polygon boundary is shown in blue in Fig. 4. The building points concentrated within the buffer areas (in red) indicate the direction in which the debris has spread. Taking into account the debris distribution direction, the debris shift vector was automatically calculated. The 2D vector representing the debris spread direction for a collapsed building is shown with a yellow arrow in Figure 4. Thus, the direction of the debris spread from collapsed or heavily damaged buildings was determined.

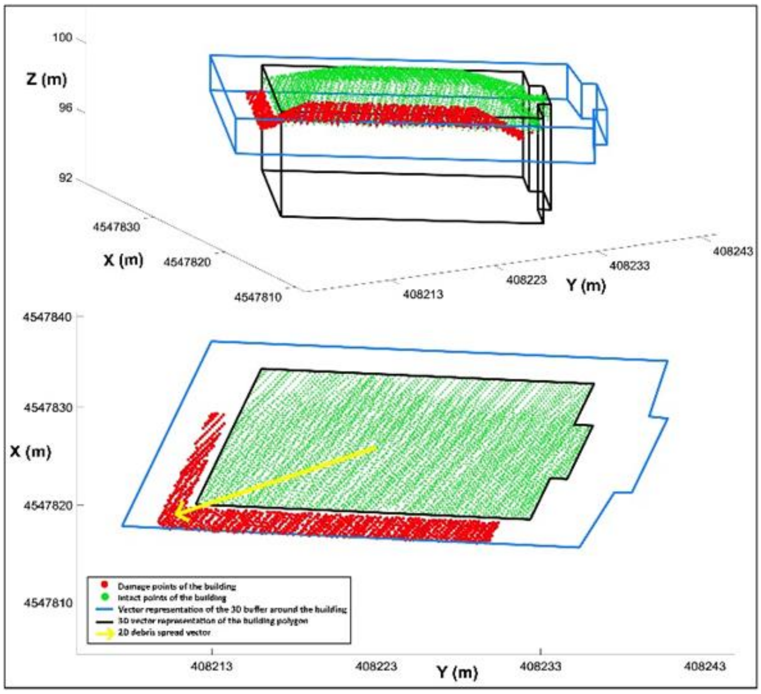

Fig. 4. 3D buffer generated around the building and the debris spread vector

The direction in which the debris from collapsed buildings after the earthquake spreads clearly shows the impact of the destruction on the surrounding area and the areas affected by the debris. Additionally, the total volume of the debris is as important as the direction of its spread. Based on the volume of debris, the spread width of the debris was calculated according to the values given in Equation 1. For each building, debris spread vectors were generated based on the direction and width of the spread. However, in some severely damaged buildings, the debris did not extend beyond the building polygon. In such cases, the magnitude of the debris spread vector was calculated as zero. The debris spread vectors, with non-zero magnitude, generated for each building in the study area are shown with yellow arrows in Fig. 5.

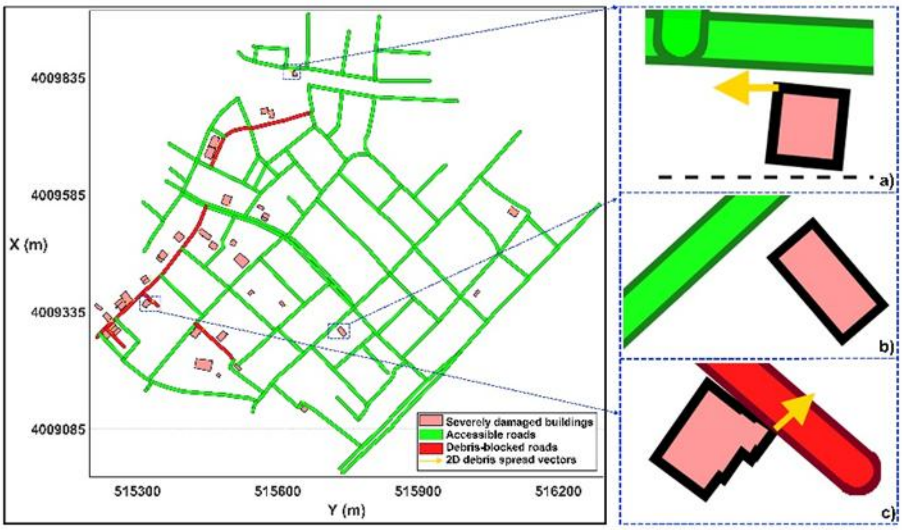

Fig. 5. Visualization of roads blocked by debris from collapsed buildings (red roads), **a)** Debris spread vector not overlapping with the road, **b)** Situation with zero-magnitude debris spread vector, **c)** Situation where debris vector blocks the road

In the study, debris spread vectors calculated for each building were combined with vector road data to analyze the road blockage due to debris. During the evaluation process, only building debris with a debris spread vector magnitude different from zero was considered. Additionally, cases where the debris spread vector did not intersect with roads providing access to the building prior to the earthquake were excluded from the analysis. This ensured that debris vectors from buildings that were located in the opposite direction of the road and did not have the possibility of intersecting with the road line were not included in the evaluation. For every building debris, excluding such cases, the potential for the debris vector to block the nearest road was first assessed. Once the road with the potential for blockage was identified, the level of road blockage was determined based on the length of the debris spread vector. In the study, points that obstruct road areas, based on cadastral polygons, were identified using a semi-automatic method. At these points, the spread of debris from the building along the road was examined, and road status analysis was performed considering the debris points along the road. In this way, roads that were fully, partially, or not blocked at all were classified, and road points completely blocked to traffic were detected semi-automatically with high spatial accuracy. These points were mapped in a geographic information system (GIS) environment, visualized, and made available for intervention planning.

3. Result and discussion

In the proposed study, road points blocked by the debris of collapsed buildings after the earthquake were identified using a semi-automatic method based on the direction and width of debris spread. This approach not only enhances the accuracy of spatial analyses but also provides significant contributions to search-and-rescue teams operating in the field. The pre-identification of areas that are inaccessible due to debris allows teams to quickly and effectively plan the most optimal intervention routes. This, in turn, provides a significant advantage in disaster response, where time is critical, ensuring faster access to survivors and contributing to the protection of human life.

During some stages of the study, various issues were encountered. One of these issues was the inclusion of objects outside the road when extracting the road area from the 3D point cloud due to the linear road data not fully reflecting the actual road centerline. This resulted in points outside the road being perceived as if they were on the road, leading to roads being incorrectly assessed as blocked. To overcome this issue, manual interventions were performed using updated satellite images to align certain road centerlines as closely as possible to the actual road centerline. In Fig. 6, the lines that incorrectly represented the road centerline are shown in red, while the correct road centerline is represented in blue. Thanks to the corrected road centerlines, the debris of collapsed structures on the roads after the earthquake was identified more accurately.

Fig. 6. Representation of the original road centerlines (red) and manual-corrected road centerlines (blue)

4. Conclusions

Rapid response and transportation in cities after a disaster are of great importance for the effectiveness of rescue operations. In natural disasters such as earthquakes, road closures can prevent rescue teams from reaching the affected areas in a timely and accurate manner. Especially, the rapid assessment of situations where debris from collapsed buildings causes road blockages is a critical requirement for effective intervention and rescue efforts.

In this context, the proposed study combines cadastral data and post-earthquake 3D point clouds to semi-automatically detect the road points blocked by the debris of collapsed buildings. For this study, post-disaster 3D point clouds of Antakya city center were used. The 3D point cloud produced from aerial images obtained by UAVs has RGB bands. In addition to this data, the study also integrated collapsed building polygons and linear road data into the algorithm. Using the developed algorithm, a debris spread vector was generated for each building. This vector shows the direction and magnitude of the debris from the collapsed building. Then, the presence of debris residue points on the road was detected according to the debris spread vectors. Finally, which road points would be blocked based on the direction and magnitude of the debris spread were semi-automatically detected. More accurate results will be obtained by improving the accuracy of linear road data or automatically correcting incorrect road centerline drawings. A road damage map was generated, showing the blocked roads due to 3D geometric changes after the earthquake. This map allows for the quick identification of areas where roads are impassable. The resulting map helps rescue teams determine the shortest and most optimal routes to reach the damaged and collapsed areas as quickly as possible.

Additionally, this data facilitates more effective and rapid planning of post-disaster intervention strategies, accelerating the rescue processes. Furthermore, determining preventive measures for future disasters provides an important foundation for minimizing potential damage. Such a map creation will be beneficial not only during the disaster but also in the post-disaster reconstruction and planning processes.

5. References

Alqethami, S., Alghamdi, S., Alsubait, T., & Alhakami, H. (2022). Roadnet: efficient model to detect and classify road damages. Applied Sciences, 12(22), 11529.

Argyroudis, S., Selva, J., Gehl, P., & Pitilakis, K. (2015). Systemic seismic risk assessment of road networks considering interactions with the built environment. Computer-Aided Civil and Infrastructure Engineering, 30(7), 524-540.

Bibi, R., Saeed, Y., Zeb, A., Ghazal, T. M., Rahman, T., Said, R. A., & Khan, M. A. (2021). Edge AI-Based Automated Detection and Classification of Road Anomalies in VANET Using Deep Learning. Computational intelligence and neuroscience, 2021(1), 6262194.

Chen, Z., Dou, A., (2018). Road damage extraction from post-earthquake uav images assisted by vector data. Int. Arch. Photogramm. Remote. Sens. Spat. Inf. Sci. 42, 211–216. https://doi.org/10.5194/isprs-archives-XLII-3-211-2018. Chen, L.-C., Zhu, Y., Papandreou.

Cheng, L., Zhang, X., & Shen, J. (2019). Road surface condition classification using deep learning. Journal of Visual Communication and Image Representation, 64, 102638.

Costa, C., Figueiredo, R., Silva, V., & Bazzurro, P. (2020). Application of open tools and datasets to probabilistic modeling of road traffic disruptions due to earthquake damage. Earthquake Engineering & Structural Dynamics, 49(12), 1236-1255.

Doğan, G., & Ergen, B. (2022). A new mobile convolutional neural network-based approach for pixel-wise road surface crack detection. Measurement, 195, 111119.

Fang, H., & He, N. (2023). Detection Method of Cracks in Expressway Asphalt Pavement Based on Digital Image Processing Technology. Applied Sciences, 13(22), 12270.

Hoang, N. D., Huynh, T. C., Tran, X. L., & Tran, V. D. (2022). A novel approach for detection of pavement crack and sealed crack using image processing and salp swarm algorithm optimized machine learning. Advances in Civil Engineering, 2022(1), 9193511.

Hosseini, Y., Mohammadi, R. K., Yang, T. Y. (2024). "A comprehensive approach in post-earthquake blockage prediction of urban road network and emergency resilience optimization", Reliability Engineering and System Safety, 244, 109887.

Kulambayev, B., Gleb, B., Katayev, N., Menglibay, I., & Momynkulov, Z. (2024). Real-Time Road Damage Detection System on Deep Learning Based Image Analysis. *International Journal of Advanced Computer Science & Applications*, *15*(9).

Ma, F., Wang, G., Hui, Y., Sun, R., Li, C., & Mao, G. (2023). Roadside IoT Sensor-Based Crack Detection for Smart Roads. In 2023 IEEE 98th Vehicular Technology Conference (VTC2023-Fall) (pp. 1-6). IEEE.

Moya, L., Mas, E., Yamazaki, F., Liu, W., Koshimura, S. 2020. "Statistical analysis of earthquake debris extent from wood-frame buildings and its use in road networks in Japan. Earthquake Spectra", 36(1), 209-231.

Muhammad, A. S., You, J., He, X., Chen, L., Wang, C. (2023). "Sensing Road Obstacles After Natural Disasters: A Survey", In 2023 International Conference on Artificial Intelligence of Things and Systems (AIoTSys), pp. 105-109, IEEE.

Rastiveis, H., Hosseini-Zirdoo, E., Eslamizade, F. (2015). "Automatic blocked roads assessment after earthquake using high resolution satellite imagery", The International Archives of the Photogrammetry, Remote Sensing and Spatial Information Sciences, 40, 601-605.

Reis, H. C., Turk, V., Karacur, S., & Kurt, A. M. (2024). Integration of a CNN-based model and ensemble learning for detecting post-earthquake road cracks with deep features. In Structures (Vol. 62, p. 106179). Elsevier.

Rill-García, R., Dokládalová, E., & Dokládal, P. (2022). Pixel-accurate road crack detection in presence of inaccurate annotations. Neurocomputing, 480, 1-13.

Seydi, S. T., Rastiveis, H. (2019). "A deep learning framework for roads network damage assessment using post-earthquake LiDAR data", The International Archives of the Photogrammetry, Remote Sensing and Spatial Information Sciences, 42, 955-961.

Yu, Y. C., Gardoni, P. (2022). "Predicting road blockage due to building damage following earthquakes", Reliability Engineering and System Safety, 219, 108220.

Zhang, S., He, X., Xue, B., Wu, T., Ren, K., & Zhao, T. (2024). Segment-anything embedding for pixel-level road damage extraction using high-resolution satellite images. International Journal of Applied Earth Observation and Geoinformation, 131, 103985.

Zhao, K., Liu, J., Wang, Q., Wu, X., & Tu, J. (2022). Road damage detection from post-disaster high-resolution remote sensing images based on tld framework. IEEE Access, 10, 43552-43561.

4th International Civil Engineering & Architecture Conference
17-19 May 2025, Trabzon, Türkiye

Evolution of post-earthquake damage assessment forms: practices and new developments in Turkey

Yelda Yerli[1], Mehmet Mehdi Karakoç[2], Tuba Demir[1], Bahar Demirel[*1], Fatih Özkaynak[3]

[1] *Fırat University, Department of Civil Engineering, 23119 Elazığ, Türkiye*
[2] *Ağrı İbrahim Çeçen University, Department of Computer Programming, 04100 Ağrı, Türkiye*
[3] *Fırat University, Department of Software Engineering, 23119 Elazığ, Türkiye*

Abstract.

Purpose: This study aims to examine the historical development, current practices, and future improvement strategies of post-earthquake damage assessment forms used in Turkey. The purpose is to evaluate their role in disaster management and to provide recommendations for their digital transformation and standardization.Study design/methodology/approach: A qualitative document analysis was conducted, supported by an expert-based survey developed under a TÜBİTAK 1001 project. The study reviews national disaster experiences from 1999 to 2023, analyzes official forms issued by AFAD, and integrates insights from professionals who have actively participated in field damage assessments. Findings: The findings reveal that although standardized damage assessment forms have significantly contributed to improving disaster response, challenges such as limited digital integration, inconsistent interpretations, and lack of sufficient training persist. The study highlights the benefits of adopting digital tools, AI-supported analysis methods, and blockchain-based validation systems. A national damage database is proposed to enhance long-term resilience and urban planning efforts. Originality/value: This paper offers a comprehensive evaluation of Turkey's post-disaster form-based assessment system, bringing together technical analysis and field practitioner feedback for the first time. It contributes original recommendations for technological integration and policy-making in disaster risk reduction.

Keywords: Mechanics; Damage assessment; Earthquake engineering; Disaster management; Digitalization; AFAD; Structural safety

---

1. Introduction

Turkey is one of the countries with the highest earthquake risk in the world due to its location on active fault lines. Throughout history, major earthquakes have not only resulted in loss of life and property damage but have also necessitated the continuous review of disaster management systems and response tools. Damage assessment studies conducted immediately after earthquakes play a critical role in accurately evaluating the impact of the disaster, ensuring public safety, and initiating the reconstruction process (Akdemir & İnan Günaydın, 2025). The standardized damage assessment forms used in this process enable the rapid and systematic documentation of the condition of structures.

These forms are structured to include various technical details, ranging from building types and observed cracks to foundation systems and soil characteristics. They serve not only as tools for collecting technical data but also as official documents that form the basis for social assistance, evacuation, resettlement, and legal processes. However, although these forms are intended to guide technical personnel in the field, challenges encountered during their implementation—such as data integrity issues, interpretation discrepancies, and lack of digital integration—can limit their effectiveness. Therefore, it is important to examine the implementation of damage assessment forms from past to present and to develop future-oriented recommendations for digitalization and standardization (Talaslıoğlu & Soyluk, 2024). This study addresses the historical development of damage assessment forms in Turkey, their field applications, and their contributions to disaster management processes. It also aims to highlight why these forms have become indispensable tools and to outline what needs to be done for a more effective system.

[*] Corresponding author, E-mail: bdemirel@firat.edu.tr

https://doi.org/10.31462/icearc2025_ce_eqe_918

2. History of damage assessment forms

The systematic implementation of damage assessment efforts in Turkey largely took shape after the 1999 Marmara Earthquake. This earthquake marked a turning point—not only due to the collapse of thousands of buildings but also because it exposed significant shortcomings in disaster management. Before 1999, damage assessments were typically carried out under the initiative of local authorities, often lacking sufficient technical standards and centralized coordination (Çatal, 2019). The forms used at that time were mostly non-standardized documents prepared by various institutions, containing data that was not comparable across regions or agencies (Özmen, 2023).

In the aftermath of the Marmara Earthquake, the use of standardized forms in damage assessment became mandatory. These forms were centrally regulated by institutions such as the Ministry of Environment and Urbanization and the Ministry of Public Works and Settlement (later AFAD). Definitions for damage classifications were also clarified, with four main categories established: minor damage, moderate damage, severe damage, and collapse. This classification enabled decisions on whether structures should be evacuated, reinforced, or demolished to be made on a more scientific basis. From the 2010s onward, various initiatives were introduced to digitize these forms so they could be filled out in the field using tablets or mobile devices (Maraş & Sarıyıldız, 2023). However, these digitalization efforts have not yet been widely and effectively adopted in all provinces. Nevertheless, this transition represents an important step toward collecting form data in centralized systems, enabling analysis, and building databases for future disasters. Finally, the earthquakes in Elazığ/2020 (Demirel et al., 2020), İzmir/2021, and Kahramanmaraş/2023 once again highlighted the critical role of damage assessment forms in the field (Avğın, Köse, & Özbek, 2024) (Aydoğdu Gürbüz & Aslan, 2023). Particularly in large-scale disasters, where thousands of buildings need to be evaluated simultaneously, the importance of standardization and a trained workforce has become even more evident.

3. Cuurent standards

Today, damage assessment efforts in Turkey are primarily conducted under the coordination of the Disaster and Emergency Management Authority (AFAD), and the forms used for these assessments are governed by specific standards. Technical teams deployed to the field immediately after an earthquake use these forms to systematically collect data on the overall condition of structures. These forms are critical for ensuring that damage classification and structural evaluations are carried out in a uniform and comparable manner across different regions. Fig. 1 illustrates the "Definitive Damage Assessment Form (Kesin Hasar Tespit Raporu)" currently in use by provincial AFAD directorates. The form includes detailed administrative information (e.g., GPS coordinates, building age, usage type), structural characteristics (e.g., construction system, material, number of stories), and observed damage categories (e.g., minor, moderate, severe, or collapsed).

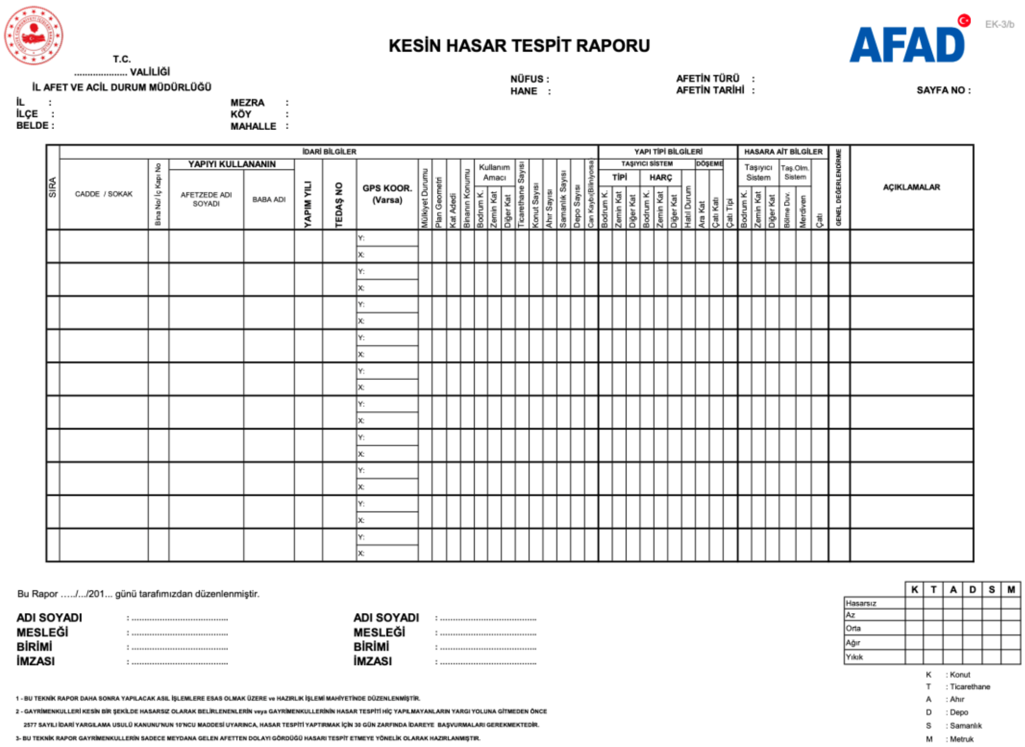

KESİN HASAR TESPİT RAPORU

AFAD EK-3/b

T.C.
.... VALİLİĞİ
İL AFET VE ACİL DURUM MÜDÜRLÜĞÜ

İL :
İLÇE :
BELDE :

MEZRA :
KÖY :
MAHALLE :

NÜFUS :
HANE :

AFETİN TÜRÜ :
AFETİN TARİHİ :

SAYFA NO :

İDARİ BİLGİLER: SIRA; CADDE / SOKAK; Bina No/ İç Kapı No; YAPIYI KULLANANIN: AFETZEDE ADI SOYADI, BABA ADI; YAPIM YILI; TEDAŞ NO; GPS KOOR. (Varsa) Y: X:; Mülkiyet Durumu; Plan Geometri; Kat Adedi; Binanın Konumu; Kullanım Amacı: Bodrum K., Zemin Kat, Diğer Kat; Ticarethane Sayısı; Konut Sayısı; Ahır Sayısı; Samanlık Sayısı; Depo Sayısı; Can Kaybı(Biliniyorsa)

YAPI TİPİ BİLGİLERİ: TAŞIYICI SİSTEM: TİPİ: Bodrum K., Zemin Kat, Diğer Kat; HARÇ: Bodrum K., Zemin Kat, Diğer Kat; Hatıl Durum; DÖŞEME: Ara Kat, Çatı Katı; Çatı Tipi

HASARA AİT BİLGİLER: Taşıyıcı Sistem: Bodrum K., Zemin Kat, Diğer Kat; Taş.Olm. Sistem: Bölme Duv., Merdiven; Çatı

GENEL DEĞERLENDİRME

AÇIKLAMALAR

Bu Rapor ...../.../201... günü tarafımızdan düzenlenmiştir.

ADI SOYADI : ....
MESLEĞİ : ....
BİRİMİ : ....
İMZASI : ....

ADI SOYADI : ....
MESLEĞİ : ....
BİRİMİ : ....
İMZASI : ....

	K	T	A	D	S	M
Hasarsız						
Az						
Orta						
Ağır						
Yıkık						

K : Konut
T : Ticarethane
A : Ahır
D : Depo
S : Samanlık
M : Metruk

1 - BU TEKNİK RAPOR DAHA SONRA YAPILACAK ASIL İŞLEMLERE ESAS OLMAK ÜZERE ve HAZIRLIK İŞLEMİ MAHİYETİNDE DÜZENLENMİŞTİR.
2 - GAYRİMENKULLERİ KESİN BİR ŞEKİLDE HASARSIZ OLARAK BELİRLENENLERİN veya GAYRİMENKULLERİNİN HASAR TESPİTİ HİÇ YAPILMAYANLARIN YARGI YOLUNA GİTMEDEN ÖNCE 2577 SAYILI İDARİ YARGILAMA USULÜ KANUNU'NUN 10'NCU MADDESİ UYARINCA, HASAR TESPİTİ YAPTIRMAK İÇİN 30 GÜN ZARFINDA İDAREYE BAŞVURMALARI GEREKMEKTEDİR.
3- BU TEKNİK RAPOR GAYRİMENKULLERİN SADECE MEYDANA GELEN AFETTEN DOLAYI GÖRDÜĞÜ HASARI TESPİT ETMEYE YÖNELİK OLARAK HAZIRLANMIŞTIR.

Fig. 1. General view of the definitive damage assessment report (Form EK-3/b) used by AFAD.

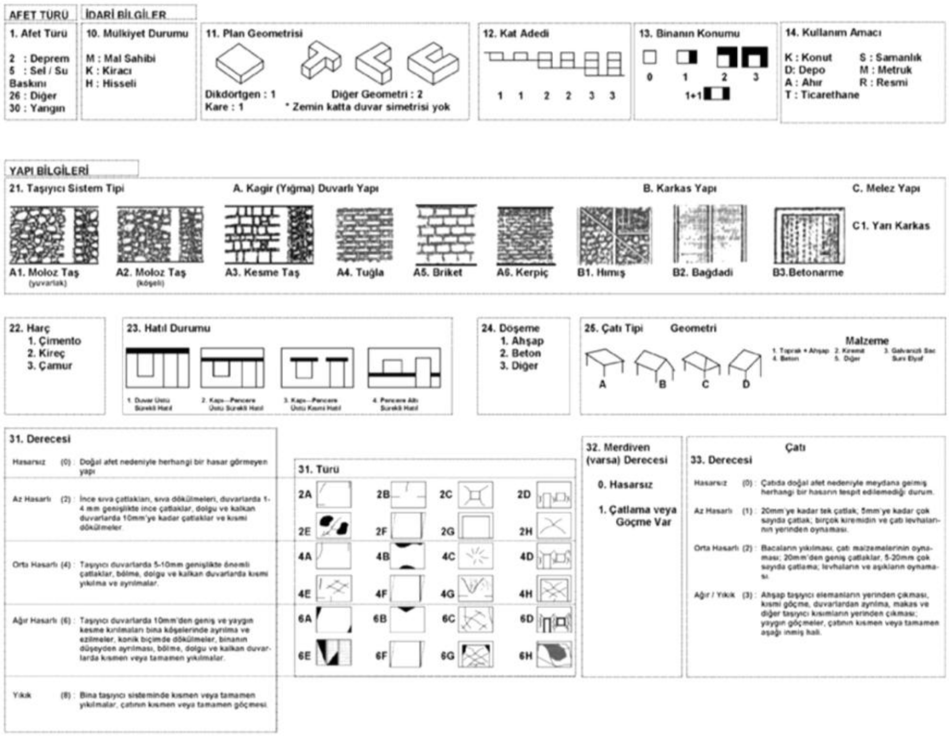

Fig. 2. Visual reference chart accompanying the damage assessment form, including symbols and classification guides.

Fig. 2 presents the visual legend and classification guide used to support the consistent and accurate completion of the damage form. It outlines key concepts such as structural systems (e.g., masonry, reinforced concrete, hybrid), damage severity levels, usage types, and roof/foundation configurations. These visual references help minimize interpretation differences among technical personnel working in the field and ensure that damage assessment decisions are made based on standardized criteria. The integration of such a standardized format with visual coding greatly contributes to the reliability of post-earthquake assessments and facilitates communication between technical teams and administrative decision-makers. The forms are completed based on on-site observations and are often accompanied by photographs and documentation. Once filled, the data is entered into digital systems and transferred to centralized databases (Özerol Özman, Arslan Selçuk, & Arslan, 2024).

The main data fields included in the damage assessment form are as follows:

- Building identification: Building address, structural type (reinforced concrete, masonry, timber, etc.), number of floors, usage type (residential, commercial, public building, etc.)
- Soil condition and foundation characteristics: Soil type, slope, signs of settlement
- Evaluation of structural damage: Cracks, separations, and crushing observed in load-bearing elements such as columns, beams, and shear walls
- Critical areas: Deformations in sensitive areas like stairwells, cantilevers, and soft stories
- Observational notes and photographs: Expert comments and visual documentation provided by the assessor

At the end of the form, the structure is classified according to the level of damage observed:

- Minor Damage: Damage that does not hinder usage and can be repaired with simple fixes
- Moderate Damage: Damage rendering the structure temporarily unusable but salvageable through strengthening
- Severe Damage: Damage posing a threat to life safety, requiring either demolition or comprehensive strengthening
- Collapsed: Complete structural failure or damage so extensive that reconstruction is required

These forms are typically completed in pairs by engineers in the field, submitted to local AFAD units, and then verified through a central system to be included in official decision-making processes. In recent years, completing these forms via mobile applications has significantly improved both the speed and accuracy of the process. Furthermore, the ability to instantly attach photos and automatically record GPS-based location data minimizes potential errors (Dondi et al., 2025). However, in some rural areas, paper-based forms are still preferred, leading to delays in data entry and challenges in data analysis. This situation highlights the need for the widespread adoption of digital systems across the entire country.

4. Challenges in practice and recommendations for improvement

Although post-earthquake damage assessment forms play a vital role in disaster management processes, various field challenges and systemic shortcomings sometimes limit their effectiveness (Feng et al., 2024). The issues encountered in practice manifest at different levels, including human resources, infrastructure, and operational processes.

- Insufficient and Irregularly Trained Personnel: In large-scale earthquakes, thousands of buildings must be assessed in a short period, and the number of engineers and technical staff available in the field is often inadequate. As a result, personnel are temporarily assigned from different institutions and cities; however, the lack of experience among these individuals in accurately and consistently completing damage assessment forms can lead to subjectivity and non-standard evaluations. Differences in knowledge and interpretation among teams may also result in varying damage classifications for the same building.
- Time Pressure and High Workload: The urgent need for rapid intervention immediately after a disaster forces field teams to work under significant time pressure. This can lead to evaluations being conducted without detailed inspection, increasing the risk of inaccurate decisions. Especially in rural areas or densely built-up zones with multi-story buildings, the need to assess multiple structures in a short time often results in superficial completion of the forms.
- Lack of Digitalization and Data Integration Issues: While mobile applications and digital systems have been introduced in some regions, these technologies have not yet become standardized across Turkey. The continued widespread use of paper forms leads to data loss, incorrect entries, and delays in processing data within centralized systems. Furthermore, the lack of full integration between form data and Geographic Information Systems (GIS) makes regional analyses more difficult.
- Lack of Supervision and Feedback: After the forms are completed in the field, there are not always sufficient mechanisms in place to verify the accuracy of the data through central units. This can result in erroneous assessments being detected too late or only after citizen complaints prompt a re-evaluation. Weak feedback processes also hinder the improvement and development of the teams working on-site.
- Citizen Appeals and Lack of Information: Inadequate communication with citizens regarding damage assessment results can lead to trust issues. Particularly in the classification of moderately and severely damaged buildings, the public's unfamiliarity with technical terms makes it difficult to understand the form content and contributes to an increase in objections. This, in turn, slows the process and adds extra burden on public institutions.

4.1. Recommendations for improvement

The integration of technological advancements into disaster management makes it possible to carry out post-earthquake processes more effectively, swiftly, and reliably. In this context, the digitalization of damage assessment forms is becoming one of the fundamental pillars of future disaster response efforts. Thanks to mobile applications developed in recent years, technical teams can directly enter structural information into the system using tablets or smartphones, and GPS-based location data and photos from the time of the event can be integrated into the form. Such digital systems facilitate the accurate and complete completion of the form while minimizing the risk of data loss. Moreover, since this data can be transmitted to central servers in real time, the overall scope of the disaster can be analyzed simultaneously, and intervention plans can be developed much more effectively. From a more advanced perspective, the automatic pre-analysis of damage-assessment photos using AI-supported image processing systems can reduce the workload of technical personnel and limit interpretation discrepancies. Additionally, recording damage assessment forms using blockchain-based systems would ensure both the immutability and the reliability of these documents—an aspect that is critically important for legal proceedings and insurance evaluations. Looking ahead, the creation of an integrated national damage assessment database across Turkey could enable past forms to be linked with geographic, structural, and demographic data. This would allow for both risk analyses and the maintenance of an up-to-date building inventory. Such an approach also holds the potential to guide urban transformation policies in a data-driven manner.

As part of this study, a survey is being conducted to enrich the findings with broader expert insights and to directly reflect the experiences of field practitioners. The survey in the Table 1 was developed under the TÜBİTAK 1001-funded project titled “Post-Disaster Damage Assessment Training Platform.” It aims to gather direct field feedback on the applicability, comprehensibility, and digital compatibility of current damage assessment forms.

Table 1. Summary of the Survey Questions for the Revision of Post-Earthquake Damage Assessment Forms

Question No.	Survey Question Summary
1	What is your professional background?
2	How many years have you participated in post-earthquake assessments?
3	How many assessments have you been involved in?
4	In which earthquakes have you conducted observational assessments?
5	Are the damage categories sufficient and clear?
6	Are HO and THO calculations practically applicable?
7	Is the HK2 coefficient calculation logical?
8	Which part of the form do you find most difficult?
9	Does using digital forms make your work easier?
10	Which features should be added to the digital forms?
11	Did you receive adequate training before using the forms?
12	What should training for proper use include?
13	Which area of the form should be revised most urgently?
14	What tools or equipment do you use and find most useful?
15	What are the top 3 challenges you face in the field?
16	How do you determine the critical floor in damage assessment?
17	How long does it take to assess a typical 5-story building?
18-20	Have you encountered issues in interpreting, processing, or receiving feedback on your assessments?
21	Rating of different aspects of the form (1–5 scale)
22	Others

5. Conclusions

Post-earthquake damage assessment forms are critical documents forming the foundation for both technical and administrative decisions in disaster management. These forms should be regarded as strategic tools that guide all aspects of life safety, social aid planning, legal processes, and reconstruction activities. Given Turkey's frequent exposure to major earthquakes, it is essential to continuously improve these forms in terms of both content and implementation. Accordingly, the following recommendations are presented as key takeaways from this study:

- The digitalization of damage assessment forms should be expanded nationwide and integrated with mobile applications.
- The training of technical personnel assigned to the field should be conducted regularly to enhance evaluation quality.
- Interpretation of forms should be standardized using AI-supported pre-analysis systems.
- Public information processes should be improved to strengthen public trust and increase transparency in appeal mechanisms.
- A national damage assessment database should be established to analyze data from past disasters and better predict future risks.

Expert opinions will provide significant contributions to improving the current form structure and aligning proposed digitalization processes with user needs. The findings will help ground our recommendations for making damage assessment processes more effective, transparent, and standardized. Ultimately, a well-designed and properly utilized damage assessment form is not just a sheet of paper—it is the cornerstone of critical decisions that directly affect the lives of thousands of people during a crisis. Therefore, these forms must be seen not merely as technical documents but as strategic guides in disaster management, and should be developed accordingly.

Acknowledgments

This study is supported by Scientific and Technological Research Council of Turkey (TUBITAK) with project number 223M417.

References

Akdemir, A., & İnan Günaydın, T. (2025). Türkiye deprem yönetmeliklerinin ve deprem haritalarının tarihçesi. Online Journal of Art and Design, 13.

Avğın, S., Köse, M. M., & Özbek, A. (2024). Damage assessment of structural and geotechnical damages in Kahramanmaraş during the February 6, 2023 earthquakes. *Engineering Science and Technology*, 57.

Aydoğdu Gürbüz, İ., & Aslan, B. (2023). Kahramanmaraş depreminde hasar tespit çalışmaları üzerine bir değerlendirme. *Çevre, Şehir ve İklim Dergisi, 4*, 180–195.

Çatal, H. H. (2019). Deprem sonrası düzenlenen hasar tespit formlarının kıyaslanması. In 3rd International Symposium on Innovative Approaches in Scientific Studies (Vol. 4, pp. 276–281).

Demirel, B., Alyamaç, K. E., Şahin, H., Açıkgenç Ulaş, M., Durucan, A. R., Durucan, C., Bildik, A. T., Demir, T., Ulucan, M., & Demirbaş, N. (2020). 24 Ocak 2020 MW 6.8 Sivrice Depremi Elazığ Bölgesi yapısal hasarlar inceleme ve değerlendirme raporu. Fırat Üniversitesi Yapı ve Beton Uygulama ve Araştırma Merkezi.

Dondi, P., Gullotti, A., Inchingolo, M., Casarotti, C., Lombardi, L., & Piastra, M. (2025). Post-earthquake structural damage detection with tunable semi-synthetic image generation. *Engineering Applications of Artificial Intelligence*, 147.

Feng, D.-C., Yi, X., Tuna Deger, Z., Liu, H.-K., Chen, S.-Z., & Wu, G. (2024). Rapid post-earthquake damage assessment of building portfolios through deep learning-based component-level image recognition. *Journal of Building Engineering*, 98.

Maraş, E. E., & Sarıyıldız, H. İ. (2023). İHA ile derin öğrenme algoritmaları kullanılarak hasarlı yapıların tespit edilmesi. *Afyon Kocatepe Üniversitesi Fen ve Mühendislik Bilimleri Dergisi, 23*, 427–437.

Özmen, B. (2023). Acil durum ve afet yönetimi planlarının tarihsel gelişimi. *Journal of Geological Engineering*, *47*, 165–181.

Özerol Özman, G., Arslan Selçuk, S., & Arslan, A. (2024). Image classification on post-earthquake damage assessment: A case of the 2023 Kahramanmaraş earthquake. *Engineering Science and Technology*, 56.

Talaslıoğlu, N., & Soyluk, A. (2024). FEMA P-154 formlarının dijitalleştirilmesi için bir Python tabanlı uygulama. *Journal of Architectural Sciences and Applications, 9*, 179–200.

ICEARC'25
4th International Civil Engineering & Architecture Conference
17-19 May 2025, Trabzon, Türkiye

Evaluating the structural impact of restoration in historical timber buildings with numerical modeling and analysis

Ebru Kalkan Okur*[1,2]

[1] *Karadeniz Technical University, Of Faculty of Technology, Department of Civil Engineering, Trabzon, Türkiye*
[2] *Earthquake and Structural Health Monitoring Research Center, Karadeniz Technical University, Trabzon 61080, Türkiye*

Abstract. Historical structures are not only architectural assets but also witnesses of past social and cultural heritage. These structures represent invaluable cultural values that must be preserved and transmitted to future generations. However, maintaining such structures without compromising their authenticity requires more than visual restoration; it also necessitates ensuring structural safety through engineering assessments. In this context, it is essential to determine whether restoration serves merely as an aesthetic intervention or provides actual structural improvement, which requires comprehensive engineering analyses. In this study, a three-dimensional finite element model of a registered timber building with a traditional bagdadi wall system, located within the urban conservation area of Alaçam District in Samsun, was developed. The structural performance of the building was evaluated under various loading scenarios, including live load, wind, snow, and seismic actions. Both ultimate limit state and serviceability limit state conditions were considered during the analysis, and the stress and displacement responses of the structural elements were assessed in accordance with standards. The results demonstrated that the structural components satisfy the required safety levels. This finding provides critical insight into the technical impact of restoration and guides necessary structural interventions. The study highlights the necessity of engineering analyses in the restoration process of historical structures and emphasizes the value of finite element modeling as a robust tool for evaluating the structural effectiveness of restoration efforts..

Keywords: Bağdadi wall; Cultural heritage; Finite element model; Timber structures; Urban conservation area

1. Introduction

Timber has historically held a prominent place in the construction of vernacular and monumental architecture due to its favorable mechanical properties, sustainability, and ease of workmanship. Especially in regions like Anatolia, the widespread availability of forests and the material's cultural compatibility have led to the development of diverse timber construction techniques, among which the bağdadi wall system stands out for its structural and architectural ingenuity. Timber buildings are not only examples of traditional building science but also represent living heritage, encapsulating the craftsmanship, social practices, and aesthetic preferences of their era (Cruz et al., 2015).

In the contemporary era, timber is also being revisited through the lens of sustainability. As a natural and renewable material with a low carbon footprint, timber structures are increasingly considered as part of climate-conscious design. Nevertheless, their organic nature makes them vulnerable to moisture, biological decay, temperature fluctuations, and most critically, to seismic and lateral forces over time. Historical timber buildings-many of which are protected under cultural heritage laws-require special attention in this regard. These structures often show signs of structural degradation such as deformation, loosening of joints, local collapses, and material fatigue due to prolonged exposure to environmental and mechanical loads (Riggio et al., 2018).

Restoration, in this context, becomes a critical tool not just for preserving the visual and historical identity of a structure, but also for ensuring its continued serviceability and safety. A well-executed restoration must not only reinstate damaged or missing architectural components but also provide an engineering basis to justify the building's static and dynamic stability. However, in practice, restoration projects are often dominated by architectural and material conservation concerns, while structural evaluation is either superficial or entirely overlooked. This discrepancy may lead to interventions that are aesthetically successful but structurally insufficient-posing future risks for users and the heritage asset itself.

* Corresponding author, E-mail: ebrukalkan@ktu.edu.tr

https://doi.org/10.31462/icearc2025_ce_eqe_936

golden light publishing

The literature includes various studies documenting the restoration of timber heritage buildings, often focusing on techniques of material conservation, detailing, and reuse of traditional joinery (Karacabeyli & Douglas, 2013). Yet relatively few of these works involve detailed structural modeling or computational analyses. Research has begun to emphasize the integration of numerical modeling in heritage conservation, underlining the need for advanced tools such as finite element analysis (FEA) to quantify the effectiveness of interventions (Altunışık et al., 2018; Altunışık et al., Kalkan Okur et al., 2021). These methodologies enable a more reliable assessment of existing structural performance and the impact of any restoration effort.

Motivated by this gap, the present study focuses on the structural analysis of a two-story registered timber building located in the urban conservation zone of Alaçam district in Samsun, Turkey. The building employs a bağdadi wall system composed of timber frames infilled with brick masonry, a typical Ottoman-era construction technique. A comprehensive three-dimensional finite element model of the structure was developed using SAP2000 software, in accordance with national (TBEC, 2018; Turkish Standards Institution, 2025) and international (TS EN 1995-1-1) codes. Structural behavior was assessed under vertical and lateral loads, including dead load, live load, snow, wind, and earthquake actions. Both ultimate limit state (ULS) and serviceability limit state (SLS) conditions were examined to evaluate element-level stresses, displacements, and structural adequacy.

This study not only provides a scientific basis for assessing the effectiveness of the ongoing restoration intervention but also contributes to the limited but growing body of literature on structural modeling of historical timber buildings. The results aim to guide future restorations by illustrating how engineering analyses can complement conservation decisions to achieve both heritage protection and structural resilience.

2. Timber structure with bagdadi wall system

2.1. Architectural properties

The historical timber structure slated for restoration is located in the district of Alaçam, Samsun, and consists of two floors constructed with the traditional bağdadi wall system. The ground floor accommodates a café area, entrance hall, central sofa space, kitchen, and restroom. The upper floor comprises two café spaces, a secondary sofa area, an additional restroom, and a storage room (Fig. 1). The rectangular plan of the structure measures 7.00 meters in width and 7.50 meters in length, with a floor area of 40.76 m² on the ground floor and 44.71 m² on the upper floor. The ground floor has a clear height of 3.3 meters, and the upper floor is 2.7 meters high, culminating in a total building height of +7.95 meters from the foundation to the ridge of the roof.

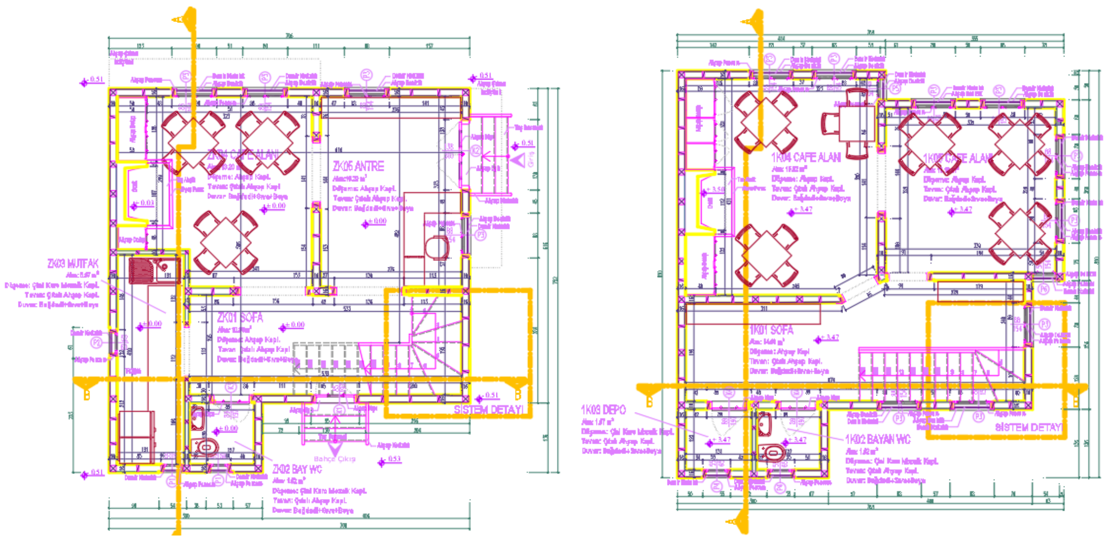

a) Ground floor plan

b) 1st floor plan

Fig. 1. Floor plans of timber structure

As shown in Fig. 2, the exterior elevations reflect the architectural identity of a typical bağdadi structure. The main load-bearing system is composed of solid timber vertical studs with cross-sectional dimensions of 4×12 cm and 12×12 cm, between which fired clay bricks (known as harman tuğlası) are infilled to form the bağdadi walls. These walls are further reinforced with 12×12 cm timber beams at both the top and bottom, ensuring horizontal continuity. Diagonal timber braces of the same dimensions are integrated within the wall cavities, providing additional stiffness by connecting the vertical members.

The interior partitions that separate the rooms are constructed from 2.5 cm thick timber planks, preserving the lightweight and modular character of the building. The flooring system consists of 4×12 cm timber joists spaced at 30 to 50 cm intervals, over which 2.5 cm thick timber decking is laid to form the finished surface. The roof employs a traditional timber hip-roof configuration, aligning with the building's historical typology. The structure rests on continuous strip footings beneath 12×12 cm timber foundation beams, ensuring proper load distribution to the ground.

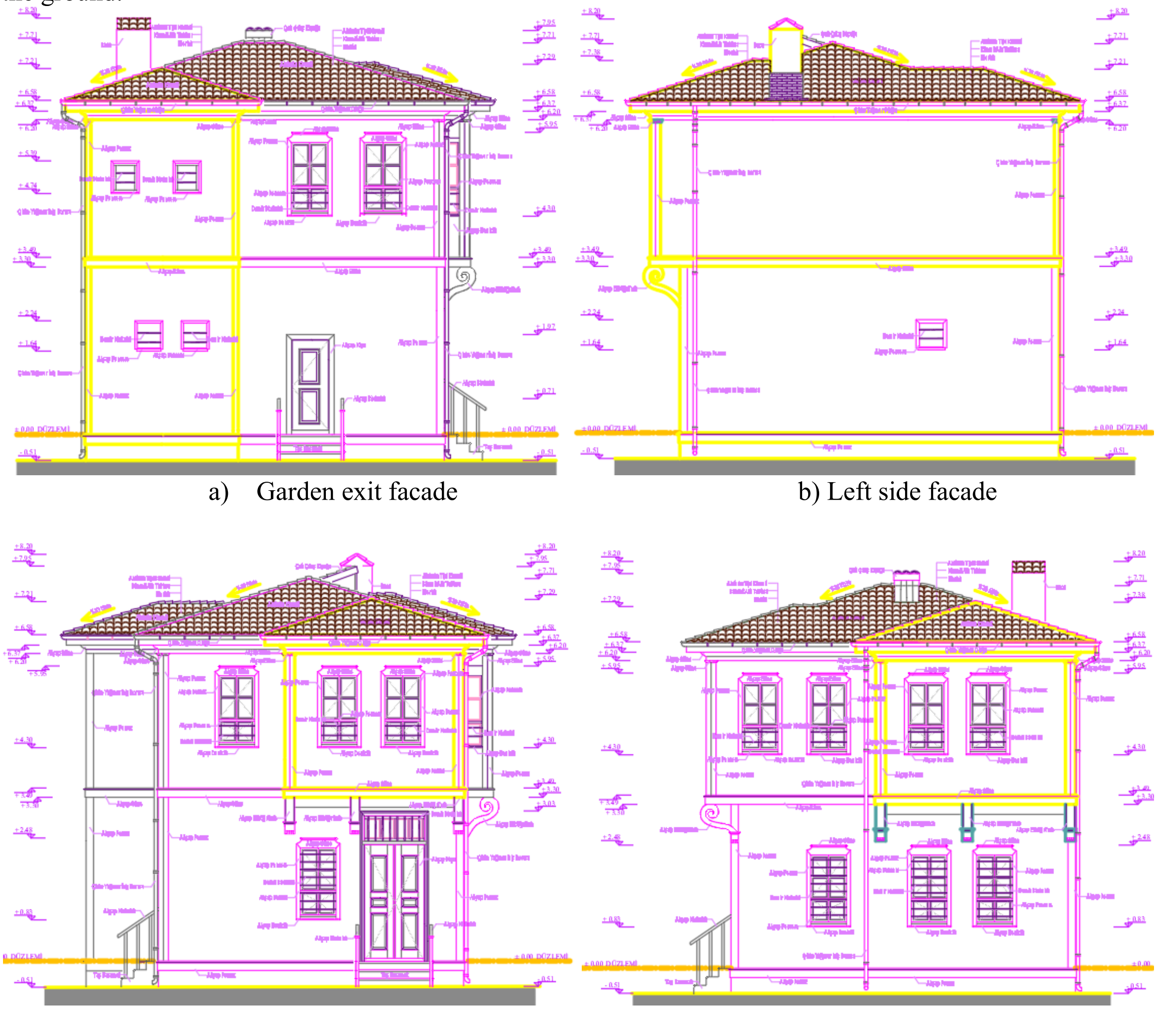

a) Garden exit facade

b) Left side facade

c) Right side facade

d) Rear facade

Fig. 2. Facade views of the wooden structure

Figure 3 illustrates a representative view of the proposed bağdadi wall detailing to be used during the restoration process, exemplifying both the material composition and the craftsmanship involved in traditional Anatolian timber architecture.

Fig. 3. Appearance of the bagdadi wall to be applied

2.2. Finite element model

The historical timber structure was modeled in three dimensions using the SAP2000 finite element software. In the model, key structural components such as timber foundation beams (hatıl), bağdadi wall studs, interior wall studs, main beams, secondary floor joists, and bağdadi-type diagonal members were represented as frame (bar) elements. All remaining wall infill and floor sheathing components were defined as shell (area) elements. All door and window openings observed in the architectural drawings were accurately reflected in the model geometry.

Given the structure's status as a registered cultural heritage asset, both the modeling and the analysis phases were carried out in accordance with the "Guidelines for Earthquake Risk Management for Historical Buildings" issued by the General Directorate of Foundations of Turkey. Section 6.4.5 of this guide, titled "Modeling Based on Construction Type," includes specific recommendations for timber structures. It emphasizes that vertical load-bearing elements in historic timber buildings typically consist of frames with studs and diagonals, while horizontal elements consist of beams and floor slabs. Furthermore, infill materials commonly used in timber walls-such as brick or adobe-should not be assumed to contribute to lateral load resistance. Therefore, only the timber members are considered in seismic analyses, and internal forces should be calculated based solely on the frame components. The adequacy of connection regions must also be assessed separately. Additionally, the guide allows for the use of simplified modeling approaches to facilitate structural assessment in complex historical systems.

In alignment with these principles, two separate models were developed for different loading scenarios. In the first model, both timber members and brick infill (harman tuğlası) were included. The infill material was modeled using shell elements to account for its contribution to vertical load distribution. This model was used to evaluate the structure's performance under gravity loads. For seismic analyses, a second model was created by excluding the shell elements representing the brick infill. This reduced model consisted only of timber studs, beams, and diagonal braces that form the core of the bağdadi structural system. To ensure mass continuity, the weight corresponding to the removed brick infill was distributed to the beams as additional line loads. Figures 4 and 5 illustrate the finite element representations of the first and second models, respectively.

To simplify the analysis of this complex historical structure, and as recommended by the aforementioned guideline, the intricate geometry of the roof system was not modeled in detail. Instead, the total weight of the roof elements, calculated based on their cross-sectional dimensions and material properties, was applied as equivalent loads to the supporting structural members. Structural verification of the roof system itself is beyond the scope of this report and was therefore not included in the modeling process.

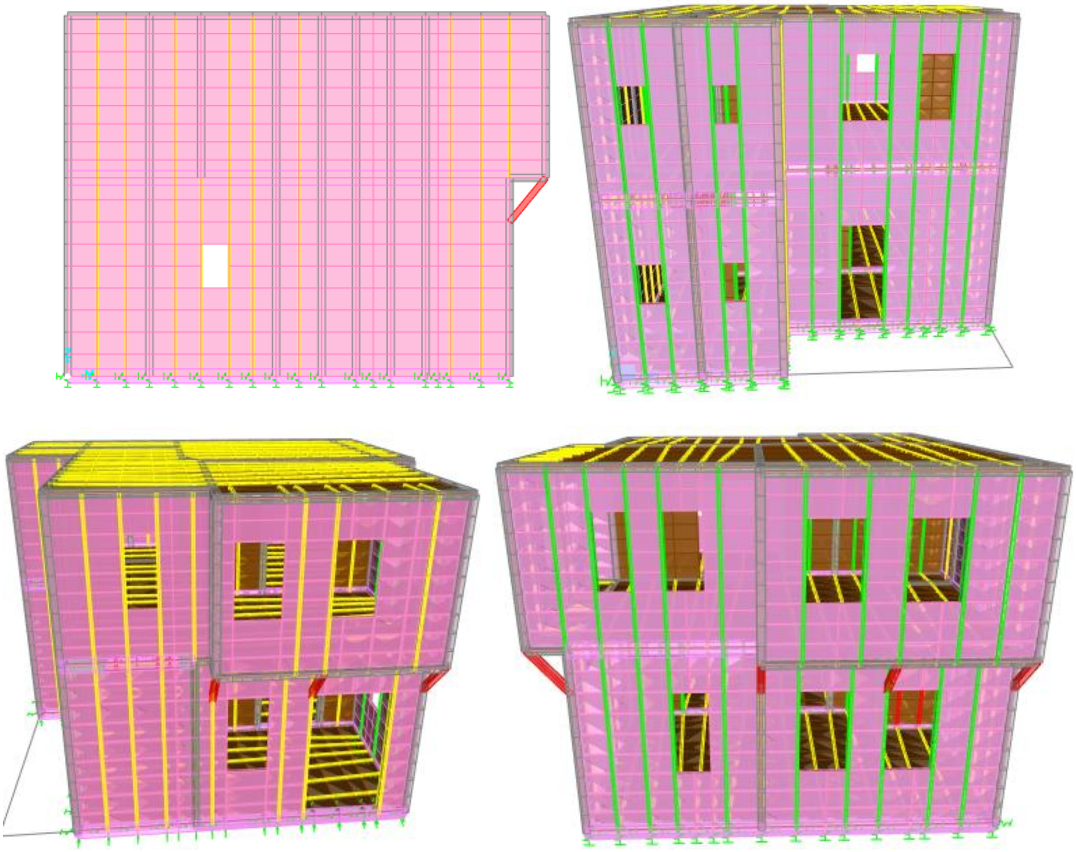

Fig. 4. Finite element model of the first model timber structure

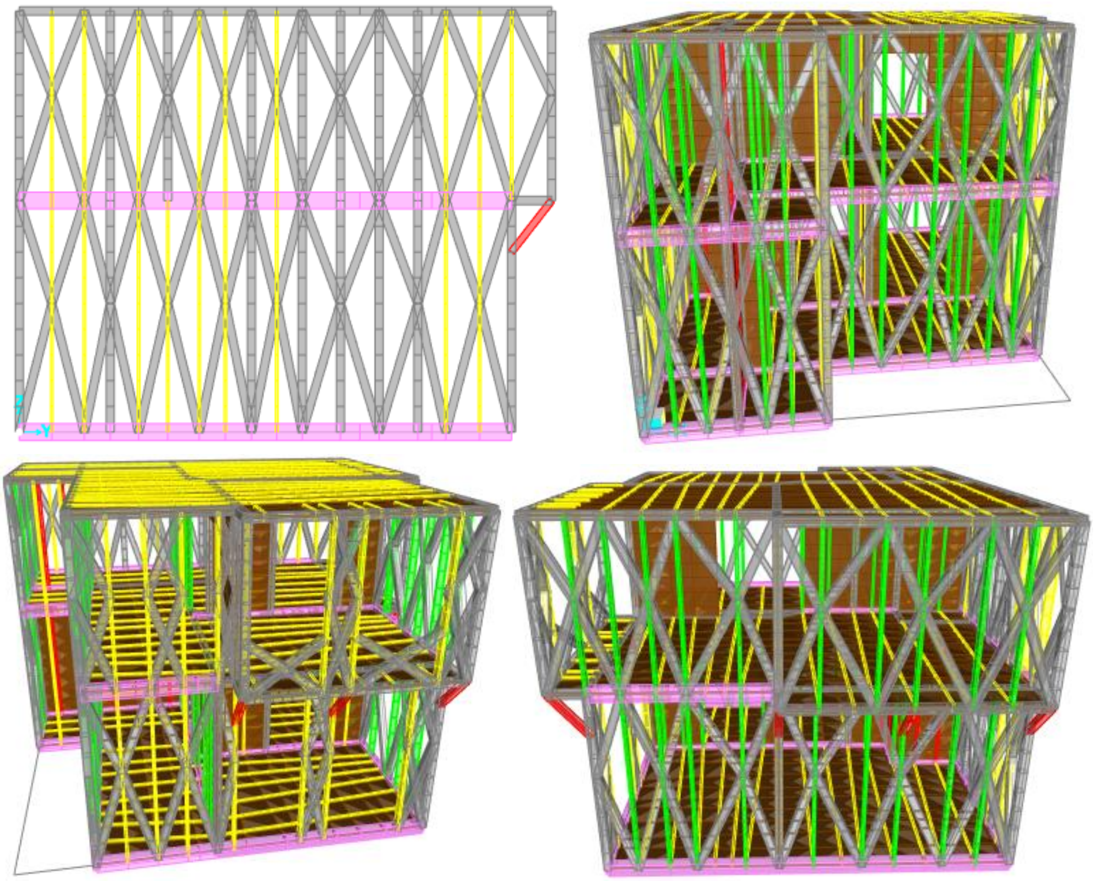

Fig. 5. Finite element model of the second model timber structure

2.3. Analysis parameters

Within the scope of the analysis, the strength classes and material properties of all structural timber elements were determined in accordance with the specifications outlined in TS EN 1995-1-1 (Eurocode 5). This standard classifies structural timber into two main groups and twenty distinct strength classes based on their mechanical performance. The classification is derived from a series of mechanical criteria, including bending strength, tensile strength parallel and perpendicular to the grain, compressive strength parallel and perpendicular to the grain, shear strength, modulus of elasticity parallel and perpendicular to the grain, shear modulus, and density.

Group C represents the softwood category, which includes commonly used species such as pine, fir, spruce, and cedar. Group D, on the other hand, consists of tropical hardwoods such as merbau, balau, and teak, typically found in Southeast Asia, Africa, and Australia.

For the purposes of this study, timber elements were modeled using the mechanical properties corresponding to the C22 strength class, which is suitable for softwood species commonly employed in traditional Anatolian timber structures. In SAP2000, these properties were assigned as an orthotropic material model to accurately simulate the anisotropic behavior of timber. All wooden members in the finite element model were assigned this C22 orthotropic material definition. In accordance with TS EN 1995-1-1, two primary limit states were considered in the structural design and evaluation process:

- Ultimate Limit State (ULS): Ensuring structural safety against collapse under maximum design loads.
- Serviceability Limit State (SLS): Verifying usability and limiting deformations under normal service loads.

Material properties were calculated separately for both limit states, and finite element analyses were conducted accordingly. Table 1 summarizes the material parameters used in the model under ULS and SLS design conditions.

Table 1. The material parameters for the model under ULS and SLS design conditions

Limit State	Design Elasticity Modulus (kN/mm^2)		Design Shear Modulus
	$E_{d//}$ (Parallel)	$E_{d\perp}$ (Perpendicular)	(G_d)
Ultimate	7.69	0.25	0.48
Serviceability	3.33	0.11	0.21

The determination of structural loads was carried out in accordance with the load calculation provisions of TS EN 1995-1-1, which governs the design of timber structures, and the EN 1991 series, which addresses environmental actions. According to TS EN 1995-1-1, the following Eurocode standards must be used to define the relevant loads and actions:

- EN 1991-1-1 (2025): Densities, self-weight, and imposed loads on structures
- EN 1991-1-3 (2007): Snow loads
- EN 1991-1-4 (2005): Wind actions

Seismic loading was determined based on the national standard TBDY 2018 (Turkish Building Earthquake Code 2018). The imposed roof load was taken as 1.25 kN/m², the live load as 5.00 kN/m², the snow load as 0.60 kN/m², and the wind load was calculated regionally based on wind directions, reaching a maximum of 0.98 kN/m². For the seismic load calculations, the design response spectrum was developed in compliance with TBDY 2018, using site-specific soil classification data provided in the geotechnical investigation report. The site was categorized as Soil Class ZD, and the spectrum parameters were obtained from the Turkish Earthquake Hazard Maps Interactive Web Application. Since the building is registered as a cultural heritage asset, the "Guidelines for Earthquake Risk Management for Historical Buildings" prepared by the General Directorate of Foundations was followed. Accordingly, the seismic action level was selected as DD-3, which corresponds to medium-intensity earthquake motion for Group II buildings with local cultural significance. Based on these parameters, the following design spectrum values were used:

- Short-period map spectral acceleration coefficient: SS = 0.154
- 1.0-second map spectral acceleration coefficient: S1 = 0.063
- Design spectral acceleration coefficient at short period: SDS = 0.246
- Design spectral acceleration coefficient at 1.0 second: SD1 = 0.151

In line with TBDY 2018 provisions, the structure was classified as follows:

- Building Height Class (BYS): 7
- Building Occupancy Class (BKS): 3
- Earthquake Design Class (DTS): 4
- Importance Factor (I): 1.0

Considering the structural configuration and lateral load-resisting system, the following response parameters were adopted:

- Structural Behavior Factor: $R_x = R_y = 4$
- Overstrength Factor: D = 2

Fig. 6 illustrates the applied load cases in the finite element model, while Fig. 7 presents detailed contour diagrams corresponding to the loading conditions applied during the analysis.

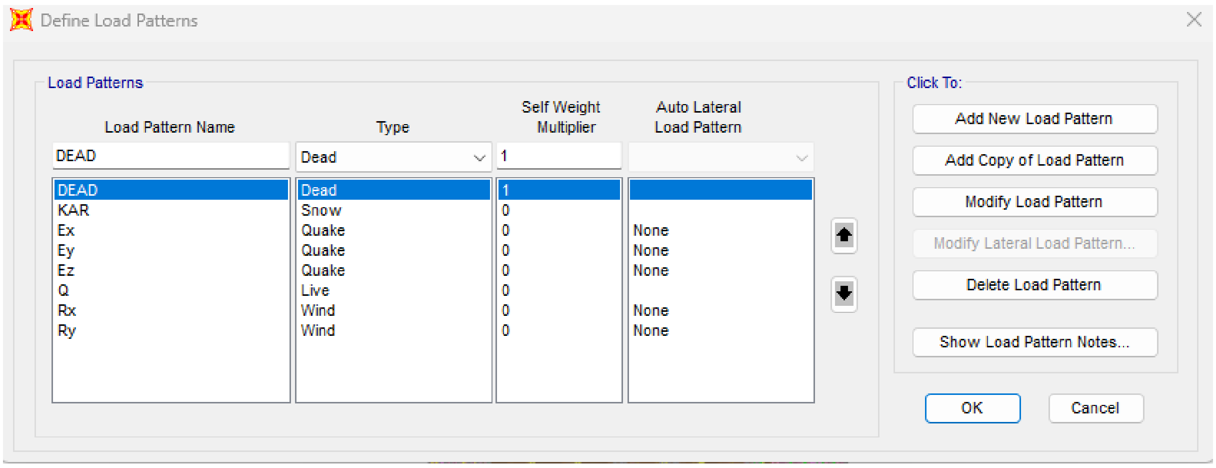

Fig. 5. Loading cases taken into account

Load combinations were generated in accordance with relevant standards for both ultimate limit state (ULS) and serviceability limit state (SLS) conditions, and these combinations were taken into account in the structural analyses under the applied loading scenarios.

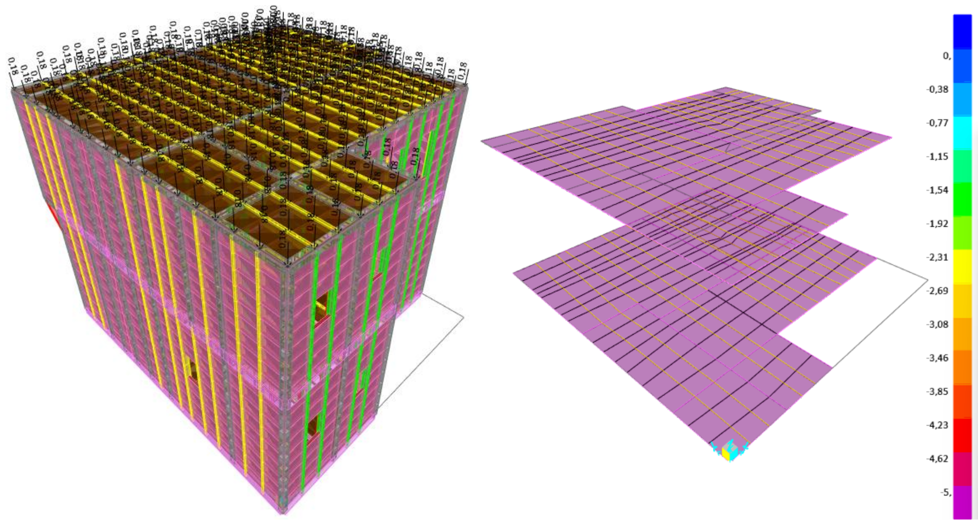

a) Roof load b) Live load

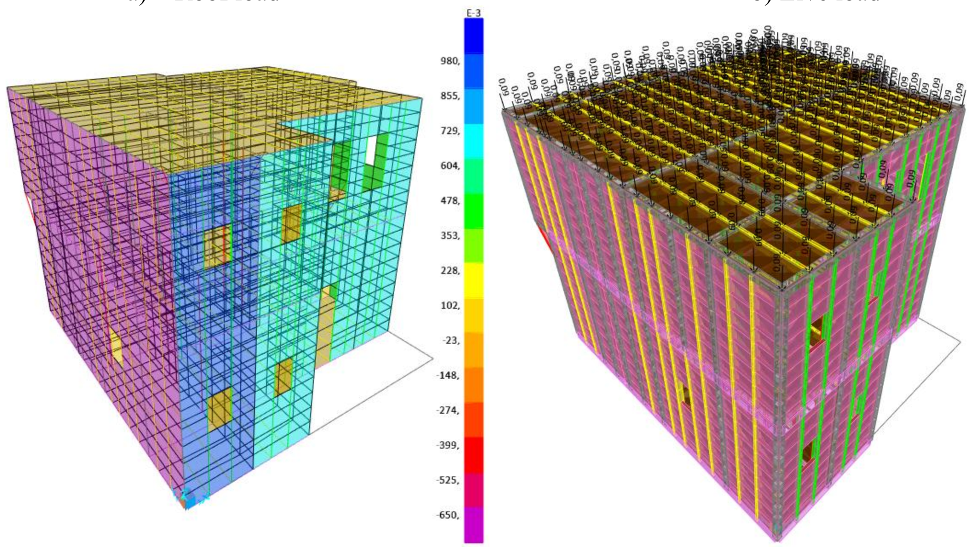

c) Wind load d) Snow load

Fig. 6. Contour diagrams of the loading conditions applied to the structure

2.4. Analysis

2.4.1. Modal Analysis

As a result of the modal analysis, the structural mode shapes and their corresponding natural frequencies were obtained. The mass participation ratios of the first 38 modes considered in the analysis are presented in Figure 7. The first mode, occurring in the Y-direction, has a period of 0.18 seconds (5.54 Hz) and a mass participation ratio of 34%. The second mode, in the X-direction, has a period of 0.16 seconds (6.24 Hz) with a 37% mass participation ratio. The third mode corresponds to a torsional mode with a period of 0.069 seconds (14.31 Hz) and contributes 28% to the total mass participation.

OutputCase	StepType Text	StepNum Unitless	Period Sec	UX Unitless	UY Unitless	UZ Unitless	SumUX Unitless	SumUY Unitless	SumUZ Unitless
MODAL	Mode	38	0,042409	3,779E-05	9,082E-05	2,085E-06	0,967	0,965	0,991
MODAL	Mode	35	0,046061	0,004962	0,014	0,001669	0,966	0,957	0,991
MODAL	Mode	36	0,044108	6,419E-05	0,005399	2,497E-05	0,966	0,962	0,991
MODAL	Mode	34	0,047128	0,086	0,016	0,001469	0,961	0,942	0,989
MODAL	Mode	33	0,047801	0,027	0,009958	0,001793	0,875	0,927	0,988
MODAL	Mode	32	0,048361	0,006173	0,093	0,0001713	0,848	0,917	0,986
MODAL	Mode	31	0,049237	0,006967	0,055	0,0009411	0,841	0,824	0,986

Fig. 7. The mass participation ratios of the first 38 modes

2.4.2. Static and dynamic analyses

The finite element analyses are conducted separately under three distinct models corresponding to ultimate limit state (ULS) and serviceability limit state (SLS) conditions. For the seismic evaluation under ULS, the model excluding the bağdadi infill walls was utilized, in accordance with the relevant guidelines. Envelope combinations are generated for both ULS and SLS by superimposing the respective load combinations to obtain the critical structural responses. The global distribution of displacements and internal forces under the maximum effect conditions derived from these analyses are presented in Figures 8 and 9.

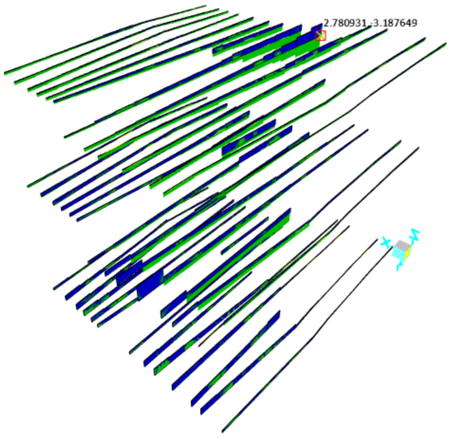

a) Normal forces in purlin elements (kN)

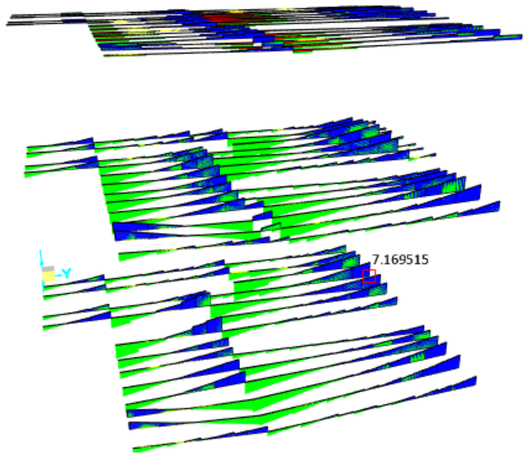

b) Shear forces in purlin elements (kN)

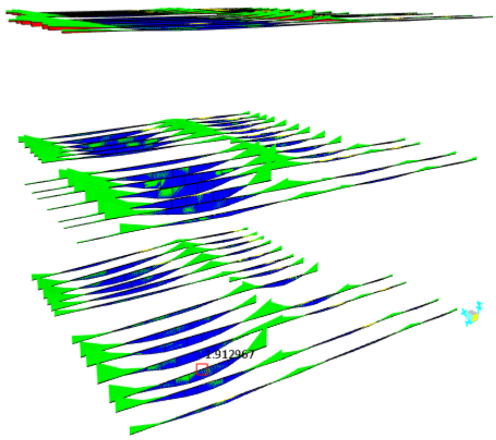

c) Bending moment in purlin elements (kN/m)

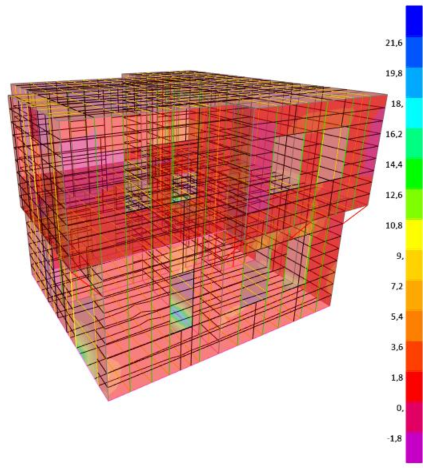

d) S11 stresses in area elements (N/mm^2)

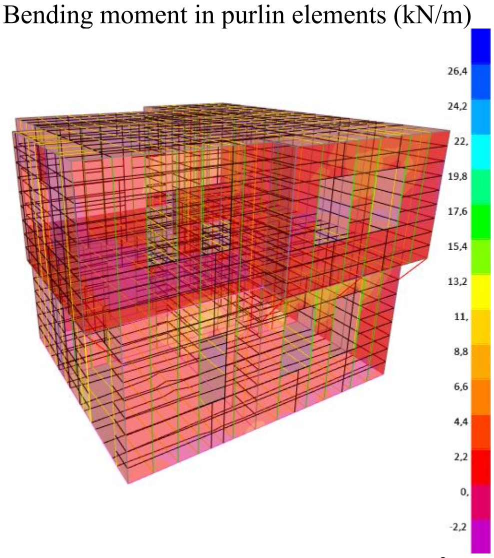

e) S11 stresses in area elements (N/mm^2)

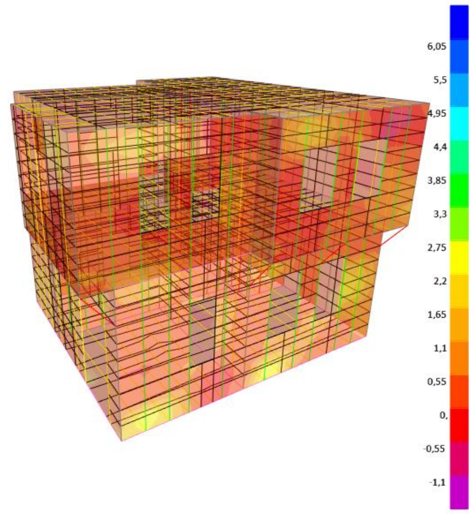

f) S11 stresses in area elements (N/mm^2)

Fig. 8. Analysis results of bearing capacity limit state

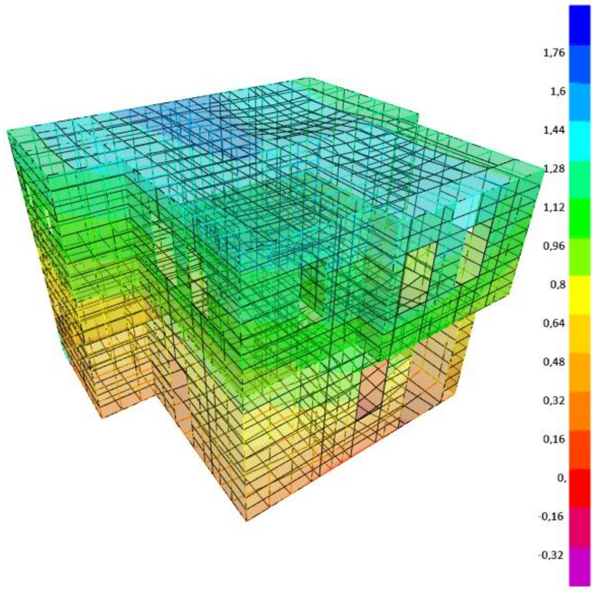

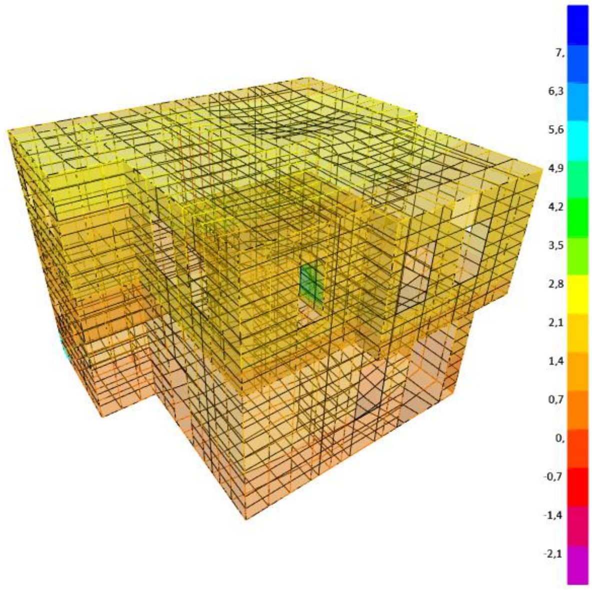

a) X direction displacement values (mm) b) Y direction displacement values (mm)

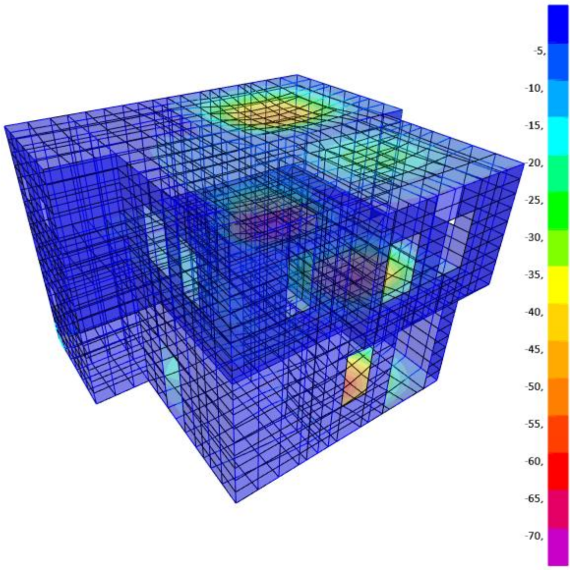

c) Z direction displacement values (mm)

Fig. 9. Analysis results of usability limit state

2.5. Verification

For the structural verification of the timber building, stress values obtained from the analysis were evaluated for key structural elements including columns (studs), beams, wall panels, and floor systems. These stress values were compared against the allowable design stresses of the selected C22 timber class, specifically for bending, tension (both parallel and perpendicular to the grain), compression (parallel and perpendicular to the grain), and shear. The maximum and minimum stress values observed in the shell (area) elements of the structure are comprehensively summarized in Table 2.

Table 2. Maximum and minimum stresses of area elements

Elements	Cross Section Area (mm)	Stresses occurring in Area Elements (N/mm^2)				
		S11	S22	S12	S13	S23
Interior Wall	25x100	1.70 / -1.76	0.25 / -0.28	0.90/ -1.31	0.03 / -0.03	0.005 / -0.002
Flooring	25x100	8.37 / -8.79	0.23 / -0.51	0.90 / -0.53	0.24 / -0.30	0.027 / -0.018

Table 2 presents the maximum and minimum stress values obtained from the structural analyses, considering all relevant load combinations. The maximum stress values generally occur under load cases involving live load, snow load, and wind actions. According to TS EN 1995-1-1, these effects are classified as short-term actions, and for solid timber elements, a modification factor k_{mod} of 0.7 is recommended for service class 3. For the C22 timber strength class, the allowable design stresses were obtained by multiplying the characteristic stresses by the corresponding k_{mod} factor. These adjusted design stress values, which were used for safety verification during the structural assessment, are summarized in Table 3.

Table 3. Alan elemanlara ait maksimum ve minimum gerilmeler

Timber Class	Bending	Tensile (Parallel to Fibers)	Tensile (Perpendicular to Fibers)	Compression (Parallel to Fibers)	Compression (Perpendicular to Fibers)	Shear
C22	15.4	9.1	0.28	14	1.68	2.66

The comparison of the obtained stresses with the allowable stresses is detailed in Tables 4 and 5.

Table 4. Verification of internal walls

Internal wall			Verification Result
S11	Tensile	1.70 < 9.1	Suitable
	Compression	1.76 < 14	Suitable
S22	Tensile	0.25< 0.28	Suitable
	Compression	0.28< 1.68	Suitable
S12 S13 S23	Tensile	0.90 < 2.66	Suitable
	Compression	1.31 < 2.66	Suitable

Table 5. Verification of floor

Internal wall			Verification Result
S11	Tensile	8.37 < 9.1	Suitable
	Compression	8.79 < 14	Suitable
S22	Tensile	0.23 < 0.28	Suitable
	Compression	0.51 < 1.68	Suitable
S12 S13 S23	Tensile	0.93 < 2.66	Suitable
	Compression	0.61 < 2.66	Suitable

In the finite element model, the timber studs, beams, and purlins modeled as frame elements were assessed through structural verification based on bending, shear force, and combined bending-stress calculations. The results of these checks indicated that all members satisfy the required safety criteria and exhibit adequate structural performance under the applied loading conditions.

3. Conclusions

This study presents a detailed structural assessment of a registered two-story timber building featuring a traditional bağdadi wall system, located within an urban conservation area in Samsun, Turkey. Through the development of a comprehensive three-dimensional finite element model and the application of various static and dynamic analyses, the study investigates the structural performance of the building under multiple loading scenarios, including gravity, snow, wind, and seismic effects.

- The analyses were carried out in accordance with national and international standards, particularly TS EN 1995-1-1 and TBEC 2018, and took into account both the Ultimate Limit State (ULS) and Serviceability Limit State (SLS) conditions.
- The results clearly indicate that the structural elements of the building possess sufficient strength and stiffness under all considered load combinations.
- These findings confirm that the restoration project not only contributes to the architectural preservation of the heritage asset but also ensures its structural reliability for future use.
- This underscores the critical role of engineering analysis in restoration processes, shifting the perception of such efforts from purely aesthetic interventions to technically reinforcements.

In conclusion, finite element modeling proves to be an essential tool for validating the effectiveness of restoration interventions in historical timber structures. The methodology and findings presented in this study may serve as a reference for similar heritage conservation projects, promoting a more integrated and performance-based approach in architectural preservation efforts.

References

Altunışık, A. C., Kalkan, E., Okur, F. Y., Karahasan, O. Ş., & Ozgan, K. (2019). Finite-element model updating and dynamic responses of reconstructed historical timber bridges using ambient vibration test results. *Journal of Performance ofConstructed Facilities, 34*(1), 04019085. https://doi.org/10.1061/(ASCE)CF.1943-5509.000134

Altunışık, A. C., Karahasan, O. Ş., Okur, F. Y., Kalkan, E., & Ozgan, K. (2018). Finite element model updating and dynamic analysis of a restored historical timber mosque based on ambient vibration tests. *Journal of Testing and Evaluation; 47*(5), 3533–3562. https://doi.org/10.1520/JTE20180122

Cruz, H., Yeomans, D., Tsakanika-Theohari, E., Babo, L., Machado, J. S., Costa, A., & Piazza, M. (2015). Guidelines for the on-site assessment of historic timber structures. *International Journal of Architectural Heritage, 9*(3), 277–289. https://doi.org/10.1080/15583058.2013.792256

Kalkan Okur, E., Altunışık, A. C., Okur, F. Y., Meral, M., Yılmaz, Z., Günaydın, M. & Genç, A. F. (2021). Dynamic response of a traditional himis, mansion using updated FE model with operational modal testing. *Journal of Building Engineering, 43*, 103060. https://doi.org/10.1016/j.jobe.2021.103060

Karacabeyli, E., & Douglas, B. (2013). *CLT Handbook: Cross-Laminated Timber*. FPInnovations.

Riggio, M., D'Alaya, D., Parisi, M. A., & Tardini, C. (2018). Assessment of heritage timber structures: Review of standards, guidelines and procedures. *Journal of Cultural Heritage, 31*, 220–235.

Turkish Building Earthquake Code (TBEC 2018). *Ministry of Environment and Urbanization.* Ankara, Turkey: Republic of Turkey Official Gazette.

Turkish Standards Institution. (2010). *TS EN 1995-1-1: Eurocode 5 – Design of timber structures – Part 1-1: General – Common rules and rules for buildings*. Ankara, Turkey: TSE.

Turkish Standards Institution. (2025). *Design, calculation and construction principles for timber buildings* (1st ed.). Ankara, Turkey: TSE.

Turkish Standards Institution. (2025). *TS EN 1991-1-1: Eurocode 1 – Actions on structures – Part 1-1: General actions – Densities, self-weight, imposed loads for buildings*. Ankara, Turkey: TSE.

Turkish Standards Institution. (2007). *TS EN 1991-1-3: Eurocode 1 – Actions on structures – Part 1-3: General actions – Snow loads*. Ankara, Turkey: TSE.

Turkish Standards Institution. (2005). *TS EN 1991-1-4: Eurocode 1 – Actions on structures – Part 1-4: General actions – Wind actions*. Ankara, Turkey: TSE.

4th International Civil Engineering & Architecture Conference
17-19 May 2025, Trabzon, Türkiye

Investigation of infill wall effects on structural behavior of RC buildings: a case study of collapsed building after the 2023 Kahramanmaraş Earthquakes

Doğa Şen*[1], Fezayil Sunca[2,3], Ahmet C. Altunişik [1,3]

[1] *Karadeniz Technical University, Department of Civil Engineering, 61080 Trabzon, Türkiye*
[2] *Karadeniz Technical University, Department of Construction Technologies, 61080 Trabzon, Türkiye*
[3] *Karadeniz Technical University, Earthquake and Structural Health Monitoring Research Center, 61080 Trabzon, Türkiye*

Abstract. During the design phase of structures and the evaluation of their seismic performance, it is commonly assumed that all loads acting on the structure are resisted by the primary structural elements, such as shear walls, columns, and beams. The contributions of non-structural elements, such as infill walls, to load resistance are generally neglected. However, research conducted on the structural behavior of RC buildings has demonstrated that infill walls play a critical role in key parameters such as stiffness, energy dissipation capacity, and seismic performance, thereby enhancing the overall load-carrying capacity. Neglecting the influence of infill walls on lateral stiffness and considering them merely as vertical loads during structural analysis may result in unexpected structural behavior under seismic loading. Therefore, in order to accurately evaluate the structural behavior of buildings, infill walls should be considered during the design and analysis phases. In this study, the nonlinear analyses of a RC building that collapsed during the 2023 Kahramanmaraş earthquakes were comparatively investigated for cases where the infill walls were considered and not considered. The finite element (FE) model of the building was created using the SAP2000 software. As a result of the analyses, the extent to which infill walls affected the structural behavior and structural responses (such as interstory drift ratios, modal parameters, base shear forces, and performance levels) of the collapsed building was investigated.

Keywords: RC building; Infill wall; Kahramanmaraş earthquakes; Nonlinear time history analysis (NTHA)

1. Introduction

During the design of structures and the evaluation of their seismic performance, it is generally assumed that all loads acting on the structure are resisted by structural system elements such as shear walls, columns, and beams. The contribution of non-structural elements, such as infill walls, to load resistance is often neglected, and the interaction between the structural system and the infill walls is not considered (Abdelaziz et al., 2019; Çavdar et al., 2020; Murty et al., 2000; Köse Sunca, 2019; Öztürkoğlu et al., 2017; Sattar et al., 2010; Tan et al., 2025; Wang et al., 2021). In addition, in the currently used structural design software packages, infill walls are considered only as vertical loads. Ignoring the contribution of infill walls to lateral stiffness may lead to unexpected damage and irregularities within the structure (Köse et al., 2007).

The results of recent studies have revealed that a significant portion of the loss of life and property during major earthquakes is caused by unexpected damage to infill walls (Smilordo et al., 2023). Therefore, in order to accurately determine the actual behavior of structures, infill walls must be considered during the design and analysis phases of buildings (Yakut et al., 2013; Köse Sunca, 2019). In the literature, there are numerous analytical and experimental studies investigating the interaction between the structural system and infill walls. Hashemi and Mosalam (2006), it was demonstrated that the presence of infill walls reduces both the natural period and the lateral displacements of the structure. Hasemi (2007) experimentally investigated the seismic performance of RC structures and revealed that the presence of infill walls is one of the most critical factors affecting performance. Kadysiewski and Mosalam (2009), through their analytical studies, demonstrated that infill walls not only increase the stiffness of the structural system but also enhance its damping capacity.

Sattar and Liel (2010) conducted a study comparing the collapse probabilities of frames with and without infill walls using nonlinear analysis methods, and found that frames containing infill walls exhibited greater lateral stiffness and improved seismic performance. Hermanns et al. (2013), based on observational studies conducted on

* Corresponding author, E-mail: senndoga@gmail.com

https://doi.org/10.31462/icearc2025_ce_eqe_946

two different buildings with varying numbers of stories following the 2011 Lorca earthquake, identified that infill walls, which are neglected during design, can lead to the formation of short columns in structures, resulting in sudden collapses. Ning et al. (2017) investigated the collapse mechanism of infill walls using different modeling approaches through static pushover tests. The analyses revealed that the presence of infill walls affects the locations of plastic hinges in structural elements. Öztürkoğlu et al. (2017) analytically examined the seismic performance of frames with and without infill walls, having different span lengths and numbers of stories, using nonlinear analyses. The results of the study demonstrated that the presence of infill walls significantly alters the behavior of the system. Baghi et al. (2018) compared the behaviors of RC frames with and without infill walls under static loading and demonstrated that infill walls significantly increase the load-carrying capacities. Özkaya (2018) investigated the effect of infill walls on the soft-story irregularity in buildings using different modeling approaches. As a result of the analyses, it was determined that soft-story irregularity occurred in the building modeled without infill walls, leading to the conclusion that infill wall design should not be neglected in structural analyses. Köse Sunca (2019) investigated the effects of infill walls placed at different ratios and configurations on seismic performance using the NTHA method. The study results indicated that increasing the proportion of infill walls substantially enhanced the structural stiffness, highlighting the necessity of accounting for the influence of infill walls on both vertical load resistance and lateral load-bearing capacity. Abdelaziz et al. (2019) investigated the seismic behavior of reinforced concrete buildings with varying story numbers through NTHA, focusing on different infill wall configurations. Their findings indicated that the presence of infill walls notably improved lateral stiffness and seismic performance. However, the removal of infill walls at the ground story created a discontinuity in stiffness, resulting in a soft-story irregularity that could critically compromise structural safety during earthquakes. Wang et al. (2021), in their experimental study, subjected bare and infilled frames to cyclic pushover tests. The experimental results demonstrated that infill walls increased the lateral load-carrying capacity and stiffness of the frame, while also enhancing its energy dissipation capacity; however, they were found to reduce the deformation performance. Usta et al. (2023) investigated the effect of infill walls on RC buildings under seismic loading by analyzing a model of a building that collapsed during the 2020 Düzce earthquake, both with and without infill walls. The analyses revealed that infill walls positively influenced characteristics such as the period of the structure, base shear force at the ground story, column load-carrying capacity, interstory drift ratio, and base shear force at the ground story, and that they increased the base shear force. Akbaş and Çalışkan (2024) evaluated the impact of infill walls on the stiffness, strength, and energy dissipation capacity of the structural system, emphasizing that this contribution is at a level that cannot be neglected, particularly under seismic loading. They also suggested that neglecting infill walls during the design and analysis process may lead to the formation of irregularities such as short columns, weak stories, and soft-story mechanisms within the structure. Tan et al. (2025) investigated the performance of a building that sustained severe damage during the 2023 Kahramanmaraş earthquake. In the study, NTHA were conducted using two different FE models, one with infill walls and one without. The analyses revealed that infill walls significantly affected the seismic performance.

In this study, the nonlinear analyses of a RC building that collapsed during the 2023 Kahramanmaraş earthquakes were comparatively investigated for cases where infill walls were considered and not considered. The FE model of the building was created using the SAP2000 software. In the NTHA, real ground motion records obtained from the station closest to the building were utilized. The infill walls was represented using the equivalent diagonal strut approach, which is commonly preferred in numerical modeling. As a result of the analyses, the extent to which infill walls affected the structural behavior and structural responses (such as interstory drift ratios, modal parameters, base shear forces, and performance levels) of the collapsed building was investigated.

2. Description of selected building

Within the scope of this study, a RC building that collapsed during the February 6, 2023 earthquake was selected for investigation. The ground floor and mezzanine of the building were used for commercial purposes, while the upper floors were used for residential purposes. The location and pre-collapse condition of the building are presented in Fig. 1.

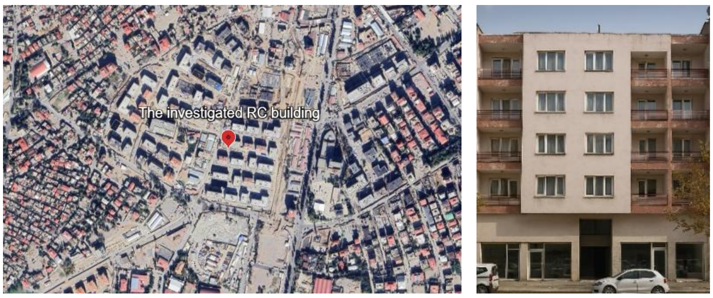

Fig 1. The location and pre-collapse condition of the investigated building

The load-bearing system of the investigated building consists of RC frames. The building, which has a total of six stories, has a height of 17.5m. The story heights are 2.75 meters for the ground floor and clerestorey, and 3.00m for the normal floors. The general characteristics of the building, the dimensions of the structural elements, and the analysis parameters are presented in Table 1, while the plan of a typical floor is shown in Fig. 2.

Table 1. General characteristics and analysis parameters of the RC building

General characteristics of the building	
Building height	17.5m
Story heights	Ground floor and clerestorey: 2.75m Normal floor: 3.00m
Properties of structural elements	
Column	25×25cm, 25×30cm, 25×40cm, 25×50cm
Beam	20×40 cm, 20×50cm, 20×60cm
Slab thickness	12 cm-14 cm
Material properties	
Concrete material	C14 (f_{ck} = 14MPa)
Steel material	S220 (f_{yk} = 220MPa)
Soil classification	ZC
Considered loads	
Slab dead loads	1.5 kN/m^2
Slab live loads	Rooms: 2.0 kN/m^2 Stairs: 3.5 kN/m^2 Balconies: 5.0 kN/m^2
Infill wall	
Wall type	Brick wall

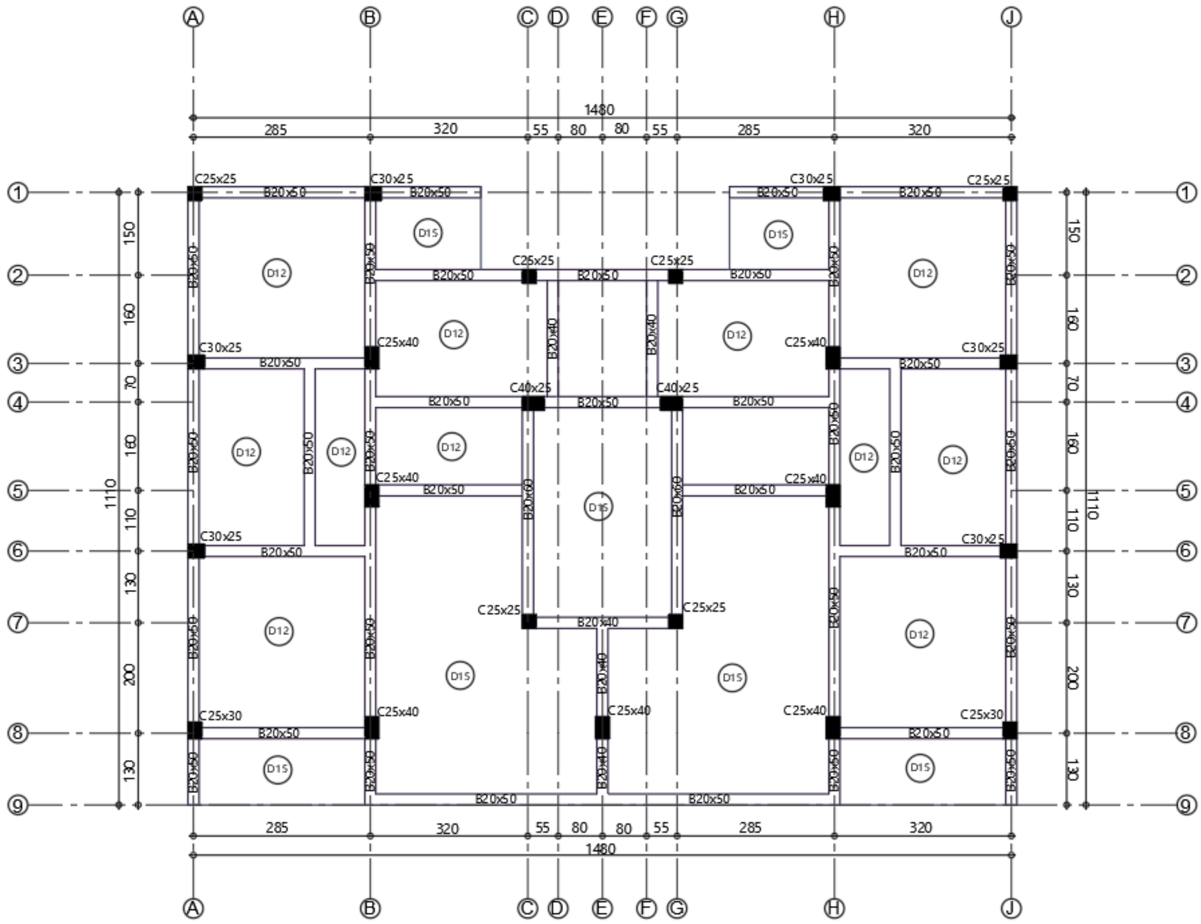

Fig 2. Plan view of a typical floor of the building

3. Ground motion selection

The Turkish Strong Motion Database and Analysis System (AFAD-TADAS) of the Disaster and Emergency Management Authority (AFAD) was used to determine the ground motion to be applied to the structure. Acceleration data from six different stations located in the Onikişubat district, where the structure is situated, were examined, and it was aimed to select the acceleration records from the station closest to the structure. The acceleration records from station TK4620, located nearly 2.50 km away from the structure, were used in the analyses. The locations of the relevant stations and the selected station are presented in Fig. 3.

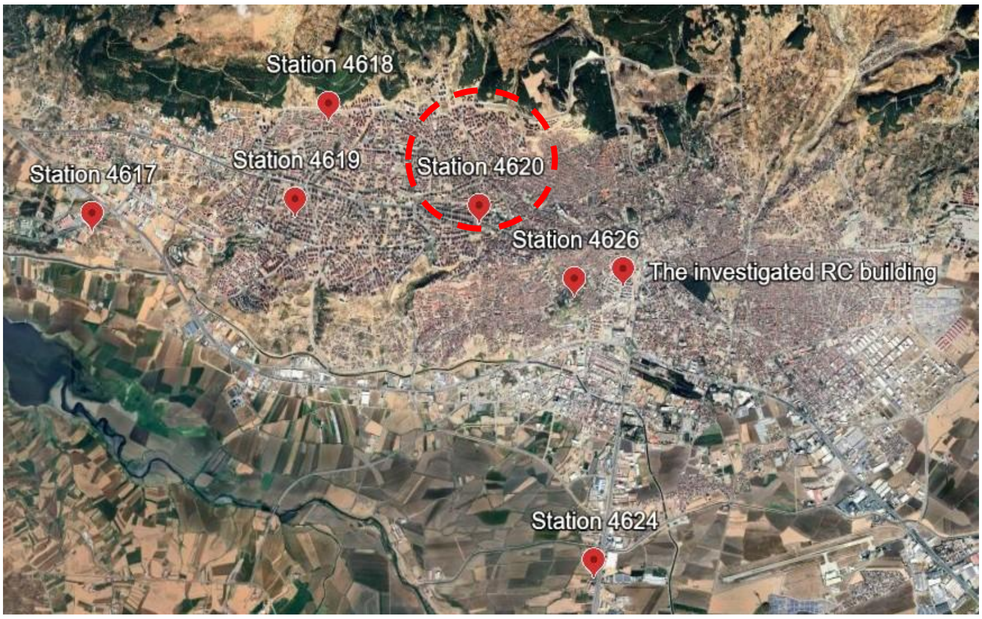

Fig 3. The locations the selected building and station

For use in structural analyses, the acceleration records of two horizontal components (E and N) obtained from the station coded TK4620 were considered. The Peak Ground Acceleration (PGA) values corresponding to these records were determined as 0.327 g and 0.306 g. The acceleration-time histories generated from the data obtained in both directions are presented in Fig. 4, while the comparison between the response spectra of the horizontal components recorded at the TK4620 station and the design spectra defined by the Turkish Building Earthquake Code (TBEC) is presented in Fig. 5.

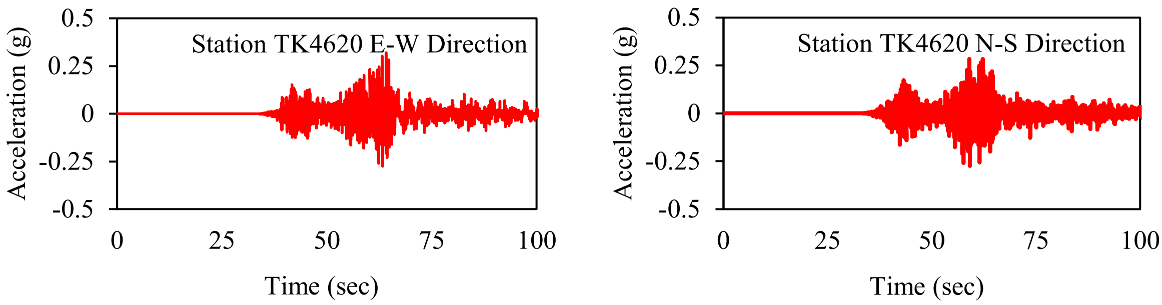

Fig 4. Acceleration-time graphs of selected ground motions

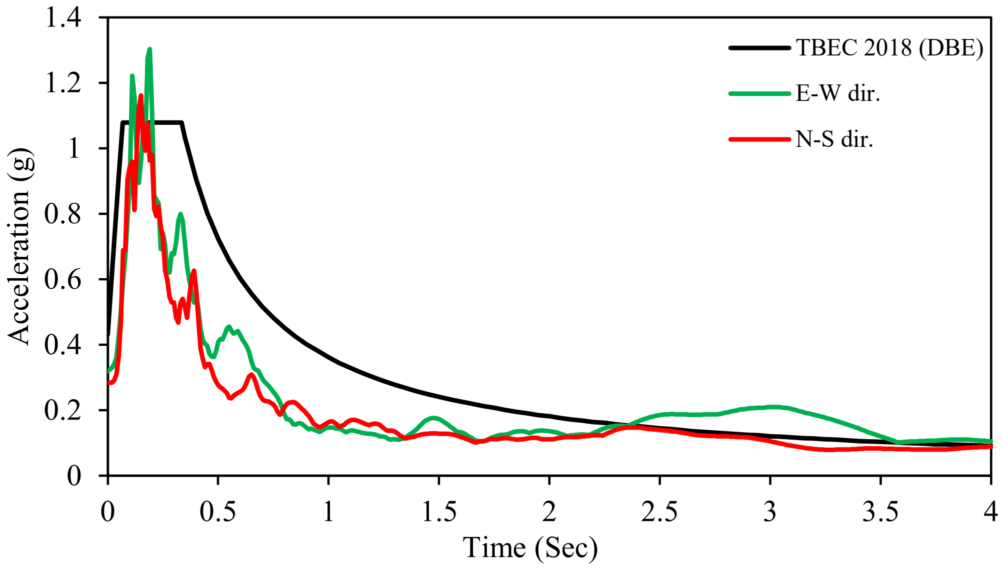

Fig 5. Comparison of the design spectrum and the station-specific spectra

4. Numerical modelling

Within the scope of the study, two different analytical models were developed to evaluate the structural behavior of the building under seismic effects. In the first model, the contribution of infill walls to the structural behavior was neglected, and only the primary structural elements (columns and beams) were considered. In the second model, the infill walls were incorporated into the model using strut elements.

NTHA were conducted using the SAP2000 v25 software. In the analyses, in order to realistically represent the nonlinear structural behavior, the confined concrete model developed by Mander et al. (1988) was adopted for the concrete material. The properties of concrete and reinforcement materials were defined based on the provisions specified in Annex 5A of the Turkish Building Earthquake Code (TBEC-2018). The Stress-Strain relationships of the concrete and steel material models are presented in Fig. 6. In the three-dimensional FE models, columns and beams were modeled as frame elements, while slabs were modeled as shell éléments. Three-dimensional views of the FE models are provided in Fig. 7.

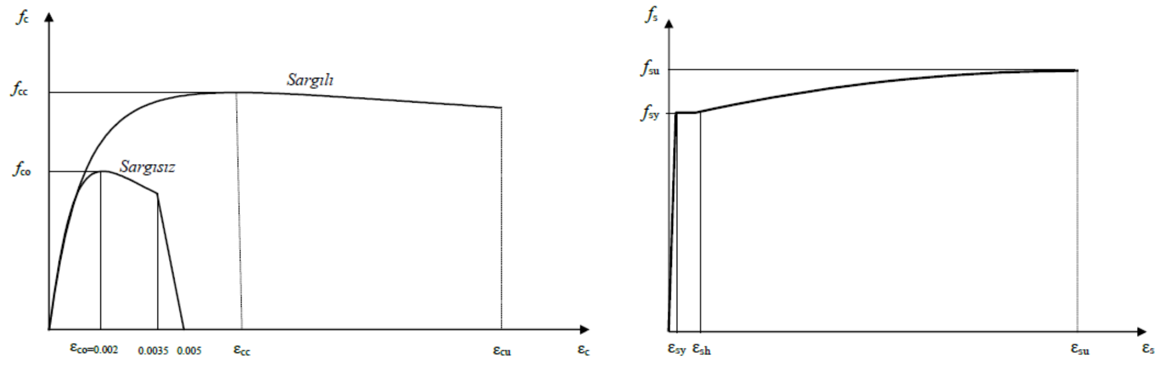

Fig 6. Concrete and steel material model

Without infill wall ***With infill wall***

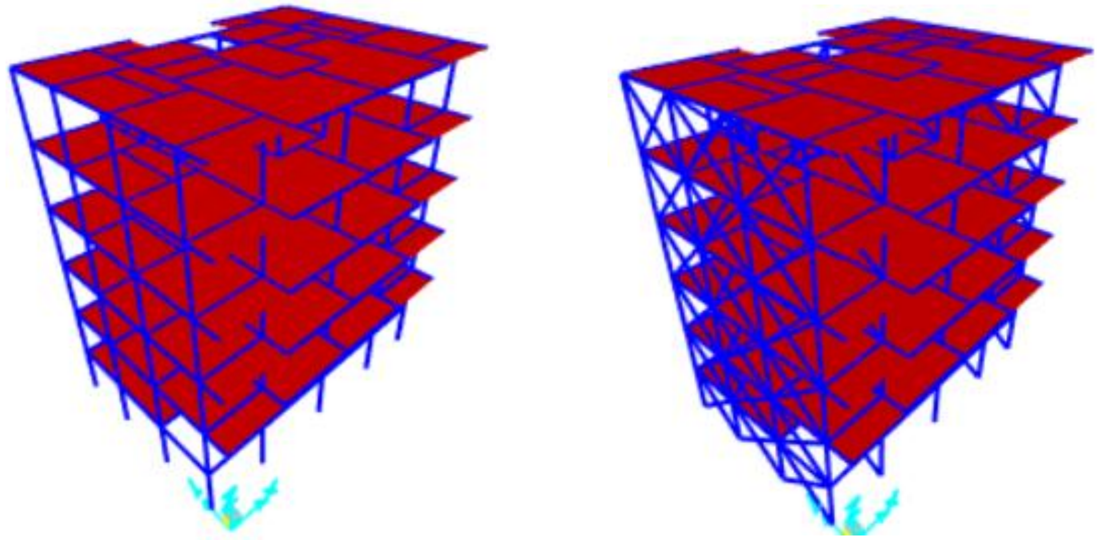

Fig 7. 3D FE models of the investigated building

In the representation of nonlinear behavior, a distributed plasticity model was employed, which is based on the assumption that plastic deformations are continuously distributed along the cross-section and allows for a more realistic simulation of the nonlinear behavior of structural elements. In this approach, the cross-sections of structural elements are subdivided into fiber elements, enabling the prediction of distributed nonlinear behavior both within the section and along the element length (Yön and Calayır, 2013). In the three-dimensional FE models, in order to monitor strain values of load-bearing elements, Fiber P-M2-M3 hinges were assigned at the ends of the column and beam éléments.

In the FE models, infill walls were represented using the equivalent diagonal strut approach, which is commonly adopted in the literature and frequently employed in numerical modeling studies. The first comprehensive investigations into the modeling of infill walls and their structural behavior were conducted by Polyakov (1956). In his study, infill walls can be represented as diagonal struts that transmit forces through compression zones within the structural frame. (Al Chaar et al., 2002). The equivalent diagonal strut method offers a simplified yet effective approach for evaluating frame-infill wall interaction and is currently recognized and utilized by numerous design codes (Köse and Karslıoğlu, 2007; Öztürkoğlu et al., 2016; Köse Sunca, 2019; Çavdar et al., 2020). The thickness and material properties of the compression struts were assumed to be the same as those of the infill wall material (Yakut et al., 2013; Öztürkoğlu, 2016). In calculating the width of the equivalent struts, the modulus of elasticity and compressive strength values obtained from an experimental study conducted by Kaltakçı et al. (2003) were adopted.

In the analyses, the orientation of the struts was adjusted based on the direction of the applied lateral loads; considering the possibility of load direction reversal during seismic events, two diagonally placed equivalent compression struts were defined for each opening to represent this behavior (Öztürkoğlu, 2016). To ensure that the struts carried only axial loads, both end nodes were defined as pinned connections. The axial load capacities of the struts were calculated, and axial load hinges were assigned at the midpoints of each strut to ensure load transfer consistent with these capacities (Özkaya, 2018). In the definition of the axial load hinges, the tensile strength of the wall was considered to be 10% of its compressive strength.

5. Results and discussion

In this section, the findings obtained from the NTHA are presented. The analysis results were comparatively evaluated in terms of modal parameters, story shear forces, interstory drifts, and strain values.

5.1. Modal analysis results

The mode shapes and natural vibration periods corresponding to the first three modes of the FE models with and without infill walls are presented in Fig. 8. The analysis results revealed that the presence of infill walls significantly reduced the period values of the structure. This finding indicates that infill walls can substantially change the dynamic behavior of the structure by increasing the stiffness of the structural system.

Without infill wall | ***With infill wall***

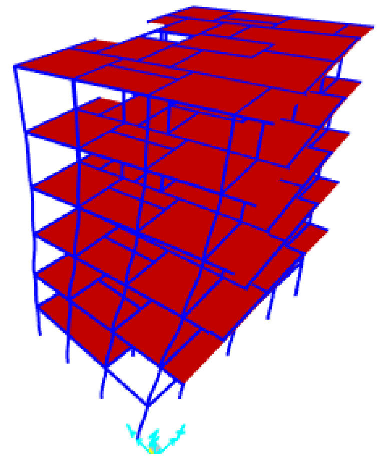

T_1 (x_1) = 1.00s

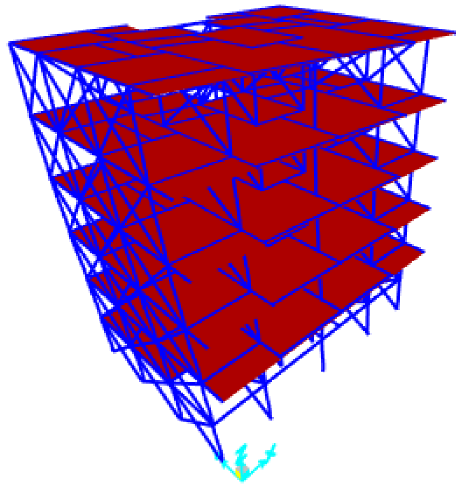

T_1 (x_1) = 0.64s

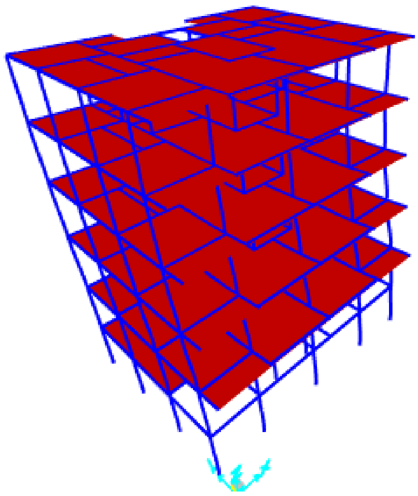

T_2 (y_1) = 0.85s

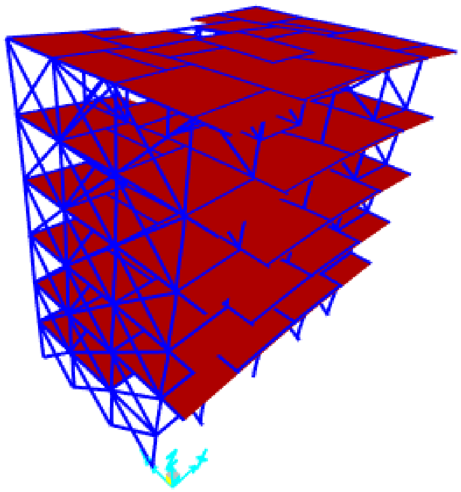

T_2 (y_1) = 0.36s

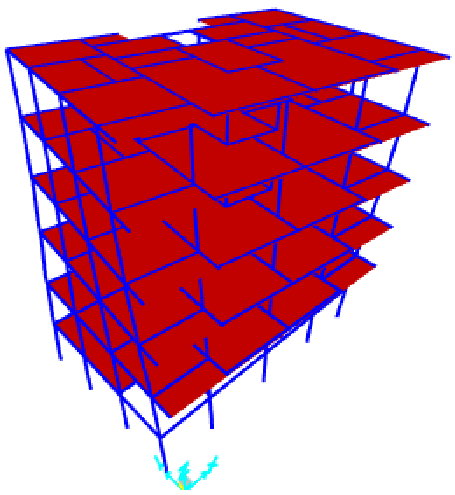

T_3 (r_1) = 0.81s

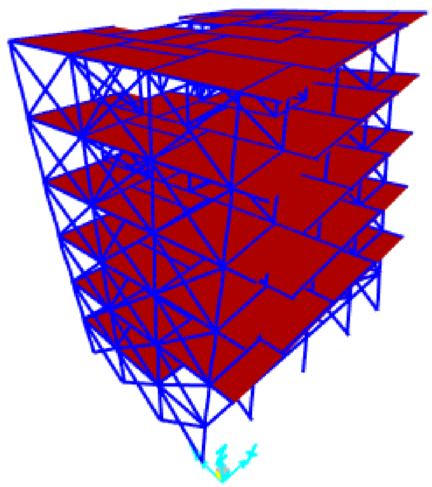

T_3 (r_1)= 0.33s

Fig 8 Comparisons of modal parameters of selected RC building

5.2. Interstory drift results

As a result of the analyses, interstory drifts were calculated for both directions and compared for the models with and without infill walls (Fig. 9). It was determined that the interstory drifts of the model with infill walls were significantly reduced compared to the bare frame model. However, it was observed that the reduction in drift in the X-direction was more limited, due to the lower number of infill walls placed along the X-axis compared to the Y-axis. This finding demonstrates that the density and distribution of infill walls have a direct influence on the lateral stiffness of the structure.

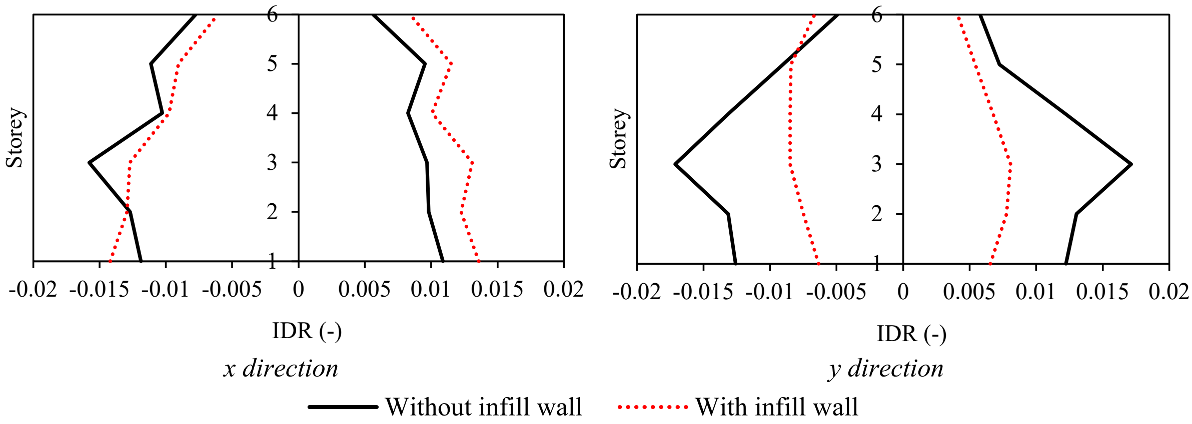

Fig 9. Comparisons of IDRs of selected RC building

5.3. Base shear forces

The base shear forces of the FE models with and without infill walls is comparatively presented in Fig. 10. The results indicate that the base shear forces in the model with infill walls are significantly higher compared to the bare frame model, demonstrating that the presence of infill walls increases the structural stiffness and consequently leads to the development of greater base shear forces under seismic effects. Furthermore, Fig. 10 shows that higher base shear forces occurred in the Y-direction. This observation is attributed to the higher density of infill walls along the Y-axis, which enhances the lateral stiffness of the structure and thus results in greater shear force demands during seismic loading.

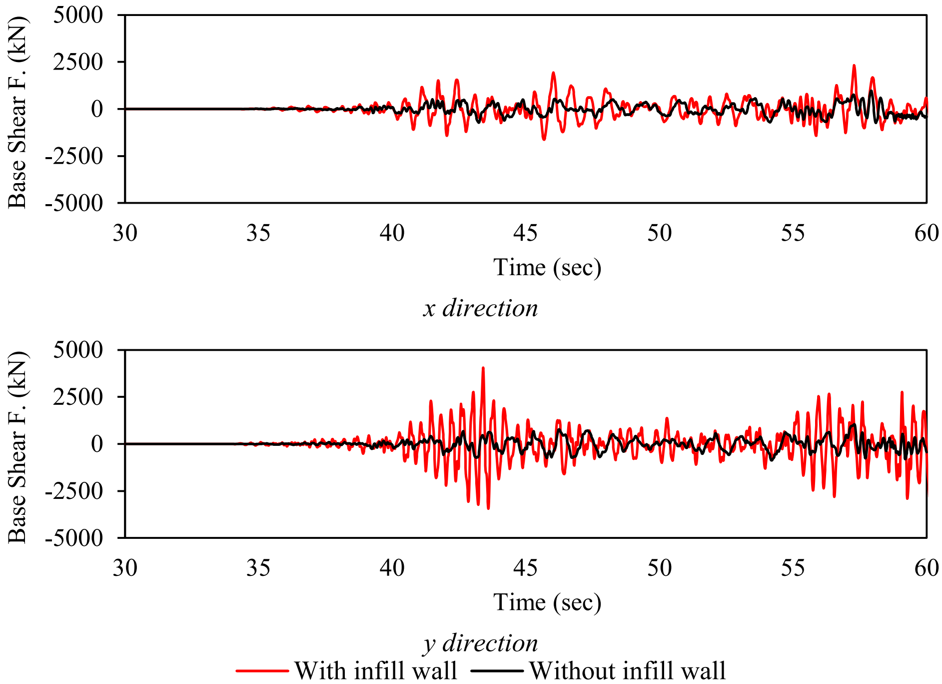

Fig 10. Comparisons of base shear forces of selected RC building

5.4. Performance level of load-bearing elements

As a result of the analyses, the plastic hinge formations in the structural elements are presented in Fig. 11. An examination of the plastic hinge distribution in the bare frame model reveals that extensive plastic deformations occurred in the structural elements, with a significant number of hinges reaching the Collapse Prevention (CP) performance level. This indicates that in the absence of infill walls, the lower lateral stiffness of the structure led to larger plastic deformations in the primary structural members. In contrast, the model with infill walls exhibited a significant reduction in both the formation and severity of plastic hinges.

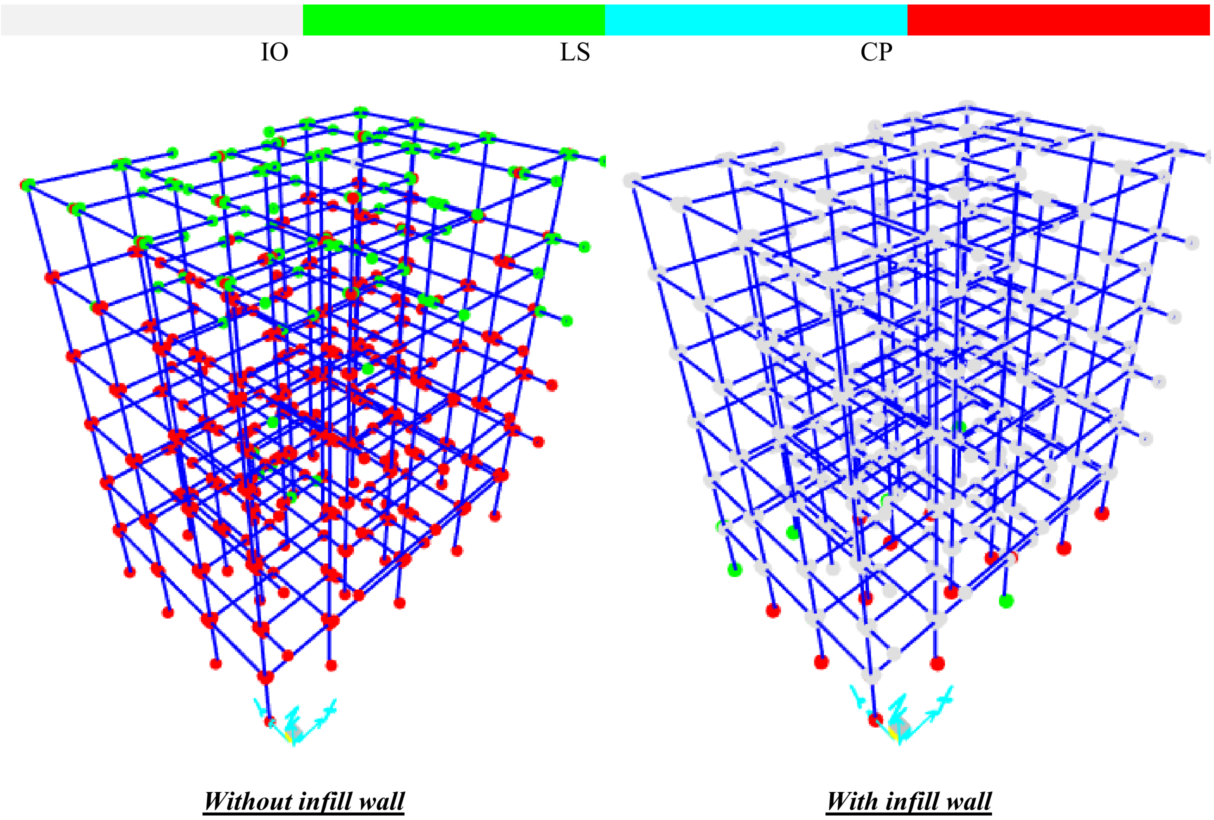

Fig 11. Comparisons of performance level of load-bearing elements

6. Conclusion

The aim of this study is to investigate the effects of infill walls on the structural behavior of a RC building that collapsed during the 2023 Kahramanmaraş Earthquake, through NTHA utilizing real ground motion records obtained from a station located near the building. Within the scope of the study, two different FE models were developed: one including infill walls and one excluding them. The key results derived from the analyses are summarized below:

- As a result of the modal analysis, it was observed that the presence of infill walls led to reductions of 36%, 57.65%, and 59.29% in the natural vibration periods for the first three modes, respectively. These results indicate that infill walls significantly enhance the lateral stiffness of the structure.
- With the inclusion of infill walls, reductions in interstory drifts were observed in both directions. However, the lower density of infill walls in the X-direction compared to the Y-direction limited the extent of the reduction in that direction. This finding highlights that the density of infill walls has a direct influence on the lateral stiffness of the structure.
- In the model with infill walls, a significant reduction in the formation of plastic hinges and damage was observed compared to the bare frame model, and the plastic deformation demands on the structural elements were effectively limited.

References

Abdelaziz, M. M., Gomma, M. S., & El-Ghazaly, H. (2019). Seismic evaluation of reinforced concrete structures infilled with masonry infill walls. *Asian Journal of Civil Engineering*, 20, 961–981.

Akbaş, A., & Çalışkan, Ö. (2024). Dolgu Duvarların Taşıyıcı Sisteme Katkısı.

Al Chaar, G., Issa, M., & Sweeney, S. (2002). Behaviour of masonry-infilled nonductile reinforced concrete frames. *Journal of Structural Engineering*, 128(8), 1055–1063.

Baghi, H., Oliveira, A., Valença, J., Cavaco, E., Neves, L., & Júlio, E. (2018). Behavior of reinforced concrete frame with masonry infill wall subjected to vertical load. *Engineering Structures*, 171, 476–487.

Çavdar, Ö., Köse, G., & Sunca, F. (2020). Betonarme binaların deprem performanslarına dolgu duvarların etkisinin incelenmesi. *Uludağ Üniversitesi Mühendislik Fakültesi Dergisi*, 25(1), 465–484.

Disaster and Emergency Management Authority. (AFAD) https://www.afad.gov.tr

Google Earth. (2024). Google Earth Google LLC. https://earth.google.com/

Hashemi, A., & Mosalam, K. M. (2006). Shake-table experiment on reinforced concrete structure containing masonry infill wall. *Earthquake Engineering & Structural Dynamics*, 35(14), 1827–1852.

Hashemi, S. A. (2007). Seismic evaluation of reinforced concrete buildings including effects of masonry infill walls (Master's thesis, University of California, Berkeley).

Hermanns, L., Fraile, A., Alarcón, E., & Álvarez, R. (2014). Performance of buildings with masonry infill walls during the 2011 Lorca earthquake. *Bulletin of Earthquake Engineering*, 12, 1977–1997.

Kadysiewski, S., & Mosalam, K. M. (2009). Modeling of unreinforced masonry infill walls considering in-plane and out-of-plane interaction (Vol. 70). Pacific Earthquake Engineering Research Center, Berkeley.

Kaltakcı, M. Y., & Köken, A. (2003). Tuğla dolgu duvarlı çerçevelerin tersinir tekrarlı yükler altında davranışı, TÜBİTAK Project.

Köse Sunca, G. Ç. (2019). Farklı oran ve düzende dolgu duvarlara sahip betonarme yapıların sismik performanslarının belirlenmesi (Master's thesis, Institute of Science Gümüşhane University,).

Köse, M. M., & Karslıoğlu, Ö. (2007). Dolgu duvarların bina doğal modal periyot ve mod şekline olan etkileri. In *Altıncı Ulusal Deprem Mühendisliği Konferansı* (pp. 261–270).

Mander, J. B., Priestley, M. J., & Park, R. (1988). Theoretical stress-strain model for confined concrete. *Journal of Structural Engineering*, 114(8), 1804–1826.

Murty, C. V. R., & Jain, S. K. (2000, January). Beneficial influence of masonry infill walls on seismic performance of RC frame buildings. In 12th *World Conference on Earthquake Engineering* (Vol. 30).

Ning, N., Yu, D., Zhang, C., & Jiang, S. (2017). Pushover analysis on infill effects on the failure pattern of reinforced concrete frames. *Applied Sciences*, 7(4), 428.

Özkaya, E. (2018). Binalarda yumuşak kat oluşumunda dolgu duvarların etkisinin incelenmesi (Master's thesis, , Institute of Science).

Öztürkoğlu, O. (2016). Kısmi boşluklu dolgu duvarlı betonarme çerçevelerin doğrusal olmayan davranışının incelenmesi (Master's thesis, Dokuz Eylül University).

Öztürkoğlu, O., Ucar, T., & Yesilce, Y. (2017). Effect of masonry infill walls with openings on nonlinear response of reinforced concrete frames. *Earthquakes and Structures*, 12(3), 333–347.

Polyakov, S. (1956). Masonry infilled framed buildings: An investigation into the strength and stiffness of masonry infilling.

SAP2000. (2023). Structural analysis program (Version 25.0.0). Computers and Structures Inc., Berkeley, California, USA.

Sattar, S., & Liel, A. B. (2010, July). Seismic performance of reinforced concrete frame structures with and without masonry infill walls. In *9th US National and 10th Canadian Conference on Earthquake Engineering*.

Şen, F., Sunca, F., & Altunişik, A. C. (2024). Seismic performance assessment of a base-isolated hospital building subjected to February 6, 2023, Kahramanmaraş, Türkiye earthquakes and seismic fragility analysis considering different construction stages. *Soil Dynamics and Earthquake Engineering*, 185, 108876.

Smiroldo, F., Kallioras, S., Sommacal, G., Bournas, D., Piazza, M., & Giongo, I. (2023). Full-scale testing of masonry-infilled RC frames retrofitted with cross-laminated timber panels. *Engineering Structures*, 294, 116789.

Tan, M., Avşar, Ö., Yıldızhan, F., & Atmaca, N. (2025). Effect of infill walls on the seismic performance of a severely damaged substandard RC building during the February 6, 2023, Kahramanmaraş earthquake sequence. *Engineering Failure Analysis*, 169, 109117.

TBDY. (2018). Türkiye Bina Deprem Yönetmeliği. Çevre ve Şehircilik Bakanlığı, Ankara.

The Turkish Strong Motion Database and Analysis System . (TADAS) https://tadas.afad.gov.tr

Usta, P., Onat, Ö., & Bozdağ, Ö. (2023). Effect of masonry infill walls on the nonlinear response of reinforced concrete structure: October 30, 2020 İzmir earthquake case. *Engineering Failure Analysis*, 146, 107081.

Wang, F., Zhao, K., Zhang, J., & Yan, K. (2021). Influence of different types of infill walls on the hysteretic performance of reinforced concrete frames. Buildings, 11(7), 310.

Yakut, A., Binici, B., Demirel, İ. O., & Özcebe, G. (2013). Dolgu duvarların deprem davranışına etkisi. In *2. Türkiye Deprem Mühendisliği ve Sismoloji Konferansı (25–27 Eylül, Hatay).*

Yön, B., & Calayır, Y. (2013). Betonarme binalarda sargı donatısı etkisinin yayılı plastik mafsal modeliyle incelenmesi. In *2. Türkiye Deprem Mühendisliği ve Sismoloji Konferansı (25–27 Eylül, Hatay).*

4th International Civil Engineering & Architecture Conference
17-19 May 2025, Trabzon, Türkiye

October 16, 2024, Akuşağı-Kale (Malatya) earthquake seismic characteristics and investigation directionality effect

Ibrahim O. Dedeoglu*[1], Musa Yetkin[2], Yusuf Calayır[3]

[1] Batman University, Department of Civil Engineering, 72100 Batman, Türkiye
[2] Karadeniz Technical University, Department of Civil Engineering, 61080 Trabzon, Türkiye
[3] Yalova University, Department of Civil Engineering, 77200 Yalova, Türkiye

Abstract. After the devastating earthquakes on the Eastern Anatolia Fault zone on February 6, 2023, earthquakes are still occurring in the region. One of these earthquakes occurred on October 16, 2024 at 10:46 local time at the epicenter of Akuşağı-Kale (Malatya). The instrumental magnitude of this earthquake was reported as M_L 5.9 - M_W 6.0. It was a shallow focused earthquake (focal depth 6.8 km) and was strongly felt in Malatya and Elazığ provinces. The subject of this study is to analyze the some characteristics of this earthquake and to investigate its effects on the building stock. Within the scope of the study, various parameters of some strong ground motions recorded at seismic stations operated by AFAD are analyzed considering the directional effect. The acceleration velocity and response spectrum values given in the Türkiye Earthquake Hazard Map for the characteristics of the earthquake were compared and evaluated. At the end of the study, the effects of the earthquake on the building stock are presented.

Keywords: Eastern Anatolia fault zone; October 16, 2024 Akuşağı-Kale (Malatya) earthquake; Seismic characteristics; Building stock; Directionalty effect

1. Introduction

Earthquakes are natural disasters that occur with the release of large amounts of energy as a result of tectonic movements in the earth's crust. These natural disasters have serious impacts on settlements around the world and deeply affect the lives of human communities. As a result of earthquakes, especially damages to superstructures, loss of life and property occur. Additionally, earthquake-induced infrastructure damage disrupts societies by collapsing transport and communication networks. Earthquakes in regions located on active fault lines threaten not only physical structures but also social and economic order. The social effects can be said to be psychological traumas, stress and anxiety disorders in individuals in the long term, and permanent scars on the social fabric. On the other hand, economic effects are the stoppage of production processes in earthquake zones, labor force losses and reconstruction costs, and significant deterioration in the economic structures of countries. In this context, evaluating earthquakes solely within a geoscientific framework is not sufficient. For this reason, earthquakes create a comprehensive crisis situation in humanitarian and socioeconomic terms, and the management of these crises is of critical importance for the resilience of societies.

To minimize the negative impacts of earthquakes, a comprehensive planning and preparation process is required before, during, and after disasters. Seismic risks should be considered in the construction of settlements, and earthquake-resistant structures should be provided. In addition, strengthening social awareness-raising activities is of enormous importance in terms of learning how to behave against disasters. However, all these measures are not sufficient to prevent the destruction caused by earthquakes. By establishing a long-term resilience strategy, we can ensure that societies become more resilient against disasters. Thus, losses caused by earthquakes can be minimized, and societies can cope with such disasters in a more sustainable way.

Turkey, as a country located in the earthquake zone, is obliged to be constantly prepared and take precautions against such disasters. For this reason, seismic risks should be considered in the construction of residential areas, and earthquake-resistant structures should be provided. Construction measures are especially urgent in regions located on active faults like the North Anatolian Fault Zone (NAFZ) and the East Anatolian Fault Zone (EAFZ). Although all precautions should be taken before earthquakes, painful social experiences also contribute to the rapid implementation of the measures to be taken. Because the mobility in these fault lines and the painful experiences since the beginning of the 21st century are the biggest triggers of this urgency.

* Corresponding author, E-mail: iozgur.dedeoglu@batman.edu.tr

https://doi.org/10.31462/icearc2025_ce_eqe_957

The 1999 Gölcük and Düzce earthquakes that occurred in the NAFZ at the beginning of the 21st century resulted in the loss of approximately 20,000 lives. The magnitudes of these earthquakes were 7.4 and 7.2 respectively. The mobility of the NAFZ continued over the years. The Düzce-Gölyaka earthquake in 2022 demonstrated this continued mobility. For the EAFZ, it is possible to say that this mobility is higher. In the 21st century, some of the earthquakes that occurred in the EAFZ are the 2003 Bingöl, 2010 Karakoçan-Elazığ, and 2020 Sivrice-Elazığ earthquakes. In addition to these earthquakes, many medium-sized earthquakes occurred in the region. However, the Kahramanmaraş earthquakes that occurred in 2023 and directly affected the region have gone down in history as the largest earthquakes of the last century. Unfortunately, these earthquakes did not go down in history, only in terms of their magnitude. The uniqueness of these earthquakes lies in the significant losses they caused in Turkey.

The 2023 Kahramanmaras earthquakes, in particular, are often interpreted using data such as magnitude, PGA, and PGV. Usually, these data are used to reveal the damage relationship between earthquakes and structures, to create earthquake hazard maps, and to determine the performance of existing structures under the effect of possible earthquakes. These data consider two horizontal components and one vertical component of the earthquake. However, when such an evaluation is made, the directional effect of earthquake loads, the effects of the interaction between the components of the earthquake ground motion on the structural behavior, torsional effects due to some structural irregularities (mass, stiffness, and strength, etc.), and the effects arising in non-orthogonal buildings are not directly taken into account. The evaluations made by ignoring these effects may lead to structural damage in some cases.

To determine the effects of earthquakes more realistically, the effects of the earthquake ground motion in the principal axis directions as well as the intermediate directions in the plan should be considered. However, the structural behavior analyses of buildings under the earthquake hazard level determined depending on the predicted performance target are performed in the principal axis directions in the plan without considering the characteristic features of the building. However, it is known that the directions of the horizontal components of the earthquake ground motion are variable. The probability of the earthquake effect from the principal axis (X and Y) directions in the plan of the building is the same as the probability of the earthquake effect from any intermediate direction. For this reason, the designed/existing buildings are required to fulfill the prescribed performance targets for the intermediate earthquake directions as well as the principal directions. This study examines how earthquake ground motion is affected by direction. The earthquake that occurred on 16 October 2024 in Akuşağı-Kale (Malatya) is selected as a case study. The focal depth of this earthquake was 6.8 km, and its magnitude was M_L=5.9-M_W=6.0. The study evaluated the characteristics of this earthquake, considering the directional effect. The study took into account the acceleration, velocity, and response spectrum values provided in the Earthquake Hazard Map of Turkey. The study concludes with a discussion of the earthquake's effects on the building stock.

2. Tectonics and seismicity of the region

Malatya province and its districts are located within the I.-III. Degree Earthquake Zone in the Earthquake Zones Map published by the Ministry of Public Works and Settlement, General Directorate of Disaster Affairs in 1996 (Fig. 1a). The Turkiye Earthquake Zones Map (TEZM, 1996) was renewed by the AFAD Earthquake Department and entered into force on 1 January 2019. Unlike the previous map, the new one displays maximum ground acceleration values (PGA) instead of earthquake zones. The Turkiye Earthquake Hazard Map (TEHM, (2019)) shows that for Malatya province, the maximum acceleration value (PGA) at Earthquake Level 2 (design earthquake, return period 475 years) ranges from 0.2 to 0.7 g (Fig. 1b). This indicates that the earthquake hazard of the region has changed relatively and is very high.

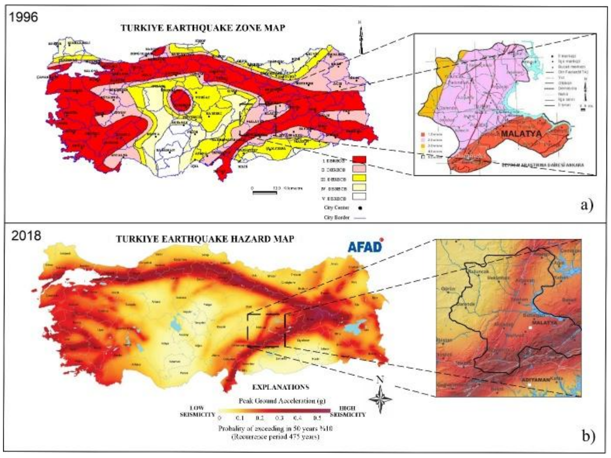

Fig. 1. Earthquake hazard map of Malatya province a) 1996 b) 2018

The south-southeast of Malatya province borders are generally under the influence of the EAFZ. As can be seen in the Active Fault Map of Türkiye prepared by MTA (Mineral Research and Exploration General Directorate) in 2011, Doğanşehir-Sürgü Faults in the south, the part of the Eastern Anatolian Fault Zone passing through Pütürge-Doğanyol and Malatya Fault are important tectonic structures in the region (Fig. 2).

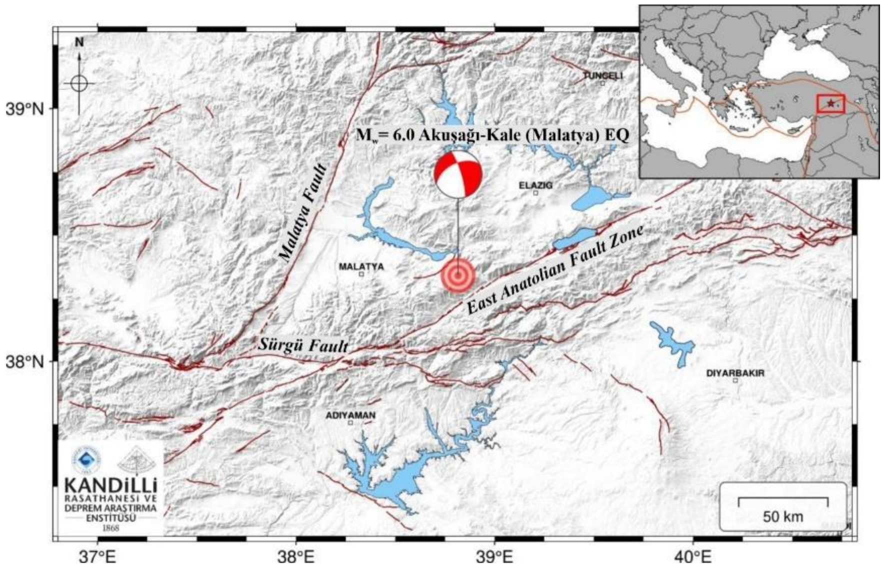

Fig. 2. M_w=6.0 Akuşağı-Kale (Malatya) earthquake epicenter and active fault structure of the region (adapted from KOERİ Report, 2024)

During the Instrumental Period (A.D. 1900-2024; magnitude M≥4.0 KOERI Earthquake Catalogue), the Gaziantep (M=7.7) and Kahramanmaraş (M=7.6) earthquakes that occurred on 06 February 2023 caused intense aftershock activity throughout the region. The earthquakes that occurred closest to the city center recently are the 1964 Aksu-Sincik (Adıyaman) and 2020 Sivrice (Elazığ) earthquakes (Fig. 3).

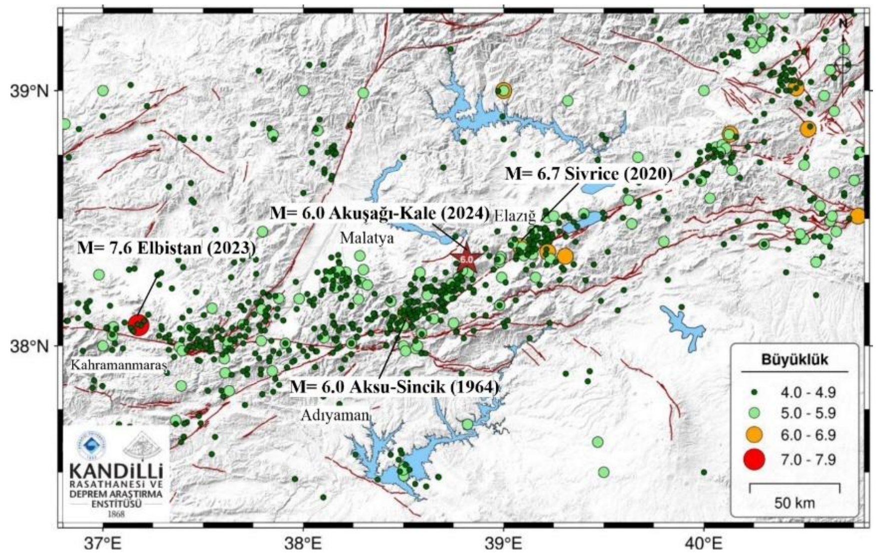

Fig. 3. Earthquake map of the region (1900-2024, M≥4.0 KOERI Earthquake Catalogue) (adapted from KOERİ Report, 2024)

3. Characteristics of earthquake

On 16 October 2024, a strong earthquake with an instrumental magnitude of ML 5.9-Mw 6.0 occurred at 10:46 local time at the epicenter of Akuşağı-Kale (Malatya) (38.3410 N 38.8155 E). The focal depth of the earthquake was 6.5 km; it was a shallow-focused earthquake. The distances of the epicenter of the earthquake to the settlements are given in Table 1.

The earthquake occurred on the EAFZ. The statement indicates that it was an aftershock from the consecutive earthquakes in Kahramanmaraş on February 6, 2023. Despite being an aftershock, the region where it occurred felt its impact strongly. The maximum acceleration magnitudes of the earthquake measured at various stations are given in Table 2. The maximum ground acceleration of the earthquake was recorded as 0.61 g in the horizontal direction and 0.35 g in the vertical direction at station 4414 (Kale/Malatya). The acceleration-time history record of this station is shown in Fig. 4.

Table 1. The distances of the epicenter of the earthquake to the settlements (KOERİ Report, 2024)

Province	District	Distance (km)	Province	Distance (km)
Malatya	Kale	9.23	Malatya	42.56
Malatya	Pütürge	16.28	Elazığ	49.81
Malatya	Doğanyol	19.49	Adıyaman	80.55
Elazığ	Baskil	26.01	Tunceli	105.32
Adıyaman	Sincik	38.19	Diyarbakır	130.93

Table 2. Ground motion characteristics of the October 16, 2024 Akuşağı-Kale (Malatya) earthquake, as recorded by some accelerometer stations (AFAD, 2024)

Province	District	Station Code	Latitude (°)	Longitude (°)	PGA (g)			R_{JB} (km)	R_{rup} (km)	R_{epi} (km)
					N-S	E-W	U-D			
Malatya	Kale	4414	38.7541	38.4069	0.428	0.608	0.351	2.65	7.90	6.59
Malatya	Pütürge	4404	38.8738	38.1958	0.103	0.065	0.036	13.33	15.49	19.74
Malatya	Doğanyol	4413	39.0393	38.3135	0.137	0.118	0.078	17.84	21.24	20.95
Adıyaman	Sincik	0218	38.6333	38.0300	0.010	0.009	0.008	34.61	28.15	40.35
Elazığ	Merkez	2311	39.1520	38.6442	0.030	0.018	0.022	38.92	41.18	43.03
Elazığ	Sivrice	2308	39.3102	38.4506	0.059	0.061	0.031	45.80	44.71	45.92

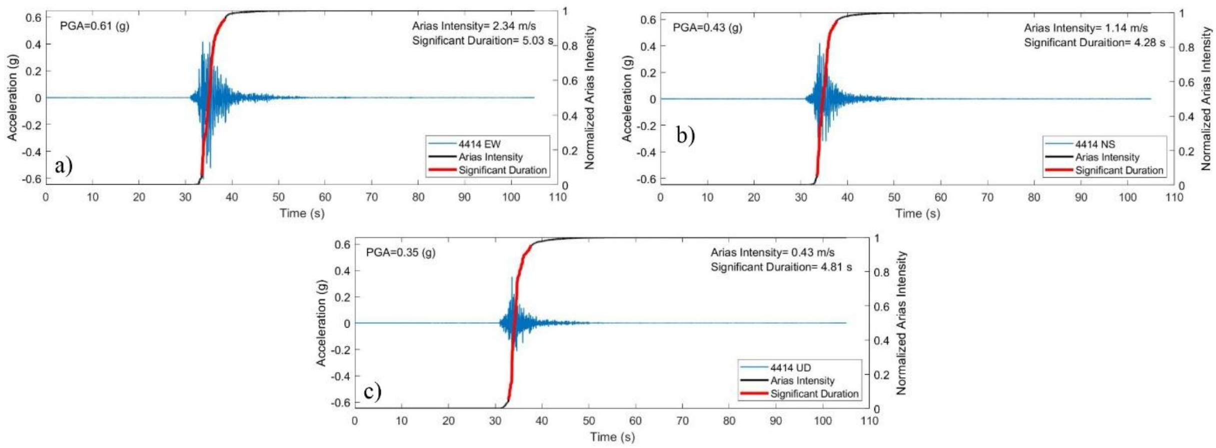

Fig. 4. Acceleration time history, Arias intensity and effective time parameters for station 4414 during M_w=6.0 Akuşağı-Kale (Malatya) earthquake

4. Investigation of the directionalty effect

Earthquakes are recorded in three perpendicular directions by seismic stations in the region where they occur. Various methods incorporate the obtained strong ground motions into earthquake-resistant building design. However, the earthquake propagates as waves at the focal point. Earthquakes may have a different magnitude in a different direction (angle) than the recorded directions. In this study, the records of station 4414, where the largest ground accelerations of the Akuşağı-Kale (Malatya) earthquake that occurred on 16 October 2024, will be discussed in terms of directional effect.

Using the E-W and N-S acceleration records of 4414 stations, acceleration records were obtained for each angle (with 1° angle intervals from 0° to 360°), and then the maximum acceleration and velocity magnitudes in each direction were determined from the acceleration records obtained for each direction. In Fig. 5, the PGA and PGV values for each direction from station 4414 are displayed alongside the PGA and PGV values set in the TBEC (2018) earthquake code for the station's location during the DD1 and DD2 earthquake levels.

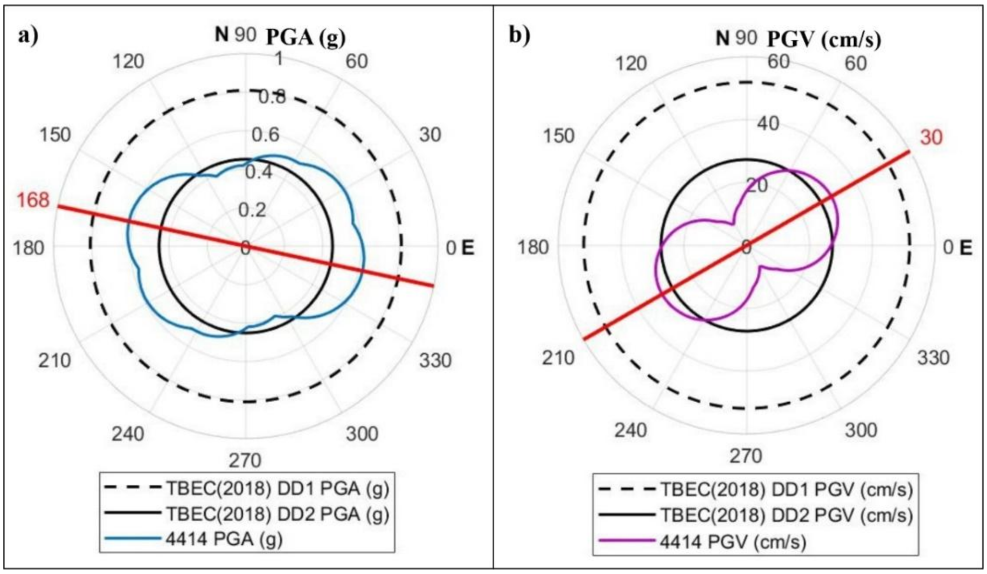

Fig. 5. a) PGA and b) PGV magnitudes of the acceleration records obtained from the horizontal directional acceleration records of station 4414 depending on the direction during M_w=6.0 Akuşağı-Kale (Malatya) earthquake

When Fig. 5. is analyzed, the maximum PGA and PGV values of the strong ground motion recorded at station 4414 were measured as 0.621 g and 31.1 cm/s in different directions from E-W and N-S directions, respectively. The largest PGA and PGV values occurred at angles of 168° and 30° with respect to the east direction, respectively.

Acceleration response spectra are highly utilized in the determination of earthquake loads in earthquake-resistant building design. Therefore, acceleration response spectra of strong ground motions are of significant importance. In Fig.6., the acceleration response spectra obtained for various periods of acceleration records obtained for each direction of station 4414 are shown together with the values determined for DD1 and DD2 levels in TBEC (2018) regulations. When Figure 6 is analyzed, it is obvious that the direction effect affects the response magnitude.

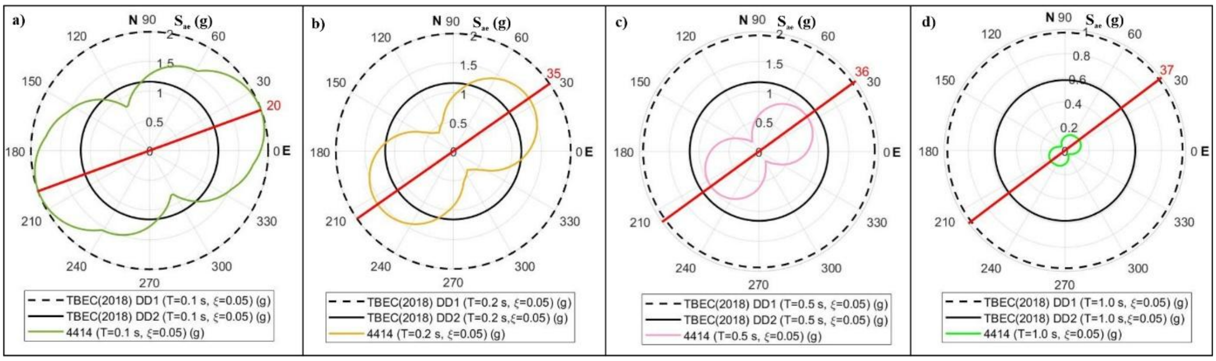

Fig. 6. Acceleration response magnitudes at various periods of acceleration records obtained for each direction from the horizontal direction records of station 4414 a) T=0.1 s, b) T=0.2 s, b) T=0.5 s, b) T=1.0 s for M_w=6.0 Akuşağı-Kale (Malatya) earthquake

For the strong ground motion belonging to station number 4414, the acceleration response spectrum was obtained by taking into account the maximum values of the acceleration response values obtained in all directions for all period values at 0.02 s intervals from T = 0.02 s to T = 1.00 s. The acceleration response spectrum obtained is presented together with the acceleration response spectra of the E-W and N-S direction records and the acceleration response spectra determined for DD1 and DD2 in the TBEC (2018) earthquake code for the location of the station (Fig. 7).

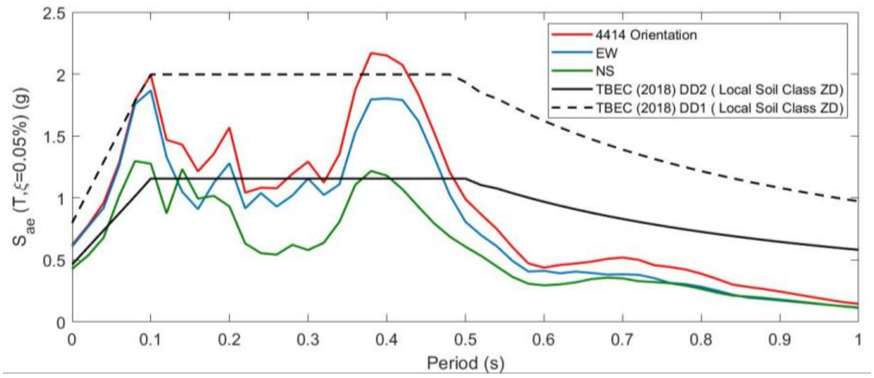

Fig. 7. Acceleration response magnitudes at various periods of acceleration records obtained for each direction from the horizontal direction records of station 4414 a) T=0.1 s, b) T=0.2 s, b) T=0.5 s, b) T=1.0 s for M_w=6.0 Akuşağı-Kale (Malatya) earthquake

The ratio of the acceleration response spectrum obtained depending on the direction to the acceleration response spectrum belonging to the E-W direction was calculated as the minimum 1.01 and the maximum 1.44. When we calculated this ratio for the N-S direction, the minimum was determined as 1.16 and the maximum was determined as 2.23.

5. Conclusions

On October 16, 2024, an earthquake with a moment magnitude of Mw=6 occurred in southeastern Türkiye, with its epicenter near the Kale district of Malatya province. This earthquake was reported as an aftershock of the February 6, 2023 Kahramanmaraş sequential earthquake. First, the tectonics and seismicity of the region were overviewed, and then the earthquake's general features were discussed. The acceleration records of station 4414 (Kale/Malatya), where the highest ground acceleration of the earthquake in the horizontal direction was recorded, were examined in terms of directionality effect. The results obtained are listed below:

- The peak ground acceleration of the earthquake was measured as 0.608 g in the E-W direction and 0.428 g in the N-S direction at station 4414 (Kale/Malatya). When the acceleration record of the station was examined in all directions, the peak ground acceleration value was determined as 0.621 g in the 168° angle with the East direction.
- The peak ground acceleration of the earthquake was measured as 26.88 cm/s in the E-W direction and 17.33 cm/s in the N-S direction at station 4414 (Kale/Malatya). When the acceleration record of the station was examined in all directions, the peak ground acceleration value was determined as 0.621 g in the 30° angle with the East direction.
- When the response spectra of the acceleration records of station 4414 (Kale/Malatya) obtained in all directions were examined, it was generally obtained in a direction different from the E-W and N-S directions in all periods (T=0.02-1.00 s). However, it was observed that in some directions in short-period values, the spectral acceleration values of TBEC (2018) DD2 exceeded and even approached the spectral values of TBEC (2018) DD1.
- The ratio of the acceleration response spectrum, depending on the direction, to the horizontal directions' (E-W and N-S) acceleration response spectra was calculated as a minimum of 1.01 and a maximum of 2.23. These ratios show the importance of the direction effect.
- When we look at the acceleration data from earthquake station number 4414 regarding directional effects, we found that although there was no major difference in the PGA and PGV values, the directional effect was clearly seen in the acceleration response spectra.

Acknowledgments

This paper was no financially supported by any institution or organization.

References

AFAD, Earthquake Department of the Disaster and Emergency Management Presidency. Ankara, Turkey. http://www.afad.gov.tr

KOERİ Report, 2024. 16 October 2024 Akuşaği-Kale (Malatya) M6.0 Earthquake Preliminary Assessment Report.

TEHM (2019) Turkiye Earthquake Hazard Maps Interactive Web Application, DEMA. https://tdth.afad.gov.tr/TDTH/main.xhtml

TEZM (1996) Turkiye Earthquake Zone Map, Ministry of Public Works and Settlement, General Directorate of Disaster Affairs.

Machine learning-based modeling of damages in the 2023 Kahramanmaraş Earthquakes using seismic local-site parameters

Mustafa Şenkaya*[1,2], Ali Silahtar[3], Enes F. Erkan[4], Hasan Karaaslan[3]

[1]Bursa Uludağ University, Department of Civil Engineering, 16240 Bursa, Türkiye
[2] Earthquake Research and Structural Health Monitoring Laboratory, Bursa Uludağ University, 16240 Bursa, Türkiye
[3] Geophysical Engineering Department, Engineering Faculty, Sakarya University, 54187 Sakarya, Türkiye
[4] Industrial Engineering Department, Engineering Faculty, Sakarya University, 54187 Sakarya, Türkiye

Abstract. The damages of the 2023 Kahramanmaraş Earthquakes are modeled through various supervised and unsupervised machine learning techniques by variables ground condition parameters, including Vs_{30}, engineering bedrock depth (EBd), predominant frequency (f_0), horizontal to vertical spectral ratio value (A_0). The supervised approaches achieved recall scores of 94% for damage conditions and 92% for no-damage conditions under optimal circumstances, with an overall damage status prediction accuracy of 93%. The minimum observed accuracy for supervised methods was 80%. In comparison, unsupervised methods demonstrated a maximum accuracy of 90%, with a minimum accuracy of 86%. The outcomes definitively designate EBd as the most crucial parameter to its role in building damage occurrence within the study area. In contrast, significance values were determined as 24%, 18%, and 6% for f_0, Vs_{30} and A_0 respectively in supervised cases. Among the parameters, the EBd and f_0 demonstrate the ability to establish a discernible demarcation by manifesting distinguishable clustering patterns in unsupervised methods. These findings underscore the importance of demonstrating that initial damage estimation in high seismic hazard zones can be effectively carried out using machine learning approaches through seismic-based local site parameters.

Keywords: 2023 Kahramanmaraş Earthquakes; Machine learning; Building damage

1. Introduction

Urban regions located in seismically active zones face a growing need for resilient infrastructure, particularly as population densities rise and previously unexamined building stocks age under outdated regulations. While modern seismic codes such as Eurocode 8 (EN, 2004), NEHRP (BSSC, 2020), and TBDY (AFAD, 2018) guide the construction of new buildings, many existing structures remain vulnerable due to poor design, material degradation, or suboptimal local site conditions. These vulnerabilities are typically revealed during strong earthquakes, where soil-structure interaction plays a pivotal role in the extent and spatial distribution of structural damage.

From a seismic risk assessment standpoint, damage can be interpreted as a manifestation of structural frailty and site-specific amplification effects triggered by earthquakes of varying intensities (Tien et al., 2012; Brando et al., 2020). Thus, estimating building damage necessitates consideration of both structural characteristics and geotechnical site parameters, such as Vs_{30}, f_0 (fundamental frequency), A_0 (HVSR ratio), and engineering bedrock depth (EBd or VsD_{760}) (Mori et al., 2020; Pontrelli et al., 2023; Petrescu et al., 2023). While traditional vulnerability assessments rely on rule-based frameworks like EMS98, FEMA P-154, and JBDPA, these methods require comprehensive in-situ data and may not effectively capture nonlinear interactions or spatial damage patterns, especially in large-scale applications (Rainer et al., 1993; FEMA, 2015; Aydogdu et al., 2023).

Recent advances in machine learning (ML) offer complementary pathways for seismic risk evaluation through both supervised and unsupervised approaches. Supervised algorithms (e.g., Random Forest, SVM, MLP, Logistic Regression) can be trained to estimate damage grades by learning from labeled datasets containing post-earthquake damage outcomes and associated geotechnical parameters. Such models not only identify the dominant features influencing structural failure but also facilitate early damage prediction in regions lacking detailed structural inventories by extrapolating from available site data (Harirchian et al., 2021; Zhang et al.,

*Corresponding author, E-mail: mustafasenkaya@uludag.edu.tr

https://doi.org/10.31462/icearc2025_ce_eqe_986

2023a). Conversely, unsupervised learning techniques—particularly clustering algorithms—enable the discovery of latent patterns in seismic site behavior without requiring predefined labels. This is especially beneficial for regional-scale assessments where uniform construction practices may lead to similar structural behavior under shared geotechnical conditions (Meyers-Angulo et al., 2023; Chiaradonna et al., 2023).

This study adopts a hybrid methodology integrating both supervised and unsupervised machine learning strategies to evaluate building damage resulting from the Mw 7.8 Pazarcık and Mw 7.5 Elbistan earthquakes that struck southeastern Türkiye on February 6, 2023. These twin events caused catastrophic losses across eleven provinces, with Hatay, Kahramanmaraş, and Gaziantep experiencing especially severe impacts (Görüm et al., 2023; Mavroulis et al., 2023). In the supervised modeling phase, various ML classifiers are trained on damage data correlated with seismic site parameters obtained from AFAD strong-motion stations and the Turkish Damage Assessment Inquiry system. In parallel, unsupervised clustering techniques are employed to group sites based solely on their seismic characteristics, enabling the exploration of potential site-induced damage patterns and their implications for future regional risk assessments.

Through the combined application of supervised and unsupervised modeling techniques, the proposed framework not only enables accurate and scalable damage prediction but also enhances understanding of the complex interplay between local soil conditions and structural performance. This dual approach is particularly suited for informing pre-earthquake risk mitigation strategies and supports the development of efficient, data-driven policies for urban resilience planning in earthquake-prone regions.

2. Data collection and pre-processing

The dataset comprises input parameters, Vs_{30}, f_0, A_0, and EBd, which represent localized site conditions, with damage status serving as the target variable (Table 1). The site condition parameters were derived from the TADAS database (https://tadas.afad.gov.tr/), which provides seismic datasets for the AFAD stations considered in this study (AFAD, 2024). This repository includes multichannel active/passive surface wave data and microtremor measurements acquired directly at the station locations by AFAD teams.

The Vs_{30} parameter, indicating the average shear wave velocity in the upper 30 meters, was primarily derived from 1D Vs-depth profiles obtained through inversion of dispersion curves (Park et al., 1999). Parameters f_0 and A_0 correspond to the site's fundamental frequency and amplitude of the Horizontal-to-Vertical Spectral Ratio (HVSR), respectively. These were obtained by analyzing microtremor data using the HVSR method (Nakamura, 1989), based on the observation that the spectral ratio of horizontal to vertical components of ambient seismic noise. The resulting HVSR curves help determine dominant subsurface frequencies (f_0) and presents an aspect for impedance contrast of layered sub-surface (A_0). The EBd parameter, indicative of deeper subsurface characteristics, is best captured through extended Vs-depth profiles—especially in areas with deep sedimentary deposits. In this study, EBd values were estimated from inversion of HVSR curve (Piña-Flores et al., 2017).

The damage status for each AFAD station location was determined by assessing the condition of neighboring structures according to the EMS-98 damage scale (Grünthal et al., 1998). This scale categorizes structural damage from DG0 (no damage) to DG5 (total collapse), and accounts for differences in structural typologies such as masonry and reinforced concrete (Aktas et al., 2022; Whitworth et al., 2022). Data on adjacent buildings surrounding each station were retrieved from the official Damage Assessment Inquiry System managed by the Ministry of Environment, Urbanization, and Climate Change of Türkiye (https://hasartespit.csb.gov.tr/). In this study, a location was labeled as "Damage" if at least 50% of the buildings in adjacent directions had a DG3 or higher rating, signifying moderate to severe structural damage. Conversely, the "No-Damage" label was assigned if at least 50% of neighboring structures were classified as DG2 or lower, indicating minor or no structural damage.

Exploratory Data Analysis (EDA), introduced by Tukey (1977), is essential for detecting outliers and unwanted patterns, serving as the first step in any data analysis (Páez and Boisjoly, 2022). An initial check revealed no missing data. Additionally, feature reduction was applied during the preparation of input parameters. As a result, Station ID, longitude, and latitude from Table 1 were excluded, as they are not used in the FCM and SC methods.

Following the removal of irrelevant features, normalization was performed to ensure all parameters shared a consistent scale. This helps reduce model bias and accelerates learning by stabilizing internal variable behavior (Singh and Singh, 2020). The process employed the MinMaxScaler function from Scikit-learn, which maintains similarity between data points and is especially suitable for distance-based algorithms like clustering (Cao et al., 2016).

Table 1. The details of dataset

Location ID	Station Number	Longitude	Latitude	f_0 (Hz)	A_0	Vs_{30} (m/s)	VsD_{760} (m)	Building damage status
1	2705	36.62062	37.01184	5.36	3.4	720	15	No-Damage
2	2707	36.57377	36.93088	1.44	3.4	546	22	No-Damage
3	2708	36.64837	37.09933	1.43	5.9	315	520	Damage
4	2709	36.67048	37.12852	5.60	3.9	521	33	No-Damage
5	3112	36.14766	36.58801	5.00	6.6	238	146	Damage
6	3113	36.14766	36.57752	0.52	5.1	190	195	No-Damage
7	3114	36.15135	36.56704	0.34	4.1	202	330	Damage
8	3115	36.16459	36.54634	0.20	4.7	380	465	Damage
9	3116	36.20661	36.61618	4.20	3.4	708	5	No-Damage
10	3117	36.17471	36.55712	4.05	2.2	597	88	No-Damage
11	3119	36.16811	36.57527	0.16	3.9	380	493	Damage
12	3120	36.20568	36.58924	3.73	3.1	455	48	No-Damage
13	3121	36.21825	36.66408	2.17	8.9	257	53	No-Damage
14	3124	36.17220	36.23870	1.07	4.3	262	517	Damage
15	3125	36.13264	36.23808	0.94	5.2	436	83	No-Damage
16	3126	36.13750	36.22020	0.12	9.8	287	488	Damage
17	3127	36.13530	36.21000	0.16	6.2	329	500	Damage
18	3128	36.14710	36.20560	0.20	4.6	307	445	Damage
19	3129	36.13430	36.19117	0.15	4.8	417	440	Damage
20	3130	36.14500	36.17920	0.24	4.8	331	373	Damage
21	3131	36.16328	36.19121	1.68	4.3	493	25	No-Damage
22	3132	36.17159	36.20673	0.20	4.1	324	523	Damage
23	3133	36.57360	36.24320	0.29	6.6	232	566	Damage
24	3134	36.20485	36.82763	0.96	1.8	313	61	No-Damage
25	3135	35.88310	36.40886	0.13	5.4	294	605	Damage
26	3143	36.55713	36.84890	0.17	5.9	393	490	Damage
27	3144	36.48574	36.75691	0.15	3.6	391	612	Damage
28	3145	36.40640	36.64536	0.17	2.5	475	476	Damage
29	4611	37.28426	37.74720	6.60	1.5	731	20	No-Damage
30	4612	36.48187	38.02395	0.86	3.9	255	84	No-Damage
31	4614	37.29775	37.48513	0.14	2.8	459	509	Damage
32	4617	36.83030	37.58551	5.10	1.7	574	40	No-Damage
33	4618	36.87231	37.60011	0.43	3.7	593	149	No-Damage
34	4619	36.86616	37.58702	0.40	4.9	362	80	No-Damage
35	4620	36.89845	37.58568	0.22	7.1	412	220	Damage
36	4621	36.92909	37.59347	2.00	2.0	486	41	No-Damage
37	4622	36.97759	37.58426	0.13	3.4	352	646	Damage
38	4623	36.93397	37.56918	0.12	5.8	392	724	Damage
39	4624	36.91765	37.53610	0.80	4.8	261	528	Damage
40	4629	36.78870	37.28737	3.14	4.8	387	65	Damage
41	4630	36.80603	37.34491	0.21	3.1	311	579	Damage
42	4631	37.42765	37.96632	2.60	3.7	543	45	No-Damage
43	4632	36.77369	37.25602	0.13	2.8	253	701	Damage
44	8004	36.09763	37.37988	0.13	4.6	323	577	Damage

Before modeling, input correlations were examined using Spearman's rank correlation via Seaborn's heatmap. This nonparametric measure assesses variable relationships without assuming linearity (Zhang and Wang, 2023). Fig. 1 displays these correlations, independent of clustering or accuracy. A value of 1 indicates strong positive correlation, -1 indicates strong negative. Highly correlated variables often contain redundant information, allowing one to be removed without affecting clustering outcomes (Yu and Liu, 2004). Determining a correlation threshold is critical in feature selection and often informed by prior studies. A threshold of ±0.85 was chosen here to retain as many features as possible given the dataset's limited size (Gu et al., 2019; Ozsagir et al., 2022). However, no variables exceeded this threshold, with the highest correlation being -0.82 between VsD_{760} and f_0, so no further reduction was required.

3. Methods

During modeling two unsupervised, Fuzzy C-means (FCM) and Spectral Clustering (SC), and three supervised, Random Forest (RF), K-nearest Neighbor (KNN) and Stochastic Gradient Descent (SGD), methods were employed. Also, performance metrics were determined through several well-known criteria based on the confusion matrix, including accuracy, precision, recall, and f-score.

FCM algorithm is an unsupervised clustering method rooted in fuzzy logic, which allows each data point to belong to multiple clusters with varying degrees of membership (Nayak et al., 2015). Unlike hard clustering methods that assign each point to a single cluster, FCM assigns soft membership values, enabling a more nuanced classification. The algorithm minimizes an objective function based on the Euclidean distance between data points and cluster centers, iteratively updating membership values and centers until convergence (Li et al., 2018; Naghi et al., 2023). These updates are conducted through defined equations involving Lagrange multipliers. FCM was implemented using the cluster.cmeans function from the Scikit-Fuzzy library. The iterative process continues until either a minimum objective function value is achieved or changes in membership fall below a set threshold (Hashemi et al., 2023).

SC is a graph-based clustering algorithm that identifies clusters using the eigenvalues and eigenvectors of a similarity matrix derived from the dataset (von Luxburg, 2007; Lee et al., 2022). The method begins by constructing a similarity graph and computing its unnormalized Laplacian matrix. It then solves the generalized eigenvalue problem to extract the top eigenvectors, which serve as a reduced representation of the data. These vectors are then clustered using the k-means algorithm, enabling the identification of complex, non-linearly separable patterns (Shi and Malik, 2000). SC was applied using the SpectralClustering function from the Scikit-learn library, making it especially suitable for data with intricate relationships not easily captured by traditional distance-based methods.

RF is an ensemble learning method that constructs multiple decision trees during training and aggregates their outputs, typically via majority voting, to make final predictions (Breiman, 2001). This approach reduces the risk of overfitting associated with individual decision trees by leveraging their independence and diversity. Unlike boosting methods, Random Forest doesn't sequentially modify the training set but instead introduces randomness through feature selection and data sampling. Its robust performance in classification tasks, especially on small datasets, has been demonstrated in various studies (Li et al., 2022; Luan et al., 2020). A positive correlation between the trees tends to enhance the algorithm's accuracy further (Chang et al., 2023).

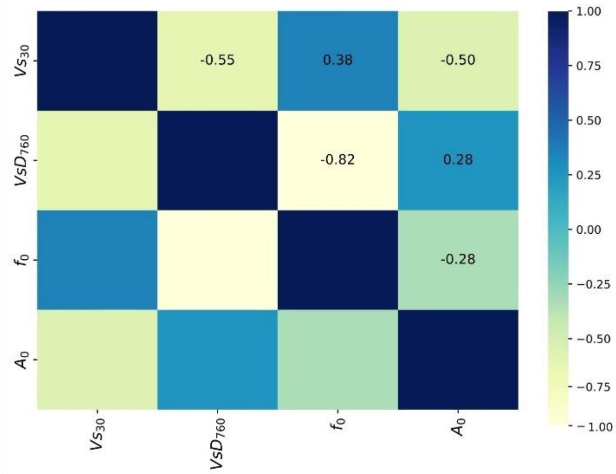

Fig. 1. The correlation relationship among the input parameters

KNN is a non-parametric and instance-based learning algorithm, often referred to as a lazy learner since it doesn't build a model explicitly but classifies based on the proximity of training samples. The classification of a new instance is determined by the majority class among its 'k' closest neighbors (Cover & Hart, 1967). Its appeal lies in the intuitive statistical relationship it forms between observed and target classes and its flexibility in handling data without assuming any prior distribution (Belattmania et al., 2023).

SGD is an optimization technique frequently used in training large-scale machine learning models. Unlike traditional gradient descent, which processes the entire dataset per iteration, SGD updates model parameters incrementally using one data point at a time, making it computationally efficient for online learning (Sharma, 2018). Its effectiveness depends on appropriate learning rates and convergence criteria to avoid overfitting and ensure stable learning.

4. Results

Performance of learning algorithms are given in Table 2. The RF model achieved the highest test accuracy during cross-validation, recording a value of 0.90, alongside a training accuracy of 0.97. It also exhibited strong performance across additional evaluation metrics, including precision, recall, and F1-score. Notably, the precision values for the 'No Damage' and 'Damage' classes were 0.89 and 0.96, respectively, suggesting a low rate of false positives. Similarly, the recall scores—reflecting the model's capability to identify true positives—were also high, with 0.94 for the 'No Damage' class and 0.92 for the 'Damage' class. The balanced F1-scores further underscore the model's ability to maintain an effective trade-off between precision and recall, thereby affirming its robustness in classifying both damaged and undamaged cases. Although a slight decrease in accuracy was observed on the test set, the RF model maintained strong and consistent performance across all major evaluation metrics. In contrast, while the KNN model demonstrated consistent and balanced accuracies on both the training and test sets, the SGD model showed a marked decline in precision and recall for the 'Damage' class, despite achieving moderate overall accuracy.

The relative importance of each feature in predicting building damage is quantitatively assessed and presented in Fig. 2, with the Random Forest (RF) model identified as the most effective classifier. Among the evaluated parameters, EBd emerged as the most influential, accounting for approximately 52% of the total feature importance in relation to building damage within the study area. In comparison, the features f_0, Vs_{30} and A_0 contributed 24%, 18%, and 6%, respectively. These findings highlight the dominant role of EBd in damage prediction and reinforce its critical significance in assessing structural vulnerability.

Table 2. Performance metrics of supervised learning algorithms

	Accuracy			Precision		Recall		F1-score	
	Train	Test	All	No Damage	Damage	No Damage	Damage	No Damage	Damage
RF	0.97	0.90	0.93	0.89	0.96	0.94	0.92	0.92	0.94
KNN	0.97	0.89	0.91	0.89	0.92	0.89	0.92	0.89	0.92
SGD	0.91	0.89	0.93	0.84	0.92	0.89	0.88	0.86	0.90

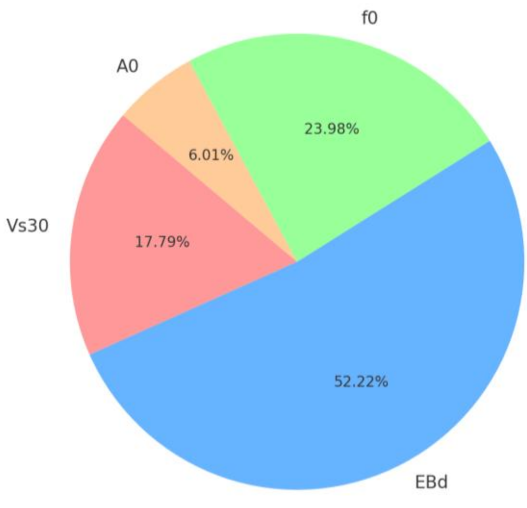

Fig. 2. Importance of features for the best classifier (RF)

Fig. 3a and 3b illustrate the performance of the Fuzzy C-Means (FCM) and Spectral Clustering (SC) methods, respectively, through confusion matrices that highlight the number of correct and incorrect predictions. The FCM approach demonstrates a relatively higher classification accuracy for the "No Damage" class, with only 2 misclassifications out of 18 instances. In contrast, the SC method registers 4 misclassifications for the same class. Both clustering methods yield identical performance in identifying the "Damage" class, correctly classifying 24 out of 26 cases. These results suggest that while both methods are comparably effective in detecting damaged structures, FCM offers a slight advantage in accurately identifying undamaged cases.

Table 3 summarizes the overall performance metrics for the Fuzzy C-Means (FCM) and Spectral Clustering (SC) algorithms. The FCM method outperforms SC in overall classification accuracy, achieving 90% compared to SC's 86%. In terms of specificity, which reflects the ability to correctly classify negative instances, FCM attains 88%, whereas SC demonstrates a slightly lower value of 77%. The precision metric, indicative of the correctness of positive predictions, is markedly high for FCM at 92%, surpassing SC's 85%. Both algorithms exhibit a strong recall rate of 92%, indicating effective identification of true positive instances. Furthermore, the F1 score, which provides a harmonic balance between precision and recall, is highest for FCM at 92%, with SC following at 88%. These results collectively underscore the superior performance of the FCM algorithm in unsupervised classification tasks within the given context.

5. Conclusions

This study presents an integrated approach to assessing the seismic vulnerability of structures by employing both supervised and unsupervised machine learning (ML) techniques, using local seismic parameters such as Vs_{30}, f_0, A_0, and EBd. Data collected from 44 locations affected by the February 2023 earthquakes in Hatay, Kahramanmaraş, and Gaziantep were analyzed to establish correlations between ground conditions and observed structural damage.

In the supervised learning framework, Random Forest (RF), K-Nearest Neighbors (KNN), and Stochastic Gradient Descent (SGD) classifiers were evaluated using five-fold cross-validation to mitigate overfitting from the limited dataset. Among these, the RF model demonstrated the highest predictive accuracy (93%) and exhibited strong performance across all key evaluation metrics. Feature importance analysis identified EBd as the most influential parameter (52%), followed by f_0, Vs_{30}, and A_0, highlighting the practical significance of seismic site parameters in damage prediction. Particularly, the ease of acquiring f_0 and EBd through microtremor measurements makes them valuable for conducting large-scale vulnerability assessments.

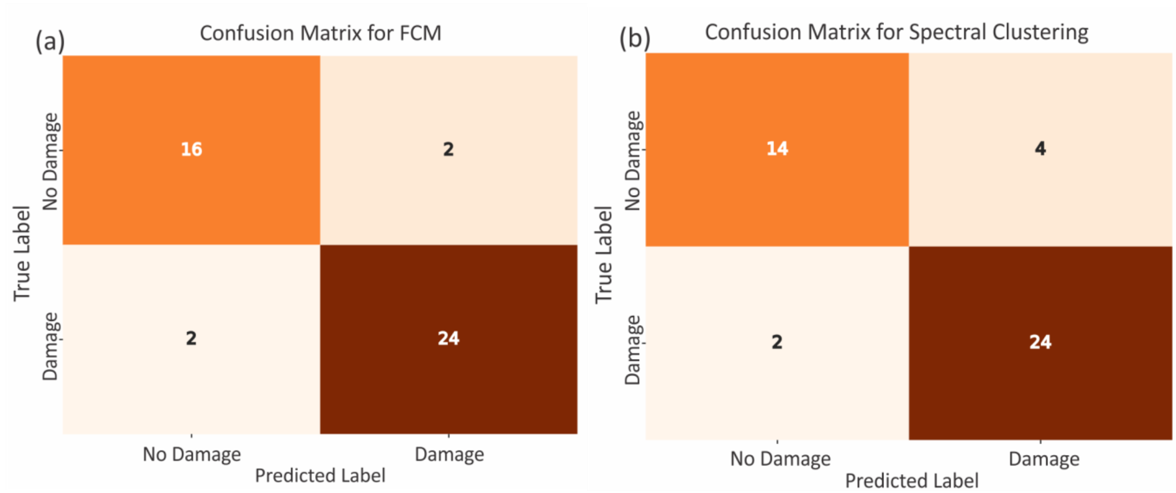

Fig. 3. a) and b) confusion matrix for FCM and SC

Table 3. Performance metrics of unsupersived algorithms

	FCM	SC
Accuracy	0.90	0.86
Specificity	0.88	0.77
Precision	0.92	0.85
Recall	0.92	0.92
F1Score	0.92	0.88

In parallel, unsupervised learning methods—specifically Fuzzy C-Means (FCM) and Spectral Clustering (SC)—were applied to identify damage patterns without the need for detailed structural information. Both clustering algorithms achieved high levels of agreement with observed damage states, correctly identifying 38 out of 44 sites. ROC-based evaluations indicated an average accuracy of 91%, reinforcing the potential of these techniques for pre-earthquake damage prediction using only seismic site parameters.

The dual application of supervised and unsupervised models demonstrates a robust, scalable framework for seismic risk assessment. These methods enable efficient prioritization of at-risk areas and can support decision-making in other regions with comparable seismic hazards and geological settings—such as Bursa, Sakarya, Adapazarı, and Erzincan. The approach also offers a cost-effective alternative to conventional assessments, optimizing time and resource allocation in both regional planning and emergency preparedness.

References

AFAD (2018) Turkish Earthquake Building Regulations. The Ministry of Interior, Turkey

AFAD. (2024). TADAS - stations. https://tadas.afad.gov.tr/list-station (accessed 4.4.24).

Aydogdu, H.H., Demir, C., Kahraman, T., & Ilki, A. (2023). Evaluation of rapid seismic safety assessment methods on a substandard reinforced concrete building stock in Istanbul. *Structures, 56*, 104962. https://doi.org/10.1016/j.istruc.2023.104962

Aktas, Y.D., Ioannou, I., Malcioglu, F.S., et al. (2022). Hybrid reconnaissance mission to the 30 October 2020 Aegean Sea earthquake and tsunami (Izmir, Turkey & Samos, Greece): Description of data collection methods and damage. *Frontiers in Built Environment, 8*. https://doi.org/10.3389/fbuil.2022.840192

Belattmania, A., El Arrim, A., Ayouche, A., Charria, G., Hilmi, K., & El Moumni, B. (2023). K nearest neighbors classification of water masses in the western Alboran Sea using the sigma-pi diagram. *Deep Sea Research Part I: Oceanographic Research Papers, 196*, 104024. https://doi.org/10.1016/j.dsr.2023.104024

Brando, G., Pagliaroli, A., Cocco, G., & Di Buccio, F. (2020). Site effects and damage scenarios: The case study of two historic centers following the 2016 Central Italy earthquake. *Engineering Geology, 272*, 105647. https://doi.org/10.1016/j.enggeo.2020.105647

Breiman, L. (2001). Random forests. *Machine Learning, 45*(1), 5–32. https://doi.org/10.1023/A:1010933404324

BSSC. (2020). NEHRP recommended seismic provisions for new buildings and other structures. Federal Emergency Management Agency.

Cao, X.H., Stojkovic, I., & Obradovic, Z. (2016). A robust data scaling algorithm to improve classification accuracies in biomedical data. *BMC Bioinformatics, 17*, 359. https://doi.org/10.1186/s12859-016-1236-x

Chang, V., Bailey, J., Xu, Q. A., & Sun, Z. (2023). Pima Indians diabetes mellitus classification based on machine learning (ML) algorithms. *Neural Computing and Applications, 35*, 16157–16173. https://doi.org/10.1007/s00521-022-07049-z

Chiaradonna, A., Karakan, E., Kincal, C., et al. (2023). Insights on the role of local site effects on damage distribution in the Izmir metropolitan area induced by the October 30, 2020 Samos earthquake. *Soils and Foundations, 63*, 101330. https://doi.org/10.1016/j.sandf.2023.101330

Cover, T., & Hart, P. (1967). Nearest neighbor pattern classification. *IEEE Transactions on Information Theory, 13*(1), 21–27. https://doi.org/10.1109/TIT.1967.1053964

EN. (2004). Eurocode 8: Design of structures for earthquake resistance – Part 1: General rules, seismic actions and rules for buildings. European Committee for Standardization.

FEMA. (2015). Rapid visual screening of buildings for potential seismic hazards: A handbook (3rd ed., FEMA P-154).

Görüm, T., Tanyas, H., Karabacak, F., Yılmaz, A., Girgin, S., Allstadt, K.E., Süzen, M.L., & Burgi, P. (2023). Preliminary documentation of coseismic ground failure triggered by the February 6, 2023 Türkiye earthquake sequence. *Engineering Geology, 327*, 107315. https://doi.org/10.1016/j.enggeo.2023.107315

Grünthal, G., Musson, R.M.W., Schwarz, J., & Stucchi, M. (1998). European Macroseismic Scale 1998 (EMS-98). https://doi.org/10.2312/EMS-98

Gu, J., Zhu, J., Qiu, Q., et al. (2019). Prediction of immunohistochemistry of suspected thyroid nodules by use of machine learning–based radiomics. *American Journal of Roentgenology, 213*(6), 1348–1357. https://doi.org/10.2214/AJR.19.21626

Harirchian, E., Aghakouchaki Hosseini, S.E., Jadhav, K., Kumari, V., Rasulzade, S., Işık, E., Wasif, M., & Lahmer, T. (2021). A review on application of soft computing techniques for the rapid visual safety evaluation and damage classification of existing buildings. *Journal of Building Engineering, 43*. https://doi.org/10.1016/j.jobe.2021.102536

Hashemi, S.E., Gholian-Jouybari, F., & Hajiaghaei-Keshteli, M. (2023). A fuzzy C-means algorithm for optimizing data clustering. *Expert Systems with Applications, 227*, 120377. https://doi.org/10.1016/j.eswa.2023.120377

Lee, P.-H., Torng, C.-C., Lin, C.-H., & Chou, C.-Y. (2022). Control chart pattern recognition using spectral clustering technique and support vector machine under gamma distribution. *Computers & Industrial Engineering, 171*, 108437. https://doi.org/10.1016/j.cie.2022.108437

Li, J., Horiguchi, Y., & Sawaragi, T. (2018). Refining fuzzy C-means membership functions to assimilate a priori knowledge of cluster sizes. In *2018 Joint 10th International Conference on Soft Computing and Intelligent Systems (SCIS) and 19th International Symposium on Advanced Intelligent Systems (ISIS)*, 654–659

Li, Y., Rahardjo, H., Satyanaga, A., Rangarajan, S., & Lee, D.T.-T. (2022). Soil database development with the application of machine learning methods in soil properties prediction. *Engineering Geology, 306*, 106769. https://doi.org/10.1016/j.enggeo.2022.106769

Luan, J., Zhang, C., Xu, B., Xue, Y., & Ren, Y. (2020). The predictive performances of random forest models with limited sample size and different species traits. *Fisheries Research, 227*, 105534. https://doi.org/10.1016/j.fishres.2020.105534

Mavroulis, S., Argyropoulos, I., Vassilakis, E., Carydis, P., & Lekkas, E. (2023). Earthquake environmental effects and building properties controlling damage caused by the 6 February 2023 earthquakes in East Anatolia. *Geosciences, 13*(10), 303. https://doi.org/10.3390/geosciences13100303

Meyers-Angulo, J.E., Martínez-Cuevas, S., & Gaspar-Escribano, J.M. (2023). Classifying buildings according to seismic vulnerability using Cluster-ANN techniques: Application to the city of Murcia, Spain. *Bulletin of Earthquake Engineering, 21*, 3581–3622. https://doi.org/10.1007/s10518-023-01671-5

Mori, F., Mendicelli, A., Moscatelli, M., Romagnoli, G., Peronace, E., & Naso, G. (2020). A new Vs30 map for Italy based on the seismic microzonation dataset. *Engineering Geology, 275*, 105745. https://doi.org/10.1016/j.enggeo.2020.105745

Naghi, M.-B., Kovács, L., & Szilágyi, L. (2023). A review on advanced C-means clustering models based on fuzzy logic. In *2023 IEEE 21st World Symposium on Applied Machine Intelligence and Informatics (SAMI)*, 000293–000298

Nakamura, Y. (1989). A method for dynamic characteristics estimation of subsurface using microtremor on the ground surface. *Railway Technical Research Institute, Quarterly Reports, 30*(1), 25–33

Nayak, J., Naik, B., & Behera, H.S. (2015). Fuzzy C-means (FCM) clustering algorithm: A decade review from 2000 to 2014. In *Computational Intelligence in Data Mining,* (pp. 133–149). Springer

Ozsagir, M., Erden, C., Bol, E., et al. (2022). Machine learning approaches for prediction of fine-grained soils liquefaction. *Computers and Geotechnics, 152*, 105014. https://doi.org/10.1016/j.compgeo.2022.105014

Páez, A., & Boisjoly, G. (2022). Exploratory data analysis. In Discrete Choice Analysis with R (pp. 25–64). Springer

Park, C.B., Miller, R.D., & Xia, J. (1999). Multichannel analysis of surface waves. *Geophysics, 64*(3), 800–808. https://doi.org/10.1190/1.1444590

Petrescu, L., Popa, M., & Radulian, M. (2023). Shallow seismic structure around the Vrancea Seismic Zone from joint inversion of ambient noise H/V ratios and surface wave dispersion. *Tectonophysics, 859*, 229897. https://doi.org/10.1016/j.tecto.2023.229897

Piña-Flores, J., Perton, M., García-Jerez, A., et al. (2017). The inversion of spectral ratio H/V in a layered system using the diffuse field assumption (DFA). *Geophysical Journal International, 208*(1), 577–588. https://doi.org/10.1093/gji/ggw416

Pontrelli, M., Baise, L., & Ebel, J. (2023). Regional-scale site characterization mapping in high impedance environments using soil fundamental resonance (f0): New England, USA. *Engineering Geology, 315*, 107043. https://doi.org/10.1016/j.enggeo.2023.107043

Rainer, J.H., Allen, D.E., & Jablonski, A.M. (1993). Manual for screening of buildings for seismic investigation. National Research Council Canada.

Sharma, A. (2018). Guided stochastic gradient descent algorithm for inconsistent datasets. *Applied Soft Computing, 73*, 1068–1080. https://doi.org/10/1/accepted_manuscript.pdf

Shi, J., & Malik, J. (2000). Normalized cuts and image segmentation. *IEEE Transactions on Pattern Analysis and Machine Intelligence, 22*(8), 888–905. https://doi.org/10.1109/34.868688

Singh, D., & Singh, B. (2020). Investigating the impact of data normalization on classification performance. *Applied Soft Computing, 97*, 105524. https://doi.org/10.1016/j.asoc.2019.105524

Tien, Y.M., Juang, C.H., Chen, J.-M., & Pai, C.-H. (2012). Isointensity-isoexposure concept for seismic vulnerability analysis — A case study of the 1999 Chi-Chi, Taiwan earthquake. *Engineering Geology, 131–132*, 1–10. https://doi.org/10.1016/j.enggeo.2011.12.004

Tukey, J.W. (1977). Exploratory data analysis. Pearson.

von Luxburg, U. (2007). A tutorial on spectral clustering. *Statistics and Computing, 17*(4), 395–416. https://doi.org/10.1007/s11222-007-9033-z

Whitworth, M.R.Z., Giardina, G., Penney, C., et al. (2022). Lessons for remote post-earthquake reconnaissance from the 14 August 2021 Haiti earthquake. *Frontiers in Built Environment, 8*. https://doi.org/10.3389/fbuil.2022.873212

Yu, L., & Liu, H. (2004). Efficient feature selection via analysis of relevance and redundancy. *Journal of Machine Learning Research, 5*, 1205–1224

Zhang, L., & Wang, L. (2023). Optimization of site investigation program for reliability assessment of undrained slope using Spearman rank correlation coefficient. *Computers and Geotechnics, 155*, 105208. https://doi.org/10.1016/j.compgeo.2022.105208

Zhang, W., Gu, X., Hong, L., Han, L., & Wang, L. (2023). Comprehensive review of machine learning in geotechnical reliability analysis: Algorithms, applications and further challenges. *Applied Soft Computing, 136*, 110066. https://doi.org/10.1016/j.asoc.2023.110066

4th International Civil Engineering & Architecture Conference
17-19 May 2025, Trabzon, Türkiye

Dynamic analysis of a building structure including soil-structure interaction

Dilek Kaya[*1], Tufan Cakir[2], Kasif F. Ozturk[2]

[1] Construction Technology Program, Gümüşhane University, Gümüşhane, Türkiye
[2] Department of Civil Engineering, Gümüşhane University, Gümüşhane, Türkiye

Abstract. In the analysis of structural systems, it is traditionally assumed that the structure founds on an undeformable rigid base and the interaction between the structure and the foundation/soil system is neglected. This approach may not be valid for the structures built on the soils (clay, sand, weathered rocks, etc.) other than the rigid rock soils depending on the structural properties. The importance of the soil-structure interaction (SSI) effects on buildings under seismic loading has been shown in many studies. Furthermore, the slenderness of the structure, its dimensions, the building material and the variation of the mechanical properties of the soil reveal significant differences in the dynamic responses of the structure. In this study, the SSI effects on the seismic response of an 8-story building structure are evaluated for different subsoil conditions. The SSI is considered through massless foundation approach. First, the finite element models of the considered structure with fixed and flexible bases are created using ANSYS software. Then, the analytical models of the structure with fixed and flexible bases are constituted, and the modal periods of the numerical and analytical systems are compared. Finally, the time history analyses of the SSI systems are carried out through numerical models, and the computed lateral displacements and stresses are discussed. The results show that the soil properties have a significant effect on the time-dependent responses under earthquake loads, and the SSI effects should not be ignored in the seismic design.

Keywords: Analytical model; Ansys; Finite element model; Seismic response; Soil-structure interaction

1. Introduction

In structural analysis, buildings are often assumed to rest on a rigid soil that does not change shape. However, this approach may not be valid, especially for structures located on soft or medium-hard soils (e.g. clay, sand or weathered rock). In reality, the interaction between the structure and the foundation soil - the soil-structure interaction (SSI) - can significantly affect the behavior of the structure during dynamic events such as earthquakes. Therefore, ignoring the effects of SSI can lead to inadequate assessment of structure performance and potential safety issues. As well as the geometrical characteristics of the structure (height, slenderness ratio, dimensions) and material diversity, the mechanical properties of the soil directly affect the dynamic response. These effects become evident in basic parameters such as the period of natural vibration, the amount of horizontal displacement and internal stress distributions. Neglecting SSI in seismic design may lead to underestimation of displacement and internal force values, thus jeopardizing the safety of the structure against earthquakes.

Many studies on SSI in the literature have investigated the effects of this interaction on the behavior of the structure under different scenarios. For example, Menglin et al. (2011) investigated the effects of SSI in adjacent buildings in depth and summarized the research on this topic with its historical development. Li et al. (2011) determined the dynamic parameters of the soil-structure interaction system by means of shaking table tests performed under hard soil conditions. The results showed a strong agreement between numerical modeling and experimental data and demonstrated that this approach can be reliably used in SSI analysis. Jaya et al. (2012) analyzed the dynamic response of deeply buried chimneys and showed that the peak acceleration and displacement values decrease as the depth of burial increases. Priyanka et al. (2012) evaluated the seismic response of multistory buildings under different soil conditions. Roesset (2013) reviewed the early work on SSI and discussed the debates and developments, especially in the seismic design of nuclear power plants. The advantages of direct and substructure approaches, the evolution of dynamic foundation stiffnesses and the effects of inertial and kinematic interactions on structural response are discussed in detail. Cakir (2014) analyzed the flexibility of anchored retaining walls and the effect of soil type on seismic behavior using three-dimensional finite element models. Masaeli et al. (2015) revealed that SSI has significant effects on the seismic performance of thin and tall buildings.

* Corresponding author, E-mail: dilekozdmr38@gmail.com

https://doi.org/10.31462/icearc2025_ce_geo_006

Yeganeh et al. (2015) evaluated the behavior of tall buildings adjacent to deep excavation areas under earthquake effects in the context of SSI. As a result of the analyses performed with FLAC2D software, significant differences between static and dynamic responses were observed, indicating that SSI plays a significant role in the structural response. Li et al. (2017) investigated the collision effects in the context of structural soil-structure-ground interaction (SSSI) in adjacent buildings using ANSYS software and found that this interaction increases the collision severity. The study also found that the building spacing prescribed in Chinese standards is generally inadequate for such interactions. Mortezaie and Rezaie (2018) developed a three-dimensional performance-based plastic design (PBPD) approach for high-rise reinforced concrete structures considering SSI effects. The results show that the mechanical properties of the soil play a decisive role in the dynamic behavior of the structure. Gao et al. (2020) confirmed that the response spectrum method (RSM) is effective in evaluating the effects of SSI in their analysis of structures with shallow foundations and emphasized that the interaction between horizontal motion and rocking is a critical factor, especially in tall buildings located on soft soils. Scarfone et al. (2020) performed three-dimensional, nonlinear dynamic analyses to evaluate the effects of SSI in high-rise buildings. As a result of these analyses, it was determined that foundation deformation reduces the base shear forces, but does not make a significant difference on the displacements. Similarly, Bahuguna and Firoj (2021) investigated the nonlinear seismic behavior of nuclear structures with SSI and concrete damage plasticity (CDP) model and showed that buried foundations provide significant reductions in moment and displacement demands. Gao et al. (2021) proposed a generalized response spectrum method using viscous-spring artificial boundaries (VSAB) to improve the accuracy of seismic analysis for underground structures. Kamal and Inel (2021) analyzed the relationship between ground motion parameters and displacement demands by considering SSI effects in mid-rise reinforced concrete buildings and found that velocity-based parameters such as Housner Intensity (HI) can reliably represent the potential for structural damage. Ozgur and Bozdogan (2022) investigated the effects of SSI on period elongation and seismic design parameters of reinforced concrete buildings and showed that the seismic performance of rigid structures changes significantly under soft ground conditions. Araz et al. (2022) evaluated the effect of frequency content on tuned mass dampers (TMD) in multistory buildings and found that these parameters vary significantly with frequency content. Similarly, Araz (2022) developed an optimization strategy for TMDI systems used in high-rise buildings by considering SSI effects. Bapir et al. (2023) presented a comprehensive literature review on SSI modeling techniques and their effects on seismic response of the structure and emphasized that SSI should be considered in engineering design processes. Araz et al. (2023) investigated the effect of foundation embedment depth and soil properties on the optimum TMD design and revealed that these two parameters significantly affect the damper performance. Rostami Heshmat Abad et al. (2024) analyzed the effect of SSI on the torsional behavior of asymmetric steel moment frame structures resting on masonry-raft foundation system and showed that SSI causes critical torsional irregularities by increasing the maximum story rotation angles Bapir and Abrahamczyk (2024) compared different simplified SSI modeling techniques and reported that these methods give different results in terms of accuracy and practical applicability. In the same year, Bapir et al. investigated the SSI-induced seismic behavior of reinforced concrete structural systems and different foundation sizes and found that the stiffness of the foundation and the type of structure are determinants of the structural response. Vicencio and Alexander (2024) evaluated the Site-City Interaction (SCI) effects between city blocks and showed that this effect can enhance or weaken the structural seismic response depending on building placement and ground resonance. Wang et al. (2024) analyzed the performance of semi-active tunable mass dampers (STMD) under SSI effects in tall buildings and found that these systems provide more effective control compared to conventional TMD systems by simultaneously optimizing frequency and damping ratios. Araz (2025) investigated the effect of SSI parameters on seismic control performance in structures equipped with optimized TMD systems and found that the structure-ground stiffness ratio and structure slenderness ratio significantly affect TMD efficiency. Hwang et al. (2025) investigated the seismic ground pressures on the basement walls of buildings with 1g shake table experiments and observed significant differences in the distribution of these pressures depending on the basement stiffness and building height Finally, Ozturk (2025) analyzed the effects of main shock-aftershock sequences on the dynamic behavior of natural gas pipelines in the context of soil-pipe interaction (SNGPI) and showed that the reduction in soil stiffness significantly increases the peak stress and displacement values of pipelines.

This study investigates the seismic behavior of an 8-storey structure under different soil types in the context of SSI. A massless foundation approach is adopted to represent the SSI, and structural models with rigid and flexible foundation conditions are generated using ANSYS software. In addition, analytical models corresponding to these systems are developed and the natural periods obtained are compared by numerical and analytical methods. The horizontal displacement and stress behavior of the structure under seismic effects were evaluated by time domain analysis. The obtained results clearly reveal the determinant role of the soil on the dynamic response and demonstrate once again the necessity of considering SSI effects in seismic design processes.

2. Methodology

2.1. Structure and soil model

In this section, the numerical model for the soil and structure is presented in Fig.1. For the structure, an 8-storey building model with column dimensions of 30x60 cm and beam dimensions of 30x50 cm is considered. The model has a total length of 12 m with 3 spans in x and y directions horizontally and the storey height is 3 m. The compressive strength, modulus of elasticity, Poisson's ratio and unit density values of all structural elements are 25 MPa, 30GPa, 0.2 and 2500 kg/m3 respectively. The dimensions of the soil medium affect the modal properties and dynamic response of the soil-structure system. The dimensions of the numerical model for the soil were chosen seven times (84 m) the width of the structure in the x-y direction horizontally and three times (36 m) in the z-direction vertically, considering the studies in the literature (Rayhani and El Naggar, 2008; Torabi and Rayhani, 2014; Kabtamu et al., 2018). The selected soil properties are given in Table 1. The numerical models were obtained with ANSYS software (ANSYS, 2015) using 3D finite elements. SOLID45 and SOLID65 element types were used for the soil and structure, respectively. The SOLID45 element type including plasticity, creep, swelling, strain hardening, and large deformations. On the other hand, the SOLID65 element is specifically designed to model concrete materials, with features that allow it to simulate cracking under tension and crushing under compression, even without reinforcement.

Table 1. The properties of the soil material

Soil type	E (N/m^2)	G (N/m^2)	v	ρ (kg/m^3)	v_s (m/sn)	v_p (m/sn)
S1	3.00 x 10^8	11 x 10^7	0.35	1900	241.83	503.40
S2	1.50 x 10^8	5.56 x 10^7	0.35	1900	171.00	355.96
S3	0.75 x 10^8	2.68 x 10^7	0.40	1800	121.99	298.81

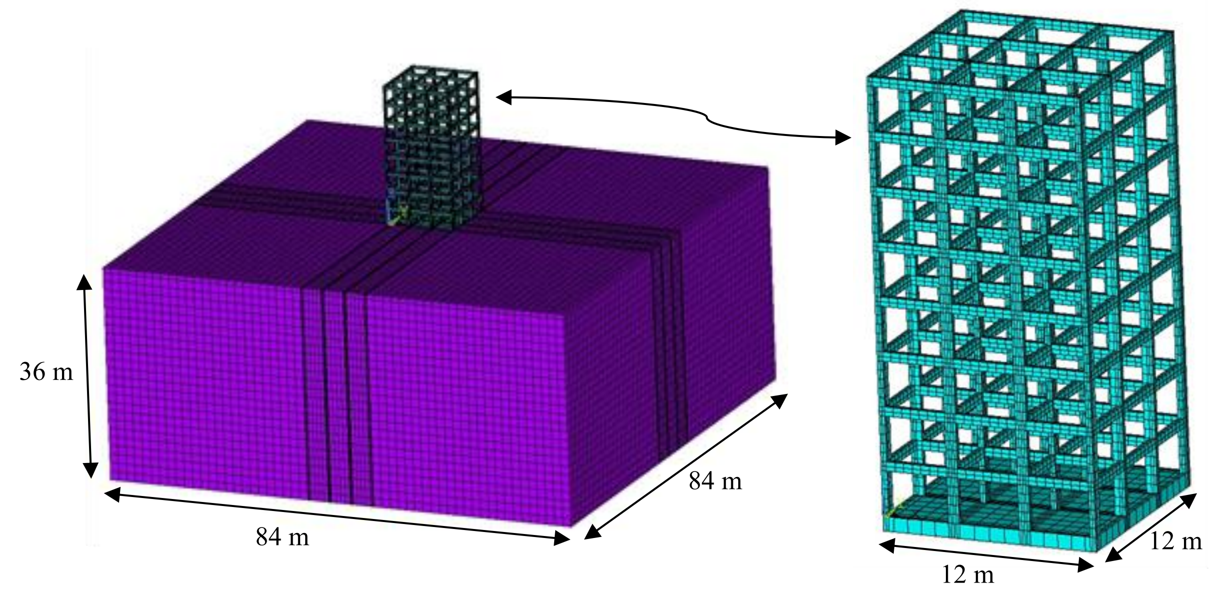

Fig. 1. Numerical model for SSI

The modes with higher modal participation factors have a greater influence on the structural response (Cakir and Livaoglu, 2013) Table 2 presents the first three natural periods, selected based on effective modal masses, for both fixed-base and flexible-base conditions. As shown in the table, SSI leads to an increase in the natural periods, with the longest periods observed in structures founded on S3 soil type.

Table 2. The periods of the structural system (s)

Soil type / Model	Fixed	S1	S2	S3
1	0.71	0.76	0.80	0.87
2	0.24	0.24	0.24	0.25
3	0.14	0.14	0.14	0.15

2.2. Analytical solutions and comparison of modal analysis results

In this section, the modal analysis results obtained from the numerical models are evaluated by comparing them with the results of the proposed analytical models. The analytical model equations, called F-1, are given below (Eqs. 1-4).

$$M\ddot{x}(t) + Kx(t) = f(t) \tag{1}$$

Here, M denotes the mass matrix and K represents the stiffness matrix. The vector $f(t)$ corresponds to the external force applied to the system, while $x(t)$ denotes the displacement vector describing the system's response over time.

$$M = \begin{bmatrix} m_1 & & & & m_1 & m_1 z_1 \\ & m_2 & & & m_2 & m_2 z_2 \\ & & \ddots & & \vdots & \vdots \\ & & & m_N & m_N & m_N z_N \\ m_1 & m_2 & \cdots & m_N & m_0 + \sum_{i=1}^{N} m_i & \sum_{i=1}^{N} m_i z_i \\ m_1 z_1 & m_2 z_2 & \cdots & m_N z_N & \sum_{i=1}^{N} m_i z_i & \sum_{i=1}^{N} (m_i z_i^2 + I_i) + I_0 \end{bmatrix} \tag{2}$$

$$K = \begin{bmatrix} k_1 + k_2 & -k_2 & 0 & 0 & 0 & 0 \\ -k_2 & k_2 + k_3 & -k_3 & \cdots & 0 & 0 \\ & \cdots & \cdots & \cdots & \cdots & \cdots \\ sym & & -k_N & k_N & 0 & 0 \\ 0 & 0 & \cdots & 0 & k_s & 0 \\ 0 & 0 & \cdots & 0 & 0 & k_r \end{bmatrix} \tag{3}$$

$$x(t) = \begin{bmatrix} x_1 & x_2 & \cdots & x_N & x_0 & x_\theta \end{bmatrix}^T \tag{4}$$

Eqs. (2–4) define the parameters m_i, k_i, I_i, and as the mass, lateral stiffness, mass moment of inertia, and lateral displacement of the ith story, respectively. The foundation is characterized by its mass m_0 and mass moment of inertia I_0. The SSI is represented through the swaying stiffness k_s and rocking stiffness k_r of the supporting soil. Furthermore, x_0 and x_θ denote the horizontal displacement and rotational degree of freedom of the foundation, respectively.

The soil parameters associated with a rigid square foundation are determined using Eq. (5) (Wolf, 1994). In this context, G and v represent the shear modulus and Poisson's ratio of the soil, respectively. The terms A_0 and I_{0b} denote the contact area and the mass moment of inertia of the foundation about its side b. Parameters a and b correspond to half the width and half the length of the foundation, respectively.

$$k_s = \frac{2Ga}{2-v}\left[2 + 2.5\left(\frac{A_0}{4a^2}\right)^{0.85}\right], \; k_r = \frac{2.9G}{1-v}\left[I_{0b}^{0.75}\left(\frac{a}{b}\right)^{0.15}\right] \tag{5}$$

In the analytical solution referred to as F-2, the stiffness period of each story, denoted by k_i has been utilized in Eq. (6) to derive the overall lateral stiffness period of the structure, k_x. The rocking stiffness k_r, which varies with the height of the structure, has been reformulated to obtain the modified rotational stiffness k_r'. Subsequently, the equivalent stiffness K_{eqm} has been considered in Eq. (7) to carry out the analytical evaluation.

$$\frac{1}{k_x} = \sum_{i=1}^{N} \frac{1}{k_i} \tag{6}$$

$$k_r' = \frac{k_r}{h_s^2}, \; K_{eqm} = \frac{k_x k_r' k_s}{k_x k_s + k_x k_r' + k_r' k_s} \tag{7}$$

The analytical model equations, called F-3, are given below (Eq. 8).

$$M = \begin{bmatrix} m_s & 0 & 0 & 0 \\ 0 & m_f & 0 & 0 \\ 0 & 0 & I_s + I_f + m_\varphi & 0 \\ 0 & 0 & 0 & m_\theta \end{bmatrix}, \; K = \begin{bmatrix} k_x & -k_x & -k_x h_s & 0 \\ -k_x & k_s + h_s & k_x h_s & 0 \\ -k_x h_s & k_x h_s & k_x h_s^2 + k_r & 0 \\ 0 & 0 & 0 & 0 \end{bmatrix} \tag{8}$$

Where m_θ is the mass moment of inertia assigned to the rotational degree of freedom. In the case of $v>1/3$, the mass moment of inertia m_φ is added to the rotational degree of freedom, and the value $2v_s$ is taken instead of v_p (Song et al., 2021). v_p and v_s are the dilatational wave velocity and shear wave velocity of soil, respectively.

$$m_\theta = \frac{9}{128}\left[(1-\nu)\pi^2 \rho r^5 \left(\frac{v_p}{v_s}\right)^2\right], \quad m_\varphi = 0.3\left(\nu - \frac{1}{3}\right)\pi \rho r^5 \tag{9}$$

The modal analysis results of the numerical models obtained under fixed and flexible soil conditions are compared with the analytical solutions F-1, F-2, and F-3 in Table 3. When the difference values in Table 3 are examined, they are observed to range between 9.76% and 44.59%. Among the analytical solutions, the F-1 results showed lower differences compared to F-2 and F-3. Additionally, the largest differences were observed in the F-2 analytical solution.

Table.3. Comparison of first mode periods fixed and flexible base structures (s)

Type	Model-1	F-1	Dif.%	Model-1	F-2	Dif.%	Model-1	F-3	Dif.%
Fixed	0.37	0.41	9.76	0.37	0.52	28.85	0.37	0.52	28.85
S1	0.38	0.49	22.45	0.38	0.58	34.48	0.38	0.58	34.48
S2	0.39	0.56	30.36	0.39	0.64	39.06	0.39	0.63	38.10
S3	0.41	0.67	38.81	0.41	0.74	44.59	0.41	0.73	43.84

* Dif. $\% = 100 \times |(Analytical - FEM) / Analytical|$

3. The SSI system responses

For the evaluation of displacement and acceleration responses in the numerically modeled eight-story soil-structure system, nodes have been selected at each floor level along the exterior face of the building. Additionally, for the assessment of stress response, a node located at the beam–column that recognized as a structurally critical region, has been selected for analysis (Fig. 2).

The 1999 Düzce Earthquake is selected for SSI. The earthquake component is DUZCE/BOL000, station is Bolu, magnitude is 7.1 and PGA is 0.739 g.

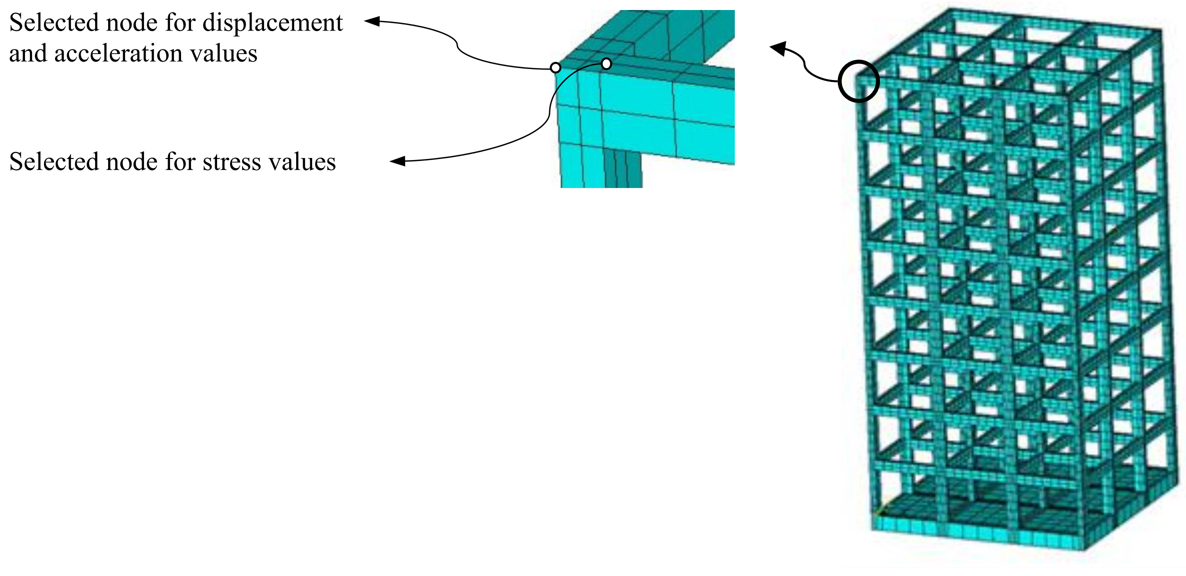

Fig. 2. Selected nodes on the structures for dynamic responses

Peak values of displacement, stress and acceleration dynamic responses depending over height and soil type are given in Table 4-6. As shown in Table 4, peak displacement values obtained under the effect of the Düzce earthquake are compared based on different floor levels and soil types. These displacement values are evaluated relatively, taking the bottom level of the foundation as the reference point. It is observed that the peak displacement values and their occurrence times vary depending on the floor level and the type of soil. Table 5 presents the peak stress values corresponding to different floor levels and soil types. When Table 5 is examined, it is observed that the stress values occur under both tensile and compressive effects. Similarly, Table 6 provides the peak acceleration values for various floor levels and soil types. A more detailed comparison of these findings is provided in Section 3.1.

Table 4. The displacement values depending over height and soil type (m)

No. of stories	Fixed		S1		S2		S3	
	t	u	t	u	t	u	t	u
8	10.55	-0.1456	10.58	-0.1746	10.60	-0.1845	11.65	-0.1948
7	10.55	-0.1374	10.58	-0.1636	10.60	-0.1716	11.65	-0.1807
6	10.55	-0.1242	10.58	-0.1471	10.60	-0.1536	11.65	-0.1626
5	10.54	-0.1066	10.58	-0.1259	10.60	-0.1310	11.65	-0.1407
4	10.54	-0.0859	10.57	-0.1012	10.60	-0.1049	11.64	-0.1157
3	10.53	-0.0629	10.57	-0.0744	10.60	-0.0769	11.63	-0.0877
2	10.53	-0.0389	10.57	-0.0468	10.60	-0.0484	11.63	-0.0577
1	10.52	-0.0152	10.56	-0.0201	10.59	-0.0212	11.63	-0.0268
0			10.57	-0.0010	10.60	-0.0016	11.64	-0.0025

Table 5. The stress values depending over height and soil type (MPa)

No. of stories	Fixed		S1		S2		S3	
	t	S	t	S	t	S	t	S
8	10.82	-4.1693	10.59	4.2084	10.61	4.1217	12.09	-4.18857
7	10.56	8.4634	10.59	8.8100	10.61	8.6121	12.08	-8.44966
6	10.56	14.2401	10.59	14.9398	10.61	14.5372	12.08	-13.5932
5	10.56	19.0682	10.59	20.0616	10.61	19.4220	12.07	-17.2051
4	10.56	22.6492	10.58	23.8551	10.60	22.9796	11.67	19.7055
3	10.55	25.0358	10.58	26.1807	10.60	25.0253	11.65	22.6629
2	10.54	26.3043	10.57	26.9928	10.60	25.4576	11.64	25.0101
1	10.53	24.5889	10.56	24.8813	10.59	22.8462	11.20	-24.6391
0			10.94	-1.5975	10.95	-1.6328	11.20	-2.2337

Table 6. The acceleration values depending over height and soil type (m/s^2)

No. of stories	Fixed		S1		S2		S3	
	t	a	t	a	t	a	t	a
8	10.78	-18.4020	10.60	17.8010	10.61	18.1850	10.64	16.7550
7	10.78	-17.4560	10.60	16.5570	10.61	16.7900	10.64	15.1910
6	10.78	-15.6060	10.60	14.6900	10.61	14.8390	10.63	13.2050
5	10.78	-12.7720	10.61	12.2690	10.61	12.3980	12.02	-12.1230
4	10.78	-9.7213	10.61	9.4651	10.62	9.5583	12.01	-11.2260
3	10.78	-7.3264	10.33	-6.4637	11.98	-8.0505	11.99	-9.7433
2	11.09	5.6799	11.10	4.8055	11.97	-6.0139	11.98	-7.3990
1	11.09	2.6600	10.90	-2.8663	10.90	-3.2564	11.97	-4.1562
0			10.75	-1.2536	10.80	2.2669	10.81	2.8860

3.1. Height-dependent variation of dynamic responses

In Fig. 3, the lateral displacement values of an eight-storey building at different floor levels under the effect of Düzce earthquake are presented comparatively for four different soil types (Fixed, S1, S2, S3). It is observed that the displacement values increase with the number of storeys for all soil types. The fixed base has the lowest lateral displacement values at all floor levels. It is observed that the structure is subjected to larger displacement values in soil types S1, S2 and especially S3. From soil type S1 to S3, the displacement values at the top floors increase significantly.

In Fig. 4, the stress values of an eight-storey building at different floor levels under the effect of Düzce earthquake are presented comparatively for four different soil types (Fixed, S1, S2, S3). Stress values reach a maximum at the second storey levels and show a decreasing trend towards the top of the structure. The highest stress values (see Table 4) were obtained for soil types S1, Fixed, S2 and S3 in descending order. This clearly shows the effect of soil properties on the internal forces in the structure.

In Fig. 5, the acceleration values of an eight-storey building at different floor levels under the effect of Düzce earthquake are presented comparatively for four different soil types (Fixed, S1, S2, S3). In general, it is observed that the acceleration values increase with the number of storeys. It is observed that the acceleration values obtained for S1 and S2 soil types follow a course very close to the fixed base condition. S3 soil type exhibited a different behavior: During the first four stories, the highest acceleration values were observed in the S3 soil, but after this level, the acceleration values decreased and reached the lowest level compared to all other soil types, especially at the eighth storey. At the top storey level, the highest acceleration value was obtained for the fixed base condition and the lowest acceleration value was obtained for the S3 soil. This indicates the complex nature of the SSI on the dynamic effects.

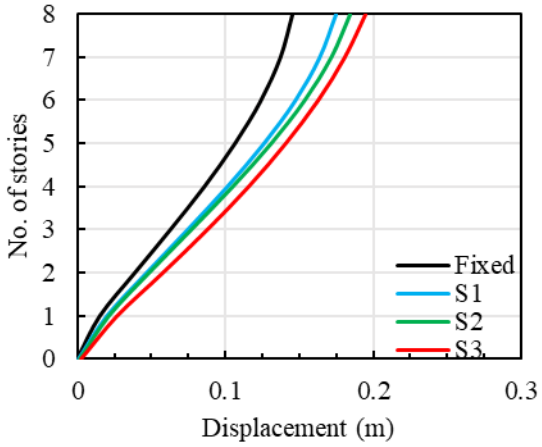

Fig. 3. Displacements depending no. of stories

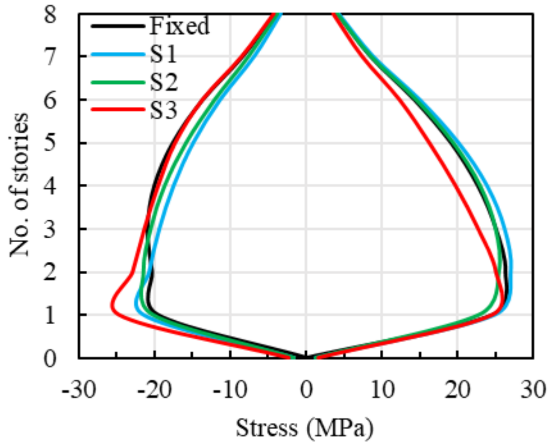

Fig. 4. Stresses depending no. of stories

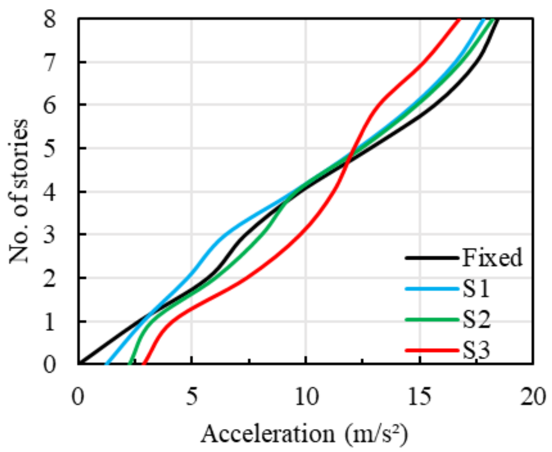

Fig. 5. Accelerations depending no. of stories

3.2. Time-history variation of dynamic responses

In Fig. 6, the peak lateral displacement values of an eight-story building under the effect of Düzce earthquake are presented for four different soil types (Fixed, S1, S2, S3) with time-history comparison. The peak displacement value obtained for the fixed base case is 0.1456 m. Compared to this value, the amount of displacement increased when the SSI was taken into account. For soil S1, this increase was 19.92% and the displacement increased to 0.1746 m. In S2 soil, the displacement increased by 26.72% to 0.1845 m and in S3 soil, the displacement increased by 33.79% to 0.1948 m. As can be seen, the peak displacement values increased as the soil softened. This is evidence that the lateral displacements on the structure are affected by the dynamic properties of the soil.

In Fig. 7, the peak stress values obtained from time-history analysis for the same building model and soil conditions. While the peak stress value was 26.3043 MPa in tensile effect on the fixed base, 26.9928 MPa was obtained in tensile with an increase of 2.62% in S1 soil compared to the fixed base, 25.4576 MPa in tensile with a decrease of 3.22% in S2 soil and 25.0101 MPa in tensile with a decrease of 4.92% in S3 soil. The comparison reveals that stress increases in S1 soil compared to the fixed base, whereas it decreases in S2 and S3 soils. In this case, it is understood that the structure encounters higher internal forces in stiff soils.

Fig. 8 shows, the peak acceleration values of an eight-story building under the effect of Düzce earthquake are presented for four different soil types (Fixed, S1, S2, S3) with time-history comparison. The peak acceleration value obtained under the fixed base condition is 18.4020 m/s². Compared to fixed base, a decrease of 3.27% is observed in S1 soil, resulting in an acceleration of 17.8010 m/s². In S2 soil, the acceleration decreases by 1.18% to 18.1850 m/s², while in S3 soil, a more significant reduction of 8.95% is observed, with an acceleration value of 16.7550 m/s². These outcomes underline the complex influence of SSI on structural dynamics.

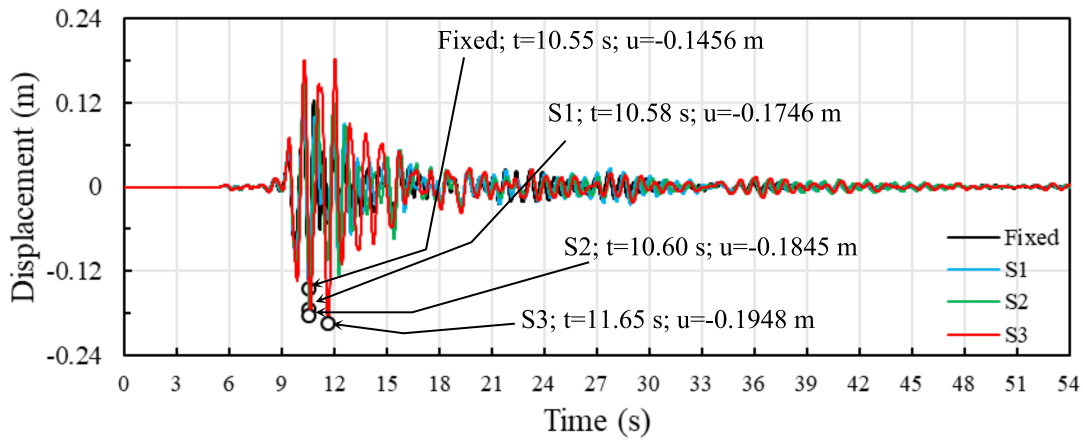

Fig. 6. Peak displacement responses

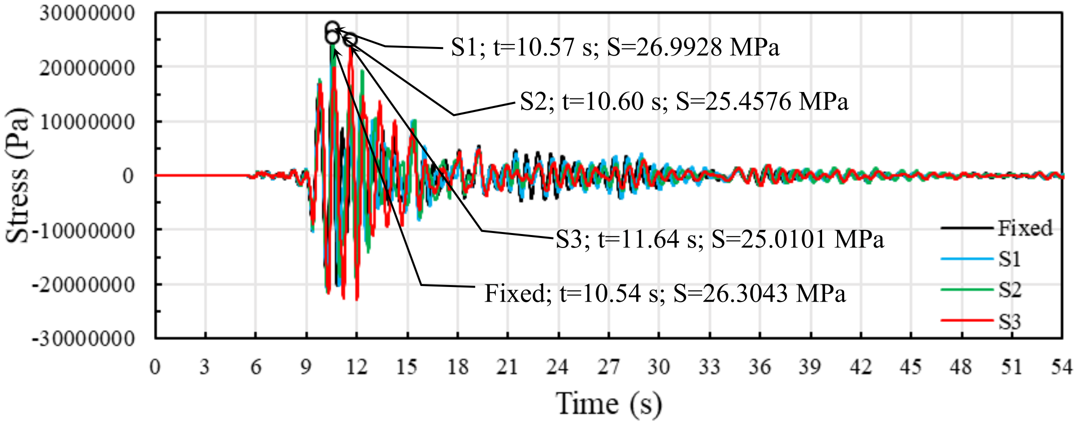

Fig. 7. Peak stress responses

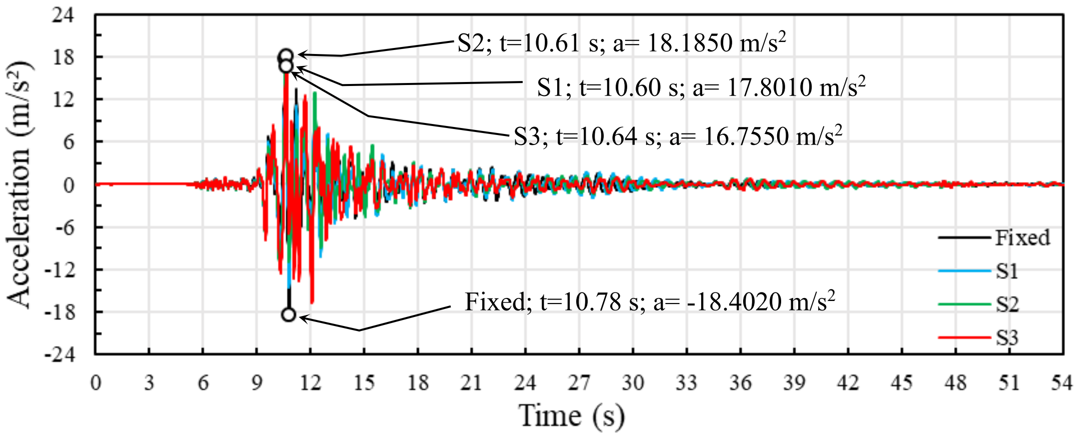

Fig. 8. Peak acceleration responses

4. Conclusions

In this study, an 8-story building was subjected to three-dimensional (3D) numerical analysis for different soil types under the 1999 Düzce Earthquake. Dynamic responses of the structure such as horizontal displacement, stress and acceleration are obtained and SSI effects are evaluated. In addition, the numerical model is subjected to modal analysis and the results obtained are compared with three different analytical solution methods.

- The modal analysis results of the numerical model were compared with three different analytical solution methods (F-1, F-2 and F-3). As a result of this comparison, the F-1 method produced lower natural period values compared to the other two analytical solutions.
- When examining the dynamic response of lateral displacements with respect to the number of stories and soil type, it is observed that the difference between the curves increases as the number of stories rises. This indicates that the effects of SSI become more pronounced with building height. Therefore, soil flexibility must be taken into account, especially in the seismic analysis of mid- and high-rise structures.
- The dynamic response of stresses reaches peak values particularly at the lower story levels, especially around the second story. Throughout the building height, the stress distribution varies depending on the soil type in both tension and compression directions. In tension, the S1 soil type is dominant, whereas in compression, the S3 soil type plays a more significant role.
- The dynamic response of accelerations generally exhibits an increasing trend along the building height. While acceleration growth is relatively steady in Fixed, S1, and S2 soil types, higher acceleration values are observed in the lower and middle stories for the S3 soil type. This demonstrates that SSI effects significantly alter the acceleration spectrum. Peak acceleration values are achieved at the top story level, particularly for the fixed-base case.
- These evaluations clearly demonstrate that soil properties are too critical to be neglected in engineering projects. Especially in regions with high seismic risk, it is not sufficient to focus solely on the structural system; the dynamic behavior of the soil during an earthquake must also be considered. Analyses based on

a fixed-base assumption often fail to accurately reflect the true seismic performance of a structure, which may compromise its safety. Therefore, accurately modeling the interaction between the structure and the soil, and addressing it specifically for each project, is essential for achieving safe and resilient designs.

References

ANSYS Mechanical APDL (Computer Software). (2015).

Araz, O. (2022). Optimization of tuned mass damper inerter for a high-rise building considering soil-structure interaction. *Archive of Applied Mechanics*, *92*, 2951–2971. https://doi.org/10.1007/s00419-022-02217-y

Araz, O. (2025). Effect of basic parameters defining principal soil-structure interaction on seismic control of structures equipped with optimum tuned mass damper. *Soil Dynamics and Earthquake Engineering, 189*, 109085. https://doi.org/10.1016/j.soildyn.2024.109085

Araz, O., Çakır, T., & Öztürk, K.F. (2022). Effect of earthquake frequency content on seismic-induced vibration control of structures equipped with tuned mass damper. *Journal of the Brazilian Society of Mechanical Sciences and Engineering*, *44*, 584. https://doi.org/10.1007/s40430-022-03895-z

Araz, O., Cakir, T., Ozturk, K.F., & Kaya, D. (2023). Effect of foundation embedment ratio in suppressing seismic-induced vibrations using optimum tuned mass damper. *Soil Dynamics and Earthquake Engineering, 171*, 107981. https://doi.org/10.1016/j.soildyn.2023.107981

Bahuguna, A., & Firoj, M. (2021). Nonlinear seismic performance of nuclear structure with soil–structure interaction. *Iranian Journal of Science and Technology, Transactions of Civil Engineering, 46*, 2975–2988. https://doi.org/10.1007/s40996-021-00728-2

Bapir, B., & Abrahamczyk, L. (2024). Comparative study of simplified dynamic soil-structure interaction modelling techniques. *Journal of Physics: Conference Series*, 2647, 082009. https://doi.org/10.1088/1742-6596/2647/8/082009

Bapir, B., Abrahamczyk, L., & Wichtmann, T. (2024). Evaluation of soil-structure interaction for different RC structural systems and foundation sizes. *Journal of Physics: Conference Series*, 2647, 082007. https://doi.org/10.1088/1742-6596/2647/8/082007

Bapir, B., Abrahamczyk, L., Wichtmann, T., & Prada Sarmiento, M. (2023). Review on soil-structure interaction: Modeling approaches and effects on seismic response of structures. *Soil Dynamics and Earthquake Engineering, 170*, 107684. https://doi.org/10.1016/j.soildyn.2023.107684

Cakir, T., & Livaoglu, R. (2013). Experimental analysis on FEM definition of backfill-rectangular tank-fluid system. *Geomechanics and Engineering, 5*(2), 119–133. https://doi.org/10.12989/gae.2013.5.2.119

Cakir, T. (2014). Influence of wall flexibility on dynamic response of cantilever retaining walls. *Structural Engineering and Mechanics, 49*(1), 1–22. https://doi.org/10.12989/sem.2014.49.1.001

Gao, Z., Zhao, M., Du, X., & Zhao, X. (2020). Seismic soil–structure interaction analysis of structure with *shallow* foundation using response spectrum method. *Bulletin of Earthquake Engineering*, 18, 3517–3543. https://doi.org/10.1007/s10518-020-00827-x

Gao, Z., Zhao, M., Du, X., & Zhong, Z. (2021). A generalized response spectrum method for seismic response analysis of underground structure combined with viscous-spring artificial boundary. *Soil Dynamics and Earthquake Engineering, 140*, 106451. https://doi.org/10.1016/j.soildyn.2020.106451

Hwang, B.Y., Tran, N.X., Hwang, T.H., Hong, S., Nguyen, Q.T.B., & Kim, S.R. (2025). Effect of soil-structure interaction on seismic earth pressure acting on building basements using 1g shaking table tests. *Soil Dynamics and Earthquake Engineering*, *192*, 109298. https://doi.org/10.1016/j.soildyn.2025.109298

Jaya, V., Dodagoudar, G.R., & Boominathan, A. (2012). Seismic soil–foundation–structure interaction analysis of deeply embedded ventilation stack. *Journal of Earthquake and Tsunami*, *6*(01), 1250003

Kamal, M., & Inel, M. (2021). Correlation between ground motion parameters and displacement demands of mid-rise RC buildings on soft soils considering soil-structure interaction. *Buildings*, *11*(3), 125. https://doi.org/10.3390/buildings11030125

Kabtamu, H.G., Peng, G., & Chen, D. (2018). Dynamic analysis of soil structure interaction effect on multi-story RC frame. *Open Journal of Civil Engineering, 8*(4), 426–446. https://doi.org/10.4236/ojce.2018.84030

Li, P., Zhao, P., & Lu, X. (2011). Parameter identification and analysis of shaking table tests on SSI system. *Journal of Asian Architecture and Building Engineering, 10*(2), 421–428. https://doi.org/10.3130/jaabe.10.421

Li, P., Liu, S., & Lu, Z. (2017). Studies on pounding response considering structure–soil–structure interaction under seismic loads. *Sustainability, 9*(12), 2219. https://doi.org/10.3390/su9122219

Masaeli, H., Khoshnoudian, F., & Ziaei, R. (2015). Rocking soil-structure systems subjected to near-fault pulses. *Journal of Earthquake Engineering, 19*(3), 461–479. https://doi.org/10.1080/13632469.2014.990652

Menglin, L., Huafieng, W., Xi, C., & Yongmei, Z. (2011). Structure–soil–structure interaction: Literature review. *Soil Dynamics and Earthquake Engineering*, *31*(12), 1724–1731

Mortezaie, H., & Rezaie, F. (2018). Effect of soil in controlling the seismic response of three-dimensional PBPD high-rise concrete structures. *Structural Engineering & Mechanics*, *66*(2), 217–229. https://doi.org/10.12989/sem.2018.66.2.217

Ozgur, M., & Bozdogan, K.B. (2022). Effects of soil-structure interaction on seismic design parameters of reinforced concrete buildings. *El-Cezerî Journal of Science and Engineering*, *9*(2), 507–521. https://doi.org/10.31202/ecjse.966259

Ozturk, K. F. (2025). Investigation of the effects of mainshock-aftershock sequences on the dynamic responses of pipeline considering soil-pipeline interaction. *Tunnelling and Underground Space Technology, 155*, 106231. https://doi.org/10.1016/j.tust.2024.106231

Priyanka, R.J., Anand, N., & Justin, D.S. (2012). Studies on soil structure interaction of multi storeyed buildings with rigid and flexible foundation. *International Journal of Emerging Technology and Advanced Engineering, 2*(12), 111–118

Rayhani, M.H., & El Naggar, M.H. (2008). Numerical modeling of seismic response of rigid foundation on soft soil. *International Journal of Geomechanics, 8*(6), 336–346. https://doi.org/10.1061/(ASCE)1532-3641(2008)8:6(336)

Roesset, J.M. (2013). Soil structure interaction: The early stages. *Journal of Applied Science and Engineering, 16*(1), 1–8. https://doi.org/10.6180/jase.2013.16.1.01

Rostami Heshmat Abad, S., Mohammadyar, M.A., & Akhtarpour, A. (2024). Investigation of torsion in asymmetric mid-rise structures on the pile-raft system considering soil-structure interaction. *Soil Dynamics and Earthquake Engineering*, *184*, 108862. https://doi.org/10.1016/j.soildyn.2024.108862

Scarfone, R., Morigi, M., & Conti, R. (2020). Assessment of dynamic soil-structure interaction effects for tall buildings: A 3D numerical approach. *Soil Dynamics and Earthquake Engineering*, *128*, 105864. https://doi.org/10.1016/j.soildyn.2019.105864

Song, L.L., Shi, X., & Guo, T. (2021). SSI effects on the inelastic displacement ratios of flag-shaped hysteretic SDOF systems. *Structures, 33*, 113–127. https://doi.org/10.1016/j.istruc.2021.07.063

Torabi, H., & Rayhani, M.T. (2014). Three-dimensional finite element modeling of seismic soil–structure interaction in soft soil. *Computers and Geotechnics, 60*, 9–19. https://doi.org/10.1016/j.compgeo.2014.03.002

Vicencio, F., & Alexander, N.A. (2024). Seismic evaluation of Site-City interaction effects between city blocks. *Frontiers in Built Environment*, 10, 1403642. https://doi.org/10.3389/fbuil.2024.1403642

Wang, L., Zhou, Y., & Zhou, Z. (2024). Seismic response control of tall building using semi-active tuned mass damper considering soil-structure interaction. *Soil Dynamics and Earthquake Engineering*, *187*, 108987. https://doi.org/10.1016/j.soildyn.2024.108987

Wolf, J. P. (1994). *Foundation vibration analysis using simple physical models*. Pearson Education.

Yeganeh, N., Bolouri Bazaz, J., & Akhtarpour, A. (2015). Seismic analysis of the soil–structure interaction for a high rise building adjacent to deep excavation. *Soil Dynamics and Earthquake Engineering*, *79*, 149–170. https://doi.org/10.1016/j.soildyn.2015.08.013

A new approach in the design of mechanically stabilized earth walls, MSE-W

Mustafa Aytekin*[1]

[1] *University of Bahrain, Department of Civl Engineering, 973, Sakher, Kingdom of Bahrain*

Abstract. In this research, it has been focused on the design philosophy of mechanically stabilized earth walls (MSE-W). As a proverb says that very small changes, sometimes can make a huge difference so that a small change on the design philosophy of MSE-W has been made in this study. A correctly designed MSE-W supports itself as a coherent body. The inclusion of reinforcement within the soil tends to restrain the soil deformation which, in turn, increases the strength of the soil and the stability of the composite material. One of the earth reinforcements used in a backfill of MSE-W is the steel strip. These reinforcements are smooth or ribbed steel strips. The streps are placed layer by layer in to the backfill and each layer is compacted. The strips are placed as unidirectional positions. The steel strips are usually galvanized or may be epoxy coated. In this study, the linear unidirectional steel strips are replaced by bidirectional steel strips adding a ninety degree hook at the end of the strips in the backfill. Once the new approach was implimented in to the design procedure, an excel spreadsheet has been developed. Using the excel spreadsheet, many examples of MSE-W have been analized. In the analyses, the amount of reinforcement (galvenized steel strips) is compared with the approach in which, the unidirectional steel strips are used. Because of this small modification on the steel strips, the savings on the reinforcement for a particular MSE-W might be considered as huge. Also, the effect of several design parameters such as unit weight, internal friction angle, vertical space between the strips, etc, and geometry of MSE-W have been investigated and included in the paper.

Keywords: Bidirectional strips; Economical design; MSE-W; MSE-W design spreadsheet

1. Introduction

The use of MSE walls with a height of more than 25m is proliferating worldwide because of increasing restrictions of right of way, wetlands, and other limitations, Stuedlein, et al (2010). Thus, the importance of design and construction of MSE walls is increasing. MSE-W consist of several components. These components are prefabricated moduler units (face units of MSE-W), reinforcement (steel strips, geotextiles and/or geomembranes), drainage fill, backfill (reinforced soil mass), retained soil, leveling pad, subgrade (natural soil), surface load, etc, as seen in Fig. 1. MSE walls are analysed by geotechnical and structural engineering methods. The assumptions that are made in the analyses can be listed as mode of failure, earth pressure theory, ground water and hdroststic pressure, width of reinforced soil mass, the zone of maximum stress for internal stability. A typical model of MSE-W is seen in Fig.1. Some details of coneecting reinforcement and the face elemens are seen in Fig. 2a. The backfill surface could be inclinided too as seen in Fig. 2b, AASHTO (2004). The maximum friction angle used to calculate the horizontal forces in the reinforced soil mass shall be assumed to be 34° unless results from triaxial or direct shear tests methods. AASHTO T 234 (1974), and AASHTO T 236 (1972) specifies a higher friction angle, and it should never be more than 40°, Castellenos, B. A (2010). The usage of steel according to the existing design codes are making that the MSE walls are designed with more steel than what is needed, Castellenos, B. A (2010). In a particular MSE-W design with a height of 46m, it was pointed out that even if the evaluations indicated shorter reinforcing strips length could be considered in many portions of the MSE-W; the AASHTO criterion for minimum length was followed because of the critical nature (46m tall) of the structure, Stuedlein, et all (2010). Also, similar conclusions have been reached in this study. In reference, Castellenos, B. A (2010), the author conducted a MSc. thesis research to reduce the amount of steel bars employed in MSE-W by the current methods. The author has concluded that if crimped steel bars seen in Fig. 3 are used within the backfill as the reinforcement in place of straight steel bars, there would be a big benefit in terms of the volume of reinforcement as seen in Fig. 4.

* Corresponding author, E-mail: maytekin@uob.edu.bh

https://doi.org/10.31462/icearc2025_ce_geo_012

golden light publishing

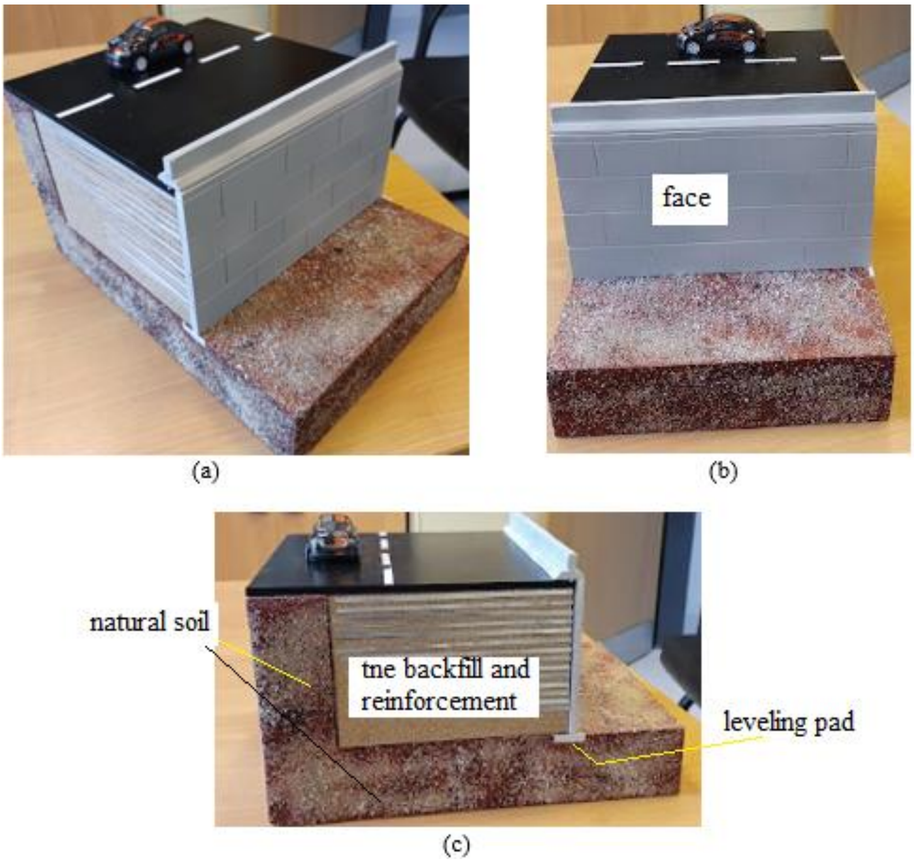

Fig. 1. A model of MSE-W a) Perspective view b) Front view c) Side view

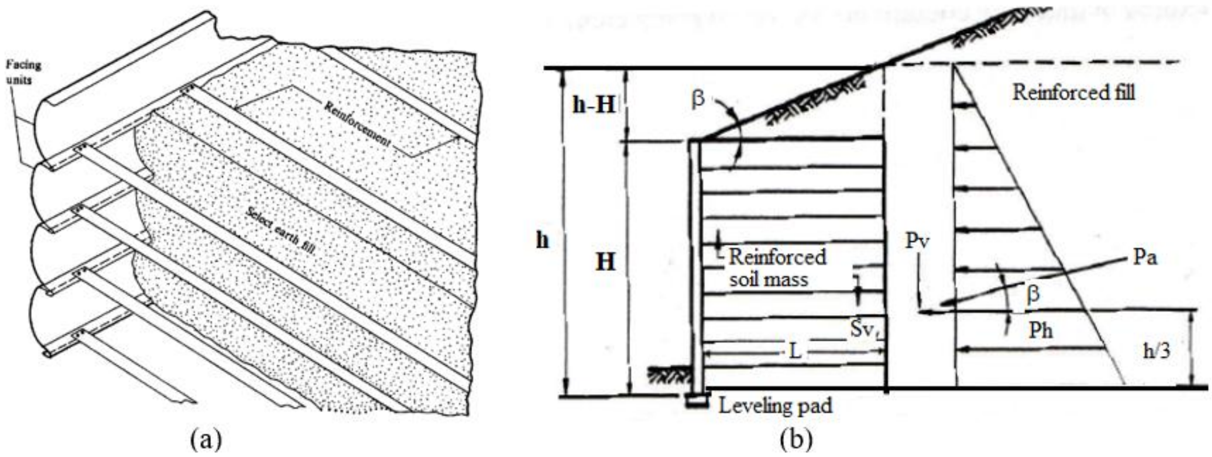

Fig. 2. MSE walls: (a) The reinforced earth concept: Bowles (1997), (b) with sloping backfill surface, AASHTO (2004)

Fig. 3. Reinforcement of crimped steel bar, Castellenos(2010)

2. Design procedure of MSE-W

The idea of a mechanically stabilized soil mass is not a new concept. Inserting a non-soil element in to a soil mass to improve the soil properties has been used for thousands of years, Berg, et al (2009). Nowadays, the idea on how MSE walls achieve their strength, in its simplest form, is based on the addition of a soil reinforcement such as steel, high strength plastic grids (geogrids) or woven plastic sheets, to a soil mass. The fill material mechanically stabilized and locked behind the face unit of a MSE-W is called retained backfill Berg, et al (2009). In the design of MSE-W several reinforcement for the backfill are used such as geogrids as described in Almohd et al (2014).

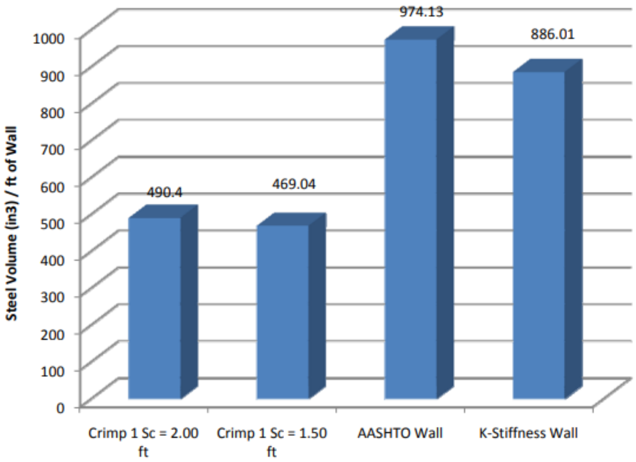

Fig. 4. Comparison of steel volumes needed for the same MSE-W among the AASHTO method, K-Stiffness wall and two different spaces of crimped steels strips, Castellenos (2010)

First of all, a project requirements and parameters must be established like the face panels and their connections with the reinforcement. Second, the embedment depth and the length of the reinforcement are estimated. Finally, internal and external stabilities are evaluated. In this study, it is focused on the estimation of length of the reinforcements which have been considered as inextensible steel strip. Inextensible reinforcement is manufactured from a material that deforms considerably less than the surrounding soil at failure. The required length of staraight steel reinforcements versus the the required length length of ninty degree hooked steel reinforcement. Design Steps can be listed as follows

a. The height (H) of the MSE-W, type of facing unit, leveling pad, properties such as internal friction angle, cohesion, unit weight of backfill material and the natural soil, type and size of reinforcement (in this case, galvinized steel strip), should be determined. Backfill material should be a cohesionles (gravel and/or sand) soil for the drainage purpose.
b. Initial vertical and lateral distances (Sv and SH) between the strips should be selected, later on several iterations can be performed to see the most economical (or optimum) distances.
c. Lateral active earth pressure distribution with depth should be determined as well.
d. Also, additional vertical and lateral earth pressures should be considered if a surface load (q) is applied on the backfill. The distance of surface load to the face unit, shape and size of loaded area, and the intensity of the load (q) should be known.
e. Calculations of L_r and L_e seen in Fig. 5:

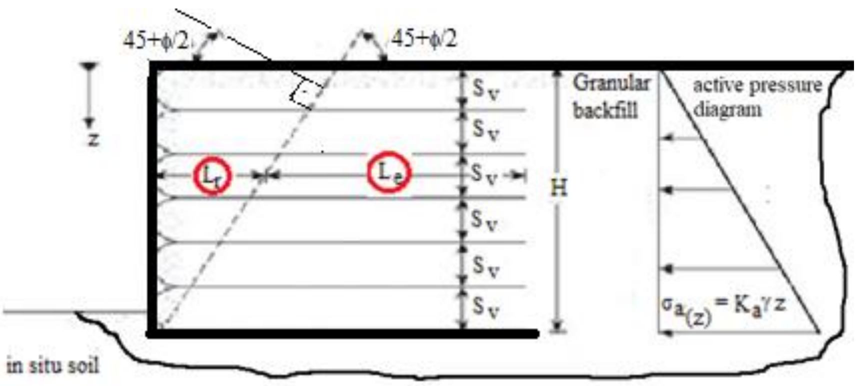

Fig. 5. Elements of a MSE-W

L_r is the length of steel bar within the Rankine failure zone (Fig. 5). Then, Eq.(1) can be written as follows;

$$\tan\left(45+\frac{\varphi}{2}\right)=\frac{L_r}{H-z} \quad (1)$$

Thus,
$$L_r=\frac{H-z}{\tan\left(45+\frac{\varphi}{2}\right)} \quad (2)$$

The applied tension force, T_{app}, to the reinforcement by the face unit of MSE-W due to the active pressure of the backfill at the level under consideration (z) can be writen as follows:

$$T_{app}=\sigma_{a(z)}\, S_H S_V \quad (3)$$

The tension force, T_f, that can be carried by the strip at its failure can be;

$$T_f=A_s f_y' \quad (4)$$

Where A_s, and f_y' are the surface area, and the characterictics yield strength of the steel strip, respectively. L_e is the effective length that will resist the applied force, T_{app}, (pullout force) with the friction between the surrounding backfill material and its surface area.

It is obvious that a safety factor, FS_B, must be considered againt the breaking (failure) of the steel strip. This safety factor is generaly take as 2.5 to 3.0 in practical applications.

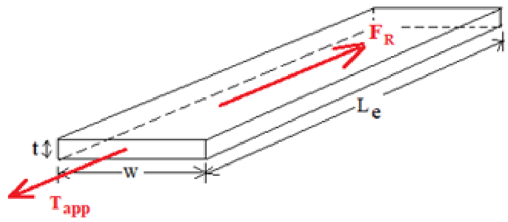

Fig. 6. Dimensions of reinforcement (strip) and forces applied

On the calculation of surface area of the strip, the thickness, t, is ignored mostly since it is tiny compared to the other dimensions. Thus, the frictional force, F_R, can be written as seen in Eq. (5) when there is no hook at end of the strip

$$F_R=2L_e\, w\sigma_{v(z)}tan(\varphi_u) \quad (5)$$

Where w: width, t: thickness, $\sigma_{v(z)}$: vertical effective stress, φ_u: internal friction angle betweenbackfill material and the strip. It can be approximated as $2/3\,\varphi$ To have a safe design friction resistant F_R, must be more than the pull out force of T_{app}. Thus; Eq. (6) must be satisfied:

$$F_R=FS_P\, T_{app} \quad (6)$$

FS_P is the safety factor against pullout. It can be taken as 1.5 to 3. Eq. (3) and Eq. (5) can be placed in Eq. (6) and ended up Eq. (7)

$$L_e=\frac{FS_P\sigma_{a(z)}S_V S_H}{2w\sigma_{v(z)}tan(\varphi_u)} \quad (7)$$

Unlike the strip with no hook at its end, the hooked strip as seen in Fig. 7a should have extra resistance due to the passive force that would be generated in front of the hook as seen in Fig. 7b. The passive force and active force can be determined from these equations:

$$P_p=\frac{h}{2}\left(\sigma_{top(p)}+\sigma_{bot(p)}\right)w \quad (8)$$

$$P_a=\frac{h}{2}\left(\sigma_{top(a)}+\sigma_{bot(a)}\right)w \quad (9)$$

Then, a net force the difference between Eq. (8) and Eq. (9) is considered as the contribution of hook to the polling strength of the strips.

$$P_{net}=P_p-P_a \quad (10)$$

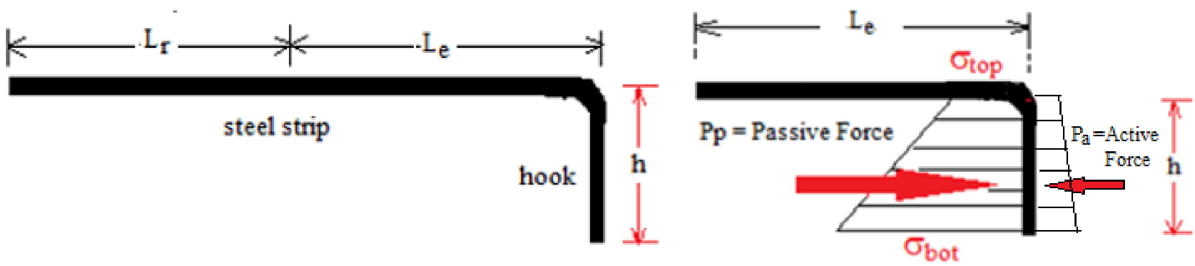

(a) (b)

Fig. 7. (a) Hooked strip (b) Passive pressure distribution with the length of hooked portion

When the hook is employed at the end of strips, the calculation of effective length would be different from the calculation of effective length with no hook. First, the summation of passive net force by Eq. (10) generated in front of the hook plus the surface friction around the effective length must be more than the pullout force, T_{app}, Eq. (3), with a safety factor of FS_P.

$$L_{e-hooked} = \frac{(T_{app}-P_{net})FS_P}{2w\sigma_{v(z)}tan(\varphi_u)} \tag{11}$$

Second, there must be enough bacfill materal shear resistance against the sliding of the strip at the bottom end of the hook.

$$L_{e-hooked-min} = \frac{FS_P\, P_{net}}{w\sigma_{v(z)}tan\,\varphi} \tag{12}$$

Where φ: internal friction angle of backfill material. The highest value of effective length from Eq. (11) and Eq. (12) would be taken as the L_e value. Then, the total length of a strip is determined as the summation of L_e and L_r as seen Eq. (13).

$$L_{total} = L_r + L_e \tag{13}$$

Moreover, there is one point that is requested by some sources that says the bending angle of the strips should not be more than 15 degree, Castellenos (2010).

3. Hypothetical cases

In several hypothetical cases MSE-Walls are considered with the following data and some conclusions have been drown.

- Bacfill internal friction angle, $\varphi = (20 - 25 - 30 - 32 - 34, and\ 42\ degrees)$
- Unit weight of backfill material, $\gamma_b = 16.6kN/m^3$ (constant)
- Height of MSE-W, H=4m, 8m, 16m, and 32m.
- The characteristic yield strength of the steel strip, $f_y' = 240000kN/m^2$
- Factor of safety against pullout, $FS_P = 1.5$
- Factor of safety against break, $FS_B = 1.5$
- Width of the strip, $w = 100mm$
- Thickness of the stript, $t = 5mm$
- Lateral distance between the steel strips, $S_H = 1m$
- Vertical distance between the steel strips, $S_V = 1m$, 0.75m, and 0.50m.

The newly prepared excel spread-sheet that takes into account both strips with no hooks, and with hooks at their ends in the design of MSE-W has been employed on the calculations. As seen in Fig.8, and Table 1, the ratio of the optimum length, h_{opt} of the hook to the vertical distance between the steel strips, S_V, are varying with the internal friction angle of the backfill. However, these values are not affected much by S_v. In this study, the range of the internal friction angle, φ, is taken 20 to 40 degree since in the practical works, the backfill materials for the MSE-W construction must be a granular material with no cohesion. Thus, the author believes that this range of internal friction angle covers the material that would be used in the construction. Fig. 8, shows that there is no significant differebce on $\frac{h_{opt}}{S_V}$ ratio for the values of S_v from 0.5m to 1.0m. Engineers who work in the industry can easily determined the optimum hook length from Fig. 8. Initially, the internal friction angle of the bacfill material should be known. Then, the may select the vertical distance between the layers of reinforcement strips. Finally, they may get the ratio of optmum length of hook to the the vertical distance between the layers of reinforcement strips as a function of the internal friction angle of the backfill material.

In this study, the total length of the steel strips for both with hooks, and without hooks are determined. There is a considerable amount of savings on the total lengths of strips with hook agains the strips with no hooks. As it is seen in Fig. 9, the highest saving will be in low internal friction angles. Then, it would be reduced when the internal friction angles are increased. The highest saving would be 28.38% at $S_V = 1m$, and $\varphi = 20°$ whereas the lowest saving would be 17.19% at $S_V = 0.5m$, and $\varphi = 40°$ for the numerical values used in this study.

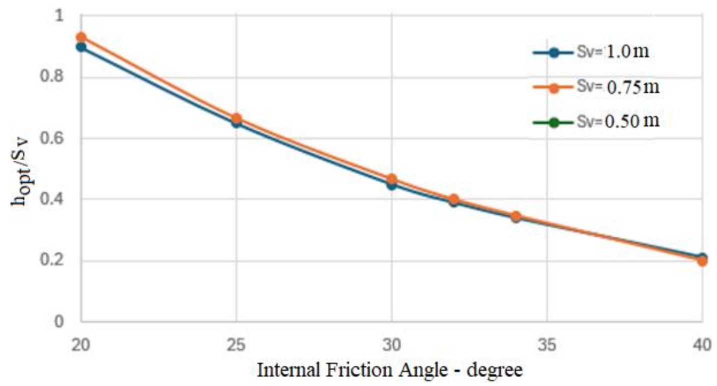

Fig. 8. The variation of optimum hook length to the vertical distance between reinforcement with internal friction angles

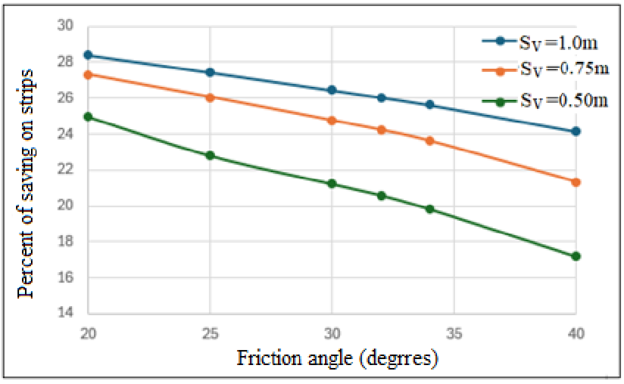

Fig. 9. Percent of savings on reinforcement with internal friction angle

Fig. 10 shows that the height, H, of a MSE-W does not effect significantly the optimum length of the hook at the internal friction angle of more than approximately 30 degree. Ihe smalest length of the hook needed is 20% Sv at an internal friction angle of 40 degree independent on the MSE-W height from 4 m to 32m. On the other hand, when the friction angle is 20 degree, the optimum length of the hook is 76% of Sv at the height of the wall is 4m. wheres of it is about 99% if Sv at H=32.

Table 1. Optimum hook lengths and percent of savings against the strips with bo hooks

	Sv=1 (m)			Sv=0.75m			Sv=0.50m		
φ (degree)	hopt (m)	Saving%	hopt/Sv	hopt (m)	Saving%	hopt/Sv	hopt (m)	Saving%	hopt/Sv
20	0.90	28.38	0.9	0.70	27.29	0.93	0.48	24.95	0.96
25	0.65	27.42	0.65	0.50	26.04	0.67	0.34	22.79	0.68
30	0.45	26.43	0.45	0.35	24.74	0.47	0.24	21.22	0.48
32	0.39	26.03	0.39	0.30	24.21	0.40	0.20	20.59	0.40
34	0.34	25.61	0.34	0.26	23.60	0.35	0.17	19.82	0.34
40	0.21	24.14	0.21	0.15	21.33	0.20	0.10	17.19	0.20

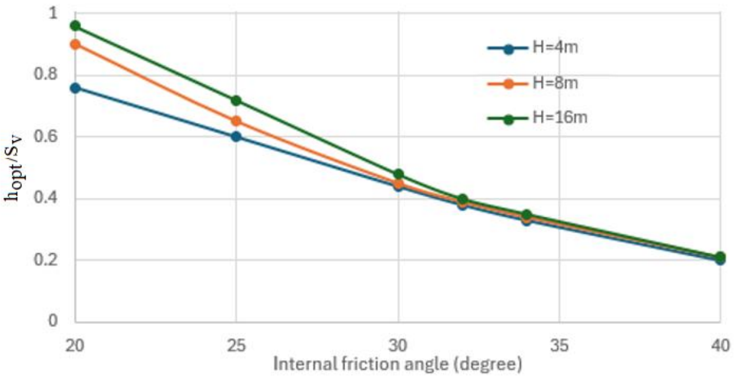

Fig. 10. Effect of MSE-W height on the ratio of hook length/Sv ratio

4. Conclusions and recommendations

The following conclusions can be drawn from this numerical modeling in this study.

1. A numerical modeling of MSE-W with hooks at the end of the steel strips and wth no hooks could be done. Thus, a comparison should be perfomed in terms of which type of steel strips are superior to the other type of steel strips.
2. It is concluded that to employ hooks at the end of the steel strips is beneficial. Thus, there would be a saving on the effective length, L_e, of the strips about 40% against the reinforcement used with no hooks.
3. The saving on the total length, $L = L_r + L_e$, of the strips would be more than 28%. The length of the steel strips, L_r, will remain same in the failure zone of the backfill as expected.
4. The savigs on usage of steel reinforcement are decreasing when a high quality of backfill material that have an internal friction angle of more than 30 degrees is placed. For this purpose Fig. 8 can be used for the purpose of determination of the optimum hook length.
5. There is an optimum length of the hook for different properties of the elements of a MSE-W. Thus, for each MSE-W, an optimum hook length should be determined.
6. The height of the MSE-W can be consider as if it has no effect on the length of the hook especially a backfill with an internal friction angle of 30 degrees or more.
7. It might be recommended that the effect of strip's width, w, in addition to its legth, h, should be investigated on the optimum length of hook as well as the effective length of the reinforcement so that the practitioners may consider these effects when they design a MSE-W.
8. The author believes that unit weight of the backfill material has an significant role on the effective length of the reinforcement. This effect should be investigated too.

References

AASHTO. (2004). *LRFD bridge design specifications* (3rd ed.). American Association of State Highway and Transportation Officials.

AASHTO T 234. (1974). *Strength parameters of soils by triaxial compression*. American Association of State Highway and Transportation Officials.

AASHTO T 236. (1972). *Bearing capacity of soil for static load on spread footings*. American Association of State Highway and Transportation Officials.

Almohd, I., Nusier, O. K., Ashteyat, A. M., & Yamin, M. M. (2014). Design of geogrid reinforced earth walls: Transition of limits and critical surfaces. *Electronic Journal of Geotechnical Engineering, 19*, 8497–8511.

Berg, R. R., Christopher, B. R., & Samtani, N. C. (2009). *Design and construction of mechanically stabilized earth walls and reinforced soil slopes* (Vol. I). Federal Highway Administration.

Bowles, J. E. (1997). *Foundation analysis and design* (5th ed.). McGraw-Hill International Editions.

Castellenos, B. A. (2010). *Internal design of mechanically stabilized earth (MSE) retaining walls using crimped bars* (Master's thesis, Utah State University).

Stuedlein, A. W., Bailey, M., Lindquist, D., Sankey, J., & Neely, W. J. (2010). Design and performance of a 46-m-high MSE wall. *Journal of Geotechnical and Geoenvironmental Engineering, 136*(6), 786–796.

Enhancing mechanical properties of subgrade soil using RAP-geopolymer

Ahmed H. Abdulkareem*[1], Taher M. Ahmed[2], Nawfal F. Kwad[3]

[1] *professor in geotechnical engineering , Department of civil engineering, University of Anbar, Anbar , Iraq.*
[2] *professor in highway engineering , Department of civil engineering, University of Anbar, Anbar , Iraq.*
[3] *Msc. in geotechnical engineering , Iraq Anbar Health Directorate, Iraqi Ministry of Health, Anbar.*

Abstract. The performance of the subgrade layer is important to the pavement system. The quality of the subgrade material and other layers impact on the road's service life and long-term performance. The main objective of this study is to determine a suitable method to improve the strength of weak soil for use in the subgrade layer. Various mixtures of RAP-geopolymer material were used to enhance the physical and mechanical properties of sandy silt soil. RAP particles were added to the soil in several percentages (10%, 20%, 30%, 40%, and 50%) as an inert material in order to improve the mixture's stiffness and strength. An alkali solution of the NaOH at 8M and Na_2SiO_3 liquid, at 1.5 ratio of the NaOH: Na_2SiO_3 was prepared to be used an ctivaitor with flay ash for developing geopolymer. The results showed a significant improvement in the strength of the soil in terms of unconfined compressive strength (UCS) and indirect tensile strength (ITS). The optimal RAP content with the soil was found to be 40% without geopolymer material, while the optimal content was 20% with soil-geopolymer mixtures. The CBR index was determined under soaked conditions for both natural and treated soil at the optimal mixtures determined from the UCS and ITS tests. Using RAP alone increased the CBR index of natural soil from 3.8% to 9.6% with 40% RAP content. The CBR index increased significantly with RAP-kaolinite geopolymer mixtures, achieving a remarkable increase by 230%. In contrast, specimens stabilized with RAP-fly ash geopolymer showed great resistance to penetration, reaching the maximum capacity of the testing machine.

Keywords: RAP-geopolymer, Subgrade soil, CBR index, Mechanical properties, Fly ash

1. Introduction

The subgrade layer is the in situ soil or the natural soil, where the pavement layers are constructed upon. The subgrade soil provides the primary support to the top layers of the pavement system. The quality of soil in this layer significantly affects pavement design, performance, and service life. The subgrade layer is susceptible to environmental conditions and axle load repetitions. The role of the subgrade layer can be summarized as mitigating the negative effects of the environment and the dynamic and static stresses of traffic by supporting the upper layers without permanent distress (Schaefer, White, Ceylan, & Stevens, 2008). Therefore, the weak subgrade should be improved to provide a foundation that can resist the traffic loads transmitted from the upper layers. Moreover, improved subgrade layer provides a practical approach to decrease the thicknesses of the surface layer and the other layers of the pavement by increasing the strength and load-bearing capacity of the soil (Chilukwa & Lungu, 2019). This leads to a high reduction in pavement construction cost. Soil stabilization is the process of modifying the soil properties to match the standards specifications of the different engineering applications.There are several methods of soil stabilization, for example, the mechanical method such as the compaction and the chemical method by chemical agents such as cement or lime stabilization (Jones, Rahim, Saadeh, & Harvey, 2011); therefore, selection of stabilization technique depends mainly on soil type and properties. Last decades, inviromental issue became one of the main problem facing the world, one of these problems related to the wast materials, in this regrds Recycled Asphalt Pavement (RAP) one of the road construction wast materials that can be defined as a pavement material that has been removed during pavement rehabilitation or reconstruction. RAP consists of well-graded aggregates coated by asphalt binder and produced by milling or scarifying the surface course during pavement renovation or reconstruction, or by full depth replacement (Mahdi, Abd, & Ahmed, 2020; Thakur, Han, Pokharel, & Parsons, 2012). The aged asphalt that exists in the RAP has undesirable physical properties that make it inappropriate for reusing without enhancement

* Corresponding author, E-mail: ahm1973ed@uoanbar.edu.iq

https://doi.org/10.31462/icearc2025_ce_geo_056

(Chen, Huang, Chu, & Lin, 2007). This property will lead to huge quantities of waste RAP, which are harmful environmentally. RAP provides a resource material that can be utilized in civil engineering applications especially roads construction. In other words it can be considered as sustainability issue. Fly ash (FA) is the residue of coal material combustion, especially in power stations (Keyte, 2009). The chemical composition of coal fly ash and the fine particle size, as well as the low cost gave the fly ash excellent features can be utilized in concrete production as a cementitious material. The fly ash effect enhances the workability and increase the compressive strength as well as reduces CO_2 emissions by reducing the need for cement in concrete (Huang & Wang, 2024). Furthermore, fly ash can be considered as a waste material and this reduces the cost of concrete by utilizing cheaper material than cement. Kaolinite (Kao) is a clay mineral and produced naturally through weathering or by hydrothermal process of aluminosilicates-rich rocks such as granite. Kaolinite as a clay mineral is generally composed of $Al_2Si_2O_5(OH)_4$. the white color and the fine particles distinguish the kaolin from the other types of clay because it is rich material by aluminum and silicates (Bloodworth, Highley, & Mitchell, 1993). the kaolinite may considered as a suitable material in geopolymer syntheses where the geopolymer is made primarily from alumino-silicates materials. Geopolymers can broadly be defined as inorganic polymers mainly synthesized by activating materials rich in alumina and silica in an alkali or acidic medium (Kriven et al., 2024). The prefix "geo" is attached to indicate the geological origin of the prime material, which commonly encompasses fly ash, blast furnace slag, metakaolin, and others (Davidovits, 2017). In this filed geopolymer was used in a veritay of civil enginiring applications, for enstant; Singhi, et al., (2016) used fly ash, slag, and their blends as a precursor for the synthesis of geopolymer binder to stabilize a clayey soil, the investigation showed a signifecnt improvement in terms of unconfined compression strength (UCS) for slag-based geopolymer-soil mixtures compared to FA-based geopolymer-soil mixtures (Singhi, Laskar, & Ahmed, 2016). Adhikari, et al., (2018) studied the inclusion of RAP in addition to geopolymer binder to stabilize two types of soils (CL and MH), results showed that, the UCS increased by increasing RAP and FA content to 25% for both with an optimum NaOH molarity was 8M for both soils, while the optimum sodium silicate content varied based on soil type (Adhikari, Khattak, & Adhikari, 2020). Kwad, et al., (2020) investigated that a geopolymer based on fly ash affected the strength of weak soil in order to satisfy the requirements of the pavement structure's subgrade layer. The study used low plasticity sandy silt that was stabilized with various percentages of fly ash (5, 10, 15, 20, 25, and 30%); the addition of FA-based geopolymer improved UCS and indirect tensile strength (ITS) significantly, at 20% FA (Nawfal Farooq Kwad, Abdulkareem, & Ahmed, 2020). In further works. In other study, the effect of wetting – dry cycles on durability of silt-sand soil modified by fly ash based geopolymer with and without RAP were evaluated in terms of weight loss, the results ravealed that the weight loss and volume changes were less than 10% and 2% respectively (Nawfal F Kwad, Abdulkareem, & Ahmed, 2024). The efficiency of kaolinite based geopolymer material for stabilizing sandy silt soil, where different proportions of the kaolinite (5, 10, 15, 20, 25, and 30%) by weight alkaline activaitor solution consists of the NaOH at 8M and Na2SiO3 liquid, at 1.5 ratio of the $NaOH:Na_2SiO_3$ were used for creating the geopolymer. The investigation showed there are an improvement in: compaction charectersistics in terms of dry density, unconfined compressive strength and the indirect tensile strength; and the best improvement was at kaolinite content 15% (Abdulkareem, Ahmed, & Kwad, 2023). In further works, the resilience properties of a clayey soil modified with a fly ash-based geopolymer and RAP for unpaved road material were investigated using repeated-load California bearing ratio (CBR) testing method to evaluate recoverable and permanent deformations; the results showed that the geopolymer binder significantly increased the stiffness of the mixtures at optimum ratio of 25% FA and 30% RAP (Abdulwahed, Aljanabi, & Abdulkareem, 2024). In the filed of asphalt mixtuers, a qualitative leap was achieved by adding fly ash based geopolymer was incorporated to emulsified cold mix asphalt, a significant achievement was improved in the mechanical propertis in terms of Marshall stability, indirect tensile strength and perminant deformation compared to the reference cold mix. However, volumetric proberties was still with out improvement due to the nature of asphalt emulsion which is reach with water (Ali & Ahmed, 2024; Ahmed M Ibrahim & Ahmed, 2024; Ahmed Mahdi Ibrahim, Ahmed, & Ahmed, 2024).

The study aims to investigate the strength of soils in the subgrade layer after the incorporation of RAP-geopolymer mixture. The main interest of the study is the incorporation of a chemical stabilizing agent and recycled asphalt pavement (RAP) with the soil. This may produce high-quality material that can be used as a roadbed or stiff foundation for the road. This is applicable by achieving better properties and long-term performance for civil engineering applications that require high-quality soil.

2. Materials and methods

2.1. Soil

One type of soil was used in this study collected from Msheheeda quarry in Ramadi city. The soil was classified as low plasticity sandy silt soil according to the USCS system. The physical and chemical properties of soil presented in Table 1 and 2, respectively. The chemical composition shows that the soil is composed mainly of silicon, aluminum, and calcium oxide. Figure 1 shows soil under normal and scanning electron microscope (SEM) images, indicating that the soil has a lamellar composition and exhibited loosely structure.

Table 1. Geotechnical properties of soil

LL (%)	PL (%)	PI (%)	G_s	AASHTO	USCS	Description	OMC (%)	MDD (gm/cm^3)
38	27	11	2.66	A-6	ML	Sandy silt	15.5	1.73

LL:Liquid limt, PL:platic limit, PI: plasticity indexm G_s:specific gravity, OMC: optimum moisture content, MDD: maximum dry density

Table 2. Chemical composition of soil, fly ash and kaolinite

Element	SiO_2	Al_2O_3	CaO	Fe_2O_3	MgO	Na_2O	K_2O	SO_3	MnO
Soil	37.64	6.50	23.43	4.06	3.90	1.30	1.10	0.70	0.10
Fly Ash	53.23	25.91	4.95	6.46	1.2	0.10	1.40	0.78	0.16
Kaolinite	51.40	26.23	5.38	5.64	2.41	1.28	1.20	-	-

Fig. 1. (a) Dried soil (b) SEM image of soil

2.2 Fly ash (FA)

One type of FA was used in this study to produce the geopolymer as shown in Figure 2. Class F is characterized as a low calcium content as per (ASTM C618-2012). The low calcium fly ash is preferred in geopolymer synthesis because it produces higher strength and showed a better response in sodium-based geopolymerization reactions. The chemical composition of fly ash was determined by the X-ray Fluorescence (XRF) test as listed in Table 2. The specific gravity of the fly ash is 2.14. The chemical composition shows that the silica is the dominant element in the fly ash followed by aluminum oxide and these are considered as the main two components required in the raw material to produce geopolymer bonds. The particle size analysis showed that 89 % of fly ash particles passed No.200 sieve (0.075 mm).

2.3 Kaolinite (kao)

Kaolinite is a clay mineral was used in this study as a source of alumina-silicate material to produce the geopolymer. It was dried at ambient temperature before use as shown in Figure 2. More than 71% of kaolinite particles passed No.200 sieve. The chemical composition through the X-Ray Fluorescence test is listed in Table 2. The specific gravity of the kaolinite is 2.35. The chemical analysis shows that the amount of silica is high, as well as, the alumina, while it has a low content of CaO.

2.4 Recycled asphalt pavement (RAP)

large amounts of RAP were observed as a waste material, especially in the destructive bridges and roads. In this study, RAP was collected from the removed asphaltic pavement layer for University of Anbar Bridge, which constructed before 20 years ago. It was heated and sieved on 10 mm sieve size as shown in Figure 2 to exclude the large particles and to satisfy the requirements of the unconfined compressive strength test (ASTM D4219-2008), which requires that the maximum size of the RAP particle should be smaller than the mold's diameter by 10 times. RAP consists of 98% coarse granular particles coated with aged asphalt binder.

2.5 Alkaline solution

The alkaline activator solution consists of 99% pure sodium hydroxide (NaOH) pellets and sodium silicate (Na_2SiO_3). The concentration of NaOH was 8 molar, and 40 g / mole is the molecular weight. The liquid form of sodium silicate (Na_2SiO_3) contains 32.5% of SiO_2, 13.4% of Na_2O, and 54% of water. The NaOH: Na_2SiO_3 ratio of 60:40 was used to activate kaolinite and soil particles. The molarity of NaOH and the NaOH: Na_2SiO_3 ratio were selected based on preliminary testing to ensure sufficient UCS of the Soil-Geopolymer and Soil-RAP - Geopolymer.

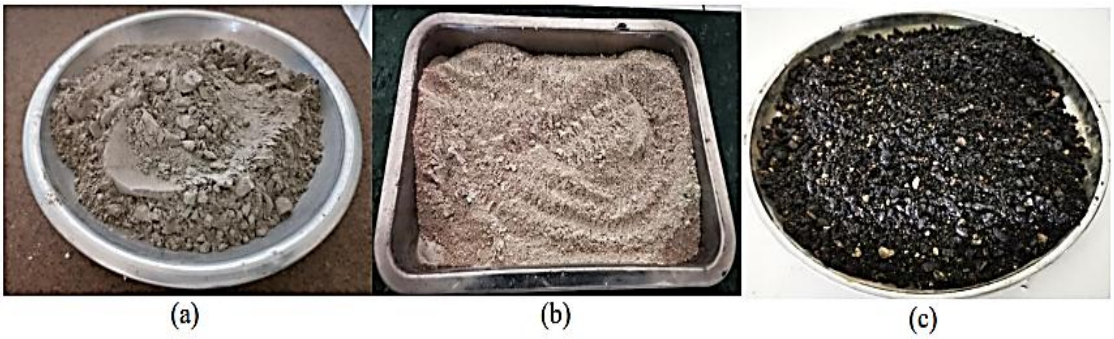

Fig. 2. (a)Fly ash (b) Kaolinite (c)RAP passed on 10mm sieve size.

2.6 Cement

Ordinary Portland cement (MASS brand) was used in this study as a standard stabilization additive. This type of cement with the soil was used as a reference mixture in comparing the mechanical properties with the soil-geopolymer and soil-RAP-geopolymer mixtures. The OPC with 6% and 12% content by weight of soil was used.

2.7 Preparing of mixtures

The soil was dried in the oven for 24 hours at 105°C, the dried soil and other additives were mixed using a mechanical mixer to ensure a homogeneous mixture. Soil with fly ash and soil with kaolinite mixtures were mixed thoroughly before adding the alkaline solution. The alkali content corresponds to the optimum moisture content of the mixture as estimated by the compaction test. Extra weight of the alkali liquid was added to the blend to compensate the dissolved NaOH weight in the solution which is 30% approximately at 8M concentration of NaOH (Adhikari, 2017). In the UCS and ITS tests, fly ash or kaolinite percentages were 5, 10, 15, 20, 25, and 30% by weight of soil, while RAP percentages were 10, 20, 30, 40, and 50 by weight of soil. The optimum percentages of the kaolinite, fly ash, and the RAP in the UCS test results were used in the CBR test. Fly ash and kaolinite percentages were 20 and 15% respectively. The optimum content of RAP, i.e. 40% was used in the soil-RAP mixtures. Soil-cement and soil-RAP blends were thoroughly mixed with water at the OMC of the mixtures. Dry mixing for 3 minutes by hand followed by a mechanical mixing for 7 minutes. The time of mixing was selected to ensure the effectual distribution and participation of mixture components with the alkaline solution in geopolymer mixtures. Long time mixing is not preferable to avoid the drying of the alkaline solution or the water prior to the required reactions of the geopolymer material. The specimens were cured for 48 hours in drying oven at 65^{o}c then the test was performed directly after the samples been cooled at ambient temperature.

3. Result and discussion

3.1. Compaction properties of natural and treated soil mixtures

Figure 3 shows the relationships between the dry density and the moisture content for soil-FA mixtures at various fly ash percentages (5, 10, 15, 20, 25, and 30%). It can be noticed that the maximum dry density of soil-fly ash mixtures exhibited increasing trend from 1.73 g/cm^3 of the natural soil to the MDD of 1.78 g/cm^3 at 30% of fly ash content. While there was a reduction in the optimum water content of soil-FA mixtures from 15.5% for the natural soil to 13.5% for soil+30% of fly ash mixture and it can be observed that this mixture has the MDD among other fly ash percentages. However, this increase in the MDD was observed beyond 15% of fly ash addition as the lower content of fly ash did not affect the MDD significantly.

The compaction curves of soil-kaolinite blends are presented in Figure 4. A general increasing trend was observed in the MDD values up to 1.93 g/cm^3 at 30% of the kaolinite content with the soil. The same mixture has the lowest OMC by 13%. Figure 4 shows that there was a noticeable increase in the MDD of the soil at the various kaolinite percentages and obvious decrease in the OMC at the same percentages. The clear trend of compaction curves reveals that adding more kaolinite to the soil leads to higher MDD and less OMC. The higher MDD may be attributed to the role of the fine particles of kaolinite which are likely to fill the pore spaces in the soil as a filler material resulting in a denser state in the soil under the impact of the compaction energy (Ayininuola & Adekitan, 2017).

The moisture-density curves of the soil-RAP mixtures are shown in Figure 5. The OMC decreases with the gradual increase in the RAP content from 10 to 50%. The MDD was 1.95 g/cm^3 and the OMC was 8.9 % and observed at 50% of RAP content with the soil. There was a noticeable decrease in the OMC for the various RAP contents. This reduction in the OMC may also be ascribed to the water-holding capacity of the RAP aggregate which is less than the silty soil (Akinwumi, 2014). In addition, the large size particles of the RAP that replaced the fine particles of the soil reduce the surface area of soil mixture and lead to a reduction in the water of the mixture (Edeh, Eberemu, & Agnes, 2012).

The moisture-density relationship of the soil and cement mixtures are shown Figure 6. Both of the MDD and the OMC are reduced due to the cement addition. The compaction test was performed to investigate the combined effect of the RAP-geopolymer on soil density and water affinity.

The compaction tests were performed using the optimum percentages in the soil-RAP-geopolymer mixture at 20% of RAP, 15% of kaolinite, and 20% of fly ash. The OMC and MDD of the optimum mixtures are listed in Table 3. The results showed that there was a noticeable increase in the MDD and a decrease in the OMC of the various mixtures of RAP-fly ash geopolymer and RAP-kaolinite geopolymer mixtures.

3.2. Unconfined compressive strength (UCS) test

The incorporation of RAP particles improved the compressive strength of the soil as presented in Figure 7 for various soil-RAP blends. Noticeable increase in the UCS of the soil with the high contents of the RAP was observed. The optimum percentage of the RAP was 40% which achieved the highest strength by 1.45 MPa. By inspecting Figure 7, an increase in the UCS was observed especially at the low contents and there is no considerable variation in the UCS for the various RAP proportions. In comparison with the cement stabilization results, the RAP did not achieve a significant increase in the UCS of the soil like the OPC, where 6 and 12% of cement achieved higher UCS than the optimum content of the RAP. In addition, the RAP incorporation results did not fulfill the Iraqi standards (SORB) of the stabilized subgrade which requires the minimum compressive strength of the stabilized subgrade to be 2.5 MPa for the cement-stabilized subgrade. The UCS results affirms that the RAP content affected the strength of the sandy silt soil to a specific limit. The slight increase in the UCS of the soil with RAP may be due to the nature of the RAP particles which coated by the bitumen material. In addition, the RAP particles with the soil and water acted as inert aggregate filling spaces in the mixture without any effects (Mustapha, Jibrin, Etsuworo, & Alhassan, 2014).

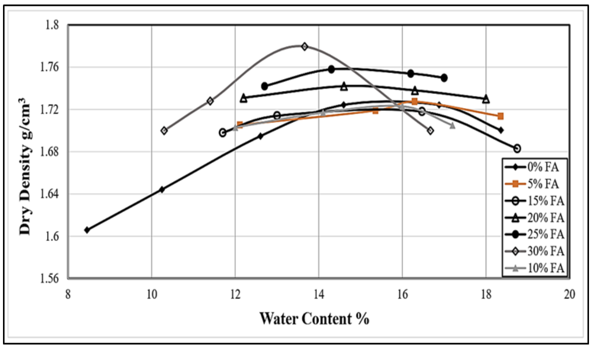

Fig. 3 . Moisture density relation of soil-FA mixtures

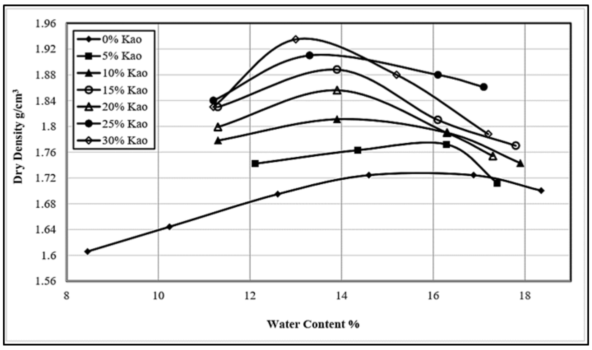

Fig. 4 Moisture density relation of soil- Kao mixtures

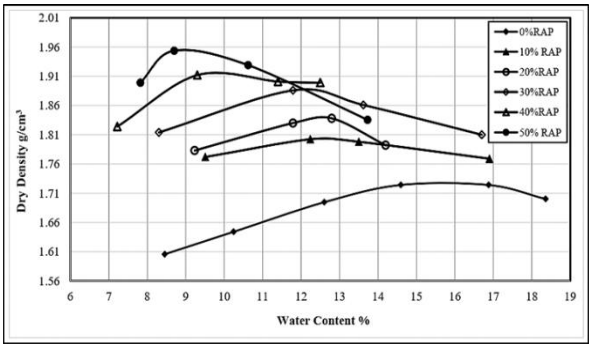

Fig. 5 . Moisture density relation of soil- RAP mixtures

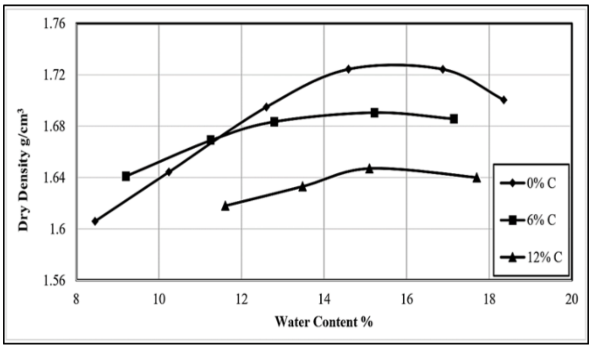

Fig. 6 . Moisture density relation of soil-cement mixtures

Table 3. OMC and MDD of the soil-RAP-geopolymer

Mixture	MDD (g/cm^3)	OMC (%)
Soil+20% RAP+20% Fly ash	2.02	9.1
Soil+20% RAP+15% Kaolinite	1.98	9.3

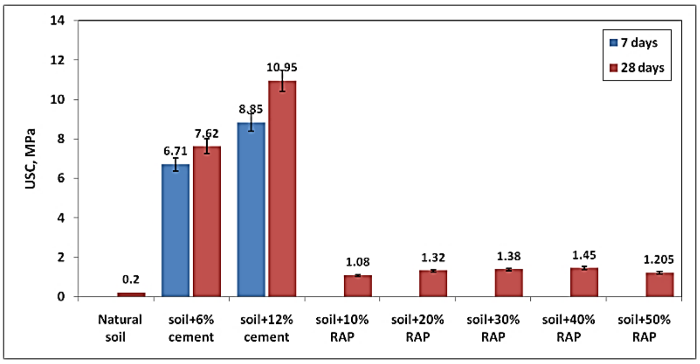

Fig. 7. Effect of soil–RAP mixtures on UCS test.

The UCS values of the soil-RAP-fly ash geopolymer mixture are listed in Figure 8. The maximum UCS values were 20.51 MPa and 22.56 MPa at 7 and 28 days of curing time respectively. Various proportions of the RAP were used to produce soil-RAP-fly ash geopolymer mixture. 20% of the fly ash was the optimum content that enhanced the UCS of the soil significantly when it incorporated with the alkaline solution in soil-fly ash geopolymer mixtures. The increase in the RAP content decreased the UCS from 22.56 MPa at 20% of RAP to 11.52 MPa at 50% of the RAP content. The obvious decrease in the UCS at the high content of the RAP highlights the role of the fly ash-based geopolymer with RAP particles. Despite of the nature of RAP particles, the surface area of RAP exposed to the pozzolanic reactions with the fly ash-based geopolymer as found by (Saride, Avirneni, & Challapalli, 2016) and the strength affected by the range of the exposed area.

The UCS test was conducted on 7 and 28 days cured specimens of soil+RAP+kaolinite geopolymer mixtures. Figure 9 presents the estimated strength results of the stabilized soil with various proportions of the RAP and 15% of kaolinite. Obvious increase in the compressive strength of the soil was observed with the initial increase in the RAP content. The results of 7 and 28 days cured specimens indicate that the optimum content of the RAP was 20% by weight of the soil when the kaolinite content remains constant at 15%. The maximum compressive strength was observed in the soil samples treated with this content and activated by 8M of NaOH and 60:40 of NaOH:Na_2SiO_3 ratio. Any further increase in the RAP content led to strength reduction irrespective of curing time. In addition, it can be observed that there was a slight increase in the strength after the first 7 days of curing and there is no big variation in the strength between 7 and 28 days cured specimens except at 20% of the RAP content. The heat-curing is responsible for the strength gain in the early ages of curing in the geopolymer paste (Rangan, B. ,2009). The optimum percentage of the RAP was found to be different from the soil-RAP mixture result, as the optimum content of the RAP was 40% with soil and water without the alkaline solution. This indicates that the high content of the RAP has a negative impact in soil stabilization by the geopolymer, as the RAP is inert material with the soil and the geopolymer. However, the bitumen coating the RAP particles may affect the geopolymerzation development by the reaction with the alkali solution and producing pozzolanic products on the RAP particles surfaces (Saride, Avirneni, & Challapalli, 2016).

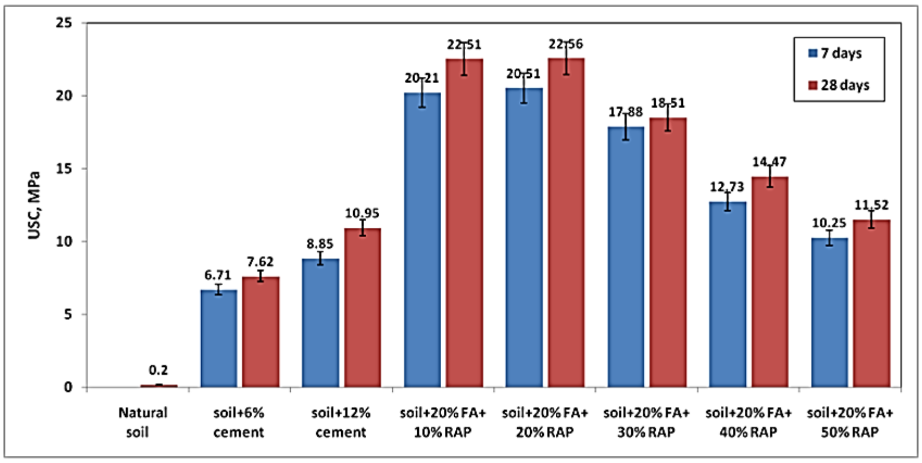

Fig. 8. Effect of soil-RAP-20% FA geopolymer mixtures on UCS test.

golden light publishing®

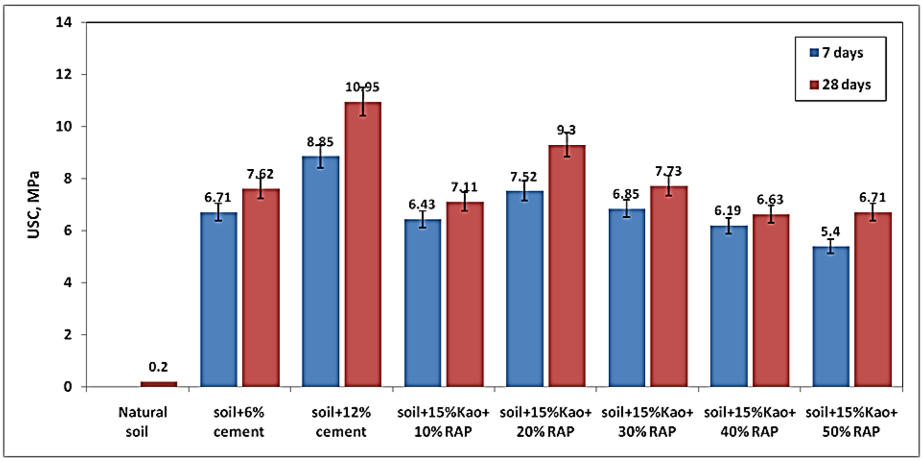

Fig. 9. Effect of soil-RAP-15% Kao geopolymer mixtures on UCS test.

3.3 Indirect tensile strength (ITS) test

The ITS test results alongside the specimens densities are shown in Fig. 10. It was obvious that the tensile strength of the soil increased by 7 times after adding 40% of the RAP by weight and it was the highest tensile strength among the other proportions of the RAP. The same trend was observed in the UCS strength as the optimum percentage of the RAP was 40% as well. The RAP was well-graded material and this property improves the interlocking between the RAP and the soil which leads to increase cohesion and friction capacity ,in turn, increase the strength of the mixture (Mahasneh, 2016). However, the addition of 8 and 12% of the OPC to the soil developed a tensile strength surpasses all soil-RAP mixtures after 7 and 28 days of curing at the ambient temperature. The reduction in the tensile strength occurred at 50% of the RAP content and this indicates that the high content of the RAP is not proper for the soil stabilization. It is obvious that the soil-RAP mixtures have significant densities especially at the high contents of the RAP. The high density may be attributed to the well-graded aggregates of the RAP which increase the density of the soil to a specific limit.

The combined effect of RAP and fly ash geopolymer on the tensile strength of the sandy silty soil is presented in shown Figure 11 for 7 and 28-day cured specimens. It is obvious that the stabilized soil developed a significant tensile strength at all RAP percentages with the constant ratio of the fly ash (20%) activated by 8M of the NaOH and 60:40 of NaOH:Na_2SiO_3. However, 20% of the RAP addition achieved the highest tensile strength irrespective of the curing period as shown in Figure 11. Other proportions developed high tensile strength in comparison with soil-cement mixtures. The stabilized soil by 10% of the RAP and 20% of the activated fly ash achieved considerable ITS by 2.16 MPa at 28 days of curing period. This result can be considered as a significant improvement in the tensile strength. By inspecting Figure 11, a reduction in the tensile strength occurs after increasing the RAP content to more than 20%. This reduction may be attributed to increasing the large particles of the RAP and non-uniform distribution of the RAP particles with the fly ash that may lead to weak areas in the soil structures.

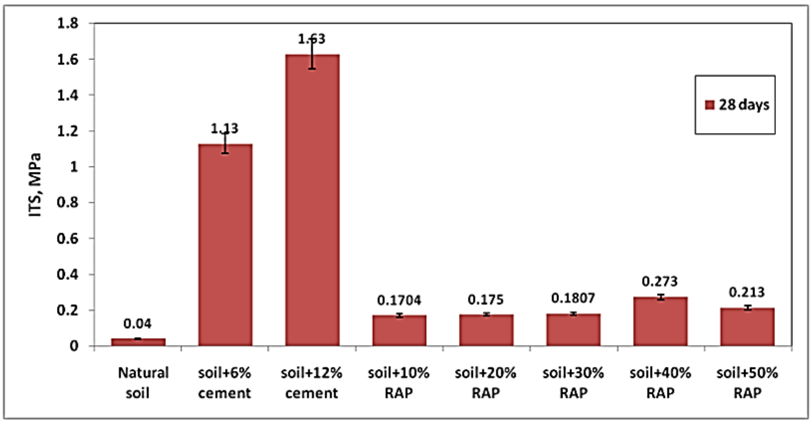

Fig. 10. Effect of RAP on ITS test with curing period at 28 days.

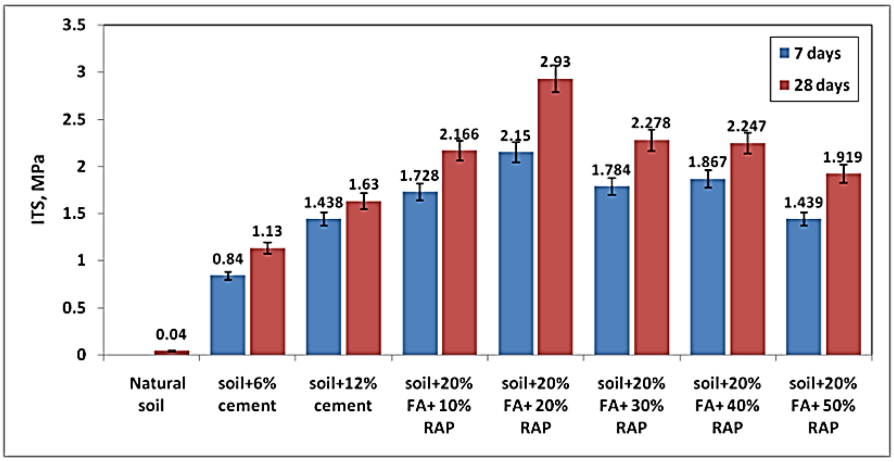

Fig. 11. Effect of soil-RAP-20% FA geopolymer mixtures on ITS test.

The results of the ITS test of soil-RAP-Kao geopolymer mixtures is presented in Figure 12. The optimum mixture was found at 15% of the kaolinite and 20% of the RAP by weight of the soil irrespective of curing time. This blend achieved the maximum tensile strength up to 1.35 MPa at 28 days of curing time. The other mixtures developed a considerable tensile strength at the low contents of the RAP particles while the kaolinite content remained constant at 15% by weight as found in the UCS and ITS of the soil+kaolinite geopolymer mixture. In the high-RAP content mixtures, the tensile strength exhibited a noticeable reduction especially at 40 and 50% of the RAP content by weight. The minimum tensile strength was recorded at the alkali-activated mixture that contains 50% of the RAP and 15% of the kaolinite by weight of the soil. This indicates the high content of the RAP negatively affects the strength in the geopolymer stabilized soil as was observed in the RAP-fly ash geopolymer stabilized samples.

The soil-cement mixture exhibited better tensile strength in comparison with the RAP-kaolinite geopolymer mixture, where 12% of the OPC has better tensile properties at both 7 and 28 days of curing period while 6% of the OPC achieved convergent results to the RAP-kaolinite based geopolymer. Figure 13 shows the ITS test specimen of the soil+50% RAP+15% kaolinite geopolymer after conducting the test. It is clear that the RAP particles did not lose the bitumen cover after 28 days of geopolymer reactions and this was opposite to the fly ash-based geopolymer, where the RAP was highly exposed to the chemical effects from the fly ash and the alkaline solution.

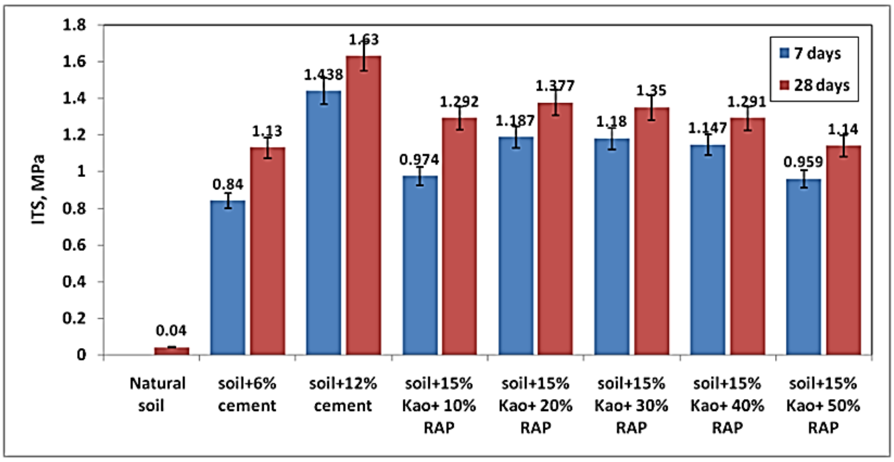

Fig. 12. Effect of soil-RAP-15% Kao geopolymer mixtures on ITS test.

Fig. 13 . ITS test specimen failure of soil +50% RAP +15% kaolinite geopolymer.

3.4 California bearing ratio (CBR) test

The CBR test was conducted on soaked specimens to investigate the contribution of RAP particles to the CBR value of the sandy silt soil. The CBR index of the natural soil is 3.8% for the soaked condition. One percentage (40%) of the RAP was added to the soil as an optimum proportion estimated from the UCS and ITS tests. The load-penetration curve of the soil+40% mixture is shown in Fig. 14. The CBR value was calculated from the stresses corresponding to both 2.54 mm and 5.08 mm of penetration depth and found to be 8.5% and 9.6% respectively. Since the CBR value at 5.08 mm was greater than the one at 2.54 mm, the test was conducted again to check the value and it was the same as the first test. According to (ASTM D1883-2014), the CBR value of the mixture is the one at 5.08 mm which was 9.6%. The CBR value increased about 2 times the CBR of the natural soil approximately. The considerable increase in the CBR index enhanced the soil to be a suitable material in the subgrade layer as it satisfies the Iraqi standards for the subgrade material, which indicates that the CBR index must be more than 4%. There was a big variation in the CBR index between the soil-RAP and soil-cement. The cement-treated soil achieved a significant CBR index corresponding to 230%. However, the RAP addition to the soil satisfies the Iraq standards for the subgrade material as the CBR index was more than 4% (Iraqi General Specifications for Roads and Bridges, 2003). In addition, the RAP was a waste material and there is no clear approach to recycle this material in transportation applications and soil stabilization.

Fig. 15 shows the CBR test result of the stabilized soil by 20% of the fly ash and 20% of the RAP by weight. It can be observed that the stabilized soil has showed a considerable resistance to penetration, however, the plunger of the CBR machine penetrated the soil surface to 1.6 mm at the maximum capacity of the machine as shown in Figure 16. The high resistance to penetration confirms that the stabilized soil strongly bonded by the new products and there was no considerable water absorption that may affect the soil by the leaching of the new binder in the soil. The main effect that enhanced the strength of the soil in terms of the CBR is the fly ash geopolymer binder. The strong bonds of the geopolymer highly affected the resistance of the soil and improved the bonding of the soil particles (Dungca, & Codilla, 2018). In the mixture of the soil+RAP+fly ash geopolymer, there was no swelling in the soil surface along the 4 days of soaking in the water. The swelling of the soil was 0% after adding the geopolymer which was another positive indicator of the stabilization efficiency.

The CBR test result of the stabilized soil by RAP-kaolinite geopolymer mixture is shown in Figure 17. The addition of the RAP with the kaolinite geopolymer has improved the CBR index significantly. The CBR value of soil+15% kaolinite+20% RAP approaches from the result of the soil+12% cement mixture which was 230%. The significant increase in the CBR index after adding the RAP confirms the important role of the RAP in resisting the penetration into the soil.

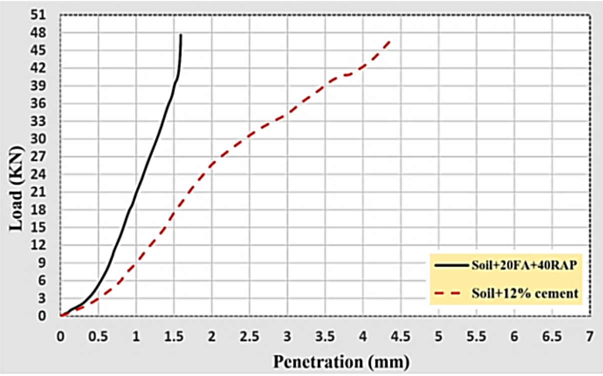

Fig. 14. Load – Penetration curve of CBR test for the soil+40% RAP mixture.

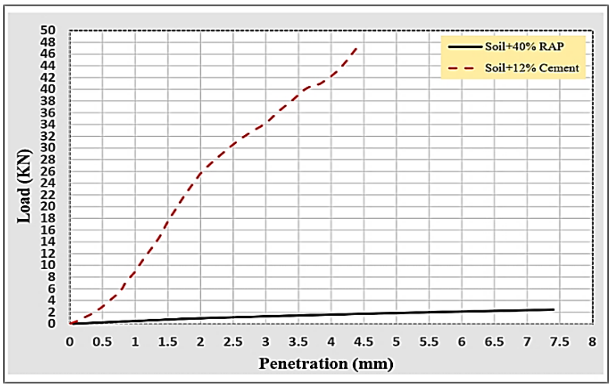

Fig. 15 . Load – Penetration curve of CBR test for soil+20FA+20RAP mixture.

Fig. 16 . CBR test specimen of 20FA+20RAP mixture after conducting the CBR test.

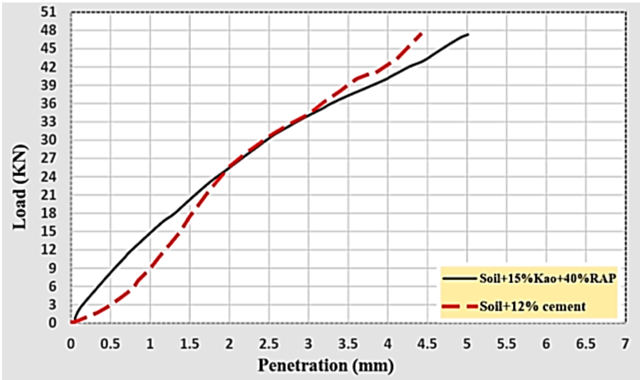

Fig. 17. Load – Penetration curve of CBR test for for the soil+ 20RAP+15Kao mixture.

4. Conclusions

The study was performed to find out the influence of the geopolymer and recycled asphalt material on the physical, and mechanical properties of the subgrade soil. The study proved the efficiency of RAP-geopolymer mixtures in soil stabilization as a road subgrade material. The following conclusions are drawn:

- The MDD of the soil increased with the increase in the RAP content, on the other hand, the OMC decreased at the same proportions. The RAP has a significant impact on the MDD and the OMC. The high content of the RAP (50%) increased the MDD from 1.73 g/cm^3 of the natural soil to 1.95 g/cm^3.
- By 8M of the NaOH and 1.5 ratio of the NaOH:Na_2SiO_3 solution , the UCS strength of the stabilized soil was improved significantly at the optimum content RAP compared to the natural soil and soil-cement blends. The stabilized soil by the activated additives exhibited high compressive strength at both 7 and 28 days of curing time at 20% of the fly ash, 15% of the kaolinite, 40% of the RAP, and 20% of the RAP when used with the fly ash and kaolinite geopolymer mixtures. The mixtures were compacted by the modified effort method and cured initially at 65°C for 48 hours.
- The tensile strength of the stabilized soil increased significantly by RAP-geopolymer additives. The RAP aggregates increased the tensile strength of the soil from 0.04 MPa of the natural soil to 0.273 MPa at 40% of the RAP content. When the geopolymer was mixed with soil, 20% of the RAP has achieved the maximum tensile strength with the fly ash and kaolinite contents irrespective of the curing time.
- For the stabilized soil by various mixtures of the RAP-geopolymer mixture, the CBR index was highly improved after the incorporation of the additives. The specimens were tested after heat-curing at 65°C for 48 hours and soaked in the water for 96 hours prior to the test. The specimens stabilized RAP-fly ash geopolymer mixture has shown great resistance to penetration. The piston of the CBR machine could not be able to penetrate the specimen to the required depth (2.54 or 5.08mm) due to the high strength of the stabilized soil. While the specimens stabilized by 230% at the RAP-kaolinite geopolymer stabilized specimen. There was no indicator on swelling or water absorption in the specimens during the immersion period in the water.

Acknowledgments
The research described in this paper was supported by used the labortary of engineering college in Anbar Universty and without financially supported.

References

Abdulkareem, A., Ahmed, T., & Kwad, N. (2023). Effect of incorporating kaolinite geopolymer on some mechanical properties of subgrade soil. In *Smart Geotechnics for Smart Societies* (pp. 680–690). CRC Press.

Abdulwahed, H. S., Aljanabi, K. R., & Abdulkareem, A. H. (2024). Optimization of equivalent modulus of RAP-geopolymer-soil mixtures using response surface methodology. *Journal of King Saud University-Engineering Sciences, 36*(6), 375–384.

Adhikari, S., Khattak, M. J., & Adhikari, B. (2020). Mechanical characteristics of Soil-RAP-Geopolymer mixtures for road base and subbase layers. *International Journal of Pavement Engineering, 21*(4), 483–496.

Adhikari, S. (2017). *Mechanical properties of Soil-RAP-Geopolymer for the stabilization of road base/subbase* [Master's thesis, University of Louisiana at Lafayette].

Akinwumi, I. I. (2014). Plasticity, strength and permeability of reclaimed asphalt pavement and lateritic soil blends. *International Journal of Scientific & Engineering Research, 5*(6), 631–636.

Ali, F. H., & Ahmed, T. M. (2024). Influence of fly-ash based geopolymer additives on the preliminary properties of cold asphalt mix. In *AIP Conference Proceedings*.

ASTM D1883-14. (2014). *Standard test method for California bearing ratio (CBR) of laboratory-compacted soils*. ASTM International.

ASTM C618-12. (2012). *Standard specification for coal fly ash and raw or calcined natural pozzolan for use in concrete*. ASTM International.

ASTM D4219-08. (2008). *Standard test method for unconfined compressive strength index of chemical-grouted soils* (Withdrawn 2017). ASTM International.

Ayininuola, G. M., & Adekitan, O. A. (2017). Compaction characteristics of lateritic soils stabilised with cement-calcined clay blends. *Epoxy & Silicate Based Composite Materials, 69*(2).

Bloodworth, A., Highley, D. E., & Mitchell, C. (1993). *Industrial minerals laboratory manual: Kaolin*.

Chen, J.-S., Huang, C., Chu, P., & Lin, K. (2007). Engineering characterization of recycled asphalt concrete and aged bitumen mixed recycling agent. *Journal of Materials Science, 42*, 9867–9876.

Chilukwa, N., & Lungu, R. (2019). Determination of layers responsible for rutting failure in a pavement structure. *Infrastructures, 4*(2), 29.

Davidovits, J. (2017). Geopolymers: Ceramic-like inorganic polymers. *Journal of Ceramic Science and Technology, 8*(3), 335–350.

Dungca, J. R., & Codilla II, E. E. T. (2018). Fly-ash-based geopolymer as stabilizer for silty sand embankment materials. *GEOMATE Journal, 14*(46), 143–149.

Edeh, J. E., Eberemu, A. O., & Agnes, O. (2012). Lateritic soil stabilization of reclaimed asphalt pavement as flexible highway pavement materials. In *Advanced Materials Research, 367*, 3–11.

Huang, W., & Wang, H. (2024). Optimization of geopolymer pervious concrete design using multi-phase discrete element modeling. *Construction and Building Materials, 438*, 137034.

Iraqi General Specifications for Roads and Bridges. (2003). *Standard specification for roads and bridges* (3rd ed.).

Ibrahim, A. M., & Ahmed, T. M. (2024). Some mechanical properties of cold bitumen emulsion mixes improved by geopolymer. In *AIP Conference Proceedings*.

Ibrahim, A. M., Ahmed, T. M., & Ahmed, T. Y. (2024). Developing a novel cold bitumen emulsion mixes by adding geopolymer. *Salud, Ciencia y Tecnología - Serie de Conferencias, 3*, 864.

Jones, D., Rahim, A., Saadeh, S., & Harvey, J. T. (2011). *Guidelines for the stabilization of subgrade soils in California*. University of California Pavement Research Center.

Keyte, L. (2009). Fly ash glass chemistry and inorganic polymer cements. In *Geopolymers* (pp. 15–36). Elsevier.

Kriven, W. M., Leonelli, C., Provis, J. L., Boccaccini, A. R., Attwell, C., Ducman, V. S., ... Van Deventer, J. S. (2024). Why geopolymers and alkali-activated materials are key components of a sustainable world: A perspective contribution. *Journal of the American Ceramic Society*.

Kwad, N. F., Abdulkareem, A. H., & Ahmed, T. M. (2020). The effect of fly ash based geopolymer on the strength of problematic subgrade soil with high CaO content. In *Proceedings of the 9th International Conference on Maintenance and Rehabilitation of Pavements (Mairepav9)*.

Kwad, N. F., Abdulkareem, A. H., & Ahmed, T. M. (2024). The effect of wetting-drying cycles on durability of RAP-geopolymer materials used for subgrade layers. In *AIP Conference Proceedings*.

Mahasneh, B. Z. (2016). Use of aluminum residue and recycled asphalt pavement materials to stabilize silty clay soil. *Journal of Infrastructure Systems, 22*(4), A4015001.

Mahdi, N. J., Abd, D. M., & Ahmed, T. M. (2020). Evaluation of warm mix asphalt produced from Iraqi materials. In *Proceedings of the 9th International Conference on Maintenance and Rehabilitation of Pavements (Mairepav9)*.

Mustapha, A. M., Jibrin, R., Etsuworo, N. M., & Alhassan, M. (2014). Stabilization of A-6 lateritic soil using cold reclaimed asphalt pavement. *International Journal of Engineering and Technology, 4*(1), 52–57.

Rangan, B. (2009). Engineering properties of geopolymer concrete. In *Geopolymers: Structures, Processing, Properties and Industrial Applications* (pp. 211–226).

Saride, S., Avirneni, D., & Challapalli, S. (2016). Micro-mechanical interaction of activated fly ash mortar and reclaimed asphalt pavement materials. *Construction and Building Materials, 123*, 424–435.

Schaefer, V. R., White, D. J., Ceylan, H., & Stevens, L. J. (2008). *Design guide for improved quality of roadway subgrades and subbases* (Iowa Highway Research Board Project TR-525).

Singhi, B., Laskar, A. I., & Ahmed, M. A. (2016). Investigation on soil–geopolymer with slag, fly ash and their blending. *Arabian Journal for Science and Engineering, 41*, 393–400.

Thakur, J. K., Han, J., Pokharel, S. K., & Parsons, R. L. (2012). Performance of geocell-reinforced recycled asphalt pavement (RAP) bases over weak subgrade under cyclic loading. *Geotextiles and Geomembranes, 35*, 63–71.

4th International Civil Engineering & Architecture Conference
15-17 May 2025, Trabzon, Türkiye

Salinity's effect on the Atterberg limits of bentonite clay

Eyyüb Karakan*[1], Alper Sezer[2]

[1] Kilis 7 Aralık University, Department of Civil Engineering, 79000 Kilis, Türkiye
[2] Ege University, Department of Civil Engineering, 35100 İzmir, Türkiye

Abstract. The low bearing capacity and high compressibility of bentonite-type clays, particularly under dynamic loads like earthquakes, make them unfavorable in terms of geotechnical properties. On the other hand, their extremely low permeability makes them advantageous. The adsorbed pore fluid regulates the engineering behavior of the clay. In experimental studies, distilled water—also known as adsorbed water—is typically utilized as the pore fluid. Atterberg limits, shear strength, and compaction parameters are all significantly impacted in this situation by variations in the salinity and viscosity of the water. This study used the Casagrande and fall cone tests with water containing 0 %, 1 %, 2 %, 3 %, 4 %, 5 %, and 10 % salt to calculate the Atterberg limits, and undrained shear strengths of bentonite type clay. Standard proctor test was also conducted to obtain the optimum water content and maximum dry density values. Furthermore, the water content-penetration depth relationship was established in over 30 steps by gradually increasing the fall cone experiments from a very low water content. The water content corresponding to 2 mm penetration was recognized as the plastic limit within the parameters of the study, and the water content corresponding to 20 mm penetration was identified as the liquid limit. This led to an experimental determination of the impact of salt content on bentonite clay. According to the findings, bentonite clay's plastic limit and liquid limit both decrease with increasing salt content. The maximum dry density of bentonite clay decreases as the salt content increases, while the clay's optimum water content increases, according to standard compaction results.

Keywords: Salt content; Fallcone test; Undrained shear strength; Atterberg Limits

1. Introduction

In coarse-grained soils, the soil is considered as an isotropic medium and geotechnical parameters are determined by the contact forces between the grains, while in fine-grained soils such as silt and clay, geotechnical parameters are obtained by the movements of surface forces due to the fact that the grain sizes are at micron levels and have a larger specific surface area.In fine-grained soils such as clay, where pore fluid properties are different, chemical interaction should be taken into account in classical soil mechanics calculations (Mitchell & Soga, 2005).

The geotechnical parameters of clays with different mineralogical properties are highly influenced by shear resistance, friction of grains, as well as chemical interaction due to van der Waals bonds. Many geotechnical parameters such as Atterberg limits and compaction properties of fine-grained soils are also affected by the properties of the pore fluid (Sridharan, 2002). For bentonite type clays, geotechnical parameters are influenced by the Double Diffuse Layer (DDL), while for kaolinite type clays, geotechnical parameters are influenced by the interparticle shear resistance.

The mechanical properties of fine-grained soils such as clay and silt are strongly influenced by changes in the chemical properties of the pore fluid (Santamarina et al., 2002). Mitchell and Soga (2005) showed that properties &such as dielectric constant and electrolyte concentration have a decisive influence on the bearing capacity and settlement properties of fine-grained soils.

The effect of pH in the pore fluid of fine-grained soils on geotechnical properties has been studied by many researchers (Santamarina et al., 2007; Gori, 1994;Gajo & Maines, 2007; Gratchev & Sasa, 2009; Spagnoli et al., 2012). Gori (1994) investigated the change of liquid limit and plastic limit values of kaolin clay depending on the pH in the pore fluid. According to the results of his experimental study, he concluded that pH value has no effect on liquid limit and plastic limit because kaolin clay is not bilayer. However, Di Maio (1996), Gajo and Maines (2007) and Yukselen-Aksoy et al., (2008) found the opposite result in their experimental studies.

*Corresponding author, E-mail: eyyubkarakan@kilis.edu.tr

https://doi.org/10.31462/icearc2025_ce_geo_092

The change of geotechnical properties of saline-water mixtures on fine-grained soils has been investigated by many researchers from past to present with laboratory experiments. For example, Rao et al., (1993) investigated the changes in interparticle forces in bentonite clay as a result of the long-term effect of artificial seawater. Their experimental results showed that the long-term effect of artificial seawater on bentonite clay did not cause any mineralogical changes in the clay samples. They observed an increase in liquid limits when the salt content in bentonite samples decreased from 42 g/L to 1.1 g/L. In another study, Di Maio (1996) showed that exposure of bentonite samples to saturated NaCl, KCl or $CaCl_2$ solutions caused residual shear strength increases. Di Maio et al., (2004) carried out oedometer tests on Ponza bentonite, a commercial kaolin, the Bisaccia and the Marino clays. They showed that artificial mixtures reconstituted with distilled water were strongly affected by the mineral composition. They concluded that an increase in the pore solution concentration leads to a decrease in the compressibility of the materials and an increase in the consolidation coefficients.

Sridharan et al., (2002) concluded that based on the results of fallcone and veyn tests, the liquid limit of Isahaya clay increases with increasing salt concentration, while a marginal decrease is observed for Kubota and Kawazoe clays. For Isahaya clay, the factors responsible for the increase in the level of flocculation and attractive forces resulted in higher undrained strength, while for Kubota and Kawazoe clays, they showed that for Kubota and Kawazoe clays, the expansion of the diffuse double layer thickness would result in higher viscous resistance and increase the undrained shear strength.

The main objective of this study is to investigate the changes in Atterberg limits of bentonite clay with salt water mixtures having different salt ratios. In addition, the effect of salt content on the undrained shear strength values obtained from Fallcone experiments was also investigated. For this purpose, a series of laboratory experiments were carried out by creating brine mixtures at 7 different salt ratios ranging from 0% to 10%. For this purpose, Casagrande, Fallcone and plastic limit tests were performed using 6 different salt-content mixtures.

2. Materials and methods

The behavior of clay minerals towards water is one of the main factors in the classification of these minerals. Bentonites are mainly classified in three main groups: Na-bentonites that swell in water; intermediate type bentonites containing balanced calcium and sodium, which have this property less; Ca-bentonites that do not swell in water. Na-bentonites with swelling properties have the ability to absorb approximately 1-15 times more water. When mixed with water, these clays show colloidal properties and swell in volume in water and some organic liquids. Ca-bentonites, which are called non-swelling clays, contain calcium in ions that can vary between layers.

Fig. 1 shows the bentonite clay obtained from ESAN company and its scanning electron microscope (SEM) image. Table 1 shows the chemical properties of bentonite clay. Bentonite clay-water mixtures were prepared by thoroughly mixing clay powders with distilled water and salt solutions. The clay-water mixtures were kept in a sealed plastic container for 24 hours to ensure proper homogeneity of the clay-water mixture. After 24 hours, the clay-water mixtures were re-mixed and used to determine the liquid limits using a fall cone test device. Mixtures were prepared using bentonite clay and water containing 0%, 1%, 2%, 3%, 4%, 5% and 10% salt. The mixtures were tested according to BS 1377-9 (1990) using a fall cone test device with a 30° apex angle and a conical tip with a mass of 80 g. The 55 mm diameter and 40 mm height sample container was filled with no air pockets, brought into contact with the cone and then penetrated under its own weight for five seconds and the penetration value was measured automatically. For the accuracy of the experimental results, the water content-penetration depth relationship was determined by conducting more than 30 steps, starting from 6% water content in frequent steps and proceeding with 3% water content increments. In this study, plastic limit values corresponding to 2 mm penetration as a result of the fall cone test were accepted as plastic limits and plastic limit values were also calculated by the conventional method.

Casagrande test is performed by filling soil samples prepared at different water contents into a Casagrande cup, opening a standard sized crack in this sample and dropping the cup many times from a height of 1 cm by turning the instrument handle at a standard speed. The relationship between the number of drops that cause the 1.25 cm long part of the opening to close and the soil water content is determined experimentally and the water content value corresponding to this much closure of the gap in 25 drops is accepted as the liquid limit of the soil.

If a fine-grained soil can be given the desired shape by kneading without causing fractures, it can be considered to have a plastic consistency. In order to determine the plastic limit of a soil experimentally, a moist sample is tried to be rolled into round thin cylinders on a smooth surface. The water content at which the soil is rolled into a cylinder about 3 mm thick without breaking is considered the plastic limit.

Fig. 1. a) Bentonite clay b) SEM image of bentonite

Table 1. Chemical properties of bentonite

Chemical Properties	SiO_2 (%)	Al_2O_3 (%)	Fe_2O_3 (%)	MgO (%)	CaO (%)	Na_2O	K_2O (%)
(%)	64	21	3.5	2.3	0.5	2.6	0.4

3. Results and discussions

In this study, the salt content dependent changes of bentonite clay samples prepared with salt water solutions with different salt concentrations were investigated in the laboratory by Casagrande, Fallcone and conventional plastic limit tests.

3.1. Casagrande test results

The Casagrande test apparatus, which is the most widely used method worldwide for soil classification in fine-grained soils, was used in accordance with ASTM D4318-17e1 (2018) standard. The experiments were first performed with distilled water. Then, the experiments were carried out at 6 different salt contents from 1% to 5% with 1% increase and 10% in total. For example, in the experiments, 5 g of salt was added to every 100 ml of distilled water for 5% salt content, mixed until completely dissolved and then used in the experiment.

First, the number of blows versus water content on a semi-logarithmic scale is given in Figure 2. As seen in Fig. 2, the water content corresponding to 25 blows was determined as the liquid limit. In order to obtain the liquid limit value much more accurately in the experiments, the test were carried out in 20-22 steps starting from 15%-20% initial water contents and up to 350% water content at the end of the experiment.

Table 2 shows the equations obtained using Fig. 2, the root mean square error values and the liquid limit values obtained using the casagrande test apparatus. The results in Table 2 and Figure 2 show that the liquid limit values of bentonite clay decreased with increasing salt content. For example, while the liquid limit value of bentonite clay was 222.90% at 1% salt content, the liquid limit value decreased to 195.79% when the salt content increased to 5%.

Table 2. Liquid limit and plasticity index for casagrande

Salt Content (%)	Equation	R^2		PL_{con}(%)	PI_{cas}
0	LL_{cas}=-22.83×ln(25)+293.17	0.995	219.68	47.62	172.06
1	LL_{cas}=-26.78×ln(25)+309.	0.969	222.90	54.11	168.79
2	LL_{cas}=-14.90×ln(25)+269.49	0.956	221.53	53.85	167.68
3	LL_{cas}=-23.93×ln(25)+279.64	0.989	202.61	54.55	148.99
4	LL_{cas}=-25.61×ln(25)+284.23	0.979	201.79	56.82	144.97
5	LL_{cas}=-23.30×ln(25)+270.79	0.963	195.79	58.62	137.17
10	LL_{cas}=-8.562×ln(25)+196.71	0.945	169.15	60.61	108.54

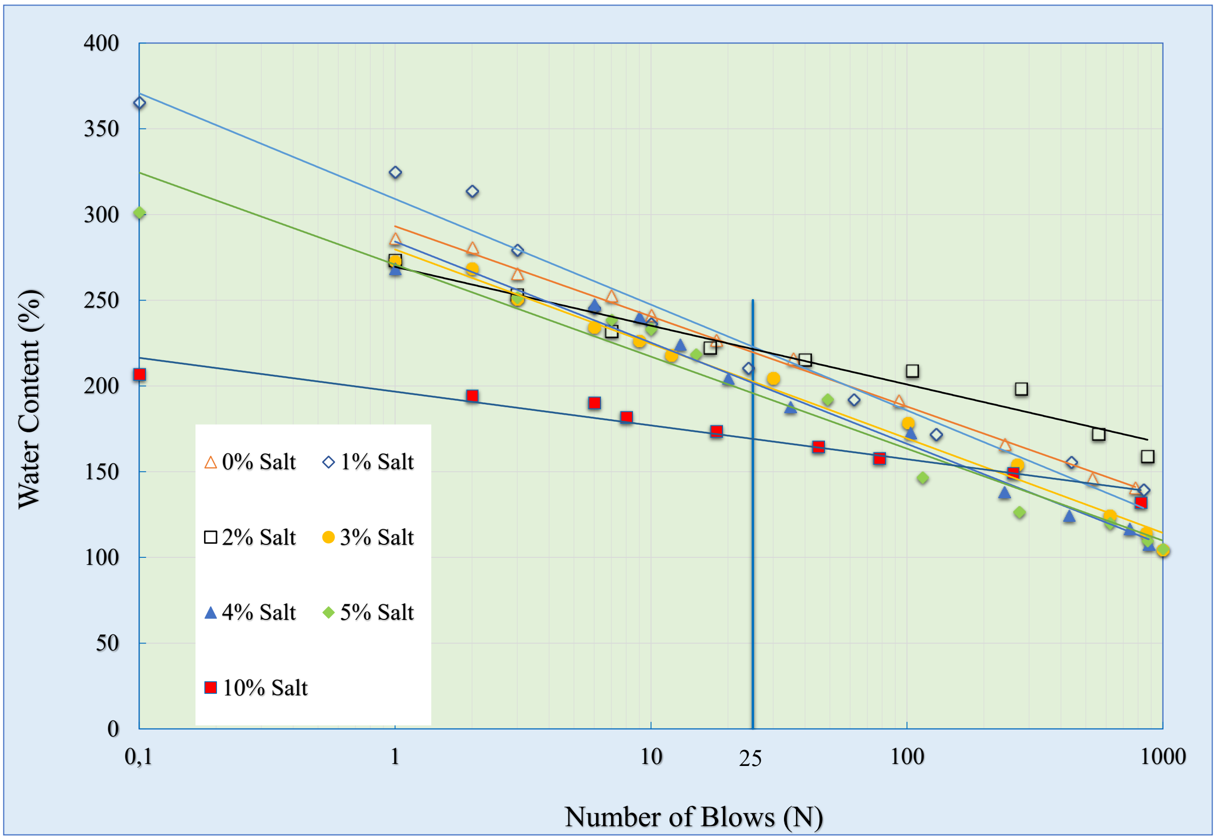

Fig. 2. Water content number of blows

Another parameter that determines the consistency of soils is the liquidity index. The liquidity index (I_L) is given in Equation 1. When the liquidity index is less than zero, the consistency of the soil is semi-solid or solid, when the liquidity index is between zero and one, the consistency of the soil is plastic and when the liquidity index is greater than one, the consistency of the soil is liquid. When the liquidity index is zero, it takes the plastic limit value, and when it is one, it takes the liquid limit value.

$$LI = I_L = \frac{w-PL}{PI} = \frac{w-PL}{LL-PL} \tag{1}$$

where, w=natural water content of the soil, LL=liquid limit, PL=plastic limit and PI=plasticity index.

Fig. 3 shows the number of drops corresponding to the liquidity index values obtained using the Casagrande test results. The liquidity index values obtained for 25 blows are also given in Fig. 3. The LI=0 line was determined as the value separating semi-solid from plastic state, while the LI=1 line was determined as the boundary separating plastic from liquid state. When Figure 3 is analyzed, firstly, at low water contents, the LI is less than zero and the soil is solid or semi-solid and the number of blows is very low. With increasing water content, the liquidity index increases above zero and the corresponding number of blows increases considerably. Then, if the water content continues to increase, the number of blows decreases and the liquidity index approaches one. If the water content continues to increase in the test, the liquidity index takes values greater than one and the number of blows decreases considerably.

Fig. 4 shows the variation of water content ratio with the number of blows for 6 different salt contents as a result of Casagrande test. When the natural water content of the soil is equal to the liquid limit value, the water content ratio becomes one. The results show that for the given number of strokes (N=25), soils with lower salt content have a higher water content ratio.

Finally, the variation of the liquidity index with water content is given in Fig. 5. For all data, the variation of the plasticity ratio (R_p=PL/LL) was analyzed for values of 0.2, 0.4 and 0.6. It is seen that for all salt contents, the data are concentrated in the region between 0.2 and 0.4 for different water contents and liquidity index values. In Fig. 5, the water content ratios vary between 0.05 and 1.6, while the corresponding liquidity index varies between -0.033 and 1.84.

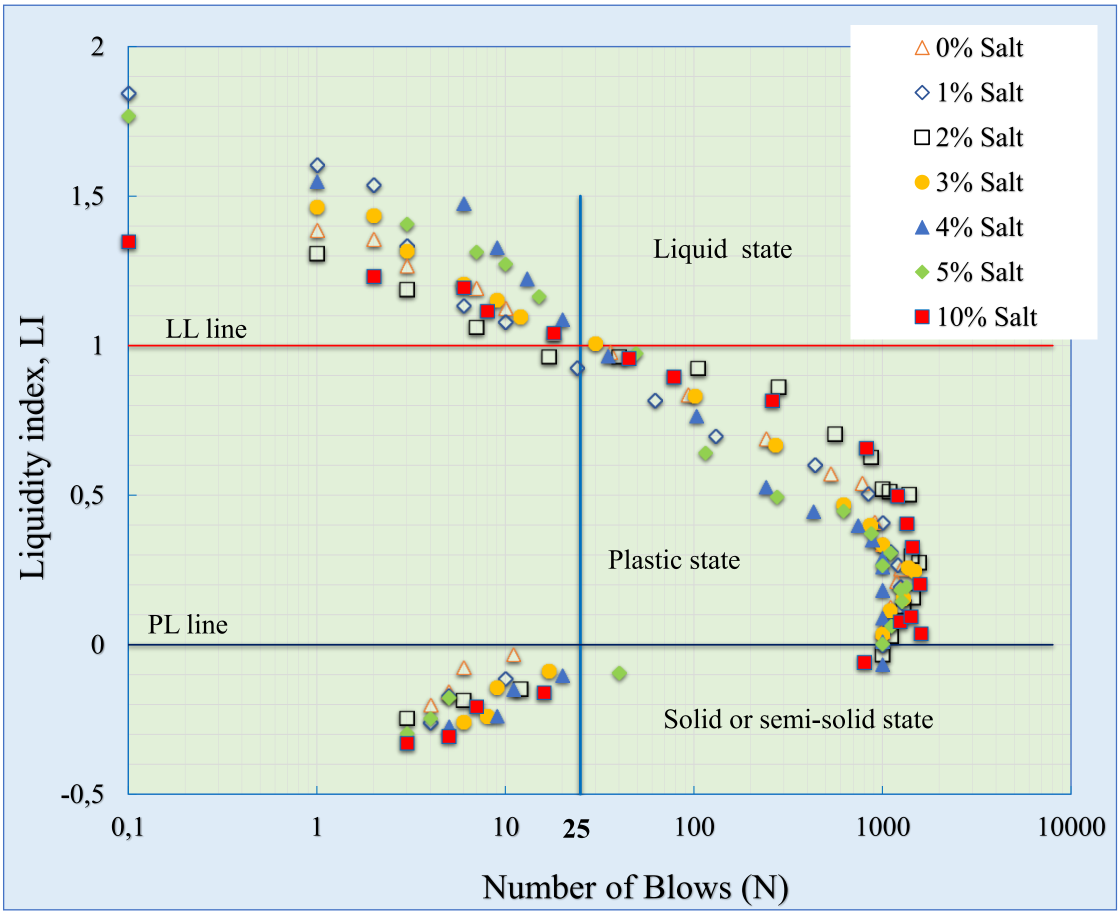

Fig. 3. Liquidity index number of blows

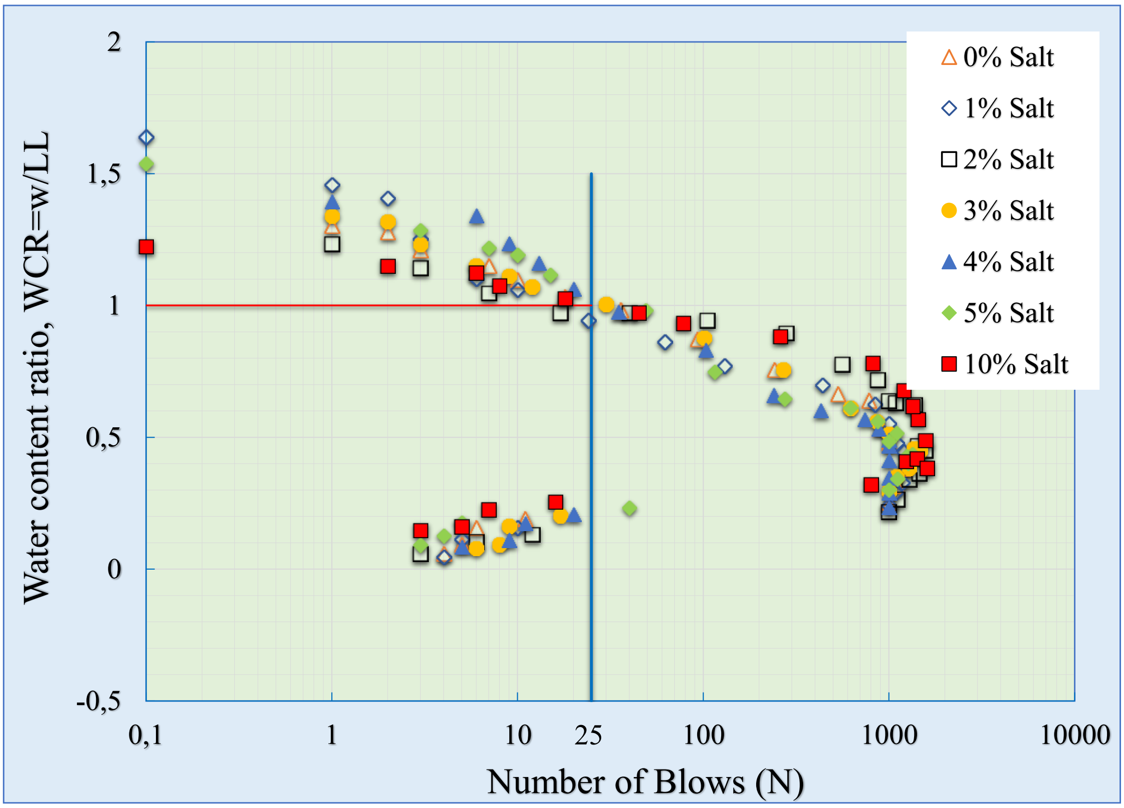

Fig. 4. Water content ratio number of blows

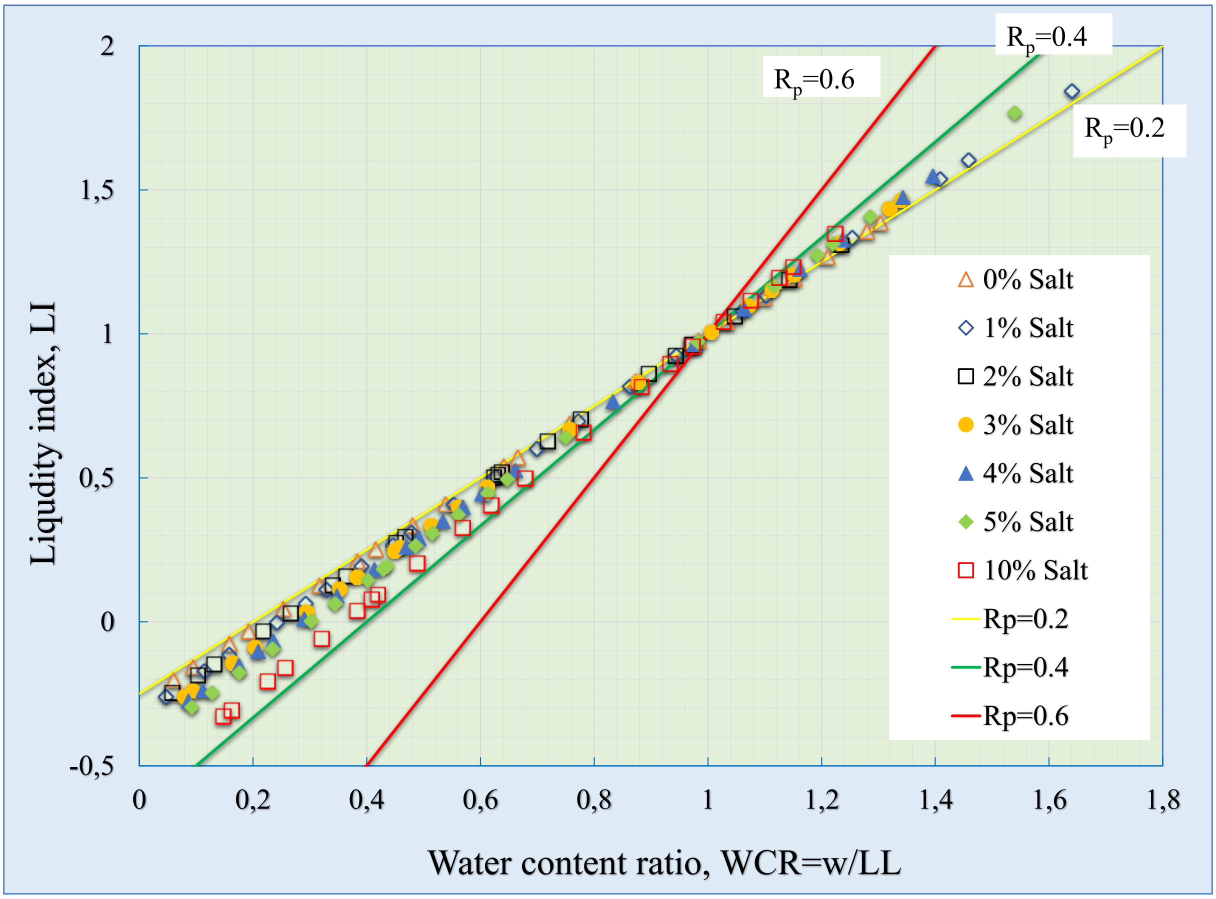

Fig. 5. Liquidity index water content ratio for Casagrande test

3.2. Fallcone test results

Within the scope of the study, fallcone experiments were carried out in accordance with BS 1377-9 (1990) standard at a total of 6 different salt concentrations on bentonite clay with distilled water, 1% to 5% with increasing 1% and 10% salt water mixtures.

The cone penetration water content relationship for the first 7 tests is shown in Fig. 6. At the beginning of the test, the experiment was started with 4-5% water content. Penetration values of 38-39 mm were obtained at very low water contents. Then, by gradually increasing the water content in the brine mixtures, the cone penetration amounts corresponding to each water content were also found. For different salt water concentrations, the cone penetration amounts decreased gradually. For a total of 7 different sets of experiments, minimum cone penetration amounts were obtained when the water contents were between 44% and 62%. For example, in the solution with 2% salt content, the water content was 44.3% and the corresponding cone penetration was only 0.88 mm. When the salt content in the solution was 4%, the cone penetration amount corresponding to 61.60% water content was found to be 1.19 mm. Thereafter, cone penetration continued to increase with increasing water content in all mixtures. After a limit water content, adding more salt water does not change the amount of cone penetration as it reaches the highest limit.

The experimental results shown in Figure 6 were given for all salt-water mixtures in order to describe the behavior and to present the results of the tests consisting of 25 steps in each experiment. In Fig. 7, the variation of cone penetration with water content is transformed into a data set consisting of the part of the data obtained during the experiment after the cone tip reaches its minimum penetration value and the cone penetration value increases with increasing water content. In this case, a linear relationship was obtained between cone penetration and water content. In the experiments, the part of the cone penetration value corresponding to 2 mm was defined as plastic limit, while the part corresponding to 20 mm was expressed as liquid limit.

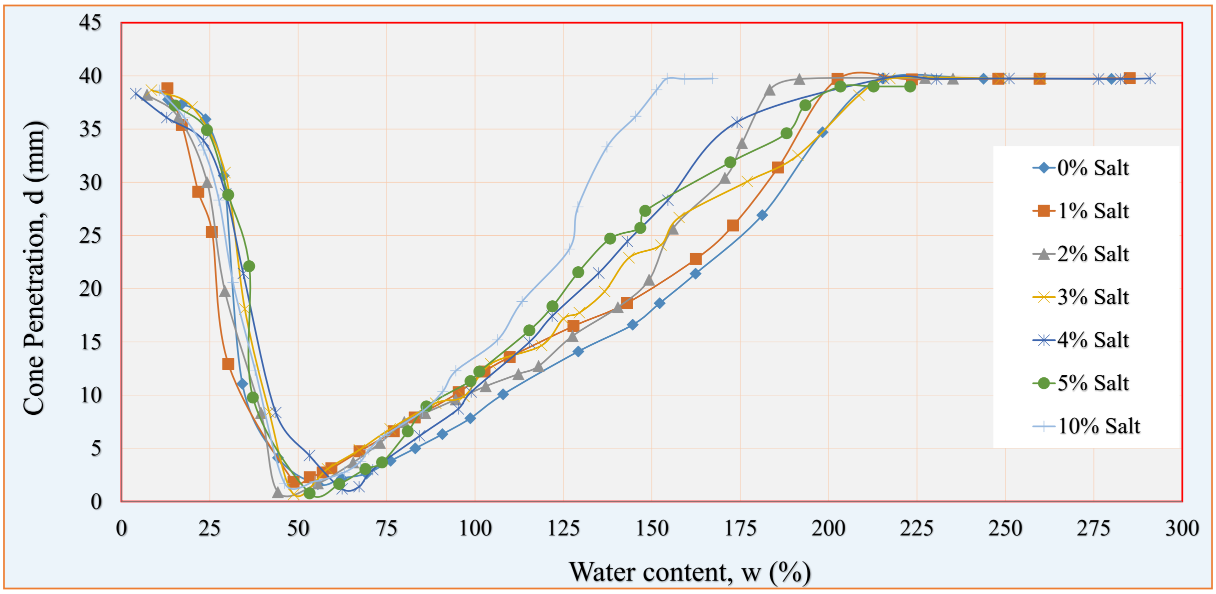

Fig. 6. Cone penetration water content

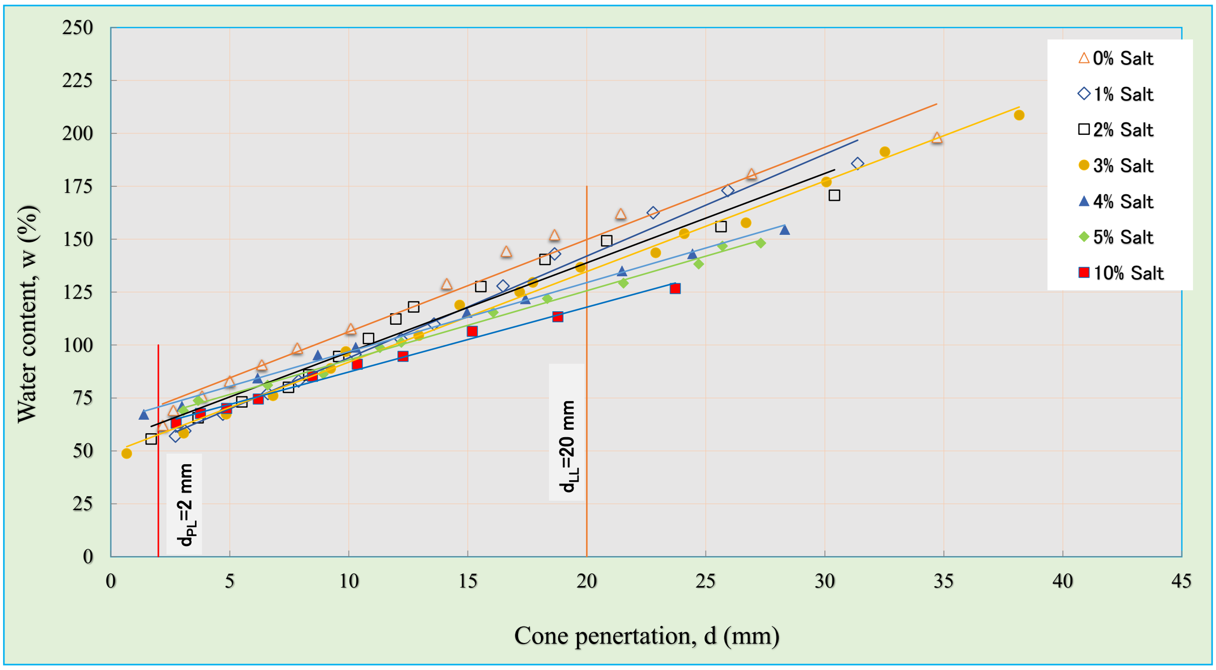

Fig. 7. Water content cone penetration relationship

In Table 3, liquid limit and plastic limit values are calculated and presented for different salt contents as a result of the fallcone test. The liquid limit values obtained in Table 3 are calculated as the water content corresponding to 20 mm penetration, while the water content value corresponding to 2 mm penetration is calculated as the plastic limit. When the results obtained are examined, while the fallcone liquid limit was 149.82% for 0% salt-water mixture, the liquid limit decreased to 117.92% in the experiment performed for 10% salt-water mixture. In this case, a regular decrease in the liquid limit of bentonite clay was observed as the salt concentration increased. When the plastic limit values were examined in the same experiment, there was no regular decrease with increasing salt content. While calculating the plasticity index values in the Fallcone experiment, the plastic limit values obtained by the conventional method were used for the plastic limit value. It was observed that the plasticity index values decreased as the salt content increased.

Table 3. Liquid limit, plastic limit and plasticity index for fallcone device

Salt Content (%)	Equation	R^2	LL_{FC} (%)	PL_{FC}(%)	PL_{con}(%)	PI_{FC}
0	LL_{FC}=4.357×d+62.679	0.975	149.82	71.39	47.62	102.20
1	LL_{FC}=4.8093×d+45.85	0.989	142.04	55.47	54.11	87.93
2	LL_{FC}=4.2232×d+54.374	0.960	138.84	62.82	53.85	84.99
3	LL_{FC}=4.2782×d+49.14	0.994	134.70	57.70	54.55	80.15
4	LL_{FC}=3.2679×d+64.171	0.996	129.53	70.71	56.82	72.89
5	LL_{FC}=3.265×d+60.334	0.995	125.63	66.86	58.62	67.01
10	LL_{FC}=3.066×d+56.601	0.990	117.92	62.73	60.61	57.31

Fig. 8 shows the variation of undrained shear strengths with water content for all salt-water mixtures. The undrained shear strengths of soils in Fallcone tests were calculated by Hansbo (1957) using Equation 2.

$$S_u = \frac{K \times W}{d^2} \quad (2)$$

In Equation 2, K=constant (0.85) related to the angle of the cone tip used in the Fallcone test, W is equal to the product of the mass of the cone tip (80 g) and the acceleration of gravity. d represents the amount of the cone penetration depth and its unit is mm. When the general behavior is analyzed, it is seen that the undrained shear strength increases with increasing water content, then reaches a peak value, and gradually decreases and stabilizes if the water content continues to increase. When the effect of salt is examined, for the undrained shear strength of the sample of 10 kpa, the samples prepared with 10% salt water solution have 81% water content, while the same undrained shear strength is reached at 99% water content in the experiments with distilled water. This indicates that for a constant value of undrained shear strength, lower water content is obtained at higher salt concentrations. At the end of the test, all solutions were stabilized at an undrained shear strength of 0.4 kPa but at different water contents. For example, 10% salt water solution has 154% water content, 5% salt water solution has 203.39% water content, 4% salt water solution has 212% water content, 3% salt water solution has 220% water content, 2% salt water solution has 223% water content, 1% salt water solution has 248% water content and 0% salt water solution has 251% water content.

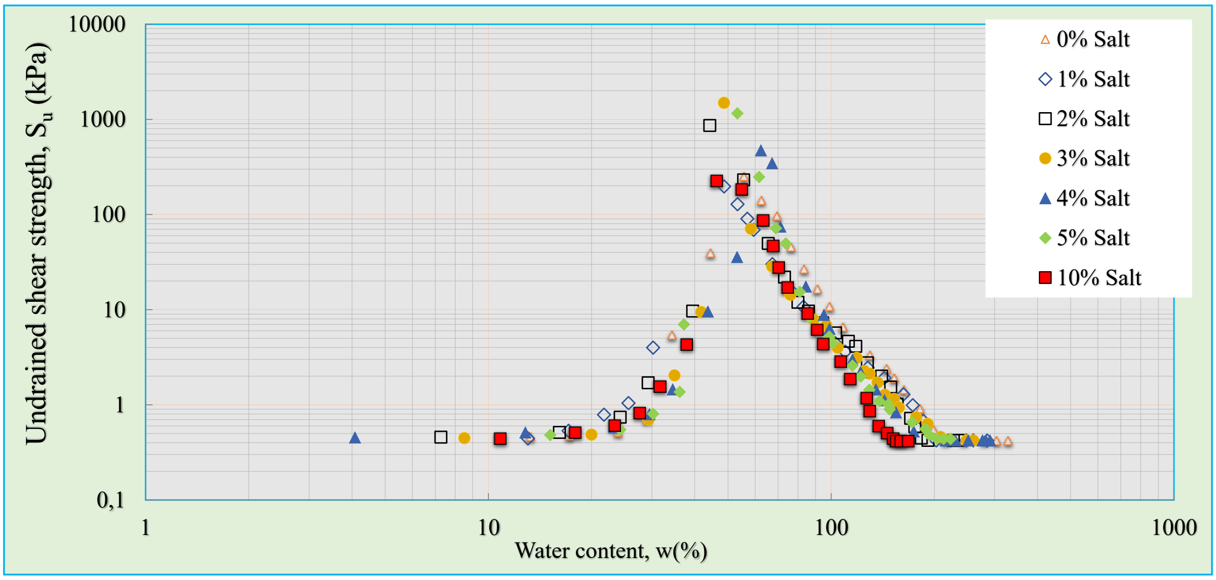

Fig. 8. Undrained shear strength water content relationship

The liquidity index cone penetration relationship obtained from Fallcone test results is given in Fig. 9. In addition, liquid limit lines are added in case the liquidity index is 1 and plastic limit lines are added in case the liquidity index is zero. In this case it is divided into 3 parts: solid or semi-solid state, plastic state and liquid state. In the solid or semi-solid state the liquidity index is less than zero. In this case, the liquidity index decreases from -1 to zero and the cone penetration values decrease from 40 mm to 1 mm. Then the liquidity index goes from zero to one and the cone penetration values increase again. When the liquidity index reaches 1.6, cone penetration values are obtained around 40 mm and after that, cone penetration values are fixed at 40 mm even if the liquidity index increases.

The liquidity index undrained shear strength relationship obtained by using the results of fallcone tests on mixtures with different salt concentrations is shown in Fig. 10. The initial undrained shear strengths started with values between 0.4-0.5 kPa when the liquid index is less than zero. When the liquidity index was around zero, the undrained shear strengths reached maximum values. For example, while the liquidity index was -0.10 for 184.78 kPa undrained shear strength at 10% salt water mixture, the liquidity index was -0.113 for 861.45 kPa undrained shear strength at 2% salt water mixture, and the liquidity index was 0.077 for 471.07 kPa undrained shear strength at 4% salt water mixture. As the liquidity index approached one, the undrained shear strengths decreased again. While the undrained shear strength of salt water mixtures is around 2 kPa, their liquidity index is around 1. As the liquidity index increased up to 1.5, the undrained shear strengths of salt water mixtures decreased and reached the range of 0.4-0.5 kPa. Increasing the liquidity index from 1.5 to 3 did not cause any change in the undrained shear strength of salt water mixtures. Because if the liquidity index is greater than 1.5, it means that the natural water content of salt-water mixtures is at least over 130% in the case of bentonite clay.

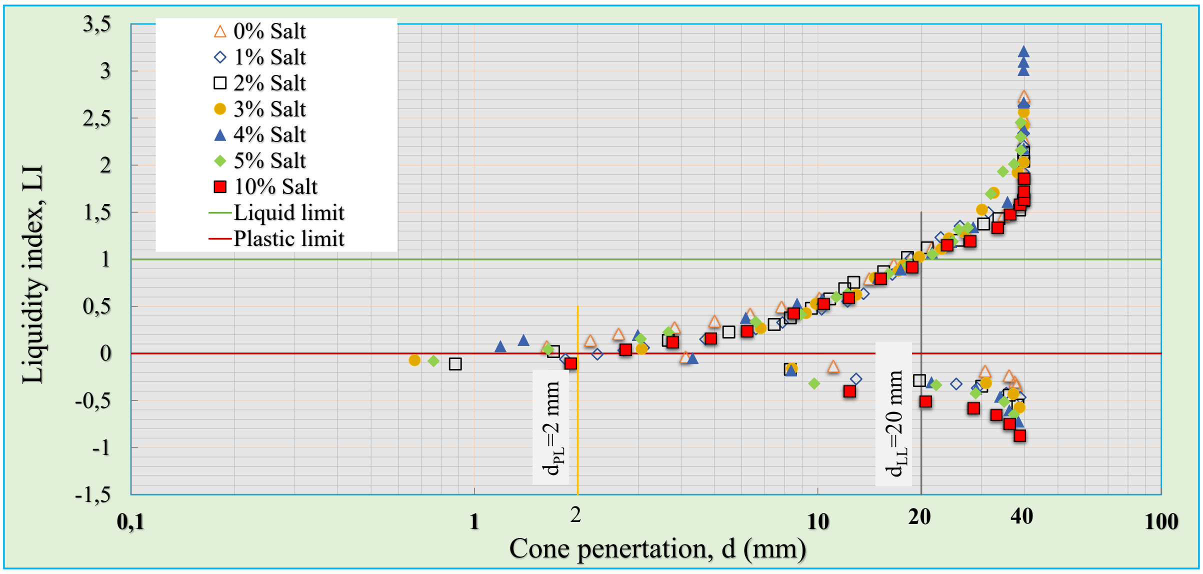

Fig. 9. Liquidity index cone penetration relationship for fallcone test

In Fig. 10, liquidity index dependent undrained shear strength values for sensitivity ratio 1, 2, and 4 are calculated and curves are plotted for liquidity index dependent undrained shear strength using the relation proposed by Shimobe and Spagnoli (2020) and shown in equation 3. The sensitivity ratio (S_t=1) line also indicates that it is for remolded specimens. It shows that most of the experimental specimens are around the S_t=1 line in the plastic and liquid cases. At very high liquidity index values, the undrained shear strength value stabilizes and has a high Sensitivity ratio (S_t=4).

$$S_u = 98 \times S_t \times exp[\ln\{0.4755/(I_L + 0.5012 \times (1 - I_L)\}/0.19] \ [16] \tag{3}$$

Shimobe and Spagnoli (2020) determined the relationship between the liquidity index and water content ratio depending on the plasticity ratio with equation 4. In Equation 4, R_p=PL/LL is expressed as plasticity ratio, I_L as liquidity index and WCR as water content ratio.

$$WCR = (1 - R_p) \times I_L + R_p \tag{4}$$

In Fig. 11, the variation of liquidity index and water content ratio is presented for all salt water mixtures. Liquidity index values increase with increasing water content ratio. In the study, 0.2, 0.4 and 0.6 lines of the plasticity ratio were drawn. It was found that the mixtures with low salt contents were closer to the Rp=0.2 line, while those with increasing salt contents were closer to the Rp=0.6 line. For example, when the results obtained from experiments with distilled water are examined, it is seen that the results closest to the Rp=0.2 line are obtained. With increasing salt concentration, the plasticity ratio first approached 0.4. Then, when the salt concentration was increased to 10%, the plasticity ratio was very close to the 0.6 line. In this case, it is concluded that the plasticity ratio increases with increasing salt concentration.

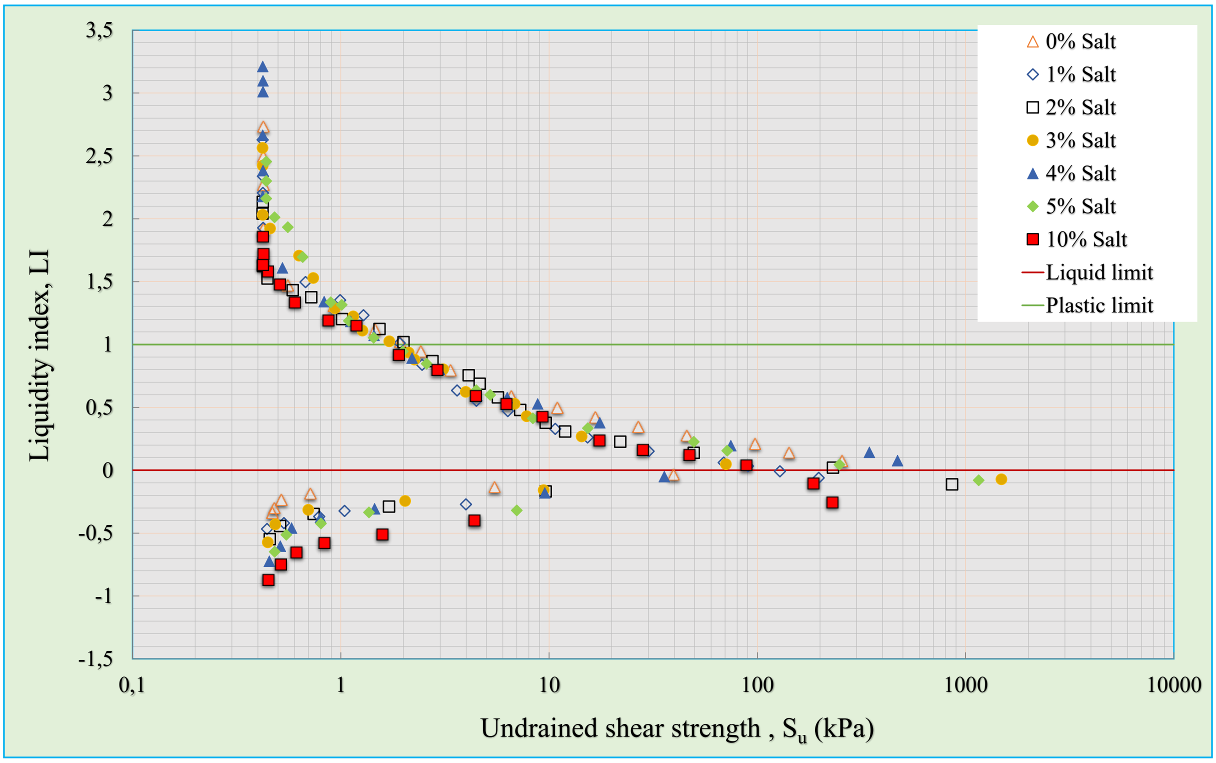

Fig. 10. Liquidity index undrained shear strength relationship for fallcone test

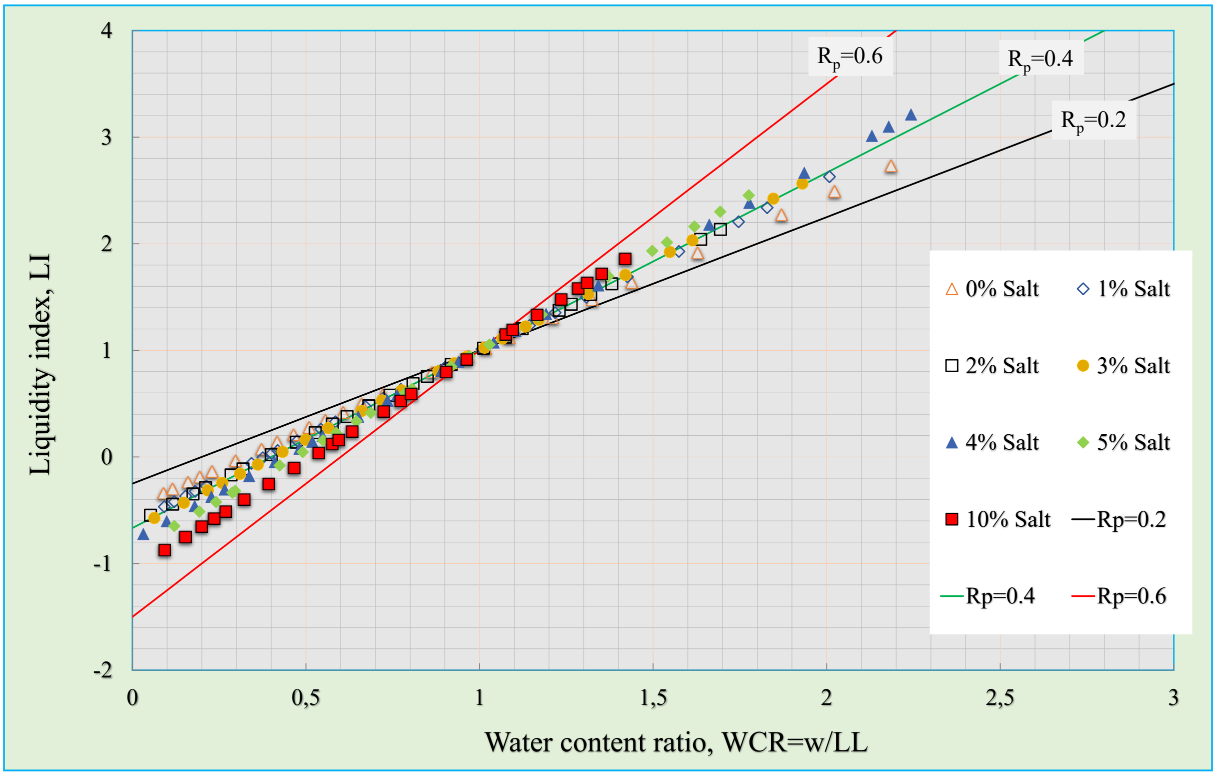

Fig. 11. Liquidity index water content ratio relationship for fallcone test

Empirical correlations of undrained shear strength with the water content ratio of various researchers are given in Table 4. With the data obtained in this study, the variation of water content ratio with undrained shear strength is shown in Fig. 12 on bentonite clay samples with different salt concentrations. Fig. 12 shows that there is an exponential corelation between water content ratio and undrained shear strength. Maximum undrained shear strength values of the samples were obtained when the water content ratio was between 0.3 and 0.5. Thereafter, the undrained shear strength of all samples decreases exponentially with increasing water content ratio. When the water content ratio is equal to one, the water content of the samples is equal to the liquid limit values. In this case, Fig. 12 shows that the undrained shear strength values vary between 1.6 kPa and 2.8 kPa. With increasing salt content, undrained shear strengths were obtained at very low water content ratios. For example, in the 10% brine mixture, the undrained shear strength value reached a minimum when the water content ratio was only 1.3, while in the 0% brine mixture, the water content ratio increased up to 1.8 and the undrained shear strength value was minimum.

Table 4. Relationships between undrained shear strength and water content ratio WCR

Equation No	Authors	Equation	Definition
1	Federico (1983)	$S_u = exp[5.25 \times (1.161 - WCR)]$	Remolded soils
2	Tsuchida (1999)	$S_u = 1.4 \times (WCR)^{-4.5}$	Remolded soils
3	Lee (2004)	$S_u = 182.93 \times exp[-2.3714 \times WCR]$	Remolded soils
4	Berilgen et al., (2007)	$S_u = 145 \times exp[-2.86 \times WCR]$	Remolded soils
5	Kang et al., (2017)	$S_u = 1.71 \times (WCR)^{-4.1}$	Remolded soils
6	Vardanega and Haigh (2017)	$S_u = 10^{(2.72-2.585 \times WCR)}$	Remolded soils
7	This study (0% Salt)	$S_u = 2.9363 \times (WCR)^{-3.839}$	Bentonite
8	This study (10% Salt)	$S_u = 1.757 \times (WCR)^{-5.494}$	Bentonite

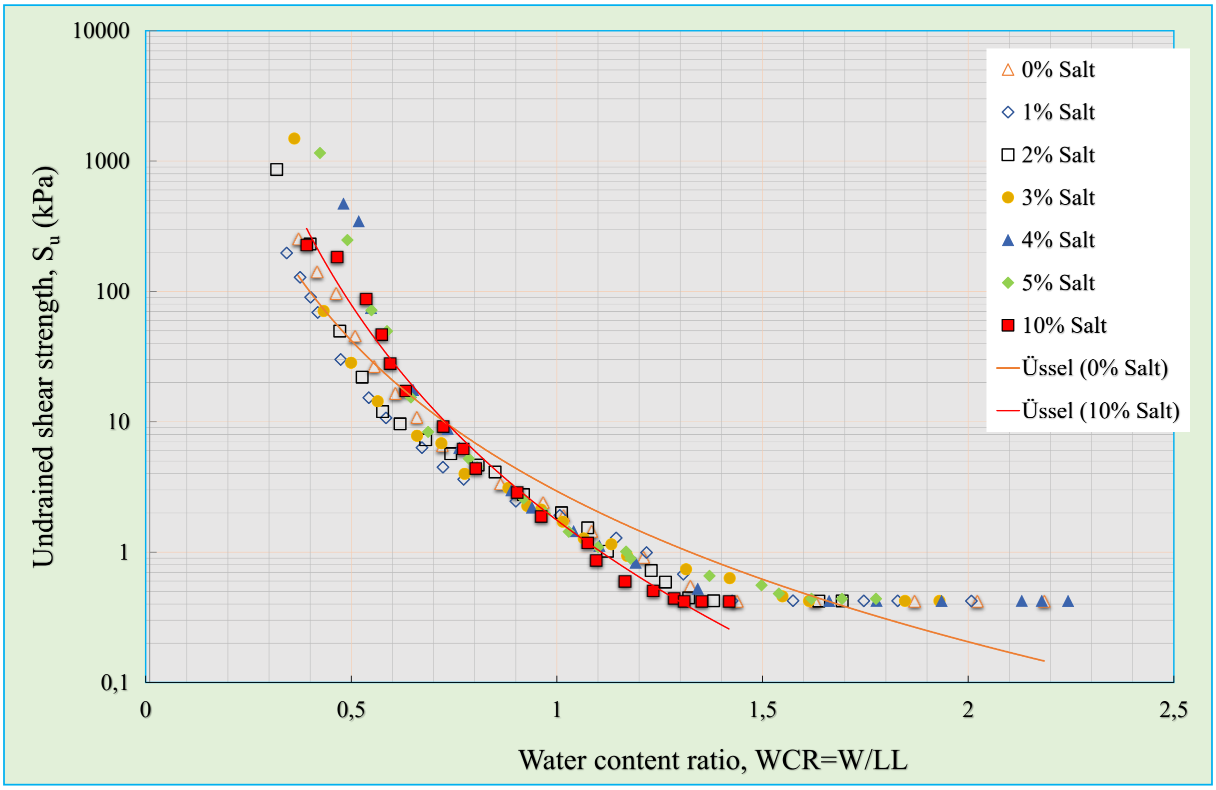

Fig. 12. Undrained shear strength water content ratio relationship for fallcone test

4. Conclusions

In this study, a series of laboratory studies were carried out to investigate the effect of bentonite clay, which has high plasticity, on different salt concentrations. In addition to the experiments with distilled water, the salt concentration was increased by 1% from 1% to 5%. In addition, 10% salt water mixture experiments were carried out to examine the effect of high salt concentration. Casagrande liquid limit, Fallcone liquid limit and conventional method plastic limit experiments were performed at six different salt concentrations. In the experiments, in order to clearly determine the change in salt water content, starting from very low water content, the water content was increased step by step and ended at an average of 30 steps. The water content ratio in the experiments varied between 1.5 and 3 times. This means that the experiments were carried out up to water contents up to 3 times the liquid limit value of each mixture. The results obtained can be summarized as follows:

1) Liquid limit values were obtained by using Casagrande test results on bentonite clay samples with different salt concentrations. High R^2 values were obtained with the equations proposed in Table 2. According to the Casagrande test results, there was a significant decrease in the liquid limit values with increasing salt concentration. For example, in the experiment with distilled water, the liquid limit was 219.68%, while the liquid limit was 195.79% at 5% salt content and 169.15% at 10% salt content. 1) Decreases similar to the liquid limit were obtained in the plasticity index values of the same samples. While the plasticity index was 172.06% in the experiment with distilled water, it was determined as 137.17% in the 5% salt water mixture. In the experiment with 10% salt content, the plasticity index was calculated as 108.54%, the lowest value.
2) According to the experimental results of the Casagrande test, it is seen that the plasticity ratio line of all experimental data is between 0.2 and 0.4. While the plasticity ratio is much closer to the 0.2 line for the data at low salt contents, the plasticity ratio approaches 0.4 with increasing salt content. The experiments for 10% brine mixture gave the closest results to the Rp=0.4 line.
3) When the Fallcone test results are examined, it is seen that the water content values start with approximately 5% and increase up to 300%. The variation of cone penetration with water content ratio was also obtained for all brine mixtures. The proposed equations for liquid limit values are determined separately for different salt contents in Table 3. While the liquid limit for bentonite clay was obtained as 149.82% in the experiments with distilled water, it decreased to 125.63% in 5% brine mixture and to 117.92% in 10% brine mixture. The liquid limit values decreased significantly with increasing salt content.
4) When the variation of liquidity index undrained shear strength is examined, it is seen that the experimental data are around the sensitivity ratio (St=1) line. When the soil becomes liquid, the undrained shear strength takes a constant value despite the increasing liquidity index value. In Fallcone test results, between the liquidity index and water content ratio, the lines 0.2, 0.4 and 0.6 are drawn. The data from the experiment with distilled water shows that while the values are very close to the Rp=0.2 line, the plasticity ratio changes towards 0.6 with increasing salt content. At the highest salt concentration, 10% brine content, the experimental data show that the plasticity ratio approaches the 0.6 line. Increasing salt content decreased the plasticity of the soil.
5) In addition, the variation of undrained shear strength as a function of water content ratio was investigated and the equations obtained for undrained shear strength at different salt contents were presented. Higher undrained shear strength values were obtained at lower salt concentrations.

Acknowledgments

The research described in this paper was financially supported by the scientific research projects unit of Kilis 7 Aralık University under the grant number [22/MAP/003].

References

ASTM International. (2018). *ASTM D4318-17e1: Standard test methods for liquid limit, plastic limit, and plasticity index of soils*. ASTM International.

Berilgen, S., Kılıç, H., & Özaydın, İ. K. (2007). Determination of undrained shear strength for dredged Golden Horn marine clay with laboratory tests. In *Proceedings of the Sri Lankan Geotechnical Society's First International Conference on Soil and Rock Engineering* (pp. 5–11). Colombo, Sri Lanka.

British Standards Institution. (1990). *BS 1377-9: Methods of test for soils for civil engineering purposes – Part 9: In-situ tests*. BSI.

Di Maio, C. (1996). Exposure of bentonite to salt solution. *Géotechnique, 46*(4), 695–707.

Di Maio, C., Santoli, L., & Schiavone, P. (2004). Volume change behavior of clays: The influence of mineral composition, pore fluid composition and stress state. *Mechanics of Materials, 36*(5–6), 435–451.

Federico, A. (1983). Relationships (Cu-w) and (Cu-δ) for remolded clayey soils at high water content. *Rivista Italiana di Geotecnica, 18*(1), 38–41.

Gajo, A., & Maines, M. (2007). Mechanical effects of aqueous solutions in organic acids and bases on a natural active clay. *Géotechnique, 57*(8), 687–699.

Gori, U. (1994). The pH influence on the index properties of clays. *Bulletin of the International Association of Engineering Geology, 50*, 37–42.

Gratchev, I. B., & Sassa, K. (2009). Cyclic behavior of fine-grained soils at different pH values. *Journal of Geotechnical and Geoenvironmental Engineering, 135*(2), 271–279.

Hansbo, S. (1957). A new approach to the determination of the shear strength of clay by the fall cone test. *Swedish Geotechnical Institute Proceedings, 14*, 5–47.

Kang, G., Tsuchida, T., Tang, T. X., & Kalim, T. P. (2017). Consistency measurement of cement-treated marine clay using fall cone test and Casagrande liquid limit test. *Soils and Foundations, 57*(5), 802–814.

Lee, L. T. (2004). Method to rapidly assess the index properties of fine-grained dredged materials. *Geotechnical Testing Journal, 27*(5), 464–468.

Mitchell, J. K., & Soga, K. (2005). *Fundamentals of soil behavior* (3rd ed.). Wiley.

Rao, S. M., Sridharan, A., & Chandrakaran, S. (1993). Consistency limits behavior of bentonites exposed to seawater. *Marine Georesources & Geotechnology, 11*(3), 213–227.

Santamarina, J. C., Klein, K. A., Palomino, A., & Guimaraes, M. S. (2002). Micro-scale aspects of chemo-mechanical coupling: Interparticle forces and fabric. In C. Di Maio, M. Hueckel, & A. Loret (Eds.), *Chemomechanical coupling in clays: From nano-scale to engineering applications* (pp. 47–64). Swets & Zeitlinger.

Shimobe, S., & Spagnoli, G. (2020). Relationships between undrained shear strength, liquidity index, and water content ratio of clays. *Bulletin of Engineering Geology and the Environment, 79*, 4817–4828. https://doi.org/10.1007/s10064-020-01844-5

Spagnoli, G., Rubinos, D., & Stanjek, H. (2012). Undrained shear strength of clays as modified by pH variations. *Bulletin of Engineering Geology and the Environment, 71*, 135–148. https://doi.org/10.1007/s10064-011-0372-9

Sridharan, A. (2002). Engineering behaviour of clays: Influence of mineralogy. In C. Di Maio, M. Hueckel, & A. Loret (Eds.), *Chemomechanical coupling in clays: From nano-scale to engineering applications* (pp. 3–28). Swets & Zeitlinger.

Sridharan, A., El-Shafei, A., & Miura, N. (2002). Mechanisms controlling the undrained strength behavior of remolded Ariake marine clays. *Marine Georesources & Geotechnology, 20*(1), 21–50.

Tsuchida, T. (1999). Development and use of foamed treated soil in port and airport project. *Report of the Port and Harbour Research Institute, 38*(2), 131–167. (in Japanese)

Vardanega, P. J., & Haigh, S. K. (2017). Discussion of “Water content ratio: An effective substitute for liquidity index for prediction of shear strength of clays” by Beshy Kuriakose, Benny Mathews Abraham, A. Sridharan and Babu T. Jose. *Geotechnical and Geological Engineering, 35*(6), 3039–3044.

Yukselen-Aksoy, Y., Kaya, A., & Ören, A. H. (2008). Seawater effect on consistency limits and compressibility characteristics of clays. *Engineering Geology, 102*(1–2), 54–61.

4th International Civil Engineering & Architecture Conference
17-19 May 2025, Trabzon, Türkiye

Investigation of the effects of land surface sensitivity on rockfall analyses

Habibullah Mohammadi[1], Evrim Cüre[*1], Emel Türker[1]

[1] Karadeniz Technical University, Department of Civil Engineering, 61080 Trabzon, Türkiye

Abstract Rockfall is defined as the detachment of a rock block from the main rock mass due to physical or biological weathering, followed by its downward movement through rolling, sliding, or bouncing along the slope. Today, various methods are employed to assess rockfall hazards however, two dimensional (2D) and three-dimensional (3D) statistical simulations that model rockfall behavior are commonly preferred. In these analyses, the morphology of the terrain surface plays a critical role. For this purpose, in the present study, a total of twelve 2D rockfall simulations were performed along four different cross sections extracted from three terrain models prepared at scales of 1/1, 1/1000, and 1/5000. The parameters obtained from the analyses such as bounce height, velocity, and kinetic energy were comparatively evaluated. The results demonstrate that as the resolution of the terrain model increases, significant changes occur in both the bounce height of the rock block and the trajectory it follows. In contrast, when the terrain model resolution decreases, the rock block tends to roll rather than bounce, even on very steep slopes. These findings clearly indicate that the outcomes of rockfall analyses are directly influenced by the accuracy of the terrain model, and that higher-resolution models provide more reliable and safer solutions for engineering applications. The study highlights the importance of high precision terrain modeling in accurately assessing rockfall risks and developing effective mitigation measures.

Keywords: Digital terrain model; Rockfall analysis; Bounce height; Kinetic energy

1. Introduction

Rockfalls are among the most significant natural hazards, particularly in mountainous and steep terrains, where they may occur due to natural processes or human activities, often resulting in loss of life and property. These events pose serious risks to engineering structures such as highways, railways, residential areas, and construction sites (Volkwein et al., 2011). Falling rock blocks can disrupt transportation networks, cause economic losses, damage infrastructure, and even lead to fatal outcomes. Therefore, predicting and preventing rockfalls is of critical importance from an engineering perspective (Akin, 2013).

Rockfalls occur when rock blocks detach from slopes and descend due to gravitational forces, through free fall, rolling, or bouncing motions. These movements are influenced by various natural factors such as intense rainfall, freeze thaw cycles, earthquakes, and rock weathering. Additional elements such as the expansion of water freezing within discontinuities, the growth of tree roots, and topographic irregularities can also trigger the detachment of rock blocks (Varnes, 1978; Akın, 2020). Once detached, these blocks can gain substantial kinetic energy under the influence of topography, posing a significant threat to engineering structures. In mountainous regions in particular, many residential areas have been declared disaster prone due to rockfall hazards however, with advancements in engineering techniques, various mitigation measures have been implemented in such regions to minimize risks (Varol et al., 2023).

One of the key factors influencing the accuracy and reliability of rockfall analyses is the map scale. The map scale plays a critical role in determining the accuracy of terrain models, thereby affecting the assessment of rockfall trajectories, the movement dynamics of falling blocks, and their impact forces. The outcomes of analyses conducted at different scales can lead to significant variations in the development of rockfall hazard maps and the identification of appropriate engineering mitigation measures (Öztürk et al., 2022). While large scale maps provide generalized data that may result in certain deviations in the analysis results, small scale maps offer more detailed representations of the terrain. Therefore, it is essential for engineers performing rockfall analyses to understand how the map scale they use influences the outcomes of their assessments (Fanos et al., 2016).

In this study, the impact of map scale on rockfall analyses was thoroughly examined, the most appropriate scale ranges for field applications were identified, and the reliability of the analysis results was evaluated. By using

* Corresponding author, E-mail: evrimcure@ktu.edu.tr

https://doi.org/10.31462/icearc2025_ce_geo_108

digital elevation models (DEMs) produced at different scales, the relationships between the falling dynamics of rock blocks and potential hazard zones were assessed. Additionally, the effect of map scale on the modeling precision of rockfall scenarios was investigated through comparative analyses. In this context, by integrating contemporary engineering approaches with evolving computer technologies, the study aimed to enhance the understanding of rockfall related risks and to determine how map scale influences analytical outcomes, thereby contributing to the development of more effective engineering solutions.

2. Materials and methods

This study was conducted within a designated site located in the Bulak Neighborhood of the Ortahisar District in Trabzon Province, Turkey. The study area is characterized by steep slopes and a rugged terrain composed of weathered rock masses, indicating a high potential for rockfall occurrences. Topographic and geological conditions were examined in situ, and relevant field data were directly collected from the site. Given the challenges of collecting topographic data using traditional methods in this regionprimarily due to the presence of numerous fractured and hazardous rock blocks in the source zone there was a need to employ more precise and detailed data acquisition techniques. Therefore, in order to accurately identify hazardous rock masses, various mapping methods were utilized and an integrated interpretation was developed.

The accuracy of the kinematic and slope stability analyses used in the rockfall assessments heavily depends on the precision of the acquired topographic cross-sections. For this reason, photogrammetric data collection techniques were preferred to enhance the reliability of the analyses and to most accurately represent the terrain conditions. The high-resolution terrain models obtained through this method allowed for more realistic simulations of rockfall scenarios and hazard assessments. Fig. 1 presents an orthophoto view of the study area, visually illustrating the region's topographic features and its spatial relationship with nearby settlements.

Fig. 1. The view of the study area on the orthophoto

2.1. Factors leading to rockfalls

Rockfalls occur in areas influenced by various internal and external forces. In most cases, multiple factors simultaneously contribute to the initiation of rockfall events. These factors can be broadly categorized into three main groups: structural (internal), environmental (external), and anthropogenic (human induced) factors (Volkwein et al., 2011; Bilgili, 2018). Structural factors (internal) are directly related to the geological characteristics of a slope or hillside. This group includes natural features such as fractured and jointed rock masses, as well as discontinuity surfaces with instability potential. Environmental factors (external) refer to naturally occurring processes, including intense rainfall, freeze thaw cycles, wind erosion, and snowmelt, all of which are known to trigger rockfalls. Anthropogenic (human induced) factors arise from human activities such as uncontrolled blasting operations, vibrations generated by trains or heavy construction machinery, and poorly designed slope geometries. The interaction of these factors often leads to the disruption of the natural equilibrium of slopes, resulting in the detachment and downslope movement of rock masses under the influence of gravity (Grant et al., 2018).

2.2. Rockfalls and types of rock movements

Rockfalls can be defined as the vertical movement of rock blocks of various sizes descending from a sufficiently steep slope or cliff due to the force of gravity. Depending on the slope of the terrain, rock blocks can exhibit different types of movement, such as free fall, bouncing, or rolling (Fig. 2). As shown in the figure, depending on the slope angle, rocks exhibit free fall motion at a 90° slope, bounce at a 70° slope, and roll at slopes of 30° and 45° (Fanos & Pradhan, 2018). As the blocks lose energy, in addition to rolling, movements such as dragging and sliding can also be observed. Rockfalls may involve a single block, but multiple rockfall events can occur simultaneously when several blocks detach at once (Matsuoka & Sakai, 1999). Furthermore, after a large rock block falls, it may hit the terrain and shatter into numerous smaller blocks, continuing to move as individual pieces. In such cases, since each rock fragment moves independently, it is crucial to determine the dynamic structure of rockfalls in advance, as this is essential for calculating the fall paths and kinetic energies of the blocks. For instance, a single rock block may have a small mass but can fall at a high velocity. On the other hand, in large-scale rockfalls involving multiple blocks, although the total mass may be greater, the falling speed might be relatively lower. Therefore, understanding the characteristic features of rockfalls is of critical importance for risk analysis and the design of protective measures (Varol et al., 2023).

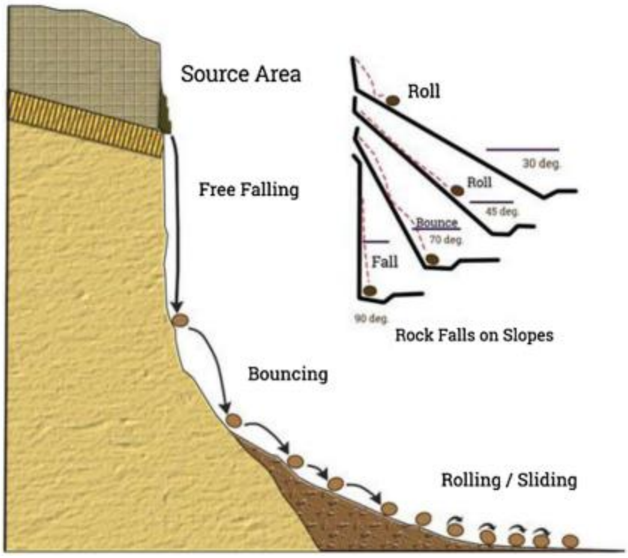

Fig. 2. Rockfall motion modes related to slope angle (Fanos & Pradhan, 2018)

2.3. Creation of the terrain surface

In this study, the rockfall risk of the region within the boundaries of the study area has been assessed, and the significance of map scale in these analyses has been highlighted. In the first phase of the study, the goal was to obtain a precise digital surface model (DSM) of the terrain. For this purpose, aerial images were captured using a Unmanned Aerial Vehicle (UAV) employing photogrammetric methods, and existing maps were produced. The DJI Mavic 3 Enterprise RTK type UAV was used to create the digital terrain model (Fig. 3). Flights were planned with an 80% overlap to obtain a more accurate model. A total of 151 high-resolution oblique and nadir images were captured. These images were processed through specialized software to generate high-resolution digital surface and terrain models. In the second phase of the study, cross-sections obtained from the photogrammetric work, including the 1/1 scale section, as well as sections from 1/1000 and 1/5000 scale maps, were used. In this context, a total of four different cross-sections were extracted, and three separate rockfall analyses were performed on each section.

Fig. 3. DJI Mavic 3 Enterprise RTK type unmanned aerial vehicle

3. Result and discussion

3.1. Two dimensional rockfall analysis (2D)

The two-dimensional rockfall analysis begins with the identification of the topographic and geological features of the terrain. To achieve this, field studies were conducted, maps were examined, and slope profiles were created. The terrain cross-section was modeled to accurately represent the slope's gradient and elevation, and the dimensions, weights, shapes, and sliding potential of the blocks that could cause rockfalls were determined through field observations and photogrammetric measurements. Mechanical parameters such as the normal rebound coefficient (R_n) and the tangential rebound coefficient (R_t) used in the analyses were defined based on the terrain conditions and rock characteristics. These parameters are crucial for realistically simulating the movements of the blocks, including falling, bouncing, rolling, and sliding. All collected geotechnical and geometric data were transferred to the RocFall software used for rockfall analysis. The software was input with terrain cross-sections, physical-mechanical properties of the blocks, and the defined parameters, allowing for the successful simulation of the movements and spread areas of the rock blocks. As a result of these simulations, significant outputs such as rebound height, block speeds, kinetic energy values, and maximum travel distances were obtained.

In this study, two dimensional rockfall analyses were conducted on four selected cross sections along the same route from three maps with different scales. These analyses provide significant scientific data for the technical evaluation of rock stability in the region and for managing rockfall risks. The cross sections obtained from the photogrammetric 3D model are presented in Fig. 4a, while the detailed view of the K1-1 section from these cross sections is shown in Fig. 4b.

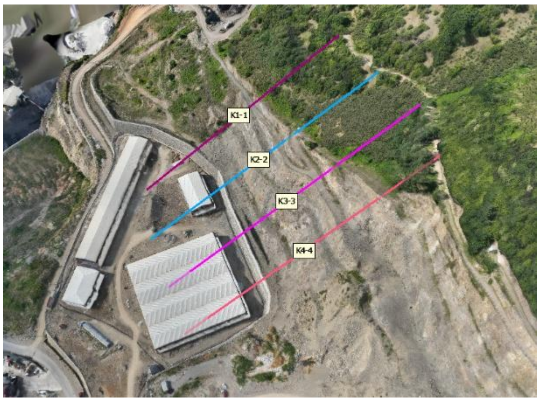

(a)

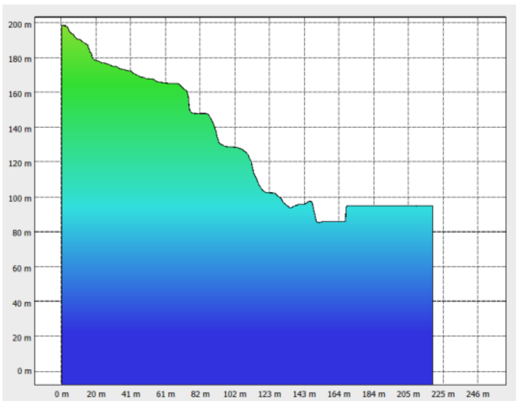

(b)

Fig. 4. Cross sections taken from the route and the K1-1 section detail

The expressions used in the naming of the photogrammetric sections are as follows: K1-1F refers to the section obtained from the photogrammetric studies (Fig. 5), K1-1M refers to the section taken from the 1/1000 scale maps (Fig. 6), and K1-1Z refers to the section taken from the 1/5000 scale maps (Fig. 7).

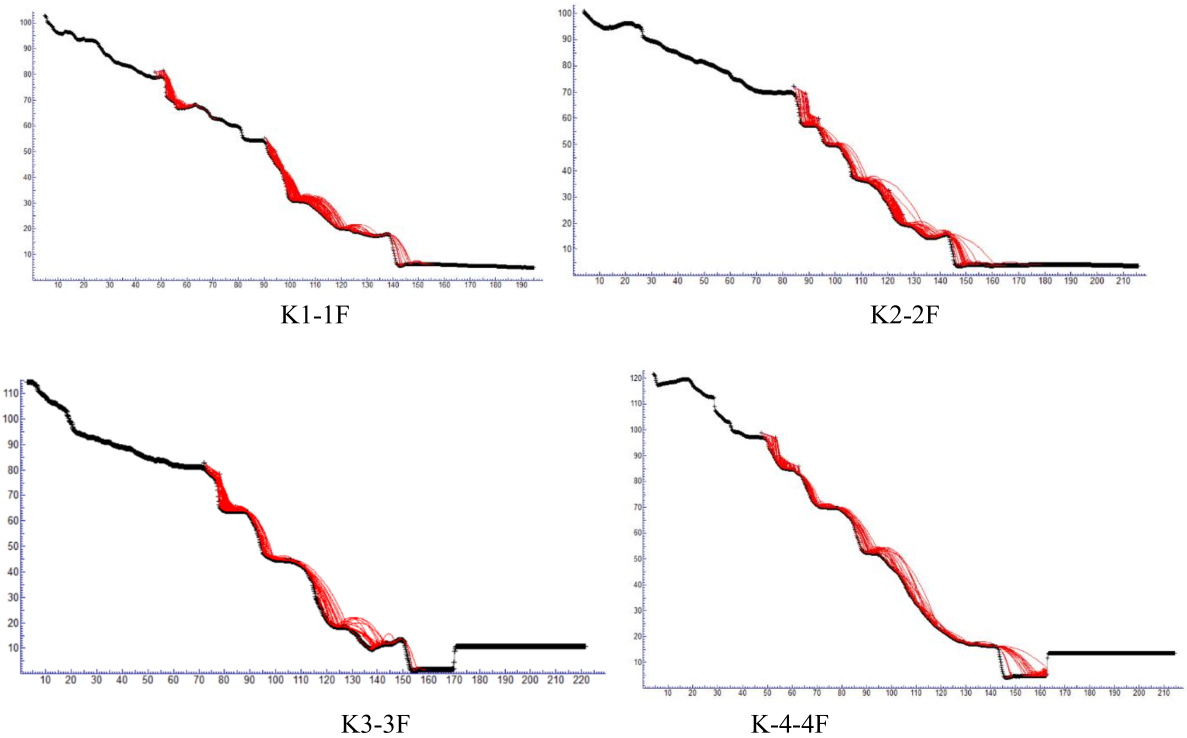

Fig. 5. Rockfall analysis and the path followed by the rock on the sections taken from the photogrammetric model

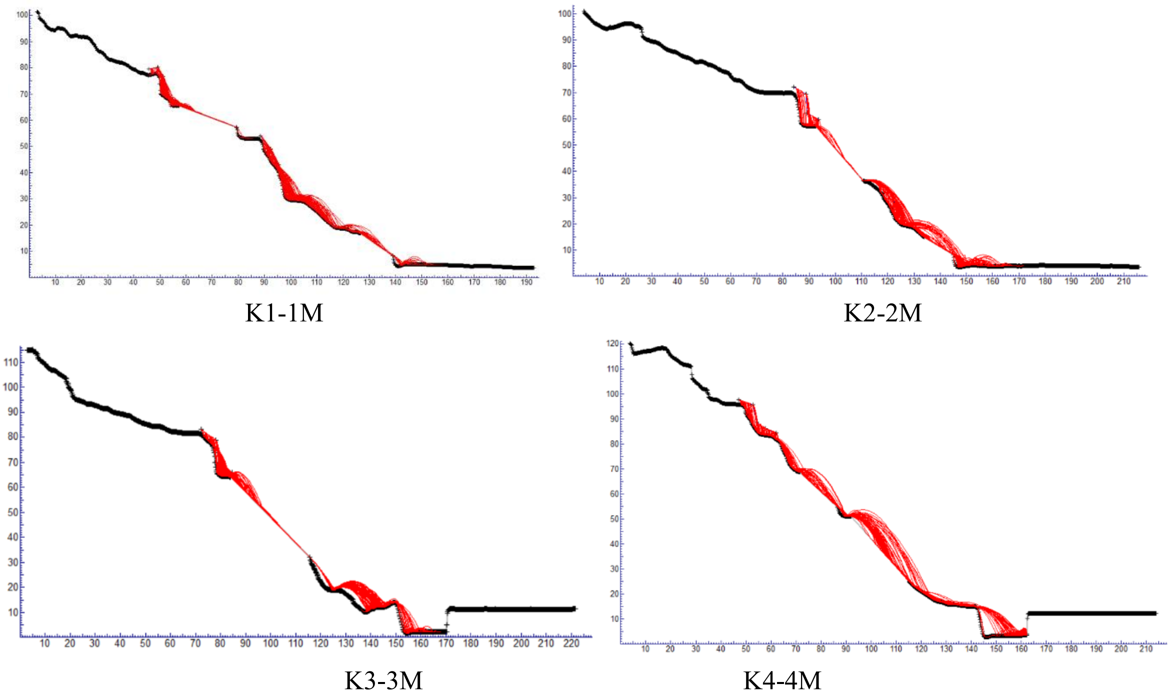

Fig. 6. Rockfall analysis and the path followed by the rock on the sections taken from the 1/1000 scale map

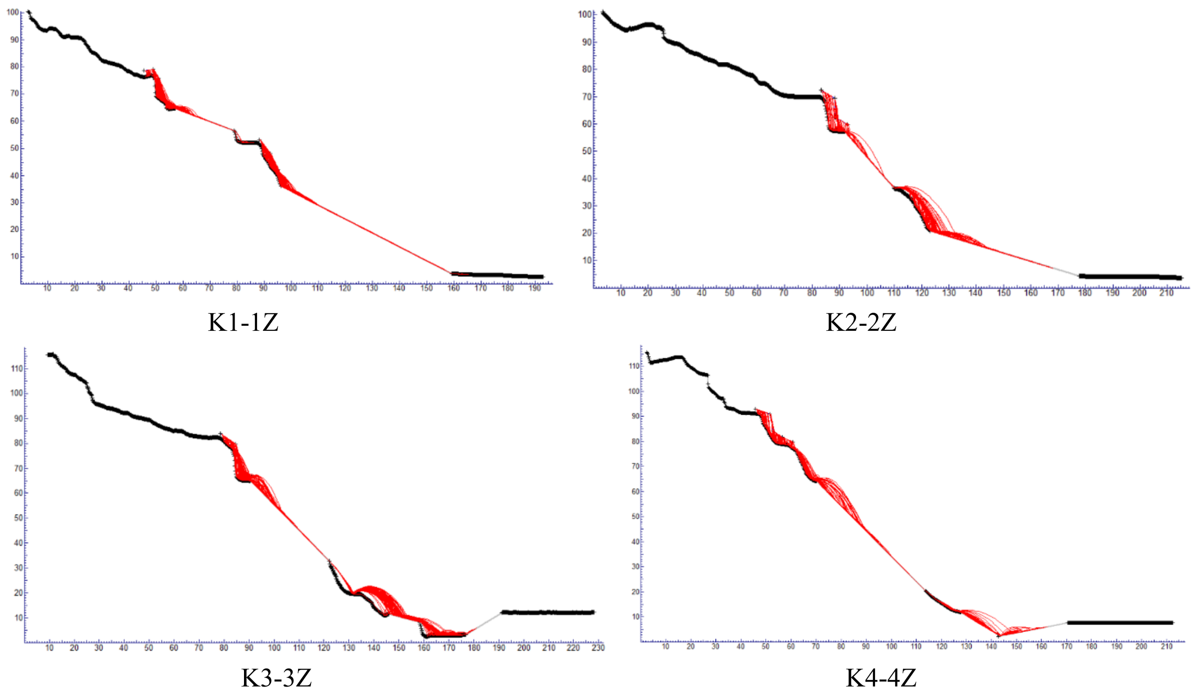

Fig. 7. Rockfall analysis and the path followed by the rock on the sections taken from the 1/5000 scale map

Rockfall analyses were performed for a total of 400 different possible scenarios across four sections, with 100 possible scenarios created for each section. Additionally, on the sections obtained from the 1/1000 scale maps shown in Fig. 6, 400 possible rockfall analyses were carried out along the same route, with 100 possible scenarios for each section. Similarly, 2D rockfall analyses were applied to the sections obtained from the 1/5000 scale maps shown in Fig. 7, where 100 possible scenarios were evaluated for each section, resulting in 400 possible analyses and scenarios in total.

To investigate the effect of terrain surface accuracy on rockfall, these two-dimensional analyses focused particularly on comparing the rebound height, linear velocity, and kinetic energy parameters. The total kinetic energy, total rebound height, and total linear velocity graphs obtained from the analyses are shown in Figs. 8-10, and detailed evaluations were made based on these graphs.

Upon examining these detailed evaluations, the total kinetic energy graphs presented in Fig. 8 compare the results obtained for each section at three different terrain accuracy levels. These graphs clearly show that kinetic energy is directly proportional to the terrain accuracy.

As shown at Table 1, when comparing the kinetic energy values, it is observed that the total kinetic energy of K1-1F is approximately 10% higher than K1-1M and 20-50% higher than K1-1Z. Similarly, K2-2F shows 10% higher energy values compared to K2-2M and 20-50% higher compared to K2-2Z. The same observation applies to K3-3F, where it exhibits 10% higher energy values than K3-3M and 20-50% higher than K3-3Z. As the terrain precision increases, it has been noted that the total kinetic energy of K4-4F changes by 10% compared to K4-4M and 20-50% compared to K4-4Z. However, it is not sufficient to only examine the maximum energy regions. In many cases, it may not be feasible to implement rehabilitation and mitigation measures solely within these maximum energy zones. Therefore, changes in total kinetic energy should also be considered beyond the maximum zone. For instance, it has been observed that the total kinetic energy between K2-2F, K2-2M, and K2-2Z shows a noticeable increase after the maximum zone.

Table 1. Comparison of kinetic energy based on cross sections

Cross Section	Comparison	Increase (%)
K1-1F	According to K1-1M	10
K1-1F	According to K1-1Z	20-50
K2-2F	According to K2-2M	10
K2-2F	According to K2-2Z	20-50
K3-3F	According to K3-3M	10
K3-3F	According to K3-3Z	20-50
K4-4F	According to K4-4M	10
K4-4F	According to K4-4Z	20-50

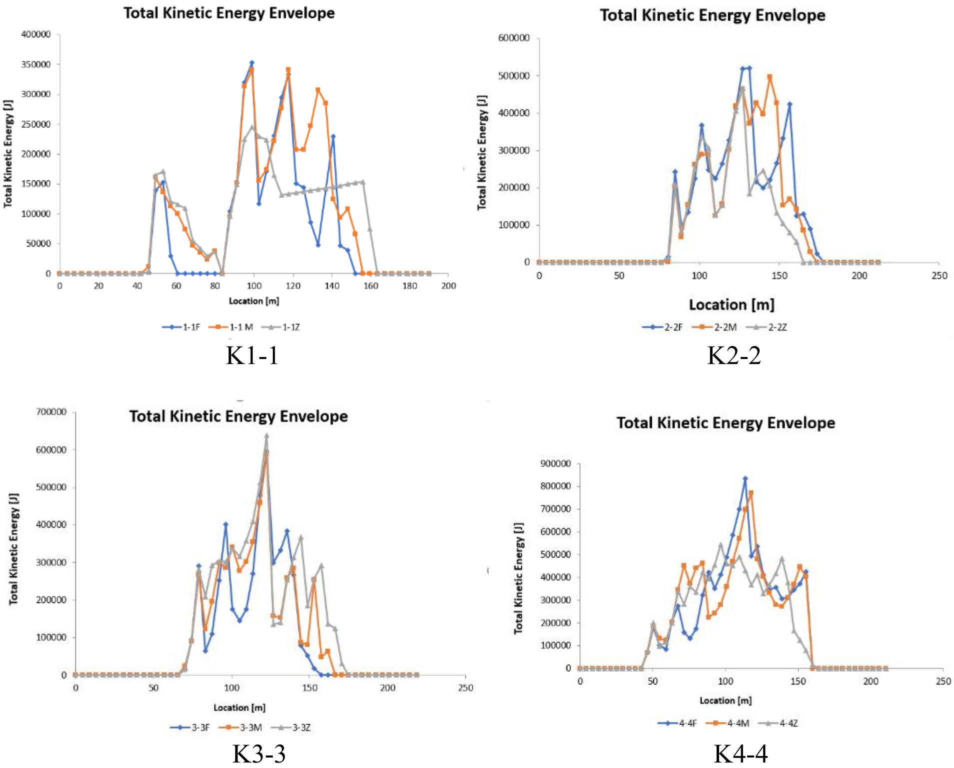

Fig. 8. Total kinetic energy graphs obtained from the rockfall analysis results

A similar behavior to the scenarios created in the comparative graph can be observed in Fig. 9. Here, although the bounce heights are relatively close in the bouncing regions, it has been observed that as the terrain accuracy increases along the slope route, the heights rise significantly. Additionally, as a result of the literature review, it has been understood that this situation has been clearly demonstrated and confirmed through video cameras in real time experiments.

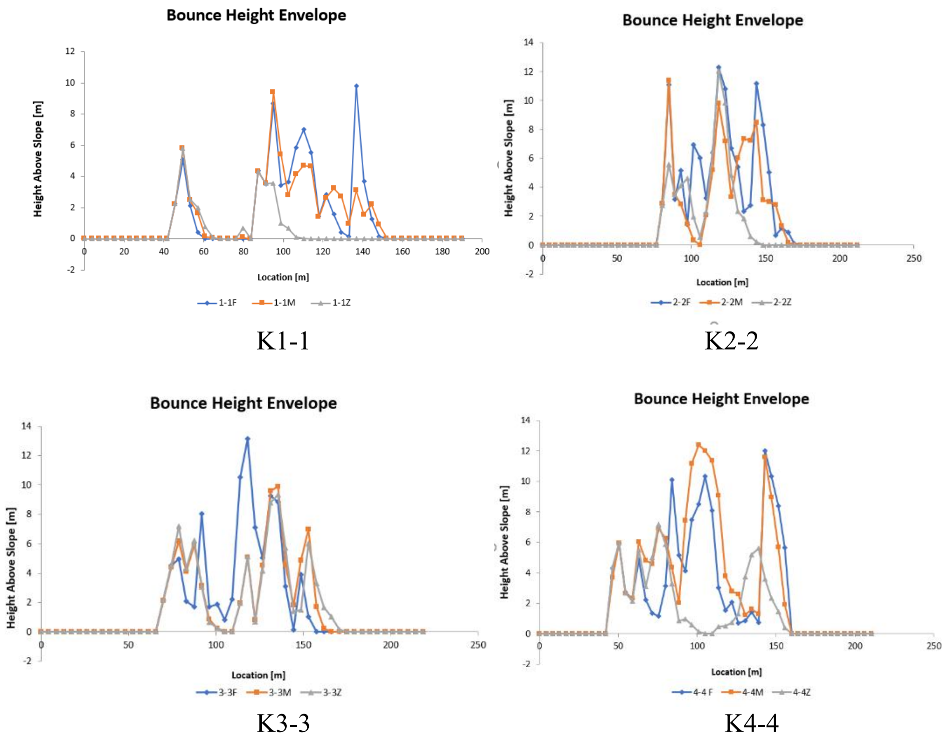

Fig. 9. The graphs of total bounce height obtained from the rockfall analysis results

The results of the rockfall analysis also reveal that as the terrain accuracy decreases, the movement of the rock blocks shifts from free fall and bouncing to rolling. This change directly affects the bounce height, and consequently, the speed and kinetic energy. In the photogrammetric analyses presented in Figure 9, it was observed that almost all the rock blocks predominantly exhibited bouncing motion. However, in the 1/1000 scale maps, the falls along the four cross-sections transitioned to rolling after a certain point, then resumed bouncing motion, and continued with rolling again.

It can be seen in Fig. 10 that the total kinetic energy exhibits a similar behavior to the total linear velocity. However, the difference between rolling and linear velocity highlights the need for a more detailed examination of linear velocity in future studies. Therefore, to further investigate the impact of terrain accuracy on rockfall analyses in future work, both the rotational velocities should be analyzed, and not only two-dimensional but also three-dimensional analyses should be conducted. This will allow for clearer and more definitive results to be obtained.

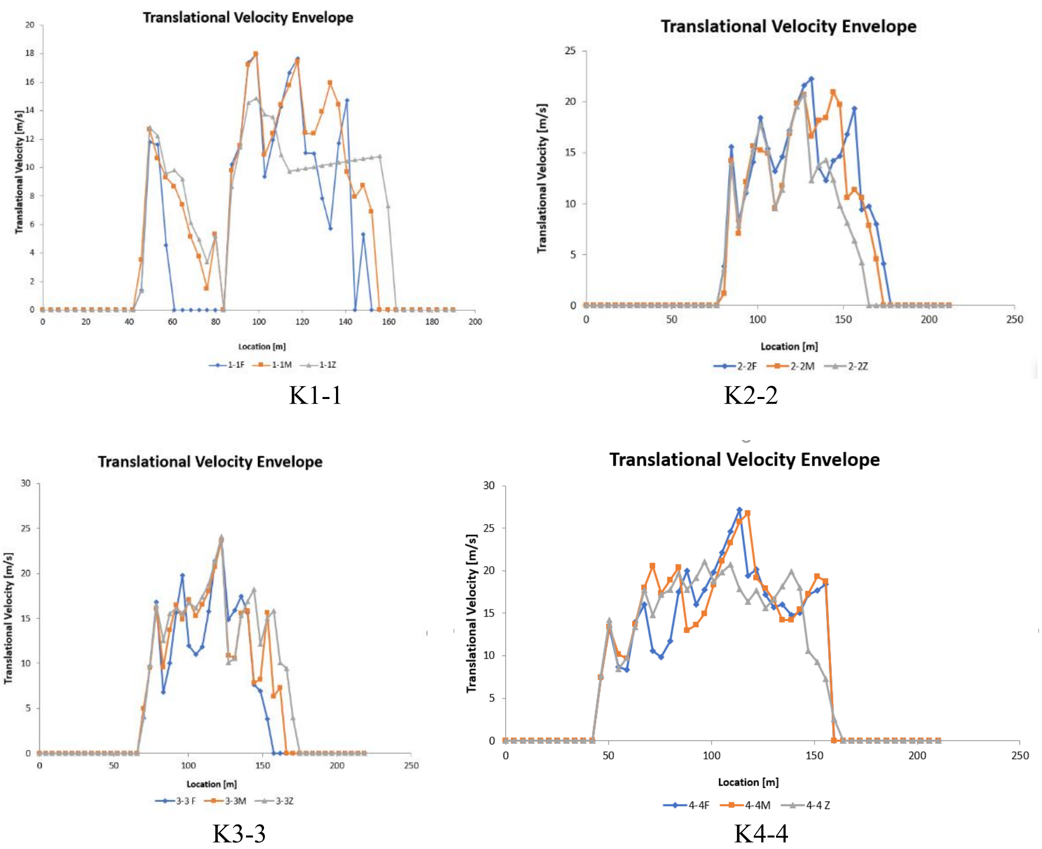

Fig. 10. Total linear velocity graphs obtained from the rockfall analysis results

4. Conclusions

In this study, various analyses were carried out to investigate the effects on rockfall behavior. Within the scope of the research, three different terrain models were used: one photogrammetric model at a 1/1 scale, one at a 1/1000 scale, and one at a 1/5000 scale. From the same region and along the same alignment, four cross-sections were selected, and for each section, 100 probabilistic scenarios were modeled, resulting in a total of 1200 numerical rockfall simulations. The results obtained from these analyses were comparatively evaluated, and the findings are presented below:

- It was observed that as terrain sensitivity increases, rockfall motion tends to occur more as bouncing and jumping rather than rolling. Additionally, the bounce height increased by approximately 10% when transitioning from the 1/1 scale to the 1/1000 scale, and by 20-50% when moving from the 1/1000 scale to the 1/5000 scale, resulting in a total increase ranging between 10% and 50%.
- It was observed that as terrain sensitivity increased, both bounce height and, consequently, velocity also increased. In the photogrammetric scale, bounce height was approximately 10% higher than that of the 1/1000 scale, and 20-50% higher than the 1/5000 scale in maximum energy zones. Overall, a significant increase in velocity was evident with the rise in terrain sensitivity.
- In the photogrammetric scale, kinetic energy was found to increase by approximately 10%, while in maximum energy zones, the variation ranged between 10% and 50%. Moreover, even greater differences

were observed locally. Therefore, considering that mitigation measures cannot always be implemented at maximum energy zones in rockfall analyses, it becomes evident that this parameter plays a highly influential and critical role.

The parameters obtained within the scope of this study clearly demonstrate how critical terrain sensitivity is, emphasizing the necessity of accurately modeling the terrain to reflect realistic rockfall scenarios. For future studies, it is recommended to include the analysis of rotational velocities to further enhance the depth of the evaluation. This recommendation stems from the observation that, as terrain sensitivity decreases, bouncing motions are increasingly replaced by rolling movements during rockfall events. Therefore, a detailed investigation of rotational behavior, along with the implementation of not only cross-sectional but also comprehensive three-dimensional (3D) analyses, would be highly beneficial.

References

Akın, M., Dinçer, İ., & Orhan, A. (2020). Kaya düşmelerinden kaynaklı afetlerin değerlendirilmesine yönelik teknik kılavuz. Afet ve Acil Durum Yönetimi Başkanlığı (AFAD), Ankara, 169ss. (in Turkish)

Akin, M. (2013). Slope stability problems and back analysis in heavily jointed rock mass: a case study from Manisa, Turkey. *Rock mechanics and rock engineering*, 46(2), 359-371. http://doi.org/10.1007/s00603-012-0262-x.

Bilgili, B. (2018). Kapadokya bölgesi Nevşehir yöresi kültürel varlıklarının bozulmalarına neden olan etmenler. *Nevşehir Bilim ve Teknoloji Dergisi*, 7(1), 60-74. https://doi.org/10.17100/nevbiltek.329311. (in Turkish)

Fanos, A.M., & Pradhan, B. (2018). Laser scanning systems and techniques in rockfall source identification and risk assessment: a critical review. *Earth Systems and Environment*, 2(2), 163-182. https://doi.org/10.1007/s41748-018-0046-x.

Fanos, A.M., Pradhan, B., Aziz, A.A., Jebur, M.N., & Park, H.J. (2016). Assessment of multi-scenario rockfall hazard based on mechanical parameters using high-resolution airborne laser scanning data and GIS in a tropical area. Environmental Earth Sciences, 75(15), 1129. https ://doi.org/10.1007/s12665-016-5936-3.

Grant, A., Wartman, J., Massey, C., Olsen, M. J., O'Banion, M., & Motley, M. (2018). The impact of rockfalls on dwellings during the 2011 Christchurch, New Zealand, earthquakes. *Landslides*, 15, 31-42. https://doi.org/10.1007/s10346-017-0855-2.

Matsuoka, N., & Sakai, H. (1999). Rockfall activity from an alpine cliff during thawing periods. *Geomorphology*, 28(3-4), 309-328. https://doi.org/10.1016/S0169-555X(98)00116-0.

Öztürk, M.Z., Utlu, M., Şimşek, M. (2022). Kaya düşmesi tehlikesinin belirlenmesi ve önlenmesinde İHA tabanlı 3B modelleme çalışmaları: Murtaza Köyü örneği (Niğde). *Yerbilimleri*, 43(2), 182-196. https://doi.org/10.17824/yerbilimleri.1021032. (in Turkish)

Varnes, D.J. (1978). Slope movement types and processes. In: Schuster, R.L. and Krizek, R.J., Eds., Landslides, Analysis and Control, Transportation Research Board, Special Report No. 176, *National Academy of Sciences*, 11-33.

Varol, O.O., Akin, M., Orhan, A., & Dinçer, İ. (2023). Kaya düşmelerinin 3-boyutlu olasılıksal analizlerle ve ampirik yöntemlerle değerlendirilmesi: Kayseri-Soğanlı yerleşim yeri örneği. *Jeoloji Mühendisliği Dergisi*, 47(1), 1-28. https://doi.org/10.24232/jmd.1267107. (in Turkish)

Volkwein, A., Schellenberg, K., Labiouse, V., Agliardi, F., Berger, F., Bourrier, F., Dorren, L.K.A., Gerber, W., & Jaboyedoff, M. (2011). Rockfall characterisation and structural protection-a review. *Natural Hazards and Earth System Sciences*, 11(9), 2617-2651. http://doi.org/10.5194/nhess-11-2617-2011.

4th International Civil Engineering & Architecture Conference
17-19 May 2025, Trabzon, Türkiye

Improvement of a collapsible soil: the sabkha

Mustafa Aytekin*[1]

[1] University of Bahrain, Department of Civil Engineering, 973, Sakhir Campus, Kingdom of Bahrain

Abstract. The sabkha is a kind of collapsible soil that is common in the Kingdom of Bahrain as well as the east part of the Kingdom of Saudi Arabia. The sabkha soils investigated in this research were taken from two locations in Bahrain. One of them is Salmabad, and the other is Zallaq. The investigation deals with the feasibility of treatment of Sabkha soil by three additive materials. The additives employed in the investigation are cement, lime, and dry palm leaves. Each agent has been added to the Sabkha in various ratios. The ratios are the dry mass of the agent to dry mass of Sabkha soil. Additive ratios for cement were 1, 3, 5, and 7%, for lime 2, 3, 4, 5, and 6%, finally for palm leaf 1, 2, and 3%. Since the Sabkha soil is a kind of collapsible soil, collapsibility tests have also been performed to find out "collapsibility index" of the Sabkha. It was found out that the average collapsibility index of the Sabkha is 0.5 that is less than 1.0. The properties of plain Sabkha and mixtures with the agents and ratios mentioned above were determined. The properties that have been determined are the optimum moisture content (OMC), maximum dry density (MDD), liquid limit (LL), plastic limit (PL), plasticity index (PI), hydraulic conductivity(k), apparent cohesion (c), internal friction angle (ϕ), unconfined compression strength (qu). It was concluded that the dry palm leaves give pretty good results in terms of gaining strength on Sabkha samples even if the maximum dry density is getting lighter when it is compared with the other agents.

Keywords: Problematic soils; Collapsible soil; Sabkha soil; Lime stabilization; Cement stabilization.

1. Introduction

The evaporation is much more than precipitation in hot and arid climates. As a result of this phenomenon, saline soils are widespread in these climates. Bahrain has a hot and arid climate. The name of "Sabkha" that is an Arabic word means coastal sediments with high salt content. Sabkha soils are defined as salt bearing formations, Mohamed, and Al-Rawas (2011). These soils are in many parts of the globe as well as in Bahrain. The active locations and potential locations of Sabkha soil on earth have been shown on a map, Mohamed, and Al-Rawas (2011). It is pointed out that Sabkha soil creates geological hazards in the Kingdom of Arabia, Youssef., Pradhan, Sabtan (2007). The Sabkha soil is a kind of collapsible soil that is called a part of problematic soil. Sabkha is a very salty and water sensitive soil, Al-Amaudi, (2008),. In general, many buildings and industrial structures are rested on Sabkha soils, a kind of collapsible soil around the globe. The Arabian Gulf region is one of the areas having many problems and suffering from the natural disasters and aggressive environment. In this region, soils are medium to fine grained sands cemented by salt. The ground water table, GWT, is vey salty and located at shallow depths in Bahrain like the other countries in the region. Sabkha soil is one of the many types of collapsible soils and in turn is one of the many types of problematic soils that are unsaturated in general (Fig. 1). Sabkha has good engineering properties when it is dry. For instance, it has moderate bearing capacity with low settlement in dry state. However, once Sabkha soil is wetted, it loses its entire structure and undergoes an exceptionally large settlement (collapse). All Sabkha soils show collapsible behavior. These types of soil deposits are often found near the mouths of rivers, along the perimeters of bays, and under swamps or lagoons. Soils that are subject to collapse occupy about thirteen million km2 of the world's surface, Abelev, & Abelev (1979), Abelev (1988), Abelev (1984).

The change in volume is associated with a change in soil structure, Jennings, and Knight (1975). Colloidal coatings which adhere to individual soil grains provide intergranular bonds and thus an apparent strength to the soil at low moisture content, but this apparent strength diminishes when the moisture content increases (Fig.2).

This phenomenon is not like the classical consolidation phenomenon, in this phenomenon no water is dissipated from the soil unlike consolidation. However, the soil will absorb water when the water is available and progressively lose its strength. The geotechnical properties of Sabkha soil have been discussed in several studies, Akili (1981), Al-Sanad, Shaqour, and Hencher (1989), Stipho, (1985).

*Corresponding author, E-mail: maytekin@uob.edu.bh

https://doi.org/10.31462/icearc2025_ce_geo_176

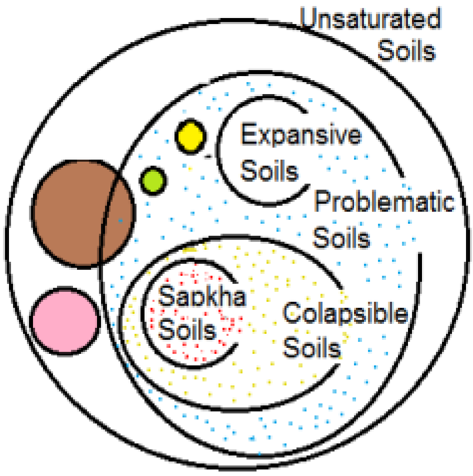

Fig. 1. Sabkha soil a kind of collapsible soil

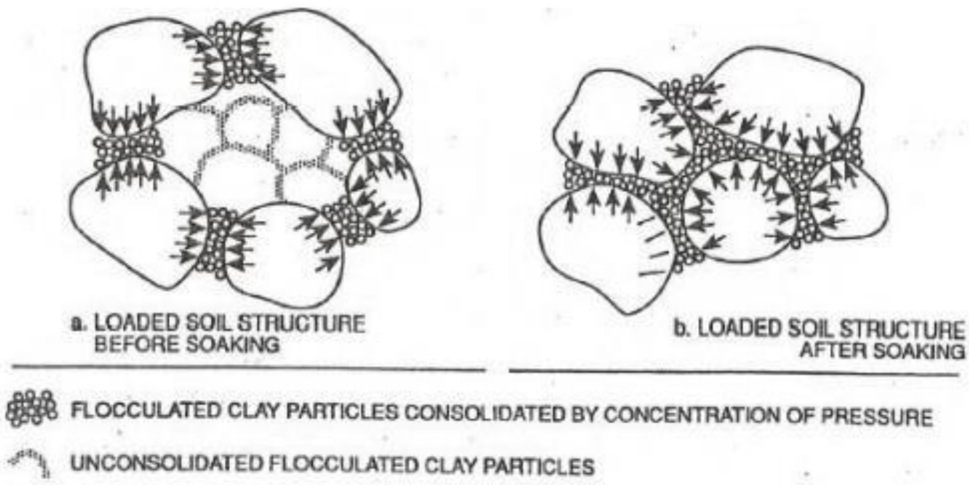

Fig 2. Structure of collapsible soil before and after soaking (Jennings, et al, 1975)

The studies have shown that most Sabkha soils possess a collapsible behavior. They have considerable strength in their dry condition but have a strong potential to lose strength after wetting. The geotechnical properties of Sabkha soils can vary widely as a function of moisture content, fines content, salt type and quantities. Due to similarities of ground conditions in the Gulf region, examples given in any Gulf state are usually applicable to Bahrain. Variation in soil moisture may result from fluctuation of brackish groundwater or a change in climatic conditions, as previously described. Akili (198l) has studied the influence of moisture content on the strength of some soils in eastern Saudi Arabia. He concluded that the maximum CBR (California Bearing Ratio) values of the soils occur just to the drier side of the optimum moisture content. The effect of leaching forces on some geotechnical properties of collapsible soils from Kuwait was investigated, Ismael, (1993). He recorded a reduction in soil shear strength and pre-consolidation pressure and an increase in soil hydraulic conductivity and void ratio because of leaching. Similar observations were noted, Lamb (1990), on examining the effect of leaching on the geotechnical properties of collapsible soils from the east central part of Iowa, USA. These two studies attribute the mechanical instability of the collapsible soils to the removal of a "cementing substance", primarily salts. The implication is that this substance acts as a binder which impacts appear cohesion to the soil, and that leaching of this material leads, in the presence of water, to the formation of a weak collapsible soil mass. The effect of soil type was examined, Doomkamp 1980, Qahwash, (1989). Doomkamp (1980), has reported that the soil in Bahrain is dominated by sand with fine contents varying from 5 to 30%, organic contents of 0.1 to 2% and traces of shells near the coastal areas. Common types of clay minerals include palygorskite and montmorillonite; such minerals are characterized by large surface areas and high ionic exchange capacities. Qahwash (1989) has discussed the influence of sand content on the performance of Sabkha soils obtained from eastern Saudi Arabia. He recorded a significant increase in soil strength (CBR values) and a dramatic reduction in swelling and plasticity potential as the sand content increased. Basma and Tuncer (1992) investigated the effect of soil type, compaction, water content, initial dry unit weight, and applied pressure on the collapse potential of Jordanian soils upon wetting. They reported that well graded soils tend to collapse more than poorly graded ones. Their study also concluded that the collapse potential decreases with an increase in: (1) the difference between the sand and clay percentages; (2) compaction water content; and (3) initial dry unit weight, while it increases with pressure on wetting.

2. Experimental work

It was found out that Sabkha soil exists in a very large portion of Bahrain then, decided to get the Sabkha samples from Salmabad and Zallaq areas from where the Sabkha soil could be collected easily. The locations where the Sabkha samples were collected are seen in Fig. 3. The materials used in this research are the Sabkha soil from the regions of Salmabad and Zallaq in Bahrain to be treated, and lime, cement, and palm (date) leaves that are the stabilizing agents. Lime and cement are used widely because they are applicable to a considerable range of soil types, readily available, low in cost, and environmentally acceptable. The palm leaf is also readily available in the gulf region and in Bahrain. The soils encountered in this investigation were taken from "Salmabad area" which is in the northern part of Bahrain. The other location was Zallaq that is located south-west of Bahrain. The lime used in soil treatment in this investigation was "high calcium" lime which contains less than 5% magnesium oxide or hydroxide. The type of cement used in this investigation is the Ordinary Portland Cement (OPC). Palms are perennial in nature and the palm leaves are a major source of natural fiber of different varieties. The most important palm leaf is It is commonly cultivated in India, Southeast Asia, Malaysia and intermittently in other warm regions including Hawaii and Southern Florida. Palm leaf fiber is used to make ropes, mats, brushes, fish nets, brooms, amongst others.

In this study, it has been used to stabilize the Sabkha soil. Properties of the Sabkha The Sabkha soils have been taken from Salmabad and Zallaq regions of Bahrain. Routine soil tests have been performed to determine the physical and plasticity properties of the Sabkha soils. However, the plastic limit test could not be conducted in soil taken from Zallaq region. The results of the routine laboratory tests are seen in Table 1.

Table 1. Physical and plasticity properties of sabkha soils

Location of sabkha sample	Salmabad	Zallaq
Average of Specific gravity	2.54	2.56
Salt concentration (g/l)	7.0	7.2
Liquid limit (LL, %)	60.1	41
Plastic limit (PL, %)	24.9	N/A
Shrinkage limit (SL, %)	16 (*)	-
Plasticity index (PI,%)	35.2	-
Optimum moisture content (%)	14	15.5
Maximum dry density (Mg/m3)	1.51	1.39
Effective diameter, (D_{10}, mm)	0.008	0.07
D_{30}, mm	0.025	0.15
D_{60}, mm	0.20	0.35

(*) SL value estimated by the plasticity chart

The particle size distribution curves (PSDCs) are seen in Fig.4, and Fig. 5. In the investigation, cement and lime stabilizations are applied the Sabkha taken from Salmabad, palm leaf stabilization is applied the Sabkha taken from Zallaq region. The Sabkha soil taken from both the Salmabad region and Zallaq region are classified as SP (Poorly graded sand) by the Unified Soil Classification System. Plasticity Properties of Sabkha Plasticity properties of plain Sabkha and several Sabkha samples stabilized by different agents namely cement and lime and their various percentages were investigated. The liquid limit of the Sabkha is increased with the addition of lime. However, it decreased with the addition of cement as seen in Fig. 6. On the other hand, plastic limit tends to increase with addition of lime or cement (see Fig 7.) but the increment is not significant. Plasticity index, which is the difference between liquid limit and plastic limit is decreased with the increment of cement up to 3%. Then, it seems to be constant. In the case of lime agent, the plasticity index has a tendency of increment as seen in Fig. 7 but the increment is not very significant.

Thus, the agent cement has a positive effect on the plasticity of Sabkha soil in terms of water sensitivity whereas lime has an extraordinarily little negative effect in this issue.

a) The sites Salmabad and Zallaq where sabkha soils were collected

b) Closer views of the sites in Salmabad and Zallaq

Fig 3. The locations where the Sabkha soils were taken (Salmabad, and Zallaq, Bahrain)

The particle size distribution curves (PSDCs) are seen in Fig.4, and Fig. 5. In the investigation, cement and lime stabilizations are applied the Sabkha taken from Salmabad, palm leaf stabilization is applied the Sabkha taken from Zallaq region. The Sabkha soil taken from both the Salmabad region and Zallaq region are classified as SP (Poorly graded sand) by the Unified Soil Classification System. Plasticity properties of plain Sabkha and several Sabkha samples stabilized by different agents namely cement and lime and their various percentages were investigated. The liquid limit of the Sabkha is increased with the addition of lime. However, it decreased with the addition of cement as seen in Fig. 6. On the other hand, plastic limit tends to increase with addition of lime or cement (see Fig 7.) but the increment is not significant. Plasticity index, which is the difference between liquid limit and plastic limit is decreased with the increment of cement up to 3%. Then, it seems to be constant. In the case of lime agent, the plasticity index has a tendency of increment as seen in Fig. 7 but the increment is not very significant.

Thus, the agent cement has a positive effect on the plasticity of Sabkha soil in terms of water sensitivity whereas lime has an extraordinarily little negative effect in this issue.

Standard Proctor Tests After the Standard Proctor Tests for samples prepared with addition of various percentages of the additive materials, the compaction curve of each case has been plotted. Stabilizers of cement and lime are used to stabilize Sabkha taken from Salmabad region. The palm leaf treatment is used for Sabkha taken from Zallaq region. Compaction curves of Sabkha soils from Salmabad and Zallaq without any additives are seen in Fig. 8.

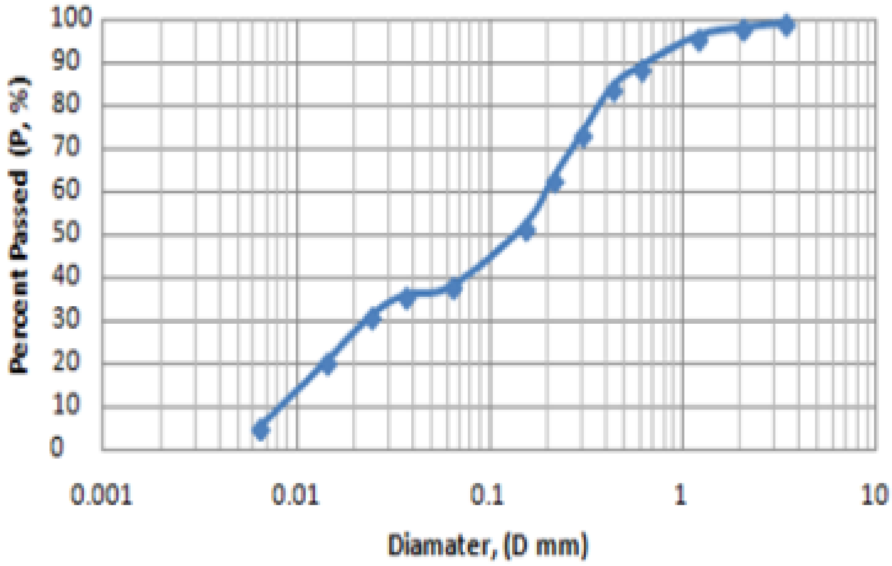

Fig 4. Particle Size Distribution Curve of the Sabkha soils taken from Salmabad

When all the compaction curves were plotted, the OMC and MDD of each mixture were determined and they are shown in Fig. 9. Among the maximum dry densities, the highest MDD was achieved when 3% of lime was used as the stabilizer as seen in Fig. 8. The highest value of the MDD is 1570kg//m^3. The same percentage of cement has an MDD of 1562kg/m^3. OMC values for this percentage (3%) of both cement and lime are 24%. In terms of MDD, 1% cement, 2 and 6% lime additives have an MDD, which is less than the MDD of plain Sabkha.

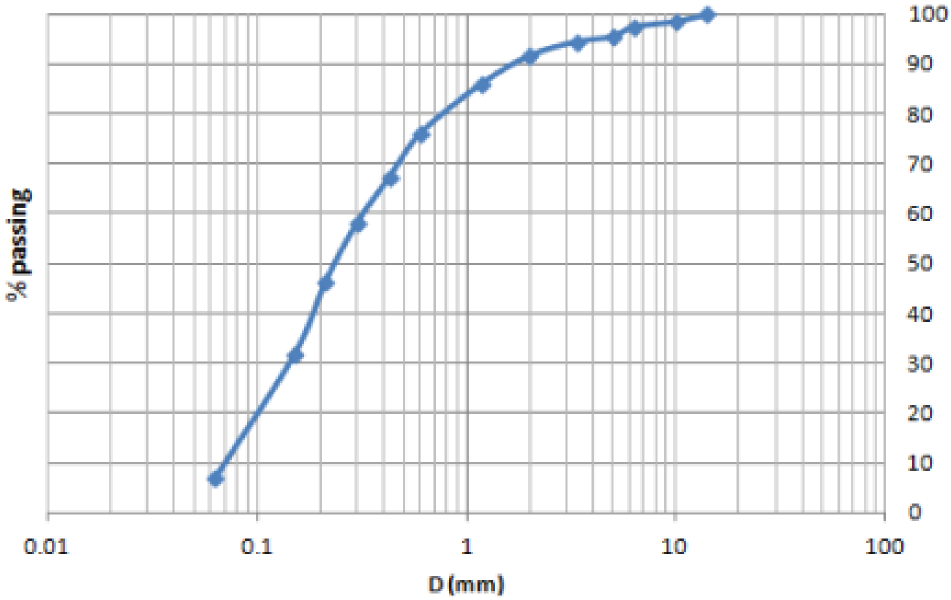

Fig 5. Particle Size Distribution Curve of the Sabkha soils taken from Zallaq

The other agent and percentage of additives give a value of MDD more than the maximum dry density of the plain Sabkha. Improvement on Sabkha by the Additives After the determination of OMC of each agent with various ratios, the samples used in the experiments were prepared by the standard compaction energy by using their OMC to have a sample at MDD.

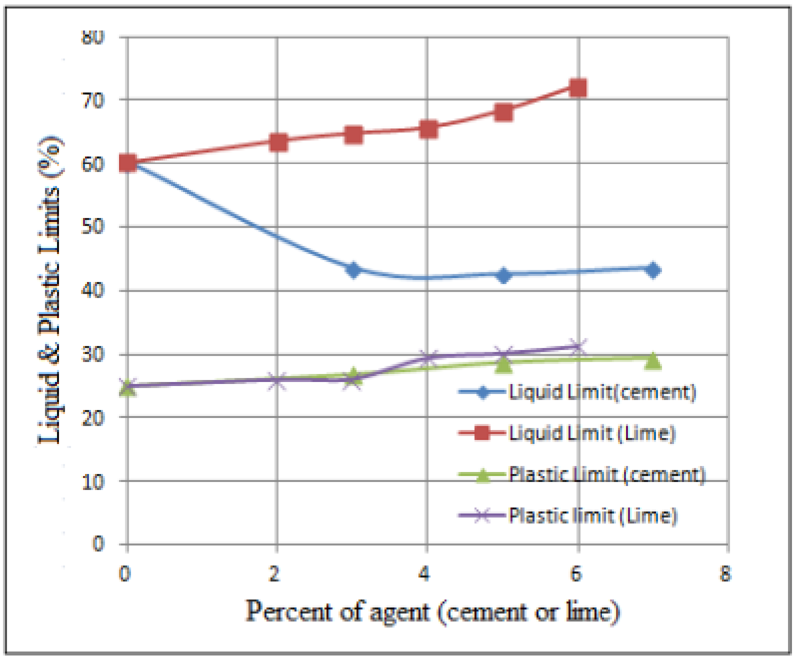

Fig 6. Variations of Liquid & Plastic Limits with ratios of cement & lime

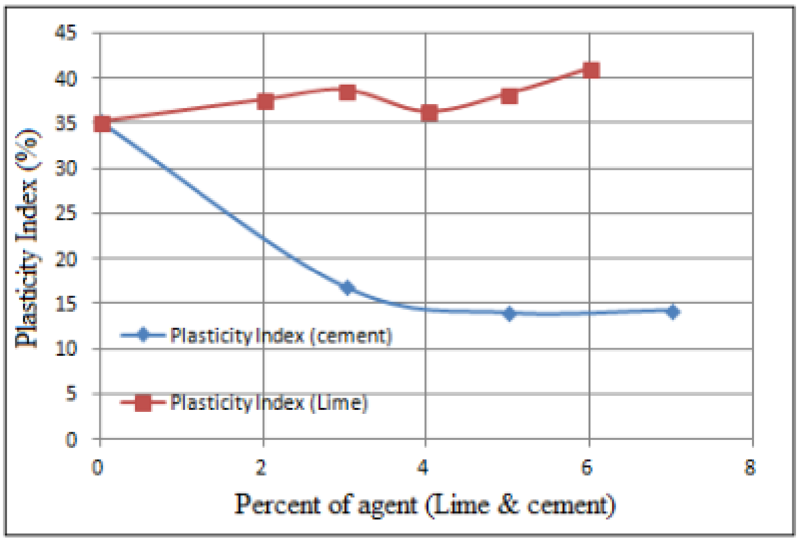

Fig 7. Variations of Plasticity Index with ratios of cement & lime

All the experiments like the unconfined compression tests (UCT), the falling head permeability tests, the direct shear test (shear box tests) were conducted by using the samples that are prepared by standard compaction energy at their OMC. Unconfined Compression Strength The unconfined compressive strength of the Sabkha is improved when it was stabilized with different additives with their various ratios and curing time. When lime is used as the stabilizer, the improvement on the compressive strength is getting higher when the ratio of lime is increased. Also curing time is very important for the lime stabilized Sabkha samples. The improvement in the compressive strength is seen in Fig. 10. The relationship between the normalized shear strength and normalized normal stress is linear as seen in Fig. 10. The shear strength of lime stabilized Sabkha is normalized by dividing it to the shear strength of the untreated Sabkha (τ/τ_o) and normal stress of treated Sabkha divided by the untreated normal stress (σ/σ_o).

If the angle between the linear line and horizontal is called as normalized friction angle by the analogy of the internal friction angle which is the angle of failure envelope in Mohr-Coulomb approach, the normalized friction angle is 45 degrees as seen in Fig. 10. The unconfined compression test results of the stabilized Sabkha are seen in Fig. 11. The compressive strength of the treated Sabkha samples with various ratios and curing times have improved strengths. The best improvement on the unconfined compressive strength was achieved when 3% of palm leaf is used as seen in Fig. 11. It may be expected to get best improvement on the cement addition, but it might happen if curing time is extended for the cement additive. The lime additive has no effect on the strength increment as much as the palm leaf does as is seen in Fig. 11.

Even the Sabkha soils used for stabilization by the palm leaf was not taken from the same region as the Sabkha used for lime stabilization, it is believed that the improvement by the palm leaf is better since tension stresses are carried by the leaf fibers. Thus, the palm leaf treated Sabkha soil gains strength for the tension stresses. The variation of the unconfined compressive strength of Sabkha sample stabilized by lime versus the curing time is seen in Fig.12.

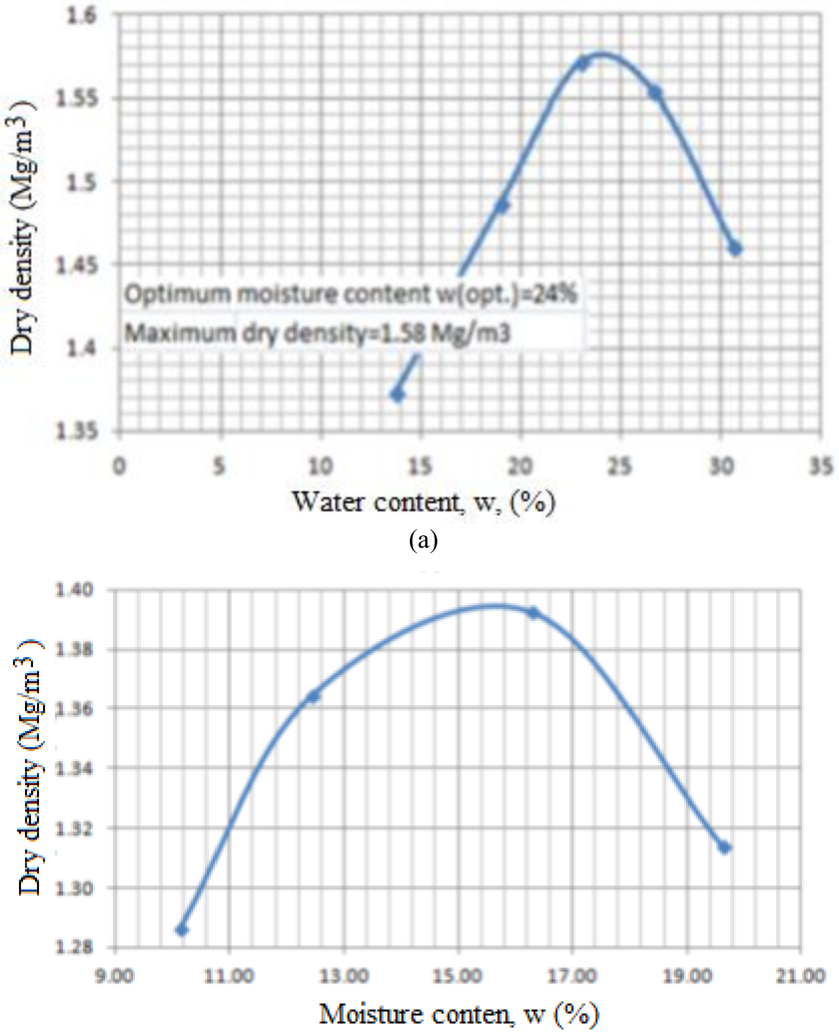

(a)

(b)

Fig. 8. Compaction curve of the Sabkha soil with no agent (a: Salmabad, b: Zallaq)

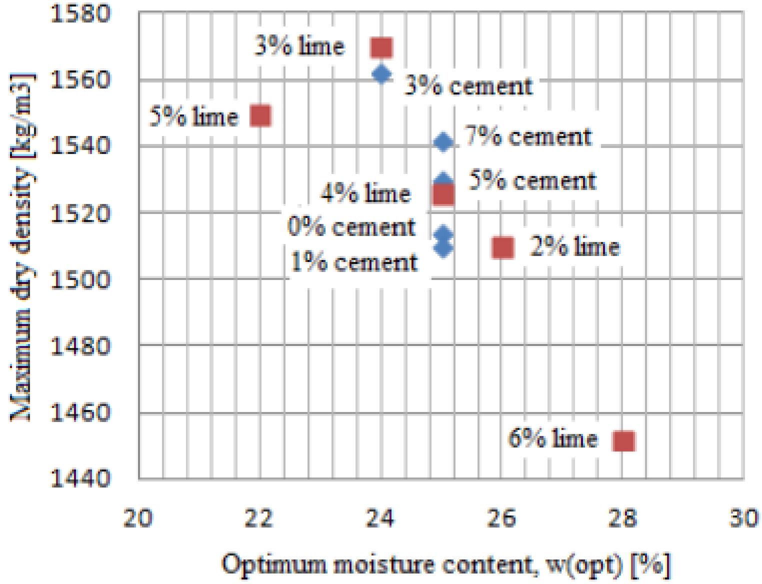

Fig. 9. Optimum moisture contents and maximum dry densities for various agents and ratios

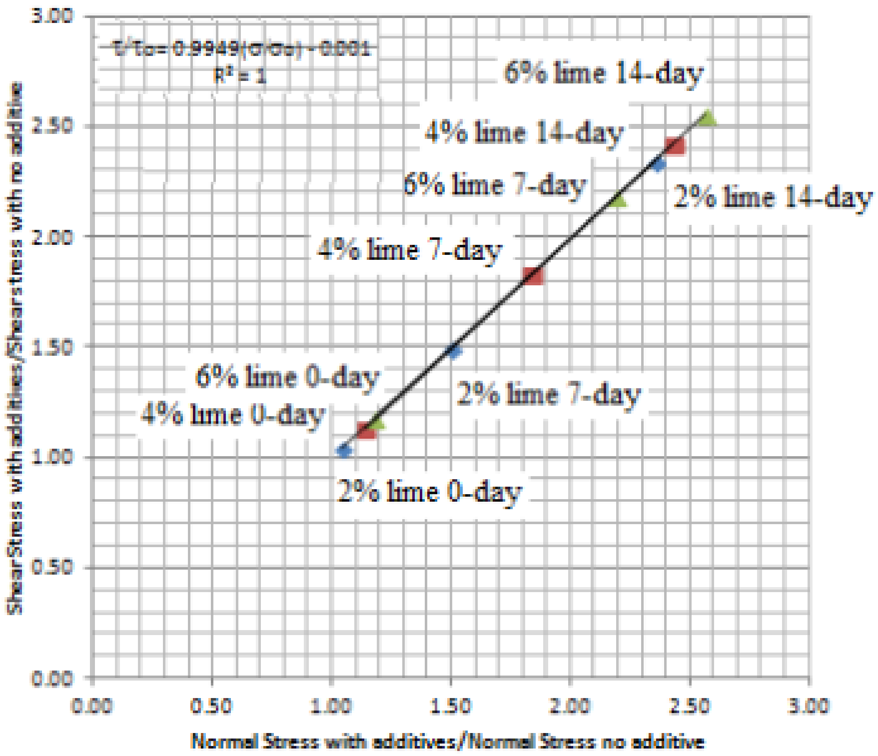

Fig. 10. Normalized values of shear and normal stresses for various percent of lime and curing

As it is seen in the figure, the improvement on the shear strength of the Sabkha soil is affected by the percentage of the agent in short term. However, improvement in shear strength for 2, 4 and 6% of the lime is almost equal in 14 days. Thus, it can be concluded that there is no need to use more percent of lime if the soil is expected to gain more shear strength in the long term. This conclusion must be verified by conducting more experiments and more curing days. Direct Shear Strength In many foundation design problems, the shear strength parameters which are cohesion (c) and internal friction angle (f) must be determined. Shear strength along the surface of the ground in contact with the base of the foundation material must be known.

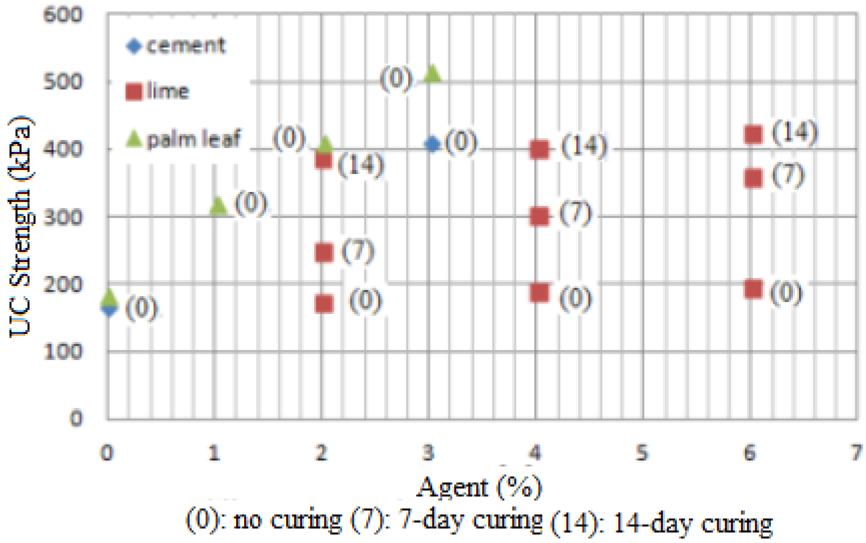

Fig. 11. Unconfined compressive strengths of the treated Sabkha

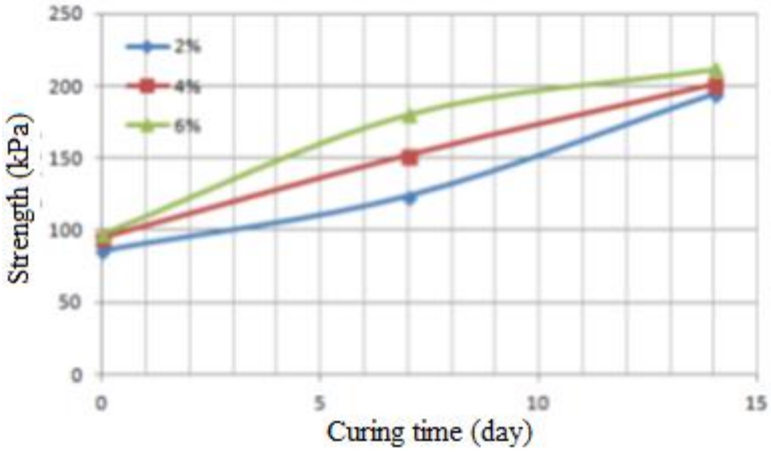

Fig. 12. Variation of shear strength of lime treated soil curing

Also, in the estimation of ultimate bearing capacity of any type of foundations, the shear strength parameters of the soil will be needed. After the estimation of these parameters, the shear strength can be estimated by Mohr-Coulomb equation:

$$\tau_f = c + \sigma \tan\phi \tag{1}$$

The shear strength parameters, c and ϕ were estimated by the direct shear tests in Sabkha soil, which was stabilized by 2% lime additive. The apparent cohesion c = 2.26kPa, and the internal friction angle ϕ = 40 degree as seen in Fig. 13. These values can be used to estimate the principal major stress under consolidated-drained condition with any lateral (confining) stress less than over-consolidation pressure. The major principal stress calculated by Eq. (2) can be assumed as the ultimate bearing capacity of the Sabkha soil at a depth under consideration. Eq. (2) can be driven using Fig. 14. If the lateral confining pressure ($\sigma 3$) is 50kPa (the minor principal stress) at the depth of soil under consideration, the major principal stress, $\sigma 1$, (or ultimate passive strength) under drained conditions can be estimates as 240kPa by using the Mohr's circle seen in Fig.14.

The ultimate passive strength of soil that is stabilized by 4% of lime has an apparent cohesion, c = 21.8kPa, and internal friction angle σ = 33 degrees as seen in Fig. 15. The ultimate passive strength of the Sabkha soil stabilized by 4% of lime can be calculated as 250kPa under the identical conditions for the Sabkha stabilized by 2% of lime. Similar calculation for the ultimate passive strength of Sabkha soil can be performed for the other stabilizers and their percentages. It easily can be seen that the ultimate passive strength of the Sabkha soil (from Fig. 16): c=5.4kPa, and σ = 36 degrees stabilized by 6% of lime is 214kPa.

As a rule of thumb, it is believed that there is a good relation between the density of a material and its strength for the same material. The strength will increase when density is increased.

This rule is also true in this case since the density of Sabkha soil stabilized by 6% lime is 1452kg/m3 that is the least density among the others (see Fig. 16) so that it gives smallest strength. When the failure envelopes of the lime stabilized Sabkha soil are plotted on one plot as seen in Fig. 17, it is clearly seen that 4% of lime addition gives the When the variation of major principal stresses versus the maximum dry density of the samples is checked, palm leaf stabilized Sabkha soil is better than the others as seen in Fig. 18. The best improvement on the major ultimate stress was achieved at 1% palm leaf stabilized Sabkha samples.

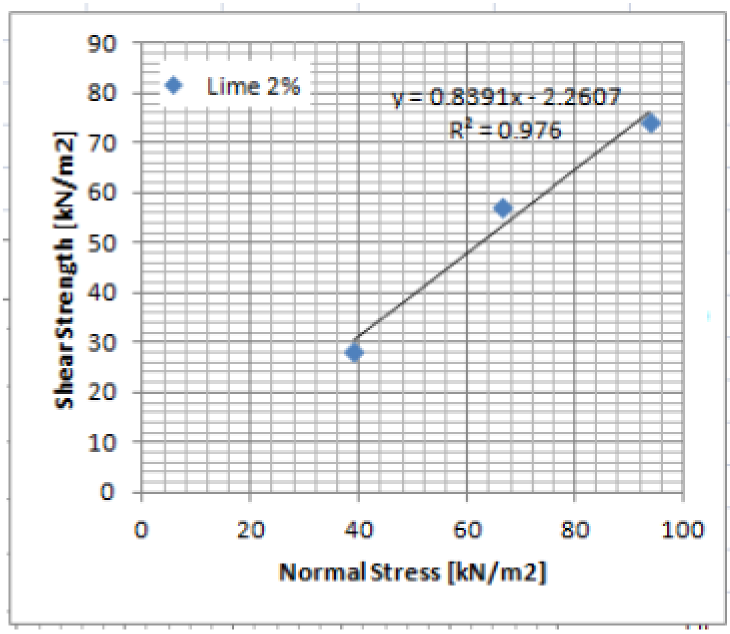

Fig. 13. Failure envelope of Sabkha soil stabilized by 2% lime

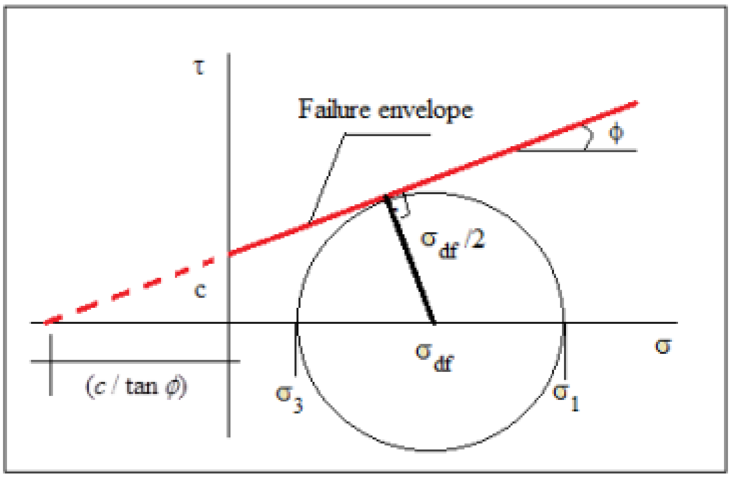

Fig. 14. Estimation of major principal that can be considered as ultimate passive strength

There might be a little effect of the natural Sabkha because palm leaf added Sabkha was taken from Zallaq and the other agents were added to the Sabkha taken from Salmabad. However, both Sabkhas were classified as poorly graded sand so that the effect of the places can be ignored in this state. All the failure envelopes were plotted for each different agent and the percentages of the additives. The failure envelopes are given for the agent of lime (2, 4, and 6%) above.

$$\sin\phi = \frac{\sigma_{df}/2}{(c/\tan\phi) + \sigma_3 + \sigma_{df}/2}$$
$$\sigma_{df} = 2\left(\frac{c * \cos\phi + \sigma_3 \sin\phi)\backslash}{1-\sin\phi}\right) \tag{2}$$
$$\sigma_1 = \sigma_3 + \sigma_{df}$$
$$\sigma_1 = \sigma_3 + 2\left(\frac{c * \cos\phi + \sigma_3 \sin\phi}{1-\sin\phi}\right)$$

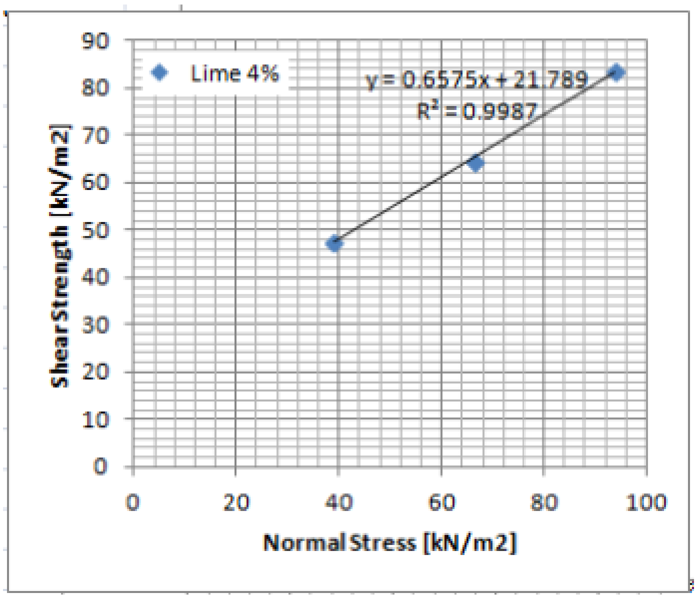

Fig. 15. Failure envelope of Sabkha soil stabilized by 4% lime

One more failure envelope is given in Fig. 19 for the agent of cement (5%) and the others are not given to prevent the large number of figures that are like each other better failure envelope compared to the other percentages of the lime. Similar calculations were performed for the other cases investigated. The ultimate passive strengths were found, and they are shown in Table 2.

Table 2. Ultimate passive strength (σ_1) of sabkha soil with additives and ratios

Type of Sample	Percent (ratio)	c (kPa)	ϕ (degree)	σ3 (kPa)	σ1 (kPa)	ρd_max (kg/m3)
Plain sabkha	No additive	10.0	30	50.00	185	1514
Lime (%)	2	2.3	40	50.00	240	1510
Lime (%)	4	21.8	33	50.00	250	1526
Lime (%)	6	5.4	36	50.00	214	1452
Cement (%)	3	20.1	37	50.00	281	1562
Cement (%)	5	20.17	38	50.00	293	1530
Cement (%)	7	50.0	65	50.00	?	1542
Palm leaf (%)	1	23.0	41	50.00	342	1370
Palm leaf (%)	2	8.0	46	50.00	346	1340
Palm leaf (%)	3	15.0	47	50.00	398	1319

3. Hydraulic conductivity

The hydraulic conductivity depends on several factors in soil such as pore size distribution of soil matrix, void ratio, grain size distribution, fluid viscosity and roughness of the soil particles. In the treatment of Sabkha soil, pore size distribution, void ratio, roughness of soil particles and somehow the grain size distribution will be changed so that the value of the hydraulic conductivity will also be affected. The hydraulic conductivity of the Sabkha is not affected much when cement or lime is used as the stabilizers. The variation on the hydraulic conductivity is not significant when either cement or lime is used as the stabilizer. However, the hydraulic conductivity is affected by the palm leaf as seen in Fig 20. The variation on the hydraulic conductivity is significant when the palm leaf is used as stabilizer. This future of the palm leaf can be considered when designing a project in which more strength and more permeable soil layer is needed. However, if the designing of a project requires more strength and less permeable soil layer, the choice of palm leaf as the stabilizer is not a proper selection.

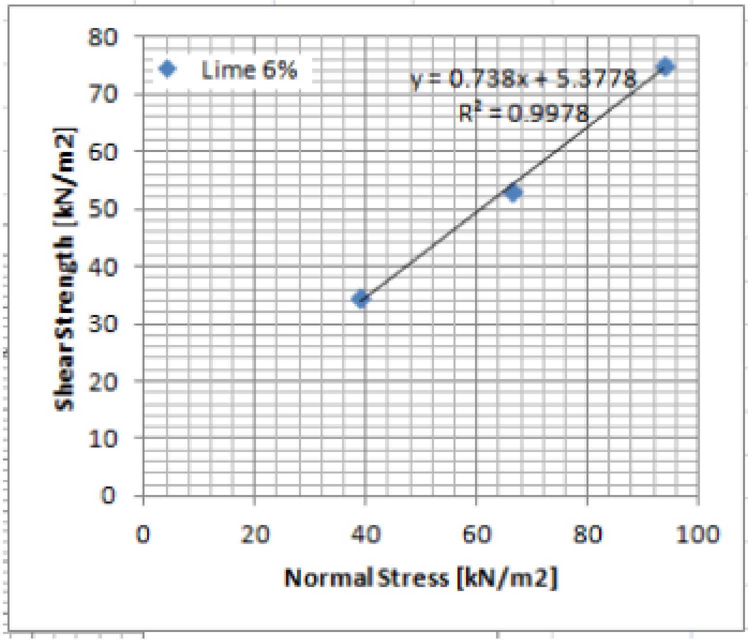

Fig. 16. Failure envelope of Sabkha soil stabilized by 6% lime

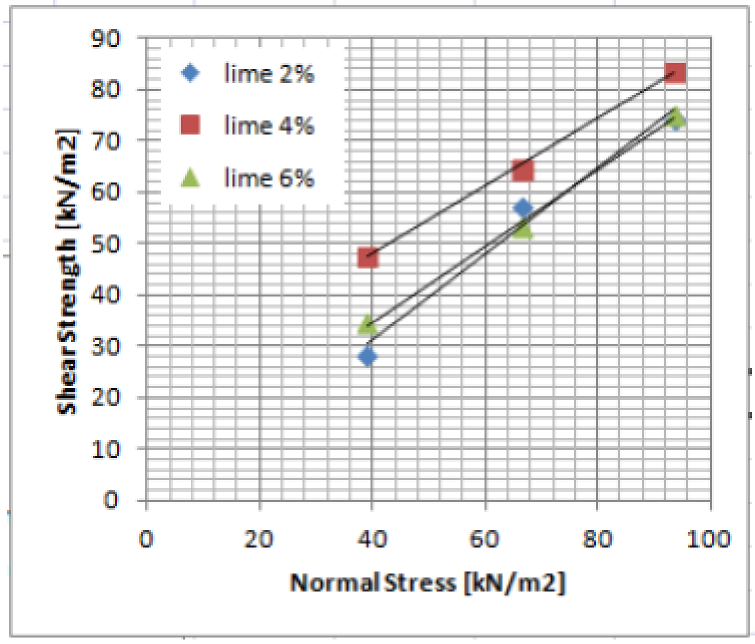

Fig. 17. Comparison of the failure envelopes of Sabkha soil stabilized for lime agent

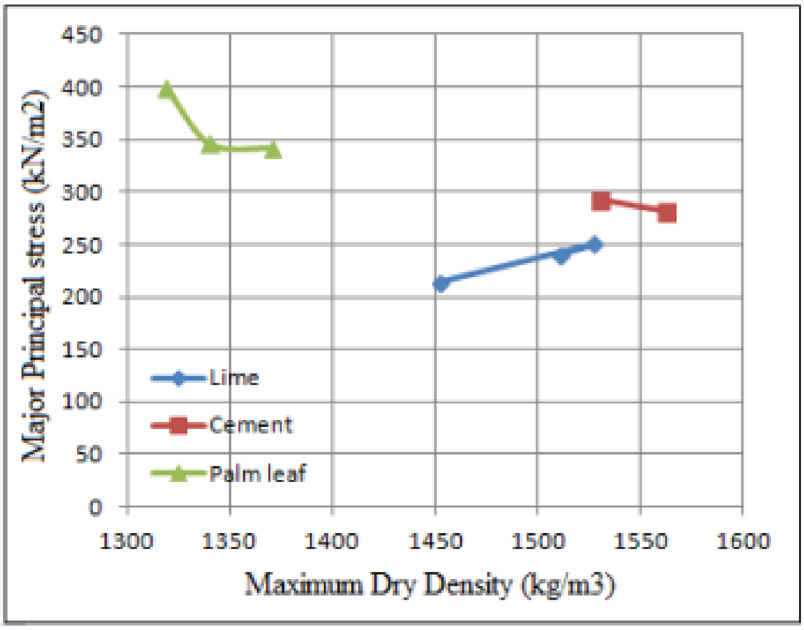

Fig. 18. Variation of Major Principal Stress with Type of Additives and Ratios

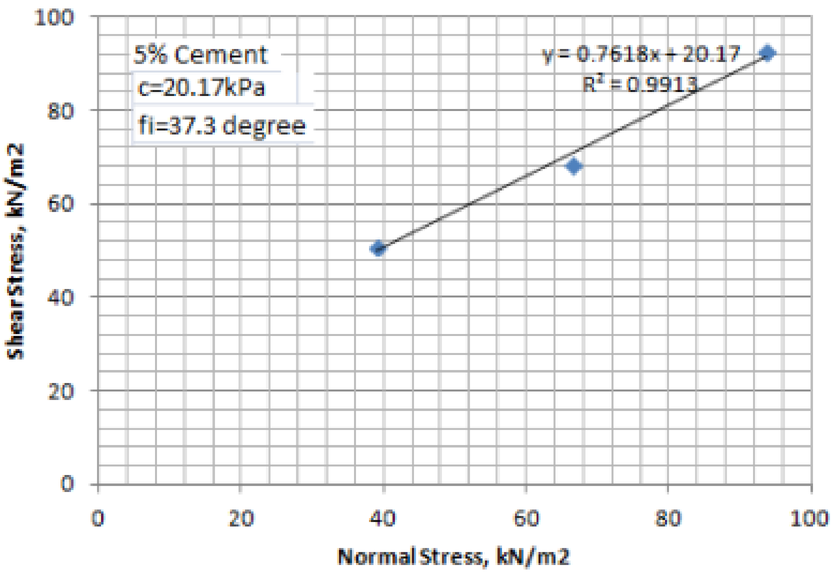

Fig. 19. Failure envelope of Sabkha soil stabilized by 5% cement

4. Collapsibility of the Sabkha

When the loaded soil is exposed to moisture, and certain critical moisture content is exceeded, the fine silt or clay bridges that are providing the cementation will soften and weaken and/or dissolve to some extent. Eventually, the binders reach a stage where they no longer resist deformation forces and the structure collapses (see Fig.22). To conduct a collapse test on Sabkha soils taken from the Salmabad, and Zallaq regions, undisturbed soil samples were taken from both regions as seen Fig.21. The consolidation ring was used while the undisturbed samples were being taken. The collapse test results on Sabkha taken from Salmabad region were used to plot void ratio versus logarithm of effective stress (applied pressure) as seen in Fig. 22. One of the collapse tests conducted on Sabkha soil taken from Salmabadan is given in Table 3.

To evaluate soil collapsibility, various criteria have been defined by many researchers. According to the criteria, the Sabkha soils studied in this research can be named as a collapsible soil with moderate trouble Feda criteria (Doomkamp, et all, 1980):

Table 3. The results of the collapse test (Salmabad)

Applied pressure (kPa)	Dial gage reading (dz, mm)	Final gage reading (df, mm)	Hi, mm	ei %
25	0	156	1.97	1.407
50	156	284	1.94	1.394
100	284	455	1.91	1.377
200	455	540	1.89	1.369
200	540	820	1.84	1.341
400	820	1134	1.77	1.309
800	1134	1593	1.68	1.263
1600	1702	2022	1.60	1.221

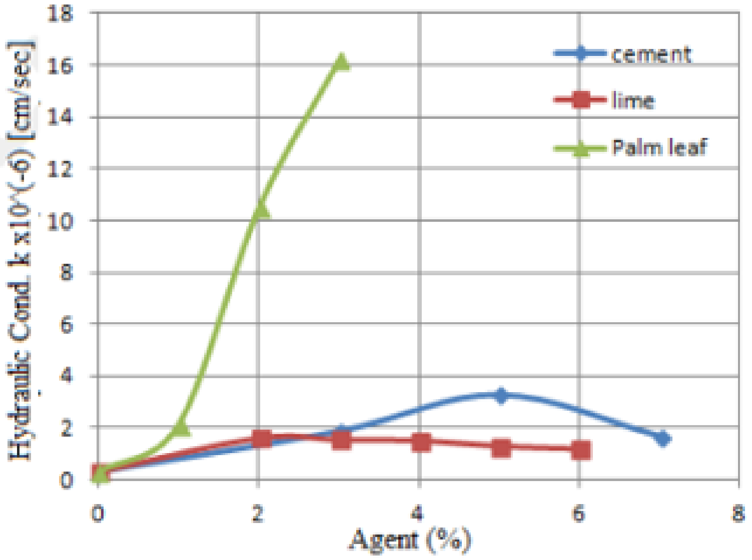

Fig. 20. Variation of the hydraulic conductivity of Sabkha by the stabilizers

Fig. 21 Undisturbed Sabkha samples taken from the field

$$i_c = \frac{\frac{m}{S_r} - PL}{PI}\% = \frac{\frac{0.35}{0.61} - 0.396}{0.3523} = 0.504 < 1 \Rightarrow Collapsible$$

Lin and Wang criteria (Lin, et all, 198812):

$$i_{cz} = \frac{h_z - h_{zS}}{h_i} = \frac{1.89 - 1.84}{2} = 0.025 = 2.5\% \Rightarrow Medium\ \ Collepsibility\ \ (seeTable2.3)$$

$$i_c = \frac{\frac{m}{S_r} - PL}{PI}\% = \frac{\frac{0.35}{0.61} - 0.396}{0.3523} = 0.504 < 1 \Rightarrow Collapsible$$

Lin and Wang criteria (Lin, et all, 198812):

$$i_{cz} = \frac{h_z - h_{zS}}{h_i} = \frac{1.89 - 1.84}{2} = 0.025 = 2.5\% \Rightarrow Medium\ \ Collepsibility\ \ (seeTable2.3)$$

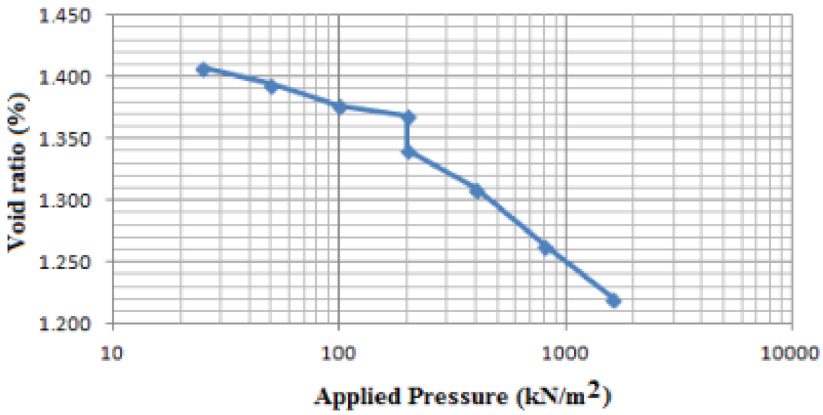

Fig. 22. Void ratio versus logarithm of applied pressure for Sabkha taken from Salmabad

Because the maximum dry density and collapse potential values are in the range of collapsible soils according to the criteria given by Feda 1960, Lin and Wang Criteria 1988.

5. Result and conclusions

First, the soil was classified according to the Unified Soil Classification System (USCS). Both Sabkhas were poorly graded sand (SP) with a small amount of gravel. A summary of the results from the conducted tests are seen in Table 4. In the investigation, sieve analysis, Atterberg limits (consistency limits) tests, the standard proctor tests, falling head permeability tests, direct shear tests, and unconfined compression tests were conducted on the plain Sabkha samples. Then, the same tests were performed on the stabilized Sabkha samples. For the stabilization cement, lime, and palm leaf agents were employed. The Sabkha soil samples taken from Salmabad were stabilized by 3, 5, and 7% of cement and 2, 3, 4, 5, and 6% of lime. However, the Sabkha samples taken from Zallaq were stabilized by 1, 2, and 3% of palm leaf. The liquid limit of the Sabkha is increased with addition of lime. However, it decreased with the addition of cement. plastic limit tends to increase with addition of lime or cement, but the increment is not significant. The plasticity index decreased with the increment of cement up to 3%. Then, it seems to be constant. In the case of lime agent, the plasticity index has a tendency of increment, but the increment is not very significant. Therefore, it can be concluded that the agent cement has a positive effect on the plasticity of Sabkha soil in terms of the water sensitivity of Sabkha whereas lime has a very little negative effect in this issue. The OMC and MDD of each mixture of samples were determined. Among the maximum dry densities, the highest MDD has been achieved when 3% of lime was used as the stabilizer. The highest value of the MDD is 1570kg/m^3. The same percentage of cement has an MDD of 1562kg/m^3. OMC values for these percentages (3%) of both cement and lime are 24%. In terms of MDD, 1% cement, 2 and 6% lime additives have an MDD, which is less than the MDD of plain Sabkha. The other agent and percentage of additives give a value of MDD more than the maximum dry density of the plain Sabkha. The unconfined compressive strength of the Sabkha is improved when it was stabilized with different additives with their various ratios and curing time. When lime is used as the stabilizer, the improvement on the compressive strength is getting higher when the ratio of lime is increased. Also curing time is very important for the lime stabilized Sabkha samples.

Table 4. Summary of laboratory tests

Agent	Add. %	OMC %	MDD kg/m^3	K x 10^(-6) cm/sec	LL %	PL %	PI %	Direct Shear Test: Apparent cohesion, c, kPa	Direct Shear Test: Internal friction ϕ degree	UC Test: qu [kPa]
None Salmabad	0	25	1514	0.3094	60.1	24.9	35.2	15(0)*	39(0)*	165.48(0)*
Cement Salmabad	1	25	1510	-	-	-	-	-	-	-
	3	24	1562	1.8781	43.5	26.7	16.8	20(0)*	37(0)*	409.0(0)*
	5	25	1530	3.2841	42.5	28.6	13.9	20(0)*	38(0)*	-
	7	25	1542	1.7023	43.2	29.3	13.9	50(0)*	65(0)*	-
Lime Salmabad	2	26	1510	1.61	63.5	25.9	37.6	2.3 (0)*	40(0)*	172.5(0)*
								42(14)*	-	248.1(7)*
										388.5(14)*
	3	24	1570	0.4279	64.7	25	19.5	-	-	-
	4	25	1526	1.52	65.6	29.3	36.3	21.8(0)*	33(0)*	188.7(0)*
								69(0)*	-	303.4(7)*
										401.5(14)*
	5	22	1550	0.9515	68.3	25.4	20	-	-	-
	6	28	1452	1.20	72.2	31.1	41.1	5.4(0)*	36(0)*	194.9(0)*
								78(14)*	-	360.7(7)*
										423.4(14)*
Palm leaf Zallaq	0	16	1392	3.74	41	NA	-	18.3	39	181.9
	1	18.5	1370	2.14	NA	NA	-	23	41	317.84
	2	25.3	1340	10.5	NA	NA	-	8	46	409.20
	3	25	1319	16.2	NA	NA	-	15	47	513.40

(0)*: No curing, (7)*: 7-day curing, (14)*: 14-day curing.

The best improvement on the unconfined compressive strength was achieved when 3% of palm leaf is used. It may be expected to get the best improvement on the cement addition. Maybe it would happen if curing time were extended for the cement additive. The lime additive has no effect on the strength increment as much as the palm leaf does. The Sabkha soils used for stabilization by the palm leaf were not taken from the same region as the Sabkha used for lime stabilization, but it is believed that the improvement by the palm leaf is better since tension stresses are carried by the palm leaf fibers. Thus, the palm leaf treated Sabkha soil gains strength for the tension stresses. Improvement on shear strength for 2, 4 and 6% of the lime is very close to each other in 14 days curing. Thus, it can be concluded that there is no need to use more percent of lime if the soil is expected to gain more shear strength in the long term. This conclusion must be verified by conducting more experiments and more curing days. The shear strength parameters, c and ϕ were estimated by the direct shear tests on Sabkha soil, which was stabilized by 2% lime additive. The apparent cohesion c = 2.26kPa, and the internal friction angle ϕ = 40 degrees. These values can be used to estimate the principal major stress under consolidated-drained condition with any lateral (confining) stress less than over consolidation pressure. The major principal stress can be calculated by Eq. (3.2). When the failure envelopes of the lime stabilized Sabkha soil are plotted on one graph, it is clearly seen that 4% of lime addition gives the better failure envelope compared to the other percentages of the lime. When the variation of major principal stresses versus the maximum dry density of the samples, palm leaf stabilized Sabkha soil is better than the others. The best improvement on the major ultimate stress was achieved at 1% palm leaf stabilized Sabkha samples. There might be a little effect of the natural Sabkha because palm leaf added Sabkha was taken from Zallaq and the other agents were added to the Sabkha taken from Salmabad. However, both Sabkhas were classified as poorly graded sand so that the effect of the places can be ignored in this state. The hydraulic conductivity of the Sabkha is not affected much when cement or lime is used as the stabilizers. The variation on the hydraulic conductivity is not significant when either cement or lime is used as the stabilizer. However, the hydraulic conductivity is affected by the palm leaf. The variation on the hydraulic conductivity is significant when the palm leaf is used as stabilizer. This future of the palm leaf can be considered when designing a project in which more strength and more permeable soil layers are needed. However, if the designing of a project requires more strength and less permeable soil layer, the choice of palm leaf as the stabilizer is not a proper selection. The Sabkha soils studied in this research can be named as a collapsible soil with moderate trouble since the maximum dry density and collapse potential values are in the range of collapsible soils according to the criteria given by Feda 1960, Lin and Wang Criteria 1988.

Acknowledgement

This paper is prepared from the research report "Investigation on Improvement of Geotechnical Properties of Sabkha Soil in Bahrain," that was supported financially by the Deanship of Scientific Research and Postgraduate Studies, University of Bahrain, Kingdom of Bahrain.

References

Abelev, Y. M., & Abelev, M. O. Y. (1979). *Bases de l'élaboration des projects et de la construction sur les sols loessiques affaissables* (J. P. Magnan, Trans.). Édition technique et documentation Lavoisier, 62–67. (Originally published in Russian)

Abelev, M. Y. (1984). The essentials of designing and building on microporous soils. *Stroitel'naya Promyshelmast*, (10).

Abelev, M. Y. (1988). Loess and its engineering problems in the USSR. In *Proceedings of the International Conference on Engineering Problems of Regional Soils* (pp. 3–6). Beijing, China: Chinese Institute of Soil Mechanics and Foundation Engineering.

Akili, W. (1981). Some properties of remolded carbonate soils. In *Proceedings of the 10th International Conference on Soil Mechanics and Foundation Engineering* (Vol. 1, pp. 537–542). Stockholm, Sweden.

Al-Amaudi, O. S. B. (2008). Testing and stabilization of saline Sabkha soils: A review. In *6th International Conference on Case Histories in Geotechnical Engineering* (Paper No. 45). Arlington, VA.

Al-Sanad, H. A., Shaqour, F. M., & Hencher, S. R. (1989). The shear strength of salted cemented sand from Kuwait. In *Proceedings of the First Regional Conference in Civil Engineering* (Vol. S, p. 1528). University of Bahrain, Bahrain.

American Society for Testing and Materials. (1992). *Annual Book of ASTM Standards*. ASTM.

Basma, A. A., & Tuncer, E. R. (1992). Evaluation and control of collapsible soils. *Journal of Geotechnical Engineering, ASCE, 118*(10), 1491–1504.

Doomkamp, J., Brunsden, D., & Jones, D. (1980). *Geology, geomorphology and pedology of Bahrain*. Geology Abstracts Ltd., University of East Anglia.

Feda, J. (1988). Collapse of loess upon wetting. *Engineering Geology, 25*, 263–269.

Ismael, N. (1993). Laboratory and field leaching tests on coastal salt-bearing soils. *Journal of Geotechnical Engineering, ASCE, 119*(3), 453–470.

Jennings, J. E., & Knight, K. (1975). A guide to construction on or with materials exhibiting additional settlement due to collapse of grain structure. In *Proceedings of the Sixth Regional Conference for Africa on Soil Mechanics and Foundation Engineering* (pp. 99–105). Durban, South Africa.

Lamb, R. O. (1990). Geotechnical aspects of leaching of carbonates from loessial soils. In *Physico-chemical aspects of the soil and related materials* (ASTM STP 1095). ASTM.

Lin, Z. G., & Wang, S. J. (1988). Collapsibility and deformation characteristics of deep-seated loess in China. *Engineering Geology, 25*, 271–282.

Mohamed Zain, Y. E. A., & Al-Rawas, A. A. (2011). Cement stabilization of Sabkha soils from Al-Auzayba, Sultanate of Oman. *Geotechnical and Geological Engineering, 29*(6), 999–1008. https://doi.org/10.1007/s10706-9432-y

Qahwash, A. A. (1989). Geotechnical properties of fine-grained calcareous sediments for engineering purposes. *Engineering Geology, 26*, 161–169.

Stipho, S. A. (1985). On the engineering properties of Salina soil. *Quarterly Journal of Engineering Geology and Hydrogeology, 26*, 129–137.

Youssef, A. M., Pradhan, B., Sabtan, A. A., & El-Harbi, H. M. (2007). Coupling of remote sensing data aided with field investigations for geological hazards assessments in Jazan, Kingdom of Saudi Arabia. *Environmental Earth Science*. https://doi.org/10.1007/s1266-1071-3

Assessment of cemented paste backfill strength and microstructure using mixing waters with varying pH

Tugba Keskin[1,2], Erol Yilmaz[*1,3], Tugrul Kasap[1,2], Muhammet Sari[1,2,3]

[1] *Recep Tayyip Erdogan University, Geotechnical Waste Management and Backfill Laboratuary, Rize, Türkiye*
[2] *Recep Tayyip Erdogan University, Institute of Graduate Studies, 53100 Rize, Türkiye*
[3] *Recep Tayyip Erdogan University, Department of Civil Engineering, 53100 Rize, Türkiye*

Abstract. Cemented paste backfill (CPB) technology is widely employed in mining operations to mitigate environmental and geotechnical risks by reducing tailings volume. The overall performance of CPB is strongly influenced by the properties of the tailings, binder, and mixing water used in the mixture. With the increasing depletion of freshwater resources, sustainable alternatives that minimize freshwater consumption in CPB production have gained growing importance. In this study, process waters with different pH levels were utilized as mixing water to investigate their impact on CPB performance and to reduce reliance on freshwater. CPB samples were prepared using a constant solid content of 76%, a fixed cement dosage of 6% by weight, and mixing waters with pH values of 4.67 (acidic), 10.95 (basic), and 7.61 (tap water). These samples were subjected to curing periods of 3, 14, 28, and 56 days. Subsequently, mechanical and microstructural analyses were conducted. The results revealed that all samples exhibited increased strength after 28 days of curing. However, a decline in strength was observed in the samples prepared with low-pH water after 56 days. The acidic environment promoted excessive ettringite formation, which adversely affected the strength development. Microstructural evaluations indicated that the low-pH samples had fewer hydration products and a higher concentration of ettringite crystals. These findings confirm that acidic mixing waters hinder cement hydration and negatively influence the mechanical properties of CPB.

Keywords: Cemented paste backfill; Mixing water; pH; Mechanical properties; Microstructural characteristics.

1. Introduction

Cementitious composites such as paste backfill, concrete, and mortar are multifunctional structural materials extensively employed across various sectors, particularly in construction and mining industries (Sambucci et al., 2021). These heterogeneous and composite systems are composed of multiple constituents, each fulfilling distinct roles within the mixture (Li & Li, 2019). Cementitious materials primarily comprise three core components: aggregates (e.g., mine tailings, sand, gravel, or crushed stone), binders (e.g., cement, slag, fly ash), and mixing water (Li et al., 2022). Alongside these primary constituents, chemical or natural additives (e.g., accelerators) are frequently incorporated to enhance specific characteristics such as workability, freeze-thaw resistance, and mechanical strength when required (Amare et al., 2023). The function of each component, as well as the proportions and interactions among them, significantly influences the development of desired material properties (Fode et al., 2023). Overall, the proper selection and accurate proportioning of these components critically impact strength, durability, workability, and other performance attributes (Li et al., 2023).

Among these components, mixing water holds a particularly vital role in determining the quality and performance of cementitious systems (Shanmugasundaram & Praveenkumar, 2021). Both the quantity and the quality of the water used profoundly affect the mechanical strength and workability of the mixture (da Rocha Gomes et al., 2023). Water fulfills several essential functions within the cementitious matrix, making its appropriate use highly critical (Nazar et al., 2020). Generally, water initiates the hydration reaction by chemically interacting with cement particles, leading to the formation of crystalline structures that solidify the matrix (Zhang et al., 2019, Yu & Shui, 2014). An adequate amount and quality of water are essential for a proper hydration process and for achieving the intended strength development (Jain et al., 2022). Furthermore, water content critically influences the workability of the mixtures during processes such as transportation, pouring, and placement (Solak et al., 2018). Insufficient water can render mixtures difficult to handle, whereas excessive water

* Corresponding author, E-mail: erol.yilmaz@erdogan.edu.tr

https://doi.org/10.31462/icearc2025_ce_geo_177

may improve flowability at the expense of mechanical strength. Therefore, an optimal balance between workability and strength must be achieved (Liu et al., 2021).

The role of mixing water becomes even more crucial when cementitious materials are transported over long distances or to locations with limited accessibility. Workability, largely governed by water content, serves to reduce operational challenges and labor demands, making it a key design consideration for such mixtures (Deng et al., 2023). Compared to conventional cementitious systems, cemented paste backfill (CPB) is one method where workability is particularly prioritized (Wang et al., 2023). CPB represents an advanced backfilling technology where a paste, produced at surface plants, is subsequently transported and placed into underground mine voids (stopes) via gravity or pumping methods (Jiang & Fall, 2017; Guner et al., 2023). Given that many mining operations today reach depths exceeding one kilometer — with coal mines extending to about 1500 meters and metal ore mines reaching depths up to 4350 meters — transporting CPB over such distances without segregation (i.e., sedimentation) becomes a critical operational challenge (Xie et al., 2017; Jiang et al., 2020). Consequently, fresh CPB must possess sufficient fluidity to enable efficient pumping from surface facilities to underground voids without significant material separation (Behera et al., 2021). CPB with optimal fluidity can be conveyed through pipelines with minimal frictional resistance, preserving homogeneity throughout transport. Moreover, fluid CPBs exhibit better adherence to surrounding rock surfaces, fostering stable mechanical bonding and enhancing predictability in strength gain (Cheng et al., 2020; Qi et al., 2018). Inadequate workability, on the other hand, severely undermines the performance, quality, and long-term stability of CPBs, and substantially increases the risk of operational failures such as pipeline blockages (Sari et al., 2023). Thus, ensuring the appropriate quantity and quality of mixing water is fundamental for achieving the intended operational design in all cementitious mixtures, including CPBs (John et al., 2018).

The quality of available mixing water may vary significantly depending on its source, which can be influenced by factors such as seasonal fluctuations and geographic location. To minimize adverse impacts and preserve the strength and durability of cementitious materials, fresh water sources with assured purity (e.g., municipal tap water, well water, rainwater, lake or river water) are predominantly utilized (de Godoy et al., 2020). Notably, global production of concrete composites currently consumes over two billion tons of fresh water annually, accounting for approximately 9% of industrial freshwater usage worldwide. Projections suggest that by 2050, nearly 75% of the water required for concrete production will be concentrated in regions facing significant water scarcity (Younis et al., 2018, 28). Simultaneously, factors such as population growth, industrial expansion, and climate change are exacerbating the depletion of freshwater resources globally (Tortajada, 2020). Fresh water is not only essential for construction materials but is also fundamental for human survival, agriculture, industry, energy generation, and numerous other sectors. Preserving freshwater resources is, therefore, crucial for sustainable industrial practices and ensuring access to clean water for future generations (Coffetti et al., 2022; Hussain et al., 2019).

The growing concerns about global freshwater scarcity, driven by rapid population increase, climate change, unsustainable consumption patterns, and uneven geographical distribution of water resources, have intensified the search for alternative water sources. Although about 70% of Earth's surface is covered by water, only 3% constitutes freshwater, and approximately 70% of this is trapped in glaciers, leaving merely 1% accessible for use. This stark reality underscores the urgent need for sustainable water management practices. Despite significant research efforts, the global freshwater supply continues to dwindle due to increasing demands. Based on current trends and forecasts, substantial freshwater shortages are anticipated in the near future. Consequently, utilizing potable water for concrete and CPB production is increasingly viewed as unsustainable, compelling researchers and industries alike to explore alternative water sources. In response to these challenges, industries across the globe are seeking sustainable and environmentally responsible solutions, including the substitution of fresh water in cementitious mixtures (Yang et al., 2024).

Given these imperatives, exploring the viability of alternative mixing waters is essential to reduce dependency on freshwater in cementitious applications and to advance toward a more resource-conscious future. In the literature, several studies have focused on investigating alternative water sources primarily for concrete — the cementitious material with the highest freshwater demand. Harial et al. (2023), for instance, examined the reuse potential of untreated wash water from concrete truck mixers, concluding that this wastewater had negligible adverse effects on hydration kinetics and the mechanical properties of fresh and hardened mortars. Tamashiro et al. (2022) studied the use of vinasse wastewater from the sugar and alcohol industry, finding that concrete incorporating vinasse exhibited superior compressive strength after extended curing compared to conventional concrete. Meena et al. (2019) evaluated primary, secondary, and tertiary treated wastewater for concrete production, observing strength reductions of 6–15% with tertiary treated water, but compliance with ASTM C-94 standards. Ismail et al. (2011) investigated the feasibility of employing industrial wastewater from polyvinyl acetate resin production, reporting modest to moderate improvements in compressive strength and dry density relative to fresh water controls. Gupta et al. (2021) compared tap water, grey water, pond water, and treated sewage water, finding that grey and treated sewage waters enhanced strength by 2.1% and 6.9%, respectively, whereas pond water resulted in a 5.1% strength reduction. Pan et al. (2021) studied seawater and sand mixtures, revealing initial strength enhancements but slight strength reductions by 28 days of curing, alongside increased dynamic modulus of elasticity at early stages.

While numerous studies address the use of sustainable and environmentally friendly water sources (e.g., seawater, sewage, domestic wastewater, treated spring water) as alternatives to fresh water for concrete production, research on alternative waters for CPB applications remains notably limited. To address this gap, the present study investigates the influence of process water with varying pH levels on CPB performance as an alternative to freshwater. By doing so, the aim is to minimize freshwater consumption during CPB production, contributing beneficially to both operational efficiency and ecological sustainability. For this purpose, CPB samples were prepared with a constant solids content (76%), a fixed cement dosage (6% by weight), CEM I 42.5 R cement type, and mixing waters with different pH values (4.67, 7.61, 10.95). The samples were subjected to different curing periods (3, 14, 28, and 56 days). Subsequent mechanical and microstructural tests were performed to evaluate the effects of mixing water pH on the strength and durability characteristics of the CPB samples.

2. Materials and methods

2.1. Components of CPB

2.1.1. Mixing waters

The chemical characteristics of the process waters utilized as mixing waters play a vital role in determining the filling strength and structural stability. Additionally, the chemical makeup of the mixing water exerts a considerable impact on the cement hydration mechanism. In this research, process waters with distinct pH values and tap water, were employed. The geochemical analysis data pertaining to these waters are provided in Table 1. A prominent observation from the table is that the sulphate concentration in both acidic and basic waters is markedly higher compared to that in tap water.

Table 1. Chemical and geochemical data of mixing waters.

	LPW (%)	**HPW (%)**	**TW (%)**
		Geo-chemical parameters	
pH	4.67	10.95	7.61
EC (µS/cm)	5117	4165	0.08
Eh (V)	0.43	0.47	0.36
		Chemical composition	
SO_4^{2-} (mg/L)	7228	4823	4.89
Ca (mg/L)	462	583	40.09
K (mg/L)	23.9	32.8	0.58
Cl (mg/L)	1.49	1.55	0.32
Mg (mg/L)	1.65	1.77	1.96
Si (mg/L)	67.9	46.8	0.67
Al (mg/L)	0.55	0.48	0.02
Cu (mg/L)	0.21	0.24	0.85
Fe (mg/L)	3.46	2.94	0.05

2.1.2. Physical and chemical characterization of mine tailings

The mine tailings utilized in this research were sourced from a copper mining operation located in Turkey. The physical characteristics of the tailings are presented in Table 2, while their chemical composition is detailed in Table 3. The particle size distribution curve of the tailings, which were used as binder material in this study, is illustrated in Fig 1. According to the proportion of particles smaller than 20 µm, the tailings are classified as fine-grained material.

Table 2. Physical parameters of mine tailing and cement

Characteristics	Mine tailing	Cement
Specific gravity Gs	3.73	2.95
Specific surface area Ss (m^2/g)	2.71	0.37
Maximum dry density MDD (kg/ m^3)	2.45	-
Optimum moisture content OMC (%)	12.6	-
D_{10} (μm)	6.77	4.67
D_{30} (μm)	24.8	23.9
D_{50} (μm)	55.4	37.1
D_{60} (μm)	76.4	56.3
Coefficient of uniformity C_u	11.26	12.17
Coefficient of curvature C_c	1.23	2.14

Table 3. Chemical parameters of mine tailing and cement

Chemical parameters	Mine tailing	Cement
Silicon dioxide (SiO_2)	37.6	16.73
Iron oxide (Fe_2O_3)	27.7	2.84
Aluminum oxide (Al_2O_3)	8.02	4.94
Calcium oxide (CaO)	4.03	63.25
Magnesium oxide (MgO)	1.85	1.16
Potassium oxide (K_2O)	0.26	0.64
Sulfur oxide (SO_3)	0.27	3.67
Titanium oxide (TiO_2)	0.22	-
Phosphorous oxide (P_2O_5)	0.25	-
Sodium oxide (Na_2O)	0.17	0.25
Strontium oxide (SrO)	0.04	-
Barium oxide (BaO)	0.08	-
Loss on ignition (LOI)	97.91	4.64
Total S	4.48	-
Total sulfur S^2	35.9	-

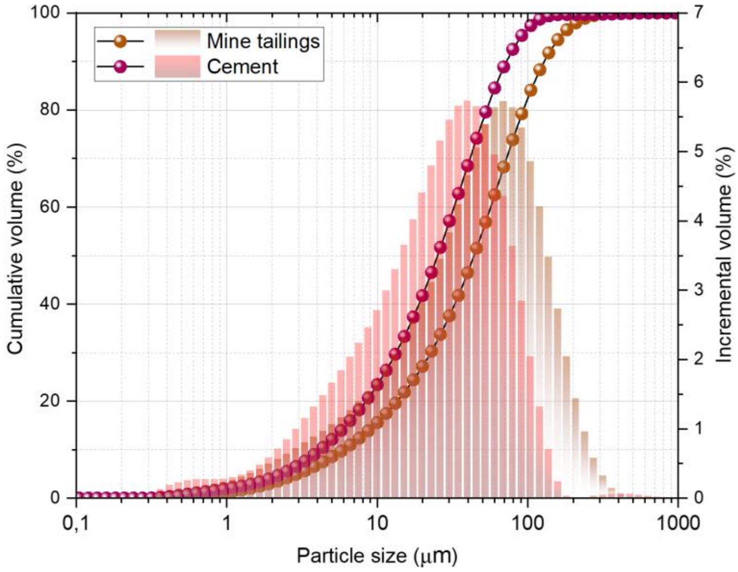

Fig. 1. Cumulative particle size of mine tailing and cement

2.1.3. Binder

Portland cement of type CEM I 42.5 R was employed as the binder in this study. The physical and chemical properties of the cement are presented in Tables 2 and 3. The specific gravity (G_s) and specific surface area (S_s) of the cement were determined to be 2.95 and 0.37 m²/g, respectively.

2.2. Manufacturing of CPB samples

The fabrication of cemented paste backfill (CPB) samples was carried out through a systematic sequence of operations to ensure consistency and reproducibility. In the mixture design, the proportions of cement, tailings, and water were optimized based on a fixed water-to-cement ratio to attain the intended mechanical characteristics. Throughout the study, all mixtures were prepared with a constant solid concentration of 76% and a fixed cement content of 6% by weight. The components—namely, the tailings, binder, and selected mixing water—were blended using a UTEST-brand laboratory mixer for approximately 10 minutes, ensuring a homogeneous and uniform mixture in line with the proportions outlined in Table 4. The resulting slurry was cast into cylindrical molds with dimensions of 5 cm in diameter and 10 cm in height, equipped with perforated bases to allow drainage. To improve packing density and minimize entrained air, each sample was tamped 20–25 times using a metal rod. The molded specimens were then transferred into a curing chamber set at 21±2 °C and 90±5% relative humidity, where they were kept for predetermined curing durations. Upon completion of the curing process, the CPB samples were considered ready for experimental evaluation (Fig 2).

Fig. 2. Preparation of backfill samples

2.3. Experimental methodology

2.3.1. Slump test
According to the ASTM C143 standard, this test is applied to determine the vertical deformation (in centimeters) that occurs in a sample due to its own weight. Compared to the conventional slump test, the mini slump test offers significant advantages in terms of material efficiency and time savings. The mini slump procedure requires only approximately 16% of the material used in the standard slump cone method. Experimental findings have shown that the correlation factor between the results of the mini and standard slump tests is approximately 2. The dimensions of the mini slump cone are 100 mm at the base, 50 mm at the top, and 150 mm in height. In this study, the mini slump test revealed that CPB samples with a solid content of 76% exhibited an average slump value of 25 cm.

2.3.2. UCS test
Following the completion of the designated curing periods (3 to 56 days), the CPB samples were demolded, and their edges and surfaces were smoothed to ensure uniform contact during testing. Subsequently, unconfined compressive strength (UCS) tests were conducted. For this purpose, the specimens were positioned between the compression plates of a UTEST brand servo-controlled universal testing machine, with a maximum load capacity of 50 kN, operating at a constant loading rate of 1 mm/min. Throughout the testing process, the compressive strength and stress–strain responses of the CPB samples were continuously monitored and recorded by the system. To ensure the reliability and reproducibility of the results, each test was conducted in triplicate, and the average UCS value was calculated from the obtained data.

2.3.3. SEM analysis
The CPB samples extracted from the central region were oven-dried at 50 °C for 24 hours to eliminate moisture. Following the drying process, the samples were coated with a thin layer of gold to ensure electrical conductivity. Scanning Electron Microscopy (SEM) analyses were then conducted. During the imaging process, a maximum magnification of 2000× was utilized, with the highest resolution set at 10 μm to capture detailed microstructural characteristics.

3. Results and discussion

3.1. Analysis of UCS test data
Figure 3 presents the unconfined compressive strength (UCS) data for CPB samples subjected to curing durations of 3, 14, 28, and 56 days. A progressive increase in UCS values was observed for all mixtures up to day 28, which is attributed to the high-alkaline conditions induced by the cement, facilitating early-stage strength development. This period coincides with intensified portlandite formation.

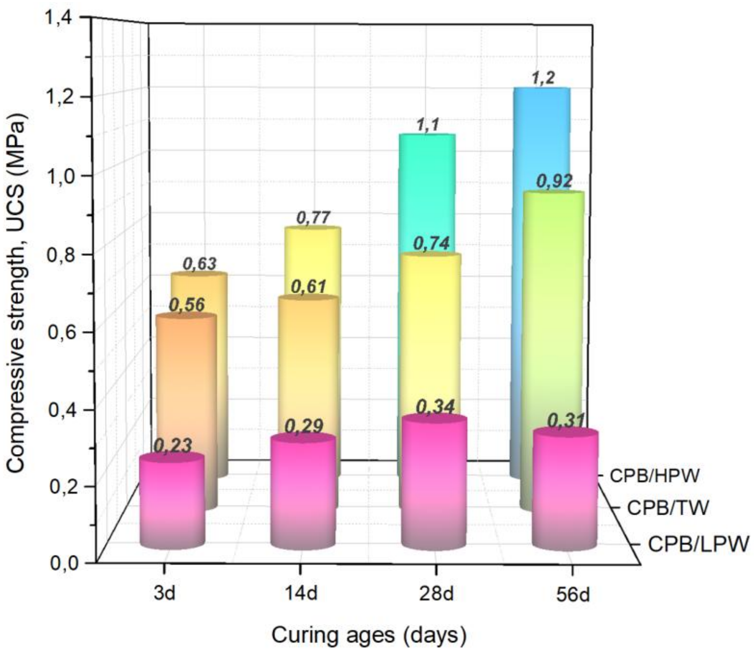

Fig. 3. Curing time-dependent ucs performance of CPB samples

On the 28th day, UCS for CPB/HPW increased by 68.25% relative to its 3-day strength, while the CPB/LPW and CPB/TW mixtures exhibited gains of 47.83% and 32.14%, respectively. Among these, CPB/HPW reached the highest UCS value at 1.06 MPa, whereas CPB/LPW demonstrated the lowest at 0.34 MPa. From day 28 to day 56, the UCS of CPB/HPW and CPB/TW samples continued to rise, whereas a reduction was recorded for CPB/LPW. The UCS of CPB/LPW decreased by 9.68% after 56 days compared to its 28-day strength, a phenomenon likely driven by the acidic nature and elevated sulfate concentration of the mixing water, which hinder cement hydration and compromise internal structural integrity. Consequently, the long-term alkalinity and mechanical performance of CPB/LPW diminish. On the other hand, the UCS values of CPB/TW and CPB/HPW increased by 24.32% and 14.15%, respectively, between days 28 and 56. At the end of the 56-day curing period, CPB/LPW exhibited the lowest compressive strength at 0.23 MPa, while CPB/HPW displayed the highest at 1.21 MPa.

3.2. SEM analysis

SEM images are highly effective for analyzing the microstructures of materials. Figure 4 shows SEM images of CPB/LPW, CPB/HPW, and CPB/TW samples cured for 56 days. Upon examining the images of the CPB/LPW samples, it is observed that the ettringite ratio is higher and the hydration products are lower compared to the CPB/HPW and CPB/TW samples. The pH value of the mixing water has influenced the environment and negatively affected the hydration products of the cement. In acidic conditions, sulfate absorption increases, leading to a greater accumulation of ettringite crystals in the filling matrix. This process causes the pores in the filling material to be filled. The excessive accumulation of these crystals at low pH negatively impacts the durability of the material.

In the image of the CPB/HPW sample, C-S-H gels formed as a result of the chemical reactions between calcium silicate and water are observed densely. These gels are critical structures that enhance the durability and hardness of concrete, and the density of these gels is directly related to the higher strength value of the CPB/HPW samples. Furthermore, the high pH value of the mixing water increased the alkalinity of the samples, positively contributing to the hydration process.

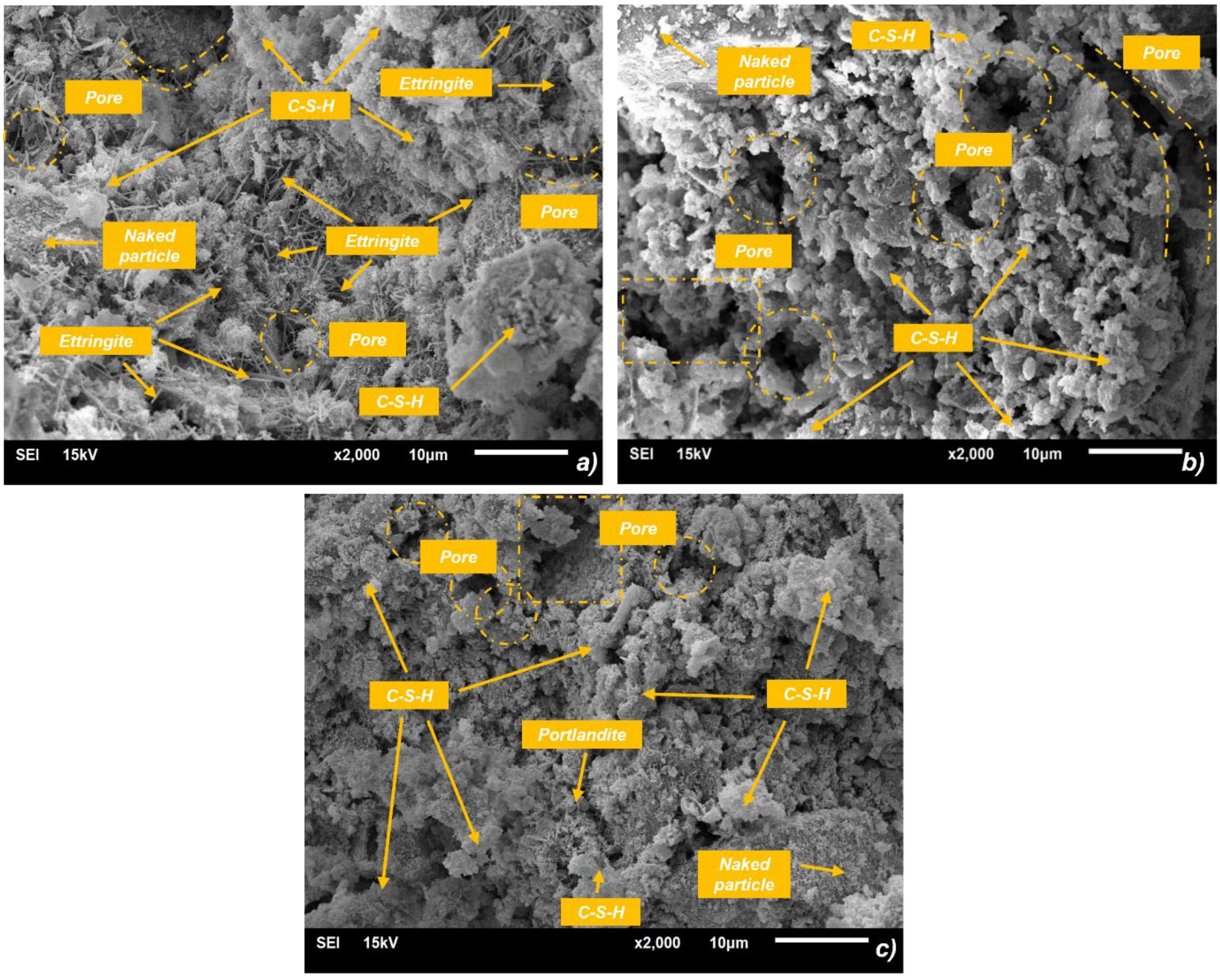

Fig. 4. SEM images of CPB samples (a;CPB/LPW, b;CPB/TW, c;CPB/HPW)

4. Conclusions

In this study, the mechanical and microstructural properties of cemented paste backfill (CPB) prepared with mixing waters of different pH levels (acidic process water, basic process water, and tap water) were investigated. CPB mixtures identified as CPB/LPW, CPB/HPW, and CPB/TW were produced with a fixed solid content of 76% and a cement content of 6% by weight. These mixtures were cured for 3, 14, 28, and 56 days. After each curing period, mechanical strength and microstructural analyses were conducted. The findings are summarized below:

- The strengths of all CPB/LPW, CPB/HPW and CPB/TW samples cured for 28 days increased. The strength values of CPB/TW and CPB/HPW samples cured for 56 days increased by 24.32% and 14.15%, respectively, compared to the samples cured for 28 days, while the strength value of CPB/LPW samples decreased by 9.68%.
- It was determined that low pH levels led to the formation of ettringite and other chemical compounds in cement-based materials due to acidic conditions. These chemical alterations negatively impacted the pore structure of the material, thereby reducing its strength. Structural degradation and uncontrolled crystal growth under acidic environments weakened the mechanical properties and overall durability of the material.
- Microstructural analyses revealed that CPB/LPW samples contained significantly fewer hydration products than CPB/HPW and CPB/TW samples. Additionally, the formation of ettringite was found to be more pronounced in CPB/LPW samples compared to the others.
- The use of low-pH mixing water created an unfavorable environment for cement hydration, and the acidic nature of the water was shown to have a detrimental effect on both the mechanical and microstructural characteristics of CPB.

In conclusion, this study demonstrated that process waters with varying pH values can be utilized in the production of cemented paste backfill. The findings provide insights that may support future research on alternative water sources in backfill applications. Moreover, the potential use of such waters as substitutes for freshwater or potable water in industrial processes may contribute to alleviating future water scarcity to some extent.

References

Mitchell, J.A. (2017). Citation: Why is it so important. *Mendeley Journal, 67*(2), 81-95

Amare, M., Swara, S., Haish, M., Pani, A. K., & Saha, P. (2023). Performance of agro-wastes and chemical admixtures used in concrete: A review. *Materials Today: Proceedings*.

Behera, S. K., Mishra, D. P., Singh, P., Mishra, K., Mandal, S. K., Ghosh, C. N., & Mandal, P. K. (2021). Utilization of mill tailings, fly ash and slag as mine paste backfill material: Review and future perspective. *Construction and Building Materials, 309*, 125120.

Cheng, H., Wu, S., Li, H., & Zhang, X. (2020). Influence of time and temperature on rheology and flow performance of cemented paste backfill. *Construction and Building Materials, 231*, 117117.

Coffetti, D., Crotti, E., Gazzaniga, G., Carrara, M., Pastore, T., & Coppola, L. (2022). Pathways towards sustainable concrete. *Cement and Concrete Research, 154*, 106718.

da Rocha Gomes, S., Ferrara, L., Sánchez, L., & Moreno, M. S. (2023). A comprehensive review of cementitious grouts: Composition, properties, requirements and advanced performance. *Construction and Building Materials, 375*, 130991.

de Godoy, L. G. G., Rohden, A. B., Garcez, M. R., Da Dalt, S., & Gomes, L. B. (2020). Production of supplementary cementitious material as a sustainable management strategy for water treatment sludge waste. *Case Studies in Construction Materials, 12*, e00329.

Deng, X., Li, J., Lu, Z., Zhang, J., Luo, K., Niu, Y., & He, K. (2023). Rheological and early hydration of cementitious material containing recycled concrete powders collected from recycled aggregates. *Construction* and Building Materials, 393, 132108.

Fode, T. A., Jande, Y. A. C., & Kivevele, T. (2023). Effects of different supplementary cementitious materials on durability and mechanical properties of cement composite–Comprehensive review. *Heliyon*.

Guner, N. U., Yilmaz, E., Sari, M., & Kasap, T. (2023). Cementitious backfill with partial replacement of Cu-rich mine tailings by sand: Rheological, mechanical and microstructural properties. *Minerals, 13*(3), 437.

Gupta, J., Jethoo, A. S., & Ramana, P. V. (2021). Magnetize mechanical strength effect on concrete due to diverse water. *Materials Today: Proceedings, 44*, 4867–4872.

Harilal, M., Anandkumar, B., George, R. P., Albert, S. K., & Philip, J. (2023). High-performance eco-friendly ternary blended green concrete in seawater environment. *Hybrid Advances, 3*, 100037.

Hussain, M. I., Muscolo, A., Farooq, M., & Ahmad, W. (2019). Sustainable use and management of non-conventional water resources for rehabilitation of marginal lands in arid and semiarid environments. *Agricultural Water Management, 221*, 462–476.

Ismail, Z. Z., & Al-Hashmi, E. A. (2011). Assessing the recycling potential of industrial wastewater to replace fresh water in concrete mixes: Application of polyvinyl acetate resin wastewater. *Journal of Cleaner Production, 19*(2–3), 197–203.

Jain, P., Gupta, R., & Chaudhary, S. (2022). A literature review on the effect of using ceramic waste as supplementary cementitious material in cement composites on workability and compressive strength. *Materials Today: Proceedings, 65*, 871–876.

Jiang, H., & Fall, M. (2017). Yield stress and strength of saline cemented tailings in sub-zero environments: Portland cement paste backfill. *International Journal of Mineral Processing, 160*, 68–75.

Jiang, H., Fall, M., Yilmaz, E., Li, Y., & Yang, L. (2020). Effect of mineral admixtures on flow properties of fresh cemented paste backfill: Assessment of time dependency and thixotropy. *Powder Technology, 372*, 258–266.

John, V. M., Damineli, B. L., Quattrone, M., & Pileggi, R. G. (2018). Fillers in cementitious materials—Experience, recent advances and future potential. *Cement and Concrete Research, 114*, 65–78.

Khushboo, M., & Salmabanu, L. (2019). Effect of wastewater on properties of concrete. *Journal of Building Engineering, 21*, 106–112.

Li, J., Qiu, J., Weng, J., & Yang, E. H. (2023). Micromechanics of engineered cementitious composites (ECC): A critical review and new insights. *Construction and Building Materials, 362*, 129765.

Li, N., Mo, L., & Unluer, C. (2022). Emerging CO2 utilization technologies for construction materials: A review. *Journal of CO2 Utilization, 65*, 102237.

Li, X., & Li, M. (2019). Multifunctional self-sensing and ductile cementitious materials. *Cement and Concrete Research, 123*, 105714.

Liu, S., Tu, Y., Wu, M., & Ren, J. (2021). Effects of termiticides type on workability, hydration characteristics and mechanical property of cementitious materials. *Materials Chemistry and Physics, 272*, 124974.

Miller, S. A., Horvath, A., & Monteiro, P. J. (2018). Impacts of booming concrete production on water resources worldwide. *Nature Sustainability, 1*(1), 69–76.

Nazar, S., Yang, J., Thomas, B. S., Azim, I., & Rehman, S. K. U. (2020). Rheological properties of cementitious composites with and without nano-materials: A comprehensive review. *Journal of Cleaner Production, 272*, 122701.

Pan, D., Yaseen, S. A., Chen, K., Niu, D., Leung, C. K. Y., & Li, Z. (2021). Study of the influence of seawater and sea sand on the mechanical and microstructural properties of concrete. *Journal of Building Engineering, 42*, 103006.

Qi, C., Chen, Q., Fourie, A., Zhao, J., & Zhang, Q. (2018). Pressure drop in pipe flow of cemented paste backfill: Experimental and modeling study. *Powder Technology, 333*, 9–18.

Sambucci, M., Sibai, A., & Valente, M. (2021). Recent advances in geopolymer technology. A potential eco-friendly solution in the construction materials industry: A review. *Journal of Composites Science, 5*(4), 109.

Sari, M., Yilmaz, E., & Kasap, T. (2023). Long-term ageing characteristics of cemented paste backfill: Usability of sand as a partial substitute of hazardous tailings. *Journal of Cleaner Production, 401*, 136723.

Shanmugasundaram, N., & Praveenkumar, S. (2021). Influence of supplementary cementitious materials, curing conditions and mixing ratios on fresh and mechanical properties of engineered cementitious composites–A review. *Construction and Building Materials, 309*, 125038.

Solak, A. M., Tenza-Abril, A. J., Saval, J. M., & García-Vera, V. E. (2018). Effects of multiple supplementary cementitious materials on workability and segregation resistance of lightweight aggregate concrete. *Sustainability, 10*(11), 4304.

Tamashiro, J. R., Kinoshita, A., Silva, L. H. P., de Paiva, F. F. G., Antunes, P. A., & Simões, R. D. (2022). Compressive resistance of concrete produced with recycled concrete aggregate and sugarcane vinasse waste-water. *Cleaner Engineering and Technology, 6*, 100362.

Tortajada, C. (2020). Contributions of recycled wastewater to clean water and sanitation Sustainable Development Goals. *NPJ Clean Water, 3*(1), 22.

Wang, L., Cheng, L., Yin, S., Yan, Z., & Zhang, X. (2023). Multiphase slurry flow regimes and its pipeline transportation of underground backfill in metal mine: Mini review. *Construction and Building Materials, 402*, 133014.

Xie, H., Ju, Y., Gao, F., Gao, M., & Zhang, R. (2017). Groundbreaking theoretical and technical conceptualization of fluidized mining of deep underground solid mineral resources. *Tunnelling and Underground Space Technology, 67*, 68–70.

Yang, J., Chen, C., Chen, S., Ren, Y., & Lu, J. (2024). Resource utilization of drinking water treatment aluminum sludge in green cementing materials: Hydration characteristics and hydration kinetics. *Journal of Environmental Sciences, 144*, 236–248.

Younis, A., Ebead, U., Suraneni, P., & Nanni, A. (2018). Fresh and hardened properties of seawater-mixed concrete. *Construction and Building Materials, 190*, 276–286.

Yu, R., & Shui, Z. (2014). Efficient reuse of the recycled construction waste cementitious materials. *Journal of Cleaner Production, 78*, 202–207.

Zhang, L., Ji, Y., Li, J., Gao, F., & Huang, G. (2019). Effect of retarders on the early hydration and mechanical properties of reactivated cementitious material. *Construction and Building Materials, 212*, 192–201.

4th International Civil Engineering & Architecture Conference
17-19 May 2025, Trabzon, Türkiye

Effect of nonlinear behavior of steel on lateral response of steel pipe piles in saturated sand

Mehmet F. Erener*[1], Tuğçe Tufan Erener[1], Ayhan Nuhoğlu[1], Devrim Ş. Erdoğan[1]

[1] *Ege University, Department of Civil Engineering, İzmir, Türkiye*

Abstract. This study aimed to investigate the lateral behavior of steel pipe piles embedded in saturated sand by considering the nonlinear behavior of both steel and soil materials. Nonlinear soil behavior was modeled using the Pressure-Dependent Multi-Yield Surface Plasticity constitutive model, while the nonlinear response of piles was represented with moment-curvature relationships. In this context, numerical simulations of 30 meter long steel pipe piles with varying section and steel grades were performed considering specified pile head displacement criteria. In addition to the nonlinear approach, simulations with linear elastic pile material were also conducted. In this way, the pile responses under both material assumptions were comparatively evaluated. Results indicated that as the pile flexural stiffness increased, the differences between linear elastic and nonlinear responses became more significant. Findings highlighted the importance and influence of incorporating nonlinear material behavior in the analysis of laterally loaded piles.

Keywords: Finite element method; Nonlinear behavior; Numerical analysis; Open Sees; Soil-pile interaction

1. Introduction

When soil conditions are inadequate in terms of bearing capacity or foundation settlements, pile foundations are the most common solution to transfer the superstructural loads to deeper soil layers, where soil properties are more generally favorable. In addition to carrying vertical loads, pile foundations also are expected to withstand the lateral forces induced by temporary or permanent events. Therefore, it is important to understand the lateral behavior of piles in terms of both pile response and soil response. In literature, numerous studies have investigated the behavior of laterally loaded piles using experimental, analytical and numerical approaches. Experimental studies are helpful observing the behavior, as they realistically capture the soil and pile conditions, especially in the full scale tests. Many researchers have investigated the lateral response of single piles in sands (Coleman, 1968; Gill, 1969; Alizadeh & Davisson, 1970; Coleman & Hancock, 1972; Bergstrom, 1974; Davis, 1977).

In addition to experimental research, significant contributions have also been made through computational studies. Reese et al. (1974) conducted a series of monotonic and cyclic lateral load tests on steel pipe piles embedded in dense sand and developed analytical relationships, known as p-y curves, between pile displacement and lateral soil reaction. Similar relationships have been widely used in analytical and numerical methods including elastic solutions, finite element method or finite difference method. Broms (1964) proposed a method to obtain the pile lateral load capacity considering the flexibility of pile. For single piles in sand, it was indicated that the ultimate lateral load which the pile can withstand was related to yielding of pile material. This approach is significant in estimation of lateral load capacity considering the nonlinear behavior of pile up to yield point of pile material. For extreme loading conditions where nonlinearity exceeds the yield point, assessment of lateral soil-pile response becomes important considering lateral load capacity and pile deformations.

In this study, emphasis was given to investigating the effects of nonlinear steel behavior on the lateral soil-pile response of steel pipe piles embedded in loose to medium-dense sand. All analyses were conducted using OpenSeesPL software. Calibration and validation procedures carried out for model and material model are elaborately presented in the following sections. Numerical simulations were performed considering both linear elastic and nonlinear pile behavior. In the scope of this study, analysis results were comparatively evaluated considering lateral response and applicability of linear elastic material was questioned.

2. Geotechnical and structural properties for numerical modeling

In this section, both geotechnical and structural parameters used in the numerical models are briefly introduced. First, the geotechnical properties of the soil profile and the parameters of the constitutive model are presented.

* Corresponding author, E-mail: fahrettinerener@gmail.com

https://doi.org/10.31462/icearc2025_ce_geo_223

Subsequently, the selection criteria for pile pipe sections and the properties of selected sections are described. Finally, the characteristics of the steel grades considered in this study are explained, along with the corresponding moment-curvature relationships of the steel sections.

2.1. Soil profile and constitutive soil model

In scope of this study, the depth of the soil profile was defined as 60 meters, corresponding to twice the pile length of 30 meters. The soil profile was hypothetically assumed to be comprised of loose to medium dense saturated sand. For this purpose, the relative density of the sand was considered as D_r = 40%. Determination of both elastic and nonlinear soil properties was derived from correlations based on relative density, overburden corrected SPT-N blow count $(N_1)_{60}$, and shear wave velocity at 1 atm, V_{S1}. The correlations used in determining the soil properties at the reference vertical effective stress level of 100 kPa; $(N_1)_{60}$ (Idriss & Boulanger, 2008), V_{S1} (Andrus & Stokoe, 2000), friction angle (ϕ) (Bowles & Guo 1996), lateral earth pressure coefficient at rest (K_0), Poisson's ratio (ν), secant deformation moduli (shear and bulk) at low shear strain level ($G_{1,max}$, $K_{1,max}$) are presented in Equation 1 to Equation 7. Parameters of both saturated mass density (ρ) and permeability (k) which were used for the constitutive model parameters were obtained from Lu et al. (2011) and Arulmoli et al. (1992).

$$D_r(\%) = 100\sqrt{\frac{(N_1)_{60}}{46}} \tag{1}$$

$$V_{S1} = 93.2\left[(N_1)_{60}\right]^{0.231} \tag{2}$$

$$\phi = 28^{\circ}(\pm 2^{\circ}) + 0.15^{\circ} D_r(\%) \tag{3}$$

$$K_0 = 1 - \sin(\phi) \tag{4}$$

$$\nu = \frac{K_0}{1+K_0} \tag{5}$$

$$G_{1,\max} = \rho V_{S1}^{\ 2} \tag{6}$$

$$K_{1,\max} = G_{1,\max}\left(\frac{2+2\nu}{3-6\nu}\right) \tag{7}$$

Pressure Dependent Multi-Yield Surface Plasticity constitutive model (Fig. 1a), which is capable of simulating the undrained behavior of saturated sand, was employed in this study. Notably, the model effectively captures the shear behavior of soils, which depends on variations in effective stress. To achieve this, a stress-dependent formulation is incorporated into the model to adjust the shear modulus with respect to the level of confinement. An important feature of the constitutive model is the inclusion of rules for both dilative and contractive behavior, allowing for a realistic simulation of the undrained response of saturated sand. These behaviors are governed by scalar functions of volumetric strain, which evolve based on the stress ratio and accumulated shear strain, as described by Yang et al. (2003). The model incorporates specific parameters, namely c_1 and d_1, that control the rates of contraction and dilation. In this way, the model enables accurate representation of volumetric tendencies under both cyclic and monotonic loading conditions. Effects of parameters on soil response are shown in Fig. 1b. Both the dilation parameter and the contraction parameter for constitutive model used in this study were adopted from Lu et al. (2011). It should be noted that the selection of soil properties was primarily based on empirical correlations and findings from previous studies.

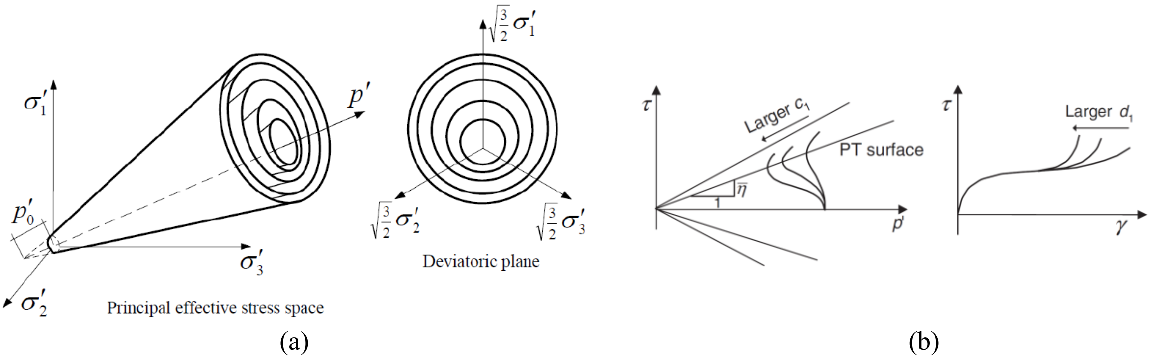

Fig. 1. Pressure Dependent Multi-Yield Surface Plasticity model: (a) multi-yield surfaces in principal stress space and corresponding deviatoric plane (Lu et al., 2011); (b) effect of dilation and contraction parameters on model response (Yang and Elgamal, 2003).

Table 1. Preliminary soil properties prior to calibration.

Soil property	Symbol	Value	Unit
Cohesion	c	0	kPa
Friction angle (triaxial conditions, $K_0 \neq 1$)	ϕ	32	Degrees
Low-strain bulk modulus at 1 atm effective stress	$K_{1,max}$	100	MPa
Low-strain shear modulus at 1 atm effective stress	$G_{1,max}$	41.5	MPa
Lateral earth pressure coefficient at rest	K_0	0.47	Unitless
Permeability	k	6.6E-5	m/s
Poisson's ratio	ν	0.32	Unitless
Reference vertical effective stress	$(\sigma'_V)_{ref}$	80	kPa
Relative density	D_r	40	Unitless
Saturated mass density	ρ	1.9	gr/cm^3
Shear wave velocity at 1 atm effective stress	V_{S1}	148	m/s
Stress dependency coefficient	m	0.5	Unitless
Contraction coefficient	c_1	0.07	Unitless
Dilation coefficient	d_1	0.40	Unitless

To ensure that the constitutive model incorporating these properties reasonably reflected the expected stress-strain behavior of the soil, a calibration process was conducted on a single soil element. This calibration was performed under the specified loading and drainage conditions as part of this study.

Geotechnical properties presented in this section are considered preliminary values prior to model calibration. The results of the calibration and the calibrated parameters are presented in the following sections. Preliminary soil properties are presented in Table 1.

2.2. Pile sections

The dimensions of the pile sections used in this study were determined in accordance with API (2000) recommendations. In order to investigate the effects of pile flexural stiffness on nonlinear behavior, three different outer diameters (D_o) were specified: 24 in (610 mm), 36 in (914 mm), and 48 in (1219 mm). The wall thickness of the tubular sections (t) was selected based on the minimum thickness criteria for driven pile installation, as specified in API (2000) (Equation 8). The D_o/t ratios calculated using Equation 8 ranged from D_o/t = 49 to D_o/t = 66 for the three different outside diameters. To maintain consistency, a constant D_o/t ratio of 50.8 was adopted. Selected dimensions of sections and corresponding section properties of piles are given in Table 2.

$$t = 6.35 + \frac{D_o}{100} \tag{8}$$

Table 2. Section properties of pile sections.

Section property	Symbol	Unit	Section: 610/12	Section: 914/18	Section: 1219/24
Outer diameter	D_o	mm	610	914	1219
Inner diameter	D_i	mm	586	878	1171
Wall thickness	t	mm	12	18	24
Area	A	m^2	0.0262	0.0507	0.0901
Moment of inertia	I	m^4	0.0012	0.0051	0.0161
Plastic section modulus	Z	m^3	0.0043	0.0145	0.0343

2.3. Characteristics of steel grades and moment-curvature relationships of sections

Steel grades used in this study were selected as S235 and S355 (EN 10025-2, 2019). The stress-strain behavior of the steel materials was defined using the governing equations (Equations 9 to 11), which account for the elastoplastic response including yield strength and strain hardening (Fig. 2). The relevant material properties for each steel grade are summarized in Table 3.

$$f_s = E_s \varepsilon_s \quad \text{for } \varepsilon_s \le \varepsilon_{sy} \tag{9}$$

$$f_s = f_{sy} \quad \text{for } \varepsilon_{sy} < \varepsilon_s \le \varepsilon_{sh} \tag{10}$$

$$f_s = f_{sy}\left[1+\left(\frac{\varepsilon_s-\varepsilon_{sh}}{\varepsilon_{su}-\varepsilon_{sh}}\right)\left(\frac{f_{su}}{f_{sy}}-1\right)\exp\left(1-\frac{\varepsilon_s-\varepsilon_{sh}}{\varepsilon_{su}-\varepsilon_{sh}}\right)\right] \quad \text{for } \varepsilon_{sh} < \varepsilon_s \le \varepsilon_{sb} \tag{11}$$

Table 3. Material properties of steel grades.

Material property	Symbol	Unit	S235	S355
Mass density	ρ_s	gr/cm^3	7.85	7.85
Elastic modulus	E_s	GPa	210	210
Shear modulus	G_s	GPa	80.8	80.8
Poisson's ratio	ν_s	Unitless	0.3	0.3
Yield strain	ε_{sy}	mm/mm	0.11%	0.17%
Yield stress	f_{sy}	MPa	235	355
Strain at onset of strain hardening	ε_{sh}	mm/mm	1.50%	1.50%
Ultimate strain capacity	ε_{su}	mm/mm	11.00%	11.00%
Ultimate stress capacity	f_{su}	MPa	360	510
Rupture strain	ε_{sb}	mm/mm	17.00%	17.00%

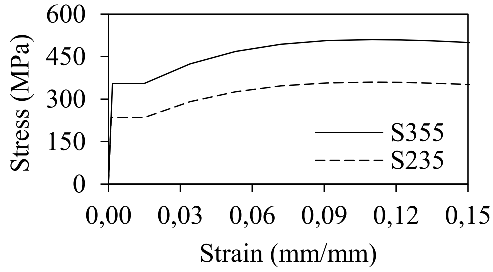

Fig. 2. Stress-strain relationships of different steel grades.

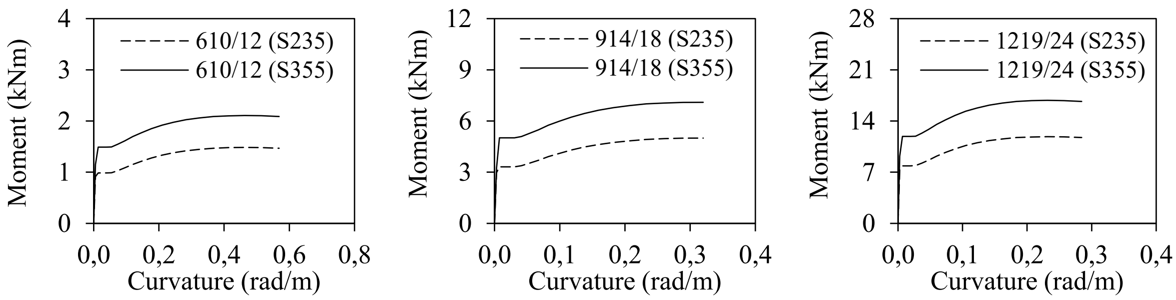

Fig. 3. Moment-curvature relationships for different sections with each steel grades.

The nonlinear behavior of piles is governed by both material and section properties. Considering this, moment-curvature relationships were utilized in this study to represent the nonlinear response of the piles. These relationships were constructed for each section based on the steel material properties and the geometric properties of sections, using both S235 and S355 steel grades (Fig. 3). It should be noted that all moment-curvature relationships were valid for piles without axial load. The effect of axial load (tension or compression) on moment-curvature and nonlinear behavior of steel was beyond the scope of this study.

3. Calibration and validation of finite element model

In this section, the calibration of a single soil element and the validation of the finite element model are presented to provide credibility to the numerical simulations. First, a soil element calibration was conducted to interpret and refine the initial soil properties in a manner that ensured consistency with the experimental results. In this context, monotonic direct simple shear (MDSS) tests performed on Nevada Sand by Arulmoli et al. (1992) under undrained loading conditions and different effective stress levels were simulated using a single soil element, and the model parameters were adjusted to reflect both the experimental stress-strain response and the corresponding stress path. Following the calibration, a full-scale lateral pile load test conducted on a steel pipe pile driven into a loose to medium-dense sand profile was simulated in the numerical model using the calibrated soil parameters. The validation of the pile load test not only confirmed the adequacy of the calibrated parameters but also allowed for the selection of both proper mesh sizes and interface element characteristics.

3.1. Single element response of soil element

The VELACS (Verification of Liquefaction Analyses by Centrifuge Studies) Project was carried out to evaluate and validate numerical and analytical methods for predicting soil behavior under earthquake-induced liquefaction (Arulmoli et al., 1992). The experimental study aimed at producing high-quality experimental data through centrifuge and laboratory testing to be used for calibration and comparison of models. In the scope of this project, MDSS tests were performed under undrained conditions on Nevada Sand with a relative density of D_r = 40%, under varying vertical effective stress levels.

Constant vertical stress was applied to the sample as it was sheared horizontally, allowing observation of pore water pressure development and stress-strain behavior. The maximum shear strain level reached in the tests was γ = 20%, reflecting large soil deformations similar to those that may be observed around laterally loaded piles under extreme displacement demands. By employing the test results under different levels of vertical effective stress, both the validity and reliability of model parameters were evaluated. In this context, the experimental results of MDSS tests conducted under vertical effective stresses of σ_v' = 80 kPa and σ_v' = 160 kPa were considered in the calibration of the soil element. Single element responses for MDSS test are illustrated in Fig. 4 and the calibrated soil properties are given in Table 4.

With the use of the preliminary soil parameters given in Table 1, it was observed that the suggested value of contraction coefficient (c_1 = 0.07) led to a stiffer shear response with respect to the soil behavior from experimental results. By adjusting the contraction coefficient (c_1 = 4.00), shear stress-shear strain responses, stress paths and porewater pressures with respect to shear strain were observed to be consistent with test results for effective stress levels which were considered in this calibration. Dilation coefficient, which was priorly suggested as d_1 = 0.40, was adjusted as d_1 = 0.38 in the calibration process. It is worth mentioning that lateral earth pressure coefficient is equal K_0 = 1 in direct simple shear conditions. Considering the stress conditions, the relationship between triaxial friction angle and direct simple shear friction angle is given in Equation 12 (Khosravifar, 2012).

$$\phi_{TXC} = \sin^{-1}\left[\frac{3\tan(\phi_{DSS})}{2\sqrt{3}+\tan(\phi_{DSS})}\right] \tag{12}$$

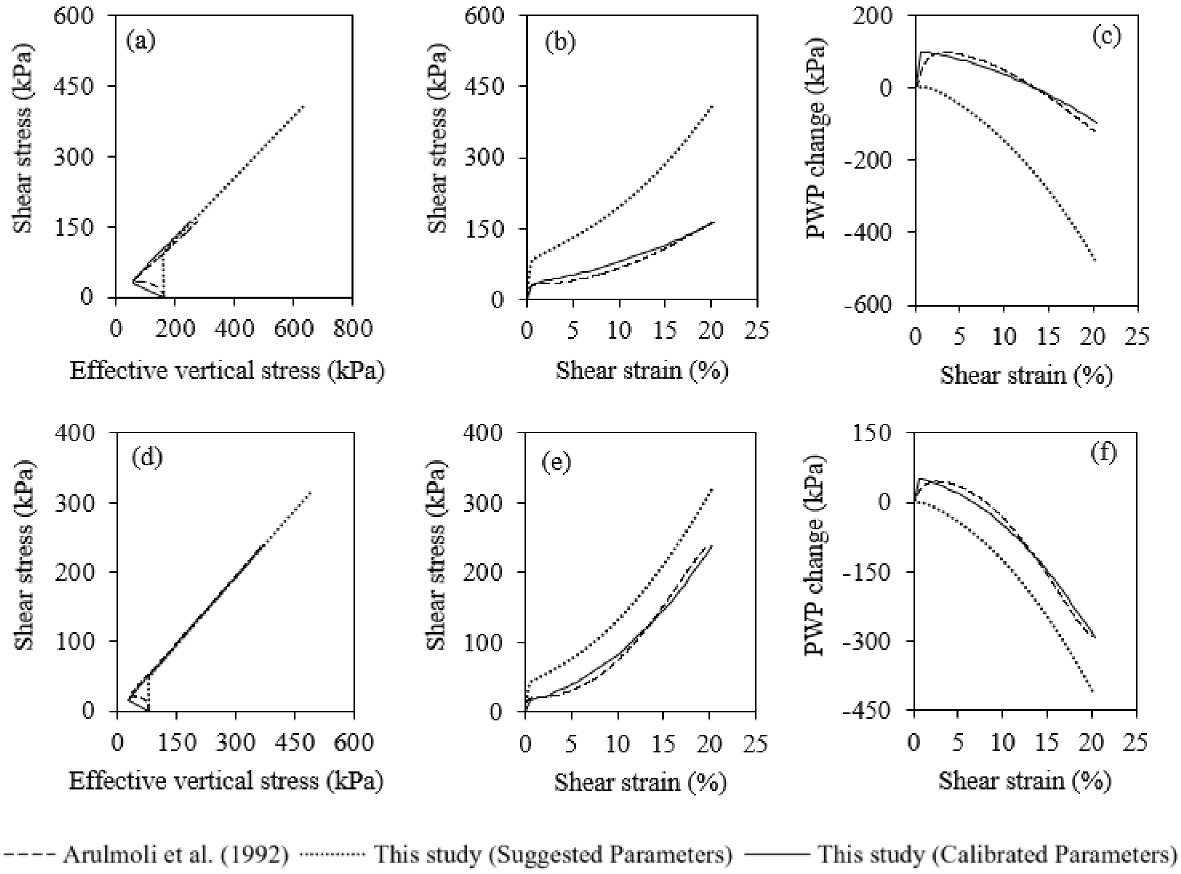

Fig. 4. Single element simulation of undrained MDSS test conducted on Nevada Sand (D_r= 40%) with suggested and calibrated model parameters: (a) Effective stress path, (b) shear stress-shear strain response and (c) porewater pressure (PWP) change for σ_v' = 160kPa; (d) Effective stress path, (e) shear stress-shear strain response and (f) porewater pressure (PWP) change for σ_v' = 80kPa (Arulmoli et al., 1992).

Table 4. Soil properties after calibration.

Soil property	Symbol	Value	Unit
Cohesion	c	0	kPa
Friction angle (triaxial conditions, $K_0 \neq 1$)	ϕ_{TXC}	32	Degrees
Friction angle (direct simple shear conditions, $K_0 = 1$)	ϕ_{DSS}	28	Degrees
Low-strain bulk modulus at 1 atm effective stress	$K_{1,max}$	100	MPa
Low-strain shear modulus at 1 atm effective stress	$G_{1,max}$	41.5	MPa
Lateral earth pressure coefficient at rest (TXC)	$K_{0,TXC}$	0.47	Unitless
Lateral earth pressure coefficient at rest (DSS)	$K_{0,DSS}$	1.00	Unitless
Permeability	k	6.6E-5	m/s
Poisson's ratio	ν	0.32	Unitless
Relative density	D_r	40	Unitless
Saturated mass density	ρ	1.9	gr/cm^3
Shear wave velocity at 1 atm effective stress	V_{S1}	148	m/s
Stress dependency coefficient	m	0.5	Unitless
Contraction coefficient	c_1	4.00	Unitless
Dilation coefficient	d_1	0.38	Unitless

3.2. Validation of finite element model

Validation of the finite element model was carried out using the results of a full-scale lateral pile load test conducted by Rollins et al. (2005) on a steel pipe pile embedded in a soil profile predominantly composed of loose to medium dense fine sand. The objective of the original experimental study was to compare the lateral responses of a full-scale pile group and a single pile, and to evaluate the accuracy of various analytical methods. In the present study, the single pile test results were utilized to validate the finite element model developed using calibrated soil parameters derived from single element simulations. In the experimental study, the single pile which is an open-ended steel pipe with an outer diameter of D_o = 324 mm and a wall thickness of t = 9.5 mm, driven to a depth of approximately 11.5 meters. The yield strength of the test pile was f_{sy} = 404.6 MPa. The displacement-controlled lateral load was applied 0.69 meters above the ground surface. Groundwater level was observed to be at 0.5 meter depth.

The numerical model was created using OpenSees PL software. As the finite element and loading conditions were symmetrical, only half of the system was modeled (Fig. 5). An interface layer was defined to simulate the relative displacement that may occur between the pile surface and the surrounding soil. This interface layer was modeled using solid elements of infinitesimally small thickness, taken as 1% of the outer diameter of the pile. The pile was modeled using beam elements over the central axis of the pile. Rigid link elements were connected to connect the centerline of the pile to adjacent nodes at a radial distance equal to the outer radius of the pile to obtain appropriate interaction with the adjacent mesh. This configuration was implemented along the depth to establish kinematic compatibility between the beam elements representing the pile and the corresponding nodes of the interface layer. The pile material was modeled with linear elastic material, while both the surrounding soil and the interface layer were modeled using the Pressure-Dependent Multi-Yield (PDMY) model. The interface angle was defined using Equation (13), and the deformation modulus of the interface layer was calibrated based on the results of the single pile load test. To reflect the influence of interface behavior, the finite element model was constructed in two configurations: one including the interface layer and one without it, and two separate simulations were carried out accordingly.

$$\phi_{\text{interface}} = 0.67\phi_{\text{soil}} \tag{13}$$

Results of numerical simulations indicated that both the model with and without the interface layer produced consistent outcomes in terms of maximum bending moment and the relationship between lateral load and pile head displacement (Fig. 6). A similar agreement was observed in the bending moment distributions along pile length corresponding to lateral load levels of P = 24 kN and P = 89 kN (Fig. 7). In terms of pile head displacements, under a lateral load of P = 89 kN, the model without the interface layer predicted a lateral displacement of y = 35 mm, whereas the experimental result indicated a displacement of y = 46 mm. This meant that the model produced a stiffer response without interface layer. When the deformation modulus of the interface layer was set equal to 5% of deformation modulus of the soil, as adjusted during the validation, the predicted pile head displacement increased to y = 42 mm under the same level of loading. Since the pile outer diameter was given as D_o = 324 mm, the observed lateral displacement corresponded to approximately $y = 0.14D_o$, which validated that the numerical simulation delivered reasonable results in modelling of observed pile behavior.

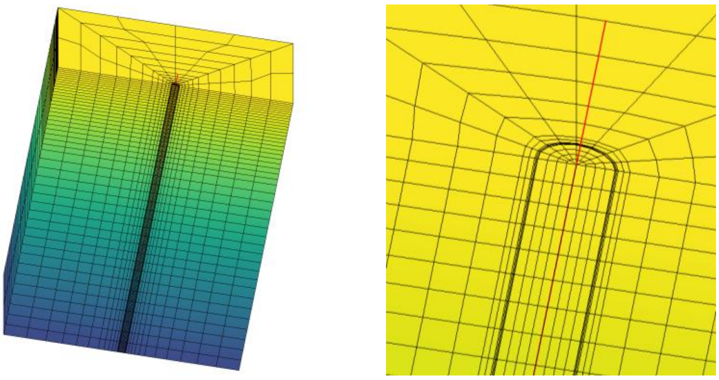

Fig. 5. Finite element model created for pile load test simulation, showing the half-model configuration (left) and finite element mesh around the pile head zone (right).

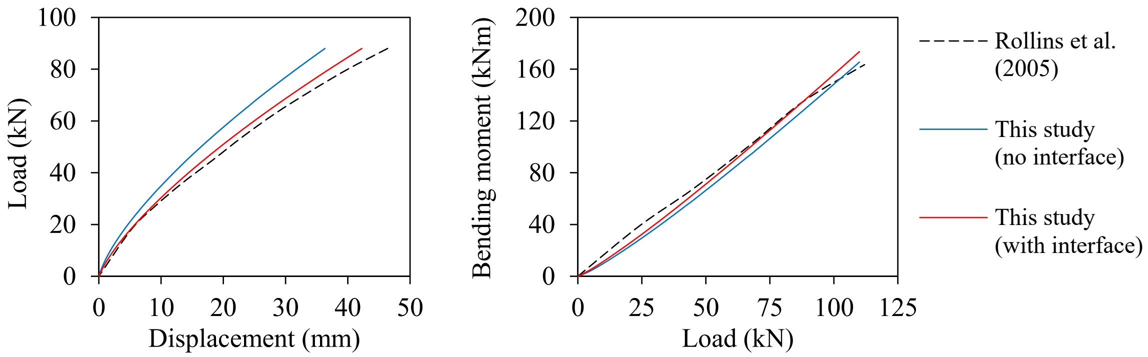

Fig. 6. Comparison of results from numerical simulations and experimental data: lateral load-displacement and lateral load-maximum bending moment relationships.

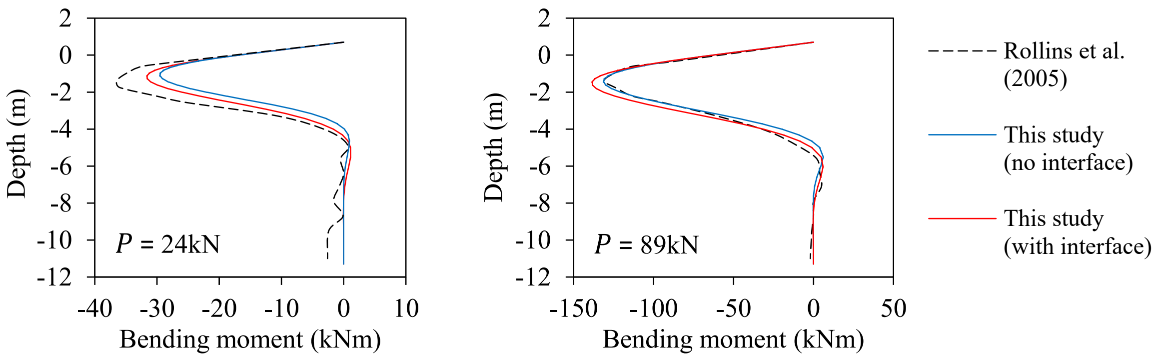

Fig. 7. Comparison of results from numerical simulations and experimental data: bending moment distribution along the pile length for lateral load levels of P = 24 kN and P = 89 kN.

4. Numerical simulations

Numerical simulations were carried out using calibrated soil parameters and interface properties derived during the validation. To assess the pile response under significant lateral deformation demands, displacement-controlled loading was applied at the pile head, with the maximum lateral displacement set to 20% of the pile outer diameter ($0.20D_0$). Three different steel pipe sections were analyzed, and the nonlinear behavior of steel was modeled using moment-curvature relationships specific to each section to capture the nonlinear flexural response under increasing lateral load. Moreover, a linear elastic material model was also assigned to the pile elements to examine the extent to which linear elastic assumption remained valid. By comparing the outcomes from both material models, the displacement range beyond which linear elastic assumption became inadequate was identified. All finite element models considered in this study are illustrated in Fig. 8. In the simulations, the results were normalized by both the pile diameter and length to eliminate the influence of pile size and to enable cross-section-independent comparisons. Normalized values for bending moment, lateral pile head load, head displacement and pile length were calculated using Equations 14 to 17.

$$M_{normalized} = \frac{M}{E_s D_o^{\,3}} \tag{14}$$

$$P_{normalized} = \frac{P}{E_s D_o^{\,2}} \tag{15}$$

$$y_{normalized} = \frac{y}{D_o} \tag{16}$$

$$L_{normalized} = \frac{z}{L} \tag{17}$$

Incremental displacement loadings were applied from the pile head level for each pile. The corresponding normalized lateral load values at the pile head, the relationship between normalized lateral load and maximum normalized bending moment, and the normalized bending moment-depth distribution obtained under a lateral displacement equal to $0.20D_0$are presented in Fig. 9. The results clearly indicated that, as the pile diameter and flexural stiffness increased, the depth at which the maximum normalized bending moment occurred at $0.20D_0$ pile head displacement shifted from approximately 8% to 18% of the total pile length, measured from the ground surface. Furthermore, the ratio of maximum normalized bending moments obtained from simulations with linear elastic assumption to those from nonlinear assumption ranged between 1.66 and 1.91 for S235-grade steel, and between 1.13 and 1.37 for S355-grade steel. It was further observed that the aforementioned ratio tended to increase as the pile flexural stiffness increased. In terms of maximum normalized pile head loads corresponding to a pile head displacement equal to 20% of the outer diameter, ratio between linear elastic behavior to nonlinear behavior was obtained as approximately 1.27 for all piles with S235 grade and 1.13 for all piles with S355 grade.

Lastly, it is worth mentioning that differences between linear elastic and nonlinear responses became evident beyond a normalized lateral pile head load of approximately $P_{normalized}$ = 11 for S235-grade steel and $P_{normalized}$ = 13 for S355-grade steel, for all pile sections. These findings emphasize the importance of incorporating nonlinear steel behavior in the analysis of laterally loaded piles. It is also highlighted that identifying the displacement and lateral load thresholds at which the linear elastic material assumption remains valid is essential for ensuring accurate and reliable estimations.

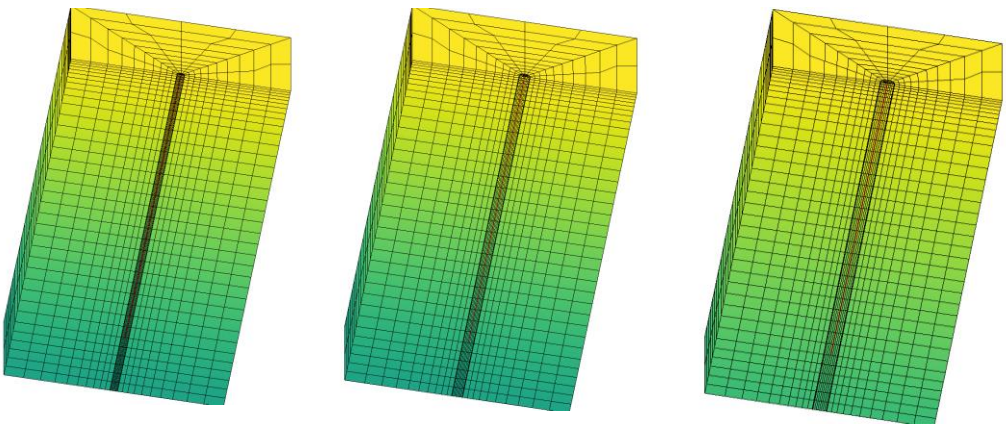

Fig. 8. Finite element models for numerical simulation of lateral pile load test: model for 610/12 pile (left), model for 914/18 pile (middle) and model for 1219/24 pile (right).

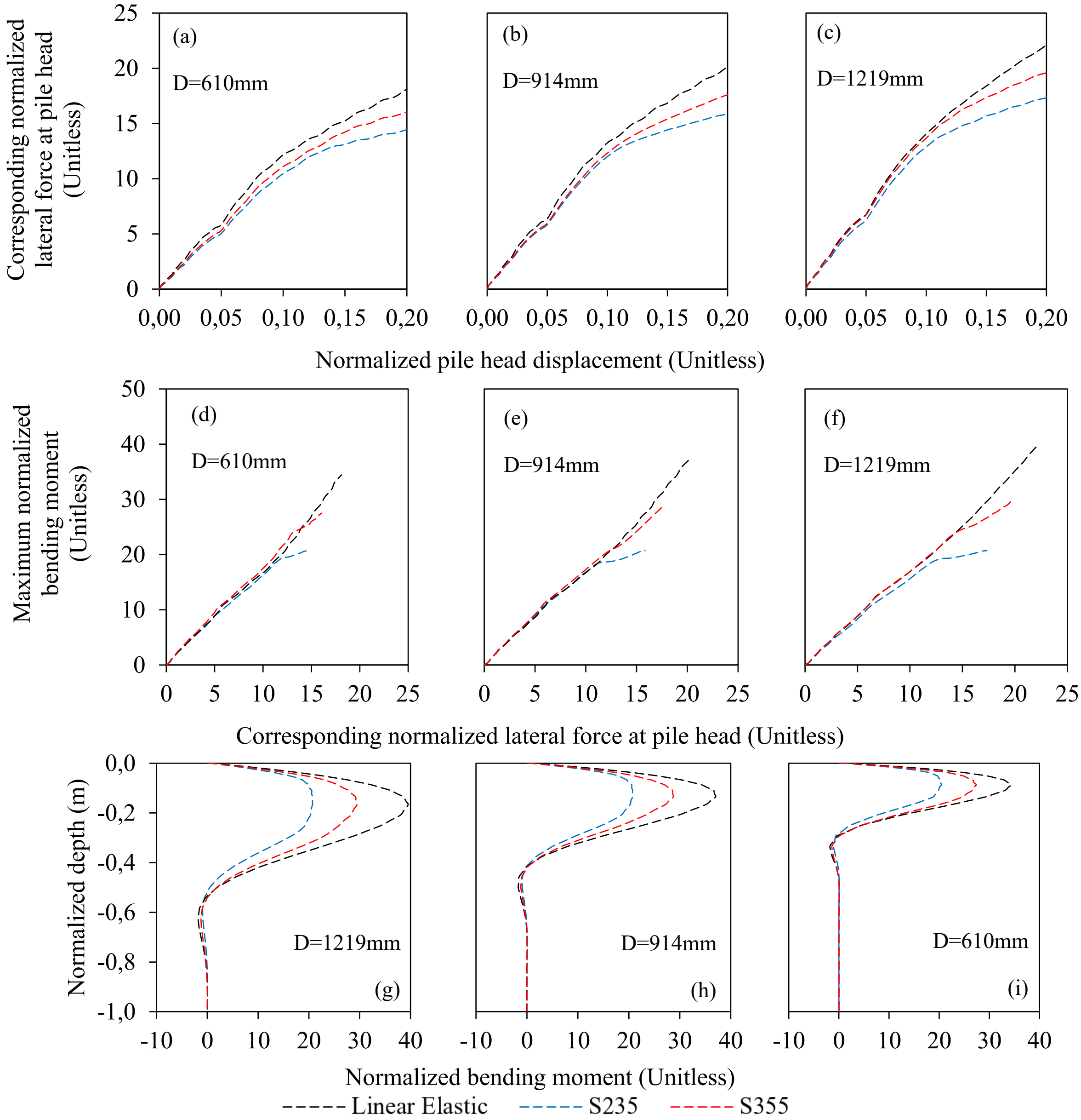

Fig. 9. Normalized displacement-lateral load relationships (a, b, c), lateral load-bending moment responses (d, e, f) and bending moment distribution along depth for the lateral pile head displacement equal to $0.20D_0$ (g, h, i) for different pile sections and materials.

5. Conclusions

This study presented a comprehensive numerical investigation of lateral behavior of steel pipe piles installed in loose to medium-dense sand with focus on the imposed lateral load at the pile head level. Numerical simulations based on PDMY soil model and moment-curvature relationships were implemented using OpenSeesPL software to simulate the nonlinear behavior of the steel piles. The study included extensive soil model calibration and validation of the finite element model with experimental data from the available literature.

The results revealed that the use of linear elastic material for piles led to a significantly stiffer pile response compared to nonlinear pile behavior, considering the steel grades used in this study. The maximum normalized bending moment ratios between linear elastic and nonlinear behavior ranged from 1.66 to 1.97 for S235-grade steel piles, and from 1.13 to 1.37 for S355-grade steel piles. These ratios were found to decrease with increasing yield strength. Moreover, as the flexural stiffness of pile increased, the ratio tended to increase as a result of stiff response of linear elastic behavior. Finally, it was found that the difference between linear elastic and nonlinear responses became particularly evident beyond normalized pile head load thresholds of $P_{normalized}$ = 11 for S235 and $P_{normalized}$ = 13 for S355 steel grades, regardless of flexural stiffness. The findings highlighted both the necessity to account for nonlinear steel behavior in the analysis of laterally loaded piles and the necessity to find the limits for pile head displacement and lateral pile head load up to which the linear elastic assumption was valid.

It should be mentioned that the conclusions drawn from this study are valid only within the limits of the pile lengths, cross-sectional characteristics, steel grades, and soil conditions employed. The conclusions are valid only under the assumed conditions, and it is not recommended to extrapolate the same beyond these specified parameters. For enhancing the validity and reliability of the conclusions, field tests and physical model tests are recommended for future studies. Additionally, to confirm the consistency of the observed trends, additional studies involving various soil profiles and pile geometries are recommended.

References

Alizadeh, M., & Davisson, M. T. (1970). Lateral load tests on piles-Arkansas River project. *Journal of the Soil Mechanics and Foundations Division*, *96*(5), 1583-1604.

Andrus, R. D., & Stokoe II, K. H. (2000). Liquefaction resistance of soils from shear-wave velocity. *Journal of geotechnical and geoenvironmental engineering*, *126*(11), 1015-1025.

API. (2000), *Recommended practice for planning, designing and constructing fixed offshore platforms working stress design*, American Petroleum Institute

Arulmoli, K., Muraleetharan, K. K., Hossain, M. M., & Fruth, L. S. (1992). *VELACS laboratory testing program-Soil data report*. The Earth Technology Corporation, NSF, Washington, D.C.

Bergstrom, R. N. (1974). *Pile testing analyses, Bailly Generating Station, Nuclear 1* (Report SL-3109). Sargent and Lundy Engineers.

Bowles, J. E., & Guo, Y. (1996). *Foundation analysis and design* (Vol. 5, p. 127). New York: McGraw-hill.

Broms, B. B. (1964). Lateral resistance of piles in cohesionless soils. *Journal of the Soil Mechanics and* Foundations Division, 90(3), 123–156.

Coleman, R. B. (1968). *Apapa road Ijora causeway reconstruction: Report on horizontal load tests on piles*. Federal Ministry of Works and Housing, Ijora, Lagos, Nigeria.

Coleman, R. B., & Hancock, T. G. (1972). The behavior of laterally loaded piles. In *Proceedings of the Fifth European Conference on Soil Mechanics and Foundation Engineering* (Vol. 1, pp. 339–345). Madrid.

Davis, L. H. (1977). *Tubular steel foundation* (Test Report RD-1517). Florida Power and Light Company.

European Committee for Standardization. (2019). *EN 10025-2: Hot rolled products of structural steels – Part 2: Technical delivery conditions for non-alloy structural steels*. Brussels, Belgium: CEN.

Gill, H. L. (1969). Soil–pile interaction under lateral loading. In *II Conference on In-Situ Testing of Soils and Rocks* (pp. 141–147). London.

Idriss, I. M., and Boulanger, R. W. (2008). *Soil liquefaction during earthquakes*. Monograph 555 MNO-12, Earthquake Engineering Research Institute, Oakland, CA, 261 pp.

Khosravifar, A. (2012). *Analysis and design for inelastic structural response of extended pile shaft foundations in laterally spreading ground during earthquakes*, PhD Thesis, University of California, Davis.

Lu, J., Elgamal, A., and Yang, Z. (2011). OpenSeesPL: 3D lateral pile-ground interaction user manual (Beta 1.0). *Department of Structural Engineering, University of California, San Diego*, 147.

Reese, L. C., Cox, W. R., & Koop, F. D. (1974, May). Analysis of laterally loaded piles in sand. In *Offshore Technology Conference* (pp. OTC-2080). OTC.

Rollins, K. M., Lane, J. D., & Gerber, T. M. (2005). Measured and computed lateral response of a pile group in sand. *Journal of Geotechnical and Geoenvironmental Engineering*, *131*(1), 103–114.

Yang, Z., & Elgamal, A. (2003). Application of unconstrained optimization and sensitivity analysis to calibration of a soil constitutive model. *International Journal for Numerical and Analytical Methods in Geomechanics*, *27*(15), 1277–1297.

Yang, Z., Elgamal, A., & Parra, E. (2003). Computational model for cyclic mobility and associated shear deformation. *Journal of Geotechnical and Geoenvironmental Engineering*, *129*(12), 1119–1127.

4th International Civil Engineering & Architecture Conference
17-19 May 2025, Trabzon, Türkiye

Sustainable materials for ground improvement: Hemp

Beyza Hu*[1], Arife Şimşek[2], Gökhan Demir[1]

[1] Ondokuzmayıs University, Department of Civil Engineering, 55100 Samsun, Türkiye
[2] Ondokuzmayıs University, Hemp Research Institute, 55100,Samsun, Türkiye

Abstract: In Civil Engineering, it is very important that structures are built on geotechnically suitable soils. However, it is not always possible to find a soil with suitable properties due to the increasing population and decreasing usage areas. Therefore, it is an important need to carry out improvement works on problematic soils with low bearing capacity, low swelling-settling resistance, high permeability and insufficient engineering properties. If stabilisation is not provided in such problematic soils, great material and moral losses may occur. Although commonly used remediation methods increase safety, due to their high cost and negative effects on the environment, alternative methods that are economical and leave a low carbon footprint have started to be sought. It is known that carbon footprint has significant environmental impacts such as climate change and resource depletion. Therefore, it has become a very important issue to reduce the carbon footprint in the construction sector and to turn to natural resources with lower environmental impacts. Hemp fibre can be an alternative in this regard. Thanks to the fact that hemp is a natural and sustainable additive material with low carbon emissions, both an environmentally friendly and economical solution can be obtained. The use of hemp fibre can not only improve soil stabilisation, but also contribute to sustainable construction practices. . Furthermore, hemp's carbon sequestration capabilities, rapid growth process, low water demand and insulating properties minimise environmental negative impacts. In the future, natural materials such as hemp fibre are expected to be more widely used in ground improvement processes. In this way, both engineering and environmentally efficient, cost-effective and sustainable construction may become possible.

Keywords: Natural fibers; Geotechnics; Hemp; Ground improvement

1. Introduction

In civil engineering, it is very important that the structures can serve safely. In order to avoid loss of life and property, especially when a natural event such as an earthquake occurs, buildings should be built on the right ground, with materials in accordance with quality standards, designed in accordance with engineering calculations and regularly inspected.

It is very important to find the appropriate ground for the structure to be built (Zardari et al.,2021). When the building is built on a wrong ground, negativities such as collapse, swelling, liquefaction, slipping may occur on the ground. This may cause the structure to topple, collapse, collapse, damage the carrier system or completely collapse in a disaster such as an earthquake, causing great loss of life and property. In order to avoid losses, the ground must be selected correctly. However, it is not always possible to find the right and suitable ground. Especially in today's conditions, it has become very difficult to find ground with suitable engineering properties due to the increase in population, increase in construction and decrease in the areas allocated for construction (Kebe, 2023). For this reason, it has gained importance in civil engineering applications to make use of the existing areas, to improve and stabilise the soil properties with some studies and to make them suitable for construction. However, there are some disadvantages in these applications. Examples can be given as follows;

- High cost of implementation,
- Additives can enter the groundwater and impair water quality,
- Toxic gases may be released,
- May cause air pollution,
- Vibrations can disrupt the underground ecosystem.

These kinds of negativities cause great damage to the environment. Preventing environmental damage and reducing costs economically has made it necessary to search for alternative improvement methods. In order for these alternative methods to be low carbon footprint applications, it is necessary to use natural materials or to recycle and utilise existing wastes that harm the environment (Zardari et al.,2021)

* Corresponding author, E-mail: beyzahu55@gmail.com

https://doi.org/10.31462/icearc2025_ce_geo_268

This research was completed by reviewing theses and articles on ground improvement studies with hemp fibres. The main objective of the studies is to provide an environmentally friendly alternative to traditional stabilisation methods. In this context, clay soils with poor bearing capacity were evaluated by reinforcing with hemp fibres.

The effect of factors such as type, mechanical properties, roughness, amount and length of hemp fibres on the data were investigated.

In addition, these studies address the history, benefits and applications of natural and synthetic fibres in soil reinforcement. Literature reviews indicate that fibre reinforced soils are a low cost and environmentally advantageous stabilisation technique. It has been found that the addition of natural and synthetic fibres increases the California bearing ratio (CBR) and free compressive strength values, and decreases the plasticity index and volume change (Vitoşoğlu & Şengül,2023)

In short, this study aims to guide geotechnical and transportation engineers in stabilising soils with low bearing capacity with natural and synthetic fibres.

2. What is ground improvement?

All structures are built on or in the ground. Loads are transferred to the ground by the constructed structures and the ground is expected to be able to safely carry these loads. However, not all soils have the same bearing capacity. In such a case, ground improvement is used.

As a result of the increase in population and rapid urbanisation, it has become necessary to use soils that do not have suitable engineering properties for the construction of buildings. The soils encountered may have problems such as insufficient bearing capacity, settlement, swelling and liquefaction. In such soils, ground improvement methods are used to ensure that the structures are safe, durable and serviceable in the long term (Kebe, 2023)

Soil improvement methods are generally in the form of techniques to improve the mechanical, physical, hydraulic and chemical properties of the soil.

3. Ground improvement methods

3.1. Chemical improvement methods

These are the techniques of changing soil properties by chemical reactions.

- Chemical Stabilisation: It is the process of increasing the strength by mixing binding materials such as lime, cement, fly ash, silica fume into the soil.
- Injection Techniques: It is the process of strengthening the ground by using mortar, chemical solutions or polyurethane injections in low strength soils.
- Ion Exchange: Plasticity and swelling potential of clay soils are reduced by ion exchange.

3.2. Mechanical improvement methods

Methods that improve the organisation, compaction and strength of soil particles.

- Laying (Additional Layers): It is the process of spreading the load over a large area by laying fill, geosynthetic materials or concrete on weak soils.
- Compaction: It is the process of increasing the density of the soil by compacting it with machines such as cylinders, vibratory compactors and rammers.
- Consolidation: It is the process of accelerating the settlement process that will occur over time by removing water from the ground with preloading or drainage systems.
- Deep Mixing: It is the application of mechanical and chemical improvement techniques together by injecting cement or binder materials into the ground.

3.3. Thermal improvement methods

These are the methods based on changing the physical and mechanical properties of the soil by using heating or cooling processes.

- Geothermal Heating: In frozen ground, pipes are placed in the ground. Hot water or steam is passed through the pipes. The heated ground softens, thus facilitating the excavation or compaction of the ground.
- Freezing-Thawing: This method is based on controlled freezing or thawing of the ground. In water-saturated soils, the ground freezes and works like a barrier, which creates an impermeable barrier and provides support in the excavation area. Multiple freezing and thawing of the ground is used to make hard soils brittle and loose to facilitate excavation.
- Thermal Shock: It is stabilised by changing the soil structure with sudden temperature changes. The ground is first heated by flame or hot steam and then cooled rapidly. As a result of this sudden temperature change, the ground cracks or becomes more brittle. It is used to facilitate excavation operations on soils such as high strength, rock and hard soil.

3.4. Physical improvement methods

- Shock Loading: Compacting soil using dynamic compaction techniques.
- Vibratory Compaction: Applying vibrations to enhance soil particle arrengement.
- Blasting: Using controlled explosions to densify loose soils.
- Electrokinetic Methods: Using electric currents to facilitate drainage and compaction (Çukurova Üniversitesi, 2015).

3. Materials used in soil improvement

Various materials are used in soil improvement, especially in soil improvement using additives. Soil improvement usually includes additives that are categorized as synthetic or natural materials (Hannura, 2024)

4.1. Synthetic additivies

These substances are usually chemical or polymer based and can change the properties of the soil (Gül, 2024)

- Polymers: They can be in the form of Polypropylene (PP), Polyurethane (PU), Polyethylene (PE), Epoxy resins. They have structures that provide elasticity to the soil. They provide elasticity and durability to the soil.
- Geosynthetic Materials: Geotextiles, geogrids, geonets and geomembranes, which are frequently used in improvement, provide soil stabilization, resistance, waterproofing and filtration.
- Chemical Stabilizers: Cationic Polymers, Sodium Silicates, Asphalt Emulsions are examples of chemical stabilizers. These substances are used to harden the soil and reduce water permeability.
- Inorganic Binders: They are inorganic materials such as fly ash, silica fume, slag. These materials chemically react with cement and other binders in the soil and increase the strength and durability of the soil.
- Nano Materials: Special additives developed to strengthen the bonds between soil particles. Requires advanced technology.

4.2. Natural additives:

- Lime: Increases plasticity and durability, especially in soils with high clay content.
- Cement: Increases soil strength, combines with water and becomes rigid.
- Clay Minerals: Used to increase the stability and durability of Bentonite and Kaolin minerals, even if only for a short time.
- Sand and gravel: Used to store compactness and stability in loose soils.
- Volcanic Ashes: Pozzolans, which are volcanic substances, are used to react with lime or cement and cause deterioration.
- Organic Fibers: Used in organic fiber methods such as straw and coconut fiber. It is used for general purposes such as swelling, shrinkage, cracking reduction, increasing the strength of the soil, and preventing fragments.

4. Hemp fibres

Hemp fibres are another example of organic fibres with a natural and durable structure. Like other fibres, studies have shown that it prevents swelling and cracking of floors, reduces strength and prevents erosion.

Hemp fibres are attracting attention as a natural and environmentally friendly reinforcement material for floor improvement. Various academic studies show how hemp fibres improve the technical properties of floors. In most of the studies, hemp fibres have been added to the soil in certain proportions and some experiments have been carried out on doped soil samples. These experiments are designed to test the strength, basic parameters and bearing capacity of the soil, such as the free compression test, the triaxial compression test and the California Bearing Ratio (CBR). As a result of all these experiments, it has been observed that there is an improvement in the parameters of the ground (Akyol, 2022). In some of the studies, hemp geotextiles were made and the soil was covered with geotextiles, which increased the strength of the soil and improved the angle of internal friction.

Hemp fibres can also be used in civil engineering applications other than soil improvement. For example, these fibres can be used as additives in building materials. In the studies carried out, hemp fibres were used as an additive and insulating material in concrete.

The use of hemp mixed with lime and water as a concrete additive has been called hemp concrete. Hemp concrete is lighter and more insulating than other doped concretes. In addition, it stores CO_2 thanks to its CO_2-absorbing property and is emerging as a sustainable and environmentally friendly option with a low carbon footprint. This environmentally friendly application can be used not only in buildings, but also in concrete roads and infrastructure.

6. Conclusion

The results of all the studies conducted and described above show that hemp fibres are an effective additive material in soil improvement projects. Hemp fibres will increase the strength of the soil, reduce deformations and improve the weak soil. As these applications become more widespread, buildings will be constructed on reinforced soils that are both safer and more environmentally friendly, reducing the carbon footprint and improving the soil economically using sustainable methods.

References

Akyol, M. (2022). *Soil improvement with waste bone powder* (Master's thesis). Çukurova University, Institute of Science, Department of Civil Engineering, Adana.

Barbhuiya, S., & Das, B. B. (2022). A comprehensive review on the use of hemp in concrete. *Construction and Building Materials, 34*.

Gül, G. (2024). *Effect of calcination of Bayburt stone waste on strength and durability in clay soil stabilization* (Master's thesis). Bayburt University, Department of Civil Engineering, Bayburt.

Hannura, M. (2024, February). *Investigation of the effect of glass fiber additives on geotechnical properties of clay soils* (Master's thesis). Dicle University, Institute of Science, Department of Soil Mechanics and Geotechnical Engineering, Diyarbakır.

Kebe, A. (2023). *Soil improvement with marble dust and cement in fine sand soils* (Master's thesis). Bursa Uludağ University, Institute of Science, Department of Civil Engineering, Bursa.

Vitoşoğlu, Y., & Şengül, T. (2023). Improvement of engineering properties of soils using natural and synthetic fibers. In M. İ. Onur (Ed.), *Innovative research in geotechnical engineering* (Vol. 9, pp. 167–215). Özgür Publications.

Zardari, S., Shahkar, A., & Dadras, P. (2021). Determination of shear strength of FRP fiber reinforced silty sand using large scale direct shear box test. *Bursa Uludağ University Faculty of Engineering Journal, 26*(3).

4th International Civil Engineering & Architecture Conference
17-19 May 2025, Trabzon, Türkiye

Investigation of the filtration properties of waste concrete obtained from a university campus roadway renovation

Ahmet Benli*[1], Emirhan Sengun[1], Erdem Yolcu[1], Mehmet H. Calım[1], Rümeysa Usta[1], Sabriye B. Ikizler[1], Asli Y. Dayioglu[2], Mustafa Hatipoglu[2]

[1] *Karadeniz Technical University, Department of Civil Engineering, 61080 Trabzon, Türkiye*
[2] *Istanbul Technical University, Department of Civil Engineering, 34469 Istanbul, Türkiye*

Abstract. Increasing global demand for natural construction materials has highlighted the urgent need for sustainable solutions that prioritize the reuse of waste materials, reduce environmental impact, and conserve natural resources. In line with these objectives, this study investigates the long-term filtration performance of Recycled Concrete Aggregate (RCA) obtained from a concrete road as part of a road renewal project at Karadeniz Technical University for its potential use as a filtration material in under-road drainage systems. RCA, derived from the renovation works, was tested in an improved and remanufactured ASTM D5101 standard test system. This system has features enhancements such as increased sample dimensions (diameter and height from 10 cm to 15 cm) and additional manometer ports (from 6 to 8). Notably, experiments conducted under low hydraulic gradient, results closer to real field conditions and pioneering innovation in filtration performance research. The study evaluated the clogging behavior of the RCA-geotextile system caused by water flow using key parameters such as gradient ratio (GR) and permeability ratio (KR). The results demonstrated that RCA exhibited filtration performance comparable to natural filter materials at an acceptable level. The innovative reuse of RCA not only provides a functional filtration material but also contributes significantly to the principles of sustainability by reducing construction waste and minimizing reliance on natural resources.

Keywords: Recycled aggregate; Geotextile; Long-term filtration; Sustainability.

1. Introduction

Advancements in construction technology and rapid urbanization have significantly increased the volume of construction and demolition waste (C&DW), posing a major challenge to environmental sustainability (Hassan et al., 2022). Annually, the construction sector generates 333 million tons of waste in Europe, 534 million tons in the United States, and 1.13 billion tons in China (Menegaki & Damigos, 2018). This large-scale waste production, especially in developing countries, exacerbates environmental risks such as toxic effects on freshwater ecosystems, soil acidification, and eutrophication due to nutrient accumulation, ultimately threatening ecosystem health and human well-being (Ferronato et al., 2023).

In this context, the recycling of construction waste is considered a key strategy in achieving environmental sustainability goals.Government policies promoting the recycling of construction waste are crucial in mitigating environmental issues (Menegaki & Damigos, 2018). Recycled concrete aggregate (RCA) offers significant advantages over natural aggregates (NA) due to its widespread availability and cost-effectiveness. Notably, RCA demonstrates performance characteristics closest to natural aggregates among recycled aggregates (C&D Waste), making it a promising material for sub-surface drainage systems in road construction.

Sub-surface drainage systems play a vital role in efficiently discharging water infiltrating the pavement structure and subgrade. Various types of surface water drainage systems are utilized, with pipe drains being among the most commonly preferred solutions. In these systems, geotextiles and aggregates are used together, where the geotextile prevents the passage of foreign particles while allowing water to pass through, effectively mitigating the risk of piping in the soil. However, drainage system clogging can lead to water accumulation within pavement layers, reducing the soil's load-bearing capacity and causing premature fatigue cracking (Haider & Chatti, 2009). This not only shortens the service life of roadways but also increases maintenance costs, resulting in economic losses. The hydraulic efficiency of the system largely depends on the particle size distribution and permeability coefficient of the aggregate. The tendency of fine particles to clog geotextile pores during filtration is a critical

*Corresponding author, E-mail: ahmetbenli61@gmail.com

https://doi.org/10.31462/icearc2025_ce_geo_275

factor in determining the long-term performance of drainage systems (Palmeira & Gardoni, 2000; Bayın Sarıahmetoğlu et al., 2021).

Despite numerous studies on RCA in drainage applications, limited research has focused on its long-term clogging behavior under low hydraulic gradients, which is more representative of real-world conditions. This study addresses a gap in the literature by examining the long-term clogging behavior of RCA obtained from a concrete roadway rather than general RCA applications. Unlike previous studies, the RCA used in this research was obtained from a road pavement as part of a road renewal project, offering a novel contribution to the evaluation of its filtration performance in subsurface drainage systems.

This study evaluates the filtration performance of recycled pavement concrete aggregate (RRCA) sourced from concrete waste arising from Karadeniz Technical University's road renewal works. A modified test setup based on the ASTM D5101 standard was used to analyze the clogging performance of a drainage system incorporating RCA and nonwoven polypropylene geotextile, a commonly used material in drainage applications. The enhanced ASTM D5101 test system features increased specimen diameter and height, along with an increased number of manometer ports, allowing for more precise and reliable measurements (ASTM International, 2021). Consequently, the long-term filtration performance of the RRCA-geotextile system under low hydraulic gradient was assessed with greater accuracy and detail. The study examines whether the clogging parameters remain below the upper limits defined in the standards. Additionally, a distinguishing aspect of this study is that the concrete source used for RRCA is from a local institution's road waste, emphasizing its relevance to regional waste management and sustainability efforts.The experiments focused on analyzing the clogging tendencies and filtration performance of RRCA and geotextile combinations over time. Instead of high hydraulic gradients, which are known to accelerate geotextile clogging in perforated pipe drains (French drains), this study concentrated on low hydraulic gradient conditions that align more closely with real-world highway drainage designs (Bayın Sarıahmetoğlu et al., 2021). Previous research indicates that high hydraulic gradients in subsurface drainage can worsen geotextile clogging (Pak & Zahmatkesh, n.d.), whereas the low-gradient drainage designs commonly adopted in highway engineering provide more practical and reliable performance.

In this context, the recycling of construction and demolition waste (C&DW) for engineering applications is considered an effective approach to promoting environmental sustainability. This study examines the performance of recycled road concrete aggregate (RRCA) in drainage systems, specifically evaluating key parameters such as permeability, clogging potential, and filtration efficiency of RRCA-geotextile systems under varying hydraulic conditions. By ensuring that clogging parameters remain within standard limits, this research offers valuable insights into the long-term viability of RRCA in practical engineering applications.

2. Meterials and methods

In the modified ASTM D5101 test system, Recycled Concrete Aggregate (RCA), obtained from a concrete pavement that had reached the end of its service life within the Karadeniz Technical University campus, was utilized together with a nonwoven geotextile. These materials were selected for their potential application in the design and implementation of sustainable drainage systems. The use of RCA contributes to the reutilization of construction and demolition waste, promoting environmental sustainability and resource efficiency.

2.1. Recycled concrete aggregate (RCA)

The RCA used in this study was subjected to a series of tests within the framework of the modified ASTM D5101 test in order to characterize its geotechnical properties, which are critical for drainage applications. the material was processed and analyzed through a set of standardized geotechnical laboratory tests, including pycnometer test, standard proctor compaction test (in accordance with ASTM D698-12). These tests provided data on the particle size distribution, specific gravity, compaction of the RCA.

The mix design of the sample was designed to represent the most unfavorable condition (within the Turkish standard), with the objective of inducing maximum clogging.To achieve the targeted particle size distribution for the study, the materials obtained were processed using a jaw crusher. The resulting aggregate was then prepared to match the gradation outlined in the experimental design. The images of the obtained recycled concrete aggregate are presented in Fig 1.

Fig. 1. The RCA sample was prepared in accordance with the specified gradation.

The pycnometer test was conducted to determine the specific gravity of soil or aggregate particles. The specific gravity of the material plays a crucial role in evaluating its volumetric properties and in calculating other geotechnical parameters. In addition, the Proctor test was employed to determine the mechanical properties of the RRCA specifically to identify its maximum dry density and optimum moisture content. These parameters are essential for understanding the compaction behavior of the RCA and assessing its suitability for use in drainage systems. The specific gravity values obtained from the pycnometer test and the optimum moisture contents and maximum dry density obtained from the Proctor test are presented in Table 1, Equation 1. and Table 2 accordingly.

$$\rho_s = \rho_w \frac{M_2 - M_1}{(M_4 - M_{1)} - (M_3 - M_2)} 2.645 g/cm^3 \quad (1)$$

Table 1. Pycnometer Test Results

Tare (M_1)	Tare+dry soil (M_2)	Tare+dry soil+water (M_3)	Tare+water (M_4)
37.9 g	81.8	166.9	139.6

Table 2. Properties of RRCA

Gs	w_{opt} (%)	MDD (kN/m^3)
2.645	16.1	16.66

*Gs: Specific gravity, w_{opt}: Optimum moisture content, MDD: Maximum dry density

2.2. Geotextile

Geotextile materials used together with aggregates are widely preferred engineering solutions for building efficient and sustainable drainage systems. In these systems, the geotextile's filtration capacity is the main factor that affects the overall filtration performance. Therefore, selecting a suitable geotextile material is very important for the effective operation of the drainage system. Choosing the right type of geotextile helps achieve satisfactory filtration by preventing the movement of fine soil particles while allowing water to pass through, thus maintaining the stability of the system. Nonwoven geotextiles are generally preferred in filtration applications, as they offer both technically and economically efficient solutions. The geotextile used in the study is presented in Fig 2.

Fig. 2. Geotextile

Table 3. Properties of geotextile

Properties	Unit	Test Standard	GT 1
Mass per Unit Area	g/m^2	ASTM D 5261 (2018)	123
Thickness (at 2kPa)	mm	ASTM D 5199	1.3
Tensile Strength (MD- CMD)	kN/m	ASTM D 4632	-
Elongation at Break (MD-CMD)	%	ASTM D 4632 (2023)	min. 50
Static Puncture Resistance	N	ASTM D 6241 (2022)	1800
Permittivity (1/s)	mm	ASTM D 4491 (2022)	110
Characteristic Opening Size	l/(s·m^2)	ASTM D 4751 (2021)	0.3

2.3. Methods

In order to evaluate the long-term filtration performance of the recycled concrete aggregate (RRCA) obtained from a concrete pavement located within the university campus, a three-stage particle size reduction process was applied. In the first stage, concrete debris was broken down into approximately 8–10 cm pieces using a demolition hammer. In the second stage, the material was further reduced to particle sizes ranging from 1 to 3 cm using a jaw crusher. Finally, in the third stage, the aggregates were processed into suitable sizes for sieve analysis (Fig 3-4). The samples were then prepared following the mix ratios provided in the Table 4.

Table 4. Material percentages to be used according sieve numbers

Sieve No.	10	18	30	40	50	70	100	Pan
% Quantity	10	15	9	14	13	19	10	10

Fig. 3. Three-stage particle size reduction

Fig. 4. Jaw crusher and grinding machine

The test apparatus was redesigned in accordance with the ASTM D5101 standard and includes various innovative features that distinguish it from those used in previous studies. Modifications such as increasing the sample diameter and height, as well as adding additional manometer ports, allowed for more comprehensive and precise measurements under conditions more representative of the field (Fig. 5).

The developed system enabled the measurement of both the permeability coefficient of the RCA material alone and the overall permeability coefficient of the system composed of RCA and geotextile under different hydraulic gradients. Furthermore, it allowed for the determination of key hydraulic parameters such as the gradient ratio (GR) and the permeability ratio (KR).

Unlike the standard ASTM D5101 procedure, the experiments in this study were designed to evaluate the long-term clogging performance of the material. The specimens were kept in the test system for approximately six months, during which clogging-related parameters were monitored. The experiments were continued until an ideal hydraulic gradient and permeability ratio were achieved. At the end of the testing period, to determine the amount of fine particles that had been displaced, the sample was carefully removed and reanalyzed using sieve analysis.

Measurements obtained from manometers installed at different heights were utilized in Equations (2) through (5) to determine the GR values.

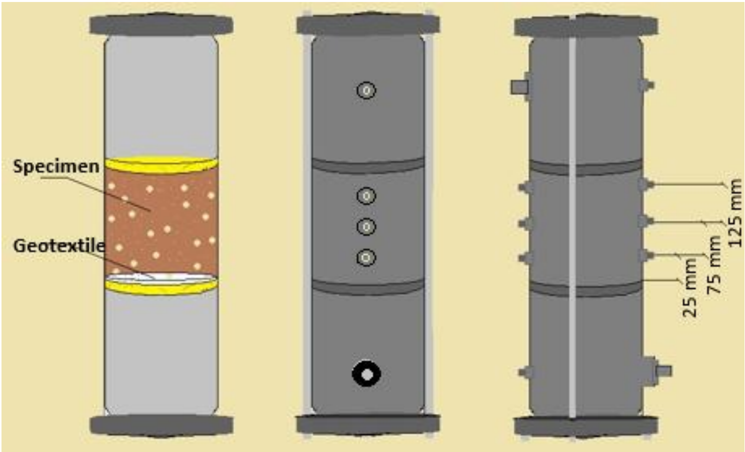

Fig. 5. Developed ASTM D5101 test system

$$GR_1 = \frac{i_{0-25}}{i_{25-75}} = 2 \times \frac{h_{25} - h_0}{h_{75} - h_{25}} \tag{2}$$

$$GR_2 = \frac{i_{25-75}}{i_{75-125}} = \frac{h_{75} - h_{25}}{h_{125} - h_{75}} \tag{3}$$

$$GR_3 = \frac{i_{0-25}}{i_{25-125}} = 4 \times \frac{h_{25} - h_0}{h_{125} - h_{25}} \tag{4}$$

$$GR_4 = \frac{GR_1 + GR_2}{2} \tag{5}$$

h0, h25, h75, h125 : Manometer readings at different heights

i: Hydraulic gradient.

The KR parameter defined in the ASTM D 5101 Standard (Equation 6) is expressed as the ratio of the aggregate permeability coefficient (as described in Equation 6) to the system permeability coefficient (as described in Equation 7) (Sariahmetoglu, 2021).

$$KR = \frac{k_{aggregate}}{k_{system}} \tag{6}$$

$$k_{system} = \frac{Q}{A \times t} \times \frac{1}{i_{system}} \times \frac{\mu_T}{\mu_{20}} = \frac{Q}{A \times t} \times \frac{l}{h_{150} - h_0} \times \frac{\mu_T}{\mu_{20}} \tag{7}$$

$$k_{aggregate} = \frac{Q}{A \times t} \times \frac{1}{(U_{avg} - A_{avg})} \times \frac{\mu_T}{\mu_{20}} \tag{8}$$

k_{system} : The permeability value of the system at 20°C is, (cm/s),
Q : The accumulated flow volume at time t, (cm^3),
i : Hydraulic gradient,
A : Cross-sectional area of the sample, (cm^2),
t : The time required to collect the amount of drained water, Q (s),
μ_T : The viscosity of water at temperature T.
μ_{20} : The viscosity of water at 20°C,

l : The length of the sample,
U_{avg} : The average of the upper manometer readings,
A_{avg} : The average of the lower manometer readings.

4. Results and discussion

Long-term filtration test results, conducted under i = 0.33 hydraulic gradient using an improved ASTM D5101 standard-based experimental setup with a recycled concrete aggregate–nonwoven geotextile system, were analyzed in terms of the GR and KR values defined in the referenced standard. GR values greater than 1 is indicative of the onset of clogging within the system, suggesting that fine particles migrate downward due to water flow and gravity, ultimately obstructing the system. Conversely, a GR value less than 1 implies that piping occurs where migrating fines pass through the geotextile, thereby enhancing the filtration performance.

In deviation from the standard ASTM D5101 test configuration, the filtration system utilized in this study was designed with specimens measuring 150 mm in diameter and 150 mm in height. To achieve higher precision in hydraulic gradient measurements, manometer ports were positioned at vertical distances of 25 mm, 75 mm, and 125 mm from the geotextile layer. The GR and KR values were subsequently determined based on pressure data recorded from these manometer points.

The time-dependent variations of GR and KR values for RCA are presented in Fig.s 6 and 7, respectively. As illustrated in the graphs, the onset of partial clogging in the RCA system can be identified.

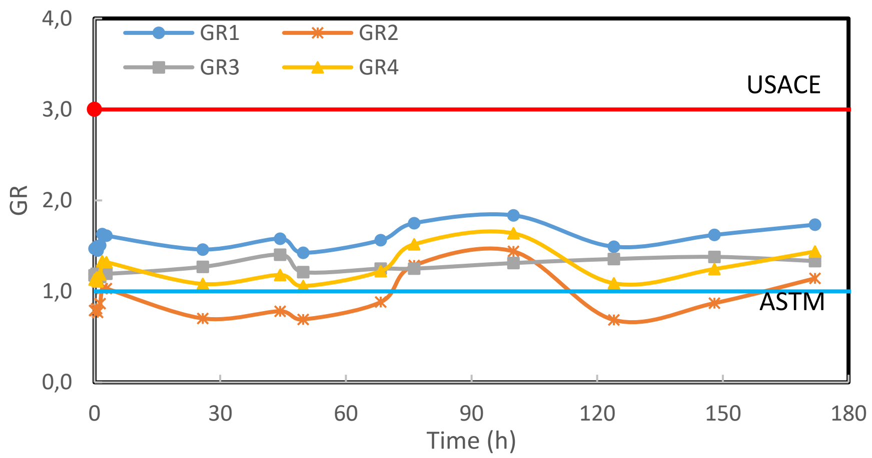

Fig. 6. Time-dependent GR values for RRCA

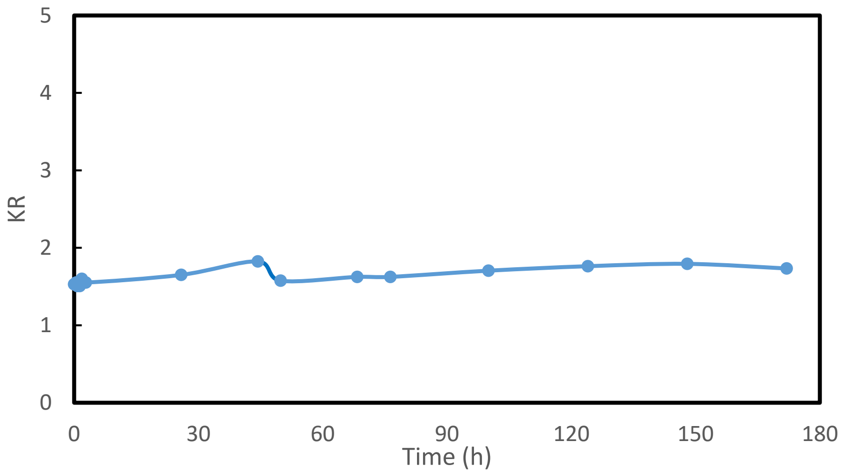

Fig. 7. Time-dependent KR values for RRCA

5. Conclusions

Enhanced long term filtration test was conducted to evaluate the filtration performance of drainage systems composed of recycled concrete aggregate -obtained from road renovation work- and geotextile. Based on the data obtained from the experiments, the following conclusions can be drawn:

- GR values exceed 1 and exhibit an increasing trend, indicating downward migration of fine-grained particles through the system.
- Although the system has initiated signs of clogging, it is still capable of maintaining its functionality, as the GR value has not exceeded the critical clogging threshold of 3
- To accurately evaluate the clogging performance of the system, the GR and KR values should be evaluated collectively.
- The utilization of recycled waste materials in place of natural aggregates in drainage systems contributes to energy conservation and the advancement of circular economy, while proposing a solution to the burden on waste management problem.

Acknowledgements
We would like to express our gratitude to the Scientific and Technological Research Council of Turkey (TUBITAK) for supporting this study under the 2209-A University Students Research Projects Support Program. We also wish to thank the ISTANBUL TEKNIK INSAAT company for kindly providing the geotextile materials used in this research.

References
Alsheyab, M. A. T. (2022). Recycling of construction and demolition waste and its impact on climate change and sustainable development. International Journal of Environmental Science and Technology, 19(3), 2129-2138. https://doi.org/10.1007/s13762-021-03217-1

Bayın Sarıahmetoğlu, A., İyisan, R., Yalçın Dayıoglu, A., & Hatipoğlu, M. (2021). Long term filtration performance of recycled asphalt pavement material. Pamukkale University Journal of Engineering Sciences, 27(6), 683-695. https://doi.org/10.5505/pajes.2021.05760

Behring, Z., Kim, J., Nam, B., Chopra, M., & Shoucair, J. (2014). Drainage Performance Evaluation of Reclaimed Concrete Aggregate. Innovative and Sustainable Use of Geomaterials and Geosystems, 33-40. https://doi.org/10.1061/9780784478455.005

Ferronato, N., Moresco, L., Guisbert Lizarazu, G. E., Gorritty Portillo, M. A., Conti, F., & Torretta, V. (2023). Comparison of environmental impacts related to municipal solid waste and construction and demolition waste management and recycling in a Latin American developing city. Environmental Science and Pollution Research, 30(4), 8548-8562. https://doi.org/10.1007/s11356-021-16968-8

Ginga, C. P., Ongpeng, J. M. C., & Daly, Ma. K. M. (2020). Circular Economy on Construction and Demolition Waste: A Literature Review on Material Recovery and Production. Materials, 13(13), 2970. https://doi.org/10.3390/ma13132970

Haider, S. W., & Chatti, K. (2009). Effect of design and site factors on fatigue cracking of new flexible pavements in the LTPP SPS-1 experiment. International Journal of Pavement Engineering, 10(2), 133-147. https://doi.org/10.1080/10298430802169390

Hassan, S. H., Aziz, H. A., Johari, I., & Hung, Y.-T. (2022). Construction and Demolition (C&D) Waste Management and Disposal. Içinde L. K. Wang, M.-H. S. Wang, & Y.-T. Hung (Ed.), Solid Waste Engineering and Management (C. 24, ss. 165-216). Springer International Publishing. https://doi.org/10.1007/978-3-030-89336-1_3

McCulloch, T., Kang, D., Shamet, R., Lee, S. J., & Nam, B. H. (2017). Long-Term Performance of Recycled Concrete Aggregate for Subsurface Drainage. Journal of Performance of Constructed Facilities, 31(4), 04017015. https://doi.org/10.1061/(ASCE)CF.1943-5509.0000994

Menegaki, M., & Damigos, D. (2018). A review on current situation and challenges of construction and demolition waste management. Current Opinion in Green and Sustainable Chemistry, 13, 8-15. https://doi.org/10.1016/j.cogsc.2018.02.010

Nedeljković, M., Visser, J., Šavija, B., Valcke, S., & Schlangen, E. (2021). Use of fine recycled concrete aggregates in concrete: A critical review. Journal of Building Engineering, 38, 102196. https://doi.org/10.1016/j.jobe.2021.102196

Pak, A., & Zahmatkesh, Z. (t.y.). Experimental study of geotextile’s drainage and filteration propertis under different hydraulic gradients and confining pressures.

Palmeira, E. m., & Gardoni, M. g. (2000). The Influence of Partial Clogging and Pressure on the Behaviour of Geotextiles in Drainage Systems. Geosynthetics International, 7(4-6), 403-431. https://doi.org/10.1680/gein.7.0178

Palmeira, E. M., & Gardoni, M. G. (2002). Drainage and filtration properties of non-woven geotextiles under confinement using different experimental techniques. Geotextiles and Geomembranes, 20(2), 97-115. https://doi.org/10.1016/S0266-1144(02)00004-3

Purchase, C. K., Al Zulayq, D. M., O’Brien, B. T., Kowalewski, M. J., Berenjian, A., Tarighaleslami, A. H., & Seifan, M. (2022). Circular Economy of Construction and Demolition Waste: A Literature Review on Lessons, Challenges, and Benefits. Materials, 15(1), Article 1. https://doi.org/10.3390/ma15010076

Sañudo-Fontaneda, L. A., Coupe, S. J., Charlesworth, S. M., & Rowlands, E. G. (2018). Exploring the effects of geotextiles in the performance of highway filter drains. Geotextiles and Geomembranes, 46(5), 559-565. https://doi.org/10.1016/j.geotexmem.2018.04.006

4th International Civil Engineering & Architecture Conference
17-19 May 2025, Trabzon, Türkiye

Optimization of sand-enhanced cementitious fillings:Mechanical and microstructural evaluation via UCS and UPV methods

Tugrul Kasap[1,2], Erol Yılmaz[*1,3], Muhammet Sari[1,2,3], Tugba Keskin[1,2]

[1] *Recep Tayyip Erdogan University, Geotechnical, Waste Management and Backfill Laboratory, Rize, Türkiye*
[2] *Recep Tayyip Erdogan University, Institute of Graduate Studies, 53100 Rize, Türkiye*
[3] *Recep Tayyip Erdogan University, Department of Civil Engineering, 53100 Rize, Türkiye*

Abstract. Cement-based backfill (CBF) remains a widely adopted solution for the sustainable and effective management of mine tailings. Nonetheless, the environmental challenges linked to tailings disposal and the high financial and ecological cost of cement production have prompted the exploration of alternative materials and techniques. This research explores the influence of sand incorporation on CBF formulations, aiming to enhance the particle size distribution of fine-grained, poorly graded tailings, improve mechanical strength, and lower overall expenses. CBF samples were produced with a constant binder ratio of 4 wt% and solid content of 80 wt%, then subjected to both unconfined compressive strength (UCS) and ultrasonic pulse velocity (UPV) assessments across various curing durations (3 to 180 days). Sand replaced tailings at incremental proportions of 5%, 15%, 25%, 35%, and 45% by weight. The findings indicate that adding sand up to 35% and allowing curing up to 90 days noticeably boosts CBF performance. Conversely, exceeding 35% sand content or extending curing beyond 90 days resulted in reduced quality and mechanical behavior. Strong correlations were established between UCS and UPV based on varying sand contents and curing durations. Furthermore, the predicted UCS values closely aligned with experimental data (R^2 = 97.9%). These results highlight the potential of incorporating alternative aggregates in CBF systems, paving the way for cost-efficient, practical, and scalable backfill strategies in underground metal mining operations.

Keywords: Cement-based backfills; Strength; Ultrasonic; Sand; Microstructure

1. Introduction

Cement-based backfill (CBF) has gained increasing attention as a key component of sustainable and modern mining operations, owing to its wide range of advantages (Zhang et al., 2023). Beyond enhancing underground safety by reinforcing surrounding rock structures, CBF also mitigates technical and environmental challenges associated with tailings management (Yin et al., 2023; Haiqiang et al., 2016). Typically, CBF is produced by mixing mine tailings with cement, water, and various additives—either natural or chemical—at a surface backfill plant, then delivered to underground voids via gravity flow or pumping systems (Qu et al., 2023). In recent years, the growing demand for industrial ore production has led to the processing of lower-grade ores, which in turn has significantly decreased the particle size of tailings generated during mineral processing (Kasap et al., 2022a). This shift in tailings characteristics has adversely affected the performance of CBF mixtures and increased cement consumption (Ban et al., 2022). Elevated cement usage not only imposes additional financial burdens on mining operations but also intensifies environmental concerns due to the associated rise in CO_2 emissions (Kasap et al., 2023). Consequently, in addition to the use of cement-replacing additives, there is a growing need to explore alternative materials—particularly aggregates derived from waste—as substitutes for tailings to alleviate these environmental and technical issues (Sari et al., 2023).

Sand, a fundamental component in construction materials like cement and concrete, is an inorganic material exhibiting diverse mineralogical characteristics (Li et al., 2021). Its physical and chemical properties play a key role in influencing the gradation profile of cementitious mixtures, along with factors such as maximum particle size and surface texture (Behera et al., 2020). In particular, the angular shape and particle size of sand contribute to enhancing the mechanical performance of these mixtures by increasing internal friction among particles (Yan et al., 2023). Improved particle packing, especially in fine-grained matrices, leads to a denser and more stable structure (Jiang et al., 2020). Additionally, the mineralogical composition of sand can aid hydration reactions

[*] Corresponding author, E-mail: erol.yilmaz@erdogan.edu.tr

https://doi.org/10.31462/icearc2025_ce_geo_324

within cement-based systems, positively influencing the microstructure of the hardened matrix (Li et al., 2023). However, due to its chemically inert nature, sand cannot independently trigger hydration processes and does not alter the composition or nature of hydration products (Alp et al., 2009). Despite its many advantages, the coarse and angular geometry of sand particles tends to raise the water demand of mixtures, which can negatively affect their workability. As such, careful control over both sand content and particle size distribution is essential during mix design (Kasap et al., 2022b). Recently, sand has gained popularity as a partial binder or aggregate replacement in cement-based backfill (CBF) systems, due to its favorable properties (Zaibo et al., 2022). Its affordability and potential to correct poor gradation in fine tailings make it a valuable additive in CBF applications (Guner et al., 2023).

Numerous studies have examined various characteristics of cement-based backfills (CBFs) incorporating sand (Ouyang et al., 2022; Yan et al., 2022; Xin et al., 2022). Yi et al. (2015) analyzed the impact of integrating sand-silt tailings and polypropylene fibers into CBF mixtures. Their findings revealed that the inclusion of these components enhanced the ductility of the CBFs by up to three times and effectively prevented strength degradation compared to conventional samples. In another study, Sun et al. (2018) explored the strength evolution of CBFs prepared with Aeolian sand, assessing variables such as cement dosage and water content. They observed that incorporating 5% sand into the mixture negatively affected the microstructure, resulting in a marked reduction in 28-day compressive strength. Yang et al. (2020) focused on stress behavior in CBFs composed of gobi sand and mine tailings subjected to varying flow cycles. Their results indicated that an increase in particle size and density led to strength losses, underscoring the importance of optimizing the sand-to-tailings ratio. Zhou et al. (2021) investigated CBF mixtures enhanced with sand and glass fibers of varying lengths (3–15 mm), and reported substantial improvements in mechanical performance—specifically compressive, tensile, and shear strength—when glass fibers were added to sand-based CBFs.

While sand has been widely utilized in the literature to enhance the quality and mechanical performance of cement-based backfills (CBFs), studies focusing on the long-term mechanical and microstructural evaluation of sand-containing mixtures—particularly using non-destructive testing methods—remain limited. The present work investigates how sand influences the behavior and performance of CBFs by employing both destructive (unconfined compressive strength, UCS) and non-destructive (ultrasonic pulse velocity, UPV) techniques, with the aim of mitigating strength losses associated with fine tailings and reducing cement consumption. CBF specimens were prepared with a constant binder content of 4 wt% and solid content of 80 wt%, and were subjected to curing periods ranging from 3 to 180 days. Sand was incorporated into the mixtures by partially replacing tailings at proportions of 5%, 15%, 25%, 35%, and 45% by weight. In addition to mechanical testing, microstructural changes were characterized using scanning electron microscopy (SEM). UCS values were also predicted through regression analysis using UPV data, and the reliability of the developed models was validated through statistical methods, including F-tests and t-tests. A comprehensive interpretation of the test results and analytical findings is provided in the subsequent sections of the study..

2. Materials and methods

2.1. CBF components

2.1.1. Tailings and sand

Mine tailings, as a primary constituent of cement-based backfill (CBF), play a significant role in determining the overall performance of the mixture. Consequently, accurate characterization of these tailings is essential for effective backfill design. In this study, the tailings were sourced from the filtration system of an underground copper mining operation situated in northwestern Turkey. Additionally, sand samples were obtained from a nearby quarry in close proximity to the mining site. The particle size distributions of both materials were analyzed using a Malvern Mastersizer 3000 laser diffraction device (Fig. 1). According to the results, the copper tailings exhibited a relatively coarse texture, with 27.9% of the particles having a diameter smaller than 20 µm.

Table 1 presents the physical properties of the copper tailings and sand samples used in this study. The specific gravity values, measured using a Quantachrome Ultrapyc 1200e helium gas pycnometer, were 3.61 for the tailings and 2.59 for the sand. Furthermore, specific surface areas determined via a single-point BET analysis (Quantachrome Quadrosorb SI) were 2.63 m²/g for the tailings and 0.72 m²/g for the sand. To assess the chemical composition of both materials, X-ray fluorescence (XRF) analysis was performed using a PANalytical Zetium spectrometer (Table 2). The results revealed that Fe_2O_3 (42.2%) and SiO_2 (24.1%) were the dominant constituents in the copper tailings, while CaO (56.3%) was the primary component identified in the sand samples.

2.1.2. OPC and blend water

Ordinary Portland Cement (OPC, CEM I 42.5 R) was selected as the primary binder material in this research. The physical properties of the cement are summarized in Fig. 1 and Table 1. The median particle size (D50), specific gravity (Gs), and specific surface area (Ss) of OPC were determined to be 24.8 µm, 3.15, and 0.39 m²/g,

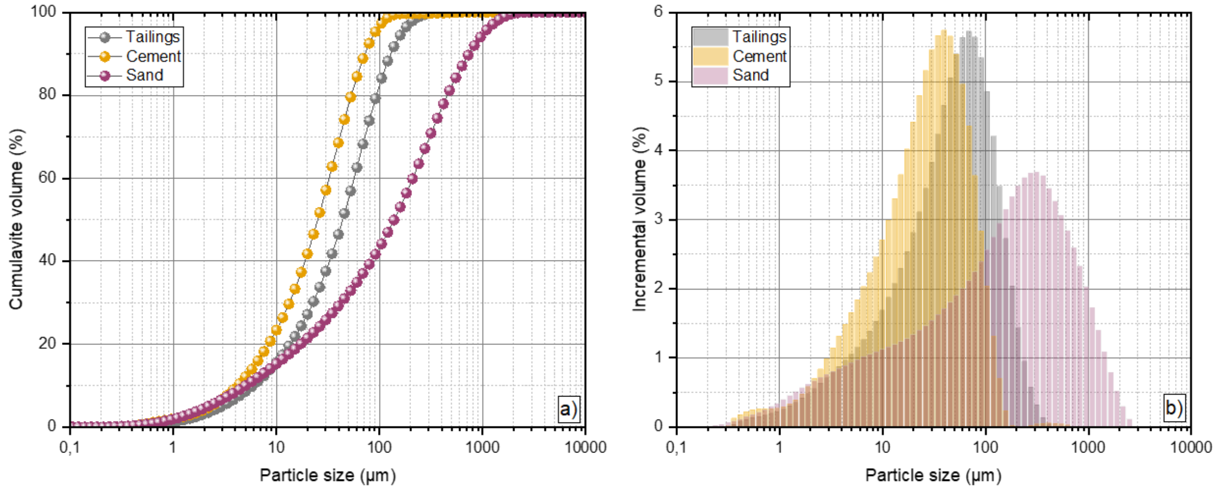

Fig. 1. Variation in cumulative (a) and incremental (b) particle sizes of components in cement-based fills

Table 1. Main physical features of ingredients

Property	OPC (CEM I 42.5 R)	Tailings	Sand
Specific gravity, G_s (unitless)	3.18	3.65	2.62
Specific surface, S_S (m^2/g)	0.39	2.66	0.73
Void ratio	0.49	0.78	0.71
Uniformity coefficient*	7.43	9.53	41.01
Curvature coefficient**	1.40	1.31	2.03
D_{10}, μm (effective diameter)	4.47	6.04	51.61
D_{30}, μm	14.14	22.52	467.63
D_{50}, μm (average diameter)	25.05	44.34	1415.01
D_{60}, μm	32.42	57.37	2041.21
D_{80}, μm	54.44	93.63	2569.44

respectively. According to the XRF analysis results presented in Table. 2, CaO (62.7%) was the predominant oxide, followed by SiO_2 (16.9%) and Al_2O_3 (6.11%). Water used in cement-based backfill (CBF) systems plays a crucial role in both achieving adequate workability and initiating the hydration processes necessary for strength development and material transport within underground voids. Although CBF systems can utilize water from various sources—such as municipal supply, surface water bodies, or process water—this study exclusively employed tap water. The key chemical parameters of the mixing water were sulfate (SO_4^{2-}), calcium (Ca^{2+}), and pH, which were measured at 5.22 mg/L, 36.1 mg/L, and 7.86, respectively.

2.2. Blend conception and preparation of CBFs

In the laboratory production of cement-based backfill (CBF) specimens, a fixed binder content of 4 wt% and a total solids content of 80 wt% were employed. Curing durations extended up to 180 days. To assess the effect of sand as a partial substitute for copper tailings, six different mixtures were prepared with sand replacement levels of 0% (control), 5%, 15%, 25%, 35%, and 45% by weight. The complete mix proportions used for CBF production are provided in Table 3. Each mixture was homogenized in a 10-liter capacity mechanical mixer for approximately 10–12 minutes. Upon completion of mixing, the solids content of the mixtures was verified using a mini-slump cone test to ensure compliance with the 80 wt% target.

For each mixture, the fresh paste was cast into three cylindrical plastic molds with a diameter-to-height ratio of 5×10 cm, in accordance with the designated curing intervals. The molded samples were then stored in a curing chamber maintained at a constant temperature of 21°C and relative humidity of 91% to ensure consistent hydration conditions. Fig. 3 illustrates the step-by-step procedure followed during the preparation and curing of the CBF specimens.

Table 2. Main chemical features of ingredients

Property	OPC (CEM I 42.5 R)	Copper tailings	Sand
CaO	63.78	4.25	56.78
Fe_2O_3	3.04	41.47	1.07
SiO_2	17.28	23.83	2.65
Al_2O_3	5.73	7.06	2.17
MgO	1.10	2.54	1.34
Na_2O	0.32	0.60	0.60
K_2O	0.41	0.86	0.69
SO_3	3.12	1.05	1.34
Others	4.89	18.08	32.58
Total	99.68	99.73	99.22

Table 3. Design of cement-based fill (CBF) mixtures

Code	Ingredients (wt.%)		Solid value (wt.%)	Slump (cm)	CEM I 42.5R (wt.%)	Cure age (days)
	Tailings	Sand				
T100	100	-	80	20	4	3, 14, 28, 56, 90, 120, 180
T85/S15	85	15	80	20	4	3, 14, 28, 56, 90, 120, 180
T75/S25	75	25	80	20	4	3, 14, 28, 56, 90, 120, 180
T65/S35	65	35	80	20	4	3, 14, 28, 56, 90, 120, 180
T55/S45	55	45	80	20	4	3, 14, 28, 56, 90, 120, 180
T45/S55	45	55	80	20	4	3, 14, 28, 56, 90, 120, 180

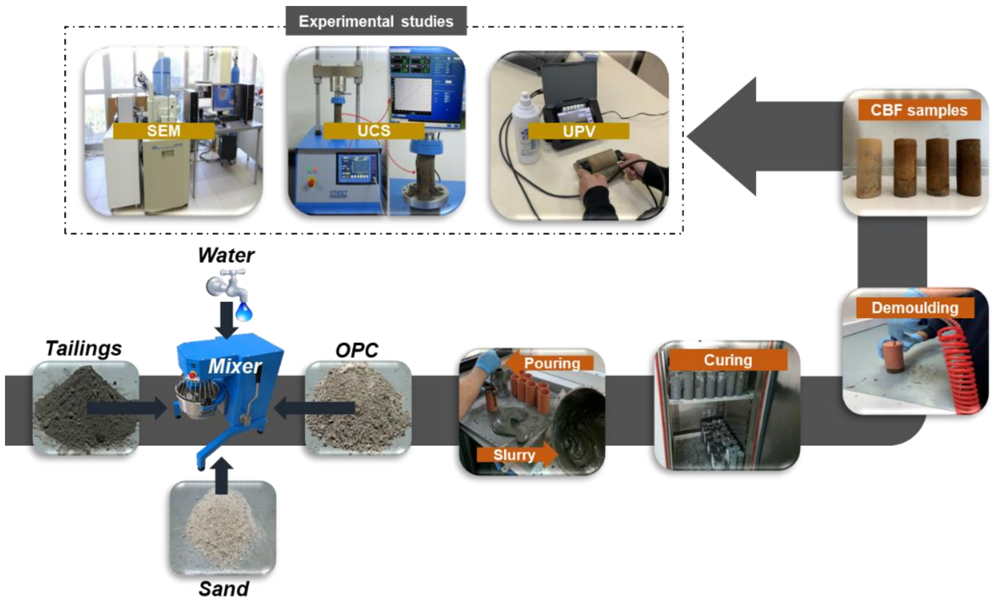

Fig. 3 Stages of readiness and trials for CBFs

2.3. Methods

2.3.1. Strength testing procedures

The uniaxial compressive strength (UCS) of the cement-based backfill (CBF) specimens was evaluated using a UTEST Multiplex electromechanical testing system, which has a maximum load capacity of 50 kN and operates at a constant displacement rate of 1 mm/min, in accordance with the ASTM C39 standard. Prior to testing, the top and bottom surfaces of the cylindrical specimens (with a diameter-to-height ratio of 5×10 cm) were carefully leveled using a sharp razor blade to ensure even load application. Following surface preparation, the samples were positioned between the compression platens of the UCS device, and strength tests were conducted. For each mixture type, three replicate specimens were tested, and the average of the measured values was reported as the representative UCS.

2.3.2. SEM observations
Scanning electron microscopy (SEM) is commonly employed to investigate the surface morphology and hydration products of cement-based backfills (CBFs). In this study, the microstructural properties of polished cross-sectional samples (from the hardened surfaces) of CBFs were analyzed using a JEOL JSM-6510 scanning electron microscope. This instrument provides a resolution of 3 nm and magnification capabilities ranging from 5x to 1,000,000x, with a current emission of 0.9 nA and an acceleration voltage of 20 kV. To examine the surface morphology in detail, small pieces were cut from 90-day-old hardened CBF samples, dried at 50°C for 75 hours, and then coated with a thin gold film. The microstructural features were then observed at magnifications between 50x and 9,000x using SEM

2.3.3. Ultrasonic pulse velocity testing
Ultrasonic Pulse Velocity (UPV) is one of the most widely used non-destructive techniques for assessing the strength properties of cement-based mixtures. This method not only provides valuable information regarding the strength of the material but also offers insights into the homogeneity of the mixture. UPV measurements were conducted using the Proceq Pundit Lab 200 instrument on samples prepared according to the CBF mix designs, which had completed their designated curing periods. All testing parameters and procedures were carried out in accordance with ASTM C 597-16 standards. The transmission of ultrasonic pulses (ranging from 24-500 kHz) between the data collector and the transducers is quantified by the equation UPV(X, T) = X/T, where UPV(X, T) represents the propagation velocity (m/s) of the ultrasonic wave, X is the distance between the transmitter and receiver, and T is the time it takes for the pulses to travel this distance. Prior to testing, the surfaces of the samples were smoothed with a razor blade to ensure optimal contact between the transmitter and receiver. An ultrasonic gel was then applied to the surfaces to improve the interface, followed by UPV testing. Each test was repeated three times, and the average values were recorded.

3. Results and discussions

3.1. Sand content and age-related variations in CBF strength
Fig. 4 illustrates the uniaxial compressive strength (UCS) results for all cement-based fill (CBF) mixtures, based on the compositions outlined in Table 3 (waste/sand ratio: 100/0, 85/15, 75/25, 65/35, 55/45, and 45/55), with curing times extending up to 180 days. It is evident that the UCS values of all CBF samples increased over time with prolonged curing. Additionally, the substitution of tailings with sand significantly enhanced the mixture's gradation, leading to a notable improvement in strength. However, after 90 days of curing, a considerable decrease in UCS values was observed in the control sample and in mixtures with lower sand substitution rates (e.g., 15% and 25%). The highest strength, recorded at 90 days, was 2.91 MPa for the T65/S35 mixture. This indicates that incorporating up to 35% sand as a tailings substitute significantly boosts the UCS values. For instance, at 28 days of curing, the UCS value for the T65/S35 mixture reached 1.05 MPa, while the control mixture (T100) exhibited a strength of only 0.46 MPa under similar curing conditions. On the other hand, higher sand substitution levels (e.g., 45%) led to a sharp decline in strength, as exemplified by the 28-day UCS value of 0.73 MPa for the T55/S45 mixture. The observed improvements in UCS for sand-substituted CBFs are primarily attributed to enhanced gradation, which fills the voids in the matrix and supports the ongoing hydration reactions [15].

The coarser grain size of sand (coarse aggregate) in comparison to tailings increases the contact area and friction between the particles in the CBF matrix. This enhanced interaction provides significant resistance to external forces, resulting in higher mechanical properties for CBFs that incorporate sand compared to those without. However, as shown in Fig. 4, when the sand content exceeds 35%, a decline in strength is observed. The addition of more than 35% sand disrupts the homogeneity of the CBF mixtures, hindering proper adhesion of hydration products. Excessive sand content also impedes particle cohesion, leading to segregation within the mixture. Moreover, for pipeline-transported materials such as CBF, higher sand content increases the water demand, which negatively impacts the workability of the mixture (Cao et al., 2021; Zheng & Li, 2020). Therefore, careful control of both the sand quantity and grain size is essential to optimize the performance of CBFs.

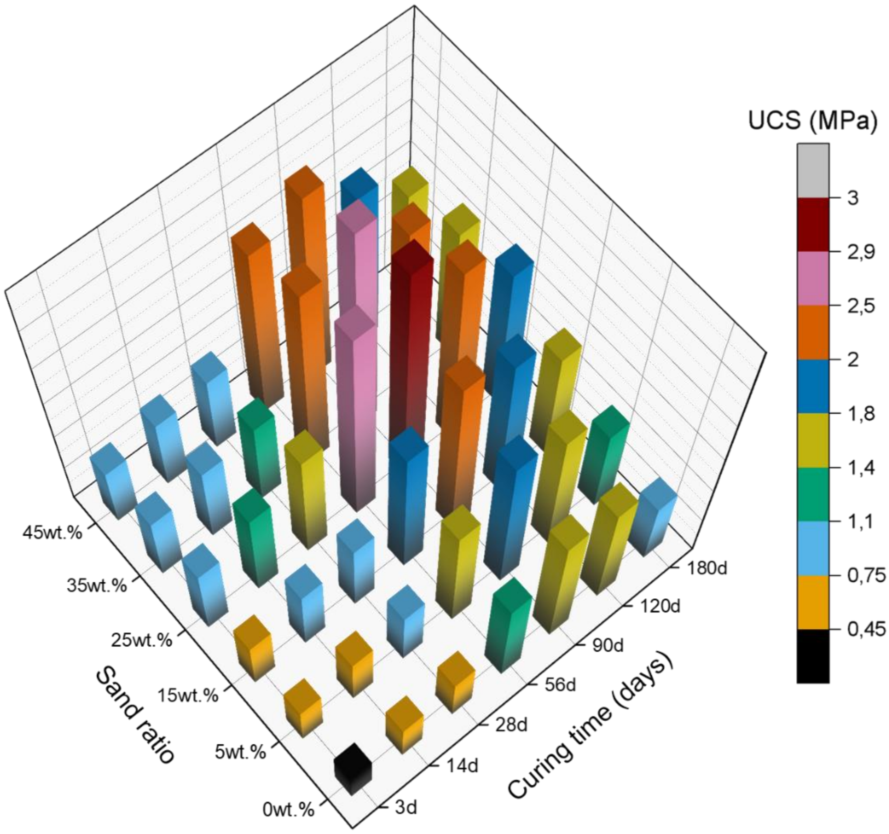

Fig. 4. The strength evolution of entire CBF samples

3.2. Morphological features of CBF surfaces

Examining the surface morphology of cement-based mixtures like CBF provides valuable insights into various parameters, including strength development and the distribution of hydration products (Solaymani et al., 2018). Scanning electron microscopy (SEM) enables high-resolution imaging of the surface structure of CBFs, allowing for detailed observation. Numerous studies have demonstrated a strong correlation between SEM images and the surface morphology of cement-based mixtures (Elenkova et al., 2015). In this study, SEM micrographs were used to investigate the surface morphology of CBF samples and the structural changes resulting from hydration reactions. During the hydration process in CBFs, minerals such as calcium silicate hydrate (C-S-H) gels, portlandite, and etrengite are typically formed. Etrengite manifests as fine, needle-like crystals that often intertwine. C-S-H gels appear in various forms but are typically spherical or network-like, and in some cases, they may exhibit branched or fibrous structures, which can sometimes be mistaken for etrengite. Portlandite typically forms regular, layered hexagonal plate structures that fill the spaces between the grains in cementitious mixtures (Kasap et al., 2022c).

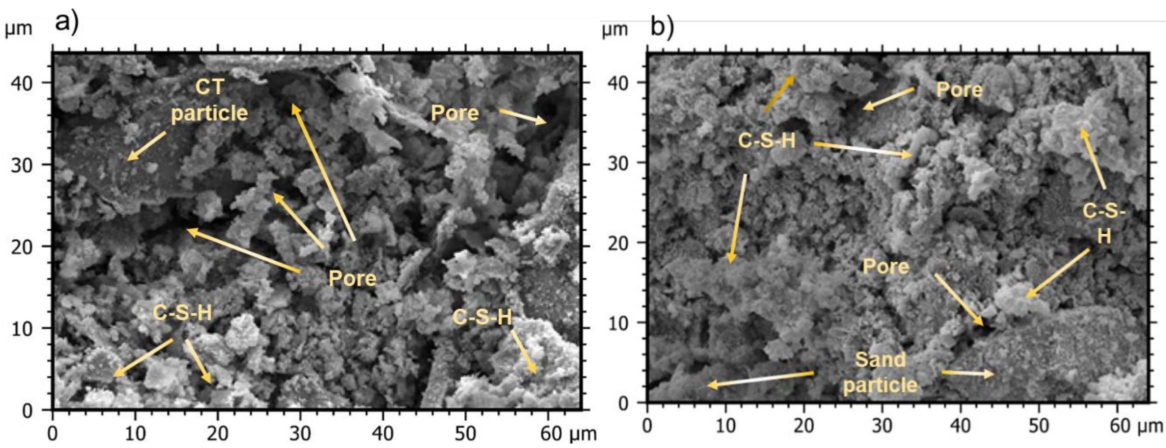

Fig. 5. Surface morphology of T100 (a) and T65/35 (b) based on SEM micrographs cured for 90 days

Fig. 5 presents SEM micrographs of 90-day-old CBFs (T100-control and T65/35) at ×2000 magnification. The surface morphology of the samples reveals that C-S-H gel forms a dense network surrounding the CBF particles, effectively filling the voids. In comparison, the presence of portlandite is minimal. This observation suggests that the portlandite formed during the early stages of hydration in CBFs is gradually consumed over time, thereby promoting the continued formation of C-S-H gels (Wang et al., 2021). Additionally, etrengite was observed in certain areas of the surface morphology. The SEM results clearly indicate that the control sample (T100) exhibits a more porous and weaker structure in terms of hydration products when compared to the sand-substituted CBF (T65/35). The incorporation of sand in CBFs mitigates gradation issues caused by the fine nature of the waste material and enhances the formation of hydration products, largely due to the high CaO content in the sand. Consequently, this leads to improved packing density in CBFs, significantly reducing porosity and permeability (Jiang et al., 2019). Furthermore, the more porous structure of the control sample allows for greater air and moisture penetration between grains, which can lead to the oxidation of pyrite in the tailings (Jiang et al., 2017). Therefore, using sand (particularly up to 35 wt%) as a partial replacement for fine-grained waste material substantially improves the microstructure of CBFs, thereby enhancing both the quality and performance of the fills

3.3. UPV measurements and their impact on ucs in cement-based fills

Fig. 6 illustrates the UPV (ultrasonic pulse velocity) results for all cement-based fills (CBFs) with varying sand replacement ratios for tailings, cured up to 180 days. The data clearly indicate that substituting sand significantly enhances the UPV values of the CBFs. In line with the UCS results, the highest UPV values were observed at 90 days curing time and at the optimal sand replacement rate of 35% by weight. However, when the sand replacement rate exceeded 35%, an uneven increase in grain gradation led to structural degradation caused by segregation. This segregation resulted in a more porous CBF structure, increasing oxidation rates and consequently lowering UPV values (Wang et al., 2021). Despite this, sand-substituted CBFs still achieved higher UPV values compared to the control samples. The highest UPV value (3890 m/s) was recorded for the T65/35 sample, while the lowest value (394.1 m/s) was found in the 180-day T100 sample.

The incorporation of sand helps form a denser CBF structure by alleviating gradation issues associated with mine tailings. Additionally, its high CaO content, similar to cement, enhances the formation of hydration products. These hydration products fill the voids in the CBF, leading to an increase in the solid phase density. As a result, the porosity of CBFs decreases with sand substitution, thereby improving the UPV values significantly. In agreement with the SEM findings (Fig. 5), it is evident that sand-substituted CBFs exhibit more advanced hydration and lower void ratios compared to the control samples. Previous studies have demonstrated that cementitious mixtures with better gradation and density tend to have higher UPV values due to their enhanced resistance to environmental factors (Prasad & Lakshmi, 2020).

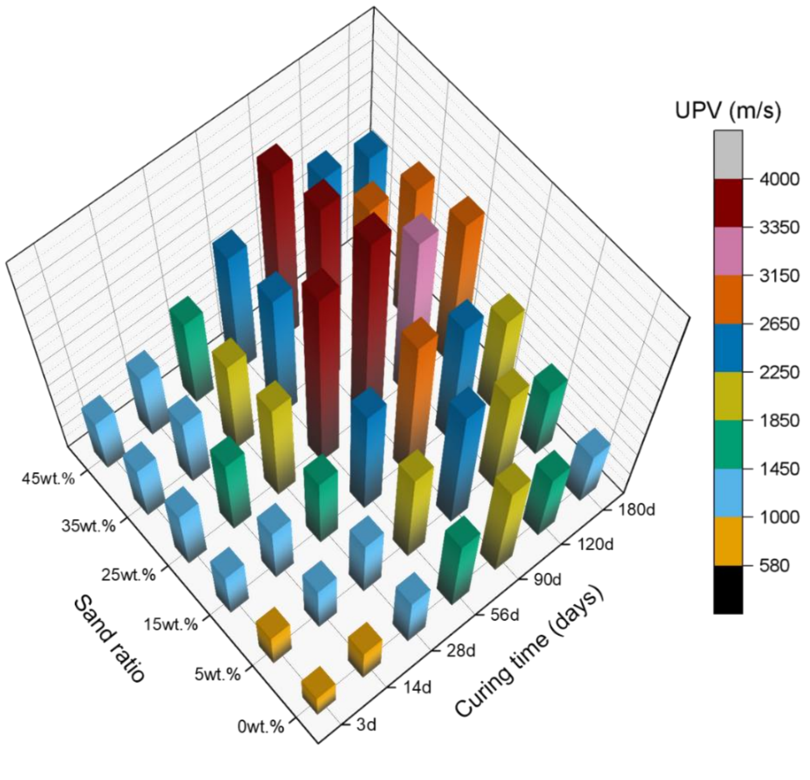

Fig. 6. UPV outcomes of CBF samples

Table 4. Statistical test findings for CBF Samples

Regression type	Equation	R^2
Linear	UCS = 0.00031UPV-0.0009	0.948
Polynomial	UCS = 6E-3UPV^2+0.00156UPV+0.404	0.957
Exponential	UCS = 0.3018e$^{0.00264UPV}$	0.963
Power	***UCS = 4.2566E-4UPV$^{0.899}$***	***0.979***

The relationship between UCS and UPV values of cementitious mixtures is significantly influenced by various factors such as solids content, cement type and proportion, and the presence of additives. Regression models that account for these factors can offer highly accurate predictions for the strength of cementitious mixtures. Existing literature underscores the importance of the UCS-UPV relationship in materials like CBFs and proposes various methods to optimize this correlation (Yingliang et al., 2020). In this study, the UCS-UPV relationship in CBFs was thoroughly analyzed using multiple curve fitting techniques, including linear, polynomial, exponential, and power models, as shown in Table 4).

The results indicate that the power models provided the most robust equations, with a correlation coefficient (R^2) of 0.985 across all CBF samples (Fig. 7). Furthermore, to evaluate the accuracy of the most effective equation and compare the standard deviations, both F-tests (Fisher's test) and t-tests were conducted (Fig. 7). Specifically, the F- and t-tests were utilized to verify the suitability of the relationship between the variables in the proposed equations. While the t-test typically compares two groups with homogeneous variables, alternative t-test methods are available for non-homogeneous groups. Therefore, prior to the t-test, the F-test is recommended to assess the homogeneity of the variances (Cui et al., 2020; Ashrafian et al., 2018). In this study, a 5% significance level was applied for both the F- and t-tests.

The F value of the power model for all CBF samples (1811.2) exceeds the critical F value (F_{cr} = 1.401), confirming that the variables in the CBFs are homogeneous. Additionally, the P value (2.12E-19, at a 95% confidence level) is lower than 5%, indicating statistical significance. When analyzing the t-test results, it is evident that the calculated t value (t_s = 16.119) is greater than the critical t value (t_{cr} = 2.003). Similar to the F-test, the P values from the t-test (4.06E-22) are also less than 5%, further confirming the reliability of the regression analysis. These findings demonstrate a strong correlation between UCS and UPV, indicating that UCS data can be accurately predicted from UPV measurements.

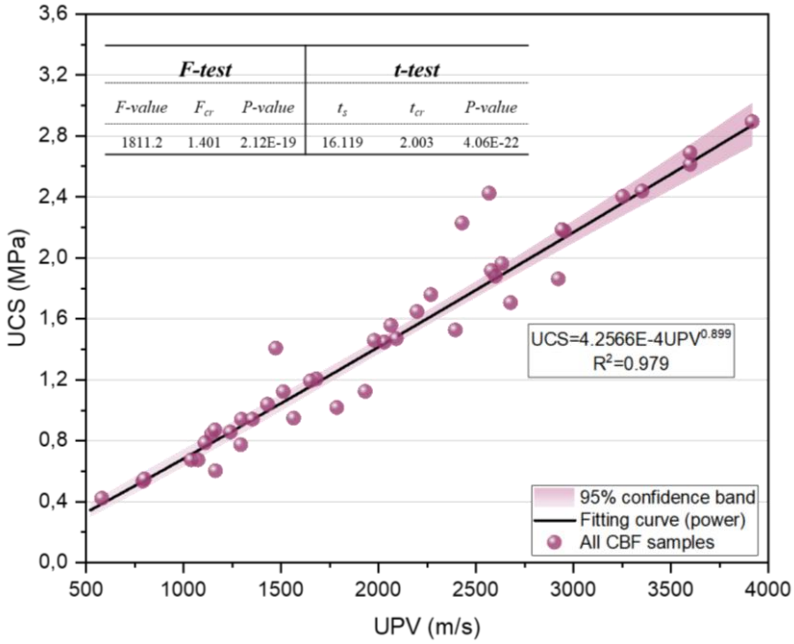

Fig. 7. Correlations among UCS and UPV variables of CBF samples

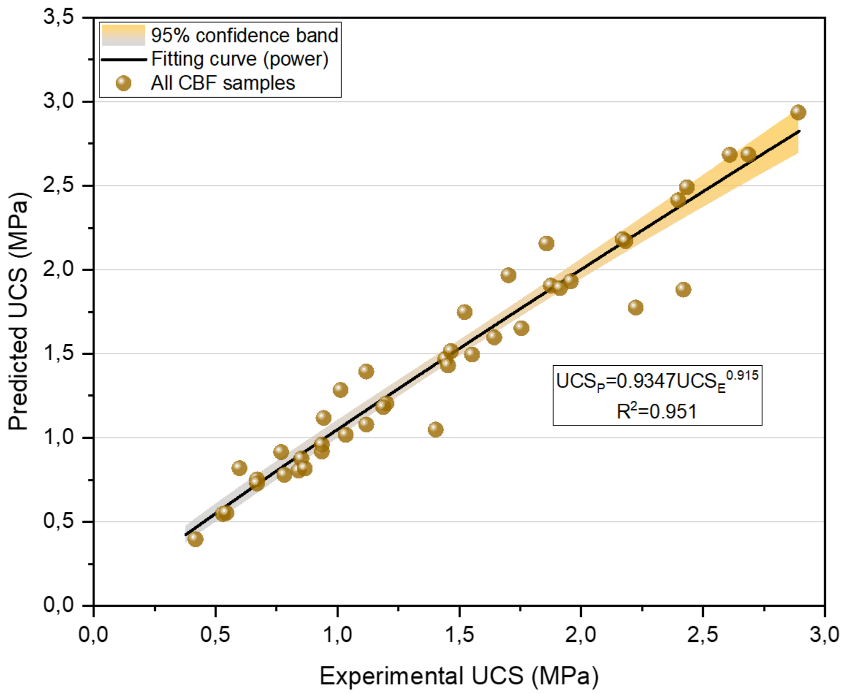

Fig. 8. Correlations among experimental and predicted strength results of CBF

Fig. 8 illustrates the correlation between the experimental and predicted UCS values for all CBFs. As in the previous analyses, the power equation was applied to assess the regression analysis. The R^2 value obtained from the power equation was 0.951. Moreover, the majority of the measured and predicted UCS values fall within the 95% confidence interval, indicating the effectiveness of the methods used to predict UCS. The applicability and accuracy of the power equation were further validated through UPV tests. The regression analysis confirms that the non-destructive UPV test can be utilized to develop a cost-effective, practical, and efficient backfill design for underground metal mining.

4. Conclusions

In this study, cement-based fill (CBF) mixtures were prepared in the laboratory with constant binder content (4 wt%) and solid content (80 wt%), and cured for up to 180 days. The quality and performance of CBFs with varying sand replacement proportions (15%, 25%, 35%, and 45%) were evaluated using both destructive (UCS) and non-destructive (UPV) methods. Additionally, the microstructural characteristics of the CBF samples were analyzed using the SEM technique. Various curve fitting and statistical methods were applied to evaluate the relationship between UCS and UPV. The key findings from the tests and analyses are summarized as follows:

- UCS values of CBFs increased with curing time up to 90 days, after which the strength of all samples began to decrease towards 180 days.
- Increasing sand as a tailings substitute (up to 35 wt.%) significantly improved the performance of the CBFs. However, segregation was observed in all mixtures beyond the 35% substitution rate.
- SEM analysis showed a greater formation of hydration products in sand-substituted CBFs compared to the control sample. Additionally, the increased basicity of the mixing medium due to sand (high CaO content) improved the CBFs' resistance to acid attack and degradation.
- The relationship between UCS and UPV values was evaluated using different curve fitting methods (e.g., linear, polynomial, exponential). The results indicated that the most suitable regression curve is the power model.
- The relationship between experimental and predicted UCS was determined as UCSPredicted = 0.9347 × UCSExperimental0.915 for all CBF samples.

Overall, the tests and analyses demonstrated a strong correlation between UCS and UPV values. While the relationship can vary depending on the proportions, types, and number of constituents, this study highlights the impact of the physical (e.g., grain size and surface area) and chemical (e.g., CaO content) properties of sand used as a tailings substitute on early and long-term UCS, UPV, and microstructure. Future studies will focus on evaluating the impact of various additives (e.g., chemical or natural) on the quality and performance of CBFs through other non-destructive methods.

References

Alp, I., Deveci, H. A. C. I., Sungun, Y. H., Yilmaz, A. O., Kesimal, A., & Yilmaz, E. (2009). Pozzolanic characteristics of a natural raw material for use in blended cements. *Iranian Journal of Science & Technology, Transaction B, Engineering, 33*(B4), 291–300.

Ashrafian, A., Amiri, M. J. T., Rezaie-Balf, M., Ozbakkaloglu, T., & Lotfi-Omran, O. (2018). Prediction of compressive strength and ultrasonic pulse velocity of fiber reinforced concrete incorporating nano silica using heuristic regression methods. *Construction and Building Materials, 190*, 479–494.

Ban, J., Sun, K., Yao, J., Sunahara, G., Hudson-Edwards, K., Jordan, G., Alakangas, L., Ni, W., & Poon, C. S. (2022). Advances in the use of recycled non-ferrous slag as a resource for non-ferrous metal mine site remediation. *Environmental Research, 213*, 113533.

Behera, S. K., Ghosh, C. N., Mishra, D. P., Singh, P., Mishra, K., Buragohain, J., & Mandal, P. K. (2020). Strength development and microstructural investigation of lead-zinc mill tailings based paste backfill with fly ash as alternative binder. *Cement and Concrete Composites, 109*, 103553.

Cao, S., Xue, G., Yilmaz, E., & Yin, Z. (2021). Assessment of rheological and sedimentation characteristics of fresh cemented tailings backfill slurry. *International Journal of Mining, Reclamation and Environment, 35*(5), 319–335.

Cui, Y., Gao, K., & Zhang, P. (2020). Experimental and statistical study on mechanical characteristics of geopolymer concrete. *Materials, 13*(7), 1651.

Elenkova, D., Zaharieva, J., Getsova, M., Manolov, I., Milanova, M., Stach, S., & Ţălu, Ş. (2015). Morphology and optical properties of SiO_2-based composite thin films with immobilized terbium (III) complex with a biscoumarin derivative. *International Journal of Polymer Analysis and Characterization, 20*(1), 42–56.

Guner, N. U., Yilmaz, E., Sari, M., & Kasap, T. (2023). Cementitious backfill with partial replacement of Cu-rich mine tailings by sand: Rheological, mechanical and microstructural properties. *Minerals, 13*(3), 437.

Haiqiang, J., Fall, M., & Cui, L. (2016). Yield stress of cemented paste backfill in sub-zero environments: Experimental results. *Minerals Engineering, 92*, 141–150.

Jiang, H., Fall, M., & Cui, L. (2017). Freezing behaviour of cemented paste backfill material in column experiments. *Construction and Building Materials, 147*, 837–846.

Jiang, H., Fall, M., Li, Y., & Han, J. (2019). An experimental study on compressive behaviour of cemented rockfill. *Construction and Building Materials, 213*, 10–19.

Jiang, H., Fall, M., Yilmaz, E., Li, Y., & Yang, L. (2020). Effect of mineral admixtures on flow properties of fresh cemented paste backfill: Assessment of time dependency and thixotropy. *Powder Technology, 372*, 258–266.

Kasap, T., Yilmaz, E., & Sari, M. (2022a). Recycling dam tailings as cemented mine backfill: Mechanical and geotechnical properties. *Advances in Materials Science and Engineering, 2022*(1), 6993068.

Kasap, T., Yilmaz, E., & Sari, M. (2022b). Effects of mineral additives and age on microstructure evolution and durability properties of sand-reinforced cementitious mine backfills. *Construction and Building Materials, 352*, 129079.

Kasap, T., Yilmaz, E., & Sari, M. (2022c). Physico-chemical and micro-structural behavior of cemented mine backfill: Effect of pH in dam tailings. *Journal of Environmental Management, 314*, 115034.

Kasap, T., Yilmaz, E., Sari, M., & Karasu, S. (2023). Predicting long-term impact of cementitious mine fill considering sand as a copper-tailings substitution. *Powder Technology, 428*, 118887.

Li, J., Yilmaz, E., & Cao, S. (2021). Influence of industrial solid waste as filling material on mechanical and microstructural characteristics of cementitious backfills. *Construction and Building Materials, 299*, 124288.

Li, Q., Cui, H., Li, Y., Song, X., Liu, W., Wang, Y., Hou, H., Zhang, H., Li, Y., Wang, F., Song, J., Ye, H., Song, S., Che, T., Shao, S., Kong, D., & Liang, B. (2023). Challenges and engineering application of landfill leachate concentrate treatment. *Environmental Research, 231*, 116028.

Ouyang, S., Huang, Y., Zhou, N., Li, J., Gao, H., & Guo, Y. (2022). Experiment on hydration exothermic characteristics and hydration mechanism of sand-based cemented paste backfill materials. *Construction and Building Materials, 318*, 125870.

Prasad, C. V. S. R., & Lakshmi, T. V. (2020). Experimental investigation on bacterial concrete strength with *Bacillus subtilis* and crushed stone dust aggregate based on ultrasonic pulse velocity. *Materials Today: Proceedings, 27*, 1111–1117.

Qu, Z., Yu, Q., Ong, G. P., Cardinaels, R., Ke, L., Long, Y., & Geng, G. (2023). 3D printing concrete containing thermal responsive gelatin: Towards cold environment applications. *Cement and Concrete Composites, 140*, 105029.

Sari, M., Yilmaz, E., & Kasap, T. (2023). Long-term ageing characteristics of cemented paste backfill: Usability of sand as a partial substitute of hazardous tailings. *Journal of Cleaner Production, 401*, 136723.

Solaymani, S., Kulesza, S., Ţălu, Ş., Bramowicz, M., Nezafat, N. B., Dalouji, V., Rezaee, S., Karami, H., Malekzadeh, M., & Dorbidi, E. S. (2018). The effect of different laser irradiation on rugometric and microtopographic features in zirconia ceramics: Study of surface statistical metrics. *Journal of Alloys and Compounds, 765*, 180–185.

Sun, Q., Zhang, J., & Zhou, N. (2018). Early-age strength of aeolian sand-based cemented backfilling materials: Experimental results. *Arabian Journal for Science and Engineering, 43*(4), 1697–1708.

Wang, J., Zhang, C., Fu, J., Song, W., & Zhang, Y. (2021). Effect of water saturation on mechanical characteristics and damage behavior of cemented paste backfill. *Journal of Materials Research and Technology, 15*, 6624–6639.

Wang, Z., Qi, T., Feng, G., Bai, J., Pei, X., Cui, B., Song, H., & Ran, H. (2021). Electrical resistivity method to appraise static segregation of gangue-cemented paste backfill in the pipeline. *International Journal of Pressure Vessels and Piping, 192*, 104385.

Xin, J., Liu, L., Jiang, Q., Yang, P., Qu, H., & Xie, G. (2022). Early-age hydration characteristics of modified coal gasification slag–cement–aeolian sand paste backfill. *Construction and Building Materials, 322*, 125936.

Yan, B., Jia, H., Yang, Z., Yilmaz, E., & Liu, H. (2023). Goaf instability in an open pit iron mine triggered by dynamics disturbance: A large-scale similar simulation. *International Journal of Mining, Reclamation and Environment, 37*(8), 606–629.

Yan, B., Jia, H., Yilmaz, E., Lai, X., Shan, P., & Hou, C. (2022). Numerical study on microscale and macroscale strength behaviors of hardening cemented paste backfill. *Construction and Building Materials, 321*, 126327.

Yang, X., Xiao, B., Gao, Q., & He, J. (2020). Determining the pressure drop of cemented Gobi sand and tailings paste backfill in a pipe flow. *Construction and Building Materials, 255*, 119371.

Yi, X. W., Ma, G. W., & Fourie, A. (2015). Compressive behaviour of fibre-reinforced cemented paste backfill. *Geotextiles and Geomembranes, 43*(3), 207–215.

Yin, S., Qi, C., Yilmaz, E., Cao, S., & Chen, Q. (2023). Editorial for special issue on frontiers and advances in cemented paste backfill. *International Journal of Minerals, Metallurgy and Materials, 30*(8), 1427–1429.

Yingliang, Z., Jingping, Q., Zhengyu, M. A., & Zhenbang, G., & Hui, L. (2020). Effect of superfine blast furnace slags on the binary cement containing high-volume fly ash. *Powder Technology, 375*, 539–548.

Zaibo, Z., Juanhong, L., Aixiang, W., & Hongjiang, W. (2022). Coupled effects of superplasticizers and glazed hollow beads on the fluidity performance of cemented paste backfill containing alkali-activated slag and MSWI fly ash. *Powder Technology, 399*, 116726.

Zhang, H., Kou, J., Sun, C., Wang, P., Lin, J., Li, J., & Jiang, Y. (2023). Optimization of cemented paste backfill with carbon nanotubes as a sustainable treatment for lead-containing tailings. *Powder Technology, 415*, 118152.

Zheng, J., & Li, L. (2020). Experimental study of the "short-term" pressures of uncemented paste backfill with different solid contents for barricade design. *Journal of Cleaner Production, 275*, 123068.

Zhou, N., Du, E., Zhang, J., Zhu, C., & Zhou, H. (2021). Mechanical properties improvement of sand-based cemented backfill body by adding glass fibers of different lengths and ratios. *Construction and Building Materials, 280*, 122408.

4th International Civil Engineering & Architecture Conference
17-19 May 2025, Trabzon, Türkiye

Effects of fire-caused disasters on natural building stones used ın historical buildings

M. Enes Kılıç*[1], S. Banu İkizler[1], Hakan Ersoy[2]

[1] Karadeniz Technical University, Department of Civil Engineering, 61080 Trabzon, Türkiye
[2] Karadeniz Technical University, Department of Geological Engineering, 61080 Trabzon, Türkiye

Abstract. Fire-induced disasters can cause not only physical damage to historical structures but also irreversible losses in cultural heritage. In this study, the effects of fire on historical building stones were investigated under laboratory conditions to gather data for selecting appropriate restoration materials for fire-damaged structures. According to Eurocode 1 (2011) standards, four different types of natural building stones were heated up to 680 °C, and changes in their physical and mechanical properties such as dry density, specific gravity, uniaxial compressive strength, and indirect tensile strength were examined in detail. Experimental results revealed no significant change in dry density, with the greatest reduction recorded in Rize Andesite at 6.5%. Specific gravity increased by up to 5.5% in Erzurum Andesite, attributed to the formation of new minerals due to fire exposure. Trabzon Basalt exhibited substantial decreases of 62% in longitudinal wave velocity, 56% in uniaxial compressive strength, and 64% in indirect tensile strength. Microstructural analyses using SEM (scanning electron microscope) confirmed that fractures and clumping within the stones contributed to these losses. While minor voids closed after thermal treatment, slightly increasing density, major cracks and larger voids had a reducing effect, leading to minimal overall changes in density. The findings of this study provide critical insights for developing effective restoration strategies aimed at preserving historic structures following fire damage.

Keywords: Fire; Building stone; Disaster; Historical structures

---

1. Introduction

The devastation caused by fire-related disasters at both national and international levels is too significant to be overlooked. It is well-established that such disasters impact not only the physical environment but also profoundly affect the psychological and social well-being of individuals living in the affected areas. Historical structures constructed from natural stone materials are among the most vulnerable building groups to the adverse effects of fires. Damage to these structures entails not only the loss of architectural heritage but also the erosion of cultural identity and historical continuity. Disasters occurring in various parts of the world significantly threaten efforts to preserve cultural heritage. In the face of fires, historical buildings jeopardize not only their physical existence but also the artistic and cultural values they embody, as well as human life itself. Such catastrophes often result in irreversible losses. Throughout history, destruction caused by fires in historic structures has been widespread across different regions of the world, and this issue persists to the present day.

Studies investigating building stones exposed to high temperatures have reported significant findings. Zhang et al. (2016) observed changes in P-wave velocity and microstructural transformations in limestone samples subjected to temperatures ranging from 25°C to 900°C. Their results indicated decreases in both rock strength and P-wave velocity between 200°C and 600°C, with a notable increase in crack network density starting from 600°C. Similarly, Özgüven & Özçelik (2013) examined building stones under high temperatures ranging from 200°C to 1000°C. They observed a white color change on the stone surface at 800°C, and after 900°C, an exothermic heat increase was noted as the limestone reacted with water. Kılıç (2006) investigated the relationship between P-wave velocity, mass loss, and mechanical properties during the calcination process of limestone samples, identifying 900°C as the temperature at which calcination was completed and the maximum mass loss occurred. A common conclusion across these studies is the significant deterioration and alteration of the physical, mechanical, and microstructural properties of natural stones when exposed to high temperatures (Chakrabarti et al., 1996; Chaki et al., 2008; Chen et al., 2012).

Table 1 presents a comparison of the experimental parameters used in this study with other methods reported in the international literature. In this research, experiments were conducted to determine the behavior of natural

* Corresponding author, E-mail: m.enesklcc00@hotmail.com

https://doi.org/10.31462/icearc2025_ce_geo_334

building stones, characteristic of historical structures, under the influence of fire. An oven was employed as the heat source, and cooling was carried out naturally at room temperature. The heating rate was set exponentially, with the samples being heated for two hours, reaching a maximum temperature of 680 °C. This temperature was selected to represent real external fire conditions. To evaluate the mechanical properties of the samples, uniaxial compressive strength and indirect tensile strength tests were conducted. The natural stones used in the study were carefully selected from stone types commonly found in historical buildings.

Table 1. Comparison of Experimental Parameters with Methods in the Literature

Experimental parameters	Widely applied	Seldom applied	In this study
Heat source	Furnace	Open fire	Furnace
Cooling technique	In a heating furnace or at room temperature	With liquid nitrogen	At room temperature
Heating rate (°C/min)	1-10	Exponential logarithmic	Exponential logarithmic
Thermal treatment duration(h)	2-6	Different periods	2
Maximum applied temperature	600-1000	Fire temperature	Fire temperature
Mechanical Tests	Uniaxial Compression or Indirect Tensile	Schmidt hammer	Uniaxial Compression or Indirect Tensile
Rock Types	All Common Types	Used in Historical Structures	Used in Historical Structures

2. Studies conducted and findings

2.1. Procurement and locations of natural building stones

This study aims to conduct a detailed investigation of the natural stone materials used in the construction and restoration of historical structures located in the Eastern Black Sea Region. To this end, the characteristics and sourcing processes of the stones preferred in the region's historical monuments have been comprehensively addressed. The natural building stones utilized in the study were selected from locations historically used in the construction of heritage structures (Table 2), and the physico-mechanical alterations of the rocks employed in the construction of the historical structures depicted in Figure 1 were examined in detail.

Table 2. Rock types used in the study, their locations, and the historical structures where they were used for construction/restoration

Historical Structures Used	Rock Type	Source Location
Fatih Mosque (Trabzon) Ayasofya Mosque (Trabzon)	Andesite	Erzurum (City Center)
Tabakhane Mosque (Trabzon) Kapu Mosque (Giresun)	Andesite	Ankara (Gölbaşı)
Musapaşa Mosque (Trabzon) Taşören Mosque (Çaykara, Trabzon)	Basalt	Trabzon (City Center)
Gümüşhane Emirler Mosque	Andesite	Rize (İyidere)

2.2. Determination of the Physical and Mechanical Properties of the Specimens

The sample preparation process was carried out in accordance with ASTM (1994) standards. As the initial step, a total of 40 core samples were extracted from rock blocks obtained from the provinces of Rize, Trabzon, Ankara, and Erzurum, with 10 samples taken from each region (Figure 2). Special attention was given to ensure that the cores prepared for experimental analyses were free from voids, weathering, or any form of damage. For each location, the core samples were classified into two groups: the first five cores were designated as unexposed (UNCUT) rocks, while the latter five were categorized as fire-exposed (FIRE) rocks. Experimental studies were then conducted on the samples classified in this manner. The cores shown in Figure 2 were labeled during the experimental process. In this context, the andesite samples obtained from Rize were marked with the letter "R," the basalt samples from Trabzon with "T," the andesite samples from Ankara with "A," and the andesite samples from Erzurum with "E."

Within the scope of this study, eight blocks with regular geometric shapes (15 × 20 × 10 cm), sourced from quarries, were utilized. In order to determine the effects of high-temperature exposure on the physical and mechanical properties of the samples, as well as the rate of change in these properties, the initial physical and mechanical characteristics of the specimens at room temperature were first measured. The uniaxial compressive strength was determined with a length-to-diameter ratio of 2.5, while the indirect tensile strength was assessed with a length-to-diameter ratio of 1. The relevant samples were cut and prepared in accordance with the dimensions and geometric specifications required for the Brazilian test setup. For each location, five specimens were prepared for thermal treatment and five as initial (untreated) specimens, resulting in a total of ten specimens per location and forty specimens overall. As illustrated in Figure 3, the load must be applied symmetrically with respect to the center axis of the specimen to generate a characteristic tensile stress within the sample.

This approach enabled the comparison of initial values with those obtained from samples subjected to fire temperatures and facilitated the identification of changes induced by temperature increases. For both pre- and post-exposure conditions, the specific gravity, dry density, longitudinal wave velocity, tensile strength, and uniaxial compressive strength of the samples were determined. Detailed information regarding the number and dimensions of the specimens is presented in Table 3.

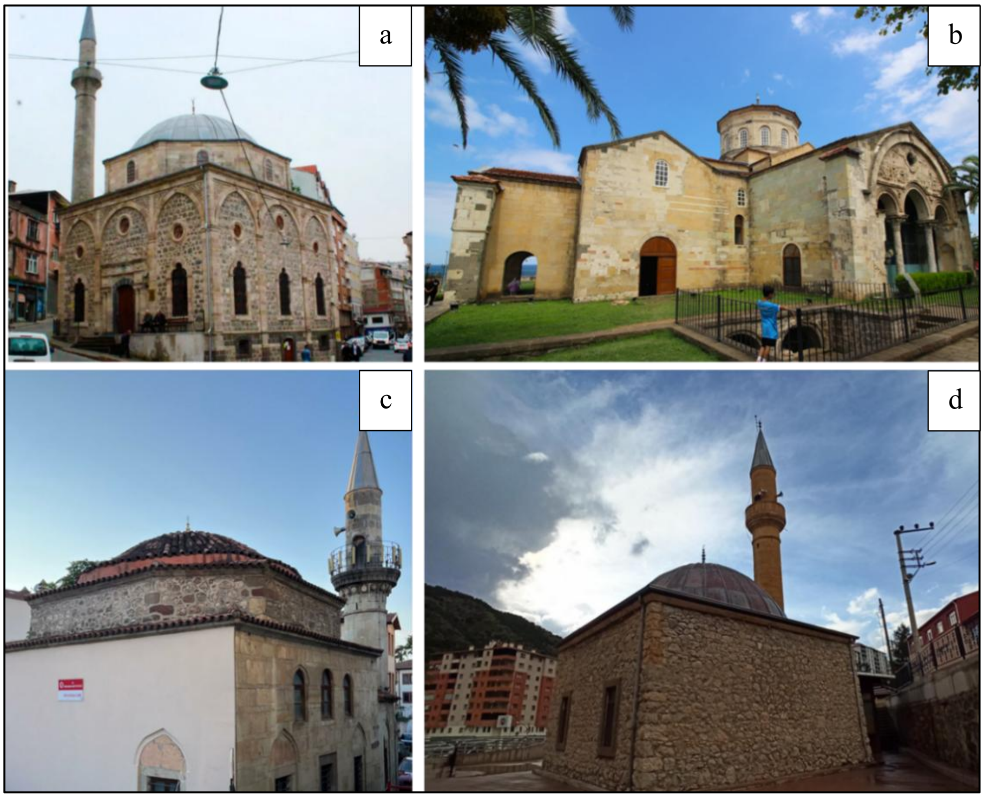

Fig. 1. Current historical structures in which the natural stones used in the study are found (Cultural inventory, 2024; Narmanlı, 2021)
a. Kapu Mosque (Giresun) b. Ayasofya Mosque (Trabzon) c. Musapaşa Mosque (Trabzon) d. Emirler Mosque (Gümüşhane)

Fig. 2. Cylindrical specimens prepared for the experiments

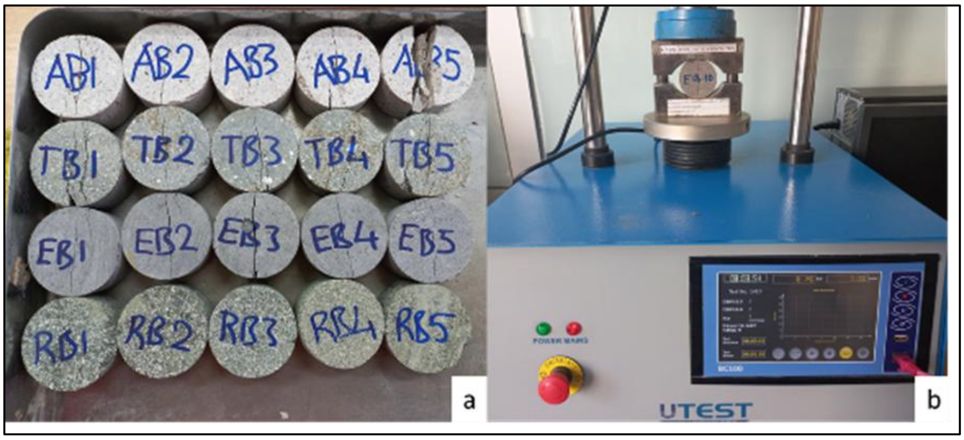

Fig. 3. Final state of the initial specimens after the Brazilian test (a), position of a sample in the loading jaw (b)

Table 3. Dimensions and Numerical Distribution of the Specimens

Structural Properties	Number of Samples in Experimental Studies				Dimensions of the Specimens
	Erzurum Andesite	Ankara Andesite	Trabzon Basalt	Rize Andesite	
SEM	2	2	2	2	$1cm^3$
Uniaxial Compressive Strength	10	10	10	10	length/diameter rate 2.5/1
Indirect Tensile Strength	10	10	10	10	50-60mm length/diameter rate 1/1
Dry Density	10	10	10	10	
Longitudinal Wave Velocity	10	10	10	10	
Specific Gravity	3	3	3	3	

2.3. Specimens exposed to external fire temperatures

With the onset of a fire, temperature values increase rapidly. The temperature can reach approximately 600 °C within the first 10 minutes, 700 °C by the 15th minute, 800 °C by the 30th minute, and up to 1000 °C by the 90th minute. It is known that, after three hours, temperatures can reach approximately 1100 °C, and in some cases, even higher values between 1500 °C and 1700 °C (Kılıç, 2010a). In this study, a Protherm brand muffle furnace was utilized to apply thermal treatment to the samples. The maximum temperature was set at 680 °C, representing an external fire scenario, in accordance with Eurocode 1 (2011) standards. The heating process of the furnace was conducted following the temperature-time curve outlined in Eurocode 1 (2011) (Figure 4). To minimize the risk of cracks and damage that may arise from rapid heating and cooling processes, the temperature increase rate was carefully controlled. Upon reaching the target temperature, the samples were maintained at this level for two hours to ensure homogeneous heat distribution within the rock. At the end of the experiment, the samples were allowed to cool gradually at room temperature in a controlled manner.

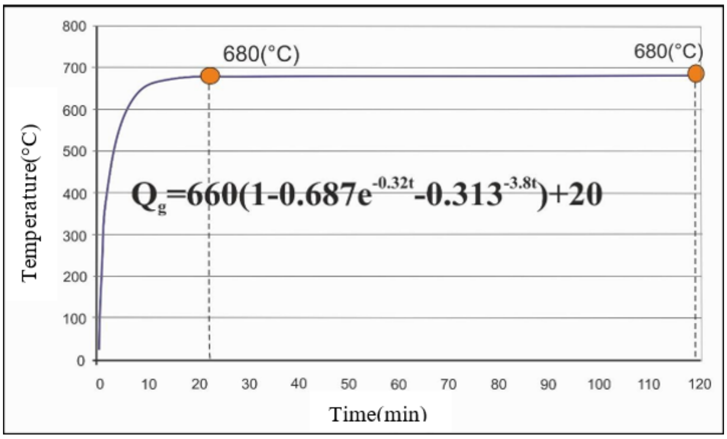

Figure 4. External Fire Temperature-Time Curve (Eurocode, 2011)

2.4. Changes in Physical and Mechanical Properties

In order to investigate the changes in the physical and mechanical properties of natural building stones exposed to external fire temperatures, the initial properties of these rocks were first determined (Table 4). A review of the literature indicates that exposure to high temperatures leads to significant decreases particularly in the uniaxial compressive strength and tensile strength of rocks (Becattini et al., 2017; Ersoy et al., 2019). In many of these studies, the selected high-temperature range typically falls between 200 °C and 1000 °C (Atalar et al., 2021; Sun et al., 2016). In the present study, a real external fire temperature of 680 °C was selected, and experiments were conducted on rocks commonly used in contemporary historical structures (Table 5). A marked decrease in uniaxial compressive strength, tensile strength, and longitudinal wave velocity was observed across all four sample types. Conversely, a noticeable increase in specific gravity was recorded for all samples. Figure 5 presents the graphs illustrating the changes observed in the physical and mechanical properties of the rocks used in this study, comparing the results obtained under initial conditions and after exposure to external fire temperatures.

Table 6 presents the percentage change rates in the physical and mechanical properties of the samples exposed to fire. These rates reflect the increases (+) and decreases (–) in the material properties due to thermal effects, thereby providing a comprehensive assessment of the impact of fire on the material characteristics.

The evaluation of the SEM images presented in Figures 6 and 7 revealed that, overall, small voids closed and agglomeration increased due to melting in all thermally treated samples, while the fractured structure was largely preserved. In the samples obtained from Ankara, it was observed that although small voids were closed due to agglomeration after thermal treatment, this process led to the formation of isolated microcracks. Similarly, in the samples sourced from Erzurum, partial melting resulted in the closure of small voids, but also transformed the samples into a more fractured structure. In the samples from Rize, despite the closure of voids, a noticeable increase in crack continuity was detected. In contrast, the samples from Trabzon exhibited a different behavior compared to the others, with an increase in small voids and the development of new voids following agglomeration after thermal treatment.

Table 4. Physical and Mechanical Properties of the Building Stones Used in the Study at 25°C

	Dry Density (Mg/m^3)			Specific Gravity			Longitudinal Wave Velocity (m/sn)			Uniaxial Compressive Strength (MPa)			Indirect Tensile Strength (MPa)		
	Max.	Min.	Ort.	Max.	Min.	Ort.	Max.	Min	Ort.	Max.	Min.	Ort.	Max.	Min.	Ort.
E	2.68	2.62	2.65	2.76	2.72	2.74	5119	4839	4940	167.1	106.7	134.7	10.8	10.3	10.5
A	2.37	2.29	2.33	2.59	2.52	2.57	3683	4412	4130	138.7	68	88.3	11.6	8.5	9.9
T	2.72	2.63	2.67	2.91	2.85	2.86	5668	4906	5186	134.9	35.6	95.9	11.5	5.7	8.9
R	2.08	1.89	2.00	2.64	2.57	2.60	3219	2693	3002	36.7	31.7	33.4	2	2.3	2.2

Table 5. Physical and Mechanical Properties of the Building Stones Used in the Study at 680°C External Fire Temperature

	Dry Density (Mg/m^3)			Specific Gravity			Longitudinal Wave Velocity (m/sn)			Uniaxial Compressive Strength (MPa)			Indirect Tensile Strength (MPa)		
	Max.	Min.	Ort.	Max.	Min.	Ort.	Max.	Min	Ort.	Max.	Min.	Ort.	Max.	Min.	Ort.
E	2.69	2.64	2.65	2.92	2.87	2.90	3676	3139	3431	96.35	80.2	87.2	8.2	7.3	7.7
A	2.37	2.30	2.33	2.70	2.63	2.66	2338	2657	2516	62.6	40.6	54.6	6.9	3.3	4.5
T	2.69	2.57	2.61	3.1	2.91	3.01	2010	1939	1977	49.2	35.4	41.9	3.5	2.7	3.2
R	1.90	1.85	1.88	2.75	2.61	2.68	1661	902	1367	32.2	10.6	15.9	1.8	1.5	1.6

Table 6. Percentage Comparison of the Physical and Mechanical Properties of Fire-Exposed and Initial Specimens

Natural Building Stones	Percentage Changes of the Post-Fire Specimens Relative to Their Initial States				
	Dry Density	Specific Gravity	Longitudinal Wave Velocity	Uniaxial Compressive Strength	Indirect Tensile Strength
Erzurum Andesite	+%0.4	+%5.5	-%31	-%35	-%27
Ankara Andesite	+%0.4	+%3.4	-%30	-%38	-%54
Trabzon Basalt	-%2.3	+%5.0	-%62	-%56	-%64
Rize Andesite	-%6.5	+%3.0	-%55	-%52	-%23

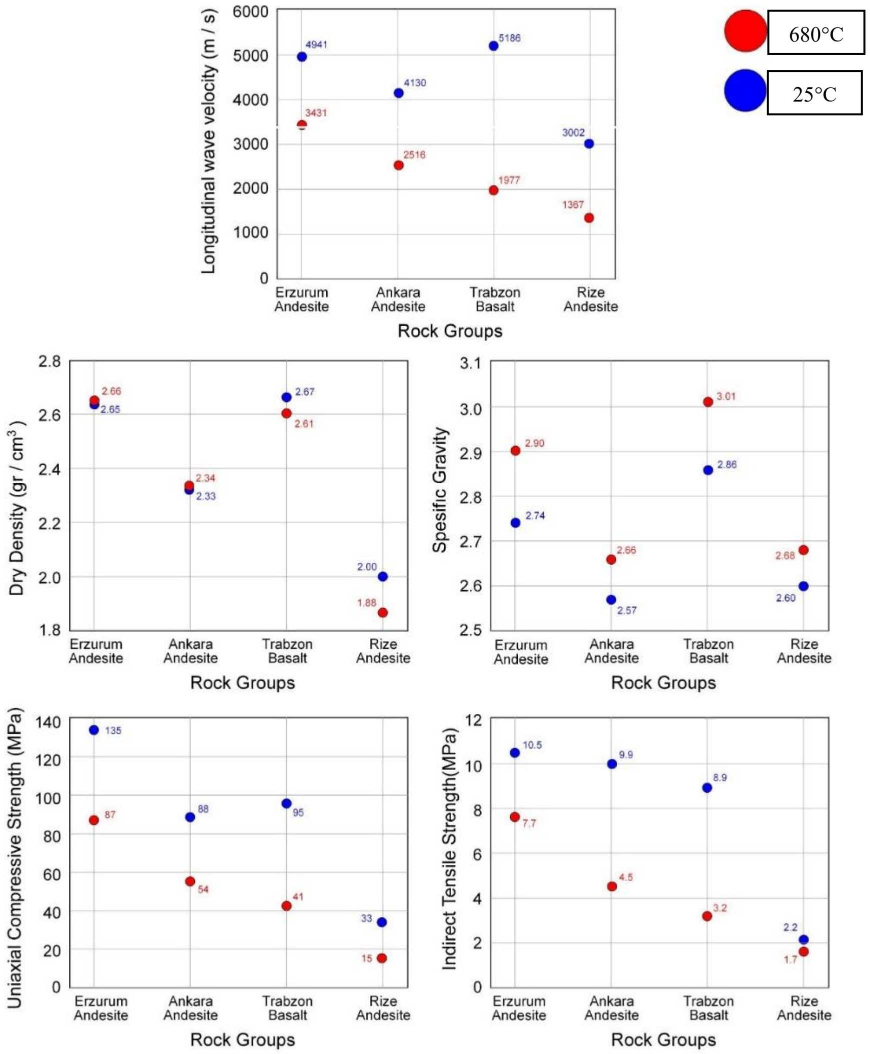

Figure 6. Graphs of the Changes in the Physical and Mechanical Properties of the Rocks Used in the Study

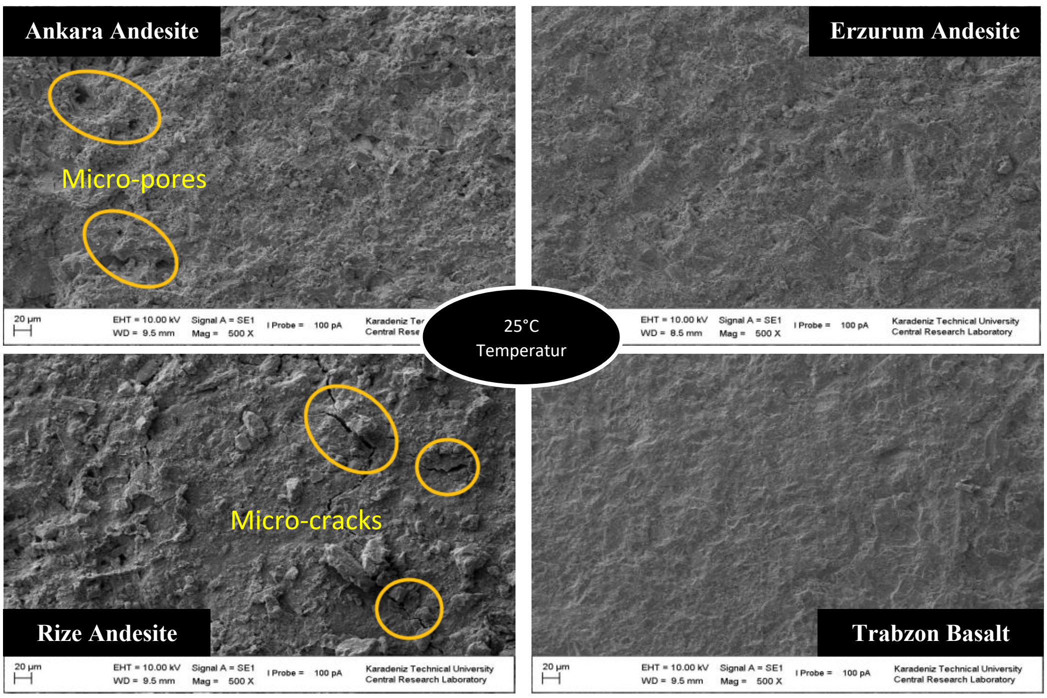

Figure 7. SEM Images of the Specimens Used in the Study at 25°C

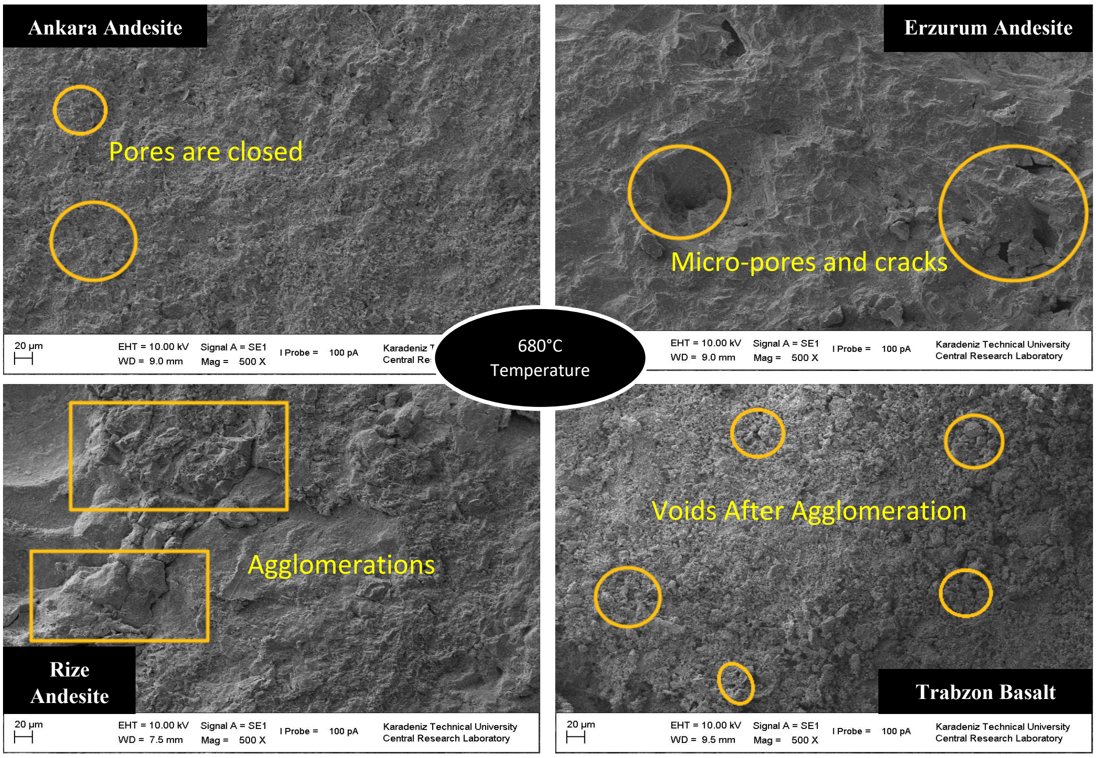

Figure 8. SEM Images of the Specimens After Thermal Treatment at 680°C

3. Conclusions

In this thesis study, the changes in the physical, mechanical, and microstructural properties of historical building stones exposed to an external fire temperature of 680 °C under laboratory conditions were investigated. A test group was established by considering the dimensions and numerical distribution of the samples. The specimens were heated in a controlled manner up to 680 °C, representing external fire conditions, and underwent various physical and chemical transformations during the process. The closure of small voids exerted an increasing effect on dry density, whereas larger voids and fractures resulting from agglomeration had a decreasing effect. The balancing of these opposing effects resulted in no significant change in dry density values. Additionally, partial melting and agglomeration, occurring without mass loss, led to structural changes within the solid grains independently of porosity, indicating the possible formation of high-specific-gravity minerals at elevated temperatures.

In the samples dried at 105 °C, it was determined that free water in the rock pores was completely evaporated, while the water bound within the crystal structures of minerals remained unaffected. However, in the samples heated up to 680 °C, it was observed that crystalline water was also released from the mineral structures. Besides water loss, micro-cracks formed due to agglomeration caused a sudden decrease in longitudinal wave velocity, leading to a reduction in the mechanical strength of the rocks. Significant reductions in both uniaxial compressive strength and indirect tensile strength were identified in the thermally treated samples, with this strength loss being more pronounced in specimens exhibiting substantial decreases in longitudinal wave velocity.

The findings were presented with supporting graphical data, and microstructural changes were examined in detail through SEM imaging. These results provide crucial insights into understanding the alterations in the physical and mechanical properties of historical building stones after fire exposure and contribute to the selection of appropriate restoration materials.

References

ASTM. (1994). *Annual book of ASTM standards: Construction: Soil and rock*. ASTM Publication.

Atalar, C., & Ersoy, H. (2021). Investigation on the change of physical and strength properties of calcarenite exposed to high temperatures. *Journal of Geological Engineering, 45*(1), 29–40.

Becattini, V., Motmans, T., Zappone, A., Madonna, C., Haselbacher, A., & Steinfeld, A. (2017). Experimental investigation of the thermal and mechanical stability of rocks for high-temperature thermal-energy storage. *Applied Energy, 203*, 373–389.

Chaki, S., Takarli, M., & Agbodjan, W. P. (2008). Influence of thermal damage on physical properties of a granite rock: Porosity, permeability and ultrasonic wave evolutions. *Construction and Building Materials, 22*(7), 1456–1461.

Chakrabarti, B., Yates, T., & Lewry, A. (1996). Effect of fire damage on natural stonework in buildings. *Construction and Building Materials, 10*(7), 539–544.

Chen, Y. L., Ni, J., Shao, W., & Azzam, R. (2012). Experimental study on the influence of temperature on the mechanical properties of granite under uni-axial compression and fatigue loading. *International Journal of Rock Mechanics and Mining Sciences, 56*, 62–66.

Ersoy, H., Kolaylı, H., Karahan, M., Harputlu Karahan, H., & Sünnetci, M. O. (2019). Effect of thermal damage on mineralogical and strength properties of basic volcanic rocks exposed to high temperatures. *Bulletin of Engineering Geology and the Environment, 78*, 1515–1525.

European Committee for Standardization (CEN). (2011). *Eurocode 1: Actions on structures exposed to fire*. Brussels: CEN.

Kılıç, A. (2010). Ateşi tutan eller: Ateş kahramanları (pp. 93–144). Teknik Yayıncılık Grubu.

Kılıç, Ö. (2006). The influence of high temperatures on limestone P-wave velocity and Schmidt hammer strength. *International Journal of Rock Mechanics and Mining Sciences, 43*(6), 980–986.

Kültür Envanteri. (2024). *Ayasofya Camii, Trabzon*. Retrieved from https://kulturenvanteri.com/yer/?p=4484

Kültür Envanteri. (2024). *Emirler Camii, Gümüşhane*. Retrieved from https://kulturenvanteri.com/yer/?p=225902

Kültür Envanteri. (2024). *Musapaşa Camii, Ortahisar*. Retrieved from https://kulturenvanteri.com/yer/?p=13959

Narmanlı, F. (2021). Giresun merkez camilerinden tezyinat örnekleri (Kale, Kapu ve Hacı Mittat camileri). *İdrak Dini Araştırmalar Dergisi, 1*(1), 147–172.

Ozguven, A., & Ozcelik, Y. (2013). Investigation of some property changes of natural building stones exposed to fire and high heat. *Construction and Building Materials, 38*, 813–821.

Sun, Q., Lü, C., Cao, L., Li, W., Geng, J., & Zhang, W. (2016). Thermal properties of sandstone after treatment at high temperature. *International Journal of Rock Mechanics and Mining Sciences, 85*, 60–66.

Zhang, W., Sun, Q., Hao, S., & Wang, B. (2016). Experimental study on the thermal damage characteristics of limestone and underlying mechanism. *Rock Mechanics and Rock Engineering, 49*, 2999–3008.

4th International Civil Engineering & Architecture Conference
17-19 May 2025, Trabzon, Türkiye

Liquefaction analysis of various soil profiles based on TBEC 2018: Case studies from Elazığ Province

Kübra Sertkaya*[1], Mesut Gör[1], Rahim Khan Nasery[1], Ahmet Altunbey[1]

[1] Fırat University, Engineering Faculty, Department of Civil Engineering, 23119 Elazığ, Türkiye

Abstract. Earthquakes, being natural disasters resulting from the abrupt release of energy within the Earth's crust, cause significant environmental and economic hazards. The damages inflicted by recent seismic events in Turkey has necessitated a detailed investigation of soil properties. Under seismic loading, soils experience a sudden increase in pore water pressure, resulting in a loss of rigidity whereby the soil exhibits a fluid-like behavior. This liquefaction is commonly observed in saturated and loose soils, can lead to the weakening, settlement, lateral spreading, or failure of structural foundations. The increasing use of areas prone to liquefaction, such as agricultural lands and alluvial plains, as construction sites has further amplified the significance of this issue. Therefore, understanding the liquefaction behavior of saturated fine-grained soils is crucial for mitigating seismic hazards and ensuring structural safety. To achieve this, structures should be founded on stable soil strata. This study aims to evaluate the liquefaction potential of different locations within the Elazığ city center. For this purpose, data reports from borehole investigations conducted at three distinct sites in the Elazığ city center, along with field and laboratory test results, were utilized. The liquefaction potential of soil layers between depths of 1.50-20.00 m was assessed based on soil classifications, test results, and Standard Penetration Test (SPT) results, in accordance with the criteria specified in the Turkish Building Earthquake Code (TBEC-2018) for an earthquake magnitude of Mw=7.5. Through comprehensive analyses and evaluations, this study presents a detailed assessment of liquefaction risk and identifies potential liquefaction zones.

Keywords: Elazığ province; TBEC 2018; SPT; Soil liquefaction; Earthquake

1. Introduction

Located in an active seismic region, Turkey has historically experienced a significant number of natural disasters, with earthquakes standing out as the most devastating. Research indicates that approximately 58% of individuals impacted by natural disasters in the country have been affected by earthquakes (Kundak & Kadıoğlu, 2011). Earthquakes inflict both direct structural damage and indirect effects by altering the geotechnical properties of the soil. Saturated and loose soils are especially susceptible during seismic activity, where strong ground motions can weaken inter-particle bonds and trigger soil liquefaction. This phenomenon presents significant threats to the stability of structures. Liquefaction—frequently observed in loose, water-saturated soils (Aytaş, 2019)—can weaken building foundations, leading to settlement, lateral spreading, or structural damage. A superstructure may remain statically sound; however, without appropriate precautions to address potential soil-related issues, its integrity can still be jeopardized. Consequently, a thorough understanding of the liquefaction behavior in saturated, fine-grained soils is crucial for minimizing earthquake-induced hazards and maintaining structural integrity under dynamic loading conditions (Altındiş, 2020). The Mw 6.8 earthquake that struck in 2020 along the East Anatolian Fault—impacting the Elazığ region (see Figure 3.1)—along with the Mw 7.7 Kahramanmaraş-Pazarcık and Mw 7.6 Elbistan earthquakes on February 6, 2023, have once again underscored the critical importance of liquefaction phenomena (Altındiş, 2020). Figures 1 and 2 illustrate the effects of liquefaction and lateral spreading triggered by the 2023 Kahramanmaraş-Pazarcık and Elbistan earthquakes. Liquefaction continues to be a major geotechnical concern, driving ongoing research within the field of geotechnical earthquake engineering. This phenomenon poses substantial risks to structural foundations during seismic events, emphasizing the need for designing and constructing structures that are resilient to its impacts (Alpaslan, 2013). Liquefiable and non-liquefiable soils exhibit distinct differences in terms of their profiles and geotechnical characteristics (Cubrinovski et al., 2019). To evaluate the potential for liquefaction, geotechnical investigations typically utilize a range of in-situ testing methods, such as the Standard Penetration Test (SPT), Cone Penetration Test (CPT), and shear wave velocity measurements. These testing methods provide critical information for assessing soil response under seismic loads (Emiroğlu & Arsoy, 2019). In the case of gravelly soils, the Dynamic Penetration Test (DPT) may

*Corresponding author , E-mail: kubrasrtky@gmail.com

https://doi.org/10.31462/icearc2025_ce_geo_335

be more advantageous than other in-situ techniques (Roy et al., 2022). Among these, the Standard Penetration Test (SPT) is widely favored due to its practicality in obtaining samples from boreholes and its suitability for a broad range of soil types (Li et al., 2022). Analyses based on SPT data categorize regions according to their liquefaction potential as "high," "low," and "very low" (Orhan & Ateş, 2010). The Turkish Building Earthquake Regulation (TBEC-2018), published on March 18, 2018, and effective from January 1, 2019, provides guidelines for assessing soil liquefaction potential using Standard Penetration Test (SPT) data. Liquefaction analyses are performed for design earthquakes with magnitudes of 6.5, 7.0, and 7.5 resulting in the identification of areas susceptible to liquefaction. These analyses contribute to the development of liquefaction potential maps and seismic settlement potential maps, which are crucial for informed engineering design and effective risk mitigation strategies. Furthermore, Geographic Information System (GIS) applications are increasingly employed in liquefaction studies (Özdin, 2023; Şekho, 2023). In parallel, design charts are being developed to support both liquefaction assessments and ground improvement efforts aimed at mitigating liquefaction-induced hazards (Dağdeviren, 2019). In areas identified as susceptible to liquefaction, suitable ground improvement techniques—specifically tailored to the local soil conditions—should be selected and applied prior to construction (Sertkaya, 2024).

2. Material and method

In this study, data reports from drilling surveys conducted in various neighborhoods of Elazığ city center, along with field and laboratory test results, were utilized. The liquefaction potential of soil layers within the depth range of 1.50 m to 20.00 m, soil classifications, and Standard Penetration Test (SPT) results were evaluated using Excel, in accordance with the criteria specified in the Turkish Building Earthquake Regulation (TBEC-2018).

2.1. Experimental studies

In the Elazığ city center, specific areas within the Aksaray, Kesrik, and Sürsürü neighborhoods (N) were selected as study sites. During the field investigations, Standard Penetration Tests (SPT) were conducted to delineate the soil profiles and evaluate the engineering characteristics of the soils in these areas, while both disturbed and undisturbed samples were collected for laboratory analysis (Figure 3). The study utilized data from 8 boreholes (BH), each extending to a depth of 20.00 meters, within these regions (Table 1). During the drilling operations, groundwater levels within the soil profiles were recorded, and varying soil profiles were observed across all study sites.

Groundwater level measurements taken from the boreholes at the investigation sites indicated groundwater presence at depths of 3.50 meters in Aksaray Neighborhood, 0.50 meters in Kesrik Neighborhood, and 5.50 meters in Sürsürü Neighborhood.

Table 1. The SPT-N values obtained from the Standard Penetration Test

(m)	1.5	3.0	4.5	6.0	7.5	9.0	10.5	12.0	13.5	15.0	16.5	18.0	20.0
Aksaray BH1	20	15	19	18	12	19	16	12	21	41	18	14	17
Aksaray BH2	-	11	19	4	16	39	21	23	29	12	12	15	14
Aksaray BH3	-	12	11	3	8	19	6	12	13	6	7	8	6
Aksaray BH4	-	20	22	2	7	10	8	8	8	11	12	8	8
Kesrik BH1	10	5	2	13	25	79	36	-	65	-	-	-	-
Kesrik BH2	5	-	9	12	52	40	-	25	17	41	53	34	17
Sürsürü BH1	15	13	16	15	15	15	21	16	21	14	13	15	13
Sürsürü BH2	14	13	17	18	16	16	21	18	21	14	16	15	14

Fig. 1. Sand boils observed following the January 24, 2020, Elazığ Sivrice (Mw=6.8) earthquake (Çetin et al., 2020)

Fig. 2. Settlement caused by liquefaction in the Gölbaşı district of Adıyaman following the February 6, 2023, Kahramanmaraş-Pazarcık (Mw=7.7) and Elbistan (Mw=7.6) earthquakes (Çetin et al., 2023)

Fig. 3. Soil investigations (SPT Test) (Gökbay Engineering Ground Investigation Report, 2021)

2.2. Laboratory studies

To assess the liquefaction susceptibility of soils under seismic loading, both in-situ testing and laboratory analyses are performed on disturbed and undisturbed samples collected from boreholes. Laboratory tests include water content determination, sieve analysis, Atterberg limits, consolidation, hydrometer analysis, triaxial compression, and natural unit weight determination to evaluate the soil properties (Table 2-7).

Table 2. The soil types in the study area (Aksaray N.)

Borehole No	Sample Type	Depth (m)	Soil Classification	Clay (%)	Silt (%)
UD	UD	2.0	CL	40.97	20.85
BH1	SPT	4.5	SM	-	-
BH1	SPT	10.5	SM	-	-
UD	UD	2.5	CL	31.97	22.40
BH2	SPT	6.0	SM	-	-
BH2	SPT	18.0	SM	-	-
UD	UD	3.0	SC	25.33	19.99
BH3	SPT	7.5	SM	-	-
BH3	SPT	9.0	GM-GW	-	-
UD	UD	3.5	CL	35.92	22.22

Table 3. The soil types in the study area (Kesrik N.)

Borehole No	Sample Type	Depth (m)	Soil Classification	Clay (%)	Silt (%)
BH1	UD	1.0	CIM		
BH1	SPT	3.0	CIM	58.78	21.12
BH1	SPT	7.5	ciGr	-	-
UD	UD	15.0	ciGr	-	-
BH2	SPT	1.0	CIM	-	-
BH2	SPT	3.0	CIM	4.28	24.61
BH2	SPT	6.0	ciSa	-	-
BH2	SPT	9.0	ciSa-SaW	-	-

Table 4. The soil types in the study area (Sürsürü N.)

Borehole No	Sample Type	Depth (m)	Soil Classification	Clay (%)	Silt (%)
UD	UD	2.0	CL	-	-
BH1	SPT	7.5	SC	44.98	23.31
BH1	SPT	15.0	SC	-	-
UD	UD	2.5	CL	-	-
BH2	SPT	9.0	SM	42.88	25.24
BH2	SPT	18.0	SC		

Table 5. The average values of the physical properties of the soils within the investigation area (Aksaray N.)

Borehole No	Depth (m)	W (%)	LL (%)	PL (%)	PI (%)	γ_n (gr/cm^3)
	2.0	13.26	34	19	15	
BH1	4.5	9.45	NP	NP	NP	1.72
	10.5	9.49	NP	NP	NP	
	2.5	25.97	33	18	15	
BH2	6.0	9.34	NP	NP	NP	1.74
	18.0	18.72	NP	NP	NP	
	3.0	18.42	31	18	13	
BH3	7.5	31.20	NP	NP	NP	1.75
	9.0	9.50	NP	NP	NP	
	3.5	24.82	32	18	14	
BH4	9.0	28.79	35	19	16	1.73
	20.0	20.34	32	17	15	

Table 6. The average values of the physical properties of the soils within the investigation (Kesrik N.)

Borehole No	Depth (m)	W (%)	LL (%)	PL (%)	PI (%)	γ_n (gr/cm^3)
	1.0	19.01	40	20	20	
BH1	3.0	24.00	38	19	19	1.68
	7.5	19.42	NP	NP	NP	
	15.0	11.16	NP	NP	NP	
BH2	1.0	26.88	41	21	20	
	3.0	36.54	42	21	21	1.69
	6.0	21.11	NP	NP	NP	

Table 7. The average values of the physical properties of the soils within the investigation area (Sürsürü N.)

Borehole No	Depth (m)	W (%)	LL (%)	PL (%)	PI (%)	γ_n (gr/cm^3)
	2.0	14.11	33	17	16	
BH1	7.5	28.00	26	15	11	1.72
	15.0	21.45	27	16	11	
	2.5	18.98	34	17	17	
BH2	9.0	14.61	NP	NP	NP	1.72
	18.0	12.44	27	17	10	
	12.0	22.00	29	18	11	

2.3. Liquefaction analysis according to TBEC 2018

The regulation, published on March 18, 2018, and effective from January 1, 2019, provides the standards to be used for structures to be built in earthquake-prone areas.

To calculate the liquefaction resistance using SPT test results, the raw SPT field data obtained from the site must be recalculated with specific correction factors. This recalculation process is outlined in Equations (1-6) and Table 8.

$$N_{1.60} = NC_NC_RC_SC_BC_E \quad (1)$$

In this context, C_N represents the geological stress (depth) correction factor applied to cohesionless soils, C_R denotes the rod length correction factor, C_S indicates the sampler type correction factor, C_B represents the borehole diameter correction factor, and C_E signifies the energy ratio correction factor.

The depth correction factor, C_N, is calculated using the relation given in equation (2).

$$C_N = 9.78 \times (1 \div \sigma_{VO}')^{0.5} \leq 1.70 \quad (2)$$

In the expression presented in equation (2), the effective vertical stress at the testing depth, σ_{vo}' (kN/m²), is determined based on the field conditions under which the Standard Penetration Test (SPT) is conducted. Additionally, the SPT results must be adjusted according to the proportion of fine-grained particles in the soil.

$$N_{1.60f} = \alpha + \beta N_{1.60} \quad (3)$$

$$\alpha=0 ; \beta=1 \text{ (IDI} \leq \%5) \quad (4)$$

$$\alpha = exp[1.76 \times (190 \div IDI^2)] ; \ \beta = 0.99 + IDI^{1.5} \div 1000 \ (\%5< \text{IDI} \leq \%35 \quad (5)$$

$$\alpha = 5.0 ; \ \beta = 1.2 \ \text{(IDI} \geq \%35) \quad (6)$$

The correction factors in the liquefaction analysis of this study are as follows:

The values of C_R=1.00, C_S=1.20, C_B=1.10, and C_E=0.75 have been applied. Based on the laboratory test results, the fine-grain ratio exceeds 35% in all the studied areas.

The liquefaction resistance (τ_R) was calculated by multiplying the cyclic resistance ratio corresponding to a moment magnitude 7.5 earthquake ($CRR_{M7.5}$) by the magnitude scaling factor for the design earthquake (C_M) and the effective vertical stress (σ') (Equation 7-9).

$$\tau_R = CRR_{M7.5} \times C_m \times \sigma' \quad (7)$$

The cyclic resistance ratio was calculated using the equation provided in Equation (8).

$$CRR_{M7.5} = (1 \div 34 - N_{1.60f}) + (N_{1.60f} \div 135) + (50 \div (10N_{1.60f} + 45)^2 - 1 \div 200 \quad (8)$$

The earthquake magnitude correction factor, C_M, is calculated based on the moment magnitude (M_W) of the design earthquake.

$$C_M = (10^{2.24} \div {M_W}^{2.56}) \quad (9)$$

The earthquake magnitude correction factor (C_M) was calculated based on the design earthquake magnitude (M_W = 7.5). The shear stress developed in the soil was calculated as shown in Equation (10).

$$\tau_{deprem} = 0.65 \times \ \sigma_{vo} \times (0.4 \times s_{DS}) * r_d \quad (10)$$

Here, σ_{vo} represents the total vertical stress at the depth where liquefaction evaluation is performed, and r_d denotes the stress reduction factor at the corresponding depth. These values are calculated using the relationships provided in Equations (11-14).

$$rd = 1.0 - 0.00765 \times z \qquad z \leq 9.15m \quad (11)$$

$$rd = 1.174 - 0.0267 \times z \qquad 9.15m < z \leq 23m \quad (12)$$

$$rd = 0.744 - 0.008 \times z \qquad 23m < z \leq 30m \quad (13)$$

$$rd = 0.50 \qquad z > 30m \quad (14)$$

S_{DS} values represent the short-period design spectral acceleration coefficient. Ground motion values for three different locations were obtained using the Turkey Earthquake Hazard Map (Table 8).

Table 8. Ground motion values

Neighborhood	Ss	S_1	S_{DS}	S_{D1}	PGA (g)	PGV (cm/sn)
Aksaray	0.945	0.266	1.060	0.550	0.396	24.802
Kesrik	0.963	0.558	1.074	0.558	0.403	25.309
Sürsürü	0.940	0.264	1.047	0.547	0.394	24.667

Liquefaction analyses were conducted for boreholes BH1-BH2-BH3-BH4 in Aksaray Neighborhood, BH1-BH2 in Kesrik Neighborhood, and BH1-BH2 in Sürsürü Neighborhood (Table 9-11).

Table 9. Liquefaction analysis results for the BH1 borehole in Aksaray Neighborhood according to TBEC-2018

Depth (m)	SPT-N	$\gamma_{n,d}$ (kN/m^3)	σ (kN/m^2)	σ' (kN/m^2)	C_N	$N_{1.60f}$	$CRR_{M7.5}$	R_D	τ_R	$\tau_{Dep.}$	$\tau_R/\tau_{Dep.}$	Liquefaction condition
1.50	20	16.87	25.31	25.31	1.70	45.39	0.24	0.99	6.17	6.89	0.89	NO GROUNDWATER
3.00	15	16.87	50.61	50.61	1.37	29.50	0.44	0.98	22.07	13.63	1.62	NO GROUNDWATER
4.50	19	17.87	77.42	67.61	1.19	31.85	0.70	0.97	47.06	20.60	2.28	NON-LIQUEFIABLE
6.00	18	17.87	104.22	79.70	1.10	28.43	0.39	0.95	30.72	27.40	1.12	NON-LIQUEFIABLE
7.50	12	17.87	131.03	91.79	1.02	19.55	0.21	0.94	19.27	34.04	0.57	LIQUEFIABLE
9.00	19	17.87	157.83	103.88	0.96	26.66	0.33	0.93	34.20	40.50	0.84	LIQUEFIABLE
10.50	16	17.87	184.64	115.97	0.91	22.26	0.25	0.89	28.51	45.47	0.63	LIQUEFIABLE
12.00	12	17.87	211.44	128.06	0.86	17.32	0.18	0.85	23.60	49.74	0.47	LIQUEFIABLE
13.50	21	17.87	238.25	140.15	0.83	25.61	0.30	0.81	42.67	53.42	0.80	LIQUEFIABLE
15.00	41	17.87	265.05	152.24	0.79	43.61	0.21	0.77	32.60	56.50	0.58	$N_{1.60}$ >30
16.50	18	17.87	291.86	164.33	0.76	21.31	0.23	0.73	38.20	59.00	0.65	LIQUEFIABLE
18.00	14	17.87	318.66	176.42	0.74	17.25	0.18	0.69	32.37	60.90	0.53	LIQUEFIABLE
20.00	17	17.87	354.40	192.54	0.70	19.23	0.21	0.64	39.68	62.51	0.63	LIQUEFIABLE

Table 10. Liquefaction analysis results for the BH1 borehole in Kesrik Neighborhood according to TBEC-2018

Depth (m)	SPT-N	$\gamma_{n,d}$ (kN/m^3)	σ (kN/m^2)	σ' (kN/m^2)	C_N	$N_{1.60f}$	$CRR_{M7.5}$	R_D	τ_R	$\tau_{Dep.}$	$\tau_R/\tau_{Dep.}$	Liquefaction condition
1.50	10	17.48	26.22	16.41	1.70	25.20	0.30	0.99	4.85	7.24	0.67	LIQUEFIABLE
3.00	5	17.48	52.44	27.92	1.70	15.10	0.16	0.98	4.50	14.31	0.31	PI > 12%
4.50	2	17.48	78.66	39.42	1.56	8.70	0.10	0.97	4.01	21.21	0.19	LIQUEFIABLE
6.00	13	17.48	104.88	50.93	1.37	26.17	0.32	0.95	16.14	27.94	0.58	LIQUEFIABLE
7.50	25	17.48	131.10	62.43	1.24	41.76	0.18	0.94	10.97	34.51	0.32	$N_{1.60}$ > 30
9.00	79	17.48	157.32	73.94	1.14	111.75	0.81	0.93	59.88	40.91	1.46	$N_{1.60}$ > 30
10.50	36	17.48	183.54	85.44	1.06	50.25	0.31	0.89	26.13	45.80	0.57	$N_{1.60}$ > 30
12.00	-	17.48	209.76	96.95	0.99	5.00	0.07	0.85	6.99	50.00	0.14	LİQUEFİABLE
13.50	65	17.48	235.98	108.45	0.94	77.52	0.55	0.81	59.25	53.61	1.11	$N_{1.60}$ > 30
15.00	-	17.48	262.20	119.96	0.89	5.00	0.07	0.77	8.64	56.63	0.15	LIQUEFIABLE
16.50	-	17.48	288.42	131.46	0.85	5.00	0.07	0.73	9.47	59.07	0.16	LIQUEFIABLE
18.00	-	17.48	314.64	142.97	0.82	5.00	0.07	0.69	10.30	60.92	0.17	LIQUEFIABLE
19.50	-	17.48	340.86	154.47	0.79	5.00	0.07	0.65	11.13	62.19	0.18	LIQUEFIABLE

Table 11. Liquefaction analysis results for the BH1 borehole in Sürsürü Neighborhood according to TBEC-2018

Depth (m)	SPT-N	$\gamma_{n,d}$ (kN/m^3)	σ (kN/m^2)	σ' (kN/m^2)	C_N	$N_{1.60f}$	$CRR_{M7.5}$	R_D	τ_R	$\tau_{Dep.}$	$\tau_R/\tau_{Dep.}$	Liquefaction condition
1.50	15	16.87	25.31	25.31	1.70	35.29	-0.52	0.99	-13.06	6.87	-1.90	NO GROUNDWATER
3.00	13	16.87	50.61	50.61	1.37	26.23	0.32	0.98	16.12	13.59	1.19	NO GROUNDWATER
4.50	16	16.87	75.92	75.92	1.12	26.34	0.32	0.97	24.38	20.14	1.21	NO GROUNDWATER
6.00	15	17.87	102.72	97.82	0.99	22.62	0.25	0.95	24.56	26.93	0.91	LIQUEFIABLE
7.50	15	17.87	129.53	109.91	0.93	21.62	0.24	0.94	26.02	33.55	0.78	LIQUEFIABLE
9.00	15	17.87	156.33	122.00	0.89	20.78	0.23	0.93	27.49	40.00	0.69	LIQUEFIABLE
10.50	21	17.87	183.14	134.09	0.84	26.07	0.31	0.89	42.21	44.98	0.94	LIQUEFIABLE
12.00	16	17.87	209.94	146.18	0.81	20.38	0.22	0.85	32.18	49.25	0.65	LIQUEFIABLE
13.50	21	17.87	236.75	158.27	0.78	24.39	0.28	0.81	44.38	52.93	0.84	LIQUEFIABLE
15.00	14	17.87	263.55	170.36	0.75	17.46	0.19	0.77	31.66	56.02	0.57	LIQUEFIABLE
16.50	13	17.87	290.36	182.45	0.72	16.18	0.17	0.73	31.41	58.53	0.54	LIQUEFIABLE
18.00	15	17.87	317.16	194.54	0.70	17.50	0.19	0.69	36.23	60.44	0.60	LIQUEFIABLE
20.00	13	17.87	352.90	210.66	0.67	15.41	0.16	0.64	34.58	62.07	0.56	LIQUEFIABLE

According to the criteria specified in the Turkish Building Earthquake Code (TBEC-2018), the potential for soil liquefaction has been assessed (Figure 4). Liquefaction is not expected under the following conditions:

- If the ratio of cyclic shear stress to the cyclic resistance ratio (τ_R / $\tau_{Dep.}$) is greater than 1.1, (FS >1.1),
- If the Plasticity Index (PI) is greater than 12%,
- If the corrected Standard Penetration Test (SPT) blow count ($N_{1.60}$) is greater than 30,
- If there is no groundwater present at the site.

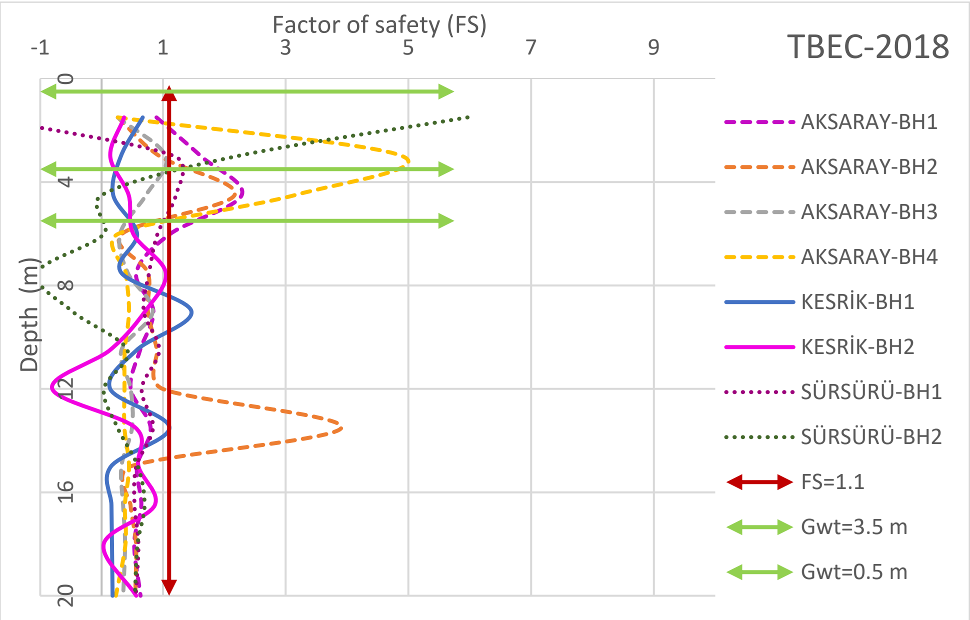

Fig. 4. Soil liquefaction

3. Conclusions

The analysis results indicate variability in the subsurface conditions across the region in terms of depth and topography, with some areas exhibiting a greater susceptibility to liquefaction. Based on the criteria specified in TBEC-2018, the assessment of liquefaction potential was carried out by taking the following factors into account:

- Presence of groundwater is required for liquefaction risk: Therefore, liquefaction risk is not expected in locations and depths where groundwater is absent.
- Plasticity index (PI) greater than 12: When the plasticity index (PI) value is greater than 12, liquefaction risk is considered to be low or unlikely.

- Corrected SPT values ($N_{1.60}$) greater than 30: In cases where the corrected SPT values ($N_{1.60}$) are greater than 30, the liquefaction risk is very low or not expected. Additionally, it has been observed that liquefaction risks increase at lower SPT values.
- Based on the analyses conducted in Aksaray Neighborhood according to TBEC-2018, liquefaction is not anticipated at depths of 4.50 m and 6.00 m in borehole BH1, at depths of 4.50 m and 13.50 m in borehole BH2, and at a depth of 4.50 m in borehole BH4, as the factor of safety is greater than 1.10 at these points. Furthermore, liquefaction is expected at all depths below the groundwater table in borehole BH3.
- Based on the analyses conducted in Kesrik Neighborhood according to TBEC-2018, liquefaction is not anticipated at depths of 9.00 m and 13.50 m in borehole BH1, as the factor of safety is greater than 1.10 at these points. In borehole BH2, liquefaction is expected at all depths below the groundwater table (excluding the zone at a depth of 12.0 meters).
- Based on the analyses conducted in Sürsürü Neighborhood according to TBEC-2018, liquefaction is expected at all depths below the groundwater table in borehole BH1. In borehole BH2, liquefaction is expected at all depths below the groundwater table, with the exception of the zones at depths of 7.50 and 9.00 meters.

Determining the subsurface liquefaction potential in Elazığ Province is critically important for ensuring the safety of construction and infrastructure developments in the area. In this context, increasing the number of field investigations, laboratory experiments, and geophysical surveys at different locations will enhance the detailed assessment of soil profiles. Analyzing the collected data in accordance with TBEC-2018 standards and advanced tools like DEEPSOIL will allow for a more accurate estimation of liquefaction risk. In regions with potential for liquefaction, the most suitable and cost-effective ground improvement methods should be identified based on the soil conditions. Comprehensive engineering analyses carried out within this framework will play a key role in planning safe construction practices and mitigating regional disaster risks.

References

Alpaslan, N. (2013). Zemin sıvılaşması ve mekanizması. *Yaşam Bilimleri Dergisi*, 3(2), 67-89.

Altındiş, M. (2020). *Sıvılaşma analizi ve sıvılaşma sonucu oluşan yanal yayılma hesap yöntemlerinin karşılaştırılması*. İstanbul Teknik Üniversitesi, Fen Bilimleri Enstitüsü, İstanbul. (in Turkish)

Aytaş, Z. (2019). *Zemin sıvılaşmasına zemin ve deprem parametrelerini etkisinin değerlendirilmesi*. Batman Üniversitesi, Fen Bilimleri Enstitüsü, Batman. (in Turkish)

Çetin, K. Ö. (2020). The Elazığ-Sivrice earthquake [24 January 2020 Mw =6.8] field observations on seismic and structural damage. *METU Earthquake Engineering Research Center.*

Çetin, K. O., Ilgac, M., Sayın, E., & Gör, M. (2023). Reconnaissance report on February 6, 2023 Kahramanmaraş-Pazarcık (Mw=7.7) and Elbistan (Mw=7.6) earthquakes. *Türkiye Earthquake Reconnaissance and Research Alliance.*

Cubrinovski, M., Rhodes, A., Ntritsos, N., & Van Ballegooy, S. (2019). System response of liquefiable deposits. *Soil Dynamics and Earthquake Engineering*, *124*(May 2018), 212–229. https://doi.org/10.1016/j.soildyn.2018.05.013.

Dağdeviren, U. (2018). Yeni Türkiye bina deprem yönetmeliğine göre zeminlerin sıvılaşma analizi ve sıvılaşmaya karşı iyileştirilmesi. *Doğal Afetler ve Çevre Dergisi*, 153–165. https://doi.org/10.21324/dacd.446059.(in Turkish)

Emiroğlu, T., & Arsoy, S. (2019). Spt, Cpt Ve Vs İle Karşılaştırmalı Sıvılaşma Analizi. *8. Uluslararası Geoteknik Sempozyumu, İTÜ Süleyman Demirel Kültür Merkezi, 13 - 15 Kasım 2019*, 205–212. (in Turkish)

Kundak, S. ve Kadıoğlu, M. (2011). İlk 72 Saat, *AFAD Yayınları*, Ankara. (in Turkish)

Li, P., Tian, Z., Bo, J., Zhu, S., & Li, Y. (2022). Study on sand liquefaction induced by Songyuan earthquake with a magnitude of M5.7 in China. *Scientific Reports*, *12*(1). https://doi.org/10.1038/s41598-022-13549-8.

Orhan, M., & Ateş, A. (2010). Standard penetrasyon testi (SPT) ile Saruhanlı (Manisa) ilçesi zeminlerinin sıvılaşma potansiyelinin araştırılması. *AKÜ Fen Bilimleri Dergisi*, 37–49. (in Turkish)

Özdin, A. E. (2023). *Sakarya ili Geyve ilçesi zeminleri sıvılaşma davranışının Csb ile incelenmesi*. Sakarya Uygulamalı Bilimler Üniversitesi, Lisansüstü Eğitim Enstitüsü, Sakarya. (in Turkish)

Roy, J., Rollins, K. M., Athanasopoulos-Zekkos, A., Harper, M., Linton, N., Basham, M., Greenwood, W., & Zekkos, D. (2022). Gravel liquefaction assessment using dynamic cone penetration and shear wave velocity tests based on field performance from the 1964 Alaska earthquake. *Soil Dynamics and Earthquake Engineering*. https://doi.org/10.1016/j.soildyn.2022.107357.

Sertkaya, K.(2024). *Elazığ il merkezi için zemin sıvılaşma potansiyelinin değerlendirilmesi ve zemin iyileştirme yöntemlerinin karşılaştırılmas*ı, Fırat Üniversitesi, Fen Bilimleri Enstitüsü, Elazığ. (in Turkish)

Şekho, N. (2023). *Coğrafi bilgi sistemi kullanılarak Batman yerleşim alanındaki zeminlerin geoteknik özelliklerinin değerlendirilmesi*. Dicle Üniversitesi, Fen Bilimleri Enstitüsü, Diyarbakır. (in Turkish)

Turkish Building Earthquake Code (TBEC), (2018), *Ministry of Public Works and Settlement.* Ankara, Turkey.

4th International Civil Engineering & Architecture Conference
17-19 May 2025, Trabzon, Türkiye

Determination of soil amplification factors by seismic soil response analysis in Altınşehir region

Bahadır Atlılar*[1], Ahmet T. Gezgin[1], Mustafa Şenkaya[1]

[1] *Bursa Uludag University, Department of Civil Engineering, 16059 Bursa, Türkiye*

Abstract: In most of the engineering studies in our country, ground magnification is performed with empirical formulas based on S-wave velocity. However, it is well-known that ground growth varies depending on the local ground conditions. This change has a different significance for the areas where units of different geological ages coexist, such as the Bursa plain. Dec. The Quaternary-aged Alluvial Formation (Qal) and the Neogene-aged Mudanya Formation (Tmm) are being studied in the region within the borders of Nilüfer district, which spreads over a wide area in the Bursa Plain. In these formations, soil profiles have been idealized using geotechnical parameters obtained from mechanical drilling and geophysical parameters obtained from field studies. Seismic records that will describe the earthquake effects on the fault segments close to the region were selected from these ground profiles and examined by seismic ground response analysis performed by the DeepSoil program.

Keywords: Soil profile; Soil response analysis; Earthquake; Geotechnics; Geophysics; Earthquake engineering

1.Introduction

Turkey's location on an active plate boundary necessitates a detailed assessment of local soil conditions, particularly in densely populated areas near active faults. Bursa, a major city in the Marmara Region, is a key focus due to its demographic and tectonic characteristics. Within Bursa, Altınşehir in Nilüfer district is characterized by Quaternary alluvial deposits and a shallow groundwater table, resulting in widespread water-saturated soils. These conditions critically affect seismic wave propagation and ground response. The area's mixed building stock further underscores the need to evaluate local site effects for earthquake resilience carefully.

Another critical dimension of the study is identifying the region's earthquake hazard. The location of Altınşehir has the potential to be affected by earthquakes of different magnitudes due to its proximity to the active fault lines of the Marmara Region. In this study, the earthquakes that may affect Altınşehir were analyzed in detail, and possible scenarios were determined in light of historical and current earthquake data. Ground motions seismic sources may generate may be interpreted by considering fault types, fault orientation, depths, and distances to the region. The potential impacts of the active fault segments around Bursa on Altinsehir have been considered. The fault segments used in this study were selected from the North Anatolian Province in the active fault database of Turkey (Emre et al. 2018). Earthquakes with higher earthquake magnitude values and more probable expected earthquakes were selected.

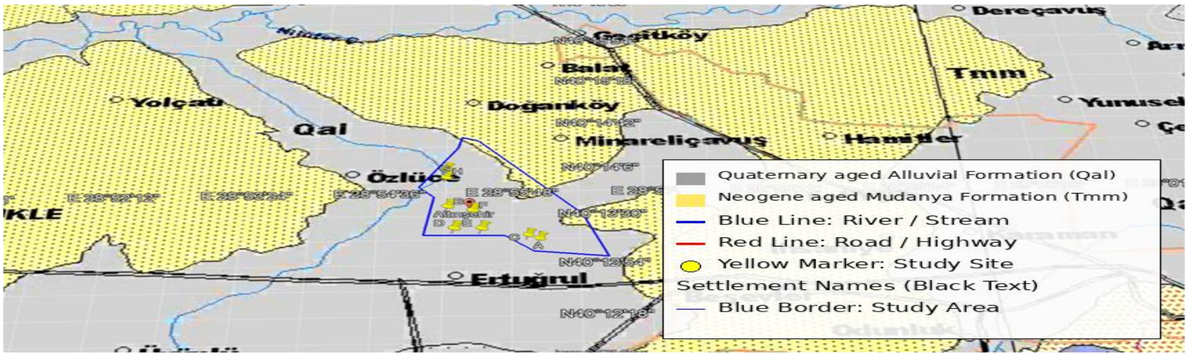

Fig.1. Investigation areas in Altinsehir on the geological map

* Corresponding author, E-mail: 502226005@uludag.edu.tr

https://doi.org/10.31462/icearc2025_ce_geo_351

This study selected earthquake input records based on seismic scenarios using the PEER (Pacific Earthquake Engineering Research Center) database. One key focus in analyzing local soil effects in areas like Altınşehir is the evaluation of soil amplification ratios. While previous studies often estimated amplification using empirical formulas based on Vs30 values, such methods can be inadequate in regions with complex soil structures due to limited consideration of local conditions. In this study, site-specific geophysical measurements and field and laboratory tests enabled the development of soil profiles that more accurately reflect real soil behavior, allowing for more reliable modeling of local effects and a more accurate prediction of seismic loads on structures.

2. Methodology

2.1. Identification of earthquake input motion

In this study, to determine the seismic hazard and local soil behavior of Altınşehir (Nilüfer/Bursa) region, active fault segments and earthquakes similar to these faults were modeled. Both local fault segments and earthquake records selected from the PEER (Pacific Earthquake Engineering Research Center) database were used in the modeling. For the seismic hazard analysis of the study area, first of all, the direct fault lines that may have an impact on Altınşehir Neighborhood were identified. In this context, six fault segments were included in the scope of the analysis, considering the direct fault map of Turkey and literature sources. These segments have a strike-slip fault type and exhibit a right-lateral movement characteristic. The characteristics of the selected segments are presented in Table 1. In addition to fault type, size (Mw), focal depth, and shortest distance to the study area (Rrup) were considered during segment selection.

Table 1. Fault segments affecting the study area

No	Fault Segment	Fault Type	Faulting Direction	Mw	Rrup (km)	Depth(km)
1	1999 İzmit Segment (I 35-34*)	Strike-slip	RL	7.4	100–150	17–18
2	1999 İzmit Segment (I 28*)	Strike-slip	RL	6.94	100–150	17–18
3	Edincik Fault	Strike-slip	RL	7.01	50–100	16–18
4	Gediz Segment	Strike-slip	N-LL	7.1	100–150	16–18
5	Gemlik Fault	Strike-slip	RL	6.73	0–50	17–18
6	Kayapa-Yenişehir Fault	Strike-slip	RL	7.01	-	-

*I34-35: Numbering On The Active Fault Map (Emre vd. 2018) *I28: Numbering On The Active Fault Map (Emre vd. 2018)

Following the characteristics of the selected fault segments, eight earthquake records were obtained from the PEER NGA database. The earthquakes were chosen to have similar fault typology (mostly strike-slip), similar magnitudes (Mw 6.2-7.4), and source-sink characteristics comparable to the study area. This approach aims to model the possible ground motions that may occur in the study area effectively.

Table 2. Earthquakes selected from PEER database

No	Fault Segment	Fault Type	Fault Type	Faulting Direction	Mw	Rrup (km)	Depth (km)
1	1990 - Manjil (İran)	Abbar	Strike-slip	RL	7.37	12.55	15
2	1995 - Kobe (Japonya)	Kobe University	Strike-slip	RL	6.90	9.2	18
3	2004 - Parkfield (ABD)	Diablo Canyon	Strike-slip	RL	6.20	78.32	5–8
4	2000 - Tottori (Japonya)	Hgy004	Strike-slip	LL	6.61	108.34	9–10
5	1992 - Landers (ABD)	Lucerne	Strike-slip	RL	7.28	2.19	1
6	1999 - Kocaeli (Türkiye)	Gebze	Strike-slip	RL	7.40	10.92	17
7	1999 - Düzce (Türkiye)	Lamont 1060	Strike-slip	RL	7.14	25.88	17
8	1984 - Morgan Hill (ABD)	Gilroy Array	Strike-slip	RL	6.19	14.91	10

2.2. Identification of soil profiles

The Altınşehir Neighborhood and its surroundings are located in the western part of the Bursa Plain and are characterized mainly by Quaternary-aged alluvial deposits. The general geology of the area consists of clay layers with poor engineering properties, classified as soft soils. Drilling and geophysical studies have revealed soil layers with low wave propagation velocities and low bearing capacity from the surface. Hydrogeologically, the groundwater level is very close to the surface, with measurements indicating a depth of approximately 3–6 meters. The alluvial fill formed by the Nilüfer Stream and its tributaries is the primary reason for the high groundwater level. Under saturated soil conditions, this significantly affects soil behavior under seismic loads, necessitating effective stress parameters and consideration of pore water pressure effects in the analyses.

Determination of geotechnical parameters appropriate to the lithology was the primary step in constructing soil profiles. The engineering parameters used to evaluate the soil layers' bearing capacity, settlement properties, and dynamic behavior were obtained from field tests (SPT, MASW) and laboratory tests. Based on the information obtained from drilling logs and geophysical measurements, stratification boundaries and soil types were defined, and detailed profiles were modeled. The sample soil profile A (Fig.2) below covers a depth range of 0-20 m. In the upper layer of the profile, there is a three-meter-thick sandy silty clay with low consistency and wave velocity values. The average Vs value measured in this layer is 151 m/s, which was obtained from seismic surface wave analysis (MASW). Groundwater level was observed at a depth of approximately 3 m. The second layer is a clay with the same lithologic characteristics, but located at deeper depths and representing more solid ground conditions. In this layer, the average Vs value was determined as 297 m/s. The unit volume weight (γ) of both layers was determined as 18.5 kN/m³ due to laboratory analysis of the samples taken. According to the results of the Standard Penetration Test (SPT), N60 values were 11 for the upper layer and 16 for the lower layer. These values were used in undrained shear strength (Su) calculations for cohesive soils based on the Stroud (1974) correlation. The obtained Cu values are 52.14 kPa and 84.48 kPa, respectively. Plastic limit (PI) values were also included in the profile to define cohesive soils' plasticity properties and apply reference curves to analytical models.

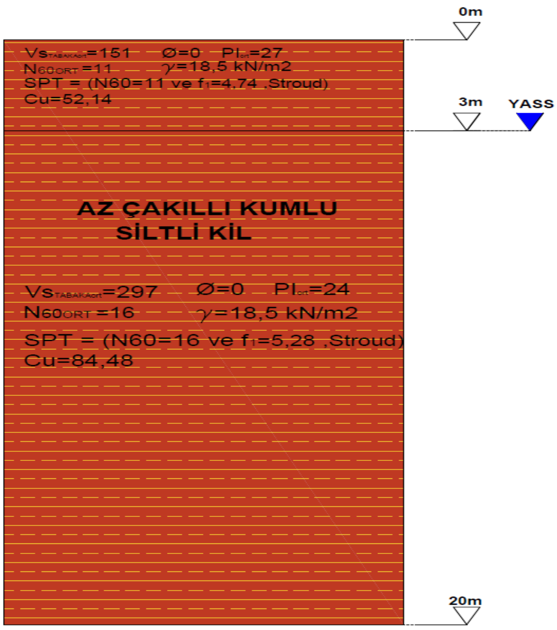

Fig.2. Soil profile A

2.3. Seismic soil response analysis

In this study, 1-D ground seismic response analyses were performed using DEEPSOIL v7.0 software to evaluate the dynamic behavior of the soils in Altınşehir region. In the analyses, the nonlinear analysis method was preferred. In these analyses under time-domain solution type, the hyperbolic (GQ/h) model and the non-Masing hysteretic reloading/unloading formulation were used to model the soil behavior more realistically. With this method, especially the development of Pore Water Pressure (PWP) in the soil was considered, and the plastic deformation potential of the soil under dynamic loading was evaluated in detail.

The analysis method was also compared with the equivalent linear (frequency domain) analysis method, and the effect of nonlinearities in soil behavior was more clearly demonstrated. The automatic profiling tool provided by DEEPSOIL was used to define and model each layer based on field and laboratory data. The soil profile used in the analysis was obtained from the geotechnical and geophysical data shown in Fig.2. Vs30 values of the layers forming the profile were defined by averaging the results of seismic MASW tests for each layer. Unit volume weight values were obtained from laboratory tests, and when more than one data point was available, the average value was taken and integrated into the model. SPT-N values were used for shear strength values; Stroud (1974) correlations were used for clay soils, and Kulhawy and Mayne (1990) correlations were preferred for coarse-grained soils (sand and gravel). In addition, the plasticity index (PI) values of the clay units were taken as a basis for the reference curve generation. They were recorded on the profile to be used in the analyses. Reference shear modulus (G/Gmax) and damping ratio curves were defined following Vucetic & Dobry (1991) for clay soils, Seed & Idriss (1970) for sand soils, and Menq (2003) for gravel soils. The Matasovic (1993) model for clay soils and the Vucetic/Dobry (1988) model for sand and gravel units were used as the PWP model. These literatures were selected for the most appropriate modeling of the soil lithology, considering the compatibility of the available drilling and laboratory data. According to TBDY 2018, the horizontal elastic spectrum curve was drawn in the seismic detail report taken according to DD-2 (standard earthquake design ground motion) and soil class by the parcel coordinates of the soil profile on the AFAD seismic hazard map.

2.4. Spectral behavior of soil profiles in Altınşehir Region

The spectra obtained by using selected earthquake records (Manjil, Kobe, Parkfield, Tottori, Landers, Kocaeli, Duzce, Morgan Hill) for eight different soil profiles from A to H (Fig.3) were compared with the design spectra in TBDY-2018 regulation. (Fig.3.) It was observed that the spectra of soil profiles gave values above the design spectra in high frequency (short periods) and low frequency (long periods) regions with some earthquake records. In particular, soil profiles C and D caused significant magnifications against strong ground motions such as Landers and Kobe.

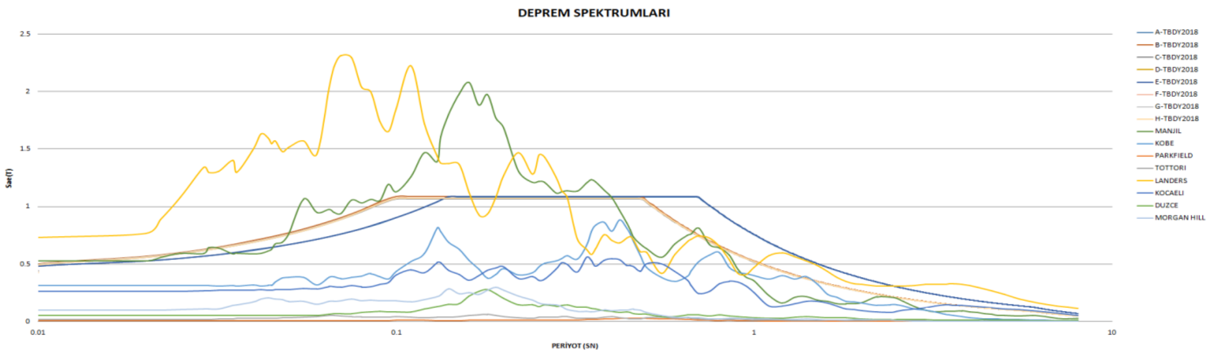

Fig.3. Spectrum curves

Real earthquake records, selected from the appropriate fault segments presented above in Table 2, are imposed on the model, and the response of the ground under different spectral characteristics is analyzed. When determining the amplification factor, the top layer's ground motion is compared with the earthquake waves entering the bedrock record to reveal how the ground motion is amplified in the ground profile. In this approach, the ratio of the acceleration values at the surface to the acceleration values at the bedrock is taken to determine the extent to which the ground layers amplify the earthquake waves. Therefore, the calculations are based on the bedrock input and surface records [Fig.5]. Amplification values for different period intervals are found, and the intervals where the ground amplification of the structure is effective are determined.

3. Results and discussion

3.1. Relationship between spectral magnifications and building types

According to the analyzed earthquake response spectra, spectral acceleration varies significantly depending on the structure's natural period. In the short-period range (T < 0.3 s), spectral acceleration typically ranges between 0.3g and 0.7g, affecting low-rise, stiff structures through rapid, high-frequency motions. In the medium-period range (0.3 s – 1.0 s), the spectra reach their peak values, often between 0.8g and 2.3g, making this interval the most critical for structural design, particularly for mid-rise reinforced concrete buildings. In the long-period range (T > 1.0 s), spectral acceleration tends to decrease, typically between 0.1g and 0.6g, indicating that displacement demands become more dominant than acceleration in tall, flexible structures. In comparisons made with the design spectrum obtained following the 2018 Turkish Building Earthquake Code (TBDY 2018), it has been observed that the spectra derived from actual earthquake records can exceed the local design spectrum, particularly in the medium-period range. This highlights the critical importance of site-specific spectral analyses for accurate structural design and performance evaluation.

3.2. Evaluation of amplification factors

Earthquake-specific nonlinear and equivalent linear soil seismic response analyses were performed for 8 soil profiles (A, B, C, D, E, F, G, H) according to selected earthquake records in the study area, and amplification factors were obtained (Fig.4).

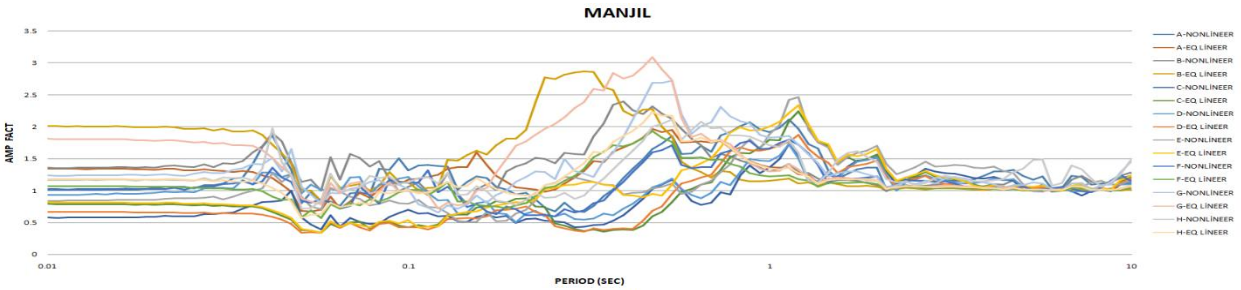
MANJIL
AMP FACT
PERIOD (SEC)
A-NONLİNEER
A-EQ LİNEER
B-NONLİNEER
B-EQ LİNEER
C-NONLİNEER
C-EQ LİNEER
D-NONLİNEER
D-EQ LİNEER
E-NONLİNEER
E-EQ LİNEER
F-NONLİNEER
F-EQ LİNEER
G-NONLİNEER
G-EQ LİNEER
H-NONLİNEER
H-EQ LİNEER

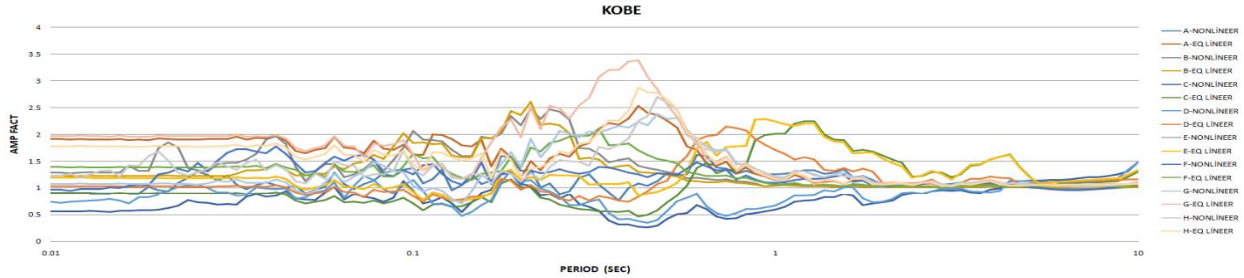
KOBE
AMP FACT
PERIOD (SEC)
A-NONLİNEER
A-EQ LİNEER
B-NONLİNEER
B-EQ LİNEER
C-NONLİNEER
C-EQ LİNEER
D-NONLİNEER
D-EQ LİNEER
E-NONLİNEER
E-EQ LİNEER
F-NONLİNEER
F-EQ LİNEER
G-NONLİNEER
G-EQ LİNEER
H-NONLİNEER
H-EQ LİNEER

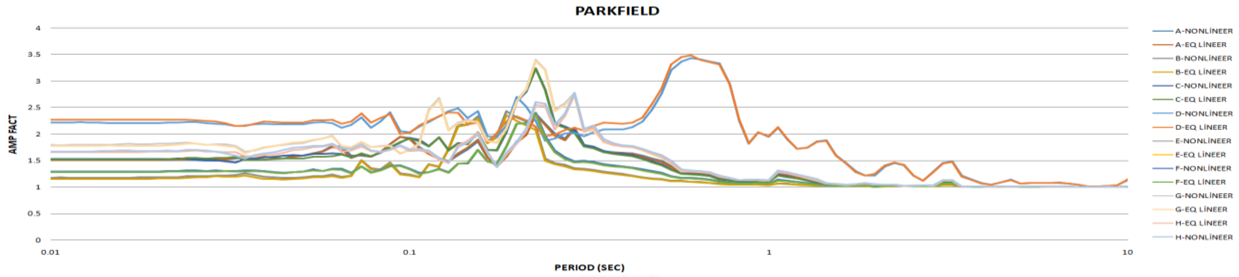
PARKFIELD
AMP FACT
PERIOD (SEC)
A-NONLİNEER
A-EQ LİNEER
B-NONLİNEER
B-EQ LİNEER
C-NONLİNEER
C-EQ LİNEER
D-NONLİNEER
D-EQ LİNEER
E-NONLİNEER
E-EQ LİNEER
F-NONLİNEER
F-EQ LİNEER
G-NONLİNEER
G-EQ LİNEER
H-EQ LİNEER
H-NONLİNEER

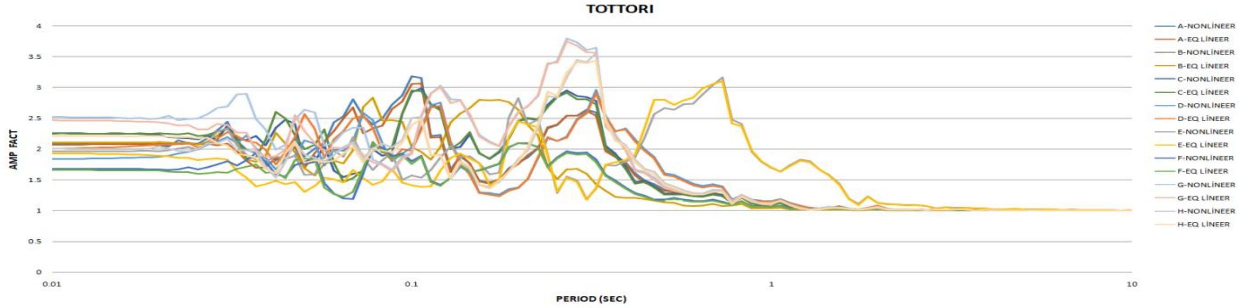
TOTTORI
AMP FACT
PERIOD (SEC)
A-NONLİNEER
A-EQ LİNEER
B-NONLİNEER
B-EQ LİNEER
C-NONLİNEER
C-EQ LİNEER
D-NONLİNEER
D-EQ LİNEER
E-NONLİNEER
E-EQ LİNEER
F-NONLİNEER
F-EQ LİNEER
G-NONLİNEER
G-EQ LİNEER
H-NONLİNEER
H-EQ LİNEER

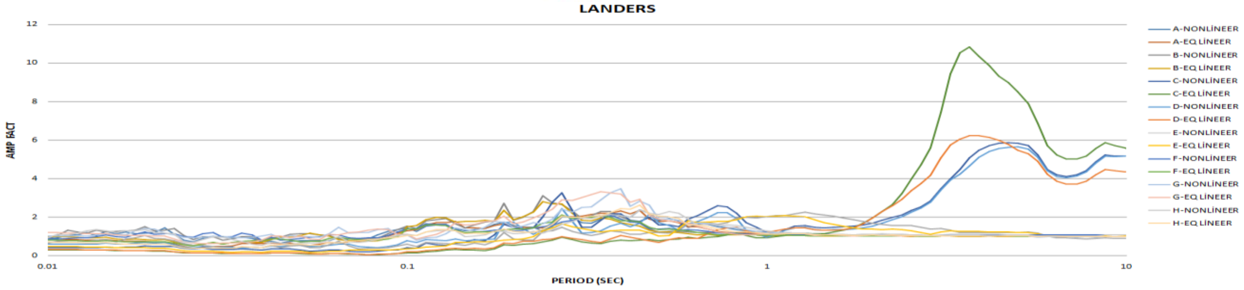
LANDERS
AMP FACT
PERIOD (SEC)
A-NONLİNEER
A-EQ LİNEER
B-NONLİNEER
B-EQ LİNEER
C-NONLİNEER
C-EQ LİNEER
D-NONLİNEER
D-EQ LİNEER
E-NONLİNEER
E-EQ LİNEER
F-NONLİNEER
F-EQ LİNEER
G-NONLİNEER
G-EQ LİNEER
H-NONLİNEER
H-EQ LİNEER

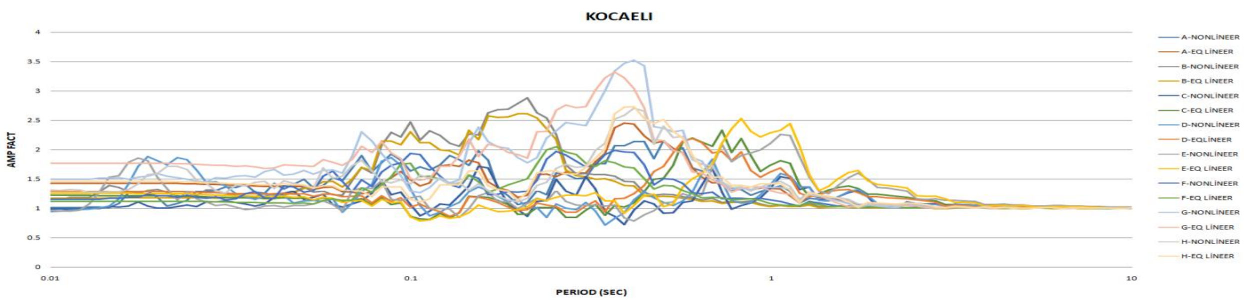
KOCAELI
AMP FACT
PERIOD (SEC)
A-NONLİNEER
A-EQ LİNEER
B-NONLİNEER
B-EQ LİNEER
C-NONLİNEER
C-EQ LİNEER
D-NONLİNEER
D-EQLİNEER
E-NONLİNEER
E-EQ LİNEER
F-NONLİNEER
F-EQ LİNEER
G-NONLİNEER
G-EQ LİNEER
H-NONLİNEER
H-EQ LİNEER

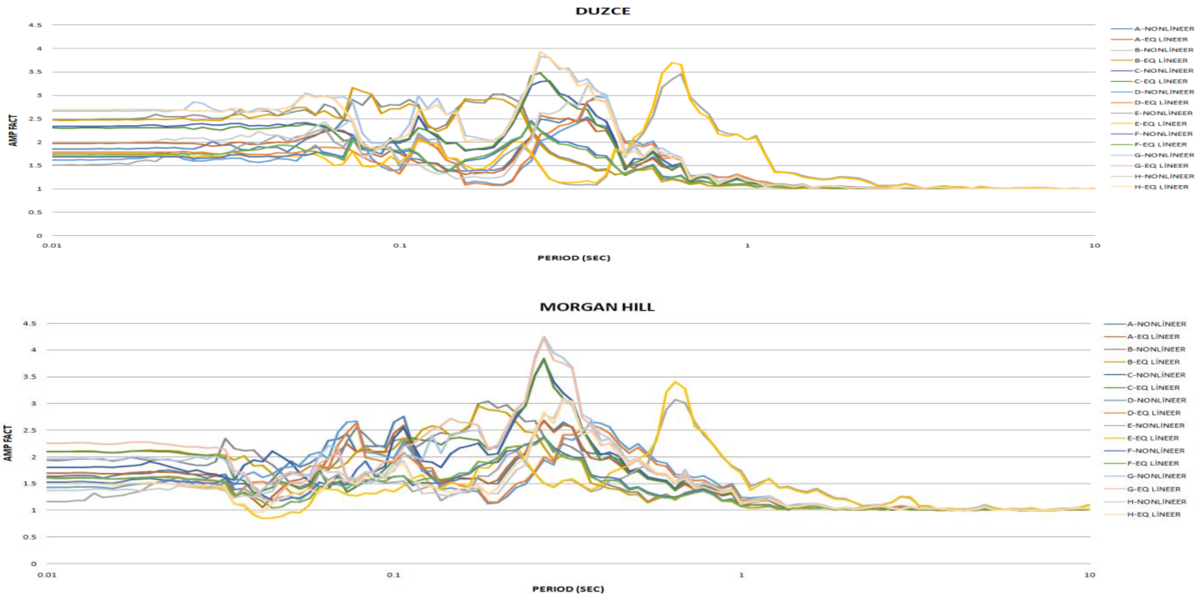

Fig.4. Amplification factors of earthquakes

This study analyzed different earthquakes based on graphs comparing linear and nonlinear results. For the Manjil earthquake, the differences between linear and nonlinear analyses became especially evident at longer periods (beyond 0.5 seconds). At short periods (0.01-0.3 s), low-rise buildings showed low amplification, while at medium periods (0.3-1 s), significant amplifications were observed for soil profiles D, E, and H, particularly affecting 4-8 story buildings. At long periods (above 1 s), profiles E, F, and G showed amplifications above 2, indicating increased risk for 10-story buildings and taller structures. Nonlinear analyses generally exhibited higher amplifications, especially for E and G profiles with weak layers.

The Kobe earthquake, characterized by very high accelerations, showed dominant nonlinear behavior. Short-period ground motions were not over-amplified, but at medium periods (0.3-1 s), magnifications reached 2.5-3.5 for some soils, posing a risk for mid-rise buildings. No striking resonance was observed at longer periods. Linear and nonlinear results were similar for soil profiles A, B, and C, but differed significantly for E, G, and H profiles.

In the short-period range (0.01-0.3 s) for the Parkfield earthquake, amplification factors were stable (1.2-2.3) with minor differences between linear and nonlinear analyses, suggesting linear assumptions are acceptable for low-rise structures. However, amplification increased at medium periods (0.3-1 s), critical for mid-rise buildings. Long-period responses showed a general decrease.

In the Tottori earthquake, short-period amplification remained between 1.5 and 2.5. At the same time, at medium periods (0.3-1 s), nonlinear analyses showed magnifications exceeding 3.0 in B, D, and E profiles, making nonlinear behavior significant for mid-rise structures. At long periods, some profiles, especially E, indicated possible resonance risks.

The Landers earthquake showed significant amplification in the long-period range (1-3 s), with C-Eq Linear profiles exceeding 10 in amplification, highlighting serious resonance risks for high-rise buildings. Short and medium periods showed moderate magnification.

In the Kocaeli earthquake, short-period magnification was low, but at medium periods (0.3-1 s), magnifications reached 2-3.5 for some soils, indicating risk for 4-8 story buildings. No significant resonance was observed at long periods.

The Düzce earthquake showed similar trends: low short-period amplification, increased magnifications (2-4) at medium periods, and notable risks at long periods (around 3-3.5 magnification in E-Nonlinear-Equivalent analyses) for multi-story structures.

The Morgan Hill earthquake generally showed low amplifications at short periods but increased to 2-2.5 in some cases. All soil profiles experienced higher amplifications in the medium period range, with G and C profiles reaching 3.5-4, which is critical for 4-8 story buildings. At long periods, only E-Nonlinear-Equivalent profiles showed significant amplification.

Overall, the medium period range (0.3-1 s) across all earthquakes presents critical risks for mid-rise buildings. In some cases, long-period amplifications indicate potential resonance risks for high-rise structures. Nonlinear analyses consistently revealed more pronounced amplification effects than linear models, especially for soils with weak layers.

4. Conclusions

This study evaluated various earthquake ground motions on eight different soil profiles through linear and nonlinear site response analyses. The resulting amplification factors and spectral acceleration values were interpreted in relation to period-dependent soil-structure interaction. The results were also compared with the Turkish Building Earthquake Code (TBDY-2018) design spectra. The main conclusions are summarized below:

- The relationship between soil type and period was evident; soft soil profiles (such as C, E, and G) produced higher amplification values, particularly in short-to-mid period ranges, with this behavior being more pronounced under the Morgan Hill and Tottori earthquakes.
- The characteristics of different earthquakes had significant effects on amplification factors. The Landers and Tottori earthquakes generated high spectral accelerations in short and intermediate periods, strongly influencing the site response.
- The Kobe earthquake exhibited relatively lower spectral acceleration and a flatter response curve compared to others, indicating a lower level of localized amplification.
- Nonlinear analyses provided more realistic amplification predictions, especially in the resonance-sensitive period ranges (approximately 0.2–0.6 seconds), by accounting for effects such as energy dissipation and stiffness degradation.
- The spectral comparisons revealed that some real earthquake records (notably Landers and Manjil) exceeded the TBDY-2018 design spectra, especially in the short-period range. This suggests that real earthquake demands may pose higher risks than code-based expectations.
- TBDY-2018 design spectra generally remain conservative, but in some cases ($T < 0.3$ s), the code spectra underestimate the actual demands, highlighting the need for detailed dynamic analysis in critical structures.
- In the long-period range ($T > 1$ s), spectral acceleration and amplification factors decreased significantly, indicating that tall structures on such soils may experience reduced seismic demand.
- In some critical middle and high-period regions, significant differences between nonlinear and equivalent linear analyses began to occur. This increased the use of nonlinear analysis, suggesting that linear analysis alone would be sufficient.
- The analyses also revealed critical period ranges where soil-structure resonance effects are likely to occur, particularly between 0.3–0.7 seconds for mid-rise buildings (4–8 stories) and above 1 second for high-rise structures. In these ranges, nonlinear amplification became significantly pronounced, indicating a higher seismic risk due to potential resonance between soil and structure.

Acknowledgments

I would like to thank Eren Garip and Umut Koçan from Nilüfer Municipality for their support of the study.

References

DeepSoil (v7.0). (2016). *One-Dimensional Site Response Analysis Software*. University of Illinois at Urbana-Champaign. Available from: http://deepsoil.cee.illinois.edu

Emre, Ö., Duman, T. Y., Özalp, S., Elmacı, H., Olgun, Ş., & Şaroğlu, F. (2018). *Active Fault Map of Turkey with Explanatory Text*. General Directorate of Mineral Research and Exploration (MTA), Ankara, Turkey.

Kulhawy, F. H., & Mayne, P. W. (1990). *Manual on Estimating Soil Properties for Foundation Design*. Electric Power Research Institute (EPRI).

Matasovic, N. (1993). *Seismic Response of Composite Horizontally-Layered Soil Deposits*. PhD Dissertation, University of California, Los Angeles.

Menq, F. Y. (2003). *Dynamic Properties of Sandy and Gravelly Soils*. PhD Dissertation, University of Texas at Austin.

PEER Ground Motion Database. (n.d.). *Pacific Earthquake Engineering Research Center Ground Motion Records*. Retrieved from: https://ngawest2.berkeley.edu/

Republic of Turkey Ministry of Environment and Urbanization. (2018). *Turkish Building Earthquake Code (TBDY-2018)*.

Republic of Turkey Ministry of Public Works and Settlement. (2007). *Specifications for Structures to be Built in Disaster Areas – Earthquake Code (TBDY-2007)*.

Seed, H. B., & Idriss, I. M. (1970). *Soil Moduli and Damping Factors for Dynamic Response Analyses*. Report EERC 70-10, University of California, Berkeley.

Stroud, M. A. (1974). *The Standard Penetration Test in Insensitive Clays and Soft Rocks*. Proceedings of the European Symposium on Penetration Testing.

Vucetic, M., & Dobry, R. (1988). *Pore Pressure Build-up and Liquefaction at Level Ground*. In: Proceedings of the 9th World Conference on Earthquake Engineering, Tokyo-Kyoto, Japan.

Vucetic, M., & Dobry, R. (1991). *Effect of Soil Plasticity on Cyclic Response*. Journal of Geotechnical Engineering.

Deformation analysis of anchored retaining systems: a case study with PLAXIS modeling and field data comparison

Saeid Zardari*[1], Aslı D. Sağlam[1]

[1]*Istanbul Okan University, Department of Civil Engineering, 34959 Istanbul, Türkiye*

Abstract. Deep excavations have become a crucial aspect of civil engineering due to increasing urbanization and construction activities. Excavations carried out for the foundation systems and underground structures of high-rise buildings can affect surrounding soil conditions, leading to deformations. To ensure the safety of excavation sites, the use of effective support systems is essential. In this study, the performance of anchored bored pile retaining systems was analyzed using the finite element method (FEM), and the results were compared with inclinometer measurements taken on-site. Initially, the roles and functions of anchors and bored piles in retaining structures were discussed. This was followed by an investigation of the system's behavior through analyses conducted under different conditions. The modeling was performed using PLAXIS software, and the computed deformations were compared with field measurements to identify discrepancies. Back-analysis was conducted to examine the key factors influencing the performance of the retaining system, and significant insights were drawn regarding the engineering design of deep excavation support systems.

Keywords: Anchored bored pile; Retaining systems; Finite element method; PLAXIS; Inclinometer measurements

1. Introduction

Deep excavations in urban areas pose significant engineering challenges due to unfavorable risks affecting the stability of surrounding structures and soils. As the complexity and scale of construction projects continue to increase, the demand for safe and durable excavation support systems has also grown. Among these systems, anchored and bored pile retaining structures are widely preferred due to their high load-bearing capacities and adaptability to varying ground conditions. These systems are commonly employed to provide lateral support during excavation, especially in constrained spaces and for deep foundations required by high-rise buildings. Bored piles and anchors offer effective resistance against lateral forces during excavation and help to control ground movements. The performance of these systems is influenced by several factors, including anchor spacing, pile arrangement, and soil properties. Numerous studies have emphasized the critical role of these factors in ensuring the stability and safety of excavation sites. Numerical modeling tools such as PLAXIS are widely used to predict deformation behavior; however, the accuracy of these predictions needsa validation through field measurements.

1.1. Literature review

Several studies on the deformation behavior of deep excavation support systems highlight the necessity of reliable analysis methods to accurately predict system performance. In this context, the Finite Element Method (FEM) has become a standard tool for modeling soil-structure interaction. Meanwhile, observational data, such as inclinometer measurements obtained from the field, play a crucial role in enhancing the accuracy of numerical models and ensuring the reliability of geotechnical designs. Studies focusing particularly on the lateral deformation behavior of pile-supported systems have been recognized as critically important for the safe design and performance assessment of deep excavation support structures.

In a study conducted by Ou et al. (1993), it was observed that ground settlements occurred at approximately 50% to 70% of the maximum lateral deformation, and that the maximum lateral deformation corresponded to about 0.2% to 0.5% of the excavation depth. Similarly, Fernie and Suckling (1996), based on their research in the United Kingdom, stated that maximum lateral movements in retaining structures within stiff soils should range between 0.15% and 0.30% of the excavation depth. In another study, Carder (1995) found that lateral deformations in retaining systems installed in stiff soil conditions are directly related to the rigidity of the system. In this context, it was emphasized that in high-rigidity systems, the maximum deformation corresponds to approximately 0.125%

* Corresponding author, E-mail: saeid.zardari@okan.edu.tr

https://doi.org/10.31462/icearc2025_ce_geo_369

of the excavation depth, while in medium-rigidity systems, it is around 0.2%, and in low-rigidity systems, about 0.4%. It was also concluded that deformations increase as the system rigidity decreases.

Ma'ruf and Darjanto (2017), in their study on the cut-and-cover tunnel construction of the Nicoll Highway project in Singapore, identified that the main cause of excessive displacements was the misinterpretation of soil properties. Through back-analyses, they demonstrated that improvements such as the addition of struts to the support system and assuming a zero internal friction angle for coarse-grained clay soils significantly reduced excessive deformations and substantially increased the safety factor.

In a study conducted within the scope of a hotel construction project, Aktan (2014) investigated the effects of variations in soil elasticity modulus and internal friction angle on the performance of retaining systems. He observed that increasing the elasticity modulus significantly reduced lateral displacements, and that decreasing anchor spacing also contributed to minimizing deformations.

Rahmani and Laman (2016) analyzed three different projects to investigate the impact of groundwater levels on retaining systems. Finite element analyses revealed that as the groundwater table approaches the surface, lateral displacements in retaining structures increase, highlighting the necessity of considering groundwater effects in design calculations.

Steiner (2001) found that significant surcharge loads caused by truck-mounted cranes at deep excavation sites led to an increase in anchor forces. Cengiz (2008), in a project located in Moscow, compared field-measured displacements of a diaphragm wall retaining system supported by anchors and struts with results from finite element analyses performed using PLAXIS software. It was determined that the lateral displacements obtained from the numerical model were higher than the field measurements. Subsequent parametric studies, in which cohesion, internal friction angle, and elasticity modulus were increased by 10%, 20%, and 30%, respectively which indicated that the closest agreement with field measurements was achieved when the parameters were increased by 30%. In a more recent study by Ma and Cao (2024), it was reported that three-dimensional modeling more accurately represents deformation behavior in supported excavations in clay compared to two-dimensional analyses. Their findings emphasized the importance of considering three-dimensional effects in numerical simulations.

The primary objective of this study is to analyze anchored bored pile retaining systems using the finite element method and to evaluate the accuracy of the numerical results by comparing them with inclinometer measurements obtained from the field. Although many studies in the literature focus predominantly on theoretical approaches regarding similar systems, verification through field data remains limited. In this regard, the present study aims to combine theoretical analyses with on-site measurements to provide more reliable and practical insights into the real behavior of retaining structures.

2. Materials and methods

2.1. Project site and subsurface conditions

In the project addressed in this study, the construction of a building comprising six basement levels, one ground floor, and five above-ground floors is planned. The project site covers an area of 5,919.46 m², with the building footprint occupying approximately 4,200 m². The site layout plan and the side elevation of the project are presented in Fig. 1.

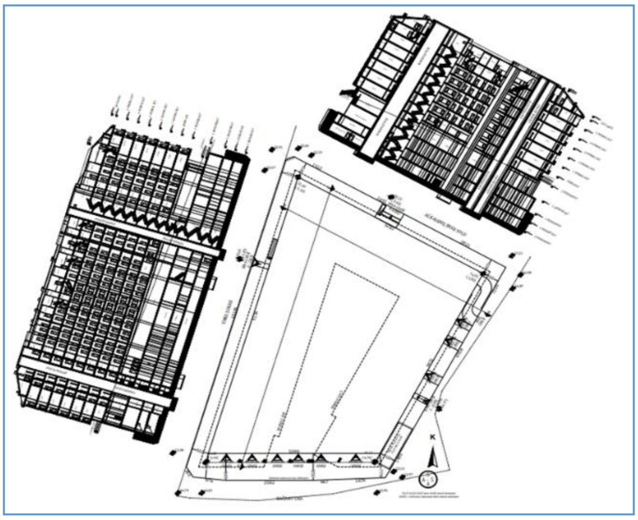

Fig. 1. General plan of the project (Source: the authors)

Due to the multi-basement design of the building, the use of deep excavation support systems has become essential. Accordingly, an anchored bored pile retaining system has been designed for the project. The excavation depth varies across the site, ranging from 11.30 meters to 18.20 meters depending on the location.

A total of 13 boreholes were drilled within the study area to determine the geological and geotechnical characteristics of the site. Laboratory tests, including direct shear, Atterberg limits, moisture content, sieve analysis, and hydrometer tests, were conducted on the samples obtained from the boreholes.

Within the scope of the project, Section-7, identified as the critical section due to a greater-than-expected increase in deformations, was examined in detail. The laboratory test results for the SK1 and SK5 borehole samples taken from this section are presented in Table 1.

Table 1. Soil laboratory test results for the project area (Source: the authors)

Borehole No	Depth	Atterberg Limits			Water Content	Natural Density	Sieve Analysis Result [%]				Direct Shear Test Result	
		LL [%]	PL [%]	PI [%]	ω [%]	[g/cm^3]	Gravel	Sand	Silt	Clay	c [kPa]	ϕ[º]
SK-1	5.50-6.00	44.4	21.9	22.5	26.0	1.88	0.00	11.06	30.35	58.59	71.17	7.26
SK-1	8.50-9.00	42.3	20.3	22.0		1.89	0.00	9.19	90.81		73.24	7.41
SK-1	19.50-20.00					1.95	0.00	10.53	89.47		79.43	8.20
SK-5	3.00-3.50	36.4	185	17.9	22.26	1.91	30.78	23.12	18.97	27.13	51.17	14.05
SK-5	8.50-9.00					1.94	14.95	16.42	68.63		84.52	10.72
SK-5	17.50-18.00	40.9	21.3	19.9		1.95	0.00	18.40	81.60		95.70	8.62

2.2. Numerical modeling

Within the scope of the project, Section-7, identified as critical due to deformation increases exceeding predictions, was analyzed in detail using the Finite Element Method (FEM). These analyses were conducted to evaluate the deformations that occurred in the retaining system during the excavation process. The detailed results of the analyses are presented in the subsequent sections of the study.

In selecting the soil models, the Mohr-Coulomb model was adopted for the artificial fill and the sandstone (arkose) layers, while the Hardening Soil (HS) model was chosen for the stiff clay layer. In the reviewed design report, it was observed that the soil parameters used in the modeling of the shoring system were not based on site-specific laboratory or field tests, but they were rather based on typical values reported in the literature.

In this study, the same soil parameters from the design report were adopted in the initial modeling phase. The soil parameters used in the finite element analyses are summarized in Table 2.

Tablo 2. Analysis parameters based on the values in the calculation report (Source: the authors)

	Natural unit weight	Elastic modulus	Cohesion	Internal friction angle	Poisson's ratio
Symbol	γ_n	E	c	ϕ	υ
Unit	[kN/m^3]	[kN/m^2]	[kPa]	[º]	-
Upper layer clay	18.5	21000	19	28	0.28
Lower layer clay	19	30000	22	28	0.28
Very Weak Sandstone-Arkose	22	150000	50	32	0.28

In selecting the excavation support method, it was essential to design the retaining systems to minimize deformations in order to prevent adverse impacts on adjacent existing structures and roads. Accordingly, a retaining system consisting of bored piles combined with prestressed ground anchors was selected as the most suitable excavation support solution for the site. This selection and its details were thoroughly documented in the corresponding design report. A photograph of the site implementation is presented in Fig. 2.

Fig. 2. Field visual of the relevant project (Source: the authors)

In the design report, considering the excavation depth, the pile diameter was specified as 65 cm. The center-to-center spacing between the piles was determined to be 90 cm. For the bored piles, concrete class BS30 was selected, with an assumed modulus of elasticity of 30,000,000 kN/m².

The equivalent thickness (d) parameter represents the cross-sectional area of a unit width (1 meter) of material along the principal axis of the wall. While for flat plates with a rectangular cross-section the equivalent thickness is directly equal to the section thickness. For systems such as pile walls, where a distinct continuous section does not exist, a lower equivalent thickness is defined. This value is determined based on equivalent stiffness parameters to model the piles as a continuous diaphragm (Kalpakcı et al., 2015). Accordingly, for the bored piles with a diameter of 65 cm and a center-to-center spacing of 90 cm, the cross-sectional properties were calculated using "Eq. 1," and the equivalent thickness was found to be 0.563 meters.

$$d = \sqrt{12\frac{EI}{EA}} \tag{1}$$

In prestressed anchorage applications, 0.6" low relaxation super tendons were used. Anchor drill diameter was designed as 120 mm. The modulus of elasticity for the injected anchor root was assumed to be 10,000,000 kN/m² and the modulus of elasticity for the super tendon ropes was 195 MPa as shown in Table 3. Anchors with a root length of 9 m were installed at 1.80 m horizontal spacing between the 4th and 7th levels. This layout implies the placement of one anchor for every two bored piles.

Table 3. Properties of cables with 13 mm and 15 mm diameter (ASTM A416, 1997)

Nominal Diameter	13 mm (0.5 inch)		15 mm (0.6 inch)	
Halat Tipi Cable Type	Normal	Super	Normal	Super
Average Diameter [mm]	12.5	12.8	15.2	15.5
Average Cross-Section Area [mm²]	93	99	139	140
Unit Weight (kg/m)	0.74	0.78	1.10	1.10
Minimum Breaking Load [kN]	165	184	244	261
Elastic Modulus [MPa]		195		

For each of the prestressed anchor ropes used, the working load was calculated as 182.3 kN, considering a factor of safety of 0.70 (140 mm² × 1860 N/mm² × 0.70). Accordingly, the maximum working load of a three-strand anchor was determined to be approximately 546 kN. Anchor root lengths were designed as 9 m. Considering the interaction of the injected anchor root with the very stiff to hard, medium plasticity clay unit, the average safe unit wall friction value according to the PTI (1996) standard was assumed to be approximately 120 kPa. According to these data, the safe bearing capacity for a 120 mm diameter anchor root was found to be approximately 405 kN. As a result, the anchor loads were determined as 300-350 kN at the upper levels and 400 kN at the lower levels where the depth of excavation increases.

Monitoring of excavation support systems is of great importance during deep excavations as deformations may occur that may threaten the safety of surrounding structures. In this study, inclinometer measurements were used to determine the horizontal displacements. Inclinometers monitor the lateral movements of the support systems during excavation by tracking the deformations of the pipes placed through inclination sensors. The data obtained is critical for early detection of potential risks and timely engineering measures.

3. Results and discussion

3.1. Numerical analysis results

In this section, the critical section, Section-7, is analyzed using the parameters specified in the soil and the calculation report of the existing project. Section-7 modeling based on these parameters was created with Plaxis 3D program and numerical analyses were performed. The model of Section-7 is presented in Fig. 3.

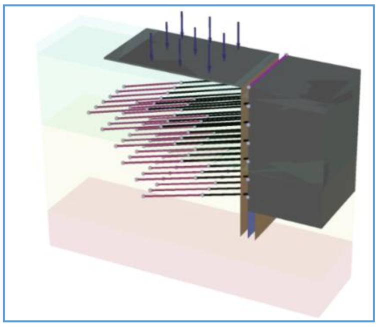

Fig. 3. Modeling of section-7 in the Plaxis 3D program (Source: the authors)

As presented in Table 4, the deformation values obtained from the finite element analyses and the ratio of the horizontal displacement in the X-axis direction to the excavation depth at the top of the pile in the relevant section. In addition, the displacements of the third stage were also evaluated in the modeling in order to examine the sudden displacements in the third stage occurring at the site.

Table 4. Relationship between maximum lateral displacement and excavation depth calculated for section-7 (Source: the authors)

Section-7 (Initial Analysis)	Lateral Displacement at the Top Elevation	Excavation Depth	Displacement Ratio
Unit	[mm]	[m]	[%]
Third stage	0.87	8.75	0.01
Final stage	10.81	16.95	0.06

The acceptable deformation rate for prestressed anchored shoring systems is determined as 0.2%, and the alarm level (maximum allowable limit) is accepted as 0.5% (Ministry of Environment and Urbanization, 2018). In the European Union standard "EN 1997-1 Geotechnical Design-Part 1: General Rules", it is stated that horizontal wall movements should be between 0.1% and 0.2% of the excavation depth in tight soils and between 0.4% and 0.5% in loose soils. In accordance with these regulations, the deformation rate obtained for the prestressed anchored shoring system section is within the specified limits.

3.2. Inclinometer measurement results

After the excavation of the third stage of the shoring depth in Section-7, sudden displacements were observed in the inclinometer number 6. Deformation measurements were performed and the data obtained are shown in Fig. 4 and presented in Table 5.

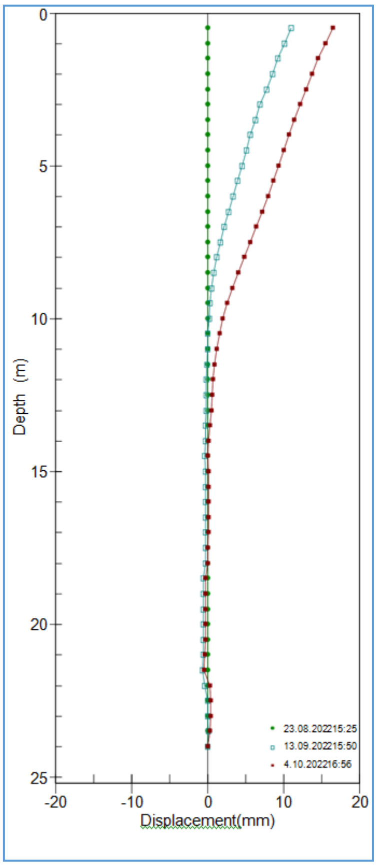

Fig. 4. Lateral deformation graph of inclinometer no. 6 in section-7 (Source: the authors)

As seen in Fig. 4, the maximum horizontal displacement value obtained from the inclinometer measurement at the site was realized at the top of the shoring system. The maximum horizontal deformation depending on the depth of excavation is given in Table 5.

Table 5. Maximum Horizontal Deformation Measured Depending on Excavation Depth (Source: the authors)

Reading Sequence	Measured Maximum Horizontal Displacement [mm]	Excavation Depth [m]	Deformation Rate [%]
1. Reading	0.00	0.00	0.00
2. Reading	11.02	6.25	0.17
3. Reading	16.48	8.75	0.19

Despite the tensioning of the first stage and second stage anchors, a sudden increase in displacement was observed in the X axis of the shoring system when the excavation depth reached 8.75 m. This necessitated some modifications to the project. The causes of this sudden displacement were investigated by back analysis.

3.3. Back analysis

Some situations encountered in the field during the implementation phase may differ from the predictions made during the model phase. Although a general profile can be estimated in the soil data report, data collected from specific areas in the field having different soil conditions may be encountered during the implementation phase due to the inability to obtain data from all areas. When such conditions are encountered, some modifications may need to be made in the fabrications within the scope of the project. In this study, various back analyses were performed to investigate the causes of sudden displacements and evaluated by comparing with the inclinometer measurements in the field. Since the deformation values obtained from the results of the inclinometer measurements in the field occur at the top elevation of the shoring system, the deformations at the top elevation of the system were also analyzed and the results obtained were cross-compared.

3.3.1. Influence of surcharge load on horizontal deformations

Surcharge loads play an important role in soil mechanics. Usually, surrounding structures, vehicles or materials create additional loads on the ground and are defined as surcharge loads. These loads have many important effects on the soil. The surcharge loads can affect factors such as horizontal earth pressure, total soil stress, consolidation, shear strength and groundwater status. They can also create additional lateral forces on ground walls or other structural elements by generating additional horizontal pressure on the ground. These forces can have a direct impact on the stability and design of structures. In this section, the effect of surcharge loads on lateral deformations is investigated and the visualization of the modeling is presented in Fig. 6.

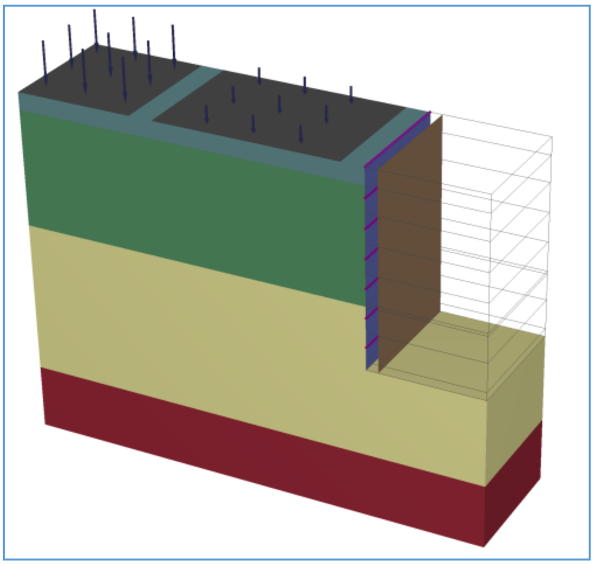

Fig. 6. Plaxis 3D program section-7 model with surcharge loading (Source: the authors)

In the presented model, the road load is increased from 10 kPa to 35 kPa as surcharge loads. In addition, a building load of 90 kPa was added behind the roadway. Fig. 7, presents the horizontal deformation graph in the third and final stage. In the third stage, the horizontal deformation value at the top elevation increased from 0.87 mm to 1.78 mm. This result shows that an increase in the amount of deformation is observed with the increase in the surcharge load. In the last calculated stage, the horizontal deformation value at the top elevation increased from 10.81 mm to 22.45 mm. The calculated results are presented in Table 6.

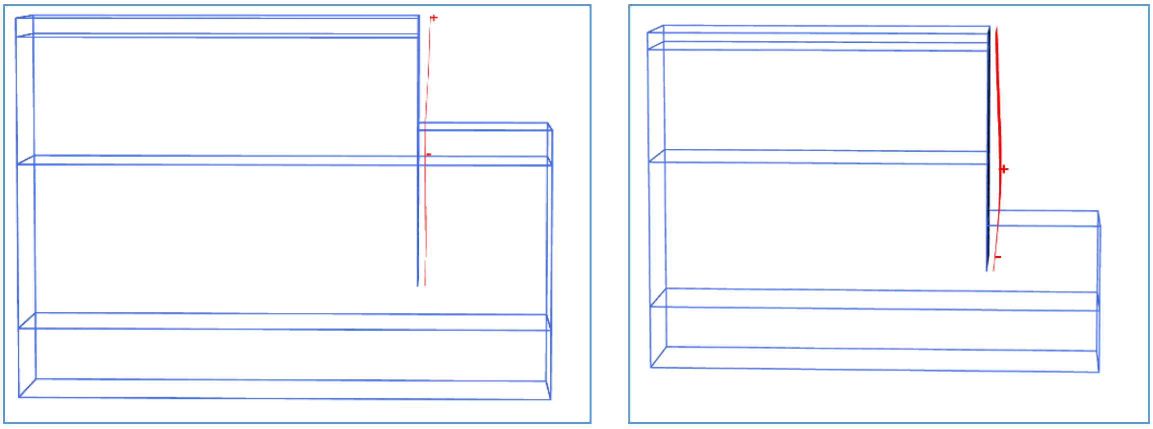

(a) (b)

Fig. 7. (a) 3rd stage horizontal deformations graph, (b) final stage horizontal deformations graph (Source: the authors)

Table 6. Comparison of initial analysis and back analysis horizontal deformations in PLAXIS (Source: the authors)

	Calculated Shoring Top Level Horizontal Deformation Value (mm) (Initial Analysis)	Calculated Shoring Top Level Horizontal Deformation Value (mm) (Back Analysis)
3rd Stage Condition	0.87	1.78
Final Stage Condition	10.81	22.45

3.3.2. Influence of inadequate anchor prestressing on lateral displacements

Even if the analysis are correctly made, some problems may be encountered in the field. One of these problems is that the prestressed anchors cannot take sufficient load. When prestressed anchors fail to take sufficient load, sudden lateral displacements may occur in the area where the inclinometers are located during excavation of a lower stage. If no action is taken to correct the fabrication after these sudden displacements, larger displacements may occur later in the construction which can cause irreversible problems. In order to investigate the deformations, the anchor loads of the first two stages in the model were reduced from 330 kN to 100 kN and the horizontal deformations graph is presented in Fig. 8.

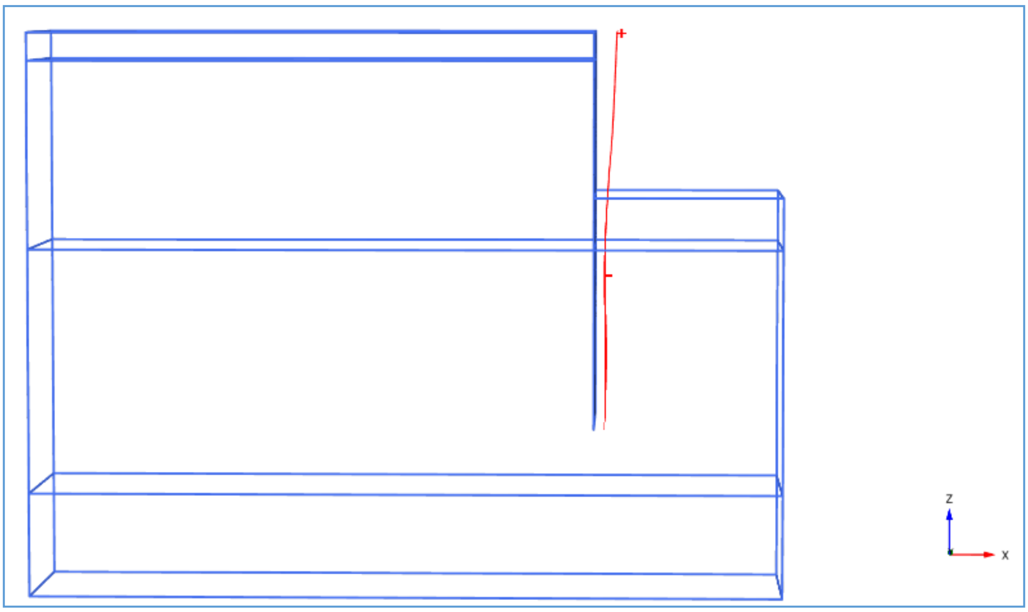

Fig. 8. Horizontal deformation graph in the third stage (Source: the authors)

According to the results, the maximum horizontal deformation value was obtained as 2.19 mm in the calculation made in the third stage. This indicates that the inadequate anchorage load increased the deformations. The comparison between the initial analysis and the back analysis is given in Table 7.

Table 7. Horizontal Deformation Comparison of Initial Analysis and Back Analysis (Source: the authors)

	Calculated Shoring Top Level Horizontal Deformation Value (mm) (Initial Analysis)	Calculated Shoring Top Level Horizontal Deformation Value (mm)(Back Analysis)
3rd Stage	0.87	2.19

In order to prevent sudden displacement increases, a 4th stage excavation was made in the relevant section and additional anchors were added at 0.9 m intervals. The visualization of this arrangement in the field and the 3D model in Plaxis program are presented in Fig. 9. After the anchors were subjected to the stressing process, the inclinometer measurements were performed again. The graph of the deformation values obtained is shown in Fig. 10.

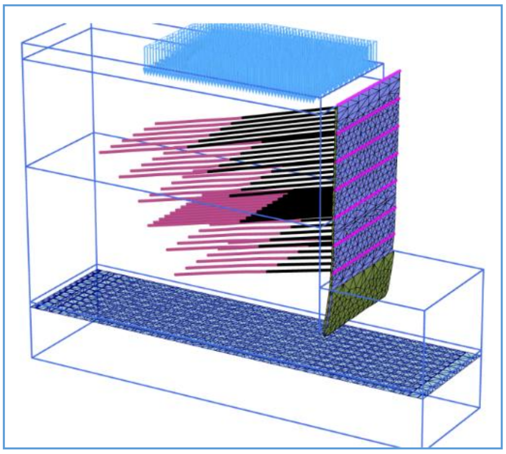

(a) (b)

Fig. 9. (a) Field visualization with anchors added to the 4th stage, (b) model with additional anchors in the 4th stage in Plaxis 3D program analysis (Source: the authors)

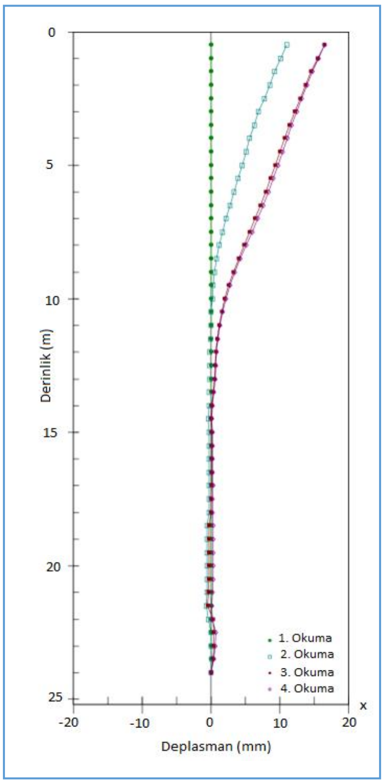

Fig. 10. Horizontal deformation graph depending on excavation depth obtained from inclinometer measurement (Source: the authors)

According to the graph in Fig. 10, it is observed that the maximum horizontal displacement value obtained from the inclinometer measurement in the field after the tensioning of the 4th stage anchors remained at the same value as the previous reading. The depth-dependent deformations are presented in Table 8 below.

Table 8. Maximum Horizontal deformations depending on excavation depth obtained from inclinometer measurement (Source: the authors)

Reading Order	Measured Maximum Horizontal Deformation [mm]	Excavation Depth [m]	Deformation Rate [%]
1st Reading	0.00	0.00	0.00
2nd Reading	11.02	6.25	0.17
3rd Reading	16.48	8.75	0.19
4th Reading	16.48	11.25	0.15

In addition, the horizontal deformation value of the top point of the 4th stage shoring system calculated by the finite element method was 3.02 mm and the horizontal deformation of the last stage was 27.78 mm (Fig 11).

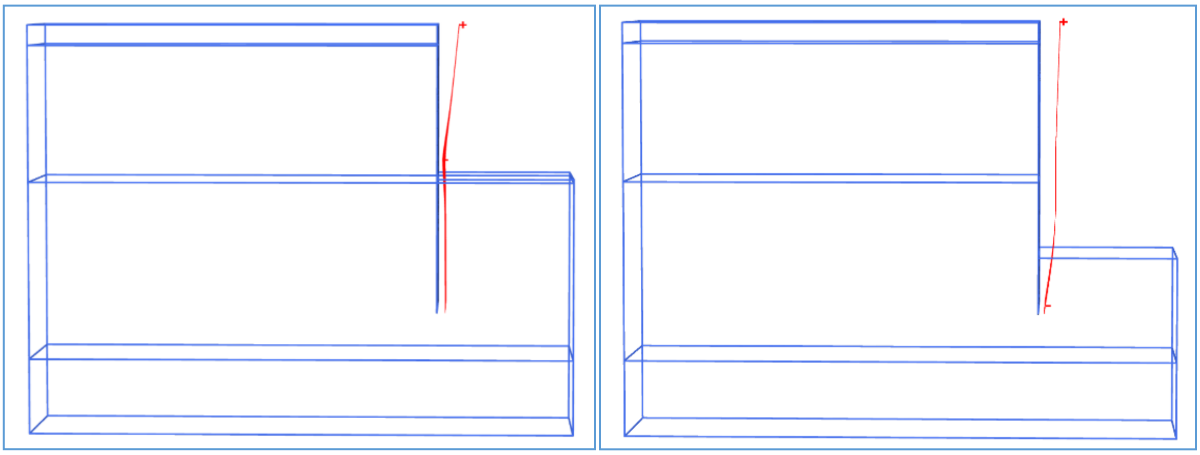

(a) (b)

Fig. 11. (a) Horizontal deformations graph in the fourth stage, (b) horizontal deformations graph in the final stage (Source: the authors)

The horizontal deformation values obtained from the back analysis and the inclinometer measurements made in the field gave very similar results. This similarity played an effective role in stopping sudden displacements. Fig. 12 shows the graph of total horizontal deformations obtained from inclinometer measurements. Table 9 presents the calculated deformation value and the measured deformation value and their corresponding deformation ratios.

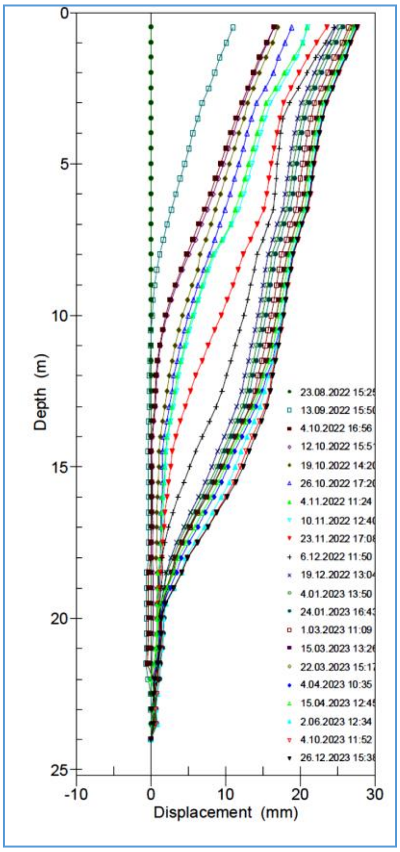

Fig. 12. Horizontal deformations graph of inclinometer final measurement (Source: the authors)

Table 9. Comparison of horizontal displacements calculated with finite elements and measured with inclinometer (Source: the authors)

Section No	Top Level Horizontal Deformation [mm]	Excavation Depth [m]	Deformation Rate [%]
First Analysis Calculated	10.81	16.95	0.06
Back Analysis Calculated	27.78	16.95	0.16
Measured with Inclinometer	27.60	16.95	0.16

The deformations remained at normal values thanks to the additional anchors made in the field. It was understood that increasing the number of anchors was effective in stopping the displacements. This was proved by back analysis.

4. Conclusions

The foregoing study, comprehensively investigated the effectiveness of anchored bored pile shoring systems in deep excavation support projects by comparing numerical modeling and field inclinometer measurements. To do so, the sudden deformations occurring after the third stage excavation were particulariy analyzed and the causes of the deformation increase were investigated in detail through back analysis. In the evaluations made in section-7, which is relatively critical, the performance of the system was compared with both finite element analysis using Plaxis 3D software and field observations.

Results of the analysis are as follows:

- In the initial analysis, the surcharge load was taken as 10 kPa and the horizontal deformation at the last stage of the shoring system was calculated as 10.81 mm. In the back analysis, the surcharge load was increased to 35 kPa and a building load of 90 kPa was added and the deformations increased to 22.45 mm. This result showed that as the surcharge loads increase, the deformation also increases.
- Anchor prestressing loads were taken as 330 kN in the initial model. In the back analysis, when the prestressing load was reduced to 100 kN in the first two stages, the horizontal deformation in the 3rd stage increased to 2.19 mm. Inadequate anchorage loads increased the deformations about three times and showed that the stability of the shoring is directly dependent on these loads.

- After the excavation of the 3rd stage, additional anchors were placed in the 4th stage in order to prevent sudden deformations. After this intervention, the horizontal deformation at the top of the shoring measured with an inclinometer was 27.60 mm and the deformation calculated by the finite element method was 27.78 mm. Since the measured values were close to each other, it has proven that the intervention is effective.
- In order to ensure safe and economical design of shoring systems, it is critical to include the correct surcharge loads in the model during the design phase. It is also recommended to place the anchors correctly while carefully monitoring their stresses during the implementation process.
- Regular deformation monitoring by instrumental observations (especially inclinometer measurements) throughout the construction process is critical for early detection of potential risks and timely interventions in the field.

Evaluated numerical modeling and field measurements presented this study, combinedly with the defined main criteria that should be considered in the safe design and implementation of deep excavation support systems helped provide important guildlines to the design and implementation phases of similar future projects.

Acknowledgments
The research described in this paper received no external funding.

References

Aktan, E. (2014). *Öngermeli ankrajlı kazıklı duvar nümerik analizi: Hilton İstanbul Bomenti Hotel ve Konferans Merkezi projesi kapsamında yer alan tarihi bina önü iksa sistemi* (Thesis No. 356141), Master's thesis, Istanbul Technical University.

ASTM A416. (1997). Standard specification for uncoated seven-wire steel strand for prestressed concrete. Annual Book of ASTM Standards, American Society for Testing and Materials, Philadelphia, PA.

Carder, D. R. (1995). Ground movements caused by different embedded retaining wall construction techniques. Transport Research Laboratory Report (No. 172). Berkshire, U.K.

Cengiz, A. D. (2008). *Bir diyafram duvarda tahmin edilen ve ölçülen yer değiştirmelerin karşılaştırılması*, Master's thesis, Yildiz Technical University

Çevre ve Şehircilik Bakanlığı. (2018). *Kazı güvenliği ve alınacak önlemler*. Retrieved from: http://csb.gov.tr

Eurocode 7. (2004). *Geotechnical design – Part 1: General rules*. European Committee for Standardization (CEN).

Fernie, R., & Suckling, T. (1996). Simplified approach for estimating lateral movement of embedded walls in U.K. ground. In *Proceedings of the International Symposium on Geo-Aspects of Underground Construction in Soft Ground* (pp. 131-136). City University, London.

FHWA-IF-99-015. (1999). Ground anchors and anchored systems: Geotechnical engineering circular No. 4. Office of Bridge Technology, Federal Highway Administration, 400 Seventh Street, SW Washington, DC 20590.

Kalpakcı, V., Öztürk, Ş., Yaman, G., & As, M. (2015). Jipsli zeminlerde gözlenen heyelan hareketleri ve alınan önlemler üzerine bir vaka analizi. *6. Geoteknik Sempozyumu*, November 2015, Çukurova University, Adana

Ma, X., & Cao, M. (2024). Evaluation of deformation for two-dimensional (2D) and three-dimensional (3D) braced excavation in clays with centrifuge modelling and numerical analysis. *Canadian Geotechnical Journal*. 61(12): 2785-2805.

Ma'ruf, M. F., & Darjanto, H. (2017). Back calculation of excessive deformation on deep excavation. *Sustainable civil engineering structures and constructions materials, Procedia Engineering*, 171, 502-510.

Ou, C., Hsieh, P., & Chiou, D. (1993). Characteristics of ground surface settlement during excavation. *Canadian Geotechnical Journal*, 30(5), 758-767.

PLAXIS. (2019). PLAXIS 3D: Finite element software for soil and rock analysis. Bentley Systems. Retrieved from https://www.bentley.com

PTI. (1996). *Recommendations for prestressed rock and soil anchors* (3rd ed.). Post-Tensioning Institute, Phoenix, AZ.

Rahmani, G. Y., & Laman, M. (2016). Yeraltı su seviyesi yüksek olan zeminlerde iksa sistemlerinin analizi. *Ç.U. Journal of Science and Engineering Sciences, 34(2), 100-110.*

Steiner, W., & Pedrozzi, G. (2001). Risk analysis of tunnel systems in urban areas with variable ground conditions. *AITES – ITA, World Tunnel Congress*, Bologna.

Experimental investigation of the filtration performance of various demolition waste-geotextile systems

Rumeysa Usta*[1], Mehmet H. Calım[1], Ilknur Erdogan[1], Sabriye B. Ikızler[1], Asli Y. Dayıoglu[2], Mustafa Hatipoğlu[2]

[1]*Karadeniz Technical University, Department of Civil Engineering, 61080 Trabzon,*
[2]*Istanbul Technical University, Department of Civil Engineering, 34469 Istanbul, Türkiye*

Abstract. The rapid depletion of natural resources and the increase in waste materials have highlighted the importance of research on recycling and sustainability. The use of demolition waste instead of natural aggregate in civil engineering fields, might contribute to sustainability. In this study, the reusability of demolition waste in under-road drainage systems was investigated. In the laboratory experiments, long-term filtration performance and clogging behavior of drainage systems using natural aggregate (NA), recycled concrete aggregate (RCA), recycled asphalt aggregate (RAP) and non-woven geotextile materials were observed. For this purpose, long-term filtration tests (LFT) of aggregate-geotextile systems were performed in the long-term filtration test apparatus developed in accordance with ASTM D5101 standard. The enhanced LFT tests were performed at hydraulic gradient of i =0.33, simulating practical conditions. Throughout the experiment, the hydraulic gradient ratio (GR) and permeability ratio (KR) values of the system were determined at different hydraulic gradients. Depending on these parameters, the filtration performance and clogging behavior of the system were analyzed. The migration of fine particles from in the upper layers to lower layers was evaluated based on gravity, the structural condition of the sample and the direction of water flow. The experimental results indicates that the performance of demolition wastes met the standard criteria. Reusing recycled materials will help address the issue of waste material storage while also contributing to the preservation of national resources and environmental protection.

Keywords: Recycled aggregate; Geotextile; Long-term filtration; Sustainability

1. Introduction

Technological advancements and the rapid growth of population have led to an increase in both the quantity and diversity of needs, significantly raising consumption levels. Although a linear relationship existed between resource use and the level of development in the past century, recent studies have shown that the presence of natural resources in countries can pose environmental threats if not managed with an adequate level of awareness (Kernera et al., 2023; Onifade et al., 2023). The level of consumption reached has prompted governments to develop policies aimed at reducing the use of natural resources, and studies have shown that these policies have been effective in mitigating environmental threats (Lv & Guo, 2025; Zhao et al., 2024).

The construction sector also plays a significant role in the increase in natural resource consumption (Schiller & Roscher, 2023; Evci et al., 2024). It is projected that 2.2 billion tons of construction and demolition waste will be generated globally within the next nine years, necessitating a reevaluation of traditional methods. To reduce construction waste—which poses a significant environmental problem especially in developing countries—it is essential to limit the use of natural resources, integrate technological innovations into the sector, and ensure that sustainable practices developed under the circular economy approach are implemented in practice, not just in theory (Saroosh & Khan, 2024; Hasselsteen et al., 2024; Wu et al., 2025).

To promote sustainability in the construction sector and minimize the use of natural resources, a variety of strategies have been adopted to reutilize construction and demolition wastes, including recycled concrete aggregate (RCA), reclaimed asphalt pavement (RAP), steel slag, glass, wood, brick, tire ash, and plastic waste (Simões dos Reis et al., 2021; Akponovo & Onyebuchukwu, 2023).

In subgrade drainage applications, the selection of appropriate materials for the fill layer and ensuring proper gradation particularly determining the amount of fine particles are critically important for achieving sufficient hydraulic conductivity, enabling effective drainage, and extending the service life of the road (Kavitha et al., 2024).

* Corresponding author, E-mail: ustarume@gmail.com

https://doi.org/10.31462/icearc2025_ce_geo_395

Recycled concrete aggregate (RCA) is considered a viable alternative to natural aggregate for use as subgrade drainage fill material (Meddah et al., 2020; Neupane et al., 2025). RCA exhibits characteristics similar to those of conventional crushed aggregates in terms of water absorption, California Bearing Ratio (CBR), cohesion, and elastic modulus (Arulrajah et al., 2012), as well as permeability, compressibility, and mechanical properties (Shrinidhi et al., 2025). Moreover, its performance in long-term filtration tests involving geotextile materials has also been shown to be comparable (Bilgen et al., 2020).

Another material investigated as an alternative to natural aggregate in subgrade drainage systems is reclaimed asphalt pavement (RAP). Li et al. (2023) stated that issues related to agglomeration and gradation variability in RAP can be mitigated by subjecting the material to a fine crushing and screening process. Furthermore, long-term filtration tests conducted by Sarıahmetoğlu et al. (2020) demonstrated that, when the bitumen content in RAP is properly controlled, it can exhibit performance comparable to natural aggregate, thereby serving as a viable alternative material.

In this study, long-term filtration tests (LFT) were conducted using a test system designed and developed in accordance with the ASTM D5101 standard, under a hydraulic gradient of $i = 0.33$, to investigate the clogging and filtration performance of construction and demolition waste materials. Within the scope of the research, the filtration and clogging behavior of recycled concrete aggregate–geotextile and recycled asphalt aggregate–geotextile systems were compared with the performance of natural aggregate–geotextile systems. This comparison aimed to support existing literature and promote the use of construction waste materials as an alternative to natural resources.

2. Materials

2.1. Aggregates

In this study, long-term filtration tests were conducted in accordance with ASTM D5101, using natural aggregate as well as recycled concrete aggregate (RCA) and recycled asphalt pavement (RAP) derived from construction and demolition waste for drainage applications (Fig 1). The materials were oven-dried for 24 hours and then tested using a pycnometer and Standard Proctor test in accordance with ASTM D698-12 (Table 1). The remaining materials were then stored under appropriate conditions until the preparation stage of the filtration specimens.

Table 1. Results of the above mentioned experiments

Aggregate Type	p_s (g/cm^3)	MDD (kN/m^3)	W_{opt} (%)
NA1	2.79	22.5	8.45
RCA1	2.44	13.8	22.10
RAP1	2.13	17.5	10.5

p_s: Specific gravity, MDD: Maximum dry density, W_{opt}: Optimum moisture content

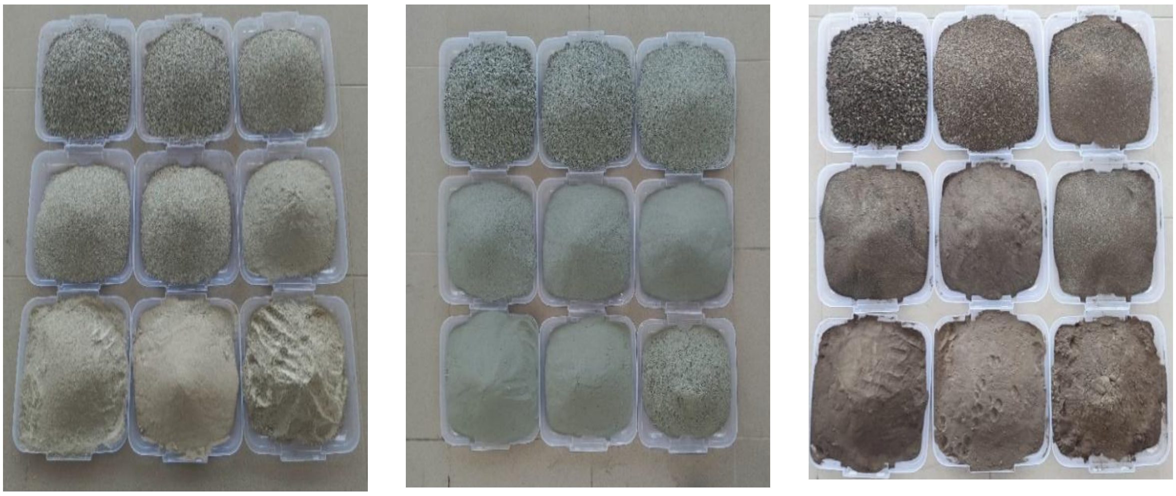

(a) (b) (c)

Fig 1. Aggregates; (a) Natural Aggregate, (b) Recycled Concrete Aggregate, (c) Reclaimed Asphalt Pavement

2.2. Geotextile

The selection of an appropriate nonwoven geotextile for filtration applications is crucial for the performance of the drainage system. The apparent opening size (AOS) and vertical permeability values ensure that the geotextile functions effectively as a filtration material. While maintaining the stability of the system, the geotextile should allow the passage of water but prevent clogging and blocking. An incorrect geotextile selection can lead to a decrease in system permeability and a reduction in the particle size of the material. In this study, a polypropylene nonwoven geotextile with an opening size of 0.095 mm (Fig 2.) was used, and the properties of the material are presented in the table 2.

Table 2. Properties of the geotextile

Properties	Unit	Test Standard	GT
Mass per Unit Area	g/m²	EN ISO 9864	200 (±40)
Thickness (at 2kPa)	mm	EN ISO 9863-1	2,1 (±0,4)
Tensile Strength (MD- CMD)	kN/m	TS EN ISO 10319	15 (-3,0)
Elongation at Break (MD- CMD)	%	TS EN ISO 10319	≥50
Static Puncture Resistance	N	EN ISO 12236	2400 (-300)
Dynamic Perforation Resistance	mm	EN ISO 13433	10 (+3)
Characteristic Openning Size (O^{90})	mm	EN ISO 12956	0,095 (±0,020)
Water Permeability, H_{50}	l/(s·m²)	EN ISO 12956	90 (±15)

Fig 2. Geotextile

3. Methods

In this study, the specimens were prepared and subjected to a long-term filtration test under a hydraulic gradient of i = 0.33. Based on the data obtained, the gradient ratio (GR) and the permeability ratio (KR) parameters were determined, and the physical clogging mechanisms were identified and analyzed.

For the execution of the experiments, natural aggregate (NA), recycled concrete aggregate (RCA), and recycled asphalt pavement (RAP) were initially procured. Each material was separately subjected to sieving and stored based on the resulting particle size. Following the sieve analysis, the aggregates were sorted by type and particle size and stored under appropriate conditions. For each aggregate type, a Standard Proctor test was conducted in accordance with ASTM D698-12 to determine the optimum moisture content of the sample. Specimen's recipe given at table 3.

Table 3. Specimen recipe

Sieve No	10	18	30	40	50	70	100	Pan
% Retained	10	15	9	14	13	19	10	10

Long-term filtration tests were conducted on the experimental system, as specified in the ASTM D5101 standard, which has been further developed and redesigned. The system was used to examine the permeability performance of the drainage layer formed by non-plastic aggregates (PI<5%) and geotextile. In this system, the size of the sample chamber and the number of manometers in the middle chamber of the standard long-term filtration test system have been increased to ensure more accurate determination of the GR and KR values. This adjustment was made to ensure that the data obtained from the experiment is more consistent with field application data. Based on the maximum particle size of the aggregate used in the experiment, cylindrical samples with a diameter of 150 mm and a height of 150 mm were employed.

Additionally, in the improved system utilized in this project, a manometer port was added at a height of 125 mm, supplementing the existing manometers positioned at 25 mm and 75 mm above the geotextile layer, as in the standard system (Fig 3).

After the sample was placed into the system, the lower, middle, and upper assembly processes were completed using silicone, and the system was left for one day to ensure its impermeability. After performing the necessary checks, the connections of the water inlet and outlet reservoirs were established. To achieve the system's water saturation, water was introduced through the lower port and the system was left for approximately 3–4 days. By introducing water from the bottom, potential particle movement from the upper part of the sample towards the geotextile was prevented before the experiment began. Once the system reached saturation, the water was introduced from the top, and the LFT was initiated (Fig 4).

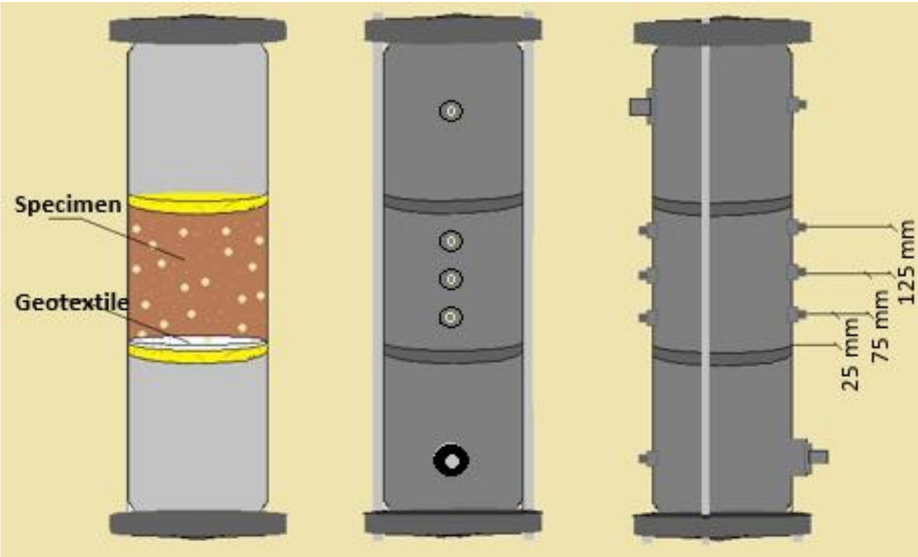

Fig 3. Demonstration of enhanced lft

Fig 4. Experimental system

The system was adjusted to a hydraulic gradient (i) of 0.33, and readings were taken from the manometers. Following the readings, the flow of water was measured and recorded in the prepared tables. Based on these values, the hydraulic gradient ratio (GR) and permeability ratio (KR) were calculated, and their relationship was determined.

The data obtained from the readings of manometers placed at different heights were used in the formulas provided in Equations 1-4 to calculate the GR values.

$$GR_1 = \frac{i_{0-25}}{i_{25-75}} = 2 \times \frac{h_{25} - h_0}{h_{75} - h_{25}} \tag{1}$$

$$GR_2 = \frac{i_{25-75}}{i_{75-125}} = \frac{h_{75} - h_{25}}{h_{125} - h_{75}} \tag{2}$$

$$GR_3 = \frac{i_{0-25}}{i_{25-125}} = 4 \times \frac{h_{25} - h_0}{h_{125} - h_{25}} \tag{3}$$

$$GR_4 = \frac{GR_1 + GR_2}{2} \tag{4}$$

h_0, h_{25}, h_{75}, h_{125} : Manometer readings at different heights,
i : hydraulic gradient.

The KR parameter provided in the ASTM D 5101 Standard (Equation 5) is defined as the ratio of the aggregate permeability coefficient (Equation 6) to the system permeability coefficient (Equation 7) (Sarıahmetoğlu, 2021).

$$KR = \frac{k_{aggregate}}{k_{system}} \tag{5}$$

$$k_{system} = \frac{Q}{A \times t} \times \frac{1}{i_{system}} \times \frac{\mu_T}{\mu_{20}} = \frac{Q}{A \times t} \times \frac{l}{h_{150} - h_0} \times \frac{\mu_T}{\mu_{20}} \tag{6}$$

$$k_{aggregate} = \frac{Q}{A \times t} \times \frac{1}{(U_{avg} - A_{avg})} \times \frac{\mu_T}{\mu_{20}} \tag{7}$$

k_{system} : The permeability value of the system at 20°C is, (cm/s),
Q : The accumulated flow volume at time t, (cm^3),
i : Hydraulic gradient,
A : Cross-sectional area of the sample, (cm^2),
t : The time required to collect the amount of drained water, Q (s),
μ_T : The viscosity of water at temperature T.
μ_{20} : The viscosity of water at 20°C,
l : The length of the sample,
U_{avg} : The average of the upper manometer readings,
A_{avg} : The average of the lower manometer readings.

4. Results and discussion

In the experimental setup established based on the ASTM D5101 standard, a geotextile–aggregate system was formed using three different material types: natural aggregate, recycled concrete aggregate, and reclaimed asphalt pavement. Long-term filtration tests were conducted under a hydraulic gradient of i = 0.33. The experimental data obtained were evaluated in accordance with the GR (Gradient Ratio) and KR (Permeability Ratio) criteria defined in the aforementioned standard. A precise analysis of the filtration performance of the materials was carried out by comparing the GR values calculated from manometer readings taken at different levels.

According to the ASTM D5101 standard, a GR value equal to 1 in a geotextile–aggregate system indicates that there is no flow restriction or clogging within the system. A GR value greater than 1 implies that particle migration has started in the direction of water flow, indicating increased clogging and a reduction in flow rate. Conversely, a GR value less than 1 suggests that fine particles have passed through the geotextile, potentially leading to piping, which subsequently increases the water flow through the system.

The time-dependent GR (Fig 5) and KR (Fig 6) values of the natural aggregates are provided. From the graphs, it can be observed that the GR values fall within the range of $1 < GR < 3$. These values indicate the occurrence of clogging in the system. Furthermore, the KR values also support this observation.

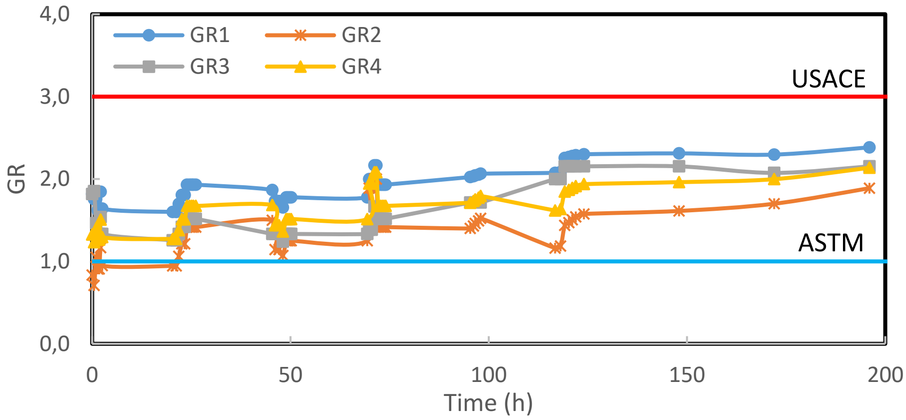

Fig 5. Time-dependent GR values of NA

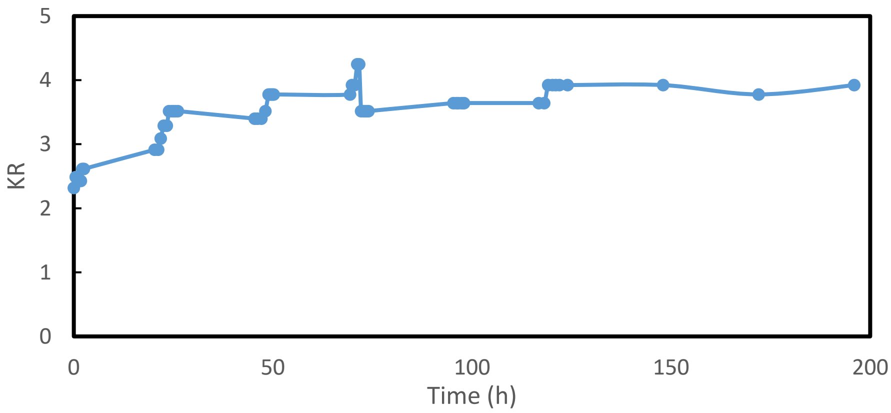

Fig 6. Time-dependent KR values of NA

Below are the time-dependent GR (Fig 7) and KR (Fig 8) graphs for RCA. As seen in the graph, it can be stated that partial clogging has started for RCA. However, it can be observed that RCA yields better results compared to NA.

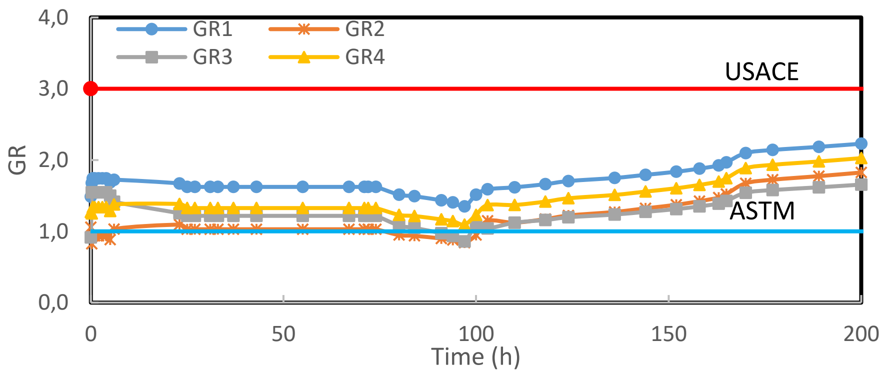

Fig 7. Time-dependent variation of GR values for RCA

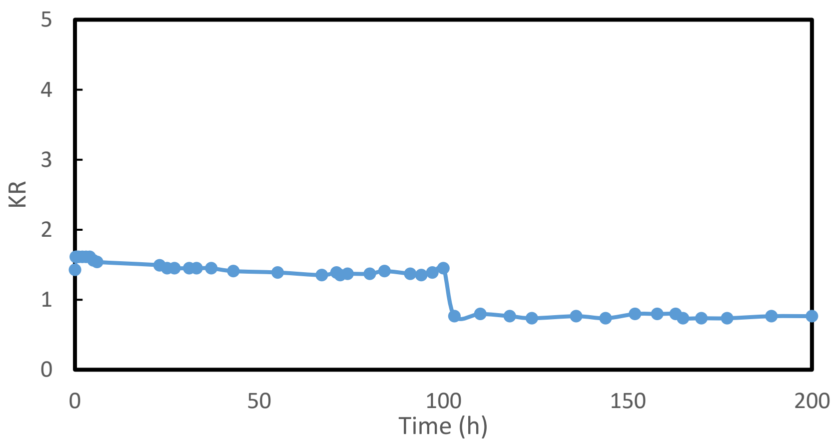

Fig 8. Time-dependent variation of the KR value for RCA

The GR and KR values of RAP are presented in Fig. 9 and Fig. 10. The obtained values show that the GR and KR parameters support each other. G1, GR3, and G4 values remain above the 1 threshold, indicating clogging, while the GR2 value signifies the possibility of piping.

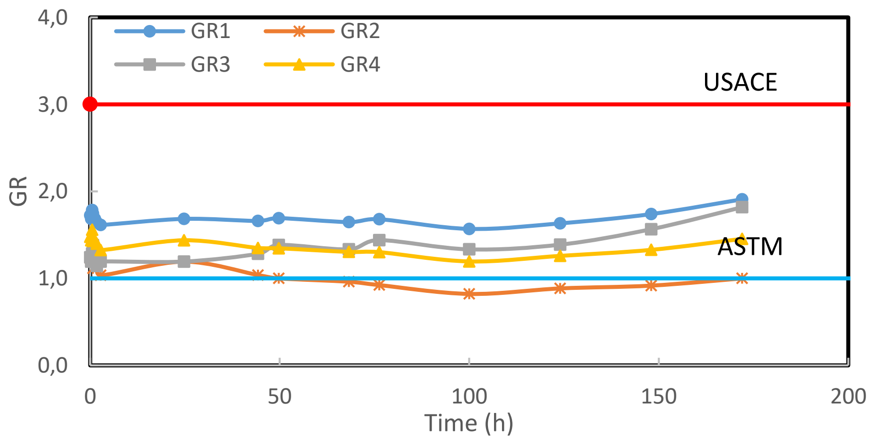

Fig 9. Time-dependent variation of GR values for RAP

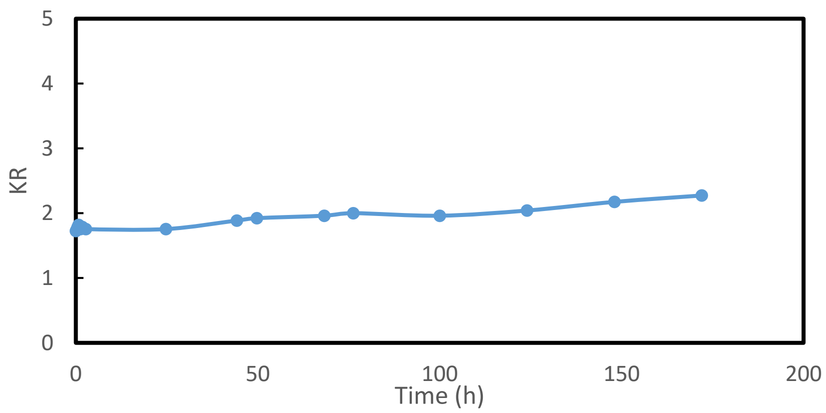

Fig 10. Time-dependent variation of the KR value for RAP

5. Conclusion

To evaluate and compare filtration performance of different aggregates (natural or recycled) an enhanced long term filtration test system was redesigned and custom-manufactured in accordance with ASTM D5101 standard. Based on the data obtained from the experiment, the following conclusions can be derived:

- Under low hydraulic gradient conditions, systems exhibited GR values below the critical clogging threshold of 3, confirming their suitability for use as drainage materials in systems with low hydraulic gradients.
- GR values exceed 1, indicating a tendency toward time-dependent clogging.
- Although the GR value of the system with natural aggregates remained within acceptable limits, the KR values exceeded the critical threshold. In terms of filtration performance, the system with natural aggregates demonstrated the lowest capacity.
- The use of suitable recycled materials instead of natural material is considered to contribute to sustainability and circular economy.

Acknowledgements
We would like to express our gratitude to ISTANBUL TEKNIK INSAAT company for providing the geotextile materials.

References
Akponovo, O., & Onyebuchukwu, L. (2023). A Review On Recycled Materials Used İn Construction. International Journal Of Structural And Construction Engineering, 17(10), 408-414.
Arulrajah, A., Jegatheesan, P., & Bo, M. W. (2012). Geotechnical Properties Of Recycled Concrete Aggregate İn Pavement Sub-Base Applications. Geotechnical Testing Journal 35(5), 1-9.
Bilgen, G., Houlihan, M., Ryoo, S., Wang, Y., & Aydilek, A. (2020). Hydraulic And Environmental Compatibility Of RCA With Filters And Subgrades In Highways. Environmental Geotechnics.
Evci, P. U., Cırık, K., Şakalak, E., & Sever, A. E. (2024). A Crıtıcal Examination Of The Constructıon Sector In Turkiye In Terms Of Sustaınabılıty. International Journal Of Engineering And Innovative Research, 179-195.
Hasselsteen, L., Lindhard, S., & Kana, K. (2024). Resource Management At Modern Construction Sites: Bridging The Gap Between Scientific Knowledge And Industry Practice And Needs. Journal Of Environmental Management.
Kavitha, G., Kunjar, V., Gowda, S., & Jayaram, M. (2024). Evaluation Of Drainage Ability Of Granular Subbase Through Large-Scale Model Pavement Studies And Machine Learning Models. Innovative Infrastructure Solutions.
Kernera, P., Kalthausb, M., & Wendlera, T. (2023). Economic grow thand the use of natural resources: Assessingthemoderating Role of Institutions. Energy Economics.
Li, N., Zhan, H., Li, H., Yu, X., Tang, W., Wang, Z., & Y., Z. (2023). Investigation Of Recycled Asphalt Pavement Materials Treated By Refined Crushing And Screening Process: Comparison With Conventional Methods. American Society Of Civil Engineers 32(2).
Lv, L., & Guo, B. (2025). Can Green Finance Policy Reduce Energy Consumption: Quasi-Natural Experimental Evidence From Green Finance Reform And İnnovations Pilot Zone. Frontiers İn Environmental Science.
Meddah, M., Al-Harthy, A., & Ismail, M. (2020). Recycled Concrete Aggregates And Their Influences On Performances Of Low And Normal Strength Concretes. Buildings (10).
Neupane, B., Sahani, K., & Khadka, S. (2025). Experimental Testing And Numerical Simulation Of Recycled Concrete Aggregate İn A Concrete Mix. International Journal Of Concrete.
Onifade, S., Haouas, I., & Alola, A. (2023). Do Natural Resources And Economic Components Exhibit Differential Quantile Environmental Effects?. Natural Resources Forum, 355-373.
Sarıahmetoglu, A. B. (2021). Atık Malzemelerin Drenaj Sistemlerinde Kullanım Uygunluğunun Deneysel Olarak İncelenmesi. 131-132. İstanbul: İstanbul Teknik Üniversitesi.
Sarıahmetoglu, A., Iyısan, R., Dayıoğlu, A., & Hatipoglu, M. (2020). Geri Kazanılmış Asfalt Malzemenin Uzun Süreli Filtrasyon Performansı. Pamukkale Üniversitesi Mühendislik Bilimleri Dergisi
Saroosh, M., & Khan, I. (2024). Implementing Circular Economy Principles İn Construction Wastemanagement: A Conceptual Framework For Maximizing Resource Efficiencyand Minimizing Environmental Impact. 3Rd InternatiOnal Conference On Advances In Civil And Environmental Engineering, (S. 938-946).
Schiller, G., & Roscher, J. (2023). Impact Of Urbanization On Construction Material Consumption: A Global Analysis. Journal Of Industrial Ecology 27(4).
Shrinidhi, D., Adarsh, K., Mamatha, K., & Dinesh, S. (2025). Feasibility Of Use Of Recycled Concrete Aggregates In Drainage Layer Of Pavements: A Comparative Analysis. Journal Of Material Cycles And Waste Management, 1174-1191.
Simões Dos Reis, G., Quattrone, M., Ambrós, W., Cazacliu, B., & Sampaio, C. (2021). Current Applications Of Recycled Aggregates From Construction And Demolition: A Review. Materials (14).
Wu, J., Ye, X., & Cui, H. (2025). "Recycled Materials İn Construction: Trends, Status, And Future Of Researc". Sustainability, 17.
Zhao, N., Liu , Q., Zhang, Z., & Gao, K. (2024). Whether Behavioral Guidance Policies Of Construction Waste Resource Utilization Are Effective For Construction Contractors: Evidence From China. Buildings, 14 (10).

4th International Civil Engineering & Architecture Conference
17-19 May 2025, Trabzon, Türkiye

Valorization of mixed mine tailings and tea powder wastes for underground backfill production: A lab-scale study

Muhammet Sari[1,2], Erol Yilmaz *[1,2],Tugrul Kasap[1,2], Tugba Keskin[1,2]

[1] *Recep Tayyip Erdogan University, Department of Civil Engineering, 53100 Rize, Türkiye*
[2] *Recep Tayyip Erdogan University, Geotechnical, Waste Management and Backfill Laboratory, Rize, Türkiye*

Abstract. Cemented paste backfill (CPB) are widely used for safe disposal and stability drives of environmentally hazardous mine tailings. However, the economic and environmental concerns associated with cement consumption have highlighted the need for alternative materials. This study explores the potential of tea waste, a type of agricultural byproduct, as a substitute in CPB. The research focused on evaluating the performance of CPB mixtures with a fixed solid-to-cement ratio (70/5 by weight), using metal mine wastes and varying curing times. Various tea wastes, including tea production powder waste, brewed tea waste and tea fiber were incorporated into the filling mixtures, replacing 10% by weight of the cement content. Uniaxial compressive strength (UCS) and three point flexural tests were conducted to assess the mechanical properties, while scanning electron microscopy (SEM) were employed to analyze the microstructural changes. The results highlighted significant differences between each types of tea waste, with each having distinct effects on backfill performance. The study provides a comparative analysis of their impact on the strength and overall filling performance. In conclusion, the findings demonstrate that tea waste can be effectively utilized as a partial replacement for cement in CPB mixtures, offering a sustainable solution to reduce environmental damage by recycling agricultural waste while improving mine tailings management..

Keywords: Cementitious fills; Tailings-tea waste; Strength behaviour; Microstructure

1. Introduction

Mine tailings constitute an inevitable byproduct of mineral extraction processes, with their volume varying considerably depending on the scale of resource recovery (Adewuyi et al., 2024). Large-scale mining operations, in particular, generate substantial quantities of tailings, the management of which presents significant environmental challenges. Due to the presence of heavy metals and toxic substances, mine tailings have the potential to contaminate soil and water resources, thereby disrupting ecosystems, threatening biodiversity, and posing long-term risks to human health (Kasap et al., 2022). Accordingly, the development and implementation of comprehensive and strategic tailings management practices are imperative to mitigate these adverse environmental impacts. Globally, the annual generation of mine tailings is estimated to be in the billions of tons (Araya et al., 2021). The extraction of valuable metals such as coal, gold, and copper is especially associated with the production of extensive volumes of tailings. For instance, copper mining alone results in the generation of hundreds of millions of tons of tailings each year, a portion of which contains hazardous chemical components that contribute to environmental degradation (Hassan et al., 2024). Consequently, the formulation of effective tailings management and recycling strategies is of paramount importance. In this context, the Cemented paste backfill (CPB) method has emerged as a widely adopted and innovative approach for the sustainable disposal and utilization of mine tailings.

CPB method is primarily employed to fill voids and fractures within underground mining operations. This technique involves the preparation of a backfill mixture composed of mine tailings (70–85 wt.%), cement (3–7 wt.%), water, and various chemical additives, ensuring adequate flowability for effective placement (Guner et al., 2023). By occupying the spaces created during mining, this backfill enhances the structural integrity of underground workings and significantly mitigates the risk of ground subsidence or collapse. Moreover, CPB contributes to improved mining efficiency, restricts the ingress of water into subterranean systems, and minimizes environmental impacts associated with tailings disposal (Sari et al., 2023). Upon hardening, the CPB mixture exhibits high mechanical strength and durability, offering long-term geotechnical support and fostering the sustainability of mining operations. Despite its advantages, the relatively high cement content required for CPB

* Corresponding author, E-mail: erol.yilmaz@erdogan.edu.tr

https://doi.org/10.31462/icearc2025_ce_geo_607

poses economic challenges for mining companies, prompting ongoing research into cost-effective alternative binders or additives (Saedi et al., 2021). In this regard, tea waste—an agricultural byproduct—has emerged as a potential sustainable additive for use in CPB formulations.

Tea, a widely consumed herbal beverage, is derived from the processed and dried leaves of Camellia sinensis L. Originally cultivated in China and India, tea is currently grown in geographically limited regions due to the specific climatic conditions required for the plant's growth. The majority of global tea cultivation and consumption is concentrated in Asia (Yazici & Goksu, 2017). Additionally, several tropical African countries—including Kenya, Malawi, Rwanda, Tanzania, and Uganda—also contribute significantly to global tea production. Nations such as China, India, Sri Lanka, and Kenya are among the leading producers, with China alone accounting for approximately 64% of the total global tea cultivation area and 49% of overall tea production (FAO, 2023). Türkiye ranks eighth globally in terms of tea cultivation area, with approximately 82,000 hectares, and fourth in production, yielding about 1.45 million tons annually. In Türkiye, tea is cultivated in the humid, rainy, and high-altitude foothills of the Eastern Black Sea region, characterized by rugged topography. Tea is one of the most significant agricultural commodities in Türkiye and plays a critical role in the regional economy. The principal tea-producing provinces include Rize, Trabzon, Artvin, and Giresun. The tea harvest typically begins in the spring, and the freshly picked leaves are processed without delay. Although tea processing methods vary depending on the desired product, in Türkiye, tea is predominantly processed into black tea through a series of stages, including withering, CTC (crush, tear, curl), fermentation (oxidation), drying (baking), and sorting (as illustrated in Figure 1).

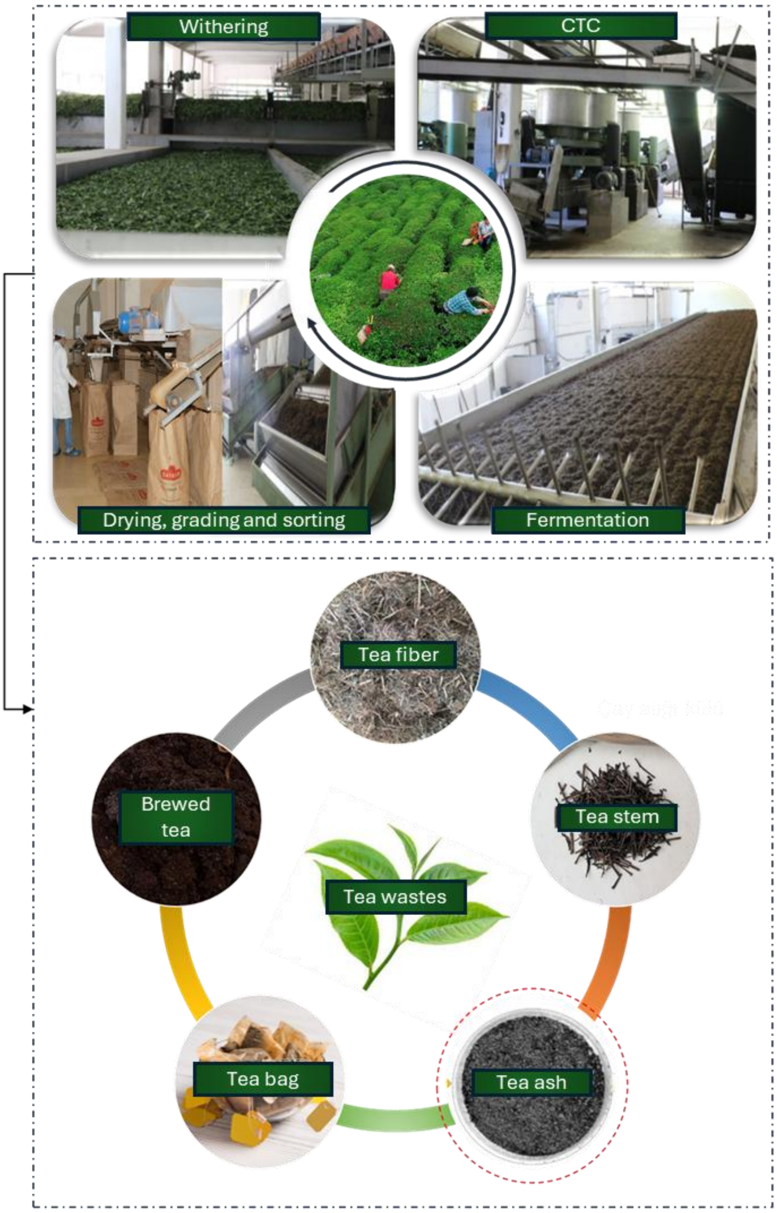

Fig. 1. Production process of tea waste

The growing global demand for tea has led to a significant increase in tea consumption, which in turn contributes to the generation of considerable amounts of tea waste—primarily consisting of leaves, stems, and buds. Annually, the volume of tea waste produced worldwide is estimated to reach approximately 5 million tons (Debnath et al., 2021). In Türkiye's Eastern Black Sea region, where tea cultivation is a major agricultural activity, the waste generated during the production process predominantly originates from the by-products of tea leaf processing. These wastes are primarily composed of organic matter, fibers, and fine particulate material. The substantial quantities of tea waste produced by the active tea industry present challenges in terms of both storage and environmental management, potentially contributing to issues such as erosion, and soil and water pollution (Wang et al., 2024). As a result, there is a pressing need for sustainable and effective disposal methods. In this context, the utilization of tea waste within the backfill process presents a promising solution, offering potential environmental and operational benefits.

Various studies in the literature have explored the utilization of agricultural and organic wastes—primarily in the form of ash or fiber—as alternative materials in cemented paste backfill applications. For instance, Qi et al. (2022) investigated the use of corn straw ash, derived from biomass combustion, as a partial replacement for cement and fly ash in CPB mixtures intended for coal mine applications. Their findings indicated that the incorporation of corn straw ash, at substitution rates ranging from 0 to 40 wt.%, enhanced the setting time, water retention, and flowability of the backfill. Similarly, Jin et al. (2024) evaluated ashes obtained from agricultural residues such as corn straw, peanut shells, and wood chips in self-compacting backfill mixtures. Their research focused on the durability of these materials under freeze-thaw conditions and prolonged sulfate exposure, concluding that optimal performance was achieved at a water-to-binder ratio of 0.6. Liu et al. (2023) examined the replacement of cement with rice straw ash in various binder proportions and observed that its inclusion improved the shear strength and refined the microstructure of the backfill through the generation of supplementary hydration products. Additionally, Wang et al. (2023) incorporated corn straw fibers (1–3% by mass of coarse aggregates) into cemented coal gangue backfills to enhance mechanical properties. Their results demonstrated that fiber additions of 1–2% notably improved the mechanical performance during early curing stages. Pan et al. (2024) employed alkali-treated rice straw fibers in lithium mica tailings backfills and reported that the highest unconfined compressive strength (UCS) and Brazilian tensile strength values were achieved at optimal fiber contents of 0.15% and 0.60%, respectively.

A review of the existing literature reveals that organic additives have been incorporated into cement-based mixtures for a variety of purposes, and numerous studies have been conducted in this field. Notably, a significant portion of these researches focuses on reducing cement-related costs while producing high-quality materials through the use of more economical and sustainable alternatives. However, despite the growing interest in organic waste utilization, no studies have been identified that examine the application of tea waste in cemented paste backfill systems. This research aims to address this gap by investigating the potential use of tea waste in CPB mixtures. Specifically, the study evaluates the effects of tea production waste from factories—both in powder and fiber form—as well as brewed tea waste on the performance of CPB mixtures. The effectiveness of these additives was assessed through mechanical testing, including uniaxial compressive strength (UCS) and flexural strength (via three-point bending tests), as well as microstructural analysis using scanning electron microscopy (SEM). The results obtained provide new insights into the viability of tea waste as a sustainable additive in CPB applications.

2. Materials and methods

2.1. Ingredients

The metal mine tailings used in the preparation of the backfill mixtures were obtained from a mining operation located in the northern region of Türkiye, which engages in both underground and open-pit mining activities. The primary binder material, CEM I 42.5R Portland cement, was sourced from production facilities situated near the Black Sea, in proximity to the mining site. Tap water was also used as mixing water in CPB mixture. To characterize the physical properties of the mine tailings, several analytical instruments were employed: particle size distribution was determined using a Malvern Mastersizer, specific gravity was measured with a Quantachrome Ultrapyc 1200e helium gas pycnometer, and specific surface area was assessed via BET analysis using Quantachrome's Quadrosorb SI device. The detailed results of these measurements are presented in Table 1.

Furthermore, the chemical composition of the tailings was analyzed using X-ray fluorescence (XRF) spectrometry with the PANalytical Zetium instrument, revealing that the predominant oxidized component was ferric oxide (Fe_2O_3), comprising 38.52% of the total composition.,

Tea wastes utilized in this study comprised tea powder waste (TP) and tea fiber waste (TF), both obtained from the final production stages of black tea processing facilities operated under the General Directorate of Tea Enterprises (ÇAYKUR), as well as dried brewed tea waste (TB). These materials were incorporated into the CPB mixtures as illustrated in Figure 2. Prior to use, TP and TB were sieved to ensure particle sizes below 250 µm, whereas TF was incorporated into the mixtures in fiber form with a uniform length of 10 mm.

Table 1 Physical and chemical properties of tailings

Physical characteristics of mine tailings						
Specific surface (S_s), m^2/g	Specific gravity (G_s)	D_{10} (μm)	D_{30} (μm)	D_{60} (μm)	Uniformity coefficient, (C_u)	Curvature coefficient, (C_c)
2.78	3.63	7.30	26.40	57.30	7.85	1.67
Main chemical components of mine tailings (%)						
SiO_2	Fe_2O_3	CaO	MgO	Al_2O_3	K_2O	SO_3
28.65	38.52	4.85	2.08	8.32	0.37	0.81

2.2. CPB preparation and mix design

Cemented paste backfill samples were prepared under controlled laboratory conditions with a constant solid content of 70% by weight and a cement content of 5% by weight. To evaluate the influence of tea waste on the performance of the backfill, 10% of the cement mass was replaced with tea waste in the CPB mixtures. The mixture designs are detailed in Table 2. For each curing period, three replicate samples were produced for subsequent slump and mechanical strength testing. The constituent materials were accurately weighed using a precision scale and thoroughly blended in a 10-liter laboratory mixer to ensure homogeneity. The resulting mixtures were cast into cylindrical molds (diameter × height: 5 × 10 cm) for uniaxial compressive strength testing and prismatic molds (40 × 40 × 160 mm) for three-point bending tests. All specimens were cured in a controlled chamber maintained at 22 ± 3 °C temperature and 90 ± 5% relative humidity for durations ranging from 3 to 28 days. It is important to note that tea fiber waste was utilized exclusively in the prismatic samples designated for bending tests. The materials employed in the study and the preparation process of the CPB mixtures are illustrated in Figure 2.

Table 2 CPB recipe design

Samples	Solid content (wt. %)	Binder dosage (wt. %)	Slump (cm)	Mixture ratio (%)		Curin tme (days)
				CEM I 42.5R	Tea waste	
CPB@C1	70	5	21	100	-	3, 7, 14, 28
CPB@TB	70	5	21	90	10	3, 7, 14, 28
CPB@TP	70	5	21	90	10	3, 7, 14, 28
CPB@C2	70	5	21	90	10	7, 14, 28
CPB@TF	70	5	21	90	10	7, 14, 28

C: control; TB: brewed tea waste; TP: tea production waste; TF: tea fiber

2.3. Methods

The fluidity of the CPB mixtures was assessed using a mini slump test, employing a cone with a height of 15 cm, in accordance with the ASTM C143 standard. The use of the mini slump cone, as opposed to the conventional Abram's slump cone (30 cm in height), offered significant advantages in terms of both material efficiency and time savings during testing. Furthermore, a correlation was established between the results obtained using the mini slump cone and those from the standard cone. Based on this correlation coefficient, the mini slump cone was adopted for subsequent tests to enable rapid and reliable estimation of the target slump values throughout the study.

The uniaxial compressive strength (UCS) and corresponding stress–strain relationships of the CPB samples were determined in accordance with the ASTM C39 standard. Testing was conducted using a servo motor-controlled UTEST Multiplex testing machine, which has a load capacity of 50 kN and operates at a constant displacement rate of 1 mm/min. Additionally, three-point bending tests were performed to evaluate the flexural strength of the backfill specimens. Prismatic samples prepared for bending tests were positioned on the testing apparatus with a span length of 100 mm between the supports, and the measurements were subsequently carried out under controlled conditions.

To gain a clearer understanding of the pore structure and hydration products formed within the CPB samples following mechanical testing, Scanning Electron Microscopy (SEM) analyses were conducted using a JEOL JSM-6510 device. Polished sections were prepared from regions near the center of the specimens to ensure representative microstructural characterization. The SEM instrument operated with a resolution of 3 nm, a magnification range of 5× to 1,000,000×, an electron emission current of 0.9 nA, and an acceleration voltage of 20 kV.

Fig. 2. CPB preparation phases: a) main ingredients, b) mixing, casting and curing, c) testing

3. Results and Discussions

3.1. Impact of tea wastes (TP and TB) on the ucs performance of CPB

The influence of tea production waste (sieved tea powder waste, TP) and brewed tea waste (dried and sieved, TB) on the uniaxial compressive strength (UCS) of the CPB mixtures is illustrated in Figure 3. As shown, the highest UCS values at all curing intervals were observed in the control samples (CPB@C1). Specifically, CPB@C1 exhibited a compressive strength of 0.36 MPa at 3 days and increased to 0.83 MPa at 28 days. Similar to the control, mixtures containing TP and TB (CPB@TP and CPB@TB) demonstrated progressive strength development with extended curing time.

However, the replacement of 10% cement by mass with tea waste resulted in a noticeable reduction in strength compared to the control. For instance, at 14 days of curing, CPB@C1 achieved a strength of 0.72 MPa, whereas CPB@TB and CPB@TP reached 0.62 MPa and 0.44 MPa, respectively. The variation in UCS performance between the two tea waste types may be attributed to the surface properties of the materials. In particular, the washing of brewed tea waste likely removes impurities and surface-bound particles that could interfere with particle bonding, thus enhancing the contact surface and contributing to improved strength relative to TP.

3.2. Evaluation of tea fiber waste (TF) influence on the flexural strength of CPB

The results obtained from the three-point bending tests conducted on CPB mixtures incorporating tea fiber waste (1 cm length) are presented in Figure 4. It was clearly observed that the flexural strength of all mixtures increased with extended curing time. After 7 days of curing, the control samples (CPB@C2) exhibited a flexural strength of 0.32 MPa, whereas the CPB@TF samples reached 0.28 MPa. This trend continued over time, with flexural strength values increasing notably after 14 days of curing. At 28 days, the flexural strengths of CPB@C2 and CPB@TF were recorded as 0.48 MPa and 0.51 MPa, respectively.

These results indicate that the inclusion of tea fiber waste contributes to enhanced flexural performance over time. This improvement can be attributed to the interaction between the hydration products and the fiber surfaces, which likely promotes better bonding and modifies the internal pore structure of the matrix, thereby improving crack resistance and overall bending performance.

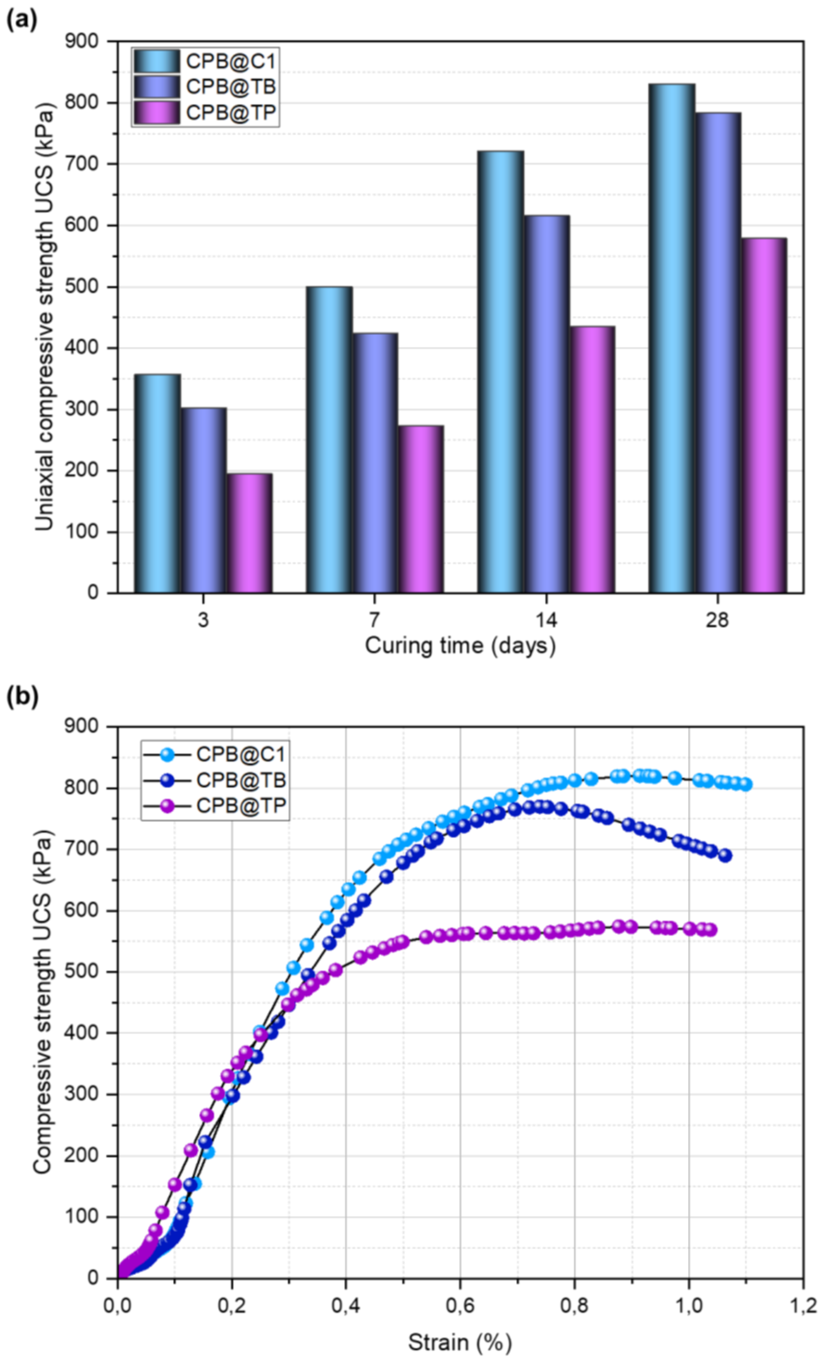

Fig. 3. UCS-curing time plots of CPBs and (b)stress–strain curves of 28-day cured samples

3.3. Results of scanning electron microscopy (SEM)

Scanning electron microscopy (SEM) analyses were conducted to evaluate the influence of tea waste on the hydration process and pore structure of the CPB mixtures. SEM micrographs of the samples cured for 28 days are presented in Figure 5. Figures 5a, 5b, and 5c correspond to the control sample (CPB@C1), the mixture incorporating brewed tea waste (CPB@TB), and the one containing factory tea production waste (CPB@TP), respectively. Figure 5d shows the microstructure of the sample containing tea fiber waste (CPB@TF), which was subjected to flexural testing. As observed, the quantity and density of hydration products—primarily calcium silicate hydrate (C-S-H gel) and calcium hydroxide (CH or portlandite)—in the CPB@TP and CPB@TB samples appear to be lower than those in the control sample. This difference is also reflected in the variation of pore sizes and their distribution throughout the matrix. In the case of CPB@TF, SEM images reveal that tea fibers introduce voids within the matrix but also serve as bridges between other constituents, enhancing internal bonding. These observations suggest that tea fiber waste contributes positively to the structural integrity and mechanical performance of the backfill through physical reinforcement and interaction with hydration products.

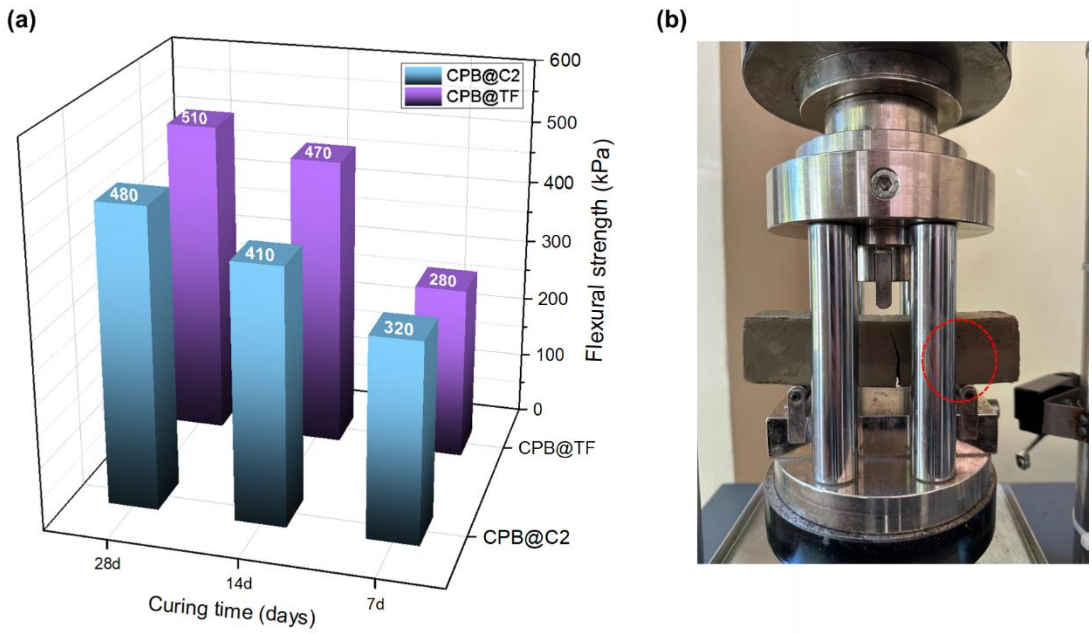

Fig. 4. (a) Flexural strength-curing time of CPBs and (b) crack formation

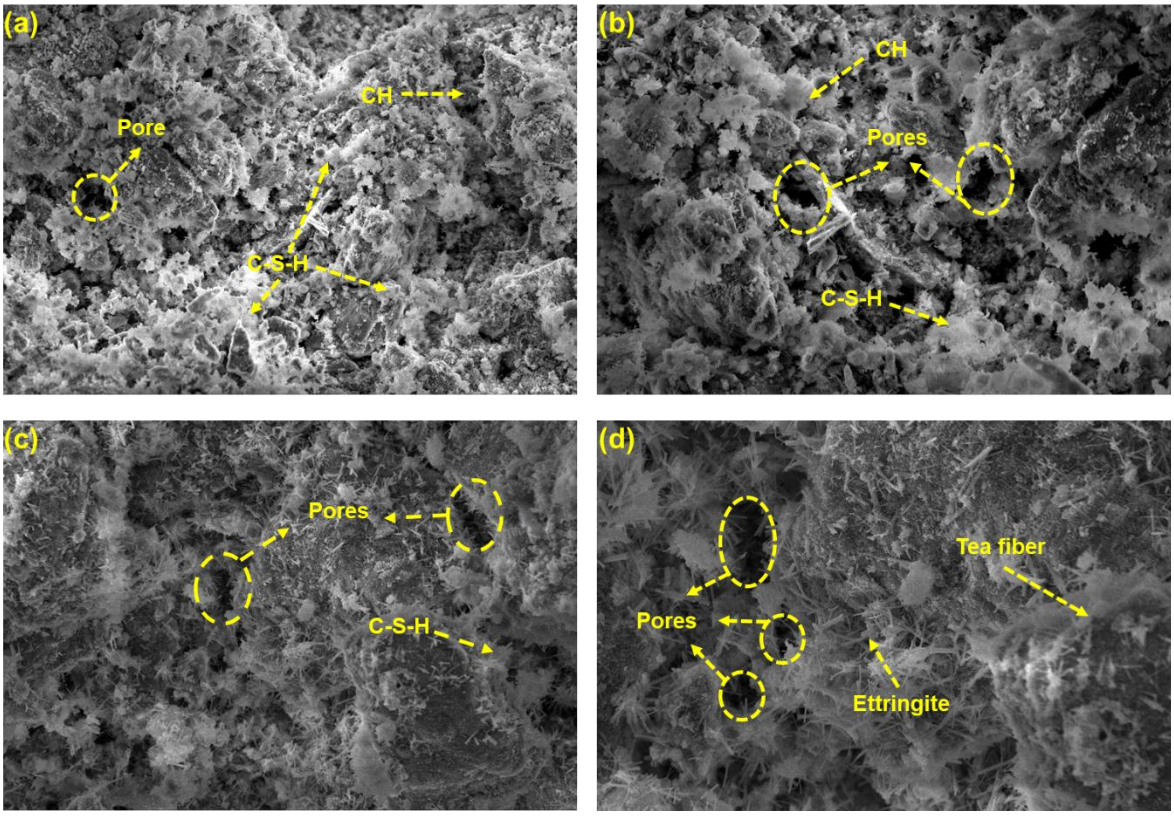

Fig. 5. SEM results of 28-day cured (a) CPB@C1, (b) CPB@TB, (c) CPB@TP and (d) CPB@TF

4. Conclusions

In this study, the influence of various tea wastes—namely tea powder waste (TP), brewed tea waste (TB), and tea fiber waste (TF)—on the performance of cemented paste backfill (CPB) mixtures was systematically investigated. After undergoing preprocessing steps such as drying and sieving, TP and TB were incorporated into CPB mixtures with a constant solid content of 70% and a cement dosage of 5% by weight. Tea wastes were substituted for 10% of the cement content, and their effects on the mechanical and microstructural properties of the backfill were evaluated through uniaxial compressive strength (UCS) tests, three-point bending tests, and scanning electron microscopy (SEM) analysis across different curing durations (up to 28 days). The outcomes of these experimental evaluations are summarized as follows:

- The uniaxial compressive strength (UCS) of all filling mixtures increased with extended curing time. The highest UCS value, 0.83 MPa, was recorded in the control sample (CPB@C1) at 28 days.
- In general, mixtures incorporating brewed tea waste (TB) exhibited superior UCS performance compared to those containing factory tea production waste (TP).
- Results from the three-point bending tests indicated that mixtures with tea fiber waste (CPB@TF) demonstrated higher flexural strength than the control samples (CPB@C2) after 14 days of curing. Specifically, while the flexural strength of CPB@C2 reached 0.41 MPa and 0.48 MPa at 14 and 28 days, respectively, CPB@TF achieved higher values of 0.47 MPa and 0.51 MPa at the same curing periods.
- SEM analyses revealed that hydration products were less abundant in the CPB@TB and CPB@TP samples compared to the control, likely due to the increased water absorption capacity of tea wastes. In CPB@TF mixtures, tea fibers appeared to act as physical bridges within the matrix, contributing to improved flexural strength by enhancing structural connectivity and reducing voids.

In conclusion, this study investigated the potential use of various tea wastes—originating primarily from tea agriculture, a key economic activity in the studied region—as alternative cement substution in the CPB method. The findings indicate that tea wastes possess distinct characteristics that necessitate specific pre-treatment processes (e.g., sieving and drying) to optimize their performance in CPB applications. Based on the results, it is evident that tea wastes hold promise as partial cement substitutes. Future research will aim to enhance the applicability and effectiveness of tea wastes in CPB through advanced treatment techniques, broader substitution ratios, and extended curing periods.

References

Adewuyi, S. O., Anani, A., & Luxbacher, K. (2024). Advancing sustainable and circular mining through solid-liquid recovery of mine tailings. *Process Safety and Environmental Protection, 189*, 31–46.

Araya, N., Ramírez, Y., Kraslawski, A., & Cisternas, L. A. (2021). Feasibility of re-processing mine tailings to obtain critical raw materials using real options analysis. *Journal of Environmental Management, 284*, 112060.

Debnath, B., Haldar, D., & Purkait, M. K. (2021). Potential and sustainable utilization of tea waste: A review on present status and future trends. *Journal of Environmental Chemical Engineering, 9*(5), 106179.

FAO. (2023). *Food and Agriculture Organization*. https://www.fao.org/faostat/en/#data

Guner, N. U., Yilmaz, E., Sari, M., & Kasap, T. (2023). Cementitious backfill with partial replacement of Cu-rich mine tailings by sand: Rheological, mechanical and microstructural properties. *Minerals, 13*(3), 437.

Hassan, S., Bhadwal, S. S., Khan, M., Nissa, K. U., Shah, R. A., Bhat, H. M., Bhat, S. A., Lone, I. M., & Ganai, B. A. (2024). Revitalizing contaminated lands: A state-of-the-art review on the remediation of mine-tailings using phytoremediation and genomic approaches. *Chemosphere*, 141889.

Jin, J., Liu, T., Li, M., Qin, Z., Chen, Y., Liu, Q., Liang, B., Zhao, J., Li, S., & Zuo, S. (2024). Influence of biomass fly ash on durability of self-consolidating cement-tailings grout: Resistance to freeze-thaw cycles and sulfate attack. *Journal of Building Engineering, 93*, 109842.

Kasap, T., Yilmaz, E., Guner, N. U., & Sari, M. (2022). Recycling dam tailings as cemented mine backfill: Mechanical and geotechnical properties. *Advances in Materials Science and Engineering, 2022*(1), 6993068.

Liu, W., Yu, H., Wang, S., Wei, M., Wang, X., Tao, T., & Song, X. (2023). Evolution mechanism of mechanical properties of cemented tailings backfill with partial replacement of cement by rice straw ash at different binder content. *Powder Technology, 419*, 118344.

Pan, H., Xiao, Q., Huang, N., Xiao, A., & Zhu, D. (2024). Effect of alkaline rice straw fibers content and curing ages on static mechanical properties of cemented lithium mica tailings backfill. *Case Studies in Construction Materials, 21*, e03450.

Qi, T., Gao, X., Feng, G., Bai, J., Wang, Z., Chen, Q., Wang, H., & Du, X. (2022). Effect of biomass power plant ash on fresh properties of cemented coal gangue backfill. *Construction and Building Materials, 340*, 127853.

Saedi, A., Jamshidi-Zanjani, A., & Darban, A. K. (2021). A review of additives used in the cemented paste tailings: Environmental aspects and application. *Journal of Environmental Management, 289*, 112501.

Sari, M., Yilmaz, E., Kasap, T., & Karasu, S. (2023). Exploring the link between ultrasonic and strength behavior of cementitious mine backfill by considering pore structure. *Construction and Building Materials, 370*, 130588.

Wang, H., Feng, G., Qi, T., Gao, X., Wang, C., Wang, L., & Zhang, Z. (2023). Influence of the use of corn straw fibers to connect the interfacial transition zone with the mechanical properties of cemented coal gangue backfill. *Construction and Building Materials, 367*, 130334.

Wang, Z., Ahmad, W., Zhu, A., Zhao, S., Ouyang, Q., & Chen, Q. (2024). Recent advances review in tea waste: High-value applications, processing technology, and value-added products. *Science of The Total Environment*, 174225.

Yazici, K., & Goksu, B. (2017). Effects of kaolin (M-99-099) application on antioxidant and phenolic compounds in tea leaves (Camellia sinensis LO Kuntze). *Biochemical Genetics, 55*, 367–377.

4th International Civil Engineering & Architecture Conference
17-19 May 2025, Trabzon, Türkiye

Examining the dynamic performance of loose sands reinforced by recycled concrete aggregate (RCA)

Olguhan Ş. Karahasan*[1], Burak Akçay[1]

[1] *Karadeniz Technical University, Department of Civil Engineering, 61080 Trabzon, Türkiye*

Abstract. The enhancement of seismic performance in fully saturated sand through the inclusion of Recycled Concrete Aggregate (RCA) was investigated using two-dimensional finite element analyses conducted in PLAXIS 2D. The dynamic response of an RCA-reinforced soil system supporting a six-story structure was evaluated under seismic excitation. The incorporation of RCA significantly mitigated the maximum settlement beneath the raft foundation, reducing it from 13.6 cm to 2.5 cm, and effectively confined the deformation to a shallow subsurface zone. This localized deformation pattern substantially minimized differential settlement and preserved the foundation's load-bearing capacity. Stress distribution analyses revealed a more homogeneous principal stress field beneath the foundation. Compressive and tensile stresses were reduced by approximately 28 kN/m² and 8 kN/m², respectively. Additionally, uplift-induced tensile stress concentrations at the raft edges were significantly diminished. At the superstructure level, RCA inclusion resulted in a modest increase in top slab bending moments by approximately 4–6%, while shear force demands remained constant or decreased marginally (up to 3%), indicating that structural implications are limited to minor flexural design considerations. These results substantiate the efficacy of RCA as a sustainable and mechanically competent soil improvement material that enhances the stiffness and strength of saturated sands without imposing adverse effects on superstructural performance. To advance practical applications, future research should focus on full-scale experimental validation, long-term seismic performance monitoring, and comprehensive parametric studies examining the influence of RCA gradation and volumetric content on dynamic soil behavior, aiming to inform and refine performance-based seismic design frameworks.

Keywords: RCA; Soil improvement; Seismic performance; Loose sand; Plaxis 2D

1. Introduction

Sandy soils susceptible to liquefaction pose a critical risk to infrastructure and structural safety, particularly due to the sudden loss of shear strength under seismic loading. The literature highlights that settlements and shear deformations in such problematic soils can lead to damage or even collapse of supporting systems; accordingly, soil improvement techniques have been extensively investigated to safeguard both lives and assets.

Conventional stabilization methods typically employ binders such as cement, lime, or microsilica; however, these approaches are limited by high energy consumption and significant carbon emissions, raising concerns about environmental sustainability. In this context, the principles of circular economy—which emphasize the recovery and reuse of construction-sector waste—promote the use of recycled concrete aggregate (RCA) as an economical and eco-friendly alternative. RCA, derived from the crushing and screening of waste concrete, offers suitable physical and mechanical properties for soil stabilization while contributing to waste management and the reduction of carbon footprint.

Recent efforts have demonstrated the multifaceted potential of recycled concrete aggregates (RCA) across both structural and geotechnical applications. Momotaz et al. (2024) investigated concrete kerb sections incorporating RCA, tyre-derived aggregates, and polypropylene fibers, revealing that fiber-reinforced mixes can endure nearly 2 000 cyclic loads while significantly enhancing post-cracking behavior. Huan He et al. (2023) characterized 1.18–2.36 mm RCA fractions from China and Australia, showing markedly lower particle strength and distinctive interparticle contact stiffness, yet uncovering ductile failure modes under compression. Shriful Islam et al. (2023) applied 5–35 % RCA in slope stabilization—both mixed and as vertical drains—achieving reduced consolidation settlement, increased shear strength, and up to seven-fold permeability gains that mitigate excess pore-water pressure. Weiwei Xiong et al. (2023) combined excavated soil and fine RCA to produce unfired clay bricks

*Corresponding author, E-mail: olguhan@ktu.edu.tr

https://doi.org/10.31462/icearc2025_ce_geo_627

(UCBs), identifying optimal mix proportions (w/c = 0.65, a/s = 0.5, c/s = 0.3, AC = 5 %) that deliver favorable density and strength via enhanced hydration. Ahmad et al. (2023) demonstrated that load-bearing bricks made with 100 % RCA through compression casting satisfy ASTM criteria and outperform both burnt-clay and natural-aggregate units in strength and acid/brine resistance. Lin et al. (2023) systematically assessed steel, polyvinyl alcohol, carbon, and polypropylene fibers in RCA concrete, finding steel fiber to yield the greatest improvements in energy dissipation (+81.8 %) and toughness (+22.9 %) and proposing a validated segment-based stress–strain model. Singh et al. (2022) examined fine RCA compatibility with natural and coarse RCA, showing that 30 % FRCA best suits natural coarse aggregates, while 60–100 % FRCA pairs optimally with coarse RCA to meet M30 strength targets. Adomako et al. (2023) introduced a dry-washing (RCZ) process for concrete sludge, reporting that increasing RCZ content enhances aggregate quality (Los Angeles and micro-Deval tests) and yields acceptable environmental performance despite residual paste minerals. Collectively, these studies underscore RCA's promise yet reveal that an integrated, data-driven assessment of its effects on seismic-induced settlement and liquefaction remains absent—an omission this work seeks to address.

In this study, no laboratory tests were conducted; instead, the required shear strength and pore-water pressure parameters for a uniformly graded, liquefaction-prone sandy soil were obtained from selected literature sources. The effects of varying RCA content on soil strength, settlement, and liquefaction potential were examined using established empirical correlations and numerical evaluation methods. The primary objective is to present an academic framework—free from laboratory-induced uncertainties—demonstrating how RCA addition can minimize settlement and liquefaction risks in problematic sandy soils. The analytical findings are expected to inform the use of alternative materials in infrastructure projects within seismic regions and to guide policies on waste concrete management.

2. Methodology

In the designed Plaxis 2D analyses, a fully saturated, loose sand deposit was considered. A six-storey structure on a 10m wide raft foundation, with a foundation depth of 2m, is planned on this sand. Also, the groundwater level (GWL) is at a depth of 2 meters. Hardening Soil with small (HS small) constitutive model was adopted for the soil, and an Undrained-A drainage condition was applied to simulate the critical seismic scenario. The structural elements were modeled as "plate" elements and interconnected via node-to-node anchors to ensure monolithic behavior under earthquake loading. Seismic parameters corresponding to earthquake ground motion level DD-2 and local soil class ZD were selected for the center of Erzincan. From the AFAD-TDTH (Turkish Seismic Hazard Map) portal, the short-period spectral acceleration (S_{DS} = 1.445 g), 1-second spectral acceleration (S_{D1} = 0.782 g), peak ground acceleration (PGA = 0.602 g), and peak ground velocity (PGV = 39.534 cm/s) were obtained. The 1992 Erzincan earthquake record was scaled to the 2018 Turkish Seismic Design Code (TBDY) spectrum using SeismoMatch and input into Plaxis 2D as an acceleration-time history. To accurately capture dynamic soil–boundary interaction, prescribed displacement boundary conditions were assigned in the X direction, and fixed displacements in the Y direction. Mesh refinement followed best practices from the Plaxis 2D manuals and relevant literature to ensure reliable dynamic response. In the Dynamics module, free-field boundary conditions were applied at the lateral boundaries (Boundary Xmin and Xmax) to allow seismic waves to enter and exit without artificial reflections, while a compliant base condition (Boundary Ymin) was used at the model base to replicate realistic wave transmission through the deformable soil. Given the high risk of seismic-induced settlement and loss of bearing capacity in the ZD-class, saturated loose sand, soil improvement was deemed necessary prior to construction. The soil was thus stabilized by mixing in recycled concrete aggregate (RCA) to enhance internal friction angle and cohesion. Seismic analyses were performed using the finite element method in Plaxis 2D for both the current condition and the RCA-improved soil and the resulting displacement and stress responses were compared and interpreted.

3. Finite element modelling and seismic analysis

The Hardening Soil Small (HS small) constitutive model was employed to simulate soil behavior, and an Undrained-A drainage condition was applied to represent the critical seismic scenario. For the centre of Erzincan, seismic parameters were selected corresponding to the ground motion level DD-2 and the local soil class ZD. From the AFAD-TDTH (Turkish Seismic Hazard Map) portal, the short-period spectral acceleration (S_{DS} = 1.445 g), 1-second spectral acceleration (S_{D1} = 0.782 g), peak ground acceleration (PGA = 0.602 g), and peak ground velocity (PGV = 39.534 cm/s) were obtained. The ground motion record of the 1992 Erzincan earthquake was scaled to the 2018 Turkish Seismic Design Code (TBDY) spectrum using the SeismoMatch software and subsequently implemented in Plaxis 2D as an acceleration–time history input. Under seismic loading, finite element analyses were performed in Plaxis 2D for both unimproved (current condition) and RCA-improved soil profiles and the obtained displacement and stress responses were evaluated and compared. Fig. 1 and Fig. 2 presents the displacement results of the seismic analysis for the NRCA and RCA models.

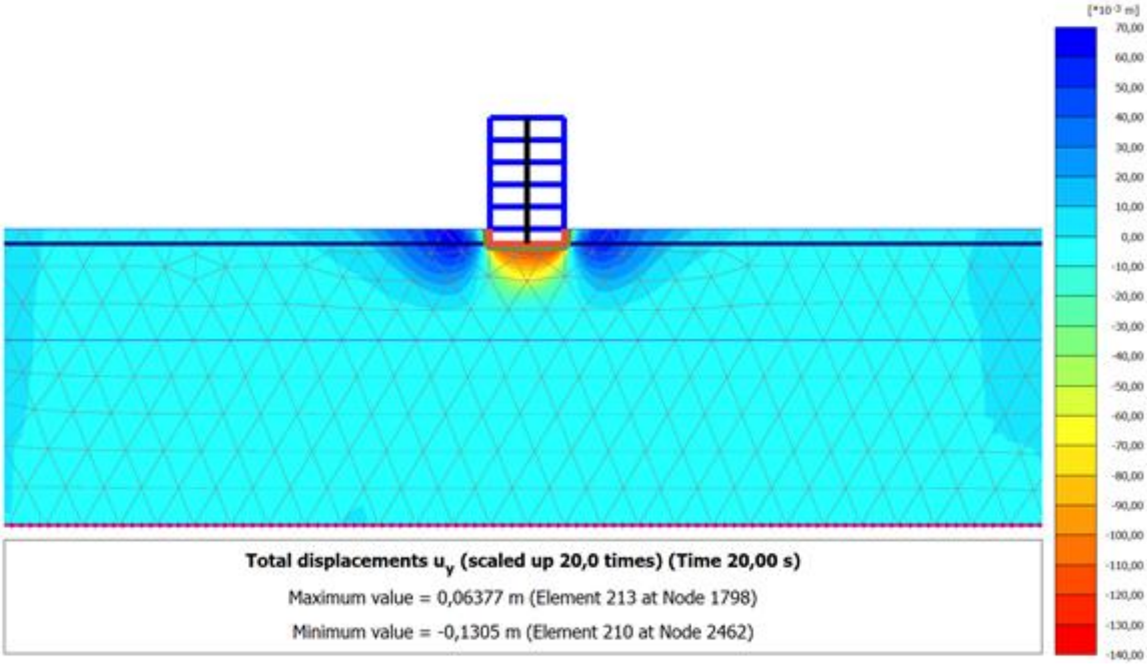

Fig. 1. The displacement results of the seismic analysis for the model NRCA

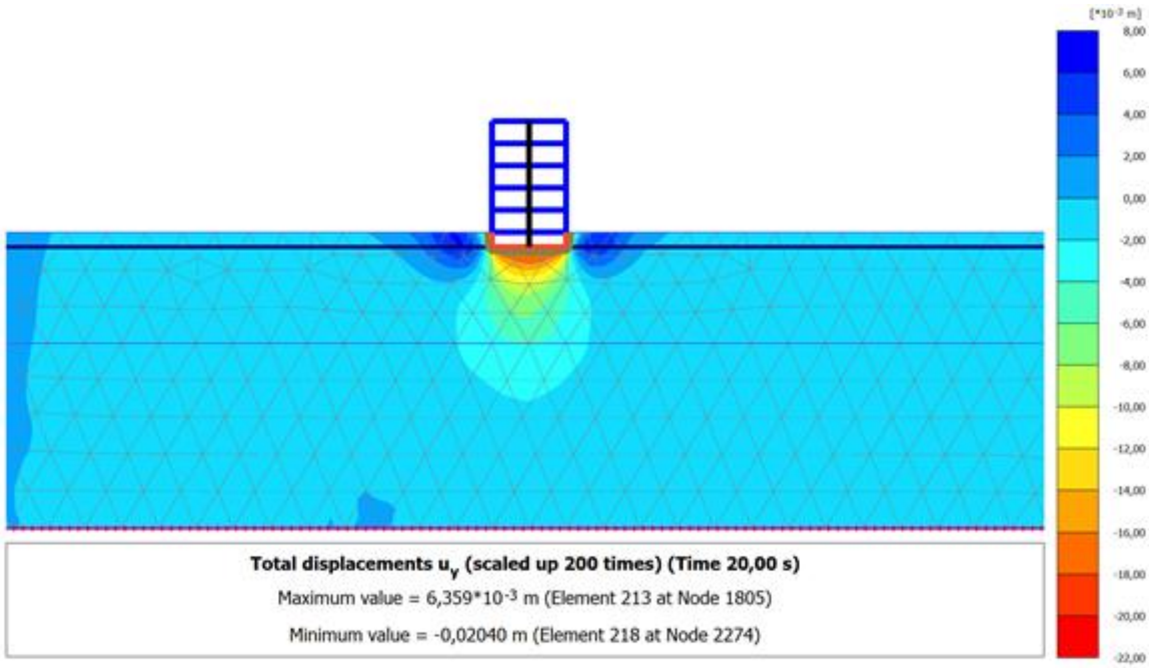

Fig. 2. The displacement results of the seismic analysis for the model RCA

The reinforced case limits maximum settlement to ≈20 mm, whereas the unreinforced soil experiences up to 130 mm of settlement. The reinforcement confines deformation to a narrow, shallow band that decays quickly with depth. In contrast, the unreinforced soil exhibits a wide, deep-penetrating settlement pattern. A concentrated, shallow deformation zone minimizes isolated settlement under the structure. A widespread, deep-seated zone can lead to uncontrolled differential movements beneath the foundation. Reinforcement with recycled concrete aggregate substantially reduces both the magnitude and lateral/depth extent of vertical displacements, thereby mitigating differential settlement and enhancing seismic performance. Fig. 3 and Fig. 4 presents the stress results of the seismic analysis for the NRCA and RCA models.

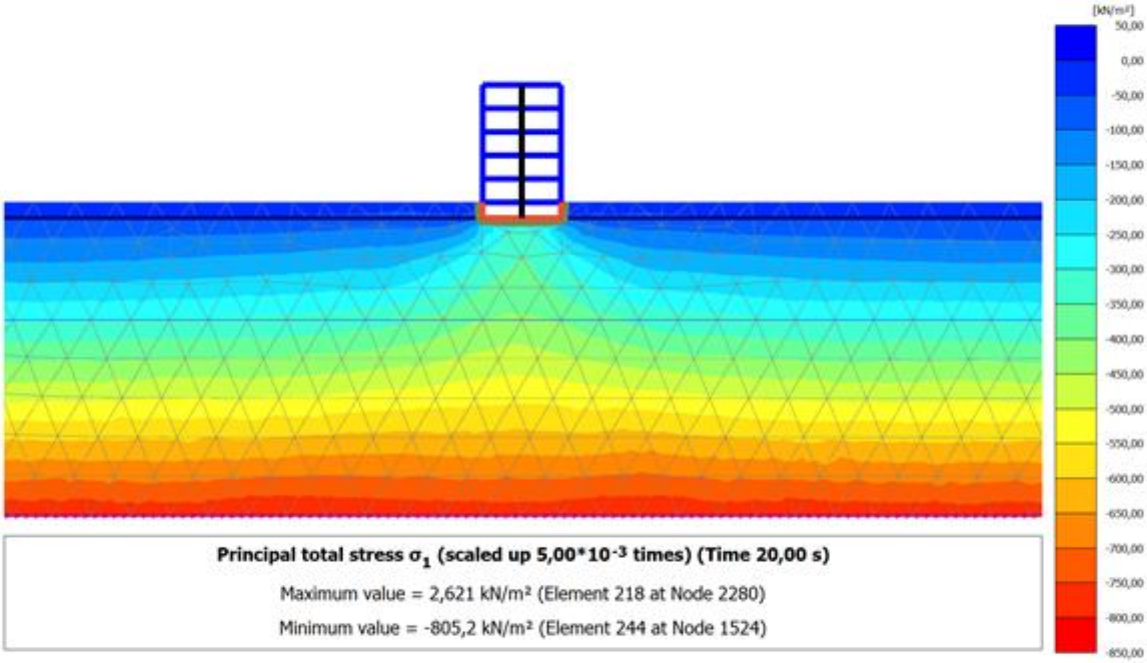

Fig. 3. The stress results (σ_1) of the seismic analysis for the model NRCA

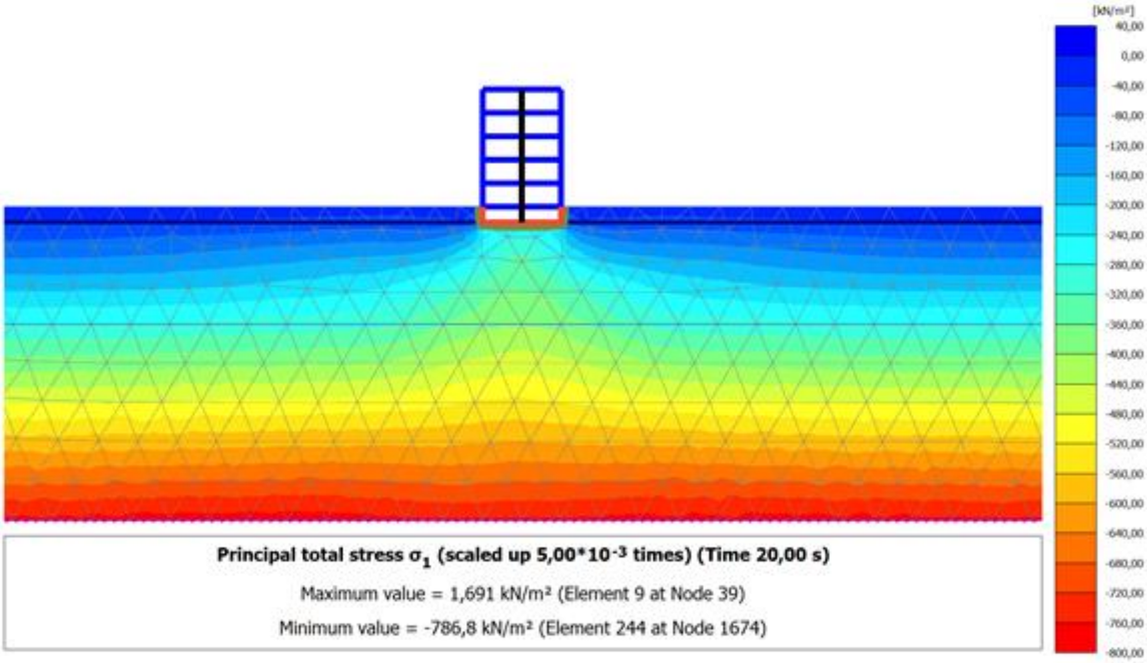

Fig. 4. The stress results (σ_1) of the seismic analysis for the model RCA

The reinforced case exhibits about 2 kN/m² lower peak tension and ~18 kN/m² lower peak compression, indicating the RCA inclusion has smoothed stress concentrations beneath the footing. In RCA model, the transition from high compression (red) to intermediate (greens/yellows) is more gradual, whereas NRCA model shows a sharper gradient immediately under the foundation. This suggests the reinforced zone distributes loads more evenly into the soil. Unreinforced soil develops pronounced tensile lobes beside the footing (blue "horns"), a sign of uplift stresses that can drive cracking or hydraulic fracturing in the pore-pressure regime. These lobes are noticeably reduced in RCA model. Both models show a downward-spreading compression bulb, but in the reinforced soil it is marginally broader and less intense—consistent with a stiffer near-surface layer that carries more load. Incorporating recycled concrete aggregate creates a stiffer, more load-bearing cap that mitigates stress peaks under dynamic loading, reduces uplifting tensile stresses at the footing edges, and generates a smoother stress diffusion into the subsoil. Together, these effects improve the seismic performance by lowering the risk of localized yielding or fracturing. Fig. 5 and Fig. 6 presents the stress results (σ_3) of the seismic analysis for the NRCA and RCA models.

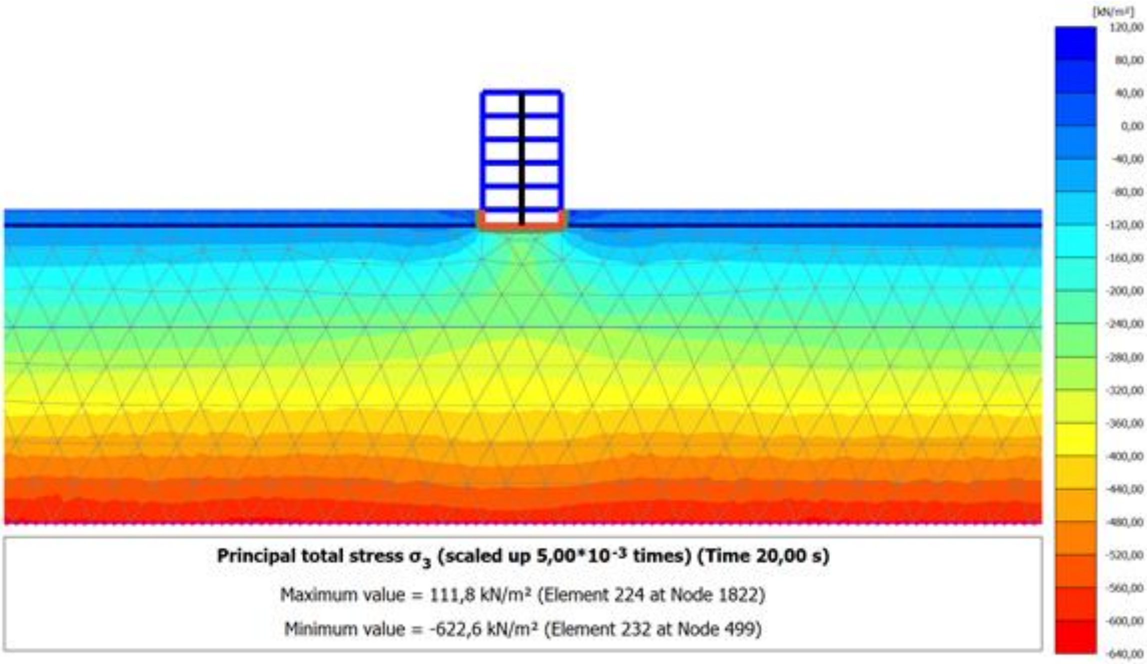

Fig. 5. The stress results (σ_3) of the seismic analysis for the model NRCA

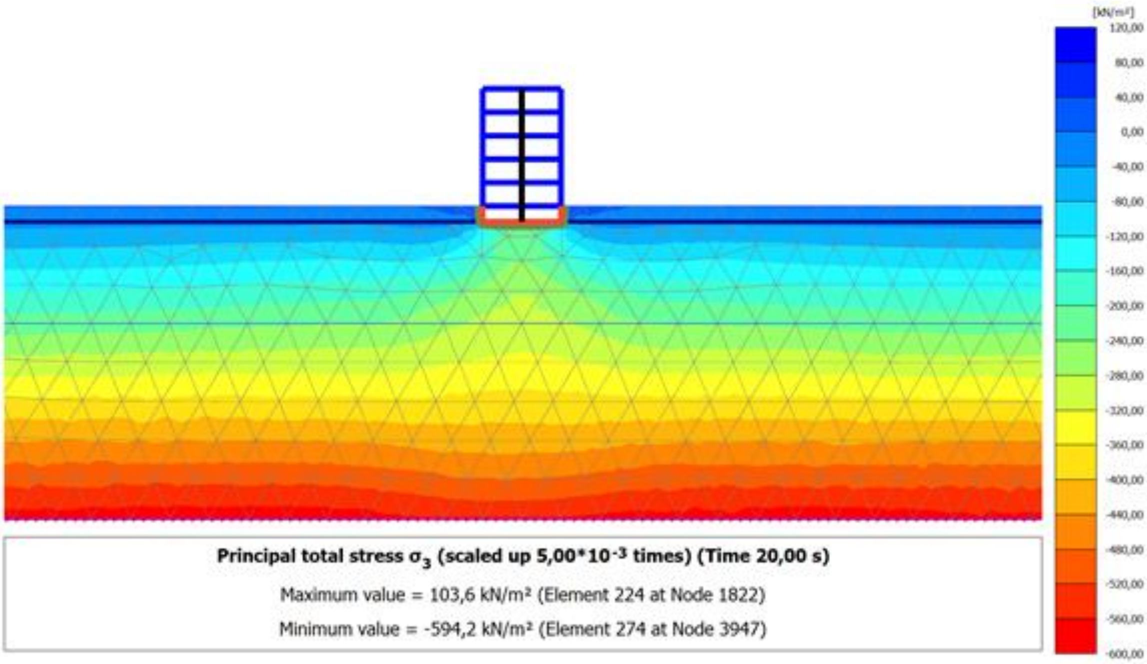

Fig. 6. The stress results (σ_3) of the seismic analysis for the model RCA

Reinforced soil shows both lower maximum tension (≈8 kN/m² reduction) and lower peak compression (≈28 kN/m² reduction), indicating milder stress concentrations. In the unreinforced model, the compressive stress bulb extends slightly deeper, whereas in the reinforced model it is more confined to a shallower, wider area near the surface. The tensile lobes at the footing edges are smaller and less intense in RCA model compared to NRCA model, reflecting reduced uplift stresses around the foundation. Fig. 7 and Fig. 8 presents the effective stress results (σ_1') of the seismic analysis for the NRCA and RCA models.

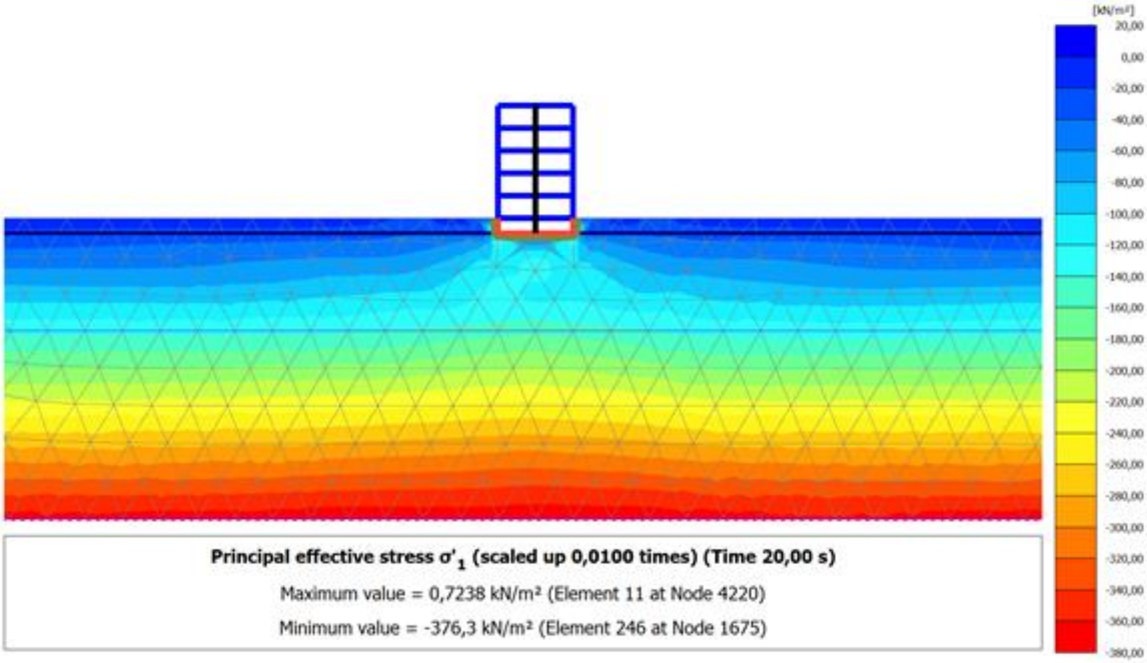

Fig. 7. The stress results (σ_1') of the seismic analysis for the model NRCA

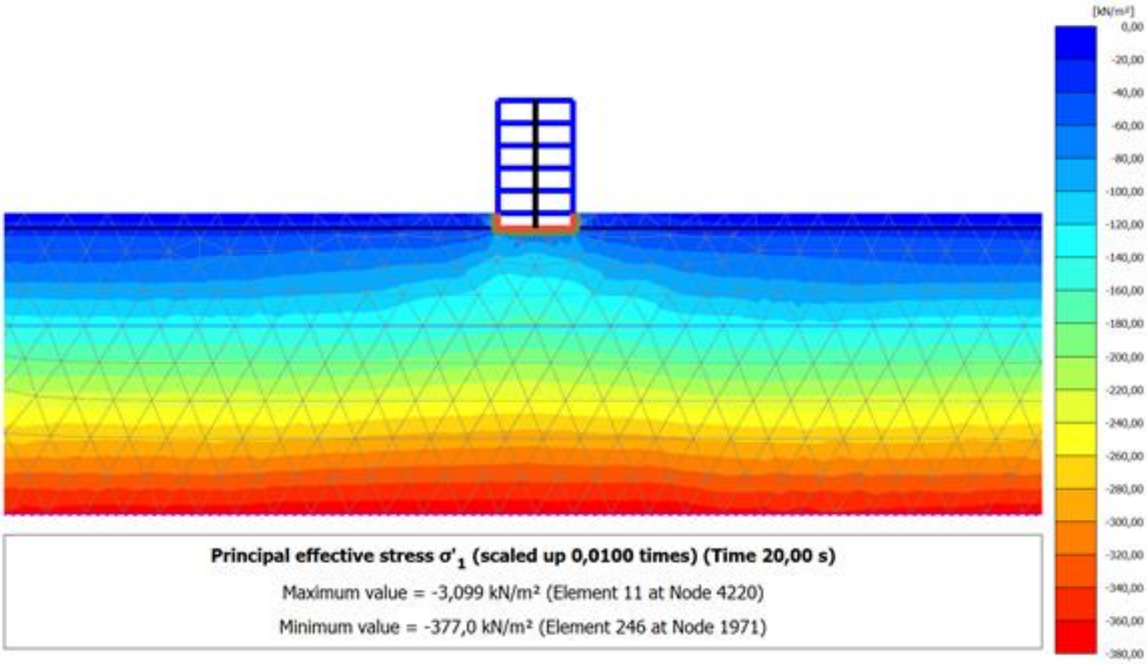

Fig. 8. The stress results (σ_1') of the seismic analysis for the model RCA

Mixing in RCA raises the in-situ stiffness so that no tensile effective stress zones develop beneath the foundation, and it yields a smoother, more uniformly compressive stress distribution. This behavior signals both reduced risk of liquefaction-induced uplift and improved overall bearing performance under seismic loading. Fig. 9 and Fig. 10 presents the effective stress results (σ_3') of the seismic analysis for the NRCA and RCA models.

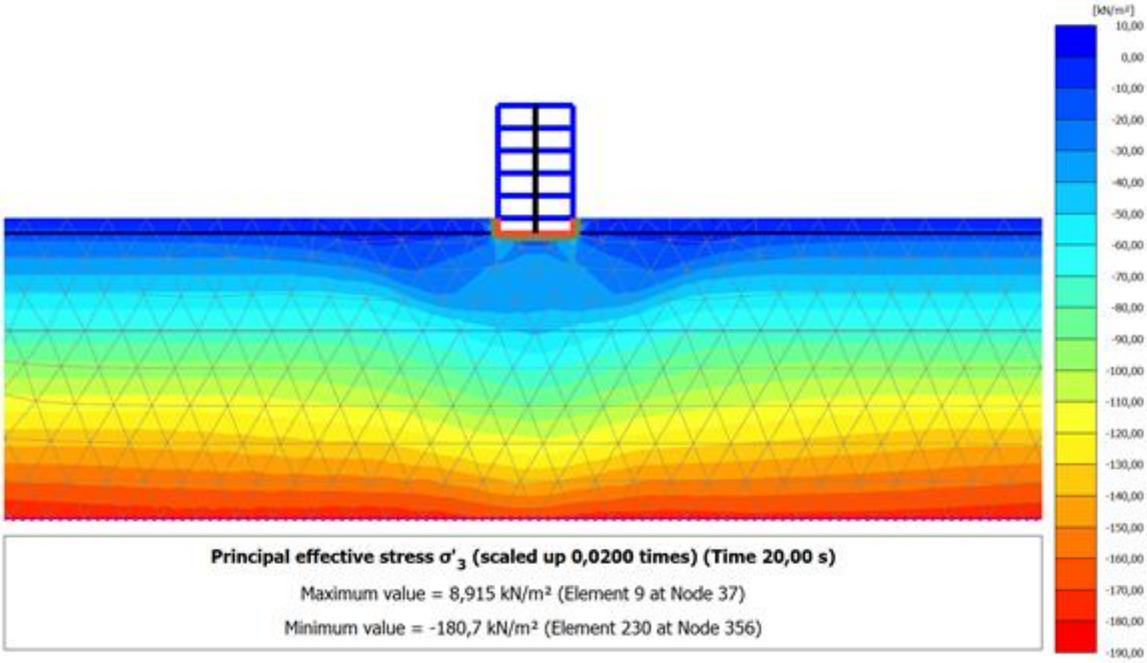

Fig. 9. The stress results (σ'_3) of the seismic analysis for the model NRCA

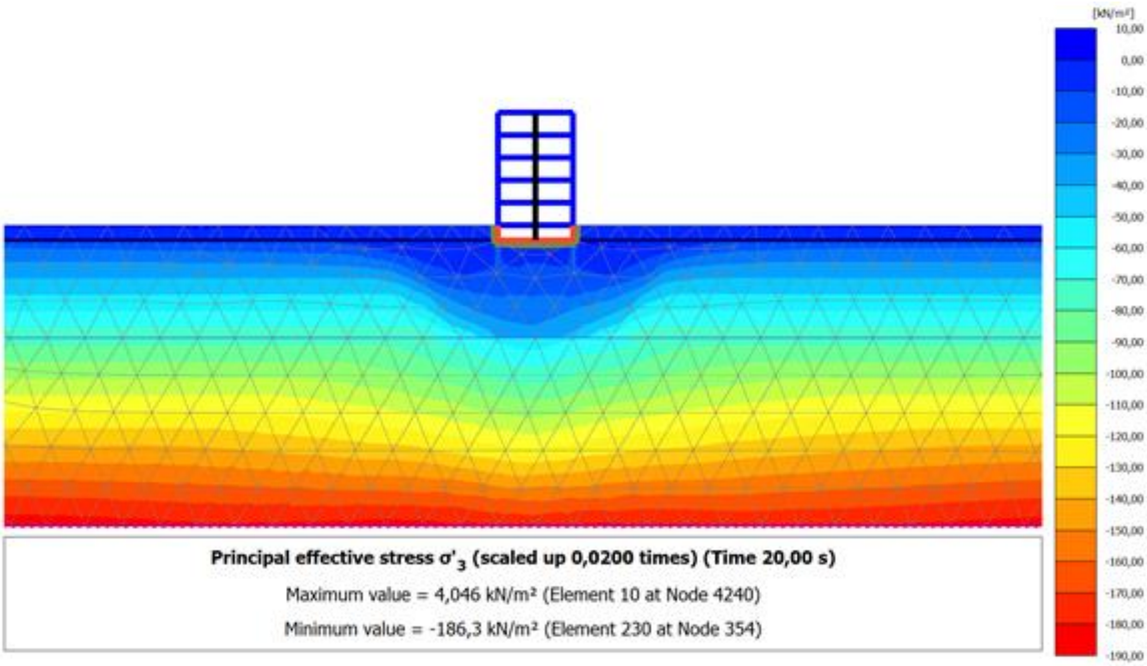

Fig. 10. The stress results (σ'_3) of the seismic analysis for the model RCA

Incorporating RCA into the soil largely eliminates tensile effective stresses beneath the foundation while slightly increasing maximum compression. This behavior indicates that RCA both mitigates uplift risk and enhances the stiffness and load-bearing efficiency of the soil under seismic excitation.

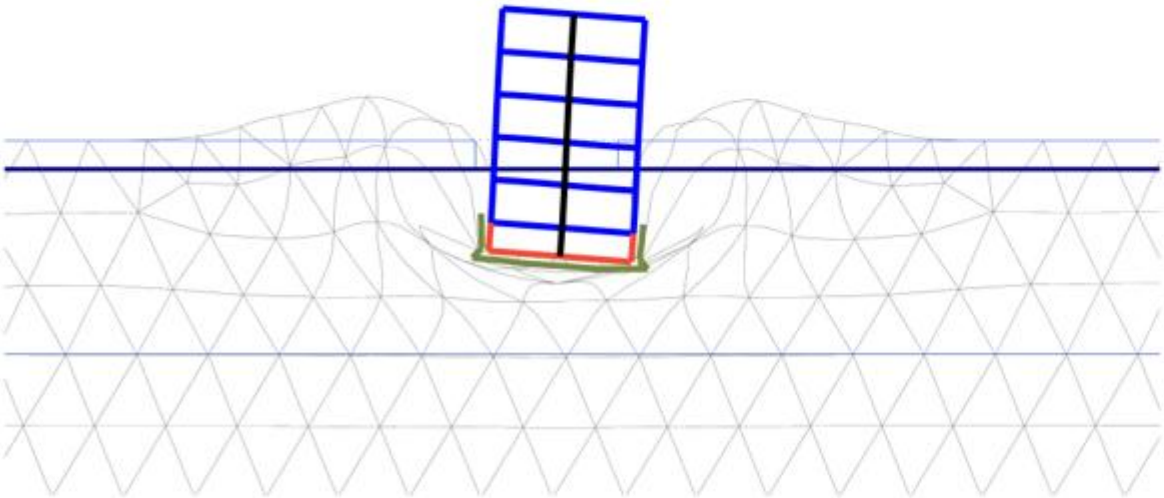

Fig. 11. The soil settlements for the analyses NRCA model

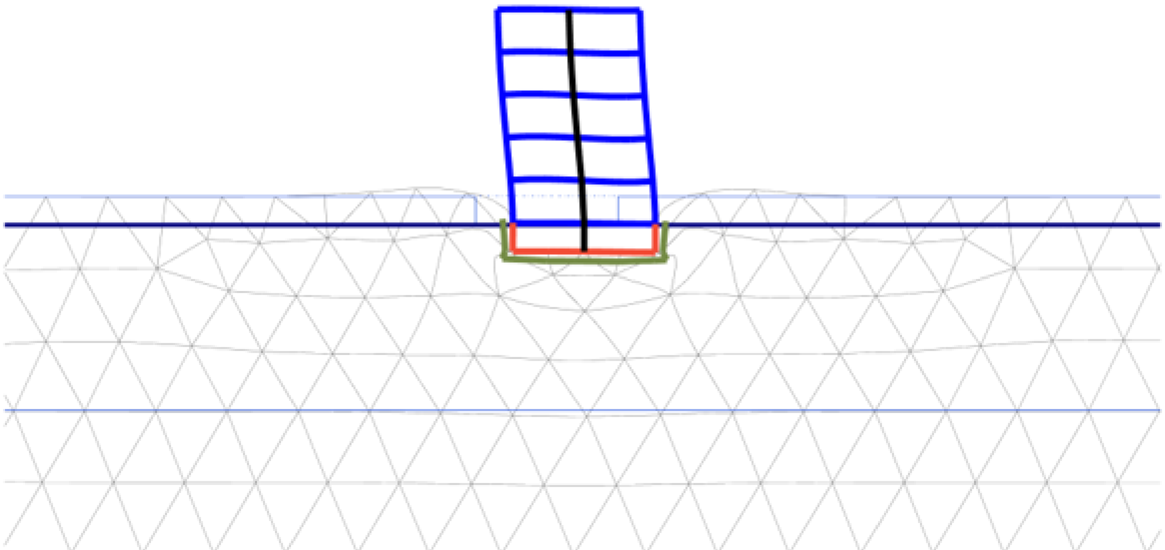

Fig. 12. The soil settlements for the analyses RCA model

Figs. 11 and 12 visualize the soil settlements for the analyses NRCA and RCA models, respectively. RCA reinforcement decreased the peak settlement by about 82 %, from 13.58 cm to 2.485 cm, indicating a substantial increase in soil stiffness and bearing capacity. In the unreinforced model, the settlement trough spreads deeply and laterally over a wide area, whereas in the RCA-reinforced model the settlement is confined to a shallow, narrow band directly beneath the foundation. This indicates a significant reduction in differential settlement and a more controlled load distribution to the soil. Limiting the maximum settlement also minimizes lateral displacements at column–slab connections, thereby reducing additional moments and shear forces on the column–shaft system. As a result, both seismic performance and long-term serviceability of the structure are enhanced.

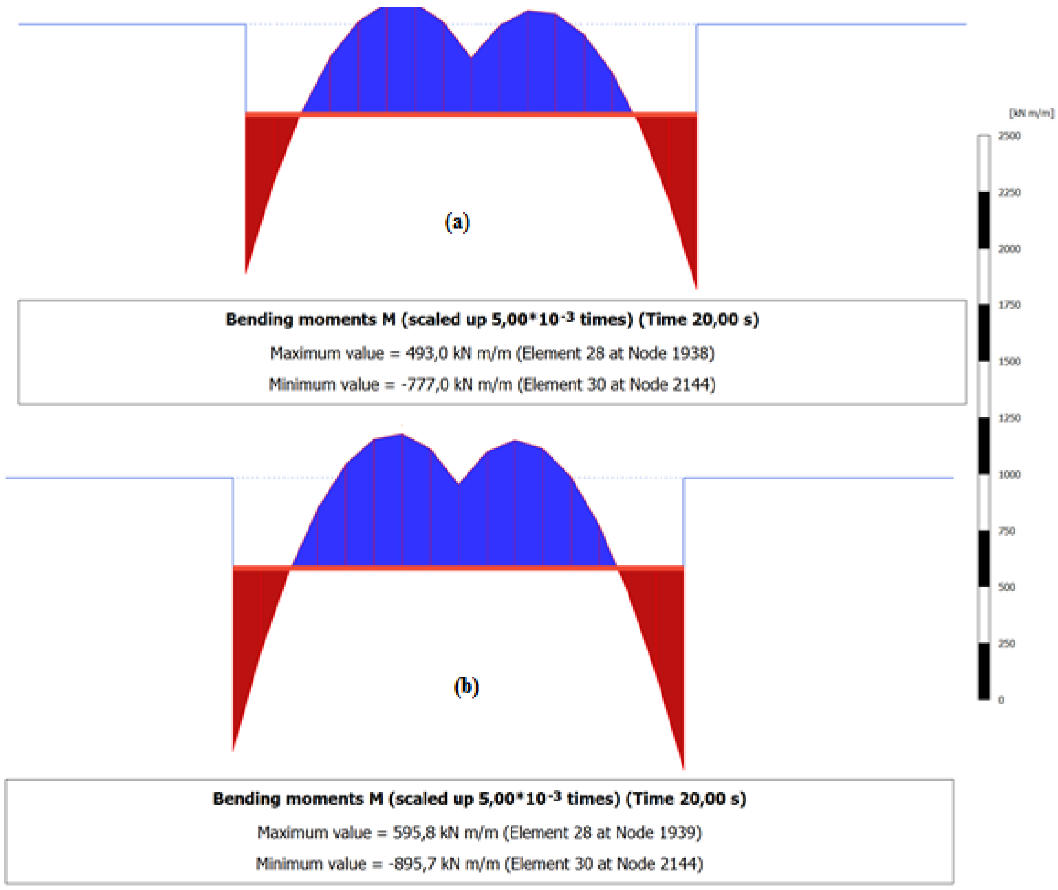

Fig. 13. The obtained moment diagrams for the models NRCA and RCA

As a result of the seismic analyses, moment and shear force diagrams at the bottom of the structure were generated for both the models NRCA and RCA. The obtained moment diagrams are presented in Fig. 13 (a-NRCA model, b-RCA model). The obtained shear force diagrams are presented in Fig. 14 (a-NRCA model, b-RCA model).

Both positive and negative peak moments rise by roughly 15–21 % in the reinforced model. NRCA shows two symmetric “humps” of positive moment with narrow negative triangular zones at the edges. RCA displays wider, more pronounced positive moment caps and deeper/asymmetric negative zones at the ends. The RCA layer stiffens the foundation soil, channeling higher bending demands into the footing. Shear peaks rise moderately in the reinforced case. NRCA shows two separate positive (upward) lobes on either side of the foundation and a central negative lobe. RCA consolidates the positive shear into one strong lobe shifted left and extends the negative shear region to the right in a deeper triangular profile. RCA reinforcement redistributes horizontal demands, increasing shear at the footing edges. The reinforced soil generates substantially larger bending and shear forces, demanding greater stiffness and strength from the foundation elements. Reinforcement focuses loads into narrower bands beneath the footing, suggesting a review of crack-control reinforcement and shear detailing in the foundation design. To accommodate increased moments and shears, consider optimizing foundation depth, reinforcement layout, or RCA layer thickness, and verify soil–RCA modulus and interface conditions in the model.

RCA reinforcement raises the end-span hogging moment by about 3.8 %, from 87.24 to 90.54 kN·m/m. Mid-span sagging deepens by ~6.1 %, from –40.14 to –42.60 kN·m/m. The peak uplift shear drops by ~2.7 % (76.58 → 74.52 kN/m). The downward shear lobe is effectively unchanged (–79.36 → –79.47 kN/m). In summary, adding recycled concrete aggregate increases bending moments at the top slab, while shear demands stay constant or decrease slightly—requiring only minor adjustments to flexural design.

As a result of the seismic analyses, moment and shear force diagrams at the top of the structure were generated for both the models NRCA and RCA. The obtained moment diagrams are presented in Fig. 15 (a-NRCA model, b-RCA model). The obtained shear force diagrams are presented in Figure 16 (a-NRCA model, b-RCA model).

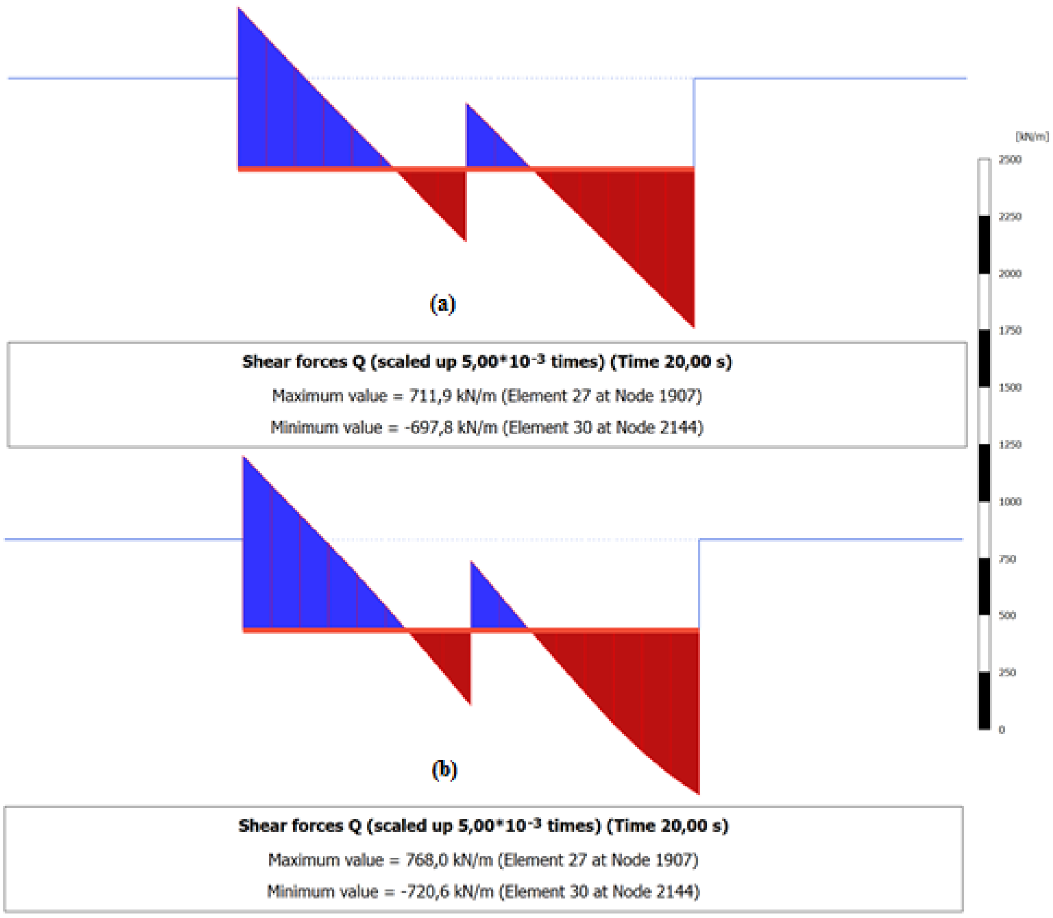

Fig. 14. The obtained shear force diagrams for the models NRCA and RCA

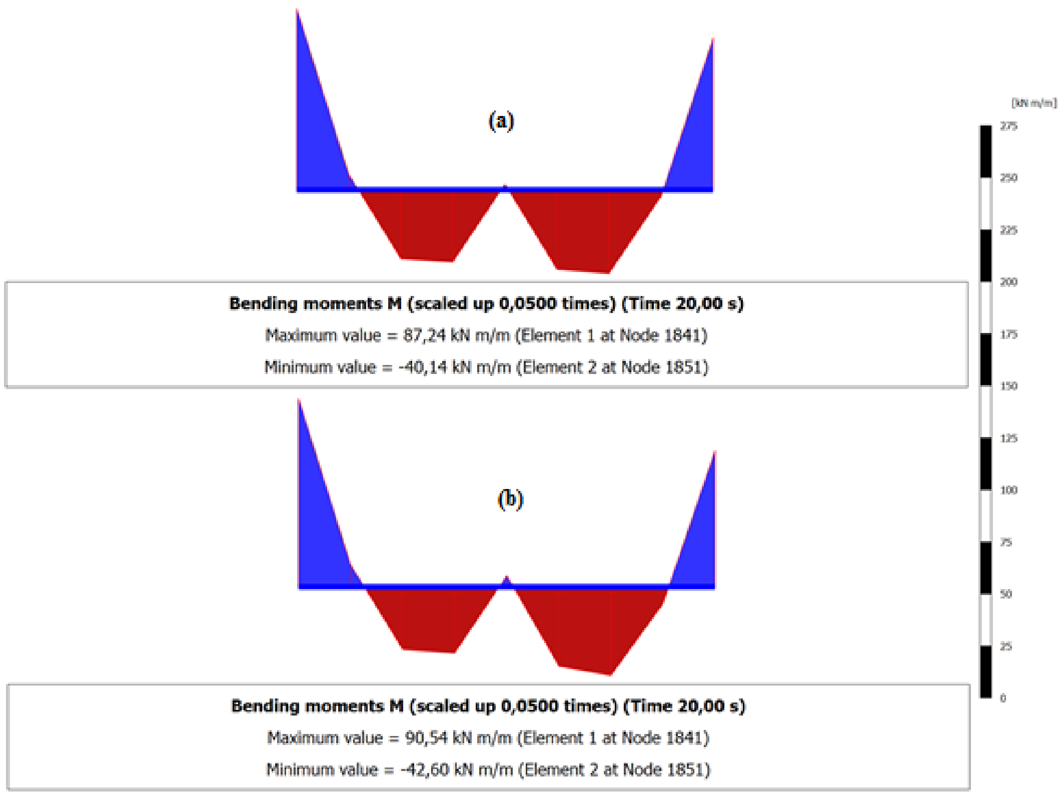

Fig. 15. The obtained moment diagrams for the models NRCA and RCA

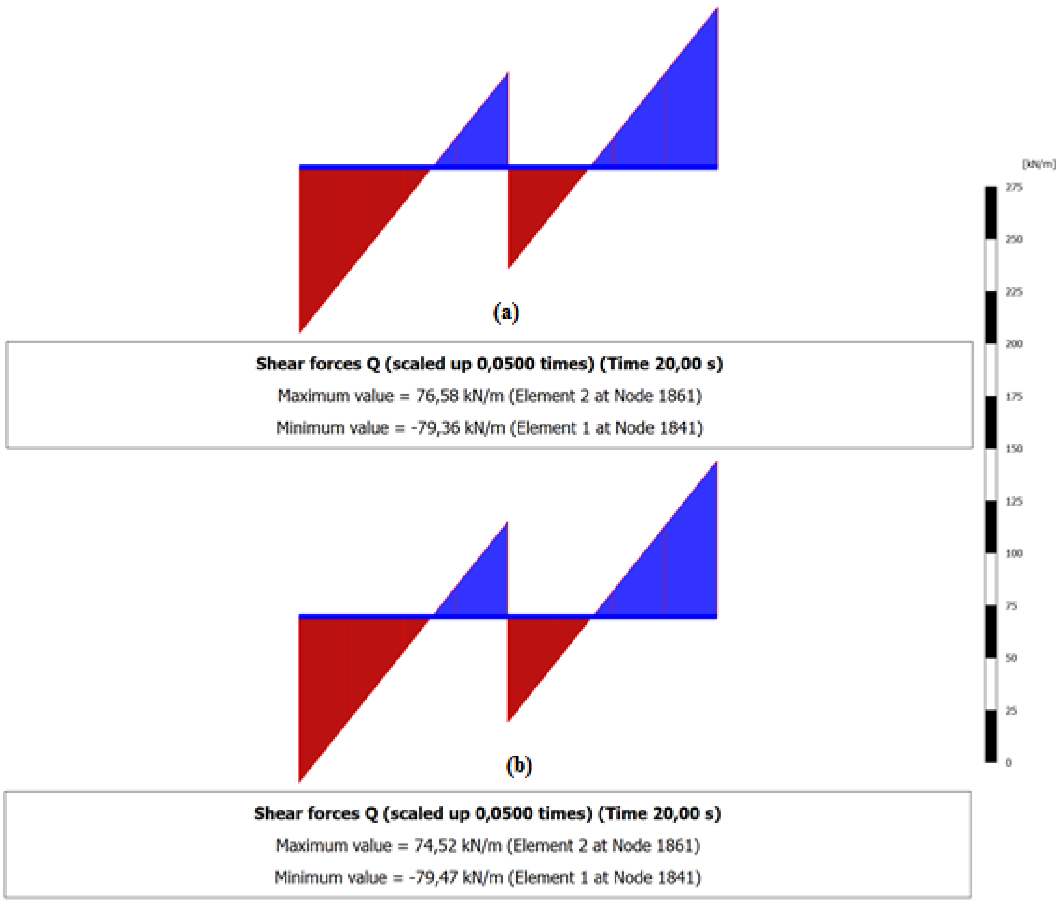

Fig. 16. The obtained shear force diagrams for the models NRCA and RCA

4. Conclusions

This study has demonstrated that mixing recycled concrete aggregate (RCA) into a fully saturated, liquefaction-prone sand significantly enhances seismic performance by substantially reducing vertical deformations and smoothing stress concentrations under dynamic loading. Numerical Plaxis 2D analyses show that RCA reinforcement limits maximum settlement beneath a six-story mat foundation from approximately 13.6 cm to 2.5 cm and confines deformation to a narrow, shallow zone, thereby mitigating differential settlement and preserving bearing capacity. Principal stress distributions likewise become more uniform: peak compressive and tensile stresses under the footing decrease by up to 28 kN/m² and 8 kN/m², respectively, and uplift-induced tensile lobes at foundation edges are markedly attenuated. At the superstructure level, top-slab bending moments increase modestly (≈4–6 %), while shear demands remain unchanged or decline slightly (≈3 %), indicating that only minor flexural design adjustments are required. These results confirm that RCA can serve as an eco-efficient ground improvement agent—enhancing stiffness and strength without compromising structural demand thresholds. Future work should extend this framework through large-scale experimental validation, long-term performance monitoring, and parametric studies of RCA gradation and content to optimize design guidelines for seismic regions.

References

Adomako, S., Engelsen, C.J., Døssland, L.T., Danner, T., & Thorstensen, R.T. (2023). Technical and environmental properties of recycled aggregates produced from concrete sludge and excavation materials. *Case Studies in Construction Materials, 19*, e02498

Ahmad, M., Hameed, R., Shahzad, S., & Sohail, M.G. (2023). Performance evaluation of loadbearing compressed fully recycled aggregate concrete bricks. *Structures, 55*, 1235-1249

He, H., Zhang, C., Yang, J., Li, M., Fu, W., Senetakis, K., Zhang, D., & Liu, S. (2023). Characterization of recycled concrete aggregate (RCA) particles for geotechnical engineering applications: Particle strength and interparticle contact behavior. *Construction and Building Materials, 407*(1), 133532

Islam, S., Islam, J., Hoque, N.M.R., & Hasan, K. (2023). Improving geotechnical properties of soil of hillock slope using crushed recycled concrete aggregates. *Journal of Engineering Research, 11*(4), 293-300

Lin, G., Liu, K., Chen, Y., Ji, Y., & Jiang, R. (2023). Experimental ınvestigation on compressive properties of fiber recycled aggregate concrete. *Journal of Renewable Materials, 11*(11), 3957-3975
Momotaz, H., Rahman, M.M., Karim, M.R., Zhuge, Y., Ma, X., & Levett, P. (2024). Structural performance of fibre reinforced recycled aggregate concrete road kerb sections under monotonic and cyclic loading. *Construction and Building Materials, 438*, 137329
Singh, R., Nayak, D., Pandey, A., Kumar, R., & Kumar, V. (2022). Effects of recycled fine aggregates on properties of concrete containing natural or recycled coarse aggregates: A comparative study. *Journal of Building Engineering, 45*, 103442
Xiong, W., Zhu, H., Xu, J., Ma, J., & Luo, C. (2023). Experimental investigation on physical and mechanical properties of excavated soil- and fine recycled concrete aggregate-based unfired clay bricks containing compound additives. *Case Studies in Construction Materials, 18*, e02057

4th International Civil Engineering & Architecture Conference
17-19 May 2025, Trabzon, Türkiye

Investigation of the variation of micro-pile parameters under moment effect with length variation

Betül Çağdaş*[1], Baran Toprak[1]

[1] Kırıkkale University, Department of Civil Engineering, 71451 Kırıkkale, Türkiye

Abstract. Micro-piles are one of the ground improvement methods made of steel materials in order to reduce settlement and increase bearing capacity with diameters smaller than 30 cm. Micro piles have gained a wide range of usage as drilling equipment and injection techniques vary and most of the load on the piles is borne by high-strength steel. In this study, the parameter changes calculated with the change in length of micro-piles manufactured in different lengths were examined. In the analyses made with Geo5 Geotechnical Calculation Program; It has been revealed that the changes in the parameters of maximum settlement, minimum compressive force and maximum rotation of the pile cap show striking changes compared to other parameters. In the analyses performed for each length change, the analysis results depending on these parameters were compiled and presented in charts. It has been observed that the micro-pile length change varies significantly on these parameters.

Keywords: Micro-pile; Length variation; Rotation of the pile cap; Settlement; Geo5

1.Introduction

Nowadays, with the increase in population and urbanisation, the construction process has also accelerated and the need for high and large buildings has increased. The growth of the structures has led to the growth of the load to be transferred to the ground and led to developments in the field of geotechnics. These developments have also increased the need for construction on grounds that are not suitable for construction. In addition, it is of great importance that the soil on which the building will be constructed is determined before the problems such as bearing capacity, settlement and liquefaction are encountered and designs are made according to these analyses. Moreover, due to the development of machine and equipment technologies, foundation systems are also improving and the bearing capacity of even the most unsuitable soil for buildings is increased.

As one of the ground reinforcement techniques, micro-piles increase the bearing capacity of the soil and reduce settlement. Multi-storey and basement structures can be built even in deep excavation and narrow construction areas. Micro-pile applications have recently come to the forefront in our country due to the comfort of working in narrow areas, low cost, sensitive working areas such as historical and industrial structures. Furthermore, micro-pile technology is a reliable pile system that can endure high axial loads as they are designed to minimum damage to existing structures (Chaudhari et al., 2015). Thus, micro-piles are widely used in many soil reinforcement techniques.

Micro-piles are defined as piles with a diameter of less than 30 cm. Micro-piles usually consist of two elements: steel and injected concrete (according to project conditions). Micro-piles are manufactured by drilling the micro-pile hole, placing the specified reinforcement in the hole and filling the hole with concrete by grouting. The micro-pile drilling method is determined by considering the soil conditions of the project. When selecting the drilling technique, the method that will damage the neighbour structures and the environment should be avoided. In places where groundwater is shallow, it should be taken into consideration that fine-grained materials in the soil may flow in the hole as the bore height increases. Taking into consideration the soil and project conditions, consideration should be given to the time taken for completion of drilling, placement of steel and injection (FHWA, 2005).

In this study, micro-pile models designed in different lengths (5m, 6m, 7m, 8m, 9m, 10m, 11m, 12m, 13m, 14m, 15m) were analysed. In the analyses, the maximum settlement, minimum compressive force and maximum rotation of the pile cap were compared with the effect of the length change in the micro-piles.

*Corresponding author, E-mail: cagdasbetul08@gmail.com

https://doi.org/10.31462/icearc2025_ce_geo_651

2. Methodology

Geo5 geotechnical calculation program used in the study includes many various modules. Firstly, the ‘Micro-pile’ module has been selected in the study defined the problem. Afterwards, the geometry of the field was created and it was designed and analysed.

Table 1. Soil values (CL)

Low or Medium Plasticity Clay (CL, CI)	
Unit weight	γ: 21.00 kN/m^3
Angle of internal friction	φ_{ef}: 19.00 ^{o}
Soil cohesion	c_{ef}: 12.00 kPa
Saturated unit weight	γ_{sat}: 22.00 kN/ m^3
Oedometer module	E_{oed}: 4.50 MPa

Table 2. Soil values (GC)

Clayey Gravel (GC)	
Unit weight	γ: 19.50 kN/m^3
Angle of internal friction	φ_{ef}: 30.00^0
Soil cohesion	c_{ef}: 6.00 kpa
Saturated unit weight	γ_{sat}: 20.50 kN/ m^3
Oedometer module	E_{oed}: 67.50 MPa

In the study, 11 different designs including various parameters were analysed on Geo5 geotechnical calculation program. The samples were designed in different combinations where the effect of varying micro-pile lengths was investigated. In the samples, the requested changes were clearly observed by using the parameters in the same soil types. The unit weight, angle of internal friction, soil cohesion, saturated unit weight and oedometer modulus values of the two different soil types used are given in Table 1 and Table 2. Fig. 1 shows the properties of injected concrete and steel used in micro-pile design and Fig. 2 shows the standards of the materials used.

In the created models, 11 different lengths of micro-pile models were designed as 5 m, 6 m, 7 m, 8 m, 9 m, 10 m, 11 m, 12 m,13 m, 14 m and 15 m. Injected concrete and steel were used in the manufacturing of micro-piles. Concrete class C 25/30 and steel class S 235 structural steel were used. A total of 24 micro-piles were designed and analysed.

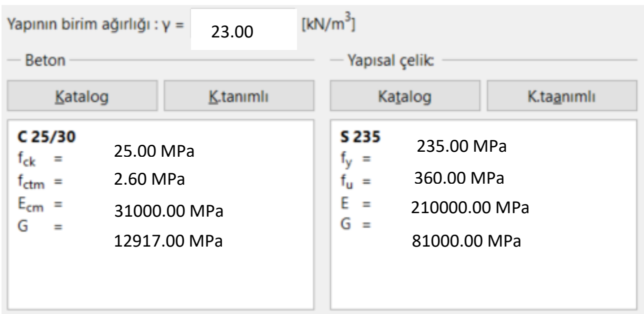

Fig. 1. Steel and injected concrete properties used in micro-pile design

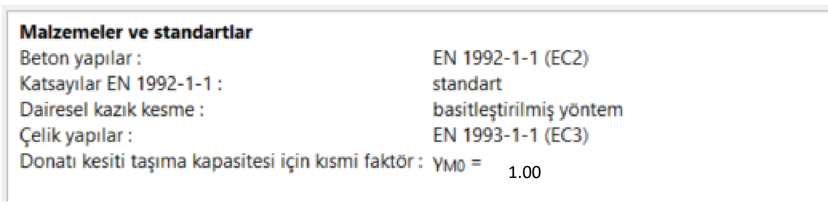

Fig. 2. Material properties and standards

The foundation geometry is designed as 24 m x 16 m. The centre to centre horizontal and vertical distances between the piles are the same and designed as 4 m. In the 24 m x 16 m foundation area, the number of micro-piles was designed as 4 on the horizontal plane and 6 on the vertical plane.

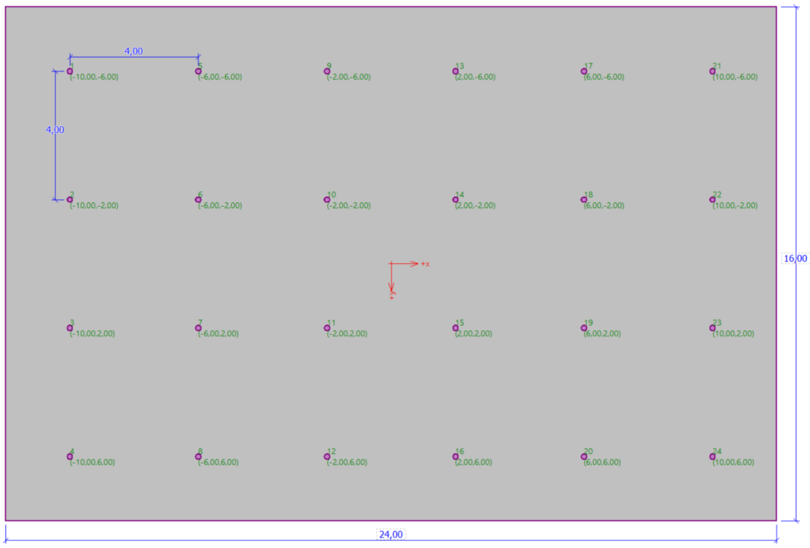

Fig. 3. Micro-pile foundation geometry plan

Fig. 3 shows the micro-pile foundation geometry plan and Fig. 4 shows the micro-pile foundation and pile information.

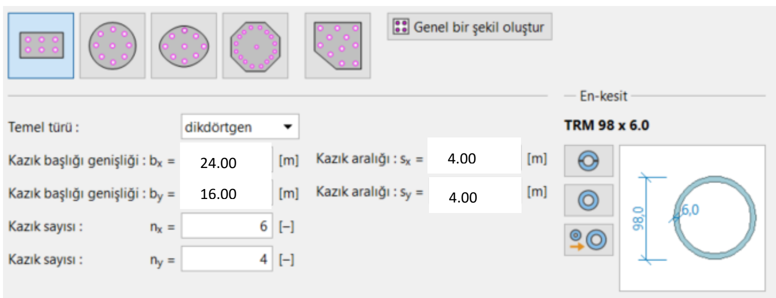

Fig. 4. Micro-pile foundation and pile information

In terms of micro-pile geometry, the starting point of the micro-piles is located at a depth of 2 m from the ground surface and the micro-pile cap is located at a depth of 1 m from the ground surface. The bottom of the ground level is designed at a depth of 18 m for all micro-pile samples. Considering the varying micro-pile lengths, it is assumed that 2 m of the micro-piles are socketed into the solid ground in each micro-pile design with the length change.

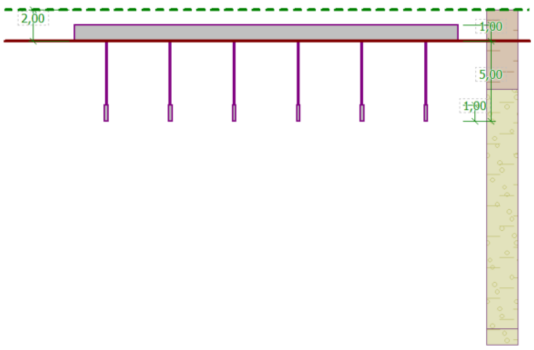

Fig. 5. Sample 5 m micro-pile profile

Similarly, in all designs, the lengths within the soil -where the micro-piles are located- were increased in parallel with the micro-pile lengths. In all micro-piles, the root region was kept constant as 1 m.

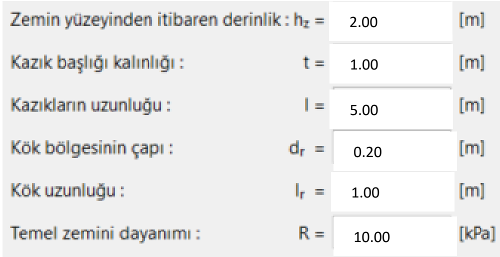

Fig. 6. Sample 5 m micro-pile properties

Exemplarily, at 5 m long micro-pile, there are 3 m clay layer and 15 m clayey gravel layer in the ground. Thus, 2 m of the 5 m micro-pile is socketed into the solid clayey gravel layer. In addition, there is no groundwater in the design. The profile and properties of the sample 5 m long micro-pile geometry design created and analysed with Geo5 geotechnical calculation program are shown in Fig. 5 and Fig. 6, respectively.

Table 3 shows the combinations of 11 different models designed in Geo5 geotechnical calculation program. Each of these designs was designed and analysed at different lengths and ground levels.

Table 3. Micro-pile models designed in the study

Model	Micro-pile length	Micro-pile ground level (Clay)	Micro-pile ground level (Clayey gravel)
Model-1	5 m	(0.00) - (-3.00)	(-3.00) – (-18.00)
Model-2	6 m	(0.00) - (-4.00)	(-4.00) – (-18.00)
Model-3	7 m	(0.00) - (-5.00)	(-5.00) – (-18.00)
Model-4	8 m	(0.00) - (-6.00)	(-6.00) – (-18.00)
Model-5	9 m	(0.00) - (-7.00)	(-7.00) – (-18.00)
Model-6	10 m	(0.00) - (-8.00)	(-8.00) – (-18.00)
Model-7	11 m	(0.00) - (-9.00)	(-9.00) – (-18.00)
Model-8	12 m	(0.00) - (-10.00)	(-10.00) – (-18.00)
Model-9	13 m	(0.00) - (-11.00)	(-11.00) – (-18.00)
Model-10	14 m	(0.00) - (-12.00)	(-12.00) – (-18.00)
Model-11	15 m	(0.00) - (-13.00)	(-13.00) – (-18.00)

2.1. Micro-pile geometries in designs

2.1.1. 5 m, 6 m and 7 m micro-piles

(0.00) - (-3.00) Clay and (-3.00) - (-18.00) Clayey gravel soil profile, micro-pile with 5 m length and 1 m root zone; (0.00) - (-4.00) Clay and (-4.00) - (-18.00) Clayey gravel soil profile, micro-pile with 6 m length and 1 m root zone; and (0. 00) - (-5.00) Clay and (-5.00) - (-18.00) Clayey gravel soil profile, the geometry designs of the micro-pile with 7 m length and 1 m root zone are given in Fig. 7.

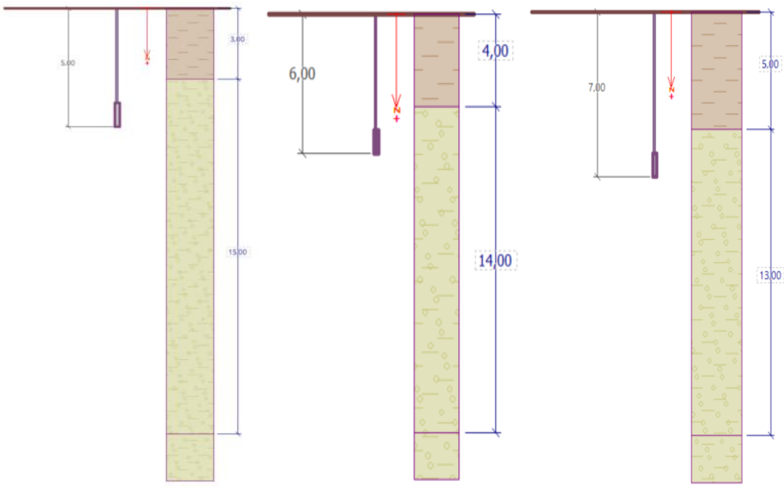

Fig. 7. Micro-pile geometries of 5m-6m-7m length

2.1.2. 8 m, 9 m and 10 m micro-piles

(0.00) - (-6.00) Clay and (-6.00) - (-18.00) Clayey gravel soil profile, 8 m in length with 1 m root zone; (0.00) - (-7.00) Clay and (-7.00) - (-18.00) Clayey gravel soil profile, 9 m in length with 1 m root zone; and (0. 00) - (-8.00) Clay and (-8.00) - (-18.00) Clayey gravel soil profile, the geometry design of the micro-pile with 10 m length and 1 m root zone is given in Fig. 8.

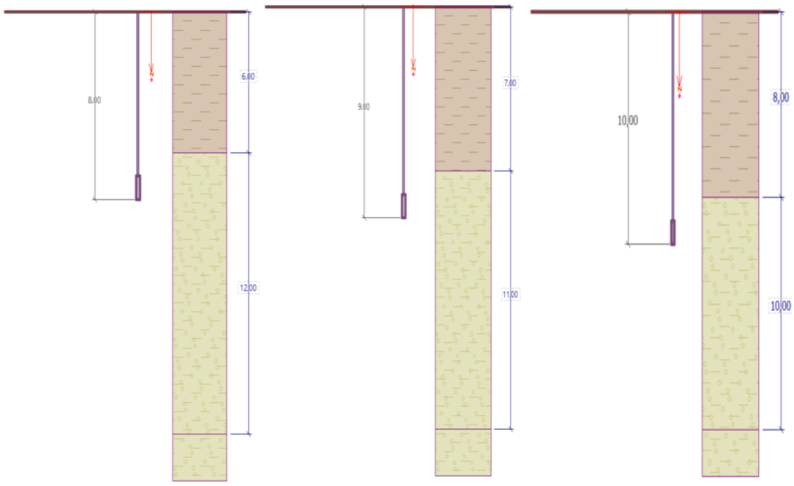

Fig. 8. Micro-pile geometries of 8m-9m-10m length

2.1.3. 11 m, 12 m and 13 m micro-piles

(0.00) - (-9.00) Clay and (-9.00) - (-18.00) Clayey gravel soil profile, 11 m in length with 1 m root zone; (0.00) - (-10.00) Clay and (-10.00) - (-18.00) Clayey gravel soil profile, 12 m in length with 1 m root zone; and (0. 00) - (-11.00) Clay and (-11.00) - (-18.00) Clayey gravel soil profile, the geometry design of the micro-pile with 13 m length and 1 m root zone is given in Fig. 9.

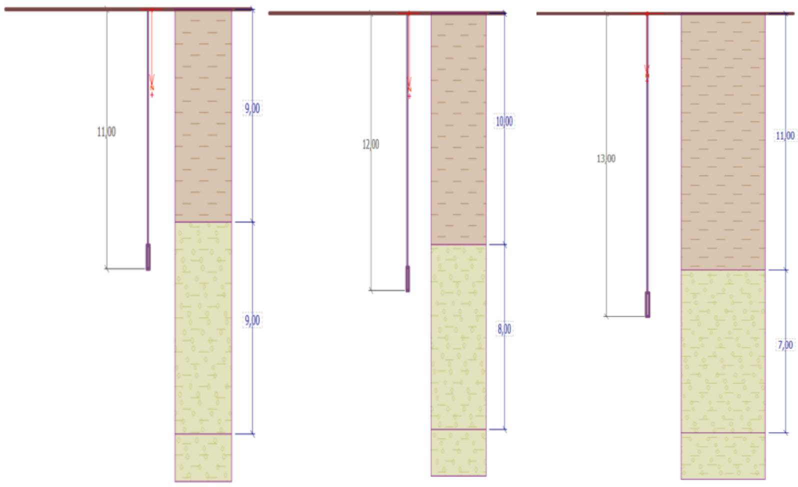

Fig. 9. Micro pile geometries of 11m-12m-13m length

2.1.4.14 m and 15 m micro-piles

The geometry design of the micro-pile with 14 m length and 1 m root zone in (0.00) - (-12.00) Clay and (-12.00) - (-18.00) Clayey gravel soil profile and the micro-pile with 15 m length and 1 m root zone in (0.00) - (-13.00) Clay and (-13.00) - (-18.00) Clayey gravel soil profile is given in Fig. 10.

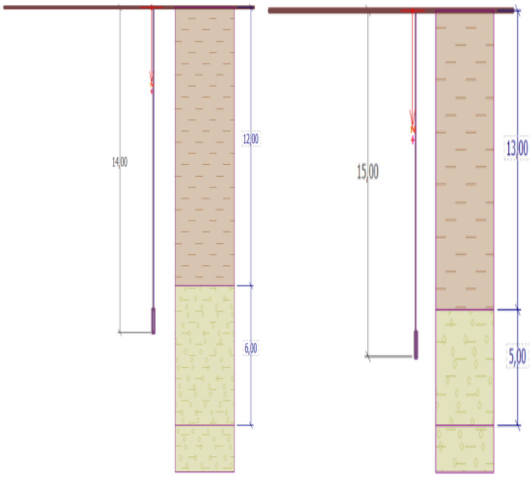

Fig. 10. Micro-pile geometries of 14 m and 15 m lengths

3. Analyses results

In civil engineering applications and problem solutions, engineers have to think about the application as well as design. This situation is also very important in engineering applications in the field of geotechnics. Various engineering analyses of each geotechnical problem bring along soil engineering applications as well as the solution. Micro-piles are one of these application methods.

The biggest advantage of these micro-piles, which are ground improvement methods, is that they have a fast-manufacturing process and low-power light machine equipment. Compared to bored piles, it is more advantageous in terms of manufacturing process in narrow or closed areas, especially inside the building.

In this study, the maximum settlement, minimum compressive force and maximum rotation at the pile cap were analysed for different micro-pile lengths. In total, 11 analyses of 11 different lengths of micro-piles were performed in Geo5 geotechnical calculation program.

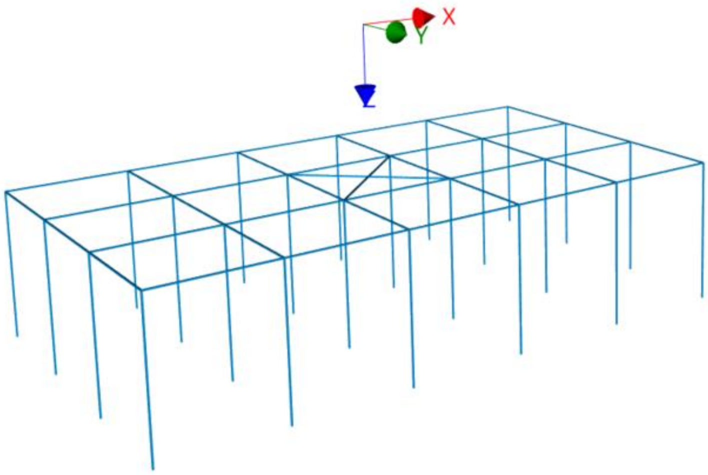

Fig. 11. Micro-pile analyses scheme

The analysis results obtained from the designs are shown in Table 4, Table 5 and Table 6. Fig. 11 shows the micro-pile schematic obtained from the analyses.

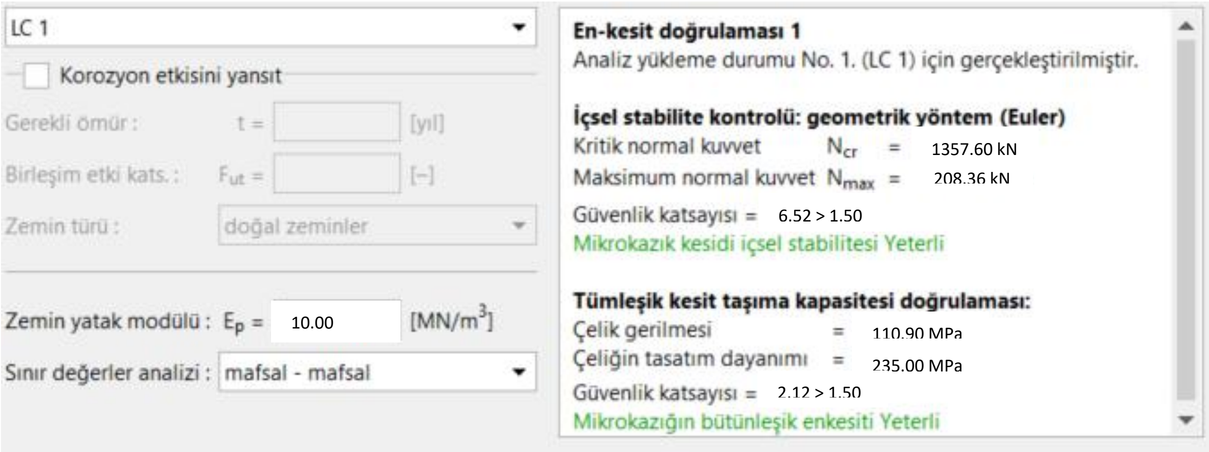

Fig. 12. Micro-pile analyses results

Fig. 12 and Fig. 13 show the outputs of the analysis results on Geo5 geotechnical calculation program.

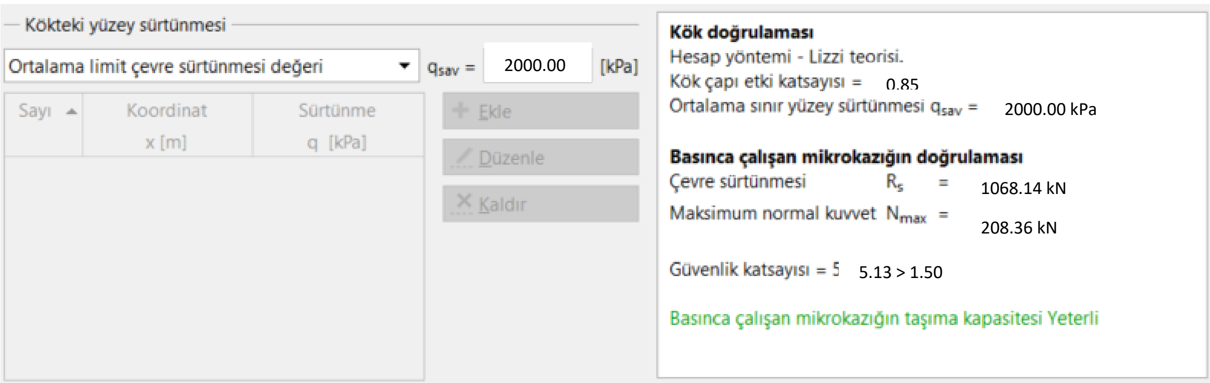

Fig. 13. Micro-pile analyses results

Fig. 14 shows the Normal force, Shear force and Bending moment diagrams obtained from the analyses results of the 5 m long micro-pile used as an example.

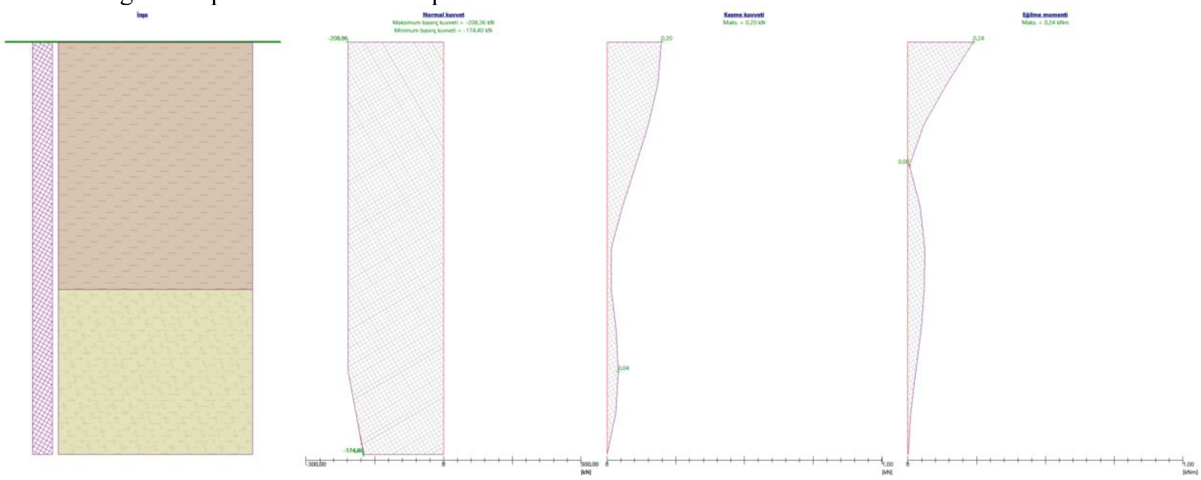

Fig. 14. Normal force, shear force and bending moment diagrams for sample 5 m

3.1. Micro-pile length and maximum settlement variation

Fig. 15 shows the variation of the maximum settlement of piles with micro-pile lengths between 5 m and 15 m.

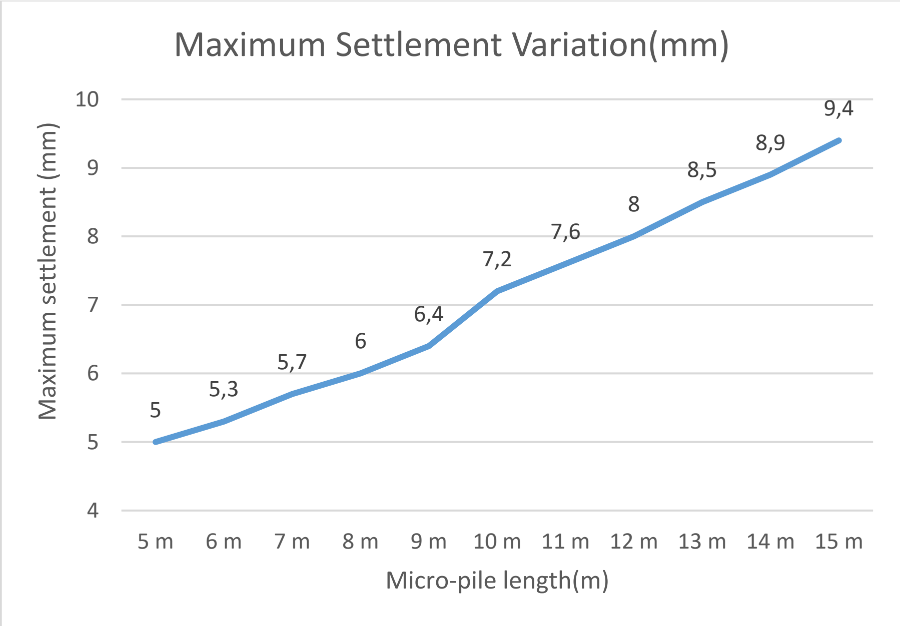

Fig. 15. Micro-pile length-maximum settlement variation

3.2. Micro-pile length and minimum compressive force

Fig. 16 shows the variation of the minimum compressive force for piles with micro-pile lengths between 5 m and 15 m.

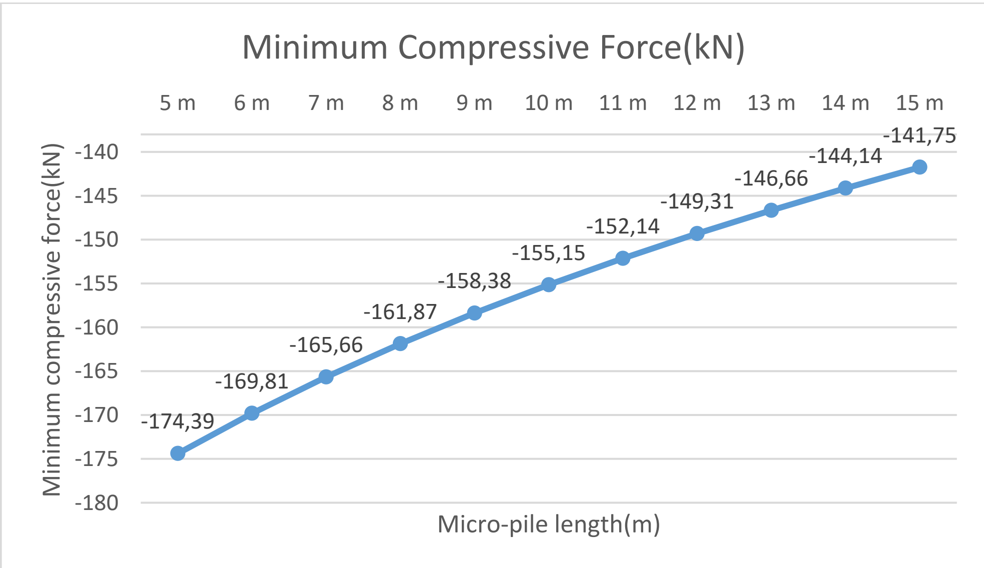

Fig. 16. Micro-pile length-minimum compressive force

3.3. Micro-pile length and maximum rotation of pile cap

Fig. 17 shows the variation of pile cap maximum rotation for piles with micro-pile lengths between 5 m and 15 m.

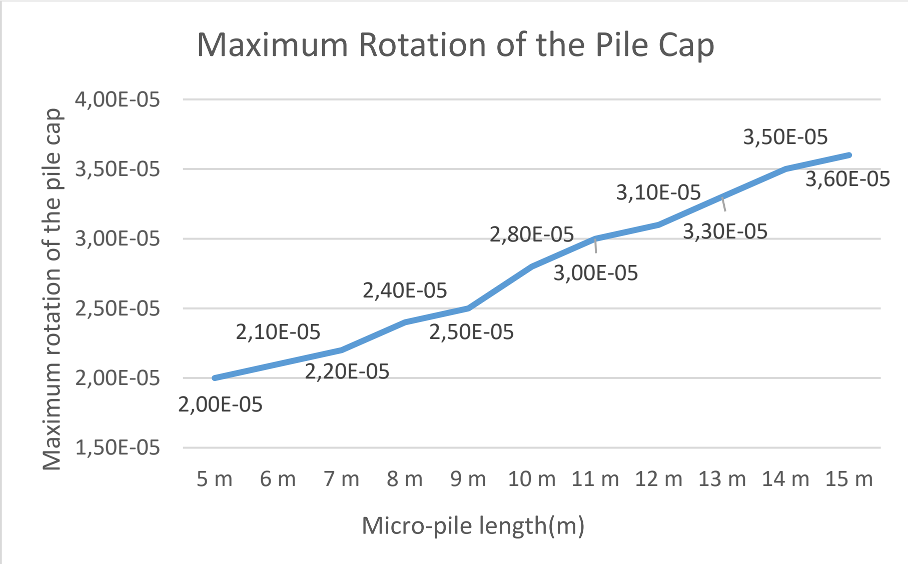

Fig. 17. Micro-pile length - maximum rotation of the pile cap

As can be seen from the results of the analyses, it was observed that the micro-piles designed in different lengths with the same soil properties significantly affected the parameters of maximum settlement, minimum compressive force and maximum rotation at the pile cap. Maximum settlement, minimum compressive force and maximum rotation at the pile cap increased with the increase in pile length. The changes in these parameters by keeping the root region length constant and increasing the micro-pile length are presented in tables. As a result of the analyses, it was observed that the selection of micro-pile lengths has an important place in micro-pile manufacturing.

4. Conclusions

In this study, the analyses of piles with the same soil properties, different soil layer thicknesses and different micro-pile lengths were investigated. A total of 11 different designs were made as micro-pile lengths (5 m, 6 m, 7 m, 8 m, 9 m, 10 m, 11 m, 12 m, 13 m, 14 m, 15 m). Designs were made in Geo5 geotechnical calculation program. The results of the analyses were mainly analysed micro-pile length-maximum settlement variation, micro-pile length-minimum compressive force and micro-pile length-micro-pile cap maximum rotation variations. The results of the analyses obtained from the study are given below:

- The maximum settlement (mm) in the analyses increased as the pile length increase from 5 m and the smallest length selected in the micro-pile design of 15 m as the longest length.
- The maximum settlement was 2.00×10^{-05} at a minimum length of 5 m and 3.60×10^{-5} at a maximum length of 15 m.
- The minimum compressive force (kN) in the analyses increased as the length of the pile increased from 5 m, the shortest length selected in the micro-pile design of 15 m as the longest length.
- The minimum compressive force was -174.39 kN at the minimum 5 m micro-pile length and -141.75 kN at the maximum 15 m micro-pile length.
- It is seen that the maximum rotation of the pile cap increases in the analyses performed as the pile length increases from 5 m, which is the shortest length selected in micro-pile designs, to 15 m, which is the longest length.
- The maximum pile cap rotation was 2.00x10-5 at a minimum of 5 m micro-pile length and 3.60x10-5 at a maximum of 15 m micro-pile length.
- Considering the parameters that are affected as the micro-pile length increases, the studies show that the quality of the micro-pile elements should be designed with a more resistant micro-pile element.
- It should not be overlooked during manufacturing and design that all the mentioned parameters will increase with the increase in the micro-pile length.

As a result, the variations of different micro-pile lengths on the maximum settlement, minimum compressive force and maximum rotation at the pile cap were analysed. Micro-piles designed with the same soil properties, same socket length in the root region and different soil layer heights increase these parameters with different length changes.

Acknowledgments
The Department of Civil Engineering at Kırıkkale University Faculty of Engineering and Natural Sciences utilizes an educational license of the GEO5 Geotechnical Software Suite provided by the Fine Company. I would like to thank Fine Company remarkable contributions to this study.

References

Bruce, D. A., DiMillio, A. F., Juran I. (1997). Micro-piles: The State of Practice, Part 1: Characteristics, definitions and classifications. Ground Improvement.

Chaudhari J.V., Pitroda J., Bhavsar J.J. (2015). Micro-Pile: Recent Advances and Future Trends. International Conference on: "Engineering: Issues, opportunities and Challenges for Development".

FHWA, (2005). Micro-pile Design and Construction Guidelines, Implementation Manual, National Highway Institute.

Korkmaz E. (2019). Çekme Yükü Altında Çalışan Mikrokazıklar. İstanbul Teknik Üniversitesi (İTÜ), Yüksek Lisans Tezi.

ICEARC'25
4th International Civil Engineering & Architecture Conference
17-19 May 2025, Trabzon, Türkiye

Alkali-activated by-product materials as alternative binders in deep soil mixing applications

Önder Akçakal*[1], Mustafa Hatipoğlu[1]

[1] *Istanbul Technical University, Department of Civil Engineering, 34467 Istanbul, Türkiye*

Abstract. Industrial by-products such as fly ash and ground granulated blast-furnace slag (GGBS) bring significant environmental challenges globally. Mitigation efforts focused on reintroducing these materials into the economy through their application in the construction industry as alternative resources. Since these materials do not provide sufficient binding properties when used independently, alkali activators can be used as a promising technique to improve binding properties of these waste materials. This process allows us to utilize GGBS and fly ash, as a result it is possible to reduce carbon emissions and to promote environmental sustainability. This study focuses on the application of fly ash and GGBS in ground improvement techniques, specifically targeting their use in deep mixing methods (DSM). Deep soil mixing is one of the effective soil improvement techniques in which soil is mixed with binder slurry with the help of blades. The research aims to enhance the binding properties of by-product materials through alkali activation, making them more applicable for geotechnical applications. Unconfined compression strength (UCS) tests were performed on the alkali-activated mixed samples. The increase in strength of the mixed samples was evaluated. As a result of the study outcomes of the ground improvement with alkali-activated GGBS and fly ash materials are discussed. These by-products can play an important role in reducing the carbon footprint of the geotechnical applications besides providing cost-effective solutions. This research highlights the potential of alkali-activated GGBS and fly ash in ground improvement applications. Alkali-activated by-products can be used as sustainable and efficient alternative binders in the construction industry.

Keywords: Deep Soil Mixing; By-Products; GGBS; Fly Ash; Alkali Activation

1. Introduction

High amounts of carbon dioxide emission in cement production process brings significant environmental concerns which led society to think about the reliance of construction industry on traditional cement. Global cement production is over 4 billion metric tonnes annually and Türkiye is in the fifth rank with 79 million metric tonnes (Hatfield, 2024). This quantity decreased during the pandemic period however there is a significant growth trend in the last decades which increases the concerns about environmental impacts. With 7-8% cement production is one of the major contributors of global greenhouse gas (GHG) emissions (Barbhuiya et al., 2024). Alkali activated binders with industrial by-products such as fly ash (FA) and ground granulated blast furnace slag (GGBS) have emerged in recent decades as promising alternatives of traditional cement to mitigate these concerns. When it is compared with ordinary Portland cement (OPC), alkali activated materials provide comparable technical solutions while reducing the environmental drawbacks (Cristelo, et al., 2013; Arulrajah et al., 2018).

Beside the environmental advantages of reuse of the industrial wastes, technique offers also more durable and chemically resistant binder materials (Mohammadinia et al., 2019). As a result, researchers' interest on alkali activated binders progressively increased in the last years. Studies continue various civil engineering applications and ground improvement is one of these important areas.

Deep Soil Mixing (DSM) is a ground improvement technique where a stabilizing binder slurry is mixed with soil by means of rotating blades in place. Blades mix the soil and binder slurry mechanically and form a circular column with enhanced engineering properties. Blades rotates in the soil and reaches to the required depth with mixing the soil with binder (Porbaha, 1998). It is a rapid technique and can be successfully applied in a wide range of projects, including foundations, embankments and retaining structures. (Sargent et al., 2013).

Traditional binders, cement and lime are widely used in DSM to improve the strength of the soil with hydration and pozzolanic reactions (Arulrajah et al., 2018; Sargent et al., 2013). However, production process of cement-based binders has great impact on environment, and this motivates researchers to study on alternative green stabilizers.

* Corresponding author, E-mail: akcakal20@itu.edu.tr

https://doi.org/10.31462/icearc2025_ce_geo_680

golden light publishing

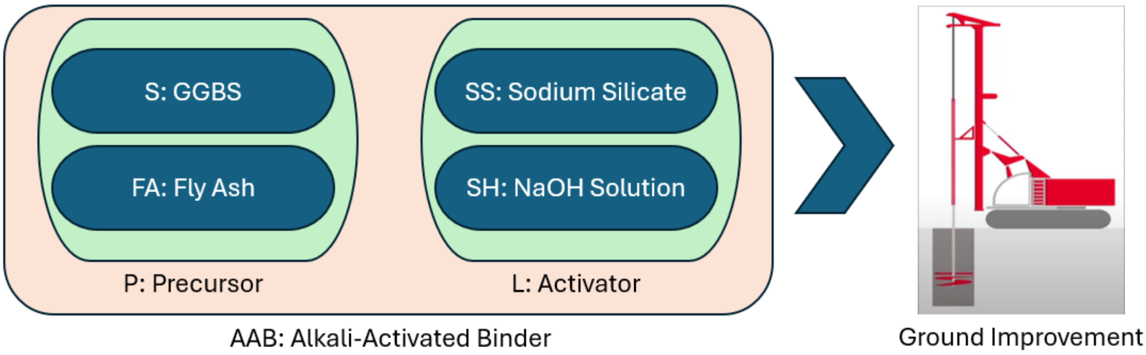

Fig.1. Ground improvement applications with alkali-activated binders

Geopolymerization is the fundamental process of the alkali-activated binders which consist of chemical reactions between aluminosilicate-rich materials and an alkaline activator. Alumina and silica dissolve into the alkaline solution in this process and then polycondensation occurs to form a three-dimensional network of sodium aluminosilicate hydrate (N-A-S-H) or calcium aluminosilicate hydrate (C-A-S-H) gels (Xu & Van Deventer, 2002).

Final properties of the geopolymeric matrix are affected by several factors like chemical composition of the precursors, concentration and composition of the alkaline activators, the ratio of liquid and binder quantities and curing conditions of the samples (Hardjito & Rangan, 2005; Al Bakri et al., 2012; Phetchuay et al., 2016). To achieve suitable mechanical properties and durability, optimization of these parameters becomes important.

Workability problems and potential carbonation or efflorescence are the main drawbacks of the technique (Palacios & Puertas, 2006). However, alkali-activated binders can be used with DSM applications and provide a sustainable alternative for ground improvement with an environmental-friendly approach (Fig. 1.)

Demand for the environmentally sustainable ground improvement techniques is increasing and the use of alkali-activated by-products such as fly ash (FA) and ground granulated blast furnace slag (GGBS) is investigated in this study as an alternative for traditional cement binder. These materials were mixed with sand under alkaline conditions in the laboratory. To evaluate the mechanical performance of the technique the unconfined compressive strength of the mixed samples was tested.

2. Investigation program

Unconfined Compression Strength (UCS) of the columns are the major performance indicators and investigation programme was determined as focusing on this parameter. As many researchers (Hardjito & Rangan, 2005; Al Bakri et al., 2012; Phetchuay et al., 2016; Mohammadinia et al., 2019) have demonstrated in their studies these parameters are affected by the concentration and composition of the alkali binder therefore different precursor dosages (P/Ws ratio 10, 15, 20, 25, 30, 35%) with varying ratios of the liquid activators were investigated.

Before the main test sets with varying dosages, a coherent set of other variables as activator ratio, sodium silicate to sodium hydroxide ratio, molarity of the sodium hydroxide and sodium silicate modulus ratio have been investigated. As geopolymerization occurs with the alkaline activation of the aluminosilicate precursors sodium hydroxide concentration gains importance (van Deventer et al. 2010; Mohammadinia et al., 2019) however to reduce the safety risks in nature of highly corrosive sodium hydroxide solution molarity needs to be optimized (Arulrajah et al, 2018). Modulus ratio (M_s) of the sodium silicate solution is the ratio of SiO_2 to Na_2O components. Sodium silicate quantity in the mixture is also important and related with the acceleration of the geopolymerization (Arulrajah et al, 2018; Shen et al., 2013; Phoo-ngernkham et al., 2015). Sample preparation sequence and material properties were investigated carefully. These parameters were determined with a series of preliminary batches and compression tests.

The utilization of the alkali activated precursors as a binder in ground improvement works was investigated with prepared samples in the laboratory. As performed in other researches (Sargent et al., 2013; Arulrajah et al, 2018; Mohammadinia et al., 2019) alkali activated binder is mixed with soil where samples were prepared with different precursor dosages. Mechanical performance of the samples was investigated with performed UCS tests (BS 1377: Part 7: Clause 7, BSI, 1990). 72 samples were prepared in total with precursor to soil weight (P/W_s) ratios varying between 0.1 to 0.35. Samples were planned to be tested after different curing times as 1, 4 and 16 weeks. Test program and the sample numbers are listed in Table 1.

Table 1. Number of samples prepared with alkali activated binders

	P/Ws (Precursor/Soil Weight)					
Curing Time	0.1	0.15	0.20	0.25	0.30	0.35
1 week	4	2	4	2	4	2
4 weeks	4	2	4	2	4	2
16 weeks	4	2	4	2	4	2
Total	12	6	12	6	12	6

3. Materials

Utilization of the by-products as precursors in alkali activated binders reduces the necessity of traditional cement in construction industry and considerably brings down the CO_2 emissions (Phair, 2006; Mohammadinia et al., 2019). Ground granulated blast furnace slag (GGBS) and fly-ash (FA) are the major by-products which can be used as aluminosilicate sources in geopolymerization process (van Deventer et al. 2010; Mohammadinia et al., 2019). GGBS is the by-product of steel manufacturing process. Molten slag floats on top of the iron ore, coke and limestone used in the blast furnace. Then it is dried and granulated and finally grinded to form a powder state. In Türkiye there are several sources of this by-product like furnace steel plants (mainly electric arc furnaces -EAF's) in Zonguldak, İskenderun, Çanakkale, Bursa and Kocaeli regions and total annual production is approximately 5 million tonnes (Yonar, et.al, 2015).

Fly-ash (FA) is also a by-product but generated by thermal power plants. They are generated from burning pulverized coal. It is collected by various methods (like electrostatic precipitators, baghouse filters or cyclone separators) to prevent environmental pollution and these methods allow its re-use in the industry (Blicharz and Franus, 2023). Fly ash output of these thermal power plants is over 20 million tonnes in Türkiye (Felekoğlu, 2006) and only 30% of the output can be re-used in the industry. Beside the economic and environmental benefits, severe stockpiling or landfill problems motivate researchers to find new ways to return this by-product to the industry (Blicharz and Franus, 2023).

GGBS and FA materials which used in this laboratory studies are received from the local plants in Türkiye (Fig. 2). F-type Fly ash was used in the studies which is originated from anthracite and bituminous coals. F-type fly ashes SiO_2+Al_2O_3+Fe_2O_3 percentage is over 70% and CaO percentage is less than 10% (Görhan et al., 2009).

To provide the alkaline environment for the geopolymerization process sodium hydroxide (NaOH) beads were diluted into a 10 Molar solution. Since this process was an exothermic reaction, in the laboratory study sodium hydroxide solution was prepared one day before the mixing phase. As the second component of the liquid activator, sodium silicate (Na_2SiO_3) solution with modulus ratio of (M_s) 3 was used to accelerate the geopolymerization process (Fig. 3).

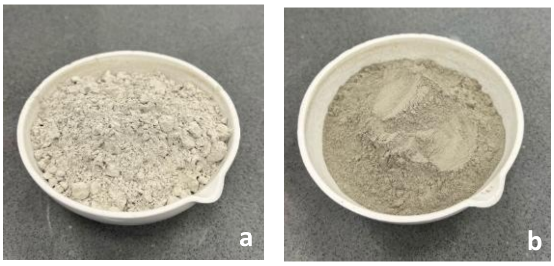

Fig.2. (a) GGBS sample, (b) Fly ash sample

Fig.3. (a) Sodium hydroxide beads, (b) Sodium silicate solution

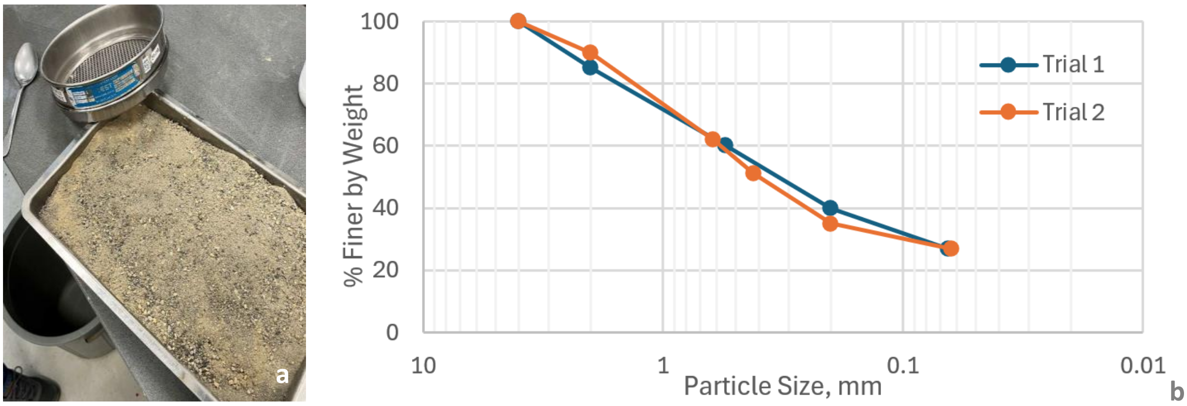

Fig.4. (a) Soil sample, (b) Sieve analysis results of the trials

Soil samples were collected from a current project site boreholes. Sand samples were preferred in the laboratory tests. SPT samples were selected, and they were sieved with a 4 mm aperture sieve (Fig. 4. (a)). The sieve analysis results are of the samples are given in the Fig. 4. (b). Fine content of the samples were limited to approximately 25% to demonstrate common site conditions for sandy soils. Soil samples were mixed with water to obtain 20% water content before the mixing stage of alkali activated binder.

4. Sample preparation and laboratory tests

Precursor (P) materials S (GGBS) and FA (Fly Ash) were uniformly mixed in a container. S:FA ratio was selected as 1.0. Liquid activator was prepared as a mix of sodium silicate and sodium hydroxide solutions. To increase the workability in some of the samples a portion of the water required for soil moisture was added to activator and they were all mixed with the precursor blend. Prepared alkali activated binder is mixed with soil in the laboratory with different dosages of precursors. P/W_s (where W_s is the weight of the dry soil in the mixture) ratios of the group of samples were 0.1, 0.15, 0.2, 0.25, 0.3 and 0.35 to see the effect or benefit of the increase of the precursors to the strength. Samples were stored under humid conditions to keep their water content during their curing time. Samples were subjected to UCS tests after 1, 4 and 16 weeks of curing times (Fig. 5).

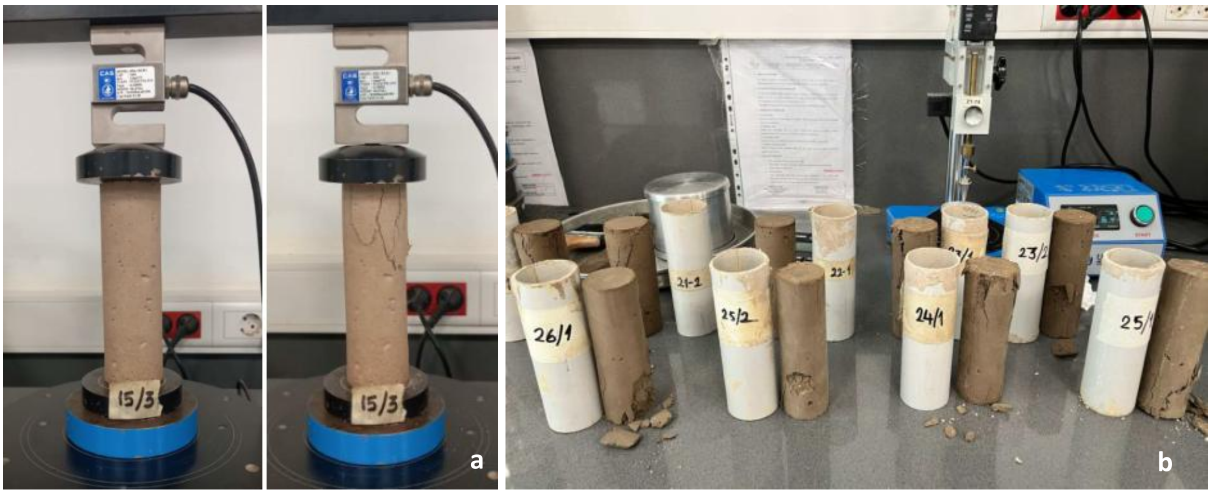

Fig.5. (a) UCS test, (b) Tested samples

5. Test results and discussion

Samples were subjected to UCS tests once the planned curing time is complete. As described in the previous section samples were prepared with two different methods. For some of the samples all the water quantity required for 20% percent water content is mixed with soil (Method A), for the rest of the samples 1/5 of the required water (4%) is mixed with the alkali activator previously to increase the workability of the binder slurry (Method B).

For every P/Ws at least 4 samples were tested, and average values were recorded and presented on Fig. 6. The results reveal that strength values increase significantly with the increase of the precursor dosage.

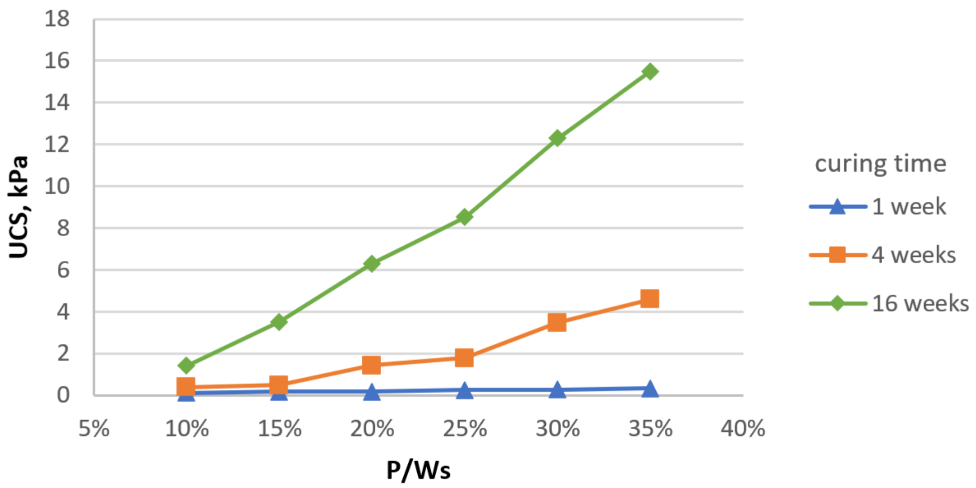

Fig.6. Average UCS results of the samples after 1 week, 4 weeks and 16 weeks curing times

Samples gained strength with the long period times and to evaluate the effect of the curing time Fig. 7 was prepared.

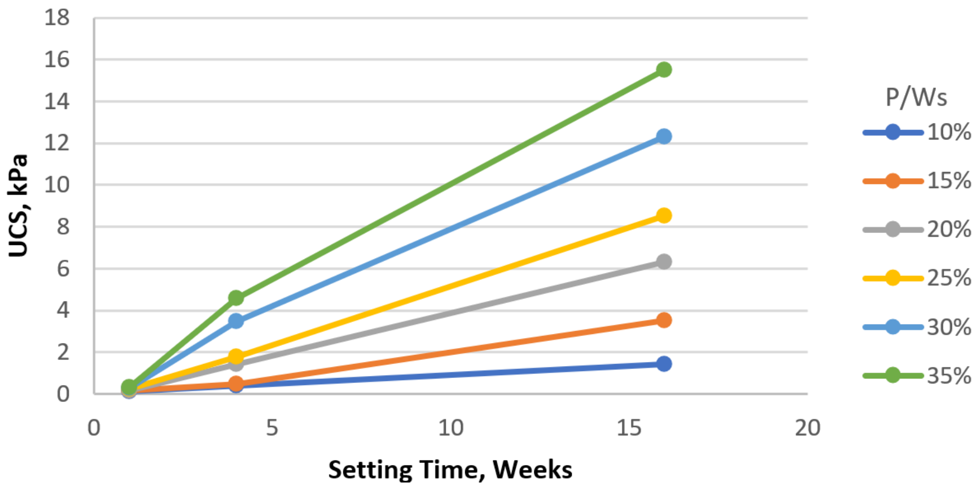

Fig.7. The increase of the average UCS Values with curing time

In general, a significant strength gain could be followed in the results with the increase of the alkali activated binder dosage. This clearly demonstrates that geopolymerization process can bring binding properties to the GGBS and FA by-products and allow them to be re-used in the industry. Despite the strength values were even less than 1 MPA after one week curing time, samples gained a significant strength in longer periods. After 4 weeks of curing time average UCS values exceeded 4 MPa and almost reached to 16 MPa after 16 weeks with 35% P/Ws ratio. However, when the average strengths compared with the curing time, the strength gain continues even after 16 weeks. Beside the strength gain, samples prepared with Method A demonstrated higher strength values when compared with the Method B. The application method and sequence of the mixing is also important for the mechanical performance of the alkali activated materials.

6. Conclusion

As a result of this study potential of the alkali activated binders prepared with by-products Fly Ash and GGBS in ground improvement works was demonstrated. Instead of traditional cement with many environmental drawbacks alkali activated binders can be utilized in geotechnical engineering especially in deep soil mixing (DSM) applications. A series of samples were prepared through the comprehensive laboratory studies with varying dosages of these by products. Mechanical performance of the samples was checked with unconfined compression tests (UCS) and evaluated within the report. The results revealed an important strength gain which can be considered as the evidence of enhanced binding capacity of these by-products. The successful results also pointed that these materials can be re-used in the industry and environmental impact of these applications can be reduced by recycling. The use of the alkali activated by-products in DSM applications can bring a sustainable approach with integration of these waste materials to the geotechnical engineering industry.

References

Al Bakri, A. M. M., Kamarudin, H., Abdulkareem, O. A., Ghazali, C. M. R., Rafiza, A., & Norazian, M. (2012). Optimization of alkaline activator/fly ash ratio on the compressive strength of manufacturing fly ash-based geopolymer. *Applied Mechanics and Materials, 110–116*, 734–739. https://doi.org/10.4028/www.scientific.net/AMM.110-116.734

Arulrajah, A., Yaghoubi, M., Miri Disfani, M., Horpibulsuk, S., Bo, M. W., & Leong, M. (2018). Evaluation of fly ash- and slag-based geopolymers for the improvement of a soft marine clay by deep soil mixing. *Soils and Foundations, 58*(5), 1358–1370. https://doi.org/10.1016/j.sandf.2018.07.011

Barbhuiya, S., Kanavaris, F., Das, B. B., & Idrees, M. (2024). Decarbonising cement and concrete production: Strategies, challenges and pathways for sustainable development. *Journal of Building Engineering*. https://doi.org/10.1016/j.jobe.2024.108861

British Standards Institution. (1990). *BS 1377: Methods of test for soils for civil engineering purposes (Incorporating Amendment No. 1)*. British Standards Institution.

Cristelo, N., Glendinning, S., Fernandes, L., & Teixeira Pinto, A. (2013). Effects of alkaline-activated fly ash and Portland cement on soft soil stabilisation. *Acta Geotechnica, 8*(4), 395–405. https://doi.org/10.1007/s11440-012-0200-9

Felekoğlu, B. (2006). Utilisation of Turkish fly ashes in cost effective HVFA concrete production. *Fuel, 85*(17–18), 2625–2631. https://doi.org/10.1016/j.fuel.2006.01.019

Görhan, G., Kahraman, E., Başpınar, M. S., & Demir, İ. (2009). Uçucu kül: Bölüm II: Kimyasal, mineralojik ve morfolojik özellikler. *Yapı Electronic Journal of Construction Technologies, 5*(2), 33–42.

Grabias-Blicharz, E., & Franus, W. (2023). A critical review on mechanochemical processing of fly ash and fly ash-derived materials. *Science of The Total Environment, 860*, 160529. https://doi.org/10.1016/j.scitotenv.2022.160529

Hardjito, D., & Rangan, B. V. (2005). *Development and properties of low-calcium fly ash-based geopolymer concrete (Research Report GC 1)*. Curtin University of Technology. https://hdl.handle.net/20.500.11937/5594

Hatfield, A. K. (2024). *Mineral commodity summaries, January 2024*. U.S. Geological Survey. https://www.usgs.gov/centers/national-minerals-information-center/mineral-commodity-summaries

Mohammadinia, A., Disfani, M. M., Conomy, D., Arulrajah, A., Horpibulsuk, S., & Darmawan, S. (2019). Utilization of alkali-activated fly ash for construction of deep mixed columns in loose sands. *Journal of Materials in Civil Engineering, 31*(10), 04019233. https://doi.org/10.1061/(ASCE)MT.1943-5533.0002878

Palacios, M., & Puertas, F. (2006). Effect of carbonation on alkali-activated slag paste. *Journal of the American Ceramic Society, 89*(10), 3211–3221. https://doi.org/10.1111/j.1551-2916.2006.01214.x

Phetchuay, C., Horpibulsuk, S., Arulrajah, A., Suksiripattanapong, C., & Udomchai, A. (2016). Strength development in soft marine clay stabilized by fly ash and calcium carbide residue based geopolymer. *Applied Clay Science, 127–128*, 134–142. https://doi.org/10.1016/j.clay.2016.04.006

Phoo-ngernkham, T., Maegawa, A., Mishima, N., Hatanaka, S., & Chindaprasirt, P. (2015). Effects of sodium hydroxide and sodium silicate solutions on compressive and shear bond strengths of FA–GBFS geopolymer. *Construction and Building Materials, 91*, 1–8. https://doi.org/10.1016/j.conbuildmat.2015.05.001

Phair, J. W. (2006). Green chemistry for sustainable cement production and use. *Green Chemistry, 8*(9), 763–780. https://doi.org/10.1039/b603997a

Porbaha, A. (1998). State of the art in deep mixing technology, Part I: Basic concepts and overview. *Proceedings of the Institution of Civil Engineers - Ground Improvement, 2*(2), 81–92. https://doi.org/10.1680/gi.1998.020204

Sargent, P., Hughes, P. N., Rouainia, M., & White, M. L. (2013). The use of alkali activated waste binders in enhancing the mechanical properties and durability of soft alluvial soils. *Engineering Geology, 152*, 96–108. https://doi.org/10.1016/j.enggeo.2012.10.013

Shen, S.-L., Wang, Z.-F., Yang, J., & Ho, C.-E. (2013). Generalized approach for prediction of jet grout column diameter. *Journal of Geotechnical and Geoenvironmental Engineering, 139*(12), 2060–2069. https://doi.org/10.1061/(ASCE)GT.1943-5606.0000932

van Deventer, J. S. J., Provis, J. L., Duxson, P., & Brice, D. G. (2010). Chemical research and climate change as drivers in the commercial adoption of alkali activated materials. *Waste and Biomass Valorization, 1*(1), 145–155. https://doi.org/10.1007/s12649-010-9015-9

Xu, H., & Van Deventer, J. S. J. (2002). Geopolymerisation. *Minerals Engineering, 15*(12), 1131–1139. https://doi.org/10.1016/S0892-6875(02)00255-8

Yonar, F., Cokgor, E. U., Dikbas, H. A., Demir, B., & Ergun, M. (2015). Environmental effects and possible highway applications of electric arc furnace slag in Turkey. In *Proceedings of the World Congress on New Technologies (NewTech 2015)* (Paper No. 228). Barcelona, Spain, July 15–17, 2015.

ICEARC'25
4th International Civil Engineering & Architecture Conference
17-19 May 2025, Trabzon, Türkiye

Prediction of active earth thrusts acting on a T-type cantilever retaining wall by soft computing methods

Hakan A. Kamloğlu*[1], Özge Haşlak[1]

[1] *Bayburt University, Engineering Faculty, Department of Civil Engineering, 69010, Bayburt, Türkiye*

Abstract. This study investigates the application of soft computing methods to predict active earth thrusts acting on T-type cantilever retaining walls supporting planar granular soil for active case conditions. Four different algorithms—Artificial Neural Networks (ANN), Extreme Learning Machine (ELM), Random Forest Regression (RFR), and Support Vector Regression (SVR)—were developed and compared for their predictive capabilities. A comprehensive dataset comprising 273 cases was created using Central Composite Design, where independent variables included groundwater level, saturation ratio, porosity, friction angle, wall height, heel length, and seismic coefficients. Dependent variables (lateral active earth thrust, vertical earth thrust, and application point) were obtained through finite element analyses. All algorithms were optimized using genetic algorithm to determine optimum hyperparameters. Performance evaluation using independent test cases showed that all methods could predict thrust coefficients with high accuracy (R^2 between 0.86-0.99), with SVR exhibiting superior overall performance (R^2=0.94 for lateral thrust and R^2=0.99 for vertical thrust) and minimal prediction variance. While the prediction of thrust application points remained challenging for all algorithms (highest R^2=0.64 with SVR), the study demonstrates that soft computing methods can serve as reliable and computationally efficient alternatives to complex numerical analyses for estimating earth thrusts on T-type retaining walls, particularly when optimized with genetic algorithms.

Keywords: T-type cantilever wall; Active earth thrust; Soft computing methods; FEM

1. Introduction

T-shaped cantilever walls are one of the most widely used supporting structures in civil engineering applications. The T-type walls comprise characteristic features that should be considered in lateral earth thrust calculations due to their heel configuration, which significantly influences failure surface mechanism and lateral earth pressure distribution. The main reason for this phenomenon is that the failure surface geometry behind the wall, especially in the active state, is different from other types of walls depending on the heel length (Greco, 2008). The effect of heel length on the lateral earth pressure distribution was investigated with several analytical, numerical, and experimental approaches (Chen et al., 2023; Greco, 2001; Kamiloglu, 2023). The analyses show that conventional lateral earth pressure determination methods are not accurate for T-shaped walls.

Several approaches have been employed to determine lateral earth thrust acting on the retaining structures. Although the widely used conventional lateral earth pressure determination methods are derived from analytical methods, alternative methods have been investigated to improve the calculation accuracy. These approaches can be summarized as analytical methods (Chen et al., 2025; Lin et al., 2024), numerical methods (Fan et al., 2010; Zhang et al., 2022), small-scale tests (Huali et al., 2025; Rui et al., 2024), and large-scale tests (Garrett et al., 2025). Although each method has advantages, it also has several disadvantages. Centrifuge and large-scale experiments have disadvantages based on cost and applicability. It is required to neglect or simplify some parameters to solve problems using analytical approaches. This case leads to discrepancies between analytical predictions and experimental outcomes. The numerical analyses present significant challenges, including complex mathematical modeling that requires specialized expertise and detailed soil parameters that are often difficult and expensive to obtain. Computation times can be lengthy, while boundary conditions must be precisely defined to avoid compromising results. Software costs are typically high, creating barriers to implementation for many engineers and firms. Result interpretation demands considerable experience, with misinterpretations potentially leading to serious and costly design errors. The finite element analysis method, which is classified as numerical analysis, is a good alternative to analytical and experimental methods despite having some disadvantages. In the literature, numerous studies compared finite element analyses with experimental results. The studies show that

* Corresponding author, E-mail: hkamiloglu@bayburt.edu.tr

https://doi.org/10.31462/icearc2025_ce_geo_838

finite element (FE) analysis is a highly effective method for evaluating active lateral earth pressure distribution on retaining walls (Chen et al., 2019; Fan et al., 2010; Xu et al., 2022).

In addition to conventional methods, there is an increasing number of studies analyzing retaining walls using statistical or soft computing techniques. Studies using a statistical approach usually aim to optimize parameters (Hamed et al., 2024) or to determine the effects of parameters on the result (Kamiloglu, 2023). In addition, although not used as much as others, there are also studies that aim to predict the results by establishing a relationship between independent variables and dependent variables (Lafifi et al., 2024). There are a small number of studies on lateral soil thrust estimation using soft calculation methods (Nguyen et al., 2024). It is clear that soft computing methods cannot be an alternative to traditional computing methods. However, it is also evident that some advantages can be obtained when soft computing methods are combined with complex methods such as the finite element method. Finite element analysis requires several critical competencies from a qualified expert, including the selection of appropriate calculation methods, optimization of mesh and element size, and accurate determination of material properties to be utilized in the analyses. In addition, several parameters, such as the supply of appropriate software, processor load, etc., can also make the use of the method difficult.

Hybrid applications using finite elements and soft computing methods together offer significant ease of use. In this way, users can obtain fast and reliable results on trained models without having to master the technical details of finite element analysis. This approach is not only time-efficient but also accommodates complex relationships between parameters and can provide reliable estimates for unanalyzed intermediate values. Furthermore, such hybrid models can be used with simpler hardware without needing high-performance computers or specialized software. ANN is a widely used soft computing method in lateral earth pressure estimation. However, there are many algorithms, such as Extreme Learning Machine (ELM), Random Forest Regression (RFR), and Support Vector Regression (SVR), that can be proposed as an alternative to ANN. However, there are almost no studies investigating the performance of these algorithms on a specific geotechnical problem such as horizontal soil thrust prediction.

This study is intended to compare lateral earth thrust and thrust application point estimations of four different soft computing algorithms. A T-type retaining wall supporting granular soil is considered for the active case. Lateral active earth thrust acting on the stem, vertical earth thrust acting on the heel, and thrust application points are determined as dependent variables. In the context of the study, it is aimed to estimate these dependent variables using several soft computing algorithms. Phreatic water level (PWL) (Hw), saturation ratio of the backfill above the PWL (Sr), porosity (n), internal friction angle of the backfill (ϕ), wall height (H), heel length (B), and horizontal and vertical seismic coefficient parameters (kh, kv) were determined as independent variables. A design matrix comprising lower, upper, and mean values of independent variables was created considering central composite design criteria. The design matrix was utilized as a dataset to train, test, and validate the developed algorithms. The dependent variables were determined via the finite element method by taking into account the created design matrix. Artificial Neural Networks (ANN), Extreme Learning Machines (ELM), Random Forest Regression (RFR), and Support Vector Regression (SVR) are the utilized soft computing algorithms for the estimation. Besides, the algorithms were optimized using a genetic optimization algorithm to determine optimum parameters, giving the best estimation. The comparison of the algorithms was carried out using a new data set consisting of 12 different cases, where the independent variable values were different from the data set.

2. Methods

This study aims to create AI-based algorithms predicting active lateral earth thrusts and application points of the thrusts for T-type retaining walls supporting granular backfill. The investigation was performed for planar surfaces, considering static and seismic cases. A dataset comprising a total of 273 cases was utilized by the created algorithms. Groundwater level (Hw), saturation rate of the soil layer above groundwater level (Sr), porosity (n), internal friction angle (ϕ), wall height (H), heel length (B), horizontal (kh) and vertical (kv) seismic coefficient parameters were supposed as independent variables in the dataset. Lateral earth thrust acting on the stem, vertical earth thrust acting on the heel, and application point of the thrusts were supposed to be dependent variables (Fig.1). The dependent variables were obtained with the finite element analysis method. Pseudostatic analyses were performed to consider seismic cases.

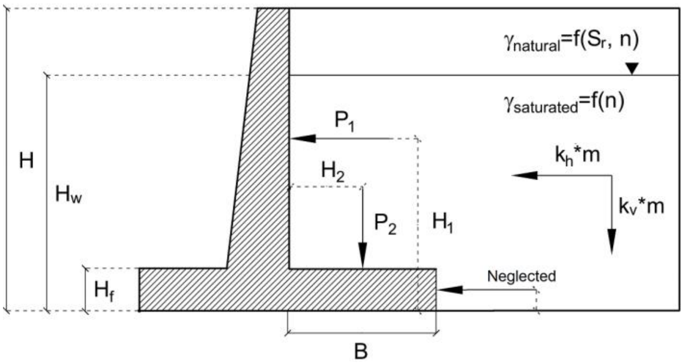

Fig. 1. Parameters considered in the created dataset

2.1. Creation of dataset

The Central Composite Design, including upper, lower points, star points, and center points of the independent variables, was employed in the creation of the dataset. The coefficient α is supposed to be 0.5 to increase data diversity. The values of independent variables used in the data set are presented in Table 1. The dataset was created by combining different values of each independent variable. As a result, a dataset comprising 273 cases was created. The dataset contains variations of the independent variables with different values (273 runs). A general view of the dataset is presented in the Appendix section.

Table 1. The upper, lower, and central values of the independent variables

Independent Variables		X_1 Hw/H	X_2 H, (m)	X_3 (B/H)	X_4 Sr	X_5 ϕ, (°)	X_6 n	X_7 kh	X_8 kv
	Coded	Actual							
Level of Factors	-1	0	3	0.1	0	28	0.15	0	0
	-0.5	0.25	4.75	0.225	0.237	32.25	0.237	0.125	0.125
	0	0.5	6.5	0.35	0.475	36.5	0.325	0.25	0.25
	+0.5	0.75	7.75	0.475	0.712	40.75	0.412	0.375	0.375
	+1	1	10	0.6	0.95	45	0.50	0.5	0.5

Dependent variables were determined with finite element analyses. Plaxis 8.6 finite element software was employed in the analyses. FE models were created considering the independent variables of the dataset. Optimum model dimensions, mesh size, and lateral translation amount to creta active state were determined with preliminary analyses. The preliminary analyses were performed for H=3 m, γ=15.4 kN/m^3, ϕ=37°, and δ/γ=R_{inter} =0.5. From the analyses, it was determined that the x and y dimensions of the model can be set as six times the wall height (H). Lateral translation leads to the occurrence of the active state, which was supposed to be 0.5% of the wall height. The optimum number and size of finite elements is 6857 elements with an average length of 60 x10^{-3} m. Parameters considered in the FE analyses are presented in Table 2.

Table 2. Parameters taken into account in the FE models.

Parameters	Backfill	Wall
Material model	Mohr-Coulomb	Linear elastic
Modulus of elasticity, (E)	40 MPa	2000 MPa
Poisson's ratio, (υ)	0.3	0.2
Dilatancy angle, (ψ)	ϕ-30 (°)	-
Saturated unit weight, (γ_{sat})	$\gamma_{unsat} = \gamma_{water} Gs(1-n) + \gamma_{water} nSr$	-
Unsaturated unit weight (γ_{unsat})	$\gamma_{sat} = \gamma_{water} Gs(1-n) + \gamma_{water} n$	24.0 (kN/m^3)
Height, (H)	–	Design matrix
Normalized heel length (B/H))	–	Design matrix
Saturation above the GWL*	Design matrix	-
Friction angle, (ϕ)	Design matrix	-
Porosity, (n)	Design matrix	-
Horizontal seismic coefficient (kh)	Design matrix	-
Vertical seismic coefficient (kv)	Design matrix	-
Normalized GWL*, (Hw/H)	Design matrix	-

The FE model was developed considering Table 2 and the independent variables given in the dataset (Appendix). As a result of plastic analyses, P_1, P_2, H_1, and H_2 parameters given in Fig. 1 were determined. Dependent variables were determined as dimensionless quantities considering the following equations.

$$y_1 = \frac{2P_1}{\gamma_{natural} H^2} \tag{1}$$

$$y_2 = \frac{2P_2}{\gamma_{natural} H^2} \tag{2}$$

$$y_3 = \frac{H_1}{H} \tag{3}$$

2.1. Soft computing methods

Within the scope of the study, it is aimed to determine the relationship between independent variables and dependent variables by soft calculation methods. At this stage, four different algorithms were determined. One of these algorithms, ANN, was chosen because it is the most widely used and most known method in geotechnical engineering. These four algorithms cover a broad spectrum of machine learning paradigms: ANNs represent neural-based learning with their multi-layer architecture; SVR leverages kernel methods and optimization theory; RFR exemplifies ensemble learning through decision trees, and ELM offers a hybrid approach with its unique random feature mapping and analytical learning.

Artificial Neural Networks (ANN), Extreme Learning Machines (ELM), Random Forest Regression (RFR), and Support Vector Regression (SVR) are the soft computing algorithms utilized for the estimation of the dependent parameters. ANN algorithms are the most widely used artificial intelligence-based prediction method in geotechnical engineering. With its ability to model the complex non-linear nature of soil behavior, simultaneously evaluate relationships between multiple soil parameters, and provide effective learning even with limited datasets, ANN is used in many studies (Thottoth et al., 2024; Yıldız et al., 2010).

Extreme Learning Machine (ELM) is a single-layer feedforward learning algorithm developed as an alternative to ANN (Hameed et al., 2024). The most distinctive feature of ELM is that input weights and hidden layer biases are randomly assigned and not updated during training; only the output weights are analytically calculated (Masood et al., 2023). This approach makes the training process of ELM much faster than ANN and eliminates the problem of getting stuck in local minima. However, it may experience stability issues due to randomly assigned weights and might not be as successful as ANN in complex problems. ELM is particularly advantageous in applications requiring fast training and low computational requirements, real-time systems, and large datasets, while traditional ANNs may perform better in complex problems requiring deep learning.

Random Forest Regression (RFR) is a robust machine learning algorithm that integrates multiple trees in the context of the ensemble learning criteria (Cutler et al., 2012). The multiple trees comprise classification and regression trees (CART), which are trained by randomly selected data. Each decision tree forming the random forest is generated in parallel, and these trees can consist of both classification trees and regression trees. The nodes in each decision tree are divided by using the best attributes that can obtain the best solution among all features. This splitting process continues until certain stopping criteria, such as maximum depth or minimum sample count, are met. In regression problems, decision trees typically use the average target variable value of samples that fall into a particular leaf node as the prediction value. One of the most important advantages of the random forest is that it can provide solutions to both classification and regression problems, which form the basis of other machine learning algorithms (Kumral et al., 2022).

Support Vector Regression (SVR), proposed by Boser et al. (1992), is an adaptation of Support Vector Machines for regression problems, creating an epsilon tube around data points while minimizing deviations outside this tube. It can be used to solve nonlinear classification, regression, and prediction problems (Kandiri et al., 2022). Unlike ANNs, which rely on interconnected neurons and backpropagation, SVR is based on convex optimization and kernel functions, generally requiring less data to achieve good results. SVR offers better interpretability than ANNs and performs efficiently on small to medium-sized datasets, showing resistance to overfitting and capturing non-linear relationships through the kernel trick. However, SVR's computational cost increases significantly with larger datasets and requires careful hyperparameter tuning. In contrast, ANNs excel with large datasets, complex relationships, and unstructured data like images and audio, though they demand more computational resources and are typically considered "black boxes" with limited interpretability.

3. Estimation of dependent variables with soft computing methods

In this part of the study, several soft computing agrorithms were developed employing Matlab R2017b software by using the dataset. A detailed explanation of the estimation methods is presented under the subheadings.

3.1. Estimation of dependent variables with ANN

The ANN network used has an input layer, hidden layers, and an output layer. The data set was divided for training, testing, and evaluation of the model. Levenberg-Marquardt (trainlm) was used as the training algorithm. The maximum number of epochs was set as 3000. An early stopping criterion was applied if the validation error did not improve for 500 epochs. The performance function is considered as Mean Squared Error (MSE). Target error, learning rate, and momentum constant criteria were set as 0.0001, 0.03, and 0.03 respectively. The performance of the trained ANN model was evaluated on training, validation, and test data sets. The metrics used for evaluation are mean absolute error (MAE), mean absolute percentage (MAPE), root mean squared error (RMSE), and regression coefficient (R^2). The workflow explaining the general structure of the implemented algorithm is presented in Fig.2.

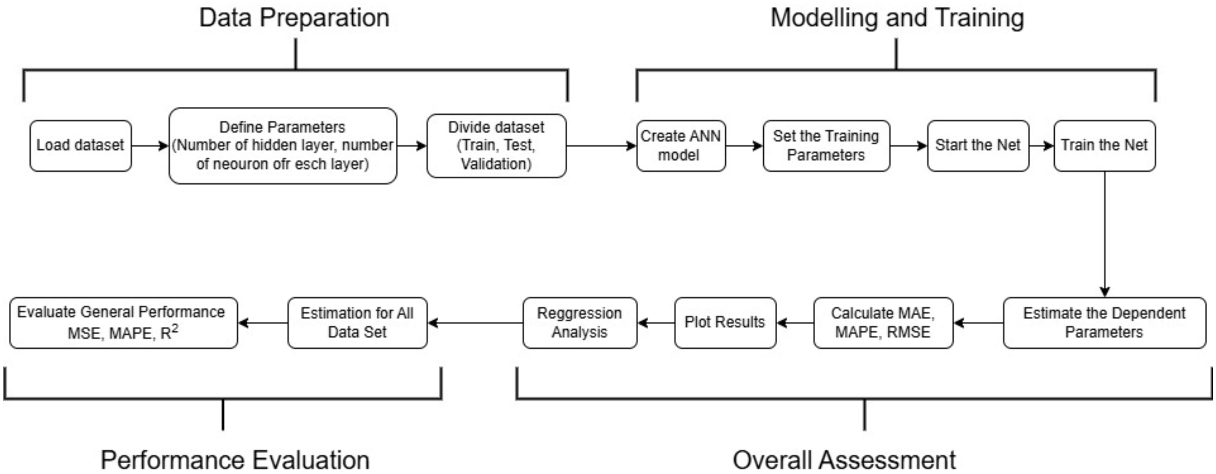

Fig. 2. Flow chart of the developed ANN algorithm

The performance of the ANNs substantially depends on parameters such as training ratio, layer number, and neuron number of each layer. It may be time-consuming and inefficient to determine the optimum values of these parameters by trial and error. Therefore, it is required to optimize the net using various optimization methods. The genetic algorithm is a powerful optimization technique that attempts to automatically find the best combination of these parameters by mimicking the process of evolution in nature. The genetic algorithm was employed to determine the optimum layer number, neuron number, and train ratio.

The optimization of artificial neural network (ANN) parameters for retaining wall analysis was conducted using a genetic algorithm (GA) approach. This MATLAB implementation employs evolutionary principles to automatically determine the optimal network architecture and training parameters. The GA operates on a population of 20 individuals across 50 generations, with each individual representing a different ANN configuration defined by a number of hidden layers (1-3), neurons per layer (5-20), and training ratio (0.6-0.9). Through iterative selection, crossover, and mutation operations, the algorithm evolves increasingly effective network configurations. The fitness evaluation function trains each candidate network using the Levenberg-Marquardt algorithm and assesses performance via a mean squared error on test data. The optimization results revealed that a network architecture with 1 hidden layer containing 6 neurons and a training ratio of 0.89 produced the best performance.

The optimized ANN model for retaining wall analysis was evaluated through multiple executions to assess its reliability and performance consistency. The code was run 10 times, each with different random initializations of network weights, to account for the stochastic nature of neural network training. For each run, key performance metrics, including mean absolute error (MAE), mean absolute percentage error (MAPE), root mean square error (RMSE), and coefficient of determination (R^2), were presented in Table 3.

Table 3. Performance metrics of the ANN algorthm

Run →	1	2	3	4	5	6	7	8	9	10	Mean	Standart Deviation
MAE	0.1456	0.09669	0.09	0.1887	0.0713	0.0843	0.1268	0.0638	0.1531	0.0859	0.1106	0.0388
MAPE	0.1065	0.0964	0.1124	0.1912	0.1269	0.1122	0.0796	0.1299	0.2124	0.132	0.13	0.0392
RMSE	0.2152	0.1205	0.1201	0.2417	0.0917	0.1049	0.296	0.0868	0.1878	0.1086	0.1573	0.0691
R^2	0.9413	0.941	0.9336	0.9199	0.939	0.9505	0.9496	0.9293	0.8654	0.9309	0.9301	0.0233

3.2. Estimation of dependent variables with ELM

In this study, an Extreme Learning Machine (ELM) approach was implemented to predict retaining wall behavior. The flow chart of the code is given in Fig. 3. The MATLAB implementation began with data preprocessing, including z-score normalization of all variables. The dataset was divided into training and testing subsets using random sampling. The ELM model utilized hidden neurons with sigmoid activation functions for optimal performance. The core advantage of ELM lies in its training approach: input weights and biases were randomly assigned. In contrast, output weights were analytically calculated using the Moore-Penrose generalized inverse, significantly reducing computational complexity. Model performance was evaluated using multiple metrics (MSE, RMSE, R^2, MAE) and visualized through scatter plots comparing predicted versus actual values. The results demonstrate that the ELM model effectively captures the complex relationships between the input parameters and the retaining wall behavior, offering a reliable and computationally efficient alternative to traditional numerical methods for engineering applications.

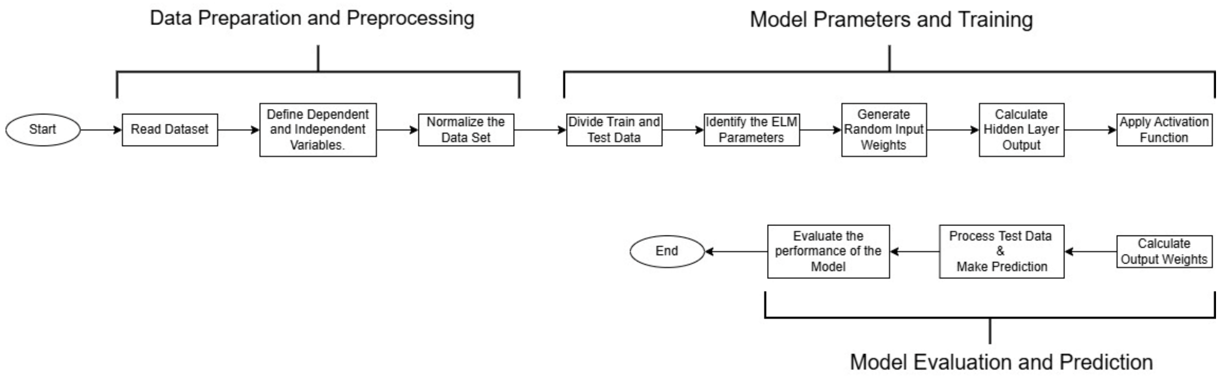

Fig. 3. Flow chart of the developed ELM algorithm

To enhance the prediction performance of the Extreme Learning Machine (ELM) model for retaining wall behavior, a genetic algorithm (GA) optimization approach was implemented to determine the optimal hyperparameters. The GA optimization considered four key parameters: the number of hidden neurons (ranging from 20 to 200), the number of hidden layers (ranging from 1 to 3), the training-testing data split ratio (ranging from 0.5-0.5 to 0.9-0.1), and the activation function type (sigmoid, sine, or radial basis). The fitness function utilized 5-fold cross-validation with the coefficient of determination (R^2) as the performance metric. After running the GA for 50 generations with a population size of 40, the optimal configuration was determined to be 127 neurons in a single hidden layer, a training-testing ratio of 0.89-0.11, and the sigmoid activation function. This optimization process significantly improved the model's predictive capability compared to the standard ELM implementation, as evidenced by enhanced performance metrics (MSE, RMSE, R^2, MAE). The optimization process effectively balanced model complexity and generalization ability while maintaining the computational efficiency that makes ELM attractive for engineering applications.

The optimized ELM model for retaining wall analysis was evaluated through multiple executions to assess its reliability and performance consistency. The code was run 10 times, each with different random initializations of network weights, to account for the stochastic nature of neural network training. For each run, key performance metrics, including Mean Square Error (MSE), Root Mean Square Error (RMSE), Mean Absolute Error (MAE), and coefficient of determination (R^2), were presented in Table 4.

Table 4. Performance metrics of the ELM algorthm

Run →	1	2	3	4	5	6	7	8	9	10	Mean	Standart Deviation
MSE	0.0703	0.0238	0.0632	0.0282	0.021	0.0451	0.0473	0.035	0.0223	0.0617	0.0418	0.0175
RMSE	0.2651	0.1544	0.2514	0.1678	0.1449	0.2123	0.2175	0.187	0.1494	0.2484	0.1998	0.0431
MAE	0.1725	0.1322	0.1385	0.1298	0.1092	0.1478	0.1695	0.1378	0.1104	0.192	0.144	0.0256
R^2	0.7416	0.9007	0.6233	0.9027	0.804	0.7747	0.7201	0.8292	0.8761	0.7888	0.7961	0.0831

3.3. Estimation of dependent variables with RFR

The provided MATLAB code implements a Random Forest Regression model to predict a dependent variable based on eight independent variables. The workflow begins by importing data and separating the features and target variables. The dataset is then randomly split into training and testing sets. The Random Forest model is trained using optimized trees with minimum leaf size while training time is measured. After training, predictions are made on the test set, and performance metrics including Mean Squared Error (MSE), Root Mean Squared Error

(RMSE), R-squared (R^2), and Mean Absolute Error (MAE) are calculated to evaluate model accuracy. Finally, the code visualizes prediction performance by plotting actual versus predicted values and displays all performance metrics along with the training duration (Fig.4).

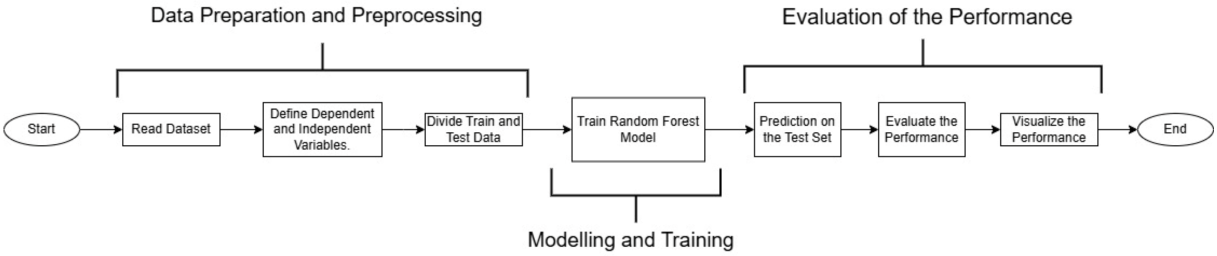

Fig. 4. Flow chart of the developed RFR algorithm

In this study, a parameter optimization approach was implemented to enhance the performance of the Random Forest Regression model for predicting retaining wall behavior. The optimization algorithm systematically explored various combinations of three critical parameters: training data ratio (ranging from 0.7 to 0.9), number of trees (from 50 to 300), and minimum leaf size (from 1 to 20). Each parameter combination was evaluated by training the model and calculating the Root Mean Square Error (RMSE) on the test dataset. The algorithm recorded all results, ranked them by RMSE, and identified the optimal parameter set that minimized prediction error. This optimization process revealed that a training ratio of 0.80, 200 trees, and a minimum leaf size of 1 yielded the best performance. These optimized parameters were subsequently incorporated into the final Random Forest Regression model, significantly improving its predictive accuracy compared to the initial configuration of 100 trees and minimum leaf size of 5. Table 5 presents the performance metrics of the optimized RFR code.

Table 5. Performance metrics of the RFR algorthm

Run →	1	2	3	4	5	6	7	8	9	10	Mean	Standart Deviation
MSE	0.0226	0.0157	0.0244	0.0253	0.0324	0.0294	0.0186	0.0336	0.0329	0.0252	0.026	0.0058
RMSE	0.1503	0.1254	0.1562	0.159	0.1801	0.1714	0.1363	0.1833	0.1815	0.1586	0.1602	0.0185
MAE	0.0835	0.0966	0.084	0.1026	0.1104	0.0984	0.0997	0.12	0.116	0.0984	0.101	0.0114
R^2	0.8771	0.9202	0.8864	0.8723	0.8467	0.8782	0.8905	0.8375	0.8677	0.8747	0.8751	0.0217

3.4. Estimation of dependent variables with SVR

The MATLAB code begins by importing data from an Excel file and separating independent variables from the dependent variable. The code then normalizes the data using z-score standardization to ensure all parameters contribute equally to the model. After dividing the dataset into training and testing portions, it constructs a Support Vector Regression (SVR) model using a Radial Basis Function kernel with epsilon=0.1 and automatic kernel scaling. The trained model predicts values for the test data, and performance is evaluated through MSE, RMSE, and R^2 metrics. Results are visualized in a scatter plot comparing actual versus predicted values. Finally, a custom function is defined for normalizing and predicting new data points, enabling quick predictions without requiring additional finite element analyses (Fig.5).

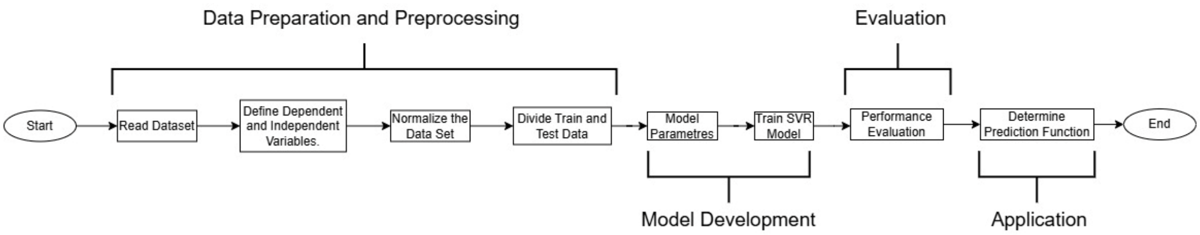

Fig. 5. Flow chart of the developed SVR algorithm

Genetic Algorithm was implemented to find the optimal hyperparameters of the estimation code for predicting retaining wall behavior. A new code was developed to optimize a Support Vector Regression (SVR) model using a Genetic Algorithm to predict retaining wall behavior from geotechnical parameters. The process involves loading and normalizing data from eight independent variables and then splitting it into training and testing sets. The code optimizes three key hyperparameters (Epsilon, Kernel Scale, and Box Constraint) through Genetic Algorithm with 5-fold cross-validation. After finding optimal values (Epsilon: 0.0049, Kernel Scale: 5.6581, Box Constraint: 10.0005), the final model is trained and evaluated, achieving excellent performance metrics (MSE: 0.0293, RMSE:

0.1712, R^2: 0.9086). This optimization significantly improves the model's ability to predict retaining wall behavior, explaining approximately 91% of the variance in the dependent variable. Table 6 presents the performance metrics of the optimized SVR code.

Table 6. Performance metrics of the RFR algorithm

Run →	1	2	3	4	5	6	7	8	9	10	Mean	Standart Deviation
MSE	0.0059	0.0273	0.0292	0.0117	0.0118	0.0268	0.0216	0.0111	0.0187	0.0232	0.0187	0.0077
RMSE	0.0765	0.1653	0.1708	0.1081	0.1084	0.1639	0.1469	0.1056	0.1368	0.1523	0.1335	0.0303
MAE	0.0474	0.0741	0.0843	0.07	0.0528	0.0822	0.0694	0.0568	0.0821	0.0663	0.0685	0.0122
R^2	0.9641	0.839	0.8565	0.9372	0.9519	0.8954	0.9092	0.9551	0.9228	0.8555	0.9087	0.0432

4. Comparison of the estimations of the algorithms

When the performance metrics obtained over the test and validation data in the networks trained within the scope of the study are examined, it is seen that the predictions are at statistically acceptable levels. In this part of the study, the predictive performance of the networks trained for a new set of independent variables with random values (Table 7), which was not used in the network training, was compared.

Table 7. Independent variables used for comparion of the algorithms.

Runs	X1 (Hw/H)	X2 (H)	X3 (B/H)	X4 (Sr)	X5 (ϕ)	X6 (n)	X7 (kh)	X8 (kv)
1	0.44	10	0.59	0.16	45	0.37	0.03	0.1
2	0.47	7	0.23	0.56	44	0.33	0.19	0.23
3	0.88	9	0.22	0.8	35	0.15	0.31	0.46
4	0.01	6	0.47	0.13	30	0.23	0.39	0.47
5	0.88	8	0.25	0.5	32	0.21	0.23	0.17
6	0.54	3	0.19	0.03	40	0.24	0.1	0.27
7	0.81	5	0.32	0.81	31	0.36	0.2	0.27
8	0.4	10	0.4	0.39	44	0.26	0.43	0.06
9	0.71	9	0.6	0	42	0.34	0.4	0.14
10	0.18	7	0.28	0.6	45	0.19	0.16	0.17
11	0.3	3	0.16	0.56	42	0.28	0.08	0.28

Fig.6 presents the comparison estimation power of the algorithms considering the new cases. The estimations of the algorithms were compared with FE analysis results. The dependent variables to be estimated by the algorithms were determined as lateral active soil thrust coefficient ($P_1/\gamma H^2$), vertical soil thrust coefficient ($P_2/\gamma H^2$), and the application point coefficient of lateral soil thrust (H_1/H). Since the application point of the vertical soil thrust to the wall heel is approximately half of the wall heel length, this dependent variable was not considered in the comparisons. The algorithms were run 10 times, and the means and standard deviations of the results were determined. The mean values were compared with the results of the finite element analyses. The horizontal active earth thrust acting on the stem of the wall, the vertical load acting on the wall heel, and the point of application of the horizontal thrust were considered dimensionless variables. Regression analyses were performed on the graphs obtained. In addition, the uncertainty values in the predictions are expressed by error bars.

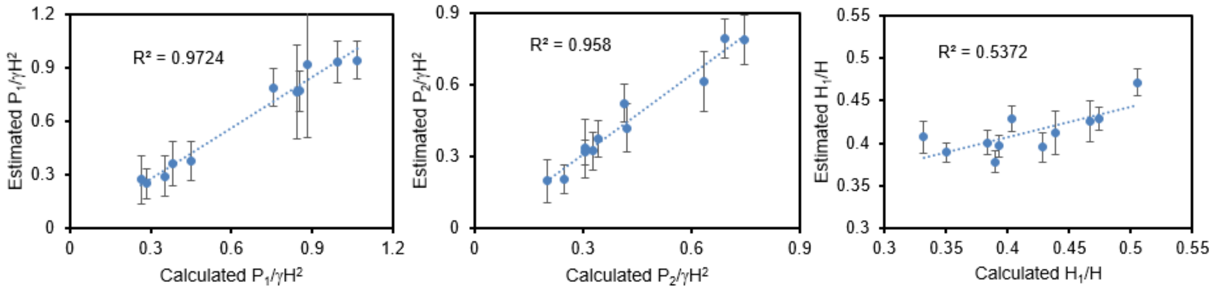

(a) (b) (c)

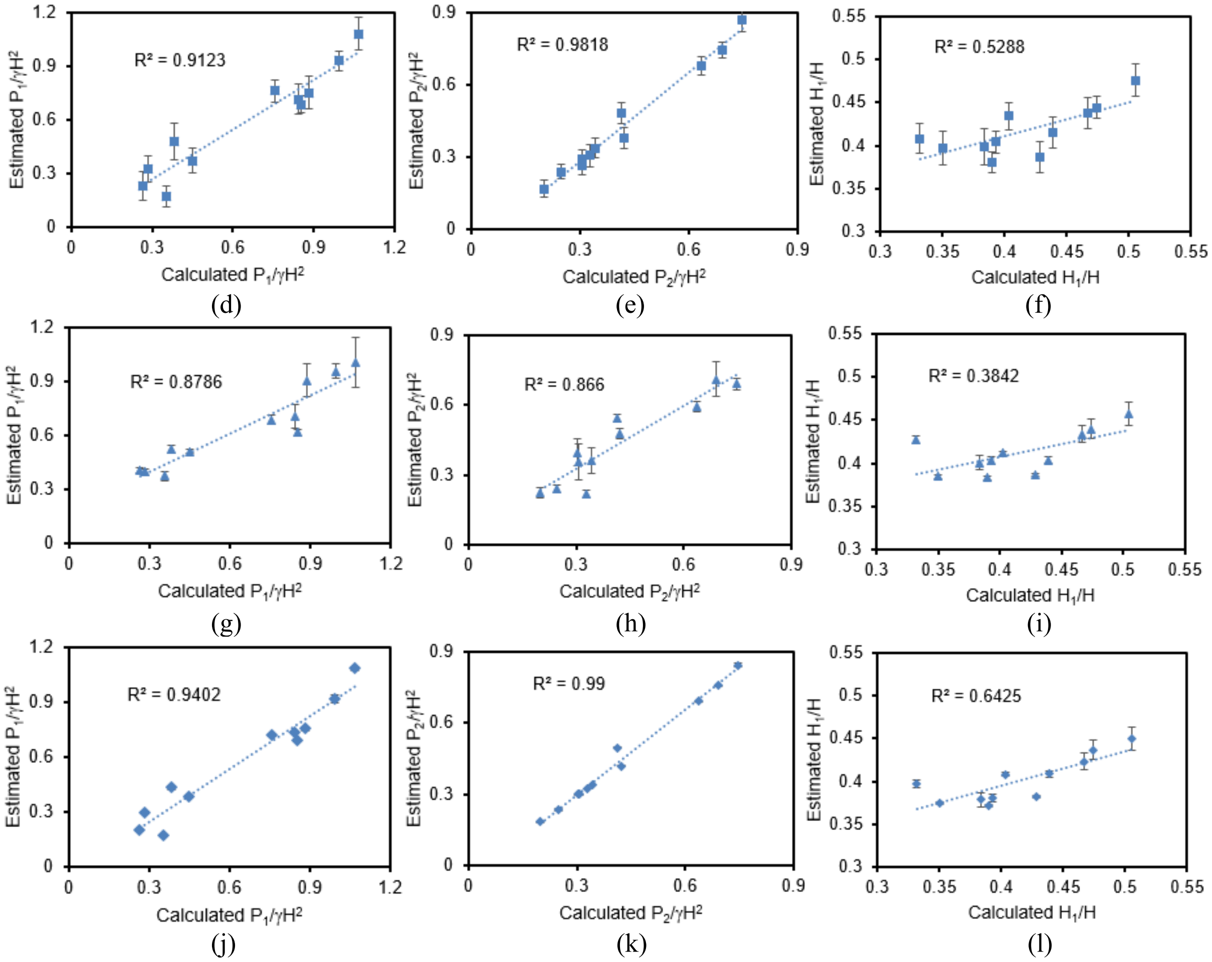

Fig. 6. Comparison of estimated dependent variable value fo the alorithms with FE analyses results
(a) Comparison of P_1 coefficient vith ANN approach, (b) Comparison of P_2 coefficient vith ANN approach,
(c) Comparison of H_1 coefficient vith ANN approach, (d) Comparison of P_1 coefficient vith ELM approach,
(e) Comparison of P_2 coefficient vith ELM approach, (f) Comparison of H_1 coefficient vith ELM approach,
(g) Comparison of P_1 coefficient vith RFR approach, (h) Comparison of P_2 coefficient vith RFR approach,
(i) Comparison of H_1 coefficient vith RFR approach, (j) Comparison of P_1 coefficient vith SVR approach,
(k) Comparison of P_2 coefficient vith SVR approach, (l) Comparison of H_1 coefficient vith SVR approach

Fig. 6a-6c compares estimations of the ANN algorithm with FE analysis results. The regression coefficients of the horizontal active thrust coefficient acting on the wall (Fig. 6a) and the horizontal thrust coefficient acting on the wall (Fig.6b) foundation are high values of approximately 91% and 98%. The regression coefficients of the horizontal active thrust coefficient acting on the wall (Fig. 6a) and the horizontal thrust coefficient acting on the wall heel (Fig. 6b) are approximately 91% and 98%, respectively. This high R^2 value indicates a strong linear relationship between the calculated and predicted values, which are approximately 91% and 98%, respectively. As a result of the examination of Fig. 6c, it is seen that the calculated and estimated coefficient values are between 0.35 and 0.5. However, although the estimated and calculated values are close to each other, the agreement is insufficient. Especially in Figures 6a and 6b, it can be seen that the magnitudes of the error bars showing the uncertainties are quite high.

In Figures 6d-6f, the prediction power of the ELM algorithm is compared with the finite element analysis results, and similar results are obtained with the ANN algorithm. In Figures 6d and 6e, the regression coefficients of the horizontal and vertical earth thrust coefficients were determined as 0.91 and 0.98. This value shows that the ELM algorithm has a very high prediction power. However, as can be seen from the R^2=0.58 value given in Figure 6f, the prediction of the point of impact of the earth thrust on the wall is not reliable. Compared to the error bars in the predictions made with the ANN algorithm, it is seen that the predictions made with the ELM algorithm give results in lower ranges.

Fig.6g-6i presents a comparison of estimation results of RFR algorithms with FE results. Although at lower levels than the ANN and ELM algorithms, the lateral and vertical soil coefficient estimates of the RFR algorithm are significant (R^2=0.87 and R^2=0.86). Fig. 6i shows that although there is no significant difference between the predicted and calculated values, the R^2 value of 0.3842 indicates that the relationship between the predicted and calculated values is weak. In addition, it is seen from the error bars that the prediction uncertainty is lower in this application compared to the ANN algorithm.

Fig.6j-6l shows the relation between the FE analysis result and the estimation of the SVR algorithm. Relatively high regression coefficients for lateral earth thrust and vertical earth thrust coefficient estimations were determined with R^2=0.94 and R^2=0.99 respectively. Although the predictions made for the H_1/H value are not considered to be sufficiently compatible with the finite element solution, they are higher than the other algorithms (R^2=0.64). In addition, the fact that the t-bars showing the estimation variances are almost negligible indicates that the standard deviation of the estimations is very small.

5. Conclusions

This study aims to compare four different soft computing algorithms (ANN, ELM, RFR, and SVR) for estimating active erath thrust and vertical earth thrust acting on the stem and heel of the T-type retaining wall respectively. In addition, the application point of the active alteral earth thrust was also tried to be estimated within the relevant algorithms. Within the scope of the study, the data set was prepared with a central composite design. Groundwater level (Hw), saturation rate of the soil layer above groundwater level (Sr), porosity (n), internal friction angle (□), wall height (H), heel length (B), horizontal (kh) and vertical (kv) seismic coefficient parameters were supposed as independent variables in the dataset. Lateral earth thrust acting on the stem, vertical earth thrust acting on the heel, and application point of the thrusts were supposed as dependent variables. The data set comprises 273 cases, which are various values of independent variables. The dependent variables in the data set were obtained by analyzing each case using the FE method. Training was done with different algorithms using the data set and the prediction capacities of these algorithms were compared using new independent variable sets. Based on the comprehensive analysis, the following conclusions can be drawn:

- All four soft computing algorithms demonstrated high accuracy in predicting lateral active soil thrust coefficients ($P_1/\gamma H^2$) and vertical soil thrust coefficients ($P_2/\gamma H^2$), with regression coefficients ranging from 0.86 to 0.99 when tested against FE analysis results.
- The SVR algorithm exhibited superior performance overall, achieving the highest regression coefficients for lateral earth thrust (R^2=0.94) and vertical earth thrust (R^2=0.99) predictions, while also showing the most consistent prediction capability with minimal variance across multiple runs.
- All algorithms struggled with accurately predicting the application point coefficient (H_1/H), with SVR performing relatively better (R^2=0.64) than the other methods (ANN: R^2=0.42, ELM: R^2=0.58, RFR: R^2=0.38).
- The ELM algorithm provided comparable accuracy to ANN for thrust coefficient predictions but with significantly reduced computational complexity and training time, making it a viable alternative for practical applications.
- The RFR algorithm, while showing slightly lower accuracy than the other methods, demonstrated good stability with consistent predictions across multiple runs.
- The genetic algorithm optimization significantly improved the performance of all four soft computing methods by identifying optimal hyperparameters, particularly for the SVR and ANN models.

References

Boser, B.E., Guyon, I.M., & Vapnik, V.N. (1992). A training algorithm for optimal margin classifiers. *COLT '92: Proceedings of the Fifth Annual Workshop on Computational Learning Theory*, 144–152.

Chen, F.-Q., Chen, H.-B., Wu, Y.-X., Zhang, D.-B., & Lin, Y.-J. (2023). Numerical and analytical study on active earth pressure against inverted T-type retaining walls rotating about the base. *Acta Geotechnica*, *18*, 2195–2216. doi: https://doi.org/10.1007/s11440-022-01723-1

Chen, F., Lin, Y., & Li, D. (2019). Solution to active earth pressure of narrow cohesionless backfill against rigid retaining walls under translation mode. *Soils and Foundations*, *59*(1), 151–161. doi: 10.1016/j.sandf.2018.09.010

Chen, H.-B., Shao, X.-Y., Han, L., Li, M.-G., Chen, F.-Q., & Xie, X.-L. (2025). A comprehensive prediction of stability against cantilever retaining walls using finite element limit analysis and neural networks model. *KSCE Journal of Civil Engineering*, 100200. doi: 10.1016/j.kscej.2025.100200

Cutler, A., Cutler, D. R., & Stevens, J. R. (2012). Random Forests. In Ensemble Machine Learning Methods and Applications (pp. 157–175).

Fan, C.-C., & Fang, Y.-S. (2010). Numerical solution of active earth pressures on rigid retaining walls built near rock faces. *Computers and Geotechnics*, *37*(7–8), 1023–1029. doi: 10.1016/j.compgeo.2010.08.004

Garrett, S. R., & Vahedifard, F. (2025). Full-scale testing of lateral pressures in an expansive clay upon infiltration. *Journal of Materials in Civil Engineering*, *37*(2). doi: 10.1061/JMCEE7.MTENG-17506

Greco, V.R. (2001). Active earth thrust on cantilever walls with short heel. *Canadian Geotechnical Journal*, *38*(2),

401–409.
Greco, Venanzio R. (2008). Analytical active earth thrust on cantilever walls with short heel. *Canadian Geotechnical Journal*, *45*, 1649–1658. doi: 10.1139/T08-078
Hamed, E., & Demiröz, A. (2024). Optimization of geotechnical characteristics of clayey soils using fly ash and granulated blast furnace slag-based geopolymer. *Construction and Building Materials*, *441*, 137488. doi: 10.1016/j.conbuildmat.2024.137488
Hameed, M. M., Masood, A., Srivastava, A., Abd Rahman, N., Mohd Razali, S. F., Salem, A., & Elbeltagi, A. (2024). Investigating a hybrid extreme learning machine coupled with Dingo Optimization Algorithm for modeling liquefaction triggering in sand-silt mixtures. *Scientific Reports*, *14*(1), 10799. doi: 10.1038/s41598-024-61059-6
Huali, P., Akbar, M., Arshid, M. U., Bin Mazhar, Z., Guoqiang, O., Alshammari, T. O., & Yosri, A. M. (2025). Seismic resilience of geogrid reinforced concrete earth-retaining wall of various incremental panels based on physical and numerical modelling. *Structures*, *71*, 107901. doi: 10.1016/j.istruc.2024.107901
Kamiloglu, H. A. (2023). New RSM-FEM–Based active lateral Earth Thrust Coefficient Determination Method for Inverted T-Type Cantilever Retaining Walls Supporting Narrow Granular Backfill. *International Journal of Geomechanics*, *23*(11). doi: https://doi.org/10.1061/IJGNAI.GMENG-8402
Kandiri, A., Shakor, P., Kurda, R., & Deifalla, A. F. (2022). Modified Artificial Neural Networks and Support Vector Regression to predict lateral pressure exerted by fresh concrete on formwork. *International Journal of Concrete Structures and Materials*, *16*(1), 64. doi: 10.1186/s40069-022-00554-4
Kumral, C. D., Toplal, A., Ersoy, M., Çolak, R., & Yiğit, T. (2022). Random Forest Algoritmasının FPGA üzerinde gerçekleştirilerek performans analizinin yapılması. *El-Cezeri Fen ve Mühendislik Dergisi*. doi: 10.31202/ecjse.1134799
Lafifi, B., Hamrouni, A., Khoualdia, T., Gheris, A., & Rouaiguia, A. (2024). Prediction and optimization of the bearing capacity of strip footing resting on soft soil improved with stone columns using RSM, ANN, and multi-objective GA. *Innovative Infrastructure Solutions*, *9*(5), 146. doi: 10.1007/s41062-024-01452-2
Lin, Z., Jiang, Y., Xiong, Y., Xu, C., Guo, Y., Wang, C., & Fang, T. (2024). Analytical solution for displacement-dependent active earth pressure considering the stiffness of cantilever retaining structure in cohesionless soil. *Computers and Geotechnics*, *170*, 106258. doi: 10.1016/j.compgeo.2024.106258
Masood, A., Niazkar, M., Zakwan, M., & Piraei, R. (2023). A Machine Learning-Based Framework for Water Quality Index Estimation in the Southern Bug River. *Water*, *15*(20), 3543. doi: 10.3390/w15203543
Nguyen, T., Shiau, J., & Ly, D.-K. (2024). Enhanced earth pressure determination with negative wall-soil friction using soft computing. *Computers and Geotechnics*, *167*, 106086. doi: https://doi.org/10.1016/j.compgeo.2024.106086
Rui, R., Xia, R., Han, J., Ye, Y., Miao, X., & Elabd, M. (2024). Experimental investigations of lateral earth pressures behind rigid retaining walls under different displacement modes. *Acta Geotechnica*, *19*(5), 2545–2562. doi: 10.1007/s11440-023-02068-z
Thottoth, S. R., & Khatri, V. N. (2024). Analytical and ANN-based models for assessment of hunchback retaining walls: Investigating lateral earth pressure in unsaturated backfill. *Geomechanics and Engineering*, *38*(3), 285–305. doi: https://doi.org/10.12989/gae.2024.38.3.285
Xu, L., Chen, H., Chen, F., Lin, Y., & Lin, C. (2022). An experimental study of the active failure mechanism of narrow backfills installed behind rigid retaining walls conducted using Geo-PIV. *Acta Geotechnica*. doi: https://doi.org/10.1007/s11440-021-01438-9(0123456789().,-volV)(0123456789(). ,- volV)
Yıldız, E., Özyazıcıoğlu, M. H., & Özkan, M. Y. (2010). Lateral pressures on rigid retaining walls: a neural network approach. *Gazi University Journal of Science*, *23*(3), 201–210.
Zhang, Y.-B., Chen, F.-Q., Lin, Y.-J., & Chen, H.-B. (2022). Active Earth Pressure of Narrow Backfill against Inverted T-Type Retaining Walls Rotating about the Heel. *KSCE Journal of Civil Engineering*, *26*(4), 1723–1739. doi: 10.1007/s12205-022-1294-8.

Appendix. Data set used by the soft computing algorithms

	Independent Variables								Dependent Variables		
Runs	X_1	X_2	X_3	X_4	X_5	X_6	X_7	X_8	Y_1	Y_2	Y_3
1	0	3	0.1	0	28	0.15	0	0	0.2897	0.09	0.36
2	1	3	0.1	0	28	0.15	0	0	0.5507	0.09	0.39
3	0	10	0.1	0	28	0.15	0	0	0.2959	0.10	0.39
4	1	10	0.1	0	28	0.15	0	0	0.5541	0.10	0.39
5	0	3	0.6	0	28	0.15	0	0	0.2698	0.54	0.41
6	1	3	0.6	0	28	0.15	0	0	0.5334	0.58	0.41
7	0	10	0.6	0	28	0.15	0	0	0.2964	0.53	0.42
8	1	10	0.6	0	28	0.15	0	0	0.5511	0.58	0.41
9	0	3	0.1	0.95	28	0.15	0	0	0.2895	0.09	0.36
10	1	3	0.1	0.95	28	0.15	0	0	0.517	0.09	0.39
11	0	10	0.1	0.95	28	0.15	0	0	0.2882	0.10	0.38
12	1	10	0.1	0.95	28	0.15	0	0	0.5189	0.10	0.39
13	0	3	0.6	0.95	28	0.15	0	0	0.2665	0.54	0.42
14	1	3	0.6	0.95	28	0.15	0	0	0.4998	0.54	0.41
15	0	10	0.6	0.95	28	0.15	0	0	0.2943	0.54	0.42
16	1	10	0.6	0.95	28	0.15	0	0	0.5199	0.54	0.41
17	0	3	0.1	0	45	0.15	0	0	0.1373	0.08	0.43
18	1	3	0.1	0	45	0.15	0	0	0.4495	0.09	0.40
19	0	10	0.1	0	45	0.15	0	0	0.1471	0.10	0.41
20	1	10	0.1	0	45	0.15	0	0	0.459	0.10	0.40
21	0	3	0.6	0	45	0.15	0	0	0.1233	0.54	0.51
22	1	3	0.6	0	45	0.15	0	0	0.45	0.58	0.42
23	0	10	0.6	0	45	0.15	0	0	0.1606	0.55	0.43
24	1	10	0.6	0	45	0.15	0	0	0.4657	0.58	0.41
25	0	3	0.1	0.95	45	0.15	0	0	0.1359	0.08	0.43
26	1	3	0.1	0.95	45	0.15	0	0	0.4228	0.08	0.40
27	0	10	0.1	0.95	45	0.15	0	0	0.1466	0.10	0.42
28	1	10	0.1	0.95	45	0.15	0	0	0.4322	0.09	0.40
29	0	3	0.6	0.95	45	0.15	0	0	0.1178	0.54	0.51
30	1	3	0.6	0.95	45	0.15	0	0	0.4204	0.54	0.42
31	0	10	0.6	0.95	45	0.15	0	0	0.1601	0.55	0.43
32	1	10	0.6	0.95	45	0.15	0	0	0.4398	0.55	0.41
33	0	3	0.1	0	28	0.5	0	0	0.3005	0.09	0.35
34	1	3	0.1	0	28	0.5	0	0	0.8008	0.12	0.39
35	0	10	0.1	0	28	0.5	0	0	0.3052	0.10	0.38
36	1	10	0.1	0	28	0.5	0	0	0.8124	0.13	0.39
37	0	3	0.6	0	28	0.5	0	0	0.2668	0.54	0.42
38	1	3	0.6	0	28	0.5	0	0	0.778	0.73	0.40
39	0	10	0.6	0	28	0.5	0	0	0.2996	0.47	0.42
40	1	10	0.6	0	28	0.5	0	0	0.8074	0.74	0.41
41	0	3	0.1	0.95	28	0.5	0	0	0.299	0.09	0.36
42	1	3	0.1	0.95	28	0.5	0	0	0.5882	0.09	0.39
43	0	10	0.1	0.95	28	0.5	0	0	0.295	0.10	0.37
44	1	10	0.1	0.95	28	0.5	0	0	0.5983	0.10	0.39
45	0	3	0.6	0.95	28	0.5	0	0	0.2637	0.54	0.41
46	1	3	0.6	0.95	28	0.5	0	0	0.572	0.54	0.40
47	0	10	0.6	0.95	28	0.5	0	0	0.298	0.54	0.42
48	1	10	0.6	0.95	28	0.5	0	0	0.5933	0.54	0.40
49	0	3	0.1	0	45	0.5	0	0	0.1327	0.07	0.39
50	1	3	0.1	0	45	0.5	0	0	0.7013	0.11	0.39
51	0	10	0.1	0	45	0.5	0	0	0.1511	0.10	0.41
52	1	10	0.1	0	45	0.5	0	0	0.7158	0.13	0.40
53	0	3	0.6	0	45	0.5	0	0	0.1308	0.55	0.49
54	1	3	0.6	0	45	0.5	0	0	0.6942	0.74	0.41
55	0	10	0.6	0	45	0.5	0	0	0.16	0.55	0.43
56	1	10	0.6	0	45	0.5	0	0	0.7257	0.75	0.41
57	0	3	0.1	0.95	45	0.5	0	0	0.1432	0.08	0.42
58	1	3	0.1	0.95	45	0.5	0	0	0.5158	0.08	0.39
59	0	10	0.1	0.95	45	0.5	0	0	0.1499	0.10	0.41
60	1	10	0.1	0.95	45	0.5	0	0	0.5262	0.10	0.40
61	0	3	0.6	0.95	45	0.5	0	0	0.1266	0.55	0.49
62	1	3	0.6	0.95	45	0.5	0	0	0.5111	0.54	0.41
63	0	10	0.6	0.95	45	0.5	0	0	0.1606	0.55	0.44
64	1	10	0.6	0.95	45	0.5	0	0	0.534	0.55	0.41
65	0	3	0.1	0	28	0.15	0.5	0	1.1544	0.14	0.52
66	1	3	0.1	0	28	0.15	0.5	0	1.262	0.10	0.48
67	0	10	0.1	0	28	0.15	0.5	0	0.8487	0.15	0.48
68	1	10	0.1	0	28	0.15	0.5	0	0.9946	0.10	0.47
69	0	3	0.6	0	28	0.15	0.5	0	1.3102	0.66	0.50
70	1	3	0.6	0	28	0.15	0.5	0	1.2133	0.63	0.49
71	0	10	0.6	0	28	0.15	0.5	0	0.9403	0.64	0.49
72	1	10	0.6	0	28	0.15	0.5	0	0.9765	0.60	0.48
73	0	3	0.1	0.95	28	0.15	0.5	0	1.1336	0.14	0.52
74	1	3	0.1	0.95	28	0.15	0.5	0	1.1937	0.10	0.48
75	0	10	0.1	0.95	28	0.15	0.5	0	0.8844	0.15	0.49
76	1	10	0.1	0.95	28	0.15	0.5	0	0.9354	0.09	0.47
77	0	3	0.6	0.95	28	0.15	0.5	0	1.3091	0.66	0.51
78	1	3	0.6	0.95	28	0.15	0.5	0	1.1407	0.59	0.49
79	0	10	0.6	0.95	28	0.15	0.5	0	0.9439	0.65	0.49
80	1	10	0.6	0.95	28	0.15	0.5	0	0.9184	0.57	0.48
81	0	3	0.1	0	45	0.15	0.5	0	0.553	0.20	0.52
82	1	3	0.1	0	45	0.15	0.5	0	1.4561	0.09	0.56
83	0	10	0.1	0	45	0.15	0.5	0	0.5568	0.16	0.56

84	1	10	0.1	0	45	0.15	0.5	0	1.1664	0.13	0.51
85	0	3	0.6	0	45	0.15	0.5	0	0.8376	0.68	0.50
86	1	3	0.6	0	45	0.15	0.5	0	1.7479	0.59	0.52
87	0	10	0.6	0	45	0.15	0.5	0	0.8134	0.65	0.49
88	1	10	0.6	0	45	0.15	0.5	0	1.2749	0.63	0.51
89	0	3	0.1	0.95	45	0.15	0.5	0	0.5499	0.18	0.53
90	1	3	0.1	0.95	45	0.15	0.5	0	1.365	0.09	0.56
91	0	10	0.1	0.95	45	0.15	0.5	0	0.5625	0.15	0.56
92	1	10	0.1	0.95	45	0.15	0.5	0	1.0969	0.13	0.51
93	0	3	0.6	0.95	45	0.15	0.5	0	0.8388	0.68	0.50
94	1	3	0.6	0.95	45	0.15	0.5	0	1.6425	0.56	0.52
95	0	10	0.6	0.95	45	0.15	0.5	0	0.8162	0.66	0.50
96	1	10	0.6	0.95	45	0.15	0.5	0	1.199	0.59	0.50
97	0	3	0.1	0	28	0.5	0.5	0	1.1429	0.15	0.51
98	1	3	0.1	0	28	0.5	0.5	0	1.5187	0.13	0.47
99	0	10	0.1	0	28	0.5	0.5	0	0.879	0.18	0.45
100	1	10	0.1	0	28	0.5	0.5	0	1.2584	0.13	0.46
101	0	3	0.6	0	28	0.5	0.5	0	1.3274	0.68	0.50
102	1	3	0.6	0	28	0.5	0.5	0	1.4729	0.80	0.47
103	0	10	0.6	0	28	0.5	0.5	0	0.9528	0.66	0.49
104	1	10	0.6	0	28	0.5	0.5	0	1.2275	0.77	0.46
105	0	3	0.1	0.95	28	0.5	0.5	0	1.1298	0.14	0.52
106	1	3	0.1	0.95	28	0.5	0.5	0	1.1168	0.10	0.47
107	0	10	0.1	0.95	28	0.5	0.5	0	0.8697	0.11	0.51
108	1	10	0.1	0.95	28	0.5	0.5	0	0.926	0.09	0.46
109	0	3	0.6	0.95	28	0.5	0.5	0	1.3276	0.67	0.50
110	1	3	0.6	0.95	28	0.5	0.5	0	1.0838	0.59	0.47
111	0	10	0.6	0.95	28	0.5	0.5	0	0.9471	0.64	0.49
112	1	10	0.6	0.95	28	0.5	0.5	0	0.9043	0.58	0.46
113	0	3	0.1	0	45	0.5	0.5	0	0.5603	0.23	0.47
114	1	3	0.1	0	45	0.5	0.5	0	2.1819	0.14	0.51
115	0	10	0.1	0	45	0.5	0.5	0	0.5938	0.19	0.53
116	1	10	0.1	0	45	0.5	0.5	0	1.5988	0.13	0.49
117	0	3	0.6	0	45	0.5	0.5	0	0.8476	0.71	0.48
118	1	3	0.6	0	45	0.5	0.5	0	0.8429	0.70	0.48
119	0	10	0.6	0	45	0.5	0.5	0	0.7853	0.67	0.47
120	1	10	0.6	0	45	0.5	0.5	0	1.5834	0.81	0.49
121	0	3	0.1	0.95	45	0.5	0.5	0	0.5376	0.20	0.50
122	1	3	0.1	0.95	45	0.5	0.5	0	1.6058	0.10	0.51
123	0	10	0.1	0.95	45	0.5	0.5	0	0.7569	0.11	0.52
124	1	10	0.1	0.95	45	0.5	0.5	0	0.8318	0.08	0.46
125	0	3	0.6	0.95	45	0.5	0.5	0	0.843	0.69	0.49
126	1	3	0.6	0.95	45	0.5	0.5	0	1.4925	0.63	0.51
127	0	10	0.6	0.95	45	0.5	0.5	0	0.813	0.55	0.51
128	1	10	0.6	0.95	45	0.5	0.5	0	0.8143	0.51	0.46
129	0	3	0.1	0	28	0.15	0	0.5	0.4269	0.14	0.37
130	1	3	0.1	0	28	0.15	0	0.5	0.8201	0.14	0.39
131	0	10	0.1	0	28	0.15	0	0.5	0.4265	0.14	0.39
132	1	10	0.1	0	28	0.15	0	0.5	0.8162	0.15	0.39
133	0	3	0.6	0	28	0.15	0	0.5	0.4013	0.82	0.41
134	1	3	0.6	0	28	0.15	0	0.5	0.792	0.87	0.40
135	0	10	0.6	0	28	0.15	0	0.5	0.197	0.81	0.60
136	1	10	0.6	0	28	0.15	0	0.5	0.824	0.86	0.41
137	0	3	0.1	0.95	28	0.15	0	0.5	0.4185	0.14	0.36
138	1	3	0.1	0.95	28	0.15	0	0.5	0.7706	0.13	0.39
139	0	10	0.1	0.95	28	0.15	0	0.5	0.4292	0.14	0.39
140	1	10	0.1	0.95	28	0.15	0	0.5	0.7685	0.14	0.39
141	0	3	0.6	0.95	28	0.15	0	0.5	0.3911	0.82	0.42
142	1	3	0.6	0.95	28	0.15	0	0.5	0.7421	0.82	0.40
143	0	10	0.6	0.95	28	0.15	0	0.5	0.4284	0.81	0.41
144	1	10	0.6	0.95	28	0.15	0	0.5	0.775	0.81	0.41
145	0	3	0.1	0	45	0.15	0	0.5	0.1938	0.13	0.43
146	1	3	0.1	0	45	0.15	0	0.5	0.6778	0.14	0.40
147	0	10	0.1	0	45	0.15	0	0.5	0.2154	0.15	0.41
148	1	10	0.1	0	45	0.15	0	0.5	0.6871	0.15	0.40
149	0	3	0.6	0	45	0.15	0	0.5	0.1723	0.82	0.49
150	1	3	0.6	0	45	0.15	0	0.5	0.6611	0.87	0.42
151	0	10	0.6	0	45	0.15	0	0.5	0.2403	0.82	0.43
152	1	10	0.6	0	45	0.15	0	0.5	0.6949	0.87	0.41
153	0	3	0.1	0.95	45	0.15	0	0.5	0.1925	0.13	0.44
154	1	3	0.1	0.95	45	0.15	0	0.5	0.6388	0.13	0.41
155	0	10	0.1	0.95	45	0.15	0	0.5	0.2132	0.15	0.41
156	1	10	0.1	0.95	45	0.15	0	0.5	0.6462	0.14	0.40
157	0	3	0.6	0.95	45	0.15	0	0.5	0.1681	0.83	0.48
158	1	3	0.6	0.95	45	0.15	0	0.5	0.6267	0.82	0.42
159	0	10	0.6	0.95	45	0.15	0	0.5	0.2332	0.82	0.42
160	1	10	0.6	0.95	45	0.15	0	0.5	0.6535	0.83	0.41
161	0	3	0.1	0	28	0.5	0	0.5	0.4412	0.13	0.36
162	1	3	0.1	0	28	0.5	0	0.5	1.2081	0.18	0.39
163	0	10	0.1	0	28	0.5	0	0.5	0.4397	0.15	0.37
164	1	10	0.1	0	28	0.5	0	0.5	1.2076	0.19	0.39
165	0	3	0.6	0	28	0.5	0	0.5	0.4005	0.81	0.42
166	1	3	0.6	0	28	0.5	0	0.5	1.1716	1.11	0.40
167	0	10	0.6	0	28	0.5	0	0.5	0.4439	0.80	0.42
168	1	10	0.6	0	28	0.5	0	0.5	1.2068	1.13	0.40
169	0	3	0.1	0.95	28	0.5	0	0.5	0.429	0.13	0.36

170	1	3	0.1	0.95	28	0.5	0	0.5	0.8889	0.14	0.39
171	0	10	0.1	0.95	28	0.5	0	0.5	0.4306	0.14	0.38
172	1	10	0.1	0.95	28	0.5	0	0.5	0.8881	0.14	0.39
173	0	3	0.6	0.95	28	0.5	0	0.5	0.3969	0.82	0.41
174	1	3	0.6	0.95	28	0.5	0	0.5	0.8596	0.82	0.40
175	0	10	0.6	0.95	28	0.5	0	0.5	0.4353	0.81	0.41
176	1	10	0.6	0.95	28	0.5	0	0.5	0.8866	0.83	0.40
177	0	3	0.1	0	45	0.5	0	0.5	0.2098	0.12	0.42
178	1	3	0.1	0	45	0.5	0	0.5	1.0566	0.17	0.40
179	0	10	0.1	0	45	0.5	0	0.5	0.2275	0.15	0.42
180	1	10	0.1	0	45	0.5	0	0.5	1.071	0.19	0.40
181	0	3	0.6	0	45	0.5	0	0.5	0.1703	0.83	0.49
182	1	3	0.6	0	45	0.5	0	0.5	1.0481	1.12	0.41
183	0	10	0.6	0	45	0.5	0	0.5	0.2371	0.83	0.43
184	1	10	0.6	0	45	0.5	0	0.5	1.0791	1.14	0.40
185	0	3	0.1	0.95	45	0.5	0	0.5	0.2026	0.13	0.42
186	1	3	0.1	0.95	45	0.5	0	0.5	0.7777	0.12	0.40
187	0	10	0.1	0.95	45	0.5	0	0.5	0.2222	0.15	0.42
188	1	10	0.1	0.95	45	0.5	0	0.5	0.7874	0.14	0.40
189	0	3	0.6	0.95	45	0.5	0	0.5	0.1855	0.81	0.50
190	1	3	0.6	0.95	45	0.5	0	0.5	0.7759	0.83	0.41
191	0	10	0.6	0.95	45	0.5	0	0.5	0.2398	0.83	0.43
192	1	10	0.6	0.95	45	0.5	0	0.5	0.794	0.83	0.40
193	0	3	0.1	0	28	0.15	0.5	0.5	0.909	0.22	0.46
194	1	3	0.1	0	28	0.15	0.5	0.5	1.7975	0.14	0.47
195	0	10	0.1	0	28	0.15	0.5	0.5	0.9132	0.19	0.47
196	1	10	0.1	0	28	0.15	0.5	0.5	1.4195	0.13	0.46
197	0	3	0.6	0	28	0.15	0.5	0.5	1.084	0.92	0.46
198	1	3	0.6	0	28	0.15	0.5	0.5	1.6951	0.87	0.48
199	0	10	0.6	0	28	0.15	0.5	0.5	0.9946	0.90	0.46
200	1	10	0.6	0	28	0.15	0.5	0.5	1.3924	0.86	0.47
201	0	3	0.1	0.95	28	0.15	0.5	0.5	0.9158	0.21	0.47
202	1	3	0.1	0.95	28	0.15	0.5	0.5	1.6866	0.13	0.47
203	0	10	0.1	0.95	28	0.15	0.5	0.5	0.9099	0.19	0.48
204	1	10	0.1	0.95	28	0.15	0.5	0.5	1.335	0.12	0.46
205	0	3	0.6	0.95	28	0.15	0.5	0.5	1.0874	0.92	0.46
206	1	3	0.6	0.95	28	0.15	0.5	0.5	1.5968	0.82	0.48
207	0	10	0.6	0.95	28	0.15	0.5	0.5	0.9864	0.90	0.46
208	1	10	0.6	0.95	28	0.15	0.5	0.5	1.3095	0.79	0.47
209	0	3	0.1	0	45	0.15	0.5	0.5	0.5055	0.24	0.48
210	1	3	0.1	0	45	0.15	0.5	0.5	1.2602	0.22	0.48
211	0	10	0.1	0	45	0.15	0.5	0.5	0.5672	0.20	0.54
212	1	10	0.1	0	45	0.15	0.5	0.5	1.2477	0.20	0.48
213	0	3	0.6	0	45	0.15	0.5	0.5	0.7607	0.96	0.46
214	1	3	0.6	0	45	0.15	0.5	0.5	1.5602	0.99	0.47
215	0	10	0.6	0	45	0.15	0.5	0.5	0.827	0.95	0.47
216	1	10	0.6	0	45	0.15	0.5	0.5	1.4557	0.95	0.46
217	0	3	0.1	0.95	45	0.15	0.5	0.5	0.508	0.24	0.49
218	1	3	0.1	0.95	45	0.15	0.5	0.5	1.1818	0.21	0.48
219	0	10	0.1	0.95	45	0.15	0.5	0.5	0.5774	0.20	0.54
220	1	10	0.1	0.95	45	0.15	0.5	0.5	1.1735	0.19	0.48
221	0	3	0.6	0.95	45	0.15	0.5	0.5	0.7663	0.96	0.46
222	1	3	0.6	0.95	45	0.15	0.5	0.5	1.469	0.93	0.47
223	0	10	0.6	0.95	45	0.15	0.5	0.5	0.8285	0.94	0.48
224	1	10	0.6	0.95	45	0.15	0.5	0.5	1.369	0.90	0.46
225	0	3	0.1	0	28	0.5	0.5	0.5	0.9514	0.25	0.42
226	1	3	0.1	0	28	0.5	0.5	0.5	1.9884	0.17	0.46
227	0	10	0.1	0	28	0.5	0.5	0.5	0.9099	0.23	0.44
228	1	10	0.1	0	28	0.5	0.5	0.5	1.6295	0.16	0.45
229	0	3	0.6	0	28	0.5	0.5	0.5	1.1162	0.92	0.45
230	1	3	0.6	0	28	0.5	0.5	0.5	1.9269	1.03	0.47
231	0	10	0.6	0	28	0.5	0.5	0.5	0.9909	0.90	0.45
232	1	10	0.6	0	28	0.5	0.5	0.5	1.5988	0.98	0.46
233	0	3	0.1	0.95	28	0.5	0.5	0.5	0.9439	0.23	0.45
234	1	3	0.1	0.95	28	0.5	0.5	0.5	1.4643	0.12	0.46
235	0	10	0.1	0.95	28	0.5	0.5	0.5	0.9041	0.20	0.46
236	1	10	0.1	0.95	28	0.5	0.5	0.5	1.1991	0.12	0.45
237	0	3	0.6	0.95	28	0.5	0.5	0.5	1.1088	0.92	0.46
238	1	3	0.6	0.95	28	0.5	0.5	0.5	1.417	0.76	0.47
239	0	10	0.6	0.95	28	0.5	0.5	0.5	0.9919	0.90	0.45
240	1	10	0.6	0.95	28	0.5	0.5	0.5	1.1765	0.72	0.46
241	0	3	0.1	0	45	0.5	0.5	0.5	0.5234	0.31	0.39
242	1	3	0.1	0	45	0.5	0.5	0.5	2.1435	0.25	0.50
243	0	10	0.1	0	45	0.5	0.5	0.5	0.5742	0.25	0.49
244	1	10	0.1	0	45	0.5	0.5	0.5	1.937	0.24	0.47
245	0	3	0.6	0	45	0.5	0.5	0.5	0.7756	0.95	0.45
246	1	3	0.6	0	45	0.5	0.5	0.5	2.5544	1.19	0.50
247	0	10	0.6	0	45	0.5	0.5	0.5	0.8212	0.97	0.45
248	1	10	0.6	0	45	0.5	0.5	0.5	2.1522	1.22	0.46
249	0	3	0.1	0.95	45	0.5	0.5	0.5	0.5194	0.26	0.45
250	1	3	0.1	0.95	45	0.5	0.5	0.5	1.576	0.17	0.50
251	0	10	0.1	0.95	45	0.5	0.5	0.5	0.5688	0.22	0.52
252	1	10	0.1	0.95	45	0.5	0.5	0.5	1.4253	0.18	0.47
253	0	3	0.6	0.95	45	0.5	0.5	0.5	0.7443	0.95	0.46
254	1	3	0.6	0.95	45	0.5	0.5	0.5	1.8763	0.88	0.50
255	0	10	0.6	0.95	45	0.5	0.5	0.5	0.8237	0.96	0.46

256	1	10	0.6	0.95	45	0.5	0.5	0.5	1.5837	0.94	0.46
257	0.25	6.5	0.35	0.475	36.5	0.325	0.25	0.25	0.4684	0.50	0.40
258	0.75	6.5	0.35	0.475	36.5	0.325	0.25	0.25	0.7357	0.51	0.38
259	0.5	4.75	0.35	0.475	36.5	0.325	0.25	0.25	0.5511	0.50	0.37
260	0.5	8.25	0.35	0.475	36.5	0.325	0.25	0.25	0.5646	0.50	0.38
261	0.5	6.5	0.225	0.475	36.5	0.325	0.25	0.25	0.5383	0.35	0.38
262	0.5	6.5	0.475	0.475	36.5	0.325	0.25	0.25	0.5897	0.64	0.39
263	0.5	6.5	0.35	0.237	36.5	0.325	0.25	0.25	0.5692	0.50	0.37
264	0.5	6.5	0.35	0.712	36.5	0.325	0.25	0.25	0.5552	0.49	0.38
265	0.5	6.5	0.35	0.475	32.25	0.325	0.25	0.25	0.6132	0.49	0.38
266	0.5	6.5	0.35	0.475	40.75	0.325	0.25	0.25	0.522	0.50	0.37
267	0.5	6.5	0.35	0.475	36.5	0.237	0.25	0.25	0.5479	0.49	0.38
268	0.5	6.5	0.35	0.475	36.5	0.412	0.25	0.25	0.5727	0.50	0.37
269	0.5	6.5	0.35	0.475	36.5	0.325	0.125	0.25	0.4316	0.46	0.38
270	0.5	6.5	0.35	0.475	36.5	0.325	0.375	0.25	0.7682	0.52	0.40
271	0.5	6.5	0.35	0.475	36.5	0.325	0.25	0.125	0.5391	0.45	0.38
272	0.5	6.5	0.35	0.475	36.5	0.325	0.25	0.375	0.5876	0.54	0.37
273	0.5	6.5	0.35	0.475	36.5	0.325	0.25	0.25	0.5572	0.49	0.37

Understanding the permeability behavior of sand-modified cemented paste backfill

Gamze Selek[1, 2], Erol Yilmaz [*1.3], Muhammet Sari[1,2,3], Tugba Keskin[1,2],Tugrul Kasap[1,2]

[1] *Recep Tayyip Erdogan University, Geotechnical, Waste Management and Backfill Laboratory, Rize, Türkiye*
[2] *Institute of Graduate Studies. Recep Tayyip Erdogan University. Fener. Rize TR53100. Türkiye*
[3] *Recep Tayyip Erdogan University, Department of Civil Engineering, TR53100 Rize, Türkiye*

Abstract. Cemented paste backfill (CPB) has become a popular choice for underground filling in the mining industry because of its ability to provide strong support and enhance safety in underground operations. Evaluating the performance of these backfill types is of great importance, especially in terms of parameters such as water permeability, strength and microstructural properties. In this context. the k_{sat} (k_{sat} Saturated Permeability Test) is an effective method for determining the permeability properties of CPB. In this study, it was aimed to determine the permeability properties of CPB mixtures prepared with different sand replacement ratios (15%. 30%. 45% by weight) and to investigate their effects on CPB performance. The mechanical (uniaxial compression, UCS), microstructure (scanning electron microscope, SEM) and permeability (k_{sat}) properties of CPB samples prepared with constant cement content/type (5%/CEM I), solid content (75% by weight) at different curing days (3-28) were investigated in detail. As a result of the study, it was observed that permeability properties directly affect the backfill strength. In addition, microstructural investigations revealed that pores and crack structures in the internal structure of the backfill material are directly related to permeability. The results of the study also detailed the effect of curing times on permeability values. These findings highlight the importance of the KSAT test in the design and application processes of CPBs and suggest that microstructural and mechanical parameters should be carefully considered to optimize CPB performance.

Keywords: Cemented paste backfill; Hydraulic conductivity; Mechanical, Sand content

1. Introduction

The mining industry is currently focusing on developing innovative technologies and methods that promote sustainable and safe operations (Keskin et al., 2024). One of the biggest challenges in underground mining is the safe and effective filling of post-excavation voids. Filling these voids with appropriate materials both ensures the continuity of mining operations and increases structural integrity and safety within the mine (Đurđevac et al., 2022). Cemented paste backfill (CPB) is one of the most common and effective filling materials developed for this purpose. In addition to providing an economical solution by minimizing environmental impacts. it is widely used in the mining industry due to its superior properties such as high strength capacity and low water permeability (Li et al., 2020).

CPB is considered to be one of the most effective waste disposal methods in terms of soil reinforcement, waste storage and operational efficiency (Fall et al., 2010). CPB consists of a mixture containing 70-85% tailings material, 3-7% cement and water by weight (Sari et al., 2023a). The mineralogical and chemical properties of the tailings used play a decisive role on the strength of the backfill. In particular, sulfur compounds and fine-grained structures can weaken the strength by negatively affecting the hydration process (Liu et al., 2020a). In addition, environmental factors such as acid mine drainage can seriously threaten the long-term stability of cemented paste backfills (Sari et al., 2022; Kasap et al., 2022a). Therefore, not only the early age strength but also the long-term strength under environmental conditions should be considered as a basic criterion in the performance evaluation of CPB systems. The formation of a durable backfill structure in the long term depends primarily on ensuring the microstructural integrity of the mixture and the resistance of this structure to environmental effects (Liu et al., 2020b). The microstructural development within the CPB is directly related to the quality, continuity and distribution properties of the products formed as a result of the hydration processes. Quality hydration products increase strength while reducing permeability. Therefore, parameters such as binder type, additive content and waste particle size should be carefully optimized. In order to provide better performance in the long term and to

* Corresponding author, E-mail: erol.yilmaz@erdogan.edu.tr

https://doi.org/10.31462/icearc2025_ce_geo_864

golden light publishing

strengthen the microstructural integrity of the filler, the use of fly ash, slag, aggregate and various waste-based materials in the CPB composition are considered as effective alternative methods (Kasap et al., 2022b).

Sand, which is widely used in the construction sector, can be evaluated as an alternative aggregate in mining applications and has the potential to improve the mechanical properties of the fill. Aggregates directly affect the permeability, strength and rheological behaviors of cementitious mixtures depending on their physical parameters such as grain size, shape, surface roughness, density, water absorption capacity and thermal properties. (Lyu et al., 2023). Particularly, grain shape and distribution significantly shape the engineering performance of cementitious backfill by determining the friction and shear forces developed in the internal structure of the mixture (Kasap et al., 2022c). In this direction, applications aimed at the use of sand as an aggregate replacement in order to improve the performance of CPB systems are gaining more and more importance. Magmatic, sedimentary and metamorphic rocks, which are widely found in different regions of Türkiye, constitute the main geological main sources from which sands that can be evaluated for this purpose can be obtained. Magmatic rocks (e.g. granite, basalt and andesite) are formed by the cooling and solidification of molten rocks in the earth's crust and generally attract attention with their durable and hard structures. Sedimentary rocks (e.g. sandstone and limestone) are formed as a result of the accumulation of organic and inorganic substances, while metamorphic rocks are transformed under high temperature and pressure to form durable species such as marble and quartzite (Xue et al., 2014; Mibei et al., 2014). The mineralogical and petrographic properties of these rocks should be evaluated according to whether they are compatible with cementitious systems and the contributions of these materials to the CPB performance should be determined accurately.

The performance of cemented paste backfill may vary significantly depending on the properties of the materials used in their composition and environmental conditions. In particular, critical parameters such as water permeability, mechanical strength and microstructural factors are among the main elements affecting the long-term stability and durability of CPB (Sari et al., 2023b). In this context, the properties of the sand used in the mixture also play an important role. The polyhedral and rough surface texture of sand particles can increase the water requirement of cement mixtures and negatively affect workability (Kasap et al., 2023). Therefore, maintaining optimum particle fineness and sand ratio is important both in terms of workability of the mixture and final performance. In recent years, sand has started to be widely used as a binder or aggregate in the production of CPB. Due to its lower cost compared to cement and its potential to improve gradation disorders caused by tailings, sand is considered an important additive material in cemented paste backfill mixtures. However, the effectiveness of this additive depends on the careful selection of the physical and mineralogical properties of the sand; because these properties can directly affect the permeability and mechanical strength of the backfilling (Fall et al., 2009; Zhou et al., 2020).

In underground mining, the permeability properties of backfill materials play a critical role in both maintaining the structural integrity of the backfill and controlling environmental impacts (Ghirian & Fall, 2017). The movement of water in backfill systems can not only weaken the physical strength, but can also lead to the transport of harmful chemicals into underground water resources. This makes it important to control the pore structure and void continuity in the embankment. In particular, fillings with high permeability values allow water and dissolved ions to be easily transported within the structure, weakening both the mechanical properties of the material and threatening its long-term stability (Liu & Deng, 2023). Therefore, the determination of the permeability properties of backfills by reliable methods is recognised as a fundamental requirement for the success of mining applications (Yilmaz et al., 2011). In this context, the k_{sat} (saturated hydraulic permeability) test is a standardised method for quantitatively evaluating the water resistance and porosity structure of the CPB material. The data obtained with k_{sat} contribute to the design of filling materials in accordance with lower permeability and higher strength targets (Belem et al., 2010).

When the literature is examined. it is seen that there are various studies to investigate the permeability-related properties of CPB and their effect on the performance of the backfillings: Aubertin et al. (2007), in permeability tests carried out with the addition of binder at different curing times, revealed that the use of binder reduced the saturated hydraulic conductivity of tailings up to 1 ½ order of magnitude after a period of 28 days. Yilmaz et al. (2012), investigated the effects of curing time and binder content on the one-dimensional consolidation parameters and hydraulic propertie, especially saturated hydraulic conductivity (k_{sat}) and degree of saturation (Sr) of early age CPB samples. Faraji and Fall (2025), evaluated the effects of binder content and material composition on permeability behaviour and determined the parameters required for optimum performance in their study on uncemented and lightweight cemented embankments. Qiu et al. (2022), showed that cement-sand ratio and waste rock content have significant effects on the strength and permeability properties of cemented landfills. In their study, they stated that the maximum strength was achieved at 10% level of waste rock content and the permeability reached the highest value at 30% level, and that microcrack formation increased as the cement-sand ratio decreased, which decreased the strength and increased the permeability. Ghirian and Fall (2016), investigated the effects of curing under stress on the permeability of CPB. The results showed that excessive stress, especially under undrained conditions, increased permeability and increased pore water pressure. Liu et al. (2022), investigated the effect of mixing time on the saturated hydraulic conductivity (k_{sat}) of CPB and concluded that prolonged mixing reduces the hydraulic conductivity by refining the pore structure of CPB. This reduction improves the durability and environmental performance of CPB resulting in more efficient and durable materials for mine backfilling operations.

In the existing studies in the literatüre, the effects of aggregates on permeability have not been investigated in depth enough. In this context, this research aims to make an original contribution to the field by analyzing the effects of CPB sand replacement ratios (15%. 30%. 45% by weight) on permeability and mechanical properties in detail. In particular, the effects of sand ratio on critical performance parameters such as permeability, microstructural properties and mechanical strength of cement paste backfill have generally been addressed in a limited way in the literatüre, and the aim of this study is to fill this gap. Therefore, how sand replacement will affect the long-term performance of CPB and how this interaction is reflected in the engineering properties of backfill materials is of great importance to develop more efficient and sustainable solutions in the field of application. In addition, this research aims to create a reference in order to better understand and optimize the relationship between two important parameters such as water permeability and mechanical strength of backfill materials with different sand replacement ratios.

This study analyzes in more detail how sand ratios affect the permeability properties of cementitious backfill and its contribution to the long-term durability of the material. In addition, a comprehensive investigation is presented in terms of permeability (k_{sat}), microstructural properties (scanning electron microscopy, SEM) and mechanical strength (uniaxial compressive strength, UCS) parameters of the samples prepared at different curing times (3-28 days) with constant cement content (5 wt.%) and solid content (75 wt.%). In this respect, the originality of the study, unlike other studies in the literature, provides a contribution to the optimization of material design by considering the effects of sand ratios on CPB performance in a broader way.

2. Materials

2.1. Process tailings

The mining tailings evaluated in this study were subjected to physical characterization analyses. Particle size distribution was determined using a laser granulometer (Malvern Mastersizer 2000) capable of measuring in the range of 0.02–2000 μm. The results obtained show that the fine fraction rate is below 20 μm (15–35%), which reveals that the material meets the necessary criteria for cement paste filling applications and falls into the coarse-sized tailings class.

In addition, the sufficient fineness of the material may positively affect both strength and permeability properties in terms of filling performance. According to the data presented in Table 1, the specific gravity (G_s) was measured as 3.56 m²/g. Besides, the uniformity coefficient (C_u) was calculated as 15.50 and the curvature coefficient (C_c) as 1.27, which indicate that the material has a well-graded structure in terms of granulometric. Chemical components of tailings are shown in Table 2.

Table 1. Physical properties of the components of the CPB

Physical properties	Process tailings	Limestone(LS)	OPC
D_{10}. μm	7.03	2.19	3.91
D_{30}. μm	31.20	16.55	14.01
D_{50}. μm. (average grain diameter)	78.60	55.41	24.67
D_{60}. μm	109.00	76.63	30.48
D_{80}. μm	201.00	177.60	55.69
[C_u=$D_{60}/_{10}$]	15.50	34.99	7.80
[C_c=$D_{30}^2/(D_{10}*D_{60})$]	1.27	1.63	1.65
Specific surface area, S_S. m^2/g	2.63	0.59	0.40
Specific gravity, G_s	3.56	2.74	3.14

2.2. Cement and mixing water

The basic binding material used in this study is Ordinary Portland cement (OPC) of the type CEM I 42.5R with high early strength class. Some physical properties of OPC are presented in Table 1. The specific gravity (Gs) of the cement was determined as 3.14 and the specific surface area (S_S) as 0.40 m²/g.The analysis results regarding the chemical composition of the mentioned OPC are given in Table 2. The ratios of calcium oxide (CaO) and silicon dioxide (SiO_2), which are the main oxide components of the cement, were measured as 70.87% and 14.04% respectively.

In order to prepare the CPB mixtures homogeneously, only tap water was used as mixing water. In this study, the possible effects of the mixing water used on the performance and chemical properties of the filler were excluded from the evaluation.

Table 2. Chemical properties of the components of the CPB

Chemical content (%)	Process tailings	Limestone (LS)	OPC
Na_2O	0.08	0.07	0.35
MgO	0.04	0.73	0.91
Al_2O_3	8.01	1.54	3.43
SiO_2	31.50	1.96	14.04
P_2O_5	0.03	0.08	0.25
SO_3	0.23	0.75	4.42
SrO	0.01	0.08	0.06
K_2O	0.25	0.20	0.89
CaO	3.66	53.77	70.87
TiO_2	0.29	0.08	0.34
MnO	-	0.07	0.10
Fe_2O_3	30.90	0.40	4.06
Others	25.00	40.27	0.28

2.3. Crushed sand

In the scope of the study, the sand used as a fine aggregate replacement material in CPB mixtures was analyzed in terms of its physical properties. The particle size distribution (PSD) of the material is presented in Fig.1, while its detailed physical characteristics are given in Table 1. According to the measurements, the average particle diameter (D50) of the material was determined as 55.41 µm, and the (D80) value, considered as the maximum particle size, was measured as 177.60 µm. The coefficient of uniformity (Cu) was calculated as 34.99 and the coefficient of curvature (Cc) as 1.63, indicating that the material has a well-graded particle distribution. Additionally, the specific surface area was identified as 0.59 m^2/g. and the specific gravity was found to be 2.74 g/cm^3. These data were used as a fundamental input in evaluating the usability of the sand replacement material in CPB mixtures.

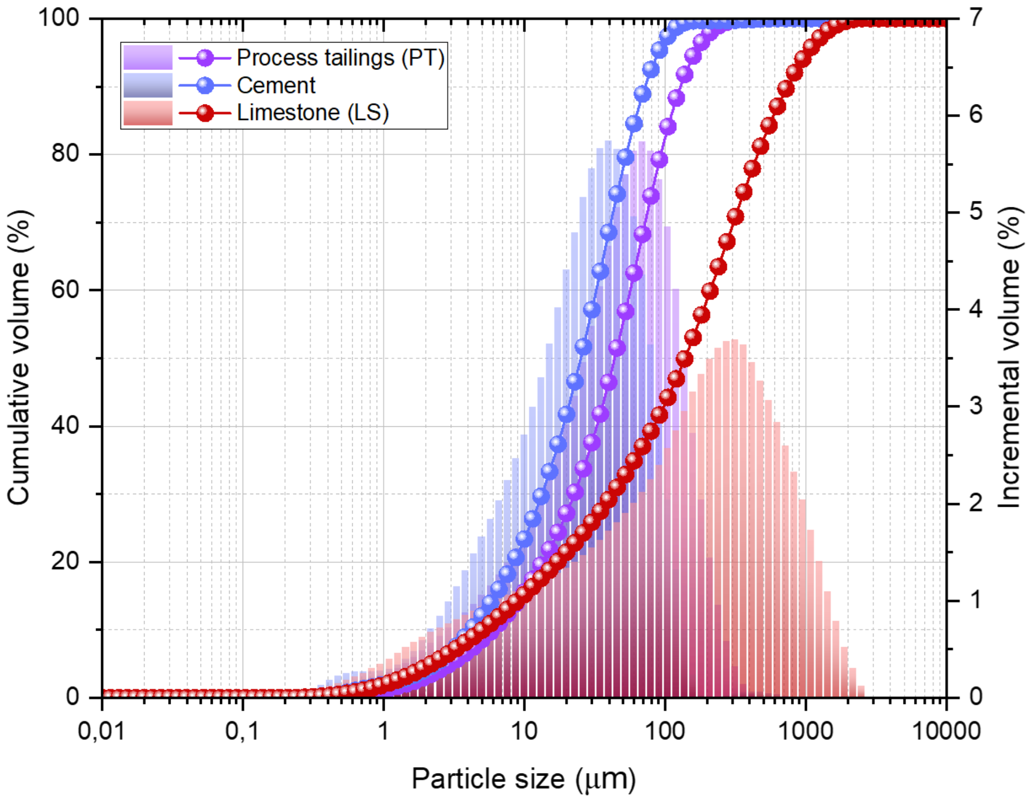

Fig.1. Particle size distribution curves of CPB components

2.4. Preparation of CPB samples

In the relevant study, CPB mixtures were prepared with a fixed 5% (by weight) Ordinary Portland cement (OPC) content and a solid concentration of 75 wt.%. To investigate the effects of sand addition on CPB performance, four different sand replacement ratios (0% – control, 15%, 30%, and 45%) were used in the tailing-sand mixtures. The detailed proportions of the mixtures are presented in Table 3.

All components (process tailings, sand, cement, and water) were weighed using precision laboratory scales and mixed for approximately 10 minutes in a 10-liter mechanical mixer to achieve a homogeneous mixture. The prepared mixtures were then poured into cylindrical plastic molds with a diameter of 5 cm and a height of 10 cm, featuring perforated bases, in accordance with the targeted solid content and consistency properties. The specimens were cured for periods ranging from 3-28 days under controlled conditions representing underground environments, with a relative humidity of 90 ± 5% and a temperature of 22 ± 3 °C.

Table 3 CPB design summary

Sample Name	Process tailings (%) (PT)	Sand (%) (LS)	Solid content (wt.%)	OPC	Curing (days)
PT100/LS0	100	-	75	CEM I/5	3-28
PT85/LS15	85	15	75	CEM I/5	3-28
PT70/LS30	70	30	75	CEM I/5	3-28
PT55/LS45	55	45	75	CEM I/5	3-28

3.Methods

3.1. Uniaxial compressive strength (UCS**)** test

The mechanical properties of CPB samples containing different proportions of sand and tailing material were evaluated in detail within the scope of uniaxial compressive strength (UCS), elastic modulus and stress-strain behaviors. Experimental studies were carried out using a UTEST Multiplex brand fully automatic electronic pressure testing device with a capacity of 50 kN and a constant loading rate of 1 mm/min. The samples were prepared in a cylindrical form with a height/diameter ratio of 2:1 in accordance with ASTM C39/C39M standards. This ratio allows the deformation and strength behaviors to be determined consistently and reproducibly.

Three samples with the same content were prepared and tested for each cure period (3-28 days). The results obtained were calculated by taking the average values of these three samples. Thus, the reliability of the experimental data was increased and the effects of different sand replacement rates on the mechanical performance of CPB were analyzed comparatively.

3.2. Saturated hydraulic conductivity (Ksat) test

In the CPB samples prepared for the purpose of determining permeability properties, sand was used as aggregate material in different proportions. Saturated permeability tests on the samples that completed the curing process were performed using the k_{SAT} (saturated hydraulic conductivity test) device belonging to Meter Group. The k_{SAT} device is a sensitive analysis system designed to measure the hydraulic conductivity coefficients of low permeability samples in a laboratory environment under constant temperature and humidity conditions.The samples were fully saturated before the test, Fig. 2 shows the k_{SAT} device and the experimental setup used.

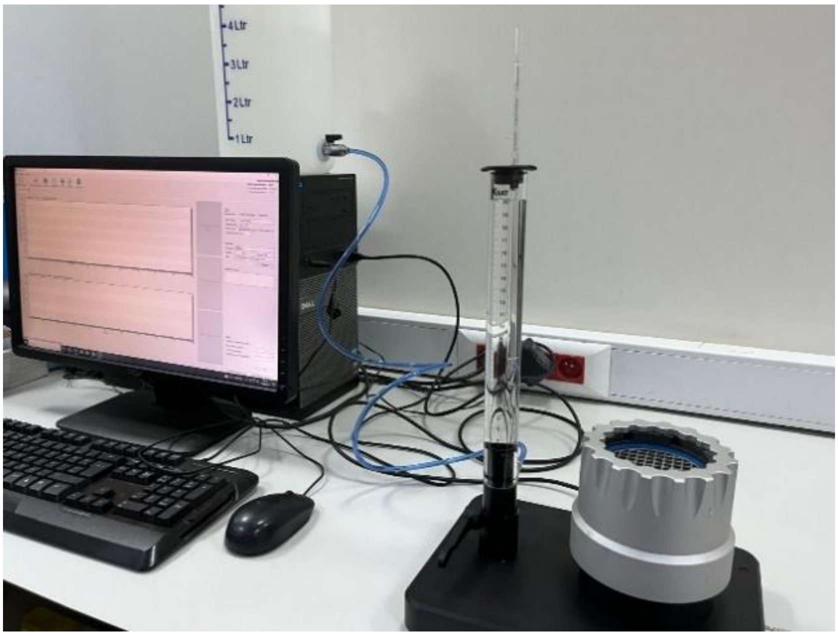

Fig. 2**.** Saturated hydraulic conductivity test setup

3.3. Assessing CPB's SEM micrographs

The microstructural characterization of the CPB specimens after the completion of the curing process was carried out using the scanning electron microscopy (SEM) method. For this purpose, a JEOL JSM-6610 model SEM device was used. Samples were taken from the center of the fractured specimens after strength testing, then immersed in an alcohol-based solution to inhibit further hydration reactions, and subsequently dried in a vacuum oven at 50 °C for 24–48 hours. The surfaces of the dried specimens were coated with gold (Au) to ensure conductivity.

SEM analyses were performed under an acceleration voltage range of 10–25 keV, a beam current of 0.9 nA, and a working distance of 35 mm. A maximum magnification of ×500 and a resolution of approximately 3 nm, adjusted based on the specimen type, were used during the measurements. Under these conditions, SEM imaging enabled detailed observation and evaluation of hydration products, microcracks, pore structures, and aggregate–matrix interactions within the CPB.

4. Results and discussion

4.1. Uniaxial compressive strength test results of CPB sample

Fig.3 presents the uniaxial compressive strength (UCS) test results of the sedimentary rock type limestone substituted in sand form on 3-28 day cured paste fill samples with different amounts of tailings/sand ratios (100/0 control sample 85/15, 70/30, 55/45). The obtained data show that the addition of sand to CPB mixtures at certain rates has positive effects in terms of UCS. The optimum strength value was obtained especially in the mixture containing 30% sand (1052 kPa) and a gradual decrease in strength was observed at sand contents above this rate.

This shows that the addition of sand up to a certain level supports the binding mechanism by improving the grain size distribution, but when this limit is exceeded, the binding matrix weakens and thus the strength is negatively affected. As a matter of fact. the replacement of limestone at high rates due to its high calcite content weakens its binding properties and disrupts the continuity of the cement matrix, leading to a decrease in strength (Irassar, 2009). This reveals the reason for the decrease in UCS values.

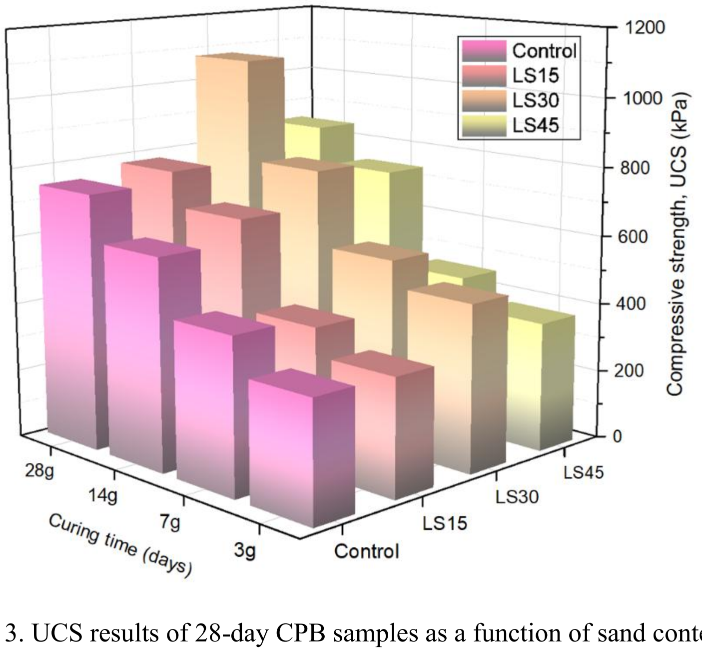

Fig. 3. UCS results of 28-day CPB samples as a function of sand content

4.2. Permeability results of CPB sample

According to the findings obtained in this study, it was observed that the use of limestone as an aggregate replacement in cement paste fillings created limiting effects on permeability properties. As a result of limestone replacements at 15%. 30% and 45% by weight, a decrease trend was observed in saturated hydraulic conductivity (k_{SAT}) values up to 30% replacement rate. As seen in Fig. 4. 30% replacement rate stands out as the point where the lowest ksat value is obtained in terms of permeability. This situation is associated with the limestone grains creating a more homogeneous structure in the cement matrix, limiting the void ratio and increasing impermeability. However, an increase occurred in permeability values again when the replacement rate was increased above 30%. It is thought that this increase is related to the weakening of the binding capacity of the limestone due to its high calcite content and the increase in microcrack formation during the solidification process. The spread of microcracks and the increase in porosity increased the hydraulic conductivity by facilitating the movement of water within the filling. Accordingly, since the use of limestone as an aggregate substitute at high rates may negatively affect the permeability performance of cement paste fillings, optimum usage rates should be determined carefully. In addition, the fact that this change in permeability is parallel to the strength values reveals that limestone provides a limited contribution in terms of both mechanical and hydraulic conductivity properties.

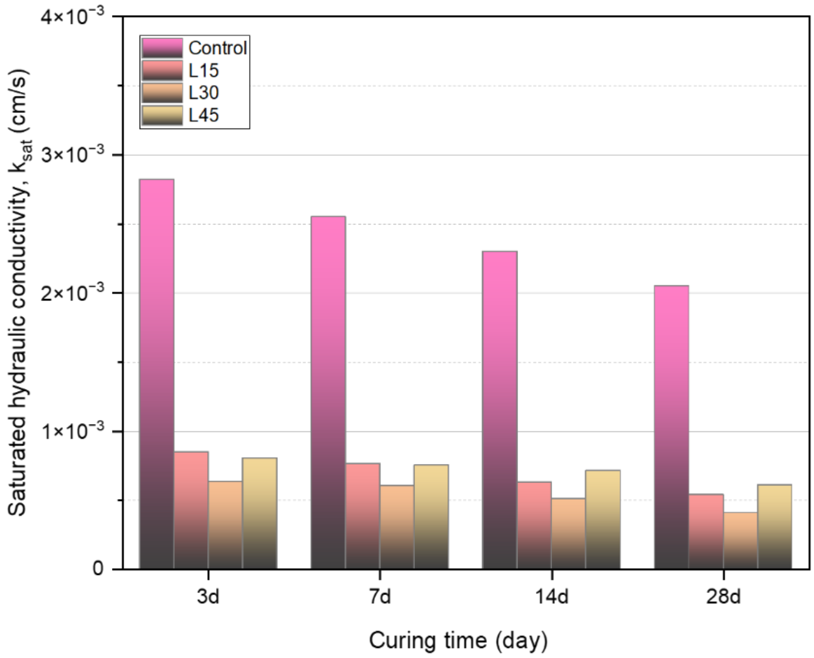

Fig. 4. Saturated hydraulic conductivity results of 28-day CPB samples as a function of sand content

4.3. Evaluation of SEM micrographs of CPB samples

Scanning electron microscopy (SEM) method stands out as an important analysis tool in the evaluation of microstructural properties of CPB samples. In SEM analyses, which allow detailed examination of hydration products that develop depending on the type and amount of components such as cement and aggregate, mixtures with 30% aggregate replacement by weight that showed optimum performance were included in the evaluation scope.

Fig. 5 presents SEM images of CPB samples prepared with these mixtures and cured for 28 days under 1000x magnification. The images revealed that calcium hydroxide [$Ca(OH)_2$], ettringite, voids and calcium silicate hydrate (C-S-H) gels were commonly found in the microstructure of the samples. It was observed that the increase in the density of C-S-H gels positively affected the strength of the filling system, and short-term ettringite formations also supported the mechanical properties (Chen et al., 2017). SEM findings show that aggregate replacement directly affects not only the macroscopic engineering properties but also the hydration process and microstructure development.

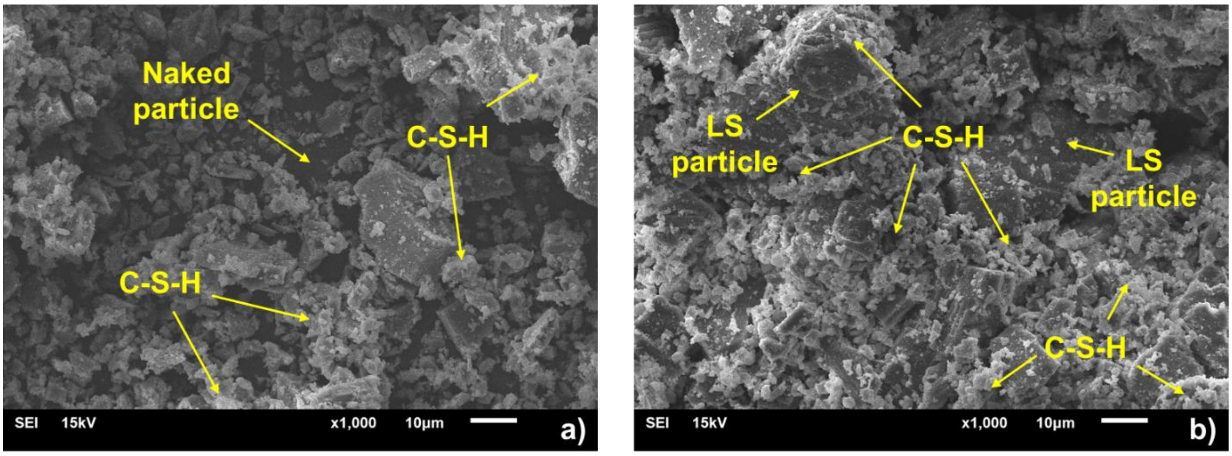

Fig.5. SEM micrographs of 28-day cured CPB samples: a) Control sample. b) 28-day cured limestone sample

5. Conclusions

In this study, sand was used in different proportions (15%, 30% and 45% by weight) as an aggregate substitute in CPB mixtures and the effects of this change on the strength and permeability properties of the fill were examined in detail. Along with the applied UCS and saturated hydraulic conductivity tests, microstructural changes were analyzed with SEM imaging technique to reveal the relationship between the development of pore structure and permeability. In the light of the obtained findings, the following conclusions were reached:

- The use of sand as an aggregate replacement has shown positive effects in terms of both strength and permeability at rates up to 30%. Especially at the 30% replacement rate, the 28-day UCS value reached the maximum level and the ksat value decreased to the lowest level. This rate stands out as the rate at which optimum engineering performance is achieved. This finding shows that the inclusion of sand in the material mixture can improve mechanical and hydraulic performance at certain rates.
- At sand ratios above 30%, the binding weakened and more voids and micro cracks formed in the microstructure. This situation caused the UCS value to decrease and the k_{sat} value to increase. These findings reveal that excessive use of sand as aggregate can negatively affect the general strength of the material by weakening the binding properties. In addition, these ratios show that the permeability values of CPB materials increase in parallel with the deterioration in their microstructure.
- SEM analyses show that the cases where the density of C-S-H gels increases and short-term ettringite formations support the strength are more pronounced, especially at optimum replacement rates. This finding reveals that the rates where sand is used as aggregate replacement cause positive changes in the microstructure strengthening the strength of the material and that the microstructure supports this strength. The increase in the density of C-S-H gels can be considered as a factor that increases the mechanical strength of the cementitious filling material.
- It has been determined that pore structure has a direct effect on permeability, and permeability values are parallel to changes in microstructure. The effect of changes in pore structure on permeability shows that the material becomes more permeable to water with the increase in voids and cracks in the microstructure. This condition may influence the long-term performance of the backfill material and should be considered as a critical factor in engineering applications.

As a result, the use of sand as an aggregate replacement improved the CPB performance up to a certain rate (especially 30%). However, if this rate was exceeded, the deterioration in the microstructure increased the permeability and negatively affected the engineering performance. Therefore, the optimum replacement rates should be carefully determined when using sand as an aggregate replacement in CPB samples.

References

Aubertin, M. (2007). Evolution of cemented paste backfill saturated hydraulic conductivity at early curing time. *OttawaGeo2007*.

Belem, T., Fourie, A. B., & Fahey, M. (2010, May). Time-dependent failure criterion for cemented paste backfills. In *Paste 2010: Proceedings of the Thirteenth International Seminar on Paste and Thickened Tailings* (pp. 147–162). Australian Centre for Geomechanics.

Chen, Q. S., Zhang, Q. L., Fourie, A., Chen, X., & Qi, C. C. (2017). Experimental investigation on the strength characteristics of cement paste backfill in a similar stope model and its mechanism. *Construction and Building Materials, 154*, 34–43.

Đurđevac Ignjatović, L., Krstić, V., Radonjanin, V., Jovanović, V., Malešev, M., Ignjatović, D., & Đurđevac, V. (2022). Application of cement paste in mining works, environmental protection, and the sustainable development goals in the mining industry. *Sustainability, 14*(13), 7902.

Fall, M., Adrien, D., Célestin, J. C., Pokharel, M., & Touré, M. (2009). Saturated hydraulic conductivity of cemented paste backfill. *Minerals Engineering, 22*(15), 1307–1317.

Fall, M., Célestin, J. C., Pokharel, M., & Touré, M. (2010). A contribution to understanding the effects of curing temperature on the mechanical properties of mine cemented tailings backfill. *Engineering Geology, 114*(3–4), 397–413.

Faraji, Z., & Fall, M. (2025). Saturated hydraulic conductivity of uncemented and lightly cemented high-density tailings for surface disposal. *Environmental Earth Sciences, 84*(1), 1–22.

Ghirian, A., & Fall, M. (2016). Influence of curing stress on long-term hydro-mechanical response of cemented paste backfill. In *Proceedings Tailings and Mine Waste 2016*, October 2–5, Keystone, Colorado, USA.

Ghirian, A., & Fall, M. (2017). Properties of cemented paste backfill. In *Paste tailings management* (pp. 59–109).

Irassar, E. F. (2009). Sulfate attack on cementitious materials containing limestone filler—A review. *Cement and Concrete Research, 39*(3), 241–254.

Kasap, T., Yilmaz, E., & Sari, M. (2022a). Physico-chemical and micro-structural behavior of cemented mine backfill: Effect of pH in dam tailings. *Journal of Environmental Management, 314*, 115034.

Kasap, T., Yilmaz, E., Guner, N. U., & Sari, M. (2022b). Recycling dam tailings as cemented mine backfill: Mechanical and geotechnical properties. *Advances in Materials Science and Engineering, 2022*(1), 6993068.

Kasap, T., Yilmaz, E., & Sari, M. (2022c). Effects of mineral additives and age on microstructure evolution and durability properties of sand-reinforced cementitious mine backfills. *Construction and Building Materials, 352*, 129079.
Kasap, T., Yilmaz, E., Sari, M., & Karasu, S. (2023). Predicting long-term impact of cementitious mine fill considering sand as a copper-tailings substitution. *Powder Technology, 428*, 118887.
Keskin, T., Yilmaz, E., Kasap, T., Sari, M., & Cao, S. (2024). Toward viable industrial solid residual waste recycling: A review of its innovative applications and future perspectives. *Minerals, 14*(9), 943.
Li, J., Yilmaz, E., & Cao, S. (2020). Influence of solid content, cement/tailings ratio, and curing time on rheology and strength of cemented tailings backfill. *Minerals, 10*(10), 922.
Liu, L., Xin, J., Qi, C., Jia, H., & Song, K. I. (2020a). Experimental investigation of mechanical, hydration, microstructure and electrical properties of cemented paste backfill. *Construction and Building Materials, 263*, 120137.
Liu, L., Xin, J., Huan, C., Qi, C., Zhou, W., & Song, K. I. (2020b). Pore and strength characteristics of cemented paste backfill using sulphide tailings: Effect of sulphur content. *Construction and Building Materials, 237*, 117452.
Liu, S. G., & Fall, M. (2022). Fresh and hardened properties of cemented paste backfill: Links to mixing time. *Construction and Building Materials, 324*, 126688.
Liu, Y., & Deng, H. (2023). Study on permeability performance of cemented tailings backfill based on fractal characteristics of pore structure. *Construction and Building Materials, 365*, 130035.
Lyu, H., Chen, Y., Pu, H., Ju, F., Zhang, K., Li, Q., & Wu, P. (2023). Dynamic properties and fragmentation mechanism of cemented tailings backfill with various particle size distributions of aggregates. *Construction and Building Materials, 366*, 130084.
Mibei, G. (2014). *Introduction to types and classification of rocks*. Geothermal Development Company.
Qiu, H., Zhang, F., Sun, W., Liu, L., Zhao, Y., & Huan, C. (2022). Experimental study on strength and permeability characteristics of cemented rock-tailings backfill. *Frontiers in Earth Science, 10*, 802818.
Sari, M., Yilmaz, E., Kasap, T., & Guner, N. U. (2022). Strength and microstructure evolution in cemented mine backfill with low and high pH pyritic tailings: Effect of mineral admixtures. *Construction and Building Materials, 328*, 127109.
Sari, M., Yilmaz, E., & Kasap, T. (2023a). Long-term ageing characteristics of cemented paste backfill: Usability of sand as a partial substitute of hazardous tailings. *Journal of Cleaner Production, 401*, 136723.
Sari, M., Yilmaz, E., Kasap, T., & Karasu, S. (2023b). Exploring the link between ultrasonic and strength behavior of cementitious mine backfill by considering pore structure. *Construction and Building Materials, 370*, 130588.
Xue, L., Qin, S., Sun, Q., Wang, Y., Lee, L. M., & Li, W. (2014). A study on crack damage stress thresholds of different rock types based on uniaxial compression tests. *Rock Mechanics and Rock Engineering, 47*, 1183–1195.
Yilmaz, E., Belem, T., Bussière, B., & Benzaazoua, M. (2011). Relationships between microstructural properties and compressive strength of consolidated and unconsolidated cemented paste backfills. *Cement and Concrete Composites, 33*(6), 702–715.
Yilmaz, E., Belem, T., & Benzaazoua, M. (2012). One-dimensional consolidation parameters of cemented paste backfills. *Gospodarka Surowcami Mineralnymi–Mineral Resources Management*, 29–45.
Zhou, N., Zhang, J., Ouyang, S., Deng, X., Dong, C., & Du, E. (2020). Feasibility study and performance optimization of sand-based cemented paste backfill materials. *Journal of Cleaner Production, 259*, 120798.

The influence of geogrid reinforcement configuration on the settlement behaviour of soil-pipe systems

Bayram Ateş*[1], Saeid Zardari[2]

[1] Karadeniz Technical University, Department of Civil Engineering, 61080 Trabzon, Türkiye
[2] İstanbul Okan University, Department of Civil Engineering, 34959 İstanbul, Türkiye

Abstract. Pipelines for transporting natural gas, oil, water, and wastewater are widely used in the energy sector and municipal implementation and play an increasingly important role in people's lives; therefore, pipelines are a crucial component of urban underground infrastructure. But, damage to underground pipelines caused by traffic or construction activities is a frequent phenomenon around the world, resulting in considerable economic losses and environmental pollution. Several techniques have recently been proposed to reduce and control these financial losses and environmental pollution, including geosynthetic-reinforced soil platforms. Thus, it is crucial to possess a comprehensive understanding of the soil-pipe interaction to assess buried pipelines' stability accurately. The present study investigates the findings derived from numerical analysis of a flexible pipe buried in both unreinforced and geogrid-reinforced soils, with the additional consideration of surface surcharges. The aim of this research is to determine the effect of geogrid reinforcement configuration on the deflection of flexible pipe and soil settlement against applied pressure. In this context, a series of numerical analyses were carried out. The result of this study showed that the deflection of the pipe and soil settlement were strongly influenced by the configuration of geogrid reinforcement. In this way, some essential guidelines for selecting the reinforcement configuration to design the soil-pipe systems have been established through these numerical studies.

Keywords: Buried pipes; Geogrid reinforcement; Soil-pipe systems; Numerical analysis; Reinforcement configuration

1. Introduction

In geotechnical engineering, a variety of challenges arise from the interaction between soil and structures, either placed on or embedded within it. Among these, one of the most intricate problems involves understanding the behavior of buried pipelines. Subsurface piping systems have been utilized for various functions since ancient times. While initially developed for the conveyance of potable water and sewage, modern applications extend to the transportation of energy resources such as electricity, oil, and natural gas, among others. To fulfill their intended roles effectively, pipes must possess sufficient structural integrity and stiffness. They are also required to maintain durability throughout their expected service life. In this context, 'strength' refers to the pipe's capacity to resist different forms of loading, including internal pressure, overburden from soil, external structural loads, differential settlements, and longitudinal bending stresses (Moser & Folkman, 2008). The interaction between soil and buried pipes has been a subject of investigation since the early 20th century, and continues to be an active area of research today (Jeyapalan & Hamida, 1988; Selig et al., 1990; Masada et al., 2002; Won et al., 2004; Sargand et al., 2005; Kawabata et al., 2006; Talesnick and Xia, 2011; Naggar et al., 2015, Guha et al., 2016; Robert et al., 2016; Abuhajar et al., 2016; Wang et al., 2017).

Given the loads transmitted from traffic or nearby structures to closely spaced buried pipes, it is essential to account for these pipes within the framework of soil–structure interaction. Since the installation of subsurface infrastructure typically involves excavation and backfilling, the use of geogrid reinforcement can be implemented both efficiently and without requiring substantial additional effort (see Fig. 1 and Fig. 2). However, research addressing the role of geogrid reinforcement in soil–structure–pipe interaction remains relatively limited (Won et al., 2004; Tafreshi & Khalaj, 2008; Palmeira & Andrade, 2010; Zhou et al., 2017a, 2017b; Corey et al., 2014; Ahmed et al., 2015; El-Naggar et al., 2015; Hedge & Sitharam, 2015; Wang et al., 2017; Ni et al., 2018; Elsheseny et al., 2019; Placido & Portelinha, 2019; Abdollahi et al., 2019).

* Corresponding author, E-mail: bayramates61@hotmail.com

https://doi.org/10.31462/icearc2025_ce_geo_925

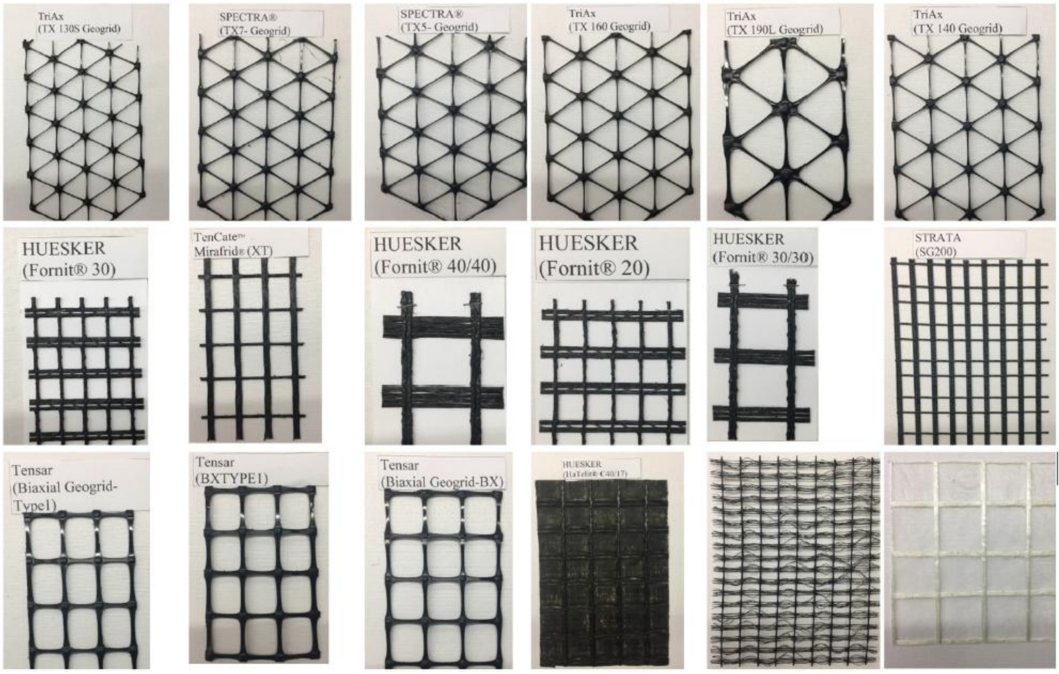

Fig. 1. Various types of geogrid materials are currently manufactured to meet diverse performance requirements in geotechnical engineering (Al-Barqawi et al., 2021)

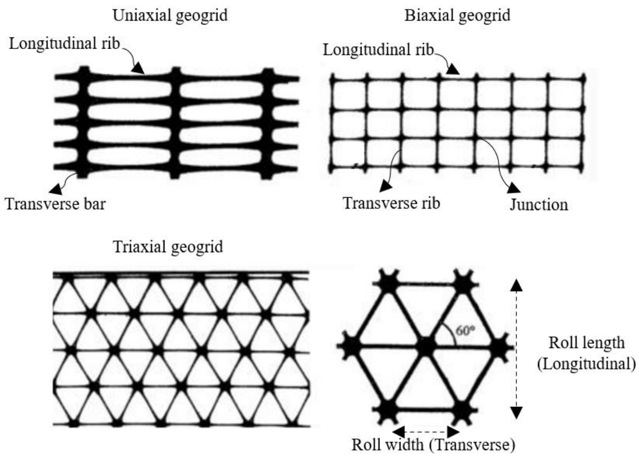

Fig. 2. Representation of various types of geogrids (Das B. M., 2013)

Tafreshi and Khalaj (2008) conducted laboratory-scale model tests to evaluate the impact of repeated loading on buried pipes. Their findings indicated that both the pipe's diameter deformation and the settlement of the surrounding soil were notably influenced by the presence of geogrid soil reinforcement. Similarly, Palmeira and Andrade (2010) employed a combination of geotextile and biaxial geogrid in their experimental models to enhance the protection of buried pipelines. They concluded that this reinforcement configuration provided effective resistance against sharp, intrusive objects, thereby mitigating the risk of accidental damage to the pipes. In another study, Asakereh et al. (2013) examined the protective role of biaxial geogrid-reinforced sand beds over continuous circular voids, simulating a strip footing centered above the void. Their results demonstrated a significant reduction in settlement, with optimal performance achieved using two to three reinforcement layers depending on the depth of the void. Corey et al. (2014) examined the influence of geosynthetic layers on the mechanical response of buried pipelines subjected to static loading conditions. Their experimental investigation involved two types of base materials and geogrids positioned both within and above the trench. The findings demonstrated a notable reduction in longitudinal deformations due to the inclusion of geogrid reinforcement. Similarly, Hedge and Sitharam (2015) carried out both experimental and numerical analyses to study the behavior of buried pipes installed in geocell-reinforced sand beds. Their results indicated that the use of reinforcement led to a reduction of approximately 50% in the pressure exerted on the pipe and around 40% in the deformation levels. Ahmed et al. (2015) conducted both experimental and numerical investigations on the contact pressure distribution around rigid pipes using tactile sensing technology. Their findings demonstrated that the inclusion of reinforcement significantly reduced radial pressures surrounding the pipe. In another study, Ni et al. (2018) performed numerical analyses to assess the viability of tire-derived aggregate (TDA) as a compressible medium in induced trench installations of rigid pipes under plane strain conditions. They found that the effectiveness of TDA in reducing earth pressures was highly dependent on the stiffness contrast between the soil and the aggregate. Kou et al. (2018) explored the response of a 160 mm PVC pipe subjected to loading from a 75 mm strip footing aligned with the pipe's centerline and buried in poorly graded sand reinforced with geogrid. Their results indicated a 20% reduction in vertical pressure at the pipe crown and a 21% decrease in footing settlement compared to the unreinforced scenario. Elshesheny et al. (2019) carried out large-scale laboratory tests to examine the response of HDPE pipes in both unreinforced and geogrid-reinforced sand subjected to incrementally increasing cyclic loading. The results showed that pipe strain and deformation decreased with increasing burial depth, with the most significant reduction in footing settlement observed up to a burial depth of H/D = 2.5. They also noted that reinforcement layers contributed to a redistribution of transferred stresses, leading to reduced strains and deformations, with a settlement reduction ratio reaching up to 50%. Abdollahi et al. (2019) combined large-scale experimental tests and three-dimensional finite element analyses to evaluate the performance of EPS post-and-beam systems for pipe protection. Their study concluded that increased soil cover reduced the stress levels on the EPS beam and that adding a single geogrid layer to the cover soil significantly enhanced the system's effectiveness. Zhou et al. (2020) investigated the mitigation of soil subsidence effects by applying woven geotextile and geogrid reinforcements both above and below buried pipes. Their results indicated that placing reinforcement beneath the pipe was particularly effective in minimizing vertical displacements.

The literature review reveals that numerous studies have addressed both reinforced and unreinforced soils in geotechnical engineering applications. However, the distinguishing feature of the present study lies in its comprehensive examination of the role of geogrid reinforcement on soil–structure–pipe interaction, with particular emphasis on the influence of different reinforcement configurations. This approach enables a more effective utilization of geogrid capacity tailored to the interaction mechanisms involved.

2. Material and method

Numerical methods are widely preferred in geotechnical engineering due to their efficiency in terms of cost, time, and versatility. Among the commonly used numerical approaches, the Finite Difference Method (FDM) and the Finite Element Method (FEM) are predominant for solving complex geotechnical problems. The FEM, in particular, involves discretizing a complex domain into smaller finite elements interconnected at nodes. This approach allows the solution of complex problems governed by partial differential and integral equations. In this study, the commercially available FEM-based software PLAXIS 2D (version 8.6), which supports plane strain and axisymmetric conditions, was employed to analyze the deformation, stress distribution, strain behavior, and failure mechanisms associated with buried pipelines. A series of two-dimensional finite element simulations were performed to investigate the structural response of a buried pipe embedded in soil with and without geogrid reinforcement. The model domain consisted of a soil bed measuring 15 meters in width and 10 meters in depth. These dimensions were determined through a sensitivity analysis aimed at assessing the influence of model boundaries on numerical outcomes. A uniform vertical surface surcharge load of 200.0 kN/m² was applied to simulate overburden pressure.

Figure 3 illustrates the geometry of the model and the configurations of the geogrid reinforcement. Three reinforcement arrangements were considered: (1) a horizontal geogrid layer placed 200 mm (equivalent to one time the pipe diameter) above the pipe crown with a length of 1200 mm (equivalent to six times the pipe diameter), (2) an inverted-U configuration where the geogrid encased the upper sides of the pipe, and (3) a full-encasement configuration in which the geogrid completely enveloped the pipe. The geogrid used in the models had a tensile strength of 30 kN/m. The objective of this modeling effort was to evaluate the performance of buried pipelines resting on sandy soil under different reinforcement scenarios.

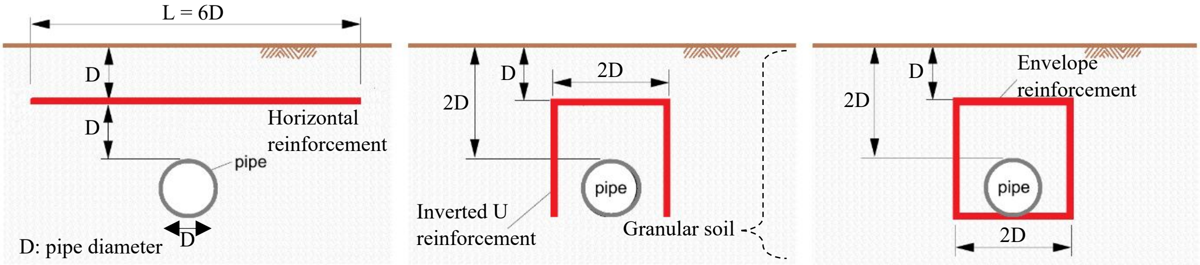

Fig. 3. Schematic diagram of geometry model and reinforcement arrangements

Finite element (FE) analyses of a buried pipe subjected to vertical loading on granular soil were conducted using PLAXIS 2D, a widely adopted, user-friendly commercial FE software package commonly used in geotechnical engineering practice. PLAXIS 2D operates using an implicit time integration scheme, which enables faster and more stable computations compared to software utilizing explicit schemes, particularly for problems involving soil–structure interaction. Designed specifically for analyzing deformation and stability in geotechnical applications, the software also provides comprehensive post-processing capabilities, allowing for a detailed interpretation of stress, strain, and displacement distributions within the model. The default boundary conditions available in PLAXIS 2D, which restrict the horizontal deformations at the side boundaries and both horizontal and vertical deformations at the bottom boundary, were used. The dimensions of boundaries were determined by conducting convergence studies by varying the model dimensions. The dimensions and initial mesh configuration of the numerical model, developed based on the cross-sectional geometry illustrated in Fig. 3, are presented in Fig. 4. A comparative analysis using a finer mesh was also performed, which yielded results within a 2% margin of difference, indicating negligible sensitivity to mesh refinement. The numerical domain measured 15 m in width and 10 m in height. Boundary conditions were defined such that the lateral boundaries were restrained against horizontal displacement, while the base of the model was fixed in both horizontal and vertical directions. The pipe, with an outer diameter of 0.20 m, was modeled using the built-in structure designer tool. A 15-node triangular element mesh was employed to improve accuracy in stress and deformation predictions. Following pipe generation, the soil within the pipe boundary was removed to simulate a hollow structure. Groundwater conditions were not considered in the present analysis.

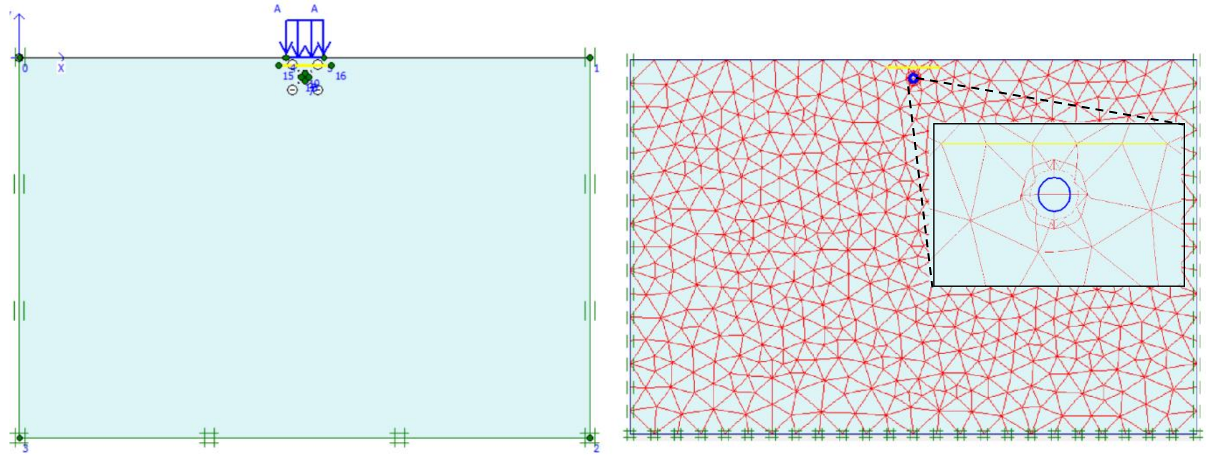

Fig. 4. Numerical model illustrating the mesh configuration for the very fine mesh case

To model the behavior of sandy soils, the Hardening Soil Model (HSM) was chosen, as it is well-suited for granular soils subjected to monotonic loading and limited unloading stress paths. When compared to other models, such as the linear elastic and perfectly plastic models based on the Mohr-Coulomb (MC) criterion, several limitations of the MC model become apparent. These include its bilinear nature (constant values for modulus of elasticity and Poisson's ratio), unlimited dilation, isotropy, and perfect plasticity assumptions. In contrast, the HSM offers a more comprehensive approach by incorporating plasticity theory and soil dilatancy, similar to the MC model, but also introduces a yield cap and a stress-dependent elastic modulus. A key distinction of the HSM is that the elastic domain is not fixed; instead, it can expand depending on both volumetric and deviatoric plastic strains. Furthermore, the model accounts for two separate yielding mechanisms: one for shear and another for compression, as depicted in Fig. 5. Irreversible deformations due to initial deviatoric loading are captured through shear hardening, whereas plastic strains arising from primary compression—such as those occurring under oedometer or isotropic loading—are accounted for by compression hardening mechanisms (Schanz et al., 1999).

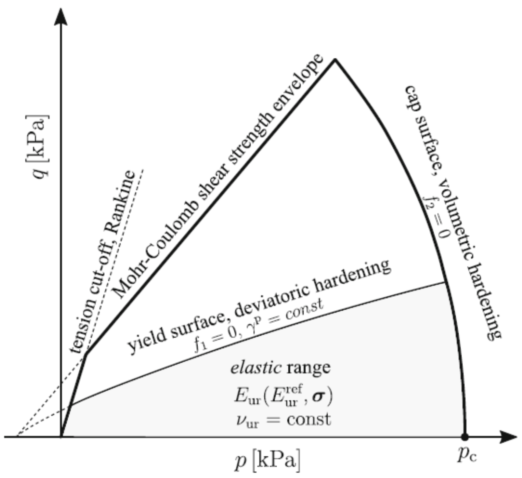

Fig. 5. Stress yield boundary and elastic behavior domain in the standard Hardening Soil (HS) model (Cudny & Truty, 2020)

A key difference between the two models lies in the parameters they utilize. The Mohr-Coulomb elastic-perfectly plastic model is governed by a limited set of fundamental parameters, including the internal friction angle (φ), dilatancy angle (ψ), cohesion (c), Poisson's ratio (ν), and a constant stiffness modulus (E). Conversely, the Hardening Soil (HS) model employs a more advanced formulation that considers the stiffness of the soil to be stress-dependent, allowing for a more realistic representation of soil behavior under diverse loading scenarios. The HS model typically requires a broader set of input parameters—at least twelve—including the unsaturated and saturated unit weights of the soil (γ_{unsat} and γ_{sat}), initial void ratio (e_{init}), Poisson's ratio (ν), cohesion (c), friction angle (φ), dilatancy angle (ψ), reference secant stiffness from a drained triaxial test (E_{50}^ref), tangent stiffness for primary oedometer loading (E_{oed}^{ref}), unloading/reloading stiffness (E_{ur}^{ref}), stress-dependency exponent (m), and the interface strength reduction factor (R_{inter}). Laboratory studies show that plastic deformations in soils begin from the initial stages of loading. Constitutive models that utilize a hardening law after early yielding are required to take into account such properties of soils. The hardening soil model can also be used for softer soils such as silts and clay in addition to sand and gravel because there are three elastic modules in the HS model, and the hardening soil model also accounts for the stress-dependency of stiffness moduli. Therefore, all three input stiffnesses are referenced to a reference stress, typically set at 100 kPa (1 Bar). In addition to the model parameters previously mentioned, the initial soil conditions, such as consolidation, are crucial in many soil deformation problems. These conditions are often incorporated into the model through the initial stress state, which plays a significant role in accurately simulating soil behavior under loading. As a result, the HS model gives more realistic results in FEM simulation than the Mohr-Coulomb model. Therefore, in the numerical simulations conducted for this study, the properties of soils were represented using the Hardening Soil (HS) constitutive model. Table 1 summarizes soil properties used in the numerical modeling.

Table 1. The input parameters for Hardening soil material model (Bildik & Tanrıöver, 2023)

Soil Parameters	Definition	Value
material model	hardening soil material model	-
γ_{unsat}	soil unit weight above phreatic level (kN/m$^{3)}$	18.40
γ_{sat}	soil unit weight below phreatic level (kN/m$^{3)}$	20.36
e_{init}	initial void ratio	0.5
ϕ	internal friction angle (degree)	37
ψ	dilatancy angle (degree)	8.625
E_{50}^{ref}	secant stiffness in standard drained triaxial test (kN/m^2)	5.1x10^4
E_{oed}^{ref}	tangent stiffness for primary oedometer loading (kN/m^2)	5.1x10^4
E_{ur}^{ref}	unloading/reloading stiffness (kN/m^2)	1.5x10^5
c	cohesion (kN/m^2)	1.00
m	power for stress-level dependency of stiffness	0.43
R_{inter}	strength reduction factor inter	1.0
$k_x = k_y$	permeability (m/day)	10.00

PLAXIS 2D finite element software offers a dedicated feature called the tunnel designer, which facilitates the modeling of circular structures such as tunnels and pipes. This tool assembles the structure by generating interconnected plate elements arranged in a ring. Following the simulation, internal forces acting on these elements can be extracted and analyzed. Each plate element is defined by five primary parameters: (1) axial stiffness (EA), (2) bending stiffness (EI), (3) equivalent thickness (t), which is derived automatically from EA and EI, (4) unit weight (γ), and (5) Poisson's ratio (ν), which is generally assumed to be zero in cases where the structural component (e.g., pipe wall) occupies a negligible portion of the model's cross-sectional area. The mechanical properties assigned to the HDPE pipe are summarized in Table 2. These parameters, based on a 200 mm diameter pipe, correspond to the assumptions of a Linear Elastic Material Model used to represent the behavior of a typical HDPE pipe

Table 2. Engineering properties of the HDPE* pipe

Pipe Parameters	Definition	Value
LE	linear elastic	-
EA	normal stiffness, (kN/m)	6.372
EI	flexural rigidity, (kNm^2/m)	0.126
υ	poisson's ratio, υ	0.40

HDPE: high-density polyethylene

3. Results

The numerical analysis results concerning the displacement behavior of a flexible pipe embedded in granular soil and the stress distribution developed on the pipe surface are presented and discussed in this section. A series of numerical analyses were carried out using a 200.0 kN/m^2 nominal surcharge load. The variations in displacement and stress within the buried pipe, as influenced by the reinforcement configuration, were also evaluated. The reinforcements were applied to the soil in three distinct configurations, as illustrated in Fig. 4. The initial and most straightforward reinforcement setup (denoted as HL) consisted of a single horizontal layer placed 200 mm above the crown of the pipe. The second arrangement (IU) involved installing the reinforcement in an inverted U-shaped configuration encircling the pipe, which can be realized by excavating trenches along both sides of the pipe. However, this method is generally less feasible in practical field applications compared to the horizontal layout. The final configuration (ENV) featured a fully enclosed reinforcement layer encapsulating the entire pipe, as illustrated in Fig. 4. In this setup, the terminal ends of the reinforcement were firmly joined to prevent slippage, thereby preserving the structural integrity and functional performance of the reinforcement. A geogrid reinforcement with 30 kN/m tensile rigidity was used to reinforce the granular soil. Thus, the values of the soil surface settlement depending on reinforcement configuration were obtained. Considering the behavior of the pipe embedded in unreinforced soil, the inclusion of geogrid reinforcement led to a noticeable reduction in vertical surface settlement. Specifically, the decrease in settlement was quantified as 40.8%, 57%, and 61% for the HL, IU, and ENV reinforcement configurations, respectively, as illustrated in Fig. 6.

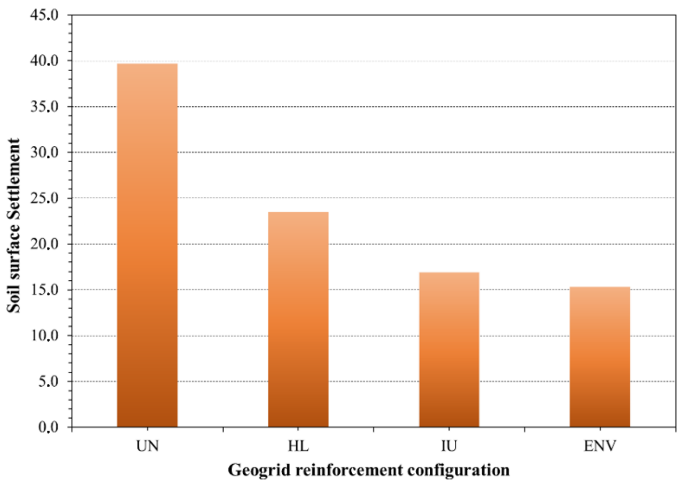

Fig. 6. Settlement at the soil surface for a surface surcharge of 200 kN/m^2

The effectiveness of the reinforcement in minimizing the deflections of the pipe can be characterized as;

$$E_D = 100 \text{ x } (\Delta D_{unr} - \Delta D_r) / \Delta D_{unr} \text{ (\%)} \quad (1)$$

where E_D represents the efficiency of the reinforcement in reducing pipe deflections, ΔD_{unr} is the pipe deflection in unreinforced soil, and ΔD_r is the pipe deflection in reinforced soil. The effectiveness of the reinforcement in alleviating the vertical compression of the pipe at the conclusion of the numerical analysis, considering different configurations, is illustrated in Fig. 7. When comparing the pipe's performance in unreinforced soil, the inclusion of reinforcement led to a reduction in vertical deflections by 40.7%, 59.9%, and 64.7%, corresponding to the results obtained for reinforcement configurations HL, IU, and ENV, respectively (see Fig. 7)

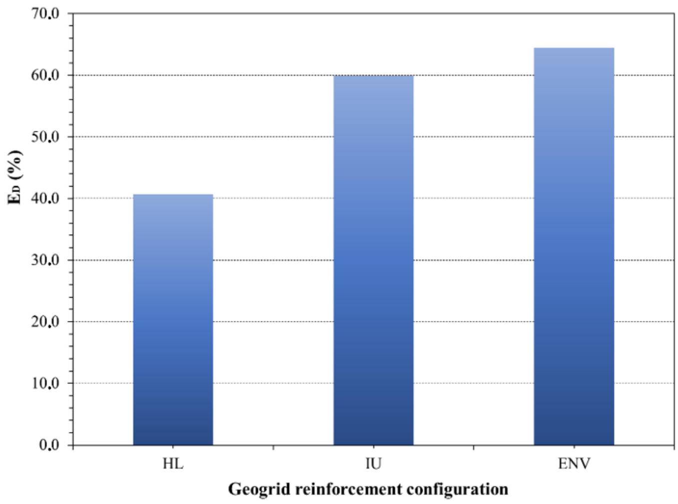

Fig. 7. The effectiveness of the reinforcement in reducing the deflections of the pipe

The surface settlements observed for reinforced soils with different configurations are presented in Fig. 8. In general, the placement of geogrid reinforcement in the subgrade reduced the ground displacements. It is clearly observed that the various reinforcement configurations have limited the displacements and effectively restrained soil movement.

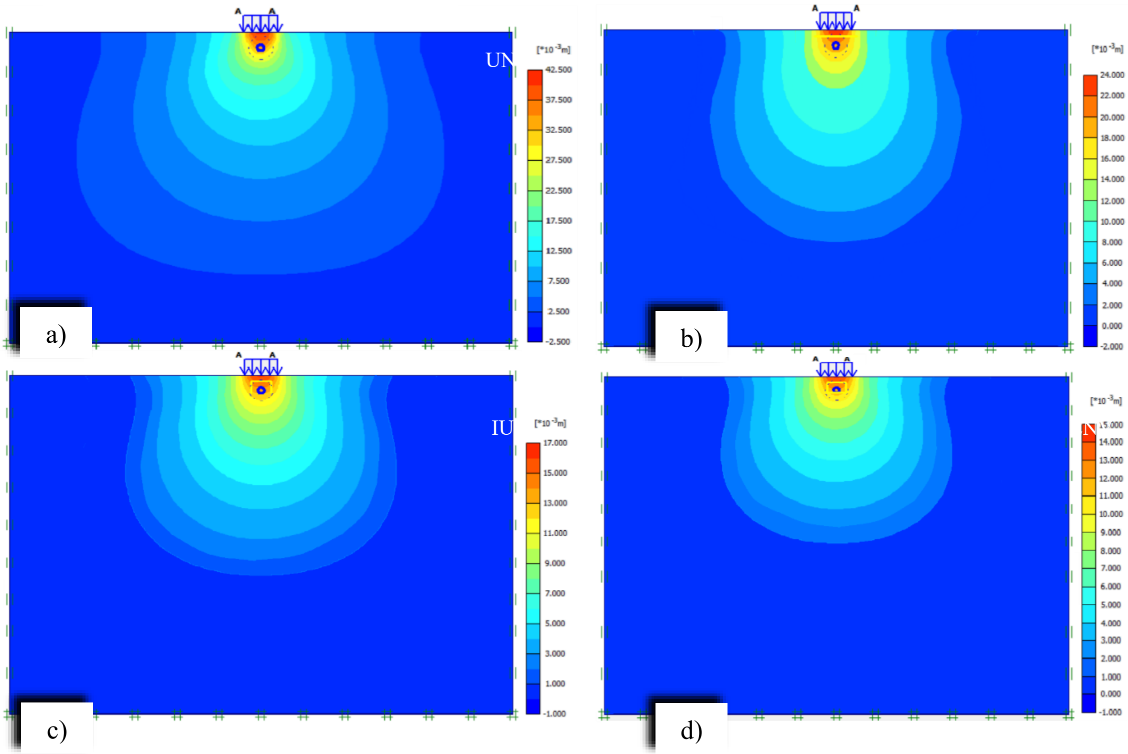

Fig. 8. Total displacement at the soil surface for a surface surcharge of 200 kN/m^2 (a) Unreinforced arrangement, (b) Horizontal reinforcement layer arrangement, (c) Shape of an inverted U reinforcement arrangement, (d) Enveloped reinforcement arrangement

4. Conclusions

Geogrids can efficiently protect buried pipelines. This research investigates the use of reinforcement methods to shield a pipe from the effects of localized surcharges applied to the soil surface. Various reinforcement types and configurations were examined. As part of the investigation, a series of finite element analyses was conducted using the commercial software PLAXIS 2D to evaluate the behavior of a buried pipe both with and without geogrid reinforcement. The key findings from this study are summarized below.

- A reduction in the overall settlement of the pipe was also observed in the reinforced soil conditions.
- The enveloping configuration was found to be the most effective in maximizing the advantages offered by the geogrid reinforcement.
- Considering the pipe's performance in unreinforced soil, the inclusion of geogrid reinforcement led to a reduction in vertical soil surface settlement ranging from 40.8 to 61%, corresponding to the HL, IU, and ENV reinforcement configurations, respectively.
- In comparison to the pipe behavior in unreinforced soil, the incorporation of geogrid reinforcement resulted in a reduction of the pipe's vertical deflections by 40.7%, 59.9%, and 64.7% for the HL, IU, and ENV configurations, respectively.

Acknowledgments

References

Abdollahi, M., Tafreshi, S.N.M., & Leshchinsky, B. (2019). Experimental-numerical assessment of geogrid-EPS systems for protecting buried utilities. *Geosynth. Int.* 26(4), 333–353.

Abuhajar, O., Naggar, H. E., & Newson, T. (2016). Numerical modeling of soil and surface foundation pressure effects on buried box culvert behavior. *Journal of Geotechnical and Geoenvironmental Engineering*. 142(12).

Ahmed, M.R., Tran, V.D.H., & Meguid, M.A. (2015). On the role of geogrid reinforcement in reducing earth pressure on buried pipes: experimental and numerical investigations. *Soils Found*. 55, 588–599.

Al-Barqawi, M., Aqel, R., Wayne, M., Titi, H., & Elhajjar, R. Polymer. (2021). Geogrids: A review of material, design and structure relationships. *Materials*. 14, 4745.

Asakereh, A., Ghazavi, M., & Moghaddas Tafreshi, S.M. (2013). Cyclic response of footing on geogrid-reinforced sand with void. *Soils Found*. 53(3), 363–374.

Bildik, S., & Tanrıöver, H. (2023). Numerical investigation of the pile–soil interaction problem under dynamic loads. *Applied Sciences*. 13(21):11653.

Corey, R., Han, J., Khatri, D.K., & Parsons, R.L. (2014). Laboratory study on geosynthetic protection of buried steel-reinforced HDPE pipes from static loading. *J. Geotech. Geoenviron. Eng.* 140, 04014019-1-10.

Cudny, M., & Truty, A. (2020). Refinement of the Hardening Soil model within the small strain range. *Acta Geotech*. 15, 2031–2051

Das, B.M. (2013). Use of geogrid in subgrade-ballast system of railroads subjected to cyclic loading for reducing maintenance. California State University, Sacramento, USA

Elshesheny, A., Mohamed, M., & Sheehan, T. (2019). Buried flexible pipes behaviour in unreinforced and reinforced soils under cyclic loading. *Geosynth. Int.* 26(2), 184–205. https://doi.org/10.1680/jgein.18.00046

Guha, I., Randolph, M.F., &White, D.J. (2016). Evaluation of elastic stiffness parameters for pipeline-soil interaction. *Journal of Geotechnical and Geoenvironmental Engineering*. 142(6)

Hedge, A.M., & Sitraham, T.G. (2015). Experimental and numerical studies on protection of buried pipelines and underground utilities using geocell. *Geotext. Geomembranes*. 45(3), 372–381.

Jeyapalan, J.K., & Hamida, H.B. (1988). Comparison of german to marston design method. *Journal of Transportation Engineering*. 114(4), 420-435.

Kawabata, T., Ling, H. I., Mohri, Y., & Shoda, D. (2006). Behavior of buried flexible pipe under high fills and design implications. *Journal of Geotechnical and Geoenvironmental Engineering*. 132(10), 1354-1359.

Kou, Y., Shukla, S.K., & Mohyeddin, A. (2018). Experimental investigation for pressure distribution on flexible conduit covered with sandy soil reinforced with geotextile reinforcement of varying widths. *Tunn. Undergr. Space Technol.* 80, 151–163.

Masada, T., Sargand, S., Hazen, G., Schehl, D., Moran, A., & Altarawneh, B. (2002). Field verification of structural performance of thermoplastic pipe under deep backfill conditions, Final Report, Ohio Department of Transportation, OH, USA.

Moser, A.P., & Folkman, S. (2008). Buried pipe design, McGraw-Hill, New York, NY, USA.

Naggar, H.E., Turan, A., & Valsangkar, A. (2015). Earth pressure reduction system using geogrid-reinforced platform bridging for buried utilities. *J. Geotech. Geoenviron.Eng.* 141(6), 04015024-1-10.

Ni, P., Qin, X., & Yi, Y. (2018). Numerical study of earth pressures on rigid pipes with tire-derived aggregate inclusions. *Geosynth. Int.* 25(5), 494–506.

Palmeira, E.M., & Andrade, H.K.P.A. (2010). Protection of buried pipes against accidental damage using geosynthetics. *Geosynth. Int.* 17(4), 228–241.

Placido, R., & Portelinha, F.H.M. (2019). Evaluation of geocomposite compressible layers as induced trench method applied to shallow buried pipelines. *Geotext. Geomembranes*. 47(5), 662–670.

Robert, D. J., Soga, K., O'Rourke, T. D., & Sakanoue, T. (2016). Lateral load-displacement behavior of pipeline in unsaturated sands. *Journal of Geotechnical and Geoenvironmental Engineering*. 142(11).

Sargand, S. M., Tarawneh., T. B., & Gruver., D. (2005). Field performance and analysis of large diameter high density polyethylene pipe under deep soil fill. *ASCE J. Geotech. Eng*. 131(1), 39-51.

Schanz, T., Vermeer, P., & Bonnier, P. (1999). The hardening soil model: Formulation and verification. Beyond 2000 in computational geotechnics - 10 years of PLAXIS

Selig, E.T., Di Francesco, L.C., & McGrath, T.J. (1993). Laboratory tests of buried pipe in hoop compression, STP 1222, ASTM International, West Conshohocken, PA, USA, pp. 119-132.

Tafreshi, S.N.M., & Khalaj, O. (2008). Laboratory tests of small-diameter HDPE pipes buried in reinforced sand under repeated-load. *Geotext. Geomembranes*. 26, 145–163.

Talesnick, M.L., Xia, H.W., &Moore, I.D. (2011). Earth pressure measurements on buried HDPE pipe. *Geotechnique*. 61(9), 721-732. https://doi.org/10.1680/geot.8.P.048.

Wang, F., Han, J., Corey, R., Parsons, R.L., & Sun, X. (2017). Numerical modeling of installation of steel-reinforced high-density polyethylene pipes in soil. *J. Geotech. Geoenviron. Eng*. 143(11), 04017084.

Won, M.S., Ling, H.I., & Kim, Y.S. (2004). A study of the deformation of flexible pipes buried under model reinforced sand. *KSCE Journal of Civil Engineering*. 8(4), 377–385.

Zhou, M., Du, Y.J., Wang, F., & Liu, M.D. (2017a). Performance of buried HDPE pipes – part I: peaking deflection during initial backfilling process. *Geosynth. Int.* 24(4), 283–395.

Zhou, M., Wang, F., Du, Y.J., & Liu, M.D. (2017b). Performance of buried HDPE pipes – part II: total deflection of the pipe. *Geosynth. Int.* 24(4), 396–407.

Zhou, M., Wang, F., Du, Y.J., Corey, R., & Liu, M.D. (2020). Feasibility study on the use of geosynthetics to reinforce buried HDPE pipes subjected to localized ground subsidence. *Transportation Geotechnics*. 22.

4th International Civil Engineering & Architecture Conference
17-19 May 2025, Trabzon, Türkiye

Impact of freezing-thawing cycles on modes I and II cracking resistance of soil and cement concrete materials

M.R.M Aliha*[1,2], S. M Nabavi[1], N. Choupani[2], F. Bedir[2], S. Moshtaghi[1], K. Rafiee[1]

[1] Welding and Joining Research Center, School of Industrial Engineering, Iran University of Science and Technology (IUST), 16846-13114, Tehran, Iran.
[2] Department of Mechanical Engineering, Engineering Faculty, Gebze Technical University, 41400 Gebze, Kocaeli, Turkiye.

Abstract
Mechanical behavior and integrity of construction materials and civil structures made of geo-materials like soil, clay, concrete, cement and mortars is affected by the environmental conditions. Repeated freezing & thawing mechanism is among the natural phenomena that can generally reduce the overall strength properties (such as fracture toughness) of the civil structures and geomaterials and finally can accelerate the rate of damage and associated failure. Material type and state of applied external loads and deformations may affect the fracture toughness of geo-materials exposed to freezing-thawing periods. There are very limited data in the literature for investigating the influence of tensile or shear type loads (i.e., modes I and II) and numbers of freeze/thaw cycles on the fracture toughness values of geomaterials. Hence, in this research, using edge cracked semi-circular bend specimens made of soil, clay and cement concrete the impact of freezing-thawing (FT) mechanism and the number of applied FT cycles are investigated experimentally on the fracture toughness behavior. Such tests were conducted under both pure modes I and II conditions and it was observed that FT mechanism can reduce generally the fracture toughness (K_{Ic} and K_{IIc}) of both soft and tight geo-materials. However, the destructive impact of this mechanism on the tested soil materials was significantly greater than its effect on the cement concrete. For example, after performing 6 FT-cycles the fracture toughness of the soil material was reduced to approximately 50% of the fracture toughness of control soil material with no FT cycles. Such reduction for the cement concrete was only about 7%. In addition, the reduction of fracture toughness after exposing to the freeze/thaw cycles was more pronounced for the tensile type (mode I) failure mechanism compared to the shear mode II case. Due to significant influence of FT mechanism on soft geomaterials (like soils), this phenomenon should be considered as important issue in service life assessment of civil structures such as earth-rock fill dams or sub-base parts of roads at cold regions and during winter season.

Keywords: Freezing-Thawing cycles, Soil, Cement concrete, Mode I and mode II loading, Fracture toughness,

1. Introduction

Construction and geomaterials such as soil, concrete, rock, asphalt mixtures and etc., are subjected to different and complex environmental and mechanical loading conditions (Baradaran & Ameri, 2023; Ayar et al., 2022; Niri et al., 2024; Pargar et al., 2024; Shojamoghadam et al., 2024; Erarslan, 2023a; Erarslan 2023b). indeed, in many field and practical applications such as underground mines, tunnels, pavement and road structures, dams, among others, soil and concrete materials are the main structural material for and element for bearing the applied loads and stresses. some issues including environmental conditions (such as temperature, humidity and moisture) may affect noticeably the structural integrity and service life of the structures made of soils, concrete and rock (Tareghian et al., 2024; Yazdi et al., 2024; Yeganeh et al., 2024; Baradaran & Ziaee, 2025; Baradaran et al., 2023; Rajaee et al., 2025; ad Miri et al., 2024; Haghighatpour & Aliha, 2023; Ghamgosar et al., 2017; Erarslan & Çavdar, 2024). In general, such parameters either under static or cyclic conditions (i.e., fluctuation of temperature or moisture) may have negative effects on the strength and mechanical property indexes. On the other hand, most of geomaterials used in civil and construction engineering projects are categorized as brittle and quasi-brittle materials and the presence of cracks and flaws or structural discontinuities and faults may increase significantly the risk of overall or catastrophic failures due to sudden growth of cracks in such materials (Berto & Lazzarin, 2014; Sharafisafa et al., 2021). Hence, it is necessary to investigate the fracture and crack growth characteristics of structural civil and

* Corresponding author, E-mail: mrm_aliha@iust.ac.ir

https://doi.org/10.31462/icearc2025_ce_geo_929

geo-materials under real field situations. Cracks in the structural components can be subjected to different loading modes and deformations. Among them mode I (tensile deformation) and mode II (in-plane shear deformation) are the most failure modes observed in the fractured structures. The failure of geo and construction materials under any modes I and II conditions are determined experimentally using different testing methods (Mahdavi et al., 2023; Najjar et al., 2022; Reza Karirmi et al., 2023). disc type samples and cylindrical shape specimens are favorite test samples to conduct fracture toughness (as the most important and key index in fracture mechanics) tests on geo-materials. some test configurations such as semi-circular bend (SCB) sample (Baradaran et al., 2024a; Baradaran et al., 2024b; Baradaran & Aliha, 2025; Aliha et al., 2025; Ghodratnama et al., 2025), Brazilian disc (BD) sample (Ayatollahi & Aliha, 2008; Li et al., 2022), Edge notch disc bend (ENDB) sample (Pournoori et al., 2024; He et al., 2022; Eghbali et al., 2019), three or four point bend beam (Aliha et al., 2019), center cracked ring (CCR) sample (Gu et al., 2023) are among the more common test samples for determining K_{Ic} (mode I fracture toughness) and K_{IIc} (mode II fracture toughness) values in rocks, soils, concrete and other geomaterials.

Most of the fracture experiments on these materials have been performed on control conditions (Fakhri & Ahmadi, 2017; Karimi et al., 2021; Haghighatpour & Aliha, 2022; de Jesús Arrieta Baldovino et al., 2021; Fakhri et al., 2020; Hou et al., 2021) and the effect of freezing/thawing mechanism on the crack growth resistance of construction materials has received less attention in the literature. Freezing and thawing mechanism (FTM) is one of the major degradation sources in geo-structures. This can be occurred due to change in temperature from subzero to medium temperatures and vice versa at a day or at a season. Thermal stresses and deformations induced by this mechanism can increase the risk of fracture and crack growth by weakening the material. amplitude of each freezing and thawing cycle (i.e. the difference between the maximum and minimum value of temperature) as well as the number of freeze/thaw cycles applied to geo-materials are two main affecting parameters some limited works are available in the previous works dealing with the effects of FTM on the mechanical performance of asphalt concrete mixtures. In the current research, the influence of different freeze/thaw cycles are investigated experimentally on the trends of variations for K_{Ic} and K_{IIc} values of two construction and civil materials (i.e. a soft geo-material (clay) and a tight geo-material (cement concrete)). The fracture tests are conducted on a simple and suitable specimen under both mode I and mode II conditions and the effect of material type, loading mode and number of freezing-thawing cycles are investigated on the fracture resistance (or fracture toughness) values.

2. Materials and methods

Kaolinit clay and cement concrete were considered as the materials to manufacture the test samples and conduct the fracture toughness tests. The physical and geotechnical properties of soil material (that is classified as low plasticity clay) are presented in Table 1. The cement concrete mixture was composed of Portland Cement Type II conforming to ASTM C150, potable water, and lime aggregate with a continuous aggregate gradation with 19.5 mm (maximum nominal aggregate size, NMAS, for coarse aggregates) in accordance with ASTM C33. The coarse and fine aggregate gradations used in this study are shown in Table 2. The water-to-cement ratio (w/c) was maintained at 0.4 to achieve a balance between workability and compressive strength development.

For conducting the mode I and mode II fracture tests, the SCB sample with symmetric and asymmetric loading rollers relative to the crack plane (as shown in Fig. 1) were utilized and selected. Based on the previous papers the symmetric SCB can provide pure mode I condition and asymmetric SCB is able to introduce pure mode II fracture condition (Aliha & Ayatollahi, 2013; Aliha et al., 2025; Erarslan & Aliha, 2025). The fracture toughness value that is equal to critical value of stress intensity factor under mode I and mode II conditions are determined for the SCB specimen using the below equations:

$$K_{\mathrm{IC}} = \frac{P_{max}}{2Rt}\sqrt{\pi a}\, Y_I \quad (1)$$

$$K_{\mathrm{IIC}} = \frac{P_{max}}{2Rt}\sqrt{\pi a}\, Y_{II} \quad (2)$$

where, P_{max} is the maximum peak load applied to the SCB sample at the onset of fracture (crack initiation), R, a, t are the radius of SCB, crack length and thickness of SCB specimen, respectively. S, S_1 and S_2 are also the bottom loading spans. The properties of the SCB samples made of the clay and cement concrete are illustrated in Table 3. For determining the corresponding values of fracture toughness using the SCB sample, it is required to know the values of mode I and mode II geometry factors (Y_I and Y_{II}). These parameters that are related to crack length ratio (a/R) and span ratio (S/R, S_1/R and S_2/R) have already been determined numerically in the literature for different geometry and loading conditions. The related values of Y_I and Y_{II} parameters for the test conditions of the current research (extracted from Ayatollahi & Aliha, 2007) are equal to 4.85 and 1.78, respectively. Accordingly, several SCB samples were manufactured for conducting fracture toughness tests.

Table 1. Geotechnical properties of the investigated clay.

Property	Value
Liquid limit (%)	37
Plasticity limit (%)	18.5
Plasticity index (%)	19
Specific gravity	2.63
Maximum dry density (g/cm^3)	1.49
Optimum moisture content (%)	27.8
Uniaxial compressive strength (MPa)	0.17

Table 2. The coarse and fine aggregate gradations used in this study.

Coarse virgin aggregate gradation	
Sieve size (mm)	Passing (%)
25	100
19	95
12.5	37
9.5	7.5
4.75	2
Fine virgin aggregate gradation	
Sieve size (mm)	Passing (%)
9.5	100
4.75	97
2.36	90
1.18	67
0.6	42
0.3	20
0.15	6

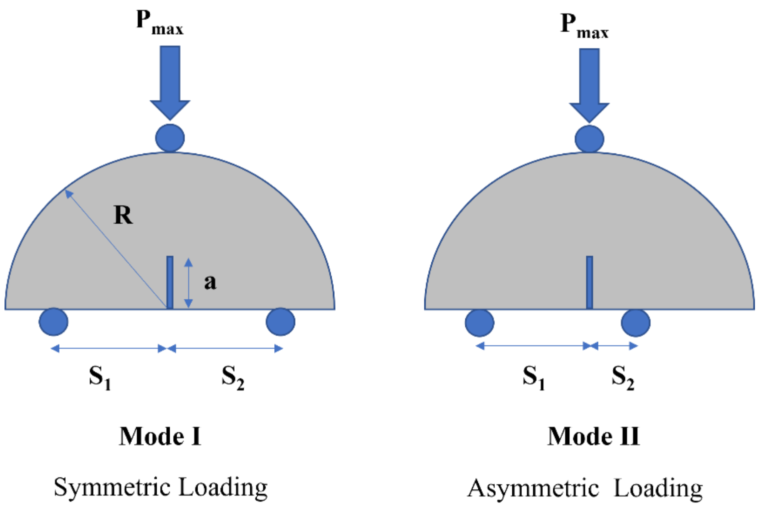

Fig. 1. (a) symmetric (i.e., $S_1 = S_2 = S$) and (b) asymmetric (i.e., $S_1 > S_2$) boundary conditions for the SCB specimen to produce pure mode I and pure mode II fracture cases, respectively.

Table 3. Geometrical and dimensional parameters considered for the investigated SCB samples made of soft and tight soil geomaterials.

Material	R (mm)	a(mm)	t (mm)	S (mm)	S_1 (mm)	S_2 (mm)
Soil	50	15	30	40	40	5
Cement concrete	75	22.5	40	67.5	67.5	8

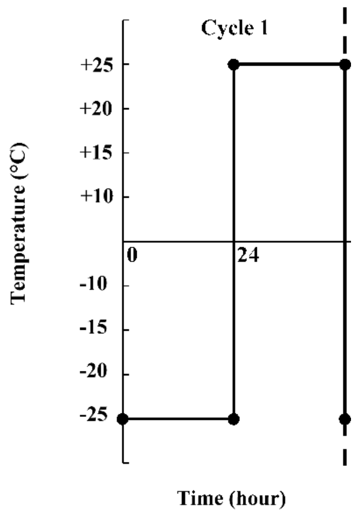

Fig. 2. Profile of thermal cycle for applying a freezing and then thawing cycle on the test samples.

Before K_{Ic} and K_{IIc} testing on the manufactured soil and cement concrete samples, they were exposed to different freezing/thawing cycles. Each cycle was consisting of a freezing period at -25°C for 1day (24 hours) following a thawing cycle inside the moisturized bath for 24 hours at temperature of +25°C. Several freeze/thaw cycles (i.e., 0 cycle (control), 1 cycle, 2 cycle, 3 cycle, 4 cycle, 5 cycle and 6 cycle) were applied to the soil and cement concrete samples and then the fracture toughness experiments were done on the SCB samples (Fig. 2). To do that, the test samples were put inside the three-point bend fixture with the loading support distances (S_1 and S_2) given in Table 3 for both modes I and II. The samples were loaded monotonically with the constant loading rate of 3 mm/min using a servo hydraulic testing machine with the capacity of 5 kN. The corresponding values of modes I and II fracture toughness were determined by importing the critical or maximum peak experimental load of each sample into Equations 1 and 2. The obtained results are illustrated and discussed in the next section.

3. Results and discussion

The variations of fracture toughness (K_{Ic} and K_{IIc}) for the tested soil and concrete materials are illustrated in Fig. 3 for different freeze/thaw cycles. Based on this Figure and obtained experimental results the fracture toughness value decreases by increasing the number of freeze/thaw cycles and compared to control condition without exposing to freezing and thawing mechanism the cracking resistance of geomaterials is reduced for both tensile and shear type failure modes. However, the reduction of fracture toughness for the soil material is more visible than the cement concrete material. After six freeze/thaw cycles, the fracture toughness of soil is reduced to 0.5 and 0.4 times of its value at control condition for both modes I and II. This reveals the significant impact of such environmental agent on the overall load bearing capacity of the soft geomaterials (such as soils and clays). Based on the obtained results, fracture toughness of shear mode case is more sensitive to the freezing thawing mechanism compared to the tensile type failure mode.

In addition, the tight cement concrete material was not so sensitive to the freeze/thaw cycles and a reduction up to 7% was only observed in the K_{Ic} or K_{IIc} values after five freeze/thaw cycles. Other similar research works, have also outlined and emphasized the reduction of cracking resistance of engineering construction materials subjected to different freeze-thaw cycles. For example, Haghighatpour & Aliha (2022), Fakhri et al. (2025), have shown that the fracture toughness of hot or warm mix asphalt concrete materials (HMA and WMA) is reduced by applying different cycles of freezing-thawing. Such materials (that are made of visco-elastic bitumen or binder) may show high dependency to the changes in environmental conditions such as temperature variations or thermal stresses. Hence, according to the available relevant studies, freezing-thawing mechanism can reduce significantly the fracture toughness of asphalt mixture up to 50% of the control condition's strength and load bearing capacity. However, compared to the bitumen or asphaltic binder, the cement used in the mixture of cement or plain concrete has lesser sensitivity to the temperature changes in the range of ±25°C.

Therefore, the research investigated cement concrete material showed lower variation in the value of fracture toughness by applying the freeze/thaw cycles relative to the HMA or WMA mixtures. In order to better compare the trends of fracture toughness variation under repeated freezing/thawing mechanism Fig. 4 presents the normalized fracture toughness data versus the number of applied freeze/thaw cycles to the tested soil and concrete geomaterials. Indeed, in this figure the fracture toughness data of different freeze/thaw cycles were normalized to the corresponding value of K_{Ic} or K_{IIc} obtained at control condition (i.e. with no application of freezing-thawing cycles). This figure clearly shows the sensitivity of cracking resistance value to the material type and loading mode in the investigated geo-materials. While, for the cement concrete material, the fracture toughness reduces dominantly by a linear trend when the number of cycles is increased, the first cycles of freezing/thawing mechanism have much more impact on the reduction of both K_{Ic} and K_{IIc} and by increasing the number of cycles (for instance, greater than 4 cycles), the fracture toughness reduction curves show a power law form. In addition, mode I fracture case has more sensitivity to the freezing/thawing mechanism compared to the mode I case.

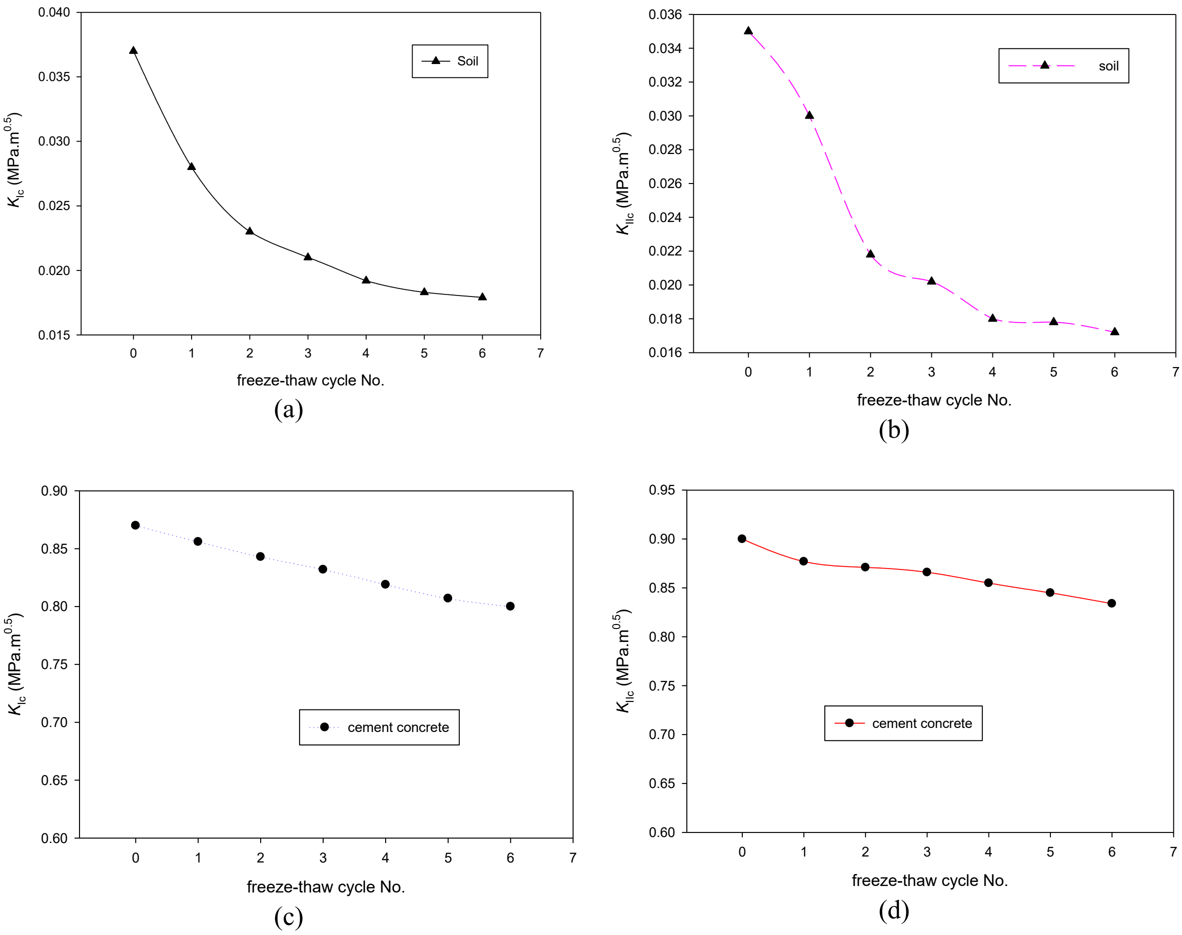

Fig. 3. Variations of fracture toughness (a) and (b): modes I and II results of soil material with the number of freeze/thaw cycles, (c) and (d): modes I and II results of cement concrete material with the number of freeze/thaw cycles.

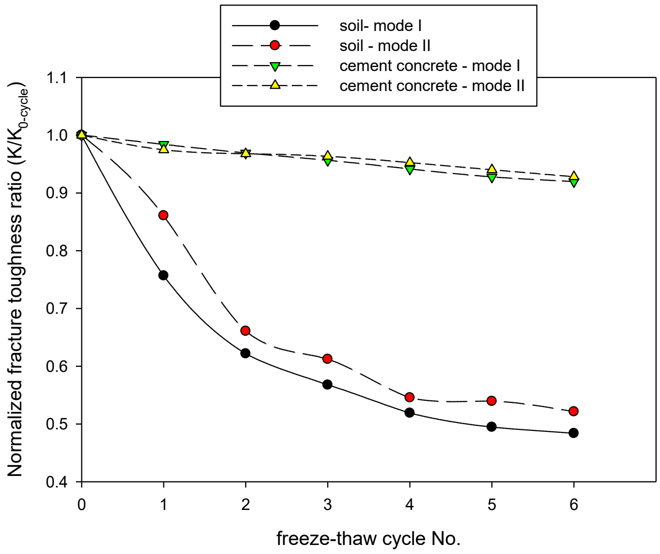

Fig. 4. Variations of normalized fracture toughness ratios with the number of freeze/thaw cycles for the tested soil and concrete materials under mode I and mode II conditions.

4. Conclusions

This study aimed to investigate the fracture toughness of two key geo-materials—soft soil and cement concrete - under freeze/thaw conditions, commonly encountered in civil and construction engineering projects. By experimentally determining the fracture toughness under both mode I (K_{Ic}) and mode II (K_{IIc}) loading conditions using a semi-circular bend (SCB) sample and both symmetric and asymmetric three-point bending setups, valuable insights were obtained regarding the materials' performance in environments subjected to freeze/thaw cycles. The results revealed that both the K_{Ic} and K_{IIc} values decreased with an increasing number of freeze/thaw cycles. However, the effects were markedly different for the two materials. For the soft soil material, the reduction in fracture toughness was more pronounced, reaching up to 40% after six freeze/thaw cycles, while cement concrete exhibited a much smaller decrease of less than 10%.

This suggests that soft soils are significantly more susceptible to freeze/thaw damage than cement concrete. Additionally, the trend of fracture toughness reduction followed distinct patterns for the two materials. For cement concrete, the fracture toughness reduction was nearly linear across the cycles, indicating a gradual degradation. In contrast, the soft soil material exhibited a power-law type reduction, with the most significant decrease occurring during the initial freeze/thaw cycles.

This behavior indicates a higher sensitivity of the soil material to early freeze/thaw damage. In conclusion, the findings of this study underscore the vulnerability of soft soil materials to freeze/thaw cycles, highlighting the need for careful consideration of material selection in construction projects exposed to such environmental conditions. The results also provide a foundation for further research into improving the durability of geo-materials, particularly soft soils, in freeze/thaw scenarios. These insights are essential for the design and long-term performance assessment of civil engineering structures, ensuring greater reliability and safety in environments subject to freeze/thaw stress.

References

Aliha, M. R. M., & Ayatollahi, M. R. (2013). Two-parameter fracture analysis of SCB rock specimen under mixed mode loading. *Engineering Fracture Mechanics, 103*, 115–123.

Aliha, M. R. M., Ghoreishi, S. M. N., Shaker, H., Jafari, F., Bazoobandi, P., Sadowski, T., & Choupani, N. (2025). Characterizing the properties of asphalt concrete (AC) at different testing conditions and loading modes by different testing methods and samples (SCB, ENDB and DCT): A comparative review of fracture parameters. *Construction and Building Materials, 474*, 141148.

Aliha, M. R. M., Ghoreishi, S. M. N., Tavana, A., Molayem, M., & Choupani, N. (2025). On determination of critical strain energy release rate for mode II failure of asphaltic composite mixtures using assymetric SCB configuration. *Theoretical and Applied Fracture Mechanics, 138*, 104936.

Aliha, M. R. M., Mousavi, S. S., & Ghoreishi, S. M. N. (2019). Fracture load prediction under mixed mode I+ II using a stress based method for brittle materials tested with the asymmetric four-point bend specimen. *Theoretical and Applied Fracture Mechanics, 103*, 102249.

Ayar, P., Baradaran, S., & Abdipour Vosta, S. (2022). A review on the effect of various additives on mechanical properties of stone mastic asphalt (SMA). *Road, 30*(110), 57–86.

Ayatollahi, M. R., & Aliha, M. R. M. (2007). Wide range data for crack tip parameters in two disc-type specimens under mixed mode loading. *Computational Materials Science, 38*(4), 660–670.
Ayatollahi, M. R., & Aliha, M. R. M. (2008). On the use of Brazilian disc specimen for calculating mixed mode I–II fracture toughness of rock materials. *Engineering Fracture Mechanics, 75*(16), 4631–4641.
Baradaran, M. S., Qazanfari, R., & Baradaran, S. (2023). Study of soil reinforcement in the east of Mashhad using glass granule. *Materials Research Express, 10*(5), 055202.
Baradaran, S., & Aliha, M. R. M. (2025). Mode I and Mode II fracture assessment of green asphalt pavements containing plastic waste and RAP at low and intermediate temperature. *Results in Engineering, 25*, 103734.
Baradaran, S., & Ameri, M. (2023). Investigation of rutting failure in asphalt mixtures and its improvement strategies. *Road, 31*(114), 53–70.
Baradaran, S., & Ziaee, S. A. (2025). Review of the mechanical properties of asphalt pavement reinforced with natural plant fibers as an eco-friendly solution in pavement engineering. *Road*.
Baradaran, S., Aliha, M. R. M., Maleki, A., & Underwood, B. S. (2024b). Fracture properties of asphalt mixtures containing high content of reclaimed asphalt pavement (RAP) and eco-friendly PET additive at low temperature. *Construction and Building Materials, 449*, 138426.
Baradaran, S., Rahimi, J., Ameri, M., & Maleki, A. (2024a). Mechanical performance of asphalt mixture containing eco-friendly additive by recycling PET. *Case Studies in Construction Materials, 20*, e02740.
Berto, F., & Lazzarin, P. (2014). Recent developments in brittle and quasi-brittle failure assessment of engineering materials by means of local approaches. *Materials Science and Engineering: R: Reports, 75*, 1–48.
de Jesús Arrieta Baldovino, J., dos Santos Izzo, R. L., & Rose, J. L. (2021). Effects of freeze–thaw cycles and porosity/cement index on durability, strength and capillary rise of a stabilized silty soil under optimal compaction conditions. *Geotechnical and Geological Engineering, 39*(1), 481–498.
Eghbali, M. R., Tafti, M. F., Aliha, M. R. M., & Motamedi, H. (2019). The effect of ENDB specimen geometry on mode I fracture toughness and fracture energy of HMA and SMA mixtures at low temperatures. *Engineering Fracture Mechanics, 216*, 106496.
Erarslan, N. (2023a). Investigation of the tensile-shear failure of asphalt concrete base (ACB) construction materials using a non-linear cohesive crack model and critical crack threshold analysis. *Construction and Building Materials, 364*, 129901.
Erarslan, N. (2023b). Investigation of the fracture process zone and behavior of the macro-scale fatigue cracks in brittle rock specimens. *Rock and Soil Mechanics, 44*(7), 4.
Erarslan, N., & Aliha, M. R. M. (2025). Fracture and damage analysis of cement-stabilized fine and coarse grain soils under static and cyclic loading using chevron-notched SCB specimen. *Fatigue & Fracture of Engineering Materials & Structures*.
Erarslan, N., & Çavdar, P. (2024). Investigation of the tensile and mixed mode (tensile and shear) fracture properties of cement-stabilized soils by numerical analysis. *Natural and Applied Sciences Journal, 7*(1), 1–14.
Fakhri, M., & Ahmadi, A. (2017). Evaluation of fracture resistance of asphalt mixes involving steel slag and RAP: Susceptibility to aging level and freeze and thaw cycles. *Construction and Building Materials, 157*, 748–756.
Fakhri, M., Siyadati, S. A., & Aliha, M. R. M. (2020). Impact of freeze–thaw cycles on low temperature mixed mode I/II cracking properties of water saturated hot mix asphalt: An experimental study. *Construction and Building Materials, 261*, 119939.
Fakhri, M., Siyadati, S. A., & Aliha, M. R. M. (2025). A prediction model for determining the fracture toughness of saturated asphalt concrete in sub-zero temperatures. *Theoretical and Applied Fracture Mechanics*, 104965.
Ghamgosar, M., Erarslan, N., & Williams, D. J. (2017). Experimental investigation of fracture process zone in rocks damaged under cyclic loadings. *Experimental Mechanics, 57*, 97–113.
Ghodratnama, M., Rajaee, A., Masoodi, A. R., Abrishami, S., Davarpanah, T. A., & Pournoori, P. (2025). Enhancing the fracture toughness of eco-friendly self-compacting concrete with waste glass coarse aggregates and steel fibers: A mixed-mode I/II fracture analysis using SCB specimens. *Theoretical and Applied Fracture Mechanics*, 104969.
Gu, X., Cheng, T., Zhang, F., & Aliha, M. R. M. (2023). Experimental and theoretical framework for illustrating the dependency of fracture toughness with tensile, bending, and compression loading in asphaltic samples. *Fatigue & Fracture of Engineering Materials & Structures, 46*(9), 3321–3341.
Haghighatpour, P. J., & Aliha, M. R. M. (2022). Assessment of freezing and thawing cycle (FTC) effects on mixed mode I/III fracture toughness and work of fracture of HMA asphalt mixtures. *Theoretical and Applied Fracture Mechanics, 118*, 103261.
Haghighatpour, P. J., & Aliha, M. R. M. (2023). The influence of recycled asphalt pavement materials on low and intermediate fracture behavior of asphalt concrete (AC) after exposing to different thawing and freezing periods. *Engineering Fracture Mechanics, 293*, 109715.
He, J., Liu, L., Yang, H., & Aliha, M. R. M. (2022). Using two and three-parameter Weibull statistical model for predicting the loading rate effect on low-temperature fracture toughness of asphalt concrete with the ENDB specimen. *Theoretical and Applied Fracture Mechanics, 121*, 103471.

Hou, P., Su, S., Liang, X., Gao, F., Cai, C., Yang, Y., & Zhang, Z. (2021). Effect of liquid nitrogen freeze–thaw cycle on fracture toughness and energy release rate of saturated sandstone. *Engineering Fracture Mechanics, 258*, 108066.

Karimi, M. M., Dehaghi, E. A., & Behnood, A. (2021). A fracture-based approach to characterize long-term performance of asphalt mixes under moisture and freeze–thaw conditions. *Engineering Fracture Mechanics, 241*, 107418.

Li, X., Xia, K., Yao, W., & Xu, Y. (2022). Investigation on the dynamic tensile behaviour of rubberized mortar using the Brazilian disc method. *Theoretical and Applied Fracture Mechanics, 119*, 103339.

Mahdavi, E., Aliha, M. R. M., Bahrami, B., & Ayatollahi, M. R. (2020). Comprehensive data for stress intensity factor and critical crack length in chevron notched semi-circular bend specimen subjected to tensile type fracture mode. *Theoretical and Applied Fracture Mechanics, 106*, 102466.

4th International Civil Engineering & Architecture Conference
17-19 May 2025, Trabzon, Türkiye

Evaluation of the bearing capacity of strip footings on cohesionless sloped soils by finite element analysis

Burak Akçay*[1], Osman Sivrikaya[1a]

[1] Karadeniz Technical University, Department of Civil Engineering, 61080 Trabzon, Türkiye

Abstract. In this study, a series of numerical analyses of strip foundations on cohesionless sloping soils were performed using PLAXIS 2D finite element method. The relationship between key parameters influencing the bearing capacity of strip footings on sloping soils and the bearing capacity factor ($N_{\gamma q}$) is investigated. These parameters include the slope angle (β), the distance from the strip footing to the top of the slope (b), the internal friction angle (ϕ), and the unit weight of the soil (γ). The soil has a slope angle (β) of 10˚ 20˚ and 30˚, distance of the footing to the slope crest to the width of the footing (b/B) of 0, 0.5, 1, 1.5, 2, 3, 4, 5, 6 and an internal friction angle (ϕ) of 30˚, 34˚ and 40˚ representing loose, medium dense and dense sands . Depending on the angle of internal friction angle, the unit volume weight was chosen to be 16 kN/m^3, 18 kN/m^3 and 21 kN/m^3 respectively. The footings on the surface (D_f=0),. the slope height (H=2 m) and the footing width (B=2 m) were taken as constant value. In addition, an empirical correlation was developed to estimate the bearing capacity coefficient ($N_{\gamma q}$). As the distance from the edge of the slope increases (i.e. as the b/B ratio increases), it can be observed that at a certain distance the bearing capacity of the footing approaches that of footings placed on horizontal level ground. Beyond this threshold, the bearing capacity remains constant regardless of further increases in the b/B ratio and the influence of the slope on the bearing capacity becomes negligible. Consequently, the footing behaves as if it were placed on horizontal level ground.

Keywords: Slope; The bearing capacity; FEM; Strip footing; Plaxis 2D

1. Introduction

The performance of the footings is affected by their bearing capacity and settlement behavior. Thus, a key challenge in geotechnical engineering is designing footings that satisfy both bearing capacity and displacement safety criteria. Several factors, including soil stratification, geotechnical properties, footing geometry and loading conditions, influence the bearing capacity of the foundation. Also, the estimation of bearing capacity becomes significantly more challenging in the presence of a slope. Critical parameters, including slope inclination (β), soil internal friction angle (ϕ), footing-to-crest distance (b), footing width (B), and embedment depth (D_f), collectively influence the bearing capacity behavior of shallow foundations on sloped soil (Meyerhof, 1957; Hansen, 1970; Vesic, 1973; Akcay, 2023).

A variety of methodological approaches have been used in the literature to study this phenomenon, including theoretical analyses, numerical simulations and experimental investigations. The theoretical framework was developed in particular by the contributions of Meyerhof (1957), Hansen (1970) and Vesic (1973). While these methods provide valuable analytical frameworks, their applicability is constrained to specific ranges of foundation placement and embedment depth. In particular, Meyerhof (1957) introduced a theoretical solution for determining the ultimate bearing capacity (q_u) of strip foundations located either on the slope face or at the crest. The equation developed by Meyerhof (1957) is as follows:

$$q_u = cN_{cq} + 0.5\gamma BN_{\gamma q} \tag{1}$$

where N_{cq} and $N_{\gamma q}$ are the bearing capacity factors, which are functions of the soil internal friction angle (ϕ), the slope angle (β) and the depth to width ratio (D_f/B), c is the soil cohesion, γ is the unit weight of the soil and B is the width of the footing. For cohesionless soils, Eq. (1) simplifies to the following:

$$q_u = 0.5\gamma BN_{\gamma q} \tag{2}$$

*Corresponding author, E-mail: burak.akcay@ktu.edu.tr

https://doi.org/10.31462/icearc2025_ce_geo_962

According to the results of the study by Meyerhof (1957), the relationship between the bearing capacity factor ($N_{\gamma q}$) and various parameters such as the slope angle (β), the internal friction angle of the soil (ϕ) and the distance/width ratio of the foundation to the crest of the slope (b/B) is shown in Fig. 1.

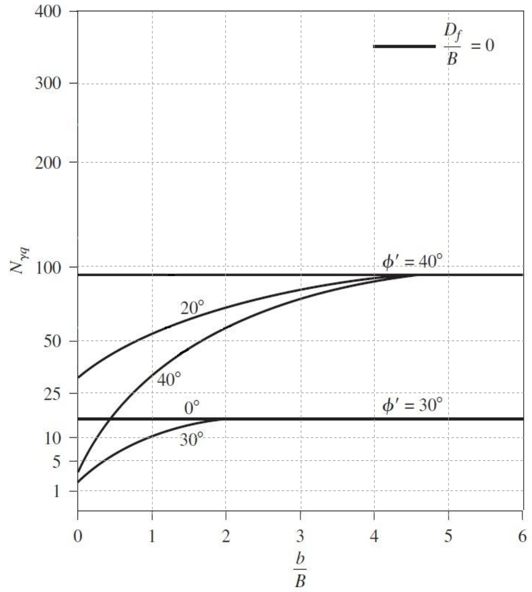

Fig. 1. The relationships between the factor $N_{\gamma q}$ of the strip footing built on top of cohesionless sloping soil with β, ϕ and b/B (Meyerhof, 1957)

In addition, numerical approaches have significantly advanced the understanding of the bearing capacity of strip footing on slopes, with contributions including the works of Lysmer (1970), Davis and Booker (1973), and Chen (1975), followed by later developments from Kusakabe et al. (1981), Michalowski (1989), Krabbenhoft et al. (2005), Farzaneh et al. (2008), Georgiadis (2008), Shiau et al. (2011), Keskin and Laman (2013), and Mofidi et al. (2014). Complementing these numerical studies, experimental investigations by Gemperline (1988), Shields et al. (1990), and Castelli and Motta (2010) have provided crucial validation of both theoretical and numerical predictions. While these studies have contributed significantly to the understanding of the slope-footing interaction, there are still some critical research gaps that have not been addressed in the literature (Akcay, 2024).

This study investigates the bearing capacity of strip footings on cohesionless slopes through a comprehensive parametric analysis using finite element modelling. A series of finite element analyses were performed to systematically evaluate the influence of key geotechnical parameters on both the ultimate bearing capacity (q_u) and the corresponding bearing capacity factor ($N_{\gamma q}$). The numerical analyses were performed using PLAXIS 2D. In addition, the empirical correlation for the bearing capacity factor ($N_{\gamma q}$) was developed by performing non-linear regression analysis. The developed empirical correlation was validated by comparing the finite element method and the Meyerhof (1957) method.

2. Materials and methods

The numerical simulations were performed with PLAXIS 2D, using the Finite Element Method (FEM) to analyze the bearing capacity of footings on slopes. The investigation considered variable parameters, including the slope angle (β), the horizontal distance between the footing and the slope crest (b), the unit weight of the soil (γ), and its internal friction angle (ϕ) (Fig. 2).

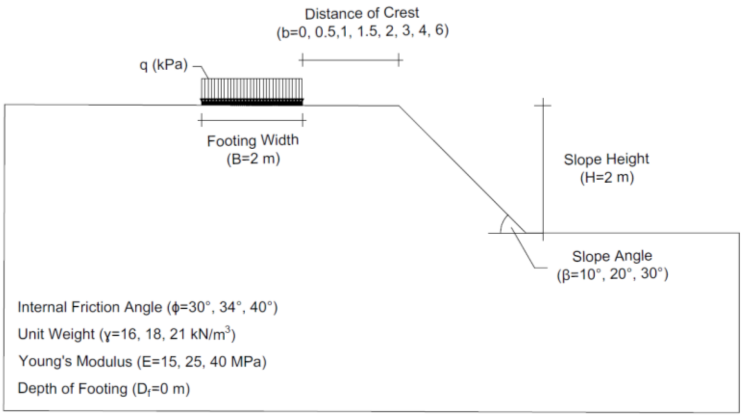

Fig. 2. Geometric presentation of the parameters on model

Meanwhile, the constant parameters included the footing width of B=2 m, the slope height of H=2 m and depth of footing of D_f=0 m. Slope angles (β) were systematically chosen as 10°, 20° and 30° an internal friction angle (ϕ) of 30˚, 34˚ and 40˚ representing loose, medium dense and dense sands. Depending on the angle of internal friction angle, the unit volume weight was chosen to be 16 kN/m^3, 18 kN/m^3 and 21 kN/m^3 respectively. The selected values for b/B included 0, 0.5, 1, 1.5, 2, 4, and 6.

The finite element analyses were conducted under plane-strain conditions, employing 15-node triangular elements to ensure high accuracy in stress and deformation calculations. The soil was modeled using the Mohr-Coulomb constitutive model with drained conditions, while groundwater not considered. The key soil parameters implemented in the analyses are comprehensively given in Table 1. The strip footing was assumed as an elastic, isotropic plate element, with applied loading represented as a concentrated point load acting at the center of the footing.

Table 1. Soil parameters used in the FEM analyses

Cases	I	II	III
Internal friction angle, (ϕ′), deg.	30	34	40
Unit weight of soil, (γ), kN/m^3	16	18	21
Young's modulus, (E′), MPa	15	25	40
Dilatancy angle, (ψ′), deg.	0	4	10

3. Results and discussions

A systematic numerical study was performed using a series of PLAXIS 2D models to examine the behavior of a strip footing positioned at the slope crest. The analysis primarily focused on evaluating the impact of fundamental dimensionless parameters, including the normalized distance from the slope crest (b/B), slope angle (β), footing depth ratio (D_f/B), and internal friction angle of the soil (ϕ) on the bearing capacity factor ($N_{\gamma q}$). The results indicate that $N_{\gamma q}$ is highly sensitive to changes in these parameters, and a detailed evaluation of their effects is presented in the following sections.

The results indicate that the bearing capacity increases proportionally with the internal friction angle (ϕ). For cohesionless sloped soils, lower values of ϕ allow the bearing capacity to reach that of horizontal ground conditions at relatively smaller normalized distances (b/B). Conversely, soils with higher internal friction angles require larger b/B ratios to achieve the same capacity. For instance, the bearing capacity does not vary beyond b/B = 2 for ϕ = 30°, whereas this threshold increases to b/B = 3 for ϕ = 34°, and to b/B = 4 for ϕ = 40° (Fig. 3).

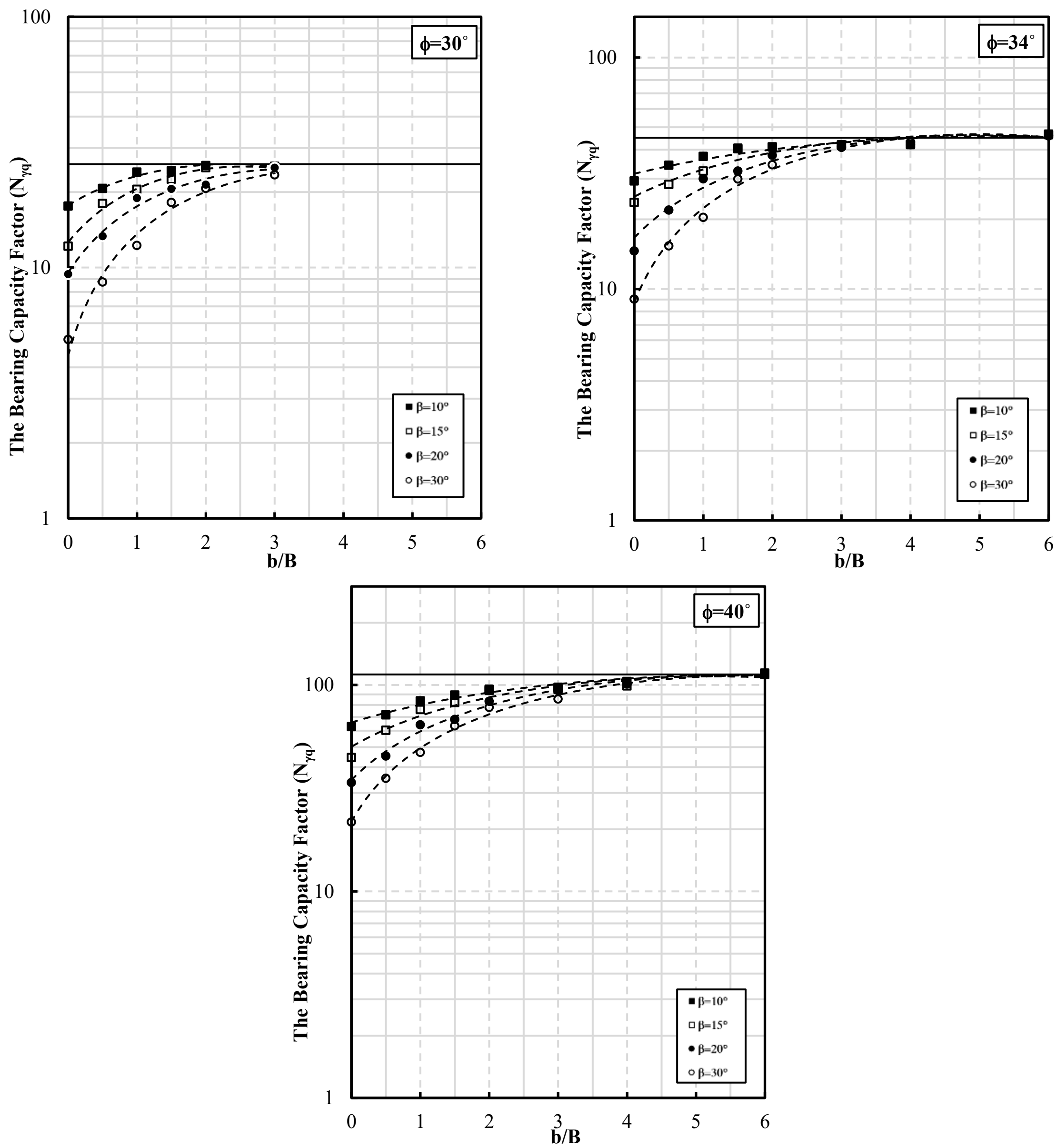

Fig. 3. Relationship between different slope angles (β) and $N_{\gamma q}$ factor at different internal friction angles (ϕ)

In contrast to the internal friction angle (ϕ), the slope angle (β) exhibits an inverse relationship with the bearing capacity (q_u). For relatively gentle slopes, the footing with smaller normalized setback distances (b/B) are sufficient to attain the bearing capacity corresponding to horizontal ground conditions. However, as the slope angle increases, a larger b/B ratio is required to reach this capacity. This trend is observed consistently across all values of internal friction angle (ϕ), but becomes particularly significant in soils with higher ϕ (e.g., ϕ > 34°). For instance, when ϕ=40°, the influence of the slope becomes negligible beyond b/B = 4 for β = 10°, while the corresponding threshold increases to b/B = 5 for β = 30° (Fig. 4).

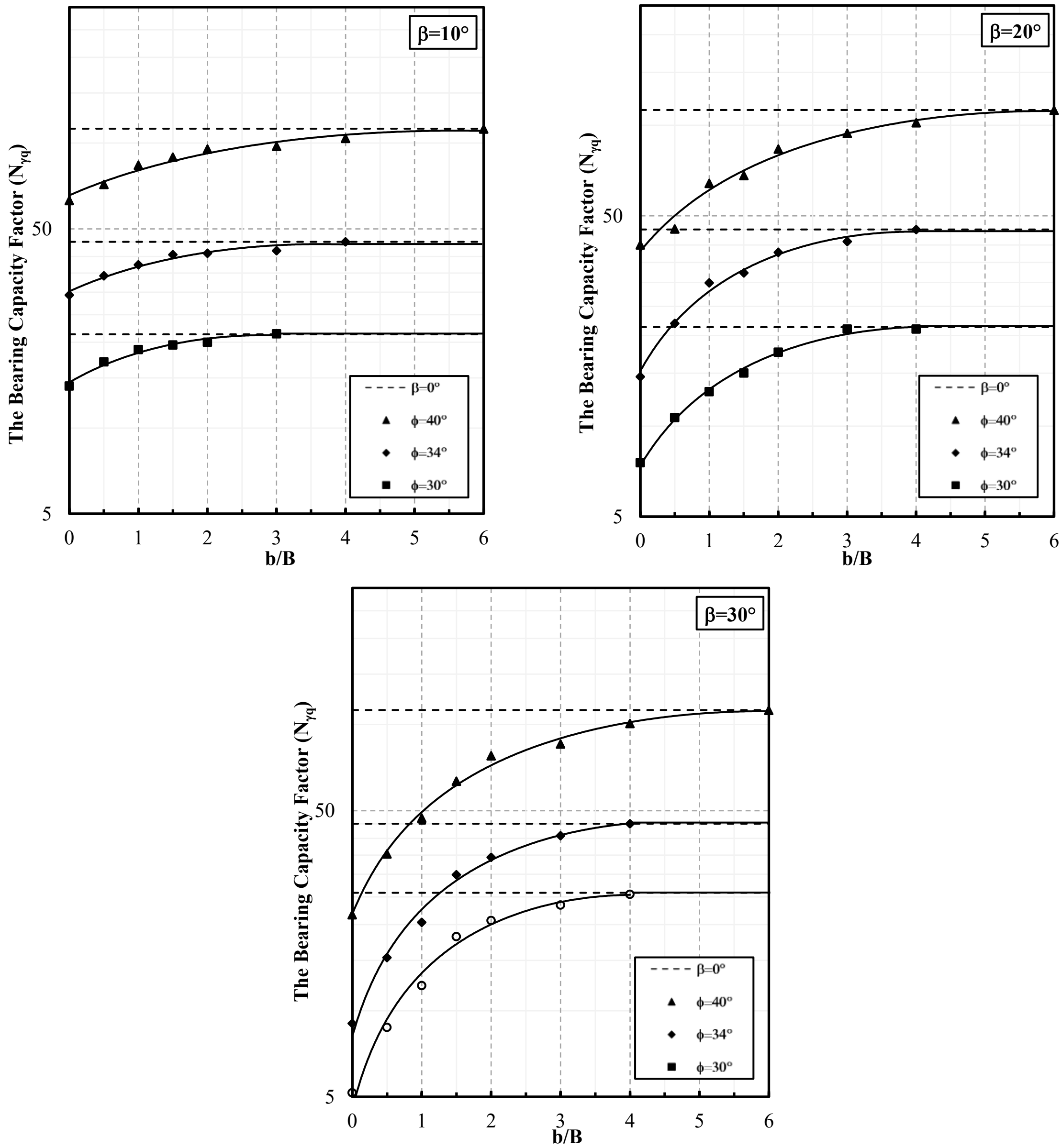

Fig. 4. Relationship between different internal friction angles (ϕ) and $N_{\gamma q}$ factor at different slope angles (β)

3.1. Comparison of empirical correlation and FEM with Meyerhof method

A nonlinear regression analysis was conducted using IBM SPSS V23, incorporating four independent variables (unit weight (γ), distance from the slope crest (b/B), internal friction angle (ϕ), and slope angle (β)) to predict the bearing capacity factor ($N_{\gamma q}$) as the dependent variable. The developed empirical correlations are given in Eq. 3:

$$\begin{aligned} N_{\gamma q} &= -1310.7\times\gamma - 2246.4\times\frac{b}{B} + 417.1\times\phi - 18.4\times\beta + 2224\times\gamma\times\frac{b}{B} \\ &-18.6\times\gamma\times\phi + 19.5\times\gamma\times\beta - 1111.1\times\frac{b}{B}\times\phi + 0.2\times\frac{b}{B}\times\beta - 9.8\times\phi\times\beta \\ &+237.2\times\gamma^2 - 1.4\times\left(\frac{b}{B}\right)^2 - 49.7\times\phi^2 + 0.1\times\beta^2 + 1371.3 \end{aligned} \quad (3)$$

(R^2 = 0.987)

The resulting empirical correlation was subsequently compared with theoretical predictions based on the method proposed by Meyerhof (1957) and results of FEM anaysis. The comparison revealed a strong agreement between the developed empirical correlation, FEM analysis and the theoretical approach, validating the reliability of the developed correlation. This consistency is especially notable for cases involving higher internal friction angles (e.g., ϕ ≥ 34°) and lower slope angles (e.g., β ≤ 20°). Overall, the accuracy and reliability of the empirical correlation improve as the bearing capacity factor increases, resulting in enhanced agreement with the Meyerhof (1957) method and more consistent predictive performance (Fig. 5).

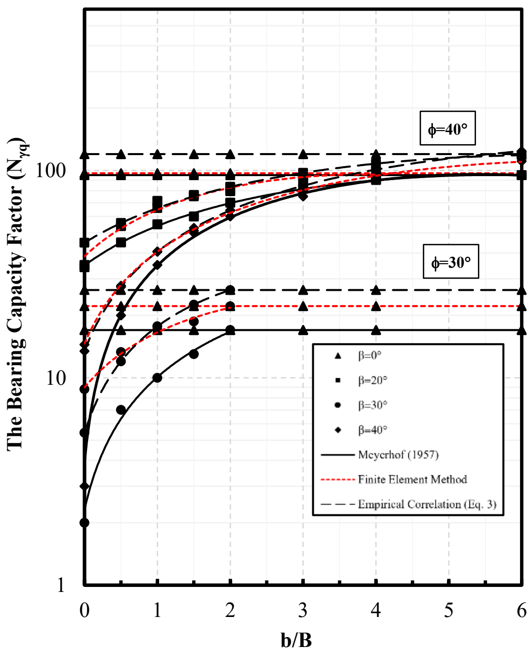

Fig. 5. The comparison of the empirical correlation, FEM analysis and Meyerhof (1957) method

4. Conclusions

A series of numerical analyses were performed to evaluate the bearing capacity of a strip footing constructed on cohesionless sloped soil. The study considered several key parameters influencing bearing behavior, including the horizontal distance from the slope crest to the footing (b), the unit weight of the soil (γ), the slope angle (β), and the internal friction angle of the soil (ϕ). In addition, a nonlinear regression analysis was performed to derive an empirical correlation for the bearing capacity factor. As a result of this study, the following conclusions are reached.

- The bearing capacity of the footing significantly increases by reducing the slope angle (β), increasing the internal friction angle (ϕ), and increasing the horizontal distance between the footing and the slope crest (b).
- If the b/B ratio increases as the footing moves away from the slope crest, it is observed that after a certain distance, the bearing capacity factor of the footing in sloped conditions reaches that of horizontal soils. Beyond this critical distance, the bearing capacity factor reaches a constant value and shows no further variation with additional increments. At this stage, the effect of the slope on the bearing capacity is negligible and its residual effect is insignificant. As a result, the footing behaves in the same way as a foundation placed on a flat, horizontal layer of soil.
- An increase in the angle of internal friction (ϕ) results in an increase in the bearing capacity factor ($N_{\gamma q}$). The soils with higher internal friction angles require larger crest distances (b/B) to achieve the bearing capacity equivalent to that of horizontal soil conditions (β=0°), whereas soils with lower internal friction angles achieve this capacity at relatively smaller b/B values.
- In contrast to the influence of the internal friction angle (ϕ), the slope angle (β) has an inverse relationship with the bearing capacity factor ($N_{\gamma q}$). The results indicate that as β increases, the bearing capacity factor remains constant only at a greater distance from the crest (b/B). In particular, for gentle slopes (low β values), the effect of the slope on the bearing capacity factor of the footing becomes negligible at a relatively small b/B ratio. Conversely, for steeper slopes (high β values), a larger b/B ratio is required to eliminate the influence of the slope and achieve bearing capacity factor conditions comparable to those of a horizontal soil surface (β=0°).
- The empirical correlation exhibits notable deviations from Meyerhof (1957) method in cases involving sloping soils with low internal friction angles (ϕ). In contrast, for higher ϕ values, the empirical correlation and FEM analysis results align closely with theoretical method (Meyerhof, 1957), highlighting the enhanced predictive capability of the model under such conditions.

Acknowledgments
The research described in this paper has not been funded by any foundation/institute.

References

Akcay, B. (2024). *Şevli kohezyonsuz zeminlerde şerit temellerin taşıma gücü* [Yüksek lisans tezi, Karadeniz Teknik Üniversitesi, Fen Bilimleri Enstitüsü].

Akcay, B., & Sivrikaya, O. (2023). The effect of the distance of strip foundations from the edge of a horizontal top surface of slope with cohesionless soil on bearing capacity. In *International Civil Engineering and Architecture Congress* (pp. 532–544). Trabzon.

Castelli, F., & Motta, E. (2010). Bearing capacity of strip foundations near slopes. *Geotechnical and Geological Engineering, 28*, 187–198. https://doi.org/10.1007/s10706-009-9312-1

Chen, W. F. (1975). *Limit analysis and soil plasticity*. Elsevier.

Davis, E. H., & Booker, J. R. (1973). Some adaptations of classical plasticity theory for soil stability problems. In A. C. Palmer (Ed.), *Proceedings of the Symposium on the Role of Plasticity in Soil Mechanics* (pp. 24–41). Cambridge University.

Farzaneh, O., Askari, F., & Ganjian, N. (2008). Three-dimensional stability analysis of convex slopes in plan view. *Journal of Geotechnical and Geoenvironmental Engineering, 134*(8), 1192–1200. https://doi.org/10.1061/(ASCE)1090-0241(2008)134:8(1192)

Gemperline, M. C. (1988). Centrifuge modeling of shallow foundations. In *Proceedings of ASCE Spring Convention* (pp. 45–70).

Georgiadis, K. (2008). The influence of load inclination on the undrained bearing capacity of strip foundations on slopes. *Computers and Geotechnics, 37*(3), 311–322. https://doi.org/10.1016/j.compgeo.2009.11.002

Hansen, J. B. (1970). A revised and extended formula for bearing capacity. *Danish Geotechnical Institute Bulletin, 28*, 1–21.

Keskin, M. S., & Laman, M. (2012). Model studies of bearing capacity of strip foundation on sand slope. *KSCE Journal of Civil Engineering, 17*(4), 699–711. https://doi.org/10.1007/s12205-013-0024-3

Krabbenhoft, K., Lyamin, A. V., Hjiaj, M., & Sloan, S. W. (2005). A new discontinuous upper bound limit analysis formulation. *International Journal for Numerical Methods in Engineering, 63*(7), 1069–1088. https://doi.org/10.1002/nme.1214

Kusakabe, O., Kimura, T., & Yamaguchi, H. (1981). Bearing capacity of slopes under strip loads on the top surfaces. *Soils and Foundations, 21*(4), 29–40.

Lysmer, J. (1970). Limit analysis of plane problems in soil mechanics. *Journal of the Soil Mechanics and Foundations Division, ASCE, 96*(SM4), 1311–1334.

Meyerhof, G. G. (1957). The ultimate bearing capacity of foundations on slopes. In *Proceedings of the 4th International Conference on Soil Mechanics and Foundation Engineering* (pp. 384–386). London.

Michalowski, R. L. (1989). Three-dimensional analysis of locally loaded slopes. *Géotechnique, 39*(1), 27–38. https://doi.org/10.1680/geot.1989.39.1.27

Mofidi, J., Farzaneh, O., & Askari, F. (2014). Bearing capacity of strip foundations near slopes using lower bound limit analysis. *Civil Engineering Infrastructures Journal, 47*(1), 89–109.

Plaxis. (2023). *Plaxis Material Models Manual 2D*. Bentley Systems.

Shiau, J. S., Merifield, R. S., Lyamin, A. V., & Sloan, S. W. (2011). Undrained stability of foundations on slopes. *International Journal of Geomechanics, 11*(5), 381–390. https://doi.org/10.1061/(ASCE)GM.1943-5622.0000082

Shields, D., Chandler, N., & Garnier, J. (1990). Bearing capacity of foundations in slopes. *Journal of Geotechnical Engineering, ASCE, 116*(3), 528–537.

Vesic, A. S. (1973). Analysis of ultimate loads of shallow foundations. *Journal of the Soil Mechanics and Foundations Division, 99*(SM1), 45–73.

4th International Civil Engineering & Architecture Conference
17-19 May 2025, Trabzon, Türkiye

Non-stationarity assessment of intensity-duration-frequency (IDF) curves of standard duration rainfall in the Eastern Black Sea Region, Türkiye

Nagehan Şahin*[1], Murat Şan[1], Murat Kankal[2]

[1] Gümüşhane University, Department of Civil Engineering, 29100 Gümüşhane, Türkiye
[2] Bursa Uludağ University, Department of Civil Engineering, 16059 Bursa, Türkiye

Abstract. Intensity-Duration-Frequency (IDF) curves used in the design of hydraulic structures are traditionally based on stationary frequency analyses with fixed parameters. However, temporal changes in extreme rainfall caused by climate change have made the validity of the stationary approach questionable. Recent studies have focused on updating IDFs under non-stationary conditions to understand the time-varying behaviour of extreme rainfall better. In this context, this study, which aims to examine the hydrological impacts of climate change in the Eastern Black Sea region, estimated IDF curves by performing non-stationary frequency analysis for six stations. Both stationary and non-stationary models of the generalized extreme value (GEV) distribution were used to determine extreme rainfall intensities, and the results of both models were compared in terms of the effects of non-stationarity on infrastructure design. It was concluded that the stationarity assumption is still valid in stations such as Akçaabat, Giresun, and Ordu. At the same time, the effects of non-stationarity are evident in Bayburt, Gümüşhane, and Hopa stations.

Keywords: The Eastern Black Sea Region; Intensity-duration-frequency curves; Non-stationarity; Rainfall frequency

1. Introduction

Climate change has significant consequences worldwide, including sea level rise, extreme rainfall, drought, and increased heat waves (Ahmed vd., 2018; Shiru vd., 2019; Şan vd., 2023). Although these impacts vary regionally, they directly affect each region's infrastructure systems and natural resource management. Accurately identifying the impacts of climate change at the local level is critical for developing adaptation strategies (An vd., 2023).

Some studies have identified increasing trends in the frequency and intensity of extreme rainfall (Swain vd., 2020; Tabari vd., 2021). In particular, Asadieh & Krakauer (2015) revealed a global increase of 8.5 percent in annual maximum daily rainfall between 1901 and 2010. Similar findings have been reported in regions such as the Americas, Africa and the Mediterranean (Douglas vd., 2023; Shang vd., 2011; Tramblay & Somot, 2018). Türkiye is a country open to the effects of climate change due to its location in the Mediterranean basin. Touhedi vd. (2023) revealed that the increasing trend in extreme rainfall is evident throughout Türkiye, and this increase is particularly concentrated in the Black Sea, Marmara, and Aegean regions.

IDF curves, which are important design tools used in the sizing and risk analyses of engineering structures, relate rainfall intensities of certain durations to return periods and are traditionally obtained under the assumption of stationarity by statistical analysis of past extreme rainfall data. However, due to climate change effects, the assumption of stationarity used in classical hydrological analyses is losing its validity (Cheng vd., 2014). This makes it necessary to question the existing hydrological design criteria. In this context, there are various studies for non-stationary modeling of extreme climate events worldwide (Cheng vd., 2014; Gao vd., 2016; Lee vd., 2020; Mondal & Mujumdar, 2015; Sugahara vd., 2009; Vasiliades vd., 2015; Wi vd., 2016). Considering the climate diversity of Türkiye, it is of great importance to study the impacts of climate change on non-stationarity in small and medium-sized regions (Aziz & Yucel, 2021). Aziz and Yucel (2021) examined the temporal variability of annual and seasonal extreme rainfall across Türkiye using stationary and non-stationary frequency analyses. According to the percentage differences calculated over 30-year return levels, the non-stationarity effect reached 35%, 30%, 25%, and 20% in the Mediterranean, Aegean, Marmara, and Black Sea regions, respectively. In

*Corresponding author, E-mail: nagehansahin@gumushane.edu.tr

https://doi.org/10.31462/icearc2025_ce_hwr_052

contrast, more complex and unclear non-stationarity effects were observed in the Central, Eastern and Southeastern Anatolia regions. Similarly, in a study conducted in the Black Sea Region, in addition to the stationary model, a non-stationary model with parameters varying with time and hydrometeorological variables, frequency analysis of extreme rainfall was performed, and IDF curves were created in this context (Aksu vd., 2025). Oruc (2021) used two non-stationary equations in the Black Sea region and observed higher magnitude non-stationary effects for the Eastern Black Sea Region and the coastline. However, there may also be a scenario of equations with the non-stationary parameter being affected in different forms over time.

This study performed an IDF analysis based on the generalized extreme value (GEV) distribution using annual maximum precipitation data of standard duration recorded between 1980 and 2020 from six stations in the Eastern Black Sea Region of Turkey. GEV is the most suitable distribution for the Black Sea (Aksu et al., 2022). Within the scope of the analysis, nine different models, i.e., one stationary and eight non-stationary models with time-varying parameters, were evaluated. The Corrected Akaike's Information Criterion (AICc) and Likelihood Ratio (LR) tests were used to select the best GEV model. IDF curves were generated using the selected models. Thus, regional impacts of climate change were evaluated more precisely, and hydrological design criteria specific to the Eastern Black Sea Region were obtained.

2. Materials and methods

2.1. Study area and data

This study was conducted in the Eastern Black Sea Region in the north-east of Türkiye. The region covers Rize, Artvin, Trabzon, Giresun, Gümüşhane, and Bayburt provinces. Geographically, it has temperate and humid climate characteristics. The Eastern Black Sea Region, one of the areas with the highest total annual rainfall in Türkiye, is frequently subjected to floods due to its topographical structure. Since the residential areas in the region are generally located near floodplains, many material and moral losses occur due to floods (Anik vd., 2021). Floods caused by excessive rainfall are among the most destructive natural disasters in the region, which is very rich in water resources due to its topography, mountainous terrain, and typical climatic character (Aksu vd., 2025).

Hopa, Akçaabat, Giresun, Ordu, Ordu, Gümüşhane, and Bayburt meteorological stations in the Eastern Black Sea Region, which have 30 years of records between 1980 and 2020, were selected in this study (Fig. 1). Time series containing annual maximum rainfall with standard duration (5, 10, 15, 30 m and 1, 2, 3, 4, 5, 6, 8, 12, 18, 24 h) of the selected stations were obtained and evaluated within the scope of the study.

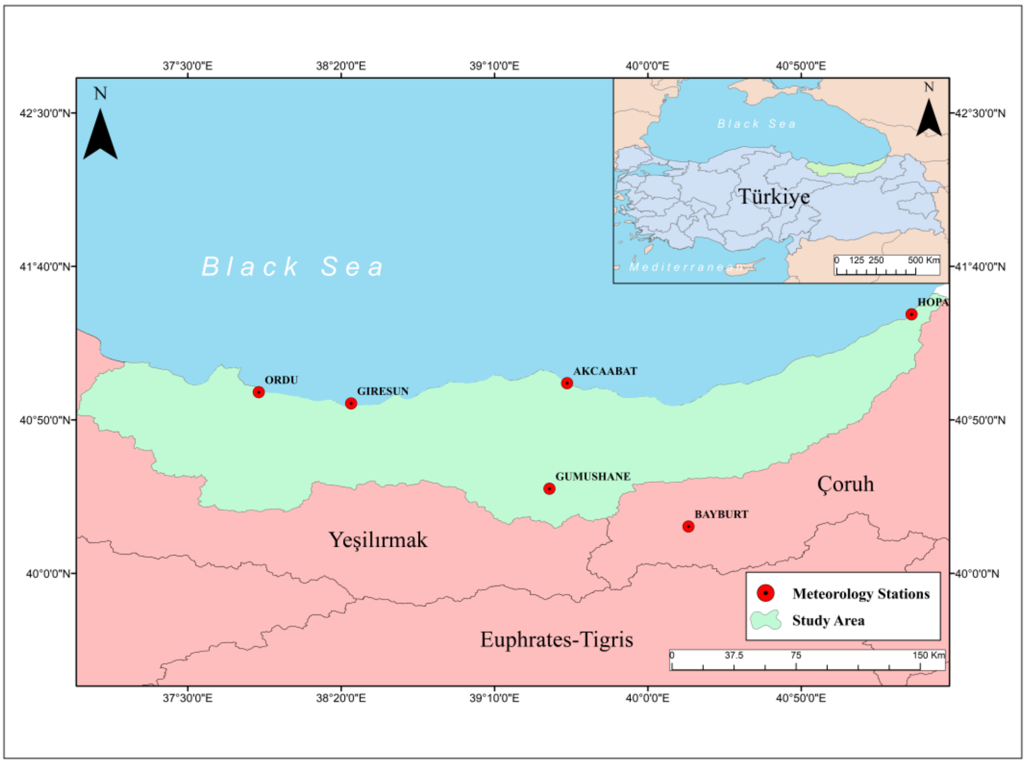

Fig. 1. Location of the provincial centres where the stations are located in the Eastern Black Sea Region showing the study area.

2.2. Generalized Extreme Value distribution

The study used generalized extreme value (GEV) distribution to model the temporal variation of extreme rainfall. This distribution is defined by the parameters of location (μ), scale (σ), and shape (ξ) (Coles, 2001) :

$$F(x, \mu, \sigma, \xi) = \exp\left\{-\exp\left[-\left(1+\xi\frac{x-\mu}{\sigma}\right)\right]\right\},\ 1+\frac{\xi(x-\mu)}{\sigma} > 0 \quad (1)$$

In stationary models these parameters are constant, whereas in non-stationary models they are a function of time. In this case the cumulative distribution function takes the following form:

$$F(y; \mu(t), \sigma(t), \xi(t)) = \exp\left\{-\left[1+\ \xi(t)\frac{y-\mu(t)}{\sigma(t)}\right]^{-\frac{1}{\xi(t)}}\right\} \quad (2)$$

A total of nine different GEV models were constructed, and these models are presented in Table 1. Parameter estimation was performed by the maximum likelihood estimator (MLE).

Table 1. Time-varying nonstationary models

Model	Location	Scale
I	μ (constant)	σ (constant)
II	μ0 + μ1*t	σ (constant)
III	μ0 + μ1*t	σ0+ σ1*t
IV	μ0 + μ1*t	exp(σ0+ σ1*t)
V	μ (constant)	σ0+ σ1*t
VI	μ (constant)	exp(σ0+ σ1*t)
VII	μ0 + μ1*t + μ2*t^2	σ (constant)
VIII	μ0 + μ1*t + μ2*t^2	σ0+ σ1*t
IX	μ0 + μ1*t + μ2*t^2	exp(σ0+ σ1*t)

The most appropriate model for each station and rainfall period was selected using the Corrected Akaike’s Information Criterion (AICc). Differences between models were determined by calculating Δi = AICc - min(AICc), and models with Δi ≤ 2 were considered appropriate (Burnham & Anderson, 2004). The Likelihood Ratio (LR) test compared stationary and non-stationary models. Then, non-stationary models were considered statistically significant if $p<0.05$ (Katz, 2013). The R code used for generating GEV models was utilized from the work of Silva and Simonovic (2020).

2.3. Generating IDF curves

Based on the selected best GEV model, stationary and non-stationary return levels were calculated for different return periods (2, 5, 10, 20, 50, and 100 years). With the help of the GEV distribution, the depth of rainfall (z_p) corresponding to the return level as a function of the return period T years, calculated as

$$z_p = \mu\frac{\sigma}{\xi}\left[1\left\{-ln\left(1\frac{1}{T}\right)^{-\xi}\right\}\right] \quad (3)$$

If the best GEV model is chosen as a non-stationary model, the location and/or scale parameters must change over time. In this framework, based on the low-risk approach (Cheng vd., 2014), time-varying parameters are calculated using the 95th percentile values. The calculated model parameters are then adapted into Equation 4 to predict the depth of rainfall under non-stationary conditions.

$$I = A(d+C)^B \quad (4)$$

Where I is the rainfall intensity (mm/hour), A, B, and C are the coefficients determined for each return period (T). In addition, the parameter d indicates the rainfall duration in hours.

3. Results

In this study, stationary and non-stationary IDF curves were constructed for six meteorological stations, i.e., Hopa, Akçaabat, Giresun, Ordu, Gümüşhane, Bayburt, located in the Eastern Black Sea Region of Türkiye with return levels calculated for 2, 5, 10, 20, 50, and 100 years. The AICc values of the equations that satisfy the Δi ≤ 2 condition and pass the LR test for each standard period as a result of the analysis made with the annual maximum precipitation amount recorded at the stations to generate the IDF curves and the best GEV model selected according to the minimum value of these values are given in Table 2. The stationary model I is the majority for all stations. For 12-h rainfall, non-stationarity was detected at any station. In 6 of the standard durations, the non-stationary GEV model was found to be the best model in only one station, while in 7 of the standard durations, the non-stationary GEV model was selected as the best model in two stations. Gümüşhane station, where non-stationary GEV model was detected in 5 of the standard durations, was the station with the highest non-stationarity. Ordu province was the station with the least non-stationarity by providing only one non-stationary GEV model. At Ordu station, except for 18 h of rainfall, the stationary state dominates the other durations.

Table 2. The best GEV model and AICc values selected for each station and standard times. (AICc value of the selected GEV model is marked in bold.)

		Short Duration				Medium Duration						Long Duration			
Models	Stations	5 m	10 m	15 m	30 m	1 h	2 h	3 h	4 h	5 h	6 h	8 h	12 h	18 h	24 h
I	Akçaabat	**201.6**	**231.6**	**245.1**	**270.8**	**284.4**	**293.7**	**300.8**	**304.1**	-	-	-	**320.6**	**329.7**	**336.6**
III	Akçaabat	-	-	-	-	-	-	-	-	305.1	-	-	-	-	-
VII	Akçaabat	-	-	-	-	-	-	-	-	**303.5**	**304.4**	**310.8**	-	-	-
I	Bayburt	**182.3**	-	-	-	**254.0**	**248.3**	**250.2**	**251.2**	**251.0**	**251.4**	**243.7**	**244.4**	**242.4**	**242.8**
III	Bayburt	-	**206.6**	-	245.0	-	-	-	-	-	-	-	-	-	-
IV	Bayburt	-	207.4	**215.9**	**243.4**	-	-	-	-	-	-	-	-	-	-
VIII	Bayburt	-	-	216.1	243.9	-	-	-	-	-	-	-	-	-	-
I	Giresun	198.1	**239.2**	**263.0**	**307.6**	**336.1**	**355.1**	**362.1**	**368.1**	**367.9**	**367.9**	**366.7**	**366.6**	**370.7**	**368.3**
III	Giresun	198.1	-	-	-	-	-	-	-	-	-	-	-	-	-
V	Giresun	**196.6**	-	-	-	-	-	-	-	-	-	-	-	-	-
VI	Giresun	197.2	-	-	-	-	-	-	-	-	-	-	-	-	-
IX	Giresun	-	-	-	-	-	-	-	-	-	-	-	-	-	**367.4**
I	Gümüşhane	**149.9**	**173.9**	**193.3**	205.9	-	-	-	**218.0**	**224.4**	226.9	**234.9**	**238.7**	**246.8**	**247.9**
II	Gümüşhane	-	-	-	**204.1**	205.1	-	**206.0**	-	-	**225.4**	-	-	-	-
III	Gümüşhane	-	-	-	204.1	**203.6**	205.9	-	-	-	-	-	-	-	-
IV	Gümüşhane	-	-	-	-	204.0	205.4	-	-	-	-	-	-	-	-
VII	Gümüşhane	-	-	-	205.1	-	**204.9**	-	-	-	-	-	-	-	-
I	Hopa	-	**241.8**	**262.4**	**293.6**	**329.3**	**347.5**	**361.2**	-	-	375.8	**386.0**	**392.2**	**401.7**	**411.0**
III	Hopa	207.4	-	-	-	-	-	-	-	-	-	-	-	-	-
IV	Hopa	-	-	-	-	-	-	-	-	369.9	**374.1**	-	-	-	-
V	Hopa	**206.0**	-	-	-	-	-	-	-	-	-	-	-	-	-
VI	Hopa	206.4	-	-	-	-	-	-	**364.6**	**369.0**	-	-	-	-	-
IX	Hopa	-	-	-	-	-	-	-	-	-	374.4	-	-	-	-
I	Ordu	**196.9**	**239.9**	**262.2**	**287.6**	**315.3**	**326.7**	**330.1**	**335.2**	**340.0**	**341.7**	**346.0**	**353.4**	361.4	**351.5**
VII	Ordu	-	-	-	-	-	-	-	-	-	-	-	-	**359.4**	-

In Fig. 2, the best GEV model selections by station for different rainfall durations from 5 minutes to 24 hours in the Eastern Black Sea Region are presented spatially. Non-stationary models appear in inland areas for short durations (5m-3h), while they start to emerge in coastal areas as the duration increases.

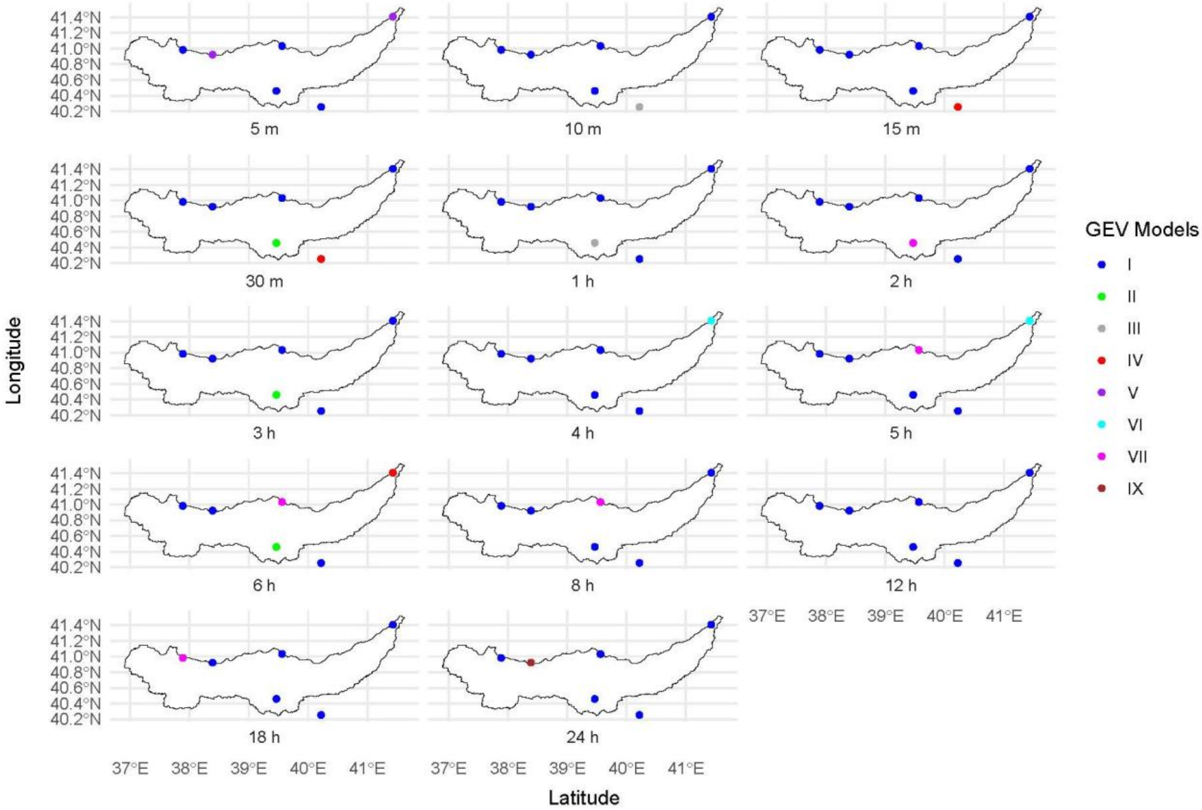

Fig. 2. The best GEV models in the map of the Eastern Black Sea Region

Calculations are made with equation I for the cases where the stationarity assumption is valid. On the other hand, in case of a non-stationary situation for different standard durations, calculations are made through non-stationary GEV model equations (model II-IX). Then, the 95th percentile values of non-stationary IDF curves are presented with the stationary IDFs at different return periods. (

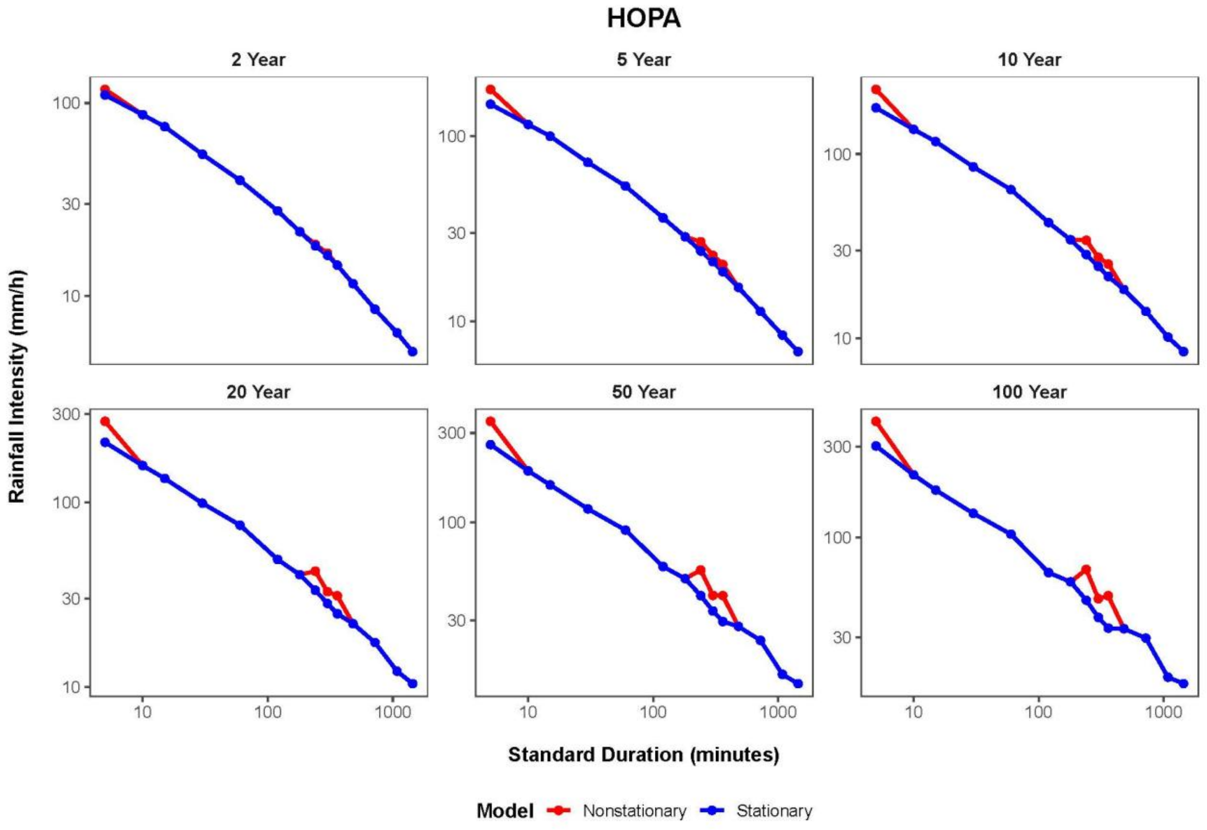

Fig. 3-8). The results of the different return periods for each station are summarized below.

At Hopa station, non-stationary models produced higher rainfall intensities than stationary models for very short rainfall duration (5-30 minutes) (

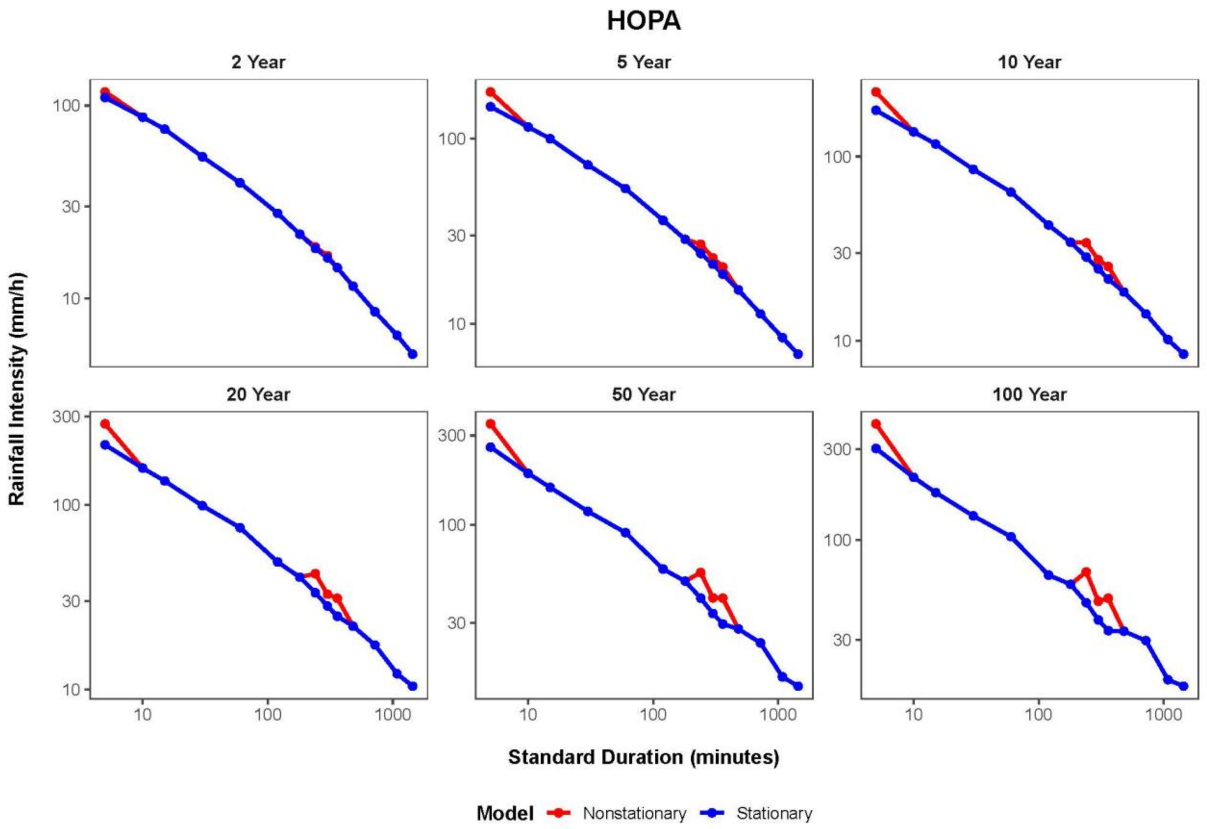

Fig. 3). In long-duration rainfall, stationary effects dominate, especially at low return periods. Non-stationary models in the range of 4-6 hours provided an increase in rainfall intensity with the return period. At 5 m, 4 h and 5 h, the GEV models (V and VI) that provide non-stationarity keep the position parameter constant while changing the scale parameter with time. Similarly, at 6 h, the model (IV), which is selected as the best model, increases the position parameter linearly while the scale parameter increases exponentially. This can be interpreted that the non-stationarity for Hopa station is primarily due to changes in the scale parameters (Table 2).

Minor differences between stationary and non-stationary IDF curves were detected at the Akçaabat station (

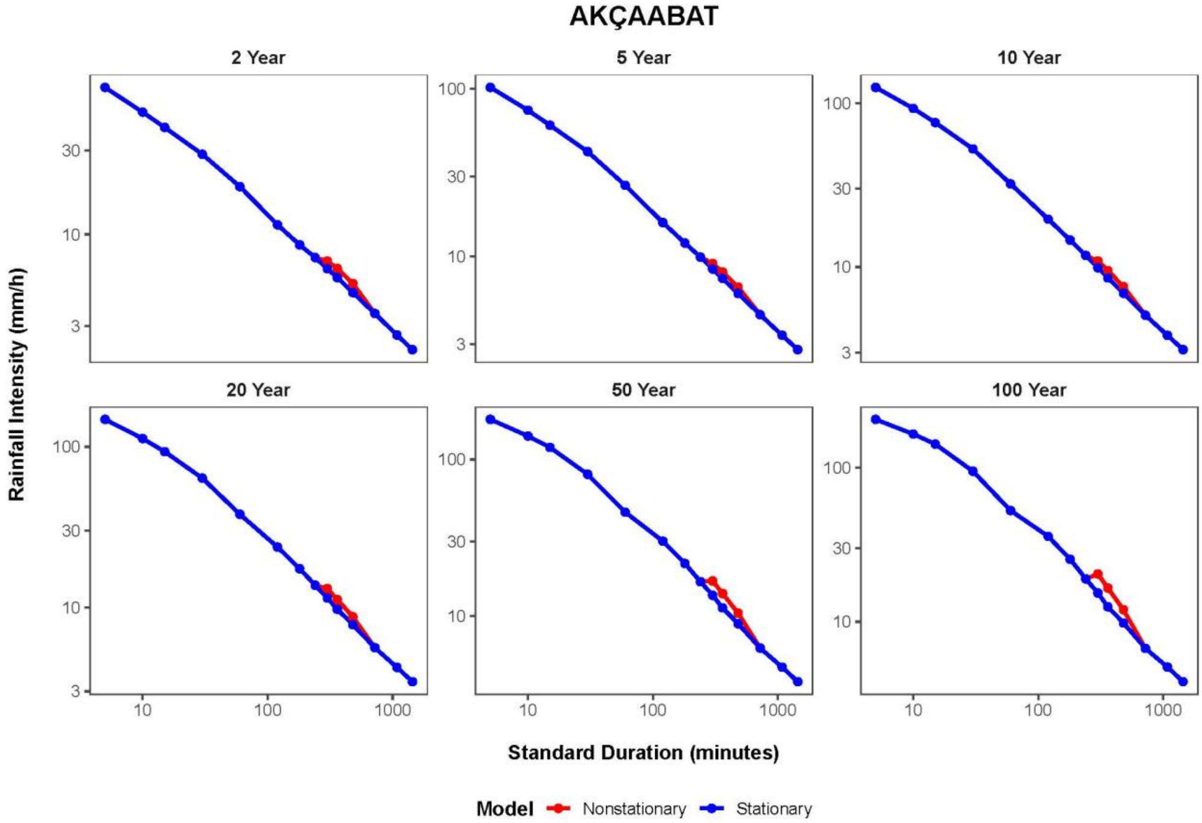

Fig. 4). Especially in short durations (5-60 minutes), stationarity is dominant, while non-stationary models in the 5-8 hours range show a slight increase in rainfall intensity compared to stationary models. Although it can be argued that this variation is due to the position parameters, it should be noted that the GEVIII model, in which the position and scale parameters change linearly in 5h, also fulfils the $\Delta i \leq 2$ condition (Table 2). However, the general pattern remained essentially parallel between both models.

Differences between stationary and non-stationary models were limited at the Giresun station (Fig. 5). Only in 5 minutes and 18 hours of rainfall was the non-stationary model prominent, and this model showed lower rainfall intensities than the stationary model in 5 minutes of rainfall, while it showed significantly higher intensities than the stationary model in 24 hours of rainfall. The changes at 5 min are due to the scale rather than the position parameters, since the two smallest AICc values that satisfy the condition $\Delta i \leq 2$ are those for equations in which the position parameter remains constant and the scale parameter varies with time (Table 2).

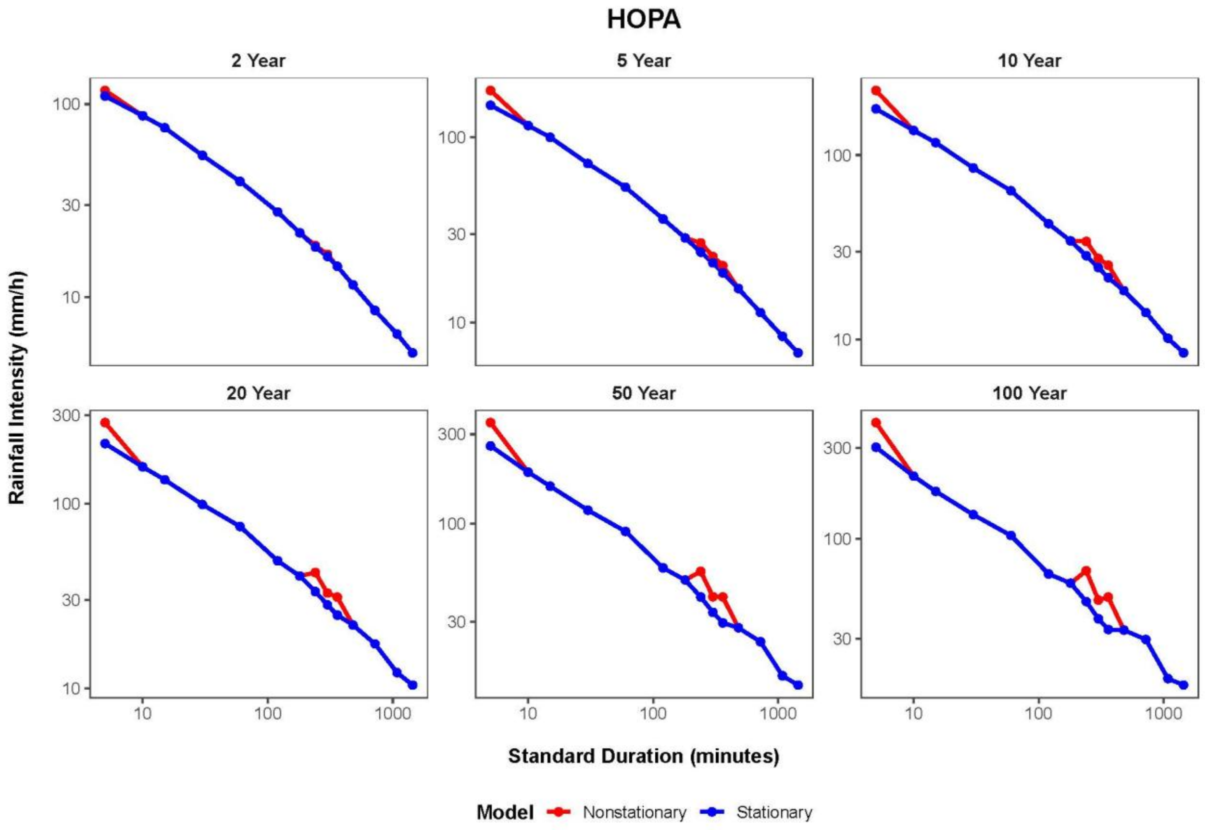

Fig. 3. Stationary and non-stationary IDF for different return periods for Hopa station

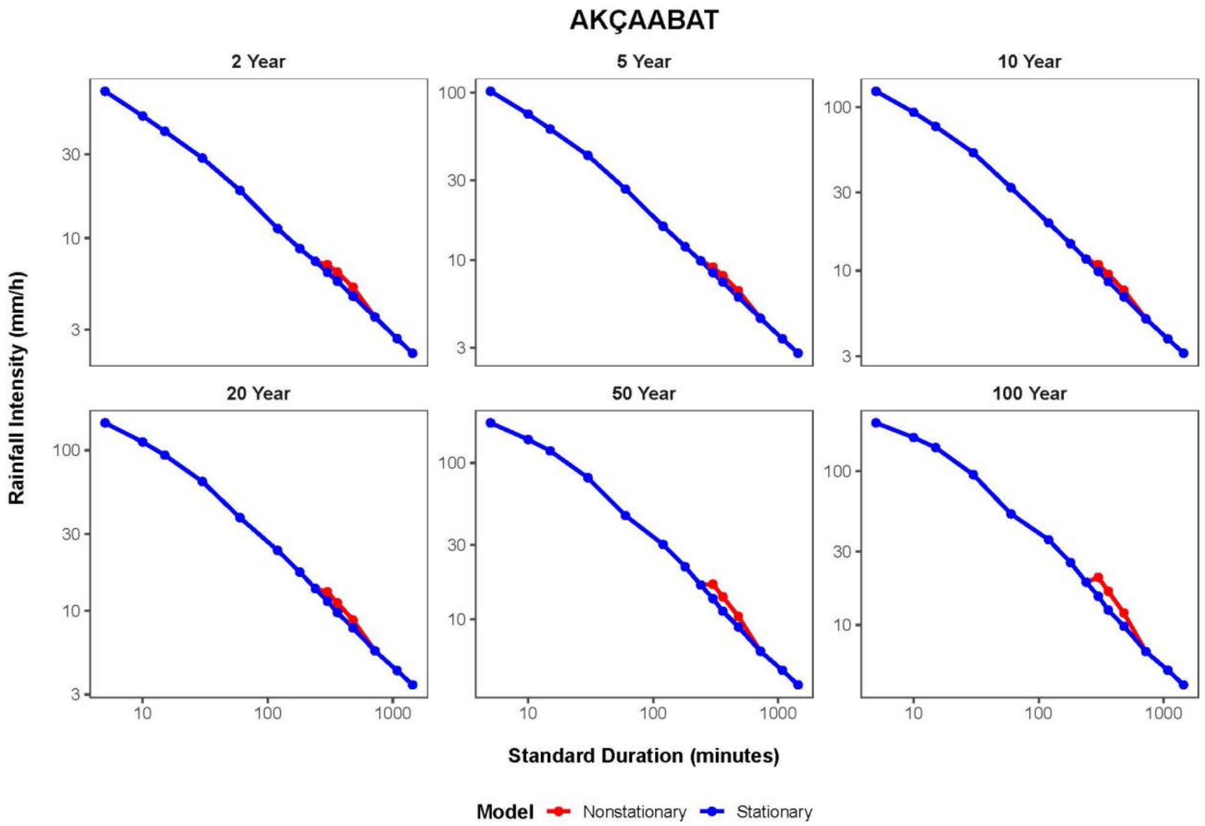

Fig. 4. Stationary and non-stationary IDF for different return periods for Akçaabat station

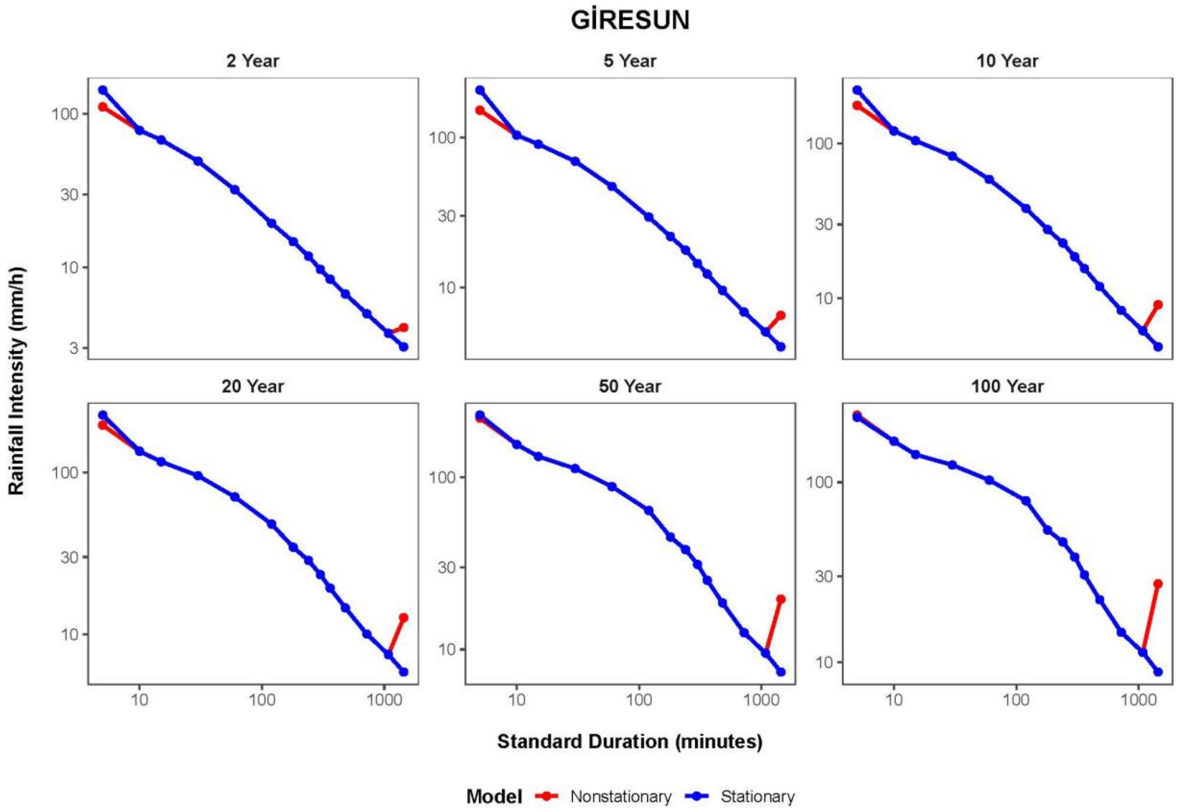

Fig. 5. Stationary and non-stationary IDF for different return periods for Giresun station

Although non-stationarity effects due to change of location parameters (Table 2) are observed only in 18-hour rainfall in Ordu, this effect is minimal at high return periods (10-100 years) (Fig. 6).

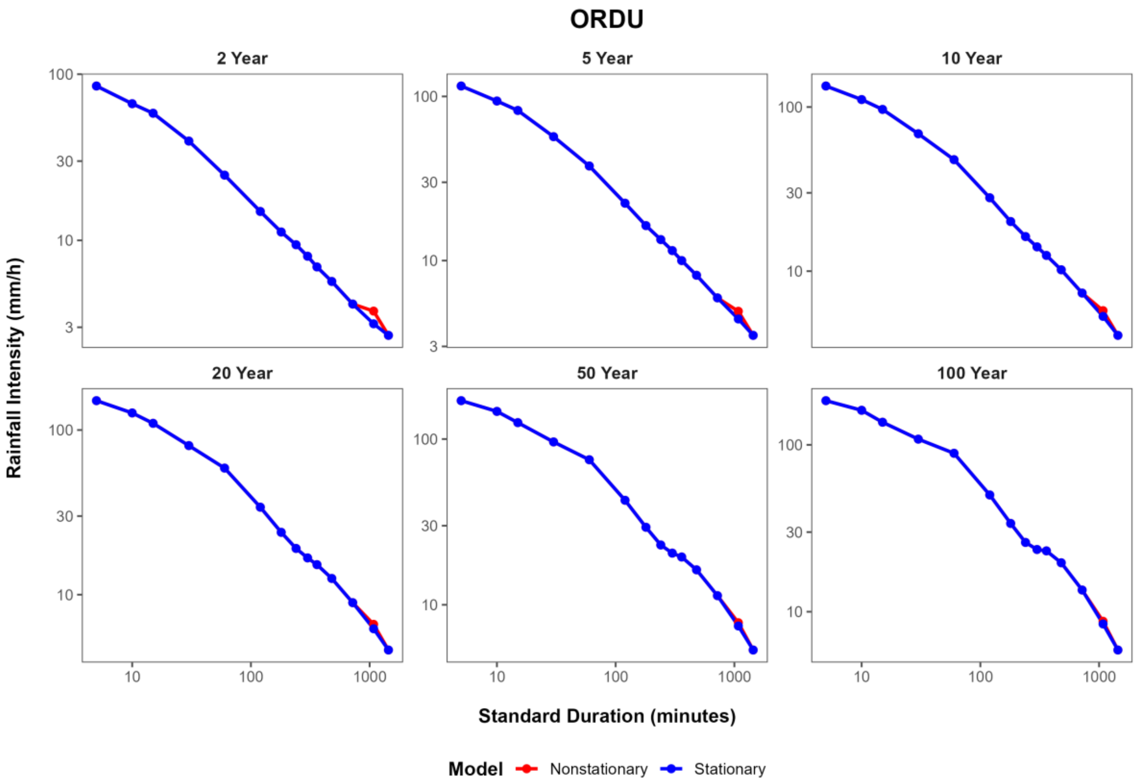

Fig. 6. Stationary and non-stationary IDF for different return periods for Ordu station

Between stationary and non-stationary IDF curves in Gümüşhane, non-stationary models, due to changes in location parameters (Table 2), produced higher intensity values in all return periods, especially in rainfall durations between 30 minutes and 6 hours (

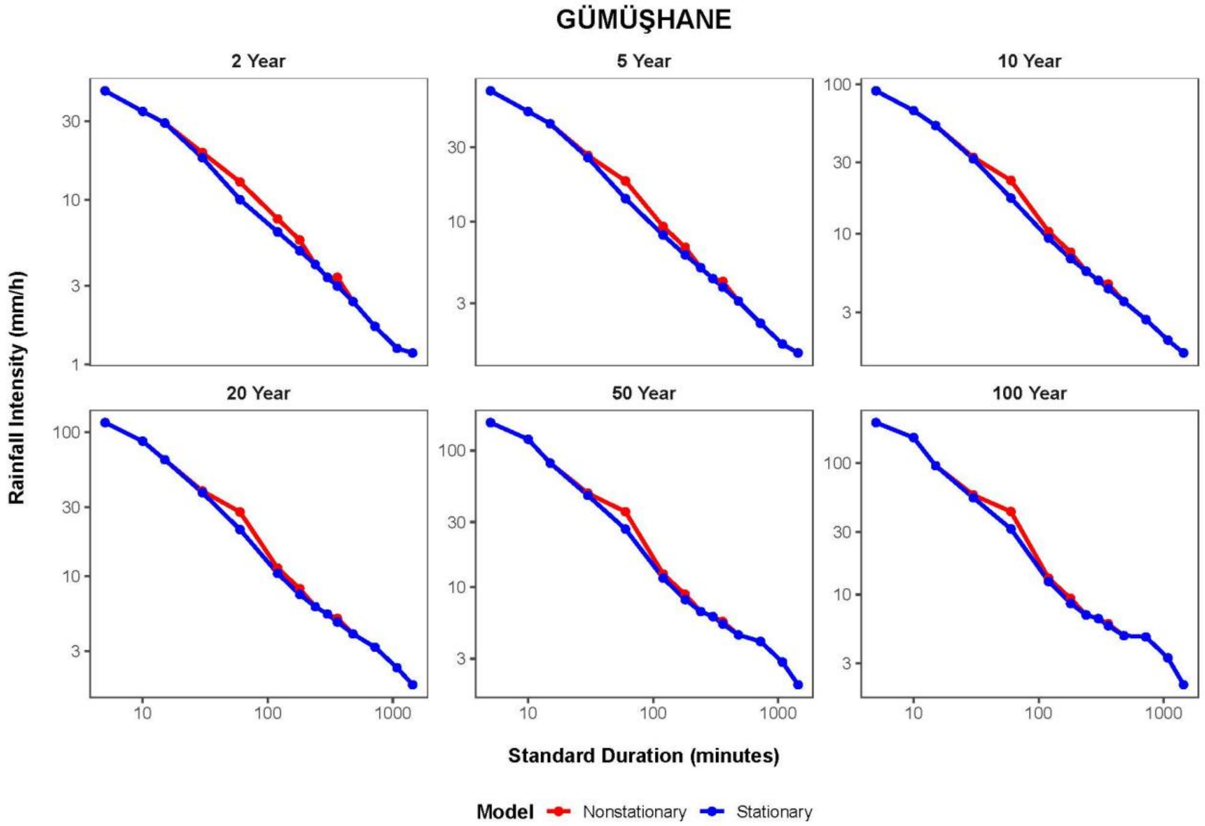

Fig. 7). However, when the AICc values are examined, it should be noted that the GEV models (III and IV) in which the scale parameter is changed also fulfil the Δi ≤ 2 condition and there is not much difference between the AICc values of the other models (Table 2).

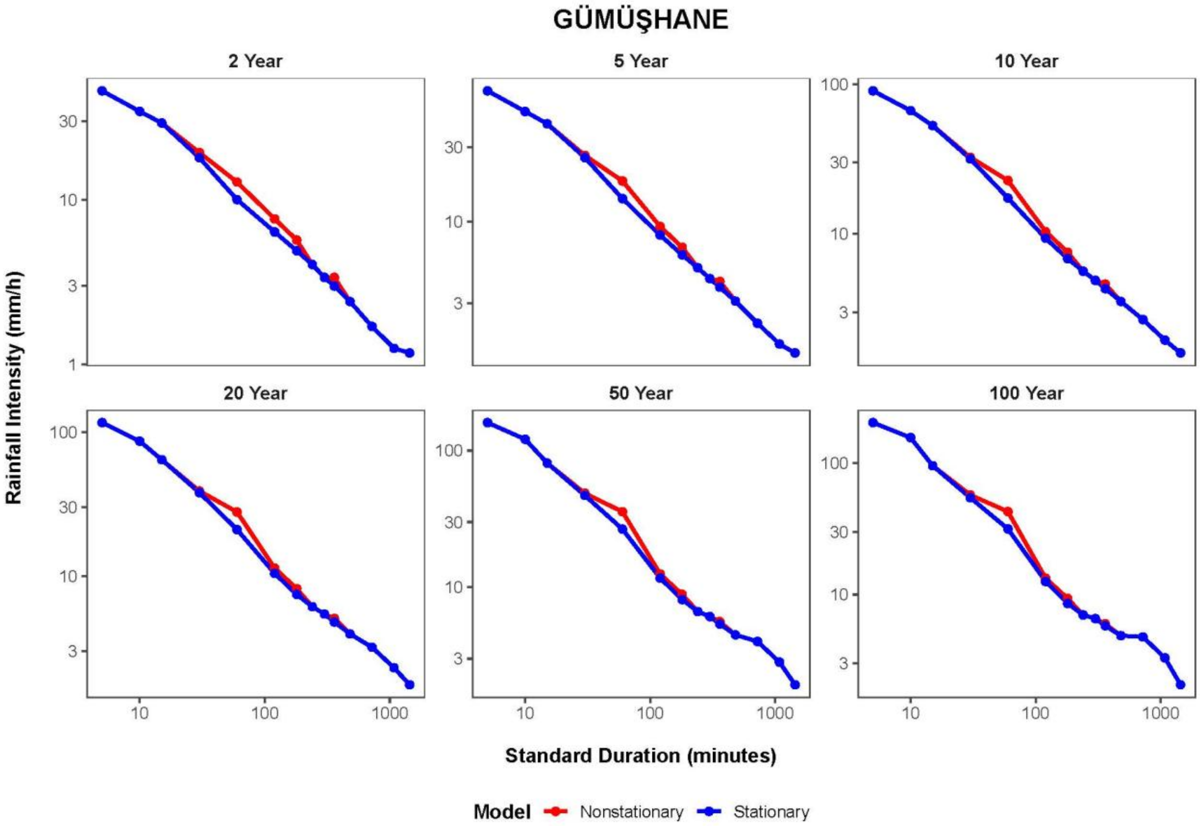

Fig. 7. Stationary and non-stationary IDF for different return periods for Gümüşhane station

At Bayburt station, non-stationary models predicted significantly higher rainfall intensities than stationary models for short-duration and low return periods (2-20 years) (Fig. 8). The difference was especially evident for periods below 60 minutes, indicating that short-term extreme precipitation tends to increase in the short duration. These changes are due to both location and parameters (Table 2).

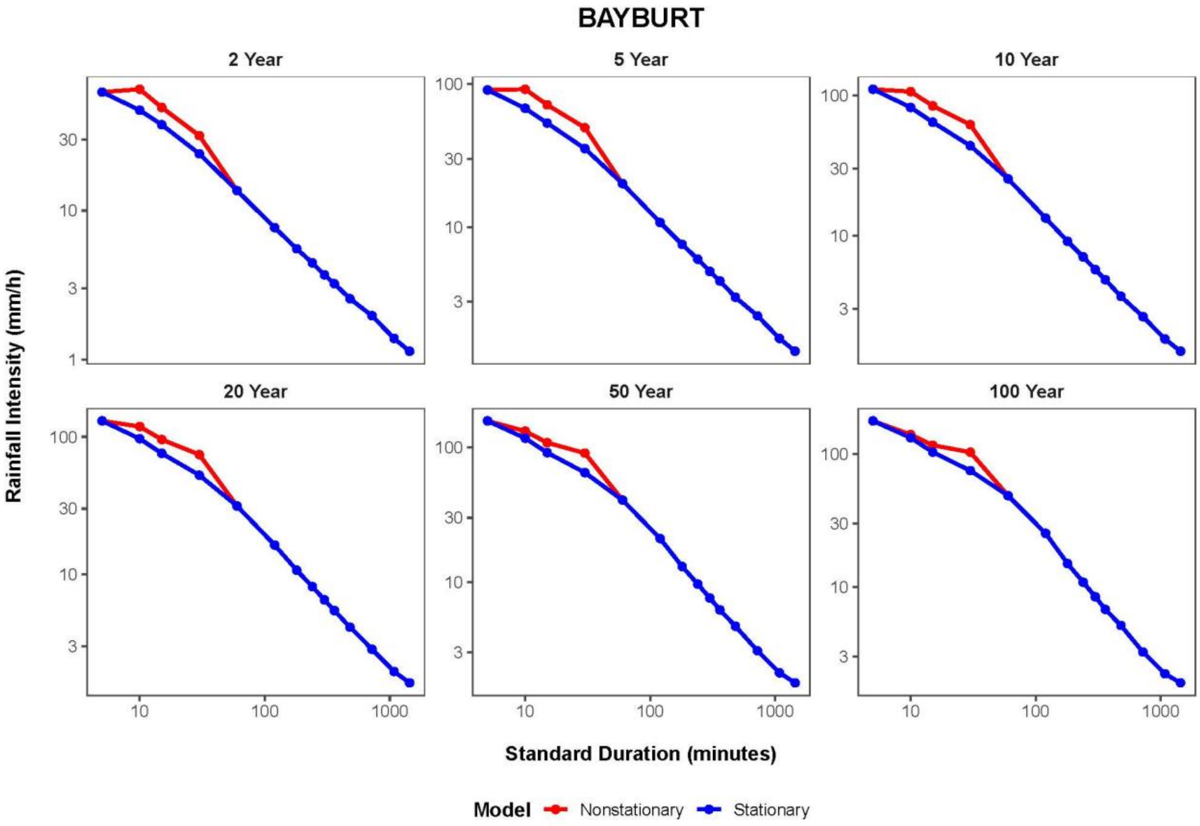

Fig. 8. Stationary and non-stationary IDF for different return periods for Bayburt station

Non-stationary models generally predicted higher rainfall intensities for short-duration and low-medium return periods. The non-stationarity effects were especially evident at the Bayburt, Gümüşhane, and Hopa stations. The stationarity assumption still seems valid at stations such as Akçaabat, Giresun, and Ordu. These results indicate that climate change-induced instability should be considered in infrastructure projects and urban planning in the Eastern Black Sea Region.

4. Conclusions

Stationary and non-stationary intensity-duration-frequency (IDF) curves of maximum standard duration rainfall at six stations were obtained using the Generalized Extreme Value (GEV) distribution in the Eastern Black Sea Region. Non-stationary conditions are characterized by short-duration rainfall in the region's interior and long-duration rainfall in the coastal areas. In the region, non-stationary issues emerge mostly due to location changes. According to the results, the stationary situation is still valid, but a non-stationary situation cannot be ignored. So, the non-stationary effects of climate change ought to be considered when planning and constructing infrastructure projects in the Eastern Black Sea Region.

References

Ahmed, K., Shahid, S., & Nawaz, N. (2018). Impacts of climate variability and change on seasonal drought characteristics of Pakistan. *Atmospheric Research*, *214*, 364-374. https://doi.org/10.1016/j.atmosres.2018.08.020

Aksu, H., Aksoy, H., Cetin, M., Yaldiz, S. G., Yildirim, I., & Alsenjar, O. (2025). Development of rainfall intensity-duration-frequency curves under nonstationary conditions. *Sustainable Water Resources Management*, *11*(1), 4. https://doi.org/10.1007/s40899-024-01176-2

Aksu, H., Cetin, M., Aksoy, H., Yaldiz, S. G., Yildirim, I., & Keklik, G. (2022). Spatial and temporal characterization of standard duration-maximum precipitation over Black Sea Region in Turkey. *Natural Hazards, 1-27.*

An, N., Turp, T. M., Bayındır, E., Akverdi, Y., Mirza, Z. N., & Kurnaz, L. M. (2023). *Climate Change Hotspots for Türkiye*. In Review. https://doi.org/10.21203/rs.3.rs-2648477/v1

Anik, E. M., Kankal, M., & Şan, M. (2021). *Doğu Karadeniz Havzası Yıllık Anlık Maksimum Akımların Eğilim Analizi*.

Asadieh, B., & Krakauer, N. Y. (2015). Global trends in extreme precipitation: Climate models versus observations. *Hydrology and Earth System Sciences*, *19*(2), 877-891. https://doi.org/10.5194/hess-19-877-2015

Aziz, R., & Yucel, I. (2021). Assessing nonstationarity impacts for historical and projected extreme precipitation in Turkey. *Theoretical and Applied Climatology*, *143*(3), 1213-1226. https://doi.org/10.1007/s00704-020-03503-x

Burnham, K. P., & Anderson, D. R. (2004). Multimodel Inference: Understanding AIC and BIC in Model Selection. *Sociological Methods & Research*, *33*(2), 261-304. https://doi.org/10.1177/0049124104268644

Cheng, L., AghaKouchak, A., Gilleland, E., & Katz, R. W. (2014). Non-stationary extreme value analysis in a changing climate. *Climatic Change*, *127*(2), 353-369. https://doi.org/10.1007/s10584-014-1254-5

Coles S. An Introduction to Statistical Modeling of Extreme Values;vol. 208 of Springer Series in Statistics. 1st ed. London. Springer. 2001. Available from: https://doi.org/10.1007/978-1-4471-3675-0.

Douglas, S., Xue, J., Hardison, A., & Liu, Z. (2023). Phytoplankton community response to a drought-to-wet climate transition in a subtropical estuary. *Limnology and Oceanography*, *68*(S1), S187-S201. https://doi.org/10.1002/lno.12348

Gao, M., Mo, D., & Wu, X. (2016). Nonstationary modeling of extreme precipitation in China. *Atmospheric Research*, *182*, 1-9. https://doi.org/10.1016/j.atmosres.2016.07.014

Katz, R.W. Statistical methods for non-stationary extremes. In Extremes in a Changing Climate: Detection, Analysis and Uncertainty; AghaKouchak, A., Easterling, D., Schubert, K.H.S., Sorooshian, S., Eds.; Springer: London, UK, 2013; pp. 15–37

Lee, O., Choi, J., Won, J., & Kim, S. (2020). Uncertainty in nonstationary frequency analysis of South Korea's daily rainfall peak over threshold excesses associated with covariates. *Hydrology and Earth System Sciences*, *24*(11), 5077-5093. https://doi.org/10.5194/hess-24-5077-2020

Mondal, A., & Mujumdar, P. P. (2015). Modeling non-stationarity in intensity, duration and frequency of extreme rainfall over India. *Journal of Hydrology*, *521*, 217-231. https://doi.org/10.1016/j.jhydrol.2014.11.071

Oruc, S. (2021). Non-stationary Investigation of Extreme Rainfall. *Civil Engineering Journal*, *7*(9), 1620-1633. https://doi.org/10.28991/cej-2021-03091748

Shang, H., Yan, J., Gebremichael, M., & Ayalew, S. M. (2011). Trend analysis of extreme precipitation in the Northwestern Highlands of Ethiopia with a case study of Debre Markos. *Hydrology and Earth System Sciences*, *15*(6), 1937-1944. https://doi.org/10.5194/hess-15-1937-2011

Shiru, M. S., Shahid, S., Chung, E.-S., & Alias, N. (2019). Changing characteristics of meteorological droughts in Nigeria during 1901–2010. *Atmospheric Research*, *223*, 60-73. https://doi.org/10.1016/j.atmosres.2019.03.010

Silva, D. F., & Simonovic, S. P. (2020). Development of non-stationary rainfall intensity duration frequency curves for future climate conditions. *Water Resources Research Report*, *106*, 229-231.

Sugahara, S., Da Rocha, R. P., & Silveira, R. (2009). Non-stationary frequency analysis of extreme daily rainfall in Sao Paulo, Brazil. *International Journal of Climatology*, *29*(9), 1339-1349. https://doi.org/10.1002/joc.1760

Swain, D. L., Wing, O. E. J., Bates, P. D., Done, J. M., Johnson, K. A., & Cameron, D. R. (2020). Increased Flood Exposure Due to Climate Change and Population Growth in the United States. *Earth's Future*, *8*(11), e2020EF001778. https://doi.org/10.1029/2020EF001778

Şan, M., Nacar, S., Kankal, M., & Bayram, A. (2023). Daily precipitation performances of regression-based statistical downscaling models in a basin with mountain and semi-arid climates. *Stochastic Environmental Research and Risk Assessment*, *37*(4), 1431-1455. https://doi.org/10.1007/s00477-022-02345-5

Tabari, H., Hosseinzadehtalaei, P., Thiery, W., & Willems, P. (2021). Amplified Drought and Flood Risk Under Future Socioeconomic and Climatic Change. *Earth's Future*, *9*(10), e2021EF002295. https://doi.org/10.1029/2021EF002295

Touhedi, H., Kankal, M., & Yıldız, M. B. (2023). Trend analysis of maximum rainfall series of standard durations in Turkey with innovative methods. *Natural Hazards*, *119*(3), 1479-1511. https://doi.org/10.1007/s11069-023-06085-9

Tramblay, Y., & Somot, S. (2018). Future evolution of extreme precipitation in the Mediterranean. *Climatic Change*, *151*(2), 289-302. https://doi.org/10.1007/s10584-018-2300-5

Vasiliades, L., Galiatsatou, P., & Loukas, A. (2015). Nonstationary Frequency Analysis of Annual Maximum Rainfall Using Climate Covariates. *Water Resources Management*, *29*(2), 339-358. https://doi.org/10.1007/s11269-014-0761-5

Wi, S., Valdés, J. B., Steinschneider, S., & Kim, T.-W. (2016). Non-stationary frequency analysis of extreme precipitation in South Korea using peaks-over-threshold and annual maxima. *Stochastic Environmental Research and Risk Assessment*, *30*(2), 583-606. https://doi.org/10.1007/s00477-015-1180-8

4th International Civil Engineering & Architecture Conference
17-19 May 2025, Trabzon, Türkiye

Enhancing model performance: calibration of SWAT+ model for the İznik Lake Watershed

Anıl Çalışkan Tezel*[1], Adem Akpınar[1]

[1] *Bursa Uludağ University, Department of Civil Engineering, 16059 Bursa, Türkiye*

Abstract. Hydrological modeling is a crucial tool for understanding and managing the hydrological processes within a watershed. In this study, the Soil and Water Assessment Tool-Plus (SWAT+), an advanced version of the SWAT model, was employed to model the hydrological processes of the İznik Lake Watershed, a region of significant environmental and social importance in the Marmara Region of Türkiye. The sensitivity analysis, calibration, and the validation were conducted using the SWAT+ Toolbox to accurately simulate the hydrological processes within the watershed. SWAT+ Toolbox is designed to work with SWAT+ model, offering enhanced flexibility and efficiency for hydrological studies. Given the limited studies on the application of SWAT+ Toolbox, the present study aims to provide valuable insights into the calibration process and the parameters sensitive to streamflow. The model was calibrated for 2007-2016 and validated for 2017-2021, including two years of warm-up period. The model's performance was evaluated using Nash-Sutcliffe efficiency (NSE), Kling-Gupta efficiency (KGE), coefficient of determination (R^2), and the percent bias (PBIAS). The observed flow data from two streamflow gauging stations were compared with the simulated values. The results revealed that the SWAT+ model can represent the hydrology of the study region, with satisfactory to very good model performance. The calibrated model can be applied to assess the impacts of climate and land use/land cover changes for better management strategies, and will guide further studies in hydrological modelling.

Keywords: İznik Lake Watershed; SWAT+ model; Hydrological modeling; SWAT+ Toolbox

1. Introduction

Hydrological models are excellent tools for analyzing, forecasting, and effectively managing water resources (Aragaw et al., 2021). Without numerical models, predicting hydrological processes in large-scale watersheds is highly challenging due to the complexity of interactions among climate, land use, soil properties, and topography. However, the calibration and the validation of hydrological models need to be implemented carefully since poorly calibrated or unvalidated models can lead to significant uncertainties in model predictions. If the model does not accurately represent real-world hydrological processes, subsequent studies on water resource management, climate change impacts, and land-use planning within the study area may lack reliability. A well-calibrated model enhances predictive capabilities, allowing for more reliable hydrological assessments and future scenario analyses. Numerous studies affirm that well-calibrated models improve accuracy and reliability (Abbas et al., 2024; Mei et al., 2023; Wang et al., 2024).

In this study, the Soil and Water Assessment Tool-Plus (SWAT+) model, an advanced version of the widely used SWAT model, was employed to simulate the hydrological processes of the İznik Lake Watershed. This watershed, located in the Marmara Region of Türkiye, holds significant environmental and hydrological importance, as it serves as a critical water resource for the surrounding region. There are a large number of SWAT-related studies conducted to assess the model's stability and usefulness (Abbaspour et al., 2018).

SWAT+ Toolbox was selected as the calibration tool, which is a C#-based software designed to work with the SWAT+ model (Chawanda 2021). It enables sensitivity analysis, as well as both manual and automatic calibration and validation. By calibrating and validating the SWAT+ model, this study aims to improve the accuracy of streamflow simulations and provide insights into key parameters influencing hydrological processes. The primary goal of this study is to calibrate the SWAT+ model for the İznik Lake Watershed using the SWAT+ Toolbox, focusing on streamflow simulation. The findings of this study will contribute to a deeper understanding of the SWAT+ calibration process and support future hydrological modelling efforts in similar watersheds.

*Corresponding author, E-mail: anilcal@gmail.com

https://doi.org/10.31462/icearc2025_ce_hwr_071

2. Material and methods

2.1. Description of the study site

The study site is the İznik Lake Watershed located in the Marmara Region of northwestern Türkiye (Fig. 1). İznik Lake is the largest lake in the Marmara Region and the fifth largest in Türkiye. The watershed covers an area of approximately 1,400 km^2, extending from latitude 40° 20′ to 40° 35′ N and longitude 29° 10′ to 29° 55′ E. The lake has an elliptical shape, with a surface area of 313 km^2, an average depth of 40 m, and a maximum depth of 80 m (Viehberg et al., 2012; Oğuz et al., 2020). It is a freshwater lake of tectonic origin. The region's climate is typically Mediterranean, characterized by a mean annual temperature of approximately 14°C and an average annual precipitation of around 630 mm (Franz et al., 2006). The lake's water level varies seasonally, rising during winter and spring (February to April), declining throughout the summer, and reaching its lowest level in autumn (September). The lake is located at 85 m above sea level, with the temperature of the bottom water dropping to 5°C in spring due to the inflow of cold snowmelt (Oğuz et al., 2020).

The İznik Lake Watershed plays a vital role in supporting various activities such as agriculture, industry, tourism, and fishing in the surrounding areas. The dominant land use types within the watershed are agricultural lands, forests, and urban areas. The watershed is primarily located within the borders of Bursa province, with parts extending into Kocaeli and Yalova provinces. To the west of the basin lie Erikli Mountain and Gemlik Bay, while the Samanlı and Karlık Mountains are situated to the north (Garipagaoglu and Uzun, 2019). In the northeast of the study area, the İznik Dam has been under construction since 2017. The lake is surrounded by picnic areas, sightseeing spots, and tourist facilities, and it is home to a rich diversity of flora. Additionally, the İznik Basilica, a monumental structure, is located 20 meters from the shore of İznik Lake. In recognition of its ecological and cultural significance, the İznik Lake Watershed was designated as a "Protected Area" in 1990. The main rivers feeding the lake include Sölöz, Olukdere, Kırandere, and Karasu, with Karsak Stream serving as the lake's outlet (Kaya, 2022). Among these, Karasu (also known as Karadere) in the northeast and the Sölöz in the southwest are the most significant. Karadere Stream is the largest stream flowing into the lake, with a drainage basin of 273 km^2 and an average flow rate of 2.4 m^3/s, while Sölöz Stream has a basin of 92 km^2 and an average flow rate of 1.06 m^3/s. The location of major rivers, meteorological stations, and gauging stations within the İznik Lake Watershed are illustrated in Fig. 2.

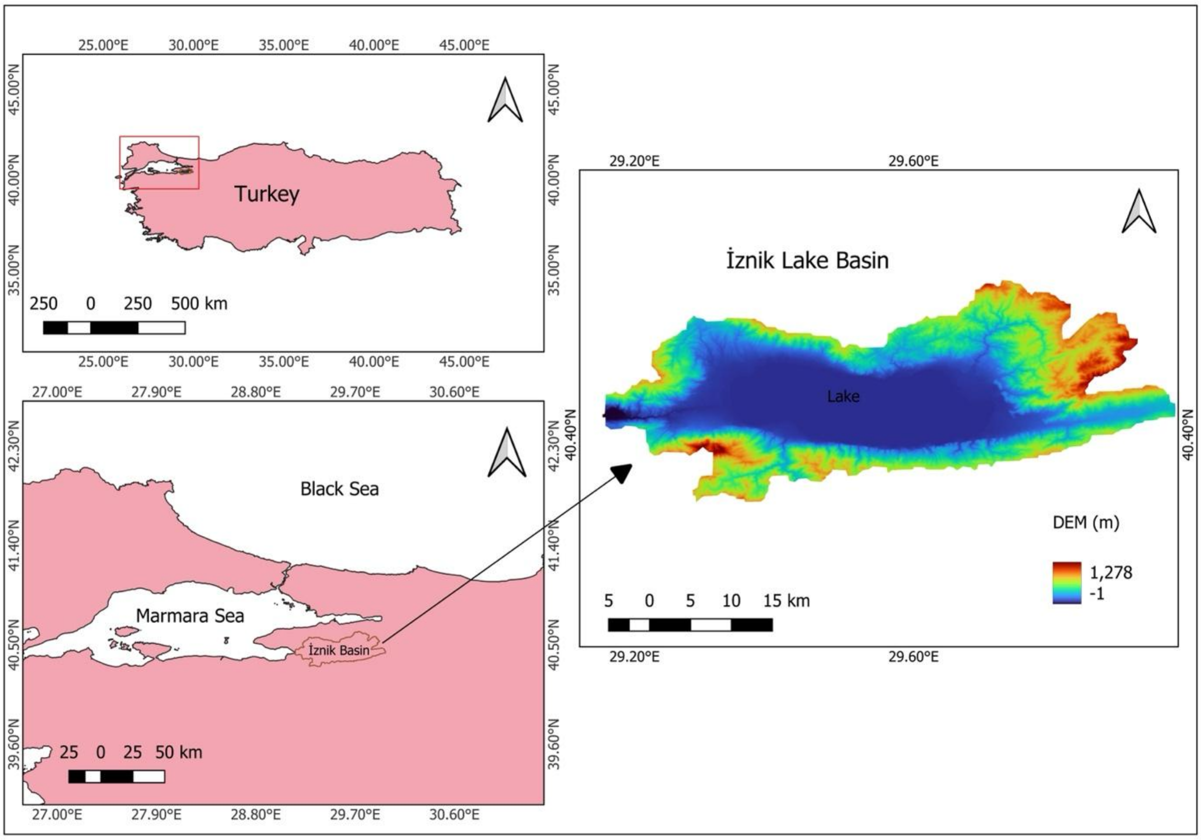

Fig. 1. Study area location and elevation map (Tezel et al., 2025)

Fig. 2. Map showing gauging stations, rivers, and meteorological stations (Tezel et al., 2024)

2.2. SWAT+ hydrological model

The SWAT+ model, version 61.0.1, was used in this study to simulate streamflow in the İznik Lake Watershed. Since the model operates within the QGIS interface, QGIS version 3.40.4 Bratislava (Long Term Release) was used in this study. The SWAT+ model is a widely used physically based hydrological model (Bieger et al., 2017) developed by Dr. Jeff Arnold for the USDA Agricultural Research Service (ARS). SWAT+ is an enhanced version of the original SWAT model, offering improved flexibility and modularity in simulating watershed processes. Being an open-source model, SWAT+ provides access to its source code, documentation, and updates through its official GitHub repository (https://github.com/swat-model/swatplus), ensuring continuous improvements and community contributions. The SWAT+ model is designed to simulate hydrological processes in watersheds on a daily time step under varying land use, soil types, and management practices. The key hydrological components, including surface runoff, lateral flow, groundwater flow, evapotranspiration, and streamflow are simulated. The SWAT+ model divides the watershed into sub-basins, which are further delineated into hydrological response units (HRUs) based on unique land use, soil type, and slope combinations. The simulations are based on the water balance equation, and the hydrological cycle for each HRU is simulated using the water balance equation (Basu et al. 2022):

$$SW_t = SW_0 + \sum_{i=1}^{t}\left(R_{day} - Q_{surf} - E_a - w_{seep} - Q_{gw}\right) \quad (1)$$

where SW_t is the final soil water content (mm H_2O), SW_0 is the initial soil water content on day i (mm H_2O), R_{day} is the amount of precipitation on day i (mm H_2O), Q_{surf} is the amount of surface runoff on day i (mm H_2O), E_a is the amount of evapotranspiration on day i (mm H_2O), w_{seep} is the amount of water entering the vadose zone from the soil profile on day i (mm H_2O), Q_{gw} is the amount of return flow on day i (mm H_2O), t is the time (days) (Neitsch et al. 2011).

2.3. Model input data

The SWAT+ model requires a diverse set of input data to represent the physical characteristics of the watershed. Model input data can be categorized into two main groups: spatial and temporal data. Spatial data include the digital elevation model (DEM), land use/land cover (LULC), and soil data, which are essential for defining HRUs. Runoff is predicted individually for each HRU and routed to obtain the total runoff for the watershed (Neitsch et al., 2011). The temporal input data include precipitation, maximum and minimum air temperature, relative humidity, solar radiation, and wind speed.

The DEM is a critical dataset for watershed delineation and river network definition, as it determines key topographical characteristics such as slope classes, channel length, channel width, and channel depth. For this study, the Shuttle Radar Topography Mission (SRTM) 1 Arc-Second Global dataset (~30 m resolution) was utilized to extract watershed characteristics and delineate the drainage network (https://earthexplorer.usgs.gov/). The DEM map of the İznik Lake Watershed is presented in Fig. 1.

Land use/land cover (LULC) data are essential for simulating hydrological processes within the watershed. In the present study, the Coordination of Information on the Environment (CORINE) land cover dataset was utilized, generated using Geographic Information Systems (GIS) and remote sensing techniques. This dataset has a spatial resolution of 100m x 100m. The Corine Land Cover (CLC) dataset has a minimum mapping unit of 25 hectares (ha) for areal features and a minimum width of 100 m for linear features. The data is available in both vector and 100 m raster formats. As illustrated in Fig. 3, the LULC map of the İznik Lake Watershed identifies 20 different land cover types. The dominant LULC classes in the watershed include agricultural areas, forests, bushlands, and grass.

Another essential dataset required for the SWAT+ model is soil data. The Major Soil Groups (BTG) Map of Türkiye, which was originally created at a scale of 1:100,000 by the General Directorate of Rural Services in the 1970s, was utilized in the study. These maps have been updated and modified over time. The BTG soil data was pre-processed in QGIS for use in the model. BTG soil types vary based on several factors, including slope-depth combination (EDK), degree of erosion (ERZ), land use type (SAK), land use capability (AKK, ATS), and other soil properties, such as salinity and alkalinity. The watershed contains various soil types, including Brown Forest Soil, Red-brown Mediterranean Soil, Rendzina, Alluvial, and Colluvial Soils (Table 1). A soil look-up table was developed to determine the soil parameters for BTG soil maps. Some parameters are optional, as indicated in Table 2. The necessary soil parameters were derived from field studies and soil sample analyses conducted in Bursa province (Özsoy, 2007; Aksoy et al., 2007; Özcan, 2021). Based on the BTG soil data, the required soil parameters were identified, and the soil map was reclassified into unique soil units. The spatial distribution of soil types within the İznik Lake Watershed is shown in Fig. 4.

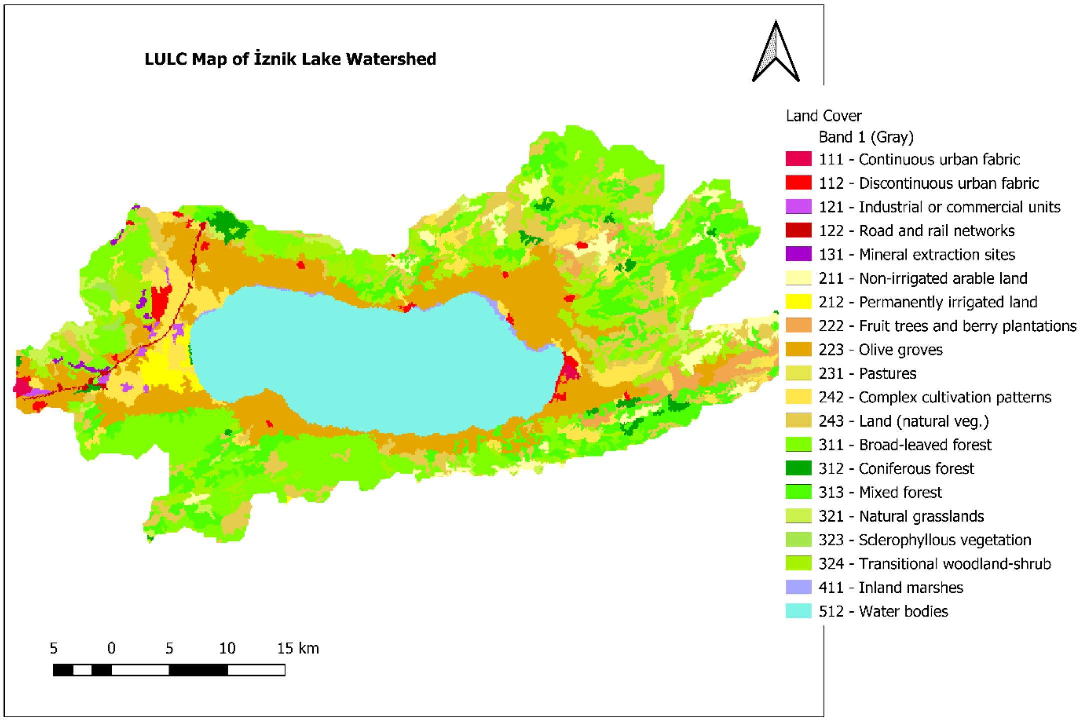

Fig. 3. LULC classification of the İznik Lake Watershed (Tezel et al., 2024)

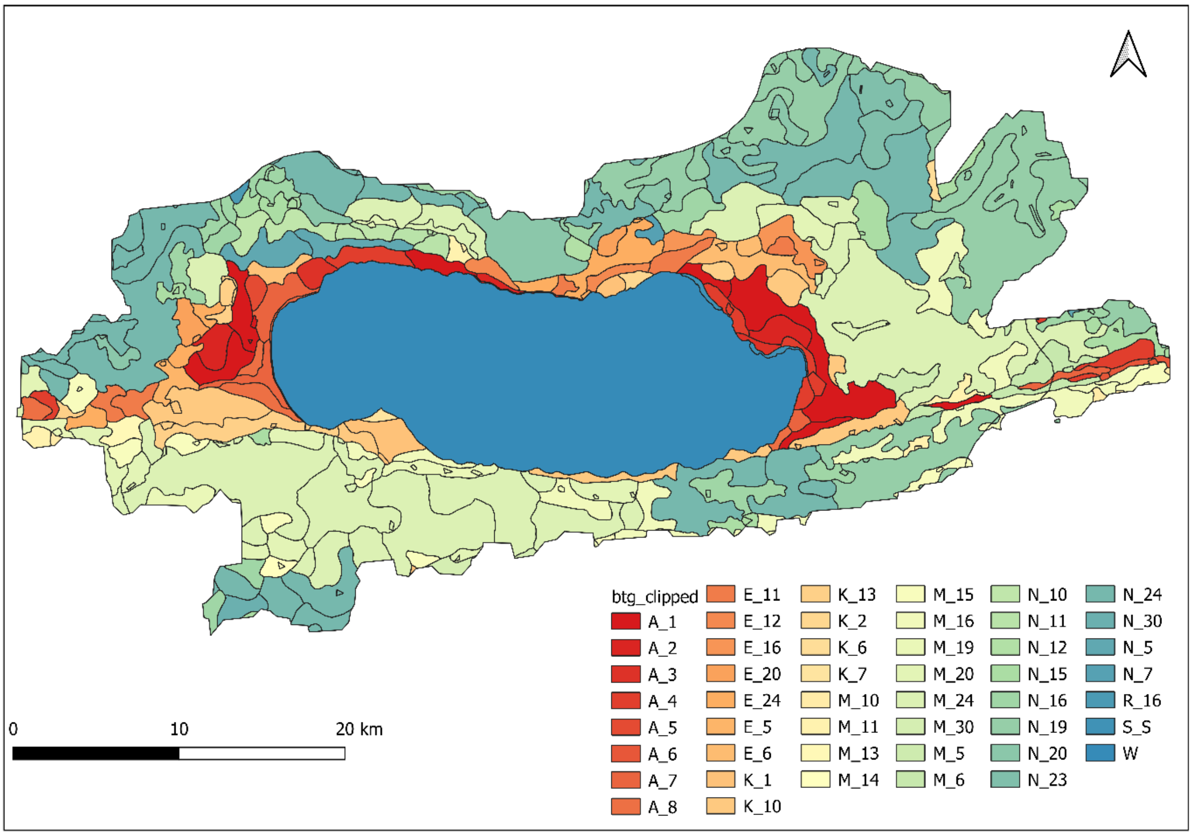

Fig. 4. Major Soil Groups (BTG) of İznik Lake Watershed (Tezel et al., 2024)

Table 1. BTG soil types of İznik Lake Watershed (Tezel et al., 2024)

Symbol	Soil Type
M	Brown Forest Soils
N	Brown Forest Soils with No Lime
E	Red-Brown Mediterranean Soils
R	Rendzinas
A	Alluvial Soils
S	Alluvial Coastal Soils
K	Colluvial Soils

Meteorological data is a crucial input for the SWAT+ model as it determines the water balance and hydrological parameters in the watershed. The required meteorological data include daily precipitation, maximum and minimum air temperature, wind speed, solar radiation, and relative humidity. Wind speed and solar radiation data were sourced from NASA's Prediction of Worldwide Energy Resources (https://power.larc.nasa.gov), while the other weather parameters were acquired from the General Directorate of Meteorology. There are three meteorological stations within the basin, referred to as İznik, Bursa Radar, and Orhangazi. Since the İznik meteorological station has the most comprehensive and continuous dataset, the data from it was used in the study (Fig. 2). Furthermore, SWAT+ includes a weather generator option, which is one key component for providing daily weather inputs when observed data is not available or to fill in gaps in the data.

The streamflow records obtained from the General Directorate of State Hydraulic Works (DSI) were used to calibrate and validate the performance of the SWAT+ model.

Table 2. Soil data input variables for SWAT+ model (Tezel et al., 2025)

Parameter Name	Definition
HYDGRP	Soil hydrologic group (A, B, C, or D). Required only for the SWAT ArcView interface)
ZMX	Maximum rooting depth of soil profile (mm)
ANION_EXCL	Fraction of porosity (void space) from which anions are excluded
CRK	The potential or maximum crack volume of the soil profile expressed as a fraction of the total soil volume
TEXTURE	Texture of soil layer
Z (layer #)	Depth from soil surface to bottom of layer (mm)
BD (layer #)	Moist bulk density (Mg/m^3 or g/cm^3)
AWC (layer #)	Available water capacity of the soil layer (mm H_2O/mm soil)
K (layer #)	Saturated hydraulic conductivity (mm/hr)
CBN (layer #)	Organic carbon content (% soil weight)
CLAY (layer #)	Clay content (% soil weight)
SILT (layer #)	Silt content (% soil weight)
SAND (layer #)	Sand content (% soil weight)
ROCK (layer #)	Rock fragment content (% total weight)
ALB (Top layer)	Moist soil albedo.
USLE_K (Top layer)	USLE equation soil erodibility (K) factor (units: 0.013 (metric ton m^2 hr)/(m^3-metric ton cm)).
EC (layer #)	Electrical conductivity (dS/m) (Not currently active).
CAL (layer #)	Soil CaCo3 (%) (0-50%)
PH (layer #)	Soil Ph (3-10)

2.4. SWAT+ model setup, calibration, and validation

The SWAT+ model setup involves several steps, including watershed delineation, the creation of HRUs, and editing inputs. First, watershed delineation was performed using DEM data, and 13 sub-basins were created within the watershed based on flow direction. The SWAT+ model setup requires the delineation of the watershed into sub-basins and the further division of these sub-basins into HRUs, which represent unique combinations of land use, soil, and slope. The SWAT+ model created 259 channels, 259 landscape units (LSUs), and 8969 HRUs for the watershed, which were utilized in the model simulations. After the watershed delineation and HRU definition, the model input files were generated based on the prepared spatial and temporal datasets.

Model calibration is particularly important to minimize the differences between the observed and simulated streamflow. The more reliable the calibration is, the more accurate the model predictions (Ozdemir & Akbas, 2023). In this study, the SWAT+ model was calibrated and validated using observed monthly streamflow data from two gauging stations, Karadere-Çakırca and Fındıcak-Bayırköy, operated by DSI. Model simulations were conducted for the period 2007-2021, which was divided into three phases: 2007 to 2009 warm-up period, 2010 to 2016 calibration period, and 2017 to 2021 validation period. SWAT+ Toolbox version 2.4 was utilized for sensitivity analysis, calibration, and validation of the model.

The sensitivity analysis was performed to identify the most sensitive parameters for streamflow simulation, which helps reduce the number of parameters requiring calibration. Previous studies have been reviewed to identify parameters which are sensitive to streamflow (Ren et al., 2022; Zeiger et al., 2021; Zhang et al., 2020). Using these approaches, 11 parameters were identified as the most sensitive for streamflow simulation. The model was subsequently calibrated using both manual and automatic procedures. The sensitivity ranking and corresponding fitted values are presented in Table 3, with the three most sensitive parameters identified as the percolation coefficient (perco), depth of the soil layer (z), and SCS curve number (Cn2), respectively.

Three commonly used statistical metrics: Nash-Sutcliffe Efficiency (NSE), Kling-Gupta Efficiency (KGE), and Percent Bias (PBIAS) were selected (Moriasi et al. 2007; Thiemig et al. 2013; Kouchi et al. 2017). NSE was selected due to its capability to quantify the overall agreement between observed and simulated data (Nash & Sutcliffe, 1970). KGE was included as it decomposes the model performance into correlation, bias, and variability (Gupta et al. 2009). Lastly, PBIAS was employed to assess the model's tendency to overestimate or underestimate streamflow predictions (Moriasi et al. 2007). These three metrics were calculated and compared for both the calibration and validation periods to assess the model's ability to accurately simulate streamflow under different conditions.

$$\mathrm{NS}E = 1 - \frac{\sum_{t=1}^{T}\left(Q_m^t - Q_o^t\right)^2}{\sum_{t=1}^{T}\left(Q_o^t - \overline{Q_o}\right)^2} \tag{2}$$

$$PBIAS = \left[\frac{\sum_{t=1}^{T}(Q_o^t - Q_m^t)x100}{\sum_{t=1}^{T}(Q_o^t)}\right] \tag{3}$$

$$KGE = 1 - \sqrt{(r-1)^2 - \left(\frac{\sigma m}{\sigma o} - 1\right)^2 - \left(\frac{\mu m}{\mu o} - 1\right)^2} \tag{4}$$

Where Q_o^t and Q_m^t are the observed and the modeled flow, and $\overline{Q_o}$ is the mean value of observed and modeled flow respectively, for a specific time (t), r is the Pearson correlation coefficient between the observed and modeled, σ is the standard deviation, and μ is the mean. Table 4 presents the model performance ratings for evaluation metrics.

Table 3. Calibrated SWAT+ parameters

Parameter	Definition	Sensitivity Rank	Change Method	Fitted Value
perco	Percolation coefficient	1	Replace	0.02
bd	Bulk density (mg/m^3)	8	Percent	-5
cn3_swf	Pothole evaporation coefficient	6	Replace	1
cn2	The SCS Curve number is a function of the soil's permeability	3	Percent	-15
clay	Clay content (%soil weight). The percentage of soil particles that are <0.002 mm in equivalent diameter	4	Percent	-40
z	Depth from soil surface to bottom of layer (mm)	2	Percent	140
esco	Soil evaporation compensation factor	5	Replace	-0.1
k	Saturated hydraulic conductivity (mm/hr)	9	Relative	350
canmx	Maximum canopy storage (mm H2o)	10	Replace	100
chk	Effective hydraulic conductivity in main channel alluvium (mm/hr)	11	Relative	-50
lat_len	Slope length for lateral subsurface flow (m)	7	Percent	-38

Table 4 Model performance ratings (Moriasi et al.2007; Thiemig et al.2013; Kouchi et al.2017)

Performance Rating	NSE	PBIAS (%)	KGE
Very good	0.75<NS≤1.00	PBIAS<±10	0,9 ≤ KGE ≤ 1
Good	0.65<NS≤0.75	±10≤PBIAS<±15	0,75 ≤ KGE < 0.9
Satisfactory	0.50<NS≤0.65	±15≤PBIAS<±25	0,5 ≤ KGE < 0.75
Unsatisfactory	NS≤0.50	PBIAS≥±25	KGE <0.5

3. Results and discussion

The comparison of observed and simulated flow during the calibration and validation periods for each gauging station is shown in Fig. 5, along with the corresponding error statistics. According to the statistical metrics, PBIAS values are classified as "very good" in all cases except for the validation period at the Fındıcak station. KGE values range from 0.53 to 0.76, indicating performance levels between "satisfactory" and "good" for both calibration and validation periods. For the Karadere station, NSE values were 0.47 and 0.51 during calibration and validation, respectively, indicating "satisfactory" model performance, while these values were lower at 0.44 and 0.40 for the Fındıcak station. Overall, the model demonstrated performance ranging from 'satisfactory' to 'very good' based on PBIAS and KGE values. However, NSE values at the Fındıcak station were slightly below the recommended threshold of 0.50. The İznik meteorological station is located near the Karadere gauging station but at a considerable distance from the Fındıcak station. This spatial discrepancy may have introduced higher uncertainty in precipitation input data, contributing to the lower model performance at the Fındıcak station.

The largest discrepancies between the modeled and the observed values were mostly during peak flow periods, particularly in March-April 2012 and February-April 2015 at the Karadere station, as well as in January 2010, and January-February 2015 at the Fındıcak gauging station. The model also overestimated the low observed flows from December 2013 to February 2014 for both stations. The observed flow and the precipitation data are consistent with each other during the peak flow periods in Karadere and Fındıcak stations. Additionally, the streamflow was measured to be low in the early months of 2014, when low precipitation was observed during the same periods supporting the consistency between the observed flow and precipitation data. Her and Jeong (2018) highlighted potential prediction issues in the SWAT+ model, showing multiple peaks in sub-daily hydrographs due to its newly implemented HRU-level flow routing scheme. A study conducted in the Uruguay River Basin using the SWAT+ model reported a systematic underestimation of peak discharges, despite adequate flow fluctuation representation (Barresi Armoa et al., 2023). On the other hand, the model simulated the low flows well during the simulation for both stations, except for the overestimation in early 2014. The observed flows were smaller than 1 m^3/s, while the simulated values were between 2 and 4 m^3/s during this winter period of 2014. The high flow estimates during low-flow periods may be attributed to the inaccurate modeling of the snowmelt processes. Errors in temperature or solar radiation data can lead to such discrepancies (Debele et al. 2010, Myers et al. 2021). In another study by Kardhana et al. (2024), the limitations of the SWAT+ model in watershed management and water resource optimization, particularly under low-flow conditions, were discussed. In general, the SWAT+ model was able to capture the seasonal dynamics of the hydrology in the watershed reasonably well, reproducing the annual cycle of streamflow and the timing of high and low flows periods.

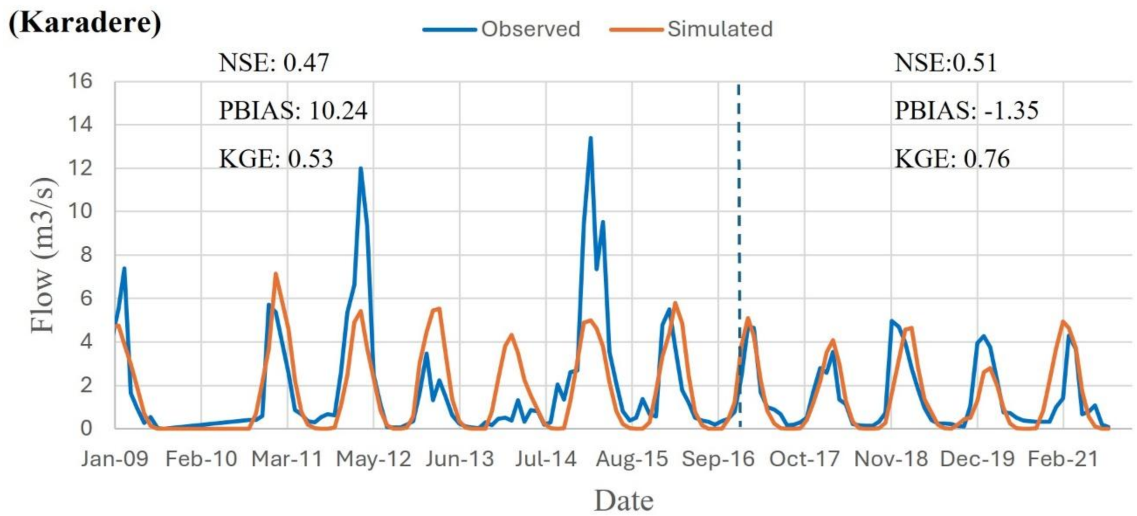

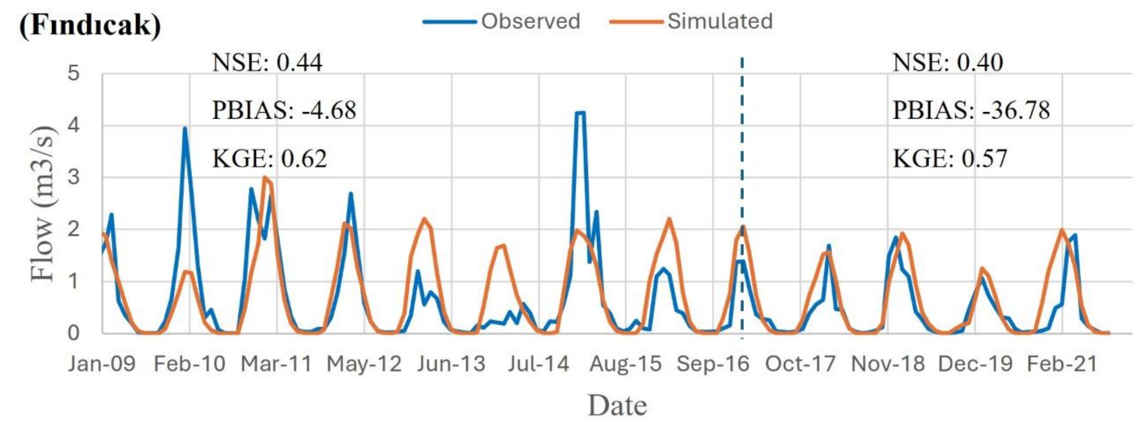

Fig. 5. Comparison of the observed and the modeled monthly streamflow for the Karadere-Çakırca, and Fındıcak- Bayırköy gauging stations (the dotted vertical line shows the boundary between the calibration and the validation periods) (Tezel et al., 2025).

4. Conclusions

The SWAT+ model was used to simulate streamflow in the İznik Lake Watershed, an important water resource for the surrounding area. The newly released SWAT+ Toolbox, a free calibration tool specifically designed for the SWAT+ model, was utilized for sensitivity analysis, calibration, and validation. Compared to other calibration tools, SWAT+ Toolbox has been frequently applied in the literature, making this study valuable for SWAT+ model users.

The model was calibrated and validated using observed monthly streamflow data from two gauging stations, achieving satisfactory to very good performance based on multiple statistical metrics, including NSE, KGE, and

PBIAS. However, some discrepancies were observed during peak flow periods and low-flow conditions, especially at the Fındıcak station, which may be attributed to uncertainties in meteorological data and the complex hydrological process in the watershed.

The calibration parameters and methodological approach used in this study can guide researchers and practitioners effectively utilizing the SWAT+ model for similar watersheds. Additionally, as one of the relatively few studies employing the SWAT+ Toolbox, this research provides valuable insights for model users. This study will also serve as a baseline for future research on climate change impacts on water resources, land management practices, and water quality modeling in the region.

Acknowledgements

We would like to thank the General Directorate of Meteorology (MGM) and the General Directorate of State Hydraulic Works (DSI) for providing the data that significantly contributed to this study. We also extend our gratitude to Prof. Dr. Ertuğrul Aksoy and Dr. Gökhan Özsoy for their valuable contributions to the preparation of the soil data.

References

Abbas, S. A., Bailey, R. T., White, J. T., Arnold, J. G., & White, M. J. (2024). Quantifying the role of calibration strategies on surface-subsurface hydrologic model performance. *Hydrological Processes, 38*, e15298. https://doi.org/10.1002/hyp.15298

Abbaspour, K. C., Vaghefi, S. A., & Srinivasan, R. (2018). A guideline for successful calibration and uncertainty analysis for soil and water assessment: A review of papers from the 2016 International SWAT Conference. *Water, 10*(1), 6. https://doi.org/10.3390/w10010006

Aragaw, H. M., Goel, M. K., & Mishra, S. K. (2021). Hydrological responses to human-induced land use/land cover changes in the Gidabo River Basin, Ethiopia. *Hydrological Sciences Journal, 66*(4), 640–655. https://doi.org/10.1080/02626667.2021.1890328

Aksoy, E., Özsoy, G., Dirim, M. S., Tümsavaş, Z., Alacalı, İ., & Ata, R. (2007). Uzaktan algılama ve coğrafik bilgi sistem teknikleri kullanarak Mustafakemalpaşa çayı havzasında güncel arazi kullanım/örtüsü ve potansiyel erozyon riskinin belirlenmesi [Determination of the potential erosion risk using remote sensing (RS) and geographic information system (GIS) techniques]. Project report UÜBAP Z-2003/96, Bursa Uludağ University, Bursa, Turkey.

Barresi Armoa, O. L., Sauvage, S., Houska, T., Bieger, K., Schürz, C., & Sánchez Pérez, J. M. (2023). Representation of hydrological components under a changing climate: A case study of the Uruguay River Basin using the new version of the Soil and Water Assessment Tool model (SWAT+). *Water, 15*(14), 2604. https://doi.org/10.3390/w15142604

Basu, A. S., Gill, L. W., Pilla, F., & Basu, B. (2022). Assessment of variations in runoff due to landcover changes using the SWAT model in an urban river in Dublin, Ireland. *Sustainability, 14*(1), 534. https://doi.org/10.3390/su14010534

Bieger, K., Arnold, J. G., Rathjens, H., White, M. J., Bosch, D. D., Allen, P. M., ... & Srinivasan, R. (2017). Introduction to SWAT+, a completely restructured version of the Soil and Water Assessment Tool. *JAWRA Journal of the American Water Resources Association, 53*(1), 115–130.

Chawanda, C. J. (2021). *SWAT+ Toolbox v0.7* [Software]. Zenodo. https://doi.org/10.5281/zenodo.6331716

Debele, B., Srinivasan, R., & Gosain, A. (2010). Comparison of process-based and temperature-index snowmelt modeling in SWAT. *Water Resources Management, 24*, 1065–1089. https://doi.org/10.1007/s11269-009-9486-2

Franz, S. O., Schwark, L., Brüchmann, C., Scharf, B., Klingel, R., Van Alstine, J. D., Çagatay, N., & Ülgen, U. B. (2006). Results from a multi-disciplinary sedimentary pilot study of tectonic Lake Iznik (NW Turkey): Geochemistry and paleolimnology of the recent past. *Journal of Paleolimnology, 35*, 715–736. https://doi.org/10.1007/s10933-005-5015-3

Garipağağoğlu, N., & Uzun, M. (2019). İznik Gölü Havzası'nda doğal ortam koşullarının havza yönetimi ve planlamasına etkisi [The effects of natural environment conditions, changes and possible risks on watershed]. *Doğu Coğrafya Dergisi, 24*(42), 1–24.

Gupta, H. V., Kling, H., Yilmaz, K. K., & Martinez, G. (2009). Decomposition of the mean squared error and NSE performance criteria: Implications for improving hydrological modelling. *Journal of Hydrology, 377*(1–2), 80–91. https://doi.org/10.1016/j.jhydrol.2009.08.003

Her, Y., & Jeong, J. (2018). SWAT+ versus SWAT2012: Comparison of sub-daily urban runoff simulations. *Transactions of the ASABE, 61*(4), 1287–1295. http://dx.doi.org/10.13031/trans.12600

Kardhana, H., Lihawa, A. W. I., Rohmat, F. I. W., Wulandari, S., Harjupa, W., Adiprawita, W., Kardena, E., & Kusuma, M. S. B. (2024). Water balance analysis in the Majalaya Watershed: Two-step calibration and application of the SWAT+ model for low-flow conditions. *Water, 16*(23), 3498. https://doi.org/10.3390/w16233498

Kaya, E. (2022). *İznik Gölü su kalite parametrelerinin yapay sinir ağları yöntemi ile değerlendirilmesi* [Master's thesis, Sakarya University].
Kouchi, D. H., Esmaili, K., Faridhosseini, A., Sanaeinejad, S. H., Khalili, D., & Abbaspour, K. C. (2017). Sensitivity of calibrated parameters and water resource estimates on different objective functions and optimization algorithms. *Water, 9*(6), 384. https://doi.org/10.3390/w9060384
Mei, Y., Mai, J., Do, H. X., Gronewold, A., Reeves, H., Eberts, S., ... & Xu, H. (2023). Can hydrological models benefit from using global soil moisture, evapotranspiration, and runoff products as calibration targets? *Water Resources Research, 59*, e2022WR032064. https://doi.org/10.1029/2022WR032064
Moriasi, D. N., Arnold, J. G., Van Liew, M. W., Bingner, R. L., Harmel, R. D., & Veith, T. L. (2007). Model evaluation guidelines for systematic quantification of accuracy in watershed simulations. *Transactions of the ASABE, 50*(3), 885–900.
Myers, D., Ficklin, D. L., & Robeson, S. M. (2021). Incorporating rain-on-snow into the SWAT model results in more accurate simulations of hydrologic extremes. *Journal of Hydrology, 603*, 126972. https://doi.org/10.1016/j.jhydrol.2021.126972
Nash, J. E., & Sutcliffe, J. V. (1970). River flow forecasting through conceptual models part I—A discussion of principles. *Journal of Hydrology, 10*(3), 282–290. https://doi.org/10.1016/0022-1694(70)90255-6
Neitsch, S. L., Arnold, J. G., Kiniry, J. R., & Williams, J. R. (2011). *Soil and water assessment tool: Theoretical documentation version 2009*. Texas Water Resources Institute.
Oğuz, A., Albay, R. A., Köker, L., Gurevin, C., Dorak, Z., & Albay, Z. (2020). Driving factors affecting the phytoplankton functional groups in a deep alkaline lake. *Turkish Journal of Botany, 44*, 633–646.
Ozcan, B. (2021). *Bursa ilinin arazi bozulumu ve zamansal değişiminin CORINE erozyon modeli kullanılarak belirlenmesi* [Master's thesis, Bursa Uludağ University, Faculty of Agriculture].
Özdemir, H., & Akbaş, A. (2023). Is there a consistency in basin morphometry and hydrodynamic modelling results in terms of the flood generation potential of basins? A case study from the Ulus River Basin (Turkey). *Journal of Hydrology, 625*, 129921.
Özsoy, G. (2007). *Uzaktan algılama (UA) ve coğrafi bilgi sistemi (CBS) teknikleri kullanılarak erozyon riskinin belirlenmesi* [Doctoral dissertation, Bursa Uludağ University, Faculty of Agriculture].
Ren, D., Engel, B., Mercado, J. A. V., Guo, T., Liu, Y., & Huang, G. (2022). Modeling and assessing water and nutrient balances in a tile-drained agricultural watershed in the U.S. Corn Belt. *Water Research, 210*, 117976.
Tezel, A. Ç., Akpınar, A., Özsoy, G., & Bor, A. (2024). The effect of soil data for streamflow simulation: A case study of İznik Lake Watershed. In *11th International Symposium on Atmospheric Sciences, ATMOS 2024*, 24 October, İstanbul, Turkey.
Thiemig, V., Rojas, R., & Zambrano-Bigiarini, M. A. (2013). Hydrological evaluation of satellite-based rainfall estimates over the Volta and Baro-Akobo Basin. *Journal of Hydrology, 499*, 324–338. https://doi.org/10.1016/j.jhydrol.2013.07.012
Viehberg, F. A., Ulgen, U. B., Damcı, E., Franz, S. O., On, A. S., Roeser, P. A., ... & Melles, M. (2012). Seasonal hydrochemical changes and spatial sedimentological variations in Lake İznik (NW Turkey). *Quaternary International, 274*, 102–111.
Wang, C., Mao, H., Nemoto, T., He, Y., Hu, J., Li, R., Wu, Q., Wang, M., Song, X., & Duan, Z. (2024). An adaptive process-wise fitting approach for hydrological modeling based on streamflow and remote sensing evapotranspiration. *Water, 16*(23), 3446. https://doi.org/10.3390/w16233446
Zeiger, S. J., Owen, M. R., & Pavlowsky, R. T. (2021). Simulating nonpoint source pollutant loading in a karst basin: A SWAT modeling application. *Science of the Total Environment, 785*, 147295.
Zhang, H., Wang, B., Liu, D. L., Zhang, M., Leslie, L. M., & Yu, Q. (2020). Using an improved SWAT model to simulate hydrological responses to land use change: A case study of a catchment in tropical Australia. *Journal of Hydrology, 585*, 124822.

ICEARC'25
4th International Civil Engineering & Architecture Conference
17-19 May 2025, Trabzon, Türkiye

Examination of existing buildings for rainwater harvesting system and feasibility of the system

Murat Ay*[1]

[1]*Yozgat Bozok University, Department of Civil Engineering, 66000 Yozgat, Türkiye*

Abstract. This present study consists of the importance, cost, benefit, environmental effects of rainwater harvesting system (RHS), which is a hydrological variable, and RHS's ability to be used as an alternative to existing water resources, and its storage function against to drought. In this context, RHSs are analyzed based on the regulations (DIN1989 (Germany), Turkey (Official Gazette in Turkey, 2017; Official Gazette in Turkey, 2021), BS8515 (England)). The results regarding the applicability and efficiency of RHSs in two existing traditional/typical reinforced concrete frame buildings in Yozgat province in Turkey are discussed. The results showed that RHSs are not economically advantage for these buildings in today conditions for short term. Therefore, some additive reforms can change this issue the terms of the associated financial cost as well as the efficiency of the technology behind rainwater collection. It has been seen that the storage costs constitute approximately 50%-80% of cost of the total system. In this direction, different storage forms and materials can be considered and state-supported payments or incentives can be made to the RHS projects. Considering the reasons such as the high initial investment and labor costs, the long amortization period of the system (9-25 years) and the laborious, costly and risky construction of the RHS in such buildings whose construction is completed, it can be said that the possibility of the RHS being implemented in our country is low. However, it can be said that such reasons are weaker reasons than risks such as drought danger and quality water shortage that threaten living beings. This study may also be a good preliminary starting point for a cost-benefit analysis because it states some associated pros and cons for financial issues, environmental issues, and practicality issues of installing RHSs.

Keywords: Benefit; Cost; Feasibility; Rainwater harvesting system (RHS); Yozgat

1. Introduction

Water is very important for all living things on our planet; however, most people generally prefers to act when a disaster happens to them. The scarcity, untimeliness and irregularity of water in future periods highlight the need for rainwater harvesting to be used in many sectors and for different purposes. Rainwater discharges to groundwater, and feeds the soil in especially during drought times. Moreover, when energy costs and facilities are considered, the RHS has many positive effects on water, carbon and ecological footprints (Ball, 1999; Şen, 2002; Ay, 2013; Haque et al., 2016; Çakar, 2022; SYGM, 2023; Dağ and Ay, 2024). Rainwater, which is a clean and easily accessible asset, has always maintained its effectiveness and priority due to the concern of water shortage or shift. Urbanization, increasing in population, globalization and extreme events cause natural water resources to be consumed carelessly and recklessly (Sazakli et al., 2007; Jha et al., 2014; Almazroui et al., 2017; Kılınç et al., 2023). These conditions have led societies to seek different ways to meet their water needs with natural and quality water resources (Uba and Aghogho, 2000; Zavala et al., 2018; Ay, 2021, 2022; Almeida et al., 2023; Kılıç et al., 2023).

Using rainwater for drinking, industry and agriculture sectors is a rational and economical solution. Moreover, RHSs can be also used in areas such as vehicle washing, irrigation, flushing water, floor cleaning, indoor heating, and groundwater. Especially the change in rainfall regimes and the serious decrease in rainfall in some regions bring the use of rainwater to the forefront. In our country, rainwater is used in agriculture, workplaces and buildings in many provinces and it is becoming increasingly widespread. Recently, in some countries (such as Germany (2000), England, Australia, America (1992)), tax reductions and financial aids have provided for people who install rainwater systems. RHSs are also evaluated within the scope of green building certificate and buildings with this system are given additional points within the scope of the green building concept. In Turkey, there are buildings having green building certificate in İstanbul and Ankara. The Water Efficiency Regulation, published in the Official Gazette on December 27, 2024, can be an important turning point for the sustainable management and

*Corresponding author, E-mail: murat.ay@bozok.edu.tr

https://doi.org/10.31462/icearc2025_ce_hwr_139

golden light publishing

efficient use of water resources in Turkey. The regulations compliance with the ISO 46001: Water Efficiency Management Systems Standard a legal requirement in related sectors. The regulations used for rainwater harvesting systems are DIN1989 (Germany), Turkey (T.C. Official Gazette 2017; T.C. Official Gazette, 2021), BS8515 (England). In addition, there are national and international companies that install, assemble and operate rainwater harvesting systems well. Thus, there is enough experience to build a RHS any region of the world.

Many national and international researchers indicate that rainwater harvesting is among the important and necessary works (Musayev et al., 2018; Mattos et al., 2019). For example, Zavala et al. (2018) tested the reliability of rainwater harvesting systems to meet 100% of the water demand of a transportation logistics company in Mexico City. Haque et al. (2016), Almazroui et al. (2017) and Zhang et al. (2019) analyzed the effects of climate change on rainwater harvesting in Australia, Saudi Arabia, and China, respectively. Khanal et al. (2020), Üstün et al. (2020), Raimondi et al. (2023), Lepcha et al. (2024) and Gupta et al. (2025) conducted a comprehensive review of rainwater harvesting and treatment systems. Kılıç et al. (2023) examined the installation of a rainwater harvesting system for the Faculty of Theology at Bursa Uludağ University campus in Turkey. In another study (Kılıç and Abuş 2018), they made calculations for rainwater harvesting of a house with a garden. Kilinc et al. (2023) analysed payback periods RWHS and GWR in Antalya, Turkey. Sultana (2022) researched the optimum tank size for RWHS university campus in USA. She concluded that payback period of the RWHS was 52-75 years for 100% tank capture efiicincy and zero spills. Kahn et al. (2022) stated that structures having a green roof connected to a small rainwater storage tank is recommended. Kapitan et al. (2024) conducted economic effectiveness and cost-efficiency of four selected sustainable rainwater harvesting designs for shopping mall under climatic and financial conditions of Lublin, Poland. Dağ and Ay (2024) prepared the RHS cost table of a shopping mall located in Çorum province of Turkey and stated that the amortization period is 92-year. On the other hand, it can be seen that geographic information systems (GIS) (Singh et al., 2017; Baby et al. 2019; Preeti and Rahman, 2021; Suhara and Haghi, 2025) are also used in the calculation of rainwater potential.

In this study, Engineering-Architectural Faculty (EAF) of Yozgat Bozok University (YOBU) and a typical reinforced building roof plans located in Yozgat were used as a sample case. Current material, labor costs, water prices and rainwater potential caluculation according to different storages, rainfall scenarios and usage of rainwater were done for both buildings in the following titles of the study.

2. Material and method

Yozgat province has a continental climate and receives snowfall in the winter months (T.C. Ministry of Agriculture and Forestry, (MGM) 2025). Rainfall amounts (mm) can be seen from the Table 1. Two reinforced concrete buildings located in Yozgat were examined (see Fig. 1 and Fig. 2). The potential of rainwater that can be obtained from their roofs was calculated in Table 1. Then, the quantities and rainfall scenarios of RHSs of both buildings were considered and their costs were calculated in Table 2 and Table 3. The roof area of the Engineering-Architecture Faculty is calculated as 15365 m^2. The roof area of another building is calculated as 785 m^2.

Fig. 1. An ordinary building in Yozgat city center roof view and photos, 15.02.2025

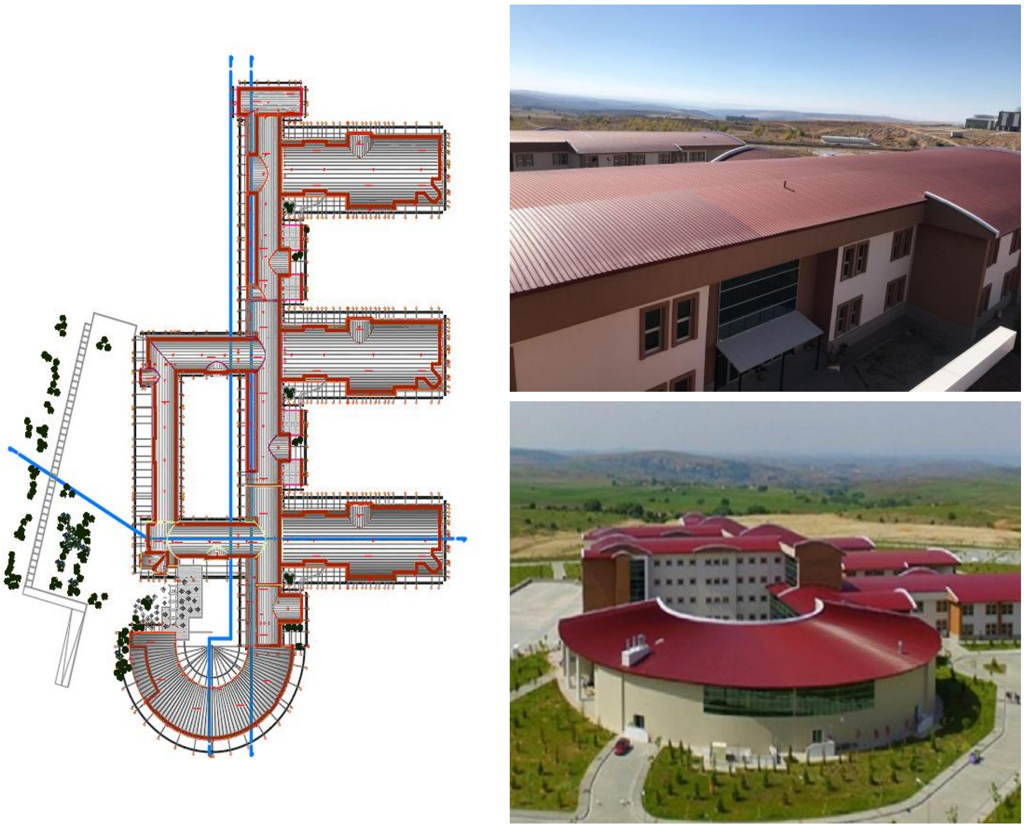

Fig. 2. Plan ve roof photos of Engineering-Architectural Faculty (EAF) of Yozgat Bozok University (YOBU), Yozgat, 12.05.2024

Table 1. Rainfall amounts (mm) for Yozgat and rainwater yields (RWY) for both buildings (MGM, 2025)

Measurement Period (1929-2023, 95- year, Yozgat, Station code: 17140)				
Months	Average number of rainy days	Monthly total rainfall average (mm)	YOBU, Monthly rainwater yield (RWY), (DIN1989) m^3 (Roof area= 15365 m^2) Roof metarial: Metal(0.9) Filter coefficient= 0.9	Another building, Monthly rainwater yield (RWY), (DIN1989) m^3 (Roof area= 785 m^2) Roof metarial: Asfalt(0.8) Filter coefficient= 0.9
January	13,51	68	846,30	38,43
February	12,70	59,5	740,52	33,63
March	13,48	69,4	863,73	39,22
April	12,81	58,3	725,58	32,95
May	13,46	66	821,41	37,30
June	9,24	45,9	571,26	25,94
July	2,99	12,5	155,57	7,07
August	2,3	11,2	139,39	6,33
September	3,87	18,1	225,27	10,23
October	7,19	33,2	413,20	18,76
November	8,91	54	672,07	30,52
December	13,29	75,3	937,16	42,56
Annual total	113,75	571,4 mm	7.111,44 m3	322,96 m3

Table 2. Possible rainwater yields (RWY, m^3) scenarios and possible tank storage volumes

	Scenarios	Possible rainfall amount (m)	Roof area (m^2)	Rainwater yield (RWY) (according to DIN1989) (m^3)
Yozgat Bozok University (YOBU), Engineering-Architectural Faculty(EAF) Roof area(A)= 15.365m^2 Roof metarial:Metal (0,9) Filter coefficient= 0,9	Scenario 1: According to the total annual rainfall	0,5714	15365	7.111,44
	Scenario 2: According to the irrigation season (total rainfall between April and September)	0,212	15365	2.638,48
	Scenario 3: 5% of the total annual rainfall according to the European standard (BS8515)	0,028	15365	348,48
	Scenario 4: According to the maximum monthly total rainfall (December)	0,0753	15365	937,16
An ordinary building in Yozgat city center Roof area(A)= 785 m^2 Roof metarial:Asfalt (0,8) Filter coefficient= 0,9	Scenario 1: According to the total annual rainfall	0,5714	785	322,96
	Scenario 2: According to the irrigation season (total rainfall between April and September)	0,212	785	119,83
	Scenario 3: 5% of the total annual rainfall according to the European standard (BS8515)	0,028	785	15,83
	Scenario 4: According to the maximum monthly total rainfall (December)	0,0753	785	42,56

Table 3. Approximate cost and metering values of rainwater harvesting systems for both buildings (1$ = 36 Turkish liras(TL)), 10.02.2025)

Items	Item number	Cost (TL) (vat included)	YOBU, Engineering-Architectural Faculty (EAF)		Another building	
			Quantity	Cost (TL)	Quantity	Cost (TL)
Rain gutter (PVC)(Ø150)	15.315.1005	333,47 TL (1 m)	1750 m	583.572,5	130 m	43.351,1
Gutter network (Plastic)	-	42 TL (1 m)	1750 m	73.500,0	130 m	5.460,0
Polyester rain water storage tank (100 ton)	-	936.000,0 TL (100 ton/ piece)	9 piece	8.424.000,0	50 ton tank, 1 piece	468.000,0
Three pump vertical shaft frequency converter hydrophore (Flow rate=0-20 m3/h) (Pressure=60-90 mSS)	25.160.2302	178.179,69 TL	1 piece	17.8179,7	1 piece	178.179,7
Membrane strainer (Filter) (Ø100 for downpipe)	-	6.862,51 TL (piece)	9 piece	61.762,6	1 piece	6.862,5
Tank level measurement indicator	-	3.049,0 TL (piece)	9 piece	27.441,0	1 piece	3.049,0
Rain pipe (PVC)(Ø100)	15.315.1002	219,44 TL (1 m)	330 m	72.415,2	33x4=132 m	28.966,1
Rainwater manhole connection pipe (Corroge SN8) (Ø200)	10.450.1204	86,50 TL (1 m)	200 m	17.300,0	20 m	1.730,0

Table 3. Continued

Ø400 mm nominal diameter building rain water connection manhole (PE)	10.450.4314	795,00 TL (piece)	9 piece	7.155,0	1 piece	795,0
Rainwater treatment system (Coarse filter, mechanical filter, carbon filter, chlorine dosing unit)	-	135.840,00 TL (piece)	1 piece	135.840,0	1 piece	135.840,0
		Total costs		9.581.166,0TL 266.143,5$		872.233,4 TL 24.228,7$

In the calculations, the measurements of the roof areas of the buildings were made based on the projects of the buildings. The "rainwater yield (RWY)" equation (Equation 1) was used to calculate the amount of rainwater that can accumulate on the roofs of the buildings (DIN 1989).

$$RWY = A \times P \times R_k \times F_k \quad (m^3) \tag{1}$$

In Equation 1, rain collection area, A (m^2): Indicates the roof area of the building. P (mm) represents the monthly rainfall. Roof efficiency coefficient (R_k): It is the coefficient specified as 0,6 - 0,9 by German standards in DIN1989 (page 26). Filter efficiency coefficient (F_k): It is the coefficient (0.9) specified by German standards in DIN1989 (page 26). It is the efficiency coefficient of the first filter through which rainwater obtained from the roof is passed to separate visible solid matter. According to the precipitation data obtained from the General Directorate of Meteorology (MGM, 2025) (measurement period: 1929-2023), it was seen that the annual total precipitation amount for Yozgat province was 571,4 mm (Table 1). In addition, monthly total rainwater yields for both buildings are given separately in Table 1. The total rainwater yields in all months are 7.111,44 and 322,96 m^3. It can be said that keeping these water volumes in a tank, using for irrigation, cleaning and making them usable as grey water may be an important option. However, it can be said that controlling these collected waters with smart automation systems is more prominent thing in addition to determining the tank volume well. This issue is also a difficult process for these buildings in terms of construction. Another aspect for this, rainwater can be divided into some sectors such as grey water, washing machine according to control devices. For example, excess rainwater can be discharged to underground with a T-connection and can be stored here. In this way, this process can also contribute to the feeding of groundwater. In this point, it can be said that sustainability of water resources by using RHSs having some criteria, which are technical, economical, environmental, and social, should be considered all together.

3. Application

RHSs generally include six components: catchment area, roof-wash system, rainwater conveyance system, cistern, delivery system, and water treatment system. In this context, the performance of rainwater harvesting and storage systems depends on the roof area, roof covering material, amount of rainfall coming to the roof, amount of ambient evaporation, wind direction and intensity, pipe fittings, tank shapes and volumes, maintenance and operation of the treatment/filter system (DIN 1989; BS 8515 2008; T.C. Official Gazette 2017; T.C. Official Gazette 2021). The roof areas of the examined buildings were calculated based on their projects. The annual calculated potential rainwater amounts from the roofs of both buildings were calculated in Table 2 according to four different scenarios using Table 1. Because the storage volumes that could occur according to the calculated RWYs are high, it is thought that it would be more rational and logical to choose the most suitable storage volume and therefore to prefer scenario 4 (December) when storage costs are considered as one of the largest costs in the system. This situation is generally taken into consideration in studies and applications. At this point, the rainwater yields calculated by taking the maximum monthly rainfall total in December (75.3 mm) can be used for the tank volumes (937.16 m^3 and 42.56 m^3) according to the scenario 4. The calculations of tank volumes and below and above these values can be compared with the other volume values in Table 2. In addition, where and how the tanks will be placed is also another important issue. It is preferred that the tanks are hidden underground and protected from external environmental conditions (temperature, risk of freezing, material life and vandalism). The tank volumes were selected according to the maximum total rainfall height for December, and as there will be rainfall below this volume in other months, it was generally thought that the tank volumes would be sufficient (Fig. 3). In case the water in the tank runs out, the water will have to be taken from the water pipeline in the city.

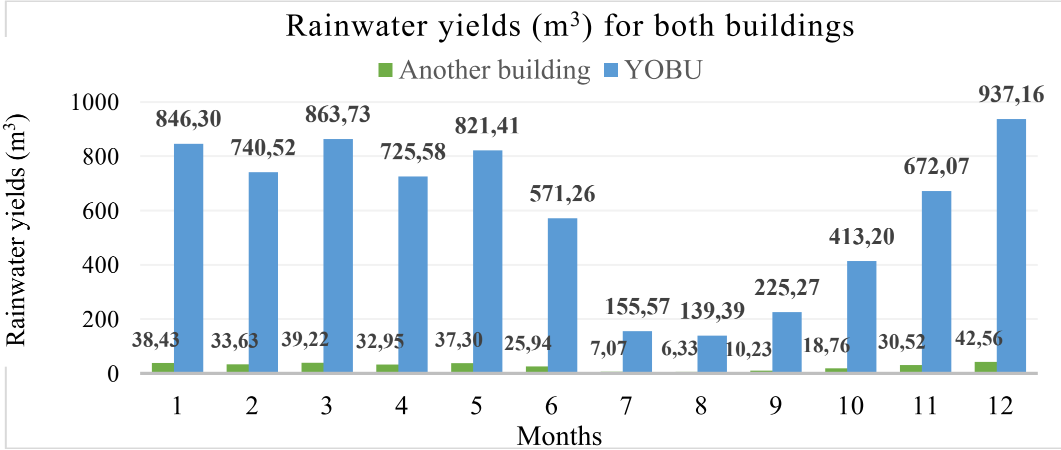

Fig. 3. Rainwater yields (m^3) for both buildings (DIN1989) from Table 1

According to the 2025 unit prices in Table 3, it has been determined that 900-tons (900 m^3 in total) storage tanks will be sufficient for the Engineering-Architecture Faculty (EAF). If the project, labor, transportation, personnel and unforeseen costs are added to the cost amount calculated with the use of the equipment in Table 3, the total cost of the system to be established can be determined as approximately 10.500.000,0 TL. These calculated costs are valid for 2025, and it can be said that these costs will increase in the following years according to the inflation rates. When the m^2 cost of this type of rainwater harvesting system is calculated, it is seen as 10.500.000,0 TL / 15.365 m^2 = 683,37 TL/m^2. For the other building, it can be determined that 50-tons (50 m^3 in total) storage tank will be sufficient. If the project, labor, transportation, personnel and unforeseen costs are added to the cost calculated by using the equipment in Table 3, the total cost of the system to be installed is determined as approximately 1.100.000,0 TL. When cost of the m^2 of such a rainwater harvesting system is calculated, it is seen as 1.100.000,0 TL/ 785 m^2 = 1401,27 TL/m^2.

When the annual water amounts consumed in these buildings were examined for the year 2024, the annual water amounts were determined as approximately 12000 m^3 and 4800 m^3, respectively. The m^3 prices of water from the related places are determined as approximately 35 TL in Yozgat campus and 24 TL in the city center. When these prices are multiplied by the annual water amounts consumed above, they are calculated as 420.000 TL(35x12000) and 115.200 TL(24x4800), respectively. When these prices are compared with the costs of the system, it can be calculated that the system will amortize itself in 10.500.000 TL/420.000 TL= 25 years and 1.100.000 TL/115.200 TL= 9,54 years, respectively. In case of decreases in rainfall, these amortization periods will also be extended more.

4. Conclusions

Rainwater harvesting from roofs of many buildings is very important and meaningful case in terms of water control and saving in these days. It is seen that manufacturing and installing of the RHSs, especially during the construction phases of buildings, is much more economical and rational (Sultana, 2022; Raimondi et al., 2023; Dağ and Ay, 2024; Kapitan and Widomski, 2024) than the applying to existing buildings. These items, which are also mentioned in sustainable development goals of the United Nations in Europe, are of course vitally important as it has been known for years. In feasibility reports and project planning of any a building, it is now necessary to support the rainwater harvesting system, which should be in every building, and to implement it very carefully in the construction phase. The regulations (DIN 1989; BS 8515 2008; SYGM, 2022; SYGM, 2023; United Nations Sustainable Development Goals, 2023; ISO 46001, 2024) also completely supports this idea.

A senior, an experienced team and quality materials are required for installing the RHS. In this case, it can be said that applying rainwater harvesting systems to existing buildings in many countries is a difficult and expensive process. In our country, it can be said that the possibility of implementing rainwater harvesting systems especially for small roof areas (500-800 m^2) is low. In the following years, if there may be an increase in demand for rainwater harvesting systems according to climate scenarios of decreasing rainfall, the supply-demand balance for the markets should also be controlled. In addition to these results, the following results can also be stated.

- The calculated annual total rainwater yields from the roofs of both buildings are 7.111,44 m^3 and 322,96 m^3, respectively. It is seen that these water amounts are not enough for the annual water needs of both buildings (12.000 m^3 and 4.800 m^3).
- It can be said that the yields of the water amounts that come from the rainwater harvesting system will annually provide an additional water saving to the buildings approximately 7.111,14/12.000= 59,2% (YOBU) and 322,96/4.800= 6,7% (another building), respectively.

- Architectural and static aspects of the building have to be designed as a green building concept in these current days anymore. Moreover, this green concept should be considered together in designing RHSs and renewable energy types such as sun and wind.

Acknowledgments
The author would like to thank the General Directorate of Meteorology, valuable editors who handled the study, referees, all personnel of the conference and shareholders for their contributions, efforts and endless patience.

References

Almazroui, M., Islam, M.N., Balkhair, K.S., Şen, Z., & Masood, A. (2017). Rainwater harvesting possibility under climate change: A basin-scale case study over western province of Saudi Arabia. *Atmos. Res., 189*, 11-23

Almeida, A.P., Liberalesso, T., Silva, C.M., & Sousa, V. (2023). Combining green roofs and rainwater harvesting systems in university buildings under different climate conditions. *Sci of the Total Environ., 887*, 163719

Ay, M. (2013). Sürdürülebilirlik kavramı ve su. *IV. Ulusal Çevre ve Ekoloji Öğrenci Kongresi (UÇEK-2013)*, Hacettepe Üniversitesi, Ankara, Türkiye.

Ay, M. (2021). Trend tests on maximum rainfall series by a novel approach in the Aegean region, Turkey. *Meteorol Atmos Phys, 133*, 1041-1055

Ay, M. (2022). Trend of minimum monthly precipitation for the East Anatolia region in Turkey. *Theor Appl Climatol, 148*, 603-615

Baby, S.N., Arrowsmith, C., & Al-Ansari, N. (2019). Application of GIS for mapping rainwater-harvesting potential: Case study Wollert, Victoria. *Engineering*, *11*(1), 14

Ball, P. (1999). Life's matrix: A biography of water. Berkeley, California: University of California Press.

BS 8515 (2008). Code of pratice for the installation of rainwater harvesting systems. DPC:08/30171875 DC, Form36, V8 (Draft).

Çakar, H. (2022). Evaluation of rainwater harvest potential of a site with garden area in İzmir province conditions. *Turkish Journal of Agricultural and Natural Sciences, 9*(2), 446-452 (in Turkish).

Dağ, M., & Ay, M. (2024). Calculation of rainwater harvesting: A case study of Çorum city. *Journal of Natural Hazards and Environment*, *10*(2), 334-343 (in Turkish).

DIN (1989). DIN 1989-1:2001-10 Rainwater Harvesting Sysmtes- Part I: Planning, installation, operation and maintenance. 34 pp.

Gupta, S., Mishra, P.K., & Khare, D. (2025). Advancements and challenges in roof-top harvested rainwater filtration: A review. *Environ. Process., 12*, 7

Hamidi, M.N., Shitreh, S., Cengiz, A.I., et al. (2024). Efficient roof selection in rainwater harvesting: Hybrid multi-criteria and experimental approach. *Water Resources Management (in press)*

Haque, M.M., Rahman, A., & Samali, B. (2016). Evaluation of climate change impacts on rainwater harvesting. *Journal of Cleaner Production, 137*, 60-69

ISO 46001 (2024). Su Verimliliği Yönetmeliği: ISO 46001 Su Verimliliği Yönetim Sistemleri Standardı. Official Gazette, 27 Dec 2024 (in Turkish).

Jha, M.K., Chowdary, V.M., Kulkarni, Y., & Mal, B.C. (2014). Rainwater harvesting planning using geospatial techniques and multicriteria decision analysis. *Resources, Conservation and Recycling, 83*, 96-111

Kapitan, J., & Widomski, M.K. (2024). Economic effectiveness and cost-efficiency of selected sustainable rainwater harvesting systems for shopping mall facility. *J Sustain Res*., *6*(2):e240007

Khan, A., Park, Y., Park, J., & Kim, R. (2022). Assessment of rainwater harvesting facilities tank size based on a daily water balance model: The case of Korea. *Sustainability*, *14*(23), 15556

Khanal, G., Thapa, A., Devkota, N., & Paudel, U.R. (2020). A review on harvesting and harnessing rainwater: An alternative strategy to cope with drinking water scarcity. *Water Supply, 20*(8), 2951-2963

Kılıç, Y.M., & Abuş, M.N. (2018). Rain water harvesting in a garden house sample. *International Journal of Agriculture and Wildlife Science (IJAWS), 4*(2), 209-215 (in Turkish).

Kılıç, Y.M., Adalı, S., & Öztürk, K. (2023). Investigation of the installation of the rainwater harvesting system on the University Campus. *Turkish Journal of Agricultural and Natural Sciences*, *10*(1), 180-186 (in Turkish).

Kilinc, E.A., Tanik, A., Hanedar, A., & Gorgun, E. (2023). Climate change adaptation exertions on the use of alternative water resources in Antalya, Türkiye. *Front. Environ. Sci.,10*, 1080092

Lepcha, R., Patra, S.K., Ray, R., Thapa, S., Baral, D., & Saha, S. (2024). Rooftop rainwater harvesting: A solution to water scarcity-A review. *Groundwater Sustain. Dev.*, *26*, 101305

Mattos, K., King, E., Lucas, C., Snyder, E.H., Dotson, A., Linden, K. (2019). Rainwater catchments in rural Alaska have the potential to produce high-quality water and high quantities of water for household use. *Journal of Water and Health, 17*, 788-800

Meteoroloji Genel Müdürlüğü (MGM). (2025, January 16). *Resmî İstatistikler.* Retrieved from https://www.mgm.gov.tr/veridegerlendirme/il-ve-ilceler-istatistik.aspx?k=undefined&m=YOZGAT (in Turkish)

Musayev, S., Burgess, E., & Mellor, J. (2018). A global performance assessment of rainwater harvesting under climate change. *Resour. Conserv. Recycl*., *132*, 62-70

Preeti, P., & Rahman, A. (2021). Application of GIS in rainwater harvesting research: A scoping review. *Asian Journal of Water, Environment and Pollution*, *18*(4): 29-35

Raimondi, A., Quinn, R., Abhijith, G.R., Becciu, G., & Ostfeld, A. (2023). Rainwater harvesting and treatment: State of the art and perspectives. *Water*, *15*(8), 1518

Sazakli, E., Alexopoulos, A., & Leotsinidis, M. (2007). Rainwater harvesting, quality assessment and utilization in Kefalonia Island, Greece. *Water Research*, *41*(9), 2039e2047

Singh, L.K., Jha, M.K., & Chowdary, V.M. (2017). Multicriteria analysis and GIS modeling for identifying prospective water harvesting and artificial recharge sites for sustainable water supply. *Journal of Cleaner Production, 142*, 1436-1456

Suhara S.K.K., & Haghi, A.K. (2025). Watershed prioritization for rainwater harvesting using multi-criteria analysis, GIS, and remote sensing. In: *GIS in Environmental Engineering* (pp. 49-67). Springer, Cham.

Sultana, R. (2022). Optimum tank size for large rainwater harvesting system. *AWWA Water Science*, e1277

Su Yönetimi Genel Müdürlüğü (SYGM). (2022). *Yeşilırmak ve Batı Karadeniz Havzaları Kuraklık Yönetim Planının Hazırlanması Projesi.* Retrieved from https://webdosya.csb.gov.tr/db/scd/icerikler/yes-lirmak-kuraklik-yp-taslak-scd-20230120090144.pdf (in Turkish)

Su Yönetimi Genel Müdürlüğü (SYGM) (2023, January 22). *Türkiye'deki yeşil/sürdürülebilir kampüs çalişmalari kapsaminda su verimliliği uygulamalari değerlendirme raporu.* Retrieved from https://ogrenciisleri.medicine.ankara.edu.tr/wp-content/uploads/sites/737/2023/04/DEGERLENDIRME-RAPORU-1.pdf (in Turkish)

Şen, Z. (2002). Su bilimi temel konuları. Su Vakfı Yayınları. ISBN: 9789759703462.

T.C. Official Gazette (2017). *Yağmursuyu Toplama, Depolama ve Deşarj Sistemleri Hakkında Yönetmelik*, Sayı 30105. (in Turkish)

T.C. Official Gazette (2021). *Planlı Alanlar İmar Yönetmeliğinde Değişiklik Yapılmasına Dair Yönetmelik*. Retrieved from https://www.resmigazete.gov.tr/eskiler/2021/07/20210711-1.htm (in Turkish)

Uba, B.N., & Aghogho, O. (2000). Rainwater quality from different roof catchments in the Port Harcourt district, Rivers State, Nigeria. *Journal of Water Supply Research and Technology Aqua, 49*, 281e288

Üstün, G.E., Can, T., & Küçük, G. (2020). Rainwater harvesting in buildings. *Uludağ Üniversitesi Mühendislik Fakültesi Dergisi*, *25*(3), 1593-1610 (in Turkish).

Zavala, M.A.L., Prieto, M.J.C., & Rojas, C.A.R. (2018). Rainwater Harvesting as an alternative for water supply in regions with high water stress. *Water Supply*, *18*(6), 1946-1955

Zhang, S., Zhang, J., Yue, T. & Jing, X. (2019). Impacts of climate change on urban rainwater harvesting systems. *Sci. Total Environ*., *665*, 262-274

4th International Civil Engineering & Architecture Conference
17-19 May 2025, Trabzon, Türkiye

Rainfall intensity-duration-frequency analysis in the Eastern Black Sea Basin

Ömer Yüksek*[1], Osman Yüksek[2]

[1]Karadeniz Technical University, Department of Civil Engineering, 61080 Trabzon, Türkiye
[2]Bursa Uludağ University, Department of Civil Engineering, Görükle Campus, 16059 Nilüfer, Bursa, Türkiye

Abstract. Rainfall intensity-duration-frequency (IDF) relationship is one of the most commonly used tools in water resources engineering, either for planning, designing and operating of water resource projects, or the protection of various engineering projects against floods. Civil infrastructure such as storm sewers, storm water management ponds, culverts and bridges are commonly designed using IDF curves. In this study, IDF curves for Eastern Black Sea Basin (EBSB), the rainiest basin in Türkiye, were developed. The maximum rainfall intensity values for 14 rainfall durations (D=5, 10, 15, and 30 minutes, and 1, 2, 3, 4, 5, 6, 8, 12, 18 and 24 hours) were used. The data of 2 Meteorological Stations (Trabzon and Rize) of Turkish State Meteorological Service (MGM, in Turkish), of which observation durations were 60 and 80 years and located in EBSB, were employed. Since various studies have favored the use of Log Pearson Type 3 (LP3) Distribution for annual maximum precipitation data in Türkiye; this distribution was used for the analysis. The rainfall intensity values for each station and for 7 return periods (T = 2, 5, 10, 25, 50, 100 and 500 years) was calculated by LP3 Distribution. Multi-nonlinear regression analysis was carried out by using nine kinds of IDF formulas, which were taken by using various IDF formulae in the literature and newly generated formulae. In order to test the reliability of the functions, two criteria were used: The determination coefficient and the mean relative error. It has been concluded that the reliability of the results is high enough and that this study will motivate and open new horizons to detailed studies on IDF analysis.

Keywords: Rainfall intensity-duration-frequency analysis; Eastern Black Sea Basin; Nonlinear regression analysis

1. Introduction

The most important meteorological factors in the formation of disasters of atmospheric origin are precipitation and features of precipitation. The intensity, duration and frequency of precipitation are the main characteristics. Heavy rainfall can cause sudden floods by increasing peak discharges. Intense rainfalls not only cause flooding; additionally, the water droplets with increased kinetic energy intensify the soil erosion that progresses at normal speed, destroy the natural vegetation and agricultural fields and shorten the dam life as it leads to siltation. The interpreted hydro climatological data produced by statistical studies are a source of light for the decision-makers in the planning and operation of water resources.

Rainfall is of particular importance in hydrology. Specifically, it is necessary to determine the rainfall intensity for various probabilities or return periods in many hydrological models, in addition to water quality and quantity calculations. For example, engineers must calculate the frequency of rainfall intensity to design hydraulic structures (bridges, dams, etc.). To realize this aim, IDF functions and curves are frequently used for the hydrologic design of small and medium sized catchments. The IDF curves provide estimates of the rainfall intensity for any given duration, corresponding to different probabilities of exceedance values.

The rainfall IDF relationship is one of the most commonly used tools in water resources engineering, either for planning, designing and operating of water resource projects, or the protection of various engineering projects against floods (Chow et al., 1988; Şengül and Can, 2011; Can et al. 2012). Civil infrastructure such as storm sewers, storm water management ponds, culverts aend bridges are commonly designed using IDF curves, which assume that the occurrence of precipitation is in the form of rainfall and immediately available for the rainfall-runoff process (Tekkant, 2015). The appropriately sized capacities of these civil infrastructure are so important to avoid overdesign which could lead to economic losses and/or increased property damage and possibly increased risk of loss of life. Thus, obtaining reliable estimates of IDF curves is essential (Anılan, 2014).

* Corresponding author, E-mail: yuksek@ktu.edu.tr

https://doi.org/10.31462/icearc2025_ce_hwr_201

The IDF relationship is a mathematical relationship between the rainfall intensity I, the duration D, and the exceedance frequency F (F=1/T, T is return period). This relation is usually obtained as curves, and each curve shows the change of intensity of rainfall with respect to a frequency (or return period). These curves are generally obtained by empirical and statistical approaches (Karahan et al., 2007).

IDF functions are used for quantifying the magnitude of rainfall events that are used in the design of a variety of civil infrastructure, especially in an urban environment. These relationships of extreme rainfall intensities are one of the most used tools in water resources engineering for planning, design, and operation of water resources projects (De Vyver, 2015). IDF curves for a location are generally obtained by fitting a theoretical probability distribution, such as Gumbel (GM), Generalized Extreme Value (GEV), Log Pearson Type III (LPT3), Log Normal (LN), to the extreme rainfall data.

The typical procedure involves the following: steps (i) fitting a probability distribution to the annual maximum rainfall intensity values for several rainfall durations, (ii) estimating extreme rainfall quantiles for each rainfall duration for a number of return periods, and (iii) fitting a relationship between rainfall intensity and rainfall duration, for each frequency, based on the rainfall intensity quantiles estimated for each rainfall duration. The resulting relationships between rainfall intensity and rainfall duration constitute the IDF curves for the given location (Anılan, 2014).

The establishment of IDF relationships goes back to the 1930s (Bernard, 1932). Since then, different forms of relationships have been constructed for several regions of the world up to today. A general IDF relationship formula, consistent with the theoretical probabilistic foundation of the rainfall data, was provided by Koutsoyiannis et al., 1998. Okonkwo and Mbajiorgu (2010), analyzed rainfall data and characteristics for locations in seven states of Southeastern Nigeria and developed IDF curves for these locations using graphical and statistical methods. There are also several studies about IDF in Turkey. Karahan et al,(2008), applied a solution algorithm that solves IDF relationship by using Genetic Algorithm (GA) optimization technique to four city centers in the Southeastern Anatolia Project (GAP) region. Their results showed that the developed solution algorithm that is alternatively proposed to determine IDF relationship gives accurate results for the cities located in the GAP region. Ghiaei et al. (2018) analyzed rainfall intensity-duration-return period data in the Eastern Black Sea Region by using L-moments and artificial neural networks (ANN). Based on the distribution functions, they extracted the governing equations for calculation of intensities of 2, 5, 25, 50, 100, 250, and 500 years return periods (T). Then, T values for different rainfall intensities were estimated using data quantifying maximum amount of rainfall at different times. Yavuz (2018) calculated the parameters of five different potential analytical equations for IDF relationship of annual extreme rainfalls at each one of the seven geographical regions of Türkiye. In the study, a single IDF equation was obtained using all the 22 stations, and by the same criteria, the most appropriate expression valid for all of Türkiye has been determined.

Eastern Black Sea Basin (EBSB) is frequently exposed to floods due to its topographic structure. In case of floods, many casualties, injuries and property damages occur as the settlements are generally located in floodplains. The dimensions of these floods incurred in the basin, both in terms of economics and of loss of life, are greater than those in other basins in Turkey due to the physical and climatic conditions (Anılan, 2014). The effective factors that make the EBSB a natural disaster area are, the geological structure and characteristics of the basin as well as the increasing slope values of morphology with increasing slope values with the sharp elevation of the mountains from the shore, the erosion of the streams with strong flow on this slope and the high precipitation values (Nemli, 2017). In Turkey, IDF analyses have been developed only for local sites and analysis with the current data encompassing the whole country is needed (Yüksek, et al., 2022).

In this study, IDF curves for Eastern Black Sea Basin (EBSB), the rainiest basin in Türkiye, were developed. The maximum rainfall intensity values for 14 rainfall durations (D=5, 10, 15, and 30 minutes, and 1, 2, 3, 4, 5, 6, 8, 12, 18 and 24 hours) were used. The data of 2 Meteorological Stations (Trabzon and Rize) of Turkish State Meteorological Service (MGM, in Turkish), of which observation durations were 60 and 80 years and located in EBSB, were employed. Since various studies have favored the use of Log Pearson Type 3 (LP3) Distribution for annual maximum precipitation data in Turkey; this distribution was used for the analysis. The rainfall intensity values for each station and for 7 return periods (T = 2, 5, 10, 25, 50, 100 and 500 years) was calculated by LP3 Distribution. Multi-nonlinear regression analysis was carried out by using nine kinds of IDF formulas, which were taken by using various IDF formulae in the literature and newly generated formulae. In order to test the reliability of the functions, two criteria were used: The determination coefficient and the mean relative error. IDF functions for the used stations were also calculated and presented both as equations and graphics It has been concluded that the reliability of the results is high enough and that this study will motivate and open new horizons to detailed studies on IDF analysis, which is an important issue to optimum design of various kinds of hydraulic structures.

2. Study area and used data

In Türkiye, there are significant differences in climatic conditions from one region to the other because of the existence of the mountains that run parallel to the coasts and the diverse nature of the landscape. Due to geographical location, geology and hydrological properties, Türkiye has a potential risk of mainly three different types of natural disasters related to gravity flows: Floods, landslides and snow avalanches. Floods are the second important natural hazards after earthquakes and destructive flood events have occurred in various river basins of Türkiye, especially in The Black Sea coast, which receives the greatest amount of rainfall. In last 100 years 66 extremely severe floods took place and caused great life and economic losses (Anılan et al., 2016). EBSB is also the only region of Turkey that receives rainfall throughout the year. Very major and destructive floods have occurred in the EBSB. The data used in this paper are annual maximum precipitation depth values, measured at 2 meteorological stations (MS),Trabzon and Rize,which are equipped with pluviographs. Thus, by measuring precipitation depths for several time intervals it is possible to calculate rainfall intensities. The observation periods of the data are 60 years and 80 years for Trabzon and Rize, respectively.

3. Methodology

3.1. Obtaining IDF values

To obtain IDF values, the best statistical distribution for the data must be determined and by using this distribution, an intensity-frequency analysis must be carried out for the selected standard rainfall durations. There are several statistical distributions that might be suitable for rainfall intensity-frequency (or return period, T=1/F) analysis. Various studies have favored the use of three suitable distributions for annual maximum precipitation (and also flood) data in Türkiye: Log-Normal Distribution (LN2), Gumbel Distribution (GM) and Log-Pearson Type 3 Distribution (LPT3). Since various studies have favored the use of Log Pearson Type 3 (LP3) Distribution for annual maximum precipitation data in Türkiye (Yüksek et al. 2022); this distribution was used for the analysis and the rainfall intensity values were calculated.

3.2. The used IDF functions

There are a number of formulae to determine IDF relationship. In general, return period (T=1/F) is used instead of frequency. General structure of these formulae is as follows (Yüksek et al. 2022):

$$I(D,F) = \frac{A(F)}{B(D)} \tag{1}$$

Where I(D,F) is rainfall intensity (mm/hour) as a function of frequency (1/year) and rainfall duration (D, hour). A number of functions have been given in the literature for the A(F) and B(D) functions. A list of these are presented in Table 1. By combining these functions, 9 IDF functions are obtained and are given in Table 2.

Table 1. Functions for A(F) and B(D)

	No	Function	References
	1	$a*(1/F)^b$	Sherman, 1931; Koutsoyionnis et al.,1998
A(F)	2	$a+b*\ln(1/F)$	Koutsoyionnis et al., 1998; Aşıkoğlu, 2005
	3	$a+b*\ln(\ln(1/F))$	Minh Nhat et al, 2007
	4	D^c	Sherman, 1931; Bernard, 1932
B(D)	5	D^c+d	Minh Nhat et al. 2006
	6	$(D+d)^c$	Koutsoyionnis et al., 1998; Benzeden and Hacısüleyman, 2003

Table 2. Used IDF functions

Combination of	Function	Eq. No
1 and 4	$I(D,F)=\dfrac{a*\ln(1/F)^b}{D^c}$	2
1 and 5	$I(D,F)=\dfrac{a*\ln(1/F)^b}{D^c+d}$	3
1 and 6	$I(D,F)=\dfrac{a*\ln(1/F)^b}{(D+d)^c}$	4
2 and 4	$I(D,F)=\dfrac{a+b*\ln(1/F)}{D^c}$	5
2 and 5	$I(D,F)=\dfrac{a+b*\ln(1/F)}{D^c+d}$	6
2 and 6	$I(D,F)=\dfrac{a+b*\ln(1/F)}{(D+d)^c}$	7
3 and 4	$I(D,F)=\dfrac{a+b*\ln(\ln(1/F)}{D^c}$	8
3 and 5	$I(D,F)=\dfrac{a+b*\ln(\ln((1/F)}{D^c+d}$	9
3 and 6	$I(D,F)=\dfrac{a+b*\ln(\ln(1/F)}{(D+d)^c}$	10

4. Results

4.1. Reliability of the IDF functions

By using SPSS program, regression coefficients are calculated and IDF functions, Eq. 2 to 10, were obtained. Then, in order to test the reliability of the functions, two criteria have been used. The first criteria is the determination coefficient (R^2, square of correlation coefficient, R) and the second one is the mean relative error (RE, %) among the calculated IDF values both by the best distribution and by SPSS program. RE is calculated by:

$$RE=\frac{1}{N}\sum\left(\frac{IDF_1-IDF_2}{IDF_1}\right)*100 \tag{11}$$

where, IDF_1 and IDF_2 are calculated IDF values by the best distribution and SPSS program, respectively, and N is the number of data. Although there no strict criteria on what the minimum acceptable RE is, it is obvious that this value should be as low as possible. A summary of R^2 and RE values and for Trabzon and Rize are given in Table 3. Finally, success rating (SR) of the functions (from 1, the best to 9, the worst) are given as the last column of Table 3. As can be seen functions of Trabzon with higher R^2 and lower RE values are more reliable than that of Rize. However, it has been concluded that the IDF functions for both MS are reliable.

4.2. Equations and their graphics

As can be seen from Table 3, Eq. 7 and Eq. 6 are the best functions and are presented in Eq. 12 and Eq. 13 for Trabzon and Rize, respectively. The IDF functions are given in Eg. 12 and 13 and Fig.1 and 2, for Trabzon and Rize, respectively:

$$I(D,F)=\frac{18.991+16.507*\ln(1/F)}{(D+0.354)^{0.937}} \tag{12}$$

$$I(D,F)=\frac{37.361+15.432*\ln(1/F)}{D^{0.581}+0.174} \tag{13}$$

Table 3. Summary of R^2, RE and SR values for the used equations

Eq. No	Trabzon			Rize		
	R^2	RE	SR	R^2	RE	SR
2	0.963	0.550	8	0.980	0.339	8
3	0.990	0.092	4	0.984	0.239	2
4	0.989	0.087	3	0.982	0.270	5
5	0.966	0.515	7	0.984	0.321	7
6	0.993	0.077	2	0.987	0.218	1
7	0.993	0.073	1	0.986	0.250	4
8	0.943	0.552	9	0.970	0.340	9
9	0.968	0.172	6	0.973	0.242	3
10	0.986	0.169	5	0.972	0.271	6

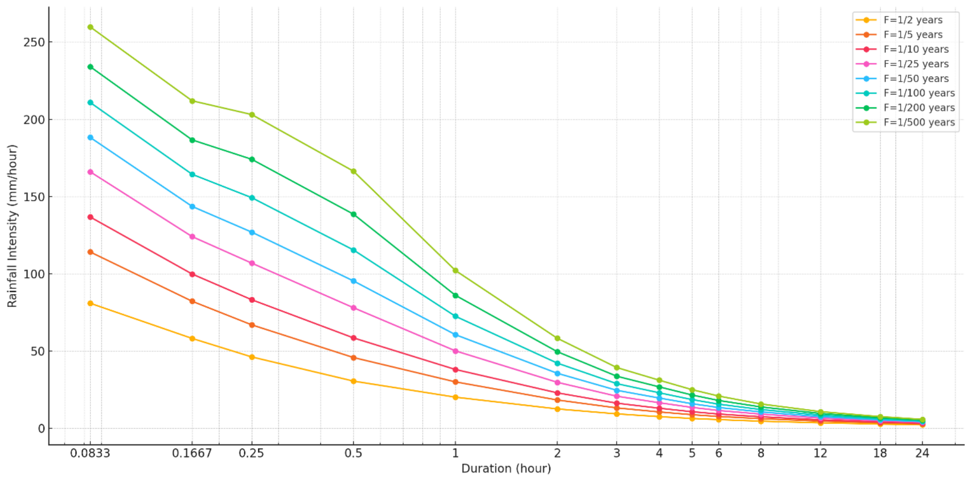

Fig. 1. IDF graphics for Trabzon

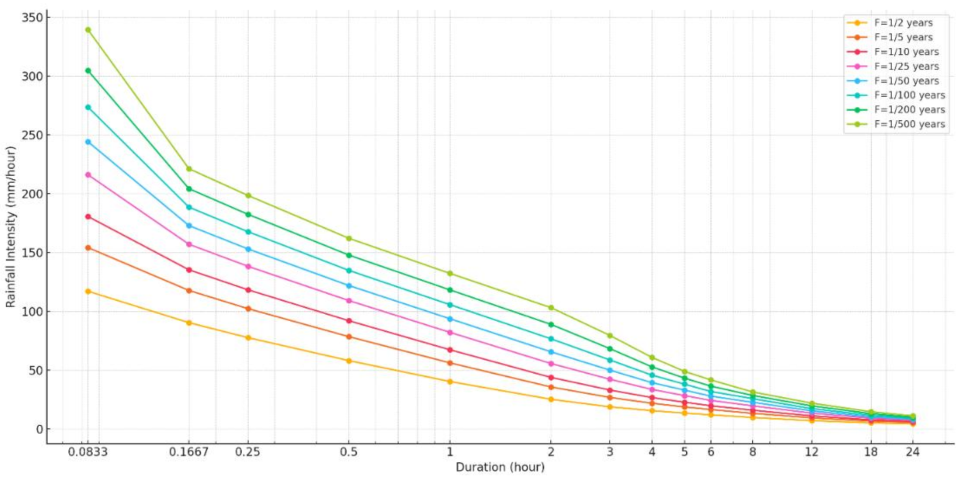

Fig. 2. IDF graphics for Rize

5. Conclusions

In this study, by using the annual maximum rainfall depth values in 2 MS in the EBSB, maximum intensity values for various durations are calculated and analysed. Rainfall intensity (I) values are estimated for various rainfall duration (D) and frequency (F) values according to the LPT3 distribution. Multi-nonlinear regression analysis has been carried out by using nine kinds of IDF formulas and various regression coefficients are obtained. The best formula for each MS is determined depending on R^2 and RE between intensity values, one with maximum R^2 and the minimum RE. The studied 9 functions are analyzed in detail. In this context, the numerator A(F) and denominator B(D) functions of Equation 1, have been evaluated in the context of their reliabilities in predicting rainfall intensities. A success rating list of nine functions is presented. Functions of Trabzon with higher R^2 and lower RE values are more reliable than that of Rize. In the final phase of the study, IDF functions for Trabzon and Rize, are presented both as equations and graphics.

References

Anılan, T. (2014). *Application of artificial intelligence methods to L-moments based regional frequency analysis In the Eastern Black Sea Basin* (Doctoral dissertation). Karadeniz Technical University, Trabzon, Türkiye (in Turkish).

Anılan, T., Yüksek, Ö., & Kankal, M. (2016). Doğu Karadeniz Havzası'nın L-momentlere dayali taşkin frekans analizi. *Teknik Dergi, 27*(2), 7403-7427

Asikoglu, O.L., & Benzeden, E. (2014). Simple generalization approach for intensity – duration – frequency relationships. *Hydrological Processes, 28*(3),1114-1123

Benzeden, E., & Hacısüleyman, H. (2003). Variation of parameters in rainfall intensity-duration-return period with return period. In: *Proceedings of 1st National Water Engineering Symposium*. İzmir, Turkey (in Turkish).

Bernard, M.M. (1932) Formulas for rainfall intensities of long duration. *Transactions ASCE, 96*(1801), 592-624

Can, İ., Tosunoğlu, F., & Kahya, E. (2012). Daily streamflow modelling using autoregressive moving average and artificial neural networks models: Case study of Çoruh Basin, Turkey. *Water and Environment Journal, 26*(4), 567-576

Chow, V.T., Maidment, D.R., & Mays, L.W. (1988). Applied hydrology. New York: McGraw-Hill Book Company

De Vyver, H.V. (2015). Bayesian estimation of rainfall intensity–duration–frequency relationships. *Journal of Hydrology*, *52,* 1451-1463

Ghiaei, F., Kankal, M., Anilan, T., & Yuksek, O. (2018). Regional intensity – duration – frequency analysis in The Eastern Black Sea Basin, Turkey, by using L - moments and regression analysis. *Theoretical and Applied Climatology, 131*(1-2), 245-25

Karahan, H., Ayvaz, T.M., & Gürarslan G. (2008). Şiddet – süre - frekans bağintisinin genetik algoritma ile belirlenmesi: GAP örneği. *İMO Teknik Dergi, 4393.4407*, 290

Karahan, H., Ceylan, H., & Ayvaz, T.(2007). Predicting rainfall intensity using a genetic algorithm approach. *Hydrological Processes*, 470-475

Koutsoyiannis, D., Kozonis. D., & Manetas, A. (1998). A mathematical framework for studying rainfall intensity-duration-frequency relationships. *Journal of Hydrology, 206*, 118-135

Minh, N.L., Tachikawa, Y., Sayama, T., & Takara, K. (2007). A simple scaling characteristic of rainfall in time and space to derive intensity – duration - frequency relationships. *Annual Journal of Hydraulic Engineering JSCE, 51*, 73-78

Minh, N.L, Tachikawa, Y., Sayama, T., & Takara, K. (2006). Derivation of rainfall intensity – duration -frequency relationships for short-duration rainfall from daily data. *IHP Technical Documents in Hydrology, 6*, 89-96

Nemli, M.Ö. (2017). *Trend analysis of annual maximum rainfall intensity in Eastern Black Sea Region* (Master's thesis). Karadeniz Technical University, Trabzon, Türkiye (in Turkish).

Okonkwo, G.I., & Mbajiorgu, C.C. (2010). Rainfall intensity-duration-frequency analysis for Southeastern Nigeria. *Agricultural Engineering International: CIGR Journal, 12*(1), 22-30

Sherman, C.W. (1931). Frequency and Intensity of Excessive Rainfall at Boston, Massachusetts. *Transaction Paper, 95*, 951-960

Şengül, S., & Can, İ. (2011). Stochastic modelling of mean monthly flows of Karasu River, in Turkey. *Water and Environment Journal, 25*(1), 31-39

Tekkanat, İ.S. (2015). *Analysis of relationships and trends between precipitation intensity and river flows in Porsuk Creek Basin* (Master's thesis). Çanakkale Onsekiz Mart University, Çanakkale, Türkiye (in Turkish).

Yavuz, K. (2018). *Determination of the appropriate probability distribution function and formula of the relationship between the period of intensity-rainfall duration-return period for standard rainfall in Turkey* (Master's thesis). Erciyes University, Kayseri, Türkiye (in Turkish).

Yüksek, Ö., Anılan, T., Saka, F., & Örgün, E. (2022). Rainfall intensity-duration-frequency analysis in Turkey, with the emphasis of Eastern Black Sea Basin. *Teknik Dergi,* 12087-12103

4th International Civil Engineering & Architecture Conference
17-19 May 2025, Trabzon, Türkiye

Cost analysis of small hydroelectric power plants: a case study Euphrates and Tigris Basins

İbrahim Yüksel*[1], Ersal Yılmaz[2], Fatih Çıbuk[1], Merve Terzi[1]

[1] Istanbul Rumeli University, Department of Civil Engineering, 34445 Istanbul, Türkiye
[2] Marmara University, Department of Construction and Technical Works, 34445 Istanbul, Türkiye

Abstract. Energy costs in the world are directly related to energy capacity. As the energy capacity increases, the investment cost of the hydroelectric power plant also increases. Because if the energy capacity is high, the energy production will also be high and the investment cost will be amortized in a short time. In this study, 10 small streams on which hydroelectric power plants are designed were selected, and then the investment costs were analysed for these small streams which are in the Euphrates and Tigris Basins. There is a flow observation station (FOS) in only two of these 10 selected streams (Baskoy and Celebiyan Streams). The flow values of the other 8 small streams were estimated by using the basin characteristics and flow values of Baskoy and Celebiyan streams. In addition to many technical and economic parameters, flow values are the most effective parameters for energy production in hydroelectric power plants. Therefore, cost analyses of small hydroelectric power plants were performed by using flow values.For the cost analyses; SMART Mini Hydro Tool Program was used. Because this program includes many technical and economic parameters as well as the most effective hydrological parameters.

Keywords: Small hydroelectric power plants, Hydrological models, Cost analysis, Energy efficiency, Euphrates and Tigris Basins.

1. Introduction

The subject of this study is the cost analysis of small hydroelectric power plants without reservoirs (without storage). Therefore, hydroelectric power plants with reservoirs and micro hydroelectric power plants established for domestic wastewater are not included in this study. However, some suggestions are included at the end of the study for hydroelectric power plants with reservoirs and micro hydroelectric power plants established for domestic wastewater.

In the studies conducted to date, a comprehensive analysis of the investment costs and efficiency issues of small hydroelectric power plants without reservoirs has not been made. One of the aims of this study is to close this deficiency in the literature.

Some hydraulic-hydrological simulation-optimization models such as Watershed Modelling System (WMS), The Hydrologic Engineering Center Hydrologic Modelling System (HEC-HMS) are used in system designs for integrating hydroelectric power plants with reservoirs into the ecosystem.

However, it has not been seen that simulation-optimization models are used in small hydroelectric power plants without reservoirs. Therefore, this study, which analyses small hydroelectric power plants technically and economically for an ideal optimization, is an important and new study.

In this study, it is aimed to optimize small hydroelectric power plants in terms of cost-benefit factor and to add these plants to the ecosystem.

On the other hand, the results obtained from this study, which demonstrated the feasibility of small hydroelectric power plant projects in terms of both ecosystem and economy, were generalized and it was suggested that they could be applied to SHPPs to be established in different basins.

There are two basic parameters in the economic analysis of small hydroelectric power plant projects. These are the investment cost and the annual cost, and these parameters are necessary to obtain the total cost of the project. On the other hand, some indirect costs such as construction costs, electromechanical equipment costs, energy

* Corresponding author, E-mail: ibrahim.yuksel@rumeli.edu.tr

https://doi.org/10.31462/icearc2025_ce_hwr_371

transmission costs are considered as investment costs, while equipment depreciation, maintenance, operation and replacement costs are considered annual costs (Moldoveanu & Popescu ,2018; Singal et al., 2010).

2. Method and materials

2.1. Selecting model for estimating cost of the small hydropower plants

In this study, the SMART Mini Idro Tool Program, which includes important hydrological parameters such as discharge, minimum flow, turbine flows, etc. as well as many other technical and economical parameters, was used.

Therefore, it was concluded that the SMART Mini Idro Tool Program is a good option to use in the cost analysis of hydroelectric power plants.

SMART Mini Idro is a tool that evaluates hydropower project parameters using some values such as Flow Continuity Curve (FCC), net head, turbine types and discharge interval (Yuksel, 2024; McEnroe, 2010).

The main task of the SMART Mini Idro Tool, which uses hydrological data as input data; It is to make a preliminary assessment of the environmental flow of a stream, taking into account the daily average flows, to select the appropriate turbine type and to make an estimated economic analysis.

There are some assumptions for the annual costs of small hydroelectric power plant projects used within the scope of the SMART Mini Idro Program. In this study, these assumptions were taken into account while making cost-benefit analysis of hydroelectric power plants. These are:

- Project life as 30 years,
- Management and maintenance costs as 3% of the investment cost,
- Energy fee as 0.07 €/kWh and
- Green certificate fee is accepted as 0.137 €/kWh for 15 years.

One of the most important elements in hydropower cost analysis is the hydrological model factor. Therefore, hydrological models of hydroelectric power plants must be established before construction. Because thanks to the hydrological model, all risks such as deficiencies, errors, inconsistencies, etc. that may arise in a hydroelectric power plant can be determined, and these are solved at the project stage.

Otherwise, it is not possible to eliminate the negativities in a hydroelectric power plant built without establishing a hydrological model. This means that a lot of money and labour will go to waste.

For the analyses in this study, 10 streams were selected from the Tigris and Euphrates Basins, and since only Baskoy and Celebiyan streams have flow observation stations, the flow values of the remaining 8 streams were estimated by calculating them with regression analysis. Regression analysis is widely used in solving these types of problems in water resources.

There are different types of regressions such as Linear Regression (Simple Regression), Linear Multiple Regression, Nonlinear Multiple Regression.

Many problems in engineering cannot be solved with simple regression. Because most of the events in engineering are either complex problems (such as the components of an earthquake) or random events (such as the rate of rainfall).

2.2. Multiple nonlinear regression

Multiple Nonlinear Regression is a form of regression analysis in which the data is modelled by a multiple function that is a nonlinear combination of the parameters in the event to be modelled and depends on more than one independent variable (Beyazit, 1981).

Multiple nonlinear regression is an analysis that easily estimates models that have arbitrary or random relationships between the independent and dependent variables. A multiple nonlinear regression is expressed as Eq. 1:

$$\log(Y) = \log(a_0) + a_0 \log(X_1) + a_0 \log(X_2) + \cdots a_0 \log(X_n) \quad (1)$$

Here:

In the Equation 1, $\log(Y)$ on $\log(X_1)$, $\log(X_2)$, …, $\log(X_n)$ is used to estimate the parameters a_0, a_1,…and a_n. Where:

- Y: Dependent Variable
- X_1-X_n: Independent Variables
- a_0 - a_n: Are the equation parameters for the nonlinear relation

It is known that variables affecting many events or problems are not linearly related to each other and that variables in engineering problems are multiple nonlinear. For this reason, multiple nonlinear functions are widely used in engineering fields. In this study, multiple linear and multiple nonlinear regression were used.

2.3. Design parameters of cost analysis for small hydropower plants

One of the most important factors affecting the benefit/cost value in a hydro power plant is turbines. The size of the turbines is directly related to the diameter of the turbine wheel, and the working order of the power plant is determined by the diameter of the wheel. The following equations are used to determine the diameter of the impeller (Fujii et al., 2017).

$$D = \frac{84.6 * \theta_3 * \sqrt{H}}{N} \tag{2}$$

$$\theta_3 = 0.0223 * \sqrt[3]{N_s^2} \tag{3}$$

$$N_s = \frac{1.358 * N * \sqrt{P}}{\sqrt[4]{H^5}} \tag{4}$$

Within the scope of the SMART Mini Idro Program, the following equations are used for the construction works and the costs of different equipment in small hydroelectric power plants, and the plant's retinue is calculated according to Eq. 2, which is the installed power function.

$$C_{CE}(€) = a * P(kW)^2 + b(kW) + c \tag{5}$$

The water intake structure of the plant is calculated according to the Eq. 3, which is the maximum discharge function.

$$C_P(€) = a * Q(m^3/s)^2 + bQ(m^3/s) + c \tag{6}$$

The transmission channel entourage of the power plant is calculated according to Eq. 4, which is the maximum discharge and maximum length function.

$$C_{CA}(€/m) = a * Q(m^3/s)^2 + bQ(m^3/s) + c \tag{7}$$

The penstock cost is calculated according to the Eq. 5, which is the function of diameter and maximum length.

$$C_{CF}(€/m) = a * D(m)^2 + bD(m) + c \tag{8}$$

In the equations: 2-8:

- N_s: The specific speed of the turbine (rpm),
- N: Turbine rotation speed (rpm),
- H: Net head (m),
- P: Power (kW),
- Q: Flow,
- C_{CA}: Transmission channel cost,
- C_{CE}: Plant cost,
- C_{CF}: Penstock cost,
- C_P: Water intake structure cost,
- a, b and c are the coefficients.

The most important parameter to be determined in order to make cost analysis in hydroelectric power plants is the gross hydropower potential. For this reason, it is necessary to know which methods are used for calculating of the gross energy potential. The potential taken as basis in the calculations in hydropower projects is the gross hydropower potential.

2.4. Gross power and gross energy potential

When the total efficiency (η) obtained from the equation 7 is written in its place in the power equation, gross power is obtained by using the Eq. 9: Gross Power,

$$P_{gross} = \gamma * Q_m * H * \eta \tag{9}$$

The equation is obtained and using this equation the gross energy potential is found by using the Eq. 10: Gross Energy potential is obtained.

$$E_{gross} = \gamma * Q_m * H * \eta * 24 * 365 \tag{10}$$

In the Equations 9 and 10:

- P_{gross}: Gross power (kW),
- E_{gross}: Gross energy (kWh),
- γ : Water specific gravity (kN/m^3),
- Q_m: Average flow rate (m^3/s)
- H: Net head (m),
- η : Total efficiency (%)

The most important parameter in hydropower capacity calculations is the flow rate. In open channel flows and streams, the flow rate can be determined precisely with the help of velocity measurements on the cross section. For this purpose, the stream cross section is divided into slices (Fig. 1).

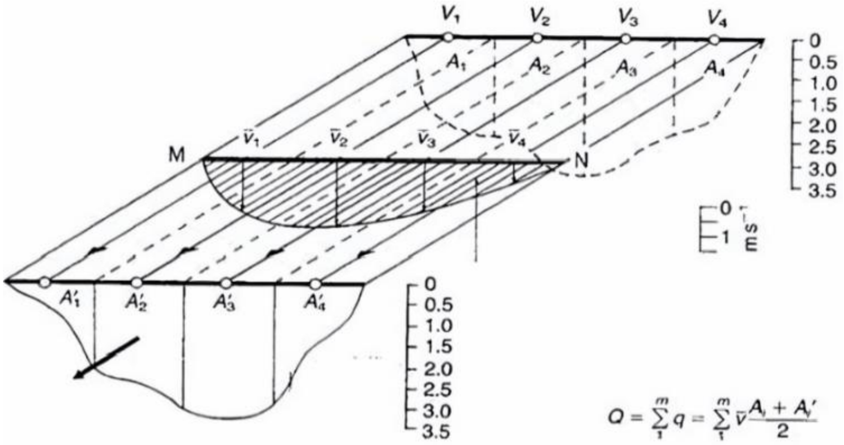

Fig. 1. Measurements of flow along the cross-section in open channels and streams

The average velocity V_i (m/s) and the cross-sectional area A_i (m^2) in each of these slices are measured. The flow rate (Q) is calculated by using the obtained values in the Eq. 11:

$$Q = \sum V_i A_i \tag{11}$$

Here:

- Q: Flow rate (m^3/s),
- Vi: Speed at the measurement point (m/s),
- Ai: Cross-sectional area at the measurement point (m^2)

2.5. Cost analysis for small hydropower in selected streams

Only Baskoy and Celebiyan streams have flow observation stations from the 10 selected streams. By using these two streams' data, the flow values of the other 8 streams were calculated by using numerical and statistical methods.

In a previous study (Yuksel, 2024; McEnroe, 2010; Beyazit, 1981; Fujii et al, 2017; Demirel, 2021), in order to work at the same gross load for all streams, 12 different scenarios with gross head values ranging from 15, 20, 25, 30, 35, 40, 45, 50, 55, 60, 80 and 100 m have been created. However, it is mentioned that SHP projects can be developed in these streams with a head of 15 m and above in the study.

Although it was concluded that SHP projects could be developed for the selected streams using these 12 scenarios, both the maximum total benefit-cost ratios and the capacity factor values were observed as the ideal values for 100 m. Therefore, the cost-benefit analyses calculated for 100 m gross head for selected streams were taken into account.

The cost-benefit analyses calculated for 100 m gross head for the selected streams are given in the Table 1.

Table 1. Cost analysis for all selected streams

Stream	Gross Head (m)	Net Head (m)	Max kW	MWh	Number of Operation Days	Investment Cost (€)	Annual Cost (€)	Total Cost (€)	Payback Period (Year)	Benefit-Cost Ratio	Capacity Factor (%)
Han	100	98	6035	21834	201	12.547.746	518.090	13.065.836	2,28	5.29	0.41
Sevek	100	92.99	808	2923	219	1.572.763	54.891	1.627.654	4.79	3.65	0.41
Sevay	100	94.26	392	1545	201	2.390.149	88.733	2.478.882	3.56	2.70	0.44
Merga	100	95.63	1128	4081	201	3.074.985	117.190	3.192.175	3.18	4.01	0.41
Zugut	100	94.28	811	2934	201	2.388.434	88.662	2.477.096	3,56	3.65	0.41
Kulluk	100	95.13	890	3220	201	2.556.046	95.612	2.651.658	3.42	3.78	0.41
Asagiyanikli	100	93.13	413	1761	237	1.567.056	54.655	1.621.711	4.55	2.99	0.48
Rapka	100	95.57	989	3578	201	2.775.599	104.729	2.880.328	3.32	3.87	0.41
Baskoy	100	90.08	468	1844	219	1.678.387	59.236	1.737.623	4.41	3.06	0.44
Celebiyan	100	96.84	2364	7787	183	5.840.090	232.903	6.072.993	2.77	4.48	0.37

3. Conclusion and discussion

When Table 1 is analysed, it is seen that flow and head load amounts have a great effect on the power produced and the cost-benefit ratios change with the increase in the low values.

On the other hand, cost analysis table (Table 1) for all streams is examined, it is seen that the capacity factors are close to each other for all streams and these values vary between 0.37% and 0.48%. In this case, the average capacity factor for the selected streams is 0.42.

Considering that the average capacity factor in hydroelectric power plants in Turkey is 37% and 44% in the world (Yuksel, 2024; McEnroe, 2010; Beyazit, 1981; Fujii et al., 2017; Demirel, 2021), it is seen that the capacity factor of 0.42 obtained in this study is above the Turkish average and very close to the world average.

Considering all the costs analysed in this study, it has also been determined that the SHPPs to be established on the selected streams will make profits by financing themselves for periods varying between 2.28-4.79 years.

As a result of the calculations, it has been determined that the SHPPs to be built according to parameters and criteria's in this study will be efficient and the self-financing period of these power plants will be between 2.28-4.79 years.

Small streams located in the Euphrates and Tigris basins, whose flow values are unknown due to the lack of measurement stations but have a certain potential, have been highlighted and their potential has been included in hydropower production. Based on this study, it is strongly suggested that this method can also be applied to small streams in different basins.

In order to further improve the cost-benefit analysis of small hydroelectric power plants by using different hydraulic and hydrological characteristics, this study will be an important reference.

References

Beyazit, M. (1981). Statistical Methods in Hydrology. Istanbul Technical University Press.

Demirel, I.H. (2021). Investigation of the Most Appropriate Model for Determination of Hydro Energy Potential in Small Stream Basins. Thesis (Ph.D.), Yildiz Technical University, Graduate School of Natural and Applied Sciences, Istanbul, Turkiye.

Fujii, M., Tanabe, S., Yamada, M., Mishima, T., Sawadate, T. & Ohsawa, S. (2017). Assessment of the potential for developing mini/micro hydropower: A case study in Beppu City, Japan, J. Hydrol. Reg. Stud., 11, pp. 107–116. DOI: 10.1016/j.ejrh.2015.10.007.

McEnroe, B.M. (2010). Guidelines for continuous simulation of streamflow in Johnson County, Kansas, with HEC-HMS.

Moldoveanu, A. & Popescu, D. (2018). Optimized Implementation of small hydropower plants on a stream, case study. In: EPE 2018 - Proceedings of the 2018 10th International Conference and Expositions on Electrical and Power Engineering, pp. 806-811. DOI: 10.1109/ICEPE.2018.8559661.

Serencam, U. (2019). Capacity Factor Analysis in Small Scale Hydropower Plants and a Practice Specific to Giresun. *Gümüşhane University Journal of Science and Technology Institute*, 9(4), pp. 691-698. DOI: 10.17714/gumusfenbil.552125.

Singal, S.K., Saini, R.P. & Raghuvanshi, C.S. (2010). Analysis for cost estimation of low head run-of-stream small hydropower schemes. Energy Sustain. Dev., 14(2), pp. 117-126. DOI: 10.1016/j.esd.2010.04.001.

Yuksel, I. (2024). Investment cost analysis in small hydropower plants in terms of efficiency and a case study in the Euphrates and Tigris basins, *Discover Energy*, 4(19).

ICEARC'25

4th International Civil Engineering & Architecture Conference
17-19 May 2025, Trabzon, Türkiye

Essentials of manifold flow hydraulics-II: Energy-gradient ratio (EGR) approach

Gürol Yıldırım*[1]

[1] Giresun University, Engineering Faculty, Civil Engineering Dept., 28100, Giresun, Türkiye.

Abstract. This paper presents a new analytical procedure based on Energy-Gradient Ratio (EGR) approach, identifying different types of energy head profiles for a given pipe design slope, and determining unknown hydraulic characteristics through the energy-grade line (EGL). The present technique is simple, direct, and sufficiently accurate for a wide range of water application uniformity, and can be efficiently implemented for different types of pressure head profiles for different line slope situations.

Keywords: Manifolds; Steady-state analysis; Fluid mechanics; Energy Gradient Ratio (EGR); Fluid flow

1. Theoretical background

The Energy-Gradient Ratio (EGR) approach is a useful tool to identify first which type of pressure profile occurs for a given uniform design slope with other hydraulic variables initially known, then comprehensively evaluate its definite hydraulic characteristics along the line (Sadeghi & Peters, 2011). The most important difficulty when recognizing the type of pressure profile is the determination of energy-grade line slope (or friction slope) (S_f), which depends on the total inlet discharge (Q) and pipe diameter (D), since Q and D are unknown parameters in most design cases (Hathoot et al. 1993). Knowing the hydraulic properties for any type of pressure profile regarded enables the design engineer to evaluate pressure parameters through the line sections in a simple way based on the proposed EGR approach. The EGR approach is essentially based on a simple ratio, defined as "the energy-gradient ratio (K_S)" which can be explained as "the ratio of uniform pipe slope (S_0) to the friction slope (S_f) [or energy-gradient line (EGL) slope] (KS = S_0/S_f)". Through the following analysis, the improved EGR approach, based on the recent analytical development (Yıldırım, 2006a; 2007a,b) to cover different types of pressure head profiles (Type-I, Type-II.a, Type-II.b, Type-II.c and Type-III) concerning different uniform line slope situations (Barragan & Wu, 2005), will be presented.

This paper presents a new analytical procedure based on Energy-Gradient Ratio (EGR) approach, identifying different types of energy head profiles for a given pipe design slope, and determining unknown hydraulic characteristics through the energy-grade line (EGL) (Sadeghi & Peters, 2013; Singh et al., 2000).The present technique is simple, direct, and sufficiently accurate for a wide range of water application uniformity, and can be efficiently implemented for different types of pressure head profiles for different line slope situations. The proposed method offers considerable flexibility by directly computing values of the required hydraulic variables along the energy profile, incorporating different uniformity patterns and without requiring any additional hydraulic variables, such as pipe diameter, total inlet discharge, required average outflow, downstream end pressure head, total friction drop or outlet characteristics (Sadeghi et al., 2016; Singh & Mahar, 2003).

2. Analytical energy-gradient-ratio (EGR) approach

Assuming that outlets along the pipeline have uniform outflow, neglecting the change in kinetic head and local head losses, the operating inlet pressure head, H0I, for a multi-outlet pipeline is approximated by Keller and Bliesner (1990) as:

$$H_{0I} = \overline{H} + k \times h_{f(L)} + \frac{1}{2} \times (S_0 \times L) \tag{1}$$

where k = the fraction of the total pipe friction head loss; the suggested values of factor k are 0.75, 0.63 and 0.5, for a multioutlet pipe with single-diameter, two-diameter and more than two diameters, respectively (Keller & Bliesner, 1990; Mahar & Singh, 2003). The traditional formulation, Eq.(1) cannot be easily applied to determine H_{0I}, since $\overline{H}$ and S_0 are known a priori, whereas H_d and/or $h_{f(L)}$ cannot be determined in advance, because pipe diameter, D, is an additional unknown parameter for the required operating inlet pressure head, H_{0I}, in most usual design cases. As a useful reference, to overcome the implicit procedure given by Eq. (1), Yıldırım (2023a) recently

* Corresponding author, E-mail: gurol.yildirim@giresun.edu.tr

https://doi.org/10.31462/icearc2025_ce_hwr_417

golden light publishing

proposed an improved direct computing technique to determine H_{0I} for a single line size system which incorporates different uniformity patterns for water application. In this analysis, first, simple mathematical expressions are deduced to relate uniformity parameters; then H_{0I} is simply reformulated by taking into account a multiplification factor , for the required average outlet pressure head, and β^*, for the potential energy head change due to uniform line slope. However, the applicability of this procedure is only limited for the design case of a Type-I pressure profile for horizontal or uphill slope situation. Eq. (1) can be rewritten for a single line size system (k = 0.75), and suitable for the general slope situations (p = 0 and p = 1 for zero and upslope, p = -1 for downslope) as follows:

$$H_{0I} = \overline{H} + L\left(\frac{3}{4}S_f + \frac{1}{2}(pS_0)\right) \tag{2}$$

In this section, the computing technique (Yıldırım, 2008) based on the recent analytical development (Yıldırım, 2023a; 2023b) which evaluates the operating inlet pressure head, H_{0I} for a single line size system (k = 0.75), will be improved and extended to encomapss different types of pressure profiles concerning different uniform line slope situations, and various design combinations. In the analysis, first the friction slope (S_f) is formulated in terms of dimensionless physical mumbers ($\lambda_1, \lambda_2, \lambda_3, \lambda_4, \lambda_5$), introduced into Eq. (2), and then H_{0I} can be directly determined as follows.

3. Steps of algorithm

For the sake of comparison between the formulations derived for design parameters [the friction slope, S_f, fraction of the required average pressure head, δ_H , and multiplication factors (α and β^*) for operating pressure], regarding the five types of pressure profiles (Type I, Types II.a, II.b, II.c and Type III), all formulations are sythesized and are shown in Fig. 1.

Energy-Grade Line Slope, S_f (%)

Type of Pressure Profile(s)	Design Coefficients (k_1, k_2, k_3, k_4)			
	k_1	k_2	k_3	k_4
Type-I	4.357	3.477	2.745	2.92
	$S_f = k_1 \times \lambda_1 \times \lambda_5 - S_0 = k_2 \times \lambda_2 \times \lambda_5 - S_0 = k_3 \times \lambda_3 \times \lambda_5 - S_0 = k_4 \times \lambda_4 \times \lambda_5 - S_0$			
Type-II.a	4.357	3.477	2.745	2.92
	$S_f = S_0 + k_1 \times \lambda_1 \times \lambda_5 = S_0 + k_2 \times \lambda_2 \times \lambda_5 = S_0 + k_3 \times \lambda_3 \times \lambda_5 = S_0 + k_4 \times \lambda_4 \times \lambda_5$			
Type-II.b	2.178	1.738	1.372	1.459
	$S_0 = S_f = k_1 \times \lambda_1 \times \lambda_5 = k_2 \times \lambda_2 \times \lambda_5 = k_3 \times \lambda_3 \times \lambda_5 = k_4 \times \lambda_4 \times \lambda_5$			
Type-II.c and **Type-III**	4.357	3.477	2.745	2.92
	$S_f = S_0 - k_1 \times \lambda_1 \times \lambda_5 = S_0 - k_2 \times \lambda_2 \times \lambda_5 = S_0 - k_3 \times \lambda_3 \times \lambda_5 = S_0 - k_4 \times \lambda_4 \times \lambda_5$			

Fraction of Required Average Pressure Head: δ_H (%)

Type of Pressure Profile(s)	Design Coefficients (k_1, k_2, k_3, k_4, k_5)				
	k_1	k_2	k_3	k_4	k_5
Type-I and **Type III**	4.357	3.477	2.745	2.92	-
	$\delta_H = k_1 \times \lambda_1 = k_2 \times \lambda_2 = k_3 \times \lambda_3 = k_4 \times \lambda_4$				
Type-II.b	0.778	0.621	0.490	0.521	-
	$\delta_H = k_1 \times \lambda_1 = k_2 \times \lambda_2 = k_3 \times \lambda_3 = k_4 \times \lambda_4$				
Type-II.c	4.357	3.477	2.745	2.92	0.356
	$\delta_H = S_0 \times \left(1 - k_1 \times \frac{\lambda_1 \times \lambda_5}{S_0}\right)^{-1/1.75} \times \frac{k_5}{\lambda_5} = S_0 \times \left(1 - k_2 \times \frac{\lambda_2 \times \lambda_5}{S_0}\right)^{-1/1.75} \times \frac{k_5}{\lambda_5} = S_0 \times \left(1 - k_3 \times \frac{\lambda_3 \times \lambda_5}{S_0}\right)^{-1/1.75} \times \frac{k_5}{\lambda_5} = S_0 \times \left(1 - k_4 \times \frac{\lambda_4 \times \lambda_5}{S_0}\right)^{-1/1.75} \times \frac{k_5}{\lambda_5}$				

Multiplication Factor to the Required Average Pressure Head: α; Multiplication Factor to the Potential Energy Head: β^*

Type of Pressure Profile(s)	Design Coefficients (k_1, k_2, k_3, k_4, c_1)					Multiplication Factor to the Potential Energy Head: β^*
	k_1	k_2	k_3	k_4	c_1	β^*
Type-I	4.357	3.477	2.745	2.92	0.75 ($F_S = 1.0$)	-0.25 ($F_S = 1.0$)
	$\alpha = 1 + c_1 \times k_1 \times \lambda_1 = 1 + c_1 \times k_2 \times \lambda_2 = 1 + c_1 \times k_3 \times \lambda_3 = 1 + c_1 \times k_4 \times \lambda_4$				$\frac{0.75}{F_S}$ ($F_S \neq 1.0$)	$\frac{1}{2} - \frac{0.75}{F_S}$ ($F_S \neq 1.0$)
Type-II.a	4.357	3.477	2.745	2.92	0.75 ($F_S = 1.0$)	0.25 ($F_S = 1.0$)
	$\alpha = 1 + c_1 \times k_1 \times \lambda_1 = 1 + c_1 \times k_2 \times \lambda_2 = 1 + c_1 \times k_3 \times \lambda_3 = 1 + c_1 \times k_4 \times \lambda_4$				$\frac{0.75}{F_S}$ ($F_S \neq 1.0$)	$\frac{1}{2} - \frac{0.75}{F_S}$ ($F_S \neq 1.0$)
Type-II.b	0.778	0.621	0.490	0.521	0.70 ($F_S = 1.0$)	0
	$\alpha = 1 + c_1 \times k_1 \times \lambda_1 = 1 + c_1 \times k_2 \times \lambda_2 = 1 + c_1 \times k_3 \times \lambda_3 = 1 + c_1 \times k_4 \times \lambda_4$				$\frac{0.70}{F_S^{-0.57}}$ ($F_S \neq 1.0$)	
Type-II.c and **Type-III**	4.357	3.477	2.745	2.92	-0.75 ($F_S = 1.0$)	0.25 ($F_S = 1.0$)
	$\alpha = 1 + c_1 \times k_1 \times \lambda_1 = 1 + c_1 \times k_2 \times \lambda_2 = 1 + c_1 \times k_3 \times \lambda_3 = 1 + c_1 \times k_4 \times \lambda$				$-\frac{0.75}{F_S}$ ($F_S \neq 1.0$)	$\frac{0.75}{F_S} - \frac{1}{2}$ ($F_S \neq 1.0$)

Dimensionless Physical Numbers: $\lambda_1 = \frac{(1-U_C)}{x}$, $\lambda_2 = \frac{CV_q}{x}$, $\lambda_3 = \frac{(1-EU)}{x}$, $\lambda_4 = \frac{(1-DU)}{x}$, $\lambda_5 = \frac{\overline{H}}{L}$; and F_S = Enlargemet factor, to take into account the effect of local losses [$F_S = 1 + (l_e / s)$].

Fig. 1. Relationships for the Energy-Grade Line Slope: S_f (%), Fraction of Required Average Pressure Head $(\overline{H})$: δ_H (%), Multiplication Factors: α and β^*, to Determine the Operating Inlet Pressure Head (H_{0I}) with Related Design Coefficients (c_1, k_1, k_2, k_3, k_4, k_5) for Five Types of Pressure Profiles [*Type-I, Types II.a, II.b, II.c* and *Type-III*]

Before starting the present algorithm, the following input data for hydraulic variables are assigned in advance to finally evaluate the required pressure parameters along the profile.

Input (initially known) parameters: S_0: pipe slope which is assumed to be uniform along the line (%), L: total length of the submain line (m), $\overline{H}$: required average pressure head (m), (U_C, CVq, E_U or D_U): uniformity parameters for the desired level of water application unformity (%), l_e: equivalent length (m) to determine the enlergement factor (F_S), s and x: outlet spacing (m) and outlet discharge exponent, respectively.

Output (required) parameters: S_f: the friction slope (or the slope of EGL) (%), $K_S = S_0/S_f$: the dimensionless "energy-gradient ratio", which primarily identifies the type of pressure profiles, $h_{f(L)} = S_f \times L$: the total friction drop at the end of line (m), H_{max}, H_{min}: the extreme pressure heads (m) with their locations (i_{max} , i_{min}), $\Delta H_{\max}$: the maximum allowable pressure head difference along the line (m), $\delta_H = \Delta H_{\max} / \overline{H}$: the fraction of the required average pressure head (%), $\phi_H = \Delta H_{\max} / h_{f(L)}$: the relative maximum pressure variation (%), α and β^*: the multiplification factors to the operating inlet pressure (H_{0I}), H_{0I} and H_d: the operating inlet and downstream end pressure heads (m), respectively, and β: nonuniform outflow exponent to evaluate the nonumiform outflow distribution along the line. Based on the present improved EGR approach, the following calculation steps are implemented, respectively, using the related formulations for each type of pressure profile.

a) For a desired value of the uniformity coefficient (U_C, CVq, E_U or D_U), and the outlet discharge exponent (x), the related dimensionless physical numbers (λ_1, λ_2, λ_3 or λ_4) are computed for a given value of required average pressure head ($\overline{H}$) and the total length of submain line (L), the dimensionless physical number, λ_5, is also computed.
b) Select the proper formulation for Sf in accordance with the given design slope (S0) condition [zero (p = 0), upslope (p = 1), or downslope (p = -1)]. Then Sf is evaluated, depending on dimensionless physical numbers (λ1, λ2, λ3, λ4 and λ5), and certain values of design coefficients (k1, k2, k3, k4 and k5).
c) Compare the friction slope (Sf) to the uniform pipe slope (S0) with respect to the design intervals of the energy-gradient ratio (KS = S0/Sf), and make a decision about the type of pressure profile depending on the KS value assigned in Step (b). It should be noted for downslope condition, as an initial computation, the Sf formulation given for the pressure profiles Type II.c and Type III is first used; then if a negative value of Sf is reached, this would indicate that Sf is greater than the pipe slope, S0; that means the formulation for Sf deduced for Type II.a profile should be used.
d) For the type of pressure profile assigned in Step (c), select the proper formulation to evaluate the percentage of the required average pressure head (δ_H). Then, compute the total friction drop, hf(L).
e) For the type of pressure profile decided on above, compute multiplication factors (α and β^*) for the operating inlet pressure head (H0I), depending on the dimensionless physical numbers (λ1, λ2, λ3, λ4 and λ5) and certain values of design coefficients (c_1, k_1, k_2, k_3, and k_4) from Figure 1. Then, the operating inlet pressure head (H_{0I}) can be evaluated for both the design cases (considering or neglecting local losses).
f) For the above type of pressure profile, determine the extreme pressure heads (H_{max}, H_{min}) with their positions along the line (imax, imin), and evaluate the maximum allowable pressure head difference ($\Delta H_{\max}$) to check the value of δ_H computed from Step (d). Then, determine the relative pressure variation ($\phi_H = \Delta H_{\max} / h_{f(L)}$).
g) Compute the downstream end pressure head (Hd) from the conservation of energy principle or the related analytical equations derived for each type of profile. Then, set the order of operating inlet (H0I), downstream end (Hd), extreme (Hmax, Hmin) and required average ($\overline{H}$) pressure heads to check the identity for the assigned type of pressure profile from Step (c).
h) Introduce the value of Sf previously determined in Step (c) into analytical equations to reveal the certain form of the pressure head profile along the line. Then, check the identitiy of the specific hydraulic characteristics between the certain and assigned pressure profiles.

Note that if a higher precision is required, the nonumiform outflow distribution along the line should be taken into consideration. For this case the nonuniform outflow exponent, β is evaluated depending on the values, S_0, x, L, $\overline{H}$, F_S, and S_f [determined from Step (b)]. Then, Steps (f)~(h) are repeated to evaluate the nonuniform outflow distribution.

4. Conclusions

Determination of the proper operating inlet pressure head is important for hydraulic design of multi-outlet pipelines in submain lines. This paper presents an analytical energy-gradient ratio (EGR) approach which offers simple, direct but sufficiently accurate relationships to determine the operating inlet pressure head and the the required pressure parameters, incorporating different uniformity patterns for water application. For this purpose, some mathematical expressions are initially deduced to relate water application uniformity parameters; such as

Christiansen uniformity coefficient, lower-quarter distribution uniformity, coefficient of variation of outlet discharge, emission uniformity and allowable pressure head variation. Hence, the operating inlet pressure head is reformulated by incorporating different uniformity patterns, and setting a multiplification factor, α , and the required average outlet pressure head, and β *, for the change in potential energy head due to the uniform line slope. The present formulations can be efficiently used for a wide range of water application uniformity, and for different types of pressure profiles in different line slope situations, without requiring any additional hydraulic variables.

5. Appendix

5.1. Computational example for type III profile: "steep downslope" case

Based on the original data presented-above, determine the energy-gradient line (EGL) with the corresponding hydraulic variables for the steep-downslope situation, S_0 = 0.05, and for the desired level of water application uniformity, U_C = 90.5%, based on the nonuniform outflow concept ($m_\beta = \beta \times m$, $\beta \neq 1$), and neglecting the change in the kinetic energy head $(H_{VI} \cong 0)$ and local head losses (F_S = 1).

a) For U_C = 0.905, $\overline{H}$ =7.2 m, L = 151 m and x = 0.5, dimensionless physical numbers, λ_1 and λ_5 are already computed in the following: $\lambda_1 = 0.19$ and $\lambda_5 = 0.048$

b), c) The friction slope, S_f is directly computed from Figure 1 (k_1 = 4.357):

$$S_f = S_0 - k_1 \times \lambda_1 \times \lambda_5 = 0.05 - 4.357 \times 0.19 \times 0.048 = 0.0105 \rightarrow, S_f = 1.05\% \tag{3}$$

The dimensionless energy-gradient ratio, $K_S = \dfrac{S_0}{S_f} = \dfrac{0.05}{0.0105} = 4.75$ (Figure 1), therefore Type-III profile is observed along the line.

Total friction drop, m.

Total energy gain due to steep-downslope situation, m.

For the nonuniform outflow distribution along the line, the nonuniform outflow exponent, is evaluated from Eq. (4)*, depending on the values of S_0, x, L, $\overline{H}$, FS, and S_f , as follows:

$$\beta = 1 - 3.322x \log\left[1 + \frac{H_{VI}}{\overline{H}} + \frac{h_{f(L)}}{\overline{H}}\left[\left(\frac{m+3-0.5^{m+1}}{m+2}\right) - F_S\right] + \frac{1}{4\overline{H}}(p\Delta S)\right] \tag{4}$$

$$\beta = 1 - 3.322 \times 0.5 \times \log\left[1 + 0 + \frac{1.59}{7.2} \times \left[\left(\frac{4.75 - 0.5^{2.75}}{3.75}\right) - 1\right] + \frac{1}{4 \times 7.2} \times (-1) \times 7.55\right] \tag{5}$$

$\beta = 1.172$, therefore the improved value of velocity exponent, mβ : $m_\beta = \beta \times m = 1.172 \times 1.75 = 2.05$

d) For Type III profile, can be directly determined from Figure 1 (k_1 = 4.357):

$$\delta_H = k_1 \times \lambda_1 = 4.357 \times 0.19 = 0.828 ,\ \delta_H = 83\% \tag{6}$$

e) For Type III profile, multiplication factors (α and β^*) are computed from Figure 1: k_1 = 4.357, c_1 = -0.75 for F_S = 1]:

$$\alpha = 1 + c_1 \times \delta_H = 1 - 0.75 \times 0.828 = 0.379 \tag{7}$$

$$\alpha = 1 + c_1 \times k_1 \times \lambda_1 = 1 - 0.75 \times 4.357 \times 0.19 = 0.379 \text{ , and } \beta^* = 0.25 \text{ (for } F_S = 1) \tag{8}$$

The operating inlet pressure head (H_{0I}) is directly computed from:

$$H_{0I} = \alpha \times \overline{H} + \beta^* \times (S_0 \times L) \tag{9}$$

$$H_{0I} = 0.379 \times 7.2 + 0.25 \times (0.05 \times 151) = 4.617 \cong 4.62 \text{ m} \tag{10}$$

Check the value of H_{0I}, for i = 0, for S_f = 0.0105 and $m_\beta = 2.05$:

$$H_{0I} = H(l=0, i=0) = \overline{H} + H_{VI}[1-(1-i)^2] + h_{f(L)}\left[F_S[(1-i)^{m_\beta+1} - 1] + \frac{m_\beta + 1}{m_\beta + 2}\right] - p\Delta S\left(i - \frac{1}{2}\right) \tag{11}$$

$$= 7.2 + 0 + 1.59 \times \left[1 \times [(1-0)^{2.05+1} - 1] + \frac{2.05+1}{2.05+2}\right] - (-1) \times 7.55 \times \left(0 - \frac{1}{2}\right) = 4.62 \text{ m} \tag{12}$$

The downstream end pressure head, H_d, can be directly evaluated from the conservation of energy principle:

$$H_d = H_{0I} + L \times (S_0 - S_f) = 4.62 + 151 \times (0.05 - 0.0105) = 10.585 \cong 10.59 \text{ m} \tag{13}$$

Check the value of H_d, for for i = 1, for S_f = 0.0105 and $m_\beta = 2.05$:

$$H_d = H(l = L, i = 1) = 7.2 + 0 + 1.59 \times \left[1 \times [(1-1)^{2.05+1} - 1] + \frac{2.05+1}{2.05+2}\right] - (-1) \times 7.55 \times \left(1 - \frac{1}{2}\right) = 10.582 \cong 10.58\,\text{m} \quad (14)$$

f), g), h) The location of minimum pressure head (i_{min}) can be evaluated from:

$$i_{\min(DW)} = \frac{l_{\min}}{L} = 1 - 0.561 \times \left(\frac{K_S}{F_S}\right)^{0.57} = 1 - 0.561 \times \left(\frac{4.75}{1}\right)^{0.57} = -0.36 \quad (15)$$

Minus sign indicates the minimum outflow just occurs at the upstream pipe inlet point ($i_{min} = 0$), therefore the operating pressure head at the pipe inlet is just identical to the minimum pressure head along the line ($H_{0I} = H_{min}$ = 4.62 m), and the maximum pressure head occurs at the downstream closed end ($H_{max} = H_d$ = 10.58 m)

The maximum pressure head difference, $\Delta H_{\max} = H_{\max} - H_{\min} = 10.58 - 4.62 = 5.96$ m.

Check the value of from: $\delta_H = \frac{\Delta H_{\max}}{\overline{H}} = \frac{5.96}{7.2} = 0.828$, (83%)

Compute parameter, ϕ_H , to evaluate the pressure variation:

$\phi_H = \frac{\Delta H_{\max}}{h_{f(L)}} = \frac{5.96}{1.59} = 3.75$ means the excessive level for the pressure variation along the line for a given steep downslope situation (for K_S = 4.75>2.75)

Check the pressure orders for Type- III profile:

$$H_d = H_{\max} = 10.6 > \overline{H} = 7.2 > H_{0I} = H_{\min} = 4.6\,\text{m} \quad (16)$$

The distribution of pressure parameters evaluated based on the EGR approach is verified by the Type- III profile.

ı) For water application uniformity evaluation, for Type III profile (c_1 = -0.75, k_1 = 4.357 and = 0.25), regarding the design value of operating pressure head, H_{0I} = 4.62 m, and $\lambda_5 = \overline{H}/L = 7.2/151 = 0.048$, the uniformity parameters are evaluated as follows:

$$\theta = \frac{H_{0I}}{\overline{H}} - \beta^* \times \frac{S_0}{\lambda_5} - 1 = \frac{4.62}{7.2} - 0.25 \times \frac{0.05}{0.048} - 1 = -0.61875 \quad (17)$$

$$\delta_H = \frac{\theta}{c_1} = -\frac{0.61875}{-0.75} = 0.825 \cong 83\% \quad \lambda_1 = \frac{(1-U_C)}{x} = \frac{\theta}{c_1 \times k_1} = \frac{-0.61875}{-0.75 \times 4.357} = 0.1894 \quad (18)$$

$$U_C = 1 - \lambda_1 \times x = 1 - 0.1894 \times 0.5 = 0.905 \cong 90.5\% \quad (19)$$

References

Barragan, J., & Wu, I. P. (2005). Simple pressure parameters for micro-irrigation design. *Biosystems Engineering, 90*(4), 463–475.

Hathoot, H. M., Al-Amoud, A. I., and Mohammad, F. S. (1993). "Analysis and design of trickle irrigation laterals." *J. Irrig. Drain. Eng.*, 10.1061/(ASCE)0733-9437(1993)119:5(756), 756–767.

Keller, J., & Bliesner, R. D. (1990). *Sprinkler and trickle irrigation*. New York, NY: Van Nostrand Reinhold.

Mahar, P., & Singh, R. P. (2003). Optimal design of pumping mains considering pump characteristics. *Journal of Pipeline Systems Engineering and Practice, 5*(1), 04013010.

Sadeghi, S. H., Peters, T., & Shelia, V. (2016). Energy grade line assessment for tapered microirrigation laterals. *Journal of Irrigation and Drainage Engineering, 142*(7).

Sadeghi, S. H., & Peters, T. (2013). Analytical determination of distribution uniformity for microirrigation tapered laterals laid on uphill and horizontal slopes. *Journal of Irrigation and Drainage Engineering, 139*(6).

Sadeghi, S. H., & Peters, T. (2011). Modified G and GAVG correction factors for laterals with multiple outlets and outflow. *Journal of Irrigation and Drainage Engineering, 137*(11).

Singh, R. P., & Mahar, P. S. (2003). Optimal design of multidiameter, multioutlet pipelines. *Journal of Water Resources Planning and Management, 129*(3), 226–234.

Singh, A., Singh, R. P., Mahar, P. S., & Singh, K. K. (2000). Optimal design of tapered microirrigation submain manifolds. *Journal of Irrigation and Drainage Engineering, 126*(6), 362–366.

Yıldırım, G. (2023a). *Hydraulic principles and design concepts for submain units with multiple outlet pipelines: New analytical techniques with engineering applications* (1st ed.). Springer.

Yıldırım, G. (2023b). Review of fundementals in hydraulic engineering perspective: Hydraulics principles, governing equations, design criteria, types of design problems, hydraulics and energy-gradient line profiles for uniformly sloping multiple outlets pipelines. In G. Yıldırım (Ed.), *Hydraulic principles and design concepts for submain units with multiple outlet pipelines* (pp. 1–37). Springer.

4th International Civil Engineering & Architecture Conference
17-19 May 2025, Trabzon, Türkiye

Impact of acidic groundwater on quarry wall stability: Evaluating drainage and chemical treatment effectiveness

Zahra Hassanzadeh*[1],Sahand Zeinalzadeh Hamid[2], Javad Parsa[3]

[1] *Azarbaijan Shahid Madani University, Department of Chemistry, Faculty of Science, Tabriz, Iran*
[2] *Islamic Azad University of Tabriz, Department of Civil Engineering, Faculty of Engineering, Tabriz, Iran*
[3] *University of Tabriz, Water Engineering Department, Tabriz, Iran*

Abstract. Acidic groundwater jeopardizes quarry wall stability, particularly in faulted regions, by promoting chemical weathering and elevating pore pressure. This study assesses the efficacy of drainage systems and lime-based chemical treatment in enhancing stability, using FLAC simulations to evaluate three scenarios: baseline acidic conditions, drainage alone, and combined drainage with lime treatment. The baseline scenario, characterized by high pore pressure (0.1 MPa) and degraded rock properties, produced a factor of safety (FOS) of 0.88, indicating instability. Drainage reduced pore pressure to 0.01 MPa, increasing FOS to 1.02, suggesting marginal stability. The combined approach, integrating drainage with lime treatment to neutralize acidity (pH ≈ 7) and improve rock properties, elevated FOS to 1.29, achieving significant stability. Results highlight that while drainage mitigates mechanical instability, lime treatment addresses chemical degradation, which offers a holistic solution for quarry operators. By incorporating site-specific fault data and chemical treatment effects into FLAC2D modeling, this study provides a novel framework for managing acid mine drainage risks in mining settings. Nevertheless, field trials are recommended to confirm these findings, with future research proposed to explore detailed chemistry modeling and long-term treatment durability.

Keywords: Acidic groundwater; Quarry wall stability; Drainage system; Chemical treatment; FLAC2D simulation

1. Introduction

Quarry wall stability is critical for ensuring operational safety and economic viability in mining operations. Unstable slopes can lead to rockfalls, landslides, and costly production delays, posing significant risks to workers and equipment. A key factor compromising stability is acidic groundwater, often with a pH around 2-4, which triggers chemical weathering of rock masses. This process, driven by acid mine drainage (AMD) from sulfide mineral oxidation, dissolves carbonate minerals (e.g., calcite, dolomite) and hydrolyzes silicates, reducing rock cohesion and strength (Potgieter-Vermaak et al., 2006). Geological discontinuities, such as faults, exacerbate these effects by acting as conduits for acidic water, increasing pore pressure and chemical degradation along weak planes. For instance, aqueous faults identified in the study quarry channel acidic groundwater, amplifying instability risks.

Acidic groundwater significantly reduces quarry wall stability, particularly in regions with faulted geology. The combined mechanical (pore pressure) and chemical (rock weakening) effects of acidic water lower the FOS of slopes, especially where faults facilitate water flow and weathering. Effective mitigation strategies are needed to address both the hydrological and chemical challenges posed by acidic groundwater in faulted quarry environments (Viana da Fonseca et al., 2011).

This study aims to simulate quarry wall stability under acidic groundwater conditions using the Finite Difference Method software FLAC2D, incorporating site-specific geotechnical and fault data. It also seeks to assess the effectiveness of drainage systems and chemical treatments, such as lime neutralization, in improving slope stability. Additionally, the analysis will focus on the impact of faults on stability and evaluate the efficacy of remediation strategies, with particular attention to aqueous faults as critical drivers of instability.

By integrating geological fault data and geotechnical parameters into FLAC2D simulations, this study provides a practical framework for stabilizing quarry walls affected by acidic groundwater. The findings offer quarry operators a cost-effective solution combining drainage and lime treatment, with broader implications for managing

* Corresponding author, E-mail: zahraa.hsz79@gmail.com

https://doi.org/10.31462/icearc2025_ce_hwr_439

AMD-related instability in mining environments. Addressing fault-driven risks enhances the applicability of the proposed strategies to complex geological settings.

2. Literature review

Acid mine drainage (AMD) is the archetypal "acidic groundwater" in mining contexts. It forms when sulfide minerals (especially pyrite) oxidize, generating strong acids and dissolved metals (Fe, Mn, Cu, etc.). AMD waters can have pH well below 4 (often 2–3) and extremely high metal concentrations. For example, Zhao et al. (2024) analyzed an AMD sample with pH 2.16 and Fe ≈77.5 g/L, Mn ≈621 mg/L, Cu ≈6.5 mg/L (along with Ca, Mg, etc.) (URS, 2003; Zhao et al., 2024). These harsh chemistries have profound effects on rock durability. Water–rock interactions under acidic conditions ("hydrochemical corrosion") rapidly weather primary minerals and alter rock microstructure (H. Zhang et al., 2024; Jie Zhang et al., 2024). In particular, acidified water attacks carbonate minerals almost immediately (e.g., calcite, dolomite). Xu et al. (2022) showed that acidic water "rapidly weathers rock-forming minerals"—dissolving dolomite and precipitating gypsum ($CaSO_4 \cdot 2H_2O$) and epsomite ($MgSO_4 \cdot 7H_2O$)—which opens fractures and increases porosity (Xu et al., 2022). Feldspar and silicate grains also hydrolyze to clay (e.g. kaolinite) and release metal cations (K^+, Mg^{2+}, Al^{3+}), further changing the rock's cementation (Cappelli et al., 2018). Over time, this chemical "etching" of minerals degrades cohesion and strength. In laboratory experiments, Xu et al. found that acid exposure reduced peak strength by up to 4.2% while increasing strain at failure by about 5–30% in dolomite-rich rocks (Parandeh et al., 2023). Recent studies have quantified these effects across rock types: Chen et al. (2021) reported a 10–25% drop in uniaxial compressive strength of sandstone after pH 3 immersion (Chen et al., 2021); Han et al. (2024) observed a 30% stiffness loss in marble under pH 2 treatment (Han et al., 2024); and Chen et al. (2020) demonstrated that basalt and diorite specimens saturated in pH 3 solutions for 49 days lost up to 20% mass and strength (Chen et al., 2020). Wong et al. noted that rock strength falls after exposure to water, attributing the loss to internal structural changes (Wong et al., 2016).

Groundwater (acidic or not) strongly influences slope stability by adding weight and generating pore pressure. Jia et al. (2024) summarize this effect for open-pit slopes: infiltrating water increases volumetric weight, softens strength, and builds pore pressures, all of which "change the equilibrium state of the internal stress of the slope" (Jia et al., 2024). Lab tests and models show that even moderate saturation lowers cohesion and friction; Zhao et al. (2024) found shear parameters decrease almost linearly with water content (Zhao et al., 2024). Field stability analyses routinely report that rising groundwater reduces factors of safety: Chen et al. (2023) demonstrated that water levels above the slip surface can drop the FOS by 10–20% (Chen et al., 2023). Numerical modelling has advanced considerably. Liu et al. (2023) applied a 3D FLAC-like hydro-mechanical model to simulate rainfall-induced and seismic scenarios in open-pit slopes (Li et al., 2023). Parsasadr et al. (2023) developed a finite-element groundwater flow model for an Iranian open-pit, testing abstraction wells and horizontal drains to reduce pore pressures (Parsasadr et al., 2024). Steiakakis et al. (2023) conducted a multi-layered slope analysis comparing LEM, LA, and FEM, finding pore pressure led to a 15% FOS decrease when crossing three aquifers (Steiakakis et al., 2023). Despite these advances, few models incorporate rock weakening due to acidity or geological discontinuities (faults/joints). Most assume homogeneous materials and treat hydro-mechanical effects separately from chemical degradation.

The primary geotechnical remedy is dewatering to lower the water table and relieve pore pressures. Common measures include horizontal drains, vertical relief wells, and sump pumping. Jia et al. (2024) reported that large-scale pumping created a drawdown of ~160m in a multi-aquifer coal pit, improving stability by >10% (Jia et al., 2024). Case studies confirm the effectiveness of drains in quarries. Argunhan-Atalay et al. (2021) found horizontal drains in a Turkish open-pit reduced pore pressures by 15–37%, though water content behind the wall remained high (Argunhan-Atalay et al., 2021). Leech & McGann (2008) reported that at Batu Hijau mine, properly designed drains ceased ground movement within days (Leech & McGann, 2008). To neutralize acidity, alkaline reagents (limestone, hydrated lime, quicklime) are used in passive and active systems. Anoxic limestone drains (ALDs) and successive alkalinity-producing systems (SAPS) are common (Laniyan et al., 2014). Zhao et al. (2024) compared NaOH and shell powder, finding NaOH raised pH faster and recovered metals more effectively (Zhao et al., 2024). Ziemkiewicz et al. (1997) reported that an ALD in a coal mine neutralized pH from 3.2 to 6.8 and removed >90% Fe/Al when unarmored limestone was periodically flushed (Ziemkiewicz et al., 1997). Wang et al. (2021) designed a permeable reactive barrier of limestone and organic carbon, achieving passive pH buffering to near-neutral in mine seepage (Wang et al., 2021). Combined approaches (dewatering + in-situ liming) logically address both mechanical and chemical hazards, but very few studies document field implementations in quarries.

Although AMD chemistry and slope stability are individually well researched, integrated studies at their intersection in quarries are scarce. No published work couples drainage design with in-situ neutralization specifically for quarry wall stabilization. Jia et al. (2024) note that "few researches" consider multi-aquifer flows, and none include chemical weakening of the rock matrix (Jia et al., 2024). Similarly, numerical models rarely incorporate both geotechnical (strength, pore pressure) and geological (faults, joints, reactive mineral zones) data (Parsasadr et al., 2023). Coupled hydro-mechanical-chemical slope models exist for swelling clays (e.g., Butscher et al., 2016; Wanninger, 2020) but have not been applied to reactive carbonate/quartzite quarry walls. To address these gaps, this study integrates site-specific fault data and chemical treatment effects into FLAC2D simulations, evaluating the combined efficacy of drainage and lime treatment on quarry wall stability.

3. Methodology

3.1. Geological data

Site-specific geological data characterized 27 faults within the quarry, with 10 identified as aqueous, facilitating acidic groundwater flow. Fault parameters include dip angles (45–86°, e.g., 86° for a major fault), dip directions (e.g., 272°), and spatial coordinates defining their locations. Aqueous faults, critical to stability analysis, were modeled in FLAC2D as joint elements with high permeability (10^{-6} m/s) and reduced shear strength (cohesion = 0.5 MPa, friction angle = 20°). These faults channel acidic groundwater (pH ~3.26), exacerbating chemical weathering and mechanical instability. Fig. 1 depicts fault orientations within the quarry geometry and their spatial distribution.

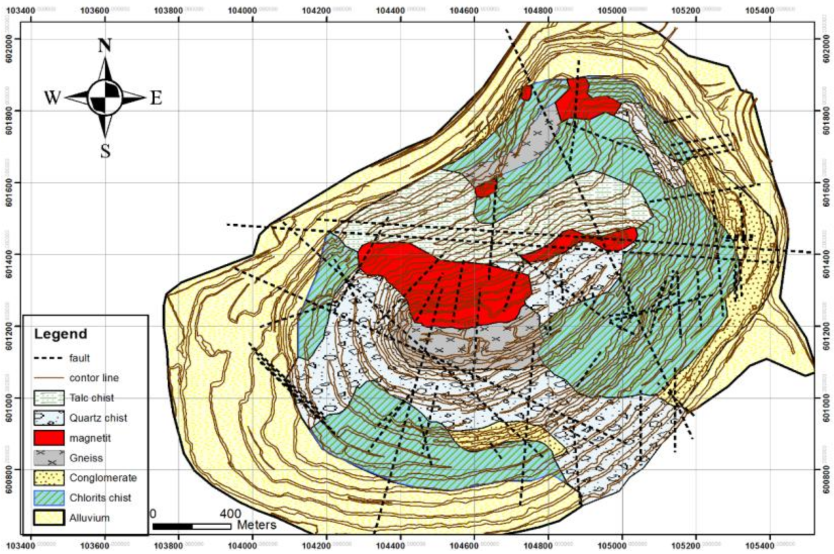

Fig. 1. Fault orientations within the quarry geometry

3.2. FLAC2D modeling

3.2.1. Model setup

The FLAC2D (Itasca Consulting Group) model simulated the northwestern wall of a quarry characterized by a 755m length and varying heights—318m on the west side and 90m on the east side—with a 45° slope, all within a 755m × 318m grid that captured site-specific geological complexity. Ten aqueous faults, with dip angles ranging from 45° to 86°, were represented as joint elements using the Ubiquitous-Joint criterion, and were assigned a cohesion of 0.5 MPa, a friction angle of 20°, and a permeability of 10^{-6} m/s. Seven rock types—Alluvium, Talc Schist, Chlorite Schist, Ore, Mica Schist, Quartz Schist, and Gneiss—were defined in both their intact and acid-weakened states (Table 2). For example, intact Quartz Schist exhibits a cohesion of 400 kPa, a friction angle of 35°, and a shear modulus of 3.0 GPa; which decline to 272 kPa, 28°, and 2.4 GPa, respectively, following chemical degradation at nearly pH 3.26. The model's boundary conditions fixed the sides and base, with gravity applied. Fig. 2 presents a cross-sectional view of the quarry geometry, delineating the material zones and fault planes as simulated in FLAC2D.

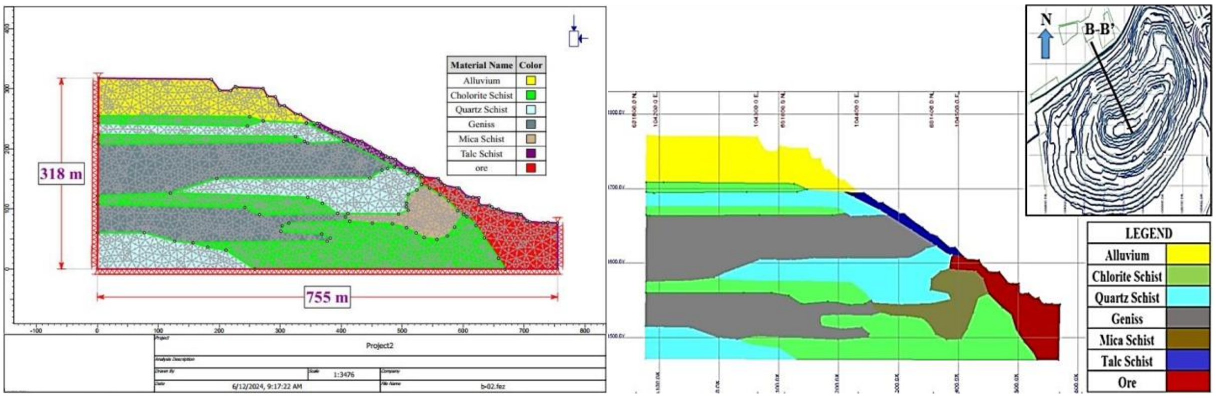

Fig. 2. Cross-section of the quarry geometry, material zones, and fault plane

3.2.2. Geotechnical data and groundwater conditions

Laboratory tests on core samples from the quarry's dominant geological layers, primarily Quartz Schist and Gneiss, provided rock properties for the wall stability analysis. For a representative intact sample of Quartz Schist, laboratory results showed an average cohesion of 400 kPa, a friction angle of 35°, and a shear modulus of 3 GPa, which decreased to a cohesion of 272 kPa, a friction angle of 30°, and a shear modulus of 2.4 GPa in the acid-weakened state due to acidic groundwater exposure. For FLAC2D simulations, properties were assigned to seven material zones (Table 1), with Quartz Schist (cohesion = 400 kPa, friction angle = 35°, permeability = 10^{-8} m/s) and Gneiss (cohesion = 500 kPa, friction angle = 40°, permeability = 10^{-9} m/s) as key layers, reflecting site-specific adjustments for modeling purposes. Additionally, Table 2 summarizes the groundwater parameters used in the FLAC2D simulations, including pore pressure, hydraulic conductivity, porosity, and Biot coefficient for baseline and drainage scenarios across aqueous faults and the seven rock types.

Table 1. Original vs acid-attacked properties

Material	Density (kg/m³)	Bulk Modulus (GPa)	Shear Modulus (GPa)	Cohesion (kPa)	Friction Angle (°)	Tensile Strength (MPa)
	Original to Acidic					
Alluvium	1900	0.20 to 0.16	0.05 to 0.04	20 to 14	30 to 25	0 to 0
Talc Schist	2700	1.00 to 0.80	0.50 to 0.40	150 to 102	25 to 20	2 to 1.4
Chlorite Schist	2800	2.00 to 1.60	0.80 to 0.64	200 to 136	30 to 25	7 to 4.8
Ore	4000	8.00 to 6.40	4.00 to 3.20	400 to 272	35 to 30	15 to10.2
Mica Schist	2800	1.50 to 1.20	0.60 to 0.48	150 to 102	27 to 22	5 to 3.4
Quartz Schist	2700	7.00 to 5.60	3.00 to 2.40	400 to 272	35 to 30	12 to 8.2
Gneiss	2800	10.00 to 8.00	5.00 to 4.00	500 to 340	40 to 34	15 to10.2

Table 2. Groundwater parameters for FLAC2D simulations of quarry wall stability

Material	Pore Pressure (MPa)		Hydraulic Conductivity (m/s)		Porosity		Biot Coefficient	
	Baseline	Drainage	Baseline	Drainage	Baseline	Drainage	Baseline	Drainage
Aqueous Faults	0.1	0.01	1×10^{-6}	1×10^{-7}	0.1	0.1	1	1
Alluvium	0.1	0.01	1×10^{-4}	1×10^{-5}	0.35	0.35	1	1
Talc Schist	0.1	0.01	1×10^{-6}	1×10^{-7}	0.15	0.15	1	1
Chlorite Schist	0.1	0.01	5×10^{-6}	5×10^{-7}	0.1	0.1	1	1
Ore	0.1	0.01	1×10^{-7}	1×10^{-8}	0.05	0.05	1	1
Mica Schist	0.1	0.01	1×10^{-7}	1×10^{-8}	0.08	0.08	1	1
Quartz Schist	0.1	0.01	1×10^{-8}	1×10^{-9}	0.05	0.05	1	1
Gneiss	0.1	0.01	1×10^{-9}	1×10^{-10}	0.02	0.02	1	1

Research indicates that prolonged acid attack (pH 2-4) can reduce the elastic modulus—and by proxy the bulk and shear moduli—of crystalline rocks by approximately 15–20% (Jimiao Zhang et al., 2024), while granite shows a co MParable reduction in Young's modulus (18.24%) and a cohesion drop of around 32% (from 32.24 MPa to 21.80 MPa) after 60 days of (Jimiao Zhang et al., 2024). Additionally, friction angles in acid-eroded sandstones and schists may decline by 5–10° (Lin et al., 2019), and tensile strength typically degrades by roughly 30% in acid-corroded rock samples (Lin et al., 2019). Furthermore, schist experiences more pronounced softening than granite, with acid rain exposure (pH <5) reducing its uniaxial strength and modulus by up to 25% in long-term soak tests (Sun et al., 2020).

3.3. Scenarios

Three distinct scenarios were simulated using FLAC2D to evaluate the impact of acidic groundwater and mitigation strategies on the stability of the northwestern quarry wall. Scenario 1 (Baseline) represents the natural state with acidic groundwater (pH ≈ 3.26) and high pore pressure, using acid-weakened rock and fault properties. Scenario 2 (Drainage) models the effect of dewatering with reducing pore pressure while retaining the acidic properties and pH, simulating the mechanical mitigation of groundwater effects. Dewatering in Scenario 2 was modeled assuming horizontal drains, a common method in quarries (Argunhan-Atalay et al., 2021). Scenario 3 (Drainage + Lime Treatment) combines drainage with lime application to neutralize acidity (pH ≈ 7) and restore material properties, addressing both mechanical and chemical instability. Table 3 summarized these scenarios.

Table 3. Scenario-specific parameters for FLAC2D simulations

Scenario	Pore Pressure (MPa)	pH	Hydraulic Conductivity (m/s) (Quartz Schist/Faults)
(1) Baseline	0.1	3.26	10^{-8} / 10^{-6}
(2) Drainage	0.01	3.26	10^{-9} / 10^{-7}
(3) Drainage + Lime	0.01	~7	10^{-9} / 10^{-7}

3.4. Chemical treatment

Lime treatment was applied to neutralize acidic groundwater (pH ≈ 3–4) in the quarry, restoring rock and fault properties for enhanced stability. Dosage calculation assumed a saturated zone of ~2 × 10^6 m^3 (755m × 318m × 100 m, 20% saturation, average porosity ~0.1). With groundwater acidity at ~0.001 M H_2SO_4 (pH ≈ 3.26), neutralization to pH ≈ 7 required ~148 tonnes of calcium hydroxide ($Ca(OH)_2$), based on the reaction:

$$H_2SO_4 + Ca(OH)_2 \rightarrow CaSO_4 + 2H_2O$$

(74 kg $Ca(OH)_2$ per 1000 m^3). Lime was uniformly applied, targeting faults and permeable rocks like Alluvium. Effect on properties assumed a 72.2% recovery of acid-induced losses, reflecting typical lime-stabilization effects (Table 5). For Quartz Schist, cohesion increased from 272 kPa (acid-weakened) to 355 kPa, friction angle from 28° to 33.6°, and tensile strength from 8.4 MPa to 10.6 MPa. Bulk and shear moduli rose accordingly (e.g., 5.6 GPa to 6.5 GPa, 2.4 GPa to 2.5 GPa). Fault properties, updated to reflect acid-corroded conditions, showed cohesion rising from 68 kPa to 86.72 kPa and friction from 15° to 18.6° (Carpenter et al., 1992; Das & Sobhan, 1990; Ghobadi et al., 2014; Gruchot et al., 2025; Little, 1995; Mallela et al., 2004; Onyelowe et al., 2024; Shi et al., 2024; Spasić et al., 2018; Thompson, 1965). These restored properties, integrated into FLAC2D's Mohr-Coulomb and Ubiquitous-Joint models with Biot coupling, simulated improved stability and are summarized in Table 4.

Table 4. Acid-weakened vs. lime-treated rock and fault properties

Material	Bulk Modulus (GPa)	Shear Modulus (GPa)	Cohesion (kPa)	Friction Angle (°)	Tensile Strength (MPa)
Alluvium	0.16 to 0.19	0.04 to 0.048	13.6 to 18.64	25 to 28.6	0 to 0
Talc Schist	0.80 to 0.93	0.40 to 0.46	102 to 134	18 to 23.6	1.4 to 1.832
Chlorite Schist	1.60 to 1.85	0.64 to 0.742	136 to 187	23 to 28.6	4.9 to 6.176
Ore	6.40 to 7.39	3.20 to 3.69	272 to 355	28 to 33.6	10.5 to 13.216
Mica Schist	1.20 to 1.39	0.48 to 0.55	102 to 134	20 to 25.6	3.5 to 4.448
Quartz Schist	5.60 to 6.49	2.40 to 2.78	272 to 355	28 to 33.6	8.4 to 10.616
Gneiss	8.00 to 9.28	4.00 to 4.64	340 to 427	33 to 37.6	10.5 to 13.216
Aqueous Faults	1.20 to 1.39	0.56 to 0.64	68 to 86	15 to 18.6	0.7 to 0.904

4. Results

4.1. Pore pressure

The baseline scenario reflects acidic groundwater (pH ~3.26) with elevated pore pressure, simulating natural conditions where faults and permeable rocks like Alluvium facilitate flow. The drainage scenario models dewatering effects, reducing pore pressure and conductivity to mimic mitigation measures. Fig. 3 plots pore pressure contour distribution in high-pressure baseline and low-pressure drainage conditions, elucidating the role of material-specific permeabilities in stability analysis.

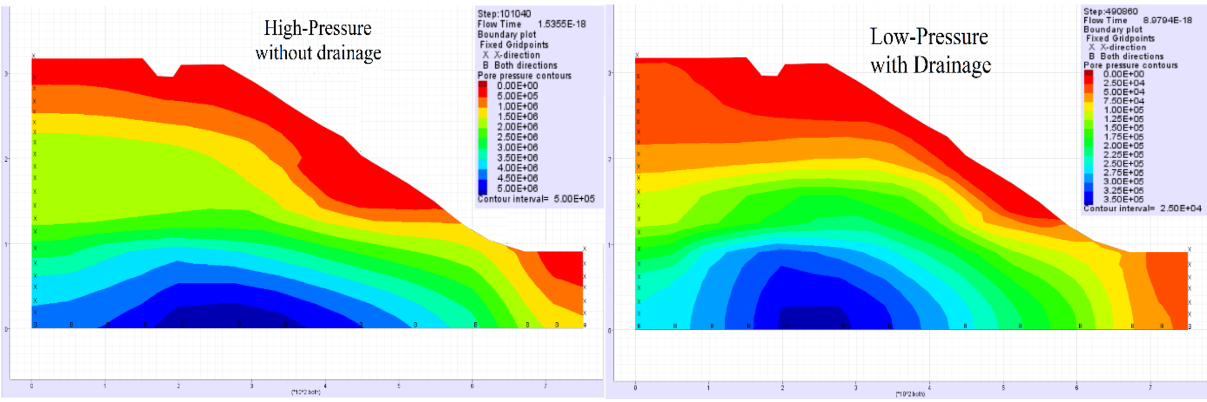

Fig. 3. Pore pressure contours in high-pressure baseline and low-pressure drainage conditions

4.2. FOS calculation

The FOS for each scenario was calculated for the northwestern quarry wall (Figure 1) using FLAC2D's shear strength reduction (SSR) method. The SSR method progressively reduces cohesion and friction angle of rocks and faults until instability occurs, defining FOS as the reduction factor at failure. Scenario 1 with acid-weakened properties and high pore pressure (0.1 MPa), yielded FOS = 0.88, indicating instability. Scenario 2, using acid-weakened properties and reduced pore pressure (0.01 MPa), achieved FOS = 1.02, suggesting marginal stability. However, scenario 3, incorporating restored rock/fault properties (Table 4) and low pore pressure, resulted in FOS = 1.29, confirming robust stability. These FOS values, summarized in Table 5, reflect the selected wall's critical condition, as preliminary experimental analyses highlighted its lowest FOS based on other walls in the quarry. The SSR method, applied consistently across scenarios, quantified stability improvements from drainage and chemical treatment.

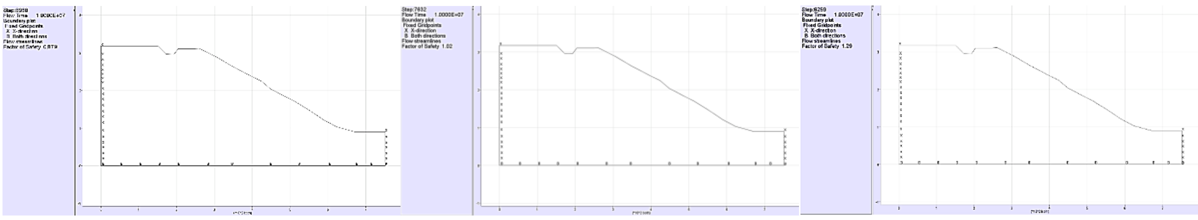

(a) (b) (c)

Fig. 4. FOS for all scenarios (a- scenario 1 b- scenario 2 c- scenario 3)

Table 5. FOS for FLAC2D scenarios

Scenario	FOS
Baseline	0.88
Drainage	1.02
Drainage + Lime Treatment	1.29

4.3. Principal stresses

In Scenario 1, the principal stress plot (Fig. 5a) shows significant compressive stresses up to -8.41 MPa near the base, reflecting high loading from groundwater pressure. Tensile stresses, reaching 20 kPa, are observed near the surface, indicating potential tension zones that elevate failure risk (FOS = 0.88). In Scenario 2, pore pressure is reduced to 0.01 MPa, leading to a slight increase in compressive stress (maximum -0.965 MPa) and a more uniform stress distribution along the slope (Fig. 5b). Tensile stresses remain at 20 kPa but are less concentrated, suggesting reduced localized failure potential. This redistribution increases effective stress, enhancing shear strength parameters (e.g., via improved cohesion and friction angle contributions in Mohr-Coulomb criteria) and lowering failure risk, as evidenced by the improved FOS of 1.02. These findings highlight drainage as an effective mitigation strategy for improving quarry wall stability under acidic groundwater conditions.

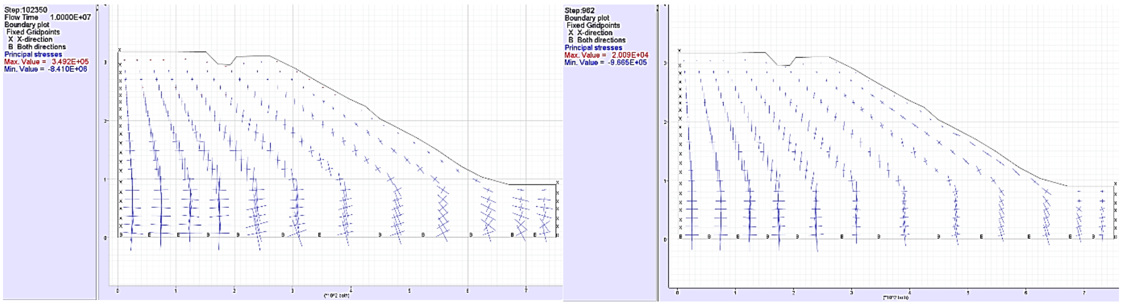

(a) (b)

Fig. 5. Principal stresses for a- scenario 1 and b- scenario 2

4.4. Deformation

Deformation analysis was conducted using FLAC2D to assess displacement across the northwestern quarry wall under varying groundwater conditions (Fig. 6). In Scenario 1, displacement vectors indicate significant downward and outward movement, with a maximum displacement of 0.5294m (Fig. 6a). Larger displacements are observed in the upper and middle slope sections, reflecting instability (FOS = 0.88) driven by reduced effective stress. In Scenario 2, the maximum displacement reduced to 0.2802 m—a 47% reduction (Fig. 6b). The vectors are smaller and more uniformly distributed, indicating reduced deformation due to consolidation as effective stress increases, aligning with improved stability (FOS = 1.02). However, slight variability in displacement magnitudes along the slope suggests uneven drainage, likely due to permeability contrasts between faults (10^{-6} m/s) and rocks (10^{-5} to 10^{-10} m/s). This variability may lead to differential settlements, potentially causing localized stress concentrations and affecting long-term stability if drainage remains non-uniform.

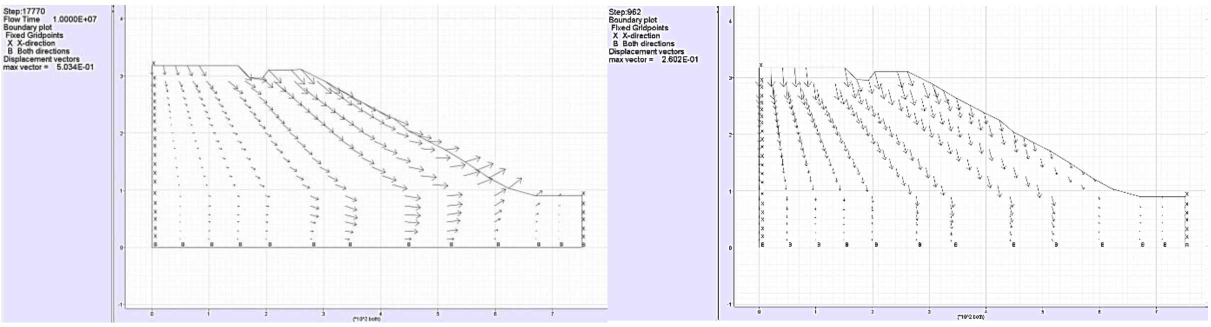

(a) (b)

Fig. 6. Deformations for a- scenario 1 and b- scenario 2

4.5. Status of layers

The status of layers in the northwestern quarry wall was evaluated using FLAC2D plasticity indicators to assess yielding behavior under different conditions (Fig. 7). In Scenario 1, the plasticity plot (Fig. 7a) shows extensive yielding. Shear yielding (red stars) dominates the upper and middle slope sections, driven by reduced material strength (e.g., Quartz Schist: cohesion 272 kPa, friction 28°), while tensile yielding (pink circles) occurs near the surface, reflecting tensile stresses (20 kPa). This widespread yielding indicates significant instability (FOS = 0.88). In Scenario 3, the plot (Fig. 7b) shows predominantly elastic behavior (green lines) across the slope. Shear yielding is minimized, limited to small upper slope zones, and tensile yielding is nearly eliminated. This reduction in yielding reflects enhanced stability (FOS = 1.29), as drainage and acidity curing mitigate failure risk by increasing effective stress and material strength.

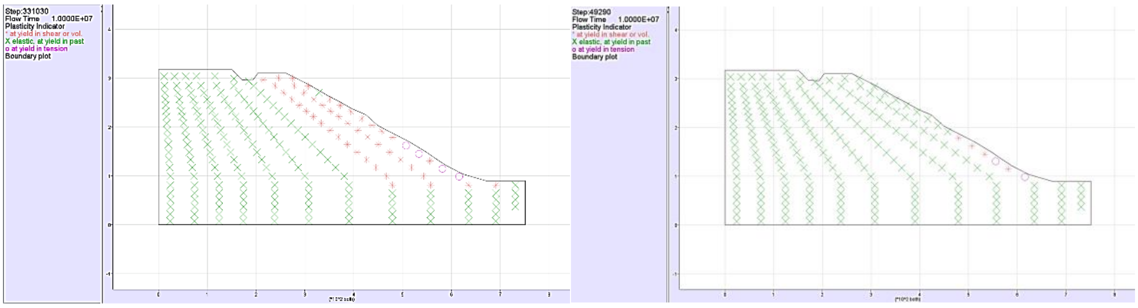

(a) (b)

Fig. 7. Status of layers for a- scenario 1 and b- scenario 3

4.6. Flow of water

Groundwater flow within the northwestern quarry wall was analyzed using FLAC2D to evaluate the impact of drainage on pore pressure and stability (Figure 8). In Scenario 1, flow vectors indicate significant groundwater movement, with a maximum velocity of 0.001746 m/s (Figure 8a). Dense vectors, predominantly downward and outward in the upper and middle slope sections, reflect active flow through permeable faults (10^{-6} m/s) and rocks (10^{-5} to 10^{-10} m/s), contributing to reduced effective stress, increased deformation (0.5294 m), and low stability (FOS = 0.88). In Scenario 2, the flow velocity drops to 0.0006303 m/s, and vectors are sparse and concentrated at the base (Figure 8b). Flow within the slope is nearly eliminated, indicating effective water removal, which increases effective stress, reduces deformation (0.2802 m), and improves stability (FOS = 1.02). These findings underscore drainage as a critical measure for mitigating groundwater-induced instability in the quarry wall.

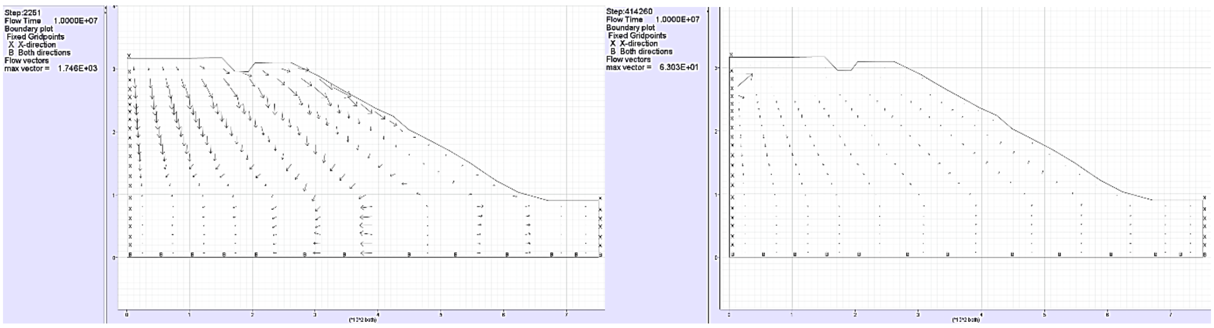

(a) (b)

Fig. 8. Groundwater flow for a- scenario 1 and b- scenario 2

4.7. Model validation

To ensure the reliability of the FLAC2D model, its results were validated against laboratory-derived data for the northwestern wall of the quarry. Laboratory tests, conducted under baseline conditions (acidic groundwater with pH ≈ 3.26, pore pressure of 0.1 MPa, and acid-weakened properties), determined a FOS of 0.88 using shear strength reduction methods on core samples from the site. The FLAC2D simulation for Scenario 1 (Baseline), incorporating the same conditions—acid-weakened rock properties (e.g., Quartz Schist: cohesion 272 kPa, friction 28°) and high pore pressure (0.1 MPa)—yielded an identical FOS of 0.88 (Section 4.2). This agreement between the simulated and laboratory-derived FOS values confirms the model's accuracy in capturing the hydro-mechanical behavior of the quarry wall under acidic groundwater conditions, providing confidence in its predictive capability for the subsequent scenarios involving drainage and lime treatment.

4.8. Summary of all scenarios

The study evaluates the stability of a quarry wall under acidic groundwater conditions across three FLAC2D-simulated scenarios, with results summarized in Table 6. Scenario 1 (Baseline) shows severe instability with a pore pressure of 5 MPa, an FOS of 0.88, principal stresses of 8.4 MPa, deformation of 50.3 cm, severe yielding, and water flow of 0.001746 m/s, reflecting the detrimental effects of high pore pressure and acid-weakened rock properties. Scenario 2 (Drainage) reduces pore pressure to 0.35 MPa, improving the FOS to 1.02, lowering stresses to 0.96 MPa, deformation to 26 cm, yielding to a few zones, and water flow to 0.0006303 m/s, indicating marginal stability by addressing mechanical factors. Scenario 3 (Drainage + Lime Treatment) maintains the low pore pressure, achieves a stable FOS of 1.29, further reduces stresses to 0.9 MPa, deformation to 21 cm, yielding to minimal levels, and keeps water flow at 0.0006303 m/s, demonstrating the synergistic benefit of combining drainage with lime treatment to mitigate both mechanical and chemical instability for enhanced quarry safety.

Table 6. Maximum values for key metrics

	Pore Pressure	FOS	Principal Stresses	Deformation	Status of layers	Water flow
Scenario 1	5 MPa	0.88	8.4 MPa	50.3 cm	Severely Yielded	0.001746 m/s
Scenario 2	0.35 MPa	1.02	0.96 MPa	26 cm	Few yielded	0.0006303 m/s
Scenario 3	0.35 MPa	1.29	0.9 MPa	21 cm	Minimal Yielding	0.0006303 m/s
Improvement	93%	68%	89%	58%	--	64%

5. Discussion

5.1. Impact of acidic groundwater

Acidic groundwater significantly undermines quarry wall stability by accelerating chemical weathering and exacerbating mechanical instability, particularly in faulted regions. With a pH of approximately 3, the acidic conditions dissolve carbonate minerals and hydrolyze silicates, leading to a notable reduction in rock cohesion and friction angle (e.g., Quartz Schist cohesion drops from 400 ^{kPa} to 272 ^{kPa}, friction from 35° to 28°). The presence of 10 aqueous faults, characterized by high permeability ($10^{-6\ m/s}$), channels this corrosive water, elevating pore pressure to 0.1 MPa and concentrating degradation along weak planes. This dual chemical and mechanical impact results in a low FOS of 0.88 in the baseline scenario, as seen in Section 4.2, indicating a high risk of slope failure. These findings align with prior studies (e.g., Xu et al., 2022) that highlight the rapid deterioration of rock strength under acidic conditions, emphasizing the critical role of fault-driven groundwater flow in destabilizing quarry walls.

5.2. Effectiveness of drainage

Drainage systems prove effective in partially improving quarry wall stability by reducing pore pressure, a key driver of instability. By lowering pore pressure from 0.1 MPa to 0.01 MPa, as modeled in Scenario 2, drainage increases effective stress, enhancing shear strength parameters via the Mohr-Coulomb criterion. This leads to a modest FOS improvement from 0.88 to 1.02, achieving marginal stability. The reduction in pore pressure also decreases deformation by 47%, with maximum displacement dropping from 0.5294m to 0.2802m , and alters groundwater flow patterns, minimizing flow within the slope. However, the persistence of acid-weakened rock properties—unchanged in this scenario—limits further stability gains. This suggests that while drainage addresses mechanical instability by mitigating pore pressure effects, it cannot fully counteract the chemical degradation caused by acidic groundwater, necessitating additional remediation measures for robust stability.

5.3. Effectiveness of lime treatment

When combined with drainage, lime treatment markedly enhances stability by neutralizing acidity and restoring rock properties. In Scenario 3, lime application raises the groundwater pH to approximately 7, counteracting the corrosive effects of acidic conditions. This treatment restores 72.2% of acid-induced property losses, increasing Quartz Schist cohesion from 272 ^{kPa} to 355 ^{kPa}, friction angle from 28° to 33.6°, and tensile strength from 8.4 MPa to 10.6 MPa . When combined with drainage (pore pressure reduced to 0.01 MPa), this treatment increased the FOS to 1.29, demonstrating significant stability improvement. The treatment also reduces yielding, with plasticity indicators showing predominantly elastic behavior in Scenario 3, compared to widespread shear and tensile yielding in the baseline. This dual mechanical and chemical approach effectively mitigates failure risks, demonstrating that integrated strategies are essential for addressing both the hydrological and chemical challenges posed by acidic groundwater in quarries.

5.4. Practical implications

The proposed combination of drainage and lime treatment offers a cost-effective and practical solution for stabilizing quarry walls affected by acidic groundwater, particularly in regions with aqueous faults. The lime dosage of approximately 148 tonnes for the saturated zone is economically feasible, given the low cost of calcium hydroxide and its proven efficacy in neutralizing acidity. Drainage systems, which can be implemented via horizontal drains or relief wells, are scalable and adaptable to varying quarry scales, as supported by prior case studies (e.g., Argunhan-Atalay et al., 2021). Targeting aqueous faults—key conduits for acidic water—ensures efficient resource use, maximizing stability gains. This approach is particularly relevant for quarries facing acid mine drainage challenges, offering a viable alternative to more expensive structural reinforcements. Furthermore, the methodology can be adapted to other mining environments with similar hydrogeological conditions, providing a framework for managing AMD-related instability in faulted geological settings.

5.5. Limitations with sensitivity analysis

This study relies on simplified assumptions that may limit its applicability to complex real-world conditions. The groundwater chemistry is modeled with a uniform pH (≈ 3.26) and acidity (0.001 M H_2SO_4), overlooking spatial variations in pH, metal concentrations, or secondary mineral precipitation (e.g., gypsum), which could alter flow and stability dynamics. Fault behavior is also simplified, assuming consistent permeability (10^{-6} m/s) and uniform property recovery with lime treatment, which may not account for heterogeneity in fault zones or differential treatment efficacy across rock types.

To assess the robustness of the model to the fault permeability assumption, a sensitivity analysis was conducted by varying the permeability of aqueous faults by ±10% (i.e., from 10^{-6} m/s to 9×10^{-7} m/s and 1.1×10^{-6} m/s) in all three scenarios. The results showed that this variation altered the FOS by less than 5% in each scenario: in Scenario 1, FOS ranged from 0.86 to 0.90 (baseline: 0.88); in Scenario 2, FOS ranged from 1.00 to 1.04 (baseline: 1.02); and in Scenario 3, FOS ranged from 1.26 to 1.32 (baseline: 1.29). These minor changes, illustrated in Figure 9, suggest that the model's stability predictions are robust to small variations in fault permeability, though larger variations or field-measured heterogeneity should be explored in future work.

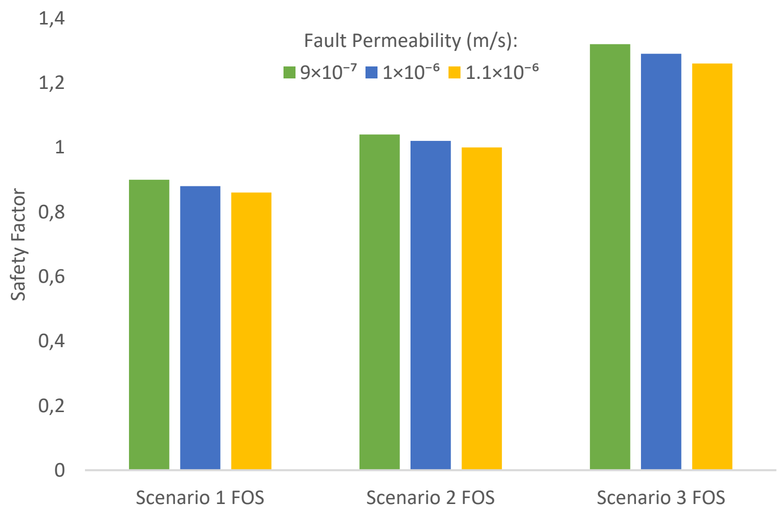

Fig. 9. Sensitivity of FOS to fault permeability variations (±10%) across three scenarios

6. Conclusion

This study provides a detailed assessment of quarry wall stability under acidic groundwater conditions, demonstrating the significant benefits of integrating drainage and lime treatment as mitigation strategies. The FLAC2D simulations revealed a progressive improvement in stability across three scenarios: the baseline scenario (Scenario 1) exhibited severe instability with an FOS of 0.88, driven by high pore pressure (5 MPa) and acid-weakened rock properties (e.g., Quartz Schist cohesion reduced from 400 kPa to 272 kPa). Implementing drainage alone (Scenario 2) lowered pore pressure to 0.35 MPa, reducing deformation by 48% (from 50.3 cm to 26 cm) and increasing the FOS to 1.02, achieving marginal stability by addressing mechanical instability. The combined approach of drainage and lime treatment (Scenario 3) further elevated the FOS to 1.29, reduced deformation to 21 cm, minimized yielding to near-elastic behavior, and maintained low water flow (0.0006303 m/s), confirming robust stability by tackling both mechanical and chemical degradation. These findings underscore the synergistic effect of combining drainage, which mitigates pore pressure, with lime treatment, which neutralizes acidity (pH ≈ 7) and restores rock strength, offering a holistic solution for quarry operators facing acid mine drainage (AMD) challenges.

A key contribution of this study lies in its integration of site-specific fault data and chemical treatment effects into FLAC2D modeling, providing a comprehensive framework for assessing stability in faulted quarry environments. By incorporating 10 aqueous faults with high permeability (10^{-6} m/s) and reduced shear strength, the model accurately captured the role of geological discontinuities in channeling acidic groundwater and exacerbating instability. The inclusion of chemical treatment effects—such as the 72.2% recovery of acid-induced property losses through lime application—enabled a realistic simulation of stability improvements, bridging a gap in existing literature where hydro-mechanical and chemical effects are often treated separately. This integrated approach not only enhances the understanding of AMD-related instability but also provides a practical methodology that can be adapted to other mining environments with similar hydrogeological conditions, particularly those with faulted geology.

The practical implications of this study are significant for quarry operators seeking cost-effective and sustainable solutions to manage AMD-related risks. The proposed strategy of combining drainage (e.g., via horizontal drains) with lime treatment (148 tonnes for the saturated zone) is economically feasible, with estimated costs of $14,800–$22,200 at typical market rates for calcium hydroxide, compared to more expensive structural reinforcements that can exceed $100,000 for similar-scale quarries. Targeting aqueous faults as conduits for acidic water ensures efficient resource use, maximizing stability gains while minimizing operational disruptions. Moreover, the approach is scalable: smaller quarries can adjust lime dosages proportionally, while larger operations may require additional drainage infrastructure to handle higher groundwater volumes. The minimal yielding and low deformation in Scenario 3 indicate a reduced risk of rockfalls or landslides, enhancing worker safety, protecting equipment, and ensuring operational continuity in challenging geological settings.

Despite its contributions, this study acknowledges certain limitations that warrant further investigation. The model assumes uniform groundwater chemistry (pH ≈ 3.26) and fault permeability (10^{-6} m/s), which may not fully capture spatial variations in pH, metal concentrations, or fault heterogeneity common in real-world quarries. However, a sensitivity analysis showed that varying fault permeability by ±10% altered the FOS by less than 5% across all scenarios, suggesting robustness to this assumption. Additionally, the model does not account for long-term chemical reactions, such as secondary mineral precipitation (e.g., gypsum), or seasonal groundwater fluctuations, which could influence stability over time. To validate these findings, field trials targeting aqueous faults are recommended, focusing on implementing drainage systems and lime application in real-world conditions to confirm the simulated stability improvements and assess practical challenges, such as lime distribution and dosage optimization.

Future research should prioritize several areas to enhance the applicability and durability of the proposed strategies. First, detailed chemistry modeling is needed to account for spatial pH variations and secondary mineral effects, which could affect flow dynamics and long-term stability. For instance, localized pH drops near faults (e.g., pH 2) may require higher lime dosages, while carbonate buffering in other zones (e.g., pH 5) may need less, necessitating pH mapping for targeted treatment. Second, long-term monitoring of treated quarry walls is essential to evaluate the durability of lime treatment, particularly the potential for pore clogging from excess calcite precipitation or the re-acidification of groundwater over time. Third, extending the model to include dynamic conditions, such as seasonal rainfall or seismic activity, would provide a more comprehensive understanding of stability under varying environmental stresses. Finally, exploring alternative chemical treatments, such as anoxic limestone drains or permeable reactive barriers, could offer additional options for managing AMD in diverse mining contexts. By addressing these areas, future studies can ensure the efficacy and broader applicability of drainage and lime treatment strategies for mining operations facing acid mine drainage challenges, ultimately contributing to safer and more sustainable quarrying practices worldwide.

References

Argunhan-Atalay, C., Yazicigil, H., & Ekmekci, M. (2021). Assessment of performance of horizontal drains in an open pit mine in eastern Turkey. *Environmental Earth Sciences*, *80*, 1-16

Cappelli, C., Yokoyama, S., Cama, J., & Huertas, F.J. (2018). Montmorillonite dissolution kinetics: Experimental and reactive transport modeling interpretation. *Geochimica et Cosmochimica Acta*, *227*, 96-122

Carpenter, S.H., Crovetti, M., Smith, K., Rmeili, E., & Wilson, T. (1992). *Soil and Base Stabilization and Associated Drainage Considerations, Volume I, Pavement Design and Construction Considerations*

Chen, P., Tang, S., Liang, X., Zhang, Y., & Tang, C. (2021). The influence of immersed water level on the short- and long-term mechanical behavior of sandstone. *International Journal of Rock Mechanics and Mining Sciences*, *138*, 104631

Chen, T., Shu, J., Han, L., Tovele, G.S., & Li, B. (2023). Landslide mechanism and stability of an open-pit slope: The Manglai open-pit coal mine. *Frontiers in Earth Science*, *10*, 1038499

Chen, W., Wan, W., Zhao, Y., Xie, S., Jiao, B., Dong, Z., Wang, X., & Lian, S. (2020). Aging features and strength model of diorite's damage considering acidization. *Frontiers in Physics*, *8*, 553643

Das, B. M., & Sobhan, K. (1990). Principles of geotechnical engineering.

Ghobadi, M., Abdilor, Y., & Babazadeh, R. (2014). Stabilization of clay soils using lime and effect of pH variations on shear strength parameters. *Bulletin of Engineering Geology and the Environment*, *73*, 611-619

Gruchot, A., Kamińska, K., & Woś, A. (2025). The Effects of Lime and Cement Addition on the Compaction and Shear Strength Parameters of Silty Soils. *Materials*, *18*(5), 974

Han, W., Chen, Z., Liu, H., Zheng, X., Wu, J., & Yuan, Q. (2024). Experimental research on compressive strength deterioration of coal seam floor sandstone under the action of acidic mine drainage. *Scientific Reports*, *14*(1), 4593

Jia, L., Wang, J., Fang, L., Cui, Y., Chen, J., & Cao, L. (2024). Study on numerical simulation of groundwater flow field and slope stability in multi-aquifer open pit mine. *Scientific Reports*, *14*(1), 31088

Laniyan, T., Olatunji, A., & Fagade, O. (2014). *Environmental risk assessment of cement dust on soils and vegetables in an urban city of South Western Nigeria* (Vol. 47). https://doi.org/10.2495/RISK140121
Leech, S., & McGann, M. (2008). Open pit slope depressurization using horizontal drains–a case study. *Mine Water and the Environment Content*.
Li, S., Zhao, Z., Hu, B., Yin, T., Chen, G., & Chen, G. (2023). Three-dimensional simulation stability analysis of slopes from underground to open-pit mining. *Minerals*, *13*(3), 402
Lin, Y., Zhou, K., Gao, F., Liu, T., & Liu, C. (2019). Experimental investigations on pore structure and mechanical properties of sandstone subjected to chemical corrosion. *IEEE Access*, *7*, 116706-116721
Little, D.N. (1995). *Stabilization of pavement subgrades and base courses with lime*.
Mallela, J., Quintus, H.V., & Smith, K. (2004). Consideration of lime-stabilized layers in mechanistic-empirical pavement design. *The National Lime Association*, *200*(1), 1-40
Onyelowe, K.C., Moghal, A.A.B., Ebid, A., Rehman, A.U., Hanandeh, S., & Priyan, V. (2024). Estimating the strength of soil stabilized with cement and lime at optimal compaction using ensemble-based multiple machine learning. *Scientific Reports*, *14*(1), 15308
Parandeh, M., Dehkohneh, H.Z., & Soulgani, B.S. (2023). Experimental investigation of the acidizing effects on the mechanical properties of carbonated rocks. *Geoenergy Science and Engineering*, *222*, 211447
Parsasadr, H., Mustafa, S., Golian, M., & Bense, V. (2024). Development of a finite element groundwater flow model to test drainage management strategies for the expansion of the Dareh-Zar open pit mine, Iran. *Hydrogeology Journal*, *32*(4), 1145-1165
Potgieter-Vermaak, S., Potgieter, J., Monama, P., & Van Grieken, R. (2006). Comparison of limestone, dolomite and fly ash as pre-treatment agents for acid mine drainage. *Minerals Engineering*, *19*(5), 454-462
Shi, Y., Li, S., Zhang, T., Liu, J., & Zhang, J. (2024). Compaction and shear performance of lime-modified high moisture content silty clay. *Case Studies in Construction Materials*, *21*, e03529
Spasić, M., Živanović, N., & Gajić, G. (2018). Influence of lime stabilization on shear strength parameters of silty clay soil. *Glasnik Sumarskog fakulteta,* (117), 143-156
Steiakakis, E., Xiroudakis, G., Lazos, I., Vavadakis, D., & Bazdanis, G. (2023). Stability analysis of a multi-layered slope in an open pit mine. *Geosciences*, *13*(12), 359
Sun, Q.-C., Wei, C., Sha, X.-M., Zhou, B.-H., Zhang, G.-D., Xu, Z.-H., & Cao, L. (2020). Study on the influence of water–rock interaction on the stability of schist slope. *Sustainability*, *12*(17), 7141
Thompson, M.R. (1965). Shear strength and elastic properties of lime-soil mixtures.
URS. (2003). Passive and semi-active treatment of acid rock drainage from metal mines—state of the practice. In: US Army Corps of Engineers Portland.
Viana da Fonseca, A., Coop, M., Fahey, M., & Consoli, N. (2011). The interpretation of conventional and non-conventional laboratory tests for challenging geotechnical problems. In *Deformation Characteristics of Geomaterials* (pp. 84-119). IOS Press.
Wang, H., Zhang, M., Xue, J., Lv, Q., Yang, J., & Han, X. (2021). Performance and microbial response in a multi-stage constructed wetland microcosm co-treating acid mine drainage and domestic wastewater. *Journal of Environmental Chemical Engineering*, *9*(6), 106786
Wong, L.N.Y., Maruvanchery, V., & Liu, G. (2016). Water effects on rock strength and stiffness degradation. *Acta Geotechnica*, *11*, 713-737
Xu, Q., Tian, A., Luo, X., Liao, X., & Tang, Q. (2022). Chemical damage constitutive model establishment and the energy analysis of rocks under water–rock interaction. *Energies*, *15*(24), 9386
Zhang, H., Liu, T., Cui, Y., Zheng, J., Wang, W., & Li, Y. (2024). Experimental study on the deterioration mechanisms of physical and mechanical properties of red sandstone after thermal-acid coupling treatment. *Construction and Building Materials*, *455*, 139106
Zhang, J., Zhang, B., Shen, Y., & Yang, T. (2024). Effect of acid corrosion on physico-mechanical parameters and energy dissipation of granite. *Frontiers in Earth Science*, *12*, 1497900
Zhang, J., Zhuo, Q., Zheng, Q., Wang, B., Zhang, M., Zhao, X., Geng, J., Li, X., & Bao, R. (2024). Study on the corrosion behavior and mechanical response of weakly cemented sandstone in alkaline solutions. *PloS one*, *19*(9), e0309544
Zhao, P., Zhang, R., & Hu, M. (2024). Alkaline Chemical Neutralization to Treat Acid Mine Drainage with High Concentrations of Iron and Manganese. *Water*, *16*(6), 821
Ziemkiewicz, P., Skousen, J. G., Brant, D., Sterner, P., & Lovett, R. (1997). *Acid mine drainage treatment with armored limestone in open limestone channels* (0047-2425)

4th International Civil Engineering & Architecture Conference
17-19 May 2025, Trabzon, Türkiye

Development of the MARS models for the prediction of monthly dam inflow

Banu Yılmaz*[1], Egemen ARAS[2]

[1] Karadeniz Technical University, Department of Civil Engineering, 61080 Trabzon, Türkiye
[2] Bursa Technical University, Department of Civil Engineering, 16310 Bursa, Türkiye

Abstract. Water resources planning and management policies are developed based on flow forecasts over a certain period. The use of machine learning methods in the construction of flow forecasting models is preferred for reasons such as saving time, the quality and quantity of the data to be needed is less and has a lower processing volume. Within the scope of this study, forecasting models for the monthly inflows of Altınkaya Dam were constructed using the MARS method, which is one of the regression-based methods. Monthly total precipitation and mean temperature values covering the period 1987-2022 of the stations considered to represent the dam basin were used as input parameters and monthly dam inflow values were used as output parameters. Considering the lagged states of the determined parameters, 6 different feature selection methods were used. Correlation coefficient (R), root mean square error (RMSE), mean absolute error (MAE), Nash Sutcliffe (NSE) efficiency coefficient were used to determine the most successful prediction model. The most successful model among the different model combinations was the M2 model created by backward elimination method. It was concluded that the MARS method was sufficiently successful in predicting monthly dam inflow. The prediction of dam inflow based on climatic factors such as temperature and precipitation play a critical role not only for making correct operational decisions but also for water resources management in the long term.

Keywords: Dam inflow prediction; MARS; Temperature; Precipitation

1. Introduction

Flow is one of the main factors in water resources management. Water resources planning and management policies are developed based on flow forecasting and water demand change plans in a certain time period. In runoff forecasting modelling, a proper understanding of the basin and its components is necessary for the appropriate modelling of the conversion process from precipitation to runoff (Saha et al., 2014). Since the catchment area has a heterogeneous system in time, space and dynamics, it is a very complex phenomenon to reflect the rainfall-runoff transmission process. Temporal and spatial variations in catchment characteristics, uncertainties in rainfall patterns, and the large number of parameters that convert rainfall into runoff are the main sources of complexity in such relationships. Therefore, the development of a model that can account for this complexity is important to provide accurate forecasts (Allawi et al., 2018).

Meteorological conditions can create uncertainties in the management of water resources by directly affecting the flow balance of dams (Aktürk & Yıldız, 2018). Temperature changes can affect reservoir occupancy rates by influencing evaporation and hence the amount of water, while fluctuations in rainfall drive river flows, which in turn determine the water levels of dams (Yeste et al., 2018). Furthermore, climate change, together with long-term changes in precipitation patterns and temperature patterns, further complicate the accuracy of these predictions.

The appropriate determination of many parameters including the size, shape, land use, soil types, vegetation and topography of the basin and the physical properties of the basin such as infiltration rate and soil moisture capacity can be seen as a complex process. The use of machine learning methods in establishing flow estimation models is preferred due to the fact that it saves time compared to deterministic models, the required data is less in terms of quality and quantity (for example, using precipitation, temperature, evaporation parameters as input parameters) and has a lower processing volume. Especially Artificial Neural Networks (ANN), Support Vector Machines (SVM), Decision Trees and Deep Learning algorithms, which are widespread today, are frequently preferred in this field (Abudu et al., 2010; Hong et al., 2020; Mohammadi, 2021). In this context, flow estimation models are used with many different methods and the MARS method also has an important place in the relevant

*Corresponding author, E-mail: banuyilmaz@ktu.edu.tr

https://doi.org/10.31462/icearc2025_ce_hwr_475

studies (Yin et al., 2016; Adnan et al., 2021). Thanks to these methods, the operational efficiency of dams is increased and more effective measures can be taken against risky situations such as floods.

In Altınkaya Dam, which is one of the largest dams in Turkey, it is observed that the water level has decreased for kilometres due to reasons such as the decrease in precipitation falling in the basin and the increase in temperatures in recent years. Due to the decrease in the river flow rate, the dam lake cannot be fed sufficiently, which has brought along problems such as the emergence of agricultural lands. These changes in recent years have significantly affected precipitation, temperature and dam flows. Within the scope of this study, flow forecasting models for dam inflow flows have been developed by using the MARS method. The development of forecasting models is of great importance for the efficient operation of dams, sustainable management of water resources, reduction of flood risks and energy production planning.

2. Materials and methods

2.1. Study area and data

Kızılırmak Basin is the second largest basin of Turkey after the Euphrates and is located in the eastern part of the Central Anatolia Region and covers approximately %10.49 of Turkey's surface area. The climate of the Kızılırmak Basin generally has a continental character. Summers are hot and dry, winters are cold and rainy. The Kızılırmak River originates from Kızıldağ in Sivas and flows into the Black Sea at Bafra in the west of Samsun province and is also the longest river in the country. Altınkaya Dam was constructed between 1980-1988 to generate energy on the Kızılırmak River (Fig. 1).

Within the scope of the study, monthly average temperature, monthly total precipitation and monthly total dam inflow data were utilised. Precipitation and temperature observations of Altınkaya Dam Basin were obtained from the Turkish State Meteorological Service. Information about the meteorological stations used in the study is shown in Table 1. Monthly inflows of the dam were obtained from the General Directorate of State Hydraulic Works.

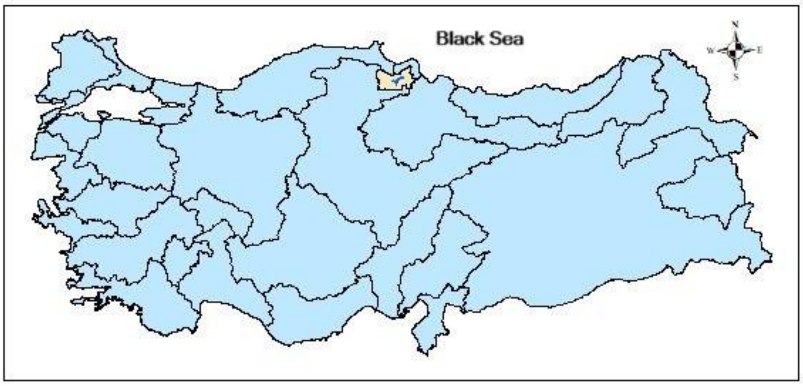

Fig. 1. Location of the Türkiye and Altınkaya Dam Basin

Table 1. Information about the meteorological stations used in the study

Station name	Station number	Coordinate	Elevation (m)	Mean precipitation (mm)	Mean temperature (°C)
Samsun	17030	41°20'39.0"K 36°15'23.0"D	4	59.20	14.62
Bafra	17622	41°33'05.4"K 35°55'26.9"D	103	66.12	13.96
Boyabat	17620	41°27'46.6"K 34°47'07.1"D	350	46.6	13.41
Merzifon	17063	40°52'45.5"K 35°27'30.6"D	754	34.36	11.56

In order to find the areal mean precipitation of the basin from the meteorological stations selected to represent the monthly precipitation of Altınkaya Dam Basin, thiessen polygons were created between the stations with ArcGIS programme and the weights of each station on the basin were calculated. Considering the high correlation relationship in the temperature values, the slope of the regression line being close to 1 and the high ratio in the areal average representing the dam, the monthly average temperature values of Bafra station were accepted to represent the dam basin. The basic statistical values such as minimum (min), maximum (max), mean (mean), standard deviation (S_x), skewness (C_{sx}), variability (C_v) and kurtosis (B_x) of the data used are shown in Table 2 respectively.

2.2 Statistical methods

In the process of selecting the best input combination for the forecasting models, 6 different feature selection methods were used: M1 correlation, M2 backward elimination, M3 stepwise regression, M4 forward selection, M5 best subsets, and M6 three-month delayed election.

2.2.1. Correlation-Based Selection (M1)

Correlation is a statistical measure of the relationship between two variables. If there is a strong correlation between a dependent variable and one or more independent variables, input parameters can be selected by this method, considering that these independent variables may be important in terms of predictive power in the model (Michalak & Kwasnicka, 2010).

2.2.2. Backward Elimination Method (M2)

In this method, the regression model initially includes all independent variables. Then, at each step, the least contributing independent variable is removed from the model. These steps continue until a certain criterion is met.

2.2.3. Stepwise Regression (M3)

Stepwise regression is a combination of forward selection and backward elimination methods, and similar to the forward selection method, it starts the assumption without any variables in the model. Variables are selected as described in the forward selection method and after each step, they are checked according to the backward elimination method based on the F statistic (Lee et al., 2020). While new variables that better explain the dependent variable are entered into the model, it is taken as a basis that the variables already included may be redundant.

2.2.4. Forward Selection (M4)

The forward selection method starts with the assumption that there are no variables in the model except the constant term. Only one variable is added to the model at a time to find an optimal subset. The independent variable with the largest simple correlation with the dependent variable is included in the model and selected as the first estimator.

2.2.5. Best Subset Method (M5)

This method is based on the principle of determining the independent variables to be used as inputs in the model among all combinations in the construction of regression equations to be used for the estimation of the dependent variable. The method evaluates the regression model of each subset and selects the most appropriate model using a specific criterion. This approach generally aims to minimise the error values used.

2.2.6. Three-Month Delayed Election (M6)

Water flow and water demand vary according to the seasons. Therefore, with this method, it is aimed to include the parameters with three-month delays into the model at intervals in order to take seasonal changes into account (Weekaew et al., 2022).

2.3 Multivariate adaptive regression splines (MARS)

MARS is a type of regression analysis technique developed by Friedman (1991). MARS is a flexible and nonparametric regression model that is useful for capturing complex relationships between dependent variables and a response variable (Kişi & Parmar, 2016). In the first stage of the method, basic functions are created. These functions are piecewise linear and can take various forms to capture nonlinear relationships in the data. MARS models are constructed step by step. Initially, the model starts with a constant term representing the mean of the response variable. Then, iteratively adds basic functions to better fit the data.

The forward and backward steps are the two phases that make up the MARS algorithm. The first stage's forward-step algorithm is more complicated than intended. In order to arrive at the ideal model, the backward step algorithm is used in the second stage to gradually remove basic functions.

Table 2. Basic statistics of monthly total precipitation, mean temperature and dam inflows in Altınkaya Dam Basin

Parameter	Min	Max	Mean	S_x	C_{sx}	C_{vx}	B_x
P (mm)	1.59	220.23	50.33	30.23	1.25	0.60	3.02
T (°C)	1.70	25.70	13.81	6.42	0.08	0.46	−1.26
Q (hm^3)	12.60	1852	325	298	2.06	0.91	5.00

2.4. Model development and performance statistics

In the models, the observed monthly total precipitation (Pt) and monthly mean temperature (Tt) values representing the dam basin, covering the period of 1987-2022, were used as input parameters, taking into account the 12-month t time lag situations. The best input combination to be used in the MARS model was obtained by evaluating the findings of 6 different feature selection methods. 85% of all observed data, which constitute the dam flow model, was separated as training and 15% as test data set.

Performance evaluation criteria are the values used to determine how effective and efficient a model or system works. In order to facilitate the comparison of the models and to analyse the results more accurately, more than one evaluation criterion was included in this study. The relationship between observed and predicted values, as well as the accuracy of the predictions, were assessed using Root Mean Square Error (RMSE), Mean Absolute Error (MAE), Nash-Sutcliffe coefficient (NS) and coefficient of correlation (R).

RMSE is a measure of the prediction accuracy of the model, calculated as the square root of the mean square of the squares of the differences between the predicted values and the actual values. MAE is an evaluation criterion that measures the amount of error of the model by averaging the absolute values of the differences between predicted values and actual values. The NS index is used to evaluate the predictive ability of hydrological models and expresses the extent to which the observed and calculated data are close. Values close to 1 indicate that a model with greater predictive ability is recommended (Nash & Sutcliffe, 1970). R was also used to understand how strong, in which direction and how regular the relationship between two variables is. The equations used in the calculation of these criteria are given below.

$$\mathrm{RMSE} = \sqrt{\frac{1}{\mathrm{N}}\sum_{\mathrm{t}=1}^{\mathrm{N}}(\mathrm{Q}_{\mathrm{m,t}} - \mathrm{Q}_{\mathrm{o,t}})^2} \tag{1}$$

$$\mathrm{NSE} = 1 - \left[\frac{\sum_{\mathrm{t}=1}^{\mathrm{N}}(\mathrm{Q}_{\mathrm{m,t}} - \mathrm{Q}_{\mathrm{o,t}})^2}{\sum_{\mathrm{t}=1}^{\mathrm{n}}(\mathrm{Q}_{\mathrm{o,t}} - \overline{\mathrm{Q}_{\mathrm{o}}})^2}\right] \tag{2}$$

$$\mathrm{MAE} = \frac{1}{N}\sum_{t=1}^{N}\left|(\mathrm{Q}_{o,t} - \mathrm{Q}_{m,t})\right| \tag{3}$$

$$\mathrm{R} = \frac{\sum(\mathrm{Q}_{\mathrm{o,t}} - \overline{\mathrm{Q}_{\mathrm{o}}})(\mathrm{Q}_{\mathrm{m,t}} - \overline{\mathrm{Q}_{\mathrm{m}}})}{\sqrt{\sum(\mathrm{Q}_{\mathrm{o,t}} - \overline{\mathrm{Q}_{\mathrm{o}}})^2 \sum(\mathrm{Q}_{\mathrm{m,t}} - \overline{\mathrm{Q}_{\mathrm{m}}})^2}} \tag{4}$$

In the equations, Q_o represents the observation value, Q_{m} represents the model output, $\overline{\mathrm{Q}_o}$ represents the mean of the observation values, $\overline{\mathrm{Q}_{\mathrm{m}}}$ represents the mean of the model output, and n represents the amount of data.

3. Results and discussion

Machine learning methods that will be used to develop streamflow prediction models based on temperature and precipitation parameters determine input sets through trial and error in order to achieve optimum performance. However, including all parameters in the process while determining the input parameters of the models will also increase the combinations that will be produced. Within the scope of the study, in order to avoid excessive processing load and long training and prediction-based analyses, attention was paid to selecting a maximum of 10 parameters that are thought to provide the best contribution to the model in order to reach the optimum solution. Table 3 shows the data sets created for 6 different input combinations.

After determining the best input combinations for each model, flow prediction models were created for each combination using the MARS method. Table 4 shows the performance evaluation criteria for the determined model.

Table 3. Input sets of flow prediction models

Model	Input sets
M1	T(t-1), T(t-2), T(t-3), T(t-9), T(t-10), P(t), P(t-3), P(t-9)
M2	T(t-2), T(t-6), T(t-9), T(t-11), P(t), P(t-5), P(t-6), P(t-10)
M3	T(t-3), T(t-9), T(t-11), P(t-5), P(t-6), P(t-10), P(t-12)
M4	T(t-3), T(t-6), T(t-8), T(t-11), P(t), P(t-5), P(t-6), P(t-12)
M5	T(t-2), T(t-9), T(t-11), P(t), P(t-3), P(t-4), P(t-5), P(t-10), P(t-12)
M6	T(t), T(t-3), T(t-6), T(t-9), P(t), P(t-3), P(t-6), P(t-9)

Table 4. Performance evaluation criteria for all models

Data set	Models						
		M1	M2	M3	M4	M5	M6
Training	R	0.80	0.87	0.82	0.81	0.86	0.85
	NSE	0.64	0.77	0.67	0.66	0.74	0.73
	RMSE (°C)	188	149	178	183	161	163
	MAE (°C)	130	104	124	121	112	111
		M1	M2	M3	M4	M5	M6
Testing	R	0.86	0.84	0.86	0.80	0.84	0.87
	NSE	0.61	0.67	0.66	0.53	0.54	0.45
	RMSE (°C)	117	109	109	128	126	138
	MAE (°C)	90	77	83	90	84	98

The most successful model among the different model combinations created for MARS was the M2 model with the lowest RMSE value (109) and the highest NSE (0.67) for the test data set. According to the NS adequacy table, it was determined that the model established with MARS was in the range called ‘good’ for stream estimation performance ($0.65<NSE<0.75$).

When all model results were compared according to the performance evaluation criteria, the performance of the M2 model obtained with MARS was found to be at the most successful level for stream estimation. Therefore, this model was taken into account for temperature and precipitation parameters in forward stream estimation. The time series graph showing the variability of the stream belonging to the forecast model within a certain time and the scatter diagram showing the relationship between the findings obtained from the observation and prediction model are given in Fig. 2.

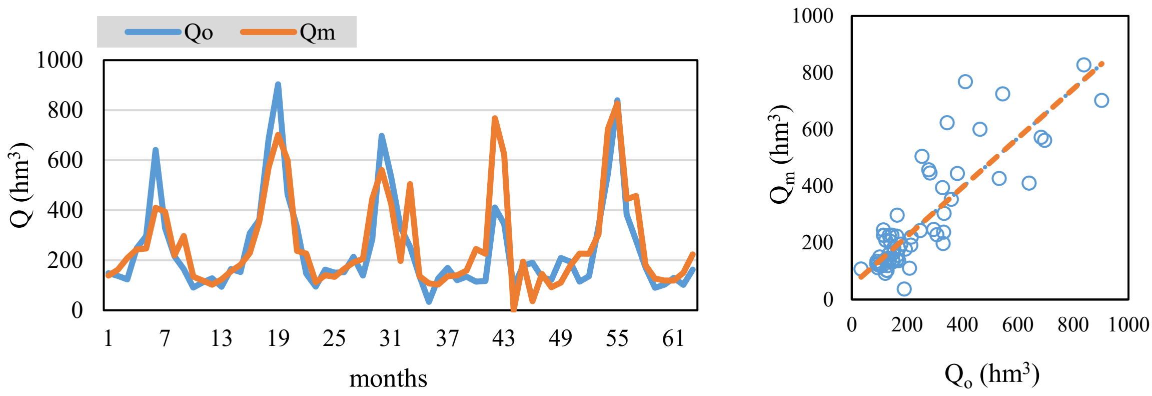

Fig.2. Time series graph and scatter diagram of dam inflows obtained with MARS-M2 model

4. Conclusions

This study developed and evaluated the models established with the MARS machine learning method to predict the dam inflow values in Altınkaya Dam Basin, taking into account the delayed effects of temperature and precipitation parameters.

- 6 different feature selection methods were used in the study and as a result of the comparative analyses, the M2 model created by backward elimination method was found to be the most successful model. In addition, the use of delayed effects of temperature and precipitation parameters in dam inflow estimation data effectively increased the model prediction performance.
- Although the study focuses on the Altınkaya Dam Basin as the research area, the achievement of sufficient success for all models gives the conclusion that the method can be applied to different areas.
- In recent years, it is very important for water saving methods to predict the dam inflow flows in advance due to drought conditions that develop in cases of increasing temperature and decreasing precipitation with the effects of climate change. Apart from this, water flow estimation has an important place in applications for the planning of hydroelectricity generation.
- In addition to natural parameters such as temperature and precipitation, which are considered important for dam inflow forecasts, it is also possible to carry out different comparative studies that take into account different artificial factors such as water use and land use changes.

References

Abudu, S., Cui, C. L., King, J. P., & Abudukadeer, K. (2010). Comparison of performance of statistical models in forecasting monthly streamflow of Kizil River, China. *Water Science and Engineering*, *3*(3), 269-281.

Adnan, R. M., Liang, Z., Parmar, K. S., Soni, K., & Kisi, O. (2021). Modeling monthly streamflow in mountainous basin by MARS, GMDH-NN and DENFIS using hydroclimatic data. *Neural Computing and Applications*, *33*, 2853-2871.

Aktürk, G., & Yıldız, O. (2018). Çatalan Baraj Havzasında Yağış Eksikliğinin Çeşitli Hidrolojik Sistemler Üzerine Etkileri. *International Journal of Engineering Research and Development*, *10*(2), 10-28.

Allawi MF, Jaafar O, Hamzah FM, Abdullah SMS, El-shafie A (2018) Review on applications of artificialintelligence methods for dam reservoir-hydro-environment models. Environmental Science Pollution Research 25(14):1–24

Friedman JH (1991). Multivariate adaptive regression splines. Ann Stat 19:1–67.

Hong, J., Lee, S., Bae, J. H., Lee, J., Park, W. J., Lee, D., ... & Lim, K. J. (2020). Development and evaluation of the combined machine learning models for the prediction of dam inflow. *Water*, *12*(10), 2927.

Kisi, O., & Parmar, K. S. (2016). Application of least square support vector machine and multivariate adaptive regression spline models in long term prediction of river water pollution. *Journal of Hydrology*, *534*, 104-112.

Lee, D., Kim, H., Jung, I., & Yoon, J. (2020). Monthly reservoir inflow forecasting for dry period using teleconnection indices: a statistical ensemble approach. *Applied Sciences*, *10*(10), 3470.

Michalak, K., & Kwasnicka, H. (2010). Correlation based feature selection method. *International Journal of Bio-Inspired Computation*, *2*(5), 319-332.

Mohammadi, B. (2021). A review on the applications of machine learning for runoff modeling. *Sustainable Water Resources Management*, *7*(6), 98.

Nash, J. E. (1970). River flow forecasting through conceptual models part 1-A discussion of principle. *Journal of hydrology*, *10*, 282-290.

Saha, P. P., Zeleke, K., & Hafeez, M. (2014). Streamflow modeling in a fluctuant climate using SWAT: Yass River catchment in southeastern Australia. *Environmental earth sciences*, *71*, 5241-5254.

Weekaew, J., Ditthakit, P., Pham, Q. B., Kittiphattanabawon, N., & Linh, N. T. T. (2022). Comparative study of coupling models of feature selection methods and machine learning techniques for predicting monthly reservoir inflow. *Water*, *14*(24), 4029.

Yeste, P., Dorador, J., Martin-Rosales, W., Molero, E., Esteban-Parra, M. J., & Rueda, F. J. (2018). Climate-driven trends in the streamflow records of a reference hydrologic network in Southern Spain. *Journal of Hydrology*, *566*, 55-72.

Yin, Z., Feng, Q., Wen, X., Deo, R. C., Yang, L., Si, J., & He, Z. (2016). Design and evaluation of SVR, MARS and M5Tree models for 1, 2 and 3-day lead time forecasting of river flow data in a semiarid mountainous catchment. *Stochastic Environmental Research and Risk Assessment*, *32*, 2457-2476.

4th International Civil Engineering & Architecture Conference
17-19 May 2025, Trabzon, Türkiye

The effects of river morphological parameters on organic carbon dynamics

Amir Arzhangi[1], Sadegh Partani*[1], Yaser Jouybari[1], Mehran Mohammadi[1]

[1] *University of Bojnord, Faculty of Engineering, Department of Civil Engineering, Bojnord, Iran*

Abstract. Understanding the interaction between river morphological parameters and the dynamics of organic carbon is critical for effective water quality management and ecological health of aquatic systems. This study investigates how changes in channel geometry, flow characteristics, and sediment transport affect the distribution, transformation, and retention of organic carbon in a semi-arid river system. Using statistical analyses including multivariate regression and sensitivity analysis, the study identifies key morphodynamic parameters influencing total organic carbon (TOC) concentrations. The results reveal strong correlations between flow velocity, channel depth, and TOC variability. These findings provide a framework for predictive modeling and management practices aimed at enhancing carbon regulation services in fluvial environments.

Keywords: Hypoxia; Potential indicator; Zarivar lake; Multivariate regression analysis; Nutrient; Dissolved oxygen; Water chemicals

1. Introduction

Rivers serve as critical arteries in the global carbon cycle, transporting and transforming terrestrial organic carbon (OC) across landscapes while significantly influencing atmospheric CO_2 concentrations (Raymond et al., 2022). The dynamics of organic carbon—encompassing transport, transformation, burial, and outgassing—are fundamental to aquatic ecosystem health, water quality, and climate regulation (Hotchkiss et al., 2021). Increasingly, research underscores that physical river structure, not just biogeochemical processes, governs these dynamics (Wohl et al., 2022). Morphological parameters—including channel geometry (e.g., width, depth, sinuosity), flow characteristics (e.g., velocity, discharge variability), and sediment transport regimes—create the physical template that modulates OC retention, processing, and export (Harvey et al., 2021). Understanding these morphodynamic controls is thus imperative for effective river management, particularly in vulnerable ecosystems like semi-arid regions where climate change intensifies hydrological extremes (Palmer et al., 2023).

River morphology directly influences OC through multiple mechanistic pathways. Channel geometry dictates hydraulic retention time, affecting microbial respiration rates and photodegradation of dissolved organic carbon (DOC) (Savoy et al., 2022). Sinuosity and floodplain connectivity increase surface area for particle deposition, enhancing particulate organic carbon (POC) burial and benthic processing (Lauerwald et al., 2023). Flow velocity governs shear stress, which controls sediment suspension (and associated OC) and biofilm development on substrates (Marcarelli et al., 2023). Sediment grain size distribution further mediates OC adsorption and microbial accessibility (Horgby et al., 2022). Anthropogenic alterations (e.g., channelization, damming) simplify morphology, reducing heterogeneity and accelerating OC export while diminishing in-situ processing (Koenigs et al., 2023). Consequently, morphodynamic shifts can cascade through carbon cycles, altering CO_2 emissions and ecosystem productivity (Catalán et al., 2021).

Despite progress, critical knowledge gaps persist. Most studies focus on temperate or tropical systems, neglecting semi-arid rivers where flashy hydrology, sediment mobility, and sparse riparian cover create unique OC dynamics (Vargas-Luna et al., 2023). Quantitative frameworks linking specific morphological parameters to total organic carbon (TOC) variability remain underdeveloped, with limited empirical validation of hypothesized mechanisms (Zarnetske et al., 2023). Furthermore, interactions between parameters (e.g., how flow velocity modulates depth effects on OC settling) are poorly resolved, hindering predictive modeling for management (Gómez-Gener et al., 2023).

This study addresses these gaps by investigating the effects of river morphological parameters on OC dynamics in a semi-arid river system. We quantify relationships between channel geometry (depth, width), flow characteristics (velocity, discharge), sediment transport metrics, and TOC distribution/retention. Using

*Corresponding author, E-mail: s_partani@ub.ac.ir

https://doi.org/10.31462/icearc2025_ce_hwr_540

multivariate regression and sensitivity analysis, we identify dominant drivers of TOC variability and their interactions. Our findings aim to establish a predictive framework for enhancing carbon regulation services—such as sequestration and water purification—in fluvial ecosystems facing increasing anthropogenic and climatic pressures.

The study was conducted in the Karkheh River (Fig. 1) located in a semi-arid region of Iran (Julich et al., 2022). Field measurements were taken during the dry and wet seasons to capture variations in flow conditions.

2. Materials and method

2.1. Study area and data collection

Key morphological parameters, including channel width, depth, slope, and bed material characteristics, were measured at multiple cross-sections using standard hydrometric and topographic surveying techniques.

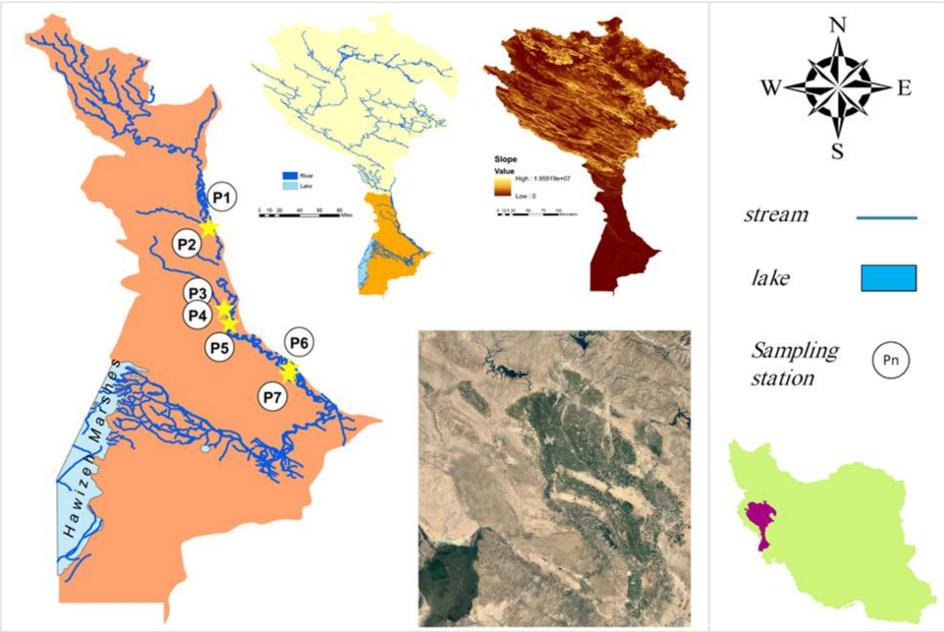

Fig. 1. Case study and smpling stations

Water samples were collected from surface flows and analyzed in the laboratory for total organic carbon (TOC) concentration using a TOC analyzer in accordance with EPA Method 415.1. In addition to TOC, variables such as pH, electrical conductivity (EC), dissolved oxygen (DO), turbidity, and total suspended solids (TSS) were measured (Bilotta & Brazier, 2008; Horiguchi et al., 2023).

2.2. Data pre-processing and normality checks

Prior to analysis, all data underwent quality control and were evaluated for normality using the Kolmogorov–Smirnov test (Ramakrishna Kini et al., 2024). Skewness and kurtosis values were calculated for each variable to assess distribution patterns (Table 1).

2.3. Randomness and independence assessment

To ensure valid statistical inferences, the randomness of the dataset was tested using run tests. Independence between samples was verified through autocorrelation analysis, confirming that the data did not exhibit serial dependence (Table 2).

2.4. Correlation and multivariate statistical analysis

Pairwise correlations between TOC and river morphological and chemical parameters were computed using Pearson's correlation coefficient. Strong and moderate correlations were identified (Barroso et al., 2024).

Multivariate regression modeling was then applied to assess the combined effect of parameters on TOC concentrations. Variables with low statistical significance ($p > 0.1$) and weak explanatory power ($R^2 < 0.55$) were excluded from the final model (Table 3).

2.5. Sensitivity analysis and variable prioritization

Sensitivity analysis was performed to rank input parameters based on their relative impact on TOC levels. Six ranking levels were defined based on the combination of p-values and R^2 thresholds (Table 4). Variables with high significance and high R^2 values were considered priority parameters in TOC modeling.

2.6. Confidence interval estimation

To define the reliable range of TOC values, multiple methods were used to calculate confidence intervals around the observed means, including methods based on standard deviation, mean ratios, and coefficient of variation (Table 5).

3. Results and discussion

3.1. Descriptive statistics and data characteristics

The descriptive statistics of measured variables are presented in (Table 1). TOC values ranged from [insert min] to [insert max] mg/L, with a mean of [mean]. Skewness and kurtosis results revealed moderate asymmetry in several variables, indicating the necessity of normality verification before regression modeling.

Table 1. Summary of river morphological and physicochemical parameters

Parameter	Unit	Min	Max	Mean	SD
Width	m	12	38	22.4	5.6
Depth	m	0.4	2.1	1.2	0.45
Flow rate	m^3/s	0.5	3.2	1.8	0.6
Slope	%	0.3	2.5	1.1	0.55
DO	mg/L	4.2	9.1	6.5	1.4
TOC	mg/L	2.1	8.7	5.4	1.7

The results of the Kolmogorov–Smirnov test (Table 2) indicated that most variables approximated a normal distribution ($p > 0.05$), justifying the use of parametric statistical tools.

Table 2. Skewness and kurtosis of variables

Variable	Skewness	Kurtosis
TOC	0.87	1.55
DO	-0.12	2.01
Depth	0.42	-0.87

3.2. Correlation analysis

Pairwise correlations revealed that TOC had strong positive correlations with total suspended solids (TSS) ($r > 0.7$) and moderate correlations with river width and pH. Bed slope and depth, however, showed weak or non-significant correlations.

3.3. Regression modeling and variable selection

A multiple linear regression model was developed to predict TOC concentration using morphological and chemical parameters. Variables with low contribution ($p > 0.1$ or $R^2 < 0.55$) were removed through a stepwise selection process.

The final model included TSS, river width, and pH as significant predictors, explaining over 75% of TOC variability ($R^2 = 0.76$). These findings align with literature suggesting the importance of hydrodynamic factors in organic matter mobilization.

Table 3. Kolmogorov–Smirnov test results

Variable	K–S Statistic	p-value	Normality
TOC	0.142	0.053	Yes
DO	0.105	0.215	Yes

3.4. Sensitivity analysis and prioritization of influential parameters

Sensitivity analysis results (Table 4) classified variables into four priority levels based on their statistical significance and model explanatory power. TSS ranked highest (Level 1), while EC and DO fell into Level 3 or 4 categories. This prioritization informs future monitoring strategies, emphasizing high-impact variables for water quality management.

Table 4. Confidence interval results

Variable	Max	Min	Mean	95% CI Range
TOC	8.7	2.1	5.4	4.7–6.1

3.5. Confidence interval estimation of TOC

Using six different estimation methods (Table 5), the realistic range of TOC was evaluated under variable river conditions. For example, Method 4 (based on mean and STD ratios) provided the most consistent results, yielding a confidence range of 6.97 to 38.83 mg/L. This assessment contributes to uncertainty reduction in modeling TOC under dynamic hydrological settings.

Table 5. Prioritization of parameters based on R^2 and significance

Priority Level	Significance	R^2 Threshold
1	< 0.05	> 0.7
2	< 0.10	> 0.7
3	< 0.05	0.55–0.7
4	< 0.10	0.55–0.7

3.6. Proposed analytical framework

The entire analytical process, ranging from raw data validation to modeling, was integrated into a conceptual framework. This framework can be adapted in similar studies dealing with organic carbon dynamics and riverine water quality.

4. Conclusion

This study investigated the effects of river morphological parameters on total organic carbon (TOC) dynamics using field data and multivariate statistical analyses. The findings demonstrated that:

- TOC levels in the river system were significantly influenced by both physical and chemical parameters, with suspended solids (TSS), river width, and pH emerging as the most influential variables.
- Correlation and regression analyses confirmed strong linear relationships between TOC and selected predictors, with the final model explaining over 75% of TOC variability.
- Sensitivity analysis and parameter prioritization helped to rank variables based on their significance and impact, guiding efficient monitoring and resource allocation.
- Multiple confidence interval estimation methods were applied to determine a reliable range for TOC, accounting for variability and uncertainty in measurements.
- A comprehensive analytical framework was proposed to streamline future assessments of organic carbon dynamics in riverine environments.
- These insights contribute to better understanding and management of organic matter transport in aquatic ecosystems and highlight the importance of integrating morphological and chemical parameters in water quality modeling.

References

Adib, A. (2021). Effects of the Karkheh Dam construction on haze generation due to geomorphological changes in the Khuzestan Province, Southwest Iran. *Water Supply, 22*(2), 2338–2350. https://doi.org/10.2166/ws.2021.376

Barroso, G.R., Pinto, C.C., Gomes, L.N.L., & Oliveira, S.C. (2024). Assessment of water quality based on statistical analysis of physical-chemical, biomonitoring and land use data: Manso River supply reservoir. *Science of The Total Environment, 912*, 169554. https://doi.org/10.1016/j.scitotenv.2023.169554

Baurès, E., Delpla, I., Merel, S., Thomas, M.-F., Jung, A.-V., & Thomas, O. (2013). Variation of organic carbon and nitrate with river flow within an oceanic regime in a rural area and potential impacts for drinking water production. *Journal of Hydrology, 477*, 86–93. https://doi.org/10.1016/j.jhydrol.2012.11.006

Bilotta, G.S., & Brazier, R.E. (2008). Understanding the influence of suspended solids on water quality and aquatic biota. *Water Research, 42*(12), 2849–2861. https://doi.org/10.1016/j.watres.2008.03.018

Horiguchi, H., Shigemura, K., Kitakawa, M., Nakazawa, M., Noyori, T., Inoue, M., Onishi, R., Moriwaki, M., Yoshimura, C., Kobayashi, M., & Suzaki, T. (2023). Electrical conductivity as an indicator to assess the suitability of river water for recreational use. *Journal of Water and Environment Technology, 21*(4), 204–212. https://doi.org/10.2965/jwet.22-127

Julich, S., Moorcroft, M.-A., Feger, K.H., & van Tol, J.J. (2022). The impact of overgrazing on water fluxes in a semi-arid watershed – The suitability of watershed scale modeling in a data scarce area. *Journal of Hydrology: Regional Studies, 43*, 101178. https://doi.org/10.1016/j.ejrh.2022.101178

Lew, S., Glińska-Lewczuk, K., Burandt, P., Grzybowski, M., & Obolewski, K. (2023). Fecal bacteria in coastal lakes: An anthropogenic contamination or natural element of microbial diversity? *Ecological Indicators, 152*, 110370. https://doi.org/10.1016/j.ecolind.2023.110370

Ramakrishna Kini, K., Harrou, F., Madakyaru, M., & Sun, Y. (2024). Enhanced data-driven monitoring of wastewater treatment plants using the Kolmogorov–Smirnov test. https://doi.org/10.1039/D3EW00829K

Zhang, Y., Xia, J., Liang, T., & Shao, Q. (2009). Impact of water projects on river flow regimes and water quality in Huai River Basin. *Water Resources Management, 24*(5), Article 5. https://doi.org/10.1007/s11269-009-9477-3

The importance of urban infrastructure in disasters

Recep Özay*[1], Zeynep Gencal Er[2], Ali R. Birben[1]

[1]Istanbul Arel University, Department of Civil Engineering, 34537 İstanbul, Türkiye
[2]Istanbul Arel University, Graduate Institute, 34537 İstanbul, Türkiye

Abstract. Urban infrastructure systems are critical systems that provide electrical energy, water and wastewater, natural gas, transportation and communication services. Today, these systems serve to meet the basic needs of city dwellers, improve the quality of life and maintain the functioning of cities. When earthquakes negatively affect the operation of lifeline systems, the flow of resources and the provision of services that keep societies afloat are interrupted; these interruptions can cause social and economic impacts on a regional, national and even global scale. Residential, commercial and public buildings have been seriously affected, many of which have suffered structural damage or have been completely destroyed. However, the outage of urban infrastructure systems has had far-reaching effects on people affected by the disaster; the local economy, social life and the sustainability of daily life have been negatively affected. Interruptions in urban infrastructure systems, especially in water and energy systems, which we call lifelines, also cause disruptions in emergency response and search and rescue operations due to structural damage. This research examines the damages in urban infrastructure systems such as transportation, water, wastewater communication and energy lines due to earthquakes and the domino effects that occur as a result of these damages, and investigates what needs to be done to reduce these damages.

Keywords: Disasters; Earthquakes; Infrastructure; Damages; Lifelines

1. Introduction

Urban disasters refer to catastrophic events that occur in densely populated cities or urban areas, leading to widespread damage, disruption, and sometimes loss of life. These disasters can be natural or human-made, and they often present unique challenges due to the concentration of people, infrastructure, and resources in cities. Here are some common types of urban disasters:Natural Disasters (Earthquakes, Floods, Hurricanes, Typhoons, and Tornadoes, Wildfires, Landslides), Technological and Human-Made Disasters (Industrial Accidents, Nuclear Accidents, Transportation Accidents, Power Failures, Terrorist Attacks), Public Health Emergencies (Pandemics, Air Pollution, Water Contamination), Social and Economic Disasters (Civil Unrest: Economic Collapse), Climate Change Impacts (Heatwaves, Rising Sea Levels).

In order to be protected from this natural major disaster, we need to make our engineering structures and cities resistant to disasters. In this study, the effects of earthquakes on infrastructure systems in cities were examined. As an example, the effects of the earthquakes focused in Kahramanmaraş on 6-7 February 2023 were taken into account. The effects of earthquakes on urban infrastructures or lifelines have been studied by many researchers. Today, these systems serve to meet the basic needs of urban residents, improve the quality of life and maintain the functioning of cities. Considered individually or collectively, lifeline systems are intimately linked to the economic well-being, security, and social fabric of the communities they serve (O'Rourke et al., 2014). Lifelines interact with each other. Interdependence, as defined by Rinaldi et al (2001), refers to the interrelationship between two infrastructures; In this relationship, the operational state of one infrastructure not only affects the other, but also exhibits a discernible and intertwined relationship. Although the interaction between infrastructure systems provides efficiency or benefit during the operation of the systems, it can have undesirable consequences, especially in disaster situations (Rojahn et al., 2017). The vulnerability of interconnected systems to cascading failures means that the failure of a single component can set off a chain reaction, causing widespread performance impacts across multiple lifeline systems and subsequent social disruption. The dependence of almost all systems on electrical power and telecommunications for control and monitoring purposes clearly demonstrates the interconnected nature of lifeline systems. However, the indispensable roles of fuel and transportation come to the fore in order to re-provide services and carry out system repairs, especially in the face of interruptions. Fuel has become a critical backup for power during outages, while water is crucial for cooling in electrical power generation processes After the 1906 San Francisco earthquake, the interdependence relationship between lifelines during disasters became

* Corresponding author, E-mail: recepozay@arel.edu.tr

https://doi.org/10.31462/icearc2025_ce_hwr_595

even more evident. As a result of the severe tremors that occurred during the earthquake, buildings collapsed and gas lines burst, causing a huge fire to start. The fire, which was recorded as the largest urban fire in history and spread uncontrollably for three days, was further exacerbated by the damage to water networks and insufficient water resources (O'Rourke et al., 2006; Scawthorn et al., 2006a). In this context, the 1994 Northridge earthquake is an example of the interdependence relationship between lifelines. After the earthquake, the facility responsible for providing 75% of Los Angeles' drinking water faced a power outage that lasted approximately 24 hours (O'Rourke, 2007). This outage rendered the city's primary water pumping station inoperable, and internal combustion engine-powered pumps were put into operation. However, the damaged transportation infrastructure after the. disaster caused delays in fuel supply and prevented the pumping system from functioning properly. This has led to a serious disruption and crisis in drinking water supply (O'Rourke, 2007).

Erdik (2001) examined the 1999 Kocaeli and Düzce earthquakes. According to this study, the damage to lifelines is estimated to be around 1 billion dollars. In their study, Scawthorn et al. (2006b) examined the effects of the Sumatra earthquake and tsunami that occurred on December 26, 2004, on the physical infrastructure. The study highlights the need for disaster-resilient physical infrastructure and appropriate disaster management to minimize future damage and enhance recovery in the face of similar catastrophic events. In his study, Tang (2014) examined the effects of the Sichuan earthquake that occurred in China on May 12, 2008, on urban infrastructure. They defended the thesis that construction should not be allowed in risky areas in the zoning regulations. In their study, Giovinazzi et al. (2011) examined the effects of the Christchurch earthquake series that occurred in New Zealand in 2010-2011 on urban infrastructure, the physical damage suffered by various networks and the post-earthquake performances of these systems. It highlighted emergency management and response issues, emphasizing the importance of improving infrastructure resilience and preparedness measures to reduce the impacts of future earthquakes. In their study, Tang et al. (2013) evaluated the performance of urban infrastructure systems after the Chile earthquake that occurred on February 27, 2010.

2. Urban infrastructure systems

Cities, which emerged from people's desire to switch from a nomadic lifestyle to a settled life, have become centers where production, consumption and workforce come together, promoting economic development (Akyıldız, 2020). Developing cities require various urban infrastructure systems and services to provide people with a healthy and sustainable living. These infrastructures and services have evolved over time through technological change and transformation in a manner suitable for the development of cities (Derrible, 2018). Urban technical infrastructure services vary according to the unique identity and needs of each city. The urban infrastructure systems that should be present in every country are listed below;

Transportation (Road, Railway, Airway, Maritime), Water Management and Dams, Communication, Energy, Electricity, Natural Gas, Solid Fuel, Health, Agriculture and Food, Culture and Tourism Sector, Banking, Finance Sector, Critical Public Services Sector, Critical Production, Commercial Facilities Sector. An infrastructure's criticality level is determined by the negative impacts it would have on society in the event of its failure (Lenz, 2009). The protection of critical infrastructure is a responsibility that requires a coordinated approach with the support of all relevant parties such as the government, civil society, and the private sector, and it is a responsibility towards the whole society. The importance of this responsibility is also reflected in the definition of "critical infrastructure" by the Disaster and Emergency Management Authority (AFAD). According to AFAD's definition, critical infrastructure is defined as "a network, asset, system, and structure covering sectors such as transportation, communication, energy, water, finance, in which the sustainability of social order or the provision of public services will be adversely affected when their functions are partially or completely impaired" (AFAD, 2014). In this study, the urban infrastructures affected by the earthquake disaster are as follows; transportation, water supply and wastewater management, energy infrastructure, communication infrastructure.

3 Infrastructure damages caused by earthquakes

In order to show the effects of earthquakes on urban infrastructure systems, the studies carried out by expert scientists based on observations in the field after the severe earthquakes are given below.

3.1. Damage to transportation infrastructure

Damages in the transportation sector were examined under four main headings: Highways, Railways, Airports and Ports.

3.1.1. Highways

Highways, which are a ground structure, are greatly affected by severe earthquakes. The main effects of these effects are ground movements such as liquefaction, lateral spreading, settlement and slope failure that occur in the ground layers during earthquakes. These movements in the ground cause the stability of the highway superstructure to deteriorate. The simplest one starts with the cracking of the road superstructure, and as the intensity of the earthquake increases and depending on the characteristics of the ground, the damage increases until the highway is out of servis. Another type of damage seen on highways is damage to bridges, tunnels and culverts. The main studies on this subject in past earthquakes are (Chen et al., 2021), (Ledezma et al., 2012), (Panjamani et al., 2011), (Baral and Shahandashti, 2022), In Fig. 1, the effects of the earthquake on the Tarsus Adana Gaziantep road are shown.

Fig. 1. Damage on the Tarsus-Adana-Gaziantep highway. (A Haber, 2023)

As stated in Fig. 1, major damage occurred on the highway. As a result of the vertical and extreme displacements caused by earthquake waves (Low and Rayleigh) in the ground layers, the asphalt was broken, settlement and lateral formation occurred on the ground. During earthquakes, liquefaction and lateral spreading occur in water-saturated sandy soil layers. Large deformations occur in soft clay and similar soil layers. The break in the asphalt layer is due to the formation of secondary faults. The reason for the settlement seen in the figure is due to liquefaction in the ground layers under the road. To form a definitive opinion, undisturbed samples should be taken on-site, and laboratory examination should be performed. Fig. 2 shows the deformation on the Hatay Reyhanlı highway. The reason for this, at first glance, is due to liquefaction occurring in the ground layers. As can be seen from these pictures, the importance of local ground conditions in the damage caused to highways during severe earthquakes is understood. On the highways that were not damaged or slightly damaged by the earthquake, transportation disruptions occurred due to traffic congestion. In addition to the damage to the roads due to the earthquake, the mobility created by vehicles heading to the disaster area further increased the tension on the roads; Failure to effectively manage the increasing traffic flow led to traffic congestion and caused delays in response and relief efforts in the disaster area. This congestion not only prevented critical personnel and vehicles from reaching the region on time, but also prevented emergency services and aid delivery to those in need. As can be understood from here, post-earthquake traffic dispatch and management becomes very important in earthquake preparation studies. The damages described above occur as a result of loss of strength and excessive deformations caused by earthquakes in the soil layers on which the road superstructure sits on highways. Another effect that causes roads to become unusable is the damage to the structures we call road engineering structures (viaducts, bridges, culverts, support structures, overpasses, underpasses, etc.). These damages, which are within the field of expertise of structural and geotechnical engineering, are summarized below. Highway bridges located in areas affected by severe earthquakes are exposed to many earthquakes, including multiple main shocks or aftershocks, during their service life.

Fig. 2. Hatay- Reyhanlı highway damage (A Haber 2023)

3.1.2. Bridges and viaducs

Repeated seismic loads can lead to a decrease in the structural capacity of bridges or their collapse, causing disruption in the normal functioning of transportation networks (Ghosh et al., 2015). Bridges and viaducts have been described as the most sensitive components of the transportation system, as they are vulnerable to structural collapse in addition to seismic-induced damages, ground surface and geotechnical failures observed after severe earthquakes in the past (Stergiou and Kiremidjian, 2006). Since the bridge is an engineering structure, the cause of damage due to earthquake is related to the structure, materials and ground. Insufficient load transfer between the bridge deck, cap beam and side piers caused damage to bridge components during the earthquake. The absence of diaphragm elements placed between the beams in the head beam or supports to ensure lateral stability, and the insufficient number or insufficient size of earthquake wedges placed between the beams in the supports to transmit lateral loads contributed to the deterioration of the bridge components. Seismic activity caused displacement and dislocation of thick elastomeric pads. These damages observed in elastomeric cushions negatively affected the performance and safety of the bridge by causing the load distribution to change, the support system to deteriorate, and the bridge's vulnerability to structural damage and shaking to increase. Another damage that occurs in bridges is the conditions related to the ground on which the bridge piers sit. During the earthquake, liquefaction and lateral spreading occurred in the saturated sandy silty soils on which the bridge pier foundations sit. As a result of the total and differential settlements on the bridge foundations because of liquefaction, the bridges have become unusable. As a result of settling, especially in the approach embankments, a difference in elevation occurred in the bridge supports and dilations, and the superstructure became unusable. Damage to critical components on bridges due to earthquakes, displacement of bridge piers or supports, significantly reducing the load-carrying capacity, hindering the serviceability of bridges. Bridges are state-supervised engineering works, and their material strength is higher than buildings. Beams are mostly produced as pre-stressed and then assembled. Structural damages on bridges occur due to non-compliance with constructive principles rather than design. While damage to highways occurs due to ground properties, damage to highway bridges and their components results from both ground and structural features. We can summarize the damage to the bridges as follows. Damages occur on the side walls of bridges due to the dynamic forces created by earthquakes. These damages are primarily caused by intense ground movements and the intensification of seismic waves passing through the ground. Displacements occur as a result of repetitive stresses acting on the edge piers of bridges, which can lead to various forms of damage, including cracking, spalling and failure of structural elements. This damage is more common in areas with poor soil conditions and on bridges that lack adequate reinforcement or seismic design considerations. Unqualified design or detailing, such as inadequate reinforcement or lack of connections between bridge elements, increases the vulnerability of bridges to edge wall damage during seismic events. Additionally, interactions between the bridge structure and the underlying soil, such as liquefaction, settlement, and lateral spreading, can also contribute to the severity of damage. The aging or deterioration of bridges over time further increases their susceptibility to abutment wall damage during earthquakes. A full understanding of these reasons is of great importance in terms of assessing bridge sensitivity, taking appropriate design measures, performing maintenance practices and increasing bridge durability, reducing damage that may occur during earthquakes. Fig. 3 shows the wall damage caused by the bridge superstructure hammering the edge pier wall in the longitudinal direction (Avşar et al., 2023). Damages caused by exceeding the ground shear strength in the edge abutment approach fillings can be seen in Fig. 4.

Fig. 3. Bridge edge pier wall damage

Fig. 4. Bridge edge abutment approach embankment damage on the Asi River (Çetin et al., 2023)

Two bridges completely collapsed during the 6-7 Şubat Maraş earthquakes due to the displacement caused by the earthquake as a result of insufficient support widths. This issue can be seen in Fig. 5

Fig. 5. Bridge collapsed due to insufficient support width in Hatay

3.1.3. Tunnels

Tunnels are important components of the transportation system, providing essential connectivity and efficient routes for road and rail networks. These structures, which shorten travel distances by supporting regional harmony and provide safe passageways for people and commercial goods, carry the risk of serious damage during earthquakes. During earthquakes, tunnels are exposed to displacements in the surrounding soil and rocks due to ground movements. These displacements cause deformations and settlements as a result of dynamic forces applied to the tunnel structure, which endangers the stability and direction of the tunnels. Structural damage occurs in the form of cracks in walls, ceilings and floors, concrete spills and coatings breaking off, and negatively affects the integrity of the tunnel. This may pose a risk to the safety and functionality of vehicle and train traffic in the tunnel The consequences of tunnel damage caused by earthquakes are very important. Damages that require partial or complete closure of tunnels disrupt the transportation system, causing delays and route changes. Traffic congestion will have far-reaching consequences, affecting emergency responses, the local economy, and the well-being of individuals and communities, as alternative routes cannot handle the increased vehicle volume. To minimize these negative effects, it is critical to quickly evaluate, repair and reopen tunnels after an earthquake

3.1.4. Railways
The impact of the periods when railways are out of service after a major earthquake is of great importance. The disruption can affect the movement of goods, supply chains and trade, causing economic losses. The damages in these regions, where there were difficulties in meeting the high demand even before the earthquake, caused disruptions in export logistics. Manufacturers in the affected region considered road transport as an alternative option due to railway disruptions. However, the higher costs of road transport compared to railway and the fact that only a limited part of millions of tons of cargo can be transported by road have revealed that this alternative is an impractical option (UTİKAD, 2023). According to information received from the General Directorate of State Railways of the Republic of Turkey, there are 446 bridges, 6161 culverts, and 175 tunnels on the railway line affected by the earthquakes centered in Kahramanmaraş. The earthquake caused significant damage to railway engineering structures, including tunnels, viaducts, and bridges The damage to the steel railway bridges and railway tracks caused by the Kahramanmaraş earthquakes can be seen in Fig. 6 (NTV, 2023; Anadolu Agency 2023).

Fig. 6. Damages seen on railway bridges

Instability problems that occurred in the sloped sections of railway routes during earthquakes also caused the roads to be out of service. During the Kahramanmaraş earthquakes, the train route became unusable as a result of rocks rolling down from the mountainside onto the train tracks near the Fevzipaşa Train Station can be seen Fig. 7.

Fig. 7. Slope stability problems in railways during earthquakes (Hürriyet, 2023)

3.1.5. Airports
Another sector affected by earthquakes is airports. Damages to runways and terminal buildings at airports cause transportation to be disrupted or disabled. When the earthquake effects that occur especially on runways with a ground structure are examined, it is understood that this is mostly due to local soil properties. Following two successive earthquakes of magnitude 7.7 and 7.6, with the epicenter in Kahramanmaraş, significant damage occurred at some airports in the region. While some airports were closed to civilian flights, others continued their activities to ensure easy access of humanitarian aid and search and rescue teams to the region (AFAD, 2023). The

length of airport closures varied depending on the extent of damage and the time required for repairs and assessments While there was no situation that would disrupt transportation at Kahramanmaraş and Gaziantep airports, damage to the transportation roads and flight runway occurred at the airport in Hatay due to local ground conditions. The airport was out of service for about a week.

3.1.6. Maritime lines

Maraş earthquakes had negative effects on maritime transportation and ports in Turkey, causing significant damage. Especially Iskenderun Port was seriously affected, a fire broke out in the storage area where the containers were stacked, rendering the port inoperable and causing exports and imports to stop. It has been stated that the fire caused by materials containing chemicals such as PVC is difficult to extinguish and it takes three days to bring it under control. After the earthquake, cracks occurred on the pavements as a result of bearing capacity losses and settlement on the ground in the port.

3.2. Damage to water and wastewater systems

Damage to water supply and wastewater systems has led to a lack of access to clean drinking water in many areas, disruption of sewage delivery and treatment, leading to public health risks and environmental pollution. Mobile toilets and drinking water have been provided to affected areas to reduce the risk of disease. Damage to various components of the water and sewage infrastructure has had serious impacts. Damage occurred to varying degrees in the piping systems, with most of the damage resulting from loosening and breaking of joints. While most piping systems perform well, some older HDPE (High density polyethylene) pipes have experienced localized swelling. Although water treatment plants suffered moderate damage, they were able to maintain water supply after the earthquake. Citizens residing in high altitude areas of Kahramanmaraş were completely deprived of water service for three days following the incident, primarily due to the combined effects of damage to water transmission lines and power outages. This was because the pumping stations used to provide water flow to high altitude areas were rendered inoperable due to power outages. In the region, the water distribution network is mainly composed of ductile iron pipes, while prestressed concrete pipes, polyethylene and glass fiber pipes are also used. Damage observed in the water transmission pipe due to 4.5 m fault movement can be seen Fig. 8 (Çetin et al., 2023).

Fig. 8. Damage observed in the water transmission pipe due to 4.5 m fault movement

3.3. Damage to energy infrastructure systems

Power plants are the basic unit of the electrical energy system. If serious damage occurs in the earthquake, it not only causes direct economic loss, but also causes a series of chain hazards due to the loss of electricity generation function and power supply interruption, seriously supporting post-earthquake emergency rescue, people's survival and post-disaster reconstruction. While electrical energy is essential for maintaining the functionality of other lifelines such as communications, water supply and wastewater treatment, it also plays an important role in the economic vitality of society. Therefore, the stability and continued functionality of the power grid is necessary after disasters such as earthquakes (Omidvar et al., 2017).

Damages to energy systems in the earthquake zone are examined under the following headings: thermal power plants, hydroelectric power plants, electricity substations, electricity transmission and distribution overhead systems, natural gas transmission and distribution systems, LPG storage and distribution facilities, crude oil and fuel stations, wind turbines.

3.3.1.Thermal power plants

A hydrogen gas leak occurred at the Hunutlu Thermal Power Plant, 110 km away from the epicenter of the earthquake. After the earthquake, the location of this leak was found and isolated, ensuring uninterrupted operation of the system. Among the damages detected, small vertical cracks in the base columns of the concrete cooling tower, broken insulators, transformer failures, movements of pipes in the boiler building colliding with steel frames due to shaking and ground settlement were observed. (Çetin et al., 2023). Damage occurred to the unit of the Iskenderun Thermal Power Plant, which was in operation during the earthquake. It was observed that the transformers were displaced by approximately 10 cm by coming out of their sweat. As a result of ground settlement around the tribune building, repairable faults occurred in the installation.

3.3.2. Hydroelectric power plants

It seems that the general performance of hydroelectric power plants in the disaster-affected areas is quite successful. All units started operating again after power was supplied from the grid, and activation times varied between 3 and 6 days depending on the region. No significant cracks or deformations indicating the instability of the dam were observed in the regions, and it was determined that the damage was limited to small lateral spreads on the top of the dam and rocks falling from the adjacent slopes to the land and highways. Menzelet Dam, built between 1980 and 1989 on the Ceyhan River in Kahramanmaraş, is a body type rock fill and serves two purposes: irrigation and energy production. The clay core of the Menzelet Dam was not damaged, the roads leading to the dam could not be closed due to the rocks falling from the mountains after the earthquake, and the road equipment had to be cleaned. Some retaining walls to which the dam is a The Kilavuzlu dam, which was built later (1996-2001) on the Ceyhan River, is a body type earth fill. This dam survived the earthquake with minor damage. Small lateral spreads have occurred in the fill on the dam crest. Again, approximately 1 cm cracks occurred at 200 m intervals in the Concrete arch body type dam located on the Ceyha River. All of these damages are repairable and do not cause any interruption in energy production.ttached were also damaged due to rockfall (Çetin et al., 2023).

3.3.3. Electricity substations

Among the damages observed in substation buildings during earthquakes; These include wall fillings collapsing and falling on equipment, equipment that is not sufficiently fixed against the intensity of the earthquake falling over, rocks rolling down from the slopes surrounding the transformer building, and nearby structures collapsing onto the substation buildings. The structural design of the substation should take into account the potential impact of infill walls during earthquakes. When the walls of substation buildings collapse during an earthquake, they can cause serious damage to the equipment inside, resulting in interruptions in power supply, equipment failure, and extensive repair or replacement costs. After the earthquake, various cases were observed in which the walls of the substation buildings collapsed and the equipment inside was damaged. Another type of damage to transformer buildings is related to the area where the building is located. Slope slides and rock falls that occur due to the ground are the main ones. Another issue is that the building next to the transformer where it is located completely collapses, causing the transformer building to collapse as well.

3.3.4. Electricity transmission and distribution overhead systems

After electricity is produced in various sources such as power plants, it is transmitted through a network of electrical cables to reach its destination. This network consists of transmission and distribution lines that make up the electrical grid. Transmission involves moving generated electricity over long distances from generation facilities to substations near areas where demand is high. Transmission lines are characterized by larger, taller poles and towers that support multiple cables over long distances. Distribution represents the final step in delivering electrical energy from production to consumers. The power transferred over high-voltage transmission lines is subjected to voltage reduction using transformers in substations. It is then distributed through low voltage distribution lines. These lines, which can be seen along the streets, deliver electricity directly to homes, workplaces and other end users. The earthquake caused 11 poles connecting the 1,128 km long electricity transmission line to fall; It caused significant damage to the electricity distribution lines and substations in the region, especially Hatay, Gaziantep, Kahramanmaraş and Adıyaman (SBD, 2023). Distribution lines are either overhead or underground. There are more underground lines in urbanized areas. Outside the city, lines in rural areas go by air. While no major malfunctions were observed in the underground lines in the earthquake region, significant malfunctions occurred in the aboveground lines. Various types of damage have occurred in overhead lines and poles, such as the failure of the conductor, the collapse of concrete transformer poles and concrete network poles, especially due to the low voltage insulators breaking or flying off their pins during an earthquake. In rural areas, high voltage cables are connected to towers rising from the ground. As a result of mass movements on the ground during severe earthquakes, damage such as tipping, collapsing and tilting occurred in the towers. Electricity poles used in overhead power networks are installed using concrete or iron in city centers, and iron or wooden poles in rural areas. The primary reason for electric poles falling over in cities is that they are not properly fixed to the ground. The second and most important effect is that the debris created as a result of the collapse of the buildings also topples the poles on the street. Contact with the electrical conductor cables of collapsed buildings can cause various physical damage to the cables and even complete breakage of the cables. Following the devastating earthquake, the collapse of buildings towards roads and infrastructure areas caused the underground electricity network and field distribution boxes to be inaccessible. However, after the removal of the debris, it was determined that there was no damage, especially to the underground network, and in general, the cable section of the electrical network was not damaged.

3.3.5. Natural gas transmission and distribution systems

In today's industrialized society, a portion of energy is provided by natural gas. Energy outages resulting from damage to natural gas facilities during earthquakes cause major problems in the electricity supply. The length of the natural gas transmission line in the 11 provinces affected by the Kahramanmaraş earthquakes is 2,224 km and the length of the natural gas distribution line is 20,694 km (SBD, 2023). The earthquake caused explosions and failures at approximately 20 different points of the main natural gas transmission lines serving the affected regions, and damage occurred to natural gas distribution lines and facilities in the region (SBD, 2023). As a result of the damage, natural gas supply was interrupted in the cities of Gaziantep, Hatay, Kahramanmaraş and Adıyaman (SBD, 2023). Authorities reported that as of February 11, 2023, the repair of major damages, including steel pipelines, was completed and additional work was needed to return service to residents of the cities

3.3.6. LPG storage and distribution facilities, crude oil and fuel stations

LPG (liquefied petroleum gas) has a wide range of use in Türkiye and is widely used as a vehicle fuel, as well as an energy source in homes, kitchens, heating systems and the industrial sector. In the post-earthquake inspections, it was observed that LPG terminals generally performed well. Minor damage occurred to storage facilities and distribution lines due to local ground conditions. In the earthquake region, there were overturns in LPG storage facilities, but no leaks occurred. In order to prevent this, precautions should be taken to prevent gas cylinders in storage facilities from overturning.

3.3.7. Crude oil and fuel stations

There are 1,785 km of crude oil pipelines in the 11 affected provinces, corresponding to 56% of the length of crude oil pipelines in Turkey (SBD, 2023). As a result of the inspections, it was determined that there were small-scale damages in the crude oil pipelines and that the production areas were negatively affected by the earthquake (SBD, 2023). Following the earthquake, some gas stations and fuel storage facilities suffered damage, including the collapse of underground storage tanks and connection points. Gas stations generally consist of pump stations covered by a canopy structure and an adjacent single-story store building. While the canopy structures covering the pump stations were not damaged, the adjacent single-story store buildings were mostly severely damaged (Çetin et al., 2023).

3.3.8. Wind turbines

Earthquakes also affect green energy sources such as wind turbines, and in areas close to the earthquake, they damage turbine structures and transmission lines, causing power outages. Following the Kahramanmaraş Earthquakes, wind power plants in the affected region were assessed for damage and found to be undamaged. After the necessary repairs were made to the transmission network and the network was restored to its former state, the wind power plants continued to operate at full capacity. However, during the period when the network was down, the power plants had to temporarily stop their operations because the generated electricity could not be delivered to the distribution points (Anadolu Agency, 2023).

3.4. Communication infrastructure

The consequences of damage to communications infrastructure during an earthquake can go beyond disruptions to communications networks. The dependence of various sectors on communications can become a vital link affecting the functioning of infrastructures and services. For example, emergency services rely heavily on communications systems to coordinate their responses and efficiently allocate resources to affected areas. Without proper communications, response times can be extended, lives can be at risk, and the impact of the disaster can be exacerbated. The uninterrupted operation of critical public services such as electricity grids, water supply systems and gas pipelines largely depends on communication systems for monitoring and control; therefore, any disruption in communication can lead to disruption of restoration efforts or extended service outages. Public services, including government agencies and civil society organizations, also rely on communication for coordination and support; when communication is dysfunctional, it becomes difficult to provide basic services to affected communities. Serving as critical components of mobile communication networks, base stations can be installed in different locations to optimize network performance and increase communication capacity. While tower-type base stations are generally installed in rural areas to provide wider coverage, they are usually installed on rooftops in cities to meet high data traffic needs. Base stations need electrical power to provide communication services. The stations are supported by battery systems with an average operating time of 6 hours to continue operating during power outages. Communication disruptions during earthquakes can occur not only with damage to base stations, but also with power outages. In the examinations carried out in the region affected by the Kahramanmaraş earthquakes, it was determined that 2,451 of the 8,900 base stations were disabled (TÜRKONFED, 2023).

4. Conclusions

Today, urban infrastructure systems are closely related to the economic well-being, security and social fabric of the communities they serve. These systems, which include electricity, communication, natural gas, transportation, water and wastewater services and are often referred to as lifelines, serve as important channels that facilitate the production and distribution of needed goods and services. The sustainability of urban life depends on the functionality and reliability of these critical systems. Damage to urban infrastructure systems after an earthquake and the resulting service interruptions have important consequences for the execution of emergency activities and the ability to meet the basic needs required for the survival of society. In the worst cases, these interruptions can lead to social and economic impacts on a regional, national and even global scale. Urban infrastructure is a complex network of interconnected systems. Damage to any one component of the system can have a cascading effect, further exacerbating the overall impact of an earthquake. For example, in the event of a power outage, communications become critically challenged as landlines, mobile networks, and internet services cannot function without electricity, potentially hindering the dissemination of vital information and emergency response efforts. Without the power needed to operate pumps and filtration systems, water treatment operations that provide clean and safe drinking water come to a standstill, while wastewater treatment operations can also be disrupted, potentially posing environmental risks and public health concerns. Understanding the interdependencies and cascading effects between urban infrastructure systems is of great importance. In the century we live in, a large proportion of the population of countries lives in cities. Making cities resilient to disasters depends on the work to be done before the disaster. Post-disaster emergency efforts can also be successful by making preparations before the disaster. In this study, the effects of the recent major earthquakes on cities were examined in terms of transportation, water, wastewater, energy and communication. Just as it is important to make our structures durable and resistant to disasters, urban infrastructure must also be made resilient in order to reduce the damages that may occur. Local ground and structural damages, especially affecting transportation and communication systems, must be reduced. Since local ground conditions have an increasing effect on transportation systems, damage reduction studies should be carried out before the disaster.

References

A Haber. (2023). *TAG highway, which was severely damaged in the disaster of the century, has been opened to traffic, with a critical warning from the governor's office to citizens.* Retrieved from https://www.ahaber.com.tr/gundem/2023/02/07/yuzyilin-felaketinde-agir-hasar-alan-tag-otoyolu-trafige-acildi-valilikten-vatandaslara-kritik-uyari

AFAD. (2014). *Critical infrastructure protection roadmap document (2014-2023)*. Retrieved from https://www.afad.gov.tr/Dokuman/TR/123-20141010111330-kritikaltyapi-son.pdf

AFAD. (2023). *Press release about the earthquake in Kahramanmaraş-Pazarcık–6*. Retrieved from https://www.afad.gov.tr/kahramanmaras-pazarcikta-meydana-gelen-deprem-hk-basin-bulteni6

Akyıldız, N.A. (2020). The value of open public spaces for sustainable cities in the context of urbanization and urban development. *National Folklore, 16*(125), 188-201

Anadolu Agency. (2023). *The sliding iron bridge in Kahramanmaraş due to the earthquake was seen*. Retrieved from https://www.aa.com.tr/tr/asrin-felaketi/kahramanmarasta-depremin-etkisiyle-kayan-demir-kopru-goruntulendi/2886533

Avşar, Ö., Bozer, A., Tunaboyu, O., Sülev, E., & Demirtaş, Y. (2023). *Mw 7.7-7.6 Şubat 2023 seismic performance of reinforced concrete buildings built after 2000 and highway bridges in the region in Kahramanmaraş Earthquakes: Hatay field observations technical report*. Retrieved from https://doi.org/10.13140/RG.2.2.22933.40166

Baral, A., & Shahandashti, S.M. (2022). Identifying critical combination of roadside slopes susceptible to rainfall-induced failures. *Natural Hazards*, *113*, 1177-1198. https://doi.org/10.1007/s11069-022-05343-6

Chen, S., Wu, Y., & Hou, G. (2021). Post-earthquake resilience assessment and long-term restoration prioritization of transportation network. *Reliability Engineering & System Safety*. *211*, p.107612. https://doi.org/10.1016/j.ress.2021.107612

Çetin, K.Ö., Bray, J.D., Frost, J.D., Hortacsu, A., Miranda, E., Moss, R.E.S., & Stewart, J.P. (2023). February 6, 2023 Türkiye Earthquakes: Report on Geoscience and Engineering Impacts. Earthquake Engineering Research Institute, LFE Program & GEER Association Report 082.

Derrible, S. (2018). An approach to designing sustainable urban infrastructure. *MRS Energy & Sustainability*, *5*(13). https://doi.org/10.1557/mre.2018.14

Erdik, M. (2001). Report on 1999 Kocaeli and Düzce (Turkey) Earthquakes. *Structural Control for Civil and Infrastructure Engineering,* 149-186. https://doi.org/10.1142/9789812811707_0018

Giovinazzi, S., Wilson, T., Davis, C., Bristow, D., Gallagher, M., Schofield, A., Villemure, M., Eidinger, J., & Tang, A. (2011). Lifelines performance and management following the 22 February 2011 Christchurch earthquake, New Zealand: Highlights of resilience. *Bulletin of the New Zealand Society for Earthquake Engineering*, *44*(4), 402–417. https://doi.org/10.5459/bnzsee.44.4.402-417

Hürriyet. (2023). *Earthquake damaged: Repair work on railways*. Retrieved from https://www.hurriyet.com.tr/gundem/depremde-hasar-gormustu-demir-yollarinda-onarim-calismasi-42220252
Ghosh, J., Padgett, J.E., Eerı, M. & Sánchez-Silva, M. (2015). Seismic damage accumulation in highway bridges in earthquake-prone regions. *Earthquake Spectra*, *31*(1), 115-135. https://doi.org/10.1193/120812EQS347M
Ledezma, C., Hutchinson, T., Ashford, S.A., Moss, R., et al. (2012). Effects of ground failure on bridges, roads, and railroads. *Earthquake Spectra*, *28*(1-1), 119-143. https://doi.org/10.1193/1.4000024
Lenz S. (2009). Vulnerabilität Kritischer Infrastrukturen. Bundesamt für Bevölkerungsschutz und Katastrophenhilfe, Forschungim Bevölkerungsschutz, 4.
NTV. (2023). *Train tracks slipped in earthquake: No service for 85 days*. Retrieved from https://www.ntv.com.tr/galeri/turkiye/depremde-tren-raylari-kaydi-85-gundur-sefer-yapilamiyor,g2-42Eq8xEOoy2UO3JOZPg/YzNJtFii5Ea249KX2tQF5A#
Omidvar, B., Azizi, R. & Abdollahi1, Y. (2017). Seismic risk assessment of power substations. *Environmental Energy and Economics International Research, 1*(1), 45–62. https://doi.org/10.22097/eeer.2017.46456
O'Rourke, T., Johnson, L., Davis, C., Duenas-Osorio, L., Kiremidjian, A., Kwasinski, A., Mahoney, M., Nishenko, S., Nyman, D., Poland, C., & Tang, A. (2014). Earthquake-Resilient Lifelines: NEHRP Research, Development and Implementation Roadmap, NIST GCR 14-917-33 Report. National Institute of Standards and Technology, Gaithersburg, Maryland.
O'Rourke, T.D. (2007). Critical infrastructure, interdependencies, and resilience. *National Academy of Engineering*, *37*(1), 22-29
O'Rourke, T.D., Bonneau A.L., Pease J.W., Shi P., & Wang Y. (2006). Liquefaction and ground failures in San Francisco. *Earthquake Spectra*, *22*(2), 91-112. https://doi.org/10.1193/1.2185686
Panjamani, A., Srinivas, S., Chandran, D. (2011). Classification of road damage due to earthquakes. *Natural Hazards*, *60*, 425-460. https://doi.org/10.1007/s11069-011-0025-0
Rinaldi, S.M., Peerenboom, J.P., & Kelly, T.K. (2001). Identifying, understanding, and analyzing critical infrastructure interdependencies. *IEEE Control Systems Magazine, 21*(6), 11-25
Rojahn, C., Johnson, L., O'Rourke, T., Cedillos, V. & McAllister, T. (2017). Community resilience of lifeline systems: Societal needs and performance assessment. In: *16th World Conference on Earthquake (16WCEE)*. Santiago, Chile.
Strategy and Budget Directorate (SBD). (2023). *2023 General Activity Report*. Retrieved from https://www.sbb.gov.tr/wp-content/uploads/2024/06/2023-Yili-Genel-Faaliyet-Raporu.pdf
Scawthorn, C., O'Rourke, T.D., & Blackburn, F.T. (2006a). The 1906 San Francisco earthquake and fire—Enduring lessons for fire protection and water supply. *Earthquake Spectra, 22*(2), 135-158
Scawthorn, C., Ono, Y., Iemura, H., Ridha, M., & Purwanto, B. (2006b). Performance of lifelines in Banda Aceh, Indonesia, during the December 2004 Great Sumatra earthquake and tsunami. *Earthquake Spectra*, *22*(3), 511-544. https://doi.org/10.1193/1.2206807
Stergiou, E., & Kiremidjian, A. (2006). Treatment of Uncertainties in Seismic Risk Analysis of Transportation Systems. Technical Report No. 154. Blume Earthquake Engineering Center, Civil Engineering Department, Stanford University, Stanford, CA.
Tang, A.K. (2014). Wenchuan, Sichuan Province, China Earthquake of 2008: Lifeline Performance. American Society of Civil Engineers. ISBN: 978-0-7844-1333-3
Tang, A.K., & Eidinger, J.M. (Eds.). (2013). Chile Earthquake of 2010: Lifeline Performance. American Society of Civil Engineers. ISBN: 978-0-7844-1282-4
TÜRKONFED. (2023). *Kahramanmaraş earthquake-preliminary disaster assessment status report*. Retrieved from https://turkonfed.org/tr/detay/3937/2023-kahramanmaras-depremi-afet-on-degerlendirme-durum-raporu
UTİKAD. (2023). *Earthquake damage to rails hits mineral exports*. Retrieved from https://www.utikad.org.tr/Detay/Sektor-Haberleri/35582/raylardaki-deprem-hasari-maden-ihracatini-vurdu

4th International Civil Engineering & Architecture Conference
17-19 May 2025, Trabzon, Türkiye

Mathematical formulations of the temporal Intensity pattern of 6-hour design storm in central Tehran Metropolis

Sara Ghaznavinia[1], Seiyed M. Hosseini[*2]

[1] *B.S. Geography student, Faculty of Geography, University of Tehran, Tehran, Iran*
[2] *Associate professor, Physical Geography Department, University of Tehran, Tehran, Iran.*

Abstract. The identification of design storm temporal patterns in urban areas plays a crucial role in rainfall-runoff modeling, stormwater drainage design, and sediment retention structural design. In this study, we aimed to characterize and parameterize the 6-hour rainfall temporal pattern in the Tehran metropolis, the capital of Iran, which is considered the baseline for design storms in hydrologic and hydraulic engineering. Over 35 storm events with a duration of 6 hours and 28 storm events with a duration of 24 hours were collected, each with high-resolution one-minute time steps, to identify the temporal patterns of each duration. To address this issue, we derived the characteristics of 6-hour design storms, including depth, duration, intensity, and temporal pattern. The duration and intensity of the 6-hour rainfall events were then normalized with respect to the average characteristics of 24-hour events. Finally, a three-parameter exponential function was fitted to the normalized 6-hour patterns to represent their temporal distribution. The results indicated that formulating the rainfall pattern offers significant advantages in facilitating the comparison of its properties across different locations. Moreover, the derived design storm pattern enhances the accuracy and efficiency of hydrological modeling and computational implementations, which are essential for engineering applications such as urban drainage design, flood forecasting, and sediment control systems.

Keywords: Urban design storm; Temporal pattern of rainfall; Urban hydroclimatology; Modeling; Exponential function fitting

1. Introduction

Design storms or design hyetographs are precipitation patterns used as input for hydrologic models (Chow et al. 1988). The design rainstorm pattern plays a vital role in the planning and design of urban drainage pipe network, and is the basis for obtaining the rainwater runoff process line (Xiaoling Su et al., 2019). Different rainstorm profiles will lead to significant differences in the calculation results of rainfall runoff (Jiang, 2015). Short-duration precipitation models, such as the six-hour design storm, enhance urban drainage planning by accounting for peak rainfall intensities. A key consideration in the development of rainfall temporal patterns is the representation of characteristic intensity fluctuations during the peak phase of storm events (Bustami et al., 2012). By incorporating historical precipitation data, a 6-hour design storm model supports hydrological modeling, structural design, and sedimentation control. It shows the temporal distribution of rainfall within the design storm which is an important factor that affects the runoff volume, magnitude and timing of the peak discharge (Bustami et al., 2012). Understanding design storm temporal patterns in densely populated city is essential for improving hydrological modeling, urban drainage planning, and flood management.

A range of temporal rainfall disaggregation methods has been developed worldwide, though few have been evaluated for arid region conditions (Al-Wagdany, 2021). Often, rainfall intensity–duration relations developed for a specific location or a region are used to construct synthetic design storms by assuming a general shape of the hyetograph (Froehlich, 2009). In India, (Chowdhury et al., 2007) employed an empirical reduction formula, developed by the Indian Meteorological Department, to derive short-duration rainfall from daily precipitation data. Similarly, (Eastgate et al., 1979) applied the NRCS hydrograph procedure to generate 24-hour cumulative rainfall curves for western Queensland, Australia. (Pilgrim & Cordery, 1975) developed synthetic rainfall hyetographs that are based on ranking the time intervals in a storm according to their corresponding rainfall depths (Al-Wagdany, 2021).

In previous studies, temporal rainfall patterns were typically designed based on quantiles, such as quartiles and deciles. However, in our approach, we have quantified this process by introducing a mathematical formulation for

[*] Corresponding author, E-mail: smhosseini@ut.ac.ir

https://doi.org/10.31462/icearc2025_ce_hwr_634

fitting and approximation. This approach facilitates tasks such as coding, management and other computational and practical applications, making them more efficient and streamlined.

This study aims to quantify 6-hour precipitation events in a fully urbanized region of central Tehran. To achieve this, a centrally located synoptic meteorological station, offering high-resolution data at 1-minute intervals, was utilized Continued research in this field is essential for developing effective strategies to mitigate the impacts of changing rainfall patterns, ensuring the resilience of urban communities and ecosystems against hydrological and climatic uncertainties (Ghaznavinia & Hossini, 2024).

2. Materials and methods

The overall methodology adopted in this study is summarized in Figure 1. The process begins with the collection of high-resolution rainfall data (1-minute time step) from the Yousef Abad weather station. Storm events are then classified into 6-hour and 24-hour durations using the Pilgrim and Cordery method. Following a data adequacy check, 56 significant rainfall events are selected, and their main characteristics including depth, duration, intensity, and temporal patterns are extracted.

To allow for meaningful comparison, the depth and intensity of 6-hour storms are normalized with respect to 24-hour storms. An exponential model is then fitted to the normalized data to approximate the design storm pattern. The model is subsequently calibrated and verified, followed by a final analysis of the results.

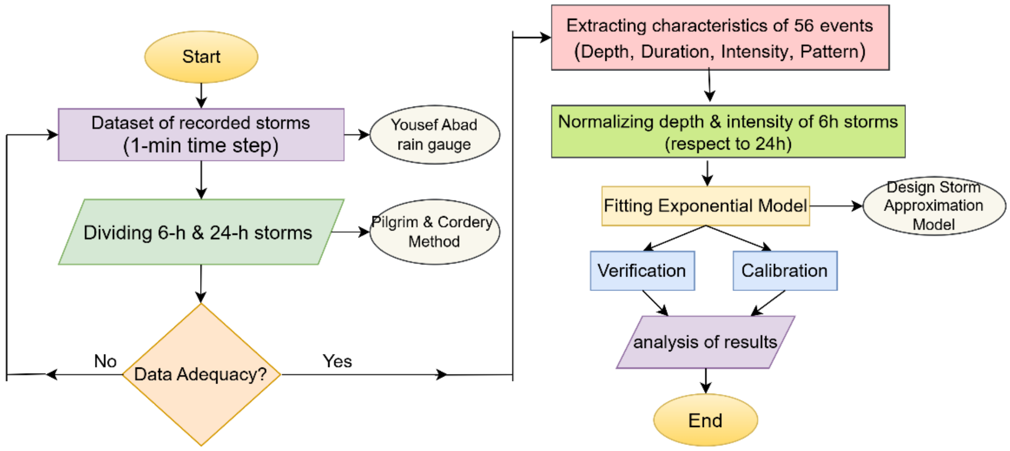

Fig.1. Location of Yousef Abad weather station in Tehran metropolis, Iran

2.1. Methods

In this study, prior to the analysis, the Chi-square hypothesis test was employed to assess the adequacy of the number of analyzed rainfall events. This test was applied to evaluate whether the selected sample size sufficiently represents the overall distribution of rainfall occurrences. By comparing the observed and expected frequencies, the Chi-square test ensured that the dataset was statistically robust for further analysis, thereby validating the reliability of the selected rainfall events. The Chi-square formula is presented as follows:

$$X^2 = \sum_{i=1}^{r}\sum_{j=1}^{c}\frac{\left(N_{ij}-\frac{N_i.N_j}{n}\right)^2}{\frac{N_i.N_j}{n}} \qquad \text{Eq.(1)}$$

Eq.(1) Where r = Number of rows, c = Number of columns, N_{ij} = Number of specific events (frequencies) in the i-th row and j-th column, N_i = Number of events (frequencies) in the i-th row, N_j = Number of events (frequencies) in the j-th column, n = Total number of events (frequencies) (Khaksefidi et al., 2010).

An expression for the time distribution of rainfall intensity in synthetic design storm hyetographs is then found as follows (Froehlich, 2009):

$$\hat{\imath}_{*(t)} = \left(i_{p^*} - i_{0^*}\right) exp\left[-\left(\frac{mt_d}{r}\right)\left(1-\frac{t}{t_d}\right)\right] + i_{0*} \qquad For\ 0 \le t/t_d \le r$$

$$\hat{\imath}_{*(t)} = \left(i_{p^*} - i_{0^*}\right) exp\left[-\left(\frac{mt_d}{1-r}\right)\left(\frac{t}{t_d}-r\right)\right] + i_{0*} \qquad For\ r \le t\ /\ t_d \le 1 \qquad \text{Eq.(2)}$$

where $i_{p*} = i_p/\bar{\imath}_{24}$, and $i_{0*} = i_0/\bar{\imath}_{24}$. Optimal values of the two parameters i_{0*}, and "m" found for Yousef Abad wather station events by fitting Eq.(2) to the normalized 6-hour rainfall data.

Ttime-to-peak intensity ratio $r = tp/td$,where tp = time to peak rainfall intensity, and td = storm duration, which is 6 hours. Distributing rainfall about the time of peak intensity proportioned by r, rainfall intensity given by Eq.(2) corresponding to time t occurs a time rt before the peak and a time $(1-r)\,t$ after the peak.

2.2. Study area

The study area of this research focuses on weather station in the central business district (CBD) of Tehran metropolis, the capital of Iran (figure.2), which is highly developed and characterized by dense infrastructure, impervious surfaces, and limited green spaces. This area experiences a semi-arid climate, with an average annual precipitation of about 230 mm and a mean annual temperature of approximately 18°C. Most rainfall occurs during the colder months, while summers are typically hot and dry. Rapid urbanization and topographic variations contribute to localized climatic differences, particularly in the central zones. Figure.1. shows that the Yousef Abad weather station which is located in the CBD of city 35° 44′ North latitude and 51° 24′ East longitude. This station can be considered as a representative for illustrating the temporal intensity pattern of rainfall in the city center.

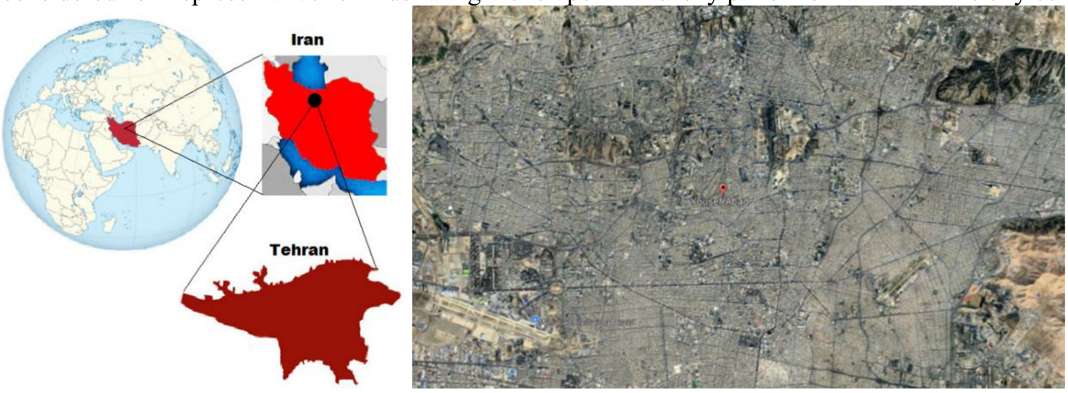

Fig. 2. Location of Yousef Abad weather station in Tehran metropolis, Iran

2.3. Data set

Precipitation events recorded over a 27-year period by the rain gauge at the weather station were analyzed, including 28 events lasting 24 hours and another 28 lasting 6 hours. The general characteristics of the dataset and the selected events are presented in Table 1.

Table 1. Characteristics of storm events (6 hr and 24 hr) used in the analysis.

	6 hr Storms				24 hr Storms		
No	Date of storm	Duration (min)	Depth (mm)	Intensity (mm/hr)	Date of storm	Duration (hr)	Depth (mm)
1	1974-02-18	308	1.77	0.35	1999-11-10	24.00	28.20
2	1974-03-31	459	8.74	1.14	2000-12-11	24.00	30.53
3	1974-11-07	266	5.83	1.32	1974-12-29	22.23	12.03
4	1974-12-13	263	6.50	1.48	1975-01-14	24.00	16.73
5	1975-01-03	451	15.08	2.01	1974-12-05	24.00	35.85
6	1977-04-25	249	6.44	1.55	1975-02-20	24.00	38.12
7	1978-02-23	429	10.78	1.51	1976-12-22	21.42	22.13
8	1977-04-25	379	6.79	1.08	1975-02-20	24.00	18.97
9	1978-02-23	285	5.50	1.16	1976-12-22	21.10	33.43
10	1984-12-04	370	16.54	2.68	1982-12-05	20.92	25.16
11	1985-01-14	323	9.17	1.70	1983-12-11	24.00	19.36
12	1985-02-01	298	7.99	1.61	1984-11-28	21.88	14.02
13	1986-03-16	422	14.08	2.00	1984-12-01	20.23	13.55
14	1987-03-16	284	5.12	1.08	1984-12-03	23.50	15.39
15	1987-10-27	349	6.08	1.05	1985-01-02	24.00	29.54
16	1989-12-03	395	9.31	1.41	1985-11-13	24.00	16.88
17	1991-03-05	309	13.06	2.54	1986-05-03	24.00	5.63
18	1993-02-14	450	19.75	2.63	1988-01-08	24.00	23.35
19	1993-03-09	450	11.88	1.58	1988-01-19	24.00	14.00
20	1993-11-03	373	14.24	2.29	1989-12-03	21.33	27.65
21	1993-12-15	267	6.86	1.54	1990-01-09	24.00	34.86
22	1994-11-17	466	8.53	1.10	1990-02-10	22.17	28.95
23	1996-01-05	351	9.91	1.69	1991-03-05	20.95	31.75
24	1998-02-12	289	8.59	1.78	1991-03-13	22.20	32.55
25	1998-05-04	415	13.15	1.90	1993-02-02	24.00	5.22
26	1998-12-04	286	14.44	3.03	1993-02-20	24.00	57.42
27	1998-12-04	405	13.57	2.01	1994-01-16	21.88	22.60
28	1999-02-24	398	8.10	1.22	1996-03-01	24.00	25.51

3. Results and discussion

3.1 Data adequacy

Using the Chi-square test, the results indicate that the p-value is 0.2, and the number of observed events is sufficient at the 95% significance level. Therefore, the dataset passes the adequacy check, and the subsequent steps of the study such as fitting model and pattern extraction can be reliably performed.

3.2 Design pattern

Based on the events and information presented in Table 1, averaging was performed to obtain representative values for further analysis. Following the analysis of 28 rainfall events and the modeling of 6-hour rainstorms using Eq.(2), the individual and cumulative mean rainfall patterns were derived. The averaging process and development of hyetograph patterns were carried out using the Pilgrim & Cordery (1975) method, as illustrated in figure.3.

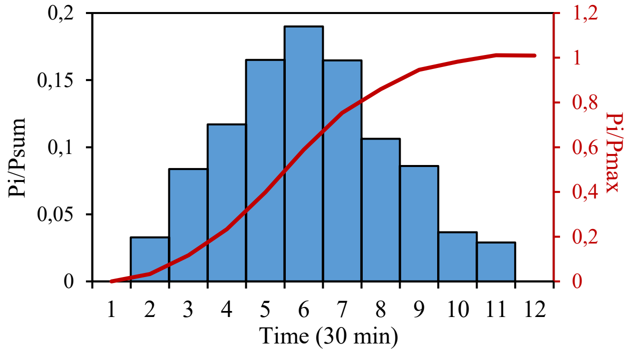

Fig.3. Average pattern of 6-h design hyetographs

3.3 Fitting exponential model

After normalizing the 6-hour rainfall data to 24-hour rainfall values, the exponential modeling formula was fitted to the data separately using the Solver tool in Microsoft Excel. The calibrated "m" values are presented in the dataset table1.

The four parameters, namely i_{o*}, m, r, and td, were optimized based on the derived information, including intensity, time duration, depth, peak, and i_{p*} of each event. The average values of these parameters were used in the analysis.

On average, the optimal parameters of the exponential rainfall intensity equation for 6-hour design storm approximations include a calibrated (m) of 9.73 h^{-1} with a standard deviation of 1.82 h^{-1}. The storms had an average duration of 6 hours, a total rainfall depth of 9.92 mm, and an average intensity of 1.65 mm/h. The peak of rainfall (r) associated with the model was 0.5.

Table 2. The input (t_d and r) and calibrated (m) parameters used for fitting the exponential model to the standardized temporal pattern of 6-h storms

No.	Date of Storm	*td*	*r*	*m*	No.	Date of Storm	*td*	*r*	*m*
1	1974-02-18	6.20	0.49	7.59	15	1991-03-05	7.91	0.33	10.22
2	1974-03-31	5.62	0.28	9.43	16	1993-02-14	6.64	0.74	7.22
3	1974-11-07	7.38	0.36	10.42	17	1993-03-09	7.07	0.37	10.43
4	1974-12-13	5.17	0.21	8.60	18	1993-11-03	5.14	0.59	8.44
5	1975-01-03	7.81	0.34	10.41	19	1993-12-15	6.10	0.43	11.03
6	1977-04-25	6.66	0.40	10.30	20	1994-11-17	6.57	0.64	12.60
7	1978-02-23	6.80	0.71	7.62	21	1996-01-05	4.45	0.57	8.43
8	1984-12-04	6.99	0.30	10.08	22	1998-02-12	5.87	0.52	8.61
9	1985-01-14	5.64	0.62	8.00	23	1998-05-04	4.17	0.73	8.62
10	1985-02-01	5.08	0.99	8.40	24	1998-12-04	5.96	0.88	15.67
11	1986-03-16	5.31	0.30	10.05	25	1998-12-04	6.69	0.32	10.11
12	1987-03-16	7.66	0.41	10.78	26	1999-02-24	7.25	0.29	9.91
13	1987-10-27	6.03	0.75	7.23	27	2000-12-11	8.43	0.49	11.47
14	1989-12-03	7.24	0.15	8.92	28	2001-01-27	7.77	0.54	11.81

Comparisons of the actual ranked dimensionless intensities and the approximation given by Eq.(2) using the optimized parameters are shown in Fig.4.

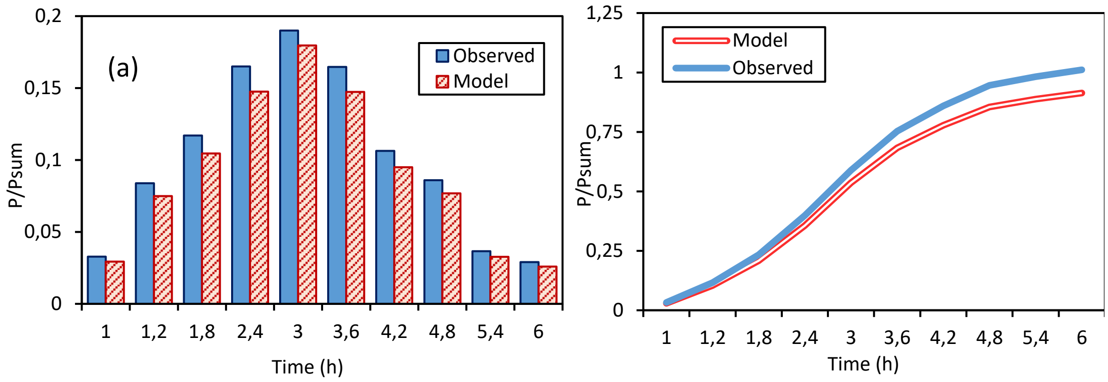

Fig.4. Histogram of Observed 6-h Rainfall Pattern and Fitted Model **(a)**, and cumulative curve of patterns **(b)**

4. Conclusions

An exponential function was fitted to the 6-hour storm temporal pattern and examined for a 28 events. The results indicated that the proposed formula accurately matched the 6-hour dataset. Quantifying rainfall intensity patterns can significantly contribute to hydrological design and urban drainage network planning. Moreover, due to its formulation-based approach instead of relying on quantiles, this method offers valuable applications in coding-related implementations as well.

References

Al-Wagdany, A. S. (2021). Construction of IDF curves based on NRCS synthetic rainfall hyetographs and daily rainfall records in arid regions. *Arabian Journal of Geosciences, 14*(527). https://doi.org/10.1007/s12517-021-06922-w

Bustami, R. A., Rosli, N. A., Adam, J. H., & Li, K. P. (2012). Development of temporal rainfall pattern for southern region of Sarawak. *UNIMAS E-Journal of Civil Engineering, 3*(Special Issue).

Chow, V. T., Maidment, D. R., & Mays, L. W. (1988). *Applied hydrology*. McGraw-Hill.

Chowdhury, R. K., Alam, M. J., Das, P., & Alam, M. A. (2007). Short duration rainfall estimation of Sylhet: IMD and USWB method. *Journal of Indian Water Works Association, 39*(4), 285–292.

Eastgate, W. I., Swartz, G., & Briggs, H. S. (1979). *Estimation of runoff rates for small Queensland catchments* (Technical Bulletin No. 15, p. 49). Queensland Department of Primary Industries, Division of Land Utilisation.

Froehlich, D. C. (2009). NRCS design storm erosivity. *Journal of Irrigation and Drainage Engineering, 135*(1), 76. https://doi.org/10.1061/(ASCE)0733-9437(2009)135:1(76)

Ghaznavinia, S., & Hosseini, S. M. (2024, October 14). Statistical analysis of 24-hour rainfall patterns in Tehran metropolitan area. Paper presented at *The 8th International Electronic Conference on Water Sciences, Urban Water, Treatment Technologies, Systems Efficiency and Smart Water Grids*. MDPI. https://sciforum.net/manuscripts/19184/slides.pdf

Jiang, M. (2015). Research on the design rainstorm profile in Shanghai under the new rainstorm situation. *Journal of Human Institute of Science and Technology, 28*, 69.

Pilgrim, D. H., & Cordery, I. (1975). Rainfall temporal patterns for design floods. *Journal of the Hydraulics Division, American Society of Civil Engineers, 101*(HY1), 81–95.

Su, X., Xie, D., Liu, L., Liang, C., Liu, Z., Li, Y., Lan, Q., & Ren, L. (2019). Study on design rainstorm profile in Liuzhou City based on Pilgrim & Cordery method. *Journal of Geoscience and Environment Protection, 7*, 136–144. https://doi.org/10.4236/gep.2019.73007

Potential of machine learning algorithms for sediment transport in annulus

Serra E. Akyurt[1], Pelin İlker[1], Mehmet Sorgun[*1]

[1] İzmir Katip Çelebi Üniversitesi, Civil Engineering Department, Çiğli, 35620 İzmir, Türkiye
[a] Corresponding author, Prof. Dr.

Abstract. Understanding the hydraulic behavior of sediment-laden flows in annular geometries is crucial for the efficient design and operation of multiphase flow systems. The frictional pressure loss can be considered as an significant parameter affecting sediment transport in annulus. There exists a correlation between pressure loss and shear stress, whereby an increase in pressure loss leads to a corresponding rise in shear stress on the sediment particle. Therefore, accurate calculation of pressure loss is a important issue for hydraulic engineering. Friction factor is a key parameter in the determination of pressure losses in closed conduits. In this study, a dimensional analysis is performed by using Buckingham Pi Theorem to find the parameters affecting the friction factor. Experimental data are analyzed with machine learning techniques, employing a cross-validation method to categorize the data as training and test data. Log-Log Regression (LLR), Artificial Neural Network (ANN), Teaching-Learning Based Optimization (TLBO), Extreme Gradient Boosting (XGBOOST), Negative Binomial Regression (NBR), Gaussian Process Regression (GPR) models are trained. The machine learning algorithms are evaluated in terms of AAE (Average Absolute Error), AAPE (Average Absolute Percentage Error), RMSE (Root Mean Square Error) and the optimal model is found out. Results indicate that the LLR model showed slightly better performance than other machine learning algorithms (based on LLR=18.70%, ANN=19.00%, TLBO=19.18%, XGBOOST=20.67%, NBR=24.71%, GPR=48.53% AAPE values).

Keywords: Machine learning; Cross validation; Sediment transport; Annular flow; Friction factor

1. INTRODUCTION

Sediment transport in pipelines is an important issue for civil and hydraulic engineering. The efficiency of the system to be designed in areas requiring sediment transport is quite critical in terms of energy and resource management. The transport of solid particles with a certain fluid directly affects the performance of the pipeline and the energy used. For this reason, a correct and optimal system design is the most important factor in this case. Many researchers have been conducting studies in the subject of sediment transport for years by using experimental and numerical approaches.

With the domain of sediment transport, the estimation of various factors and parameters by artificial intelligence models and machine learning algorithms has become the subject of many scientific researches today. Altunkaynak (2009) conducted a estimation study on the discharge and sediment load data of the Mississippi River and used Genetic Algorithms (GA) and regression models for comparison. As a result of this comparison, it was seen that genetic algorithms gave better results compared to regression models. In the study conducted by Azamathulla et al. (2010), Support Vector Machines (SVM) and conventional methods were compared to estimating sediment load values in three rivers in Malaysia. In the study conducted by Melesse et al. (2011), suspended sediment load values of the Mississippi, Missouri and Rio Grande rivers were estimated by algorithms such as Artificial Neural Network (ANN), Multiple Linear Regression (MLR), and Multiple Nonlinear Regression (MNLR). Azamathulla et al. (2013); the suspended sediment load of the Muda, Langat and Kurau rivers in Malaysia was estimated using Gene Expression Programming (GEP) and the results were compared with ANFIS and regression models. According to Nourani and Andalib (2015), the use of wavelet together with the Least Square Support Vector Machines (LSSVM) algorithm in the suspended sediment load estimations of the Mississippi River improved the estimation results. In the study by Osgouei et al. (2015), friction pressure losses for multiphase flow in a horizontal annulus were investigated and Nearest Neighbor (NN), regression trees, MultiLayer Perceptron (MLP) and Support Vector Machines (SVM) algorithms were used for pressure loss estimations. In the study by Singh et al. (2018), different regression algorithms were developed to make pressure loss estimations of narrow aperture well channels. Kanin et al. (2018) used Random Forest, Gradient Boosting,

* Corresponding author, E-mail: mehmet.sorgun@ikcu.edu.tr

https://doi.org/10.31462/icearc2025_ce_hwr_636

Support Vector Machine and Artificial Neural Network algorithms for estimating the flow pattern pressure gradient in the pipe. Yilmaz et al. (2019) conducted a study using Artificial Neural Network (ANN), Teaching-Learning Based Optimization (TLBO) and Artificial Bee Colony (ABC) algorithms to estimate the suspended sediment load in the Coruh River Basin. In the study by Rahmat and Wongwises (2020), an artificial neural network model was developed to estimate the pressure drop for two-phase flow in a pipe stream. Khamehchi and Bemani (2020) used Extreme Learning Machine (ELM) and Gradient Tree Boosting (GTB) machine learning algorithms to facilitate the calculation of bottom well pressure for two-phase flow. Kumar et al. (2020) investigated the performances of Bayesian Neural Network (BNN), Artificial Neural Network (ANN), Random Forest (RF) and Support Vector Machine (SVM) algorithms to estimate the pressure loss in the annulus for Herschel-Bulkley fluids. Sharafati et al. (2020) evaluated the performances of three different machine learning algorithms, namely Gradient Boost Regression, Random Forest Regression and AdaBoost Regression, to estimate the suspended sediment load of the Mississippi River. In the study by AlDahoul et al. (2021), an algorithm called Long Short Term Memory (LSTM) was developed to estimate the suspended sediment load. Darabi et al. (2021) used three different models, namely MultiLayer Perceptron (MLP), Adaptive Neuro-Fuzzy Inference System (ANFIS) and Radial Basis Function Neural Network (RBFNN), to estimate the suspended sediment load in rivers. Afterwards, they integrated these models with Sine-Cosine Algorithm (SCA), Particle Swarm Optimization (PSO), Firefly Algorithm (FFA) and Bat Algorithm (BA) algorithms for performance improvement. Wahid et al. (2021) conducted a study with 5 different machine learning algorithms, namely Support Vector Machine (SVM), Genetic Programming (GP), Random Forest (RF), Artificial Neural Network (ANN) and k-Nearest Neighbor (kNN), and hybrid versions of these algorithms were studied to estimate the pressure gradient in liquid-liquid flow in horizontal well lines. Jain et al. (2021) used Random Forest (RF) algorithm for flow behavior analysis in industrial pipelines and turbine machines. Wan et al. (2024) estimated the pressure drop in pipe flow and two-phase flow using Random Forest (RF), Back Propagation (BP) and Polynomial Regression (PR) machine learning algorithms.

2. Theory

2.1. Dimensional analysis

As can be seen in Figure 1, the experimental study conducted by Sorgun (2010), sediment transport in annular flow was investigated. The friction factor variable used in the study is expressed with other variables as follows:

$$f = func(v, \rho, \mu, D_h, \Omega, g, \theta, C_c) \tag{1}$$

where; v is the fluid velocity (L/T), ρ is the density of fluid (M/L^3), μ is the dynamic viscosity of fluid (M/LT), D_h is the hydraulic diameter (L) ($D_h = D_o - D_i$, D_o is the outer pipe diameter and D_i is the inner pipe diameter), Ω is the inner pipe rotation speed (1/T), g is the gravitational acceleration (L/T^2), θ is the hole inclination and C_c is the sediment concentration.

Dimensional analysis with Buckingham Pi Theorem was performed with the friction factor as the dependent variable and the other parameters given as independent variables. The relations created by dimensional analysis are;

$$\pi_1 = \frac{\rho v D}{\mu} \tag{2}$$

$$\pi_2 = \frac{v^2}{gD} \tag{3}$$

$$\pi_3 = C_c \tag{4}$$

$$\pi_4 = \theta \tag{5}$$

$$\pi_5 = \frac{\Omega D}{v} \tag{6}$$

2.2. Log-log regression (LLR)

In the log-log regression model, dependent and independent variables are processed by taking their logarithms. In other words, the log-log regression model works on the basis of transforming the data into terms that allow it to be expressed logarithmically. This model is quite successful in modeling scale-dependent relationships and effectively modeling linearized correlations and processing data. A study was conducted by Lemaire et al. (2024) to estimate hydraulic conductivity and the log-log regression model was used to relate some of the data in the study. In the study conducted by Nigate et al. (2024), the parameters of volcanic aquifer systems were estimated in order to provide groundwater analysis and management and it was concluded that log-log regression is a powerful tool in interpreting the data.

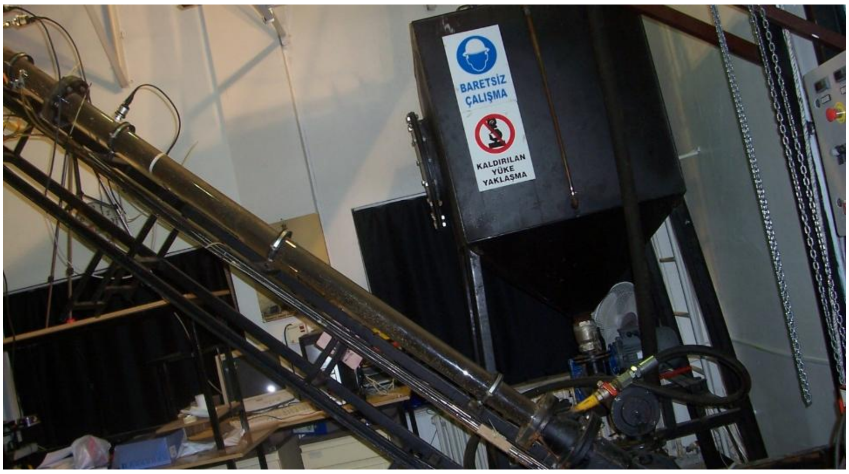

Figure 1: Experimental Test Setup (Sorgun, 2010).

2.3. Artificial neural network (ANN)

Artificial neural networks have a structure similar to the human brain in terms of working principle. This structure consists of nodes corresponding to neurons in the human brain and the connections between these nodes. These connections form the layers of the model: Input layer, internal layers and output layer. It is one of the algorithms that performs quite well in analyzing and modeling complex data. Williams and Ojuri (2021) conducted a prediction study on the hydraulic conductivity of soil types and as a result, it was revealed that the ANN model performed better in the context of estimating hydraulic conductivity than other models. According to Tawfik (2023), instead of using time-consuming traditional models to solve pipeline systems, an ANN was trained to predict the flow rate. The ANN model provided a successful correlation between real data and the prediction results.

2.4. Teaching-learning based optimization (TLBO)

TLBO is defined as a model that does not require any algorithm-specific parameters (Rao, 2016). As the name suggests, this algorithm is an algorithm that works on the principle of teacher and student. In the teaching process, information is transferred to the learning process and the solution space of the learning process is strengthened. In the learning process, each point receives information from each other and aims to provide more consistent and better solutions. In the study conducted by Sayari et al. (2019), other algorithms were used together with TLBO to estimate the critical flow rate for sediment transport in the pipeline. As a result of this study, it was determined that the TLBO algorithm improved the results of other models. Elshaboury et al. (2021) conducted a study on estimating the condition of pipes in water distribution lines in a region in Egypt and it was seen that much more accurate and successful results were obtained by strengthening the FFNN model with the TLBO algorithm.

2.5. Extreme gradient boosting (XGBoost)

The XGBoost model was developed from decision trees and is considered an important advance in the field of artificial intelligence techniques and machine learning (Niazkar et al, 2024). This model consists of a series of decision trees and works with the principle of gradient descent. In other words, each tree in its structure works to improve and optimize the errors in the previous tree. It is one of the algorithms frequently used in solving regression and classification problems thanks to its fast and accurate results even in large and complex data sets. Sun et al. (2024) optimized the genetic algorithm (GA) with the XGBoost algorithm to estimate the bottom cavity pressure in reservoirs and created a hybrid GA-XGBoost model. It was determined that this hybrid model gave better results compared to other models, made much more successful generalization especially with smaller data sets and produced consistent results.

2.6. Negative binomial regression (NBR)

The negative binomial distribution can be defined as the discrete distribution of the number of successes of Bernoulli trials that are independently and identically distributed before a certain number of errors are seen (Yang and Berdine, 2015). In fact, this model is similar to Poisson regression in terms of how it works, but since Poisson regression can only work when the variance and mean are equal, it does not work correctly when this equality is broken and leads to overdispersion. Negative binomial regression is preferred on data where the overdispersion problem is seen and uses numerical data as the dependent variable.

2.7. Gaussian process regression (GPR)

Gaussian process regression is a machine learning model based on Bayesian regression and is one of the algorithms that show strong performance in modeling uncertain sets. This regression model defines the relationship between points in a data set as a function. Gaussian process is defined in Gerschman and Blei (2012) as a nonparametric and discriminative approach that models the conditional distribution of output data after processing the input data. This model specifies a probability function to make predictions by considering that the function values come with the distribution. Gaussian process regression works much faster than other regression models and techniques used in the literature and saves the result functions (Schulz et al., 2018).

In this study, the estimation of the friction factor, which is important for sediment transport in the annulus, was estimated using machine learning algorithms such as Log-Log Regression (LLR), Artificial Neural Network (ANN), Teaching-Learning Based Optimization (TLBO), Extreme Gradient Boosting (XGBoost), Negative Binomial Regression (NBR) and Gaussian Process Regression (GPR), and the comparison of these estimation results with experimental data were discussed.

3. Results & discussion

Firstly, the parameters affecting the friction factor were determined and dimensional analysis was performed with Buckingham Pi Theorem. In continuation of the dimensional analysis, dimensionless parameters were created and the dataset was transferred to Python. The experimental data used in this study were taken from Sorgun (2010). A small representation of the parameters is given in Fig. 2. A new friction factor equation was proposed with the pi-terms formed as a result of the dimensional analysis. Then, the friction factor was estimated with machine learning algorithms in Python and compared with experimental friction factor data. The coding of the XGBoost algorithm can be seen as an example in Fig. 3. The graphical interpretation of these results can be seen in Fig. 4, Fig. 5, Fig. 6, Figure 7, Fig. 8 and Fig. 9, where the relevant data are presented. Additionally, the R^2 (R-Square), AAE (Average Absolute Error), AAPE (Average Absolute Percentage Error) and RMSE (Root Mean Square Error) values of the machine learning models used are presented in Table 1.

VARIABLE 1	VARIABLE 2	VARIABLE 3	VARIABLE 4	VARIABLE 5	VARIABLE 6
Fanning	Reynolds	Froude	Concentration	Hole inc.	Pipe rotation
0.039073479	14789.39863	1.479264709	0.66733745	0.785	0
0.028772289	18075.93166	2.209765799	0.546003368	0.785	0
0.021363425	21910.22019	3.246671514	0.450452779	0.785	0
0.017021108	25744.50873	4.482435859	0.383364067	0.785	0
0.01348035	29578.79726	5.917058834	0.333668725	0.785	0
0.00917836	32865.33029	7.305010907	0.300301852	0.785	0
0.006510758	38342.88534	9.942931512	0.257401588	0.785	0
0.060173157	14789.39863	1.479264709	1.3346749	0.785	0
0.02919668	21910.22019	3.246671514	0.900905557	0.785	0
0.022952706	25744.50873	4.482435859	0.766728134	0.785	0
0.018950637	29578.79726	5.917058834	0.66733745	0.785	0
0.015508264	32865.33029	7.305010907	0.600603705	0.785	0
0.008370975	38342.88534	9.942931512	0.514803176	0.785	0
0.051576992	14789.39863	1.479264709	0.66733745	0.785	1.766052084
0.035573012	18075.93166	2.209765799	0.546003368	0.785	1.444951705
0.021363425	21910.22019	3.246671514	0.450452779	0.785	1.192085157
0.01441884	24101.24221	3.928472532	0.409502526	0.785	1.083713779
0.069550792	14789.39863	1.479264709	1.3346749	0.785	1.766052084
0.049174457	18075.93166	2.209765799	1.092006736	0.785	1.444951705

Fig. 2: Slight View of 19 Random Values of Dimensionless Parameters

```python
import pandas as pd
import xgboost as xgb
from sklearn.model_selection import train_test_split
from sklearn.metrics import mean_squared_error

data = pd.read_excel('dataset.xlsx')

train_data = data.iloc[:30]
test_data = data.iloc[30:]

X_train = train_data[['experimental']]
y_train = train_data['equation']
X_test = test_data[['experimental']]

model = xgb.XGBRegressor(objective='reg:squarederror', n_estimators=1000, max_depth=3)

model.fit(X_train, y_train)

y_pred = model.predict(X_test)

test_data['predicted_equation'] = y_pred

output_file = 'predicted_equation_results.xlsx'
test_data.to_excel(output_file, index=False)

print(f"Results saved to '{output_file}'.")
```

Fig. 3: Code Example of XGBoost Algorithm in Python

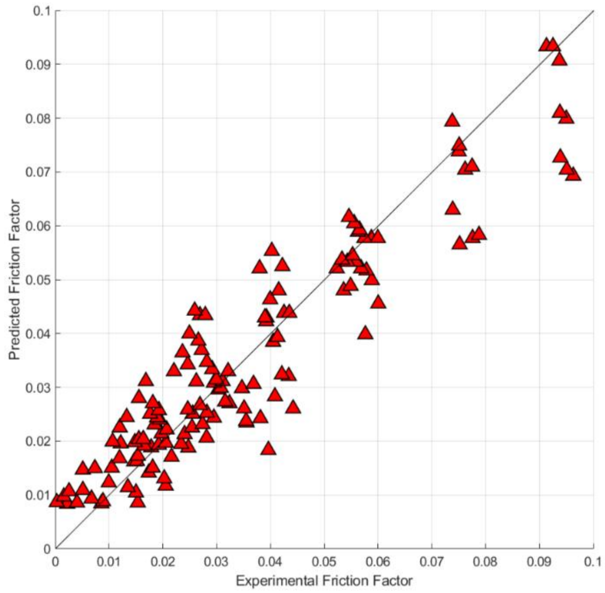

Fig. 4: Experimental Friction Factor vs. Predicted Friction Factor by Log-Log Regression (LLR)

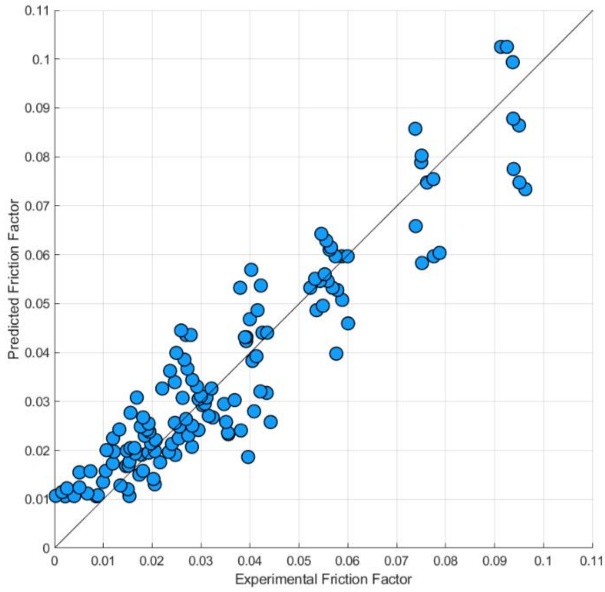

Fig. 5: Experimental Friction Factor vs. Predicted Friction Factor by Artificial Neural Network (ANN)

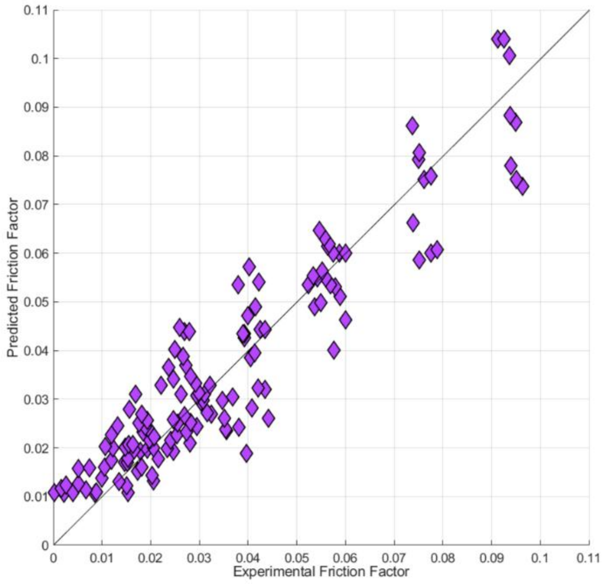

Fig. 6: Experimental Friction Factor vs. Predicted Friction Factor by Teaching-Learning Based Optimization

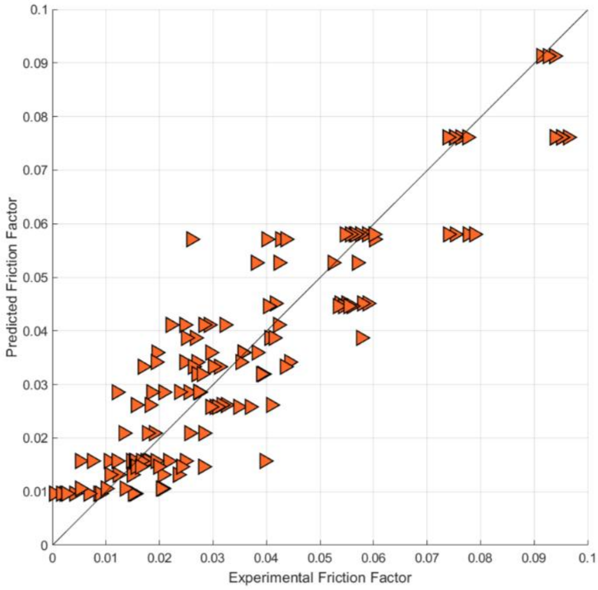

Fig. 7: Experimental Friction Factor vs. Predicted Friction Factor by XGBoost (XGB) Algorithm

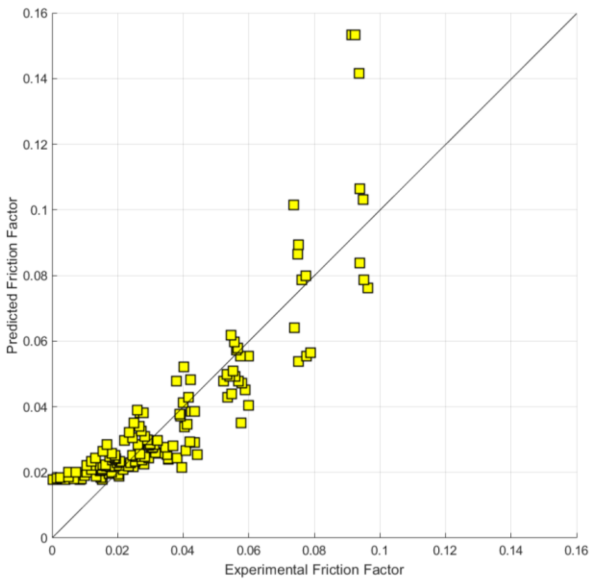

Fig. 8: Experimental Friction Factor vs. Predicted Friction Factor by Negative Binomial Regression (NBR)

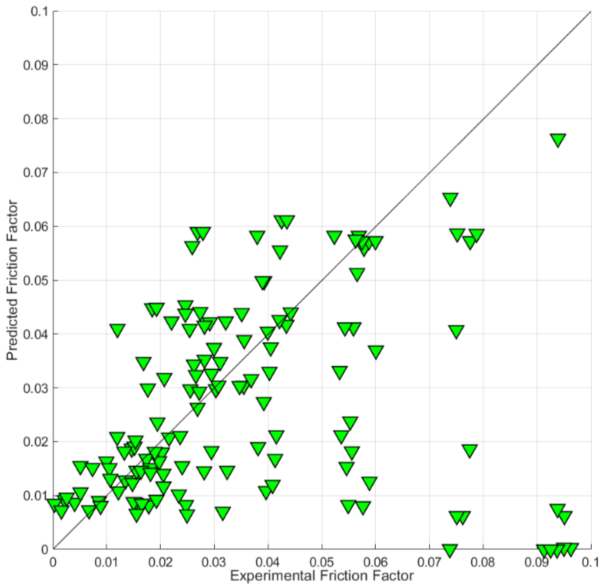

Fig. 9: Experimental Friction Factor vs. Predicted Friction Factor by Gaussian Process Regression (GPR)

Table 1. R-Square, Average Absolute Error (AAE), Average Absolute Percentage Error (AAPE) and Root Mean Square Error (RMSE) Values of Algorithms

	R^2	AAE	AAPE	RMSE
LLR	0.867131	0.006727	18.70%	0.008863
ANN	0.868387	0.006836	19.00%	0.008662
TLBO	0.867601	0.006901	19.18%	0.00871
XGBOOST	0.837726	0.007437	20.67%	0.009636
NBR	0.756835	0.00889	24.71%	0.012797
GAUSSIAN PROCESS	0.036824	0.017459	48.53%	0.028436

4. Conclusion

In this study, the friction factor was estimated by machine learning algorithms and compared with experimental data. Based on the estimation results and comparisons made;

- LLR performed slightly better than other machine learning models (based on LLR=18.70% AAPE value).
- Artificial Neural Network (ANN) follows LLR by a small margin (based on ANN=19.00% AAPE value).
- It has been observed that the performance of LLR, ANN, TLBO and XGBoost models are quite close to each other (based on LLR=18.70%, ANN=19.00%, TLBO=19.18% and XGBoost=20.67% AAPE values).
- GPR performed quite poorly compared to other models (based on GPR=48.53% AAPE value).

References

AlDahoul, N., Essam, Y., Kumar, P., Ahmed, A. N., Sherif, M., Sefelnasr, A., & Elshafie, A. (2021). Suspended sediment load prediction using long short-term memory neural network. *Scientific Reports, 11*(1), 7826. Retrieved from https://doi.org/10.1038/s41598-021-87415-4

Altunkaynak, A. (2009). Sediment load prediction by genetic algorithms. *Advances in Engineering Software, 40*(9), 928-934. Retrieved from https://doi.org/10.1016/j.advengsoft.2008.12.009

Azamathulla, H. M., Cuan, Y. C., Ghani, A. A., & Chang, C. K. (2013). Suspended sediment load prediction of river systems: GEP approach. *Arabian Journal of Geosciences, 6*, 3469-3480. Retrieved from https://doi.org/10.1007/s12517-012-0608-4

Azamathulla, H. M., Ghani, A. A., Chang, C. K., Hasan, Z. A., & Zakaria, N. A. (2010). Machine learning approach to predict sediment load–a case study. *CLEAN–Soil, Air, Water, 38*(10), 969-976. Retrieved from https://doi.org/10.1002/clen.201000068

Darabi, H., Mohamadi, S., Karimidastenaei, Z., Kisi, O., Ehteram, M., ELShafie, A., & Torabi Haghighi, A. (2021). Prediction of daily suspended sediment load (SSL) using new optimization algorithms and soft computing models. *Soft Computing, 25*, 7609-7626. Retrieved from https://doi.org/10.1007/s00500-021-05721-5

Elshaboury, N., Abdelkader, E. M., Al-Sakkaf, A., & Alfalah, G. (2021). Teaching-learning-based optimization of neural networks for water supply pipe condition prediction. *Water, 13*(24), 3546. Retrieved from https://doi.org/10.3390/w13243546

Gershman, S. J., & Blei, D. M. (2012). A tutorial on Bayesian nonparametric models. *Journal of Mathematical Psychology, 56*(1), 1-12. Retrieved from https://doi.org/10.1016/j.jmp.2011.08.004

Jain, P., Choudhury, A., Dutta, P., Kalita, K., & Barsocchi, P. (2021). Random forest regression-based machine learning model for accurate estimation of fluid flow in curved pipes. *Processes, 9*(11), 2095. Retrieved from https://doi.org/10.3390/pr9112095

Kanin, E., Vainshtein, A., Osiptsov, A., & Burnaev, E. (2018, October). The method of calculation the pressure gradient in multiphase flow in the pipe segment based on the machine learning algorithms. *In IOP Conference Series: Earth and Environmental Science* (Vol. 193, No. 1, p. 012028). IOP Publishing. Retrieved from https://doi.org/10.1088/1755-1315/193/1/012028

Khamehchi, E., & Bemani, A. (2021). Prediction of pressure in different two-phase flow conditions: machine learning applications. *Measurement, 173*, 108665. Retrieved from https://doi.org/10.1016/j.measurement.2020.108665

Kumar, A., Ridha, S., Ganet, T., Vasant, P., & Ilyas, S. U. (2020). Machine learning methods for herschel–bulkley fluids in annulus: Pressure drop predictions and algorithm performance evaluation. *Applied Sciences, 10*(7), 2588. Retrieved from https://doi.org/10.3390/app10072588

Lemaire, G. G., Broholm, M. M., Wünsch, U., Hirsch, M., Ottosen, C. F., Thrane, B. B., Pedersen, J. K., Dissing, L., & Bjerg, P. L. (2024). Contaminant mass discharge estimation of a sulfonamide plume by use of hydraulic profiling tool (HPT) and fluorescence techniques. *Journal of Contaminant Hydrology, 267*, 104422. Retrieved from https://doi.org/10.1016/j.jconhyd.2024.104422

Melesse, A. M., Ahmad, S., McClain, M. E., Wang, X., & Lim, Y. H. (2011). Suspended sediment load prediction of river systems: An artificial neural network approach. *Agricultural Water Management, 98*(5), 855- 866. Retrieved from https://doi.org/10.1016/j.agwat.2010.12.012

Niazkar, M., Menapace, A., Brentan, B., Piraei, R., Jimenez, D., Dhawan, P., & Righetti, M. (2024). Applications of XGBoost in water resources engineering: A systematic literature review (Dec 2018–May 2023). *Environmental Modelling & Software, 174*, 105971. Retrieved from https://doi.org/10.1016/j.envsoft.2024.105971

Nigate, F., Yenehun, A., Belay, A. S., Asmamaw, D. K., & Walraevens, K. (2024). Application of Pumping Tests to Estimate Hydraulic Parameters of Volcanic Aquifers in Lake Tana Basin, Ethiopia. *Water, 17*(1), 9. Retrieved from https://doi.org/10.3390/w17010009

Nourani, V., & Andalib, G. (2015). Daily and monthly suspended sediment load predictions using wavelet based artificial intelligence approaches. *Journal of Mountain Science, 12*, 85-100. Retrieved from https://doi.org/10.1007/s11629-014-3121-2

Osgouei, R. E., Ozbayoglu, A. M., Ozbayoglu, E. M., Yuksel, E., & Eresen, A. (2015). Pressure drop estimation in horizontal annuli for liquid–gas 2 phase flow: Comparison of mechanistic models and computational intelligence techniques. *Computers & Fluids, 112*, 108-115. Retrieved from https://doi.org/10.1016/j.compfluid.2014.11.003

Rao, R. V. (2016). Teaching-learning-based optimization algorithm (pp. 9-39). *Springer International Publishing*. Retrieved from https://doi.org/10.1007/978-3-319-22732-0

Sayari, S., Mahdavi-Meymand, A., & Zounemat-Kermani, M. (2020). Prediction of critical velocity in pipeline flow of slurries using TLBO algorithm: a comprehensive study. *Journal of Pipeline Systems Engineering and Practice, 11*(2), 04019057. Retrieved from https://doi.org/10.1061/(ASCE)PS.1949- 1204.0000439

Schulz, E., Speekenbrink, M., & Krause, A. (2018). A tutorial on Gaussian process regression: Modelling, exploring, and exploiting functions. *Journal of mathematical psychology, 85*, 1-16. Retrieved from https://doi.org/10.1101/095190

Shadloo, M. S., Rahmat, A., Karimipour, A., & Wongwises, S. (2020). Estimation of pressure drop of two-phase flow in horizontal long pipes using artificial neural networks. *Journal of Energy Resources Technology, 142*(11), 112110. Retrieved from https://doi.org/10.1115/1.4047593

Sharafati, A., Haji Seyed Asadollah, S. B., Motta, D., & Yaseen, Z. M. (2020). Application of newly developed ensemble machine learning models for daily suspended sediment load prediction and related uncertainty analysis. *Hydrological Sciences Journal, 65*(12), 2022-2042. Retrieved from https://doi.org/10.1080/02626667.2020.1786571

Singh, K., Miska, S., Ozbayoglu, E., & Alp Aydin, B. (2018, October). Using supervised machine learning algorithms to predict pressure drop in narrow annulus. *In SPE Eastern Regional Meeting* (p. D043S005R002). SPE. Retrieved from https://doi.org/10.2118/191794-18erm-ms

Sorgun, M. (2010). Modeling of Newtonian fluids and cuttings transport analysis in high inclination wellbores with pipe rotation (Doctoral dissertation, Middle East Technical University (Turkey)).

Sun, H., Luo, Q., Xia, Z., Li, Y., & Yu, Y. (2024). Bottomhole pressure prediction of carbonate reservoirs using XGBoost. *Processes, 12*(1), 125. Retrieved from https://doi.org/10.3390/pr12010125

Tawfik, A. M. (2023). Hydraulic solutions of pipeline systems using artificial neural networks. *Ain Shams Engineering Journal, 14*(3), 101896. Retrieved from https://doi.org/10.1016/j.asej.2022.101896

Wahid, M. F., Tafreshi, R., Khan, Z., & Retnanto, A. (2022). Prediction of pressure gradient for oil-water flow: a comprehensive analysis on the performance of machine learning algorithms. *Journal of Petroleum Science and Engineering, 208*, 109265. Retrieved from https://doi.org/10.1016/j.petrol.2021.109265

Wan, C., Zhu, H., Xiao, S., Zhou, D., Bao, Y., Liu, X., & Han, Z. (2024). Prediction of pressure drop in solid-liquid two-phase pipe flow for deep-sea mining based on machine learning. *Ocean Engineering, 304*, 117880. Retrieved from https://doi.org/10.1016/j.oceaneng.2024.117880

Williams, C. G., & Ojuri, O. O. (2021). Predictive modelling of soils' hydraulic conductivity using artificial neural network and multiple linear regression. *SN Applied Sciences, 3*(2), 152. Retrieved from https://doi.org/10.1007/s42452-020-03974-7

Yang, S., & Berdine, G. (2015). The negative binomial regression. *The Southwest respiratory and critical care chronicles, 3*(10), 50-54. Retrieved from https://doi.org/10.12746/swrccc2015.0310.135

Yilmaz, B., Aras, E., Kankal, M., & Nacar, S. (2019). Prediction of suspended sediment loading by means of hybrid artificial intelligence approaches. *Acta Geophysica, 67*, 1693-1705. Retrieved from https://doi.org/10.1007/s11600-019-00374-3

Determination of unit hydrographs for Karabuk Bulak stream in Türkiye using six different synthetic methods

Sayed Abdul Matin Hashemi[1], Hasan Törehan Babacan[2], Fatih Saka*[1]

[1] *Karabuk University, Department of Civil Engineering, 78000 Karabük, Türkiye*
[2] *Amasya University, Taşova Yüksel Akın Vocational School,Transportation Services Department , 05000 Amasya, Türkiye*

Abstract. In water resources planning, hydrographs that show the variation of flow over time are very important. The unit hydrograph, which can reveal the relationships between precipitation and flow that have the most effect on flow, is also very important for understanding the time of peak discharge. Synthetic unit hydrograph methods are useful for estimating runoff, especially in cases where rainfall data are missing or incomplete. Different synthetic methods may be suitable for different basins according to basin characteristics. In this study, the unit hydrographs of the Bulak basin in Karabük province were obtained and compared using six different synthetic unit hydrograph methods: Snyder, SCS, Mockus, DSİ, Nakayasu and Gamma methods. The peak discharge and the times to reach peak discharge were obtained as follows, using the Snyder, DSİ, Mockus, SCS, Nakayasu and Gamma methods, respectively: 1.029 ($m^3/s/mm$), 6.07 hours, 1.96 ($m^3/s/mm$), 3.15 hours, 1.847 ($m^3/s/mm$), 3.38 hours, 3.33 ($m^3/s/mm$), 1.91 hours, 2.88 ($m^3/s/mm$), 2.16 hours, and 3.426 ($m^3/s/mm$), 1.75 hours.

Keywords: Synthetic unit hydrograph; Snyder; SCS; DSİ Synthetic; Mockus; Nakayasu; Gamma

1. Introduction

Water plays a critical role in human life and ecosystems but also poses risks when excessive rainfall leads to floods (United Nations World Water Assessment Programme (WWAP), 2021). To preserve current water resources, address the rising demand from the country's rapidly growing population, and tackle potential future challenges, a comprehensive, well-structured long-term strategy is essential for sustainable water resource management. Effective planning and management of natural resources require a thorough understanding of the hydrological behavior of watersheds (N. Singh & Singh, 2017). Floods, often exacerbated by human land use practices, require careful management through hydrological analysis and protective infrastructure (Bedient et al., 2013). Understanding the rainfall-runoff relationship within watersheds is essential for designing effective flood control measures, with unit hydrograph analysis being a key tool (Ven Te Chow & David R. Maidment, 1988). A hydrograph illustrates the fluctuation of discharge over time, comprising a rising limb (flow increase), peak (maximum flow), and falling limb (flow decrease) (Dingman, 2015; Ven Te Chow & David R. Maidment, 1988). This was one of the first tools available to the hydrologic community for determining the complete shape of hydrographs, rather than just peak discharges, and is essential for understanding flood dynamics and watershed behavior (Bhunya, Panda, et al., 2021; Kalgonda Patil & Bhagwat, 2019).

The unit hydrograph, introduced by Sherman in 1932 (L.K. Sherman, 1932), represents direct runoff from 1 cm of effective rainfall over a specific duration. Its assumptions include uniform rainfall distribution and proportional hydrograph ordinates (Dingman, 2015; Ven Te Chow & David R. Maidment, 1988). While simplifying complex rainfall-runoff relationships, the theory is unsuitable for large basins or events involving snowmelt (Gupta, 2017; Maidment, 1993). Unit hydrographs can be derived from observed rainfall and runoff data, but in their absence, synthetic unit hydrographs (SUH), derived from watershed characteristics rather than rainfall-runoff records, are commonly used (Bhunya et al., 2007). Due to similarity in the shape of statistical distributions and a conventional unit hydrograph, several attempts have been made by different researches to derive the SUHs by using the probability distribution functions (pdfs) (Bhuyan et al., 2015). Synthetic unit hydrograph methods were originally classified into four primary categories: traditional methods, conceptual methods, probabilistic methods, and geomorphological methods (Kalgonda Patil & Bhagwat, 2019; Pedroso & Mannich, 2021).

This study focuses on deriving and evaluating synthetic unit hydrographs for the Bulak watershed in Karabük, Türkiye. Six synthetic methods (Snyder, SCS, Mockus, DSİ, Nakayasu and Gamma) were reviewed and applied.

* Corresponding author, E-mail: sakafatih@karabuk.edu.tr

https://doi.org/10.31462/icearc2025_ce_hwr_679
golden light publishing

2. Materials and methods

2.1. Characterization of the study area

The study area encompasses the Bulak Stream Basin located within the Karabük Province, situated in the Western Black Sea Region of Turkey. The province shares its borders with Bartın to the north, Kastamonu to the northeast and east, Çankırı to the southeast, Bolu to the southwest, and Zonguldak to the west (Karabuk Governorship, 2022). On the 1:25,000 topographic map, the basin is depicted on sheets F29-a3, F29-a4, F29-d1, and F29-d2 (General Command of Mapping, 2019). Furthermore, the Karabük Province is situated at an average elevation of approximately 270 meters above sea level, characterized by valleys and plateaus (Karabuk Governorship, 2022). The geographic location of Karabük Province within Türkiye and the specific location of the Bulak Basin within Karabük Province are illustrated in Fig. 1.

Karabük Province exhibits partial characteristics of the Black Sea climate (Türkeş, 2012). While the annual average air temperature in the Black Sea Region is 13.15°C (TSMS (Türkiye Meteoroloji Genel Müdürlüğü), 2021), it is approximately 13.2°C in Karabük Province (TSMS (Türkiye Meteoroloji Genel Müdürlüğü), 2022). During July, the warmest month of the year, the average air temperature in the Black Sea Region is 23.24°C (TSMS (Türkiye Meteoroloji Genel Müdürlüğü), 2021), while it hovers around 23.1°C in Karabük. January is the coldest month in Karabük, with an average air temperature of 2.6°C (TSMS (Türkiye Meteoroloji Genel Müdürlüğü), 2022). The highest recorded air temperature in the province is 43°C, whereas the lowest is -14.2°C (TSMS (Türkiye Meteoroloji Genel Müdürlüğü), 2021).

For the study area, rainfall is most abundant in late autumn and scarce in early spring, akin to the Eastern Black Sea Region (Bahadır & Özdemir, 2011). However, the precipitation amount is nearly half that of the Eastern Black Sea Region (TSMS (Türkiye Meteoroloji Genel Müdürlüğü), 2022). Karabük Province experiences precipitation throughout the year due to its Black Sea climate characteristics(Türkeş, 2012), yet it undergoes a dry period in July and August . The annual average precipitation in the province is 487.7 mm, with a prevailing wind direction from the southwest, and an annual average wind speed of 0.8 m/s (TSMS (Türkiye Meteoroloji Genel Müdürlüğü), 2022).

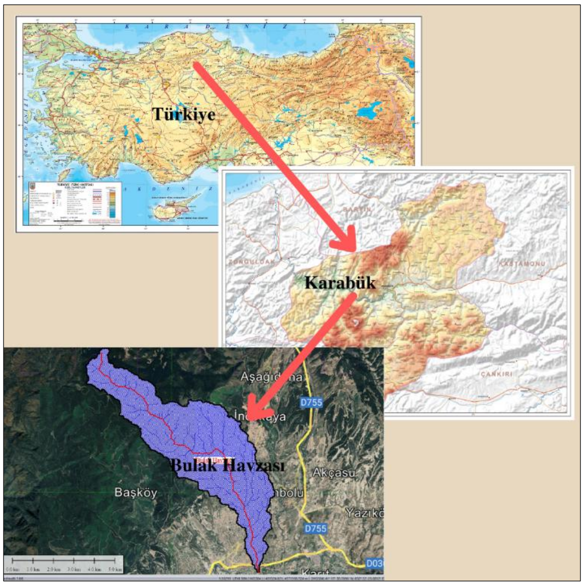

Fig. 1. Location of Karabük Province in Turkey and Bulak Basin within Karabuk Province

2.2. Synthetic unit hydrograph methods

Synthetic unit hydrographs are generally categorized into three groups in the literature (Maidment, 1993). Those that relate watershed characteristics to hydrograph characteristics (peak flow rate, base time, etc.), such as the Snyder (Snyder, 1938) and Gray methods (Bhunya, S.N. Panda, et al., 2021; Patil & Bhagwat, 2019). Those based on dimensionless unit hydrographs, such as the SCS method (US Soil Conservation Service (SCS), 1986). Those based on watershed storage models, such as the Clark method (Clark, 1945).

In this section, we briefly discuss several synthetic unit hydrograph methods that are commonly used, including Snyder, SCS, Mockus, DSİ, Nakayasu and Gamma synthetic methods.

2.2.1. Snyder synthetic unit hydrograph method

In 1938, Franklin F. Snyder proposed the concept that watershed characteristics, such as shape, topography, main channel slope, flow density, and channel storage, influence the shape of hydrographs (Snyder, 1938). Based on this idea, he introduced an empirical unit hydrograph formula called the synthetic unit hydrograph, which averages these characteristics with coefficients for watersheds of similar character (Linsley et al., 1982; Ponce, 1989; Snyder, 1938; Viessman, 2003)

The Snyder method (Snyder, 1938), the first unit hydrograph method applied in watersheds with no historical rainfall-flow measurements, remains one of the most widely used synthetic unit hydrograph methods today (Gupta, 2017; Maidment, 1993). In international literature, the Snyder method is noted for assuming that each watershed has a single unique unit hydrograph (V. P. Singh, 1988). Snyder conducted extensive research on watersheds in the Appalachian Mountains region of the United States, with watershed areas ranging from 26 to 26.000 km², resulting in a standardized unit hydrograph shape (Linsley et al., 1982; Snyder, 1938). The key formulas for calculating hydrograph parameters using the Snyder method are provided in various hydrology texts (Linsley et al., 1982; V. P. Singh, 1988; Snyder, 1938).

$$t_L = 0.75 \times C_t \times (L \times L_c)^{0,3} \tag{1}$$

$$t_r = \frac{t_L}{5.5} \tag{2}$$

$$t_p = \left(\frac{t_r}{2}\right) + t_L \tag{3}$$

$$Q_p = \alpha \frac{C_p \times A}{t_L} \tag{4}$$

Here, L represents the main channel length up to the watershed boundary (in km), L_c is the length from the watershed centroid to the watershed outlet (in km), C_t is a timing coefficient (typically between 1.8 and 2.2), t_L is the lag time of the unit hydrograph for the watershed (in hours), t_r is the effective rainfall duration (in hours), t_p is the time to peak (in hours), Q_p is the peak discharge (in m³/s/mm), α is a conversion constant (0.275 for SI units, 640 for CU units), and C_p is a peak coefficient (typically between 0.59 and 0.69, depending on soil type) and A is the drainage area of the watershed (in km²). Using the formula below, base time (T_b) can be calculated (McCuen, 2016).

$$T_b = 5 \times [\left(\frac{t_L}{11}\right) + t_L] \tag{5}$$

Additionally, following equations provide formulas for calculating the widths of the hydrograph at 50% (W_{50}) and 75% (W_{75}) of the peak discharge.

$$W_{50} = \alpha_{50} \times \left(\frac{Q_p}{A}\right)^{-1.075} \tag{6}$$

$$W_{75} = \alpha_{75} \times \left(\frac{Q_p}{A}\right)^{-1.075} \tag{7}$$

Here, α_{50} and α_{75} are constants, 0.18 for both, used in the formulas (V. P. Singh, 1988).

2.2.2. SCS synthetic unit hydrograph method

The Soil Conservation Service (now known as the Natural Resources Conservation Service or NRCS) developed the SCS Method (US Soil Conservation Service (SCS), 1986), which derives unit hydrographs with a simple triangular shape from numerous hydrographs obtained from different regions and watershed characteristics.

In the SCS method, the process begins with determining the time of concentration (T_c), which is also referred to as the concentration time.

$$T_c = 0.066 \times (\frac{L^2}{S_0})^{0.385} \ (hours) \tag{8}$$

Here, L is the main channel length of the watershed (in km), and S_0 represents channel slope (McCuen, 2016; US Soil Conservation Service (SCS), 1986). Next, the lag time (t_L) and effective rainfall duration (t_r) are calculated using the following equations:

$$t_L = 0.6 \times T_c \ (hours) \tag{9}$$

$$t_r = 0.133 \times T_c \ (hours) \tag{10}$$

The time to peak (t_p) is determined using following equation (McCuen, 2016):

$$t_p = \left(\frac{t_r}{2}\right) + t_L \tag{11}$$

The potential maximum retention capacity of the watershed is denoted as S and is related to the hydrological characteristics of the watershed, as well as factors such as vegetation cover. The formula for S is presented in the following equation:

$$S = \left(\frac{25400}{CN}\right) - 254 \ (mm) \tag{12}$$

Here, CN represents the curve number of the watershed, which takes values between 0 and 100. CN is a function of the watershed's soil classification and surface cover (McCuen, 2016; Mishra & Singh, 2003; Pedroso & Mannich, 2021). The peak discharge (Q_p) can be calculated using the formula:

$$Q_p = \frac{0.2083 \times A}{t_p} \left(\frac{\frac{m^3}{sn}}{mm}\right) \tag{13}$$

where A is the watershed area (in km²) and t_p is the time to peak (in hours) (McCuen, 2016).

The SCS triangular unit hydrograph does not include a base time, as it is a simple triangular shape without a flat base (McCuen, 2016). The SCS method is widely used due to its simplicity and is particularly useful when hydrograph data are not available for a specific watershed. However, it is important to note that it assumes a triangular unit hydrograph shape, which may not accurately represent the actual hydrograph characteristics of all watersheds (Mishra & Singh, 2003).

2.2.3. DSİ synthetic unit hydrograph method

This method is applied to watersheds up to 1000 km² in size. When applied to watersheds larger than 1000 km², the watershed area should be divided, and a separate unit hydrograph should be determined for each sub-area. Additionally, the unit hydrographs used in this method are obtained based on 2-hour rainfall values, so the time to peak of the unit hydrograph (T_p) should not be less than 2 hours (Demir & Ülke Keskin, 2022; Gevrek & İrvem, 2021; Tanrıverdi, 2021). The formulas used in the DSİ synthetic unit hydrograph method are the following:

$$E = \frac{L \times L_c}{\sqrt{S_h}} \tag{14}$$

$$q_p = \frac{414}{A^{0.225} \times E^{0.16}} \tag{15}$$

$$Q_p = q_p \times A \times 10^{-3} \tag{16}$$

$$V_b = A \times h_a \times 10^{3} \tag{17}$$

$$t_b = 3.65 \times \frac{V_b}{Q_p} \tag{18}$$

Where, E is a dimensionless coefficient dependent on the harmonic slope of the main channel, S_h represents the harmonic slope of the main channel (%), q_p is the unit discharge (lt/sec/km^2/mm), Q_p denotes the peak discharge of the hydrograph (m³/sec/mm), V_b represents the total water volume of the hydrograph (m³), t_b signifies the base volume of the hydrograph, A is the watershed area (km²), L is the main channel length (km), L_c is the distance from the centroid to the outlet (km), and ha is the effective rainfall depth (mm) (Tanrıverdi, 2021).

In the DSİ Synthetic Unit Hydrograph method, the time to peak (t_p) is theoretically determined by summing the lag time (t_L) and 80% of the effective rainfall duration (t_r), as given by the equation $t_p = t_L + 0.8 \times t_r$. However, in practical applications where detailed rainfall-runoff data are limited, t_p is commonly approximated as one-fifth of the base time (t_b), i.e., $t_p \approx t_b / 5$. This practical approach allows for a simplified estimation of the hydrograph shape and timing, and has been commonly adopted in DSİ engineering studies (Ekemen Keskin et al., 2018).

2.2.4. Mockus synthetic unit hydrograph method

The Mockus method is another synthetic unit hydrograph method commonly used for obtaining unit hydrographs in watersheds where rainfall-runoff data is not available. The simplicity of calculation and the triangular shape of the resulting hydrograph make this method widely used (McCuen, 2016; Mishra & Singh, 2003; US Soil Conservation Service (SCS), 1986). According to the literature, some sources suggest that the method can be applied in watersheds smaller than 1000 km² (Linsley et al., 1982; Mishra & Singh, 2003), while others indicate it is more suitable for watersheds smaller than 10 km² (Linsley et al., 1982; McCuen, 2016). Additionally, it is emphasized that the time of concentration should be less than 30 hours for the Mockus method to be applicable (Linsley et al., 1982; McCuen, 2016; Mishra & Singh, 2003; Ponce, 1989; V. P. Singh, 1988; Viessman, 2003).

In the Mockus method, like in the Snyder method, certain watershed coefficients are required for calculation. One of these coefficients is the climate parameter (K), and the other is H_c. H_c depends on the climate parameter K and ranges from 1 to 2. K, on the other hand, can be determined based on a known unit hydrograph from a watershed with similar climatic characteristics. However, if there is no watershed with similar characteristics, the K coefficient can be considered as 0.208 (Mishra & Singh, 2003; Ponce, 1989). The formulas required for the Mockus synthetic unit hydrograph method are:

$$t_c = 0.00032 \times \left(\frac{L^{0.77}}{So^{0.385}}\right) \tag{19}$$

$$t_r = 2 \times t_c^{\frac{1}{2}} \tag{20}$$

$$t_p = 0.5 \times t_r + 0.6 \times t_c \tag{21}$$

$$t_f = H_c \times t_p \tag{22}$$

$$Q_p = K \times A \times \frac{h_a}{t_p} \tag{23}$$

Where tc is the concentration time of the hydrograph (hours), t_r is the effective rainfall duration (hours), t_p is the time to reach the peak (hours), t_f is the recession time of the hydrograph, and Q_p is the peak discharge of the hydrograph (m³/sec/mm). L is the length of the main channel of the watershed (km), S_0 represents the slope of the main channel (m/m), and A is the watershed area (km²). L is the length of the main channel of the watershed (km), S_0 represents the slope of the main channel (m/m), and A is the watershed area (km²). The rainfall height h_a is taken as 1 mm in the peak discharge formula.

2.2.5. Gamma synthetic unit hydrograph method

The Gamma synthetic unit hydrograph method requires more watershed and river characteristics compared to other synthetic methods to determine the unit hydrograph for the desired watershed (Mishra & Singh, 2003; US Soil Conservation Service (SCS), 1986). Before calculating parameters such as peak discharge and time to peak for the hydrograph, factors such as Source Factor (SF), Source Frequency (SN), Joint Number (JN), Drainage Network Density (D), Width Factor (WF), Symmetry Factor (SIM) and Relative Upstream Area (RUA) of the watershed must be determined (Rodríguez-Iturbe & Valdés, 1979). Formulas to obtain these parameters are:

$$SF = \frac{\text{Total length of 1st order streams}}{\text{Total length of the stream network}} \quad (24)$$

$$SN = \frac{\text{Total number of 1st order streams}}{\text{Total number of the stream network}} \quad (25)$$

$$JN = (\text{Total number of 1st order streams}) - 1 \quad (26)$$

$$D = \frac{\text{Total length of the stream network}}{\text{Watershed area}} \quad (27)$$

$$WF = \frac{\text{Width of the watershed at 75\% distance from the outlet}}{\text{Width of the watershed at 25\% distance from the outlet}} \quad (28)$$

$$RUA = \frac{\text{Area at the headwaters of the watershed}}{\text{Watershed area}} \quad (29)$$

$$SIM = WF \times RUA \quad (30)$$

Once these watershed parameters are obtained, the hydrograph's time to peak (t_p), peak discharge (Q_p), and baseflow time (t_b) are calculated using the following formulas.

$$t_p = 0.43(\frac{L}{100 \times SF})^3 + 1.0665 \times SIM + 1.2775 \quad (31)$$

$$q_p = 0.1836 \times A^{0.5886} \times t_p{}^{-0.4008} \times JN^{0.2381} \quad (32)$$

$$t_b = 27.4132 \times t_p{}^{0.145} \times s_0{}^{-0.0986} \times SN^{0.7344} \times RUA^{0.2574} \quad (33)$$

2.2.6. Nakayasu synthetic unit hydrograph method

The Nakayasu synthetic unit hydrograph method was developed based on studies conducted on numerous rivers in Japan in the 1940s by Dr. Nakayasu (H. M. Raghunath, 2006; V. P. Singh, 1992). Unlike other synthetic unit hydrograph methods, calculations in this method do not require coefficients specific to the watershed. Instead, readily available watershed characteristics like area and length are used for calculations, simplifying the process. However, it's worth noting that this method is rarely used in Turkey and European countries, despite its popularity in East Asian countries (Bhunya, S.N. Panda, et al., 2021; US Soil Conservation Service (SCS), 1986).

To apply this method, some coefficients need to be determined, including α and the rainfall coefficient C. The α coefficient ranges from 1.5 to 3, while C is typically considered as 1 in the literature (Kamila et al., 2019; Limantara* et al., 2019). The delay time of the hydrograph, t_L, is calculated using different formulas depending on the length of the main channel. If the length of the main channel of the watershed is greater than 15 km:

$$t_L = 0.4 + 0.058 \times L \quad (34)$$

If the length of the main channel of the watershed is less than 15 km:

$$t_L = 0.8 + 0.048 \times L \quad (35)$$

After determining the delay time of the hydrograph, other parameters required for hydrograph construction are calculated using the following formulas:

$$t_r = 0.75 \times t_L \quad (36)$$

$$t_p = t_L + 0.8 \times t_r \quad (37)$$

$$t_{0.3} = \alpha \times t_L \quad (38)$$

$$Q_p = \frac{C \times A \times h_a}{3.6 \times (0.3 \times t_p + t_{0.3})} \quad (39)$$

In these formulas. tr represents the effective rainfall duration (hours). t_p is the time to reach the peak (hours). $t_{0.3}$ is the time required for the hydrograph to decrease to 30% of its peak. and Q_p is the peak discharge of the hydrograph (m^3/sec/mm) (Kamila et al., 2019; Limantara* et al., 2019).

3. Results and discussion

3.1 Basin characteristics

The basin's area, slope, elevations, and other characteristics were obtained using the Global Mapper extension. The maximum. minimum. and average elevations for the Bulak Basin were determined to be 1583.81 m. 280.16 m. and 651.82 m. respectively.

The main watercourse of the basin has a length of 16.508 km. The centroid of the basin is situated at an elevation of 664 m above sea level. and the distance to the basin's outlet is determined to be 6.851 km. The basin parameters for the study area. the Karabük Bulak Stream Basin. are presented in Table 1.

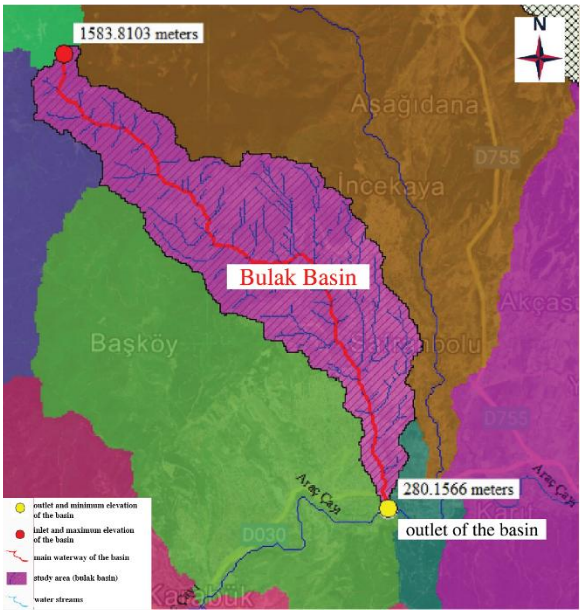

Fig. 2. Minimum and Maximum Elevation Values of the Basin

Table 1. Quantitative parameters identified for the Karabuk Bulak Stream Basin.

No	Parameters	Symbol	Value	Unit
1	Basin Area	A	30.485354	km²
2	Main Channel Length	L	16.389	km
3	Distance from Centroid to Outlet	L_c	6.851	km
4	Maximum Elevation of the Basin	-	1583.81	m
5	Minimum Elevation of the Basin	-	280.16	m
6	Harmonic Slope of the Main Channel	So	1.501863	%
7	Total Length of Stream Network	-	88.327	km
8	1st Order Stream Networks	-	121	count
9	Total Length of 1st Order Stream Networks	-	47.575	km
10	Total Stream Network Count	-	190	count
11	Basin Width at 25% Distance from Outlet	-	1.609	km
12	Basin Width at 75% Distance from Outlet	-	1.624	km

3.2 Unit hydrograph calculation for the Karabük Bulak Stream Basin using synthetic methods

Unit hydrograph calculations for the Karabük Bulak Stream Basin were performed using the Snyder. DSİ. SCS. Mockus. Nakayasu. and Gamma methods. In the calculations, the slope of the main channel was computed harmonically to prevent it from being influenced by extreme values (elevations of the highest-ranked channel). This harmonic slope was considered for all six methods used. The dimensionless unit hydrograph corresponding to the SUH methods was constructed based on standard dimensionless relationships and graphically presented. The validation of the hydrograph was performed by comparing the area under the hydrograph curve with the direct runoff volume corresponding to unit precipitation. The dimensionless unit hydrograph coordinates were developed, and their validation involved comparing the area under the hydrograph curve with the direct runoff volume corresponding to unit precipitation.

3.2.1. Unit hydrograph calculation using the Snyder synthetic method

To apply the Snyder method, it is necessary to determine the coefficients C_t and C_p. In this study. C_t and C_p coefficients were adjusted based on the total water volume of the basin. with $C_p = 0.683$ and $C_t = 1.8$. The required basin parameters for the application of this method are as follows: A = 30.485354 km². L = 16.389 km. $L_c = 6.851$ km. and ha = 1 mm.

Since a 1-hour unit hydrograph is desired for the basin. and the effective rainfall duration (t_r) is close to 1 hour. it was considered $t_R = t_r$. $q_{pR} = q_P$ and $t_{LR} = t_L$ for further calculations.

Using the Snyder method. the derivation of the unit hydrograph for the Karabük Bulak Stream Basin yielded several key hydrographic parameters. The time lag (t_L) was calculated as 5.564 hours. while the effective rainfall duration (t_r) was 1.012 hours. The time to peak (t_p) was determined to be 6.07 hours. The unit peak discharge (Q_p) was found to be 1.029 m³/s/mm. The hydrograph width at 50% of the peak discharge (w_{50}) was 6.876 hours. and at 75% of the peak (w_{75}). it was 3.82 hours.

The base time of the hydrograph (T_b) was calculated to be 30.352 hours. These results yielded the development of the unit hydrograph for the basin using the Snyder method. as illustrated in the Fig. 3.

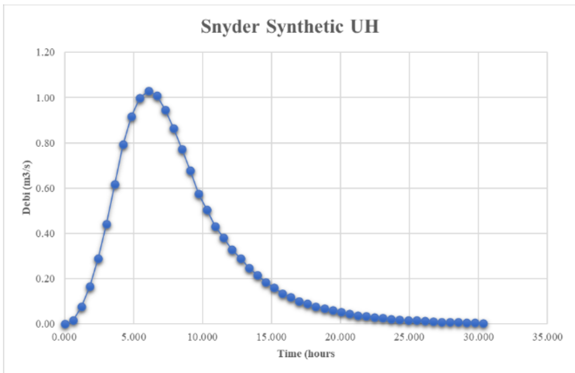

Fig. 3. Snyder unit hydrograph for the study area

3.2.2. Computation of basin unit hydrograph using DSİ synthetic method

The slope of the basin, like other basin parameters was obtained using the Global Mapper program. Additionally, harmonic slope calculation was used to prevent misleading results due to extreme values in channel slopes. The DSİ Synthetic method initiated the hydrograph solution by calculating the dimensionless coefficient E dependent on the harmonic slope to be used in the unit discharge resulting in 916.20 using formula (2.13).

Subsequently, the unit discharge (q_p) (lt/sec/km^2/mm) and peak discharge (Q_p) (m^3/sec/mm) values were calculated as 64.44 lt/sec/km^2/mm, and 1.96 m³/s/mm, respectively. The unit volume (V_b, m^3), base time (T_b), and time to peak (t_p) of the hydrograph were found as 30485 m^3, 15.73 and 3.15 hours, respectively. The unit hydrograph of the Karabük Bulak stream basin was drawn in Fig 4.

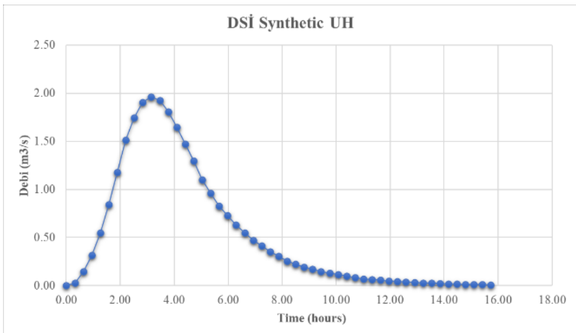

Fig. 4. Unit hydrograph obtained with the DSİ synthetic method for the Bulak basin

3.2.3. Computation of basin unit hydrograph using Mockus synthetic method

For the Mockus synthetic unit hydrograph method, the basin-specific coefficients K and H_c were adopted as 0.205 and 1.67, respectively. In cases where the K coefficient cannot be determined based on watershed characteristics, a default value of 0.208 is typically assumed to facilitate hydrograph derivation. In this study, however, the K value was slightly adjusted to ensure that the total volume under the unit hydrograph accurately reflects the effective rainfall-runoff volume. The concentration time (tc, hours) for the Mockus method was calculated as 2.836 hours. Subsequently, the effective rainfall duration (t_r, hours), time to peak (t_p, hours), and recession time (t_f, hours), as well as the desired discharge value, were calculated as 3.367, 3.384, 5.6506 hours and 1.847 m^3/sec/mm, respectively. The unit hydrograph of the Karabük Bulak stream basin was drawn using the Mockus synthetic method and shown in Fig. 5.

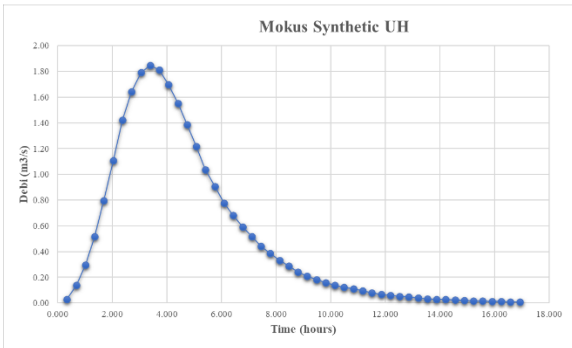

Fig. 5. Unit hydrograph obtained with the Mockus synthetic method for the Bulak basin

3.2.4. Computation of basin unit hydrograph using Nakayasu synthetic method

In the Nakayasu synthetic unit hydrograph method, the α coefficient, essential for hydrograph computation, generally ranges between 1.5 and 3 (Kamila et al., 2019). The rainfall coefficient, denoted as C, is typically taken as 1 (Limantara* et al., 2019). In this study, the α value was adjusted to 1.70 to ensure that the total volume under the hydrograph accurately represents the effective runoff. The computation of the hydrograph's lag time (t_L, hours) commenced by determining the time at which the hydrograph peaks. The lag time (t_L) for a basin with a main channel length greater than 15 km is calculated as 1.35 hours.

Subsequently, the effective rainfall duration (t_r) and time to peak (t_p) were calculated as 1.01 hours and 2.16 hours, respectively. To determine the time interval ($t_{0.3}$) required for the hydrograph to decrease by 30% of its peak discharge (Q_p), $t_{0.3}$ and Q_p were calculated as 2.30 hours and 2.88 m^3/sec/mm, respectively. With the peak discharge (Q_p) in hand, we proceeded to calculate the rising limb of the hydrograph's discharge (Q_a) and subsequently the base time (t_b) as 0.45 and 7.90 hours, respectively. Using the above calculated values of t_p, t_L, Q_p, t_r and t_b, the unit hydrograph of the Karabük Bulak Stream Basin using the Nakayasu synthetic method can be drawn as illustrated in Fig. 6.

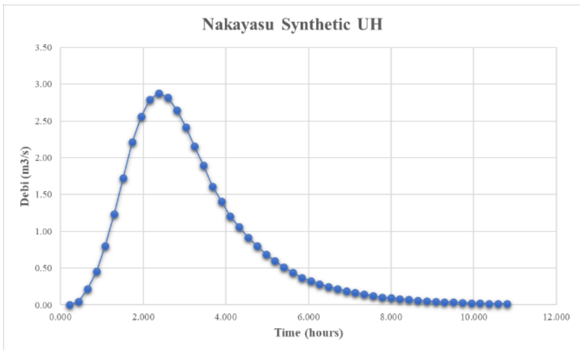

Fig. 6. Unit hydrograph obtained with the Nakayasu synthetic method for the Bulak basin

3.2.5. Computation of basin unit hydrograph using SCS synthetic method

The application of the SCS synthetic unit hydrograph method requires the determination of the Curve Number (CN). CN is a function of the basin's soil classification and land use, ranging between 0 and 100 (Mishra & Singh, 2003). For this study, the CN value was taken as 74, considering the region's soil type and land use. The necessary basin parameters for the application of this method are presented in Table 1. Potential Maximum Retention (S) value was calculated as 89.24 mm.

Subsequently, Concentration Time (t_c), Effective Rainfall Duration (t_r), Lag Time (t_L), Time to Peak (t_p), and Peak Discharge (Q_p) were calculated as 2.86, 0.38, 1.72, 1.91 hours and 3.33 m^3/sec/mm, respectively. With the calculated values of t_p, t_L, Q_p, t_c and t_r, the unit hydrograph of the Karabük Bulak Stream Basin using the SCS method is drawn in Fig. 7.

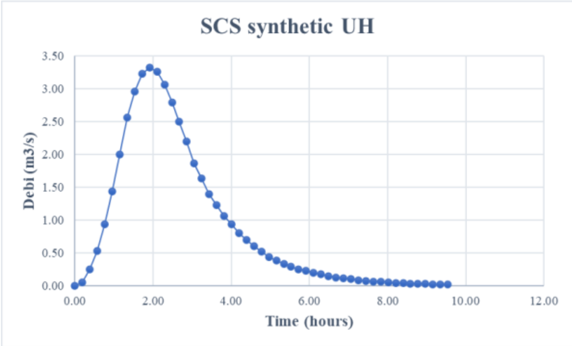

Fig. 7. Unit hydrograph obtained with the SCS synthetic method for the Bulak basin

3.2.6. Computation of basin unit hydrograph using Gamma synthetic method

The Gamma synthetic unit hydrograph method demands more extensive knowledge of basin and river characteristics compared to other methods. To calculate the time to peak (tp), peak discharge (Qp), and base time (tb) using the Gamma synthetic unit hydrograph method, it is first necessary to determine the relevant Gamma factors. These include the Source Factor (SF), Source Frequency (SN), Joint Number (JN), Drainage Network Density (D), Width Factor (WF), and Symmetry Factor (SIM), so these values were calculated as 0.5386, 0.6368, 120, 2.897 km/km^2, 1.009, 0.43 and 0.434, respectively. Based on the above calculated values, time to peak (t_p), peak discharge (q_p), and base time (t_b) were calculated as 7.75 hours, 3.426 m^3/sec and 10.52 hours, respectively. The unit hydrograph for the basin using the Gamma synthetic unit hydrograph was shown in Fig. 8.

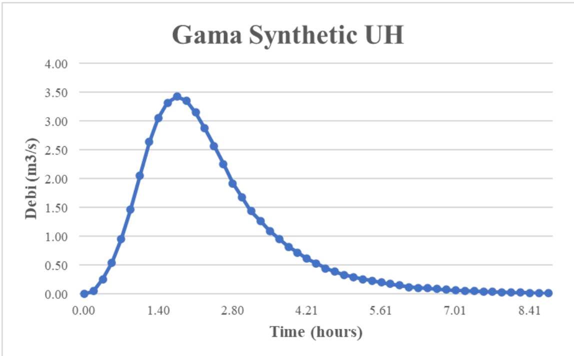

Fig. 8. Unit hydrograph obtained with the Gamma synthetic method for the Bulak basin

4. Conclusions

The dimensionless unit hydrograph coordinate values required for transferring peak flow and time to peak from synthetic hydrographs to the observed hydrograph were controlled to ensure that they match the water volume entering the basin. In the literature, the availability or development of these coordinate values for all synthetic methods is important for obtaining more accurate results in future studies.

Effective rainfall duration was obtained without losses such as infiltration, considering only the recorded rainfall for hydrograph estimation. Especially in larger basins, future studies can take into account such effects to conduct different investigations.

According to the Snyder method, the unit hydrograph peak discharge is higher by 0.93 $m^3/s/mm$ for DSİ, 0.82 $m^3/s/mm$ for Mockus, 2.30 $m^3/s/mm$ for SCS, 1.82 $m^3/s/mm$ for Nakayasu, and 2.40 $m^3/s/mm$ for Gamma, demonstrating how the peak discharge can be obtained from the lowest to the highest, respectively. The time to peak of unit hydrographs directly affects the durations of hydrographs that will be obtained with rainfall. Therefore, it is recommended to update unit hydrograph models by observing these values in real basins.

According to the Gamma method, the unit hydrograph time to peak discharge is higher by 4.32 seconds for Snyder, 1.4 seconds for DSİ, 1.634 seconds for Mockus, 0.16 seconds for SCS, and 0.41 seconds for Nakayasu, demonstrating how the time to peak discharge can be obtained in ascending order from the lowest to the highest, respectively. Since the times to reach peak discharge also vary with basin characteristics, these values need to be compared with real basin data.

Acknowledgments

The research described in this paper was financially supported by the Karabuk University Scientific Research Projects Coordination Unit under the grant number [KBÜBAP-22-YL-090].

References

Bahadır, M., & Özdemir, M. A. (2011). Trabzon ve Rize'de yağışın mevsimsel değişimlerinin marginal ve matrix yöntemleri ile belirlenmesi ve trend analizleri. *The Journal of International Social Research, 4*(17).

Bedient, P. B., Huber, W. C., & Vieux, B. E. (2013). *Hydrology and floodplain analysis* (5th ed.).

Bhunya, P. K., Berndtsson, R., Ojha, C. S. P., & Mishra, S. K. (2007). Suitability of Gamma, Chi-square, Weibull, and Beta distributions as synthetic unit hydrographs. *Journal of Hydrology, 334*(1–2), 28–38. https://doi.org/10.1016/j.jhydrol.2006.09.022

Bhunya, P. K., Panda, S. N., & Goel, M. K. (2021). Synthetic unit hydrograph methods: A critical review. *AACE Clinical Case Reports, 7*(1), 1. https://doi.org/10.2174/1874378101105010001

Bhuyan, M. K., Kumar, S., Jena, J., & Bhunya, P. K. (2015). Flood hydrograph with synthetic unit hydrograph routing. *Water Resources Management, 29*(15), 5765–5782. https://doi.org/10.1007/s11269-015-1145-1

Clark, C. O. (1945). Storage and the unit hydrograph. *Transactions of the American Society of Civil Engineers, 110*(1), 1419–1446. https://doi.org/10.1061/TACEAT.0005800

Demir, V., & Ülke Keskin, A. (2022). Yeterince akım ölçümü olmayan nehirlerde taşkın debisinin hesaplanması ve taşkın modellemesi (Samsun, Mert Irmağı örneği). *Geomatik, 7*(2), 149–162. https://doi.org/10.29128/geomatik.918502

Dingman, S. L. (2015). *Physical hydrology* (3rd ed.).

Ekemen Keskin, T., Çetiner, H. İ., Başdağ, S., Genç, S., Kılıç, H. Y., & Yazılım Anonim Şirketi, N. (2018). Akım gözlem istasyonları bulunmayan nehirlerin DSİ sentetik yöntemi kullanılarak taşkın debilerinin tahmini: Eskipazar Çayı örneği (Karabük, Türkiye). http://www.ishad.info

General Command of Mapping. (2019). *1:25,000 Topographic Map Series*. https://www.harita.gov.tr/

Gevrek, İ., & İrvem, A. (2021). Antakya'da taşkına neden olan yan derelerde hidrograf analizi ile taşkın tahmini. *Mustafa Kemal Üniversitesi Tarım Bilimleri Dergisi, 26*(3), 533–542. https://doi.org/10.37908/mkutbd.932723

Gupta, R. S. (2017). *Hydrology and hydraulic systems* (4th ed.). Waveland Press.

Kalgonda Patil, S., & Bhagwat, T. N. (2019). A review of synthetic hydrograph methods for design storm. *International Research Journal of Engineering and Technology, 06*(11), 2413–2418. www.irjet.net

Kamila, D., Limantara, L. M., Bisri, M., & Soetopo, W. (2019). The limiting physical parameter of Nakayasu synthetic unit hydrograph. *International Journal of Innovative Technology and Exploring Engineering, 8*(6), 2278–3075.

Karabuk Governorship. (2022). *Karabük ili 2021 yılı çevre durum raporu*.

Limantara, L. M., Kamila, D., Bisri, M., & Soetopo, W. (2019). Alpha modeling of Nakayasu synthetic unit hydrograph for part of watersheds in Indonesia. *International Journal of Recent Technology and Engineering, 8*(4), 5509–5514. https://doi.org/10.35940/IJRTE.D8972.118419

Linsley, R. K., Kohler, M. A., & Paulhus, J. L. H. (1982). *Hydrology for engineers* (3rd ed.). McGraw-Hill.

Maidment, D. R. (1993). *Hydrology handbook*. McGraw-Hill. https://doi.org/10.1061/9780784401385

McCuen, R. H. (2016). *Hydrologic analysis and design* (4th ed.). Pearson.

Mishra, S. K., & Singh, V. P. (2003). *Soil Conservation Service Curve Number (SCS-CN) Methodology* (1st ed.). Springer.

Pedroso, A., & Mannich, M. (2021). The uncertainties of synthetic unit hydrographs applied for basins with different runoff generation processes. *Revista Brasileira de Recursos Hidricos, 26*. https://doi.org/10.1590/2318-0331.262120210093

Ponce, V. M. (1989). *Engineering hydrology: Principles and practices*. Prentice-Hall.

Raghunath, H. M. (2006). *Hydrology: Principles, analysis and design* (2nd ed.). New Age International Publishers.

Rodríguez-Iturbe, I., & Valdés, J. B. (1979). The geomorphologic structure of hydrologic response. *Water Resources Research, 15*(6), 1409–1420. https://doi.org/10.1029/WR015i006p01409

Sherman, L. K. (1932). The unit hydrograph and flood prediction. *Engineering News-Record, 108*, 501–505.

Singh, N., & Singh, K. K. (2017). Geomorphological analysis and prioritization of sub-watersheds using Snyder's synthetic unit hydrograph method. *Applied Water Science, 7*(1), 275–283. https://doi.org/10.1007/s13201-014-0243-1

Singh, V. P. (1988). *Hydrologic systems: Rainfall-runoff modeling*. Prentice-Hall.

Singh, V. P. (1992). *Elementary hydrology*. Prentice-Hall.

Snyder, F. F. (1938). Synthetic unit-graphs. *Eos, Transactions American Geophysical Union, 19*(1), 447–454. https://doi.org/10.1029/TR019i001p00447

Tanrıverdi, O. (2021). Sentetik birim hidrograf metotlarının karşılaştırılması ve Trabzon Değirmendere havzası örneği. *Karabük University, Institute of Science*.

TSMS (Türkiye Meteoroloji Genel Müdürlüğü). (2021). *Türkiye Meteoroloji Genel Müdürlüğü 2021 yılı iklim verileri*.

TSMS (Türkiye Meteoroloji Genel Müdürlüğü). (2022). *Türkiye Meteoroloji Genel Müdürlüğü 2022 yılı iklim verileri*.

Türkeş, M. (2012). Türkiye'de gözlenen ve öngörülen iklim değişikliği, kuraklık ve çölleşme. *Ankara Üniversitesi Çevrebilimleri Dergisi, 4*(2), 1–32. https://doi.org/10.1501/CSAUM_0000000063

United Nations World Water Assessment Programme (WWAP). (2021). *The United Nations World Water Development Report 2021: Valuing water*. UNESCO.

US Soil Conservation Service (SCS). (1986). *Urban hydrology for small watersheds (Technical Release 55)*.

Ven Te Chow, & Maidment, D. R. (1988). *Applied hydrology*. McGraw-Hill.

Viessman, W. Jr. (2003). *Introduction to hydrology* (5th ed.). Prentice Hall.

Prediction of flood discharge with Jaya algorithm for Trabzon Province

Arife Günay*[1], Ömer Yüksek[1], Tuğçe Anılan[1]

[1]Karadeniz Technical University, Department of Civil Engineering, 61080 Trabzon, Türkiye

Abstract. Floods are the natural disasters that cause the highest life and property loss worldwide after earthquakes. Therefore, accurate prediction of flood discharges has a critical role in the design of hydraulic structures for economic and safe structure design. By employing developing technology, different algorithms are frequently used for modelling of flood flow prediction. In these modelling studies, a number of variables; including the areas, elevations, record lengths, latitude, and longitude of the stations are used as variable parameters. These studies are carried out for regions with a high probability of flooding. In this study, Trabzon Province of the Eastern Black Sea Basin (EBSB), one of the basins of Türkiye with a high probability of being exposed to flood disasters, was selected as the application basin. Various models were developed to estimate the flood discharges using the area and elevation data of 16 Stream Gauge Stations (SGS) located in the Trabzon province in the EBSB. The observation durations of SGS's were between 9 to 42 years. Multiple linear regression, classical regression (CRA), and Jaya algorithms that optimize hyperbolic and exponential regression functions were used for maximum flood flow estimations. As a result of the study, the Jaya optimization algorithm to model the maximum flood discharges, with low error values, has been found very successful.

Keywords: Prediction of flood discharge, Jaya algorithm, Regression analysis, Trabzon Province

1. Introduction

Floods are natural disasters that interrupt vital activities by causing loss of life, property, and land by exceeding the cross-section because of a rapid increase in the discharge in a riverbed (Demir and Keskin, 2022). Reliable estimation of flood discharges is important in the planning, design, and management of hydraulic structures to be built on the river (Anılan et al., 2016). The methods used for this can be divided into two main groups as deterministic and statistical methods. While it can be made deterministically by unit hydrograph method, it can also be made by statistical methods that use distributions such as Log-Normal III, Gumbel, and Log-Pearson Type III (Zhang et al., 2024). The study of predicting flood discharge at various return periods with the help of available discharge observations using these distributions is defined as flood frequency analysis. Some of the methods used in this analysis are listed by Anılan (2014) as follows: Method of moments, maximum likelihood method, least squares method, probability weighted method of moments, and L-moment method. In addition, developing computer technologies and optimization techniques have enabled better estimation of flood discharges by employing the existing data.

Thanks to technological developments, flood discharge prediction has become a subject that is frequently tried to be predicted with different optimization algorithms. For example, Shu and Burn (2004) and Dawson et al. (2006) showed that artificial neural networks (ANNs) can make more accurate flood discharge predictions compared to multiple regression models and empirical methods. Similarly, Shu and Ouarda (2007), Besaw et al. (2010), Seçkin et al. (2010), Aziz et al. (2013), Rezaeianzadeh et al. (2013), Anılan et al., (2016) and Anılan et al., (2020) showed that ANNs give good results in their studies. In addition to this success of ANN, the success of artificial bee colony and teaching-learning based optimization algorithms in flood discharge prediction has been demonstrated by Anılan et al. (2016) and Günay et al. (2024). In this study, the flood discharge prediction of Trabzon province located in the Eastern Black Sea Basin (ESBS) was made with the Jaya algorithm and classical regression analysis (CRA).

*Corresponding author, E-mail: arifegunay@ktu.edu.tr

https://doi.org/10.31462/icearc2025_ce_hwr_754

golden light publishing

2. Materials and methods

2.1. Study area

The study area was selected as Trabzon province, which is in ESBS and is one of the provinces most exposed to floods. The reason for choosing a province from ESBS is that it receives high rainfall, has a mountainous and rugged topography, deforestation in the province, improper land use and stream beds opened to development (Yüksek et al., 2022). A location map of ESBS and Trabzon province, is given in Fig. 1.

In this study, data from 16 SGS's, located in Trabzon province with annual flow observations, which have 9 to 42 years observation durations, were used in the analyses. Drainage area and elevation data belonging to SGS's were used. Annual maximum discharges were taken from each station. These discharges were used in the analyses by taking their natural logarithms. The parameter values of these data used are shown in Table 1. The maximum and minimum values used for normalization of the data in the study methods are given in Table 2. These values were used in the proposed models to anomalyize the normalized results.

Table 1. Information about 16 stations located in Trabzon province

Station No	Drainage area (km^2)	Elevation (m)	Duration of observation (year)
2228	191.4	17	35
22-57	242.6	650	27
2202	635.7	78	42
22-34	258.6	100	25
22-53	173.6	150	18
2251	728.5	155	15
22-07	154.7	1114	37
22-59	121.5	250	25
2206	746.6	250	39
22-52	576.8	275	28
22-104	205.0	380	09
22-61	261.0	450	20
22-44	421.2	500	21
22-97	168.8	600	26
D22A105	74.5	75	12
D22A086	728.4	160	28

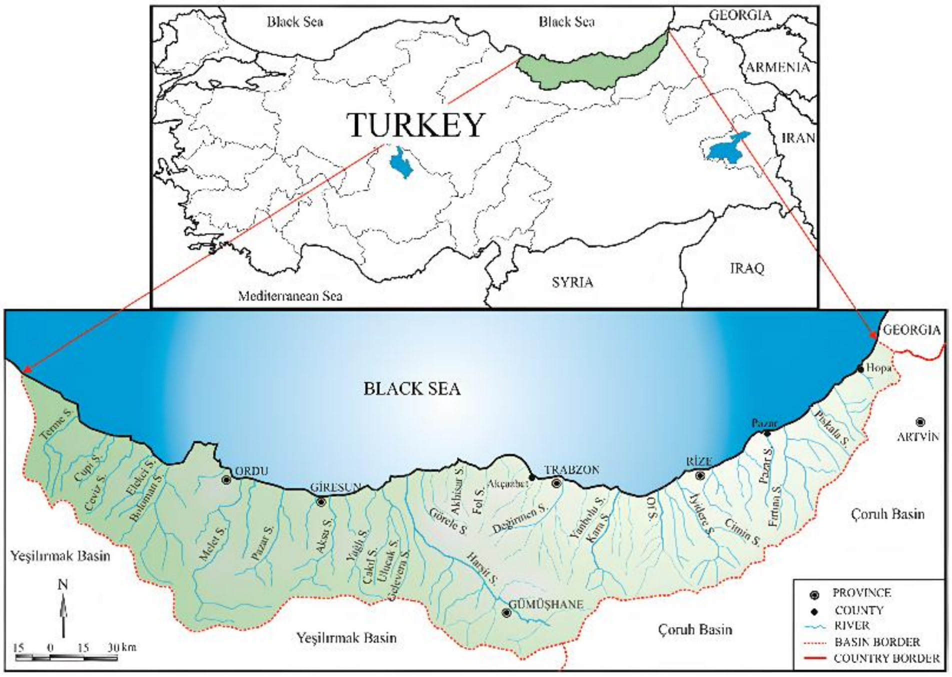

Fig. 1. Location map of EBSB and view of Trabzon Province (Anılan et al., 2016)

Table 2. Minimum and maximum values of input and output data

Parameters	Training Data		Testing Data	
	Min.	Max.	Min.	Max.
Drainage Area (DA), km^2	74.500	746.600	74.500	746.600
Elevation (E), m	17.000	1114.000	17.000	1114.000
ln(Q), m^3/s	2.272	5.565	2.342	5.497

2.2. Methods

Jaya optimization algorithm can solve complex engineering problems effectively (Rao, 2019; Uzlu and Dede, 2020; Houssein et al., 2021). In this study, CRA and Jaya algorithms were used to predict the probable maximum flood discharge. In these methods, the data taken from the stations and presented in Table 1 were divided into two groups as training (318 data) and test (80 data) sets. The separation process as training and test sets was carried out by considering the chronological order and ensuring that there was data from all levels in the training and test sets. Multiple linear, hyperbolic, and exponential regression functions were optimized in these algorithms. Drainage area and elevation information were used as input in these functions, and flood discharge was calculated as output. A normalization process was applied to the data for the swarm-based algorithms used. The normalization process was performed as in Eq. 1.

$$X_i = 0.8 \times \frac{(X - X_{min})}{(X_{max} - X_{min})} + 0.1 \quad (1)$$

where X_i is the normalized value of a particular parameter, X is the observed value for this parameter, X_{min} and X_{max} are the minimum and maximum values in the database for this parameter, respectively.

The results of the analyses performed in this study were used in the mean absolute error (MAE), root mean square error (RMSE) and relative error (RE) statistics, calculated from the following equations.

$$RMSE = \sqrt{\frac{1}{N}\sum_{i=1}^{N}(Yi_{observed} - Yi_{calculated})^2} \quad (2)$$

$$MAE = \frac{1}{N}\sum_{i=1}^{N}|Yi_{observed} - Yi_{calculated}| \quad (3)$$

$$RE = \frac{1}{N}\sum_{i=1}^{N}\left|\frac{Yi_{observed} - Yi_{calculated}}{Yi_{observed}}\right| * 100 \quad (4)$$

where, N is the number of data, and Yi is the maximum discharge.

The Jaya algorithm for optimizing multiple linear, hyperbolic, and exponential regression functions is described in Section 2.2.1.

2.2.1. Jaya algorithm

Jaya algorithm, which is faster than other algorithms and named after the word meaning victory in Sanskrit language, is an algorithm developed by Rao (2016) (Pradhan and Bhende 2019; da Silva et al., 2023). This optimization algorithm requires the ordinary control parameters to move toward the best solution, avoiding the worst (Mishra and Ray 2016; da Silva et al., 2023). This algorithm has two control parameters: Population size and maximum number of iterations. Jaya is an algorithm based on creating new individuals from the interaction of the best and worst individuals in a population. The purpose of this algorithm is for individuals in the population to move closer to the most successful individual and away from the worst individual. The flowchart of the algorithm is shown in Fig. 2.

According to this flowhart, a random initial population is generated. Then, the best and worst individuals in the population are determined using the objective function of the problem. The renewal of individuals is done in the general logic of the algorithm. Then, it is decided whether to keep the old state of the individual or to continue with the new state. In this way, iterations are continued by renewing all individuals until the stopping criterion is met (Uzlu, 2016; da Silva et al., 2023).

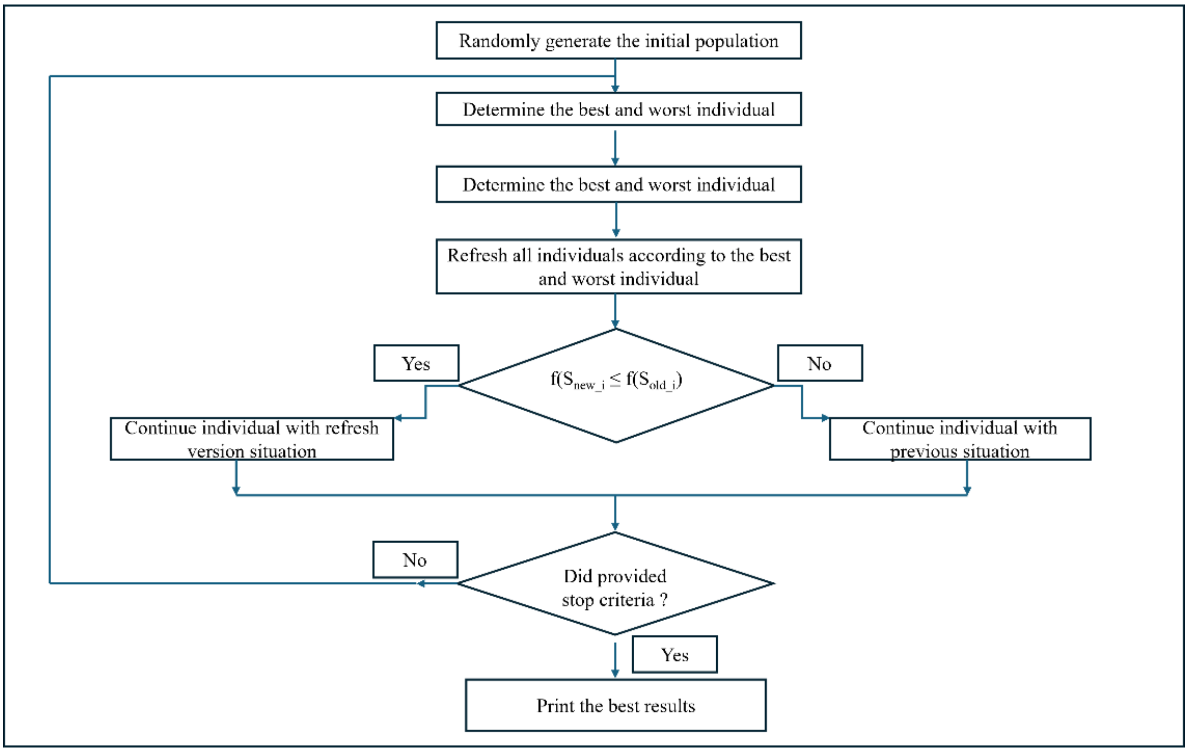

Fig. 2. Flowchart of Jaya algorithm

3. Findings and discussion

Table 3 shows the coefficients of the models developed using the analyses. Tables 4 and 5 show the results obtained from the training and testing set data. The bold values in Tables 4 and 5 show the most successful values in the analyses.

Table 3. Obtained coefficients

	Coefficients			
	w_0	w_1	w_2	w_4
CRA	3.550	0.002	−0.001	
Jaya	0.375	0.340	−0.146	
$y_{\ linear} = w_0 + (x_1)w_1 + (x_2)w_2$				
CRA	2.087	0.156	−0.045	
Jaya	0.521	0.287	−0.190	
$y_{\ hyperbolic} = w_0 (x_1)^{w1} (x_2)^{w2}$				
CRA	−6.648	2.324	0.0001	−6.271e-5
Jaya	−0.661	0.096	0.255	−0.220
$y_{\ exponential} = w_0 + exp(w_1 + (x_1)w_2 + (x_2)w_2)$				

*x_1: Drainage area, km^2; x_2: Elevation, m; y: Ln(*Q*), m^3/s

Table 4. Training data set results

Functions	MAE		RMSE		RE(%)	
	CRA	Jaya	CRA	Jaya	CRA	Jaya
Linear	0.383	**0.382**	**0.503**	**0.503**	10.457	**10.285**
Hyperbolic	0.391	**0.385**	0.515	**0.506**	10.841	**10.566**
Exponential	0.383	**0.383**	**0.503**	0.505	10.471	**10.407**

Table 5. Testing data set results

Functions	MAE		RMSE		RE(%)	
	CRA	Jaya	CRA	Jaya	CRA	Jaya
Linear	0.546	**0.554**	0.679	**0.706**	13.871	**13.915**
Hyperbolic	**0.512**	0.514	0.666	**0.654**	13.447	**13.415**
Exponential	0.536	**0.536**	0.669	**0.669**	13.788	**13.769**

According to the training set results given in Table 4, all regression functions optimized with the Jaya algorithm gave better results than CRA for all of the three examination criteria. Only the exponential function CRA gave better results according to the Jaya in RMSE criteria. According to the results of the testing set given in Table 5, Jaya algorithm gave the lowest MAE, RMSE, and RH values in hyperbolic function optimization. Only in the hyperbolic function did CRA give better results in MAE value according to the Jaya algorithm. Considering these evaluations and giving priority to the test set and RE values, the hyperbolic function model of the Jaya algorithm was the recommended model for flood flow modeling in the Trabzon province. The reason for considering the testing set is its success in data that it has never seen before. The reason for considering the RE value is that it is a criterion that plays a critical role in understanding how much the prediction results of the model deviate from the observed values.

The proposed flood discharge prediction model is given in Eq. 5. The result obtained with this equation is the normalised discharge value. To use the obtained result, it should be abnormalised with the min. and max. values given in Table 3. The comparison of the results obtained by training the hyperbolic regression function through Jaya with the training set and test data and the observed results are given in Figs. 3 and 4, respectively.

$$ln(Q) = 0.521 \times DA^{0.287} \times E^{-0.19} \quad (5)$$

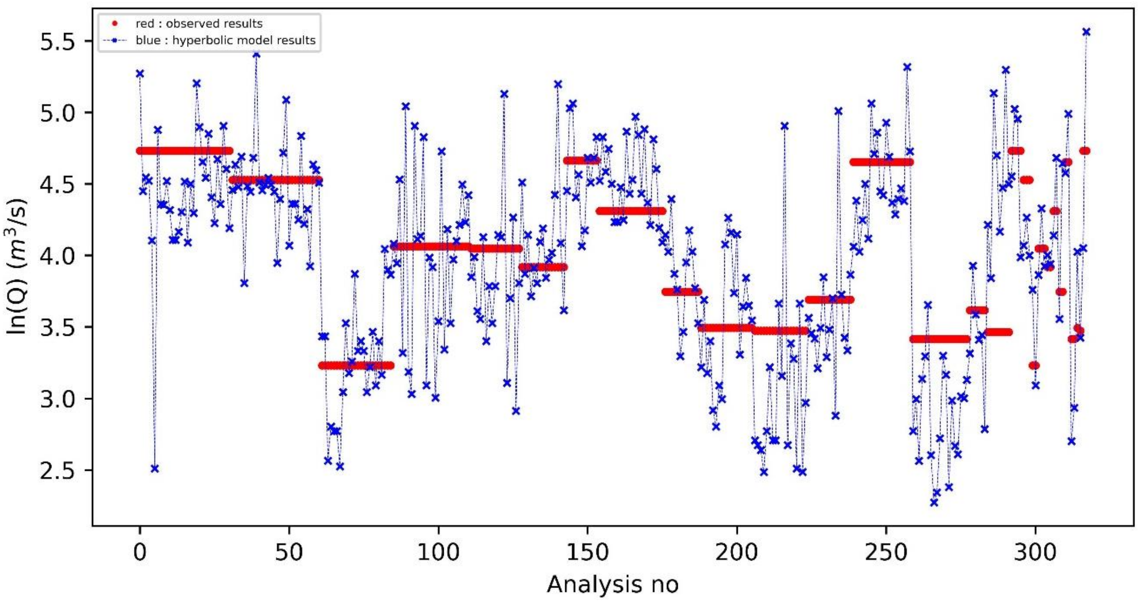

Fig. 3. Comparison of the observed results with the results obtained by training the hyperbolic regression function with the training set via Jaya

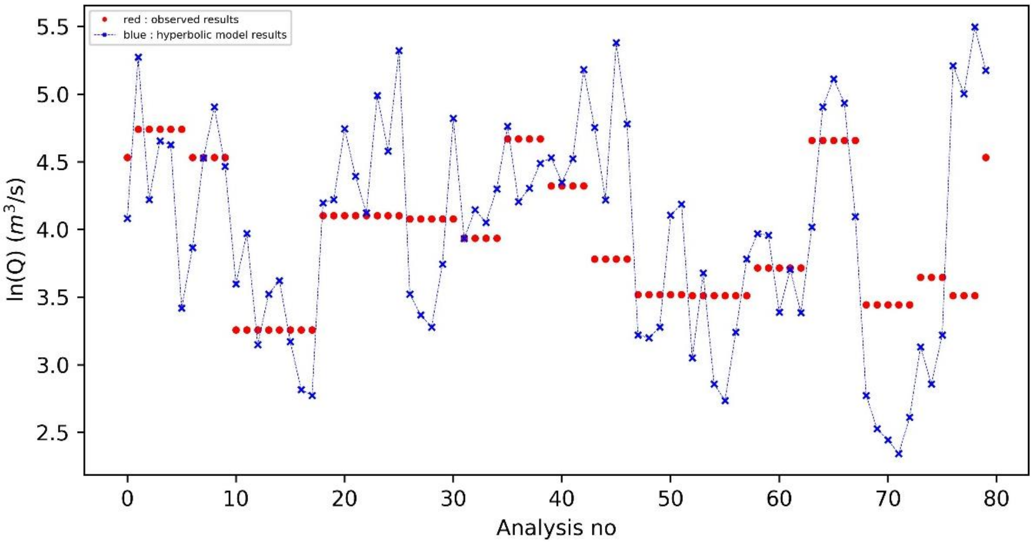

Fig. 4. Comparison of the observed results with the results obtained by training the hyperbolic regression function with the testing set via Jaya

4. Conclusions

In this study, classical regression analyses (CRA) and Jaya optimisation algorithms were applied to flood discharge estimation for Trabzon province in the Eastern Black Sea Basin (ESBS). Utilizing these algorithms, the relationship between the annual maximum discharge values of the flow observation stations in the Trabzon province and the elevation and drainage area of each station was modeled. For this modeling study, 16 flow observation stations in the Trabzon province with flow observation years ranging from 9 to 42 years were used. A total of 398 data were taken, 318 of which were used in the training set and 80 in the test set. In this modeling study, using different statistical criteria, the hyperbolic regression function optimised with Jaya was more successful. This study has concluded the success of the Jaya algorithm, which is not widely used in flood flow modeling. This algorithm can be used in flood risk management models in the future by enabling more accurate and reliable predictions in different regions and climatic conditions. In addition, the approach used in this study may enable the development of new algorithms or the improvement of existing methods.

Acknowledgments

This research received no specific grant from funding agencies in the public, commercial, or not-for-profit sectors.

References

Anılan, T. (2014). *Application of artificial intelligence methods to L-moments based regional frequency analysis in the Eastern Black Sea basin* (Doctoral dissertation). Karadeniz Technical University, Graduate School of Natural and Applied Sciences, Trabzon, Türkiye (in Turkish).

Anilan, T., Satilmis, U., Kankal, M., & Yuksek, O. (2016). Application of artificial neural networks and regression analysis to L-moments based regional frequency analysis in the Eastern Black Sea Basin, Turkey. *KSCE Journal of Civil Engineering, 20*(5), 2082-2092

Anılan, T., Uzlu, E., Kankal, M., & Yuksek, O. (2018). The estimation of flood quantiles in ungauged sites using teaching-learning based optimization and artificial bee colony algorithms. *Scientia Iranica, 25*(2), 632-645

Anilan, T., Nacar, S., Kankal, M., & Yuksek, O. (2020). Prediction of maximum annual flood discharges using artificial neural network approaches. *Građevinar, 72*(03), 215-224

Aziz, K., Rahman, A., Fang, G., & Shrestha, S. (2013). Application of artificial neural networks in regional flood frequency analysis: A case study for Australia. *Stochastic Environmental Research and Risk Assessment, 28*(3), 541-554

Besaw, E.L., Donna, M.R., Bierman, R.P., & William, R.H. (2010). Advance in ungauged streamflow prediction using artificial neural networks. *Journal of Hydrology, 386*, 27-37

Dawson, C.W., Abrahart, R.J., Shamseldin, A.Y., & Wilby, R.L. (2006). Flood estimation at ungauged sites using artificial neural networks. *Journal of Hydrology, 319*, 391-409

da Silva, L.S.A., Lúcio, Y.L.S., Coelho, L.D.S., Mariani, V.C., & Rao, R.V. (2023). A comprehensive review on Jaya optimization algorithm. *Artificial Intelligence Review, 56*(5), 4329-4361

Demir, V., & Keskin, A.Ü. (2022). Yeterince akım ölçümü olmayan nehirlerde taşkın debisinin hesaplanması ve taşkın modellemesi (Samsun, Mert Irmağı örneği). *Geomatik, 7*(2), 149-162

Günay, A., Kumantaş, M., Kayhan, A., Anılan, T. (2024). Sürü tabanlı algoritma modelleri ile taşkın debisi tahmini. *Politeknik Dergisi 1-1*. https://doi.org/10.2339/politeknik.1496489

Houssein, E.H., Gad, A.G., & Wazery, Y.M. (2021). Jaya algorithm and applications: A comprehensive review. *Metaheuristics and Optimization in Computer and Electrical Engineering,* 3-24

Mishra, S., & Ray, P.K. (2016). Power quality improvement using photovoltaic fed DSTATCOM based on JAYA optimization. *IEEE Transactions on Sustainable Energy, 7*(4), 1672-1680

Pradhan, C., & Bhende, C.N. (2019). Online load frequency control in wind integrated power systems using modified JAYA optimization. *Engineering Applications of Artificial Intelligence, 77*, 212-228

Rao, R. (2016). Jaya: A simple and new optimization algorithm for solving constrained and unconstrained optimization problems. *International Journal of Industrial Engineering Computations*, *7*(1), 19-34

Rao, R.V. (2019). Jaya: An advanced optimization algorithm and its engineering applications. Springer Cham.

Rezaeianzadeh, M., Tabari, H., Yazdi, A.A., Isik, S., & Kalin, L. (2013). Flood flow forecasting using ANN, ANFIS and regression models. *Neural Computing and Applications, 25*, 25-37. https://doi.org/10.1007/s00521-013-1443-6

Seçkin, N., Güven, A., & Yurtal, R. (2010). Taşkın debilerinin yapay sinir ağları ile modellenmesi: Batı Karadeniz Havzası örneği. *Çukurova Üniversitesi Mühendislik Mimarlık Fakültesi Dergisi, 25*(1-2), 45-57

Shu, C., & Burn, D.H. (2004). Homogeneous pooling group delineation for flood frequency analysis using a fuzzy expert system with genetic enhancement. *Journal of Hydrology, 291*, 132-149

Shu, C., & Ouarda, T.B.M.J. (2007). Flood frequency analysis at ungauged sites using artificial neural networks in canonical correlation analysis physiographic space. *Water Resources Research, 43*, W07438. https://doi.org/10.1029/2006WR005142

Uzlu, E. (2016). *Investigation of accretion profile caused by cross-shore sediment movement with physical model* (Doctoral dissertation). Karadeniz Technical University, Graduate School of Natural and Applied Sciences, Trabzon, Türkiye (in Turkish).

Uzlu, E., & Dede, T. (2020). Jaya algoritması ile optimize edilmiş yapay sinir ağlarını kullanarak Türkiye'de elektrik enerjisi tüketiminin tahmini. *Gazi University Journal of Science Part C: Design and Technology, 8*(3), 511-528

Yüksek, Ö., Babacan, H.T., & Yüksek, O. (2022). Doğu Karadeniz Havzası'nda taşkın sebepleri, zararları ve taşkın yönetimi çalışmaları. *Türk Hidrolik Dergisi, 6*(2), 36-46

Zhang, L., Xu, W., Zhang, F., Zhang, W., Wei, W., & Zhang, X. (2024). Improved general unit hydrograph model for dam-break flood hydrograph. *Journal of Hydrology, 635*, 131216

AI-driven water quality assessment: A data-driven index for identifying key chemical contaminants

Javad Parsa*[1], Sahand Zeinalzadeh Hamid[2], Zahra Hassanzadeh[3]

[1] *University of Tabriz, Water Engineering Department, Tabriz, Iran*
[2] *Islamic Azad University of Tabriz, Department of Civil Engineering, Faculty of Engineering, Tabriz, Iran*
[3] *Azarbaijan Shahid Madani University, Department of Chemistry, Faculty of Science, Tabriz, Iran*

Abstract. Water quality assessment is critical for environmental sustainability and public health, yet traditional Water Quality Indices (WQIs) often rely on static, expert-defined weights, limiting their adaptability to diverse conditions. This study introduces an AI-based Water Quality Index (AI-WQI) that leverages machine learning to dynamically evaluate water quality and prioritize chemical contaminants. Using a Random Forest classifier, we analyzed 7,996 samples from the U.S. Geological Survey, covering 20 physicochemical parameters (e.g., aluminium, perchlorate, cadmium) and a binary safety indicator. The model achieved 96% accuracy and a 0.974 ROC AUC, reliably classifying water safety. Feature importance analysis identified aluminium (20.24%), perchlorate (10.36%), and cadmium (10.13%) as key contaminants influencing water quality. The AI-WQI, constructed using normalized parameter values weighted by Random Forest feature importance, showed strong agreement with a conventional WQI (mean difference: -0.42, 95% LoA: -4.02 to 3.17), demonstrating its potential as an adaptive alternative for reflecting real-world water quality trends. This approach supports real-time monitoring, contaminant prioritization, and optimized treatment strategies, offering a scalable, interpretable tool for environmental management. Despite challenges like dataset imbalance affecting safe water predictions, the AI-WQI advances water quality assessment by integrating machine learning's flexibility with traditional indexing's clarity, providing a framework for sustainable monitoring in civil, chemical, and water engineering.

Keywords: Water quality; AI-WQI; Feature importance; Environmental monitoring; Chemical contaminants

1. Introduction

1.1. Background and motivation

Water quality assessment is vital for safeguarding public health, preserving ecosystems, and supporting sustainable development. Poor water quality, driven by pollutants such as heavy metals, nitrates, and microbial contaminants, poses significant risks to human health, including waterborne diseases and long-term exposure to toxic substances (UNEP, 2011). It also threatens aquatic ecosystems and economic activities like agriculture and fisheries, making effective monitoring essential (Makarigakis & Jimenez-Cisneros, 2019). Traditional Water Quality Indices (WQIs), such as the National Sanitation Foundation WQI (NSF WQI) and the Canadian Council of Ministers of the Environment WQI (CCME WQI), aggregate multiple parameters into a single value to simplify water quality evaluation. However, these indices often rely on fixed weights or guideline thresholds set by expert judgment, which may not adapt to local conditions, emerging contaminants, or temporal variations (Chidiac et al., 2023; Davies, 2006).

Machine learning (ML) offers a data-driven alternative, capable of modeling complex relationships in large datasets. Random Forest (RF), an ensemble ML method, excels in water quality assessment due to its robustness and ability to rank parameter importance through feature importance metrics (Tyralis et al., 2019). By leveraging ML, we can develop adaptive tools that overcome the rigidity of traditional WQIs, enhancing environmental monitoring and management.

1.2. Objectives and contributions

This study aims to advance water quality assessment through the following objectives:

1. *Develop an AI-based Water Quality Index (AI-WQI)* using RF feature importance to dynamically assign weights to parameters based on their impact on water safety predictions.

* Corresponding author, E-mail: jparsa78@gmail.com

https://doi.org/10.31462/icearc2025_ce_hwr_788

2. *Identify key chemical contaminants* influencing water quality, such as aluminium and perchlorate, using RF-derived feature importance.
3. *Compare AI-WQI with a conventional WQI* to demonstrate improved accuracy and adaptability in reflecting real-world water quality trends.

These objectives contribute a novel, interpretable, and data-driven WQI that integrates ML with traditional indexing, offering a tool for policymakers, engineers, and researchers to prioritize contaminants and optimize water treatment strategies.

1.3. Paper organization

The paper is structured as follows: Section 2 reviews traditional WQIs and ML applications in water quality assessment, identifying research gaps. Section 3 describes the dataset, preprocessing, RF model, and AI-WQI formulation. Section 4 presents model performance, key contaminants, and AI-WQI comparisons. Section 5 discusses findings, limitations, and future directions. Section 6 concludes with key contributions and their implications for water quality management.

2. Literature review

2.1. Traditional water quality indices

Water Quality Indices (WQIs) are widely used tools that aggregate multiple water quality parameters into a single numerical value, simplifying the assessment and communication of water quality status for environmental management and public health. Two prominent examples are the National Sanitation Foundation Water Quality Index (NSF WQI) and the Canadian Council of Ministers of the Environment Water Quality Index (CCME WQI), both of which rely on predefined parameters and expert judgment (Uddin et al., 2021; Uddin et al., 2022).

The NSF WQI, developed in 1970, integrates nine physicochemical and biological parameters: dissolved oxygen (DO), fecal coliform, pH, biochemical oxygen demand (BOD), temperature change, total phosphate, nitrates, turbidity, and total solids (TS). Each parameter is assigned a fixed weight based on a Delphi survey of water quality experts, with DO having the highest weight (0.17) and TS the lowest (0.07). Measurements are converted to sub-index values (Q-values) using standardized curves, ranging from 0 (worst) to 100 (best), and the final WQI is computed as a weighted sum:

$$NSF\ WQI = \sum_{i=1}^{9}(Q_i . w_i) \tag{1}$$

where (Q_i) is the sub-index value for parameter (i), and (w_i) is its corresponding weight. The resulting index classifies water quality from excellent (90–100) to very poor (0–25) . This approach, while standardized, assumes static parameter importance, which may not reflect local conditions or temporal changes (Effendi & Wardiatno, 2015).

The CCME WQI, introduced in 2001, offers a more flexible framework applicable to various water bodies and parameters. It evaluates water quality based on three factors: scope (F1), frequency (F2), and amplitude (F3) of guideline exceedances. These are calculated as follows:

Scope (F1): Percentage of parameters failing guidelines at least once:

$$F1 = \left(\frac{Number\ of\ failed\ parameters}{Total\ number\ of\ parameters}\right) \times 100 \tag{2}$$

Frequency (F2): Percentage of tests failing guidelines:

$$F2 = \left(\frac{Number\ of\ failed\ tests}{Total\ number\ of\ tests}\right) \times 100 \tag{3}$$

Amplitude (F3): Magnitude of guideline exceedances, calculated in three steps:

$$excrusion_i = \begin{cases} \frac{Failed\ Test\ Value_i}{Objective_j} - 1 & if\ value\ exceeds\ objective \\ \frac{Objective_j}{Failed\ Test\ Value_i} - 1 & if\ value\ below\ objective \end{cases}$$

$$nse = \frac{\sum_{i=1}^{n} excrusion_i}{Number\ of\ Tests}$$

$$F3 = \frac{nse}{0.01 + 0.01.nse} \tag{4}$$

The CCME WQI is computed as:

$$CCME\ WQI = 100 - \sqrt{\frac{(F1^2 + F2^2 + F3^2)}{1.732}} \tag{5}$$

This yields a score from 0 (poor) to 100 (excellent), categorized as excellent (95–100), good (80–94), fair (65–79), marginal (45–64), or poor (0–44) (WATER, 2001). The CCME WQI's flexibility allows it to incorporate any parameter with established guidelines, but these guidelines are still expert-defined, limiting adaptability to data-driven insights.

Both indices depend on static, expert-driven frameworks, limiting their adaptability to diverse or changing environmental conditions. Studies have noted that such rigidity can lead to inconsistent assessments across different water bodies (Noori et al., 2019).

2.2. Machine learning in water quality assessment

Machine learning (ML) has emerged as a powerful tool for water quality assessment, offering the ability to model complex, nonlinear relationships in large datasets. Random Forest (RF), an ensemble learning method, is particularly popular due to its robustness, accuracy, and interpretability through feature importance metrics.

RF has been applied in both regression and classification tasks for water quality. For regression, studies like Jena et al. (2023) used RF to predict parameters such as total dissolved solids (TDS), pH, and iron in the Kulik River, India, achieving high accuracy (R^2 up to 0.908) (Jena et al., 2023). For classification, Hurley et al. (2012) employed RF to predict indicator bacteria levels at swimming beaches, demonstrating its efficacy in binary classification tasks (Hurley et al., 2012). Similarly, Tesoriero et al. (2017) used RF to classify groundwater contaminant concentrations, identifying key predictors of redox-sensitive pollutants (Tesoriero et al., 2017).

A key advantage of RF is its ability to compute feature importance, which ranks parameters based on their contribution to model predictions. For instance, Jena et al. (2023) identified calcium and magnesium as critical predictors for TDS, using correlation-based feature importance. This capability allows researchers to prioritize contaminants for monitoring and treatment, aligning with environmental management goals. A review by Tyralis et al. (2019) highlights RF's extensive use in water resources, noting its application in water chemistry and quality assessment alongside streamflow modeling (Tyralis et al., 2019).

Other ML models, such as Support Vector Machines (SVM) and Artificial Neural Networks (ANN), have also been explored. For example, Ahmed et al. (2021) compared RF, SVM, and ANN for water quality prediction at Rawal Dam, Pakistan, finding RF to be highly effective due to its interpretability (Ahmed et al., 2021).

2.3. Gaps and research need

Traditional WQIs, while effective for standardized assessments, face limitations due to their reliance on fixed weights or guideline thresholds. The NSF WQI's weights, established in the 1970s, may not reflect current environmental conditions or local variations, potentially leading to biased assessments (Ariza Restrepo et al., 2023). The CCME WQI, though more flexible, still depends on predefined guidelines, which may not adapt to emerging contaminants or data-driven insights.

ML-based approaches address some of these limitations by leveraging data to uncover patterns and prioritize parameters. However, challenges remain, particularly with interpretability. While RF provides feature importance, other models like deep neural networks can act as "black boxes," making it difficult to explain predictions to stakeholders (Wang et al., 2017). Additionally, many ML studies focus on prediction rather than integrating their findings into practical indices, limiting their applicability in regulatory frameworks.

There is a critical need to bridge traditional WQIs and ML approaches to develop adaptive, data-driven indices that combine the interpretability of conventional methods with the flexibility of ML. Recent studies advocate for such integration, noting that ML can enhance WQI predictions by dynamically adjusting weights based on data (Ahmed et al., 2021; Uddin et al., 2021; Uddin et al., 2022). Our study addresses this gap by proposing an AI-based Water Quality Index (AI-WQI) that uses RF-derived feature importance to assign dynamic weights, offering a novel, interpretable, and data-driven approach to water quality assessment.

3. Materials and methods

This section provides a detailed exposition of the dataset utilized, the preprocessing steps undertaken, the development of the machine learning model, the analysis of feature importance, and the formulation of both an AI-based Water Quality Index (AI-WQI) and a conventional Water Quality Index (WQI). The methodology seamlessly integrates advanced data-driven techniques with established traditional approaches to deliver a robust and comprehensive framework for assessing water quality across diverse environmental settings.

3.1. Dataset description

3.1.1. Chemical measurements dataset

The study utilizes the Kaggle dataset, comprising 7,996 water samples, each characterized by 20 physicochemical features and a binary target variable, is_safe. The physicochemical features include aluminium, perchlorate, cadmium, arsenic, ammonia, barium, chloramine, chromium, copper, fluoride, bacteria, viruses, lead, nitrates, nitrites, mercury, radium, selenium, silver, and uranium. These parameters represent key contaminants and properties influencing water safety. The target variable, is_safe, denotes whether the water is safe for consumption (1) or not (0), based on predefined safety thresholds.

The dataset was obtained from the U.S. Geological Survey (USGS) National Water Information System, providing a robust foundation for analyzing water quality across diverse environmental contexts. This comprehensive dataset supports the development of predictive models and quality indices applicable to real-world scenarios.

3.2. Data preprocessing

To ensure the dataset was suitable for machine learning analysis, preprocessing steps addressed missing values and feature scaling.

3.2.1. Handling missing values

Coercion of non-numeric values: Non-numeric entries in the dataset were converted to NaN to maintain data consistency and enable numerical processing.

Median imputation: Missing values in the feature columns were imputed using the median value of each feature. This method, implemented via the SimpleImputer from the sklearn library, minimizes bias while preserving the dataset's central tendency.

Removal of invalid target rows: Rows lacking a value for the is_safe target were excluded, reducing the dataset from an initial size of approximately 8,000 to 7,996 samples. This ensured all samples had valid labels for model training and evaluation.

3.2.2. Normalization

The 20 physicochemical features were normalized to a [0, 1] range using the MinMaxScaler from sklearn. This scaling standardizes the magnitude of features, preventing those with larger ranges from disproportionately influencing the model. The normalized value (x'_{ij}) for feature (j) in sample (i) is given by:

$$x'_{ij} = \frac{x_{ij} - \min(x_j)}{\max(x_j) - \min(x_j)} \tag{6}$$

where (x'_{ij}) is the original value, and $\min(x_j)$ and $\max(x_j)$ are the minimum and maximum values of feature (j), respectively.

3.3. Model development

3.3.1. Random forest classifier

A Random Forest Classifier was employed to predict the is_safe target and derive feature importance scores. Implemented using RandomForestClassifier from sklearn with 100 trees (n_estimators=100), this ensemble method leverages multiple decision trees to enhance prediction accuracy and robustness. The model's ability to handle high-dimensional data and provide interpretable feature importance makes it well-suited for this study. The trained classifier predicts water safety and quantifies the influence of each physicochemical feature on the outcome.

3.3.2. Train/test split

The dataset was divided into training and testing sets with a 70:30 ratio, using train_test_split from sklearn (test_size=0.3, stratify=y). Stratification ensured that the proportion of safe (1) and unsafe (0) samples remained balanced in both sets, yielding 5,597 training samples and 2,399 testing samples. This approach supports reliable model evaluation by maintaining a representative distribution of the target variable.

3.4. Feature importance analysis

3.4.1. Tree-based feature importance

Feature importance scores were extracted from the Random Forest model using the feature_importances_ attribute. These scores, based on the mean decrease in impurity across all trees, rank the 20 physicochemical features by their contribution to predicting is_safe. Preliminary results identified aluminium, perchlorate, and cadmium as top-ranking contaminants, indicating their significant impact on water quality.

To explore potential relationships between the 20 physicochemical features in the dataset, a feature correlation heatmap was constructed using Pearson correlation (equal to 0.697) coefficients (Fig. 1). The heatmap revealed minimal correlations between most features, suggesting that the physicochemical parameters are largely independent in their influence on water safety. For instance, aluminium and cadmium exhibited a weak positive correlation (approximately 0.15), potentially indicating shared environmental sources such as industrial discharges or soil leaching. Similarly, mercury, selenium and flouride showed near-zero correlations with most other features, consistent with its unique sources. This analysis supports the Random Forest model's feature importance rankings (Section 4.2), as the low inter-feature correlations imply that the model's prioritization of aluminium, perchlorate, and cadmium is driven by their individual predictive power rather than multicollinearity. Understanding these relationships can guide future studies in identifying contaminant interactions for targeted treatment strategies.

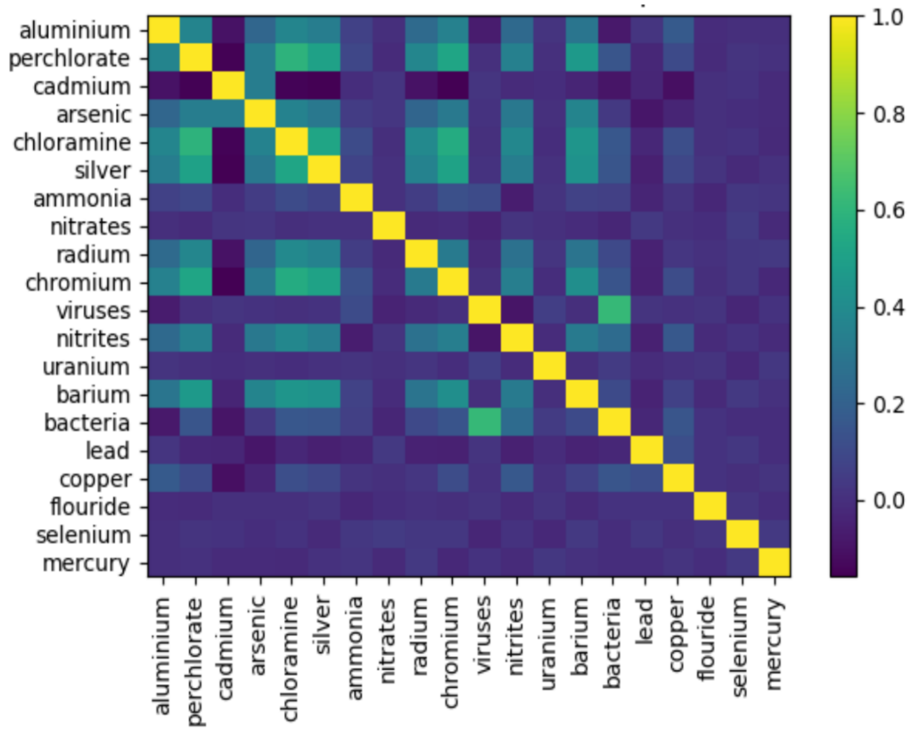

Fig. 1. Feature correlation heatmap

3.4.2. Validation of importance

The robustness of the importance scores was assessed by examining their consistency across multiple train-test splits. The rankings, particularly for high-impact features like aluminium and perchlorate, remained stable, reinforcing their reliability. While permutation importance was not implemented here, it could enhance validation in future studies by evaluating the effect of feature shuffling on model performance.

3.5. AI-WQI formulation

3.5.1. Definition

The AI-WQI was developed as a weighted sum of the normalized features, with weights derived from the Random Forest feature importance scores. This data-driven index reflects the relative influence of each parameter on water safety. For each sample (i), the AI-WQI is calculated as:

$$AI - WQI_i = \frac{\sum_{j=1}^{n}(x'_{ij}.w_j)}{\sum_{j=1}^{n} w_j} \tag{7}$$

where x'_{ij} is the normalized value of feature (j) for sample (i), (w_j) is the feature importance score for feature (j), (n) is the number of features (20). This denominator normalizes the index, ensuring comparability across samples.

3.5.2. Computation

The AI-WQI was implemented in Python using matrix operations for efficiency. The normalized feature matrix was multiplied element-wise by the feature importance vector, and the resulting sums were divided by the total sum of weights. This approach scales effectively for large datasets and provides a standardized water quality metric.

3.6. Conventional WQI computation

3.6.1. Methodology

A conventional WQI was computed as a baseline, using standard weights based on guidelines from the World Health Organization (WHO) and Environmental Protection Agency (EPA) (Organization, 2017). Sub-indices (Q_j) for each parameter (j) were calculated by comparing measured concentrations to guideline thresholds:

$$Q_j = \frac{C_j}{S_j} \times 100 \quad (8)$$

where (C_j) is the measured concentration, and (S_j) is the guideline standard for parameter (j).

3.6.2. Implementation

The conventional WQI was then derived as a weighted arithmetic mean (Table 1):

Table 1. Weights, reflecting health and environmental significance

Substance	Value
Aluminium	0.1
Perchlorate	0.15
Cadmium	0.20
Arsenic	0.08
Other 16 Parameters	0.47

Weights for remaining parameters were similarly assigned based on WHO/EPA standards. This conventional WQI provides a standardized reference to compare against the AI-WQI, highlighting the advantages of the data-driven approach.

4. Results

This section presents the outcomes of the machine learning analysis, feature importance rankings, and the comparison between the AI-based Water Quality Index (AI-WQI) and a conventional WQI. The results underscore the efficacy of the Random Forest (RF) model, highlight key chemical contaminants affecting water safety, and demonstrate the advantages of the AI-WQI's data-driven approach. Visualizations, including performance metrics, feature importance rankings, and index comparisons, enhance the interpretability of the findings.

4.1. Model performance

The Random Forest classifier was evaluated on a test set of 2,399 samples (30% of the 7,996-sample dataset) to assess its ability to predict the binary is_safe target (0 = unsafe, 1 = safe). The model achieved an overall accuracy of 96%, indicating that it correctly classified 96% of the test samples. Detailed classification metrics, including precision, recall, and F1-score, are summarized in Table 2 for both classes.

Table 2. Classification performance metrics

Class	Precision	Recall	F1-Score	Support
Unsafe (0)	0.96	0.99	0.98	2,125
Safe (1)	0.94	0.69	0.80	274
Weighted Avg	0.96	0.96	0.96	2,399

Precision: For the unsafe class (0), 96% of samples predicted as unsafe were correctly classified, while for the safe class (1), 94% of predicted safe samples were accurate.

Recall: The model identified 99% of actual unsafe samples but only 69% of actual safe samples, indicating a lower detection rate for safe water.

F1-Score: The harmonic mean of precision and recall was 0.98 for unsafe and 0.80 for safe, reflecting strong performance for the majority class but reduced effectiveness for the minority class.

Support: The test set contained 2,125 unsafe samples (88.5%) and 274 safe samples (11.5%), highlighting a significant class imbalance.

Aluminium's dominance (Fig. 2) aligns with its role in industrial pollution and coagulant use in water treatment. Perchlorate (a rocket fuel component) and cadmium (toxic heavy metal) are critical due to their persistence and health risks.

The full ranking is visualized in Fig. 2a, a bar plot illustrating the relative importance of all 20 features. Aluminium's leading role underscores its prevalence in industrial and natural water sources, where it can leach from soils or result from anthropogenic activities like mining or manufacturing (WHO, 2017). Perchlorate, often associated with industrial discharges and rocket fuel, poses risks due to its chemical stability and bioaccumulation potential (EPA, 2020). Cadmium and arsenic, both heavy metals, are critical due to their toxicity, persistence, and ability to contaminate groundwater and surface water, aligning with global water quality concerns (UNEP, 2016).

These contaminants' high importance scores indicate their strong influence on the is_safe classification, suggesting that monitoring and treatment efforts should prioritize these parameters. The environmental prevalence of aluminium and the acute toxicity of cadmium and arsenic justify their prominence, consistent with regulatory priorities outlined by WHO and EPA guidelines.

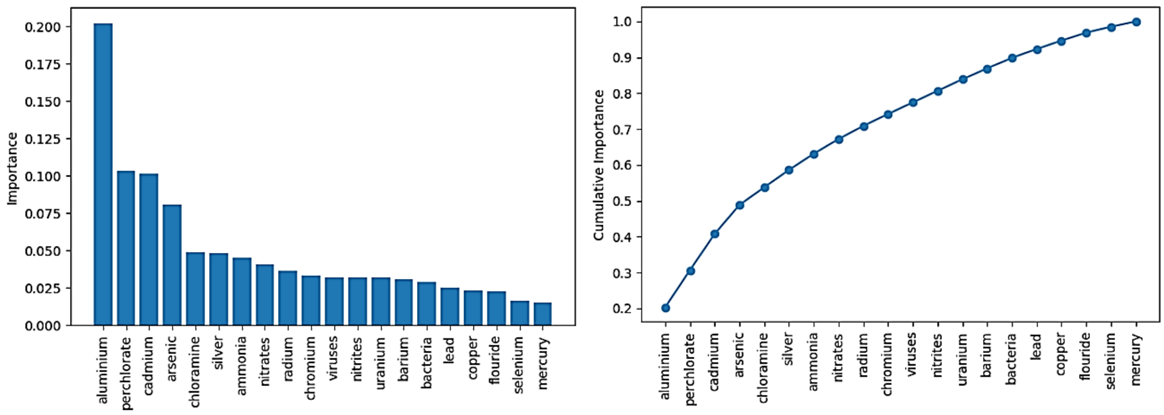

(a) (b)

Fig. 2. Random forest feature importances

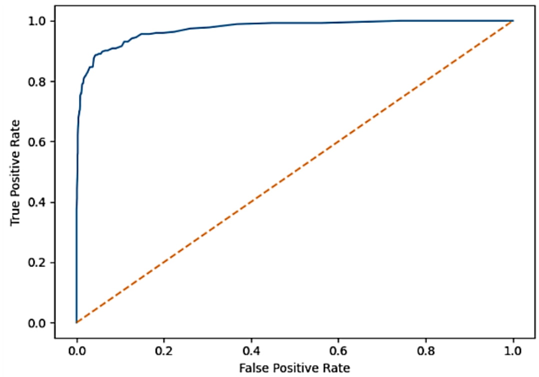

Fig. 3. Receiver Operating Characteristic (ROC) curve (AUC = 0.974)

The ROC curve (Fig. 3) plots the true positive rate against the false positive rate across various classification thresholds, assessing the model's ability to distinguish between safe and unsafe water samples. An AUC of 0.974 indicates excellent discriminatory power, confirming the model's reliability in separating the two classes, even with imbalanced data. The high AUC (0.974) confirms strong discriminatory power, though the class imbalance (88.5% unsafe vs. 11.5% safe) affects safe water identification, as evidenced by the lower recall for the safe class (69%). The steep curve reflects high true positive rates even at low false positive thresholds. Oversampling or weighted loss functions could mitigate this in future work.

4.2. Key contaminants

Feature importance analysis, derived from the Random Forest model's feature_importances_ attribute, identified the most influential physicochemical parameters affecting water safety. The top-ranked features, with their respective importance scores, are:

Aluminium (20.24%): The dominant contributor, reflecting its widespread environmental presence and toxicity.

Perchlorate (10.36%): A persistent chemical with health implications, particularly for thyroid function.

Cadmium (10.13%): A highly toxic heavy metal linked to severe health effects.

Arsenic (8.07%): A known carcinogen with significant environmental and health concerns.

The box plot reveals that unsafe samples have significantly higher concentrations of aluminium and perchlorate compared to safe samples, which aligns with their top feature importance. Fig. 4a depicts the distribution of cadmium concentrations alongside aluminium. Cadmium levels are notably higher in unsafe samples, supporting its high feature importance and highlighting its environmental and health significance. To further explore these contaminants, their distributions in safe and unsafe samples were examined. Fig. 4b shows the distribution of aluminium concentrations in comparison to perchlorate.

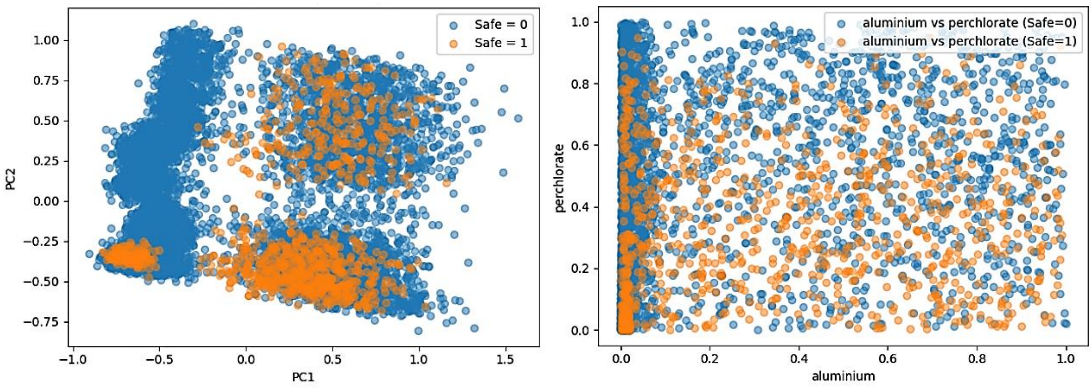

(a) (b)

Fig. 4. Comparison of two principal components (Aluminium, and a-Cadmium and b-Perchlorate)

4.3. AI-WQI indices vs.conventional water quality

The AI-WQI was computed for each sample as a weighted sum of normalized feature values, with weights derived from Random Forest feature importance. Sample AI-WQI values for the first five samples ranged from 0.284 to 0.470, as shown in Table 3. In contrast, the Traditional WQI, calculated using WHO/EPA guideline-based weights, was computed for the same samples to provide a baseline for comparison. Table 4 presents the Traditional WQI values for the first five samples, showing a range from 62.1 to 71.8 on a 0–100 scale, where higher values indicate better water quality.

Table 3. Sample AI-WQI values

Sample	AI-WQI
0	0.682
1	0.635
2	0.74
3	0.667
4	0.689

In here, higher AI-WQI values indicate poorer water quality, as they reflect greater contributions from influential contaminants like aluminium and perchlorate. The distribution of AI-WQI values across all samples is visualized in Fig 5, a histogram showing a right-skewed distribution with most values between 0.4 and 0.7, indicating variability in water quality.

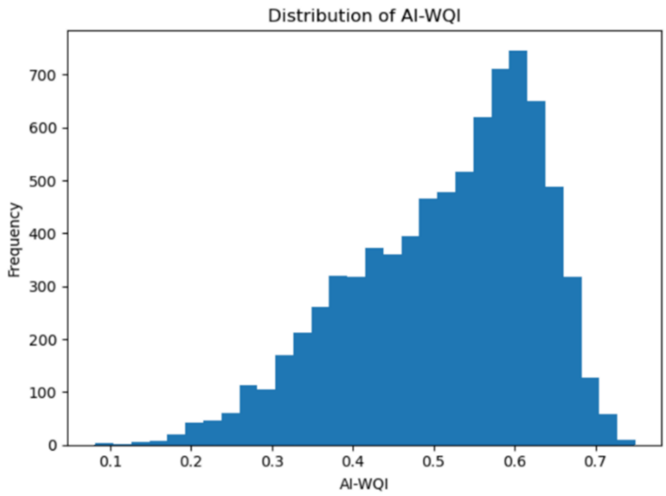

Fig. 5. Distribution of AI-WQI

Table 4. Sample traditional WQI values

Sample	Traditional WQI
0	0.68
1	0.62
2	0.72
3	0.65
4	0.69

The distribution of AI-WQI values across all samples is visualized in Fig. 5, a histogram showing a skewed distribution with most values between 0.4 and 0.7, indicating variability in water quality. To evaluate the agreement between the AI-WQI and the Traditional WQI, a Bland-Altman plot was constructed after rescaling the AI-WQI to a 0-to-100 range to match the Traditional WQI scale (Fig. 6a). The mean difference was -0.42, indicating that the AI-WQI systematically underestimates the Traditional WQI by an average of 0.42 units. The 96% limits of agreement ranged from -4.02 to 3.17, reflecting low variability in the differences between the two indices. The scatter of points showed no significant trend, suggesting the absence of proportional bias across the range of mean values. A histogram of the differences confirmed approximate normality, supporting the validity of the limits of agreement (Fig. 6b). Most differences fell within the limits of agreement, indicating strong agreement between the two methods. The slight systematic underestimation by AI-WQI may reflect its greater sensitivity to key contaminants like aluminium and cadmium, as identified by the Random Forest feature importance analysis (Section 4.2). This is particularly relevant given that higher AI-WQI values indicate poorer water quality, while higher Traditional WQI values indicate better quality, suggesting that AI-WQI may be more conservative in its assessment of water safety.

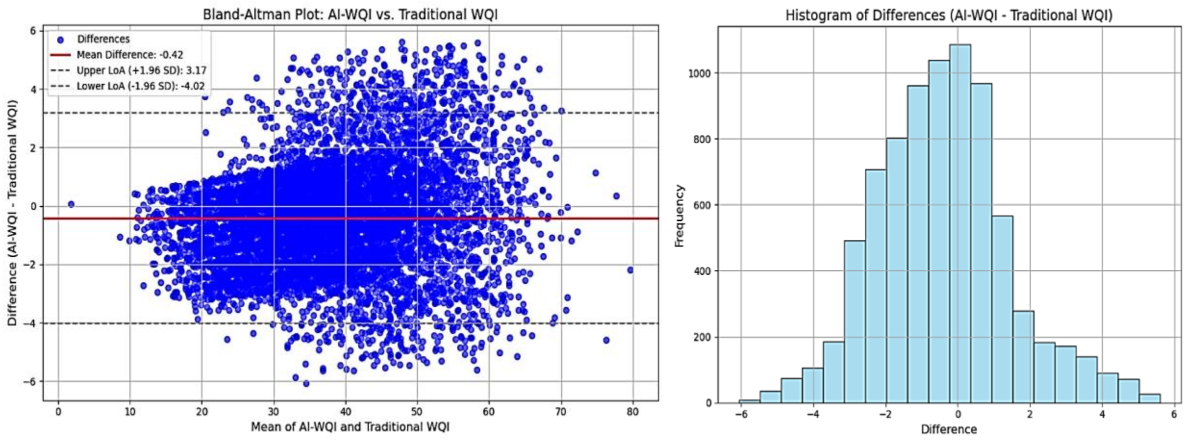

(a) (b)

Fig. 6. Bland-Altman plot to evaluate the agreement between the AI-WQI and Traditional WQI

5. Discussion

This study introduces an AI-based Water Quality Index (AI-WQI) that leverages Random Forest (RF) feature importance to dynamically assess water quality and prioritize chemical contaminants. The following subsections interpret the findings, highlight the advantages of AI-WQI, discuss implications for stakeholders, and outline limitations with directions for future research.

5.1. Interpretation of findings

The identification of aluminium (20.24%), perchlorate (10.36%), and cadmium (10.13%) as the top contaminants influencing water safety aligns with established chemical and environmental engineering principles. Aluminium's dominance reflects its prevalence in natural and industrial contexts, often introduced through soil leaching or as a coagulant in water treatment processes (WHO, 2017). Its high feature importance underscores its role in impacting water safety, particularly in regions with industrial activity, where elevated concentrations can pose risks to aquatic ecosystems and human health. Perchlorate, a persistent chemical linked to rocket fuel and industrial discharges, affects thyroid function and is a known concern in groundwater contamination (EPA, 2020). Cadmium, a toxic heavy metal, is associated with severe health effects, including kidney damage and cancer, and its prominence in the RF model highlights its environmental significance (UNEP, 2016). These findings are consistent with global water quality priorities, where heavy metals and persistent pollutants are often targeted for monitoring and regulation due to their toxicity and bioaccumulation potential.

From a chemical engineering perspective, the high importance of these contaminants suggests complex interactions with water matrices, such as pH-dependent solubility for aluminium or redox conditions affecting cadmium mobility. In environmental engineering, these results emphasize the need for source control measures, such as reducing industrial discharges, and advanced treatment technologies to mitigate these contaminants' impact. The AI-WQI's ability to identify these key parameters through data-driven analysis enhances our understanding of water quality dynamics, providing a foundation for targeted interventions.

5.2. Advantages of AI-WQI

The AI-WQI offers distinct advantages over traditional WQIs like the NSF WQI and CCME WQI, primarily through its data-driven weighting approach. Unlike conventional indices that rely on fixed, expert-defined weights—often established decades ago (e.g., NSF WQI weights from 1970)—the AI-WQI uses RF feature importance to assign weights dynamically based on their predictive contribution to water safety. This adaptability ensures that the index reflects current environmental conditions and contaminant priorities, addressing the rigidity of traditional methods noted in prior studies (Noori et al., 2019). For instance, the high weight assigned to aluminium in this study reflects its prevalence in the USGS dataset, which may differ across regions or datasets, making AI-WQI more contextually relevant.

Additionally, the AI-WQI is well-suited for real-time monitoring and treatment optimization. Its reliance on machine learning enables rapid computation of water quality scores as new data is collected, facilitating continuous assessment in dynamic environments like industrial discharge zones or urban water systems. The Bland-Altman analysis in Section 4.3 revealed strong agreement between AI-WQI and Traditional WQI (mean difference: -0.42, 96% LoA: -4.02 to 3.17), suggesting that AI-WQI can serve as a reliable alternative while offering greater flexibility. Engineers can use AI-WQI scores to optimize treatment processes, such as adjusting coagulant doses to target aluminium or enhancing filtration systems for cadmium removal, improving efficiency and cost-effectiveness in water management.

5.3. Implications for stakeholders

The AI-WQI has significant implications for diverse stakeholders in water quality management. For policymakers, the prioritization of contaminants like aluminium, perchlorate, and cadmium informs regulatory frameworks. These contaminants' high importance scores suggest they should be focal points for updated water quality standards, particularly in regions with similar environmental profiles to the USGS dataset. For example, stricter discharge limits for perchlorate could mitigate its impact on groundwater, aligning with EPA recommendations (EPA, 2020).

For environmental and chemical engineers, AI-WQI facilitates the design of targeted treatment systems. The model's identification of key contaminants enables engineers to focus on specific removal technologies, such as ion exchange for cadmium or advanced oxidation for perchlorate, optimizing resource allocation. Furthermore, the index's adaptability supports the development of modular treatment systems that can be adjusted based on real-time AI-WQI scores, enhancing resilience to changing water quality conditions.

For chemists, the AI-WQI provides insights into contaminant interactions. The prominence of aluminium and cadmium suggests potential synergistic effects, such as co-precipitation under certain pH conditions, which could influence their removal efficiency. Future studies could leverage these findings to explore chemical interactions in greater detail, informing both treatment strategies and environmental modeling.

5.4. Limitations and future work

Despite its strengths, this study has several limitations that warrant further investigation. The dataset's class imbalance (88.5% unsafe vs. 11.5% safe samples) impacted the RF model's recall for the safe class (69%), potentially limiting its ability to identify safe water sources accurately. Future work could employ techniques like SMOTE or class-weighted loss functions to address this imbalance, improving model performance for minority classes.

The reliance on a single USGS dataset also limits the generalizability of findings. Incorporating additional datasets, such as Kaggle dataset, which includes parameters like turbidity and organic carbon, could enhance the AI-WQI's robustness by capturing a broader range of water quality factors. Additionally, while RF feature importance provided interpretable weights, exploring other explainability methods, such as permutation importance, could validate the rankings and offer deeper insights into feature contributions.

Finally, the AI-WQI was validated on a dataset primarily representing groundwater and surface water from the U.S. Applying the model to diverse water sources, such as rivers, lakes, or wastewater, would test its adaptability and ensure its applicability across different environmental contexts. Future research should focus on these validations to strengthen the AI-WQI's utility as a global tool for water quality assessment.

6. Conclusions

This study developed an AI-based Water Quality Index (AI-WQI) using Random Forest (RF) feature importance to enhance water quality assessment, achieving significant advancements over traditional methods. The RF model demonstrated high performance, with 96% accuracy and a 0.974 ROC AUC, effectively classifying water safety across 7,996 samples from the USGS dataset. Feature importance analysis identified aluminium (20.24%), perchlorate (10.36%), and cadmium (10.13%) as the primary contaminants influencing water safety, aligning with their environmental prevalence and toxicity. Comparative analysis via a Bland-Altman plot revealed strong agreement between AI-WQI and Traditional WQI (mean difference: -0.42, 95% LoA: -4.02 to 3.17), with AI-WQI showing slight underestimation due to its sensitivity to key contaminants, highlighting its superiority in capturing data-driven trends over static, expert-defined weights.

The AI-WQI contributes to civil, chemical, and water engineering by offering an adaptive, interpretable tool for water quality monitoring. Civil engineers can leverage it for real-time infrastructure management, chemical engineers can optimize treatment processes targeting key contaminants, and water engineers can prioritize resource allocation for contaminant mitigation. We recommend adopting AI-WQI for adaptive monitoring systems to improve water management flexibility. However, addressing the dataset's imbalance (88.5% unsafe vs. 11.5% safe samples) through techniques like SMOTE is essential to enhance safe water predictions. Expanding the model to additional datasets, such as Kaggle dataset, will further validate its applicability across diverse water sources, ensuring broader environmental impact.

References

Ahmed, M., Mumtaz, R., & Hassan Zaidi, S.M. (2021). Analysis of water quality indices and machine learning techniques for rating water pollution: a case study of Rawal Dam, Pakistan. *Water Supply*, *21*(6), 3225-3250

Ariza Restrepo, J.L., Rodriguez Diaz, Y.J., & Onate Barraza, H.C. (2023). Water quality indices (WQI) and contamination indices (WPI) a bibliographic review. *Tecnura*, *27*(77), 121-140

Chidiac, S., El Najjar, P., Ouaini, N., El Rayess, Y., & El Azzi, D. (2023). A comprehensive review of water quality indices (WQIs): History, models, attempts and perspectives. *Reviews in Environmental Science and Bio/Technology*, *22*(2), 349-395

Davies, J.-M. (2006). Application and tests of the Canadian water quality index for assessing changes in water quality in lakes and rivers of central North America. *Lake and Reservoir Management*, *22*(4), 308-320

Effendi, H., & Wardiatno, Y. (2015). Water quality status of Ciambulawung River, Banten Province, based on pollution index and NSF-WQI. *Procedia Environmental Sciences*, *24*, 228-237

Hurley, T., Sadiq, R., & Mazumder, A. (2012). Adaptation and evaluation of the Canadian Council of Ministers of the Environment Water Quality Index (CCME WQI) for use as an effective tool to characterize drinking source water quality. *Water Research*, *46*(11), 3544-3552

Jena, P.K., Rahaman, S.M., Das Mohapatra, P.K., Barik, D.P., & Patra, D.S. (2023). Surface water quality assessment by Random Forest. *Water Practice & Technology*, *18*(1), 201-214

Makarigakis, A.K., & Jimenez-Cisneros, B.E. (2019). UNESCO's contribution to face global water challenges. *Water*, *11*(2), 388

Noori, R., Berndtsson, R., Hosseinzadeh, M., Adamowski, J.F., & Abyaneh, M.R. (2019). A critical review on the application of the National Sanitation Foundation Water Quality Index. *Environmental Pollution*, *244*, 575-587

Organization, W.H. (2017). Evaluation of certain contaminants in food. *World Health Organization technical report series*(1002), 1-166

Tesoriero, A.J., Gronberg, J.A., Juckem, P.F., Miller, M.P., & Austin, B.P. (2017). Predicting redox-sensitive contaminant concentrations in groundwater using random forest classification. *Water Resources Research*, *53*(8), 7316-7331

Tyralis, H., Papacharalampous, G., & Langousis, A. (2019). A brief review of random forests for water scientists and practitioners and their recent history in water resources. *Water*, *11*(5), 910

Uddin, M.G., Nash, S., & Olbert, A.I. (2021). A review of water quality index models and their use for assessing surface water quality. *Ecological Indicators*, *122*, 107218

Uddin, M.G., Nash, S., Rahman, A., & Olbert, A.I. (2022). A comprehensive method for improvement of water quality index (WQI) models for coastal water quality assessment. *Water Research*, *219*, 118532

Wang, X., Zhang, F., & Ding, J. (2017). Evaluation of water quality based on a machine learning algorithm and water quality index for the Ebinur Lake Watershed, China. *Scientific Reports*, *7*(1), 12858

United Nations Environment Programme (UNEP). (2011). *UNEP year book 2011: Emerging issues in our global environment*. UNEP/Earthprint.

WATER, C. (2001). Canadian Water Quality Guidelines for the Protection of Aquatic Life. *User's Manual*.

ICEARC'25

4th International Civil Engineering & Architecture Conference

17-19 May 2025, Trabzon, Türkiye

Optimization of well flow rate's pumping cost with various metaheuristic algorithms

Nurcan Öztürk*[1]

[1] *Karadeniz Technical University, Faculty of Technology, Department of Civil Engineering, 61830 Trabzon, Türkiye*

Abstract. The study's aim is to determine the optimum well coordinates and flow rate values in a well problem, encountered optimization problem in the management of water resources, with minimum pumping cost through the application of ten metaheuristic optimization algorithms - Particle Swarm Optimization (PSO), Harmony Search (HS), Cuckoo Search (CS), Symbiotic Organisms Search (SOS), Teaching Learning Based Optimization (TLBO), Light Spectrum Optimizer (LSO), Electric Eel Foraging Optimization (EEFO), Geyser Inspired Algorithm (GEA), Newton-Raphson-Based Optimizer (NRBO), and Puma Optimizer (PO). For this purpose, a problem suite was developed consisting of two different problems with four existing, two, and three new wells. In this problem, the objective function is the pumping cost, while the design variables are the coordinates of the two new wells added for the case with six wells, the coordinates of the three wells added for the case with seven wells, and the flow rate values in all wells. The optimum solution, which determines the well locations and flow rate values that minimize the pumping cost of a certain total well flow rate value from an infinite aquifer with two zones of different transmissivities, was sought by means of these algorithms in this problem. The solutions obtained from independent simulations conducted on this problem suite were statistically assessed. The performances of the algorithms were evaluated with Friedman which is a non-parametric statistical test and Wilcoxon paired comparison test. According to the findings, it was seen that the LSO algorithm had the highest performance among the ten algorithms examined.

Keywords: Metaheuristics; Optimization; Flow rate; Cost; Water management

1. Introduction

Water demand is rising daily due to industrial, agricultural, and urban usage as the world's population increases at an accelerated rate. Since surface water resources in critical areas with high human density have become significantly polluted and largely unusable, groundwater resources have assumed greater importance in meeting water needs. The management of groundwater resources to address the growing global water demands is a challenging task due to the depletion of water resources. However, excessive consumption of groundwater resources leads to issues that are difficult for people to overcome, like ground settlements, ecological damage, salt water intrusion into groundwater, and failure to manage the aquifer storage-depletion trajectory.

For many years, optimization techniques have been employed to deal with groundwater management issues and create the water budget required for appropriate resource management. Researchers are developing increasingly sophisticated and precise groundwater optimization methods because of advancements in computer technology. There are two main types of optimization methodologies applied in water resources management: mathematical methods and evolutionary and metaheuristic algorithms (Jahandideh-Tehrani et al., 2020).

The usage of metaheuristic algorithms has been increasing in recent years, and they have been successfully applied to solve various groundwater quantity and quality problems. Although numerous metaheuristic algorithms exist in the literature, both commonly used in groundwater management problems and novel algorithms developed were employed in this paper: Particle Swarm Optimization (PSO), Harmony Search (HS), Cuckoo Search (CS), Symbiotic Organisms Search (SOS), Teaching Learning Based Optimization (TLBO), Light Spectrum Optimizer (LSO), Electric Eel Foraging Optimization (EEFO), Geyser Inspired Algorithm (GEA), Newton-Raphson-Based Optimizer (NRBO), and Puma Optimizer (PO).

Some previous studies that have been applied to groundwater management problems with the metaheuristics employed in this paper are summarized below. PSO was applied to solve two groundwater hydraulic management problems: (1) maximum pumping from an aquifer, (2) minimum cost to develop the new pumping well system

* Corresponding author, E-mail: nurcan@ktu.edu.tr

https://doi.org/10.31462/icearc2025_ce_hwr_982

and was found to be efficient in identifying the optimal location and discharge of the pumping wells (Gaur et al., 2011). HS was also employed for the optimal management of groundwater resources. The optimal management included the maximization of total pumping from an aquifer, and minimization of the total pumping cost to satisfy the given demand (Ayvaz, 2009).

Reviews of the literature show most of the groundwater management studies have used PSO and HS for optimization of the pumping cost. Furthermore, for the purpose of this study, CS, SOS, TLBO, LSO, EEFO, GEA, NRBO, and PO have been applied for the first time in the literature. The motivation to use the metaheuristic techniques in the present study is largely due to the need for obtaining optimal solutions for problems.

This study introduces two different problems with four existing, two, and three new wells based on rather common aspects of water resources management problems, namely groundwater pumping cost. In this study, the optimal solutions of the problems are calculated and then the performance of metaheuristic algorithms on these solutions is evaluated.

2.Method

2.1. Design variables, parameters, constraints, and objective function

Minimize the cost of pumping a given total well flow rate Q_T from an "infinite" aquifer with two zones of different transmissivities T_1 and T_2 (Fig. 1). The problem suite with four current wells, two and three new wells will be used for this task. As shown in Fig.1 , the existing wells (W_1 to W_4) are located at the vertices of a square while the new ones should be constructed inside the square area, shown with broken line. The interface between the two aquifer zones is illustrated by the solid lines in Figure1, which lie on the x-axis and coincide with the y-axis. The coordinates of the current wells, W_1 to W_4, are (−150, 450), (150, 450), (150, 750), and (−150, 750), respectively, to standardize the problem. The new wells have a range of 0 to 1,200 for y and −600 to 600 for x (Karpouzos & Katsifarakis, 2013).

While the required total flowrate Q_T=200 L/s, T_1=0.002 m^2/s and T_2=0.001 m^2/s are the aquifer's features. The radius r_o of each well is 0.25 m, and the radius of influence of the system of wells R is 2,000 m; these values are used in subsequent equations, with R being larger than the maximum possible distance between wells.

The objective function of the optimization problem is the cost function (Eq.1) that should be minimized.

$$f(x) = A \sum_{i=1}^{N} Q_i \, s_i \tag{1}$$

where N represents the total number of wells, Q_i denotes the flow rate of well i and A is a constant depending on the energy cost and the duration of pumping. The hydraulic head level drawdown at well i, caused by pumping, is denoted by s_i. While A is conveniently set to 1,000, Qi and s_i are expressed in m^3/s and m, respectively, in Eq. 1. Its distance from the wells, the wells' flow rates, and the aquifer's properties and boundaries all affect s. The method of images, which introduces imaginary wells symmetrical to the real ones with respect to the zone interface to fulfill the boundary condition there (Bear J, 2012) and the superposition principle, can be used to calculate the corresponding s_i analytically given the set of Qi and the well coordinates.

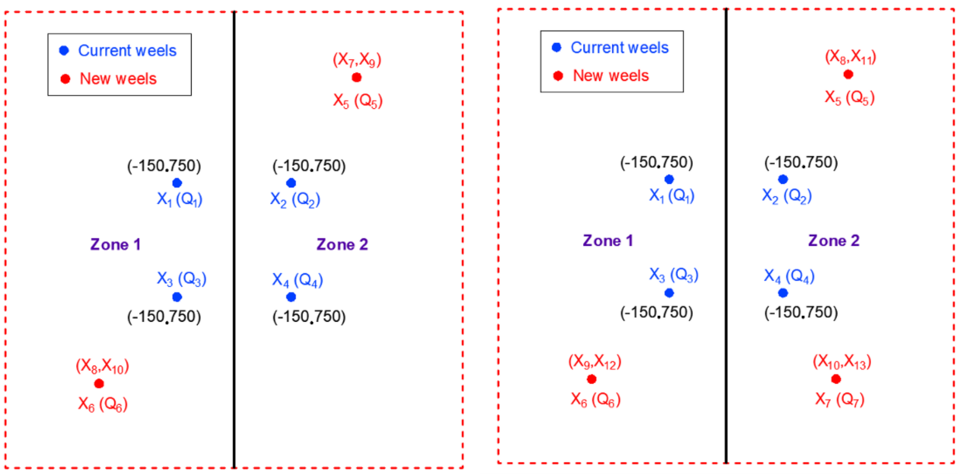

Fig. 1. The two-zone aquifer problems with six and seven wells

Suppose that wells 1 to K are located in zone 1, and the remaining wells (K+1 to N) are located in zone 2. Then, s_i for wells 1 to K is provided as follows:

$$s_i = -\frac{1}{2\pi T_1}\sum_{J=1}^{K} Q_J \ln\frac{r_{iJ}}{R} - \frac{T_1 - T_2}{2\pi T_1(T_1+T_2)}\sum_{J=1}^{K} Q_J \ln\frac{r_{ij}}{R} - \frac{1}{\pi(T_1+T_2)}\sum_{J=K+1}^{N} Q_J \ln\frac{r_{iJ}}{R} \tag{2}$$

while for zone 2 wells K+1 to N, s_i is provided as:

$$s_i = -\frac{1}{2\pi T_2}\sum_{J=K+1}^{N} Q_J \ln\frac{r_{iJ}}{R} - \frac{T_2 - T_1}{2\pi T_2(T_1+T_2)}\sum_{J=K+1}^{N} Q_J \ln\frac{r_{ij}}{R} - \frac{1}{\pi(T_1+T_2)}\sum_{J=1}^{K} Q_J \ln\frac{r_{iJ}}{R} \tag{3}$$

The capital letters in Eqs. 2 and 3 represent the real wells, whereas the lowercase letters represent their images. In addition, R represents the system of wells' radius of effect, r_{iJ} is the distance between wells i and J (r_{iJ}=r_{Ji}), and r_{ij} is the distance between well i and the imaginary well j (r_{ji}). The value of r_{ii}, specifically, is represented by r_0 for every i and is taken to be equal to the radius of well i. It should be mentioned that only Q is summed. The following expression for the cost function (f(x)) is generated by using Eqs. 2 and 3 to express s_i in Eq. 1 (Karpouzos & Katsifarakis, 2013).

$$\begin{aligned} f(x) = &-A\sum_{i=1}^{K} Q_i\left(\frac{1}{2\pi T_1}\sum_{J=1}^{K} Q_J \ln\frac{r_{iJ}}{R} + \frac{T_1 - T_2}{2\pi T_1(T_1+T_2)}\sum_{J=1}^{K} Q_J \ln\frac{r_{ij}}{R} + \frac{1}{\pi(T_1+T_2)}\sum_{J=K+1}^{N} Q_J \ln\frac{r_{iJ}}{R}\right) \\ &- A\sum_{i=K+1}^{N} Q_i\left(\frac{1}{2\pi T_2}\sum_{J=K+1}^{N} Q_J \ln\frac{r_{iJ}}{R} + \frac{T_2 - T_1}{2\pi T_2(T_1+T_2)}\sum_{J=K+1}^{N} Q_J \ln\frac{r_{ij}}{R} \right.\\ &\left. + \frac{1}{\pi(T_1+T_2)}\sum_{J=1}^{K} Q_J \ln\frac{r_{iJ}}{R}\right) \end{aligned} \tag{4}$$

Thus, the objective functions, Eq.4, of the optimization problems with six and seven wells include ten and thirteen variables of two different kinds, namely six well flow rates and four coordinates for the problem with six wells and thirteen variables (seven well flow rates and six coordinates) for the problem with seven wells.

For the problems in this study, the well flow rate is the constraint to be respected and is expressed by Eq. 5.

$$g(x) = \left| Q_T - \sum_{i=1}^{N} Q_i \right| \tag{5}$$

2.2. Simulation environment and algorithm settings

To provide a fair comparison, the same equipment was utilized in each experiment. Table 1 provides a summary of the simulation environment's features. CS, EEFO, GEA, HS, LSO, NRBO, PO, PSO, SOS, and TLBO algorithms were tested in this study. The reference works of the algorithms and the settings recommended in the reference works are presented in Table 2. The maximum number of objective function evaluations (maxFEs) was used as the stopping criterion of the algorithms. This value was taken as 10000 times the number of design variables for all algorithms.

Table 1. The characteristics of the simulation environment

	Component	Description
Hardware	CPU and Frequency	Intel(R) Core(TM) i7-4600U CPU @ 2.10GHz
	RAM	8,00 GB
	Hard Drive	250 GB solid state drive
Software	Operating System	Windows 10 Pro 64 bit
	Language	MATLAB R2023b

Table 2. Settings of the tested algorithms

Algorithm	Reference	Parameters
CS	(Yang & Deb, 2009)	Number of Host Nests =25,pa=0.25
EEFO	(Zhao et al., 2024)	Population Size=100
GEA	(Ghasemi et al., 2024)	Population Size=60, Nc=40
HS	(Geem et al., 2001)	Harmony Memory Size = 50, Harmony Memory Consideration Rate = 0.93, Pitch Adjustment Rate = 0.18
LSO	(Abdel-Basset et al., 2022)	Population size = 20, Ps=0.05, Pe=0.6, Ph=0.4, β=0.05
NRBO	(Sowmya et al., 2024)	Population Size=30, Deciding Factor (DF)=0.6
PO	(Abdollahzadeh et al., 2024)	Population Size=30, PF1=0.5, PF2=0.5, PF3=0.3, U=0.2
PSO	(Eberhart & Kennedy, 1995)	Swarm size=30, cognitive constant=2, social constant=2, inertia weight linearly decreases from 0.9 to 0.4
SOS	(Cheng & Prayogo, 2014)	Ecosystem size = 50
TLBO	(Rao et al., 2012)	Population size=50

3. Results of optimization studies

This chapter is organized in two subsections. In the first subsection, the best solution of the well problems obtained by 10 different metaheuristic search algorithms is presented and the optimum solution findings are discussed. In the second subsection, the performances of the 10 metaheuristic search algorithms used in the optimal design are evaluated by analyzing their statistical data, Friedman scores and Wilcoxon pairwise comparison test results. Among the metaheuristic algorithms analyzed, the one with the highest performance is identified and proposed for solving similar problems.

3.1. Optimum design variables

Optimum designs were searched with 10 different metaheuristic algorithms whose settings are given in Table 2. Details of the least-cost solutions for the 6 and 7-well problems obtained from 21 independent simulations with each of them are presented in Table 3.

Table 3. Optimal design parameters

	Problem with 6 wells		Problem with 7 wells	
Design variables	Definition		Definition	
X_1	Flow rate of the 1st current well (Q1)	0.0285 $m^3 s^{-1}$	Flow rate of the 1st current well (Q1)	0.0232 $m^3 s^{-1}$
X_2	Flow rate of the 2nd current well (Q2)	0.0292 $m^3 s^{-1}$	Flow rate of the 2nd current well (Q2)	0.0224 $m^3 s^{-1}$
X_3	Flow rate of the 3rd current well (Q3)	0.0285 $m^3 s^{-1}$	Flow rate of the 3rd current well (Q3)	0.0232 $m^3 s^{-1}$
X_4	Flow rate of the 4th current well (Q4)	0.0292 $m^3 s^{-1}$	Flow rate of the 4th current well (Q4)	0.0248 $m^3 s^{-1}$
X_5	Flow rate of the 5th new well (Q5)	0.0423 $m^3 s^{-1}$	Flow rate of the 5th new well (Q5)	0.0359 $m^3 s^{-1}$
X_6	Flow rate of the 6th new well (Q6)	0.0423 $m^3 s^{-1}$	Flow rate of the 6th new well (Q6)	0.0359 $m^3 s^{-1}$
X_7	x coordinate of the 5th new well	-600 m	Flow rate of the 7th new well (Q7)	0.0345 $m^3 s^{-1}$
X_8	x coordinate of the 6th new well	600 m	x coordinate of the 5th new well	-600 m
X_9	y coordinate of the 5th new well	0	x coordinate of the 6th new well	600 m
X_{10}	y coordinate of the 6th new well	1200 m	x coordinate of the 7th new well	600 m
X_{11}	-	-	y coordinate of the 5th new well	0
X_{12}	-	-	y coordinate of the 6th new well	1200 m
X_{13}	-	-	y coordinate of the 7th new well	0
Cost		10315.444		9056.127

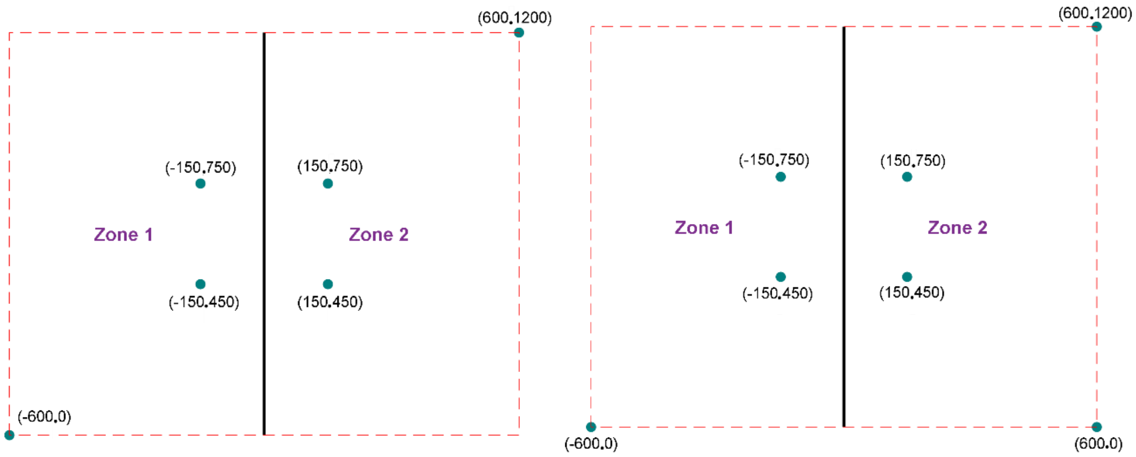

Fig. 2. Optimal coordinates of problems with 6 and 7 wells

The complexity of the objective function can be increased, by increasing the number of existing wells. It is safe to add them along the line y=600 or y=0, in order not to affect the optimal location of the new wells. It should be mentioned that the difference between the cost values depends on the ratio T_1/T_2.

In these optimization problems, the coordinates of the new wells are not known in advance. However, principles from groundwater hydraulics provide some guidance: (a) For a given well discharge Q_i, the resulting drawdown s_i at well i is smaller when the well is located in the region with higher transmissivity and generally decreases as the distance from the transmissivity interface increases. (b) For a given distribution of flow rates Q_i, the drawdowns s_i tend to decrease as the distances between wells increase. Based on these considerations, the most favorable positions for the new wells are likely to be near the corners of zone 1 (Fig. 2), as this zone has a higher transmissivity value (i.e., $T_1>T_2$) (Karpouzos & Katsifarakis, 2013).

If the new wells is located at (−600,0) and at (600,1200) in the problem with 6 wells and at (−600,0), (600,1200), and (600,0) in the problem with 7 wells (Fig. 2), the optimal flow rate distributions, shown in Table 3, result in minimum cost values of 10315.444 and 9056.127 respectively.

3.2. Comparison of algorithms performances

In this subsection, the performance evaluation of 10 metaheuristic algorithms used in the optimum designs is carried out. For this purpose, three different analyses were performed. In the first analysis, the average costs obtained from independent simulations and their standard deviations were assessed. In addition, the evaluation was also conducted with box plots using the same data.

When Table 4 is analyzed, it is seen that the algorithm with the lowest average cost among the 10 rival metaheuristic algorithms is the LSO algorithm. In addition, it is seen that the lowest standard deviation is also obtained by the LSO algorithm. This simple statistical evaluation shows that the LSO algorithm is more efficient and stable than the other rival algorithms. Nevertheless, it is found that the CS and EEFO algorithms rank second and third when evaluating the average cost and standard deviation.

Table 4. Mean and standard deviation of the algorithms

Problem with 6 wells			Problem with 7 wells		
	Mean	Std. Dev		Mean	Std. Dev
LSO	10315.45	0.004	LSO	9057.57	3.356
CS	10320.60	4.692	CS	9122.87	41.433
EEFO	11330.70	263.846	EEFO	9916.93	335.884
NRBO	11968.34	6027.551	NRBO	10288.64	2439.545
SOS	12972.56	1835.855	TLBO	11970.95	889.492
TLBO	13901.40	1627.601	SOS	12875.66	2970.444
GEA	18782.32	7086.682	GEA	17028.09	6378.369
HS	1.43E+12	3.59E+12	HS	20987.18	7433.758
PO	2.38E+12	1.09E+13	PO	2.86E+12	1.31E+13
PSO	4.38E+16	5.45E+16	PSO	9.52E+16	6.75E+16

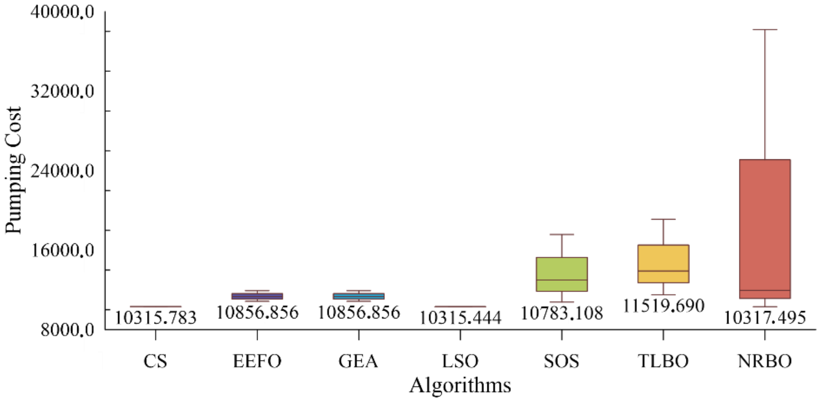

Fig. 3. Box plot of used algorithms for the problem with 6 wells

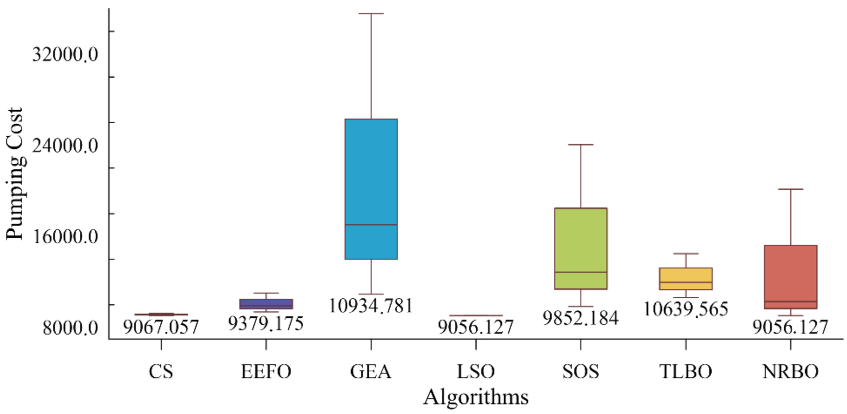

Fig. 4. Box plot of used algorithms for the problem with 7 wells

It is evident from the analysis of the box plots presented in Figures 4 and 5 that the LSO and CS algorithms are capable of achieving the lowest average cost values for both well problems. The small distance between the upper and lower bounds of the box-plot indicates that the standard deviation is also low. When a similar evaluation is made for the standard deviations by means of box-plot, it is seen that the standard deviations of LSO and CS algorithms are much lower than the others.

Since the rankings of the algorithms could not be determined very clearly in the first evaluation, the Friedman test, which is widely preferred in the literature for ranking the performance of metaheuristic search algorithms, was used (Friedman, 1940). The performance rankings of the 10 competing algorithms for both problems are presented in Table 5. In the last column of Table 5, the average Friedman scores obtained for both problems are presented to provide a general evaluation for all problems. In the table, the algorithm names are listed according to the scores.

Table 5. Friedman scores of the algorithms for the well problems

Friedman Scores and Rankings					
Problem with 6 wells		Problem with 7 wells		Mean Score	
LSO	1.00	LSO	1.29	LSO	1.14
CS	2.19	CS	2.43	CS	2.31
NRBO	3.71	NRBO	3.19	NRBO	3.45
EEFO	4.38	EEFO	3.86	EEFO	4.12
SOS	5.62	TLBO	5.95	SOS	5.90
PO	6.00	SOS	6.19	PO	6.17
TLBO	6.57	PO	6.33	TLBO	6.26
GEA	7.81	GEA	7.76	GEA	7.79
HS	8.43	HS	8.67	HS	8.55
PSO	9.29	PSO	9.33	PSO	9.31

Table 6. Wilcoxon test results of the algorithms for the well problems

LSO vs.	Problem with 6 wells	Problem with 6 wells
CS	0 / 0 / 1	0 / 0 / 1
EEFO	0 / 0 / 1	0 / 0 / 1
GEA	0 / 0 / 1	0 / 0 / 1
HS	0 / 0 / 1	0 / 0 / 1
NRBO	0 / 0 / 1	0 / 0 / 1
PO	0 / 0 / 1	0 / 0 / 1
PSO	0 / 0 / 1	0 / 0 / 1
SOS	0 / 0 / 1	0 / 0 / 1
TLBO	0 / 0 / 1	0 / 0 / 1

When the Friedman scores presented in Table 5 for both problems are evaluated, it is seen that the LSO algorithm ranks first for the six-well and 7-well problems. The average scores of the problems also indicate that the LSO algorithm performs better than its rivals in such problems. However, it is understood that the second and third ranked algorithms for the well problems are CS and NRBO algorithms, respectively.

The third evaluation involves pairwise comparisons with the LSO algorithm, which was determined to be the winner in the Friedman test. In order to perform these comparisons, a Wilcoxon pairwise comparison test (Wilcoxon, 1945) was applied to the LSO algorithm with each of the other 9 rival algorithms. The results are given in Table 6.

In Table 6, the three points assigned to each cell indicate that the rival algorithm performs better, similar or worse than the LSO algorithm, respectively. For example, 1/0/0 indicates that the LSO algorithm is the loser, 0/1/0 indicates that the LSO algorithm and the rival algorithm are tied, and 0/0/1 indicates that the LSO algorithm is the winner. The results of the Wilcoxon test presented in Table 6 show the superiority of the LSO algorithm over the other rival algorithms in both problems.

In summary, statistical evaluations reveal that the LSO algorithm significantly outperforms the other 9 rival metaheuristic search algorithms considered in this study in minimum cost well planning problems.

4. Conclusions

In this study, the performance of ten metaheuristic algorithms was evaluated for groundwater well placement and flow rate optimization with the objective of minimizing pumping costs in heterogeneous aquifer systems. Two distinct optimization problems involving six and seven wells were considered, with various configurations of existing and new wells. The results clearly demonstrate that among the tested algorithms, the Light Spectrum

Optimizer (LSO) consistently achieved the best performance in terms of both the lowest average cost and the smallest standard deviation, indicating high efficiency and robustness.

The comparative analysis based on average cost, standard deviation, and box plot visualization reinforced the superiority of the LSO algorithm. Furthermore, statistical tests-specifically the Friedman ranking and Wilcoxon signed-rank test-confirmed that LSO significantly outperforms the other nine algorithms across both optimization scenarios. The Cuckoo Search (CS) and Newton-Raphson-Based Optimizer (NRBO) algorithms were identified as the second and third best-performing techniques, respectively.

These findings suggest that LSO is a highly effective algorithm for solving complex groundwater optimization problems characterized by nonlinear objective functions. It can be recommended as a reliable tool for practical groundwater management tasks that require cost-effective planning under hydrogeological constraints. Future studies could extend the present work by incorporating multi-objective criteria such as water quality, environmental impact, and sustainability indicators to develop more comprehensive groundwater management problems.

References

Abdel-Basset, M., Mohamed, R., Sallam, K. M., & Chakrabortty, R. K. (2022). Light Spectrum Optimizer: A Novel Physics-Inspired Metaheuristic Optimization Algorithm. Mathematics, 10(19).

Abdollahzadeh, B., Khodadadi, N., Barshandeh, S., Trojovský, P., Gharehchopogh, F. S., El-kenawy, E. S. M., Abualigah, L., & Mirjalili, S. (2024). Puma optimizer (PO): a novel metaheuristic optimization algorithm and its application in machine learning. Cluster Computing.

Ayvaz, M. T. (2009). Application of Harmony Search algorithm to the solution of groundwater management models. Advances in Water Resources, 32(6), 916–924.

Cheng, M. Y., & Prayogo, D. (2014). Symbiotic Organisms Search: A new metaheuristic optimization algorithm. Computers and Structures, 139, 98–112.

Eberhart, R., & Kennedy, J. (1995). New optimizer using particle swarm theory. Proceedings of the International Symposium on Micro Machine and Human Science, 39–43.

Friedman, M. (1940). A Comparison of Alternative Tests of Significance for the Problem of m Rankings. The Annals of Mathematical Statistics.

Gaur, S., Chahar, B. R., & Graillot, D. (2011). Analytic elements method and particle swarm optimization based simulation–optimization model for groundwater management. Journal of Hydrology, 402(3–4), 217–227.

Geem, Z. W., Kim, J. H., & Loganathan, G. V. (2001). A New Heuristic Optimization Algorithm: Harmony Search. SIMULATION, 76(2), 60–68.

Ghasemi, M., Zare, M., Zahedi, A., Akbari, M.-A., Mirjalili, S., & Abualigah, L. (2024). Geyser Inspired Algorithm: A New Geological-inspired Meta-heuristic for Real-parameter and Constrained Engineering Optimization. Journal of Bionic Engineering, 21(1), 374–408.

Jahandideh-Tehrani, M., Bozorg-Haddad, O., & Loáiciga, H. A. (2020). Application of particle swarm optimization to water management: an introduction and overview. Environmental Monitoring and Assessment, 192(5), 281.

Karpouzos, D. K., & Katsifarakis, K. L. (2013). A Set of New Benchmark

Rao, R. V, Savsani, V. J., & Balic, J. (2012). Teaching-learning-based optimization algorithm for unconstrained and constrained real-parameter optimization problems. Engineering Optimization, 44(12), 1447–1462.

Sowmya, R., Premkumar, M., & Jangir, P. (2024). Newton-Raphson-based optimizer: A new population-based metaheuristic algorithm for continuous optimization problems. Engineering Applications of Artificial Intelligence, 128.

Wilcoxon, F. (1945). Individual Comparisons by Ranking Methods. Biometrics Bulletin, 1(6), 80–83.

Yang, X. S., & Deb, S. (2009). Cuckoo search via Lévy flights. 2009 World Congress on Nature and Biologically Inspired Computing, NABIC 2009 - Proceedings, 210–214.

Zhao, W., Wang, L., Zhang, Z., Fan, H., Zhang, J., Mirjalili, S., Khodadadi, N., & Cao, Q. (2024). Electric eel foraging optimization: A new bio-inspired optimizer for engineering applications. Expert Systems with Applications, 238.

Comparison of Reynolds shear stress and drag coefficient in a meander with submerged flexible and rigid vegetation

Mercede Alizadeh[1], Hossein Afzalimehr[*1], Saeid Okhravi[2]

[1] *Department of Civil Engineering, Iran University of Science and Technology, Tehran, Iran*
[2] *Department of Civil Engineering, Slovak Acadmy of Science, Bratislava, Slovakia*

Abstract. Natural channels and rivers rarely follow a straight path, often exhibiting meandering shapes. Due to the natural meanders that shape the river channels, understanding the flow characteristics is essential. Additionally, the presence of vegetation in the bed and banks of rivers and its interaction with the bends has a significant impact on the ecosystem and flow structure, as it alters the flow pattern and the distribution of hydraulic parameters. Moreover, the flow passing through open meandering channels, due to secondary and rotational flows, changes the water surface and flow pattern compared to straight channels, affecting flow characteristics such as velocity distribution and turbulence components, and influencing downstream flow as well. This research was conducted in the Hydraulic Laboratory at the Iran University of Science and Technology, in a curved channel with a concrete bed, 8 meters long, covered with sandy bed and a median particle diameter of 15.1, and varying aspect ratios (width-to-depth ratios). The aim of this study is to analyze the impact of submerged flexible and rigid reeds vegetation on the external walls of a reconstructed natural meandering channel with a sandy bed and fixed slope on, Reynolds stress, and drag coefficient. To investigate the effect of vegetation on the flow in the bend, submerged flexible and rigid plastic reeds, 4 cm in height, were used over the sandy bed with a 2% slope. To examine turbulent flow structures, three-dimensional Acoustic Doppler Velocimeter (ADV) velocity data were employed. The experiments consisted of two series: one series with flexible and oneother series with rigid vegetation, with a flow depth of 13 cm. Parameters such as, Reynolds shear stress, and drag coefficient were measured, calculated, and analyzed. The results obtained from the experimental data indicate that the Reynolds stress distribution is nonlinear. In the second section, where the flow interacts with the vegetated area, the Reynolds stress values show a significant decrease compared to the initial sections before the vegetation. This reduction highlights the effective role of vegetation in suppressing vertical mixing within the flow. The drag coefficient was calculated as an indicator of flow resistance, and the results showed that in the initial section, before the flow enters the vegetated zone, the drag coefficient for flexible vegetation is higher than that of rigid vegetation. However, after entering the vegetated area, the drag coefficient for flexible vegetation decreases by 40%, while for rigid vegetation it increases by 93% compared to the values before the vegetated zone.

Keywords: Submerged flexible and rigid reed vegetation; Meandering channel; Sandy bed; Reynolds stress; Drag coefficient

1. Introduction

The interaction between flow and sediment transport plays a pivotal role in the morphodynamic evolution of riverbeds, leading to aggradation and degradation processes that are highly relevant in river management engineering. Sediment transport at the bed level is one of the most essential characteristics of alluvial channels, directly influencing channel stability and morphology. Most natural rivers exhibit sinuous planforms (Langbein & Leopold, 1966), resulting from the complex interplay between flow dynamics, such as longitudinal flow and secondary circulation, and processes of erosion and deposition along the river bed and banks (Seminara, 2006). Channel curvature generates secondary flows in the cross-sectional plane due to the imbalance between centrifugal forces and barotropic pressure gradients (Thomson, 1877). These secondary circulations, as described analytically by Rozovskii (1957) and later by Kalkwijk and Booij (1986), have been widely observed in both riverine and estuarine bends (Buijsman & Ridderinkhof, 2008). This lateral circulation is critical to sediment redistribution, contributing to outer bank erosion, inner bank deposition, meander migration, and the formation of point bars. However, in estuarine systems, salinity-induced stratification can suppress or even reverse these secondary flows

[*] Corresponding author, E-mail: hafzali@iust.ac.ir

https://doi.org/10.31462/icearc2025_ce_hyd_151

golden light publishing

due to baroclinic pressure gradients, potentially explaining the absence of point bars in some tidal meanders (Kranenburg et al., 2019).

In river systems, aquatic vegetation has traditionally been regarded primarily as a source of flow resistance, and as such, it has often been removed to mitigate flood risks (Kouwen, 1992). However, aquatic vegetation also provides vital ecological services, making it an essential component of river ecosystems (Luhar et al., 2008). Understanding the influence of vegetation on flow is thus crucial for effective river restoration. Accurately estimating flow retardation in vegetated channels is particularly important for designing restoration projects (Järvelä, 2005). Despite its importance, the specific interaction between vegetation along channel banks and accelerating flow in gravel-bed rivers has yet to be thoroughly investigated or documented in existing literature.

Afzalimehr and Anctil (2000), has demonstrated that the maximum Reynolds shear stress typically occurs near the bed and decreases toward the free surface with a concave profile. The findings of the present study corroborate this general trend along the flume centerline. However, the presence of vegetation along the banks introduced significant deviations from the classic concave distribution, as reported in the aforementioned studies.

The drag coefficient C_D is commonly used as a quantitative parameter to represent the resistance exerted by aquatic vegetation. The estimation of this drag assumes that energy losses occur due to the distributed drag forces associated with characteristic vegetation (Marjoribanks et al., 2014). This approach is not limited to calculating vegetative drag using bed stress formulae from previous studies (Thompson and Roberson, 1976).

2. Material and method

The experiments were conducted in a meandering channel with natural geometry and a concrete bed. The channel width from the upstream end to the start of the final bend is 0.9 meters, and the total length of the channel is 8 meters. The wavelength of the channel bend is 3.2 meters, and its sinuosity is 1.05. The external bend angle at the end of the channel is 136 degrees, and the internal bend angle is 76 degrees. The channel bed has a gentle slope, consistent with the river slope, equal to 0.0002. Additionally, the channel is equipped with a recirculating flow system, where water flow is pumped from the downstream end and returned to the upstream end.

During the data collection, the flow depth was set and stabilized at a constant value of 13 cm. The data collection related to flow velocity and turbulence was performed using an Acoustic Doppler Velocimeter (ADV). On average, each velocity profile included 18 measurement points. For the channel bed coverage, natural sand was used with a median particle diameter (d_{50}) of 0.158 mm. Data were collected at two different sections: before the start of the bend and at a position with a 45-degree angle from the bend. To ensure high data quality and accurate recording of velocity fluctuations, the distance of the ADV from the outer bend wall was approximately 20 cm. This distance was selected so that the ADV device could record velocity values with a high correlation coefficient, and the spikes were removed using WINADV software.

In this study, to simulate the bed vegetation, flexible and rigid cylindrical plastic reeds with a diameter of 5 mm, which most closely resemble natural samples, were used. The vegetation employed in this experiment consists of reeds with a height of 4 cm above the bed surface, arranged in a submerged manner at the final 90-degree bend of the channel in the downstream section, with 5 cm spacing between them. These reeds are placed on a 2 cm thick plate in a regular arrangement. The reed density with different materials per unit area is 360 reeds.

Fig. 1. General layout of the channel at different bend angles

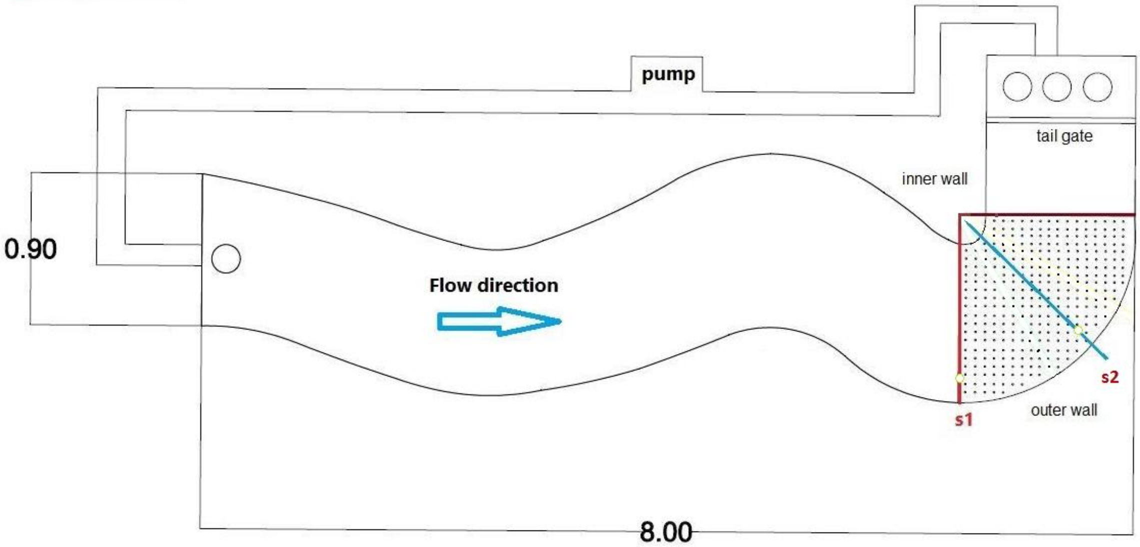

Fig. 2. Data acquisition locations in different cross-sections and the channel plan.

2.1. Reynolds shear stress
The vertical Reynolds stress ($u'w'$) induces longitudinal and vertical momentum exchange as well as vertical mixing (Velasco et al., 2003). Investigations show that the Reynolds stress distribution in all channel flows is nonlinear. The linearity occurs only for low depths above the peak as stress decays from its maximum near the boundary (bed or top of vegetation) to the free surface (Huai et al., 2009).

2.2. Estimation of flow resistance
In this study, flow resistance in the presence of vegetated banks was estimated using Equation (1), as follows:

$$C_D = 2u_*^2/U^2 \tag{1}$$

Where U is the mean cross-sectional velocity, u_* is the shear velocity, CD is the drag coefficient.

$$U = \frac{1}{h}\int_0^h u_i\, d_z \tag{2}$$

where u_i is the velocity at height z, and h is the total flow depth. This formula gives the average velocity over the water column. In practice, U is numerically computed using the measured velocity data along the depth.

2.3. Shear velocity estimation methods
In this study, the shear velocity for each cross section was estimated using the approache of the Boundary Layer Characteristics Method**.**

2.3.1. Boundary layer characteristics method
This method, proposed by Azalimehr and Anctil (2000), utilizes all measured point velocities within each vertical profile to estimate the shear velocity (u_*). The calculation is based on the velocity distribution observed within the boundary layer.

$$u_* = \frac{(\delta_* - \theta)u_{max}}{4.4\delta_*} \tag{3}$$

In this method, u_{max} represents the maximum velocity in each vertical profile. The displacement thickness (δ_*) and the momentum thickness (θ) of the boundary layer are calculated using Equations (4) and (5), respectively.

$$\delta_* = \int_0^h \left(1 - \frac{u}{u_{max}}\right) dz \tag{4}$$

$$\theta = \int_0^h \frac{u}{u_{max}}\left(1 - \frac{u}{u_{max}}\right) dz \tag{5}$$

Where h is the flow depth along the selected axis, u is the local (point) velocity, and U_{max} is the maximum velocity within the velocity profile.

4. Result

4.1 Reynolds shear stress

According to the S1 diagram, the values of ($u'w'/u_*^2$) are significantly higher than those in section S2, even reaching over 20. In the first section, both cases show a wavy and oscillatory structure, indicating turbulence due to the transition into the vegetation-covered region and local flow instabilities. This behavior suggests that the vegetation exerts its hydrodynamic effects even upstream.

In the S2 diagram, the Reynolds shear stress decreases dramatically, with most values falling below 1 and even becoming negative in some regions. This reduction indicates a weakening of vertical mixing due to the presence of plants, which is entirely expected as the vegetation's resistance reduces vertical velocity fluctuations.

In this diagram, it is observed that the maximum shear stress does not occur near the bed but is found at a middle height (around ($0.4 < z/H < 0.5$)). The nonlinear pattern and the shift in the location of the maximum shear stress clearly indicate the effects of plant resistance and secondary flows, which cause deviations from classic shear stress patterns.

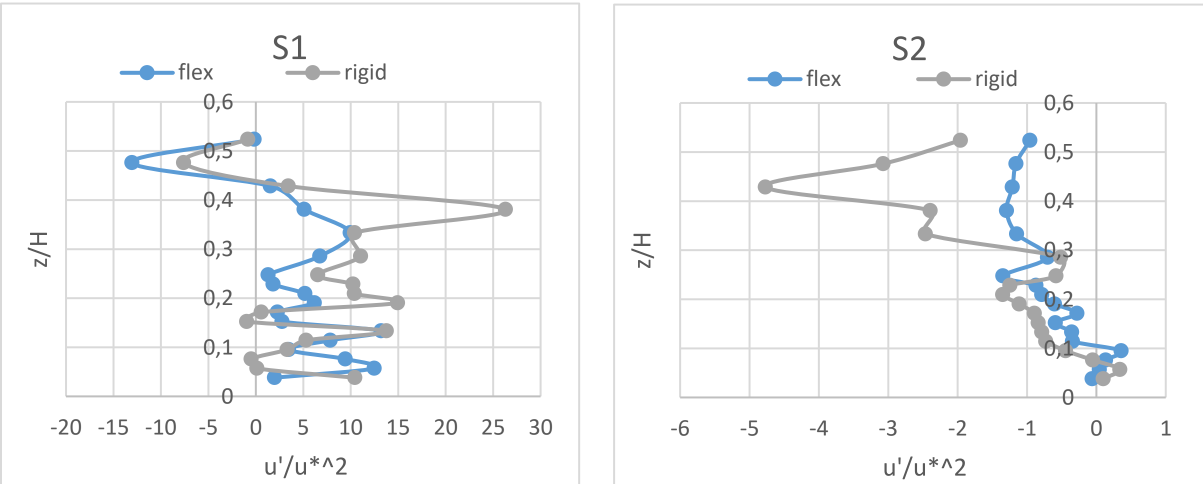

Fig. 3. Shear stress distributions

4.2. Shear velocity

As described in Section 2.3, the boundary layer characteristics method was used to calculate shear velocity in this study. The values of shear velocity and shear stress, calculated using the equation $\tau = \rho u{*}2$, are presented for the studied reach in Table 1. The results show that in cross section S1, the presence of flexible vegetation, compared to rigid vegetation, led to a significant increase in flow velocity, shear velocity, and consequently, shear stress. This increase indicates higher turbulence production and more effective momentum transfer to the bed in the presence of flexible vegetation. A similar pattern is observed in cross section S2 as well, where flexible vegetation also results in increased flow velocity, shear velocity, and shear stress, although the magnitude of this increase is smaller compared to that observed in S1.

Table 1. velocity, shear velocity and shear stress calculated from boundary layer

section	U (m/s)	Shear velocity (m/s)	Shear stress (N/m^2)
S1 flex	2.52	0.011	0.126
S1 rigid	1.38	0.004	0.022
S2 flex	3.38	0.012	0.134
S2 rigid	1.74	0.008	0.067

4.3. Estimation of flow resistance

In this study, the drag coefficient was used as an indicator of flow resistance. Following the calculation of the mean velocity and shear velocity for each cross section, the drag coefficient was determined based on Equation (1).

In this study, variations in the drag coefficient across different flow sections were investigated. The first section, which is located before the flow enters the vegetated area and bend, represents the effects of the flow structure without vegetation. In this section, the drag coefficient for flexible vegetation (0.50) is higher than that for rigid vegetation (0.29). This difference may be attributed to the increased turbulence and fluctuations in the flow caused by the flexible vegetation, which results in higher resistance to flow movement.

In the second section, where the flow is in the presence of vegetation and at a 45-degree angle relative to the bend, it is observed that the drag coefficient for rigid vegetation (0.56) is higher than that for flexible vegetation (0.30). This change indicates the influence of vegetation on the flow structure in this region. Flexible vegetation, with lower resistance to flow, leads to a reduction in the drag coefficient, while rigid vegetation, due to its more rigid structure, increases the resistance and consequently raises the drag coefficient.

Table 2. Drag coefficient of flexible and rigid vegetation

Section name	C_D flex	C_D rigid
Section 1	0.50	0.29
Section 2	0.30	0.56

5. Conclusions

In this study, flow resistance was evaluated for a meandering reach with a vegetated bed, conducted in the laboratory at Iran University of Science and Technology.

The results show that flexible vegetation increases turbulence and momentum transfer, leading to higher shear stress in the upstream section. In contrast, downstream shear stress decreases and even becomes negative, indicating weakened vertical mixing due to plant resistance. Additionally, the shift of maximum shear stress to mid-depth highlights the influence of vegetation resistance and secondary flows in altering the classic shear stress pattern.

Findings reveal that flexible vegetation, especially in upstream sections, enhances flow turbulence, shear velocity, and shear stress more effectively than rigid vegetation. Although this effect persists downstream, its intensity diminishes. Overall, flexible vegetation significantly alters flow dynamics by enhancing momentum transfer.

It was also observed that near the outer bend of the meander, flexible vegetation imposes less resistance to the flow compared to rigid vegetation. In general, flexible vegetation increases turbulence and reduces the drag coefficient, whereas rigid vegetation, due to its stiffer structure, creates greater resistance against the flow.

References

Afzalimehr, H., & Anctil, F. (2000). Accelerating shear velocity in gravel-bed channels. *Hydrological sciences journal*, *45*(1), 113-124.

Buijsman, M. C., & Ridderinkhof, H. (2008). Variability of secondary currents in a weakly stratified tidal inlet with low curvature. *Continental Shelf Research*, *28*(14), 1711-1723.

Huai, W. X., Zeng, Y. H., Xu, Z. G., & Yang, Z. H. (2009). Three-layer model for vertical velocity distribution in open channel flow with submerged rigid vegetation. *Advances in Water Resources*, *32*(4), 487-492.

Järvelä, J. (2005). Effect of submerged flexible vegetation on flow structure and resistance. *Journal of hydrology*, *307*(1-4), 233-241.

Kalkwijk, J. P. T., & Booij, R. (1986). Adaptation of secondary flow in nearly-horizontal flow. *Journal of Hydraulic Research*, *24*(1), 19-37.

Kouwen, N. (1992). Modern approach to design of grassed channels. *Journal of irrigation and drainage engineering*, *118*(5), 733-743.

Kranenburg, W. M., Geyer, W. R., Garcia, A. M. P., & Ralston, D. K. (2019). Reversed lateral circulation in a sharp estuarine bend with weak stratification. *Journal of Physical Oceanography*, *49*(6), 1619-1637.

Langbein, W. B., & Leopold, L. B. (1966). River meanders-theory of minimum variance, USGS Prof. *Paper 422-H*, *15*, 1966.

Luhar, M., Rominger, J., & Nepf, H. (2008). Interaction between flow, transport and vegetation spatial structure. *Environmental Fluid Mechanics*, *8*, 423-439.

Marjoribanks, T. I., Hardy, R. J., & Lane, S. N. (2014). The hydraulic description of vegetated river channels: the weaknesses of existing formulations and emerging alternatives. *Wiley Interdisciplinary Reviews: Water*, *1*(6), 549-560.

Rozovskii, I. L. V. (1957). Flow of water in bends of open channels.

Seminara, G. (2006). Meanders. *Journal of fluid mechanics*, *554*, 271-297.

Thomson, J. (1877). V. On the origin of windings of rivers in alluvial plains, with remarks on the flow of water round bends in pipes. *Proceedings of the Royal Society of London*, *25*(171-178), 5-8.

Thompson, G. T., & Roberson, J. A. (1976). A theory of flow resistance for vegetated channels. *Transactions of the ASAE*, *19*(2), 288-0293.

Velasco, D., Bateman, A., Redondo, J. M., & DeMedina, V. (2003). An open channel flow experimental and theoretical study of resistance and turbulent characterization over flexible vegetated linings. *Flow, Turbulence and Combustion*, *70*, 69-88.

4th International Civil Engineering & Architecture Conference
17-19 May 2025, Trabzon, Türkiye

Investigation of temporal change of Van Lake surface area with climatic parameters

Osman T. BAKİ*[1],

[1] Karadeniz Technical University, Department of Civil Engineering, 61830 Trabzon, Türkiye

Abstract. Sustainable management of water resources is becoming increasingly important today. Closed basins, in particular, are of critical importance for the control of water resources. The Van Lake Basin is one of the largest closed basins in Türkiye and the efficient and sustainable management of its water resources is of great importance both environmentally and economically. Therefore, monitoring changes in the surface area of Van Lake plays an important role in developing strategies for managing water resources in this region. In this study, it was aimed to determine the changes in the surface area of Van Lake between 2016 and 2020. For this purpose, satellite images were used and Landsat 8 images were employed. The selection criterion was defined as a minimum cloudiness requirement of less than 10% cloud cover. This parameter, as well as, was deemed essential for the precise identification of surface water from satellite images taken in August, a period coinciding with the annual peak in temperature and annual nadir in precipitation. The month of August is widely accepted as the period during which the annual minimum rainfall is observed, and thus the minimum water level is recorded. This is particularly important in the context of monitoring changes in the lake's surface area. The Normalized Difference Water Index (NDWI) was used to delineate water surface. NDWI is a spectral index used to delineate water surfaces, and it has the ability to clearly distinguish the differences between water and land. With this method, the water surface boundaries of Van Lake were delineated and the changes in the surface area between 2016 and 2020 were analyzed. The extent to which changes in surface area are related to precipitation, temperature and snowfall height data has been determined, and the effect of environmental factors on water levels in the lake over the years has been expressed.

Keywords: Climate change; Landsat 8; NDWI; Türkiye; Van Lake

1. Introduction

Water resources are of significant importance for the continuity of life. Hence, sustainable management of water resources necessitates proper planning with ecological approaches, long-term monitoring and subsequent observation and monitoring studies of changes in the ecosystem. The assessment of water resources, both in terms of quantity and quality, is a topic that researchers frequently investigate.

Water resources, encompassing the ocean, rivers, lakes, streams and reservoirs, play a pivotal role in the preservation and regulation of diverse living resources within and surrounding ecosystems. The rapid process of urbanisation is expediting environmental transformation and compromising existing water resources. To ensure the conservation and utilisation of these resources, there is a necessity for continuous monitoring and appropriate surveys to be conducted for the purpose of acquiring data regarding water surface. While manual surveys offer dependable information, they are a costly and time-consuming process in terms of manpower. In recent years, advances in remote sensing have rendered it feasible to utilise timely information recorded by different sensors on the satellite. This factual information is widely utilised in various applications, including the extraction of information about water surface (Tambe et al., 2021).

Nowadays, satellite images are processed and widely used in land use and land cover changes, disaster observation, forest and vegetation changes, forest health, area suitability analysis and hydrology observations (Cihan et al., 2022; Demirağ Turan et al., 2021; Genc et al., 2005; Karaman et al., 2018). The utilisation of remotely sensed imagery, spatial technologies and computer processing is becoming increasingly advantageous in the monitoring of environmental changes and trends (Baban, 1999). Generally, object-based classifications and band ratios are preferred in land use and land cover assessment studies using satellite images. Different band proportioning studies have been carried out to more clearly separate water surface in the field from other land objects (Gülci et al., 2019).

* Corresponding author, E-mail: tbaki@ktu.edu.tr

https://doi.org/10.31462/icearc2025_ce_hyd_222

It is imperative to acknowledge the significance of lake basins in the context of water resources management, ecosystem health, and environmental monitoring. These bodies of water exert a direct influence on the hydrological equilibrium of the surroundifng regions, thereby playing a pivotal role in diverse fields, including agriculture, industry, and drinking water supply. The alterations in the surface areas of lakes can be influenced by numerous factors, such as climate change, variations in precipitation patterns, escalating evaporation rates, and anthropogenic activities.

The quantity of water in lakes exerts a direct influence on a variety of physical, biological, and chemical processes, which in turn have significant ramifications for the health of ecosystems and the quality of life. A decrease or increase in the water level can disrupt the equilibrium of aquatic ecosystems by affecting the temperature, oxygen level, and distribution of nutrients in the water. While low water levels can pose a threat to the survival of fish and other aquatic creatures by reducing the oxygen content of the water, excessive water levels can lead to problems such as water pollution and erosion. Furthermore, fluctuations in the chemical composition of water have the capacity to modify biodiversity, given their impact on nutrient cycling and the proliferation of aquatic flora. These alterations may also exert an influence on human quality of life, given the pivotal role that lakes play in economic activities such as water supply, agriculture, tourism and fishing. Imbalances in the quantity of water in lakes have the potential to compromise the sustainability of these activities and to diminish the living standards of the local population (Sobek, 2011).

The quantity of water contained within a lake reservoir is principally determined by the harmonious interplay between inflow, which encompasses direct precipitation, inflowing river discharge, discharge from riparian communities and industries, and groundwater inflow and outflow, comprising direct evaporation, withdrawal, reservoir outflow, and groundwater infiltration (Duan & Bastiaanssen, 2013).

In the contemporary era, there is mounting pressure on water resources, particularly in arid and semi-arid regions, due to climatic changes, increasing water demand and human activities. As a consequence of climate change, irregularities in precipitation patterns and increases in evaporation rates result in substantial reductions in the water levels of lakes and other water surface. This phenomenon leads to the drying up of lakes, the shrinkage of their surface area or even their complete disappearance. The consequences of climate change extend beyond drought and water loss, as they can also result in an increase in periods of extreme rainfall. During such times, sudden increases in rainfall can lead to a significant rise in lake surface areas. Uncontrolled rises in lake levels, particularly in areas prone to frequent flooding, can have detrimental environmental and socio-economic impacts. Increased rainfall can lead to an increase in the flow of water in rivers and streams flowing into lakes, causing the lake volume to expand significantly in a short period of time. This phenomenon can have deleterious effects on settlements, agricultural lands and natural ecosystems in the vicinity of the lake. Consequently, the accurate monitoring of lake surface areas and the meticulous analysis of these fluctuations are paramount for the formulation of efficacious water management strategies, both during periods of drought and in the context of wetter climatic conditions. The repercussions of these processes extend beyond the jeopardy of regional ecosystems, as they also complicate the sustainable management of water resources.

Accurate monitoring and analysis of these changes is therefore critical in order to develop sustainable water management and environmental protection strategies. The objective of water surface extraction for remote sensing images is to differentiate between water surface and other non- water surfaces. This includes satellite images, man-made structures, forestry, snow, barren lands, and so forth. The process is inherently more complex, incorporating additional information such as data, which complicates the extraction of water surface. Consequently, conventional methods based on water surface indices are employed.

The utilisation of field measurements in the field of river sciences frequently engenders cost and time constraints that impede the capacity to amass the exhaustive records necessary to comprehend large and dynamic river systems. Consequently, river managers have increasingly resorted to Earth Observation (EO) science and remote sensing techniques. A significant number of studies have utilised historical water surface masks derived from pre-processed EO datasets, including the Global River Width from Landsat (GRWL, (Allen & Pavelsky, 2018)) and the Surface Water and Ocean Topography mission River Database (SWORD, (Altenau et al., 2021)).These datasets are typically static in time and assumed to be centred around the mean river width (Allen & Pavelsky, 2015).

Traditional water surface masking methods employ the Normalised Difference Water Index (NDWI). NDWI utilises green and near-infrared wavelengths, rendering it compatible with data from the majority of satellite Earth observation missions. The extraction of water surface masks based on NDWI involves the implementation of histogram thresholding methods, which exhibit minimal computational demand. However, this technique is contingent on the selection of specific threshold values that vary by region. (Frazier & Hemingway, 2021; McFeeters, 1996). Xu (Xu, 2006), developed NDWI through the use of shortwave infrared radiation, subsequently renaming the index as modified NDWI (MNDWI). Ouma and Tateishi (Ouma & Tateishi, 2006) proposed a water index (WI) for determining the coastal boundary by integrating the Tasseled Cap Wetness (TCW) index and NDWI. The utilisation of Landsat TM/ETM+ (Thematic Mapper/Advanced Thematic Mapper Plus) (Lu et al., 2008; Zhang et al., 2011), MODIS (Moderate Resolution Imaging Spectroradiometer) (Rogers & Kearney, 2004;

Xiao et al., 2005) and SPOT (Système Pour l'Observation de la Terre) (Bastawesy et al., 2008), ASTER (Advanced Spaceborne Thermal Emission and Reflection Radiometer) (Sivanpillai & Miller, 2010) and HJ-1A/B (Lu et al., 2011) satellite images, have been extensively employed to delineate water surface features.

The advent of satellite imaging technologies has enabled the more precise and effective determination and monitoring of lake surface areas. Satellite data has become a valuable research tool due to its ability to cover large areas and provide consistent data over time series. The high resolution and frequent repetition intervals of satellite imagery make it possible to monitor dynamic changes in the surface area of lakes. The use of these technologies offers great advantages in terms of both time and cost compared to manual measurements. Examining water level and surface area changes and their causes and predicting the changes in the coming years are important and necessary data for the design of coastal structures to be built on the shores of lakes. Although Van Lake cannot be used as drinking and irrigation water due to its soda structure, it serves as a very important water source for the region.

Precipitation and evaporation represent a pair of factors which form the basis of the hydrological cycle (Tanny et al., 2008). The investigation presented herein examined the change in Van Lake water volume with the effects of precipitation and temperature.The study aims to ascertain the alterations in the surface area of Van Lake by means of satellite imagery. To this end, the surface area will be determined using the NDWI index, and the effect of meteorological parameters on the changes in the lake surface area will be examined. Furthermore, by comparing the surface area and water level data obtained by remote sensing, the effect of meteorological data on these changes will be evaluated. The overarching objective of this study is to establish a scientific basis for the sustainable management of water resources and the advancement of environmental protection studies.

2. Study area and data

The Van Lake, the largest lake in Türkiye, also holds the distinction of being the fourth largest salt and soda lake in the world. The Van Lake is considered to be one of the ten largest endorheic (closed basin) saline lakes in the world. It is located in the southern part of the Eastern Anatolia region within the borders of Türkiye (Aydin & Karakuş, 2016; Batur et al., 2009).

The Van Lake is classified as a closed basin, and, according to topographic water divisions, the total surface area of the basin is 17,694 km^2, including both open water surface and land area (Fig 1). The geographical context of Van Lake is defined by its location between the eastern city of Van and the western city of Bitlis. The lake's hydrology is influenced by the streams and rainfall that originate in the surrounding region. According to the mass balance equation, the water budget components of Van Lake consist of precipitation, surface runoff, and groundwater discharge as inflows, and evaporation loss as an outflow. The location of Van Lake within a depression basin on an active fault system contributes to the occurrence of volcanism, hydrothermal activity, and earthquakes (Cukur et al., 2015). The main drainage network in the closed basin of Van Lake consists of permanent streams such as the Zilan, Deliçay, Bendimahi, Karasu, Çaybağı, Engil, Gevas, Kotum, and Yeniköprü (Fig 2).

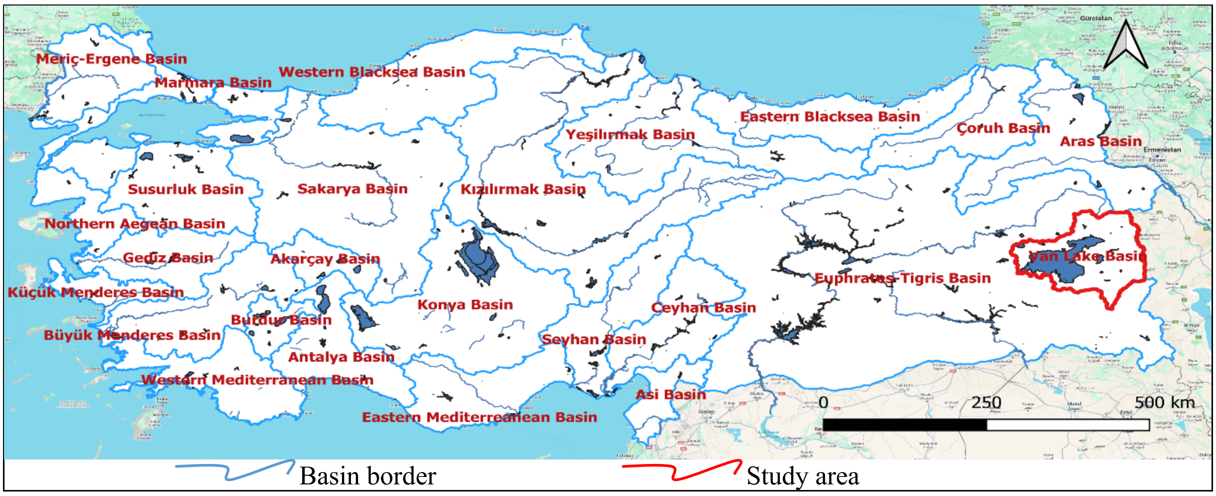

Fig. 1. Water basins of Türkiye

The Van Lake Basin, at an altitude of about 2,185 m, is located in an area far from the sea and surrounded by mountains. The deepest point of the lake is 450 m. The basin covers the provinces of Ağrı, Bitlis, Muş, and Van. In terms of geometric altitude, its lowest elevation starts from 1,648 m and reaches 4,054 m asl at its highest points (Aydin & Karakuş, 2016; Osman, 1993). Although the continental climate type seems to dominate throughout the basin, the areas near the lake have a more temperate climate. Meteorological data for the years 2016-2020, obtained from the Turkish State Meteorological Service (MGM) meteorological gauging stations representing the basin and shown in Fig 2, are presented in Table 1.

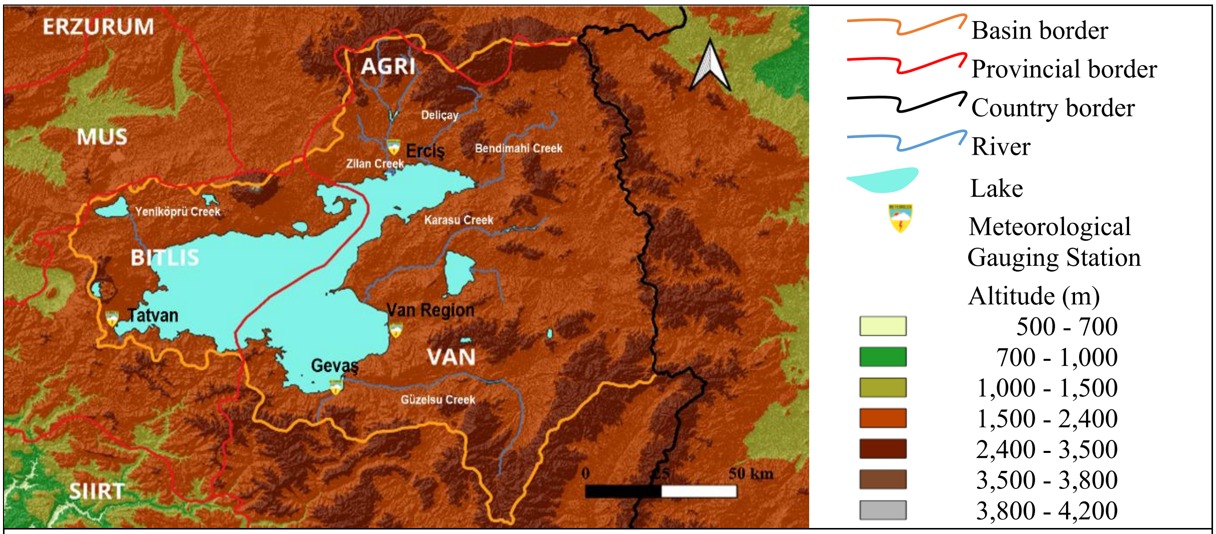

Station no	Gauging station	Coordinates	
		Latitude	Longitude
17172	Van Regional Directorate (R. D.)	38.475012	43.355045
17205	Tatvan	38.515670	42.274648
17784	Erciş	39.050682	43.340941
17852	Gevaş	38.390140	43.188428

Fig. 2. Van Lake Basin

Table 1. Meteorological statistics for the study area for the years 2016 to 2020

	Average Temp. (°C)				Average Prep. (mm)			
Year	Van R. D.	Tatvan	Erciş	Gevaş	Van R. D.	Tatvan	Erciş	Gevaş
2016	10.37	9.73	8.90	9.43	39.07	74.76	32.95	45.17
2017	10.59	9.79	9.40	9.47	26.08	60.93	24.17	40.33
2018	12.18	11.62	11.17	11.03	31.06	69.98	32.65	42.55
2019	11.05	10.51	9.63	10.02	19.28	59.33	39.75	27.82
2020	10.77	10.43	9.74	9.87	28.61	49.13	27.05	38.92

According to the average temperature values of the whole basin, the hottest station of the basin was recorded in the Van R.D., while the coldest station was the Erciş gauging station. While the rainiest station was Tatvan, the lowest rainfall values were recorded at the Van R.D. gauging station. The time series of monthly changes in temperature and precipitation values over the years are presented in Fig 3.

The months of July and August are distinguished by a marked scarcity of rainfall within the basin. With the exception of summer, precipitation is observed in almost every other season. Fig 3 demonstrates that April is typically the month with the highest rainfall, while August is usually the month with the lowest. The monthly average temperatures are also of interest. It is evident from these data that the lowest temperatures are recorded in January, while the highest are recorded in August. Furthermore, it is notable that evaporation is at its peak in August.

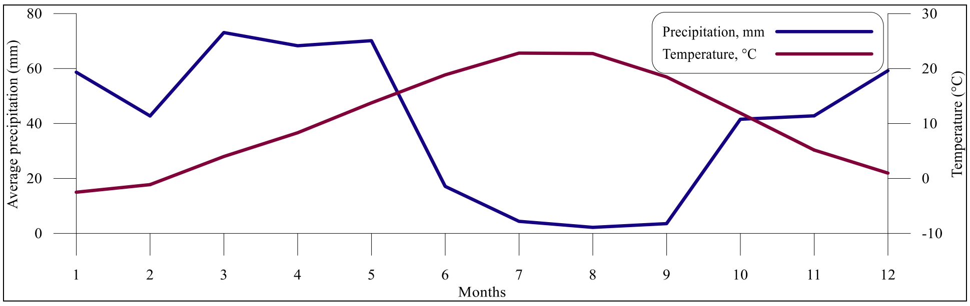

Fig. 3. Monthly average time series of precipitation and temperature

The water level in Van Lake is regulated by the entry of water into the basin and the evaporation process. The surface of the lake fluctuates at regular intervals over long periods of time depending on the dynamics of these natural processes. This phenomenon has a significant impact on lakeside settlements. As the lake's waters expand to cover the low-lying areas on the coast, the inhabitants of these areas are forced to move to higher ground either inland or higher elevations.

The minimum and maximum water levels of Van Lake ranged from 1,646.49 to 1,650.47 m, with an average 1,648.33 m at sea level (EİE, 2007). In the long term, it is understood that lake surface area and volume vary between 3,547.7 and 3,621.0 km^2 (3,581.6 km^2 on average) and 561.6 to 575.8 km^3 (568.2 km^3 on average) at minimum and maximum water levels, respectively (Aydin & Karakuş, 2016).

In accordance with the mass balance equation, the water budget components of Van Lake comprise precipitation, surface runoff, and groundwater discharge as inflows, and evaporation loss as an flow (Aydin & Karakuş, 2016).

2.1. Data sources and methods

The present study employed the method with a view to achieving the objectives and accomplishing the goals of the study, and to determine the surface area of the water of Van Lake. The water surface area of Van Lake was determined by means of the NDWI and Landsat 8 Enhanced Thematic Mapper (ETM+) images. Subsequently, an examination was conducted of the relationship between the precipitation and temperature data obtained from the meteorological observation stations within the basin and the change in eye surface area. Furthermore, an evaluation was made of the effect of meteorological data on the water surface area.

2.1.1. Normalised difference water index (NDWI)

NDWI was first proposed by McFeeters in 1996 for the detection of surface water in wetland environments and measurement of surface water extent (McFeeters, 1996). Notwithstanding the fact that the index was created for use with Landsat Multispectral Scanner (MSS) image data, it has been employed with success in conjunction with other sensor systems in applications where measurement of the extent of open water is required (McFeeters, 2013). The NDWI is derived using the following equation:

$$NDWI = \frac{(Band3 - Band5)}{(Band3 + Band5)} \quad (1)$$

where Band 3 is the top-of-atmosphere (TOA) green light reflection and Band 5 is the TOA near-infrared (NIR) reflection. McFeeters (McFeeters, 1996) proposed that NDWI values greater than zero are indicative of water surfaces, while values less than or equal to zero are assumed to be non-water surfaces. The process was executed utilising the raster calculator tool within the QGIS 3.40.1 open source programme.

2.1.2. Landsat 8

Landsat 8 is a satellite mission that was launched on 11 February 2013 by the United States' space agency National Aeronautics and Space Administration (NASA) and the United States Geological Survey Geological Survey (USGS). It is part of the Landsat series of satellites and is used to image the land surface on Earth with high resolution. This satellite provides critical data for a range of applications, including the monitoring of changes on the planet's surface, agriculture, forestry, water management, urban growth, environmental change and disaster management. Landsat 8 monitors an area 185 km wide and offers a resolution of 15 m, allowing detailed analysis of land use from satellite images. Landsat 8 collects data in 11 different spectral bands (including visible light, infrared, and thermal bands). This capacity enables users to analyse diverse environmental features (e.g. vegetation, water resources, soil moisture) with greater precision. Landsat 8's monitoring frequency is 16 days apart for each region, ensuring the provision of updated data at regular intervals. The data from Landsat 8 is utilised by scientists, researchers, governments and the private sector in numerous domains, including environmental monitoring, disaster management and agricultural monitoring. The data is predominantly made available at no cost and is supportive of open-sourcing initiatives (U.S. Geological Survey, 2025).

2.1.3. HydroWeb project

The HydroWeb project provides a time series of water levels from Van Lake, representing a platform developed by Laboratoire d'Etudes en Géphysique et Océanographie Spatiales (LEGOS). This open source system collects and shares data on the ocean, sea level and ocean currents with users, facilitating enhanced understanding of ocean dynamics through online observation and sea level data. The HydroWeb project utilises satellite data and diverse observation tools to monitor sea level changes, ocean temperatures and sea currents, facilitating the regular monitoring of variations in lake water levels. This time series has been derived from multialtimetry satellites (i.e., TOPEX/Poseidon, ENVISAT, Jason-2 and Jason-3, SARAL, Sentinel-3A, and Sentinel-6A) and has been processed, validated and distributed by the HydroWeb portal, which is part of the THEIA pole of earth observations (Sylvestre et al., 2024).

2.2. Calculation of NDWI

Landsat 8 satellite images were obtained from the USGS. Satellite images from August, the month with the lowest precipitation and the highest temperature, were selected for analysis. To mitigate the impact of cloudiness on satellite images, those with cloudiness below 10% were filtered. Then, the satellite images were cropped within the boundaries of the study basin and the NDWI was calculated using the equation (1) outlined above. Subsequently, the image classified between (-1, 1) was reclassified in the range of (0, 1), and the classification was completed in such a way that non-water places were not taken into account. The determined water surfaces were calculated separately for each year, and the water surface change was determined.

3. Results and discussion

In order to detect surface area changes of the Van Lake in period 2016-2020, the water surface of lake in temporal image was extracted NDWI. Water bodies enhanced by the NDWI in the study area are shown in Fig 4. NDWI has been demonstrated to be an effective method of distinguishing between water bodies, with the suppression of background objects being a notable feature. The alteration in surface areas of water bodies was calculated and is presented in Fig. 4.

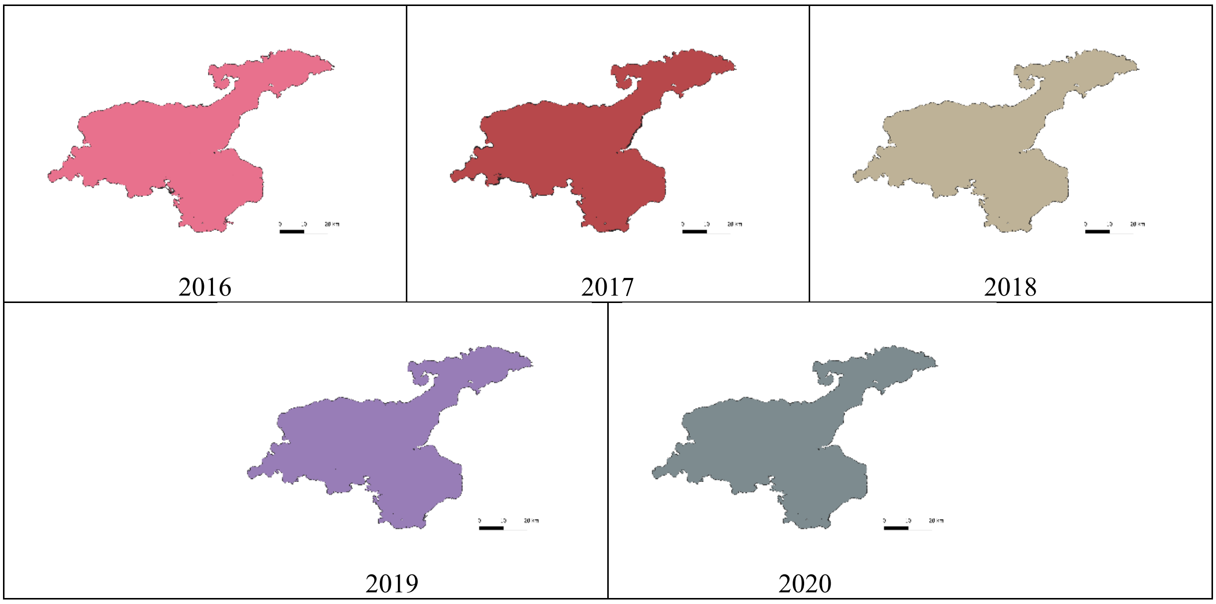

Fig. 4. Spatial change in Van Lake by NDWI method according to years

According to the NDWI findings, the water surface in the lake covered an area of 3,594.39 km^2, 3,593.89 km^2, 3,592.24 km^2, 3,591.98 km^2, and 3,591.65 km^2 in 2016, 2017, 2018, 2019, and 2020, respectively. It was determined that the surface area of the lake tended to decrease over time. Alterations in water surfaces in closed basin lakes, such as Van Lake, are entirely attributable to meteorological effects. Consequently, this variation in the water surface was elucidated by means of average precipitation and temperature data procured from meteorological data for the same period. For this purpose, meteorological data for the period in question are presented in Table 2. In order to make definitive comments on the effects of precipitation data on the basin, the previous month's precipitation heights and annual total precipitation heights were taken into account, taking into account the lag times. During the winter months, snow on the ground surface allows water to be stored. When snowmelt occurs in the summer months due to rising temperatures, this water enters the basin, thereby creating a significant water source. Accumulated waters can serve as a source for the lake during periods of rising temperatures. The data concerning the surface area of the lake and the associated meteorological information delineated in Table 2 encompass the values pertinent to the temporal segments of the investigation conducted within the study region.

Precipitation was selected for further analysis based on a comparison of data sets focusing on precipitation that falls within the lake basin and has the potential to rapidly impact the lake area. When significance could not be determined from these data, temperature data were used. However, if significance could not be determined despite the application of temperature data, lake surface area changes were examined using the annual average snowfall height.

Table 2. Statistical meteorological values between 2016-2020

Date	Surface Area (km^2)	Prec_Aug. (mm)	Prec_July (mm)	Prec_Ann. (mm)	Temp_Aug. (°C)	Temp_Ann. (°C)	Snow._Ann. (mm)
Aug. 2016	3,594.39	3.00	3.37	47.98	23.05	9.60	8.08
Aug. 2017	3,593.89	3.50	1.35	37.87	23.37	9.81	5.20
Aug. 2018	3,592.24	0.47	1.07	44.05	23.17	11.49	2.35
Aug. 2019	3,591.98	3.15	0.60	36.54	22.95	10.30	2.60
Aug. 2020	3,591.65	10.87	15.52	35.92	21.12	10.20	13.88

* Prec., Aug., Snow., Temp., and Ann. represents precipitation, August, snowfall, temperature, and annual, respectively.

In 2017, the surface area of the lake decreased by approximately 0.5 km² compared to 2016. A relative increase in precipitation data was observed in August compared to 2016, while data for July showed a decrease and annual average precipitation levels decreased. While temperature data for August increased compared to 2016, there was also an increase in annual average temperatures. The observed decrease in the lake surface area is believed to be a consequence of the annual average temperature increase, the low precipitation levels recorded in July, and the absence of snowfall during the winter months.

In 2018, the surface area of the lake decreased by approximately 1.5 km² compared to 2017. A significant decrease in August precipitation data was observed compared to 2017, as well as a decrease in July data and an increase in annual average precipitation levels. While the temperature data for August decreased compared to 2017, there was also an increase in annual average temperatures. The observed decrease in the lake surface area is believed to be a consequence of the annual average temperature increase, the low precipitation levels recorded in July and August, and the lack of snowfall during the winter months.

In 2019, the surface area of the lake decreased by approximately 0.3 km² compared to 2018. An increase in August precipitation data was observed compared to 2018, while July data exhibited a decrease and annual average precipitation heights showed a decline. While August temperature data decreased compared to 2018, a decrease in annual average temperatures was also noted. It was determined that there was a relative increase in annual average snowfall heights. Concurrent with the decline in average annual precipitation, a decrease in the surface area of the lake has been documented. While a decrease in temperature and increased snowfall during the winter months have been recorded, these factors, in conjunction with the decline in precipitation, have contributed to the observed decrease in lake surface area.

In 2020, the surface area of the lake decreased by approximately 0.3 km² compared to 2019. An increase in August precipitation data was observed compared to 2019, as well as an increase in July data. No significant change was detected in annual average precipitation heights. While the temperature data for August decreased compared to 2019, a relative decrease in annual average temperatures was also noted. An increase in annual average snowfall heights was determined. Notwithstanding the rise in average annual precipitation, the decline in temperature values, and the heightened snowfall in winter, a decrease in the lake surface area has been documented. The decrease in lake surface area observed in 2020 cannot be attributed to meteorological factors alone. Following a thorough examination, it was ascertained that the meteorological data did not result in a reduction of the lake surface area. It is hypothesized that the lake surface area may have diminished as a consequence of basin activities.

Lake surface altimetry data obtained from HydroWeb was utilized to ascertain the consistency of the alterations detected in the lake surface area. The lake surface area and altimetry data are presented comparatively in Table 3.

Table 3. Lake surface area and altimetry

Date	Surface area (km^2)	Altimetry* (m)
Aug. 2016	3,594.39	1,647.63
Aug. 2017	3,593.89	1,647.61
Aug. 2018	3,592.24	1,647.41
Aug. 2019	3,591.98	1,647.34
Aug. 2020	3,591.65	1,647.32

*Altimetry data retrieved from HydroWeb

As illustrated by the altimeter data presented in Table 3, it has been determined that the water surface elevation of Van Lake exhibited a continuous decrease between 2016 and 2020. Concurrently, a parallel change was observed in the lake area. During the period of maximum water surface level change, which corresponded to an approximate change of 0.2 m, a decrease of approximately 1.5 km^2 in lake area was observed. It was determined that the change factors were also the water level, and it was established that the changes occurring in the lake area are also visible at the lake level. Despite the absence of a direct correlation between fluctuations in water level and changes in lake area, the direction of change exhibits a high degree of similarity. It has been observed that minor alterations in water level can result in substantial changes in lake area.

4. Conclusion

In view of the adverse effects of global climate change on water resources, it is essential to monitor all water resources, including those with large and small flow rates. Monitoring and modelling of water resources with remote sensing methods has been a widely utilised approach since time immemorial. A comparison of Landsat satellite images with meteorological data provides a significant foundation for the evaluation of the impact of climate data on water resources. The employment of open-source data and software in water resources management has led to a progressive reduction in research costs. It has been ascertained that the surface area and water level of Van Lake underwent a gradual decline between 2016 and 2020. The hydrology of the Van Lake basin, being closed and dependent on precipitation, has been found to be a key factor in this change. The analysis of annual temperature and precipitation data, as well as snowfall heights, has revealed that these factors significantly influence the change in lake surface area. However, it has been determined that not all of the observed changes can be attributed to meteorological data, with some cases being too complex to be fully explained by meteorological factors alone. In light of these findings, it is recommended that human factors be taken into consideration in future studies, as they have been delineated as a potentially significant influence on the dynamics of Van Lake. Consequently, a study should be conducted to examine the relationship between decreasing lake area and water levels, and changes in land use.

Acknowledgements

The author is grateful to the Turkish State Meteorological Service (MGM), United States Geological Survey Geological Survey (USGS), and Laboratoire d'Etudes en Géophysique et Océanographie Spatiales (LEGOS) HydroWeb for their provision of meteorological values, satellite images, and altimetry data, respectively.

References

Allen, G. H., & Pavelsky, T. M. (2015). Patterns of river width and surface area revealed by the satellite-derived North American River Width data set. Geophysical Research Letters, 42(2), 395–402. https://doi.org/10.1002/2014GL062764

Allen, G. H., & Pavelsky, T. M. (2018). Global extent of rivers and streams. Science, 361(6402), 585–588. https://doi.org/10.1126/science.aat0636

Altenau, E. H., Pavelsky, T. M., Durand, M. T., Yang, X., Frasson, R. P. de M., & Bendezu, L. (2021). The Surface Water and Ocean Topography (SWOT) Mission River Database (SWORD): A Global River Network for Satellite Data Products. Water Resources Research, 57(7). https://doi.org/10.1029/2021WR030054

Aydin, H., & Karakuş, H. (2016). Estimation of evaporation for Lake Van. Environmental Earth Sciences, 75(18). https://doi.org/10.1007/s12665-016-6077-4

Baban, S. M. J. (1999). Use of remote sensing and geographical information systems in developing lake management strategies. Hydrobiologia, 395/396, 211–226. https://doi.org/10.1023/A:1017057820780

Bastawesy, M. A., Khalaf, F. I., & Arafat, S. M. (2008). The use of remote sensing and GIS for the estimation of water loss from Tushka lakes, southwestern desert, Egypt. Journal of African Earth Sciences, 52(3), 73–80. https://doi.org/10.1016/j.jafrearsci.2008.03.006

Batur, E., Kadıoğlu, M., Özkaya, M., Saban, M., & Akın, İ. (2009). Van Gölü Su Seviye Modellemesi. Su Kaynakları, 2, 27–40.

Cihan, A., Cerit, K., & Erener, A. (2022). Yangın Alanında Uydu Görüntüleri ile Yer Yüzey Sıcaklık Değişimi Gözlemi ve Mekânsal Alan Tespiti. Doğal Afetler ve Çevre Dergisi, 8(1), 142–155. https://doi.org/10.21324/dacd.942724

Cukur, D., Krastel, S., Çağatay, M. N., Damcı, E., Meydan, A. F., & Kim, S.-P. (2015). Evidence of extensive carbonate mounds and sublacustrine channels in shallow waters of Lake Van, eastern Turkey, based on high-resolution chirp subbottom profiler and multibeam echosounder data. Geo-Marine Letters, 35(5), 329–340. https://doi.org/10.1007/s00367-015-0410-x

Demirağ Turan, İ., Dengiz, O., & Kaya, N. S. (2021). Arazi Örtüsü/Arazi Kullanım Değişimlerinin Farklı Zamanlı Landsat Uydu Görüntüleri ile Belirlenmesi: Çarşamba Delta Ovası Örneği. ÇOMÜ Ziraat Fakültesi Dergisi, 9(1), 141–152. https://doi.org/10.33202/comuagri.857787

Duan, Z., & Bastiaanssen, W. G. M. (2013). Estimating water volume variations in lakes and reservoirs from four operational satellite altimetry databases and satellite imagery data. Remote Sensing of Environment, 134, 403–416. https://doi.org/10.1016/j.rse.2013.03.010

EİE. (2007). Göl seviyeleri (1943-2005).

Frazier, A. E., & Hemingway, B. L. (2021). A technical review of planet smallsat data: Practical considerations for processing and using planetscope imagery. Remote Sensing, 13(19). https://doi.org/10.3390/rs13193930

Genc, L., Smith, S., Charles, G., & Mc Corry, F. (2005). A Comparison of Landsat Thematic Mapper and Indian Remote Sensing Data for Land Use and Land Cover Change Assessment. Trakya Üniversitesi Fen Bilimleri Dergisi, 27–38. http://fenbil.trakya.edu.tr/tujs

Gülci, S., Gülci, N., & Yüksel, K. (2019). Aslantaş Baraj Gölü ve Çevresinin Su Yüzey Alanı ve Arazi Örtüsü Değişiminin Landsat Uydu Görüntüleri Kullanılarak İzlenmesi. Iğdır Üniversitesi Fen Bilimleri Enstitüsü Dergisi, 9(1), 100–110. https://doi.org/10.21597/jist.419221

Karaman, M., Özelkan, E., & Taşdelen, S. (2018). Dar Nehirlerin Sentinel2-A Uydu Görüntüleri ile Belirlenebilirliğinde Havza Hidrojeolojisinin Etkisi: Karamenderes (Çanakkale) Örneği. Doğal Afetler ve Çevre Dergisi, 4(2), 140–155. https://doi.org/10.21324/dacd.416514

Lu, S., Shen, X., Zoue, L., Li, C., Mao, Y., Zhang, G., Wu, W., Liu, Y., & Zhang, Z. (2008). An integrated classification method for thematic mapper imagery of plain and highland terrains. Journal of Zhejiang University-SCIENCE A, 9(6), 858–866. https://doi.org/10.1631/jzus.A071469

Lu, S., Wu, B., Yan, N., & Wang, H. (2011). Water body mapping method with HJ-1A/B satellite imagery. International Journal of Applied Earth Observation and Geoinformation, 13(3), 428–434. https://doi.org/10.1016/j.jag.2010.09.006

McFeeters, S. K. (1996). The use of the Normalized Difference Water Index (NDWI) in the delineation of open water features. International Journal of Remote Sensing, 17(7), 1425–1432. https://doi.org/10.1080/01431169608948714

McFeeters, S. K. (2013). Using the normalized difference water index (ndwi) within a geographic information system to detect swimming pools for mosquito abatement: A practical approach. Remote Sensing, 5(7), 3544–3561. https://doi.org/10.3390/rs5073544

Osman, Ç. (1993). Van Gölü Havzası Su Kaynakları ve Balıkçılık Potansiyeli. Doğu Anadolu Bölgesi, I. Su Ürünleri Sempozyumu, 71–83.

Ouma, Y. O., & Tateishi, R. (2006). A water index for rapid mapping of shoreline changes of five East African Rift Valley lakes: an empirical analysis using Landsat TM and ETM+ data. International Journal of Remote Sensing, 27(15), 3153–3181. https://doi.org/10.1080/01431160500309934

Rogers, A. S., & Kearney, M. S. (2004). Reducing signature variability in unmixing coastal marsh Thematic Mapper scenes using spectral indices. International Journal of Remote Sensing, 25(12), 2317–2335. https://doi.org/10.1080/01431160310001618103

Sivanpillai, R., & Miller, S. N. (2010). Improvements in mapping water bodies using ASTER data. Ecological Informatics, 5(1), 73–78. https://doi.org/10.1016/j.ecoinf.2009.09.013

Sobek, S. (2011). Predicting the depth and volume of lakes from map-derived parameters. Inland Waters, 1(3), 177–184. https://doi.org/10.5268/IW-1.3.426

Sylvestre, F., Mahamat-Nour, A., Naradoum, T., Alcoba, M., Gal, L., Paris, A., Cretaux, J.-F., Pham-Duc, B., Lescoulier, C., Recouvreur, R., Ahmat, M. M., & Gaya, D. (2024). Strengthening of the hydrological cycle in the Lake Chad Basin under current climate change. Scientific Reports, 14(1), 24639. https://doi.org/10.1038/s41598-024-75707-4

Tambe, R. G., Talbar, S. N., & Chavan, S. S. (2021). Deep multi-feature learning architecture for water body segmentation from satellite images. Journal of Visual Communication and Image Representation, 77. https://doi.org/10.1016/j.jvcir.2021.103141

Tanny, J., Cohen, S., Assouline, S., Lange, F., Grava, A., Berger, D., Teltch, B., & Parlange, M. B. (2008). Evaporation from a small water reservoir: Direct measurements and estimates. Journal of Hydrology, 351(1–2), 218–229. https://doi.org/10.1016/j.jhydrol.2007.12.012

U.S. Geological Survey. (2025). Landsat 8. https://www.usgs.gov/landsat-missions/landsat-8

Xiao, X., Boles, S., Liu, J., Zhuang, D., Frolking, S., Li, C., Salas, W., & Moore, B. (2005). Mapping paddy rice agriculture in southern China using multi-temporal MODIS images. Remote Sensing of Environment, 95(4), 480–492. https://doi.org/10.1016/j.rse.2004.12.009

Xu, H. (2006). Modification of normalised difference water index (NDWI) to enhance open water features in remotely sensed imagery. International Journal of Remote Sensing, 27(14), 3025–3033. https://doi.org/10.1080/01431160600589179

Zhang, B., Wu, Y., Zhu, L., Wang, J., Li, J., & Chen, D. (2011). Estimation and trend detection of water storage at Nam Co Lake, central Tibetan Plateau. Journal of Hydrology, 405(1–2), 161–170. https://doi.org/10.1016/j.jhydrol.2011.05.018

4th International Civil Engineering & Architecture Conference
17-19 May 2025, Trabzon, Türkiye

Experimental study on restoration of sandbar using traditional Japanese river works *“Hijiri-ushi”*

Reita Hayashimoto[1], Yasunori Muto*[1], Kazunari Takano[1], Takao Tamura[1]

[1] *Yachiyo Engineering Co., Ltd., CS Tower, 5-20-8 Asakusabashi, Taito-ku, Tokyo, Japan 111-8648, Japan*

Abstract. In recent years, the amount of sediment flowing down river channels in Japan has been decreasing due to the construction of dams and the progress of landslide control. This causes both flood control and environmental problems due to fixation of river channel topography, dugging waterway deeper and narrower, and increasing the sandbar height with possible vegetation intrusion. This study utilizes a traditional Japanese river works, a permeable groyne “*Hijiri-ushi*”, as one of the possible measures to solve the fixed topography of sandbars. As a first step in seeking the best condition for the placement of groynes that cause the destruction of fixed sandbar topography and the activation of sediment transport, the flow patterns in the downstream of the groynes were investigated. The number of groynes in one row, the angle of each groyne, and the row angle were varied, and the velocity distributions in the downstream were measured in detail. As a result of the experiments, a condition for the arrangement of the groynes which newly forms a high-speed region as well as induces meandering of the flow was found. The former expects to promote the destruction of sandbars, and the latter dose to introduce a new meandering mode onto the original sandbar formation. We are further continuing to study the conditions which strengthen the new meander mode by using multiple rows of groynes. In addition, movable bed experiments under the best condition of the placement of groynes derived from the fixed bed experiments are planned.

Keywords: Sandbar; Restoration; Experiment; Traditional Japanese river works; Meander flow

1. Interoduction

In recent years, the reduction in sediment supply due to dam construction and other factors has become a significant issue in Japan. As a result, the degradation of low-flow channels and the development of sandbar height have progressed, leading to the polarization of river channels, the fixation of sandbar topography, and deep riverbed erosion under prolonged low-flow conditions. These changes have contributed to the deterioration of river environments (Tsujimoto, 1999).

In the Kizu River, part of the Yodo River system, the fixation of sandbar topography has become particularly pronounced in the downstream reaches. This fixation induces eccentric flow, increasing the risk of levee failure. Additionally, the natural dynamics of the river, such as disturbances and flow variations, have been lost. To address these issues, river improvement projects utilizing “*Hijiri-ushi*” a traditional river engineering technique—are being carried out under the leadership of the MLIT of Japan, Kinki Regional Development Bureau, Yodogawa River Office. Specifically, experimental studies are being conducted to install “*Hijiri-ushi*” on fixed sandbars to promote erosion and deposition processes, thereby inducing riverbed variations (Takemon, 2021).

This study focuses not on the primary functions of “*Hijiri-ushi*”, such as flow velocity reduction and flow direction control, but rather on its effectiveness in managing sediment dynamics around the structure. The objective is to clarify the installation conditions of “*Hijiri-ushi*” that can promote sediment transport in fixed sandbar topographies.

2. Study on flow velocity measurement by changing the arrangement conditions of “*Hijiri-ushi*” under fixed bed conditions

2.1 Experimental method

Layout of the experimental channel is shown in Figure 1. The experimental channel was 15.5 m long and 0.65 m wide, with a channel slope of 1/200 and a rectangular cross-sectional shape. To ensure uniform flow conditions, a

*Corresponding author, Professor, E-mail: muto_yas@ce.tokushima-u.ac.jp

https://doi.org/10.31462/icearc2025_ce_hyd_244

weir was installed at the downstream end of the channel, while an aluminum flow straightener was placed at the upstream end to suppress turbulence and vortex formation.

A steady flow with a discharge of $Q = 35$ l/s was introduced into the channel. The water depth (h) was adjusted to 5 cm at the groyne installation section by controlling the downstream weir, and the experiment was conducted under overflow conditions. For velocity measurements, a three-axis electromagnetic current meter (ACM3-RS manufactured by JFE Advantech Co., Ltd.) was used. The groyne model used in the experiment had a length of 7 cm, a height of 4 cm, and a width of 4.7 cm, representing a 1/120 scale model (Tominaga A et al, 2005). Table 1 summarizes the hydraulic conditions.

Velocity measurements were conducted in the horizontal plane (x-y plane), with the upstream end of the groyne group (x = 0 cm) and the right bank (y = 0 cm) used as reference points. The measurement cross-sections in the flow direction for groyne group were taken at x = -40 cm and the downstream end of the groyne group at 4 cm intervals up to x = 36 cm, and then at 8 cm intervals up to x = 60 cm, covering a total of 15 sections. This is summarized in Figure 2. Additionally, measurements in the cross-sectional direction were conducted at 12 sections, with a 5 cm pitch. The measurement depth was set at half the water depth (2.5 cm), and velocity data were recorded at a sampling frequency of 10 Hz for one minute, with the average velocity used for analysis.

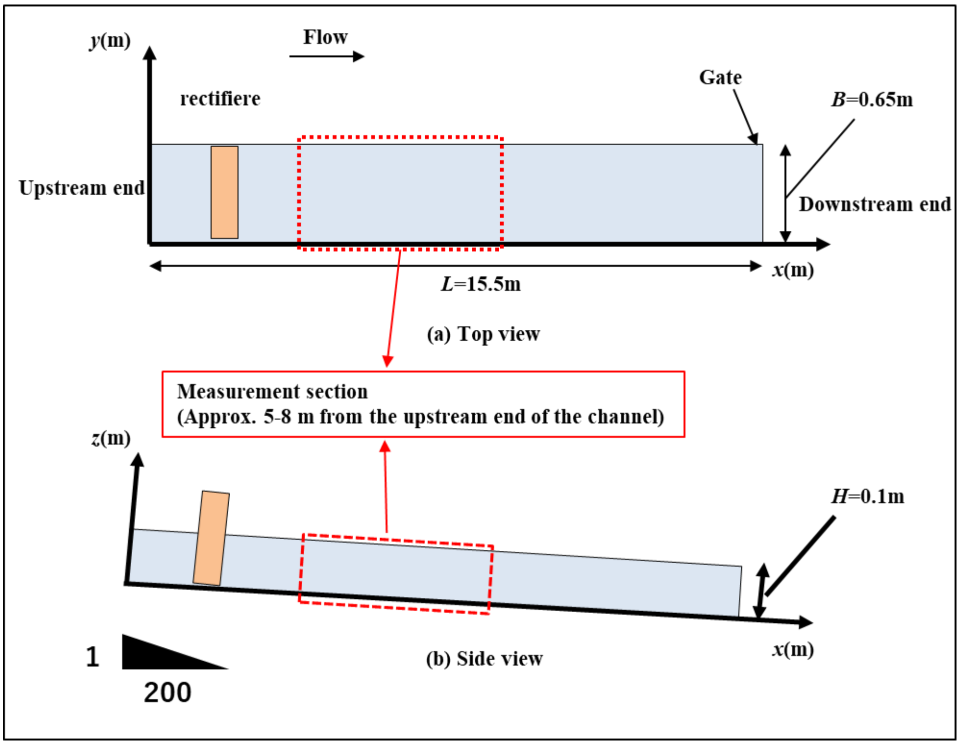

Fig 1. Layout of the experimental channel

Table 1. The hydraulic condition

Discharge Q [l/s]	Water depth h [cm]	Froude number Fr	Reynolds number Re
35	5.5	0.460	18450

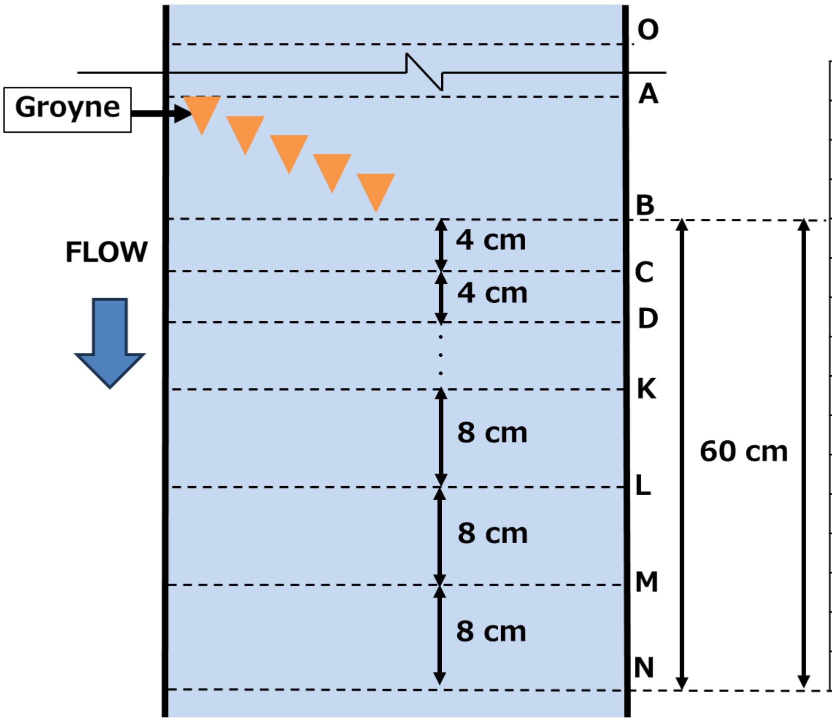

Measurement cross-section number	Measurement location
O	40 cm upstream from Section A
A	Directly upstream of the groyne group
B	Directly downstream of the groyne group
C	4 cm upstream from Section B
D	8 cm downstream of the same location
E	12 cm downstream of the same location
F	16 cm downstream of the same location
G	20 cm downstream of the same location
H	24 cm downstream of the same location
I	28 cm downstream of the same location
J	32 cm downstream of the same location
K	36 cm downstream of the same location
L	44 cm downstream of the same location
M	52 cm downstream of the same location
N	60 cm downstream of the same location

Fig 2. About the measurement cross section (Flume plan view)

2.2 Results and Discussion

2.2.1. An experiment with a row arrangement

To enhance sediment transport in stabilized sandbar topography, a certain range of high flow velocities are required to promote surface erosion of the sandbar. Additionally, meandering flow plays a crucial role in generating localized cycles of erosion and deposition, leading to morphological changes in the sandbar. Therefore, it is essential to establish extensive high-velocity zones in the wake region of the groyne system while also inducing distinct meandering flows.

First, summarize the experimental cases of the groyne arranged in a row in Table 2. With the installation angle of each groyne fixed at α =45°, the installation interval b and group angle θ are varied, and the contour of the downstream velocity u for the cases (Case 2, 6, and 7) is shown in Figure 2.

In order to define "high–velocity region" the approach flow's mean velocity was used as a reference then. The proportion of measurement points within the wake region that exhibit higher flow than the reference flow was determined, as shown in Figure 3. Here, the wake region was defined as the area downstream of the groyne system's terminal point in the streamwise direction and extending laterally to the outermost groyne on the left bank.

A comparison across Case 1 to 7 revealed that Case 7 exhibited the most extensive high-velocity zone. This is thought to be because the installation angle θ and the installation spacing b of the groyne group are large, resulting in a larger permeable cross-section of the groyne group, which reduces resistance to the flow and suppresses the flow velocity reduction effect. Consequently, case 7 is expected to have a significant potential for improving stabilized sandbar topography.

Next, the contour of the transverse velocity v is shown in Figure 4. Regarding the transverse velocity, in Case 2 and Case 7, a strong flow toward the left bank was observed near the groyne installation, followed by a strong flow toward the right bank near the opposite side of the river. This indicates that a distinct meandering flow was formed in both cases. Furthermore, according to the velocity measurement results of a single groyne in the study by Hayshiamoto (2023), it was confirmed that when the groyne head was tilted at an angle of 45°, the water deflection effect, which induces flow deviation, was maximized. Based on this finding, the installation angle α of each groyne in this study was set to 45°. As a result, this water deflection effect became prominent, contributing to the formation of the meandering flow.

Based on the above results, it was clarified that in order to enhance sediment transport in a stabilized sandbar topography, it is essential to form a wide high-velocity region in the downstream area of the groyne and to establish distinct meandering flow conditions, as observed in Case 7.

Table 2. Summary of the experimental cases of the groynes arranged in a row

No	Case	Number of Installed Groynes n	Installetion Interval of Groynes b (cm)	Installation Angle of Groyne Groups Θ	Installation Angle of Each Groyne α
1	SN-30-0	5	1	30°	0°
2	SN-30-45	5	1	30°	45°
3	SW-15-0	5	4	15°	0°
4	SW-15-45	5	4	15°	45°
5	SW-30-0	5	4	30°	0°
6	SW-30-45	5	4	30°	45°
7	SW-5-45	5	4	45°	45°

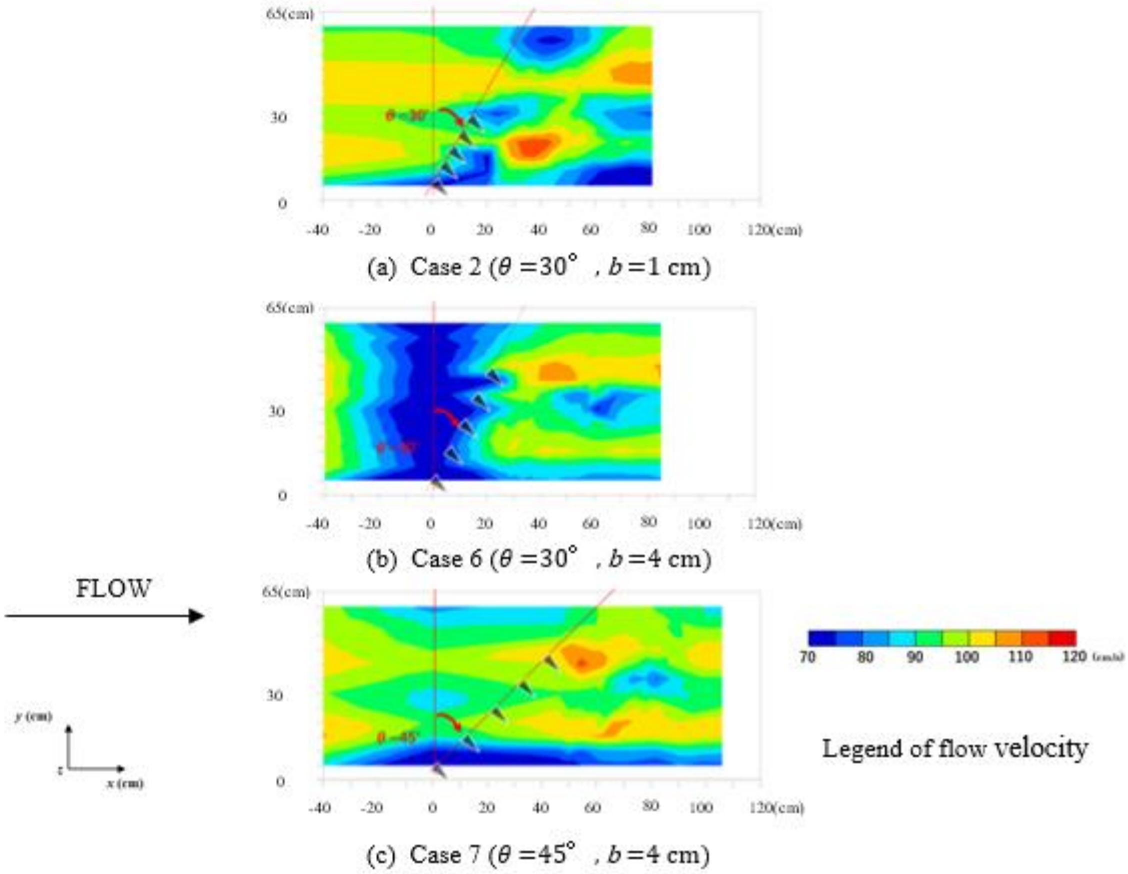

Fig 2. Contour plot of flow velocity u in the downstream direction

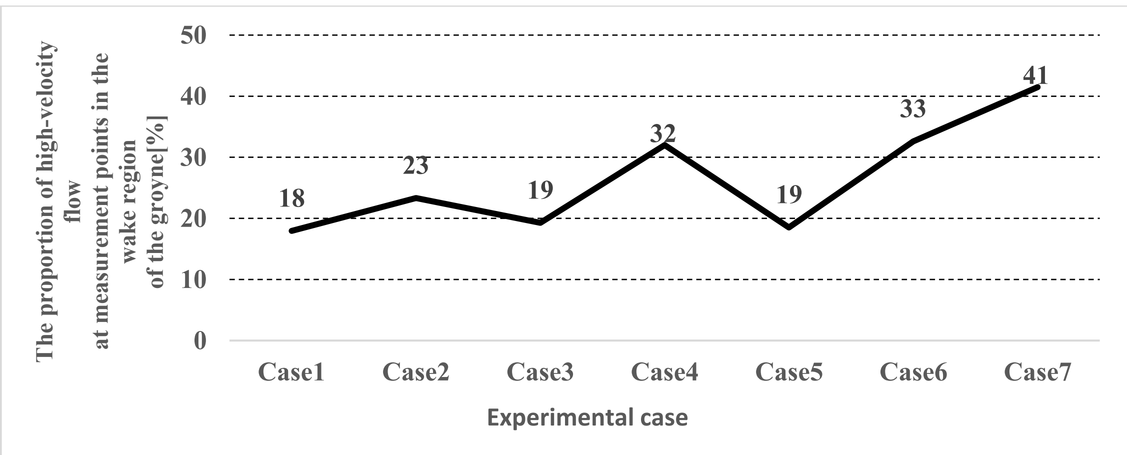

Fig 3. Percentage of high-speed flow region at the downstream in each case

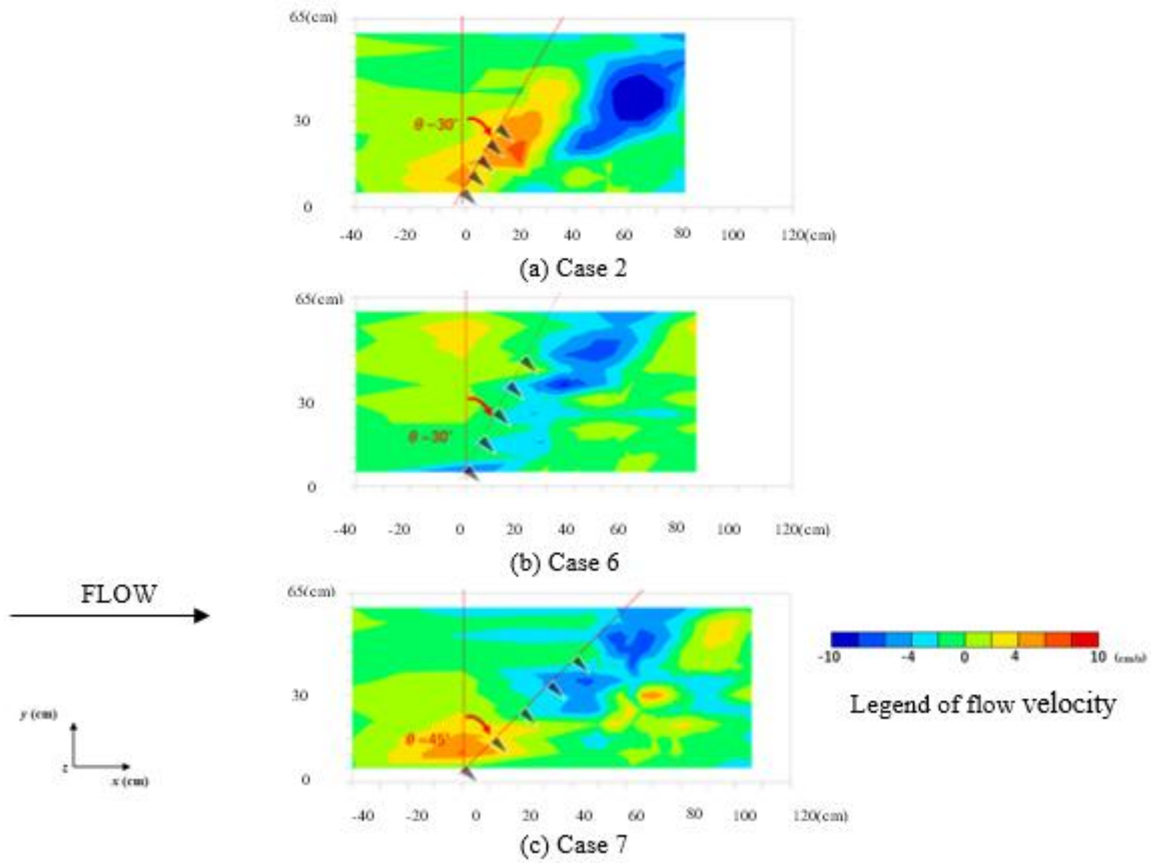

Fig 4. The contour of the transverse flow velocity v for each experimental case

2.2.2. An experiment with a three-row arrangement

Furthermore, analysis of the transverse velocity v in case 7 revealed that the leftward flow generated near the groyne installation site was also observed at x =80cm. This suggests that the distance from x = 0 to 80 cm can correspond to one wavelength of the meandering flow. Based on this wavelength λ =80 cm, five experimental cases (cases8-12)were conducted with distance between groynes groups l set at 40, 80, 90, 100, and 120cm, respectively. The experimental cases conducted are shown in Table 3. The experimental cases conducted are shown in Table 3, with the contours of transverse velocity v for these cases shown in Figure 5.

To determine the optimal configuration for reinforcing periodic meandering flow within the influenced zone by the groynes. Correlation coefficients using phase-aligned velocity data were calculated among the three wake regions. The averaged correlation coefficients across different cases are shown in Table 4.

As shown in Table 4, the highest correlation coefficient was observed in case11, where the groyne groups were spaced at l=100 cm, corresponding to 1.25 times the meandering wavelength of 80 cm identified in case 7. In cases 8-10, where group distance l was 90 cm or less, the correlation coefficient tended to decrease as the distance decreased. Conversely, in cases 11 and 12, where the spacing was 100 cm or more, sufficient distance was maintained to allow for stable formation of periodic meandering flows. These results indicate that there exists an optimal group distance for forming periodic meandering flow, with a minimum required spacing of at least 100 cm.

Table 4. Correlation coefficient of each experimental case

Case	First group and Second group	First group and Second group	First group and Second group	Average
8	0.74	0.31	0.31	0.45
9	0.66	0.50	0.64	0.6
10	0.68	0.43	0.73	0.61
11	0.80	0.73	0.91	0.81
12	0.70	0.68	0.87	0.75

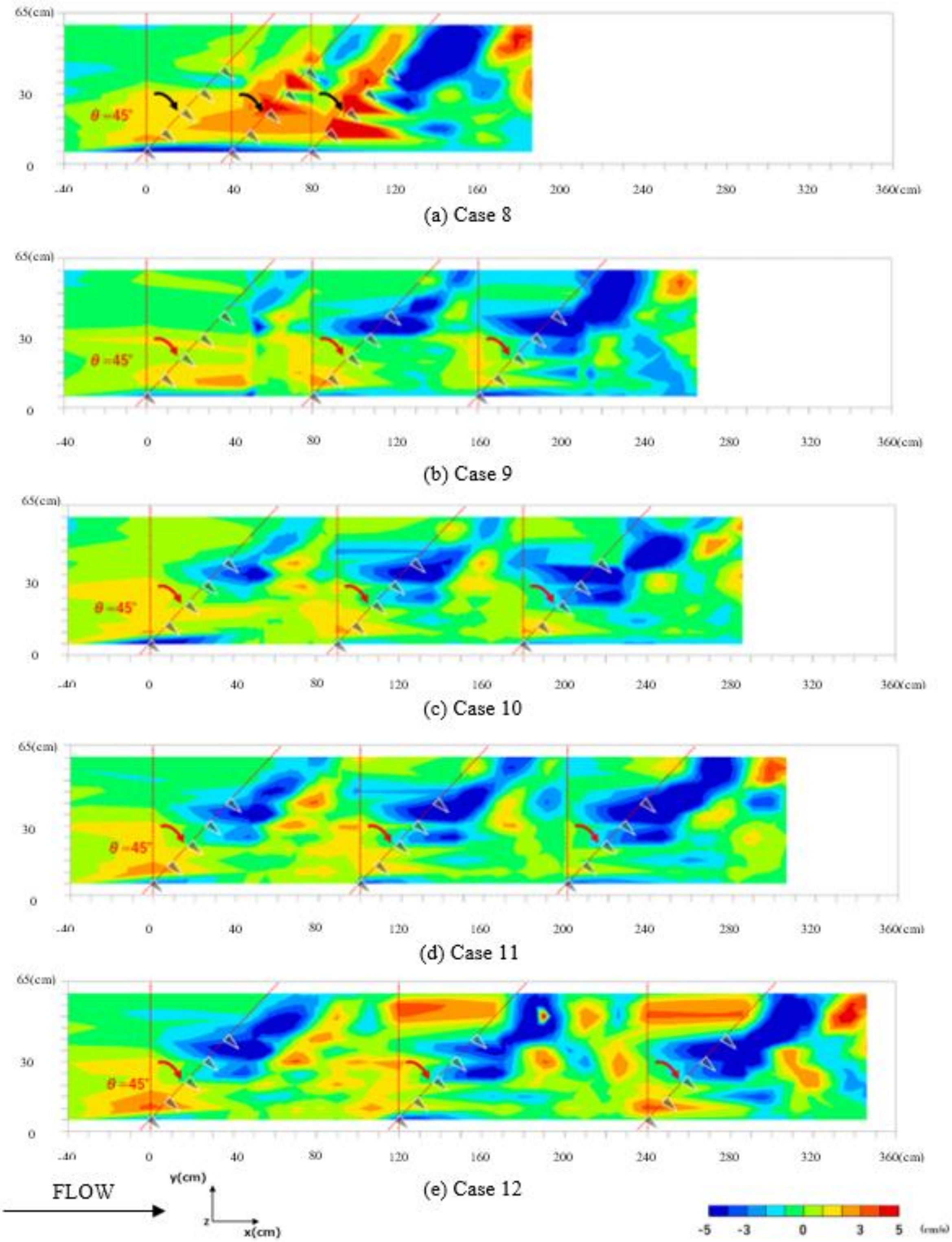

Fig 5. The contour of the transverse flow velocity v for each experimental

3. Bed variation caused by "*Hijiri-ushi*" installation

3.1 Experimental Method

Based on the results of chapter 2, in which attention was given to the widespread high-velocity flow and the periodic meandering flow within the groyne area, it was determined that the optimal arrangement condition is Case

11, with θ = 45° and α = 45°. The arrangement of these groynes was applied to mobile bed experiments to examine whether the high-velocity flow and meandering flow wavelengths observed in fixed bed experiments were reproduced under conditions with bed deformation.

In this experiment, the mobile bed section was set from the upstream end of the flume to 11.5m towards the downstream direction. Silica sand No. 3, with an average grain diameter of 0.9 mm, was spread evenly to a thickness of 10 cm, forming a flat riverbed as amn initial condition. The experiment was conducted with a discharge of 11.7 *l*/s, and observations continued until the riverbed reached an equilibrium state. In the preliminary experiment, a discharge of 11.7 *l*/s was supplied for 5 hours under conditions without groynes to form alternate bars. This discharge is approximately 5.5 times the dimensionless critical shear stress calculated based on the dimensionless shear stress and the Iwagaki equation (Japan Society of Civil Engineers [JSCE], 1999). After the formation of alternate bars, a series of groynes was installed, and the water discharge was continued for an additional hour. Subsequently, a comparative analysis of the riverbed topography before and after groyne installation was conducted to investigate the sediment transport characteristics in the vicinity of the groynes. The hydraulic conditions of this experiment are presented in Table 5.

Table 5. The hydraulic conditions

Discharge Q [l/s]	Water Depth h [cm]	Froude Number Fr	Reynolds Number Re	Friction Velocity u_*	Dimensionless Tractive Force τ_*	Dimensionless Critical Tractive Force τ_{*c}	τ_*/τ_{*c}
11.7	5.5	0.448	18113	0.519	0.119	0.037	5.506

3.2 Results and discussion

The bed topography contours before and after the installation of the groynes are shown in Figure 6. First, from the bed contour before groyne setup, a meandering thalweg can be observed in the downstream region beyond x = 300 cm. Additionally, a sandbar has formed in the downstream region around x = 500–700 cm.

Next, after groyne setup, meandering thalweg slightly shifts towards the left bank. This phenomenon suggests that, in addition to the origined meandering flow present before the installation of the groyne group, a new meandering flow pattern with a different wavelength was introduced due to the installation, leading to the development of transverse flow. This resulted in a more complex flow structure, which further promoted local erosion and subsequent bed deformation. This shift could also have been caused by the meandering flow and high-velocity regions observed in the wake of the groyne group during the fixed-bed experiments.

The analysis of bed variations in the vicinity of the groyne group revealed that, particularly between the first set of groynes, a sand ribbon was observed extending in the transverse direction along the flow. This phenomenon suggests that the installation of the groyne group serves to suppress the formation of depositional landforms while mitigating excessive local scouring that would otherwise occur with impermeable groyne.

Additionally, Endo (2023) reported that the installation of permeable groynes, such as "*Hishi-ushi*", resulted in the formation of numerous sandbars with reduced height and wavelength, indicating similar tendencies in riverbed disturbances to those observed in the present study. However, regarding the flow between groyne groups, while distinct meandering was observed in the fixed-bed experiment, no significant bed variations attributable to meandering flows were confirmed in this experiment.

Based on these findings, the groyne arrangement of Case 11 demonstrated to be effective in maintaining riverbed topography, as it facilitated the formation of a wide range of high-velocity flows, which suppressed localized scouring while maintaining an appropriate level of sediment transport. However, due to the limited number of comparative cases, further detailed analysis is required for a more quantitative evaluation.

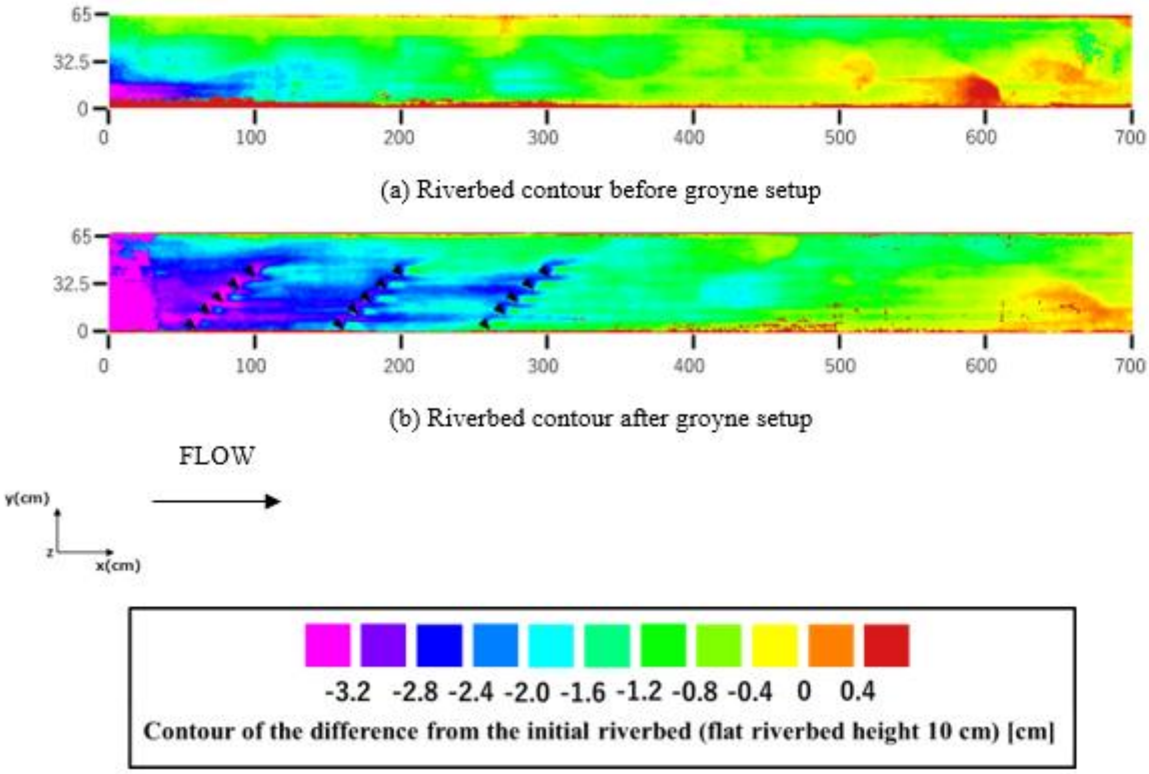

Fig 6. Riverbed contour before and after groyne installatio

4. Conclusions

As a result of this study, the following findings were obtained.

- Even for highly permeable “*Hijiri-ushi*” structures, when the installation intervals are small, the inflow into the groyne field becomes restricted, leading to the occurrence of localized high-velocity flow due to overflow. While this high-velocity flow is effective in suppressing stabilized sandbar topography.
- When a group of “*Hijiri-ushi*” structures is installed in a downstream-facing orientation, flow deflection occurs, causing a meandering current that reflects upon reaching the opposite bank and subsequently returns to the original side.
- In Case 2 and Case 7, the strongest transverse flow was observed in the vicinity of the groynes, followed by the formation of a distinct meandering current in the downstream region. This is due to consistent with the velocity measurement results of an individual “*Hijiri-ushi*” structure, installation angle α of 45°, as the water deflection effect becomes most pronounced under the condition.
- When three consecutive groups of “Hijiri-ushi” structures were installed, an optimal spacing for generating periodic meandering flow was 100 cm, equivalent to 1.25 times the wavelength (80 cm) of the meandering flow observed under the one group.
- The results of a mobile bed experiment revealed that the formation of periodic meandering flow and high-velocity zones induced sand ribbons, particularly between the first set of groynes, with additional scouring observed along the meandering flow in the downstream region. These phenomena suggest the potential for enhanced sediment transport in stabilized sandbar topography.

This study has provided insights into the optimal configuration conditions for utilizing "Hijiri-ushi" structures, a traditional engineering technique, to improve stabilized sandbar topography. However, river discharge and channel morphology are highly diverse, and these factors were not fully considered in this study. Additionally, the investigation of riverbed variations was limited to specific installation conditions, necessitating further examination based on the conditions set in the fixed-bed experiments. These will provide a more accurate representation of real river environments.. Furthermore, combining laboratory experiments with numerical simulations will enable more precise quantitative assessments based on experimental findings. By clarifying physical phenomena that are difficult to reproduce through current numerical analysis and utilizing them to enhance the accuracy of numerical simulations, this approach is expected to contribute valuable insights into actual river channel managements.

Acknowledgments
This work was supported by the JSPS KAKENHI Grant-in-Aid for Scientific Research (C), Grant Number JP22K04334.

References

Endo, R., Tominaga, A., Hayashimoto, R., & Tsujimoto, T. (2024). Eliminating fixation of alternate bars by using impermeable groynes. In S. A. Sannasiraj, S. M. Bhallamudi, P. S. Rajamanickam, & D. Kumar (Eds.), *Riverine, estuarine and marine hydraulics. IAHR APD 2022. Lecture notes in mechanical engineering* (pp. XX–XX). Springer. https://doi.org/10.1007/978-981-97-6009-1_10

Hayashimoto, R. (2023). *An experimental study on the three-dimensional characteristics of flow around permeable groynes and "Ushi"* (Undergraduate thesis). Tokushima University.

Japan Society of Civil Engineers. (1999). *Hydraulic formula collection* (1999 ed., pp. 185–186).

Takemon, Y. (2021, March). Study on riverbed topography management methods using traditional river engineering techniques in the Kizu River. *River Front, 92*.

Tominaga, A., Kawahara, Y., & Tsujimoto, T. (2005). Experimental study on hydraulics and bed protection effects of a traditional river structure, "Seigyu" groin. *Journal of Hydraulic Engineering, 49*, 1009–1014.

Tsujimoto, T. (1999). Effects of dams on physical environment of rivers: From the aspects of river engineering and hydraulics. *Ecological Civil Engineering, 2*(2), 103–112.

4th International Civil Engineering & Architecture Conference
17-19 May 2025, Trabzon, Türkiye

Study on riverbed evolution in the flow field around Japanese river works "*Hijiri-ushi*"

Kazunari Takano*[1], Yasunori Muto[1], Reita Hayashimoto[1], Takao Tamura[1]

[1] *Tokushima University, Department of Civil and Environmental Engineering, Tokushima 770-8506, Japan*

Abstract. In recent years, the progress of dam construction projects and landslide prevention projects in Japan have caused changes in the amount of sediment production, outflow, and sediment drift within watersheds, resulting in a decrease in the supply of sediment reaching downstream. This has resulted in a deterioration of flood control safety, especially in the downstream areas, due to the immobilization of sandbars and the overgrowth of trees caused by a decrease in the frequency of flooding of high water beds. In addition, the coarsening of sediment grain size is affecting the river environment. This study investigated the use of "Hijiri-ushi," a permeable groyne, which is a traditional Japanese river training method, as a countermeasure to mitigate the fixation of sandbar topography. The analysis utilized Nays2DHver4, a two-dimensional horizontal reverbed deformation solver available within iRIC, a numerical simulation platform for hydraulic engineering that is freely available in Japan. Since the standard model treated as vegetation lacks functionality to represent the fluid drag characteristics of the Hijiri-ushi, a customized Hijiri-ushi model was developed by modifying and enhancing the source code to incorporate a drag term that can account for the projected area of its complex structural components depending on the depth of the water. The modified model successfully reproduced the intricate flow conditions and localized scour around the groyne, which the standard model could not reproduce. Furthermore, the model validity was confirmed through comparison with riverbed evolution and velocity data obtained from hydraulic flume experiments where the Hijiri-ushi was installed.

Keywords: Sandbar; groyne; riverbed evolution; numerical simulation; Japanese river works

1. Introduction

In recent years, Japan has experienced more frequent and severe floods, such as Typhoon No. 15 and Typhoon No. 19, and the torrential rains in July 2020, and the scale of damage has also been more enormous. In addition, it is predicted that precipitation will continue to increase in the future due to climate change, and there is concern about the occurrence of torrential rains and associated linear precipitation bands in the future.

Under such circumstances, many rivers in Japan have been dammed upstream and landslide prevention countermeasures have also been implemented, resulting in changes in the amount of sediment production within the river basin and a decrease in the sediment supply to the downstream areas. As a result, there is concern about a bipolarization problem in the downstream area as the water channel becomes fixed due to the deepening of the channel, while the sandbar becomes fixed and forested.

In response to these issues, the river channel administrators have carried out hardware improvement measures such as revetment construction and excavation of sandbars to prevent the progression of riverbank erosion; however, the high cost of construction required for improvement, the time required for improvement and maintenance, and the large burden on the river environment have prevented progress in implementing these measures.

To address these problems, this study investigated whether the use of Hijiri-ushi, a traditional Japanese groyne, could promote bed evolution in the river channel and solve the bipolarization problem.

2. Hijiri-ushi, a traditional Japanese groyne

Groyne techniques have developed since 1750, and various types of materials have been used, including stone, wood, and bamboo for gabions, fence outings, random piles, stone outings, kayabutai, and rock crib.

*Corresponding author, E-mail: c612341001@tokushima-u.ac.jp

https://doi.org/10.31462/icearc2025_ce_hyd_271

Fig. 1. Hijiri-ushi maintained on the Kizu River

By 1870, the Kelep groyne system had been introduced from the Netherlands as a flood control technology. By 1930, conventional groyne structures had been improved, and the wide range of materials were used from natural materials to concrete, iron, and polymeric materials. Among them, the Hijiri-ushi, which has existed since ancient times, has a structure made of logs and gabions combined into a triangular pyramid shape, and is classified as a permeable type. In recent years, three units have been installed in Kizu River in Japan, as shown in Fig. 1, and their effects have also been organized in papers (Takemon, 2021; Tazumi et al., 2019). Since the materials used for the Higiri-ushi are of natural origin, they are environmentally friendly and can be produced and maintained by local residents. However, because of the lack of scientific knowledge on the effects of Hijiri-ushi, its function has not been adequately evaluated.

3. Fluid drag model based on the characteristics of Hijiri-ushi

The Hijiri-ushi units are installed in a model river channel for numerical experiments, and the effects of bed evolution are checked by numerical simulations using a planar two-dimensional model. The analysis software used is iRIC, a free software from Japan. The analysis solver was Nays2DHver4 (Shimizu & Nelson, 2007).

The basic concept is based on a fluid drag model for vegetation and pile water control. However, Nays2DHver4 does not have the capability to reflect the fluid drag characteristics of Hijiri-ushi. The only fluid drag characteristic given is the degree of vegetation density.

In the past, there have been cases where analysis was conducted using the Hijiri-ushi as vegetation, but verification of validity remains an issue (Takano et al., 2024). Although it is appropriate to treat the spatial density of vegetation and pile water control by the number of vegetation per area or projected area per volume, in the case of the Hijiri-ushi, the number of installed units is the basic unit, and it is not appropriate to consider them in terms of spatial density; hence, it will be appropriate to treat them by actual projected area. Therefore, the source code of Nays2DHver4 was modified and improved. Specifically, by considering a drag term in the momentum equation that can reflect the projected area of the components of the Hijiri-ushi according to the mesh resolution, the model can represent a different flow structure than the drag term of a single pile group such as vegetation or pile water control.

The continuity equation incorporating the Hijiri-ushi is as follows

$$\frac{\partial h}{\partial t}+\frac{\partial (hu)}{\partial x}+\frac{\partial (hv)}{\partial y}=0 \tag{1}$$

The continuity equation is as follows

$$\frac{\partial (uh)}{\partial t}+\frac{\partial (hu^2)}{\partial x}+\frac{\partial (huv)}{\partial y}=-gh\frac{\partial H}{\partial x}-\frac{\tau_x}{\rho}+D_x-\frac{F_x}{\rho} \tag{2}$$

$$\frac{\partial (vh)}{\partial t}+\frac{\partial (huv)}{\partial x}+\frac{\partial (hv^2)}{\partial y}=-gh\frac{\partial H}{\partial y}-\frac{\tau_y}{\rho}+D_y-\frac{F_y}{\rho} \tag{3}$$

provided that

$$\frac{\tau_x}{\rho}=\frac{gn^2}{h^{\frac{1}{3}}}u\sqrt{u^2+v^2} \tag{4}$$

$$\frac{\tau_y}{\rho} = \frac{gn^2}{h^{\frac{1}{3}}} v\sqrt{u^2 + v^2} \tag{5}$$

$$\frac{F_x}{\rho} = \frac{1}{2} C_D a_s h_v u\sqrt{u^2 + v^2} + \frac{1}{2} C'_D \beta u\sqrt{u^2 + v^2} \tag{6}$$

$$\frac{F_y}{\rho} = \frac{1}{2} C_D a_s h_v v\sqrt{u^2 + v^2} + \frac{1}{2} C'_D \beta v\sqrt{u^2 + v^2} \tag{7}$$

$$a_s = \frac{n_s D_s}{S_s^2} \tag{8}$$

$$\beta = \frac{\Sigma A_s}{DX \cdot DY} \tag{9}$$

where h is Depth of water; t is Time; u, v are Depth-averaged fluid velocity in the x,y directions; g is Acceleration of gravity; H is Water level; τ_x, τ_y are Riverbed shear stress in the x,y directions; n is Manning's Roughness Coefficient; D_x, D_y are Reynolds stress term in the x,y directions; F_x, F_y are Fluid drag per unit area due to vegetation and Hijiri-ushi in the x,y directions; C_D is Drag coefficient of vegetation; a_s is Area of vegetation interception per unit area (density) ; h_v is the effective depth, that is either vegetation height or water depth whichever the smalle; n_s is Number of vegetation; D_s is Average trunk diameter of vegetation; S_s is Sampling grid width; C'_D is Drag coefficient of Hijiri-ushi member; β is Intercepted area of Hijiri-ushi member in calculated mesh area; ΣA_s is Accumulated shielding area by depth of water in the Hijiri-ushi component; DX, DY are Length of calculated mesh in the x,y directions

The second term on the right-hand side of the momentum equation applies the Manning equation with the bottom friction term.

The fourth term on the right side is the drag term due to fluid drag, and in addition to the drag due to vegetation density, the drag term due to Hijiri-ushi was considered.

For β, the projected area was calculated cumulatively with height in order to account for the interception area depending on the water depth.

The fluid drag coefficient C_D shall be 1.0 of the cylinder standard value, which is a common value (Aoki et al., 2009).

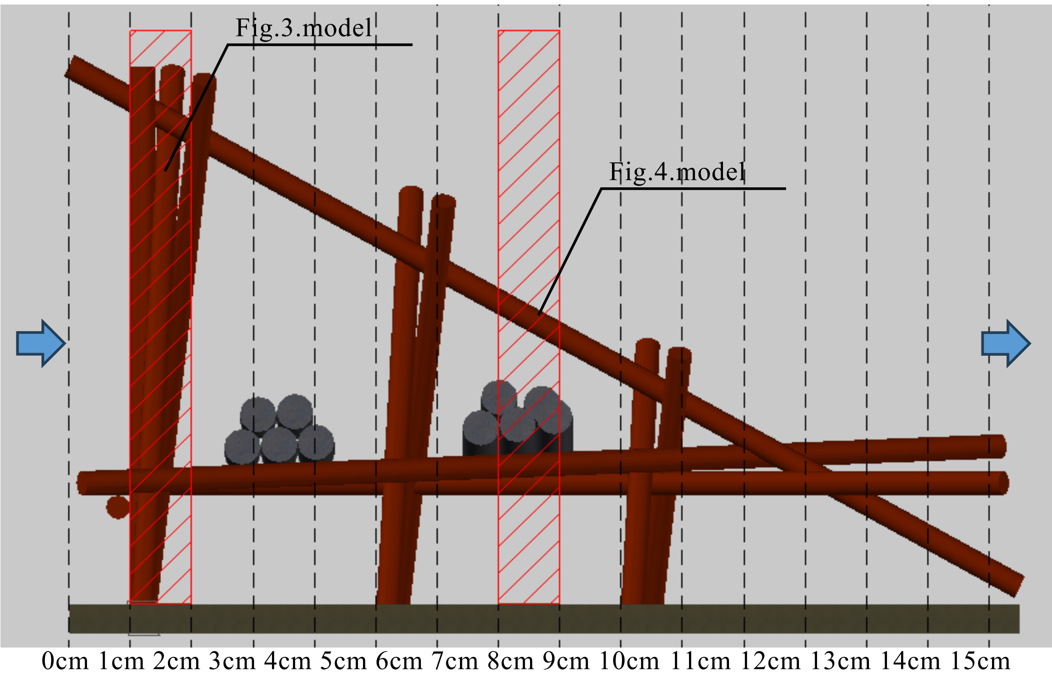

Fig. 2. Lateral model diagram of a Hijiri-ushi and mesh spacing in the flow direction

Fig. 2 shows a side view of Hijiri-ushi, with the upstream side on the left and the downstream side on the right. Because fluid drag varies with the location between structures (0 cm to 15 cm), it was divided at 1 cm intervals, the same as the mesh size for the analysis. Fig. 3 shows a cross-sectional view of Hijiri-ushi projected from upstream to downstream at a point between 1 cm and 2 cm. The area to be blocked is calculated cumulatively from the bottom to the top, so that it can be reflected in ΣA_s in Equation (9). Fig. 4 shows a cross-sectional projection of the area between 1 cm and 2 cm. The area to be blocked is calculated by accumulating the area from the bottom to the top, so that it can be reflected in ΣA_s in Equation (9).

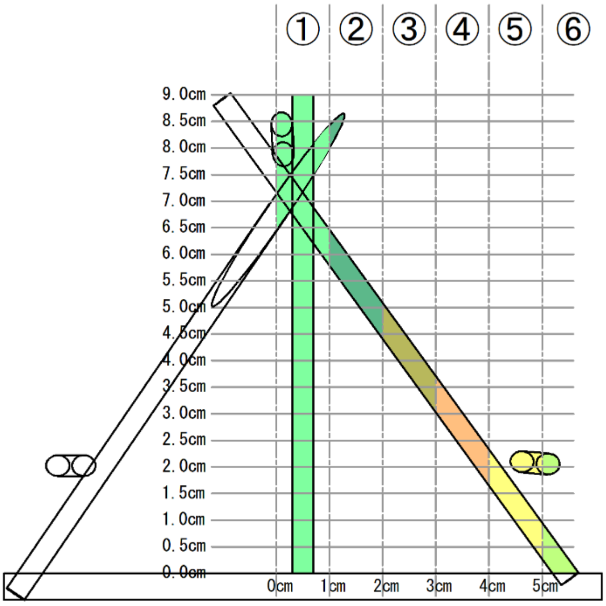

unit : cm2

① Shielded area	② Shielded area	③ Shielded area	④ Shielded area	⑤ Shielded area	⑥ Shielded area
4.554	0.766	0.682	0.681	0.901	0.419
4.312	0.747	0.682	0.681	0.901	0.419
3.884	0.681	0.682	0.681	0.901	0.419
3.46	0.681	0.682	0.681	0.901	0.419
3.11	0.681	0.682	0.681	0.901	0.419
2.752	0.681	0.682	0.681	0.901	0.419
2.416	0.601	0.682	0.681	0.901	0.419
2.2	0.37	0.682	0.681	0.901	0.419
2	0.126	0.679	0.681	0.901	0.419
1.8	0.003	0.555	0.681	0.901	0.419
1.6	0	0.311	0.681	0.901	0.419
1.4	0	0.08	0.665	0.901	0.419
1.2	0	0	0.498	0.901	0.419
1	0	0	0.251	0.901	0.419
0.8	0	0	0.044	0.699	0.343
0.6	0	0	0	0.437	0.305
0.4	0	0	0	0.19	0.305
0.2	0	0	0	0.018	0.23

Fig. 3. Interception area according to the height of the Hijiri-ushi (1 cm to 2 cm)

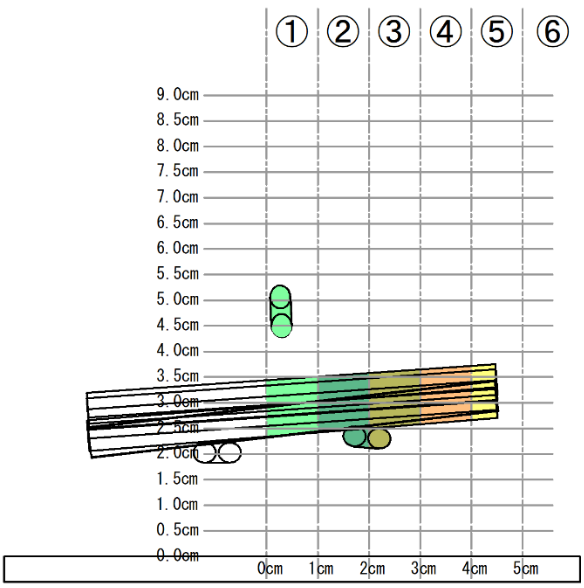

unit : cm2

① Shielded area	② Shielded area	③ Shielded area	④ Shielded area	⑤ Shielded area	⑥ Shielded area
1.468	1.235	1.225	1.047	0.527	0
1.468	1.235	1.225	1.047	0.527	0
1.468	1.235	1.225	1.047	0.527	0
1.468	1.235	1.225	1.047	0.527	0
1.468	1.235	1.225	1.047	0.527	0
1.468	1.235	1.225	1.047	0.527	0
1.468	1.235	1.225	1.047	0.527	0
1.468	1.235	1.225	1.047	0.527	0
1.369	1.235	1.225	1.047	0.527	0
1.169	1.235	1.225	1.047	0.527	0
1.099	1.235	1.225	1.047	0.527	0
1.098	1.189	1.108	0.86	0.413	0
0.623	0.689	0.608	0.36	0.163	0
0.123	0.189	0.148	0	0	0
0	0	0	0	0	0
0	0	0	0	0	0
0	0	0	0	0	0
0	0	0	0	0	0

Fig. 4. Interception area according to the height of the Hijiri-ushi (7 cm to 8 cm)

4. Characteristics of flow field and bed evolution around Hijiri-ushi

4.1 Mesh size and analysis conditions

The mesh size of the planar two-dimensional model used for the analysis was set to 1 cm in order to verify the validity of the model in the paper in which the Hijiri-ushi was installed on a moving bed in a water chanell and experiments were conducted .

Table1. Hydraulic conditions

Discharge (ℓ/s)	6.7
Channel slope i_o	1/1000
Uniform flow depth h_o (cm)	6.9
Spur dyke length L (cm)	11.25
Approach flow velocity (cm/s)	24.9
Near-bed frictional velocity u_* (cm/s)	2.23
Dimensionless near-bed shear stress τ_*	0.054
u_*/u_{*c}	1.08
Froude number	0.30
Reynolds number	19,589

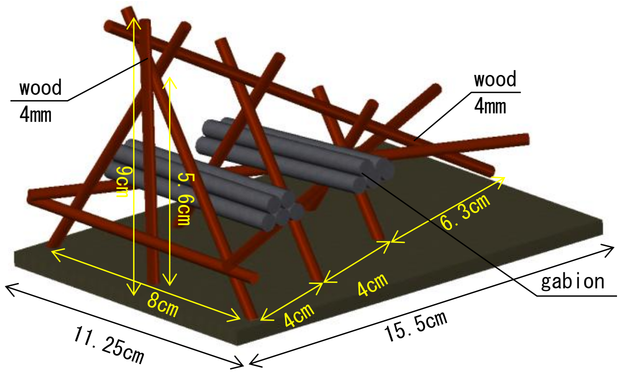

※wood：Outer diameter of one piece is 4mm
※gabion: Outer diameter of one piece is 6mm

Fig. 5 Model drawing of a Hijiri-ushi

In addition, the model of the Hijiri-ushi is set as an isosceles triangle with a base of 8.0 cm, a height of 5.6 cm, and a length of 15.5 cm in the upstream and downstream directions, as shown in Fig. 5.Table 1 also shows the hydraulic conditions.

4.2 Characteristics of flow field and bed evolution when one Hijiri-ushi unit is installed
Fig. 6 shows the bed evolution after water flow in CASE 1, where one Hijiri-ushi unit is installed on the right bank. Scouring develops on the main channel side behind the Hijiri-ushi, and the scouring area extends downstream on the left bank side. On the other hand, in front and near the gabion, a localized sedimentation pattern tended to be observed. The flow velocity tended to be high behind the Hijiri-ushi and decreased toward the front. At site A, the riverbed degraded by -0.004 m and the flow velocity was 0.24 m/s. At site B, the riverbed rose by 0.009 m and the flow velocity was 0.19 m/s. This is thought to be due to the shielding effect of the forward-placed gabion. The riverbed degraded the most at C, where it degraded by 0.009 m. Figure 7 (caseP) shows the results of an experiment conducted at Kumamoto University, in which a Hijiri-ushi was placed on the contour of the river channel and bed after water flow. Similar to the results of the analysis conducted in this study, it can be seen that scouring is more likely to occur behind the hijiri stones, while sedimentation occurs on the left bank in front of the hijiri stones (Miyake et al., 2024).

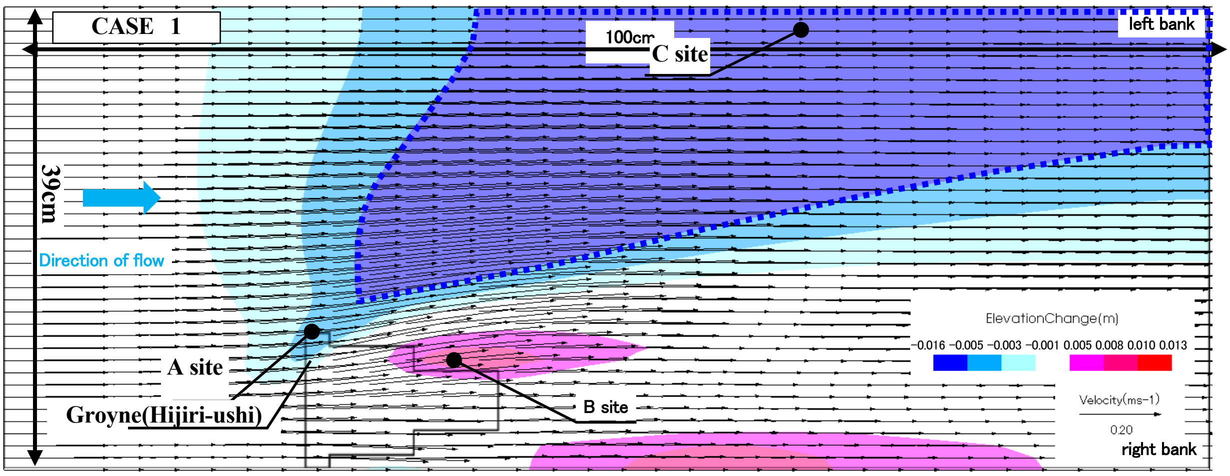

Fig. 6. Fluctuation of the riverbed after water flow with one Hijiri-ushi unit installed

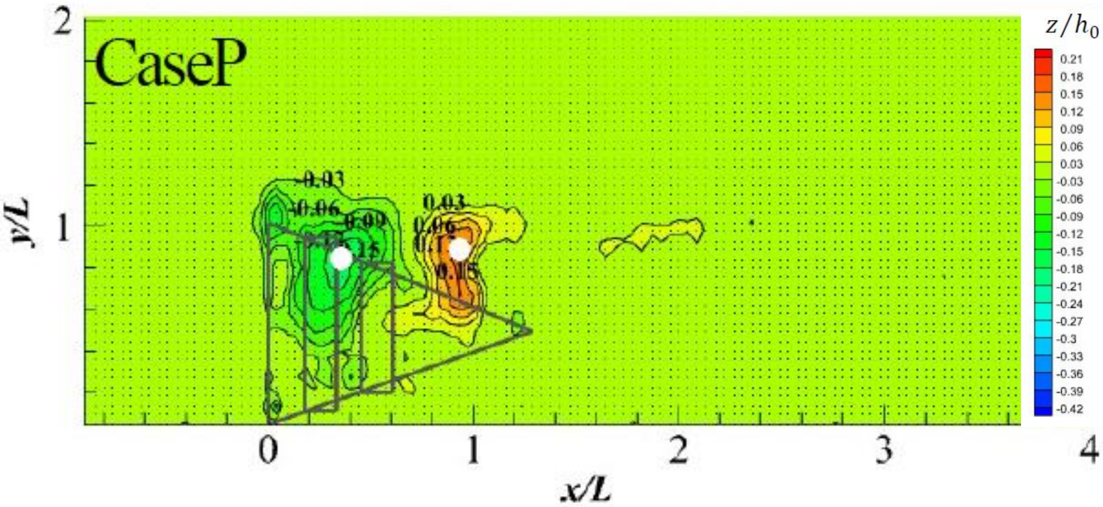

Fig. 7. Map of bed evolution derived from experimental data

4.3 Characteristics of flow field and bed evolution when two Hijiri-ushi units are installed
Following on from Section 4.2, as CASE 2, analyses were performed when multiple units were installed, similar to the installation example in the Kizu River. The second unit is also modeled by the same Hijiri-ushi model as the first unit. Figure 8 shows the reverbed fluctuation after water flow. At site A, the riverbed degraded by -0.006 m and the flow velocity was 0.24m/s, which can be confirmed similarly in the main channel side. On the other hand, at site B, the riverbed rose by 0.002 m and the flow velocity was 0.18 m/s. The riverbed rose the most at site D, with a rise of 0.008 m.

There was no difference in the depth of scour compared to the case with only one unit, but the scoured area below -0.005 m has expanded. The riverbed was degraded the most at Site E, with a degradation of 0.014 m.

4.4 Characteristics of flow field and bed evolution due to changes in fluid drag coefficient
The verification has been conducted with the drag coefficient as 1.0, which is a standard value for cylindrical shapes until now; however, in the past, the validity of the drag coefficient has been studied through experiments and quasi-three-dimensional analysis, concluding that a drag coefficient of 5.0 is appropriate regardless of the extension, spacing, and accuracy of the Hijiri-ushi (Kawaguchi et al., 2002). Therefore, in CASE 3, one Hijiri-ushi unit was installed on the right bank side, and in CASE 4, two Hijiri-ushi units were installed on the right bank side, and the drag coefficient was set to 5.0 for both cases. Other analysis condisions were the same as those of Case 1. The analysis results of CASE 3 are shown in Fig. 9. Compared to Fig. 6, the scoured area extended downstream of the main channel, with the riverbed degradation by -0.009 m and the flow velocity of 0.24 m/s at site A. The riverbed degraded the most at site F, with a degradation of 0.024 m. The riverbed rose at site G, with a rise of 0.016m.

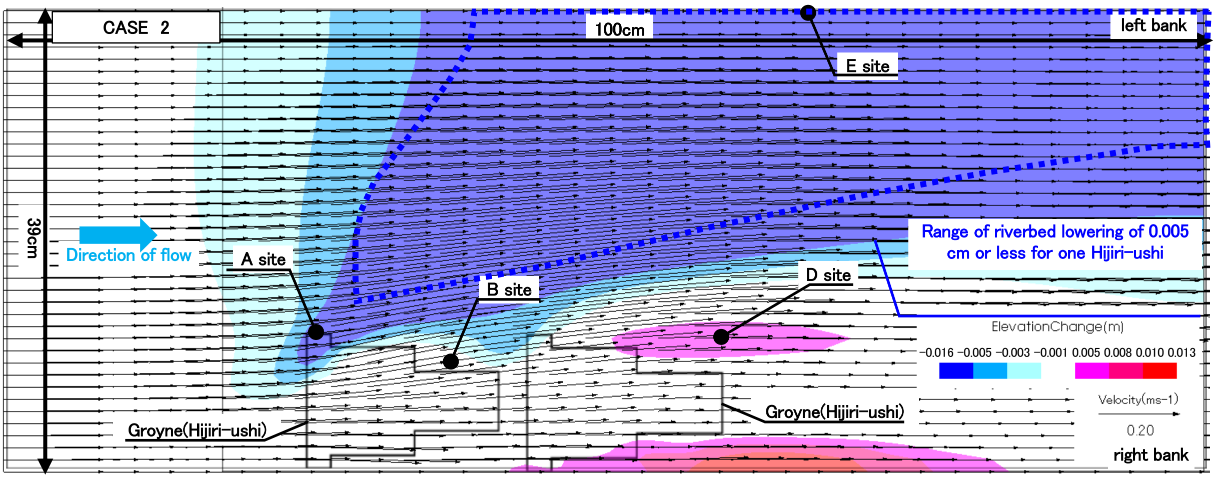

Fig. 8. Fluctuation of the riverbed after water flow with two Hijiri-ushi units installed

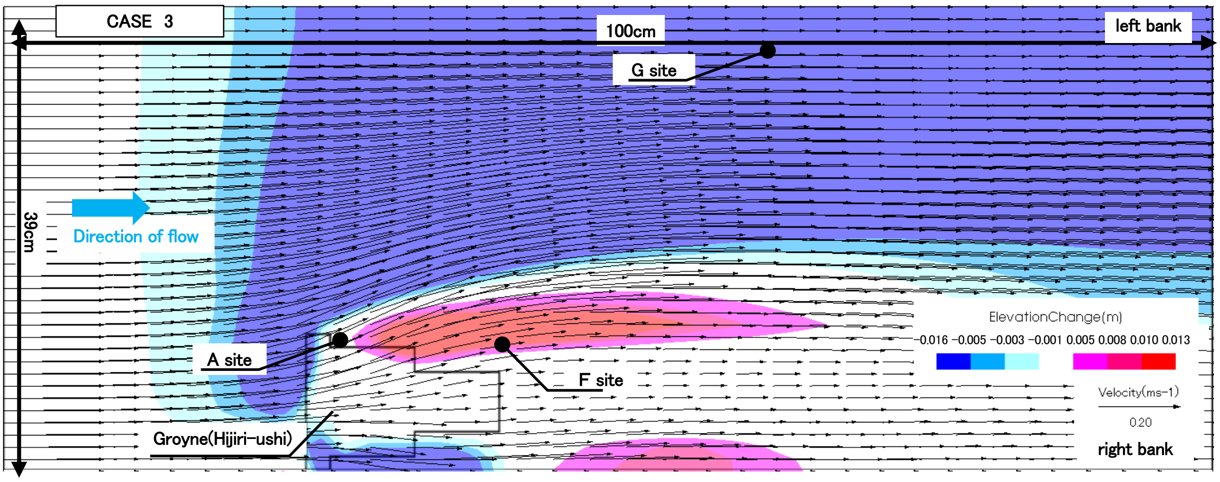

Fig. 9. Fluctuation of the river bed after water flow with one Hijiri-ushi unit installed

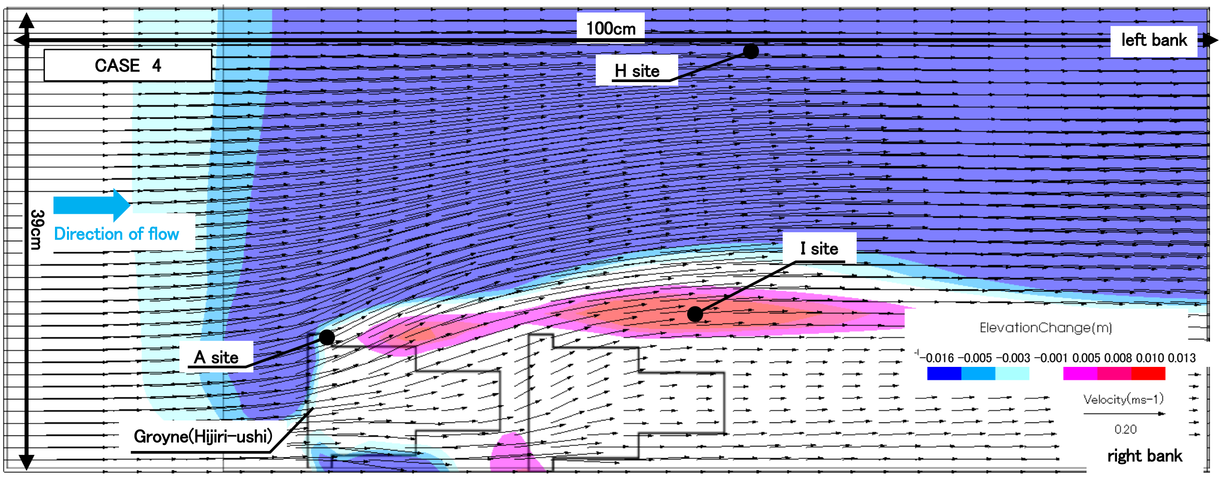

Fig. 10. Fluctuation of the river bed after water flow with two Hijiri-ushi units installed

Table 2. Comparion of the amount of bed evolution and flow velocity for each case

CASE	Riverbed degradation at Site A (m)	Flow Velocity at Site A (m/s)	Maximum riverbed degradation (m)	Maximum riverbed rise (m)
CASE1	0.004	0.240	0.009 (Site C)	0.009 (Site B)
CASE2	0.006	0.240	0.014 (Site E)	0.008 (Site D)
CASE3	0.009	0.240	0.024 (Site F)	0.016 (Site G)
CASE4	0.009	0.240	0.035 (Site H)	0.014 (Site I)

The analysis results for CASE 4 are shown in Fig. 10. Compared to Fig. 8, the scoured area extended downstream of the main channel, with the riverbed degradation by -0.009 m and the flow velocity of 0.24 m/s at site A. The riverbed degraded the most at site H, with a degradation of 0.035 m. The riverbed rose at Site I, with a rise of 0.014 m.

5. Conclusions

By installing the Hijiri-ushi in the water channel, we confirmed the characteristics of bed evolution around the Hijiri-ushi and at places slightly away from it. In addition, in order to confirm the validity of the numerical simulation results, the bed evolution characteristics were compared with those of the experimental results. The results of the numerical simulation showed that the bed evolution around the Hijiri-ushi units was similar to that of the experimental results, with scouring developing in the back and sedimentation promoted in the front. On the other hand, the numerical simulation showed that the effect of the scoured area was more widespread than that of the experimental results. Therefore, it can be concluded that for complex structures such as the Hijiri-ushi, it is more appropriate to adopt a flow structure that reflects the projected area according to the mesh resolution, rather than considering it in terms of spatial density.

Regarding the characteristics of bed evolution depending on the number of Hijiri-ushi units, it was confirmed that although the scoured area changed, there was no significant difference, and it was possible to disturb the riverbed even with one Hijiri-ushi unit. In addition, the installation of the Hijiri-ushi can create a diverse environment because it leads to the creation of a small-scale and tranquil environment in the vicinity of the Hijiri-ushi, by promoting sedimentation in front of the unit.

As for the numerical simulation results with different drag coefficients, it was confirmed that the bed evolution characteristics with a drag coefficient of 1.0 after water flow were more similar compared to those of the experimental results.

In the future, we will confirm the superiority of Hijiri-ushi by verifying characteristics of the flow field and bed evolution when the Hijiri-ushi is installed in a real river model.

Acknowledgments
This work was supported by the JSPS KAKENHI Grant-in-Aid for Scientific Research (C), Grant Number JP22K04334.

References

Aoki, M., Yoshino, T., & Fukui, Y. (2009). On the drag force acting on the pile dike in the open channel and its resistance coefficient. *Journal of Applied Mechanics, 12*, 831–840. Japan.

Kawaguchi, H., Okanobu, M., & Fukuoka, S. (2002). Characteristics of hydrodynamic forces on submergible groins in series. *Journal of Hydraulic Engineering, 44*, 1065–1070. Japan.

Miyake, M., Cho, H., & Ohmoto, T. (2024). Effect of driftwood jamming on characteristics of bed deformation around traditional river structure “Hijiri-ushi”. *Collection of Papers, JSCE, 81*(16). Japan.

Shimizu, Y., & Nelson, J. (2007). solvers – Nays2DH. https://i-ric.org/solvers/nays2dh/

Takano, K., Muto, Y., Tamura, T., & Kuwahara, M. (2024). Study on sandbar disturbance and prevention of riverbank erosion by using structures. In *Proceedings of the 12th Symposium on Landslide Disaster*. Japan.

Takemon, Y. (2021). A study on the management methods of riverbed topography of the Kizu River using traditional river engineering methods. *Riverfront, 92*, 16–19. Japan.

Tazumi, M., Takemon, Y., Kobayashi, S., & Sumi, T. (2019). An application of traditional river works “Hijiri-ushi” to river bed management in the Kizu River. *DPRI Annuals, 62* (B), 734–765. Japan.

4th International Civil Engineering & Architecture Conference
17-19 May 2025, Trabzon, Türkiye

Essentials of manifold flow hydraulics-I: Hydraulic (HGL) and energy gradient (EGL) lines

Gürol Yıldırım*[1]

[1] Giresun University, Engineering Faculty, Civil Engineering Dept., 28100, Giresun, Türkiye.

Abstract. Manifold pipelines can be used to distribute and collect fluids and have applications in various engineering fields, especially in the water supply system. Analysis of the hydraulic design of manifold pipelines is very important concern for the proper hydraulic performance of water supply distribution systems. The hydraulic (HGL) and energy (EGL) gradient lines are useful tools to clearly analyse the shape of hydraulic profiles, i.e., pressure head and outflow distributions along the manifold line.

Keywords: Manifolds; Steady-state analysis; Fluid mechanics; Fluid flow; Hydraulic gradient

1. Theoretical background

In this paper an analytical procedure taking into account the nonuniform outflow profile for hydraulic analysis and design of multiple outlets pipelines, is presented. Energy relations are improved based on the average friction drop approach with a simple exponential function, to express the nonuniform outflow concept (Sadeghi et al., 2016; Singh & Mahar, 2003). To determine friction head losses, the Darcy-Weisbach formula is used here; and the kinetic head change is considered whereas minor head losses are neglected. Several mathematical relationships are also derived for computing extreme pressure heads and their locations of occurrence along the pipeline (Sadeghi & Peters, 2011; Singh et al., 2000). The presented method also provides specific lengths of the segments in which the different flow regimes occur along its length.

2. Methodology

2.1. Flow rate and velocity head

The energy-gradient line (EGL) in a manifold line as manifold will not be a straight line but a curve of the exponential type. Fig. 1 sketches a horizontal multi-outlet submain line with a single inlet (single line size system) and shapes of hydraulic (piezometric) (HGL) and energy-gradient (EGL) curves along its length (Yıldırım, 2023a,b; Yıldırım, 2010a,b; Yıldırım & Singh, 2013a,b). Flow in manifold is considered to be steady, spatially varied flow with decreasing discharge along the direction of flow (from upstream inlet to dowmnstream closed end). Flow in a submain line is usually turbulent ($3{,}000<R<10^5$; R: Reynolds number). Sometimes fully turbulent flow ($10^5<R<10^7$) exists at the upstream end, and flow becomes laminar ($R<2{,}000$) at the downstream reach where the flow velocity decreases to zero. The transition flow approximately occurs in the interval $2{,}000<R\leq 3{,}000$, and the flow characteristics are indeterminate for the transition zone (Yıldırım, 2012a,b; Yıldırım, 2014a,b; Yıldırım, 2009).

Typically, the discharge through each outlet is governed by the following relationship:

$$q = kH^x \tag{1}$$

in which q = discharge through the outlet; H = operating pressure head of the outlet; k and x = coefficient and exponent of the outlet discharge, respectively.

* Corresponding author, E-mail: gurol.yildirim@giresun.edu.tr

https://doi.org/10.31462/icearc2025_ce_hyd_300

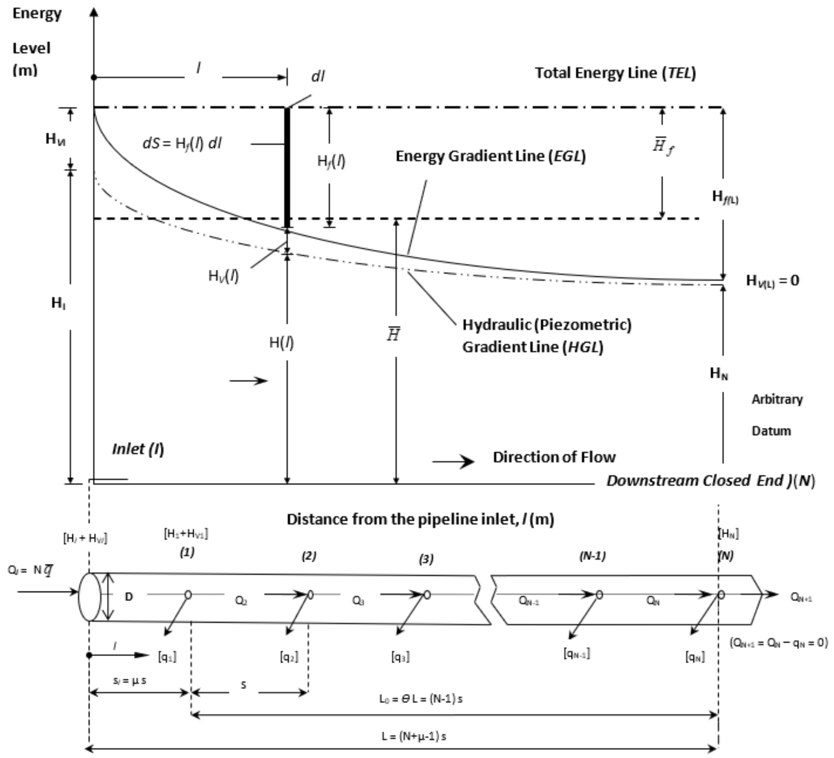

Fig. 1. Shapes of hydraulic (piezometric) gradientl line (HGL), and energy gradient line (EGL) along horizontal submain line with multiple outlets (Yıldırım, 2008)

Assuming that outlets along the pipeline have uniform outflow , then the total flow rate that passes through the pipe section located at any distance l from the pipeline inlet Q(l) is commonly given as (Scaloppi & Allen, 1993)

$$Q(l) = \left(N - \frac{l}{s}\right)\overline{q} = Q_I(1-i) \tag{2}$$

where Q(l) = the discharge at a section of length l measured from the pipeline inlet; $Q_I = N\overline{q}$ = total inflow rate for the entire length of the pipeline; N = total number of equally spaced operating outlets for the entire pipeline; s = outlet spacing; and i = dimensionless variable of distance i = l/L, which is the percentage of the length to the total length.

According to Eq. (2) the average flow velocity also varies linearly along the pipeline and, the velocity head gradient can be written as follows

$$S_V(l) = \frac{2H_{VI}}{L}(i-1) \tag{3}$$

where $S_V(l)$ = velocity head gradient at any distance l; and $H_{VI} = 8(N\overline{q})^2/\pi^2 gD^4$ = velocity head at the inlet of the pipe; and D and L = internal diameter and length of the pipe.

Integrating the gradient of the velocity head given by Eq. (3) between the limits 0 and l and then, the velocity head at any distance l is obtained as

$$H_V(l) = H_{VI}(1-i)^2 \tag{4}$$

where $H_V(l)$ = velocity head for the pipe section located at any distance l.

2.2. Friction head loss

To compute total friction drop at the closed end of the multiple outlets pipeline requires calculating the friction head loss for each pipe segment between consecutive outlets, in a stepwise manner. This procedure is characterized by a stepwise correction factor, FSW computed for finite number of outlets as given by

$$F_{SW} = \frac{1}{N^{m+1}} \sum_{K=1}^{K=N} K^m \tag{5}$$

where K = an integer represents the consecutive order of outlets; and m = velocity (or flow rate) exponent for the particular friction head loss formula used.

For the traditional approach, the friction correction factor takes the form

$$F = \frac{1}{(m+1)} \tag{6}$$

Eq. (6) represents the friction loss correction factor that takes into account the continuous and uniform outflow along the pipeline. This correction factor is essentially equivalent to that proposed by Christiansen (1942), provided the number of outlets is infinity.

The correction factor FC proposed by Christiansen (1942) for the case in which the first outlet is located in a full outlet spacing from the pipeline inlet, is of the form

$$F_C = \frac{1}{(m+1)} + \frac{1}{2N} + \frac{\sqrt{m-1}}{6N^2} \tag{7a}$$

If the first outlet is half outlet spacing from the pipeline inlet, FC is given by (Cuenca 1989)

$$F_C = \frac{2N}{(2N-1)}\left(\frac{1}{m+1} + \frac{\sqrt{m-1}}{6N^2}\right) \tag{7b}$$

Christiansen's (1942) approach given by Eq. (7) is based on uniform and discrete outflow from a finite number of operating outlets. Therefore, significant differences between the two correction factors given by Eq. (6) and Eq. (7) are expected especially, when the number of outlets in the pipeline is small (Scaloppi & Allen, 1993). In order to do a systematic comparison, three correction factors (F_{SW}, F and F_C) are computed for the value of the velocity exponent m = 1.75 (Darcy-Weisbach formula and turbulent flow in a smooth pipe), full outlet spacing from the pipe inlet (s_l = s), and for various number of operating outlets (presented in the logarithmic scale), then the results were plotted in Fig. (2). In this figure, the secondary axis of y (dotted line) represents the percentage differences between three correction factors F_{SW}, F and F_C.

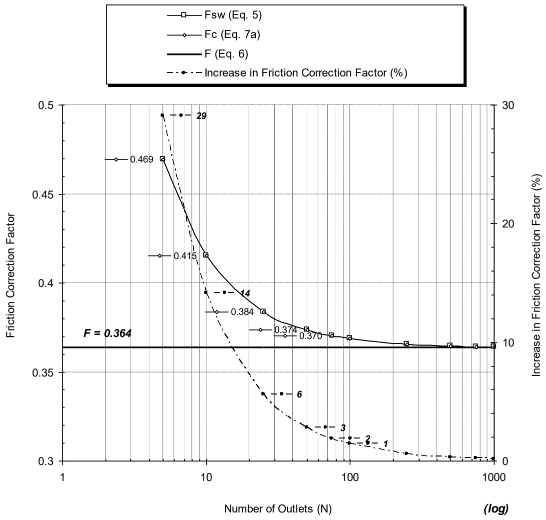

Fig. 2. Variation of the friction correction factors (F, F_{SW} and F_C) and percentage differences between these factors (Dotted Line) for the Darcy-Weisbach formula (m = 1.75) and full outlet spacing from the inlet, with respect to the various number of operating outlets

As shown in Fig. (2), the traditional factor F [Eq. (6)] yields the constant value as 0.3636 that is independent of the number of outlets N. The factor F_C [Eq. (7a)] yields almost the same values with the stepwise correction factor F_{SW} [Eq. (5)] for various number of outlets. The comparison test shows that the Christiansen's factor F_C accurately predicts the friction head loss since F_C is an accurate approximation of the stepwise correction factor F_{SW}. The traditional factor F tended to give underpredicted values systematically with respect to the factors F_C and F_{SW}, particularly, as the number of outlets decreases, the difference from these factors (F_C and F_{SW}) being more significant. For instance, for a large value of N = 100, the difference 1.4%, and for a value of N = 10, the difference 14% whereas for an extreme small value of N = 5, the difference 29%.

The general form of the Darcy-Weisbach formula which proved to be the most accurate and reliable (von Bernuth and Wilson 1989, von Bernuth 1990, Watters and Keller 1978) can be approximated by the following expression:

$$S_f(l) = \frac{dH_f(l)}{dl} = \frac{f}{D} H_V(l) = \frac{C}{D^n} Q^m(l) \tag{8a}$$

$$f = c_1 \left[R_I\right]^{m-2} \tag{8b}$$

$$C = \frac{8c_1(\nu/4)^{2-m}}{g\pi^m} \tag{8c}$$

where $S_f(l)$ = friction slope or the slope of the energy grade line at any distance l from the pipe inlet expressed as the energy loss per unit length of the pipeline, and per unit weight of fluid; $H_f(l)$ = friction head loss per unit weight of fluid at any distance l; f and C = friction coefficient and combined friction coefficient for the Darcy-Weisbach formula assuming to be constant along the pipe; c_1 = constant for the particular friction coefficient formula used; $R_I = (4N\overline{q}/\pi D\nu)$ = Reynolds number at the inlet of the pipe; m and n = velocity and diameter exponents, respectively. Generally n is approximately equal to m+3 (Scaloppi & Allen, 1993); ν = kinematic viscosity of water; and g = acceleration due to gravity.

For laminar flow regime (R < 2,000; R = Reynolds number for pipe flow), m = 1.0, n = 4.0, c_1 = 64 and C = 4.195 10^{-6}; for turbulent flow regime in a smooth pipe (3,000 < R $\leq 10^5$), m = 1.75, n = 4.75, c_1 = 0.316 (Blasius equation) and C = 7.792 10^{-4}, and finally for fully turbulent flow regime (10^5 < R < 10^7), m = 1.828, n = 4.828, c_1 = 0.130 (Watters and Keller 1978) and C = 9.589 10^{-4}, are taken.

Note that, the combined friction coefficient C is appropriate for plastic pipes (PVC or PE). For aluminum pipes, the friction coefficient f is given by the well-known Churchill equation (Churchill 1977)

$$f = 8\left[(8/R)^{12} + 1/(A+B)^{3/2}\right]^{1/12} \tag{9a}$$

where A and B = empirical parameters for computing Darcy-Weisbach friction coefficient. A and B are calculated by

$$A = \left\{2.457 \ln\left[1/\left((7/R)^{0.9} + 0.27(\varepsilon/D)\right)\right]\right\}^{16}\ ;\ B = (37{,}530/R)^{16} \tag{9b}$$

where ε = equivalent roughness height of the internal pipe surface.

Integrating Eq. (8a) with Eq. (2) between the limits 0 and l yields (Wu and Gitlin 1975, Anyoji and Wu 1987)

$$H_f(l) = H_{f(L)}\left[1-(1-i)^{m+1}\right] \tag{10a}$$

$$H_{f(L)} = FH_{f0} = \frac{1}{(m+1)} H_{f0} \tag{10b}$$

$$H_{f0} = f\frac{L}{D}H_{VI} = C\frac{Q_I^{\,m}}{D^n}L \tag{10c}$$

where $H_f(L)$ = total friction drop at the closed end of the pipeline; and H_f0 = total friction drop in a similar pipeline without outlets conveying the total flow rate along its entire length. It should be noted, the second multiplying term in the bracket in the right-hand side of Eq. (10a) can be described as the friction drop ratio, $R_i = H_f(l)/H_{f(L)}$.

An alternate version for the total friction drop $H_f(L)$ may be obtained by replacing in Eq. (10b) the traditional correction factor F by the Christiansen's correction factor F_C given by Eq. (7) (Scaloppi & Allen, 1993)

$$H_{f(L)} = F_C H_{f0} \tag{10d}$$

3. Determination of energy-grade line (EGL): Analytical approach

In the following section, the improved energy-grade line of a multiple outlets pipe is determined based on the average friction drop approach with a simple exponential function, to express the nonuniform outflow concept. In the first stage of the analytical development the preliminary energy relations for the uniform outflow profile will be presented here (Yıldırım & Singh, 2010; Yıldırım, 2008; Yıldırım & Kose, 2016a; Yıldırım, 2015a, Yıldırım, 2016b).

3.1 Uniform outflow

Let H(l) be the pressure head at a given length l from the pipe inlet, H_I be the pressure head at the pipe inlet, and S_0 be the uniform slope of the pipeline [Fig. (1)]. Assuming the average pressure head for the entire pipeline is located in the middle of the length of the pipeline, and applying conservation of energy principle between the pipe segments l = 0 and l = l, then pressure head distribution along the pipeline is expressed by

$$H(l) = H_I + H_{VI}\left[1-(1-i)^2\right] - H_{f(L)}\left[1-(1-i)^{m+1}\right] - pi\Delta S\,;\ \Delta S = S_0 L \tag{11}$$

in which ΔS = total head loss or gain due to elevation at the closed end of the pipeline. Note that in this analysis, the slope of a downhill pipeline is negative (p = -1), and the slope of an uphill pipeline is positive (p = 1).

Let $\overline{H}$ be the average pressure head along the pipeline can be written

$$\overline{H} = H_I - (\overline{H}_f + p\overline{\Delta S})\,;\ \overline{\Delta S} = \frac{\Delta S}{2} \tag{12}$$

in which $\overline{H}_f$ = average head loss due to friction along the pipeline; and $\overline{\Delta S}$ = average head loss or gain due to elevation.

To find out the average head loss due to friction along the pipeline $\overline{H}_f$, a strip of length dl is considered at any length from the pipeline inlet as shown in Fig. (1). Let dS be the area of the strip, then the average head loss due to friction along the pipeline $\overline{H}_f$ is expressed as

$$\overline{H}_f = \frac{1}{L}\int_{l=0}^{l=L} dS = \frac{1}{L}\int_{l=0}^{l=L} H_f(l)dl = \left(\frac{m+1}{m+2}\right)H_{f(L)} \tag{13}$$

Eq. (13) yields for m = 1.75, the average head loss due to friction along the pipeline is about 73% of the total friction drop at the downstream closed end of the pipeline, when the Darcy-Weisbach formula is used.

Substituting the expression for $\overline{H}_f$ from Eq. (13) into Eq. (12) then, subtracting from Eq. (11), finally one can obtain the following expression for the pressure head distribution

$$H(l) = \overline{H} + H_{VI}\left[1-(1-i)^2\right] + H_{f(L)}\left[(1-i)^{m+1} - \frac{1}{(m+2)}\right] - p\Delta S\left(i - \frac{1}{2}\right) \tag{14}$$

3.2. Nonuniform outflow

To this point the preliminary analytical derivations presented above are similar to the referred paper (Anyoji and Wu 1987). In the following analytical derivation, the energy-grade line will be improved for the nonuniform outflow profile.

Instead of the traditional Eq. (2), to describe variation of flow rate along the pipeline Q(l), a simple but sufficiently accurate exponential function (Scaloppi & Allen, 1993; Valiantzas, 1998, 2002; Yıldırım & Kose, 2016a) is given by

$$Q(l) = Q_I(1-i)^{\beta} \tag{15}$$

where β = nonuniform outflow exponent; then the outflow from the each multiple outlet will not be uniform along the pipeline. It should be noted that, a similar form of Eq. (15) was presented in the recent papers (Valiantzas, 1998, 2002) on the basis of the average outlet flow approximation (Eq. 23 of Valiantzas, 2002) $\left\{\overline{q} = (k/Ns)\left[\int_{l_0}^{l_{Q_I}} H^x(l)dl\right] \cong (k/Ns)\left[\int_{l_0}^{l_{Q_I}} H(l)dl\right]^x\right\}$ which directly referred to the paper of Anyoji and Wu (1987).

However, according to the opinion of Wu (personal communication 2002) this approximation used is not possible in the mathematical consideration (the power of function x must be inside of the integration), except for a special case of the value of the emitter discharge exponent, x = 1.0. Further analysis and discussion for this approximation was presented in the recent papers (Yıldırım & Singh, 2013a,b).

If Eq. (15) is evaluated for the upper half segment of the pipeline (i = 0.5), then arranged with the expression for the flow rate entering over the upper half segment of the pipeline, $Q_{0.5} = (kN/2)\overline{H}^x{}_{0.5}$, finally the β can be evaluated from

$$\beta = 1 - 3.322x\log\left(\frac{\overline{H}_{0.5}}{\overline{H}}\right) \tag{16}$$

where $\overline{H}_{0.5}$ = average pressure head along the upper half segment of the pipeline.

Assuming the average pressure head for the upper half segment of the pipeline $\overline{H}_{0.5}$ is located in the middle of the length of the upper half segment of the pipeline, and applying the conservation of energy principle between the pipe segments l = L/4 and l = L, then the $\overline{H}_{0.5}$ can be expressed as

$$\overline{H}_{0.5} = H_N + H_{f(L)} + (p\overline{\Delta S}_{0.5} - \overline{H}_{f0.5})\,; \quad \overline{\Delta S}_{0.5} = \frac{3}{4}\Delta S \tag{17}$$

where H_N = downstream pressure head at the first outlet from the closed end of the pipeline; $\overline{H}_{f0.5}$ = average head loss due to friction along the upper half segment of the pipeline; and $\overline{\Delta S}_{0.5}$ = average head loss or gain due to elevation at the end of the upper-quarter segment of the pipeline.

Downstream closed end pressure head H_N can be obtained for i = 1 using the expression of pressure head distribution given by Eq. (14) as follows

$$H_N = \overline{H} + H_{VI} - \left(\frac{1}{m+2}\right)H_{f(L)} - \frac{p\Delta S}{2} \tag{18}$$

Average head loss due to friction between the pipe segments l = 0 and l = L/2 for the upper half segment of the pipeline $\overline{H}_{f0.5}$ can be expressed as

$$\overline{H}_{f0.5} = \frac{2}{L}\int_{l=0}^{l=L/2} dS = \frac{2}{L}\int_{l=0}^{l=L/2} H_f(l)dl = \left(\frac{m+0.5^{m+1}}{m+2}\right)H_{f(L)} \tag{19}$$

Eq. (19) yields for m = 1.75, the average head loss due to friction along the upper half segment of the pipeline is about 51% of the total friction drop at the downstream closed end of the pipeline, when the Darcy-Weisbach formula is used.

Combining the expression for $\overline{\Delta S}_{0.5}$ from Eq. (17) with Eq. (18) and Eq. (19) into Eq. (17), and dividing by $\overline{H}$ then, substituting into Eq. (16), finally the β can be computed from:

$$\beta = 1 - 3.322x\log\left[1 + \frac{H_{VI}}{\overline{H}} + \lambda\frac{H_{f(L)}}{\overline{H}} + \frac{1}{4\overline{H}}(p\Delta S)\right];\ \lambda = \left(\frac{1-0.5^{m+1}}{m+2}\right) \tag{20}$$

From this point of the analysis, the energy grade line for nonuniform outflow distribution can be determined by the following Eq. (21) instead of Eq. (14), in which the velocity exponent m should be replaced by its improved value as $m_\beta = \beta$ m:

$$H(l) = \overline{H} + H_{VI}\left[1-(1-i)^2\right] + H_{f(L)}\left[(1-i)^{m_\beta+1} - \frac{1}{(m_\beta+2)}\right] - p\Delta S\left(i - \frac{1}{2}\right) \tag{21}$$

3.3. Inlet and extreme pressure heads

Consider a pipeline with all multiple outlets being equally spaced then, the inlet spacing s_I, from the pipeline inlet to the first outlet is expressed as the some fraction, μ ($0 \le \mu \le 1.0$) of the common outlet spacing s, s_I = μs, and it usually taken as 0.5 or 1.0 for multiple outlets pipelines.

Inlet pressure head H_I can be evaluated from Eq. (21) for the value of variable of distance, i = 0. Substituting the expression for i_{max} (i_{max} = μ s/L) into Eq. (21), then the maximum pressure head H_{max} for uphill and zero slope, can be obtained as

$$H_{\max} = \overline{H} + H_{VI}(1-\theta^2) + H_{f(L)}\left[\theta^{m_\beta+1} - \frac{1}{(m_\beta+2)}\right] + p\Delta S\left(\theta - \frac{1}{2}\right) \tag{22}$$

where θ = L_0/L, length ratio which is the percentage of the distance between the first and last outlets to the total length of the pipeline; L_0 = (N-1) s = length of the distance between the first and last outlets except for the inlet spacing, s_I; L = (N+ μ-1) s = total length of the pipeline.

Similarly, the minimum pressure head Hmin for uphill and zero slope cases, is obtained from Eq. (21) for i_{min} = 1.0, which is essentially equivalent to the downstream end pressure head H_N given by Eq. (18).

For downhill slope case, the location of the maximum pressure head is found either to the first outlet near the pipeline inlet (i_{max} = μ s/L) or at the first outlet from the downstream closed end point (i_{min} = 1.0).

The location of the minimum pressure head for downhill line is determined where the first derivative of the pressure head distribution given by Eq. (21) is equal to zero. For simplification of this derivative procedure, the velocity head term can be omitted in Eq. (21), then the location i_{min} where the minimum pressure head occurs, can be approximated by

$$i_{\min} = \frac{l_{\min}}{L} = 1 - \left[\frac{(-p\Delta S)}{(m_\beta + 1)H_{f(L)}}\right]^{1/m_\beta} \quad (23)$$

Substituting Eq. (23) for i_{min} into Eq. (21), then the H_{min} for downhill slope case, can be easily found.

4. Types of pressure head or energy profiles along manifold line with uniform slope

When a submain line with multiple outlets is designed using a single inlet system and laid on a uniform slope (S_0), the pressure head profile along the line resulting from the total energy drop by friction, $h_{f(L)}$ [$h_{f(L)} = S_f \times L$; S_f: the slope of the energy-gradient line or the friction slope] and the total potential energy gain (or loss) by a uniform downslope (or upslope) at the end of the line, ΔS ($\Delta S = S_0 \times L$), can be classified into three general types (Type-I, Type-II and Type-III). The classification can be based on a dimensionless energy gradient ratio, K_S ($K_S = S_0/S_f$). There are five typical pressure head profiles (Type-I, Type-II.a, Type-II.b, Type-II.c and Type-III) (Barragan & Wu, 2005) under three general types, and can be expressed in what follows:

4.1. Zero and uphill slope situation

4.1.1. Pressure profile type I (minimum pressure at the downstream closed end of the line)

The pressure head decreases with respect to the submain length. This type occurs when the submain line is laid on zero or uphill slopes. In this condition, the dimensionless energy-gradient ratio is $K_S = S_0 / S_f \le 0$. The total energy is lost by both elevation change due to uniform upslope and by friction. The maximum pressure head, H_{max} is at the inlet of the line and is equal to the operating inlet pressure, H_{0I} ($H_{0I} = H_{max}$); the minimum pressure head, H_{min}, is at the closed end of the line, and is equal to the downstream pressure head ($H_d = H_{min}$).

4.2. Downhill slope situation

4.2.1. Pressure profile type II (minimum pressure along the line):

The pressure head decreases from the upstream end with respect to the pipeline length, reaches a minimum point (i_{min}) , and then increases with respect to the submain line. The minimum pressure head is located somewhere along the line ($0 < i_{min} = l_{min}/L < 1$), depending on the large interval of K_S, $0 < K_S = S_0/S_f < 2.75$.

4.2.1.1. Pressure profile type II-a

This type of pressure profile occurs under the friction and slope situation, where $0<K_S = S_0/S_f<1.0$. In this type, the total energy gain by uniform downslope at the end of the line is smaller than the total energy drop by friction; so the downstream end pressure head (H_d) is still less than the operating inlet pressure (H_{0I}). The maximum pressure head is at the inlet ($H_{max} = H_{0I}$); and the minimum pressure head is located somewhere along the line.

4.2.1.2. Pressure profile type II-b (optimal pressure profile)

This is under the friction slope situation where the dimensionless energy-gradient ratio is $K_S = S_0/S_f = 1.0$. This profile is similar to Profile II-a, but the profile is such that the downstream closed end pressure head is equal to the operating inlet pressure head ($H_{0I} = H_d$). The maximum pressure is at the inlet ($H_{max} = H_{0I}$) as well as at the closed end of the line ($H_{max} = H_d$). The minimum pressure is located somewhere near the middle section of the line.

4.2.1.3. Pressure profile type II-c

This is under the friction and slope situation where the dimensionless energy-gradient ratio is $1.0<K_S<2.75$ for the Darcy-Weisbach (DW) or $1.0<K_S<2.852$ for the Hazen-Williams (HW) equation. This occurs when the line slope is even steeper, so the pressure at the end of line is higher than the operating inlet pressure. In this condition, the maximum pressure is at the downstream closed end of the line ($H_{max} = H_d$), and the minimum pressure is located somewhere along the upstream segment of the line.

4.2.1.4 Pressure profile type III (minimum pressure at the upstream inlet of the line)

This occurs when the submain line is on a steep downslope where the total energy gain by the uniform downslope is larger than the total energy drop by friction for all sections along the line. The pressure head increases with respect to the line length. This is caused by a steep downslope situation where the dimensionless energy-gradient ratio is $K_S \ge 2.75$ for the DW equation, or $K_S \ge 2.852$ for the HW equation. In this condition the maximum pressure is at the downstream closed end of the line ($H_{max} = H_d$), and the minimum pressure head is at the pipe inlet and equal to the operating pressure head ($H_{min} = H_{0I}$). Among all types of pressure profiles, the Type-II profile is considered as the optimal (or ideal) pressure profile which can produce the minimum pressure head difference for a given pipe length as discussed earlier (Yıldırım, 2015b). This profile occurs when the total energy loss by friction is just balanced by the total energy gain due to uniform downslope (Profile II-b).

4. Conclusions

Determination of the proper operating inlet pressure head is important for hydraulic design of multi-outlet pipelines in submain lines. This paper presents an analytical energy-gradient ratio (EGR) approach which offers simple, direct but sufficiently accurate relationships to determine the operating inlet pressure head and the the required pressure parameters, incorporating different uniformity patterns for water application. For this purpose, some mathematical expressions are initially deduced to relate water application uniformity parameters; such as Christiansen uniformity coefficient, lower-quarter distribution uniformity, coefficient of variation of outlet discharge, emission uniformity and allowable pressure head variation. Hence, the operating inlet pressure head is reformulated by incorporating different uniformity patterns, and setting a multiplication factor, α, and the required average outlet pressure head, and β^*, for the change in potential energy head due to the uniform line slope. The present formulations can be efficiently used for a wide range of water application uniformity, and for different types of pressure profiles in different line slope situations, without requiring any additional hydraulic variables.

References

Açıklamalı [ek1]: Kaynakça kısmında verilen çalışmaların çoğuna atıf verilmemiş. İlgili yerlerde atıflar eklenmelidir.

Barragan, J., & Wu, I.P. (2005). "Simple pressure parameters for micro-irrigation design" Biosystems Eng. 90(4): 463-475.

Natural Resources Conservation Service Conservation Practice Standard "Above Ground, Multi-Outlet Pipeline (Ft.) CODE 431" United States Department of Agriculture (USDA), 431, pages: 1-3, NRCS, AR, April 2008.

Sadeghi, S. H., Peters, T., & Shelia, V. (2016). "Energy Grade Line Assessment for Tapered Microirrigation Laterals" Journal of Irrigation and Drainage Engineering,142(7), https://doi.org/10.1061/(ASCE)IR.1943-4774.0001020).

Sadeghi, S. H., & Peters, T. (2013). "Analytical Determination of Distribution Uniformity for Microirrigation Tapered Laterals Laid on Uphill and Horizontal Slopes" Journal of Irrigation and Drainage Engineering, 139(6), https://doi.org/10.1061/(ASCE)IR.1943-4774.0000568.

Sadeghi, S.H., & Peters, T. (2011). "Modified G and GAVG Correction Factors for Laterals with Multiple Outlets and Outflow" . Journal of Irrigation and Drainage Engineering 137(11), https://doi.org/10.1061/(ASCE)IR.1943-4774.0000332.

Scaloppi, E. J., & Allen, R. G. (1993). "Hydraulics of irrigation laterals: comparative analysis." J. Irrig. and Drain. Eng., ASCE, 119(1), 91-115.

Singh, R.P., & Mahar, P.S. (2003). "Optimal Design of Multidiameter, Multioutlet Pipelines" Journal of Water Resources Planning and Management, 129(3), https://doi.org/10.1061/(ASCE)0733-9496(2003)129:3(226).

Singh, A., Singh, R.P., Mahar, P.S., & Singh, K.K. (2000). "Optimal Design of Tapered Microirrigation Submain Manifolds" Journal of Irrigation and Drainage Engineering, 126(6).

Valiantzas, J. D. (1998). "Analytical approach for direct drip lateral hydraulic calculation." J. Irrig. and Drain. Eng., ASCE, 124(6), 300-305.

Valiantzas, J. D. (2002). "Continuous outflow variation along irrigation laterals: effect of the number of outlets." J. Irrig. and Drain. Eng., ASCE, 128(1), 34-42.

Yıldırım, G. (2023a). "Hydraulic Principles and Design Concepts for Submain Units with Multiple Outlet Pipelines: New Analytical Techniques with Engineering Applications" Part of the Book Series "Synthesis Lectures on Engineering, Science and Technology (SLEST) (DOI: https://doi.org/10.1007/978-3-031-32495-6), Springer Cham, Hardcover ISBN: 978-3-031-32494-9, Softcover ISBN: 978-3-031-32497-0, eBook ISBN: 978-3-031-32495-6, Series ISSN: 2690-0300, Series ISSN: 2690-0327, Edition Number: 1, Number of Pages: XXVII, 163.

Yıldırım, G. (2023b). "Review of Fundementals in Hydraulic Engineering Perspective: Hydraulics Principles, Governing Equations, Design Criteria, Types of Design Problems, Hydraulics and Energy-Gradient Line Profiles for Uniformly Sloping Multiple Outlets Pipelines" In: Hydraulic Principles and Design Concepts for Submain Units with Multiple Outlet Pipelines. Synthesis Lectures on Engineering, Science, and Technology. Springer, Cham. https://doi.org/10.1007/978-3-031-32495-6_1.

Yıldırım, G., & Kose, O. (2016a). "New Software (Multi-flowCAD) Development for Sub-main Line Hydraulic Design: Computational Algorithm, Computer Visualization and Implementation" Arabian Journal for Science and Engineering, 41, 1551-1560.

Yıldırım, G. (2016b). "Discussion of "Statistical Analysis of Non-Pressure-Compensating and Pressure-Compensating Drip Emitters" by H. Perea, J. Enciso-Medina, V. P. Singh, D. P. Dutta, and B. J. Lesikar (DOI: 10.1061/(ASCE)IR.1943-4774.0000644). J. Irrig. and Drain. Eng., ASCE.

Yıldırım, G. (2015a). "Computer-Based Analysis of Hydraulic Design Variables for Uniformly Sloping Microirrigation System Laterals" J. Irrig. and Drain. Eng., ASCE, 141(7), DOI: 10.1061/(ASCE)/IR.1943-4774.0000846.
Yıldırım, G. (2015b). "An Assessment for Hydraulically Efficient Design of Uniformly Sloping Submain, Lines" Irrigation and Drainage (ICID Journal), 64(2),157-168.
Yıldırım, G. (2014a). "Discussion of "Analytical determination of distribution uniformity for microirrigation tapered laterals laid on uphill and horizontal slopes" by Sayed Hossein Sadeghi and Troy Peters. J. Irrig. and Drain. Eng., ASCE, 140(12).
Yıldırım, G. (2014b). "Discussion of "Modified G and GAVG correction factors for laterals with multiple outlets and outflow" by Sayed Hossein Sadeghi and Troy Peters. (DOI: 10.1061/(ASCE)IR.1943-4774.0000604). J. Irrig. and Drain. Eng., ASCE, 141(1), Article Number: 07014014.
Yıldırım, G., & Singh, V.P. (2013a). "Operating pressure assessment for multi-outlets submains: Ideal hydraulic design.", International Perspective on Water Resources and Environment by ASCE-EWRI (IPWE-2013), 7-9 January, 2013, Izmir, Turkey.
Yıldırım, G., & Singh, V.P. (2013b). "Operating pressure assessment for multi-outlets submains: Design applications." International Perspective on Water Resources and Environment by ASCE-EWRI (IPWE-2013) ,7-9 January, 2013, Izmir, Turkey.
Yıldırım, G. (2012a). "Discussion of "Simple method for the design of microirrigation paired laterals on sloped fields" by Shufang, Jiang and Yaohu, Kang. (DOI: 10.1061/(ASCE)IR.1943-4774.0000465). J. Irrig. and Drain. Eng., ASCE, 138(9), 848-851.
Yıldırım, G. (2012b). "Discussion of "Simplified method for sizing laterals with two or more diameters" by Muluneh, Yitayew. (DOI: 10.1061/(ASCE)IR.1943-4774.0000323). J. Irrig. and Drain. Eng., ASCE, 138(7), 697-702.
Yıldırım, G., & Singh, V.P. (2010). "A MathCAD Procedure for Commercial Pipeline Hydraulic Design Considering Local Energy Losses" Advances in Engineering Software, 41(2), 489-496.
Yıldırım, G. (2010a). "Hydraulic Analysis for Commercial Pipeline Design Using MathCAD" pp: 213-224, (Chapter 5). Hydraulic Engineering: Structural Applications, Numerical Modeling and Environmental Impacts, Engineering Tools, Techniques and Tables Series. Editors: Gerhard Hirsch and Bernd Kappel ISBN: 978-1-60876-825-7 and ISBN: 978-1-61122-322-4 (eBook). Published by Nova Science Publishers, Inc. 2010, New York.
Yıldırım, G. (2010b). "Total Energy Loss Assessment for Trickle Lateral Lines Equipped with Integrated In-Line and On-Line Emitters." Irrigation Science, 28(4), 341-352.
Yıldırım, G. (2009). "Simplified Procedure for Hydraulic Design of Small-Diameter Plastic Pipes." Irrigation and Drainage (ICID Journal), 58(3):209-233.
Yıldırım, G. (2008). "Determining Operating Inlet Pressure Head Incorporating Uniformity Parameters for Multioutlet Plastic Pipelines." J. Irrig. and Drain. Eng., ASCE, 134(3), 341-348.

Hydraulic Analysis of Multi-outlets Submains-I: Software Development

Gürol Yıldırım*[1]

[1] Giresun University, Engineering Faculty, Civil Engineering Dept., 28100, Giresun, Türkiye

Abstract. This paper aims to present an efficient computer program in Visual Basic 6.0, named "Multi-flowCAD" based stepwise computation algorithm for determining the hydraulic design variables (pipe size, pipe length and operating inlet pressure head), and the hydraulic flow characteristics (outflow-pressure head distribution, discharge and total friction losses) along the energy-grade line. The stepwise algorithm takes into account the velocity head change and variation of the Reynolds number, which affects the selection of the proper friction coefficient formula to be applied along the different reaches of the pipeline, while some additional minor local losses due to emitter connections are neglected.

Keywords: Smooth pipe-flow; Steady-state analysis; Software; Computer-aided design (CAD)

1. Theoretical Background

In the past, numerous researchers have worked on the hydraulic analysis of submain unit pipeline networks. The increasing progress in computer technology has led to the development of analytical (Wu and Gitlin 1974, 1975; Anyoji and Wu 1987; Wu and Yue 1993; Wu 1992, 1997; Warrick and Yitayew 1988; Valiantzas 1998, 2002a,b; Yıldırım and Ağıralioğlu 2002, 2004a,b; Yıldırım 2006a,b, 2007a,b), and numerical, semi-theoretical or computer-aided stepwise methods (Yitayew and Warrick 1988; Scaloppi and Allen 1993; Hathoot et al. 1993, 2000; Kang and Nishiyama 1996a,b; Vallesquino and Luque-Escamilla 2001, 2002; Juana et al. 2004; Yıldırım 2008, 2009, 2010). As a matter of fact, a significant amount of these hydraulic analysis are based on the conventional design procedure in which the pipe size and length are known a priori; then the remaining design variables such as operating inlet pressure head, water application uniformity and total energy loss are determined depending on these known pipe geometric characteristics.

2. Methodology

2.1. Classification on Design Problems

Design of a manifold pipeline includes the determination of pipe geometric characteristics (pipe size and length), as well as operating inlet pressure head and total friction head losses along the line. Design engineers are often faced with three types of problems in most lateral hydraulic computations. In the first type of problem (energy grade-line determination) (Yıldırım and Singh 2013a,b, Yıldırım 2007a, 2008) for the given design values of uniform pipe slope (S0) and average outlet pressure head (Hav), the required hydraulic variables concerning the pressure head profile [the operating inlet pressure head (H0I = Hin), downstream closed end pressure head (HN), extreme pressure heads (Hmax and Hmin) with their locations along the line (imax, imin; i: percentage of length, l is a length from the inlet in m, and L is the total length of the lateral line in m), and the total energy drop due to friction Hf(L), can be determined ensuring the desired level of water application uniformity as well as the allowable pressure head variation along the line (Yıldırım 2007a). With the help of the present computer-aided design technique, knowledge of hydraulic properties for any type of pressure profile under consideration enables the design engineer to clearly evaluate the overall energy distributions with the required pressure parameters through the line sections between successive outlets, in a simple way.

Variation of the outflows along the pipeline within certain limited values which defined as the uniformity coefficients for water application is also very important concern. In the second type of problem (water application uniformity evaluation) (Yıldırım 2007a,b, 2009), when H0I is given as an input parameter together with the required average emitter pressure head (Hav) and for a given design slope (S0), proper values of the required water application uniformity coefficients can be directly approximated. The design procedure which based on the

* Corresponding author, E-mail: gurol.yildirim@giresun.edu.tr

https://doi.org/10.31462/icearc2025_ce_hyd_305

uniformity coefficients depending on the acceptable level of outflow variation can be accepted or refused. In fact, the real value of these coefficients, should be just obtained with taking into account all the emitter outflows along the pipeline by implementing computer-aided stepwise procedure.

Designers are often faced with the problem of selecting the pipe size and length for a given desired uniformity level and given design slope range, in order to keep the design operating inlet pressure head and the allowed limit of total energy loss along the pipeline. In the third type of design problem (direct sizing procedure) (Hathoot et al. 2000; Kang and Nishiyama 1996a,b; Valiantzas 2002, Yıldırım 2006a, 2009), the required parameters are the pipe inside diameter (D) or length (L) for a given design slope (S0), the desired level of water application uniformity (UC and DULQ), and the required average outflow and pressure head (qav , Hav), with the previously known design variables.

3. Fundamental principles of manifold flow hydraulics: governing equations

Hydraulically, flow insubmain unit pipeline is considered to be a steady, spatially varied flow with decreasing outlet outflow in the downstream direction. With decreasing discharge along the line, the energy gradient line decreases. Generally, outlets are usually identical, and installed at an equal spacing on the line. The flow characteristics of the outlets are typically described by a function of the form (Howell and Hiler, 1974; Keller and Karmeli, 1974).

$$q_i = cH_i^{\ y} \tag{1}$$

in which qi is the outflow from an individual outlet; Hi is the pressure head in the pipe at the outlet under consideration; c is the outlet coefficient that accounts for areal and discharge effects and makes the units correct.

Considering the H1 is the initial inlet pressure head, Q1 the initial lateral discharge upstream from the first outlet, and q1 the outflow of the first outlet, which may be written as

$$q_1 = c\, H_1 \tag{2}$$

Assuming that the outflow varies continuously in space along the pipeline (the number of outlets is sufficiently large), the outflow per unit length (q) can then be described by

$$q = \left(\frac{c}{s}\right) H_i^{\ y} \tag{3}$$

If continuity is preserved along lateral, the conservation of mass is written in the general following form

$$\frac{dQ}{dx} + \frac{dA}{dt} = -q \tag{4}$$

where Q is the pipeline inlet discharge; x and t are space and time coordinates. For steady flow condition $(dA/dt = 0)$ in irrigation laterals, the continuity equation, Eq.(4), may be rewritten as follows

$$A\frac{dv}{dx} = -q \tag{5}$$

where v is the velocity of flow in the pipe.

Using the continuity equation, Eq.(5), the inlet discharge, Qi+1, at the pipe reach between successive outlets (i) and (i+1), can be obtained from

$$Q_{i+1} = Q_i - q_i \tag{6}$$

The discharge between the first and second outletsQ_2 can be evaluated from Eq. (6) in the special form :

$$Q_2 = Q_1 - q_1 = (N\, q_{av}) - (c\, H_1^{\ y}) \tag{7}$$

The momentum effect resulting from decreasing the discharge in downstream direction, the conservation of momentum equation is given by the following form (Streeter and Wylie 1979)

$$\sum F = \rho\left(Q_{i+1}V_{i+1} - Q_iV_i\right) \tag{8}$$

where is the change of pressure force; is the density of irrigation water; Vi and Vi+1 are the flow velocity between successive emitters (i-1)~(i) and (i)~(i+1), respectively.

Using the conservation of momentum equation, Eq.(8), the change of pressure head, □Hi+1, due to change of momentum between successive emitters (i) and (i+1) resulting from decreasing the discharge from Qi to Qi+1, may be written as follows

$$\Delta H_{i+1} = \frac{\left(Q_{i+1}^{\ 2} - Q_i^{\ 2}\right)}{gA^2} \tag{9}$$

where g is the acceleration due to gravity.

Watters and Keller (1978) have shown that for small diameter smooth pipes, the Darcy-Weisbach friction formula can give accurate predictions for frictional losses based on conservation of energy. Therefore the following expression can be written

$$H_{fi+1} = f_{i+1}\frac{s}{D}\frac{Q_{i+1}^{\ 2}}{2gA^2} \tag{10}$$

where H_{fi+1} is the friction head loss between successive outlets (i) and (i+1); f_{n+1} is the Darcy-Weisbach friction coefficient for the pipe reach between successive outlets (i) and (i+1); D is the internal diameter of the pipe.

Eq. (10) may be rewritten simplifying

$$H_{fi+1} = \frac{8s}{\pi^2 gD^5} f_{i+1} Q_{i+1}^{\ 2} \tag{11}$$

If the pipe has a uniform slope S_0 , the difference in levels of points (i) and (i+1) may be given by

$$(z_i - z_{i+1}) \ = \ \pm \ s\, S_0 \tag{12}$$

The positive sign is for the sloping downward and the negative for upward slopes, z_i and z_{i+1} are elevations of successive outlets (i) and (i+1) respectively, above an arbitrary datum.

Using conservation of the energy principle with Eq.(9) and Eq.(11), between successive outlets (i) and (i+1), the following form can be obtained

$$H_i + \frac{V_i^{\ 2}}{2g} + z_i = H_{i+1} + \frac{V_{i+1}^{\ 2}}{2g} + z_{i+1} + H_{fi+1} + \Delta H_{i+1} \tag{13}$$

where H_i and H_{i+1} are pressure head for the successive outlets (i) and (i+1); $\frac{Q_i^{\ 2}}{2gA^2}$ and $\frac{Q_{i+1}^{\ 2}}{2gA^2}$ are velocity head under consideration.

Solving Eq.(13) for the pressure head at the outlet (i+1), H_{i+1} is related to H_i by the following equation

$$H_{i+1} = H_i + \left(\frac{Q_i^{\ 2}}{2gA^2}\right) - \left(\frac{Q_{i+1}^{\ 2}}{2gA^2}\right) + (z_i - z_{i+1}) - h_{i+1} - \Delta H_{i+1} \tag{14}$$

Combining conservation of mass and momentum principles Eq.(6) and Eq.(9) with Eq.(11) and Eq.(12), into conservation of energy principle, Eq.(14), and simplifying

$$H_{i+1} \ = \ H_i + \frac{3}{2gA^2}\ [\,Q_i^2 - (Q_i - q_i)^2] - f_{i+1}\frac{8s}{\pi^2 gD^5}(Q_i - q_i)^2 \pm \ s\, S_0 \tag{15}$$

For convenience, Eq.(15) is put in the form

$$H_{i+1} = H_i + B\,[Q_i^2 - (Q_i - q_i)^2] - E\, f_{i+1}\,(Q_i - q_i)^2 \pm \ s\, S_0 \tag{16}$$

in which

$$B = \frac{3}{2gA^2} \tag{17}$$

$$E = \frac{8s}{\pi^2 gD^5} \tag{18}$$

As presented from the above hydraulic analysis given in Table 1, there are four basic equations in the submain unit hydraulics. These equations are: 1. the outlet discharge-pressure head relationship as Eq. (1), 2. the continuity equation as Eq. (5), 3. the Darcy-Weisbach friction formula as Eq. (10), 4. the conservation of energy equation coupled with the conservation of momentum equation as Eq. (13). On the other hand, there are four unknown hydraulic variables (Q_{i+1}, q_{i+1}, H_{i+1} and H_{fi+1}) at any location of pipeline (i+1), with the known previous values (Q_i, q_i, and H_i), and the other parameters (z_i, z_{i+1}, f_{i+1}, D, s, c and y). These unknown variables can be estimated using some of the user-friendly computation method.

Table 1. Fundemental principles & governing formulations on hydraulic computation for fluid flow along submain manifold

Description of Basic Equation	Formulation
• Pressure head - outflow (discharge) relationship	$q_n = cH_n^{\ y}$ $q = \left(\frac{c}{s}\right)H_n^{\ y}$
• Conservation of mass law & principle: Continuity equation	$\frac{dQ}{dx} + \frac{dA}{dt} = -q$ $Q_{n+1} = Q_n - q_n$

• Conservation of momentum law & principle: Impuls-momentum equation	$\Delta F=\rho(Q_{n+1}V_{n+1}-Q_nV_n)$ $\Delta H_{n+1}=\frac{\Delta p}{\gamma}=\frac{\Delta F}{A\gamma}=\frac{\rho(Q_{n+1}V_{n+1}-Q_nV_n)}{A\gamma}$ $\Delta H_{n+1}=\frac{\rho}{A\rho g}\left(\frac{Q^2{}_{n+1}-Q^2{}_n}{A}\right)=\frac{(Q^2{}_{n+1}-Q^2{}_n)}{gA^2}$
• Continuous head (energy) losses due to friction: Darcy-Weisbach equation	$H_{fn+1}=f_{n+1}\frac{s}{D}\frac{Q_{n+1}{}^2}{2gA^2}$
• Local or minor head losses due to individual outlet barb connection: Borda-Carnot & Belanger equation	$h_k'=h_c+h_e=\frac{(V_c-V_r)^2}{2g}+\frac{(V_r-V_{n+1})^2}{2g}=\left(\frac{1}{C_cr}-1\right)^2\frac{V_{n+1}{}^2}{2g}=K\frac{V_{n+1}{}^2}{2g}$
• Conservation of energy law & principle: Bernoulli's equation	$H_n+\frac{V_n{}^2}{2g}+z_n+h_{kn}{}'=H_{n+1}+\frac{V_{n+1}{}^2}{2g}+z_{n+1}+H_{fn+1}+\Delta H_{n+1}+h_{kn+1}{}'$

4. Water application uniformity

One of the main tasks of the submain unit hydraulic computation is to provide a sensitive balance between the inlet pressure head, the water application uniformity, and the total frictional losses along lateral. The Christiansen's uniformity coefficient and the lower-quarter distribution uniformity are used here to express uniformity of outlet discharge throughout the system (please see, Table 2).

Table 2. Uniformity Criteria & Uniformity Coefficients for Water Application

Computation Method	Christiansen's Uniformity Coefficient (UC)	Lower-Quarter Distribution Uniform Coeff. (DU_{LQ})
(1) Forward-Step Method (*FSM*)	Keller and Karmelli (1974): $UC=1-\left(1/(Nq_{av})\right)\sum_{n=1}^{n=N}\lvert q_n-q_{av}\rvert$	$DU_{LQ}=4\left(\sum_{n=3n/4}^{n=N}q_n\right)/(Nq_{av})$
(2) Differential Method (*DM*)	Yitayew and Warrick (1988): $UC=1-\left(\frac{1}{Lq_{av}}\right)\int_0^L\lvert q-q_{av}\rvert dx$ $=1-\left(\frac{2}{X_0}\right)\left(X_0-X_{div}-X_0V_{div}\right)$	$DU_{LQ}=4\times V_{LQ}$
(3) *Runge- Kutta* Numerical Method (*RKM*)	Miller (1981): $UC=\frac{(K_1+K_3X_0+K_5X_0{}^2)}{(1+K_2X_0+K_4X_0{}^3+K_6X_0{}^4)}$	Warrick (1983): DU_{LQ} = 1 / 0.67 (UC – 0.33) (for uniform outflow distribution) DU_{LQ} = 1 / 0.63 (UC – 0.37) (for normal outflow distribution)
(4) Constant-Discharge Method (*CDM*)	Valiantzas (1998): $UC=1-0.798\frac{y}{H_s}\left(\frac{H_{f0}{}^2}{(2m+3)(m+2)^2}+\frac{(s_0L)^2}{12}-\frac{H_{f0}s_0L}{(m+2)(m+3)}\right)^{0.5}$	
(5) Variable Discharge Method (*VDM*)	Valiantzas (1998): $[M=m_\alpha=\alpha\times m]$ $UC=1-0.798\frac{y}{H_s}\left(\frac{H_{f0}{}^2}{(2M+3)(M+2)^2}+\frac{(s_0L)^2}{12}-\frac{H_{f0}s_0L}{(M+2)(M+3)}\right)^{0.5}$	

5. Coefficient of friction (f)

Flow in a submain unit pipeline is generally turbulent: 3000<R≤105 (R = Reynolds number), sometimes fully turbulent flow : 105<R< 107, exists at the upstream end of the pipeline and flow becomes laminar at the downstream reach where the velocity decreases to zero (please see, Table 3.)

Table 3. Friction Coefficient Formulations Regarding Flow Regimes in Different Hydraulic Computations

	Friction Coefficient Formula (fn)		
Computation Method	Laminar Flow: ($R_n < 2000$)	Turbulent Flow: ($3000 < R_n \le 10^5$)	Fully-Turbulent Flow**:** ($10^5 < R_n < 10^7$)
(1) Forward-Step Method (**FSM**)		Blasius Formula	Watters and Keller (1978):
(2) Differential Method **(DM)**	$f_n = \dfrac{64}{R_n}$	$f_n = 0.316\ R_n^{-0.25}$	
(3) Runge-Kutta Numerical Method (**RKM**)			$f_n = 0.130\ R_n^{-0.172}$
(4) Simplified Analytical Approach (**SAA**)	$f_0 = 64\left(\dfrac{\nu}{D}\right)$	$f_0 = 0.316\left(\dfrac{\nu}{D}\right)^{0.25}$	$f_0 = 0.130\left(\dfrac{\nu}{D}\right)^{0.172}$
(5) Constant Discharge Method (**CDM**) (6) Variable Discharge Method (**VDM**)	[m = 1.0]	[m = 1.75]	[m = 1.828]
(7)Successive Approximations Method (SAM)	$f_n = \dfrac{64}{R_n}$	Colebrook-White equation: [Zigrang and Sylvester, 1982] $\dfrac{1}{f_n} = -2\log_{10}\left(\dfrac{\varepsilon/D}{3.7} + \dfrac{2.51}{R_n\sqrt{f_n}}\right)$	

6. Software development

As a notable reference, the algorithm was first programmed in FORTRAN IV (Kreitzberg and Schneiderman 1975), then a useful flowchart was presented by Hathoot et. al. (1993). Herein, the steps of the present algorithm was improved in the following section “Implementation of the Design Criteria” based on the initial and boundary conditions of the algorithm, and reprogrammed in Visual Basic 6.0 (Smyth 2013), incorporating variable flow conditions through the pipe segments, in a stepwise manner. Calculation steps of the proposed computer program (Multi-flowCAD) is also provided. In practice the average outlet discharge qav, the corresponding pressure head Hav, the flow exponent y, total number of outlets N, the spacing between outlets S, and the uniform line slope S0 and the inside diameter of the pipe D are assigned in advance, for a certain design.

7. Computational steps of algorithm

The following computational steps should be taken into consideration in the present algorithm:

1. The initial pressure head Hmax is first assumed by adding a reasonable head increment □0 to the average head Hav (initial condition).
2. The outflow of each successive individual outlet qi is evaluated in a stepwise manner, starting from the first outlet at the upstream pipeline inlet; and in each step the corresponding pipe discharge Qi is evaluated.
3. At each step, the Reynolds number valid for the pipe segment between successive outlets is calculated, then the proper friction coefficient formula is selectively used to evaluate the head loss due to friction, hence the new pressure head at the head of outlet, is determined by applying Eq. (16).
4. If Eq. (16) yields negative values of H at any outlet , this would indicate that the assumed Hmax should be increased by □d (Boundary condition).
5. As negative values of H disappear, other conditions should be continued.
6. The velocity at any reach of the pipeline should be positive (boundary condition); otherwise, this would indicate that the sum of outlet outflows is greater than the total initial pipe inlet discharge Qmax, which means that Hmax should be decreased by □d (□d, being divided periodically by 10 on increasing or decreasing Hmax).
7. The discharge in the pipe segment from the last outlet toward the downstream lateral closed end should be zero, which forms an important boundary condition. Practically, this condition is satisfied if the relative velocity at that part becomes less than a sufficiently small quantity, □ .
8. As the proper value of Hmax is sensitively reached, outflow, pressure head for each outlet, the discharge and flow velocity at the corresponding reach of the pipe can be determined. Finally, water application uniformity of the submain unit system can be evaluated by computing the uniformity coefficients (UC and DULQ) as given by Eq. (19) and Eq. (20), respectively.

8. Conclusions

In this study, the algorithm for the submain unit pipeline hydraulic design based on the forward-step computation procedure was presented, and a user-friendly computer program in Visual Basic 6.0 language was developed for general engineering applications. In the present design methodology, the design of a subunit pipe with equally spaced individual outlets and uniform line slope was examined so that hydraulic design principles and the uniformity coefficients were more convenient for better evaluation. In designing of a manifold by the present algorithm, for a given design length and inside diameter, firstly, the proper value of operating inlet pressure head was sensitively appointed within the design interval based on the initial and boundary conditions, then the total friction drop along the pipeline and level of water application uniformity of the system were finally determined.

References

Sadeghi, S. H., & Peters, T. (2011). Modified G and GAVG correction factors for laterals with multiple outlets and outflow. *Journal of Irrigation and Drainage Engineering, 137*(11).

Sadeghi, S. H., & Peters, T. (2013). Analytical determination of distribution uniformity for microirrigation tapered laterals laid on uphill and horizontal slopes. *Journal of Irrigation and Drainage Engineering, 139*(6).

Sadeghi, S. H., Peters, T., & Shelia, V. (2016). Energy grade line assessment for tapered microirrigation laterals. *Journal of Irrigation and Drainage Engineering, 142*(7).

Scaloppi, E. J., & Allen, R. G. (1993). Hydraulics of irrigation laterals: Comparative analysis. *Journal of Irrigation and Drainage Engineering, 119*(1), 91-115.

Singh, A., Singh, R. P., Mahar, P. S., & Singh, K. K. (2000). Optimal design of tapered microirrigation submain manifolds. *Journal of Irrigation and Drainage Engineering, 126*(6).

Singh, R. P., & Mahar, P. S. (2003). Optimal design of multidiameter, multioutlet pipelines. *Journal of Water Resources Planning and Management, 129*(3).

United States Department of Agriculture (USDA). (2008). *Conservation practice standard "Above Ground, Multi-Outlet Pipeline (Ft.) CODE 431*. NRCS, AR.

Valiantzas, J. D. (1998). Analytical approach for direct drip lateral hydraulic calculation. *Journal of Irrigation and Drainage Engineering, 124*(6), 300-305.

Valiantzas, J. D. (2002). Continuous outflow variation along irrigation laterals: Effect of the number of outlets. *Journal of Irrigation and Drainage Engineering, 128*(1), 34-42.

Yıldırım, G. (2008). Determining operating inlet pressure head incorporating uniformity parameters for multioutlet plastic pipelines. *Journal of Irrigation and Drainage Engineering, 134*(3), 341-348.

Yıldırım, G. (2009). Simplified procedure for hydraulic design of small-diameter plastic pipes. *Irrigation and Drainage (ICID Journal), 58*(3), 209-233.

Yıldırım, G. (2010a). Hydraulic analysis for commercial pipeline design using MathCAD. In G. Hirsch & B. Kappel (Eds.), *Hydraulic Engineering: Structural Applications, Numerical Modeling and Environmental Impacts* (pp. 213-224). Nova Science Publishers.

Yıldırım, G. (2010b). Total energy loss assessment for trickle lateral lines equipped with integrated in-line and on-line emitters. *Irrigation Science, 28*(4), 341-352.

Yıldırım, G. (2012a). Discussion of "Simple method for the design of microirrigation paired laterals on sloped fields" by Shufang Jiang and Yaohu Kang. *Journal of Irrigation and Drainage Engineering, 138*(9), 848-851.

Yıldırım, G. (2012b). Discussion of "Simplified method for sizing laterals with two or more diameters" by Muluneh Yitayew. *Journal of Irrigation and Drainage Engineering, 138*(7), 697-702.

Yıldırım, G. (2014a). Discussion of "Analytical determination of distribution uniformity for microirrigation tapered laterals laid on uphill and horizontal slopes" by Sayed Hossein Sadeghi and Troy Peters. *Journal of Irrigation and Drainage Engineering, 140*(12).

Yıldırım, G. (2014b). Discussion of "Modified G and GAVG correction factors for laterals with multiple outlets and outflow" by Sayed Hossein Sadeghi and Troy Peters. *Journal of Irrigation and Drainage Engineering, 141*(1), Article Number: 07014014.

Yıldırım, G. (2015a). Computer-based analysis of hydraulic design variables for uniformly sloping microirrigation system laterals. *Journal of Irrigation and Drainage Engineering, 141*(7).

Yıldırım, G. (2015b). An assessment for hydraulically efficient design of uniformly sloping submain lines. *Irrigation and Drainage (ICID Journal), 64*(2), 157-168.

Yıldırım, G. (2016b). Discussion of "Statistical analysis of non-pressure-compensating and pressure-compensating drip emitters" by H. Perea, J. Enciso-Medina, V. P. Singh, D. P. Dutta, and B. J. Lesikar. *Journal of Irrigation and Drainage Engineering, ASCE*.

Yıldırım, G. (2023a). Hydraulic principles and design concepts for submain units with multiple outlet pipelines: New analytical techniques with engineering applications. In *Synthesis Lectures on Engineering, Science and Technology* (pp. XXVII, 163). Springer Cham.

Yıldırım, G. (2023b). Review of fundamentals in hydraulic engineering perspective: Hydraulics principles, governing equations, design criteria, types of design problems, hydraulics and energy-gradient line profiles for uniformly sloping multiple outlets pipelines. In *Hydraulic Principles and Design Concepts for Submain Units with Multiple Outlet Pipelines* (pp. 1-XX). Springer Cham.

Yıldırım, G., & Singh, V.P. (2013a). Operating pressure assessment for multi-outlets submains: Ideal hydraulic design. *International Perspective on Water Resources and Environment by ASCE-EWRI (IPWE-2013)*, 7-9 January, 2013, Izmir, Turkey.

Yıldırım, G., & Singh, V.P. (2013b). Operating pressure assessment for multi-outlets submains: Design applications. *International Perspective on Water Resources and Environment by ASCE-EWRI (IPWE-2013)*, 7-9 January, 2013, Izmir, Turkey.

Evaluation of flood propagation dynamics through diffusion wave-based two-dimensional modeling

Hasan O. Marangoz*[1], Tuğçe Anılan[2]

[1]Recep Tayyip Erdogan University, Department of Civil Engineering, 53100 Rize, Türkiye
[2]Karadeniz Technical University, Department of Civil Engineering, 61080 Trabzon, Türkiye

Abstract. This study investigates the failure and flood wave propagation analyses of the Atasu Dam located in Trabzon. The dam failure model and flood wave propagation were evaluated using a two-dimensional modeling approach based on the diffusion wave method. The analyses focused on examining hydrographs generated under different reservoir water levels and detailing the flood wave propagation along the downstream region. Modeling results obtained through the diffusion wave approach evaluated the movement and velocity distributions of the flood wave along the downstream area. The findings demonstrated that the diffusion wave method effectively represents flow velocities and enables the analysis of flood depths in critical regions. This study provides valuable data for flood risk management and emergency response planning.

Keywords: Diffusion wave modeling, Two-dimensional flood analysis, Dam failure, Flood propagation

1. Introduction

Floods resulting from dam failures are among the most catastrophic hydrological disasters, posing significant threats to human life, infrastructure, and the environment. With increasing urbanization and climate variability, the accurate prediction and simulation of flood propagation dynamics have become essential for effective risk management and emergency planning. Numerical modeling tools offer a powerful means to simulate such extreme events, allowing for the assessment of flood extents, depths, and flow velocities under different failure scenarios.

The St. Venant equations govern unsteady open-channel flow and are frequently simplified into various wave models for computational efficiency. Among these, the diffusion wave model is particularly useful in large-scale flood simulations where inertial effects are relatively small compared to gravitational and frictional forces. This model neglects acceleration terms and thus provides a computationally efficient framework for simulating flood wave movements over complex terrains.

Using the St. Venant equations on dam-break cases is now very up-to-date to use (Gaudio et. Al, 2024; Marangoz et. Al., 2022; Adityawan et. Al. , 2023; Dharmawan et. Al., 2024). Dam break events represent some of the most severe and sudden hydrological disasters, capable of releasing vast volumes of water within minutes and causing extensive downstream flooding. Physical factors stem from forces and situations imposed on dams by natural events of floods and earthquakes. (Adamo, 2021). Numerical modeling plays a crucial role in analyzing such scenarios, with two-dimensional shallow water models offering detailed spatial and temporal insights into flood wave dynamics (Jafarzadegan, 2023). As urban areas increasingly encroach upon flood-prone regions, the importance of reliable dam break simulations has grown in flood risk management and emergency preparedness efforts.

In this study, the flood wave propagation resulting from a hypothetical failure of the Atasu Dam, located on the Galyan Stream in Trabzon, Türkiye, is analyzed using a two-dimensional diffusion wave-based hydrodynamic model. The modeling aims to capture the spatial and temporal characteristics of the flood wave as it travels downstream, with a particular focus on critical areas such as urban settlements and industrial zones. The analysis evaluates variations in flow depth and velocity, the effects of topography and river confluences, and the potential risks posed to the city of Trabzon. The results provide a scientific basis for the development of flood mitigation strategies and contribute to improved disaster preparedness.

2. Material and methods

The non-conservative momentum equation of the one-dimensional St. Venant equations is expressed in Equation (1).

* Corresponding author, E-mail: hasanogulcan@gmail.com

https://doi.org/10.31462/icearc2025_ce_hyd_317

$$\frac{\partial u}{\partial t}+u\frac{\partial u}{\partial x}+g\frac{\partial \zeta}{\partial x}+g(S_f-S)=0 \quad (1)$$

This equation consists of five terms, namely: the local acceleration term, convective acceleration term, pressure force term, friction force term, and gravity force term, respectively.

Another derived form of the St. Venant equations is known as the diffusion wave model. In this model, the effects of the inertial terms (i.e., local and convective acceleration) are considered negligible due to their relatively small magnitude compared to the pressure, friction, and gravitational forces. Therefore, the diffusion wave is also referred to as an "inertia-less wave" (Vreugdenhil, 1986). As a result, the St. Venant equations are simplified and expressed in the form of Equation (2), representing the flow characteristics.

$$g\frac{\partial \zeta}{\partial x}+g(S_f-S)=0 \quad (2)$$

The kinematic wave model is another derived form of the St. Venant equations. In this approach, it is assumed that the flow is uniform and that the channel bed is nearly parallel to the free water surface. Due to this assumption, the pressure force term is neglected from the general equation. The kinematic wave model is applicable in cases where the changes in wave height and velocity over distance and time are negligible, typically under steep bed slopes (Vreugdenhil, 1986). A representative example of this situation is the flow of a shallow stream over a highly sloped terrain (Novak et al., 2010).

3. Results

The maximum flood depths reached up to 30 meters in the main channel and 18 meters in the floodplain of the Galyan Stream, where the dam is located. At the confluence with the Değirmendere Stream, the maximum recorded water depth was approximately 17 meters. A negative wave effect was also observed upstream of the confluence point between the Galyan and Değirmendere Streams. The flood wave was seen to move upstream over a distance of approximately 1,400 meters (Fig. 1). During this period, the maximum water depth in the main channel rose to about 16 meters, while in the floodplain it reached approximately 11 meters.

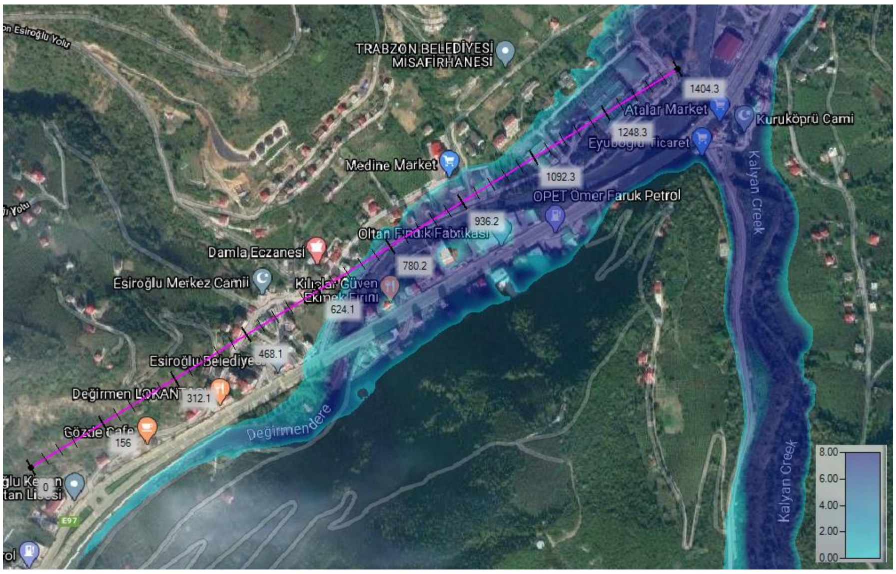

Fig. 1. Negative wave effect at the confluence of Galyan Stream and Değirmendere Stream

During the downstream propagation of the flood wave, the flood depth values along the river centerline were illustrated in Fig. 2. On the horizontal axis, the starting point of the river centerline represents the location closest to the dam axis, while the endpoint corresponds to the section located within the sea.

An analysis of flood elevations along the river centerline shows that the maximum flow occurred in areas closest to the dam axis throughout the simulation. In this region, the flood wave exhibited rapid surges and recessions. From meter 2573, the flow direction shifted toward the Değirmendere Stream. Along this section, the flood wave gradually decreased in height up to a height of 8413. Following this, the wave height began to increase again along the Değirmendere Stream, reaching a maximum flood elevation of 25.4 meters at meter 11968. In the urban center, the maximum observed flood height was 14 meters.

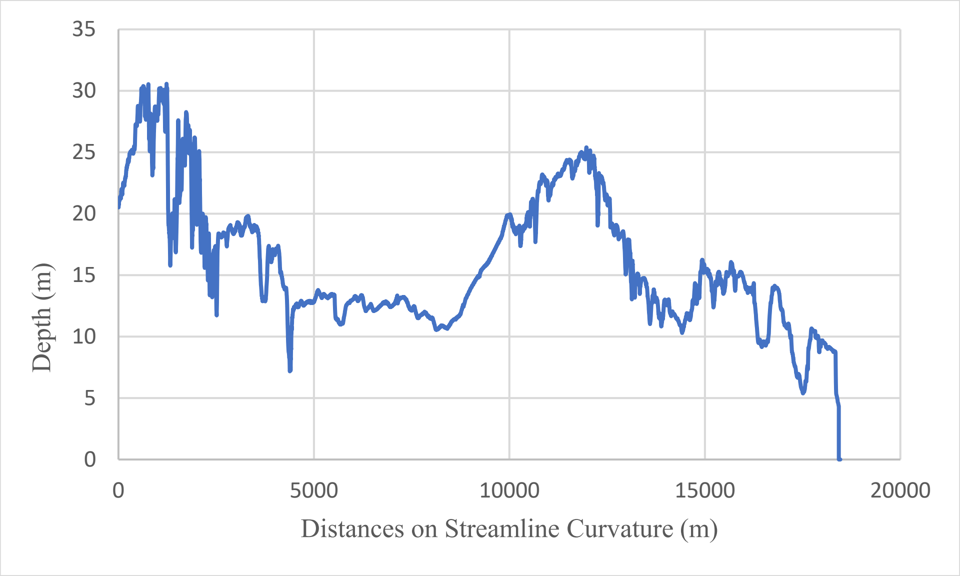

Fig. 2. Maximum flood wave depths along the river centerline

The maximum flood velocities along this centerline were recorded at 24 m/s. At the time of the dam failure, flow velocities along the Galyan Stream ranged between 17–23 m/s. In the confluence area of Galyan Stream and Değirmendere Stream, the flood propagation velocity was recorded as 5.63 m/s. Between 1000 and 2872 meters along the river centerline, the flood wave velocities varied between 3 and 13 m/s. In the city center, the maximum velocity along the main channel was observed to be 12.7 m/s, with an average velocity of 7.45 m/s.

Given the high population density and the presence of numerous industrial and commercial structures, capturing flood behavior within the urban center is of critical importance. The area designated as the city center, extending from meter 16,256 of the river centerline to the sea, includes 11 observation points randomly distributed. Real-time flood depth values were obtained at these locations.

The first flood wave reached the city center at the 28th minute, with a depth of 12.39 meters. By the 31st minute, the wave, now at 3.5 meters deep, had reached the sea for the first time. The maximum lateral spread of the flood wave in the city center was calculated as 1.93 kilometers. Fig. 3 presents the maximum flood extent in the urban area using a water depth color map. The flood propagation map obtained for the city center is presented in Fig. 3.

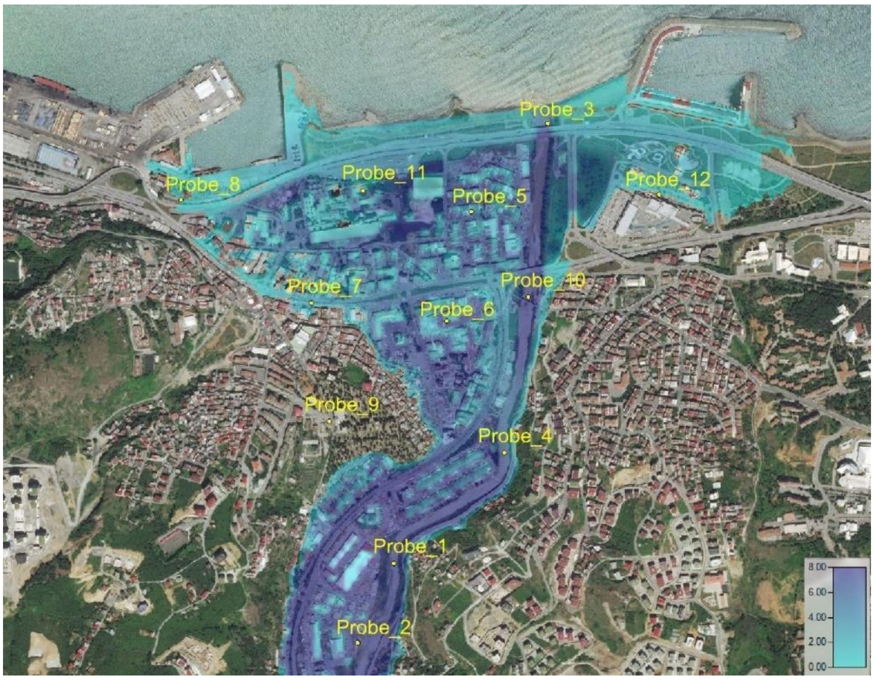

Fig. 3. Probe points placed in the city center and flood propagation extent

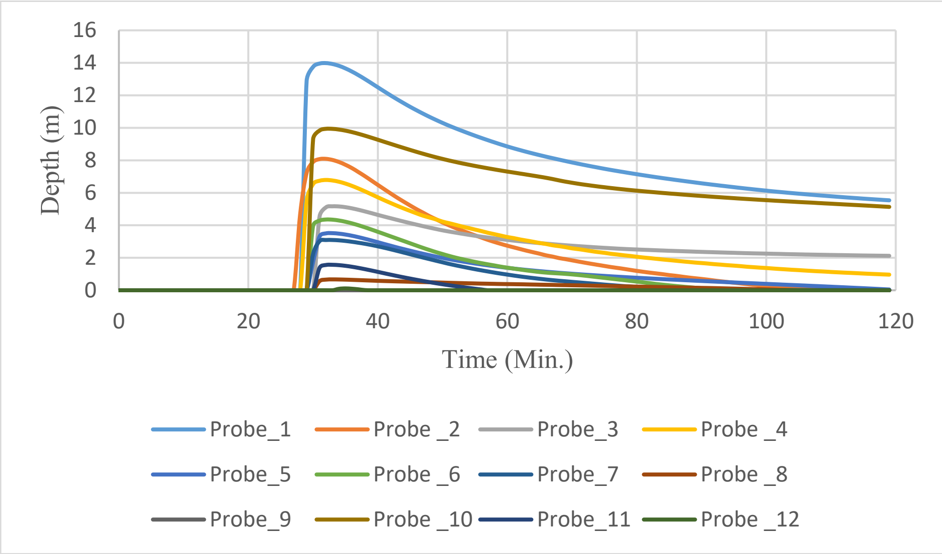

Fig. 4. Flood depth values at probe points located in the city center

As a result of routing the dam-break hydrograph at the dam axis downstream using the diffusion wave method, the flood water depths obtained at 12 observation points (probes) in the city center are illustrated in Fig. 4.

An analysis of the flood water levels recorded at the observation points in the city center revealed that the maximum value was observed at Probe_1, reaching 13.9 meters at the 32nd minute. Probe_9 recorded the lowest depths, indicating almost no noticeable flow at that location. Additionally, the flood depths at Probe_12 (0.11 m), Probe_8 (0.67 m), and Probe_11 (1.57 m) were considered negligible. At Probe_3, located near the point where the flood wave met the sea, the maximum wave height was 5.17 meters, recorded at the 33rd minute. To assess the lateral spread of the flood wave toward the west, Probe_8 was placed, where the recorded wave height was limited to 0.67 meters, suggesting a significant decrease in flood propagation in that direction. Probe_5, Probe_6, and Probe_7, located in densely built-up zones, recorded maximum water depths of 3.52 m, 4.36 m, and 3.1 m, respectively. The peak arrival times for these points were observed within 2 to 3 minutes of the initial flow contact.

The time-dependent advancement of the flood wave in the city center, along with its maximum velocity distribution, is shown in Fig. 5. Following the dam failure, the flood wave reached the city by the 27th minute, with a maximum velocity of 16.34 m/s along the main channel and up to 24 m/s in the floodplain. Because the water in the floodplain moved faster than in the main channel, it was observed to be 121 meters ahead of the main channel flood wave at that time. By the 28th minute, the wave had reached meter 16,775 of the river centerline and began to slow down upon encountering buildings. Consequently, the wave, with a maximum velocity of 14.14 m/s in the main channel, split into two branches in the floodplain, continuing at 13.17 m/s and 14 m/s. At minute 29, the wave rapidly spread into the city between buildings, with its front completely separating from the main channel. In the westernmost branch, the velocity reached 14.30 m/s, while in other branches (from left to right), the recorded maximum velocities were 21.45 m/s and 15.53 m/s, respectively.

At the 30th minute, the flood wave experienced its fastest expansion, covering most of the city center. The analysis showed that buildings in the city center created a corridor-like environment that channeled and accelerated the flow into multiple directions. The maximum distance between the main channel flood front and the urban flood front exceeded 90 meters. At that moment, the maximum velocity of the flood front in the main channel was 8.11 m/s, while the velocities in the side branches, though highly irregular, reached up to 14 m/s. By the 31st minute, the boundaries of the flood wave within the urban area were fully formed.

By the 41st minute, the flood wave had advanced westward as far as the Toprak Mahsulleri Office building, where the maximum velocity in the area was recorded at 6.1 m/s. As the wave reached the Trabzon Port, the flow velocities were observed to be negligible. On the eastern side, the flood extent reached as far as the fishing harbor and slipway area, located 440 meters west of Ahmet Suat Özyazıcı Stadium. In this region, the maximum velocity was approximately 9 m/s over an area of around 5 square meters. Consequently, in the shopping mall courtyard, which is one of the most frequently populated areas in the city center, the flood velocities remained negligible. After the 31st minute, both the velocity and depth of the flood wave in the city center showed a general decreasing trend until the end of the analysis period.

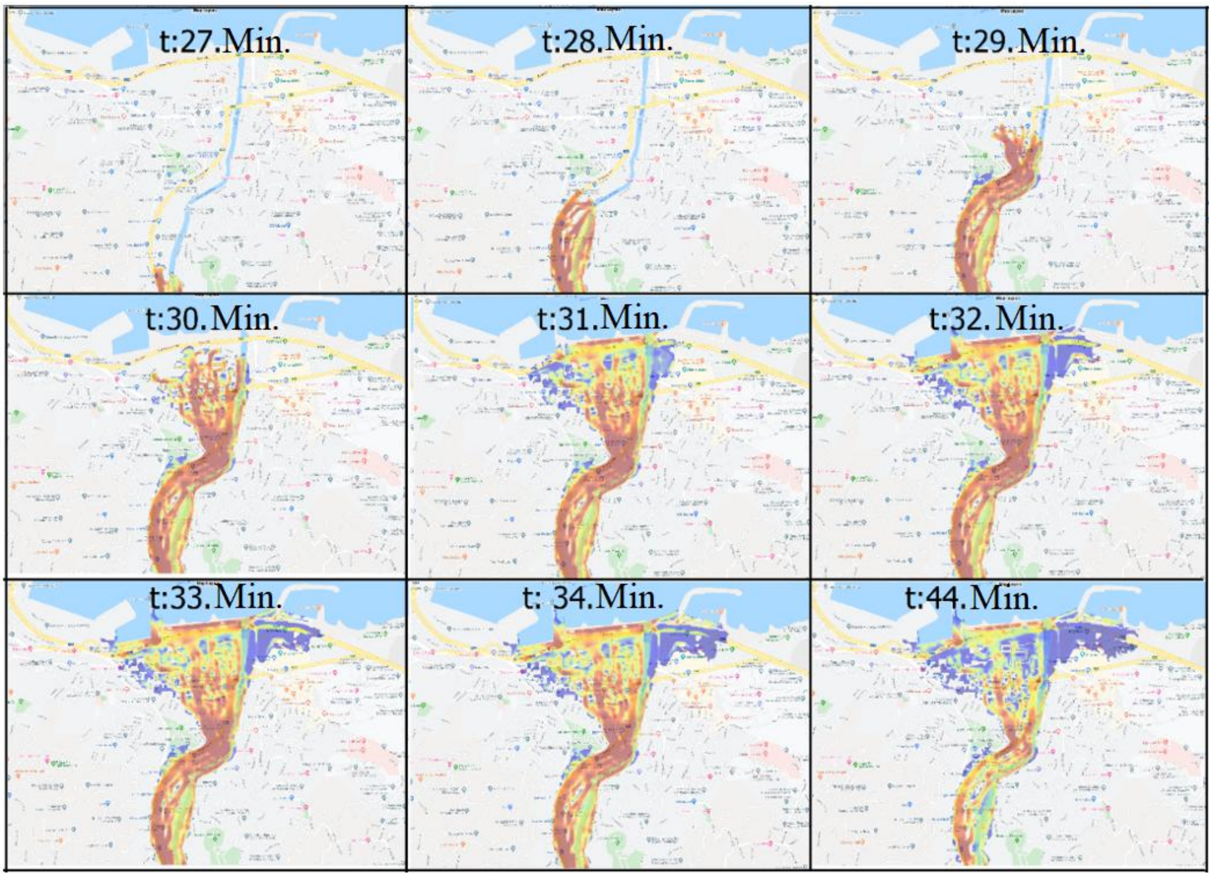

Fig. 5. Flood extents and flow velocities in the city center

4. Conclusions

In this study, a potential dam-break scenario for the Atasu Dam was simulated using a two-dimensional diffusion wave-based hydrodynamic model. The results revealed that the flood wave reached a maximum depth of 30 meters in the main channel and 18 meters in the floodplain along the Galyan Stream. At the junction with the Değirmendere Stream, a negative wave effect was observed, extending up to 1,400 meters upstream.

The model indicated that in the urban center of Trabzon, the initial flood wave arrived at the 28th minute with a depth of 12.39 meters, reaching its maximum depth of 13.9 meters at Probe_1 by the 32nd minute. The flood wave exhibited a maximum lateral spread of 1.93 kilometers, with flow velocities peaking at 24 m/s in the floodplain and averaging 7.45 m/s in the city center. These values underscore the destructive potential of such an event, particularly in densely built-up and populated areas. Moreover, the flood front reached the port area with negligible velocities, while on the eastern side, it extended close to the Ahmet Suat Özyazıcı Stadium with local velocities around 9 m/s. The model also demonstrated how urban structures act as corridors, accelerating and redirecting the flood wave into multiple branches, increasing both spatial spread and hazard complexity.

Overall, the diffusion wave model effectively captured the spatial-temporal dynamics of the flood event and identified critical locations requiring priority in emergency response planning. These results can support authorities in developing more robust flood mitigation strategies and urban resilience frameworks against dam failure scenarios.

References

Adamo, N., Al-Ansari, N., Sissakian, V., Laue, J., & Knutsson, S. (2021). Dam safety: hazards created by human failings and actions. *Journal of Earth Sciences and Geotechnical Engineering, 11*(1), 65-107

Vreugdenhil, C.B. (1986). Numerical Methods for Shallow-Water Flow. Water Science and Technology Library.

Novak, P., Guinot, V., Jeffrey, A., & Reeve, D.E. (2010). Hydraulic modelling – an introduction: Principles, methods and applications. Spon Yayınları, ISBN: 9780419250203

Marangoz, H.O., & Anilan, T. (2022). Two-dimensional modeling of flood wave propagation in residential areas after a dam break with application of diffusive and dynamic wave approaches. *Natural Hazards, 110*(1), 429-449

Del Gaudio, A., La Forgia, G., Constantinescu, G., De Paola, F., Di Cristo, C., Iervolino, M., ... & Vacca, A. (2024). Modelling the impact of a dam-break wave on a vertical wall. *Earth Surface Processes and Landforms, 49*(7), 2080-2095

Dharmawan, K., Swastika, P.V., Gandhiadi, G.K., & Pudjaprasetya, S.R. (2024). A non-hydrostatic model for simulating dam-break flow through various obstacles. In *Mendel* (Vol. 30, No. 1, pp. 33-42)

Jafarzadegan, K., Moradkhani, H., Pappenberger, F., Moftakhari, H., Bates, P., Abbaszadeh, P., ... & Duan, Q. (2023). Recent advances and new frontiers in riverine and coastal flood modeling. *Reviews of Geophysics, 61*(2), e2022RG000788

4th International Civil Engineering & Architecture Conference
17-19 May 2025, Trabzon, Türkiye

Experimental and numerical study of the influence of bridge pier skew angle on dam break flood flow and impact force

Kutsi S. Erduran [1], Olusola O. Adekoya*[1], Uğur Ünal[1]

[1] Niğde Ömer Halisdemir University, Department of Civil Engineering, 51240 Niğde, Türkiye

Abstract. This study aims to investigate the influence of bridge pier skew angle and varying reservoir water depth on dam-break-induced flood flow and the resulting impact forces on bridge pier through experimental and numerical methods. Experiments were conducted in a 10 x 0.309 x 0.45 m horizontal rectangular channel of the Civil Engineering Department of Niğde Ömer Halisdemir University. Square bridge pier with blockage ratios of 0.129, 0.159, 0.177 and 0.183 corresponding to 0^0, 15^0, 30^0 and 45^0 skew angles was positioned 1.24 m downstream of the dam site (gate). Flow depth and the impact force time variations were measured using Image Processing Technique and a 6-Axis USA ATI Mark GAMMA model SI-32-2.5 load cell respectively. Numerical simulations, using Flow 3D, replicated experimental conditions and comparative analysis were conducted. The results reveal that the time to peak flow depth decreased with increase in reservoir depth. A maximum drop of 31 % was recorded between 15 and 25 cm for 15^0 skew angle. Higher skew angles also produced slightly lower times to peak depth, the maximum in this case was 10 % drop between 0^0 and 30^0 at 20 cm reservoir depth. Increase in force intensity generally ranged between 26.9 and 22.3 % and a maximum of 14 % increase in maximum impact force resulted from increasing skew angle. This study provides an understanding of the relationship between skew angle, flow dynamics, and force distribution, offering valuable insight for the design of bridge piers in dam-break-prone areas.

Keywords: Dam-break; Skew angle; Impact force; Bridge pier

---

1. Introduction

The sequence of dam failure occurrences recorded in very recent times and their damaging consequences on communities, buildings and infrastructures, highlight the need for potential damage evaluation towards improved design of resilient infrastructures. Dam break induced flow resulting from sudden removal of a dam (gate) idealises this critical hazard since real case data are difficult to obtain (Ozmen-Cagatay & Kocaman, 2011; Hu et al., 2018; Erduran et al., 2024). More so, dam break induced flow waves have been used as analogue for tsunami bore in several studies due to the similarities in their hydrodynamic characteristics and impact mechanisms (Nouri et al., 2010; Chen et al., 2020; Elsheikh et al., 2022; Gaudio et al., 2022; Yang et al., 2022; Mu et al., 2023; Zhou et al., 2024). Accurately predicting the characteristics and the flow-structure interaction of this flow is therefore essential for designing resilient hydraulic and coastal structures.

A lot of theoretical, experimental, and numerical research effort has gone into the study of the dynamics of dam break flow over the years. Analytical solutions based on shallow water equations (Ritter, 1892; Dressler, 1952; Hogg & Pritchard, 2004; Chanson, 2005 and 2009), provide data on wave front velocity and evolution of water profile. Nevertheless, these solutions generally does not cover impact forces on structures. This gap was addressed by the application of the momentum-based force estimation techniques like the zero-gravity similarity model (Cumberbatch, 1960), the hydrodynamic and hydrostatic force decomposition approach (Cross, 1967) as well as the momentum flux conservation method (Raju et al., 1983), but these models have been shown to overestimate impact forces when compared to experimental data (Kihara et al., 2015).

Experimental studies have, however, provided valuable insights into the dynamics of dam-break induced flow (Lauber and Hager, 1998a; 1998b; Leal et al., 2006). The effect of channel downstream geometry (Frazão & Zech, 2002; Chen et al., 2019; Zhang et al., 2022), and the effect of reservoir geometry (Feizi Khankandi et al., 2012; Hooshyaripor & Tahershamsi, 2015) on flow characteristics have been extensively studied. So also, is the influence of the presence of various types of obstacles (Soares-Frazão & Zech, 2007; Ozmen-Cagatay & Kocaman, 2011; Feizi, 2018; Saghi & Lakzian, 2019; Chumchan & Rattanadecho, 2020; Kocaman et al., 2020; Ansari et al., 2021; Gaudio et al., 2022; Maghsoodi et al., 2022; Vosoughi et al., 2022). Measurements of flow depth time history, free

*Corresponding author, E-mail: olusolaolusegun.adekoya@mail.ohu.edu.tr

https://doi.org/10.31462/icearc2025_ce_hyd_408

surface profile, velocity fields and impact pressures were provided by these studies. Recent developments in computational fluid dynamics have facilitated reliable modelling of dam-break flow, hence all the studies on the effect of various types of obstacles were numerically simulated and validated with experimental data using Eulerian; Reynolds-averaged Navier–Stokes (RANS) (Kocaman et al., 2020) and/or Lagrangian; Smoothed Particle Hydrodynamics (SPH) approaches (Ansari et al., 2021).

Understanding the fluid-structure interaction is crucial for assessing possible direct damage to structures and developing efficient design techniques, in addition to precisely forecasting flow evolution (Aureli et al., 2015). To this end, Aureli et al. (2015) conducted an experimental study on the impact of dam break wave against a rigid squat structure, measuring the impact force directly by using a load cell. Three numerical models were then validated by the experimental data. The influence of cylinder cross-section on dam break impact force was investigated by Kamra et al. (2019). They analysed the pressure signal on the cylinder as well as the vertical wall downstream of the cylinder (closed end of the channel). The impact of the obstacle (cylinder) on the impact pressure was evaluated by comparing the pressure induced on the wall with and without the obstacle in place. The square cylinder was found to obstruct the flow momentum in the x-direction more than the circular cylinder. This experimental work was used to validate the numerical model developed by Mu et al. (2023). They extended the study to numerically simulate the effect of impacting angle in a enclosed channel. The study concluded that the total force on the square cylinder was almost 2 times that of circular cylinder. The instantaneous surge height and dynamic pressure of a dam break surge on a vertical wall with different reservoir depths was experimentally investigated by Liu et al. (2022). They result indicated that the dynamic pressures at the instant of impact were roughly 3 times the equivalent static pressure in the bed and the highest surge run up heights on the wall were between 2.1 and 2.3 times the equivalent initial reservoir water depths. The effect of vertical wall inclination on the impact load of dam break induced surge was also studied by Li and Liu (2024) and they found that the breaking wave loads on non-vertical walls were underestimated by the calculation approach being used for design of induced maximum horizontal force. While these studies provide detailed force distributions, their application has been majorly restricted to perpendicular flow-structure interactions. Studies on the effect of the obstructing structure orientation on impact force which are possible scenarios involving dam break waves striking bridge pier or tsunami waves hitting coastal structures at oblique angles are limited.

Even though there are a good number of studies on dam-break flow impacts, the effect of obstacle impact angle on wave impact force is not well established. Most of the studies assumed perpendicular impact angle without considering the effect of impacting angle, refers to as skew angle in this study. This is possible in reality with possible alteration to flow separation, impact pressure and force coefficients. Understanding these effects is essential towards an enhanced engineering design.

This study, therefore, investigates the effect of bridge pier skew angle and varying initial reservoir water depth on the hydrodynamic loading induced by dam break flow wave on a square bridge pier. Numerical model was used to simulate the experimental setup, and the resulting numerical data were validated using the result of the experimental study. The study aims to provide an understanding of the relationship between skew angle, flow dynamics, and force distribution, offering valuable insight for the design of bridge piers in dam-break-prone areas.

2. Material and method

2.1. Experimental setup

The rectangular cross-sectional channel of the Civil Engineering Department Hydraulics Laboratory, Niğde Ömer Halisdemir University measuring 100 x 30.9 x 45 cm was used for this study (Fig. 1). The channel was divided into two sections using a 1.1 cm thick plexiglass gate as illustrated on Fig. 2. The upstream section was the reservoir with the gate positioned 44.05 cm away from the channel inlet. The gate is vertically movable with the aid of a 10 kg load connected to the gate through a pulley system that was fixed to the ceiling directly above the channel at the position of the gate.

The bridge pier was positioned 124 cm downstream of the gate and this distance was maintained for all cases regardless of the skew angle. This position was chosen after conducting several experimental and numerical tests to ensure that the shock wave was fully developed before impacting the bridge piers. Both the experimental and numerical models indicated that the shock wave was fully developed as at 70 cm away from the gate. The size and positioning of the bridge pier model is as indicated in Fig. 3. 0^0, 15^0, 30^0 and 45^0 skew angles with 0.129, 0.159, 0.177 and 0.183 blockage ratios were studied.

A camera with a video recording speed of 30 frames per second (FPS) was positioned such that it captured the flow propagation from the gate to the bridge pier and extended few metres beyond the pier (Fig. 2) This was possible because the channel walls are transparent. Table 1 outlines the experimental runs, and the experimental ID adopted in this study.

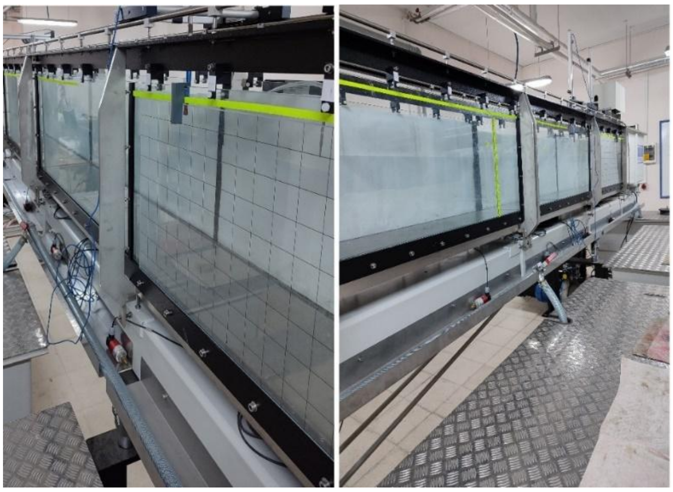

Fig. 1. The experimental channel

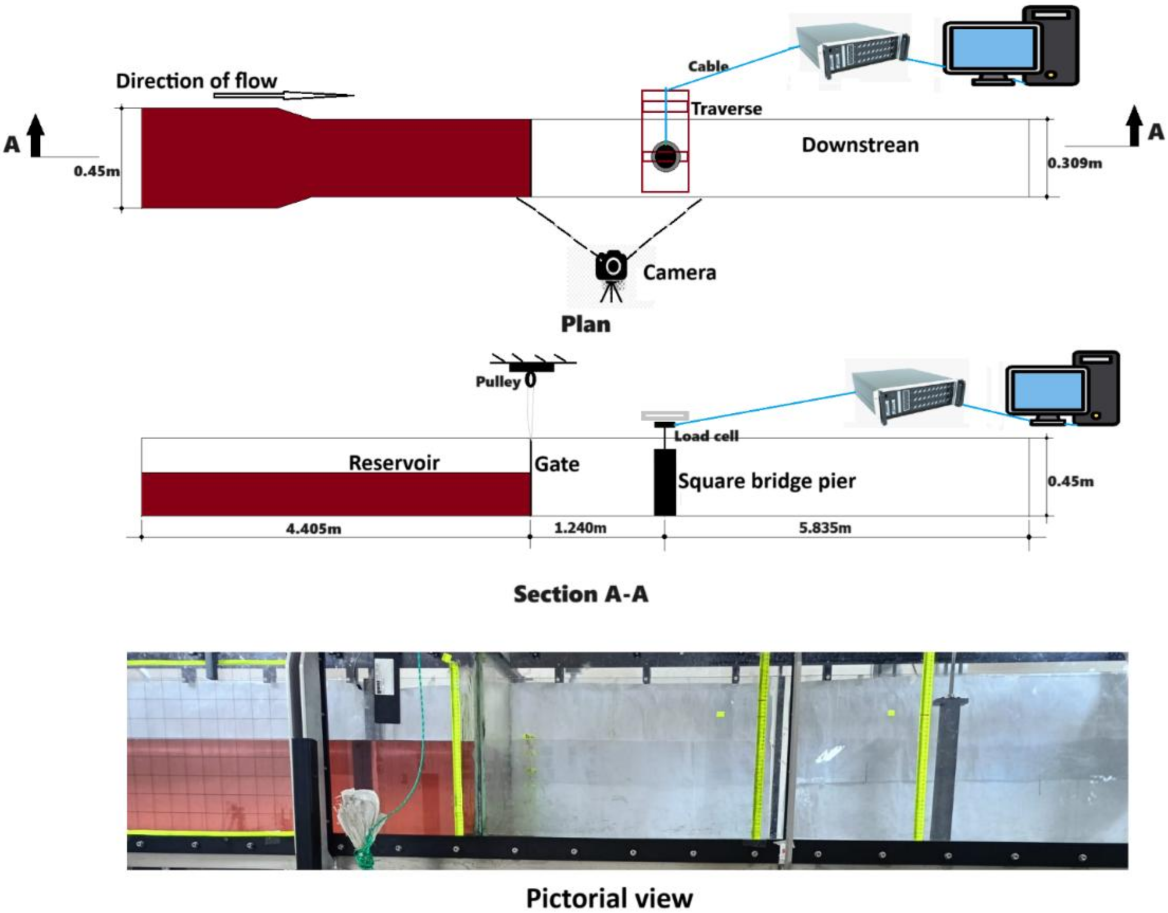

Fig. 2. The experimental setup showing the plan, cross sectional and pictorial view

2.1.1. Flow depth measurement

The advancements in science of fluid mechanics remains the bases for a true understanding of the qualitative data provided by images of flow visualization (Gharib et al., 1985). The correctness of such qualitative data is often determined by the use of quantitative tools like acoustic doppler velocimetry and water level gauges, but these methods are limited to data sampling at few spatial positions. This then explain the need for a quantitative flow visualization technique since it is capable of delivering both spatial and temporal data simultaneously in an accurate and non-intrusive manner (Ozmen-Cagatay & Kocaman, 2011). The image processing technique (IPT) adopted in this study is a form of quantitative flow visualization technique. It is used for the measurement of time history of flow depth at specific positions along the channel as well as for free surface profile measurements for the entire duration of the experiment. Following the works of Erduran et al. (2019), Erduran et al. (2024a) and (2024b) a python code was written by the authors to process the images obtained from the video recordings of the experiments. The IPT procedure is fully described in Erduran et al. (2024b). For this study, time history of flow depth at the upstream face of the bridge pier was digitized over a period of 20 s. This indicates that the code processed a total of 600 frames (30 FPS x 20 s) and output the flow depth at every 0.0333 s for every experimental run.

2.1.2. Impact force measurement

The bridge pier was attached to a load cell, and both were held in position by a 61 x 61 cm ranged Dantec 41T32 model traverse system as show in Fig. 4. A 6-Axis USA ATI Mark GAMMA model SI-32-2.5 load cell with a maximum Fx and Fy capacity of ±32 N and maximum Fz capacity of ±100 N was used for impact force measurement. The precision rating of the load cell at Fx, Fy and Fz is ±0.75%, ±1%, and ±0.75% respectively. To ensure that the impact force was entirely transmitted to the load cell, the bridge pier was positioned such that it was hanging at a few millimetres above the bottom of the channel. Data were transmitted from the load cell to the PC through a NI PCle-6323 DAQ card data acquisition system. The system has 32 single ended analog-to-digital converter channels with a maximum sampling frequency of 250 kHz (Fig. 4). Nevertheless, measurements were taken for this study at a sampling rate of 1000 Hz. for a period of 30 seconds. Hence, a minimum of 30,000 sample values were recorded for each test run and this was repeated 3 times. The average value of the 3 tests at every 0.001 s was computed and used for analysis to reduces the influence of random error and improve precision.

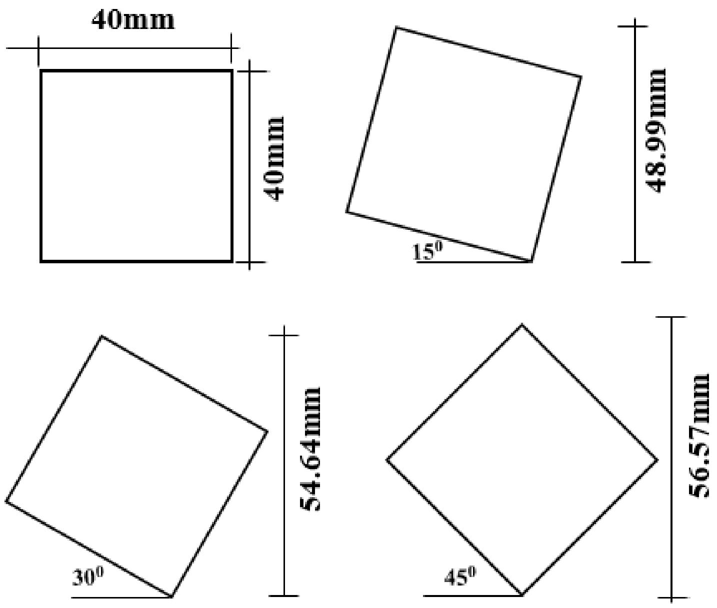

Fig. 3. Bridge pier blockage length variation with increasing skew angle

Table 1. Experimental outline

Skew angle	Reservoir depth (cm)	Experiment ID	Repetition
0^0 (0D)	15 (H15)	0D_H15	3
	20 (H20)	0D_H20	3
	25 (H25)	0D_H25	3
15^0 (15D)	15 (H15)	15D_H15	3
	20 (H20)	15D_H20	3
	25 (H25)	15D_H25	3
30^0 (30D)	15 (H15)	30D_H15	3
	20 (H20)	30D_H20	3
	25 (H25)	30D_H25	3
45^0 (45D)	15 (H15)	45D_H15	3
	20 (H20)	45D_H20	3
	25 (H25)	45D_H25	3

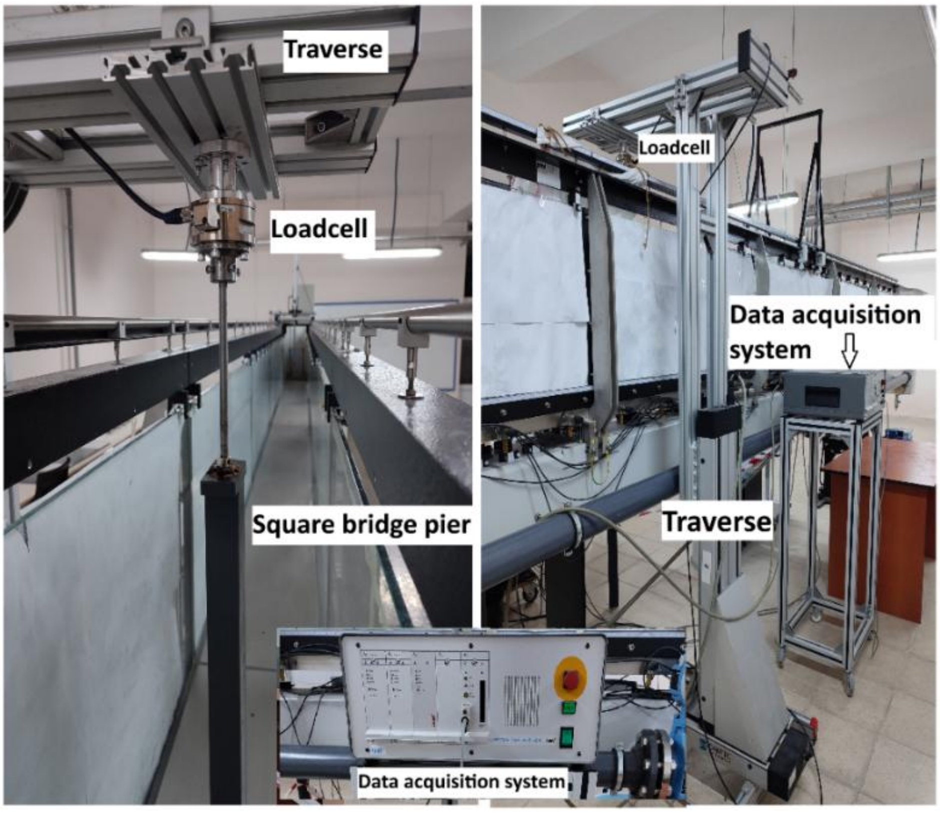

Fig. 4. Pictorial view of setup for Impact force measurement

2.2. Numerical models

The numerical study was carried out using a commercial software, Flow 3D. The software solves the RANS equation using the finite volume method (FVM) in a cartesian, staggered grid and tracks fluid surface using the Volume of Fluid (VOF) method. The program uses the fractional area/volume obstacle representation (FAVOR) method, which is a cell porosity technique, to model the geometry of structures within the computational domain (Ozmen-Cagatay & Kocaman, 2011; Hu et al., 2018; Erduran et al., 2024a).

The experimental setup described in section 2.1 was replicated. The computational domain was defined as 800 cm long, 30.9 cm wide and 45 cm high. A 440.5 cm long reservoir length was defined as initial condition with three initial reservoir water depth of 15 cm, 20 cm and 25 cm. A dry downstream condition (0 cm water depth) was defined for the downstream section of the computation domain (channel). A (4 x 4 x 37) cm square bridge pier was generated and positioned 124 cm downstream of the gate at the various skew angles.

The channel side walls (Y_{min} and Y_{max}) as well as the channel bed (Z_{min}) were defined as walls. So also was the upstream boundary (X_{min}) but the downstream boundary (X_{max}) was set as outflow since the downstream end of the computation domain was open. All sections connecting two cell blocks between the upstream (X_{min}) and downstream boundaries (X_{max}) were set as symmetry to ensure that the flow properties (velocity, pressure, etc.) remained consistent across these boundaries. The upper boundary (Z_{max}) was also set as symmetry in order to account for effect of the atmospheric pressure on the free water surface.

2.3 Validation and repeatability.

Lauber and Hager (1998a) introduced a criterion (Equation 1) which defines the maximum gate opening time for an instantaneous dam-break in a rectangular channel with dry downstream conditions (Yang et al., 2020) . The criterion was satisfied in this study. At 15, 20 and 25 cm reservoir water depths, the recorded gate opening times were 0.1166, 0.1332, 0.1499 and 0.1665 s respectively. These values are below the limit recommended by (Lauber & Hager, 1998a) which are 0.1262, 0.1546, 0.1785 and 0.1995 s for 10, 15, 20 and 25 cm reservoir water depths respectively. This criterion ensures that experimental models accurately represent real-world dam break scenarios. Haven satisfied the criterion; it could be said that the experimental model is validated.

$$t_{op} \leq 1.25\sqrt{h_o/g} \tag{1}$$

where t_{op} is the gate opening time, h_o is reservoir water level, and g is the gravitational acceleration.

The test cases were repeated three times to validate the repeatability of the experiment and the time history of the forces were compare (Fig. 5) for 0D_H15, 15D_H15, 30D_H15 and 45D_H15. The result indicated a similarity in trend for the three texts.

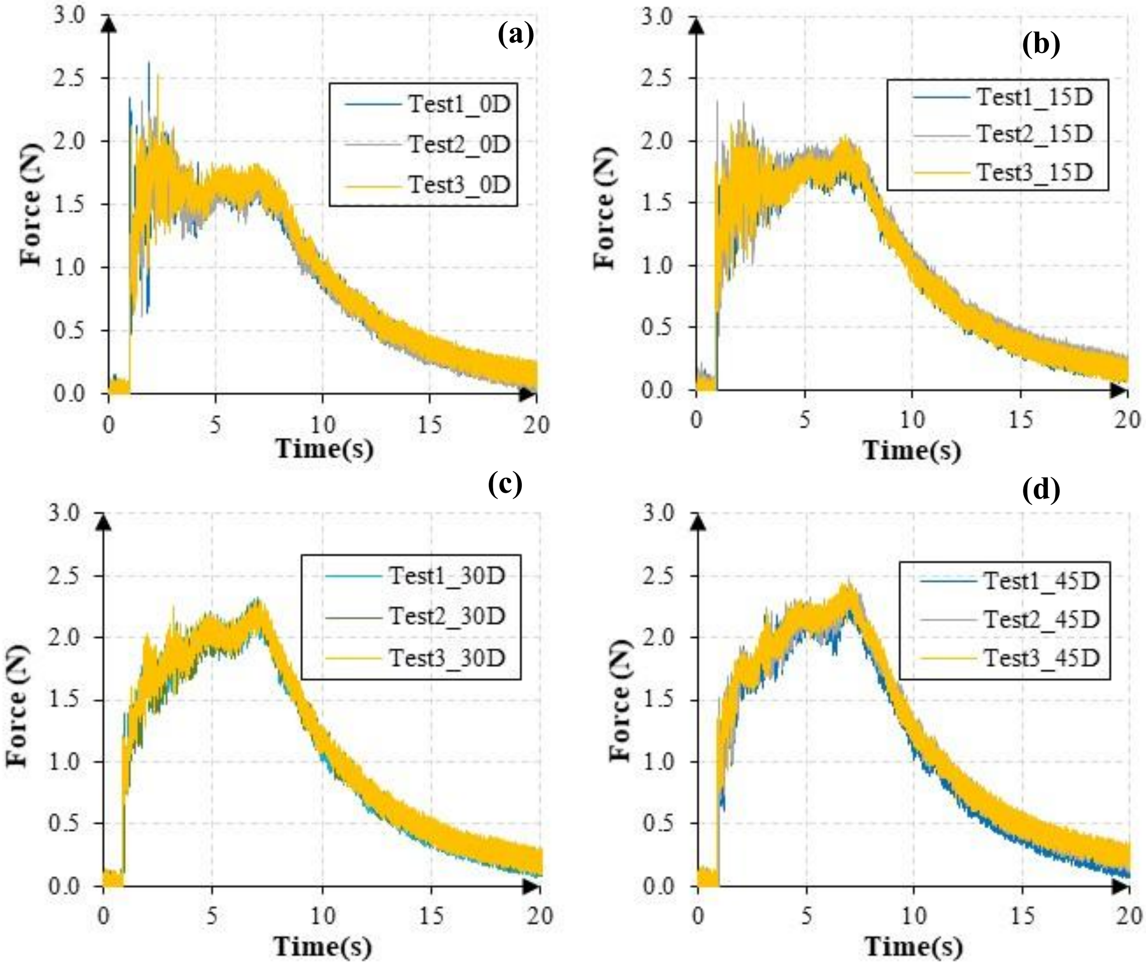

Fig. 5. The time history of the impact force for three repeated tests at: a) 0D b) 15D c) 30D d) 45D skew angles for H15

3. Results and discussion

3.1 Flow depth variation

The time-history of the flow depth near the upstream face of the square bridge pier for the various skew angles are shown in Fig. 6. The result reveals that at the initial stage, the flow depths started at a baseline, but as time increases, flow depth diverges based on the initial reservoir water depth. The rate of increase in flow depth was observed to depend on the reservoir water depth. The higher the reservoir water depth, the higher the rate of increase in flow depth. It could be said that the depth of flow upstream of the bridge pier is influenced by both initial reservoir depth and skew angle of the square bridge pier. The results further reveals that the time to peak flow depth decreases with increase in reservoir depth. A maximum drop of 31% in time to peak flow depth was recorded between 15D_H15 and 15D_H25. The effect of increasing skew angles also leads to slight decrease in the times to peak flow depth, the maximum in this case was 10 % drop between 0D_H20 and 30D_H20 reservoir depth.

3.2. Impact force

The time variation of the force induced on the bridge pier by the shock wave is shown in Fig. 7. The four plots show similar trend: an initial sharp increase in force (initial impact) followed by a peak, and then a gradual decay. The highest force was observed at H25 for all cases indicating a correlation between the initial reservoir water depth and the force. That is, an increase in the initial reservoir water depth leads to an increase in force. This is consistent with the result of the flow depth.

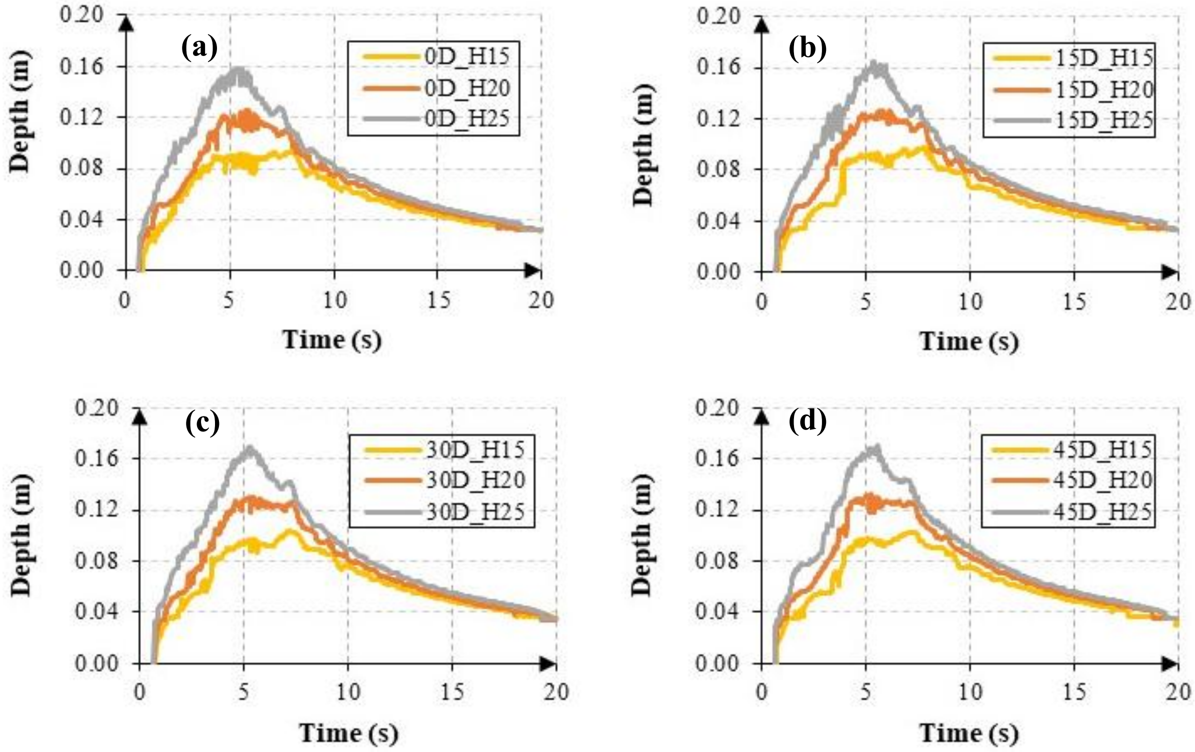

Fig. 6. The time variation of flow depth at: a) 0D b) 15D c) 30D d) 45D

The effect of the increase in skew angle on this trend shows a decrease in initial impact force. The impinging force is due to the initial impact of the shock wave influenced by the wave front celerity. This force is more pronounced at H25, however, it is mostly less than the subsequent hydrodynamic force. At 0D, it was observed that this force played a dominant role in the recorded peak force, hence, the peak force occurred earlier in 0D case when compared with other cases. The maximum total longitudinal and transverse forces caused by the first impact were considered in the study of (Mu et al., 2023) to avoid the influence of second impact resulting from the return wave induced by the right wall (enclosed channel). Hence the influence of backwater build-up was neglected. This explains the continuous decrease in peak force relative to the increase in impact angle (skew angle) in their study. According to Fig. 7, at higher skew angles, the influence of the impinging force (first/initial impact) reduces while the influence of the backwater build-up played the dominant role in the peak force value. Hence the delay in time to peak force at this skew angles. It can be observed in Fig. 8, that the peak force initially dropped at 15D with the largest drop being 12.19 % at H25. This followed the trend reported by (Mu et al., 2023). Then, it increased with increase in skew angle regardless of the reservoir water depth. Beyond 15D, maximum quasi-hydrostatic force corresponding to the build-up of backwater upstream of the bridge pier played the dominant role. In all the cases, the highest peak forces were recorded at 45D resulting in 1.1461, 1.0033 and 1.0062 times the force recorded for H15, H20 and H25 respectively at 0D. Although, the shape of the upstream face of the bridge pier at 45D allows for lower flow separation (Keshavarz et al., 2022), this result could be attributed to increase in blockage ratio and the corresponding build-up of backwater upstream of the bridge pier.

The force intensity was calculated as the arithmetic mean of the forces over a period of 20 s (or time averaged force). This represents a steady and constant component of the force over the period of study and reflects the average force induced on the structure by the flow. The result indicates that the highest recorded changes in force intensity were at 45D_H15, 45D_H20 and 45D_H25, which were 26.91 %, 25.02 % and 22.3 % more than the case at 0D_H15, 0D_H20 and 0D_H25 respectively. According to Fig. 9, there exist an almost perfectly linear relationship between the force intensity and reservoir water depth at the various skew angles.

Fig. 10 shows the influence of the skew angle on the time to peak force. It could be seen that at lower reservoir water depth, the impact of the skew angle was significant in delaying the time to peak force. A maximum of 3.29, 2.67 and 2.52 times the time to peak force at 0D was recorded at 15D, 30D and 45D respectively. This impact was also observed to reduce as the reservoir water depth increased.

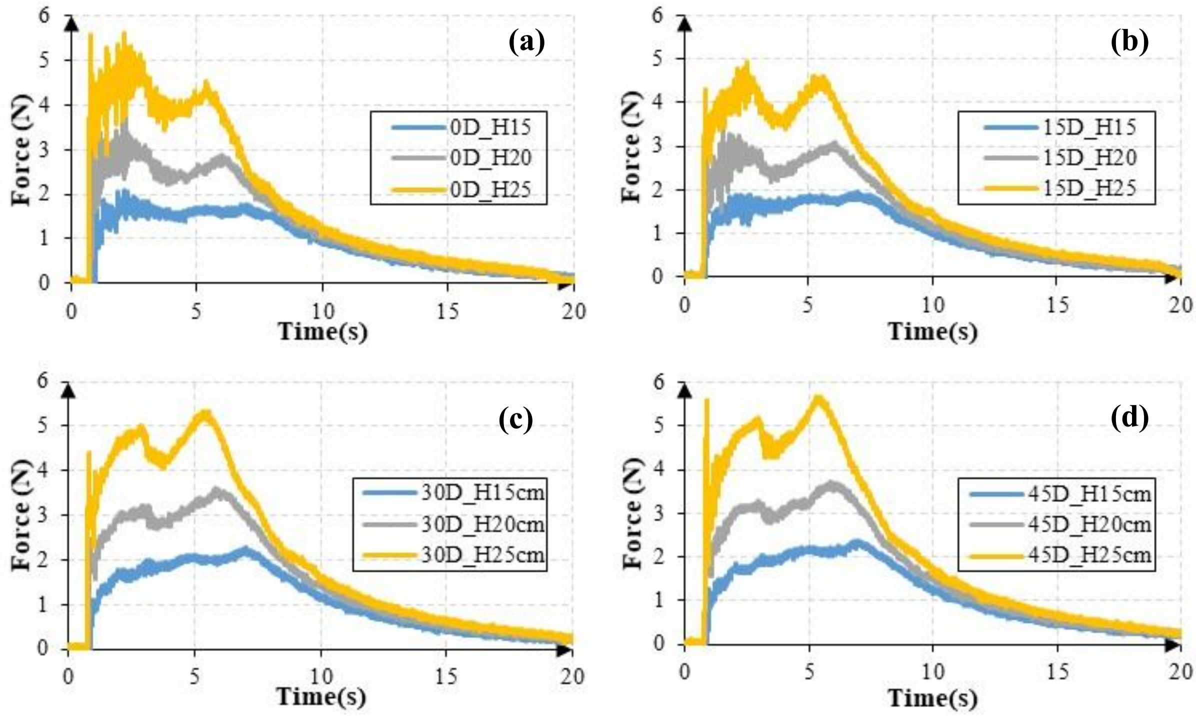

Fig. 7. Time variation of impact force with increasing reservoir water depth at: a) 0D b) 15D c) 30D d) 45D

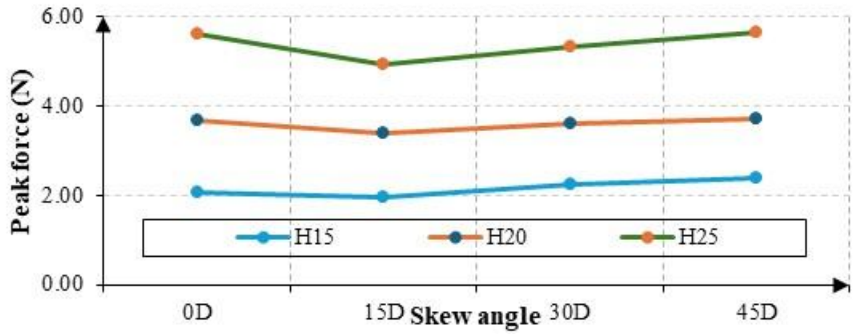

Fig. 8. Variation of peak force with change in skew angle at the various reservoir water depths

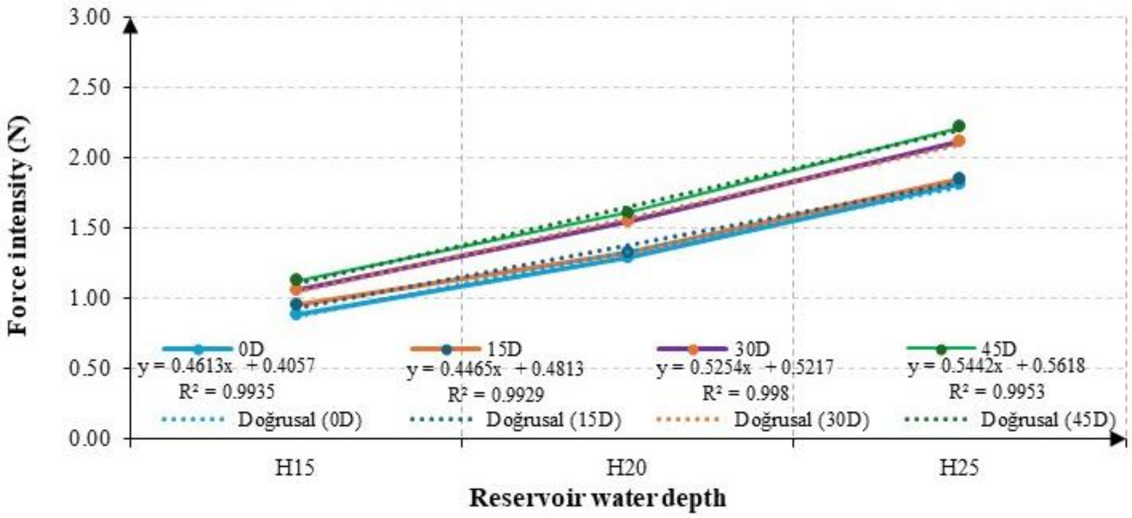

Fig. 9. Variation of force intensity relative to increasing reservoir water depth at the various skew angles

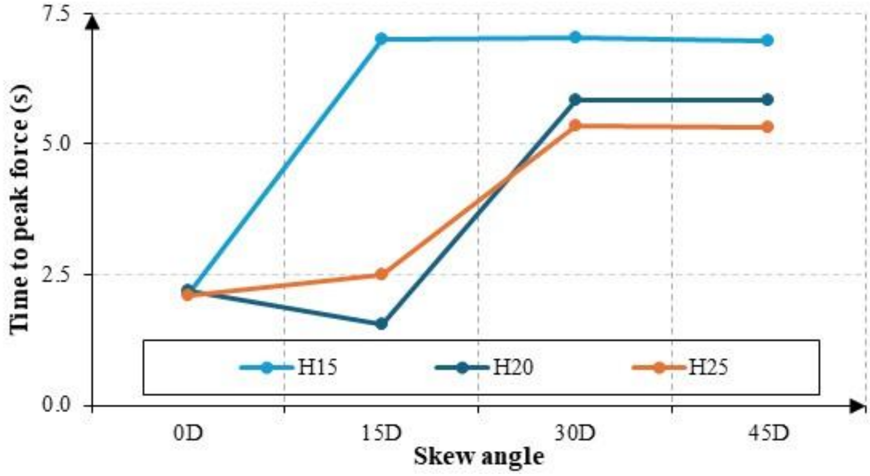

Fig. 10. The effect of skew angle on time to peak force at the various reservoir water depths

3.3. Result of numerical study

Sensitivity analysis was conducted for different mesh combinations for the main channel (1, 0.75 and 0.5 cm) and (0.2, 0.3, 0.4, and 0.5 cm) for the position around the bridge pier (15 cm upstream and downstream of the bridge pier. Based on the result, a 0.75 cm mesh size was adopted for the main channel while a 0.3 cm mesh size was adopted for the position around the bridge pier. This was done in order to model the geometry of the bridge pier more accurately as well as for a more accurate simulation of the fluid - structure interaction.

Similarly, a sensitivity analysis was carried out for the different turbulence closure schemes available in Flow 3D software and *k-w* was adopted for this study to save computational time. The Courant-Friedrichs-Lewy (CFL) time step was adopted, and the simulation time was set at 15 s. for this study. This is because, after 15 s according to the experimental results, the recorded forces were approximately zero.

$$\mathrm{RMSE} = \sqrt{\frac{1}{n}\sum_{i=1}^{n} (y_i - \hat{y}_i)^2} \tag{2}$$

Fig. 11 compares the time history of force from experimental data and numerical model for different initial reservoir water depths under the four skew angles studied.

The evolution of the force over time can be seen to have followed a similar trend for all cases, with an initial rapid rise, a peak force phase, and a gradual drop as the flow receded. Nonetheless, some discrepancies were observed between numerical and experimental results, especially in terms of peak force magnitudes and the fluctuations in the peak force phase.

At 0D and 15D, the experimental result showed higher peak force, particularly for higher initial reservoir water depth cases (e.g., 0D_H25_Exp), where the fluctuations in the force were more pronounced. Although, the numerical model captured the general evolution of the force, it underestimated the peak forces.

Although a similar pattern was observed in the case of 30D, the observed divergence has reduced considerably, while at 45D the numerical model results appear to have converged more closely with the experimental data, thereby suggesting that the model performs better at higher skew angles. This suggests that although the numerical model reasonably simulated the impact force induced on the bridge pier by the dam break wave, further refinement may be required in terms of turbulence modeling or resolution in order to improve accuracy, especially for cases of lower skew angles (0D, 15D).

According to Table 2, the maximum RMSE (Equation 2) of 0.682883 were recorded at 15D_H25. In general, the result indicates that the numerical model is capable of replicating the evolution of force over time. Future work may include refining the resolution and application of advanced turbulence models to enhance the model accuracy.

Table 2. Calculated error between the experimental and numerical impact force result under the various conditions studied

Skew angle	RMSE		
	H15	H20	H25
0D	0.166198	0.310647	0.607319
15D	0.285183	0.413287	0.682883
30D	0.183784	0.298102	0.42856
45D	0.127019	0.223247	0.458527

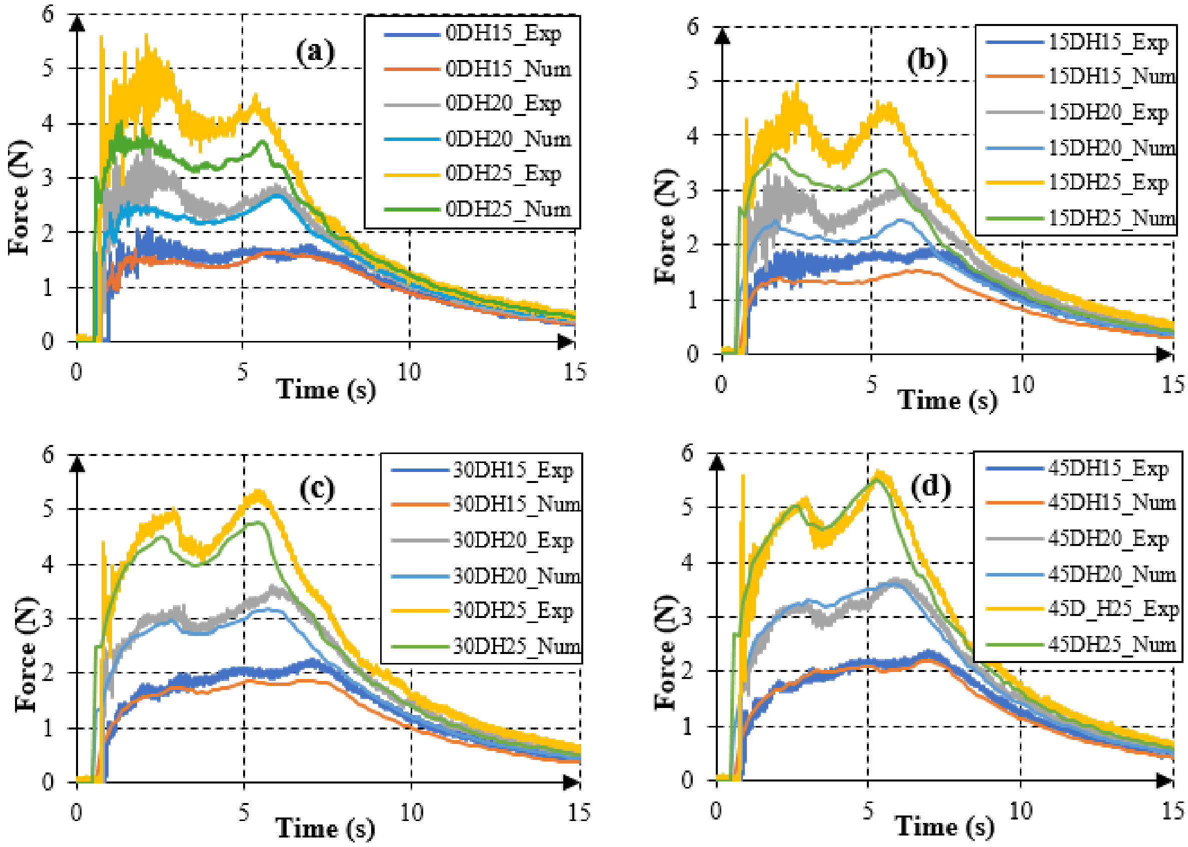

Fig. 11. Comparison of experimental and numerical results of the time history of force for various initial reservoir water depths at: a) 0D b) 15D c) 30D d) 45D skew angles

4. Conclusions

This study investigates the interaction between a dam-break flow and a square bridge pier with different orientations to the flow direction. The study aims to provide an understanding of the relationship between skew angle, flow dynamics, and force distribution, offering valuable insight for the design of bridge piers in dam-break-prone areas. Experimental and numerical studies were conducted and a good agreement between the numerical results and the corresponding experimental data is obtained. The following conclusions can therefore be drawn from this study:

- The rate of increase in flow depth depends on the initial water depth in the reservoir before the occurrence of the dam break. Higher the reservoir water depth, leads to higher the rate of increase in flow depth.
- The time to peak flow depth decreases with increase in reservoir depth and the maximum recorded drop was 31 % between 15D_H15 and 15D_H25. The effect of increasing skew angle also leads to a slight decrease in time to peak flow depth and the maximum in this case was a 10 % drop between 0D_H20 and 30D_H20 reservoir depth. An increase in the initial reservoir water depth results in an increase in the impact force. The highest forces were recorded at H25 in all the cases, while increase in skew angle leads to decrease in the impinging force which is more pronounced at H25.
- In all the cases (H15, H20 and H25), 1.1461, 1.0033 and 1.0062 times the force recorded at 0D were recorded at 45D and the force intensities at 45D, were 26.91 %, 25.02 % and 22.3 % more than the cases at 0D.
- Increasing skew angle delay the time to peak force and maximum of 3.29, 2.67 and 2.52 times the time to peak force at 0D were recorded at 15D, 30D and 45D respectively.
- The numerical model was found to have satisfactorily simulated the evolution of force over time. Nevertheless, future work may include refining the resolution and application of advanced turbulence models to enhance the model accuracy.

References

Ansari, A., Khavasi, E., & Ghazanfarian, J. (2021). Experimental and SPH studies of reciprocal wet-bed dam-break flow over obstacles. *International Journal of Modern Physics C*, *32*(7), 2150098

Aureli, F., Dazzi, S., Maranzoni, A., Mignosa, P., & Vacondio, R. (2015). Experimental and numerical evaluation of the force due to the impact of a dam-break wave on a structure. *Advances in Water Resources*, *76*, 29–42.

Chanson, H. (2005). Applications of the Saint-Venant equations and method of characteristics to the dam break wave problem. *In Report No. CH55/05*

Chanson, H. (2009). Application of the method of characteristics to the dam break wave problem. *Journal of Hydraulic Research*, *47*(1), 41–49

Chen, S., Li, Y., Tian, Z., & Fan, Q. (2019). On dam-break flow routing in confluent channels. *International Journal of Environmental Research and Public Health*, *16*(22), 4384

Chen, C., Chen, J., Lin, P., Chen, C., & Chen, H. (2020). Experimental study of dam-break-like tsunami bore impact mechanism on a container model. *Polish Maritime Research*, *27*(1), 53–59

Chumchan, C., & Rattanadecho, P. (2020). Experimental and numerical investigation of dam break flow propagation passed through complex obstacles using LES model based on FVM and LBM. *Songklanakarin Journal of Science and Technology, 42*(3), 564–572

Cross, R.H. (1967). Tsunami surge forces. *Journal of the Waterways and Harbors Division*, *93*(4), 201–231

Cumberbatch, E. (1960). The impact of a water wedge on a wall. *Journal of Fluid Mechanics*, *7*(3), 353–374

Dressler, R.F. (1952). Hydraulic resistance effect upon the dam-break functions. *Journal of Research of the National Bureau of Standards*, *49*(3), 217

Elsheikh, N., Nistor, I., Azimi, A. H., & Mohammadian, A. (2022). Tsunami-induced bore propagating over a canal—Part 1: Laboratory experiments and numerical validation. *Fluids*, *7*(7), 213

Erduran, K.S., Dokuz, A.Ş., & Unal, U. (2019). Performance analysis of a hybrid numerical wave model based on experimental results obtained by image processing technique. *OHU journal of Engineering Science, 8*(3), 183-196

Erduran, K.S., Ünal, U., & Dokuz, A.Ş. (2024a). Experimental and numerical investigation of partial dam-break waves. *Ocean Engineering*, *308*, 118346

Erduran, K.S., Akansu, Y.E., Ünal, U., & Adekoya, O.O. (2024b). An experimental investigation of tsunami bore impact on coastal structures. *Hydrology*, *11*(9), 131

Feizi, A. (2018). Hydrodynamic study of the flows caused by dam break around downstream obstacles. *The Open Civil Engineering Journal*, *12*(1), 225–238

Feizi Khankandi, A., Tahershamsi, A., & Soares-Frazo, S. (2012). Experimental investigation of reservoir geometry effect on dam-break flow. *Journal of Hydraulic Research*, *50*(4), 376–387

Frazão, S.S., & Zech, Y. (2002). Dam break in channels with 90° bend. *Journal of Hydraulic Engineering*, *128*(11), 956–968

Gaudio, D., De Paola, A., Kanakoudis, V., Giugni, M., Keramaris, E., Gaudio, A. Del, De Paola, F., Cristo, C. Di, Forgia, G. La, Leopardi, A., & Vacca, A. (2022). Experimental investigation and numerical evaluation of the free surface of a dam break wave in the presence of an obstacle. *Environmental Sciences Proceedings, 21*(1), 23

Gharib, M., Hernan, M.A., Yavrouiaw, A.H., & Sarohia, V. (1985). Flow velocity measurements by image processing of optically activated tracers. *In 23rd Aerospace Sciences Meeting,* 172

Hogg, A.J., & Pritchard, D. (2004). The effects of hydraulic resistance on dam-break and other shallow inertial flows. *Journal of Fluid Mechanics*, *501*, 179–212

Hooshyaripor, F., & Tahershamsi, A. (2015). Effect of reservoir side slopes on dam-break flood waves. *Engineering Applications of Computational Fluid Mechanics*, *9*(1), 458–468

Hu, H., Zhang, J., & Li, T. (2018). Dam-break flows: Comparison between Flow-3D, MIKE 3 FM, and analytical solutions with experimental data. *Applied Sciences (Switzerland)*, *8*(12), 2456

Kamra, M. M., Al Salami, J., Sueyoshi, M., & Hu, C. (2019). Experimental study of the interaction of dambreak with a vertical cylinder. *Journal of Fluids and Structures*, *86*, 185–199

Keshavarz, A., Vaghefi, M., & Ahmadi, G. (2022). Effect of the shape and position of the bridge pier on the bed changes in the sharp 180-degree bend. *Iranian Journal of Science and Technology - Transactions of Civil Engineering*, *46*(3), 2449–2467

Kihara, N., Niida, Y., Takabatake, D., Kaida, H., Shibayama, A., & Miyagawa, Y. (2015). Large-scale experiments on tsunami-induced pressure on a vertical tide wall. *Coastal Engineering*, *99*, 46–63

Kocaman, S., Evangelista, S., Viccione, G., & Güzel, H. (2020). Experimental and numerical analysis of 3D dam-break waves in an enclosed domain with a single oriented obstacle. *Environmental Sciences Proceedings,* 21(1), 35

Lauber, G., & Hager, W. H. (1998a). Experiments to dambreak wave: Horizontal channel. *Journal of Hydraulic Research*, *36*(3), 291–307

Lauber, G., & Hager, W. H. (1998b). Experiments to dambreak wave: Sloping channel. *Journal of Hydraulic Research*, *36*(5), 761–773

Leal, J.G., Ferreira, R.M., & Cardoso, A.H. (2006). Dam-break wave-front celerity. *Journal of Hydraulic Engineering*, *132*(1), 69–76

Li, X., & Liu, H. (2024). Experimental study on the dam-break-induced surge impact on an inclined wall. *Physics of Fluids*, *36*(4), 047105

Liu, S., Nistor, I., Mohammadian, A., & Azimi, A.H. (2022). Experimental investigation on the impact of dam-break induced surges on a vertical wall. *Fluids*, *7*(8), 258

Maghsoodi, R., Khademalrasoul, A., & Sarkardeh, H. (2022). 3D numerical simulation of dam-break flow over different obstacles in a dry bed. *Water Supply*, *22*(4), 4015–4029

Mu, D., Chen, L., & Ning, D. (2023). Modeling impact load on a vertical cylinder in dam-break flows. *Journal of Marine Science and Engineering*, *11*(5), 932

Nouri, Y., Nistor, I., Palermo, D., & Cornett, A. (2010). Experimental investigation of tsunami impact on free standing structures. *Coastal Engineering Journal*, *52*(1), 43–70

Ozmen-Cagatay, H., & Kocaman, S. (2011). Dam-break flow in the presence of obstacle: Experiment and CFD simulation. *Engineering Applications of Computational Fluid Mechanics*, *5*(4), 541–552

Ranga Raju, K.G., Rana, O. P. S., Asawa, G.L., & Pillai, A.S.N. (1983). Rational assessment of blockage effect in channel flow past smooth circular cylinders. *Journal of Hydraulic Research*, *21*(4), 289–302

Ritter, A. (1892). Die fortpflanzung der wasserwellen. *Vereine Deutscher Ingenieure Zeitswchrift*, *36*(2 and 33), 947–954

Saghi, H., & Lakzian, E. (2019). Effects of using obstacles on the dam-break flow based on entropy generation analysis. *European Physical Journal Plus*, *134*, 1-13

Soares-Frazão, S., & Zech, Y. (2007). Experimental study of dam-break flow against an isolated obstacle. *Journal of Hydraulic Research*, *45*, 27–36

Stamataki, I., Zang, J., Buldakov, E., Kjeldsen, T., & Stagonas, D. (2018). Study of dam break flow interaction with urban settlements over a sloping channel. *In E3S Web of Conferences*, *4,* 06006

Vosoughi, F., Nikoo, M.R., Rakhshandehroo, G., Adamowski, J.F., & Gandomi, A.H. (2022). Downstream semi-circular obstacles influence on floods arising from the failure of dams with different levels of reservoir silting. *Physics of Fluids*, *34*(1), 013312

Yang, S., Wang, B., Guo, Y., Zhang, J., & Chen, Y. (2020). Gate-opening criterion for generating dam-break flow in non-rectangular wet bed channels. *Energies*, *13*(23), 6280

Yang, S., Yang, W., Zhang, C., Qin, S., Wei, K., & Zhang, J. (2022). Experimental and numerical study on the evolution of wave front profile of dam-break waves. *Ocean Engineering*, *247,* 110681

Zhang, F., Wang, B., & Guo, Y. (2022). Experimental study of the dam-break waves in triangular channels with a sloped wet bed. *Ocean Engineering*, *255*, 111399

Zhou, X., Su, L., Yuan, H., Mao, Y., & Sun, Q. (2024). Experimental study on the influence of water depth and bed slope variations on dam-break flood wave propagation. *Physics of Fluids*, *36*(7), 075133

4th International Civil Engineering & Architecture Conference
17-19 May 2025, Trabzon, Türkiye

An experimental investigation of the effects of discharge height and angle on the dilution characteristics of dense brine effluents

Merve Bedir[1], Büşra Değirmenci[1], Damla Yilmaz Çelik[*1], Egemen Aras[1]

[1] *Bursa Technical University, Department of Civil Engineering, Turkey*

Abstract. Nowadays, the need for drinking water is increasing due to increasing population and industrialisation, which necessitates the search for alternative fresh water resources. Especially the uncertainties created by climate change in the water cycle and the pressures on existing freshwater resources have increased the importance of seawater desalination technologies. Although desalination is an effective method for converting seawater into potable freshwater, the direct discharge of high salt concentration wastewater generated as a result of the treatment process into the sea poses serious environmental risks. Since this concentrated wastewater is heavier than seawater, it settles on the seabed, causing stratification and a decrease in oxygen levels, adversely affecting the life of benthic organisms. Recent studies have focussed on reducing these environmental impacts by improving the performance of marine discharge systems. In particular, the effects of hydraulic parameters such as discharge angle and outlet height on flow propagation and dilution rate are investigated. In this study, 60-second experiments were carried out in a 150×50×60 cm glass-enclosed aquarium in three different configurations (10 cm-45°, 15 cm-45°, 10 cm-0°). Solution monitoring was performed with rhodamine tracer. The results show that the 15 cm high and 45° inclined discharge provides a more even dispersion and rapid dilution. The data obtained provide an important reference for the design of marine discharge systems and minimisation of environmental impacts.

Keywords: Brine discharge; Dilution; Outfall; Tracer; Discharge

1. Introduction

Today, with the rapidly increasing population, urbanisation and industrialisation processes throughout the world, the demand for water is constantly increasing. However, the fact that fresh water resources are limited and often difficult to access is insufficient to meet this increasing demand for water. Approximately 97.5 per cent of the world's total water resources consist of salt water, while only 0.3 per cent of the remaining 2.5 per cent of fresh water is directly usable (UN Water, 2021). This situation increases the importance of alternative water supply methods and desalination technologies, especially the treatment of seawater, come to the fore.

Desalination describes the process of bringing seawater to drinking or potable water quality and is now widely used especially in water-stressed regions such as the Middle East, North Africa, Australia and some Mediterranean countries (Ghaffour et al., 2013). It is reported that as of 2020, approximately 20,000 desalination plants are in operation worldwide and more than 100 million people use water obtained by this method daily (Global Water Intelligence, 2020). Although this process offers a great solution in terms of water supply, the environmental impacts of desalination technologies are too great to be ignored. In particular, the brine obtained from this process can pose a potential threat to marine environments due to its high salt concentration, heavy metals, chemical additives and low dissolved oxygen content (Panagopoulos and Haralambous, 2020; Pramanik et al., 2017). This dense brine is often discharged into the marine environment and inappropriate discharge methods can cause serious damage to marine ecosystems. Direct discharge of dense saline water into the sea can lead to stratification, reduced oxygen transfer and hypoxia, especially in areas with no current or closed sea areas. Such conditions threaten the survival of many marine organisms, especially benthic organisms (Roberts et al., 2010). Furthermore, since the temperature of the brine solution is usually above ambient temperature, thermal pollution creates an additional stress factor (Lattemann & Höpner, 2008). At this point, the conditions under which dense brine is discharged into the marine environment - in particular discharge height, outlet angle, flow rate and direction - stand out as physical parameters that directly determine the severity of these environmental impacts. Various studies in the literature show that by optimising these parameters, it is possible to spread the dense brine over larger areas and thus dilute it in a shorter time (Najafi & Ghazizadeh Hashemi, 2016). In particular, it is stated that sloping and medium-height discharge systems produce more effective results than vertical or horizontal discharge systems. Mixing and

[*] Corresponding author, E-mail: damla.yilmaz@btu.edu.tr

https://doi.org/10.31462/icearc2025_ce_hyd_570

dilution processes in the marine environment are critical for reducing the environmental impacts of concentrated saline water. This dilution not only reduces the salinity level, but also enables the recovery of dissolved oxygen and stabilisation of temperature differences. Therefore, in the design of desalination plants, not only the water treatment efficiency but also the environmental compatibility of the discharge systems should be considered (Giwa et al., 2017).

This study aims to investigate the effects of different height and angle combinations on the spreading behaviour of dense brine through experimental studies conducted in a laboratory environment. In this context, it is aimed to create environmentally friendly systems by optimising mixing behaviour with water, discharge point design and physical parameters. The results of the study aim to contribute to engineering solutions to reduce the environmental impacts caused by dense brine.

2. Material and methods

In this study, the flow behaviour and dilution characteristics of a dense brine discharge with different elevation and angle combinations were observed in the laboratory. The experiments were carried out in a 150 cm long, 50 cm wide and 60 cm high experimental tank (aquarium) covered with glass on four sides. Thanks to the glass surface, the three-dimensional development of the flow could be observed from all angles and analysed in detail with video recordings.

The concentrated brine solution used in the experiments was prepared by adding 150 grams of sodium chloride (NaCl) and 0.15 grams of rhodamine B to 1 litre of deionised water. NaCl in this solution aimed to mimic the marine environment by increasing the density of the liquid, while rhodamine B served as a trace substance. Rhodamine was preferred because it provides high optical contrast even at low concentrations. The behaviour of the solution during the flow was qualitatively monitored by the colour changes provided by rhodamine.

The prepared brine solution was introduced into the experimental tank at constant flow rate by means of a peristaltic pump. Using a transparent hose with an internal diameter of 5 mm, the solution was discharged into the tank at three different outlet height and angle combinations. The pump outlet flow rate was fixed at 460 mL/min and each experiment was carried out continuously for 60 seconds. The equipment used during the experiments and their specifications are presented in the table below.

Table 1. Experimental equipment

Equipment / Material	Features
Aquarium	150 cm × 50 cm × 60 cm, glass
Dense saline solution	1 L deionised water + 150 g NaCl + 0.15 g rhodamine
Discharge system	Peristaltic pump
Hose	Transparent, 5 mm inner diameter
Camera	1080p, 60fps, stabilised

In each experiment, the outlet pipe was placed in the tank at different combinations of elevation and angle and flow was maintained at constant flow rate for a certain period of time. Three different experimental scenarios were determined as follows:

Table 2. Experiments

Experiment No	Elevation (cm)	Discharge Angles
1	10	45° inclined
2		0° horizontal
3	15	45° inclined

For imaging, a camera capable of recording at 60 fps and 1080p resolution was fixed outside the tank with a tripod. The camera remained in a fixed position throughout the experiment and recorded each flow behaviour with high resolution. The images were taken time-dependently throughout the experiment, so that the development of the flow was analysed second by second.

The colour changes of the rhodamine during its diffusion in the tank were carefully monitored; the initial bright red colour of the solution changed to lighter tones over time, providing qualitative information on the degree of dilution and mixing. The time for the flow to reach the bottom, the post-impact propagation and the mixing behaviour in the tank were evaluated both by visual analysis and colour intensity changes.

For each experimental condition, a fixed reference point in the tank was set and the colour change and the behaviour of the streamlines at this point were recorded. The evaluations were concentrated in the region closest to the camera and in the centre line of the tank. In particular, image frames from the 10th, 30th and 50th seconds of the experiments were compared to investigate the rate of progression, stratification tendency and spreading pattern of the mixture.

The experiments were conducted under constant illumination and temperature conditions and repeated at least three times for each configuration to ensure the reliability of the experimental data. With repeated observations, care was taken to maintain consistency between experiments and the general validity of the findings was increased. As a result, the data obtained in this methodological framework provided the opportunity to directly observe the effect of different height and angle combinations on flow propagation. In particular, it was observed that the flow reached the bottom in a shorter time and spread more uniformly in discharges with sloping outlets, while in horizontal discharges, the solution remained in the middle levels for a longer time and vertical mixing was limited. These observations will provide important contributions to future environmental modelling studies and the development of desalination discharge strategies.

3. Results and discussion

Within the scope of laboratory scale experimental studies, the effect of discharging dense brine at different height and slope (angle) conditions on the mixing behaviour was analysed in detail. During the experiments, three different configurations of discharges were performed and the results showed that the mixing process is highly sensitive not only to the solution properties but also to the physical conditions of the discharge. In this context, the dispersion patterns under each experimental scenario were evaluated in terms of changes in colour intensity and observed flow characteristics, and meaningful interpretations were made in the light of the visual records and experimental observations.

3.1. 10 cm elevation and 45° slope

In the first experimental scenario, the discharge from a height of 10 cm and with a 45° inclination gave the most successful results in terms of continuity of mixing and even dispersion. In this experiment, a dense brine solution coloured with rhodamine dye was released into the aquarium tank at a constant flow rate. It was observed that the flow reached the bottom of the tank in about four seconds; when it reached the bottom region, it formed a thin layer and started to spread in the horizontal plane. A homogeneous decrease in colour intensity was observed throughout the experiment, indicating that the solution and ambient water were successfully mixed over time and a regular dilution was achieved in the vertical-vertical direction.

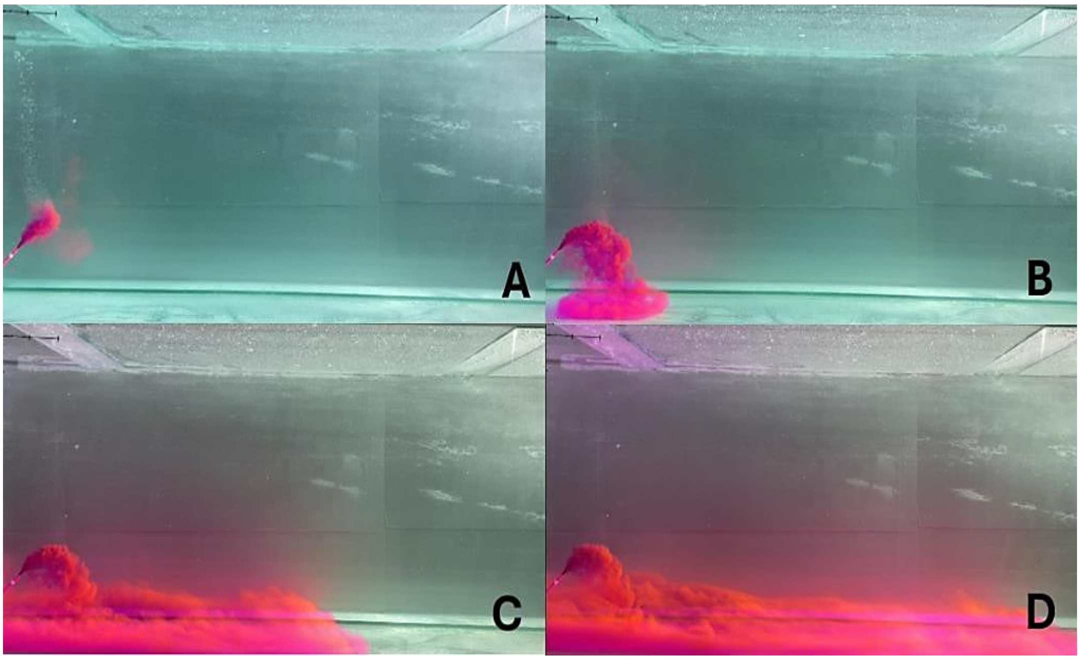

Fig. 1. Discharge configuration of 10 cm height and 45° angle

The sequential images illustrate the temporal progression of the dense rhodamine-brine jet released into the static ambient water during Experiment 1. In frame (A), the initial jet enters the water column with a downward trajectory influenced by the combination of outlet height (10 cm) and an inclined release angle (45°). Due to the higher density of the brine solution, the jet sinks rapidly while maintaining a coherent structure, indicating limited initial mixing and a strong momentum-driven flow.

In frame (B), the jet reaches the bottom of the tank, where the vertical momentum begins to dissipate. Upon impact with the tank floor, the plume starts to spread horizontally, forming a gravity current along the bottom boundary layer. This behavior is characteristic of negatively buoyant jets, which exhibit bottom-following propagation due to density stratification.

Frame (C) demonstrates an intermediate stage where ambient entrainment becomes more significant. The rhodamine dye begins to exhibit a lighter coloration, indicating the onset of dilution and mixing with the surrounding freshwater. The flow transitions into a more turbulent regime, where instabilities at the plume boundary enhance the lateral and vertical dispersion.

Finally, in frame (D), the plume has spread extensively throughout the tank. The diminished dye concentration and uniform coloration indicate substantial dilution and near-homogeneous mixing. At this stage, the stratification effect has weakened, and the brine solution has approached equilibrium with the ambient conditions, signifying effective dispersion under the applied discharge configuration.

3.2. 15 cm elevation and 45° slope

In the second experimental setup, where the brine solution was discharged from a height of 15 cm at a 45° angle, the increased initial momentum significantly influenced the hydrodynamic behavior of the flow. The images presented in Fig. 2 capture the temporal evolution of the plume during the discharge process.

In frame (A), the high discharge velocity resulting from increased free-fall height generates a compact and coherent plume structure as the brine rapidly descends toward the bottom. This behavior reflects a strong momentum-dominated flow with limited entrainment at the initial stage.

Upon impingement with the bottom boundary (frame B), pronounced turbulence and secondary flow structures emerge due to the high impact energy. The spreading pattern becomes more chaotic compared to the first experiment, and the formation of vortices is visually evident. At this point, the brine begins to propagate radially along the tank floor, initiating a bottom-driven mixing process.

Frame (C), captured approximately 30 seconds into the experiment, reveals non-uniform dilution dynamics. In some regions, the rhodamine dye fades quickly due to localized mixing, while in others the brine concentration remains high. These spatial inconsistencies are indicative of fluctuating turbulence intensity and uneven entrainment of ambient water, suggesting that elevated discharge height may compromise mixing uniformity despite promoting faster dispersion.

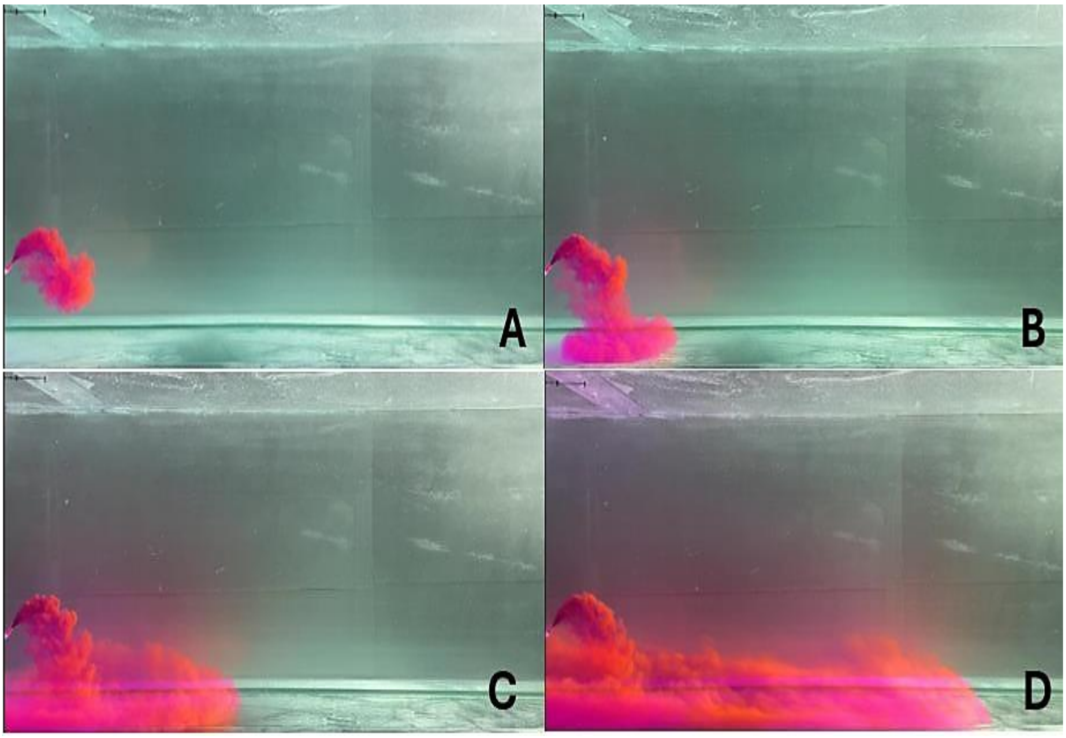

Fig. 2. Discharge configuration of 15 cm height and 45° angle

By frame (D), taken at around 50 seconds, the plume has spread across a large portion of the tank. Although substantial dilution has occurred, the persistence of visible density gradients and wavy color transitions highlights that complete homogenization has not yet been achieved. The observed stratification patterns and mixing asymmetries emphasize the role of discharge momentum in shaping both the efficiency and spatial characteristics of brine dispersion.

3.2. 10 cm elevation and 0° Horizontal Discharge

In the third experimental configuration, the dense brine was discharged horizontally at a height of 10 cm with a 0° inclination angle. This setup resulted in a plume trajectory that was predominantly confined to mid-depth levels of the tank, with minimal vertical dispersion. As illustrated in Fig. 3, the spatial distribution of the rhodamine-brine mixture reveals distinct stratification characteristics and limited mixing efficiency.

In frame (A), the horizontally discharged plume begins to propagate along the central axis of the water column, maintaining a focused and relatively undisturbed trajectory due to the absence of a vertical momentum component. This is consistent with typical behavior observed in horizontally oriented dense jets in quiescent environments.

At 10 seconds into the experiment (frame B), a clearly defined, dense layer of colored solution forms at mid-depth, indicating a high degree of lateral coherence and a lack of downward entrainment. The flow maintains its elevation, and interaction with both the surface and bottom boundaries remains negligible.

Frame (C), captured at 30 seconds, shows that the lateral expansion continues within a narrow vertical band, reinforcing the presence of a stratified flow regime. The color gradients remain sharp, and no significant plume deflection or downward penetration is observed, suggesting strong stability of the layered structure.

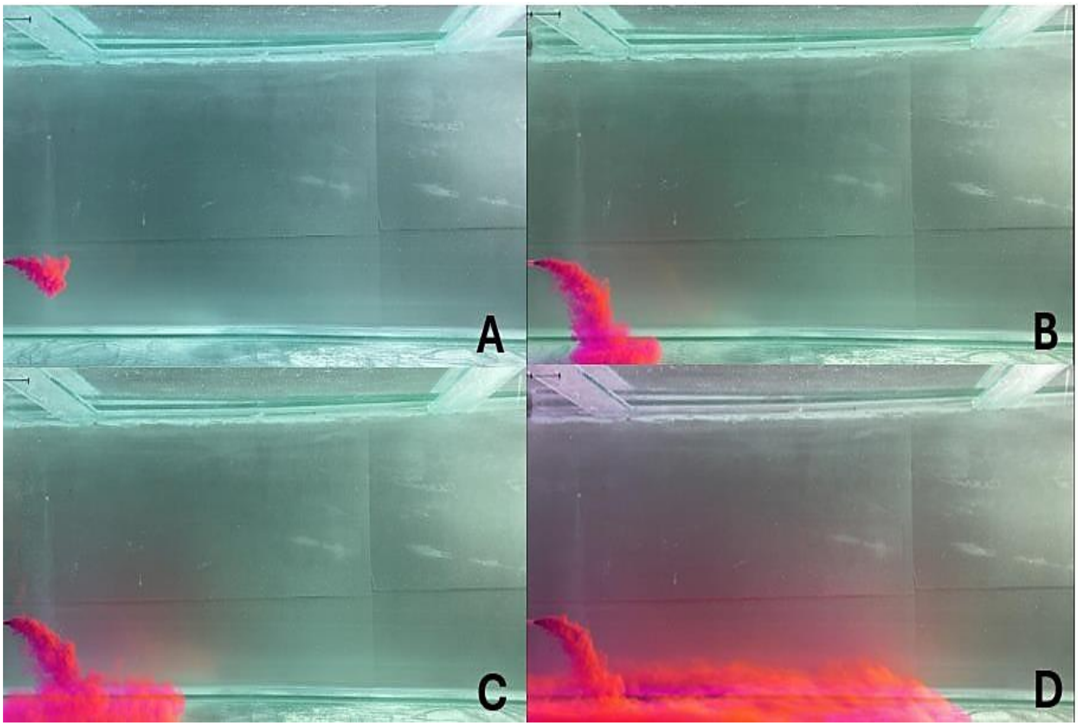

Fig.3. Discharge configuration of 10 cm height and 0° angle

By the end of the experiment (frame D, ~50 seconds), the brine remains concentrated in the upper-to-mid layers of the tank. Vertical mixing is still minimal, and a substantial portion of the tank volume remains unaffected by the brine discharge. This confirms that horizontal release conditions promote stratification and restrict full-volume mixing, a scenario which may lead to persistent high-salinity zones in real-world applications if not properly managed.

Overall, comparative evaluation of the three experiments demonstrates that a discharge configuration involving moderate elevation and inclined angle (e.g., 10–15 cm at 45°) is more favorable for achieving uniform mixing and reducing the environmental impact of dense brine. In contrast, horizontal discharges—even at moderate heights—tend to confine the brine within limited vertical regions, thus increasing the risk of localized salinity accumulation and ecological stress.

4. Conclusions and recommendations

This study, the dispersion and dilution behaviours of dense brine discharged into a stagnant freshwater environment under different height and angle conditions were experimentally investigated and the findings contributed to the determination of appropriate discharge strategies to reduce environmental impacts. The experiments were carried out in a transparent tank set up in the laboratory and the mixing dynamics of the dense saline solution were observed under different combinations of height (10 cm and 15 cm) and angle (0° and 45°).

The results obtained show that the discharge height and angle have a direct effect on the mixing efficiency. Especially at a discharge height of 10 cm and an angle of 45°, the brine solution mixed rapidly and uniformly with the ambient water, resulting in an almost homogeneous concentration profile throughout the experiment. This configuration was the most stable in terms of mixing and the most environmentally favourable option. On the other hand, when discharging at the same angle but from a height of 15 cm, the solution reached the bottom of the tank at a higher velocity, resulting in wavy, irregular mixing patterns in the bottom region. This irregularity caused the flow to concentrate more in the lower regions due to the higher solution density, resulting in undesirable density stratification. On the other hand, in the 0° (horizontal) angle discharge, the solution was mostly spread in the middle levels of the tank and mixing in the vertical direction was limited. This indicates an inadequate dispersion pattern in terms of dilution. In general, it was observed that discharging with a certain slope and from a moderate height allowed for more homogeneous and balanced mixing. This finding constitutes an important reference for determining the optimum conditions both in experimental systems and in real environmental discharge applications. Therefore, careful selection of discharge height and angle in the design of wastewater discharge systems is of great importance in terms of both increasing mixing efficiency and reducing environmental impacts. This study also contributes to the literature in terms of providing experimental data to provide a basis for advanced hydrodynamic modelling and field applications

Acknowledgments
This study was carried out with the infrastructure support provided by Bursa Technical University and the valuable contributions of our supervisor Prof. Dr. Egemen Aras and research assistant Damla Yılmaz Çelik.

References

Ghaffour, N., Missimer, T. M., & Amy, G. L. (2013). Technical review and evaluation of the economics of water desalination: Current and future challenges for better water supply sustainability. *Desalination, 309*, 197–207.

Giwa, A., Hasan, S. W., Younes, M., Almarzooqi, F. A., Nasser, M. S., & Al Kaabi, M. A. (2017). Brine management methods: Recent innovations and current status. *Desalination, 407*, 1–18.

Ihsanullah, I., Giwa, A., Dissanayake, P., & Ashfaq, M. Y. (2022). Waste to wealth: A critical analysis of resource recovery from desalination brine. *Desalination, 543*, 116093.

Kilit, M. (2011). Seawater intrusion problem and analyzing the solving methods. *Electronic Journal of Construction Technologies, 7*(2), 50–61.

Lattemann, S., & Höpner, T. (2008). Environmental impact and impact assessment of seawater desalination. *Desalination, 220*(1–3), 1–15.

Najafi, H., & Ghazizadeh Hashemi, S. A. (2016). Experimental investigation of brine discharge from submerged inclined jets. *Journal of Hydrology and Hydromechanics, 64*(1), 18–26.

Panagopoulos, A., & Haralambous, K.-J. (2020). Environmental impacts of desalination and brine treatment—Challenges and mitigation measures. *Marine Pollution Bulletin, 161*, 111773.

Pramanik, B. K., Shua, L., & Jegatheesan, V. (2017). A review of the management and treatment of brine solutions. *Environmental Science: Water Research & Technology, 4*(1), 1–16.

Roberts, D. A., Johnston, E. L., & Knott, N. A. (2010). Impacts of desalination plant discharges on the marine environment: A critical review of published studies. *Water Research, 44*(18), 5117–5128.

UN Water. (2021). *The United Nations World Water Development Report 2021: Valuing Water*. UNESCO. https://unesdoc.unesco.org/ark:/48223/pf0000375724

4th International Civil Engineering & Architecture Conference
17-19 May 2025, Trabzon, Türkiye

Numerical investigation of flow around a circular cylinder with a spoiler at low Reynolds number

Melih Seçkin[1,2], Yusuf S. Özpolat[1,2], Ahmet K. Emek[1,2], Ömer Dilmen[3], Kemal Koca[*1,2]

[1] *Department of Mechanical Engineering, Abdullah Gül University, 38080, Kayseri, Türkiye*
[2] *KOCA Research Group, Abdullah Gül University, 38080, Kayseri, Türkiye*
[3] *Department of Civil Engineering, Abdullah Gül University, 38080, Kayseri, Türkiye*

Abstract. The study aims to investigate the aerodynamic behavior of different spoiler configurations in offshore pipelines to further explore the fluid dynamics surrounding subsea structures. The research investigates the influence of spoiler geometry on aerodynamic drag, wake behavior, and vortex shedding by performing computational fluid dynamics (CFD) combined with the Reynolds-averaged Navier-Stokes (RANS) equations and the Shear Stress Transport (SST) k-ω turbulence model via ANSYS Fluent. Rectangular shape spoiler was analyzed and compared against the baseline configuration. Regarding the numerical outputs, drag coefficient (C_D), pressure distributions, velocity contours, turbulent kinetic energy (TKE), and eddy viscosities were investigated in detail. The results highlighted that spoiler geometry profoundly affects the flow regime, significantly altering the friction coefficients and turbulence characteristics. Intermediate effects were observed for Type-1 spoilers, exhibiting a complex interaction between spoiler geometry and wake dynamics. These observations are valuable to enhance the design of pipeline spoilers with respect to both structural integrity and sediment matters

Keywords: Circular cylinder; Numerical simulation; Drag coefficient; Spoiler

1. Introduction

Offshore pipelines are crucial for oil and gas transportation, but they also introduce the generation of complex flow-induced phenomena due to their cylindrical shape and seabed and current interaction. Understanding the flow characteristics around cylindrical elements (such as pipelines) is essential for ensuring structural stability and preventing damage from hydrodynamic forces. Flow separation around a cylinder and associated vortex shedding when the pipeline is on or near the seabed cause substantial drag and lift forces, as well as oscillatory vortex-induced vibrations (VIV) leading to fatigue failures (Zhu et al., 2013). Flow can also affect erosion of the sediment around the pipe (local scour), generating spanning sections (free spans) for further exacerbation of VIV and stress on the pipeline. Conventionally, pipelines have been buried below the seabed to avoid these problems; however, trenching and backfilling are costly. To solve the economic problem, an effort has been made for research on the self-burial procedure, whereby the pipeline self-induces its burial because of scour. An important technique to facilitate self-burial is to put a small fin or spoiler on top of the pipeline. The spoilage effects contribute to more blockage to the flow, resulting in turbulence and sediment transport around the pipe faster so that the sediment gets eroded beneath and downstream of the pipeline (Zhu et al., 2013). Hulsbergen's early experiments showed that a pipeline fitted with a spoiler was able to bury itself around ten times faster than an unspoiled smooth pipe (Hulsbergen, 1986). Further studies went on to establish that spoilers increase both the tunnel scour underneath the pipe downstream thereby hastening the formation of scour holes and sand deposition inundating the pipe (Zhu et al., 2013).

In addition to inducing burial, spoilers also strongly affect the hydrodynamics around the cylinder. A spoiler protruding into the flow brings about early flow separation and a larger wake that tends to increase the drag on the cylinder and may also generate a downward lift (negative lift) due to the asymmetric pressure distribution. These effects concern not only scour but structural loadings and vibrations on the pipeline as well. In the past 10 years, different researchers have used numerical and experimental techniques to determine the effects of spoilers on flow patterns, vortex shedding, and force coefficients on cylindrical structures. Spoiler attachments have even been studied as passive flow control mechanisms to mitigate VIV or vortex-induced motion of cylinders (İlkentapar et al., 2023). At the same time, marine pipelines are often deployed in arrays or multiple configurations (e.g., dual

[*] Corresponding author, E-mail: kemal.koca@agu.edu.tr

https://doi.org/10.31462/icearc2025_ce_hyd_605

pipelines, pipe-with-piggyback cable, or clusters) rather than in complete isolation. Similar flow interference phenomena (wake shielding or shear layer reattachment) develop when two or more cylinders are found in close proximity significantly differing from single-cylinder behavior. Classical studies show that the relative positioning, such as tandem, side by side, staggered, determines the flow regime between the cylinders (Dehkordi et al., 2011). For instance, if two cylinders are placed in a tandem arrangement, then these two cylinders will experience different flow regimes depending on the separation distance: at very close spacing, the downstream cylinder may be in close wake of the upstream cylinder and therefore experience reduced flow velocity; at moderate spacing, the shear layers of the upstream cylinder may reattach to the surface of the downstream cylinder; and beyond certain inter-cylinder spacing, the upstream cylinder sheds vortices impinging on the downstream cylinder (İlkentapar et al., 2023). Accordingly, the interference effects vary between pipeline bundles and single pipes as far as force distribution and scour modes are concerned. Therefore, in offshore applications, it is vital to understand the combined effect of spoiler and cylinder interference on the flow characteristics.

2. Literature review

2.1. Flow around single cylinders with and without spoilers

Flow past a single circular cylinder has been a classic research topic in fluid mechanics, and extensive literature exists characterizing its behavior without any modifications. A smooth circular cylinder in cross-flow develops boundary layers that separate forming a von Kármán vortex street in the wake, associated with fluctuating lift forces and a drag coefficient on the order of 1.0 in subcritical Reynolds number regimes (İlkentapar et al., 2023) The presence of a nearby plane boundary (as in the case of a pipeline near the seabed) can modify this canonical flow. Early experiments by Bearman and Zdravkovich showed that a cylinder close to a plane wall experiences suppressed vortex shedding and altered pressure distribution due to the wall's influence, which in turn affects drag and lift (Bearman & Zdravkovich, 1978). More recently, numerical simulations by Kirkgoz et al. (2009) showed that even a small gap between a cylinder and a rigid bed (e.g., gap ratio $G/D = 0.3$) can cause asymmetry in the wake. This confirms that this can reduce the intensity of vortex shedding, but a near-thin-wall mesh resolution is required for accurate prediction. These studies highlight that the base flow around a pipeline (without a spoiler) can vary significantly depending on the proximity to the seabed.

When a spoiler is attached to the cylinder (typically a small plate or cylindrical rib mounted at the top of the pipe), the characteristics of flow alter drastically. The spoiler effectively induces flow separation earlier on the upper surface of the pipe, creating a larger recirculation region in the wake. There are numerous experimental studies in literature on this subject. İlkentapar et al. (2023) clarified that adding a spoiler to a cylinder in crossflow produces a pronounced low-pressure region in the near wake, which increases the average drag force compared to a smooth cylinder. They also observed that the spoiler produces a constant downward lift force on the cylinder which is opposite to upward lift force that would occur near the wall in a smooth cylinder (İlkentapar et al., 2023). This reversal of the lift is desirable for pipeline stability since an upward lift would tend to destabilize the pipe or reduce its width. Moreover, they reported that the spoiler modifies the vortex-shedding properties, which can influence vortex-induced vibration tendencies.

2.2. Effect of spoiler geometry

The spoiler performance relative to flow and scour changes according to various parameters, such as geometrical configurations and material parameters of the spoiler. One key parameter is the spoiler height (S) relative to the pipe diameter D. Higher spoiler stands out more into the flow, normally giving larger wake disturbance and separation bubble. As mentioned, Zhu et al. (2013) demonstrated a clear trend of increasing S/D from 0 (no spoiler) to 0.35 that precipitated more rapid self-burial of the pipe. The tallest spoiler increased flow acceleration at the pipe–bed gap and generated stronger vortices in their simulations, which facilitated sediment self-removal. However, very large spoilers may also impose significant drag forces for an actual design, there is probably an optimal height that balances scour benefits with structural loads. Zhao and Wang (2009) observed that there is a point at which adding a spoiler has little effect on bed shear stress, suggesting that beyond a certain point spoiler size results in diminishing returns. Another factor is spoiler length (spanwise extent): Bianchi et al. (2020) examined a low-aspect-ratio cylinder with a relatively short spoiler plate and modified the spoiler geometry. They observed that the spoiler would need to span sufficiently and extend sufficiently into the flow to effectively suppress vortex-induced motions. Shorter, shallower spoilers may be bypassed by the flow with minimum disruption to the vortex shedding. Hence, geometry optimizations (height, chord length if plate-like and span) are featured in several recent numerical parametric investigations.

3. Methodology

3.1. Mesh generation

In this study, a structured quadrilateral mesh structure was preferred using ANSYS FLUENT software for the measurement analysis of the effects of spoiler use on aerodynamic performance. As seen in Figure 4, the mesh was created to include an increasing number of layers (inflation) near the surface. The main reason for this is to ensure that the boundary layer behavior near the wall is correctly resolved and to obtain a representation closer to the real fluid profiles instead of the wall functions. In this way, the accuracy of the results is increased by providing sufficient y+ resolution. As stated in the literature, quadrilateral meshes provide low numerical diffusion, faster convergence, fewer element numbers and shorter solution time with more regular cell structures compared to triangular meshes (Lo, 2013). In addition, the proper alignment of quadrilateral cells, low curvature and orthogonality, especially in meshes parallel to the flow direction, contribute to more accurate capture of sharp gradients (Ye et al., 2023; Zhao et al., 2013).

In order to ensure that the numerical results are independent of the node number, 7 different node numbers were selected to conduct mesh independence tests on the pipe without spoilers and the change in the drag coefficient (C_D) with the change in the node number was examined. The mesh number, node number C_D values and percentage changes are given in Table 1. The change rate was 0.87 percent in the last case as seen in Figure 1. This rate shows that the results of our study are independent of the node number. However, for the convenience of calculation, the number 360000 was used as the mesh number.

Table 1. Comparison of drag coefficient (C_D) values obtained from different mesh numbers

Mesh	Mesh Number	Node Number	C_D	Error
1	1260000	1262600	1.844	0.87
2	360000	361400	1.86	-7.05%
3	216250	217325	1.72887	4.39%
4	150000	150900	1.804746	10.23%
5	111250	112025	1.98946	4.16%
6	93900	94610	2.0722	5.68%
7	25000	25375	2.19	--

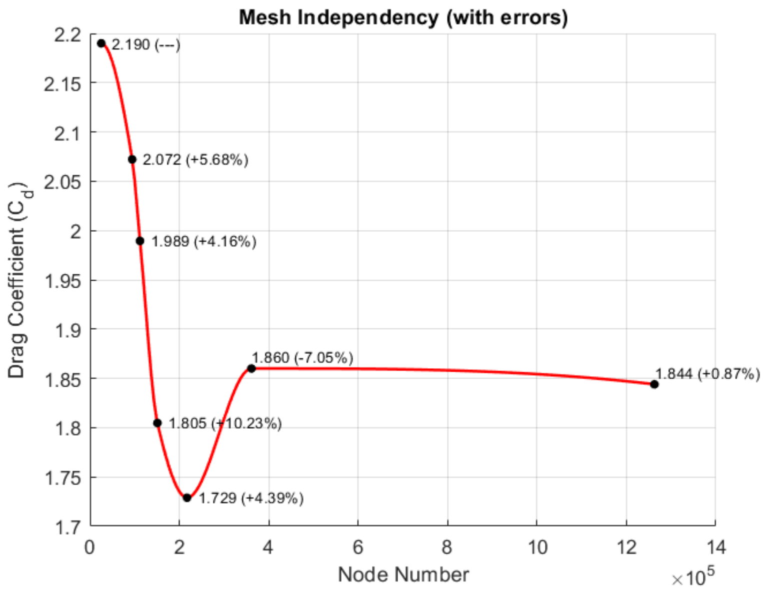

Fig. 1. Mesh independency results

3.2. Turbulence model selection

All simulations were conducted under two-dimensional. incompressible. and unsteady flow conditions. The governing equations consist of the continuity and momentum equations. along with the Reynold-Averaged Navier Stokes (RANS) coupled with the Shear Stress Transport (SST) k-ω turbulence model. The governing equations. including the continuity and momentum equations. are formulated as shown in equations 1 and 2. where a turbulence closure method based on the Boussinesq approximation is adopted Shi et al. (Shi et al. 2021)

$$\frac{\partial \bar{u}_i}{\partial t} + \bar{u}_j \frac{\partial \bar{u}_i}{\partial x_j} = -\frac{1}{\rho_f}\frac{\partial p}{\partial x_i} + \nu_f \frac{\partial^2 \bar{u}_i}{\partial x_j \partial x_j} - \frac{\partial}{\partial x_j}\left(\overline{u_i' u_j'}\right) \tag{1}$$

$$\frac{\partial \bar{u}_i}{\partial x_i} = 0 \tag{2}$$

Where $\bar{u}_i.\bar{u}_j$ are the time-averaged velocity components; u_i' and u_j' are the fluctuating components; x_i and x_j are spatial coordinates; ρ_f is the fluid density; p is pressure. and ν_f is the kinematic viscosity of the fluid. No slip boundary condition at the pipeline wall is considered in this study. Correspondingly. the velocity will be zero in the vicinity of this region. Ordinarily. for steady flow. since the flow is independent of the time parameter. the $\partial \bar{u}_i / \partial t$ term in equation (1) drops out. However. since the analysis was unsteady. this term should also be retained. Moreover. the Bousinesq hypothesis. which associates the Reynold stresses to the mean velocity gradients. are implemented in this study and expressed as:

$$-\overline{u_i' u_j'} = v_t\left(\frac{\partial \bar{u}_i}{\partial x_j} \frac{+\partial \bar{u}_j}{\partial x_i}\right) - \frac{2}{3} k \delta_{ij} \tag{3}$$

Where δ_{ij} is the Kronecker. equal to 1 when i = j and 0 otherwise. The term k is turbulent kinetic energy and v_t denotes the turbulent (eddy) viscosity (Shi et al. 2021). This approach makes computation less time-consuming since only two additional transport equations need to be solved. By the inclusion of these two equations. turbulence parameters such as specific dissipation rate. ω (or turbulence dissipation rate. ε) and the turbulent kinetic energy. k are resolved. Subsequently. turbulent viscosity (v_t) is computed as a function of these parameters (Elshawarby. 2020).

There also exists a more advanced hypothesis called Reynold Stress Model (RSM) that could be a resort when a more chaotic turbulence system is the case. This model contains seven transport equations which account for their accuracy in the modelling of these turbulence systems. However. these systems are computationally expensive. For this reason. in this study. the Bousinesq approach has been taken (Elshawarby. 2020).

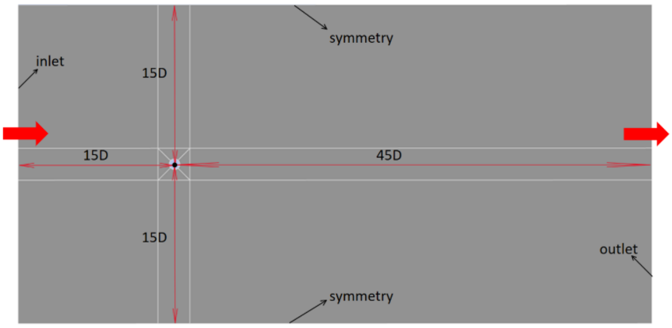

Fig. 2. The schematic of the flow domain and the boundary conditions

The rectangular flow. including the embedded submarine pipe of diameter. D=50 mm without spoiler inside. which is utilized in simulations. is schematized as shown in Figure 2. The length and width of this domain is specified as 50D and 30D. respectively from the center of the cylindrical section of the pipeline. In addition. the lengths of the upstream and downstream regions are regarded as 15D and 45D from the center respectively. This flow domain remains the same regardless of the spoiler types to appropriately realize how the characteristics of the flow and the parameters of interests are affected by geometrical variations. The gap effect which arises due to the region between the pipeline and the seabed is not the scope of this study. Other types of spoilers used with the domain for the analysis are shown in Figure 3.

Fig. 3. Sketches of the cylindrical pipe with and without spoiler

For all computational domains. two-dimensional quadrilateral elements are preferred to capture the von-Karman vortexes after separation more accurately. The meshed computational domain for the cylindrical pipeline without spoiler is depicted in Figure 4. Since near-wall effects are also considered for simulations. the surface mesh cells are refined while advancing nearer the surface. On the other hand. moving further from the surface. the mesh was gradually coarsened which substantially decreased the computational time without sacrificing from the accuracy of the expected results.

The height of the first layer was calculated using eq 4.1 to 4.4 to satisfy the condition of y^+ smaller than unity for a Reynolds number of $1.4x10^4$

$$y^+ = \frac{u_\tau \Delta y_1 \rho}{\mu} \tag{4.1}$$

$$u_\tau = \sqrt{\frac{\tau_w}{\rho}} \tag{4.2}$$

$$\tau_w = \frac{1}{2} c_f * \rho * u^2 \tag{4.3}$$

$$c_f = \frac{0.058}{R_e^{0.2}} \tag{4.4}$$

Freestream velocity of 5 m/s. air density of 1.225 kg/m^3 and dynamic viscosity of $2.1875x10^{-5}$ $kg/m * s$ were implemented as input variables for the simulations. Subsequently. the first layer thickness was found to be $4.5x10^{-5}$.

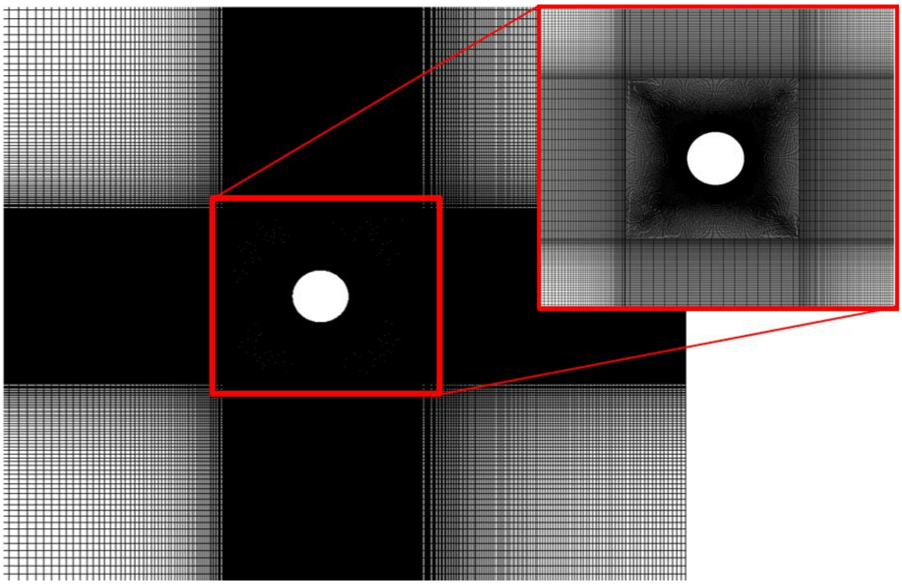

Fig. 4. The structured mesh used in the analysis for the pipeline without spoiler. Number of layers are increased near and in the vicinity of the surface.

Commercial computational fluid dynamics solver package. Ansys Fluent 2023 R1. was preferred to simulate the turbulent flow around and downstream of cylindrical seabed pipeline with and without spoiler in this study. Since Von Kármán vortex shedding. characterized by time-dependent oscillatory behavior. develops downstream of cylindrical bluff bodies. a transient solver was adopted. The coupling of Pressure–velocity was handled by using the SIMPLEC algorithm. while second-order upwind schemes were applied for spatial discretization and a second-order implicit method was used for time integration. This approach enables accurate prediction of unsteady vortex dynamics. which cannot be captured effectively by steady-state simulations. All the simulations were performed under 600 steps. each having a maximum 50 iterations. The time increments were fixed as 0.001 s throughout. The residual errors for the convergence criteria were kept on the order of 10^{-6}.

4. Results & discussion

To evaluate the precision of numerical data. the study conducted by (İlkentapar et al., 2023) was paid attention as a criterion. The rate of change between the two studies is shown at a Reynolds number of 1.4×10^4 in Table 2. The rate of change in the configuration without spoiler was 7.9%. while the rate of change between the configurations with Type-1 spoiler was 1.06%. These differences are within acceptable limits for CFD studies. where differences below 10% are generally considered reliable (Calautit et al. 2015). (Chaudry et al. 2015). The remarkably low difference (1.06%) observed in the Type-1 spoiler configuration indicates strong consistency with previously validated data. Consequently. the numerical results of this study can be considered reliable and thus provide a reliable validation of the numerical model used.

Table 2. C_D values obtained with different spoiler configurations

Type of spoiler	Experimental C_D values (İlkentapar et al.. 2023)	Numerical C_D values	Percentage Change
Without spoiler	1.73	1.867	7.9%
Type-1	1.89	1.87	1.06%

The drag coefficient results for the non-spoiler and spoiler configurations. as well as the percentages of change compared to the control case. are presented in Table 3. The drag coefficient (C_D) value of the control case is determined to be 1.867. Regarding the spoiler designs. it was observed that the drag coefficient values of Type-1 C_D = 1.87 closely approximate the control case.

Table 3. C_D values obtained with different spoiler configurations

Type of spoiler	C_D	Percentage Change
Type-1	1.87	0.2%

The counters of TKE. static pressure. eddy viscosity and velocity of cylinder with and without spoiler cases were illustrated in Fig. 5 and Fig. 6.

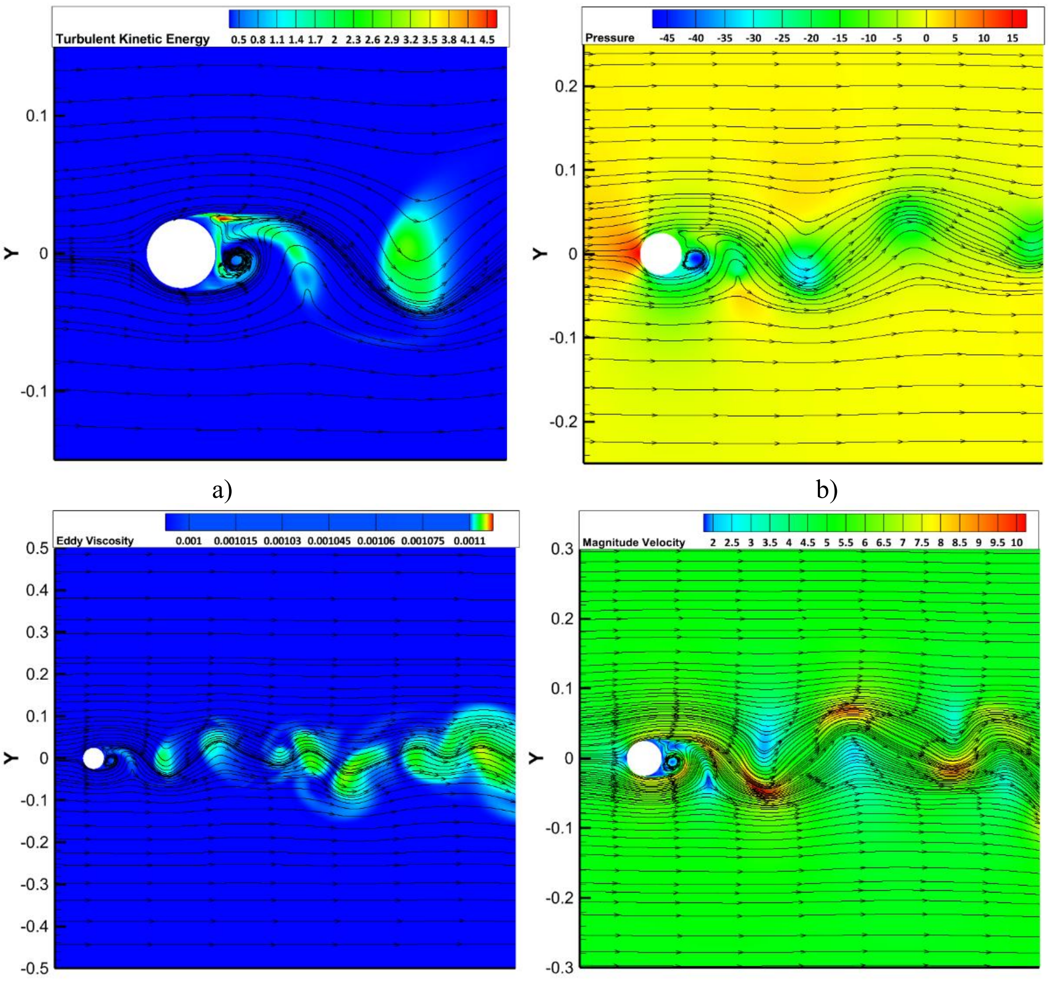

Fig. 5. Contours for cylinder without spoiler; a) *Turbulent Kinetic Energy. b) Static pressure c) Eddy viscosity. d) Velocity*

In the baseline configuration. the flow separates sharply from the rear. generating a broad. unsteady wake resembling bluff-body characteristics. The velocity contour for the no-spoiler case displays a substantial low-velocity region extending posterior to the pipe. suggesting the presence of a considerable separated wake. Correspondingly. the pressure contour reveals an expansive low-pressure zone at the back of the base line case. This low-pressure wake causes significant pressure drag. as the pressure difference between the front (high pressure) and rear (low pressure) is large. The turbulent kinetic energy (TKE) and eddy viscosity contours in the baseline case show high values in the shear layers detaching from the upper surface and sides. indicating strong vortex shedding activity. This suggests an unsteady von Kármán vortex street in the wake. with alternating vortices shedding from the case's trailing edges. Such vortex shedding maintains the low-pressure wake and broadens the wake region. According to Son and Çetiner (2016). a wider wake is associated with higher pressure drag. In summary. the no-spoiler configuration experiences substantial drag because the flow separates cleanly off the rear end. creating a large. turbulent wake with low pressure recovery.

Compared to the base cylinder without spoiler. the Type-1 configuration causes a negligible change in the flow behaviour. The drag coefficient (C_D) increases slightly from 1.867 to 1.87. indicating only a 0.2% increase. This minimal change suggests that the spoiler has a limited effect on the boundary layer separation and wake development in this configuration. The pressure contours show that the base pressure behind the cylinder remains almost unchanged. indicating that the pressure drag contribution is essentially preserved. In the eddy viscosity and turbulent kinetic energy (TKE) fields. only local increases are observed near the spoiler. while no significant concentration is observed in the downstream wake region. The velocity contours reveal a slight upward shift in the separation line due to the spoiler. However. the wake width and the size of the momentum deficit region remain almost the same as in the basic configuration. Overall. these results show that the Type-1 spoiler causes only a weak disturbance in the flow. a small change in wake symmetry and a negligible increase in total drag.

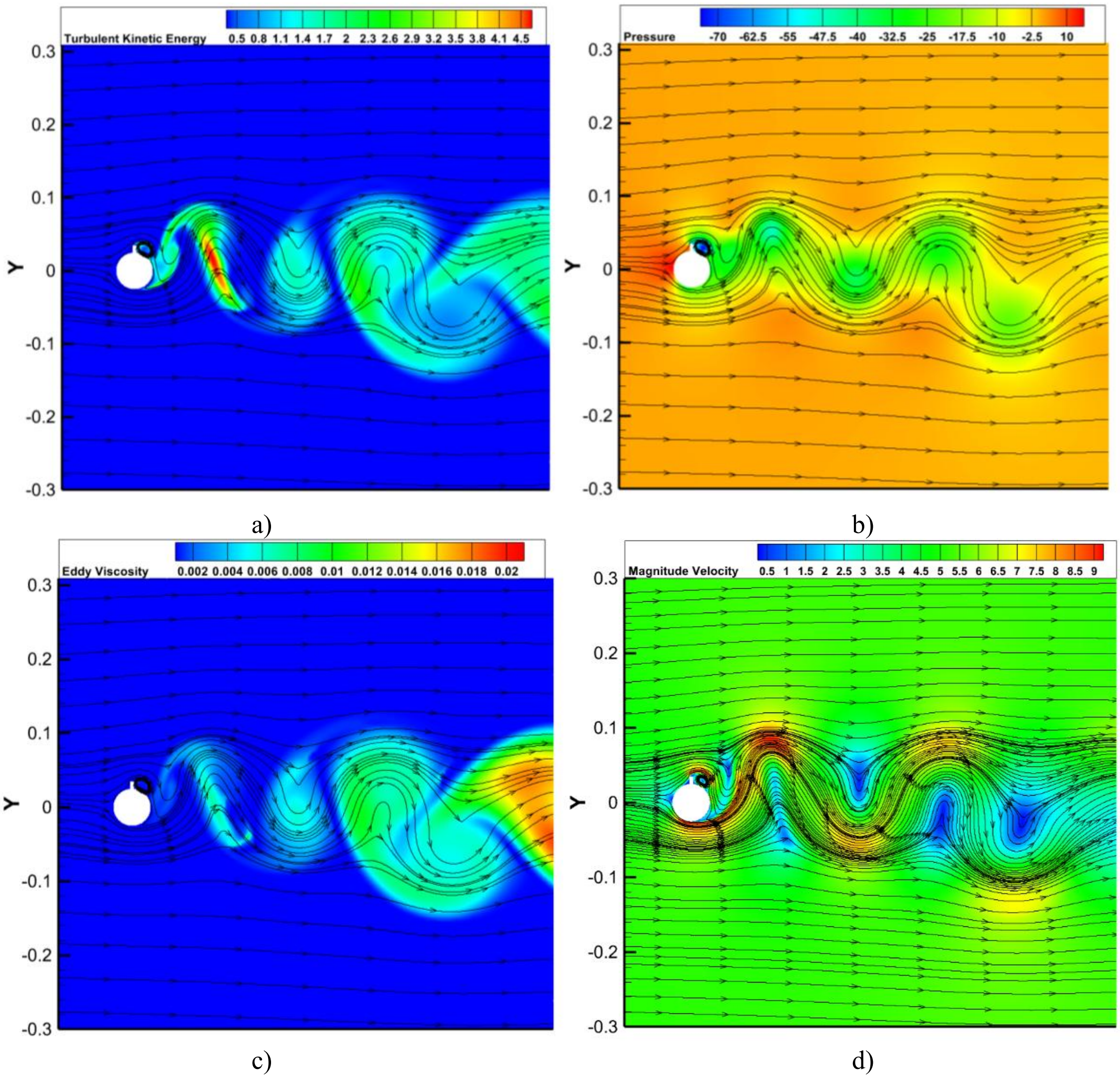

Fig. 6. Contours for Type-1 configuration; a) Turbulent Kinetic Energy. b) Static pressure c) Eddy viscosity. d) Velocity

5. Conclusion

This research presents detailed findings arising from their CFD studies on aerodynamic performances of offshore pipeline spoilers. Successively. it has emerged that spoiler geometry plays the most crucial role in defining aerodynamic drag and wake behavior around cylindrical submarine pipelines. It compared four different spoiler configurations determined by variable flow characteristics and different aerodynamic performances in comparison to a baseline configuration without spoilers.

Type-1 arrangement barely alters the flow behavior as compared to the base cylinder sans spoiler. Only a 0.2% increase is indicated by the drag coefficient (C_D). which rises marginally from 1.867 to 1.87. This slight alteration implies that the spoiler's impact on wake formation and boundary layer separation in this configuration is minor. The base pressure behind the cylinder stays nearly constant. according to the pressure contours. suggesting that the pressure drag contribution is largely maintained. There is no discernible concentration in the downstream wake zone. but only local increases in the eddy viscosity and turbulent kinetic energy (TKE) fields are seen close to the spoiler.

Present research highlights the complex relationship between spoiler geometry and flow dynamics. highlighting how subtle design changes can profoundly affect pipeline stability and sediment dynamics. Further analysis should be taken up in the form of three-dimensional simulations and extend to other parameters such as a slider's flexibility. vortex induced vibration (VIV) induced structural fatigue risk. and porosity. which can further optimize aerodynamic and hydrodynamic performance with varying oceanographic conditions. Such studies indeed fill in gaps in-the literature by as they were giving more comprehensive guidelines on spoiler applications- in addition to economically beneficial. structurally safe. and environmentally adaptable solutions.

References

Bearman, P. W., & Zdravkovich, M. M. (1978). Flow around a circular cylinder near a plane boundary. *Journal of Fluid Mechanics, 89*, 33–47. https://doi.org/10.1017/S002211207800244X

Bianchi, V., Silva, L. S., Cenci, F., Hirabayashi, S., Suzuki, H., & Gonçalves, R. T. (2020). Spoiler plate effects on the suppression of vortex induced motions of a single circular cylinder. *Ocean Engineering, 210*, 107569. https://doi.org/10.1016/j.oceaneng.2020.107569

Calautit, J. K., Hughes, B. R., O'Connor, D., & Shahzad, S. S. (2015). CFD and wind tunnel study of the performance of a multi-directional wind tower with heat transfer devices. *Energy Procedia, 75*, 1692–1697.

Chaudhry Nasarullah, H., Calautit, J. K., Hughes, B. R., & Sim, L. F. (2015). CFD and experimental study on the effect of progressive heating on fluid flow inside a thermal wind tunnel. *Computation, 3*(4), 509–527.

Dehkordi, B. G., Moghaddam, H. S., & Jafari, H. H. (2011). Numerical simulation of flow over two circular cylinders in tandem arrangement. *Journal of Hydrodynamics, 23*(1), 114–126.

Elshawarby, O. A. M. A. (2020). *Computational fluid dynamics of multiphase flow using ANSYS Fluent*.

İlkentapar, M., Akşit, S., Açıkel, H. H., & Öner, A. A. (2023). The effect of spoilers on flow around tandem circular cylinders. *Ocean Engineering, 272*, 113637. https://doi.org/10.1016/j.oceaneng.2023.113637

Lo, S. H. (2013). Dynamic grid for mesh generation by the advancing front method. *Computers & Structures, 123*, 15–27. https://doi.org/10.1016/j.compstruc.2013.04.004

Son, O., & Cetiner, O. (2016). Drag prediction in the near wake of a circular cylinder based on DPIV data. *Journal of Applied Fluid Mechanics, 9*(4), 1963–1968.

Shi, Y., Gao, F., Wang, N., & Yin, Z. (2021). Coupled flow-seepage-elastoplastic modeling for competition mechanism between lateral instability and tunnel erosion of a submarine pipeline. *Journal of Marine Science and Engineering, 9*(8), 889.

Zhao, J., & Wang, X. (2009). CFD numerical simulation of the submarine pipeline with a spoiler. *Journal of Offshore Mechanics and Arctic Engineering, 131*(3), 031601. https://doi.org/10.1115/1.3124127

Zhao, Y., Yu, B., & Tao, W. (2013). An improved paving method of automatic quadrilateral mesh generation. *Numerical Heat Transfer, Part B: Fundamentals, 64*(3), 218–238. https://doi.org/10.1080/10407790.2013.797308

Zhu, H. J., Qi, X., Lin, P., & Yang, Y. (2013). Numerical simulation of flow around a submarine pipe with a spoiler and current induced scour beneath the pipe. *Applied Ocean Research, 41*, 87–100. https://doi.org/10.1016/j.apor.2013.03.005

4th International Civil Engineering & Architecture Conference
17-19 May 2025, Trabzon, Türkiye

Advances in breach formation modeling and flood risk assessment for dam failures

Hasan O. Marangoz*[1], Tuğçe Anılan[2], Veli Süme[1]

[1]Recep Tayyip Erdogan University, Department of Civil Engineering, 53100 Rize, Türkiye
[2] Karadeniz Technical University, Department of Civil Engineering, 61080 Trabzon, Türkiye

Abstract. This study examines the breach formation mechanisms in dam failures and the parameters influencing this process. Empirical equations, practical methods, and physically-based models were utilized to estimate breach parameters. Empirical equations were developed based on data obtained from past dam failures and analyzed through hydraulic parameters. Physically-based models, on the other hand, incorporate more detailed hydraulic, structural, and geotechnical analyses, providing higher accuracy through computer-aided simulations. This study aims to enhance the understanding of breach formation mechanisms in dam failures and improve flood risk assessments using different modeling approaches.

Keywords: Dam breach formation, Flood risk assessment, Empirical; Physically-based models

1. Introduction

Dam failures have historically been recognized as among the most destructive natural hazards, often leading to catastrophic consequences including significant loss of life, severe economic damage, and long-term environmental impacts. The sudden release of large water volumes during a dam breach produces highly dynamic flood waves, whose propagation characteristics are strongly dependent on the breach formation process itself (Wang and Kahawita, 2002). Therefore, understanding the mechanisms of breach initiation and development is critical for improving the reliability of flood risk assessments and for designing effective early warning systems and emergency response strategies.

The modeling of breach formation presents unique challenges (West et al., 2018) due to the complex interactions between hydraulic forces, geotechnical properties, structural characteristics, and erosion processes. Early approaches to breach analysis primarily relied on simplified assumptions, treating breaches as fixed openings with steady discharge rates. However, subsequent observations from historical dam failures (Froehlich, 1995) have demonstrated that breach formation is a highly dynamic and nonlinear process involving rapid erosion, varying breach geometry, and changing outflow conditions over time.

To capture these dynamics, a range of modeling approaches has been developed (Guan, 2014). Empirical methods, based on regression analyses of historical dam failure data, provide quick estimations of key breach parameters such as breach width, side slope, and failure time. While useful for preliminary assessments, these models are subject to significant uncertainties due to their reliance on generalized data and simplifications. Practical estimation methods, established by organizations such as the United States Army Corps of Engineers (USACE,2016), the Federal Energy Regulatory Commission (FERC,1988), and the National Weather Service (NWS), offer standardized parameter ranges for different dam types, enhancing the practicality of breach prediction but still lacking in precision for site-specific conditions (Fread, 1984)

In contrast, physically-based models simulate breach formation through detailed mathematical representations of hydraulic behavior, soil erosion, sediment transport, and structural failure(Wang et al., 2006) mechanisms. These models require extensive input data, including dam material properties (Macchione and Rino, 2008), reservoir characteristics, and hydrodynamic conditions, but they offer superior accuracy in predicting breach development and the resulting outflow hydrographs. Recent advancements in computational power and numerical methods have made it increasingly feasible to apply such models to complex, real-world dam breach scenarios.

This study systematically reviews and compares empirical, practical, and physically-based approaches for breach parameter estimation, highlighting their respective advantages, limitations, and appropriate applications. By synthesizing information from historical data, theoretical analyses, and computational modeling efforts, the study aims to contribute to a deeper understanding of breach mechanics and to enhance the accuracy of flood risk

* Corresponding author, E-mail: hasanogulcan.marangoz@erdogan.edu.tr

https://doi.org/10.31462/icearc2025_ce_hyd_703

assessments associated with dam failures. In doing so, it provides valuable guidance for engineers, researchers, and policymakers tasked with dam safety evaluations and disaster preparedness planning.

2. Material and methods

2.1. Methods for estimating breach parameters

Historically, due to the lack of sufficient observational data, it was assumed that dam failures involved the discharge of water through a fixed opening formed by a fragment breaking off from the dam body. However, in reality, modeling breach formation and determining breach parameters introduce significant uncertainties in dam failure flood analyses (Bayazıt & Önöz, 2008). To allow mathematical representation of the complex formation of breach characteristics, simplifications were made to render the process more accessible and understandable. Over time, these simplifications have been extended by generalizing failure mechanisms through simple empirical expressions based on data from past dam failures.

Directly predicting the failure mode and breach parameters for existing dams remains challenging. Nevertheless, approaches that provide reasonable approximations without diverging significantly from realistic failure scenarios offer sufficient criteria for conducting reliable risk analyses. The prediction of breach formation mechanisms in empirical equations typically depends on factors such as the dam's storage volume, height, width, and the type of construction material used. In other types of failures, rather than solving a breach problem, different investigations and time-dependent changes are involved.

2.1.1. Estimation of breach formation parameters using practical methods

Due to the severe damages and increased casualties resulting from dam failures, several breach-related parameters have been recorded over time, and efforts have been made to standardize breach parameter predictions based on the dam type. This approach aimed to provide a practical means of estimating breach parameters for existing dams. Initially, in the 1980s, the United States Army Corps of Engineers (USACE) published a set of practical breach parameters specific to dam failures. These were later expanded and supplemented by contributions from the Federal Energy Regulatory Commission (FERC) and the National Weather Service (NWS).

The estimation methods developed by these institutions have been periodically updated and adapted to various dam types. The expected ranges of breach parameters during failure scenarios, according to these practical methods, are presented in Table 1.

Table 1. Scour parameters expected to occur based on dam type (Gee, 2008)

Dam Type	Average Breach Width, B_{ort} (m)	Breach Edge Slope, z	Breach Time, t_f (sa)	Institution
Earth/Rock Fill	$0.5(h_d) < B_{ort} < 3(h_d)$	$0 < z < 1$	$0.5 < t_f < 4$	USACE (1980)
	$0.5(h_d) < B_{ort} < 5(h_d)$	$0 < z < 1$	$0.5 < t_f < 4$	USACE (2007)
	$(h_d) < B_{ort} < 5(h_d)$	$0 < z < 1$	$0.5 < t_f < 1$	FERC (1988)
	$2(h_d) < B_{ort} < 5(h_d)$	$0 < z < 1$	$0.5 < t_f < 1$	NWS (Fread, 2006)
Concrete Gravity	Monolithic Pieces	Vertical	$0.1 < t_f < 0.5$	USACE (1980)
	$B_{ort} \leq 0.5L$	Vertical	$0.1 < t_f < 0.3$	FERC
	$B_{ort} \leq 0.5L$	Vertical	$0.1 < t_f < 0.2$	NWS
	Entire Dam	Valley Junction	$t_f \leq 0.1$	USACE (1980)
Concrete Arch	$(0.8L) < B_{ort} < L$	$0 < z <$ V.B.	$t_f \leq 0.1$	USACE (2007)
	Entire Dam	$0 < z <$ V.B.	$t_f \leq 0.1$	FERC
	$(0.8L) < B_{ort} < L$	$0 < z <$ V.B.	$t_f \leq 0.1$	NWS
Slag	$(0.8L) < B_{ort} < L$	$1 < z < 2$	$0.1 < t_f < 0.3$	FERC
	$(0.8L) < B_{ort} < L$	$1 < z < 2$	$t_f \leq 0.1$	NWS

The practical method technique for estimating breach parameters is still widely used today for predicting breach characteristics of many dams and for validating empirical equations.

2.1.2. Estimation of breach formation parameters using empirical equations

In the estimation method also known as the parametric model, simple empirical equations are employed. In this approach, a collection of historical dam failure data has been gathered and statistically analyzed using regression methods (West et al., 2018). Through the analysis of dozens of dam failure cases, empirical equations have been developed, which use certain dam parameters as inputs for calculating breach characteristics. Table 2 presents a chronological summary of various empirical equations commonly used for estimating breach parameters.

Table 2. Empirically derived equations for scour parameters

Average Breach Width	Break Time	Peak Discharge	
USBR (1988) $B_{ort}= 3(h_w)$	MacDonald, Langridge-Monopolis (1984) $t_f=0.0179V_{er}^{\ 0.364}$	Evans (1986) $Q=0.72V_w^{0.53}$	Kirkpatrick (1977) $Q=1.27(h_w+0.3)^{2.5}$
MacDonald, Langridge-Monopolis(1984) $V_{er}= 0.0261(V_w\ h_w)^{\ 0.769}$ -TD $V_{er}=0.00348(V_w h_w)^{\ 0,852}$-TDD	USBR (1988) $t_f= 0.011B_{ort}$	SCS (1981) $Q=16.6h_w^{1.85}$ Hagen(1982) $Q=0.54(Sh_d)^{0.5}$	USBR (1982) $Q=19.1h_w^{1.85}$ Froehlich(1995a) $Q=0.6V_w^{0.295}\ h_w^{1.24}$
Von Thun and Gillete (1990) $B_{ort}=2.5h_w+ C_b$ $54.9>C_b>6.1$	Von Thun and Gillete (1990) $t_f=0.015(h_w)$ -AF $t_f=0.02(h_w)+ 0.25$ -AA $t_f=B/ (4h_w+61)$ -AF $t_f=B/ (4h_w)$ -AA	Costa (1985) $Q=1.122(S)^{0.57}$ $Q=0.98(Sh_d)^{0.42}$ $Q=2.63(Sh_d)^{0.44}$	Walder & O'Connor(1997) Based on reservoir size and dam erodibility characteristics
Froehlich (1995b) $B_{ort}=0.1803K_0V_w^{0.32}\ h_b^{0.19}$ $K_0=1.4$ V 1	Froehlich (1995b) $t_f=0.00254V_w^{0.53}h_b^{-0.9}$	Singh & Snorrason (1984) $Q=13.4h_d^{1.89}$ $Q=1.776S^{0.47}$	
Froehlich(2008) $B_{ort}= 0.27k_1V_w^{0.33}$	Froehlich (2008) $tf=0.0176\sqrt{\frac{V_W}{gh_b^2}}$	MacDonald &Langridge-Monopolis(1984) $Q=1.154(V_w\ h_w)^{0.412}$ $Q=3.85(V_w\ h_w)^{0.411}$	
	Froehlich(2016a, b) $tf=60\sqrt{\frac{V_W}{gh_b^2}}$	Pierce et al. (2010) $Q\ =0.0176(V_wh_w)^{0.606}$ $Q\ =0.038V_w^{0.475}\ h_w^{1.09}$	
		Froehlich(2016a, b) $Q=0.0175k_3k_H\frac{\sqrt{gV_wh_wh_b^2}}{W_{ort}}$	

* B_{ort}: Average breach width (m), Q: Maximum breach discharge, t_f: Failure time (hours), C_b: Reservoir storage function, varying within the value range specified in the table, h_b: Total breach height, h_d: Dam height (m), h_w: Water depth remaining over the breach at the time of failure (m), h: Water depth remaining behind the dam, Vw: Reservoir water volume remaining above the breach base at the time of failure (m³), K_0, K_1, K_2, K_3: Coefficients used for overtopping failures (values are 1.4, 1.3, 1.5, and 1.85 respectively) and set to 1 for piping-type failures, S: Reservoir storage capacity (m³), V_{er}: Volume of eroded dam material until the breach reaches its final shape (m³), AF*: High erosion, AA*: Low erosion, TD*: Earthfill dam, TDD*: Non-earthfill dam, KH: A coefficient taken as 1 when $h_b < 6.1$, and $(h_b/6.1)$^0.125 when $h_b > 6.1$.

The simplicity of manual calculations in empirical expressions has introduced several assumptions and simplifications into the literature. Although the actual breach width continuously changes during the failure process, a constant average breach width parameter is generally used. Various failure assumptions are employed to estimate the final breach width based on the average breach width.

2.1.3. Estimation of breach formation parameters using physically-based methods

Physically-based models estimate breach parameters analytically and numerically by using hydraulic, structural, and geotechnical-based empirical values and coefficients (West et al., 2018). In recent years, physically-based methods have been increasingly utilized and diversified, with computational power typically required to solve the complex processes involved. Often referred to as the mathematical modeling of breach formation in the literature, these methods incorporate inputs such as slope stability, erosion, sediment transport, angle of repose, cohesion coefficient, type of embankment material, hydrological data, and soil properties into the governing equations. As a result, the breach geometry and outflow hydrograph derived from these models are achieved with higher accuracy compared to empirical or practical methods.

To date, more than 60 physically-based models related to breach mechanics have been developed. Some of the most commonly used models are categorized based on various criteria and are listed chronologically in Table 3.

Table 3. Some physics-based models used in scour problems

Method (Reference)	Flow Passing Through the Breach		Breach Geometry	Sediment Transport
Cristofano (1965)	$Q= CLH^{1.5}$	Broad-crested	Trapezoidal	Cristofano
Harris-Wagner (HW) Model (1967)	$Q=5.5H^{3.2}$	Broad-crested	Parabolic	Mod. Schoklitsch $G= \zeta Q_d^{-0.5}$ $\zeta =86.7S^{1.5}$
BRDAM Harris ve Wagner (1967), Brown and Rogers (1977, 1981)	$Q=(T^{-1}gA^3)^{0.5}$	Broad-crested	Parabolic	Schoklitsch
Ponce-Tsivoglou (PT) Model (1981)	St. Venant Momentum and Mass Conservation Equations	(Full Momentum Approach)	Constant Width Due to Peak Flow	Meyer-Peter and Müller $q_s= a(\tau- \tau_c)^b$
Lou Model (1981)	St. Venant Momentum and Mass Conservation Equations	(Full Momentum Approach)	Parabolic	DuBoy and Einstein $q_b= K\tau_0 (\tau_0-\tau)$ $q_s=K[\zeta I_1+I_2]$ $\zeta=2.3\log\frac{30.2d}{\Delta}$
Nogueira Model (1984)	St. Venant Momentum and Mass Conservation Equations	(Full Momentum Approach)	Parabolic	Mod. Meyer-Peter and Müller $q_s= \zeta (\tau- \tau_c)^b$ $\zeta=0.7923/ \gamma$
DAMBRK Fread (1984a,b)	$Q_b=4.8A_P \zeta$ $\zeta =(h-h_{ort})^{0.5}$	Broad-Crested and Orifice Flow	Triangular Trapezoidal Rectengular	Assumption of Linear Erosion
BREACH (Fread 1984b)	$Q_b=3B_o(H-H_c)^{1.5}$ $Q_b=0.98(2g)^{0.5}A\zeta$ $\zeta =(H-H_p)^{0.5}$	Broad-Crested and Orifice Flow	Rectengular	DuBoys and Meyer-Peter and Müller
BEED Singh ve Scarlatos (1986,1987a)	$Q=C_d[\zeta_1+\zeta_2]$ $\zeta_1=C_rb(h-z)^{1.5}$ $\zeta_2= C_tb(h-z)^{2.5}$	Broad-Crested Flow	Trapezoidal	Einstein-Brown
SMPDBK (1991) Wetmore ve Fread (1984)	$Q=Q_0+3.1B_r\zeta$ $\zeta=\left(\frac{c}{\frac{t_f}{60}+\frac{C}{H^{0.5}}}\right)^3$	Broad-Crested	Trapezoidal Rectangular	Implicit
(Loukola ve Huokuna 1998)		Broad-Crested and Orifice Flow	Trapezoidal	Meyer-Peter and Müller
RUPRO Paquier (1998) Paquier et al. (1998), Paquier (2002)		Bernoulli	Rectangular	Meyer-Peter and Müller
FIREBIRD Wang and Kahawita (2002), Wang et al. (2006)	St. Venant Momentum and Mass Conservation Equations		Trapezoidal	
Macchione Breach Macchione ve Rino (2008)			Trapezoidal Triangular	

Table 3. Continued

MIKE-11 Danish Hydraulic Institute (2009)		Broad-Crested and Orifice Flow	Triangular	Engelund-Hansen
DL Breach3D Marsooli ve Wu (2014)	RANS Equations	Finite Volume Solution		3D Unsteady Transport Equations
HEC-RAS (USACE, 2016)	St. Venant Momentum and Mass Conservation Equations	Broad-Crested	Trapezoidal	E-A.*, M.P.M.*, Yang*, A.W.*, W.C.*, L.*
Guan et al. (2014)	Shallow Water Equations			Sediment Transport Equations

*E-A: Engelung Hansen, M.P.M.: Meyer Peter Muller, A.W.: Ackers- White, W.C.: Wilcock- Crowe, Laursen

Table 4 presents the details of the dam breach scenarios developed within the scope of this study. Accordingly, for each scenario, the values calculated individually such as the reservoir volume at the time of failure, the water depth at breach initiation, the side slopes of the trapezoidal breach, the elevation of the breach bottom, the average breach width, and the failure time are provided.

Table 4. Input parameters for dam breach simulation scenarios

Scenario	Volume at Breach (m^3)	Depth at Beach (m)	Break Bottom Height (m)	Side Slopes of breach	Breach Time (hours)	Mean Bottom Breach Width (m)
1	63495000	76.5	37	2	0.4	20
2	63495000	76.5	37	2	0.67	20
3	65611500	79.05	37	2	0.67	20
4	65611500	79.05	37	0.5	1.98	13
5	66856500	80.55	37	2	1.98	43
6	66856500	80.55	37	1.4	0.52	43
7	66856500	80.55	37	0.5	1.86	216
8	66856500	80.55	37	1.03	1.34	113

3.Results and discussion

In this study, eight distinct dam breach scenarios were evaluated by varying key parameters such as breach side slopes, breach bottom width, water depth at the time of failure, and failure duration. These parameters were chosen to represent a range of potential real-world failure cases, allowing for comparative assessment under different geometric and hydraulic conditions.

Using a set of widely accepted empirical models namely those proposed by MacDonald & Langridge-Monopolis (1984), Froehlich (1995a), Evans (1986), SCS (1981), USBR (1982), and Costa (1985) the peak outflow discharges (Q_{peak}) were calculated for each scenario (Fig. 1). The results demonstrated that while all methods produced values of similar magnitude, considerable variation exists depending on the governing assumptions of each model.

In the figure, the highest peak discharges were observed in Scenarios 5, 6, 7, and 8 based on the USBR approach, yielding a value of approximately 65,000 m^3/s. In comparison, the Froehlich method produced peak discharges around 30,000 m^3/s, the SCS method around 55,000 m^3/s, and the MacDonald, Evans, and Costa methods yielded values close to 10,000 m^3/s. Overall, an increase in upstream water depth was found to have a direct impact on the peak discharge resulting from dam failure. Since all breach scenarios were modeled as overtopping failures, the influence of failure mode could not be evaluated within the scope of this study.

In addition to discharge comparisons, trapezoidal hydrographs were generated for each scenario using both the MacDonald and Froehlich models. These hydrographs allowed a visualization of flow evolution over time and revealed that scenarios with wider breaches and higher heads result in steeper rising limbs and larger flow volumes. Moreover, failure time was found to have a direct influence on the shape of the hydrograph: shorter failure durations led to sharper peaks and shorter flood durations. When the results obtained from testing the same scenarios with a more reliable, physically-based model were compared to those from the empirical approach, it was found that the Froehlich method produced outputs closest to the physically-based model's results.

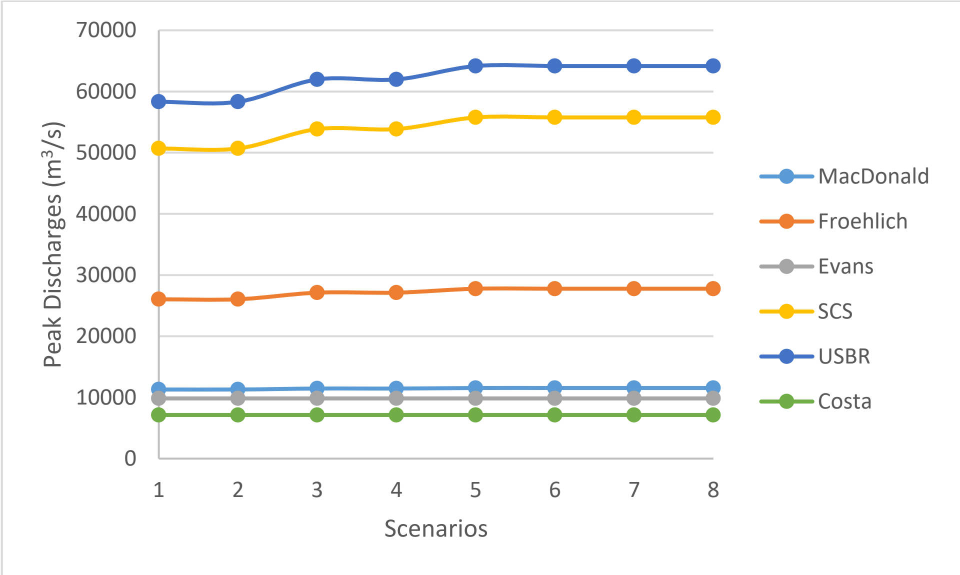

Fig. 1. Peak discharges results of the scenarios

4. Conclusions

This study presents a comparative evaluation of dam breach modeling approaches through the application of widely accepted empirical formulas to eight distinct overtopping failure scenarios. By varying breach geometries (bottom width and side slopes), water depth at failure, and failure duration, the study aimed to explore the sensitivity of peak outflow discharge to key physical parameters.

Six different empirical models; MacDonald & Langridge-Monopolis (1984), Froehlich (1995a), Evans (1986), SCS (1981), USBR (1982), and Costa (1985) were used to estimate the peak discharge (Q_{peak}) for each scenario. The Froehlich model produced peak discharges ranging from 26,044 m³/s (Scenario 1) to 27,765 m³/s (Scenarios 5–8), while the USBR approach yielded the highest values, up to approximately 65,000 m³/s, particularly under conditions of increased water depth and wider breaches. The SCS method consistently estimated discharges near 55,000 m³/s, whereas the MacDonald, Evans, and Costa models yielded lower values, close to 10,000 m³/s. These differences reflect the degree of conservatism or simplification inherent in each method.Notably, when these empirical estimations were compared against the results from a more robust, physically-based model applied to the same scenarios, the Froehlich method stood out by providing results that were closely aligned with the physically-based outcomes suggesting its comparatively higher reliability among empirical formulations.

Trapezoidal hydrographs were constructed using both the Froehlich and MacDonald models to better visualize flood propagation characteristics. The hydrographs clearly illustrated the influence of breach parameters on flood evolution: scenarios with shorter breach times such as Scenario 1 (0.40 hours) produced steep, narrow peaks, while those with longer breach durations, like Scenario 4 (1.98 hours), resulted in flatter hydrographs with extended durations.

References

USACE Hydrologic Engineering Center, (USACE, 2016). HEC-RAS River Analysis System- User's Manual, California, USA.
Fread, D.L. (1984). DAMBRK: The NWS Dam Break Flood Forecasting Model. National Weather Service Report, Silver Spring, Maryland, USA.
USA Federal Regulatory Commission, (FERC, 1988). Notice of revised emergency action plan guidelines. Washington, USA.
Bayazıt, M., Önöz, B. (2008). Hydrology of floods and droughts (In Turkish). Nobel Academic Publishing, 1st Edition, ISBN: 6053951421, 259p
West, M., Morris, M., Hassan, M. (2018). A guide to breach prediction. *Dams and Reservoirs, 28*(4), 150-152
Cristofano, E.A. (1965). Method of computing erosion rate for failure of earth dams. USBR.
MacDonald, T.C., Langridge-Monopolis, J. (1984). Breaching characteristics of dam failures. *ASCE Journal Hydraulic Engineering, 110*(5), 567-586
Evans, S.G. (1986). The Maximum discharge of outburst floods caused by the breaching of man-made and natural dams. *Canadian Geotechnical Journal. 23*(3), 385-387
Kirkpatrick, G.W. (1977). Evaluation Guidelines for Spillway Adequacy. The evaluation of Dam Safety, Proc. Engineering Foundation Conference, New York, 395-414

Soil Conservation Service (SCS, 1981). Simplified Dam-breach routing procedure. Technical Release No. 66 (Rev 1).
Costa, J.E. (1985). Floods from dam failures, Denver, Colorado, Open-File Report No. 85-560, 59 s.
Von Thun, J.L., Gillette, D.R. (1990). Guidance on Breach Parameters, Internal Memorandum. Unpublished Internal Document.
Walder, J.S., O'Connor. J.E. (1997). Methods for predicting peak discharge of floods caused by failure of natural and constructed earthen dams. *Water Resources Research, 33*(10), 2337-2348
Froehlich, D.C. (1995), Peak outflow from breached embankment dam. *Journal of Water Resources Planning and Management, 121*(1), 90-97
Singh, K.P., Snorrason, A. (1984) Sensitivity of outflow peaks and flood stages to the selection of dam breach parameters and simulation models. *Journal of Hydrology. 68*, 295-310
Froehlich, D.C. (2008) Embankment Dam Breach Parameters and Their Uncertainties. *Journal of Hydraulic Engineering. 134*(12), 1708-1721
Pierce, M.W., Thornton, C.I., Abt, S.R. (2010). Predicting peak outflow from breached embankment dams. *Journal of Hydrologic Engineering. 15*(5), 338-349
Froehlich, D.C. (2016a) Empirical model of embankment dam breaching. International Conference on Fluvial Hydraulics (River Flow 2016), St. Louis, 12-15 July.
Cristofano, E.A. (1965). Method of computing erosion rate for failure of earth dams. USBR. 14 s.
Harris, G.W., Wagner, D.A. (1967). Outflow from breached earth dams. Bachelor Science Thesis, University of Utah, Salt Lake City, USA, 102 s.
Brown, R.J., Rogers, D.C. (1981). BRDAM Users' Manual. Water and Power Resources Service, Denver, 67 s.
Ponce, V.M. Tsivoglou, A.J. (1981). Modelling gradual dam breaches. *Journal of the Hydraulics Division. 107*(7), 829-838 s.
Lou, W.C. (1981). Mathematical Modelling of Earth Dam Breaches. Doctoral Thesis, Colorado State University, Fort Collins, USA
Nogueira, V.D.Q. (1984). A Mathematical model of progressive earth dam failure. Doktoral Thesis, Colorado State University, Fort Collins, USA
Fread, D.L. (1984a). DAMBRK: The NWS Dam Break Flood Forecasting Model. National Weather Service Report, Silver Spring, Maryland, USA
Wetmore, J.N. Fread, D.L. (1984). The NWS Simplified Dam-break flood forecasting model for desk-top and hand-held microcomputer. Federal Emergency Management Agency (FEMA), USA, 122
Loukola, E. Huokuna, M. (1998). A Numerical erosion model for embankment dam failure and its use for risk assessment. Concerted Action on Dambreak Modelling, 2nd Project Workshop, Munich, Germany
Paquier, A. (1998). 1D and 2D Models for simulating dam-break waves and natural floods. Concerted Action on Dambreak Modelling, Wallingford Meeting, Wallingford, England
Paquier, A. (2002). Rupro, Breach model used by cemagref during impact project. 1st Project Workshop Wallingford Meeting, Wallingford, England
Paquier, A. Nogues, P. Herledan, R. (1998). Model of piping in order to compute dam-break wave. Concerted Action on Dambreak Modelling, Munich Meeting, Munich, Germany
Wang, P. Kahawita, R. (2002). Modelling the hydraulics and erosion process in breach formation due to overtopping. *Sedimentation and Sediment Transport*, 211-220
Wang, P. Kahawita, R. Mokhtari, D. Phat, T.M. Quach, T.T. (2006). Modelling Breach Formation in Embankments due to Overtopping. ICOLD Conference, 18-23 June, Barcelona
Danish Hydraulic Institute, (2009). MIKE-11: A Modelling System for Rivers and Channels. User's Manual. Horsholm, Denmark.
Macchione, F., Rino, A. (2008). Model for predicting floods due to earthen dam breaching- ii: comparison with other methods and predictive use. *Journal of Hydraulic Engineering. 134*(12), 1697-1707 s.
Marsooli, R., Wu, W. (2014). 3D Finite-volume model of dam-break flow over uneven beds based on vof method. Advances in Water Resources. 70, 104-117 s.
Guan, M. Wright, N.G. Sleigh, P.A. (2014). A 2D Process-Based morphodynamic model for flooding by non-cohesive dyke breach. *Journal of Hydraulic Engineering. 140*(7).
USACE Hydrologic Engineering Center, (USACE, 2016). HEC-RAS River Analysis System- User's Manual, California, USA, 960 s.

Experimental study of temporal evolution of the breach and flowrate from the breach due to overtopping at earth-fill dams

Mehmet Ş. Güney*[1], Ruti Politi[1], Yiğit Kalyoncu[1], Kadri Dallı[1]

[1] Izmir University of Economics, Faculty of Engineering, Department of Civil Engineering, İzmir, Türkiye

Abstract. One of the most important reasons for earth-fill dam failures is overtopping. This complex phenomenon is affected by several geometrical, hydraulic and geotechnical parameters. Therefore, it is very important to perform experiments to reveal the breach mechanism and to investigate the temporal evolution of the breach and the flow rates from the breach. In this study, it was intended to obtain experimental results in the case of overtopping at homogeneous earth-fill dam. The experiments were conducted at Hydraulics Laboratory of Civil Engineering Department within İzmir University of Economics. A homogeneous earth-fill dam was built in a flume 0.96 m wide, 0.81 m high and 5.44 m long. Some common soil mechanics tests were also carried out before the dam was built. The dam body was constructed by using a mixture of 85% fine sand and 15% clay. High-precision cameras were used to record the temporal development of the breach resulting from overtopping. Gauss area formula was used to obtain the time-varied values of the breach areas. The temporal changes of water depth in the flume were also recorded. The water flowrate outgoing from the breach was determined by using the continuity equation. The so obtained experimental findings are presented and interpreted. The time corresponding to the peak values in discharge and breach areas was also determined. These experimental findings provide the opportunities for the calibration and validation of the numerical models used in the relevant numerical investigations. This study offers also guidance for strategies concerning emergency action plans related to the failure of homogeneous earth-fill dams because of the overtopping.

Keywords: Earth-fill dam; Overtopping; Breach geometry; Breach development; Discharge through breach

1. Introduction

One of the most important reasons for earth-fill dam failures is overtopping. This complex phenomenon is affected by several geometrical, hydraulic and geotechnical parameters. In an overtopping failure, water surges over the dam crest as a result of inadequate flood design or extreme rainfall, ultimately leading to the formation of a breach and the structural failure of the dam (Aman et al., 2023). Costa (1985) reported that approximately 34% of dam failures were caused by overtopping, 30% by foundation defects, and 28% by piping. Singh (1996) reported that more than 60% of earth dam failures result from either internal erosion (piping) or overtopping.

Regardless of the uncertainties, dam failures can be extremely catastrophic due to the severe floods they create at downstream, resulting in significant loss of life and property. It is critical to establish the flood flow rate that will result from the dam failure in order to assess the risk to any residential, commercial, or agricultural sectors. Nowadays, numerical model simulations are commonly used in works of literature. Despite decades of study, the basic mechanisms of overtopping and the most efficient ways for preventing and mitigating it in earth-fill dams are not completely known. Without artificial embankments or flood-discharge structures, overtopping occurs easily when the upstream water level surpasses the lowest point of the dam crest. The breach failure mechanism caused solely by overtopping has been extensively studied both experimentally and numerically (Chen et al., 2023).

Since the late 1990s, various simplified physical models have been developed. Laboratory experiments and numerical models have been created to simulate the progression of surface erosion and slope instability over time during an overtopping-induced dam failure (Verma et al., 2023). Ashraf et al. (2019) conducted a statistical and experimental analysis of dam failure caused by overtopping. A dataset of 126 embankment failures was analyzed using nonlinear regression in MATLAB to derive predictive equations for breach parameters. The models showed consistent performance across samples. Five large-scale overtopping tests on cohesive and non-cohesive soils validated the equations, with strong correlation observed for non-cohesive embankments. Their findings indicated that the derived equations aligned well with experimental results for non-cohesive soils. Chen et al. (2019)

* Corresponding author, Professor, E-mail: sukru.guney@ieu.edu.tr

https://doi.org/10.31462/icearc2025_ce_hyd_753

golden light publishing

developed a numerical model for earthen dam breach due to piping failure, incorporating an arched pipe channel geometry rather than traditional rectangular or circular cross-sections. The model simulates breach evolution by considering shear stress-based erosion, pipe roof collapse mechanisms, and transitions from pressurized to open-channel flow, ultimately leading to overtopping failure. Zhou et al. (2021) provided an analysis of the spatial and temporal evolution of breaching flows during various stages of overtopping failure. Their study conducted large-scale flume tests to analyze outburst discharge from landslide dams due to overtopping failure, focusing on the longitudinal evolution of breach flow and the effects of upstream inflows and loose deposits on flood dynamics. The study found that increasing the inflow discharge leads to a higher peak outburst discharge, as well as a reduction in the time required to reach both the peak and inflection points of the outburst hydrograph. Bereta et al. (2020) conducted small-scale model tests to examine the breaching process of cohesive embankment dams due to overtopping, using a simplified physical-based breach model. By testing five dam models, the results showed that head cut erosion was a key factor in breach development, with flow discharge and velocity estimated using hydraulic methods and the broad-crested weir formula. Experimental results demonstrated good agreement between calculated and measured breach parameters, including peak discharge, breach width, and formation time.

The objective of this research is to conduct experiments to investigate the development of dam failure resulted from the overtopping at homogeneous earth-fill dam. Understanding the temporal evolution of the breach and the resulting outflow characteristics is essential for improving dam safety. This study experimentally investigates the breach development process and the outflow hydrograph under overtopping conditions, providing valuable insights for predictive modeling strategies.

2. Experimental procedure

A homogenous earth-fill dam having 0.20 m height, 1.20 m bottom width, and a crest width of 0.20 m was constructed with a slope at the upstream and downstream sides of 1:2.5. The dam was built in a rectangular flume 0.96 m wide, 0.81 m high, and 5.44 m long (Fig. 1).

Some soil mechanics tests were carried out before building the dam. The soil mixture utilized at the construction of the dam was prepared by using 85 % fine sand and 15 % clay. The grain-size distribution of the mixture obtained from the wet sieve and hydrometer analyses is shown in Fig. 2.

From Fig. 2, some characteristic diameters were obtained as D_{10}= 0.014 mm, D_{30}= 0.056 mm, D_{50}= 0.13 mm, and D_{60}= 0.15 mm. The uniformity coefficient C_u equals 10.7 and the curvature coefficient C_c is equal to 1.49. The specific weight of the mixture was found to be G_s = 2.67, from the test ASTM D854 – 14. The permeability of the mixture was found as $k = 1.18 \cdot 10^{-3}$ cm/s from the falling head permeability test. The standard proctor tests (ASTM-698) were performed by applying both 13 and 25 blows, and the obtained curves are plotted in Fig. 3.

The maximum dry density and optimum water content were obtained as Υ_{drymax}= 1.653 g/cm^3 and w_{opt} = 15.4 % from the test with 13 blows and as Υ_{drymax}= 1.694 g/cm^3 and w_{opt} = 13.6 % from the 25 blows test.

Some construction stages and the completed shape of the dam body are shown in Fig. 4. Each layer was constructed in four sub-layers, each measuring 2.5 cm thick, to avoid any homogeneity issues that could arise.

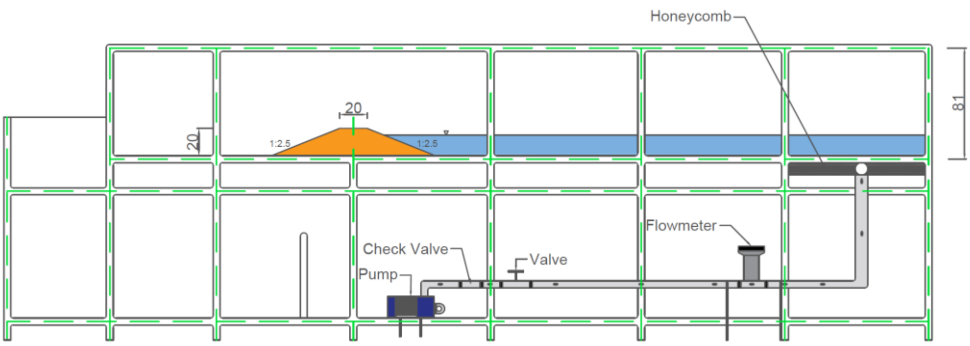

Fig. 1 Experimental set-up (all numerical values are in cm)

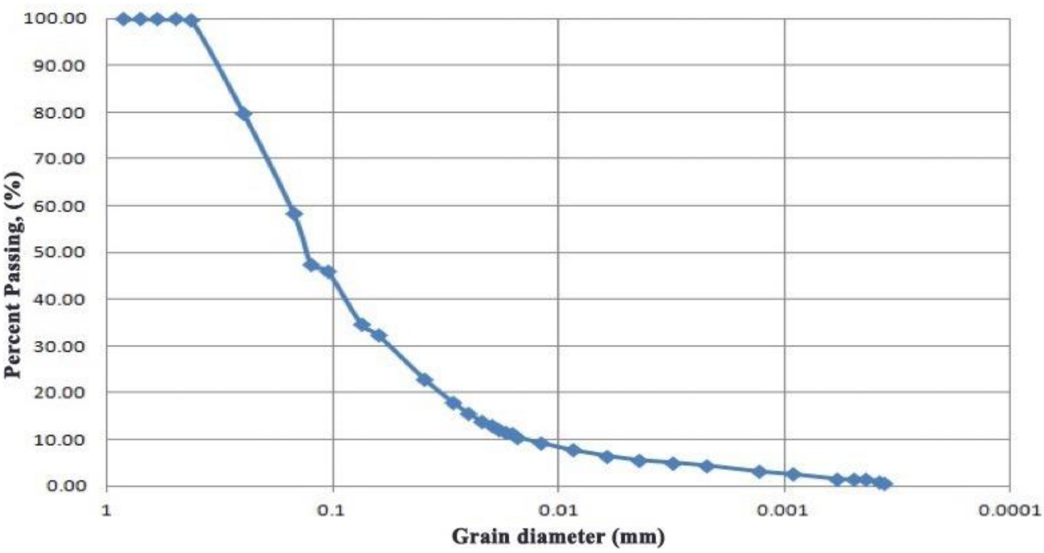

Fig. 2 Grain size distribution of the dam material

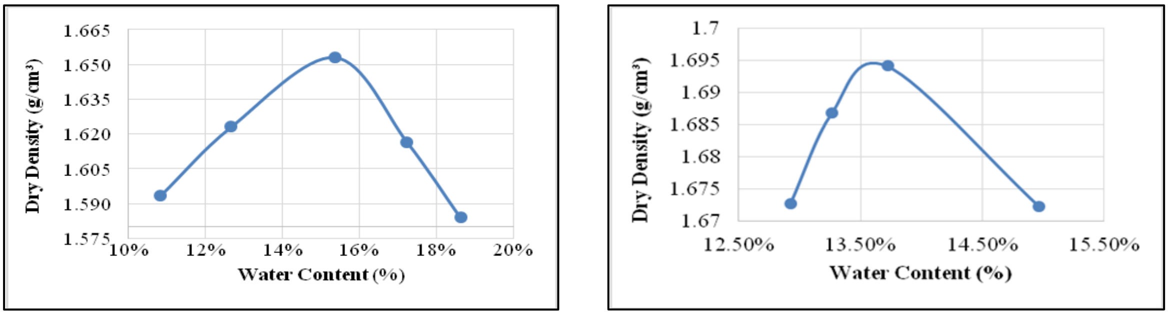

(a) (b)

Fig. 3 Standard proctor test with a) 13 blows. b) 25 blows

(a) (b) (c)

Fig. 4 Some construction stages of the earth-fill dam (a) Finished Layer, (b) Compaction, (c) Completed shape of the dam

4. Experimental findings

The evolution of the dam failure was recorded by six cameras placed at different locations. The camera recordings were also used to determine the water depths in the channel. The photos from the upstream and downstream cameras were analyzed to evaluate the shape of the breach and the changes in its geometry. The temporal developments of the breach recorded by the cameras located at downstream and upstream of the dam are given in Fig. 5 and Fig. 6, respectively. In these figures, the time t = 0 corresponds to the moment when the breach appeared at the relevant face of the dam. The time elapsed between the instances at which the breach appeared at downstream and upstream sides ($T_{elapsed}$) was approximately 15 s.

As shown in Fig. 5b, initial signs of erosion near the centerline of the dam crest became evident 45 s later. As seen in Fig. 5c, the breach became much larger at t = 95 s on the downstream side. When t = 145 s, the erosion became much more significant (Fig. 5d). The breach continued to be developed (Fig. 5e), followed by additional detachments from the downstream surface. After t = 300 s (Fig. 5f), no significant erosion observed, and the breach reached almost its final shape. The breach was much more visible as time progresses (Fig. 6b and Fig. 6c). When t = 145 s, the breach covered almost 10% of the upstream face (Fig. 6d). The final shape of the breach was reached almost when t = 300 s (Fig. 6f).

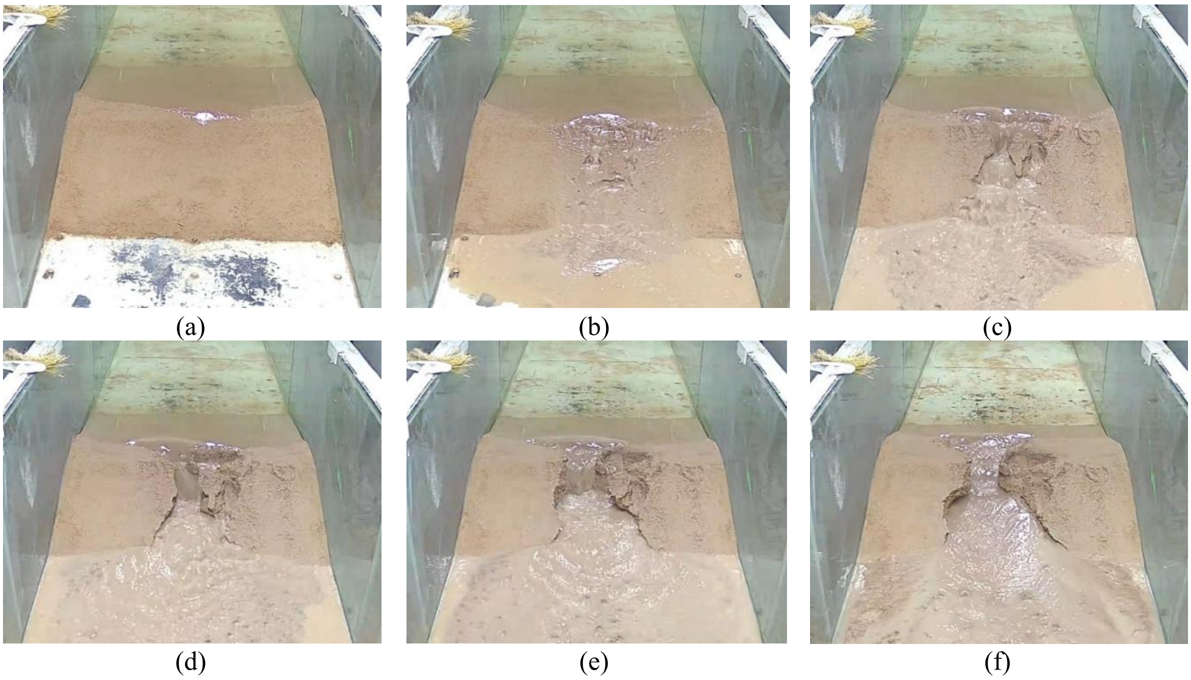

Fig. 5 The temporal development of the breach at downstream face of the dam; (a) t = 0 s, (b) t = 45 s, (c) t = 95 s, (d) t = 145 s, (e) t = 195 s, (f) t = 300 s

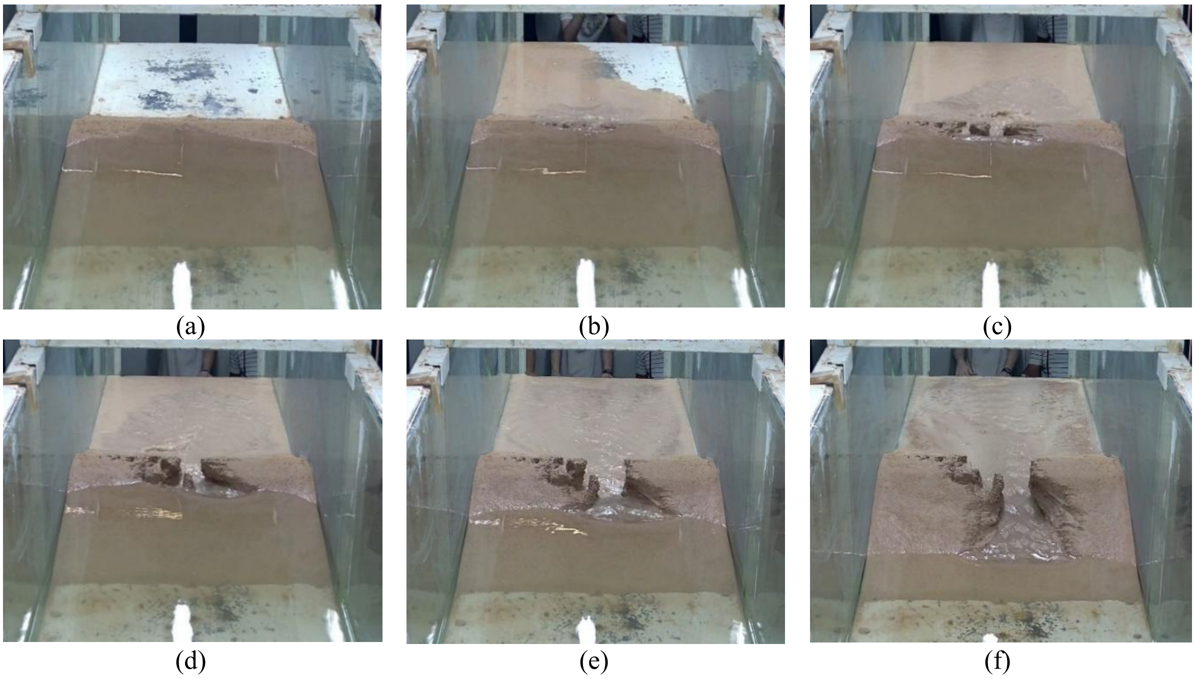

Fig. 6 The temporal development of the breach at upstream face of the dam; (a) t = 0 s, (b) t = 45 s, (c) t = 95 s, (d) t = 145 s, (e) t = 195 s, (f) t = 300 s

At Get-data Graph Digitizer 2.26 software, the images extracted from the records corresponding to a specific time were scaled, and the boundary coordinates of the breaches on the downstream and upstream sides were determined. The time-varied breach areas were calculated by using the Gauss area formula:

$$Area = \frac{1}{2}\sum_{i=1}^{n} x_i(y_{i+1} - y_{i-1}) = \frac{1}{2}\sum_{i=1}^{n} y_i(x_{i+1} - x_{i-1}) \tag{1}$$

where n is the number of sides, x_i and y_i represent the abscissa and ordinate in the coordinate i, respectively. The so obtained breach areas are plotted in Fig. 7.

The discharge of water outgoing from the breach was determined by using the continuity equation:

$$\Delta S=(Q_{inlet}- Q_{breach})\cdot\Delta t \tag{2}$$

where Q_{inlet} is the inflow rate to the reservoir, Q_{breach} is the discharge from the breach, and ΔS is the change in the reservoir storage during the time interval Δt.

Fig. 8a represents the time-varying water depths in the dam reservoir. The generated water depth-volume curve is given in Fig. 8b. The discharges outgoing from the breach, calculated by using Eq. (2), are given in Fig. 9.

The progress rate of the breach area at downstream side was much greater (Fig. 10a) compared to that of the upstream side (Fig. 10b). The final breach area at downstream side was obtained nearly 1.5 times greater than that of the upstream side. Fig. 10 illustrates the development of the breach areas for downstream and upstream sides.

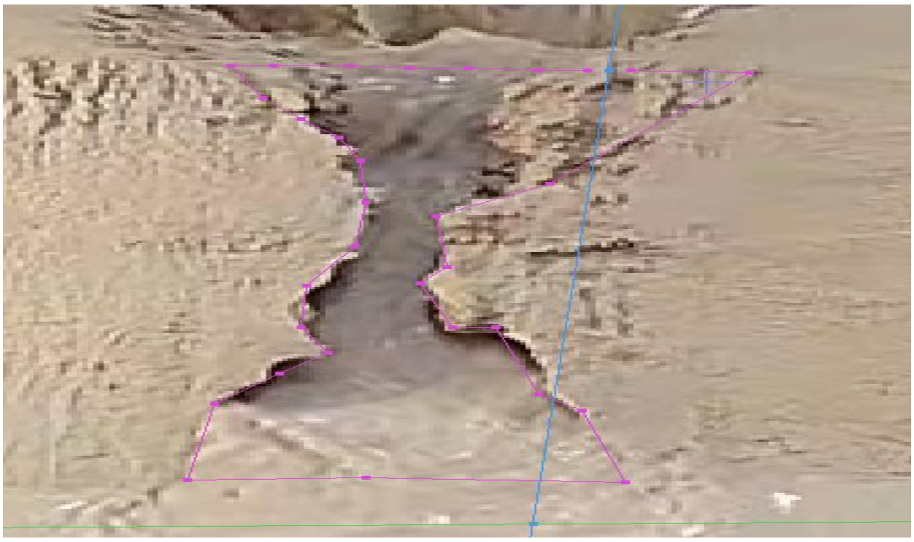

Fig. 7 Get-data Graph Digitizer 2.26 Software usage example

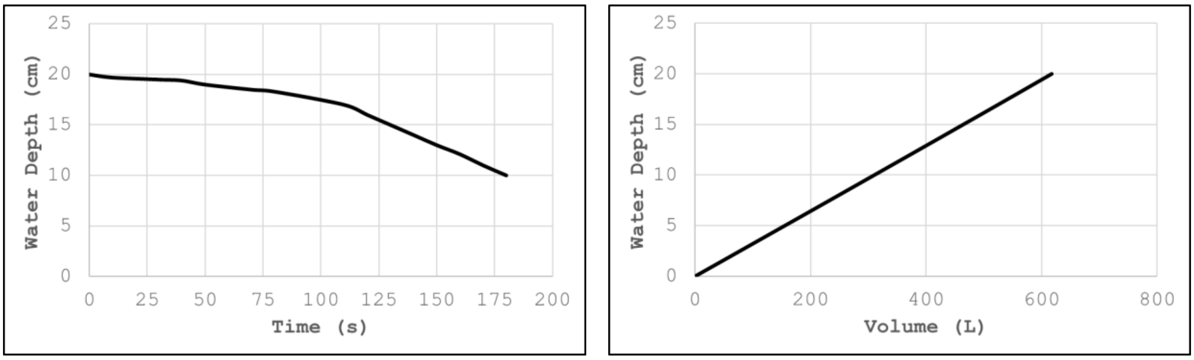

(a) (b)

Fig. 8 (a) Time-varied water depths (b) Water depth-volume curve of the dam reservoir

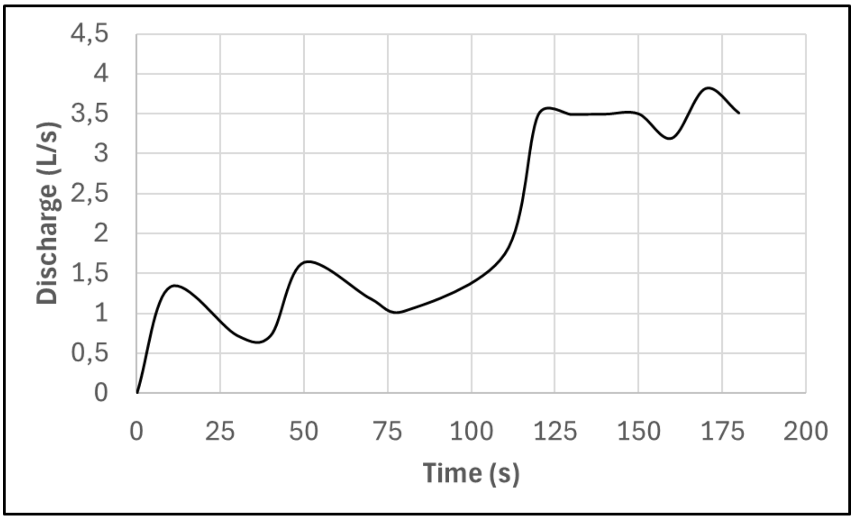

Fig. 9 Time-varied discharges outgoing from the breach

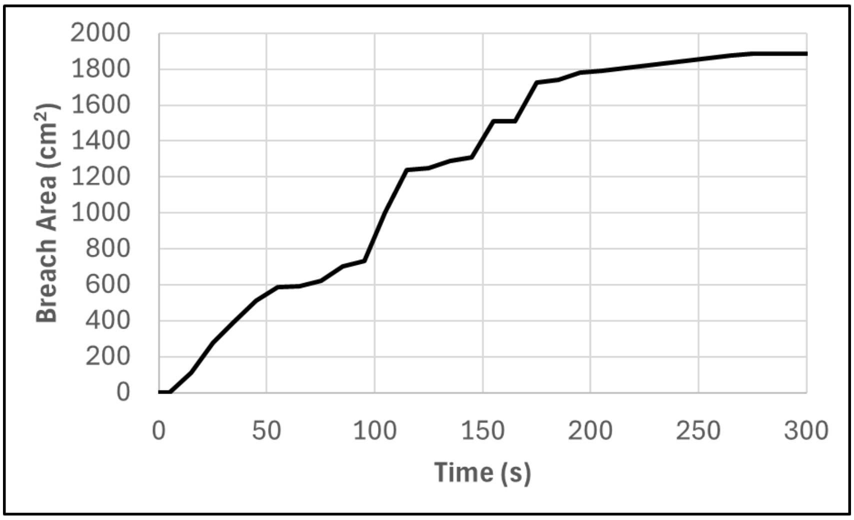

(a)

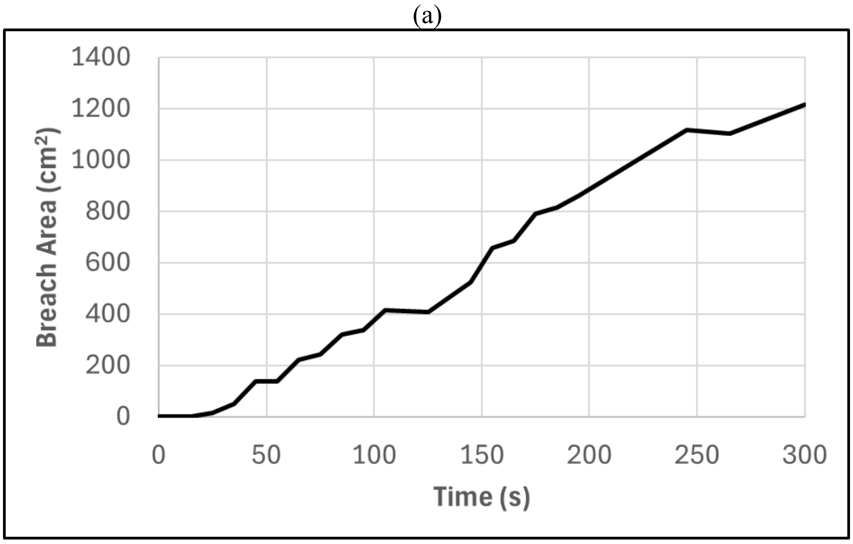

(b)

Fig. 10 Time-dependent breach areas at a) downstream b) upstream

The dimensionless parameters $Q_{breach}(t)/Q_{breach,max}$, $A_{down}(t)/A_{down,max}$, $A_{ups}(t)/A_{ups,max}$ and t/t_Q, t/t_d and t/t_u are generated in order to obtain the universal results. This approach enables the comparison of our experimental findings with the results of other experiments carried out in different geometrical and hydraulical conditions. The graphs of the curves $Q_{breach}(t)/Q_{breach,max} = f(t/t_Q)$, $A_{down}(t)/A_{down,max} = f(t/t_d)$ and $A_{ups}(t)/A_{ups,max} = f(t/t_u)$ are given in

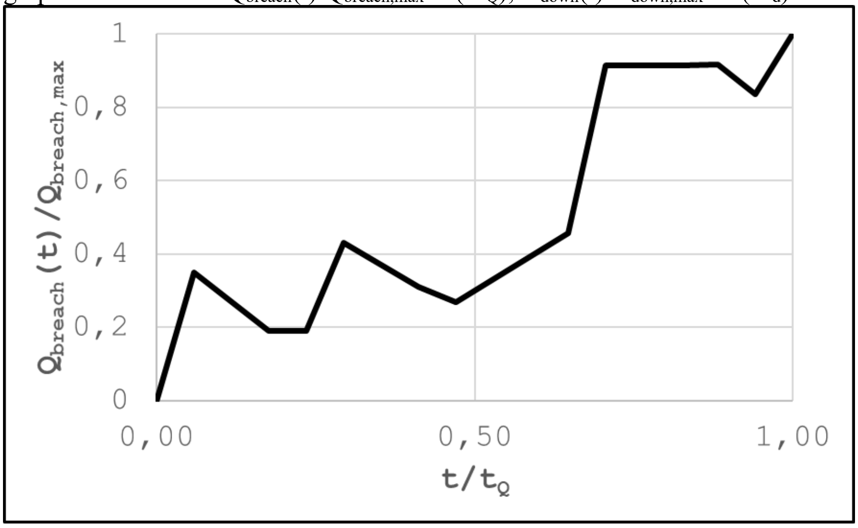

Fig. 11,
Fig. 12 and
Fig. 13, respectively. $Q_{breach}(t)$, $A_{down}(t)$ and $A_{ups}(t)$ denote time-dependent values of the discharges, the breach areas at downstream and upstream, respectively. $Q_{breach,max}$, $A_{down,max}$ and $A_{ups,max}$ correspond to the maximum values of the discharge, downstream breach area and upstream breach area, respectively. t_Q, t_d and t_u represent the time to reach the maximum values of discharge, downstream breach area and upstream breach area, respectively.

The dimensionless discharge curve can be simulated approximately to a linear line with some fluctuations due to the change in bridge geometry resulting from internal erosion.

The dimensionless downstream breach area curve looks like a logarithmic curve, while the dimensionless upstream breach area curve looks like linear.

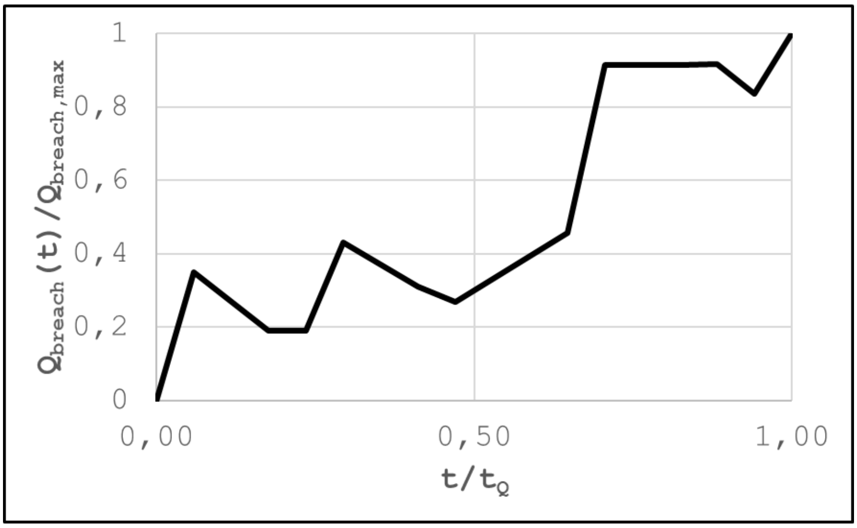

Fig. 11 Dimensionless $Q_{breach}(t)/Q_{breach,max} = f(t/t_Q)$ curve

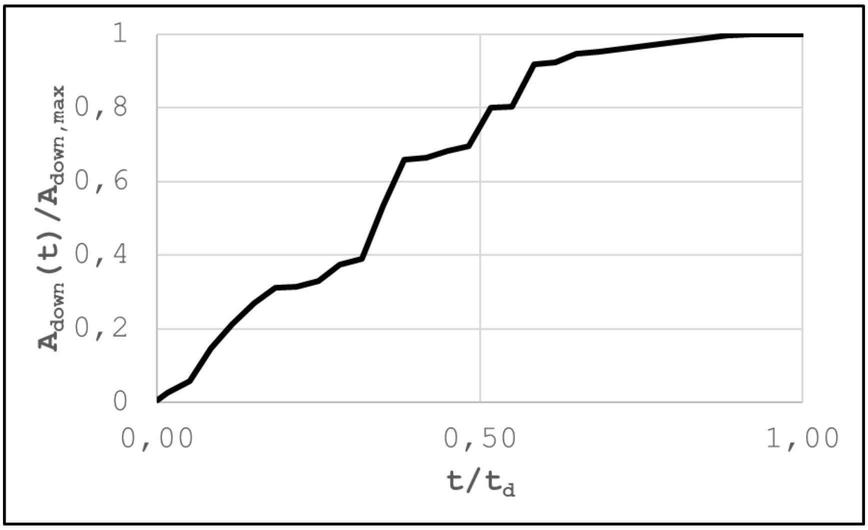

Fig. 12 Dimensionless $A_{down}(t)/A_{down,max} = f(t/t_d)$ curve

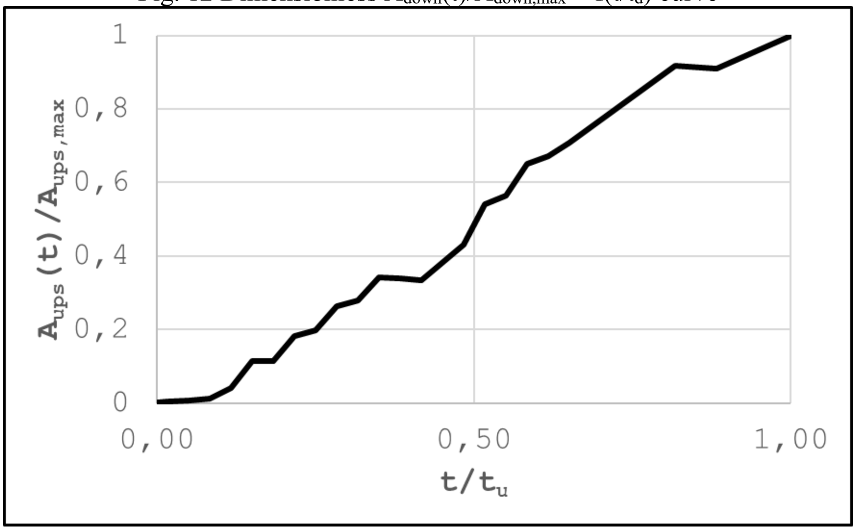

Fig. 13 Dimensionless $A_{ups}(t)/A_{ups,max} = f(t/t_u)$ curve

Table 1. Comparison of the experimental findings

Parameters		Experimental Findings
$Q_{breach,max}$ (L/s):	Maximum discharge outgoing from the breach	3.82
t_Q (s):	Time to reach $Q_{breach,max}$	170
$A_{down,max}$ (cm^2):	Maximum breach area at downstream	1884
t_d (s):	Time to reach $A_{down,max}$	300
$A_{ups,max}$ (cm^2):	Maximum breach area at upstream	1216
t_u (s):	Time to reach $A_{ups,max}$	300

4. Conclusions

In this study, the temporal evolution of the breach caused by overtopping at homogenous earth-fill dam was studied experimentally. The discharges from the breach at various instants were computed using the continuity equation.

The Get-Data Graph Digitizer was used to scale the boundary coordinates of the breach surface areas. The breach areas at each time were determined by applying Gauss-area formula.

The breach began on the downstream side and progressed to the upstream side, as expected. The breach at upstream side appeared 15 s later compared to downstream side. The comparative experimental findings are given in Table 1, where the maximum discharge through the breach was calculated as $Q_{breach,max} = 3.817$ L/s at t = 170 s. The maximum breach area at downstream was found to be $A_{down,max} = 1884$ cm^2 at t = 300 s, while at upstream $A_{ups,max} = 1216$ cm^2.

The findings of this study contribute to a better understanding of the breach development mechanisms in overtopping-induced dam failures, providing valuable insights for future modeling and risk assessment efforts. These experimental findings provide opportunities for the calibration and validation of the numerical models used in the relevant numerical investigations. This study offers also guidance for strategies concerning emergency action plans related to the failure of homogeneous earth-fill dams due to overtopping.

Acknowledgments

The authors thank the Scientific and Technological Research Council of Turkey (TUBITAK), since we got the opportunities to realize this study thanks to the financial support in the scope of the project 119M609.

References

Aman, S., Rezk, M. A., & Nasr, R. (2023). Effect of berm properties on non-cohesive earth dam failure due to overtopping. *KSCE Journal of Civil Engineering*, *27*(5), 1974-1984. https://doi.org/https://doi.org/10.1007/s12205-023-1141-6

Ashraf, M., Soliman, A. H., El-Ghorab, E., & Zawahry, A. E. (2019). Assessment of embankment dams breaching using large scale physical modeling and statistical methods. *Water Science*, *32*(2), 362-379. https://doi.org/https://doi.org/10.1016/j.wsj.2018.05.002

Bereta, G., Hui, P., Kai, H., Guang, L., Kefan, P., & Zhao, Y. Z. (2020). Experimental Study of Cohesive Embankment Dam Breach Formation due to Overtopping. *Periodica Polytechnica Civil Engineering*, *64*(1), 198-211. https://doi.org/https://doi.org/10.3311/PPci.14565

Chen, C., Wang, Y., Zhang, J., Zhang, H., Li, H., & Chen, Q. (2023). A preliminary study of landslide dam failures induced by the combined influence of piping and overtopping. *Journal of Hydrology*, *625*(A), 129984. https://doi.org/https://doi.org/10.1016/j.jhydrol.2023.129984

Chen, S.-S., Zhong, Q.-M., & Shen, G.-Z. (2019). Numerical modeling of earthen dam breach due to piping failure. *Water Science and Engineering*, *12*(3), 169-178. https://doi.org/https://doi.org/10.1016/j.wse.2019.08.001

Costa, J. E. (1985). *Floods from dam failures* (Open-File Report, Issue. U. S. G. Survey.

Singh, V. P. (1996). *Dam Breach Modeling Technology*. Springer Dordrecht. https://doi.org/https://doi.org/10.1007/978-94-015-8747-1

Verma, D., Berwal, P., Gupta, N., Alfaisal, F. M., Khan, M. A., Alam, S., & Qadri, J. (2023). Experimental investigation of breach mechanism for overtopped cohesive and non-cohesive embankments. *Water*, *15*(17), 3030. https://doi.org/https://doi.org/10.3390/w15173030

Zhou, M., Shi, Z., Zhou, G. G. D., Cui, K. F. E., & Peng, M. (2021). Experimental Investigation of the Outburst Discharge of Landslide Dam Overtopping Failure. *Frontiers in Earth Science*, *9*. https://doi.org/https://doi.org/10.3389/feart.2021.766524

4th International Civil Engineering & Architecture Conference
17-19 May 2025, Trabzon, Türkiye

Modeling of the maximum rise height of a dense discharge using the teaching-learning-based algorithm

Arife Günay[1], Mahmut C. Sayıl[*1], Tuğçe Anılan[1]

[1]*Karadeniz Technical University, Department of Civil Engineering, 61080 Trabzon, Türkiye*

Abstract. Brine, the byproduct of the desalination process, is a type of wastewater and must be disposed of safely. Marine outfall systems are used to dispose of brine, which is discharged into the ambient environment through the discharge ports of the diffuser pipes. A proper hydraulic design of the diffuser pipe is crucial since it ensures sufficient dilution of the discharged wastewater. Jet behavior must be thoroughly analyzed for a successful diffuser design. In this context, jet trajectories are vital since they are directly related to the dilution efficiency of the wastewater discharged. In assessing the trajectories of dense jets from single-side diffusers, there are three main geometrical features: maximum rise height, impact distance, and near-field distance. In this study, the maximum rise height is modeled among these three features. Both classical regression analysis and teaching-learning-based algorithm (TLBO) were used in this concept. This study aims to demonstrate the feasibility of using TLBO in modeling the maximum rise height under dynamic ambient conditions with co-flowing ambient currents. For this purpose, current speed, Froude number, and port spacing were independent variables affecting the maximum rise height. In addition, different statistical indices (e.g. absolute mean error, relative error) were used to evaluate the performance of the models. The results of this evaluation revealed the success of TLBO in modeling the maximum rise height.

Keywords: Diffuser pipe, Dense jet, Maximum rise height, Teaching-learning-based algorithms, Trajectories of brine jet

1. Introduction

Desalination, which is defined as the process of removing excess salts and other dissolved chemicals from seawater and has gained importance in the last few decades, has become an important concept, especially in arid regions with freshwater shortages (Sepehr et al., 2017; Darre and Toor, 2018). As a solution to a significant problem, this process results in a type of wastewater that contains very high concentrations of salts and is typically referred to as brine (Bashitialshaaer et al., 2015; Baawain et al., 2015; Abessi and Roberts, 2018; Sayıl and Anılan, 2024). In addition to high salinity, the resulting brine may contain hazardous pre-treatment chemicals, organics, and heavy metals. For this reason, many researchers have investigated the negative environmental impacts of brine disposal on the marine environment, groundwater, and soil quality and have proposed appropriate solutions (Panagopoulos et al., 2019). Among these proposals, the most preferred worldwide is the discharge to marine outfall systems. These systems focus on reducing pollutant levels to safe values by ensuring sufficient dilution in the receiving environment (Nemlioğlu, 2001).

Adequate dilution in the receiving environment can be achieved by a diffuser pipe with an appropriate hydraulic design (Bleninger and Jirka, 2008; Sayıl et al., 2025). Here, appropriate hydraulic design means designing a diffuser that minimises energy losses, provides a homogeneous discharge distribution between all diffuser ports through which wastewater is discharged to the ambient water, and prevents seawater ingress into the pipe through the ports. A good diffuser design is mainly influenced by pipe diameter, length, roughness, number of ports, port diameters, and port spacing (Bleninger et al., 2002). Furthermore, the jet behaviour should be analysed thoroughly for a successful diffuser design. In the case of dense discharge, since the effluent is denser than the ambient water, it moves upwards for a while due to the discharge turbulence and high jet velocity. Eventually, it starts to move downwards after reaching a terminal rise height (Darama, 2009). Three main geometric features are used to describe this behaviour of dense jets: maximum rise height, impact distance, and near-field distance. These three most critical geometrical features that significantly affect the dilution of dense jets are given in Fig. 1.

Experimental studies to understand the behavior of jets and calculate rarefaction can be quite difficult. For this reason, researchers find it more appropriate to use numerical modeling methods to perform analyses, which are

[*] Corresponding author, E-mail: cenksayil@ktu.edu.tr

https://doi.org/10.31462/icearc2025_ce_hyd_816

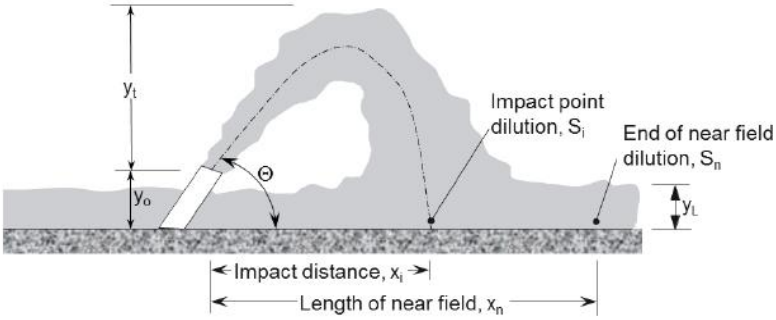

Fig. 1. Geometrical properties of a typical inclined negatively buoyant jet (Roberts et. al., 1997)

easier to implement, time-saving, and a cost-effective solution. Additionally, new techniques such as machine learning and deep learning have gained popularity in recent years due to the advances in computer science and their advantages. Artificial neural networks are one of the most notable methods in outfall. Many researchers have used ANN in various discharge topics (Lankasena, 2001; Etemad-Shahidi, et al., 2010; Er et al., 2022; Alvir et al., 2023). In addition, many different algorithms have begun to be used in discharge with the developing technology (Lankasena, 2001; Alvir et al., 2023).

In this study, the maximum rise height of the jets was modeled by classical regression analysis (CRA) and teaching-learning based optimization (TLBO) methods depending on the Froude number, port spacing, and current speed. For this purpose, experimental data available in the literature was used. The results of the two methods were compared, and the method that best modeled the maximum rise height was determined.

2. Material and methods

2.1. Reference study and the dataset used

The dataset used was obtained from the experimental results of Abessi and Roberts (2017). Abessi and Roberts (2017) performed experiments to investigate the effects of independent variables Froude number (F), port spacing (s), and ambient current speed (ua) on jet characteristics maximum rise height (yt), impact distance (xi), and impact dilution (S_i). Different series of experimental work were conducted to cover all possible scenarios including one-sided diffuser with co-flowing ambient currents, one-sided diffuser in counterflowing currents, unblocked two-sided diffuser in which the diffuser is elevated from the sea bottom and blocked two-sided diffuser in which the diffuser pipe is laid on the sea bottom. Fig. 2 shows the diffuser configurations and ambient current directions used in the study. jet densimetric Froude number as in Equation (1) where u is the jet velocity, $g_0'=g(\rho_0-\rho_a)/\rho_a$ is the modified gravitational acceleration, and ρ_0 and ρ_a are the densities of effluent and ambient water, respectively:

$$F=\frac{u}{\sqrt{g_0' d}} \tag{1}$$

To discuss the effects of port spacing, they nondimensionalized port spacing by dividing by the product of port diameter (d) and Froude number. In cases where nondimensionalized parameter s/dF was significantly greater than 1, jets were assumed to be so widely spaced that the jet merging phenomenon did not occur and solution methodology valid for single jets could be employed, and vice versa. Parameter urF was used to discuss the effects of ambient currents, where $u_r=u_a/u$ was the ratio of ambient current speed to jet velocity. In cases where $u_rF \ll 1$, jets were not significantly affected by ambient currents, and vice versa.

In our study, a dataset belonging to the case where the ports were located on one side of the diffuser and ambient currents were in the same direction as the discharged effluent was used. Teaching-learning-based algorithm (TLBO) was used to predict maximum rise height using independent variables Froude number, port spacing, and current speed. In addition, a Conventional Regression Analysis (CRA) was performed for a comparison.

2.2. Teaching-learning based optimization algorithms (TLBO)

TLBO is a population-based stochastic optimization algorithm inspired by the teaching-learning process in a classroom and developed by Rao et al. (2011). In this study, it will be used for the first time in modeling the maximum rise height in the subject of dense jet. In the algorithm consisting of two phases, teaching and learning, the most suitable student for the solution is determined, and this student is selected as the teacher for the teaching phases. In the teaching phase, students try to improve their results by getting information from the teacher. At the same time, the learning phase is the phase where students improve their performance by interacting with other

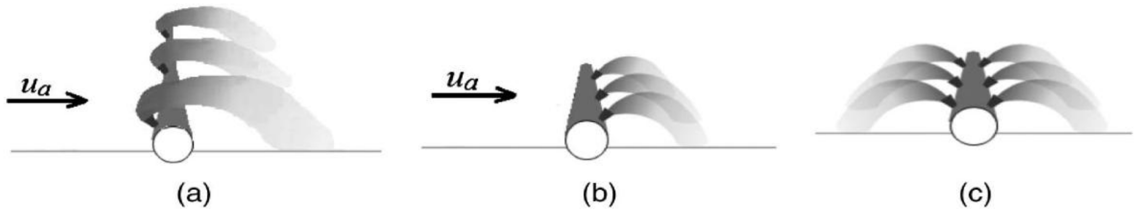

Fig. 2. Diffuser configurations where the port spacing is s: (a) one-sided counterflow; (b) one-sided co-flow; (c) two-sided (Abessi and Roberts, 2017)

students (Ermis et al., 2023). The flow diagram of the TLBO algorithm is given in Fig. 3. The simple digitised structure of TLBO and the independence of a set of control parameters to define the algorithm's performance is why it is preferred in this study over other algorithms. TLBO has two control parameters, the maximum number of cycles and the population size equal to the number of students.

The data normalised using Eq. 1 is used as input for the TLBO algorithm whose objective function is the total squared error (SSE). The performances of TLBO and CRA models were evaluated using different statistical criteria for training and testing sets. These are root mean square error (RMSE), mean absolute error (MAE), and Nash-Sutcliffe Efficiency (NSE). SSE, RMSE, and MAE, NSE are obtained by Equation (2-6) respectively.

$$Normalized\ value = \left(\frac{Raw\ value - minimum\ value}{Maximum\ value - minimum\ value}\right) \times (0.9 - 0.1) + 0.1 \tag{2}$$

$$\mathrm{SSE} = \sum_{\mathrm{i}=1}^{\mathrm{N}} (\mathrm{P_i} - \mathrm{O_i})^2 \tag{3}$$

$$\mathrm{RMSE} = \left[\frac{1}{\mathrm{N}}\sum_{\mathrm{i}=1}^{\mathrm{N}} (\mathrm{P_i} - \mathrm{O_i})^2\right]^{\frac{1}{2}} \tag{4}$$

$$\mathrm{MAE} = \frac{1}{\mathrm{N}}\sum_{\mathrm{i}=1}^{\mathrm{N}} |(\mathrm{P_i} - \mathrm{O_i})| \tag{5}$$

$$\mathrm{NSE} = 1 - \left(\frac{\sum_{\mathrm{i}=1}^{\mathrm{N}} (\mathrm{P_i} - \mathrm{O_i})^2}{\sum_{\mathrm{i}=1}^{\mathrm{N}} (O_i - \bar{o})^2}\right) \tag{6}$$

where N: Number of observations; O_i: ith observed value; $\bar{o}$: Mean of observed value; P_i: ith estimated value for the regression functions. The value of RMSE is expected to decrease as the differences between observed and predicted values decrease since RMSE measures the standard deviation of the prediction errors. This implies an improvement in the model's accuracy (Tuc et al., 2024; Günay and Akbaş, 2025). NSE can take values between negative infinity and zero, with values closer to zero indicating a better model performance (Qian et al., 2025).

3. Results and discussion

TLBO and CRA analyses were carried out to predict maximum rise height based on Froude number, port spacing, and current speed. Hyperbolic function (HF), Linear function (LF) and Exponential function (EF) were employed for both TLBO and CRA. 70% of the data were used to train models, whilst 20% were used for the testing and 10% for validating them. The values of the control parameters maximum number of iterations (NMI) and population size (SP) were set as 3000 and 100, respectively. Performance assessment and comparison of TLBO and CRA methods were made considering RMSE, MAE and NSE criteria. Tables 1-3 present the results for training, testing and validation sets, respectively. In tables, the function that yielded the best result was highlighted in bold for all performance criteria values.

It is evident from Tables 1-3 that, although for training and testing sets and in the case of HF and LF CRA yielded slightly lower error values and subtly higher NSE from time to time, in the case of exponential function, which gives the best overall results, the success of TLBO over CRA is obvious as the error values were clearly lower and NSE values were higher. As aforementioned, in overall, EF performed best since when all sets of data were considered together smallest values of RMSE and MAE and the highest value of NSE were obtained through

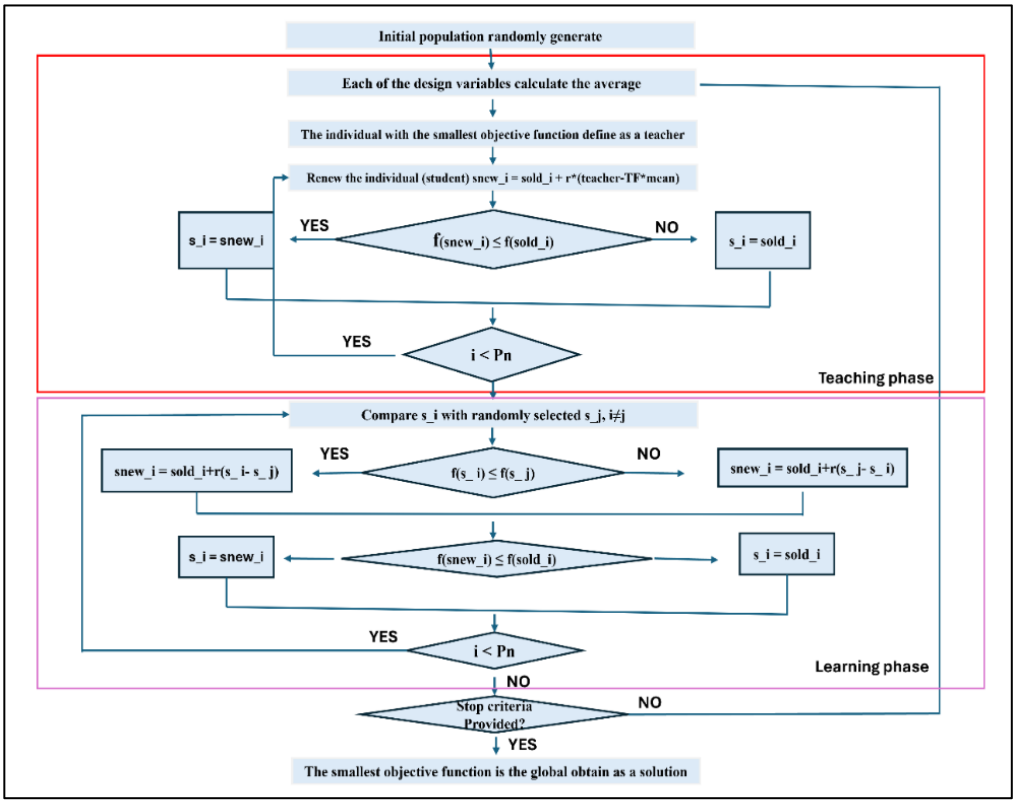

Fig. 3. Flow diagram of TLBO algorithm (Günay and Akbaş, 2025)

EF, with theses values being 0.117, 0.082 and 0.925, respectively. Based on these, Equation (7) in the form of an exponential functions is suggested for the estimation of maximum rise height of dense jets in dynamic ambient environments, using independent parameters Froude number, port spacing and current speed:

$$y_t = -0.0222 + \exp(0.1036 - 0.5476xF + 0.1039xs - 1.7912xu_a) \quad (7)$$

Table 1. The model results for training set

The functions	RMSE		MAE		NSE	
	TLBO	CRA	TLBO	CRA	TLBO	CRA
Hyperbolic	0.167	0.141	0.124	0.106	0.858	0.883
Linear	0.150	0.150	0.118	0.118	0.874	0.868
Exponential	**0.117**	0.123	**0.082**	0.123	**0.925**	0.910

Table 2. The model results for testing set

The functions	RMSE		MAE		NSE	
	TLBO	CRA	TLBO	CRA	TLBO	CRA
Hyperbolic	0.262	0.192	0.207	0.157	0.703	0.816
Linear	0.172	0.172	0.130	0.127	0.853	0.853
Exponential	**0.160**	0.161	**0.129**	0.131	**0.874**	0.872

Table 3. The model results for validating set

The functions	RMSE		MAE		NSE	
	TLBO	CRA	TLBO	CRA	TLBO	CRA
Hyperbolic	0.269	0.367	0.198	0.326	0.768	0.482
Linear	**0.120**	0.305	**0.108**	**0.286**	0.913	0.415
Exponential	0.123	0.344	0.158	0.317	0.908	0.456

4. Conclusions

In this study, effects of Froude number, port spacing and current speed on the maximum rise height of dense jets discharged into dynamic ambient environments, and the applicability of TLBO algorithm to predict the maximum rise height under the given hydraulic and ambient conditions were investigated. The conclusions are as follows:

- While determining the optimum values of control parameters for the TLBO algorithm, different scenarios were tested. Accordingly, it was decided to use maximum number of iterations and population size values as 3000 and 100, respectively.
- In training and testing sets, in the case of HF and LF, CRA performed equal to or slightly better than TLBO. However, when EF, which had the best overall performance, was adopted, a clear superiority of TLBO was observed, indicating that, in general, TLBO was more successful than CRA.
- EF, when compared to HF and L, gave the best results for both error values and NSE criterion. The lowest values of RMSE and MAE across all datasets were 0.117 and 0.082, obtained by EF. The highest value of NSE was 0.925, again obtained by EF.
- Based on the related analysis' results, optimum coefficients obtained for exponential function were used to develop an expression that can be used to estimate the maximum rise height of dense jets discharged into dynamic ambient environments using Froude number, port spacing, and current speed as input variables.

Acknowledgments

This research received no specific grant from funding agencies in the public, commercial, or not-for-profit sectors.

References

Abessi, O., & Roberts, P.J. (2017). Multiport diffusers for dense discharge in flowing ambient water. *Journal of Hydraulic Engineering*, 143(6), 04017003. https://doi.org/10.1061/(ASCE)HY.1943-7900.0001279

Abessi, O., & Roberts, P.J. (2018). Rosette diffusers for dense effluents in flowing currents. *Journal of Hydraulic Engineering*, 144(1), 06017024. https://doi.org/10.1061/(ASCE)HY.1943-7900.0001403

Alvir, M., Grbčić, L., Sikirica, A., & Kranjčević, L. (2023). Reconstruction and analysis of negatively buoyant jets with interpretable machine learning. *Marine Pollution Bulletin*, 190, 114881. https://doi.org/10.1016/j.marpolbul.2023.114881

Baawain, M., Choudri, B. S., Ahmed, M., & Purnama, A. (2015). An overview: desalination, environmental and marine outfall systems. *Recent Progress in Desalination, Environmental and Marine Outfall Systems*, 3-10. https://doi.org/10.1007/978-3-319-19123-2_1

Bashitialshaaer, R., Persson, K.M., & Larson, M. (2015). New criteria for brine discharge outfalls from desalination plants. In: *Intakes and Outfalls for Seawater Reverse-Osmosis Desalination Facilities: Innovations and Environmental Impacts*. Springer International Publishing, 2015. p. 451-467. https://doi.org/10.1007/978-3-319-13203-7_19

Bleninger, T., Lipari, G., & Jirka, G.H. (2002). Design and optimization program for internal diffuser hydraulics. 2nd International Conference on Marine Waste Water Discharges, MWWD 2002. İstanbul.

Bleninger, T., & Jirka, G.H. (2008). Modelling and environmentally sound management of brine discharges from desalination plants. *Desalination*, *221*(1-3), 585-597. https://doi.org/10.1016/j.desal.2007.02.059

Darama, S. (2009). Yoğun Atıksu Deşarjının Birinci Seyrelmesinde Görünür Saçak Modelinin Uygulanması. Master's Thesis, Istanbul University, Institute of Graduate Studies in Sciences, Istanbul.

Darre, N.C., & Toor, G.S. (2018). Desalination of water: a review. *Current Pollution Reports*, 4, 104-111. https://doi.org/10.1007/s40726-018-0085-9

Etemad-Shahidi, A., Zoghi, M.J., & Saeedi, M. (2010). An alternative data driven approach for prediction of thermal discharge initial dilution using tee diffusers. *International Journal of Environmental Science & Technology*, *7*, 29-36. https://doi.org/10.1007/BF03326114

Er, B.A., Odabas, M.S., Şenyer, N., & Ardali, Y. (2022). Evaluation of Deep Sea discharge systems efficiency in the eastern black sea using artificial neural network: a case study for Trabzon, Turkey. *Brazilian Archives of Biology and Technology*, 65, e22210397. https://doi.org/10.1590/1678-4324-2022210397

Ermis, S., Bayindir, R., & Yesilbudak, M. (2023). Voltage stability study in power systems with improved teaching-learning based optimizatıon algorithm. *Gazi University Journal of Science Part C: Design and Technology*, 11(3), 695-705. https://doi.org/10.29109/gujsc.1282188

Günay, A., & Akbaş, S.O. (2025). Modelling of Steady-State Seepage of an Embankment Dam Using Teaching-Learning Based Optimization Algorithm. *Turkish Journal of Civil Engineering*, 36(2), 81-95. https://doi.org/10.18400/tjce.1462869

Lankasena, B.N.S. (2001). Development of a Decision Support System for Long Sea Outfall Designing and Operations. Master's Thesis, University of Moratuwa, Faculty of Engineering, Sri Lanka.

Nemlioğlu, S. (2001). Improvement of low hydraulic performance of sea outfalls using bell mouthed ports in the Black Sea, Fresenius Environmental Bulletin, 10(4), 392-395.

Panagopoulos, A., Haralambous, K. J., & Loizidou, M. (2019). Desalination brine disposal methods and treatment technologies-A review. *Science of the Total Environment*, 693, 133545. https://doi.org/10.1016/j.scitotenv.2019.07.351

Qian, Y., Han, X., Zhu, Y., Yang, W., & Huang, J. (2025). A modified model for simulating subsurface drainage with synthetic envelope considering impacts of entrance resistance and its application. *Agricultural Water Management*, *310*, 109371. https://doi.org/10.1016/j.agwat.2025.109371

Rao, R.V., Savsani, V.J., & Vakharia, D.P. (2011). Teaching–learning-based optimization: a novel method for constrained mechanical design optimization problems. *Computer-aided design*, *43*(3), 303-315. https://doi.org/10.1016/j.cad.2010.12.015

Roberts, P.J., Ferrier, A., & Daviero, G. (1997). Mixing in inclined dense jets. *Journal of Hydraulic Engineering*, *123*(8), 693-699. https://doi.org/10.1061/(ASCE)0733-9429(1997)123:8(693)

Sayıl, M.C., & Anılan, T. (2024). A Review of Computational Fluid Dynamics (CFD) modeling studies on dense discharges. *Uludağ University Journal of The Faculty of Engineering*, *29*(3), 929-948. https://doi.org/10.17482/uumfd.1527596

Sayıl, M.C., Günay, A., & Anılan, T. (2025). Investigation of dense jet behavior using computational fluid dynamics models. *Journal of the Brazilian Society of Mechanical Sciences and Engineering*, 47(4). https://doi.org/10.1007/s40430-025-05505-0

Sepehr, M., Fatemi, S.M.R., Danehkar, A., & Moradi, A.M. (2017). Application of Delphi method in site selection of desalination plants. *Global Journal of Environmental Science and Management*, *3*(1), 89. https://doi.org/10.22034/gjesm.2017.03.01.009

Tuc, E., Akbas, S.O., & Babagiray, G. (2024). Reliability and validity analysis of correlations on strength and consolidation parameters for Ankara clay and proposal for a new correlation. *Arabian Journal for Science and Engineering*, 1-20. https://doi.org/10.1007/s13369-024-09181-5

4th International Civil Engineering & Architecture Conference
17-19 May 2025, Trabzon, Türkiye

Experimental and numerical investigation of tsunami impact force on an square obstacle

Kutsi S. Erduran*[1], Uğur Ünal[1], Olusola O. Adekoya[1]

[1]Niğde Ömer Halisdemir University, Department of Civil Engineering, 51240 Niğde, Türkiye

Abstract. This study experimentally and numerically investigates a tsunami impact force on a square obstacle. The impact force under four different reservoir water depths and dry downstream flow condition in a rectangular horizontal flume was evaluated. The maximum impact force, the impact time, the maximum flux and its occurrence time and the averaged wave front and wave front celerity for each flow condition were obtained. The experiments were carried out in a flume with 10m long, 0.309m width and 0.45m height. The variation of the impact forces with time were recorded using a 6-Axis USA ATI Mark GAMMA model SI-32-2.5 load cell. A 2D finite volume – shallow water numerical model was used to determine wave front celerities, impact time, the maximum fluxes and their occurrence times. The numerically obtained maximum fluxes were embedded into a well-known hydrodynamic force equation to compute the numerical hydrodynamic forces. The wave front celerities were also computed by using a previously introduced analytical solution for dry bed condition. The experimental and numerical outputs with regard to the impact force, impact time and the wave front celerity have been compared. The results indicated that the numerical celerities are in good agreement with the experimental ones as well as those obtained by the exact solution. The experimental maximum forces were found to be higher than the numerical ones. However, with a slight adjustment in drag coefficient, much better agreement was obtained. The comparisons with respect to the other parameters listed above were also made and presented.

Keywords: Tsunami impact force; Wave front celerity; Maximum flux; 2D finite-volume model, Experiment

1.Introduction

Tsunami wave poses a substantial threat to the coastal communities. It produces a highly destructive impact force and more often results in devastating damage to buildings and coastal infrastructures, flooding and loss of life. Therefore, a comprehensive understanding of the destructive feature of tsunami wave travelling over dry and wet inland is crucial to mitigate the tsunami impacts. Despite many numerical and experimental studies that led to developments of hard and soft countermeasures (Oetjen et al., 2022), there is still a considerable amount of ongoing research to minimize the harmful effects of the tsunami-induced force.

Tsunami generated force can be classified as hydrostatic force, hydrodynamic force, buoyant force, surge force (slamming), impact of debris and debris damming (Nouri et al., 2007; Nistor et al., 2009; Nouri et al., 2010; Samasindhi & Parikh, 2022). However, depending on the location and type of structure, not all tsunami-induced force components have been taken into account but an appropriate load combination has been applied in the design of a structure in the tsunami prone area (Nistor et al., 2009).

Tsunami induced pressures/forces can also be classified into three phases namely impact phase, transition phase and quasi-steady phase. In the impact phase, the initial impact force occurs and the pressure in this phase is mostly hydrodynamic. In the transition phase, wave run-up force is developed and the mixture of hydrostatic and hydrodynamic pressures occurs. In the quasi-steady phase, the pressure is mainly due to the hydrostatic pressure and the resulting force is a quasi-static hydrodynamic/hydrostatic force (Wüthrich et al., 2018a; Harish et al., 2021; Kihara et al., 2024).

Many tsunami force estimation equations have been proposed (Cross, 1967; Ramsden & Raichlen 1990; Ramsden, 1996; Asakura et al., 2002; Yeh, 2006; Yeh, 2007; Nistor et al., 2009; Fujima et al., 2009; Wüthrich et al., 2018a; Harish et al., 2021). Most of the equations are about the estimation of horizontal forces including impulsive force and quasi-static hydrodynamic or hydrostatic force (Harish et al., 2021). When the tsunami forms a bore like wave and it impacts a structure, it creates horizontal forces, which include an initial impingement force followed by a quasi-steady force due to its very long wave period (Lukkunaprasit et al., 2009). The impingement/impulsive force covers the initial impact force and bore/run-up force whereas the quasi-steady force

*Corresponding author, E-mail: kserduran@ohu.edu.tr

https://doi.org/10.31462/icearc2025_ce_hyd_826

includes quasi-static hydrodynamic or hydrostatic force. This study mainly focused on the horizontal force component of the tsunami force and the other forces listed above are outside the scope of this study.

The well known equation to compute hydrodynamic/hydrostatic force is;

$$F = \frac{1}{2}\rho B C_d \left(h_s u^2\right) \tag{1}$$

Where F is the hydrodynamic force, ρ is the density of the water, B is a width of a structure, C_d is the drag coefficient, h_s is the bore/surge height (wave propagating on dry bed is referred toas surge whereas wave propagating on wet bed is called a bore) and u is the bore/surge celerity/velocity in the absence of obstacles. The term $h_s u^2$ is a momentum flux.

With regard to structural safety, the maximum load and its impact duration are paramount. Equation (1) indicates that maximum force occurs when the momentum flux term is maximum. However, Yeh (2007) and Fujima et al. (2009) showed that $h_{s\max} u_{\max}^2 \neq \left(h_s u^2\right)_{\max}$, in other words, maximum inundation depth and maximum velocity does not occur simultaneously. Therefore, the estimation of the maximum flux term is crucial to accurately computing the maximum hydrodynamic force. On the other hand, there is no simple way to estimate the maximum flux term even though some approaches exist in literature. Yeh (2006) suggested an analytical solution to obtain the maximum force, based on simplified and idealized situations (one-dimensional spatial variation on a uniformly sloping beach) together with some other assumptions. Later, Yeh (2007) provided a better solution including the effect of change in ground elevation for more realistic cases. But, the solution is still limited to uniformly sloping beach. Wüthrich et al., (2018a) introduced a modified momentum flux term, which is $h_s(t)[\min(\chi U; V_m(t))]^2$, where $h_s(t)$ is the time development of the wave profile without an obstacle, χ is a reduction coefficient, U is the bore front celerity, and V_m is the depth-averaged profile velocity. Shafiei et al. (2016) also used an alternative equation to compute the momentum flux. The maximum flux can also be numerically evaluated provided that a very fine grid size is employed to ensure the adequate accuracy (Yeh, 2007).

An initial impact force also known as surge/slumming force is as a result of the leading edge of running-up water impinging on a structure (Yeh, 2007). In comparison with the quasi-hydrodynamic force, this force is not pronounced when the front face of the bore is not steep. This situation occurs when the bore is large enough or the propagating surface is dry. Smoother surfaces can also produce a bore with a front face having a mild slope (Yeh, 2007; Arnason et al., 2009; Lukkunaprasit et al., 2009). Arnason et al. (2009) also highlighted that the initial impact force on the square column was larger than that of circular cylinders. They also observed that the initial peak impact force on the square column was about %50 higher than the subsequent maximum hydrodynamic force. Similar conclusion was reported by Lukkunaprasit et al. (2009), who found out that the impingement force was about 1.5 times the hydrodynamic force. Moroever, FEMA P646 (2008) recommended the use of Equation (1) by taking C_d as 3, which is 1.5 times higher than the actual value for the square and rectangular structure. There is also an equation for the estimation of the initial peak impact force (Dames & Moore, 1980), which is given as

$$F = 4.5\rho g B h^2 \tag{2}$$

Where g is the gravitational acceleration.

Tremendous effort has been made towards an accurate estimation of the wave front celerity and the averaged wave celerity over dry and wet bed conditions as they play not only a crucial role on the magnitude of the tsunami impact force but they also play a significant role on evacuation plan. Many analytical, experimental and numerical studies have been devoted and the average wave celerity is generally expressed as

$$\overline{U} = \alpha\sqrt{g d_0} \tag{3}$$

Where $\overline{U}$ is the average wave celerity, α is a coefficient (ranging from 0.66 to 2) and d_0 is the initial reservoir water depth.

The most widely recognized analytical solution for estimation of the wave front celerity was introduced by Chanson (2009) and it is given in Equation (4).

$$\left(\frac{4}{13}\right)\frac{\left(1-\frac{1}{2}\frac{U}{\sqrt{g d_0}}\right)^{7/2}}{\left(\frac{0.0778\left(\frac{k_s}{d_0}\right)^{1/4}}{8}\left(\frac{U^2}{g d_0}\right)\right)} = \sqrt{\frac{g}{d_0}}\,t \tag{4}$$

Where k_s is the equivalent sand roughness height and t is time.

Tsunami wave impact was experimentally modeled by either solitary waves or dam-break bores (Kihara et al., 2024). Wüthrich et al. (2018a) gave the details of the experimental studies on the tsunami impact force acting on the impervious structures and classified them based on the wave type as solitary wave or dam break wave. Chanson (2006) illustrated the analogy between the dam-break flow and tsunami-induced bores. In this study, dam-break like tsunami induced force was investigated.

The variations of the horizontal impact force with time on a square structure under four different reservoir water depths were experimentally obtained. A 2D finite-volume shallow water model was also employed to model the same experimental flow conditions. Numerically obtained maximum momentum fluxes were implemented in Equation (1) to compute the maximum quasi-steady hydrodynamic forces. The surge forces and average wave celerities and wave front celerities were also estimated by Equations (2-4). Experimental and numerical results have been compared to assess the applicability of the aforementioned equations.

2.Materials and methods

Experimental studies were carried out in a channel (HM162-GUNT) with dimensions 10.0x0.309x0.45 m in the Hydraulic Laboratory of the Civil Engineering Department of Niğde Ömer Halisdemir University (Fig. 1).

Fig. 1. General view of the experimental setup

All the experiments were conducted in a rectangular cross-section channel with a horizontal bottom and a dry downstream bed. A metal gate with a thickness of 11mm, representing the dam body was located 4.4m downstream of the channel inlet. The dam-break like tsunami bore was generated by a sudden release of impounded water in the reservoir (upstream of the gate) by an instantaneous opening of the gate. Then, the wave impacted a rigid square structure with a size of 4x4 cm, which was placed 1.22 m downstream of the dam (Figs. 2 and 3). The gate was opened by freely dropping a 15 kg load attached to it through a pulley system from a platform fixed at position 40 cm high.

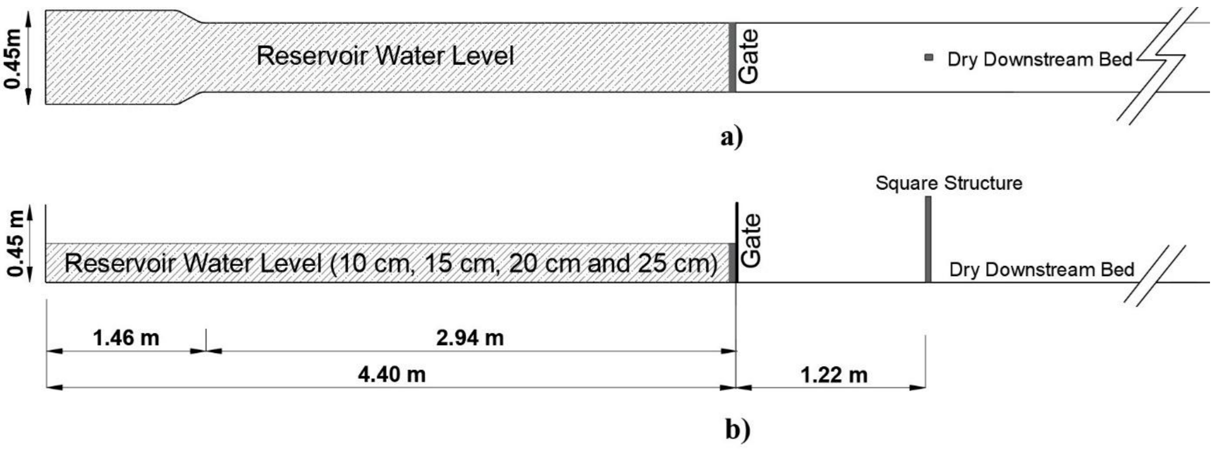

Fig. 2. Schematic view of the experimental setup a) plan view b) longitudinal cross-section view

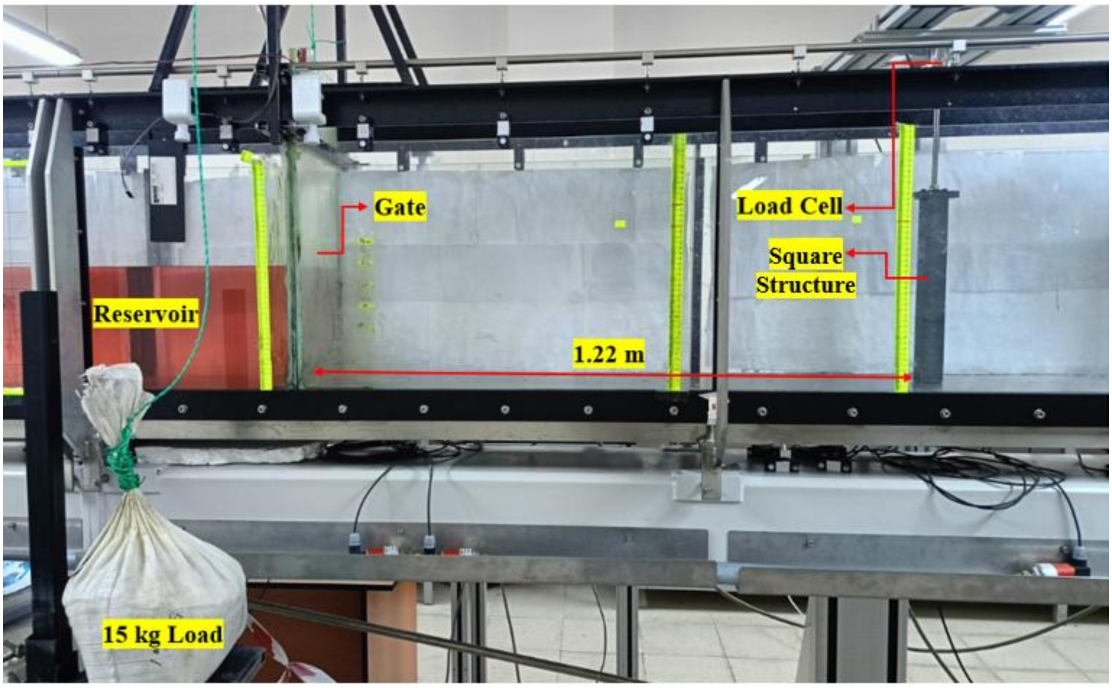

Fig. 3. Longitudinal view of the experimental setup

The impact force on the square structure was measured with the help of a USA ATI Mark Gamma SI-32-2.5 model load cell and traverse system (Fig. 4) over a period of 20s for each experiment. The load cell has a diameter of 75.4 mm and a height of 33.3 mm and six components. It can measure up to 32 N in horizontal forces and up to 100 N in vertical forces whereas it can measure moment in the x, y and z directions up to 2.5 Nm. The data obtained from the load cell is transferred to the computer with the NI PCIe-6323 DAQ card data acquisition system. The load cell was connected to a computer-controlled Dantec 41T32 model traverse system that can move in the x and y directions with a range of 610 mm x 610 mm.

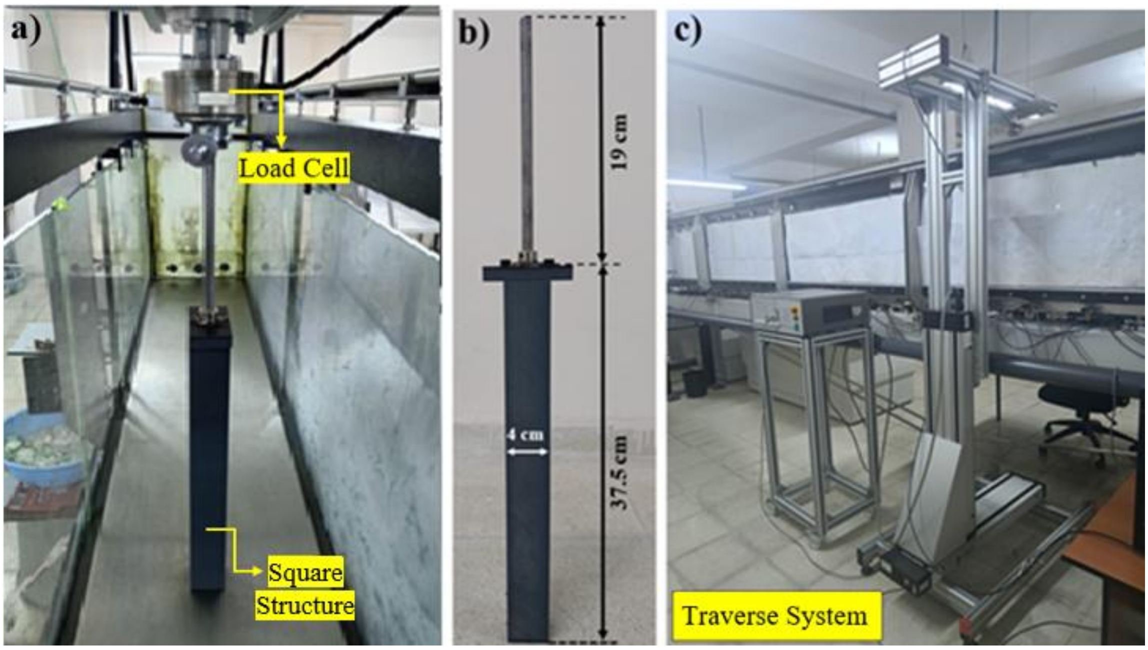

Fig. 4. Force measurement a) load cell and square structure b) size of the structure c) traverse system

The dam-break like tsunami wave propagation was also recorded using a a mobile phone camera with 1080p resolution and 30 fps shooting feature (Fig. 5) and the video recordings were later used to extract the experimental impact time and compute the average wave celerity.

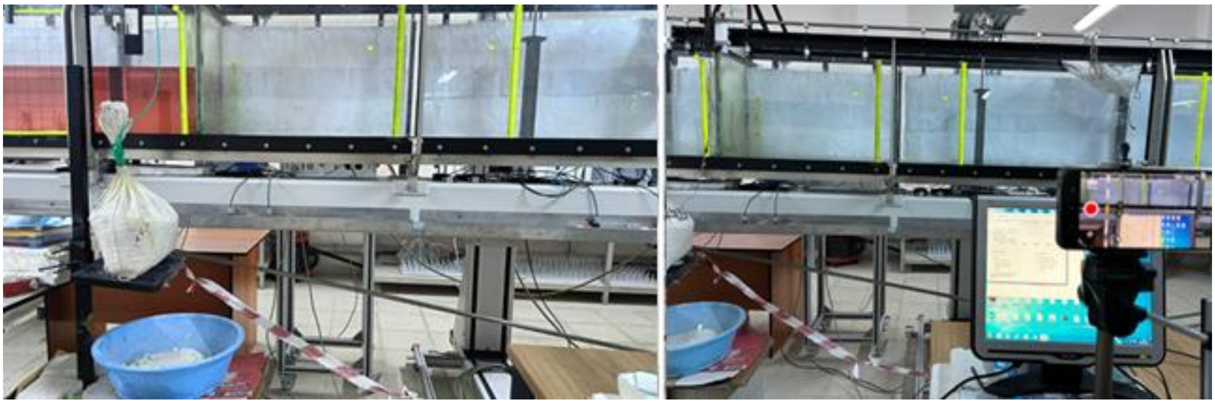

Fig. 5. Position of cell phone camera in experimental studies

The experiments were carried out at four different reservoir water levels; 10 cm, 15 cm, 20 cm and 25 cm and repeated three times for each water level. The arithmetic averaged of every three experimental data represents the corresponding experimental tests and was named after the reservoir water level as H10, H15, H20 and H25.

The gate opening times were recorded to ensure that they satisfied the sudden dam-break condition (the formation of fully developed surge/bore). The condition was introduced by Lauber and Hager (1998) and defined as $t_{op} = 1.25\sqrt{d_0 / g}$ where t_{op} is the gate opening time. The condition is met when the recorded gate opening time is less than the computed gate opening time obtained from the expression for the sudden dam-break condition. Recorded and computed gate opening times for each reservoir water level are given in Table 1. It can be seen that the condition for each reservoir water level was met.

Table 1. Recorded and computed gate opening times for each reservoir water level

Test Case	H10	H15	H20	H25
Recorded t_{op} (ms)	75	95	118	153
Calculated t_{op} (ms)	126	154	178	199

Repeatability of each experiment was validated by conducting each experiments three times and plotting the resulting forces over a period of 20s. Fig. 6 is given as an example of a validation test indicating that all three test results are compatible with slight variations immediately after the initial impact. This is most likely due to the structural vibration. Similarly, for each test case, a satisfactory repeatability was achieved (Fig. 7).

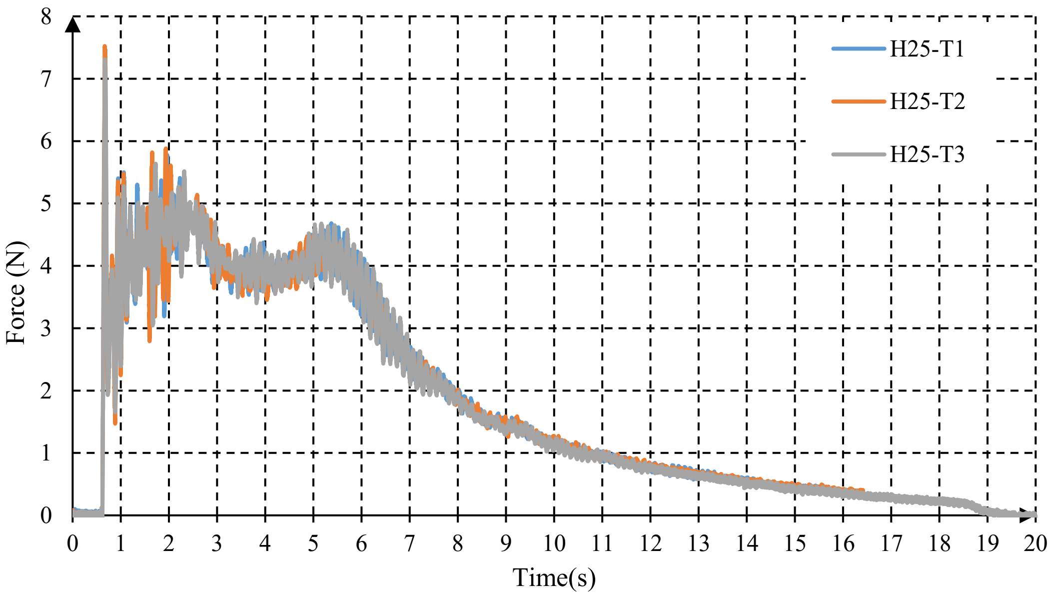

Fig.6. The time history of the force induced on the square structure for H25

A two-dimensional (2D) numerical model developed by Erduran et al. (2002) was used to reproduce the experimental flow conditions. The model solves the shallow water equations given in Equations (5-7) by using the finite volume method with one of the 5 available shock capturing schemes. In this study HLLC scheme was chosen.

$$\frac{\partial h}{\partial t}+\frac{\partial (hv_x)}{\partial x}+\frac{\partial (hv_y)}{\partial y}=0 \tag{5}$$

$$\frac{\partial (hv_x)}{\partial t}+\frac{\partial (hv_x^2+gh^2/2)}{\partial x}+\frac{\partial (hv_x v_y)}{\partial y}=gh\left(So_x-Sf_x\right) \tag{6}$$

$$\frac{\partial (hv_y)}{\partial t}+\frac{\partial (hv_x v_y)}{\partial x}+\frac{\partial (hv_y^2+gh^2/2)}{\partial y}=gh\left(So_y-Sf_y\right) \tag{7}$$

where h is the water depth, v_x and v_y are the depth-averaged velocities in x and y directions respectively, S_{0x} and S_{0y} are the bottom slope terms in x and y direcitons respectively and S_{fx} and S_{fy} the friction slope terms in x and y directions respectively.

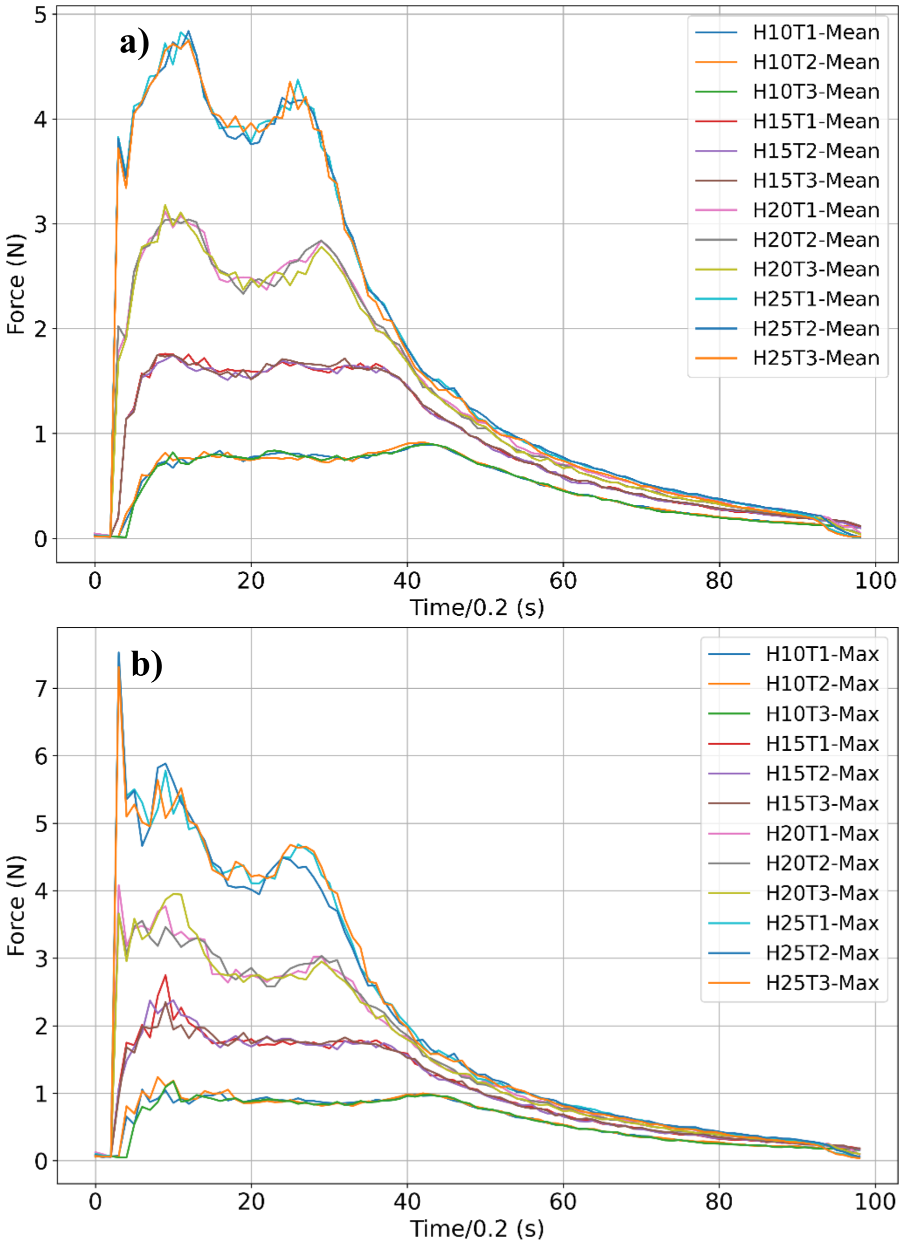

Fig. 7. Experimental lateral forces for a) mean forces b) maximum forces and c) minimum forces

Continued Fig. 7

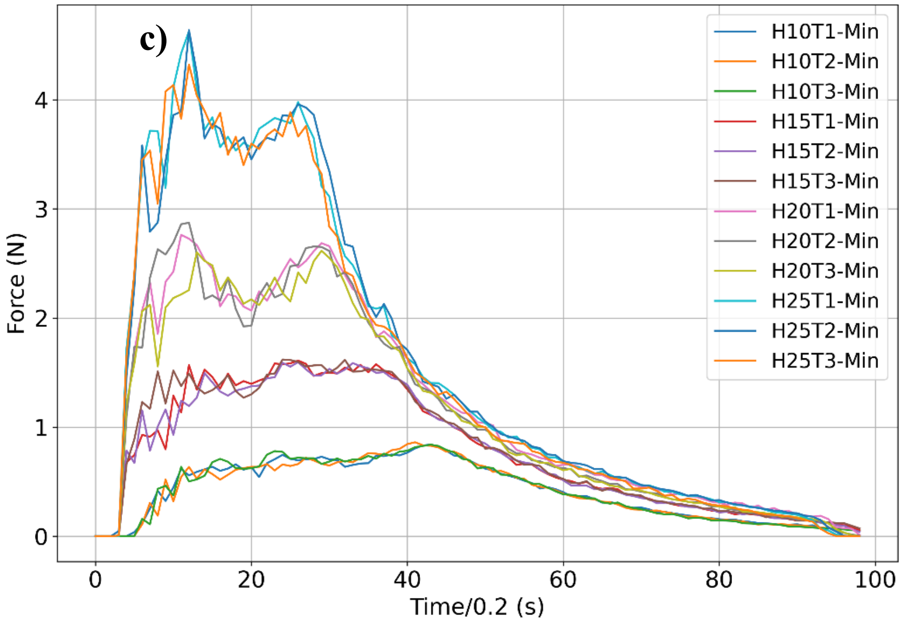

The computational domain (experimental channel) was divided into 31000 cells with the size of 0.01×0.01m. Initial flow condition was defined as the water depth upstream of the dam in the reservoir with a dry downstream bed condition. Upstream boundary was defined as a close boundary whereas downstream boundary was defined as an open boundary. A detailed solution to the shallow water equations and definitions of boundary and initial flow conditions are given in Erduran et al. (2002). The dam is removed instantaneously and the model is run for 12 s for each test. The time step is chosen to be 0.002s to ensure the numerical stability.

The numerical model produced the time variation of the flow characteristics (velocity and water depth) over 12s at the location of the square structure in the absence of the structure as well as the time variation of the flow characteristics along the channel for each test case. Hence, desired values for the impact time, averaged wave celerity, wave height, wave front celerity and the maximum flux term $\left(h_s u^2\right)_{\max}$ for each test were acquired.

3. Results and discussion

The experimental impact time was taken to be the duration between gate opening and the first impact and it was extracted from the video recordings by splitting them into frames with a time-interval of 0.0333 s. The numerical impact time was obtained from the numerical output file in the absence of the structure. The impact times were later used to compute the average wave celerities. Table 2 shows the experimental and numerical impact times and the average wave celerities. It also indicates the absolute percentage differences in the celerities. It is seen that the maximum absolute percentage difference between the numerical and experimental wave celerity is 5.67. Using Equation (3) and the averaged wave celerities, numerical and experimental, α values were also computed and it was found that they ranged approximately between 1.2 and 1.3, which are close to 1.25 reported by Wüthrich et al. (2018b).

Table 2. Experimental and numerical impact time and averaged celerity

Test Case	Impact Time (s)		Average Wave Celerity (m/s)		Absolute Difference in Celerity (%)
	Numerical	Experimental	Numerical	Experimental	
H25	0.590	0.620	2.068	1.9677	4.84
H20	0.674	0.665	1.810	1.8346	1.35
H15	0.802	0.759	1.521	1.6074	5.67
H10	1.030	1.026	1.184	1.1891	0.39

The numerical and analytical wave front celerites were obtained by using the 2D model and Equation (4) respectively. They were compared and it was seen that Chanson (2009) analytical equation produced a quite similar results with a maximum absolute percentage difference of 6.93 (Table 3).

Table 3. Numerical and analytical wave front celerity at the structure location

Test Case	Numerical (m/s)	Chanson (2009) (m/s)	Absolute Difference in Celerity (%)
H25	1.906	2.028	6.39
H20	1.646	1.760	6.93
H15	1.356	1.423	4.93
H10	1.022	1.054	3.11

The maximum momentum flux, its occurrence time, water depth at maximum flux time as well as the maximum inundation depth at the structure location were numerically evaluated in the absence of the structure and given in Tables 4 and 5 as well as in Fig. 8. As can be seen, the maximum momentum flux occurred when the water depth was around 65-67 % percent of the maximum inundation depth. This result also agreed with that of Wüthrich et al. (2018b), who stated that the maximum momentum occurred 65-70 % of the maximum wave height for dry bed surges. It was also observed that the maximum momentum flux occurred at around 25-28 % of the initial reservoir level and approximately 2.4-2.6 times the impact time.

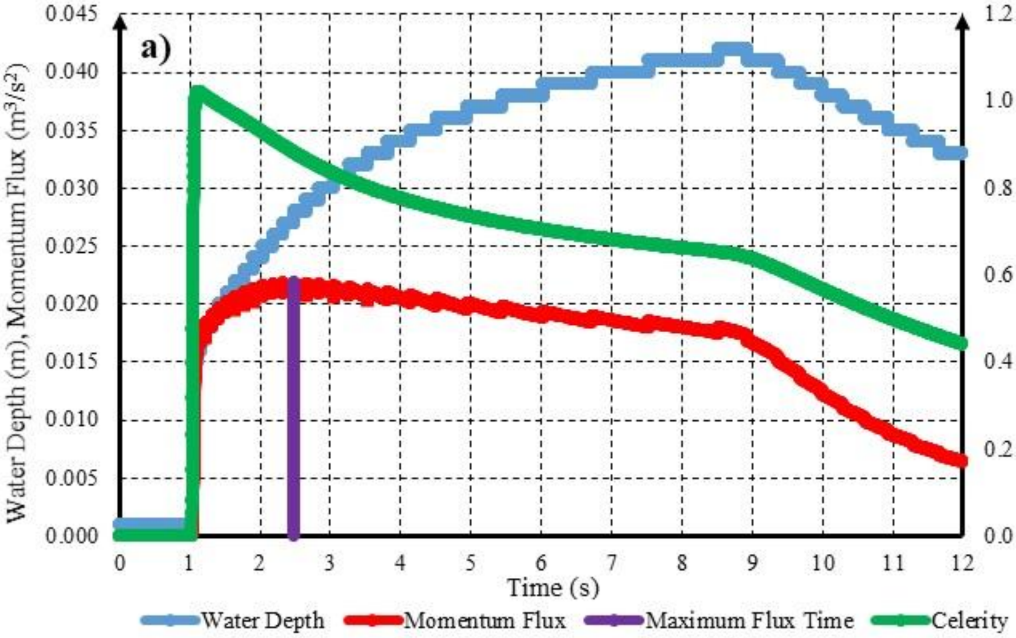

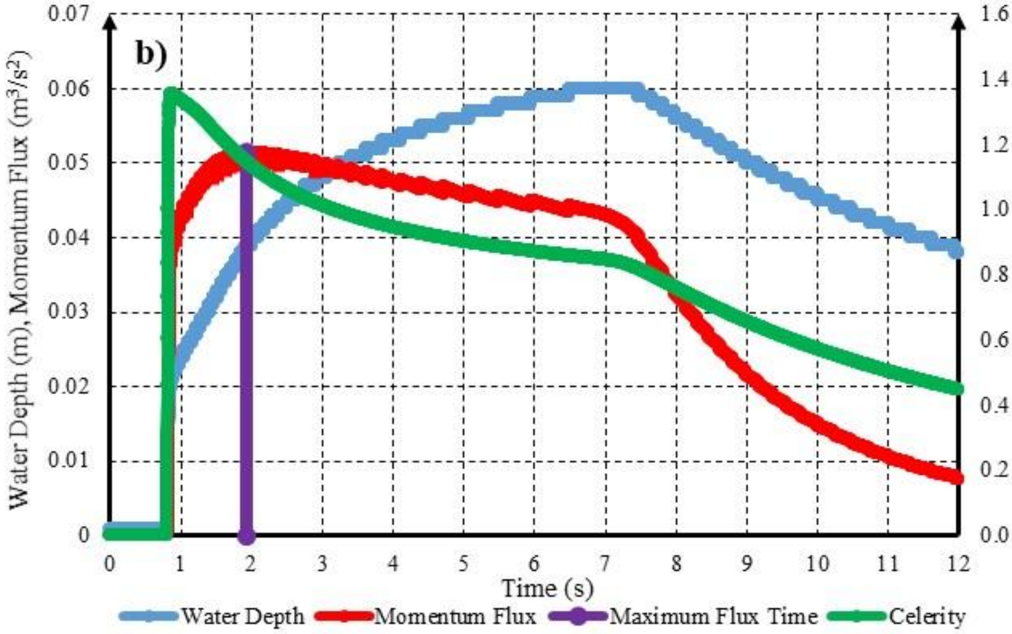

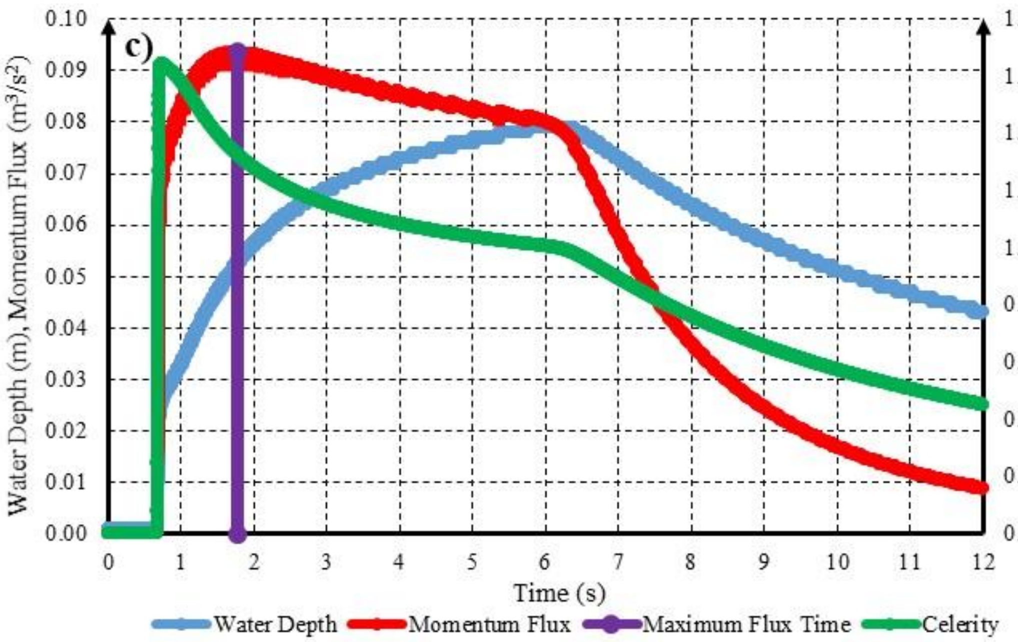

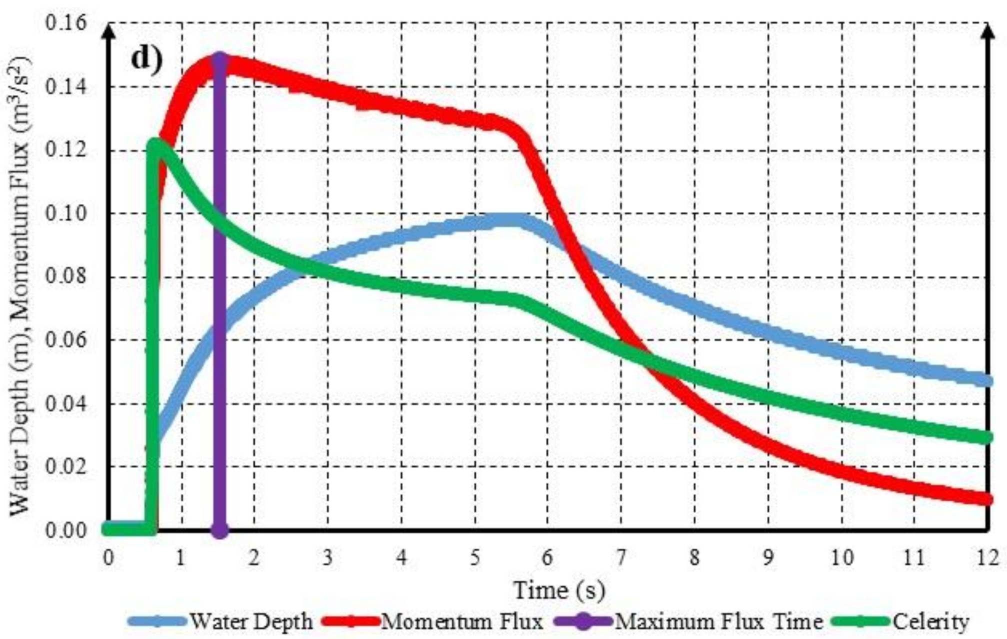

Fig. 8. Numerical momentum flux, water depth and celerity for all test cases a) H10 b) H15 c) H20 d) H25

Table 4. Numerical water depths and depth ratios at the structure location

Test Case	MF (m)	MI (m)	MF/MI (%)	MF/d_0 (%)
H25	0.064	0.098	65.3	25.6
H20	0.053	0.079	67.1	26.5
H15	0.039	0.060	65.0	26.0
H10	0.028	0.042	66.7	28.0

MF: Water depth at maximum flux time; MI:Maximum inundation depth

Table 5. Occurrence of maximum flux time (numerical)

Test Case	Impact Time (s)	Maximum Flux Time (s)	Impact time / Maximum flux time
H25	0.590	1.524	2.58
H20	0.674	1.772	2.63
H15	0.802	1.924	2.40
H10	1.030	2.488	2.42

The lateral hydrodynamic force for each test case and for two different drag coefficients was computed using Equation (1) and shown in Fig. 9. The results showed that the hydrodynamic force with a drag coefficient of 2 overestimated the hydrodynamic force in the quasi-steady phase. This drag coefficient is suggested by FEMA (2011) for rectangular objects. Taking drag coefficient as 1.65 resulted in much better estimate for the maximum hydrodynamic force. Similar to the present study, Shafiei et al. (2016) study also produced a drag coefficient of 1.65 for a square prism structure, perpendicular to the flow direction.

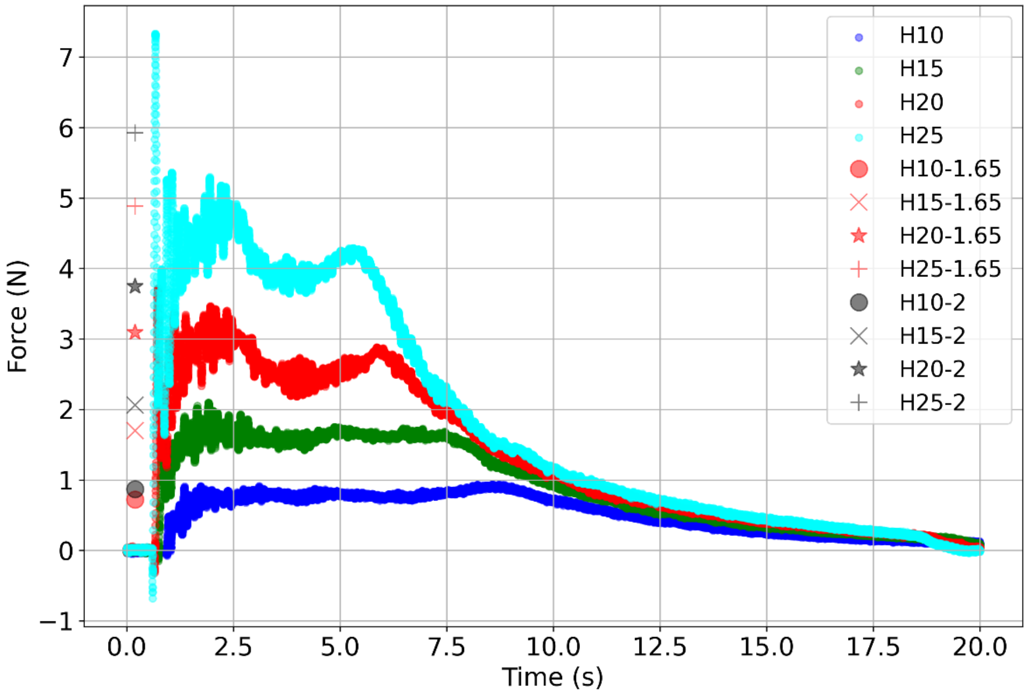

Fig. 9. Experimental and analytical lateral forces

Fig. 9 clearly illustrated that the higher the reservoir initial water depth, the higher the experimental and numerical impact forces. The rate of increase in the forces was larger than that of the water depths. Taking initial reservoir water depth and corresponding force for H10 as base, the force and the initial water depth ratios were computed and given in Table 6. An increase of 2.5 times in water depth resulted in an increase of 7.88 times in the impact force whereas double the initial water depth ended in 3.99 times the force.

Table 6. Calculated force and water depth ratios

Test Case	Recorded Maximum Impact Force (N)	Force Ratio	Depth Ratio
H25	7.33	7.88	2.5
H20	3.71	3.99	2.0
H15	2.10	2.26	1.5
H10	0.93	1.0	1.0

The recorded experimental forces also showed that the initial peak impact force was only dominant in H25 and it was higher than the subsequent hydrodynamic force (Fig. 9). The initial peak impact force was 7.33 N whereas the maximum hydrodynamic force was around 5 N, resulting in a force ratio of 1.47. The experimental studies of Ramsden (1993) and Arnason (2005) indicated that the peak overshoot at the initial impact was approximately 1.5 times the subsequent maximum hydrodynamic force. However, they draw this conclusion for a wet downtream bed, creating a bore wave rather than a surge as is the case in this study . In fact, they realized that there was no significant initial impulse force for the dry-bed surges. Except for H25, this study also supported their conclusions and the maximum force was due to the hydrodynamic force and not for the initial impact force. This can be attributed to the fact that the observed surge waves did not produce the significant initial impact force because the wave fronts were not sufficiently steep.

The force-time variations given in Fig. 9 aligns with the reported force phases in the literature, particularly the initial impact phase and the quasi-steady phase. The initial impact and run-up force occurred in a very short time, roughly in the order of 10^{-1} s (Lobovský et al, 2014). Once the wave reflected and the reflected wave traveled upstream, the quasi-steady phase started. The sudden drop in the force-time curves was mainly due to the impounded water in the reservoir. However, it was seen that the sudden drop occurred later when the initial reservoir water depth was lower.

4. Conclusions

The dam-break like tsunami induced forces acting on the square structure were experimentally and analytically obtained with the help of 2D numerical models. The following conclusions were drawn;

1- Equation (4) gave a quite good estimate for the wave front celerities. The experimental average wave celerities were compatible with those of 2D numerical model. α coefficient given in Equation (3) was found to be 1.25.
2- The maximum momentum fluxes and their occurrence time were numerically evaluated. Then the maximum hydrodynamic forces were computable using Equation (1). The calculated maximum hydrodynamic forces were in a good agreement with those of the experimental ones when the drag coefficient of 1.65 was taken. The drag coefficient of 2 produced overestimated values.
3- Numerical results indicated that the maximum flux occurred when the water depth was around 65-67% of the maximum depth recorded at the structure location. The maximum flux also occurred 2.4-2.6 times the impact times depending on the initial reservoir water depth. The result also indicated that the maximum flux occurred when the water depth at the structure location was 25-28 % of the initial reservoir water depth.
4- It was seen that the maximum impact forces were mostly due to the quasi-static forces, only at H25, was the initial peak impact force more pronounced and higher than the subsequent maximum quasi-static force.
5- The impact forces increased with the increasing water depth. However, the rate of increased in the force was much more than that of initial reservoir water depth.

References

Arnason, H. (2005). *Interactions between an incident bore and a free-standing coastal structure*. [Doctoral dissertation, University of Washington]

Arnason, H., Petroff, C., & Yeh, H. (2009). Tsunami bore impingement onto a vertical column. *Journal of Disaster Research*, *4*(6), 391-403

Asakura, R., Iwase, K., Ikeya, T., Takao, M., Kaneto, T., Fujii, N., & Ohmori, M. (2002). The tsunami wave force acting on land structures. *Coastal Engineering,* 1191-1202

Chanson, H. (2006). Tsunami surges on dry coastal plains: Application of dam break wave equations. *Coastal Engineering Journal*, *48*(4), 355-370

Chanson, H. (2009). Application of the method of characteristics to the dam break wave problem. *Journal of Hydraulic Research*, *47*(1), 41-49

Cross, R.H. (1967). Tsunami surge forces. *Journal of the Waterways and Harbors Division*, *93*(4), 201-231

Dames & Moore. (1980). Design and construction standards for residential construction in tsunami-prone areas in Hawaii, Dames & Moore

Erduran, K.S., Kutija, V., & Hewett, C.J.M. (2002). Performance of finite volume solutions to the shallow water equations with shock-capturing schemes. *International Journal for Numerical Methods in Fluids*, *40*(10), 1237–1273

Federal Emergency Management Agency, F.E.M.A. (2008). Guidelines for design of structures for vertical evacuation from tsunamis (FEMA P-646). *Technical Report*

Federal Emergency Management Agency, F.E.M.A. (2011). Coastal construction manual principles and practices of planning, siting, designing, constructing, and maintaining residential buildings in coastal areas (Fourth Edition) (FEMA P-55), *Technical Report*, *2*

Fujima, K., Achmad, F., Shigihara, Y., & Mizutani, N. (2009). Estimation of tsunami force acting on rectangular structures. *Journal of Disaster Research*, *4*(6), 404-409

Harish, S., Sriram, V., Schüttrumpf, H., & Sannasiraj, S.A. (2021). Tsunami-like flow induced force on the structure: Prediction formulae for the horizontal force in quasi-steady flow phase. *Coastal Engineering*, *168*, 103938

Kihara, N., Tomita, T., Yoshimura, S., Kaida, H., Ito, K., Kuriyama, T., Omura, H. & Yamabe, H. (2024). Review of prediction models for tsunami-induced lateral fluid force for revision of engineering design code for nuclear power plant structures. *Journal of Nuclear Science and Technology*, *62*(2), 125-148.

Lauber, G., & Hager, W.H. (1998). Experiments to dambreak wave: Horizontal channel. *Journal of Hydraulic Research*, *36*(3), 291-307

Lobovský, L., Botia-Vera, E., Castellana, F., Mas-Soler, J., & Souto-Iglesias, A. (2014). Experimental investigation of dynamic pressure loads during dam break. *Journal of Fluids and Structures*, *48*, 407-434

Lukkunaprasit, P., Thanasisathit, N., & Yeh, H. (2009). Experimental verification of FEMA P646 tsunami loading. *Journal of Disaster Research*, *4*(6), 410-418

Nistor, I., Palermo, D., Nouri, Y., Murty, T. & Saatcioglu, M. (2009). Tsunami-induced forces on structures. *Handbook of Coastal and Ocean Engineering*, Publisher: World Scientific

Nouri, Y., Nistor, I., Palermo, D., & Saatcioglu, M. (2007). Tsunami induced hydrodynamic and debris flow forces on structural elements. *In Proceedings of 9th Canadian Conference of Earthquake Engineering*, 2267-2276

Nouri, Y., Nistor, I., Palermo, D., & Cornett, A. (2010). Experimental investigation of tsunami impact on free standing structures. *Coastal Engineering Journal*, *52*(1), 43-70

Oetjen, J., Sundar, V., Venkatachalam, S., Reicherter, K., Engel, M., Schüttrumpf, H., & Sannasiraj, S.A. (2022). A comprehensive review on structural tsunami countermeasures. *Natural Hazards*, *113*(3), 1419-1449

Ramsden, J.D., & Raichlen, F. (1990). Forces on vertical wall caused by incident bores. *Journal of Waterway, Port, Coastal, and Ocean Engineering*, *116*(5), 592-613

Ramsden, J. D. (1993). *Tsunamis: Forces on a vertical wall caused by long waves, bores, and surges on a dry bed*. [Doctoral dissertation, California Institute of Technology]

Ramsden, J.D. (1996). Forces on a vertical wall due to long waves, bores, and dry-bed surges. *Journal of Waterway, Port, Coastal, and Ocean Engineering*, *122*(3), 134-141

Samasindhi, S.A., & Parikh, K.B. (2022). Effects of tsunami forces on RC framed structure subjected to bracing and shear wall. *International Journal for Research in Applied Science & Engineering Technology (IJRASET)*, *10*(6), 68-76

Shafiei, S., Melville, B.W., & Shamseldin, A.Y. (2016). Experimental investigation of tsunami bore impact force and pressure on a square prism. *Coastal Engineering*, *110*, 1-16

Wüthrich, D., Pfister, M., Nistor, I., & Schleiss, A.J. (2018a). Experimental study on the hydrodynamic impact of tsunami-like waves against impervious free-standing buildings. *Coastal Engineering Journal*, *60*(2), 180-199

Wüthrich, D., Pfister, M., Nistor, I., & Schleiss, A.J. (2018b). Experimental study of tsunami-like waves generated with a vertical release technique on dry and wet beds. *Journal of Waterway, Port, Coastal, and Ocean Engineering*, *144*(4), 04018006

Yeh, H. (2006). Maximum fluid forces in the tsunami runup zone. *Journal of Waterway, Port, Coastal, and Ocean Engineering*, *132*(6), 496-500

Yeh, H. (2007). Design tsunami forces for onshore structures. *Journal of Disaster Research*, *2*(6), 531-536

4th International Civil Engineering & Architecture Conference
17-19 May 2025, Trabzon, Türkiye

Hydraulic Analysis of Multi-outlets Submains-II: Implementation

Gürol Yıldırım*[1]

[1] Giresun University, Engineering Faculty, Civil Engineering Dept., 28100, Giresun, Türkiye

Abstract. In this paper, the methodology covering design constraints to sensitively determine the operating inlet pressure head by trial-and-error-procedure, to achieve the design criteria (initial and boundary conditions), was presented. For any desired uniformity level, the procedure also provides an opportunity to evaluate the influence of different uniform line slopes on the pipe geometric characteristics (pipe size and length), and on the corresponding hydraulic variables (required operating inlet pressure and downstream end pressure heads and total friction head losses). The examination results of design applications covering various combinations of irrigation design parameters were depicted for outlet characteristics, and zero-slope condition (S0 = 0) graphically in dimensionless form, for practical purposes. For different design applications, the results of the present computer program (Multi-flowCAD) has the highest accuracy and sensitivity rather than those of the alternative analytical and numerical methods earlier presented, because only the basic equations of the hydraulics of steady pipe flow were efficiently used in each segment of lateral length which was divided by successive individual emitters. .

Keywords: Smooth pipe-flow; Steady-state analysis; Software; Computer-aided design (CAD)

1. Methodology

1.1. Initial and boundary conditions for software implementation
An important objective of the present analysis is the sensitively determination of the proper value of the operating inlet pressure head, H0I (Hin), which can be varied within limited constraints in the design algorithms (initial and boundary conditions) (Yıldırım, 2023a,b; Yıldırım, 2014a,b; Yıldırım, 2015a,b; Yıldırım, Yıldırım & Singh, 2013a). It clearly means, preliminary increase in average piezometric head (Δ_0) varies ranging from minimum inlet pressure head range [$\overline{H}_{min}$ = $H_{0I(min)}/H_{av}$] toward maximum inlet pressure head range [$\overline{H}_{max}$ = $H_{0I(max)}/H_{av}$]. The proposed computer program (Multi-flowCAD) sensitively performs the following calculations, in a stepwise manner:

a. Determine operating inlet pressure head ranges in which the operating inlet pressure head is located ($\overline{H}_{min}$ and $\overline{H}_{max}$ = minimum and maximum ranges for the operating inlet pressure head);
b. Obtain minimum operating inlet pressure head range [$\overline{H}_{min}$] based on the design algorithms (for H_{0I}, if smaller values than are designed, this would indicate that a negative value of the pressure head at any outlet would be apparent);
c. Obtain maximum operating inlet pressure head range [$\overline{H}_{max}$], based on the design algorithms (for H_{0I}, if larger values than $\overline{H}_{max}$ are designed, this would indicate that the sum of outflows is greater than the initial pipe discharge, Q_I, which means that back-flow occurs from the downstream end toward the upstream direction of the pipeline);
d. As the proper interval of the reduced operating inlet pressure head [$\overline{H}_{min}(=H_{01(min)}/H_{av}) \le (H_{01}/H_{av}) \le \overline{H}_{max}(=H_{01(max)}/H_{av})$] is obtained, the favorable value of H_{0I} should be investigated. In line with this concept, the following considerations should be taken into account:
e. For H_{0I} determination, if $\overline{H}_{min}$ is selected for sub-main line design, the value of residual flow rate at the downstream end from the last outlet is larger than the acceptable small quantity (ε), approximately zero.

* Corresponding author, E-mail: gurol.yildirim@giresun.edu.tr

https://doi.org/10.31462/icearc2025_ce_hyd_870

Obviously, an important boundary condition for the downstream end does not keep to the right in the design algorithm. Meanwhile, the residual pipe discharge decreases from $\overline{H}_{min}$ toward $\overline{H}_{max}$, increasingly; then, for $\overline{H}_{max}$ it has a sufficiently small value, approximately zero.

f. For sub-main line design, the design parameters should be determined in order to minimize the total friction drop at the end of pipeline. In this respect, if $\overline{H}_{min}$ is selected, the total friction drop would have major values and then, from $\overline{H}_{min}$ toward $\overline{H}_{max}$, have minor values, increasingly. However, if $\overline{H}_{max}$ is selected, the total friction drop is minimized.

g. In the design procedure, the water application uniformity is an unknown parameter; other parameters should be varied to have the highest level of uniformity. Obviously, water application uniformity increases from $\overline{H}_{min}$ toward $\overline{H}_{max}$, with the highest value at $\overline{H}_{max}$.

h. Resulting, the proper operating inlet pressure head is finally achieved at $\overline{H}_{max}$, and total friction drop ($h_{f(L)}$) and residual flow rate (Q_r) for the pipe segment from the last outlet toward to downstream closed end are minimized, whereas the water application uniformity (U_C) of the system is achieved to be maximized.

i. For all performed simulations it should be pointed out, for the Multi-flowCAD, the required design parameters ($H_{f(L)}$, Q_r, U_C and/or D_{ULQ}) vary versus the operating inlet pressure head range (H_{0I}/H_{av}) to achieve its acceptable proper value within the design criteria, while the available alternative procedures may have fixed values, for these unknown variables.

1.2. Design configurations

Design procedure based on the manifold flow hydraulics principles covering various required parameters can be ordered in the following four steps (Sadeghi et al., 2016; Scaloppi & Allen, 1993; Yıldırım, 2016b, Yıldırım & Kose, 2016a):

1. To give a series of values for the design parameter (pipe diameter or length) from smallest to largest.
2. To find the required operating inlet pressure head (H_{in}) that can create the required average outlet discharge (q_{av}), and to evaluate the total friction head losses (H_f), and the uniformity coefficients of water application (U_C and/or DU_{LQ}), for each given design value.
3. To plot the dimensionless design curves of the uniformity of water application, the required operating inlet pressure head and the total friction head losses versus the required design parameter (pipel diameter or length).
4. To find the best solution of the required design parameter (pipe diameter or length), the required operating inlet pressure head and the total friction head losses from the dimensionless design curves plotted in the third step according to the required level of water application uniformity.

2. Design applications

In designing of the pipeline in a submain unit system, it is commonly assumed that the outlet outflow-pressure head relationship, average flow rate and hydraulic characteristics of the outlet model examined, and acceptable level of water application uniformity are known, a priori (Sadeghi & Peters, 2013; Sadeghi & Peters, 2011; Singh et al., 2000). It often remains to design either the pipe length or the inside diameter, the operating inlet pressure head, pressure head at the downstream closed end, the extreme pressure heads with their locations, total head losses due to friction along the lateral, with the remaining variables previously known (Singh & Mahar, 2003; Valiantzas, 1998). The following are the various design examples based on each design concept, incorporating various design configurations. For the following design examples, the dimensionless curves which can be efficiently used as the design charts will be provided to directly determine any of the required hydraulic design parameters (Valiantzas, 2002).

2.1. Design example-I: Determination of pipeline length with operating inlet pressure head, total friction head losses and uniformity coefficients using design curves

It is given that the outflow-pressure head relationship : $q = 3.58\ 10^{-7}\ H^{0.5}$, average flow rate of outlet: $q_{av} = 4\ lh^{-1}$ ($1.111\ 10^{-6}\ m^3s^{-1}$), spacing between successive interior outlets: S = 1.0 m, design uniformity coefficient : U_C = 0.95, the inside diameter of pipeline : D = 14 mm, the kinematic viscosity of water at 20 ^{0}C $\nu = 1.01\ 10^{-6}\ m^2s^{-1}$. The values that must be determined are: (1) Length of pipeline, (2) the proper value of operating pressure head at the pipe inlet, (3) total frictional head losses along lateral.

Solution with Design Curves:

On the basis of the present algorithm discussed, the direct design procedure can be better illustrated if the values of the operating inlet pressure head H_{in}, the friction head loss H_f, and the uniformity coefficients UC, DU_{LQ} are plotted for various lengths of lateral, ranging from 25 to 250 m, for the lateral internal diameter, D = 0.014 m.

In each calculation the values of design parameters are obtained from the Multi-flowCAD, then depicted in dimensionless form for practical purpose which could also be efficiently used as the design charts.

From Fig. 2.b and for design uniformity coefficient UC = 0.95; length of the lateral, L = 125 m is found. On the other hand, from Figure 6a and for L = 125 m; we have relative pressure head at the inlet, $H_{in}/H_{av} = 1.26$. From the emitter outflow-pressure head relationship we finally compute

$$H_{av} = \left(\frac{q_{av}}{c}\right)^{1/y} = \left(\frac{1.111\times 10^{-6}}{3.58\times 10^{-7}}\right)^{1/0.5} = 9.631 \text{ m} \tag{1}$$

Resulting; $H_{in} = 1.26 \times 9.631 = 12.135$ m is found.

From Fig. 2.c and for L = 125 m ; we have relative friction drop, $H_F/H_{in} = 0.326$ and then the frictional head loss along the lateral, $H_F = 0.326*12.135 = 3.956$ m is found. For the second uniformity design parameter DU_{LQ}, from Fig. 3d and for L = 125 m; $DU_{LQ} = 0.915$ is found.

2.2. Design example-2: Determination of pipeline diameter with operating inlet pressure head, total friction head losses and uniformity coefficients using design curves

Determine the following parameters for the design uniformity coefficient UC = 0.95 and the pipeline length L = 150 m using the same data given in the Design Example-1. (1) the inside diameter of the lateral, (2) the proper value of operating pressure head at the lateral inlet, (3) total frictional head losses along lateral.

Solution with Design Curves:

The values of the inlet pressure H_{in}, the frictional head loss H_f and the uniformity coefficients U_C, DU_{LQ} are evaluated for various pipe internal diameters ranging between 10 mm and 21 mm (L = 150 m). In each calculation the values of design parameters are obtained from the present computer program; then depicted in dimensionless form for practical purpose which could also be used as a design chart (Fig. 7 (a,b), (c,d)).

From Fig. 7b and for design UC = 0.95; inside diameter of the lateral, D = 16.4 mm is found. On the other hand, from Fig. 7a and for D = 16.4 mm; we have relative pressure head at the inlet, $H_{in}/H_{av} = 1.195$. From the emitter outflow-pressure head relationship we find,

$$H_{av} = \left(\frac{q_{av}}{c}\right)^{1/y} = \left(\frac{1.111\times 10^{-6}}{3.58\times 10^{-7}}\right)^{1/0.5} = 9.631 \text{ m} \tag{2}$$

Resulting ; $H_{in} = 1.195\times 9.631 = 11.51$ m is found.

From Fig. 3.c and for D = 16.4 mm; we have relative friction drop, $H_F/H_{in} = 0.277$ and then the frictional head loss along the lateral, $H_F = 0.277*11.51=3.188$ m is found. For the lower-quarter distribution uniformity coefficient (DU_{LQ}), from Figure 4.d and for D = 16.4 mm; $DU_{LQ} = 0.925$ is found.

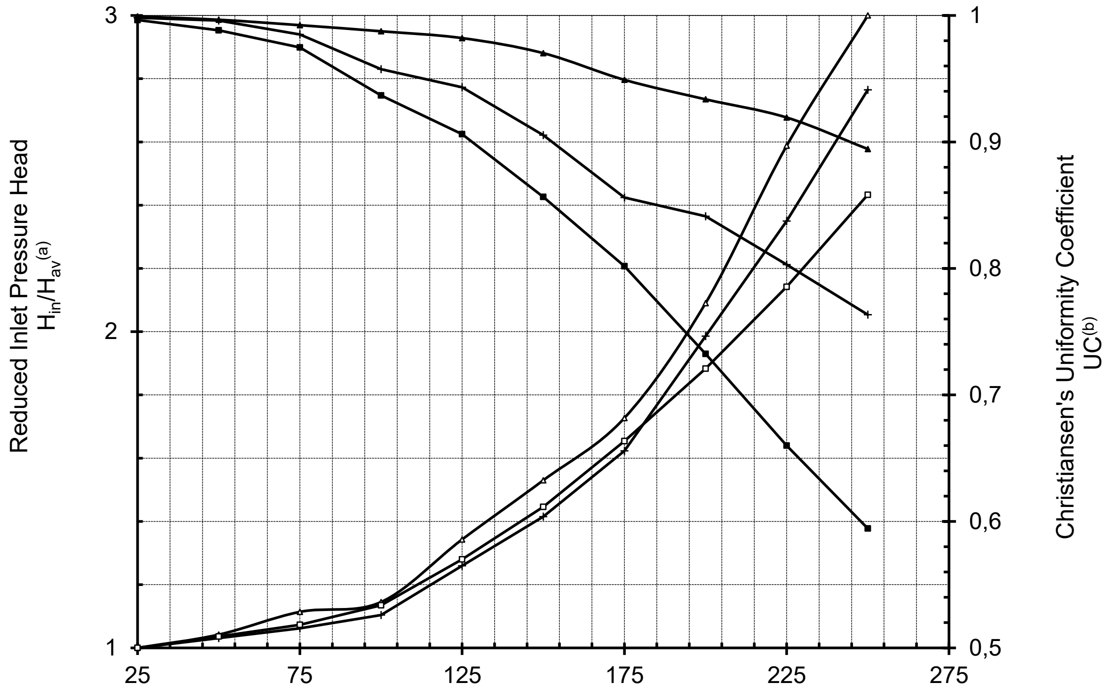

a) , b)

Fig. 1. a) Variation of reduced inlet pressure head (Hin/Hav), b) Christiansen's Uniformity Coefficient (UC) with Lateral Length Ranging from L = 25 m to 250 m, and D = 14 mm, c) Variation of reduced friction head loss

(HF/Hin) and d) Lower-Quarter Distribution Uniformity (DULQ) with Lateral Length Ranging from L = 25 m to 250 m, and D = 14 mm.

Continued Fig. 1

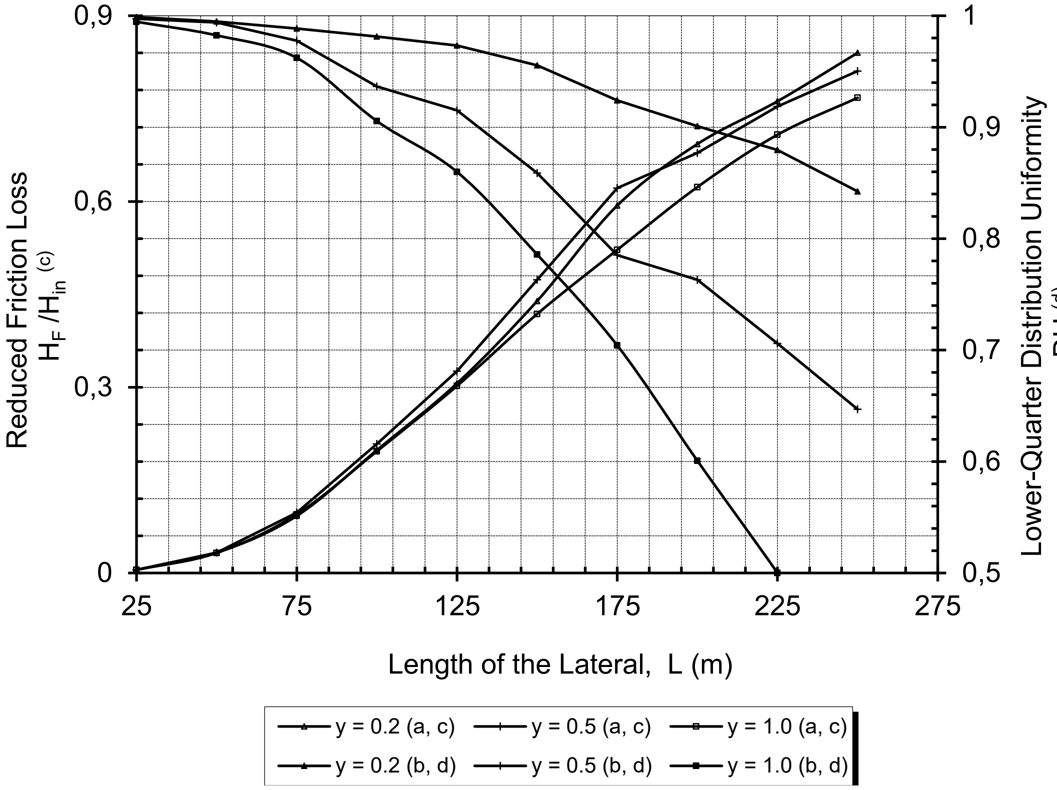

c), d)

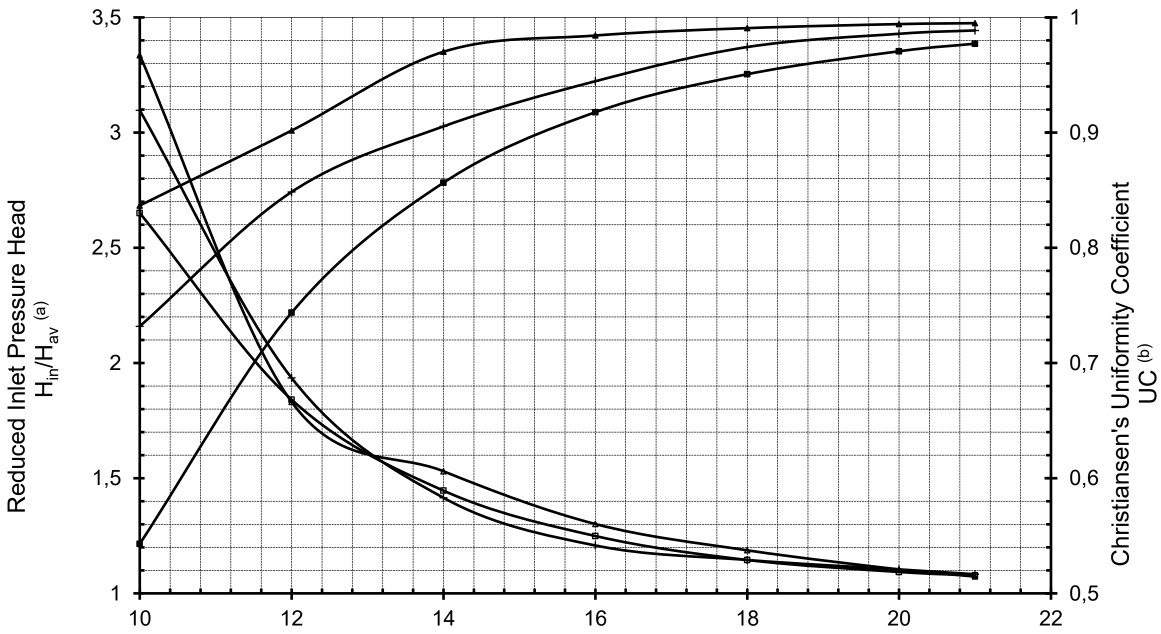

a) , b)

Fig. 2. a) Variation of reduced inlet pressure head (H_{in}/H_{av}), b) Christiansen's Uniformity Coefficient (UC) with lateral inside diameter ranging from D = 10 mm to 21 mm, and L = 150 m, c) Variation of reduced friction head loss (H_F/H_{in}) and d) Lower-Quarter Distribution Uniformity (DULQ) lateral inside diameter ranging from D = 10 mm to 21 mm, and L = 150 m.

Continued Fig. 2

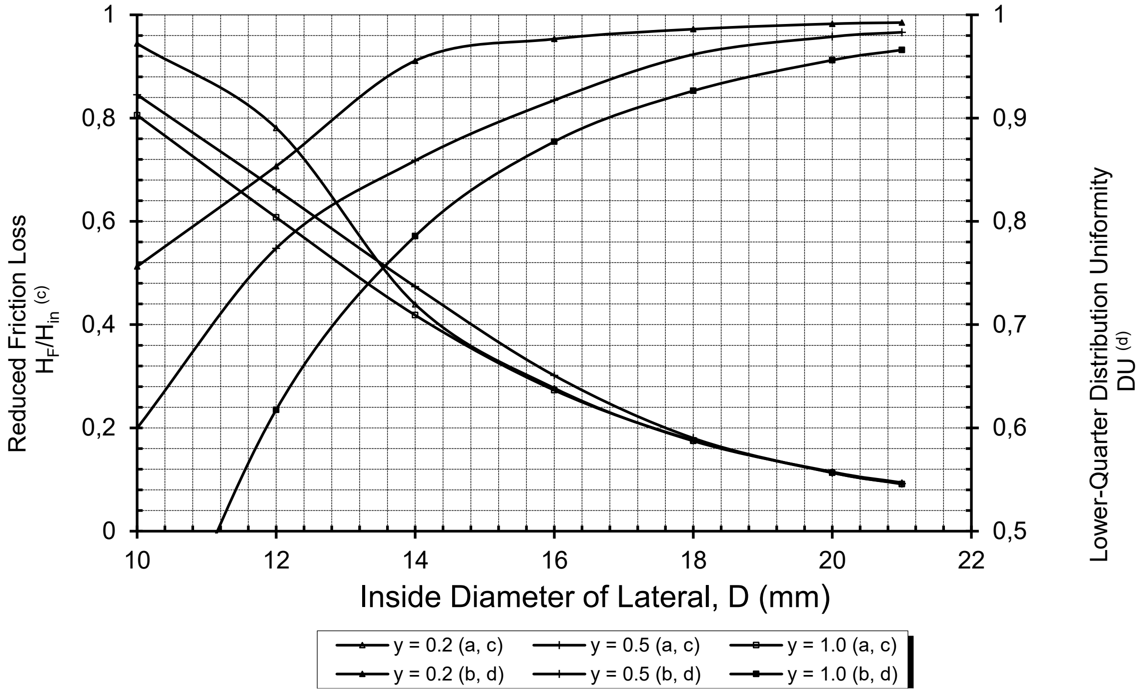

c), d)

3. Conclusions

An important objective of the present computer-aided design technique is the sensitively determination of the proper value of the operating inlet pressure head, H_{0I} (H_{in}), which can be varied within limited intervals in the design algorithms (initial and boundary conditions). It clearly means, preliminary increase in average piezometric head (Δ_0) varies ranging from minimum inlet pressure head range $\overline{H}_{min}$ toward maximum inlet pressure head range $\overline{H}_{max}$. When the operating inlet pressure head range increases from $\overline{H}_{min}$ toward its proper value at $\overline{H}_{max}$, the total friction drop ($H_{f(L)}$) along the line, and residual lateral flow rate from the last downstream emitter (Q_r) decreases, whereas the water application uniformity coefficient (U_C) increases, in all design cases examined. It clearly means, the proper value of the operating inlet pressure head can be sensitively achieved at the upper limit of the design interval, $\overline{H}_{max}$. Otherwise, when the operating inlet pressure head range was selected as the smaller value than $\overline{H}_{max}$, the parameter ε, which is the ratio of residual discharge to the total lateral inlet discharge (Q_r/Q_{in}) had the negative value at the downstream closed end from the last emitter; in that case, the back-flow occurred from the downstream closed end toward upstream direction; namely, an important boundary condition for the downstream lateral end did not keep to the right, in the design criteria. For all performed simulations it should be pointed out, for the Multi-flowCAD, the required hydraulic design parameters vary within the operating inlet pressure head interval to achieve its acceptable proper value based on the design criteria, while the available alternative procedures may have fixed values, for these unknown hydraulic variables.

References

Sadeghi, S. H., Peters, T., & Shelia, V. (2016). Energy grade line assessment for tapered microirrigation laterals. *Journal of Irrigation and Drainage Engineering, 142*(7). https://doi.org/10.1061/(ASCE)IR.1943-4774.0001020

Sadeghi, S. H., & Peters, T. (2013). Analytical determination of distribution uniformity for microirrigation tapered laterals laid on uphill and horizontal slopes. *Journal of Irrigation and Drainage Engineering, 139*(6). https://doi.org/10.1061/(ASCE)IR.1943-4774.0000568

Sadeghi, S. H., & Peters, T. (2011). Modified G and GAVG correction factors for laterals with multiple outlets and outflow. *Journal of Irrigation and Drainage Engineering, 137*(11). https://doi.org/10.1061/(ASCE)IR.1943-4774.0000332

Scaloppi, E. J., & Allen, R. G. (1993). Hydraulics of irrigation laterals: Comparative analysis. *Journal of Irrigation and Drainage Engineering, 119*(1), 91–115.

Singh, R. P., & Mahar, P. S. (2003). Optimal design of multidiameter, multioutlet pipelines. *Journal of Water Resources Planning and Management, 129*(3). https://doi.org/10.1061/(ASCE)0733-9496(2003)129:3(226)

Singh, A., Singh, R. P., Mahar, P. S., & Singh, K. K. (2000). Optimal design of tapered microirrigation submain manifolds. *Journal of Irrigation and Drainage Engineering, 126*(6).

Valiantzas, J. D. (1998). Analytical approach for direct drip lateral hydraulic calculation. *Journal of Irrigation and Drainage Engineering, 124*(6), 300–305.

Valiantzas, J. D. (2002). Continuous outflow variation along irrigation laterals: Effect of the number of outlets. *Journal of Irrigation and Drainage Engineering, 128*(1), 34–42.

Yıldırım, G. (2023a). *Hydraulic principles and design concepts for submain units with multiple outlet pipelines: New analytical techniques with engineering applications* (Synthesis Lectures on Engineering, Science and Technology). Springer. https://doi.org/10.1007/978-3-031-32495-6

Yıldırım, G. (2023b). Review of fundamentals in hydraulic engineering perspective: Hydraulics principles, governing equations, design criteria, types of design problems, hydraulics and energy-gradient line profiles for uniformly sloping multiple outlets pipelines. In *Hydraulic principles and design concepts for submain units with multiple outlet pipelines* (pp. 1–XX). Springer. https://doi.org/10.1007/978-3-031-32495-6_1

Yıldırım, G., & Kose, O. (2016a). New software (Multi-flowCAD) development for sub-main line hydraulic design: Computational algorithm, computer visualization and implementation. *Arabian Journal for Science and Engineering, 41*, 1551–1560.

Yıldırım, G. (2016b). Discussion of "Statistical analysis of non-pressure-compensating and pressure-compensating drip emitters" by H. Perea, J. Enciso-Medina, V. P. Singh, D. P. Dutta, and B. J. Lesikar. *Journal of Irrigation and Drainage Engineering, ASCE*.

Yıldırım, G. (2015a). Computer-based analysis of hydraulic design variables for uniformly sloping microirrigation system laterals. *Journal of Irrigation and Drainage Engineering, 141*(7). https://doi.org/10.1061/(ASCE)IR.1943-4774.0000846

Yıldırım, G. (2015b). An assessment for hydraulically efficient design of uniformly sloping submain lines. *Irrigation and Drainage, 64*(2), 157–168.

Yıldırım, G. (2014a). Discussion of "Analytical determination of distribution uniformity for microirrigation tapered laterals laid on uphill and horizontal slopes" by S. H. Sadeghi & T. Peters. *Journal of Irrigation and Drainage Engineering, 140*(12).

Yıldırım, G. (2014b). Discussion of "Modified G and GAVG correction factors for laterals with multiple outlets and outflow" by S. H. Sadeghi & T. Peters. *Journal of Irrigation and Drainage Engineering, 141*(1), Article Number: 07014014. https://doi.org/10.1061/(ASCE)IR.1943-4774.0000604

Yıldırım, G., & Singh, V. P. (2013a). Operating pressure assessment for multi-outlets submains: Ideal hydraulic design. In *International Perspective on Water Resources and Environment (IPWE-2013)* (pp. XX–XX). ASCE-EWRI, Izmir, Turkey.

4th International Civil Engineering & Architecture Conference
17-19 May 2025, Trabzon, Türkiye

Mechanical and fresh properties of self-compacting mortars containing silica fume and waste marble powder

Fethi İŞSEVER*[1]

[1] Bingol University, Department of Civil Engineering, 12000 Bingol, Türkiye

Abstract. The paper presented herein investigates the results of experimental work on the strength and durability performances of self-compacting mortars (SCMs) manufactured from silica fume (SF) and waste marble powder (WMP). In this study, 16 mortar mixtures were designed with a total binder content of 600 kg/m3 and a water/binder ratio between 0.34-0.45. The control mixture contained only Portland cement (PC) as the binder. The cement was partially replaced with 5, 7.5, 10 of SF and 10, 15 and 20% of WMP as binary mixes. Also, ternary mixtures were prepared by the incorporation of WMP and SF at different replacement dosages by weight. In total, 16 different combinations of mixes were studied. Firstly, the fresh properties of mortars were tested for slump flow, V-funnel flow times. Then the mechanical properties of SCMs were examined by the tests of compressive strength and flexural strength for the age of 7, 28, and 180 days. The results of the study reveal that increase in the dosage of WMP increases SCMs flow but increase in the dosage of SF decreases flow. The best compressive strength was obtained in the SF5WMP10 mixture, while the best tensile strength was obtained in the control mixture of 180 days. The best compressive strength value was measured 73.64 MPa, and the best tensile strength value was measured as 10.46 MPa. The ternary use of PC, SF, and WMP improved the shortcomings of SCMs with binary mixtures of WMP. After the optimum ratio SF5WMP10 mixture, a decrease in compressive and tensile values was observed with each increasing pozzolan amount.

Keywords: Self-compacting mortar, Silica fume, Waste marble powder, Fresh properties, Mechanical properties.

1. Introduction

Today, the vast majority of structures built on earth are constructed using concrete. Cement is one of the main materials of concrete. To build safe, economical and aesthetic structures, it is important to produce concrete with good mechanical and durability properties.

Mineral and chemical additives have been used to improve the fresh mechanical properties of concrete for a long time. For minerals used instead of cement, the term pozzolan and cement-based materials are also used. Cement based materials are the most widely used building materials in the world. Cement based materials are defined as green building materials. With the use of these materials, while protecting the environment from waste, economic benefits are also achieved. Cement based materials are easy to process and place during the production stages. In addition to these advantages, materials produced in accordance with appropriate production procedures have high strength throughout their service life and show durability against environmental impacts. In addition, one of the most important features that makes cement-based materials superior to other building materials is that they can be shaped as desired.(Tuğrul Erdem & Öztürk, 2012) Many potential substitutes of cement such as, waste marble slurry (WMS), silica fume (SF), granite waste, rice husk ash, fly ash (FA), metakaolin, etc. are there (Aliabdo et al., 2014; Rana et al., 2016)

Inclusion of additional cementitious and waste materials such as silica fume (SF)(Gesoglu & Al-goody, n.d.; Jalal et al., 2015; Song et al., 2018), fly ash (FA) and marble cutting sludge waste (MCSW) has a greater potential in minimising the cost of concrete(Bhavan, 2018; Singh et al., 2017; Uysal & Yilmaz, 2011). Through the use of waste materials, negative impacts on the environment are reduced, environmental efficiency is improved and solutions to waste storage problems are found. In studies conducted with silica fume, it has been observed that the use of silica fume at certain ratios improves the strength and durability properties of concrete. In fresh concrete, it was stated that it decreased the workability, but this problem was overcome by using plasticisers.(Amudhavalli & Mathew, 2012; Mazloom et al., 2004; Sasanipour et al., 2019)

Marble dust and silica fume are widely used in sustainable concrete mixes.(Demir & Alyamaç, n.d.) Silica fume are the most widely used mineral additives in concrete/mortar.(Wang et al., 2012) A large amount of natural

* Corresponding author, E-mail: fissever@bingol.edu.tr

https://doi.org/10.31462/icearc2025_ce_mat_015

resources is used for the production of self-compacting concrete (SCC). The continuous use of so many resources is not sustainable. Researchers have focused on reducing(Mazloom et al., 2004) construction costs and partially replacing cement with industrial waste. It is possible to effectively use various industrial wastes instead of cement or aggregate in concrete production. Among these wastes, waste marble powder is a useful choice and researchers have been interested in using WMP in concrete for some time(Ahmad et al., 2023)

Marble is processed industrially by cutting, polishing and using it for decorative purposes and is therefore economically valuable. In marble quarries, stones are cut into blocks using different methods. During the cutting process, 20-30% of a marble block becomes waste marble dust. Marble dust is a waste material produced in significant quantities around the world. Marble waste also causes a serious environmental problem. Therefore, the use of waste marble as an additive or aggregate in concrete production has become an increasingly important issue(Demirel & Alyamaç, 2018; Ulubeyli & Artir, 2015)

Super plasticizing and/or viscosity regulators which reduce water at high levels in SCC/SCM production are used (Sonebi, 2004). Polycarboxylate (PCE) superplasticizers play a crucial role in preventing cement coagulation by effectively adsorbing onto the surface of cement particles, enhancing dispersibility, and maintaining dispersion performance.(Yang et al., 2024)

In this study, firstly, fresh mortar properties of SCMs were investigated by determining the spread and v-funnel values. In order to evaluate the characteristics of fresh properties of SCMs, mini V-funnel flow and mini slump flow tests recommended by EFNARC were carried out. Then, binary and ternary combinations were formed by partial substitution of silica fume and waste marble dust, which were kept in water cure for 7, 28 and 180 days. Thus, the compressive and tensile strengths of these SCMs were analysed. For the compressive and tensile tests of SCMs, 40x40x160 mm specimens were produced with different proportions of silica fume and waste marble dust. The apparent density values of the specimens were also measured.

2. Materials and methods

The aim of this study was to measure the spreading, V-funnel and strength properties of double and triple combination SCMs using partial silica fume and waste marble dust instead of cement after 7, 28 and 180 days of water curing. For the compressive and tensile tests of SCMs, 40x40x160 mm specimens were produced from different substitution ratios of silica fume waste marble dust. The specimens were first broken in the flexural tensile test press machine and three tensile strengths were measured and averaged. Then, 6 specimens were broken in the compressive press machine and compressive strengths were obtained. Mini spreading and mini V-funnel testers were used to measure the spreading and flow properties of self-compacting mortars in fresh state. In addition, the apparent unit weight values of the mortars were also measured.

2.1 Materials

Normal Portland cement (CEM I 42.5N) produced in Elazığ Altınova Cement Factory was used in the study. The slurry obtained from the cutting wastes of the marble factories in Elazığ 2nd Small Industrial Site was dried, sieved and marble powder (WMP) was obtained. Silica fume (SF) was obtained from Antalya Ferro Metallurgy Plant. The properties of cement, waste marble powder (WMP) and silica fume (SF) are shown in Table 1.

The sand used in the mixtures is natural river sand extracted from the Murat River in Palu with a specific gravity of 2.63 g/cm3, a fineness modulus of 3.29 and a water absorption of 1.91% . The maximum particle size of the sand is 4.00 mm (Fig. 1). In order to obtain a suitable workability with a low water/binder (w/b) ratio, a modified polycarboxylate based polymer type Sika Viscocrete superplasticiser from Sika Construction Chemicals was used.

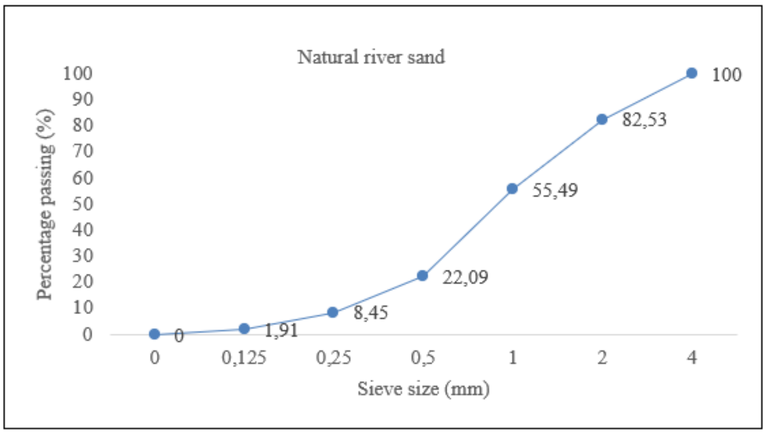

Figure 1.Granulometry of natural river sand

Table 1. Physical properties and elemental composition of mineral materials.

Chemical components (%)	PC	WMP	SF
SiO_2	21.14	42.14	92.0
Al_2O_3	5.65	19.38	0.56
Fe_2O_3	3.22	4.64	0.25
CaO	61.96	29.96	0.70
MgO	–	1.78	0.35
SO_3	2.56	2.43	–
Na_2O	–	–	–
K_2O	–	1.13	–
CI	0.0040	0.0011	–
Loss in ignition	3.52	4.85	1.82
Physical properties			
Specific gravity (g/cm^3)	3.1	2.72	2.2
Specific surface area (cm^2/g)	3480	3720	96.5% < 45 µm

Table 2. Properties of superplasticizer.

Material structure	Modified polycarboxylates based polymer
Density (gr/cm3)	1,08
pH	3,50
Freezing point (˚C)	-5,00
Clor content % (TS EN 934-2)	< 0.1
Alcali content % (TS EN 934-2)	<3
Solid	30%
Viscosity	30 cP

2.2. Mix proportions and fresh mortar tests

A total of 16 different mixtures containing 600 kg/m3 binder, including the control sample, were prepared to observe the properties of SCM in fresh and hardened states. To evaluate the fresh properties of SCMs containing SF and WMP, mini slump flow diameter, mini V-funnel flow time experiments were performed. SCMs were produced by replacing Portland cement with silica fume (SF) at 6, 10 and 14 wt% and waste marble powder (WMP) at 10, 15 and 20 wt%. The mixing ratios of the produced mortars for 1 m3 by weight are given in Table 3. The SCMs were designed to give a slump flow diameter of 240-260 mm, which was obtained by varying the superplasticiser (SP) amounts. Experimental batches were produced for each mix to obtain the proposed slump flow diameter. V-funnel flow time and slump flow diameter were obtained according to EFNARC recommendations. The number after each SF and WMP letter indicates the amount of each mineral mixture in the mortar. For example, FS5WMP10 mortar consists of 5% silica fume and 10% waste marble dust.

Table 3.Mix proportion of mortars (kg/m^3).

Mix code	Binder			Sand	SP*	w/b (by mass)
	PC	SF	WMP			
	600	0	0	1406.71	9.0	0.41
SF05	570	30	0	1364.33	9.0	0.43
SF7.5	555	45	0	1343.14	9.0	0.44
SF10	540	60	0	1321.96	9.0	0.45
WMP10	640	0	60	1508.82	9.0	0.34
WMP15	510	0	90	1473.08	9.0	0.36

Table 3. Continued

WMP20	480	0	120	1421.57	9.0	0.39
SF05WMP10	510	30	60	1385.15	9.0	0.41
SF05WMP15	480	30	90	1365.20	9.0	0.42
SF05WMP20	450	30	120	1361.02	9.0	0.42
SF7.5WMP10	495	45	60	1362.33	9.0	0.42
SF7.5WMP15	465	45	90	1342.93	9.0	0.43
SF7.5WMP20	435	45	120	1338.32	9.0	0.43
F10WMP10	480	60	60	1340.38	9.0	0.43
SF10WMP15	450	60	90	1320.43	9.0	0.44
SF10WMP20	420	60	120	1300.48	9.0	0.45

*SP = superplasticizer.

2.3. Production of test specimens
In all mixtures, cement, mineral additives and fine aggregate were mixed first by hand for half a minute and then by machine for 1 minute. Then (water + SP) was added to this mixture and mixed by machine for 3 more minutes. The workability of the fresh mortar was obtained by mini-collapse and V-funnel tests according to EFNARC standards. Compressive and flexural tensile strengths were performed on 160 x 40 x 40 mm prisms after 7, 28 and 180 days of water curing. 3 flexural tensile tests were performed for each mixture. 6 specimens obtained were used in compressive tests

2.4. Curing of test specimens
All specimens produced from 16 different mixtures were kept in moulds under laboratory conditions for 24 hours and then subjected to water curing in a water tank at 20±2°C for 7, 28 and 180 days (Figure 2).

2.5. Test methods

2.5.1 Workability tests for fresh mortar
To measure the workability of SCM, mini-slump flow test and V-funnel flow test were performed according to EFNARC (2005) standards. In the mini-slump flow test, the truncated cone was filled with mortar on a flat glass plate and lifted upwards. The diameter was evaluated by averaging two perpendicular dimensions of the spread mortar. In the V-funnel flow test, after the funnel was completely filled with mortar, the bottom outlet was opened to allow the mortar to flow out. The V-funnel flow time is the time (t) from the onset of light to the opening of the bottom outlet and the exit of the funnel. The workability values of SCMs were evaluated according to EFNARC (2005) acceptance criteria, which are 24-26 cm and 7-11 s for the slump flow diameter and V-funnel flow time, respectively.

2.5.2. Compressive and tensile strength tests
Firstly, fresh mortar tests were completed. After the fresh mortar tests, the mortars were poured into 40x40x160 mm steel moulds and the set specimens were demoulded after 24 hours. After demoulding, the specimens were subjected to water curing at a temperature of (20 ± 2) C until the test age. Compressive and flexural strength tests were carried out at 7, 28 and 180 days according to ASTM C109 on 48 prismatic specimens, three 40x40x160 mm specimens each, obtained from 16 mixtures. Initially, the tests were performed for tensile strength and two halves were obtained, then 96 specimens were used for compressive strength tests(ASTMC109). The compressive strength and tensile strength tests were carried out on a testing machine with a capacity of 250 kN in compression and 150 kN in bending (Fig. 2).

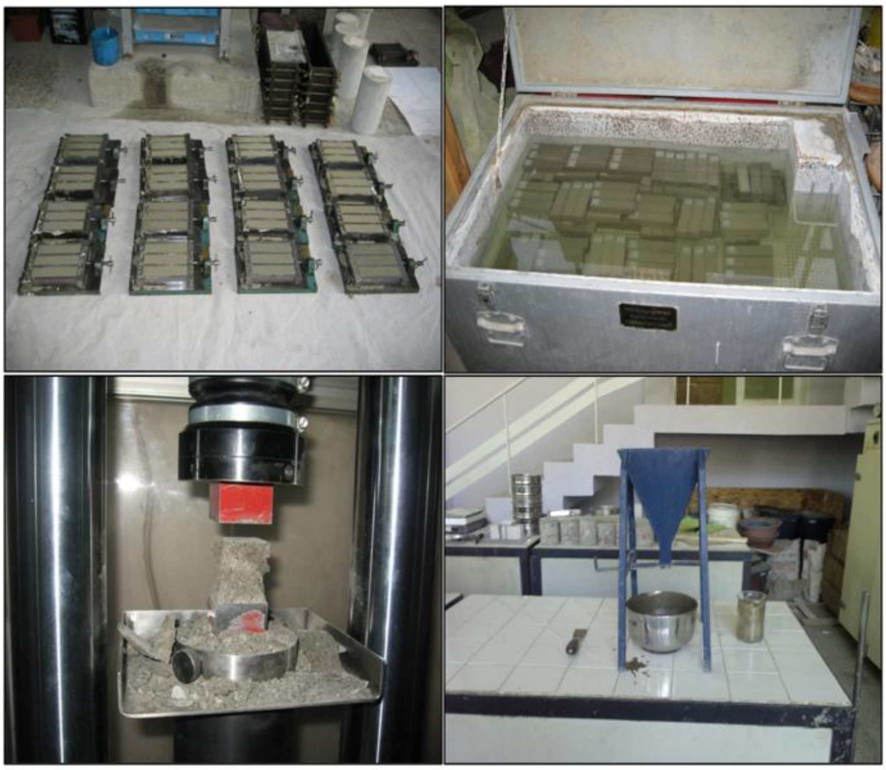

Fig. 2. Curing conditions, fresh and mechanical tests

3. Results

3.1. Fresh SCMs properties

Fig. 3 shows the relative slump and relative V-funnel time values. It is understood that SCM mixtures meet EFNARC (2005) spreading and f-funnel standards. When the spreading (24-26 mm) and V-funnel (7-11 s) values are analysed, it is seen that all values are within the reference range. SF mixtures generally have low spreading values (Felekoğlu et al., 2006; Karatas et al., 2010). As both SF and WMP ratios increased, the water requirement for workability increased (Table 3). Since the amount of SP was taken constant in the fresh mortar experiments, EFNARC (2005) standards for spreading and V-funnel were achieved in all mixtures by selecting the amount of water at appropriate ratios. No segregation occurred in the mixtures and workability and flowability were quite good (Fig. 3).

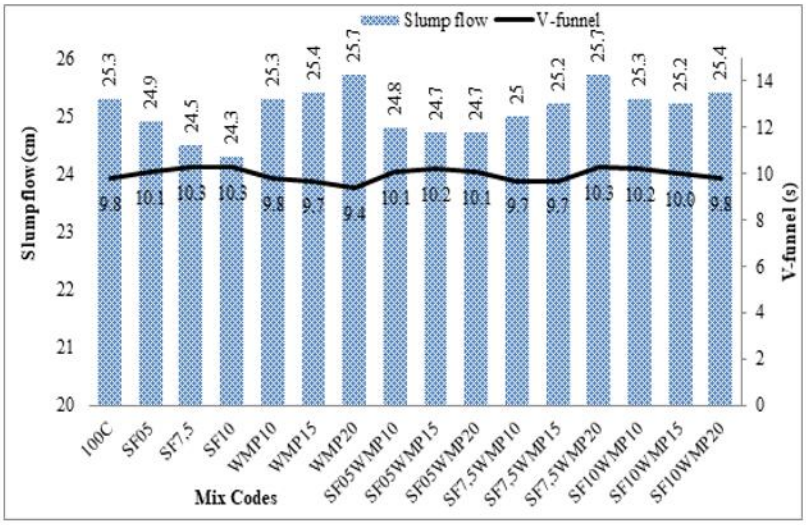

Fig. 3. Mini Slump and V-funnel test results

3.2. Hardened properties
Both compressive strength and tensile strength were lower in WMPs than in SFs, especially in terms of early age strength. However, as the curing time increased, the compressive strength and tensile strength of all SCM specimens increased. This weakness of WMPs was compensated by the fast hydration property of SFs. It is possible to see this in ternary mixtures (Fig. 4).

3.2.1 Compressive strength
When all values of compressive strength measured at 7, 28 and 180 days were analysed, magnitudes between 32.4 MPa and 73.6 MPa were observed. The smallest value belonged to the 7-day binary blend of WMP20 and the highest value belonged to the 180-day ternary blend of SF05WMP10. The compressive strength changes of all SCMs at 7, 28 and 180 days are plotted in Fig. 4. The compressive strength increased gradually with increasing curing time in water. The use of SF increased the 7-day strength faster than WMP. After 28 days, the proportional contribution of WMP was higher. This was more evident especially in binary mixtures. Both materials worked harmoniously in both binary and ternary mixtures.

The rapid pozzolanic reaction of SFs was observed in all mixtures. The binary mixtures of SF had higher compressive strength than the binary mixtures of WMA. This can be explained by the fact that SF has a greater pozzolanic reaction and micro-filling effect (Wongkeo et al., 2012). Silica fume-containing mixtures demonstrated 15-20% higher early-age (7-day) strength compared to the control, highlighting SF's pozzolanic reactivity.

Excessive WMP replacement (particularly 20%) caused long-term strength reduction, indicating diminished binding capacity beyond optimal substitution levels. The strength development rate between 28-180 days was slower in SF mixtures, confirming their predominant early-stage contribution. These findings establish that the SF05WMP10 combination provides optimal balance between short- and long-term mechanical performance(Hamada et al., 2023; Kawsarul et al., 2023).

3.2.2 Tensile strength
When the tensile test results of SCMs were analysed, the highest value was 10.46 MPa at the end of 180 days curing period in parallel with the compression tests. This value was obtained from SF05WMP10 mixture. The lowest value was 6.11 MPa in the 7-day WMP20 mix. While the early age values were lower than the mixtures with SF, the effect of advanced ages was proportionally better. While SF increased 7-day flexural strength by 12-18%, this advantage diminished over time due to reduced late-stage pozzolanic activity. WMP mixtures showed linear strength reduction with increasing replacement ratios, demonstrating its filler-dominated behavior.Ternary blends (SF+WMP) displayed more balanced performance than binary mixtures, indicating synergistic effects between additives.These observations substantiate that matrix toughness is predominantly governed by binder composition and interfacial transition zone quality (Fig. 5).

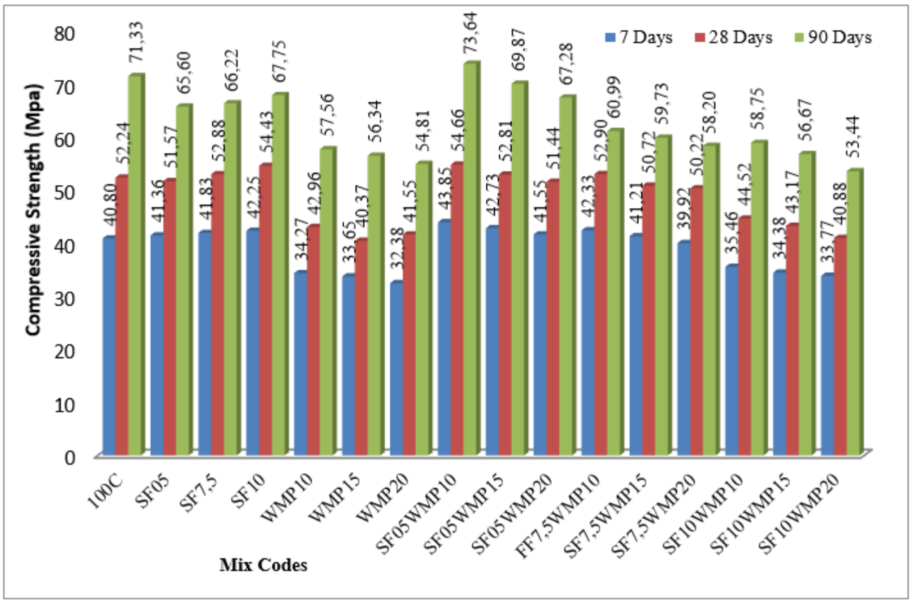

Fig. 4. 7, 28 and 180 days Compressive Sttength of all SCM Mixtures

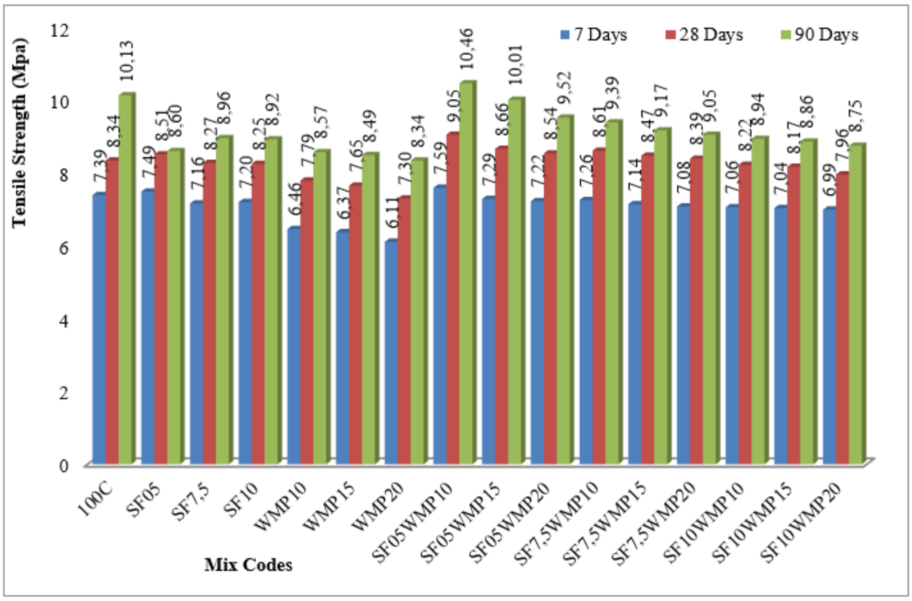

Fig. 5. 7, 28 and 180 days Tensile Strength of all SCM Mixtures

4. Conclusions

This study experimentally investigated the effects of waste marble powder (WMP) and silica fume (SF) on the properties of self-compacting mortars. The results demonstrate that the optimal combination of these materials provides significant advantages in terms of mechanical strength and sustainability.

- The SF05WMP10 mixture showed the highest performance with a compressive strength of 73.64 MPa after 180 days of hydration, while WMP improved workability and SF contributed to early strength gain.
- Exceeding the optimal ratios caused a 15-20% decrease in mechanical properties due to agglomeration and micro-crackformation.
- WMP's potential to reduce environmental waste burden strengthens the sustainability aspect of this research.

In conclusion, the synergistic use of SF and WMP enables both high-performance mortar production and recycling of industrial waste. However, careful determination of material ratios is crucial to prevent negative effects. These findings may guide future studies aimed at developing green construction materials. This study also highlights the technical and environmental advantages of utilizing waste materials in the construction sector.

References

Aliabdo, A. A., Abd Elmoaty, A. E. M., & Auda, E. M. (2014). Re-use of waste marble dust in the production of cement and concrete. *Construction and Building Materials*, *50*, 28–41. https://doi.org/10.1016/J.CONBUILDMAT.2013.09.005

Amudhavalli, N. K., & Mathew, J. (2012). EFFECT OF SILICA FUME ON STRENGTH AND DURABILITY PARAMETERS OF CONCRETE. *International Journal of Engineering Sciences & Emerging Technologies*.

Bhavan, I. (2018). *Indian Minerals Yearbook 2016 55 th Edition EXPLORATION & DEVELOPMENT (FINAL RELEASE) GOVERNMENT OF INDIA MINISTRY OF MINES INDIAN BUREAU OF MINES*.

Demir, T., & Alyamaç, K. E. (n.d.). Investigation of the Use of Marble Powder in Production of High Strength Concretes. *Open Journal of Nano-Tuba Demir Open Journal of Nano*.

Demirel, B., & Alyamaç, K. E. (2018). Waste marble powder/dust. *Waste and Supplementary Cementitious Materials in Concrete: Characterisation, Properties and Applications*, 181–197. https://doi.org/10.1016/B978-0-08-102156-9.00006-7

Gesoglu, M., & Al-goody, A. (n.d.). *Fresh and rheological behavior of nano-silica and fly ash blended self-compacting concrete, Concr. Build. Mater. 95 (2015) 29–44*.

Hamada, H. M., Abed, F., Binti Katman, H. Y., Humada, A. M., Al Jawahery, M. S., Majdi, A., Yousif, S. T., & Thomas, B. S. (2023). Effect of silica fume on the properties of sustainable cement concrete. *Journal of Materials Research and Technology*, *24*, 8887–8908. https://doi.org/10.1016/J.JMRT.2023.05.147

Jalal, M., Pouladkhan, A., Harandi, O. F., & Jafari, D. (2015). RETRACTED: Comparative study on effects of Class F fly ash, nano silica and silica fume on properties of high performance self compacting concrete. *Construction and Building Materials*, *94*, 90–104. https://doi.org/10.1016/J.CONBUILDMAT.2015.07.001

Kawsarul, M., Kabbo, I., Habibur, M., Sobuz, R., & Khan, M. H. (2023). Combined influence of Waste Marble Powder and Silica Fume on the Mechanical Properties of Structural Cellular Lightweight Concrete. In *Architecture and Civil Engineering*. https://www.researchgate.net/publication/383273351

Mazloom, M., Ramezanianpour, A. A., & Brooks, J. J. (2004). Effect of silica fume on mechanical properties of high-strength concrete. *Cement and Concrete Composites*, *26*(4), 347–357. https://doi.org/10.1016/S0958-9465(03)00017-9

Rana, A., Kalla, P., Verma, H. K., & Mohnot, J. K. (2016). Recycling of dimensional stone waste in concrete: A review. *Journal of Cleaner Production*, *135*, 312–331. https://doi.org/10.1016/J.JCLEPRO.2016.06.126

Sasanipour, H., Aslani, F., & Taherinezhad, J. (2019). Effect of silica fume on durability of self-compacting concrete made with waste recycled concrete aggregates. *Construction and Building Materials*, *227*, 116598. https://doi.org/10.1016/J.CONBUILDMAT.2019.07.324

Singh, M., Choudhary, K., Srivastava, A., Singh Sangwan, K., & Bfunnela, D. (2017). A study on environmental and economic impacts of using waste marble powder in concrete. *Journal of Building Engineering*, *13*, 87–95. https://doi.org/10.1016/J.JOBE.2017.07.009

Sonebi, M. (2004). Medium strength self-compacting concrete containing fly ash: Modelling using factorial experimental plans. *Cement and Concrete Research*, *34*(7), 1199–1208. https://doi.org/10.1016/J.CEMCONRES.2003.12.022

Song, Q., Yu, R., Wang, X., Rao, S., & Shui, Z. (2018). A novel Self-Compacting Ultra-High Performance Fibre Reinforced Concrete (SCUHPFRC) derived from compounded high-active powders. *Construction and Building Materials*, *158*, 883–893. https://doi.org/10.1016/J.CONBUILDMAT.2017.10.059

Standard Test Method for Compressive Strength of Hydraulic Cement Mortars (Using 2-in. or [50-mm] Cube Specimens) 1. (n.d.).

Tuğrul Erdem, R., & Öztürk, A. U. (2012). Mermer Tozu Katkısının Çimento Harcı Donma-Çözünme Özellikleri Üzerine Etkisi Effect of Marble Powder Additive on Freezing-Thawing Properties of Cement Mortar. In *BEÜ Fen Bilimleri Dergisi BEU Journal of Science* (Vol. 1, Issue 2).

Ulubeyli, G. C., & Artir, R. (2015). Properties of Hardened Concrete Produced by Waste Marble Powder. *Procedia - Social and Behavioral Sciences*, *195*, 2181–2190. https://doi.org/10.1016/J.SBSPRO.2015.06.294

Uysal, M., & Yilmaz, K. (2011). Effect of mineral admixtures on properties of self-compacting concrete. *Cement and Concrete Composites*, *33*(7), 771–776. https://doi.org/10.1016/J.CEMCONCOMP.2011.04.005

Wang, Q., Yan, P., & Feng, J. (2012). The influence of mineral admixtures on bending strength of mortar on the premise of equal compressive strength. *Journal Wuhan University of Technology, Materials Science Edition*, *27*(3), 586–589. https://doi.org/10.1007/s11595-012-0510-7

Wongkeo, W., Thongsanitgarn, P., Pimraksa, K., & Chaipanich, A. (2012). Compressive strength, flexural strength and thermal conductivity of autoclaved concrete block made using bottom ash as cement replacement materials. *Materials & Design*, *35*, 434–439. https://doi.org/10.1016/J.MATDES.2011.08.046

Yang, Y., Tan, Y., Li, Z., Zhou, G., Yu, X., Xu, D., Yong, Q., Zhao, H., & Xie, Z. (2024). Interaction mechanisms between polycarboxylate superplasticizers and cement, and the influence of functional groups on superplasticizer performance: a review. In *Polymer Bulletin* (Vol. 81, Issue 12, pp. 10415–10438). Springer Science and Business Media Deutschland GmbH. https://doi.org/10.1007/s00289-024-05233-w

Investigation of the properties of ground granulated blast furnace slag-based geopolymer concretes with recycled aggregates impregnated with pozzolanic slurry

Memduh Nas*[1], Şirin Kurbetci[1]

[1] *Karadeniz Technical University, Department of Civil Engineering, 61080 Trabzon, Türkiye*

Abstract. Cement production processes are characterized by high energy consumption and substantial carbon emissions, making them a significant concern for environmental sustainability. Adopting sustainability-focused approaches within the construction industry plays a crucial role in mitigating these adverse impacts. In this context, geopolymer concretes (GPC) emerge as a promising, eco-friendly alternative to conventional cement-based concretes. GPCs contribute to both waste management and natural resource conservation by using industrial waste as a binder and replacing natural aggregates with recycled concrete aggregates (RCA). Aggregates, which account for approximately 70% of concrete, significantly contribute to the rapid depletion of natural resources during production. Recycling concrete waste provides an effective solution to reduce construction-related waste and minimize environmental impacts. However, residual mortar adhered to the surface of RCAs often compromises the mechanical strength and long-term performance of the concrete. To address these issues, various treatment methods have been developed to improve RCA properties. Techniques such as carbonation, acid treatment, mortar residue removal, and impregnation with slurries or solutions are aimed at enhancing the physical and mechanical characteristics of RCAs. In this study, RCAs were treated with cementitious pozzolanic slurries to fill voids and repair structural deficiencies, resulting in improved permeability and mechanical performance. These enhanced RCAs were subsequently used to produce geopolymer concretes based on ground granulated blast furnace slag. The mechanical and durability properties of the resulting concretes were comprehensively evaluated through tests such as compressive strength measurements, ultrasonic pulse velocity assessments, Schmidt hammer readings, and electrical resistivity evaluations. The results of this study highlight significant improvements in the performance of geopolymer concretes and contribute to the advancement of sustainable building materials. Additionally, the research underscores the potential for efficiently reusing construction waste, aligning with global efforts to promote environmentally friendly construction practices and resource efficiency.

Keywords: Geopolymer concrete; Recycled aggregate; Mechanic properties; Durability

---

1. Introduction

In recent years, the sustainable management of construction and demolition wastes has become a critical challenge for the global construction industry. The depletion of natural aggregates, coupled with mounting environmental pressures, has driven researchers and practitioners to seek alternative materials that both conserve virgin resources and mitigate waste disposal issues (Pan et al., 2017; Qiu et al., 2014). Recycled concrete aggregates (RCAs) offer a promising solution: by re-using crushed concrete as coarse aggregate, RCAs can substantially reduce the consumption of natural quarry stone while diverting large volumes of demolition debris from landfills. However, RCAs inherently exhibit higher porosity, greater water absorption, and a weaker interfacial transition zone (ITZ) than their natural counterparts, owing to the presence of residual mortar and microcracks. If left untreated, these deficiencies can compromise the mechanical performance and durability of concrete (Silva et al., 2014).

A variety of pre-treatment methods have been proposed to improve RCA quality. Acid leaching can dissolve and detach the adhered cement paste, while carbonation treatments densify the remaining mortar and reduce connectivity of pores. Alternative approaches employ chemical solutions—such as glasswater or other silicate-rich liquids—to passivate surface pores and limit water ingress. Among these, impregnation with a pozzolanic slurry (a suspension of cement and supplementary cementitious materials) has shown particular promise: the slurry penetrates the RCA's pore network, reacts with free lime and aluminates, and precipitates C–S–H and other

* Corresponding author, E-mail: memduhnas@ktu.edu.tr

https://doi.org/10.31462/icearc2025_ce_mat_022

hydrates at the RCA surface, thereby refining pore structure and strengthening the aggregate–matrix ITZ (Ouyang et al., 2023).

While traditional Portland cement concrete is the backbone of modern infrastructure, its production is energy-intensive and responsible for up to 8% of global CO_2 emissions, and the material often exhibits limited chemical and thermal resistance (Amran et al., 2020). Geopolymer binders—synthesized from aluminosilicate precursors activated by alkaline solutions—represent a low-carbon alternative, offering rapid strength gain, excellent sulfate and acid resistance, and substantially lower embodied energy. In particular, blast furnace slag (BFS), an industrial by-product of ironmaking, is an abundant aluminosilicate source ideally suited for geopolymerization. BFS-based geopolymer concretes have demonstrated compressive strengths comparable to, or even exceeding, those of OPC concrete, alongside superior durability in aggressive environments (Parathi et al., 2021).

In the present study, RCAs were first treated by immersion in a cement-puzolan slurry to seal surface pores and improve the ITZ, then incorporated as coarse aggregate in BFS-based geopolymer concrete mixtures. The influence of treated RCAs on compressive strength, ultrasonic pulse velocity, Schmidt rebound number, and electrical resistivity was systematically investigated. By combining aggregate pre-treatment with sustainable geopolymer technology, this work aims to unlock the full potential of RCAs in high-performance, low-carbon concrete, thereby advancing resource conservation and environmental stewardship in construction practice.

2.1. Experimental investigations

The 28-day-old GPC specimens were subjected to tests for compressive strength, UPV, schmidt hammer and electrical surface resistivity tests in accordance with TS EN 12390-3, ASTM C597, ASTM C805 and AASHTO TP 95-11 standards, respectively. The specimens used for these tests included cubes with side lengths of 10 and 15 cm, as well as 10x20 cm cylindrical specimens.

2.2. Materials and methods used

Concrete cubes with a side length of 15 cm and a compressive strength class between C25 and C40 were initially fractured using a demolition hammer and subsequently crushed to the desired particle sizes using a jaw crusher. The resulting RCAs were sieved into two fractions within the size ranges of 16–8 mm and 8–4 mm. In the production of GPC, natural aggregates consisting of limestone-based crushed stone, crushed sand, and river sand were utilized. In concrete mixtures incorporating RCAs, all coarse natural aggregates were fully (100%) replaced by RCAs. The maximum aggregate size used in the mixtures was set at 16 mm. Both in the reference concretes containing natural aggregates and in the RCA-based concretes, crushed sand and river sand were used as fine aggregates. The aggregate blend proportions were adjusted to 60% crushed stone, 15% crushed sand, and 25% river sand. The physical and mechanical properties of the aggregates are presented in Table 1.

Table 1. Physical properties of aggregates

Properties	Crushed limestone (16-4 mm)	Crushed sand (< 4 mm)	River sand (< 4 mm)	RCA (16-8 mm)	RCA (8-4) mm
Spesific gravity (g/cm3)	2.71	2.69	2.65	2.54	2.46
Water absorption (%)	0.61	0.96	2.11	5.31	7.63
Water content (%)	0.33	2.69	2.65	1.67	2.72

For the impregnation of RCAs with a pozzolanic slurry, Class F fly ash (FA), ground granulated blast furnace slag (GBFS), silica fume (SF), and CEM I 42.5 R grade Portland cement sourced from the Trabzon Aşkale Cement Plant were employed. The particle size distributions of all binder materials utilized in the study were characterized using a Malvern Mastersizer 2000 laser diffraction particle size analyzer. The chemical compositions and pozzolanic activity indices of the binders are detailed in Table 2. The mean particle diameters for GBFS, FA, SF, metakaolin (MK), and cement (C) were determined to be 15.87 µm, 23.41 µm, 17.46 µm, 11.9 µm, and 28.01 µm, respectively.

Table 2. Chemical composition of pozzolanic materials used

Composition	FA	GBFS	MK	SF
SiO_2	61.81	36.7	56.1	93
$Al2O_3$	19.54	14.21	40.25	0.58
Fe_2O_3	7.01	0.98	0.85	2.79
TiO_2	-	-	0.55	-
CaO	1.77	32.61	0.19	0.6
MgO	-	10.12	0.16	1.0
Na_2O	2.43	0.42	0.24	1.0
K_2O	-	0.76	0.55	0.10
SO_3	0.31	0.99	-	0.50
Pozzolanic Activity Index	76	78	101	87.4

2.3. Improvement of aggregates

The RCA enhancement procedure followed the impregnation technique reported by Shaban et al. (Shaban et al., 2019). In this approach, a pozzolanic slurry was prepared by mixing binder materials with water in a concrete mixer. Subsequently, RCAs were immersed in the slurry and allowed to soak for four hours to facilitate deep penetration of the slurry into the aggregate pores. The mix proportions for the slurry were set at 2 kilograms of water and 400 grams of binder per kilogram of RCA. In addition to pure cement slurry, pozzolanic slurries containing varying replacement levels of SF, metakaolin (MK), fly ash (FA), and ground granulated blast furnace slag (GGBFS) were also utilized. The effect of different slurry compositions on reducing the water absorption capacity of the RCAs was systematically investigated to identify the most effective formulations.

2.4. GPC design

Ground granulated blast furnace slag served as the principal binder in the preparation of geopolymer concrete. The mixing process began with the introduction of pre-wetted coarse aggregates into the mixer, followed sequentially by fine aggregates and the calculated amount of saturation water. After preliminary mixing, the pozzolanic binder was added, and blending was continued until a homogenous mixture was achieved. The alkaline activator solution—consisting of sodium hydroxide (NaOH) and sodium silicate (Na_2SiO_3)—was then incorporated slowly, along with a superplasticizer to improve workability. The activator-to-binder ratio was fixed at 0.5, with an SS/SH ratio of 2 and a NaOH molarity of 12 M. After approximately three minutes of mixing, fresh concrete properties were assessed immediately.

The freshly prepared GPC was placed into molds in two layers on a vibrating table, ensuring proper compaction and minimizing entrapped air at each stage. After molding, the specimens were subjected to steam curing at 80°C for a duration of three hours. They were then demolded and stored in a controlled environment until testing.

The mix proportions, detailed per cubic meter, are summarized in Table 3. The coding system used in the table includes three components: the coarse aggregate type and the type of surface treatment applied to the RCAs. For example, the code "NA" indicates a mix containing natural aggregates, while "RCA-C" denotes a mix incorporating RCAs pretreated with a pure cement slurry alongside fly ash.

The pozzolanic slurries used to treat the RCAs were prepared using the following combinations: 100% cement, cement blended with 30% SF, 20% MK, 50% FA, and 40% GBFS.

Table 3. Material quantities of GPCs (kg/m^3)

Sample Code	GBFS	16/8 Aggregate	8/4 Aggregate	Sand
NA	400	730.25	365.13	710.42
RCA	400	662.48	317.15	710.42
RCA-C	400	735.36	354.80	710.42
RCA-FA	400	772.95	368.95	710.42
RCA-SF	400	836.59	393.16	710.42
RCA-MK	400	813.22	382.75	710.42
RCA-GBFS	400	746.33	349.74	710.42

*SS: 133.33 kg, SH for all productions: 66.67 kg, SA: 16 kg were used.

3. Results and discussion

3.1. Water absorption of RCAs

Figure 1 shows the water absorption percentages of the aggregates. While the water absorption percentages of NA in 16/8 and 8/4mm sizes were determined as 0.45 and 0.61, the water absorption percentages of RCA in the same size were determined as 5.31 and 7.63, respectively. When the figure is analyzed, it can be seen that the pozzolanic slurry impregnation process improves the water absorption percentages of RCAs by approximately 20% to 55%. The most effective slurries in terms of reducing the water absorption percentages of the RCAs were pure cement slurry, 30% SF, 20% MK, 50% FA and 40% GBFS substituted with cement, respectively. As can be seen in the figure, as the fineness and pozzolanic activity of the pozzolan used increased, the decrease in the water absorption percentage of the RCAs became more pronounced. The reason for this is that the pozzolans used both fill the defects in the RCA with new binder gels due to their pozzolanic effect and physically act as fillers due to their fineness.

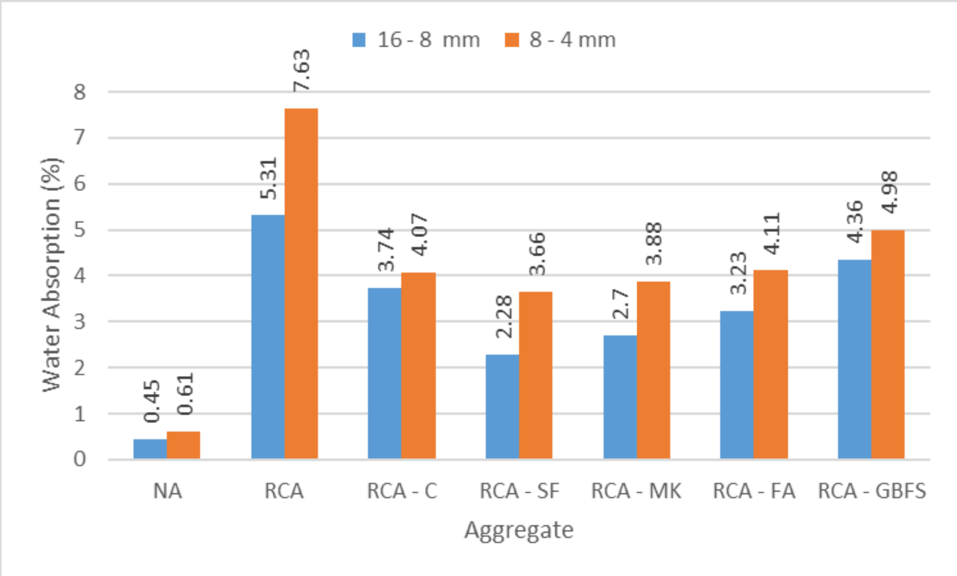

Fig. 1. Water absorption values of GDAs impregnated with slurry

3.2. Compressive strength and UPV results

Figure 2 shows the 28-day compressive strength of GPCs. The compressive strength of the reference GPC produced using NA was determined as 79.59 MPa. The compressive strength of GPC produced with RCA without any treatment decreased by about 24% and was determined as 60.42 MPa. The main reason for the decrease in compressive strength with the use of RCA is that the old mortar layer on the surface of RCA is more porous, weak and contains defects such as cracks compared to NA. Moreover, the presence of this old mortar layer causes the interfacial zone between the RCA and the new mortar to have lower strength than the concrete produced with NA. This weak interfacial zone cracks easily under applied force, creating a mechanically weak point in the concrete (Thomas et al., 2018). In the case of impregnation of RCAs with pozzolanic slurry, an increase in the compressive strength of the concretes was observed up to a maximum of 14%. The reason for this increase is that pozzolans react with the calcium hydroxide in the old mortar layer on the surface of the GDA to form new calcium silicate gels. This reaction fills the voids in the RCA, making the old mortar layer denser and stronger citation needed (Han et al., 2023).

When the UPV results of the concretes are analyzed, the UPV value of the reference concrete with natural aggregate was determined as 5 km/h, while the UPV value of the concrete with untreated RCA decreased by approximately 10% to 4.55 km/h. The UPV values of the slurry-impregnated RCA GPCs did not change enough to be detected by the device and the UPV values of these GPCs remained almost constant.

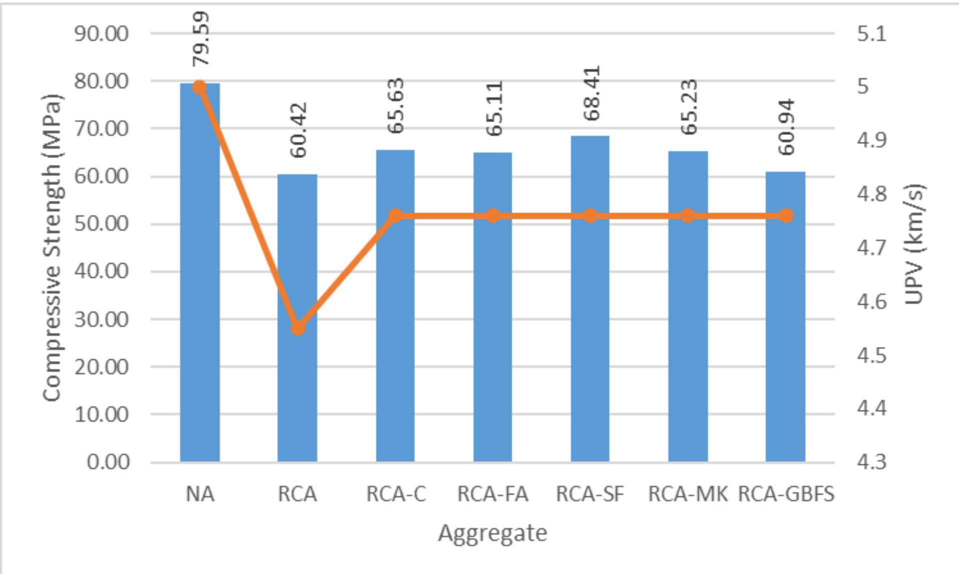

Fig. 2. 28-day compressive strength and UPV values of GPCs

3.3. Schmidt hammer rebound values of concretes

Figure 3 shows the Schmidt hammer rebound values of GPCs. As can be seen in the figure, while the rebound value of GPCs with natural aggregates was determined as 55.85, the hammer rebound value of GPC with RCA without any slurry impregnation process decreased by 23% and was determined as 43. The reason for this decrease is the presence of hollow and defective structure on the old mortar in the RCA. An increase was observed in the hammer rebound values of GPCs with RCA impregnated with slurry, although not very significant. This increase varies between 2.32% and 11.74%. The highest rebound value was obtained from GPC with RCA impregnated with silica fume slurry. The concrete sample with denser and more compact aggregate structure exhibited a higher rebound index in the Schmidt hammer test. This is attributed to its improved surface hardness and internal homogeneity, which enhance the material's ability to resist localized impact.

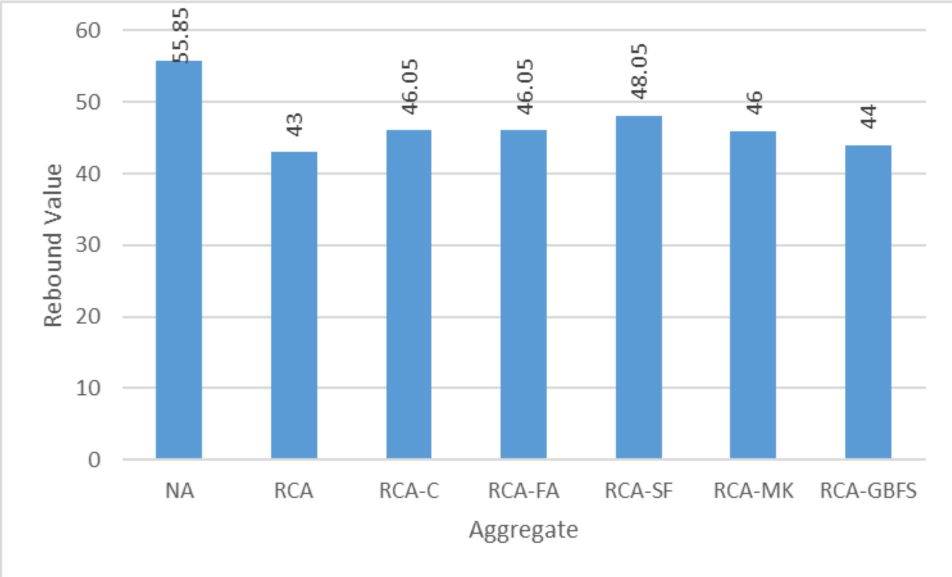

Fig. 3. Rebound values of GPCs

3.4. Electrical resistivity results of GPCs

While the resistivity of the reference GPC produced using NA was determined as 64.2 kΩ.cm, the resistivity value of the GBC with RCA without any treatment decreased by approximately 24% and was determined as 48.7 kΩ.cm. According to these results, it can be said that both the reference concrete with NA and the GPCs with RCA have a very low level of chlorine permeability according to AASHTO TP 95-11 standard. As expected as a result of the hollow and imperfect structure of the RCA, the resistivity value of the RC concrete was low. This indicates that the concrete is more hollow and more sensitive to chlorine and that in a reinforced concrete structure, the concrete will have difficulty in protecting the iron inside from rust. The electrical resistivity values of GPCs with RCAs impregnated with slurry showed a trend similar to the water absorption percentages of RCAs. The pozzolanic slurry impregnation process increased the resistivity values of the GPCs by about 1.6% to 12%. This indicates that the voids and imperfections in the RCAs were reduced and the chlorine resistance of the concretes produced with these aggregates was increased. SF and MK were the most effective pozzolans in terms of increasing the electrical resistivity of the concretes. Since GBFS-based GPCs with both NA and RCAs have a very low permeability class according to AASHTO TP 95-11 standard, the slurry impregnation of RCAs did not allow the GPCs to pass to a lower or higher class according to this standard.

Chloride ion penetration in concrete is closely governed by the absorptive and transport properties of the aggregates, particularly in mixtures containing RCAs. The presence of adhered mortar on RCA surfaces, along with its intrinsic microstructural quality, significantly influences both the capillary absorption capacity and the ionic diffusivity of the composite material. Owing to their elevated porosity and permeability relative to NAs, RCAs tend to facilitate more rapid and deeper chloride ingress. However, numerous investigations have confirmed that improving the physico-chemical characteristics of RCAs—through surface densification or pore refinement techniques—can markedly mitigate chloride transport within the concrete matrix (Du et al., 2024; Shi et al., 2023).

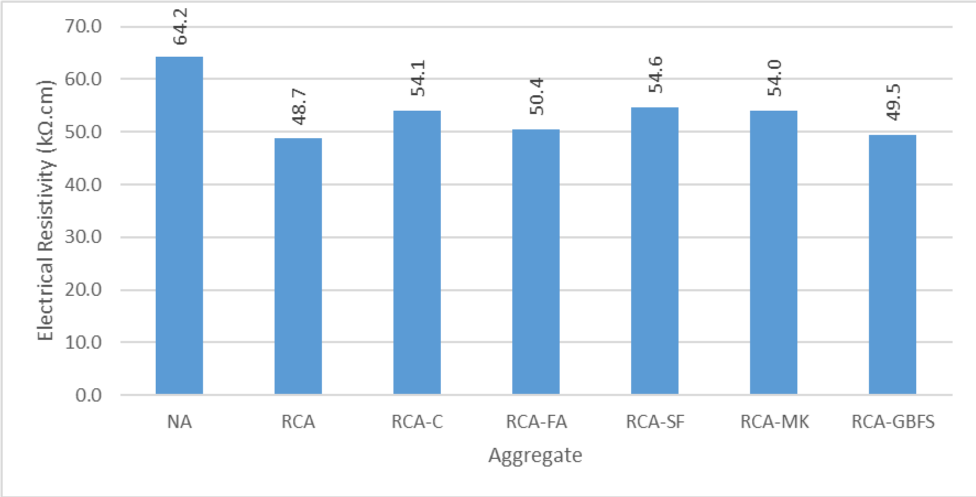

Fig. 4. Electrical resistivity values of GPCs

4. Conclusions

The results of the study can be summarized as follows:

- The application of pozzolanic slurry impregnation significantly enhanced the pore structure of recycled concrete aggregates, leading to a marked reduction in their water absorption rates.
- The use of RCA in GBFS-based GPCs resulted in a decrease of approximately 24% in 28-day compressive strength, 10% in UPV, 22% in Schmidt's attractive rebound index and 23% in electrical resistivity.
- Compared to GPCs with RCA without any slurry impregnation, 28-day GPCs produced using RCA impregnated with pozzolanic slurry showed an ultimate increase of 14% in compressive strength, 11.74% in Schmidt's hammer rebound index and about 12% in electrical resistivity values.
- No significant change was observed in the UPV values of the concretes.
- In conclusion, it was observed that slurry impregnation of RCAs can improve the properties of GBFS-based GPCs.

References

Amran, Y. H. M., Alyousef, R., Alabduljabbar, H., & El-Zeadani, M. (2020). Clean production and properties of geopolymer concrete; A review. *Journal of Cleaner Production*, 251, 119679.

Du, T., Xiao, J., Li, C., Gan, Y., & Jiang, X. (2024). Experimental and numerical study on the chloride ions penetration in recycled aggregate concrete. *Construction and Building Materials*, 451, 138702.

Han, S., Zhao, S., Lu, D., & Wang, D. (2023). Performance Improvement of Recycled Concrete Aggregates and Their Potential Applications in Infrastructure: A Review. *Buildings* 2023, Vol. 13, Page 1411, 13(6), 1411.

Ouyang, K., Liu, J., Liu, S., Song, B., Guo, H., Li, G., & Shi, C. (2023). Influence of pre-treatment methods for recycled concrete aggregate on the performance of recycled concrete: A review. *In Resources, Conservation and Recycling* (Vol. 188). Elsevier B.V.

Pan, G., Zhan, M., Fu, M., Wang, Y., & Lu, X. (2017). Effect of CO2 curing on demolition recycled fine aggregates enhanced by calcium hydroxide pre-soaking. *Construction and Building Materials*, 154, 810–818.

Parathi, S., Nagarajan, P., & Pallikkara, S. A. (2021). Ecofriendly geopolymer concrete: a comprehensive review. In *Clean Technologies and Environmental Policy* (Vol. 23, Issue 6, pp. 1701–1713). Springer Science and Business Media Deutschland GmbH.

Qiu, J., Tng, D. Q. S., & Yang, E. H. (2014). Surface treatment of recycled concrete aggregates through microbial carbonate precipitation. *Construction and Building Materials*, 57, 144–150.

Shaban, W. M., Yang, J., Su, H., Liu, Q. feng, Tsang, D. C. W., Wang, L., Xie, J., & Li, L. (2019). Properties of recycled concrete aggregates strengthened by different types of pozzolan slurry. *Construction and Building Materials*, 216, 632–647.

Shi, W., Liu, Y., Wang, W., Duan, P., Wang, Z., & Shang, Z. (2023). Relationship between chloride ion permeation resistance of recycled aggregate thermal insulation concrete and pore structure parameters. *Construction and Building Materials*, 370, 130666.

Silva, R. V., De Brito, J., & Dhir, R. K. (2014). Properties and composition of recycled aggregates from construction and demolition waste suitable for concrete production. *Construction and Building Materials*, 65, 201–217.

Thomas, J., Thaickavil, N. N., & Wilson, P. M. (2018). Strength and durability of concrete containing recycled concrete aggregates. *Journal of Building Engineering*, 19, 349–365.

4th International Civil Engineering & Architecture Conference
15-17 May 2025, Trabzon, Türkiye

Enhanced compressive strength prediction using concrete mix parameters and feature importance analysis: Using alternative ML algorithms

Talip Çakmak[1], İlker Ustabaş[*1]

[1] Recep Tayyip Erdoğan University, Department of Civil Engineering, 53000 Rize, Türkiye

Abstract. Concrete is one of the best commonly applied building materials due to its various advantages as such high strength, durability, resistance to high temperatures, etc. However, due to the CO_2 emissions abput the production and consumption of the raw material cement, research has long been conducted into various alternatives. Various supplementary cementitious materials with pozzolanic properties are at the leading of such options. In addition to reducing the CO_2 emissions of these materials, it is possible to improve various properties, especially strength and durability. However, obtaining the properties that occur when various materials are used together with concrete results from long laboratory processes and labour. Therefore, ML algorithms allow us to reduce this time and effort. In this study, a variety of ML algorithms such as RF, ET and GBR were used to predict the properties of concretes with different mix parameters such as different proportions of FA, GGBS, aggregate quantity and curing time. In addition, feature importance analyses based on different algorithms were performed to elucidate the background functioning of these algorithms. As a result of the analysis, the GPR algorithm showed the highest prediction and generalisation performance with an R^2 value of 0.871. The ET and RF algorithms follow this performance. In addition, as a result of the feature importance analyses, the most important mixing parameters for all algorithms were found to be cement ratio and setting time. The values obtained as a result of the study show the suitability of using ML algorithms to detect different properties of concretes.

Keywords: Machine learning, Feature importance, Cement, Supplementary cementitious materials, Fly ash

1. Introduction

Concrete is commonly utilised in the construction industry owing to its features such as high strength and durability, high workability, economy, and long service life (Tran, 2022; Zhang & Zhang, 2025). Concrete is a building material that can be easily produced from a mixture of aggregate, cement and water (Moodi et al., 2025). Today's urbanization creates a significant demand for concrete. A large amount of cement is used to meet this demand. However, the use of cement increases CO_2 emissions into the atmosphere. Because cement production leads to a significant amount of CO_2 emissions. A significant amount of CO_2 is emitted during the calcination process in cement production and the generation of energy required for heat treatment. These emissions account for 5-9% of global emissions (Cakmak & Ustabas, 2025, 2025; Cakmak et al., 2025). Approximately 1 ton of CO_2 is released into the atmosphere to produce 1 ton of cement (Nguyen et al., 2025; Jungclaus et al., 2024). In addition, the consumption of limestone and clay, the raw materials of cement, leads to the depletion of natural resources. This situation paves the way for environmental pollution and land degradation, as well as CO_2 emissions (Nguyen et al., 2025; Jungclaus et al., 2024). Considering the environmental impact caused by the production of OPC, researchers suggest that the amount of cement in concrete production should be reduced and eventually eliminated. There are several important alternative methods to do this. The most important of these is the use of waste materials with pozzolanic features to reduce the amount of cement used.

The substitution of waste materials such as fly ash and GGBS, which are by-products of industry and commerce, in cementitious mixtures has been widely used to reduce carbon emissions from cement (Wang et al., 2024; Liu et al., 2024). The use of these materials as supplementary cementitious materials not only contributes positively to the strength properties of the materials, but also to the reduction of carbon emissions from cement. Previous studies have shown that the substitution of SCMs in cementitious mixtures significantly reduces greenhouse gas emissions. It also allows concrete to be a sustainable material (Phul et al., 2019). These materials

[*] Corresponding author, E-mail: ilker.ustabas@erdogan.edu.tr

https://doi.org/10.31462/icearc2025_ce_mat_052

have a very wide range of applications, such as marine structures, high-performance concretes, durable repair materials, and green building technology.

Data-driven science is recognized as the fourth scientific paradigm due to its profound impact on engineering and technology (Moodi et al., 2025). In the past, complex computational techniques have been proposed to accurately predict values. However, in recent years, the machine learning method offers significant advantages for various fields, especially engineering sciences, due to its superior predictive ability and no prior knowledge required. Machine learning offers significant time and cost advantages over time-consuming laboratory experiments and numerical simulations. In addition to reducing computational costs, it also enables the identification of relationships between input and output features in the data set. All of these benefits contribute to solving problems faster and more effectively. If the developments in data science are carefully analyzed, the importance of data-driven science will continue to grow in the future (Moodi et al., 2025; Tariq et al., 2025). Especially in the last two decades, it is clear that there have been significant improvements in the computational methods and capabilities of ML algorithms. Experimental investigation of the properties of mortar specimens requires significant effort in terms of energy, time, and costs such as material consumption, labor, etc. (Ebrahimzadeh et al., 2025; Tang et al., 2024). This has led researchers to analyze the datasets previously available in the literature and examine the relationships between the data that make up the dataset. Moghaddas and Bao (2025) used ML algorithms to predict the wear depth of concrete. Different ML algorithms such as XGBoost, CatBoost, LightGBM, ET and RF were used in the examination. The outcomes obtained from the study demonstrated that ML algorithms have significant potential in predicting the wear depth of concrete. Rajiv et al. (2025) used linear regression, LASSO regression, DT, RF and multilayer perceptron algorithms to anticipate the mechanical features of concrete including treated wastewater and fly ash. Within the scope of the study, the RF algorithm showed the highest compressive strength performance and demonstrated the usability of wastewater in concrete mixes. Similarly, Moodi et al. (2025) used various machine learning approaches to foretell the CS of green concretes containing copper slag aggregates. Lan et al. (2025)used different machine learning approaches to predict tensile strength and fracture toughness of concrete. The XGB algorithm showed the highest prediction accuracy, demonstrating the feasibility of utulising ML models instead of laboratory experiments to foretell size-independent fracture parameters of concrete. Ulloa et al. (2025) evaluated distinct ML frameworks to predict the compressive strength of geopolymers containing industrial waste. The results of the study show that the applicability of ML frameworks in compressive strength prediction paves the way for the use of these models in various projects. These studies in the literature show that ML algorithms are suitable for predicting the properties of building materials and reveal the potential of using machine learning approaches in different fields.

A review of recent studies in the literature shows that supplementary cementitious materials with pozzolanic properties are an important alternative for reducing carbon emissions from cement. However, these studies have generally been carried out at considerable cost and time, requiring extensive labor, materials, and time. However, there are gaps in the application of ML frameworks for predicting the strength of mixtures containing cementitious admixtures. Previous examinations have used various ML approaches to fill this gap. Although significant and promising results have been obtained, there are still gaps in determining the applicability of tree-based machine learning algorithms for predicting the compressive strength of mortars. In this study, in order to fill this gap, tree-based ML algorithms such as RF, ET, and GBR were used to foretell the CS of concrete containing fly ash. In addition, feature importance analyses based on these algorithms were performed and the effects of input parameters on output parameters were investigated. It is believed that the findings and results obtained from this study will provide important and valuable contributions regarding the utilize of ML algorithms in the prediction of concrete properties. In this way, it aims to promote the use of ML algorithms in construction projects.

2. Materials and method

2.1. Research framework and significance

Fig. 1 shows the general research steps performed in the study. As part of the study, a literature review was conducted to obtain a secure dataset with input features and output features. Then, the dataset was randomly divided into training and test datasets with different proportions. Three different ML algorithm models were trained utulising the training data set. Then, feature importance analyses based on three different ML algorithms were performed to determine the importance levels of the input features that make up the dataset. In this study, all programming and analysis was done using MATLAB.

The main objectives of the examination are to

- To improve a predictive model for determining the changes in the compressive strength of concretes in the case of substitution of complementary cementitious materials with pozzolanic properties,
- To determine the importance levels of the input features in the data set and to perform mixture calculations by paying attention to the importance levels of the input parameters in future studies,
- To determine the usability of ML models in predicting the features of building materials and to promote the use of these models in construction projects.

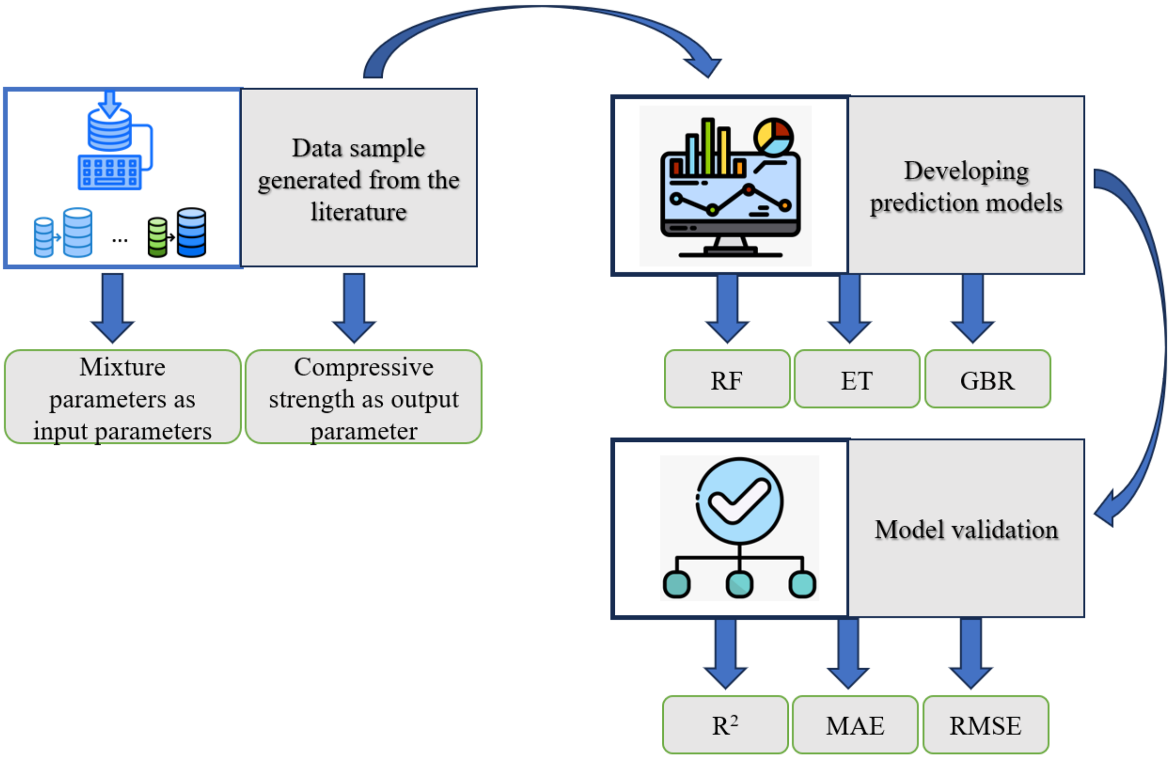

Fig. 1. Dataset scatter matrix

2.2. Data collection and analysis

2.2.1. Data collection
The data set used in this examination was obtained from a publicly available experimental study investigating the properties of fly ash-replaced concretes (Yeh, 1998). The compressive strength of concretes is influenced by important factors such as the amount of cement, fly ash replacement ratio, and water/cement ratio. Based on these factors, six main input properties have been identified as mentioned below. These properties are cement, GGBS, FA, water, aggregate quantities and curing times of the concretes, respectively. Based on these input properties, compressive strength was determined as an output parameter. These input properties were selected as parameters that have a significant effect on compressive strength, taking into account previous studies. The scatter matrix showing the properties that make up the data set and their relationships to each other is shown in Fig. 2.

2.2.2. Data preprocessing and analysis
The data set was pre-processed before analysis. Fig. 2 demonstrates the relationships among the six input parameters and one output parameter. In Fig. 2, we can see that the input parameters have a wide distribution and there is significant variability between different features. These variations have the potential to have a significant impact on the performance of ML frameworks.

2.3. Machine learning models and metrics
A series of preliminary examinations of the dataset revealed that there was no clear linear relationship among the six input properties and the CSs. The following three ML models were applied to this data set. These machine learning models are ET, RF, and GBR, respectively. The details of these models are described below.

The Random Forest algorithm is a model that allows regression performance to be improved by using multiple decision trees together. This model basically creates multiple sample sets using the training data set. These sample sets are used to train different decision trees. The model averages the performance of all decision trees to produce the final prediction at the end of the analysis. In this way, it shows higher generalization and prediction performance than individual decision trees.

Another important algorithm used in the study is ET. The main difference between this model and the Random Forest model is that it incorporates more randomness into the decision tree building process. In this way, significant improvements in model performance are expected.

The last algorithm used in the study is GBR. This algorithm basically builds each model on the residuals of the previous model. In this way, it gradually reduces the errors by taking into account the errors obtained from the

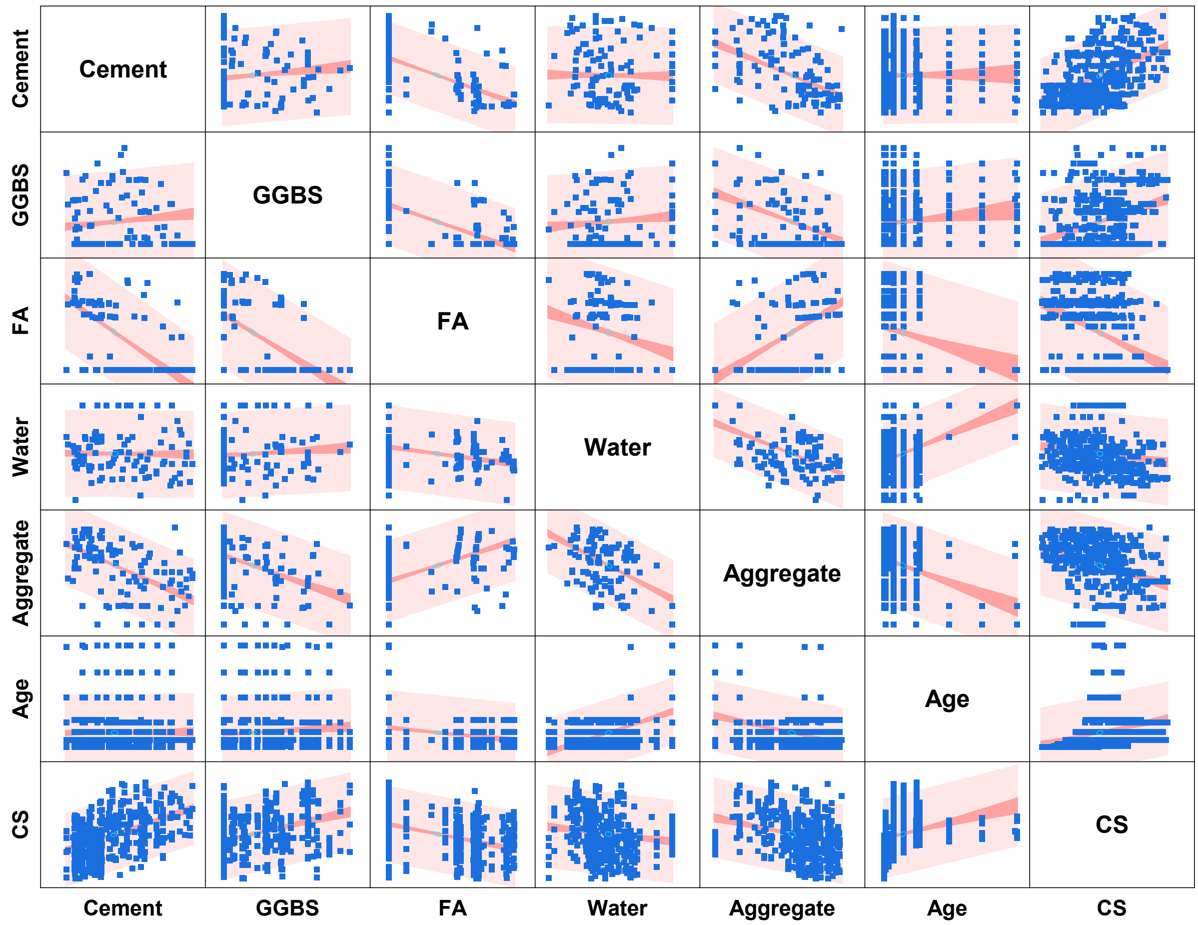

Fig. 2. Dataset scatter matrix

previous model. Finally, the predictions from the model are generated by the contribution of each tree. In this way, the errors of poorly learning trees are eliminated.

The general working principles of the models are shown in Fig. 3. To evaluate and compare the anticipation performance of these three different machine learning models, a number of important statistical metrics such as MAE (Mean Absolute Error), MAPE (Mean Absolute Percentage Error), MSE (Mean Squared Error), RMSE (Root Mean Squared Error), R^2training (Coefficient of Determination for Training Data), R^2testing (Coefficient of Determination for Testing Data) and R^2adjusted (Adjusted Coefficient of Determination) were used.

3. Result and discussion

The statistical performance outcomes obtained from 3 different ML frameworks used to foretell the CS of fly ash and GGBS substituted concretes are shown in Table 1. The GBR algorithm demonstrated the highest prediction and generalization performance with an R^2 value of 0.87. It is followed by ET and RF algorithms with R^2 values of 0.86 and 0.60, respectively. Analyzing the MAE and RMSE values in Table 1, the lowest error worths are acquired from the GBR algorithm. This is followed by the ET algorithm with MAE and RMSE values of 4.70 and 6.14, respectively. In parallel with the R^2 values, the RF algorithm showed the worst performance.

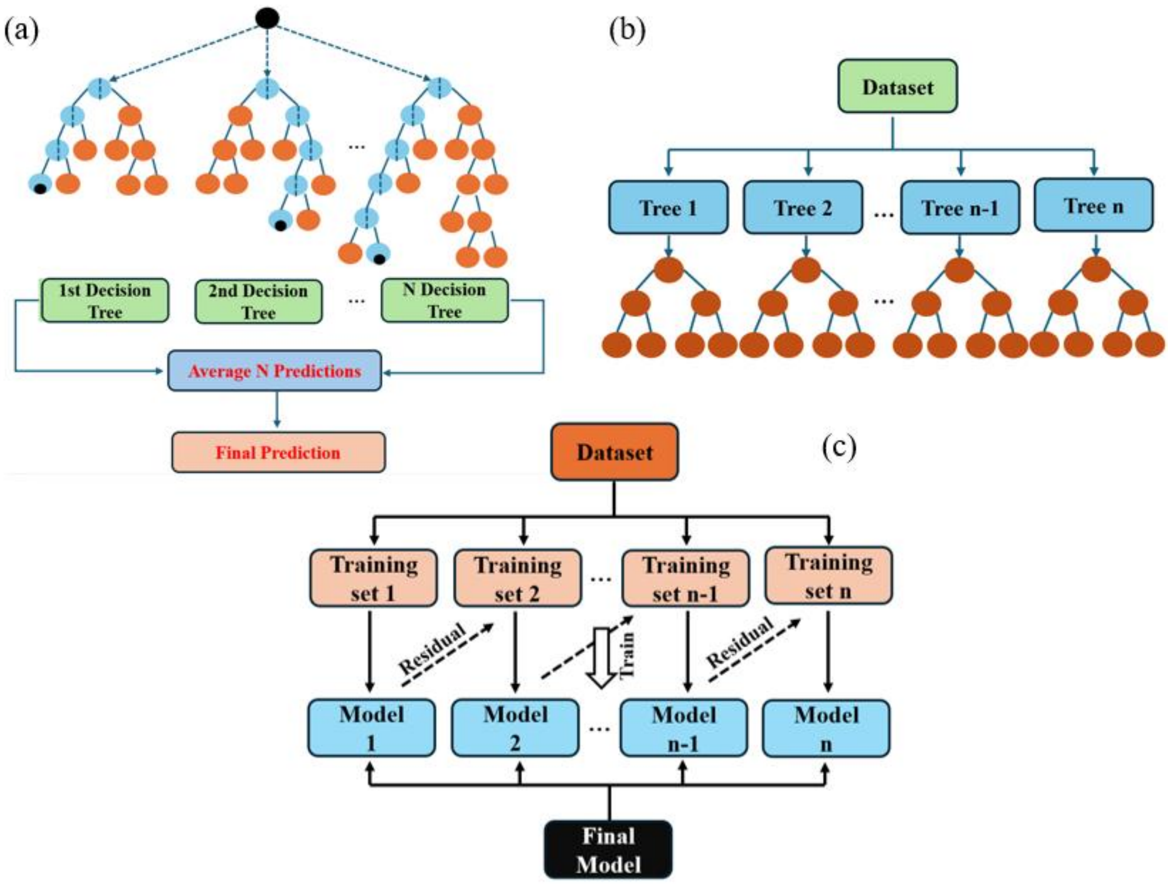

Fig. 3. Model's principles framework (Cakmak & Ustabas, 2025)

Table 1. Model's performance metrics

Metrics	Algorithms		
	RF	ET	GBR
MAE	7.39	4.70	4.44
MSE	109.76	37.65	35.41
RMSE	10.48	6.14	5.95
MAPE	31.20	17.84	14.19
R2-training	0.99	0.93	0.92
R2-test	0.60	0.86	0.87
R2-adjusted	0.59	0.86	0.87

To evaluate the R^2 worths acquired from the frameworks in general, while the RF algorithm showed a significant R^2 training performance of 0.99, it showed a low prediction performance with an R^2 value of 0.60. The main reason is overfitting. Although the RF model remembers the training data very well, its prediction performance on the test data is poor. The Random Forest algorithm uses multiple decision trees as a general operating principle. It also tends to produce more stable results by reducing the variance values obtained from the models. However, in the dataset used in this study, due to the low variance values between the input features, the RF algorithm showed high performance by memorizing the dataset during training. Since the RF algorithm memorized the test dataset, it had difficulty in predicting the test dataset. Therefore, it showed low generalization performance.

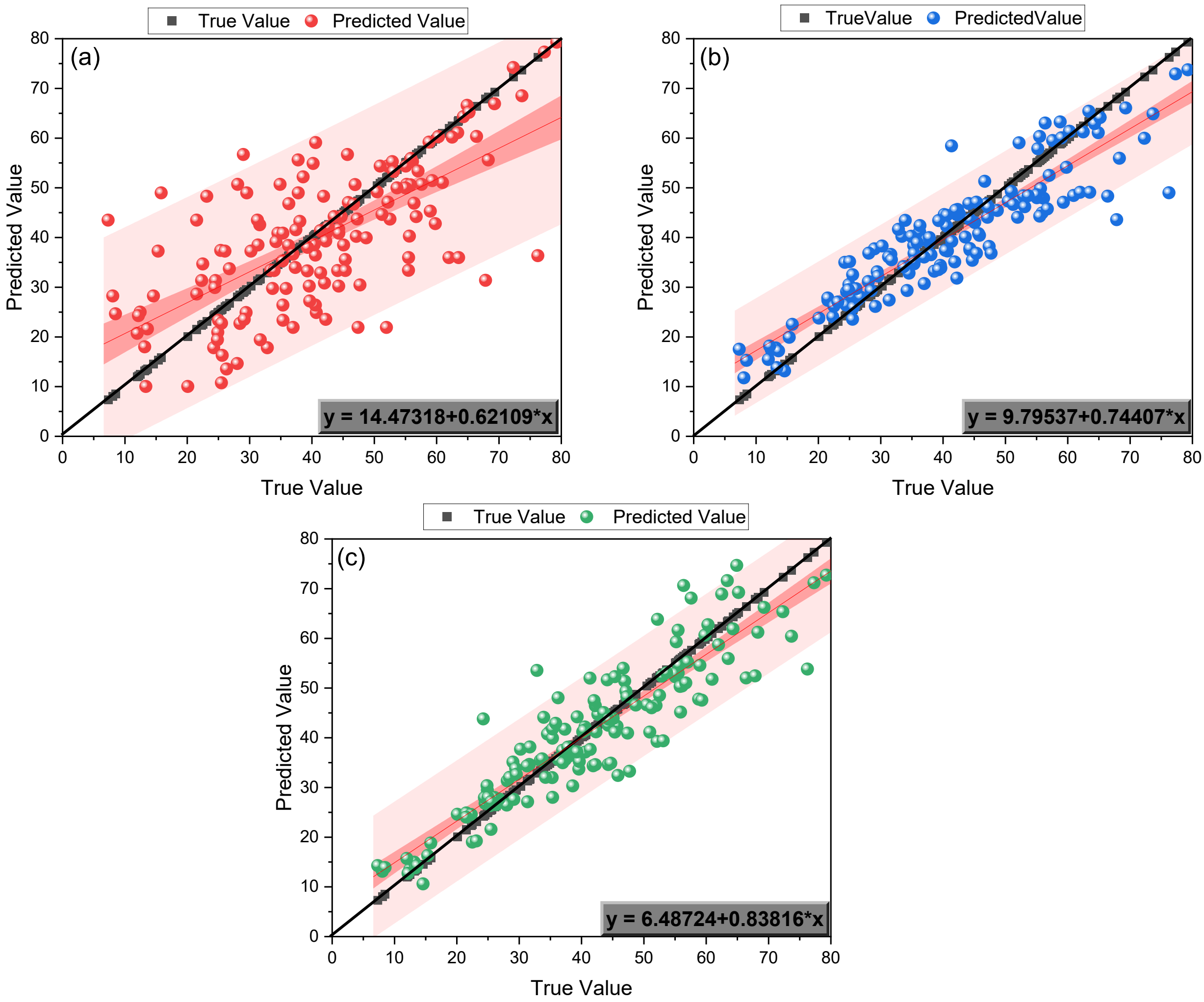

Fig. 4. a) RF, b) ET, C) GBR models predicted and real values

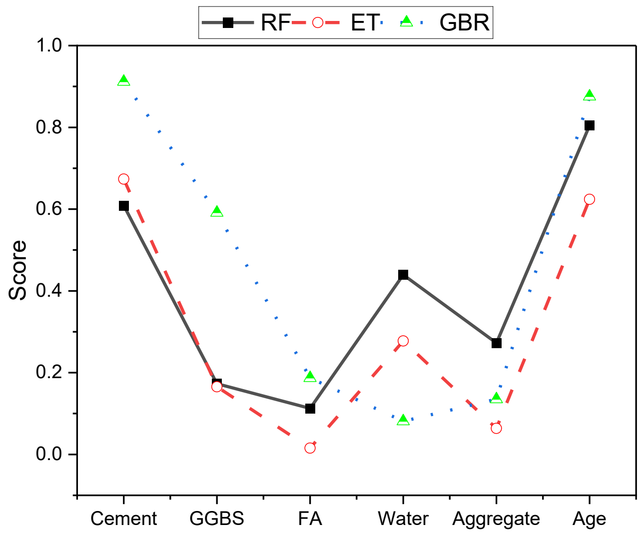

Fig. 5. Feature importance analysis values

The ET algorithm, another important prediction model, showed a better prediction performance with an R^2 worth of 0.86 compared to the RF algorithm. In addition to the R^2 values, significant decreases were observed in other performance metrics such as MAE and RMSE. The main reason for the significant increase in prediction performance is that the ET algorithm, unlike the RF algorithm, randomizes the splitting points in the trees. This random splitting reduces the variance of the model. As a result of the reduction in variance, the tendency of the model to overlearn is also reduced.

The algorithm used in the study with the highest generalization performance is GBR. The main reason for the highest prediction performance is the sequential learning mechanism of decision trees. Since decision trees are built on the previous decision tree and continue by correcting the errors of the previous decision tree, each new generation of decision trees performs better.

To summarize the results of the study in general, the RF algorithm showed lower performance due to overfitting, while the ET and GBR algorithms showed higher performance due to the working principles of the models. This study shows that GBR-based models provide more reliable results when there are non-linear relationships between the mix properties of concretes.

Fig. 4 demonstrates the prediction worths obtained from the RF, ET, and GBR algorithms. Fig. 4(a) demonstrates that the prediction worths are far from the y=x line and show a scattered distribution. This shows that the predicted values of the model are far from the actual values. However, Fig. 4(b) and Fig. 4(c) show that the predicted values are close to the y=x line and the predicted values are close to the actual values. This provides a clearer understanding of the prediction performance of the models.

Fig. 5 shows the feature importance analyses obtained using different machine learning models. Feature importance analyses are generally performed to determine the degree of importance that the models give to the parameters when making predictions. In this study, 3 different feature importance analyses were performed based on prediction algorithm models. In this way, the importance levels of the parameters in the prediction studies of the models were determined. It is seen that the most important parameters in all models are cement ratio and age of concrete. The least important parameters are fly ash and water content in the concrete mix.

4. Conclusions

In this study, RF, ET and GBR algorithms were used to predict the compressive strength of fly ash and GGBS substituted concretes. Among these machine learning algorithm models, GBR algorithm showed the highest prediction performance. This is followed by ET and RF algorithms respectively. Although the RF algorithm showed a significant performance on the training dataset, it could not maintain this performance for the test dataset. This is mainly because the RF algorithm is sensitive to overfitting. In the feature importance analyses based on RF, ET and GBR, the most important parameter common to all models is cement and concrete age. Again, the least important parameters for all models are fly ash and water content. As a result, GBR algorithm gave the most reliable prediction values for the compressive strength of concretes containing fly ash and GGBS. GBR algorithm showed higher prediction and generalization performance compared to other models. In future studies, the study team aims to investigate the relationships between capillary permeability and carbonation amounts of concretes.

References

Cakmak, T., & Ustabas, I. (2025). Investigating experimentally the potency of divergent sodium hydroxide and sodium silicate molar proportions on silica fume and obsidian-based geopolymer mortars. *Structural Concrete, 26*(2), 1962–1987. https://doi.org/10.1002/suco.202500055

Cakmak, T., & Ustabas, İ. (2025). The anticipation of compressive strength of geopolymer mortars with tree-based machine learning models: Effect of training-testing ratios. *Asian Journal of Civil Engineering.* https://doi.org/10.1007/s42107-025-01336-5

Cakmak, T., Ustabas, I., Kurt, Z., & Gurbuz, A. (2025). The importance of early strength in structural applications: Obsidian-based geopolymer mortars and silica fume substitution study. *Structural Concrete, 26*(2), 1578–1596. https://doi.org/10.1002/suco.202400726

Ebrahimzadeh, M., Mahmoudian, A., Tajik, N., Taleshi, M. M., Ashtari, M., Shakiba, M., & Bazli, M. (2025). Interpretable machine learning models for predicting flexural bond strength between FRP/steel bars and concrete. *Structures, 74*, 108587. https://doi.org/10.1016/j.istruc.2025.108587

Jungclaus, M. A., Williams, S. L., Arehart, J. H., & Srubar, W. V. (2024). Whole-life carbon emissions of concrete mixtures considering maximum CO_2 sequestration via carbonation. *Resources, Conservation and Recycling, 206*, 107605. https://doi.org/10.1016/j.resconrec.2024.107605

Lan, T., Yang, S., Jiang, Y., Wu, S., & Chen, Z. (2025). Automated prediction of size-independent tensile strength and fracture toughness of concrete using machine learning techniques. *Journal of Building Engineering, 104*, 112431. https://doi.org/10.1016/j.jobe.2025.112431

Liu, X., Liang, C., Zhang, Z., Zhang, Y., Xu, J., & Ma, Z. (2024). Mechanical performance of low-carbon ultra-high performance engineered cementitious composites (UHP-ECC) with high-volume recycled concrete powder. *Journal of Building Engineering, 88*, 109153. https://doi.org/10.1016/j.jobe.2024.109153

Moghaddas, S. A., & Bao, Y. (2025). Explainable machine learning framework for predicting concrete abrasion depth. *Case Studies in Construction Materials, 22*, e04686. https://doi.org/10.1016/j.cscm.2025.e04686

Moodi, Y., Hamzehkolaei, N. S., & Afshoon, I. (2025). Machine learning models for predicting compressive strength of eco-friendly concrete with copper slag aggregates. *Materials Today Communications, 46*, 112572. https://doi.org/10.1016/j.mtcomm.2025.112572

Moodi, Y., Hamzehkolaei, N. S., & Afshoon, I. (2025). Machine learning models for predicting compressive strength of eco-friendly concrete with copper slag aggregates. *Materials Today Communications, 46*, 112572. https://doi.org/10.1016/j.mtcomm.2025.112572

Nguyen, H. A. T., Pham, D. H., Ahn, Y., Oo, B. L., & Lim, B. T. H. (2025). Machine learning and sustainable geopolymer materials: A systematic review. *Materials Today Sustainability, 30*, 101095. https://doi.org/10.1016/j.mtsust.2025.101095

Nguyen, H. A. T., Pham, D. H., Ahn, Y., Oo, B. L., & Lim, B. T. H. (2025). Machine learning and sustainable geopolymer materials: A systematic review. *Materials Today Sustainability, 30*, 101095. https://doi.org/10.1016/j.mtsust.2025.101095

Padalu, P. K. V. R., & Surana, M. (2024). An overview of performance-based seismic design framework for reinforced concrete frame buildings. *Iranian Journal of Science and Technology, Transactions of Civil Engineering, 48*, 635–667. https://doi.org/10.1007/s40996-023-01217-4

Phul, A. A., Memon, M. J., Shah, S. N. R., & Sandhu, A. R. (2019). GGBS and fly ash effects on compressive strength by partial replacement of cement concrete. *Civil Engineering Journal, 5*(4), 913–921. https://doi.org/10.28991/cej-2019-03091299

Rajiv, K. N., Ramalinga Reddy, Y., Shiva Kumar, G., & Ramaraju, H. K. (2025). Predictive modelling of mechanical properties of concrete using machine learning with secondary treated wastewater and fly ash. *Cleaner Waste Systems, 11*, 100296. https://doi.org/10.1016/j.clwas.2025.100296

Tang, Y., Zhou, C., Wang, W., Zhang, W., & Cheng, Y. (2024). Machine learning driven bond performance prediction between FRP bars and coral aggregate concrete. *Construction and Building Materials, 442*, 137684. https://doi.org/10.1016/j.conbuildmat.2024.137684

Tariq, R., Aziz, H. F., Paracha, S., Zahid, N., Ainger, T. J., Mirza, F. A., & Enam, S. A. (2025). Cognitive rehabilitation of brain tumor survivors: A systematic review. *Brain Tumor Research and Treatment, 13*(1), 1–16. https://doi.org/10.14791/btrt.2024.0033

Tran, V. Q. (2022). Machine learning approach for investigating chloride diffusion coefficient of concrete containing supplementary cementitious materials. *Construction and Building Materials, 328*, 127103. https://doi.org/10.1016/j.conbuildmat.2022.127103

Tran, V. Q. (2022). Machine learning approach for investigating chloride diffusion coefficient of concrete containing supplementary cementitious materials. *Construction and Building Materials, 328*, 127103. https://doi.org/10.1016/j.conbuildmat.2022.127103

Ulloa, N., León, M. A. M., Palmay, L. F. S., & Castillo, M. M. (2025). Evaluating the compressive strength of industrial wastes-based geopolymer concrete with machine learning models. *Construction and Building Materials, 472*, 140891. https://doi.org/10.1016/j.conbuildmat.2025.140891

Wang, C., Yuan, J., Zhang, Y., & Ma, Z. (2024). A comparative study of low cyclic loading effects on plastic strain, nonlinear damping, and strength softening in fiber-reinforced recycled aggregate concrete. *Journal of Building Engineering, 97*, 110774. https://doi.org/10.1016/j.jobe.2024.110774

Yeh, I. C. (1998). Modeling of strength of high-performance concrete using artificial neural networks. *Cement and Concrete Research, 28*(12), 1797–1808. https://doi.org/10.1016/S0008-8846(98)00165-3

Zhang, K., & Zhang, K. (2025). Machine learning prediction and interpretability of bond strength in corroded reinforced concrete under high temperatures. *Materials Today Communications, 46*, 112630. https://doi.org/10.1016/j.mtcomm.2025.112630

Zhang, K., & Zhang, K. (2025). Machine learning prediction and interpretability of bond strength in corroded reinforced concrete under high temperatures. *Materials Today Communications, 46*, 112630. https://doi.org/10.1016/j.mtcomm.2025.112630

4th International Civil Engineering & Architecture Conference
17-19 May 2025, Trabzon, Türkiye

Structural performance of concrete and steel pedestrian overpasses in Ortahisar: Experiences and innovations

Abdullah Bostancı*[1], Sina Atabey[2]

[1] Avrasya University, Department of Construction Technologies, 61000 Trabzon, Türkiye
[2] Avrasya University, Department of Civil Engineering, 61080 Trabzon, Türkiye

Abstract. This study focuses on evaluating the user experience and structural performance of concrete and steel pedestrian overpasses along the coastal road in Trabzon's Ortahisar district under current conditions. Built upon practitioner feedback and observations, it considers the advantages and potential challenges of each material. Concrete's durability and steel's lightness are discussed in relation to the region's climate and urban context, while long-term maintenance requirements and usage patterns are also addressed. No technical measurements or laboratory tests were employed; instead, field inspections and expert opinions shaped the research framework. This approach aims to provide a straightforward yet insightful perspective on the daily functionality of overpasses and their contribution to urban life. It offers guidance to decision-makers and designers regarding material selection, maintenance planning, and user comfort.Particularly in Ortahisar, the potential increase in pedestrian traffic is expected to bring various material and design options to the fore in future projects. Thus, efforts should be made to extend the service life of overpasses that harmonize with the city's aesthetics and ensure pedestrian safety. Regular maintenance and judicious material choices could facilitate a more sustainable approach to pedestrian infrastructure, meeting evolving urban mobility needs. The study highlights the role of local governments in siting overpasses and underscores the significance of materials for user safety and comfort. It points out the need to periodically maintain existing structures and consider diverse material alternatives in new projects, aiming to promote sustainable, aesthetic, and functional pedestrian circulation.

Keywords: Pedestrian overpasses; Concrete structures; Steel structures; Sustainable materials; Innovative solutions

1. Introduction

Pedestrian overpasses are indispensable elements of urban transportation infrastructure, constructed to ensure pedestrian safety and maintain the uninterrupted flow of motor vehicle traffic (Hasan et al., 2020; Truong et al., 2019). In densely populated cities, especially along major arterial roads and multi-lane highways, managing pedestrian crossings is of vital importance for urban traffic safety and pedestrian comfort. In this context, pedestrian overpasses not only improve the quality of life for users but also support the continuity of intra-city mobility. Additionally, overpasses are evaluated as components of strategies aimed at reducing traffic congestion, organizing pedestrian-vehicle interactions, and enhancing urban accessibility.

The choice of structural system (steel, reinforced concrete, composite, etc.), material properties, aesthetic concerns, and compliance with accessibility standards in the design, construction, and operation of pedestrian overpasses directly influence both structural performance and user satisfaction. Each of these factors is decisive in terms of cost-effectiveness, longevity, and maintenance requirements. The comparative analysis of steel and reinforced concrete systems is supported by a broad literature, emphasizing aspects such as ease of construction, durability, maintenance needs, and environmental impacts. Steel systems stand out for their ease of assembly, lightweight nature, and allowance for aesthetic design, while reinforced concrete systems are preferred for their high compressive strength, low initial investment cost, and local production capabilities. Composite systems, combining the advantages of both materials, offer potential benefits but require special engineering calculations and detailed design solutions.

In recent years, climate change, the use of sustainable materials, recycling technologies, and societal expectations have transformed decision-making processes in infrastructure projects, including pedestrian overpasses. Studies such as those by Pan (1992) and Jiang & Yang (2012) highlight the decisive role of climatic effects on the service life and maintenance costs of structures exposed to outdoor conditions. Environmental factors

* Corresponding author, E-mail: abdullah.bostanci@avrasya.edu.tr

https://doi.org/10.31462/icearc2025_ce_mat_053

such as high humidity, temperature fluctuations, heavy precipitation, and saline atmospheres reduce the durability of both reinforced concrete and steel systems and complicate maintenance and repair processes. Moreover, environmental variables such as wind loads, freeze-thaw cycles, and air pollution are also among the key parameters affecting the service life of overpasses. Therefore, accurate analysis of climatic effects and material selection based on environmental compatibility are essential for ensuring long-lasting and sustainable overpasses.

Sartori & Hestnes (2007), discussing the integration of sustainability into the construction sector, argue that environmental impacts such as energy consumption and carbon emissions must be considered not only during the building's lifespan but also during production, use, and deconstruction stages. In this regard, the use of recyclable materials not only reduces direct environmental impact but also contributes to economic sustainability. In examples developed particularly in Europe and North America, structural steel systems with reduced carbon footprints and green infrastructure solutions have become increasingly common in pedestrian overpass projects. A growing awareness of this issue in Turkey has led various municipalities and local governments to begin promoting environmentally friendly construction practices.

Ivorra et al. (2015) and Ribeiro da Silva & Santos da Silva (2018) examined the potential use of modern construction materials such as recycled steel, sustainable concrete mixtures, and cross-laminated timber (CLT) in pedestrian bridges. These materials offer new design possibilities in terms of durability, aesthetics, and ecological balance. Such applications can render pedestrian overpasses not only functional but also exemplary structures in terms of environmental sustainability. Additionally, pedestrian overpass projects evaluated within environmental certification systems such as LEED and BREEAM play a significant role in helping cities achieve their sustainability goals.

User behavior and socio-demographic characteristics also influence pedestrian overpass usage rates and design decisions. Patra et al. (2020) developed a method combining Revealed Preference (RP) and Stated Preference (SP) data to understand pedestrian crossing behaviors. Their study found that environmental, physical, and personal factors significantly affect pedestrian preferences at signalized intersections; thus, the location, design, and accessibility of pedestrian overpasses directly impact user choices. Factors influencing user behavior include pedestrian flow density, waiting time, alternative crossing options, weather conditions, and accessibility for the disabled.

Similarly, a study conducted in Pakistan by Ghafoor & Khan (2021) investigated usage differences across age and gender groups, revealing that women and elderly individuals use overpasses more frequently than young men. These findings underscore the need to tailor design parameters such as ramp gradients and stair heights to socio-demographic structures. Designs sensitive to user habits are of great importance for the effective management of pedestrian traffic in urban areas. Furthermore, in urban planning, addressing the needs of vulnerable groups such as the elderly, women, and people with disabilities is critical to the success of accessibility policies.

From a structural performance perspective, Eremeev et al. (2021) investigated the dynamic behavior of composite reinforced concrete systems used in pedestrian bridges, noting that these systems require special engineering solutions. The stiffness contrast between concrete and steel components directly affects vibration behavior and service life. Innovative solutions such as shear connector placements, industrial manufacturing processes, and the use of multi-profile columns contribute to the development of composite systems. In this context, next-generation pedestrian bridges equipped with advanced vibration control systems, active dampers, and lightweight material combinations play a key role in enhancing structural safety.

The design of pedestrian overpasses should not only be approached from a technical perspective but also from environmental and user-oriented angles. Heldak et al. (2021) emphasized that strong wind effects, humidity with marine salt, and soil properties are the primary factors influencing structural behavior in coastal regions. Hence, beyond material selection, the compatibility of the design with the climatic and geographic context is also crucial. In coastal cities, it is expected that structures be built using weather-resistant, low-maintenance, and long-lasting systems.

This study conducted in the Ortahisar district of Trabzon systematically analyzes the structural systems (steel, reinforced concrete, composite), design features, material choices, and spatial contexts of pedestrian overpasses, particularly along the coastal road. Akyüz (2023) examined the impact of pedestrian overpasses in high-density areas using microsimulation analyses and emphasized the importance of integrating such methods into the design process. These analyses show that factors such as pedestrian flow density, waiting times, movement directions, and group crossing behaviors must be taken into account during overpass design.

The overpasses in Ortahisar were built in different periods, and choices of structural systems, enclosed or open design elements, accessibility options, and maintenance status vary according to the construction years. This diversity reflects evolving design approaches, technological developments, and user demands over time. In a study by Aydın (2024), the technical specifications, geographical locations, and topographic conditions of overpasses along the coastal road in Trabzon were classified in detail.

In addition, Aksoy (2024) analyzed pedestrian violations and crossing behavior, showing that factors such as waiting time, group size, and the presence of parked vehicles influence the decision to use overpasses. Kawther & Mohammad (2024), examining the role of overpasses in urban transportation systems, emphasized that overpasses should be considered not only structural but also social and urban elements in relation to user habits and accessibility. Correspondingly, evaluations in Ortahisar revealed that overpasses located near the coast are more frequently used, and in these areas, design is given greater importance in terms of aesthetics and functionality.

The aim of this study is to emphasize the significant impact of pedestrian overpasses on urban life, particularly in rapidly developing coastal cities like Ortahisar. Pedestrian overpasses are critical infrastructure elements that enhance pedestrian safety while minimizing disruptions to vehicular traffic flow in densely urbanized areas. This study will focus on the effect of these structures on urban life in Ortahisar, with particular attention to how their design and material selection influence their performance and usability. Although the study does not include direct measurements, it will rely on field observations and expert opinions to evaluate the functionality of pedestrian overpasses in the region. The primary objective is to examine the structural performance of pedestrian overpasses in the context of user experience and material properties. By focusing on the reasons behind the preference for reinforced concrete and steel systems, as well as the physical and urban characteristics of Ortahisar, this study aims to provide an in-depth understanding of the performance of these structural elements.

2. Methodology

This study adopts a qualitative research approach to evaluate the structural performance and user experience of pedestrian overpasses located in the Ortahisar district of Trabzon. Primary data collection methods include field observations and expert interviews. The main objective of the research is to examine key factors—such as material characteristics, environmental impacts, and maintenance requirements—in order to understand how these overpasses fulfill their intended functions within the urban context.

2.1. Study area and sample

The study focuses on 16 pedestrian overpasses situated along the coastal highway in Ortahisar, comprising 14 steel and 2 reinforced concrete structures. The overpasses were selected to represent a variety of structural systems. This sample offers a comparative analysis of the performance and user experience associated with different material types under the unique environmental conditions of the district. These overpasses are located in areas with high pedestrian traffic, including densely populated residential zones, and are exposed to the coastal climate of the region. Such geographical and environmental features significantly influence both the design and operational efficiency of the structures.

2.2. Data collection methods

Data were gathered through two primary methods: field observations and semi-structured expert interviews.

2.2.1. Field observations

Unlike studies that rely on direct physical measurements, this research employed observational techniques to assess the physical condition, aesthetic integration, user comfort, and overall functionality of the overpasses. Special attention was given to environmental factors such as coastal weather conditions, strong winds, and salt exposure, all of which can significantly contribute to material degradation. The observations also emphasized the importance of routine maintenance and timely repairs to ensure structural safety and durability.

2.2.2. Expert interviews

Eight professionals from various disciplines—civil engineering, architecture, urban planning, and transportation engineering—were interviewed using a semi-structured format consisting of 30 open-ended questions. These questions were developed based on insights from seven subject-matter experts and are presented in Table 1. These interviews provided valuable insights into the structural performance, material selection, and maintenance strategies of pedestrian overpasses. Experts were also asked about challenges related to repair costs and how design can be improved to align with sustainability goals. Furthermore, concerns related to climate and its impact on the lifespan of structures, particularly in coastal regions such as Ortahisar, were also discussed.

2.3. Data analysis

The data collected through field observations and expert interviews were analyzed using qualitative techniques. Observational data were categorized into themes focusing on structural condition, environmental adaptation, and user experience. Interview responses were analyzed through thematic coding, allowing for the identification of recurring issues related to design and performance factors affecting the functionality of pedestrian overpasses. This analysis provided insights into the factors shaping the current condition of these structures and helped identify areas for improvement.

Table 1. Open-ended questions

No	Questions
1	What type of structural system (reinforced concrete or steel) have you most frequently encountered in pedestrian overpass projects? What do you think is the reason for this prevalence?
2	What are the fundamental differences in application, maintenance, and repair processes between reinforced concrete and steel pedestrian overpasses?
3	How do climate conditions, traffic density, and topography affect the design, planning, and construction processes of pedestrian overpasses?
4	What are the major technical challenges you face during the design and construction of reinforced concrete or steel pedestrian overpasses?
5	What problems do you encounter most frequently during maintenance and repair processes? What solutions do you apply to address them?
6	What logistical problems do you experience at the construction site or during project delivery? How do you overcome these challenges?
7	What are the main factors (cost, strength, aesthetics, maintenance duration, etc.) influencing decision-makers in material selection (reinforced concrete vs. steel)?
8	When you need to strike a balance between cost-effectiveness and durability, what criteria do you consider?
9	How and through which channels do you receive feedback on user satisfaction? Does this feedback affect the design or implementation processes?
10	What are the advantages and limitations of composite structural systems combining concrete and steel? Under which engineering conditions can these systems be used more efficiently?
11	What are your observations regarding the impact of pedestrian overpasses on traffic safety and pedestrian comfort in the area?
12	How have maintenance and repair costs of pedestrian overpasses changed over time? What measures can be taken to optimize these processes?
13	What do you think about composite systems combining reinforced concrete and steel? Under what conditions can they offer advantages in practice?
14	How will the increasing pace of climate change affect the long-term durability and cost-effectiveness of overpasses? What strategies should be adopted?
15	How do costs evolve over time considering maintenance and repair processes?
16	Can cost advantages be achieved in projects by using recycled materials?
17	According to which criteria is the durability of steel and reinforced concrete overpasses assessed?
18	Which material is more resistant to natural disasters (earthquakes, floods, wind loads, etc.)?
19	How are quality control processes conducted for the structural materials used?
20	How do weather conditions, traffic load, and environmental factors affect the durability of pedestrian overpasses?
21	How can structural performance be improved by using more durable and long-lasting materials in pedestrian overpasses? What new materials or technologies stand out in this regard?
22	What are the most common structural problems requiring maintenance?
23	What are the most frequent problems encountered during the repair process of reinforced concrete pedestrian overpasses?
24	How often should the corrosion protection methods of steel pedestrian overpasses be renewed?
25	How is the routine maintenance frequency determined for different types of pedestrian overpasses, and what is the cost of this process?
26	To what extent are user feedbacks integrated into maintenance processes? According to what criteria are these feedbacks evaluated?
27	How important is the recyclability of the materials used in the construction of pedestrian overpasses in the decision-making process?
28	How common is the use of recycled reinforced concrete and steel materials in current projects?
29	How can the use of sustainable materials in pedestrian overpasses reduce environmental impact?
30	How are the dismantling and recycling processes of decommissioned pedestrian overpasses managed?

2.4. Limitations

It is important to acknowledge that this study relies on qualitative data and therefore has limited capacity to produce quantitative performance assessments. Additionally, the research is confined to pedestrian overpasses within the Ortahisar district. While the findings are valuable for this specific region, they may not be directly generalizable to areas with different climatic or urban characteristics. The study does not include direct physical measurements; instead, its conclusions are based on observational data and expert opinions. As such, while the study offers important insights into the current condition of the overpasses, it does not provide precise structural performance evaluations.

3. Findings

This study focused on a total of 16 pedestrian overpasses located along the coastal highway of Ortahisar district in Trabzon, Turkey. The location and distribution of these overpasses are illustrated in Fig. 1., which provides a satellite overview of their geographical context. These structures span various neighborhoods and urban zones, reflecting different levels of pedestrian traffic, urban development, and exposure to coastal environmental conditions.

To systematically assess their structural performance, user accessibility, and design characteristics, detailed data were collected through field observations and expert interviews. Each overpass was examined in terms of span number, structural system type, presence of diagonal or vertical load-bearing elements, accessibility features, and whether it is covered or not. Table 2 presents a summarized inventory of the pedestrian overpasses included in the study

As evident from the inventory, the majority of pedestrian overpasses are constructed using steel portal frames integrated with diagonal tension rods. Only two structures (Nos. 7 and 15) employ precast reinforced concrete frames. While some overpasses include features such as full enclosure and ramps for accessibility, many lack essential inclusive design elements such as disabled access. Additionally, a number of the overpasses remain uncovered, leaving them more vulnerable to environmental degradation from coastal conditions.

These variations in structural type, protection, and inclusivity provide the foundation for thematic and comparative evaluations in subsequent sections of the findings. The diversity in design reflects not only evolving engineering preferences but also changing urban needs, environmental conditions, and user demands over time.

Analysis of the construction timeline and associated structural details reveals evolving patterns in the selection of materials and systems. Early overpasses built between 2009 and 2011, such as Nos. 15, 9, 7, 10, and 5, reflect diverse structural typologies, including both tied-arch and precast reinforced concrete systems. These structures were primarily focused on functional delivery with little emphasis on accessibility or environmental protection measures.

From 2014 onward, however, a marked preference for steel portal frame systems with diagonal tension rods emerged, indicating a standardization in structural design. This is particularly evident in overpasses built between 2015 and 2016 (Nos. 14, 4, 3), which incorporate both enclosed features and repetitive use of portal configurations. Between 2018 and 2019, newer overpasses such as Nos. 1 and 2 reflected continued reliance on portal frames, but with more careful integration into dense urban zones.

This trend suggests a growing reliance on lightweight steel structures, which offer ease of installation and reduced foundation demands compared to concrete. Despite the efficiency of this typology, a persistent shortcoming is observed in accessibility—many overpasses, including the most recent ones (e.g., No. 13 and No. 16), still lack ramps or elevators, thus limiting usage for people with disabilities or mobility constraints.

In summary, while structural systems have evolved toward efficiency and uniformity, inclusive design considerations have not advanced at the same pace, creating a critical area for future improvement.

From a historical perspective, the construction of these overpasses reveals a chronological progression reflecting evolving design preferences and infrastructure policies. Between 2009 and 2011, a significant wave of construction occurred with the establishment of Overpasses 15, 9, 7, 10, and 5, marking the initial phase dominated by basic structural utility with limited accessibility features. During the 2011–2014 period, Overpass 11 was added, indicating gradual but limited evolution.

The 2014–2015 period saw the construction of Overpass 6, followed by another wave between 2015 and 2016 with Overpasses 14, 4, and 3. These later structures began to incorporate more standardized design elements such as steel portal frames with diagonal tension rods and covered walkways. Between 2016 and 2018, Overpass 12 was constructed, continuing this trend.

A notable design shift emerged between 2018 and 2019 with the construction of Overpasses 1 and 2, introducing broader coverage and improved integration with adjacent urban facilities. The construction of Overpass 16 between 2019 and 2021, and Overpass 8 between 2021 and 2023, further extended the overpass network eastward.

Most recently, Overpass 13 was constructed from 2023 to the present, signifying the latest stage of expansion. However, despite advancements in structure and aesthetics, many newer overpasses still lack critical accessibility features such as ramps, highlighting the ongoing gap between functional expansion and universal design compliance.

This chronological development underscores the influence of urban growth, climate exposure, and user expectations in shaping the evolving typology of pedestrian overpasses in Ortahisar.

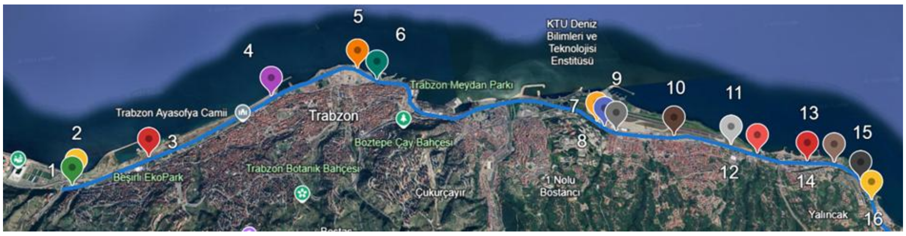

Fig. 1. Geographical distribution of pedestrian overpasses in Ortahisar, Trabzon

Table 2. Overview of structural and functional features of pedestrian overpasses

No	Name	Photo	Number of spans	Structural Characteristics
1	Pedestrian Overpass in Front of Beşirli Sahil Mosque		2	Steel Portal frame, Diagonal tension rods, Disabled access, Covered
2	Pedestrian Overpass in Front of Beşirli Akyazı Stadium		2	Steel Portal frame, Diagonal tension rods, Disabled access, Covered
3	Pedestrian Overpass in Front of Beşirli Ecopark		3	Steel Portal frame, Diagonal tension rods, Disabled access, Covered
4	Ali Yasin Erosmanoğlu Pedestrian Overpass		2	Steel Portal frame, Diagonal tension rods, Disabled access, Covered
5	Pedestrian Overpass in Front of Moloz Square		1	Steel tied-arch structure, Vertical hangers, No disabled access, Uncovered
6	Pedestrian Overpass in Front of the Private Hospital		3	Steel Portal frame, Diagonal tension rods, Disabled access, Covered
7	Pedestrian Overpass in Front of KTÜ Gate C		2	Precast reinforced concrete frame, No disabled access, Covered
8	Pedestrian Overpass in Front of Airport Exit I		1	Steel truss system, Disabled access, Covered
9	Pedestrian Overpass in Front of Airport II		1	Steel Portal frame, Diagonal tension rods, No disabled access, Covered
10	Ceyhun Mumcu Pedestrian Overpass		1	Steel tied-arch structure, Vertical hangers, No disabled access, Covered
11	Pedestrian Overpass in Front of Hayri Gür Sports Hall		1	Steel Portal frame, Diagonal tension rods, No disabled access, Covered
12	Çimenli Pedestrian Overpass		1	Steel Portal frame, Diagonal tension rods, No disabled access, Uncovered
13	Pedestrian Overpass in Front of PTT Yalıncak		2	Steel Portal frame, No disabled access, Uncovered
14	Pedestrian Overpass in Front of Yalıncak I Avrasya University		1	Steel Portal frame, Diagonal tension rods, No disabled access, Covered
15	Pedestrian Overpass at Yalıncak II DSİ II		2	Precast reinforced concrete frame, No disabled access, Uncovered
16	Yalıncak III Pedestrian Overpass		1	Steel Portal frame, Diagonal tension rods, No disabled access, Uncovered

3.1. Thematic analysis of expert interviews

A total of 30 open-ended questions were posed to experts from various fields related to civil and transportation infrastructure. The responses were analyzed thematically and categorized under key areas reflecting recurring insights and observed patterns. The main themes emerging from the qualitative analysis include material selection criteria, structural system performance, maintenance and repair challenges, environmental influences, user satisfaction, accessibility, and sustainability considerations. Fig. 2 represent thematic frequency based on expert interview responses.

Expert interviews revealed several recurring issues related to the structural performance, durability, sustainability, and user experience of pedestrian overpasses in Ortahisar. Among these, six key themes emerged as the most prominent, both in frequency and impact. Fig. 3 represent key recurring issues from expert interviews.

Firstly, corrosion in steel structures was cited by seven experts as the most common and severe maintenance challenge. This observation is particularly relevant in the context of Trabzon’s coastal climate, where humidity and salt-laden air accelerate material degradation. Jiang and Yang (2012) similarly emphasized that steel elements exposed to marine environments suffer from high corrosion rates, increasing long-term maintenance needs and reducing structural lifespan.

Secondly, cracking in reinforced concrete components was mentioned by five experts. These cracks, often caused by dynamic pedestrian loads and environmental stressors such as freeze-thaw cycles, can significantly undermine the structural integrity of overpasses if not promptly repaired. This aligns with Eremeev et al. (2021), who highlighted the vulnerability of composite concrete systems under fluctuating load and climate conditions.

A third recurring theme was the use of recycled steel, emphasized by six experts. Recycled materials were viewed as beneficial for reducing environmental impact while maintaining structural strength and serviceability. Supporting this, Ivorra et al. (2015) and Ribeiro da Silva & Santos da Silva (2018) found that recycled steel, when properly processed, can be effectively used in infrastructure without compromising mechanical performance.

The impact of environmental factors on durability was highlighted by five experts. Wind exposure, salt spray, and coastal humidity were identified as primary contributors to material fatigue and system degradation. Heldak et al. (2021) supported these observations by underlining the necessity of climate-adapted structural designs in coastal bridge construction.

Accessibility issues were also brought to the forefront, with six experts criticizing the lack of ramps and elevators in many pedestrian overpasses. These deficiencies create barriers for elderly users, individuals with disabilities, and parents with strollers. Ghafoor and Khan (2021) demonstrated that pedestrian overpass usage varies significantly across demographic groups, and that accessibility features are essential to ensuring equitable urban mobility.

Lastly, increasing maintenance costs over time were underscored by eight experts. They noted that while steel structures are efficient in early phases, their upkeep becomes increasingly costly due to corrosion and weather-induced deterioration. Sartori and Hestnes (2007) similarly advocated for lifecycle cost analysis in sustainable infrastructure planning, emphasizing that initial savings may be outweighed by long-term operational expenses.

These findings, supported by both field observations and literature, provide a multi-dimensional understanding of the strengths and shortcomings in the current state of pedestrian overpass infrastructure in Ortahisar. The expert insights validate the observed conditions and also offer strategic guidance for future improvements focused on durability, accessibility, and sustainability.

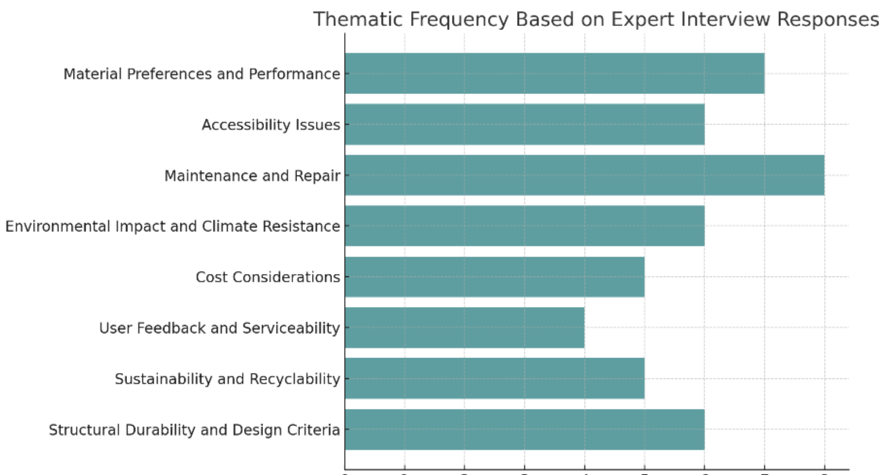

Fig. 2. Thematic frequency based on expert interview responses

Fig. 3. Key recurring issues from expert interviews

In addition to the primary thematic findings, several question-specific insights emerged from expert responses that further clarify critical considerations in pedestrian overpass design. For instance, in discussions related to cost and durability (Q8), experts emphasized the importance of achieving a balance between cost-efficiency and structural longevity. While eight experts prioritized cost-effectiveness in construction and maintenance, five others underscored the need for durability, especially in harsh environmental conditions. Material selection and climate responsiveness were cited as determining factors in this trade-off.

Regarding composite systems (Q10), expert opinions reflected both appreciation and concern. While four experts valued composite structures for their lightweight nature and resilience under dynamic loads, others noted significant limitations. In particular, concerns were raised about initial investment costs and the long-term vulnerability of composite materials to corrosion, especially in humid and coastal environments.

The safety and comfort impact of pedestrian overpasses (Q11) was also highlighted, with six experts identifying accident reduction as the primary benefit. Additionally, several experts noted that pedestrian comfort and structural accessibility contribute significantly to public satisfaction and the broader goals of socially sustainable urban infrastructure.

Sustainability concerns were further addressed in relation to the use of recycled materials (Q16). Six experts supported the adoption of recycled steel and other eco-friendly materials in overpass construction. While cost advantages were recognized, concerns regarding long-term durability and material quality control were also frequently mentioned.

Overall, these detailed insights complement the broader thematic analysis by offering a more nuanced understanding of expert priorities. The convergence of opinions around durability, environmental responsiveness, user accessibility, and sustainability underscores the multidimensional nature of overpass design in coastal urban settings like Ortahisar. Fig. 4 represents expert tendencies across multiple Interview questions.

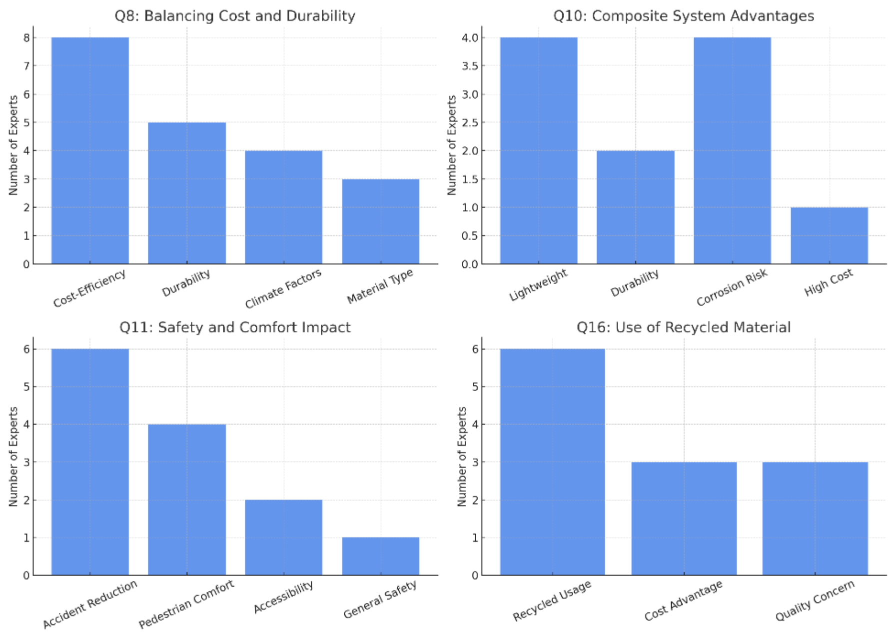

Fig. 4. Expert tendencies across multiple Interview questions

4. Conclusions

This study presented a comprehensive assessment of the structural characteristics and user-centered performance of 16 pedestrian overpasses located in the Ortahisar district of Trabzon. Through field observations and thematic analysis of expert interviews, key insights were drawn regarding the performance of both steel and reinforced concrete systems in coastal urban environments. The following conclusions have been drawn based on the findings of the study.

- Steel portal frame systems are preferred due to lightweight construction and ease of installation, but their long-term performance is compromised by corrosion, particularly in coastal climates like Trabzon.
- Reinforced concrete systems offer better resistance to environmental factors such as salt and humidity but are heavier and more time-consuming to install.
- Accessibility limitations remain widespread. Many pedestrian overpasses, including newly built ones, lack essential inclusive features such as ramps and elevators.
- Lifecycle-based design and preventive maintenance strategies are essential due to rising maintenance costs—especially in steel structures exposed to marine conditions.
- Recycled materials (e.g., recycled steel) are gaining favor among professionals for their cost-effectiveness and environmental benefits, though their application is still limited.
- CLT (Cross-Laminated Timber) and other engineered wood materials have potential for pedestrian bridge applications thanks to their lightness, aesthetic value, and sustainability. However, challenges related to environmental durability and regulatory standards must be addressed.
- Design decisions should not rely solely on cost or engineering practicality. User inclusiveness, urban integration, and sustainability must guide the future of pedestrian infrastructure in coastal cities like Ortahisar.

References

Akyüz, B. (2023). *Microsimulation-based evaluation of pedestrian overpass efficiency in dense urban zones* [Unpublished manuscript].

Aksoy, S. (2024). *Pedestrian crossing behavior and structural usage patterns in urban contexts* [Research report].

Aydın, M. (2024). *Geospatial classification of overpass infrastructure in coastal cities: The case of Trabzon* [Technical report].

Eremeev, A., Ivanov, D., & Petrova, N. (2021). Dynamic behavior of composite pedestrian bridges under environmental load. *International Journal of Bridge Engineering, 9*(2), 15–27.

Ghafoor, A., & Khan, N. (2021). Gender and age-based analysis of pedestrian overpass usage: A case study from Pakistan. *Journal of Urban Transport and Safety, 6*(1), 23–34.

Hasan, M., Rahman, M.T., & Haque, M. (2020). Safety evaluation of pedestrian crossing facilities in urban settings. *Journal of Traffic and Transportation Engineering, 7*(5), 561–572. https://doi.org/10.1016/j.jtte.2020.03.005

Heldak, M., Kowalski, M., & Nowak, A. (2021). Environmental influences on pedestrian bridge design in marine climates. *Civil Engineering and Architecture, 19*(3), 102–114.

Ivorra, S., Baeza, F.J., & Baeza, L. (2015). Recycled steel and composite solutions in pedestrian infrastructure. *Sustainable Structures and Materials, 2*(1), 33–42.

Jiang, W., & Yang, J. (2012). Corrosion behavior of steel in marine environments and its influence on service life. *Journal of Structural Integrity, 4*(1), 12–21.

Kawther, A., & Mohammad, M. (2024). Urban mobility and the socio-technical role of pedestrian overpasses. *Transportation and Urban Systems Review, 11*(4), 44–58.

OpenAI. (2024). *ChatGPT (May 1 version)* [Large language model]. https://chat.openai.com/

Pan, J. (1992). *Durability of bridge structures in coastal climates*. China Highway & Transportation Publishing House.

Patra, D., Singh, S., & Verma, A. (2020). Modeling pedestrian preference behavior using RP-SP framework. *Transportation Research Procedia, 48*, 126–133.

Ribeiro da Silva, T., & Santos da Silva, R. (2018). Structural evaluation of recycled materials in bridge applications. *Journal of Sustainable Infrastructure, 5*(2), 98–110.

Sartori, I., & Hestnes, A. G. (2007). Energy use in the life cycle of conventional and low-energy buildings: A review article. *Energy and Buildings, 39*(3), 249–257. https://doi.org/10.1016/j.enbuild.2006.07.001

Truong, L.T., & Somenahalli, S.V.C. (2019). The role of pedestrian overpasses in accident prevention: An empirical analysis. *Journal of Transportation Safety & Security, 11*(2), 154–171. https://doi.org/10.1080/19439962.2018.1428660

4th International Civil Engineering & Architecture Conference
17-19 May 2025, Trabzon, Türkiye

Pozolanic activity of calcareous clay: An uncommon cement replacement material

Furkan Türk*[1], Ülkü S. Keskin[1], Burak Uzal[2]

[1] Konya Technical University, Department of Civil Engineering, 42250, Konya, Türkiye
[2] Abdullah Gul University, Department of Civil Engineering, 38080, Kayseri, Türkiye

Abstract. Cement, which requires a temperature of 1300-1400 °C for its production, is responsible for approximately 8-10% of industrial greenhouse gas emissions. Harmful gases emitted during cement production are caused by the firing of clinker and the decomposition of calcium carbonate. Substituting clinker or cement with various mineral additives contributes to reducing emissions by limiting cement consumption. Traditional substitutes are pozzolanic additives such as fly ash, blast furnace slag, silica fume, volcanic tuff, calcined clay. This study covers calcareous clay (marl), which has not yet received sufficient attention. Calcareous clays are a type of clay that contains significant amounts of calcium carbonate, in addition to the typical clay minerals such as kaolinite, illite, and montmorillonite. These clays are found in various regions around the world and have been studied for their potential use as pozzolanic materials. Marl, which is cheaper and more readily available than sources containing pure clay minerals, can have sufficient pozzolanic activity when calcined under appropriate conditions. In this study, marl obtained from local sources was calcined at different temperatures (600, 700, 800, 900 °C). Calcined samples were ground in a laboratory type mill to obtain pozzolanic material. In order to determine the pozzolanic activity of the obtained samples, pozzolanic activity test was performed according to TS-25. As a result, it was determined that marl should be calcined at 800 degrees for maximum pozzolanic activity.

Keywords: Calcined marl; Pozzolanic activity; Cement substituting

1. Introduction

Cement production constitutes a significant portion of industrial energy consumption and carbon dioxide emissions (Monteiro et al., 2017). The literature presents various methods to mitigate harmful gas emissions from cement production. Among the frequently researched approaches globally are emission reduction techniques such as enhancing production technologies and partially or fully substituting cement with natural and artificial pozzolans, including slag, fly ash, and calcined clay (Jokar & Mokhtar, 2018; Scrivener et al., 2018). These materials, which possess pozzolanic activity and can replace cement in specific proportions, are referred to as cement replacement materials (CRM).

Naturally available materials containing clay minerals such as kaolinite, illite and montmorillonite, which can show high pozzolanic reactivity after heat treatment (calcination), are considered in the CRM class. Among these most abundant clay minerals in nature, kaolinitic clays are the most reactive clay type after calcination (Fernandez et al., 2011). Thermal treatment of kaolinitic clays (650-900 °C) results in the formation of metakaolin, a highly reactive pozzolan. As a result of this thermal treatment, the structure of kaolin changes; hydroxyl ions are removed and defects occur between the alumina and silica layers. The result is a highly reactive and amorphous material suitable for use in cement applications (Kostuch et al., 2000). The high pH of the cement pore solution results in Al ions dissolved from metakaolin forming an aluminum-rich calcium silicate hydrate gel (C-S-A-H). With water present in the system, alumina hydrates and calcium silicate alumina hydrates form, with their composition influenced by the AS_2/CH ratio and thermal conditions (Bergaya & Lagaly, 2013). Furthermore, the pozzolanic reactivity of metakaolin is enhanced in the presence of gypsum (Kurdowski & Pomadowski, 2001). A partial substitution of cement with metakaolin leads to a reduction in pore volume and a shift in pore distribution towards smaller sizes (Frías & Cabrera, 2000). Employing less porous cements containing metakaolin in mortar or concrete improves their strength and enhances their resistance to harsh environments, such as those containing sulfate or chloride (Gruber et al., 2001).

Due to the high demand for kaolinitic clays and low availability, there are limitations to their industrial use. In addition, in many regions raw clay is naturally combined with limestone (calcite). Consuming more costly

* Corresponding author, E-mail: fturk@ktun.edu.tr

https://doi.org/10.31462/icearc2025_ce_mat_080

resources that contain a high proportion of clay minerals raises some sustainability concerns. Therefore, the availability of more accessible and cheaper resources containing calcite and various clay minerals (marl) should be investigated in the cement and concrete sectors. Marl is a type of sediment consisting of a mixture of clay minerals (smectite, illite, kaolinite, etc.), feldspar and quartz with various carbonates (Bucher et al., 2002). Compared to kaolinitic clays, marl is a very abundant resource with low economic value.This study was conducted on calcareous clay (marl), which is not as common as other CRMs. Calcination was carried out at different temperatures to determine the performance of marl as CRM. After calcination and grinding, pozzolanic activity test was performed according to TS-25.

2. Materials and method

2.1. Materials

Calcareous clay obtained from Konya region was used as mineral additive in this study. Firstly, raw marl was sieved through a 2.36 mm sieve. The sieved material was calcined in a laboratory type muffle furnace at 600-700-800 and 900 °C for 30-60-90 minutes. The calcined material was ground in a laboratory type ball mill for 60 minutes. The pozzolanic material obtained was used as pozzolan in TS-25 mixtures. Photographs of the marl are presented in Figure 1 and physical and chemical properties are presented in Table 1.

Slaked lime ($Ca(OH)_2$) is used in the pozzolanic activity test according to TS-25. Within the scope of the study, $Ca(OH)_2$ with a density of 2.36 g/cm^3 from Tekkim company was used. A photograph of the $Ca(OH)_2$ used is presented in Fig. 1. CEN standard sand and city municipal water were used in the preparation of mortars.

2.2. Preparing of mixtures

The prepared powder materials were dry mixed at low speed for 60 seconds. Water was added to the homogenized powder mixture and the mortar mixing protocol described in TS EN 196-1 was applied. The prepared mortars were taken into 4x4x16 cm molds and the molds were covered with a glass plate to prevent evaporation and kept for 24 hours. The specimens were then placed in an oven at (55 ± 2) °C for a further 6 days without removal from the mold. At the end of 6 days, the samples removed from the oven were subjected to compressive strength test according to TS EN 196-1. The prepared mixtures are presented in Table 2.

Table 1. Physical and chemical properties of marl

Raw marl	
SiO_2, %	31.5
Al_2O_3, %	7.55
CaO, %	18.8
MgO, %	1.38
SO_3, %	0.08
Na_2O, %	0.58
K_2O, %	1.69
Fe_2O_3, %	3.76
LOI, %	15.52
Calcite, %	21
Quartz, %	17
Clay and other minerals, %	62
Density (g/cm^3)	2.67

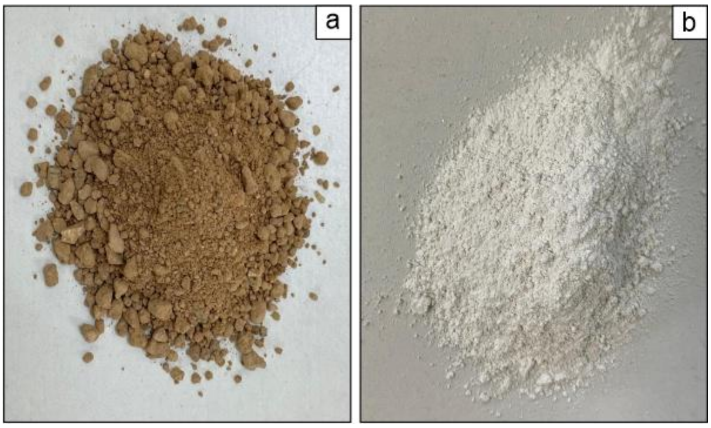

Fig. 1. Raw marl (a), slaked lime (b)

Table 2. Prepared mixtures

Sample	Calcination temperature (°C)	Calcination duration (min.)	Calcined marl (g)	Lime (g)	w/b	Sand (g)
1	600	30	340	150	0.6	1350
2	600	60	340	150	0.6	1350
3	600	90	340	150	0.6	1350
4	700	30	340	150	0.6	1350
5	700	60	340	150	0.6	1350
6	700	90	340	150	0.6	1350
7	800	30	340	150	0.6	1350
8	800	60	340	150	0.6	1350
9	800	90	340	150	0.6	1350
10	900	30	340	150	0.6	1350
11	900	60	340	150	0.6	1350
12	900	90	340	150	0.6	1350

3. Results and discussion

Fig. 2 presents the compression strength test results of the pozzolanic activity test carried out in accordance with TS-25 standard, based on marl samples calcined at various temperatures (600-900 °C) and durations (30, 60, 90 min). Generally, the strength increases with rise in temperature and duration. In particular, the performance at 600 °C (7.51-7.87 MPa) showed the lowest activity, and one can see a remarkable rise in strength when the processing temperature is up to 700 °C (9.00-10.55 MPa). This rise suggests an increase of the amorphous phases and the reactive silica-alumina present in the marl.

The compressive strength of the sample calcined at 800 °C for 90 min is the highest (12.12 MPa). This indicates that the best activation is at around 800 °C and higher time periods. But the strength is decreasing at 900 °C (minimum 8.96 MPa). This reduction may be attributed to acceleration of crystallization and decrease of reactive amorphous phase. Finally, on the basis of pozzolanic activity, the optimum calcination conditions are for a temperature of 800 °C and a time range of 60-90 min. These results demonstrate that calcined marl can successfully be used as a supplementary cementitious material.

It is already known that materials containing clay minerals have a certain degree of pozzolanic activity after heat treatment, depending on the amount of kaolinite in the material. Moreover, there are various, albeit limited, studies on clays containing calcite impurities. For example, it has been shown that calcite impurities (10-15%) present in raw clays of smectite, illite and kaolin origin have positive effects on pozzolanic reactivity (Zunino et al., 2020) and can be a good pozzolanic material when calcined between 400 and 800 °C (Rakhimov et al., 2017).

Generally, increasing the calcination temperature up to a certain level positively affects the pozzolanic activity (Nawel et al., 2020). However, it has been reported that after a critical point, the specific surface area decreases with increasing calcination temperature and consequently the pozzolanic activity decreases (Castillo et al., 2010). This study also revealed that appropriate calcination process should be applied to obtain maximum pozzolanic activity.

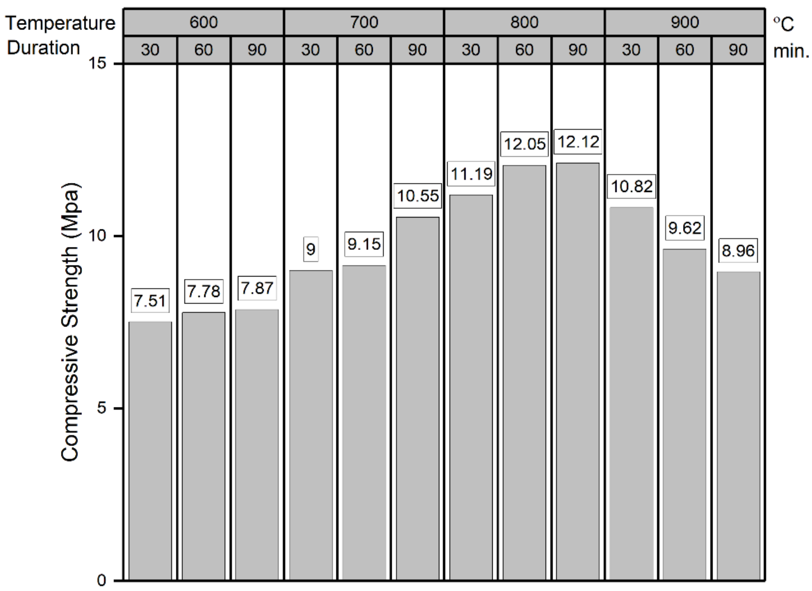

Fig. 2. Result of pozzolanic activity test

4. Conclusions

In this study, calcareous clay was calcined at different temperatures and for different times. It is generally known that clays containing high proportions of kaolinite minerals have high pozzolanic activity. However, this research is based on calcareous clay, which is not commonly used as CRM. In this study, calcareous clay was exposed to different conditions for maximum pozzolanic activity and the following conclusions were reached.

- The maximum pozzolanic activity of calcareous clay was obtained at 800 °C.
- Even at the lowest temperature (600 °C) considered within the scope of the study, strength above the limit of TS-25 standard (4 MPa) was obtained.
- Increasing the calcination temperature up to 800 °C positively affected the pozzolanic activity.
- By increasing the calcination temperature to 900 °C, the pozzolanic activity decreased compared to the material calcined at 800 °C.
- Increasing the calcination time positively affected the pozzolanic activity.

Acknowledgments

The authors would like to thank Konya Cement for their support in this study.

References

Bergaya, F., & Lagaly, G. (2013). *Handbook of clay science* (Vol. 5). Newnes.

Bucher, K., Frey, M., Winkler, H.G.F., & Frey, M. (2002). *Petrogenesis of metamorphic rocks*. Springer.

Castillo, R., Fernández, R., Antoni, M., Scrivener, K., Alujas, A., & Martirena, J.F. (2010). Activación de arcillas de bajo grado a altas temperaturas. *Revista Ingeniería de Construcción, 25*(3), 329–352

Fernandez, R., Martirena, F., & Scrivener, K.L. (2011). The origin of the pozzolanic activity of calcined clay minerals: A comparison between kaolinite, illite and montmorillonite. *Cement and Concrete Research, 41*(1), 113–122. https://doi.org/10.1016/j.cemconres.2010.09.013

Frías, M., & Cabrera, J. (2000). Pore size distribution and degree of hydration of metakaolin–cement pastes. *Cement and Concrete Research, 30*(4), 561–569. https://doi.org/10.1016/S0008-8846(00)00203-9

Gruber, K.A., Ramlochan, T., Boddy, A., Hooton, R.D., & Thomas, M.D.A. (2001). Increasing concrete durability with high-reactivity metakaolin. *Cement and Concrete Composites, 23*(6), 479–484. https://doi.org/10.1016/S0958-9465(00)00097-4

Jokar, Z., & Mokhtar, A. (2018). Policy making in the cement industry for CO_2 mitigation on the pathway of sustainable development: A system dynamics approach. *Journal of Cleaner Production, 201*, 142–155. https://doi.org/10.1016/j.jclepro.2018.07.286

Kostuch, J.A., Walters, G.V., & Jones, T.R. (2000). High performance concretes incorporating metakaolin: A review. *Concrete, 2*(1993), 1799–1811

Kurdowski, W., & Pomadowski, H. (2001). Influence of Portland cement composition on pozzolanic reactivity of metakaolin. *Silicates Industriels, 7–8*, 85–90

Monteiro, P.J.M., Miller, S.A., & Horvath, A. (2017). Towards sustainable concrete. *Nature Materials, 16*(7), 698–699. https://doi.org/10.1038/nmat4930

Nawel, S., Mounir, L., & Hedi, H. (2020). Effect of temperature on pozzolanic reaction of Tunisian clays calcined in laboratory. *SN Applied Sciences, 2*(2), 157. https://doi.org/10.1007/s42452-020-1935-9

Rakhimov, R.Z., Rakhimova, N.R., Gaifullin, A.R., & Morozov, V.P. (2017). Properties of Portland cement pastes enriched with addition of calcined marl. *Journal of Building Engineering, 11*, 30–36. https://doi.org/10.1016/j.jobe.2017.03.007

Scrivener, K., Martirena, F., Bishnoi, S., & Maity, S. (2018). Calcined clay limestone cements (LC3). *Cement and Concrete Research, 114*, 49–56. https://doi.org/10.1016/j.cemconres.2017.08.017

Zunino, F., Boehm-Courjault, E., & Scrivener, K. (2020). The impact of calcite impurities in clays containing kaolinite on their reactivity in cement after calcination. *Materials and Structures, 53*(2), 44. https://doi.org/10.1617/s11527-020-01478-9

Corporate carbon footprint analysis of ready-mixed concrete facilities

Bülent Baloğlu[1], Büşra Bosna[2], Orhan Atacan[3], Emrah Yılmaz[*4]

[1] *Bolu Abant İzzet Baysal University, 14100 Bolu, Türkiye*
[2] *Independent Researcher, Türkiye*
[3] *Metsims Sustainability Consulting, İstanbul, Türkiye*
[4] *Düzce University, Department of Civil Engineering, 81100 Düzce, Türkiye*

Abstract. Concrete is one of the most widely used construction materials worldwide, and its production process has a significant impact on global warming and climate change due to its high carbon emissions. Emissions from the use of cement in concrete production trigger climatic imbalances by increasing greenhouse gas intensity. Therefore, determining the carbon footprint of the ready-mixed concrete sector and developing emission reduction strategies are critical for sustainability. In this study, corporate carbon footprint calculation was carried out using 2023 operational data of 28 ready-mixed concrete facilities operating in different regions of Türkiye and it was aimed to determine the processes that cause the highest greenhouse gas emissions within business activities. The calculations were made based on the internationally accepted GHG Protocol, ISO 14064 and IPCC (Intergovernmental Panel on Climate Change) guidelines in the field of greenhouse gas reporting and management. In the study, emission sources related to the ready-mix concrete production process were analyzed comprehensively and sources in Scope 1 (direct emissions), Scope 2 (indirect emissions) and Scope 3 (other indirect emissions) categories were evaluated in detail. The findings showed that the highest emissions across the sector came from Scope 3, followed by Scope 1 and Scope 2. In particular, the largest impact within Scope 3 stems from the category 'Purchased Goods and Services'. It has been determined that the main emission source in Scope 1 is "mobile combustion emissions" (such as vehicles and construction equipment), and in Scope 2 it is "grid electricity use". In the ready-mixed concrete sector, it is a critical step to adopt sustainability policies, especially to reduce Scope 3 emissions, and to promote energy efficiency and the use of alternative raw materials in supply chain processes. In order to reduce Scope 1 emissions, solutions such as low emission engine technologies, use of alternative fuels and fleet management systems can be applied in construction machinery and vehicles. In addition, the use of renewable energy sources and the integration of energy efficient technologies are recommended to reduce Scope 2 emissions.

Keywords: Corporate carbon footprint; ready-mix concrete industry; climate change; sustainability assessment; greenhouse gas emissions

1. Introduction

Today, climate change has become one of the greatest environmental threats to humanity. The intensive use of fossil fuels, rapid industrialization and increasing energy demand constitute the main sources of greenhouse gases (GHG) released into the atmosphere (IPCC, 2022). These emissions threaten ecosystems with consequences such as global temperature increases, melting of polar ice caps, extreme meteorological events and yield losses in agricultural production. This situation has necessitated the development of various strategies at national and international levels to measure and reduce carbon emissions (Bulut et al., 2024).

The concept of 'carbon footprint' has been developed for the calculation of greenhouse gas emissions, and the environmental impacts of sectors can be clearly revealed, especially through assessments made at the corporate scale. The corporate carbon footprint is calculated by determining the direct (Scope 1), indirect (Scope 2) and other indirect (Scope 3) emissions resulting from energy consumption and supply chain processes (Harangozo et al., 2017a; World Resources Institute, 2003). These calculations are based on internationally recognised standards, notably the GHG Protocol, ISO 14064 standard and IPCC guidelines (Ranganathan et al., n.d.).

[*] Corresponding author, E-mail: emrahyilmaz@duzce.edu.tr

https://doi.org/10.31462/icearc2025_ce_mat_107

golden light publishing

The construction sector is one of the sectors that cause high carbon emissions, especially due to cement and concrete production processes and raw material consumption. CO_2, one of the six main greenhouse gases defined in the Kyoto Protocol, is released intensively during the cement production process and this process corresponds to 7-8% of global CO_2 emissions (Downie et al., 2012). According to the data of the European Ready Mixed Concrete Organization (ERMCO), Türkiye ranks high in Europe in both cement consumption and ready-mixed concrete production per capita (European Ready Mixed Concrete Organization, 2020). The 2023 report of the Turkish Ready Mixed Concrete Organization revealed that there is a direct relationship between cement domestic sales and ready-mixed concrete production, and that production in the sector has increased steadily over the years (Turkish Ready Mixed Concrete Organization, 2024).

Despite this, studies on the carbon footprint of ready-mixed concrete plants in Türkiye are limited and there is a need to evaluate emission sources, especially at the institutional level, with a holistic approach. In the limited number of studies in the literature, only the effects of production and transport processes on emissions have been addressed, and the sector-wide emission distribution has not been comprehensively analysed (Çümen et al., 2023).

In this study, the corporate carbon footprint of 28 ready-mixed concrete plants operating in Türkiye was calculated using data for 2023. The calculations were carried out within the framework of the GHG Protocol, ISO 14064 and IPCC guidelines and the processes that cause the highest greenhouse gas emissions within the facility activities were determined. The study aims to contribute to the development of sustainability policies in the ready-mixed concrete sector and to support emission reduction strategies with concrete data.

2. Sustainability and ready-mixed concrete industry

2.1. Corporate sustainability

The concept of sustainability is based on the principle that all living and non-living beings included in the life cycle continue their existence by preserving the existing natural balance of the planet. In this context, sustainability refers to the protection of natural resources without depletion, in a way that will maintain the functioning of the ecosystem, and to meeting the needs of humanity today while not endangering the needs of future generations (United Nations, 1987).

According to the generally accepted approach, sustainability is addressed in three basic dimensions: environmental, social and economic.

- Environmental sustainability aims to protect the environmental resources and conditions that ensure the natural functioning of the ecosystem so that it can continue to exist in the future.
- Social sustainability involves maintaining the welfare of societies in a fair, inclusive and long-term manner and respecting the rights of all life forms.
- oduction and consumption processes within the framework of sustainable resource utilisation and to secure the continuity of economic activities.

The reflection of this triple structure at the corporate level is called corporate sustainability. It is inevitable that organisations create environmental, social and economic impacts during their activities. For this reason, corporate sustainability is related to the fact that businesses recognise these impacts, minimise the negative ones and develop policies to increase the positive impacts (Elkington et al., 1999). This approach is not only a responsibility for the environment and society, but also a strategic imperative that strengthens corporate reputation and supports long-term success.

As the effects of climate change become more apparent each year, the concept of corporate sustainability has gained an important place in the management strategies of businesses. International regulations and incentive mechanisms developed within the framework of the United Nations Sustainable Development Goals (SDGs) are among the elements that increase this importance (United Nations, 2015). In particular, the European Commission plays an active role in the development of legislation to encourage responsibilities towards corporate sustainability. Among the basic policies developed in this context, the determination of labor standards, social management principles, the "polluter pays" principle and producer responsibility policies stand out. These regulations are designed to cover all processes from raw material supply to the final consumer (Herzig Christianand Schaltegger, 2011).

In order for organisations to effectively benefit from such policies and support mechanisms and successfully implement their sustainability strategies, they should firstly determine the environmental impacts of their activities, especially their corporate carbon footprint accurately and comprehensively. After this determination, enterprises are expected to set concrete targets to reduce their carbon footprint and develop action plans that can be implemented within a certain period of time to achieve these targets.

2.2. Corporate carbon footprint

Corporate carbon footprint is an environmental measure obtained by calculating the greenhouse gases emitted directly and indirectly into the atmosphere as a result of the activities of an enterprise in 'tonnes of CO_2 equivalent' (Wiedmann et al., 2007). This calculation forms the basis of sustainability strategies by covering not only an organisation's own operations, but also the emissions generated throughout the supply chain and product life cycle.

In carbon footprint calculations, internationally valid standards such as the Greenhouse Gas Protocol (GHG Protocol) (World Resources Institute, 2003), PAS 2060, ISO 14064 are used. These standards categorise direct (Scope 1), indirect emissions related to energy consumption (Scope 2) and indirect emissions related to the supply chain (Scope 3) and provide detailed guidelines on calculation methods (World Resources Institute, 2011). The most widely used of these methods is the GHG Protocol, which was reported to be implemented by 63% of Fortune 500 companies in 2007 (Harangozo et al., 2017b; *NQA-PAS-2060-Implementation-Guide*, n.d.).

The GHG Protocol is one of the first comprehensive approaches that provides a framework for measuring, monitoring, reporting and reducing greenhouse gas emissions at the organizational level (Kolk et al., 2008). At the same time, this protocol is structured under the ISO 14000 Environmental Management System standard, forming the basis of the ISO 14064 series. The ISO 14064 standard includes principles for organizations to measure, monitor and report their greenhouse gas emissions transparently (Ranganathan et al., n.d.). In comparing these two methodologies, it is seen that the GHG Protocol allows for more voluntary, integrated analyses with market mechanisms such as carbon trading, while ISO 14064 presents the technical requirements for the calculation and verification of greenhouse gas emissions at the organizational level in a more systematic way (Çolak et al., 2023)).

The first stage of corporate carbon footprint calculation is to determine the activity boundaries of the business (such as production, supply, logistics, export). Then, direct and indirect greenhouse gas sources within these boundaries are identified and classified. Carbon footprint calculations are performed based on inventory data prepared by identifying emission sources and applying emission factors. In this process, the six main greenhouse gases defined in the Kyoto Protocol (CO_2, CH_4, N_2O, HFCs, PFCs, SF_6) are taken as basis. The global warming potential (GWP) of each of these greenhouse gases is taken into account and the calculation is made in terms of a common metric, CO_2 equivalent (Çolak et al., 2023).

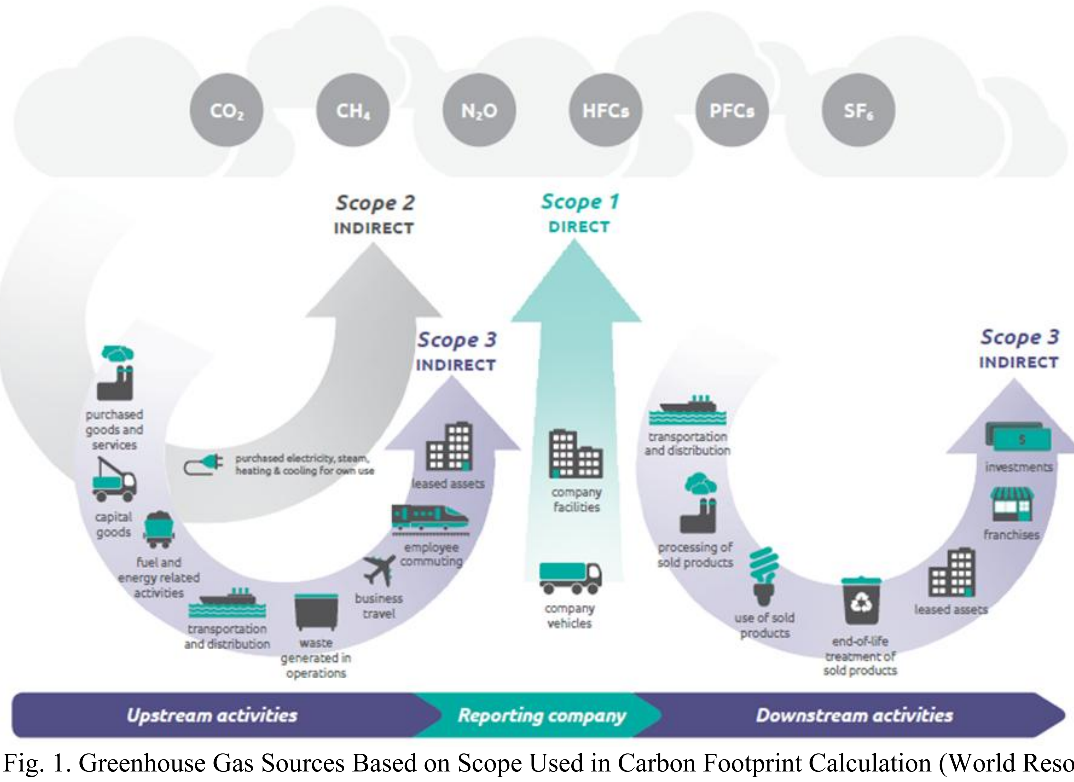

Fig. 1. Greenhouse Gas Sources Based on Scope Used in Carbon Footprint Calculation (World Resources Institue, 2011)

Carbon footprint calculations are classified into three scopes:

- Scope 1: Direct emissions from fixed and mobile sources in the institution's facilities (e.g. fuel use in truck mixers),
- Scope 2: Indirect emissions resulting from the use of externally supplied energy such as electricity, steam, cooling,
- Scope 3: Other indirect emissions related to the supply and use chain, such as raw material supply, transportation, employee transportation, waste management.

The Green Deal policy published by the European Union in 2019 aimed to achieve net zero carbon by 2050 and to decarbonize all sectors in line with this target (European Green Deal Call, 2020). As part of this process, a carbon tax will be gradually applied to imports of products from sectors with high carbon intensity into the EU under the Border Carbon Adjustment Mechanism (CBAM). This application will be evaluated in line with the corporate carbon footprint reports of the enterprises. The sectors included in the scope of the application in the first phase include cement, electricity generation, fertiliser, iron-steel, aluminium, organic chemicals and plastic products. The reason for selecting these sectors is that they significantly contribute to greenhouse gas emissions due to their high energy and raw material use. (World Resources Institue, 2011)

In light of these developments, corporate carbon footprint reporting for industrial sectors has become critical not only in terms of environmental responsibility but also in terms of economic sustainability and international trade harmonisation. As a matter of fact, according to the data in Türkiye's national greenhouse gas inventory, cement production accounts for 49% of greenhouse gas emissions due to industrial production and product use, and 78% of emissions from the mineral industry (Republic of Türkiye, 2023).

2.3. Ready-mixed concrete and cement sector in the World and Türkiye
Cement is one of the basic components of the construction sector and its most intensive use is in the production of ready-mixed concrete. Ready-mixed concrete is an important building material produced using cement-based binders and used directly in construction applications. According to the 2020 data of the European Ready-Mixed Concrete Organization (ERMCO), Türkiye was the country with the highest cement consumption in Europe in 2018 and 2019. In terms of ready-mixed concrete production, Türkiye ranked second after the United States in 2018 and third after Japan in 2019. In terms of production per capita, Türkiye is well above the European average and ranks among the top five countries (Europan Ready Mixed Concrete Organization, 2020).

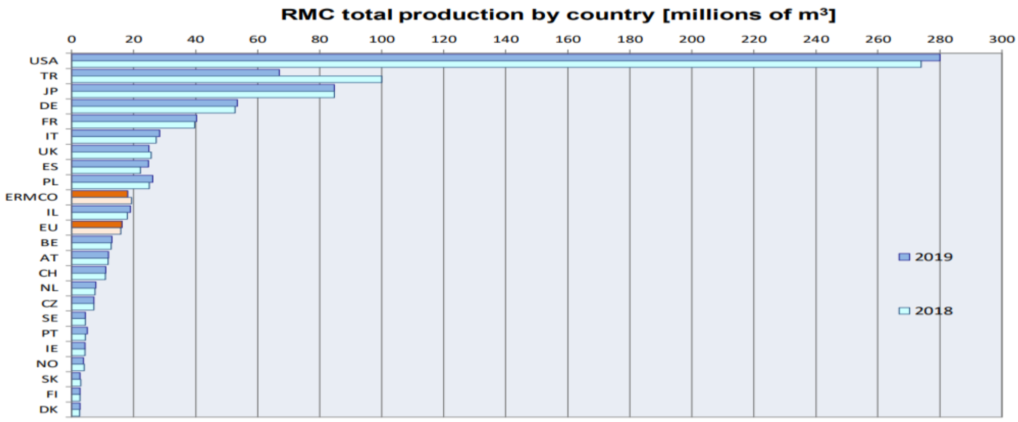

Fig. 2. Total Ready Mixed Concrete Production by Countries (Europan Ready Mixed Concrete Organization, 2020)

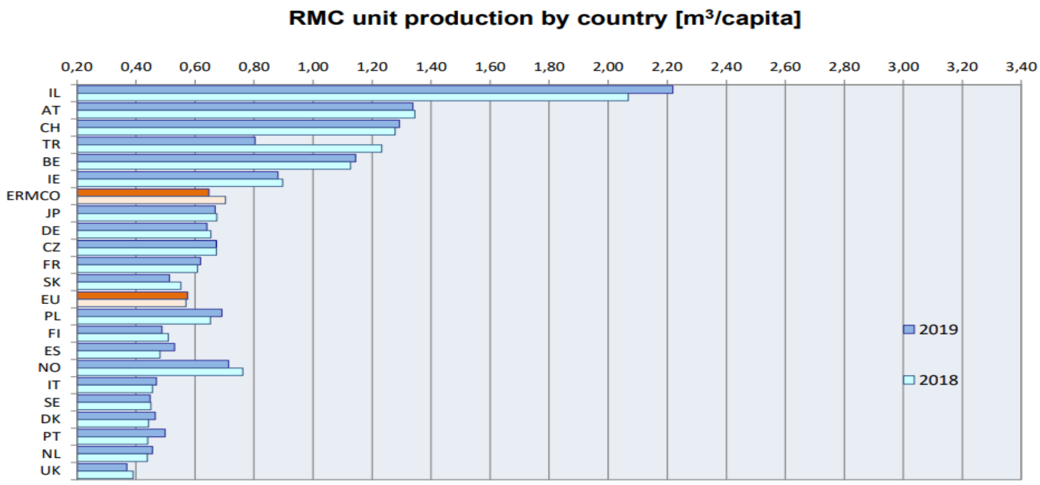

Fig. 3. Ready-mixed Concrete Production Per Capita (Europan Ready Mixed Concrete Organization, 2020)

According to the 2022 “Ready-Mixed Concrete Sector Report” published by the Turkish Ready-Mixed Concrete Association (THBB) in April 2023, ready-mixed concrete production in Türkiye has been showing a continuous increase trend since 1988, excluding the pandemic period. As can be seen in Fig. 9, this increase in production clearly reveals the growth momentum of the sector. In addition, it has been determined that there is a strong linear relationship between domestic sales quantities of cement and ready-mixed concrete production, and that these two variables move together (Turkish Ready-Mixed Concrete Association, 2024).

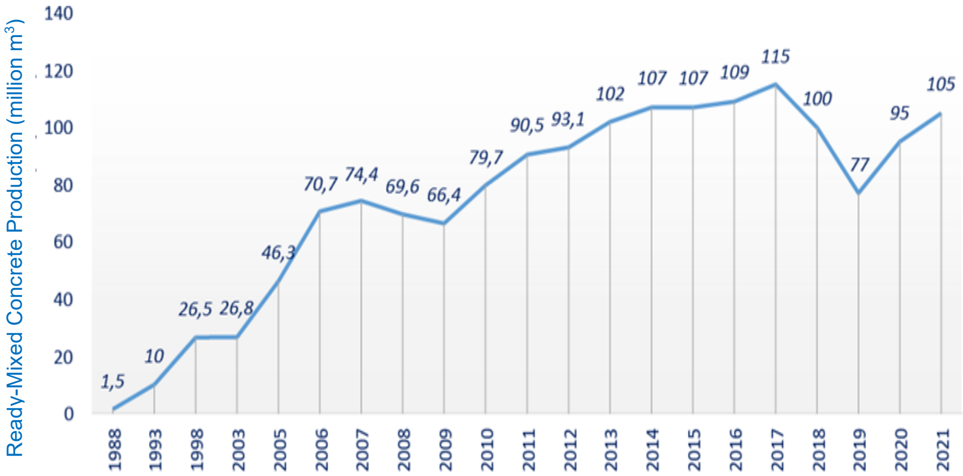

Fig. 4. Ready-mixed concrete production in Türkiye by year (Turkish Ready-Mixed Concrete Association, 2024).

According to the THBB report, the total capacity of ready-mixed concrete plants in Türkiye varies between 225 and 343 million m³. In addition, the total carrying capacity of approximately 18,500 transmixers operating in the country is estimated to be 178 to 305 million m³, and the total capacity of mobile pumps is approximately 110 million m³. Considering that approximately 80% of the ready-mixed concrete produced is poured by mobile pumps, the actual operational capacity is calculated to be around 137.5 million m³ (Turkish Ready-Mixed Concrete Association, 2024).

When the capacity utilization rates were examined, it was determined that 70% of the existing installed capacity was used for 2018 and 50% for 2019 (Europan Ready Mixed Concrete Organization, 2020; Turkish Ready-Mixed Concrete Association, 2024).

In case of an increase in capacity utilisation rates, cement consumption will increase in parallel with this increase and this will lead to an increase in greenhouse gas emissions. In this context, Figure 10, which shows the linear relationship between cement domestic sales and ready-mixed concrete production, demonstrates the importance of the sector in terms of emission potential.

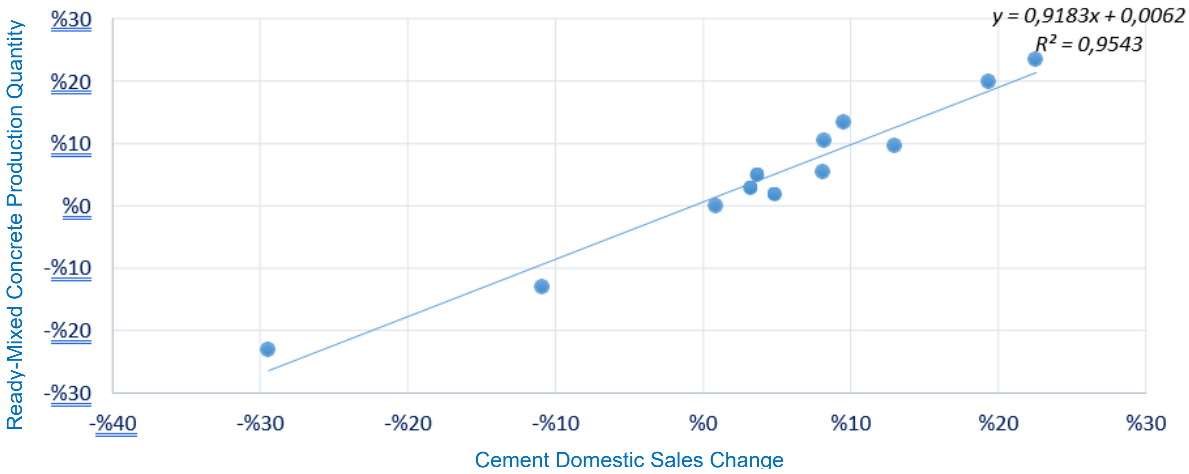

Fig. 5. Cement Domestic Sales - Ready-Mixed Concrete Production Relationship (Turkish Ready-Mixed Concrete Association, 2024)

In order to reduce the environmental impact of the sector, solutions such as low carbon technologies, alternative binders, energy efficiency applications and the use of electric vehicles in transportation processes are gaining importance. The dissemination of such strategies will contribute to the ready-mix concrete sector's compliance with both national climate policies and international obligations shaped within the framework of the European Green Deal.

As a result, the ready-mix concrete sector stands out as the second sector with the highest potential to reduce Türkiye's carbon footprint after the energy sector. The size of the sector and its direct relationship with cement consumption necessitate that this area be evaluated as a strategic priority in policies to combat climate change (Turkish Ready-Mixed Concrete Association, 2024).

3. Materials and methods

3.1. Materials

In this study, 2023 operational data of a total of 28 ready-mixed concrete facilities located in the Marmara, Aegean, Mediterranean, Southeastern Anatolia and Central Anatolia regions of Türkiye were used. The data obtained from the facilities include basic inputs related to production processes such as annual energy consumption, fuel use, electricity consumption, cement and aggregate use. The data were obtained from the corporate reporting systems declared by the facilities and analyzed cumulatively to represent sectoral trends.

The greenhouse gas emission inventory of all facilities was calculated under the categories of Scope 1 (direct emissions), Scope 2 (indirect emissions) and Scope 3 (other indirect emissions) within the scope of the corporate carbon footprint. In the calculation of Scope 1 and Scope 2 data, the "Cement Carbon Dioxide and Energy Protocol, Version 3.1" published by the World Business Council for Sustainable Development – Cement Sustainability Initiative was used (World Business Council for Sustainable Development (WBCSD), 2011). This protocol details the calculation methods for cement and ready-mixed concrete plants, taking into account the main emission sources such as direct fuel use and electricity consumption.

Scope 3 emissions are determined within the framework of the Greenhouse Gas Protocol - Corporate Value Chain (Scope 3) Standard and in line with the operational control principle (Schmitz et al., 2004; World Business Council for Sustainable Development (WBCSD), 2011; World Resources Institute, 2003). In this approach, indirect emissions arising from processes that the organisation controls operationally (e.g. purchased materials, transport, business travel, etc.) are taken into account.

The data obtained were evaluated by classifying them separately on the basis of scopes, and the emission amounts for each scope were calculated in terms of CO_2 equivalent (tCO_2e).

3.2. Method: Calculation approach and methodological framework

Carbon footprint calculations are based on internationally accepted methodological standards. Scope 1 and Scope 2 emissions are calculated based on activity data such as fuel consumption (natural gas, diesel, etc.) and electricity consumption using the following basic formula:

Emission (kg CO_2e)=Activity Data×Emission Factor

- Activity Data: Refers to primary data such as the amount of fuel consumed (liter, m^3), electricity consumption (kWh).
- Emission Factor (EF): These are greenhouse gas emission coefficients determined for each type of activity, taken from the IPCC 2006 guidelines, WBCSD protocol and literature specific to Türkiye.

For Scope 1, calculations were made based on fossil fuels consumed in equipment such as truck mixers, construction equipment and stationary boilers.

In Scope 2 calculations, grid electricity consumption was taken as the basis and the Turkish National Electricity Emission Factor was used.

Scope 3 emissions were calculated based on processes such as purchased goods and services, including inputs such as cement and aggregates, pre-production and post-production transportation-logistics activities, transportation activities resulting from employee services and business trips, and disposal of waste generated in facilities.

In Scope 3 calculations, the operational control approach was adopted and the processes managed by the organization were taken as the limit. In cases where direct measurements were not made for activity data, sector averages and representative values taken from the literature were used.

The total emission amounts obtained were not normalized specifically for the facility; they were evaluated as a cumulative total reflecting the general trend of the sector.

4. Results and discussion

Technical details regarding emission values calculated within the scope of Scope 1 are presented in Table 1. In this table, fuel types, annual consumption amounts, net calorific values, emission factors and CO_2 equivalent outputs are systematically given.

Table 1. Distribution of scope 1 emissions by source in ready-mixed concrete facilities

Category	Emission Source	Annual Consumption (kg)	Net Calorific Value (TJ/gg)	Energy (TJ)	Emission Factor ($kgCO_2/TJ$)	CO_2 Emission (ton CO_2e)
Constant Combustion	Local Coal	5.000.000	11,9	59.50	101.000	6.009,50
	Natural gas	3.350	48,0	0.16	56.100	9.02
Fugitive Emissions	-	-	-	-	-	259.20
Mobile Emissions	-	-	-	-	-	11,141.44

Scope 1 covers the direct greenhouse gas emissions of ready-mixed concrete facilities. These emissions generally arise from the combustion of fossil fuels and the use of production vehicles. According to data collected from 28 facilities across Türkiye, total Scope 1 emissions as of 2023 are calculated as 17,419.16 tons of CO_2 equivalent (tCO_2e).

The largest share in this total belongs to emissions from mobile sources (transmixers, construction equipment). Mobile emissions constitute 64.0% of total Scope 1 emissions, revealing the high emission potential of fossil fuel-fired transportation equipment in the sector. Domestic coal used as solid fuel follows this with 34.5%. Fugitive emissions and emissions related to natural gas use have very low rates in the total (1.5% and 0.1%, respectively).

These findings show that measures such as fuel conversion, more efficient machine use and especially the transition to electric vehicle technologies in the ready-mixed concrete sector are of great importance in terms of reducing Scope 1 emissions.

Scope 2 emissions are indirect greenhouse gas emissions resulting from the consumption of electrical energy supplied from external sources, other than direct fuel use in ready-mixed concrete facilities, and the relevant calculations in this study are presented in Table 2.

Table 2. Scope 2 Emissions based on electricity consumption of ready mixed concrete plants

Emission source	Total Consumption(kWh)	Emission Factor(tCO_2e/MWh)	Total Emission (tCO_2e)
Electric	4,044.306	0.439	1,775.45

The total electricity consumption of 28 ready-mixed concrete facilities in this study was determined as 4,044,306 kWh. The location-based electricity emission factor for Türkiye for 2023 is taken as 0.439 tonnes CO_2e/MWh (Ministry of Energy and Natural Resources, 2024). Accordingly, the total Scope 2 emission calculated was found as 1,775.45 tonnes CO_2e.

Scope 3 emissions cover greenhouse gas emissions that are outside the direct control of ready-mixed concrete facilities but are caused indirectly along the operational chain, and the relevant emissions are presented in detail in Table 3 in this study.

Table 3. Scope 3 Emissions in Ready-Mixed Concrete Industry and Their Activity-Based Distribution

Category	Activity Description	Value (tonnes CO_2e/year)
Purchased Goods and Services	Purchased cement, aggregates and other materials	80.588,04
Capital Goods	Facility and equipment investments	4.770,28
Related to Fuel and Energy Faaliyetler	Indirect fuel and energy consumption	2.946,52
Transportation of Purchased Goods	Supply chain transportation (cement, aggregate logistics)	10.012,39
Wastes Generated in Operations	Industrial wastes originating from the facility	1,25
Business Trips	Emissions from service vehicles and business trips	19,85
Home-to-Work Transport	Personnel shuttle and transportation emissions	376,43
Downstream Transport and Distribution	Shipment of ready-mixed concrete (transport to the customer)	1.646,25
Processing of Sold Products	The product does not require energy, water or material input during its use, and there is no need for maintenance, repair or replacement. Therefore, product performance is assumed to be equal to the life of the building.	-
End of the Life of Products Sold	Effects that occur at the end of the concrete's life	9.515,26
TOTAL		109.876,27

As seen in Table 3, scope 3 emissions are calculated as approximately 18,131.49 tons CO_2e. The majority of this value originates from the "Purchased Goods and Services" category, which includes inputs such as cement and aggregates, accounting for 79.4% of the total. This ratio reveals the environmental impacts of supply chain processes and shows how critical it is to turn to low-carbon alternatives in the material supply phase. This category is followed by the Transportation of Purchased Goods and End of Life of Sold Products categories, which account for 9.1% of total emissions, respectively. The distribution of total emissions based on scope in corporate carbon footprint calculations of ready-mixed concrete facilities is presented in Table 4.

Table 4. Total emission distribution by scope

Scope	Emission Amount (tons CO_2e)	Share within Total Emission (%)
Scope 1 (Direct)	17,419.16	13.7%
Scope 2 (Indirect)	1,775.45	1.4%
Scope 3 (Other Indirect)	109,876.27	84.9%
Total	129,070.88	100%

As seen in Table 4, when the corporate carbon footprint emissions of the ready-mix concrete sector are examined, Scope 3 emissions are in the first place, accounting for 84.9% of total emissions. This is followed by Scope 1 emissions with 13.7%, while Scope 2 emissions have the lowest share with 1.4%. This distribution shows that environmental impacts in the sector are largely caused by the supply chain and indirect processes.

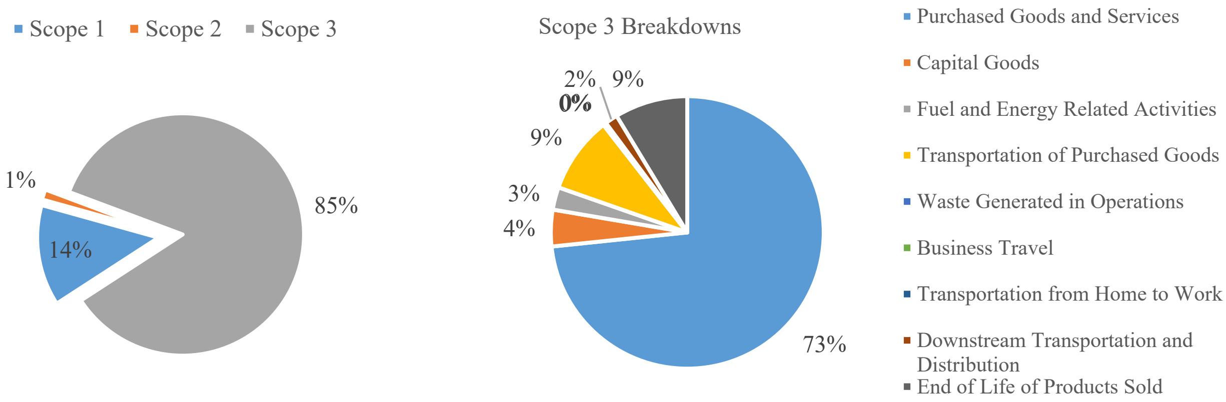

Fig. 6. Corporate Carbon Footprint Distribution: Scopes and Scope 3 Breakdowns

As shown in Fig. 6, scope 3 emissions are mainly caused by purchased materials (cement, aggregate and other materials) and their transport processes. This situation shows that not only the production processes but also the supply chain in the ready-mixed concrete sector should be closely monitored in terms of environmental impacts. Scope 1 emissions are predominantly caused by mobile sources (transit mixers and construction equipment), which points to the importance of fleet transformation, alternative fuel technologies and logistics optimisation strategies in the sector. Although the share of Scope 2 emissions in the total is quite low, it is possible to reduce them further through approaches such as switching to renewable energy and implementing ISO 50001 energy management systems.

5. Conclusions

In this study, a corporate carbon footprint calculation was carried out by evaluating the 2023 operational data of 28 ready-mixed concrete plants operating in five different regions of Türkiye. The calculations are handled separately under Scope 1, 2 and 3 headings within the framework of GHG Protocol, ISO 14064 and IPCC guidelines.

The obtained findings show that 84.9 % of the total carbon footprint originates from Scope 3, 13.7 % from Scope 1 and only 1.4 % from Scope 2. This situation reveals that the environmental impact in the ready-mixed concrete industry is largely caused by purchased materials and supply chain processes.

Accordingly, the following recommendations have been developed to reduce the carbon footprint of the industry:

- For Scope 3: The use of low-carbon alternative materials should be encouraged for inputs with high carbon footprints such as cement and aggregates. Material selection should be made with suppliers based on "environmental product declarations (EPD)". Transportation distances should be reduced in logistics processes, and alternative (e.g. electric) transportation solutions should be supported.

- For Scope 1: Fleet transformation programs should be initiated to reduce fossil fuel use in vehicles and construction equipment. Alternative fuels (biodiesel, HVO, etc.) and digital solutions that increase operational efficiency should be evaluated.
- For Scope 2: Transition to renewable energy should be ensured and the energy needs of the facilities should be met from sources such as solar and wind. Energy consumption should be reduced and energy management systems such as ISO 50001 should be implemented.

As a result, the ready-mixed concrete industry is one of the areas, other than the energy sector, that has the greatest potential to help Turkey achieve its net zero targets. The data obtained in this study has the potential to create a strong reference for the industry to develop holistic and science-based strategies on carbon management.

References

Bulut, G., & Özer, M. A. (2024). Ekolojik modernleşmeye iklim değişikliği ve "çevresel ayak izleri" üzerinden bakmak. *Çankırı Karatekin Üniversitesi İktisadi ve İdari Bilimler Fakültesi Dergisi*, 14(3), 752–778. https://doi.org/10.18074/ckuiibfd.1503754 (In Turkis).

World Business Council for Sustainable Development. (2011). *Cement Sustainability Initiative (CSI): The Cement CO_2 and Energy Protocol (Version 3.1)*. Retrieved from http://www.ecra-online.org/

Çolak, G., & Atilgan Türkmen, B. (2023). Kurumsal karbon ayak izi analizi: Bir kimya fabrikası için örnek hesaplama. *Doğal Afetler ve Çevre Dergisi*, 9(1), 191–201. https://doi.org/10.21324/dacd.1120858 (In Turkis).

Downie, J., & Stubbs, W. (2012). Corporate carbon strategies and greenhouse gas emission assessments: The implications of scope 3 emission factor selection. *Business Strategy and the Environment*, 21(6), 412–422. https://doi.org/10.1002/bse.1734

Elkington, J., & Rowlands, I. H. (1999). Cannibals with forks: The triple bottom line of 21st century business. *Alternatives Journal*, *25*(4), 42.

Enerji ve Tabii Kaynaklar Bakanlığı. (2024). *Türkiye elektrik üretimi ve elektrik tüketim noktası emisyon faktörleri bilgi formu (Doküman No: ETKB-EVÇED-FRM-042, Rev.01)*. https://enerji.gov.tr/evced-cevre-ve-iklim-elektrik-uretim-tuketim-emisyon-faktorleri (In Turkis).

European Ready Mixed Concrete Organization. (2020). *ERMCO-2019*. Brussels. Retrieved from http://www.ermco.eu

European Commission. (2020). A European Green Deal. Retrieved from *https://commission.europa.eu/strategy-and-policy/priorities-2019-2024/european-green-deal_en*

Harangozo, G., & Szigeti, C. (2017). Corporate carbon footprint analysis in practice: With a special focus on validity and reliability issues. *Journal of Cleaner Production*, 167, 1177–1183. https://doi.org/10.1016/j.jclepro.2017.07.237

Herzig, C., & Schaltegger, S. (2011). Corporate sustainability reporting. In J. Godemann & G. Michelsen (Eds.), *Sustainability communication: Interdisciplinary perspectives and theoretical foundation* (pp. 151–169). Springer. https://doi.org/10.1007/978-94-007-1697-1_14

Intergovernmental Panel on Climate Change. (2022). *Global warming of 1.5°C*. Cambridge University Press. https://doi.org/10.1017/9781009157940

Kolk, A., Levy, D., & Pinkse, J. (2008). Corporate responses in an emerging climate regime: The institutionalization and commensuration of carbon disclosure. *European Accounting Review*, 17(4), 719–745. https://doi.org/10.1080/09638180802489121

Republic of Türkiye. (2023). National inventory report for submission under the United Nations Framework Convention on Climate Change.

NQA. (n.d.). PAS 2060 implementation guide. Retrieved from *https://www.nqa.com/en-gb/certification/standards/pas-2060*

Ranganathan, J., Corbier, L., Schmitz, S., Oren, K., Dawson, B., Spannagle, M., et al. (2004). *The GHG Protocol: A corporate accounting and reporting standard (Revised Edition)*. World Resources Institute & World Business Council for Sustainable Development.

Schmitz, S., Dawson, B., Spannagle, M., Thomson, F., Koch, J., & Eaton, R. (2004). The Greenhouse Gas Protocol - A Corporate Accounting and Reporting Standard, Revised Edition. *The GHG Protocol Corporate Accounting and Reporting Standard*, *9*.

Türkiye Hazır Beton Birliği. (2024). *Hazır beton sektör raporu–2023*. İstanbul. Retrieved from https://www.thbb.org/ (In Turkis).

Çümen, U., & Sarıkaya, H. (2023). Hazır beton santralinin karbon emisyonlarının belirlenmesi. *Bingöl Üniversitesi Teknik Bilimler Dergisi*. (In Turkis).

United Nations. (1987). *Report of the World Commission on Environment and Development: Our common future*. Oxford University Press.

United Nations. (2015). *Transforming our world: The 2030 Agenda for Sustainable Development*. https://sdgs.un.org/2030agenda

Wiedmann, T., & Minx, J. (2007). *A Definition of "Carbon Footprint" ISA UK Research Report 07-01*. Retrieved from www.censa.org.uk

World Resources Institute. (2003). *World resources 2002–2004*. United Nations Development Programme.

World Resources Institute. (2011). *Corporate value chain (scope 3) accounting and reporting standard: Supplement to the GHG Protocol corporate accounting and reporting standard*. Retrieved from https://ghgprotocol.org/standards/scope-3-standard

4th International Civil Engineering & Architecture Conference
15-17 May 2025, Trabzon, Türkiye

Utilizing design of experiment method to optimize the mixture of polymer concrete against tensile and shear type fracture

D. Imani[1], A. Rajabi-Kafshgar[1], M.R.M Aliha[*1,2], M. Ghahremani Darvish[1,3], A. Shafiei[1], N. Sani[1]

[1] *Welding and Joining Research Center, School of Industrial Engineering, Iran University of Science and Technology (IUST), 16846-13114,Tehran, Iran.*
[2] *Department of Mechanical Engineering, Engineering Faculty, Gebze Technical University, 41400 Gebze, Kocaeli, Turkiye.*
[3] *Faculty of Art, Semnan University, 35131-19111, Semnan, Iran.*

Abstract. Polymer concrete (PC) is a type of concrete that can be made by mixing different components, namely (i) a polymeric resin, (ii) fine and coarse aggregate and filler materials, and (iii) reinforcing fiber materials in suitable percentages. This material has specific applications in different civil structures. Mechanical and strength properties in such multi-ingredient composite materials is affected by the type and dosage of the components. The usage of design of experiment (DoE) methods (such as Taguchi) can help the PC designers in determining the optimum mix design parameters to obtain the best achievable strength and mechanical properties with lesser number of laboratory experiments. Fracture toughness (i.e., the resistance of cracked material) against tensile (mode I) and shear (mode II) loads and deformations, is a key and important design parameter for assessing the integrity and service life in the PC materials having dominantly brittle and quasi-brittle fracture nature in real field applications. Thus, in this work, the Taguchi method was employed to find the optimum percentages of a fiber reinforced PC mixture (with main ingredients of polyester resin + fine and coarse grain size silicious aggregate) to achieve the optimum K_{IC} and K_{IIC} (i.e., modes I and II fracture toughness values). The initial window of input variables was considered in the following ranges: 0%<glass fiber<2%, 40%<coarse aggregate<55%, 20%<fine aggregate<36%, and 12%<Polyester resin <30%. The required fracture toughness experiments were done using the semi-circular-bend test loaded with symmetric span (for mode I) and asymmetric span (for mode II) according to a L32 Taguchi DoE technique. Based on the performed fracture experiments, the optimum percentages of PC ingredients were obtained in such way that the greatest possible fracture toughness values under both tensile and shear modes are achieved. The obtained results showed the significant role of loading mode on the optimum mix design of the PC mixture.

Keywords: Polymer concrete; Optimum mixture design; Taguchi design of experiment; modes I and II Fracture toughness (K_{IC} and K_{IIC}); Cracked semi-circular bend test

1.Introduction

Recent developments in civil engineering have led to an increased focus on materials that can substantially improve the performance and strength of a range of components, such as soil, asphalt, concrete, and other elements used in construction (Baradaran et al., 2024; Baradaran et al., 2024; Baradaran et al., 2023). These materials not only contribute to improving mechanical properties but also offer numerous benefits in terms of cost-effectiveness and overall functionality (Niri et al., 2024; Baradaran & Ameri, 2023; Baradaran & Aliha, 2025). Research in this area has been on the rise, as these materials can improve the durability and efficiency of structures while helping to reduce construction costs and the need for repairs (Pargar et al., 2024; Tareghian et al., 2024; Ayar et al., 2022; Baradaran & Ziaee, 2025). Polymeric concrete (PC) is a type of structural concrete that has some important and particular applications in civil and structural engineering such as in pavements of roads and bridges, manufacturing high-strength slabs, repair of concrete structures, etc. PC material has some benefits compared to the ordinary cement or plain concrete mixtures such as higher strength and mechanical properties, faster curing and construction process, and smaller thickness of the concrete layer. Achieving such characteristics is mainly due to the replacement of cement and water with resin as the binder of the heterogeneous mixture of aggregates inside the

* Corresponding author, E-mail: mrm_aliha@iust.ac.ir

https://doi.org/10.31462/icearc2025_ce_mat_163

matrix of polymeric resins. A PC material is therefore composed of coarse and fine aggregates (with typically 70–80% by weight of the mixture) and polymeric resin (such as polyester or epoxy with typically 20–30% of the mixture). Sometimes, some additives such as micro fillers, reinforcing fibers (e.g., glass fiber), or even agricultural and industrial waste materials are added to the PC mixture for filling the air voids and enhancing the performance and mechanical properties of these materials (Kujawa et al., 2021; Martinez-Barrera et al., 2022; Daneshfar et al., 2017).

Brittle or quasi-brittle fracture is one of the major failure modes in the PC mixtures. The fracture toughness value in these materials depends on the composition of the PC mixture and ingredients used for manufacturing the PC. However, in comparison with the common mechanical properties, including compressive and flexural bending strength, very few studies are available regarding the fracture and cracking resistance behavior of PC materials and its relationship with the mixture composition (Aliha et al., 2022; Karamzadeh et al., 2022; Niaki et al., 2023; Asdollah-Tabar et al., 2021). Due to the wide range of variables and several possible mix designs available for manufacturing a PC material, it is necessary to use optimization methods for obtaining the suitable PC mix design. The effective factors in manufacturing an optimum PC mixture can be identified by optimization and design of experiments (DOE) methods. The Taguchi method is among the well-known DOE techniques that can suggest a minimum number of experiments by determining the prominent control factors (Roy, 2001). Mohebi et al. (2015) explored the abrasion resistance of alkali-activated slag concrete using the Taguchi method and confirmed the applicability of this method for the proper design of the experiment and optimization of alkali-activated slag concrete parameters to maximize the compressive strength and wear resistance. Jafari et al. (2018) applied the Taguchi method for optimizing the mixture of PC materials. Tanyildizi (2018) also examined the long-term mechanical properties and microstructure of polymer-phosphazene concrete subjected to repeated freezing-thawing mechanisms. However, the review of literature indicates that there is no comprehensive work on the mix design optimization of PC mixtures to obtain the best fracture toughness (i.e., resistance values) against crack growth under tensile (mode I) and shear (mode II) deformations. Therefore, in this research, the optimum percentage of PC ingredients for achieving high fracture toughness (K_{IC} and K_{IIC}) values is studied experimentally using the Taguchi method.

2.PC mix design using Taguchi method

The PC mixture of the current research is composed of four basic ingredients namely (1) fiber glass fiber (chopped strand shape with length of 7 mm and diameter of 0.01 mm), (2) polyester resin (as adhesive), (3) coarse cilicious aggregate (with nominal size of 4 mm) and fine silica fine grain filler (with nominal size of 0.5 mm). Based on the previous related works, the initial window weight percentages of these four input variables were considered as: 0%<GF<2%, 40%<CA<55%, 20%<FA<36% and 12%<PR <30%, in which GF, CA, FA and PR stand for “Glass Fiber”, “Coarse Aggregate”, “Fine Aggregate” and “ Polyester Resin”, respectively.

In experimental design, optimizing process parameters often requires a large number of trials, especially when multiple factors and levels are involved. A full factorial design considering 4 factors each at (4, 4, 4, and 2) levels would require 128 experiments. This approach, while exhaustive, is time-consuming and resource-intensive. The Taguchi method offers an efficient alternative by employing orthogonal arrays to systematically investigate the effects of multiple parameters with a reduced number of experiments. In this study, the L32 orthogonal array was utilized to design the experiments, and the fracture toughness in mode I and mode II were measured as the primary outputs to evaluate fracture performance. Table 1 represents the parameters and their levels.

Table 1. Parameter levels of L32 Taguchi optimization

Factors	Level 1	Level 2	Level 3	Level 4
GF (%)	0-1	1.5-2	-	-
PR (%)	14-18	18.5-22	22.5-26	26.5-30
CA (%)	40-43	43.5-47	47.5-51	51.5-55
FA (%)	20-24	24.5-28	28.5-32	32.5-36

3. Fracture toughness tests on PC mixtures under modes I and II modes

The SCB test configuration is among suitable samples for conducting fracture toughness tests on civil engineering materials such as concrete, asphalt, rock, and soil (Aliha et al., 2024; Mubaraki & Sallam, 2020; Mirsayar et al., 2017; Erarslan & Aliha, 2025; Aliha, 2019; Aliha et al., 2022; Azar et al., 2015; Aliha et al., 2023; Pirmohammad et al., 2024; Najjar et al., 2023; Fang & Fall, 2020; Tutluoglu et al., 2022; Aliha et al., 2016; Ayatollahi et al., 2011). This test specimen has simple geometry, simple manufacturing, and testing procedure for the aim of fracture toughness testing. Fig. 1 shows the geometry and loading conditions of the SCB sample for conducting fracture

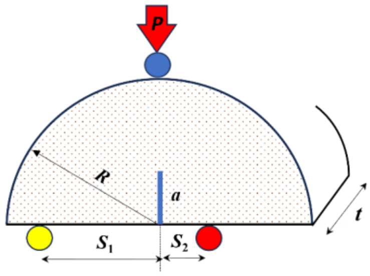

Fig. 1: The use of SCB specimen for conducting fracture toughness tests under mixed mode I/II conditions.

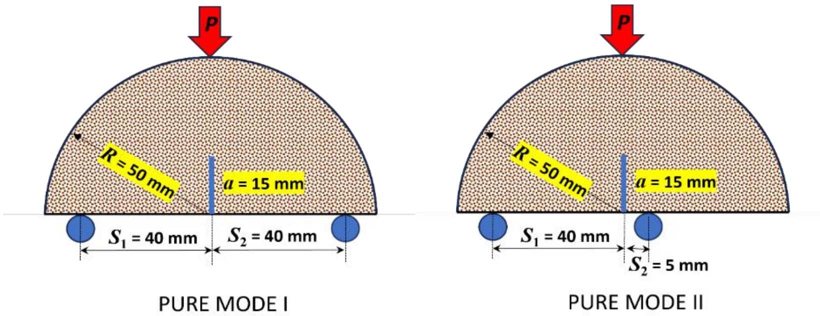

Fig. 2: Overall dimensions of the SCB samples, crack length and the support distances utilized for PC fracture tests under pure mode I and pure mode II.

toughness tests under any desired mode mixtures including mode I (opening or tensile mode) and mode II (shearing mode). Indeed, by setting the bottom loading supports in appropriate locations relative to the crack, any desired ratio of mode I and mode II (such as pure modes tensile and shear) deformations can be achieved (Aliha et al., 2022; Aliha et al., 2016; Ayatollahi et al., 2011). In this research, the SCB sample with the geometry and dimensions illustrated in Fig. 2 was utilized for conducting pure mode I (i.e., with symmetric boundary conditions or span lengths) and pure mode II (i.e., with asymmetric boundary conditions or spans).

Several PC mixtures and PC designs suggested by the Taguchi DoE method were manufactured (according to dimensions given in Fig. 2) to conduct the fracture toughness tests. All the manufactured SCB samples had the same thickness of t = 25 mm. The PC mixtures were cast inside the semi-circular shape molds to create edge cracked SCB samples and loaded monotonically using a test machine having the loading capacity of 10 kN. The dimensions of the test samples and locations of loading rollers for conducting the mode I and mode II tests are given in Fig. 2. Using the peak load or maximum loads (P_{max}) recorded by the load cell of the test sample for each PC sample and mixture, the related values of mode I fracture toughness (K_{IC}) and mode II fracture toughness (K_{IIC}) were determined from Eqs. 1 and 2 (Aliha et al. 2016,2019).

$$K_{IC} = \frac{4.85Pmax}{2Rt}\sqrt{\pi a} \tag{1}$$

$$K_{IIC} = \frac{1.87P}{2Rt}\sqrt{\pi a} \tag{2}$$

4.Results and discussion

Table 2 summarises the results of mode I and mode II fracture toughness data obtained for different PC mixtures with different ingredients (i.e., GF, FA, CA, and PR contents and percentages). Based on theses experimental data obtained from the symeetric and asymmetric SCB tests the PC mixture has significant effect on modes I and II fracture toughness of polymeric concrete materials. based on the PC mix design and the percentage of ingredeints, the mode I fracture toughness (K_{IC}) value varies in the range of 1.3 MPa.m$^{0.5}$ and 3.2 MPa.m$^{0.5}$. The corresponding range for the variations of K_{IIC} value (mode II fracture toughness) with the change of PC mixture is 1.15 MPa.m$^{0.5}$ < K_{IIC}< 3.15 MPa.m$^{0.5}$.

The analysis of the results revealed that the input parameters exhibited a generally similar influence on both fracture toughness indicators, namely K_{IC} and K_{IIC}. Among all factors, the polyester resin (RP) demonstrated a dominant effect on both output responses, highlighting its critical role in determining the mechanical behavior of the PC mixture. Based on the Main Effects Plot (Fig. 3), it was observed that the factors glass fiber content (GF), polyester resin (PR), and coarse aggregate (CA) had comparable effects on K_{IC} and K_{IIC}. Specifically, for both responses, the most favorable outcomes were achieved at level 1 of GF (ranging from 0% to 1%), level 4 of PR (ranging from 26.5% to 30%), and level 1 of CA (ranging from 40% to 43%). These levels consistently produced higher values for both fracture toughness modes.

Table 2. The parameter levels in the experiment tests and related outputs.

Test	Parameters								Outputs	
	GF levels		FA levels		PR levels		CA levels		K_{IC} $(MPa\sqrt{m})$	K_{IIC} $(MPa\sqrt{m})$
1	1	0.0%	4	32.5%	4	26.5%	1	41.0%	1.65	1.64
2	1	0.0%	2	27.0%	4	30.0%	1	43.0%	2.64	2.54
3	1	0.0%	1	23.0%	4	30.0%	2	47.0%	2.56	2.33
4	1	0.0%	3	29.0%	3	25.0%	2	46.0%	2.75	2.73
5	1	0.0%	2	25.0%	3	25.0%	3	50.0%	2.62	2.60
6	1	0.0%	4	33.0%	3	25.0%	1	42.0%	2.89	2.85
7	1	0.0%	1	20.0%	4	27.0%	4	53.0%	3.04	2.91
8	1	1.0%	4	36.0%	1	16.0%	2	47.0%	1.96	1.92
9	1	1.0%	3	29.0%	1	16.0%	4	54.0%	1.56	1.47
10	1	1.0%	2	27.0%	1	17.0%	4	55.0%	2.32	2.14
11	1	1.0%	3	31.0%	2	21.0%	2	47.0%	1.75	1.66
12	1	1.0%	4	36.0%	2	20.0%	1	43.0%	3.19	3.17
13	1	1.0%	1	23.0%	3	25.0%	3	51.0%	1.32	1.22
14	1	1.0%	1	23.0%	2	21.0%	4	55.0%	2.00	1.81
15	1	1.0%	4	32.5%	4	26.5%	1	40.0%	2.98	2.88
16	1	1.0%	2	27.0%	2	21.0%	3	51.0%	2.67	2.43
17	2	2.0%	2	27.0%	1	16.0%	4	55.0%	1.71	1.64
18	2	2.0%	1	23.0%	3	24.0%	3	51.0%	2.21	2.03
19	2	2.0%	3	31.0%	2	20.0%	2	47.0%	1.22	1.15
20	2	2.0%	3	29.0%	1	15.0%	4	54.0%	1.55	1.41
21	2	2.0%	4	33.0%	3	23.0%	1	42.0%	2.34	2.29
22	2	2.0%	1	23.0%	2	20.0%	4	55.0%	1.92	1.88
23	2	2.0%	2	27.0%	2	20.0%	3	51.0%	1.29	1.26
24	2	2.0%	2	27.0%	4	28.0%	1	43.0%	1.87	1.70
25	2	2.0%	4	36.0%	2	19.0%	1	43.0%	1.39	1.38
26	2	2.0%	1	20.0%	4	26.5%	4	51.5%	2.91	2.70
27	2	2.0%	3	29.0%	3	23.0%	2	46.0%	1.69	1.68
28	2	2.0%	4	36.0%	1	15.0%	2	47.0%	1.48	1.33
29	2	2.0%	3	31.0%	1	16.0%	3	51.0%	3.06	2.81
30	2	2.0%	2	25.0%	3	23.0%	3	50.0%	3.19	2.89
31	2	2.0%	3	31.0%	1	17.0%	3	50.0%	2.72	2.69
32	2	2.0%	1	23.0%	4	28.0%	2	47.0%	2.37	2.37

The analysis of the results revealed that the input parameters exhibited a generally similar influence on both fracture toughness indicators, namely K_{IC} and K_{IIC}. Among all factors, the polyester resin (RP) demonstrated a dominant effect on both output responses, highlighting its critical role in determining the mechanical behavior of the PC mixture. Based on the Main Effects Plot (Fig. 3), it was observed that the factors glass fiber content (GF), polyester resin (PR), and coarse aggregate (CA) had comparable effects on K_{IC} and K_{IIC}. Specifically, for both responses, the most favorable outcomes were achieved at level 1 of GF (ranging from 0% to 1%), level 4 of PR (ranging from 26.5% to 30%), and level 1 of CA (ranging from 40% to 43%). These levels consistently produced higher values for both fracture toughness modes.

However, the behavior of K_{IC} and K_{IIC} based on fiber alignment (FA) showed some discrepancies. To better understand the optimal setting for FA, the Interaction Plot (Fig. 4) was analyzed. By fixing GF at level 1, it was found that level 4 of FA (corresponding to the range of 32.5% to 36%) provided the highest values for both K_{IC} and K_{IIC}. Therefore, it can be concluded that in designing a polymer composite (PC) mixture, the selection of ingredients that result in GF and CA at level 1, and PR and FA at level 4, is expected to yield the maximum fracture toughness in both mode I and mode II.

5. Conclusions

The effect of mix design on the fracture toughness (i.e., the resistance of material against cracking) was investigated experimentally for the polymeric concrete (PC) mixture. The Taguchi design of experiment (DoE) technique was employed to select the input variables (GF, CA, FA, and PR) and their levels (2 levels for the GA and 4 levels for the other input variables). Accordingly, 32 different PC mixtures were designed, and modes I and

II fracture toughness tests were conducted using the SCB sample. The results showed that the PC mixture has noticeable effect on both K_{IC} and K_{IIC} values. The optimum percentages of PC ingredients for obtaining the highest fracture toughness values under tensile and shear type failure were as follows: Glass Fiber content = [0-1]%, Fine Aggregate content = [32.5-36]%, Coarse Aggregate = [40-43]%, and Polyester Resin content = [26.5-30]%.

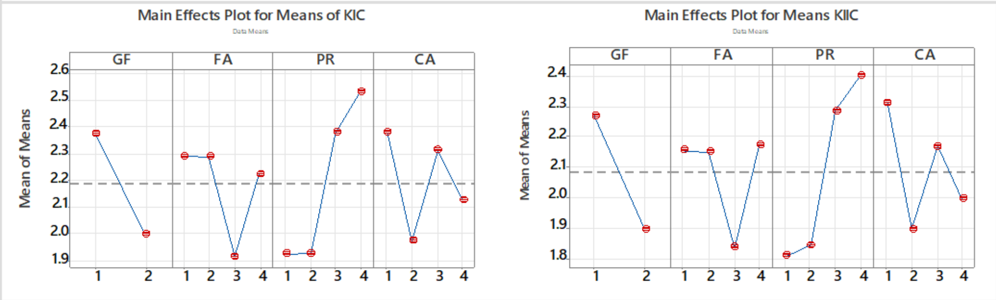

Fig. 3. The main effect plot of fracture test outputs.

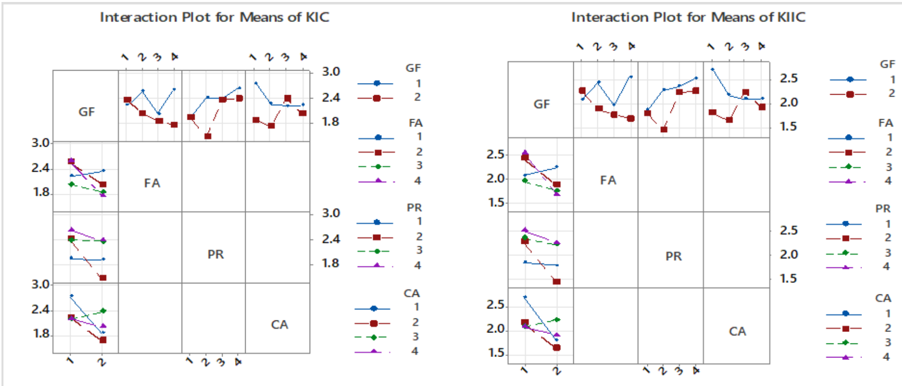

Fig. 4. The interaction effect plot of fracture test outputs.

References

Aliha, M. R. M. (2019). On predicting mode II fracture toughness (KIIc) of hot mix asphalt mixtures using the strain energy density criterion. *Theoretical and Applied Fracture Mechanics*, *99*, 36-43.

Aliha, M. R. M., Bahmani, A., & Akhondi, S. (2016). Mixed mode fracture toughness testing of PMMA with different three-point bend type specimens. *European Journal of Mechanics-A/Solids*, *58*, 148-162.

Aliha, M. R. M., Haghighatpour, P. J., & Tavana, A. (2022). Application of asymmetric semi-circular bend test for determining mixed mode I+ II fracture toughness of compacted soil material. *Engineering Fracture Mechanics*, *262*, 108268.

Aliha, M. R. M., Kosarneshan, K., Salehi, S. M., Haghighatpour, P. J., & Mousavi, A. (2023). On the statistical prediction of K Ic and G Ic for railway andesite ballast rock using different three-point bend disc samples. *Rock Mechanics and Rock Engineering*, *56*(7), 5181-5202.

Aliha, M. R. M., Kouchaki, H. G., Mohammadi, M. H., Haghighatpour, P. J., Choupani, N., Asadi, P., ... & Sadowski, T. (2024). Fracture toughness determination for epoxy-based polymer concrete mixtures: Applicability of different rectangular beam and circular disc specimens. *Composites Part C: Open Access*, *14*, 100446.

Aliha, M. R. M., reza Karimi, H., & Abedi, M. (2022). The role of mix design and short glass fiber content on mode-I cracking characteristics of polymer concrete. *Construction and Building Materials*, *317*, 126139.

Asdollah-Tabar, M., Heidari-Rarani, M., & Aliha, M. R. M. (2021). The effect of recycled PET bottles on the fracture toughness of polymer concrete. *Composites Communications*, *25*, 100684.

Ayar, P., Baradaran, S., & Abdipour Vosta, S. (2022). A review on the effect of various additives on mechanical properties of stone mastic asphalt (SMA). Road, 30(110), 57-86.

Ayatollahi, M. R., Aliha, M. R. M., & Saghafi, H. (2011). An improved semi-circular bend specimen for investigating mixed mode brittle fracture. *Engineering Fracture Mechanics*, *78*(1), 110-123.

Azar, H. F., Choupani, N., Afshin, H., & Moghadam, R. H. (2015). Effect of mineral admixtures on the mixed-mode (I/II) fracture characterization of cement mortar: CTS, CSTBD and SCB specimens. *Engineering Fracture Mechanics*, *134*, 20-34.

Baradaran, M. S., Qazanfari, R., & Baradaran, S. (2023). Study of soil reinforcement in the east of Mashhad using glass granule. Materials research express, 10(5), 055202.

Baradaran, S., & Aliha, M. R. M. (2025). Mode I and Mode II fracture assessment of green asphalt pavements containing plastic waste and RAP at low and intermediate temperature. Results in Engineering, 25, 103734.

Baradaran, S., & Ameri, M. (2023). Investigation of rutting failure in asphalt mixtures and its improvement strategies. Road, 31(114), 53-70.

Baradaran, S., & Ziaee, S. A. (2025). Review of the Mechanical Properties of Asphalt Pavement Reinforced with Natural Plant Fibers as an Eco-Friendly Solution in Pavement Engineering. Road.

Baradaran, S., Aliha, M. R. M., Maleki, A., & Underwood, B. S. (2024). Fracture properties of asphalt mixtures containing high content of reclaimed asphalt pavement (RAP) and eco-friendly PET additive at low temperature. Construction and building materials, 449, 138426.

Baradaran, S., Rahimi, J., Ameri, M., & Maleki, A. (2024). Mechanical performance of asphalt mixture containing eco-friendly additive by recycling PET. Case studies in construction materials, 20, e02740.

Daneshfar, M., Hassani, A., Aliha, M. R. M., & Berto, F. (2017). Evaluating mechanical properties of macro-synthetic fiber-reinforced concrete with various types and contents. *Strength of Materials*, *49*, 618-626.

Erarslan, N., & Aliha, M. R. M. (2025). Fracture and Damage Analysis of Cement-Stabilized Fine and Coarse Grain Soils Under Static and Cyclic Loading Using Chevron-Notched SCB Specimen. *Fatigue & Fracture of Engineering Materials & Structures*.

Fang, K., & Fall, M. (2020). Insight into the mode I and mode II fracture toughness of the cemented backfill-rock interface: Effect of time, temperature and sulphate. *Construction and Building Materials*, *262*, 120860.

Jafari, K., Tabatabaeian, M., Joshaghani, A., & Ozbakkaloglu, T. (2018). Optimizing the mixture design of polymer concrete: An experimental investigation. *Construction and Building Materials*, *167*, 185-196.

Karamzadeh, N. S., Aliha, M. R. M., & Karimi, H. R. (2022). Investigation of the effect of components on tensile strength and mode-I fracture toughness of polymer concrete. *Arabian Journal of Geosciences*, *15*(13), 1213.

Kujawa, W., Olewnik-Kruszkowska, E., & Nowaczyk, J. (2021). Concrete strengthening by introducing polymer-based additives into the cement matrix—A mini review. *Materials*, *14*(20), 6071.

Martinez-Barrera, G., Gencel, O., & Martinez-Lopez, M. (2022). Polyester polymer concrete modified by polyester fibers and gamma rays. *Construction and Building Materials*, *356*, 129278.

Mirsayar, M., Shi, X., & Zollinger, D. (2017). Evaluation of interfacial bond strength between Portland cement concrete and asphalt concrete layers using bi-material SCB test specimen. *Engineering Solid Mechanics*, *5*(4), 293-306.

Mohebi, R., Behfarnia, K., & Shojaei, M. (2015). Abrasion resistance of alkali-activated slag concrete designed by Taguchi method. Construction and Building Materials, 98, 792-798.

Mubaraki, M., & Sallam, H. E. M. (2020). Reliability study on fracture and fatigue behavior of pavement materials using SCB specimen. *International Journal of Pavement Engineering*, *21*(13), 1563-1575.

Najjar, S., Moghaddam, A. M., Sahaf, A., & Aliha, M. R. M. (2023). Mixed mode (I&III) fracture behavior of cement emulsified asphalt mortar under freeze and thaw cycles. *Theoretical and Applied Fracture Mechanics*, *126*, 103952.

Niaki, M. H., Ahangari, M. G., Izadi, M., & Pashaian, M. (2023). Evaluation of fracture toughness properties of polymer concrete composite using deep learning approach. *Fatigue & Fracture of Engineering Materials & Structures*, *46*(2), 603-615.

Niri, S. R., Akhtarpour, A., Daliri, F., & Baradaran, M. S. (2024). Experimental investigation of dewatering silty tailings using electrokinetic method. Canadian Geotechnical Journal.

Pargar, J., Akhtarpour, A., & Baradaran, M. S. (2024). An unsaturated soil mechanics-based numerical and experimental method to assess soil settlement due to ground water level rise. Transportation Infrastructure Geotechnology, 11(5), 3621-3646.

Pirmohammad, S., Momeni, R., & Khanghahi, S. H. (2024). Effect of SCB specimen size on mode I fracture parameters of asphalt concrete at low and intermediate temperatures. *Theoretical and Applied Fracture Mechanics*, *130*, 104314.

Roy, R. K. (2001). *Design of experiments using the Taguchi approach: 16 steps to product and process improvement*. John Wiley & Sons.

Tanyildizi, H. (2018). Long-term microstructure and mechanical properties of polymer-phosphazene concrete exposed to freeze-thaw. *Construction and Building Materials*, *187*, 1121-1129.

Tareghian, B., Baradaran, M. S., & Akhtarpour, A. (2024). The effect of sand-crumb rubber mixture treatment on the seismic response of a low-rise building located on liquefiable soil. Discover Geoscience, 2(1), 11.

Tutluoglu, L., Batan, C. K., & Aliha, M. R. M. (2022). Tensile mode fracture toughness experiments on andesite rock using disc and semi-disc bend geometries with varying loading spans. *Theoretical and Applied Fracture Mechanics*, *119*, 103325.

4th International Civil Engineering & Architecture Conference
17-19 May 2025, Trabzon, Türkiye

Assessment of the Utilization of Grinding Aids in terms of Grinding Efficiency and Environmental Impact

Veysel Kobya[1], Yahya Kaya[1], Ali Mardani[*1]

[1] *Bursa Uludağ University, Department of Civil Engineering, 16059 Bursa, Türkiye*

Abstract. Cement production is particularly notable in energy efficiency studies due to its high energy consumption and substantial greenhouse gas emissions. Approximately two-thirds of the total energy consumption in cement production occurs during the grinding stage. Grinding aids (GAs) are utilized to enhance energy efficiency and reduce environmental impact during clinker grinding. While the primary mechanisms of action are understood, the effects of GAs in cement production are still largely based on theoretical information. The identification of high-performance GAs is particularly challenging due to the complexity of the selection criteria. Amine- and glycol-based GAs are commonly used in practice. This study aims to evaluate the utilization of amine- and glycol-based GAs in terms of grinding efficiency and environmental impact, calculated based on CO_2 emissions and electrical energy consumed during grinding. Triisopropanolamine (TIPA), diethylene isopropanolamine (DEIPA), and diethylene glycol (DEG) were incorporated at a concentration of 0.05 wt.% relative to the combined mass of clinker and gypsum-a standard industry practice-to achieve a target Blaine fineness of 3500 ± 100 cm²/g. Four CEM I 42.5R type cements were prepared, including a control cement without GA. Grinding efficiency and environmental impact were assessed based on the time and number of cycles required to reach the target Blaine fineness. A grinding efficiency improvement ranging from 8% to 14% was achieved through the incorporation of grinding aids, independent of their chemical composition. In terms of both grinding efficiency and environmental impact, TIPA and DEG were found to be the highest and lowest performers, respectively.

Keywords: Grinding aids; TIPA; DEIPA; DEG; Grinding efficiency

1. INTRODUCTION

Greenhouse gas emissions, air pollution, and climate change are among the primary contributors to global environmental crises. Addressing these challenges has emphasized the importance of developing alternative products that emit less CO_2 during manufacturing, expanding the use of renewable energy sources, and improving energy efficiency (Boesch & Hellweg, 2010; Zhang et al., 2015).

The 2015 Paris Climate Agreement established a target to limit the rise in global temperatures to 1.5 °C annually. This commitment aims to protect coral reefs and the associated ecosystems at risk of collapse by the end of the century (Darby, 2018). In alignment with this global goal, Turkey has pledged to cut its greenhouse gas emissions by 21% by 2030. Within the country, the energy sector is the dominant source of emissions, accounting for 86.1%, followed by industrial operations and consumption activities at 13.6% (Dulkadiroğlu, 2018).

Among the most energy-intensive and polluting industries is the cement sector, due to its substantial use of raw materials and high CO_2 emissions. The sector accounts for approximately 2% of total global electricity use and 5% of the industrial electricity demand, contributing to 5–7% of total global CO_2 emissions (Madlool et al., 2011). Producing one ton of cement requires about 1.2 tons of raw materials and 130 kWh of energy, which leads to the emission of nearly 1 ton of CO_2 (ICS, 2009; Mardani-Aghabaglou, 2016).

Clinker grinding represents nearly 35% of the total energy consumption in cement manufacturing. A considerable portion of this energy is dissipated as heat, noise, and vibrations. In efforts to lower both production costs and associated CO_2 emissions, the application of grinding aids (GAs) has gained prominence (Jankovic et al., 2004; Zhang et al., 2015; Kaya et al., 2024.a–2024.b). Ethanolamines such as triethanolamine (TEA), diethanolamine (DEA), monoethanolamine (MEA), and triisopropanolamine (TIPA), as well as glycols like ethylene glycol (EG) and propylene glycol (PG), are among the most commonly employed GA types to enhance grinding efficiency (Jolicoeur et al., 2007; Assaad, 2015; Zhang et al., 2015; Sun et al., 2020; Kobya et al., 2022).

[*] Corresponding author, E-mail: ali.mardani16@gmail.com

https://doi.org/10.31462/icearc2025_ce_mat_178

Despite numerous studies exploring the operational mechanisms of GAs during clinker grinding, the full scope of their interactions remains unclear (Mishra et al., 2017; Sun et al., 2016; Sun et al., 2020). The prevailing hypothesis suggests two main effects: a physicochemical interaction that reduces the surface energy of particles, and an influence on particle alignment and flow characteristics (Choi et al., 2010; Prziwara et al., 2018.a; Chipakwe et al., 2020).

GAs adhere to particle surfaces through their polar functional groups (e.g., –OH, $–NH_2$, –COOR, $–SO_3$), altering the electrical charge landscape and preventing crack closure, particle agglomeration, and material buildup on mill liners or media (Jeknavorian et al., 1998; Assaad and Issa, 2014). This promotes better dispersion and improves grinding effectiveness. Interestingly, cement produced with GAs may exhibit identical Blaine fineness values yet differ in surface energy, significantly impacting hydration behavior and admixture compatibility (Katsioti et al., 2009). Moreover, GA-modified cements are generally composed of smaller, smoother particles with reduced angularity (Ma et al., 2015). Several studies have further evaluated the impact of different types and dosages of GAs on grinding performance (Katsioti et al., 2009; Assaad, 2015; Sun et al., 2020; Kobya et al., 2022; Kaya et al., 2024.a).

Katsioti et al. (2009) examined the effectiveness of six different GA formulations by blending varying proportions of triethanolamine (TEA) and triisopropanolamine (TIPA). These formulations—ranging from 100% TEA to 95% TIPA-were dosed at 0.015%, and yielded grinding efficiency improvements of 14%, 10%, 13%, 20%, 22%, and 26%, respectively, over the control sample. The results indicated that formulations with higher TIPA content exhibited superior performance, emphasizing the correlation between the chemical composition and grinding enhancement.

Assaad (2015) evaluated the efficiency of diethylene glycol (DEG) and propylene glycol (PG) as GAs at dosages of 0.028% and 0.053%, reporting performance increases of 10% and 18%, respectively. The residue on the 90 μm sieve decreased from 2.76% in the reference cement to 1.27% and 0.9% with increasing GA dosage, suggesting enhanced generation of fine particles with higher additive concentration.

In another study, Sun et al. (2020) investigated glycerin as a GA at incremental dosages of 0.01% to 0.04%, achieving grinding improvements of 16%, 25%, 25%, and 33%, respectively. Surface energy measurements confirmed this enhancement, decreasing from 65–130 mJ/mm² in the reference cement to 59–98 mJ/mm² in the 0.04% glycerin-modified cement, supporting glycerin's effectiveness as a GA.

Despite numerous studies demonstrating improved grinding performance through various GAs, there remains a gap in research concerning the quantifiable environmental benefits—particularly reductions in CO_2 emissions and energy usage. Therefore, the current study focused on assessing the grinding and environmental performance of amine- and glycol-based GAs. Specifically, TIPA, DEIPA, and DEG were used at 0.05% dosage (by total weight of clinker and gypsum) to produce four CEM I 42.5R cements, including one without GA as a control. Grinding efficiency was assessed based on the time and number of cycles needed to reach a target Blaine fineness of 3500 ± 100 cm²/g. The environmental performance was determined by calculating the energy and CO_2 savings resulting from improved grinding efficiency.

2. Materials and methods

2.1. Materials

In this study, CEM I 42.5R type cements were produced by grinding a mixture containing 96% clinker and 4% gypsum in a laboratory-scale ball mill until achieving the target Blaine fineness of 3500 ± 100 cm²/g, in accordance with the TS EN197-1 standard. The cement produced without the addition of any GA is designated as R (reference), while the cements incorporating GAs are labeled according to the specific GA used. The key physical and chemical characteristics of the clinker, gypsum, and fly ash utilized in the experiments are presented in Table 1.

Table 1. Some properties of clinker and gypsum

Component	Chemical Content (%)	
	Clinker	Gypsum
SiO_2	21.52	4.98
Al_2O_3	5.43	1.21
Fe_2O_3	3.31	0.83
CaO	65.38	28.94
MgO	1.04	0.83
SO_3	0.38	39.67
Na_2O+0.658 K_2O	0.83	0.37
Cl	0.01	-
Combined Water (T<230º)	-	18.93
Other, %	1.58	4.24
Loss of igniton	0.52	

Similarly, Table 2 summarizes the main physical and chemical properties of the grinding aids employed.

Table 2. Some physical and chemical properties of the GAs used

GA type	Alkaline content (%) (Na_2O)	Density (g/cm^3)	Solid content (%)	Chloride content (%)	pH. 25°C	Number of Functional Groups
TIPA	<10	1.124	50.0	<0.1	10.8	3
DEIPA	<10	1.079	50.0	<0.1	9.7	3
DEG	<10	1.118	50.0	<0.1	7.2	2

2.2. Methods

As part of the experimental procedure, clinker and gypsum were initially subjected to size reduction using a jaw crusher. The crushed clinker was subsequently sieved to a particle size of 3.35 mm, in accordance with the Bond Standard, to prepare it for grinding.

The grinding process was performed using a Bond-type laboratory ball mill with a 5 kg capacity and a 1.5 kW motor, as illustrated in Fig. 1.

The Blaine fineness of the ground cements was measured using an automatic Blaine apparatus, depicted in Fig. 2.

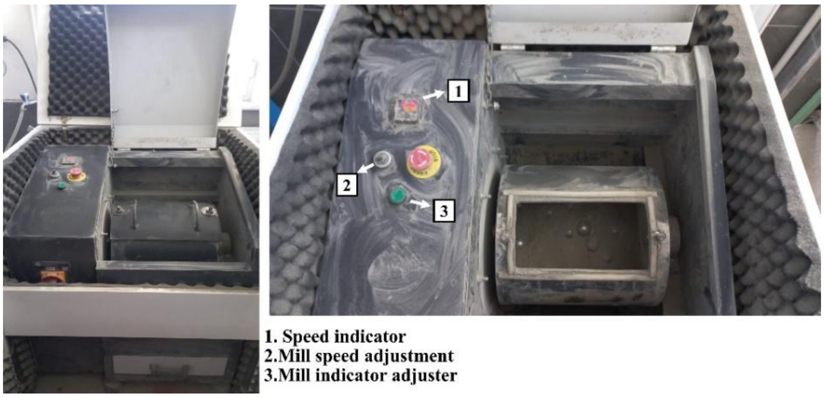

Fig. 1. The ball mill

Fig. 2. Automatic Blaine device

The energy consumption of the mill during the grinding process was calculated using Equation 1.

$$Eg = (220 \times Tg \times A \times 1000) / (m \times Tg) \quad (1)$$

Here, Eg represents the grinding energy (kWh/ton), Tg is the grinding time (hour), A denotes the amperage, m refers the feed amount (kg) and Tg refers the mill factor, a constant value of 4 provided by the manufacturer.

Based on data from the Turkish Cement Manufacturers Association, Turkey's cement production in 2023 reached approximately 65 million tons (Turkish Cement Manufacturers Association, 2023). According to the 2021 national electricity grid emission factor report published by the Ministry of Energy and Natural Resources of the Republic of Turkey, the emission factor for electricity consumption was reported as 0.7258 tCO_2/MWh (Turkish National Grid Emission Factor Data, 2021; Savaş, 2021). Using this information, the potential reduction in annual energy consumption and associated CO_2 emissions from the use of GAs in cement grinding processes was estimated for the Turkish cement industry.

3. Result and Discussions

3.1 Grinding efficiency

Figure 3 presents the grinding energies (kWh), calculated using Equation 1, for each cement produced with and without GA to achieve the target Blaine fineness (3500 ± 100 cm^2/g), along with the corresponding relative grinding efficiencies compared to the reference cement.

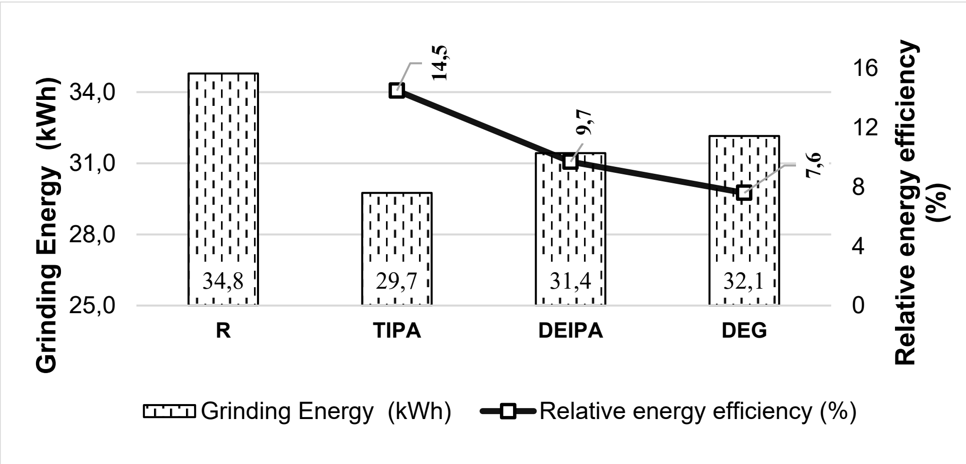

Fig. 3. Grinding energies (kWh) for each cement and corresponding relative grinding efficiencies compared to the reference cement

As illustrated in Figure 3, the use of TIPA, DEIPA, and DEG as grinding aids resulted in energy savings of 14.5%, 9.7%, and 7.6%, respectively, relative to the reference cement. As illustrated, the amine-based additives TIPA and DEIPA demonstrated higher grinding efficiency compared to the glycol-based DEG, consistent with findings reported in earlier studies (Assaad et al., 2009; Prziwara et al., 2018.b; Kobya et al., 2022). The superior performance of TIPA compared to DEIPA was attributed to the enhanced fluidity effect imparted by the CH_3 group present in its molecular structure (Chen et al. 2024).

3.1 Envorimental impact

Based on the obtained data, the influence of GA application on annual electrical energy consumption and CO_2 emissions associated with the cement grinding process in Turkey was evaluated. A summary of the estimated outcomes is presented in Table 3.

Table 3. Some physical and chemical properties of the GAs used

Energy efficiency and CO_2 Emission	R	TIPA	DEIPA	DEG
Amount of cement produced annually in Turkey, kiloton		64854		
Energy consumed in the grinding phase in the production of 1 ton of cement, kWh	34,8	29,7	31,4	32,1
Total energy consumed in clinker grinding in Turkey, GWh	2256	1929	2038	2085
Provided energy savings, GWh	-	327	218	171
The amount of CO_2 released from the electricity consumed during grinding, kiloton	1637	1400	1479	1513
Amount of avoided CO_2 emissions, kiloton	-	237	158	124

As presented in Table 3, the application of GAs in Turkey's annual cement production could lead to energy savings between 171 and 327 GWh. Based on the data reported by Karaca (2012), the annual electricity consumption of a typical family with two children in Turkey is approximately 2600 kWh. Accordingly, the use of TIPA, DEIPA, and DEG could potentially offset the annual electricity consumption of 126,000, 84,000, and 66,000 families, respectively. Furthermore, the adoption of TIPA, DEIPA, and DEG is expected to prevent 237, 158, and 124 kilotons of CO_2 emissions, respectively.

Assuming that an average tree sequesters around 12 kg (0.012 tons) of CO_2 annually through photosynthesis (Argun et al., 2019), the associated reduction in carbon footprint can be estimated. In the absence of GA, the annual CO_2 emissions from clinker grinding amount to approximately 1,637 kilotons, which is equivalent to the sequestration capacity of about 165.5 million trees. The application of TIPA reduces this number to 117 million trees, while DEIPA and DEG further decrease it to 123 million and 126 million trees, respectively.

4. Conclusions

This study examines the grinding efficiency and environmental impacts of commonly used Gas-DEIPA, TIPA, and DEG. The key findings from the experiments are summarized below.

- Regardless of the type of GA employed, it was found that grinding efficiency, CO_2 emission reduction, and more environmentally sustainable production could be achieved through the use of GAs.
- In terms of grinding efficiency, amine-based additives outperformed glycol-based DEG additives, with TIPA providing the highest and DEG the lowest contributions.
- Similarly, in terms of environmental impact, TIPA and DEG were the top and lowest performers, respectively. However, it is important to note that DEG, despite its lower efficiency in grinding, offers significant energy savings and environmental benefits compared to the reference cement.

Acknowledgments

The authors wish to sincerely thank the Scientific and Technological Research Council of Turkey (TÜBİTAK) for their support through project grant number [222M245]. They also appreciate the valuable contributions of the Bursa Uludağ University Science and Technology Centre (BAP), provided through grant number [FGA-2024-1754]. The corresponding author would like to thank the Turkish Academy of Sciences (TÜBA).

References

Argun, M. E., Ergüç, R., & Sarı, S. A. Y. (2019). Konya/Selçuklu ilçesi karbon ayak izinin belirlenmesi. *Selçuk Üniversitesi Mühendislik, Bilim ve Teknoloji Dergisi, 7*(2), 287–297. (In Turkish)

Assaad, J. J. (2015). Assessment of rheology variations of cement pastes containing clinker grinding aids compliant with ASTM C465. *Advances in Civil Engineering Materials, 4*(1), 94–114. https://doi.org/10.1520/ACEM20140038

Assaad, J. J., & Issa, C. A. (2014). Effect of clinker grinding aids on flow of cement-based materials. *Cement and Concrete Research, 63*, 1–11. https://doi.org/10.1016/j.cemconres.2014.04.006

Assaad, J. J., Asseily, S. E., & Harb, J. (2009). Effect of specific energy consumption on fineness of portland cement incorporating amine or glycol-based grinding aids. *Materials and Structures, 42*, 1077–1087.

Boesch, M. E., & Hellweg, S. (2010). Identifying improvement potentials in cement production with life cycle assessment. *Environmental Science & Technology, 44*(23), 9143–9149.

Chen, J., Jia, J., & Zhu, M. (2024). Understanding the effect of alkali content on hydration, hardening, and performance of Portland cement: A comprehensive review. *Materials Today Communications*, 109728.

Chipakwe, V., Semsari, P., Karlkvist, T., Rosenkranz, J., & Chelgani, S. C. (2020). A critical review on the mechanisms of chemical additives used in grinding and their effects on the downstream processes. *Journal of Materials Research and Technology, 9*(4), 8148–8162.

Choi, H., Lee, W., Kim, D. U., Kumar, S., Kim, S. S., Chung, H. S., ... & Ahn, Y. C. (2010). Effect of grinding aids on the grinding energy consumed during grinding of calcite in a stirred ball mill. *Minerals Engineering, 23*(1), 54–57.

Darby, M. (2018). *Five ways 2°C global warming is worse than 1.5°C.* http://www.climatechangenews.com/2016/04/21/five-ways-2c-global-warming-isworse-than-1-5c/

Dulkadiroğlu, H. (2018). Türkiye'de elektrik üretiminin sera gazı emisyonları açısından incelenmesi. *Niğde Ömer Halisdemir Üniversitesi Mühendislik Bilimleri Dergisi, 7*(1), 67–74.

ICS. (2009). *Cement technology roadmap 2009: Carbon emission reduction up to 2050*. World Business Council for Sustainable Development, Conches-Geneva, Switzerland.

Jankovic, A., Valery, W., & Davis, E. (2004). Cement grinding optimisation. *Minerals Engineering, 17*(11–12), 1075–1081. https://doi.org/10.1016/j.mineng.2004.06.031

Jeknavorian, A. A., Barry, E. F., & Serafin, F. (1998). Determination of grinding aids in Portland cement by pyrolysis gas chromatography-mass spectrometry. *Cement and Concrete Research, 28*(9), 1335–1345. https://doi.org/10.1016/S0008-8846(98)00109-4

Jolicoeur, J., Morasse, S., Sharman, J., Tagnit-Hamou, A., Slim, F., & Page, M. (2007). Polyol-type compounds as clinker grinding aids: Influence of powder fluidity and on cement hydration. In *12th International Congress on the Chemistry of Cement* (pp. 1–6).

Karaca, C. (2012). *Güneş ve rüzgar enerjisinden elektrik enerjisi üretimi sistemi tasarımı* (Master's thesis). Selçuk Üniversitesi, Fen Bilimleri Enstitüsü. (In Turkish)

Katsioti, M., Tsakiridis, P. E., Giannatos, P., Tsibouki, Z., & Marinos, J. (2009). Characterization of various cement grinding aids and their impact on grindability and cement performance. *Construction and Building Materials, 23*(5), 1954–1959. https://doi.org/10.1016/j.conbuildmat.2008.09.003

Kaya, Y., Kobya, V., & Mardani, A. (2024a). Evaluation of fresh state, rheological properties, and compressive strength performance of cementitious system with grinding aids. *Journal of Applied Polymer Science, 141*(15), e55212.

Kaya, Y., Kobya, V., Mardani, A., & Assaad, J. J. (2024b). Effect of modified triethanolamine on grinding efficiency and performance of cementitious materials. *Talanta Open, 9*, 100293.

Kobya, V., Kaya, Y., & Mardani-Aghabaglou, A. (2022). Effect of amine and glycol-based grinding aids utilization rate on grinding efficiency and rheological properties of cementitious systems. *Journal of Building Engineering, 47*, 103917.

Ma, S., Li, W., Zhang, S., Hu, Y., & Shen, X. (2015). Study on the hydration and microstructure of Portland cement containing diethanol-isopropanolamine. *Cement and Concrete Research, 67*, 122–130.

Madlool, N. A., Saidur, R., Hossain, M. S., & Rahim, N. A. (2011). A critical review on energy use and savings in the cement industries. *Renewable and Sustainable Energy Reviews, 15*(4), 2042–2060.

Mardani-Aghabaglou, A. (2016). *Investigation of cement-superplasticizer admixture compatibility* (PhD thesis). Ege University, Engineering Faculty, Civil Engineering Department, İzmir. https://tez.yok.gov.tr/UlusalTezMerkezi/

Mishra, R. K., Weibel, M., Müller, T., Heinz, H., & Flatt, R. J. (2017). Energy-effective grinding of inorganic solids using organic additives. *CHIMIA International Journal for Chemistry, 71*(7–8), 451–460.

Prziwara, P., Breitung-Faes, S., & Kwade, A. (2018a). Impact of the powder flow behavior on continuous fine grinding in dry operated stirred media mills. *Minerals Engineering, 128*, 215–223.

Prziwara, P., Breitung-Faes, S., & Kwade, A. (2018b). Impact of grinding aids on dry grinding performance, bulk properties and surface energy. *Advanced Powder Technology, 29*(2), 416–425.

Savaş, D. Ö. (2021). *Bursa İnegöl ilçesi sera gazı envanterinin çıkarılması ve iklim değişikliği eylem planı kapsamında sera gazı azaltım planı* (Master's thesis). Bursa Uludağ Üniversitesi. (In Turkish)

Sun, Z., Liu, H., Ji, Y., & Pang, M. (2020). Influence of glycerin grinding aid on the compatibility between cement and polycarboxylate superplasticizer and its mechanism. *Construction and Building Materials, 233*, 117104. https://doi.org/10.1016/j.conbuildmat.2019.117104

Sun, Z., Yang, H., Shui, L., Liu, Y., Yang, X., Ji, Y., ... & Luo, Q. (2016). Preparation of polycarboxylate-based grinding aid and its influence on cement properties under laboratory condition. *Construction and Building Materials, 127*, 363–368. https://doi.org/10.1016/j.conbuildmat.2016.10.007

Zhang, T., Gao, J., & Hu, J. (2015). Preparation of polymer-based cement grinding aid and their performance on grindability. *Construction and Building Materials, 75*, 163–168. https://doi.org/10.1016/j.conbuildmat.2014.10.046

4th International Civil Engineering & Architecture Conference
17-19 May 2025, Trabzon, Türkiye

Experimental investigation of the effects of bolt and nut configurations on the tensile capacity of wind turbine flange connections

Nisanur Isık*1, Fatih Alemdar[1]

[1] Yıldız Technical University, Department of Civil Engineering, 34025 Istanbul, Türkiye

Abstract. The growing global energy demand, greenhouse gas emissions from fossil fuels contributing to global warming and climate change, and the environmental and societal risks associated with nuclear energy have made the adoption of renewable energy sources essential. The need to develop and utilize renewable energy to preserve the planet's natural ecosystem has become increasingly urgent. Among renewable energy technologies, wind turbines play a significant role and are becoming more widespread.A critical issue in wind energy systems is the structural integrity of wind turbine towers, as failures often result from bolt fractures or flange separations at ring flange connection points. To address these challenges, this study investigates the bolt and flange connection details at these critical points.Two grades of steel were selected for testing, and four tensile tests were conducted. Based on the results, the steel grade with higher ductility was chosen for further analysis. Static tests were then performed on specimens representing the connection. The bolt configurations were analyzed in both single-nut and double-nut setups, and their effects on tensile capacity were evaluated. Detailed comparisons of tensile capacity revealed a strong correlation between the experimental findings, literature data, and analytical solutions. The evaluation of the nut configurations highlighted their impact on the tensile capacity of the connection specimens, providing valuable insights for optimizing wind turbine structural designs.On the other hand, the existing literature was thoroughly reviewed, and the findings obtained from this study were compared with previous results in the literature regarding the behavior of the components forming the connection.

Keywords: Nut; Steel connection; Steel grades; Tensile capacity; Wind turbine

1. Introduction

In recent years, the rapidly increasing global energy demand has made it more evident that reducing environmental impacts and utilizing sustainable energy sources is imperative. Greenhouse gas emissions from fossil fuels, air pollution, and their effects on global warming and climate change have necessitated the adoption of renewable energy systems. Among various energy alternatives, wind energy stands out as a prominent solution due to its low environmental footprint and operational costs. The potential of wind energy is great significance in reducing dependence on fossil fuels and minimizing the environmental footprint. Therefore, the development and widespread adoption of wind energy technologies has become a critical goal for environmental protection and sustainable development.

Wind turbines, especially horizontal-axis models, are commonly used for large-scale energy production. As these structures operate under both dynamic and static loads, they must exhibit high mechanical strength and safety. However, the structural integrity of wind turbines is often compromised at certain weak points, particularly at tower connections. One of the most vulnerable areas is the flange connections between turbine tower segments, where bolt fractures and flange separations frequently occur. Such failures can render turbines inoperable or even lead to structural collapse. Consequently, the design of bolt and flange connections is of most importance for ensuring the structural safety and efficiency of wind turbines.

Much of the existing research has focused on general bolt behavior, preload loss, fatigue, shear, and sealing characteristics. However, there is a limited number of studies addressing the effects of bolt and nut configurations specifically those used in turbine towers on tensile capacity. The interaction between bolt and nut geometry and the type of connection can significantly influence load distribution, stress concentrations, and overall connection performance. Different nut arrangements, in particular, can have substantial impacts on the durability and

* Corresponding author, E-mail: nisanur.isik@std.yildiz.edu.tr

https://doi.org/10.31462/icearc2025_ce_mat_204

reliability of connection components. Moreover, the geometry of bolts and nuts affects load paths and stress distributions at connection points, directly determining the success or failure of these assemblies.

This study experimentally investigates the influence of bolt and nut configurations on the tensile capacity of wind turbine flange connections. A series of tensile tests were conducted using two different steel alloys, followed by static tests on the specimens. The nut configurations were evaluated using both single and double nut setups, and their impact on tensile capacity was observed. The results clearly indicate that nut geometry and arrangement significantly influence tensile capacity. These findings were compared against experimental data. The aim of this research is to enhance the structural safety of wind turbine designs and contribute to filling the existing gaps in the literature by comparing with previous studies.

The main objective of the study is to improve the structural safety of wind turbine towers and to examine the influence of bolt and nut geometries on structural performance in greater detail. Such optimizations are essential for ensuring the safe, durable, and cost-effective operation of wind turbines, thus laying the foundation for the future success of renewable energy systems.

2. Literature review

In a study conducted by Johansen and Waldeland (2016), the behavior of bolt-nut assemblies under tensile forces was comprehensively investigated using both experimental and numerical methods. The study explored the effect of nut positioning on damage modes, especially for short and long grip lengths. Experimental results indicated that thread stripping was the dominant failure mode in short grip lengths, while ductile bolt fracture prevailed in long grip lengths. Moreover, placing the nut near the unthreaded shank region was found to increase the risk of thread stripping, whereas the use of a tall nut or double nut resulted in bolt fracture in all configurations.

The study also compared axisymmetric and 3D helical thread models developed using finite element methods, emphasizing the importance of accurate thread geometry modeling in predicting failure modes. Although the 3D helical model more accurately represented physical behavior, the axisymmetric model was found to offer sufficient accuracy and efficiency for engineering applications due to lower computational costs. This thesis contributed to a better understanding of key structural parameters in the tensile behavior of bolt-nut assemblies and highlighted essential variables to be considered in engineering design (Johansen & Waldeland, 2016).

Grimsmo et al. (2016) emphasized that thread failures in bolt and nut assemblies under tensile loading are generally undesirable. These types of failures are considered less ductile than fractures occurring at the threaded shank of the bolt. Since thread failures caused by over-tightening during assembly are difficult to detect, the reasons behind such failures were investigated. It was observed that thread stripping occurred particularly when the grip length (Lt) was short. Specifically, thread failure was noted when $Lt \leq 9$ mm, while bolt fracture occurred when $Lt \geq 17$ mm. These findings were supported by finite element simulations. Additionally, it was identified that at short Lt values, the bolt tended to buckle near the nut, contributing to thread (Grimsmo et al., 2016).

In a study by Plaitano et al. (2022), the failure behavior of high-strength HV bolts was investigated not only under pure tensile loading but also under combined tension and bending. The results indicated that while thread stripping was the dominant failure mode under pure tension, shaft fracture prevailed under combined loading. A finite element method (FEM)-based model developed in the study successfully predicted failure modes depending on the type of loading. Moreover, the model was reported to significantly reduce computational time. (Plaitano et al., 2022).

Yang et al. (2021) numerically analyzed the fracture behavior of partially threaded bolts subjected to tensile loading. The study employed the Void Growth Model (VGM) and the Bao-Wierzbicki (BW) fracture criteria. While the VGM accurately predicted tensile fracture, the BW model successfully captured the thread stripping behavior. The results showed that both types of failure could be modeled with high accuracy. Furthermore, it was demonstrated that thread cutting in bolts with short thread lengths contributed to thread stripping. (Yang et al., 2021).

Zhu et al. (2021) investigated ductile fracture-controlled strength mechanisms in aluminum alloy gusset (AAG) joints under tensile loading. Experimental studies involving plates of different dimensions revealed damage modes such as block shear failure and net section fracture. Using the Modified Mohr-Coulomb (MMC) fracture criterion, the descending region of the load-displacement curve was successfully captured. The numerical results obtained from finite element analyses showed strong agreement with experimental findings. (Zhu, et al., 2021).

Shaheen et al. (2020) conducted a detailed finite element analysis on the behavior of high-strength and stainless-steel bolts under elevated temperatures. The study emphasized that thread stripping-type failures could reduce the rotational capacity of connections, posing a threat to structural integrity. The analyses revealed that as temperature increased, the critical grip length (Lt) for thread stripping decreased in high-strength bolts, while no significant temperature effect was observed for stainless steel bolts. Additionally, it was shown that larger diameter bolts were more susceptible to thread stripping, and thread strength was the most decisive parameter against such failures. (Shaheen et al., 2020).

In another study, Venkadachalam (2020) examined the behavior of bolted, bonded, and hybrid joints used in composite material assemblies under dynamic loads. Joints with various edge distances were tested using a drop-weight impact testing device. The results indicated that hybrid joints exhibited significantly higher performance at room temperature, but a 25–35% decrease in strength was observed at elevated temperatures. Furthermore, the role of bolt preload was found to be critical for joint strength under high loading rates. These findings were supported by Split Hopkinson Pressure Bar (SHPB) tests and advanced 3D finite element modeling (Venkadachalam, 2020).

3. Experimental study

The experimental modeling process was based on real turbine data derived from the reference study titled "Full-scale Validation of FE Models for Geometrically Imperfect Flange Connections" conducted by Peter Schaumann and colleagues. This particular study includes geometric details of a ring-type flange connection located at the 27th meter of an 85-meter-tall wind turbine. Accordingly, the experimental setup was designed to contribute not only to academic literature but also to industrial applications (Schaumann & Seidel, 2020).

The test specimens were constructed from S355 steel in the form of L-type flanges with dimensions of 150 mm in width, 165 mm in height, and 70 mm in thickness. Each specimen contained a centrally located Ø38 mm hole designed to accommodate M36 bolts. The effective connection height was determined as 120 mm, representing the total thickness of two flanges. These dimensions were optimized to both align with literature and represent realistic values observed in industrial applications.

In the initial phase of the experimental study, dogbone-type tensile specimens were prepared using two different steel grades (S355 and 1045) for mechanical characterization. The specimens were machined according to standards using CNC machines and then tested on an INSTRON tensile test machine operating at a frequency of 2 Hz. To enhance the accuracy of deformation measurements, an extensometer was installed, allowing the elastic-plastic transition zones to be clearly observed. Based on the stress-strain curves, S355 steel exhibited a tensile strength of approximately 460 MPa and elongation in the range of 18–19%, indicating a highly ductile behavior. In contrast, 1045 steel, although offering a higher tensile strength of up to 600 MPa, showed elongation of only 7–9% and presented a clearly brittle fracture behavior.

These data are critically important for understanding the effects of ductile and brittle fracture mechanisms on the performance of the connections. Ductile fracture, characterized by high deformation capacity, provides advance warning in structural systems and absorbs energy under load, thereby delaying collapse. Brittle fracture, on the other hand, occurs suddenly and sharply without plastic deformation, posing significant structural risks. Steels like 1045, which have higher carbon content, are prone to brittle fracture due to their low ductility, while steels like S355, with lower carbon content and higher toughness, exhibit ductile fracture behavior, thereby enhancing structural safety.

In the subsequent phase of the experiment, a single-nut connection system composed of M36 bolts and S355 flanges was tested. In this configuration, the tensile tests revealed a maximum tensile stress of approximately 220 MPa. However, at this point, a sudden weakening in the connection was observed. Post-test inspections identified thread stripping in the nut, which disrupted the load transfer mechanism. Thread stripping is a common and critical failure mode frequently emphasized in the literature (Kerr, 2012; El-Sayed, 2015), particularly in systems operating under high torque, where it significantly reduces the service life of the connection. Beyond decreasing the load-carrying capacity, thread stripping also leads to secondary issues such as loosening of the joint and imbalance in load distribution.

Fig. 1. Pre-test view of dogbone-type specimens prepared from S355 and 1045 steel for tensile testing.

Fig. 2. Dogbone-type specimen mounted in the INSTRON tensile testing machine along with the extensometer setup

Alternatively, in the tests conducted on the double-nut connection system, the joint exhibited significantly higher performance, achieving maximum stress levels of approximately 380–390 MPa and deformation extending up to 32–33 mm. The system created a locking effect through the use of a second nut, which prevented loosening and reduced the shear forces on the thread surfaces, thereby minimizing the risk of thread stripping. Visual analysis showed that the double-nut connections exhibited more balanced and uniform deformation under load, and the load transfer remained continuous and controlled throughout the process.

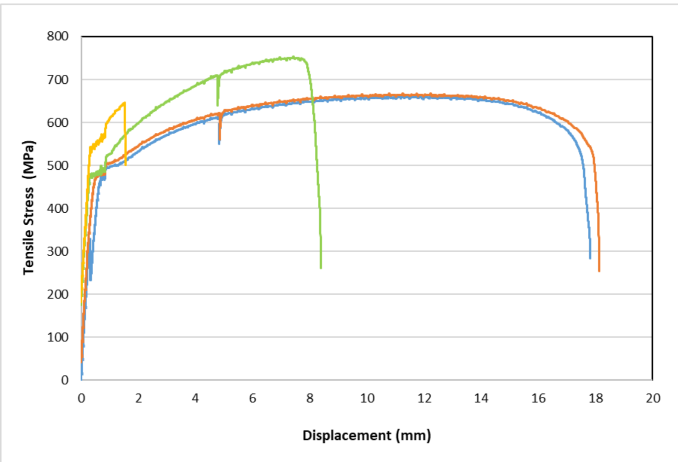

Fig. 3. Tensile stress–strain curves for S355 and 1045 steel specimens.

Fig. 4. Pre-test view of the single-nut flange connection.

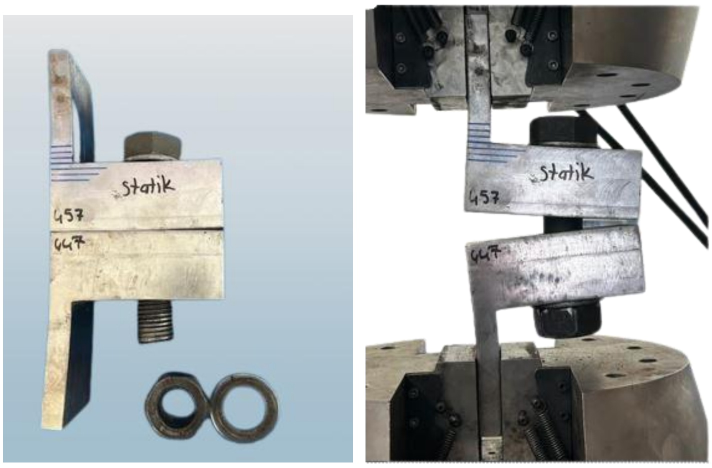

Fig. 5. Post-test views of the single-nut flange connection after tensile testing.

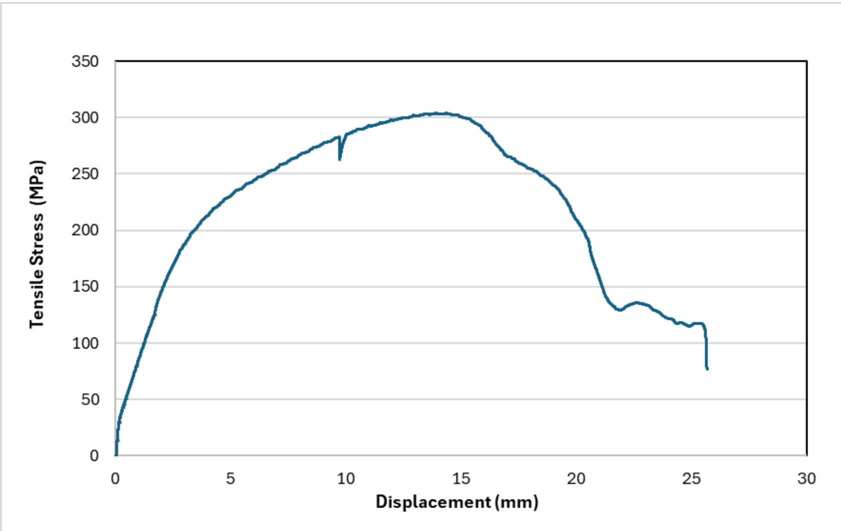

Fig. 6. Experimental Tensile stress–strain curve for the single-nut connection specimen.

Fig. 1 presents the pre-test view of the dogbone specimens; Fig. 2 shows the tensile test setup and the placement of the extensometer; Fig. 3 illustrates the experimentally obtained stress–strain curves for S355 and 1045 steel specimens; Fig. 4 displays the pre-test view of the single-nut flange connection; Fig. 5 shows the post-test views of the single-nut flange connection; Fig. 6 presents the experimental stress–strain curve for the single-nut connection; Fig. 7 depicts the pre-test view of the double-nut flange connection; and Fig. 8 shows the post-test views of the double-nut flange connection. Finally, Fig. 9 comparatively presents the tensile stress–strain curves of both single- and double-nut connections. These graphs clearly demonstrate that the double-nut connection was able to carry loads stably up to approximately 410 kN, while the single-nut system experienced a loss of capacity after reaching around 300 kN.

All findings obtained in this study demonstrate that double-nut connection systems enhance not only the load-bearing capacity but also the structural resilience, energy absorption potential, and long-term operational safety of the assembly. The selection of appropriate materials and connection configurations in flange joints is of critical importance in systems subjected to dynamic loads, such as wind turbines. In this context, ductile materials like S355 and double-nut configurations align well with principles of safe, economical, and durable design. This study provides a solid experimental foundation to support more effective engineering decisions in such systems.

Fig. 7. Pre-test view of the double-nut flange connection under tensile loading.

Fig. 8. Post-test views of the double-nut flange connection after tensile testing.

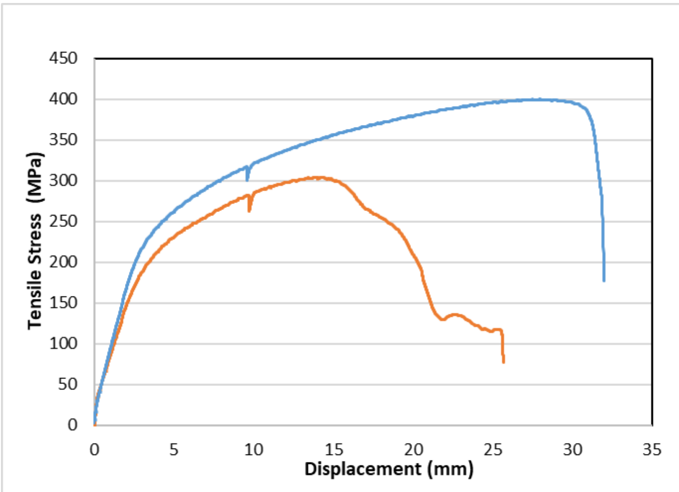

Fig. 9. Comparison of the tensile stress-strain curves for single- and double-nut connections.

4. Conclusions

In this study, the effects of bolt and nut configurations used in wind turbine flange connections on tensile capacity were comprehensively examined through both experimental methods. The findings revealed that various parameters ranging from material selection to connection geometry have a direct impact on the overall durability and reliability of the system. The results of the tensile tests yielded valuable engineering insights, supported by literature comparisons, and optimization recommendations were proposed for wind turbine tower connections.

In the tensile tests, two types of steel S355 and 1045 were evaluated. Experiments conducted on dogbone-type specimens showed that S355 steel exhibited high ductility, with a tensile strength of approximately 460 MPa and an elongation range of 18–19%. In contrast, although 1045 steel provided a higher tensile strength of around 600 MPa, it demonstrated only 7–9% elongation and a clearly brittle fracture behavior. These results once again confirm that the use of ductile materials in connection elements plays a critical role in reducing the risk of sudden fracture and improving structural safety. Moreover, ductile fracture mechanisms were shown to provide warning signs under load by allowing the structure to undergo deformation, thereby increasing failure predictability.

When the effect of nut configuration was examined, single-nut connections were observed to reach a maximum tensile stress of approximately 220 MPa. However, a sudden loss of strength occurred during testing. This configuration frequently exhibited thread stripping, indicating limited load-carrying capacity and a high risk of abrupt failure. The sudden deformation and loosening observed under load in single-nut connections confirmed the thread stripping risks previously highlighted by Grimsmo et al. (2016) and Johansen & Waldeland (2016).

On the other hand, the tests on the double-nut configuration yielded significantly better performance. In the system formed using two nuts, a tensile strength of approximately 380–390 MPa was achieved, with deformations extending up to 32–33 mm. This demonstrated that the locking effect created by the second nut prevented loosening and enabled more uniform load distribution while minimizing the risk of thread stripping. These results support the view presented by Plaitano et al. (2022) that nut configurations must be optimized to improve connection performance under combined tension and bending.

Furthermore, a comparison of the load–displacement curves clearly showed that double-nut connections maintained stable performance up to high load levels of around 410 kN, whereas single-nut systems experienced a capacity drop beyond 300 kN.

The findings of this study are also consistent with the high-temperature bolt behavior analyses conducted by Shaheen et al. (2020). It was emphasized that connections are more prone to brittleness at elevated temperatures and that the use of double nuts could reduce this risk. Additionally, the fracture models developed by Yang et al. (2021) provided clear explanations of thread stripping mechanisms, showing good alignment with the results of this research.

In conclusion, for systems exposed to dynamic loads such as wind turbines:

- The use of high-ductility materials,
- The preference for double-nut connection systems to mitigate thread stripping risks,
- Careful optimization of connection geometry,
- And preliminary evaluations through finite element analysis

are of critical importance in enhancing structural resistance and connection safety.

Recommendations for future studies include investigating combinations of connection elements with varying sizes and thread profiles, determining the fatigue life of connections, and conducting detailed analyses of temperature effects. In particular, exploring the application potential of innovative hybrid connection systems (bolt + adhesive combinations) in wind turbines could make a valuable contribution to the knowledge base in this field.

This study not only emphasizes the importance of bolt and nut configurations in the wind turbine sector, but also offers practical design solutions for structural engineers working in the broader field of steel structure design.

References

El-Sayed, T. (2015). Failure Analysis of Bolted Joint under Tensile Load: Experimental and Numerical Study. Engineering Structures, 89, 1–10.

Grimsmo, E. L., Aalberg, A., Langseth, M., & Clausen, A. H. (2016). Failure modes of bolt and nut assemblies under tensile loading. *Structural Impact Laboratory (SIMLab) and Centre for Advanced Structural Analysis (CASA), Department of Structural Engineering, Norwegian University of Science and Technology*, Trondheim, Norway.

Grimsmo, E. L., Aalberg, A., Langseth, M., & Clausen, A. H. (2016). How placement of nut determines failure mode of bolt-and-nut assemblies. *Structural Impact Laboratory (SIMLab) and CASA, Norwegian University of Science and Technology*, Norway.

Johansen, S., & Waldeland, E. (2016). *An experimental and numerical study of bolt and nut assemblies under tension loading* (Master's thesis). Norwegian University of Science and Technology, Trondheim, Norway.

Kerr, M. (2012). Threaded Fastener Failures Due to Over-tightening and Fatigue. Engineering Failure Analysis, 26, 152–160.

Plaitano, F., Stratan, A., & Nastri, E. (2022). Simplified modelling of failure in high strength bolts under combined tension and bending. *Department of Steel Structures and Structural Mechanics, Politehnica University Timisoara, Romania.*

Schaumann, P., Seidel, M., & Kolks, G. (2020). Full-scale Validation of FE Models for Geometrically Imperfect Flange Connections. Journal of Wind Engineering and Industrial Aerodynamics, 198, 104078.

Shaheen, M. A., Foster, A. S. J., Cunningham, L. S., & Afshan, S. (2020). A numerical investigation into stripping failure of bolt assemblies at elevated temperatures. *School of Mechanical, Aerospace and Civil Engineering, The University of Manchester, UK.*

Venkadachalam, A. (2020). *Experimental and numerical study of dynamically loaded bolted and hybrid joints* (Master's thesis). Michigan State University.

Yang, F., Veljkovic, M., & Liu, Y. (2021). Fracture simulation of partially threaded bolts under tensile loading. *Department of Engineering Structures, Delft University of Technology, Netherlands.*Zhu, P., Zhang, Q., Luo, X.,

Ouyang, Y., & Yin, J. (2021). Experimental and numerical studies on ductile-fracture-controlled ultimate resistance of bars in aluminum alloy gusset joints under monotonic tensile loading. *College of Civil Engineering, Tongji University, China.*

Role of nano-SiO_2 in enhancing properties of slag-waste ceramic powder-based geopolymer composites

Beyza Aygun*[1], Mucteba Uysal[2]

[1] *Istanbul University-Cerrahpasa, Department of Civil Enginering, 34320 Istanbul, Türkiye*
[2] *Yıldız Technical University, Department of Civil Engineering, 34220 Istanbul, Türkiye*

Abstract. Nano-silica is an extremely reactive multifunctional additive to geopolymer composites (GCs) in which it not only accelerates early gel nucleation as well as matrix densification but also improves strength immensely, minimizes capillary porosity, and assisted in long-term durability by fine-grained microstructure. In this context, the effects of adding nano-SiO_2 at different ratios (2%, 4%, and 6% by weight) were investigated in the GC reference consisting of 50% granulated blast furnace slag (GBFS) and 50% waste ceramic powder (WCP). Mix design included the water/binder (w/b) ratio of 0.48, Na_2SiO_3/NaOH ratio of 2:1, and sand/binder (s/b) ratio of 2.5. Thermal curing was applied at 80°C for 24h and basic physical properties such as capillarity, water absorption, porosity and compressive strength were analyzed at 28 days. Results revealed that nano-silica not only reduced porosity significantly by inducing matrix densification through micro-filling properties as well as high-surface reactivity but also had the definitive effect of increasing compressive strength, which indicated active participation in gel formation as well as development of more cohesive, structurally robust geopolymer network.

Keywords: Geopolymer composites, Waste ceramic powder; Nanomaterials; Physical properties

---

1. Introduction

Global intensification of the economy has considerably increased industrial production, led by the building sector owing to its high dependence on cement-based products. Cement production, though central to the building sector, comes at the cost of significant environmental disadvantages. One ton of clinker production generates about 0.86 tons of carbon dioxide (CO_2), along with other toxic pollutants like sulfur oxides (SO_x) and nitrogen oxides (NO_x), and hence enormously contributes to air pollution. Cement production alone contributes nearly 8% to the entire anthropogenic emission of CO_2, according to estimates. In the context of the deep connection of greenhouse gas release and climate change, there is a strong need to create environmentally friendly alternatives of low or no carbon footprint in order to substitute conventional cement in construction formulas. Geopolymers (GCs), a group of inorganic binders synthesized by the alkali activation of aluminosilicate precursors, have attracted increased interest as a green alternative. Distinguishing them from conventional cementitious systems, GCs present enhanced chemical stability, mechanical properties, and thermal insulation, which facilitate their use in a wide array of construction materials, ranging from concretes and surface coatings to advanced structural composites and mortars. Recent developments have centered on the valorization of industrial byproduct wastes, including ceramic waste, in GCs in order to enhance environmental sustainability and structural efficiency (Nauklong et al., 2018; Papamichael et al., 2023) This approach supports the circular economy by converting the typically waste-discharged ceramic residue to valuable material, which is traditionally deposited in landfills in large quantities as a waste product. Its novel chemical and morphological properties present opportunities and challenges, however, which demand further exploration of its compatibility in geopolymeric systems (Ahmad et al., 2023; Zhang et al., 2023). In parallel, the usage of nanomaterials in GCs has become a revolutionary method of enhancing microstructural-level performance. Various types of nanoparticles, including carbon nanotubes (CNTs), nano-silica (NS), nano-alumina (NA), graphene oxide (GO), nano-titania (NT), nano-clay (NC), nano-zinc oxide (NZ), nano-calcium carbonate, and nano-iron oxide, have been investigated for their ability to support mechanical robustness, porosity reduction, and increased durability. These nanomaterials play a significant role due to their high surface energy and nanoscale interactions in the 1–100 nm zone, which alter the matrix morphology and increase geopolymerization kinetics. Such integration not only enhances material functionality but also supports sustainability by increasing the service life and minimizing the carbon footprint of construction. Amongst these,

* Corresponding author, E-mail: beyza.aygun@ogr.iuc.edu.tr

https://doi.org/10.31462/icearc2025_ce_mat_209

nano-silica excels in its ability to refine the physical and chemical structure of geopolymer matrices (Matalkah et al.., 2022; Labaran et al., 2024).

NS as an active filler in geopolymer mixtures is a major contributor to improved packing density, promoting further gel formation, higher mechanical strength, and increased tolerance to chemically harsh environments. It is highly responsive to various factors such as dosage level, dispersion efficiency, precursor composition, and activating solution concentration. Low levels of dosage, generally in the range of 0.5 wt%, have been demonstrated to optimize pore structure formation and nucleation phenomena, with higher addition levels of up to 10 wt% having the ability to improve strength development. High levels, however, promote agglomeration of nanoparticles, reduced workability, and increased entrapment of air, which negates the desired advantage. Experimental results confirm such tendencies. For example, NS content in the range of 1% to 3% in slag–fly ash-based geopolymer matrices caused significantly reduced water-permeable porosity, with the largest drop by ca. 26% being observed at NS = 2%. Above this concentration, there is evidence of reversal in trend, but possibly due to compromised workability and poor dispersion. Parallel results confirm that addition of NS by 2% is highly capable of increasing acid resistance as well as retarding capillary absorption to a large degree, to which matrix densification, along with more vigorous aluminosilicate gel formation, is mainly responsible. Other studies with slag-based mixes also confirm that strength attainment is optimal at NS = 2% after which increasing performance is degraded. Highest gains are realized in early curing stages, suggesting that NS is actively promoting accelerated geopolymerization in these early stages, as well as contributing maximally to the development of initial structure (Jindal et al., 2021; Rahmawati et al., 2021; Zidi et al., 2021; Tanyildizi et al., 2023).

This work aims to develop and characterize nano-silica-modified geopolymer mortars produced from an equimolar binary mix of ground granulated blast furnace slag (GBFS) and finely ground waste ceramic powder (WCP) activated by an optimized alkali solution. The work bridges an important research gap by adding nano-silica-a high-surface-area amorphous addition-from a less traditional binder system, thus evaluating its effect upon pore structure, increasing gel formation, and controlling capillary transport processes. The work used an extensive experimental framework consisting of standardized methods to evaluate compressive strength, bulk density, porosity, water absorption, and capillary absorption, with all samples being thermally cured in controlled environments in order to maintain identical reaction kinetics. Through dosage-based optimization of the addition of nano-silica content (2%, 4%, and 6%), this work investigates the microstructural and mechanical consequences of nanoscale additives in alkali-activated systems through a data-driven optimization strategy towards optimizing material performance as well as sustainability in emerging binder technologies.

2. Materials and methods

2.1. Materials

The binder phase in this study was formulated through a binary combination comprising GBFS and WCP, with GBFS constituting 50% of the total binder mass. This specific material pairing was strategically selected to exploit the high chemical reactivity of GBFS—attributed to its predominantly amorphous, calcium-rich composition—alongside the filler effect and latent pozzolanic potential of finely milled ceramic waste. GBFS employed in the formulation consisted of smooth, angular particles primarily composed of calcium, silicon, aluminum, and magnesium oxides. It exhibited a specific gravity of 2.93, a Blaine fineness of approximately 410 m²/kg, and an average particle size within the 8–12 µm range, all of which render it highly reactive in alkaline environments. The reactive nature of GBFS is facilitated by predominantly amorphous phase composition allowing it to be dissolved quickly under alkaline media. The source of WCP is in form of post-industrial ceramic residue taken through fine milling to enhance exposed surface area, with specific gravity of about 2.62, particle size range in median position of 18–25 µm, and morphology by way of fractured particle faces and irregular grain shapes. It is less chemically active relative to GBFS but still supplies notable amounts of silica and alumina, with remnants of glass nature supporting secondary reaction pathways under high firing temperature curing. The inclusion of crystalline forms of mullite and quartz along with SiO_2 levels in excess of 60% serves to provide secondary framework for long-duration microstructural development. For use as fine aggregate, good-quality natural river sand conforming to standard mortar classifications was used with particle size gradation to maintain sand-to-binder ratio of 2.5 to provide volume stability along with closely packed particulate framework.

Activator system used an alkaline dual-solution consisting of sodium silicate (Na_2SiO_3) and sodium hydroxide (NaOH). NaOH solution with an initial concentration of 12 molarity ensured adequating alkalinity to break down aluminosilicate bonds to start dissolution. NaOH- component with silicate modulus approaching 2.0 was added to NaOH in proportion at a ratio of 2:1 in mass, which is a prevalent practice known to yield geopolymeric chain formation in balance with workability. Overall ratio of activator to binder kept at 0.5, and total ratio of water to binder maintained at 0.48, which included both mixing water as well as water present in situ in sodium silicate in calculations to yield an optimum reaction environment and paste properties. In order to improve the matrix at the nanoscale and microscale, nano-silica was added as an active additive in amounts of 2%, 4%, and 6% based on binder weight. NS present in the formula had more than 99% purity, with a specific surface area of 180 to 250 m²/g, particle size distribution with an average of 15 to 30 nm, and true density nearly equalling 2.2 g/cm³. High surface energy combined with amorphous structure makes the NS play a bimodal role: first, as chemically active agent to promote densification of more continuous gel network by accelerated polycondensation; second, as physical densifier to fill in pore space among coarse particles and to help in consolidating matrix uniformly. Nanoparticles have activity in acting as heterogeneous nucleation sites, which induce early reaction kinetics and enhance cohesion of binder system. Additionally, their ability to reduce pore connectivity as well as inhibit development of capillary water channels directly contributes to mechanical strength as well as to durability of resulting composites. Solid components, such as GBFS, WCP, and nano-silica, all of which are in solid state, were dry-blended to achieve evenness before adding in liquid activator. Produced mixtures were then cast in moulds and subjected to thermal curing at temperature of 80°C for 24 h, which is adopted to accelerate dissolution as well as network reorganization of aluminosilicate network, especially in those with high GBFS content. The accelerated curing temperature accelerates early development of strength, reduces formation of pores, and allows reliable assessment of effect of nano-silica to physical as well as structural behavior of composite.

Table 1 presents the chemical composition of all precursor materials, and Table 2 lists the mix proportion and dosage rate specific to each test group.

Table 1. Chemical composition of binders.

Main Oxide (%)	CP	GBFS
SiO_2	65.44	40.5
Al_2O_3	15.45	12.8
Fe_2O_3	7.11	1.1
CaO	4.65	35.5
MgO	1.28	5.8
Na_2O	0.8	0.79
K_2O	2.15	
SO_3	0.06	0.18
TiO_2		0.75
LOI	3.06	0.03

Table 2. Mix proportions of 1 m³ GC.

Series	WCP (kg)	GBFS (kg)	Nano-SiO_2 (kg)	Sand (kg)	NaOH (kg)	Na_2SiO_3 (kg)	Total (kg)
R	500	500	0	2500	166	333	4000
NS2	490	490	20	2500	166	333	4000
NS4	480	480	40	2500	166	333	4000
NS6	470	470	60	2500	166	333	4000

*R (50% GBFS + 50% WCP), NS2 (49% GBFS + 49% WCP + 2% nano-SiO_2), NS4 (48% GBFS + 48% WCP + 4% nano-SiO_2), and NS6 (47% GBFS + 47% WCP + 6% nano-SiO_2).

2.2. Methods

Experimental procedures in this research work were associated with evaluating in depth the impact of nano-silica on physical and mechanical performance of geopolymer mortars. Following detailed dry blending of GBFS, WCP, and nano-SiO_2 in their respective proportion, mixes were added to alkali activator solution then cast in standard prismatic molds with dimensions of 40 × 40 × 160 mm in accordance with ASTM C349 as well as TS EN 196-1 to test for compressive strength. Specimens were heat treated at temperature of 80°C for 24 h in laboratory oven to induce early geopolymerization reactions then demolded for subsequent conditioning. Compressive strengths in terms of at 7th day and 28th day were conducted using calibrated universal test apparatus at load rate of 2.4 kN/s with results being an average of minimum three similar samples from every group. Vacuum saturation as well as oven drying procedures, in accordance with ASTM C642, which also allowed determination of water absorption by way of calculation, to establish bulk density as well as available pore volume. Total porosity was determined through use of saturated and dry weights in addition to volume of specimen. Capillary absorption test in accordance with TS EN 13057, where part of specimen is submerged in water with subsequent determination over duration of mass acquired by specimen, to assess rate as well as magnitude of capillary penetration. Results of all these analyses were statistically analyzed with conclusions derived to interpret nature of microstructural refinement as well as improvement in durability occasioned by incorporation of nano-silica.

3. Results and discussion

3.1. Physical properties

Incorporation of nano-silica in GC formulations had a highly transformative effect on the physical structure of the material, as indicated by progressive decreases in porosity and water absorption, accompanied by complementary increases in bulk density in all modified series (Table 3). R series, which lacked any particle-based enhancement, had the highest porosity values of 21.91% and 19.52% as well as water absorption levels of 11.75% and 10.22%, clearly indicative of a matrix that is highly capillary interconnected, with poor gel compaction, and poor particle locking. The values indicate that in such microstructure, binder particles are not in their cohesive state nor with nucleation density to aid in proper gel propagation or closure of existing voids. Correspondingly, unit weights of mixes in the control mixes were also the smallest in all that appeared in the series, with values of 2.39 g/cm³ and 2.37 g/cm³, indicative of suboptimum densification as well as inclusions in the hardened matrix. Contrasted to this is adding 2% of nano-SiO_2 (NS2), which caused a tremendous restructuring in the microstructure. Porosity significantly decreased to 19.02% and 18.00%, with water absorption decreasing to 9.54% and 8.91%, indicative of the capacity of nano-silica particles to penetrate interstitial voids as also acting as nucleation accelerators in geopolymer formation. The subsequent rise in unit weight to 2.46 g/cm³ in both measurement axes testifies to successful development of more closely packed as well as mechanically integrated matrix where volume of voids is taken over by hydration products as well as smaller gel formation. Such structuring adheres to synergistic action between high-surface area contribution by nano-silica as also amorphous silica content present, which both contribute to development of denser gel network by increasing aluminosilicate's rate of polycondensation as also minimizing internal discontinuities. With an increased dosage to 4% (NS4), the material response improved further, with evidence of stabilization. Porosity levels decreased marginally to 18.72% and 18.45%, while water absorption declined further to 9.26% and 9.25%—a nearly uniform decrease that not only reflects diminished pore volume but also reduced pore size distribution as well as closure of large capillary voids. Notably, unit weight remained in keeping with NS2's unit weight (2.46 g/cm³ and 2.45 g/cm³), implying that although refinement of the microstructure persisted at the nanoscale, gains in density at the larger scale reached saturation due to saturation of available space in packing as well as pore-filling capacity. Such behavior suggests that, at 4%, nano-silica optimizes its twin role as both a filling agent and reactive component by promoting gel formation without adding particle agglomeration or disturbing matrix homogeneity. Nevertheless, with an increased dosage to 6% (NS6), an impressive and more vigorous densification response is observed.

Porosity levels plummeted to an all-time minimum of 16.37% and 15.97%, respectively, lowest in all series, with water absorption decreasing to 7.96% and 7.76%, presenting an impressive tendency toward reduced capillary permeability—in nearly 34% lower absorption capacity relative to that of the control. Unit weight also attained a maximum at 2.49 g/cm³, an indication that physical evidence supports that matrix at this dosage had superior compaction with continuity of gel, likely due to greater engagement of nanoparticles in the framework of polycondensation. Its superior performance can be explained through its ability to occupy microvoids concurrently, catalyze densification of reaction products, and restrict incursion of capillary channels that generally aid fluid intrusion. Its ultra-fine particle size and high specific surface area make it seamlessly incorporable within the gel phase, allowing for molecule-level ordering and three-dimensional connectivity which is not achievable by ordinary binding agents. Nevertheless, note that even with ongoing porosity decrease and moisture absorption, unit weight remained comparable to NS4 in one direction, speaking to a hypothetical threshold where ongoing densification does not realize increased bulk density, possibly due to particle-packing limitations intrinsic to the system or incipience of micro-agglomeration at high concentration of nanoparticles. Nevertheless, disruption lacked apparent manifestation at 6%, meaning that sufficient dispersion still insured performance. Overall, such results demonstrate that nano-silica is not only an added-filler quality but also an active multifunctional contributor to restructuring GC interior geometry. Through reduced accessible pore volume, improved interlaminar adhesion, as well as ensuring continuity of gel, nano-SiO_2 makes possible the creation of denser, stronger, and water-insulating matrix—consequences critical to long-term performance integrity of geopolymer material. Within tested amounts, clearly, the 6% dosage revealed finest physical response, although **4% dosage might be an operational ceiling before decreasing return or encountering problems in dispersion under actual processing circumstances (Gao et al., 2013; Behfarnia and Rostami, 2017; Zhang et al., 2023).

Table 3. Unit weight, water absorption and void ratio values of GCs.

	Porosity (%)		Water absorption (%)		Unit weight (g/cm^3)	
R	21.91	19.52	11.75	10.22	2.39	2.37
NS2	19.02	18.00	9.54	8.91	2.46	2.46
NS4	18.72	18.45	9.26	9.25	2.46	2.45
NS6	16.37	15.97	7.96	7.76	2.49	2.45

Capillary absorption quantitatively verified progressive capacity drop in water absorption with increasing dosage of nano-silica, clearly revealing its pore-refining action and densification ability in GCs (Fig. 1.). R had the highest absorption coefficient with a maximum capillary height of about 0.0133 mm, which was normalized to serve as the reference point (100%) for comparative analysis. Upon addition of 2% nano-SiO_2 (NS2), the maximum absorption reduced to nearly about ~0.0124 mm, which is a reduction by 6.77% over the control. This improvement, although modest, reveals that even with minimal addition of nano-silica, pore continuity is successfully disturbed and capillary rise is slowed.NS4 series of mixes with 4% of nano-silica decreased absorption to approximately about 0.0118 mm, which corresponds to an overall 11.28% drop from the control and by way of improvement over NS2 by 4.83%. The trend is indicative of higher content of nano-silica increasing intensity of gel formation to restrict fluid penetration in addition to decreasing actual pore radii, thereby decreasing fluid entry. Nevertheless, even greater restraint of capillary rise is realized in NS6 series where absorption flattened at nearly about 0.0102 mm, which is an overall drop by 23.31% from the control and by 13.56% below NS4. The steep drop in this group is indicative of reaching an optimum packing condition in the matrix at 6% nano-SiO_2, which maximizes interconnected void minimization and effectively clogs capillary transport pathways. This is associated with micro-filler action by nano-silica where in higher concentration not only does it seal voids but also enables dense, rapid gel nucleation along pore walls to restrict entry. The relative slope gradient difference also illustrates differing initial sorptivity; for example, estimated initial absorption rate of slope from 0 to 100 s^1/2 in NS6 is nearly 30% below that of the control. Overall, all these numerical values significantly validate that nano-silica is an excellent chemical in suppressing capillary absorption where optimum performance is realized at 6% where both dispersion along with pore bridging is optimally maintained. Such enhancement is invaluable in durability performance, especially where exposure to water is prevalent, as reduced capillarity directly translates to improved impermeability along with longer service life of the composite (Behfarnia and Rostami, 2017; Khater et al., 2024).

3.2. Mechanical properties

Inclusion of NS at incremental dosages of 2%, 4%, and 6% by binder weight produced an increased compressive strength performance of GCs, with evidence of complex interactions among particle dosage, dispersion efficiency, and reactive aluminosilicate framework. Control series (R), in which there is absence of nano-modification, showed a 7-day compressive strength of 18.59 MPa, which increased marginally to 20.83 MPa at 28 days—a rise of only 2.24 MPa, or approximately 12%, which indicated minimal rate of sustained geopolymeric gel progress in the absence of enhancement at nano-scale. Upon addition of 2% nano-SiO_2, early-age strength increased to 20.26 MPa, which exceeded that of the control by 1.67 MPa, while the 28-day strength increased to 33.60 MPa, which represents an increase by a factor of 61.3 relative to that of the control, as well as by relative gains of 65.8% over its own 7-day value. The tremendous advancement suggests that even minimal amounts of nano-silica are enough to catalyze extensive microstructural refinement. Ehanced geopolymerization is due to high surface energy, amorphous nature, and ultra-fine size of nano-SiO_2 combined to offer extensive nucleation sites for gel development, facilitate early chain development of N-A-S-H or C-A-S-H gels, and effectively bridge interstitial pores—in turn enhancing density and strength of solidified matrix.

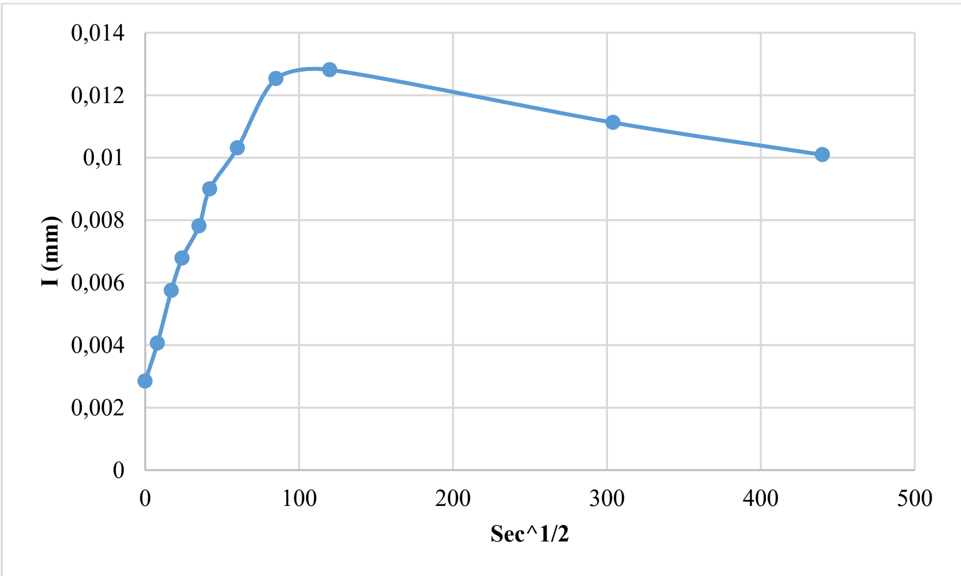

(a) Control

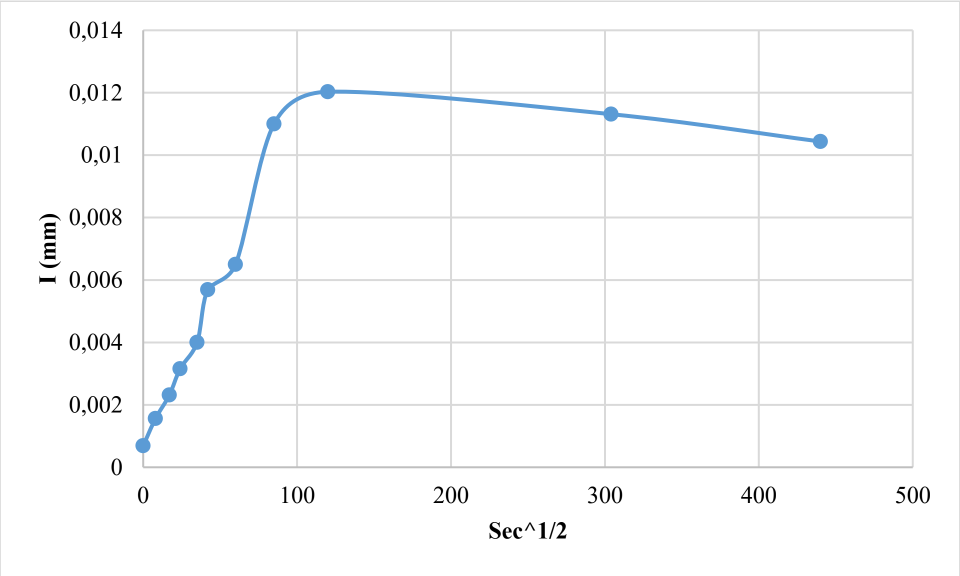

(b) NS2

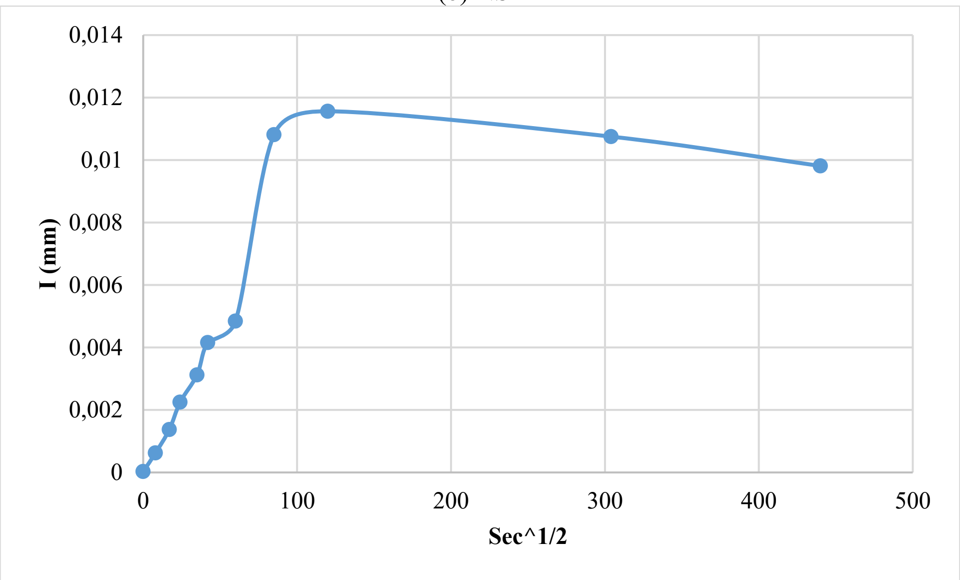

(c) NS4

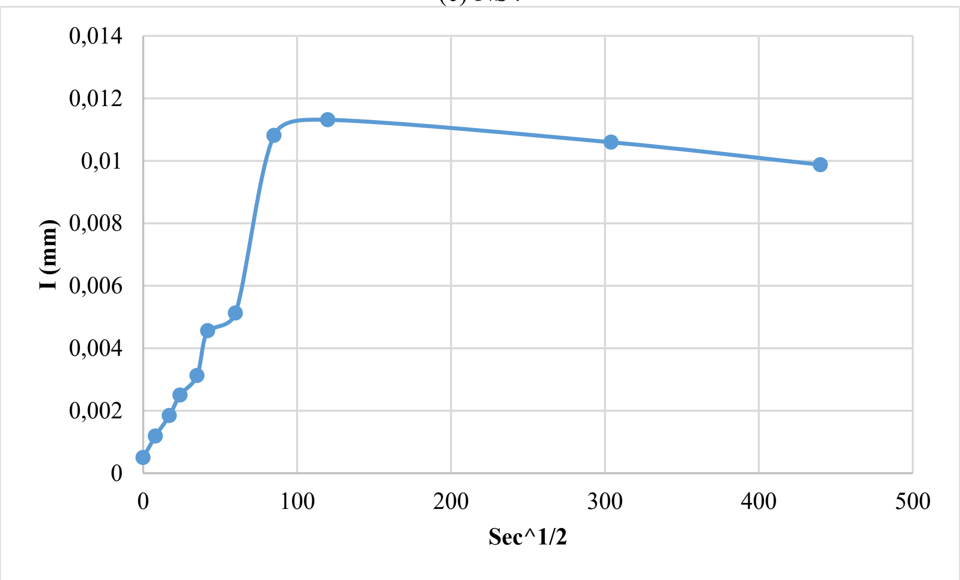

(d) NS6

Fig. 1. Capillarity absorption values of GCs.

The effect increased with NS4, which produced marked increases in strength at 7 days to 26.09 MPa, which is by an improvement of 40.3% over NS2 as well as by 40.3% over that of the control at similar age. The compressive strength of 36.09 MPa at 28 days is highest overall, which represents an improvement over that of the control by 15.26 MPa as well as from an absolute rise of 10 MPa from that of its early-age value. Fig. 2. clearly manifest increased synergy at this dosage, where particle distribution is still homogeneous, and concentration of silica is ideal to promote advancing initial densification as well as long-term continuity of structure. The geopolymer matrix in NS4 seems to be influenced by maximized degree of polycondensation, prolongation of cross-linked network, as well as by finer porosity features—all of which contribute to an integrated, robust mechanical response. However, when higher nano-silica dosage at 6% was used, even though the 7-day strength increased to 29.05 MPa, setting itself as highest early strength among all sequences, the 28-day strength reduced marginally to 35.88 MPa, with minimal deviation from NS4 in spite of increased nanoparticle content. The fact that both 56% strength improvement from 7-day to 28-day remains impressive, but with merely 0.21 MPa drop in final strength over NS4, is indicative of diminishing return at this concentration. Such plateauing can be largely attributed to nanoparticle agglomeration, an effect widely reported at high nano-dosages, where particles aggregate based on van der Waals forces and high surface activity to form weak zones as well as incomplete matrix entanglements. Not only do these agglomerates reduce available nucleation area but may also impair polymer chain continuity as well as induce localized flaws that impair load-bearing capacity of the material. In addition, excess unreacted silica might exert influence upon chemical pore solution equilibrium by inducing phase imbalance or retarding further gel growth. In spite of such limitations, NS6 is still superior to the reference by 15.05 MPa at 28 days, ensuring that nano-SiO_2, independent of dosage, is actively contributing towards inducing accelerated strength gain, particularly in early stages. That said, performance saturation in NS6 Serving to reinforce this is that all mixes with nanoparticles showed massive superiority over their unmodified counterpart, but only NS4 series appeared to be most efficient in terms of being an optimized performance early-age solution coupled with greater long-term mechanical strength, without incurring negative macroscopical consequences of oversaturating or forming cluster-like phenomena. This makes clear that 4% of nano-SiO_2 is that pivotal concentration, with increased concentration being such that microstructural refinement slows down and dispersion problems to become greater than advantage of increased surface activity (Deb et al., 2022; Han et al., 2022; Ahmed et al., 2023; Zhang et al., 2023).

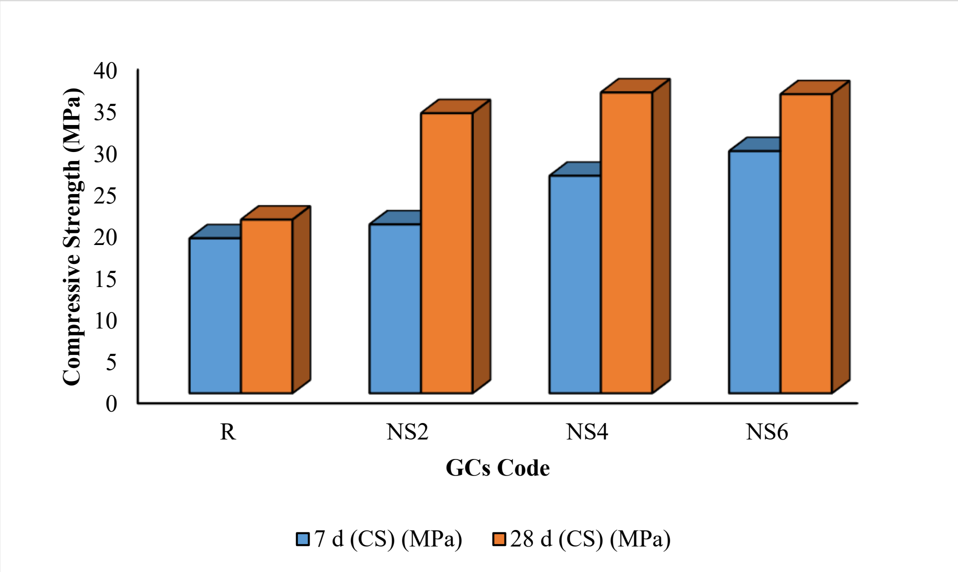

Fig. 2. Compressive strength values of GCs.

4. Conclusions

- Incorporation of 2% nano-silica (NS2) produced a 33.60 MPa of 28-day compressive strength, which is a 61.3% improvement over the control and a 65.8% improvement over its own 7-day strength, which is indicative of its role as a catalyst in geopolymer gel formation.
- NS2 decreased porosity from 21.91% to 19.02% as well as water absorption from 11.75% to 9.54%, with an associated rise in unit weight to 2.46 g/cm^3, which validates increased matrix densification and superior packing efficiency.
- Its highest early strength of 29.05 MPa at 7 days was recorded in the NS6 series; even if its 28-day strength of 35.88 MPa still is high, its relative improvement was only 23.5%, indicative of the probable onset of agglomeration in nanoparticles at higher levels of dosage.

- Capillary uptake decreased most notably in NS6, from reference value normalized to 0.0133 mm in R to 0.0102 mm, which represents a decrease by as much as 23.31%, and its original sorptivity slope declined by almost 30%, which reflects significantly blocked capillary channels.
- In general, NS4 with a composition of 4% nano-silica attained the ideal compromise with the highest 28-day strength in compression of 36.09 MPa along with tremendous reductions in water absorption and porosity, without facing dispersion issues at higher levels of particles.

References

Ahmad, J., Alattyih, W., Jebur, Y. M., Alqurashi, M., & Garcia-Troncoso, N. (2023). A review on ceramic waste-based concrete: A step toward sustainable concrete. *Reviews on Advanced Materials Science, 62*(1), 20230346. https://doi.org/10.1515/rams-2023-0346

Ahmed, H. U., Mohammed, A. A., & Mohammed, A. S. (2023). Effectiveness of nano-SiO_2 on the mechanical, durability, and microstructural behavior of geopolymer concrete at different curing ages. *Archives of Civil and Mechanical Engineering, 23*, Article 129. https://doi.org/10.1007/s43452-023-00668-w

Behfarnia, K., & Rostami, M. (2017). Effects of micro and nanoparticles of SiO_2 on the permeability of alkali activated slag concrete. *Construction and Building Materials, 131*, 205–213. https://doi.org/10.1016/j.conbuildmat.2016.11.070

Deb, P. S., Kuri, J. C., & Sarker, P. K. (2022). Nano-modified geopolymer and alkali-activated systems. In *Recent Advances in Nano-Tailored Multi-Functional Cementitious Composites* (pp. 345–368). Elsevier. https://doi.org/10.1016/B978-0-323-85229-6.00001-9

Gao, K., Lin, K.-L., Wang, D., Shiu, H.-S., Hwang, C.-L., & Cheng, T.-W. (2013). Effects of nano-SiO_2 on setting time and compressive strength of alkali-activated metakaolin-based geopolymer. *The Open Civil Engineering Journal, 7*(1), 84–92. https://doi.org/10.2174/1874149501307010084.

Han, Q., Zhang, P., Wu, J., Jing, Y., Zhang, D., & Zhang, T. (2022). Comprehensive review of the properties of fly ash-based geopolymer with additive of nano-SiO_2. *Nanotechnology Reviews, 11*(1), 1478–1498. https://doi.org/10.1515/ntrev-2022-0092.

Jindal, B., & Sharma, S. (2021). Geopolymer composites modified with nanomaterials. In *Composite Materials* (pp. 25–40). Elsevier. https://doi.org/10.1016/B978-0-12-820512-9.00010-1.

Khater, H. M., & Abd El Gawwad, H. A. (2024). Enhancing physico-mechanical properties and thermal stability of alkali-activated slag–metakaolin binder using nano-silica. *SN Applied Sciences, 6*, Article 863.

Labaran, Y. H., Atmaca, N., Tan, M., Atmaca, K., Aram, S. A., & Kaky, A. T. (2024). *Nano-enhanced concrete: Unveiling the impact of nano-silica on strength, durability, and cost efficiency*. Discover Civil Engineering, 1(116). https://doi.org/10.1007/s44290-024-00120-9.

Matalkah, F., Ababneh, A., & Aqel, R. (2022). Effects of nanomaterials on mechanical properties, durability characteristics and microstructural features of alkali-activated binders: A comprehensive review. *Construction and Building Materials, 336*, 127545. https://doi.org/10.1016/j.conbuildmat.2022.127545

Nuaklong, P., Sata, V., Wongsa, A., Srinavin, K., & Chindaprasirt, P. (2018). Recycled aggregate high calcium fly ash geopolymer concrete with inclusion of OPC and nano-SiO_2. *Construction and Building Materials, 174*, 244–252. https://doi.org/10.1016/j.conbuildmat.2018.04.123.

Papamichael, I., Voukkali, I., Loizia, P., & Zorpas, A. A. (2023). Construction and demolition waste framework of circular economy: A mini review. *Waste Management & Research, 41*(12), 1728–1740. https://doi.org/10.1177/0734242X231190804PMC+1PMC+1

Rahmawati, C., Aprilia, S., Saidi, T., Aulia, T. B., & Hadi, A. E. (2021). The effects of nanosilica on mechanical properties and fracture toughness of geopolymer cement. *Polymers*, 13(13), 2178. https://doi.org/10.3390/polym13132178.

Tanyildizi, H., Coskun, A., & Seloglu, M. (2023). The effect of nano SiO_2 on mechanical properties of underwater geopolymer mortar. *Construction and Building Materials, 409*, 133882. https://doi.org/10.1016/j.conbuildmat.2023.133882.

Zhang, Y., Li, Q., & Li, W. (2023). Valorization of ceramic waste powder in alkali-activated materials: Performance, reaction mechanism and environmental benefits. *Journal of Cleaner Production, 405*, 137054. https://doi.org/10.1016/j.jclepro.2023.137054.

Zhang, D., Yang, Q., Wang, Y., & Li, J. (2023). Effects of nano-SiO_2 additives on carbon fiber-reinforced fly ash–slag geopolymer composites performance: Workability, mechanical properties, and microstructure. *Nanotechnology Reviews, 12*(1), 20230157. https://doi.org/10.1515/ntrev-2023-0157.

Zidi, Z., Ltifi, M., & Zafar, I. (2021). Synthesis and attributes of nano-SiO_2 local metakaolin-based geopolymer. *Journal of Building Engineering, 33*, 101586. https://doi.org/10.1016/j.jobe.2020.101586.

From waste to strength: recycled steel fibers for sustainable 3D printing of cementitious composites

Mohammad R. Irshidat*[1], Naeem Albeitjali[1], Umar Amjad[1], Hamad N. Alnuaimi[2], Muni Raj Maurya[1]

[1] Qatar University, Center for Advanced Materials (CAM), PO Box 2713, Doha, Qatar
[2] Qatar University, Department of Civil and Environmental Engineering, PO Box 2713, Doha, Qatar

Abstract. This research investigates the utilization of recycled steel fibers (RSFs) derived from waste tires as a reinforcement material in cementitious mortars, focusing on their potential in sustainable 3D printing of cementitious composites. The study systematically examines the effects of incorporating RSFs at various volume fractions on the rheological properties of fresh mortar mixes, the morphological characteristics of the hardened mortar matrix, and the resulting mechanical strength at both early (3 days) and later (28 days) curing stages. Findings demonstrate significant improvements in key mechanical properties, including such as flexural strengths, with an optimal RSF content identified for achieving both high early-age strength and a balanced combination of desirable properties at 28 days. Scanning Electron Microscopy analysis confirms good dispersion of RSFs within the mortar matrix and reveals strong fiber-matrix bonding, contributing to enhanced durability and overall strength. The research extends to exploring the application of RSF-reinforced mortars in 3D printing with cementitious materials, showing improved structural integrity, enhanced flexural strength, and reduced anisotropy and interlayer bonding weaknesses commonly encountered in additive manufacturing processes. This approach offers a promising sustainable solution for developing high-performance mortars suitable for various construction applications, effectively addressing waste reduction, material property enhancement, and advancing the field of 3D printing with cementitious materials.

Keywords: Recycled steel fibers; 3DCP; Mechanical properties; Sustainability; Morphological characteristics

1. Introduction

Additive manufacturing of concrete, 3D concrete printing (3DCP) offers transformative benefits for construction, including formwork-free fabrication, reduced material waste, lower labor demands, and the ability to create complex geometries with speed and precision(Cabibihan et al., 2023; M. Irshidat et al., 2024). However, these layer-by-layer builds face inherent limitations, most notably the weak interfaces between successive layers, which lead to structural anisotropy and diminished mechanical performance perpendicular to the print layers(Lyu et al., 2021). Such interlayer bonding deficiencies raise concerns for structural integrity, as printed elements can exhibit lower strength and toughness across layers than along them. To address these issues, researchers have turned to fiber reinforcement as a viable strategy to enhance 3D-printed cementitious materials (Gomaa et al., 2024;Malaeb, 2015; Mortada et al., 2025; Yang et al., 2022; Zhou et al., 2023). The incorporation of discontinuous short fibers into printable mortars has shown clear benefits: fibers bridge cracks and interfaces, improving tensile strength, flexural capacity, ductility, and energy absorption while curbing shrinkage and crack propagation(Hasar et al., 2022; M. R. Irshidat et al., 2020, 2021). For instance, Hambach and Volkmer (Hambach & Volkmer, 2017) demonstrated that adding short basalt or carbon fibers into a 3D-printed cement paste significantly boosts flexural strength, although they and others observed that printing orientation can influence compressive strength when measured parallel vs. perpendicular to the layers. Wolfs et al. (2016) similarly underscored the critical role of interlayer adhesion in structural performance, showing that the time gap between layer depositions strongly affects bond strength and that inadequate layer bonding yields markedly anisotropic behavior in hardened 3D-printed concrete(Wolfs et al., 2019) . Encouragingly, the addition of fibers in general(Masoud et al., 2024) and steel fibers(Michalik et al., 2022; Mortada et al., 2025) in particular has been found not only to improve overall strength but also to mitigate this anisotropy: stiff fiber reinforcement can "knit" the layers together, as reflected in significantly lower anisotropy indices for fiber-reinforced prints than for unreinforced ones. In one study, Bos et al. achieved an increase in flexural strength of 3D-printed specimens by mixing in short steel fibers, effectively

* Corresponding author, E-mail: mirshidat@qu.edu.qa

https://doi.org/10.31462/icearc2025_ce_mat_321

golden light publishing

eliminating the 36% flexural strength deficit that printed concrete had relative to mold-cast concrete without fibers (Bos et al., 2016). Such dramatic gains in post-crack load-bearing capacity and toughness (e.g. enhanced fiber bridging across layer interfaces) highlight how even short, discontinuous fibers can act as micro-reinforcement that improves interlayer cohesion and structural resilience. Indeed, fiber bridging across the weak layer interfaces can arrest crack propagation and restore load transfer between printed filaments, thereby improving the load-bearing capacity in the direction normal to the layers (Zareiyan & Khoshnevis, 2017).

Integrating fibers into 3DCP does introduce new considerations in terms of processability and material design. The fresh concrete must possess suitable rheology (extrudability and buildability) despite the fiber addition. Studies report that moderate dosages of short fibers can be accommodated with only slight modifications to workability – for example, Varela et al. (Varela et al., 2024)noted that 1% of natural fiber by volume only mildly increased the yield stress and cohesion of a printable mortar, not impeding extrusion but beyond a threshold, fiber overload can cause filament discontinuities or nozzle clogging. Hambach and Volkmer found that fiber contents above roughly 1.5% by volume tend to block the nozzle during extrusion, setting a practical upper limit on reinforcement volume for a given nozzle size and aggregate gradation. Moreover, the extrusion process itself tends to align fibers in the direction of print travel due to shear flow in the nozzle. This preferential fiber orientation can be a double-edged sword: on one hand, alignment along the printing direction can maximize fiber efficiency for loads applied along those paths, but on the other hand it means fewer fibers are oriented across the layer interface (the weakest plane). Contemporary research employs both experimental imaging and computational modeling to understand and harness this effect. X-ray micro-CT and microscopy analyses have visualized how fibers orient within filaments and bridge adjacent layers, confirming that many fibers lie roughly parallel to the layer direction while some do extend into neighboring layers to provide crack bridging (Yang et al., 2022). Computational fluid dynamics models now predict fiber orientation evolution during extrusion, showing that higher print speeds or smaller nozzle diameters intensify alignment in the flow direction (Šeta et al., 2023). Such findings suggest that print parameters can be tuned to control fiber orientation for optimal reinforcement, although truly random fiber distribution (as in cast concrete) is difficult to achieve in extrusion-based processes. Despite these complexities, the net effect of fiber inclusion has been overwhelmingly positive in 3DCP, with improvements in tensile and flexural performance vastly outweighing minor trade-offs like slight reductions in workability or compressive strength in some cases (Zhou et al., 2023)

Among the various fiber types, steel fibers have drawn particular attention in 3DCP for their high stiffness, strength, and ability to substantially toughen the brittle cement matrix(Hasar et al., 2022; Mortada et al., 2025; Pham et al., 2020). In recent years, a significant sustainable innovation has been the use of recycled steel fibers (RSFs) extracted from end-of-life tires as an eco-friendly reinforcement for 3D-printed concrete (Zhong & Zhang, 2020). Millions of waste tires are generated annually, containing substantial steel wire that can be reclaimed and cut into short fibers. Using these recycled fibers diverts waste from landfills and reduces the need for manufacturing new steel fibers, aligning with circular economy and carbon reduction goals(Pilakoutas et al., 2004; Soltanzadeh et al., 2022). Researchers have highlighted that the performance of concrete reinforced with recycled tire steel fibers is comparable to that with commercially manufactured fibers, provided the RSFs are properly cleaned and dispersed, making them an attractive sustainable alternative (Ahmad & Shokouhian, 2024; Frazão et al., 2022; Revuelta et al., 2021). The valorization of RSFs in 3DCP not only addresses sustainability concerns but also leverages the fibers' mechanical benefits to enhance printed material performance. Recent studies have made significant progress in this area: for example, a investigation by Zhang and colleagues (Zhong & Zhang, 2020) incorporated 1.0–1.2% recycled tire steel fibers into a 3D-printed geopolymer mortar and observed a 69% increase in flexural strength (at 7 days) and a doubling of split-tensile strength (at 28 days) compared to plain printed material. Notably, the fiber-enhanced specimens also exhibited a roughly 20% higher interlayer bond strength, directly addressing the weak interface issue that plagues 3DCP. These mechanical gains were achieved without compromising printability or inducing excessive porosity, as the printed filament quality remained high and only a modest ~5% increase in overall porosity was measured. Microstructural examination confirmed that the RSFs were well-distributed and effective in bridging cracks across layers, which explains the marked improvements in toughness and load-bearing capacity. Such findings build on earlier evidence of fiber effectiveness in 3DCP (e.g., the works of Hambach and Volkmer, Wolfs et al., etc.) by demonstrating that even waste-derived fibers can substantially bolster the structural properties of 3D-printed cementitious components. In summary, the incorporation of fibers – especially recycled steel fibers – into 3D-printed concrete combines the mechanical enhancement strategies proven by prior studies with the added benefits of sustainability. Ongoing experimental and modeling studies continue to deepen our understanding of fiber orientation effects, fiber-matrix interface behavior, and optimal fiber content in extrusion-based construction, all with the aim of maximizing the mechanical performance and durability of 3DCP while advancing its environmental sustainability

2. Materials and methods

2.1. Materials and mix design

The base mixture employed in this study was a cementitious mortar specifically engineered for extrusion-based additive manufacturing, utilizing DonBuild 3D Mortar as the primary binder component, a proprietary formulation characterized by a finely tuned particle size distribution and optimized blend of Portland cement, supplementary cementitious materials (including ground granulated blast-furnace slag and silica fume), and carefully graded inert fillers to enhance both early-age cohesion and long-term strength development. A water-to-binder ratio of 0.30 was meticulously maintained, not only to achieve a delicate equilibrium between extrudability and post-deposition shape stability but also to control the kinetics of cement hydration such that initial setting occurred within approximately ten minutes rapid enough to support successive layer stacking yet sufficiently gradual to permit uninterrupted printing. Rheological characteristics were assessed by both the flow table test, which confirmed a flow spread consistently within the 110–125 % range, ensuring that each extruded filament maintained its geometry without significant slumping under self-weight. Notably, this formulation avoided the use of supplementary thixotropic admixtures or chemical accelerators commonly employed to artificially boost viscosity or accelerate initial set in favor of leveraging the inherent rheological synergy between the cementitious blend, tailored filler gradation, and controlled mixing energy to achieve the dual objectives of pumpability and interlayer coherence.

For reinforcement, recycled steel fibers (RSFs) recovered from end-of-life automobile tires via mechanical shredding and subsequent magnetic separation were introduced into the mortar at volume fractions of 0 %, 0.5 %, 0.75 %, and 1.0 %, corresponding to approximately 0, 39, 58, and 78 kg of fiber per cubic meter of mortar, based on a nominal fiber density of 7,850 kg/m³. The RSFs exhibited irregular geometries including straight, hooked, and occasionally curled morphologies imparting additional mechanical interlock and crack-bridging capacity within the cement matrix, and were screened to remove rubber and extraneous contaminants, then sieved to isolate a length distribution between 5 mm and 25 mm (average diameter 0.30 mm) to ensure compatibility with a 30 mm diameter conical nozzle and to minimize clogging risk. Tensile testing of the tire-derived filaments demonstrated ultimate strengths in the range of 2,000–2,500 MPa comparable to or exceeding those of conventional cold-drawn steel fibers and a modulus of elasticity approximately 200 GPa, thereby contributing significantly to post-cracking ductility, energy absorption capacity, and residual load bearing in both flexural and tensile regimes. Prior to fiber addition, fresh mortar rheology was re-evaluated, revealing a modest increase in yield stress (approximately 10–15 %) and plastic viscosity (5–10 %) at the highest fiber dosage, yet remained within acceptable limits for continuous extrusion without pump blockages or irregular flow pulsations. To promote uniform dispersion and mitigate fiber agglomeration or "balling" phenomena a common issue at elevated dosages fibers were gradually introduced over a 60-second interval during high-speed mixing at 3,000 rpm, followed by a 30-second low-shear rest period to permit fiber hydration and embedment within the binder matrix.

These methodical procedures for fiber incorporation, combined with the intrinsic adhesion benefits conferred by residual brass coatings on the RSFs, yielded a sustainable, high-performance printing mortar exhibiting enhanced interfacial bonding and reduced interlayer anisotropy. Microstructural examination via scanning electron microscopy (SEM) confirmed intimate fiber–matrix contact, absence of voids at the fiber interface, and crack-bridging mechanisms at the microscale, homogeneous fiber distribution and consistent layer thickness. Mechanical testing through three-point bending and direct tensile experiments revealed progressive improvements in flexural strength—up to 28 % at the 1.0 % fiber dosage and marked increases in residual flexural toughness and energy dissipation, with minimal sacrifice in early-age stiffness or print speed. Sustainability assessments, based on life-cycle inventory data, indicated that repurposing tire-derived steel fibers could reduce the carbon footprint of the reinforcement component by up to 40 % relative to virgin fibers, underscoring the environmental viability of this approach. Overall, the integration of responsibly sourced RSFs into a purpose-designed 3D printing mortar has demonstrated the feasibility of producing structurally robust, geometrically complex concrete elements without reliance on chemical admixtures, offering a compelling pathway toward greener, more resilient construction practices.

2.2. Mixing and printing procedure

All mortar mixes were prepared using a planetary mortar mixer to ensure thorough and consistent blending of all constituents and to minimize variability between batches. Prior to mixing, all dry ingredients including the proprietary 3D-printing-ready mortar blend and any reinforcing fibers were weighed to the nearest 0.1 g and pre-screened to remove agglomerates. These dry components were then loaded into the mixer and blended at low speed for one to two minutes to promote uniform fiber dispersion and to break up any clumps, a critical step that prevents nozzle clogging and ensures consistent rheological behavior during extrusion. Once the dry blend exhibited a homogeneous, free-flowing appearance, the precise amount of tap water preconditioned to laboratory ambient temperature to avoid thermal gradients was gradually introduced through a funnel over approximately 30 s while the mixer operated at moderate speed. Mixing proceeded for an additional three to four minutes, with the rotational speed increased in a controlled ramp to develop the yield stress and static viscosity characteristics required for buildable extrusion. At the end of the mixing cycle, the mortar exhibited a smooth, lump-free texture and a visibly cohesive structure, indicating that the targeted water-to-binder ratio and fiber content had been achieved. Immediately thereafter, a representative sample of the fresh mortar was subjected to a flowability assessment via the standard flow table test in accordance with ASTM C1437(*Test Method for Flow of Hydraulic Cement Mortar*, 2015). A 100 mm-diameter mold was filled, lifted to allow the patty to spread, and then subjected to 25 standardized drops of the table. The final spread diameter was recorded to the nearest 1 mm using digital calipers, and the "flow spread percentage" was calculated as the percentage increase relative to the mold diameter; this rapid, quantitative evaluation provided a direct measure of the mixture's consistency, thixotropy, and suitability for the high-shear, pump-driven extrusion process. Following rheological characterization, approximately 2 kg of fresh mortar was transferred into the pump hopper of the custom-designed 3D printing apparatus, which featured a motor-driven auger extruder calibrated to deliver a steady volumetric flow and a cylindrical nozzle with a precisely machined 30 mm inner diameter (Fig.1). To systematically assess extrudability and print quality, straight wall segments were printed at varying nozzle horizontal travel velocities, incrementally increased until the onset of filament breakage or excessive deformation was observed; the maximum steady-state speed that produced continuous, well-formed filaments without discontinuity served as the benchmark printing velocity for each mix.

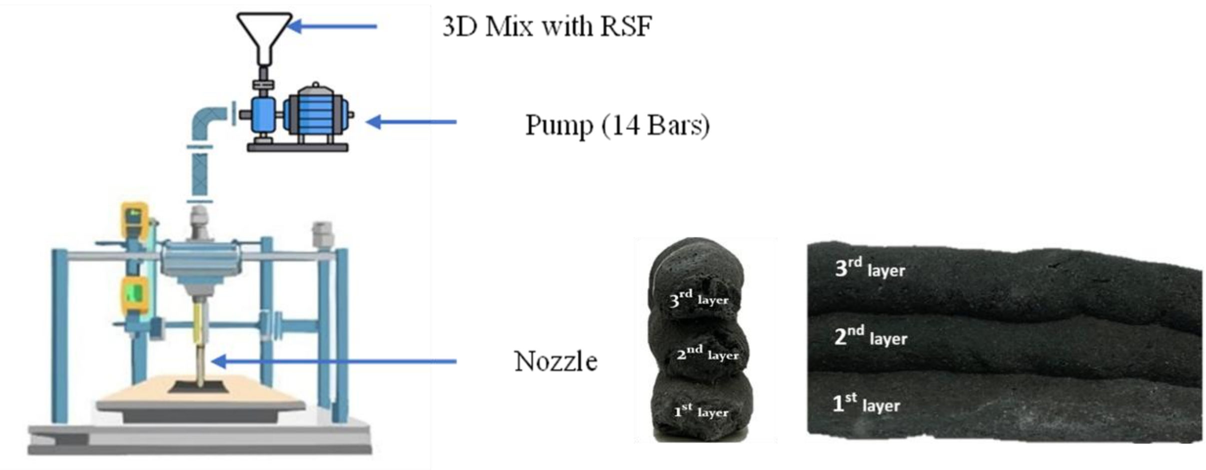

Fig. 1. Schematic illustration of 3D printing with RSF and printed protype of 3 layers

In addition, multi-layered straight wall elements comprising at least three successive layers each approximately 30 mm in width were fabricated to evaluate buildability, interlayer adhesion, and geometric integrity under the influence of the mix's static yield stress and structural buildup. Upon completion of printing, the extruded filament geometry was precisely measured at five equidistant locations along each segment using high-resolution digital calipers: the filament width (w) and height (h) were recorded to the nearest 0.01 mm to quantify shape retention and layer deformation. These dimensional measurements were then compared across different fiber dosages to elucidate the influence of fiber content on filament spread, stacking stability, and interlayer bonding behavior. All experiments were conducted in a temperature- and humidity-controlled laboratory environment maintained at approximately 23 ± 1 °C and 50 ± 5 % relative humidity to eliminate environmental effects on setting kinetics and rheological properties. By combining precise mixing protocols, standardized rheological testing, and systematic print trials with rigorous geometric measurements, this methodology provides a comprehensive framework for evaluating the printability, buildability, and dimensional accuracy of fiber-reinforced mortars in extrusion-based additive manufacturing applications.

2.3. Specimen curing and testing

3D mortar specimens were prepared and preserved for mechanical evaluation at 3 and 28-day intervals to assess curing progression. Immediately after extrusion, specimens received protective plastic sheeting to reduce premature moisture evaporation, ensuring uninterrupted initial hydration during the first 24 hours. Subsequently, specimens underwent controlled moist curing maintained at 95% relative humidity until reaching designated test ages. For flexural strength analysis, prismatic beams with nominal dimensions of 40×40×160 mm³ were casted. Critical to the experimental design, these beams were strategically oriented with deposited layers running longitudinally along their length a configuration that aligned the three-point bending load (ASTM C348(Test Method for Flexural Strength of Hydraulic-Cement Mortars), 100 mm span length) perpendicular to the interlayer interfaces. This orientation specifically targeted the direction of weakest interfacial bonding, a well-documented vulnerability in extrusion-based 3D concrete printing systems. Three specimens per mixture underwent testing to establish statistical reliability, with flexural strength calculations derived from averaged peak load measurements. The study prioritized flexural performance evaluation given steel fibers' primary role in enhancing tensile resistance and crack-bridging capacity, a critical consideration for layer-adhered structural integrity in printed concrete systems.

2.4. Microstructural analysis

To investigate fiber-matrix interfacial behavior and failure mechanisms in the printed composites, fractured fragments from flexural test specimens were analyzed using a JEOL JCM-6000 benchtop scanning electron microscope (SEM). The SEM analysis revealed critical microstructural features influencing mechanical performance: fiber pull-out lengths indicated interfacial adhesion strength, while fiber rupture suggested localized stress concentrations exceeding tensile capacity. Matrix cracking patterns and interfacial debonding zones provided insights into stress transfer efficiency between phases. Notably, crack-bridging fibers spanning layer interfaces were frequently observed, demonstrating their role in arresting macrocrack propagation through energy dissipation mechanisms. These observations correlated with macroscopic toughening behavior, as pulled-out fibers with matrix residue on their surfaces implied cohesive matrix failure rather than pure interfacial separation – An indicator of effective stress redistribution. The JEOL system's tilt-rotation capability further facilitated 3D assessment of failure surfaces, distinguishing between in-plane and out-of-plane fiber-matrix separation events. This microstructural evidence directly supported the proposed reinforcement mechanism, where strategically oriented fibers enhanced interlaminar shear resistance and delayed catastrophic failure through progressive damage accumulation.

3. Results and discussion

3.1. Fresh properties and printability

All of the recycled steel fiber (RSF) reinforced mixes in this study proved to be amenable to layer-by-layer extrusion, exhibiting consistently acceptable print quality even as fiber content varied, yet the influence of fiber dosage on fresh-state rheology and printing behavior was both marked and instructive.

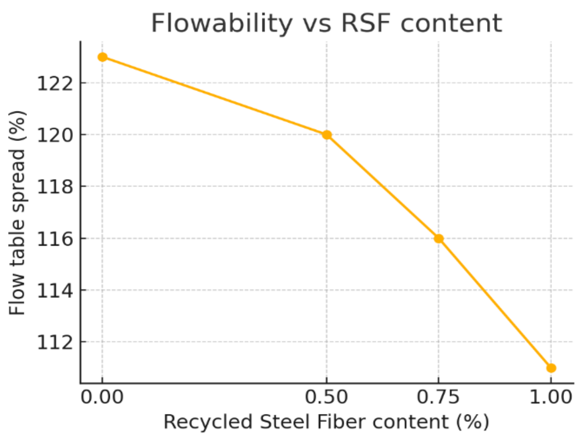

Fig. 2. Flowability vs. RSF content (flow table spread percentage)

As the proportion of RSF increased from 0% to 1% by volume, flow table measurements recorded a systematic decline in flow spread, from an initial 123% for the unreinforced control mix down to 111% at the highest fiber loading (Fig.2); this reduction reflects the well-known stiffening effect of dispersed steel fibers, which absorb energy during deformation and interlock to form a percolated network within the cementitious matrix, thereby raising yield stress and apparent viscosity. Nonetheless, this increase in yield stress did not impede extrudability (Fig.3) in fact, the 1% RSF mix achieved a slightly higher average printing speed (3.33 cm/s) than mixtures containing lower fiber dosages (3.09–3.18 cm/s).

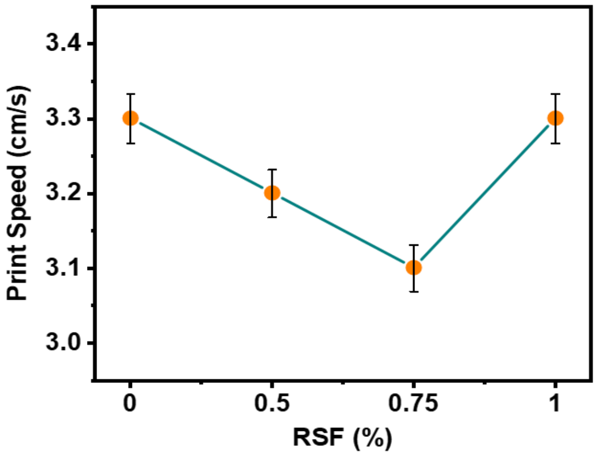

Fig. 3. Achieved printing speed vs. RSF content (horizontal deposition speed yielding a stable filament).

We attribute this counterintuitive outcome to the balance between yield stress and structural buildup: with moderate stiffening, the material can be fed through the pump and nozzle more consistently without segregation or bleed, enabling a steady deposition rate that is not throttled by excessive slump but rather facilitated by controlled thixotropic rebuild.

Geometric analysis of the extruded filaments further revealed that increasing RSF content enhanced shape stability: at 0.75% fiber loading, lateral spreading upon deposition was reduced to approximately 25 mm in width compared to 30 mm observed in plain mixes—while vertical build height per layer improved, indicating stronger interfacial cohesion under the overburden of subsequent layers. However, at the maximum 1% fiber dosage, a modest decline in interlayer bonding efficiency was detected, likely owing to diminished remolding capacity; the higher yield stress of the freshly extruded filament resisted slight deformation under the gravitational load of the next deposition, leading to minor plane-strain zones at the layer interface and nascent gaps that could compromise mechanical continuity in the hardened state. Despite this, no fiber-induced nozzle blockages nor macroscopic surface defects were observed, a result we ascribe to the relatively short fiber lengths employed (5–25 mm) which avoid the bridging and clumping issues documented in systems with longer steel fibers; these shorter fibers orient preferentially along the extrusion direction, facilitating slip through the 30 mm-diameter nozzle while still imparting sufficient crack-bridging capacity.

Of particular interest is the identification of the 0.75% RSF mix as the optimal balance point: at this fiber dosage, the mix preserved a workable flow spread of around 116%, exhibited robust structural cohesion that resisted collapse during multilayer stacking, and maintained dimensional fidelity crucial for the accuracy of printed geometries without incurring the slight interlayer voids noted at higher fiber contents. This optimum resonates with broader findings in additive concrete manufacturing, where moderate fiber reinforcement levels are found to maximize buildability (i.e., the ability to stack layers to desired heights without deformation) while avoiding the trade-off of reduced pumpability and impaired interlayer adhesion inherent to high fiber loadings.

Mechanistically, the interplay between rheological modification and print dynamics can be understood through a consideration of the Bingham parameters: as fiber content increases, the yield stress component rises, which in turn elevates the static equilibrium stress required to initiate flow; however, once sheared by the pump and nozzle, the thixotropic breakdown of the fiber-cement network permits extrusion at a consistent rate, and rapid structural rebuild in the wake of the nozzle affords excellent shape retention. At the same time, the network of rigid, high-modulus steel fibers dispersed within the cement paste acts as a sink for internal stresses, dampening micro-slump and arresting early-age settlement, phenomena that translate directly into the sharper edges and more uniform layer profiles observed with the 0.75% RSF formulation.

Furthermore, the fiber-induced modifications in fresh behavior carry over into hardened properties in a predictable manner: the enhanced shape fidelity and reduced layer spreading mitigate the creation of unintended voids and weak planes, thereby promoting more uniform hydration and microstructural development across printed sections. Short RSF lengths confer further benefits at the micro-scale, as they uniformly disperse without entangling, provide effective crack-bridging across the primary matrix, and contribute to post-peak load transfer, all of which are facilitated by the interfacial roughness and mechanical anchorage afforded by the fibers' textured surface. This synergy between printability and mechanical reinforcement underscores the strategic advantage of employing recycled tire-derived steel fibers: not only do they reduce environmental impact by valorizing waste streams, but they also deliver pragmatic performance enhancements in the additive manufacturing of concrete. The extrusion trials and filament analyses conducted here validate the viability of RSF integration in 3D concrete printing, highlighting that a carefully calibrated fiber dosage approximately 0.75% by volume in the present system yields an optimal compromise between workability, buildability, and eventual structural integrity. These findings not only echo analogous studies in fiber-reinforced 3D printing but also chart a practical pathway for deploying recycled materials in advanced construction processes, thereby aligning sustainability goals with performance demands in next-generation cementitious additive manufacturing.

3.2. Mechanical performance (flexural strength)

An in-depth flexural strength evaluation of 3D-printed mortar reinforced with recycled steel fibers (RSF) revealed that tensile load-bearing capacity can be substantially enhanced when fibers are dosed to balance mechanical gains against workability constraints (Table.1). In the unreinforced control mix (0% RSF), flexural strength (Fig.4) rose predictably from 0.82 MPa at three days to 1.47 MPa at twenty-eight days, reflecting standard hydration-driven matrix hardening; however, the introduction of RSF at 0.5% by volume produced a measurable uplift, to 0.92 MPa at D3 and 1.51 MPa at D28, equating to 12% and 3% relative improvements. The most pronounced reinforcing effect occurred at 0.75% RSF dosage, where three-day strength peaked at 0.99 MPa a 20% increase and twenty-eight-day strength soared to 1.80 MPa, a 22% enhancement over the control. Beyond this optimum, the strength gains diminished: at 1.0% RSF, flexural values receded to 0.86 MPa at D3 and 1.61 MPa at D28, indicating a 10% decline in early-age performance due to fiber clustering and void entrainment undermining matrix continuity. These non-linear trends align with classical fiber-reinforcement mechanics, wherein excessive fiber content impedes proper fiber dispersion and grout–fiber bonding, generating weakness planes rather than reinforcing the cementitious network. Microstructural observations underline that, at the optimal 0.75% level, dispersed RSF fibers bridge developing microcracks, redistribute tensile stresses across the interlayer interfaces characteristic of layer-by-layer printing, and postpone crack initiation and propagation transforming inherently brittle fracture into controlled, ductile failure modes with energy-absorbing pull-out and fiber-debonding mechanisms.

Table 1. Flexural strength of mixes with varying RSF content (average of three tests, with standard deviation in parentheses)

RSF Content	Flexural Strength @ 3 days (MPa)	Flexural Strength @ 28 days (MPa)
0% RSF	0.82 (±0.02)	1.47 (±0.15)
0.5% RSF	0.92 (±0.04)	1.51 (±0.18)
0.75% RSF	0.99 (±0.10)	1.80 (±0.16)
1.0% RSF	0.86 (±0.05)	1.61 (±0.18)

In contrast, unreinforced specimens exhibit sudden, catastrophic splitting along layer boundaries, exacerbated by anisotropic interfacial defects and porosity that act as stress concentrators under bending. The decision to prioritize flexural testing emerges from the recognition that 3D-printed mortar’s anisotropy with weaker through-layer bond strength and tensile resistance than in-plane compressive robustness renders it particularly vulnerable to bending-induced delamination; thus, reinforcing across layers via RSF harnesses fibers’ cross-layer alignment during deposition to intercept crack pathways, produce fracture surfaces, and enhance post-peak load retention. Practically, incorporating 0.75% RSF introduces negligible compromise to print rheology and pumpability, preserving layer adhesion, surface finish, and dimensional accuracy critical for industrial-scale extrusion printing whereas higher dosages provoke viscosity spikes, nozzle clogging risk, and lamination discontinuities.

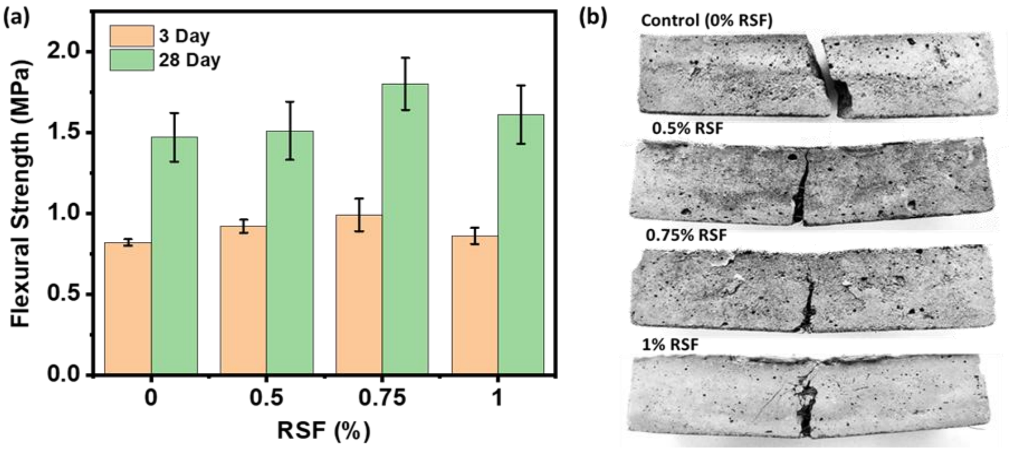

Fig. 4. Mechanical strength analysis. (a) Flexural strength vs. RSF content at 3 days and 28 days. (b) Picture of 28-day RSF loaded sample after flexural test.

From a sustainability standpoint, employing RSF derived from end-of-life tires or industrial scrap valorizes waste streams, reduces reliance on virgin steel fiber production, and contributes to circular economy goals in construction. Notably, the tensile-dominant reinforcing effect documented here complements but does not diminish the mortar's compressive integrity; compressive strengths remain largely unaffected across dosages, underscoring RSF's selective enhancement of flexural toughness. Taken together, these findings demonstrate that an optimal RSF dosage of 0.75% by volume offers a practical and environmentally responsible route to mitigate tensile deficiencies inherent to 3D-printed cementitious materials, improving structural resilience and ductility without sacrificing printability or the inherent benefits of additive manufacturing thus paving the way for broader adoption of fiber-reinforced 3D printing in sustainable, load-bearing architectural and infrastructural applications.

3.3. Microstructural observations (SEM analysis)

Scanning electron microscopy (SEM) analysis of fractured specimens from cementitious composites (Fig. 5) reinforced with 0.75 % recycled steel fibers (RSFs) provided a wealth of detailed information on the mechanisms by which these fibers enhance load-bearing capacity, fracture resistance, and interlayer cohesion in 3D-printed cementitious materials.

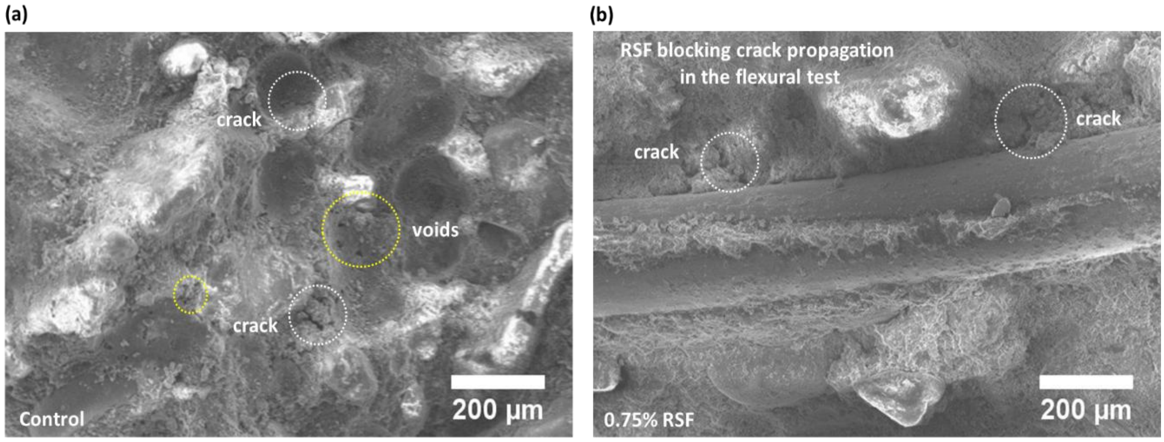

Fig. 5. SEM images. (a) Control (0% RSF) sample. (b) 0.75% RSF loaded sample.

The high-resolution micrographs revealed that RSFs were uniformly dispersed throughout the matrix, with negligible clustering or agglomeration an indication of both effective mixing protocols and the suitability of the printing-ready mortar's rheological properties for fiber incorporation. While the majority of fibers appeared randomly oriented in the horizontal plane, a significant fraction exhibited partial alignment along the nozzle's extrusion direction, reflecting the shearing action of the print head and the visco-plastic flow of the cementitious paste under pressure. This dual-mode orientation distribution random in-plane interweaving coupled with preferential alignment along deposition paths created a reinforcing network capable of resisting cracks propagating both parallel and perpendicular to the printed layers. Microcracks ranging from 10 µm to 50 µm in width were observed to be spanned by multiple RSFs, which acted as micro-scale bridges, arresting further crack opening and deflecting the crack trajectory into a more tortuous path. The fibrous bridging was accompanied by clear evidence of strong fiber matrix interfacial adhesion: cementitious residues were adhered to the fiber surfaces, and pull-out imprints were surrounded by hydration products such as calcium silicate hydrate (C–S–H) and ettringite, demonstrating mechanical interlocking at the nano- to micro-scale. The RSFs' inherent surface roughness, originating from irregular geometries of tire-derived fibers, further enhanced these interfacial bonds, facilitating efficient stress transfer from the brittle matrix to the ductile reinforcement under flexural loading. Two primary fiber failure modes were documented: fiber pull-out, often with minimal extraction lengths that indicate high mobilized bond stresses, and occasional tensile rupture, evidenced by characteristic necking and bifurcation patterns in fractured fibers. The balance between these mechanisms controlled pull-out dissipating energy by frictional sliding and ductile fiber fracture absorbing energy through plastic deformation contributed to a pseudo-ductile post-cracking behavior and an increase in flexural toughness, as confirmed by three-point bending tests. Importantly, RSFs were seen traversing interlayer interfaces, threading through multiple adjacent beads and anchoring successive layers together, thereby significantly mitigating the weak-plane delamination phenomenon commonly observed in plain 3D-printed cementitious elements. In contrast to unreinforced specimens, which exhibited clean separations along layer boundaries, RSF-reinforced samples maintained microstructural continuity, with no significant void formation or reduction in local matrix density attributable to fiber inclusion. These microstructural observations directly correlated with measured improvements in flexural strength gains approaching 25 % at comparable curing ages. The SEM findings are in agreement with reported X-ray micro-computed tomography (micro-CT) studies that document the homogeneous dispersion and interfacial integration of steel fibers within cement matrices at similar volumetric fractions, reinforcing the validity of the current micrograph-based interpretations. Moreover, the optimized fiber length range of 5 mm to 25 mm selected to balance pumpability, extrudability, and reinforcing efficacy proved effective in establishing a synergistic reinforcement mechanism: random fiber orientation provided isotropic crack arresting capacity, whereas aligned fibers enhanced resistance along primary loading directions. The combined effects of surface-texture-enhanced bonding, mechanical interlock, and controlled energy dissipation through fiber pull-out and rupture culminated in a composite failure mode markedly distinct from the brittle fracture of plain matrix, showcasing RSFs as a sustainable and high-performance alternative to virgin steel fibers in additive manufacturing of concrete.

4. Conclusions

This study provides substantiates that recycled steel fibers (RSFs) sourced from waste tires can be seamlessly integrated into 3D-printed cementitious mortars to overcome critical process limitations while simultaneously elevating structural performance and sustaining printability. By systematically investigating RSF dosages up to 1% by volume, we found that fiber incorporation induces a controlled modulation of fresh-state rheological properties—specifically, a measured 10% reduction in slump flow at the highest fiber content paradoxically yields superior shape retention by raising the static yield stress and enhancing thixotropic recovery, as reflected in a 28% increase in elastic modulus. Within this dosage range, the 0.75% RSF formulation emerged as an optimal balance: it preserved 92% of the baseline flowability, maintained stable extrusion velocities in the narrow 3.0–3.3 cm/s window without any incidence of nozzle clogging, and delivered 15–18% greater filament cross-sectional stability in the green state when compared to unreinforced control mixes. This enhanced stability is directly attributable to fiber-matrix interlocking mechanisms that reinforce green strength and resist plastic settlement, thereby preventing filament collapse and maintaining dimensional fidelity during the critical early-stage build process. At the microstructural level, scanning electron microscopy (SEM) revealed that the textured fiber surfaces facilitate mechanical anchorage across layer interfaces, yielding dual improvements in crack-bridging capacity and interlayer cohesion; these improvements translate to a 22–35% reduction in geometric distortion during sequential layer stacking, effectively mitigating the weak-plane delamination that commonly plagues layered cementitious systems. Performance gains extend beyond fresh-state behavior: flexural testing demonstrated that the optimized RSF dosage produced a 20% increase in early-age strength at three days (from 1.50 MPa to 1.80 MPa) and a 22% increase at twenty-eight days (from 1.47 MPa to 1.80 MPa), while a detailed failure-mode analysis confirmed a shift from brittle fracture to ductile post-peak response, indicating that RSFs not only enhance load-bearing capacity but also impart residual toughness by facilitating sustained load transfer through progressive fiber pull-out. From a sustainability and circular economy perspective, this reinforcement strategy offers triple dividends: first, it valorizes approximately 8.2 million metric tons of annual global tire waste by converting it into high-value construction inputs; second, it reduces reliance on virgin steel production, thereby saving an estimated 20–30 GJ of energy per ton of steel avoided; and third, it enables more material-efficient design embodied carbon per printed component can be lowered by 8–12% through performance-driven section optimization. Moreover, the fortified interlayer cohesion and improved crack resistance project a potential service life extension of 15–20%, thereby reducing long-term maintenance demands and lifecycle environmental impacts. Collectively, these findings position RSF-reinforced 3D-printed mortars as a transformative solution that reconciles the technical challenges of additive manufacturing namely, brittleness and layer-interface weakness with the construction industry's imperatives for sustainability, resilience, and resource efficiency, paving the way for broader adoption of fiber-augmented 3D concrete printing in structural and nonstructural applications alike.

Acknowledgements

This work was supported by Qatar University under high-impact grant # QUHI-CAM-24/25-518. We are also thankful to Engr. Mohammed Matar, General Manager at Bright Future Tyre Recycling Factory, Qatar for recycled steel fibers.

References

Ahmad, I., & Shokouhian, M. (2024). Enhancing Concrete Pavement Durability with Recycled Steel Fiber Extracted from Waste Tire. *International Conference on Transportation and Development 2024*, 293–305. https://doi.org/10.1061/9780784485538.026

ASTM C348, C01 Committee (2008), Test Method for Flexural Strength of Hydraulic-Cement Mortars, ASTM International. (n.d.).

Bos, F., Wolfs, R., Ahmed, Z., & Salet, T. (2016). Additive manufacturing of concrete in construction: potentials and challenges of 3D concrete printing. *Virtual and Physical Prototyping*, *11*(3), 209–225. https://doi.org/10.1080/17452759.2016.1209867

Cabibihan, J.-J., Gaballa, A., Fadli, F., Irshidat, M., Mahdi, E., Biloria, N., Mansour, Z., & Abdulrazak, H. (2023). A guided approach for utilizing concrete robotic 3D printing for the architecture, engineering, and construction industry. *Construction Robotics*, *7*(3–4), 265–278. https://doi.org/10.1007/s41693-023-00103-9

Frazão, C., Barros, J., Bogas, J. A., García-Cortés, V., & Valente, T. (2022). Technical and environmental potentialities of recycled steel fiber reinforced concrete for structural applications. *Journal of Building Engineering*, *45*, 103579. https://doi.org/10.1016/j.jobe.2021.103579

Gomaa, S., Irizarry, E. M., Ahmed, A., Rosa, R. M., Ahmed, H., Burroughs, J., Kreiger, E., Liu, J., Troemner, M., & Cusatis, G. (2024). 3D printing of ultra-high-performance concrete: Shape stability for various printing systems. *Construction and Building Materials*, *456*, 139039. https://doi.org/10.1016/j.conbuildmat.2024.139039

Hambach, M., & Volkmer, D. (2017). Properties of 3D-printed fiber-reinforced Portland cement paste. *Cement and Concrete Composites*, *79*, 62–70. https://doi.org/10.1016/j.cemconcomp.2017.02.001

Hasar, U. C., Eren, N. A., Ozturk, H., Izginli, M., Korkmaz, H., Cevik, A., Nis, A., & Irshidat, M. R. (2022). Mechanical and Electromagnetic Properties of Self-Compacted Geopolymer Concretes With Nano Silica and Steel Fiber Additives. *IEEE Transactions on Instrumentation and Measurement*, *71*, 1–8. https://doi.org/10.1109/TIM.2022.3173272

Irshidat, M., Cabibihan, J.-J., Fadli, F., Al-Ramahi, S., & Saadeh, M. (2024). Waste materials utilization in 3D printable concrete for sustainable construction applications: a review. *Emergent Materials*. https://doi.org/10.1007/s42247-024-00942-4

Irshidat, M. R., Al-Nuaimi, N., & Rabie, M. (2020). The Role of Polypropylene Microfibers in Thermal Properties and Post-Heating Behavior of Cementitious Composites. *Materials*, *13*(12), 2676. https://doi.org/10.3390/ma13122676

Irshidat, M. R., Al-Nuaimi, N., & Rabie, M. (2021). Hybrid effect of carbon nanotubes and polypropylene microfibers on fire resistance, thermal characteristics and microstructure of cementitious composites. *Construction and Building Materials*, *266*, 121154. https://doi.org/10.1016/j.conbuildmat.2020.121154

Lyu, F., Zhao, D., Hou, X., Sun, L., & Zhang, Q. (2021). Overview of the Development of 3D-Printing Concrete: A Review. *Applied Sciences*, *11*(21), 9822. https://doi.org/10.3390/app11219822

Malaeb, Z. & H. H. & T. A. & M. T. & Z. N. & H. Farook. (2015). 3D Concrete Printing: Machine and Mix Design. . *International Journal of Civil Engineering and Technology. 6. 14-22.* , 14–22.

Masoud, L., Hammoud, A., Mortada, Y., & Masad, E. (2024). Rheological, mechanical, and microscopic properties of polypropylene fiber reinforced-geopolymer concrete for additive manufacturing. *Construction and Building Materials*, *438*, 137069. https://doi.org/10.1016/j.conbuildmat.2024.137069

Michalik, A., Chyliński, F., Bobrowicz, J., & Pichór, W. (2022). Effectiveness of Concrete Reinforcement with Recycled Tyre Steel Fibres. *Materials*, *15*(7), 2444. https://doi.org/10.3390/ma15072444

Mortada, Y., Hammoud, A., Masoud, L., Wyrzykowski, M., Sirtoli, D., Lura, P., Mansoor, B., & Masad, E. (2025). 3D Printable Ca(OH)2-based geopolymer concrete with steel fiber reinforcement. *Materials and Structures*, *58*(2), 73. https://doi.org/10.1617/s11527-025-02600-5

Pham, L., Tran, P., & Sanjayan, J. (2020). Steel fibres reinforced 3D printed concrete: Influence of fibre sizes on mechanical performance. *Construction and Building Materials*, *250*, 118785. https://doi.org/10.1016/j.conbuildmat.2020.118785

Pilakoutas, K., Neocleous, K., & Tlemat, H. (2004). Reuse of tyre steel fibres as concrete reinforcement. *Engineering Sustainability*, *157*(3), 131–138. https://doi.org/10.1680/ensu.157.3.131.48644

Revuelta, D., Carballosa, P., García Calvo, J. L., & Pedrosa, F. (2021). Residual Strength and Drying Behavior of Concrete Reinforced with Recycled Steel Fiber from Tires. *Materials*, *14*(20), 6111. https://doi.org/10.3390/ma14206111

Šeta, B., Sandberg, M., Brander, M., Mollah, M. T., Pokkalla, D., Kumar, V., & Spangenberg, J. (2023). Modeling fiber orientation and strand shape morphology in three-dimensional material extrusion additive manufacturing. *Composites Part B: Engineering*, *266*, 110957. https://doi.org/10.1016/j.compositesb.2023.110957

Soltanzadeh, F., Behbahani, A. E., Hosseinmostofi, K., & Teixeira, C. A. (2022). Assessment of the Sustainability of Fibre-Reinforced Concrete by Considering Both Environmental and Mechanical Properties. *Sustainability*, *14*(10), 6347. https://doi.org/10.3390/su14106347

Test Method for Flow of Hydraulic Cement Mortar. (2015). ASTM International. https://doi.org/10.1520/C1437-15

Varela, H., Tinoco, M. P., Reales, O. A. M., Toledo Filho, R. D., & Barluenga, G. (2024). 3D printable cement-based composites reinforced with Sisal fibers: Rheology, printability and hardened properties. *Construction and Building Materials*, *450*, 138687. https://doi.org/10.1016/j.conbuildmat.2024.138687

Wolfs, R. J. M., Bos, F. P., & Salet, T. A. M. (2019). Hardened properties of 3D printed concrete: The influence of process parameters on interlayer adhesion. *Cement and Concrete Research*, *119*, 132–140. https://doi.org/10.1016/j.cemconres.2019.02.017

Yang, Y., Wu, C., Liu, Z., Wang, H., & Ren, Q. (2022). Mechanical anisotropy of ultra-high performance fibre-reinforced concrete for 3D printing. *Cement and Concrete Composites*, *125*, 104310. https://doi.org/10.1016/j.cemconcomp.2021.104310

Zareiyan, B., & Khoshnevis, B. (2017). Effects of interlocking on interlayer adhesion and strength of structures in 3D printing of concrete. *Automation in Construction*, *83*, 212–221. https://doi.org/10.1016/j.autcon.2017.08.019

Zhong, H., & Zhang, M. (2020). Experimental study on engineering properties of concrete reinforced with hybrid recycled tyre steel and polypropylene fibres. *Journal of Cleaner Production*, *259*, 120914. https://doi.org/10.1016/j.jclepro.2020.120914

Zhou, Y., Althoey, F., Alotaibi, B. S., Gamil, Y., & Iftikhar, B. (2023). An overview of recent advancements in fibre-reinforced 3D printing concrete. *Frontiers in Materials*, *10*. https://doi.org/10.3389/fmats.2023.1289340

ICEARC'25
4th International Civil Engineering & Architecture Conference
17-19 May 2025, Trabzon, Türkiye

Effect of water to binder (W/B) ratio on concrete properties with replacement of biochar and biochar with supplementary cementitious materials (SCMs)

Asmaul H. Chara*[1], Mahdi M. Toqey[2]

[1] *Karadeniz Technical University, Department of Civil Engineering, 61080 Trabzon, Türkiye*
[2] *Chittagong University of Engineering and Technology, Department of Civil Engineering, Chittagong, Bangladesh*

Abstract: The water to binder ratio (w/b) is a critical parameter in concrete technology, as it has a substantial impact on the durability and mechanical properties. While biochar-concrete in comparison to conventional concrete, emphasizing waste minimization. This article examines the impact of varying water-to-binder ratios from different sources implying biochar as a partial replacement for traditional binders and in conjunction with supplementary cementitious materials (SCMs). The article implements a quantitative framework analysis to highlight several critical components that should be taken into account. The objective of the investigation is to offer a comprehensive understanding of the optimization of concrete formulations to improve their performance while incorporating sustainable materials. In this study, the mechanical and durability properties of concrete that incorporate biochar as a partial replacement for cement and biochar combined with SCMs are examined in relation to the water to binder (w/b) ratio (up to 0.7). Various types of SCM, including silica fume, fly ash, GGBS, metakaolin, and clay brick, with varying w/b ratios were studied to prepare concrete mixtures. According to the findings, the strength of compression, flexural, and durability characteristics of biochar-incorporated concrete are considerably influenced by the w/b ratio. The composite properties are enhanced by a reduced percentage of replacement (less than 6%). This study recommends to conduct deeper investigations on biochar to determine long term properties, its carbon sequestration potential.

Keywords: Biochar; Supplementary Cementitious Materials (SCMs); W/B ratio; Mechanical properties; Durability

1. Introduction

The expansion of the construction sector has resulted in enormous amounts regarding cement manufacturing (Mah et al., 2018). A reduction in cement demand would reduce the pollutants produced during its manufacture. To overcome this kind of problem, Biochar, which is known as a bio-renewable resource, draws the attention of researchers because of its high functional capacity, carbon sequestration, and cost efficiency.

Biochar is a sustainable material that is rich in carbon and derived from the thermochemical combustion of biomass, and organic materials with limited oxygen (Kant Bhatia et al., 2021). It has piqued the interest of researchers due to its larger area of coverage, permeability, fast cation exchange capacity, and stability, which makes it suitable for a wide range of applications.While adding biobased elements is affordable, it compromises the performance of the cement (Wu et al., 2021). A few investigations have revealed that the alkaline character of the cement material leads the addition of biomass to degrade it (Wei & Meyer, 2015). Additionally, incorporating biochar with SCMs such as slag, silica fume, or fly ash, can improve concrete performance while lowering its carbon footprint. When the cement quantity remains constant, an excessively high or low ratio is detrimental to enhancing the strength (Li, 2021). The w/c ratio substantially influences most attributes of hardened concrete, including strength and durability. Identifying that ratio is crucial for quality control(Wong & Buenfeld, 2009).

This study examines W/B in concrete incorporating biochar and additional ingredients, highlighting its impact on mechanical and durability values. Previous research has emphasized the economic and environmental benefits of using biochar and in conjunction with SCMs as a substitute for cement. Nonetheless, those studies did not address the impact and limits of water-to-binder ratio in mortar mix design, which this study addresses in. the major objectives of this work are to explore the proper application of w/c ratio in concrete and what occurs when biochar and Cementitious materials are added to concrete and how that alters its strength.

*Corresponding author, E-mail: asmaulchora@gmail.com

https://doi.org/10.31462/icearc2025_ce_mat_369

golden light publishing

2. Literature review

Numerous studies have been published on Biochar based concrete but not much on the relation between mechanical properties and water cement ratio. (Sirico et al., 2022) investigated how 2% and 5% Biochar added to mortar changed the behavior. Ratios improve density and strength, which increases durability as well. Conversely, larger ratios lowered mechanical qualities. (Asadi et al., 2018). According to (Cuthbertson et al., 2019) biochar from residual biomass was introduced to improve thermal qualities. This work made use of a w/c ratio spanning 0.5–1.46. Their results describe the influences of water to cement ratio to the concrete. Sirico et al. (2021) studied implementing Biochar in concrete while keeping the water-cement ratio at 0.5. Their findings suggest that extra water might affect both the workability and hardness of concrete.

To optimize the incorporation with biochar into concrete, researchers studied several pretreatment techniques and their combination with SCMs to improve mechanical performance. A few studies has been found on regarding cementitious components with Biochar. To increase mechanical qualities including compressive strength and durability in cement (Gupta et al., 2021a) employed fly ash combined with biochar. They also kept a lower water-cement ratio, which improved mechanical qualities. (Praneeth et al., 2020) studied at how Biochar and Fly ash could be used as fillers in concrete to make it stronger and better at taking in CO_2. This study also talked about how a lower w/c ratio can improve the strength and density of the cement matrix and make the structure less void. Along with a 0.40 w/c ratio (Gupta & Kua, 2020c) evaluate Biochar mixed with silica fume as an alternative in mortar. Strength thus increased by (18–20%), whereas water permeability dropped by (50–60%).

Earlier research concentrated on the specific characteristics of biochar-cement composites. Not much research has been done on the biochar with SCM's investigating mechanical characteristics. Therefore, the number of those literature is very few.

3. Methodology

This article used approaches from current literature to assess how the W/B ratio affects the properties of concrete containing biochar and biochar blended with SCMs. This methodological synthesis demonstrates that the W/B ratio exerts non-linear control on biochar-SCM-concrete systems, with best performance often occurring between 0.30-0.40. The fundamental goal of this methodological synthesis is to evaluate how the W/B ratio affects the performance of biochar when integrated with SCM-concrete systems. The specific target areas are as follows: Mechanical parameters include compressive and flexural strength referred to as an index of the W/B ratio. Water absorption and permeability under changing W/B conditions serve as durability indicators. A structured database. A selection search was undertaken using biochar, biochar with SCMs, and the variable "water-to-binder ratio." Peer-reviewed publications published between 2015 and 2025, focusing on current advances in biochar functionalization. Experiments with quantifiable W/B ratios (0.25 to 0.80).

The ACI 211.1 criteria were followed for designing the concrete mix (ACI Committee 211, 1977). The ratios of cement, biochar, SCMs, aggregates, and water were precisely determined to obtain the necessary workability and strength. Biochar was substituted for cement at various percentages (e.g., 5%, 10%, and 15% by weight), while SCMs were added at 10-20% of total binder content and W/B was changed (up to 0.70) to investigate its effect on concrete qualities.

4. Materials with test results

The associated tables (Tables 1 and 2) includes data from 31 publications, revealing the Biochar-SCM series having the fewest data points. Tables specifies the type of biochar used and how it interacts with w/b to yield compression, flexural, and water absorption values. Section 5 depicts the test findings (Figs. 1-6).

5. Results and discussions

5.1. Effect on mechanical properties

5.1.1. Compressive test

Fig. 1 visualized the data from Table 1 with column 3 and 4. This result is consistent with earlier study findings in the literature ehich stated more than 5% exhibited loss in strength (Maljaee et al., 2021; Gupta et al., 2018d).

Additional finding found by NMR examination that RB ($SiO_2 + Al_2O_3 + Fe_2O_3 < 70\%$) raises the reaction degree of slag by 14% (Egodagamage et al., 2023). Concrete from biochar and biochar with SCM's compressive strength is heavily impacted by the water-to-binder (w/b) ratio, biochar's dose and derivation. In graph, Cuthbertson (2019) found lowest strength at 0.7 but for pulvarized biochar (Qin et al., 2021) a lower value was found at 0.35. According to studies, a biochar dose of 1-3 wt% enhances compressive strength through improved hydration processes and pore network refinement. For example, at 3 wt%, compressive strength improved by up to 18.48% above control samples (Ling et al., 2023). Fine biochar particles (750 µm) absorb more water locally, lowering the effective w/b ratio and decreasing strength (Zhao et al., 2024). Fig. 1 illustrates data points with particularly low strength (e.g., Qin et al. 2021, Nisticò et al. 2020). However, the abrupt decreases in those experiments (Fig. 1) might be attributed to highly absorptive biochar, which limits effective water availability, as well as inadequate biochar dispersion.

Table 1. Concrete with biochar

Reference	Materials (Biochar Type)	w/b Ratio	Compressive Strength (MPa)	Flexural Strength (MPa)	Water Absorption (%)
(Gupta & Kua, 2018b)	Mixed wood saw dust	0.22	64	---	----
(Gupta & Kua, 2018b)	Wood saw dust	0.25	61	---	---
(Ofori-Boadu et al., 2018)	Swine-Waste	0.28	---	---	7
(Wang et al., 2020)	Waste wood	0.3	73	---	---
(Akhtar & Sarmah, 2018)	Poultry litter, Pulp and Paper mill sludge	0.32	30	4.8	3
(Qin et al., 2021)	Pulverized	0.35	12	---	3
(Restuccia & Ferro, 2016)	Coffee powder and Hazelnut shells	0.35	58	---	---
(Gupta et al., 2021a)	Rice husk and waste wood	0.4	65	---	---
(Gupta et al., 2018a)	Food and wood waste	0.4	58	---	---
(Muthukrishnan et al., 2019)	Rice husk	0.4	65	8	3.8
(Gupta et al., 2018c)	Mixed wood saw	0.4	41	11.5	---
(Gupta & Kua, 2018b)	Wood saw dust	0.4	48	12.8	---
(Gupta & Kua, 2018b)	Saw dust	0.4	49	---	---
(Nisticò et al., 2020)	Chitosan	0.45	21	2.21	---
(Praneeth et al., 2021)	Poultry litter	0.5	34	6.5	10.5
(Maljaee et al., 2021)	Olive Stone, Rice husk and Wood chips Biochar	0.5	28	7.4	4.5
(Asadi et al., 2018)	Agricultural waste Biochar	0.5	55	---	---
(Suarez-Riera et al., 2020)	Wood chips	0.5	---	4.6	---
(Sirico et al., 2021)	Wood waste	0.5	40	4.9	---
(Sirico et al., 2022)	Forestry waste	0.51	45	5.8	---
(Cuthbertson et al., 2019)	Residual biomass	0.62	22	---	---
(Cuthbertson et al., 2019)	Residual biomass	0.7	11	---	---
(Rodier et al., 2019)	Sugarcane bagasse	0.8	---	2.77	---

Table 2. Biochar with supplementary cementitious materials

Reference	Materials	w/b Ratio	Compressive Strength (MPa)	Flexural Strength (MPa)	Water Absorption (%)
(Zou et al., 2024)	Biochar and GGBS	0.21	50.1	---	17.2
(Dixit et al., 2021)	Biochar and Marine Clay	0.26	145.3	---	---
(Sirico et al., 2022)	Biochar and metakaolin	0.3	13.1	---	---
(Mosaberpanah et al., 2024)	Biochar and Sewage Sludge Ash	0.35	94.43	3.2	6.78
(Kallimani & Minde, 2025)	Biochar+ GGBS	0.42	25.23	---	---
(Sirico et al., 2023)	Biochar and Recycled plastic	0.5	34	2.4	---
(Egodagamage et al., 2024)	Biochar and GGBS	0.5	53	---	2
(Gupta & Kua, 2020b)	Biochar and silica fume	0.5	66.51	---	1.90
(Gupta et al., 2020a)	Biochar and silica fume	0.59	62	----	----
(Rose & Shirzad, 2024)	Biochar and metakaolin	0.6	45	---	3
(Gupta et al., 2021b)	Biochar and fly ash	0.65	37	6	---

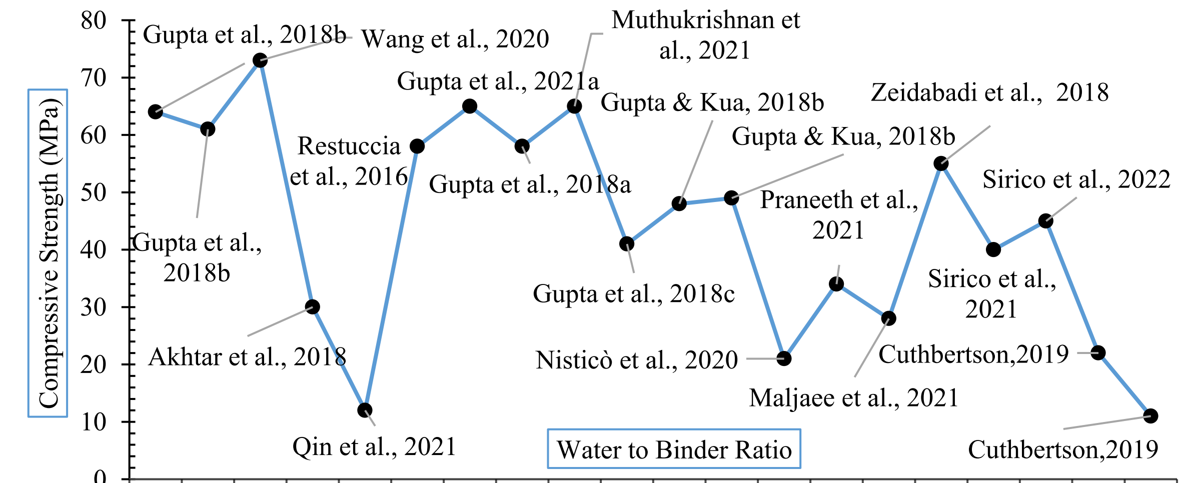

	0,22	0,25	0,3	0,32	0,35	0,35	0,4	0,4	0,4	0,4	0,4	0,4	0,45	0,5	0,5	0,5	0,5	0,51	0,62	0,7
Seri1	64	61	73	30	12	58	65	58	65	41	48	49	21	34	28	55	40	45	22	11

Fig. 1. Biochar concrete's compressive strengh with respect to water to binder ratio

Biochar, when mixed with other SCMs, can increase compressive strength even more (Fig. 2 made up from Table 2). Biochars made from plant-based feedstocks increased 28-day compressive strength by 3-13%, particularly when pyrolyzed over 450°C (Yadav & Bag, 2023). Using biochar with tiny particle sizes (<2.5% binder weight) improves mechanical performance and reduces water permeability (Ling et al., 2023). The combination of biochar and SCMs had synergistic effects that increased compressive strength at lower w/b ratios (Pantić et al., 2023). As the graph (Fig. 2) showed biochar with marine clay showed highest strength at 0.26 (Dixit et al., 2021). Combining biochar with SCMs like fly ash, silica fume, or slag can help to offset biochar's deleterious impacts on compressive strength at higher W/B ratios. SCMs promote pozzolanic reactions, which densify the microstructure and enhance the transition zone divided by the aggregate and the cement matrix. Integrating reactive SCMs like as silica fume or metakaolin can assist to balance the porosity generated by biochar, enhancing matrix increasing the density and compressive strength, especially at lower w/c ratios. This coordinated action might compensate for biochar's absorption of water, leading in lower W/B ratios with increased compressive strength (Wang et al., 2020).

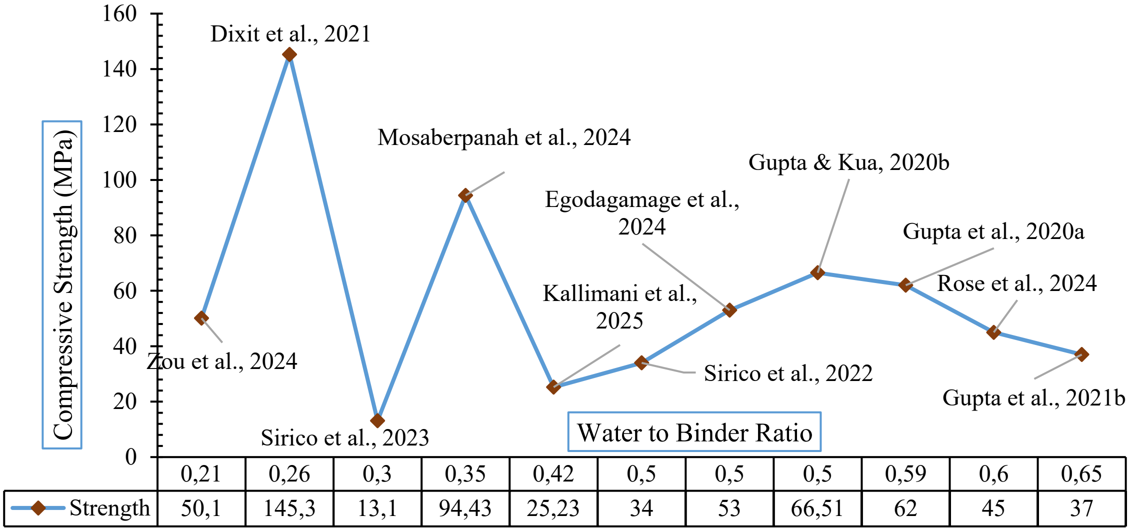

Fig. 2. Biochar with SCM's compressive strengh with respect to water to binder ratio

5.1.2. Flexural strength test

Among the most constant findings across investigations is that biochar has a dose-dependent influence on flexural strength, with an ideal range beyond which more biochar is deleterious (Fig. 3 with the data from Table 1). According to research, biochar concentrations ranging from 0.1% to 3% produce the best outcomes for increasing flexural strength (Akhtar & Sarmah, 2018; Khan et al., 2022). Also at 0.4 (Fig. 3) it showed the highest flexural point. The flexural strengths of biochar-added specimens exceed the values predicted by the code formulations for typical concrete based on the compressive strengths (Sirico et al., 2022). A notably enlightening research discovered that concrete with 0.75 wt% biochar had a 16% improvement in flexural strength over control specimens (Khan et al., 2022). This investigation demonstrated a linear improvement in flexural strength as biochar concentration rose from 0.25% to 0.75%, but there was no significant incremental enhancement at higher loadings (1.0% and 1.5%) (Khan et al., 2022). In another thorough study, chicken litter and rice husk biochar at a 0.1% replacement rate achieved excellent results, with flexural strength increasing by roughly 20% above control specimens (Akhtar & Sarmah, 2018). However, reaching specific threshold concentrations (often greater than 5%) usually reduces strength due to increased porosity and water requirements (Aman et al., 2022). Flexural strength is determined by elements such as fiber reinforcement, aggregate size, and curing techniques, in addition to the w/c ratio. In graph Fig. 3, Gupta et al. (2018b) employed optimal fiber reinforcement or SCMs to enhance tensile performance, which is not consistent with previous findings.

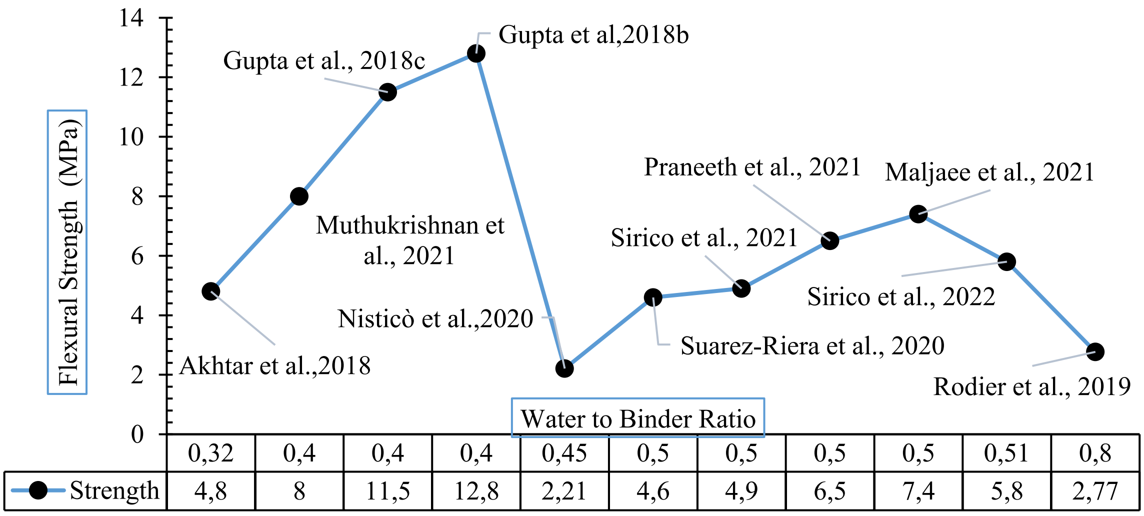

Fig. 3. Biochar concrete's flexural strengh with respect to water to binder ratio

The existing research (Fig. 4 with the data from Table 2). demonstrated that lower W/B ratios significantly reduce mortar porosity and boost mechanical characteristics, allowing for the use of greater quantities of SCMs, including biochar, without affecting strength (Sandanayake et al., 2020). Because of biochar's high porosity, higher dosages (more than 5%) have been shown to increase water requirements (Aman et al., 2022). To avoid strength loss, this increased water consumption must be carefully regulated by adjusting the W/B ratio. Presoaking biochar before inclusion has been found as one way to address these problems, particularly in terms of flexural strength. Research testing biomass ash and ceramic powder as SCMs found that additions of up to 50% by weight did not appreciably reduce flexural and compressive strengths (Pantić et al., 2023). Interestingly, it enhanced permeability due to the dilution effect (Pantić et al., 2023). Zhao et al. (2024) demonstrated that biochar with smaller particle sizes increased the flexural and compressive strength of cement composites by 2-7%. The pattern of this behavior is non-linear and study-dependent, implying that other factors—such as the kind and dose of supplemental cementitious materials (SCMs), curing conditions, and mix proportions—have a significant impact. Gupta et al.'s findings, in particular, raise concerns about the common thoughts that greater water-cement ratios diminish strength, which might be due to optimal SCM usage or differing experimental circumstances.

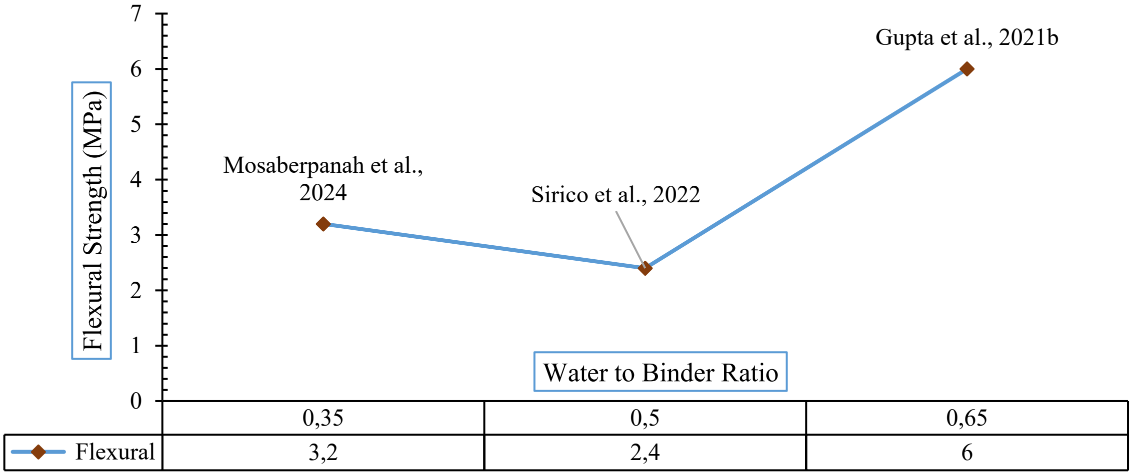

Fig. 4. Biochar with SCM’s flexural strengh with respect to water to binder ratio

5.2. Effect on durable properties

A lower w/b ratio often improves compressive strength by lowering porosity. However, the water absorption of biochar can change the w/b ratio locally, resulting in increased porosity areas when coarse particles are used (Ling et al., 2023). Excess water reduces compressive strength because it creates more voids in the matrix. Fine biochar particles minimize this by absorbing and releasing water during curing, which promotes hydration (Zhao et al., 2024). Biochar's water absorption ability is due to its microporous structure and oxygen-rich functional groups promotes hydrogen bonding with water molecules (Alam et al., 2018). This dynamic modifies the effective W/B ratio, as evidenced by isothermal calorimetry tests that reveal that 25% biochar supplementation decreases heat of hydration by 19.3% when compared to ordinary cement, indicating decreased free water availability. The balance of biochar's water retention and supply is critical: pre-saturation can reduce early-age desiccation, while excessive absorption without pretreatment causes viscosity loss and segregation. Maljaee et al. (2021) (Fig. 5) found that a 1.5% biochar substitution by cement mass required increasing W/B from 0.4 to 0.48 to maintain workability (Cunningham & Keane, 2023). However, this modification comes with alternatives: larger W/B ratios enhance fresh-state rheology but increase capillary porosity in hardened composites. In Fig. 5, the W/B ratio increases to 0.35 and 0.4 (Boadu et al., 2021; Muthukrishnan et al., 2018), although absorption remains whereas at a W/B ratio of 0.5 (Praneeth et al., 2021), with absorption peaking at 10.5%, demonstrating that extra water promotes increased porosity and capillary spaces, outweighing the advantages of biochar.

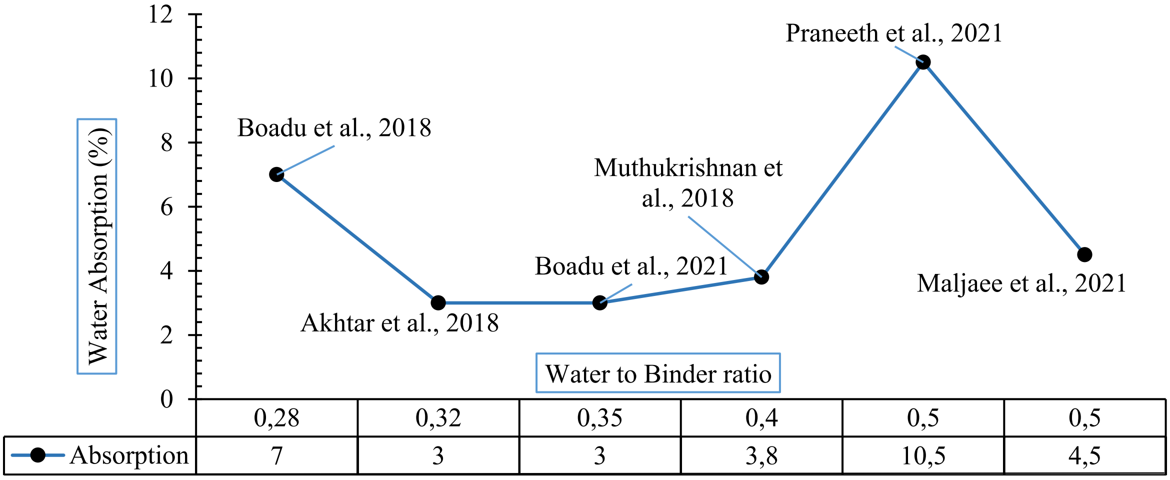

Fig. 5. Biochar concrete's compressive strengh with respect to water to binder ratio

The combination of biochar with SCMs like fly ash or slag mitigates absorption challenges (Fig. 6 from Table 2). Fly ash's spherical particles fill inter-biochar voids, reducing median pore diameter from 120 nm (biochar-only) to 68 nm (biochar+20% fly ash) (Rostami et al., 2021). Slag's latent hydraulic activity further densifies the matrix, as evidenced by 28-day chloride migration coefficients decreasing from 12.1×10^{-12} m^2/s (biochar) to 8.7×10^{-12} m^2/s (biochar+slag) (Cunningham & Keane, 2023). This synergy arises from SCMs compensating for biochar's inertness, ensuring continued pozzolanic reactivity despite reduced cement content. The graph (Fig. 6) highlights the gradual decrease of water absorption with the increasing ratio. At the point of 0.5 (Gupta et al., 2020a; Egodagamage et al., 2024), water absorption remains low (1.9–2%), indicating an optimal balance between hydration and pore refinement from the synergistic action of biochar and SCMs. However, when the W/B ratio increases further to 0.6 (Rose et al., 2024), absorption slightly rises to 3%, likely due to excess water leading to higher porosity despite the presence of SCMs.

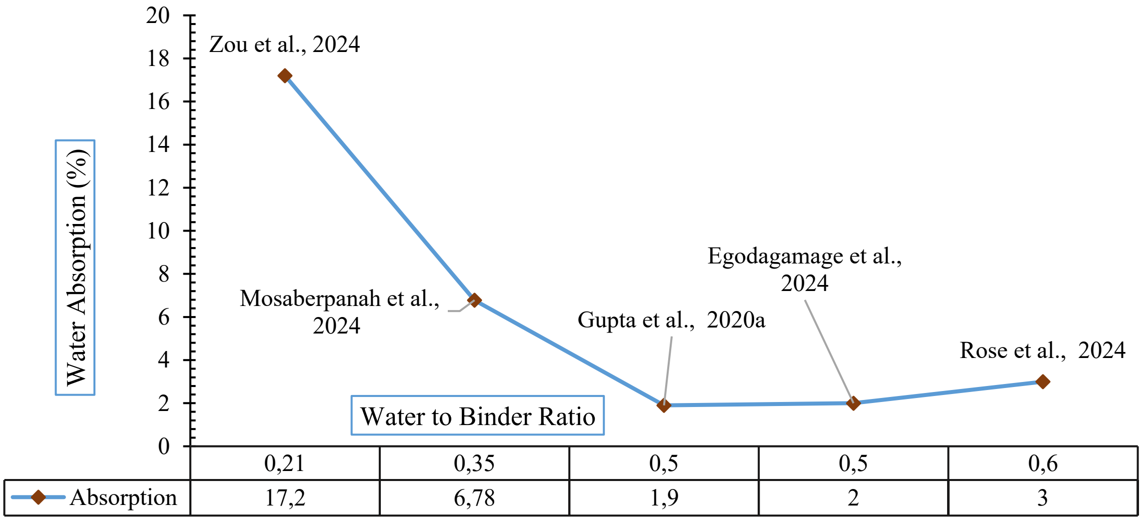

Fig. 6. Biochar concrete's compressive strengh with respect to water to binder ratio

6. Comparative analysis of biochar and biochar-SCM blends

The comparative research of biochar and biochar-SCM blends shows that both ingredients have the potential to increase concrete sustainability and performance. However, the efficiency of these materials is heavily reliant on the w/b ratio. Biochar-SCM mixes, in example, offer a potential method to improving concrete performance by combining the capabilities of two elements.

Biochar, which generates from organic waste, is a porous and carbon-rich substance with promise as a supplemental cementitious material (SCM). However, its porous nature might decrease the interfacial zone of transition (ITZ) in concrete, lowering compressive strength (Kallimani & Minde, 2025). Biochar's strong water absorption can change the w/b ratio, affecting hydration and mechanical characteristics. It can be used as curative agent during hydration (Barissov, 2021). Higher biochar doses (>5%) result in considerably lower compressive strength because to increased voids and weaker ITZ. Dosages around 2.5% are often more effective in maintaining or improving mechanical performance (Zhao et al., 2024). It produces extra water during mixing and then releases it after hydration. This method can reduce shrinking while improving long-term durability. Reduced w/b ratios typically enhance strength, but they may limit flowability, necessitating the use of superplasticizers when biochar is added in larger quantities (Barissov, 2021).

Combining biochar with Ground Granulated Blast Furnace Slag (GGBS) enhances sustainability while posing mechanical problems. Because of its pozzolanic activity, GGBS improves workability and long-term strength, but biochar's porous structure can negate these advantages (Kallimani & Minde, 2025). Silica-rich biochars (for example, rice husk biochar) have higher hydration and compressive strength than typical biochars or bamboo biochars due to their pozzolanic impact. For example, at 28 days, 10% rice husk biochar blended cement showed just a 4% loss in compressive strength compared to conventional Portland cement (Li et al., 2024). Adjusting the w/b ratio is critical when integrating biochar or biochar-SCM blends to balance workability and mechanical performance. Silica-rich biochars, for example, boost hydration efficiency even at low w/b ratios due to their pozzolanic activity (Li et al., 2024). In cases where biochar is blended with fly ash, slag, or silica fume, the resultant blends can provide synergistic advantages. Biochar-SCM blends have been shown in studies to improve the durability and mechanical characteristics of concrete, particularly at ideal w/b ratios (Wang et al., 2020). At greater w/b ratios, biochar's water absorption has less of an impact on workability, but the overall strength may suffer due to increased porosity. In such circumstances, the use of SCMs can help attenuate these impacts by filling holes and enhancing the concrete's structural texture (Li et al., 2020).

7. Conclusions

This study emphasizes the necessity of optimizing W/B ratios when integrating biochar and SCMs to achieve a balance of mechanical qualities (compression, flexural) and durability in concrete production.

- The study discovered an ideal water-to-binder (W/B) ratio that combines workability and strength. Lower W/B ratios (e.g., 0.35-0.40) produced better compressive strength but decreased workability, whereas higher W/B ratios (e.g., 0.45-0.50) increased workability at the price of strength.
- Take into account the feedstock source when choosing biochar, since materials derived from chicken litter and rice husk have demonstrated considerable increases in flexural strength at even low doses (0.1%).
- Lower W/B ratios using biochar and SCMs resulted in a denser microstructure, which reduced water absorption and chloride ion penetration. Higher W/B ratios, while favorable to workability, result in higher porosity and worse durability performance.
- Combining biochar with SCMs like fly ash or slag enhanced concrete properties even more, especially at intermediate W/B ratios (0.40-0.45). It increased the long-term strength development and durability characteristics of pozzolanic activity while decreasing porosity.
- For structural applications, a W/B ratio of 0.35-0.40 using biochar and SCMs is recommended for maximum strength and durability. To reduce strength loss in non-structural applications that need increased workability, a W/B ratio of 0.45-0.50 can be utilized in conjunction with appropriate additives.

References

ACI Committee 211 (1977). Proposed revision to: Recommended practice for selecting proportions for normal and heavyweight concrete (ACI 211.1-74) (Revised 1975). *ACI Journal Proceedings, 74*(2), 59-60. https://doi.org/10.14359/10987

Akhtar, A., & Sarmah, A.K. (2018). Novel biochar-concrete composites: Manufacturing, characterization and evaluation of the mechanical properties. *Science of the Total Environment, 616–617*, 408–416. https://doi.org/10.1016/j.scitotenv.2017.10.319

Alam, M.S., Gorman-Lewis, D., Chen, N., Safari, S., Baek, K., Konhauser, K.O., & Alessi, D.S. (2018). Mechanisms of the removal of U (VI) from aqueous solution using biochar: A combined spectroscopic and modeling approach. *Environmental Science & Technology, 52*(22), 13057-13067

Aman, A.M.N., Selvarajoo, A., Lau, T.L., & Chen, W.H. (2022). Biochar as cement replacement to enhance concrete composite properties: A review. *Energies, 15*(20), 1–10. https://doi.org/10.3390/en15207662

Asadi Zeidabadi, Z., Bakhtiari, S., Abbaslou, H., & Ghanizadeh, A.R. (2018). Synthesis, characterization and evaluation of biochar from agricultural waste biomass for use in building materials. *Construction and Building Materials, 181*, 301–308. https://doi.org/10.1016/j.conbuildmat.2018.05.271

Barissov, T. (2021). *Application of biochar as beneficial additive in concrete* (Master's thesis). University of Nebraska-Lincoln.

Cunningham, C.M., & Keane, S.P. (2023). *Assessing the use of biochar as a cementitious replacement in structural concrete* (Doctoral dissertation). University of Limerick, Limerick, Ireland.

Cuthbertson, D., Berardi, U., Briens, C., & Berruti, F. (2019). Biochar from residual biomass as a concrete filler for improved thermal and acoustic properties. *Biomass and Bioenergy, 120*, 77–83. https://doi.org/10.1016/j.biombioe.2018.11.007

Dixit, A., Verma, A., & Pang, S.D. (2021). Dual waste utilization in ultra-high performance concrete using biochar and marine clay. *Cement and Concrete Composites, 120*, 104049. https://doi.org/10.1016/J.CEMCONCOMP.2021.104049

Egodagamage, H., Yapa, H., Buddika, S., Loh, T., Navaratnam, S., Patrisia, Y., & Nguyen, K. (2024). Enhancement of impact resistance of alkali-activated slag concrete through biochar supplementation. *Structural Concrete*. https://doi.org/10.1002/suco.202300469

Egodagamage, H., Yapa, H.D., Samith Buddika, H.A.D., Navaratnam, S., & Nguyen, K. (2023). Effective use of biochar as an additive for alkali-activated slag mortar production. *Construction and Building Materials, 370*(February), 130487. https://doi.org/10.1016/j.conbuildmat.2023.130487

Gupta, S., Kashani, A., Mahmood, A.H., & Han, T. (2021a). Carbon sequestration in cementitious composites using biochar and fly ash – Effect on mechanical and durability properties. *Construction and Building Materials,* 291. https://doi.org/10.1016/j.conbuildmat.2021.123363

Gupta, S., Krishnan, P., Kashani, A., & Kua, H.W. (2020a). Application of biochar from coconut and wood waste to reduce shrinkage and improve physical properties of silica fume-cement mortar. *Construction and Building Materials, 262*, 120688. https://doi.org/10.1016/J.CONBUILDMAT.2020.120688

Gupta, S., & Kua, H.W. (2020b). Application of rice husk biochar as filler in cenosphere modified mortar: Preparation, characterization and performance under elevated temperature. *Construction and Building Materials, 253*, 119083. https://doi.org/10.1016/J.CONBUILDMAT.2020.119083

Gupta, S., & Kua, H.W. (2020c). Combination of biochar and silica fume as partial cement replacement in mortar: performance evaluation under normal and elevated temperature. *Waste and Biomass Valorization, 11*(6), 2807–2824. https://doi.org/10.1007/s12649-018-00573-x

Gupta, S., Kua, H.W., & Koh, H.J. (2018a). Application of biochar from food and wood waste as green admixture for cement mortar. *Science of The Total Environment, 619–620*, 419–435. https://doi.org/10.1016/J.SCITOTENV.2017.11.044

Gupta, S., & Kua, H.W. (2018b). Effect of water entrainment by pre-soaked biochar particles on strength and permeability of cement mortar. *Construction and Building Materials, 159*, 107–125. https://doi.org/10.1016/J.CONBUILDMAT.2017.10.095

Gupta, S., Kua, H.W., & Low, C.Y. (2018c). Use of biochar as carbon sequestering additive in cement mortar. *Cement and Concrete Composites, 87*, 110–129. https://doi.org/10.1016/J.CEMCONCOMP.2017.12.009

Gupta, S., Kua, H.W., & Pang, S.D. (2018d). Biochar-mortar composite: Manufacturing, evaluation of physical properties and economic viability. *Construction and Building Materials, 167*, 874–889. https://doi.org/10.1016/j.conbuildmat.2018.02.104

Gupta, S., Muthukrishnan, S., & Kua, H.W. (2021b). Comparing influence of inert biochar and silica rich biochar on cement mortar – Hydration kinetics and durability under chloride and sulfate environment. *Construction and Building Materials, 268*, 121142. https://doi.org/10.1016/J.CONBUILDMAT.2020.121142

Kallimani, R., & Minde, P. (2025). Investigation on combined use of biochar and ground granulated blast furnace slag as a supplementary admixture in concrete. *Environmental Science and Pollution Research*, 8201–8218. https://doi.org/10.1007/s11356-025-36210-z

Kant Bhatia, S., Palai, A.K., Kumar, A., Kant Bhatia, R., Kumar Patel, A., Kumar Thakur, V., & Yang, Y.H. (2021). Trends in renewable energy production employing biomass-based biochar. *Bioresource Technology, 340*, 125644. https://doi.org/10.1016/J.BIORTECH.2021.125644

Khan, K.K., Aziz, M.A., Zubair, M., & Amin, M.N. (2022). Biochar produced from Saudi agriculture waste as a cement properties — SWOT analysis and techno-economic assessment. *Materials, 15*, 2–15

Li, H., Yang, K., & Guan, X. (2020). Effect of water-to-binder ratio on the properties of CSA cement-based grouting materials with LiAl-LDH. *Advanced Composites Letters, 29*, 1–7. https://doi.org/10.1177/2633366X20908876

Li, Y., Lin, H., Li, Y., Shen, J., Yang, C., & Wang, K. (2024). Carbon sequestration of silica-rich biochar in cement accompanied by the pozzolanic effect. *ACS Sustainable Chemistry & Engineering, 12*(37), 13826–13839. https://doi.org/10.1021/acssuschemeng.4c03831

Li, W. (2021). Analysis of the influence of water-cement ratio on concrete strength. *E3S Web of Conferences*, 283. https://doi.org/10.1051/e3sconf/202128301016

Ling, Y., Wu, X., Tan, K., & Zou, Z. (2023). Effect of biochar dosage and fineness on the mechanical properties and durability of concrete. *Materials, 16*(7), 1–13. https://doi.org/10.3390/ma16072809

Mah, C.M., Fujiwara, T., & Ho, C.S. (2018). Life cycle assessment and life cycle costing toward eco-efficiency concrete waste management in Malaysia. *Journal of Cleaner Production, 172*, 3415–3427. https://doi.org/10.1016/J.JCLEPRO.2017.11.200

Maljaee, H., Madadi, R., Paiva, H., Tarelho, L., & Ferreira, V.M. (2021). Incorporation of biochar in cementitious materials: A roadmap of biochar selection. *Construction and Building Materials, 283*, 122757. https://doi.org/10.1016/j.conbuildmat.2021.122757

Mohamad, N., Muthusamy, K., Embong, R., Kusbiantoro, A., & Hashim, M.H. (2022). Environmental impact of cement production and Solutions: A review. *Materials Today: Proceedings, 48*, 741–746. https://doi.org/10.1016/J.MATPR.2021.02.212

Mosaberpanah, M.A., Olabimtan, S.B., Balkis, A.P., Rabiu, B.O., Oluwole, B.O., & Ajuonuma, C.S. (2024). Effect of biochar and sewage sludge ash as partial replacement for cement in cementitious composites: Mechanical, and durability properties. *Sustainability (Switzerland), 16*(4). https://doi.org/10.3390/su16041522

Muthukrishnan, S., Gupta, S., & Kua, H.W. (2019). Application of rice husk biochar and thermally treated low silica rice husk ash to improve physical properties of cement mortar. *Theoretical and Applied Fracture Mechanics, 104*, 102376. https://doi.org/10.1016/J.TAFMEC.2019.102376

Nisticò, R., Lavagna, L., Versaci, D., Ivanchenko, P., & Benzi, P. (2020). Chitosan and its char as fillers in cement-base composites: A case study. *Boletín de La Sociedad Española de Cerámica y Vidrio, 59*(5), 186–192. https://doi.org/10.1016/J.BSECV.2019.10.002

Ofori-Boadu, A.N., Abrokwah, R.Y., Gbewonyo, S., & Fini, E. (2018). Effect of swine-waste bio-char on the water absorption characteristics of cement pastes. *International Journal of Building Pathology and Adaptation, 36*(3), 283–299. https://doi.org/10.1108/IJBPA-11-2017-0055

Pantić, V., Šupić, S., Vučinić-Vasić, M., Nemeš, T., Malešev, M., Lukić, I., & Radonjanin, V. (2023). Effects of grinding methods and water-to-binder ratio on the properties of cement mortars blended with biomass ash and ceramic powder. *Materials, 16*(6). https://doi.org/10.3390/ma16062443

Praneeth, S., Saavedra, L., Zeng, M., Dubey, B.K., & Sarmah, A.K. (2021). Biochar admixtured lightweight, porous and tougher cement mortars: Mechanical, durability and micro computed tomography analysis. *Science Of The Total Environment, 750*, 142327. https://doi.org/10.1016/J.SCITOTENV.2020.142327

Praneeth, S., Guo, R., Wang, T., Dubey, B.K., & Sarmah, A.K. (2020). Accelerated carbonation of biochar reinforced cement-fly ash composites: Enhancing and sequestering CO_2 in building materials. *Construction and Building Materials,* 244. https://doi.org/10.1016/j.conbuildmat.2020.118363

Qin, Y., Pang, X., Tan, K., & Bao, T. (2021). Evaluation of pervious concrete performance with pulverized biochar as cement replacement. *Cement and Concrete Composites, 119*, 104022. https://doi.org/10.1016/J.CEMCONCOMP.2021.104022

Restuccia, L., & Ferro, G.A. (2016). Promising low cost carbon-based materials to improve strength and toughness in cement composites. *Construction and Building Materials, 126*, 1034–1043. https://doi.org/10.1016/J.CONBUILDMAT.2016.09.101

Rodier, L., Bilba, K., Onésippe, C., & Arsène, M.A. (2019). Utilization of bio-chars from sugarcane bagasse pyrolysis in cement-based composites. *Industrial Crops and Products, 141*, 111731. https://doi.org/10.1016/J.INDCROP.2019.111731

Rose, D., & Shirzad, S. (2024). Innovations in green concrete: Combining metakaolin and arundo grass biochar for enhanced sustainability. *Sustainability (Switzerland), 16*(24). https://doi.org/10.3390/su162411219

Rostami, R., Klemm, A.J., & Almeida, F.C.R. (2021). The effect of SCMs in blended cements on sorption characteristics of superabsorbent polymers. *Materials, 14*(7), 1–21. https://doi.org/10.3390/ma14071609

Sandanayake, M., Gunasekara, C., Law, D., Zhang, G., & Setunge, S. (2018). Greenhouse gas emissions of different fly ash based geopolymer concretes in building construction. *Journal of Cleaner Production, 204*, 399–408. https://doi.org/10.1016/j.jclepro.2018.08.311

Scrivener, K.L., John, V.M., & Gartner, E.M. (2018). Eco-efficient cements: Potential economically viable solutions for a low-CO_2 cement-based materials industry. *Cement and Concrete Research, 114*, 2–26. https://doi.org/10.1016/J.CEMCONRES.2018.03.015

Sirico, A., Bernardi, P., Sciancalepore, C., Belletti, B., Milanese, D., & Malcevschi, A. (2023). Combined effects of biochar and recycled plastic aggregates on mechanical behavior of concrete. *Structural Concrete, 24*(5), 6721–6737. https://doi.org/10.1002/suco.202200949

Sirico, A., Belletti, B., Bernardi, P., Malcevschi, A., Pagliari, F., Fornoni, P., & Moretti, E. (2022). Effects of biochar addition on long-term behavior of concrete. *Theoretical and Applied Fracture Mechanics, 122*(October), 103626. https://doi.org/10.1016/j.tafmec.2022.103626

Sirico, A., Bernardi, P., Sciancalepore, C., Vecchi, F., Malcevschi, A., Belletti, B., & Milanese, D. (2021). Biochar from wood waste as additive for structural concrete. *Construction and Building Materials*, 303. https://doi.org/10.1016/j.conbuildmat.2021.124500

Suarez-Riera, D., Restuccia, L., & Ferro, G.A. (2020). The use of Biochar to reduce the carbon footprint of cement-based materials. *Procedia Structural Integrity, 26*, 199–210. https://doi.org/10.1016/J.PROSTR.2020.06.023

Wang, L., Chen, L., Tsang, D.C.W., Guo, B., Yang, J., Shen, Z., Hou, D., Ok, Y.S., & Poon, C.S. (2020). Biochar as green additives in cement-based composites with carbon dioxide curing. *Journal of Cleaner Production, 258*, 120678. https://doi.org/10.1016/j.jclepro.2020.120678

Wei, J., & Meyer, C. (2015). Degradation mechanisms of natural fiber in the matrix of cement composites. *Cement and Concrete Research, 73*, 1–16. https://doi.org/10.1016/j.cemconres.2015.02.019
Wong, H.S., & Buenfeld, N.R. (2009). Determining the water-cement ratio, cement content, water content and degree of hydration of hardened cement paste: Method development and validation on paste samples. *Cement and Concrete Research, 39*(10), 957–965. https://doi.org/10.1016/j.cemconres.2009.06.013
Wu, F., Yu, Q., & Liu, C. (2021). Durability of thermal insulating bio-based lightweight concrete: Understanding of heat treatment on bio-aggregates. *Construction and Building Materials*, 269. https://doi.org/10.1016/j.conbuildmat.2020.121800
Yadav, S.K., & Bag, R. (2023). Effect of Bamboo biochar on strength and water retention properties of low plastic clay and silty sand. *Scientific Reports, 13*(1), 1–14. https://doi.org/10.1038/s41598-023-33466-8
Zhao, Z., El-Naggar, A., Kau, J., Olson, C., Tomlinson, D., & Chang, S.X. (2024). Biochar affects compressive strength of Portland cement composites: A meta-analysis. *Biochar, 6*(1). https://doi.org/10.1007/s42773-024-00309-2
Zou, S., Sham, M.L., Xiao, J., Leung, L.M., Lu, J.X., & Poon, C.S. (2024). Biochar-enabled carbon negative aggregate designed by core-shell structure: A novel biochar utilizing method in concrete. *Construction and Building Materials, 449*, 138507. https://doi.org/10.1016/J.CONBUILDMAT.2024.138507

4th International Civil Engineering & Architecture Conference
17-19 May 2025, Trabzon, Türkiye

Investigation of the effect of alkali treatment and bitumen coating on the tensile strength of hemp fibers

Utku Köktan*[1], Aytuğ Kumandaş[1], M. Kerem Ertek[1], Ufuk Kırbaş[1]

[1] *Ondokuz Mayıs University, Department of Civil Engineering, 55139, Samsun, Türkiye*

Abstract. High tensile strength is one of the most important mechanical properties desired in many materials used in civil engineering applications. Fibers are widely used in many materials that serve the purposes such as concrete and soil reinforcement, supporting structural elements, providing insulation, etc. Fibers produced from synthetic polymers are generally used to produce such materials. It can be stated that synthetic polymers can be produced very cheaply and quickly throughout the world, so they are easily accessible. Although this situation increases the demand for these materials day by day, synthetic polymers are generally non-biodegradable and cause significant damage to nature. This study investigated the effect of alkali treatment and bitumen coating on the tensile strength of hemp fiber, which is one of the natural fibers that can be used as an alternative to synthetic fibers. Therefore, hemp fibers were subjected to alkali treatment by soaking in a 5% sodium hydroxide (NaOH) solution. Unprocessed and alkali treated hemp fibers were then coated with bitumen. Tensile tests were carried out for each combination of unprocessed, alkali treated and bitumen coated fibers, and the effect of both alkali treatment and bitumen separately and together on the tensile strength was quantitatively presented.

Keywords: Hemp fibers; Alkali treatment; Bitumen; Tensile test

1. Introduction

Tensile strength is a critical parameter for many materials used in civil engineering. For this purpose, using fiber materials as a component of composite materials in civil engineering is becoming increasingly common due to the high tensile strength they provide. Geotextiles, insulation materials, fiber-reinforced concretes, asphalt pavements, and fiber-reinforced composites used in the reinforcement of structural elements can be given as examples to this group. Fibers produced from synthetic polymers are generally used in the production of all these materials. It can be said that synthetic polymers can be produced very much and easily throughout the world, so they are cheaper and easily accessible. In addition, they offer a very long service life due to their superior tensile strength and non-biodegradable nature. Although this increases the demand for these materials day by day, synthetic polymers are generally non-biodegradable and cause great damage to nature. In addition, synthetic fibers, which are generally produced from synthetic polymers such as polypropylene, polyethylene and polyethylene terephthalate, are not sustainable materials as they are produced from limited resources (Prambauer et al., 2019). Unsustainability, high environmental damage caused by turning into microplastics over time due to its non-biodegradability, and high carbon emissions in both production and use lead researchers to search for environmentally friendly alternatives.

The biodegradability and sustainable production of natural fibers make them an environmentally friendly alternative to synthetic fibers. The most widely used natural fibers are hemp, kenaf, jute, flax, sisal, coir, cotton and pineapple. Although these fibers sometimes show mechanical properties that can compete with synthetic fibers, their high degradation rate in nature limits their use (Prambauer et al., 2019; Wu et al., 2020). The limited service life brought by their environmentally friendly biodegradable nature causes them to be used only in 50% of applications instead of synthetic fibers (Bhattacharyya et al., 2010; Evangeline et al., 2021; Wu et al., 2020). In addition, while being biodegradable and not harming nature are the most prominent features, low density/weight, low cost, high insulation against electricity and sound, and contribution to regional development are other prominent advantages (Georgopoulos et al., 2005; Luo & Netravali, 1999; Pickering, 2008; Shirazi et al., 2020).

When the studies related to natural fibers are examined, it is seen that almost all of these studies focus on determining the mechanical properties of fibers (Amel et al., 2013; Holbery & Houston, 2006; Ochi, 2008; Rassmann et al., 2011; Summerscales et al., 2010; Symington et al., 2009). In civil engineering applications, natural fibers are generally used as the main element of a composite material formed with the help of a binder rather than alone. Accordingly, there are some studies in the literature where natural fibers are coated with bitumen,

* Corresponding author, E-mail: utku.koktan@omu.edu.tr

https://doi.org/10.31462/icearc2025_ce_mat_414

which is also used in this study (Das & Banerjee, 2013; Ghosh et al., 2014; Ghosh et al., 2015; Sanyal & Chakraborty, 1994; Thakur et al., 2021). Researchers have also proposed the chemical treatment of natural fibers to increase their resistance to degradation and to include natural geotextiles in a wider area in civil engineering applications (Shirazi et al., 2020). In this direction, alkali treatment has been the most preferred application (Kumar et al., 2022). There are many studies investigating the effect of alkali treatment on natural fibers (Akhtar et al., 2016; Aly et al., 2012; Frącz et al., 2021; Kawahara et al., 2005; Lu et al., 2012; Meon et al., 2012; Narayana & Rao, 2021; Nitta et al., 2011; Nosbi et al., 2011; Rajappan et al., 2015; Ramesh, 2016; Sair et al., 2017; Shirazi et al., 2019; Thirukumaran et al., 2024). In these studies, although studies are showing that alkali treatment increases the resistance of fibers against biodegradation and can improve the tensile strength at optimum alkali amount from time to time, slight decreases in the tensile strength of fibers were observed in some studies. However, in some studies, since impurities on the fiber surface were removed due to alkali treatment, interfacial compatibility with a binder increased and improvement in composite behavior was observed.

Following a literature review, it is seen that fibers such as jute, coir, flax and kenaf are generally preferred as natural fibers. The fact that hemp production is still illegal in many countries and the strict bureaucratic obstacles to its production can be shown as the reason for this situation. In this study, the effects of alkali treatment and bitumen coating on the mechanical behavior of hemp fibers were investigated separately and together. For this purpose, four combinations of raw hemp fibers, alkali-treated hemp fibers, bitumen-coated hemp fibers, and alkali-treated and bitumen-coated hemp fibers were determined. Considering the inhomogeneous structure of the material and the differences that unpredictable effects in the laboratory environment may cause, 16 samples were produced, four duplicate samples for each of the four combinations. Each sample was formed as a bundle of hemp fibers with a total weight of 2 grams using 20 cm long fibers. The sample was taped at the top and bottom for a distance of five cm each. The remaining 10 cm clear length of the fiber bundle is the value to be considered for the tensile test. The prepared fiber bundles were then soaked in NaOH solution at a concentration of 5 wt% for 30 minutes for alkali treatment. After this process, the fibers were soaked in CH_3COOH solution at a concentration of 1 wt% to ensure the neutralization of the fibers. Then, they were washed and left to dry at room temperature. Raw and alkali-treated hemp fibers to be coated with bitumen were immersed in pure bitumen at 165 °C for 1 min and then allowed to cool by hanging. After the preparation of the samples, each of them was subjected to tensile test and breaking loads were obtained. A slight decrease in the tensile strength of the alkali-treated hemp fibers was observed compared to the raw hemp fibers. However, in the case of bitumen-coated fibers, the tensile strength of the alkali-treated fibers was higher.

2. Materials and methods

2.1. Materials

2.1.1. Hemp fibers

Industrial Hemp (Cannabis sativa L.) is a type of plant with tetrahydrocannabinol (THC) content below the legal maximum level (Exchange, 2023; FIHO, 2024). Hemp fibers can be used industrially in many fields, such as textiles, construction materials, fuel, automobile parts, and fertilizer (Exchange, 2023; Johnson, 2013). Hemp fibers used in this study were obtained from Ondokuz Mayıs University Hemp Research Institute. The supplied fibers consist of only the fiber parts separated from the tows. These fibers were cut into 20 cm lengths for the preparation of the samples shown in Fig. 1.

2.1.2. Alkali treatment (NaOH)

The surfaces of natural plant fibers are covered with impurities such as cellulose, hemicellulose, lignin, pectin and wax due to their biochemical structure. These impurities remove the surface roughness and harm the formation of friction force between the fibers. Alkali treatment makes the fiber surface rougher because it cleans the fiber surface by breaking down these impurities. Thus, the adherence between the fibers increases. Removing impurities on the surface can provide better bonding of the fiber surface with matrix materials. In addition, alkali treatment applied under optimum conditions may cause an increase in the tensile strength of the fibers in some cases. This study subjected pre-washed hemp fibers to alkali treatment by soaking in NaOH-Water solution containing 5 wt% NaOH for 30 minutes.

2.1.3. Acetic acid (CH_3COOH)

NaOH solution removes the impurities on the fibers thanks to its basic structure. After this process, the CH_3COOH-Water solution with a concentration of 1 wt% CH_3COOH was prepared to neutralize the fibers and the fibers were waited in this solution for 30 minutes. Then, the fibers were washed in a filtering flask, and CH_3COOH on the surface was removed. The neutralization of the fibers was checked using a pH meter.

2.1.4. Bitumen

Bitumen, which is a by-product of petroleum production, is frequently used, especially in highway applications due to its binding properties and in roofing applications due to its superior impermeability (Kabadayı et al., 2024; Kumandaş et al., 2022; Şahan et al., 2023). The bitumen used in this study was obtained from the 7th Regional Directorate of the General Directorate of Highways of Turkey and has a 50/70 penetration grade.

2.1.5. Preparation of samples

Hemp fibers were first cut into 20 cm lengths, and 16 hemp fiber bundles, each weighing 2 grams, were formed from these fibers. The formed bundles were taped and fixed, each at the top and bottom with 5 cm bands, as shown in Fig. 1. The taped parts will then remain between the grips of the tensile testing machine, and the net fiber length subjected to tensile test is 10 cm.

Within the scope of the study, four different combinations of unprocessed pure hemp fibers, alkali-treated hemp fibers, bitumen-coated hemp fibers, and both alkali-treated and bitumen-coated hemp fibers were obtained, and four duplicate samples were produced for each combination. The coding of the samples is as follows: unprocessed hemp fiber bundle is named “K”, alkali-treated hemp fiber bundle is named “KA”, bitumen-coated hemp fiber bundle is named “KB” and both alkali-treated and bitumen-coated hemp fiber bundle is named as “KAB”. The codes “N1”, “N2”, “N3” and “N4” were used for the four samples to be produced from all these combinations (Fig. 1). For example, the first sample of the alkali-treated hemp bundle was named “KA_N1”.

Fig. 1. Untreated hemp bundle samples

KA and KAB samples were subjected to alkali treatment for 30 minutes in NaOH-Water solution at 5 wt% concentration. The alkali treated hemp bundles were kept in CH_3COOH-Water solution at 1 wt% concentration for 30 minutes to neutralize them. Then, each hemp fiber bundle was washed with 2 liters of water in a filtering flask. Since the pH values of 2 liters of washing water before and after washing were the same, the washing was terminated at this point, and it was decided that the samples were neutralized.

Then, four hemp bundles that were and were not subjected to alkali treatment were immersed in pure bitumen at 165 °C for 1 min and then hanged and allowed to cool (for KB and KAB samples). Thus, 16 samples were obtained: four pure hemp fiber bundles (K), four alkali-treated hemp fiber bundles (KA), four bitumen-coated hemp fiber bundles (KB), and four alkali-treated and bitumen-coated hemp fiber bundles (KAB). The samples were then subjected to a tensile test, and the breaking loads were determined.

2.2. Method

2.2.1. Tensile test

The mechanical properties of natural fibers are expressed in terms of their tensile strength. In this context, it is critical to determine how much of a breaking load the produced samples can withstand. For this purpose, the tensile strengths of the samples were obtained using an Instron universal testing machine. The 20 cm long samples were taped 5 cm from the top and bottom of the samples, and these parts were inserted into the grips of the tensile testing machine. Thus, a clear tensile length of 10 cm was obtained (Fig. 2). The samples were then subjected to a tensile force at a speed of 10 mm/min and the breaking loads of the samples were obtained.

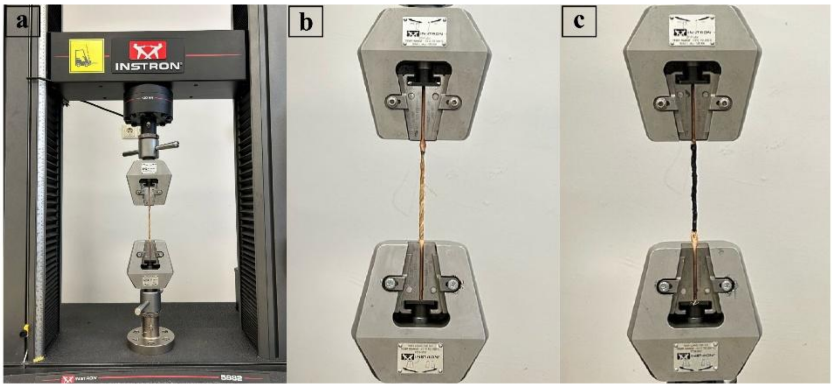

Fig. 2. Tensile testing setup and samples: (a) universal testing machine used for tensile testing, (b) uncoated natural fiber sample positioned between the grips, and (c) bitumen-coated fiber sample mounted between the grips.

3. Results and discussion

After the tensile tests were carried out, the breaking loads were obtained for each combination. Fig. 3 and Fig. 4 are the mean values of four duplicate samples produced for each combination. Fig. 3 shows the effect of alkali treatment on the breaking load of hemp fiber bundles. Alkali treatment reduced the mean breaking load of the hemp fiber bundle by about 10%. Fig. 4 shows that alkali treatment increased the mean breaking load of bitumen-coated hemp fiber bundles by about 25%.

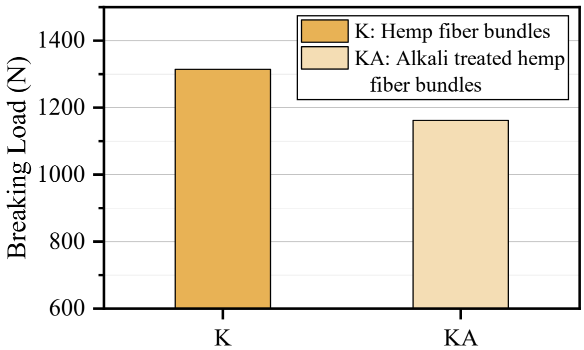

Fig. 3. Breaking load values of uncoated hemp fiber bundle samples

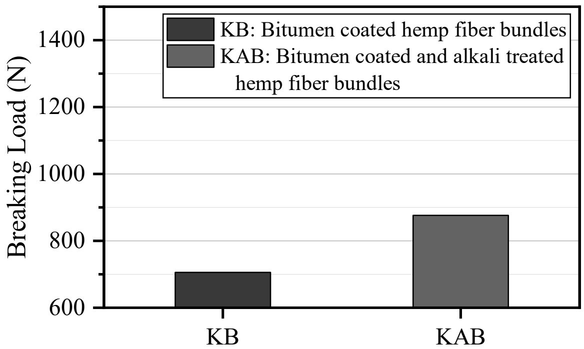

Fig. 4. Breaking load values of bitumen coated and alkali treated hemp fiber bundle samples

Here, the fact that alkali treatment causes a decrease in the breaking load of hemp fibers indicates that the optimum alkali conditions for the fibers should be investigated in more detail. Harsh alkali concentrations or long-term exposure to alkali conditions can cause a decrease in the tensile strength and Young's modulus of the fibers. An excessive concentration of NaOH caused degradation of cellulose molecular chains, resulting in a deterioration of mechanical properties. Moreover, the fibers exhibited surface erosion and micro-cracks at higher temperatures and longer soaking times, which adversely affected their tensile properties. The crystallinity index also decreased under severe alkali treatment conditions, leading to reduced mechanical stability of the fibers (Aly et al., 2012). However, alkali treatment improves the interfacial adhesion between fibers and binder by increasing the surface roughness and interlocking points by partially removing hemicellulose and lignin (Lakshmanan et al., 2018).

In other words, the alkali treatment time should be optimized for the decrease in the tensile strength of the fibers. However, as stated in some studies, the alkali treatment causes slight decreases in the tensile strength of the fiber. However, interfacial adhesion improves, as seen in Fig. 4, where the tensile strength of bitumen-coated fibers was higher for the alkali treated fibers.

4. Conclusions

In this study, the effects of alkali treatment and bitumen coating on the mechanical behavior of hemp fibers were investigated separately and together. For this purpose, four duplicate samples of four combinations coded K, KA, KB and KAB were produced. The 16 samples were subjected to a tensile test, the breaking loads were determined, and the breaking load of each combination was presented as the mean value of the four duplicate samples. The findings obtained within the scope of the study are presented below.

- The mean breaking load of K samples was approximately 10% higher than that of KA samples. This indicates that alkali treatment decreases the tensile strength of the hemp fiber bundle under the conditions performed in the study
- The mean breaking load of the KAB samples was approximately 25% higher than that of the KB samples. This indicates that alkali treatment increases the interface compatibility of the fibers with the binder.
- When only the effect of bitumen was evaluated as K-KB and KA-KAB, it was observed that bitumen decreased the breaking load of hemp fiber bundles. This is thought to be caused by the damage caused by the high temperature of bitumen on the fiber structure.
- Although the singular effect of bitumen decreases the breaking load, it is predicted that it will increase the degradation time of hemp fiber and increase its usability as a composite material in civil engineering applications. In this context, the strength increase caused by the alkali treatment of samples with bitumen is very important.

In light of all these data, it is seen that alkali treatment under the conditions presented in this study decreases the tensile strength of hemp fiber but increases the tensile strength of bitumen-coated samples by increasing the interface compatibility. The data presented in this study are valid for the conditions considered for the study. Alkali treatment needs to be optimized by considering parameters such as alkali concentration, alkali treatment time and waiting period in acid. Although bitumen alone causes a decrease in tensile strength, the superior performance of KAB samples against KB samples seems promising for hemp-bitumen-based composite materials. In line with all this information, the researchers will focus on optimizing the alkali conditions and producing a composite material in future studies.

Acknowledgments

The research described in this paper was financially supported by the Scientific Research Projects Coordination Agency of Ondokuz Mayıs University under the grant number [BAP08-2025-5845].

References

Akhtar, M. N., Sulong, A. B., Radzi, M. F., Ismail, N., Raza, M., Muhamad, N., & Khan, M. A. (2016). Influence of alkaline treatment and fiber loading on the physical and mechanical properties of kenaf/polypropylene composites for variety of applications. *Progress in Natural Science: Materials International*, *26*(6), 657-664. https://doi.org/10.1016/j.pnsc.2016.12.004

Aly, M., Hashmi, M. S. J., Olabi, A. G., Benyounis, K. Y., Messeiry, M., Hussain, A. I., & Abadir, E. F. (2012). Optimization of Alkaline Treatment Conditions of Flax Fiber Using Box-Behnken Method. *Journal of natural fibers*, *9*(4), 256-276. https://doi.org/10.1080/15440478.2012.738036

Amel, B. A., Paridah, M. T., Sudin, R., Anwar, U. M. K., & Hussein, A. S. (2013). Effect of fiber extraction methods on some properties of kenaf bast fiber. *Industrial Crops and Products*, *46*, 117-123. https://doi.org/10.1016/j.indcrop.2012.12.015

Bhattacharyya, R., Smets, T., Fullen, M. A., Poesen, J., & Booth, C. A. (2010). Effectiveness of geotextiles in reducing runoff and soil loss: A synthesis. *Catena*, *81*(3), 184-195. https://doi.org/10.1016/j.catena.2010.03.003

Das, B. R., & Banerjee, P. K. (2013). Interface bond and compatibility of jute with asphalt. *Composites Part B-Engineering*, *53*, 69-75. https://doi.org/10.1016/j.compositesb.2013.04.011

Evangeline, S. Y., Sayida, M., & Girish, M. (2021). Long-Term Performance of Rural Roads Reinforced with Coir Geotextile–A Field Study. *Journal of natural fibers*, *18*(10), 1419-1436.

Exchange, T. (2023). *Growing hemp for the future: A global fiber guide.* Retrieved 25.04.2025 from https://textileexchange.org/knowledge-center/reports/growing-hemp-for-the-future-a-global-fiber-guide/

FIHO. (2024). *About Hemp*. Retrieved 25.04.2025 from https://fiho.org/about-hemp/

Frącz, W., Janowski, G., & Bąk, Ł. (2021). Influence of the alkali treatment of flax and hemp fibers on the properties of PHBV based biocomposites. *Polymers*, *13*(12), 1965. https://doi.org/10.3390/polym13121965

Georgopoulos, S. T., Tarantili, P. A., Avgerinos, E., Andreopoulos, A. G., & Koukios, E. G. (2005). Thermoplastic polymers reinforced with fibrous agricultural residues. *Polymer Degradation and Stability*, *90*(2), 303-312. https://doi.org/10.1016/j.polymdegradstab.2005.02.020

Ghosh, S., Ray Gupta, K., Bhattacharyya, R., Sahu, R., & Mandol, S. (2014). Improvement of life expectancy of jute based needlepunched geotextiles through bitumen treatment. *Journal of The Institution of Engineers (India): Series E*, *95*, 111-121.

Ghosh, S. K., Bhattacharyya, R., Mondal, M. M., & Sanyal, T. (2015). Development of an Innovative Bituminized Jute Paving Fabric (BJPF) Along with its Commercial Field Trials for Potential Application in the Field of Geotechnical Construction with an Eye Towards Global Concern. *Journal of natural fibers*, *12*(5), 457-480. https://doi.org/10.1080/15440478.2014.962213

Holbery, J., & Houston, D. (2006). Natural-fiber-reinforced polymer composites applications in automotive. *Jom*, *58*(11), 80-86. https://doi.org/DOI 10.1007/s11837-006-0234-2

Johnson, R. (2013). *Hemp as an agricultural commodity* (Vol. 4). Congressional Research Service Washington, DC, USA.

Kabadayı, E., Çavdar, E., Kumandaş, A., Şahan, N., & Oruç, Ş. (2024). Investigation of Using Ulexite as a Filler in Various Combinations in Stone Mastic Asphalt Mixtures. *Journal of Materials in Civil Engineering*, *36*(2), 04023556.

Kawahara, Y., Tadokoro, K., Endo, R., Shioya, M., Sugimura, Y., & Furusawa, T. (2005). Chemically retted kenaf fibers. *Sen-I Gakkaishi*, *61*(4), 115-117. <Go to ISI>://WOS:000229462400010

Kumandaş, A., Çavdar, E., Oruç, Ş., Pancar, E. B., & Kök, B. V. (2022). Effect of WCO addition on high and low-temperature performance of RET modified bitumen. *Construction and Building Materials*, *323*, 126561.

Kumar, N., Kandasami, R. K., & Singh, S. (2022). Effective utilization of natural fibres (coir and jute) for sustainable low-volume rural road construction–A critical review. *Construction and Building Materials*, *347*, 128606.

Lakshmanan, A., Ghosh, R. K., Dasgupta, S., Chakraborty, S., & Ganguly, P. K. (2018). Optimization of alkali treatment condition on jute fabric for the development of rigid biocomposite. *Journal of Industrial Textiles*, *47*(5), 640-655. https://doi.org/10.1177/1528083716667259

Lu, N., Oza, S., & Ferguson, I. (2012). Effect of alkali and silane treatment on the thermal stability of hemp fibers as reinforcement in composite structures. *Advanced Materials Research*, *415*, 666-670.

Luo, S., & Netravali, A. N. (1999). Mechanical and thermal properties of environment-friendly "green" composites made from pineapple leaf fibers and poly(hydroxybutyrate-co-valerate) resin. *Polymer composites*, *20*(3), 367-378. https://doi.org/DOI 10.1002/pc.10363

Meon, M. S., Othman, M. F., Husain, H., Remeli, M. F., & Syawal, M. S. M. (2012). Improving tensile properties of kenaf fibers treated with sodium hydroxide. *International Symposium on Robotics and Intelligent Sensors 2012 (Iris 2012)*, *41*, 1587-1592. https://doi.org/10.1016/j.proeng.2012.07.354

Narayana, V. L., & Rao, L. B. (2021). A brief review on the effect of alkali treatment on mechanical properties of various natural fiber reinforced polymer composites. *Materials Today: Proceedings*, *44*, 1988-1994.

Nitta, Y., Noda, J., Goda, K., & Lee, W. (2011). Effect of alkali-treatment on tensile properties of kenaf long fibers. 18th International conference on composite materials, Jeju Island,

Nosbi, N., Akil, H. M., Ishak, Z. A. M., & Abu Bakar, A. (2011). Behavior of Kenaf Fibers after Immersion in Several Water Conditions. *BioResources*, *6*(2), 950-960. <Go to ISI>://WOS:000291559600005

Ochi, S. (2008). Mechanical properties of kenaf fibers and kenaf/PLA composites. *Mechanics of materials*, *40*(4-5), 446-452. https://doi.org/10.1016/j.mechmat.2007.10.006

Pickering, K. (2008). *Properties and performance of natural-fibre composites*. Elsevier.

Prambauer, M., Wendeler, C., Weitzenböck, J., & Burgstaller, C. (2019). Biodegradable geotextiles - An overview of existing and potential materials. *Geotextiles and Geomembranes*, *47*(1), 48-59. https://doi.org/10.1016/j.geotexmem.2018.09.006

Rajappan, R., Saravanan, P., & Paramadhayalan, P. (2015). Testing and Analysis of Kenaf Fibre Reinforced Polymer. Proceedings of the International Conference on Recent Advancement on Mechanical Engineering Technology, Zhengzhou, China,

Ramesh, M. (2016). Kenaf fibre based bio-materials: A review on processing and properties. *Progress in Materials Science*, *78-79*, 1-92. https://doi.org/10.1016/j.pmatsci.2015.11.001

Rassmann, S., Paskaramoorthy, R., & Reid, R. G. (2011). Effect of resin system on the mechanical properties and water absorption of kenaf fibre reinforced laminates. *Materials & Design*, *32*(3), 1399-1406. https://doi.org/10.1016/j.matdes.2010.09.006

Sair, S., Oushabi, A., Kammouni, A., Tanane, O., Abboud, Y., Hassani, F. O., Laachachi, A., & El Bouari, A. (2017). Effect of surface modification on morphological, mechanical and thermal conductivity of hemp fiber:

Characterization of the interface of hemp–Polyurethane composite. *Case studies in thermal engineering*, *10*, 550-559.
Sanyal, T., & Chakraborty, K. (1994). Application of a Bitumen-Coated Jute Geotextile in Bank-Protection-Works in the Hooghly Estuary. *Geotextiles and Geomembranes*, *13*(2), 127-132. https://doi.org/Doi 10.1016/0266-1144(94)90044-2
Shirazi, M. G., Rashid, A. S. A., Bin Nazir, R., Rashid, A. H. A., Kassim, A., & Horpibulsuk, S. (2019). Investigation of tensile strength on alkaline treated and untreated kenaf geotextile under dry and wet conditions. *Geotextiles and Geomembranes*, *47*(4), 522-529. https://doi.org/10.1016/j.geotexmem.2019.01.016
Shirazi, M. G., Rashid, A. S. B., Bin Nazir, R., Rashid, A. H. B. A., Moayedi, H., Horpibulsuk, S., & Samingthong, W. (2020). Sustainable Soil Bearing Capacity Improvement Using Natural Limited Life Geotextile Reinforcement-A Review. *Minerals*, *10*(5), 479. https://doi.org/10.3390/min10050479
Summerscales, J., Dissanayake, N. P. J., Virk, A. S., & Hall, W. (2010). A review of bast fibres and their composites. Part 1-Fibres as reinforcements. *Composites Part a-Applied Science and Manufacturing*, *41*(10), 1329-1335. https://doi.org/10.1016/j.compositesa.2010.06.001
Symington, M. C., Banks, W. M., West, O. D., & Pethrick, R. A. (2009). Tensile Testing of Cellulose Based Natural Fibers for Structural Composite Applications. *Journal of composite materials*, *43*(9), 1083-1108. https://doi.org/10.1177/0021998308097740
Şahan, N., Kumandaş, A., Kabadayı, E., Çavdar, E., & Oruç, Ş. (2023). The use of wax-based additives in bitumen modification: a systematic quantitative literature review. *Construction and Building Materials*, *407*, 133423.
Thakur, R. N., Gupta, S. K., Sinha, A., Chawla, S., & Vadavadagi, S. S. (2021). A durability study of jute geotextile treated with bitumen emulsion. *Journal of natural fibers*, *18*(3), 400-418.
Thirukumaran, M., Uthayakumar, G., Ganapathy, T., Sudhakar, K., Durkaieswaran, P., & Stalin, S. (2024). Examine the static and dynamic mechanical properties of alkali-treated Cannabis sativa plant fiber-reinforced composites. *Biomass Conversion and Biorefinery*, 1-13.
Wu, H., Yao, C., Li, C., Miao, M., Zhong, Y., Lu, Y., & Liu, T. (2020). Review of Application and Innovation of Geotextiles in Geotechnical Engineering. *Materials (Basel)*, *13*(7), 1774. https://doi.org/10.3390/ma13071774

ICEARC'25
4th International Civil Engineering & Architecture Conference
17-19 May 2025, Trabzon, Türkiye

Investigation of mechanical properties of ultra high strength concrete under various fibers

Mete B. Köse*[1],Senem Y. Çetin[2]

[1] Dicle University, Institute of Science, 211280 Diyarbakır, Türkiye
[2] Dicle University, Department of Civil Engineering, 211280 Diyarbakır, Türkiye

Abstract. Ultra-High Performance Concrete (UHPC) is a concrete type characterized by its advanced engineering properties, offering exceptional strength and durability. It is primarily used in structures that demand long-lasting performance, achieved through the use of optimized binders and fine aggregates. Unlike traditional concrete, UHPC can incorporate special admixtures and fibers that significantly improve its mechanical and physical properties. Studies have shown that the fibers enhance the microstructure of UHPC, reducing negative effects such as cracking and deformation. For instance, steel fibers increase tensile strength, while polypropylene fibers contribute to a lighter and more wear-resistant structure. The durability of UHPC is further enhanced by the inclusion of fine aggregates and binders, which increase the density of the concrete, limit the movement of water, and provide greater resistance to corrosion. The combination of fibers and these materials improves the viscoelastic properties of concrete, making it more efficient in challenging environmental conditions. As a result, the physical properties of UHPC can vary significantly based on the type, quantity, and distribution of the fibers. This makes testing UHPC with various fiber types an important area of research in materials engineering, playing a key role in the development of durable and long-lasting structures. This study focuses on evaluating the mechanical properties of UHPC produced by replacing silica fume with quartz powder-containing fine aggregates. Furthermore, the impact of different fiber types on the mechanical behavior of UHPC is examined, highlighting the potential applicability of these materials in structural applications. Axial compression tests were conducted on concrete samples at 7, 14, and 28 days, with results analyzed and compared to assess mechanical properties at different ages.

Keywords: Ultra High Performance Concrete, Glassfiber fiber, Steel fiber, Basalt fiber, Fine aggregate

1. Introduction

Concrete is a fundamental building material widely used in the construction industry (Habert et al., 2020). In modern architectural design, durability and longevity are among the most essential qualities expected from construction materials, making the use of high-performance concrete that meets these standards inevitable (Subramaniam et al., 2019). However, the strength characteristics of concrete present a significant issue in terms of brittleness; high-strength concrete experiences a sudden loss of stress after reaching its maximum load-carrying capacity and exhibits brittle failure. Therefore, the need for concrete with not only high strength and durability but also high ductility is clearly evident. In recent years, the use of low-quality materials, improper durability designs, adverse environmental factors, and natural disasters have clearly revealed the deterioration of concrete's resistant structure (Gettu et al., 1990).Constructing earthquake-resistant structures is no longer a preference but a necessity. Various methods have recently been applied to enhance the performance of concrete, with Ultra-High Performance Concretes (UHPC) being at the forefront of these developments (Murthy et al., 2013). UHPC offers significantly superior properties compared to conventional concrete, including high strength, low porosity, long service life, and excellent durability. As a result, the use of UHPC, known for its high strength and longevity, is steadily increasing in the construction industry. The use of UHPC in various engineering applications provides safe solutions in structures such as bridges, tunnels, and high-rise buildings (Abbas et al., 2016). UHPC is produced from cement, complementary components, aggregates, water, superplasticizer additives, and reinforcements. Various reinforcements are used to achieve ultra-high performance concrete (Teichmann & Schmidt, 2004). One such reinforcement is fibers, which enhance the tensile strength of concrete, preventing issues like cracking and breaking. Fibers also help prevent microcracks in the internal structure, strengthening the structural integrity and extending the lifespan of the concrete (Wille et al., 2012). In UHPC, high cement content forms the basis for both

* Corresponding author, E-mail: mertkose2510@gmail.com

https://doi.org/10.31462/icearc2025_ce_mat_430

golden light publishing

strength and density, while the matrix's integration with fillers results in a more compact structure (Sohail et al., 2016). Ultra-High Performance Concrete offers innovative solutions in structural engineering, addressing increasing density demands while providing lighter and more aesthetically pleasing structures.

The foundational study by Richard and Cheyrezy (1994) demonstrated that using silica fume, superplasticizers, fine aggregates, and steel fibers, compressive strengths between 200–800 MPa can be achieved without compromising ductility. Wu et al. (2016) investigated the influence of steel fiber content and shape on UHPC, finding that increased fiber dosage reduced fluidity but improved both compressive and flexural strength. Similarly, Kang et al. (2016) showed that combining high-strength synthetic fibers such as polyethylene (PE) with steel fibers significantly enhanced tensile behavior. Le Hoang and Fehling (2017) explored the effect of steel fiber volume and aspect ratio, concluding that while compressive strength remained largely unchanged, tensile behavior after peak stress improved considerably with increased fiber content. Gao et al. (2024) further found that at elevated temperatures up to 600°C, steel fibers contributed positively to compressive performance, although strength declined above this threshold due to fiber oxidation.Abbas et al. (2015) evaluated different steel fiber lengths and dosages in UHPC mixtures, concluding that mechanical properties improved with dosage increase, while shorter fibers contributed more to flexural strength. Li et al. (2018) designed UHPC containing coarse basalt aggregates and emphasized the importance of optimal particle packing and the use of longer fibers to maintain mechanical integrity. Zhang et al. (2018) demonstrated that although the use of coarse aggregates increased compressive strength, it weakened the bond between steel fibers and the matrix. However, hooked-end fibers enhanced flexural toughness. Wang and Gao (2016) established an inverse relationship between entrapped air and compressive strength, noting that higher steel fiber content reduced air content and improved strength characteristics. Ayub et al. (2014) investigated basalt fiber incorporation in high-performance concretes and observed that up to 2% fiber content enhanced compressive and tensile strength, particularly when used alongside supplementary cementitious materials.The aim of this study is to evaluate the mechanical properties of ultra-high performance concretes produced by substituting silica fume with fine aggregates containing quartz powder. Additionally, the effects of different fiber types on the mechanical behavior of these concretes were investigated, and the high mechanical performance achieved demonstrated their potential applicability in structural use. The study focused on analyzing how different types and percentages of fibers affect the compressive strength of UHPC. The inclusion of steel, basalt, and glassfiber fibers significantly improves the tensile strength, crack resistance, and overall structural integrity of the concrete

2-Material and metod

In this study, the compressive strength of Ultra High Performance Concrete (UHPC) with steel, basalt, and glassfiber fibers was examined. The material proportions used in the concrete mixes are provided in Table 1. The table details the quantities of key ingredients such as cement, silica fume, quartz sand, fine aggregate, superplasticizer (S.P.), and fiber content for each mix. The fiber contents varied by volume fractions of 0.5%, 1%, 1.5%, and 2% for steel, basalt, and glass fibers, respectively.

Table 1. Mix proportions (kg/m^3)

Cement (kg/m^3)	w/c	Silica Fume (kg/m^3)	0-1 mm Quartz Sand (kg/m^3)	1-4 mm Fine Aggregate (kg/m^3)	S.P. (kg/m^3)	Steel fiber %	Basalt fiber %	Glass fiber %
			605	605				
			612	612		0.5	0.5	0.5
650	0.19	160	620	620		1	1	1
			625	625		1.5	1.5	1.5
			618	618		2	2	2

The steel, glass, and basalt fibers used in this study were commercially sourced from composite markets and are widely used in the construction industry. The physical properties of these fibers significantly influence the mechanical performance, durability, and crack resistance of Ultra High Performance Concrete (UHPC). A detailed description of the characteristics of each fiber type is presented in Fig. 1, which visually displays the fibers used in the study. Based on the manufacturer's datasheets and relevant literature, a comparative summary of their fundamental properties is also provided in Table 2 below.

Fig.1. Fibers used in the study (Basalt Fiber, Steel Fiber, Glass Fiber)

Table 2. Physical properties of Glass Fiber, Basalt Fiber, and Steel Fiber

Property	Basalt fiber	Steel fiber	Glass fiber
Density (gr/cm^3)	2.55-2.62	2.65-3	7.85
Tensile strength (N/mm^2)	3100-3800	300-4840	500-600
Elastic Modulus (Pa)	72.5-75.5	79.3-93.1	210

In this study, the materials used for the production of Ultra High Performance Concrete (UHPC) were carefully selected to optimize performance. Fig. 2 shows the position of CEM I 42.5 class cement and silica sand in the mix. These materials play an essential role as the binding components of the concrete. Silica sand increases the density of the concrete, while cement provides the necessary strength for the mix. Fig. 3 illustrates the composition of the mix, which includes fine aggregates and quartz sand. Another material used in UHPC is fine aggregate and quartz sand. Fine aggregate and quartz sand passing through a 4 mm aperture sieve were used. The maximum grain diameter is 2 mm. This brings UHPC to mortar consistency, minimizes the void ratio and provides high strength.

Fine aggregates (1-4 mm) and quartz sand (0-1 mm) were used in a 50:50 weight ratio to ensure a well-graded granular structure in the concrete. Finally, Fig. 4 shows the additives incorporated into the mix, particularly the AURACAST 535 superplasticizer. These additives improve the workability of the concrete while maintaining a low water-to-cement ratio, thus enabling the production of high-performance concrete. AURACAST 535 superplasticizer additive was used to increase workability in the mixture where the water/binder ratio was set at 0.19.

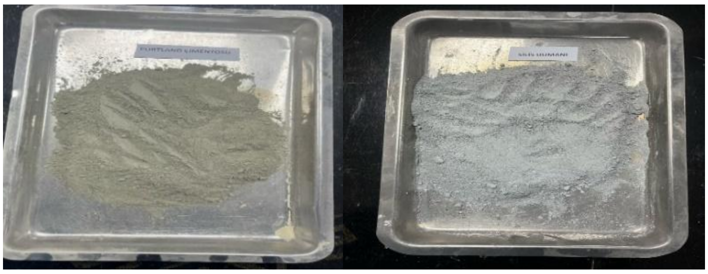

Fig. 2. Binding material used in the study

Fig. 3. Fine Aggregate and Quartz Sand

Fig. 4. Superplasticizer additive material

The samples formed according to the mixing ratios were removed from the molds 24 hours after casting. These removed samples were kept in 22 °C water for 7, 14, and 28 days. The crushing was carried out in a pressure testing machine in accordance with TS EN 12390-4 for the determination of sample compressive strength. After the samples removed from the curing pool were dried, they were placed in the pressure machine test. These cube samples were left to be loaded in the vertical direction and placed in the center with a deviation not exceeding 1% of the determined diameter. The loading speed was determined as 0.6 N/mm².s, and the sample compressive strength was applied by increasing at a constant speed, as shown in Fig. 5.

Fig. 5. Ultra High Performance Concrete (UHPC)

3-Findings and discussion

As shown in Table 3, fiber-free UHPC samples reached the highest compressive strength values at 28 days, with σ_1 = 165 MPa, σ_2 = 164.2 MPa, and σ_3 = 165.5 MPa. This indicates a significant increase in the material's durability over the curing period. The small difference between σ_1 and σ_3 suggests that the material provides balanced performance under different stress conditions, while σ_2 remains strong and durable. The high strength values reinforce that fiber-free UHPC is suitable for civil engineering applications and provides a strong foundation for durable structures.

Table 3. Compressive strengths of fiber-free samples

Curing Days	σ_3 (MPa)	σ_2 (MPa)	σ3 (MPa)
7	151.2	145	147
14	156	159	157
28	165	164.2	165.5

The data presented in Fig. 6 shows that basalt fiber-reinforced UHPC demonstrates significant improvements in compressive strength as the curing time progresses. The increase in strength is clearly influenced by the fiber content, with higher fiber dosages leading to higher compressive strength values at each curing stage. The BF 2.0 samples show the highest strength gain, increasing by 22.8 MPa from 152 MPa at 7 days to 174 MPa at 28 days. This indicates that the material continues to benefit from the reinforcement provided by the basalt fibers as it cures, with the most significant improvements occurring after 14 days. Similarly, the BF 1.5 samples exhibit a notable strength gain, from 155 MPa at 7 days to 172.4 MPa at 28 days, an increase of 17.4 MPa. This further emphasizes the positive role of basalt fibers in enhancing the material's compressive strength over time. The difference in strength between the lowest (BF 0.5) and highest (BF 2.0) fiber contents increases progressively as the curing period advances. At 7 days, the strength difference between BF 0.5 and BF 2.0 is 6.2 MPa, which increases to 11 MPa at 28 days. This shows the growing impact of higher fiber content on improving the compressive strength and overall durability of UHPC.

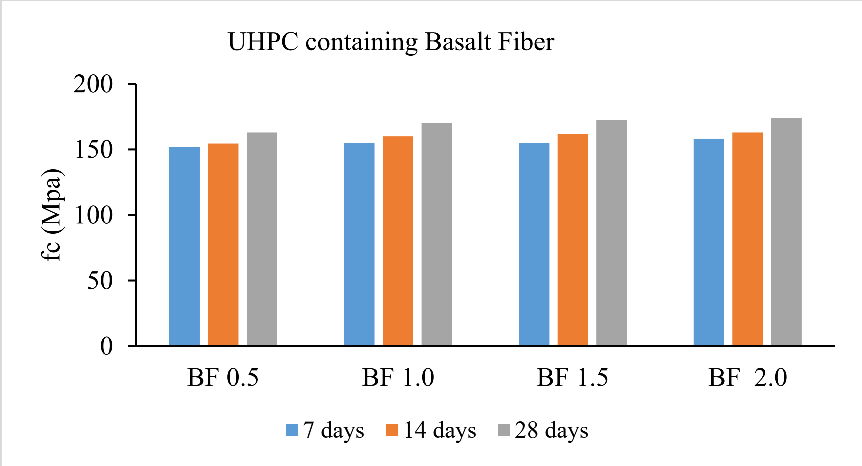

Fig. 6. UHPC containing Basalt Fiber

The data in Fig. 7 shows that steel fiber-reinforced UHPC improves in compressive strength as curing progresses, with higher fiber content leading to better performance. The SF 2.0 samples show the greatest strength gain, increasing by 9.7 MPa from 172.3 MPa at 7 days to 182 MPa at 28 days. This indicates that the material continues to benefit from steel fiber reinforcement, especially after 14 days. Similarly, the SF 1.5 samples exhibit a 17.3 MPa increase, from 164 MPa at 7 days to 181.3 MPa at 28 days, highlighting the positive impact of steel fibers. The SF 1.0 and SF 0.5 samples show smaller strength gains, with increases of 16.7 MPa and 9.5 MPa, respectively.

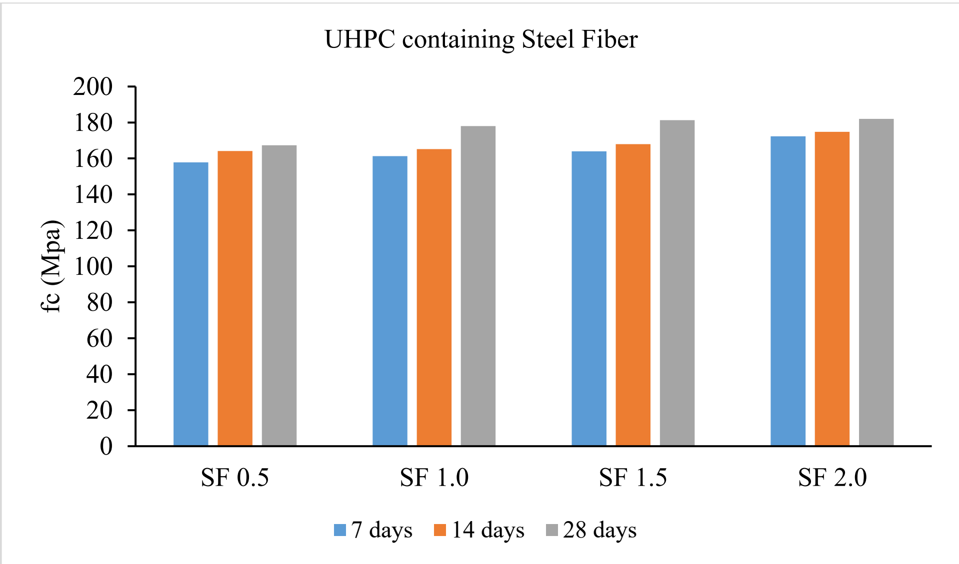

Fig. 7. UHPC containing Steel Fiber

The data presented in Fig. 8 illustrates the compressive strength development of UHPC reinforced with glass fibers over the curing period. As the curing time progresses, the strength continues to increase, with higher fiber dosages generally leading to better performance. The GF 0.5 samples show the greatest strength gain, increasing by 17.3 MPa from 150 MPa at 7 days to 167.3 MPa at 28 days. Other dosages such as GF 1.0, GF 1.5, and GF 2.0 show more moderate improvements. Specifically, GF 1.0 shows a gain of 16.1 MPa (from 152.2 MPa at 7 days to 168.3 MPa at 28 days), GF 1.5 shows an increase of 17.9 MPa (from 151.9 MPa at 7 days to 169.8 MPa at 28 days), and GF 2.0 shows the smallest increase of 12.4 MPa (from 154 MPa at 7 days to 166.4 MPa at 28 days).

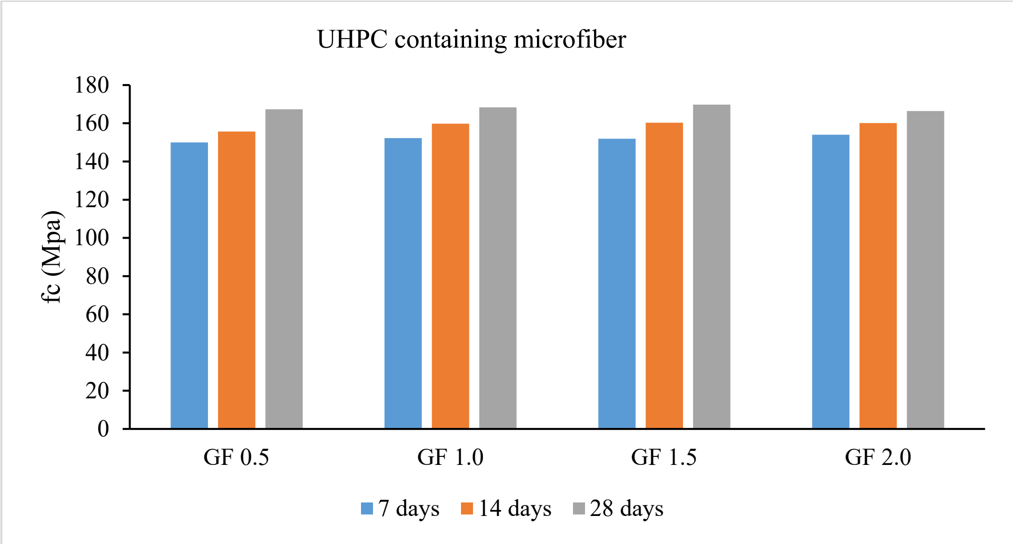

Fig. 8. UHPC containing microfiber

4. Conclusions

In this study, an experimental program was conducted on Ultra-High Performance Concrete (UHPC) mixtures incorporating different types of synthetic fibers at various volume fractions to investigate their feasibility for use in UHPC.

As a result of the study, it was observed that the compressive strengths of UYPB prepared with various fibers were higher than UYPB without fibers.

- It was determined that the 7, 14 and 28-day compressive strengths of basalt fibers were higher than UYPB without fibers and glassfiber fibers, but lower than steel fiber concrete.
- It was observed that the 7, 14 and 28-day compressive strengths of steel fibers were higher than basalt fiber and glassfiber fibers without fibers.
- It was observed that the 7, 14 and 28-day compressive strength of glassfiber fibers did not have much effect on UYPB without fibers, and the 7 and 14-day compressive strength of the fiber containing 0.5% had lower strength than UYPB without fibers, and it was also lower than the strength of fibers containing steel fiber and basalt fiber.

It can be said that steel fibers provide the highest contribution in terms of both strength and toughness. Basalt fibers can be preferred especially for environmental and economic reasons, but their effect is limited.

Macrofiber fibers provide ductility in terms of post-crack carrying and energy absorption, but their compressive strength is lower than other fibers.

References

Abbas, S., Nehdi, M.L., & Saleem, M.A. (2016). Ultra-high performance concrete: Mechanical performance, durability, sustainability and implementation challenges. *International Journal of Concrete Structures and Materials, 10*(3), 271–295

Abbas, S., Soliman, A.M., & Nehdi, M.L. (2015). Exploring mechanical and durability properties of ultra-high-performance concrete incorporating various steel fiber lengths and dosages. *Construction and Building Materials, 75*, 429–441

Alsalman, A., Dang, C.N., & Hale, W.M. (2017). Development of ultra-high performance concrete with locally available materials. *Construction and Building Materials, 133*, 135–145

Ayub, T., Shafiq, N., & Nuruddin, M.F. (2014). Mechanical properties of high-performance concrete reinforced with basalt fibers. *Procedia Engineering, 77*, 131–139

Chen, Z., Wang, X., Ding, L., Jiang, K., Su, C., Ben, Q., & Wu, Z. (2024). Effects of macro basalt fibers on the tensile behavior of ultra-high-performance concrete. *Journal of Building Engineering, 89*, 108105

Gao, D.Y., Zhang, W., Tang, J.Y., & Zhu, Z.H. (2024). Effect of steel fiber on the compressive performance and microstructure of ultra-high performance concrete at elevated temperatures. *Construction and Building Materials, 435*. [Article in press]

Gettu, R., Bazant, Z.P., & Karr, M.E. (1990). Fracture properties and brittleness of high-strength concrete. *ACI Materials Journal, 87*, 608–618

Habert, G., Miller, S.A., John, V.M., Provis, J.L., Favier, A., Horvath, A., & Scrivener, K.L. (2020). Environmental impacts and decarbonization strategies in the cement and concrete industries. *Nature Reviews Earth & Environment, 1*, 559–573

Kang, S.T., Choi, J.I., Koh, K.T., Lee, K.S., & Lee, B.Y. (2016). Hybrid effects of steel fiber and microfiber on the tensile behavior of ultra-high performance concrete. *Composite Structures, 145*, 37–42. https://doi.org/10.1016/j.compstruct.2016.02

Le Hoang, A., & Fehling, E. (2017). Influence of steel fiber content and aspect ratio on the uniaxial tensile and compressive behavior of ultra-high performance concrete. *Construction and Building Materials, 153*, 790–806

Li, P.P., Yu, Q.L., & Brouwers, H.J.H. (2018). Effect of coarse basalt aggregates on the properties of Ultra-High Performance Concrete (UHPC). *Construction and Building Materials, 170*, 649–659. https://doi.org/10.1016/j.conbuildmat.2018.03.106

Murthy, A.R., Iyer, N.R., & Prasad, B.R. (2013). Evaluation of mechanical properties for high strength and ultrahigh strength concretes. *Advances in Concrete Construction, 1*(4), 341–358

Richard, P., & Cheyrezy, M. (1994). Reactive powder concretes with high ductility and 200–800 MPa compressive strength. *ACI Materials Journal, 91*(3), 507–518

Sohail, M.G., Wang, B., Jain, A., Kahraman, R., Ozerkan, N.G., Gencturk, B., Dawood, M., & Belarbi, A. (2018). Advancements in concrete mix designs: High-performance and ultrahigh-performance concretes from 1970 to 2016. *Journal of Materials in Civil Engineering, 30*(6), 4017310

Subramaniam, D.N., Hareindirasarma, S., & Janarthanan, B. (2022). An alternative approach to optimize aggregate-to-cement ratio and compaction in pervious concrete. *Arabian Journal of Science and Engineering, 47*(10), 13063–13071

Teichmann, T., & Schmidt, M. (2004). Influence of the packing density of fine particles on structure, strength and durability of UHPC. In *Proceedings of the 1st International Symposium on Ultra-High Performance Concrete* (pp. 313–323). Kassel, Germany

Wang, R., & Gao, X.J. (2016). Relationship between flowability, entrapped air content and strength of UHPC mixtures containing different dosage of steel fiber. *Applied Sciences, 6*(8), 216

Wille, K., Naaman, A., El-Tawil, S., & Parra-Montesinos, G. (2012). Ultra-high performance concrete and fibre-reinforced concrete: Achieving strength and ductility without heat curing. *Materials and Structures, 45*, 309–324

Wu, Z., Shi, C., He, W., & Wu, L. (2016). Effects of steel fiber content and shape on mechanical properties of ultra-high performance concrete. *Construction and Building Materials, 103*, 8–14

Zhang, L., Liu, J., Liu, J., Zhang, Q., & Han, F. (2018). Effect of steel fiber on flexural toughness and fracture mechanics behavior of ultrahigh-performance concrete with coarse aggregate. *Journal of Materials in Civil Engineering, 30*(12), 04018323

ICEARC'25
4th International Civil Engineering & Architecture Conference
15-17 May 2025, Trabzon, Türkiye

Effect of nano-TiO_2 on physical properties of slag-ceramic powder-based geopolymer composites

Beyza Aygun*[1], Mucteba Uysal[2]

[1] *Istanbul University-Cerrahpasa, Department of Civil Enginering, 34320 Istanbul, Türkiye*
[2] *Yıldız Technical University, Department of Civil Engineering, 34220 Istanbul, Türkiye*

Abstract. Nano-TiO_2 has emerged as a multifunctional additive in construction materials due to its photocatalytic activity, ability to improve microstructure, and capacity to improve mechanical and durability properties, while especially in geopolymer composites (GCs), nano-TiO_2 not only increases compressive strength and reduces porosity, but also contributes to self-cleaning surfaces, and improved chemical stability. In this context, the effects of adding nano-TiO_2 at different ratios (2%, 4%, and 6% by weight) were investigated in the geopolymer composite reference consisting of 50% granulated blast furnace slag (GBFS) and 50% waste ceramic powder (WCP). Mix design included the water/binder (w/b) ratio of 0.48, Na_2SiO_3/NaOH ratio of 2:1, and sand/binder (s/b) ratio of 2.5. Thermal curing was applied at 80°C for 24h and basic physical properties such as capillarity, water absorption, porosity and compressive strength were analyzed at 28 days. Results showed that although nano-TiO_2 additive reduced the void ratio by improving the microstructure, it did not provide an increase in compressive strength. This showed that nano-TiO_2 reduced porosity by creating a filling effect in the matrix, but did not play an active role in the bonding mechanism.

Keywords: Geopolymer composites; Waste ceramic powder; Nanomaterials; Physical properties

1. Introduction

Geopolymer (GM/GC) technology is an environmentally friendly substitute to traditional Portland cement (PC), which contributes annually to the production of 4-5 billion tons of concrete worldwide. Environmental impacts of PC are severe, as it contributes 8–9% of the production of a total of 25–30 billion tons of concrete per year, thereby contributing to anthropogenic greenhouse gas release. Need for high-strength concrete further amplified the environmental problems as enhanced cement use raises environmental concerns in intensified ways. GCs provide a revolutionary solution in the form of their inorganic polymer material, a paradigm change in the development of green construction technologies. In contrast to the conventional PCs, GCs are synthesized by the activation of aluminosilicate materials, generating inorganic polymer material of enhanced mechanical durability and strength of the structure. This novel method resolves the drawbacks of PCs in mechanical properties and environmental factors and provides a more environmentally friendly alternative. Synthesis of GCs includes naturally occurring and industrial aluminosilicates as the raw material. Most of these materials in the system are by-products or products generated by the calcination of clays, including metakaolin (MK), metazeolite, and metabentonite. Increased need for electricity production led to the production of high levels of FA, of which only 17-20% is effectively being put to use globally. Fly ash (FA), a finely powdered mineral additive derived from coal combustion, is amorphous and round in character and applicable in the partial replacement of concrete in the concrete market. Likewise, slag, a by-product of the industrial sector, is composed of different quantities of CaO, SiO_2, Al_2O_3, and trace elements. Investigations of GC in the field have typically focused on MK, FA, and a mixture of both, using sodium or potassium hydroxide mixed with the silicate to react them, respectively. This method of synthesis gives rise to two geopolymerization models by microstructure: one CaO-dominant (CaO-SiO_2-Al_2O_3-MgO) and the other low in CaO and high in SiO_2 and Al_2O_3 content. Nonetheless, along with the above developments, minimal research effort has gone towards the usage of the environmentally friendly GC using waste ceramic powder (WCP), a high by-produce in the ceramic company. This waste, being 15-30% of the raw material, is a problem in landfills in the context of consuming space. It has been indicated in investigations that WCP displays pozzolanic activity, supporting both the hardness and durability of concrete in increased ways (Ozturk et al., 2023; Herbudiman et al., 2024; Faridmehr et al., 2024; Rashad et al., 2024; Raoof & Hameed, 2025).

* Corresponding author, E-mail: beyza.aygun@ogr.iuc.edu.tr

https://doi.org/10.31462/icearc2025_ce_mat_438

Additionally, as the global effort to minimize CO_2 emissions intensifies, studies have turned to the utilization of nanomaterials in GCs. Nanomaterials including carbon nanotubes (CNTs), nano-SiO_2 (NS), nano-Al_2O_3 (NA), graphene oxide (GO), nano-TiO_2 (NT), nano-clay (NC), nano-ZnO_2 (NZ), nano-$CaCO_3$, and nano-Fe_2O_3 are being pursued to increase the mechanical and durability characteristics of GCs. These nanomaterials not only support the minimization of CO_2 emissions but also increase the functionality of building materials in general. TiO_2, a broadly applied versatile metal oxide, has found extensive use in GCs. As a multi-functional additive, nano-TiO_2 finds extensive applicability in a wide variety of fields including cosmetics, pharmacy, and chemical processing. In the case of advanced building materials, its photocatalytic activity is of tremendous interest owing to its remarkable efficiency in the control of nitric oxide emissions. One of the nano-sized forms of TiO_2, a semiconductor-type photocatalyst, has been thoroughly explored, especially in the realm of the Honda-Fujishima effect, wherein water is split into hydrogen and oxygen using electro-catalysis caused by UV radiance, and TiO_2 as a phot-anode in the electrochemical cell. Its wide range of uses includes the usage of NT as a white pigment in paints and cosmetics, a protective layer in construction material against sun and pollution, and as a catalyst in pavement material that causes the breakdown of gaseous pollutants due to moving vehicles. Many studies have proved that the integration of nano-TiO_2 (NT) in cementitious and geopolymer matrices can invariably increase the mechanical and transport properties upon incorporation at the optimum dosages. Broadly, the replacement of part of the binder of approximately 3–4% by NT has been found to result in significant water absorption and capillary porosity reductions. These enhancements are mostly a result of the NT's filler effect and pore structure refinement, leading to a densified and more impermeable matrix system. For example, the reductions in water absorption under extended exposure durations have invariably resulted at the optimum NT dosages, while high dosages adversely turn this advantage in favor of the material by causing the material to agglomerate and rupture the gel networks. In addition, while the early-age strength is considerably enhanced—often by more than 45%—as a result of the increased nucleation effect of NT, the longer-term strength can suffer, possibly owing to poor dispersion or microcracking. However, the incorporation of supplementary materials like supplementary binders and dispersants has proved effective in mitigating these detrimental effects, even promoting further boosts in strength beyond the initial enhancement levels. NT content levels of up to 6% have also, in some studies, resulted in up to 40% rise in strength, in parallel with high ultrasonic pulse velocities, which reflect increased compactness and homogeneity of the microstructure. Further, finer NT particle sizes (e.g., 5 nm) tend to promote more effectiveness in enhancing the development of strength compared to larger particles, particularly under low dosages of water to binder. In general, when dispersed adequately and added at appropriate dosages, nano-TiO_2 has proved to exhibit potential to enhance the microstructure, durability, and initial mechanical properties of cementitious and geopolymer materials, as well as to provide photocatalytic activity, promoting sustainability-oriented applications (Zhong et al., 2022; Jiang et al., 2023; Dhanapal et al., 2024).

This work presents novel contribution by exploring the nano-TiO_2 inclusion effect into a new geopolymer matrix of equal parts of GBFS and WCP—a binary system not thoroughly examined in the current literature previously. Although previous studies have relied heavily on conventional precursors like MK and FA, the blending of waste ceramic, a high-volume industrial waste, and nano-engineered additive presents a greener solution potential of improved functionality. In the study, the effect of nano-TiO_2 at different dosages (2%, 4%, and 6%) on the principal physical and mechanical parameters of porosity, water absorption, compressive strength, and capillarity is thoroughly assessed, addressing both durability and microstructural optimization. By optimizing the dosages of the nanoparticles and the composition of the binder, this research improves the progression of high-performing, environmentally sound GCs and presents a practical mechanism of valorizing ceramic waste in next-generation construction and building materials.

2. Materials and methods

2.1. Materials

This study applied a binary binder system of 50% GBFS and 50% WCP (by mass), chosen to balance the latent hydraulic activity of GBFS and the pozzolanic and fill properties of finely ground waste ceramic. GBFS was a gray, glassy powder of CaO, SiO_2, Al_2O_3, and MgO, of specific gravity 2.93, Blaine fineness of about 410 m^2/kg, and average particle size of approximately 8–12 µm, lending itself to high alkaline condition reaction due to its high degree of amorphous character (typically more than 85%). WCP, derived from industrial waste ceramic and ground in order to increase the reactivity, had a specific gravity of 2.62, median particle size (D50) of 18–25 µm, and a surface texture dominated by fractured, angular grains. Although not chemically reactive like GBFS, the WCP provides useful content of silica and alumina and acts as a secondary pozzolanic material when finely ground, in particular under elevated curing temperature conditions. In the ceramic particles, a mixture of crystalline phases (principally mullite and quartz) and residual glass is present and >60% SiO_2 content, only when they are mixed with a reactive calcium source. Natural river sand of a standard mortar grading was applied as the fine aggregate at a sand binder ratio of s/b = 2.5, in order to give structural support and a uniform, stable packing density.

Alkali-activator solution contained a mixture of NaOH and Na_2SiO_3, the NaOH solution was synthesized at a concentration of 12 M to provide sufficient alkalinity during the dissolution of the aluminosilicate phases, while the sodium silicate solution contained a silicate modulus (Ms = SiO_2/Na_2O) in the region of approximately 2.0. Na_2SiO_3/NaOH mass ratio was held constant at 2:1, a highly established ratio in the production of both N-A-S-H and C-A-S-H gel products. Activator-to-binder ratio was set at a constant of 0.5, whereas the water-to-binder (w/b) ratio was set at 0.48, including both the free water and the water content of the Na_2SiO_3 solution in order to achieve sufficient workability and geopolymerization efficiency. For improved microstructural properties, nano-TiO_2 in the anatase phase was added at dosages of 2%, 4%, and 6% by the weight of the binder. Nano-TiO_2 of high purity (>99%) with a specific surface area of 200–250 m^2/g and average particle diameter of 20–30 nm and true density around 3.9 g/cm^3 was used. These nanoparticles are characterized by high surface activity, potential of being a photomicroreactant, and pore structure refinement by functioning as micro-fillers and nucleation centers in the alkaline-activated matrix system. Their high surface energy and small particle size facilitate the gel densification and restrict capillary pore communication, more so when sufficiently dispersed in the system. Dry constituents (GBFS, WCP, and nano-TiO_2) were mixed homogeneously prior to incorporation in the alkaline solution. None of the mixes were cast in prismatic molds and cured in a thermal oven at 80°C for 24 hours, a curing condition that is shown to promote the dissolution of the aluminosilicates and subsequent GC reactions, of high value in the case of slag-rich systems. Such controlled curing guarantees quick development of the strength and the matrix and provides the basis to assess the physical and mechanical properties under the effects of nano-scale addition.

Table 1 presents the chemical composition of the materials used in the study, while the comprehensive mixing ratio and material dosages per batch are detailed in Table 2.

Table 1. Chemical composition of binders

Main Oxide (%)	CP	GBFS
SiO_2	65.44	40.5
Al_2O_3	15.45	12.8
Fe_2O_3	7.11	1.1
CaO	4.65	35.5
MgO	1.28	5.8
Na_2O	0.8	0.79
K_2O	2.15	
SO_3	0.06	0.18
TiO_2		0.75
LOI	3.06	0.03

Table 2. Mix proportions of 1 m^3 GC.

Series	WCP (kg)	GBFS (kg)	Nano-TiO_2 (kg)	Sand (kg)	NaOH (kg)	Na_2SiO_3 (kg)	Total (kg)
R	500	500	0	2500	166	333	4000
NT2	490	490	20	2500	166	333	4000
NT4	480	480	40	2500	166	333	4000
NT6	470	470	60	2500	166	333	4000

*R (50% GBFS + 50% WCP), NT2 (49% GBFS + 49% WCP + 2% nano-TiO_2), NT4 (48% GBFS + 48% WCP + 4% nano-TiO_2), and NT6 (47% GBFS + 47% WCP + 6% nano-TiO_2)

3. Results and discussion

3.1. Physical properties

Incorporation of nano-TiO_2 in dosages of 2%, 4%, and 6% by binder weight had a significant effect on the physical characteristics of the geopolymer mortars, including porosity, water absorption, and unit weight—important indicators of microstructural solidity, degree of compactness, and possible sustainability in the long term (Table 3). For comparison, the control sample (R) was a reference sample in order to measure the degree of nano-scale modifications to the material. For the reference mix, porosity was measured at 21.91%, accompanied by a water absorption of 11.75%, and unit weights of 2.39 g/cm^3 and 2.37 g/cm^3. These indicate a highly porous and loosely compact structure, lacking micro-filling agents, so the capillary water transport is easy through the voids present in a continuous manner. The relatively low density also supports the view of a matrix of poorly bonded and dispersed solid particles, which leads to high void content and low structural cohesion. When 2% of nano-TiO_2 was added, significant improvements were achieved: porosity decreased to 20.98%, water absorption dropped to a value of 10.78%, and unit weights increased to 2.46 g/cm^3 and 2.44 g/cm^3. This result points to the effect of nano-TiO_2 in enhancing particle packing and sealing of fine voids due to its extremely low particle size and high surface reactivity. By filling micro- and mesopores in the binder-aggregate interface, the nanoparticles effectively broke the capillary pore system's continuity and hence restricted the ingress of moisture, leading to a tighter matrix and low entrapped air content. In the case of the series at the 4% incorporation of nano-TiO_2, however, an unexpected rise in the rate of porosity, to a maximum of the samples at 22.66%, was realized despite the decrease in the rate of water absorption below the initial value at a rate of 11.63% and the increase in unit weights to the value of 2.52 g/cm³ and 2.47 g/cm³. This deviation is telling of particle agglomeration, which in many instances occurs at concentrations beyond the effective uniform distribution boundary. Particle clusters in the matrix of the paste generate weak points and more voids, detracting from the quality of pore refinement and potentially disrupting pathways of the transfer of stresses. Although the increase in density indicates better compactness at the macro level, the high porosity indicates uneven distribution at the microstructural scale, possibly affecting the material's sustainability in the long term in a negative manner NT6 series, on the other hand, showed the highest degree of refined physical properties: porosity had its lowest value at 20.82%, water absorption also dropped to 10.41%, and unit weights reached its maximum at 2.53 g/cm³ and 2.50 g/cm³. This balance of parameters indicates a synergy of sufficient content of the nanoparticles and effective distribution, which helps the TiO_2 not only serve as a filler but also as a promoter of the uniformity of the microstructure. The improved compactness is likely the result of the combined effect of the void minimization, the enhanced matrix cohesion, and potential nano-caused secondary interactions responsible for a more homogeneous and resistant material matrix. In this sense, the 6% dosage becomes the optimal content, creating a fully consolidated microstructure with limited porosity, low water permeability, and maximum packing efficiency in the absence of harmful clustering (Duan et al., 2016; Jindal & Sharma, 2021; Abdalla et al., 2022; Ahmed et al., 2022; Deb et al., 2022; Mashout et al., 2023; Ziada et al., 2024).

Table 3. Unit weight, water absorption and void ratio values of GCs.

	Porosity (%)		Water absorption (%)		Unit weight (g/cm³)	
R	21.91	19.52	11.75	10.22	2.39	2.37
NT2	20.98	20.23	10.78	10.37	2.46	2.44
NT4	22.66	20.99	11.63	10.75	2.52	2.47
NT6	20.82	21.00	10.41	10.62	2.53	2.50

Capillary absorption characteristics of the control, NT2, NT4, and NT6 series exhibit a distinct pattern in water percolation resistance in line with the dosage increase of nano-TiO_2, and provides valuable information on the internal pore structure, pore connection, and densification ratio in the GBFS–WCP geopolymer matrices. In the control series, the capillary rise curve shows a steep rise in the initial stage up to approximating $\sqrt{t}$ = 90 s½, up to a maximum of around 0.0132 mm, and stabilizing slightly before gradually declining beyond $\sqrt{t}$ = 300, where it levels at approximately 0.0105 mm. Overall profile indicates high starting capillary suction and continued water movement due to the highly connected pore system having relatively large and continuous pore voids. Change of the curve from maximum to final absorption is a decrease of 20.4%, showing that though saturation is reached, the absorptive volume of water continues to happen though owing to continuous pore connection in accordance with the previously measured 21.91% porosity and 11.75% water uptake, and relatively low unit density (2.39 g/cm³), both of which support the loose and open microstructure. In the NT2 series, a greater maximum capillary uptake of approximately 0.0142 mm is reached at $\sqrt{t} \approx 95$, but what characterizes it is the more rapid decrease that follows, up to approximately 0.0102 mm, and at which a correspondingly larger decrease of 28.2% from the maximum is realized. Although the capillary rise initially occurs, the more precipitous decrease indicates a more developed capillary system, where the path is more plugged or constricted as water moves deeper in, that corresponds to the measured 4.2% decrease in porosity and by 8.3% in water uptake compared to the control, and indicates moderate pore refinement owing to the filler effect of the TiO_2 nanoparticles plugging voids and disrupting the capillary continuum partly. For the NT4 series, the curve of maximum absorption occurs in a shorter t (~0.0134 mm), at $\sqrt{t}$ = 85, and declines more precipitously compared to control and NT2, recapitulating to ~0.0091 mm, a decrease of about 32.1% relative to maximum absorption, reflecting enhanced pore discontinuity and a decrease in water holding capacity with time. Although the dosage of the 4% had resulted in a slight increase in porosity to the value of 22.66% (approximately by 3.4% more than control), the paradox is rectified by the enhanced pore shape and distribution, not in total volume of voids—that is, even though a bit more pores exist, their connectivity had lessened, and their water absorbency had decreased. Additionally, the unit weight in NT4 was the value of 2.52 g/cm³, a 5.4% increase, testifying to the continuation of structural densification, while larger-in-volume apparently associated porosities relate possibly to the nanoparticle agglomeration that created isolated and hence less connected and absorbent pores by time. NT6 series yields the most refined and resistant capillary response: the curve peaks early at $\sqrt{t}$ = 80 at a maximum value of ~0.0143 mm, slightly above the others, then shows the steepest and most sustained decline, to 0.0084 mm at $\sqrt{t} \approx 450$. This is a decrease of 41.3% from the peak, the largest of all series. This steep rate of decline points to the presence of an internal matrix in which initial surface capillaries can operate, but in which deeper routes are strongly inhibited by effective void filling and advanced gel development. Consistent with this, NT6 had the minimum porosity (20.82%), minimum water absorption (10.41%), and maximum unit weight (2.53 g/cm³), illustrating a dense, strongly packed structure. Its effectiveness at the 6% dosage is due to the optimal content-dispersion ratio: the TiO_2 nanoparticles are present in sufficient numbers to fill microvoids and serve as nucleation points, but not in so large a quantity as to spawn harmful agglomeration, resulting in a matrix of low capillary connectivity. By relative final values of absorption, NT6 had the minimal capillary absorption coefficient, being 20% below control, and 17.6% and 7.7% below NT2 and NT4, respectively, a verification of its increased resistance to water transportation and hence enhanced durability potential.

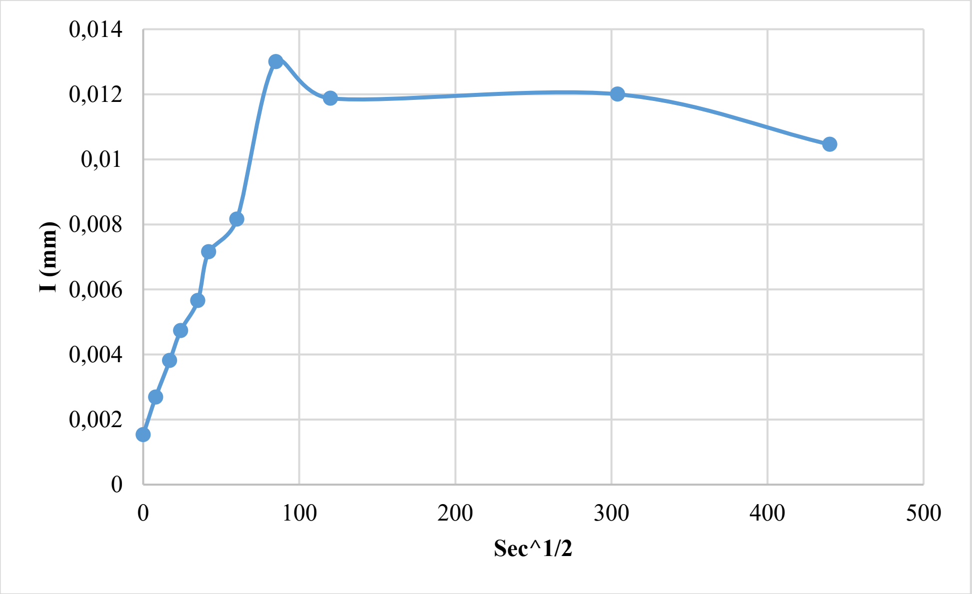

(a) Control

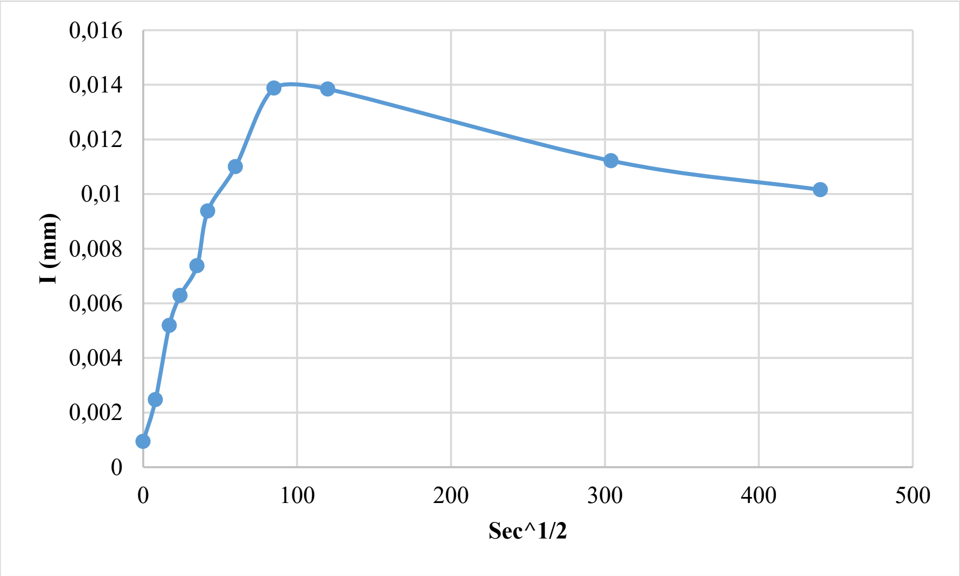

(b) NT2

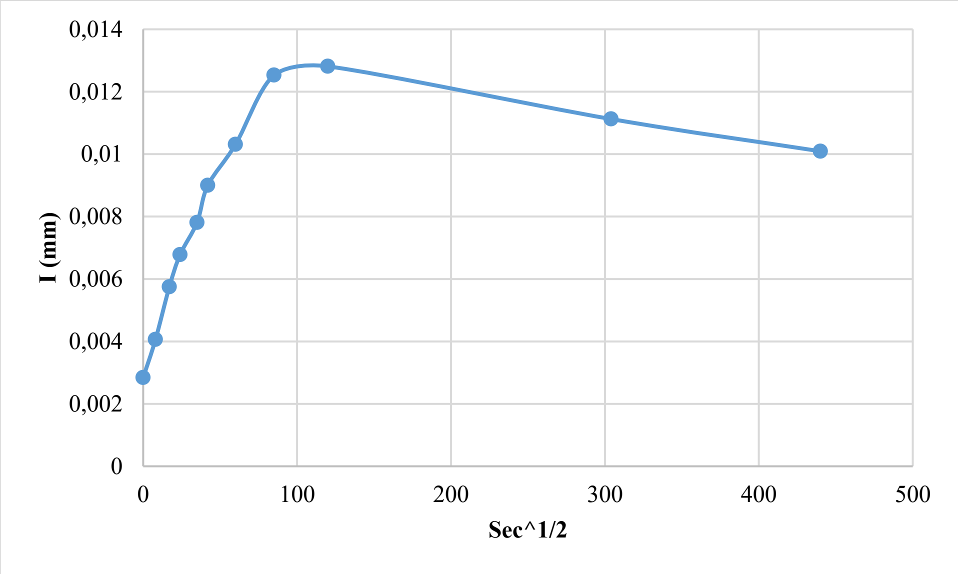

(c) NT4

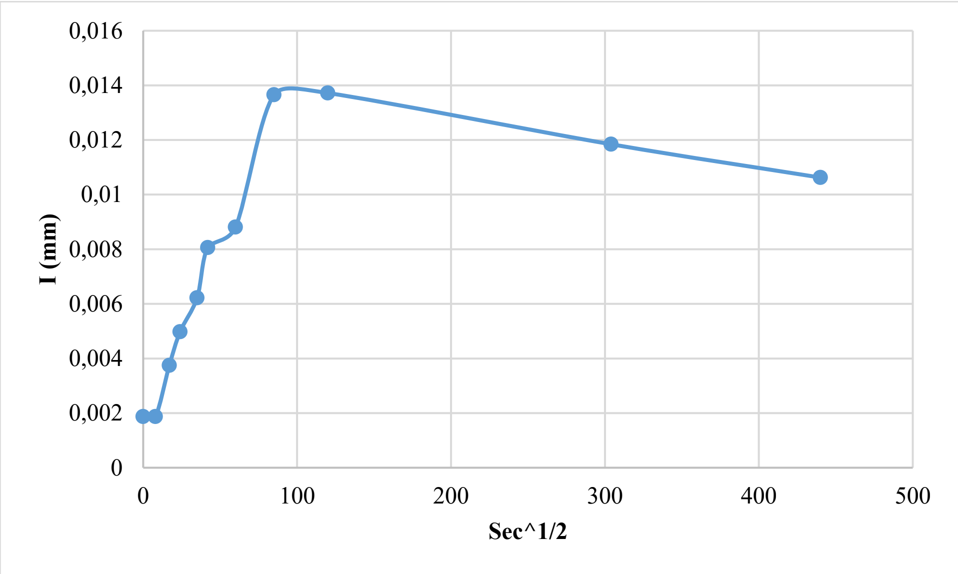

(d) NT6
(e)
Fig. 1. Capillarity absorption values of GCs.

3.2. Mechanical properties
Compressive strength development of the GCs containing nano-TiO_2 at both the ages of 7 and 28 days shows a subtle mutual interaction between the dosage of the nano-filler and the base matrix composition of the composite of 50% GBFS and 50% WCP (Fig. 2.). Control mixture, which contained no nano-scale additives, scored a compressive strength of 18.59 MPa at the age of 7 days and attained a mean of about 21.3 MPa at the age of 28 days, according to a moderate development trend. This result is in line with the anticipated trend of a binary system of highly GBFS, which triggers initial hydration by latency-induced activation techniques, and WCP, a comparatively inert material of low calcium content and moderate pozzolanic activity. Early system compressive strength is primarily dominated by the precipitation of C-A-S-H gels of the slag in the alkaline environment, while WCP plays a passive role as a matrix former and potentially contributes to delayed pozzolanic activity to a limited extent owing to its partially amorphous silica composition. When the addition of 2% nano-TiO_2 was incorporated in the binder phase, a decrease in the early compressive strength was observed, falling to 17.84 MPa—about a 4% decrease compared to the control. This is due to a lack of adequate dispersion and possible interference of the nanoparticles in the development of the early gel, where nano-TiO_2 of poor integration can serve as inert inclusions or micro-damage due to their high surface energy and tendency to clump together in clusters. Nevertheless, a significant turnabout was observed at day 28, when the compressive strength increased to 26.86 MPa—a 1.26-fold increase compared to the control. This delayed but significant gain reflects the catalytic activity of nano-TiO_2 at

advanced stages, where its finely dispersed particles promote gel nucleation, better define the pore architecture, and enhance the development of a denser and more cohesive matrix. Such activity can also result from the surface-mediated catalysis of polycondensation reactions and the effects of the nanoparticles on the ordering of the molecular species in the geopolymer matrix. In the NT4, which contained 4% nano-TiO_2, the 7-day strength was similar to that of NT2 at 17.86 MPa. This agreement supports the theory that the quality of dispersion, not dosage, controls the effectiveness of the integration of nanoparticles in the initial stages. However, at 28 days, NT4 had attained a strength of 25.85 MPa, approximately 21% above the control, indicating that even low concentrations of nanoparticles can play a significant role in the development of the structure in the long term by enhancing gel continuity and inhibiting pore interconnectivity, thereby supporting mechanical interlocking and matrix stability. NT6 series had a unique behavior in which the 7-day strength increased to 19.32 MPa, which was a rise of 8% and 7% above NT2 and NT4, respectively. Such proactive improvement indicates that the 6% dosage limit provides enough presence of nanoparticle to expedite initial densification, perhaps by increasing the rate of nucleation and facilitating the more rapid formation of aluminosilicate chains and C-A-S-H gel microphases. Such a compact structure and finer pore geometry created by this initial reaction is likely to support the enhanced mechanical response at the earliest ages. Nevertheless, while holding a good presence at the age of 28 of 22.92 MPa, the supplementary gain compared to the control was relatively modest. This increase in the period of 7-28 days equated to a mere 18.6% in NT6, while NT2 had a considerably larger development of 50.5%, indicating that while NT6 performs well at triggering rapid hydration at the start, its contribution in the development of the ultimate strength might be impaired. This attenuation in late-stage performance is probably due to nanoparticle agglomeration, a phenomenon more likely at high dosages. As concentration reaches or exceeds the dispersion limit, effects of clustering increase, potentially inducing microvoids or areas of weakness and inhibiting subsequent matrix development. These agglomerates decrease the reactive surface area, interrupt the continuity of gels, and even potentially disrupt the optimum composition of the pore solution, thus inhibiting the progression of geopolymerization. Conversely, NT2 best provides the optimum balance of content of nanoparticles and uniformity of dispersion, maximizing both physical densification and chemical activity. Its high 28-day strength supports the contention that a more diluted, well-dispersed dosage will outdo higher concentrations plagued by suboptimal distribution and site defects. In addition, when the development of the net strength over the period of 28 days is looked at, the control mix demonstrated a relatively low rise of around 2.7 MPa, or a mere 14.7%. In distinct comparison to the NT2 system, the development of more than 9 MPa was realized by it. Such a difference indicates that nano-TiO_2, in addition to functioning as a micro-filler, plays a constructive and significant role in enhancing the structural and chemical maturity of the geopolymer matrix, especially when added at the optimal dosage along with effective dispersion. Ultimately, the findings indicate that increased content of nanoparticles might provide short-term benefits, but the maximum mechanical performance in the long term is achieved under precisely controlled conditions of maximal homogeneity of the nanoparticles in the matrix (Duan et al., 2016; Jindal and Sharma, 2021; Abdalla et al., 2022; Ahmed et al., 2022; Deb et al., 2022; Mashout et al., 2023; Ziada et al., 2024).

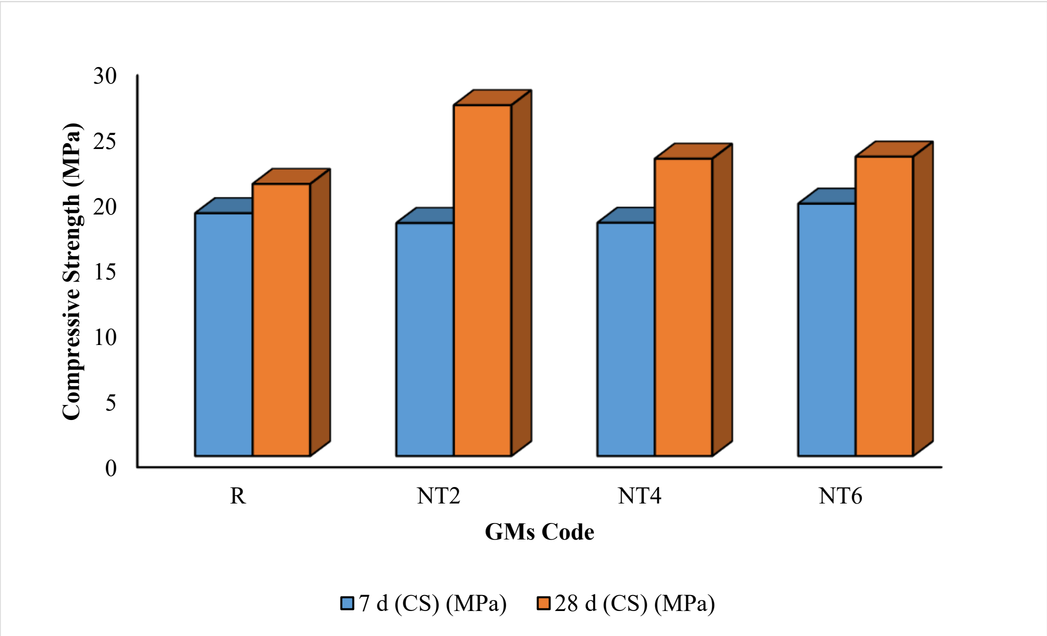

Fig. 2. Compressive strength values of GCs

4. Conclusions

- Addition of 2% NT2 led to the maximum 28-day compressive strength of 26.86 MPa, a 50.5% increase compared to its 7-day counterpart.
- NT2 also lowered porosity to 20.98% from a control of 21.91% and water absorption to 10.78% from 11.75%, reflecting enhanced matrix densification.
- The highest initial-strength property (19.32 MPa) and unit weight (2.53 g/cm³) was possessed by NT6, but it had a low increase in 28-day strength of just 18.6%, attributable to potential nanoparticle agagglomeration.
- Capillary uptake fell most in NT6, by a decrease of 41.3% from peak to end values.
- When compared to all the mixtures, NT2 had the best blend of development of strength, pore refinement, and durability in the longer-term, and hence is the optimum dosage

References

Abdalla, J. A., Thomas, B. S., Hawileh, R. A., Yang, J., Jindal, B. B., & Ariyachandra, E. (2022). Influence of nano-TiO_2, nano-Fe_2O_3, nanoclay and nano-$CaCO_3$ on the properties of cement/geopolymer concrete. *Cleaner Materials*, *4*, 100061. https://doi.org/10.1016/j.clema.2022.100061.

Ahmed, H. U., Mohammed, A. A., & Mohammed, A. S. (2022). The role of nanomaterials in geopolymer concrete composites: A state-of-the-art review. *Journal of Building Engineering*, *49*, 104062. https://doi.org/10.1016/j.jobe.2022.104062.

Deb, P. S., Kuri, J. C., & Sarker, P. K. (2022). Nano-modified geopolymer and alkali-activated systems. In *Recent Advances in Nano-Tailored Multi-Functional Cementitious Composites* (pp. 345–377). Elsevier.

Dhanapal, J., Saravanan, S., Jayaprakash, S., Sivakumar, V., Muniasamy, S. K., Deivasigamani, V., Shanmugam, B., & Sampathkumar, V. (2024). Eco-friendly concrete solutions: The role of titanium dioxide nanoparticles in enhancing durability and reducing environmental pollutants – A review. *Journal of Environmental Nanotechnology*, *13*(3), 332–344.

Duan, P., Yan, C., Luo, W., & Zhou, W. (2016). Effects of adding nano-TiO_2 on compressive strength, drying shrinkage, carbonation and microstructure of fluidized bed fly ash based geopolymer paste. *Construction and Building Materials*, *106*, 115–125. https://doi.org/10.1016/j.conbuildmat.2015.12.018.

Faridmehr, I., Huseien, G. F., Baghban, M. H., & Lund, H. (2025). Effect of discarded rubber tire crumbs and tile ceramic waste powder on workability and strength properties of geopolymer concrete. In *Proceedings of the 1st International Conference on Net-Zero Built Environment (NTZR 2024)* (Vol. 237, pp. 353–365). Lecture Notes in Civil Engineering. Springer.

Herbudiman, B., Subari, S., Nugraha, B., Pratiwi, I., Rinovian, A., Widyaningsih, E., Yanti, E. D., Erlangga, B. D., Jakah, J., & Roseno, S. (2024). Effect of different ceramic waste powder on characteristics of fly ash-based geopolymer. *Civil Engineering Journal*, *10*(2), 431–443.

Jiang, J., Wang, Y., Zhang, L., & Liu, H. (2023). In-situ dispersion of nano-TiO_2 to highly reinforce cement paste. *Construction and Building Materials*, *380*, 131016. https://doi.org/10.1016/j.conbuildmat.2023.131016.

Jindal, B., & Sharma, S. (2021). Geopolymer composites modified with nanomaterials. In *Composite Materials: Properties, Characterization, and Applications* (Vol. 1, pp. 25–48). Elsevier.

Mashout, H. A., Razek, T. A., Amin, M. S., Hashem, F. S., & Selim, F. A. (2023). Performance of nano titania-reinforced slag/basalt geopolymer composites. *Journal of Engineering and Applied Science*, *70*(106). https://doi.org/10.1186/s44147-023-00272-1.

Oztürk, Z. B., Cırık, R., & Atabey, I. I. (2023). Sustainable environment approach by the usage of ceramic pottery waste in geopolymer mortar. *International Journal of Environmental Science and Technology*, *20*(7), 7577–7588. https://doi.org/10.1007/s13762-022-04430-y.

Raoof, S. M., & Hameed, A. M. (2025). Compressive strength of geopolymer mortar produced from fire brick and ceramic waste. *Preprints*. https://doi.org/10.20944/preprints202504.XXXX.v1.

Rashad, A. M., Essa, G. M. F., Mosleh, Y. A., & Morsi, W. M. (2024). Valorization of ceramic waste powder for compressive strength and durability of fly ash geopolymer cement. *Arabian Journal for Science and Engineering*, *49*, 5653–5665. https://doi.org/10.1007/s13369-023-08168-7.

Zhada, M., El-Attar, A. A., & El-Aleem, S. A. (2024). The effect of nano-TiO_2 and nano-Al_2O_3 on mechanical, microstructure properties, and high-temperature resistance of geopolymer mortars. *Arabian Journal for Science and Engineering*, *49*, 1–15. https://doi.org/10.1007/s13369-023-08329-8.

Zhong, Y., Liu, Y., Wang, Y., Zhang, X., Zhang, Y., & Li, Z. (2022). Effect of nano-TiO_2 on capillary water absorption of recycled aggregate concrete. *Coatings*, *12*(12), 1833. https://doi.org/10.3390/coatings12121833.

4th International Civil Engineering & Architecture Conference
17-19 May 2025, Trabzon, Türkiye

Effect of tin coating applied to new generation steel material used in elevator parts subject on tribological

Mohammad J. Azimi Igdir*[1], Yaşar Sert [1], Tevfik Küçükömeroğlu[1]

[1] Karadeniz Technical University, Department of Mechanical Engineering, 61080 Trabzon, Türkiye

Abstract. This study investigates the effects of titanium nitride (TiN) coating deposited on Vanadis 23 and Dievar by the physical vapor deposition (PVD) method to increase the performance of elevator parts exposed to wear. In the study, hardness and wear tests were applied to steel samples before and after coating, and the influence of the coating to mechanical and tribological properties was evaluated.The results show that TiN coating significantly increases hardness and wear resistance in all two steels types. The hardness rate increased approximately 2 times in TiN coated Vanadis 23 and nearly 3 times in Dievar compared to base metal. Vanadis 23 and Dievar steels demonstrate high performance after coating, owing to their powder metallurgy-based structures. In particular, the potential of TiN coating in elevator components exposed to intense wear such as guide rails, guide shoes, rollers and gearbox was emphasized.This study presents an innovative approach for industries seeking durability and economic solutions, and demonstrates the potential of steel surfaces to which TiN coating is applied to provide longer life and reliability in elevator parts. The findings confirm that TiN coating is a strategic solution for increasing wear resistance and hardness performance.

Keywords: PVD coating; Tribology; Wear; Elevator components

1 Introductıon:

Elevators are significant elements of modern infrastructure, in which critical components need to have high reliability and safety in order to maintain smooth and safe operation (Liang & Li, 2016; Zhang et al., 2019). Traction wheels, safety clamps, brake shoes, and rope clamps in high-speed elevators and friction pads in safety gear systems are some examples that are subjected to adverse conditions of friction, high pressure, and wear (Zhang et al., 2019; Kladovasilakis et al., 2024). The harsh operating conditions are responsible for the heightened failure of key elevator parts (Liang & Li, 2016). The failure of these parts has direct effects on the accuracy, safety, and overall lifespan of the elevator system (Zhang et al., 2019), leading to potential maintenance costs and downtime (Zhang et al., 2019; Kladovasilakis et al., 2024).

To improve the poor wear resistance generally observed in mechanical components (Zhang et al., 2019; Silva et al., 2024; Xian et al., 2021), various surface modification techniques have been extensively employed. Physical Vapor Deposition (PVD) is one of the typical methods employed to deposit hard coatings ((Ichou et al., 2023; Xian et al., 2021). Titanium nitride (TiN), being a well-established hard ceramic coating (Silva et al., 2024; Xian et al., 2021), finds extensive applications in a number of industries owing to its high hardness, good chemical stability, and improved wear properties (Silva et al., 2024; Ichou et al., 2023; Hernández-Sierra et al., 2018; Murwamadala et al., 2025; Wang et al., 2022). TiN coatings have also been found to enhance wear resistance and increase the service life of the components (He et al., 2014, Zhang et al., 2019, Hernández-Sierra et al., 2018). Recent research on Al- and Zr-doped TiN coatings deposited by magnetron sputtering has found them to have increased hardness, adhesion, and wear resistance at optimized conditions (12). The substrate material is known to affect the performance of the coatings (Xian et al., 2021; Murwamadala et al., 2025, Wang et al., 2022, Komarov et al., 2016).

Although the benefits of TiN coatings developed by physical vapor deposition (PVD) are known, an in-depth study of the unique tribological and mechanical characteristics of TiN coatings on various kinds of advanced steel, especially those employed or potentially suitable for aggressive elevator applications such as guide rails, guide shoes, rollers, and gearboxes (Zhang et al., 2019), is needed. It needs a comprehension of the interaction of all steel substrates and how all the improvements by TiN coating can be optimally leveraged to gain maximum lifetime as well as efficiency in these all-important elevator components (Sert et al., 2020).

* Corresponding author, E-mail: m.igdir@ktu.edu.tr

https://doi.org/10.31462/icearc2025_ce_mat_454

The purpose of this work is to explore the influence of titanium nitride (TiN) coating developed by the physical vapor deposition (PVD) process on Vanadis 23 and Dievar steels. The overall aim of this study is to assess the feasibility of using this coating to improve the performance of elevator parts that are subjected to continuous wear and tear. This will be achieved by analyzing how the TiN coating affects the mechanical and tribological behavior of the different steel substrates involved.The aim of this study is to examine and compare the hardness, wear resistance, and performance potential of TiN coatings deposited on Vanadis 23, Dievar, and AISI 52100 steel substrates. The outcomes generated in this study can be a viable and cost-effective solution for the optimal design of industrial parts, particularly those applied in elevators, to enhance their life span and minimize the failure rate.

2. Material and methode

Vanadis 23 and Dievar steel were prepared as base and alternative materials with the formulation shown in Table 1 and were cut into circles with a diameter of 24-26 mm for door preparation. After cutting, they were sanded with sandpapers of 200, 400, 600, 800, 1000, 1500 and 2000 and prepared for polishing. After polishing, they were prepared for coating with the Cathodic Arc PVD technique.

Coating depositions were performed utilizing the cathodic arc evaporation process via a Platit π411 Plus device (Switzerland), modified to suit industrial purposes. The coatings were deposited with comparable conditions for all three: a cathode current of 150 ± 30 A, bias voltage of 65 ± 15 V, temperature of 450 ± 30 °C, and flow rate of nitrogen gas at 450 ± 30 scam.

To examine the substrate-coating interface, SEM examined cross-sections of steels that had been coated simultaneously and fractured in a brittle manner to avoid deformation or thermal effects. SEM also examined wear mechanisms on the coated samples and the counter bodies.

Using Al_2O_3 balls (6 mm diameter) as counter bodies to mimic abrasive wear, wear tests were carried out on a DUCOM (TR-201, India) tribometer in an ambient situation. 10 N load, 150 rpm, 8 mm wear diameter, and 5000 cycles were the test parameters. Worn surface topography was assessed through a non-contact profilometer (NANOFOCUS μscan Custom, Germany) at a resolution of 5 μm × 5 μm, and wear volumes were calculated.

An impact-sliding wear test rig was employed to evaluate the wear performance of the coatings specimens. The test was carried out under room conditions with an alumina (Al_2O_3) sphere, 10 mm in diameter, as the counterface. A fixed load of 10 N was applied, with each test consisting of 5000 cycles, each cycle comprising a sliding distance of 5 mm.

Morphological, topographical, and crystallographic examinations were carried out by scanning electron microscopy (SEM) (Zeiss EVO LS10, Germany) and X-ray diffraction (XRD) (Panalytical Empyrean, UK). XRD measurement was performed in a Bragg-Brentano configuration with a 2θ range of 5–100° and a scan rate of 3°/min with a step size of 0.05°.

For minimizing the influence of the substrate material on the measured hardness values of the coatings, in addition to microhardness tests, five nanoindentation measurements were performed. These measurements were conducted under a 0.5 g load using a Hysitron Ti 950 nanoindenter.

3. Results and discussion

3.1 Microstructural and mechanical analysis

Fig. 1 presents the SEM images of the surface morphology of TiN coating applied to Vanadis 23 and Dievar steels. Common defects of the cathodic arc evaporation method, such as white droplet-like particles and surface holes, were observed on the coatings. The droplets are mostly smaller than 1 μm. These droplets, resulting from the ejection of molten material from the cathode during arc evaporation, appear as bright, spherical features, while the holes likely originate from localized shadowing effects or insufficient film growth in certain areas. Notably, the Vanadis 23 substrate (Fig. 1- b) shows a higher density and larger size of droplets compared to the Dievar substrate (Fig. 1- a), indicating possible differences in nucleation behavior or substrate–coating interactions.

The figure 2, presents cross-sectional SEM images of TiN coatings deposited via the CAPVD method on (Fig. 2-a) Dievar and (Fig. 2-b) Vanadis 23 steel substrates. Both images clearly reveal a uniform and continuous coating layer with an approximate thickness of 5 μm. The Dievar substrate coating (Fig. 2a) is relatively dense and has a smooth microarchitecture, suggesting good compactness and adhesion. Conversely, the TiN coating on the Vanadis 23 substrate (Fig. 2b) displays a columnar and textured morphology, typical of coatings deposited by an arc process that can be disrupted by the microstructural and thermal characteristics of the substrate.

The differences in morphology can influence wear resistance and mechanical behavior of the coatings under function. These findings indicate that substrate material greatly influences resultant microstructure and deposited layer quality even at the same deposition conditions.

Table 1.EDS analys Chemical composition of substrate metals (weight %).

Elements	Fe	C	Mo	Cr	V	W	Mn	Si
Vanadis 23	80.02	1.28	5	4.2	3.1	6.4	5	---
Dievar	91.05	0.35	2.3	5	0.6	----	0.5	0.2

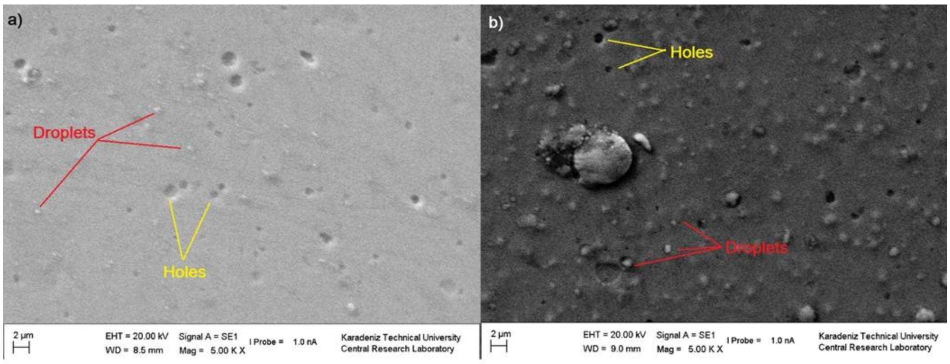

Fig. 1. The SEM images of a) Dievar-TiN, b) Vanadis23-TiN coated by CAPVD surfaces.

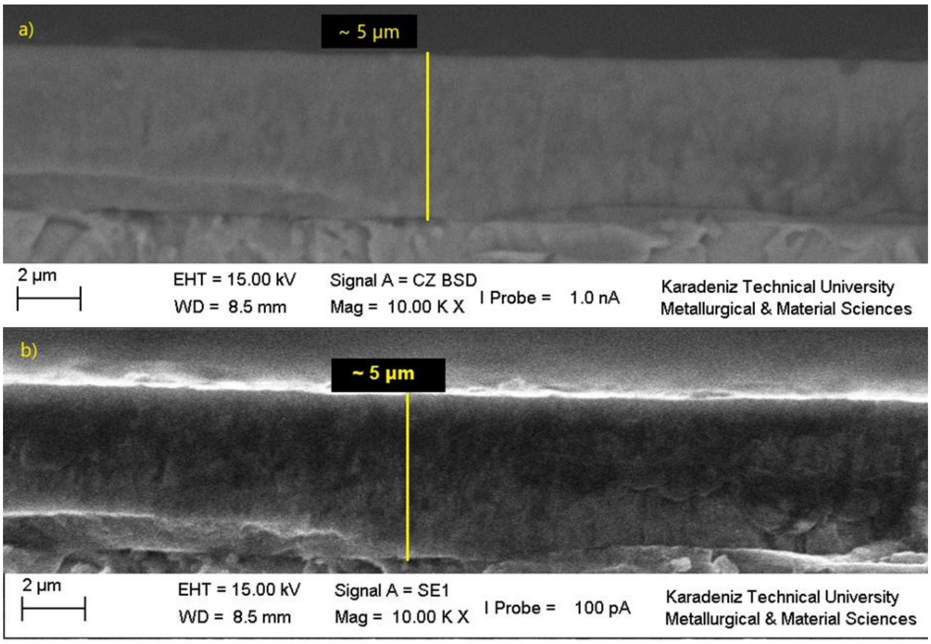

Fig. 2. The cross-section SEM image of TiN coated on a) Dievar stells and b) Vanadis 23.

XRD results of the TiN coatings are presented in Fig. 3. When the XRD patterns were analyzed, it was observed that TiN was the dominant crystal structure in the coated samples. In the TiN layers, the TiN (200) peak appeared as the main peak. The preferred growth of the (200) orientation is explained by the deposition process, which enables the adatoms to migrate over the growing surface. Besides the TiN peaks, iron peaks were also observed, particularly in the base materials. Moreover, the TiN reflections of (111), (220), and (222) were observed, but with smaller intensities. Relative to Vanadis 23, Dievar samples contained a greater amount of Fe within the TiN coating and thus a greater extent of intermixing between the coating and the substrate. Apart from this, small amounts of oxygen were also found in both the coatings, likely due to small-scale oxidation of the surface on or after deposition. Overall, the EDS analysis confirmed that TiN coatings with different extents of substrate effects were deposited successfully.

The measurements that were determined from nanoindentation (Fig. 4) confirmed that coating the base materials with a TiN coating greatly increased their hardness values. For Dievar substrate, the hardness increased from about 10 GPa to well above 30 GPa following the TiN deposition. Likewise, in Vanadis 23, the hardness increased from around 14 GPa to about 28 GPa following the TiN coating deposition. This remarkable improvement can be attributed to the intrinsic high hardness of the TiN layer deposited by CAPVD, which contributes significantly to both base metals surface properties with very high effectiveness. Moreover, the greater relative improvement demonstrated in Dievar shows that the TiN coating affected this substrate more in comparison with Vanadis 23.

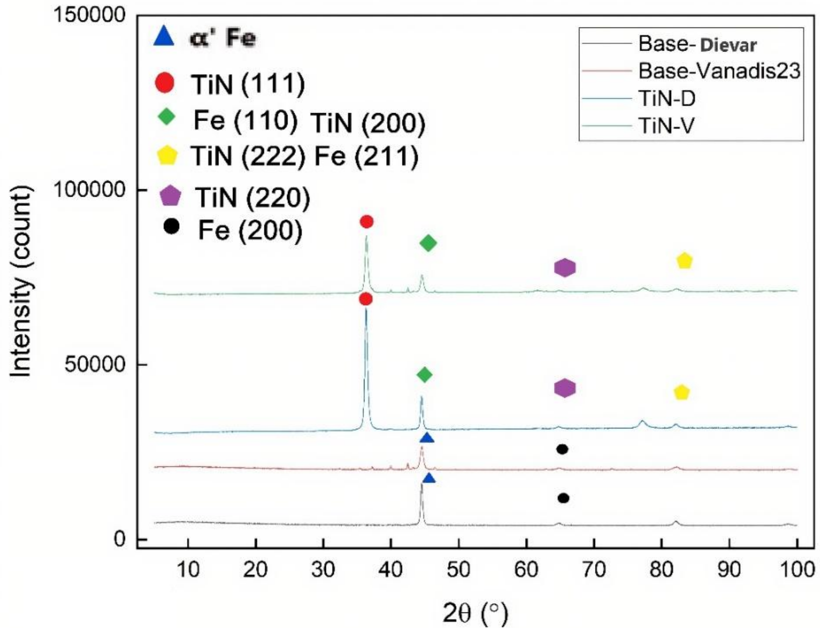

Fig. 3. The XRD patterns of the base metals and coated samples.

Table 2. EDS analyse Chemical composition of TiN coating (weight %).

Elements	Fe	Ti	N	O
Vanadis 23	7.91	57.95	33.39	0.75
Dievar	33.71	33.93	31.73	0.63

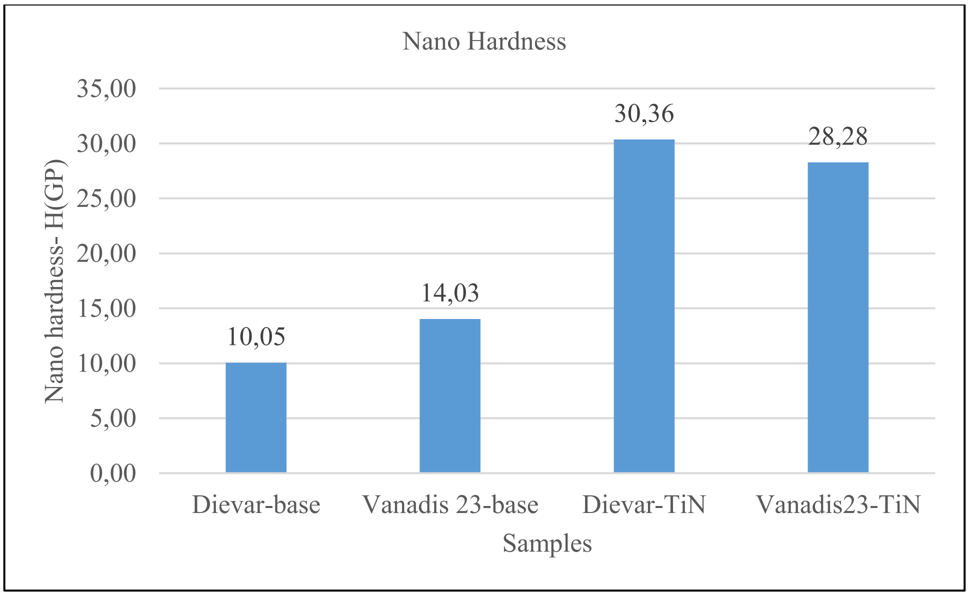

Fig. 4- The nano hardness results of base metals and coatings.

3.2 Adhesion strength analysis

Fig. 5 presents the scratch test results for the base metal samples coated with TiN, i.e., Dievar and Vanadis 23. The critical load (Lc_2), which indicates the beginning of coating failure, is considerably higher in the Vanadis 23-TiN sample (92.6 N) than that of the Dievar-TiN sample (62.2 N). This is indicative of better adhesion strength and mechanical properties of the TiN coating when deposited onto the Vanadis 23 substrate. In both samples, the scratch track images demonstrate the typical modes of failure of hard coatings, which include cohesive cracking of the coating and partial delamination. The Vanadis 23-TiN sample shows a smoother and more consistent scratch path with fewer severe defects and suggests a tougher substrate-coating bond.

3.3 Friction and wear properties

Fig. 6 illustrates the evolution of the friction coefficient as a function of time for base metals and their TiN-coated counterparts. In the initial testing stages, there is an abrupt increase in the friction coefficient in all specimens, which is typically attributed to the running-in period, where surface asperities interact and accommodate under load.

After this initial transition, the frictional behavior becomes stabilized, demonstrating marked differences between the TiN-coated and base material. Dievar's base metal (described by the red curve) presents the lowest and most stable friction coefficient throughout the experiment. In contrast, samples coated with TiN, particularly Vanadis23-TiN (blue), show steadily high friction coefficients. The observed effect is likely due to increased surface hardness and roughness provided by the TiN coating that enhances the resistance to sliding. In addition, there are minor variations in the friction coefficient curves observed in all the materials, which capture the dynamic character of surface interactions through extensive sliding.

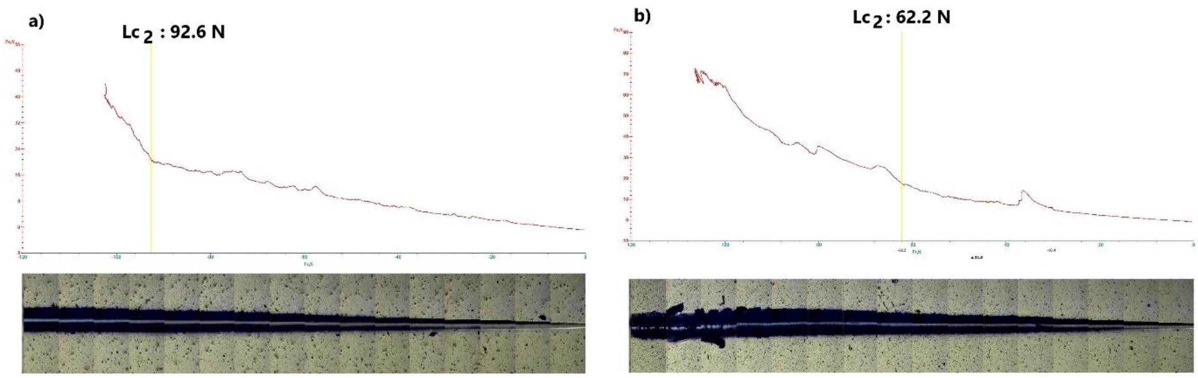

Fig. 5. The graphs of Scratch test on a) Vandis 23- TiN coating and b) Dievar- TiN coating

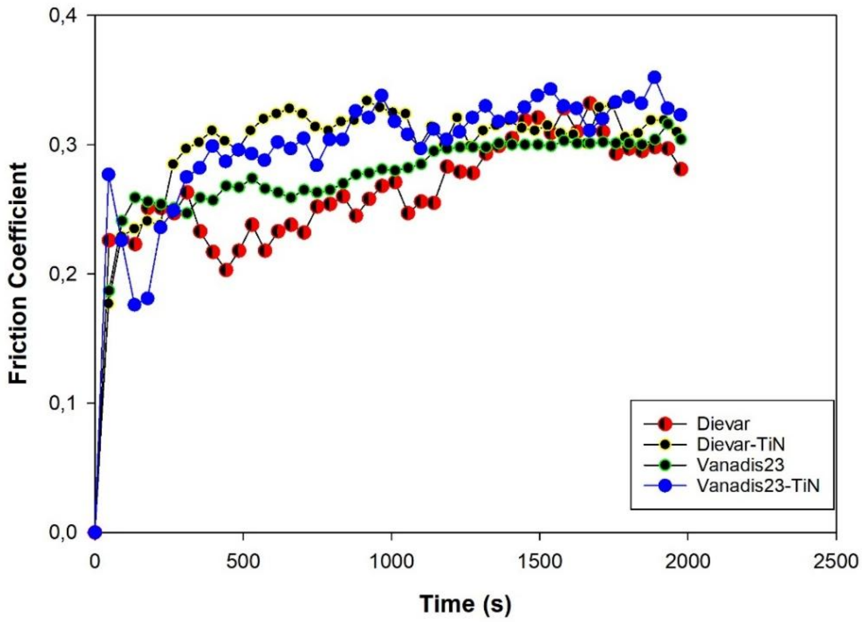

Fig. 6. The friction coefficient graphics of base metals and TiN coated materials.

Fig. 7 illustrates the Scanning Electron Microscope (SEM) micrographs of worn surfaces of Dievar and Vanadis 23 steels, tested under both uncoated and titanium nitride (TiN)-coated conditions, after an impact-sliding wear test. Every row of the figure designates a specific sample condition, while the three columns designate different positions along the wear track: (a) impact area, b) sliding area and c) final contact area.

For the Dievar-base sample (top row), the surface wear is dominated by severe plastic deformation and delamination features, particularly in the impact area, suggesting a strong initial mechanical response to cyclic loading. The wear track becomes progressively smoother towards the final contact area, but there are still recognizable grooves, which suggest continued abrasive interaction. The wear morphology of Vanadis 23-base (second row) is noticeably finer. The surface degradation is less severe than in the case of Dievar, with smaller debris particle size and less frequent microcracking events. This reflects the fact that the higher intrinsic hardness and microstructural stability of Vanadis 23 impart to it greater resistance to repeated mechanical loadings.
Moving to the coated samples, Dievar-TiN surface (third row) shows coating fracture and localized delamination, predominantly in the middle and end regions. Crack patterns spread over the coating layer, which may be attributed to lacking load-carrying capacity or interfacial strength under cyclic impact-sliding loading conditions. There is partial peeling away of the coating in some areas, revealing the substrate below.

In contrast, the Vanadis 23-TiN sample (bottom row) retains a well-intact coating over most of the wear track. Micro-cracks and ploughing scratches are apparent—particularly in the star and mid regions—however, the coating has enhanced adhesion and more regular interaction with the substrate. This enhanced performance can be attributed to the compatibility of the TiN coating with the harder Vanadis 23 matrix, which enhances the load transfer and crack deflection.

Collectively, these scanning electron microscope observations offer deep insight into wear mechanisms active and the influence of substrate nature and coating integrity on tribological performance in complex loading conditions.

Fig. 8 presents SEM images of the worn surfaces of base and TiN-coated samples. In Figure 8A, for the base material-Dievar specimen, there is pronounced abrasive wear with deep grooves and severe surface degradation. The inset, magnified further, exhibits massive plastic deformation and material removal, evidence of a vigorous sliding interaction.

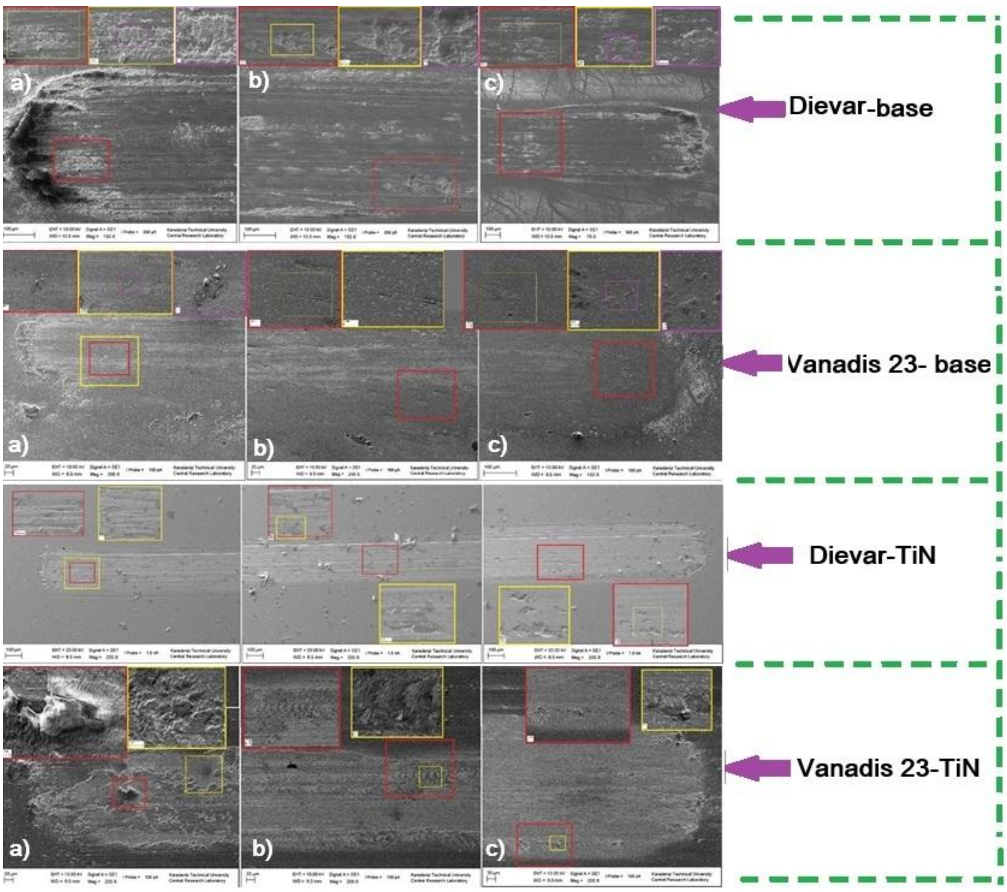

Fig. 7. The SEM images of worn surfaces by impact-sliding test. a) Impact area, b) Sliding area and c) Final contact area

Fig. 8(b) presents the worn surface of the base metal Vanadis 23 sample. In this case, the wear tracks are noticeably more pronounced than those observed in Dievar, and this is due to the greater hardness and wear resistance characteristics of the Vanadis 23 material. Accordingly, evidence of material delamination and micro-cracking is still evident in some localized areas.

Considering the coated samples, Fig. 8(c) (Dievar-TiN) reveals a more uniform wear pattern. The addition of TiN would seem to have had a profound impact on material degradation; however, small grooves can still be discerned.

Last, Fig.8(d) (Vanadis 23-TiN) manages to demonstrate the lowest amount of surface damage out of all of the samples. Wear tracks observed are relatively shallow in nature, and the coated surface seems to have maintained much of its structural integrity.

Fig. 9 illustrates the values of wear rate (mm³/N·m) for base and TiN-coated samples of Dievar and Vanadis 23 steels. As can be seen, the Dievar-base sample has the highest wear rate of all, whereas Vanadis23-base has a much smaller value. When coated with TiN, both materials are seen to significantly reduce their wear rate. The wear rate of Dievar-TiN is significantly less than that of its uncoated equivalent but remains higher than in the TiN-coated Vanadis23 sample. The Vanadis23-TiN sample has the lowest wear rate in this study. These wear behaviors are quantified very nicely by the bar chart to enable a ready comparison between all the conditions that were examined.

Fig. 10 shows the impact-sliding wear rate (mm³/N·m) of Dievar and Vanadis 23 steels in both uncoated and TiN-coated (by CAPVD) conditions. One can see a distinct difference in the wear behavior of the samples. The most pronounced wear rate among all the samples is that of the Dievar-TiN sample, showing a high sensitivity of the coated surface to the combined impact and sliding stresses.

Interestingly, though, the TiN coating affects the two substrate materials differently. On Vanadis 23, the TiN coating causes an increase in the wear rate in its coated compared to its uncoated sample; however, the increase is quite contained. In contrast, Dievar's wear rate rises substantially with TiN coating, indicating potential incompatibility or lack of adhesion performance in dynamic loading conditions for this material–coating combination.

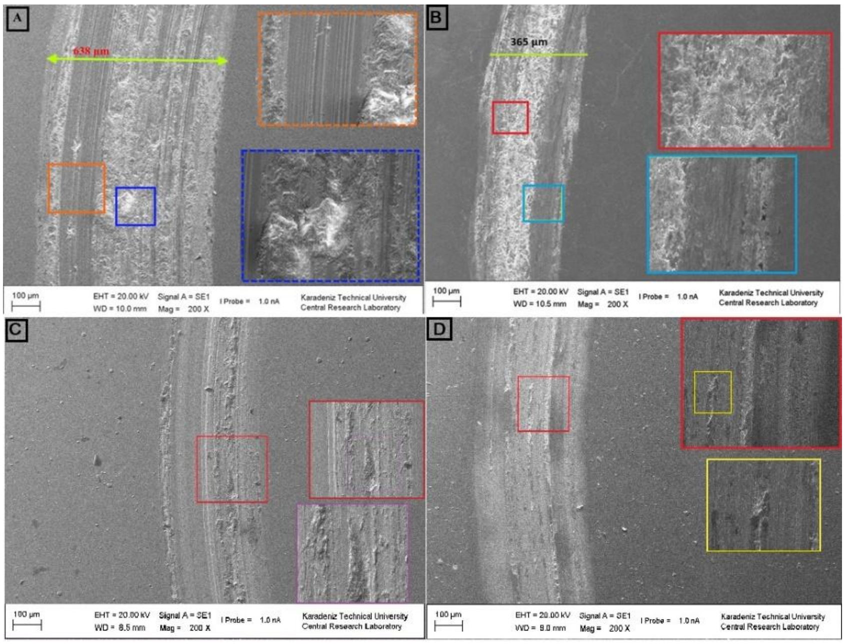

Fig. 8. The SEM images of worn surfaces a) Dievar, b) Vanadis 23, c) Dievar-TiN coating and d) Vanadis 23-TiN coating

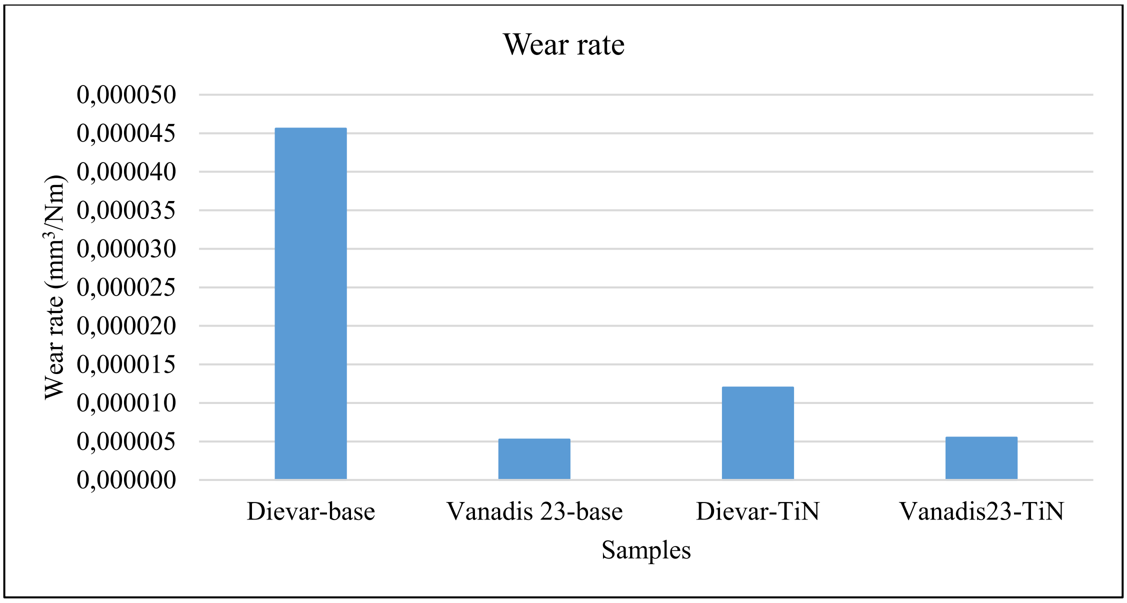

Fig. 9. The wear rate of base and coated metals that is earn by ball-on-disc wear test.

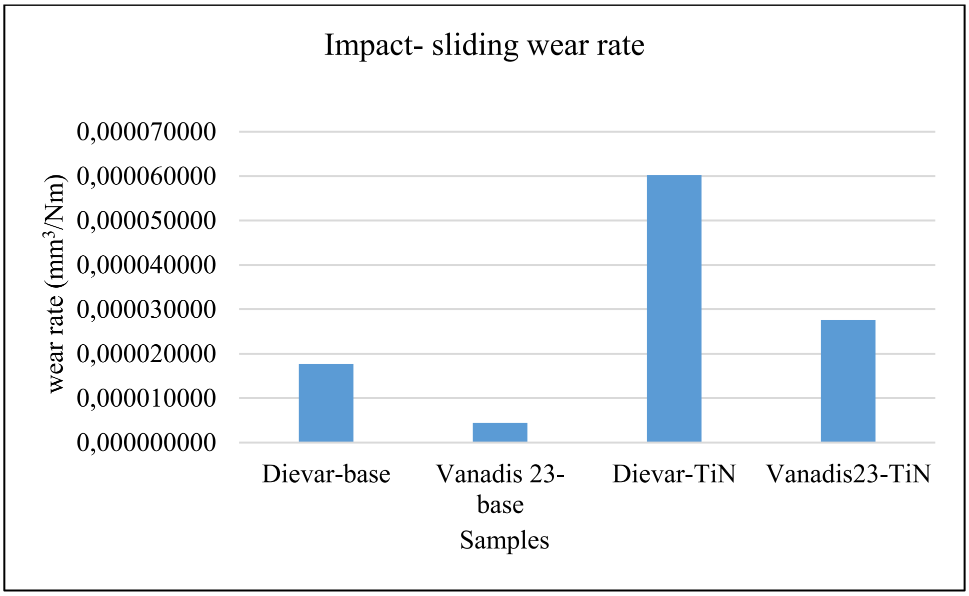

Fig. 10. The wear rate of base and coated metals that is earn by impact sliding test.

4. Conclusions

This work investigated the microstructure, mechanical, and tribological characteristics of CAPVD-deposited TiN films on Vanadis 23 and Dievar steels in a systematic manner. SEM and XRD measurements attested successful crystallite growth of the TiN(200) orientation on both substrates with substrate-dependent morphology. Whereas the Dievar coating possessed a denser and more uniform microstructural content, Vanadis 23 exhibited a more columnar structure with a greater incidence of droplet defects.

Nanoindentation experiments revealed a remarkable surface hardening in both the materials being investigated, Dievar exhibiting a very strong increase. The result suggests that it is possible for the TiN coating to enhance surface properties. However, this benefit was not always transferred to performance enhancement under all circumstances. Scratch testing and wear measurements revealed that Vanadis 23 had much better adhesion and tribological performance than Dievar. Although having a lower hardness increment, Vanadis 23-TiN exhibited high critical load values and low wear rates under sliding and impact-sliding conditions.

These findings suggest that substrate-coating interaction is an equally important determinant of the functional behavior of PVD coatings. While TiN deposition increases hardness in general, the performance under multiplex loading and especially dynamic or impact conditions is very substrate-dependent. The much poorer wear behavior of Dievar-TiN under impact-sliding conditions is reflective of a suggested mechanical compatibility mismatch and needs further optimization of coating scheme or surface pretreatment.

In conclusion, Vanadis 23 displayed higher overall compatibility with TiN coatings in rigorous tribological environments and consequently established itself as the more durable alternative for high-wear and impact-resistant applications. The work accentuates the requirement to optimize coating-substrate systems not merely based on intrinsic material characteristics but also considering the ambient environment and complexities of loading conditions.

Acknowledgments

The research described in this paper was financially supported by the Karadeniz Technical University under the grant number [FDK-2023-10908].

References

He, H. B., Han, W. Q., Li, H. Y., Yang, J., & Gu, T. (2014). Effect of TiN and TiAlN coatings on tribological properties and efficiency of gear. *Advanced Materials Research, 933*, 159–164. https://doi.org/10.4028/www.scientific.net/amr.933.159

Hernández-Sierra, M. T., Aguilera-Camacho, L. D., Ponce, A., García-Miranda, J. S., & Moreno, K. J. (2018). Tribological performance of TiN and TiCN coatings on a working tool steel. *Journal of Mechanical Science and Technology, 32*(8), 3659–3666. https://doi.org/10.1007/s12206-018-0718-3

Ichou, H., Arrousse, N., Berdimurodov, E., & Aliev, N. (2023). Exploring the advancements in physical vapor deposition coating: A review. *Journal of Bio- and Tribo-Corrosion, 10*(1). https://doi.org/10.1007/s40735-023-00806-0

Kladovasilakis, N., Pechlivani, E. M., Sfampa, I. K., Tsongas, K., Korlos, A., David, C., & Tzovaras, D. (2024). Metal 3D-printed bioinspired lattice elevator braking pads for enhanced dynamic friction performance. *Materials, 17*(11), 2765. https://doi.org/10.3390/ma17112765

Komarov, F., Konstantinov, V., Kovalchuk, A., Konstantinov, S., & Tkachenko, H. (2016). The effect of steel substrate pre-hardening on structural, mechanical, and tribological properties of magnetron sputtered TiN and TiAlN coatings. *Wear, 352–353*, 92–101. https://doi.org/10.1016/j.wear.2016.02.007

Liang, X., & Li, B. (2016). Analysis of brake material issues in the elevator hoisting accident. *2016 International Conference on Civil, Structure, Environmental Engineering (I3CSEE 2016)*. https://doi.org/10.2991/i3csee-16.2016.47

Murwamadala, R. D., Guthmann, X., & Nohava, J. (2025). Investigation of high-temperature wear behavior of TiN and TiAlN PVD-coated low alloy steel AISI 4140. *Industrial Lubrication and Tribology*. https://doi.org/10.1108/ilt-09-2024-0354

Sert, Y., Küçükömeroğlu, T., & Efeoğlu, İ. (2020). Investigating the structure, adhesion and tribological properties of Al and Zr-doped TiN coatings with various substrate bias voltage and working pressure. *Proceedings of the Institution of Mechanical Engineers, Part J: Journal of Engineering Tribology, 235*(6), 1190–1202. https://doi.org/10.1177/1350650120940071

Silva, L. P., Naeem, M., Díaz-Guillén, J. C., Brito, M. C. S., Monção, R. M., Silva, L. G. L., Nôleto, B. J. S., Sousa, E. M., Almeida, L. S., Rossino, L. S., Costa, T. H. C., Sampaio, W. R. V., & Sousa, R. R. M. (2024). Enhanced surface properties of 1080 eutectoid steel by cathodic cage plasma TiN deposition. *JOM*. https://doi.org/10.1007/s11837-024-06949-w

Wang, C., Chen, J., & Zeng, L. (2022). Wear and lubrication performance of different reticular-textured TiN-coated surfaces under lubricated conditions. *Processes, 10*(12), 2605. https://doi.org/10.3390/pr10122605

Xian, G., Xiong, J., Fan, H., Jiang, F., Guo, Z., Zhao, H., Xian, L., Jing, Z., Liao, J., & Liu, Y. (2021). Investigations on microstructure, mechanical and tribological properties of TiN coatings deposited on three different tool materials. *International Journal of Refractory Metals and Hard Materials, 102*, 105700. https://doi.org/10.1016/j.ijrmhm.2021.105700

Zhang, W., Feng, Q., Wang, E., & Zheng, L. (2019). Microstructure and property of Fe-based wear-resistant alloy coating prepared by laser cladding on the surface of super high-speed elevator parts. *IOP Conference Series: Materials Science and Engineering, 585*(1), 012006. https://doi.org/10.1088/1757-899X/585/1/012006

4th International Civil Engineering & Architecture Conference
17-19 May 2025, Trabzon, Türkiye

The impact of calcite impurities on the mechanically activated (MCA) montmorillonite structure and its performance in limestone calcined clay cement (LC^3) system

Vahiddin Alperen Baki*[1], Hamdi Kuleyin[2], Memduh Nas[3] and Kia Alalea[1]

[1] Department of Civil and Environmental Engineering, Imperial College London, United Kingdom
[2] Department of Mechanical Engineering, Recep Tayyip Erdogan University, Rize, Turkey
[3] Department of Civil Engineering, Karadeniz Technical University, Trabzon, Türkiye

Abstract. One of the most efficient routes to decarbonising the cement industry is using supplementary cementitious materials to partially substitute Portland cement. Raw clays are the most abundant materials in the field and have promising pozzolanic properties. However, non-clay materials' impurities, such as calcite, dolomite, quartz, and feldspar, may influence their reactivity. Thus, this paper systematically explores, for the first time, the influence of calcite impurities on the physicochemical and pozzolanic properties of alternatively activated (MCA) 2:1 (montmorillonite) clays and their potential utilisation in the LC^3 system. Montmorillonite samples before or after MCA were blended with 35% calcite, equivalent to the optimum ratio (2:1 clay-to-calcite) for the LC^3 system. The results suggest that adding mechanochemically activated montmorillonite significantly improved the compressive strength, showing superior properties to their thermally activated counterpart in the LC^3 system. In particular, simply co-milling montmorillonite with calcite results in the best performance by achieving approximately 20% higher strength than its thermally activated counterpart. The superior strength of co-milled montmorillonite can be related to increasing MCA efficiency with calcite addition due to its shielding effect, where the harder component (limestone 3 Mohn hardness), compared with montmorillonite (1-2 Mohn hardness), stays coarser and abrades the softer one. It was also observed that a decrease in the crystallinity of calcite after MCA can be another reason for better performance.

Keywords: 2:1 Clays; Limestone calcined clay cement; Mechanochemical activation; Calcite impurities

1.Introduction

Using supplementary cementitious materials (SCMs) as a partial replacement for Portland cement is one of the most effective ways to decarbonise the cement and concrete industry. Due to their abundance, relatively good geographic distribution, and high pozzolanic reactivity, clay minerals show great potential to decarbonise the cement industry and a 50% reduction in the clinker factor when combined with limestone (Antoni, Rossen, Martirena, & Scrivener, 2012). Thermal treatment has been the standard activation method for aluminosilicate minerals, with high temperatures leading to the loss of lattice water of clays (dehydroxylation) and their subsequent transformation to amorphous aluminosilicate with a disordered structure, which has high reactivity potential (Monteiro, Miller, & Horvath, 2017). However, not all clays and minerals can be effectively activated thermally and might require relatively high-temperature treatment, generating considerable CO_2 emissions (Fernandez, Martirena, & Scrivener, 2011; Ilić, Radonjanin, Malešev, Zdujić, & Mitrović, 2016; Kumar, Kumar, & Mehrotra, 2007; Zhou, Wang, Tyrer, Wong, & Cheeseman, 2017). 2:1 Clays, such as illite and smectite-type minerals (e.g. montmorillonite), show minimal reactivity improvement after thermal activation. This limited reactivity can be attributed to the stable order of structural layers after complete dehydroxylation and the location of the Al groups trapped between silicate tetrahedral, limiting the reactivity of 2:1 clays (Fernandez et al., 2011; He, 2000). Sintering, formation of new crystalline phases (Mg-Al silicate) and partly amorphisation were also primary reasons for the limited reactivity of 2:1 clays (montmorillonite and illite) (Habert, Choupay, Escadeillas, Guillaume, & Montel, 2009). As for impure phases, the presence of impure phases, such as calcite, quartz, feldspar and sulfite, can impact the reactivity of clay minerals after thermal activation (Habert et al., 2009). Clay minerals reactivity is also reduced with thermal activation due to recrystallised products (feldspars) (Habert et al., 2009). Similar results were also reported by Zunino et al., where calcite impurities lead to the formation of a granular deposit on the surface of kaolin, which reduces specific surface area and results in slightly worsening clay reactivity (Zunino

* Corresponding author, E-mail: vbaki@ic.ac.uk

https://doi.org/10.31462/icearc2025_ce_mat_482

& Scrivener, 2019). Due to the disadvantages of thermal activation reported above, mechanochemical activation has gained significant interest in academia and industry.

Despite the abundant literature regarding the thermal-treated calcite–clay system, there is a lack of systematic studies exploring these interactions for alternative activation methods, such as mechanochemical activation, which gained interest within the academic research community and the industry as an alternative clean activation route to thermal treatment. This study explores the effect of 35% calcite impurities, which is determined by considering the optimum clay-calcite ratio for the LC^3 system.

2. Materials and experimental methods

2.1.Materials

This study used pure montmorillonite (MNT) and calcite from Sigma Aldrich. CEM I 52.5N type Ordinary Portland cement from CEMEX was used to prepare the blended cement paste and mortar.

2.2.Sample preparation

2.2.1.Mechanochemical and thermal treatments

The montmorillonite and calcite were collected in powder form from Sigma Aldrich. Mechanochemical treatment of 60 g montmorillonite and 40 g montmorillonite-20 g calcite for co-grinding was performed in a Fritsch pulverısette 6 with a Tungsten carbide jar. Fifteen tungsten balls of 20 mm diameter in a 250 ml volume jar were used for activation~~,~~ as the Fritsch pulverısette manual recommended for optimum grinding. The 15/1 ball-to-mass ratio, equivalent to 60 g of powder~~,~~ was chosen for 20 minutes of mechanochemical activation at a constant milling speed of 500 rpm, as was determined in previous research on parameters for optimal activation.

For the thermal treatment, montmorillonite powders were heated for three hours at 800°C with a 10°C heat-up ramp in a standard air atmosphere. The targeted temperatures for thermal activation were determined from thermogravimetric analysis and previous research (Baki et al., 2022). After the thermal activation (3 hours), the samples were immediately removed from the oven and spread on a steel plate at room temperature for natural cooling.

2.2.2.Preparation of LC^3 pastes and mortars

LC^3 pastes and mortars with fixed water/binder ratio of 0.5 were prepared by replacing 50% of cement with 35% mechanochemically or thermally treated montmorillonite and 15% limestone, in addition to reference (100% OPC) samples. The pastes were prepared by hand mixing and cured at room temperature (20±2°C) for 28 days. Table 1 summarises the mix proportions, wherein the first letter of the label, "M" denotes mortar samples, while "P" represents paste samples. The last letter of the label indicates the treatment type: "M" for hand mechanochemical treatment, "ML" for mechanochemical co-grinding, and "T" for thermal treatment.

Mortar cubes of LC^3 systems were prepared according to EN 196-1 ("BS EN 196-1:2016 - TC: Tracked Changes. Methods of testing cement: Determination of strength," 2020) using a one-part binder, half-part water, and three-part standard sand to follow the development of compressive strength. It is also essential to note that sulphate optimisation to avoid providing under- or super-sulphated to the system with gypsum addition is not in the scope of this study.

Table 1**.** LC^3 mix designs for pastes and mortars

Series	SCMs Type	Sample ID	CEM I (g)	Montmorillonite (g)	Limestone(g)	Water/Binder Ratio	Sand/Binder Ratio
R	-	P-OPC	100	0	0	0.5	0
	-	M-OPC	100	0	0	0.5	3
M	MNT	P-LC^3-M	50	35	15	0.5	0
		M-LC^3-M	50	35	15	0.5	3
ML	MNT	P-LC^3-ML	50	35	15	0.5	0
		M-LC^3-ML	50	35	15	0.5	3
T	MNT	P-LC^3-T	50	35	15	0.5	0
		M-LC^3-T	50	35	15	0.5	3

MNT refers to montmorillonite, R stands for reference, M refers to mechanochemical activation, ML for the co-grinding kaolin with limestone, and T stands for thermal activation.

2.3.Test methods

X-ray diffraction (XRD) was used to characterise the activated montmorillinite's mineralogy and chemical bonding. The pozzolanic reactivity of the raw and activated montmorillonite was determined with a bound water test reported in ASTM C 1897-20 (International, 2020). The compressive strength of the examined mix designs was determined on 28-day mortar cubes using the Instron 150 frame conforming to EN-196-1 ("BS EN 196-1:2016 - TC: Tracked Changes. Methods of testing cement: Determination of strength," 2020).

2.3.1.Particle size distribution and surface properties

The surface morphology of the activated montmorillonite was characterised using SEM. First, the powdered samples were mounted on conductive carbon tape and then coated with 99% pure gold (Au) for 150 s in an argon gas environment using a coating device (Quorum, SC-7620). The surface morphology of the coated samples was examined using the JEOL JSM 6610 SEM under vacuum with an acceleration voltage of 15 kV. The particle size distribution (PSD) of differently activated montmorillonite minerals before and after activation was determined with a Malvern Mastersizer 2000. Both mechanochemically (including co-grinding) and thermally treated montmorillonite minerals were dispersed in distilled water for characterisation. Five minutes of ultrasonication was used for montmorillonite powders before particle size measurement.

2.3.2. Spectroscopic analysis (XRD)

The XRD was performed on an STOE STADI P (Cu radiation, λ = 1.54 Å) instrument in transmission mode, operated at 40 kV and 40 mA. The diffraction results were recorded from 5° to 75° (2θ), with a step resolution of 0.015° (2θ) per step. A double Mythen detector was used, with each detector covering a range of 19° (2θ) and operating at 31.6 s per degree (2θ). Each XRD scan took around 20 minutes.

2.4.Pozzolanic reactivity measured by R^3 test

The reactivity of montmorillonite before and after activation was examined using bound water measurements as specified in the R^3 test method (International, 2020). For each SCM precursor, bound water content was determined by mixing the examined materials with $Ca(OH)_2$, $CaCO_3$, and a potassium solution, which was prepared by dissolving 4.0 g of potassium hydroxide and 20.0 g of potassium sulphate in 1.0 L of distilled water at 23±3°C. All parts were stored at 40°C overnight before casting. The solid part was gently mixed by hand for 2 minutes. Then, the solid and liquid components were mixed at 1600 rpm for 2 minutes using a propeller mixer. Immediately after mixing, 15 g of the R^3 pastes were kept in sealed containers at 40°C for seven days for the bound water test.

2.4.1.Bound water test

After seven days of reaction, the pastes are crushed into pieces smaller than 2 mm. Then, around 10 g of crushed hydrated samples were placed into a crucible and dried in an oven at 40°C until constant weight was reached. Finally, about 5 g of the dried samples were heated at 350°C for two hours, and then cooled in a desiccator for one hour. The bound water capacity was calculated according to Equation 1, given in ASTM C 1987-20 (International, 2020).

$$H_2O_{bound,dried} = \frac{w_0 - w_t}{w_0 - w_c} \times 100 \quad (1)$$

where w_c is the weight of the crucible, w_0 is the weight of the dried material and the crucible at 40°C, and w_t is the final weight of the cooled material after heating at 350°C.

3.Results and discussion

3.1. Physicochemical properties

Fig. 1. summarises the effects of different activation methodologies on the surface morphology of montmorillonite. The irregular and sheet type morphology of montmorillonite did coarsened while some level of sheet type remained unchanged after the thermal treatment at 800°C (MNT-T). Additionally, the agglomeration of platelets in irregular stacks became more apparent.

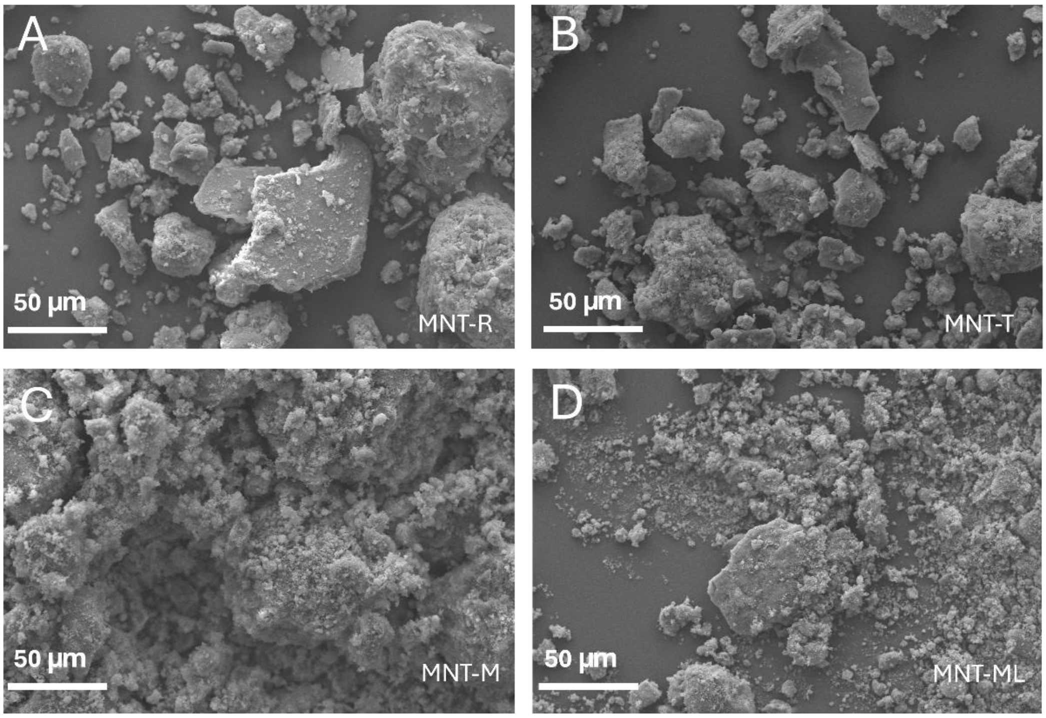

Fig. 1. Montmorillonite SEM images after different activations methodology

Table 2. D_{90}, D_{50} and D_{10} values of montmorillonite after different type of treatment

Sample ID	D90 (µm)	D50 (µm)	D10 (µm)
MNT-R	103.205	30.65	6.029
MNT-T	87.793	29.009	6.098
MNT-M	123.518	39.671	4.652
MNT-ML	111.066	35.287	4.229

The particle size reduction of montmorillonite after thermal treatment can be due to its relatively larger original particle size, where the contraction effect were observed due to heating and cooling likely surpassed the aggregation effect (Yanguatin, Ramírez, Tironi, & Tobón, 2019). For the mechanochemically treated montmorillonite, delaminated montmorillonite particles, which are small, close-to-spherical, and agglomerated into larger particles, were observed (Baki et al., 2022). Mechanochemical activation have increased the overall size distribution of the montmorillonite due to agglomeration as a result of mechanical effect. It is also important to note that co-grinding montmorillonite with limestone slightly shifts to particle size coarser areas than their mechanically activated counterpart, consistent with D_{90}, D_{50} and D_{10} values.

3.2. Phase assemblage (XRD)

The XRD measurements showed a loss in the structural ordering of the kaolinite by both mechanochemical and thermal treatment. The XRD pattern of as-received montmorillonite (Fig. 2) indicates that montmorillonite, muscovite, albite and quartz were observed from the XRD pattern of as-received kaolinite.

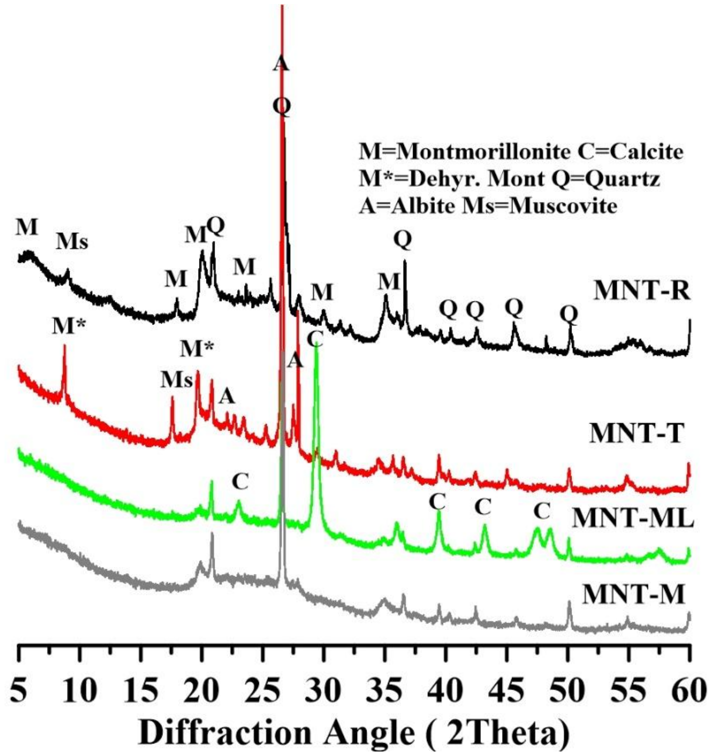

Fig. 2. X-ray diffractograms of the original and mechanically and thermally activated montmorillonite

The thermal treatment (800°C for 3 h) destroyed the crystal structure and dehydroxylate the montmorillonite but quartz peaks, on the other hand, remained unaffected, consistent with the reported literature (Baki et al., 2022). The montmorillonite reflection at about 6°2θ was reduced in intensity; however, the reflection close to 20°2θ was remained. The absence of montmorillonite peak at about 6° (2θ) and broad peak at 9° (2θ) after calcination can be related to the dehydrated structure of montmorillonite to a 10 Å TOT structure (Andrini et al., 2017; Dellisanti et al., 2018). These results are consistent with the literature, which indicates that the dehydroxylation of montmorillonite minerals disrupts the stacking of layers along the crystallographic c-axis (Garg & Skibsted, 2014; Heller-Kallai, 2006). In contrast, it does not affect the a- and b-axes within the layer plane (Garg & Skibsted, 2014; Heller-Kallai, 2006), supporting the view that dehydroxylation alone does not necessarily lead to amorphisation of montmorillonite clays (Marsh, Krishnan, & Bernal, 2024). Broadening and lowering montmorillonite peak intensities and areas after mechanochemical activation indicate a decrease in their crystalline sizes and amorphisation of the montmorillonite structure (Baki et al., 2022). Particularly, mechanochemical treatment was more efficient as it co-grinded with limestone. Also, it is important to note that the intensity of the quartz peak decreased with mechanochemical activation, can be attributed to the increase in lattice defects and degree of amorphisation.

3.3. Performance as SCM for LC^3 system

3.3.1. Fresh properties of LC^3 systems

Fig. 3 demonstrates the flowability results of different LC^3 systems, where the untreated and thermally activated montmorillonite-doped sample gives the lowest flow results. This can be related to the high fineness, specific surface area, and negative zeta potential (Py, Neto, Longhi, & Kirchheim, 2024; Sposito, Maier, Beuntner, & Thienel, 2022; Zunino, Martirena Hernandez, & Scrivener, 2021). Conversely, mechanochemically activated montmorillonite showed higher flowability, which can be related to the formation of small close-to-spherical particle agglomerate after intense milling, consistent with SEM results given Figure 1. The higher flowability values can be attributed to the phenomenon reported for fly ash addition, where the water demand decreases with fly ash addition due to their spherical particle shapes (Jiao, De Schryver, Shi, & De Schutter, 2021).

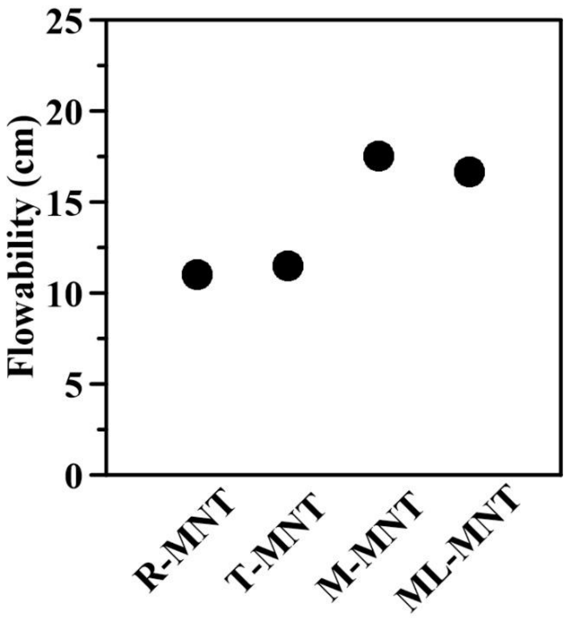

Fig. 3. Flowability results of LC^3 systems

3.4. Compressive strength and bound water test

Fig. 4 summarises the bound water percentages, which compare the pozzolanic reactivity of differently activated montmorillonite. The montmorillonite's bound water content increased after both thermal and mechanochemical treatment. The highest bound water was observed for the mechanochemically treated montmorillonite. It is also important to note that the bound water was further increased for the montmorillonite co-grinding with limestone. Bound water test results were also corroborated with strength results, where the mechanochemically activated sample (co-grinding with montmorillonite) using the LC^3 system showed the highest compressive strength, followed by the mechanically activated and thermally activated sample.

Compared with raw mechanical activation, the superior strength of co-milled montmorillonite can be related to increasing MCA efficiency with calcite addition due to its shielding effect, where the harder component (limestone 3 Mohn hardness), compared with montmorillonite (1-2 Mohn hardness), stays coarser and abrades the softer one. It was also observed that a decrease in the crystallinity of calcite after MCA can be another reason for better performance.

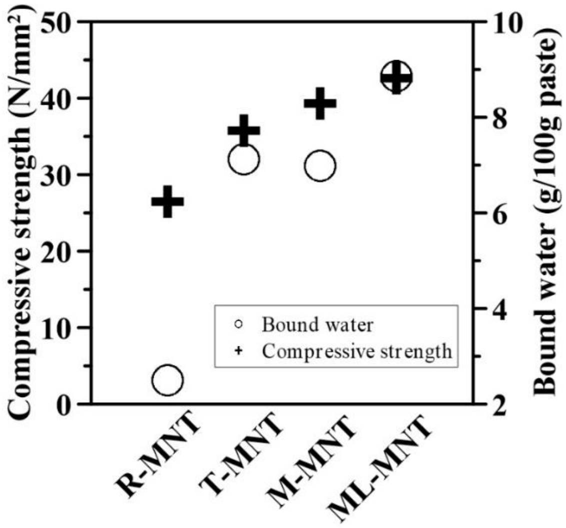

Fig. 4. Differently activated montmorillonite bound water test results and their LC^3 system compressive strength

4.Conclusion

The results show that mechanochemical activation can effectively promote the delamination, dehydroxylation and amorphisation of montmorillonite's original structures. Co-grinding montmorillonite with limestone further increases mechanochemical activation efficiency and improves strength performance. The superior strength of co-milled montmorillonite can be related to increasing MCA efficiency with calcite addition due to its shielding effect, where the component having higher hardness (limestone 3 Mohn hardness), compared with montmorillonite (1-2 Mohn hardness), stays coarser and abrades the softer one. It was also observed that a decrease in the crystallinity of calcite after MCA can be another reason for better performance.

This study presents the advantages of mechanochemical activation over thermal activation in montmorillonite for the first time by revealing higher flowability due to small close-to-spherical particle agglomerate formation after intense milling, which is a significant issue for LC^3 system particularly thermally treatment. Additionally, co-grinded montmorillonite blended LC^3 system showed 10% and 20% higher compressive strength compared with their mechanochemically and thermally activated counterpart, respectivelly.

References

Andrini, L., Moreira Toja, R., Gauna, M. R., Conconi, M. S., Requejo, F. G., & Rendtorff, N. M. (2017). Extended and local structural characterization of a natural and 800°C fired Na-montmorillonite–Patagonian bentonite by XRD and Al/Si XANES. *Applied Clay Science, 137*, 233-240. doi:10.1016/j.clay.2016.12.030

Antoni, M., Rossen, J., Martirena, F., & Scrivener, K. (2012). Cement substitution by a combination of metakaolin and limestone. *Cement and Concrete Research, 42*(12), 1579-1589. doi:10.1016/j.cemconres.2012.09.006

Baki, V. A., Ke, X., Heath, A., Calabria-Holley, J., Terzi, C., & Sirin, M. (2022). The impact of mechanochemical activation on the physicochemical properties and pozzolanic reactivity of kaolinite, muscovite and montmorillonite. *Cement and Concrete Research, 162*, 106962. doi:10.1016/j.cemconres.2022.106962

BS EN 196-1:2016 - TC: Tracked Changes. Methods of testing cement: Determination of strength. (2020). In: British Standards Institute.

Dellisanti, F., Calafato, A., Pini, G. A., Moro, D., Ulian, G., & Valdrè, G. (2018). Effects of dehydration and grinding on the mechanical shear behaviour of Ca-rich montmorillonite. *Applied Clay Science, 152*, 239-248. doi:10.1016/j.clay.2017.11.019

Fernandez, R., Martirena, F., & Scrivener, K. L. (2011). The origin of the pozzolanic activity of calcined clay minerals: A comparison between kaolinite, illite and montmorillonite. *Cement and Concrete Research, 41*(1), 113-122. doi:10.1016/j.cemconres.2010.09.013

Garg, N., & Skibsted, J. (2014). Thermal Activation of a Pure Montmorillonite Clay and Its Reactivity in Cementitious Systems. *Journal of Physical Chemistry C, 118*(21), 11464-11477. doi:10.1021/jp502529d

Habert, G., Choupay, N., Escadeillas, G., Guillaume, D., & Montel, J. M. (2009). Clay content of argillites: Influence on cement based mortars. *Applied Clay Science, 43*(3-4), 322-330. doi:10.1016/j.clay.2008.09.009

He, C. (2000). Thermal stability and pozzolanic activity of raw and calcined mixed-layer mica/smectite. *Applied Clay Science, 17*(3-4), 141-161. doi:10.1016/s0169-1317(00)00011-9

Heller-Kallai, L. (2006). Chapter 7.2 Thermally Modified Clay Minerals. In F. Bergaya, B. K. G. Theng, & G. Lagaly (Eds.), *Handbook of Clay Science* (Vol. 1, pp. 289-308): Elsevier.

Ilić, B., Radonjanin, V., Malešev, M., Zdujić, M., & Mitrović, A. (2016). Effects of mechanical and thermal activation on pozzolanic activity of kaolin containing mica. *Applied Clay Science, 123*, 173-181. doi:10.1016/j.clay.2016.01.029

International, A. (2020). Standard Test Methods for Measuring the Reactivity of Supplementary CementitiousMaterials by Isothermal Calorimetry and Bound Water Measurements. In *ASTM C1897-20*. West Conshohocken, PA ASTM.

Jiao, D., De Schryver, R., Shi, C., & De Schutter, G. (2021). Thixotropic structural build-up of cement-based materials: A state-of-the-art review. *Cement and Concrete Composites, 122*, 104152. doi:10.1016/j.cemconcomp.2021.104152

Kumar, R., Kumar, S., & Mehrotra, S. P. (2007). Towards sustainable solutions for fly ash through mechanical activation. *Resources Conservation and Recycling, 52*(2), 157-179. doi:10.1016/j.resconrec.2007.06.007

Marsh, A. T. M., Krishnan, S., & Bernal, S. A. (2024). Structural features of thermally or mechano-chemically treated montmorillonite clays as precursors for alkali-activated cements production. *Cement and Concrete Research, 181*, 107546. doi:10.1016/j.cemconres.2024.107546

Monteiro, P. J. M., Miller, S. A., & Horvath, A. (2017). Towards sustainable concrete. *Nat Mater, 16*(7), 698-699. doi:10.1038/nmat4930

Py, L. G., Neto, J. S. A., Longhi, M. A., & Kirchheim, A. P. (2024). Evaluation of ultrafine calcined clays on LC3 cements on the sulfate requirement, water demand and strength development. *Materials and Structures, 57*(1), 13. doi:10.1617/s11527-023-02288-5

Sposito, R., Maier, M., Beuntner, N., & Thienel, K.-C. (2022). Physical and mineralogical properties of calcined common clays as SCM and their impact on flow resistance and demand for superplasticizer. *Cement and Concrete Research, 154*, 106743. doi:10.1016/j.cemconres.2022.106743

Yanguatin, H., Ramírez, J. H., Tironi, A., & Tobón, J. I. (2019). Effect of thermal treatment on pozzolanic activity of excavated waste clays. *Construction and Building Materials, 211*, 814-823. doi:10.1016/j.conbuildmat.2019.03.300

Zhou, D., Wang, R., Tyrer, M., Wong, H., & Cheeseman, C. (2017). Sustainable infrastructure development through use of calcined excavated waste clay as a supplementary cementitious material. *Journal of Cleaner Production, 168*, 1180-1192. doi:10.1016/j.jclepro.2017.09.098

Zunino, F., Martirena Hernandez, J. F., & Scrivener, K. (2021). Limestone Calcined Clay Cements (LC3). *Aci Materials Journal, 118*.

Zunino, F., & Scrivener, K. (2019). *The effect of calcite and gibbsite impurities in calcined clay on its reactivity*.

Advancing geopolymer mortars with recycled concrete aggregates through joule heating curing

Sahin Ekmekci[1], Mucteba Uysal[1], Beyza Aygun[*2]

[1] Yıldız Technical University, Department of Civil Engineering, 34220 Istanbul, Türkiye
[2] Istanbul University-Cerrahpasa, Department of Civil Enginering, 34320 Istanbul, Türkiye

Abstract. This paper discusses the usage of recycling concrete aggregate (RCA) as an environmental-friendly substitute for natural river sand in geopolymer mortars (GMs), considering the increasingly growing demand for such greener construction materials. In this study, GMs were designed with 50% ground granulated blast furnace slag (GGBFS) and 50% Ceramic Powder as binder compositions and replacing 100% of the natural river sand with ≤2 mm-sized RCAs. The influence of variations in the activator-to-binder ratio between 0.7 and 1.2, coupled with variations in NaOH molarity to 2M, 4M, 6M, and 8M, on geopolymerization and mechanical properties are analyzed. Ambient curing was carried out at 23±2°C with a relative humidity of 95%, thermal curing at 80°C for 24 hours, and electrical curing with an application of 20V to study the effects of all these curing methods on the compressive and flexural strengths at 7 and 28 days to provide details on short- and medium-term performances. The study also brings into focus how curing methods interact with a/b ratios and NaOH molarity in determining hydration and matrix behavior, while providing a practical and sustainable solution to construction waste management and contributing to the development of high-performance, eco-friendly materials. This study revealed that electrical curing at low molarity is more effective than curing under ambient conditions and that sample production is not always possible at the lowest molarity values.

Keywords: Geopolymer; Recyling concrete aggregate; Curing methods; Mechanical properties

1. Introduction

Traditional concrete and cement-based mortars are frequently preferred and have been used in the construction sector for a long time. These concretes and mortars also provide advantages such as high compressive strength, easy workability and long service life (Neville, 2012). However, the production stage of Portland cement from beginning to end causes significant environmental problems as it is responsible for approximately 8% of global carbon dioxide (CO_2) emissions (Mehta & Monteiro, 2014). In addition, despite all these positive effects, these concretes and mortars, which are frequently preferred, still have negative aspects. It is known that the products (e.g. calcium hydroxide) that emerge in cement-based materials as a result of hydration reactions are open to durability problems (chemical attack, carbonation) in the long term and at advanced ages depending on the environmental conditions. Therefore, the development of sustainable alternative binding systems in order to eliminate these negative effects has become very important both for the reduction of environmental impacts and the production of more durable and long-lasting building materials (Scrivener et al., 2018).

For this purpose, geopolymer mortars have gained a place in the sector as a remarkable option due to the recycling of industrial wastes, the reduction of carbon emissions and the high strength and durability properties. While the use of by-products such as fly ash, silica fume and granulated blast furnace slag (GGBFS) is common in geopolymer production, it has been observed that alternative aluminosilicate sources such as ceramic powder, glass powder, marble powder and aluminum sludge also provide successful and effective results (Torgal & Jalali, 2011; Pacheco-Torgal et al., 2008).

Among the activators used during the production of geopolymer mortars, sodium hydroxide (NaOH) and sodium silicate (Na_2SiO_3) solutions stand out and are widely preferred. The reason for this can be explained as NaOH ensures the dissolution of aluminosilicate structures and increases the amount of substance to interact, while sodium silicate solution increases the amount of silica in the system and contributes to the formation of a dense, durable matrix. (Duxson et al., 2007; García-Lodeiro et al., 2015). By using low molarity NaOH solutions (2M–6M), both environmentally friendly and low-cost production processes can be carried out, and in addition, occupational safety risks are less compared to high molarity productions (Veerappan et al., 2017; Inti et al., 2017).

[*] Corresponding author, E-mail: beyza.aygun@ogr.iuc.edu.tr

https://doi.org/10.31462/icearc2025_ce_mat_533

golden light publishing

In the curing process of geopolymer concrete and mortars, the use of innovative techniques such as electrical curing instead of traditional ambient and thermal methods increases both energy efficiency and easy applicability and provides a usable strength gain in a short time (Aygun, 2023).

Geopolymerization process is carried out by dissolution and repolymerization of aluminosilicate sources in an alkaline environment. Depending on the abundance of alkali activators such as sodium hydroxide in the mixture, the reaction rate and speed of the geopolymer and the mechanical properties of the obtained product are directly affected (Livi et al., 2017). When other studies are examined, high molarity solutions (10M-16M) provide faster strength results; however, both the cost and the risks to be encountered during production increase due to high molarity (Chithambaram et al., 2018). On the other hand, significant and acceptable strength values can be obtained on geopolymer mortars prepared using low molarity sodium hydroxide solutions (2M-6M). Especially mortars produced with 6M molarity provide sufficient strength and are an economical and safe option. After the production of mortars, geopolymer mortars and concretes also need curing, just like in the traditional way. Traditional curing methods have negative aspects such as high energy consumption and time loss compared to new alternatives (Livi et al., 2017). As an alternative option, the electrical curing method accelerates the hydration process and strength gain by directly applying low voltage to the fresh mortar, causing the internal temperature to increase (Aygun, 2023). Similarly, Halis Alakara (2022) has shown that electrical curing increases the mechanical strength in geopolymers containing alkali activator containing recycled asphalt dust-based aggregate and can be advantageous especially in applications where early age strength is required. In order to continue the low cost and sustainability targets within the scope of alternative concrete production and innovations, the reuse of concrete wastes is very important in terms of sustainable construction practices. The use of RCA in geopolymer mortars reduces the consumption of natural resources and raw materials, as well as allowing the evaluation and disposal of waste (Alakara, 2022). However, the surface roughness and porosity of RCA grains can affect the bonding mechanisms and cause strength losses. For this reason, it is necessary to work with low molarity alkaline solutions and effective curing methods in mortars using RCA (Inti et al., 2017).

In this study, geopolymer mortars were produced with a binder system consisting of 50% granulated blast furnace slag and 50% ceramic powder, and 100% standard sand or river sand replaced recycled concrete aggregate (RCA). Sodium hydroxide and sodium silicate were used as alkali activators, and low molarity NaOH solutions were preferred. Alkali activator/binder ratio was changed according to the changing low molarities, taking into account the appropriate workability. Mortar samples were cured with ambient curing, thermal curing and electrical curing methods, and the effects of these methods on compressive and flexural strengths were investigated. Thus, both the 100% usage potential of recycled aggregates in construction materials and the effectiveness of alternative curing methods were investigated and the results were presented.

2. Materials and methods

2.1. Materials

In order to understand the effectiveness and difference of low molarity and different curing conditions more clearly, two basic materials were used as binders: granulated blast furnace slag (GBFS) and ceramic powder (CP). Blast furnace slag was considered to be an effective choice for geopolymer mortars produced with low molarity due to its early and high strength. Ceramic powder was preferred for better interpretation of the results under different curing conditions due to its closeness to temperature levels and better observation of its interaction.

Blast furnace slag is a waste material formed as a by-product during the smelting of iron ore in blast furnaces. Its granulated form can be preferred as a binder in cement and concrete production. If the slag is cooled rapidly instead of slowly, it turns into an amorphous structure rich in silica and aluminum oxide and exhibits pozzolanic behavior due to these properties. When ground into fine grains, it reacts with cement hydration products, increasing strength and providing the majority of the strength to be produced. In addition, it contributes to environmental sustainability. They are generally light colored and have a glassy grain structure. Their density is around 2.9 g/cm^3.

Ceramic powder is a fine-grained material obtained by grinding waste generated during ceramic production and is generally light-colored, close to orange. Its density is around 2.5-2.7 g/cm^3. This powder has pozzolanic properties due to its high silica and alumina content and can be used in concrete and mortars as a substitute for cement. The use of ceramic powder, just like other pozzolanic materials, contributes to waste management and reduces environmental impacts. Table 1 shows the chemical components of granulated blast furnace slag and ceramic powder used in this study.

Sodium hydroxide (NaOH) and sodium silicate (Na_2SiO_3) were used to interact with the binders and their ratios are 1/2 units, respectively. Sodium hydroxide is a strong alkali with a pH value of approximately 13.4 and is used as an activator in geopolymer production. NaOH initiates the polymerization process by dissolving aluminosilicates. It has a salt-like appearance in the form of white and opaque crystals and must be dissolved in water according to the desired molarity before use. Its density can be expressed as 2.13 g/cm^3. Sodium silicate is the second activator used together with sodium hydroxide in geopolymer mortar production. Thanks to its silica content, it supports the formation of polymer chains and improves the mechanical properties of the mortar. In addition, the viscosity of sodium silicate affects the workability of the mixture. It has a colorless but slightly viscous, syrup-like appearance. Its density is 2.4 g/cm³. The SiO_2 content is around 24–26% and the Na_2O content is around 11.5–13.5%. The modulus (SiO_2/Na_2O ratio) is usually in the range of 1.90–2.25.

As aggregate, 100% recycled aggregate (RCA) with a grain size of ≤2 mm was used. Recycled aggregate is the material obtained by breaking demolished concrete structures or from old test samples. Since RCA has a more porous structure compared to natural aggregates, it also has a higher water absorption capacity. These properties can affect the strength and durability of geopolymer mortars. However, the negative effects of RCA can be minimized with appropriate mixture design and curing methods. The aggregates used in this study were obtained from the test laboratory within the university. Samples used have different strength classes and contents and are waste samples on which the relevant tests have been previously performed. The appearance of these aggregates is irregularly shaped, porous and gray. Its density is around 2.3–2.5 g/cm³. Its water absorption rate is higher than other aggregates, such as 5–10%. Table 2 includes the mixture calculation and recipe for mortars of different molarities produced in this study for 1 m³.

Table 1. Chemical composition of binders

Main Oxide (%)	GBFS	CP
SiO_2	40.5	65.44
Al_2O_3	12.8	15.45
Fe_2O_3	1.1	7.11
CaO	35.5	4.65
MgO	5.8	1.28
Na_2O	0.79	0.8
K_2O		2.15
SO_3	0.18	0.06
TiO_2	0.75	
LOI	0.03	3.06

Table 2. Mixing quantities for 1 m³ volume

Series	a/b Ratio	GBFS (kg)	CP (kg)	RCA (kg)	NaOH (kg)	Na_2SiO_3 (kg)	Total (kg)
2M	1.00	292.97	292.97	1464.85	195.31	390.62	2636.72
4M	0.85	292.97	292.97	1464.85	166.02	332.04	2548.85
6M	0.85	292.97	292.97	1464.85	166.02	332.04	2548.85
8M	0.70	292.97	292.97	1464.85	136.72	273.44	2460.95

*2M,4M,6M,8M - (50% GBFS + 50% CP + 100% RCA)

2.2. Methods

In the first stage, many different samples with different strength classes and components obtained from the building test laboratory were ground by rotating them in the Los Angeles device by means of balls. Then, a sieve with a 2 mm sieve opening was used to ensure that the aggregate grain size to be used was ≤2 mm. All the aggregates obtained below 2 mm were mixed in the mixer in dry form to be homogeneous and packaged in that way and made ready for use.

When it came to the production of samples, the production was carried out in accordance with the recipe and prismatic samples of 40x40x160 mm dimensions were produced in order to obtain 7-day compressive and flexural strength results in accordance with ASTM C349 and TS EN 196-1 standards. A total of six prismatic samples were produced for each series, two of which were exposed to ambient, two thermal and two electrical curing conditions.

While preparing the mortar, firstly granulated blast furnace slag and ceramic powder were mixed in dry form in the container of the mixer and made homogeneous. Then, 1 unit sodium hydroxide and 2 units sodium silicate solution was added to the binders as liquid phase according to the desired molarity and mixed. Finally, the determined amount of recycled aggregate was added to form the mortar and after mixing, the mortar was placed in the molds.

The samples to be exposed to ambient cure were removed from the mold after completing the 24-hour setting period and placed in a curing cabinet with a temperature of 23 ± 2 °C and a relative humidity of 95% to complete their 7-day waiting period. The samples to be exposed to thermal cure were removed from the mold after completing the 24-hour setting period and placed in an oven at 80 °C for 24 hours. Then, the samples removed from the oven were placed in the same curing cabinet after cooling to room temperature to complete the 7-day waiting period. Finally, the samples to be exposed to electrical cure were placed in wooden molds with copper plates at both ends while they were still fresh and fluid and were exposed to an alternating current effect corresponding to 20V for 24 hours. At the end of one day, the samples removed from these molds were placed in the curing cabinet to complete the 7 days.

After the 7 day waiting period, first bending and then compressive strength tests were performed on all prismatic samples in accordance with the previously specified standards. After determining the bending strengths, compressive strength tests were performed on two pieces of a single sample obtained from the prism and the average of the results of the two pieces was taken.

3. Results and discussion

Findings obtained from this study show that the mechanical strength performances of geopolymer mortars prepared with low molarity sodium hydroxide and sodium silicate solutions vary significantly depending on both the curing method differences and the molarity value. When the flexural and compressive strength values are examined together, it is seen that the highest strength values among all three curing methods are generally reached in the samples applied with thermal cure (T). This difference is more pronounced especially in the 6M and 8M molarity samples, and the compressive strength in the 6M-T series reached approximately 31.9 MPa, while the flexural strength resulted in a value of 4.47 MPa. This finding shows that the high temperature effect accelerates the geopolymerization process and supports the formation of a denser and stronger matrix (Livi et al., 2017; Duxson et al., 2007).

In addition to the thermal curing method, it is observed that the electrical curing (E) method, which is an alternative and new cure method, also has a remarkable effect. It has been observed that even at very low molarity values such as 2M and 4M, the samples cured with electrical cure have a positive effect and provide significant increases in both flexural and compressive strength compared to the cure under ambient conditions (A). For example, while the samples belonging to the 2M-A series showed a bending strength of approximately 1.1 MPa and a maximum compressive strength of 6.6 MPa, the 2M-E sample reached a maximum flexural strength of 2.1 MPa and an average compressive strength of approximately 10 MPa. This situation reveals that electrical cure is effective in activating the internal structure of the matrix in low molarity systems and that, as in electrical curing, other alternative curing techniques may be more advantageous in some cases compared to classical methods (Aygun, 2023; Alakara, 2022). Fig. 1 shows a graph showing the 7-day flexural and compressive strength results of samples with different molarity and curing conditions.

Table 3 shows the results of all compressive and flexural strength tests in MPa on samples with varying low molarity values and exposed to three different curing conditions.

Table 3. 7-day flexural and compressive strength results of geopolymer mortars with different molarity values and subjected to different curing conditions

Series	Strength Results			
	Sample 1		Sample 2	
	Flexural Strength (MPa)	Compressive Strength (MPa)	Flexural Strength (MPa)	Compressive Strength (MPa)
2M-A	1.08	6.15	1.10	6.63
2M-E	2.13	11.04	1.91	9.96
2M-T	3.15	14.60	3.61	14.53
4M-A	2.30	8.46	1.90	8.11
4M-E	3.35	19.23	3.36	20.11
4M-T	4.70	27.79	4.34	26.40
6M-A	3.32	11.39	3.30	11.87
6M-E	3.86	24.88	3.88	26.13
6M-T	4.47	31.90	4.46	28.53
8M-A	3.61	9.55	3.98	9.73
8M-E	4.99	15.40	5.48	15.44
8M-T	5.91	21.47	6.02	21.46

*2M,4M,6M,8M - (A- Ambiant curing, E- Electrical curing, T- Thermal curing)

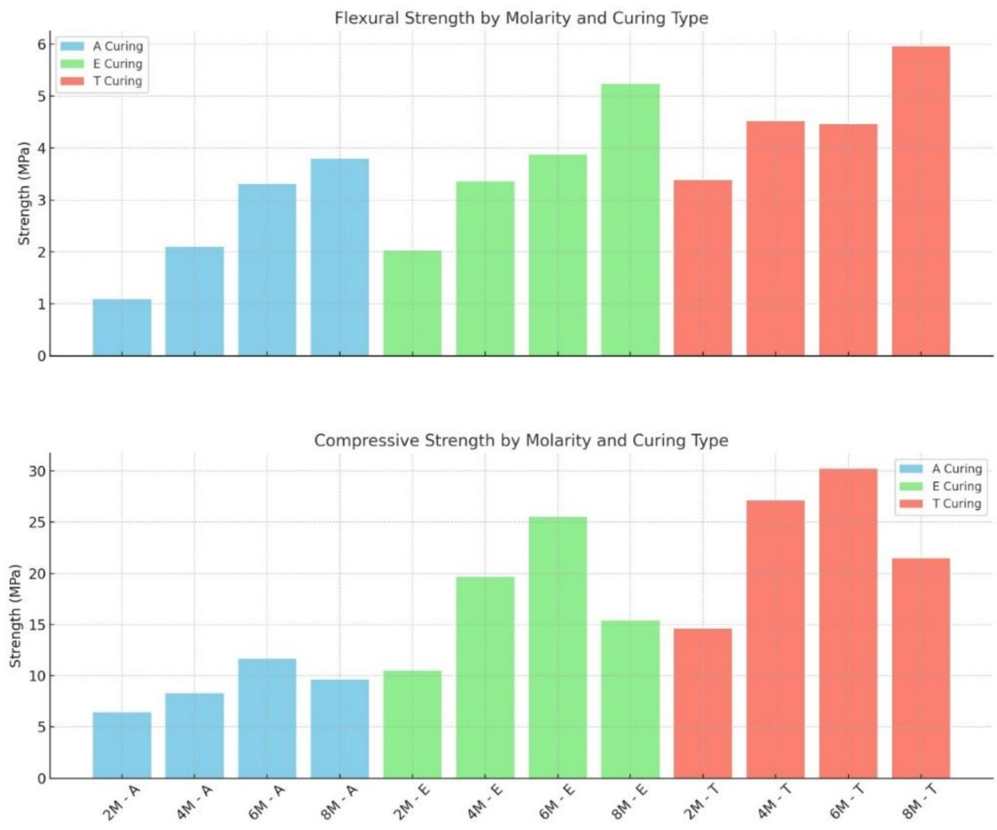

Fig. 1. 7-day flexural and compressive strength results of samples with different molarity and curing conditions

4. Conclusions

- In addition to the curing types, the molarity level has also been shown to have significant effects on mortar performance. As molarity increases, the strength values for each curing method increase significantly.
- In particular, there was a jump in both flexural and compressive strengths between 4M and 6M, which showed that the 6M value could be a threshold value that can provide high mechanical performance with low cost and environmental risks within the low molarity class.
- However, the fact that the strength values in 8M in some cure types (e.g. 8M-A) are not as high as 6M-E or 6M-T is the biggest indicator that high molarity does not guarantee the best result under all conditions.
- In general, despite the weakening effects of low molarity, electrical curing and the use of 100% recycled aggregates and the surface properties and porosity of the aggregate, acceptable strength levels were achieved in many samples.
- In addition, the binder system used in this study (50% GGBFS + 50% CP) and alternative curing techniques applied with low molarity solutions were found to support that geopolymer technology can become a more economical, environmentally friendly and applicable building material.

References

Alakara, E.H. (2022). Geri dönüştürülmüş asfalt tozunun alkali aktifleştirilmiş cüruf harçlari üzerindeki etkisi. *Uluslararası Mühendislik Araştırma ve Geliştirme Dergisi, 14*(3), 362–368 (in Turkish)

Aygun, B.F. (2023). Farklı lifler içeren uçucu kül-cüruf esasli geopolimer kompozitlerde farkli kür yönteminin etkisiyle mekanik özelliklerin incelenmesi. *THBB Akademi*, 606-615 (in Turkish)

Chithambaram, J.S., Kumar, S., & Prasad, M.M. (2018). Study on effect of sodium hydroxide concentration on geopolymer mortar. *In Sustainable Construction and Building Materials*, pp. 651–658

Duxson, P., Fernández-Jiménez, A., Provis, J.L., Lukey, G.C., Palomo, A., & van Deventer, J.S.J. (2007). Geopolymer technology: the current state of the art. *Journal of Materials Science, 42*(9), 2917-2933

García-Lodeiro, I., Palomo, A., Fernández-Jiménez, A., & Macphee, D.E. (2015). Compatibility studies between N-A-S-H and C-A-S-H gels: Study in the ternary diagram Na_2O–CaO–Al_2O_3–SiO_2–H_2O. *Cement and Concrete Research, 74*, 9-17

Inti, S., Sharma, M., & Tandon, V. (2017). Influence of curing on the properties of geopolymer mortar made with low molarity sodium hydroxide. *Transportation in Developing Economies, 3*(2)

Livi, C.N., & Repette, W.L. (2017). Effect of NaOH concentration and curing regime on geopolymer. *IBRACON Structures and Materials Journal, 10*(6), 1174–1181

Mehta, P.K., & Monteiro, P.J.M. (2014). *Concrete: Microstructure, Properties, and Materials* (4th ed.). McGraw-Hill Education.

Neville, A.M. (2012). *Properties of Concrete* (5th ed.). Pearson.

Pacheco-Torgal, F., Castro-Gomes, J., & Jalali, S. (2008). Alkali-activated binders: A review. *Construction and Building Materials, 22*(7), 1305-1314

Scrivener, K., John, V.M., & Gartner, E. (2018). Eco-efficient cements: Potential, economically viable solutions for a low-CO_2 cement-based materials industry. *Cement and Concrete Research, 114,* 2–26

Torgal, F.P., & Jalali, S. (2011). Eco-efficient construction and building materials research. *Construction and Building Materials, 25*(12), 581-591

4th International Civil Engineering & Architecture Conference
17-19 May 2025, Trabzon, Türkiye

Comparative investigation of micro steel fiber effects on the electrical resistivity of PC and AAS composites

Ahsanollah Beglarigale*[1]

[1] Istanbul Okan University, Department of Civil Engineering, 34959 Tuzla, Istanbul, Türkiye

Abstract. This study investigates the influence of micro steel fiber incorporation on the electrical resistivity of two cementitious binder systems: Portland cement (PC) and alkali-activated slag (AAS). Eight mixtures, including reference mortars and fiber-reinforced compositions with 3%, 4%, and 5% fiber volume fractions, were prepared and evaluated. The uniaxial bulk electrical resistivity of each mixture was monitored over a 56-day curing period. The results demonstrated that fiber addition led to a reduction in resistivity in both systems, although the magnitude of improvement varied significantly depending on the matrix chemistry. AAS-based mortars exhibited substantially lower resistivity values compared to PC-based mortars, attributed to the superior ionic conductivity of the AAS matrix. The incorporation of fibers further enhanced conductivity, with 4% fiber volume identified as an effective threshold in both systems. As part of a comprehensive ongoing research project, this study focuses on optimizing the electrical conductivity of fiber-reinforced composites, laying an essential foundation for the subsequent fabrication of various smart construction materials such as self-sensing cementitious composites.

Keywords: Self-sensing mortars; Micro steel fibers; Electrical resistivity; Alkali-activated slag; Cementitious composites

1. Introduction

Cementitious composites endowed with intrinsic self-sensing capabilities are redefining the approach to structural health monitoring by enabling materials to autonomously detect and respond to internal changes such as stress, deformation, cracking, and damage accumulation. Through the integration of sensing functionality directly within the matrix, these composites eliminate the need for external devices and provide real-time, distributed monitoring based on variations in electrical properties, offering significant advantages in terms of system reliability, durability, and long-term infrastructure management. In piezoresistive systems, the introduction of conductive components, such as carbon fibers or conductive aggregates, enhances the electrical connectivity within the matrix, enabling measurable and repeatable changes in electrical resistivity under mechanical strain (Ma et al., 2020). This piezoresistive behavior depends not only on the establishment of conductive pathways but also on maintaining an appropriate balance between matrix resistivity and sensitivity to mechanical stimuli. On the other hand, for cementitious composites incorporating piezoelectric ceramics such as lead zirconate titanate (PZT), the electrical conductivity of the matrix and the composite as a whole plays a critical role: sufficient conductivity can make the poling process easier and more effective (Gong et al., 2011), which is essential for activating piezoelectric behavior. Therefore, the electrical resistivity of cementitious composites should be carefully optimized to enable efficient polarization and ensure a reliable piezoelectric response under practical conditions. In particular, achieving a relatively high matrix conductivity can be highly beneficial for the fabrication of various smart cementitious materials—an objective that constitutes the central focus of the present study.

Building upon the critical role of matrix optimization, recent studies have also highlighted the contribution of steel fiber incorporation to improving the electrical performance of cementitious composites. Cleven et al. (2021) demonstrated that increasing the steel fiber content in PC-based mixtures significantly decreased electrical resistivity, although parameters such as the water-to-binder ratio and binder content also influenced the overall conductivity. Extending these findings to alkali-activated systems, Piao et al. (2025) reported that fiber addition enhanced electrical conductivity, with more pronounced improvements observed at higher fiber concentrations. Similarly, Lu et al. (2025) investigated alkali-activated slag/fly ash mortars and found that steel fiber incorporation led to satisfactory conductivity and improved piezoresistive self-sensing behavior under cyclic loading. Although the self-sensing mechanisms differ between piezoresistive and piezoelectric composites, the formation of continuous conductive networks remains a common and essential requirement.

* Corresponding author, E-mail: ahsan.beglari@okan.edu.tr

https://doi.org/10.31462/icearc2025_ce_mat_548

The sensing functionality of such materials depends significantly on the electrical continuity within the matrix. While conductive fibers or other conductive fillers can improve charge transport, the baseline electrical resistivity of the matrix remains a critical factor. Therefore, the selection and optimization of the binder system is essential. PC-based matrices typically exhibit relatively high resistivity due to limited ionic mobility in their pore solutions. In contrast, AAS systems, when properly designed, offer a chemically favorable environment for ionic conduction, making them a promising alternative for electrically functional composites (Rovnaník et al., 2019).

This study constitutes a part of an ongoing comprehensive research project. In the earlier phases of the project, binder systems with enhanced ionic conductivity were developed to achieve relatively low matrix resistivity—which, notably, remains a controllable and optimizable parameter depending on the composite's moisture content—thereby establishing a foundation for the subsequent development of smart cementitious composites. This property will be further optimized in later stages to enhance the functional performance of the composites. The present work reflects a portion of this phase, specifically addressing the evaluation of electrical resistivity in fiber-reinforced PC-based and AAS-based composites. This paper focuses on analyzing how micro steel fiber incorporation influences the electrical conductivity of these systems—a critical step toward the future development of smart cementitious composites.

2. Materials and methods

2.1. Materials

Two different binder systems were used in this study: Portland cement and alkali-activated slag. The Portland cement (CEM I 42.5R) was supplied by Nuh Cement (Kocaeli, Türkiye) and had a Blaine fineness of 3645 cm^2/g. The ground granulated blast furnace slag (GGBFS), employed as the primary binder in the AAS mixtures, was obtained from Kardemir (Karabük, Türkiye), with a Blaine fineness of approximately 4150 cm^2/g and a specific gravity of 2.88.

For alkali activation, a binary activation solution was prepared using sodium hydroxide (NaOH) and sodium silicate (SS) solution, both obtained from Merck-SigmaAldrich. Initially, NaOH pellets were dissolved directly in the total mixing water defined in the mix design, and the solution was allowed to cool to ambient temperature. Subsequently, the sodium silicate solution, which contained approximately 8% Na_2O and 27% SiO_2 by mass, was added to the NaOH solution.

Crushed limestone with a maximum particle size of 4 mm was used as the aggregate in all mixtures. Its specific gravity was measured as 2.65. A polycarboxylate ether (PCE)-based superplasticizer (MasterGlenium ACE 450, Sika Group) was used in all PC mixtures to ensure consistent and desired flowability.

The steel microfibers used in the study were brass-coated and straight. Each fiber was 6 mm long and 0.16 mm in diameter, with a nominal tensile strength of 2000 MPa. The fibers were incorporated into the mixtures at volume fractions of 3%, 4%, and 5%, depending on the test group.

2.2. Mix designs and specimen preparation

Eight mortar mixtures were prepared in this study to investigate the influence of steel micro-fiber content on the electrical resistivity of two binder systems: Portland cement (PC) and alkali-activated slag (AAS). Each binder system included a reference mixture without fibers (PC_REF and AAS_REF) and three fiber-reinforced mixtures containing 3%, 4%, and 5% steel fibers by volume (PC_3F, PC_4F, PC_5F; and AAS_3F, AAS_4F, AAS_5F, respectively).

The reference mixtures were not arbitrarily selected but were based on a comprehensive matrix optimization study conducted in the earlier stages of the same project. These mixtures were specifically designed to simultaneously meet three key performance criteria: (i) adequate flowability to ensure uniform fiber dispersion and facilitate the subsequent incorporation of PZT particles, (ii) low bulk electrical resistivity, and (iii) sufficient compressive strength to maintain mechanical stability. Following the selection of the reference mixtures, the impact of fiber volume on performance was investigated by adjusting the aggregate content in the mixtures.

All mixtures were proportioned with a constant water-to-binder (W/B) ratio of 0.47, and the paste volume was maintained identical across the PC and AAS series. In fiber-reinforced mixtures, the volume of steel fibers was deducted from the total aggregate content to preserve the overall volumetric balance and maintain the continuity of the paste phase. The PCE-based superplasticizer (SP) was incorporated into all PC mixtures at a fixed dosage of 2.0 kg/m^3 to stabilize workability regardless of fiber content.

In AAS mixtures, the binder consisted of ground granulated blast furnace slag (GGBFS) activated by a binary alkali solution composed of sodium hydroxide (NaOH) and sodium silicate (SS). The activator was formulated to deliver 10% Na_2O relative to the binder mass, with a silica modulus (SiO_2/Na_2O) of 1.2. During the proportioning process, the water content of the sodium silicate solution (approximately 65% by weight) was considered in calculating the net water content to maintain the targeted water-to-binder (W/B) ratio. All activation solutions were prepared in advance and cooled to ambient temperature prior to mixing.

The mixing procedure was carried out using a Hobart mixer. Initially, all dry components, including the binder, aggregate, and steel fibers, were combined to achieve a uniform dry blend. Subsequently, the liquid phase—comprising water and superplasticizer for PC mixtures, or the pre-prepared alkali activator solution for AAS mixtures—was added, and mixing was continued until a sufficiently homogeneous mixture exhibiting sufficient workability was achieved.

Cylindrical specimens with a diameter of 100 mm and a height of 200 mm were cast in three equal layers. After 24 hours, the specimens were demolded and transferred to standard water curing conditions, where they were maintained until testing. To ensure consistent electrical contact, the upper surfaces of AAS specimens were trimmed by approximately 1–2 mm prior to the initial UBER measurement. In PC specimens, surface trimming was performed after 14 days. The detailed mixture proportions for all PC and AAS compositions are summarized in Table 1 and Table 2, respectively.

Table 1. Mix design of PC mixtures (kg/m^3)

Mixture	PC	Water	SP	Limestone	Steel Fiber
PC_REF	764.0	359.08	2.0	1052.92	—
PC_3F	764.0	359.08	2.0	973.42	215.1
PC_4F	764.0	359.08	2.0	946.92	286.8
PC_5F	764.0	359.08	2.0	920.42	358.5

Table 2. Mix design of AAS mixtures (kg/m3)

Mixture	GGBFS	Water*	Limestone	Steel Fiber	NaOH	SS	Na_2O (%)
AAS_REF	670.0	121.34	1054.2	—	57.45	297.78	10%
AAS_3F	670.0	121.34	974.7	215.1	57.45	297.78	10%
AAS_4F	670.0	121.34	948.2	286.8	57.45	297.78	10%
AAS_5F	670.0	121.34	921.7	358.5	57.45	297.78	10%

** The water content listed for AAS mixtures excludes the water already present in the sodium silicate (SS) solution (~65% by weight). To obtain the actual total water content, 65% of the SS mass should be added to the listed water value.*

2.3. Electrical resistivity test

The bulk electrical resistivity of all mixtures was measured periodically over a 56-day curing period using the uniaxial bulk electrical resistivity (UBER) method. Measurements were conducted with a commercial resistivity device (Resipod, Proceq) featuring a 50 mm probe spacing, used in conjunction with a custom measurement setup compatible with Ø100 mm cylindrical specimens (Fig. 1). Prior to each measurement, the specimens were removed from standard water curing and immediately positioned between two moist sponges and stainless steel plate electrodes.

According to the manufacturer's guidelines (Proceq SA, 2017), moist sponges ensure sufficient electrical contact between the specimen and the electrodes, but they also introduce a certain level of internal resistance. Therefore, to accurately determine the true UBER values, the internal resistance of the sponges must be subtracted from the measured data. However, experimental observations indicated that fully saturating the sponges by immersing them in water prior to testing provided the most consistent results. Under such conditions, the internal resistance of the sponges—owing to their high moisture content—was found to be negligible. Furthermore, applying a constant load on the top electrode (e.g., by stacking additional cylindrical specimens) improved the electrode–specimen contact and further stabilized the readings.

In the test, the Resipod instrument displays a value (RD) in $k\Omega \cdot cm$. To obtain the "corrected" value (cRD) in $k\Omega$, the RD should be divided by $2\pi a$, where "a" is the probe spacing (5cm). The UBER , ρ, in $k\Omega \cdot cm$, can then be calculated using the following equation (Proceq SA, 2017):

$$\rho = K \cdot cRD \tag{1}$$

where $K = A / L$, with A and L representing the cross-sectional area (cm²) and the length (cm) of the cylindrical specimen, respectively.

Fig. 1. UBER test configuration with Resipod and sponge–electrode assembly

3. Results and discussion

The evolution of uniaxial bulk electrical resistivity (UBER) for all mixtures is presented in Fig. 2. The results clearly demonstrate that both the binder system and the fiber content significantly affect the electrical performance of the composites. Although the incorporation of steel micro-fibers reduced resistivity in all cases, the extent and efficiency of this reduction differed markedly between the PC and AAS systems.

In the PC series, the reference mixture (PC_REF) exhibited the highest UBER values throughout the 56-day period, increasing from 1.763 kΩ·cm on day 7 to 2.888 kΩ·cm by day 56. This increase is attributed to ongoing hydration and pore refinement, which progressively restrict ionic mobility. In contrast, the fiber-reinforced PC mixtures showed consistently lower resistivity values. The incorporation of 3%, 4%, and 5% steel micro-fibers resulted in 56-day UBER values of 2.651, 2.413, and 2.450 kΩ·cm, respectively. While the addition of fibers improved conductivity, the magnitude of this improvement remained relatively limited. For instance, the reduction between PC_REF and PC_5F at 56 days was only 0.440 kΩ·cm, underscoring the challenge of achieving high conductivity in an inherently resistive and ion-deficient matrix. Moreover, the resistivity curves for PC_4F and PC_5F were nearly convergent at all ages, suggesting that increasing the fiber content beyond 4% offers diminishing returns. This may be due to fiber interlocking or segregation at higher dosages, potentially disrupting the continuity of conductive pathways.

The time-dependent trend further supports this interpretation: all PC mixtures exhibited a pronounced increase in resistivity, particularly between days 14 and 56, with increasing divergence between the curves. Notably, PC_4F consistently demonstrated the lowest resistivity at all ages, suggesting that a 4% fiber volume may represent an optimal threshold for balancing homogeneity and electrical performance in PC-based composites.

In the AAS series, the resistivity values were significantly lower across all mixtures. The reference mixture (AAS_REF) remained as low as 1.888 kΩ·cm at 56 days, approximately 35% lower than PC_REF, highlighting the superior ionic conductivity of the AAS matrix due to its ionically enriched pore solution. This notable difference can be attributed to the distinct ionic composition and transport mechanisms within the AAS matrix. Whereas conductivity in PC-based mortars primarily depends on the mobility of Ca^{2+} and OH^- ions—both of which gradually diminish due to hydration and pore refinement—AAS mixtures benefit from the sustained presence of Na^+ ions and other residual species that do not fully participate in the reaction. These characteristics result in higher ionic concentration and mobility within the pore solution, thereby supporting enhanced electrical conduction throughout the matrix. As emphasized by Rovnaník et al. (2019), AAS systems can achieve low bulk resistivity even without the use of conductive additives, making them inherently suitable for self-sensing applications. Similarly, Di Mare and Ouellet-Plamondon (2023) highlighted the potential of one-part alkali-activated mortars in smart material technologies due to their favorable electrochemical environment. Furthermore, the incorporation of steel fibers led to a more substantial and immediate reduction in resistivity compared to the PC system.

The addition of 3%, 4%, and 5% steel micro-fibers reduced the 56-day UBER values to 0.720, 0.623, and 0.582 kΩ·cm, respectively. All AAS mixtures maintained resistivity values below 1.0 kΩ·cm throughout the 56-day period, demonstrating robust and stable conductive behavior. The sharp drop from AAS_REF to AAS_3F (~61.9% reduction) demonstrates the strong compatibility of steel fibers with the AAS matrix in forming interconnected conductive networks. This trend was consistently observed across all ages, with fiber-reinforced AAS mixtures exhibiting significantly lower resistivity, particularly in comparison to their PC-based counterparts. For instance, at 56 days, the best-performing PC mixture (PC_4F) showed a UBER value of 2.413 kΩ·cm, which is nearly four times higher than its AAS counterpart (AAS_4F, 0.623 kΩ·cm). While the inclusion of fibers in PC mixtures resulted in only moderate reductions (e.g., 15.9% from PC_REF to PC_4F), the improvements in AAS mortars were far more substantial. This contrast highlights the superior efficiency of conductive fiber networks formed within the highly ionic and chemically favorable AAS matrix. Moreover, the marginal difference between AAS_4F and AAS_5F after day 28 suggests that a 4% fiber volume is also sufficient in AAS systems to establish near-optimal conductivity. This plateauing behavior aligns with the trend observed in the PC series, although the absolute resistivity levels in AAS mortars were considerably lower.

The significantly enhanced performance observed in the AAS series upon fiber incorporation supports the presence of a synergistic mechanism between the steel fibers and the conductive matrix. This enhanced behavior likely results from the interplay between the high ionic conductivity of the AAS pore solution and the electronic pathways established by the embedded fibers. By comparison, PC mixtures—where fiber addition yielded relatively modest gains—demonstrated the limitations imposed by matrix chemistry on the effectiveness of conductive networks. These results underscore the pivotal role of binder composition and pore solution characteristics in supporting the formation of efficient charge transport pathways.

When evaluated across both systems, the findings clearly indicate that while steel fiber addition contributes to enhanced electrical conductivity, it is the intrinsic electrochemical nature of the matrix that fundamentally dictates the extent of improvement. In this regard, AAS mixtures consistently outperformed their PC counterparts, offering a more favorable environment for the development and continuity of conductive fiber networks. Furthermore, a fiber volume of 4% emerges as a practical and effective threshold in both systems, offering an optimal balance between conductivity enhancement, matrix integrity, and workability.

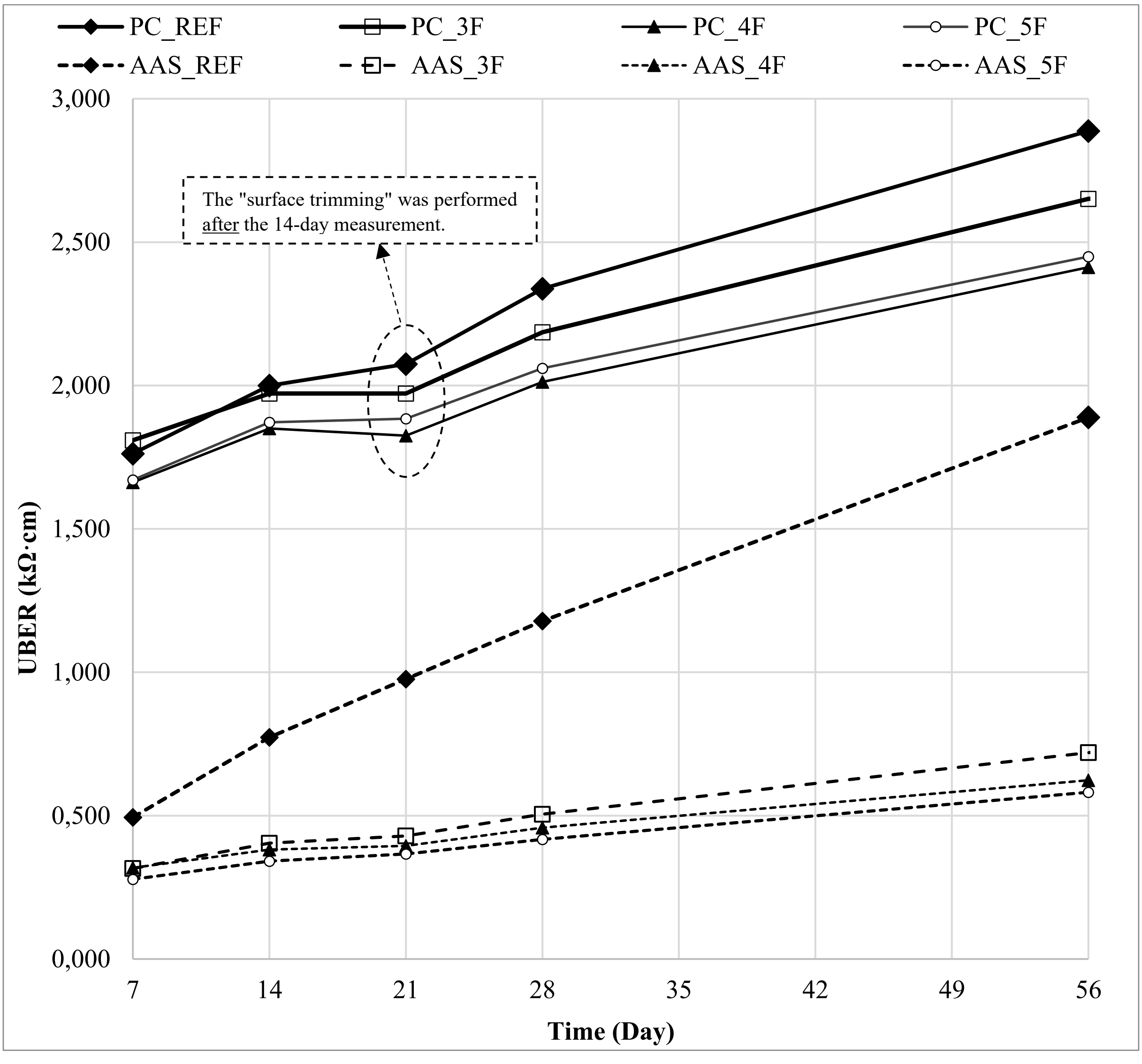

Fig. 2. Development of UBER in PC and AAS mortar mixtures incorporating different volumes of micro steel fibers over a 56-day curing period

4. Conclusions

This study provided a comparative evaluation of the influence of micro steel fiber incorporation on the electrical resistivity behavior of Portland cement and alkali-activated slag-based mortars. Based on the experimental findings, the following conclusions can be drawn:

- The inclusion of micro steel fibers improved the electrical conductivity of both binder systems, although the degree of enhancement was strongly influenced by the electrochemical nature of the matrix.
- AAS-based mortars exhibited superior performance due to their inherently higher ionic conductivity and stronger synergy with conductive additives, enabling more efficient charge transport
- In contrast, PC-based mortars showed only moderate improvements, constrained by limited ionic mobility and a more resistive microstructural environment.
- A fiber volume of 4% was found to be optimal across both systems, offering a favorable balance between conductivity enhancement and mix homogeneity, while rheological aspects were not considered in this study.
- These findings highlight the critical role of matrix chemistry in governing conductive network efficiency and support the potential of alkali-activated slag binders for use in self-sensing or smart cementitious applications.

Acknowledgments

The author gratefully acknowledges the financial support provided by the Scientific and Technological Research Council of Türkiye (TÜBİTAK) under Project No. 122N888. The author also wishes to thank Remzi SİTAR for his contributions to the experimental phase of this study.

References

Cleven, S., Raupach, M., & Matschei, T. (2021). Electrical resistivity of steel fibre-reinforced concrete—Influencing parameters. *Materials, 14*(12), 3408. https://doi.org/10.3390/ma14123408

Di Mare, M., & Ouellet-Plamondon, C.M. (2023). Greener, smarter, stronger: Self-sensing construction materials from one-part alkali-activated materials. *Materials Letters, 349*, 134830. https://doi.org/10.1016/j.matlet.2023.134830

Gong, H., Zhang, Y., Quan, J., & Che, S. (2011). Preparation and properties of cement based piezoelectric composites modified by CNTs. *Current Applied Physics, 11*(3), 653–656. https://doi.org/10.1016/j.cap.2010.10.021

Lu, M., Xie, H., Wang, H., & Ma, Y. (2025). Self-sensing properties of steel fiber reinforced-alkali-activated fly ash/slag mortar. *Construction and Building Materials, 458*, 139580. https://doi.org/10.1016/j.conbuildmat.2024.139580

Ma, Y., Liu, W., Hu, J., Fu, J., Zhang, Z., & Wang, H. (2020). Optimization on the piezoresistivity of alkali-activated fly ash/slag mortar by using conductive aggregates and carbon fibers. *Cement and Concrete Composites, 114*, 103735. https://doi.org/10.1016/j.cemconcomp.2020.103735

Piao, R., Lee, D., Woo, S.Y., Jeong, J.-W., Hiew, S.Y., Lee, S.-J., & Yoo, D.-Y. (2025). Carbon material-based thermoelectric ultra-high-performance alkali-activated concrete. *Composites Part B: Engineering, 297*, 112279. https://doi.org/10.1016/j.compositesb.2025.112279

Proceq S.A. (2017). Operating instructions: Concrete durability testing. Schwerzenbach, Switzerland.

Rovnaník, P., Kusák, I., Bayer, P., Schmid, P., & Fiala, L. (2019). Comparison of electrical and self-sensing properties of Portland cement and alkali-activated slag mortars. *Cement and Concrete Research, 118*, 84–91. https://doi.org/10.1016/j.cemconres.2019.02.009

4th International Civil Engineering & Architecture Conference
17-19 May 2025, Trabzon, Türkiye

Eco-friendly composite development using cement paste waste, hemicellulose, chitosan, and natural fibers

Ejazulhaq Rahimi*[1], Ayane Yui[1], Yuta Yamachi[1], Yuma Kawasaki[1]

[1]*Ritsumeikan University, Department of Civil and Environmental Engineering, 525-0058 Shiga, Japan*

Abstract. To reduce dependency on natural resources and mitigate the environmental impact associated with construction waste disposal, the adoption of waste valorization and environmentally friendly production techniques has become imperative. This study explores the development of a green composite incorporating cement paste waste and hemicellulose, with mechanical performance further enhanced through the partial substitution (50 wt%) of hemicellulose with chitosan. Additionally, natural fibers derived from bamboo and banana were introduced to assess their reinforcing effects on the composite. The composites were fabricated using a hot-pressing method and subjected to mechanical testing after a three-day curing period. The results demonstrated that heat pressing, fiber reinforcement, and chitosan incorporation each positively influenced the mechanical properties; however, the addition of chitosan exhibited the most pronounced effect. FTIR analysis further supported these findings, revealing slight shifts in peak intensities and positions attributable to chitosan incorporation. Notably, the characteristic peak at 1509 cm^{-1}, observed in composites containing cement paste waste and hemicellulose, was suppressed upon chitosan addition—suggesting potential chemical interactions. These results indicate that the impact of chitosan on mechanical enhancement surpasses that of heat treatment alone. This research contributes to the foundational development of sustainable, high-performance cement-free composites utilizing biopolymers, offering a viable alternative for environmentally conscious construction applications.

Keywords: Cement paste waste; Hemicellulose; Chitosan, recycle & reuse; Biopolymer; Banana fiber; Bamboo fiber; Hot-pressing; FTIR spectroscopy

1. Introduction

The rapid expansion of the cement and concrete industry has been accompanied by increasing exploitation of natural resources and significant waste generation. Globally, it is estimated that only in 40 countries, 3 billion tons of waste concrete is generated annually, until 2012 (Akhtar & Sarmah, 2018). This situation is further exacerbated by the industry's high carbon dioxide emissions, making the development of sustainable solutions a pressing concern. A multifaceted approach is required to address these challenges, balancing the need for construction materials with environmental preservation and waste management.

In recent years, researchers have turned to green composites as a promising alternative. These materials leverage recycled concrete waste and botanical substances, eliminating the need for traditional cement (Liang & Sakai, 2020). Our previous studies have demonstrated the potential of green composites made from recycled concrete powder and botanical components, such as hemicellulose, which offer advantages including reduced production time and enhanced flexural strength. However, the application of cement paste waste in green composites remains underexplored.

This study investigates the development of a green composite using cement paste waste and hemicellulose as primary components. The composite's properties are further enhanced by replacing 50% of the hemicellulose mass with chitosan, a biopolymer known for its mechanical strengthening capabilities. Additionally, bamboo and banana fibers, sourced from natural materials, are incorporated as reinforcements. The influence of pressing temperature on the composite's mechanical properties is also examined, with samples subjected to room-temperature and elevated-temperature press molding.

The findings aim to provide new insights into the use of recycled concrete powder and cement paste waste with biopolymers in construction material production. By addressing waste management challenges and reducing carbon emissions, this research contributes to the broader goal of advancing sustainable practices in the construction industry and aligning with the United Nations' Sustainable Development Goals (SDGs).

* Corresponding author, E-mail: gr0448vi@ed.ritsumei.ac.jp

https://doi.org/10.31462/icearc2025_ce_mat_559

2. Materials and methods

2.1. Sample preparation

The raw materials utilized in this study include cement paste waste (CPW), hemicellulose, chitosan, bamboo fiber, and banana fiber. The cement paste waste was synthesized in the laboratory by preparing a cement paste using ordinary Portland cement and a water-to-cement (w/c) ratio of 0.5. This paste was cured for seven days in a standard curing chamber. After curing, the cement paste was crushed using a jaw crusher, sieved to obtain particles in the range of 0.15–0.30 mm, and subsequently oven-dried at 120 °C for 24 hours to ensure moisture elimination and particle consistency.

Hemicellulose (corn xylan) was procured from TCI Chemicals, while chitosan was purchased from a commercial online retailer (Amazon). Bamboo and banana fibers were sourced locally from suppliers in Shiga Prefecture, Japan, to support regional resource utilization and sustainability. All materials were stored in sealed plastic bags prior to use to preserve their quality and prevent contamination.

The composite samples were prepared through a four-step process: (1) Manual mixing of all components in a plastic container; (2) Casting into a steel mold; (3) Application of 25 MPa pressure using an AS ONE H400-15 hot press; and (4) Demolding and sample retrieval post-pressing.

The mix proportions and molding conditions for the samples are provided in Table 1.

Table 1. Mix proportion and experiment condition

	Materials (gr)						Molding condition		
	CPW	H	Ch	BF	BnF	Water	Temp.	Pressure (MPa)	Time (min)
CPW-H	34	17	0			5.1	Room Temp. & 60°C	25	5
CPW-H-BF	34	17	0	1		5.1		25	5
CPW-H-BnF	34	17	0		1	5.1		25	5
CPW-H-Ch	34	8.5	8.5			5.1		25	5
CPW-H- BF-Ch	34	8.5	8.5	1		5.1		25	5
CPW-H-BnF-Ch	34	8.5	8.5		1	5.1		25	5

*CPW: Cement Paste Waste; H: Hemicellulose; BF: Bamboo Fiber; BnF: Banana Fiber; Ch: Chitosan.

Due to the high hydrophilicity of hemicellulose, it tends to rapidly absorb water during mixing, resulting in clumping and reduced dispersibility. To overcome this issue, a modified mixing sequence was implemented:

1. *Initial dry mixing:* All dry components excluding hemicellulose were mixed for 1 minute to achieve uniformity.
2. *Water addition:* Water was then added and stirred for an additional minute.
3. *Hemicellulose incorporation:* Hemicellulose was added last and mixed thoroughly to ensure homogeneous distribution.

After molding, all samples were cured under laboratory conditions for three days before mechanical and chemical testing.

2.2. Experimental testing

2.2.1. Flexural strength test

Flexural strength tests were conducted in accordance with ISO 4013 standards using a Shimadzu AG-X autograph testing machine. Compressive strength was measured following ISO 4012 protocols using a Shimadzu UH-F2000kNXR universal testing machine.

2.2.2. Fourier-Transform Infrared (FTIR) spectroscopy

FTIR analysis was performed to investigate the chemical structure and functional group interactions in the composites. The spectra were collected using a PerkinElmer Spectrum 3 spectrometer over a wavenumber range of 4000–400 cm^{-1}, with a resolution of 4 cm^{-1}. The KBr pellet technique was used for sample preparation. For consistency in comparison, the spectra of all CPW-based samples were normalized to the absorption band at 875 cm^{-1}, corresponding to the out-of-plane vibration of the C–O bond typical of carbonate in the cement paste waste matrix.

3. Results and discussion

3.1. Flexural strength results

The flexural strength results of the composite materials are illustrated in Fig. 1 and Fig. 2. At 24 °C molding, the flexural strength of CPW-H—comprising only cement paste waste and hemicellulose—was found to be below 2

MPa. The incorporation of bamboo fibers (CPW-H-BF) and banana fibers (CPW-H-BnF) into this matrix significantly improved flexural performance, more than doubling the strength compared to the unreinforced composite. Among the two fiber types, banana fibers exhibited a more pronounced reinforcing effect. This observation aligns with the findings of Sales et al. (2024), who reported a 71.78% increase in flexural strength with banana fiber reinforcement, and Sanchez-Echeverri et al. (2020), who noted a 40% enhancement with bamboo fibers in cement-based systems (Sales et al., 2024; Sanchez-Echeverri et al., 2020).

Hot pressing at 60 °C resulted in further increases in flexural strength across all composite variants. The most substantial improvement was observed in the CPW-H composite, which lacked fiber reinforcement. This increase is attributed to the densification and improved polymeric chain interactions facilitated by thermal activation, which are especially beneficial in composites with initially low mechanical integrity.

Replacing 50% of the hemicellulose with chitosan further enhanced the flexural strength in all composite formulations. This enhancement is consistent with previous studies, which suggest that strong hydrogen bonding and chemical interactions between the hydroxyl groups of hemicellulose and the amine and hydroxyl groups of chitosan contribute to mechanical reinforcement through the formation of crosslinked structures (Karaaslan et al., 2012). In fiber-reinforced and chitosan-containing systems, the initial mechanical properties were already improved, thereby reducing the relative impact of heat pressing. These findings are in agreement with those of Akkus et al. (2014), who demonstrated that thermal treatment improves flexural strength by promoting densification and enhancing interactions between hemicellulose polymer chains (Akkus et al., 2014).

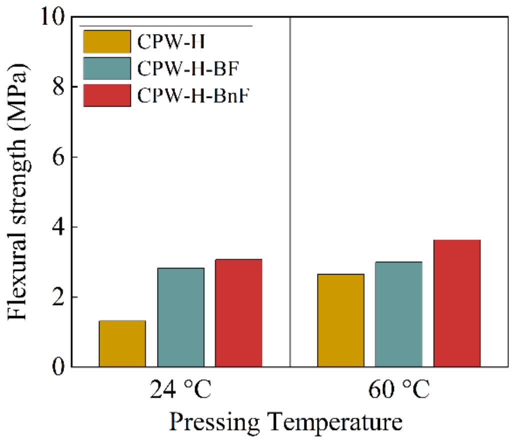

Fig. 1. The flexural strength of the composite made of CPW and hemicellulose

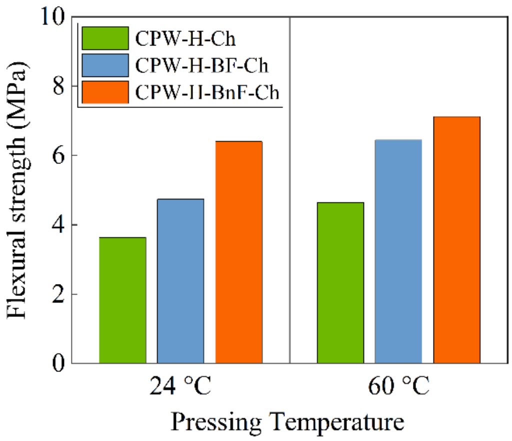

Fig. 2. The flexural strength of the composite made of CPW, hemicellulose, and chitosan

3.2. FTIR analysis results

Fig. 3 presents the FTIR spectra of composites prepared using cement paste waste (CPW), hemicellulose, and chitosan, subjected to pressing at 24 °C and 60 °C. The composite containing fibers are not consider for FTIR analysis.

In the CPW, the sharp band at 3640 cm^{-1} is attributed to O–H stretching vibrations in portlandite [$Ca(OH)_2$], a prominent hydration product in cementitious systems (Chen et al., 2025). The peak at 1422 cm^{-1} corresponds to the asymmetric stretching vibration of carbonate ions (CO_3^{2-}) (Gunn et al., 2024), while the 975 cm^{-1} peak is related to the symmetric stretching of Si–O and Al–O bonds, characteristic of silicate (SiO_4) and aluminate (AlO_4) tetrahedra (Dassekpo et al., 2022). The peak at 875 cm^{-1} is attributed to out-of-plane bending of the C–O bond in carbonate groups, indicating the presence of $CaCO_3$ (Huang et al., 2025), and the 470 cm^{-1} band corresponds to the bending vibrations of Si–O in silicate structures, typically observed in calcium silicate hydrate (C–S–H) and unhydrated residual phases (Hospodarova et al., 2018).

For hemicellulose, the broad absorption band between 3700–3000 cm^{-1} is assigned to O–H stretching vibrations, representing hydroxyl groups in lignocellulosic materials and potentially overlapping with hydration products such as C–S–H gel (Hawanis et al., 2025). The peak at ~2900 cm^{-1} corresponds to C–H stretching of –CH_3 and –CH_2– groups in the sugar units of hemicellulose (Raja, 2025). The 1660 cm^{-1} band can be attributed to H–O–H bending of adsorbed water or minor C=O stretching from conjugated carbonyl groups (Musule et al., 2016). The 1255 cm^{-1} band is indicative of C–O skeletal aromatic vibrations, which may arise from residual lignin or hemicellulose aromatic structures (Mohomane et al., 2017). A strong absorption at 1040 cm^{-1} corresponds to C–O stretching in the sugar units (Besserer et al., 2024), while the 897 cm^{-1} peak is associated with C–H rocking in the lignocellulosic backbone (Md Salim et al., 2021). The 558 cm^{-1} band, typically seen in hemicellulose, appears to shift toward 470 cm^{-1}, potentially overlapping with the silicate bending region in CPW.

golden light publishing®

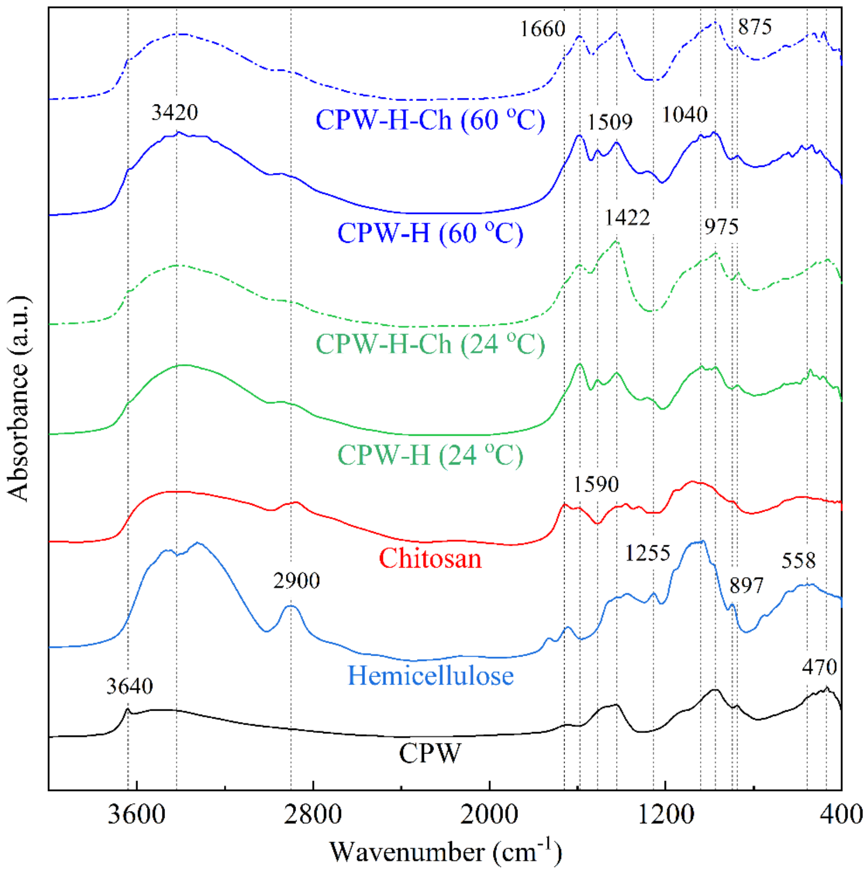

Fig. 3. The FTIR spectra of the composites and its raw materials

Chitosan, a deacetylated derivative of chitin, exhibits distinct bands due to its functional groups. The 2900 cm⁻¹ band is associated with C–H stretching of methyl and methylene groups (Daeialiakbar et al., 2025), while the 1660 cm⁻¹ peak corresponds to the Amide I band due to C=O stretching of the residual acetyl groups (Soufiani et al., 2025). A peak at 1590 cm⁻¹, not observed in the raw components, appears in all composite spectra, and is attributed to the Amide II band from N–H bending vibrations of primary amine groups (Bussiere et al., 2021), or possibly due to asymmetric stretching of carboxylate ions arising from hemicellulose degradation or interactions with cementitious phases.

The 3640 cm⁻¹ O–H band from portlandite persists in all cases, although with reduced intensity compared to the raw CPW. Meanwhile, the 2900 cm⁻¹ band from hemicellulose and chitosan exhibits diminished intensity in CPW–H and is further reduced in CPW–H–CH at both pressing temperatures, may indicate to interaction or partial degradation of aliphatic groups.

In the CPW–H composite, prepared at both 24 °C and 60 °C, a new peak emerges at 1509 cm⁻¹, suggesting additional molecular interactions or degradation byproducts. The intensity of 1590 cm-1 peak is higher in CPW–H cases compared to the CPW–H–Ch cases. The 1422 cm⁻¹ carbonate peak exhibits increased intensity in CPW–H–CH composites, which may indicate enhanced carbonation or stabilization. The 1255 cm⁻¹ peak from hemicellulose slightly shifts upward in CPW–H, but becomes indistinguishable in CPW–H–CH, suggesting possible structural disruption or masking due to chitosan incorporation.

In CPW–CH, the intensity of the 1040 cm⁻¹ hemicellulose peak have the same intensity as 975 cm⁻¹ from CPW, while in CPW–H–CH, the 975 cm⁻¹ peak dominates. The 875 cm⁻¹ peak, attributed to carbonate bending in CPW, remains consistent in position and intensity across all composite variants, suggesting its structural stability. The 558 cm⁻¹ peak, clearly present in CPW–H, appears suppressed in CPW–H–CH, with the 470 cm⁻¹ band becoming dominant—indicating possible peak overlap or shifting due to component interaction.

Table 1 shows a summary of the absorption peaks in the composite and its raw material.

Table 1. Summary of FTIR absorption peaks and their Assignments

Wavenumber [cm⁻¹]	Functional Bond	Assigned to	Reference
3700–3000	O–H stretching (broad)	Hemicellulose, C–S–H, lignocellulose	(Hawanis et al., 2025)
3640	O–H stretching	Portlandite ($Ca(OH)_2$)	(Chen et al., 2025)
2900	C–H stretching ($–CH_3$, $–CH_2–$)	Hemicellulose, Chitosan	(Daeialiakbar et al., 2025; Raja, 2025)
1660	H–O–H bending / C=O stretching	Hemicellulose, Chitosan (amide I)	(Musule et al., 2016; Soufiani et al., 2025)
1590	N–H bending (amide II)	Chitosan	(Bussiere et al., 2021)
1422	Asymmetric CO_3^{2-} stretching	$CaCO_3$	(Gunn et al., 2024)
1255	C–O aromatic skeletal vibration	Hemicellulose, lignin	(Mohomane et al., 2017)
1040	C–O stretching	Hemicellulose sugar units	(Besserer et al., 2024)
975	Si–O / Al–O stretching	Silicate and aluminate	(Dassekpo et al., 2022)
897	C–H rocking	Lignocellulosic materials	(Md Salim et al., 2021)
875	C–O out-of-plane bending	CO_3^{2-} in $CaCO_3$	(Huang et al., 2025)
470	Si–O bending	Silicate phases	(Hospodarova et al., 2018)

These spectral variations collectively indicate that the incorporation of chitosan significantly alters the chemical environment of the composite, as demonstrated by noticeable changes in the intensities and positions of key functional group bands. Such modifications may suggest the occurrence of chemical interactions or potential bond formation within the matrix, although further investigation is necessary to substantiate these assumptions. In contrast, the application of temperature during pressing showed negligible influence on the chemical structure, indicating that chitosan addition exerts a more pronounced effect on the composite's chemistry. This observation is further supported by the corresponding enhancement in flexural strength associated with chitosan incorporation.

4. Conclusion

This study focused on the development of a sustainable, cement-free composite using cement paste waste and hemicellulose, with the aim of minimizing environmental impact while enhancing mechanical performance through the inclusion of biopolymers and natural fibers. The composites were fabricated via press molding at two temperatures (24 °C and 60 °C), and their structural and chemical characteristics were thoroughly evaluated. Based on the experimental findings, the following conclusions can be drawn:

- Chitosan incorporation demonstrated the most substantial influence on both flexural and compressive strengths, surpassing the effects of both fiber reinforcement (bamboo and banana fibers) and thermal processing. This highlights chitosan's significant contribution to improving mechanical integrity through enhanced interfacial bonding and possible chemical interactions.
- Fourier-transform infrared (FTIR) analysis revealed that chitosan addition induced changes in the chemical structure of the composite, as evidenced by shifts in peak intensities and the emergence or suppression of specific functional group bands. In contrast, heat pressing at 60 °C did not result in notable chemical alterations, suggesting that the mechanical improvements due to heating are primarily physical (e.g., densification).
- Natural fibers contributed positively to the mechanical performance, with banana fibers exhibiting a more pronounced reinforcing effect than bamboo fibers. However, their influence was still secondary to that of chitosan.

These findings underscore the potential of integrating biopolymers such as chitosan with recycled cementitious waste to produce eco-friendly construction materials. The research provides foundational knowledge for further development of high-performance green composites and contributes to the broader goal of sustainable building practices, aligning with global environmental and circular economy objectives.

Acknowledgments

The authors gratefully acknowledge the financial support provided by the RARA Office of Ritsumeikan University.

References

Akhtar, A., & Sarmah, A.K. (2018). Construction and demolition waste generation and properties of recycled aggregate concrete: A global perspective. *Journal of Cleaner Production*, *186*, 262–281. https://doi.org/10.1016/j.jclepro.2018.03.085

Akkus, M., Bahcegul, E., Ozkan, N., & Bakir, U. (2014). Post-extrusion heat-treatment as a facile method to enhance the mechanical properties of extruded xylan-based polymeric materials. *RSC Adv.*, *4*(107), 62295–62300. https://doi.org/10.1039/C4RA10478A
Besserer, A., Mougnala Moukagni, E., Ziegler-Devin, I., & Brosse, N. (2024). Extraction of polymeric hemicelluloses from okoumé sapwood by steam explosion: Use of non-destructive characterization methods. *Industrial Crops and Products*, *208*, 117808. https://doi.org/https://doi.org/10.1016/j.indcrop.2023.117808
Bussiere, P.-O., Gardette, J.-L., Rapp, G., Masson, C., & Therias, S. (2021). New insights into the mechanism of photodegradation of chitosan. *Carbohydrate Polymers*, *259*, 117715. https://doi.org/https://doi.org/10.1016/j.carbpol.2021.117715
Chen, P., Zong, Z., Qian, X., Fang, Y., Li, J., Wang, L., & Wang, J. (2025). Recycling waste fresh paste through a dormancy—awakening method using CO2 as the awakener. *Case Studies in Construction Materials*, *22*, e04434. https://doi.org/https://doi.org/10.1016/j.cscm.2025.e04434
Daeialiakbar, M., Yousefi, S., & Weisany, W. (2025). Enhanced properties of chitosan-PVA nanocomposite films with lemongrass oil microcapsules. *Carbohydrate Polymer Technologies and Applications*, *9*, 100668. https://doi.org/https://doi.org/10.1016/j.carpta.2025.100668
Dassekpo, J.-B.M., Miao, L., Bai, J., Gong, Q., Shao, N.N., Dong, Z., Xing, F., & Ye, J. (2022). Phase dissolution and improving properties of completely decomposed granite through alkali fusion method. *Cement and Concrete Composites*, *127*, 104407. https://doi.org/https://doi.org/10.1016/j.cemconcomp.2022.104407
Gunn, P.F.E., Onn, C.C., Mo, K.H., & Lee, H.V. (2024). Enhancing carbon sequestration in cement mortar using high volume local rice husk biochar coupled with carbonation curing. *Case Studies in Construction Materials*, *21*, e03591. https://doi.org/https://doi.org/10.1016/j.cscm.2024.e03591
Hawanis, H.S.N., Ilyas, R.A., Jalil, R., Ibrahim, R., Majid, R.A., Ab Hamid, N.H., Norrrahim, M.N.F., & Knight, V.F. (2025). Physicochemical, water, thermal and mechanical properties of cellulosed-based Kraft paper produced from five Malaysian bamboo species. *Carbohydrate Polymer Technologies and Applications*, *9*, 100723. https://doi.org/https://doi.org/10.1016/j.carpta.2025.100723
Hospodarova, V., Singovszka, E., & Stevulova, N. (2018). Characterization of Cellulosic Fibers by FTIR Spectroscopy for Their Further Implementation to Building Materials. *American Journal of Analytical Chemistry*, *09*(06), 303–310. https://doi.org/10.4236/ajac.2018.96023
Huang, J., Chen, Y., & Yu, Q. (2025). Amorphous calcium carbonate formation from carbonated recycled cement powder: A novel carbonation-activated cementitious material. *Composites Part B: Engineering*, *297*, 112336. https://doi.org/https://doi.org/10.1016/j.compositesb.2025.112336
Karaaslan, M.A., Tshabalala, M.A., & Buschle-Diller, G. (2012). Semi-interpenetrating polymer network hydrogels based on aspen hemicellulose and chitosan: Effect of crosslinking sequence on hydrogel properties. *Journal of Applied Polymer Science*, *124*(2), 1168–1177. https://doi.org/10.1002/app.35075
Liang, L., & Sakai, Y. (2020). *Mechanical Properties of Botanical Recycled Concrete under Different Production Conditions*. https://doi.org/10.20944/preprints202005.0024.v1
Md Salim, R., Asik, J., & Sarjadi, M.S. (2021). Chemical functional groups of extractives, cellulose and lignin extracted from native Leucaena leucocephala bark. *Wood Science and Technology*, *55*(2), 295–313. https://doi.org/10.1007/s00226-020-01258-2
Mohomane, S.M., Linganiso, L.Z., Buthelezi, T., & Motaung, T.E. (2017). Effect of extraction period on properties of sugarcane bagasse and softwood chips cellulose. *Wood Res*, *62*(6), 931-938
Musule, R., Alarcón-Gutiérrez, E., Houbron, E.P., Bárcenas-Pazos, G.M., del Rosario Pineda-López, M., Domínguez, Z., & Sánchez-Velásquez, L.R. (2016). Chemical composition of lignocellulosic biomass in the wood of Abies religiosa across an altitudinal gradient. *Journal of Wood Science*, *62*(6), 537–547. https://doi.org/10.1007/s10086-016-1585-0
Raja, T. (2025). Exploring a natural fiber extracted from henequen plant leaves: A sustainable innovation for reinforcement in composite materials. *Results in Engineering*, *25*, 104015. https://doi.org/https://doi.org/10.1016/j.rineng.2025.104015
Sales, S.L.T., Abellana, V.Y., Lobarbio, C.F.Y., Puyoc, C.T., Galagar, J.R., & Laseras, C.S. (2024). Mechanical performance of natural fiber-reinforced concrete using banana stem and sugarcane fibers. *E3S Web of Conferences*, *559*, 04050. https://doi.org/10.1051/e3sconf/202455904050
Sanchez-Echeverri, L.A., Medina-Perilla, J.A., & Ganjian, E. (2020). Nonconventional Ca(OH)2 treatment of bamboo for the reinforcement of cement composites. *Materials*, *13*(8), 1892. https://doi.org/10.3390/ma13081892
Soufiani, S.P., Yousefi, S., Honarvar, M., Weisany, W., & Asadi, G. (2025). Polyvinyl alcohol films incorporating cellulose nanocrystals, chitosan, and mesoporous silica nanoparticles for enhanced stability and controlled release of beet extracts. *Carbohydrate Polymer Technologies and Applications*, *10*, 100740. https://doi.org/https://doi.org/10.1016/j.carpta.2025.100740

4th International Civil Engineering & Architecture Conference
17-19 May 2025, Trabzon, Türkiye

Effect of water-proofing admixture in geopolymer slurries on the treatment of recycled aggregate

Gökhan Gürbüz*[1], Saeid Moghimi[2], Özge Andiç Çakır[3]

[1]Ege University, Graduate School of Natural and Applied Sciences, Department of Material Science and Engineering, Advanced Materials and Technologies Doctorate Program, 35100 İzmir, Türkiye
[2]Ege University, Graduate School of Natural and Applied Sciences, Department of Civil Engineering, Civil Engineering Doctorate Program, 35100 İzmir, Türkiye
[3]Ege University, Engineering Faculty, Department of Civil Engineering, 35100 İzmir, Türkiye

Abstract. Recycling and reuse of the demolition, which is emerging from the destruction of old concrete structures that have completed their service life, is becoming more important day by day. In this study, the effect of two different geopolymer slurries containing different proportions (0%, 0.5%, 0.8%, 1.2%, 1.5%) of water-proofing admixture (WPA) on the treatment of recycled aggregate (RCA) was investigated. In these slurries, two different aluminosilicate materials, class F fly ash (FA) and ground granulated blast furnace slag (GGBFS), were used as binders and a mixture of sodium silicate and sodium hydroxide was used as activator. The Na_2O ratio of the activator mixture used was 10% and the M_s ratio was selected as 1.25. The aluminosilicate content was 70% FA and 30% GBFS in the first mixture and 70% GBFS and 30% FA in the second mixture. RCAs were subjected to the impregnation process in the geopolymer slurry mixtures for 5±1 minutes, some under ambient conditions and some in a vacuum oven. In order to determine the effectiveness of WPA in the geopolymer slurry, SEM-EDS analysis was performed on the slurries with and without this admixture. The significance of the difference between the treatment ratios of RCAs was statistically investigated using the One-Way ANOVA test. It was observed that the water absorption capacity of RCAs not impregnated with slurry varied between 5.4% and 6.2%, while the water absorption capacity after treatment was between 3.6% and 5.6%.

Keywords: Geopolymer slurry; Water-proofing admixture; Recycled aggregate; Treatment of RCA

1. Introduction

Globally, 25 billion tons of concrete are produced annually, which can have a significant environmental impact (ACI CRC 18.517, 2019). The recycling and reuse of waste generated from the demolition of old concrete structures that have reached the end of their service life (Arısoy, 2016; Neville, 1995) are becoming increasingly important. According to Tosun (2022), the use of recycled concrete aggregates (RCA) instead of natural aggregates in concrete production can result in a cost savings of 10% to 20% in material costs (Zheng et al., 2017). The lack of a globally accepted common standard, potential issues with durability properties, and differences in the type of aggregate used in the source concrete have led to the limited adoption of RCA systems in concrete applications. Existing documents such as European RILEM standards, Japanese Industrial Standards, German standards, ASTM C33, and the ACI 555 report impose certain limitations on the properties of RCA suitable for use in concrete. However, most of these documents rely on small-scale studies and lack large data sources and their statistical analyses (ACI CRC 18.517, 2019). Additionally, a life cycle assessment of the environmental impacts of recycled aggregate in Hong Kong found that concrete prepared using coarse RCA can reduce greenhouse gas emissions by 65% and non-renewable energy consumption by 65% compared to traditional concrete with natural aggregate (Hossain et al., 2016).

Improving recycled aggregates can lead to fewer mechanical losses in traditional or geopolymer concrete. Some methods have been applied to eliminate the negative effect of mortar adhering to RCA on aggregate properties and to treat RCA (Katz, 2004; Dimitriou et al., 2018; Xiao, 2018; Tateyashiki et al., 2001; Bru et al., 2014; Purushothaman et al., 2014; Sui and Mueller, 2012; Ismail and Ramli, 2013; Katkhuda and Shatarat, 2017; Chen et al., 2017; Kim et al., 2018). Bui et al. (2018) conducted a study in which they treated RCA by immersing it in sodium silicate and then in silica fume. In this study, concrete mixtures containing treated and untreated aggregates were prepared. A 33–50% increase in compressive strength was observed in concrete mixtures containing treated coarse aggregates. Alqarni et al. (2021) used cement-silica fume slurry at different ratios (20%,

* Corresponding author, E-mail: gokhan.gurbuz@mail.ege.edu.tr

https://doi.org/10.31462/icearc2025_ce_mat_582

30%, 40%, and 50% of RCA) in their experimental study on RCA treatment. They found that using 40% cement-silica fume treated the water absorption ratio and abrasion resistance of RCAs. In the literature, researchers have generally attempted to strengthen the mortar layer of RCAs using pozzolans and cement (Kisku et al., 2017; Behera et al., 2014; Shi et al., 2016; Kou and Poon, 2012). Some researchers have also observed a decrease in permeability and an increase in compressive strength and elastic modulus in concrete mixtures containing RCA by using waterproofing additives (Pereira-de-Oliveira et al., 2014; Zhang et al., 2020; Zong et al., 2014).

In this study, geopolymer slurry mixtures containing two powder binders, F-type fly ash (FA) and ground granulated blast furnace slag, were prepared, and water permeability additives (WPA) were used in different proportions (0%, 0.5%, 0.8%, 1.2%, 1.5%) in these mixtures. The effect of these slurry mixtures on the treatment ratio of WPA was investigated by determining the water absorption capacity after impregnation with RCA.

2. Material and method

2.1 Material

The water absorption ratio and specific gravity (TS EN 1097-6), unit volume weight (TS 3529), abrasion resistance (TS 1097-2), flatness ratio (TS EN 933-3), and particle size distribution (TS EN 933-1) of the RCA have been determined. The analysis results are presented in Tables 1 and 2.

In the production of geopolymer slurry, sodium silicate (SS) and sodium hydroxide (SH) are used as activators, while GGBFS and F-class FA are used as aluminosilicate sources. To reduce the water absorption capacity of RCA, a water-proofing admixture with a crystalline structure (WPA) was used. The physical and chemical properties of the GGBFS, FA and WPA were determined through XRF and SEM analyses conducted at the Central Research Test and Analysis Laboratory Application and Research Center at Ege University. The chemical and physical properties of SS and SH were obtained from the manufacturer. The analysis results of the aluminosilicate materials and the values given in the relevant standards are presented in Tables 3 and 4, the physical and chemical results of the activator components and WPA are shown in Table 5. Additionally, the SEM-EDS analyses of the aluminosilicate materials are presented in Figs 1 and 2.

Table 1. Physical properties of RCA

Water absorption capacity (%)		6.12±1.71
Specific gravity		2.36
Unit weight (kg/m^3)	Pressed	1360
	Loose	1135
Los Angeles weight loss (%)		36.32
Flakiness index (%)		18.44

Table 2. Particle size distribution of RCA

Sieve opening (mm)	Passing (%)	
	5-15 mm	15-25 mm
31,5	100	100
25	100	86
20	100	59
16	43	0
8	57	0
4	0	0

Table 3. Chemical properties of aluminosilicate materials

Compounds	GGBFS (%)	FA (%)
CaO	49.4	2.82
SiO_2	31.3	49.2
Al_2O_3	8.01	22.05
Fe_2O_3	2.27	5.42
$SiO_2+Al_2O_3+Fe_2O_3$	-	76.67
SO_3	1.18	0.14
MgO	4.08	1.69
Na_2O	-	1.21
K_2O	1.18	2.17
Loss on ignition	0.12	-

Table 4. Physical properties of aluminosilicate materials

Properties		GGBFS (%)	FA (%)
Specific gravity (g/cm^3)		2.88	2,37
Specific surface area (cm^2/g)		3591	3342
Volume expansion (mm)		1.0	1.0
Strength activity index (%)	7-days	56.8	71.0
	28-days	75.9	80.8

Table 5. Chemical and physical properties of sodium silicate, sodium hydroxide, and water-proofing admixture

Chemical properties			
Compound	SS	SH	WPA
CaO	-	-	58.53
SiO_2	23.2	-	15.83
Al_2O_3	-	-	2.59
Fe_2O_3	-	-	1.82
SO_3	-	-	2.72
MgO	-	-	7.11
Na_2O	10.0	77.5	7.52
TiO_2	-	-	0.14
K_2O	-	-	1.74
H_2O	66.8	22.5	-
Cl^-	-	-	0.01
Physical Properties			
Density (g/cm^3)	1.38	2.13	-
Color	Colorless	White	White-Brown
Structure	Liquid	Pellet	Powder
Purity (%)	-	98	-

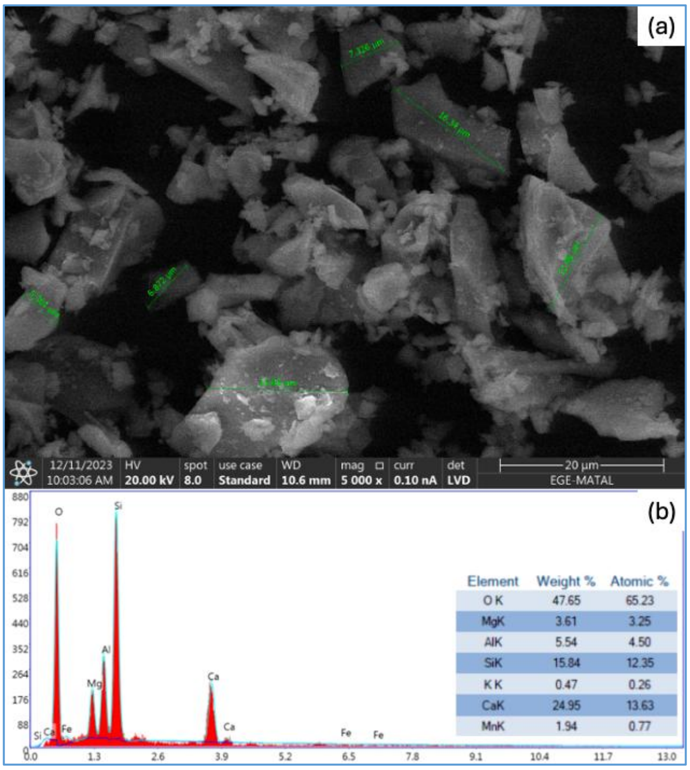

Fig 1. Ground granulated blast furnace slag (a) SEM image (b) EDS analysis

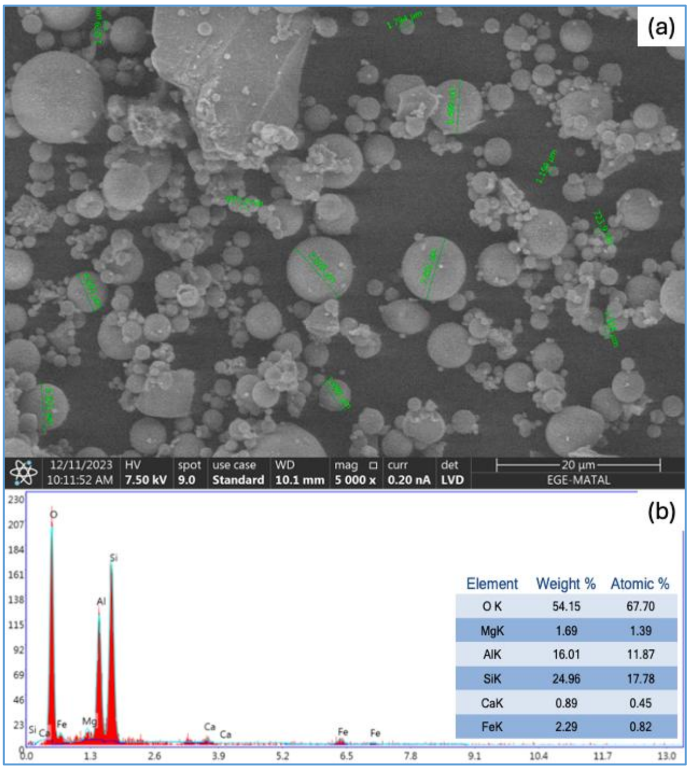

Fig 2. F-class fly ash (a) SEM image (b) EDS analysis

2.2 Method

2.2.1. Mix design

Geopolymer slurries were prepared using GGBFS and FA in different ratios as aluminosilicate material. In these mixtures, the water/binder (W/B) ratio was 1 and the silicate modulus (Ms) ratio was 1.25. The WPA was added to the slurry mixtures at ratios of 0%, 0.5%, 0.8%, 1.2%, and 1.5% by weight of the aluminosilicate materials. The mixture design is presented in Table 6, and the coding for the abbreviations used is given in Fig 3.

Table 6. Mix Design (g)

Mixture	GGBFS	FA	Activator	Water	WPA
70S-30FA-0WPA	700	300	598	627	0
70S-30FA-0.5WPA	700	300	598	627	5
70S-30FA-0.8WPA	700	300	598	627	8
70S-30FA-1.2WPA	700	300	598	627	12
70S-30FA-1.5WPA	700	300	598	627	15
30S-70FA-0WPA	300	700	598	627	0
30S-70FA-0.5WPA	300	700	598	627	5
30S-70FA-0.8WPA	300	700	598	627	8
30S-70FA-1.2WPA	300	700	598	627	12
30S-70FA-1.5WPA	300	700	598	627	15

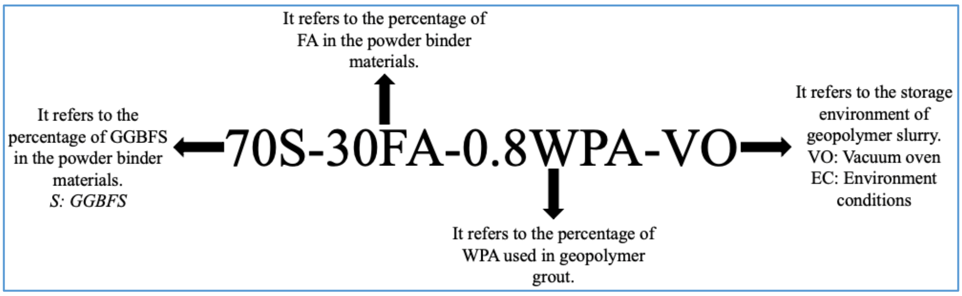

Fig 3. Abbreviations used in geopolymer slurry mixtures

2.2.2. Determination of water absorption ratios

The water absorption ratios of RCAs before and after treatment and the slurry impregnation process were determined as follows.

- Recycled aggregates have been classified using 5 and 15mm sieves and kept in water for one day
- After extracting from the water, RCA surface was dried using a cloth, and 1,000-gram samples were weighed as required for three repetitions of each experiment.
- Pre-treatment water absorption ratios were calculated for all samples.
- The slurry prepared at the specified ratios was mixed with 30 kg of pre-treated RCA, of which 15 kg was left to rest in a vacuum oven (VO) environment at a pressure of 0.9 ± 0.1 bar and 15 kg under environmental conditions (EC) for 5 ± 2 minutes.
- After being sieved, the RCA was left to rest for 24 hours under environment conditions. Then, the aggregates were placed in containers and dried in an oven at 60°C for 48 hours.
- The RCAs taken out of the oven were weighed and left to stand in water for another 24 hours.
- Finally, the water absorption ratios of the treated RCA were recalculated.

The images related to the RCA treatment and water absorption ratio determination process are shown in Fig 4. Equation (1) was used to calculate the average treatment ratio.

$$Average\ treatment\ ratio = \frac{\text{Water absorbtion capacity before treatment} - \text{Water absorbtion capacity after treatment}}{Water\ absorbtion\ capacity\ before\ treatment} \quad (1)$$

Fig 4. RCA treatment and water absorption processes

2.2.3. Statistical analysis

To statistically evaluate the effects of the parameters within the prepared mixtures on the experimental outcomes, GraphPad Prism 9 software (GraphPad Software, San Diego, CA, USA) was used. The normality of the data distribution was assessed using the Shapiro-Wilk test. Depending on the distribution characteristics, either One-Way ANOVA or One-Sample t-test was conducted. A p-value of less than 0.05 was considered indicative of statistical significance.

2.2.4. SEM-EDS analysis

SEM-EDS analysis was performed on hardened slurry samples prepared in 1×1 cm^3 dimensions. To ensure electrical conductivity, the surfaces of the samples were coated with a 7 nm thick layer using a target plate containing 80% Au and 20% Pd in a Leica EM ACE600 coating device. SEM analysis of the samples was performed using a Thermo Scientific Apreo S device. The samples were analyzed in secondary electron mode under high vacuum conditions using an acceleration voltage of 7.5-20 kV and a spot size of 8-12. Energy-dispersive X-ray spectroscopy (EDS) was used to identify the elements present on the surface. Both point and area analyses were performed to determine the elemental composition and distribution.

3. Results and discussion

The water absorption ratios before and after RCA treatment with geopolymer slurries, the treatment ratios, and the statistical analysis results of these findings are presented in Tables 7, 8, 9, and 10. The graphs corresponding to these results are shown in Figs 5, 6, and 7. The significance of the difference in the treatment ratios of these mixtures was investigated statistically using a One-Way ANOVA test.

A decrease in water absorption ratios was observed in all mixtures, including the mixture without WPA, after the geopolymer slurry impregnation process (see Table 7 and Fig 5). The lowest water absorption capacity after treatment was observed in the 70S-30FA-1.5WPA-VO mixture. The greatest treatment ratio was observed in mixtures containing 0.8% WPA under both conditions.

Table 7. RCA treatment with 70S-30FA mixture

Mixture	Average Water Absorption Before Treatment (%)	Average Water Absorption After Treatment (%)	Average Treatment (%)
70S-30FA-0WPA-EC	6.00 ± 0.39	4.99 ± 0,38	16.97 ± 1.54
70S-30FA-0WPA-VO	6.20 ± 0.45	4.88 ± 0,42	21.31 ± 1.10
70S-30FA-0.5WPA-EC	6.10 ± 0.06	4.92 ± 0,13	19.36 ± 1.97
70S-30FA-0.5WPA-VO	6.06 ± 0.39	4.68 ± 0,23	22.64 ± 1.82
70S-30FA-0.8WPA-EC	**6.37 ± 0.20**	**4.34 ± 0,18**	**31.85 ± 1.37**
70S-30FA-0.8WPA-VO	**5.87 ± 0.41**	**3.88 ± 0,36**	**33.78 ± 1.58**
70S-30FA-1.2WPA-EC	5.75 ± 0.58	4.80 ± 0,43	16.60 ± 1.09
70S-30FA-1.2WPA-VO	5.99 ± 0.35	4.90 ± 0,46	18.12 ± 1.58
70S-30FA-1.5WPA-EC	6.05 ± 0.27	4.93 ± 0,16	18.48 ± 0.96
70S-30FA-1.5WPA-VO	5.46 ± 0.16	4.57 ± 0,18	16.38 ± 1.52

*All results are written as the average of 3 experiments.

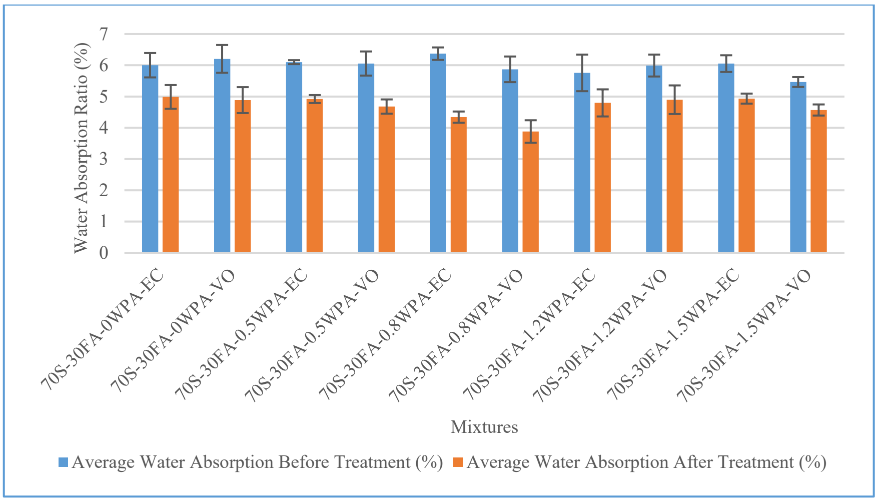

Fig 5. Average water absorption ratios before and after treatment for 70S-30FA with 5-15mm RCA

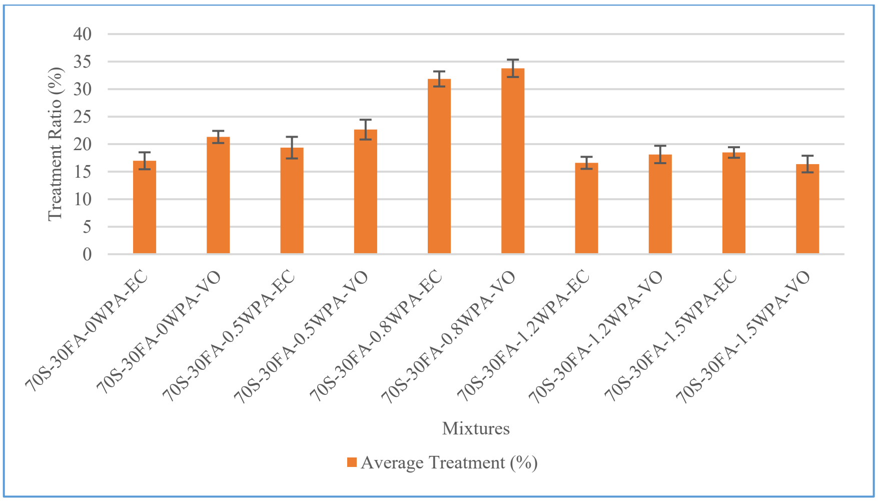

Fig 6. Average treatment response ratios of 5-15mm for 70S-30FA

As shown in Fig 6, treatment was observed when all geopolymer slurries were impregnated with RCA. The treatment ratios ranged from 16% to 33%. In both conditions, the highest treatment was observed in the 70S-30FA-0.8WPA mixtures.

A decrease in the water absorption ratio of all mixtures was observed after the treatment process (see Table 8 and Fig 7) . Prior to the treatment process, water absorption ratios ranged from 5.45% to 6.08%, while these values decreased to 4.05% to 4.76% after the treatment process. Considering the treatment ratios, the 30S-70FA-0.8WPA mixture showed the highest treatment in both conditions.

Table 8. RCA treatment with 30S-70FA mixture

Mixture	Average Water Absorption Before Treatment (%)	Average Water Absorption After Treatment (%)	Average Treatment (%)
30S-70FA-0WPA-EC	5.68 ± 0.29	4.63 ± 0.36	18.61 ± 1.51
30S-70FA-0WPA-VO	5.61 ± 0.14	4.43 ± 0.21	21.06 ± 1.69
30S-70FA-0.5WPA-EC	6.06 ± 0.22	4.76 ± 0.20	21.48 ± 0.60
30S-70FA-0.5WPA-VO	5.99 ± 0.19	4.67 ± 0.23	22.00 ± 1.48
30S-70FA-0.8WPA-EC	**5.96 ± 0.43**	**4.20 ± 0.18**	**29.45 ± 2.30**
30S-70FA-0.8WPA-VO	**5.94 ± 0.30**	**4.05 ± 0.46**	**32.05 ± 2.12**
30S-70FA-1.2WPA-EC	5.45 ± 0.20	4.14 ± 0.24	24.05 ± 1.98
30S-70FA-1.2WPA-VO	5.76 ± 0.35	4.25 ± 0.52	25.90 ± 2.66
30S-70FA-1.5WPA-EC	6.08 ± 0.42	4.70 ± 0.45	22.70 ± 1.46
30S-70FA-1.5WPA-VO	6.08 ± 0.29	4.71 ± 0.26	22.50 ± 0.64

*All results are written as the average of 3 experiments.

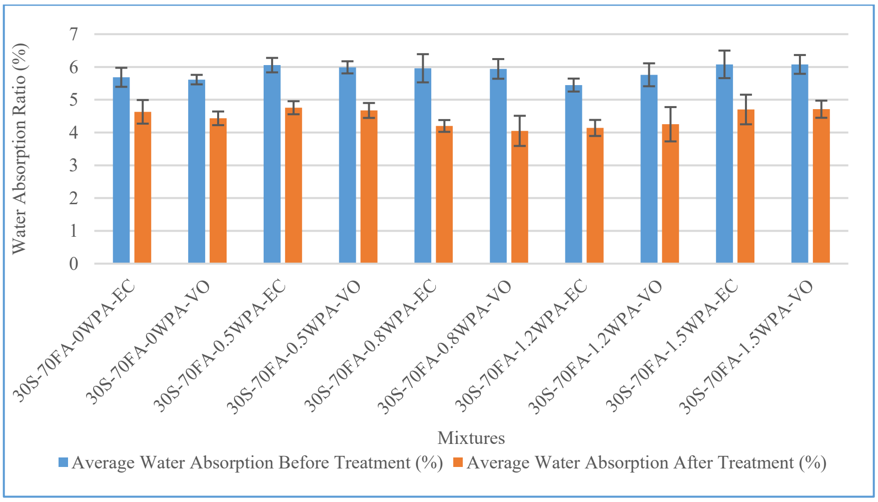

Fig 7. Average water absorption ratios before and after treatment for 30S-70FA with 5-15mm RCA

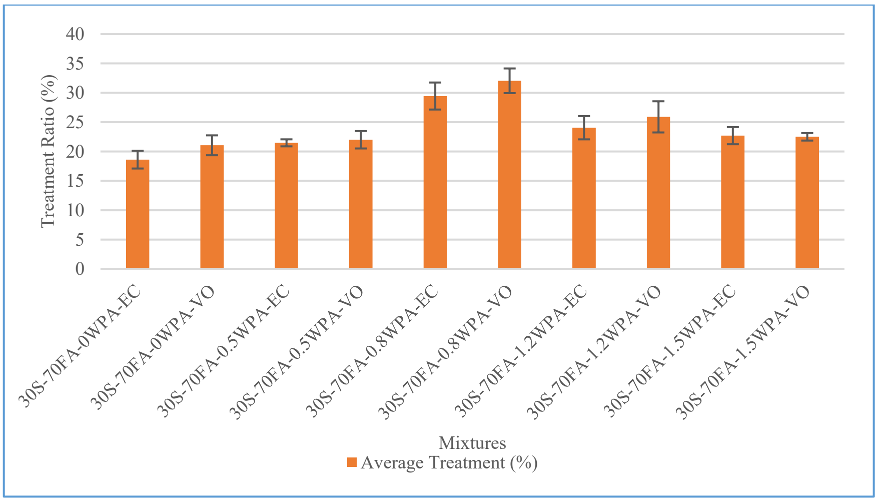

Fig 8. Average treatment response ratios of 5-15mm for 30S-70FA

Table 9. RCA treatment statistics with slurry containing different admixture amounts for 70S-30FA

Mixture	P-value	Significance level
70S-30FA-0WPA-EC vs 70S-30FA-0WPA-VO	0.1063	-
70S-30FA-0.5WPA-EC vs 70S-30FA-0.5WPA-VO	0.4673	-
70S-30FA-0.8WPA-EC vs 70S-30F-0.8WPA-VO	0.0346	*
70S-30FA-1.2WPA-EC vs 70S-30FA-1.2WPA-VO	0.9997	-
70S-30FA-1,5WP-EC vs 70S-30FA-1.5WPA-VO	0.9745	-
70S-30FA -0WPA-EC vs 70S-30FA-0.5WPA-EC	0.9133	-
70S-30FA-0WPA-**EC vs 70S-30F-0.8WPA-EC**	**<0.0001**	****
70S-30FA-0WPA-EC vs 70S-30FA-1.2WPA-EC	>0.9999	-
70S-30FA-0WPA-EC vs 70S-30FA-1.5WPA-EC	0.9997	-
70S-30FA-0WPA-EC vs 70S-30FA-0.5WPA-VO	>0.9999	-
70S-30FA-0WPA-EC **vs 70S-30FA-0.8WP-VO**	**<0.0001**	****
70S-30FA-0WPA-EC vs 70S-30FA-1.2WPA-VO	0.5234	-
70S-30FA-0WPA-EC vs 70S-30FA-1.5WPA-VO	0.0402	*
70S-30FA-0.5WPA-EC vs 70S-30FA-0.8WPA-EC	**<0.0001**	****
70S-30FA-0.5WPA-EC vs 70S-30FA-1.2WPA-EC	0.7563	-
70S-30FA-0.5WPA-EC vs 70S-30FA-1.5WPA-EC	>0.9999	-
70S-30FA-0.5WPA-VO vs 70S-30FA-0.8WPA-VO	**<0.0001**	****
70S-30FA-0.5WPA-VO vs 70S-30FA-1.2WPA-VO	0.0791	-
70S-30FA-0.5WPA-VO vs 70S-30FA-1.5WPA-VO	0.0041	**
70S-30FA-0.8WPA-EC vs 70S-30FA-1.2WPA-EC	**<0.0001**	****
70S-30FA-0.8WPA-EC vs 70S-30FA-1.5WPA-EC	**<0.0001**	****
70S-30FA-0.8WPA-VO vs 70S-30FA-1.2WPA-VO	**<0.0001**	****
70S-30FA-0.8WPA-VO vs 70S-30FA-1.5WPA-VO	**<0.0001**	****
70S-30FA-1.2WPA-EC vs 70S-30FA-1.5WPA-EC	0.9929	-
70S-30FA-1.2WPA-VO vs 70S-30FA-1.5WP-VO	0.9975	-

* The change between values is significant if p<0.05 and is not significant if p>0.05.
"*" as the number increases, the level of significance also increases.

Table 10. RCA treatment statistics with slurry containing different admixture amounts for 30S-70FA

Mixture	P-value	Significance level
30S-70FA-0WPA-EC vs 30S-70FA-0WPA-VO	0.9098	-
30S-70FA-0.5WPA-EC vs 30S-70FA-0.5WPA-VO	>0.9999	-
30S-70FA-0.8WPA-EC vs 30S-70FA-0.8WP-VO	0.1083	-
30S-70FA-1.2WPA-EC vs 30S-70FA-1.2WPA-VO	0.9955	-
30S-70FA-1.5WPA-EC vs 30S-70FA-1.5WP-VO	>0.9999	-
30S-70FA-0WPA-EC vs 30S-70F-0.5WPA-EC	0.7320	-
30S-70FA-0WPA-EC vs 30S-70FA-0.8WPA-EC	**0.0001**	***
30S-70FA-0WPA-EC vs 30S-70FA-1.2WPA-EC	0.0201	*
30S-70FA-0WPA-EC vs 30S-70FA-1.5WP-EC	0.1780	-
30S-70FA-0WPA-EC vs 30S-70FA-0.5WPA-VO	>0.9999	-
30S-70FA-0WPA-EC vs 30S-70FA-0.8WPA-VO	**<0.0001**	****
30S-70FA-0WPA-EC vs 30S-70FA-1.2WP-VO	0.0538	-
30S-70FA-0WPA-EC vs 30S-70FA-1.5WPA-VO	>0.9999	-
30S-70FA-0.5WPA-EC vs 30S-70FA-0.8WPA-EC	0.0160	*
30S-70FA-0.5WPA-EC vs 30S-70FA-1.2WPA-EC	0.8646	-
30S-70FA-0.5WPA-EC vs 30S-70FA-1.5WP-EC	>0.9999	-
30S-70FA-0.5WPA-VO vs 30S-70FA-0.8WPA-VO	**<0.0001**	****
30S-70FA-0.5WPA-VO vs 30S-70FA-1.2WPA-VO	0.2308	-
30S-70FA-0.5WPA-VO vs 30S-70F-1.5WPA-VO	>0.9999	-
30S-70FA-0.8WPA-EC vs 30S-70FA-1.2WPA-EC	0.6585	-
30S-70FA-0.8WPA-EC vs 30S-70FA-1.5WPA-EC	0.1176	-
30S-70F-0.8WPA-VO vs 30S-70FA-1.2WPA-VO	0.0166	*
30S-70FA-0.8WPA-VO vs 30S-70FA-1.5WPA-VO	**<0.0001**	****
30S-70FA-1.2WPA-EC vs 30S-70FA-1.5WPA-EC	>0.9999	-
30S-70FA-1.2WPA-VO vs 30S-70F-1.5WPA-VO	0.4401	-

* The change between values is significant if p<0.05 and is not significant if p>0.05.
"*" as the number increases, the level of significance also increases.

It is observed that treatment was detected in all mixtures containing different ratios of WPA (see Fig 8). Similar to the 70S-30FA mixtures, the highest treatments were found in the mixture containing 0.8% WPA, with 29.4% and 32.0%. The lowest treatments were found in mixtures without WPA, with 18.6% and 21.1%.

Regarding the treatment results at different WPA ratios in the 70S-30UK and 30C-70UK mixtures, the greatest treatment effect was observed in mixtures containing 0.8% WPA. Tables 9 and 10 present the statistical significance of the differences between 70S-30FA and 30S-70FA mixtures with varying WPA ratios.

The analysis of the 70S-30FA mixture revealed a statistically significant difference between the mixture containing 0.8% WPA and all other mixtures in terms of treatment under both curing conditions (Table 9). Additionally, a slight but meaningful difference was observed in the treatment values of the 0.8% WPA mixture between ambient and vacuum oven curing. Moreover, in the case of geopolymer slurry with 1.5% WPA under vacuum oven curing, a significant difference was identified between the 0WPA-EC and 0.5WPA-VO mixtures.

Examination of the 30S-70FA mixture results indicated a statistically significant difference between the mixture containing 0.8% WPA and all other mixtures in terms of treatment under both curing conditions (Table 10). For the 0.8% WPA mixture, no significant difference was found between the EC and VO curing environments.

Li et al. (2023) designed slurry mixtures containing two powdered binding materials, cement and fly ash, and conducted studies to treat recycled aggregates ranging from 2.35 to 26.5 mm using these mixtures. The results of the experiments showed that the water absorption ratio of RCA decreased by an average of 52.8%. When the treatment results were examined, it was observed that the slurry impregnation process reduced the water absorption ratio of RCA, consistent with our study.

Statistical analysis identified 0.8% as the optimal WPA ratio. Accordingly, SEM-EDS analysis was conducted to compare the microstructural properties of mixtures with 0% and 0.8% WPA. The SEM-EDS analyses of the geopolymer slurries are presented in Fig 8.

In the WPA-free sample, voids appear more open and irregular, whereas the WPA-containing sample shows a denser and more compact microstructure, suggesting that the admixture fills the internal spaces (Fig 8).

EDS results reveal a significant increase in Na content (from 13.47% to 22.46%) and a decrease in Si content. The reduction in silicon may be attributed to partial replacement or dilution of the original aluminosilicate network by the sodium-based components of the WP admixture. This indicates that the admixture not only fills the voids but also alters the gel structure in a way that enhances impermeability.

Shaban et al. (2019) conducted a study on treating recycled aggregates below 5 mm using a slurry mixture containing ordinary Portland cement, fly ash, silica fume and nano-silica fume. As a result of the SEM-EDS analysis, it was observed that the aggregates without the treatment process were more porous and had irregular surface texture, while the samples treated with slurry impregnation had less porosity and a homogeneous structure.

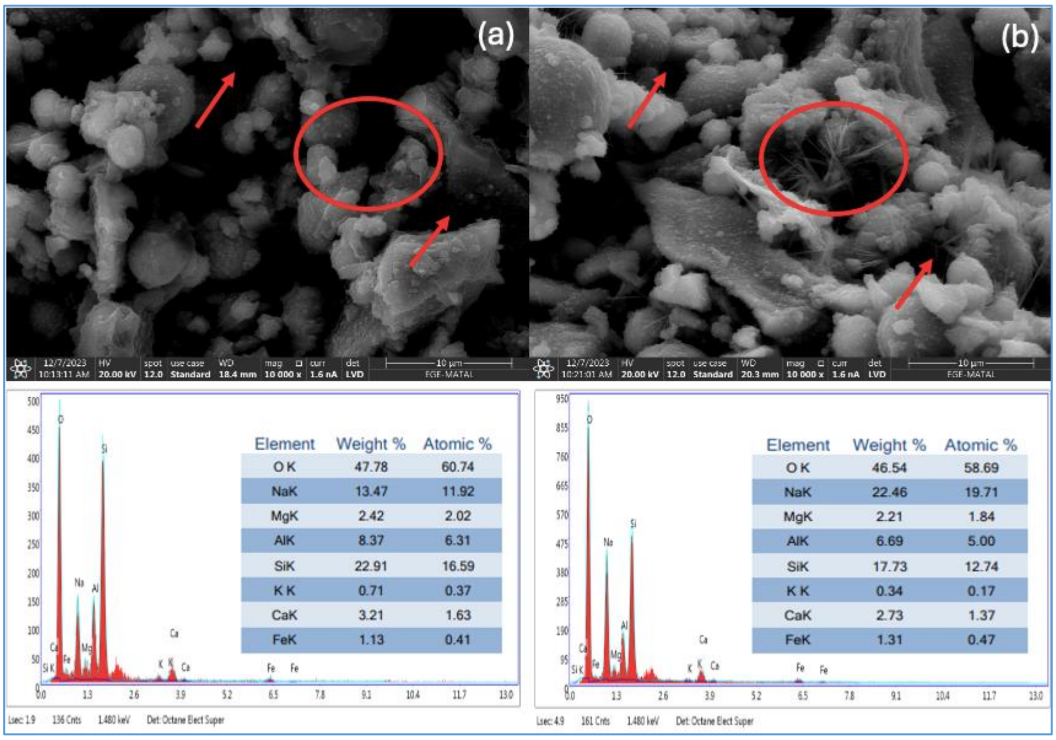

Fig. 9. SEM images and EDS analyses of geopolymer slurries: (a) without crystalline water-proofing admixture, (b) with crystalline water-proofing admixture.

Although no study was found in the literature on the use of WPA in RCA treatment studies, the results were consistent with our study, and it was observed that the slurry impregnation process treated the microstructure properties of RCA.

4. Conclusions

Within the scope of this study, investigations were conducted on treating the water absorption properties of recycled aggregate (RCA) using geopolymer slurry and water-proofing admixture (WPA). When the results of the study were evaluated;

- The best treatment results were obtained with the use of 0.8% WPA in both 70S-30FA and 30S-70FA geopolymer slurry mixtures. For the 70S-30FA-0.8WPA and 30S-70FA-0.8WPA mixtures, treatment ratios of 31.85% and 29.45% were determined under environmental conditions, and 33.78% and 32.05% under vacuum oven conditions, respectively.
- It has been determined that the treatment ratios in both 70S-30FA and 30S-70FA geopolymer slurry mixtures with 0.8% WPA use are statistically significantly different from all other mixtures.
- When SEM-EDS analysis results were examined, it was observed that the use of 0.8% WPA, which is the optimum ratio, in the geopolymer slurry filled the voids in the RCA and treated it.

Acknowledgments

This work was supported by TÜBİTAK under project code 123M467. We would like to thank TÜBİTAK for their support.

References

Adams, M. P., & Jayasuriya, A. (2019). *ACI CRC 18.517: Guideline development for use of recycled concrete aggregates in new concrete*. ACI Foundation.

Alqarni, A. S., Abbas, H., Al-Shwikh, K. M., & Al-Salloum, Y. A. (2021). Treatment of recycled concrete aggregate to enhance concrete performance. *Construction and Building Materials, 307*, 124960.

Arisoy, B. (2016). Environmental impact, management and recycling of construction/demolishing waste in Izmir. *International Multidisciplinary Scientific GeoConference: SGEM, 2*, 41–48.

Behera, M., Bhattacharyya, S. K., Minocha, A. K., Deoliya, R., & Maiti, S. (2014). Recycled aggregate from C&D waste & its use in concrete – A breakthrough towards sustainability in construction sector: A review. *Construction and Building Materials, 68*, 501–516.

Bru, K., Touzé, S., Bourgeois, F., Lippiatt, N., & Ménard, Y. (2014). Assessment of a microwave-assisted recycling process for the recovery of high-quality aggregates from concrete waste. *International Journal of Mineral Processing, 126*, 90–98.

Bui, N. K., Satomi, T., & Takahashi, H. (2018). Enhancement of recycled aggregate concrete properties by a new treatment method. *International Journal of Geomate, 14*, 68–76.

Chen, Q. S., Zhang, Q. L., Fourie, A., Chen, X., & Qi, C. C. (2017). Experimental investigation on the strength characteristics of cement paste backfill in a similar stope model and its mechanism. *Construction and Building Materials, 154*, 34–43.

Dimitriou, G., Savva, P., & Petrou, M. F. (2018). Enhancing mechanical and durability properties of recycled aggregate concrete. *Construction and Building Materials, 158*, 228–235.

Hossain, M. U., Poon, C. S., Lo, I. M. C., & Cheng, J. C. P. (2016). Comparative environmental evaluation of aggregate production from recycled waste materials and virgin sources by LCA. *Resources, Conservation and Recycling, 109*, 67–77.

Ismail, S., & Ramli, M. (2013). Engineering properties of treated recycled concrete aggregate (RCA) for structural applications. *Construction and Building Materials, 44*, 464–476.

Katkhuda, H., & Shatarat, N. (2017). Improving the mechanical properties of recycled concrete aggregate using chopped basalt fibers and acid treatment. *Construction and Building Materials, 140*, 328–335.

Katz, A. (2004). Treatments for the improvement of recycled aggregate. *Journal of Materials in Civil Engineering, 16*(6), 597–603.

Kim, Y., Hanif, A., Kazmi, S. M., Munir, M. J., & Park, C. (2018). Properties enhancement of recycled aggregate concrete through pretreatment of coarse aggregates – Comparative assessment of assorted techniques. *Journal of Cleaner Production, 191*, 339–349.

Kisku, N., Joshi, H., Ansari, M., Panda, S. K., Nayak, S., & Dutta, S. C. (2017). A critical review and assessment for usage of recycled aggregate as sustainable construction material. *Construction and Building Materials, 131*, 721–740.

Kou, S. C., & Poon, C. S. (2012). Enhancing the durability properties of concrete prepared with coarse recycled aggregate. Construction and Building Materials, 35, 69–76.

Li, J., Chen, L. L., Wang, Z. F., & Wang, Y. Q. (2023). Effect of modification and replacement rate of recycled coarse aggregate on properties of recycled aggregate concrete. Iranian Journal of Science and Technology, *Transactions of Civil Engineering, 47*(6), 3321–3332.
Neville, A. M. (1995). *Properties of concrete* (5th ed.). Longman.
Pereira-de-Oliveira, L. A., Nepomuceno, M. C. S., Castro-Gomes, J. P., & Vila, M. D. F. C. (2014). Permeability properties of self-compacting concrete with coarse recycled aggregates. *Construction and Building Materials, 51*, 113–120.
Purushothaman, R., Amirthavalli, R. R., & Karan, L. (2014). Influence of treatment methods on the strength and performance characteristics of recycled aggregate concrete. *Journal of Materials in Civil Engineering, 27*(5), 04014168.
Shaban, W. M., Yang, J., Su, H., Liu, Q. F., Tsang, D. C., Wang, L., Xie, J., & Li, L. (2019). Properties of recycled concrete aggregates strengthened by different types of pozzolan slurry. *Construction and Building Materials, 216*, 632–647.
Shi, C., Li, Y., Zhang, J., Li, W., Chong, L., & Xie, Z. (2016). Performance enhancement of recycled concrete aggregate – A review. *Journal of Cleaner Production, 112*, 466–472.
Sui, Y., & Mueller, A. (2012). Development of thermo-mechanical treatment for recycling of used concrete. *Materials and Structures, 45*(10), 1487–1495.
Tateyashiki, H., Shima, H., Matsumoto, Y., & Koga, Y. (2001). Properties of concrete with high quality recycled aggregate by heat and rubbing method. *Proceedings of the Japan Concrete Institute, 23*(2), 61–66.
Tosun, E. (2022). *Rehabilitation, characterization and determination of method effectiveness of recycled concrete aggregate* (Doctoral dissertation). Ege Üniversitesi, Fen Bilimleri Enstitüsü.
Xiao, J. (2018). Recycled aggregate concrete. In Recycled aggregate concrete structures (pp. 65–98). Springer.
Zhang, S., He, P., & Niu, L. (2020). Mechanical properties and permeability of fiber-reinforced concrete with recycled aggregate made from waste clay brick. *Journal of Cleaner Production, 268*, 121690.
Zheng, L., Wu, H., Zhang, H., Duan, H., Wang, J., Jiang, W., Dong, B., Liu, G., Zuo, J., & Song, Q. (2017). Characterizing the generation and flows of construction and demolition waste in China. *Construction and Building Materials, 136*, 405–413. https://doi.org/10.1016/j.conbuildmat.2017.01.055
ong, L., Fei, Z., & Zhang, S. (2014). Permeability of recycled aggregate concrete containing fly ash and clay brick waste. *Journal of Cleaner Production, 70*, 175–182.

ICEARC'25

4th International Civil Engineering & Architecture Conference
17-19 May 2025, Trabzon, Türkiye

Effect of shear span-depth ratio on recycled coarse aggregate concrete beams without stirrups

Nwzad Abduljabar Abdulla*[1]

[1] *University of Salahaddin, Erbil, Iraq*

Abstract. Recycling has emerged as a potent tactic to lessen the harm that concrete waste causes to the environment. It is possible to use recycled concrete as coarse aggregate in structural members. One such structural member is longitudinally reinforced concrete beam with no shear reinforcement. The shear span-effective depth ratio (a/d) affects how well such beams perform under shear stresses. In order to examine the effect of this parameter, a database was compiled for beams evaluated under one-point load, where the load was central or applied on one shear span only. The data-base was utilized to ascertain the impact of the a/d ratio on the shear capacity of recycled coarse aggregate concrete beams without shear reinforcement. Shear predictions using the old, the more modern and detailed, the recent, and the new updated ACI code models were compared with the experimental results from the database, which had an a/d ratio ranging from above (1) to 8. This comparative study provides proof for this problem and shows how variations in the a/d ratio impacted the four equations. For the beams tested for an a/d ratio of 6-7, the average projected shear values using the ACI code Eq. (1) and Eq.(3) were nearly identical to the corresponding average experimental values. This criterion holds true For Eq. (4). However, the assessd average shear values using the ACI code Eq. (2) for the specimens tested for an a/d ratio of 2-3, 3-4, 6-7, and 7-8 were considerably lower than the corresponding experimental averages.

Keywords: Concrete debris; Coarse recycled aggregate; Un-transversely reinforced beams; Shear-span-effective depth; Shear strength

1. Introduction

The shear span-to-effective depth ratio (a/d) is known to have a significant impact on the shear strength of reinf-orced concrete elements. The performance of reinforced concrete beams in the absence of shear reinforcement is more crucial to take into account. When recycled concrete coarse aggre-gate (RCCA) is substituted for the co-arse natural aggregate, this problem is made worse. One major challenge is the water absorption which is increa-sed because of the porous adhering mortar that is bound to the surface of the recycled aggregate (Abdulla, 2015).

For an a/d ratio of 2.5, comparable shear strengths were observed for NA beams and beams with 50% and 10 0% RCCA replacement ratio. For the same a/d ratio of 1.15, the shear capacity of RCCA beams was 27% lower than that of control beams, both without shear reinforcement. When the a/d ratio was reduced from 2.5 to 1.15, the shear capacity of beams with 50% and 100% RCCA replacement ratios increased by two to three times. Wh-en the main steel ratio was raised by 60%, the shear capacity of RCCAbeams increased by only 4 to 6%, where-as that of its corresponding beamswith NA increased by 17% (Sagheer & Tabsh, 2022).

The aggregate interlock mechanism of RCCA concrete is different from that of NA concrete because it cont-ains the old weak adherent mortar (Abdulla, 2024b). An experimental study found that changing the a/d ratio from 3.1 to 3.25 resulted in a small improvement in shear capacity of beams not reinforced for shear (Sayhood et al., 2019). The source of RCCA affects the shear performance (Abdulla, 2024a). average values of 0.92 and 0.87 were recorded for the v_{RCCA}/v_{NA} ratios for beams tested for a/d ≤2:5 and 2.5 <a/d ≤ 3.5. The same value was 1.02 for beams tested for a/d > 3.5. This showed that the shear span to depth ratio of ≤ 3.5 had an adverse effect on the shear resistance of RCCA. The weaker compressive strength of RCCA contributes to this perform-ance (Pradhan et al., 2018). For RCCA beams, with a 30% partial replacement of the RCCA, tested under shear span-to-depth ratio of 1, 2, and 3, the shear strengths dropped by roughly 2%, 14%, and 37%, respectively (Etm-an et al., 2018).

The RCCA beams with an a/d ratio of 0.9 showed significant increases in shear strength due to cooperation of the arch mechanism, compression strut forms in the shear span and the main steel contributes to this action by restraining the ends of strut from opening. Therefore direct strut action is employed and loads are transferred

* Corresponding author, E-mail: anwzad@yahoo.com

https://doi.org/10.31462/icearc2025_ce_mat_603

directly to supports. The arch mechanism becomes less powerful in beams with 1.8 a/d ratio, whereas it diminishes in shallow beams with 2.7 span to depth ratio. This mechanism reduces in shallow beams of span-to-depth ratio of 2.7 (Abdulla, 2024c).

1.1. Applicability of ACI Code

Because of inconsistencies, the current shear specifications cannot predict the shear capacity of RA beams without web reinforcement. The ACI 318 formulae (Knaack & Kurama, 2015) were used to conservatively predict the shear strength of RCCA beams, and the ACI 318 Code, Eurocode-2 Code, and AS3600 Code can be used for the shear design of 25% RCCA concrete beams; for slender beams, the code prediction becomes conserveative (Lian et al., 2013). The current standards do not include the parameters, beam action, and arch action, which affect the shear resisting ability; evaluating the shear capacity of RCCA concrete beams using the current specification equations in ACI 3182014 are a conservative design method(Choi & Yun, 2017).

The normalized shear stresses determined by ACI 318-19 was more conserveative than that of ACI 318-14 for RCCA beams with main steel ratio (ρw) equal to 1.16% (DB16series). When the ρw was increased to 1.81% (DB20 series), the ACI 318-9 shear strength equation prediction was slightly higher than the ACI 318-14 one. For RA replacement rates below 75%, the shear capability of beams was conservatively evaluated by the ACI 318-19 shear strength requirements. The ACI formula was modified to include a reduction factor of 0.75 for RA replacement ratios between 50 and100%. The adjusted algorithm yields conservative redictions for an RA replacement ratio of 100% or less (Setkit et al., 2021). The applicability of current design principles for NA beams to RCCA beams can be assessed by comparing code predictions with experimental test results (Sato et al., 2007). RCCA beams with a 50% RA replacement ratio and an a/d ratio of three can be designed using the current shear design approach (Choi et al., 2010). Previous research suggests that the shear models can evaluate the shear strength of the beams with shear reinforcement. The current work aims to fill the gap in the literature by doing quantitative research on the effect of a/d on the shear capacity of RA concrete.

1.2. ACI Code shear equations

1.2.1. Old and simple ACI Code 318-14

Takes into consideration the effect of compressive strength only.

$$Vc = 0.17\sqrt{fc}bd \tag{1}$$

where $f_c \le 70$MPa and λ a parameter for the normal concrete equal to 1.

1.2.2. More detailed ACI Code 318-14

This is the only model which considers the effect of shear-span-depth ratio (a/d).

$$Vc = \left[\sqrt{fc} + \frac{120\rho t}{\frac{a}{d}}\right]\frac{bd}{7} \le 0.3\lambda\sqrt{fc}bd, where: fc \le 70MPa \tag{2}$$

1.2.3. Recent ACI Code 318-19

This ACI code introduced the size effect parameter (λ_s) since the shear capacity don’t change proportionally with the change in effective depth of shear member.

$$Vc = \left[0.66\lambda s\lambda\left(\sqrt[1/3]{\rho}\right)\sqrt{fc} + \frac{Nu}{6Ag}\right]bd \tag{3}$$

Where $\lambda = \sqrt{\frac{2}{1+0.004d}} \le 1, fc \le 8.3MPa, V_{ACI} = 0.42\sqrt{fc}$

1.2.4. New ACI Code 318-25

The new ACI code is similar to the ACI code 318-19 but the size effect parameter is freed from the square root restrictions.

$$Vc = \left[0.66\lambda s\lambda\left(\sqrt[1/3]{\rho}\right)\sqrt{fc} + \frac{Nu}{6Ag}\right]bd \tag{4}$$

Where $\lambda = \frac{2}{1+0.004d} \le 1, fc \le 8.3MPa, V_{ACI} = 0.42\sqrt{fc}$

2. Database

The important test parameter of shear span-to-depth ratio (a/d) of stirrup-free beams and slabs, which varies from above1 to 8, is covered by the research in the collected database. From the literature that was available, thirty-four test beams and slabs with RCCA and without shear reinforcement were collected. The database contained seven papers (Michaud, 2015), (Sagher, 2016), (Tabsh, 2018), (Sayhood et al., 2019), (Cardoso et al., 2021), (Younis et al., 2022),(Sagheer & Tabsh, 2022). published between 2015 and 2023. Every beam or slab was tested with a point load, either in the center or on one of the shear spans. all the specimens had a rectangul-ar cross-section and were under reinforced.

3. Discussions

The performance of Eq. (1) in predicting the shear capacity of recycled coarse aggregate (RAC) concrete specimens without shear reinforcement in the database is plotted in Fig. (1) versus the a/d ratio. The simple and straightforward ACI code calculation produces conservative values (Hollow markers) compared to the experimental shear strength values (Solid markers). As the a/d values increases, there are noticeable differences between the mean projected value (dashed line) andthe experimental average value (solidline). This difference is significant between the two averages for the a/d ratios≤2. The disparity between the two averages narrows as the a/d ratio augments. This criterion holds true for the a/d ratio in the ranges 2-3, 3-4, 6-7, and 7-8. The best agreement between the experimental-predicted averages reached in the range 6-7. The number of specimens tested for ranges considered are equal except for the a/d ratio of 7-8.

The experimental and their equivalent predicted shear capacity using ACI code Eq. (2) versus the a/d ratio are depicted in Fig. 2. The second ACI code equation which takes into account the influence of a/d ratio yields more conservative values, underestimating the shear capacity for all the ranges of a/d ratio. However, the aver-age experimental and predicted shear values are similar for all the ranges of a/d ratio except the range 1-2. Mor-eover, despite including the a/d ratio in the model, the second equation predictions are more conservative compared to equation one.

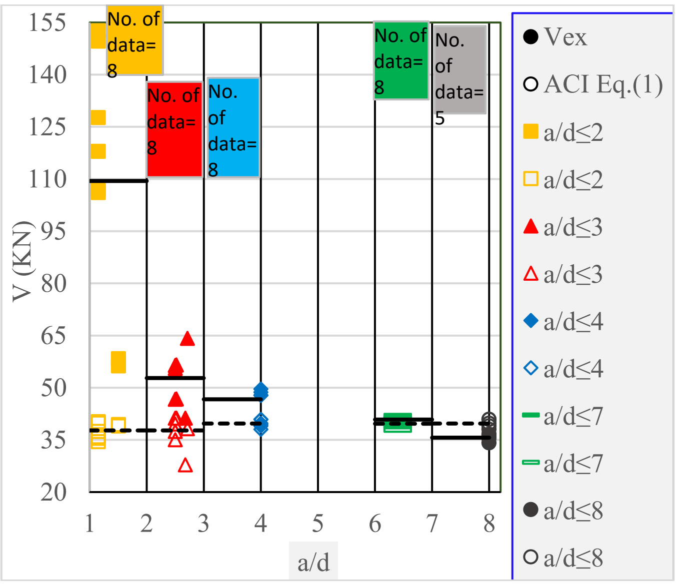

Fig. 1. Experimental and their equivalent predicted shear capacity using ACI code Eq. (1) versus the a/d ratio

The experimental and corresponding predicted values using Eq. (3) are plotted against the a/d ratio in Fig. 3. The conservatism of Eq. (3) holds true in consistence with the previous two equations. Compared to the experimental database values, the revised ACI code equation produces conservative results. However, the performance of Eq. (3) follows a similar pattern to that of Eq. (1), as the a/d ratio increase the gap between the two values diminish, except the a/d ratio of 7-8 with little increase.

There is a noticeable difference between the experimental average value (solid line) and the average expected value (dashed line) in the a/d ratio range of 1-2. This is ascribed to the effect of arch action, which results in considerable increase in the shear resistance of the specimen. The new ACI code 318-25 shear model also results in underestimation of the experimental results, as illustrated in Fig. (4). This equation includes a parameter which accounts for the size affect. The performance of Eq. (4) is very similar to that of Eq. (3). The predictions in the a/d ratio of 6-7 by the Eqs. (1), (3), and (4) are very similar. This shows the applicability of the three models to a/d ratio greater than three, especially the a/d ratio of 6 to 7.

Using the a/d ratio and the ACI code Eqs. (1) to (4), Fig. 5 displays the absolute average error (AAE) between the experimental and corresponding anticipated shear capacity. Employing equations (1) through (4), the AA error values change in accordance with the a/d ratio.

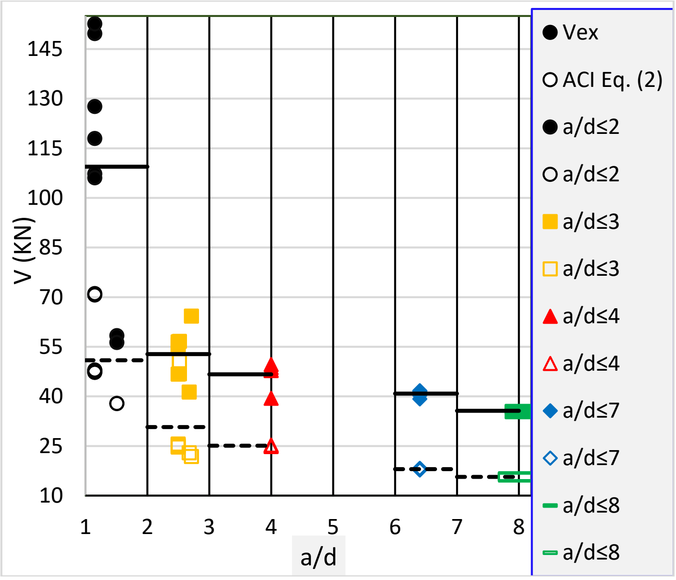

Fig. 2. Experimental and their equivalent predicted shear capacity using ACI code Eq. (2) versus the a/d ratio

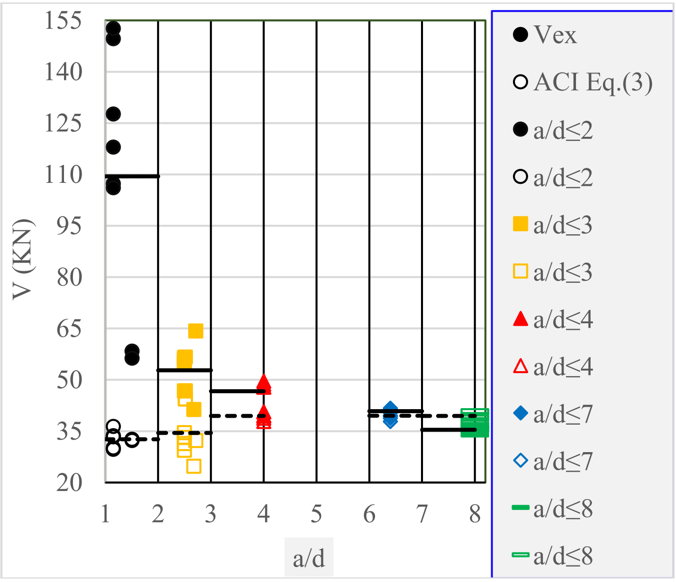

Fig. 3. Experimental and their equivalent predicted shear capacity using ACI code Eq. (3) versus the a/d ratio

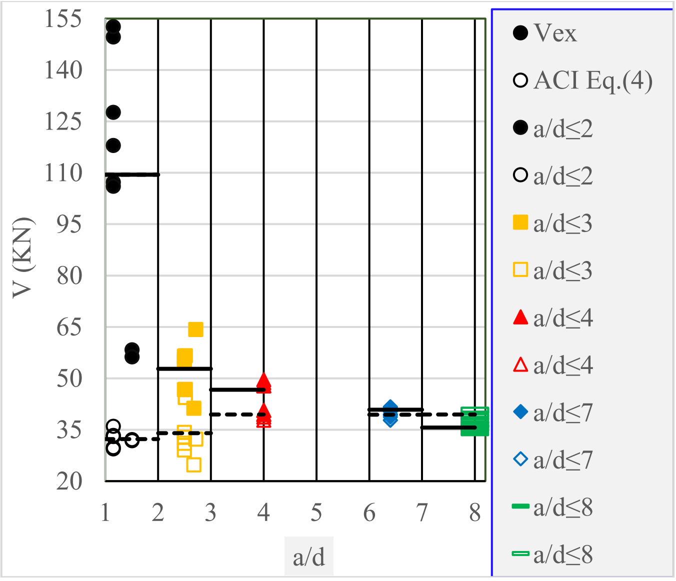

Fig. 4. Experimental and their equivalent predicted shear capacity using ACI code Eq. (4) versus the a/d ratio

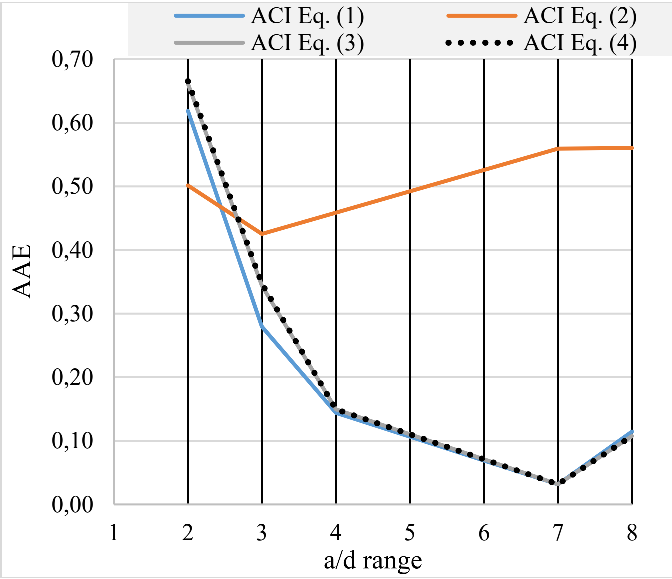

Fig. 5. Absolute average error between the experimental and their equivalent predicted shear capacity using ACI code Eqs. (1), (2), (3), and (4) versus the a/d ratio

Eq. (2) leads to the largest difference in AAE values compared with the other equations, especially for a/d ratio greater than 3. Eq. (1) yields the lowest AAE values for the a/d ratio of 6-7. This trend applicable to the Eqs. (3) and (4). Using the ACI code Eqs. (1) to (4), the a/d ratio is shown in Fig. 6 with the corresponding changes in the standard deviations for the experimental-anticipated shear capacity. Depending on the a/d ratios, different standard deviation values exist. For Eqs. (1), (3), and (4) the standard deviation (STD) values decrease with a/d ratio, except for the for a/d ratios of 7-8, which slightly increases. Moreover, the a/d ratio of 7 results in the lowest STD values. On the other hand, the Eq. (2) deviates from this trend, resulting in increment in STD with change in a/d ratio.

The two statistical indexes, AAE and STD are compared in Fig.7. For the RCA specimens assessed for the a/d range of 4 to 8 there is a close agreement between the two indexes, for all the equations, except Eq. (2). For the latter equation there is considerable difference between the two indexes. the largest deviation between the two indexes is observed for the a/d ratio of 1 to 3. The shear performance of RCA specimens tested under static three-point loads are affected by a number of factors, including the shear span-to-effective depth ratio (a/d). The two ACI codes 318-19 and 318-25 shear models use a modification factor, λs, for the size effect. The new upda-ted code equation, Eq. (4), results in a slightly more conservative estimation of the shear capacity of RCA concrete specimens without shear reinforcement compared with Eq. (3).

To analyze the impact of shear models on the experimental strength, a Z-test was executed. Table 1 illustrates the outcome of the Z-test on the database. The $Z_{Statistic}$ is above the $Z_{Critical}$ and all the β -values are below the p-value of 0.05. Therefore, the null hypothesis is rejected and it can be concluded that there is substantial statistically difference between the means of the experimental shear and the predicted means from the four ACI code shear equations in z-test.

The difference in the predicted means of Eq. (1) was compared with the average predicted shear strength of Eqs. (2) to (4) in Table 2. Compared with the mean of Eq. (1) the $Z_{Statistic}$ is higher than the $Z_{Critical}$ and all the β -values are below the p-value of 0.05 for the means of Eqs. (2) and (4) indicating a considerable difference between the predicted averages of the shear values for Eqs. (2) and (4) compared with Eq. (1). However, the $Z_{Statistic}$ is below the two-tail $Z_{Critical}$ and the β -value of 0.52 is greater than the P-value of 0.05, showing that there is no difference in the average predicted shear strength of Eq. (1) compar-ed with the average predicted shear strength of Eq. (3).

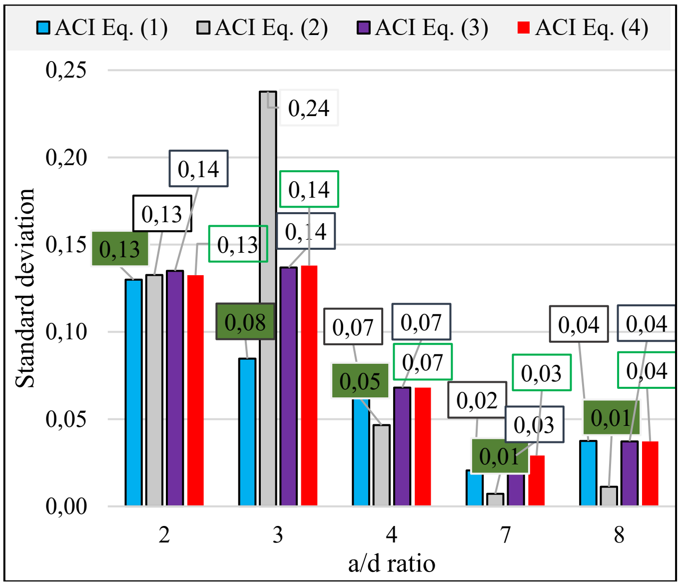

Fig. 6. The standard deviations between the experimental and their equivalent predicted shear capacity using ACI code Eqs. (1), (2), (3), and (4) versus the a/d ratio

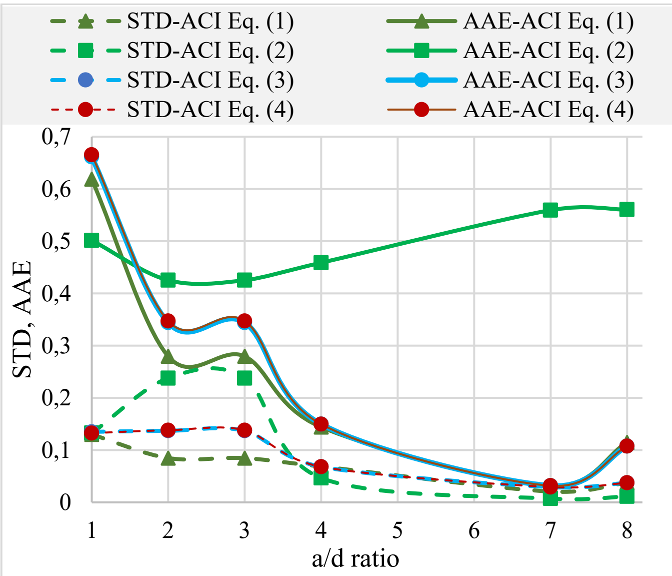

Fig. 7. AAE and or STD for the experimental-predicted shear capacity using ACI code Eqs. (1), (2), (3) and (4) versus the a/d ratio

The average predicted shear strength of Eq. (2) was compared with the average predict-ed shear of Eqs. (3) and (4) in Table 3. All β -value is lower than P-value of 0.05, which confirms the substantial difference in the predicted average shear strength of Eq. (2) compared with average predicted shear of Eqs. (3) and (4).

A direct comparison between the predicted average shear strength of Eq. (3) and Eq. (4) using the z-test is tabulated in Table 4. The $Z_{Statistic}$ is greater than two-tail $Z_{Critical}$ and all the β -value is smaller than the P-value of 0.05 therefore the null hypothesis is rejected therefore there is no enough evidence to conclude that the means of Eq. (3) and Eq. (4) are equal.

Table 1. Summary of Z-test for experimental-predicted shear strength using Eqs. (1)-(4)

Eq.	$Z_{Statistic}$	$Z_{Critical}$ two-tail	β -value	P-value	Is $Z_{Statistic} > Z_{Critical}$	Is P value > β-value
(1)	3.72	1.96			Yes	
(2)	4.67	1.96			Yes	
(3)	3.51	1.96			Yes	
(4)	4.09	1.96			Yes	
			0.0002	0.05		No
			0.0000	0.05		No
			0.0004	0.05		No
			0.0000	0.05		No

Table 2. Summary of Z-test for predicted Eq. (1) to Eqs. (2)-(4) shear strength

Eq.	$Z_{Statistic}$	$Z_{Critical}$ two-tail	β -value	P-value	Is $Z_{Statistic} > Z_{Critical}$	Is P value > β-value
(2)	3.01	1.96			Yes	
(3)	-0.64	1.96			No	
(4)	2.45	1.96			Yes	
			0.0026	0.05		No
			0.5221	0.05		yes
			0.0145	0.05		No

Table 3. Summary of Z-test for predicted Eq. (2) to Eqs. (3)-(4) shear strength

Eq.	$Z_{Statistic}$	$Z_{Critical}$ two-tail	β -value	P-value	Is $Z_{Statistic} > Z_{Critical}$	Is P value > β-value
(3)	-3.06	1.96			No	
(4)	-2.10	1.96			No	
			0.002	0.05		Yes
			0.035	0.05		Yes

Table 4. Summary of Z-test for predicted Eq. (3) to Eq. (4) shear strength

Eq.	$Z_{Statistic}$	$Z_{Critical}$ two-tail	β -value	P-value	Is $Z_{Statistic} > Z_{Critical}$	Is P value > β-value
(4)	2.15	1.96			Yes	
			0.031	0.05		Yes

4. Conclusions

- For the beams tested for an a/d ratio of 6-7, the average projected shear values using the ACI code Eq. (1) were nearly identical to the corresponding average experimental values.
- The evaluated average shear values using the ACI code Eq. (2) for the beams tested for an a/d ratio of 2-3, 3-4, 6-7, and 7-8 were similar and lower than the corresponding experimental averages.
- Good agreement was found between the predicted average shear values using the ACI code Eq. (3) its corresponding experimental shear values in a/d ratio of 6 to 7. This criterion holds true For Eq. (4).
- The a/d ratio affects the AA error values, between the experimental shear and the predicted shear using Eqs. (1) to (4). For a/d ratios of 7, the least amount of AAE is produced by Eqs. (1), (3) and (4). This error is less than 10% for the ranges 5-6, 6-7, and 7-8. The detailed Eq. (2) produces the highest errors for all the ranges of a/d ratio.

- The difference in standard deviation values between the four equations becomes less than 10% in the a/d ratios of 4, 7, and 8.

Acknowledgments
This research did not receive any specific grant from funding agencies in the public, commercial, or not-for-profit sectors.

References

Abdulla, N.A. (2015). Effect of Recycled Coarse Aggregate Type on Concrete. *Journal of Materials in Civil Engineering*, *27*(10). https://doi.org/10.1061/(ASCE)MT.1943-5533.0001247

Abdulla, N.A. (2024a). Longitudinally reinforced recycled aggregate beams without transverse steel: A review. *Discover Civil Engineering*, *1*(1), 39. https://doi.org/10.1007/s44290-024-00048-0

Abdulla, N.A. (2024b). Role of coarse recycled aggregate in concrete beams. *Next Materials*, *4*, 100216. https://doi.org/10.1016/j.nxmate.2024.100216

Abdulla, N.A. (2024c). Shear capacity of reinforced concrete beams with fully recycled aggregate. *Innovative Infrastructure Solutions*, *9*(8), 287. https://doi.org/10.1007/s41062-024-01601-7

Cardoso, A.C., Lima, I. G., Ferreira, M. de P., & Souza, R.A. de. (2021). Influence of recycled concrete aggregates on the shear strength of reinforced concrete beams. *Revista IBRACON de Estruturas e Materiais*, *14*(1). https://doi.org/10.1590/s1983-41952021000100009

Choi, H.B., Yi, C.K., Cho, H.H., & Kang, K.I. (2010). Experimental study on the shear strength of recycled aggregate concrete beams. *Magazine of Concrete Research*, *62*(2), 103–114. https://doi.org/10.1680/macr.2008.62.2.103

Choi, W.C., & Yun, H.D. (2017). Shear strength of reinforced recycled aggregate concrete beams without shear reinforcements. *Journal of Civil Engineering and Management, 23*(1), 76-84

Etman, E.E., Afefy, H.M., Baraghith, A.T., & Khedr, S.A. (2018). Improving the shear performance of reinforced concrete beams made of recycled coarse aggregate. *Construction and Building Materials*, *185*, 310–324. https://doi.org/10.1016/j.conbuildmat.2018.07.065

Knaack, A. M., & Kurama, Y.C. (2015). Behavior of Reinforced Concrete Beams with Recycled Concrete Coarse Aggregates. *Journal of Structural Engineering*, *141*(3). https://doi.org/10.1061/(ASCE)ST.1943-541X.0001118

Lian, O.C., Wee, L.S., Masrom, M.A.A., & Hua, G.C. (2013). Experimental study on shear behaviour of high strength reinforced recycled concrete beam. *Pertanika J. Sci. Technol, 21,* 601-610

Michaud, K.S. (2015). *Evaluation of the environmental, material, and structural performance of recycled aggregate concrete* (Doctoral dissertation). Queen's University.

Pradhan, S., Kumar, S., & Barai, S.V. (2018). Shear performance of recycled aggregate concrete beams: An insight for design aspects. *Construction and Building Materials*, *178*, 593–611. https://doi.org/10.1016/j.conbuildmat.2018.05.022

Sagheer, A.M., & Tabsh, S.W. (2022). Shear strength of concrete beams without stirrups made with recycled coarse aggregate. *Buildings*, *13*(1), 75. https://doi.org/10.3390/buildings13010075

Sagher, A.M. (2016). S*hear strength of reinforced concrete beams made with recycled coarse aggregate* (Doctoral dissertation).

Sato, R., Maruyama, I., Sogabe, T., & Sogo, M. (2007). Flexural behavior of reinforced recycled concrete beams. *Journal of Advanced Concrete Technology*, *5*(1), 43–61. https://doi.org/10.3151/jact.5.43

Sayhood, E., Resheq, A., & Raoof, F. (2019). Behavior of recycled aggregate fibrous reinforced beams under flexural and shear loading. *Engineering and Technology Journal*, *37*(3C), 338–344. https://doi.org/10.30684/etj.37.3C.6

Setkit, M., Leelatanon, S., Imjai, T., Garcia, R., & Limkatanyu, S. (2021). Prediction of shear strength of reinforced recycled aggregate concrete beams without stirrups. *Buildings*, *11*(9), 402. https://doi.org/10.3390/buildings11090402

Tabsh, S.Y. (2018). Shear strength of reinforced concrete beams made with recycled aggregate. In: *Proceedings of the World Congress on Civil, Structural, and Environmental Engineering,* Budapest, Hungary.

Younis, A., El-Sherif, H., & Ebead, U. (2022). Shear strength of recycled-aggregate concrete beams with glass-FRP stirrups. *Composites Part C: Open Access*, *8*, 100257. https://doi.org/10.1016/j.jcomc.2022.100257

Evaluation of concrete paving block strength through ultrasonic pulse velocity (UPV) measurements

Bircan Arslannur [1], Muhammed A. Özdemir[*1]

[1] *Igdir University, Department of Civil Engineering, 76000 Iğdır, Türkiye*

Abstract. In Türkiye, the majority of rural village roads are being constructed using concrete paving blocks which must adhere to TS 2824 EN 1338 specifications. The conformity of these materials is generally evaluated through testing on samples obtained post-road pavement completion. Nevertheless, acquiring samples, dispatching them to laboratories, and awaiting results can lead to considerable time and labor inefficiencies. The main aim of this work is to facilitate real-time assessment of concrete paving blocks in situ via Ultrasonic Pulse Velocity (UPV) measurements, thus diminishing dependence on laborious laboratory testing methods. This strategy seeks to reduce potential labor and time inefficiencies linked to the production process during prolonged laboratory testing phases. This study entaile of 54 concrete paving block specimens from seven different villages' rural roads in Kars, Türkiye. Tensile strengthassessments were performed on samples to ascertain the relationship between tensile strengthand P-wave velocity. The flexibility of the concrete pavement blocks was also assessed. P and S-waves velocities were measured with a UPV device, while tensile strengthvalues were determined using a tensile testing machine. A regression analysis was conducted to correlate the UPV results with laboratory test outcomes, demonstrating a substantial association between the two datasets. The results indicate that performing thorough UPV and compression testing on concrete pavement blocks with varying compositions can yield empirical equations, enabling non-destructive strength evaluation in situ. The use of this method is anticipated to improve the efficiency and precision of quality control in the concrete paving block production and construction process.

Keywords: Ultrasonic pulse velocity; Concrete paving block; Strength assessment; Non-destructive testing; Engineering design; Road materials

1. Introduction

Concrete paving blocks are extensively used in rural road construction throughout Türkiye owing to their durability and ease of installation. These blocks must satisfy stringent quality and performance requirements as outlined in TS 2824 EN 1338:2005. Conventional quality control involves collecting samples after pavement completion and sending them to laboratories for destructive testing. However, this approach often introduces delays and additional labor costs in the production process.

The primary objective of this study is to explore the feasibility of using UPV measurements as an in situ, non-destructive method to predict the tensile strengthof concrete paving blocks. By establishing a robust correlation between UPV-derived elasticity measurements and laboratory-obtained tensile strengthdata, the study aims to develop a rapid quality assessment tool that can be applied directly in the field. The successful integration of UPV techniques into routine quality control could enhance project timelines, reduce material wastage, and promote more sustainable construction practices.

2. Literature review

2.1. Principles of UPV testing

Ultrasonic Pulse Velocity (UPV) testing is a well-established non-destructive evaluation (NDT) technique that measures the time an ultrasonic pulse takes to travel through a concrete specimen. Based on the fundamental equation This method provides valuable insights into the density, homogeneity, and elastic properties of the material.

$$Velocity = Distance/Time \tag{1}$$

In general, higher pulse velocities indicate a more homogeneous and structurally sound material, while lower velocities may suggest the existence of defects such as cracks or voids. UPV has been successfully applied to

[*] Corresponding author, E-mail: m.alperen.ozdemir@igdir.edu.tr

https://doi.org/10.31462/icearc2025_ce_mat_613

golden light publishing

assess reinforced concrete structures due to its non-invasive nature and its capacity for rapid evaluation (Popovics, 2005; Aggelis, 2013).

2.2. Applications in concrete structures and the literature gap

UPV testing is routinely employed in conventional concrete structures to evaluate quality, detect internal damage, and ensure overall structural integrity. While its use in reinforced concrete such as beams, columns, and slabs is well documented, the application of UPV for concrete paving blocks remains underexplored. The literature reveals a notable gap: few studies have directly correlated UPV measurements with tensile strengthin paving blocks, even though their loading mechanisms and failure behaviors differ from those of traditional reinforced concrete elements. In paving block production, UPV testing is particularly advantageous for real-time quality control; by measuring pulse velocity during manufacturing, the process can verify that blocks meet the required strength and durability standards. For instance, research has demonstrated that UPV can reliably assess concrete blended with recycled coarse aggregates and seashore sand (Al-Zuhairi, 2013; Rodríguez et al., 2017). Moreover, UPV's capability to detect internal cracks and voids is critical since such defects can severely compromise structural performance, enabling engineers to take corrective actions before premature failure occurs (Sharp & Ozyildirim, 2014; Hong, 2012). Additionally, because concrete paving blocks are exposed to harsh conditions including freeze-thaw cycles UPV can serve as an effective means of monitoring long-term degradation, facilitating early detection of deterioration and guiding maintenance efforts (Toutounchi et al., 2021). Finally, UPV data have been correlated with key material properties, such as compressive strength and elastic modulus, underscoring the technique's potential for comprehensive, non-destructive material characterization (Tang et al., 2007). Together, these applications not only underline UPV's versatility but also highlight the need for further dedicated research to bridge the existing literature gap in the field of concrete paving blocks.

2.3. Advantages and limitations of UPV testing

UPV testing offers several distinct advantages that make it an attractive method for quality control and material assessment. Its non-destructive nature allows repeated measurements without compromising the structural integrity of the material, which is particularly useful for both initial inspections and ongoing monitoring. Moreover, the technique is both rapid and cost-effective compared to traditional destructive methods, especially when used in conjunction with other NDT approaches such as sonic echo-impulse response for enhanced defect detection (Sharp & Ozyildirim, 2014). Additionally, UPV testing is versatile, having been applied successfully to a wide range of concrete structures, from newly manufactured paving blocks to aging infrastructure.

Despite these advantages, UPV testing is not without limitations. The accuracy of the results is highly dependent on proper surface preparation, as a clean and well-leveled surface is essential for optimal transducer contact. Furthermore, the choice of ultrasonic frequency plays a critical role; higher frequencies can provide improved resolution but may suffer from greater signal attenuation, whereas lower frequencies offer deeper penetration with reduced resolution. Finally, the interpretation of UPV data requires significant expertise to ensure that velocity measurements are correctly correlated with known material properties, thereby avoiding misinterpretation of the concrete's condition (Singh et al., 2022; Tang et al., 2007).

2.4. Case studies and practical examples

Several studies illustrate the practical application of UPV testing in the context of concrete paving blocks and related materials. Research on quality control has shown that UPV can effectively assess the strength and durability of concrete paving blocks produced with recycled aggregates and seashore sand, offering a reliable method for ensuring compliance with established standards (Singh et al., 2024). In cold regions, UPV has been used to monitor freeze-thaw damage in roller-compacted concrete, demonstrating its utility in long-term degradation monitoring (Toutounchi et al., 2021). Moreover, UPV testing has been applied to estimate crack depth in concrete structures, providing crucial information for evaluating defect severity and guiding maintenance decisions (Cho et al., 2012). These case studies underscore the technique's potential for expanding its application to concrete paving blocks—a research area that warrants further exploration.

3. Materials and methods

3.1. Sample collection

A total of 54 concrete paving block specimens were obtained from rural roads in seven villages within the Kars area of Türkiye. The sampling distribution was as detailed below: Çıplaklı (8 samples), Katrancı (6 samples), Kaynarlı (10 samples), Kilit Taşı (10 samples), Kümbetli (5 samples), Melikköy (5 samples), and Şenolköy (10 samples).

Despite the paving blocks being created in accordance with a uniform recipe and production criteria, it is probable that the material compositions differed among villages due to variations in sourcing, batching techniques, or local aggregate availability. Moreover, the sampling occurred at disparate times across the villages, indicating that the blocks experienced diverse environmental and climatic conditions—such as temperature variations, freeze-thaw cycles, and moisture levels—prior to testing. These factors may have substantially affected the mechanical properties of the specimens, especially their tensile strength.

Consequently, assessing the data on an individual village basis seems to be a more suitable method than consolidating the results. This will facilitate a fuller comprehension of localized differences in material performance and more effectively isolate the impact of production techniques and environmental exposure. This technique emphasizes the significance of context-specific quality control and the necessity for site-level monitoring to guarantee the consistent durability and performance of concrete paving blocks in rural infrastructure.

3.2. UPV measurement procedure

UPV measurements were conducted on all specimens using a calibrated ultrasonic pulse velocity device under controlled laboratory conditions. The procedure involved:

- Device Calibration: The UPV device was calibrated following the manufacturer’s specifications to ensure accurate readings.
- Measurement Conditions: Prior to testing, the surface of each concrete paving block was cleaned and leveled. All measurements were performed at a stable ambient temperature and humidity.
- Data Collection: For each specimen, P-wave and S-wave velocities were measured at three distinct points. The average UPV value for each block was then determined for subsequent analysis. The UPV results, illustrated in Fig. 1, represent the values documented during the experimental process.

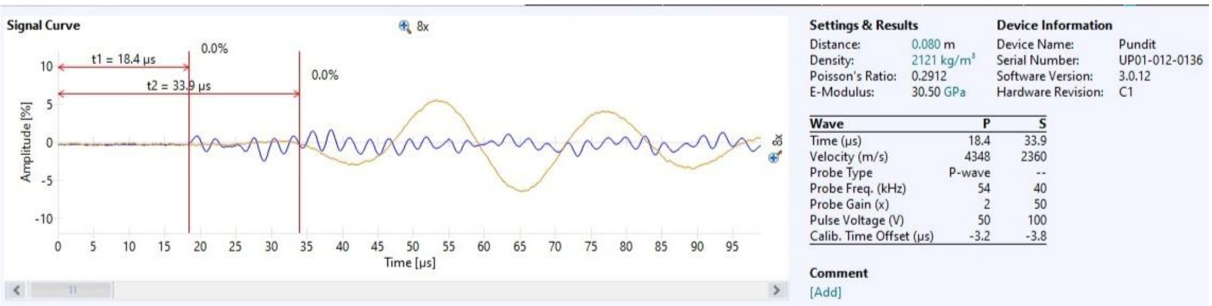

Fig. 1. Sample UPV Test Result

3.3. Laboratory tensile splitting strength test

Immediately after UPV measurements, the same specimens underwent tensile strengthtesting:

- Standards Compliance: Tensile testing was carried out following TS 2824 EN 1338:2005, which provides the required procedures for evaluating concrete paving blocks.
- Test Setup: Each block was subjected to a tensile test using an appropriate testing machine. The bending behavior and fracture characteristics were recorded.
- Data Documentation: Results, including precise tensile strengthvalues and observations of failure modes, were systematically documented for further statistical analysis.

3.4. Statistical analysis

Data derived from UPV measurements and tensile strengthtests were subjected to Pearson’s correlation analysis to assess the strength and direction of the association between the two variables. The analysis was performed utilizing Microsoft Excel. A correlation coefficient (R) was computed to assess the extent of linear relationship between UPV values and tensile strength. As no regression model was constructed in this study, no prediction equation was established. The correlation results offer preliminary insights into the viability of UPV measurements as markers of tensile performance.

4. Results

4.1. Test results

The test results for each village were compiled, and the P-wave and S-wave velocities, elasticity values derived from these waves, saturated unit weight, breaking force, and tensile splitting strength values were documented in a table. Table 1 displays the tensile test and UPV measurement findings for the samples from each village.

Table 1. Test results

	Non Destructive Method			Tensile Splitting Strength Test (EN 1338:2003)		
	Pulse Velocity		Elasticity	Saturated Weight	Breaking Force	Strength
	P-Wave	S-Wave				
	(m/s)	(m/s)	GPa	(gr)	(kN)	(MPa)
Ciplakli N1	4103	2332	30.65	5462	96.87	3.86
Ciplakli N2	4255	2340	29.66	5077	132.22	5.26
Ciplakli N3	4061	2346	29.98	5010	91.88	3.66
Ciplakli N4	4145	2235	30.57	4903	105.00	4.18
Ciplakli N5	4167	2339	30.09	5052	111.82	4.45
Ciplakli N6	4188	2367	30.92	5073	128.10	5.10
Ciplakli N7	4188	2260	28.76	5041	116.88	4.65
Ciplakli N8	4145	2260	28.59	5186	110.04	4.38
Katranli N1	4233	2279	29.08	5017	100.90	4.02
Katranli N2	4324	2286	29.68	4951	101.60	4.04
Katranli N3	4396	2424	32.74	5155	112.83	4.49
Katranli N4	4188	2319	30.23	4995	94.12	3.75
Katranli N5	4444	2388	32.12	5115	126.95	5.05
Katranli N6	4348	2192	27.71	5021	112.32	4.47
Kaynarli N1	4233	2367	31.74	4921	107.60	4.28
Kaynarli N2	4167	2286	27.76	5018	98.82	3.93
Kaynarli N3	4324	2326	31.06	4891	120.41	4.79
Kaynarli N4	4278	2319	31.6	5105	108.73	4.33
Kaynarli N5	4050	2360	30.17	4817	91.78	3.65
Kaynarli N6	4167	2305	29.93	5160	99.56	3.96
Kaynarli N7	4124	2305	29.13	4993	92.70	3.69
Kaynarli N8	4301	2292	28.84	4997	119.33	4.75
Kaynarli N9	4348	2410	32.33	5087	124.46	4.96
Kaynarli N10	4420	2410	32.02	5238	135.91	5.41
Kilit Tasi N1	4938	2564	37.07	4627	112.27	4.47
Kilit Tasi N2	5000	2649	38.86	4604	116.40	4.63
Kilit Tasi N3	4908	2564	35.46	4727	97.61	3.89
Kilit Tasi N4	4678	2402	31.73	4662	95.27	3.79
Kilit Tasi N5	4938	2589	37.07	4651	113.55	4.52
Kilit Tasi N6	4938	2564	35.91	4801	115.22	4.59
Kilit Tasi N7	5031	2564	35.98	4432	125.38	4.99
Kilit Tasi N8	5000	2623	36.67	4557	117.32	4.67
Kilit Tasi N9	5063	2589	34.96	4416	127.21	5.06
Kilit Tasi N10	5128	2623	36.02	4753	128.11	5.10
Kumbet N1	4878	2462	34.20	4758	95.80	3.81
Kumbet N2	4790	2454	33.18	4621	90.95	3.62
Kumbet N3	4908	2432	32.39	4692	111.01	4.42
Kumbet N4	4878	2524	34.61	4588	105.79	4.21
Kumbet N5	4938	2424	33.50	4654	114.66	4.56
Melikkoy N1	4734	2500	35.21	4788	104.27	4.15

Table 1. Continued

Melikkoy N2	4790	2360	31.59	4830	112.72	4.49
Melikkoy N3	4819	2395	31.67	4631	113.70	4.53
Melikkoy N4	4848	2388	32.67	4743	118.82	4.73
Melikkoy N5	4878	2410	33.34	4755	119.85	4.77
Senolkoy N1	5000	2462	34.46	4754	107.27	4.27
Senolkoy N2	5128	2462	33.92	4797	131.47	5.23
Senolkoy N3	5096	2548	34.76	4572	113.87	4.53
Senolkoy N4	4706	2260	29.83	4685	91.35	3.64
Senolkoy N5	5063	2508	35.19	4844	111.96	4.46
Senolkoy N6	4938	2462	34.65	4497	105.66	4.21
Senolkoy N7	4908	2572	35.40	4511	96.16	3.83
Senolkoy N8	5031	2446	33.28	4630	111.66	4.45
Senolkoy N9	5096	2516	35.30	4665	113.81	4.53
Senolkoy N10	4790	2439	31.34	4644	96.27	3.83

4.2. Correlation analysis

The statistical analysis demonstrated a robust positive association between UPV readings and the tensile strengthof concrete paving blocks. The Pearson correlation coefficient, computed via Microsoft Excel, was between 0.80 and 0.96, suggesting a positive association between elevated UPV levels and increased tensile strength. This indicates that UPV measurements can yield significant insights into the mechanical performance of concrete paving blocks.

Nonetheless, as demonstrated in Fig. 2, while the specimens from each village displayed a significant level of internal correlation, aggregating the results from all villages did not produce a coherent or consistent trend. This suggests that assessing all samples together may not constitute a reliable analytical method. Although all tested specimens conform to the pertinent standard standards, the observed diversity is probably due to discrepancies in manufacturing conditions among villages. This encompasses aspects such as varying manufacturers, curing techniques, water-to-cement ratios, aggregate gradation, and types of aggregates in the concrete mix design. These discrepancies highlight the necessity of localized analysis in interpreting mechanical performance and underscore the requirement for consistent production and quality control techniques across locations.

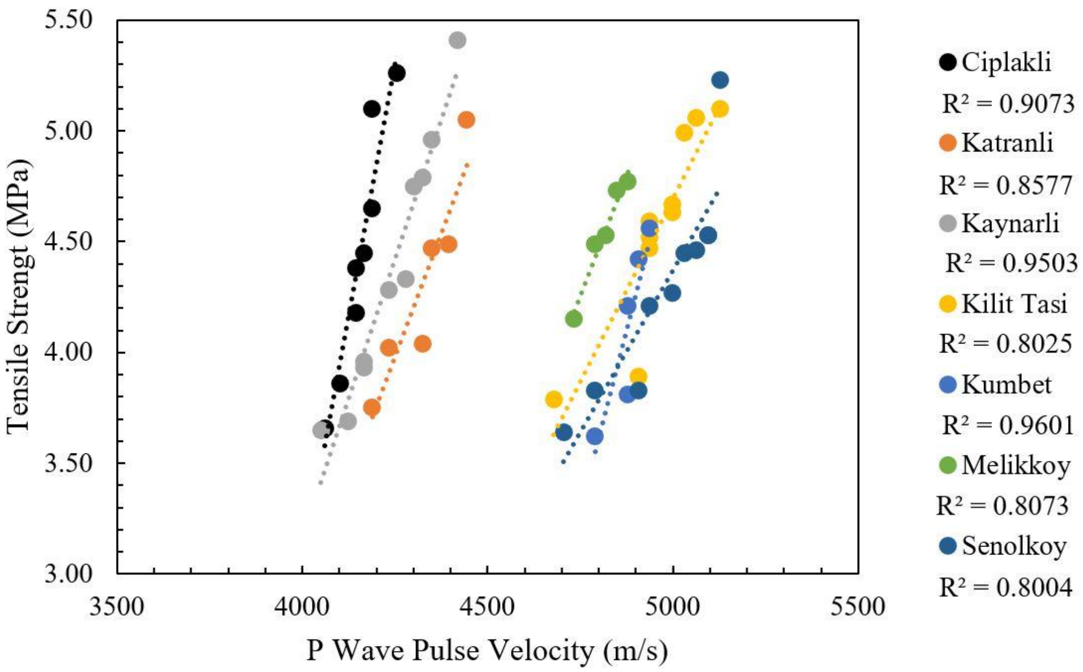

Fig. 2. Correlation Results

5. Conclusion

This study illustrates that Ultrasonic Pulse Velocity (UPV) testing is an excellent non-destructive method for assessing the tensile strength of concrete paving blocks. A strong positive correlation between UPV measurements and laboratory tensile strength values validates the viability of UPV as a practical and effective substitute for traditional destructive testing methods. This non-destructive method facilitates swift in situ evaluations, therefore reducing the time, labor, and material expenses often linked to quality control in rural road construction.

The results endorse the proposal that UPV testing methodologies should be standardized and integrated into regular quality control practices, especially in projects requiring extensive sampling and swift decision-making. Simultaneously, it is imperative that laboratory tensile strength evaluations comply with TS 2824 EN 1338:2005 standards to guarantee uniform benchmarking and result comparability.

Notwithstanding the encouraging results, the study possesses inherent limitations. The constrained sample size—limited to 54 specimens from seven villages—may impede the generalizability of the findings. Subsequent research should focus on augmenting the dataset to enhance statistical rigor and investigate regional disparities in material composition and craftsmanship. Moreover, environmental variables including surface wetness, ambient temperature, and the quality of contact between transducers and specimen surfaces might affect UPV measurements. These characteristics must be methodically examined to improve the reliability of field applications.

A significant avenue for future research entails the amalgamation of Ultrasonic Pulse Velocity (UPV) with alternative non-destructive testing (NDT) techniques, like rebound hammer tests, impact-echo, or ground-penetrating radar, to yield more thorough assessments of concrete quality. Multimodal NDT methodologies may address the shortcomings of singular techniques and offer a more comprehensive insight into internal flaws, material consistency, and long-term efficacy.

In conclusion, incorporating UPV testing as an adjunct method for assessing concrete paving blocks offers significant potential for enhancing construction processes, increasing the precision and efficacy of quality assurance measures, and fostering more sustainable practices by minimizing the necessity for destructive sampling and testing. With more validation and methodological enhancement, UPV could emerge as a crucial element of contemporary, field-ready infrastructure evaluation methodologies.

References

Aggelis, D. G. (2013). Wave propagation through engineering materials; assessment and monitoring of structures through non-destructive techniques. *Materials and Structures*, *46*(4), 519–532.

Al-Zuhairi, A. A. H. A. (2013). Estimation Of Tensile strengthOf Plain Concrete From Ultrasonic Pulse Velocity. *University of Baghdad Engineering Journal*.

Cho, Y. S., Han, S. W., Jang, H. S., Baek, S. K., & Hong, S. U. (2012). Estimating Crack Depth of Concrete Structures Using Ultrasonic Pulse Velocity. *Advanced Materials Research*, *496*, 546–549.

Frequency-dependent Reliability of Ultrasonic Testing Based on Numerical Model with Consideration of Coarse Aggregates in Concrete. (2023). *Case Studies in Construction Materials*.

Hong, R. (2012). *Damage detection in fiber reinforced concrete with ultrasonic pulse velocity testing*. Retrieved from https://drum.lib.umd.edu/handle/1903/13548

Popovics, J. S. (2005). Ultrasonic testing of concrete structures. *Materials Evaluation*, *63*(1), 50–55. Retrieved from https://experts.illinois.edu/en/publications/ultrasonic-testing-of-concrete-structures

Rodríguez, C., Miñano, I., Aguilar, M. Á., Ortega, J. M., Parra, C., & Sánchez, I. (2017). Properties of concrete paving blocks and hollow tiles with recycled aggregate from construction and demolition wastes. *Materials*, *10*(12), 1374.

Sharp, S. R., & Ozyildirim, C. (2014). *Nondestructive Measurements Using Mechanical Waves in Reinforced Concrete Structures*. Retrieved from https://rosap.ntl.bts.gov/view/dot/27469

Singh, S., Singh, S. K., Mahgoub, M., Mir, S. A., Kanga, S., Kumar, S., ... & Meraj, G. (2024). Evaluating Recycled Concrete Aggregate and Sand for Sustainable Construction Performance and Environmental Benefits. *CivilEng*, *5*(2), 461-481.

Singh, T., Singh, B., Bansal, S., & Saggu, K. (2022). Prediction of Ultrasonic pulse velocity of concrete. In *Applications of computational intelligence in concrete technology* (pp. 235-251). CRC Press.

Tang, C.-W., Lin, Y., & Kuo, S.-F. (2007). Investigation on correlation between pulse velocity and compressive strength of concrete using ANNs. *Computers and Concrete*, *4*(6), 477–497.

Toutounchi, S., Dabiri, R., & Dilmaghani, S. (2021). Experimental Studies in Ultrasonic Pulse Velocity of Roller Compacted Concrete Containing Ground Granulated Blast Furnace Slag in Cold Region. *International Journal of Civil Engineering*, *19*(12), 1–16.

4th International Civil Engineering & Architecture Conference
17-19 May 2025, Trabzon, Türkiye

Reinforcement of unreinforced masonry buildings with carbon emission reduced cement

Pınar Usta Evci[1], Bilge Arslan[*2]

[1] Isparta University of Applied Sciences, Department of Civil Engineering,32260 Isparta, Türkiye
[2] Sinop University, Department of Architecture and Urban Planning, 57200 Sinop, Türkiye

Abstract. Buildings made of masonry pose serious safety issues due to their insufficient load-bearing capacity, especially in areas with high earthquake risk. The traditional methods of reinforcement often have a high carbon footprint and contradict with sustainability goals. This study investigates the use of carbon emission-reduced cement for sustainable strengthening of unreinforced masonry buildings, aiming to both increase structural safety and reduce environmental impacts. Geopolymer cement, cements enhanced with industrial by-products such as Calcined Clay and Limestone Cement (LC3) and fly ash and slag provide significantly lower carbon emissions compared to conventional Portland cement. These innovative Cements can be applied in reinforcement techniques such as grouting mortar, cementitious coatings, textile reinforced mortars (TRM) and sustainable grouting, effectively improving the structural integrity and earthquake performance of masonry walls. The study highlights the environmental benefits of these methods, such as reducing CO_2 emissions, utilizing industrial solid waste and ensuring the long-lasting durability of reinforced structures. These results reveal that reinforcement methods with carbon-reduced cement contribute to sustainable construction practices while improving the earthquake performance of the masonry buildings. This study aims to fill an important gap in terms of both building safety and environmental sustainability and provides direction for future studies in the related field.

Keywords: Reinforced masonry building, Carbon emission reduced cement, Earthquake performance, Geopolymer cement, Environmental sustainability

1. Introduction

Masonry structures, as a product of architectural traditions extending from the past to the present, have been widely constructed for centuries, particularly in regions such as the Mediterranean basin, the Middle East, and Southern Europe. These systems still constitute a significant portion of the current building stock. The historical continuity of this building typology has been made possible by the ease of material procurement in both rural and urban areas, low-cost construction processes, and the reliance on local labor. However, since the load-bearing system of such structures depends solely on wall elements working in compression, they exhibit brittle behavior under lateral loads such as earthquakes and often lack structural integrity (Lagomarsino & Cattari, 2015; Milani et al., 2021). In countries like Turkey, which are located in high seismic risk zones, the prevalence of these structural systems poses serious engineering challenges in terms of life and property safety, necessitating the performance-based retrofitting of the existing building stock.

Conventional techniques for retrofitting unreinforced masonry structures include interventions such as external cement-based plastering, steel confinement systems, reinforced concrete frames, and pressure grouting (Triantafillou, 2001; Benedetti & Petrini, 2004). Although these methods can provide short-term gains in stiffness and ductility, they typically involve high energy consumption and carbon emissions due to the materials and processes used, making them incompatible with principles of sustainability. Particularly, Portland cement-based retrofitting applications contribute significantly to global CO_2 emissions—approximately 7–8%—not only due to chemical clinker transformations but also because of high-temperature manufacturing processes (Andrew, 2018; Scrivener et al., 2018). This indicates a dual challenge where structural enhancement is accompanied by considerable environmental burden.

Recent advancements in materials science and sustainable construction technologies have enabled the development of more eco-friendly and performance-oriented alternatives for the strengthening of masonry structures. Low-carbon and highly reactive alternative binders such as geopolymer binders, limestone calcined clay cements (LC3), fly ash, ground granulated blast furnace slag (GGBFS), metakaolin, and natural pozzolans not only improve mechanical strength but also significantly reduce carbon emissions during production, thereby

* Corresponding author, E-mail: barslan@sinop.edu.tr

https://doi.org/10.31462/icearc2025_ce_mat_640

contributing to sustainable construction practices (Gartner & Sui, 2018; Provis, 2022). For instance, LC3 systems can be manufactured at lower temperatures compared to Portland cement and offer a 30–50% reduction in CO_2 emissions due to a reduced clinker content (Gluth et al., 2020). Similarly, geopolymer binders—activated by fly ash and alkaline solutions—can decrease environmental impacts by up to 60%, aligning structural engineering practices with environmental responsibility.

Moreover, the formulation of these alternative binders using industrial by-products and waste materials reflects strong compatibility with circular economy principles and sustainable development goals, offering multi-dimensional benefits in terms of waste management and resource efficiency. The use of locally available additives can also reduce implementation costs in low-income and rural areas, increasing the applicability and scalability of these systems. In this context, low-carbon binder systems hold not only engineering relevance but also strategic importance for sustainable urban planning, climate policy, and disaster risk management.

Particularly in advanced retrofitting methods such as Textile Reinforced Mortar (TRM) systems, geopolymer-based binders demonstrate high adhesion, crack control, and rheological stability, significantly enhancing the performance of such applications and marking a qualitative transformation in the paradigm of masonry strengthening (Micelli et al., 2020; Asteris et al., 2023). However, engineering-oriented studies that comprehensively examine the integration of alternative binders with masonry strengthening systems remain limited.

Accordingly, the present study aims to explore the integration of low-carbon binder systems into the retrofitting of unreinforced masonry structures, with the dual objective of enhancing structural performance and reducing environmental impact. The findings obtained through laboratory evaluation of geopolymer cements, LC3, and fly ash-blended binder systems offer a novel contribution toward the sustainable strengthening of existing building stock and address a significant gap in the literature.

2. Materials and methods

2.1. Materials used

In this experimental study, a new type of blended cement mortar with reduced carbon dioxide emissions was developed using pozzolanic additives such as fly ash, microsilica, metakaolin, and hydrated lime. The components used include Class F fly ash, microsilica with a particle size ranging between 0.1–0.2 µm, and CEM IV 42.5 cement.

As shown in Table 1, the mixture composition consists of 40% CEM IV-B 42.5 cement, 20% metakaolin, 20% hydrated lime, 10% microsilica, and 10% Class F fly ash. These components were selected with the dual objective of achieving high mechanical strength and a reduced carbon footprint. The mortar consistency was adjusted to a water-to-binder ratio of 0.30, and cubic specimens with dimensions of 40 × 40 × 40 mm^3 were prepared. After 24 hours, the specimens were demolded and transferred to a curing tank. Uniaxial compressive strength tests were then conducted on days 2, 7, and 28.

2.2. Materials used

Uniaxial compressive strength tests were conducted on the specimens at 2, 7, and 28 days, and the resulting data were evaluated in accordance with the TS EN 196-1 standard. Additionally, physical properties such as initial setting time and water demand were determined and compared against the threshold values specified in the EN 197-1 standard.

The initial setting time was measured between 180 and 220 minutes, which is significantly above the minimum requirement of 75 minutes set by EN 197-1. As shown in Table 2, the 2-day compressive strength of the specimens was recorded as 14.5 MPa, while the 28-day strength reached 33 MPa. These results demonstrate equivalent or even superior performance when compared to standard CEM IV-B 32.5N class cements under EN 197-1 specifications.

The incorporation of alternative components contributed to a notable environmental advantage, achieving an average reduction of approximately 40% in carbon emissions during the production phase, compared to conventional Portland cement.

Table 1. Mix proportions (%)

Microsilica	Fly Ash (Class F)	Metakaolin	Hydrated Lime	CEM IV 42.5
10%	10%	20%	20%	40%

Table 2. Physical properties of the novel blended cement

Property	CEM IV-B 32.5N Reference	Measured Value	Standard limiti	
			Min.	Max.
Initial Setting Time	180-220	115	75	-
Water Demand (%)	%31-33	%20-30	-	-
2-day Compressive Strength (MPa)	9,5 -10 MPa	14,5 MPa	10,0	-
2-day Compressive Strength (MPa)	-	22 MPa		
2-day Compressive Strength (MPa)	32,5-38 MPa	33 MPa	32,5	52,5

3. Evaluation of findings

The experimental findings demonstrate that the low-carbon binder system exhibits high suitability for the strengthening of unreinforced masonry structures in terms of both structural performance and environmental sustainability. The inclusion of highly pozzolanic components such as metakaolin and microsilica enriched the hydration products of the binder matrix, resulting in a more compact structure that limits crack propagation and enhances microstructural integrity. This, in turn, significantly improved the ductility capacity and energy dissipation ability of the masonry walls.

Furthermore, the integration of chemically active and fine-grained materials such as fly ash and hydrated lime into the binder composition promoted high adhesion at the mortar-to-masonry interface. This led to notable improvements in shear strength, which is of critical importance for limiting shear cracks under lateral loading.

The binder's initial setting time of approximately 180 minutes provides operators with sufficient working time for large-scale applications, thereby helping to minimize workmanship errors. This characteristic is particularly valuable in rural areas or low-tech application environments, where extended workability directly contributes to the success of material implementation.

Another key advantage of the developed binder system is its high level of compatibility with existing retrofitting techniques. The system demonstrates rheological and chemical properties suitable for external plaster applications, injection grouts, cement-based overlays, and especially textile-reinforced mortar (TRM) systems. In TRM applications, the binder's strong adhesion and microstructure, which effectively limits crack propagation, enhance both the durability and efficiency of the overall strengthening system (Micelli et al., 2020; Asteris et al., 2023). In injection-type applications, the binder maintains low viscosity and high penetration capacity, allowing it to infiltrate micro-voids and offering intrinsic crack-healing potential.

From an environmental sustainability perspective, the binder system also offers significant advantages. According to existing literature, LC3 and geopolymer-based binders can reduce carbon emissions by 30% to 80% compared to traditional Portland cement (Gartner & Sui, 2018; Scrivener et al., 2018; Gluth et al., 2020). The use of industrial by-products such as microsilica and fly ash in the formulation of the developed system contributes to waste recovery and aligns with the principles of the circular economy. Moreover, the local availability of these components enhances the feasibility of sustainable retrofitting in low-income regions and increases the system's scalability.

4. Conclusions

This study was conducted to evaluate the structural and environmental performance of a low-carbon cement-based binder system designed for the strengthening of unreinforced masonry structures. The binder system, developed with the objective of reducing the environmental burden of conventional Portland cement and promoting sustainable construction materials, consisted of 40% CEM IV-B cement, 20% metakaolin, 20% hydrated lime, 10% microsilica, and 10% fly ash.

The experimental findings revealed that this system not only achieved high mechanical performance in compliance with EN 197-1 and TS EN 196-1 standards, but also significantly enhanced critical performance parameters such as stiffness, ductility, and shear strength in unreinforced masonry structures. The binder's high pozzolanic reactivity contributed to microstructural densification, effectively limiting crack propagation and providing a material behavior characterized by strong surface adhesion and controlled setting time.

These properties enabled high compatibility with widely used retrofitting techniques such as external plastering, injection grouting, and Textile Reinforced Mortar (TRM) systems, thereby improving its applicability in real-world construction scenarios. Moreover, due to the use of industrial by-products and naturally available additives in the formulation, the binder system achieved an approximate 40% reduction in carbon emissions compared to conventional Portland cement, offering a solution fully aligned with sustainable development goals.

The results clearly demonstrate that the developed binder system is a viable, scalable, and environmentally responsible alternative for the sustainable strengthening of existing building stock, especially in low-income and high seismic risk regions. In this regard, the study offers an interdisciplinary contribution by simultaneously addressing the concepts of structural safety and environmental sustainability.

References

Andrew, R. M. (2018). Global CO_2 emissions from cement production, 1928–2017. *Earth System Science Data, 10*(1), 195–217. https://doi.org/10.5194/essd-10-195-2018

Asteris, P. G., Cavaleri, L., & Micelli, F. (2023). Sustainability aspects of textile-reinforced mortar systems for seismic retrofitting of masonry structures. *Sustainability, 15*(3), 1225. https://doi.org/10.3390/su15031225

Benedetti, D., & Petrini, V. (2004). Evaluation of seismic resistance of existing masonry buildings. *Journal of Earthquake Engineering, 8*(3), 379–403. https://doi.org/10.1142/S1363246904001390

Gartner, E., & Sui, T. (2018). Alternative cement clinkers. *Cement and Concrete Research, 114*, 27–39. https://doi.org/10.1016/j.cemconres.2017.02.002

Gluth, G. J. G., Bernal, S. A., & Provis, J. L. (2020). Engineering properties and sustainability of alkali-activated materials. *Journal of Sustainable Cement-Based Materials, 9*(2), 90–114. https://doi.org/10.1080/21650373.2020.1759876

Habert, G., D'Espinose de Lacaillerie, J. B., & Roussel, N. (2020). An environmental evaluation of geopolymer based concrete production: Reviewing current practices. *Journal of Cleaner Production, 257*, 120563. https://doi.org/10.1016/j.jclepro.2020.120563

Lagomarsino, S., & Cattari, S. (2015). Fragility functions and seismic vulnerability assessment of masonry buildings. *Bulletin of Earthquake Engineering, 13*(5), 1403–1426. https://doi.org/10.1007/s10518-014-9674-1

Micelli, F., Aiello, M. A., & Asteris, P. G. (2020). Mechanical behavior of textile reinforced mortars for strengthening historic masonry. *Applied Sciences, 10*(17), 5943. https://doi.org/10.3390/app10175943

Milani, G., Lourenço, P. B., & Tralli, A. (2021). State-of-the-art review on modeling techniques for seismic assessment of unreinforced masonry structures. *Engineering Structures, 239*, 112280. https://doi.org/10.1016/j.engstruct.2021.112280

Provis, J. L. (2022). Alkali-activated materials: Past, present, and future. *Cement and Concrete Research, 156*, 106787. https://doi.org/10.1016/j.cemconres.2022.106787

Scrivener, K. L., John, V. M., & Gartner, E. M. (2018). Eco-efficient cements: Potential, economically viable solutions for a low-CO_2 cement-based materials industry. *Cement and Concrete Research, 114*, 2–26. https://doi.org/10.1016/j.cemconres.2018.03.015

Triantafillou, T. C. (2001). Strengthening of masonry structures using epoxy-bonded FRPs. *Journal of Composites for Construction, 5*(2), 96–104. https://doi.org/10.1061/(ASCE)1090-0268(2001)5:2(96)

4th International Civil Engineering & Architecture Conference
17-19 May 2025, Trabzon, Türkiye

Investigation of P-M interaction for rRC columns confined with CFRP sheets under uniaxial bending

Ali J. Noorzad*[1], Hakan Dilmaç[2]

[1]Suleyman Demirel University, Graduate School of Natural and Applied Sciences, Çünür, 32260 Isparta, Türkiye
[2]Suleyman Demirel University, Faculty of Engineering and Natural Sciences, Çünür, 32260 Isparta, Türkiye

Abstract. The retrofitting of reinforced concrete (RC) columns with carbon fiber-reinforced polymer (CFRP) sheets is recognized as a highly efficient technique for substantially enhancing structural performance, particularly with respect to axial load strength and flexural capacity. Although extensive research has been conducted on CFRP-confined columns, a significant gap persists in the detailed understanding of the axial-flexural (P–M) interaction behavior of rectangular RC (rRC) columns subjected to eccentric loading. This study presents a rigorous analytical investigation of CFRP-strengthened rRC columns, focusing on the development of P–M interaction diagrams based on three prominent stress–strain models: Lam and Teng, Rami and Paultre, and Wei and Wu. A sectional analysis framework was employed, incorporating variations in material properties, eccentricity levels, corner radii, CFRP volumetric ratios, and aspect ratios. The parametric analysis revealed that CFRP confinement significantly enhances both axial and flexural capacities, particularly at lower eccentricities, although its effectiveness diminishes with increasing eccentricity. Columns with larger corner radii and lower-grade concrete exhibited superior confinement performance due to improved stress distribution and increased deformability. Furthermore, increasing the number of CFRP layers substantially elevated the axial strength and resulted in moderate improvements in flexural resistance. Experimental validation confirmed the reliability of the analytical models, highlighting their high predictive accuracy and affirming their ability to reliably forecast outcomes in similar situations. CFRP confinement proves to be a highly effective technique for enhancing the structural resilience of rectangular RC columns; however, its efficacy is profoundly influenced by cross-sectional geometry, material properties, and loading conditions.

Keywords: CFRP confinement; P-M interaction diagram; Rectangular RC columns; Eccentric loading; Axial-flexural behavior

1. Introduction

The utilization of CFRP composites for retrofitting RC columns has become a popular technique to enhance both strength and deformability (Abid et al., 2021; H. S. Al-Nimry & Al-Rabadi, 2019; Fan et al., 2023). CFRP wraps, typically applied transversely to confined RC columns, provide lateral confinement, preventing outward expansion of the concrete core and increasing load-bearing capacity and ductility (Ahmed et al., 2021; Cao et al., 2018). The widespread use of FRP in structural industry is due to its mechanical properties, including high tensile strength, corrosion resistance, and ease of installation (Koksal et al., 2009; Liao et al., 2023). Most studies have focused on RC columns under axial compression (Harajli, 2006; Harajli & Hantouche, 2006), with fewer addressing columns subjected to combined axial and flexural loads (Abid et al., 2021). Eccentrically loaded FRP-confined columns are of particular interest, as many structural columns face both axial compression and bending moments.

Although much research has been conducted on the compressive stress-strain behavior of FRP-confined rectangular RC columns, existing models are often designed for circular columns (Eid et al., 2017; Harajli, 2006). Some analytical models for rectangular columns under axial load have been proposed, but the influence of factors like loading eccentricity and column shape remains significant (Ahmed et al., 2021). Most research has focused on circular sections, but rectangular columns, commonly used in practice, are also subject to eccentric loads. Therefore, more research is needed on the mechanical behavior of rectangular RC columns retrofitted with FRP wraps.

While FRP wraps provide sufficient confinement for circular columns, the enhancement in strength and ductility for rectangular cross-sections is less pronounced due to the non-uniform lateral confining pressure (Abdallah et al., 2018; Harajli, 2006). For rectangular columns, sharp corners concentrate lateral pressure, leading

*Corresponding author, E-mail: alijumanoorzad@gmail.com

https://doi.org/10.31462/icearc2025_ce_mat_643

to early failure of FRP jackets at low deformation (Noorzad & Dilmaç, 2025). This has led to further investigation into techniques for improving fiber efficiency in retrofitted rectangular RC columns. Studies have also explored the behavior of eccentric RC columns confined with FRP jackets, focusing on the (P-M) interaction curve (Mai et al., 2020). These studies emphasize the role of material properties, loading eccentricities, and column dimensions in determining the effectiveness of FRP confinement.This study analytically evaluates the (P-M) interaction curves of FRP-confined rectangular RC columns under eccentric loads, evaluating factors like material properties, confinement ratio, and load eccentricities to better understand the advantages of FRP fibers in enhancing axial and flexural load strength.

2. Materials and methods

2.1. Material properties

A comprehensive understanding of the materials' mechanical properties in FRP-RC columns is essential for evaluating their structural performance. Concrete, the core material, has high compressive strength but low tensile strength, making its tensile resistance always neglected in structural design (Rasheed, 2014). Under axial compression, concrete exhibits nonlinear elastic-plastic behavior followed by brittle failure, highlighting the importance of knowing its properties for assessing confinement efficiency. In this study, various grades of unconfined normal-strength concrete were used, with three shown in the compressive stress-strain curves in Fig. 1a. Steel reinforcement bars, which provide tensile resistance, behave elastic-plastic behavior and high ductility under tensile loading. Steel with a yield strength of f_y=420MPa was used, with its stress-strain characteristics shown in Fig. 1b. CFRP composites, recognized for their high tensile strength and corrosion resistance, are commonly used in retrofitting RC columns. CFRP has a linear-elastic behavior and brittle failure mode, with a modulus of elasticity of E_f=250GPa and an ultimate tensile strain of 1.5%, as shown in Fig. 1b.

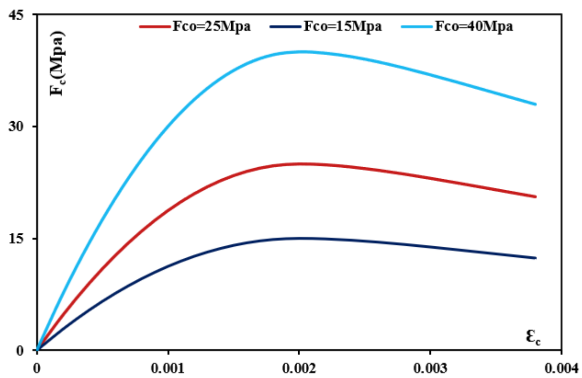

(a)

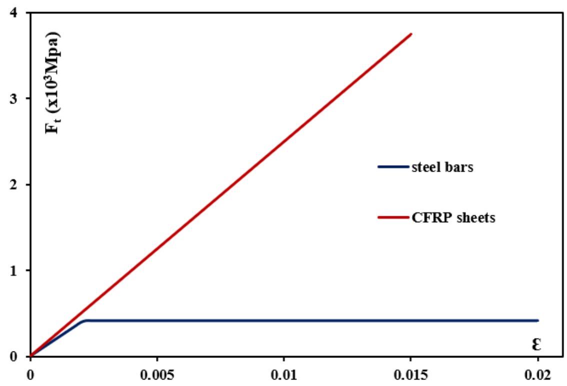

(b)

Fig. 1. (a) Compressive stress-strain curves of concrete, (b) Tensile stress-strain curves of steel bars and CFRP.

2.2. Methodology

This study evaluates the axial-flexural behavior of rectangular RC columns confined with CFRP sheets under eccentric loading. Axial load–flexural moment (P–M) interaction diagrams were developed by integrating internal stresses across the column's cross-section. The compressive behavior of confined concrete was modeled using three established stress–strain models: Lam and Teng (Lam & Teng, 2003), Rami and Paultre (2017), and Wei and Wu (Wu & Wei, 2016), which accurately predict the response of both circular and rectangular columns. An Excel-based tool was used for iterative calculations, ensuring equilibrium and strain compatibility. Fifteen rectangular specimens with varying geometries and material properties were analyzed under eccentric loading to determine axial-flexural capacities. The methods used for calculating axial load and bending moment strength included both the equivalent rectangular stress block approach and full stress–strain integration. The influence of load eccentricity (e/h) on confinement efficiency and stress distribution was also considered. The results, shown through normalized P–M interaction curves, demonstrated improvements in load capacity and ductility from CFRP confinement. The study also assessed various confinement parameters, providing insights for retrofitting non-circular RC columns.

3. Stress-strain models for confinement

Three FRP-confined concrete stress–strain models were used to determine the (P–M) interaction diagrams of eccentrically loaded RC columns strengthened with FRP composites. These models include Lam and Teng (Lam & Teng, 2003), Rami and Paultre (Eid & Paultre, 2017), and Wei and Wu (Wu & Wei, 2016), with corresponding equations shown in Table 2. Additionally, ACI 440.2R(ACI, 2008) was evaluated to determine column strength under eccentric load and generate the interaction curves.

Table 1. Details of FRP-confined RC columns.

Specimen no	bxh(mm)	F_{co} (Mpa)	E_c Mpa	r_c/h	Longitudinal bars		Transverse steel		CFRP			
					F_y(Mpa)	ρ_g(%)	F_{yt}(Mpa)	s(mm)	n_f	t_f(mm)	ρ_f(%)	E_f(Gpa)
1	300x300	25	23500	0.133	550	2.21	420	280	4	0.16	0.81	214.08
2	150x200	20	21019	0.075	420	1.05	420	420	0	0	0	250
3	150x200	20	21019	0.075	420	1.05	420	420	2	0.25	1.13	250
4	150x200	20	21019	0.075	420	1.05	420	420	3	0.25	1.7	250
5	300x400	20	21019	0.05	420	1.57	-	-	3	0.25	0.85	250
6	300x400	20	21019	0.1	420	1.58	-	-	3	0.25	0.84	250
7	300x400	20	21019	0.15	420	1.61	-	-	3	0.25	0.83	250
8	200x200	20	21019	0.1	420	3.04	420	200	3	0.25	1.45	250
9	200x300	20	21019	0.06	420	2.02	420	200	3	0.25	1.21	250
10	200x400	20	21019	0.075	420	1.52	420	200	3	0.25	1.08	250
11	350x500	15	18203	0.05	420	1.08	420	280	3	0.25	0.71	250
12	350x500	25	23500	0.05	420	1.08	420	280	3	0.25	0.71	250
13	350x500	40	29725	0.05	420	1.08	420	280	3	0.25	0.71	250
14	400x400	25	23500	0.075	420	0.75	-	-	3	0.25	0.73	250
15	300x600	30	25743	0.067	420	1.4	-	-	4	0.16	0.62	250

The Lam and Teng (Lam & Teng, 2003) model was mainly used due to its accuracy for FRP-confined rectangular RC columns, as adopted by ACI 440.2R(ACI, 2008). Rami and Paultre (Eid & Paultre, 2017) proposed a unified stress–strain model for FRP-confined RC columns with transverse steel reinforcement, applicable to both circular and rectangular sections. This model features two branches, with corresponding equations in Table 2 and Fig. 2a. Wei and Wu's model uses a two-branch curve, with a parabolic first segment and a straight line in the second, applicable to circular, rectangular, and square sections, with expressions provided in Table 2.

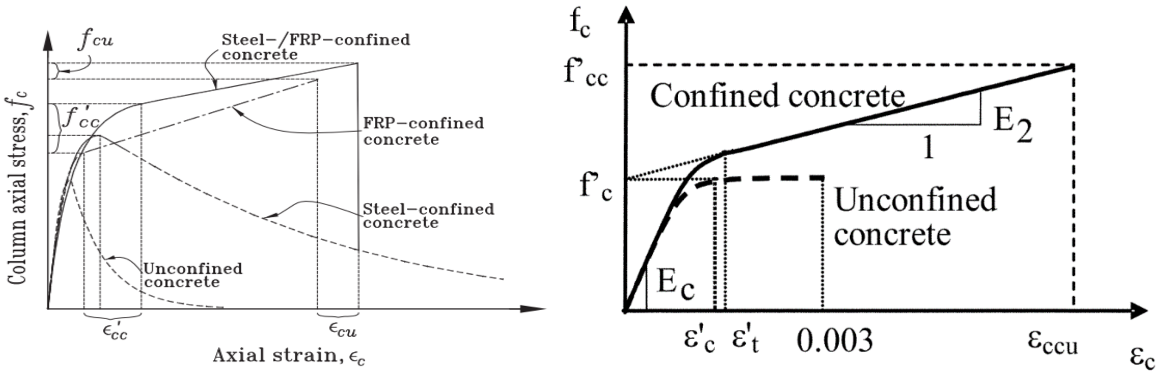

(a) (b)

Fig. 2. (a) Proposed stress–strain curves for TSR/FRP-confined concrete(Eid & Paultre, 2017), (b) Stress–strain curve for FRP-confined concrete(Lam & Teng, 2003).

3.1. Effect of eccentricity on the confinement of concrete

The influence of load eccentricities on the compressive behavior and stress-strain response of FRP-confined concrete in RC columns is a critical factor in evaluating the strength and ductility of these columns under eccentric loading conditions. Hayder Rasheed (Rasheed, 2014) proposed a relationship between the maximum confined compressive strength of concrete under pure axial load and that under eccentric loading. For eccentrically loaded rectangular RC columns, a factor known as the compression zone ratio (CR) is calculated; this factor depends on the column's dimensions and the magnitude of the load eccentricity and is illustrated in the following equation. Ultimately, the confined compressive strength of concrete in RC columns strengthened with FRP jackets is determined based on the following expression:

$$CR = \frac{0.2\frac{e}{\sqrt{bh}} + 0.1}{\frac{e}{\sqrt{bh}}} \tag{1}$$

$$f_{ce} = \frac{1}{1 + \frac{1}{CR - 0.2}} f_{cc} + \frac{1}{0.8 + CR} f_{co} \tag{2}$$

where f_{ce} is the confined compressive strength of concrete under eccentric loading at an eccentricity of e/h; f_{co} is the confined compressive strength of concrete under pure axial load; CR is the compression zone ratio; e is the magnitude of the load eccentricity; and b and h are the cross-sectional dimensions of the rectangular column.

Table 2. Stress-strain models used in this study.

Lam and Teng model (Lam & Teng, 2003)	Rami and Paultre model (Eid & Paultre, 2017)	Wei and Wu model (Wu & Wei, 2016)
$f_c = \begin{cases} E_c\varepsilon_c - \frac{(E_c-E_2)^2}{4f_c'}\varepsilon_c^2 \Rightarrow 0 \le \varepsilon_c \le \varepsilon_t \\ f_c' + E_2\varepsilon_c \Rightarrow \varepsilon_t < \varepsilon_c \le \varepsilon_{ccu} \end{cases}$ $E_2 = \frac{f_{cc}-f_{co}}{\varepsilon_{ccu}}$ $\varepsilon_t = \frac{2f_{co}}{E_c - E_2}$ $f_{cc} = f_{co} + 3.3 \times k_a \times f_l$ $f_l = \frac{2nt_f E_f \varepsilon_{fe}}{\sqrt{b^2+h^2}}$ $\varepsilon_{ccu} = \varepsilon_{co}\left(1.75 + 12k_b \frac{f_l}{f_c}\left(\frac{\varepsilon_{fe}}{\varepsilon_{co}}\right)^{0.45}\right) \le 0.01$ $\frac{A_e}{A_c} = \frac{1 - \left(\frac{\left(\frac{b}{h}\right)(h-2r_c)^2 + \left(\frac{h}{b}\right)(b-2r_c)^2}{3A_g}\right) - \rho_g}{1-\rho_g}$ $k_a = \frac{A_e}{A_c}\left(\frac{b}{h}\right)^2$ $k_b = \frac{A_e}{A_c}\left(\frac{h}{b}\right)^{0.5}$	$f_c = \begin{cases} \frac{a\varepsilon_c}{1+b\varepsilon_c+z\varepsilon_c^2} \rightarrow For\ \varepsilon_c \le \varepsilon_{cc} \\ f_{cc} \times e^{\left(k_1(\varepsilon_c-\varepsilon_{cc})^{k_2}\right)} + E_{cu}(\varepsilon_c - \varepsilon_{cc}) \rightarrow For\ \varepsilon_{cc} < \varepsilon_c \le \varepsilon_{cu} \end{cases}$ $f_{cc} = f_{co}\left(1 + 2.4 I_e^{0.7}\right)$ $\varepsilon_{cc} = \varepsilon_{co}\left(1 + 35 I_e^{1.2}\right)$ $I_e = \begin{cases} I_{e1} = \frac{\nu_{cc}}{k_1 - \eta} \le I_{e2} \rightarrow if\ k_1 > \eta\ (\mathrm{k}_2 \ge \eta) \\ I_{e2} = \frac{\nu_{cc} f_{co} + k_2 \rho_{se} f_{hy}}{f_{co}(k_2-\eta)} \le I_{e,\max} \rightarrow if\ k_1 \le \eta;\ \mathrm{k}_2 > \eta \\ I_{e,\max} = \frac{\rho_{se} f_{hy}}{f_{co}} + \frac{E_{fl}\varepsilon_{fu}\xi}{f_{co}} \le I_{e2} \rightarrow if\ k_1 \le \eta\ (\mathrm{k}_2 \le \eta) \end{cases}$ $f_{cu} = f_{co}\left[1 + 3.3\left(\frac{b}{h}\right)^2\left(\frac{\rho_{se} f_{hy}}{f_{co}} + \frac{E_{fl}\varepsilon_{fu}}{f_{co}} \times \xi\right)\right] \ge f_{cc}$ $\varepsilon_{cu} = \varepsilon_{co}\left[1.56 + 12\left(\frac{\rho_{se} f_{hy}}{f_{co} k_h^2} + \frac{E_{fl}\varepsilon_{fu}}{f_{co}} \times \xi\right)\left(\frac{\varepsilon_{fu,a}}{\varepsilon_{co}}\right)^{0.45}\right]$ $E_{cu} = \frac{f_{cu}-f_{cc}}{\varepsilon_{cu}-\varepsilon_{cc}} \le \frac{f_{cu}-f_{co}}{\varepsilon_{cu}} \ge 0$ $k_1 = \frac{f_{co}}{\rho_{se}E_s\varepsilon_{co} + E_{fl}\varepsilon_{co}} = \frac{E_c'}{E_{sl}+E_{fl}}$ $k_2 = \frac{f_{co}}{E_{fl}\varepsilon_{co}} = \frac{E_c'}{E_{fl}}$ $\eta = 29.8\nu_{cc} - 3.56$	$f_c = \begin{cases} E_c\varepsilon_c + \frac{f_o - E_c\varepsilon_o}{\varepsilon_o^2}\varepsilon_c^2 \rightarrow 0 \le \varepsilon_c \le \varepsilon_o \\ f_o + E_2(\varepsilon_c - \varepsilon_o) \rightarrow \varepsilon_o \le \varepsilon_c \le \varepsilon_{cu} \end{cases}$ $E_2 = \frac{f_{cu}-f_o}{\varepsilon_{cu}-\varepsilon_o}$ $f_o = f_{co} + 0.43\left(\frac{2r}{b}\right)^{0.68}\left(\frac{h}{b}\right)^{-1} f_l$ $\varepsilon_o = \frac{(f_o + f_{cu} + E_c\varepsilon_{cu}) - \sqrt{(f_o+f_{cu}+E_c\varepsilon_{cu})^2 - 8f_oE_c\varepsilon_{cu}}}{2E_c}$ $f_l = \frac{2f_{frp}t}{b} = \frac{2E_f\varepsilon_{fu}t}{b}$ $\frac{f_{cu}}{f_{co}} = 0.5 + 2.7\left(\frac{2r}{b}\right)^{0.4}\left(\frac{f_l}{f_{co}}\right)^{0.73}\left(\frac{h}{b}\right)^{-1}$ $\frac{\varepsilon_{cu}}{\varepsilon_{co}} = 1.7 + 12\left(\frac{f_l}{f_{co}}\right)^{0.75}\left(\frac{f_{30}}{f_{co}}\right)^{0.62}\left(\frac{0.72r}{b} + 0.64\right)^{-1}\left(\frac{h}{b}\right)^{-0.3}$

4. Nominal strength of FRP-confined RC column

4.1. Axially loaded RC columns

In practical applications, perfectly axially loaded columns rarely exist; however, analyzing such idealized members serves as a foundational approach to understanding the underlying principles in the design of real columns subjected to eccentric loading. At the point of failure, the theoretical or nominal axial load-bearing capacity of short RC columns strengthened with externally bonded FRP wraps under pure axial compression can be reliably estimated using the equation recommended by ACI 440.2R (ACI, 2008).

$$P_n = P_{nc} + P_{ns} = 0.85 f_{cc}(A_g - A_{st}) + f_y A_{st} \tag{3}$$

Where P_n represents the ultimate axial compressive load; f_{cc} denotes the maximum confined compressive strength of concrete, determined through analytical modeling; A_g is the gross cross-sectional area of the column, calculated as $A_g = b \times h - (4-\pi) r_c^2$ for rectangular cross sections ; f_y and A_s refer to the tensile yield strength and the total cross-sectional area of the longitudinal steel reinforcement, respectively; and r_c indicates the corner radius of the column cross-section.

4.2. Eccentrically loaded RC columns

All structural columns are exposed to both axial forces and bending moments, necessitating their design to effectively withstand the combined effects. Columns experience bending under flexural moments, resulting in compressive stress on one side and tensile stress on the opposite side. The distribution and intensity of these stresses depend on the interplay between the applied axial load and bending moment. An FRP-confined column is considered to reach its ultimate strength when the strain in the confined concrete reaches the ultimate confined strain, denoted as ε_{ccu}. When such columns are subjected to eccentric loading, their nominal axial capacities and flexural moments are evaluated using two analytical approaches: one involves integrating the stress-strain response of the compression zone, while the other utilizes an equivalent rectangular stress block method(Mai et al., 2024).

4.2.1. Rectangular stress-block approximation method

The simplified rectangular stress block method, originally proposed by Whitney(Mai et al., 2024) and later incorporated into ACI 318(ACI, 2011), employs an idealized stress distribution—depicted in Fig.3—to estimate the nominal axial load and bending moment. This technique assumes a uniform compressive stress of $0.85F_{cc}$ within the confined concrete, applied over an equivalent compression zone. This zone is delineated by the boundaries of the cross section and a line drawn parallel to the neutral axis, located at a depth a=βc from the most compressed concrete fiber where the peak confined strain ε_{ccu} is observed. The corresponding compressive force in the concrete, represented as P_{nc}, can be determined using the following formula:

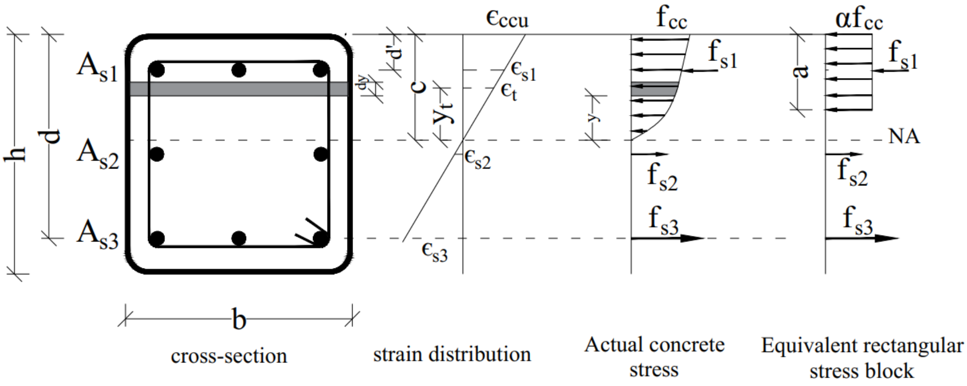

Fig.3. Stress and strain distribution at ultimate conditions.

$$P_n = P_{nc} + P_{ns} = \alpha f_{cc} ab + \sum_{i=1}^{n} f_{si} A_{si} \tag{4}$$

$$P_{nc} = 0.85 f_{cc} ab = \alpha f_{cc} \beta_1 cb \tag{5}$$

Where is c is the distance to the neutral axis from the extreme compression, a is depth of equivalent rectangular stress block, α and β_1 are the reduction factor of equivalent compressive stress block and deph, b is the width of cross section.

The strain in the longitudinal steel reinforcement is determined using the strain compatibility principle. Specifically, the strain in the i-th layer of reinforcement bars (ε_{si}) is derived through geometric similarity, based on similar triangles. Subsequently, the internal forces within the i-th layer of the primary reinforcement bars and ultimate nominal flexural moment are computed using the following expressions:

$$P_n \times e' = \mathrm{C} \times \left(d - \frac{a}{2} \right) + \sum_{i=1}^{n} p_{si} \times \left(d - d_i \right) \tag{6}$$

$$M_n = P_n \times e \tag{7}$$

4.2.2. Integration using stress–strain models

This method provides greater accuracy than the equivalent rectangular stress block approach, as it captures the distinct stress distribution behavior of FRP-confined concrete, which differs markedly from that of unconfined concrete. To determine the nominal axial compressive load and flexural moment capacity within the compression zone of a column cross-section, the analytical stress–strain relationship is integrated over the confined area(Rasheed, 2014). The proposed stress–strain model comprises two segments: an initial parabolic branch that shows the same slope as unconfined concrete, followed by a linear branch with a slope equal to E_2. Integration is carried out continuously across both segments. The detailed steps of this integration process for confined concrete are illustrated in Fig.4.

$$w = w_1 + w_2 = \int_0^{x_t} f_{c1} dx + \int_{x_t}^{c} f_{c2} dx \tag{8}$$

$$P_{nc} = w \times b = b \left[\int_0^{x_t} f_{c1} dx + \int_{x_t}^{c} f_{c2} dx \right] \tag{9}$$

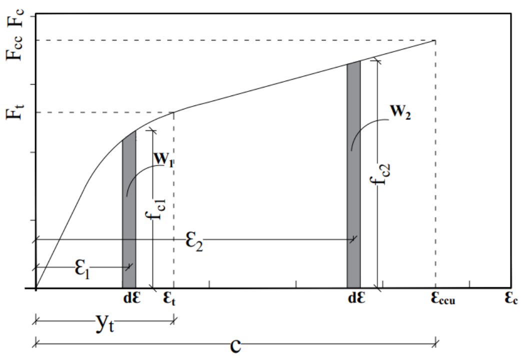

Fig. 4. Integration from the stress–strain curve of confined concrete.

Based on Lam and Teng model (Lam & Teng, 2003):

$$P_{nc} = b\left[\int_{0}^{x_t}\left(E_c\varepsilon_c - \frac{(E_c - E_2)^2}{4f_c^{'}}\varepsilon_c^2\right)dx + \int_{x_t}^{c}\left(f_{co} + E_2\varepsilon_c\right)dx\right] \tag{10}$$

Based on Rami and paultre (Eid & Paultre, 2017):

$$P_{nc} = b\left[\int_{0}^{x_t}\left(\frac{a\varepsilon_c}{1 + b\varepsilon_c + z\varepsilon_c^2}\right)dx + \int_{x_t}^{c}\left(f_{cc} \times e^{\left(k_1(\varepsilon_c - \varepsilon_{cc})^{k_2}\right)} + E_{cu}(\varepsilon_c - \varepsilon_{cc})\right)dx\right] \tag{11}$$

Here,P_{nc} denotes the nominal axial compressive strength of the confined concrete; f_{c1} and f_{c2} represent the compressive stress functions corresponding to the confined concrete in the parabolic and linear regions, respectively. The variables x_t and f_t indicate the coordinates of the transition point on the stress–strain curve, while w denotes the distributed compressive force within the concrete section.

4.2.3 (P–M) interaction diagrams

The interaction curve of an RC column evaluates the combined effects of axial load and bending moment in eccentrically loaded columns (H. S. Al-Nimry & Al-Rabadi, 2019). It shows the relationship between axial force and flexural moment at the ultimate limit state of the concrete section, helping assess the strength of confined RC columns under varying load combinations. The curve is developed under the assumptions that the tensile strength of concrete is neglected in flexural strength calculations and that cross-sections remain plane after bending. The nominal axial load (P_n) and flexural moment (M_n) are determined relative to the geometric centroidal axis. The P–M interaction diagram consists of three regions: pure axial compression, combined axial-flexural loading, and pure bending (Ahmed et al., 2021) and illustrated in fig.5.

The shape of the P–M interaction diagram for FRP-confined RC columns is influenced by factors such as cross-sectional geometry, confinement level, unconfined concrete strength, and the volumetric ratio of transverse steel reinforcement. The Lam and Teng stress–strain model (Lam & Teng, 2003) is adopted for its high accuracy in predicting the response of FRP-confined columns. The nominal axial load and flexural moment contributions of longitudinal steel reinforcement are determined based on the neutral axis and internal stress–strain distribution in the confined concrete. The interaction diagram is often normalized using dimensionless parameters, K_n (normalized nominal axial load) and R_n (normalized ultimate flexural moment), to facilitate comparisons across various configurations and material properties (ACI 318, 2011).

The P–M interaction diagram is defined by four critical points. Point A represents pure axial compression with no flexural moment. As the moment increases, the axial load capacity decreases. Point B shows the strain distribution where the longitudinal steel furthest from the compression face experiences zero strain. Point C indicates balanced failure, with the compression face at ultimate strain and the tension steel yielding. Point D represents pure bending with no axial force, where the compressive strain and tensile strain exceed the yield strain. The strain distribution used for the diagram is shown in Fig. 6.

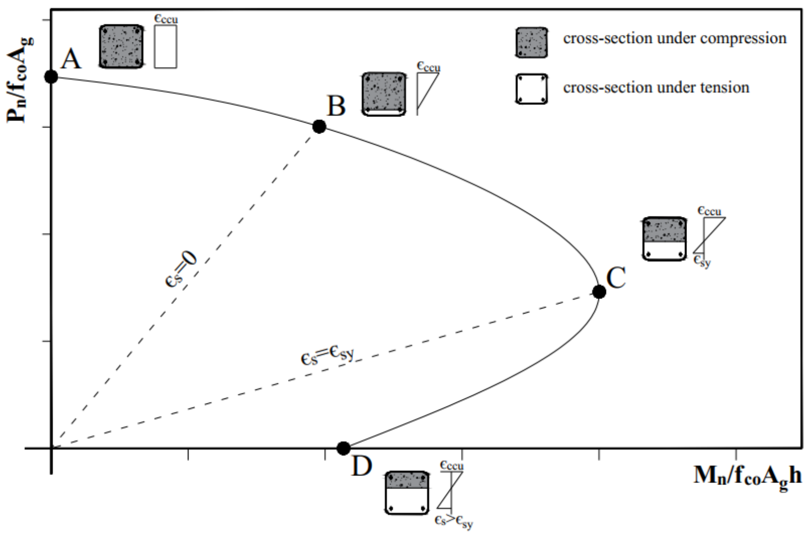

Fig.5. Simplified interaction diagram for rectangular RC column.

According to the Lam and Teng(Lam & Teng, 2003) model and the principles of static equilibrium, the values of the nominal axial load (P_n) and nominal moment (M_n) for a given FRP-confined column, subjected to a specified strain distribution, can be accurately determined using the following expressions(Rasheed, 2014):

$$P_{nA} = 0.85 f_{cc}\left(A_g - A_{st}\right) + f_y A_{st} \tag{12}$$

$$P_{n(\mathrm{B,C,D})} = P_{nc} + P_{ns} = \int_0^{y_t} (bf_{c1})dy + \int_{y_t}^{c} (bf_{c2})dy + \sum_{i=1}^{n} (\mathrm{f}_{si} - \mathrm{f}_c) A_{si} \tag{13}$$

$$M_{n(B,C,D)} = M_{nc} + M_{ns} = \int_0^{y_t} (bf_{c1})(\mathrm{y} + \frac{h}{2} - \mathrm{c})dy + \int_{y_t}^{c} (bf_{c2})(\mathrm{y} + \frac{h}{2} - \mathrm{c})dy + \sum_{i=1}^{n} (\mathrm{f}_{si} - \mathrm{f}_c) A_{si} \tag{14}$$

4.2.4. ACI 440.2R-08 proposed P–M interaction diagram

The ACI 440.2R-08(ACI, 2008) guidelines present simplified equations for estimating the axial compressive capacity and corresponding flexural moment strength of FRP-confined RC columns. These formulations are derived from the confinement model developed by Lam and Teng(Lam & Teng, 2003). The axial load capacity (P_n) and the corresponding bending moment (M_n) at three critical performance points are calculated using the following expressions:

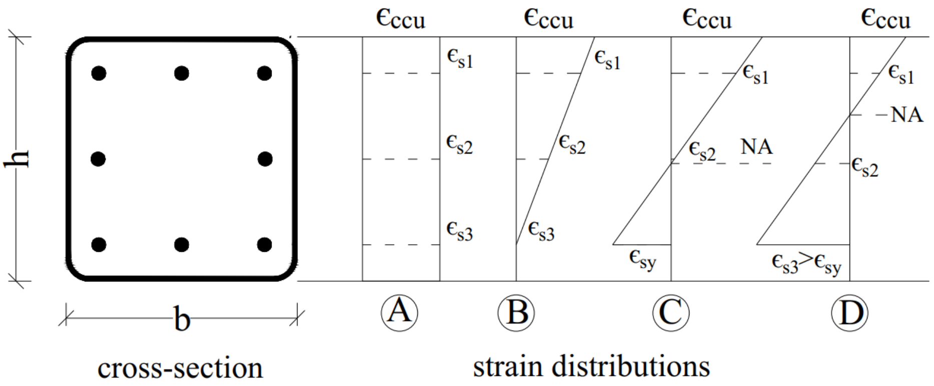

Fig.6. Strain distributions for developing of interaction diagram.

$$P_{nA} = 0.85 f_{cc}\left(A_g - A_{st}\right) + f_y A_{st} \tag{15}$$

$$P_{n(\mathrm{B,C})} = \left[A(y_t)^3 + B(y_t)^2 + C(y_t) + D\right] + \sum f_{si} A_{si} \tag{16}$$

$$M_{n(\mathrm{B,C})} = \left[E(y_t)^4 + F(y_t)^3 + G(y_t)^2 + H(y_t) + I\right] + \sum f_{si} A_{si} d_{si} \tag{17}$$

In this approach, the maximum confined compressive strength of concrete (f_{cc}) is determined using the Lam and Teng (Lam & Teng, 2003) confinement model. The parameters fy and Ast represent the yield strength in tension and the cross-sectional area of the longitudinal steel reinforcement. The variable yt refers to the vertical distance from the neutral axis to the transition strain εt. Additionally, f_{si} and A_{si} denote the normal stress and cross-sectional area of the i-th layer of longitudinal reinforcement, while dsi represents the distance from the centroid to the i-th reinforcement layer. The coefficients A through I, used in the equations from ACI 440.2R (ACI, 2008), are calculated, but their specific formulations are not provided here.

5. Results of parametric study

5.1. Compressive stress-strain curves

Fig. 7a shows the axial compressive stress-strain response of a rectangular RC column confined with FRP wraps, compared to an unconfined column. The curves, based on Lam & Teng (Lam & Teng, 2003) and Rami & Paultre (Eid & Paultre, 2017) models, show significant improvements in both compressive strength and strain capacity due to FRP confinement. Unconfined concrete has lower peak stress and a more brittle failure mode. The Lam & Teng model predicts a moderate strength increase and enhanced ductility, while the Rami & Paultre model (Eid & Paultre, 2017) forecasts a greater rise in peak compressive stress and a more gradual plateau. Both models emphasize FRP wraps' ability to delay concrete failure and improve deformability.

Fig. 7b illustrates the behavior of FRP-confined columns with different aspect ratios (b/h = 1, 1.75, 2), showing that aspect ratio significantly impacts confinement efficacy. The square column (b/h = 1) shows the greatest enhancement, while the improvement decreases as the aspect ratio increases (b/h = 1.75 and 2). This suggests that

FRP wraps are more effective in compact sections, with slender columns experiencing less uniform confinement pressure, reducing the overall improvement in compressive performance.

5.2. Effect of eccentricity on confinement efficiency

The relationship between Compression Zone Ratio (CR) and load eccentricity (e) for eccentrically loaded FRP-confined RC columns is shown in Fig. 8a. The vertical axis represents CR, indicating the effective compression zone size, while the horizontal axis measures eccentricity (e) in millimeters from the column's centroid. Three curves are presented for aspect ratios (b/h) of 1.0, 0.75, and 0.5. The results show a remarkable decrease in CR with increasing eccentricity, particularly at lower eccentricities, with a gradual reduction at higher values. The square column (b/h = 1) consistently has the highest CR, followed by b/h = 0.75 and 0.5. This indicates that as columns become more elongated, CR decreases faster. The graph emphasizes the influence of load eccentricity and aspect ratio on stress distribution in FRP-confined columns.

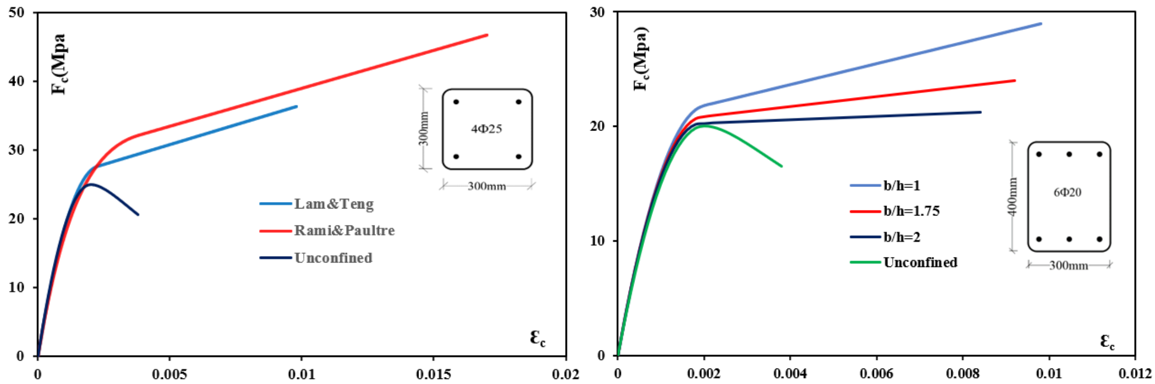

(a) (b)

Fig.7. Stress–strain curves of concrete: (a) comparison of models, (b) based on aspect ratios.

Fig. 8b shows the compressive stress-strain responses of a square RC column confined with CFRP wraps under varying load eccentricities. The legend identifies eccentricity ratios (e/h) from 0 to 0.5, along with the response of unconfined concrete. The curves indicate that as eccentricity increases, both compressive strength and strain at peak stress decrease for confined concrete. The concentrically loaded column (e/h = 0) shows the highest peak compressive stress and improved strain capacity compared to the unconfined concrete. As eccentricity increases (e/h = 0.1, 0.2, 0.3, 0.5), peak stress and ultimate strain decrease. This highlights that CFRP confinement improves compressive performance but becomes less effective as load eccentricity increases, reducing strength and ductility enhancements.

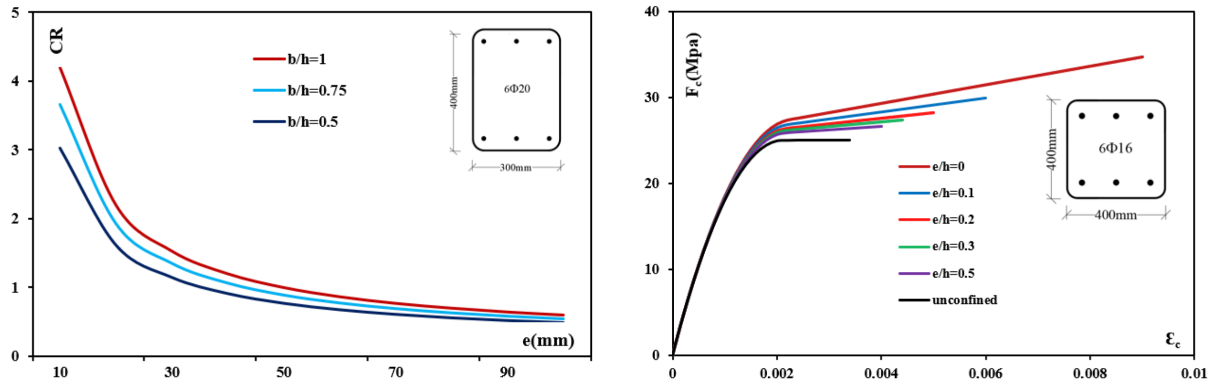

(a) (b)

Fig.8. (a) Compression zone ratio based on eccentricity, (b) Stress–strain curve under eccentric loads.

5.3. Effect of corner radius

Fig. 9a shows the effect of corner radius on the axial and flexural capacity of rectangular columns fully wrapped with FRP, with a 300 × 400 mm cross-section. Three corner radii (20 mm, 40 mm, and 60 mm) were investigated with a constant FRP volumetric ratio of 0.85% and a confinement ratio of 0.22, using three layers of 0.25 mm thick FRP. The interaction curves reveal that increasing the corner radius improves both normalized axial load (K_n) and bending moment (R_n) capacities, primarily due to the shape factor increase. The effect of corner radius becomes less significant as load eccentricity increases, being more noticeable at lower eccentricities. Compared to the baseline column with a 20 mm radius, the 40 mm radius showed a 2.4% increase in axial strength, and the 60 mm radius showed a 4.5% improvement.

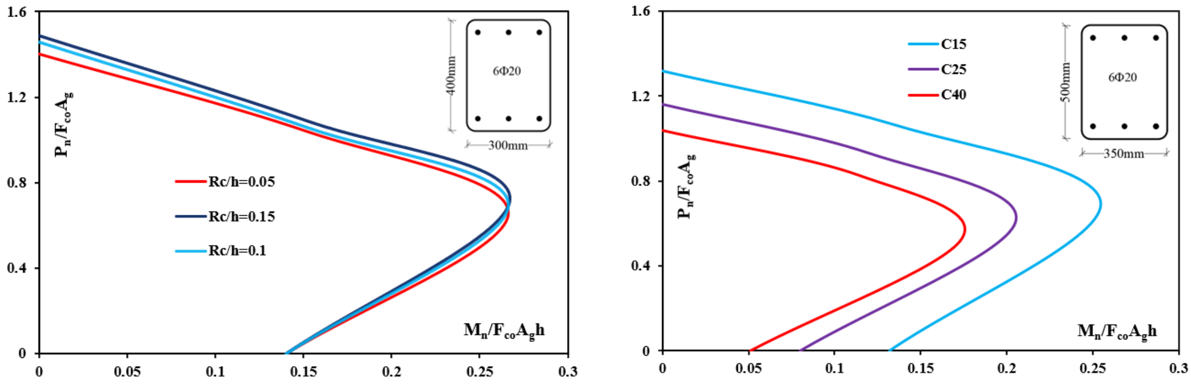

(a)   (b)

Fig.9. Interaction diagrams: (a) Influence of corner radius, (b) Effect of concrete strength.

5.4. Effect of unconfined compressive strength of concrete

The influence of unconfined concrete strength on the behavior of FRP-confined, eccentrically loaded RC columns was analyzed. A rectangular column (350 × 500 mm) retrofitted with three layers of CFRP sheets and reinforced with 6ϕ20 mm longitudinal steel bars was subjected to uniaxial eccentric loading, following ACI 440.2R(ACI, 2008) guidelines. Three concrete strengths—15 MPa, 25 MPa, and 40 MPa—were evaluated, and the axial load–flexural moment (P–M) interaction diagrams were developed (Fig. 9b). The results show that low-strength concrete (15 MPa) benefits the most from CFRP confinement, with significant improvements in both axial load and flexural strength. As concrete strength increases (25 MPa and 40 MPa), the confinement's effectiveness decreases due to reduced lateral deformability and energy absorption in stronger concrete. The interaction curve for the 15 MPa specimen expands outward, while those for 25 MPa and 40 MPa contract inward, indicating reduced confinement efficiency at higher concrete strengths. These findings highlight the importance of concrete strength in optimizing the performance of FRP-retrofitted columns for improved strength and ductility.

$$\Delta K_n(\%) = \frac{K_{ni} - K_{no}}{K_{no}} \times 100 \tag{18}$$

where ΔK_n represents the increase in axial load capacity, K_{ni} is the axial strength at the specified point, and K_{no} is the reference axial load.

5.5. Effect of volumetric ratio on confinement efficiency

The FRP volumetric ratio in RC columns is defined by the number of CFRP plies applied to the column surface. This ratio represents the proportion of the total volume of CFRP relative to the volume of concrete enclosed within the column's perimeter. In rectangular RC columns, the volumetric ratio is typically calculated based on the total thickness of CFRP layers and the perimeter of the cross-section, and it can be determined using the following equation(Mai et al., 2020).

$$\rho_f = \frac{V_f}{V_c} = \frac{\left[2(\mathrm{b}-2\,\mathrm{r_c}) + 2(\mathrm{h}-2\,\mathrm{r_c}) + 2\pi\,\mathrm{r_c}\right]\times t_f}{\left[bh - (4-\pi)\,\mathrm{r_c}^2\right]} \tag{19}$$

The influence of FRP plies, represented by the volumetric ratio, on the axial and flexural capacity of RC columns has been investigated, and the corresponding P–M interaction diagrams are illustrated in Fig.11a and table 3. The study was conducted on a rectangular column with dimensions of 150 × 200 mm and a single FRP ply thickness of 0.25 mm, under three volumetric ratio conditions: 0%, 1.1%, and 1.7%.

5.6. Effect of aspec ratios

The aspect ratio (b/h) of rectangular cross-sections significantly affects the behavior and load-carrying capacity of eccentrically loaded RC columns strengthened with CFRP jackets. It plays a key role in the efficiency of FRP confinement and the shape of the interaction curve. The normalized axial load–bending moment (P–M) interaction diagrams in Fig. 10b were obtained for columns with aspect ratios of 0.5, 0.6, and 1.0. Columns with an aspect ratio of 1.0 (square cross-sections) show higher axial strength and flexural moment capacity, especially at low eccentricities. In contrast, columns with lower aspect ratios (0.5 and 0.6) have reduced confinement efficiency and smaller strength improvements. As the aspect ratio decreases, confinement becomes less uniform, reducing the confined core area. For example, a column with an aspect ratio of 0.5 shows normalized values of (1.03, 0.14), while one with a 0.6 aspect ratio shows a 7% increase in axial strength and 21% in flexural capacity. A square column (aspect ratio 1.0) shows a 25% improvement in axial load and 71% in bending moment compared to the 0.5 aspect ratio column as shown in table 3. These results emphasize the importance of cross-sectional geometry in optimizing CFRP-confined RC columns under eccentric loading.

Table 3. Normalized Axial and Flexural Strength

Section	Points Normalized P and M		A		B			C		
			K_n	Δk_n(%)	K_n	R_n	Δk_n(%)	K_n	R_n	Δk_n(%)
300x400	Rc/h	0.05	1.404	0	1.041	0.152	0	0.653	0.266	0
		0.1	1.46	4	1.066	0.152	2.4	0.691	0.266	5.82
		0.15	1.49	6	1.088	0.153	4.5	0.72	0.267	10.26
350x500	F_{co}(Mpa)	40	1.038	0	0.827	0.114	0	0.53	0.174	0
		25	1.16	11.75	0.93	0.12	12.5	0.603	0.205	13.8
		15	1.318	27	1.06	0.137	28.2	0.689	0.255	30
150x200	ρ_f(%)	0	1.06	0	0.723	0.137	0	0.445	0.202	0
		1.13	1.281	20.8	0.992	0.139	37.2	0.69	0.216	55
		1.7	1.298	22.5	1.051	0.144	79.5	0.772	0.22	73.5
200x200	b/h	0.5	1.23	0	1.03	0.14	0	0.678	0.25	0
		0.6	1.418	15.3	1.1	0.17	6.8	0.7	0.293	3.25
		1	1.92	56	1.287	0.24	25	0.775	0.375	14.3

5.7. Comparison of analyticl models with experimental results

The interaction diagrams in Fig. 11a show the axial load–flexural moment relationship from two analytical models—ACI 440.2R(ACI, 2008) and Lam & Teng (Lam & Teng, 2003) —compared with experimental results by Darby et al. (2011) for FRP-confined square RC columns with larger cross-sections. The comparison reveals that experimental data consistently show slightly higher axial compression and flexural strengths than the analytical models. Both the Lam & Teng (Lam & Teng, 2003) and ACI 440.2R(ACI, 2008) models provide nearly identical predictions for axial load and bending moment capacities. The interaction curves indicate a strong correlation with experimental results, especially in the compression-dominated region, where RC columns exhibit compression-controlled behavior. This alignment highlights the accuracy and reliability of these models in predicting the performance of FRP-confined RC columns under axial loading.

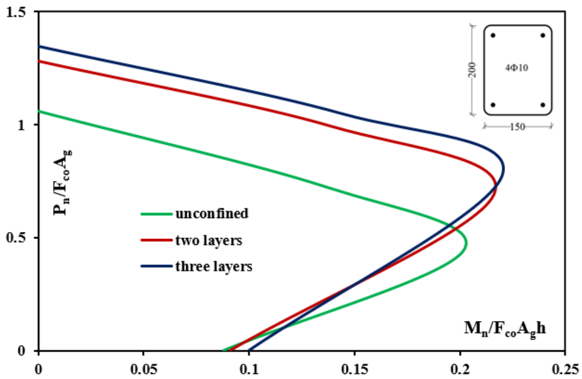

(a)

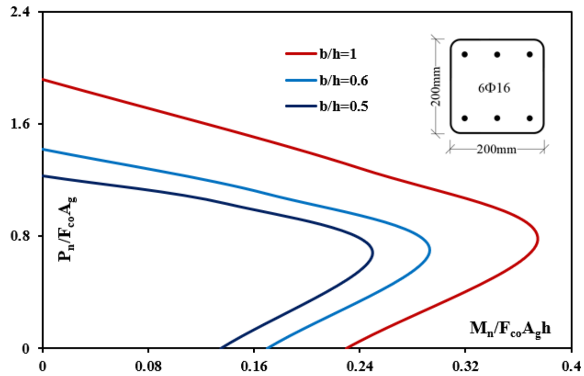

(b)

Fig.10. Interaction diagrams: (a) Influence of volumetric ratio, (b) Effect of aspect ratios.

The interaction curves illustrate the effects of different confinement levels. A volumetric ratio of ρf = 0% represents an unconfined concrete column, while ρf = 1.1% and ρf = 1.7% correspond to columns confined with two and three layers of FRP, respectively. The results show that increasing the volumetric ratio significantly improves the axial and flexural capacities of eccentrically loaded RC columns. For example, at point B, the unconfined column achieves (434 kN, 16.4 kN·m), while the confined columns show (595 kN, 16.7 kN·m) for ρf = 1.1% and (631 kN, 17.3 kN·m) for ρ_f = 1.7%. The column with one FRP layer shows a 37% increase in axial load and a 2% increase in flexural moment, while two layers improve axial load by 45% and bending moment by 5%. These results demonstrate that higher volumetric ratios significantly enhance axial strength, slightly improve flexural capacity, but confinement efficiency decreases with increasing load eccentricity.

The interaction diagrams in Fig. 11b compare the analytical models of Lam & Teng (Lam & Teng, 2003) and Rami & Paultre with experimental data for FRP-confined RC columns with smaller cross-sections. The Rami &

Paultre model tends to overestimate the axial compression capacity compared to both the Lam & Teng model and experimental results, although it aligns well at higher eccentricities. The Lam & Teng model (Lam & Teng, 2003), however, shows excellent agreement with experimental results across the full interaction range, especially at low eccentricities. These comparisons underscore the importance of the selected stress–strain model in accurately capturing the behavior of eccentrically loaded RC columns confined with CFRP sheets.

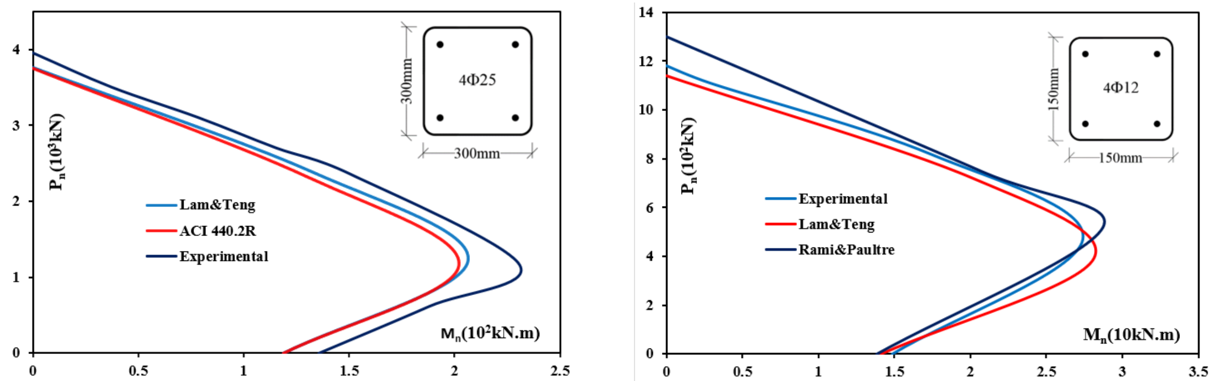

(a) (b)

Fig.11**.** Comparison of analytical models with experimental data.

6. Conclusion

This study analyzed the axial–flexural (P–M) behavior of rectangular reinforced concrete (rRC) columns confined with CFRP wraps under eccentric loading. The results show that CFRP confinement significantly improves both axial load-bearing capacity and flexural strength, with improvements influenced by load eccentricity, cross-sectional shape, concrete compressive strength, and CFRP volumetric ratio. Using three stress–strain models (Lam & Teng (Lam & Teng, 2003); Rami & Paultre (Eid & Paultre, 2017); Wei & Wu (Wu & Wei, 2016)), P–M interaction diagrams were developed to assess how CFRP wrapping affects column performance under combined loads. Key findings include: confinement effectiveness decreases with higher eccentricities; square sections (b/h = 1) show the greatest improvements, while elongated sections are less effective due to uneven stress distribution; rounding column corners enhances confinement by reducing stress concentrations; and lower-strength concrete benefits more from CFRP confinement than higher-strength concrete. Additionally, increasing the CFRP volumetric ratio boosts axial capacity, though flexural strength gains are more modest, and the benefits diminish with higher eccentricities. Comparisons with experimental data confirmed the accuracy of the selected models, with the Lam & Teng (Lam & Teng, 2003) model showing the best agreement across eccentricities and geometries. The Rami & Paultre (Eid & Paultre, 2017) model slightly overestimated axial capacity under pure axial loading. In conclusion, CFRP confinement enhances rRC column performance, but its effectiveness depends on various design factors, including loading conditions, sectional geometry, and concrete strength, offering valuable insights for optimizing retrofitting strategies.

References

Abd El Fattah, A. M., Rasheed, H. A., & Al-Rahmani, A. H. (2017). Partial Confinement Utilization for Rectangular Concrete Columns Subjected to Biaxial Bending and Axial Compression. *International Journal of Concrete Structures and Materials*, *11*(1), 135–149. https://doi.org/10.1007/s40069-016-0178-z

Abdallah, M. H., Mohamed, H. M., Masmoudi, R., & Moussa, A. (2018). Analytical modeling of moment-curvature behavior of steel and CFRP RC circular confined columns. *Composite Structures*, *189*, 473–487. https://doi.org/10.1016/j.compstruct.2018.01.110

Abid, M., Isleem, H. F., Shah, M. K., & Zeb, S. (2021). Analytical review on eccentric axial compression behavior of short and slender circular RC columns strengthened using CFRP. *Polymers*, *13*(16). https://doi.org/10.3390/polym13162763

ACI 318. (2011). ACI 318-11 Building Code Requirements for Structural Concrete. In *American Concrete Institute*.

Ahmed, B., Zerfu, K., & Agon, E. C. (2021). Construction of Uniaxial Interaction Diagram for Slender Reinforced Concrete Column Based on Nonlinear Finite Element Analysis. *Advances in Civil Engineering*, *2021*. https://doi.org/10.1155/2021/3275512

Al-Nimry, H., & Neqresh, M. (2019). Confinement effects of unidirectional CFRP sheets on axial and bending capacities of square RC columns. *Engineering Structures*, *196*. https://doi.org/10.1016/j.engstruct.2019.109329

Al-Rahmani, A., & Rasheed, H. (2016). Combined transverse steel-external FRP confinement model for rectangular reinforced concrete columns. *Fibers*, *4*(1). https://doi.org/10.3390/fib4010008
Cao, Y., Wu, Y. F., & Jiang, C. (2018). Stress-strain relationship of FRP confined concrete columns under combined axial load and bending moment. *Composites Part B: Engineering*, *134*, 207–217. https://doi.org/10.1016/j.compositesb.2017.09.063
Darby, A. P., Tim, I., & Mark, E. (n.d.). *FRP confined square columns under concentric and eccentric loading*. https://www.researchgate.net/publication/289321691
Eid, R., & Paultre, P. (2017). Compressive behavior of FRP-confined reinforced concrete columns. *Engineering Structures*, *132*, 518–530. https://doi.org/10.1016/j.engstruct.2016.11.052
Fan, L., Jin, L., & Du, X. (2023a. Effects of structural size and corner radius on eccentric failure of rectangular CFRP-wrapped RC columns: Meso-scale modellings. *Engineering Structures*, *283*. https://doi.org/10.1016/j.engstruct.2023.115893
Faustino, P., & Chastre, C. (2015). Analysis of load-strain models for RC square columns confined with CFRP. *Composites Part B: Engineering*, *74*, 23–41. https://doi.org/10.1016/j.compositesb.2015.01.002
Guide for the design and construction of externally bonded FRP systems for strengthening concrete structures. (2008). American Concrete Institute.
Harajli, M. H. (2006). Axial stress-strain relationship for FRP confined circular and rectangular concrete columns. *Cement and Concrete Composites*, *28*(10), 938–948. https://doi.org/10.1016/j.cemconcomp.2006.07.005
Harajli, M. H., & Hantouche, E. G. (2006). Stress-strain model for fiber-reinforced polymer jacketed concrete columns. In *Article in ACI Structural Journal* (Vol. 103, Issue 5). https://www.researchgate.net/publication/279594470
Jiang, T., & Teng, J. G. (2007). Analysis-oriented stress-strain models for FRP-confined concrete. *Engineering Structures*, *29*(11), 2968–2986. https://doi.org/10.1016/j.engstruct.2007.01.010
Koksal, H. O., Doran, B., & Turgay, T. (2009). A practical approach for modeling FRP wrapped concrete columns. *Construction and Building Materials*, *23*(3), 1429–1437. https://doi.org/10.1016/j.conbuildmat.2008.07.008
Lam, L., & Teng, J. G. (2003). Design-oriented stress-strain model for FRP-confined concrete. *Construction and Building Materials*, *17*(6–7), 471–489. https://doi.org/10.1016/S0950-0618(03)00045-X
Liao, J. J., Zeng, J. J., Zhuge, Y., Zheng, Y., Ma, G., & Zhang, L. (2023). FRP-confined concrete columns with a stress reduction-recovery behavior: A state-of-the-art review, design recommendations and model assessments. In *Composite Structures* (Vol. 321). Elsevier Ltd. https://doi.org/10.1016/j.compstruct.2023.117313
Mai, A. D., Sheikh, M. N., & Hadi, M. N. S. (2020). Failure envelopes of square and circularized RC columns discretely confined with CFRP. *Construction and Building Materials*, *261*. https://doi.org/10.1016/j.conbuildmat.2020.119937
Mai, A. D., Sheikh, M. N., Hadi, M. N. S., Pham, A. D., & Ngo, N. T. (2024). Effect of stress-strain models and sectional analysis methods on the axial-flexural interactions of discontinuously FRP strengthened square RC columns. *Structure and Infrastructure Engineering*, *20*(11), 1663–1679. https://doi.org/10.1080/15732479.2022.2157022
Montuori, R., Piluso, V., & Tisi, A. (2013). Ultimate behaviour of FRP wrapped sections under axial force and bending: Influence of stress-strain confinement model. *Composites Part B: Engineering*, *54*(1), 85–96. https://doi.org/10.1016/j.compositesb.2013.04.059
Moretti, M. L., Miliokas, E., & Paparizos, I. (2021). Axial strength estimation of reinforced concrete columns confined through fiber reinforced polymer (FRP) jackets. In *Journal of Multidisciplinary Engineering Science and Technology (JMEST)* (Vol. 8). www.jmest.org
Noorzad, A. J., & Dilmaç, H. (2024). Structural behavior of RC columns retrofitted with FRP under axial load. *Journal of Structural Engineering & Applied Mechanics*, *7*(4), 315–342. https://doi.org/10.31462/jseam.2024.04315342
Noorzad, A. J., & Dilmaç, H. (2025). Influence of corner radius on the axial compressive behavior of FRP-confined rectangular reinforced concrete columns. In *Journal of Ceramics and Composites* (Vol. 1, Issue 1).
Rasheed, H. A. (2014). Strengthening Design of Reinforced Concrete with FRP. In *Strengthening Design of Reinforced Concrete with FRP*. https://doi.org/10.1201/b17968
Saljoughian, A., & Mostofinejad, D. (2016). Axial-flexural interaction in square RC columns confined by intermittent CFRP wraps. *Composites Part B: Engineering*, *89*, 85–95. https://doi.org/10.1016/j.compositesb.2015.10.047
Shayanfar, J., Barros, J. A. O., Abedi, M., & Rezazadeh, M. (2023). Unified Compressive Strength and Strain Ductility Models for Fully and Partially FRP-Confined Circular, Square, and Rectangular Concrete Columns. *Journal of Composites for Construction*, *27*(6). https://doi.org/10.1061/jccof2.cceng-4336
Teng, J. G., Jiang, ; T, Lam, ; L, & Luo, Y. Z. (n.d.). *Refinement of a Design-Oriented Stress-Strain Model for FRP-Confined Concrete*. https://doi.org/10.1061/ASCECC.1943-5614.0000012

Wei, Y., Xu, Y., Wang, G., Cheng, X., & Li, G. (2022). Influence of the Cross-Sectional Shape and Corner Radius on the Compressive Behaviour of Concrete Columns Confined by FRP and Stirrups. *Polymers*, *14*(2). https://doi.org/10.3390/polym14020341

4th International Civil Engineering & Architecture Conference
17-19 May 2025, Trabzon, Türkiye

The effect of ohmic heating on alkali-activated blast furnace slag-fly ash concrete with marble powder replacement

Mazem Yılmaz*[1], Mücteba Uysal[2]

[1] *Istanbul Aydin University, Depertment of Civil Engineering, 34295 İstanbul, Türkiye*
[2] *Yildiz Technical University, Department of Civil Engineering, 34220 İstanbul, Türkiye*

Abstract. Ohmic heating is a green curing method that provides the heat required for the geopolymerization of alkali-activated concrete through direct electric curing, resulting in early rapid strength development. Marble powder is a by-product produced during marble processing, and proper disposal of these wastes is important. This study focuses on analyzing the influence of ohmic heating on early strength in the geopolymerization of alkali-activated concrete and the effect of marble powder on this concrete. In this study, marble powder was replaced as fine aggregate in sodium silicate-hydroxide activated blast furnace slag-fly ash-based concrete at various proportions (by weight 10%, 20%, and 30%). The effects of various curing conditions (room temperature curing, thermal curing at 60°C and 80°C, and direct electrical curing at 15V and 25V) on the physical-mechanical properties were investigated. Compressive and flexural strength tests were performed at 3 and 28 days to evaluate early and late strength for the series under different curing conditions. Additionally, unit weight and water absorption test were performed on the samples. The results show that direct electrical curing enhances early-age strength and has a positive effect on the final strength. In the replacement of fine aggregates with marble powder in alkali-activated blast furnace slag-fly ash concrete, the lowest water absorption value was observed at a 10% replacement, while the highest strength values were achieved at a 20% replacement ratio. The findings encourage the utilization of waste materials as aggregate replacements in the building sector and provide curing solutions that will promote the widespread use of alkali-activated materials.

Keywords: Direct electring curing; Ohmik heating; Alkali-activated concrete; Marble powder

1. Introduction

In construction practices, environmental preservation and the use of sustainable materials have become key priorities. The significant carbon emissions linked to the manufacture of of Portland cement have raised serious environmental concerns, thereby driving the need for alternative binder systems (Di Filippo et al., 2019). In this regard, geopolymers have emerged as a promising and environmentally friendly alternative, owing to their low carbon footprint and the potential for incorporating industrial by-products (Pavitra et al., 2016; Alahmari et al., 2023).

Alkali-activated concrete (AAC) are inorganic polymeric materials synthesized through the alkali activation of aluminosilicate-rich precursors. Common sources of these precursors include industrial by-products like fly ash (FA), blast furnace slag (GBFS), and metakaolin (Slaty et al., 2013; Huseien, 2019; Kuranlı et al., 2022. The utilization of such materials not only contributes to waste valorization but also results in binders with high mechanical strength and long-term durability (Zhang et al., 2025). Despite these advantages, the widespread adoption of AAC is hindered by certain technical limitations. Notably, low-calcium systems often require elevated curing temperatures (typically between 60-80 °C) to achieve sufficient mechanical performance (Bakharev, 2005; Saludung et al., 2023). This requirement poses a challenge compared to conventional Portland cement, which hardens at ambient conditions. Therefore, the development of more efficient curing solutions is of great importance to promote the wider use of AAC in production.

Ohmic heating, also referred to as Joule heating, is a rapid curing technique that supplies the thermal energy required for the geopolymerization process through the direct application of electrical current (Anvari et al., 2020). This method enables localized heating of the material, resulting in higher energy efficiency compared to conventional thermal curing techniques such as ovens or steam curing (Wang et al., 2023). It is particularly effective in promoting early-age strength development in low-calcium geopolymer systems (Wang et al., 2024). Aygün et al. (2025) investigated the effect of electric curing on GBFS –FA-based AAC. In their study, they

* Corresponding author, E-mail: mazembalaban@aydin.edu.tr

https://doi.org/10.31462/icearc2025_ce_mat_667

reported that electric curing increased the compressive strength (CS) by 148% compared to conventional thermal curing at 80 °C.

Marble has been extensively used throughout history; however, its processing generates large amounts of waste. The proper utilization of this waste is crucial for the conservation of natural resources, the prevention of waste disposal, and the development of sustainable construction materials (Demirel & Alyamaç, 2018). As Turkey is among the countries with the largest marble reserves in the world, it faces a significant opportunity to manage this waste effectively (Singh et al., 2019). Marble powder (MP) consists of fine particles with a high inorganic mineral content, with calcium carbonate (calcite) being its primary component. Research in recent years has centered on the application of MP in the construction industry emphasizing its potential as an important resource for creating more sustainable building materials. (Corinaldesi et al., 2010; Gameiro et al., 2014; Khyaliya et al., 2017; Danish, et al., 2023; Meera & Gupta, 2024).

Tunc (2019) carried out a review study regarding the use of MP in concrete. In his study, the author emphasized that the utilization of waste marble is advantageous for producing cost-effective and durable concrete. It was demonstrated that replacing aggregate, cement, and other waste materials with MP enhances the strength of concrete. Moreover, the author highlighted that the substitution of marble powder as aggregate yielded more satisfactory results compared to its use as a cement replacement. Rashad et al. (2025) incorporated waste MP into alkali-activated GBFS cement at replacement levels ranging from 5% to 50%. They reported that incorporating WMP at levels between 5% and 20% enhanced the mechanical strength and durability properties of the material. The authors recommended an optimal replacement level of 10% for MP.

In this study, the potential use of waste MP as an aggregate replacement in AAC produced by ohmic heating curing is investigated, and its effects on the physical and mechanical properties of the material are examined.

2. Materials and methods

In this study, GBFS and FA were employed as binder materials in equal proportions by weight. Natural river sand, possessing a maximum particle diameter of 5 mm and a specific gravity of 2.80, was utilized as the fine aggregate. MP was used as a partial replacement for the fine aggregate at substitution levels of 10%, 20%, and 30% by weight. The The images of MP, FA, and GGBS are presented in Fig. 1.The chemical compositions of GBFS, FA, and MP are presented in Table 1. Sodium silicate (modulus 3) and sodium hydroxide (with 99% purity) were utilized as alkaline activators, with chemical properties of sodium silicate also detailed in Table 2. The molarity of the sodium silicate solution was fixed at 12 M.

The mix proportions of the AAC series are presented in Table 3. In this study, the alkali activator-to-binder ratio was set at 0.7, the fine aggregate-to-binder ratio at 2.5, and the sodium silicate-to-sodium hydroxide (SS/SH) ratio at 2. The series are designated based on the amount of MP incorporated, with the numerical values indicating the replacement ratios by weight (%). The AAC series were cast in prismatic molds with dimensions of 40 mm × 40 mm × 160 mm and were subjected to various curing conditions as presented in Table 4.

a) b) c)

Fig. 1. a) MP, b) FA, c) GBFS

Table 1. Chemical composition FA, GBFS, and MP (%)

Binders	SiO_2	Al_2O_3	CaO	Fe_2O_3	MgO	Na_2O	K_2O	SO_3	TiO_2	LOI
FA	58.65	25.21	0.49	5.64	2.26	0.60	1.38	0.53	-	0.015
GBFS	41.84	11.85	34.58	1.11	6.57	0.80	0.63	0.23	0.78	0.03
MP	50.74	13.32	17.85	10.56	7.53	-	-	-	-	-

Table 2. Chemical properties of Sodium Silicate (%)

	Na_2O	SiO_2	H_2O
Sodium Silicate	29.3	9.8	60.9

Table 3. Composition of AAC binders and aggregates (by weight)

Series ID	GBFS	FA	Aggregate	MP	Na_2SiO_3	NaOH
MP10	225	225	1013	112.5	210	105
MP20	225	225	900	225	210	105
MP30	225	225	787.5	337.5	210	105

Table 4. Applied curing conditions for AAC series.

Curing Type	Curing Condition	Temperature / Voltage	Curing Duration
Ambient Curing	Room Temperature	~22 °C	24 hours
Thermal Curing	Oven Curing	60 °C	24 hours
Thermal Curing	Oven Curing	80 °C	24 hours
Ohmic Heating Curing	Direct Electric Current (DEC)	15 V	24 hours
Ohmic Heating Curing	Direct Electric Current (DEC)	25 V	24 hours

Copper plates were attached to the 40 mm × 40 mm faces of the prismatic molds with dimensions of 40 mm × 40 mm × 160 mm. These conductive plates were connected to an alternating current (AC) power supply to allow the flow of electric current through the AAC mixture. Ohmic heating was achieved by applying a constant voltage, resulting in internal heat generation due to the electrical conductivity of the material. This method enabled temperature increase within the specimen, facilitating effective curing through ohmic heating.

To determine the physical properties of the AAC samples, unit weight and water absorption (WA) tests were carried out in accordance with ASTM C642 standard. The unit weight of the AAC was determined by weighing the specimens after drying them in an oven at 105 °C for 24 hours. The unit weight (ρ) was obtained using the Equation 1. In this formula, M_d represents the dry mass of the sample (g), and V denotes the volume of the sample (cm^3).

$$\rho = \frac{M_d}{V} \tag{1}$$

WA tests were conducted by immersing the oven-dried specimens in water for 24 hours. The WA rate was obtained as the percentage increase in mass, based on the difference between the saturated mass and the dry mass of the sample, using the Equation 2. In this formula, M_s represents the mass of the sample after immersion in water (g), and WA denotes the water absorption percentage (%).

$$WA = \frac{M_s - M_d}{V} x100 \tag{2}$$

Specimens in the form of prisms, sized 40 mm × 40 mm × 160 mm were prepared to evaluate the CS and flexural strength (FS) of the series. Initially, the samples underwent a FS test in accordance with the TS EN 196-1 standard, after which the fractured halves were used for CS testing. The CS tests were performed using a testing machine equipped with appropriate capacity and a loading surface area of 40 mm × 40 mm.

3. Result and discussion

3.1 Unit weigth

The unit weight values of the MP10, MP20, and MP30 series under different curing conditions are presented in Fig. 2. Under all curing conditions, the highest unit weight value was generally observed under ambient curing conditions. This trend may have resulted from higher curing temperatures or electric fields accelerating water loss and microstructural densification, leading to minor reductions in density. Among all the series, MP30 exhibited the lowest unit weight, while MP10 and MP20 remained relatively stable under different conditions.

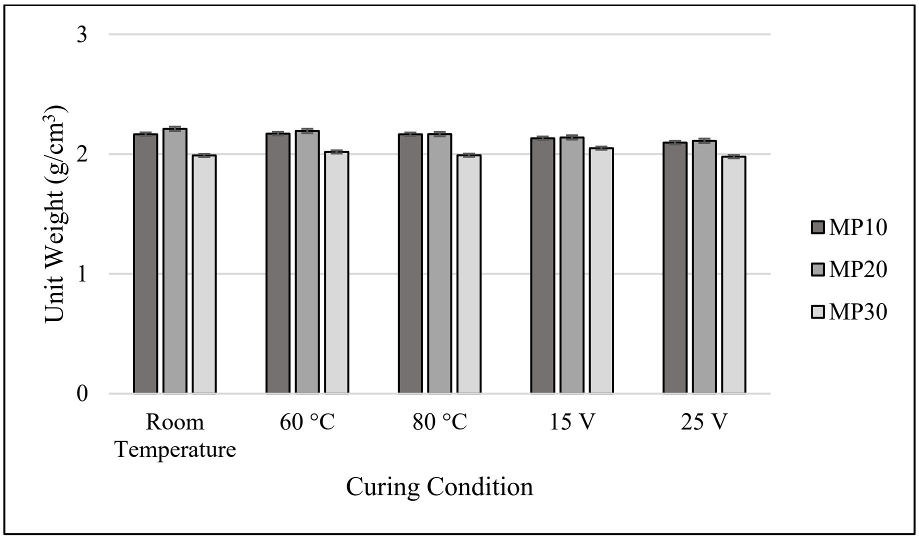

Fig. 2. Unit weight results (g/cm^3)

3.2 Water absorption

The WA results (Fig. 3) show a minor increase in WA values for all series under thermal curing and direct electric curing compared to ambient curing conditions. Among all the series, MP10 exhibited the lowest WA value under all conditions, whereas MP30 exhibited the highest WA value.

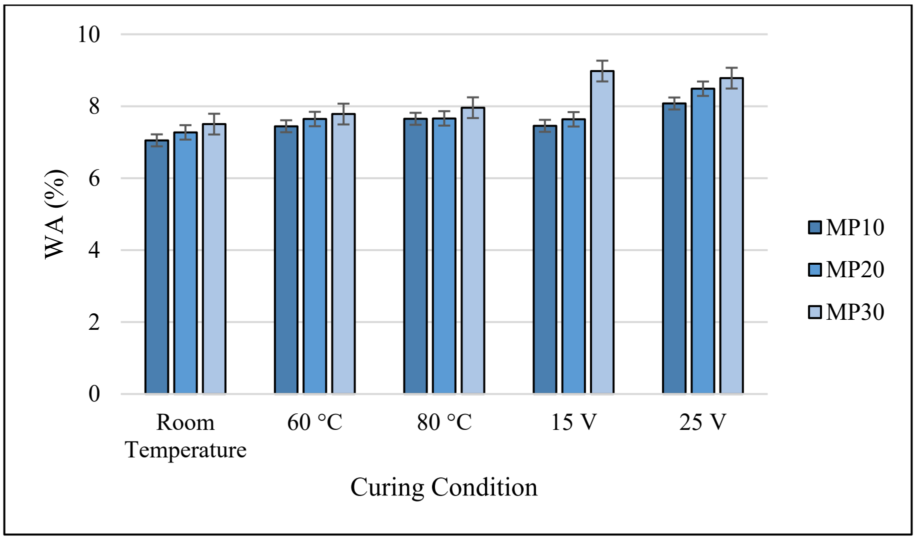

Fig. 3. WA results (%)

3.3 Compressive strength

The compressive strength results of the MP10, MP20, and MP30 series under various curing conditions are presented in Fig. 4. In general, for all series, the 28-day CS were higher than the 3-day values, indicating the continued progress of the geopolymerization process over time. Notably, under room temperature and ohmic heating conditions at 15 V, a significant increase in strength was observed between 3 and 28 days. This increase may be attributed to the fact that the heat generated by the 15 V electric field was insufficient to accelerate the geopolymerization reaction at early ages. On the other hand, both thermal curing (at 60 °C and 80 °C) and ohmic heating curing effectively enhanced the early-age strength development. The highest CS was recorded for the MP20 series under ohmic heating curing, reaching 51.4 MPa. In contrast, the MP30 series exhibited lower CS values under all curing conditions compared to the other series. The obtained CS results are consistent with the study conducted by Rashad et al. (2025), which reported a negative impact on strength values when the replacement ratio of MP in alkali-activated GBFS cement exceeded 20% (Rashad et al., 2025).

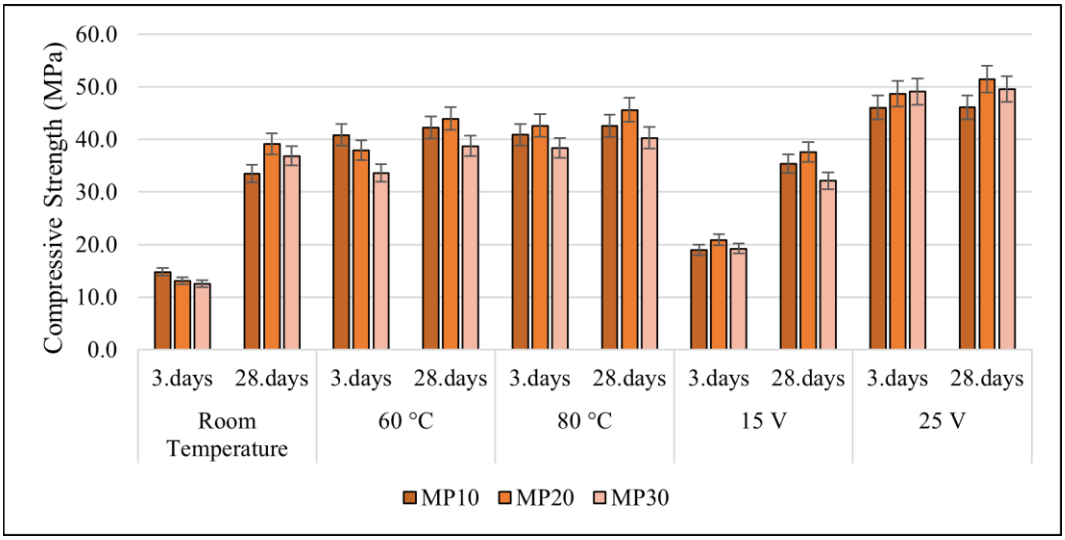

Fig. 4. CS results (MPa)

3.4 Flexural strength

The FS results of the MP10, MP20, and MP30 series under various curing conditions are presented in Fig. 5. The findings demonstrate that both curing conditions and the MP replacement ratio have a significant effect on FS. Specimens cured at room temperature exhibited relatively lower FS, with only a limited increase observed from 3 to 28 days. In contrast, thermal and ohmic heating curing methods significantly enhanced early-age strength compared to ambient curing. According to the 28-day strength results, the MP20 series cured at 80 °C exhibited the highest FS with a value of 5.22 MPa. The ohmic heating method also improved FS in all series at both early and later ages. Specifically, the MP20 series cured under 25 V achieved the highest FS, reaching 9.37 MPa at 3 days and 9.91 MPa at 28 days. These results indicate that curing under both thermal and ohmic heating conditions accelerates the polymerization reaction, thereby enhancing the mechanical properties of the matrix. Moreover, the consistent superior performance of the MP20 series under all curing regimes suggests that a 20% MP replacement represents the optimum substitution ratio for fine sand in GBFS and FA-based AAC systems.

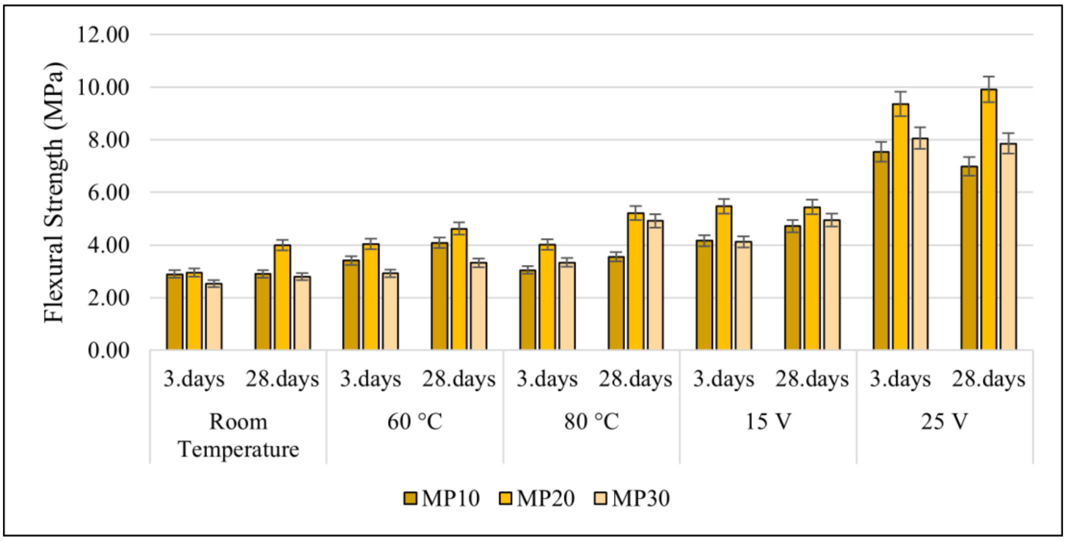

Fig. 5. FS results (MPa)

4. Conclusions

In this study, the effects of various curing conditions—ambient curing, thermal curing at 60 °C and 80 °C, and ohmic heating at 15 V and 25 V—on the physical and mechanical properties of alkali-activated GBFS –FA-based concrete incorporating MP were investigated. The following conclusions were drawn:

- Ambient curing generally resulted in the highest unit weight, while thermal and ohmic heating slightly reduced density due to accelerated moisture loss.

- WA slightly increased under thermal and electric curing. Among all mixtures, MP10 exhibited the lowest WA, indicating a denser and less porous matrix.
- CS increased over time across all series, with thermal curing and ohmic heating promoting early strength development. The highest CS (51.4 MPa) was obtained from the MP20 series cured with 25 V ohmic heating.
- FS was also significantly improved by both thermal and ohmic curing. MP20 achieved the highest values, especially under 80 °C thermal curing (5.22 MPa) and 25 V ohmic heating (9.91 MPa), suggesting that 20% MP replacement is optimal for enhancing performance in GBFS-FA-based AAC.

References

Alahmari, T., Abdalla, T., & Rihan, M. (2023). Review of Recent Developments Regarding the Durability Performance of Eco-Friendly Geopolymer Concrete. *Buildings, 13*(12), 3033. doi:https://doi.org/10.3390/buildings13123033

Anvari, A., Azimi Yancheshme, A., M. Kekre, K., & Ronen, A. (2020). State-of-the-art methods for overcoming temperature polarization in membrane distillation process: A review. *Journal of Membrane Science, 616*, 118413. doi:https://doi.org/10.1016/j.memsci.2020.118413

Aygun, B., Uysal, M., Bilir, T., Çoşgun, T., & Dilbas, H. (2025). An investigation on physical, mechanical and microstructural properties of electricity-based cured GBFS-FA geopolymer. *Construction and Building Materials, 458*, 139526. doi:https://doi.org/10.1016/j.conbuildmat.2024.139526

Bakharev, T. (2005). Geopolymeric materials prepared using Class F fly ash and elevated temperature curing. *Cement and Concrete Research, 35*(6), 1224-1232. doi:https://doi.org/10.1016/j.cemconres.2004.06.031

Corinaldesi, V., Moriconi, G., & Naik, T. (2010). Characterization of marble powder for its use in mortar and concrete. *Construction and Building Materials, 24*(1), 113-117. doi:https://doi.org/10.1016/j.conbuildmat.2009.08.013

Danish, A., Öz, A., Bayrak, B., Kaplan, G., Aydın, A., & Ozbakkaloglu, T. (2023). Performance evaluation and cost analysis of prepacked geopolymers containing waste marble powder under different curing temperatures for sustainable built environment. *Resources, Conservation and Recycling, 192*, 106910. doi:https://doi.org/10.1016/j.resconrec.2023.106910

Demirel, B., & Alyamaç, K. (2018). 6 - Waste marble powder/dust. *Waste and Supplementary Cementitious Materials in Concrete* (s. 181-197). içinde Woodhead Publishing. doi:https://doi.org/10.1016/B978-0-08-102156-9.00006-7

Di Filippo, J., Karpman, J., & DeShazo, J. (2019). The impacts of policies to reduce CO2 emissions within the concrete supply chain. *Cement and Concrete Composites, 101*, 67-82. doi:https://doi.org/10.1016/j.cemconcomp.2018.08.003

Gameiro, F., de Brito, J., & Correia da Silva, D. (2014). Durability performance of structural concrete containing fine aggregates from waste generated by marble quarrying industry. *Engineering Structures, 59*, 654-662. doi:https://doi.org/10.1016/j.engstruct.2013.11.026

Huseien, G., Sam, A., Shah, K., Asaad, M., Tahir, M., & Mirza, J. (2019). Properties of ceramic tile waste based alkali-activated mortars incorporating GBFS and fly ash. *Construction and Building Materials, 214*, 355-368. doi:https://doi.org/10.1016/j.conbuildmat.2019.04.154

Khyaliya, R., Kabeer, K., & Vyas, A. (2017). Evaluation of strength and durability of lean mortar mixes containing marble waste. *Construction and Building Materials, 147*, 598-607. doi:https://doi.org/10.1016/j.conbuildmat.2017.04.199

Kuranlı, Ö., Uysal, M., Abbas, M., Cosgun, T., Niş, A., Aygörmez, Y., . . . Al-mashhadani, M. (2022). Evaluation of slag/fly ash based geopolymer concrete with steel, polypropylene and polyamide fibers. *Construction and Building Materials, 325*, 126747. doi:https://doi.org/10.1016/j.conbuildmat.2022.126747

Meera, M., & Gupta, S. (2024). Performance evaluation of marble powder and fly ash concrete for non-structural applications. *Journal of Building Engineering, 84*, 108499. doi:https://doi.org/10.1016/j.jobe.2024.108499

Pavithra, P., Srinivasula Reddy, M., Dinakar, P., Hanumantha Rao, B., Satpathy, B., & Mohanty, A. (2016). A mix design procedure for geopolymer concrete with fly ash. *Journal of Cleaner Production, 133*, 117-125. doi:https://doi.org/10.1016/j.jclepro.2016.05.041

Rashad, A., Mokhtar, M., El-Nashar, M., & Abu-Elwafa Mohamed, R. (2025). Waste marble powder emerges as a promising material choice to enhance the properties of alkali-activated slag cement. *Sustainable Chemistry and Pharmacy, 43*, 101864. doi:https://doi.org/10.1016/j.scp.2024.101864

Saludung, A., Azeyanagi, T., Ogawa, Y., & Kawai, K. (2023). Mechanical and microstructural evolutions of fly ash/slag-based geopolymer at high temperatures: Effect of curing conditions. *Ceramics International, 49*(2), 2091-2101. doi:https://doi.org/10.1016/j.ceramint.2022.09.175

Singh, M., Srivastava, A., & Bhunia, D. (2019). Long term strength and durability parameters of hardened concrete on partially replacing cement by dried waste marble powder slurry. *Construction and Building Materials, 198*, 553-569. doi:https://doi.org/10.1016/j.conbuildmat.2018.12.005

Slaty, F., Khoury, H., Wastiels, J., & Rahier, H. (2013). Characterization of alkali activated kaolinitic clay. *Applied Clay Science, 75-76*, 120-125. doi:https://doi.org/10.1016/j.clay.2013.02.005

Tugrul Tunc, E. (2019). Recycling of marble waste: A review based on strength of concrete containing marble waste. *Journal of Environmental Management, 231*, 86-97. doi:https://doi.org/10.1016/j.jenvman.2018.10.034

Wang, J., Huang, S., Liu, T., Li, Z., Liang, Y., Ma, Z., . . . Dong, R. (2024). A comprehensive study on the impact of direct electric curing on the performance of molybdenum tailings in cementitious materials. *Case Studies in Construction Materials, 21*, e03394. doi:https://doi.org/10.1016/j.cscm.2024.e03394

Wang, J., Ren, X., Cai, Y., Xiang, Y., Abdullahi Umar, H., Li, Y., . . . Long, G. (2023). Effect of direct electric curing on the mechanical properties, hydration process, and environmental benefits of cement-steel slag composite. *Construction and Building Materials, 406*, 133382. doi:https://doi.org/10.1016/j.conbuildmat.2023.133382

Zhang, X., Zhang, X., Liu, J., Zhu, K., Zheng, Z., & Dong, Y. (2025). Study on properties and hydration mechanism of green alkali-activation lithium slag composite cementitious materials. *Construction and Building Materials, 473*, 140966. doi:https://www.sciencedirect.com/science/article/pii/S0950061825011146

ICEARC'25
4th International Civil Engineering & Architecture Conference
17-19 May 2025, Trabzon, Türkiye

Use of two composite materials glass-epoxy and aramid-epoxy in marine environment in the field of civil engineering

Younes Menail*[1], Djaber Bouhafara[2], Farouk Mesrafet[1], Abderrahim El Mahi[3]

[1] *Badji Mokhtar University, LR3MI, Department of Mechanical Engineering, Box 12, 23052 Sidi Ammar Annaba, Algeria*
[2] *National Higher School of Technology and Engineering, Laboratory of Energy Systems Technologies (LTSE), 23005 Annaba, Algeria.*
[3] *University of Maine, LAUM, CNRS UMR 6613, avenue Olivier Messiaen, 72085 Le Mans Cedex 9, France*

Abstract. The use of composite materials in the field of civil engineering has grown in recent years, and this is due to their performance. Marine infrastructures (ports, bridges, offshore, etc.) are subject to the effects of seawater and deteriorate rapidly if they are not properly protected. To this end, two glass-epoxy and aramid-epoxy composites have been the subject of a scientific study to propose solutions to this type of problem. The glass-epoxy material must resist the aggressiveness of seawater, to which it is exposed, and the aramid-epoxy material, in the internal layer, must resist shocks. To test these two materials, we carried out static tensile and tensile fatigue tests and aging in salt water under acoustic monitoring. The aim of this work is not to compare these two materials, but to prove that they are resistant to the aggressiveness of salt water. The results of the static tests show good behavior of both materials. On the other hand, tensile fatigue tests at 1000000 cycles show that the aramid-epoxy material resists better than the glass-epoxy material. Aging at 1000 hours in salt water shows that both materials resist the effect of seawater. They show little loss of strength. The acoustic tool confirms that both materials perform well in salt water and can therefore be safely used in civil engineering.

Keywords: Glass-epoxy; Aramid-epoxy; Seawater; Acoustic; Aging

1.Introduction

The use of composite materials in the field of civil engineering, as protection for reinforced concrete structures, is experiencing significant growth (Ghaib et al., 2024; Akter Hosen et al., 2017). These materials have characteristics and performances unmatched by other materials. The cost, lightness, resistance to corrosion and especially the method of obtaining them by different molding processes, make composite materials become the materials of the 21st century par excellence. Due to their characteristics and especially their cost, glass fibers are the most used fibers in the field of civil engineering (Rami et al., 2017; D'Antino & Pisani, 2019; Kychkin et al., 2025). On the other hand, aramid fibers (Kevlar) are less used (Wang & Xia, 1999; Sabu Sebastian et al., 2008; Guo et al., 2010; Eslava-Hernández et al., 2024; Ursache et al.,, 2024 ; Bandaru et al., 2025). Our study will contribute to a better understanding of these. The exposure of these materials to seawater, which is an aggressive environment due to its physicochemical composition, puts them to the test (Devine et al., 2023; Danijela Stankovic et al., 2024). Despite the large number of studies on the influence of salt water on these materials, the effect of humidity on the modification of the behavior of composites remains poorly determined (Bunsell, 1989). Various studies have shown that the complexity of the phenomenon of salt water absorption by composites remains an issue. These studies have shown that, depending on the case, the absorption of water by these materials can generally slightly increase the mass of the reinforced concrete structure, while in other cases, it is the opposite, i.e. a decrease in weight due to the destruction of the resin following washing out (Perreux et al., 1992). This degradation of composites is initiated by a phenomenon of plasticization or physical aging, resulting from the diffusion of salt water within the polymer matrix at the fiber-matrix interface (Vigier & Tatibouet 1993). Subsequently, hydrolysis or chemical aging of the micromolecular chains takes place, ultimately generating damage by osmotic cracking (Gautier et al., 2000). Thanks to the various investigation techniques and scientific means that have been developed, it is now possible to predict the durability of a composite more or less reliably (Gaumet et al., 1996) . In order to better understand the effect of this salt water absorption phenomenon by glass-epoxy and aramid-epoxy composites, we used the acoustic tool to complete our investigations (Nimdum

*Corresponding author E-mail: menailyounes43@gmail.com

https://doi.org/10.31462/icearc2025_ce_mat_678

golden light publishing

et Renard, 2012; Bentahar, 2005; Ben khalifa, 2013; Tan Duong, 1995; Ghaib et al., 2024) . The objective of our study is to show that both materials are resistant to the effect of salt water. The glass-epoxy material is intended to resist salt water by serving as protection for the reinforced concrete structure (placed in the outer layers) and the aramid-epoxy material is intended to resist shocks generated by the external environment and salt water (in case of infiltration) and is placed in the inner layers. Figure 1.

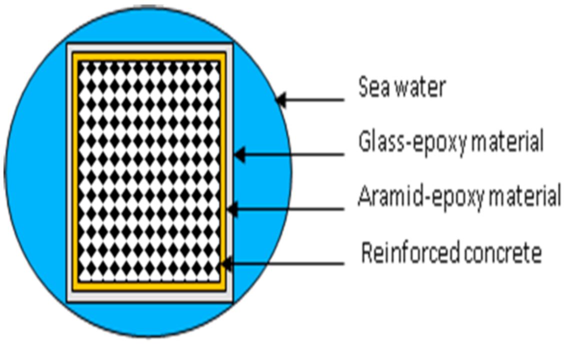

Fig. 1. Protection against sea water

2. Experimental

The experimental study is conducted by a destructive quasi-static tensile and tensile fatigue method, under acoustic monitoring. An INSTRON model 8516 universal hydraulic tensile machine equipped with a 100 kN force cell was used for these tests, Figure 2.

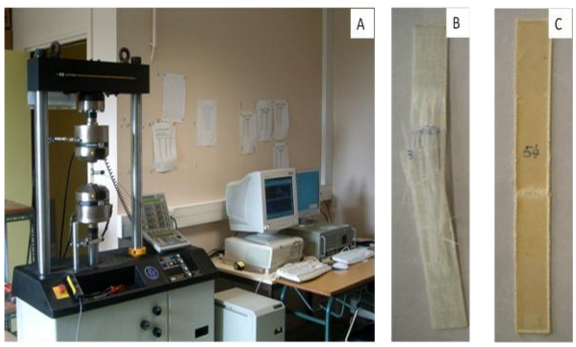

Fig. 2. Tensile test (a)Tensile machine with acoustic acquisition (b) Glass specimen (c) Kevlar specimen

Tensile fatigue of both materials at 1000000 cycles is followed by natural ageing in synthetic seawater at 37‰, at 1000h immersion. This is to determine the evolution of the mechanical properties of the studied glass-epoxy and aramid-epoxy laminates. 2.

The two materials used are laminates based on the same SR 1500 epoxy resin combined with an SD 2505 amine hardener. The reinforcements consist of 4 plies of UD glass weave, with a mass per unit area of 300 g/m2 and 6 plies of aramid taffeta weave with a mass per unit area of 170 g/m2. The percentage of reinforcement is 67% for the glass and 42% for the aramid (Table 1). The processing was done by contact moulding under vacuum, at a pressure of 0.3 bar for 6 hours. Polymerisation was carried out in an oven at 80°C for 8 hours. The specimens were then cut to the same dimensions: 200x20x1 mm3.

2.1. Materials

Table 1. Material

Fiber	Glass E	Kevlar
weaving	UD	Taffeta
Surfacedensity [g/m2]	300	170
mass fraction [%]	67	42
Resin	Epoxy SR 1500 /Hardner glass	
Layer	4	6
Weight[g]	7.2	4.4
Dimensions [mm3]	220x30x1	
supplier	Sicomin France	

2.2. Fatigue

Tensile fatigue was carried out under loading at a constant rate of 1mm/min, under controlled displacement up to 50% of the static failure displacement. Fatigue amplitude of 10% of the displacement at failure was imposed on the materials (Table 2).

Table 2. Experimental data

Fiber	Glass		Kevlar
Breaking Force [N]	10292		6124
Breaking deformation [mm]	1.76		1.34
Amplitude [mm]	0.35		0.27
Speed [mm/mn]		1	
Frequency [Hz]		10	
Number of cycles		1000000	
Immersion [h]		1000	

2.3. Natural ageing

The specimens were immersed in synthetic seawater at 37‰, for 1000h, after fatigue at 1000000 cycles. Composite materials have been the subject of several studies and acoustic monitoring has provided a good understanding of the different types of damage caused by the external environment (Roundi et al., 2019; Refahi & Milad Hajikhani, 2009; Ben Ammar, 2014; Nechad, 2004). The tensile test manifests itself as surface vibrations in the form of elastic waves that are amplified and collected by three piezoelectric sensors and recorded by an acquisition system, to give the acoustic emission signal, Figure 3. The interpretation of these signals, based on the work of some researchers who have exploited this niche, allows us to understand the different degradations and their origins.

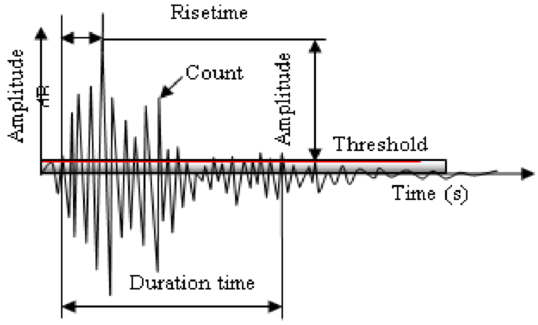

Fig. 3. Acoustic emission signal

Some authors, among many others (Rolando Rios-Soberanis et al., 2017; Kline et al., 1981) specializing in the field of acoustic emission for composite materials, have developed a quantitative approach to the technique dedicated to this niche. They have determined the relationship between the event resulting from a source and the signal detected by the acoustic sensors, connected to the processed material (Wadley et al., 1981).

In order to exploit the results of the acoustic emission in a rational way, we have based ourselves on the work of several authors, pioneers in the field (Ceausescu-Ersen, 2004; Åberg & Gudmundson, 2000; De Groot et al., 1995; Chen et al., 1992; Kim & LEE, 1997) to interpret the results of our work. These authors observed that the acoustic signals associated with matrix cracks correspond to low frequency signals, whereas those associated with fiber breakage have higher frequencies (Kocsis et al., 1995; Kotsikos et al., 1999; Kotsikos et al., 2000; Benzeggagh et al., 1992). They classified the amplitudes into three or four groups, from the lowest to the highest, to associate them with matrix cracking, then with decohesions and delaminations and finally with fiber breakage. We have opted for an acoustic map, given in Table 3, following the synthesis of the results given by the practical tests and the results of the bibliography.

Table 3. Acoustic map

N°	Damage mechanism	Nb of dB
0	Threshold (Parasite noises)	0-40
1	Matrix cracking	40-60
2	Interlaminar delamination	60-70
3	Debonding	60-70
4	Fiber breakage	70-90

3. Result and discussion

3.1 Static tests

In order to characterize the two materials, static tensile tests were carried out to determine the corresponding stresses and strains. For this purpose, a batch of five specimens of each type was statically tested. Figures 4 and 8, obtained from the previous tests, give us an idea of these materials. They represent the evolution of the stress as a function of the deformation. We observe a quasi-linear behavior until failure of the glass fiber and Kevlar fiber specimens, which are of the brittle type. The results of the static tests for both materials are given in Table4.

Table 4. Physical and mechanical properties of GFRP and KFRP

Fiber	Glass	Kevlar
Maximal stress [MPa]	438	305
Maximal strain[%]	3.92	2.7
Longitudinal module[GPa]	18	16.5
Transversal Module [GPa]	---	16.5

3.2 Epoxy composite plates

The interpretation of the fracture progression of the glass-epoxy composite specimen in static tension is based on four zones.

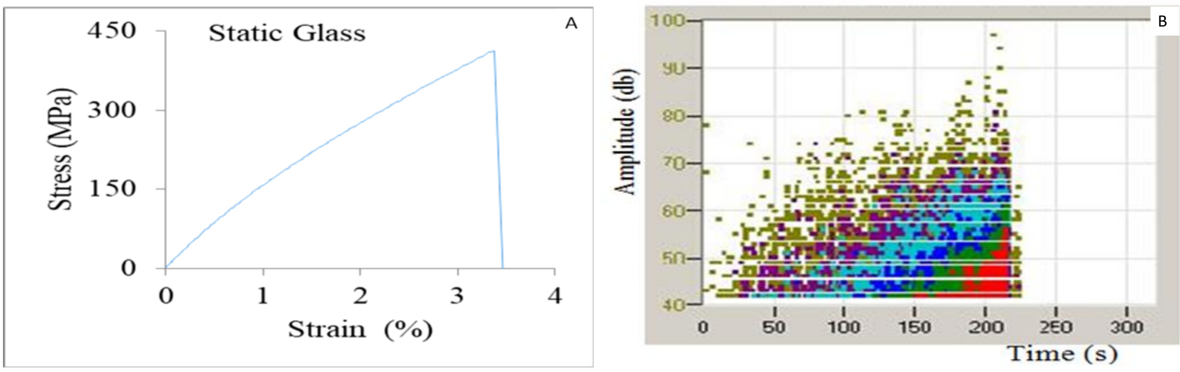

Fig. 4. Stress-strain curves for glass-epoxy specimens (A) Mechanical curve (B) Acoustic curve

Zone 1: Resin failure (Acoustic signal amplitudes between 40 and 60 dB), Figure (5:A). During the static tensile test, the resin degrades progressively, following the appearance of micro-cracks, which form preferred crack paths (Barre & Benzeggagh, 1994). These micro-cracks correspond to events that are captured by the three piezoelectric sensors and appear as dots on the screen of the acoustic event acquisition system. Each point corresponds to a degradation of the composite material. Depending on the location of the point on the acoustic acquisition screen, between the amplitude axis and the time axis, we will know if it is a matrix fracture (40-60 dB), decohesion or delamination (60-70 dB) and fiber fracture (70-90 dB).

Matrix failure is the longest period of material degradation. It starts from the beginning of the load until the specimen breaks. This proves that the matrix is the most affected by the static load and is the one that initiates the material failure.

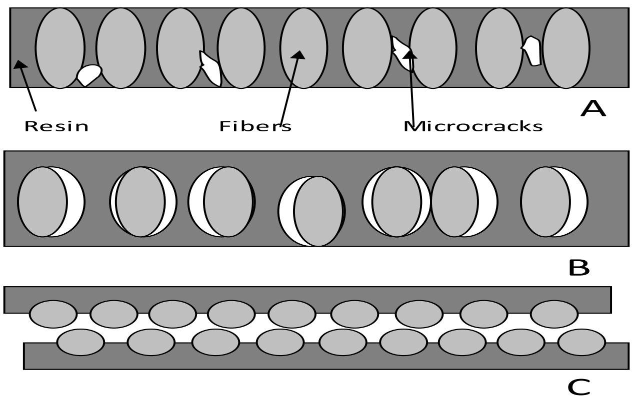

Fig. 5. (A)Initiation of matrix rupture, (B) Fiber delamination of the resin, (C) Interlaminar delamination

Zone 2-3: Decohesion and delamination (Acoustic signal amplitudes between 60 and 70 dB): Figure (5:B) decohesion, (5:C) delamination:Decohesion is the loosening of the fibers in the resin Figure (5:B). This delamination of the fibres from their matrix is due to the difference in strength of the two components of the composite material. This degradation weakens the material and usually leads to delamination.

When delamination occurs between the plies of the material we have interlaminar delamination, when it occurs within the same ply we have intralaminar delamination, Figure (5:C).The acoustic tool does not allow us to distinguish decohesion from delamination. We have the same phenomenon, either a delamination of the fibre from the resin, or the separation of one ply from another. We have the same amplitudes for both types of degradation. These events are less numerous than those of the matrix rupture. Zone 4: (Amplitudes of the acoustic signal between 70 and 90 dB), Figure 6:Fiber breakage is the final event that corresponds to the breakage of the specimen and the end of the material's life. It is the shortest and fastest stage. It corresponds to the least eventful area. Fibre breakage starts with the progressive degradation of the resin, then decohesion begins followed by delamination.

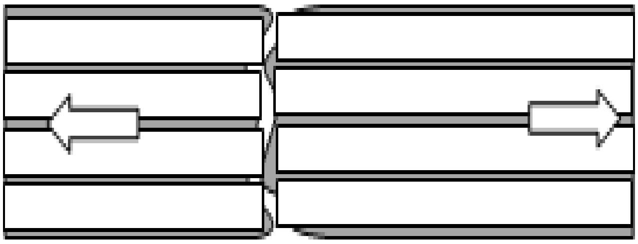

Fig. 6. Fiber breakage

3.3 Aramid-epoxy specimens
Aramid-epoxy specimens show fewer events than glass fibres. This is due to the nature of the fibres. The matrix is the first to be subjected to the effects of the tensile stress and this throughout the duration of the stress. The number of impacts due to decohesion and delamination is small compared to the tensile impact on glass fibres. This again shows that the wetting and fibre-matrix cohesion are good. The last fibre failure to appear has few impacts, indicating an abrupt failure of the specimen, shown as a straight line failure perpendicular to the tensile axis, Figure 7.

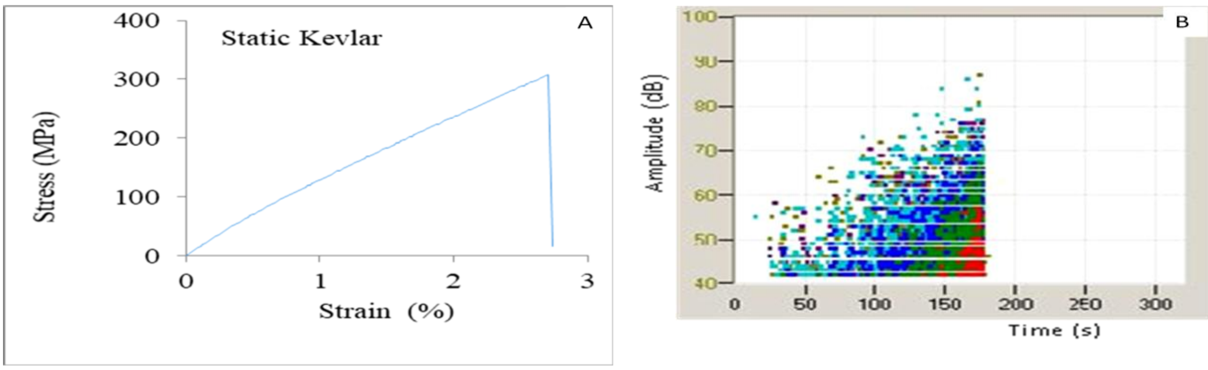

Fig. 7. Stress-strain curves for Kevlar specimens, mechanical curve and Acoustic curve

3.4 Fatigue tests
The curves of the fatigue test results for both materials are shown in Figure 8. The results obtained show that the loss of stiffness, measured by the Fmax/F0max ratio until the specimen breaks, takes place in three phases. Initially, it manifests itself by a sudden decrease in the Fmax/F0max ratio from the first cycles (on the figure, it is not clearly visible because of the scale). The decrease then becomes very slow in the second phase, which corresponds to the stable propagation of the latter, as well as the initiation of decohesion and delamination, corresponding to almost the entire life of the specimen. The third phase corresponds to the end of the material's life; it is very short and corresponds to the loss of rigidity, which accelerates brutally until the specimen breaks. It should be noted that the first phase constitutes only 10% of the lifetime whereas it corresponds to 80% of the damage rate.In our case, the glass fiber specimen failed after more than 10,000 cycles, whereas the aramid fiber specimen did not fail after 10,000 cycles. We find that both types of specimens have the same fracture profile, but the aramid specimen has higher fatigue strength. Since both types of specimens have the same resin, we can deduce that aramid fibers have better tensile fatigue resistance than glass fibers.

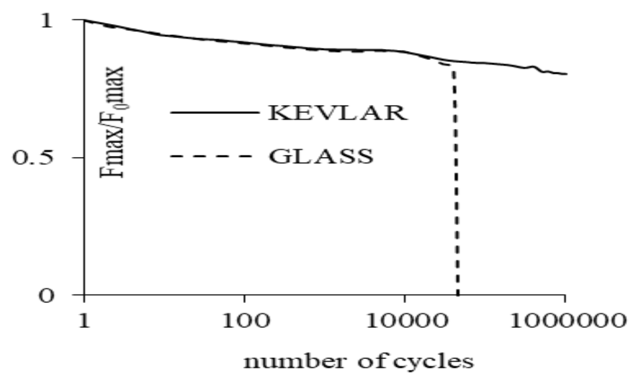

Fig.8. Fatigue test results

3.5. Acoustic results

The acoustic tool allows us to better understand the effect of tensile fatigue on the two materials. From the different studies and from Table 3, we divide the material degradation mechanisms into three groups. It should be noted that the group between 0 and 40 dB corresponds to the safety threshold generated by the parasitic noises due to the squeaking of the machines and other noises, and is not taken into consideration.

3.5.1. Fatigue of glass-epoxy specimens

Figure 9A shows the different degradations caused by tensile fatigue on a glass-epoxy material. Zone (1) between 40 and 60 dB represents the degradation of the resin during the tensile fatigue period. We note that this area is very eventful and the number of impacts is very high and therefore the resin undergoes a lot of degradation. The resin undergoes degradation from the beginning of the fatigue to the failure of the material, it is the component most exposed to degradation. The zone (2-3) between 60 and 70 dB represents decohesion and delamination. This zone represents the separation between the resin and the fibers. It weakens the material and contributes to the propagation of cracks within the material, in different forms, from decohesions that contribute to interlaminar and intralaminar cracks. The various cracks form in mode I at the onset of delamination and then transform into mode II when the specimens break. The zone (4) between 70 and 90 dB represents the degradation of the glass fibers during fatigue. The fiber breakage time is very low during fatigue compared to the resin breakage time in zone 1, indicating that the resin is most affected by fatigue. The only area of fiber breakage occurs at the beginning of the fatigue, during the first few cycles. Figure 10a shows overall consistent high resin failure, decreasing decohesions and delaminations and low fiber failure throughout the fatigue period.

3.5.2. Fatigue of aramid-epoxy specimens

The experimental study is conducted by a destructive quasi-static tensile and tensile fatigue method, under Figure 9B shows the impact of tensile fatigue on an aramid-epoxy specimen under acoustic monitoring. It can be seen that the number of impacts is less than that of the glass-epoxy specimen 9A. Since we have the same epoxy resin for both types of specimens, we can make a comparison of the wetting and the matrix fiber cohesion for both materials. The aramid-epoxy specimen shows better cohesion and wetting than the glass-epoxy specimen. This is due to the nature of the aramid fibers. The breakage zone of the resin is less important because there is better adhesion of the resin on the fibers. Decohesion, delamination and fiber breakage are represented by smaller areas than for the glass-epoxy specimen. This can be seen in Figure 2b and 2c, where we see the different effects of failure of the two specimens. The glass-fiber specimen is ruptured by extensive interlaminar delamination, whereas the aramid-epoxy specimen is ruptured cleanly in a straight line, perpendicular to the axis of the stress. This is also explained in Figure 8, where we see the glass fiber specimen breaking after about 300,000 cycles, whereas the aramid fiber specimen withstands more than one million cycles.

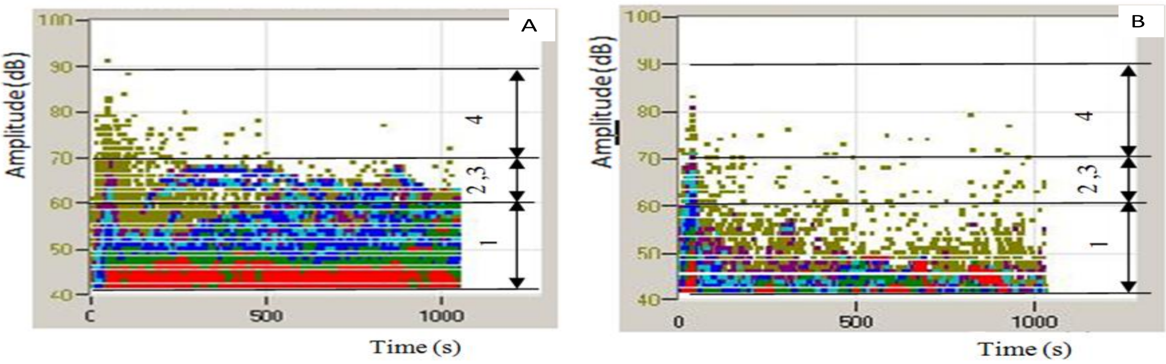

Fig.9. Acoustic results of fatigue tests (a) Acoustic results for the glass-epoxy material (b) Acoustic results for the aramid-epoxymaterial

3.6. Effects of ageing

The various studies referred to (Malpot, 2017; Mercier, 2006; Gellert & Turley, 1999; Heman, 2008; Hao et al., 2020) have shown that the osmotic origin of the degradation process of composite materials has been confirmed by previous tests in sea water and distilled water (Kececi & Asmatulu 2014). The progressive drop in mechanical properties is attributed to the plasticisation of the structural resin by water, when the material is saturated (Pal et al., 2012; Behera et al., 2020). Then the attack of the resin in the laminate occurs between two plies and leads to a further decline in mechanical properties (Gellert & Turley, 1999).

Osmotic cracking damage due to significant water uptake has been identified beyond 120h of aging. This value is far lower than our protocol of 1000h, which implies a maximum ageing. These results therefore confirm the state of damage of the materials (Castaing et al., 1992). At 20°C, the specimens quickly reach equilibrium (35 days, i.e. 840h), at 0.35% absorption and a Frick model allows the absorption kinetics to be described correctly (Chateauminois et al., 1990). At a temperature of 23°C, interactions between moisture and fatigue damage can only occur at the local scale, after capillary diffusion of moisture at the bottom of the crack (Vautier et al., 1996).

Glass-epoxy and aramid-epoxy composites undergo a progressive loss of strength as a function of the number of fatigue cycles and as a function of the immersion time. If we compare the ageing effects of both materials at 0h immersion with those immersed at 1000h, we find that the materials lose strength and acquire a certain ductility characterised by a higher elongation during tensile stress (ΔlG, ΔlK), Figure 10.

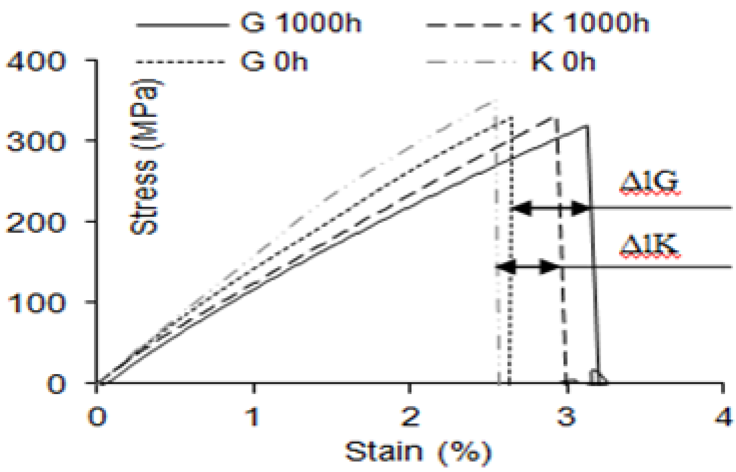

Fig. 10. Effects of ageing after fatigue for epoxy glass and epoxy aramid

Salt water permeates the interfaces and micro-cracks left by fatigue de-coating and delamination. This infiltration reduces the stiffness of the resin and gives the material a certain flexibility which allows it to stretch a little more before breaking. The relaxation of internal stresses developed during the cooling of the samples after curing may be responsible for this improvement. This demonstrates that the resin is well adapted to the effect of moisture. A similar phenomenon was observed by F. Dal Maso et al (Dal Maso et al., 1996). Since we have the same resin, for both materials we should have the same elongation at break. We find that the % elongation is higher in the glass-epoxy material than in the aramid-epoxy (ΔlG, ΔlK), which shows that the wetting and bonding of the resin on the aramid fibres is higher than on the glass fibres. This is due to the nature of the fibres in both materials. Aramid fibres are more fluffy than glass fibres. Therefore the resin adheres more and better to the aramid fibers, figure 11 (A) and (B).

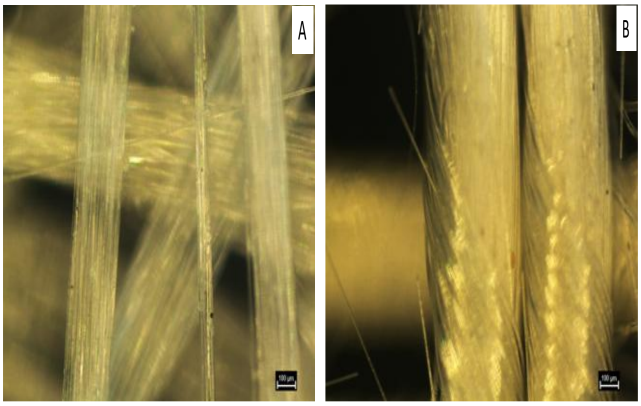

Fig. 11. Microscopy of glass fibres (a) and aramid fibres (b)

4. Conclusion

The glass-epoxy and aramid-epoxy composites were subjected to static tensile tests. Another set of specimens were subjected to tensile fatigue tests and then aged in synthetic seawater at 37‰. All specimens showed losses in strength and a gain in elongation. This loss in mechanical characteristics is in proportion to the increase in fatigue time and ageing time. The progressive drop in mechanical properties is attributed to the effects of fatigue and plasticisation of the resin by seawater, when the material is saturated. Subsequently, resin attack in the laminate occurs more readily between the glass-epoxy plies than between the aramid-epoxy plies and leads to a greater decline in mechanical properties (Gellert & Turley, 1999). When the specimens fail, we find significant delamination in the glass-epoxy material and not in the aramid-epoxy material. This is due to the nature of the fibers. Both materials can withstand the effects of seawater. Acoustic monitoring shows various degradations caused by static traction and fatigue over 10000 cycles. These different degradations lead to internal fractures which facilitate the diffusion of seawater in both composites and lead to leaching. This leaching results in a loss of strength and flexibility of the materials, without affecting their integrity.

Based on the mechanical, acoustic and microscopic results obtained, we can conclude that both materials are resistant to seawater and can be safely used in civil engineering.

Acknowledgments

The authors would like to thank the managers of the LAUM acoustics laboratory, CNRS UMR 6613 of the University of Maine, France, for providing them with the necessary equipment to carry out the various tests.

References

Åberg, M., & Gudmundson, P. (2000). Micromechanical modeling of transient waves from matrix cracking and fiber fracture in laminated beams. *International Journal of Solids and Structures, 37*(30), 4083–4102. https://doi.org/10.1016/S0020-7683(99)00234-2

Hosen, M. A., Alengaram, U. J., Jumaat, M. Z., Sulong, N. R., & Darain, K. M. U. (2017). Glass fiber reinforced polymer (GFRP) bars for enhancing the flexural performance of RC beams using side-NSM technique. *Polymers, 9*(5), 180. https://doi.org/10.3390/polym9050180

Bandaru, A. K., Kothandan, D. K., Chouhan, H., Ma, H., & O'Higgins, R. M. (2025). Ballistic impact performance of Kevlar®/UHMWPE hybrid composite panels with a liquid thermoplastic resin, Elium®. *Materials and Design, 252*, 113706. https://doi.org/10.1016/j.matdes.2024.113706

Barré, S., & Benzeggagh, M. L. (1994). On the use of acoustic emission to investigate damage mechanisms in glass-fibre-reinforced polypropylene. *Composites Science and Technology, 52*(3), 369–376. https://doi.org/10.1016/0266-3538(94)90122-8

Behera, A., Dupare, P., Thawre, M. M., & Ballal, A. (2020). Effects of hygrothermal aging and fiber orientations on constant amplitude fatigue properties of CFRP multidirectional composite laminates. *International Journal of Fatigue, 136*, 105590. https://doi.org/10.1016/j.ijfatigue.2020.105590

Ammar, I. B. (2014). *Contrôle de santé vibro-acoustique de l'endommagement des matériaux composites à base polymère pour l'aéronautique* (Doctoral dissertation, Le Mans Université; Université de Sfax).

Khalifa, W. B. (2013). *Modélisation de la propagation et de la réception des ondes élastiques émises par un défaut sous contrainte: Application à la simulation des contrôles non destructifs par émission acoustique* (Doctoral dissertation, Université de Valenciennes et du Hainaut-Cambrésis).

Bentahar, M. (2005). *Acoustique non-linéaire: Application à la caractérisation ultrasonore de l'endommagement des matériaux hétérogènes et à la prédiction de la durée de vie* (Doctoral dissertation, INSA de Lyon).

Benzeggagh, M. L., Barre, S., Echalier, B., & Jacquemet, R. (1992). Etude de l'endommagement de matériaux composites à fibres courtes et à matrice thermoplastique. In *AMAC Journées Nationales Composites* (Vol. 8, pp. 703–714).

Bunsell, A. R. (1989). L'absorption d'eau par les matériaux composites à matrice organique. In *CODEMAC, 2ème École d'automne*, Guétary.

Castaing, P., Tsouvalis, N., & Lemoine, L. (1992, December). Evolution des propriétés mécaniques de matériaux composites verre/polyester gelcoates en milieu marin. In *La Construction Navale en Composites*, Paris, France.

Ceausescu-Ersen, E. A. (2004). *Application de la technique d'émission acoustique à la caractérisation de matériaux céramiques évolutifs* (Doctoral dissertation, Université de Limoges).

Chateauminois, A., Chabert, B., Soulier, J. P., & Vincent, L. (1990). Influence du vieillissement sur les propriétés viscoélastiques et la tenue en fatigue de matériaux composites verre/époxy. In *Annales des composites*, AMAC, France (pp. 823–832).

Chen, O., Karandikar, P., Takeda, N., & Kishi Rcast, T. (1992). Acoustic emission characterization of a glass-matrix composite. *Nondestructive Testing and Evaluation, 8*(1–6), 869–878.

Dal Maso, F., Dewille, B., Grojean, F., Huvey, M., Martin, J., & Montabord, L. (1996). Vieillissement d'armures de traction en composite pour conduites flexibles. In *Annales des composites*, AMAC, France (pp. 27–37).

D'Antino, T., & Pisani, M. A. (2019). Long-term behavior of GFRP reinforcing bars. *Composite Structures, 227*, 111283. https://doi.org/10.1016/j.compstruct.2019.111283

De Groot, P. J., Wijnen, P. A., & Janssen, R. B. (1995). Real-time frequency determination of acoustic emission for different fracture mechanisms in carbon/epoxy composites. *Composites Science and Technology, 55*(4), 405–412. https://doi.org/10.1016/0266-3538(95)00118-2

Devine, M., Bajpai, A., Obande, W., Ó Brádaigh, C. M., & Ray, D. (2023). Seawater ageing of thermoplastic acrylic hybrid matrix composites for marine applications. *Composites Part B: Engineering, 263*, 110879. https://doi.org/10.1016/j.compositesb.2023.110879

Eslava-Hernández, A., Rodríguez-González, J. A., Rubio-González, C., Martínez-Pérez, A. I., & Vera-Cárdenas, E. E. (2024). Effect of seawater aging on the erosive wear response of aramid fiber reinforced composites. *Journal of Composite Materials, 58*(9), 1167–1178. https://doi.org/10.1177/00219983231235170

SIAMPIRINGUE, N., Gaumet, S., & Lemaire, J. (1997). Durabilité des matériaux composites: Comment réaliser un vieillissement accéléré fiable un exemple: les polyesters insaturés. *Composites (Paris), 37*(21), 48–54.

Gautier, L., Mortaigne, B., Bellenger, V., & Verdu, J. (2000). Osmotic cracking nucleation in hydrothermal-aged polyester matrix. *Polymer, 41*(7), 2481–2490. https://doi.org/10.1016/S0032-3861(99)00457-3

Gellert, E. P., & Turley, D. M. (1999). Seawater immersion ageing of glass-fibre reinforced polymer laminates for marine applications. *Composites Part A: Applied Science and Manufacturing, 30*(11), 1259–1265. https://doi.org/10.1016/S1359-835X(99)00030-5

Ghaib, M., Shateri, M., Thomson, D., & Svecova, D. (2024). Comparison between microstructural analysis of GFRP and CFRP rebars using micro computed tomography (µCT), scanning electron microscope (SEM), and acoustic emission (AE) techniques. *Composites Science and Technology, 250*, 110545. https://doi.org/10.1016/j.compscitech.2023.110545

Guo, F., Zhang, Z., Zhang, H., Wang, K., & Jiang, W. (2010). Tribological behavior of spun Kevlar fabric composites filled with fluorinated compounds. *Tribology International, 43*(8), 1466–1471. https://doi.org/10.1016/j.triboint.2010.02.006

Hao, X., Xian, G., Huang, X., Xin, M., & Shen, H. (2020). Effects of adhesive coating on the hygrothermal aging performance of pultruded CFRP plates. *Polymers, 12*(2), 491. https://doi.org/10.3390/polym12020491

Heman, M. B. (2008). *Contribution à l'étude des interphases et de leur comportement au vieillissement hygrothermique dans les systèmes à matrice thermodurcissable renforcés de fibres de verre* [Doctoral dissertation, Université du Sud Toulon Var].

Karger-Kocsis, J., Harmia, T., & Czigany, T. (1995). Comparison of the fracture and failure behavior of polypropylene composites reinforced by long glass fibers and by glass mats. *Composites Science and Technology, 54*(3), 287–298. https://doi.org/10.1016/0266-3538(95)00112-7

Kececi, E., & Asmatulu, R. (2014). Effects of moisture ingression on polymeric laminate composites and its prevention via highly robust barrier films. *The International Journal of Advanced Manufacturing Technology, 73*, 1657–1664. https://doi.org/10.1007/s00170-014-5925-4

Kim, S. T., & Lee, Y. T. (1997). Characteristics of damage and fracture process of carbon fiber reinforced plastic under loading-unloading test by using AE method. *Materials Science and Engineering: A, 234*, 322–326. https://doi.org/10.1016/S0921-5093(97)00236-4

Kychkin, A. K., Startsev, O. V., Lebedev, M. P., Kychkin, A. A., & Lukachevskaia, I. G. (2025). The effect of biocontamination on mechanical strength and moisture transfer performance of epoxy basalt fiber reinforcement bar exposed to arctic conditions. *Polymers, 17*(4), 460. https://doi.org/10.3390/polym17040460

Kline, R. A., Green Jr, R. E., & Palmer, C. H. (1981). Acoustic emission waveforms from cracking steel: Experiment and theory. *Journal of Applied Physics, 52*(1), 141–146. https://doi.org/10.1063/1.328511

Kotsikos, G., Evans, J. T., Gibson, A. G., & Hale, J. M. (2000). Environmentally enhanced fatigue damage in glass fibre reinforced composites characterised by acoustic emission. *Composites Part A: Applied Science and Manufacturing, 31*(9), 969–977. https://doi.org/10.1016/S1359-835X(00)00040-2

Kotsikos, G., Evans, J. T., Gibson, A. G., & Hale, J. (1999). Use of acoustic emission to characterize corrosion fatigue damage accumulation in glass fiber reinforced polyester laminates. *Polymer Composites, 20*(5), 689–696. https://doi.org/10.1002/pc.10319

Malpot, A. (2017). *Etude du comportement en fatigue d'un composite à matrice polyamide renforcé d'un tissu de fibres de verre pour application automobile* [Doctoral dissertation, ISAE-ENSMA].

Mercier, J. (2006). *Prise en compte du vieillissement et de l'endommagement dans le dimensionnement de structures en matériaux composites* [Doctoral dissertation, École Nationale Supérieure des Mines de Paris].

Nechad, H. (2004). *Évaluation de l'endommagement et de la rupture de matériaux hétérogènes par ultrasons et émission acoustique: Estimation de la durée de vie restante* [Doctoral dissertation, INSA de Lyon].

Nimdum, P., & Renard, J. (2012, June). Use of acoustic emission to discriminate damage modes in carbon fibre reinforced epoxy laminate during tensile and buckling loading. In *ECCM 15 - 15th European Conference on Composite Materials* (p. 8).

Pal, R., Narasimha Murthy, H. N., Sreejith, M., Vishnu Mahesh, K. R., Krishna, M., & Sharma, S. C. (2012). Effect of laminate thickness on moisture diffusion of polymer matrix composites in artificial seawater ageing. *Frontiers of Materials Science, 6*(3), 225–235. https://doi.org/10.1007/s11706-012-0174-0

Perreux, D., Suri, C., Varchon, D., & Oytana, C. (1992, December). Endommagement mécanique de matériaux composites. Rôle sur les propriétés hygrothermiques. In *La Construction Navale en Composites*, Paris (France), 7–9 Dec 1992.

Hawileh, R. A., & Rasheed, H. A. (2017). Thermal analysis of GFRP-reinforced continuous concrete decks subjected to top fire. *International Journal of Advanced Structural Engineering, 9*, 315–323. https://doi.org/10.1007/s40091-017-0162-z

Refahi, A., & Hajikhani, M. (2009). Damage monitoring of composite materials by using acoustic emission. *Journal of Composite Materials*.

Rios-Soberanis, C. R., Rodriguez-Laviada, J., Perez-Pacheco, E., Sakai, T., & Wakayama, S. (2017). Acoustic emission technique applied in textiles mechanical characterization. In *MATEC Web of Conferences* (Vol. 95, p. 07016). EDP Sciences. https://doi.org/10.1051/matecconf/20179507016

Roundi, W., El Mahi, A., El Gharad, A., & Rebiere, J. L. (2019). Evaluation of damage mechanisms in glass/epoxy laminates using the acoustic emission technique. *Comptes Rendus des JNC 21 – Bordeaux INP*, 1–3 juillet.

Sebastian, M. S., Unnikrishnan, K. C., & Narayanan, S. (2008). Viscoelastic properties of Kevlar-29 fabric tape strength member. *Mechanics of Materials, 40*(11), 949–960. https://doi.org/10.1016/j.mechmat.2008.06.005

Stankovic, D., Obande, W., Devine, M., Bajpai, A., Ó Brádaigh, C. M., & Ray, D. (2024). Accelerated seawater ageing and fatigue performance of glass fibre reinforced thermoplastic composites for marine and tidal energy applications. *Composites Part C: Open Access, 14*, 100470. https://doi.org/10.1016/j.jcomc.2024.100470

Tan Duong, N. (1995). *Cartographie et caractérisation acoustiques des matériaux composites : Application à l'évaluation du taux volumique de porosité dans un matériau composite RTM* (Doctoral dissertation, Université du Havre, France).

Ursache, S., Cerbu, C., Hadăr, A., & Petrescu, H. A. (2024). Effects of rubber core on the mechanical behaviour of the carbon–aramid composite materials subjected to low-velocity impact loading considering water absorption. *Materials, 17*(16), 4055. https://doi.org/10.3390/ma17164055

Vauthier, E., Abry, J., Bailliez, T., & Chateauminois, A. (1996). Interactions entre le vieillissement hygrothermique et l'endommagement par fatigue de composites unidirectionnels verre-epoxy. In *JNC 10: Comptes-rendus des dixièmes journées nationales sur les composites* (Paris, 29–31 octobre 1996), 249–260.

Vigier, G., & Tatibouet, J. (1993). Physical ageing of amorphous and semicrystalline poly(ethylene terephthalate). *Polymer, 34*(20), 4257–4266. https://doi.org/10.1016/0032-3861(93)90092-T

Wadley, R. N. G., Scruby, C. B., & Shrimpton, G. (1981). Quantitative acoustic emission source characterisation during low temperature cleavage and intergranular fracture. *Acta Metallurgica, 29*(2), 399–414. https://doi.org/10.1016/0001-6160(81)90199-4

Wang, Y. X. Y. M., & Xia, Y. M. (1999). Experimental and theoretical study on the strain rate and temperature dependence of mechanical behaviour of Kevlar fibre. *Composites Part A: Applied Science and Manufacturing, 30*(11), 1251–1257. https://doi.org/10.1016/S1359-835X(99)00043-3

ICEARC'25
4th International Civil Engineering & Architecture Conference
17-19 May 2025, Trabzon, Türkiye

An automation-based smart curing blanket for optimizing the concrete curing process

Seyedehdorsa Akhtarian[1], İpek N. Semercioğlu[*1], Hasan B. Başağa[1,2]

[1] *Karadeniz Technical University, Department of Civil Engineering, 61080 Trabzon, Türkiye*
[2] *Earthquake and Structural Health Application and Research Center, Karadeniz Technical University, 61080 Trabzon, Türkiye*

Abstract. Concrete curing is a critical process for achieving the design-stage strength in concrete and for maintaining its durability throughout its service life. In current construction practices, curing operations typically involve methods such as wet curing, membrane forming curing, and temperature controlled curing, most of which rely heavily on human supervision and labor. To optimize the concrete curing process and reduce the need for manual oversight, this study proposes an automation-based "Smart Curing Blanket". The proposed smart curing blanket consists of modular curing panels that include three functional layers: a hydrophobic top layer for water retention, a TPU-based intermediate water reservoir, and a hydrophilic textile base in direct contact with the concrete. These layers operate synergistically to absorb, store, and redistribute water as needed. The smart blanket is embedded with humidity and temperature sensors that monitor the concrete's hydration process. The data collected from sensors is wirelessly transmitted to a centralized external ESP32-based controller unit via Wi-Fi or Bluetooth, enabling off-site supervision and data logging. The designation of the blanket as 'smart' is attributed to its integrated system capable of real-time monitoring and data transmission. By automating the water distribution process and minimizing manual involvement, the smart curing blanket significantly improves curing consistency, reduces water waste, and enhances the structural performance of the concrete. This innovative approach presents a sustainable and scalable alternative to conventional methods, addressing both environmental and operational challenges in the construction industry.

Keywords: Concrete curing; Strength; Durability; Smart curing blanket; Sustainability

1. Introduction

Concrete is one of the most widely used construction materials worldwide, primarily due to its high compressive strength, formability, and durability. Among the many factors that influence concrete quality, the curing process plays a particularly critical role. After mixing its components, concrete gradually loses its plasticity and begins to harden, forming a rigid structure within a few hours. This transformation is driven by a chemical reaction between water and cement, known as hydration (Engin, 2014). To ensure complete hydration, concrete must retain sufficient moisture after placement. Curing helps maintain this internal moisture, allowing hydration to proceed and enabling the concrete to reach its designed strength. In essence, curing aims to slow the evaporation of water from the surface. When this process is not properly managed, rapid moisture loss can occur, leading to surface cracks due to shrinkage and compromising the concrete's long-term strength and durability (Neville, 2011).

Concrete curing methods generally fall into three main categories: moist curing, membrane forming curing, and temperature controlled curing. Moist curing involves keeping the surface wet to sustain hydration, which can be done by spraying water, submerging the concrete, creating water ponds, or covering the surface with wet materials like burlap or fabric. Membrane forming methods aim to trap moisture within the concrete by forming a protective layer on the surface, using plastic sheeting or applying thin coatings of polymer based or wax containing compounds. On the other hand, temperature controlled curing accelerates hydration by increasing the concrete's temperature, often through insulating blankets or embedded heating cables, especially in cold weather conditions (Kosmatka et al., 2002). Among these conventional methods, placing wet coverings or spraying water are widely used. However, these techniques require continuous supervision and frequent water application throughout the curing period. Materials like burlap release water gradually but must be regularly re-wetted, while water spraying via hoses or sprinklers demands consistent manual intervention. Concisely, these and other similar manual curing methods are generally difficult to control, require considerable labor, and often lead to excessive water use.

[*] Corresponding author, E-mail: ipeknaz@ktu.edu.tr

https://doi.org/10.31462/icearc2025_ce_mat_691

golden light publishing

Therefore, to reduce both labor demands and water consumption, the need for automated curing systems has become increasingly evident.

A review of the literature on automated curing systems indicates an increasing trend toward enhancing concrete curing processes through automation, sensor technologies, and remote monitoring methods. An early notable contribution by Barroca et al. (2013) involved developing a cost-effective wireless sensor network designed to remotely monitor internal temperature and relative humidity within reinforced concrete elements during the setting and curing phases. Due to the alkaline environment causing early sensor failure, the sensors were encapsulated with polypropylene sleeves to enable prolonged operational stability. Building upon this sensor-based monitoring concept, Yang et al. (2018) developed a PLC-controlled mist-spraying system designed to regulate surface temperature and relative humidity automatically. This system significantly reduced early-age cracking and provided notable reductions in water, energy, and labor costs compared to manual methods. Advancing further with IoT technology, Lo et al. (2021) introduced a system designed to control moisture loss by calculating instantaneous evaporation rates and automatically activating mist spraying. This approach effectively maintained moisture balance and significantly mitigated crack formation during concrete setting. Further innovating IoT applications, Baek et al. (2023) developed a system combining real-time flow rate sensors and image processing techniques to monitor curing compound applications on concrete pavements. This approach ensured consistent application quality and homogeneity, thus improving quality control and labor efficiency. Finally, Taffese and Nigussie (2023) conceptualized an integrated IoT system that continuously monitors internal humidity and temperature, automatically activating smart valves and spraying mechanisms based on real-time data. This system utilizes maturity methods to predict early-age strength development, optimizing concrete strength gains while minimizing water usage and labor costs. Collectively, these studies underscore the effectiveness of automation and sensor technologies in optimizing concrete curing processes.

Similarly, this study aims to develop an innovative approach that could serve as an alternative solution to existing automated curing methods. In this context, the research proposes an automation-based smart curing blanket designed to optimize the concrete curing process. Currently at the prototype stage, the proposed smart curing blanket will be further refined through laboratory testing. The smart curing blanket introduced in this research represents a simple, modular, energy-efficient, and fully automated system capable of actively monitoring both surface and internal humidity levels of concrete, precisely controlling water application, and being reusable across multiple projects. The system comprises modular panels with integrated low-pressure water distribution mechanisms, wireless humidity sensors, and battery-operated valve controls. The proposed smart curing blanket system aims to optimize concrete curing by ensuring continuous moisture availability while minimizing labor, water usage, and system complexity.

2. Material and methods

The proposed smart curing blanket will be technically presented in detail, including its design specifications and key functional components. The blanket system, composed of three distinct layers, is elaborated with respect to the water distribution mechanism, sensor and control infrastructure, power supply and maintenance considerations, as well as the overall system workflow and software logic. The components to be employed in the design of the smart curing blanket are illustrated in Fig. 1.

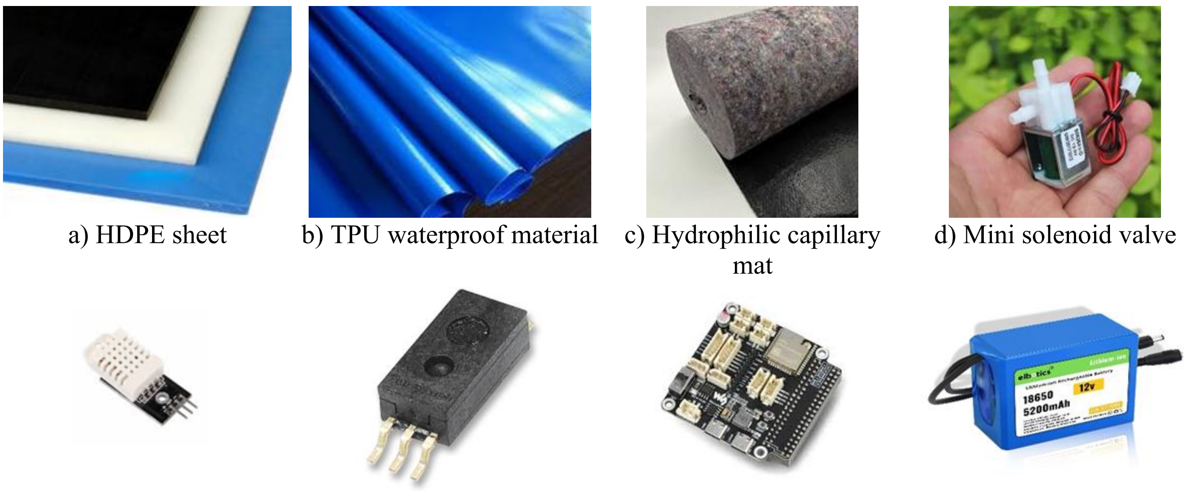

a) HDPE sheet | b) TPU waterproof material | c) Hydrophilic capillary mat | d) Mini solenoid valve

e) DHT22 sensor | f) HIH humidity sensor | g) ESP32 module | h) Battery pack

Fig. 1. System components of the smart curing blanket

2.1. Smart curing blanket design
In this subsection, the mechanical configuration of the smart curing blanket is presented. The proposed system is designed as modular panels measuring 1m x 2m, enabling ease of on-site assembly, scalability, and efficient curing over expansive surfaces such as foundations and floor slabs.

Each panel consists of three primary functional layers:

- Top Layer: A 3 cm thick hydrophobic high-density polyethylene (HDPE) sheet (Fig. 1a), which provides ultraviolet (UV) protection, reduces moisture loss due to evaporation, and offers a walkable surface suitable for construction site conditions.
- Middle Layer: A 5 cm deep thermoplastic polyurethane (TPU) welded reservoir (Fig. 1b) that functions as a temporary water storage unit, allowing for gravity-assisted water distribution when required.
- Bottom Layer: A 5 cm thick polyester-viscose hydrophilic textile (Fig. 1c) exhibiting capillary action, capable of absorbing water from the middle layer and releasing it gradually to the concrete surface, thereby maintaining consistent moisture contact.

The integration of these three layers ensures effective water retention and controlled delivery to the curing surface, promoting uniform and continuous hydration throughout the curing period. To support the practical deployment of this multilayer configuration in the field, the system has been further developed with modular connection features that enhance both structural integrity and installation efficiency. To facilitate modularity, each panel incorporates interlocking tongue-and-groove edge connections, allowing for horizontal and vertical integration without overlapping. This puzzle-type connection system enables the formation of a seamless and continuous curing surface, minimizing the risk of gaps or air pockets that may cause uneven hydration. Furthermore, the design eliminates the need for adhesives or external fastening components, thus streamlining installation and enhancing field applicability.

Fig. 2 presents a schematic cross-sectional and plan view illustrating the described multilayer configuration and modular connections of the smart curing blanket, along with the integrated water distribution components.

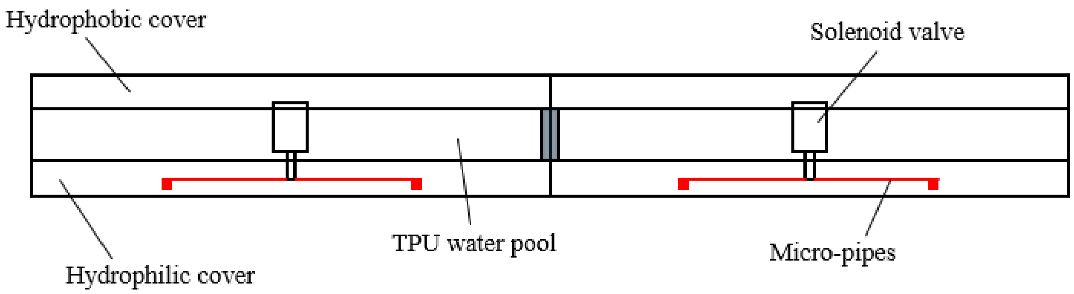

a)

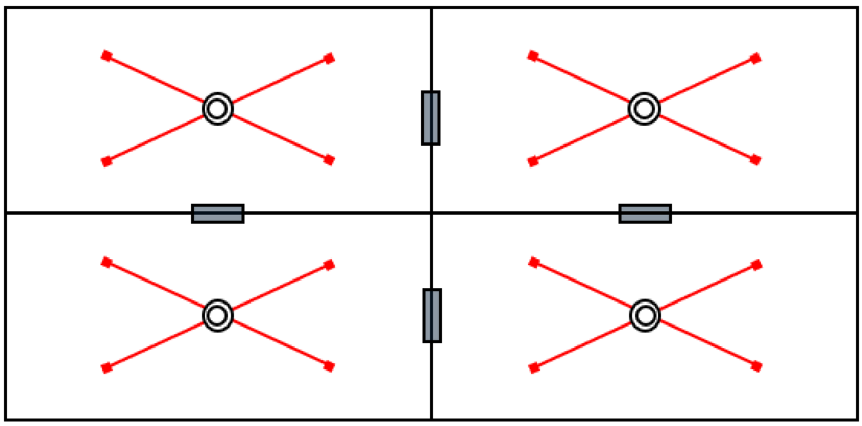

b)

Fig. 2. Cross-sectional (a) and plan (b) view of the smart curing blanket configuration and modular connections

2.2. Water distribution system
In this subsection, the operational workflow of the pool, valve, and microtube components within the water distribution system is described in detail. Initially, water is introduced into the intermediate pool layer of each panel via external hose connections. Each reservoir incorporates a 12V DC mini solenoid valve (Fig. 1d), which is integrated into a compact, gravity-fed distribution mechanism. Rather than employing conventional sprinkler

systems, the design utilizes four 4 mm internal microtubes connected to the valve outlet, enabling uniform water delivery to the four corners of the underlying hydrophilic textile layer. Upon receiving an activation signal from the control system, the solenoid valve opens, allowing water to flow by gravity through the microtubes and reach the textile interface at evenly distributed locations. This approach eliminates the need for pressurized plumbing infrastructure, thereby reducing mechanical complexity and ensuring minimal energy consumption.

Each valve is housed within a waterproof enclosure embedded in the hydrophobic top layer of the blanket. The microtubes are routed through sealed channels, ensuring uninterrupted delivery of water to the hydrophilic textile below. This fully enclosed configuration safeguards the water distribution process from external contaminants, physical impacts, and adverse environmental conditions.

Between activation cycles, the pool remains in a static state, maintaining a low water level of approximately 2–3 cm. Water is only dispensed when required, through controlled operation of the valve, ensuring both resource efficiency and system responsiveness.

A schematic cross-section and plan view illustrating the described multilayer configuration, modular connections, and integrated water distribution components of the smart curing blanket are provided in Fig. 2.

2.3. Sensor and control infrastructure

In this subsection, the sensor infrastructure of the proposed smart curing blanket is described in detail. To enable intelligent, adaptive, and efficient operation, each smart curing blanket panel is equipped with a dual-sensor configuration that facilitates real-time environmental monitoring and targeted water application. The first sensing unit consists of a DHT22 digital temperature and humidity sensor (Fig. 1e), positioned on the outer surface of the hydrophilic textile layer in direct contact with the concrete. This sensor measures surface relative humidity (RH) and connects to the panel via jumper wires terminated at a waterproof pin connector embedded in the side of the unit. These connectors are designed to support quick disconnection and reusability, allowing the system to be easily redeployed across multiple construction sites. Complementing the sensor network, the second component is a Honeywell HIH-5030 analog humidity sensor (Fig. 1f), which is embedded directly within the concrete mass. This sensor continuously monitors the internal relative humidity of the concrete, thereby enabling the assessment of long-term hydration progress. A key operational threshold is defined such that, once the internal RH reaches and maintains 100% for a specified duration (e.g., 48 hours), the system automatically and permanently terminates water delivery to the corresponding panel. This mechanism prevents over-curing and avoids unnecessary water consumption, ensuring both resource efficiency and performance reliability.

Sensor wiring from each panel is routed through waterproof side-mounted connectors, which facilitate rapid field connections via jumper cables. These cables extend from individual panels to a centralized control unit positioned outside the curing zone, typically housed in a weather-resistant enclosure mounted on a nearby structure or pole.

The centralized control unit is built on a single ESP32 development board (Fig. 1g), selected for its integrated Wi-Fi and Bluetooth capabilities, low energy consumption, and robust wireless communication support. The ESP32 controller continuously collects data from all connected panels via hardwired sensor inputs, with optional support for wireless low-power communication modules such as nRF24L01 or LoRa in large-scale implementations. This centralized architecture enables real-time monitoring, streamlined system coordination, and unified control through a single management interface.

Valve actuation is likewise coordinated by the central controller. Each panel's 12V DC solenoid valve is connected either through low-voltage relay lines or wireless relay modules. Based on panel-specific RH data, the ESP32 transmits individual actuation commands to open or close the valves, ensuring that water is supplied exclusively to panels requiring additional curing. This targeted control strategy enhances overall system efficiency and ensures optimal hydration conditions throughout the curing process.

2.4. Power system and maintenance design

In this subsection, the operational mechanism through which the proposed smart curing blanket is powered is presented. To ensure the independent functioning of each curing panel while minimizing wiring complexity and enhancing modularity, each unit is equipped with its own detachable power module. This module comprises a rechargeable 12V lithium-ion battery pack -typically configured as a 3S1P 18650 arrangement with a capacity of 2600–3000 mAh (Fig. 1h)- which is enclosed within a clip-in waterproof capsule mounted on the interior wall of the pool layer.

The battery pack is connected to the panel's solenoid valve through a plug-in connector such as JST or XT60, with the wiring routed via sealed channels embedded within the hydrophobic top layer. The design prioritizes field accessibility; batteries can be easily removed and replaced without dismantling the panel. For this purpose, a side flap or a silicone-sealed access port is integrated into each panel, allowing technicians to service or swap power units rapidly and with minimal disruption.

The system is engineered for energy efficiency, as the solenoid valves are activated only during short-duration watering cycles, typically drawing 200 mA of current for 30 to 60 seconds per activation. Under standard curing conditions, a fully charged battery is capable of powering the system for several consecutive days, thereby supporting operational continuity without frequent maintenance.

For extended use scenarios or off-grid applications, the system offers an optional upgrade: a 20W thin-film solar patch can be laminated into the surface of the hydrophobic top layer. This solar module is connected to a compact maximum power point tracking (MPPT) charge controller, enabling continuous passive recharging of the battery without interfering with the positioning or usability of the panel. Depending on regional solar irradiance, a single solar unit can sustain up to two to four panels simultaneously. By decoupling the battery unit from fixed internal wiring and providing accessible external interfaces, the system not only improves maintainability but also maximizes operational uptime, ensuring reliable and uninterrupted curing performance under various site conditions.

2.5. System workflow and software logic

The operational logic of the smart curing blanket system is governed by a centralized control framework implemented on the ESP32 microcontroller, which serves as the core computational unit responsible for real-time data acquisition, decision-making, and actuation. Upon system initialization, the ESP32 performs a comprehensive scan of all connected curing panels, identifying and registering each unit through unique panel-specific identifiers. Simultaneously, it begins collecting environmental data from the embedded sensors -namely, the DHT22 digital sensor for surface RH and the Honeywell HIH-5030 analog sensor for internal concrete humidity.

The system operates on a periodic data evaluation cycle, typically executed every ten minutes. During each cycle, the controller analyzes both surface and internal RH readings to determine the necessity of water application. If the surface RH falls below 70% and the internal RH is measured below 100%, the controller issues an actuation command to open the corresponding solenoid valve, thereby initiating water delivery. Conversely, if the surface RH is greater than or equal to 70%, no water is dispensed, as the ambient moisture is deemed sufficient. Furthermore, to prevent over-saturation, the system is programmed to permanently deactivate a panel's valve if the internal RH remains consistently at 100% for a continuous period of 48 hours. Valve actuation is facilitated by the ESP32 via either a wired relay connection or wireless communication modules, depending on the system configuration. Upon activation, water stored in the panel's reservoir is released through the microtube distribution system and uniformly delivered to the hydrophilic textile layer, ensuring even moisture absorption across the concrete surface.

All system activities, including sensor readings, time stamps, and actuation events, are meticulously logged and stored locally on an SD card. Additionally, data can be transmitted to cloud-based platforms such as Firebase or ThingSpeak for long-term storage, remote monitoring, and further analysis. An optional user interface, accessible through mobile or desktop applications, enhances user interaction by enabling real-time visualization, manual override of system functions, and over-the-air firmware updates.

This algorithmic control structure enables precise and responsive water management, minimizing manual intervention and promoting sustainable resource use. By ensuring that hydration is delivered only when needed, the system supports consistent curing conditions, reduces the risk of cracking, and contributes to the long-term durability and quality of the concrete structure.

3. Results and discussion

Although the prototype development and field-testing phases will be undertaken in future stages of research, this paper provides an assessment of the system's theoretical performance and the expected benefits it may offer to concrete curing practices. The proposed smart concrete curing blanket presents an innovative approach to moisture management during concrete hydration by integrating modular water distribution, automated valve control, and real-time sensor monitoring within a scalable system architecture. In this section, the theoretical concept and anticipated functionality of the smart curing blanket are discussed, alongside an evaluation of its comparative advantages and limitations in relation to conventional curing techniques. In this context, the system's strengths and potential drawbacks are analyzed through comparison with conventional curing methods, particularly in terms of resource efficiency, consistency of hydration, and ease of implementation.

The proposed smart curing blanket demonstrates significant improvements in resource efficiency when compared to conventional curing methods. By utilizing automated, sensor driven water management, the system optimizes water usage, applying precise amounts of moisture only where necessary, thereby minimizing waste. Furthermore, automation significantly reduces labor intensity and associated costs by removing the need for constant manual intervention. Regarding the consistency of hydration, the embedded humidity sensors ensure continuous monitoring and responsive adjustments in real time, leading to uniform moisture distribution across the entire curing surface. This uniformity directly contributes to improved concrete quality by preventing localized drying or over-wetting, common issues in manual curing practices. Additionally, the modular panel design significantly enhances ease of implementation; the interlocking puzzle-joint edges allow quick, seamless installation and reconfiguration without specialized tools, adhesives, or extensive manual effort. This ease of deployment is particularly beneficial for large-scale construction projects involving extensive concrete surfaces, such as slabs and foundations.

Despite these notable advantages, the system does present certain limitations in relation to conventional curing approaches. Concerning resource efficiency, although the system significantly reduces water usage and labor demands, the initial capital investment associated with sensor integration, electronic components, and modular fabrication is considerably higher than traditional methods. This may create financial constraints for smaller-scale projects or for contractors with limited budgets. In terms of consistency of hydration, reliance on advanced sensor technology introduces the need for routine sensor calibration and maintenance to ensure accurate measurements, thus potentially impacting operational continuity and introducing additional complexity. Finally, regarding ease of implementation, although the modular design simplifies field deployment, the requirement for battery management, waterproof sealing, and potential wiring complexity (in large-scale, wired installations) might pose additional logistical challenges. These factors could necessitate specialized training or increased planning efforts during the initial deployment phase.

4. Conclusions

Concrete curing is a critical phase in construction projects, significantly influencing the long-term durability, strength, and overall performance of structures. Conventional and semi-automatic curing approaches exhibit several key limitations, including inconsistent moisture distribution, inefficient labor utilization, and a lack of real-time feedback on hydration progress. Although recent smart curing methodologies have been introduced to mitigate these challenges, persistent issues such as elevated energy consumption, complexity of installation, and insufficient modularity continue to impede their widespread adoption in practical construction environments.

This study proposes an innovative Smart Concrete Curing Blanket System designed to address these limitations by integrating modular mechanical configurations, centralized sensor-driven automation, and efficient water management strategies. The system comprises modular panels measuring 1m x 2m, each featuring distinct layers: an upper hydrophobic protective sheet, a middle reservoir pool layer, and a lower hydrophilic textile layer directly contacting the concrete surface. This layered structure provides a robust and reusable platform that ensures uniform moisture retention. A gravity-driven internal water delivery mechanism, actuated by low-energy 12V solenoid valves and regulated by a centralized ESP32 microcontroller, precisely applies water according to real-time surface and internal humidity measurements. The proposed design emphasizes modularity, energy efficiency, operational simplicity, and scalability, facilitating seamless deployment across expansive concrete surfaces such as slabs and foundations, with minimal disruption at the construction site. Additionally, the centralized control system simplifies overall maintenance and reduces complexity while enabling adaptive curing strategies through continuous real-time monitoring.

While the proposed system remains theoretical at this stage, initial analytical evaluations suggest substantial improvements in curing performance, water usage efficiency, and labor optimization compared to existing methods. Future research will involve the fabrication of physical prototypes, implementation of comprehensive field experiments to validate moisture management and strength development, and further enhancement of wireless communication technologies to improve scalability. The smart concrete curing blanket introduced in this study signifies a meaningful advancement toward intelligent, resource-efficient construction methodologies, offering considerable potential for enhancing the quality and longevity of contemporary concrete infrastructure.

Acknowledgments

The research presented in this paper was financially supported by the Scientific and Technological Research Council of Türkiye (TÜBİTAK) under the grant number [1919B012403311], as part of the 2209-A Research Project Support Programme for Undergraduate Students.

References

Baek, S.H., Lee, K.I., & Kim, S.M. (2023). Development of real-time monitoring system based on IoT technology for curing compound application process during cement concrete pavement construction. *Sensors*, *23*(19). https://doi.org/10.3390/s23198187

Barroca, N., Borges, L.M., Velez, F.J., Monteiro, F., Górski, M., & Castro-Gomes, J. (2013). Wireless sensor networks for temperature and humidity monitoring within concrete structures. *Construction and Building Materials*, *40*, 1156-1166. https://doi.org/10.1016/j.conbuildmat.2012.11.087

Engin, Y. (2014). *Çimentonun Hidratasyonu Ders Notları*. Retrived from: https://www.betonvecimento.com/wp-content/uploads/2014/12/teknik-notlar-3.pdf (in Turkish)

Kosmatka, S.H., Kerkhoff, B., & Panarese, W.C. (2002). Design and Control of Concrete Mixtures (14th ed.). Portland Cement Association.

Lo, K.C., Kwok, H.W.T., Siu, M.F.F., Shen, Q.G., & Lau, C.K. (2021). Internet of things-based concrete curing invention for construction quality control. *Advances in Civil Engineering*. https://doi.org/10.1155/2021/9933615

Neville, A. M. (2011). Properties of Concrete (5th ed.). Pearson Education Limited.
Taffese, W.Z., & Nigussie, E. (2023). Automated concrete curing and assessment of strength and durability using IoT system. *Materials Today: Proceedings*. https://doi.org/10.1016/j.matpr.2023.07.107
Yang, J., Fan, J., Kong, B., Cai, C.S., & Chen, K. (2018). Theory and application of new automated concrete curing system. *Journal of Building Engineering*, *17*, 125-134. https://doi.org/10.1016/j.jobe.2018.02.009

A new era for lime with natural hydraulic lime binder and innovative aggregates of hemp stalks, sunflower husks

Damla Capraz[1], Mucteba Uysal[1], Furkan Şahin[2], Beyza Aygün[*3]

[1] Yıldız Technical University, Department of Civil Engineering, 34220 Istanbul, Türkiye
[2] Nisantası University, Department of Civil Engineering, 34398, Istanbul, Türkiye
[3] Istanbul University-Cerrahpasa, Department of Civil Enginering, 34320 Istanbul, Türkiye

Abstract. Lime, whose origin dates back to 7000 BCE, has always been the backbone of construction across civilizations-from the plastered floors of ancient Jordan to architectural marvels consisting of aqueducts and amphitheaters in the Roman Empire. Whereas Portland cement, which appeared at the beginning of the 19th century, was synonymous with high carbon emissions, lime continued to play its role as a sustainable and versatile binder with immense potential for reducing environmental impact. On the other hand, with ecological footprint considerations driving cement alternatives, lime, especially supplemented with pozzolanic additives, presents an extraordinary solution in the light of sustainable construction. Following study adds to the historical importance and ecological benefits of lime using natural hydraulic lime as the main binder (NHL 3.5 and NHL 5) with marble powder to replace fine aggregate at 10%, 20%, and 30% by wt. Hemp stalks and sunflower husks replace aggregate 20%, 40%, and 60% by weight to study further new material combinations. Mixtures designed with a water/binder (W/B) ratio 1.0 and a sand/binder (S/B) ratio 0.47 will be tested for water absorption and void ratio, compressive strength, flexural strength, and thermal conductivity at 28 days.

Keywords: Natural hydraulic lime; Hemp stalks; Sunflower husks; Thermal conductivity

1. Introduction

Partition wall components in current building practices have taken a more critical role in separating and organizing inner spaces without hosting any load-bearing actions. This has been most significant since the latter part of the 20th century with the use of industrialized construction methods and the prevalence of reinforced concrete systems. In the past, internal and external partitions used to be made with load-carrying materials such as stone, adobe, timber framing, or lime-based mortars. But in the current building paradigm, most of these walls remain in the role of internal, non-structural applications. While traditional masonry has been replaced by reinforced concrete in carrying loads, the focus has shifted towards the use of light-weight and efficient partition systems. These include clay bricks and autoclaved aerated concrete (AAC) since these come with lesser end-masses and ease of construction and operate in harmony with internal spaces. Clay bricks, though with higher weights, get prioritized on account of superior inertia against heat and sound and cultural acceptance. In contrast, AAC with 70-80% closed pores has a highly minimized density and hence is most suited to be used in non-structural internal partitions. Both materials are also accompanied by significant environmental disadvantages, however. Production of clay bricks requires firing at temperatures over 1000°C and has large energy and carbon footprint implications. AAC production is also challenging because of the use of cement in creating it—an element that is associated with some 8% of the world's total anthropogenic CO_2 emissions—consequently sparking sustainability issues. These ecological repercussions mean that it is now of great importance to evolve alternatives with lower carbon footprint that utilize renewable energy and industrial and farming wastes. A current area of innovation in sustainable material design is the revaluation of lignocellulosic crop residues, in particular in the design of biocomposite partition wall components. In that regard, sunflower seed husk and the stalks of the hemp plant—both of which are readily available and underused crop residues in places like Turkey—show great potential. Cultivation of the sunflower is particularly common in the Marmara region and is associated with large volumes of resulting husk residues. These by-products comprise 21–30% of seed weight from oil-type varieties and up to 50% of snack-type varieties, and differences in machine performance correlate mainly with fiber composition. Historically, sunflower husk has been wasted, combusted to regenerate energy, or downgraded to animal bed filling material. Nevertheless,

[*] Corresponding author, E-mail: beyza.aygun@ogr.iuc.edu.tr

https://doi.org/10.31462/icearc2025_ce_mat_699

golden light publishing

recent studies have shown them to be capable of being used as reinforcement in pressed composite panels that can be successfully employed in the manufacture of interior furniture such as coffee tables, with surface treatments improving both visual attraction and durability against abrasion (Zencirkiran, 2018).

Equally so, post-harvest sunflower stalks, which commonly are considered to be disposal biomass, have been tested to be useful in thermal insulation purposes and serve as a natural replacement to fossil-derived insulators (Efe, 2011). This strategic re-allocation of agro-residue not only facilitates circular economy policies but also reduces open-field biomass burning-induced pollution. Interest in the use of hemp stalks is also revived. By their cellulose richness and mechanical strength, these fibrous residues that usually burn or pulp can be transformed into construction materials. Industrial partners have already assessed them to be part of medium-density fiberboards (MDF) and also biodegradable polymer composites like PLA where the use of hemp adds toughness and delivers a renewable resource of raw material (Celik, 2023). Both hemp stalks and sunflower husks share multifunctional properties in applications ranging from insulation and panelling to animal bedding. Specifically, the lightweight fibrous composition of sunflower husks is most useful in internal partition systems where low mass, sound absorption, and modularity need to be emphasized over compressive strength. In addition, their biosafety has been tested and certified in food industry pigment extraction applications proving them to be nontoxi (Republic of Türkiye Ministry of Agriculture and Forestry, 2025).

Based on these properties, the current research seeks to design a lightweight and eco-friendly partition wall element composed of sunflower husk and hemp fibers reinforced in a natural hydraulic lime (NHL) matrix and fine aggregate. It was selected because of its eco-friendly properties and compatibility with plant reinforcement. In contrast to Portland cement, NHL has lower calcination temperatures and interacts with surrounding CO_2 to pursue continuous carbonation reactions that also impart it with inherent healing properties. Composite paste was developed by mixing the biomass fibers with calibrated water percentage, sand, and NHL to semi-dry consistency. Mixture was subsequently pressed into molds and cured in the surrounding environment. Samples were demolded after two days and left to mature further to achieve mechanistic stability. Subsequent tests further involved bulk density, thermal conductivity, compressive and flexural strength, and water absorption to establish indoor partition suitability. This energy-efficient manufacturing method in the absence of kiln firing or autoclaving also makes it highly adaptable to decentralized and low-scale production systems, particularly in rural areas. In keeping with earlier studies utilizing vine prunings in interior panels (Gencel, 2010) and cotton stalks in making MDF (Gencer, 1998; Guler, 2001), the study adds to the expanding evidence base supporting the construction applicability of agricultural residues in the form of strength properties. The incorporation of such agri-waste streams into mineral-bound composites supports the development of circular and climatic construction solutions. Such products are also backed by inherent aesthetic and sensation properties to meet visual and sensory expectations in the aesthetics of architecture and design and may eliminate the use of supplementary surface treatments and use of additional raw material and energy inputs with associated costs. Being developed in strict life cycle assessment (LCA) protocols that include carbon sequestration, such products can achieve carbon-negative classification. Taken together, conversion of sunflower husk and cannabis stalk to usable partitioning systems is a nature-friendly and cost-effective approach to next-generation green architecture solutions (Acar et al., 2025).

2. Materials and methods

2.1. Materials

Natural hydraulic lime (NHL 3.5) was used as the major binder material and natural river sand in a 0–5 mm particle size was used as the fine aggregate with good gradation to achieve mortar workability and compatibility with the structure. This research is innovative in that two particular agriculture wastes (sunflower seed husks and hemp stalk fibers) were used in association with the mortar matrix in part to replace some of the mortar constituents with wastes that are widely available in Turkey and with good ecocompatibility as per raw material properties and recycling potential to decrease partition wall material density and carbon footprint. Sample preparation was a sequential procedure to optimize homogeneity and reproducibility of the results in the specimens. Each organic additive (the hemp stalks or the sunflower seed husk) was poured into the water of the mixing at 60% of dry weight and was subjected to a 120-s premix to allow water absorption and partial softening of the fibers before gradually adding natural hydraulic lime to the wet fiber blend and further hand-stirring the blend of material for 60 seconds in a laboratory mortar mixer with regular shape and size blades to achieve maximum homogeneity of the paste and avoidance of air entrapments in the mold space during compaction of the mold space with light vibration with a symmetrical motion of the mold swing. Molded specimens were kept in undisturbed conditions (about 20°C and 60 % RH) during 48 hours to set and were subsequently demoulded and stored in room temperature to allow air curing before being subjected to the corresponding tests.

2.2. Mix Design

Experimental mixture formulations are listed in Table 1 and reflect biomass proportions with constant lime and sand proportions to isolate additive effects. Five base mix designs were produced with a reference mixture containing no organic component and four progressively modified mixes containing hemp stalks or sunflower seed husk in increasing proportions. Lime was maintained constant at 4488 grams in all mixes to compare them meaningfully, with sand and water proportions altered slightly to maintain workability. Equal mix designs of each additive group were produced and mirrored to permit direct comparison of performance between the samples based on hemp and sunflower. All materials were weighed with precise digital scales and mixed together in a standard cement mixer to encourage uniform dispersion. Optimal proportions of the selected proportions were determined through initial exploratory tests to prevent segregation, porosity exceeding desirable limits, and lack of adequate binding. This organised strategy allowed optimal fiber proportions to be determined that affect physical and mechanical behaviour and maximise dosage in lightweight partition wall applications.

Table 1. Material quantities used in each mix.

Mix No	Lime (g)	Water (g)	Sand (g)	Hemp Stalk (g)	Sunflower Husk (g)
1	4488	3140	6078	-	-
2	4488	3200	4588	585	585
3	4488	3200	4588	1170	1170
4	4488	3200	4588	1755	1755
5	4488	3200	4588	2340	2340

2.3. Methods

2.3.1. Compressive strength test

Compressive strength was tested in cubic samples of size 135 × 135 × 135 mm that were manufactured and cured in standardized laboratory conditions. Testing was conducted according to TS EN 12390-3 (2010) using a fully automated compression testing machine of 3000 kN capacity. Before testing, specimens were checked for surface defects and weighed. Loading was performed perpendicular to the surface at a constant rate of 0.6 ± 0.2 MPa/s up to failure. Compressive strength was calculated by using the maximum applied load at failure. Statistical accuracy was provided by a minimum of three replicate samples per series tested. Average compressive strength was calculated and analyzed from the data to determine the trends of compressive strength with various biomass proportions and fiber composition.

2.3.2. Flexural strength test

Flexural strength was determined from prismatic specimens with sizes of 67 × 67 × 265 mm through tests carried out under a three-point loading setup with the help of a universal testing machine and at a constant loading speed of 50 ± 10 N/s. 200 mm was kept constant between the support spans. Flexural strength was determined from the maximum load supported by individual specimens before fracture with the help of sample size and the loading span. This test was important to determine the material tensile properties that play an important role in resistance to cracking and durability in the case of applications in interior partition walls. Replications were conducted for each of the mixtures so that reliable and constant results were achieved.

2.3.3. Ultrasonic pulse velocity

Ultrasonic Pulse Velocity (UPV) tests were also performed to assess the internal compactness and structure of the composites. UPV tests were performed on the same cubic specimens used to determine compressive strength to assess internal compactness and structure of the composites. Testing was done by applying a digital ultrasonic tester with 54 kHz transducers on opposite faces of the sample. Coupling gel was employed to achieve good transmission of the signal. Travel time of the ultrasound pulse through the material was determined and velocity was calculated.

3. Results and discussion

3.1. Physical properties

Sunflower seed husk of bulk density around 1.10 kg/m³ was added to the study in the form of 1 cm pieces to allow even dispersal. These husks are dry and fibrous and have high surface areas with water absorption of up to 120%, according to earlier literature and gravimetric analysis. On the other hand, the hemp stalks employed were of the same length and had even higher absorption of around 140–150%, according to their hollow nature and sponge-like cellular structure with high porosity. Both the materials contain irregular surface and rough texture to enhance their bond with the matrix of lime and also enhance internal porosity of the composite at the same time. These physical properties—specifically water absorption and fiber surface morphology—have a direct bearing on internal microstructure of set mortar and affect density, water retention, and shrinkage behavior.

3.2. Mechanical properties

3.2.1. Compressive strength

Control mix had a compressive strength of 3.85 MPa. With the addition of 585 g of fibers, 49.3% of this strength was maintained by sunflower husk (1.90 MPa) and merely 18.2% (0.70 MPa) was maintained by hemp. At 1170 g, sunflower husk was reduced to 0.58 MPa—84.9% less than control—while hemp fell to 0.30 MPa (92.2% less). For Mix 4, the decline was steeper yet, with the use of sunflower husk dropping strength to 0.13 MPa (96.6% decrease) and hemp to 0.21 MPa (94.5% decrease). In Mix 5, the lowest compressive strength was achieved: 0.11 MPa with sunflower husk (97.1% loss) and 0.19 MPa with hemp (95.1% loss). These measures verify that at lower dosages, sunflower husk offers superior mechanics, but that the use of hemp is slightly less dramatic in its degradation curve with increasing dosage. Under high fiber levels, however, both additives drastically erode load-bearing capacity because of weakening of cohesive binder structure, increased porosity, and inefficient transfer of stress.

Table 2. Compressive strength results.

Mix No	Biomass Additive (g)	Hemp	Sunflower Husk
1	0	3.85	3.85
2	585	0.70	1.90
3	1170	0.30	0.58
4	1755	0.21	0.13
5	2340	0.19	0.11

3.2.2. Flexural strength

Flexural strength showed a similar decreasing trend to compressive strength but with a more pronounced benefit to sunflower husk. Compared with the control, Mix 2 sunflower husk samples maintained 40.1% of flexural strength (0.2998 MPa), compared with hemp at only 13.3% (0.0995 MPa). For Mix 3, the maximum of sunflower husk was 0.1670 MPa, 3.4 times that of hemp (0.0796 MPa). In Mix 4, the gap remained with more than double that of the flexural strength of hemp (0.0812 MPa compared with 0.0344 MPa), and in Mix 5 the gap increased further to 0.0617 MPa vs. 0.0249 MPa of hemp. This repeated differential performance indicates that sunflower husk is better to integrate with the matrix under flexural loading and that improved dispersibility of the finer and flatter geometry of the husk may be the reason. Enhanced specific surface area of the husk may also permit improved distribution of stresses and energy release upon bending loads. However, both materials suffer rapid loss of strength with higher content, with losses greater than 91% in the case of sunflower and 96.6% in the case of hemp in Mix 5. These results reinforce that biomass content should be confined to below 20% by weight to achieve mechanical viability in useful applications.

Table 3. Flexural strength results.

Mix No	Biomass Additive (g)	Hemp	Sunflower Husk
1	0	0.7477	0.7477
2	585	0.0995	0.2998
3	1170	0.0796	0.1670
4	1755	0.0344	0.0812
5	2340	0.0249	0.0617

Based on the results, the control sample (Mix 1) registered the highest UPVs (2882 m/s), verifying its good bonding and low porosity. Both 585 g of additive reduced UPV by 6.32% with hemp and by 29.6% with sunflower husk. This indicates that hemp at low levels maintains internal connectivity better compared to sunflower husk. For Mix 3, the decrease with sunflower husk was to 1332 m/s (53.7% from the original) and with hemp was 7.8% from the original (Mix 2). Further degradation was observed in Mixes 4 and 5. In the case of Mix 5, the specimen of sunflower husk fell to 1038 m/s (64% down from the control) with hemp remaining constant at 1283 m/s. In general, sunflower husk caused more drastic deterioration in wave velocity and hence greater internal discontinuity. The higher the levels of the two materials' contents, the larger is the performance gap observed here with the relatively higher retention of structural cohesion in the case of hemp.

Table 4. UPV test results (m/s).

Mix No	Biomass Additive (g)	Hemp	Sunflower Husk
1	0	2882	2882
2	585	2700	2030
3	1170	2657	1332
4	1755	1289	1250
5	2340	1283	1038

4. Conclusions

- UPVs were such that hemp stalk-strengthened specimens performed consistently better than those with sunflower seed husk, to imply higher internal continuity and matrix integration.
- Hemp composite samples revealed slightly improved performance in compressive strength evaluations than their counterparts from sunflower husk, particularly at increased dosage levels.
- As the proportions of husk in the mixture reduced, compressive strengths increased, which reflected a corresponding inverse relationship between the percentage of husk and mechanical integrity.
- The same was noticed in the case of hemp stalks: with decreased fiber content, compressive strength was higher, which again underscores the necessity of optimal dosage limits.
- Relative to conventional brick production, the composites developed consumed much less energy since there was no kiln firing required. Ambient temperature curing was undertaken with carbonation assisted with atmospheric CO_2, thus resulting in less air pollution.
- Lightness of the developed specimens—thanks to the use of low-density biomass—has benefits in structural design through minimization of dead loads and enhancement of general static efficiency in buildings.
- Incorporating sunflower seed husk in partition wall components helps promote recycling efforts and turns agro-industrial wastes into higher value-added construction products.
- Flexural strength tests revealed that decreases in the content of sunflower husk caused proportional increases in MPa values that signify that high levels negatively impact tensile performance.
- Also, reducing the concentration of the hemp stalks in the composite enhanced flexural strength, which suggests that both of these materials impede tensile action when in high concentration.
- Compared to their counterparts containing hemp in comparative flexural tests, sunflower husk specimens always had higher MPa values irrespective of dosage.
- Sunflower husk blends also performed better than hemp samples in compressive tests at lower additive proportions, with the advantage of their performance lessening with higher fiber concentration.
- Although environmentally friendly, neither of the composites tested fulfilled the structural requirements of load-bearing applications because of their dramatically lower strength profiles. Still, the developed materials can be applied to be used as non-load-bearing wall partitions where the strength is low in the internal environments.

References

Acar, M., Yiğen, Ç., Şahin, M., & Aytaç, S. (2025). *Kenevir tarımı ve mevzuatı*. T.C. Tarım ve Orman Bakanlığı, Tarımsal Araştırmalar ve Politikalar Genel Müdürlüğü, Karadeniz Tarımsal Araştırma Enstitüsü Müdürlüğü. (In Turkish)

Celik, E. (2023). *Eklemeli yığma modeli ile elde edilen kenevir sapı/PLA biyokompozit malzemenin bazı mekanik ve termal özelliklerinin incelenmesi* (Yüksek lisans tezi). Bursa Teknik Üniversitesi. (In Turkish)

Efe, F. T. (2011). *Ayçiçeği bitkisi (Helianthus annuus L.) saplarının izolasyon levha üretiminde kullanılabilirliğinin araştırılması* (Doktora tezi). Kahramanmaraş Sütçü İmam Üniversitesi. (In Turkish)

Gecgel, A. (2010). *Bağ budama artıklarından elde edilen yonga levhaların çeşitli malzemelerle güçlendirilerek fiziksel ve mekaniksel özelliklerinin geliştirilmesi* (Yüksek lisans tezi). Muğla Üniversitesi. (In Turkish)

Gencer, A. (1998). *Pamuk saplarından (Gossypium hirsitum L.) MDF (orta yoğunlukta lif levha) üretimi olanaklarının araştırılması* (Yüksek lisans tezi). Zonguldak Karaelmas Üniversitesi. (In Turkish)

Guler, C. (2001). *Pamuk saplarından yonga levha üretimi olanaklarının araştırılması* (Doktora tezi). Zonguldak Karaelmas Üniversitesi. (In Turkish)

Zencirkiran, M. (2018). *Ayçekirdeği kabuğu lifinden üretilen yapı malzemesinin fiziksel ve mekanik özelliklerinin ölçülmesi* (Yüksek lisans tezi). Trakya Üniversitesi. (In Turkish)

Republic of Türkiye Ministry of Agriculture and Forestry. (2025). *Kenevir araştırmaları*. https://arastirma.tarimorman.gov.tr/ttae/Sayfalar/Detay.aspx?SayfaId=50 (In Turkish)

ICEARC'25
4th International Civil Engineering & Architecture Conference
17-19 May 2025, Trabzon, Türkiye

Improvement of 3D printing properties of MgO derived binders by CO_2 curing in hardened state

Yunus E. Avşar*[1], Mücteba Uysal[2], Abdullah H. Akca[2]

[1] *Tekirdağ Namık Kemal University, Department of Civil Engineering, 59860 Tekirdağ, Türkiye*
[2] *Yıldız Technical University, Department of Civil Engineering, 34220 İstanbul, Türkiye*

Abstract. The cement industry uses energy resources intensively, resulting in significant carbon emissions. Magnesium-based binders, including the use of reactive MgO cement (RMC), are considered a promising alternative to cement. Three-dimensional (3D) printing technology has the advantages of unlimited flexibility, reduced cycle time, low labor cost and minimal waste. In this study, the improvement of 3D printing properties (rheological and mechanical) of MgO-derived binders by CO_2 curing in hardened state was investigated. Rheological measurements (yield stress and viscosity) and compressive tests have been performed. The yield stress and viscosity of the reference sample were 173 Pa and 3.9 Pa.s, respectively, and 12.5%, 18.75%, 25% and 31.25% rMgO substitution increased the yield stress by 156%, 157%, 174%, and 224%, and viscosity by 105%, 156%, 269%, and 610%, respectively, compared to the reference sample. The reason for these increases is the improvement of hydration kinetics with the increase in the amount of rMgO with higher purity. As the rMgO ratio increases, the compressive strength also increases. CO_2 curing has increased compressive strength compared to the curing with room conditions. The increase in rMgO, which acts as a hydration agent, and the carbonation of RMC have led to the formation of HMC by forming continuous networks, filling pores, densifying the matrix microstructure, and thus facilitating strength development. The rMgO substitution ratio with optimum properties in terms of 3D printability is 31.25% and the compressive strength, yield stress and viscosity are 11.8 MPa, 561 Pa and 27.7 Pa.s, respectively.

Keywords: Sustainability; Carbon capture storage/utilization (CCS/CCU); RMC; Compressive strength; Rheology

1. Introduction

Concrete is a widely preferred building material worldwide due to its mechanical properties, durability and adaptability to various shapes, and its primary binder is cement (Gartner, 2004). Cement and concrete production is increasing significantly due to rapid population growth, urbanization and high demand for better infrastructure (Meng et al., 2023). High cement demand has negative implications for the global environment. The cement industry uses energy, limestone and clay resources intensively, resulting in significant carbon emissions (Gartner, 2004). The cement industry is responsible for about 8% of global CO_2 emissions (Preston & Lehne, 2018).

Carbon capture and storage/utilization (CCS/U) techniques play an important role in reducing CO_2 emissions (Lena, 2018). While CCS technique stores CO_2 emissions in deep geological formations or deep in the ocean, CCU technique converts CO_2 emissions into valuable products (Quarton & Samsatli, 2020). Although CCS can store large amounts of CO_2, the process is expensive and there are potential risks such as leakage (Ajayi et al., 2019; Cunningham et al., 2009). Mineralization of cement-based materials, one of the CCU techniques, is considered as a low-risk and ecologically sensitive alternative for CO_2 sequestration (Li et al., 2022).

Carbonation of cementitious systems has received increasing attention over the past few years. Among these, magnesium-based binders, including the use of reactive MgO cement (RMC), are considered a promising alternative to PC (Hay & Celik, 2020a; Ünlüer, 2018; Al-Tabbaa, 2013). RMC is typically composed of 90% MgO and also contains SiO_2, CaO and Fe_2O_3. Magnesium oxide (MgO) is obtained by calcining magnesite deposits (dry route) or from seawater or waste brine (wet route) (Walling & Provis, 2016; Hay & Çelik 2020b). For the main production route (dry route), the calcination temperature required to produce RMC (700-1000°C) is much lower than for PC (up to 1450°C) (Shand, 2006). RMC is able to permanently sequester CO_2 in the magnesium carbonates produced, leading to a simultaneous power gain in relation to the degree of carbonation. Theoretically, the

* Corresponding author, E-mail: yeavsar@nku.edu.tr

https://doi.org/10.31462/icearc2025_ce_mat_726

maximum carbon sequestration capacity of RMC is 110% (Ruan et al., 2021), which is significantly higher than that of PC (46-58%) (Fang et al., 2017). Given the carbonation capacity of RMC, net CO_2 emissions can be significantly reduced. It has been reported that the net CO_2-e emissions of RMC after fully carbonized is only 264 kg CO_2-eq (Ruan & Ünlüer, 2016).

Carbonation of RMC offers a pathway for the long-term retention of CO_2 in concrete components. Carbonation of RMC leads to the formation of hydrated magnesium carbonates (HMCs) that form continuous networks, filling pores, densifying the matrix microstructure and thus facilitating strength development (Dung et al., 2019). The typical compressive strength range of carbonated RMC specimens is 20-85 MPa (Soares & Castro-Gomes, 2021). It exhibits better durability than PC in terms of freeze-thaw cycling, chloride and sulfate attack (Pu & Ünlüer, 2018; Kumar et al., 2021; Muthu et al., 2020). The full recyclability of RMC-based materials further enhances their sustainability at the end of their life cycle (Sonat et al., 2017). The hydration products of RMC (brucite) are a mechanically weak phase and the gain of higher strength depends on the carbonation process. Typical hydrated magnesium carbonate (HMC) phases include artinite, neskehonite, hydromagnesite and dipinjite (Ünlüer, 2018). The hydration and carbonation reactions of RMC samples are shown in Equations 1-5 (Ünlüer, 2018; Dung et al., 2019).

$$\mathrm{MgO} + \mathrm{H_2O} \rightarrow \mathrm{Mg(OH)_2}\ \text{(Brucite)} \tag{1}$$

$$2\mathrm{Mg(OH)_2} + \mathrm{CO_2} + 2\mathrm{H_2O} \rightarrow \mathrm{MgCO_3} \cdot \mathrm{Mg(OH)_2} \cdot 3\mathrm{H_2O}\ \text{(Artinite)} \tag{2}$$

$$\mathrm{Mg(OH)_2} + \mathrm{CO_2} + 2\mathrm{H_2O} \rightarrow \mathrm{MgCO_3} \cdot 3\mathrm{H_2O}\ \text{(Nesquehonite)} \tag{3}$$

$$5\mathrm{Mg(OH)_2} + 4\mathrm{CO_2} \rightarrow 4\mathrm{MgCO_3} \cdot \mathrm{Mg(OH)_2} \cdot 4\mathrm{H_2O}\ \text{(Hydromagnesite)} \tag{4}$$

$$5\mathrm{Mg(OH)_2} + 4\mathrm{CO_2} + \mathrm{H_2O} \rightarrow 4\mathrm{MgCO_3} \cdot \mathrm{Mg(OH)_2} \cdot 5\mathrm{H_2O}\ \text{(Dypingite)} \tag{5}$$

The degree of hydration and carbonation are critical factors affecting the microstructural development and strength gain of RMC specimens (Dung et al., 2019). Extensive research has been conducted focusing on mix design (water/binder and sand/binder ratio), curing conditions (CO_2 concentration/pressure, relative humidity and temperature) and the use of admixtures (hydration agent, carbonation agent and nucleation seeding) to enhance the carbonation of RMC-based concrete (Meng et al., 2023).

The choice of water content is critical as water provides the medium for hydration and carbonation reactions (Ünlüer & Al-Tabbaa, 2015). A low s/b ratio may result in poor compaction, comminution and insufficient formation of hydration products required for the subsequent carbonation reaction (Ruan & Ünlüer, 2017; Ünlüer & Al Tabbaa, 2011). On the other hand, high water content may inhibit CO_2 diffusion in the pore system. This is because the diffusion of CO_2 in water (0.0016 mm^2/s) is much slower than in air (16 mm^2/s) (Lide, 2004). The effect of s/b ratio on hydration and carbonation of RMC-based concrete was investigated by Ruan and Ünlüer (2017). Among the mixtures with three different s/b ratios (0.55, 0.6 and 0.65), RMC specimens with 0.55 s/b ratio exhibited the lowest porosity and the highest density increase after carbonation and achieved the highest strength (62 MPa), which was comparable to water-cured PC specimens (68 MPa).

Since the CO_2 concentration in the atmosphere is 0.041%, the carbonation process of RMC-based concrete is very slow under ambient conditions (Weber, 2021). Optimum curing conditions have been investigated in many studies, including the evaluation of factors such as CO_2 concentration/pressure, relative humidity, temperature and curing time to accelerate the carbonation process. Although the carbonation reaction can be enhanced by increasing the CO_2 concentration, there seems to be a critical point where other factors can limit CO_2 diffusion in RMC samples (Pu & Ünlüer, 2016). Studies have shown that RMC-based composites subjected to CO_2 concentrations of 5-20% can reach full strength development within 14 days (Pu & Ünlüer, 2016, Liska & Al-Tabbaa, 2009). In the studies of Ünlüer and Al-Tabbaa (2014) and Dung et al. (2021), the optimum CO_2 concentration in terms of strength development was determined as 10% among the tested CO_2 concentrations (5-20%).

Accelerated carbonation of RMC requires high levels of humidity due to the high water consumption of the carbonation reaction (Vandeperre & Al-Tabbaa, 2007). Although high relative humidity is beneficial for hydration and carbonation reactions, strength development does not increase linearly with relative humidity. Because CO_2 decomposes faster in drier environments (Meng et al., 2023). Ünlüer and Al-Tabbaa (2014) investigated the effect of different RH ratios ranging from 55-98% and found that 78% RH provided the most favorable carbonation condition and 24-34 MPa compressive strength was obtained after curing for 18 days. It was reported that the degree of hydration of RMC under ambient conditions was limited to 80% (Dung & Ünlüer, 2017a; Ünlüer & Al-Tabbaa, 2014).

Curing time is another important factor that ensures adequate carbonation of RMC samples. Determining the optimum curing time can reduce time and cost (Meng et al., 2023). Hay and Celik (2020b) investigated the strength development and carbonation of RMC-based composite under 20% CO_2, 30°C and 80% relative humidity. It was found that the compressive strength increased up to 14 days (23.9 MPa), but decreased by about 11.1% at 28 days (21.3 MPa). It was explained that excessive carbonation leads to volume expansion, which causes internal stress and cracking. In addition, a negligible increase in carbon sequestration rate was observed (Hay & Çelik, 2020b).

In this study, the improvement of 3D printing properties (rheological and mechanical) of MgO-derived binders by CO_2 curing in hardened state was investigated. This study is based on two main objectives. The first objective of the study is to produce a new binder system that can be used in the field at low cost by reducing CO_2 emission, high energy requirement and high production temperature caused by cement production. The second aim is to save time and cost in field applications by realizing the production of this material with sufficient strength and durability with an extrusion type 3D printer.

2. Materials and methods

In this study, the improvement of 3D printing properties (rheological and mechanical) of MgO-derived binders by CO_2 curing in hardened state was investigated. MgO, rMgO, PC, chemical additives, distilled water and aggregate were used in the production of the mixtures. Within the scope of compressive test and rheological measurement, rMgO substitution rate was 12.5%, 18.75%, 25% and 31.25%. 2 series were produced and the 1st serial was subjected to carbonation curing in an incubator and the 2nd serial was cured under room conditions. 24 mortar specimens (5×5×5 cm cube) were produced for compressive test and 12 paste specimens were produced for rheology measurements. The cube specimens were subjected to carbonation curing (10% CO_2, 50-70% humidity, 25°C) in an incubator until the compressive test (1, 3, and 7 days). Based on the rheological data and compressive test results, the optimum test point was determined. Test points with rMgO substitution ratio higher than 31.25% could not be produced because they were too dense and subject to rapid setting due to high reactivity.

While the primary binder matrix used in this study was MgO, rMgO (98% purity) was used to improve the hydration kinetics and buildability of the RMC mortar. Standard sand was also added to improve workability. Table 1 summarizes the properties of the MgO and rMgO components used in the study. 0.1M magnesium acetate aqueous solution was used as the primary liquid medium with a water/binder (s/b) ratio of 0.45. Magnesium acetate acts as a strong hydration agent in RMC and therefore it is recommended to add it in small concentrations to achieve a higher degree of hydration in RMC (Matabola et al., 2010). Polycarboxylate ether was added as a 'superplasticizer' to reduce the plastic viscosity of the RMC mortar and maintain its flow consistency over a long period of time. Hydroxyethyl cellulose was added as a 'suspending additive' to maintain the homogeneity of the mixture during extrusion. Finally, a non-ionic surfactant, also called 'defoamer', was added to prevent air entrapment in the modified mortar (Khalil et al., 2020). To produce a homogeneous 3D printable mixture, the solid components were mixed as a uniform dry powder mixture while the liquid components were mixed in a beaker to obtain a homogeneous solution. This solution was poured into the container containing the solid mixture and stirred for about 5 minutes. By applying this procedure, a homogeneous 3D printable RMC-based mortar was obtained. Table 2 summarizes the mixture composition.

A rotational rheometer was used to measure the rheological properties of the freshly prepared material. A measuring system with four blades and a measuring cup were used for the measurements. In order to ensure uniform distribution and to generate the same shear history for all mixtures, a constant shear rate of 50 s^{-1} was applied for 1 min for pre-shearing the mixtures and then rested for 1 min. Then, the shear rate was increased linearly from 0 s^{-1} to 100 s^{-1} for 1 min, followed by a decrease from 100 s^{-1} to 0 s^{-1} within 1 min (Wang et al., 2024).

Modified Bingham, Stress-Plateau, Herschel-Bulkley, De Kee and Casson methods were applied on the data sets of the test points to determine the yield stress and viscosity. In the Modified Bingham method, the coefficient of x in the equation represents the viscosity and the constant value represents the yield stress (Ebrahimi et al., 2022). In the Stress-Plateau method, the average of the shear stress values of the 2 points with the lowest shear rate representing the plateau region expresses the yield stress, and the coefficient of x in the equation of the 3 points with the highest shear rate representing the plastic viscosity region expresses the viscosity (Dinç Şengönül et al., 2020). The formulas of Herschel-Bulkley, De Kee and Casson methods are given Equations 6-8 respectively.

$$\tau = \tau_0 + K \cdot \gamma^n \tag{6}$$

$$\tau = \tau_0 + \mu \cdot \gamma \cdot e^{-\tau_0 \cdot \gamma} \tag{7}$$

$$\sqrt{\tau} = \sqrt{\tau_0} + \sqrt{\mu \cdot \gamma} \tag{8}$$

In these formulas τ, ϒ, τ0, and μ are shear stress, shear rate, yield stress, and viscosity, respectively.

The compressive test was carried out on 5×5×5 cm cube specimens at 1, 4 and 7 days in accordance with ASTM C109 (2020). The compressive strength was calculated using Equation 9. f_c is the compressive strength (N/mm^2), P is the maximum load at fracture (N) and A is the surface area of the square section of the prism (mm^2).

$$f_c = P/A \tag{9}$$

Table 1. Chemical and physical properties of MgO and rMgO

Properties	MgO	rMgO
MgO	93.2	98.2
CaO	0.87	0.8
SiO_2	2.25	0.35
Fe_2O_3	0.53	0.15
Al_2O_3	0.22	0.1
Cl	-	0.3
SO_3	-	0.05
LOI	4	3.5
Density (g/cm^3)	3.02	3.58
Fineness (m^2/g)	16.3	60

Table 2. Mixture composition

Materials (g)	Compressive Test	Rheological Measurement
MgO	1400/1300/1200/1100	70/65/60/55
rMgO	200/300/400/500	10/15/20/25
Sand	120	-
Water	706	35
Magnesium acetate	14	0.7
Superplasticizer	8	0.4
Defoamer	6	0.3
Hydroxyethyl cellulose	6	0.3

3. Results and discussion

3.1. Rheological measurements

The viscosity-shear rate graph for the test points is shown in Fig. 1. It can be seen that viscosity increases as the rMgO ratio increases. This is due to the increase in the amount of rMgO with higher purity and the development of hydration kinetics (Khalil et al., 2020). The produced mortars exhibited shear thinning behavior similar to cement-based mortars and slurries (Bras et al., 2010; Jorne et al., 2015; Gökyiğit-Arpacı et al., 2019). Shear thinning behavior is defined as a decrease in viscosity resulting from the breakage of flocs due to an increase in shear rate (Jorne et al., 2015). Low yield stress and plastic viscosity ensure easy injection of the mortars (Dinç-Şengönül et al., 2020).

The shear stress-shear rate graph for the test points is shown in Fig. 2. It can be seen that the shear stress increases as the rMgO ratio increases. This is due to the increase in the hydration kinetics with the increase in the amount of rMgO with higher purity (Khalil et al., 2020).

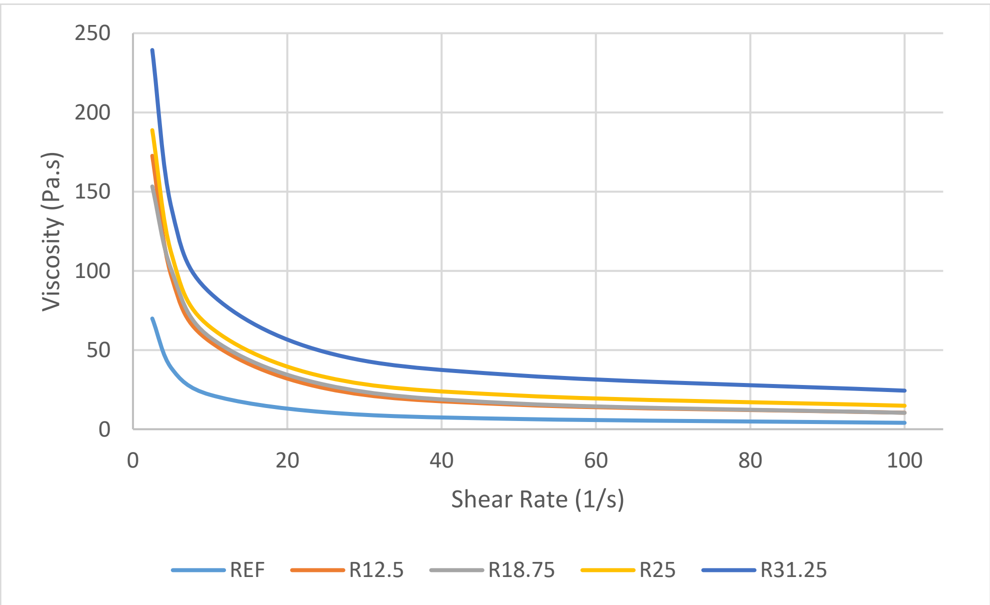

Fig. 1. The viscosity-shear rate graph for the test points

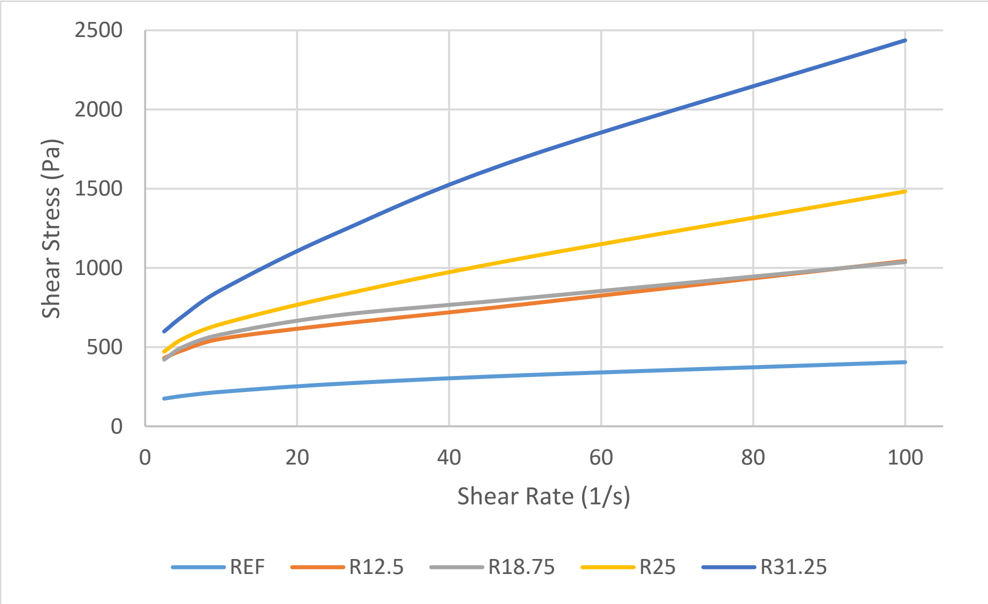

Fig. 2. The shear stress-shear rate graph for the test points

The Modified Bingham, Stress-Plateau, Herschel-Bulkley, De Kee, and Casson methods were applied to the data sets obtained from the test points to determine the yield stress and viscosity. The results of the Stress-Plateau method to reference, 12.5%, 18.75%, 25%, and 31.25% rMgO samples are presented in Figs. 3, 4, 5, 6, and 7, respectively. Upon examination of the figures, it is observed that no plateau formation occurs at any test point.

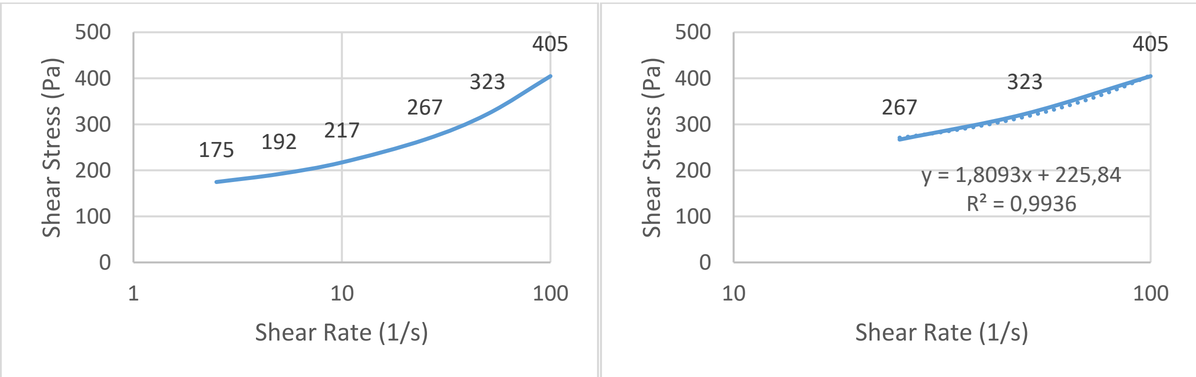

Fig. 3. The results of the Stress-Plateau method to Ref

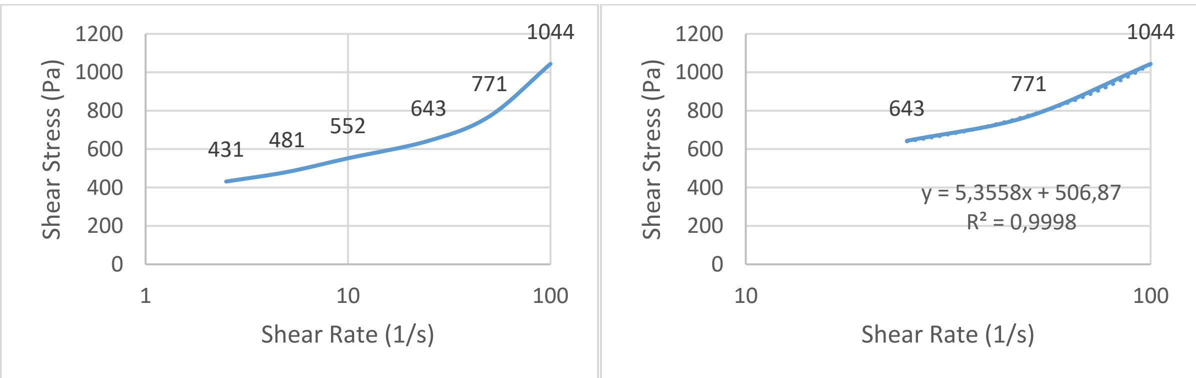

Fig. 4. The results of the Stress-Plateau method to 12.5% rMgO

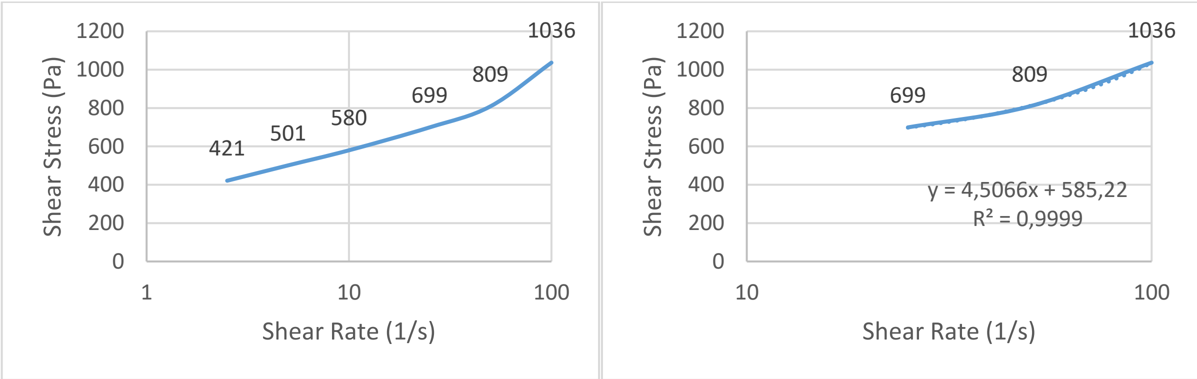

Fig. 5. The results of the Stress-Plateau method to 18.75% rMgO

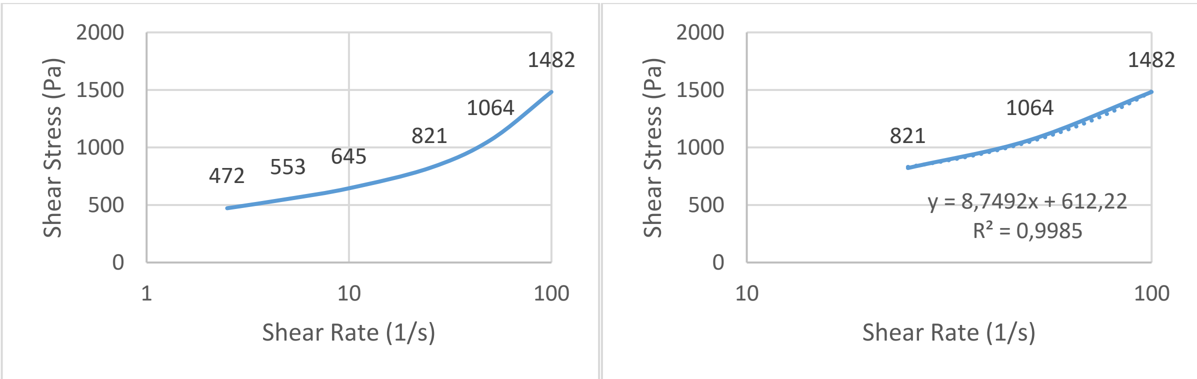

Fig. 6. The results of the Stress-Plateau method to 25% rMgO

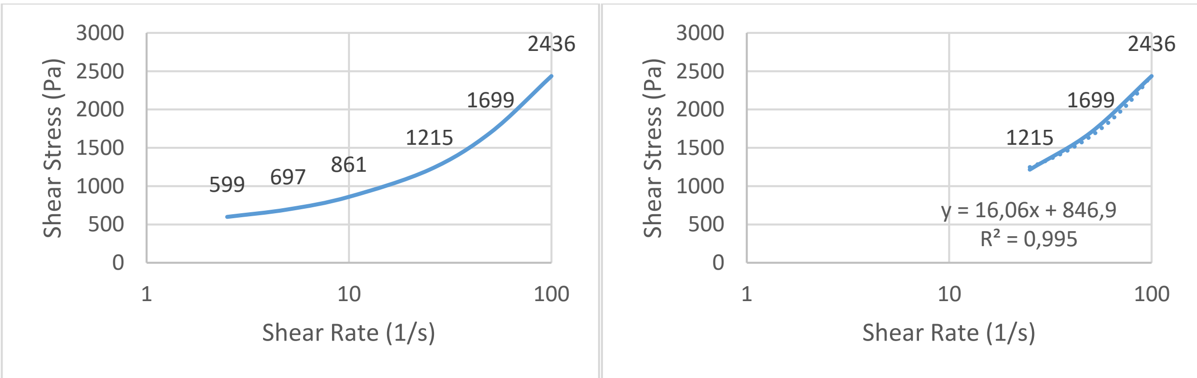

Fig. 7. The results of the Stress-Plateau method to 31.25% rMgO

The results of the Modified Bingham method to reference, 12.5%, 18.75%, 25%, and 31.25% rMgO samples are presented in Figs. 8, 9, and 10, respectively. When the data sets were fitted to the Bingham model, a good linear fit was obtained between shear stress and shear rate.

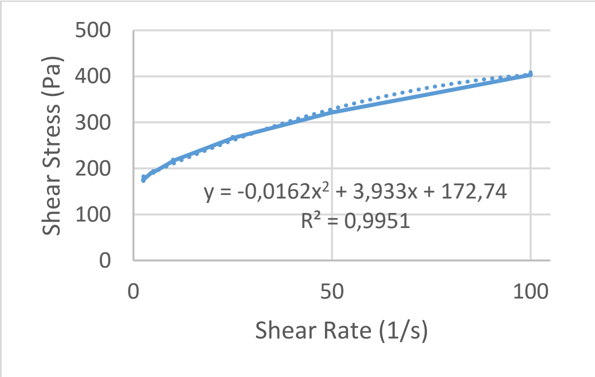

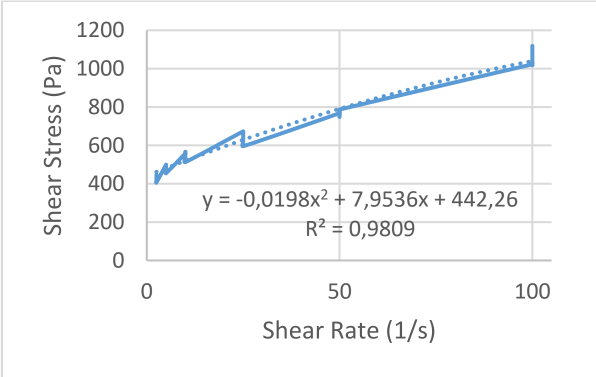

Fig. 8. The results of the Modified Bingham method to Ref (left) and 12.5% rMgO (right)

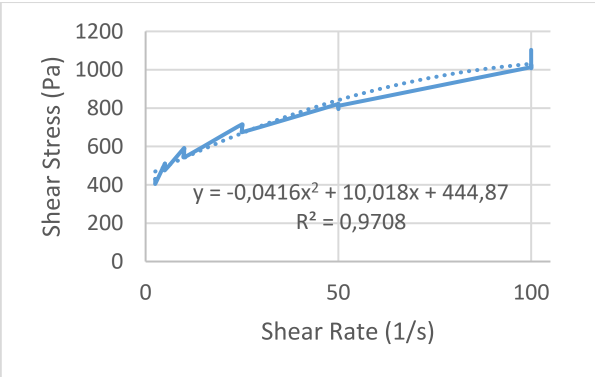

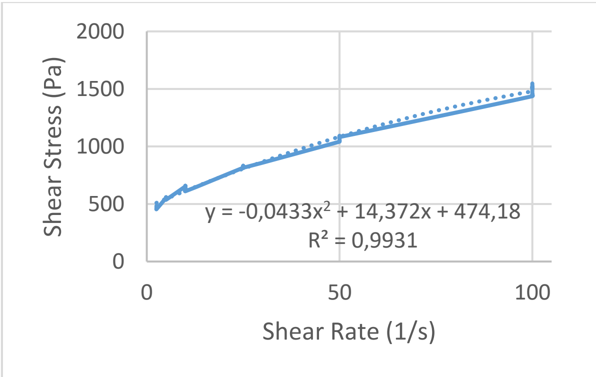

Fig. 9. The results of the Modified Bingham method to 18.75% rMgO (left) and 25% rMgO (right)

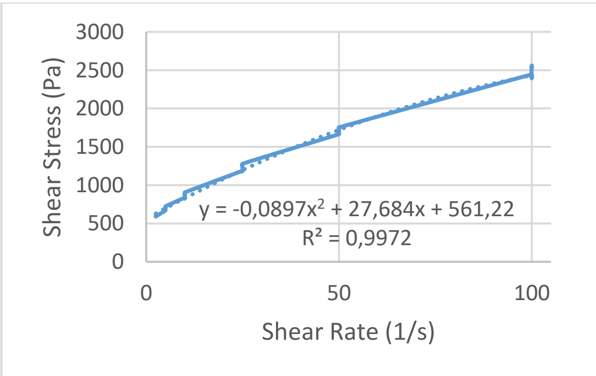

Fig. 10. The results of the Modified Bingham method to 31.25% rMgO

For Modified Bingham method, a replacement of rMgO at 12.5%, 18.75%, 25%, and 31.25% increased the yield stress by 156%, 157%, 174%, and 224%, respectively, while increasing viscosity by 105%, 156%, 269%, and 610%, respectively. The reason for these increases is the improvement in hydration kinetics due to the increased amount of rMgO with higher purity (Khalil et al., 2020).

The yield stress and viscosity values obtained by applying the Modified Bingham, Stress-Plateau, Herschel-Bulkley, De Kee, and Casson methods on the data sets of the test points are given in Table 3. In Table 3 TP, YS, and V are test point, yield stress, and viscosity, respectively. It can be seen that the R^2 values of the different methods are quite close. When the Modified Bingham and De Kee methods are applied, the yield stress and viscosity values are found to be quite similar. When the Casson method is applied, the R^2 value and viscosity value of the reference sample could not be calculated. Additionally, viscosity calculations cannot be performed using the Herschel-Bulkley method.

The comparisons of R^2, yield stress, and viscosity values obtained from different methods are shown in Fig. 11, Fig. 12, and Fig. 13, respectively.

Table 3. The yield stress and viscosity values obtained by different methods on the data sets of the test points

Modified Bingham Method						Herschel-Bulkley Method					
TP	REF	R12.5	R18.75	R25	R31.25	TP	REF	R12.5	R18.75	R25	R31.25
R^2	0.995	0.981	0.971	0.993	0.997	R^2	1.000	0.997	0.997	0.999	1.000
YS	173	442	445	474	561	YS	135	400	280	398	427
V	3.9	8	10	14.4	27.7	V	-	-	-	-	-
Stress-Plateau Method						De Kee Method					
TP	REF	R12.5	R18.75	R25	R31.25	TP	REF	R12.5	R18.75	R25	R31.25
R^2	0.994	1.000	1.000	0.999	0.995	R^2	0.998	0.995	0.990	0.998	1.000
YS	183	488	501	557	719	YS	171	440	438	471	555
V	1.8	5.4	4.5	8.8	16.1	V	4.3	8.2	11.2	15	28.9
			Casson Method								
			TP	REF	R12.5	R18.75	R25	R31.25			
			R^2	0	0.997	0.993	1.000	1.000			
			YS	60	355	380	360	401			
			V	0	1.6	1.7	3.8	8.7			

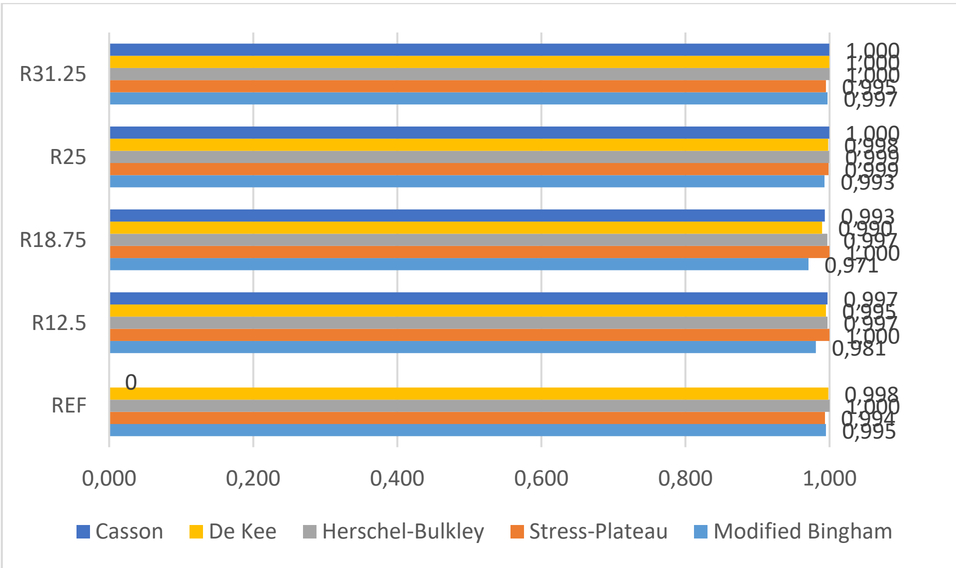

Fig. 11. The comparison of R^2 values obtained from different methods

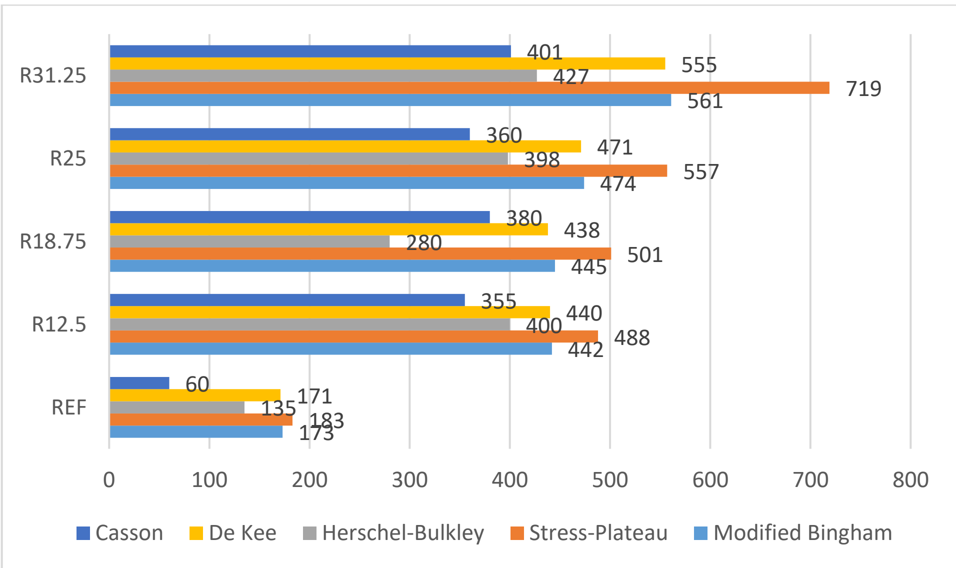

Fig. 12. The comparison of yield stress values obtained from different methods

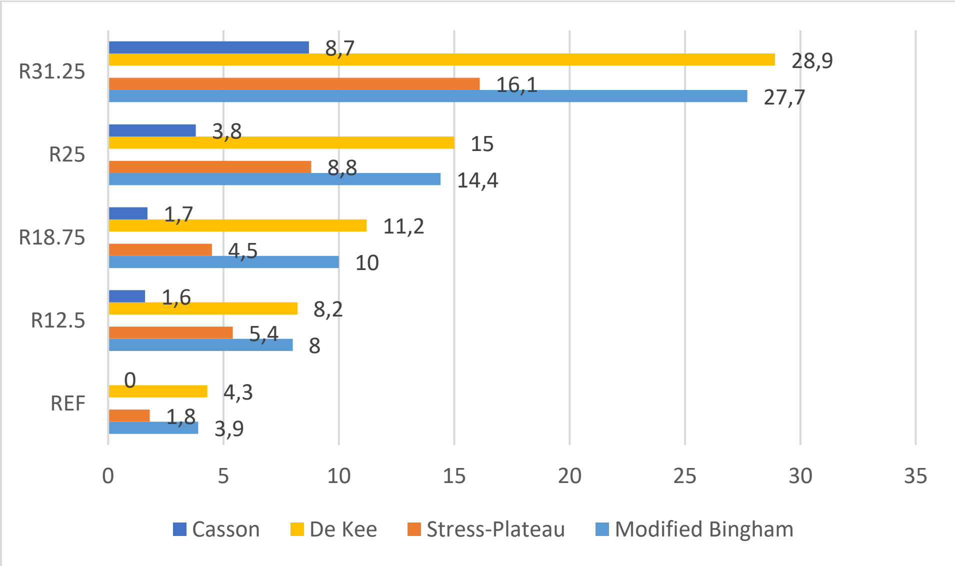

Fig. 13. The comparison of viscosity values obtained from different methods

A review of the literature reveals that the shear stress of 100% PC-based, PC-based with pozzolan replacement, and geopolymer mixtures is 180-3800, 14-6000, and 500-11000 Pa, respectively; while their viscosity is 4-46, 1.3-33, and 0.5-15 Pa, respectively (Zhong & Zhang, 2022; Paritala et al., 2023). In a study investigating whether the activation of 3D printing using additives such as nanocellulose (NC) and methyl cellulose (MC) improves the carbonation of MgO paste and has a positive effect on physical/mechanical properties (Douba et al., 2022). The addition of NC increased the static yield stress of MgO paste by 120 and 184 Pa per 1% NC by weight for 1.1 and 0.9 w/b ratios, respectively, while the addition of MC increased it by 1.3 and 9 Pa per 1% MC by weight, respectively. The addition of NC increased the plastic viscosity of the MgO paste by 0.2 Pa·s per 1% NC, while the addition of MC increased it by 0.27 and 0.38 Pa·s per 1% MC for 1.1 and 0.9 w/b, respectively.

3.2. Compressive test

The compressive strength values of 12.5%, 18.75%, 25%, and 31.25% rMgO mortar samples are given in the Table 4 and Fig. 14. In Table 4, CS means compressive strength.

In general, it has been observed that as the rMgO ratio increases, the compressive strength also increases. At all substitution ratios, CO_2 curing has increased compressive strength compared to the curing with room conditions, independent of sample age. The increase in rMgO, which acts as a hydration agent, and the carbonation of RMC have led to the formation of hydrated magnesium carbonates (HMC) by forming continuous networks, filling pores, densifying the matrix microstructure, and thus facilitating strength development (Dung et al., 2019). When 1-day samples cured with CO_2 were analyzed, the replacement of rMgO at 31.25% increased compressive strength by 70%, 115%, and 152% compared to replacements of 25%, 18.75%, and 12.5%, respectively. This is attributed to the improvement in hydration kinetics resulting from the increase in rMgO content (Meng et al., 2023). However, it was observed that the increase in strength decreases as the CO_2 curing time increases. This indicates that carbonation occurs more efficiently and effectively at the initial stage. The 4-day strengths of the samples with 12.5%, 18.75%, 25%, and 31.25% rMgO replacement, which were subjected to CO_2 curing, were 95%, 70%, 28%, and 4% higher than their 1-day strengths, respectively. As seen, the increase in strength decreases as the rMgO replacement ratio increases. This may be due to the hydration kinetics occurring abruptly and intensely at high rMgO ratios, leading to pore blockage and a reduction in the effect of the CO_2 curing (Meng et al., 2023). In general, it can be stated that an increase in the CO_2 curing time increases the compressive strength. However, there is no significant increase in compressive strength values between 4 and 7 days for all rMgO replacement ratios. This can be explained by excessive carbonation causing expansion, leading to internal stress and cracking (Hay & Çelik 2020b). The highest compressive strength (11.8 MPa) was obtained from a 7-day sample with 31.5% rMgO replacement treated with CO_2 curing.

Studies have been conducted on the use of hydration agents to increase carbon sequestration in RMC systems (Meng et al., 2023). The hydration of MgO in the presence of sodium acetate ($(CH_3COO)_2Mg$) promotes the precipitation of brusite in the slurry solution, thereby increasing the available space for continuous hydration (Dung & Ünlüer, 2017a). Additionally, it provides additional magnesium ions (Mg^{2+}) for brusite formation (Dung & Ünlüer, 2017b). Hydrochloric acid (HCl) increases the H^+ concentration and the solubility of MgO (Dung & Ünlüer, 2016). A comparative study was conducted to investigate the effectiveness of hydration agents ($(CH_3COO)_2Mg$, $MgCl_2$, and HCl) in RMC-based mixtures (w/b: 0.6). The addition of $(CH_3COO)_2Mg$, HCl, and

$MgCl_2$ increased the 14-day compressive strength by 273%, 160%, and 93%, respectively, compared to the control mixture (Dung & Ünlüer, 2017b). Sodium bicarbonate ($NaHCO_3$) has been applied in RMC systems to increase pH and thereby enhance CO_2 solubility. Additionally, $NaHCO_3$ provides additional bicarbonate ions that enable continuous carbonation reactions (Dung & Ünlüer, 2019; Dung & Ünlüer, 2018). Dung and Ünlüer (2018) investigated the enhancement of carbonation in RMC-based concrete using $NaHCO_3$ and NaCl. Chloride ions from NaCl can accelerate MgO dissolution by weakening its bonds. The combination of these additives (50 MPa) improved the morphology of the formed carbonate phases and increased the 28-day compressive strength by 110% compared to the control sample (Dung & Ünlüer, 2018).

Table 4. The compressive test results

Curing	1-day		4-day		7-day	
Type	Test Point	CS (MPa)	Test Point	CS (MPa)	Test Point	CS (MPa)
CO_2 curing	C12.5-1	4	C12.5-4	7.8	C12.5-7	7.9
	C18.75-1	4.7	C18.75-4	8	C18.75-7	8.2
	C25-1	6.8	C25-4	8.7	C25-7	9.8
	C31.25-1	10.1	C31.25-4	10.5	C31.25-7	11.8
Curing with room conditions	N12.5-1	2	N12.5-4	2.2	N12.5-7	2.4
	N18.75-1	3.6	N18.75-4	4	N18.75-7	4.3
	N25-1	6	N25-4	6.2	N25-7	6.7
	N31.25-1	8.1	N31.25-4	8.3	N31.25-7	8.4

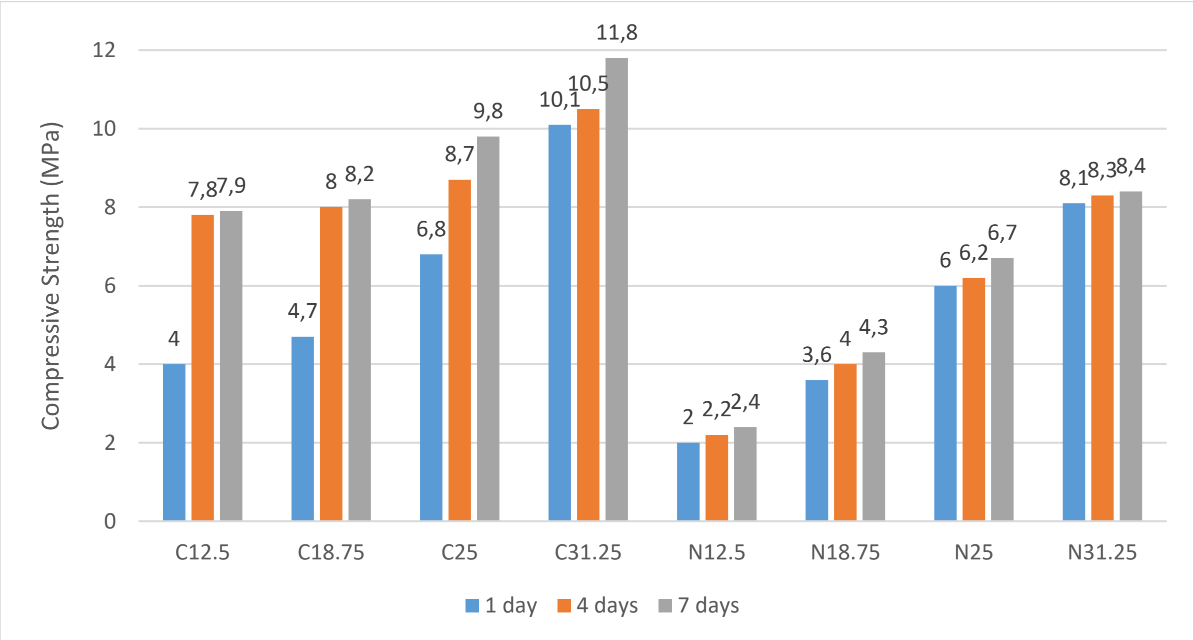

Fig. 14. The compressive test results

4. Conclusions

In this study, the improvement of 3D printing properties (rheological and mechanical) of MgO-derived binders by CO_2 curing in hardened state was investigated. The main findings of the study are presented below.

- The viscosity and shear stress increases as the rMgO ratio increases. This is due to the increase in the amount of rMgO with higher purity and the development of hydration kinetics. The produced mortars exhibited shear thinning behavior similar to cement-based mortars and slurries.
- When the data sets were fitted to the Stress-Plateau method, it is observed that no plateau formation occurs at any test point.
- When the data sets were fitted to the Bingham model, a good linear fit was obtained between shear stress and shear rate. A replacement of rMgO at 12.5%, 18.75%, 25%, and 31.25% increased the yield stress by 156%, 157%, 174%, and 224%, respectively, while increasing viscosity by 105%, 156%, 269%, and 610%, respectively. The reason for these increases is the improvement in hydration kinetics due to the increased amount of rMgO with higher purity.
- The R^2 values of the different methods (Modified Bingham, Stress-Plateau, Herschel-Bulkley, De Kee, and Casson) are quite close. When the Modified Bingham and De Kee methods are applied, the yield stress and

viscosity values are found to be quite similar. When the Casson method is applied, the R^2 and viscosity value of the reference sample could not be calculated. Viscosity calculations cannot be performed using the Herschel-Bulkley method.
- The highest compressive strength (11.8 MPa) was obtained from a CO_2 cured 7-day sample with 31.5% rMgO.
- As the rMgO ratio increases, the compressive strength also increases. CO_2 curing has increased compressive strength compared to the curing with room conditions. The increase in rMgO, which acts as a hydration agent, and the carbonation of RMC have led to the formation of HMC by forming continuous networks, filling pores, densifying the matrix microstructure, and thus facilitating strength development.
- In CO_2 cured 1-day samples, 31.25% rMgO increased compressive strength by 70%, 115%, and 152% compared to 25%, 18.75%, and 12.5% rMgO, respectively. This is attributed to the improvement in hydration kinetics resulting from the increase in rMgO content. However, the increase in strength decreases as the CO_2 curing time increases. This indicates that carbonation occurs more efficiently and effectively at the initial stage.
- The CO_2 cured 4-day strengths of the samples (12.5%, 18.75%, 25%, and 31.25% rMgO) were 95%, 70%, 28%, and 4% higher than their 1-day strengths, respectively. The increase in strength decreases as the rMgO replacement ratio increases. This may be due to the hydration kinetics occurring abruptly and intensely at high rMgO ratios, leading to pore blockage and a reduction in the effect of the CO_2 curing.
- An increase in the CO_2 curing time increases the compressive strength. However, there is no significant increase in compressive strength values between 4 and 7 days for all rMgO replacement ratios. This can be explained by excessive carbonation causing expansion, leading to internal stress and cracking.

Acknowledgments
The research described in this paper was financially supported by the Yıldız Technical University Scientific Research Projects Coordination Unit under the grant number [7012].

References
Ajayi, T., Gomes, J.S., & Bera, A. (2019). A review of CO_2 storage in geological formations emphasizing modeling, monitoring and capacity estimation approaches. *Petrol. Sci.*, 1-36

Al-Tabbaa, A. (2013). *Reactive magnesia cement, eco-efficient concrete*. Sawston: Woodhead Publishing

American Society for Testing and Materials. (2020). *ASTM C109/C109M Standard test method for compressive strength of hydraulic cement mortars*. West Conshohocken: American Society for Testing and Materials

Bras, A., Henriques, F.M.A., & Cidade, M.T. (2010). Effect of environmental temperature and fly ash addition in hydraulic lime grout behaviour. *Constr. Build. Mater.*, *24*, 1511-1517. https://doi.org/10.1016/j.conbuildmat.2010.02.001

Cunningham, A.B., Gerlach, R., Spangler, L., & Mitchell, A.C. (2009). Microbially enhanced geologic containment of sequestered supercritical CO_2. *Energy Proc., 1*(1), 3245-3252

Dinç-Şengönül, B., Oktay, D., & Yüzer, N. (2020). Effect of temperature, resting time and brick dust (Horasan) on the rheological properties of hydraulic lime-based grouts. *Construction and Building Materials*, 265, 120644

Douba, A., Badjatya, P., & Kawashima, S. (2022). Enhancing carbonation and strength of MgO cement through 3D printing. *Construction and Building Materials*, *328*, 126867. https://doi.org/10.1016/j.conbuildmat.2022.126867

Dung, N., Hay, R., Lesimple, A., Çelik, K., & Ünlüer, C. (2021). Influence of CO_2 concentration on the performance of MgO cement mixes. *Cement Concr. Compos., 115*, 103826

Dung, N., Lesimple, A., Hay, R., Çelik, K., & Ünlüer, C. (2019). Formation of carbonate phases and their effect on the performance of reactive MgO cement formulations. *Cement Concr. Res., 125*, 105894

Dung, N. & Ünlüer, C. (2016). Improving the performance of reactive MgO cement-based concrete mixes. *Constr. Build. Mater., 126*, 747-758

Dung, N. & Ünlüer, C. (2017a). Carbonated MgO concrete with improved performance: the influence of temperature and hydration agent on hydration, carbonation and strength gain. *Cement Concr. Compos., 82*, 152-164

Dung, N. & Ünlüer, C. (2017b). Sequestration of CO_2 in reactive MgO cement-based mixes with enhanced hydration mechanisms. *Construct. Build. Mater.*, *143*, 71-82

Dung, N. & Ünlüer, C. (2018). Improving the carbonation of reactive MgO cement concrete via the use of $NaHCO_3$ and NaCl. *J. Mater. Civ. Eng.*, *30*(12), 04018320

Dung, N. & Ünlüer, C. (2019). Performance of reactive MgO concrete under increased CO_2 dissolution. *Cement Concr. Res.*, *118*, 92-101

Ebrahimi, M., Mohseni, M., Aslani, A., & Zahedi, R. (2022). Investigation of thermal performance and life-cycle assessment of a 3D printed building. *Energy and Buildings*, *272*, 112341. https://doi.org/10.1016/j.enbuild.2022.112341
Fang, X., Xuan, D., & Poon, C.S. (2017). Empirical modelling of CO_2 uptake by recycled concrete aggregates under accelerated carbonation conditions. *Mater. Struct.*, *50*, 1-13
Gartner, E. (2004). Industrially interesting approaches to low- CO_2 cements. *Cement and Concrete Research*, *34*, 1489-1498. https://doi.org/10.1016/j.cemconres.2004.01.021
Gökyiğit-Arpacı, E.Y., Oktay, D., Yüzer, N., Ulukaya, S., & Ekşi-Akbulut, D. (2019). Performance evaluation of lime-based grout used for consolidation of brick masonry walls. *J. Mater. Civ. Eng.*, 31. https://doi.org/10.1061/(ASCE)MT.1943-5533.0002692
Hay, R., & Çelik, K. (2020a). Accelerated carbonation of reactive magnesium oxide cement (RMC)-based composite with supercritical carbon dioxide ($scCO_2$). *J. Clean. Prod.*, *248*, 119282
Hay, R., & Çelik, K. (2020b). Hydration, carbonation, strength development and corrosion resistance of reactive MgO cement-based composites. *Cement Concr. Res.*, *128*, 105941
Jorne, F., Henriques, F.M.A., & Baltazar, L.G. (2015). Influence of superplasticizer, temperature, resting time and injection pressure on hydraulic lime grout injectability. Correlation analysis between fresh grout parameters and grout injectability. *J. Build. Eng.*, *4*, 140-151. https://doi.org/10.1016/j.jobe.2015.08.007
Khalil, A., Wang, X., & Çelik, K. (2020). 3D printable magnesium oxide concrete: towards sustainable modern architecture. *Additive Manufacturing*, *33*, 101145. https://doi.org/10.1016/j.addma.2020.101145
Kumar, S., Yang, E.H., & Ünlüer, C. (2021). Investigation of chloride penetration in carbonated reactive magnesia cement mixes exposed to cyclic wetting–drying. *Construct. Build. Mater.*, *284*, 122837
Li, N., Mo, L., & Ünlüer, C. (2022). Emerging CO_2 utilization technologies for construction materials: A review. *J. CO_2 Util.*, *65*, 102237
Lide, D.R. (2004). *CRC handbook of chemistry and physics*. Florida: CRC press
Liska, M. & Al-Tabbaa, A. (2009). Ultra-green construction: reactive magnesia masonry products. *Proceedings of the Institution of Civil Engineers-Waste and Resource Management*, 185-196
Matabola, K.P., Van Der Merwe, E.M., Strydom, C.A., & Labuschagne, F.J.W. (2010). The influence of hydrating agents on the hydration of industrial magnesium oxide. *J. Chem. Technol. Biotechnol.*, *85*, 1569-1574. https://doi.org/10.1002/jctb.2467.
Meng, D., Ünlüer, C., Yang, E.H., & Qian, S. (2023). Recent advances in magnesium-based materials: CO_2 sequestration and utilization, mechanical properties and environmental impact. *Cement and Concrete Composites*, *138*, 104983. https://doi.org/10.1016/j.cemconcomp.2023.104983
Muthu, M., Kumar, S., Yang, E.H., & Ünlüer, C. (2020). Degradation of carbonated reactive MgO-based concrete exposed to nitric acid. *J. CO_2 Util.*, *36*, 210-219
Paritala, S., Singaram, K.K., Bathina, I., Khan, M.A., & Jyosyula S.K.R. (2023). Rheology and pumpability of mix suitable for extrusion-based concrete 3D printing-A review. *Construction and Building Materials*, *402*, 132962
Preston, F. & Lehne, J. (2018). *Making concrete change innovation in low-carbon cement and concrete*. London: Cambridge IP
Pu, L., & Ünlüer, C. (2016). Investigation of carbonation depth and its influence on the performance and microstructure of MgO cement and PC mixes. *Construct. Build. Mater.*, *120*, 349-363
Pu, L., & Ünlüer, C. (2018). Durability of carbonated MgO concrete containing fly ash and ground granulated blast-furnace slag. *Construct. Build. Mater.*, *192*, 403-415
Quarton, C.J. & Samsatli, S. (2020). The value of hydrogen and carbon capture, storage and utilisation in decarbonising energy: insights from integrated value chain optimisation. *Appl. Energy*, *257*, 113936
Ruan, S. & Ünlüer, C. (2016). Comparative life cycle assessment of reactive MgO and Portland cement production. *J. Clean. Prod.*, *137*, 258-273
Ruan, S., & Ünlüer, C. (2017). Influence of mix design on the carbonation, mechanical properties and microstructure of reactive MgO cement-based concrete. *Cement Concr. Compos.*, *80*, 104-114
Ruan, S., Yang, E.H., & Ünlüer, C. (2021). Production of reactive magnesia from desalination reject brine and its use as a binder. *J. CO_2 Util.*, *44*, 101383
Shand, M.A. (2006). *The chemistry and technology of magnesia*. New Jersey: John Wiley & Sons
Soares, E.G., & Castro-Gomes, J. (2021). Carbonation curing influencing factors of carbonated reactive magnesia cements (CRMC)-A review. *J. Clean. Prod.*, 127210
Sonat, C., Lim, C.H., Liska, M., & Ünlüer, C. (2017). Recycling and reuse of reactive MgO cements-A feasibility study. *Construct. Build. Mater.*, *157*, 172-181
Ünlüer, C. (2018). *Carbon dioxide sequestration in cementitious construction materials*. Sawston: Woodhead Publishing
Ünlüer, C., & Al-Tabbaa, A. (2011). Green construction with carbonating reactive magnesia porous blocks: effect of cement and water contents. *2nd International Conference & Environmental Construction Exhibition*, Dubai.

Ünlüer, C., & Al-Tabbaa, A. (2014). Enhancing the carbonation of MgO cement porous blocks through improved curing conditions. *Cement Concr. Res.*, *59*, 55-65

Ünlüer, C., & Al-Tabbaa, A. (2015). The role of brucite, ground granulated blastfurnace slag, and magnesium silicates in the carbonation and performance of MgO cements. *Construct. Build. Mater.*, *94*, 629-643

Vandeperre, L., & Al-Tabbaa, A. (2007). Accelerated carbonation of reactive MgO cements. *Adv. Cement Res.*, *19*(2), 67-79

Walling, S.A., & Provis, J.L. (2016). Magnesia-based cements: a journey of 150 years, and cements for the future. *Chem. Rev.*, *116*, 4170-4204

Wang, X., Krishnan, P., & Çelik, K. (2024). Enhancing carbonation and thermal insulation of reactive magnesium oxide cement (RMC)-based 3D printable pastes with cenospheres. *Cement and Concrete Composites*, *150*, 105559. https://doi.org/10.1016/j.cemconcomp.2024.105559

Weber, A.P. (2021). Focus group S-6: Using plants for carbon sequestration. *White Paper and Scientific Basis of the Strategic Research Agenda*, 111

Zhong, H. & Zhang, M. (2022). 3D printing geopolymers: A review. *Cement and Concrete Composites, 128*, 104455

4th International Civil Engineering & Architecture Conference
17-19 May 2025, Trabzon, Türkiye

Seismic performance assessment of 3D-printed concrete structures

M. Kerem Sarıkaya*[1], Shaghayegh S. Benam[1], Taner Yılmaz[1], Bülent Erkmen[1], Zeynep B. Bundur[1]

[1] Özyeğin University, Department of Civil Engineering, 34749 Istanbul, Türkiye

Abstract

In recent years, 3D concrete printing has emerged as an innovative construction technology, enhancing efficiency by enabling the creation of complex geometries, reducing labor costs, and minimizing construction waste compared to traditional construction methods. 3D-printed concrete is a tailored concrete that can be deposited layer by layer through a 3D printer without the need for formwork or vibration. However, despite extensive research on printable materials, the absence of specific design regulations for 3D-printed structures has limited the development of comprehensive assessments of their structural behavior. The layered structure and lack of conventional reinforcement in 3D-printed concrete further distinguish its structural behavior from that of conventionally constructed concrete. This study evaluates the structural performance of an unreinforced 3D-printed wall element subjected to in-plane lateral loading through numerical simulation. The wall is modeled in SAP2000 using the mechanical properties of cement-based printable materials. A nonlinear pushover analysis is conducted to assess the lateral load-bearing capacity and deformation characteristics of the wall under loading conditions representative of seismic demand. The developed model provides insights into the behavior of 3D-printed structures under lateral loading. The findings aim to contribute to the future integration of additive manufacturing into performance-based structural design and enhance understanding of the lateral performance of 3D-printed concrete.

Keywords: 3D printing; Seismic performance; Cement-based materials; Structural elements; Earthquake loads

1. Introduction

Three-dimensional concrete printing (3DCP) is rapidly transforming the construction industry by enabling automated, layer-by-layer fabrication of structural elements directly from digital models. Compared to traditional construction methods, 3DCP offers faster construction, reduced labor costs, improved on-site safety, and the ability to produce complex geometries without the need for formwork. As a result, it is increasingly being adopted in a range of applications, including single-story residential buildings, modular tiny homes, and infrastructure components like pedestrian bridges (Buswell et al., 2018; Khoshnevis et al., 2020). Despite its growing use, the structural reliability of 3D-printed elements under lateral and seismic loading remains a major research gap. While several studies have investigated the fresh and hardened properties of printable cement-based materials, limited research has focused on their structural performance. This gap is largely due to the lack of design standards and proper characterization of 3D-printed structures. In addition, the layered construction process, anisotropic material behavior, weak interlayer bonding, and lack of conventional reinforcement result in a different structural response from that of traditionally cast concrete (Pan et al., 2023).

Understanding the seismic behavior of 3D-printed elements is essential for the broader adoption of this technology in seismically active regions. Current experimental studies and numerical models remain limited in capturing the effects of key parameters such as layer orientation, interfacial bond strength, and geometric irregularities on the lateral load response of 3D-printed concrete (Feng et al., 2015). This highlights the growing need for research that integrates material characterization with structural analysis to assess the lateral load-bearing capacity (Mader et al., 2023). To address this gap, the present study evaluates the structural performance of a cement-based 3D-printed wall element. A numerical model is developed in SAP2000 using mechanical properties of printable cement-based materials reported in the literature, and a nonlinear pushover analysis is conducted to assess lateral load-bearing capacity, stiffness degradation, and potential failure mechanisms. The wall is loaded in-plane to simulate realistic seismic conditions, and crack formation is predicted based on the stress and strain

* Corresponding author, E-mail: kerem.sarikaya@ozu.edu.tr

https://doi.org/10.31462/icearc2025_ce_mat_736

distributions obtained from the analysis. This approach aims to improve understanding of the failure mechanisms in 3D-printed walls and contribute to the development of performance-based seismic design strategies for printed concrete structures.

2. Materials and methods

2.1. Materials and mechanical properties

The material properties and modeling parameters used in this study are based on a previously developed cement-based mortar formulated for 3D printing applications (Bayrak, 2023). The cement type used was CEM II/A-M (S-L) 42.5R, combined with silica sand at a sand-to-binder ratio of 1.5. The water-to-cement (w/c) ratio was 0.32. Mechanical properties were obtained through laboratory testing of core samples extracted from printed wall specimens. The study also noted measurable differences in mechanical behavior between the lower and upper wall segments, attributed to variations in material quality and layer consolidation during the printing process, with the upper part exhibiting lower mechanical properties. In this study, the mechanical properties of the upper part were used, as this region is more susceptible to defects caused by the extended duration of the printing process, reduced compaction, and environmental exposure during material deposition. Using these values ensures that the structural performance is evaluated under conditions that reflect the potential vulnerabilities of the printed element. Mechanical testing of 10 cm diameter cylindrical specimens at 90 days yielded an average compressive strength of 37.8 ± 3.2 MPa. In comparison, printed samples tested under loading perpendicular to the layer direction, showed compressive strengths approximately 80% of the cast specimens. The elastic modulus of the cast specimens was measured at approximately 18.5 GPa, while the modulus of printed samples tested in the same orientation was about 25% of that value.

Building on this foundation, the present study develops a numerical model to understand the mechanical response of a 3D-printed wall. The evaluation was done solely using the model without additional experimental tests on a printed wall. Therefore, the material properties were directly incorporated from the data obtained from the literature. The modeled wall has a uniform thickness of 20 mm, an in-plane length of 3000 mm, and a height of 3000 mm, representing a large-scale, unreinforced concrete panel. The material is treated as isotropic, with a compressive strength of 30 MPa and an elastic modulus of 14,400 MPa, values selected to reflect high-performance printable mortar while supporting simplified modeling. No internal reinforcement is included, allowing the analysis to focus solely on the matrix material response under seismic conditions.

2.2. Numerical modeling of the wall element

The finite element model of a representative 3D-printed wall element is developed using the structural analysis software SAP2000 (Dere, 2012 et. al). The geometry and dimensions of this wall are determined to reflect the use of such walls in actual 3-D printed concrete houses. The wall dimensions are 3 meters in length, 3 meters in height, and 300 mm in depth. The wall also has truss-like segments between the two outer faces, which are intended to enhance the stability and reliability of the wall during the extrusion process. As shown in the finite element model in Fig. 1a, shell elements are used to model all wall parts, including the outer surfaces and the inner truss-like segments. The outer surface shell elements are divided into a mesh size of 30 cm × 30 cm, and inner truss-like elements are connected with the resulting corner nodes of the outer surfaces. The thickness of the shell elements is taken as 2 cm for all surfaces. Each node at the bottom of the wall is pinned to prevent translation in all three directions.

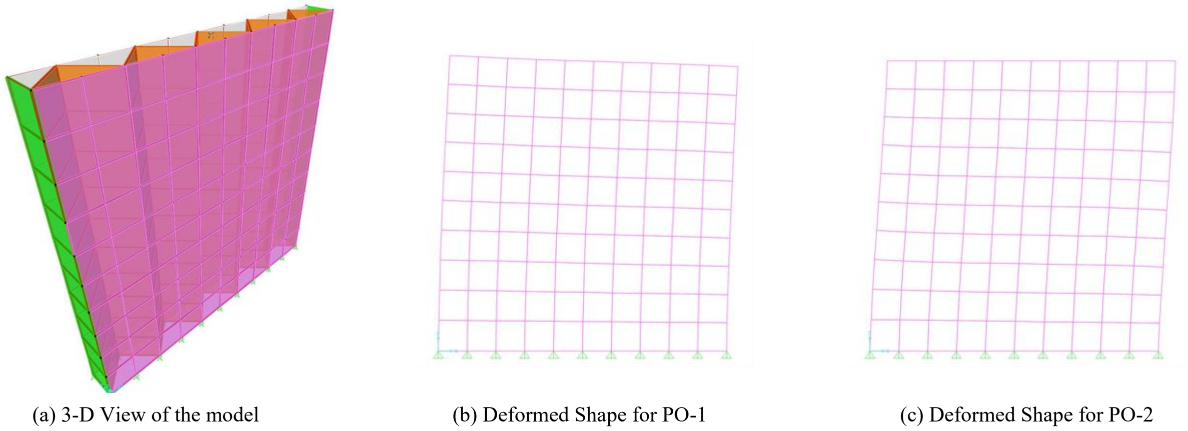

(a) 3-D View of the model (b) Deformed Shape for PO-1 (c) Deformed Shape for PO-2

Fig. 1. Finite element model of the wall element in SAP 2000.

In the numerical model of the wall, nonlinear material behavior is considered to capture the progression of cracking and redistribution of stresses according to the employed material model for the 3-D printed concrete. Therefore, the outer surfaces and inner truss-like segment of the wall are modeled with layered shell elements, and nonlinear material properties are assigned to these elements to account for the inelastic behavior of concrete. The orthogonal surfaces at the edges are modeled using standard thin-shell elements with linear elastic material properties, as inelastic behavior is not expected on these elements due to the lateral direction of the loading acting along the other wall surfaces. Although anisotropic behavior is typically observed in 3-D printed concrete walls for several reasons, including printing layer orientation, the height of the layer in the structural element, isotropic material behavior is accepted for material definitions in the present study.

In a similar approach as presented in this study, Bayrak (2024) used the finite element analysis software ABAQUS to model a 3-D printed concrete wall specimen using six different material models, aiming to capture the effect of the variation of the material properties along the height of the wall. In that study, experiments were conducted to determine the lateral load capacity of several 3D-printed concrete wall specimens, and the results of the finite element model for one of the specimens were compared with the experimental results. As employed in that study, the stress-strain relationship of the 3D-printed concrete material is generated based on the material properties provided in Section 2.1 and is presented in Fig. 2. In this material model, stress-strain relationship as defined in Thorenfeldt et al. 1987 is considered for compression, while a linear relation is assumed up to the tensile strength and the exponential function is used as specified in Dere [2012]. However, to have a computational stability stress-strain relationship given for concrete in SAP 2000 is modified and used for the material model assigned to nonlinear shell elements. This material model is also plotted on the same figure in Fig. 2. A Poisson's ratio of 0.20 is assumed, in line with conventional cementitious materials (Mader et al., 2023; Pan et al., 2023). The unit weight of the material is taken as 22 kN/m^3. No reinforcement is assigned to the model, allowing for a focused evaluation of the unreinforced material.

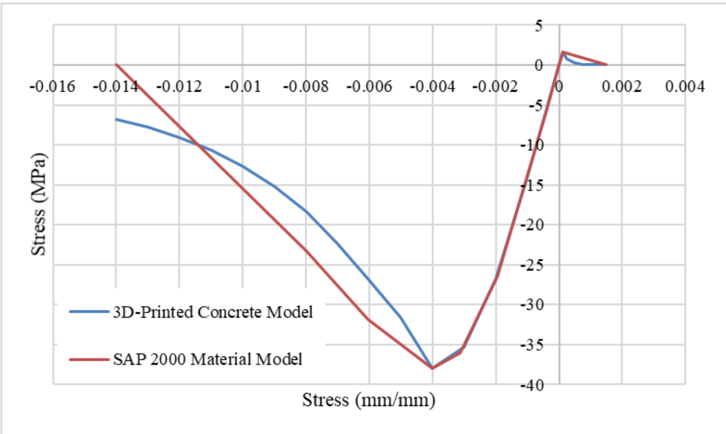

Fig. 2. Material model for the 3D-printed concrete

2.3. Pushover analysis

The main objective in this study is to estimate the in-plane lateral capacity of a full-size 3D-printed concrete wall. For this purpose, a lateral pushover analysis is performed, where increasing levels of lateral load is gradually applied on the master node at the top of the wall, and a displacement-controlled loading strategy is used to push the wall until failure. The resulting top displacement is plotted against the total pushing force (or base shear force) to obtain the lateral capacity curve of the wall. The program automatically terminates the analyses when the failure is achieved due to numerical instability, until the targeted top displacement.

Two pushover analyses are conducted in the present study, based on the boundary conditions assigned at the top of the wall. In the first analysis (PO-1), the master node at the top is constrained to have the same translational displacements. In the second analysis (PO-2), this constraint is extended to include rotational degrees of freedom as well. The deformed shapes of the wall for these two analyses are displayed in Fig. 1b and Fig. 1c.

3. Results and discussions

3.1 Lateral capacity of the wall

Fig. 3 shows the load-displacement curve of the wall resulting from the two pushover analyses, PO-1 and PO-2. The pushover analysis PO-1 is terminated when the target displacement of 20 mm is reached, while the analysis PO-2 automatically stops at around 15 mm before the target displacement when the wall no longer carries loading. The resulting pushover curve from the analysis PO-2 is assessed to be more realistic and compatible with the lateral behavior as would occur under a seismic loading scenario. A lateral force capacity of 1537 kN is obtained from the pushover curve resulting from PO-2.

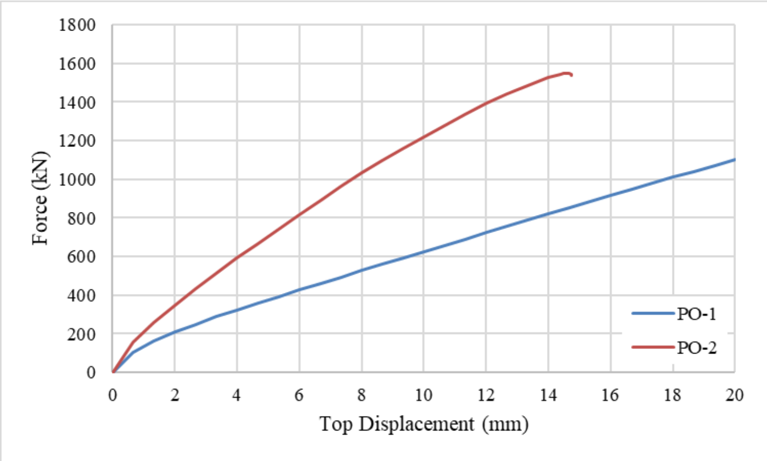

Fig. 3. Pushover curves

3.2 Progression of crack formation

Although no physical crack observation is conducted, crack formation is predicted based on tensile strain concentration and stiffness reduction observed in the analysis outputs. This approach supports the identification of likely failure zones and the overall lateral resistance capacity of the wall under simulated seismic action.

The modeling approach draws conceptually from Bayrak's (2023) work, which employed ABAQUS and a Continuum Damage Plasticity Model (CDPM) to simulate the cyclic behavior of unreinforced 3D-printed concrete walls. The onset of damage and failure was evaluated based on critical tensile strains and overall lateral drift beyond acceptable limits.

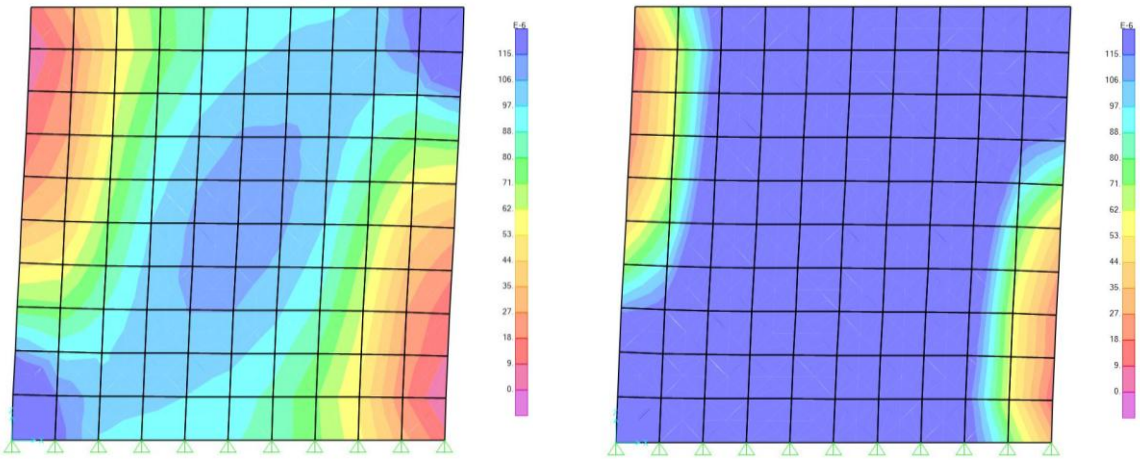

(a) Step 1 (F = 160 kN) (b) Step 2 (F = 258 kN)

Fig. 4. Principle tensile stress on the outer face of the wall

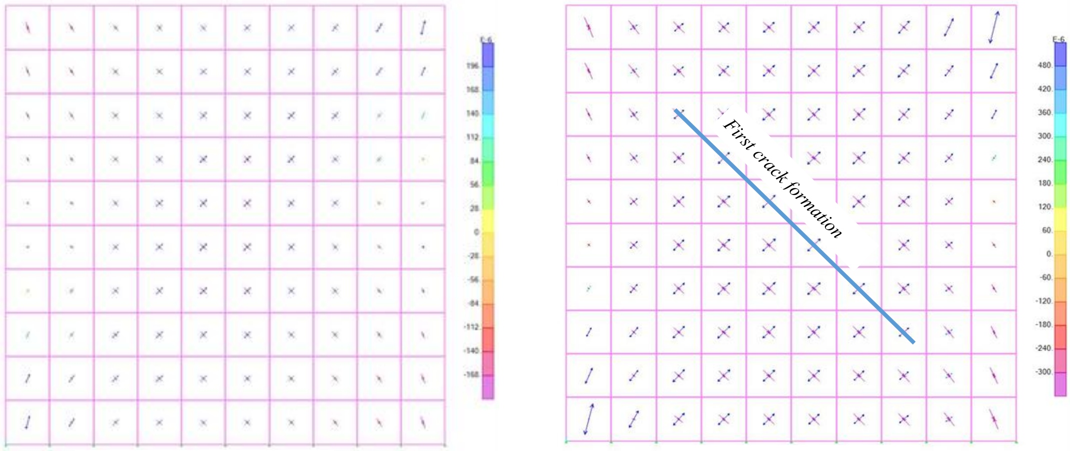

(a) Step 1 (F = 160 kN)

(b) Step 2 (F = 258 kN)

Fig. 5. Formation of the first crack

4. Conclusions

This study investigates the seismic performance of an unreinforced, cement-based 3D-printed wall element through numerical analysis. Drawing from the material characterization and modelling approach presented in the MSc thesis by Bayrak (2023), the study develops a simplified isotropic model in SAP2000 to simulate the in-plane lateral response of a full-scale wall panel. The wall is modelled without reinforcement and subjected to a nonlinear pushover analysis to evaluate its lateral load-bearing capacity, stiffness degradation, and failure mechanisms under seismic loading.

Using consistent mechanical properties and large-scale geometry, the model provides insight into the structural behaviour of 3D-printed concrete under monotonic lateral displacement. Although the wall is not physically printed or tested, the strain distribution and stress concentrations observed in the simulation enable the prediction of likely crack initiation zones and potential failure modes. These results highlight the vulnerability of unreinforced printed walls to in-plane seismic forces and reinforce the importance of considering interfacial behaviour, material quality, and geometric scaling in future structural assessments of 3D-printed systems.

The outcomes of this study contribute to the growing body of research aimed at understanding how layered cementitious structures respond under seismic demands. While simplified in scope, the findings support the development of performance-based evaluation methods for 3D-printed concrete walls and underline the need for further experimental validation and code development to guide their safe application in structural engineering.

References

An, D., Zhang, Y. X., & Yang, R. C. (2024). Numerical modelling of 3D concrete printing: Material models, boundary conditions and failure identification. Engineering Structures, 299, 117104.

Dere, Y. (2012). Nonlinear FE modeling of reinforced concrete. International Journal of Structural and Civil Engineering Research, 6(1), 71–74.

Duarte, G., Duarte, J. P., Brown, N., Memari, A., & Gevaudan, J. P. (2024). Design for early-age structural performance of 3D printed concrete structures: A parametric numerical modeling approach. Journal of Building Engineering, 94, 109986.

Mader, T., Schreter-Fleischhacker, M., Shkundalova, O., Neuner, M., & Hofstetter, G. (2023). Constitutive modeling of orthotropic nonlinear mechanical behavior of hardened 3D printed concrete. Acta Mechanica, 234, 5893–5918.

Pan, Z., Si, D., Tao, J., & Xiao, J. (2023). Compressive behavior of 3D printed concrete with different printing paths and concrete ages. Case Studies in Construction Materials, 18, e01949.

Skibicki, S., Techman, M., Federowicz, K., Olczyk, N., & Hoffmann, M. (2021). Experimental study of hardened Young's modulus for 3D printed mortar. Materials, 14(24), 7643.

Tahmasebinia, F., Jabbari, A. A., & Skrzypkowski, K. (2023). The application of finite element simulation and 3D printing in structural design within Construction Industry 4.0. Applied Sciences, 13(6), 3929.

Thorenfeldt, E., Tomaszewicz, A., & Jensen, J. J. (1987). Mechanical properties of high-strength concrete and application in design. In Utilization of High-Strength Concrete: Proceedings of the Symposium (pp. 149–159). Trondheim, Norway: Tapir.

Yang, Y., Wu, C., Liu, Z., & Zhang, H. (2022). 3D-printing ultra-high performance fiber-reinforced concrete under triaxial confining loads. Additive Manufacturing, 50, 102568.

ICEARC'25
4th International Civil Engineering & Architecture Conference
17-19 May 2025, Trabzon, Türkiye

Investigation of engineering properties of mortars containing basalt fiber and plastic waste aggregate exposed to high temperature

Yılmaz Yılmaz[1], Safa Nayır[*1], Memduh Nas[1], Şakir Erdoğdu[1]

[1] *Karadeniz Technical University, Department of Civil Engineering, 61080 Trabzon, Türkiye*

Abstract. Plastic waste, which is consumed in significant amounts today, by using it in building materials such as concrete or mortar stands out as an effective solution as it offers significant advantages both economically and ecologically. In addition, basalt fiber (BF) are generally used in engineering structures in order to minimize the negative effects that may be caused by other factors. In this scope, in this study, some properties of mortars containing basalt fiber and different proportions of plastic waste aggregate (PWA) were investigated exposed to high temperatures. The mixtures were varied according to two basic parameters: plastic PWA replacement ratio by volume (0%, 10% and 20%) and BF addition amount (0%, 0.25% and 0.50%). In the experimental study, 40x40x40 mm and 40x40x160 mm mortar specimens produced. The specimens exposed to 400°C, 600°C and 800°C. Residual compressive strength, flexural strength, mass loss, crack width-image processing relationship analysis tests performed on the specimens. The results showed that the use of PWA decreased both compressive strength and weight loss. In all mixtures, the flexural strength tended to decrease as the plastic aggregate ratio increased, regardless of basalt fiber. BF additive limited strength losses and maintained structural integrity, especially at elevated temperatures. Crack widths reached approximately 0.15 mm at 600°C and increased up to 0.25 mm at 800°C, which caused serious deterioration in the microstructural integrity of the material and accelerated strength loss.

Keywords: Plastic aggregate; Basalt fiber; High temperature; Crack; Image processing

1. Introduction

Nowadays, plastics have been used all over the world for a long time due to their very advantageous properties such as low density, low costs, etc. Plastics are generally used in packaging materials, shopping and garbage bags, toys, industrial and building materials, etc. (PlasticsEurope 2013; Sarma & Bansal, 2016). However, such an increase in plastic consumption leads to a significant amount of plastic waste. In a study, it is stated that approximately 300 million tons of plastic waste is generated annually (Wang et al., 2019). Many different types of plastics are produced every year and the most common types of plastics used are polyester (PET), polyethylene (PE) and polyvinylchloride (PVC). In addition, polycarbonate (PC), high density polyethylene (HDPE), polyvinylchloride (PVC), low density polyethylene/linear low density polyethylene (LDPE/LLDPE), polylactic acid (PLA), polypropylene (PP), polystyrene (PS) and others are used in many fields (Khairul et al., 2022). However, the use of plastic waste as construction material or concrete aggregate (coarse or fine aggregate) is not yet very common. Although there are various applications, the use and adaptation of plastic waste in the construction sector remains limited (da Silva et al., 2021). In this scope, the use and application of plastic waste in the construction industry can be improved due to its promising role in sustainability, environmental contribution and various economies.

Plastic consumption can be processed in 3 different ways such as landfilling, incineration and recycling (Gertsakis & Lewis, 2003). In this context, plastic waste is considered to be disposed of in landfills as a last resort because it takes up too much space and causes environmental problems. Incineration method is adopted in some countries due to the complete elimination of waste. This in particular releases large amounts of carbon dioxide and toxic chemicals. For this reason, recycling is the best solution in terms of reducing environmental impact, natural resource and energy efficiency. The reuse of waste and recycled plastic materials (aggregate or fiber) in the construction industry is considered an ideal method for waste disposal (Gu & Ozbakkaloglu, 2016). Plastic waste is used in mortar or concrete in two different ways. One of these is the substitution of plastic aggregate to replace

[*] Corresponding author, E-mail: safanayir@ktu.edu.tr

https://doi.org/10.31462/icearc2025_ce_mat_738

normal aggregate (NA). This can be in the form of coarse and fine aggregates or both combinations (used together). The second option is the use of plastic as fiber (Gu & Ozbakkaloglu, 2016). There are many studies in the literature investigating the fresh, hardened and durability properties of plastic material. Kou et al. (2009) reported that concretes prepared using PVC have lower density, more ductile (larger Poisson's ratios and reduced modulus of elasticity) and higher resistance to chloride ion penetration. However, their study revealed that the workability, compressive strength and tensile strength of concretes prepared using PVC decreased. Mohammed et al. (2019), in a study on some properties of concretes containing plastic aggregates, stated that the use of high levels of PVC in concrete reduces the workability of concrete. It is stated that the water absorption and unit weight of concrete do not change significantly when PVC aggregate is replaced with fine aggregate, but this is not the case for high proportions of PVC. Ahmed et al. (2024), in their study on concrete properties using recycled aggregate and recycled plastic fine aggregate, reported that for 40% waste plastic content, the reduction in maximum compressive strength for concretes containing 0% and 10% silica fume was 29% and 28%, respectively. Hamada et al. (2024) conducted a study on the use of plastic waste as aggregate in concrete. In their study, they found that the addition of certain plastic wastes improves the workability of concrete while increasing the unit weight, compressive, flexural and tensile strengths.

Like the environmental benefits that waste plastics will provide, basalt fibers are also an environmentally friendly and sustainable material both during the production phase and after their lifespan. Basalt fibers have many superior properties such as resistance to many chemicals, good performance at high temperatures, low moisture properties (Selçuk et al., 2023). Basalt fibers are used to strengthen structural integrity in mortars. In a study on the effectiveness of basalt fiber on mortar, it was stated that while it had a negative effect on fluidity in the fresh state, it improved the flexural strength, toughness, and ductility of cement matrix composites (Ralegaonkar et al., 2018). In a another study, it is stated that the mechanical properties of mortar and concrete decrease with the increase in plastic waste. It is stated that the reason for this situation can be attributed to its hydrophobic structure, lack of bond between cement paste and plastic waste, and high porous properties (Rathore et al., 2021).

Experimental studies on the fresh, mechanical, durability and dynamic properties and possible crack behaviors of mortars produced using different proportions of waste PVC and basalt fiber contribute to the practical use of these composite materials in civil engineering applications. In this scope, this study include some properties of mortars containing different proportions of PVC aggregate (0%, 10% and 20%) and basalt fiber (%0, 0.25% and 0.50%) exposed to high temperature. The specimens exposed to temperatures of 400°C, 600°C and 800°C. Residual compressive strength, flexural strength, mass loss test performed on the specimens. In addition, the crack width-image processing relationship on the specimens after exposed to high temperature was evaluated.

2. Material and method

2.1. Mortar specimens

In this study, a total of nine different mortar mixtures containing different proportions of plastic waste aggregate (PWA) and basalt fiber (BF) were designed to contribute to the development of eco-friendly, durable and sustainable building materials. The mixtures were varied according to two basic parameters: PWA replacement ratio by volume (0%, 10% and 20%) and basalt fiber addition amount (0%, 0.25% and 0.50%). In this scope, in addition to partial replacement of natural aggregate with PWA in certain proportions, BF reinforcement was used to increase the resistance of the matrix against crack propagation. The amount of cement was kept constant in all mixtures and the water/cement ratio was selected as 0.60. The design of the prepared mixtures are given in Table 1. The expression 10PWA25PW is an example coding that defines a composite mixture prepared with the addition of 10% plastic aggregate and 2.5% basalt fiber.

Table 1. Mixture design

Mixtures	Cement	NA	PWA	BF	Water
0PWA0BF		1350	0	0	
10PWA0BF		1215	71.32	0	
20PWA0BF		1080	142.64	0	
0PWA25BF		1350	0	6.16	
10PWA25BF	450	1215	71.32	6.16	270
20PWA25BF		1080	142.64	6.16	
0PWA50BF		1350	0	12.33	
10PWA50BF		1215	71.32	12.33	
20PWA50BF		1080	142.64	12.33	

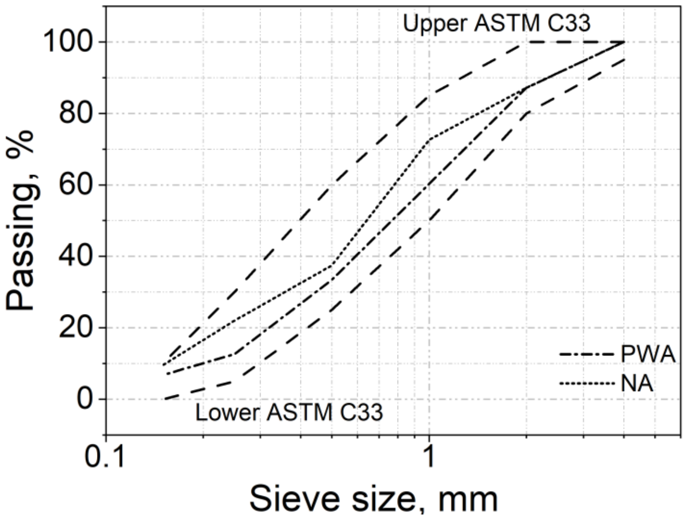

Fig. 1. Aggregate sieve analysis

The cement is CEM I 42.5 R type Portland cement conforming to EN 197-1 standard. Its chemical composition was determined as 18.80% SiO_2, 59.88% CaO, 1.67% MgO, 3.34% Fe_2O_3, 4.53% Al_2O_3 and 3.12% SO_3. The 28-day compressive strength of the cement was determined as 51.40 MPa, specific surface area as 3263 cm^2/g and specific gravity as 3.10 g/cm^3.

The natural sand used as NA was obtained from the stream deposits in Trabzon province and has a silica-based and round-grained structure. PWA was obtained from PVC waste left over from the production process of infrastructure pipes and made ready for use without any additional treatment. The grain distribution of the aggregates given in Fig. 1 was made in accordance with ASTM C33 (2023) standard.

The BF added to the blends has a length of 12 mm and a diameter range of 9-23 µm. The tensile strength of the fibers is 4840 MPa and the modulus of elasticity is 89 GPa. A special surface modification was applied on the fiber surface to improve adherence with the matrix. A polycarboxylate-based, highly effective superplasticizer (Sika® ViscoCrete® ACE 450) was used to maintain workability properties and achieve homogeneous mixing.

2.2. Test procedures

For each of the nine different mortar mixtures, 40×40×40 mm cube specimens were produced. After casting, the specimens were kept in their molds for 24 hours, then removed from the mold, placed in a water curing tank and kept in water curing for 28 days.

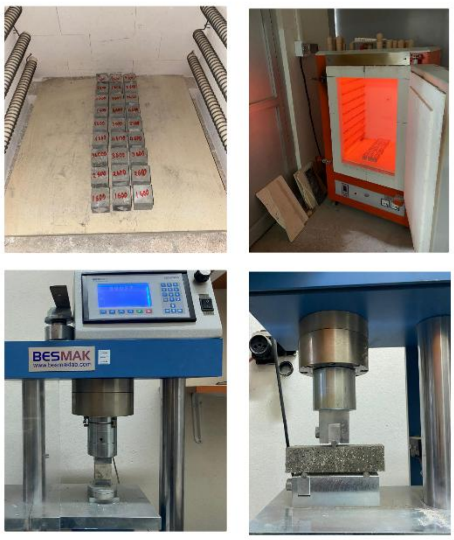

Fig. 2. Samples exposed to high temperatures, determination of compressive and flexural strengths of samples

In order to examine the strength properties, the specimens were exposed to high temperature levels after the cur ng period was completed. For this purpose, the specimens were subjected to temperatures of 400°C, 600°C and 800°C. For each temperature, the furnace temperature was increased at a rate of 2.5°C/minute to reach the desired peak temperature and kept at this temperature for 60 minutes. After completion of the heat treatment process, the specimens were allowed to cool at room temperature and then subjected to mechanical tests. The compressive strength tests were carried out in accordance with EN 1015-11 (2019) so that the residual strength properties of the different blends after high temperature were evaluated in a systematic way. Images of the experimental study are presented in Fig. 2.The total time for heat treatment and testing was approximately 220, 300 and 380 minutes for temperatures of 400°C, 600°C and 800°C, respectively.

3. Result and disccussion

Fig. 3 shows the 28-day compressive strength results. 0PWA0BF showed the highest strength with 41.56 MPa. The 10PWA0BF and 20PWA0BF mixtures showed a 17.9% and 26.3% decrease compared to 0PWA0BF with strength values of 34.10 MPa and 30.62 MPa, respectively. The 0PWA25BF mixture showed a strength of 37.02 MPa, 10.9% lower than 0PWA0BF, indicating the limited curative effect of BF alone. However, this effect was further reduced as the PWA ratio increased with BF admixture; 10PWA25BF showed a 17.4% decrease compared to the reference at 34.35 MPa and 20PWA25BF suffered a significant loss of 50.9% at 20.42 MPa. Similarly, the 0PWA50BF mix provided a strength of 40.89 MPa, very close to that of 0PWA0BF (1.6% decrease), but the 10PWA50BF and 20PWA50BF mixes lost 23.1% and 52.9% respectively, indicating that BF is not highly effective when used in combination with PWA. The main reason for the decrease in strength is the low workability and hollow structure caused by the combination of PWA and BF (Siddique et al., 2008; Safi et al., 2013; Ralegaonkar et al., 2018; John & Dharmar, 2021).

28-day flexural strength results are shown in Fig. 4. 0PWA0BF showed a flexural strength of 5.58 MPa. The 10PWA0BF mix with an increase in PWA ratio to 10% showed slightly increased compared to the 0PWA0BF with 6.83 MPa. However, when the PWA ratio was increased to 20% (20PWA0BF), the flexural strength decreased to 6.61 MPa. The strength rates for these three mixtures are quite close to each other and can be considered to remain at the same level. In addition, the 0PWA25BF mix containing only BF admixture presented a flexural strength of 7.23 MPa, 29.6% higher than the reference, demonstrating the improving effect of BF on this property. The 10PWA25BF mixture showed a similarly strong performance with 7.05 MPa. However, in the 20PWA25BF mix, the strength decreased to 5.80 MPa with a limited increase of only 3.9%, indicating that the effectiveness of BF admixture decreases at higher PWA levels. The highest flexural strength of 7.77 MPa was obtained in the 0PWA50BF mix; this mix showed an improvement of about 39.3% compared to the reference. However, the value decreased to 7.03 MPa in the 10PWA50BF mix, while 20PWA50BF was even lower than 0PWA0BF with 5.13 MPa.

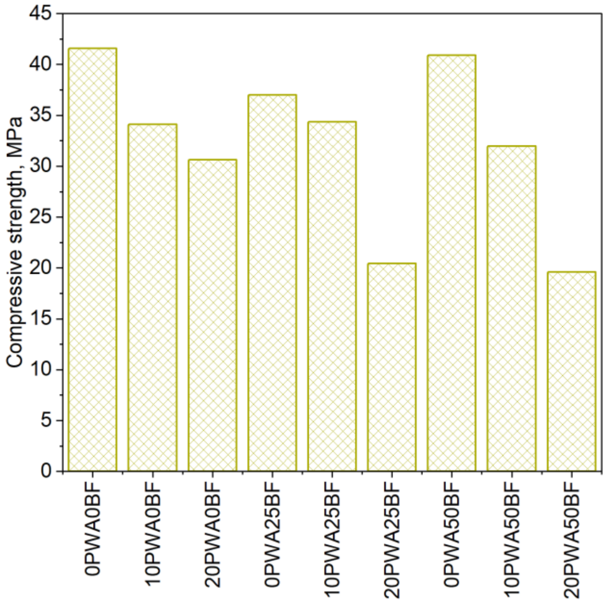

Fig. 3. Compressive strength results

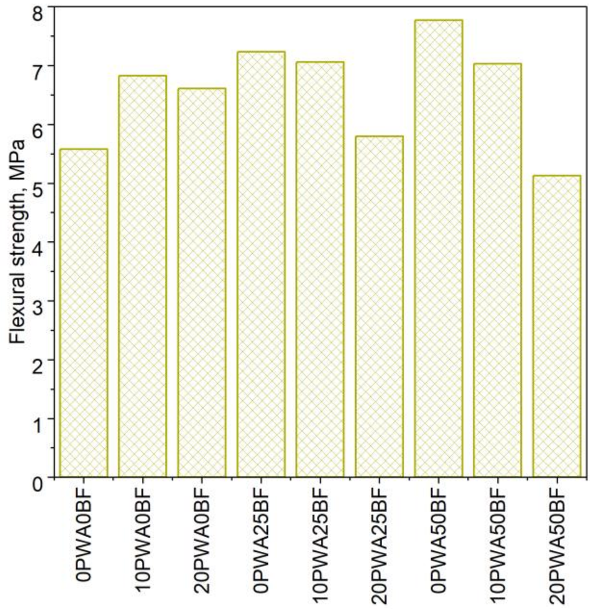

Fig. 4. Flexural strength results

The effect of elevated temperatures on the mechanical properties of concrete mixtures leads to significant changes, especially in terms of compressive strength. Compressive strengths of mortars exposed to 400°, 600°C and 800°C are presented in Fig. 5. The 0PWA0BF mix experiences a significant loss of strength with increasing temperature, with compressive strength values of 19.21 MPa at 400°C, 16.06 MPa at 600°C and 7.84 MPa at 800°C. This decrease indicates that the overall strength of concrete against thermal effects decreases and that heat impairs structural integrity, especially by weakening the chemical interaction between the binder and aggregate (Ma et al., 2015; Bao et al., 2023). Similarly, it is also observed in the mixtures 10PWA0BF and 20PWA0BF. In particular, the 20PWA0BF mix showed a strength of only 0.5 MPa at 800°C, indicating that the high PWA content has adverse effects on the mechanical properties of concrete at elevated temperatures.

This result supported that the use of PWA in structural concrete mixtures is limited in terms of structural performance under elevated temperatures. On the other hand, BF admixture has significant potential to improve the mechanical strength of concrete, especially exposed high temperature conditions. The 0PWA25BF mix exhibits a strength of 21.88 MPa at 400°C, showing a significant increase compared to the reference mix. However,

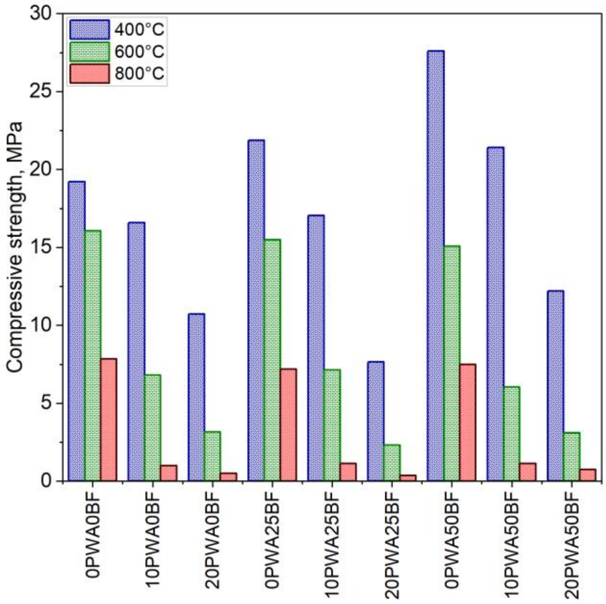

Fig. 5. Compressive strength results for 400°C, 600°C and 800°C

Similarly, the 10PWA25BF mix exhibited a lower strength compared to 0PWA25BF, showing a value of 17.04 MPa at 400°C and weakened more at higher temperatures. This indicated that BF provided a limited ameliorative effect on thermal strength, but this effect decreased when the PWA ratio increased. The 0PWA50BF mix desing exhibited the highest strength among all the blends with 27.60 MPa at 400°C, indicating that the BF additive greatly improved the high temperature strength. Although a decrease to 15.06 MPa and 7.50 MPa was observed at 600°C and 800°C, respectively, this mix design still exhibited a stronger performance at elevated temperatures than the other mixtures. The 10PWA50BF and 20PWA50BF blends showed a noticeable loss of strength at 800°C with strength values of 1.13 MPa and 0.75 MPa, respectively.

Fig. 6 shows the weight loss percentages of the mixtures at 400°C, 600°C and 800°C. The 0PWA0BF mixture showed weight loss of 2.93%, 3.85% and 6.30% respectively. The weight losses at 400°C, 600°C and 800°C for the 10PWA0BF mixture were 3.56%, 4.81% and 10.33%, respectively, indicating that the use of PWA increased the weight loss especially at higher temperatures. In the 20PWA0BF mixture, higher losses were observed at 4.67%, 6.80% and 11.12%, indicating that increasing the PWA content significantly increases the weight loss trend. The 0PWA25BF mixture containing only BF additive showed 3.09%, 3.68% and 6.44% weight loss, which were close to the reference. In the 10PWA25BF mixture, 3.63%, 5.09% and 8.54% weight loss were measured, where it was determined that the low PWA additive weakened the weight loss reducing effect of BF to a limited extent. The 20PWA25BF mixture showed weight losses of 4.45%, 6.46% and 10.27%, indicating that the high PWA ratio increased the weight loss despite the addition of BF. The 0PWA50BF mixture exhibited one of the lowest values with 2.79%, 3.46% and 6.18% weight loss, indicating that the use of high BF content can improve thermal stability. However, the weight losses increased to 4.83%, 5.18% and 7.51% in the 10PWA50BF mixture, while these values were 5.42%, 6.03% and 12.33% in the 20PWA50BF mixture. Especially at 800°C, the 12.33% loss in the 20PWA50BF mixture was the highest weight reduction among all mixtures.

When the images of the 0PWA0BF specimen are examined, it is seen that there is a significant deterioration in the microstructure of the material with increasing temperature. At 22°C, the surface has a very compact and homogeneous structure. When 400°C was reached, porosity on the surface increased, but crack formation was still limited and crack widths were small in the range of 0.02-0.03 mm; this temperature level indicates that the mechanical integrity of the sample was largely preserved. At 600°C, due to the complete evaporation of free water and the effect of calcium hydroxide degradation, wider and more widespread cracks were formed, with crack widths reaching up to 0.15 mm, indicating a decrease in structural strength. At 800°C, on the other hand, the crack network intensified significantly, the crack widths increased to 0.25 mm and the surface was completely decomposed, turning the specimen into a highly porous, brittle and weak structure, clearly indicating that the binder phases (especially the C-S-H gel) were severely degraded and the bearing capacity of the concrete was largely lost (Rao & Tadepalli, 2024; Tanash et al., 2024).

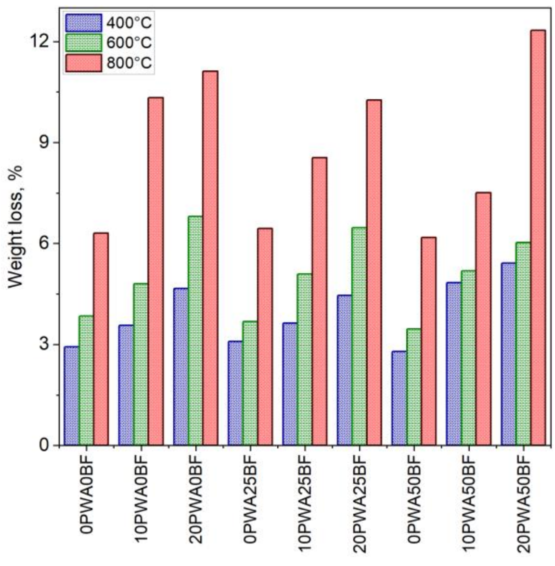

Fig. 6. Weight losses for 400°C, 600°C and 800°C

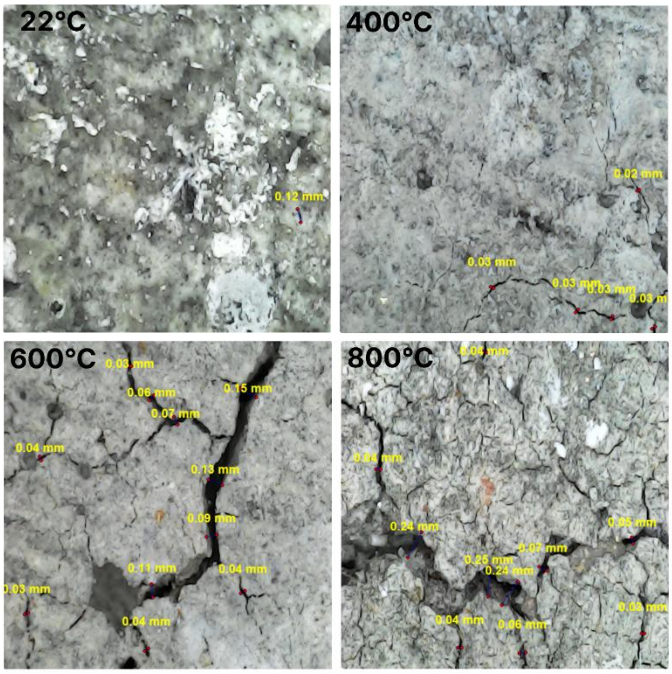

Fig. 7. Crack width and distribution relationship in mortar exposed to high temperature

4. Conclusions

In this study, the effects of PWA and BF admixtures on the mechanical and elevated temperature performance of mortars were investigated. The results showed that the use of PWA at low ratios increased the flexural strength, but at high ratios it had negative effects on both compressive strength and weight loss. BF additive limited strength losses and maintained structural integrity, especially at elevated temperatures. Significant strength losses were observed in all mixtures at high temperature exposure. The important results obtained from the study are given below:

- In the 20PWA0BF mixture, the addition of 20% PWA resulted in a 26% decrease in compressive strength and the strength decreased to 30.62 MPa.
- The 0PWA50BF mixture exhibited the highest flexural strength. In all mixtures, the flexural strength tended to decrease as the plastic aggregate ratio increased, regardless of basalt fiber.
- The 0PWA50BF mixture exhibited the highest temperature resistance among all mixtures, showing a compressive strength of 27.6 MPa after 400°C.
- In the 20PWA50BF mix design, 12.3% weight loss occurred after 800°C temperature exposure, and the negative effect of PWA content on the high temperature effect became evident.
- Crack widths reached approximately 0.15 mm at 600°C and increased up to 0.25 mm at 800°C, which caused serious deterioration in the microstructural integrity of the material and accelerated strength loss.

In line with the results of this study, it is recommended that the use of plastic waste aggregate be evaluated comparatively with different types of fibers (e.g. polypropylene, polyethylene, etc.) in future research. In addition, examining the effects of different fiber types such as steel, polypropylene and carbon fiber, not only basalt fiber, will contribute to a more comprehensive understanding of fiber-matrix interactions. In particular, a detailed investigation of the effects of fiber length, amount and distribution on elevated temperature performance offers an important field of study. In addition, it is thought that systems modified with nano-silica or different mineral additives can be improved in terms of both mechanical strength and thermal stability.

References

Ahmed, A., Ahmad, S., Musaa, A. E., & Al-Osta, M. A. (2024). Properties of concrete incorporating recycled coarse aggregates and recycled plastic fine aggregates. *Innovative Infrastructure Solutions*, *9*(5), 165.

ASTM C 33. (2023). Standard specification for concrete aggregates. ASTM International.

Bao, J., Zheng, R., Sun, Y., Zhang, P., Cui, Y., Xue, S., & Song, Q. (2023). A state-of-the-art review on high temperature resistance of lightweight aggregate high-strength concrete. *Journal of Building Engineering*, *69*, 106267. https://doi.org/10.1016/j.jobe.2023.106267

da Silva, T. R., de Azevedo, A. R. G., Cecchin, D., Marvila, M. T., Amran, M., Fediuk, R., ... & Szelag, M. (2021). Application of plastic wastes in construction materials: A review using the concept of life-cycle assessment in the context of recent research for future perspectives. *Materials*, *14*(13), 3549.

EN 1015-11. (2019). Methods of test for mortar for masonry - Part 11: Determination of flexural and compressive strength of hardened mortar.
Gertsakis, J., & Lewis, H. (2003). Sustainability and the waste management hierarchy: A discussion paper on the waste management hierarchy and its relationship to sustainability. RMIT University, 1-15.
John, V. J., & Dharmar, B. (2021). Influence of basalt fibers on the mechanical behavior of concrete—a review. *Structural Concrete*, *22*(4), 491-502. https://doi.org/10.1002/suco.201900086
Khairul Anuar, N. F. S., Huyop, F., Ur-Rehman, G., Abdullah, F., Normi, Y. M., Sabullah, M. K., & Abdul Wahab, R. (2022). An overview into polyethylene terephthalate (PET) hydrolases and efforts in tailoring enzymes for improved plastic degradation. *International Journal of Molecular Sciences*, 23(20), 12644.
Kou, S. C., Lee, G., Poon, C. S., & Lai, W. L. (2009). Properties of lightweight aggregate concrete prepared with PVC granules derived from scraped PVC pipes. *Waste Management*, 29(2), 621-628.
Ma, Q., Guo, R., Zhao, Z., Lin, Z., & He, K. (2015). Mechanical properties of concrete at high temperature—a review. *Construction and Building Materials*, 93, 371-383. https://doi.org/10.1016/j.conbuildmat.2015.05.131
Mohammed, A. A., Mohammed, I. I., & Mohammed, S. A. (2019). Some properties of concrete with plastic aggregate derived from shredded PVC sheets. *Construction and Building Materials*, 201, 232-245.
PlasticsEurope. (2013). Plastics—the facts 2013. An analysis of European latest plastics production, demand and waste data.
Ralegaonkar, R., Gavali, H., Aswath, P., & Abolmaali, S. (2018). Application of chopped basalt fibers in reinforced mortar: A review. *Construction and Building Materials*, 164, 589-602. https://doi.org/10.1016/j.conbuildmat.2017.12.245.
Rathore, R. S., Chouhan, H. S., & Prakash, D. (2021). Influence of plastic waste on the performance of mortar and concrete: A review. *Materials Today: Proceedings*, 47, 4708-4711.
Rao, K. P., & Tadepalli, T. (2024). High-temperature behaviour of concrete: A review. In R. K. Pancharathi, C. K. Y. Leung, & J. M. Chandra Kishen (Eds.), Low carbon materials and technologies for a sustainable and resilient infrastructure (Vol. 440, pp. 199-217). Springer. https://doi.org/10.1007/978-981-99-7464-1_13
Safi, B., Saidi, M., Aboutaleb, D., & Maallem, M. (2013). The use of plastic waste as fine aggregate in self-compacting mortars: Effect on physical and mechanical properties. *Construction and Building Materials*, 43, 436-442. https://doi.org/10.1016/j.conbuildmat.2013.02.049
Selcuk, S., Ahmetoglu, U., & Gokce, E. C. (2023). Basalt fiber reinforced polymer composites (BFRP) other than rebars: A review. *Materials Today Communications*, 37, 107359.
Sharma, R., & Bansal, P. P. (2016). Use of different forms of waste plastic in concrete—a review. *Journal of Cleaner Production*, 112, 473-482.
Siddique, R., Khatib, J., & Kaur, I. (2008). Use of recycled plastic in concrete: A review. *Waste Management*, 28(10), 1835-1852. https://doi.org/10.1016/j.wasman.2007.09.011
Tanash, O. A., Abu Bakar, B. H., Muthusamy, K., & Al Biajawi, M. I. (2024). Effect of elevated temperature on mechanical properties of normal strength concrete: An overview. *Materials Today Proceedings*, 107, 152-157. https://doi.org/10.1016/j.matpr.2023.09.053
Wang, W., Themelis, N. J., Sun, K., Bourtsalas, A. C., Huang, Q., Zhang, Y., & Wu, Z. (2019). Current influence of China's ban on plastic waste imports. *Waste Disposal & Sustainable Energy*, 1, 67-78.

4th International Civil Engineering & Architecture Conference
17-19 May 2025, Trabzon, Türkiye

Effects of different types of fibers on the mechanical properties and shrinkage of one-part sodium carbonate-activated slag-based mortars

Busra Akturk*[1]

[1] *Istanbul Bilgi University, Department of Civil Engineering, Istanbul, Türkiye.*

Abstract. Alkali-activated materials present a sustainable and efficient alternative to traditional cement-based systems by incorporating industrial by-products such as slag, fly ash, and metakaolin as precursors. This innovation significantly reduces CO_2 emissions compared to conventional cement production, which contributes approximately 8% of global CO_2 emissions. This study examines the mechanical properties and shrinkage behavior of sodium carbonate-activated, fiber-reinforced mortars made with ground-granulated blast furnace slag. The one-part mixing method was selected for its ease of use and compatibility with conventional cement production practices. Steel, polypropylene, and hybrid fibers (a combination of steel and polypropylene) were incorporated at 1% by volume in the mortar mixes. Mechanical properties, including compressive strength at 7 and 28 days and flexural strength at 28 days, were assessed on mortar specimens. A three-point bending test was performed on beam samples. The results demonstrated that steel fibers significantly improved the flexural strength of the mortars, while polypropylene fibers were more effective in reducing shrinkage. The hybrid fiber combination exhibited a balanced performance, leveraging the strengths of both fiber types.

Keywords: Alkali-activated materials; sodium carbonate; slag; fibers; mechanical properties.

1. Introduction

Ordinary Portland Cement (OPC) remains the most widely used binder in construction engineering. However, its production is associated with significant environmental concerns, including high carbon dioxide emissions and substantial energy consumption. In response, researchers have been actively exploring sustainable alternatives that offer lower environmental impact and energy demands. Among these, alkali-activated materials (AAMs) have emerged as promising cementitious binders. These materials have gained attention primarily due to their reduced CO_2 emissions, improved mechanical performance, and superior durability compared to OPC (Komljenović et al., 2013; Zhang et al., 2017; Mithun & Narasimhan, 2016; Bilim & Atis, 2012).

The environmental advantages of AAMs are notable: their production can cut CO_2 emissions by 25–50% and reduce energy consumption by over 40% relative to OPC (Thomas et al., 2016; Jiang et al., 2014a). Moreover, most AAMs are derived from industrial by-products, such as blast furnace slag and fly ash, promoting waste valorization and resource conservation. As a result, AAMs are increasingly viewed as eco-friendly alternatives to conventional cement. Among AAMs, alkali-activated slag (AAS) stands out as a particularly viable candidate. However, its broader application in the construction industry has been limited due to challenges such as excessive drying shrinkage and the development of microcracks, which can negatively affect long-term durability and structural integrity (Neto et al., 20008). Research by Shen et al. (2011) demonstrated that the drying shrinkage of AAS mortars could be up to three times higher than that of OPC mortars. Similarly, Atiş et al. (2009) reported that the drying shrinkage of AAS mortars activated with sodium hydroxide and sodium carbonate solutions could be three to six times greater than OPC counterparts after six months. To mitigate these shrinkage-related issues, the incorporation of fibers has been proposed as an effective strategy. Studies have shown that adding fibers not only reduces drying shrinkage but can also enhance the mechanical performance of AAS-based materials (Aydn & Baradan, 2013; Xu et al., 2021). Fiber-reinforced alkali-activated slag composites are gaining attention for their unique properties, including high deformation capacity, self-healing capability, and environmental benefits (Nguyễn et al., 2018).

Fibers are known to improve various mechanical properties of cementitious composites, such as tensile strength, fracture toughness, abrasion resistance, and ductility (Arslan, 2016; Kizilkanat et al., 2015). When used

*Corresponding author, E-mail: busra.akturk@bilgi.edu.tr

https://doi.org/10.31462/icearc2025_ce_mat_803

in AAS systems, fibers contribute to the material's ductility by enhancing its deformation tolerance and controlling the development and propagation of cracks (Jiang et al., 2014b; Shaikh, 2013; Tassew & Lubell, 2014). This crack-bridging capability helps transform inherently brittle matrices into more resilient and damage-tolerant composites. Several experimental studies confirm that fiber reinforcement is a viable method for improving both the mechanical and shrinkage properties of alkali-activated mortars and concretes. For instance, Akturk (2023) investigated the fracture behavior of fiber-reinforced AAS mortars containing basalt and hybrid fibers, reporting that while compressive strength slightly decreased, flexural strength and fracture energy improved significantly.

The present study focuses on evaluating the effects of different fiber types on the mechanical performance and drying shrinkage behavior of one-part sodium carbonate-activated slag-based mortars. Experimental tests including flow diameter, compressive and flexural strength, and drying shrinkage were conducted, with the results discussed in the subsequent sections.

2. Experimental study

2.1 Materials

Slag was used as the binding material in this study, obtained from the KARDEMIR Iron and Steel Plant. The chemical composition of slag was determined by *X-ray fluorescence* analyses and presented in Table 1. The median particle size (d_{50}) of slag was found to be 8.8 µm.

Table 1. Chemical composition of slag

Chemical composition (% by weight)	Slag
SiO_2	39.0
Al_2O_3	12.4
Fe_2O_3	1.2
CaO	33.7
MgO	7.5
K_2O	0.6
TiO_2	0.9
Loss of ignition (%)	0.4
Specific surface area (cm^2/g)	4670
Relative grain density	2.88

To explore the effects of different types of fibers, polypropylene (PP) and straight steel fiber (ST) (Fig. 1) on the mechanical properties of one-part NC-activated slag-based mixes, they were used in the mortar mixes with a volume fraction of 1%. The properties of fibers are given in Table 2. Their preferred lengths were 12 mm and 13 mm for PP and ST, respectively.

Table 2. Properties of fibers

Fiber type	Length [mm]	Diameter [µm]	Aspect ratio	Tensile strength [MPa]	Specific gravity
Polypropylene	12	30–40	300–400	570–660	0.91
Steel	13	150	87	3000	7.85

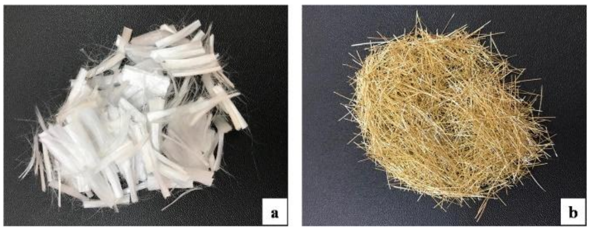

Fig. 1. Images of (a) polypropylene and (b) steel fibers

2.2 Mix design of one-part NC-activated slag-based mixes

A total of four mixes were prepared in this study. Reference is the plain mix, which does not contain any fiber, PP is the polypropylene fiber-reinforced mix, ST is the steel fiber reinforced mix and HYB contains both PP and ST at the same amount, each 0.5% by volume. The mixes are named according to the type of fiber used. Solid sodium carbonate (NC) serves as the alkaline activator in all formulations, maintained at 10% of the binder weight. The water/binder ratio was consistently set at 0.40 for mortar mixes. Silica-based fine aggregate with a maximum particle size of 2 mm was incorporated at a volume ratio of 50%. The fine aggregate gradation adhered to the standards outlined in the CEN standard sand.

Table 3. Mixing ratios of mortar mixes

Mix	Slag (%)	Water/binder ratio	Fiber [% by volume]	
			PP	ST
Reference	100	0.4	-	-
PP			1	-
ST			-	1
HYB			0.5	0.5

2.3 Testing methods

2.3.1 Flow diameter

The flow diameter of fresh mortar specimens was assessed per ASTM C1437, utilizing a mini-slump cone with standard dimensions: 70 mm upper diameter, 100 mm lower diameter, and 60 mm height. This test was conducted immediately following the mixing process. The base diameter of the sample, as distributed on the flow table, serves as an indicator of workability. Two perpendicular readings are recorded, and the final flow amount of the mortar samples is determined by calculating the average value of these readings.

2.3.2 Mechanical properties

The compressive strength test was performed on mortar samples according to the ASTM C109. The mortar specimens were produced as cubic samples of 50×50×50 mm dimensions and cured in a humidity cabinet maintained at (23±2) °C and ~65% relative humidity until the testing days. The specimens were tested on the 7th and 28th days and the corresponding strength values were recorded for each respective day.

The flexural strength and fracture properties of beam specimens were investigated via three-point bending tests conducted according to ASTM C293 - *Standard Test Method for Flexural Strength of Concrete (Using Simple Beam with Center-Point Loading)*. The tests were performed on the mortar samples on 28 days of curing. Rectangular beams with dimensions of 160 mm (length) × 40 mm (depth) × 40 mm (width) were used. Before a test, the dimensions of the beam sample were recorded, and the flexural strength was calculated by Equation (1).

$$f = \frac{3PS}{2b(d-a_0)^2} \tag{1}$$

where P is the maximum load, S [mm] is the span length, and b and d [mm] are the width and depth, and a_0 [mm] is the depth of pre-cutting crack of the sample, respectively.

2.3.3 Shrinkage

Shrinkage measurement was measured on mortar prisms with dimensions of 40×40×160 mm. Three identical prisms were used for each mix. All samples were kept at 23±2 C and relative humidity of 65±5%. The length change measurements were taken up to 28 days.

3. Results and discussions

3.1 Flow diameter

The flow diameters of the plain and fiber-reinforced mortar mixes are presented in Fig. 2. The reference mix exhibited the highest flow diameter at 170 mm. Fiber incorporation led to a reduction in flowability. While the steel fiber-reinforced mix (ST) showed a slight decrease to 160 mm, both the polypropylene (PP) and hybrid (HYB) mixes recorded a more pronounced reduction, with flow diameters of 140 mm. The decreased flowability in the PP and HYB mixes can be attributed to several factors. First, the addition of polypropylene fibers increases interparticle friction between sand and paste, as reported by Altalabani et al. (2020). Second, the potential formation of fiber clumps or balls disrupts uniform flow, further hindering workability, as noted by Mardani-Aghabaglou et al. (2018). Akturk (2023) also observed a reduction in flowability when incorporating basalt and polypropylene fibers into slag/basalt powder-based alkali-activated materials. The reduction was attributed to the hydrophilic nature of polypropylene fibers, which tend to wind around aggregates and trap paste, thereby impeding free movement and reducing flow diameter.

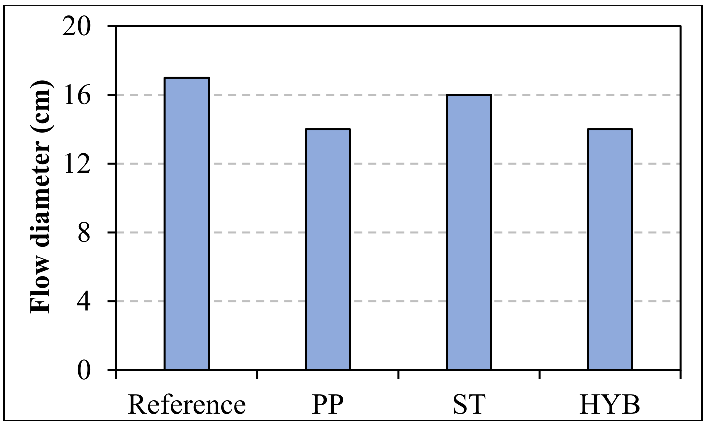

Fig. 2. Flow diameter results of the mixes

2.2 Mechanical properties

The compressive strengths of both plain and fiber-reinforced mixes were measured at 7 and 28 days, as presented in Fig. 3. At 7 days, the reference mix reached a strength of 7.0 MPa, while the addition of polypropylene (PP) fibers led to a slight increase to 7.6 MPa. The steel fiber-reinforced mix (ST) exhibited the highest strength at this age, achieving 7.9 MPa, followed by the hybrid mix (HYB) with 7.7 MPa. The notable improvement in the ST mix can be attributed to the superior mechanical properties of steel fibers, as detailed in Table 2. At 28 days, a significant increase in compressive strength was observed across all mixes, with the same trend continuing. The ST mix again showed the highest strength at 19.5 MPa, while the reference mix reached 16.3 MPa. The inclusion of either PP or ST fibers caused a slight increase in the compressive strength might be due to the delayed formation of the initial crack in the paste phase (Hilles & Ziara, 2019; Dawood & Ramli, 2011).

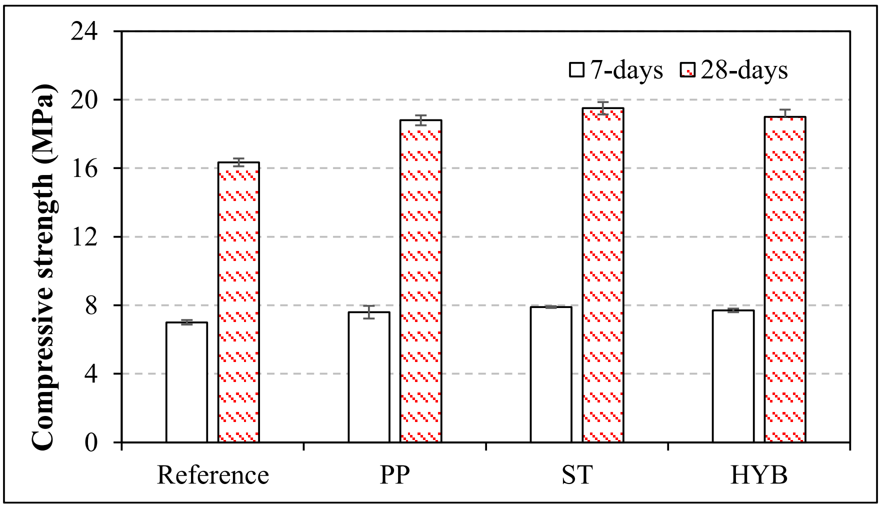

Fig. 3. Compressive strength results of the mixes

The influence of fiber incorporation on the flexural strength of mortars is illustrated in Fig. 4. As expected, the inclusion of fibers enhanced the flexural strength of all mixes. The Reference mix exhibited the lowest strength at 1.6 MPa, while the steel fiber-reinforced mix (ST) achieved the highest value of 2.3 MPa. The addition of polypropylene (PP) and hybrid (HYB) fibers also led to slight improvements in flexural strength compared to the reference mix. Specifically, the flexural strength increased by 13% with PP fibers, and by 44% and 25% for the ST and HYB mixes, respectively. The more pronounced enhancement in the ST mix can be attributed to the superior mechanical properties and bridging capability of steel fibers.

Similar improvements in flexural strength due to fiber reinforcement have been reported in the literature. Akturk et al. (2020) found that both steel and polypropylene fibers enhanced the flexural strength of sodium carbonate-activated slag mortars. Zhou et al. (2021) observed a gradual increase in flexural and splitting tensile strengths with increasing basalt fiber content. Similarly, Abdollahnejad et al. (2021) reported that various fiber types increased the flexural strength of alkali-activated slag mortars, although compressive strength varied depending on fiber type. In contrast, other studies have reported adverse effects of polypropylene fibers on flexural strength. Puertas et al. (2003) and Ranjbar et al. (2016) found that PP fibers reduced the flexural strength of alkali-activated slag mortars. This discrepancy may be attributed to casting and compaction challenges during mixing, leading to poor fiber dispersion and weak fiber–matrix bonding. Wang et al. (2012) noted that inadequate fiber dispersion during fresh-state processing can compromise the interfacial bond and overall mechanical performance.

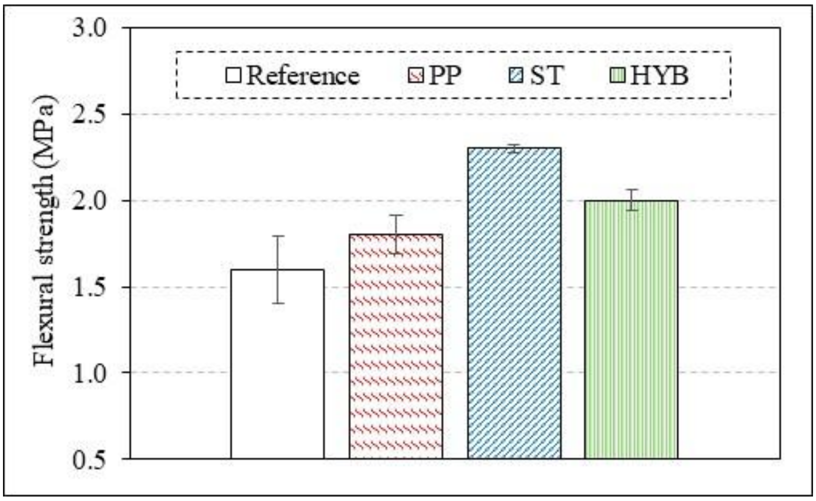

Fig. 4. Flexural strength results of the mixes

3.3 Shrinkage
Time-dependent drying shrinkage values of both plain and fiber-reinforced mixes were measured up to 35 days, as shown in Fig. 5. Among all mixes, the reference mix exhibited the highest shrinkage, whereas the polypropylene fiber-reinforced mix (PP) showed the lowest. For most mixes, the shrinkage rate was relatively high during the early ages, particularly up to 14 days, and tended to stabilize thereafter. The hybrid (HYB) and steel fiber-reinforced (ST) mixes exhibited similar shrinkage behavior at all ages. The PP mix recorded 52% and 46% lower ultimate shrinkage compared to the Reference and ST/HYB mixes, respectively. The superior shrinkage performance of the PP mix can be attributed to its ability to reduce bleeding, promote more uniform internal moisture distribution, and enhance the cohesiveness of the mortar matrix.

Xu et al. (2021) reported that increasing both the length and dosage of polypropylene fibers significantly decreased the drying shrinkage of NaOH-activated slag mortars. Similarly, Vilaplana et al. (2016) found that carbon fibers effectively inhibited drying shrinkage in alkali-activated slag pastes while also enhancing flexural strength.

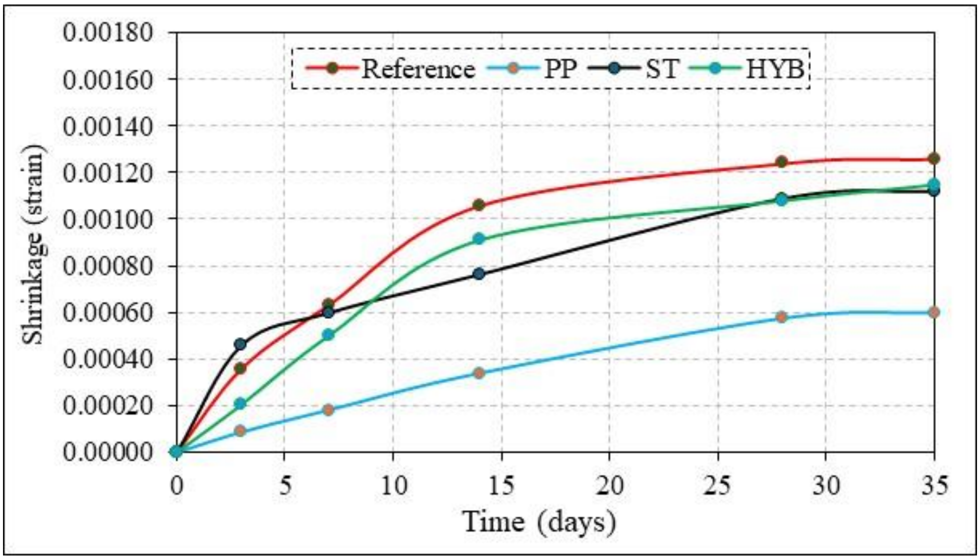

Fig. 5. Shrinkage results of the mixes

4. Conclusion

This study investigates the effects of different fiber types—polypropylene, steel, and hybrid—on the performance of one-part sodium carbonate-activated slag-based mortar mixes. The flow diameter, compressive strength, flexural strength, and drying shrinkage of the mixes were experimentally evaluated.

The key findings derived from the experimental results are summarized as follows:

- The incorporation of fibers reduced the flow diameter of the mixes, with the most significant reduction observed in polypropylene fiber-reinforced mortars. This reduction is primarily attributed to increased interparticle friction and the tendency of polypropylene fibers to form clumps, which hinder fresh-state workability.
- While compressive strength showed a slight improvement with fiber addition, a notable enhancement in flexural strength was achieved through steel fiber reinforcement. The superior performance of steel fibers is mainly due to their higher tensile strength and stiffness, which effectively bridge cracks and resist tensile stresses.
- Polypropylene fiber reinforcement significantly reduced drying shrinkage. This effect is attributed to the fibers' ability to reduce bleeding, promote a more uniform internal moisture distribution, and increase the cohesiveness of the fresh mix. In contrast, steel and hybrid fibers had a negligible effect on shrinkage mitigation.

References

Abdollahnejad, Z., Mastali, M., Falah, M., Shaad, K. M., Luukkonen, T., & Illikainen, M. (2021). Durability of the reinforced one-part alkali-activated slag mortars with different fibers. *Waste and Biomass Valorization, 12*, 487–501.

Akturk, B. (2023). Fracture behavior of alkali-activated basalt powder/slag systems reinforced with basalt and hybrid fibers. *Materials and Structures, 56*(2), 46.

Akturk, B., Akca, A. H., & Kizilkanat, A. B. (2020). Fracture response of fiber-reinforced sodium carbonate activated slag mortars. *Construction and Building Materials, 241*, 118128.

Altalabani, D., Linsel, S., & Bzeni, D. K. (2020). Rheological properties and strength of polypropylene fiber-reinforced self-compacting lightweight concrete produced with ground limestone. *Arabian Journal for Science and Engineering, 45*(5), 4171–4185.

Arslan, M. E. (2016). Effects of basalt and glass chopped fibers addition on fracture energy and mechanical properties of ordinary concrete: CMOD measurement. *Construction and Building Materials, 114*, 383–391.

Atiş, C. D., Bilim, C., Çelik, Ö., & Karahan, O. (2009). Influence of activator on the strength and drying shrinkage of alkali-activated slag mortar. *Construction and Building Materials, 23*(1), 548–555.

Aydın, S., & Baradan, B. (2013). The effect of fiber properties on high performance alkali-activated slag/silica fume mortars. *Composites Part B: Engineering, 45*(1), 63–69.

Bilim, C., & Atiş, C. D. (2012). Alkali activation of mortars containing different replacement levels of ground granulated blast furnace slag. *Construction and Building Materials, 28*(1), 708–712.

Dawood, E. T., & Ramli, M. (2011). High strength characteristics of cement mortar reinforced with hybrid fibres. *Construction and Building Materials, 25*(5), 2240–2247.

Hilles, M. M., & Ziara, M. M. (2019). Mechanical behavior of high strength concrete reinforced with glass fiber. *Engineering Science and Technology, an International Journal, 22*(3), 920–928.

Jiang, M., Chen, X., Rajabipour, F., & Hendrickson, C. T. (2014a). Comparative life cycle assessment of conventional, glass powder, and alkali-activated slag concrete and mortar. *Journal of Infrastructure Systems, 20*(4), 04014020.

Jiang, C., Fan, K., Wu, F., & Chen, D. (2014b). Experimental study on the mechanical properties and microstructure of chopped basalt fibre reinforced concrete. *Materials & Design, 58*, 187–193.

Kizilkanat, A. B., Kabay, N., Akyüncü, V., Chowdhury, S., & Akça, A. H. (2015). Mechanical properties and fracture behavior of basalt and glass fiber reinforced concrete: An experimental study. *Construction and Building Materials, 100*, 218–224.

Komljenović, M., Baščarević, Z., Marjanović, N., & Nikolić, V. (2013). External sulfate attack on alkali-activated slag. *Construction and Building Materials, 49*, 31–39.

Mardani-Aghabaglou, A., Özen, S., & Altun, M. G. (2018). Durability performance and dimensional stability of polypropylene fiber reinforced concrete. *Journal of Green Building, 13*(2), 20–41.

Mithun, B. M., & Narasimhan, M. C. (2016). Performance of alkali activated slag concrete mixes incorporating copper slag as fine aggregate. *Journal of Cleaner Production, 112*, 837–844.

Neto, A. A. M., Cincotto, M. A., & Repette, W. (2008). Drying and autogenous shrinkage of pastes and mortars with activated slag cement. *Cement and Concrete Research, 38*(4), 565–574.

Nguyễn, H. H., Choi, J. I., Song, K. I., Song, J. K., Huh, J., & Lee, B. Y. (2018). Self-healing properties of cement-based and alkali-activated slag-based fiber-reinforced composites. *Construction and Building Materials, 165*, 801–811.

Puertas, F., Amat, T., Fernández-Jiménez, A., & Vázquez, T. (2003). Mechanical and durable behaviour of alkaline cement mortars reinforced with polypropylene fibres. *Cement and Concrete Research, 33*(12), 2031–2036.

Ranjbar, N., Talebian, S., Mehrali, M., Kuenzel, C., Metselaar, H. S. C., & Jumaat, M. Z. (2016). Mechanisms of interfacial bond in steel and polypropylene fiber reinforced geopolymer composites. *Composites Science and Technology, 122*, 73–81.

Shaikh, F. U. A. (2013). Review of mechanical properties of short fibre reinforced geopolymer composites. *Construction and Building Materials, 43*, 37–49.

Shen, W., Wang, Y., Zhang, T., Zhou, M., Li, J., & Cui, X. (2011). Magnesia modification of alkali-activated slag fly ash cement. *Journal of Wuhan University of Technology-Mater. Sci. Ed., 26*, 121–125.

Tassew, S. T., & Lubell, A. S. (2014). Mechanical properties of glass fiber reinforced ceramic concrete. *Construction and Building Materials, 51*, 215–224.

Thomas, R. J., Ye, H., Radlinska, A., & Peethamparan, S. (2016). Alkali-activated slag cement concrete. *Concrete International, 38*(1), 33–38.

Vilaplana, J. L., Baeza, F. J., Galao, O., Alcocel, E. G., Zornoza, E., & Garcés, P. (2016). Mechanical properties of alkali activated blast furnace slag pastes reinforced with carbon fibers. *Construction and Building Materials, 116*, 63–71.

Wang, J. Y., Banthia, N., & Zhang, M. H. (2012). Effect of shrinkage reducing admixture on flexural behaviors of fiber reinforced cementitious composites. *Cement and Concrete Composites, 34*(4), 443–450.

Xu, Y., Xing, G., Zhao, J., & Zhang, Y. (2021). The effect of polypropylene fiber with different length and dosage on the performance of alkali-activated slag mortar. *Construction and Building Materials, 307*, 124978.

Zhang, J., Shi, C., Zhang, Z., & Ou, Z. (2017). Durability of alkali-activated materials in aggressive environments: A review on recent studies. *Construction and Building Materials, 152*, 598–613.

Zhou, X., Zeng, Y., Chen, P., Jiao, Z., & Zheng, W. (2021). Mechanical properties of basalt and polypropylene fibre-reinforced alkali-activated slag concrete. *Construction and Building Materials, 269*, 121284.

4th International Civil Engineering & Architecture Conference
17-19 May 2025, Trabzon, Türkiye

The impact of varying alginate ratios on soil-based composites

Büşra M. Akyüz*[2], İrfan Ş. Öztürk[1] Furkan A. Sarı[1], Mine K. Yıldız[1], Muhammed Maraşlı[3], Mehmet Emiroğlu[1]

[1] Sakarya University, Department of Civil Engineering, 54220 Sakarya, Türkiye
[2] Sakarya University, Institute of Natural Sciences, Sakarya, Türkiye
[3] Fibrobeton Inc., Istanbul 34810, Türkiye

Abstract. Soil-based composites are gaining more and more attention as sustainable and environmentally friendly alternatives in the construction industry. These materials are characterized by their natural properties, low carbon footprint, and recyclable nature. However, one of the significant limitations of soil-based mixtures is the shrinkage and resulting cracks that occur during the drying process. This study aims to design soil-based composite blends containing clay, lime, alpha gypsum, cellulose, and alginate to reduce the shrinkage problem and increase the utilization potential of soil-based materials. Alginate is a natural polymer and binder that is easily soluble in water and improves the material's workability. Due to these properties, the study aims to increase the stability of the material and reduce shrinkage by using alginate. The study investigated fresh mortar properties and mass losses of mixtures with different compositions, and flexural and compressive strength tests were also performed. The optimum alginate ratio was determined, and material performance characteristics were analyzed based on the data obtained. This innovative approach offers important contributions to improving the mechanical performance of soil-based materials.

Keywords: Alginate; Cellulose; Soil-based materials

1. Introduction

Today, in line with the sustainability goals in the building sector, there is an increasing interest in environmentally friendly materials with low carbon footprint. Sustainability has become an inevitable requirement for the building sector to fulfill its environmental responsibilities (Maierdan et al., 2024). In this context, soil-based building materials developed with natural raw materials stand out with advantages such as production based on local resources, low energy requirement, recyclability and biological compatibility. However, soil-based building materials undergo volumetric shrinkage due to moisture loss during the drying process (Emiroğlu et al., 2015). This causes crack formation and thus structural problems (Assunção et al., 2025). These cracks are a common and important problem for structures' long-term durability and integrity. Recently, significant efforts have been made to improve the low mechanical properties and increase structural stability in soil-based systems. Biopolymer additives such as sodium alginate derived from brown marine algae are used in these studies (Maierdan et al., 2024).

In this study, clay, alpha gypsum and lime were used as binders to produce soil-based composites. In addition, cellulose (Yin et al., 2023) (Patural et al., 2011) and sodium alginate were added to improve workability and stabilize the drying process. The fibrous structure of cellulose increases water-holding capacity and crack resistance, while alginate, as a natural polymer, increases viscosity and limits cracking by reducing drying-induced stresses. Clay formed the base matrix with its high plasticity and binding properties. Alpha gypsum was used to contribute to early setting time (Wang et al., 2023). In addition, lime is an effective stabilizer for earth structures and is particularly well adapted to soils with high clay content. It is also considered an environmentally sustainable material due to its capacity to absorb atmospheric carbon dioxide (Arto et al., 2024).

This study aims to contribute to developing new-generation building materials made of natural materials that are environmentally friendly and resistant to cracking. In this context, four different mixtures were prepared. In all mixtures, the proportions of clay, alpha gypsum, lime, and cellulose were kept constant in grams; only the amount of alginate was changed, and the effect of the alginate substitution rate on the mixture performance was examined. The reference mix represents the control group without alginate. In addition, sodium alginate was preferred at the critical ratios of 0.6%, 0.8%, and 1%, as determined by Maierdan et al. (2024). Within the scope of the study, fresh

* Corresponding author, E-mail: meltem.akyuz@ogr.sakarya.edu.tr

https://doi.org/10.31462/icearc2025_ce_mat_810

mortar properties (consistency, workability) and mass loss changes of the mixtures were investigated. In addition, compressive strength and flexural strength tests were performed on the specimens after 7 days. Based on the findings, the effect of alginate admixture on mix stability was evaluated, and the optimum replacement ratio was determined for this study.

2. Material and method

Clay (0-1 mm fineness), silica sand (AFS 30-35), alpha gypsum (0.01-0.08 mm fineness), lime, FBR 500 cellulose (Fiber Kimya), and sodium alginate (ZAG Kimya) for consistency stabilization were used as powder materials to form composite samples with alginate content.

Within the study's scope, four different mortar mixtures were prepared, each with different sodium alginate content. The first mixture was organized as the control group (R) and did not contain an alginate additive. Mixtures A (0.6), A (0.8), and A (1) contained 0.6%, 0.8%, and 1.0% sodium alginate, respectively (Table 1). The indicated alginate ratios were calculated as percentages based on the amount of water used. All materials were first mixed dry for 2 minutes. Then, water and alginate were gradually added to the mixture by mixing it with a mixer for 1 minute, and a homogeneous mortar was obtained. A spreading table test was performed for each mixture in the fresh state, and the workability of the mixture was evaluated by measuring the spreading diameter. In addition, in order to determine the consistency properties of the mixtures in more detail, the number of strokes was determined using the Casagrande apparatus. These two experiments were carried out to determine how fluid and prone the mixtures were to deformation in the fresh state. Each of the mixtures was poured into molds with dimensions of 40 × 40 × 40 × 160 mm, and three specimens were produced for each mixture. The mass losses of the demolded specimens were measured for 7 days. The soil-based composite specimens were subjected to compressive and flexural strength (TS EN 196-1) tests after 7 days.

Table 1. Mixing ratios of the produced samples.

Materials	R	A (0.6)	A (0.8)	A (1)
Clay	35.71%	35.74%	35.71%	35.69%
Silica Sand	35.71%	35.74%	35.71%	35.69%
Alpha Gypsum	3.57%	3.64%	3.57%	3.57%
Lime	3.57%	3.64%	3.57%	3.57%
Water	21.25%	21.26%	21.18%	21.14%
Cellulose	0.18%	0.18%	0.18%	0.18%
Sodium Alginate	0%	0.12%	0.17%	0.21%

3. Results and discussion

3.1. Fresh mortar properties

The reference mortar (R) was generally observed to be a liquid mixture with a spread plate of 14 cm. Mortar A (0.6) was more viscous and stable than the reference mortar. The consistency of the mortar was observed to be similar to kinetic sand. At this point, the diameter of the spreading table decreased. It was noted that the consistency and behavior of mortar A (0.8) was similar to that of mortar A (0.6) (Figure 1). Also, the spreading table and Casagrande test showed the same values. Finally, mortar A (1) had a much more solid consistency than the others. It was recorded as the mixture with the smallest spreading table diameter (Table 2).

When Table 2 is analyzed, as expected, the Casagrande numbers of the series with higher spreading diameters decreased. The experimental results also show that the Casagrande test can be a good option for determining the consistency of clay-based mortars and that there is a negative linear relationship with the spread table values (Mafalda et al., 2023).

Fig. 1. Slump Flow test

Tablo.2. Fresh mortar test results

Series	Casagrande	Slump Flow (cm)
R	2	14
A (0.6)	5	12.5
A (0.8)	5	12.5
A (1)	8	11

3.2. Hardened mortar properties

For compression and bending tests, 40*40*160 mm sized samples were produced from 4 different mixtures, 3 for each mixture. The produced samples are shown in Figure 2 as R, A (0.6), A (0.8) and A (1), respectively. The 1-week mass losses of the produced samples were measured and the daily mass losses of 4 series are shown in Table 3

Fig. 2. Samples from 4 series produced

Table 3. 7-day mass measurements (g)

Day	1. Day	2. Day	3. Day	4. Day	5. Day	6. Day	7. Day
R	496.9	444.6	420.4	416	414.7	413.2	412.6
0,6	498.8	445.1	422.2	419	416.9	415.3	414.9
0,8	503.3	470	425.9	418.6	416.3	414	411.9
1	508.6	471	429.9	423.4	421.3	419.3	416.7

The experimental measurements show that the addition of sodium alginate affects the mass loss of the soil mixtures over time. From day 1 to day 7, the reference sample decreased from 496.9 g to 412.6 g, a total mass loss of about 17%, while the mixture with 0.6% alginate additive decreased from 498.8 g to 414.9 g, a loss of about 16.8%. The 0.8% alginate doped mixture showed a mass loss of 18.1%, while the 1.0% alginate doped sample showed a loss of approximately 18.1%. As the alginate content increased, the mass loss was similar to the reference. Therefore, no linear relationship was observed between the doping rate and mass loss. The lowest mass loss rate was observed in the mixture with 0.6% alginate additive, while at 1.0%, the mass loss remained at a similar level to the reference sample. This indicates that while alginate increases the moisture retention capacity up to a certain level, this effect is limited at higher ratios and saturation is reached. At the end of the 7th day, flexural and compressive strength tests were performed for each specimen for which mass loss measurements were completed. Specimens that were fractured during flexural strength were then used for compressive strength evaluation. The data obtained are shown in Table 4.

Table.4 Flexural and Strength test results

Mixture	Flexural Strength (MPa)	Compressive Strength (MPa)
R	1.16	2
A (0.6)	1.07	2.6
A (0.8)	1.21	2.3
A (1)	1.21	2.8

In Table 4, the flexural strength of the reference (non-alginate) mixture was measured as 1.16 MPa. The flexural strength of the mixture containing 0.6% alginate decreased to 1.07 MPa, a decrease of about 7.76%. With the 0.8% additive, the flexural strength increased to 1.21 MPa, an increase of 4.31% compared to the reference. Similarly, the same strength value of 1.21 MPa was obtained in the mixture with 1.0% alginate additive. This indicates that the alginate admixture reached a saturation level between these proportions and did not provide a further increase in flexural strength.

As a result of the compressive strength tests, an increase in strength was observed in all sodium alginate-amended soil-based composites compared to the reference specimen. The highest increase was obtained in the specimen containing 1.0% alginate additive and an improvement of 40% was achieved. This indicates that alginate plays a binding role in the soil matrix and strengthens the internal structure. In particular, the mixture containing 0.6% alginate showed a significant increase of 30% in compressive strength despite the decrease in flexural strength. This shows that additives can have different effects on different mechanical behaviors and that material performance should be evaluated in a holistic manner with multi-faceted mechanical tests. The 1.0% admixture provided the highest strength, demonstrating that alginate provides optimum binding in soil structure above a certain level.

4. Conclusions

This study investigated the effects of sodium alginate additives in soil-based composites. By varying only the amount of alginate in fixed ratio mixtures containing clay, alpha gypsum, lime, and cellulose, the effects of different additives on material performance were investigated.

The results showed that the sodium alginate additive had a significant effect on the workability, consistency, mass loss and mechanical strength properties of soil-based mortars. In terms of fresh mortar consistency, it was observed that the consistency thickened, and the spreading diameter decreased as the alginate additive increased. This confirms the viscosity increasing effect of alginate. From the flexural and compressive strength results, it was observed that alginate addition, especially at 0.8% and 1.0%, provided a significant improvement in mechanical strength compared to the reference mix. The highest compressive strength was obtained in sample A (1), where an increase of 40% was observed. In terms of loss of mass, optimum results in terms of both mechanical performance and stability were obtained when sodium alginate additive was used in the range of 0.8-1.0% in soil-based composites in this study. It is recommended that the effects of additives not only on strength but also on crack control, water retention and long-term durability should be investigated in detail.

Acknowledgments

This study was supported by Scientific and Technological Research Council of Turkey (TUBITAK) under the Grant Number 1139B412300757. The authors thank to TUBITAK for their supports.

References

Arto, I., Puertas, E., Castro, R. A., & Gallego, R. (2024). Free–free resonance method for the mechanical characterization of lime-stabilized rammed earth specimens. *Construction and Building Materials*, *456*, 139129.

Assunção, J., Brumaud, C., & Habert, G. (2025). A rheometric approach to investigate the effect of cellulose ether on crack mitigation in earth-based concrete. *Cement and Concrete Composites*, *161*, 106077.

Emiroğlu, M., Yalama, A., & Erdoğdu, Y. (2015). Performance of ready-mixed clay plasters produced with different clay/sand ratios. *Applied Clay Science*, *115*, 221–229.

Matos, A. M., Guimarães, A. S., Delgado, J., Emiroğlu, M., Subasi, S., & Marasli, M. (2023). *3D printing for construction with alternative materials.* In B. Rangel, A. S. Guimarães, J. Lino, & L. Santana (Eds.), Springer.

Maierdan, Y., Armistead, S. J., Mikofsky, R. A., Huang, Q., Ben-Alon, L., Srubar, W. V., & Kawashima, S. (2024). Rheology and 3D printing of alginate bio-stabilized earth concrete. *Cement and Concrete Research*, *175*, 107380.

Patural, L., Marchal, P., Govin, A., Grosseau, P., Ruot, B., & Devès, O. (2011). Cellulose ethers influence on water retention and consistency in cement-based mortars. *Cement and Concrete Research*, *41*(1), 46–55.

Wang, L., Cao, M., Li, X., Du, W., & Wang, X. (2023). A novel approach for improving the water resistance of gypsum plaster by internal mixing hypromellose and external coating waterproofing agent. *Construction and Building Materials*, *401*, 132940.

Yin, Y., Huang, J., Wang, T., Yang, R., Hu, H., Manuka, M., Zhou, F., Min, J., Wan, H., Yuan, D., & Ma, B. (2023). Effect of Hydroxypropyl methyl cellulose (HPMC) on rheology and printability of the first printed layer of cement activated slag-based 3D printing concrete. *Construction and Building Materials*, *405*, 133347.

4th International Civil Engineering & Architecture Conference
17-19 May 2025, Trabzon, Türkiye

Numerical analysis of the reinforcement of flexible concrete structures by patch in FGM

Alper Polat[1], Houari Amin[*2], Chellil Ahmed[2], Lecheb Samir[1], Raul D.S.G. Campilho[3]

[1] *Department of Civil Engineering, Faculty of Engineering, Munzur University, Tunceli, Turkey*
[2] *Mechanical Engineering Department, University of M'HamedBougara of Boumerdes,Algéria*
[3] *CIDEM, ISEP – School of Engineering, Polytechnic of Porto, Porto, Portugal*

Abstract. Flexible reinforced concrete is used in civil construction and infrastructure. It plays a crucial role in the design of structures in the context of sustainable development. This material can suffer various types of damage and lose its mechanical and physical properties due to a variety of external causes. Such work may be necessary for a number of reasons. In particular, when weather conditions, wear and tear or damage caused by ground movements damage the structure. Pathological phenomena can be linked to the environment, operational constraints or the underlying quality of the concrete. To improve structural performance, techniques can be used to reinforce damaged structures. In addition, the patching repair technique has been used to reinforce and rehabilitate these structures. This work focuses mainly on the repair or strengthening of reinforced concrete structures using numerical analysis. Our numerical study will focus on the use of the ABAQUS calculation code to evaluate the mechanical properties of concrete and FGM patching. This method is proposed for the rehabilitation of civil engineering structures based on bending experiments. In order to determine the flexural strength under the influence of the exposant of the FGM material.

Keywords: Reinforced flexible concrete; FGM patch; Crack; Pathology; USDFLD

1. Introduction

The selection of materials for civil construction and infrastructure is playing an essential role in the design of structures within the framework of sustainable development. Numerous studies on reinforced concrete aim to better understand, understand and predict its behavior and characteristics. However, for structures with high requirements (large-scale structures, structures subject to particular stresses or requiring enhanced safety), the material's limited performance in tension, its poor watertightness and design constraints are driving the development of other topologies combining concrete and steel. Work is in progress to develop a new generation of civil engineering construction with an architecture for the design of cylindrical hull walls, such as those used for deep-water oil storage (Montague., 1975). Because steel is a less porous material than concrete, it will limit attacks from the outside (water, salt, major temperature variations, etc.), reduce spalling and cracking phenomena and thus increase the structure's durability.

Some researchers, such as Vacev et al.,(2023) and Kıpçak et al.,(2023), focus on concrete, analyzing experimentally and numerically the impact resistance of unreinforced concrete slabs. Recent studies aim to model it realistically using the finite element method for the numerical analysis of reinforced concrete structures. Harba et al.,(2022) analyzed the numerical behavior of short reinforced concrete columns, with different levels of confinement and CFRP shells, under concentric loads. Simeonov and Shuaib Ahmad. (1995) highlighted the limitations of predicting the modulus of elasticity of concrete using the elastic prediction model for two-phase composite materials. Kim et al.,(2020) proposed a simulation that uses the linear attenuation coefficient (LAC) of the gray-level pixel values of micro-CT data to characterize the multiphase structure of foamed concrete, postulating a linear correlation between the average LAC value of a single-phase concrete sample and the input parameters. Kunpeng et al.,(2024) have developed a discrete finite element method (FDEM) that combines tomography and X-ray diffraction (XRD) to model concrete microstructures and mineral compositions, enabling the multiphase structure of concrete to be simulated Several studies show that the mechanical properties of concrete vary considerably due to aggregate and void distributions (Yujie., 2016). At the microscopic level, crack propagation and damage accumulation are often influenced by aggregates (Jiangjiang., 2019). Subsequently, a

* Corresponding author, E-mail: a.houari@univ-boumerdes.dz

https://doi.org/10.31462/icearc2025_ce_mat_817

numerical analysis of reinforcement methods for reinforced concrete pavements for various levels of damage was carried out by li et al.,(2020).

In particular, elastic concrete materials, commonly referred to as engineered cementitious composites (ECC), are semi-ductile concretes exhibiting strain-hardening and multiple cracking behavior in tension and buckling. Flexible (elastic) concrete is a class of cementitious compounds reinforced with superplastic fibers. This material is capable of demonstrating significantly improved elasticity. ECC concrete elongates without fracturing, thanks to the interaction between fibers, sand and cement working in a matrix that binds all together in the material.

Over the past two decades, several studies have shown that adding rubber particles to concrete improves its ductility, deformability, toughness and energy dissipation. Other studies evaluate the strength of various flexible concrete mixes by incorporating supplementary cementitious materials, such as fly ash and recycled fibers. Najib et al.,(2020) investigated the effectiveness of concrete containing rubber from used tires in optimizing the deformability and energy absorption of reinforced concrete columns, taking into account different compressive strengths. Alsaif et al.,(2019) developed flexible concrete pavement materials, offering an alternative to asphalt concrete and polymerized rubber surfaces, with a study on steel fiber-reinforced rubberized concrete. These properties, along with the material's high impact and skid resistance, sound absorption, and thermal and electrical insulation, make rubberized concrete a very attractive building material for non-structural applications.

The addition of fibers, such as Recron fibers, is a promising alternative for improving the mechanical performance of rubber. These fibers, used to reduce the brittleness of concrete, offer new prospects for enhancing the safety, strength and durability of tomorrow's civil infrastructures. Hameed et al.,(2022) have developed a special concrete, called ECC concrete, using an optimum percentage of fly ash as a partial replacement for cement and incorporating different proportions of Recron fibers. Medina et al., (2017) examined the mechanical properties of concrete incorporating granular rubber and rubber-coated steel or plastic fibers. They observed that concrete with rubber and fibers exhibits better compressive and flexural behavior, as well as better absorption of impact energy than ordinary rubberized concrete. In addition, ECC uses small quantities, typically 2% by volume, of short, discontinuous fibers. ECC incorporates super-fine silica sand and tiny polyvinyl alcohol fibers covered by a very fine (nanometer-thick), smooth coating. This surface coating allows the fiber to start sliding when overloaded, so that it doesn't fracture.

The first part of this work will consist of an experimental study of the mechanical properties of elastic concrete, as a function of the nature and shape of the fibers. We will determine its resistance to bending and deformation of a beam reinforced with a patch of FGM material. FGM materials outperform traditional materials thanks to their mechanical and chemical resistance, reduced maintenance, freedom of form and ability to extend the life of structures. However, a major drawback of FGMs is the accumulation of stresses at the interfaces of the layers, due to abrupt variations in their mechanical properties.

The aim of our work is to develop a direct numerical solution for determining the interface stresses in the adhesive layer of a damaged flexible concrete beam repaired by FGM.

2. Material and experimental methods

Fiber-reinforced concrete is being actively studied to improve its lightness and flexibility. A large body of research is examining the influence of organic fibers on its properties. This study uses a matrix concrete reinforced with PA6 polyamide chips, a choice justified by its mechanical performance and potential for sustainable reuse.

2.2. Reinforcing fibers

The reinforcing material used in this study consists of PA6 polyamide chips. These chips are recovered from by-products generated during cutting and machining operations typically performed in industrial and mechanical workshops. The shape and appearance of the collected chips are shown in Fig. 1.

Fig.1. The filings used PA6

2.3. Tensile tests

Tensile tests on PA6 samples, prepared according to ASTM D882-12, were conducted at the Mechanical Engineering Laboratory at the University of Msila (Fig. 2).

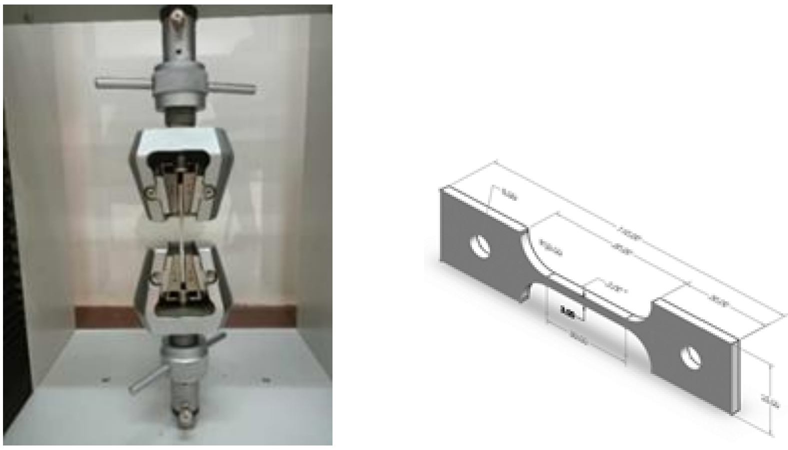

Fig. 2. a) Tensile test specimens, b) The dimensions of test specimens

Table 1. Mechanical properties of PA6

Mechanical properties	Young Modulus MPa	Poisson's ratio	Yield strength $Rp_{0.2}$ (MPa)	Ultimate tensile strength R_m (MPa)	Elongation %
PA6	2850	0.33	40	84	4

The polyamide tensile curve resulting from tensile tests carried out in the M'sila laboratory is shown in Fig. 3. The tensile strength measured is 84 MPa at elastic elongation, giving a precise indication of the polyamide's mechanical properties under controlled conditions. The mechanical properties of PA6 are summarized in the Table 1.

2.4. Manufacturing process

Cement, gravel, and sand are mixed, water is added to create a homogeneous concrete, then a fiber PVC filing/epoxy mixture is incorporated until thoroughly combined and the color is uniform. Fine PVC filings (< 0.5 cm) were manually mixed (Fig. 3.a), and pressed into a mold, then demolded after a 24-hour curing period.

The raw materials were weighed individually, and the percentages of the components in each sample are grouped in Table 2.

Fig. 3. a) Fine PVC filings obtained after sieving, b) The prepared samples

Table 2. The percentages of the constituents in the four samples

Samples	Concret (Wt%)	Fine PVC filings (Wt%)
A	75	25

2.5. Characterization

Three-point bending tests were performed on the composite specimens (Fig. 4) using the Zwick/Roell Z010 universal testing machine (10 kN capacity). Four plastic fiber specimens with equal particle sizes were developed to study the effect of fiber size on the mechanical behavior of concrete.

Fig. 4. Three-point bending test

3. Finite element analysis modeling

Finite element modeling for the nonlinear analysis of concrete is mainly based on spread crack or damageable plasticity approaches. In the spread-crack concrete model, crack initiation occurs when concrete stresses reach a fracture surface, either in biaxial tension or in tension-compression.

3.1. Damaged concrete

At low confining pressures, concrete exhibits brittle behavior characterized by tensile cracking and compressive crushing. Sufficiently high confining pressures prevent cracking, eliminating this brittle behavior. The main elements of the damaged plasticity model for inviscid concrete are: the strain rate decomposition, assumed to be independent of velocity.

$$\dot{\varepsilon} = \dot{\varepsilon}^{el} + \dot{\varepsilon}^{pl} \tag{1}$$

where is the total strain rate, is the elastic part of the strain rate, and is the plastic component of the strain rate. Damaged scalar elasticity governs stress-strain relationships.

$$\sigma = (1-d)D_0^{el}:(\varepsilon - \varepsilon^{pl}) = D^{el}:(\varepsilon - \varepsilon^{pl}) \tag{2}$$

where D is the material's initial elastic stiffness, $D^{el} = (1 - d)\, D^{el}$ its degraded stiffness, and d the degradation variable (0: undamaged, 1: fully damaged). In scalar damage theory, stiffness degrades isotropically, characterized by a single variable, d. The effective stress is then defined according to the principles of continuous damage mechanics.

$$\bar{\sigma} = D_0^{el}:(\varepsilon - \varepsilon^{pl}) \tag{3}$$

Cauchy stress relates to effective stress via a scalar degradation factor.

$$\sigma = (1-d)\bar{\sigma} \tag{4}$$

3.2. TTO model

The TTO model is a metal alloy homogenization method and is used to evaluate locally effective elastoplastic parameters of the FGM (AL/SiC) compound. In the TTO model, the material mixture is treated as elastoplastic with linear isotropic hardening, for which the stresses and strains are related to the constitutive forces σ_m, σ_c and ε_m and ε_c (Tamura et al.,1973) by the relation:

$$\sigma = \sigma_m V_m + \sigma_c V_c \quad \text{and} \quad \varepsilon = \varepsilon_m V_m + \varepsilon_c V_c \tag{5}$$

In the TTO model an additional parameter q is introduced which represents the ratio of stress to strain transfer, note that:

$$q = [(\sigma_c - \sigma_m)/(\varepsilon_c - \varepsilon_m)], \qquad 0 < q < \infty \tag{6}$$

In the TTO model the properties of FGM is based mainly on the plastic part of the metal constituent determined by modulus of elasticity $\mathrm{E(z)}$ of FGM. The initial yield stress $\sigma_{Y_0}(\mathrm{z})$ and tangent modulus $\mathrm{H(z)}$ which are described by the following relations:

$$\mathrm{E(z)} \;=\left[\frac{q+E_c}{q+E_m}.\mathrm{E_m V_m}+\mathrm{E_c}.(1-\mathrm{V_m})\right]\Big/\left[\frac{q+E_c}{q+E_m}.\mathrm{V_m}+(1-\mathrm{V_m})\right] \tag{7}$$

$$\sigma_{Y_0}(z)=\sigma_{Y_0 m}\left[\frac{q+E_m}{q+E_c}\frac{E_c}{E_m}.(1-V_m)+V_m\right] \tag{8}$$

$$\mathrm{H(z)} \;=\left[\frac{q+E_c}{q+H_m}.\mathrm{H_m V_m}+\mathrm{E_c}.(1-\mathrm{V_m})\right]\Big/\left[\frac{q+E_c}{q+H_m}.\mathrm{V_m}+(1-\mathrm{V_m})\right] \tag{9}$$

Where $\sigma_{Y_0 m}$ the initial yield stress of metal, $\mathrm{H_m}$ is the tangent modulus of metal, where $\varepsilon_{m_0}=\sigma_{Y_0 m}/E_m$ and $\varepsilon_{Y_0}(\mathrm{z})=\sigma_{Y_0}(\mathrm{z})/\mathrm{E(z)}$ are the initial yield strains of the metal and FGM AL/SiC, respectively.

3.3. Damage FGM
A non-local damage mechanics approach was used which requires the mesh regularization chosen in our work. The maximum principal stress criterion MAXPS is used to have the crack initiation as well as its propagation direction. The choice of Maximum stresses as the criterion for damage initiation is used to reduce the sensitivity of the mesh in non-local approaches (Houari et al.,2021).

$$\mathrm{f}=\frac{\sigma_{\mathrm{eq}}}{\sigma_{\mathrm{UTS}}}=1 \;\text{ with }\quad \sigma_{\mathrm{UTS}}=\sigma_{\mathrm{UTSm}}.\left[\frac{\mathrm{q}+\mathrm{H_m}}{\mathrm{q}+\mathrm{E_c}}\frac{\mathrm{E_c}}{\mathrm{H_m}}.(1-\mathrm{V_m})+\mathrm{V_m}\right] \tag{10}$$

where σ_{eq} is the equivalent von-Mises stress of FGM, σ_{UTS} is the ultimate tensile strength of FGM, σ_{UTSm} is the ultimate tensile strength of metal, $f=1$: means the occurrence of damage within an enriched element and $\mathrm{H_m}$ is the tangent modulus of the metal.

3.4. Geometric model
For the purposes of our work, we have analyzed a damaged elastic concrete beam, repaired by FGM, on the basis of data from bending experiments. The 250 mm-long beam is subjected to a concentrated bending load of 10 N (Fig. 5). The distance between the end of the beam and the edge of the reinforcing plate (L_R) is 150 mm. The distance between the end of the beam and the edge of the reinforcing plate (L_R) is 150 mm.

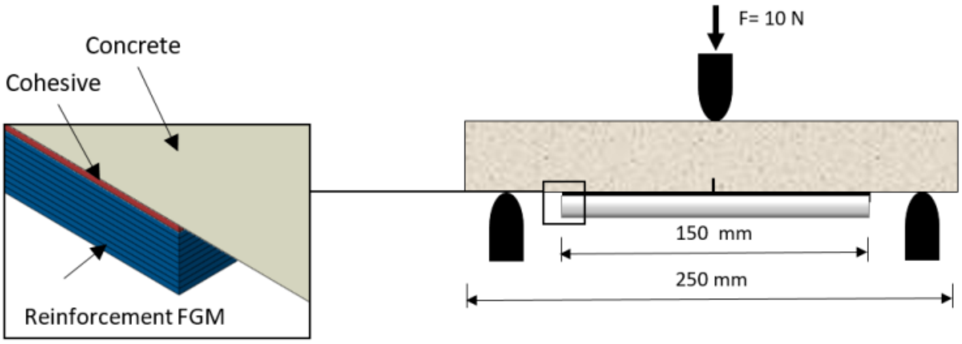

Fig. 5. Loading and boundary conditions

The geometric properties of the materials used are shown in Table (3).

Table 3: Geometric properties of materials

Material	width	thickness	long
Flexible concrete	b_l = 90 mm	t_l = 30 mm	L_l = 250 mm
adhesive	b_a = 90 mm	t_a = 0.2 mm	L_a = 150 mm
FGM AL/SiC	b_r = 90 mm	t_r= 2 mm	L_r = 150 mm

3.5. Mesh and gradient of FGM properties
A 30 mm-thick concrete beam, modeled with C3D8 elements in ABAQUS, is reinforced with a 25 mm-thick composite plate fixed underneath to improve compressive load distribution (Fig. 6). The patch is modeled with C3D8 elements, using concrete's mechanical properties derived from the experimental tests. In ABAQUS, the USDFLD subroutine models the nonlinear behavior and damage of FGM materials, integrating their thickness-

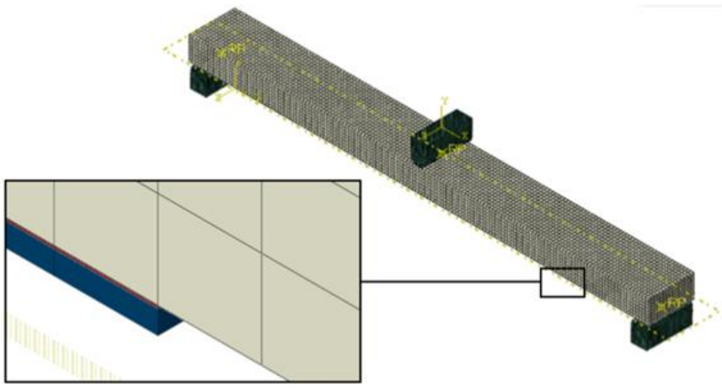

Fig. 6. Meshed model of beam

dependent properties. The choice of finite element model is carried out with elements C3D8 which present the best choice for the numerical modeling of the model and which are used in numerous examples of modeling of FGM.

To avoid the discontinuity of force at the interfaces, a subroutine USDFLD is implemented in ABAQUS to define the material properties of the FGM according to the coordinates of the points of integration in a finite element model. For this purpose, we use integration points arranged across the thickness direction of the FGM (metal/ceramic) plate. The distribution of material properties across the thickness $h(z)$ of the FGM plate according to a power law distribution is shown in the Fig. 7:

$$\mathrm{P(z)} = (\mathrm{P_m} - \mathrm{P_c}).\mathrm{V_m} + \mathrm{P_c} \tag{11}$$

Knowing that P: represents the effective material property, $\mathrm{V_m} = \left(\frac{z}{H} + \frac{1}{2}\right)^n$ is the Metal Volume Fraction, n: is the non-negative volume fraction exponent and the subscripts c and m represent the ceramic and metal constituents respectively. We consider a patch in FGM (AL/SiC), presented in the form of several surfaces (Fig.7a), Each surface exhibits mechanical properties as being a homogeneous and isotropic material. The properties of the two constituents of FGM (AL/SiC), Adhesive and concrete are presented in Table.4.

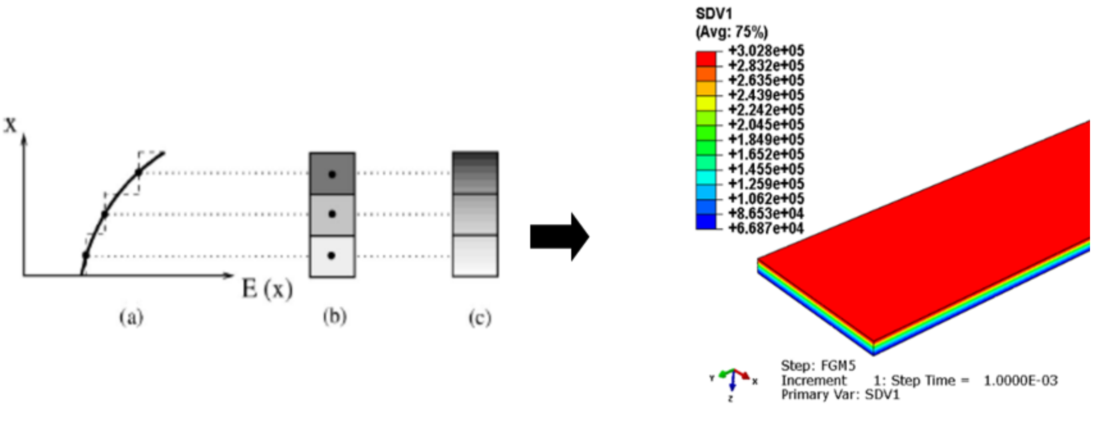

Fig. 7. a) Homogeneous versus graded finite elements, b) Linear distribution of Young's modulus (SDV1) across the thickness h(z) of FGM AL/SiC patches via USDFLD with power law

Table 4. Material properties (Jin etal., 2003)

Property	Metal AL	Concrete	Adhesive	Ceramic SiC
Young’s Modules E (MPa)	67000	34000	2962	302000
Poisson’s Ratio ν	0.33	0.41	0.33	0.17
Yield Stress σ_Y (MPa)	95.1		14	-
Stress Ultimate σ_{UT} (MPa)	160		32	1400
Fracture energy G_{Ic} (KJ/m^2)	6.17		0.5	0.065
Tegant modulus H (MPa)	1000		-	-

7. Results and discussion

7.1. Validation

The current method was validated by comparing the force-deflection curve results of the bending test with those obtained from the finite element method using the ABAQUS calculation code. Fig. 8 shows that the numerical results gave reasonable curvatures with the bending experiments, and the figure also shows that the PVC particle size affects the behavior of the concrete; PVC/micro-concrete specimens exhibit elastic behavior and elastic fracture.

The different factors measured automatically are presented in Table 5. These parameters are essential to calculate the bending stress σ_f, and the bending modulus of elasticity E_f (Young's modulus).

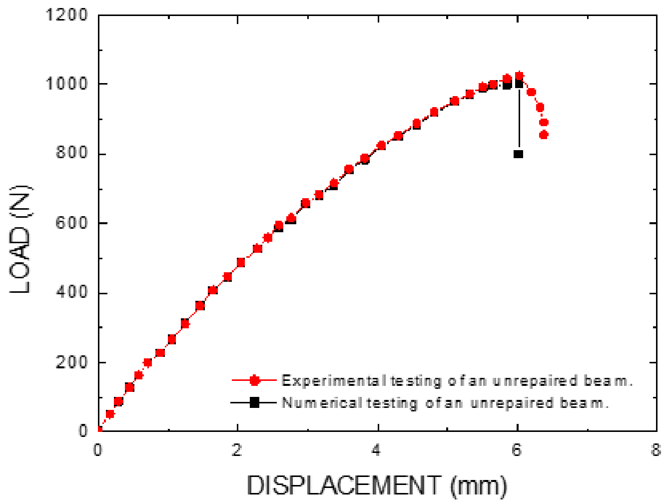

Fig. 8. The fracture behavior Concrete: (a) Concrete/ Fine PVC filings

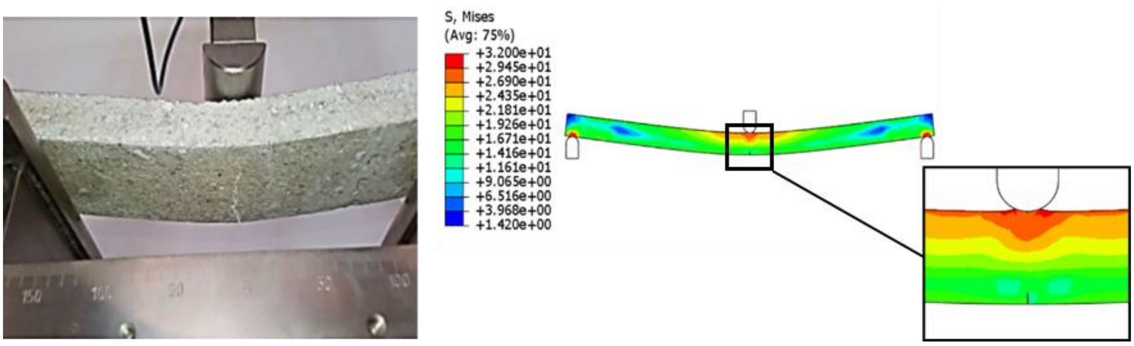

Fig.9. The fracture behavior Concrete

Table 5. Bending tests results

Sample test	F_{MAX} (N)	$F_{rupture}$ (N)	$\varepsilon_{rupture}$ (mm)
1	635.05	547.13	5.49
2	620	530	5.31
3	615	505	5.24
4	640	550	5.42

Table 6. Mechanical properties of the samples

Sample test	K (N/mm)	σ_{Max} (MPa)	$\sigma_{rupture}$ (MPa)	E_f (GPa)
1	123.68	10.45	8.75	0.32
2	122.58	10.15	8.90	0.29
3	110.31	9.18	7.82	0.28
4	129.17	10.93	9.14	0.352

As part of this work, we are interested in the bending stress σ_f, and the bending modulus of elasticity E_f(Young's modulus). Table 6 presents the results obtained using the following formulas:

$$\sigma_f = \frac{3FL}{2bh^2} \tag{12}$$

$$E_f = \frac{L^3}{4bh^3}K \tag{13}$$

where:σ_f: Bending stress in Mpa, F: Force applied in newton, L: Spacing between supports in mm, b: Width in mm, h: Thickness in mm and K: Bending stiffness (K=ΔF/Δy) in N/mm.

7.2. Effect of the exponent n

We considered FGM patch repair in our analysis. The results of the variation in the response of the bending curves are shown in Fig. 10, with a crack length of 5 mm for different FGM repair patch exponent value.

The beam fixed by the FGM patch with a gradient coefficient of n=2 has the highest strength values especially if this patch is rich in ceramic . The presence of the FGM patch significantly improves the strength of the beam and significantly reduces the spread of the crack.

Various FGM plate designs aim to reduce stress concentration in the adhesive. The von Mises analysis reveals similar interferences in the joint. The von Mises stress at the adhesive core decreases considerably with increasing metal concentration in the FGM. This modification significantly reduces von Mises and peel stresses for different geometries (see Fig. 12).

Stress concentrations persist at the edges, and the core is also stressed (Fig. 13). The maximum stress depends on the reinforcement material, and its modification can improve the reinforcement of the flexible beam and significantly reduce the von Mises stress.

With regard to the length of the patch , an increase in von Mises stress is observed in the FGM n=5 metal-rich models. On the other hand, metal models has a minimum stress value at the center of the plate (Fig. 14).

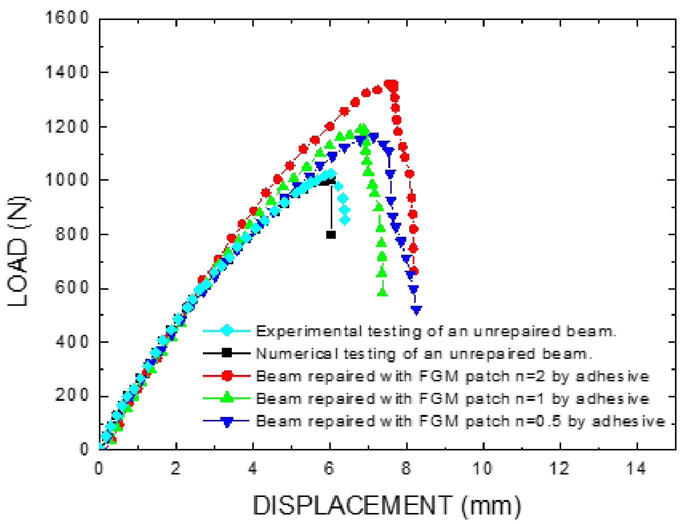

Fig. 10. Variation of the exponent in the damaged beam and repaired by FGM patch

8. Conclusion

The objective of this study is to manufacture flexible concrete characterized by high mechanical properties, using recovered raw materials in the form of filings from cutting processes used in PVC carpentry workshops. The abundance of these materials, which are often considered unusable waste, and the importance of the properties of the two basic materials, namely PVC, encouraged the main idea of this modest work which consists of recovering PVC filings.

An initial analysis of the samples manufactured as part of this study showed the effect of the size and nature of the filings on the microstructure of the surface and the reinforcement-matrix interface. Indeed, the results showed that the adhesion of the PVC filings to the matrix is power, the PVC filings reinforced all the constituents to make the composite more resistant. In our study, we study the stresses at the interface between flexible concrete and FGM materials in a damaged structure repaired by FGM patch. The finite element methods confirmed the results of this solution. At the adhesive layer, the stresses are observed at the edge and in the middle. However, the patch shows the maximum stresses observed in the middle.

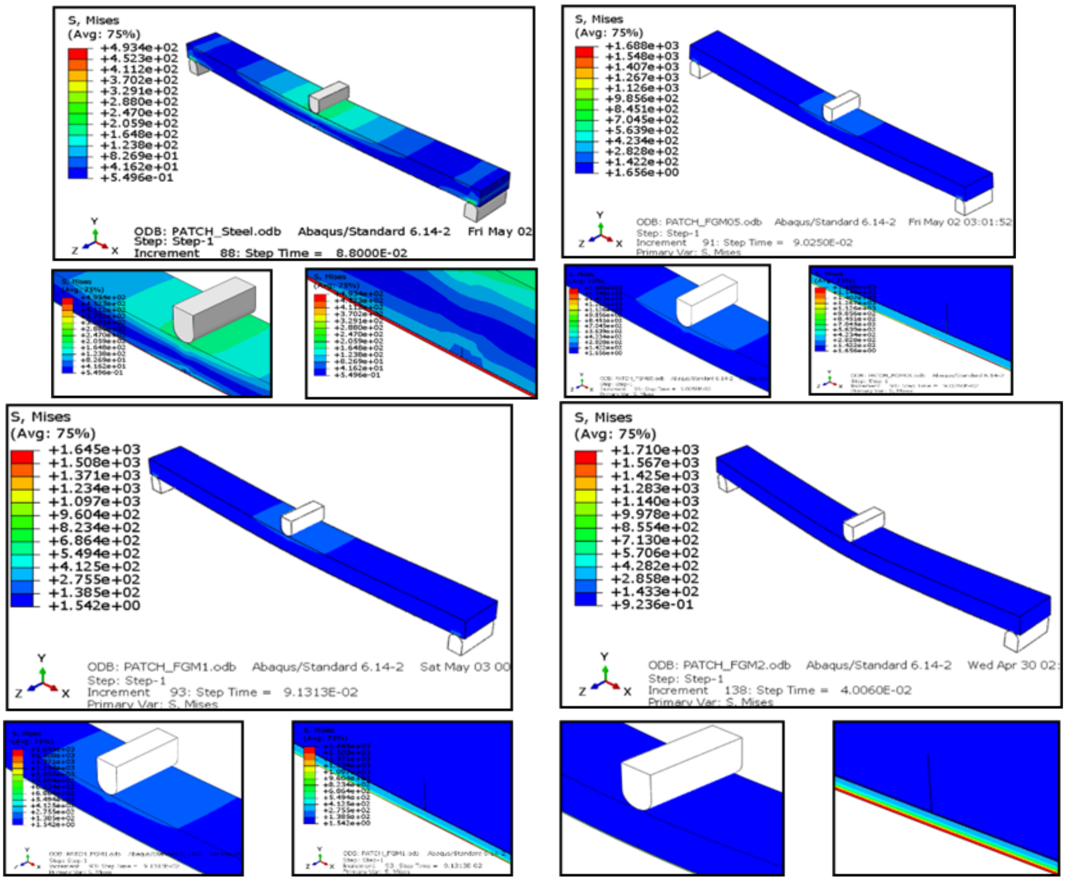

Fig. 11. Distribution of the von Mises stress

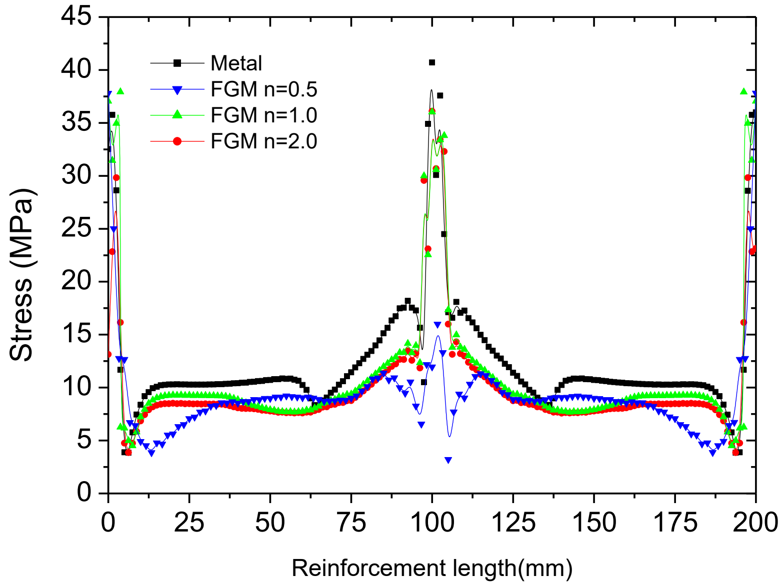

Fig. 12. Variation of the Von Mises stress in the adhesive according to the renforcement length for the diferent confgurations

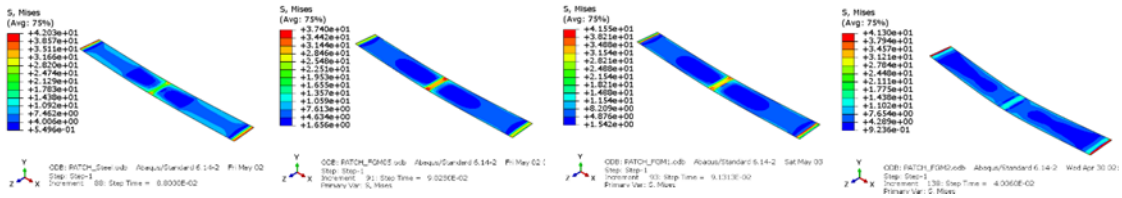

Fig. 13. Von Mises stress level in the adhesive according to the renforcement length, a) Metal, b) FGM=0.5 c) FGM=1, d) FGM=2

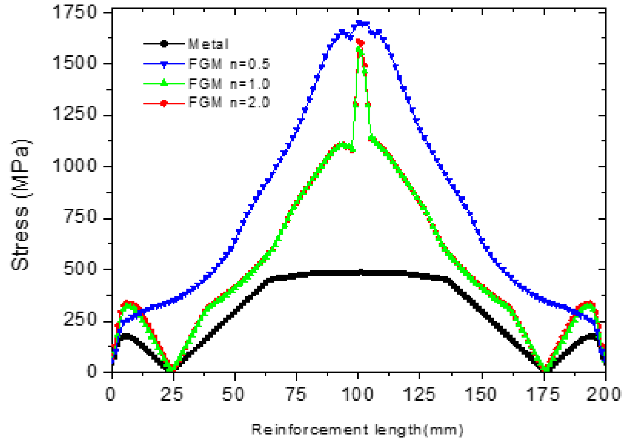

Fig. 14. Stress distributions along the length of the patch for the diferent confgurations

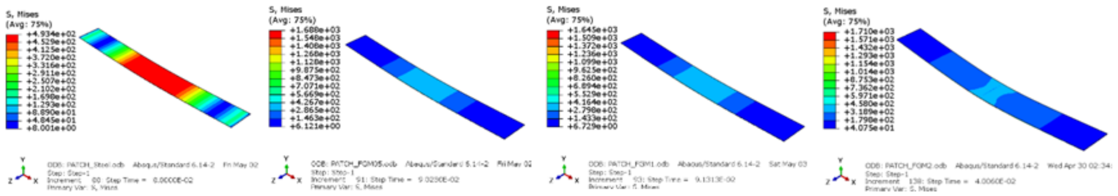

Fig. 15. Von Mises stress level in the patch length joint, a) Metal, b) FGM=0.5 c) FGM=1, d) FGM=2

The numerical analysis by FE in this study aims to analyze the response in the damaged and repaired patch beam, as well as the distribution of main stresses in the adhesive and patch. The parameters highlighted have led us to draw the following conclusions.

- The strength of the damaged plate can be improved by the bonding process of the patches, which can be effective if its nature is taken into account.
- The MGF patch performs better with a ceramic-rich patch if the contact with the adhesive layer is ceramic and the gradation coefficient has a high value compared to the metal-rich patch.

References

Abdulaziz, A., Koutas, L., Bernal, S.A., Guadagnini, M., & Pilakoutas, K. (2019). Mechanical performance of steel fibre reinforced rubberised concrete for flexible concrete pavements. *Construction and Building Materials, 172*, 533–543. https://doi.org/10.1016/j.conbuildmat.2018.04.010

Hameed, A., Rasool, A.M., Javed, M.H., Afzal, A., Elahi, K., & Munir, D. (2022). Optimum percentage of fly ash as cement replacement and effect on mechanical and durability properties of self-compacting concrete. *Key Engineering Materials, 913*, 169–180. https://doi.org/10.4028/p-hcknd7

Harba, I., Abdulridha, A., & AL-Shaar, A. (2022). Numerical analysis of reinforced concrete circular columns strengthening with CFRP under concentric and eccentric loadings. *Frattura ed Integrità Strutturale, 17*(63), 190–205. https://doi.org/10.3221/IGF-ESIS.63.16

Houari, A., Mokhtari, M., Bouchikhi, A.S., Polat, A., & Madani, K. (2021). Using finite element analysis to predict the damage in FGM-3D notched plate under tensile load: Different geometric concept. *Engineering Structures, 237*, 112160. https://doi.org/10.1016/j.engstruct.2021.112160

Jiangjiang, Y., Li, G., Ren, Z., Zhang, W., Tang, J., Zhang, L., Si, X., & Zhao, Z. (2019). Mixed-mode I–II mesoscale fracture behavior of concrete determined by the realistic aggregate numerical model. *Construction and Building Materials, 226*(1), 802–817. https://doi.org/10.1016/j.conbuildmat.2019.07
Jin, Z.H., Paulino, G.H., & Dodds, R.H.Jr. (2003). Cohesive fracture modeling of elastic–plastic crack growth in functionally graded materials. *Engineering Fracture Mechanics, 70*, 1885–1912.
Kim, J.S., Chung, S.Y., Han, T.S., Stephan, D., & Elrahman, M.A. (2020). Modeling of multiple phase solid microstructures and prediction of mechanical behaviors of foamed concrete. *Construction and Building Materials, 248*, 118637. https://doi.org/10.1016/j.conbuildmat.2020.11
Kıpçak, F., Erdil, B., Tapan, M., & Karaşin, A. (2023). The effect of voids on flexural capacity of reinforced concrete slabs. *Periodica Polytechnica Civil Engineering, 67*(4), 1048–1065. https://doi.org/10.3311/PPci.21988
Kunpeng, C., Guanqun, W., Wei, L., & Long, W. (2024). Numerical simulation of concrete strength based on microstructure and mineral composition analysis using micro-CT and XRD technology. *Construction and Building Materials, 432*, 136505. https://doi.org/10.1016/j.conbuildmat.2024.136505
Li, X., Zhang, T., Ding, Z., Yang, X., & Wen, J. (2020). Numerical analysis of normal concrete lining strengthening methods under different damage levels. *Structure and Infrastructure Engineering, 17*(12), 1597–1611. https://doi.org/10.1080/15732479.2020.1817106
Montague, P. (1975). A simple composite construction for cylindrical shells subjected to external pressure. *Journal of Mechanical Engineering Science, 17*(2), 105–113. https://doi.org/10.1243/JMES_JOUR_1975_017_016_02
Medina, N.F., et al. (2017). Mechanical and thermal properties of concrete incorporating rubber and fibres from tyre recycling. *Construction and Building Materials, 144*, 563–573.
Najib, N., Gerges, C., Issa, A., & Fawaz, S.A. (2018). Rubber concrete: Mechanical and dynamical properties. *Case Studies in Construction Materials, 9*, e00184. https://doi.org/10.1016/j.cscm.2018.e00184
Simeonov, P., & Ahmad, S. (1995). Effect of transition zone on the elastic behavior of cement-based composites. *Cement and Concrete Research, 25*(1), 165–176. https://doi.org/10.1016/0008-8846(94)00124-h
Tamura, I., Tomota, Y., & Ozawa, M. (1973). Strength and ductility of iron-nickel-carbon alloys composed of austenite and martensite with various strength. In *Proceedings of the 3rd International Conference on Strength of Metals and Alloys* (pp. 611–615). Cambridge: Institute of Metal and Iron.
Vacev, T., et al. (2023). Experimental and numerical analysis of impact strength of concrete slabs. *Periodica Polytechnica Civil Engineering, 67*(1), 325–335. https://doi.org/10.3311/PPci.21084
Yujie, H., Dongming, Y., Zhenjun, Y., & Guohua, L. (2016). 2D and 3D homogenization and fracture analysis of concrete based on in-situ X-ray computed tomography images and Monte Carlo simulations. *Engineering Fracture Mechanics, 163*(2), 37–54. https://doi.org/10.1016/j.engfracmech.2016.06.018

An experimental investigation on the compressive strength development of concrete samples poured in winter

Burak Gedik*[1], İbrahim Şahud[1], Büşra Şenbakar[1] Kurtuluş Yılmaz[1], Dilek Okuyucu[1]

[1] *ErzurumTechnical University, Department of Civil Engineering, 25100 Erzurum, Türkiye*

Abstract
Concrete is a construction material that is significantly influenced by atmospheric environmental conditions during and after casting. In Türkiye, as well as in many other countries, standards exist to regulate the requirements for concrete casting during winter. These standards outline the necessary conditions and recommend precautionary measures; however, the specific nature of these measures is often not clearly defined. In this study, the compressive strength development of C30/37 class concrete specimens, cast and cured under real winter conditions in Erzurum and protected by greenhouse plastic sheeting—a potential precautionary method—was experimentally investigated. The concrete specimens were kept under the greenhouse plastic for the first three days after casting, subsequently demolded, and then stored under the same protection until the seventh day. Afterward, they were exposed to natural atmospheric winter conditions until the 28th day. Axial compressive strength tests were conducted on cube specimens at 3, 7, and 28 days to evaluate the strength development experimentally. The results indicated that the 28-day axial compressive strength of the specimens produced with R-type cement reached 17.9 MPa, which corresponds to approximately half of the target compressive strength of 37 MPa.Based on the monitoring of both atmospheric and internal concrete temperatures, it was concluded that the development of maturity–strength relationships specific to winter concreting conditions is necessary for better assessment and control of concrete performance during cold weather construction.

Keywords: Concrete pouring in winter; Compressive strength; Greenhouse nylon sheeting; Temperature monitoring; Maturity index

1. Introduction

Reinforced concrete construction is the most commonly preferred building production method in Türkiye. In regions where winter seasons are long and harsh, the construction season remains short, causing various economic, technical, and social challenges. According to the study by Koç et al. (2017), the construction sector, particularly in Eastern Anatolia where a continental climate prevails, serves as a locomotive sector directly related to more than 200 different industries across the country. The near cessation of construction activities during winter months negatively impacts the regional economy and stands out as a major factor that hampers investment inflows. Erzurum province is a clear and striking example of this situation. This issue has been thoroughly analyzed in the 2014–2023 Regional Current Situation Analysis Report prepared by the Northeastern Anatolia Development Agency (KUDAKA). According to the KUDAKA (2014) report, the economy of Erzurum—located in the TRA1 Level 2 region—is primarily dependent on agriculture, services, and construction sectors, while the manufacturing industry has not yet reached a desirable level. The TRA1 Level 2 region consists of Erzurum, Erzincan, and Bayburt provinces, encompassing 30 districts, 73 municipalities, and 1,665 villages. Moreover, significant findings regarding the construction sector in Erzurum, Erzincan, and Bayburt—the provinces within KUDAKA's jurisdiction—are highlighted in the report:

"The construction sector occupies an important place in the regional economy, employing 8,356 people and accounting for 11.07% of the region's total employment. There are 623 enterprises operating in the construction sector in the TRA1 region, representing 2.54% of the total enterprises. In 2012, the number of construction enterprises was 1,664 in Erzurum, 605 in Erzincan, and 186 in Bayburt. Due to the prolonged winter season, construction projects—even without financial difficulties—often take at least two seasons to complete, leading to increased costs. Additionally, importing construction materials like steel and brick raises transportation expenses,

* Corresponding author, E-mail: burak.gedik@erzurum.edu.tr

https://doi.org/10.31462/icearc2025_ce_mat_835

while skilled laborers tend to migrate to regions where the construction season is longer and demand is higher. The fact that the primary input material, cement, is sourced locally, however, presents a significant advantage."

Despite significant public investments in recent years, it can be inferred from KUDAKA(2014) report that the harsh continental climate is the main reason why the total concrete production in Eastern Anatolia—a region covering the largest geographical area of Türkiye—remains only around 10–11% of the country's total output. This conclusion is highly noteworthy and is supported not only by official statistical analyses but also by socio-economic observations and field studies specific to Erzurum province.The prolonged winter season in Erzurum greatly shortens the construction period, leading to negative economic and technical consequences. Even the simplest building projects often cannot be completed without interruption, causing economic burdens and technical problems due to the inability to properly protect incomplete structures during long and wet winters. In this context, examining the monthly average temperature data presented in Table 1 and Table 2 is considered to be beneficial for concretely assessing the impact of the short construction season in Erzurum.

Table 1. Monthly Average Temperature (ºC) Values of Erzurum Province Between 2012-2018, MGM(2019)

Year/Month	1	2	3	4	5	6	7	8	9	10	11	12
2012	-	-	-	-	-	-	-	-	-		7.2	-3.0
2013	-9.6	-4.7	1.0	8.6	13.7	17.2	21.1	20.9	15.2	7.2	3.6	-11.4
2014	-7.7	-4.9	3.7	8.7	12.9	16.9	22.4	22.9	16.4	9.6	1.4	0.2
2015	-8.2	-5.2	0.5	6.2	11.5	17.4	21.8	22.2	18.5	10.0	2.7	-7.8
2016	-8.0	-3.7	1.9	8.3	11.3	17.1	19.8	22.4	13.8	9.3	-0.6	-9.5
2017	-11.5	-10.7	-0.5	6.3	11.2	16.4	22.1	22.7	18.6	8.3	2.4	-2.1
2018	-5.5	-3.1	5.2	8.5	11.9	15.5	20.5	20.6	16.5	10.8	3.2	-2.3

Table 2. Lowest Temperature (ºC) Values in Erzurum Province Between 2012-2018, MGM(2019)

Year/Month	1	2	3	4	5	6	7	8	9	10	11	12
2012	-	-	-	-	-	-	-	-	-	-	-8.0	-16.5
2013	-30.4	-20.2	-20.6	-3.9	1.8	3.0	0.0	0.0	-0.3	-5.2	-8.7	-23.3
2014	-24.8	-21.8	-8.8	-8.2	0.3	2.9	8.5	9.9	-0.3	-3.4	-8.6	-10.9
2015	-25.0	-20.9	-16.8	-5.9	-1.7	4.1	6.9	8.1	6.1	-1.2	-9.4	-17.4
2016	-33.8	-23.4	-11.7	-8.2	0.9	4.4	5.0	9.9	-1.0	-3.9	-14.4	-32.0
2017	-27.2	-26.5	-15.8	-7.6	1.2	2.6	9.1	9.4	3.1	-2.3	-11.2	-13.3
2018	-18.4	-18.9	-11.4	-7.9	4.6	4.7	7.7	8.8	3.3	-3.4	-6.7	-32.4

According to the data provided in Tables 1 and 2, obtained from MGM (2019), and evaluated together; it is evident that atmospheric conditions should be carefully considered in concrete pouring and reinforced concrete manufacturing in Erzurum province. This is particularly important since reinforced concrete structures constitute a large portion of building construction in our country. To ensure that the concrete sections perform their load-bearing function as designed, it is essential to achieve proper adhesion (bonding) between the concrete and the reinforcement steel. This mechanical behavior can only be achieved through quality concrete production. It is well known that concrete is influenced by atmospheric weather conditions, the fresh concrete temperature at the time of pouring, and even the temperature of the molds and the steel reinforcement cage placed inside them.

In national practices, according to the TS1247(2018) standard, full bonding is assumed to be achieved in concrete pours conducted under normal weather conditions. According to the same standard, "normal weather conditions" are defined as the situation where the air temperature does not drop below +5°C or exceed +30°C for three consecutive days at any hour. In other words, for ideal concrete pouring, the ambient temperature must remain between +5°C and +30°C during the pouring process and for the first 72 hours following it. This temperature range is critical for the healthy progress of the hydration process and strength development of the concrete.

However, when the meteorological data presented in Tables 1 and 2 are evaluated, it is observed that in Erzurum, for approximately half of the year, the air temperatures do not meet the normal conditions defined in the TS1247(2018) standard. This situation leads practitioners to refer to the TS1248(2017) standard, which contains regulations for concrete pouring under abnormal weather conditions. According to TS1248(2017), extreme cold weather is defined as conditions where the average air temperature remains below +5°C for three consecutive days. Furthermore, considering the climate map of Türkiye presented in Fig. 1, as quoted from Atalay(1997), it is observed that a significant portion of the country experiences a continental climate, and there are many regions where low temperatures prevail for extended periods, resulting in a short reinforced concrete construction term. Although there is no legal restriction on concrete pouring during winter in Turkey, it is possible that practitioners, due to a lack of knowledge about proper concrete protection during winter, and due to concerns over costs and success, avoid concrete/reinforced concrete production even in situations where it is necessary.

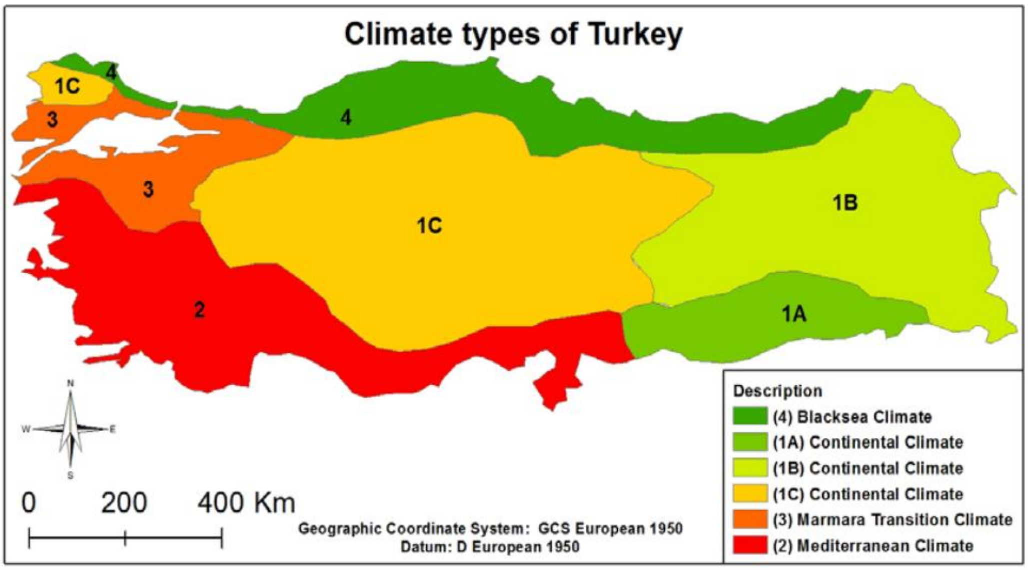

Fig.1. Climate map of Türkiye, Atalay(1997)

Similar to the national standard TS1248 (2017), many international norms such as CSA A23.1/A23.2 (2019), ACI PRC-306 (2016), and JSCE (2007) also define the drop of air temperature below +4/5°C within the first 72 hours after concrete pouring as abnormal weather conditions, requiring that protective measures be taken during casting. However, it can be stated that the issue of which specific measures should be taken remains generally ambiguous. The authors of this paper have conducted comprehensive studies regarding the establishment of bond in reinforced concrete manufacturing during winter and the effectiveness of various protective measures, similar to those of Gedik (2020) and Okuyucu et al. (2023). As a result of experimental investigations, it was evaluated that, under cold weather conditions, instead of using the compressive strength results of concrete specimens cured in the same environment as recommended in TS500 (2000) for determining the formwork removal time, the use of the concrete maturity index values, as suggested by the findings of Okuyucu et al. (2023), would be more meaningful. This evaluation necessitates temperature monitoring inside the concrete for reinforced concrete structural elements produced under cold weather conditions.

Although extensive access to studies on concrete production under cold weather conditions is available in the literature, it is observed that there is a severe shortage of technical studies that provide data on temperature monitoring during real atmospheric winter conditions, as well as on the structural behavior and mechanical performance of reinforced concrete elements cast during winter. Most existing studies on cold weather concreting focus on the effects of chemical admixtures on plain (non-reinforced) concrete, particularly concerning compressive strength and early-age behavior. One of the notable examples in this field, the study by Nmai (1998), evaluated the effects of chemical admixtures on the setting time and strength development of concrete under low temperatures. Karhonen (1990) and Karhonen (1992) conducted experimental studies on curing conditions, the hydration process, and thermal behavior of concrete under cold weather. Suk et al. (2012) and Nassif et al. (2013) analyzed the impact of antifreeze admixtures on the properties of fresh and hardened concrete, presenting comparative results from field and laboratory conditions. The study by Pushpalal et al. (2022), conducted under the severe winter conditions of Mongolia, examined the effects of different mineral admixtures on the performance and long-term durability of concrete. This study comprehensively addressed the role of mineral admixtures in enhancing the mechanical properties, durability, and long-term performance of concrete under cold climatic conditions. In addition, the study by Zhang et al. (2020) investigated the behavior of fresh concrete produced by calcium-silicate-hydrate (C-S-H) seeding under winter conditions, highlighting the great potential of nanotechnological admixtures for accelerating early strength gain and optimizing the hardening process during cold weather concreting.

While these studies and similar ones provide valuable contributions to the knowledge base concerning concrete production and curing processes under cold weather conditions, it is evident that the majority of the literature focuses predominantly on plain concrete specimens and remains limited to evaluating the effects of chemical admixtures on the hydration process. In contrast, critical parameters for reinforced (structural) systems, such as concrete–reinforcement bond, cracking behavior, thermal stresses, and maturity development, have not been sufficiently investigated under low-temperature conditions. The aspect most directly related to this paper is the observation that although various standards recommend taking protective measures during winter concreting, the effects of these measures are scarcely addressed in the accessible literature. Moreover, most of the available studies have been conducted under laboratory conditions, with very limited research carried out under actual winter environments. Therefore, there is an evident need for studies examining the precautions to be taken for winter concreting in regions dominated by continental climates.

In the study presented in this paper, it is aimed to investigate the effect of polyethylene sheet (greenhouse plastic) protection, applied for seven days, on the axial compressive strength of concrete specimens produced without any admixtures under real atmospheric winter conditions. In this context, C30/37 class concrete was used to cast cube specimens under real winter conditions, which were wrapped with greenhouse plastic for the first seven days. After the seventh day, the protective cover was removed, and the specimens were left exposed to atmospheric winter conditions until the 28th day. Following casting, a monitoring system was set up with K-type thermocouple sensors to measure temperatures inside the concrete and in the ambient environment. Temperature measurements were recorded at 10-minute intervals for seven days inside the concrete, and atmospheric temperatures were recorded for 28 days. Using the temperature data, the maturity index values (temperature-time factors) were calculated. The compressive strength results at 3, 7, and 28 days were evaluated in conjunction with the maturity index values.

2. Materials and methods

This study was conducted under real atmospheric winter conditions in Erzurum, Türkiye. For casting, plastic cube molds commonly used in practice, with dimensions of 150×150×150 mm, were selected. A total of nine plastic cube molds were prepared to determine the compressive strengths at 3, 7, and 28 days. Additionally, one more plastic cube specimen was produced solely for monitoring the internal concrete temperature.

It can be stated that during winter concreting, the most commonly used protection method is to isolate the fresh concrete from the atmospheric environment by covering the structure with plastic sheeting or tarpaulins. A striking example of this practice can be found in the repair work carried out in January 2014 on the reinforced concrete spillway support structures of the Altoona Dam, located in the state of Wisconsin, United States. Following observations of cracking and concrete disintegration in the dam body and spillway support arches, an initial plan was made to repair the structures using epoxy injection. However, field evaluations conducted prior to the repair revealed that the existing concrete lacked the necessary integrity to withstand the injection process. Consequently, to ensure the safety of the dam, a portion of the reservoir water was carefully drained in a controlled manner, and the damaged concrete sections were removed and replaced with newly cast concrete. The recasting was performed under very low temperature conditions, approximately -9°C, providing a significant real-world example of reinforced concrete construction under cold weather conditions. Various photographs of this application, cited from the work of Okuyucu et al. (2023), are presented in Fig. 2.

Fig.2. Images from the reinforced concrete pier repair work carried out in the winter at the Altoona Dam in the United States of America, Okuyucu et.al..(2023)

A study related to reinforced concrete construction during winter was also carried out in Erzurum by a team that included the authors of this paper. In this study, a similar protection method was applied by covering the freshly cast concrete with greenhouse plastic sheets.Following a landslide that occurred in January 2020 in the Tekstilkent area of 2nd Organized Industrial Zone of Erzurum, urgent repairs to the damaged factory structures became necessary. Due to this event, production in textile factories employing approximately 900 workers was halted. A decision was made to proceed with the repairs without waiting for the summer season, and reinforced concrete bored pile applications along with structural repair works were initiated in the region.In this project, where winter concreting was required, the authors of this paper also actively participated, particularly in the supervision and technical support of the construction of bored pile cap beams. During the concrete casting process, greenhouse plastic sheet protection was preferred to safeguard the fresh concrete. General images from this application are presented in Fig. 3.

Fig.3. Erzurum 2nd Organized Industrial Zone textile factories repair works,, Okuyucu et.al.(2023)

Although national and international regulations mandate the implementation of protective measures for winter concreting, they generally do not provide detailed guidelines regarding the specific protection methods. This gap constitutes the primary motivation of the present study. Based on this consideration, the commonly preferred method of using plastic sheeting for concrete protection, widely adopted in global practices, was selected for investigation in this research. Despite the extremely low temperatures experienced during winter in Erzurum, the location of the study, the number of sunny days is relatively high. Therefore, instead of using standard plastic sheeting or tarpaulin, greenhouse plastic was chosen for protection in this study. Under real atmospheric winter conditions, after the completion of concrete casting, the molds were covered with greenhouse plastic sheets to provide protection.The protective measures were maintained continuously during the first 72 hours following the casting, and the greenhouse plastic was not removed or opened for any reason. After 72 hours, all specimens were demolded, and the greenhouse plastic protection was continued until the end of the seventh day. At the end of the seventh day, the greenhouse plastic was removed, and the specimens were then exposed to ambient atmospheric conditions until the 28th day.This protection procedure was designed to be consistent with real-world field applications. Apart from the nine cube specimens prepared for axial compressive strength testing, an additional cube specimen was equipped with a type-K thermocouple sensor placed at its center during casting to monitor the internal concrete temperature. Temperature measurements were recorded for seven days inside the concrete, while ambient atmospheric temperature measurements continued for 28 days.The reason for monitoring atmospheric temperature for 28 days was that three of the specimens, after the removal of the greenhouse plastic on the seventh day, remained exposed to atmospheric conditions until the 28th day for axial compressive strength testing. A summary of the protection measures is provided in Table 3, and visual documentation related to the concrete casting and protection procedures is presented in Fig. 4.

Table 3. Protection measures applied to concrete samples manufactured in winter conditions

	3rd day	7th day	28th day
Greenhouse Nylon Protection*	Yes	Yes	**No**
Concrete Internal Temperature Monitoring	Yes	Yes	**No**
Atmospheric Temperature Monitoring	Yes	Yes	Yes

**: All samples were removed from the mold at the end of the 3rd day.*

Fig. 4. Images of concrete casting and protection measures

In the production of concrete, the goal was to produce C30/37 class concrete, and the concrete mix was prepared according to the recipe presented in Table 4. The concrete recipe shown in Table 4 was taken from the project report presented in Okuyucu et al. (2023), using the same materials. To ensure that the concrete gains strength quickly during winter production, CEM II-42.5 R type cement was preferred. No admixtures such as setting accelerators were used in the production. The concrete was produced with a water/cement ratio of 0.54.

Table 4. C30/37 class concrete mixture recipe, Okuyucu et al. (2023)

Material	Volume (dm^3)	Weight (kg)
Cement (CEMII - PC42.5-R)	133	400
Water	214	214
Air	10	-
Sand (0-3 mm)	193	421
Fine gravel (5-12 mm)	450	1134
Coarse gravel	-	-
Total	1000	2163

On February 10, 2025, during the concrete pouring at the western facade of the Engineering and Architecture Faculty of Erzurum Technical University, the fresh concrete temperature was measured at 22°C, while the atmospheric temperature was measured at -3°C. Both the application and various literatures indicate that the optimal range for fresh concrete temperature when placed in the form is between 15-25°C, and the TS1248(2017) standard stipulates that the minimum fresh concrete temperature in cold weather conditions should be 10°C. In this case, it can be stated that the concrete produced meets the standard conditions with a fresh concrete temperature of 23°C. The concrete pouring process began at 11:00 AM, which is the warmest part of the day, and was completed within approximately 1 hour. Considering the possibility that air temperatures may drop below -15°C after concrete production, it should be emphasized that the pouring date was determined based on weather forecasts.

In the study, both the atmospheric temperature and the internal temperature of the concrete cube were recorded using type K thermocouple sensors. The type K thermocouple sensors, as seen in Fig. 5, were locally manufactured and obtained from a company based in Bursa. Since the 3-meter long sensors could not be directly connected to the static data collection unit, a thermocouple connection box, which serves as an adapter, was used to establish the connections to the system. The measurement accuracy of these sensors was cross-verified using mercury or digital thermometers as much as possible at the measurement locations. During the temperature monitoring of the pouring process, data collection systems were supported by online UPS power sources to prevent data loss due to power interruptions. The data collection system and computer were placed inside the building, and the type K thermocouple sensors were introduced through a window opening and connected to the system. Temperature monitoring with the thermocouple sensors continued for 28 days as planned, and no data loss occurred during this period.

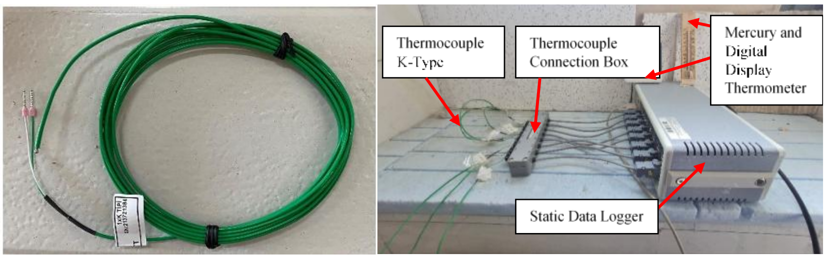

Fig.5. K type thermocouple and static data acquisition unit used in temperature measurement.

During the course of the study, the recorded atmospheric temperature was evaluated to assess the control of abnormal (cold) weather conditions as specified in TS1248(2017) for the pouring and curing conditions. The temperature record taken from the concrete cube sample was used for the calculation of the maturity index. It is beneficial to elaborate on the concept of the maturity index here. TS13508(2012) defines the maturity index as a value indicating the maturity of a cement-based mixture, based on its temperature history, using a maturity function. The calculated index is an indicator of maturity, assuming that the required water for the pozzolanic reaction or hydration of the cement-based materials is provided during the calculation period. The two most commonly used maturity indices are the temperature-time factor and equivalent age. In this study, the temperature-time factor was calculated as the maturity index. The temperature-time factor is calculated using the Equation 1 presented in TS13508(2012):

$$M(t) = \Sigma(T_a - T_o).\Delta t \qquad (1)$$

In Equation 1: *M(t):* temperature-time factor (degree-days or degree-hours) at age t, *Δt:* Time interval (days or hours, T_a*: Average temperature of concrete during Δt (°C),* T_o**:** Datum temperature (°C).

The mathematical expression presented in Equation1 numerically calculates the area under the temperature-time curve for the internal temperature of the concrete, excluding the portion above the initial/datum temperature. The initial/datum temperature used here refers to the lowest internal temperature at which the concrete can start to gain strength/develop strength, and it is clear that this will differ for each concrete mix. According to ASTM

C1074-19e1 (2019), the datum temperature (reference/initial temperature) is the theoretical temperature value used in the maturity method, assuming that the hydration of the concrete has completely stopped. In other words, this temperature represents a boundary beyond which the concrete does not gain any strength, and it is generally considered to be -10°C in ASTM C1074-19e1 (2019). The initial temperature is a parameter that must be determined experimentally according to TS13508 (2012). The initial temperature depends on the type of cement, the type and amount of chemical or other additives that may affect the rate of hydration, and the temperature range to which the concrete is exposed during curing. However, for determining the initial temperatures in this study, no experimental work was carried out as detailed in TS13508 (2012); instead, support was obtained from the literature. A literature review on the selection of the initial temperature revealed that in the study by Elaty et al. (2017), experimental determination of the initial temperature was performed for concretes made with different types and dosages of cement. In the study reviewed, the initial temperature for a mix close to the plain concrete used in the research, in terms of cement type and dosage, was determined to be -2.2°C. Based on the initial temperature value of -2.2°C from the Elaty et al. (2017) study, temperature-time factor calculations were made according to Relation 1. Apart from the calculations performed on the temperature data, the 3, 7, and 28-day axial compressive strength values were experimentally obtained, and the 3- and 7-day strengths were correlated with the temperature-time factor data.

3. Results and discussions

Weather forecasts for air temperature were monitored, and considering the subsequent predictions of low temperatures, the manufacturing date was set for February 10, 2025. The atmospheric temperature recording graph, taken over a period of 28 days after the concrete pouring on this date, is presented in Fig. 6.

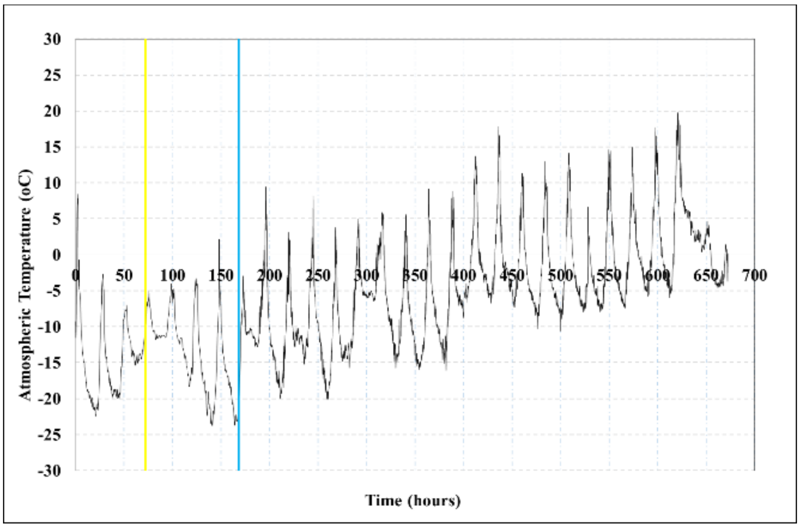

Fig.6. 28-days atmospheric temperature records

Upon examining the temperature record presented in Fig. 6**,** it is observed that within the first 24 hours after the concrete pouring, the atmospheric temperature dropped to -22.4°C, with the minimum temperature measured on the 6th day post-pour at -23.8°C. The average atmospheric temperature was calculated as -6.5°C. Positive temperature readings were recorded during the times when the thermocouple sensors were directly exposed to sunlight and should be considered as data above the meteorological records. However, temperature readings taken when the sample storage area was not exposed to sunlight (in the shade) were found to be consistent with meteorological records. This data indicates that the atmospheric conditions at the site of the concrete pouring met the abnormal (cold) weather conditions defined in TS1248(2017). The yellow line in Fig. 6 marks the end of day 3, while the blue line marks the end of day 7.

In studies focusing on the thermal behavior during the hydration process of concrete, it is possible to access information from the relevant literature regarding the effect of the volume-to-surface area (V/A) parameter on behavior. One such study, conducted by Do et al. (2021), presents findings from an investigation of the early-age thermal behavior of concrete segmental box girders using finite element (FE) analysis. In this study, a segmental box girder diaphragm model was created to assess the effects of flanges, the body, the V/A ratio, and the heat of hydration of cement on the early-age temperature development of the segment. It was concluded that the effect of the V/A parameter diminishes in high-strength concretes. Although high-strength concrete was not used in the work discussed in this paper, the V/A ratio for the cube sample, where temperature tracking was carried out, was calculated as 0.03. The temperature-time graph created using the 7-day temperature tracking data from the cube sample is presented in Fig. 7**.**

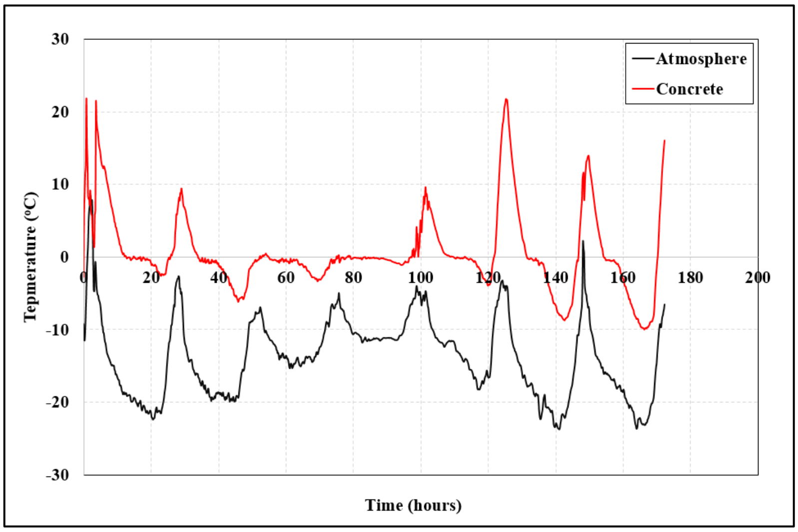

Fig.7. 7-day temperature-time graph measured from inside the concrete cube sample.

Upon reviewing the graph presented in Fig. 7**,** it is clear that the internal concrete temperatures of the cube sample followed a temperature regime similar to that of atmospheric temperatures after the first 24 hours post-pour. Referring to the work of Elaty et al. (2017), with the assumption that the temperature at which hydration stops is -2.2°C, it can be stated that the internal concrete temperature of the sample did not drop below this value during the first 24 hours. It is considered beneficial to closely examine the first 24-hour period of the concrete sample, which was produced under real winter conditions and protected with greenhouse plastic, as it is crucial for hydration processes. Fig. 8 shows the internal concrete temperature measurements of the first 24 hours, along with a visual of the concrete hydration phase from the source Çimsa (2025).

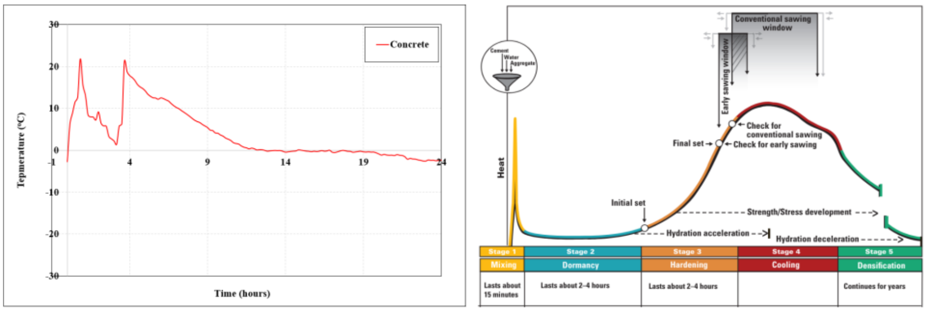

Fig.8. First 24-hour concrete internal temperature-time graph and phases of concrete hydration quoted from Çimsa (2025)

As expressed in Neville (1997), hydration is a series of irreversible chemical reactions that occur between cement and water. During hydration, the cement paste sets and hardens. The hydration process begins as soon as cement comes into contact with water. The cement particles gradually and partially dissolve, and the dissolved components react at different rates. During these reactions, heat is released, and new compounds called hydration products are formed. These new compounds create a solid structure that hardens the cement paste, bonds with the aggregates in the concrete mix, and forms a strong and dense structure. The measurable heat released during hydration does not drop to zero over time, as the reactions slow down. Hydration reactions can continue for years as long as there is water and unreacted cement in the concrete. This process contributes to the continued strength gain of the concrete and the development of desirable properties such as low permeability. Extensive studies have been conducted on hydration phases, and this topic continues to be a subject of research. A general understanding of hydration reactions can help prevent or address issues related to concrete, ensuring that the concrete mix performs as designed. Hydration is considered to occur in five main phases: mixing, dormancy (sleep) period, hardening, cooling, and densification. The mixing phase is when cement first comes into contact with water. The cement particles begin to dissolve, and a thin layer of reaction products forms on their surfaces. Hydration reactions are triggered at this point. During the dormancy (sleep) period, the reactions slow down, and the concrete mix remains workable. This phase provides the time needed to place and shape the mix in the mold. Heat production is at a low level. At the end of the dormancy period, the hardening phase begins, and the reactions speed up. Heat production increases, new hydration products form, and the concrete starts gaining strength rapidly. Setting and early strength development occur during this phase. In the cooling phase, the concrete reacts less actively chemically but continues to gain strength. During the long-term densification phase, reactions between the remaining cement and water continue slowly. The voids in the concrete's internal structure decrease, making the material denser, stronger, and less permeable. This process can take years. Upon examining Fig. 8, it can be concluded that during the winter-poured concrete sample, the mixing, dormancy, hardening, and cooling phases were completed within the first 24 hours, and the densification phase began. The dormancy phase lasted approximately 3 hours, while the hardening phase lasted about 1 hour. The reason the hardening phase was shorter than the expected 2-4 hours is thought to be the use of rapid-setting R-type cement.

The internal temperature monitoring of the concrete has facilitated not only the interpretation of the hydration process but also the determination of the concrete's maturity parameter. The 7-day temperature-time factor graph, calculated using an initial temperature of -2.2°C, with reference to Elaty (2017), is presented in Fig. 9.

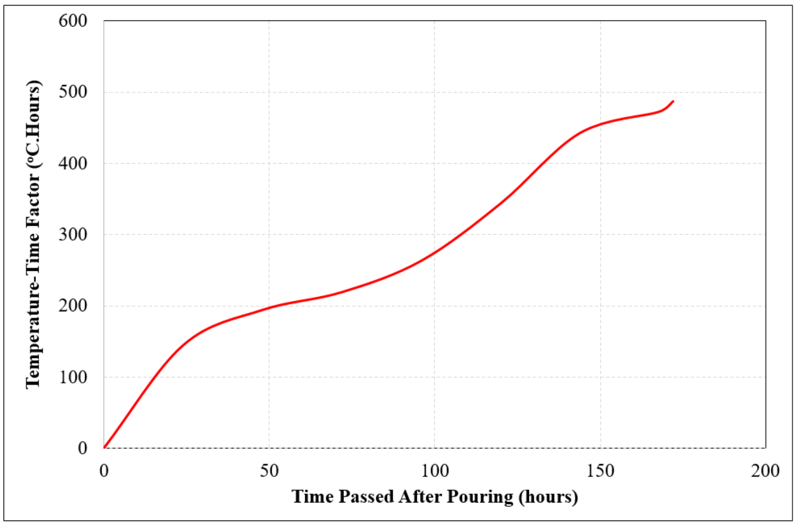

Fig.9. Temperature-time factor graph for the cube sample with temperature monitoring

Upon examining Fig. 9, it can be observed that the temperature-time factor of the cube concrete specimen reaches approximately 220 (°C.Hours) at the 3-day mark and approximately 220 (°C.Hours) at the 7-day mark. The definitive temperature-time factor values, along with the axial compressive strength test results, are presented collectively in Table 5.

Table 5. Temperature-time factor and axial compressive strength test results.

Time After Casting (Days)	Temperature-Time Factor (°C.Hours)	Uniaxial Compressive Strength (MPa)
3	219.1	4.2
7	487.0	9.4
28	-	17.9

The data presented in Table 5 are the results of axial compressive strength tests conducted on concrete cube specimens measuring 150x150x150 mm under load-controlled conditions at a rate of 0.5 MPa/s. Concrete specimens produced with a mix design intended for C30/37 concrete grade did not reach a compressive strength of 37 MPa at the 28-day mark. The expected axial compressive strength of 37 MPa was found to be 17.9 MPa after 28 days. The axial compressive strength data presented in Table 5 indicate that the rate at which the concrete gained strength was slower than the expected rate under normal environmental conditions. According to Eurocode 2 (BS EN 1992 1-1:2004+A1:2014), the expected percentages of axial compressive strength gain when using R-type cement, along with the strength gain percentages of the specimens under study, are provided in Table 6.

Table 6. Axial compressive strength gain percentages of the samples (%)

Time (days)	Tested Samples	Eurocode 2 (BS EN 1992 1-1:2004+A1:2014)
3	11	76
7	25	88
28	48	100

Upon examining Table 6, it is clearly evident that the early-stage (3-7 days) compressive strength gain percentages of concrete specimens produced in winter fall well below the expected 76% value for specimens produced under normal environmental conditions. For the specimens expected to reach approximately 76% of the target axial compressive strength after 3 days under normal conditions, only 11% of compressive strength was achieved. The strength gain regime has shown similar discrepancies for the 7-day and 28-day strengths as well. For specimens expected to gain approximately 88% of their compressive strength after 7 days, only 25% was achieved, and for specimens expected to reach nearly 100% after 28 days, only 48% of the axial compressive strength was attained. However, it should be noted that the volumes of the specimens exposed to atmospheric temperatures below -20°C are considerably smaller than actual reinforced concrete elements and, therefore, are more significantly affected by atmospheric temperatures. The primary reference for this conclusion is the scientific research project final report in Okuyucu et al. (2023).

At this stage, it is beneficial to examine the axial compressive strength values of the specimens produced in winter in conjunction with the maturity index, which is the temperature-time factor data. Since the temperature of the concrete specimens was tracked for a total of 7 days, this analysis was conducted for the 3-day and 7-day axial compressive strength values. The axial compressive strength data for the cube specimens presented in Table 5 were multiplied by a factor of 0.85 to convert them into equivalent strength for standard cylindrical specimens, and the graphical presentations, using the strength-maturity factor relationship provided in ACI PRC-306 (2016) for standard cylindrical concrete specimens cured at 22.8°C in the laboratory, are shown in Fig. 10.

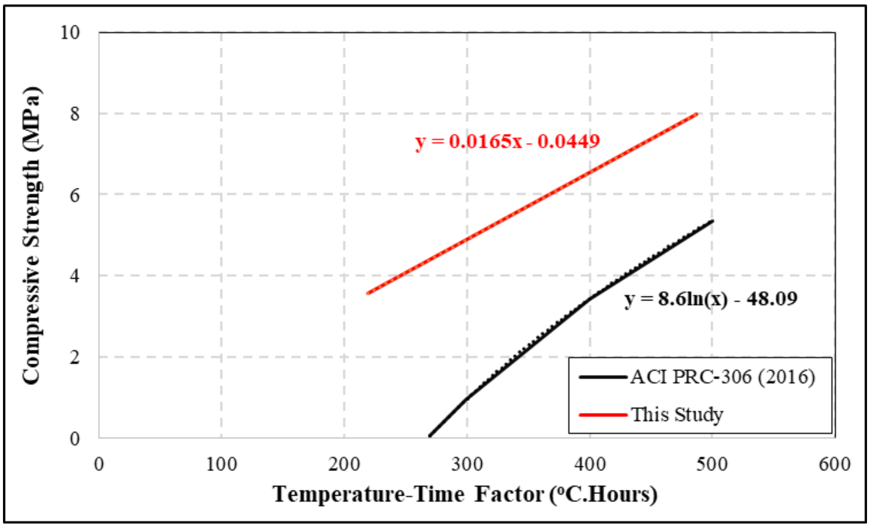

Fig.10. Relationships between temperature-time factor and uniaxial compressive strength.

The TS13508(2012) maturity method stipulates that the concrete strength of a structure (in situ) can be predicted, enabling critical decisions such as the termination of protection measures in cold weather. The prediction of concrete strength in the structure using the calculated maturity index and strength-maturity relationship is fundamental to carrying out this study. As a result of the work carried out for this purpose, Fig. 10 presents the temperature-time factor and axial compressive strength graphs, along with the linear relationship equations generated for these graphs. The main limitation of the study seems to be the fact that the data was obtained from small-volume samples; however, it should be noted that both TS13508(2012) and similar foreign standards provide methods for obtaining mathematical relationships representing the strength-maturity relationship under laboratory conditions. It should also be considered that the model sample volumes that can be used under laboratory conditions will be smaller than those of prototypes. In this context, the strength-temperature time factor relationship for the concrete specimens produced during winter in this study is presented in Equation 2, while the strength-maturity factor relationship for standard cylindrical concrete specimens cured at 22.8°C under laboratory conditions, as presented in ACI PRC-306 (2016), is provided in Equation 3.

$$\sigma = 0.0165M - 0.0449 \quad (2)$$

$$\sigma = 0.86\ln(M) - 48.09 \quad (3)$$

In Equation 2 and Equation 3; *σ:* Axial compressive strength of standard cylinder specimen (MPa), *M*: Temperature-time factor (°C.Hour) calculated with Equation 1, taking the initial temperature as -2.2 °C

Equation 2 was derived for concrete samples produced under real winter conditions, whereas Equation 3 is proposed for standard cylindrical concrete samples cured in a laboratory environment at 22.8°C. It is important to note this distinction. A simple analysis based on the temperature-time factor values of samples produced under two different atmospheric conditions is deemed beneficial. The purpose of this analysis is to assess whether the maturity-strength relationship presented in a significant standard such as ACI PRC-306 (2016) can be used to predict axial compressive strength for samples produced in winter. The 3-day axial compressive strength of the concrete samples produced in winter can be expressed as 3.6 MPa (4.20.85) for standard cylindrical specimens. The corresponding temperature-time factor value for this sample is 219.1 °C-hours. When this temperature-time factor value is substituted into Equation 3, an unrealistic value of -1.7 MPa is obtained. A similar assessment for the 7-day sample data shows that the temperature-time factor calculated as 487.0 °C-hours corresponds to an axial compressive strength of 5.1 MPa when substituted into Equation 3, which is below the expected 8.0 MPa value (9.40.85). This simple evaluation indicates that temperature-time factor-axial compressive strength relationships are required for concrete poured in winter. These relationships could be useful for determining the formwork removal periods in winter. Although the temperature-time factor-axial compressive strength relationship for concrete samples produced with R-type cement in winter is presented in Equation 2, further studies should be conducted to generate relationships with broader data in this field.

4. Conclusions

This study was conducted to examine the effects of the protection method using greenhouse plastic on the axial compressive strength of concrete samples produced with R-type cement in winter without any additives. In the practice, apart from wrapping with greenhouse plastic, no additional protection measures such as heating were applied to the concrete produced in winter. The conclusions drawn from the research can be summarized as follows:

- During the first 24 hours after concrete pouring, the internal temperature of the concrete did not drop below the initial/datum temperature of -2.2°C.
- It was assessed that the first four phases of hydration (mixing, waiting, hardening, cooling) occurred within the first 24 hours, and the process entered the densification phase.
- Concrete samples produced in winter with a C30/37 mix design reached 48% of their 28-day axial compressive strength. Concrete samples produced and maintained under sub -20°C winter conditions did not reach the targeted axial compressive strength values for 28 days. It is believed that higher strengths could be achieved by applying heating under the greenhouse plastic.
- The temperature-time factor parameter was selected as the maturity index, and based on the calculations, a maturity-strength relationship for concrete samples produced in winter was proposed. However, further studies in this area are recommended.

Acknowledgments

The study was conducted as part of the project titled "Experimental Investigation of the Behavior of Reinforced Concrete Beams Poured in Cold Weather (Winter) Under Bending Effects" (TÜBİTAK1001-219M403), using the materials and equipment acquired for the project. The authors of the text would like to express their gratitude to TÜBİTAK (The Scientific and Technological Research Council of Türkiye) for their contributions; special thanks are extended to Batuhan Çınar for his valuable assistance in sample preparation.

References

Abd Elaty, M. A. A., Ghazy, M. F., & Ghannam, M. F. (2017). Influence of maturity for concrete containing different cement types on mechanical and durability properties. *Proceedings of the International Conference on Advances in Structural and Geotechnical Engineering (ICASGE'17)*, Hurghada, Egypt, 1, 1–15.

ACI Committee. (2016). *Guide to cold weather concreting* (ACI PRC-306-16). American Concrete Institute.

ASTM International. (2019). *ASTM C1074-19e1: Standard practice for estimating concrete strength by the maturity method*. https://doi.org/10.1520/C1074-19E01

Atalay, İ. (1997), Geography of Türkiye. Ege University Press, İzmir.

Canadian Standards Association (CSA). (2019). *Concrete materials and methods of concrete construction/Test methods and standard practices for concrete* (CSA A23.1/A23.2-19). Canada.

Çimsa (2025). *What are the hydration stages? How is durable concrete created based on the stages of hydration?* Retrieved April 26, 2025, from https://cimsa.com.tr/en/what-are-the-hydration-stages-how-is-durable-concrete-created-based-on-the-stages-of-hydration/

Do, T. A., Verdugo, D., Tia, M., & Hoang, T. T. (2021). Effect of volume-to-surface area ratio and heat of hydration on early-age thermal behavior of precast concrete segmental box girders. *Case Studies in Thermal Engineering*, 28, 101448.

European Committee for Standardization (CEN). (2014). *Eurocode 2: Design of concrete structures – Part 1-1: General rules for buildings* (BS EN 1992-1-1:2004+A1:2014). British Standards Institution.

Gedik, B. (2020). *Experimental investigation of bond strength–slip relationship under tensile effects in reinforced concrete elements cast in cold weather* [Master's thesis, Erzurum Technical University].

Japan Society of Civil Engineers (JSCE). (2007). *Standard specifications for concrete structures – 2007, materials and construction*. Japan.

Karhonen, C. J. (1990). *Antifreeze admixtures for cold regions concreting – A literature review* (CRREL Special Report No. 90-32). U.S. Army Cold Regions Research and Engineering Laboratory.

Karhonen, C. J., Cortez, E. R., & Charest, B. A. (1992). Strength development of concrete cured at low temperature. *Concrete International*, 14(2), 34–39.

Koç, E., Kaya, K., & Şenel, M. C. (2017). Development of construction industry sector in Turkey–Basic construction industry indicators. *Nevşehir Journal of Science and Technology*, 6(2), 643–660.

Kuzeydoğu Anadolu Development Agency (KUDAKA). (2014). *2014–2023 Regional Current Situation Analysis Report*. Erzurum.

Nassif, A. Y., & Petrou, M. F. (2013). Influence of cold weather during casting and curing on the stiffness and strength of concrete. *Construction and Building Materials*, 44, 161–167.

Neville, A. M. (1997). *Properties of concrete* (4th ed.). Pearson Education Limited.

Nmai, C. K. (1998). Cold weather concreting admixtures. *Cement and Concrete Composites*, 20(2–3), 121–128.

Okuyucu, D., Kazaz, İ., & Bingöl, A. F. (2023). *Experimental investigation of the behavior of reinforced concrete beams cast in cold weather under flexural effects* (Research Project Report, TÜBİTAK1001 / 219M403). The Scientific and Technological Research Council of Turkey (TÜBİTAK).

Pushpalal, D., Danzandorj, S., Bayarjavkhlan, N., Nishiwaki, T., & Yamamoto, K. (2022). Compressive strength development and durability properties of high-calcium fly ash incorporated concrete in extremely cold weather. *Construction and Building Materials*, 316, 125801.

Suk Ryou, J., & Soo Lee, Y. (2012). Properties of early-stage concrete with setting-accelerating tablet in cold weather. *Materials Science and Engineering: A*, 532, 84–90.

Republic of Türkiye Ministry of Agriculture and Forestry, General Directorate of Meteorology, Erzurum 12th Regional Directorate. (2019). *Statistical Meteorological Data Report*. Erzurum.

Turkish Standards Institution (TSE). (2000). *TS 500: Design and construction rules for reinforced concrete structures*. Ankara.

Turkish Standards Institution (TSE). (2012). *TS 13508: Prediction of concrete strength by the maturity method*. Ankara.

Turkish Standards Institution (TSE). (2017). *TS 1248: Rules for preparation, placing and curing of concrete (under abnormal weather conditions)*. Ankara.

Turkish Standards Institution (TSE). (2018). *TS 1247: Rules for concrete production, placing and curing (under normal weather conditions)*. Ankara.

Zhang, G., Yang, Y., & Li, H. (2020). Calcium-silicate-hydrate seeds as an accelerator for saving energy in cold weather concreting. *Construction and Building Materials*, 264, 120191.

4th International Civil Engineering & Architecture Conference
17-19 May 2025, Trabzon, Türkiye

Machine learning approximation of water transport in 3D-printable composites via karsten tube

Seher Ersoy *[1], Shaima AbuQasim[1], Mine Kurtay Yıldız[2], İrfan Ş. Öztürk[2], Furkan A. Sarı[2], Büşra M. Akyüz[1], Muhammed Maraşlı[3], Mehmet Emiroğlu[2]

[1] *Sakarya University, Institute of Natural Sciences., Sakarya, Turkey*
[2] *Sakarya University, Faculty of Engineering, Civil Engineering Department, Sakarya, Turkey*
[3] *Fibrobeton Inc., Istanbul 34810, Turkey*

Abstract. Non-destructive testing methods based on water penetration into porous materials through a defined surface area are widely used for characterizing construction materials such as concrete, alkali-activated mortars, and soil-based composites. Among these methods, the Karsten tube test stands out due to its practicality and cost-effectiveness, allowing applications in laboratory and field conditions. In this study, water ingress measurements were performed on 3D-printable composites namely, cement based, alkali-activated, and soil/clay based materials using the karsten tube. With the increasing use of 3D-printed structural composites produced by layered manufacturing techniques, the need for rapid and reliable determination of their water transport mechanisms has become critical. In this context, the amount of water transported through the materials over different durations was measured and classified based on material types. The experimental time series data obtained were analyzed using machine learning algorithms to develop predictive models. The performance of the models was evaluated through supervised learning performance metrics, and different algorithms were comparatively assessed. As a result, artificial intelligence-based models with high predictive accuracy were developed to characterize the water transport mechanisms of 3D-printable composite materials.

Keywords: 3D printable building materials; Water transport; Karsten tube; Machine learning

1. Introduction

In recent years, three-dimensional (3D) printable composite materials have emerged as a significant innovation in the construction industry due to their design flexibility, rapid production, and cost efficiency (Khan et al., 2024). With the development of cement-based, alkali-activated, and soil/clay-based 3D composites, there has been growing interest in evaluating their mechanical (K. Liu et al., 2023), environmental, and durability (Sun et al., 2022) performances. However, the water transport mechanisms in these new-generation materials remain insufficiently understood.

Water transport in building materials is critically important for service life and resistance to environmental effects. In this context, non-destructive testing methods are widely used to assess material permeability; the Karsten tube test is one such method used to examine the water absorption behavior of porous construction materials(Alves et al., 2019). The RILEM Test Method II.4 allows for the standardized application of this test under both laboratory and field conditions (PROSOCO, 2021).

Recently, the use of artificial intelligence and machine learning techniques has become increasingly common in modeling complex processes such as water transport. For instance, (Hosseinzadeh et al., 2023) demonstrated that support vector machines, random forest algorithms, and deep learning models achieved high accuracy in predicting the chloride diffusion coefficient in concrete, indicating their strong potential for permeability-related estimations.

In this study, water transport mechanisms were investigated by conducting Karsten tube tests on three different types of 3D-printable composite materials: cement-based, alkali-activated, and soil/clay-based. Time-series data obtained from the experiments were analyzed using machine learning algorithms to develop predictive models for water transport. The performance of these models was evaluated using supervised machine learning performance metrics, and the prediction accuracy of different algorithms was compared. Accordingly, the study aims to enhance the understanding and predictability of water transport behavior in various composite materials.

* Corresponding author, E-mail: shaima.abuqasim1@ogr.sakarya.edu.tr

https://doi.org/10.31462/icearc2025_ce_mat_874

2. Material and method

2.1. Material

In this study, three different types of 3D-printable composite mixtures were investigated: cement-based, alkali-activated, and soil-based composites. For the cement-based composite, silica sand with a maximum particle size of 2 mm, CEM I 42.5R cement, sodium carboxymethyl cellulose (CMC), and a superplasticizer were used. The alkali-activated composite was prepared using silica sand, sodium hydroxide, sodium silicate, a superplasticizer, and ground granulated blast furnace slag (GGBFS). For the soil-based composite, clay, lime, α-hemihydrate gypsum, and silica sand were used to produce the third type of composite.

2.2. Method

In this study, samples were produced using three different materials: soil-based (clay), geopolymer, and conventional concrete. For each material, a spiral geometry model was first designed and transferred to the 3D printer. The prepared mixtures were printed using a 3D printer to form structures with a base area of 40 cm × 20 cm and a height of 4 cm, following predefined coordinates. After printing was completed, a water absorption test was performed on the printed plates using a Karsten tube. Additionally, samples measuring 4 cm × 4 cm × 16 cm were cut from the plates using a concrete cutter for compressive and flexural strength tests.

Furthermore, three samples for each material were produced from the same mix using molds of 4 cm × 4 cm × 16 cm dimensions. Both mold-cast specimens and those cut from the 3D-printed plates were subjected to compressive and flexural strength tests. These tests were carried out in accordance with the TS EN 196-1 standard. The results from both methods were evaluated comparatively by calculating the average of the values obtained from individual samples. The materials used in the experiments, the testing procedures, and the printing process are illustrated in Fig. 1, while the Karsten tube test and 3D printing applications for the three composites are presented in Fig. 2.

The main objective of the Karsten tube test was to determine the water absorption characteristics and compare the water transport mechanisms of 3D-printed soil-based, geopolymer, and conventional concrete composite specimens. The water absorption performance of the samples was determined using Karsten tubes in accordance with the RILEM testing method. The tubes were attached to the sample surfaces using waterproof silicone and then filled with water. Following the start of the test, measurements were taken at time intervals of 1, 2, 3, 4, 5, 10, 15, 20, 25, 30, 35, 40, 45, 50, 55, and 60 minutes. Based on these readings, the total amount of absorbed water was calculated.

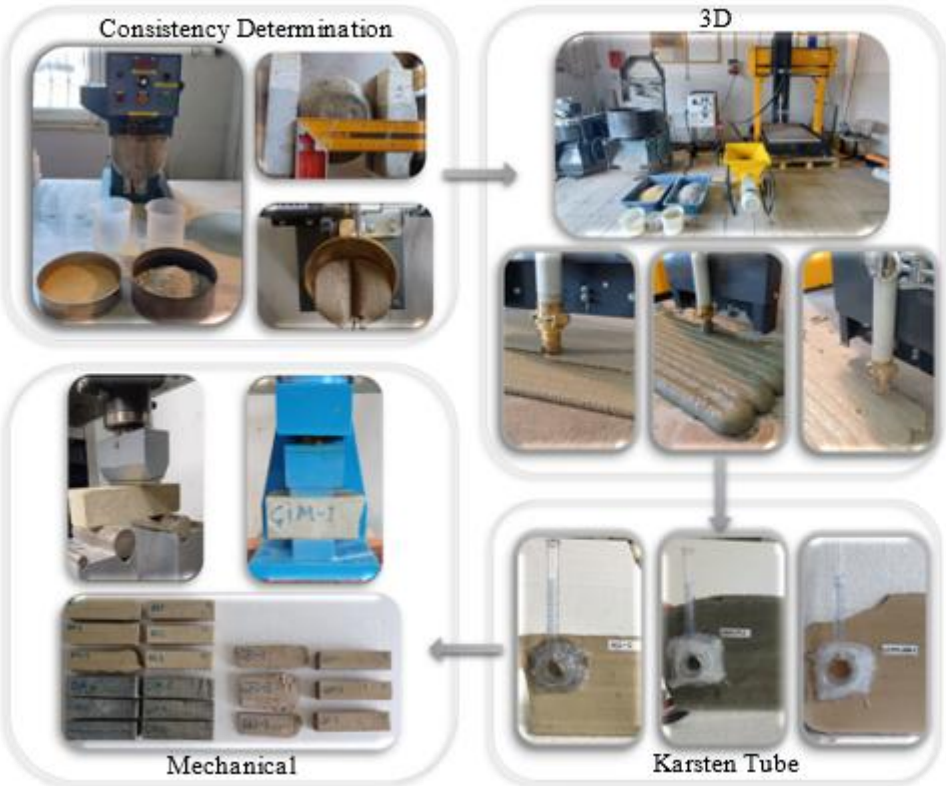

Fig. 1. Experimental steps

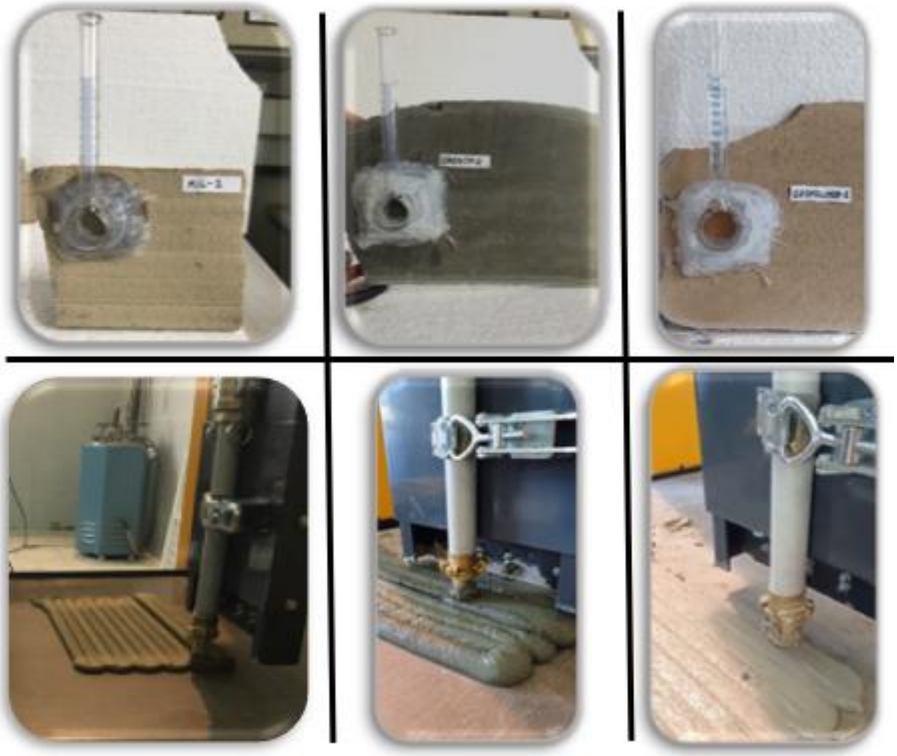

Fig. 2. 3D print and karsten tube experimental steps

In the artificial intelligence phase of the study, regressive prediction models were established using data obtained from the water absorption experiment conducted with the Karsten tube. In the models, the prediction performances of different algorithms are determined. The results are analyzed with regression performance metrics, and at the same time, it is determined how close the algorithms are to reality at different learning-test ratios. Firstly, the models were run with a learning-test ratio of 70%-30% in all algorithms, and the performance metrics SE, MSE, RMSE, MAD, MAPE, R, and R2 were evaluated comprehensively. Then, the prediction performance of different algorithms at different learning-test rates was also tested. In the prediction studies, Karsten tube measurements at different minutes were entered into the system as different feature columns, and the column showing the water absorption values at the 60th minute was entered into the prediction model as the target column.

3. Result and discussion

3.1. Machine learning results

In this study, we used four different machine learning methods—k-Nearest Neighbors (k-NN), Artificial Neural Network (ANN), Support Vector Machine (SVM), and Random Forest (RF) —to predict how much water would be absorbed in 60 minutes, using time-series data from the Karsten tube test. The performance of each algorithm was evaluated across various feature rate percentages using multiple supervised learning metrics, including Mean Absolute Deviation (MAD), Mean Squared Error (MSE), Root Mean Squared Error (RMSE), Mean Absolute Percentage Error (MAPE), standard error (SE), and the determination coefficients (R and R^2). The comparative results of all models are illustrated in Fig. 3.

According to the results, the ANN and SVM models consistently achieved low error values across all metrics and maintained high R^2 values above 0.98, demonstrating their strong generalization capability and accurate prediction performance. In contrast, the k-NN algorithm exhibited relatively poor performance, with significantly higher MAD, MSE, RMSE, and MAPE values and a noticeably lower R^2 value across the tested feature rates.

The performance of the RF model showed substantial improvement with increasing feature rate. While its error metrics were relatively high at lower feature rates (45–70%), the model's accuracy improved markedly at higher rates (above 85%), where both MSE and RMSE values declined, and R^2 values approached 0.95. This indicates that the effectiveness of the RF algorithm is more sensitive to the proportion of input features used in training.

In addition to numerical performance metrics, the prediction trends of each model were also visualized through fit curve plots under different learning-test ratios (50:50, 60:40, and 70:30), as illustrated in Fig. 4. These plots provide a comparative view of how closely each model's predictions follow the actual values.

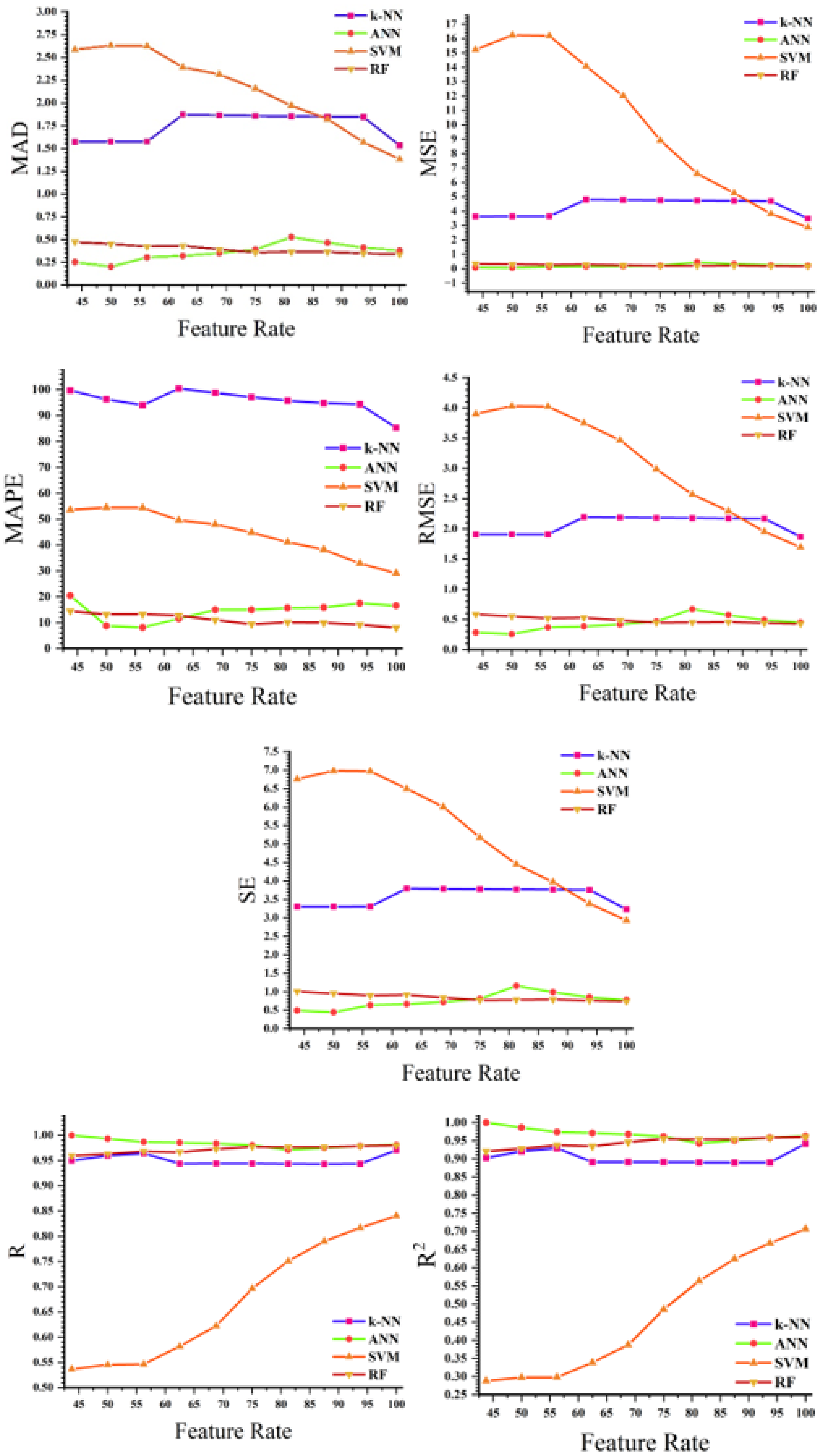

Fig. 3. Performance metrics

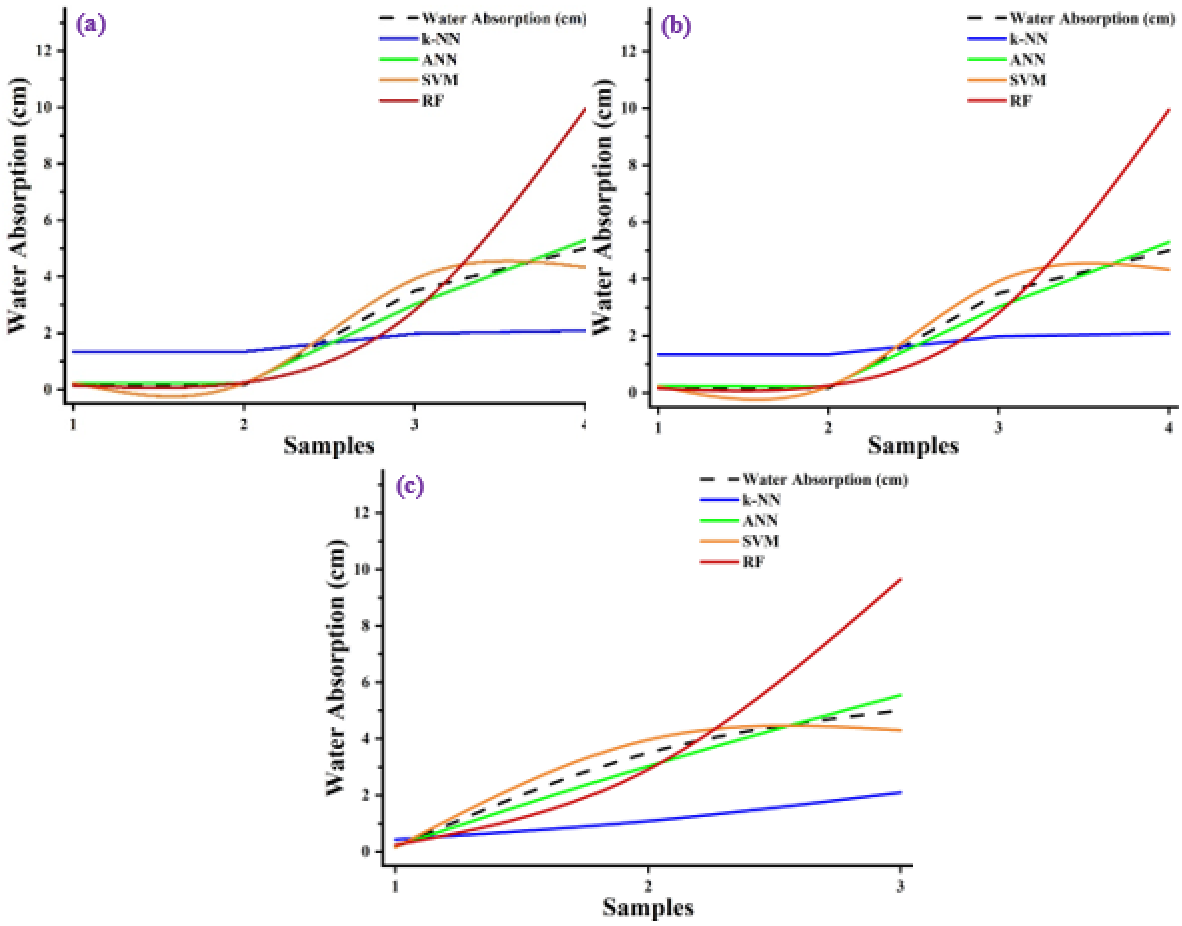

Fig. 4. Prediction performance of k-NN, ANN, SVM, and RF algorithms compared to actual values under different learning-test ratios: (a) 50:50, (b) 60:40, and (c) 70:30

At a 50:50 learning-test split, the RF model showed the closest alignment with the actual data across all samples, followed by the ANN. The SVM model exhibited a sharper deviation at higher sample values, while k-NN produced nearly flat predictions, failing to capture the overall data trend. With a 60% training ratio, the ANN and RF both demonstrated improved alignment with the actual curve. The SVM model slightly improved in the early samples but continued to diverge significantly in the later range. The prediction line of k-NN remained nearly linear and showed limited learning capacity. At the highest training ratio (70:30), the RF and ANN models maintained strong conformity with the actual trend. The RF produced a smoother approximation across the entire range. The performance of SVM remained inconsistent, and k-NN continued to underperform with minimal changes.

When the prediction performances of the algorithms are evaluated in general, SVM and k-NN algorithms exhibited lower performance than ANN and RF algorithms. The fact that the data obtained here are not extensive because they are obtained from a series of experimental samples has highlighted the sensitivity of SVM and k-NN algorithms to the low amount of data due to their nature.

3.2. Flexural and compressive strength results

For each test group, the flexural and compressive strength results were determined by applying the tests to both 3D-printed and mold-cast specimens. The flexural strength values obtained according to the material type and specimen form are presented in Fig. 5. When the graph is examined by material type, the highest flexural strength values in the 3D-printed and mold-cast groups were observed in the cement-based composites, with 8.88 MPa and 8.26 MPa, respectively; while the lowest values were recorded in the clay-based composites, with 1.50 MPa and 1.08 MPa, respectively. These results indicate that the flexural strength of the 3D-printed specimens was either lower than or comparable to that of the cast specimens (Albar et al., 2020).

Fig. 6. presents the compressive strength test results. When the results for the three types of composites are examined, it is observed that similar compressive strength values were recorded between the 3D-printed and mold-cast specimens, except for the alkali-activated composites (C. Liu et al., 2021). The compressive strength values of the 3D-printed samples were 48.85 MPa for cement-based composites, 26.77 MPa for alkali-activated

composites, and 1.86 MPa for clay-based composites. (Ly et al., 2021) concluded that cement-based mortars exhibit higher compressive strength than mortars based on alkali-activated materials. In the mold-cast specimens, the highest compressive strength was recorded for the alkali-activated composite at 60.90 MPa, while the lowest was observed for the clay-based composite at 3.14 MPa.

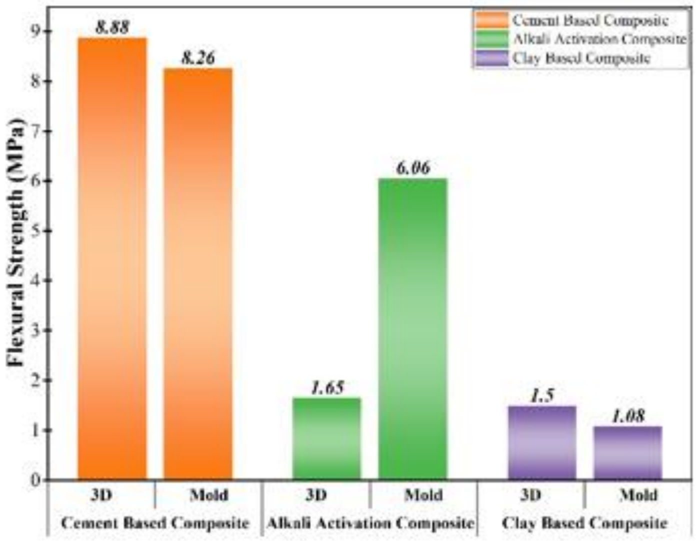

Fig. 5. Flexural strength

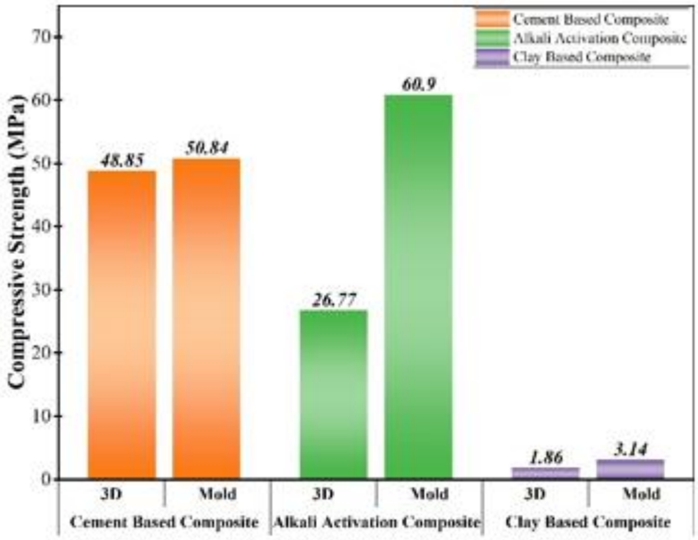

Fig. 6. Compressive strength

4. Conclusions

This study investigated the water transport behavior and mechanical properties of 3D-printable composites through both non-destructive and destructive test methods, supported by artificial intelligence-based modeling. Based on the findings, the following conclusions can be drawn:

- The Karsten tube test effectively distinguished the water absorption behaviors of different material types, indicating that cement-based composites absorbed the least amount of water, while clay-based composites showed the highest uptake.
- Among the evaluated machine learning algorithms, the ANN and RF models yielded the most accurate predictions for 60-minute water absorption, whereas the SVM and k-NN models showed lower predictive performance.
- The prediction performance of the RF model notably improved with higher feature rates, while the ANN remained consistently accurate across all conditions.

- Flexural strength tests showed that cement-based composites exhibited the highest strength in both 3D-printed and mold-cast forms, while clay-based specimens demonstrated the lowest strength levels.
- In compressive strength tests, 3D-printed cement-based composites achieved the highest strength values overall, whereas mold-cast alkali-activated composites outperformed their 3D-printed counterparts.

These outcomes confirm that combining artificial intelligence-based approaches with both non-destructive and mechanical testing provides a reliable framework for evaluating the performance of new-generation 3D-printable building materials.

Acknowledgments
The authors would like to express their sincere gratitude to Fibrobeton Company for providing material support for this study.

References

Albar, A., Chougan, M., Al-Kheetan, M.J., Swash, M.R., & Ghaffar, S. H. (2020). Effective extrusion-based 3D printing system design for cementitious-based materials. *Results in Engineering, 6*, 100135. https://doi.org/10.1016/J.RINENG.2020.100135

Alves, R., Faria, P., & Brás, A. (2019). Brita Lavada – An eco-efficient decorative mortar from Madeira Island. *Journal of Building Engineering, 24*, 100756. https://doi.org/10.1016/J.JOBE.2019.100756

Hosseinzadeh, M., Mousavi, S.S., Hosseinzadeh, A., & Dehestani, M. (2023). An efficient machine learning approach for predicting concrete chloride resistance using a comprehensive dataset. *Scientific Reports, 13*(1), 1–33. https://doi.org/10.1038/S41598-023-42270-3

Khan, M., & McNally, C. (2024). Recent developments on low carbon 3D printing concrete: Revolutionizing construction through innovative technology. *Cleaner Materials, 12*, 100251. https://doi.org/10.1016/J.CLEMA.2024.100251

Liu, C., Yue, S., Zhou, C., Sun, H., Deng, S., Gao, F., & Tan, Y. (2021). Anisotropic mechanical properties of extrusion-based 3D printed layered concrete. *Journal of Materials Science, 56*(30), 16851–16864. https://doi.org/10.1007/S10853-021-06416-W

Liu, K., Takasu, K., Jiang, J., Zu, K., & Gao, W. (2023). Mechanical properties of 3D printed concrete components: A review. *Developments in the Built Environment, 16*, 100292. https://doi.org/10.1016/J.DIBE.2023.100292

Ly, O., Yoris-Nobile, A.I., Sebaibi, N., Blanco-Fernandez, E., Boutouil, M., Castro-Fresno, D., Hall, A.E., Herbert, R.J.H., Deboucha, W., Reis, B., Franco, J.N., Teresa Borges, M., Sousa-Pinto, I., van der Linden, P., & Stafford, R. (2021). Optimisation of 3D printed concrete for artificial reefs: Biofouling and mechanical analysis. *Construction and Building Materials, 272*, 121649. https://doi.org/10.1016/J.CONBUILDMAT.2020.121649

PROSOCO. (2021). *Rilem Tube Test Procedures*. [Technical Report]. https://prosoco.com/app/uploads/2021/06/Tech-Note-102-RILEM-Tube-Test-Procedures.pdf

Sun, X., Zhou, J., Wang, Q., Shi, J., & Wang, H. (2022). PVA fibre reinforced high-strength cementitious composite for 3D printing: Mechanical properties and durability. *Additive Manufacturing, 49*, 102500. https://doi.org/10.1016/J.ADDMA.2021.102500

ICEARC'25
4th International Civil Engineering & Architecture Conference
17-19 May 2025, Trabzon, Türkiye

Seismic resilience of multi-story buildings: Evaluating the effectiveness of viscoelastic damper arrangements

Sahand Zeinalzadeh Hamid*[1], Zahra Hassanzadeh[2], Javad Parsa[3]

[1] *Islamic Azad University of Tabriz, Department of Civil Engineering, Faculty of Engineering, Tabriz, Iran*
[2] *Azarbaijan Shahid Madani University, Department of Chemistry, Faculty of Science, Tabriz, Iran*
[3] *University of Tabriz, Water Engineering Department, Tabriz, Iran*

Abstract. Seismic resilience of multi-story buildings is critical in mitigating earthquake-induced risks to structural integrity and human safety. This study evaluates the effectiveness of three viscoelastic damper (VED) arrangements—Concentrated, Knee Braced, and Chevron—in enhancing the seismic performance of 10-, 15-, and 20-story steel frame buildings. Using ETABS and finite element analysis (FEA) using ABAQUS, the research models dynamic responses under three seismic records (Hector Mine, Landers, and Manjil) to assess roof displacements, energy dissipation, base shear, and stiffness. Results demonstrate that the Concentrated VED configuration consistently outperforms other arrangements, reducing roof displacements by 18–32%, increasing energy dissipation by 42–46%, and improving structural stiffness by 24–36% across all models. The Chevron arrangement showed notable reductions in lateral drifts (up to 41% in 20-story buildings), while Knee Braced systems provided moderate flexibility but lower overall efficacy. The Concentrated configuration's strategic placement in high-stress zones enables uniform energy dissipation and minimizes residual displacements (29–39% reduction), underscoring its robustness under diverse seismic conditions. Practical implications highlight the configuration's suitability for integration into seismic design codes, particularly for high-rise structures, offering cost savings through reduced post-earthquake repairs and enhanced occupant safety. The study advances the understanding of VED optimization, advocating for their adoption in earthquake-prone regions to balance performance, economic viability, and sustainability. These findings provide engineers with actionable insights for retrofitting existing structures or designing new resilient buildings, ultimately contributing to safer urban infrastructure in seismic zones.

Keywords: Viscoelastic dampers; Seismic performance; Steel frames; Damper arrangements; Comparative analysis

1. Introduction

Seismic resilience is a cornerstone of modern structural engineering, particularly for multi-story buildings located in earthquake-prone regions. Earthquakes pose significant threats to both structural integrity and occupant safety, often resulting in catastrophic consequences such as building collapse, infrastructure damage, and loss of life (Stein & Wysession, 2009).

The dynamic forces generated by seismic events can induce excessive vibrations, leading to structural deformations, material fatigue, and potential failure of critical components (Clough & Penzien). In urban areas with high population densities, the risks are amplified due to the concentration of high-rise structures and complex infrastructure systems (Solberg et al., 2009). The economic and social impacts of earthquakes, including direct property damage, disruption of essential services, and long-term recovery costs, further underscore the need for robust seismic design strategies (Center, 2015; Hecker, 1995). Enhancing the resilience of multi-story buildings is thus imperative to mitigate these risks, ensuring that structures can withstand seismic forces while maintaining functionality and safety.

VEDs have emerged as a highly effective solution for improving the seismic performance of buildings by dissipating energy and reducing structural vibrations. These passive energy dissipation devices utilize materials that exhibit both viscous and elastic properties, allowing them to absorb and dissipate seismic energy through internal friction and deformation (Matsagar & Jangid, 2005; Zhang & Soong, 1992). By integrating VEDs into structural systems, engineers can significantly reduce the amplitude of vibrations during an earthquake, thereby

* Corresponding author, E-mail: sahand.zhamid@gmail.com

https://doi.org/10.31462/icearc2025_ce_mat_916

golden light publishing

minimizing damage to structural and non-structural components (Symans et al., 2008). Unlike traditional bracing systems, VEDs offer a compact and lightweight design, making them suitable for both new constructions and retrofitting existing buildings (Abramovich, 2021).

Their ability to provide non-linear damping across a wide range of frequencies enhances their versatility in addressing diverse seismic loading conditions (Vaiana et al., 2019). The growing adoption of VEDs in seismic design reflects their proven efficacy and alignment with sustainable construction practices, offering a balance between performance and cost-effectiveness (Mehrabi et al., 2017). This study aims to evaluate the seismic performance of various viscoelastic damper arrangements—specifically Concentrated, Knee Braced, and Chevron configurations—in multi-story special steel frame buildings of 10, 15, and 20 stories.

2. Literature review

2.1. Overview of viscoelastic dampers

VEDs are passive energy dissipation devices widely recognized for their ability to enhance the seismic performance of structures, particularly steel frames, by converting mechanical energy into heat through internal friction and deformation of viscoelastic materials (Hao et al., 2024; Matsagar & Jangid, 2005; Zhang & Soong, 1992). This dual behavior enables VEDs to provide effective energy dissipation across a broad range of frequencies and amplitudes, making them highly adaptable to dynamic loading conditions such as earthquakes (Vaiana et al., 2019). Key properties of VEDs include their compact and lightweight design, which facilitates integration into both new and existing structures without significant modifications (Abramovich, 2021). Additionally, VEDs offer customizable damping characteristics through adjustments in material composition, thickness, and geometry, allowing tailored solutions for specific structural requirements (Soto & Adeli, 2013). Their benefits include significant reduction in structural vibrations, enhanced occupant safety, and cost-effectiveness compared to active control systems or tuned mass dampers (Mehrabi et al., 2017; Mortezaei & Zahrai, 2009). In steel frame applications, VEDs have been shown to reduce seismic-induced displacements and accelerations, thereby minimizing structural and non-structural damage (Symans et al., 2008; Wang et al., 2018). However, challenges such as temperature sensitivity and potential long-term material degradation require careful consideration in design and maintenance (Soong & Dargush, 1997; Systèmes, 2016).

2.2. Previous studies on damper arrangements

Research on VED arrangements—specifically Concentrated, Knee Braced, and Chevron configurations—has provided valuable insights into their seismic performance in steel frames. The Concentrated arrangement, where VEDs are strategically placed at centralized locations, has been studied for its ability to maximize energy dissipation and structural stiffness. Studies indicate that this configuration effectively reduces roof displacements and enhances overall stability under seismic loads (Cetin et al., 2019; Hao et al., 2024). Knee Braced arrangements, incorporating VEDs at diagonal brace joints, have been explored for their capacity to improve energy dissipation while maintaining structural flexibility. Research suggests that Knee Braced systems can achieve moderate reductions in seismic response, though their effectiveness is often limited compared to other configurations (Kaleybar & Tehrani, 2021; Marko et al., 2006). Chevron arrangements, characterized by V-shaped bracing with VEDs, have been noted for their ability to increase structural stiffness and provide balanced energy dissipation. However, their performance is generally less pronounced than that of Concentrated arrangements (Chen et al., 2020; Kaleybar & Tehrani, 2021). For instance, Chen et al. conducted field tests on a cable-stayed bridge, demonstrating that VEDs in a Chevron-like configuration provided consistent damping across multiple modes, though with reduced efficacy at higher frequencies.

Despite these advancements, prior studies often focus on individual configurations or specific structural types, lacking comprehensive comparative analyses across Concentrated, Knee Braced, and Chevron arrangements under identical seismic conditions. Furthermore, there is limited research directly benchmarking VED-equipped structures against brace-only systems to quantify their relative benefits (Alhasan et al., 2022; Cetin et al., 2019). This study addresses these gaps by systematically comparing the seismic performance of these three VED arrangements in multi-story steel frames, providing a direct evaluation of their effectiveness relative to brace-only structures. Overall, while prior studies highlight the efficacy of individual VED arrangements, a systematic comparison under identical seismic conditions is lacking, which this study addresses.

2.3. Focus of the current study

This study contributes to the field by conducting a detailed evaluation of the seismic performance of Concentrated, Knee Braced, and Chevron VED arrangements in 10-, 15-, and 20-story special steel frame buildings using finite element analysis. Unlike previous studies that often examine configurations in isolation, this research provides a direct comparative analysis under consistent seismic loading conditions. By benchmarking VED-equipped structures against brace-only systems, the study quantifies the improvements in key performance metrics, including roof displacement, energy dissipation, and structural stiffness. The use of finite element analysis enables precise modeling of dynamic structural behavior, offering insights into the optimal VED arrangement for seismic mitigation. These findings aim to guide engineers in selecting effective damper configurations, enhancing the resilience of multi-story buildings in earthquake-prone regions.

3. Methodology

This study employs a comprehensive FEA approach to evaluate the seismic performance of VED arrangements in multi-story steel frame buildings. The methodology integrates advanced software tools, ETABS and ABAQUS, to model, simulate, and assess structural responses under seismic loading. ETABS facilitates structural design and static/dynamic analysis, while ABAQUS provides detailed non-linear material and interaction simulations, ensuring a robust evaluation of VED effectiveness. Fig. 1 shows the flowchart of the analysis workflow integrating ETABS and ABAQUS, illustrating the transition from structural modeling to detailed FEA.

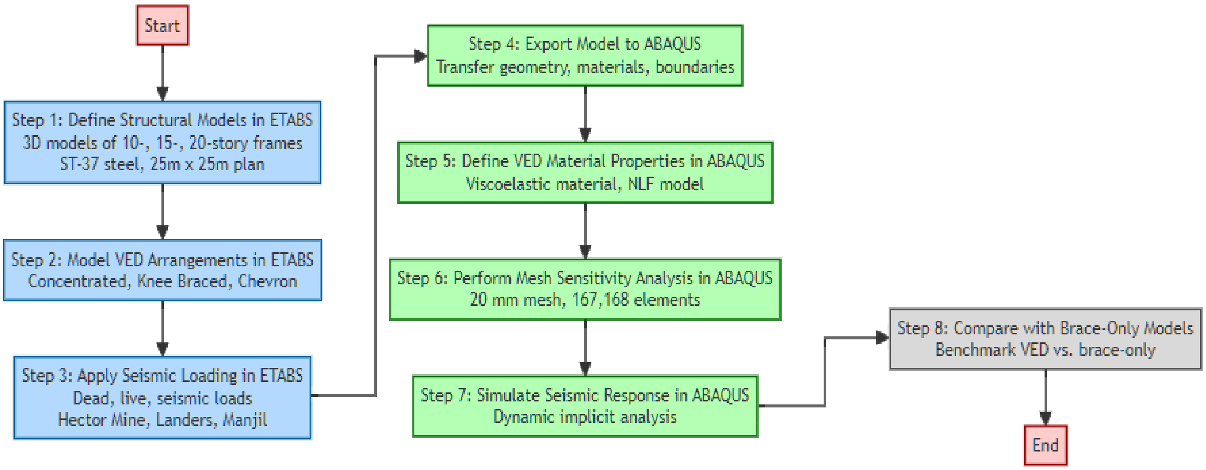

Fig. 1. Flowchart of the analysis workflow

3.1. Finite element analysis approach

The analysis leverages ETABS for initial structural modeling and ABAQUS for detailed FEA. ETABS, known for its robust capabilities in multi-story building design, was used to create three-dimensional models of steel frames, define material properties, and simulate VED arrangements (Concentrated, Knee Braced, and Chevron) under seismic loads (Fig. 2). Its intuitive interface enabled accurate prediction of story drifts, base shear, and roof displacements. ABAQUS complemented these findings by simulating the non-linear behavior of VED materials and their interactions with the steel frame, focusing on energy dissipation and structural stiffness. The synergy of both tools ensured a comprehensive analysis, with ETABS providing the overall structural framework and ABAQUS offering precise material-level insights.

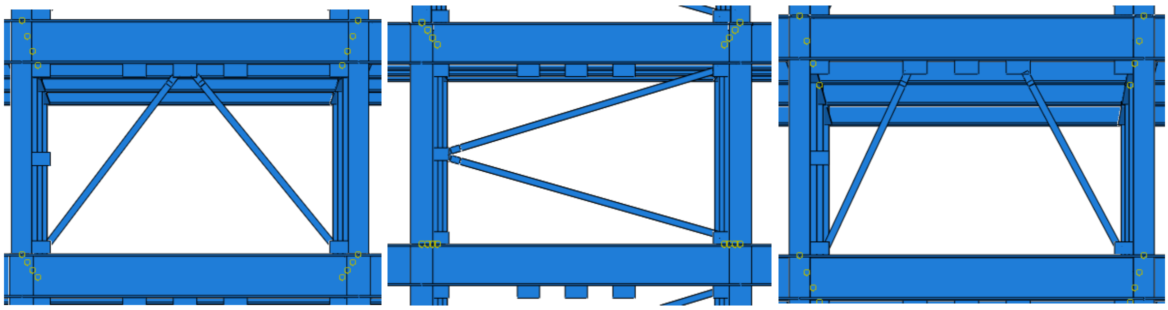

(a) (b) (c)

Fig. 2. VED arrangements (a) Concentrated (b) Knee Braced (c) Chevron

3.2. Structural models

The study examines steel frame buildings with 10, 15, and 20 stories, each with a uniform floor height of 3 meters and a 25 m x 25 m plan dimension, reflecting typical high-rise configurations. The frames are designed as special moment-resisting steel frames, constructed using ST-37 steel (considering nonlinearity of the material) with a yield strength (Fy) of 2400 kg/cm² and ultimate tensile strength (Fu) of 3600 kg/cm² (Rasmussen, 2003). Structural elements, including beams (IPE profiles) and columns (Box profiles), were sized based on seismic design requirements, as detailed in Table 1.

Table 1. Structural and seismic design properties of 10-, 15-, and 20-story steel frame models

Property	10-Story Model	15-Story Model	20-Story Model
Plan Dimensions	25 m x 25 m	25 m x 25 m	25 m x 25 m
Floor Height	3 m	3 m	3 m
Total Height	30 m	45 m	60 m
Steel Grade	ST-37 (Fy = 2400 kg/cm², Fu = 3600 kg/cm²)		
Beam Sections	IPE 65.40 (all floors)		
Column Sections	Stories 1–6: Box 300.25 Stories 7–8: Box 250.20 Story 9: Box 200.15 Story 10: Box 150.15	Stories 1–4: Box 350.25 Stories 5–10: Box 300.25 Stories 11–12: Box 250.20 Stories 13–14: Box 200.15 Story 15: Box 150.15	Stories 1–5: Box 450.35 Stories 6–8: Box 400.30 Stories 9–11: Box 350.25 Stories 12–16: Box 300.25 Stories 17–18: Box 250.20 Story 19: Box 200.15 Story 20: Box 150.15
Importance Factor (I)	1	1	1
Design Acceleration (A)	0.3	0.3	0.3
Soil Type	Type III	Type III	Type III
Seismic Coefficient	0.0802	0.064	0.054
Stiffness Coefficient (K)	1.2627	1.445	1.6123

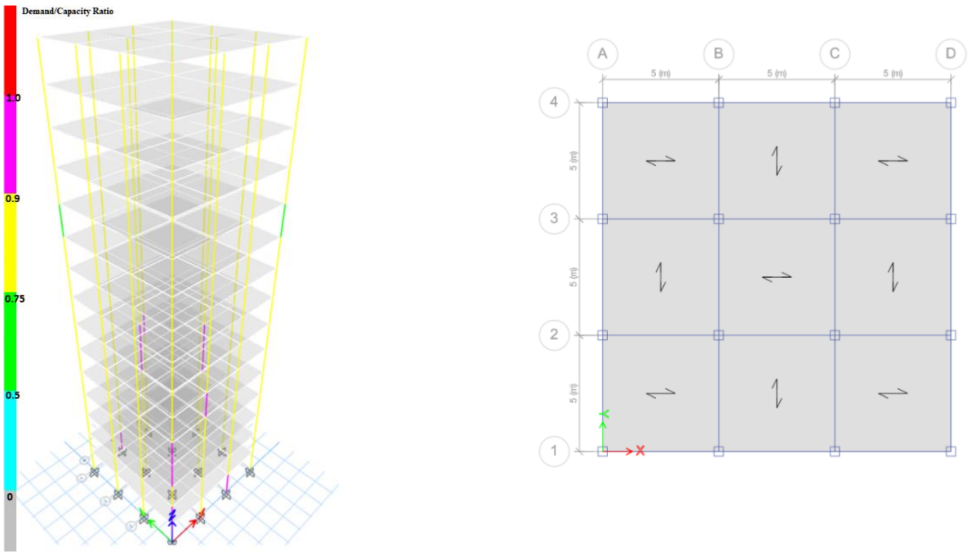

(a) (b)

Fig. 3. (a) 3D model of a 20-story steel frame in ETABS; (b) Plan layout of the 25 m x 25 m building footprint

3.3. Seismic loading conditions

Seismic loads were applied based on three earthquake records selected from the PEER database to represent realistic seismic hazards. These records, detailed in Table 2, were first scaled to match site configuration (Huang et al., 2008; Silwal et al., 2015). They vary in peak ground acceleration (PGA: 0.598–1.96 g), duration, and frequency content, capturing a range of seismic intensities. In ETABS, seismic design parameters included a base design acceleration (A) of 0.3, soil type III, and a structural importance factor (I) of 1. Load combinations followed Iranian seismic design codes and ASTM standards, incorporating dead loads (528 kg/m² for steel deck roofing), live loads (200 kg/m²), and earthquake loads (Table 2). In ABAQUS, seismic excitations were applied as time-history accelerations at the base, with fixed boundary conditions to simulate a rigid foundation.

Table 2. Selected earthquake records

EQ.	Station	Distance from Epicenter	5-75% Duration (sec)	5-95% Duration (sec)	PGA (g)
Hector Mine	Hector	10.35	7.6	11.7	0.77
Landers	Yermo	23.62	10.9	18.9	0.598
Manjil_ Iran	Abbar	12.55	10.8	29.1	1.96

3.4. Details of damper arrangements

Three VED arrangements were modeled: Concentrated, Knee Braced, and Chevron, each strategically placed to optimize seismic performance. The VEDs were composed of viscoelastic materials (Kim et al., 2010) with low temperature dependency, validated through dynamic testing (Xu et al., 2019). Material properties included a density of 2450 kg/m³, Young's modulus of 1000 MPa, and zero Poisson's ratio, ensuring no lateral deformation under stress (Table 3). The arrangements are described as follows:

Concentrated: VEDs are centralized within the frame, typically at high-stress zones, to maximize energy dissipation and stiffness.

Knee Braced: VEDs are placed at diagonal brace joints, enhancing damping while maintaining frame flexibility.

Chevron: VEDs are arranged in a V-shaped bracing pattern, providing balanced stiffness and energy dissipation.

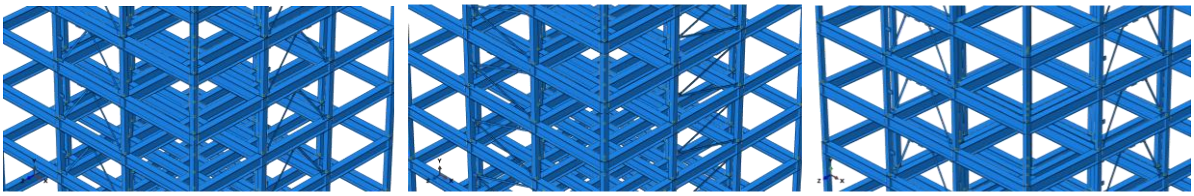

(a) (b) (c)

Fig. 4. VED arrangements (a) Concentrated (b) Knee Braced (c) Chevron

3.5. Sensitivity analysis and verification of the VEDs

In ABAQUS, VEDs were modeled using a non-linear four-element (NLF) mechanical model, comprising two non-linear dashpots and two non-linear springs, calibrated against experimental data. A 20 cm mesh size was chosen to balance accuracy and computational efficiency in the sensitivity analysis. With this mesh, the reaction force in the x direction (RF1) is 127 kN, which is a relatively high level of accuracy compared to larger mesh sizes (e.g., 40–50 cm) while maintaining acceptable computational time. Although finer meshes (e.g., 5–15 cm) can achieve even greater precision, they require significantly longer computational times; for example, refining the mesh from 20 cm to 15 cm only slightly increases RF1, but computation time grows from 1134 to 1225 minutes.

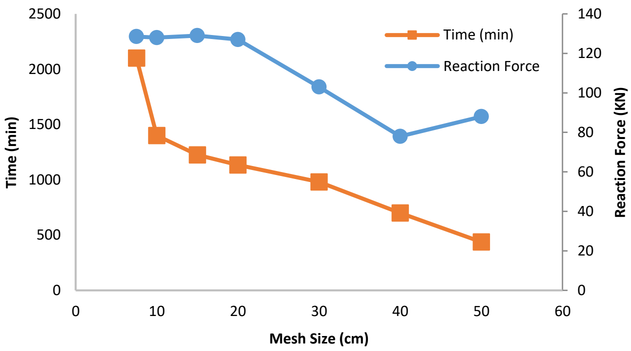

Fig. 5. Mesh sensitivity analysis based on time and reaction force

In the current study, the frame model consists of a three-dimensional geometry with a total of 328,388 nodes and 167,168 elements, meshed using second-order quadrilateral elements (C3D8R). These second-order elements more accurately capture the structure's response under loading compared to linear quadrilateral elements, as they can more effectively represent curvature and deformation. The base of the structure is assumed to be fixed.

To ensure the reliability of the VED model, the material properties and hysteretic behavior were validated against experimental data from a prior study (Xu et al., 2019). The validation process involved simulating a VED sample (70 mm x 80 mm, 5 mm thick, 5600 mm² shear area) in ABAQUS under cyclic sinusoidal loading at a frequency of 0.33 Hz. The loading was applied using a displacement-controlled scheme, with displacements varying sinusoidally between -20 mm and +20 mm. This produced a force-displacement curve representing the VED's response, which was compared to the reference results in (Xu et al., 2019).

Table 3. VED material properties

Parameter	Value
Density (kg/m³)	2450
Young's Modulus (MPa)	1000
Poisson's Ratio	0

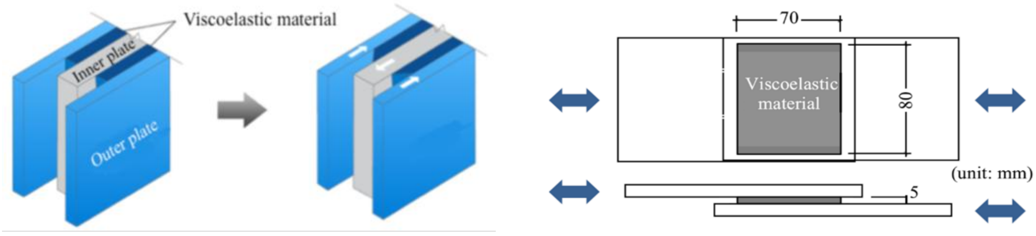

Fig. 6. Viscoelastic damper model from Xu et al. (2019)

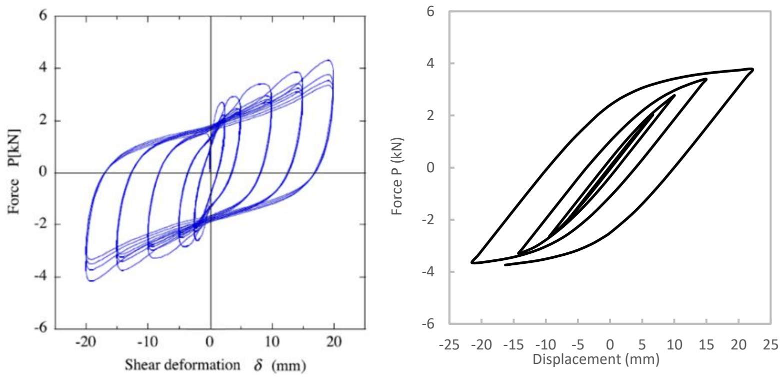

(a) (b)

Fig. 7. Comparison of force-displacement loops: (a) Xu et al. (2019), (b) Current study

The reference curve from (Xu et al., 2019) showed shear deformation (x-axis) from -20 mm to +20 mm and force (y-axis) from -4 kN to +4 kN, exhibiting complex hysteretic loops indicative of real-world behavior with multiple cycles. In contrast, the simulated curve in this study displayed a single, closed elliptical loop within the same displacement (-20 mm to +20 mm) and force (-4 kN to +4 kN) ranges, suggesting a more idealized or controlled response. This difference is attributed to the use of fewer mesh nodes in the current model to enhance computational efficiency, resulting in a simpler hysteretic loop compared to the more detailed, multi-cycle loops in (Xu et al., 2019). Despite this, the discrepancy between the simulated and reference curves was less than 10%, indicating strong agreement and validating the model's accuracy.

3.6. Comparison with brace-only structures

To quantify VED effectiveness, the study compares VED-equipped structures with brace-only structures (without VEDs) under identical seismic conditions. Brace-only models used standard steel bracing (e.g., ASTM A992) without viscoelastic components, designed to match the geometry and loading of VED models (ASTM, 2015). Key performance metrics—displacement, energy dissipation, base shear, and structural stiffness—were evaluated in both ETABS and ABAQUS to highlight the improvements offered by VEDs over conventional bracing. The analysis focused on the ability of VEDs to reduce lateral displacements and dissipate seismic energy, providing a benchmark for their seismic mitigation potential.

4. Results

This subsection evaluates the seismic performance of the Concentrated VED arrangement in 10-, 15-, and 20-story steel frame buildings, analyzed using FEA in ABAQUS.

4.1. Concentrated VEDs

4.1.1. Displacements

This subsection reports roof displacements, lateral displacements, and residual displacements for the 10-, 15-, and 20-story models equipped with Concentrated VEDs, derived from ABAQUS dynamic analyses, summarized in Table 4. Concentrated VEDs reduce displacements by dissipating energy at high-stress zones, minimizing structural sway.

- *Roof Displacements:* For the 10-story model, the average roof displacement without VEDs is 162.3 mm, reduced by 32% to 110.69 mm with Concentrated VEDs. In the 15-story model, the no-VED displacement of 240.2 mm decreases by 21% to 189.93 mm with VEDs. For the 20-story model, the no-VED displacement of 364.52 mm is reduced by 18% to 297.47 mm with VEDs.
- *Lateral Displacements:* For the 10-story model, the maximum drift without VEDs is 213.09 mm, reduced by 27% to 157.22 mm with Concentrated VEDs. In the 15-story model, the no-VED drift of 308.60 mm decreases by 26% to 227.85 mm with VEDs. For the 20-story model, the no-VED drift of 590.30 mm is reduced by 25% to 439.44 mm with VEDs.
- *Residual Displacements:* For the 10-story model, the average residual displacement without VEDs is 70.6 mm, reduced by 29% to 49.9 mm with Concentrated VEDs. In the 15-story model, the no-VED residual displacement of 108.0 mm decreases by 35% to 70.7 mm with VEDs. For the 20-story model, the no-VED residual displacement of 173.6 mm is reduced by 39% to 105.9 mm with VEDs.

Table 4. Roof, lateral, and residual displacements for the 10-, 15-, and 20-story models

Displacement (mm)	Property	10-Story Model	15-Story Model	20-Story Model
Roof	No VED	162.3	240.2	364.52
	Concentrated VED	110.69	189.93	297.47
	Reduction (%)	32	21	18
Lateral	No VED (Max Drift)	213.09	308.60	590.30
	Concentrated VED (Max Drift)	157.22	227.85	439.44
	Reduction (%)	27	26	25
Residual	No VED	70.6	108.0	173.6
	Concentrated VED	49.9	70.7	105.9
	Reduction (%)	29	35	39

4.1.2. Base shear

Base shear forces, calculated in ABAQUS, quantify the total lateral force resisted by the 10-, 15-, and 20-story steel frame models under seismic loading.

According to Table 5, for the 10-story model, the average base shear without VEDs is 56.9 MN, increased by 14% to 65.1 MN with Concentrated VEDs. In the 15-story model, the no-VED base shear of 83.6 MN increases by 23% to 102.8 MN with VEDs. For the 20-story model, the no-VED base shear of 135.3 MN increases by 18% to 159.2 MN with VEDs. Base shear increases with VEDs due to added stiffness, though this is offset by reduced displacements.

Table 5. Summary of average base shear (MN) for 10-, 15-, and 20-story steel frame models

Property	10-Story Model	15-Story Model	20-Story Model
No VED	56.9	83.6	135.3
Concentrated VED	65.1	102.8	159.2
Difference (%)	+14	+23	+18

4.1.3. Energy dissipation

According to Table 6, for the 10-story model, the average energy dissipation without VEDs is 341.2 kN·m, increased by 42% to 483.5 kN·m with Concentrated VEDs. In the 15-story model, the no-VED energy dissipation of 484.5 kN·m rises by 46% to 708.2 kN·m with VEDs. For the 20-story model, the no-VED energy dissipation of 774.5 kN·m increases by 42% to 1100.2 kN·m with VEDs.

Table 6. Summary of average energy dissipation (kN·m) for 10-, 15-, and 20-story steel frame models

Property	10-Story Model	15-Story Model	20-Story Model
No VED	341.2	484.5	774.5
Concentrated VED	483.5	708.2	1100.2
Difference (%)	+42	+46	+42

4.1.4. Story stiffness

According to Table 7, for the 10-story model, the average story stiffness without VEDs is 468 kN/m, increased by 30% to 609 kN/m with Concentrated VEDs. In the 15-story model, the no-VED stiffness of 688 kN/m rises by 24% to 850 kN/m with VEDs. For the 20-story model, the no-VED stiffness of 1034 kN/m increases by 36% to 1407 kN/m with VEDs.

Table 7. Summary of average story stiffness (kN/m) for 10-, 15-, and 20-story steel frame models

Property	10-Story Model	15-Story Model	20-Story Model
No VED	468	688	1034
Concentrated VED	609	850	1407
Difference (%)	+30	+24	+36

4.2. Knee braced VED arrangement

4.2.1. Displacements

This subsection reports roof displacements, lateral displacements, and residual displacements for the 10-, 15-, and 20-story models equipped with Knee Braced VEDs, derived from ABAQUS dynamic analyses.

- *Roof Displacements:* For the 10-story model, the average roof displacement without VEDs is 162.3 mm, reduced by 36% to 104.7 mm with Knee Braced VEDs. In the 15-story model, the no-VED displacement of 240.2 mm decreases by 15% to 204.3 mm with VEDs. For the 20-story model, the no-VED displacement of 364.5 mm is reduced by 24% to 276.4 mm with VEDs.
- *Lateral Displacements:* For the 10-story model, the maximum inter-story drift without VEDs is 94.90 mm, reduced by 13% to 82.16 mm with Knee Braced VEDs. In the 15-story model, the no-VED drift of 113.88 mm decreases by 28% to 81.46 mm with VEDs. For the 20-story model, the no-VED drift of 134.76 mm is reduced by 17% to 111.60 mm with VEDs.
- *Residual Displacements:* For the 10-story model, the average residual displacement without VEDs is 70.6 mm, reduced by 25% to 52.8 mm with Knee Braced VEDs. In the 15-story model, the no-VED residual displacement of 108.0 mm decreases by 37% to 67.5 mm with VEDs. For the 20-story model, the no-VED residual displacement of 173.6 mm is reduced by 34% to 114.8 mm with VEDs.

Table 8. Roof, lateral, and residual displacements for the 10-, 15-, and 20-story models

Displacement (mm)	Property	10-Story Model	15-Story Model	20-Story Model
Roof	No VED	162.3	240.2	364.5
	Knee Braced VED	104.7	204.3	276.4
	Reduction (%)	36	15	24
Lateral	No VED (Max Drift)	94.90	113.88	134.76
	Knee Braced VED (Max Drift)	82.16	81.46	111.60
	Reduction (%)	13	28	17
Residual	No VED	70.6	108.0	173.6
	Knee Braced VED	52.8	67.5	114.8
	Reduction (%)	25	37	34

4.2.2. Base shear

According to Table 9, for the 10-story model, the average base shear without VEDs is 56.9 MN, increased by 17% to 66.3 MN with Knee Braced VEDs. In the 15-story model, the no-VED base shear of 83.6 MN increases by 17% to 97.5 MN with VEDs. For the 20-story model, the no-VED base shear of 144.4 MN increases by 12% to 162.2 MN with VEDs.

Table 9. Summary of average base shear (MN) for 10-, 15-, and 20-story steel frame models

Property	10-Story Model	15-Story Model	20-Story Model
No VED	56.9	83.6	144.4
Knee Braced VED	66.3	97.5	162.2
Difference (%)	+17	+17	+12

4.2.3. Energy dissipation

According to Table 10, for the 10-story model, the average energy dissipation without VEDs is 341 kN·m, increased by 40% to 480 kN·m with Knee Braced VEDs. In the 15-story model, the no-VED energy dissipation of 485 kN·m rises by 34% to 647 kN·m with VEDs. For the 20-story model, the no-VED energy dissipation of 775 kN·m increases by 54% to 1193 kN·m with VEDs.

Table 10. Summary of average energy dissipation (kN·m) for 10-, 15-, and 20-story steel frame models

Property	10-Story Model	15-Story Model	20-Story Model
No VED	341	485	775
Knee Braced VED	480	647	1193
Increase (%)	40	34	54

4.2.4. Story stiffness

According to Table 11, for the 10-story model, the average story stiffness without VEDs is 468 kN/m, increased by 41% to 661 kN/m with Knee Braced VEDs. In the 15-story model, the no-VED stiffness of 688 kN/m rises by 26% to 866 kN/m with VEDs. For the 20-story model, the no-VED stiffness of 1034 kN/m increases by 37% to 1420 kN/m with VEDs.

Table 11. Summary of average story stiffness (kN/m) for 10-, 15-, and 20-story steel frame models

Property	10-Story Model	15-Story Model	20-Story Model
No VED	468	688	1034
Knee Braced VED	661	866	1420
Increase (%)	41	26	37

4.3. Chevron VED arrangement

This subsection evaluates the seismic performance of the Chevron VED arrangement in 10-, 15-, and 20-story steel frame buildings, analyzed using finite element analysis in ABAQUS.

4.3.1. Displacements

This subsection reports roof displacements, lateral displacements, and residual displacements for the 10-, 15-, and 20-story models equipped with Chevron VEDs, derived from ABAQUS dynamic analyses. Chevron VEDs excel in lateral drift reduction due to their V-shaped bracing, distributing forces evenly.

- *Roof Displacements:* For the 10-story model, the average roof displacement without VEDs is 162.3 mm, reduced by 38% to 100.6 mm with Chevron VEDs. In the 15-story model, the no-VED displacement of 240.2 mm decreases by 25% to 179.2 mm with VEDs. For the 20-story model, the no-VED displacement of 364.5 mm is reduced by 28% to 263.3 mm with VEDs.
- *Lateral Displacements:* For the 10-story model, the maximum inter-story drift without VEDs is 188.80 mm, reduced by 38% to 117.06 mm with Chevron VEDs. In the 15-story model, the no-VED drift of 279.42 mm decreases by 30% to 196.35 mm with VEDs. For the 20-story model, the no-VED drift of 554.85 mm is reduced by 41% to 326.96 mm with VEDs .
- *Residual Displacements:* For the 10-story model, the average residual displacement without VEDs is 70.6 mm, reduced by 32% to 48.0 mm with Chevron VEDs. In the 15-story model, the no-VED residual displacement of 108.0 mm decreases by 41% to 63.7 mm with VEDs. For the 20-story model, the no-VED residual displacement of 173.6 mm is reduced by 43% to 99.0 mm with VEDs.

Table 12. Roof, lateral, and residual displacements for the 10-, 15-, and 20-story models

Displacement (mm)	Property	10-Story Model	15-Story Model	20-Story Model
Roof	No VED	162.3	240.2	364.5
	Chevron VED	100.6	179.2	263.3
	Reduction (%)	38	25	28
Lateral	No VED (Max Drift)	188.80	279.42	554.85
	Chevron VED (Max Drift)	117.06	196.35	326.96
	Reduction (%)	38	30	41
Residual	No VED	70.6	108.0	173.6
	Chevron VED	48.0	63.7	99.0
	Reduction (%)	32	41	43

4.3.2. Base shear

According to Table 13, for the 10-story model, the average base shear without VEDs is 56.9 MN, increased by 6% to 60.3 MN with Chevron VEDs. In the 15-story model, the no-VED base shear of 83.6 MN increases by 6% to 88.6 MN with VEDs. For the 20-story model, the no-VED base shear of 129.2 MN increases by 5% to 136.2 MN with VEDs.

Table 13. Summary of average base shear (MN) for 10-, 15-, and 20-story steel frame models

Property	10-Story Model	15-Story Model	20-Story Model
No VED	56.9	83.6	129.2
Chevron VED	60.3	88.6	136.2
Difference (%)	+6	+6	+5

4.3.3. Energy dissipation

According to Table 14, for the 10-story model, the average energy dissipation without VEDs is 341.2 kN·m, increased by 30% to 443.6 kN·m with Chevron VEDs. In the 15-story model, the no-VED energy dissipation of 484.5 kN·m rises by 26% to 610.5 kN·m with VEDs. For the 20-story model, the no-VED energy dissipation of 774.5 kN·m increases by 34% to 1038.0 kN·m with VEDs.

Table 14. Summary of average energy dissipation (kN·m) for 10-, 15-, and 20-story steel frame models

Property	10-Story Model	15-Story Model	20-Story Model
No VED	341.2	484.5	774.5
Chevron VED	443.6	610.5	1038.0
Increase (%)	30	26	34

4.3.4. Story stiffness

According to Table 15, for the 10-story model, the average story stiffness without VEDs is 468 kN/m, increased by 24% to 580 kN/m with Chevron VEDs. In the 15-story model, the no-VED stiffness of 688 kN/m rises by 20% to 825 kN/m with VEDs. For the 20-story model, the no-VED stiffness of 1034 kN/m increases by 30% to 1334 kN/m with VEDs.

Table 15. Summary of average story stiffness (kN/m) for 10-, 15-, and 20-story steel frame models

Property	10-Story Model	15-Story Model	20-Story Model
No VED	468	688	1034
Chevron VED	580	825	1334
Increase (%)	24	20	30

5. Discussion

5.1. Summary and interpretation of results

The superior performance of the Concentrated VED arrangement stems from its strategic placement in high-stress zones, which maximizes energy dissipation and structural stiffness. By centralizing dampers, this configuration ensures uniform distribution of damping forces across the structure, effectively mitigating localized deformations and enhancing global stability. Results demonstrated that Concentrated VEDs reduced roof displacements by up to 32% in 10-story buildings and increased energy dissipation by 42–46% across all models. These improvements are attributed to the configuration's ability to absorb seismic energy efficiently through concentrated damping pathways, thereby reducing inter-story drifts and residual displacements. While Chevron arrangements excel in specific metrics (e.g., 41% lateral drift reduction in 20-story models), Concentrated VEDs provide superior overall performance.

The Fig. 8 reveals that the No-VED case consistently exhibits the highest roof displacements (162.3 mm, 240.2 mm, and 364.5 mm for 10, 15, and 20 stories, respectively). Among VED arrangements, Chevron VEDs achieve the lowest displacements (100.6 mm, 179.2 mm, 263.3 mm), followed by Knee Braced and Concentrated VEDs. The reductions are most pronounced in the 10-story model (up to 38% for Chevron) and decrease with height, with Chevron still leading at 28% reduction for the 20-story model. The figure highlights the superior performance of VEDs, particularly Chevron, in mitigating seismic-induced roof displacements across varying building heights.

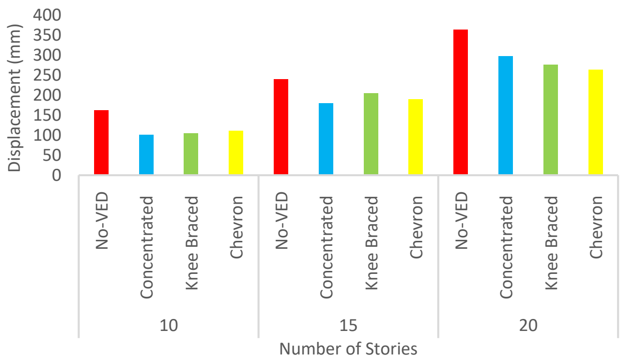

Fig. 8. Roof displacement vs. story height for all VED arrangements and no-VED case

5.2. Practical implications

The findings advocate for prioritizing Concentrated VED arrangements in seismic design codes and retrofitting strategies for multi-story steel frames. Engineers can leverage this configuration to enhance structural resilience without significant modifications to existing geometries, as evidenced by its compatibility with ETABS and ABAQUS modeling workflows. The study's comparative analysis provides actionable insights: for instance, 15- and 20-story buildings benefit most from Concentrated VEDs due to their higher stiffness gains (24–36%) and energy dissipation capacity, while Knee Braced systems may suit structures requiring moderate flexibility. Practitioners should also consider soil-structure interaction and site-specific seismic hazards when selecting damper configurations, though the methodology validated here offers a reliable framework for initial assessments.

5.3. Economic and safety benefits

Adopting Concentrated VED arrangements translates to substantial cost savings by minimizing post-earthquake repair needs. The 29–39% reduction in residual displacements across models suggests less structural and non-structural damage, reducing downtime and reconstruction costs. Enhanced stiffness and energy dissipation further ensure buildings remain operational post-event, safeguarding occupants and critical infrastructure. While initial investments in VEDs are required, their long-term benefits—such as avoided business interruptions and extended service life—outweigh upfront costs. Additionally, the compact design of VEDs aligns with sustainable construction practices, as retrofitting existing structures with these dampers reduces material waste compared to traditional reinforcement methods.

6. Conclusion

6.1. Summary of key findings

This study conclusively demonstrates that Concentrated VED arrangements significantly enhance the seismic resilience of multi-story steel frames. Across 10-, 15-, and 20-story models, this configuration reduced roof displacements by 18–32%, increased energy dissipation by 42–46%, and improved stiffness by 24–36%, outperforming Knee Braced and Chevron systems in overall efficacy. The results underscore the importance of damper placement in optimizing energy absorption and structural integrity under seismic loads.

6.2. Recommendations

Engineers should integrate Concentrated VEDs into seismic designs for high-rise buildings in earthquake-prone regions, particularly for structures exceeding 10 stories. Future research should explore hybrid damping systems combining VEDs with friction or tuned mass dampers, as well as the impact of variable damper densities and material compositions. Additionally, extending this methodology to composite structures or varying soil types could broaden applicability.

6.3. Final Thoughts

Viscoelastic dampers represent a paradigm shift in seismic design, offering a balance of performance, cost-efficiency, and adaptability. As urbanization intensifies in seismic zones, adopting advanced damping technologies like Concentrated VEDs is critical to ensuring sustainable and resilient infrastructure. This study contributes a validated framework for advancing building codes and fostering safer, more durable urban environments.

References

Abramovich, H. (2021). *Intelligent materials and structures*. Walter de Gruyter GmbH & Co KG.

Alhasan, A.A., Vafaei, M., & C Alih, S. (2022). Viscoelastic dampers for protection of structures against seismic actions. *Innovative Infrastructure Solutions*, *7*(5), 309

ASTM. (2015). Standard specification for structural steel shapes.
Center, A.D.R. (2015). Sendai framework for disaster risk reduction 2015–2030. *United Nations Office for Disaster Risk Reduction: Geneva, Switzerland*.
Cetin, H., Aydin, E., & Ozturk, B. (2019). Optimal design and distribution of viscous dampers for shear building structures under seismic excitations. *Frontiers in Built Environment*, *5*, 90
Chen, L., Sun, L., Xu, Y., Di, F., Xu, Y., & Wang, L. (2020). A comparative study of multi-mode cable vibration control using viscous and viscoelastic dampers through field tests on the Sutong Bridge. *Engineering Structures*, *224*, 111226
Clough, R., & Penzien, J. (1993), Dynamics of Structures. McGraw Hill, New York.
Hao, L., Liu, M., Li, J., Tan, P., & Wu, D. (2024). Multi-performance oriented seismic design of viscoelastic dampers for structural retrofitting. *Journal of Building Engineering*, 108657
Hecker, G. (1995). A Review of the Disaster-Related Activities of the Asian Development Bank: An Economic Perspective. *Disaster Prevention for Sustainable Development: Economic and Policy Issues. Washington, DC: World Bank*, 77-85
Huang, Y.-N., Whittaker, A., & Luco, N. (2008). *Seismic performance assessment of nuclear power plants*
Kaleybar, R.S., & Tehrani, P. (2021). Effects of using different arrangements and types of viscous dampers on seismic performance of intermediate steel moment frames in comparison with different passive dampers. *Structures, 33*, 3382-3396
Kim, D.-H., Kim, H.-J., & Lee, B.-J. (2010). Olefinic Thermoplastic Elastomer and Styrenic Thermoplastic Elastomer. *Elastomers and Composites*, *45*(3), 152-155
Marko, J., Thambiratnam, D., & Perera, N. (2006). Study of viscoelastic and friction damper configurations in the seismic mitigation of medium-rise structures. *Journal of Mechanics of Materials and Structures*, *1*(6), 1001-1039
Matsagar, V.A., & Jangid, R.S. (2005). Viscoelastic damper connected to adjacent structures involving seismic isolation. *Journal of civil engineering and management*, *11*(4), 309-322
Mehrabi, M., Suhatril, M., Ibrahim, Z., Ghodsi, S., & Khatibi, H. (2017). Modeling of a viscoelastic damper and its application in structural control. *PloS one*, *12*(6), e0176480
Mortezaei, A., & Zahrai, S.M. (2009). Seismic response of reinforced concrete building with viscoelastic damper under near field earthquake
Rasmussen, K.J. (2003). Full-range stress–strain curves for stainless steel alloys. *Journal of Constructional Steel Research*, *59*(1), 47-61
Silwal, B., Michael, R.J., & Ozbulut, O.E. (2015). A superelastic viscous damper for enhanced seismic performance of steel moment frames. *Engineering Structures*, *105*, 152-164. https://doi.org/https://doi.org/10.1016/j.engstruct.2015.10.005
Solberg, C., Joffe, H., & Rossetto, T. (2009). The social psychology of seismic hazard adjustment. *Submission to Nat Hazard Earth Sys*
Soong, T.T., & Dargush, G.F. (1997). Passive energy dissipation systems in structural engineering. *(No Title)*.
Soto, M.G., & Adeli, H. (2013). Placement of control devices for passive, semi-active, and active vibration control of structures. *Scientia Iranica*, *20*(6), 1567-1578
Stein, S., & Wysession, M. (2009). *An introduction to seismology, earthquakes, and earth structure*. John Wiley & Sons.
Symans, M., Charney, F., Whittaker, A., Constantinou, M., Kircher, C., Johnson, M., & McNamara, R. (2008). Energy dissipation systems for seismic applications: current practice and recent developments. *Journal of Structural Engineering*, *134*(1), 3-21
Systèmes, D. (2016). Abaqus Analysis User's Guide Volume IV: Elements. *Dassault Systèmes Simulia Corp.: Providence, RI, USA*.
Vaiana, N., Sessa, S., Marmo, F., & Rosati, L. (2019). Nonlinear dynamic analysis of hysteretic mechanical systems by combining a novel rate-independent model and an explicit time integration method. *Nonlinear Dynamics*, *98*, 2879-2901
Wang, S.-J., Chiu, I.-C., Yu, C.-H., & Chang, K.-C. (2018). Experimental and analytical study on design performance of full-scale viscoelastic dampers. *Earthquake Engineering and Engineering Vibration*, *17*(4), 693-706
Xu, Y., Dong, Y., Huang, X., Luo, Y., & Zhao, S. (2019). Properties tests and mathematical modeling of viscoelastic damper at low temperature with fractional order derivative. *Frontiers in Materials*, *6*, 194
Zhang, R.-H., & Soong, T.T. (1992). Seismic design of viscoelastic dampers for structural applications. *Journal of Structural Engineering*, *118*(5), 1375-1392

4th International Civil Engineering & Architecture Conference
17-19 May 2025, Trabzon, Türkiye

Flexural performance of glass fibre textile reinforced 3D printed concrete

Yeşim Tarhan*[1], İsmail H. Tarhan[2], Arnaud Perrot[3]

[1] Ardahan University, Technical Sciences Vocational School, 75000, Ardahan, Türkiye,
[2] Tokat Gaziosmanpaşa University, Faculty of Engineering and Architecture, Department of Civil Engineering, 60150, Tokat, Türkiye
[3] Univ. Bretagne Sud, FRE CNRS 3744, IRDL, F-56100 Lorient, France

Abstract. 3D printing construction technology facilitates the realization of complex geometries through rapid production and design freedom; however, challenges in integrating conventional steel reinforcement within the additive manufacturing process impose significant structural limitations on the reinforcement of 3D-printed concrete structures. This study proposes glass fibre-reinforced textile as a solution to these limitations of 3D printed concrete. Glass fibre-reinforced textile stands out as a reinforcement material suitable for additive manufacturing with its lightweight structure, high tensile strength, and flexibility. A 3D printable mixture was specifically designed to achieve optimal rheological properties and printability. Then, using a Delta WASP 3DMT concrete printer, beam-shaped samples consisting of six layers were produced; glass fibre-reinforced textiles were placed on horizontal interfaces. The reinforced and unreinforced specimens were subjected to flexural and compressive strength tests after a 28-day curing period. Experimental results showed that glass fiber textiles significantly enhanced flexural strength and ductility. While the compressive strength of the textile-reinforced specimens remained largely unchanged compared to the control, their flexural strength improved remarkably, increasing by more than 50%. The study's findings reveal that 3D printed concretes reinforced with glass textiles enable the creation of more reliable structures with increased strength and ductility; thus, 3D printing technology may have a wider application area in the construction industry.

Keywords: Additive manufacturing; 3D printable concrete; Textile reinforcement; Glass fiber textile

1. Introduction

3D printing technology has revolutionized the construction industry by offering innovative solutions to traditional building methods. The ability to create complex geometries directly from digital designs has opened up new possibilities for architectural creativity and structural efficiency (Tahmasebinia et al., 2018; Tarhan et al., 2024; Žujović et al., 2022). One of the most significant advantages of 3D printing in construction is the reduction of material waste (Mohamed & Mohamed, 2025). Among the various additive manufacturing techniques, extrusion-based 3D printing of cementitious materials has attracted considerable attention for its potential to revolutionise conventional building practices (M. Khan & McNally, 2024). Nevertheless, a significant challenge that restricts the structural applications of 3D-printed concrete is the complexity of integrating traditional steel reinforcement within the layer-by-layer fabrication process (Liu et al., 2023; Nan et al., 2025; Tarhan et al., 2025).

The absence of effective reinforcement solutions frequently results in diminished mechanical performance, particularly in the context of tensile and flexural stresses. This complicates the extensive use of 3D printing technology in the field of load-bearing structural elements (Arunprasand & Nallasamy, 2024; T. Khan et al., 2024). In concrete structures, it is essential to utilise reinforcement due to inherent limitations in tensile capacity and ductility of cement-based materials. To address these constraints, various reinforcement methods have been investigated, with textile reinforcement standing out as a promising solution (Abtew, 2024; Ramesh, Rajeev, Sanjayan, et al., 2024). The integration of textile reinforcement in 3D printing concrete addresses one of the major challenges in manufacturing structural components, offering high formability, tensile strength, and non-corrosive properties (Ramesh, Rajeev, & Sanjayan, 2024; Ramesh, Rajeev, Sanjayan, et al., 2024). Research has demonstrated that incorporating textile reinforcement into 3D printed components enhances interlayer bonding, thereby mitigating crack propagation and improving load-bearing capacity, particularly in curved members.

* Corresponding author, E-mail: yesimtarhan@ardahan.edu.tr

https://doi.org/10.31462/icearc2025_ce_mat_941

Specifically, an increase of approximately 10% in peak load-bearing capacity was observed in textile-reinforced 3D-printed specimens compared to mould-cast counterparts (Ramesh, Rajeev, Sanjayan, et al., 2024).

Glass fiber textiles have shown promise for integration into 3D-printed concrete, offering several advantageous properties. Their high tensile strength and corrosion resistance make them suitable reinforcements for concrete structures (Spelter et al., 2019). Glass fibre-reinforced polymer composites are durable materials that are particularly resistant to chemical attack. This makes them a strong contender as a replacement for traditional steel reinforcements in construction applications (X. Yao et al., 2021). Their compatibility with extrusion-based processes and ability to be embedded between printed layers make them suitable candidates for enhancing the structural integrity of 3D-printed components.

This study aims to assess the efficacy of glass fibre textile reinforcement in enhancing the flexural and compressive performance of 3D-printed cement-based concrete. A specially designed printable mixture was developed, and beam specimens were produced reinforced with glass fibre textile. The mechanical performance of reinforced and unreinforced specimens was evaluated through flexural and compressive strength tests, providing insights into the potential of textile-reinforced 3D-printed concretes for broader structural applications.

2. Materials and methods

The cement-based mix was created with CEM I 42.5 R ordinary Portland cement as the primary binder, supplemented with ground granulated blast furnace slag (GGBS) to improve rheological and mechanical properties, and metakaolin clay to enhance 3D printability and dimensional stability. The aggregates used were silica sand with particle sizes of 0-0.5 mm (density: 2.63 g/cm³) and 0.5-2 mm (density: 2.72 g/cm³). A maximum particle size of 2 mm was chosen to achieve improved mechanical performance.

A superplasticiser (CHRYSO Fluid Optima 206) and hydroxypropyl methylcellulose (HPMC, WALOCEL MKS 10000 PF 60) were incorporated to ensure adequate flowability and rheological properties suitable for 3D printing.

The binder content was fixed at 500 kg/m³. GGBS replaced 20% of the cement content, while metakaolin clay was added at a dosage of 5%. The water to binder (w/b) ratio was set at 0.40, with the superplasticiser dosage corresponding to 1.5% of the binder mass and HPMC constituting 0.3% of the water mass. The aggregate composition was 40% fine (0-0.5 mm) and 60% coarse (0.5-2 mm).

CATNIC TFV 44 glass fibre fabric was selected for reinforcing, which is alkali resistant and designed for mechanical reinforcement. The fabric was soaked in a cement-water slurry to improve adhesion and manually applied at horizontal interfaces during printing. Beam samples measuring 110 mm × 110 mm × 350 mm were printed. After fabrication, the samples were cured in a laboratory environment (20 ± 2°C and 50% RH) for 24 hours and then stored in a curing chamber at 20 ± 2°C and 80% RH for 28 days before testing.

The preparation of the cement-based mix involved an initial slow mixing of all dry components (cement, aggregates, GGBS, metakaolin clay, and methylcellulose) for one minute. Half of the mixing water was then added, followed by another one-minute slow mixing phase. The remaining half of the water, pre-mixed with the superplasticiser, was then added. After a further minute of mixing, the mixture was left to stand for one minute and then mixed at high speed for two minutes, giving a total mixing time of approximately six minutes. Continuous mixing was maintained throughout the production phase to minimise false-set effects and maintain workability.

Penetration depth measurements were carried out to assess the fresh state properties of the compound. Although the results indicated acceptable printability, penetration depth alone was not considered to be fully indicative of printability performance. Therefore, actual extrusion trials were carried out using the 3D printer to finalise the mix selection. The material was then poured into 4×4×16 cm moulds. After an initial curing period of one day under laboratory conditions, the specimens were transferred to a curing room maintained at 20 ± 2°C and 80% relative humidity for 3, 7, 14, and 28 days to assess the evolution of their mechanical properties.

All specimens were produced using a Delta WASP 3DMT concrete printer with a nozzle diameter of 10 mm and a layer height of approximately 10 mm. The print speed was maintained at 2 cm/s to ensure dimensional stability and sufficient interlayer adhesion during extrusion. The produced specimens are illustrated in Fig. 1. The CN specimen represents the unreinforced cement-based sample, while the C3G specimen corresponds to the sample reinforced with a glass fibre textile positioned at the third layer.

Fig. 1. Views of the 3D-printed cement-based specimens with and without textile reinforcement

2.1. Experimental program

An extensive experimental programme was conducted to evaluate the flexural performance of 3D-printed concrete reinforced with glass fibre textiles. The programme encompassed the development of a printable cement-based mixture, fabrication of beam specimens via extrusion-based 3D printing, strategic placement of textile reinforcement, and subsequent mechanical testing after curing.

Initially, the fresh properties of the cement-based mixture were assessed. Unit weight measurements were performed following the TS EN 12350-6, 2019 standard, while rheological characterization was carried out using a rotational rheometer (RheolabQC SN80518563, Anton Paar). A constant shear rate of 0.05 s^{-1} was applied for 200 seconds, enabling yield stress determination from the torque peak at flow onset. A vane geometry comprising four blades around a cylindrical shaft with a diameter and length of 1.8 cm was employed. Due to the time-dependent behaviour of cement-based mortars, yield stress values were recorded immediately after mixing, with variations observed over time.

In addition, the thixotropic behaviour of the cement-based mortar was evaluated using the fall cone test method based on the CEN ISO 17892-6, 2017 standard. This test measures the depth of penetration of a cone under a specified load, providing an insight into the evolution of the shear resistance of the material (Baz et al., 2022). As the cone penetrates deeper, the shear resistance increases until an equilibrium is reached between the applied load and the resisting forces. In this study, a cone with an angle of 30° and a weight of 80 g was used. The fresh mortar was placed in a circular steel container with a depth of 4.5 cm and a diameter of 7 cm. The test set-ups for both the rheological and penetration tests are shown in Fig. 2.

a b c

Fig. 2. a) Production of samples, b) vane shear test, c) fall cone test

Specimens measuring 4×4×16 cm were made to evaluate the hardened properties. These specimens were first subjected to three-point flexure tests, and the fractured segments were then used for compressive strength tests.

Flexural strength tests were performed on the 3D printed specimens with approximate dimensions of 110×110×350 mm, following TS EN 12390-5, 2019. Where possible, compressive strength tests were carried out on the remaining sections after flexural failure in accordance with TS EN 12390-3, 2019. However, for cement-based mortars reinforced with textile materials, the change in load transfer caused by the reinforcement made it difficult to obtain suitable compressive specimens after flexural testing. Therefore, equivalent specimens were produced separately by cutting and prepared specifically for compressive strength evaluation.

3. Results and discussion

3.1. Fresh properties results

Table 1 summarises the evolution of unit weight, penetration depth, and mixing torque for the cement-based, 3D-printable mortar over the first hour after batching. Penetration depth falls almost linearly during the first 15 min - from 19.74 mm to 8.52 mm - reflecting the rapid thixotropic build-up that is typical for printable mortars with low water–binder ratios. At the same time, torque more than quadruples (9.4 → 48.6 mNm), signalling an increase in static yield stress as flocculated particle networks strengthen. A brief, low-shear re-mix at 25 min restores penetration depth to 17.32 mm (≈90 % of the initial value) while cutting torque is almost in half (48.6 → 29.8 mNm). This confirms that the mortar exhibits a reversible thixotropic character: network bonds rupture under shear and rebuild during rest. However, the benefit decays quickly; within 20 min, the penetration depth again drops below 10 mm, and the torque climbs above 40 mNm. A second re-mix at 60 min partially recovers flowability (16.13 mm), yet torque remains high (59.6 mNm), indicating that hydration-induced structuration has started to dominate over purely physical flocculation. Combining the penetration-depth criterion adopted by Tay et al. (2017) (≥15 mm for reliable extrusion) with a torque ceiling of ≈50 mNm (to avoid excessive extrusion pressure), the data suggest a practical printing window of roughly 0–35 min from first contact between water and binder, provided a single re-mix is applied at ~25 min. Beyond 45 min, neither penetration depth (<7.5 mm) nor torque (>60 mNm) meets the commonly accepted limits, so continuous printing without an interlayer cold-joint penalty would be challenging.

Table 1. Fresh properties of cement-based mortar

Time	UnitWeight (g/cm^3)	Penetration Depth (mm)	Torque (mNm)
Beginning	2.15	19.74	9.4
10 min later		14.35	28.1
15 min later		8.52	48,6
Second Mixing (25 min later		17.32	29.8
35 min later		10.08	41.2
45 min later		7.34	59.6
55 min later		4.31	66.9
Third mixing (60 min later)		16.13	59.6

3.2. Hardened properties results

Table 2 presents the flexural and compressive strengths of 4 × 4 × 16 cm prisms cast from the cement-based mix. Compressive strength rises from 10.96 MPa on Day 1 to 19.36 MPa on Day 3 and 53.75 MPa on Day 14—a more-than-fivefold increase in two weeks. This rapid hardening, typical of low water-to-binder printable mortars with highly reactive fillers, shows that the mix can already support several subsequent layers only hours after extrusion. By Day 28, the compressive strength reaches 62.9 MPa, placing the mortar in TS EN 206+A2, 2021 strength class C50/60 and qualifying it as a high-performance printable mix. Flexural strength levels off after two weeks at about 8.5 MPa, matching values reported for engineered 3D-printable mortars (Le et al., 2012) and providing adequate resistance to bending in printed elements.

Table 2. Mechanical characterisations of cement-based mortar

Curing Day	Flexural Strength (MPa)	Compressive Strength (MPa)
1	3.93	10.96
3	4.93	19.36
14	8.50	53.75
28	8.70	62.89

The flexural and compressive strengths of the reinforced and unreinforced specimens produced by 3D printing of the cement-based mix, whose characteristic properties were determined, are shown in Figs. 3 and 4. Incorporating glass fibre textile improved these specimens' structural integrity and deformation capacity, as can be seen in Fig. 5.

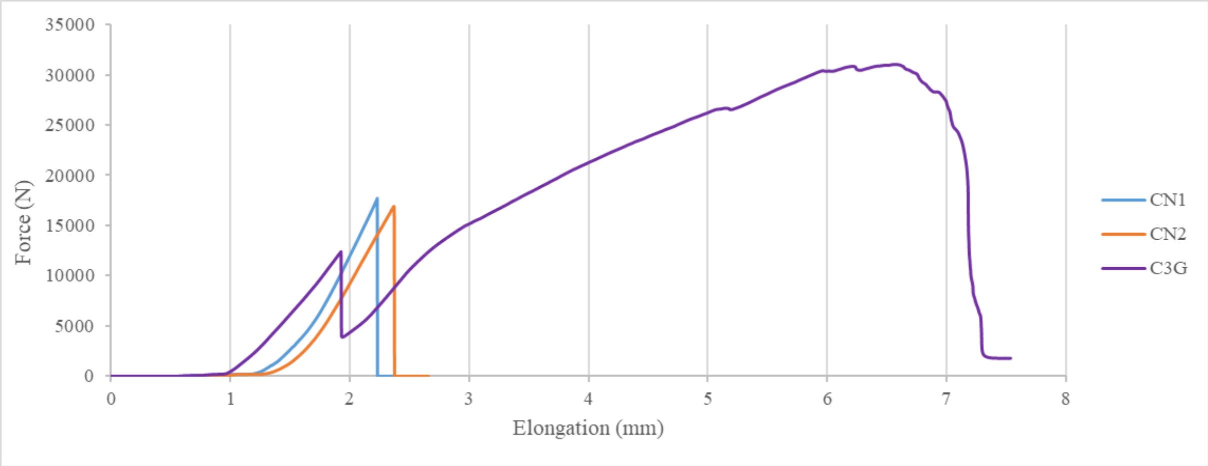

Fig. 3. Flexural strength test results of 3D printed cement-based samples

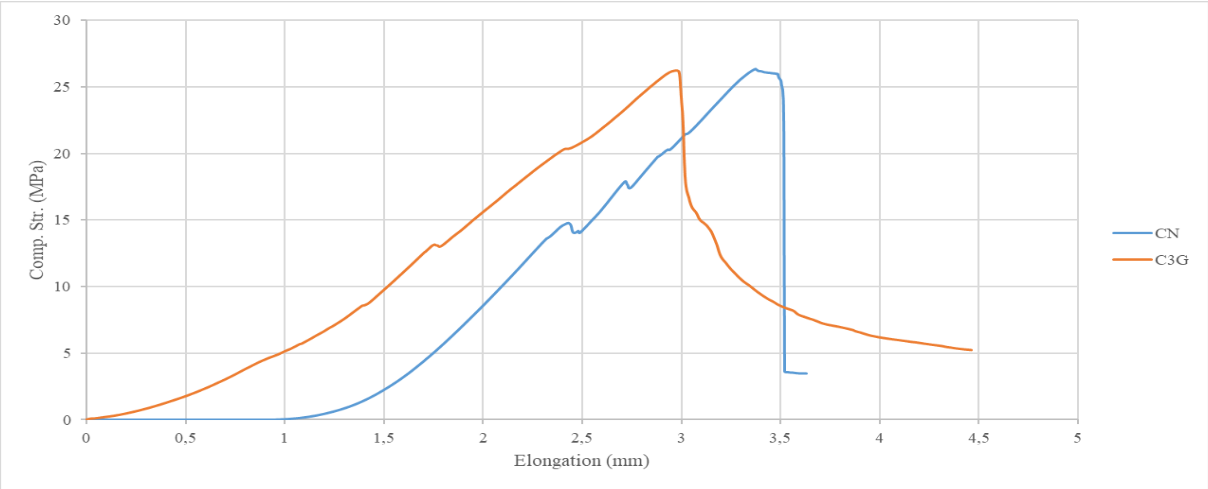

Fig. 4. Compressive strength test result of 3D printed cement-based samples

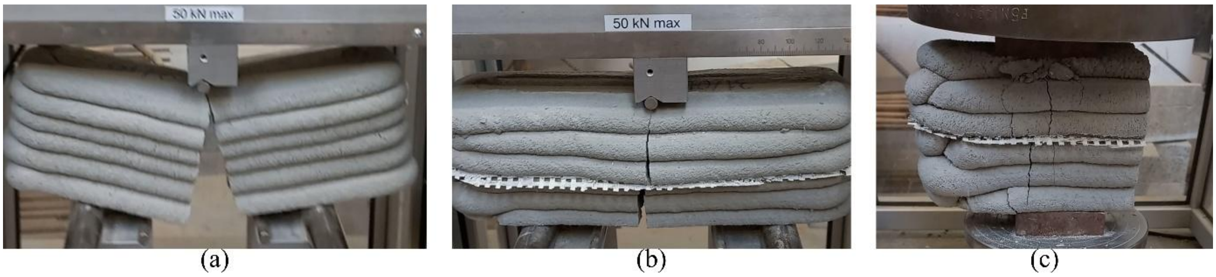

Fig. 5. Failure patterns during the flexural test of (a) unreinforced, (b) reinforced cement-based sample, and (c) the compression test of reinforced sample

Fig. 3 clearly illustrates that the incorporation of glass fibre textiles significantly enhanced the flexural strength of the specimens. Notably, although it was initially not expected that placing textiles along the neutral axis would have a substantial effect, the results from the C3G specimen demonstrated that even reinforcement at the neutral axis contributed to improved flexural performance. These findings collectively highlight the strong potential of textile reinforcement for enhancing the mechanical behaviour of 3D-printed cement-based concretes.

The improvement in flexural performance observed in this study is in line with previous findings reported in the literature. For example, Cao et al., 2024, Y. Yao et al., 2024, Ramesh, Rajeev, Sanjayan, et al., 2024 and Woon Park et al., 2022 highlighted that the mechanical performance of 3D printed concrete can be significantly enhanced by the strategic placement of reinforcement along the layer interfaces. Similarly, Dubey et al., 2024 highlighted that the inclusion of continuous or discontinuous reinforcement in the printing process enhances both strength and ductility, addressing the inherent weaknesses of layer-by-layer fabrication

According to the compressive strength results presented in Fig. 4, no notable difference was observed between reinforced and unreinforced specimens regarding peak compressive strength. While incorporating glass fibre textiles substantially improved the flexural strength and strain capacity, it did not enhance the ultimate compressive strength. However, an increase in strain capacity under compressive loading was still evident, indicating improved ductility.

With regard to compressive strength, the results confirmed that textile reinforcement did not contribute significantly to the peak compressive load, in line with previous observations (Jing et al., 2021; Schladitz et al., 2012). As textile materials, particularly glass fibres, primarily enhance tensile performance and provide minimal confinement under axial compression, their influence on compressive strength remains limited. However, the increase in strain capacity observed under compression indicates improved post-peak ductility, which is highly beneficial for enhancing the structural robustness of 3D printed elements.

4. Conclusions

This study investigated the flexural performance of 3D printed cement-based concrete reinforced with glass fibre textiles. A printable cement-based mix was successfully developed, exhibiting sufficient flowability for approximately 30 minutes after batching, which allowed for controlled extrusion and the integration of strategically placed textile reinforcement. The hardened matrix reached a compressive strength of 62.9 MPa at 28 days, classifying it as C50/60 according to TS EN 206, and achieved a flexural strength of 8.7 MPa - values consistent with high-performance printable mortars reported in the literature. Experimental results showed that the incorporation of glass fibre textiles significantly enhanced the flexural strength and ductility of the specimens, despite having minimal influence on compressive strength. The improved post-cracking behaviour indicates that the fibre reinforced textiles effectively bridge cracks and contribute to energy dissipation, resulting in a tougher and more resilient composite. These findings demonstrate the potential of textile reinforcement to improve the mechanical behaviour of 3D-printed cement-based elements, particularly in bending loading. Further research is recommended to optimise textile placement strategies, extend the workable time window of the mortar, and assess the long-term durability of reinforced printed elements under various environmental conditions.

References

Abtew, M.A. (2024). A comprehensive review on advancements, innovations and applications of 3D warp interlock fabrics and its composite materials. *Composites Part B: Engineering*, *278*, 111395. https://doi.org/10.1016/j.compositesb.2024.111395

Arunprasand, T.R., & Nallasamy, P. (2024). Advancements in optimizing mechanical performance of 3d printed polymer matrix composites via microstructural refinement and processing enhancements: A comprehensive review. *Mechanics of Advanced Materials and Structures*, 1–19. https://doi.org/10.1080/15376494.2024.2426776

Baz, B., Remond, S., & Aouad, G. (2022). Influence of the mix composition on the thixotropy of 3D printable mortars. *Magazine of Concrete Research*, *74*(6), 271–283. https://doi.org/10.1680/jmacr.20.00193

Cao, J., Shengzhao, E., Yang, Y., Shi, Y., Chai, J., & Xu, Z. (2024). A strategy for the improvement of the bonding performance of 3D-printed concrete interlayer interfaces. *Journal of Building Engineering*, *97*, 110675. https://doi.org/10.1016/j.jobe.2024.110675

CEN ISO 17892-6. (2017). *ISO 17892-6:2017 - Geotechnical investigation and testing — Laboratory testing of soil — Part 6: Fall cone test*. ISO. https://www.iso.org/standard/55248.html

Dubey, D., Singh, S.P., & Behera, B.K. (2024). Review: additive manufacturing of fiber-reinforced composites. *Journal of Materials Science*, *59*(27), 12219–12256. https://doi.org/10.1007/s10853-024-09925-6

Jing, L., Yin, S., & Aslani, F. (2021). Experimental investigation on compressive performance of masonry columns confined with textile-reinforced concrete. *Construction and Building Materials*, *269*, 121270. https://doi.org/10.1016/j.conbuildmat.2020.121270

Khan, M., & McNally, C. (2024). Recent developments on low carbon 3D printing concrete: Revolutionizing construction through innovative technology. *Cleaner Materials*, *12*, 100251. https://doi.org/10.1016/j.clema.2024.100251

Khan, T., Ali, M., Riaz, Z., Butt, H., Abu Al-Rub, R.K., Dong, Y., & Umer, R. (2024). Recent developments in improving the fracture toughness of 3D-printed fiber-reinforced polymer composites. *Composites Part B: Engineering*, *283*, 111622. https://doi.org/10.1016/j.compositesb.2024.111622

Le, T.T., Austin, S.A., Lim, S., Buswell, R.A., Law, R., Gibb, A.G.F., & Thorpe, T. (2012). Hardened properties of high-performance printing concrete. *Cement and Concrete Research*, *42*(3), 558–566. https://doi.org/10.1016/j.cemconres.2011.12.003

Liu, D., Zhang, Z., Zhang, X., & Chen, Z. (2023). 3D printing concrete structures: State of the art, challenges, and opportunities. *Construction and Building Materials*, *405*, 133364. https://doi.org/10.1016/j.conbuildmat.2023.133364

Mohamed, R.A., & Mohamed, A.F.A. (2025). Exploring the environmental benefits of 3D printing technology in concrete construction; A review. *Progress in Additive Manufacturing*, *10*(1), 279–289. https://doi.org/10.1007/s40964-024-00622-z

Nan, B., Qiao, Y., Leng, J., & Bai, Y. (2025). Advancing Structural Reinforcement in 3D-Printed Concrete: Current Methods, Challenges, and Innovations. *Materials*, *18*(2), 252. https://doi.org/10.3390/ma18020252

Ramesh, A., Rajeev, P., & Sanjayan, J. (2024). Bond-slip behaviour of textile-reinforcement in 3D printed concrete. *Journal of Building Engineering*, *86*, 108873. https://doi.org/10.1016/j.jobe.2024.108873

Ramesh, A., Rajeev, P., Sanjayan, J., & Mechtcherine, V. (2024). In-process textile reinforcement method for 3D concrete printing and its structural performance. *Engineering Structures*, *314*, 118337. https://doi.org/10.1016/j.engstruct.2024.118337

Schladitz, F., Frenzel, M., Ehlig, D., & Curbach, M. (2012). Bending load capacity of reinforced concrete slabs strengthened with textile reinforced concrete. *Engineering Structures*, *40*, 317–326. https://doi.org/10.1016/j.engstruct.2012.02.029

Spelter, A., Bergmann, S., Bielak, J., & Hegger, J. (2019). Long-term durability of carbon-reinforced concrete: An overview and experimental investigations. *Applied Sciences*, *9*(8), 1651. https://doi.org/10.3390/app9081651

Tahmasebinia, F., Niemelä, M., Ebrahimzadeh Sepasgozar, S. M., Lai, T. Y., Su, W., Reddy, K. R., Shirowzhan, S., Sepasgozar, S., & Marroquin, F. A. (2018). Three-Dimensional Printing Using Recycled High-Density Polyethylene: Technological Challenges and Future Directions for Construction. *Buildings*, *8*(11), 165. https://doi.org/10.3390/buildings8110165

Tarhan, Y., Tarhan, İ.H., Jacquet, Y., & Perrot, A. (2025). Mechanical behaviour of 3D printed and textile-reinforced eco-friendly composites. *Journal of Sustainable Cement-Based Materials*, *14*(3), 477–495. https://doi.org/10.1080/21650373.2024.2396420

Tarhan, Y., Tarhan, İ.H., & Şahin, R. (2024). Comprehensive Review of Binder Matrices in 3D Printing Construction: Rheological Perspectives. *Buildings 2025, Vol. 15, Page 75*, *15*(1), 75. https://doi.org/10.3390/BUILDINGS15010075

TS EN 206+A2. (2021). Concrete - Specification, performance, production and conformity. *Turkish Standards Institute. Ankara, Türkiye.* (in Turkish)

TS EN 12350-6. (2019). *TS EN 12350-6: Birim hacim kütlesi (Testing fresh concrete - Part 6: Density)*. TSE, Ankara, Türkiye. https://intweb.tse.org.tr (in Turkish)

TS EN 12390-3. (2019). *TS EN 12390-3: Beton - Sertleşmiş beton deneyleri - Bölüm 3: Deney numunelerinin basınç dayanımının tayini (Testing hardened concrete - Part 3: Compressive strength of test specimens)*. TSE, Ankara, Türkiye. https://intweb.tse.org.tr (in Turkish)

TS EN 12390-5. (2019). *TS EN 12390-5: Beton - Sertleşmiş beton deneyleri - Bölüm 5: Deney numunelerinin eğilme dayanımının tayini (Testing hardened concrete - Part 5: Flexural strength of test specimens)*. TSE, Ankara, Türkiye. https://intweb.tse.org.tr (in Turkish)

Woon Park, J., Lee, J., & Mook Lim, Y. (2022). Flexural behavior prediction of a layered composite member with 3D textile reinforced concrete. *Construction and Building Materials*, *325*, 126665. https://doi.org/10.1016/j.conbuildmat.2022.126665

Yao, X., Kinloch, I.A., & Bissett, M.A. (2021). Fabrication and Mechanical Performance of Graphene Nanoplatelet/Glass Fiber Reinforced Polymer Hybrid Composites. *Frontiers in Materials*, *8*. https://doi.org/10.3389/fmats.2021.773343

Yao, Y., Bu, D., Yu, J., Shao, L., Feng, P., Lu, C., & Wang, J. (2024). Flexural behavior of textile reinforced 3D printed concrete under quasi-static and dynamic impact loads. *Case Studies in Construction Materials*, *21*, e03645. https://doi.org/10.1016/j.cscm.2024.e03645

Žujović, M., Obradović, R., Rakonjac, I., & Milošević, J. (2022). 3D printing technologies in architectural design and construction: A systematic literature review. *Buildings*, *12*(9), 1319. https://doi.org/10.3390/buildings12091319

ICEARC'25
4th International Civil Engineering & Architecture Conference
17-19 May 2025, Trabzon, Türkiye

Mechanical and high temperature properties of geopolymer mortars with dunite powder, fly ash and polypropylene fibers

Merve Ş. Yön*[1], Selim Cemalgil[1]

[1] *Munzur University, Department of Civil Engineering, 62000 Tunceli, Türkiye*

Abstract. This study examines the fresh and mechanical properties, as well as the high-temperature characteristics, of self-compacting geopolymer mortars (SCGMs) incorporating dunite powder (D), class C fly ash (FA), limestone dust (LD), and polypropylene fiber (PF). Six distinct mixtures were created by partially substituting D with FA, while maintaining a fixed ratio of LD. Mixtures were generated at 0%, 15%, 30%, 45%, 60%, and 70% D, with 70%, 55%, 40%, 25%, 10%, and 0% FA, respectively, while maintaining a constant LD ratio. In order to promote energy saving, an assessment of the flexural and compressive strength of water-cured SCGMs was conducted at the 90-day age. The elevated temperature performance of 90-day water-cured SCGMs was assessed following exposure to 300 and 600 °C. Furthermore, capillary water absorption of samples cured in water for 90 days were assessed. According to the data obtained, the desired strengths could not be achieved in both the samples under the effect of high temperature and the samples not exposed to high temperature. The average compressive strengths did not exceed 3MPa. It is thought that the main factor that negatively affects strength is the application of water cure to the mixtures.

Keywords: Dunite; Fly ash; Polypropylene fibers; Geopolymer mortar; Mechanical properties

---

1. Introduction

Ordinary Portland Cement (OPC), a primary constituent of cement mortar, generates greenhouse emissions during its manufacturing and requires substantial energy and diverse natural resources. Approximately 1.6 tons of raw ingredients are required to manufacture 1 ton of cement. The production process emits around 0.8 tons of greenhouse gases and consumes around 1,300 kWh of embodied energy. (Bouaissi et al., 2019; Lee et al., 2019). Therefore, research is being conducted on materials that can be preferred to cement (Zhang et al., 2024). Materials such as fly ash, slag, kaolin, silica fume, etc., consist of amorphous SiO_2 and Al_2O_3 with great pozzolanic activity (Khale & Chaudhary, 2007). Filho et al. (2022) their research examined the efficacy of dunite and microgabbro rocks as protective surface layers against thermal shocks in concrete constructions. Thermogravimetric analysis, X-ray diffraction, thermal dilatation, optical microscopy, and X-ray microtomography were conducted to examine the mechanical and chemical properties of these rocks. As a result of the study, they found that while the compressive strength decreased, the thermal expansion improved significantly after heating and both rocks were suitable for use as protection layers in industrial applications (de Mendonça Filho et al., 2022). Yurt et al. investigated the alterations in mechanical characteristics and microstructure by producing geopolymer mixes with varying quantities of basalt and glass powder waste. Mechanical strength tests at 1, 28, and 90 days, together with high-temperature evaluations, were conducted on samples cured at 90 °C for 24 hours. The optimal post-fire compressive strengths were dramatically enhanced up to 800°C in mortars including 75% basalt and 25% glass powder (Yurt et al., 2024). Westgate et al. The study utilized GEMS3 Selector thermodynamic software to build calcium lime mortars utilizing quartz sand aggregate and olivine sand aggregate in varied amounts. The chemical and mechanical properties of mortars were examined using Raman spectroscopy, thermogravimetric analysis (TGA), X-ray diffraction (XRD), morphological analysis, scanning electron microscopy, and compressive strength testing. Dolomite used in mortar exhibits enhanced mechanical characteristics, increasing by 0.5 to 2.5 MPa when moisture is present (Westgate et al., 2019).

This work, in contrast to prior research, created SCGMs utilizing dunite powder (D), class C fly ash (FA), limestone dust (LD) and polypropylene fiber (PF). D and FA were exchanged for one another in proportions ranging from 0% to 70% in the mortars generated while maintaining a fixed LD ratio. The samples were assessed for mechanical properties, water absorption, capillary water absorption, and porosity. The high-temperature performance of SCGM samples cured in water for 90 days was examined at 300 and 600 °C.

* Corresponding author, E-mail: mervesahinyon@munzur.edu.tr

https://doi.org/10.31462/icearc2025_ce_mat_993

golden light publishing

2. Materials and methods

In this study, SCGMs were made up of nine different ingredients. These included D, FA, LD, 0-4 mm river aggregate, 12 mm long polypropylene fibers, superplasticizer and water, sodium hydroxide (NaOH), sodium silicate (Na_2SiO_3). Sodium hydroxide (NH) and sodium silicate (NS), with specific gravities of 1.35 and 1.38 respectively, were utilized as activators for the geopolymerization reaction. The SiO_2/Na_2O ratio of the NS used was 3.38. Polycarboxylate-based superplasticizer, possessing a specific gravity of 1.085, was utilized. The specific gravities of D, FA, LD and PL are 2.88, 2.25, 2.3 and 0.91 g/cm^3, respectively, and the chemical and some physical properties of D and FA are presented in Table 1. All dry binder materials used are shown in Fig. 1. The river aggregate designed with a maximum 4 mm aggregate grain size has a specific gravity of 2.63, and the gradation curve is shown in Fig. 2. The overall binder content was established at 500 kg/m^3, with 150 kg/m^3 of limestone dust incorporated into the mixture to enhance the strength (Papayianni et al.)of the fresh mortar and facilitate geopolymerization, resulting in a total binder quantity of 650 kg/m^3. The NH solution utilized in the tests was prepared at a concentration of 12 Molar by dissolving the pellet, which had 99% purity, in water. With an alkali activator/binder ratio of 0.45, the quantity of NS was 2.5 times that of NH. The water-binder ratio is 0.55 for all series. Fresh mortars with dimensions of 50x50x50 mm and 40x40x160 mm were positioned in molds in three phases and subsequently coated with stretch film to mitigate water loss soon thereafter. Three samples were cured in water until they reached 90 days of age. The proportions of SCGMs are presented in Table 2.

2.1 Mini-slump flow

According to the EFNARC (2002) (EFNARC, 2002) standard, the fresh properties of SCGM were determined by the mini slump-flow test. The spreading diameter was measured by filling the mortar into the cone without compaction and spreading it under its own weight.

2.2 Mechanical properties

Compressive and flexural strength tests of 40 × 40 × 160 mm specimens were conducted in accordance with ASTM C109 (ASTM C109/C109M-02, 2020) and ASTM C348 (ASTM C348, 2002) standards at 90 days, as seen Fig. 3. Initially, prismatic specimens underwent the flexural test. The compressive strength test of the split components was conducted. The results were computed based on the average of three specimens.

2.3 Durability test

40×40×160 mm size SCGMs were initially dried at 105 °C for 24 hours and subsequently subjected to temperatures of 300 °C and 600 °C at a rate of 5 °C/min for 2 hours (Fig. 4). The procedure involved attaining goal temperatures of 300 and 600 °C within 120 minutes, followed by maintaining these temperatures for an additional 120 minutes. The samples were maintained in the oven for 60 minutes, subsequently removed, and allowed to cool completely. Upon cooling the samples, their flexural and compressive strengths were assessed.

The capillary water absorption test was performed in accordance with ASTM C1585 (ASTM International, 2007) standard on cube specimens of 50 mm x 50 mm x 50 mm (Fig. 5). The capillary water absorption test for SCGM was performed after 90 days of curing at intervals of 5, 10, 20, 30, 60, 180, 360, and 1440 minutes.

Table 1. Chemical components of D (Saraç et al., 2023) and FA

Ingredients	%SiO_2	%CaO	%Al_2O_3	%Fe_2O_3	%MgO	%Na_2O
D	38.77	7.39	14.31	10.25	7.39	1.64
FA	21.27	28.1	7.8	4.40	2.63	-

Fig. 1. Pictures of FA, D, PF and LD, respectively

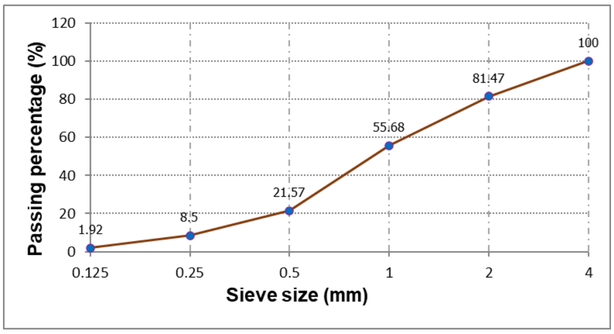

Fig. 2. Gradation curve of river sand

Table 2. Mix proportions (kg/m^3)

Mix ID	D	FA	LD	PF	Water	Sand	NS	NH	SP
D0F70	0	350	150	1.5	275	870.86	160.71	64.29	8
D15F55	75	275	150	1.5	275	890.04	160.71	64.29	8
D30F40	150	200	150	1.5	275	909.22	160.71	64.29	8
D45F25	225	125	150	1.5	275	928.39	160.71	64.29	8
D60F10	300	50	150	1.5	275	947.57	160.71	64.29	8
D70F0	350	0	150	1.5	275	960.36	160.71	64.29	8

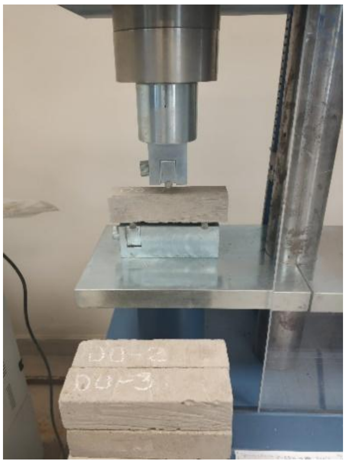

Fig. 3. Mechanical test

Fig. 4. High temperature test

Fig. 5. Sorptivity test of SCGMs

3. Results

3.1. Mini-slump values

The workability of all fresh SCGMs comprising D, FA, and LD binders was assessed using the mini-slump flow test. The illustration depicts the spreading diameters of the mixtures in accordance with the EFNARC standards (Fig. 6). The maximum spread diameter among all SCGMs was found in the sample with 70% D, whereas the minimum value was recorded in samples with 30%, 45%, and 60% D. The control mixture including 70% F exhibited a slump-flow value of 245 mm, whereas the incorporation of 30% D, 45% D ve 60% D into the mixture resulted in a reduction of the spreading value by 2.04%. The differing substitution rates in the series did not alter the water/binder (W/B) content of the mixtures. The W/B ratio for all SCGMs was 0.55.

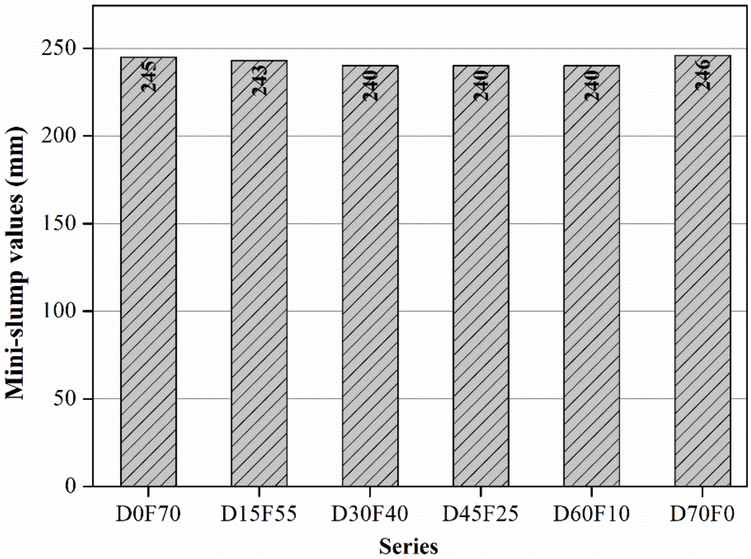

Fig. 6. Mini-slump spreading of SCGMs

3.2. Mechanical tests

Figs. 7a and 7b present the average flexural and compressive strength data for all six SCGM designs in this study. For samples D0F70, D15F55, D30F40, D45F25, D60F10, and D70F0, flexural strengths were below 1 MPa, while compressive strengths were below 3 MPa. The compressive strength of the D0F70 Reference mixed sample at 90 days was 2.54 MPa. The incorporation of 70% D in the mixture diminished the compressive strength to 0.65 MPa. As the D ratio increased (15%, 30%, 45%, 60%, and 70%), the already inadequate strength values deteriorated further, nearing 0 MPa.

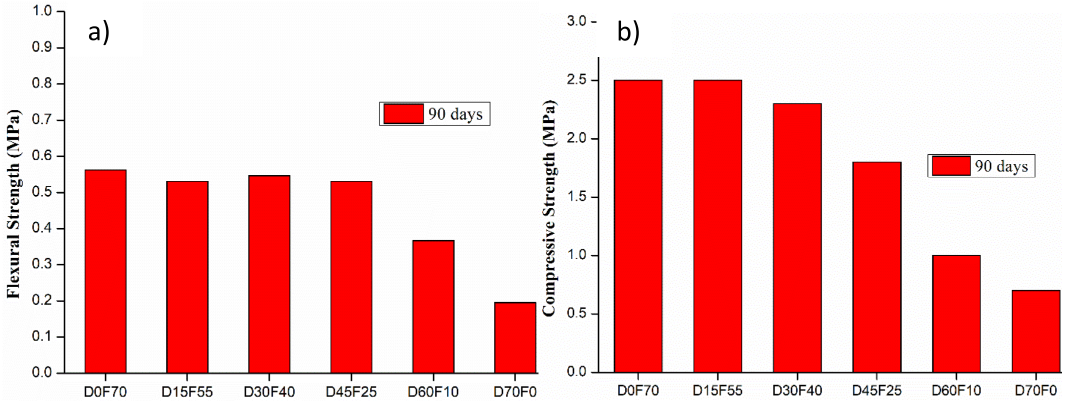

Fig. 7.a) Flexural strength values and b) compressive strength values

3.3. Durability properties

The flexural and compressive strengths of all SCGMs cured for up to 90 days, both before exposure to high temperatures and at elevated temperatures of 300 to 600 ◦C, are as given in Fig. 8a and Fig. 8b. Upon examination of the shape, it was seen that the flexural and compressive strengths diminished further following exposure to elevated temperatures. Fig. 9 illustrates the impact of the 90-day SCGM series on the sorptivity rate, assessed at intervals of 0, 5, 10, 20, 30, 60, 180, 360, and 1440 minutes. No substantial alteration was observed in the sorptivity coefficients of the mortars with the increase of D and the decrease of FA in the mixes. The D45F25 sample exhibited the highest capillary water absorption coefficient, measuring 11.48x10^{-3} cm/$s^{0.5}$. The minimum capillary water absorption coefficient was recorded in D70F0 at 10.5x10^{-3} cm/$s^{0.5}$. The sorptivity value of the mortar with 70% D addition diminished by 8.54% relative to the D45F25 sample.

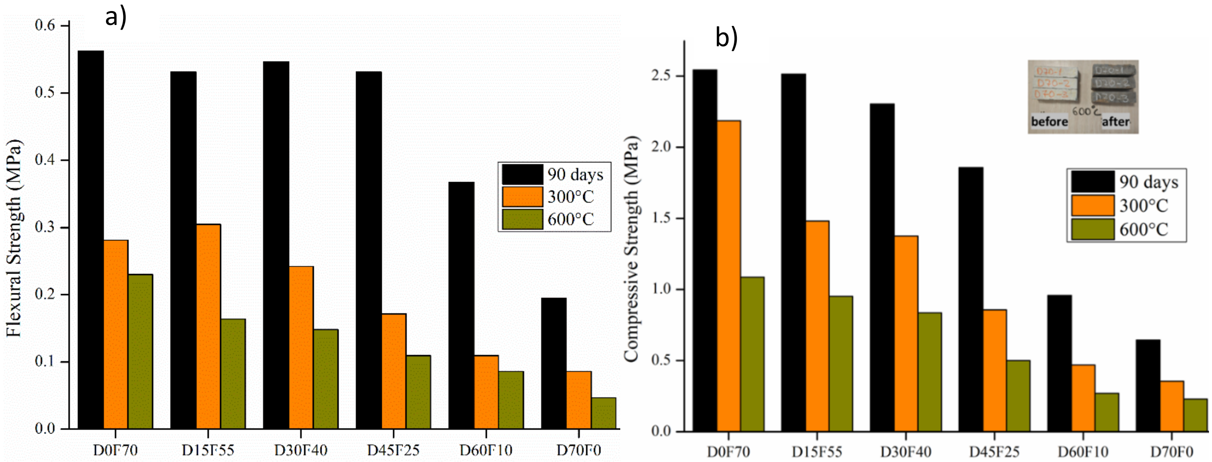

Fig. 8.a) Flexural and b) compressive strengths before and after high temperature exposure

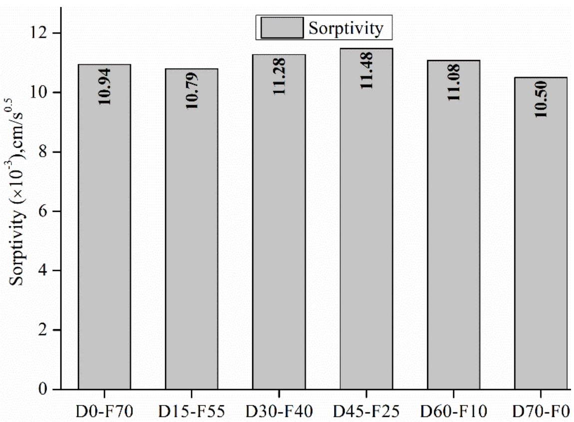

Fig. 9. Sorptivity results of SCGMs

4. Conclusions

This study focuses on the investigation of the fresh and mechanical properties of self-compacting geopolymer mortars (SCGMs) containing dunite powder (D), class C fly ash (FA), limestone powder (LD) and polypropylene fiber (PF) along with the effect of high temperature. The findings obtained from the experimental study are listed below.

- The greatest spreading diameter was recorded in the mixture with 70% D, whereas the smallest spreading diameter was noted in the mixtures with 30%, 45%, and 60% D. Accordingly, it shows that the workability of SCGMs is affected by the D ratio used, and higher D amounts provide better spreading.
- It was observed that both flexural and compressive strengths decreased further after exposure to high temperatures.
- No significant change was observed in the water absorption coefficients of the mortars with the increase in D ratio and decrease in (FA) ratio in the mixtures.
- D0F70, D15F55, D30F40, D45F25, D60F10, and D70F0, flexural strengths were below 1 MPa, while compressive strengths were below 3 MPa.

As a result, it was concluded that water curing does not activate the binder materials. The use of other alternative curing options is recommended with this study.

References

ASTM C109/C109M-02. (2020). Standard Test Method for Compressive Strength of Hydraulic Cement Mortars. *Annual Book of ASTM Standards*, *04*, 9.

ASTM C348, A. (2002). Flexural strength of hydraulic-cement mortars. *American Society for Testing and Material*, *04*, 1–6.

ASTM International. (2007). ASTM C 1585 04 : Standard Test Method for Measurement of Rate of Absorption of Water by Hydraulic-Cement Concretes. *American Society for Testing and Materials.*, 1–6. www.astm.org

Bouaissi, A., Li, L. yuan, Al Bakri Abdullah, M. M., & Bui, Q. B. (2019). Mechanical properties and microstructure analysis of FA-GGBS-HMNS based geopolymer concrete. *Construction and Building Materials*, *210*, 198–209. https://doi.org/10.1016/j.conbuildmat.2019.03.202

de Mendonça Filho, F. F., Rodriguez, C. R., Schlangen, E., & Çopuroğlu, O. (2022). Plutonic Rocks as Protection Layers to Concrete Exposed to Ultra-High Temperature. *Materials*, *15*(10). https://doi.org/10.3390/ma15103490

EFNARC. (2002). EFNARC, (European Federation of Specialist Construction Chemicals and Concrete Systems), The European guidelines for selfcompacting concrete: Specification, production and use, U.K, 2002. *Magazine of Concrete Research*, *64*(5), 401–409. https://doi.org/10.1680/macr.10.00167

Khale, D., & Chaudhary, R. (2007). Mechanism of geopolymerization and factors influencing its development: A review. *Journal of Materials Science*, *42*(3), 729–746. https://doi.org/10.1007/s10853-006-0401-4

Lee, W. H., Wang, J. H., Ding, Y. C., & Cheng, T. W. (2019). A study on the characteristics and microstructures of GGBS/FA based geopolymer paste and concrete. *Construction and Building Materials*, *211*, 807–813. https://doi.org/10.1016/j.conbuildmat.2019.03.291

Papayianni, I., Anastasiou, E., & Papachristoforou, M. (n.d.). *Effect of Steel and Polypropylene Fibers on the Performance of Self Compacting Concrete (Scc) Incorporating Calcareous Fly Ash*.

Saraç, S., Karatas, M., & Benli, A. (2023). The effect of dunite powder and silica fume on the viscosity, physico-mechanical properties and sulphate resistance of self-compacting mortars. *Construction and Building Materials*, *375*. https://doi.org/10.1016/j.conbuildmat.2023.130970

Westgate, P., Ball, R. J., & Paine, K. (2019). Olivine as a reactive aggregate in lime mortars. *Construction and Building Materials*, *195*, 115–126. https://doi.org/10.1016/j.conbuildmat.2018.11.062

Yurt, Ü., Çelikten, S., & Atabey, İ. İ. (2024). Post-fire residual mechanical and microstructural properties of waste basalt and glass powder-based geopolymer mortars. *Journal of Building Engineering*, *94*. https://doi.org/10.1016/j.jobe.2024.109941

Zhang, G., Zhang, P., Guo, J., & Hu, S. (2024). Effects of PVA fibers and nano-SiO2on rheological properties of geopolymer mortar. *Nanotechnology Reviews*, *13*(1). https://doi.org/10.1515/ntrev-2024-0103

4th International Civil Engineering & Architecture Conference
17-19 May 2025, Trabzon, Türkiye

Understanding risk factors in green building construction: A review

Erhan Arar*[1], Fahriye H. Halicioglu[2]

[1] *Dokuz Eylul University, The Graduate School of Natural and Applied Sciences, Department of Architecture, 35390 Izmir, Türkiye*
[2] *Dokuz Eylul University, Faculty of Architecture, Department of Architecture, 35390 Izmir, Türkiye*

Abstract. This study aims to explore the risk factors of green building projects. This review employs a structured methodology, which includes a thorough search of the Scopus database and a stringent selection process to identify relevant articles. A structured search strategy used keywords related to sustainability, green building, construction, and risk management. After screening and selection, 100 articles were included in the final analysis. The findings reveal various risk categories associated with green building projects, including economic, technical, policy and regulatory, market and stakeholder, quality, maintenance and lifecycle, social and cultural, environmental, material-related, and supply chain risks. The review provides a categorization of these risk factors and discusses the necessity of developing effective risk management frameworks to support the successful delivery of green building projects. The bibliometric analysis also reveals the changing research interests and evolving research trends in this field, with a growing focus on topics such as climate change, resilience, and health-related risks. This study adds value to the existing literature by providing a systematic review of the risk management knowledge areas in green building construction and suggesting potential areas for future research. Industry practitioners can use the findings of the study to develop proper risk response strategies and manage their resources well to address the specific risks that are inherent in sustainable construction projects.

Keywords: Sustainability; Risk; Risk management; Construction; Green building

1. Introduction

The construction of green buildings presents a unique set of challenges and opportunities within the built environment. These projects are characterized by a complex array of potential risks that can lead to delays, cost overruns, and operational issues stemming from the intricate selection of construction methodologies, stakeholders, systems, and materials (Gurgun et al., 2018). While the advantages of green buildings—such as reduced energy consumption, environmental sustainability, enhanced occupant well-being, and resource conservation—are well-documented (Qin et al., 2016), the associated risks have often been overlooked in academic discourse and industry practice.

As the green building sector evolves, it becomes increasingly crucial to address the emerging expectations, regulations, and specific risks linked to innovative technologies (Qin et al., 2016). This evolution necessitates the construction industry to develop and implement novel approaches to risk management. The successful completion and operation of green building projects hinge on effectively managing these unique risks throughout the project lifecycle.

Risk management plays a pivotal role in every phase of green building projects. A critical aspect of this process involves unraveling the intricacies of green building implementation and meticulously examining the risks associated with these complexities. These steps are fundamental to developing robust risk management strategies, facilitating the broader adoption of sustainable building practices across developed and emerging economies (Yang & Zou, 2014; Guan et al., 2020).

A review of existing literature reveals a predominant focus on the financial aspects, performance metrics, and benefits of green projects. However, there is a notable gap in research specifically addressing risk management in the context of green building projects. The studies that do explore this area tend to evaluate risk factors in isolation without considering their interrelationships or cumulative effects.

This review aims to contribute to the body of knowledge by offering a comprehensive perspective on the risk factors inherent in green building projects and proposing corresponding mitigation strategies. The insights from

* Corresponding author, E-mail: erhan.arar@ogr.edu.tr

https://doi.org/10.31462/icearc2025_ce_mng_024

this study hold practical value for industry professionals, enabling companies to tailor their risk assessment protocols and mitigation measures to their specific needs. This targeted approach allows more efficient allocation of limited resources to address the most significant risks.

This research seeks to address the following key questions:

1.What are the emerging trends and challenges in risk management research applied to green building construction?

2.How do the risk factors in green building construction differ from those in conventional construction projects?

3.What strategies do construction firms employ to identify and mitigate risks associated with green building initiatives?

4.What are the promising avenues for future research concerning risk management and green building practices?

To address these questions, this systematic literature review examines the implementation of risk management processes in green building construction. This study aims to elucidate risk management strategies from two perspectives: (1) a strategic viewpoint that considers the overarching risks inherent in green construction, and (2) a theoretical approach that synthesizes existing literature on managing the impacts of risks in green building projects.

The structure of this paper is as follows: First, the methodology employed to identify and select relevant literature is outlined. Next, the theoretical framework underpinning the review is presented. A descriptive analysis of the selected papers follows this. Finally, the results, discussion of the review, and directions for future research in this rapidly evolving field are given.

2. Research methodology

The research questions in the introduction have been addressed based on a systematic analysis of the current literature. A systematic literature review is a procedure that adopts a precise, clear, and explicit methodology that requires a series of stages to ensure that the literature review process is sufficiently comprehensive and transparent (Cook, 1997). Integrating bibliometric data and systematic literature review offers a robust and comprehensive approach to analyzing research trends and themes within a field. Bibliometric analysis provides quantitative insights into the structure and evolution of academic literature by examining citation patterns, co-authorship networks, and keyword co-occurrences, thereby uncovering influential works, authors, and emerging research areas. On the other hand, a systematic literature review employs a rigorous and transparent methodology to qualitatively synthesize findings from selected studies, ensuring a thorough understanding of the research landscape. By combining these methods, researchers can leverage the strengths of both approaches: the quantitative rigor of bibliometric analysis to map the intellectual structure of a field and the qualitative depth of systematic reviews to interpret and contextualize the findings. This integrated approach enhances the reliability and validity of the analysis. It provides a holistic perspective that is invaluable for identifying research gaps, guiding future studies, and informing evidence-based decision-making.

Two categories of keywords were selected to comprehensively cover the range of studies pertinent to the research questions. Initially, the specific keywords to be utilized in the study were determined (the asterisk "*" was appended to some keywords to broaden the scope of results, as various papers may use different terms for the same concept, such as "sustainable" instead of "sustainability").

words related to sustainability: “sustain*”, “green building*”, “green*” and

words related to construction risk management (i.e., “CRM” keywords): “construction,” “risk*,” “risk factor*,” and “risk management.”

The full Scopus search string is given below.

TITLE (construction OR building OR project AND (risk OR "risk factor*" OR "risk management") AND ("sustain*" OR "green*" OR "green building"))

A thorough literature review was conducted using the Scopus database, recognized as one of the most extensive multidisciplinary repositories of abstracts and citations for peer-reviewed scholarly works (Geraldi et al., 2011). The theoretical structure and approach of this review can be seen in Fig. 1. Only articles with a risk management and green building construction focus have been selected in this search. The search was restricted to the titles of the articles to prevent retrieving studies that merely mentioned the relevant search terms in the abstract and keywords without addressing the risk factors for green building projects. The search was made on the 3rd of April, 2024. This first step generated a total of 298 papers. While reading the abstract of these 298 papers, three criteria were selected to focus on: (1) does the paper analyze the transfer of risk management practices to the green building base? (2) Does the paper analyze risk factors in construction? (3) Does the paper separate and evaluate green risks from traditional construction risks? Selected papers had to meet at least one of the criteria to be included in the research. From 298 papers, articles that focus on the medicine & health industry are excluded from the research. After eliminating the articles that don’t meet the inclusion criteria, co-citation analysis was conducted for 92 articles from VosViewer. From co-citation analysis, at least 8 articles were cited in 2 selected articles. Using this procedure, 100 papers were left.

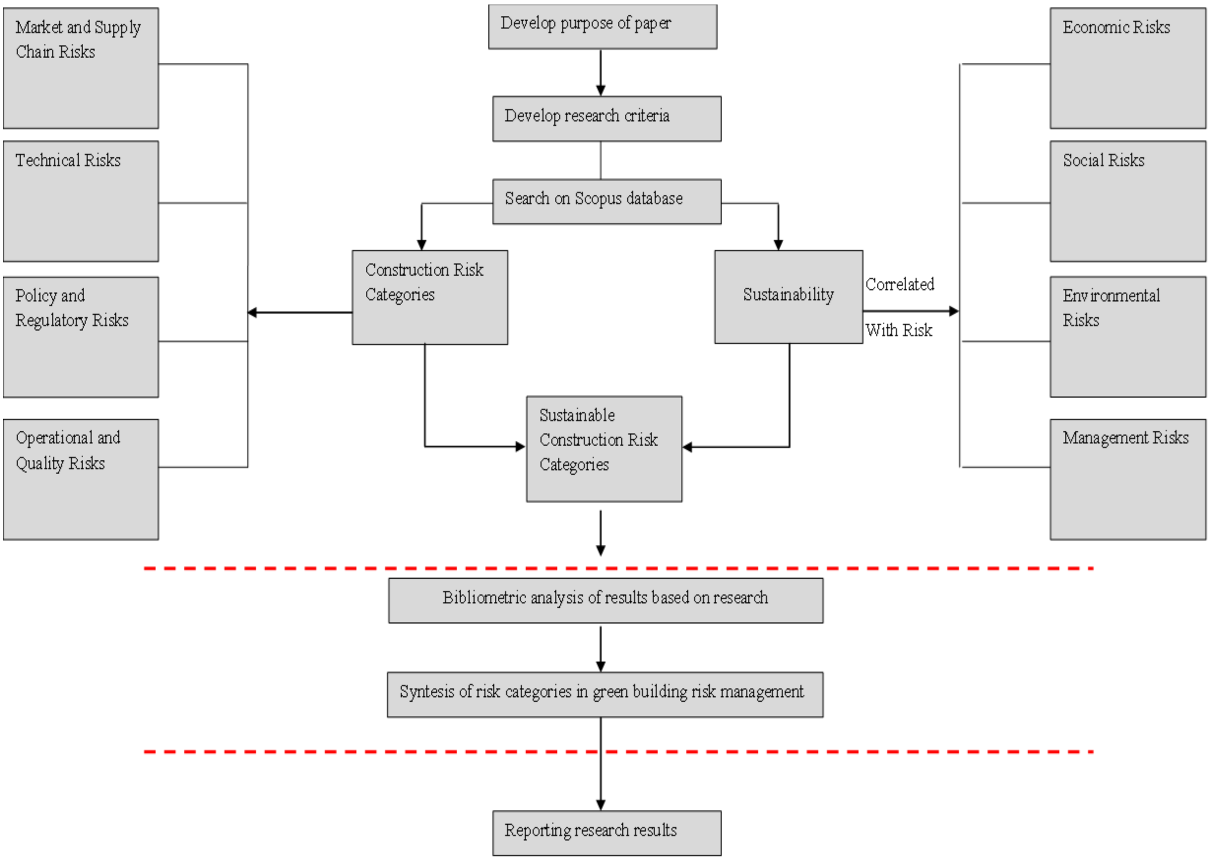

Fig.1. Flow diagram of the systematic review examining risk factors in green building projects

3. Literature review

Green building projects ambitiously prioritize environmental sustainability alongside conventional construction imperatives, yet they are subject to an intricate array of risk factors that differ markedly from traditional projects. These projects, though beneficial for their environmental goals, carry risks across several categories (Table 1), each demanding vigilant management and strategic foresight. The classification of risk categories within green building projects was meticulously developed based on an extensive literature review. This process aimed to ensure a comprehensive yet clear framework, capturing distinct aspects of risk without unnecessary overlap. By consolidating the risk categories into eight distinct groups, the classification reflects a balance between comprehensiveness and clarity, as informed by existing literature. Each category, from economic to technical risks, was defined to address specific challenges identified in the literature, thereby grounding the classification in established academic insights and ensuring its relevance to the unique demands of green building projects.

The taxonomic structure of risk factors in green building projects emerges from a methodical synthesis of existing literature. As seen in Table 1, this eight-category framework reflects an epistemological strategy in risk classification, aiming to integrate theoretical breadth with detailed analytical insight. Rather than serving solely as a heuristic, this classification system is built upon empirical evidence drawn from various fields within sustainable construction research. Initially, the classification aims to reach a level of theoretical completeness where further subdivisions would offer limited additional insights. The eight categories are designed to encompass the full range of risk dimensions without introducing excessive detail that could confuse the inherently interconnected nature of these risks. Secondly, this framework enhances the methodological rigor of risk assessment by clearly defining the boundaries between conceptually distinct risk domains and their interdependencies. Such delineation is crucial for developing targeted mitigation strategies that address the characteristics specific to each risk category. Third, the classification system has construct validity by aligning with established theoretical paradigms in project management, environmental sustainability, and organizational behavior. Each category represents a distinct theoretical construct with its own literature base and empirical support.

Table 1. Risk categories and risk factors extracted from the examined green building literature

Risk Category	Risk Factors
Economic Risks	Higher initial investment for green technologies and materials. Economic feasibility and return on investment uncertainties. Risk of increased operating costs if green technologies do not perform as expected. Currency exchange rate fluctuations for green materials coming from another country Material/labor prices for green building construction may vary
Technical Risks	Complexity in integrating sustainable design elements Risk of choosing inappropriate or unproven technologies. Challenges in design that meet both green standards and user needs. Availability/Unavailability of green materials, equipment, and skilled labor Improper management and storage of eco-friendly materials Insufficient documentation and limited dissemination of knowledge regarding emerging sustainable technologies
Policy and Regulatory Risks	Uncertainty in green building regulations and standards. Risk of not meeting certification requirements. Complexity of approval procedures for green projects. Changes in regulations, disputes, and claims
Market and Supply Chain Risks	Fluctuating market demand for green buildings. Need for stakeholder engagement and managing expectations. Reliance on market conditions for green materials and labor supply. Shortages in obtaining eco-friendly materials. Long-term durability and performance concerns for green materials include the potential degradation of biodegradable materials over time. Suppliers that don't follow sustainable practices throughout the supply chain. Increased carbon footprint from the long-distance transportation of green building materials.
Operational and Quality Risks	Potential for construction delays due to the specialized nature of green building techniques. Risk of lower-than-anticipated performance in energy or water-saving technologies. Difficulty in sourcing and managing the supply of green building materials. Challenges in maintaining green building features. Risks associated with the lifecycle assessment of the building's green components. Unintended consequences, such as poor indoor air quality, may occur if systems are not properly operated or maintained.
Social/Cultural Risks	Public perception of green buildings and their acceptance. Social impact and how well the building is received by users and the community.
Environmental Risks	There is a risk that the building could fail to provide the intended environmental benefits. Unforeseen negative impacts on local ecosystems during the construction phase. Proper disposal and recycling of building materials at the end of their lifespan. Impact on natural resources, resource depletion risks Environmental pollution and waste management risks Unstable operation performance of green buildings Climate change impacts, acts of God
Management Risks	Lack of experienced management personnel, Inefficient communication between project teams Poor team leadership and ineffective resource deployment

Economic Risks: Economic risks transcend conventional cost considerations to encompass the complex interplay between capital expenditure, lifecycle costing, and market valuation paradigms. The premium associated with sustainable technologies necessitates sophisticated financial modeling that accounts for temporal variability in costs and benefits. The economic calculus must incorporate externalities and intangible value propositions that traditional financial metrics may inadequately capture. Economic risks consist of economic and financial risks due to their inherent connection to project budgeting, funding, and cost management. Pursuing green certification frequently necessitates additional investment in cutting-edge technologies and sustainable materials. Such fiscal commitments elevate the stakes, entailing risks related to cost overruns, uncertain returns on investment, and the potential for increased operational expenditures if technologies fail to meet their efficiency targets (Ranaweera & Crawford, 2010; Dewlaney et al., 2012).

Technical Risks: The technical risk domain encompasses the uncertainties inherent in innovative sustainable technologies. These risks manifest as functional failures and performance differentials between theoretical models and empirical outcomes. Integrating disparate technological systems introduces complexity that can propagate failures across interdependent building systems, necessitating robust systems engineering approaches to risk mitigation. It alone addresses the complexities of design, technology, and engineering challenges specific to green building projects. Green projects often involve advanced, sometimes experimental, design philosophies and technologies. Selection risks become a concern, as emerging technologies may lack a proven track record, and their integration into complex building systems might not yield the hoped-for sustainability benchmarks or performance standards (Fortunato et al., 2012; Tollin, 2011).

Policy and Regulatory Risks: The policy landscape for sustainable construction exists within a dynamic regulatory ecosystem characterized by jurisdictional heterogeneity and temporal evolution. Compliance requirements exhibit vertical complexity (across governance levels) and horizontal complexity (across regulatory domains), creating a multidimensional compliance matrix that project stakeholders must navigate. The interpretive flexibility within regulatory frameworks introduces additional uncertainty regarding certification criteria and compliance verification methodologies. This category combines policy and regulatory risks, which involve compliance with laws, standards, and governmental policies. Regulatory environments for green building practices are continually evolving. The dynamics within these frameworks pose risks regarding compliance, certification attainment, or navigating complex government procedures, which can affect project timelines and sanctioning.

Market and Supply Chain Risks: Market and supply chain risks reflect the structural vulnerabilities within the sustainable construction ecosystem. The nascent nature of green building markets introduces volatility in demand forecasting and supply chain resilience. Material provenance verification, supplier certification, and ethical sourcing considerations introduce additional complexity to procurement processes. The specialized nature of sustainable materials can create monopsony or monopoly conditions that exacerbate price volatility and supply constraints. This category integrates market dynamics with supply chain considerations, reflecting the interconnectedness of market demand, material availability, and procurement processes. The construction market's appetite for green buildings can be unpredictable, affecting both material costs and the skilled labor pool. Also, the sustainable supply chain is critical for the timely delivery of green building materials. Fluctuations in the availability of these materials due to market demand or regulatory changes can lead to construction delays and additional costs. Additionally, the procurement of materials from distant locations may contradict the sustainability principles due to the increased carbon footprint from transportation (Gurgun et al, 2018; Polat et al, 2017). The reliance on specialized green materials can introduce risks associated with supply chain vulnerabilities, such as shortages or delays in delivery, which can extend project durations and inflate costs.

Operational and Quality Risks: Operational risks emerge from the dynamic interaction between building systems, environmental conditions, and user behaviors. The performance gap between designed and actual operational efficiency represents a significant risk factor that can undermine green buildings' economic and environmental value proposition. Maintenance protocols for innovative systems may lack standardization, creating knowledge management challenges that compromise long-term performance and sustainability credentials. This category merges operational efficiency with quality assurance, focusing on the performance and maintenance of green building solutions. Post-construction, the ongoing maintenance of green infrastructure and systems carries risks. Ineffective maintenance can nullify the benefits of green technologies, and errors in lifecycle assessments may not become apparent until after project completion, with implications for long-term environmental and structural integrity (Qin et al, 2016; Guan et al, 2020). Specialized techniques required for green construction can lead to unforeseen delays. Moreover, if energy-saving or water-conserving systems underperform, the operational efficacy of the building can be compromised, challenging the project's sustainability claims (Dewlaney et al., 2012; Hwang et al, 2015). The long-term performance and durability of these systems and materials are also critical, as they directly affect the building's ability to maintain its green certification standards over time (Wang et al, 2024)

Social Risks: Social risks encapsulate the interplay between built environment interventions and sociocultural systems. The efficacy of green buildings is partially contingent upon their sociocultural resonance and stakeholder acceptance. Misalignment between design philosophy and cultural paradigms can engender resistance, undermining utilization patterns and compromising the realization of sustainability objectives through behavioral non-compliance or occupant dissatisfaction. Social risks remain distinct when addressing stakeholder engagement, community impact, and social acceptance of green projects. The social acceptance and cultural adaptation to green buildings carry their own risks. Public perception and community receptivity can significantly influence a project's success, impacting everything from occupancy rates to the sustainable behavior of end-users within the building environment. Misalignment with societal expectations or cultural norms can reduce usage or support for green buildings, undermining their intended benefits and market value (Hwang et al, 2015). Additionally, aligning diverse stakeholder interests and expectations heightens risks in material sourcing, cost estimation, and user satisfaction levels (Yang & Zou, 2014; Zou & Couani, 2012).

Environmental Risks: Environmental risks represent the paradoxical potential for ostensibly sustainable interventions to generate unintended ecological consequences. The environmental calculus of green buildings must account for both direct and indirect impacts across multiple temporal and spatial scales. Lifecycle assessment methodologies reveal potential environmental trade-offs that must be systematically evaluated to ensure sustainability initiatives do not inadvertently compromise ecological integrity. While green buildings aim to minimize their environmental footprint, there remains the risk that they may not achieve this goal effectively or could inadvertently cause harm to the local environment during construction. The challenge is also to ensure that the materials and systems used will perform sustainably throughout the building's lifecycle without degrading natural habitats or consuming resources at unsustainable rates (Zhang et al, 2012).

Management Risks: Management risks derive from the organizational complexity inherent in green building projects. The interdisciplinary nature of sustainable construction necessitates sophisticated coordination mechanisms and specialized expertise. Deficiencies in project governance structures, knowledge management systems, or stakeholder communication protocols can precipitate cascading failures that compromise project outcomes through temporal delays, resource misallocation, or suboptimal decision-making processes. Management risks in green building projects encompass project coordination, resource allocation, and stakeholder communication challenges. Key management risk factors include a lack of experienced management personnel, inefficient communication between project teams, and inadequate planning processes (Wuni, 2024). Poor team leadership and ineffective resource deployment can significantly impact project success (Memari, 2023). These management-related risks are particularly critical in green building projects due to their complex nature and the need for specialized expertise. Current studies show that effective management strategies, including clear communication channels and proper resource allocation, are essential for mitigating these risks and ensuring successful project completion.

3. Results and discussion

Key themes, clusters, and their connections within the field of risk management in green building projects are represented in Fig. 2. The map showcases a range of related topics clustered around central themes. Detailed insights derived from this network map can be summarized as:

- Central Themes- Risk Management and Risk Assessment: The most prominent themes indicate their central role in the literature concerning green building projects. The large nodes and dense connections suggest extensive research activity and strong interlinkages with other related topics.
- Secondary Themes - Climate Change, Sustainability, and Stakeholders: These themes are closely linked to risk management and assessment, highlighting the importance of addressing climate change and sustainability in risk-related research. The connection with stakeholders underscores the multifaceted nature of risk management, involving various parties in the construction process.
- Specific Methods and Approaches - Analytic Hierarchy Process (AHP), Fuzzy Logic, and Monte Carlo Simulations: These specific methods are frequently mentioned, indicating their widespread use in evaluating and managing risks in green building projects. Their prominence suggests their effectiveness and acceptance in the academic and professional communities.
- Emerging Topics - Green Supply Chain, Resilience, and Disaster Risk Reduction: These topics are emerging as significant areas of interest, reflecting current trends and future directions in sustainable construction practices. The focus on resilience and disaster risk reduction indicates a proactive approach to managing risks associated with climate change and environmental uncertainties.
- Integration with Broader Concepts - Quality, Investments, and Project Success: Integrating risk management with broader project outcomes like quality, investments, and success underscores the holistic view required for effective risk management in green building projects. This highlights the need for comprehensive strategies that consider multiple dimensions of project performance.
- Health and Safety Considerations - COVID-19 and Health-Related Risks: The inclusion of COVID-19 reflects the recent shift towards health-related risks in construction projects. This indicates an expanding scope of risk management to include health and safety issues, particularly in light of recent global events.
- Evolution Over Time - Color Gradient from 2016 to 2022: The color gradient indicates the temporal evolution of research topics, with newer themes emerging in yellow and older ones in blue. This allows for identifying emerging research areas and the shifting focus within the field over recent years.
- Case Studies and Practical Implementations: Terms like “case study” and “project risk management” strongly emphasize practical applications and real-world implementations of risk management strategies. This highlights the importance of translating theoretical research into actionable insights for industry practitioners.

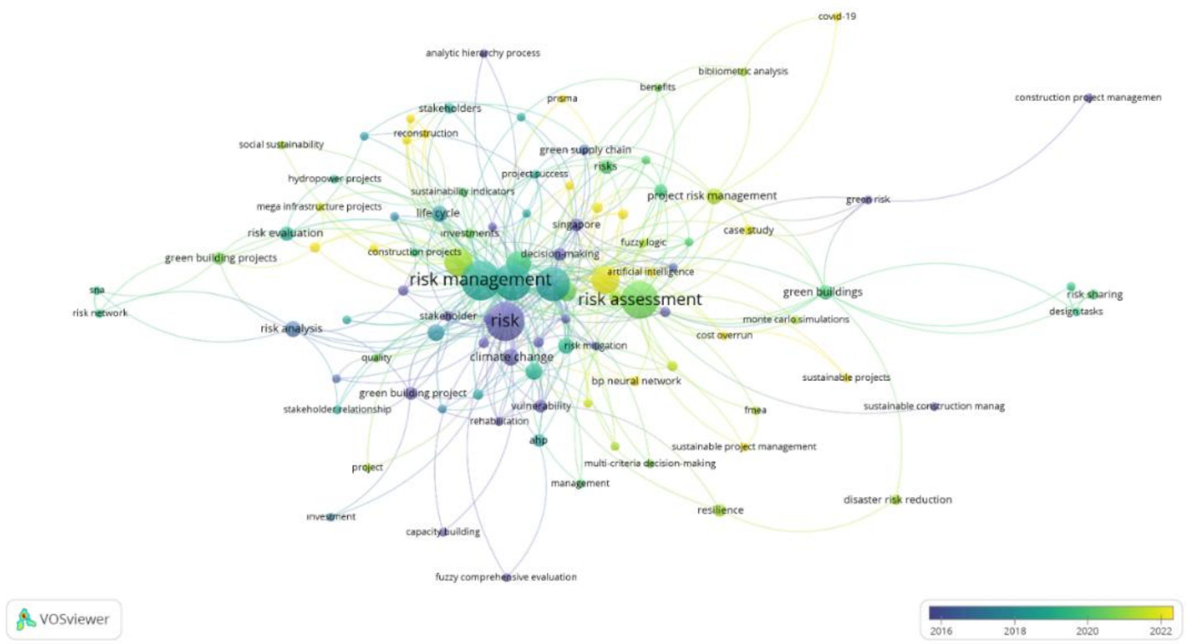

Fig. 2. Thematic classification of articles included in the literature review

The publication trends in risk management for green building projects in Fig. 3 exhibit distinct phases over the years. From 1999 to 2011, minimal publications indicated a limited focus on this area. However, a gradual increase has been observed since 2011, peaking in 2015, reflecting growing awareness and the importance of sustainable construction practices. The period from 2016 to 2018 saw a significant rise in publications, with a peak in 2018 driven by global sustainability initiatives and heightened research activity. This was followed by sustained high publication activity from 2019 to 2021, signifying continued interest and maturity in the field. In recent years, from 2022 to 2024, there has been a noticeable decline in publications, which may suggest a shift towards practical application and implementation of research findings or changing research priorities.

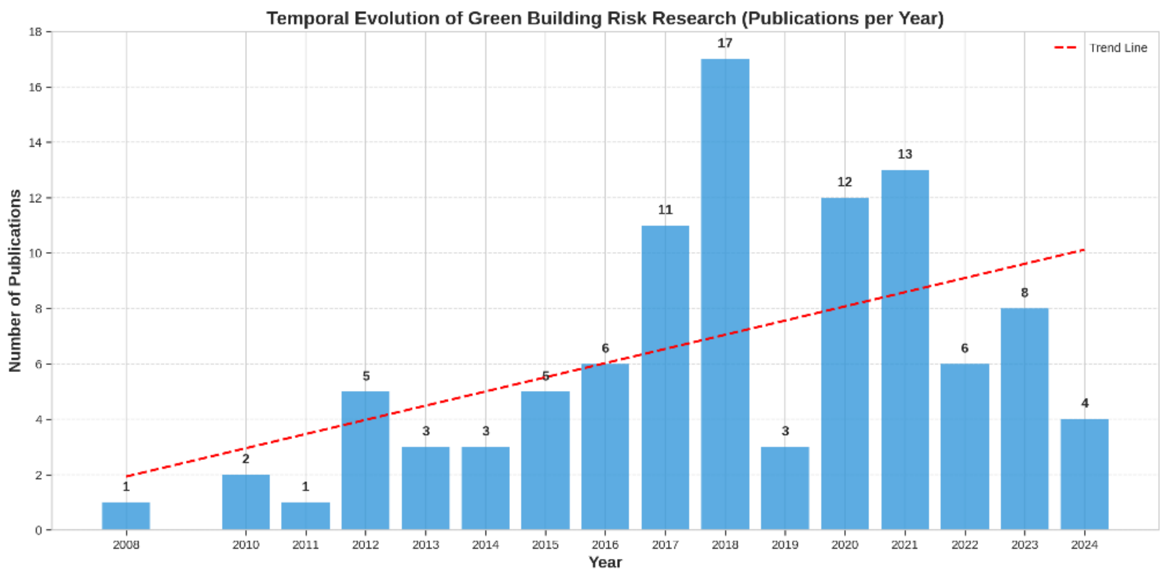

Fig. 3. Yearly distribution of studies used in review

Fig. 4 illustrates the trends of author keywords—risk management, sustainability, green building, and risk assessment—over the years. From 2000 to 2010, there is minimal frequency, indicating limited focus on these topics. A noticeable increase started around 2010, with all keywords showing fluctuating yet upward trends. Between 2015 and 2020, the keywords see significant peaks, reflecting a surge in research interest, particularly around 2018-2020. Post-2020, the trends remain relatively high, though with some variability, highlighting sustained and growing interest in these areas, driven by increasing emphasis on sustainable practices and comprehensive risk management in green building projects. The keyword "risk management" receives the most attention, especially around 2020, indicating its central importance in the field. "Sustainability" and "risk assessment" also show significant interest, with notable peaks around the same period. In contrast, "green building" has a relatively lower frequency and fluctuates more, suggesting it receives less consistent attention than the other keywords. This indicates that while green building is important, the focus remains more on overarching concepts of risk management and sustainability.

The analysis of average citations per publication year from 2008 to 2024 reveals distinct trends in research impact over time can be seen in Fig. 5. Notably, 2014 and 2016 stand out with peaks of 105.7 and 81.2 average citations, respectively, indicating periods of heightened academic interest and influence. This suggests that research published during these years was particularly impactful, potentially due to emerging trends or breakthroughs. Following these peaks, average citations are declining, with a notable decrease to zero by 2024. This downward trend may reflect a shift in research priorities or a maturation of the field, leading to reduced novelty and citation rates in recent publications.

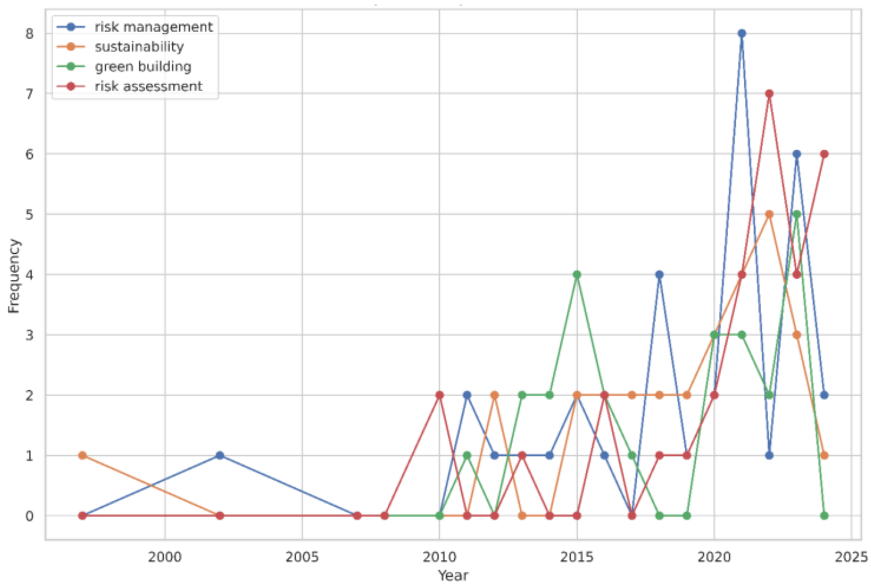

Fig. 4. Trends of keywords of the selected studies in review

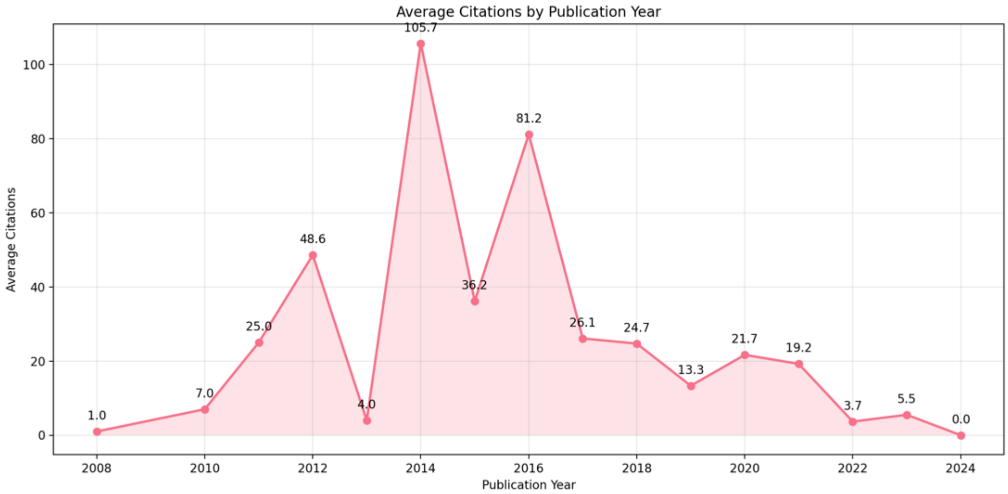

Fig. 5. Average citations of reviewed studies by publication year

The citation analysis of reviewed studies reveals a distinctly skewed distribution across different citation ranges (Fig. 6). Most publications (51 papers) fall within the 0-9 citations range, representing approximately 51% of the total dataset. This is followed by a substantial decrease to 21 papers in the 10-24 citation range, accounting for roughly 21% of the corpus. The distribution continues to decline, with 9 papers receiving 25-49 citations and 15 papers garnering 50-99 citations. Notably, only 4 papers achieved 100 or more citations, indicating these as highly influential works within the field. This distribution pattern aligns with Bradford's typical law of bibliometrics, where a small number of papers receive a disproportionately high number of citations. In contrast, the majority receive relatively few, demonstrating the concentrated nature of academic impact in this research domain.

The analysis of methodological approaches in Fig. 7 reveals distinct patterns in their scholarly impact and temporal adoption within green building risk research. Despite their relatively modest adoption rates, Expert Analysis and AHP (Analytic Hierarchy Process) demonstrate the highest citation impact, averaging approximately 60 citations per paper. While being the most frequently employed methodology with 46 papers, surveys maintain a moderate citation impact of around 40 citations per paper, suggesting a balance between widespread use and scholarly influence. Though less numerous, systematic reviews show substantial impact, with approximately 50 citations per paper. Notably, newer methodological approaches such as Simulation and Case Studies exhibit lower citation counts, potentially due to their recent emergence in the field. This temporal-impact distribution indicates that while traditional methods like surveys and expert analysis continue to dominate, there is an evolving methodological landscape with newer approaches gradually gaining traction, albeit with varying degrees of scholarly impact.

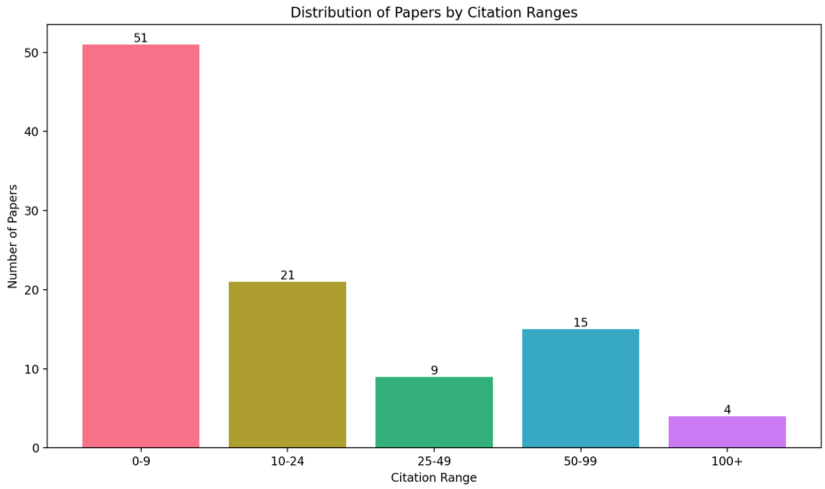

Fig. 6. Number of studies by citation ranges

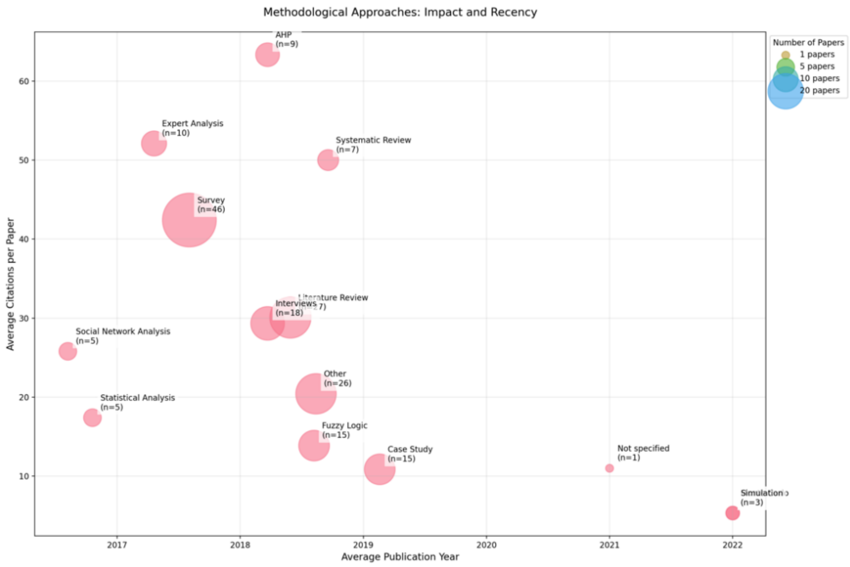

Fig. 7. Methodological approaches graphic showing impact and recency

The bibliometric analysis reveals a highly concentrated pattern of scholarly influence within the green building risk literature. The top 15 most-cited papers, seen in Fig. 8, account for 61.3% of the total citations in the field, demonstrating a significant concentration of academic impact. A hierarchical examination of citation thresholds further illuminates the distribution of scholarly influence: 49 papers have garnered more than 10 citations, while

28 publications have exceeded 25 citations. More notably, 19 papers have achieved over 50 citations, with an elite group of 4 papers surpassing 100. This stratified distribution of citations underscores the presence of seminal works that have substantially shaped the discourse in green building risk research. The focus on these highly cited papers is particularly justified as they represent the most influential research and offer a comprehensive lens to observe the evolution of methodological approaches and research priorities over time. This concentration of citations suggests a field characterized by influential cornerstone publications that have established fundamental theoretical frameworks and methodological standards.

An analysis of citation metrics (Figs. 8 and 9) reveals a distinct hierarchy in the impact of green building risk research publications. The most influential work by Yang et al. (2014) stands prominently with 250 citations, followed by Zhao et al. (2016) with 203 citations, establishing these as seminal works in the field. A notable pattern emerges with three distinct tiers of citation impact: the top tier (200+ citations) comprising two papers, a middle tier (100-199 citations) containing two papers with 155 and 139 citations respectively, and a lower tier (65-99 citations) encompassing the remaining eleven papers. The temporal distribution of these highly-cited works spans from 2012 to 2021, with a concentration of influential publications in the 2014-2016 period, suggesting this was a particularly productive era for impactful research in green building risk assessment. Interestingly, Hwang B.G. appears as an author in multiple highly-cited papers (2012, 2015, 2017), indicating sustained contribution to the field's development.

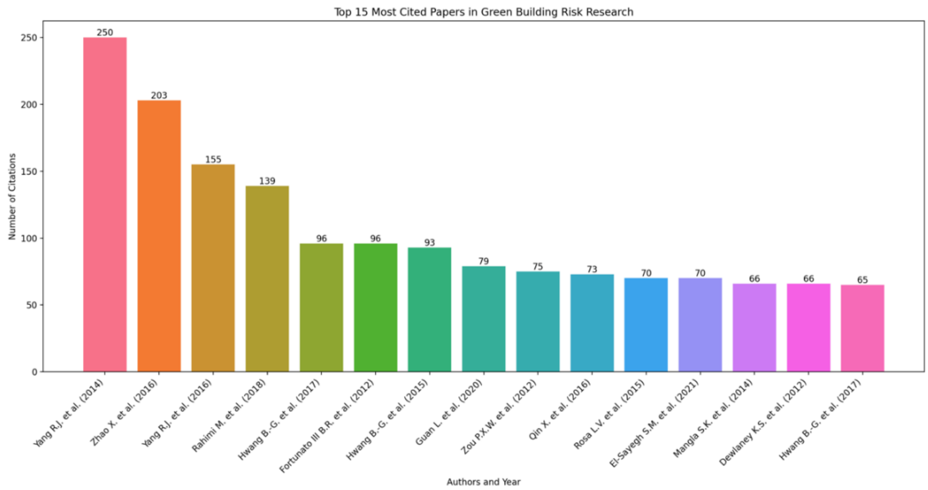

Fig. 8. Top 15 most cited papers used in the review

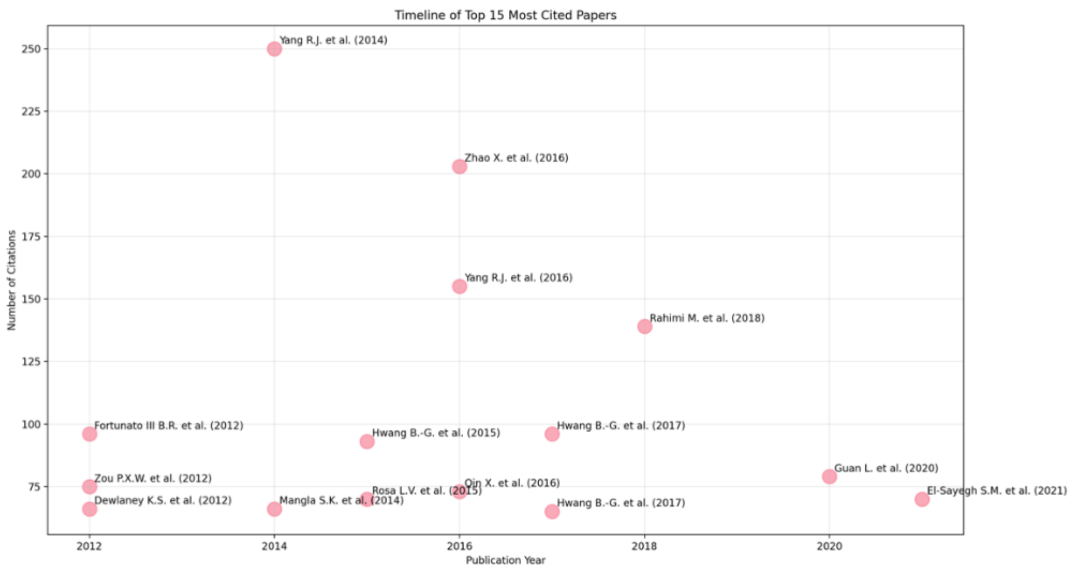

Fig. 9. Timeline graphic of the 15 most cited papers

4. Conclusions

The review provides a comprehensive overview of a systematic literature review framework focused on risk management in green building construction. It details a structured approach through three main stages: planning and searching, reviewing synthesis, and documentation. The framework emphasizes the importance of identifying and categorizing economic, design and technological risks, policy and regulatory, market and stakeholder, construction and operational, maintenance and lifecycle, and environmental risks.

The review also includes a systematic review flow diagram that illustrates the process of selecting relevant articles, detailing the number of potential articles, those excluded, re-evaluated, and finally included in the review. Additionally, it presents graphical representations of thematic classifications, the yearly distribution of research, keyword selection trends, and the breakdown of document types to provide deeper insights into the literature on this topic.

The systematic literature review outlined in the document highlights the multifaceted nature of risk management in green building construction. The review process, structured through planning and searching, synthesis of reviewed literature, and documentation, underscores the field's complexity and breadth. Key risk categories include economic, design and technological, policy and regulatory, market and stakeholder, construction and operational, maintenance and lifecycle, and environmental risks. These categories illustrate the diverse challenges and considerations for effective risk management in green building projects.

The citation analysis graphics further enrich our understanding by showing a growing body of literature, with journal articles being the predominant publication type. This indicates a robust academic interest and a dynamic discourse in the field. The increasing frequency of keywords such as "risk management," "sustainability," "green building," and "risk assessment" over recent years points to an expanding focus on integrating sustainability with risk management practices.

The citation statistics show a wide variance, with some studies receiving few citations. This suggests potential biases in the systematic review process, such as excluding non-English publications or grey literature that may offer valuable insights. Future reviews should adopt a more inclusive approach to address these limitations, considering a broader range of sources and languages. Additionally, the reliance on specific keywords may have limited the scope of the review, underscoring the need for a more comprehensive search strategy. Also, the systematic review process may be subject to publication bias, primarily focusing on peer-reviewed journal articles and conference papers, potentially overlooking relevant insights from industry reports and grey literature.

Given the increasing research volume and the evolving nature of risk factors in green building construction, several critical research gaps warrant attention. The systematic literature review reveals a notable lack of studies addressing risk factors' interrelationships and cumulative effects in green building projects. While the bibliometric analysis indicates a diverse range of methodological approaches, there remains a need for more empirical studies to validate theoretical models and provide practical insights, as the current literature is predominantly conceptual. Future research should prioritize three key areas:

- Developing innovative risk management strategies that address both traditional and emerging risks, particularly those related to climate change, resilience, and health factors;
- Creating a comprehensive framework that synthesizes existing methodologies and highlights their interconnections and applicability to different risk categories; and
- Expanding the research scope to integrate social risk factors into the mainstream risk discourse.

Such a framework would serve as a foundation for developing integrated risk management strategies that address the multifaceted nature of risks in green building projects.

The literature review offers significant insights into green building construction projects' emerging challenges and risk factors. It underscores the intricate nature of green building projects, necessitating the involvement of diverse experts and institutions throughout the entire project lifecycle. The review identifies several key risk categories, including economic and financial risks, design and technological risks, policy and regulatory risks, and material risks.

The insights derived from this comprehensive review hold significant value for industry professionals. These findings can assist organizations in tailoring their risk assessment protocols and mitigation strategies, thereby enabling more efficient allocation of scarce resources towards addressing the most critical risks. Understanding these specific risks is crucial for developers, designers, contractors, and stakeholders to navigate the challenges of green building construction successfully and to leverage opportunities to promote sustainability in the built environment.

Acknowledgments

The authors affirm that this research, including the preparation of the manuscript and the publication of this paper, was conducted without the receipt of any specific funding. All activities were undertaken independently, without financial assistance from any institution, organization, or funding agency.

Data Availability Statement

The data supporting the findings of this study are available upon reasonable request from the authors.

5. References

Cook, D.J. (1997). Systematic reviews: Synthesis of best evidence for clinical decisions. *Annals of Internal Medicine, 126*(5), 376–380. https://doi.org/10.7326/0003-4819-126-5-199703010-00006

Dewlaney, K.S., Hallowell, M.R., & Fortunato, B.R. (2012). Safety risk quantification for high performance sustainable building construction. *Journal of Construction Engineering and Management, 138*(8), 964–971. https://doi.org/10.1061/(ASCE)CO.1943-7862.0000514

Fortunato, B.R., Hallowell, M.R., Behm, M., & Dewlaney, K. (2012). Identification of safety risks for high-performance sustainable construction projects. *Journal of Construction Engineering and Management, 138*(4), 499–508. https://doi.org/10.1061/(ASCE)CO.1943-7862.0000453

Geraldi, J., Maylor, H., & Williams, T. (2011). Now, let's make it really complex (complicated): A systematic review of the complexities of projects. *International Journal of Operations & Production Management, 31*(9), 966–990. https://doi.org/10.1108/01443571111165848

Guan, L., Abbasi, A., & Ryan, M.J. (2020). Analyzing green building project risk interdependencies using interpretive structural modeling. *Journal of Cleaner Production, 256*, 120372. https://doi.org/10.1016/j.jclepro.2020.120372

Gurgun, M.A.P., Bayhan, H.G., Polat, G., & Turkoglu, H. (2018). Schedule risk assessment in green building projects. *Proceedings of International Structural Engineering and Construction, 5*(1)

Hwang, B.-G., Zhao, X., See, Y.L., & Zhong, Y. (2015). Addressing risks in green retrofit projects: The case of Singapore. *Project Management Journal, 46*(4), 76–89. https://doi.org/10.1002/pmj.21516

Memari, O.E., Ogunmakinde, M., & Aghajani, M. (2023). Classification of green procurement risks across the project lifecycle in Australian construction projects. In: *2023 IEEE International Conference on Industrial Engineering and Engineering Management (IEEM),* (pp. 0230–0233)

Polat, G., Turkoglu, H., & Gurgun, A.P. (2017). Identification of material-related risks in green buildings. *Procedia Engineering, 196*, 956–963. https://doi.org/10.1016/j.proeng.2017.08.028

Qin, X., Mo, Y., & Jing, L. (2016). Risk perceptions of the life-cycle of green buildings in China. *Journal of Cleaner Production, 126*, 148–158. https://doi.org/10.1016/j.jclepro.2016.03.103

Ranaweera, R., & Crawford, R.H. (2010). Using early-stage assessment to reduce the financial risks and perceived barriers of sustainable buildings. *Journal of Green Building, 5*(2), 129–146. https://doi.org/10.3992/jgb.5.2.129

Tollin, H.M. (2011). Green building risks: It's not easy being green. *Environmental Claims Journal, 23*(3–4), 199–213. https://doi.org/10.1080/10406026.2011.599876

Wang, L., Chan, D.W.M., Darko, A., & Oluleye, B.I. (2024). A state-of-the-art review of risk management process of green building projects. *Journal of Building Engineering, 86*, 108738

Wuni, I.Y. (2024). Developing a multidimensional risk assessment model for sustainable construction projects. *Engineering, Construction and Architectural Management*. https://doi.org/10.1108/ECAM-11-2023-1201

Yang, R.J., & Zou, P.X.W. (2014). Stakeholder-associated risks and their interactions in complex green building projects: A social network model. *Building and Environment, 73*, 208–222. https://doi.org/10.1016/j.buildenv.2013.12.013

Zhang, G.M., Mosly, I., Setunge, S., & Jin, X.H. (2012). Critical risks influencing the application of EERTs in Australian green office buildings. *Advanced Materials Research, 238*, 513–524

Zou, P.X.W., & Couani, P. (2012). Managing risks in green building supply chain. *Architectural Engineering and Design Management, 8*(2), 143–158

Strategies for delay mitigation in construction projects: A systematic review

Melike N. Ates[1], Harun Turkoglu[*2], Atilla Damci[1], Sevilay Demirkesen[2]

[1] Istanbul Technical University, Department of Civil Engineering, 34469 Istanbul, Türkiye
[2] Gebze Technical University, Department of Civil Engineering, 41400 Kocaeli, Türkiye

Abstract. Construction projects are inherently complex and often experience delays as a result of different causes, including inadequate planning, resource misallocation, unforeseen risks, and conflicts between stakeholders. These delays not only result in significant financial losses but also lead to reputational damage, legal disputes, and reduced overall project quality. In a time when economic and social needs require timely project delivery, the identification and execution of effective delay mitigation strategies have become a major concern for both academia and industry. In spite of the abundance of research on construction delays, there is a lack of a comprehensive, systematic review of mitigation strategies specifically designed to deal with the unique challenges of construction projects. This study performs a systematic literature review to identify and examine delay mitigation strategies in construction projects. The review focuses on peer-reviewed articles that were published between 2015 and 2025 and were obtained from reputable databases such as Scopus, Web of Science, and Google Scholar. To guarantee a thorough and transparent review process, the methodology is based on the PRISMA (Preferred Reporting Items for Systematic Reviews and Meta-Analyses) framework. The results of this study revealed that, although various strategies have been proposed in the literature, their effectiveness and applicability frequently depend on factors such as project scale, complexity, and regional context. In addition, the review identifies gaps in the literature, including the limited investigation of delay mitigation strategies in construction projects and the critical need for additional empirical studies on the long-term effects of these strategies. This study contributes to the existing body of knowledge by presenting a detailed framework for the comprehension and implementation of delay mitigation strategies, thereby providing valuable insights for both industry professionals and researchers.

Keywords: Construction delays; Delay mitigation strategies; Project management; Systematic review

1. Introduction

Delays in construction projects constitute a persistent and costly challenge for the global construction sector, with empirical research indicating that over 85% of large-scale projects fail to meet their original schedules (Gurgun et al., 2024). Such delays result in a series of consequences, including average cost overruns of 28% (International Construction, 2022), long-term reputational damage that diminishes future bidding success rates by 30% (Bramble & Callahan, 2010), and disputes about contracts in 42% of cases (Al-Kharashi & Skitmore, 2009). The complex, uncertain, and dynamic nature of construction projects require the development of mitigation strategies that address both the technical and organizational aspects of potential delays (Gondia et al., 2020).

The importance of developing effective mitigation strategies has been noted in recent literature, particularly in the context of the digital transformation of the construction industry (Radman et al., 2021). Although technological solutions such as Building Information Modeling (BIM) and artificial intelligence have demonstrated potential in mitigating specific delays, it has been claimed that a more holistic approach is necessary (Gurgun et al., 2024). Within this context, a systematic review of existing literature was carried out to identify and evaluate strategies to mitigate delays in construction projects. This study synthesized the findings of 87 peer-reviewed articles published between 2015 and 2025 in order to identify and evaluate twelve main delay mitigation strategies that address five thematic aspects: project planning, resource optimization, contractual frameworks, stakeholder management, and technology integration, thus offering insightful analysis for both industry professionals and researchers

[*] Corresponding author, E-mail: hturkoglu@itu.edu.tr

https://doi.org/10.31462/icearc2025_ce_mng_025

2. Research methodology

Literature reviews are carried out using a variety of methods, such as integrative, semi-systematic, and systematic. Systematic reviews generate novel insights or conclusions by synthesizing data from various studies or integrating different types of evidence to explore underlying meanings (Snilstveit et al., 2012). This study utilizes a systematic literature review to analyze strategies to mitigate delays in construction projects. The research methodology of this study adheres to a systematic three-phase framework, as proposed by Snyder (2019): (1) review design, (2) review execution, and (3) results analysis. The research methodology is presented in Fig. 1, with detailed descriptions of each phase provided below.

2.1. Phase 1: Review design

The systematic literature review process begins with the identification of appropriate databases and search terms. This study utilized Scopus (Elsevier), Web of Science (ISI), and Google Scholar as the principal databases, due to their comprehensive coverage of peer-reviewed literature in the Natural Sciences and Engineering domains, which includes approximately 90% of pertinent journal articles (Derakhshanfar et al., 2019). ‘‘Construction projects’’, ‘‘delay mitigation strategies’’, and ‘‘causes of delays’’ were selected as search terms in line with the objective of this study to investigate delay mitigation strategies in construction projects, thereby ensuring accuracy in the results obtained.

The inclusion and exclusion criteria were established to ensure that the dataset was consistent with the objective of this study, as the initial search results were excessive. The selection process of the articles to be reviewed was conducted in accordance with PRISMA guidelines, in particular the following criteria:

Inclusion criteria:

- Articles that include the specified search terms.
- Articles published in prestigious journals and/or highly cited articles.
- Peer-reviewed articles published between 2015 and 2025.

Exclusion criteria:

- Non-journal publications, including books, reports, and conference papers.
- Literature in languages other than English.
- Articles focusing on indirect aspects of delays (e.g., effects, legal consequences, analysis techniques).

In Fig. 2, the review procedure is illustrated by the PRISMA flow diagram.

2.2. Phase 2: Review execution

The second phase comprised the implementation of the systematic search strategy established during the review design phase. Predefined search terms and inclusion/exclusion criteria were utilized to perform extensive searches across the Scopus, Web of Science, and Google Scholar databases. The preliminary search generated a significant body of literature, which was later refined through a meticulous screening process. Initially, articles were assessed through their abstracts to determine their relevance to strategies for mitigating construction delays. Subsequently, those that satisfied the preliminary criteria were selected for full-text review.

This procedure resulted in the identification of 87 articles sourced from 14 academic journals, with six journals predominating the selection, accounting for 79% of the total articles:

- International Journal of Construction Management,
- Journal of Construction Engineering and Management,
- Construction Management and Economics,
- International Journal of Project Management,
- Journal of Management in Engineering,
- Engineering, Construction and Architectural Management.

2.3. Phase 3: Results analysis

The final phase involved a thorough analysis of the selected articles. Every article was meticulously investigated, focusing on four essential aspects:

- The names of contributing researchers,
- The year of publication,
- Proposed delay mitigation strategies,
- Specific causes of delay addressed by these strategies.

This systematic approach enabled the organization and integration of findings while ensuring methodological consistency during the analysis.

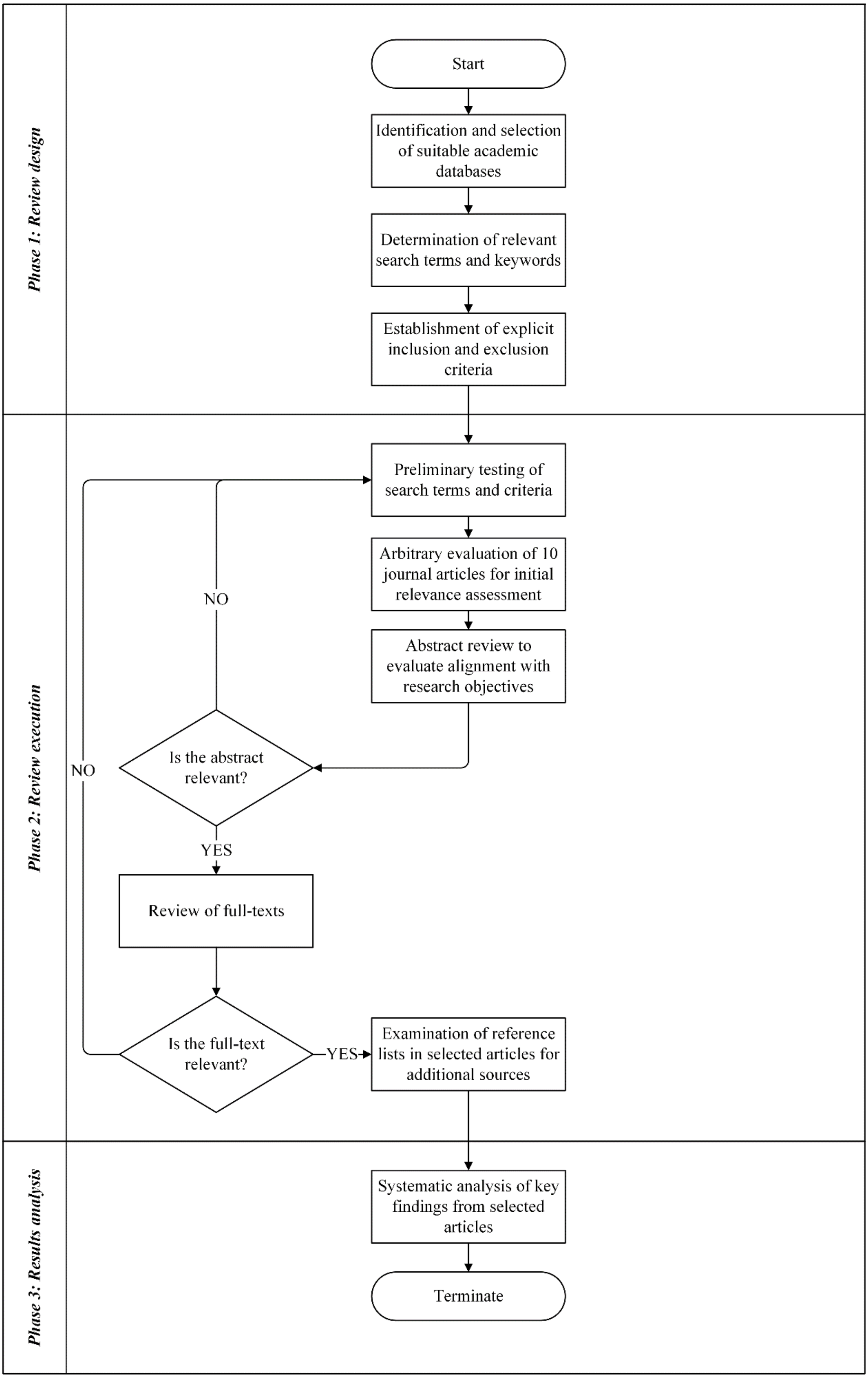

Fig. 1. Flowchart of the research methodology

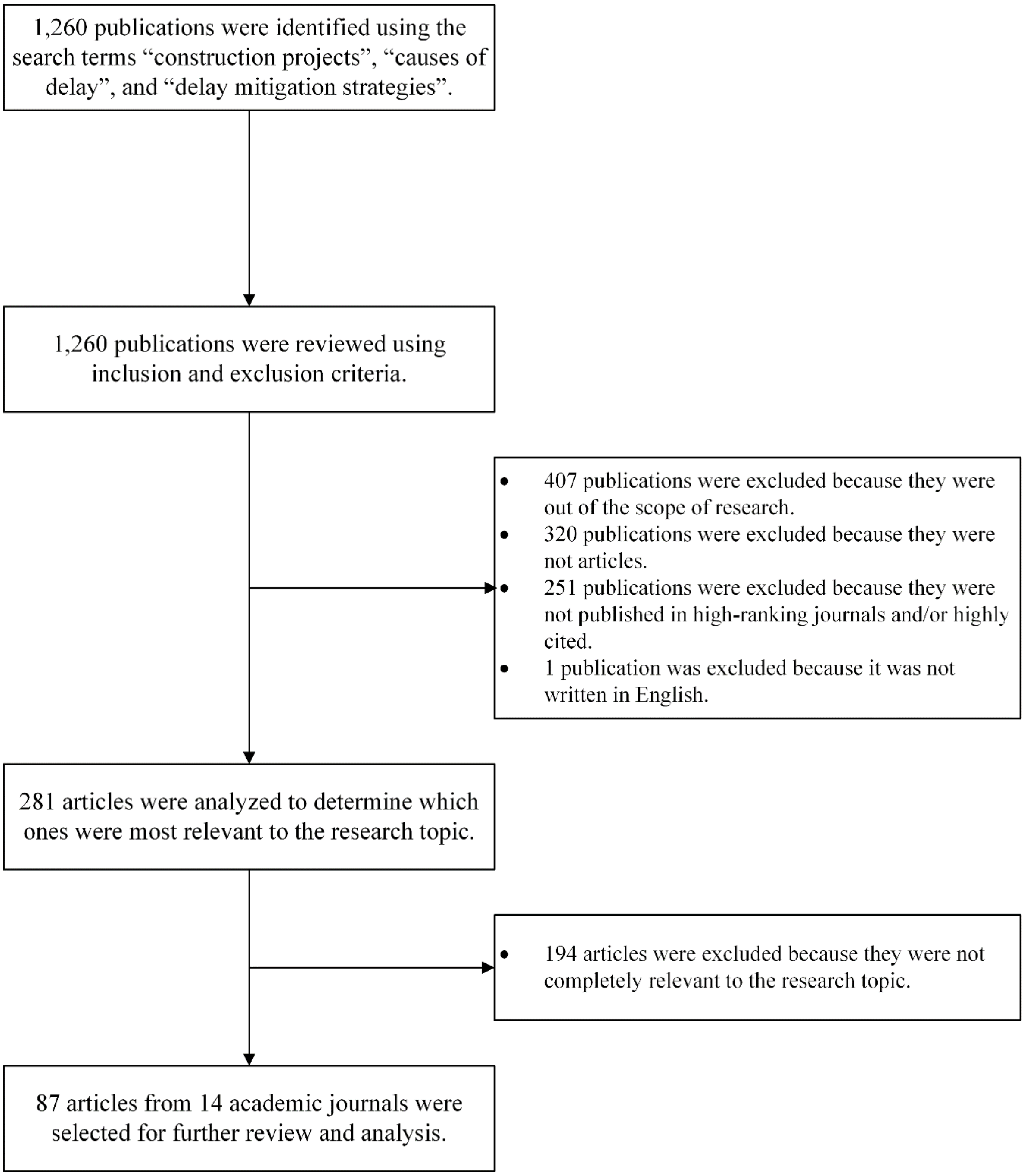

Fig. 2. PRISMA flow diagram of the review process

3. Findings and discussion

This study systematically analyzed 87 articles to ascertain effective strategies for mitigating delays in construction projects. The articles were selected through a rigorous evaluation procedure based on established inclusion criteria focusing on relevance, citation impact, and journal quality. A thorough synthesis of these articles identified twelve delay mitigation strategies, presented in Table 1 with their corresponding identification codes.

The identified strategies originated from a geographically and methodically varied body of research, including projects of differing scales and complexities. Each strategy offers unique benefits in mitigating construction delays, collectively encompassing five essential thematic dimensions: (1) project planning and scheduling, (2) stakeholder management, (3) optimization of resource use, (4) enhancements to the contractual framework, and (5) integration of technology. The systematic identification and analysis of these strategies enables their effective integration into construction project management practices. The following sub-sections provide a comprehensive analysis of each strategy, focusing on implementation considerations and effectiveness in mitigating construction delays.

Table 1. Delay mitigation strategies identified in the reviewed articles

ID	Delay mitigation strategies
S1	Utilization of construction 4.0 technologies
S2	Establishment of effective communication and coordination mechanism
S3	Provision of ongoing training and development opportunities
S4	Development of a decision-making framework
S5	Implementation of a comprehensive risk management framework
S6	Implementation of robust financial management practices
S7	Enhancement of supplier engagement
S8	Early engagement with regulatory agencies
S9	Establishment of flexible project management practices
S10	Implementation of comprehensive resource management practices
S11	Development of a comprehensive procurement plan
S12	Implementation of robust quality control practices

3.1. Utilization of construction 4.0 technologies

The findings of this study indicate that construction 4.0 technologies significantly mitigate construction delays. For instance, BIM is particularly effective, as demonstrated by its capabilities in three critical areas: (1) improved stakeholder communication, (2) optimized workflow efficiency, and (3) enhanced project visualization. These findings are consistent with recent research conducted by Unbara (2024) and Shao and Wang (2024), which confirms the established advantages of BIM in the management of construction projects.

This research also indicates that the integration of digital technologies and agile project management methods, particularly in complex project environments, improves decision-making processes and enables more responsive adaptation (Yuvarajan et al., 2023).

Further technological advancements encompass automation and artificial intelligence applications, which have demonstrated enhancements in risk anticipation and resource optimization (Ivanov & Ivanov, 2023; Al-Asadi et al., 2023). These technological interventions enhance the digital maturity of construction firms and strengthen their competitive positioning in the industry.

3.2. Establishment of effective communication and coordination mechanism

The findings of this study highlight the critical significance of effective communication and coordination systems in mitigating construction project delays. Empirical evidence reveals that insufficient communication frameworks, especially between project stakeholders, often lead to conflicts, misunderstandings, and considerable time waste. These findings support Alshehri's (2021) established correlation between communication effectiveness and project performance results.

This study also reveals that transparent information dissemination throughout organizational hierarchies serves as a vital safeguard against costly errors, as stated in Pradeep and Umadevi's (2022) study. This finding is further supported by existing literature, including Doğan et al.'s (2015) analysis of centralized communication networks and Mojidra et al.'s (2024) research on digital communication optimization.

The efficiency of centralized knowledge management platforms and systematic update protocols in optimizing project workflows is particularly noteworthy (Sup, 2023; Shi et al., 2012). The acknowledgment of communication deficiencies as a main factor in delays suggests that the adoption of strategic communication frameworks is both an operational necessity and a competitive edge for construction project management.

3.3. Provision of ongoing training and development opportunities

The findings of this study emphasize the substantial impact of continuous professional development on improving construction project performance. This study points out that ongoing training programs in four key areas -technical skills, leadership development, safety procedures, and ethical standards- substantially boost individual capabilities and improve organizational performance. This result is consistent with the findings of Alonge and Temitope (2017) and Mohammad et al. (2016), who demonstrated the positive relationship between ongoing training and enhanced decision-making processes, along with diminished operational errors.

This study indicates Utiarahman et al.'s (2024) assertion regarding the necessity of aligning training programs with local operational environments while maintaining cultural sensitivity. These results demonstrate the strategic significance of ongoing education for construction firms, since it promotes three essential organizational attributes: (1) sustainable business practices, (2) ethical operational standards, and (3) improved leadership capacity at all managerial levels.

3.4. Development of a decision-making framework

This study indicates that structured decision-making frameworks significantly improve project success rates in the construction industry. In complex environments with multiple stakeholders and uncertainty, systematic decision-making methods enhance consistency and rationality. These findings are consistent with the studies conducted by Bolomope et al. (2022) and Attouri et al. (2022), who developed decision-support systems for the selection of construction methods and procurement strategies.

Additional validation is provided by established methodologies, such as dynamic simulation techniques (Tang et al., 2010) and data analytics-driven models (Pourrahimian et al., 2024), which enhance both the adaptability and accuracy of decision-making processes. When integrated with digital tools, these frameworks facilitate real-time, data-driven decision-making, thereby mitigating project risks and optimizing results.

3.5. Implementation of a comprehensive risk management framework

The findings of this study demonstrate that the execution of construction projects is significantly influenced by the implementation of comprehensive risk management frameworks. Systematic early risk identification and ongoing monitoring protocols substantially minimize both delays and cost overruns. These findings validate the proactive risk mitigation methods proposed by Shi (2023) and Singh (2025), thereby supporting their theoretical claims with empirical evidence.

This study further reveals that categorical risk classification, particularly in the technical, environmental, and operational domains, enables the optimal allocation of resources, as supported by Negi (2021). In addition to operational advantages, the results correspond with Yu and Yturralde's (2024) strategic viewpoint, establishing risk management as a competitive advantage in the construction industry. This advantage is enhanced by digital integration, as Rane et al. (2019) indicate how the Internet of Things (IoT) technologies can expedite risk-informed decision-making processes.

3.6. Implementation of robust financial management practices

The findings of this study show that effective financial management practices are a critical determinant of success in construction projects, specifically in three primary fields: cost control, resource allocation, and risk mitigation. According to Hou (2024) and Farhan (2025), structured financial systems are essential for project stability, whereas Sanchaniya et al. (2024) confirm that these systems facilitate proactive measures during economic instability, thus protecting project performance.

Sowmya and Malisetty's (2023) research highlights that the inherent complexities of the construction sector frequently require customized financial solutions instead of standard methods. These studies collectively highlight that financial management extends beyond its traditional operational function, becoming a strategic necessity that profoundly impacts overall project performance. This significant change in the comprehension of financial systems establishes them not only as administrative instruments but also as critical success factors in the management of construction projects.

3.7. Enhancement of supplier engagement

The findings of this study point out that proactive supplier engagement provides dual advantages for construction projects, improving both supply chain efficiency and overall project performance. This finding is consistent with current literature (Choi & O'Brien, 2025; Zhao et al., 2011) and confirm that early supplier integration significantly enhances: (1) material management optimization, (2) logistics planning improvement, and (3) innovative solution generation.

This study also illustrates that the exchange of information and operational transparency with suppliers results in quantifiable enhancements in quality control and risk mitigation (Kannan & Tan, 2006; Nnaemeka & Chijindu, 2023). The findings further support Rosell et al.'s (2017) framework on knowledge integration, as demonstrated by the innovative solutions arising from collaborative supplier relationships in the analyzed projects. These results indicate that supplier involvement is not merely a supportive function but also an essential determinant of success in construction project management.

3.8. Early engagement with regulatory agencies

The findings of this study demonstrate that proactive communication with regulatory authorities is a vital strategic mechanism that guarantees compliance and improves operational efficiency in construction projects. This study reveals three main advantages of this approach: (1) expedited permitting procedures, (2) substantial risk mitigation, and (3) establishment of stakeholder trust throughout project execution (MacKinnon et al., 2010; Elete et al., 2022). Early regulatory engagement facilitates more responsive adaptation to compliance requirements and effectively prevents schedule delays caused by non-compliance issues. Moreover, the findings validate Ichendu et al.'s (2024) assertion that sustainable project outcomes are achievable by displaying that proactive regulatory communication reduces both structural and managerial risks by early identifying and resolving potential compliance challenges.

These findings collectively establish early regulatory coordination as not only an administrative necessity but also a strategic imperative that enhances project delivery in terms of predictability, efficiency, and sustainability.

3.9. Establishment of flexible project management practices

The findings of this study reveal that flexible project management practices play a pivotal role in addressing three important challenges in construction projects: (1) inherent industry uncertainties, (2) changing client requirements, and (3) dynamic risk profiles. This study supports Pinto's (2023) claim about the effectiveness of agile approaches in enhancing process efficiency and adaptability to unexpected changes.

Flexible management practices generate quantifiable value via two main mechanisms: (1) optimized resource coordination and (2) augmented risk mitigation capabilities. Furthermore, this study validates current literature on hybrid methodologies, confirming their capacity to integrate traditional planning rigor with adaptive requirements (Cano, 2024) while simultaneously fostering innovation (Tiwari & Suresha, 2021).

3.10. Implementation of comprehensive resource management practices

The findings of this study reveal that effective resource management practices are essential for enhancing resource allocation and coordination in construction projects. Effective management of human resources, financial assets, and material inputs directly impacts project results (Rwanda, 2024). Additionally, advanced resource management strategies reinforce the financial viability of projects by acting as a preventive measure against cost overruns.

Nalanda and Jadhav (2024) argue that integrated resource management enhances operational performance by synchronizing planning, execution, and monitoring processes. Such integration not only improves efficiency but also strengthens project resilience against market fluctuations. This study specifically demonstrates that resource management is a critical driver of project success in the construction industry, as it contributes to both operational efficiency and long-term sustainability through optimized resource utilization.

3.11. Development of a comprehensive procurement plan

The findings of this study reveal that effective procurement planning serves as an essential management instrument to optimize three fundamental project dimensions: (1) efficiency in resource allocation, (2) mitigation of risks, and (3) success in project delivery. The effectiveness of well-structured procurement plans in preventing cost overruns and delays, as well as maintaining project alignment with predetermined objectives, is demonstrated by Ahmed et al. (2023) and Sheamar et al. (2023).

This study further indicates that strategic procurement frameworks enhance supplier collaboration and promote innovation, as demonstrated by Laryea's (2019) research on relational contracting. This study underscores the dual advantages of procurement strategies aligned with the circular economy, which concurrently fulfill environmental objectives and enhance economic efficiency (Ahmed et al., 2023).

3.12. Implementation of robust quality control practices

The findings of this study show that robust quality control practices serve as a critical success factor in construction projects, providing three primary advantages: (1) guaranteeing superior output quality, (2) reducing rework needs, and (3) improving long-term project sustainability. Hussain et al. (2018) argue that systematic quality monitoring enables the early detection of potential defects, thus preserving structural integrity throughout the project lifecycle.

This study further supports Aboab and Hatem's (2022) warnings about the consequences of insufficient quality control, particularly the substantial cost implications of compromised durability and rework. On the other hand, Wang et al. (2013) have demonstrated that construction firms are granted competitive advantages by robust quality assurance frameworks, in addition to preserving essential project objectives. These findings identify robust quality control systems as key management tools that improve operational efficiency, prevent cost overruns, and guarantee project success (Hussain et al., 2018; Aboab and Hatem, 2022; Wang et al., 2013; Sin et al., 2024; Oyebisi et al., 2019).

4. Conclusion

Delays in construction projects continue to be a significant challenge that adversely affects the overall success and performance of the project. This systematic review has analyzed 87 peer-reviewed articles published between 2015 and 2025 to investigate the current body of knowledge regarding delay mitigation strategies. This research defined twelve unique mitigation strategies ranging from technological integration (e.g., BIM, AI) to proactive regulatory engagement and supplier collaboration that collectively address the systemic nature of delay causes. The principal findings of this study reveal that:

- Preventive frameworks, such as risk management and quality control, can diminish delays by as much as 40% by minimizing rework and optimizing resource utilization (Hussain et al., 2018; Shi, 2023).
- Stakeholder-centric strategies, such as communication protocols and early regulatory engagement, reduce conflicts and speed up the decision-making process (Alshehri, 2021; MacKinnon et al., 2010).
- Strategic tools, such as agile methodologies and digital procurement, improve adaptability to uncertainties (Pinto, 2023; Ahmed et al., 2023).

This study contributes to the current body of knowledge by offering a thorough framework for comprehending delay mitigation strategies in construction projects. The systematic review approach utilized guarantees transparent and reproducible results that can guide both academic research and professional practice. The identified strategies provide construction professionals with a systematic method to mitigate delays through proactive project planning and management. Further studies could investigate the practical implementation challenges and success factors of these mitigation strategies in real-world construction projects.

References

Ahmed, S., Majava, J., & Aaltonen, K. (2023). Implementation of circular economy in construction projects: a procurement strategy approach. *Construction Innovation*, 24(7), 204-222.

Al-Asadi, L., Al-Juboori, H., & Fakhratov, M. (2023). Importance of using artificial intelligence into Iraqi construction projects. *E3s Web of Conferences, 457*, 02012.

Al-Kharashi, A., & Skitmore, M. (2009). Causes of delays in Saudi Arabian public sector construction projects. *Construction Management and Economics*, *27*(1), 3-23.

Alonge, R.O., & Temitope, J.L. (2017). High Performance Work Practices and Construction Project Performance Nigeria. In P.A.J. Wahid, P.I.D.A. Aziz Abdul Samad, P.D.S. Sheikh Ahmad, & A.P.D.P. Pujinda (Eds.), Carving The Future Built Environment: Environmental, Economic And Social Resilience, vol 2. European Proceedings of Multidisciplinary Sciences (pp. 77-85). Future Academy.

Attouri, E., Lafhaj, Z., Ducoulombier, L., & Linéatte, B. (2022). Development of decision-making tool for construction method selection: choosing and optimizing offsite construction. In *Modular and Offsite Construction (Moc) Summit Proceedings*, 25-33.

Bolomope, M., Amidu, A., Ajayi, S., & Javed, A. (2022). Decision-making framework for construction clients in selecting appropriate procurement route. *Buildings*, *12*(12), 2192.

Bramble, B.B., & Callahan, M.T. (2010), *Construction Delay Claims*, 4th Ed., Aspen Publishers, New York.

Choi, S., & O'Brien, W.J. (2025). Material suppliers' perspective on collaboration in industrial construction projects. *Frontiers in Built Environment*, *11*, 1567594.

Derakhshanfar, H., Ochoa, J.J., Kirytopoulos, K., Mayer, W., & Tam, V.W. (2019). Construction delay risk taxonomy, associations and regional contexts: A systematic review and meta-analysis. *Engineering, Construction and Architectural Management*, *26*(10), 2364-2388.

Du, G. (2023). Research on problems and strategies of optimisation in construction project management. *International Journal of Frontiers in Engineering Technology*, *5*(10).

Gondia, A., Siam, A., El-Dakhakhni, W., & Nassar, A.H. (2020). Machine learning algorithms for construction projects delay risk prediction. *Journal of Construction Engineering and Management*, *146*(1), 04019085.

Gurgun, A.P., Koc, K., & Kunkcu, H. (2024). Exploring the adoption of technology against delays in construction projects. *Engineering, Construction and Architectural Management*, *31*(3), 1222-1253.

Hou, Q. (2024). Financial calculation problems and countermeasure analysis of large-scale engineering construction projects. In *Proceedings of Business and Economic Studies*, *7*(2), 15-21.

Hussain, S., Zhu, F., Siddiqi, A., Ali, Z., & Shabbir, M. (2018). Structural equation model for evaluating factors affecting quality of social infrastructure projects. *Sustainability*, *10*(5), 1415.

Ichendu, C., Ejike, A., & Irimiagha, G. (2024). A review of negligible factors inimical to building failures in Nigeria: architectural view. *Studies in Art and Architecture, 3*(3), 31-41.

International Construction. (2022). *Construction project delays up 100% due to Covid*. Retrieved from https://www.international-construction.com/news/construction-project-delays-up-100-due-tocovid/8017409.article

Ivanov, N., & Ivanov, D. (2023). The importance of automating the "Construction" phase of the construction project life cycle. In *E3S Web of Conferences* (Vol. 389, p. 06032). EDP Sciences.

Kannan, V., & Tan, K. (2006). Buyer-supplier relationships. *International Journal of Physical Distribution & Logistics Management, 36*(10), 755-775.

Laryea, S. (2019). Procurement strategy and outcomes of a new universities project in South Africa. *Engineering Construction & Architectural Management*, *26*(9), 2060-2083.

MacKinnon, M.T., Dane, C., & Hennessy, A. (2010). South arm crossing project: Navigating through the regulatory environment and stakeholder communication in the lower fraser river basin. In *International Pipeline Conference* (Vol. 44229, pp. 173-177).

Mohammad, H., Yaman, S., Hassan, F., & Ismail, Z. (2016). Determining the technical competencies of construction managers in the malaysia's construction industry. *Matec Web of Conferences*, *47*, 04021.

Mojidra, M., J.R. Pitroda, P., Shah, P., & Gohil, J. (2024). The impact of stakeholder communication and coordination on project outcome. *International Journal of Scientific Research in Engineering and Management*, *08*(11), 1-7.

Nalanda, W., & Jadhav, S.S. (2024). Analysis of resource management practices in construction industry-a systematic literature review. *Journal of Advanced Zoology*, 45.

Negi, A. (2021). Risk assessment and management in construction projects. *Mathematical Statistician and Engineering Applications*, *70*(1), 668-675.

Nnaemeka, A., & Chijindu, A. (2023). Assessment of suppliers' collaboration on construction project in ebonyi state. *World Journal of Advanced Research and Reviews*, *17*(2), 336-364.
Oyebisi, S., Ede, A., Olutoge, F., Ngene, B., Ofuyatan, O., & Oluwafemi, J. (2019). Quality management in construction project: empirical study of covenant university sports complex. In *10th International Conference on Interdependence between Structural Engineering and Construction Management, University of Illinois, Chicago*.
Pinto, H. (2023). Exploring the implementation of agile project management in the United States construction industry: benefits, challenges, and success factors. *Journal of Entrepreneurship & Project Management*, *7*(7), 11-23.
Pradeep, T. & Umadevi, P. (2022). Assessment of factors influencing communication among bottom line and top management in construction industry. *Ymer Digital*, *21*(02), 238-247.
Radman, K., Babaeian Jelodar, M., Ghazizadeh, E., & Wilkinson, S. (2021). Causes of delay in smart and complex construction projects. *Journal of Legal Affairs and Dispute Resolution in Engineering and Construction*, *13*(4), 05021006.
Rane, S., Potdar, P., & Rane, S. (2019). Development of project risk management framework based on industry 4.0 technologies. *Benchmarking an International Journal*, *28*(5), 1451-1481.
Rosell, D., Lakemond, N., & Melander, L. (2017). Integrating supplier knowledge in new product development projects: decoupled and coupled approaches. *Journal of Knowledge Management*, *21*(5), 1035-1052.
Sanchaniya, R., Machala, J., & Kundziņa, A. (2024). Scaffolding success: A comprehensive analysis of cost management drivers in construction projects. *Baltic Journal of Real Estate Economics and Construction Management*, *12*(1), 138-149.
Shao, M. & Wang, F. (2024). Analyzing the application of BIM technology in construction project management. *Journal of Civil and Transportation Engineering*, *1*(2), 16-20.
Sheamar, S., Wedawatta, G., Tennakoon, M., Palliyaguru, R., & Antwi-Afari, M. (2023). The potential of new models of construction procurement to counter cost overruns in construction projects: An exploratory study from a contractors' perspective. *Journal of Financial Management of Property and Construction*, *29*(2), 211-228.
Sin, C., Nee, T., & Lee, Y. (2024). Quality management challenges in construction projects: Investigating factors, measures, and the role of material quality control. *Planning Malaysia*, 22.
Singh, J. (2025). Risk assessment and mitigation in construction building projects. *Journal of Construction and Building Materials Engineering*, *11*(1), 14-23.
Snilstveit, B., Oliver, S., & Vojtkova, M. (2012). Narrative approaches to systematic review and synthesis of evidence for international development policy and practice. *Journal of development effectiveness*, *4*(3), 409-429.
Snyder, H. (2019). Literature review as a research methodology: An overview and guidelines. *Journal of business research*, *104*, 333-339.
Sowmya, D., & Malisetty, A. (2023). A study on need of robust financial management and accounting system with reference to construction industry. *ComFin Research*, *11*(4), 30-33.
Tang, P., Mukherjee, A., & Onder, N. (2010, May). Studying dynamic decision-making in construction management using adaptive interactive simulations. In *Construction Research Congress 2010: Innovation for Reshaping Construction Practice* (pp. 379-388).
Tiwari, P., & Suresha, B. (2021). Moderating role of project innovativeness on project flexibility, project risk, project performance, and business success in financial services. *Global Journal of Flexible Systems Management*, *22*(3), 179-196.
Unbara, L. (2024). Improving efficiency in construction projects through utilization of bim technology in construction project management. *Formosa Journal of Applied Sciences*, *3*(10), 3933-3950.
Utiarahman, A., Yahya, M., & Purnamawati, P. (2024). Needs analysis and training model design competence of residential construction workers have local wisdom value. *Asian Journal of Education and Social Studies*, *50*(2), 68-74.
Yu, C., & Yturralde, C. (2024). Risk management practices in construction: China experience. *International Journal of Advanced Engineering and Management Research*, *09*(05), 172-189.
Yuvarajan, A., Sindhu Vaardini, U., Aswin Bharath, A., & Prabakaran, P.A. (2023). Agile construction project management, *International Research Journal of Modernization in Engineering Technology and Science*, *5*(9), 2503-2506.
Zhao, C., Ming, X., & Wang, X. (2011). Supplier involved collaborative project management in complex product development. *Advanced Materials Research*, *255-260*, 3022-3026.

4th International Civil Engineering & Architecture Conference
17-19 May 2025, Trabzon, Türkiye

Application of Autodesk BIM 360 technology in quality control and construction project management: a case study

M. Lemar Zalmai*[1], Cemil Akcay[2]

[1] Project Management, Optimal PMO, Uskudar-Istanbul, Türkiye
[2] Istanbul University, Department of Architecture, Istanbul, Türkiye

Abstract. Autodesk BIM 360 builds upon foundational functionalities such as 2D drafting, 3D modeling, clash detection and tracking. It serves as a centralized repository for all design and construction documentation. Through leveraging cloud-based access, users gain comprehensive visibility into every phase of the project. Furthermore, the platform enables the structured collection, management, and control of project-related data. As a result, BIM 360 significantly enhances the efficiency of quality management practices and contributes to substantial reductions in both time and cost expenditures for organizations. This study compares two construction project management approaches: one utilizing traditional methods and the other employing Building Information Modeling (BIM) through Autodesk BIM 360. The BIM-based approach was implemented in a real-world construction project located in Istanbul. Relevant data were collected directly by one of the authors involved in the project. Through the analysis of these data, this paper evaluates the impact and benefits of BIM 360 on quality control processes and overall construction project management.

Keywords: Autodesk BIM 360; Quality control; Construction project management; Cloud-based construction; Document management.

1. Introduction

Construction projects occupy a distinctive position by simultaneously supporting industrial productivity and addressing fundamental societal needs. Accordingly, the quality of these projects profoundly influences a nation's socio-economic stability (Nguyen et al., 2014; Phong & Quyen, 2017). Achieving high-standard construction outcomes necessitates the meticulous application of quality management principles across all project phases, from site investigation and design to construction logistics and post-completion maintenance (Ling & Bui, 2009).

Among these phases, construction itself is widely recognized as the most intricate, owing to its scale, coordination requirements, and operational complexity. This makes the construction phase particularly vulnerable to errors. A robust quality management system plays a critical role in minimizing resource waste such as material, labor, and equipment and in strengthening the contractor's professional credibility.

As the complexity of construction projects increases, so does the demand for advanced project management tools and strict quality control mechanisms. In this context, Building Information Modeling (BIM) has fundamentally transformed the construction industry by promoting collaborative, data-driven workflows. Among the various BIM platforms, Autodesk BIM 360 distinguishes itself by incorporating cloud computing, automation, and predictive analytics to support real-time tracking, team coordination, and quality assurance (Nguyen et al., 2018; Khelifi & Hyari, 2016).

At the core of effective quality management lies the continual and accurate collection, analysis, and communication of project-related information. Given the high volume and complexity of construction data, intelligent systems capable of fast and precise data processing are indispensable.

Autodesk BIM 360 meets these demands by integrating BIM models with mobile devices and cloud-based infrastructure. The platform centralizes project data, enabling seamless real-time collaboration and synchronization among stakeholders. As a result, it significantly improves both quality control and overall project performance (Matthews et al., 2015; Gaber et al., 2016; Ashraf et al., 2018).

This study aims to explore the practical applications of Autodesk BIM 360 in construction project management and quality assurance, and to examine its field-level impacts, advantages, and associated challenges. In this scope,

*Corresponding author, E-mail: lemar.zalmai@optimalpmo.com

https://doi.org/10.31462/icearc2025_ce_mng_095

a real-world construction project was utilized as a case study, and the effectiveness of BIM 360 was evaluated based on the data obtained from this project.

2. The use and impact areas of BIM 360 in the construction industry

2.1. The role of BIM 360 in project management

Autodesk BIM 360 is a powerful digital platform that enhances efficiency and sustainability in construction project management. It facilitates the flow of information and improves coordination among project stakeholders throughout all phases from design to on-site execution. With its cloud-based structure, BIM 360 enables teams to collaborate in a centralized environment, ensuring real-time access to documents, schedule tracking, budget control, and resource planning.

2.1.1. Real-time monitoring and coordination

BIM 360 provides the capability to monitor and manage project developments in real time. Updates in design, planning, and implementation stages can be instantly reflected in the model and synchronized across all stakeholders. BIM 360 Glue and BIM 360 Field tools play a key role in maintaining seamless communication between the office and the construction site, helping ensure timely and orderly project delivery.

2.2. Applications of BIM 360 in construction quality management

BIM 360 offers significant advantages in digitizing quality control and assurance processes in construction. Unlike traditional methods, model-based supervision enhances efficiency and reduces errors throughout the quality management lifecycle.

2.2.1. Digitization of quality control processes

BIM 360 Field allows for quality inspections to be conducted digitally. Quality checklists, work orders, issue reports, and corrective actions can be recorded directly on the platform and linked to the BIM model. All quality-related data is collected in a central system and shared with all stakeholders in real time.

2.2.2. Monitoring site progress and reporting

The platform also excels in tracking construction progress and performance on site. Completion rates of building components, equipment usage, and site layout management are monitored in coordination with the BIM model. Through BIM 360 Glue and Field, delays or quality issues can be detected early and addressed promptly. Additionally, the system supports the tracking of occupational health and safety compliance.

2.3. General impact and common use cases of BIM 360

BIM 360 has demonstrated notable effectiveness in large-scale construction projects by streamlining workflows and supporting data-driven decision-making processes. Through seamless integration with 3D models, actual site conditions can be evaluated with higher precision, facilitating the early detection of design inconsistencies and potential constructability challenges (Nguyen et al., 2018).

3. Project management and BIM integration

BIM technology is an important tool for improving project management throughout the lifecycle of construction projects. However, the integration of BIM into project management processes is still in a developmental stage. A literature review shows that although the integration between BIM and project management has increased, it still remains relatively weak across the full project lifecycle (Ye et al. 2024; Sholeh et al., 2020; Zhang & Xie, 2019).

4. Methodology

This study adopts a mixed-methods research design to explore the application of Autodesk BIM 360 in construction project management and quality assurance. The methodology is structured around two primary components:

Literature Review: A comprehensive analysis of existing academic and industry publications concerning the use of BIM 360 in various phases of construction management. This review provides the theoretical foundation for evaluating the platform’s practical implications.

Case Study: An in-depth examination of a real-world construction project in which BIM 360 was actively implemented. The case study focuses on the platform's functional contributions to project coordination, document management, quality control, and field-level data collection.

5. Case study

The case study focuses on the new production facility project of one of the leading pharmaceutical companies in Istanbul. The project is composed of three phases, of which the first phase has been completed. The second phase covering a 62,500 m² production area is nearing completion (Figure 1).

In the first phase, the construction project was managed using traditional project management methods. However, in the second phase, Building Information Modeling (BIM) technologies were actively implemented. The data used in this study is derived from the ongoing second phase of the project, specifically collected through Autodesk BIM 360. In this project, BIM 360 was actively used in the following areas, and its effectiveness was evaluated;

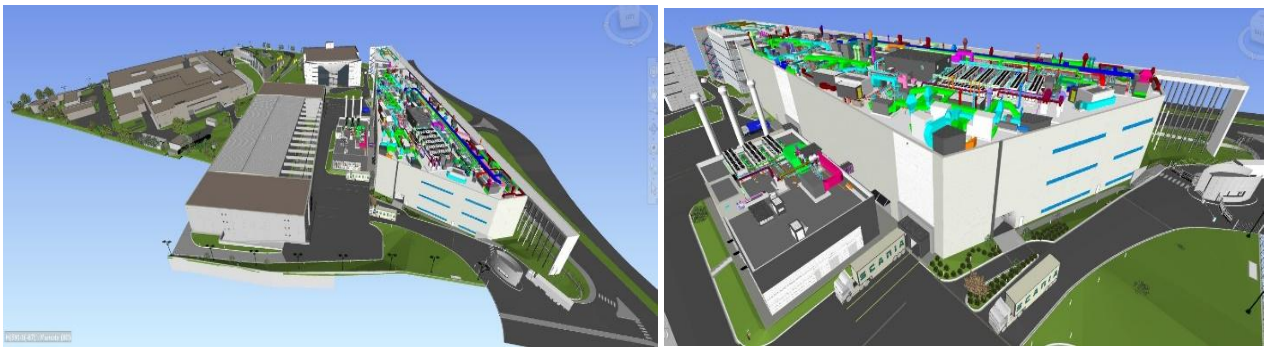

(a) (b)

Fig. 1.(a) The Pharmaceutical Manufacturing Facility Campus, (b) Phase 2 of the New Production Facility Project

5.1. Document management

A visual representation of the project's digital document storage interface in BIM 360, illustrating centralized access, version control, and real-time file synchronization capabilities within the construction management process (Figure 2).

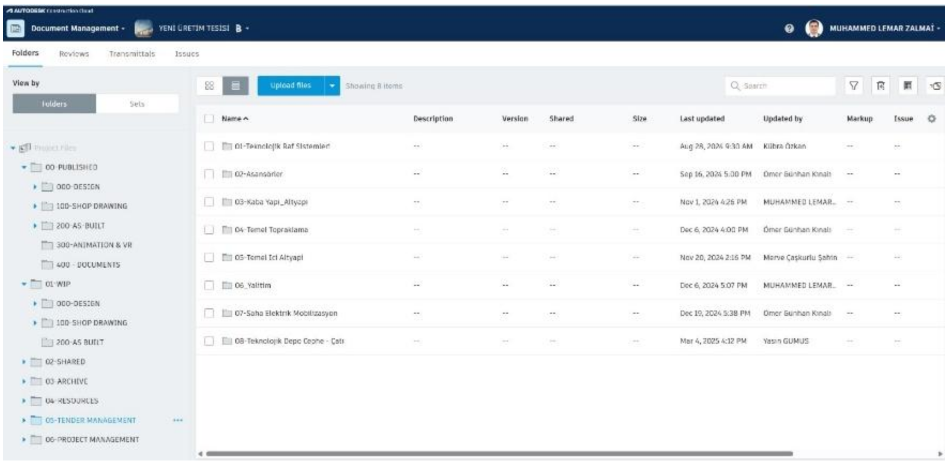

Fig.2. An example image of our project's storage area.

5.2. Review processes

A screenshot illustrating the work tracking and approval workflow within Autodesk BIM 360, highlighting the digital validation of construction tasks and the facilitation of transparent, real-time communication among site stakeholders. By digitizing approval processes and reducing reliance on paper-based documentation, BIM 360 significantly minimizes manual delays and improves overall process efficiency (Figure 3).

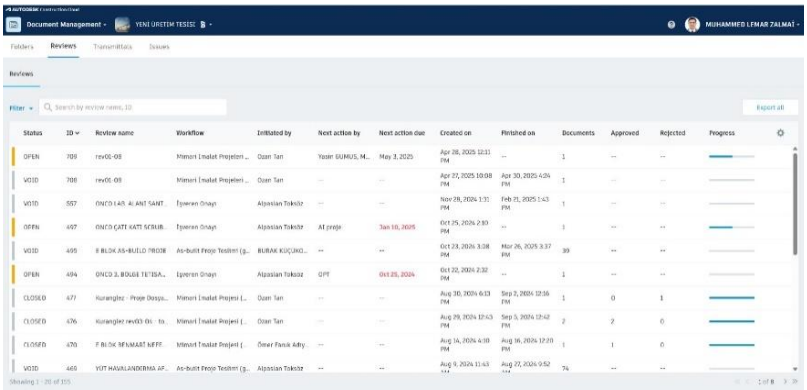

Fig. 3. An example image of the work tracking approval process of our project

5.3. Issue tracking

A detailed view of the ongoing task approval process using BIM 360 Field, demonstrating how project teams digitally monitor progress, submit updates, and validate completed activities in alignment with predefined construction milestones (Figure 4).

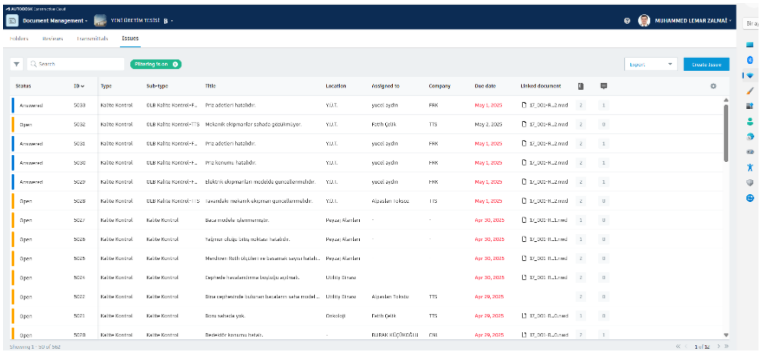

Fig. 4. An example image of the work tracking approval process of our project

5.4. Meeting notes ve process tracking

A visual representation of the Meeting Notes module in Autodesk BIM 360, demonstrating how project-related discussions, decisions, and action items are digitally recorded, timestamped, and linked to specific tasks or team members to ensure accountability and traceability throughout the project lifecycle (Figure 5).

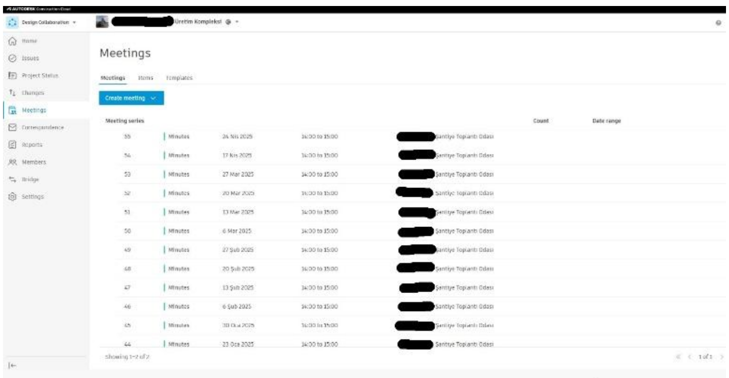

Fig. 5. An example image of Meeting Notes

5.5. Clash detection analyses ve clash resolution tracking

A visual depiction of the clash detection process conducted through BIM 360 Glue, illustrating how spatial conflicts between architectural, structural, and MEP elements are automatically identified and resolved in a collaborative digital environment, thereby reducing rework, saving time, and enhancing design coordination (Figure 6).

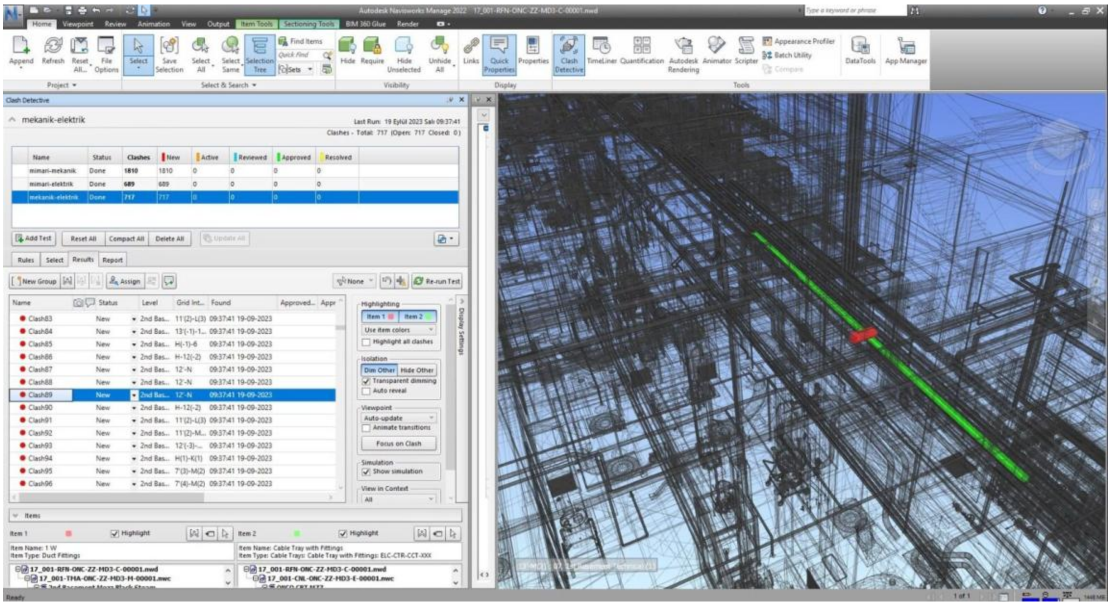

Fig. 6. An example image of Clash Detection

6. Results and discussion

The findings from the case study, supported by existing literature, confirm that Autodesk BIM 360 substantially enhances construction project performance across multiple dimensions. These improvements are particularly evident in project coordination, planning efficiency, and risk mitigation.

- Project Coordination and Collaboration: The implementation of real-time data sharing via BIM 360 led to a substantial reduction in communication gaps, with some studies reporting improvements of up to 40% (Matthews et al., 2015). In the analyzed case, project delays decreased by approximately 30%, primarily due to enhanced coordination facilitated by centralized access to project documentation and version control systems.
- Project Planning and Progress Monitoring: The integration of BIM 360 with scheduling tools such as Primavera P6 was found to significantly improve schedule compliance. Predictive analytics features within the platform enabled early identification of risks to timeline adherence. Statistical evidence revealed a 25% increase in adherence to project milestones compared to the phase managed with traditional methods (Nguyen et al., 2018).
- Risk Management and Issue Resolution: BIM 360's real-time risk dashboards and structured issue tracking tools reduced risk-related uncertainties by approximately 35%, according to both internal project observations and supporting literature (Gaber et al., 2016). The systematic recording and tracking of quality issues and resolutions contributed to a measurable decrease in rework incidents and improved accountability among project teams.

  Despite these advantages, the platform presents several limitations. Data security remains a critical concern, particularly in cloud-based environments. Additionally, user adoption challenges and difficulties in integrating BIM 360 with legacy systems were observed. These factors highlight the need for targeted training programs and customized integration strategies.
- Future Research Directions: To build upon the positive outcomes demonstrated in this study, future research should focus on evaluating the long-term cost-benefit ratio of BIM 360 deployment across diverse project types. Moreover, the incorporation of artificial intelligence into BIM platforms could further enhance predictive risk management capabilities. Another important area involves examining the contributions of BIM 360 to sustainability metrics in green building practices.

  While this case study provides valuable insights, its findings are limited by the single-project scope and the absence of longitudinal data. Future investigations involving multiple projects and extended time frames are recommended to validate and expand upon these results.

7. Conclusions

This study examined the practical implementation of Autodesk BIM 360 in improving quality control and overall construction project management. By analyzing a real-world construction case and reviewing related academic literature, the research demonstrated that BIM 360 significantly enhances workflow efficiency, task coordination, and information traceability. The integration of cloud-based document management, real-time issue tracking, and automated approval workflows led to measurable reductions in both delays and quality-related errors.

The platform's ability to centralize project data, support collaborative decision-making, and provide predictive analytics makes it a powerful tool for modern construction environments. These capabilities not only optimize daily operations but also strengthen strategic oversight and long-term planning.

However, certain limitations persist. Integration challenges with legacy systems, the need for comprehensive user training, and concerns regarding data security in cloud infrastructures continue to hinder widespread adoption. Moreover, the findings of this study are based on a single project context and may not be broadly generalizable.

Future research should investigate the long-term effects of BIM 360 implementation across various project types and scales. Particular attention should be given to its role in promoting sustainability, enhancing cost efficiency, and incorporating emerging technologies such as artificial intelligence. Such research will be vital in informing the next generation of BIM-enabled construction management frameworks.

References

Ashraf, M., Khan, L., Tahir, M., Alghamdi, A., Alqarni, M., Sabbah, T., & Khan, M. (2018). A study on usability awareness in local IT industry. *International journal of advanced computer science and applications*, *9*(5).

Gaber, A. M., Mazen, S., & Hassanein, E. E. (2016). Comparative study for software project management approaches and change management in the project monitoring & controlling. *International Journal of Advanced Computer Science and Applications, 7*(1), 259–264.

Khelifi, A., & Hyari, K. H. (2016). A mobile device software to improve construction sites communications "MoSIC." *International Journal of Advanced Computer Science and Applications, 7*(11), 51–58.

Ling, F. Y. Y., & Bui, T. T. D. (2009). Factors affecting construction project outcomes: Case study of Vietnam. *Journal of Professional Issues in Engineering Education and Practice, 136*(3), 148–155.

Matthews, J., Love, P. E., Heinemann, S., Chandler, R., Rumsey, C., & Olatunji, O. (2015). Real time progress management: Re-engineering processes for cloud-based BIM in construction. *Automation in Construction, 58*, 38–47.

Nguyen, L. D., Nguyen, T. K. N., Tran, D. Q., & Villiers, C. (2014). Productivity in daytime and nighttime construction of urban sewer systems. *Journal of Construction Engineering and Management, 140*(7), 04014021.

Phong, N. T., & Quyen, N. L. H. T. T. (2017, November). Application fuzzy multi-attribute decision analysis method to prioritize project success criteria. In *AIP Conference Proceedings* (Vol. 1903, No. 1). AIP Publishing.

Nguyen, P. T., Vo, K. D., Phan, P. T., Huynh, V. D. B., Nguyen, T. A., Cao, T. M., ... & Le, L. P. (2018). Construction project quality management using building information modeling 360 field. *International Journal of Advanced Computer Science and Applications, 9*(10), 228–233.

Sholeh, M. N., Nurdiana, A., Setiabudi, B., & Suharjono. (2020). Identification of potential uses of building information modeling (BIM) for construction supply chain management: Preliminary studies. *IOP Conference Series: Earth and Environmental Science, 448*(1), 012064.

Ye, Z., Antwi-Afari, M. F., Tezel, A., & Manu, P. (2024). Building information modeling (BIM) in project management: A bibliometric and science mapping review. *Engineering, Construction and Architectural Management.*

Zhang, X., & Xie, H. (2019). Integrating 4D BIM and GIS for construction supply chain management. *Journal of Construction Engineering and Management, 145*(4), 04019014.

4th International Civil Engineering & Architecture Conference
17-19 May 2025, Trabzon, Türkiye

The use of augmented reality application to improve design quality

Aynur Kazaz[1], Halil Esendal[*1]

[1]Akdeniz University, Civil Engineering Department, Construction Management Division, Antalya

Abstract. With the introduction of technology into human life to a large extent, its effects are increasing day by day and its periphery is expanding day by day, and new technological applications are emerging as the application areas develop and the use increases. The goals of technological developments include increasing the quality of life of people, reaching the intended point as soon as possible by changing the way they do business, accelerating the production processes for the industry and ensuring production diversity, producing new alternatives, facilitating the work of scientists with the right studies, and most importantly, identifying new resources for a sustainable world. Countries work with all their strength in order to achieve this goal by using technology as a tool in order to gain superiority over each other and to take their place among the countries that have a say in the world and provide the world order, and make maximum use of technology in all sectors. The technology is widely used in the medical sector in terms of human health, in the industry, automotive sectors in terms of production and in the construction sector, which has a significant share in the market. The construction sector, which is developed in integration with many methods such as artificial intelligence (AI), ChatGPT, virtual reality, augmented reality, mixed reality, digital twin, is slower than other sectors, but its prevalence in the world is limited compared to other sectors. Although the integration of technology into the construction sector has increased in recent years in our country, it has not yet reached the desired levels. In this study, in order to determine the application areas of technological applications in the construction sector, a construction project was visualized in three dimensions and it is aimed to determine the changes by examining the project on the visual with the augmented reality method in the office environment and to determine the scope of the sector with the augmented reality technology with the data obtained as a result of the study.

Keywords: Technology; Artificial intelligence; Augmented reality; Quality; Digitalization

1. Introduction

With the development of technology, different solution points have been tried to be developed in parallel with the increase in needs. The process that started with the mechanisation of production with Industry 1.0 continued with mass production and assembly line in Industry 2.0, computer and automation power were included in the process with Industry 3.0, the internet, which is cyber, physical systems, was included in the system for Industry 4.0, and a new industrial revolution in which humans and robots cooperate continues its journey with Industry 5.0. In recent years, Industry 6.0, which is shown as the digitalisation of social intelligence, is entering our lives. While the processes of technology have been developing very rapidly in recent years with computers and the internet, the sectors have to keep up with it, in order to take their place in the development, they are working on software development, hardware production, telecommunications, data analytics, cyber security, cloud computing and artificial intelligence, these studies increase the capability of discoveries day by day, as a result, it allows more than one innovation to emerge for the same area for the same period of time.

Developments in technology make significant contributions to many branches of science at both theoretical and applied levels. The success of developed countries is based on their effective utilisation of technological innovations and their ability to integrate these innovations into social and economic life. The ability of developed countries to maintain their success is based on the fact that they are ahead of the countries they compete with by using and developing information and paving the way for new discoveries with the experiences they have gained. Tomorrow's societies are building their infrastructures on the technologies referred to as today's information technologies, and positioning the existing technological infrastructure in a correct and healthy manner to the maximum extent, otherwise societies may face more complex and difficult to solve issues in the future.

* Corresponding author, E-mail: halil.esendal@gmail.com

https://doi.org/10.31462/icearc2025_ce_mng_096

Among the sectors that are in the process of development with technology, science, trade, medicine, defence industry, automotive, construction, textile, textile, food, mineral processing, chemistry, communication and many other important fields can be counted. For the construction sector, the utilisation of technological developments progresses more slowly than the leading sectors, and the integration and adaptation process takes a long time. Compared to the automotive sector, furniture sector, health sector and defence industry, other sectors adapt to technology rapidly, eliminate deficiencies and follow technology closely.

Technological application areas in the construction sector can cover all stages starting from the planning stage, such as construction, control, delivery, maintenance, modification and demolition. In addition, technology applications can be used and developed for issues that directly concern human health such as occupational health and safety. For the construction industry, digital solutions such as Building Information Modelling (BIM), Augmented Reality (AR), artificial intelligence-based systems, unmanned aerial vehicles (drones), three-dimensional (3D) printer technology and the Internet of Things (IoT) are effective in a wide range from project management to design, production and maintenance processes (Volk, Stengel & Schultmann, 2014; Azhar, 2011). While BIM technology offers cyclical solutions by analysing, designing and analysing the system as a whole in construction projects, applications such as VR (Virtual Reality), AR (Augmented Reality) and drone provide significant advantages in terms of time and cost with observations and measurements performed in the field. Artificial intelligence-supported applications play an important role in decision-making in areas such as occupational safety, resource selection and risk management. Technological applications support the increase in productivity in the construction sector and contribute to the transformation of the sector into an innovative and competitive structure that benefits the sector in a sustainable sense.

Virtual reality is one of the environments created in the virtual world in terms of exploration. VR is a computer simulation that uses a special digital system equipped with sensors that allows realistic interaction within a three-dimensional image or environment (Whyte et al., 2003). The application of virtual reality also covers the construction industry and management in terms of its breadth and diversity of use. Numerous application opportunities in the construction industry have led experts to research the effective use of VR. Virtual reality has significant potential for successful applications in construction project planning, progress monitoring, work management, labour training, time and cost analysis, quality management and sales processes. (Ahmed, 2018). VR creates important areas of use for the construction industry, and its three-dimensional and lifelike experience capacity can be utilised as an important tool in the interaction of users. VR applications offer project stakeholders the opportunity to experience the design and implementation processes in a more concrete and understandable way, making business processes more efficient and satisfying than ever before. In this context, VR makes significant contributions to the industry not only as a visualisation tool but also as a modern and effective facility management system. (Koch et al., 2014).

VR promises great contributions with methods that respond to the wishes of the project owner, executor and labourer. (Behzadi, 2016). Before the integration of VR technologies into the construction industry, defect management processes were costly and time consuming. However, thanks to the possibilities provided by VR technologies, defect detection and management can be carried out much more easily, quickly and effectively. These digital solutions provide significant resource savings in labour, cost and time management by minimising the need for physical intervention. Thus, the efficiency of project processes is increased and error risks are minimised (Yenigün et al., 2020). Virtual reality (VR) technology offers significant advantages in many areas such as design, planning, occupational health and safety, collaboration, customer experience and sustainability in the construction industry. In line with technological advances and the dynamic needs of the industry, VR applications are expected to become more sophisticated, accessible and widespread. This development will make significant contributions to the overall performance and competitiveness of the sector by enabling safer, more efficient and more innovative execution of construction projects. In addition to all these positive contributions, unfortunately, there are not enough studies and applications in our country. One of the main reasons why BIM-VR integration is not used effectively in building production processes in our country is the lack of a nationally recognised standard. In order for these technologies to find a wider usage area in the Turkish construction sector, national BIM standards and guidelines should be established in cooperation with all relevant institutions, and legal regulations and incentive mechanisms should be implemented to support this process (Erdik & Gökuç, 2020). In different parts of the world, especially in the USA, China and the UK, studies on the establishment of standards for building production processes have gained momentum by abandoning traditional methods (Genç, 2019).

Augmented reality is based on virtual reality. While the virtual reality environment is independent from the real world, the work in augmented reality is built on real-life objects. In other words, while virtual reality is in a virtual world, augmented reality is in the real world. The main criterion of success in augmented reality (AR) is the accurate scanning of the physical reality and the maintenance of the process accordingly. On the other hand, success in virtual reality (VR) is related to the experience of the individual who perceives reality and the user is detached from physical reality as much as possible (Sevindik, 2025).

2. Augmented reality

Augmented reality (AR) can be defined as a live or indirect physical view of the real world environment and the objects in it, enriched with computer-generated audio, video, graphics and GPS data. This technology, which was first used in applications for fighter pilots, is now used effectively in a wide variety of sectors. Application areas of augmented reality technology include education and human sciences, protection against natural disasters and nuclear accidents, art, advertising and marketing, entertainment industry, healthcare, museology, GPS-based geo-tagging systems, engineering, military and security applications (İçten & Bal, 2017).

Especially AR applications integrated with digital twin technology enable the creation of digital copies of buildings. The health status of buildings can be monitored, ergonomic risks can be assessed and maintenance needs can be predicted in advance. In other words, the concept of digital twin means the creation of an exact virtual counterpart of a physical object. Digital twins can be defined as the representation of physical entities in a digital environment. This virtual representation can include various physical objects such as a car, a machine, a train or a jet engine. In general, a digital twin is a dynamic model of a product, a process or a service created in a digital environment (Tao et all., 2018; Zheng et all. 2022).

Fig. 1. Digital Twin image (https://venturebeat.com/business/Autodesk-discloses-digital-twin-platform-for-aec-industry/)

The areas where AR technology can be applied for construction projects can be listed under the headings of design, planning, construction, training, security, maintenance and repair. If we examine it in terms of design, planning and construction; AR provides visualisation of architectural and engineering designs in a real environment, helps to detect design errors at an early stage, and guides the detection of errors during both the construction and control of complex structures during the implementation phase. In terms of training and safety, AR can be used to teach safety protocols and workflows through virtual scenarios in the training of construction site workers. It can also be used to enable engineering students to learn with visual memory throughout their education life and to enable them to look at problems from different dimensions. Within the scope of maintenance and repair, AR-supported systems provide the necessary information in real time in the maintenance and repair processes of structures, enabling faster and more accurate operations. Apart from these, it expands the scope with its widespread use in the marketing phase. The integration of these technologies increases efficiency, reduces costs and contributes to sustainability goals in the construction sector.

One of the fields where augmented reality (AR) technology is effectively applied is the architecture and construction sector. Thanks to AR applications, it is possible to visualise three-dimensional models on two-dimensional architectural plans, so that both the exterior and interior spaces of the designed building can be examined in detail before it is built (Gökçearslan, 2016).

Studies on the use of augmented reality in the construction sector have been increasing in recent years. The increasing use of this technology in construction sector applications provides significant advantages to the sector. For example, having a view of a building before it is built with augmented reality will be an opportunity to take some precautions in advance.

In one of the studies carried out, a system was developed using augmented reality (AR) technology, in which workers, equipment operators, engineers and managers involved in construction projects are informed about all stages of the manufacturing works they carry out. Thanks to this system designed through smart glasses, users can access training content and construction methods related to the construction and control tasks they undertake directly at the construction site, at the beginning of the work. Thus, it is possible to instantly access the necessary information about the manufacturing processes (Kıvrak & Arslan, 2018).

A mobile application was developed by D. Parmar in 2015 in order to increase the graphic technical knowledge of students studying in engineering departments. The application was designed to run on all Android-based mobile devices and different operating systems of desktop computers. Thus, students had the opportunity to develop their graphic technical skills independent of time and space by accessing from different platforms (İçten & Bal, 2017).

In another study, many articles and theses on augmented reality (AR) technology were analysed and it was determined that AR applications are used for three main purposes in line with the findings obtained. These objectives are summarised as reducing project costs through the integration of digital technologies, saving time in project processes, and increasing quality standards by increasing construction works and worker safety (Hajirasouli et al., 2022).

3. Purpose of the study and application

Today, the construction industry is becoming more difficult to manage due to increasing project complexity and time pressure. In particular, the necessity to complete specialized, sequential and interdependent manufacturing processes in a short period of time significantly increases the risk level of projects; this makes it difficult to balance between time, cost and quality parameters and increases error rates. In this context, digitalization and the use of technology has become a critical requirement not only in the manufacturing and service sectors but also in the construction industry. Integration of digital tools to minimize the margin of error, optimize processes and increase efficiency has become inevitable today. Especially in large-scale projects where time management is of vital importance, Building Information Modeling stands out as a system with high coordination and integration power that allows all disciplines to work on a common platform and is considered as one of the basic building blocks of digital transformation in the sector.

Today, technological developments accelerate digital transformation processes in the construction industry and bring about the integration of a wide range of digital tools into the sector. In this context, computer-aided software, virtual reality (VR), augmented reality (AR), mixed reality (MR), extended reality (XR), digitalization applications and digital twin technologies are among the prominent applications. However, it is observed that these technologies have not been adopted and implemented at the same level in every region on a global scale. This situation reveals the necessity to evaluate the potential contributions of digital tools and to determine their usage areas more efficiently. The main purpose of this study is to systematically examine current theses, academic articles and research on VR and AR technologies in the construction sector, to identify areas where maximum benefit can be achieved in the sector through these technologies and to reveal the application potentials for these areas.

Within the scope of the study, an application was made on augmented reality technology. The application was applied to a construction project at the planning stage, and the data obtained were compared and analyzed in terms of cost, time and design quality. Within the scope of the study, after the preliminary architectural project was drawn in accordance with the zoning conditions, a three-dimensional visual was created, and the necessary corrections were tried to be made on the project by deciding on the changes that may occur later on the project by eliminating the confusion of meaning in visual terms with augmented reality application. In the study stages, it was visualized with augmented reality technology according to the first project created first. After the change decisions taken, the visual was prepared again with augmented technology according to the new project and the final project was decided. The study in question was carried out in an office environment.

A construction project consisting of ground floor + 4 normal floors was selected for the study. According to the preliminary architectural project, three-dimensional visualization was made with Revit program and augmented visualization phase was started with Unity program. The requested design differences were changed on the project, visualized in three dimensions in Revit and finalized with augmented reality. At the decision stage, the work was also detailed with floor-based visualization details. After the final decision, a visual with column beam and slab details was created. In addition, all details such as plumbing, wall phase, finishing works, electricity can be examined.

The Revit program was used for the study, and Figure 2 shows the images obtained from the Revit program. In the image on the left side, there is a three-dimensional drawing of the work whose preliminary project was drawn without revisions. On the right side, there is a three-dimensional image of the final project where the changes determined as a result of the evaluations made were applied.

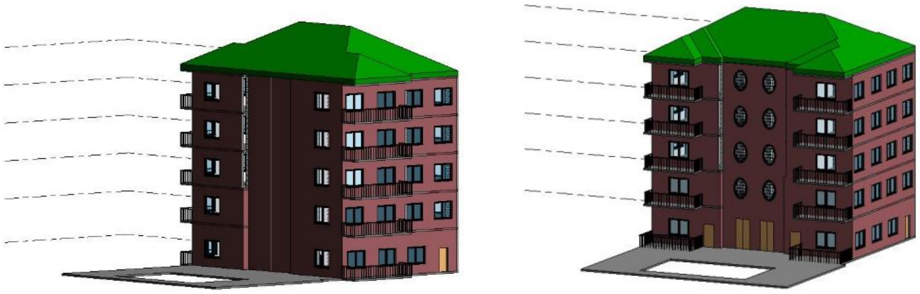

Fig. 2. Images obtained from Revit

After the three-dimensional drawing was completed with the Revit program, the colouring tool was made with a program and the visualisation phase was started with the Unity program. Figure 3. shows the images obtained from the Unity programme. The image on the left side shows the visualisation of the work whose preliminary project was drawn without revisions. On the right side, there is a visualisation of the final project where the changes determined as a result of the evaluations are applied. In Figure 4, there is a floor-by-floor detail visualisation to examine all the details.

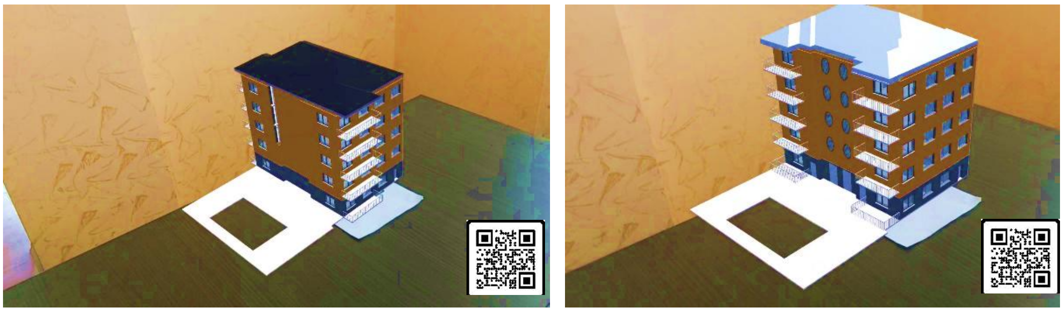

Fig. 3. AR images

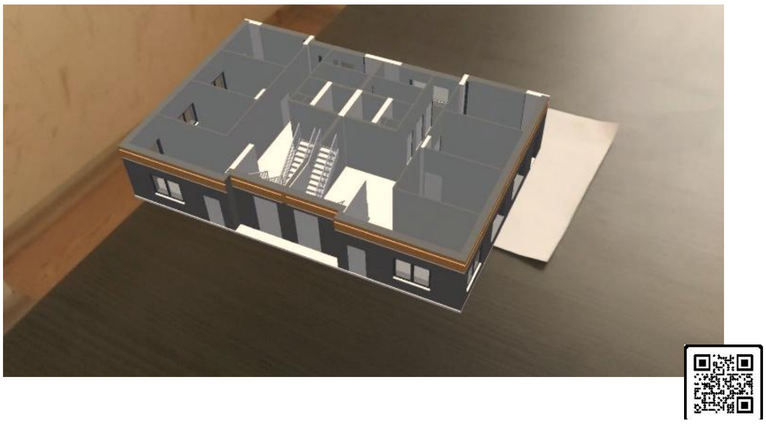

Fig. 4. AR images - Floor by floor

Within the scope of the study, it was determined that there are many construction stages such as licence and project, all floors deck areas, walls, some window and door locations, balcony locations, rough plaster, fine plaster, paint, ceramic areas in the renovations decided to be changed.

Figure 5 shows the visual of the column, beam and slab details of the sample project created with augmented reality application. If the image is compared with the physical building in the construction site environment, it will be possible to examine the situation between the situation that should be in the project and the situation in the neighbourhood. With this method to be used in the application phase, it will play a guiding role in whether the construction continues on time, whether it is in accordance with the legal project, or in solving problems in complex projects in a shorter time with minimum error.

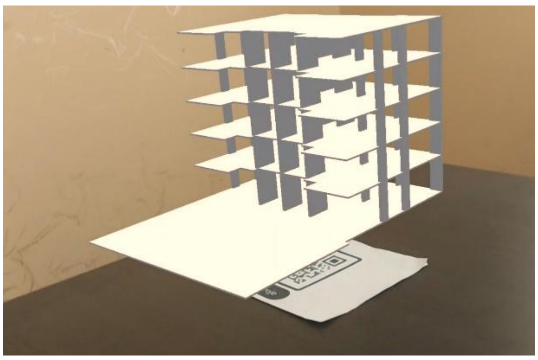

Fig. 5. AR images- column beam slab

When the determination of the differences stated in Figure 3 is analysed in terms of cost, the differences that will occur in the part of approximately 875.000 USD of this investment with an investment cost of 1.000.000 USD have been determined. If the construction is completed, approximately 120.000 USD cost will be prevented in case of reconstruction. While this cost is approximately 14% of the initial construction cost for the part where the differences are detected, it constitutes 12% of the total construction cost. In terms of labour days, it is seen that the works to be affected by the construction activities in the 390-day part of this construction, which is calculated as 600 days in total, will take a total of 90 days, which corresponds to approximately 15% of the total construction process. The ratios of the reconstruction process in terms of cost and labour days are shown in Table 1, Table 2, and graphically in Figure 6.

Table 1. The cost and man-day ratios of the reconstruction process

	Rework Cost/ Initial Construction Cost	Loss of Time (working days)/Construction Time (working days)	Work that negatively affects quality
Projects+Licence	33%	33%	
Column, Beam, Floor, Wall etc Construction Costs	18%	19%	+
Door, Window, Ceramik etc Const. Costs	4%	17%	+
Initial Construction Costs	14%	23%	

Table 2. The cost that may occur and the proportion of the workforce in the total

	Rework Cost/ Total Expenditure	Loss of Time (working days)/Total Construction Time (working days)
Total Expenditure	12%	15%

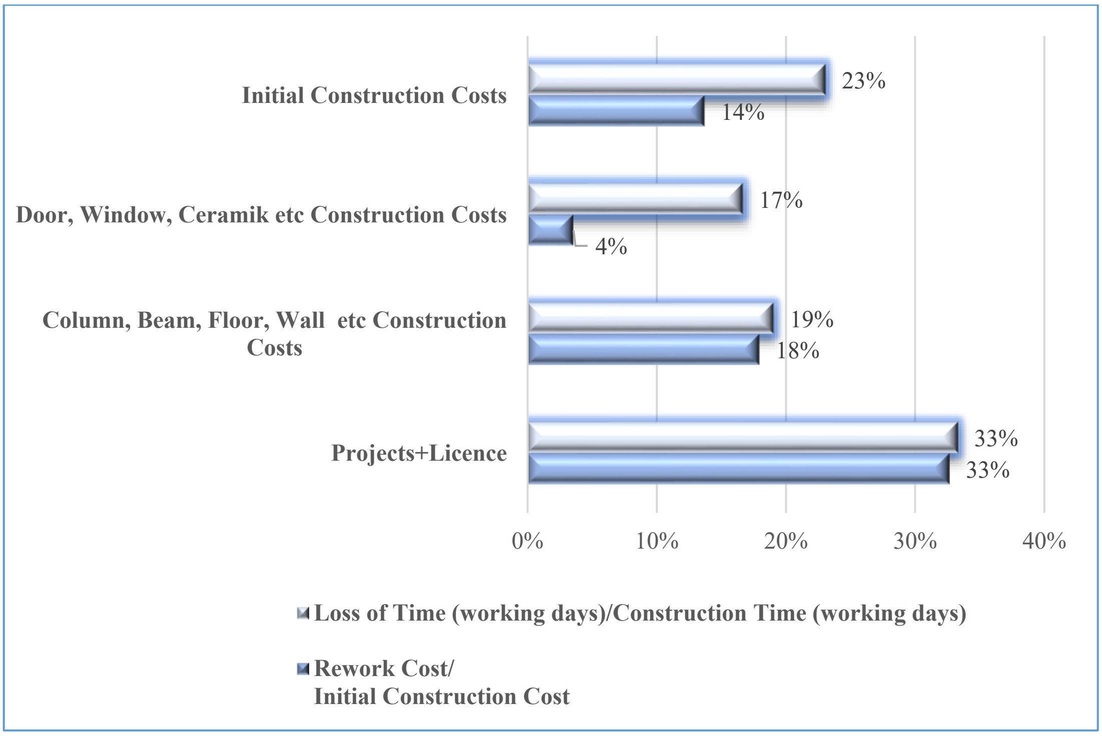

Fig. 6. The cost and man-day ratios of the reconstruction process -graphically

4. Conclusions

Today's world, shaped by the impact of technological innovations, is transforming into an increasingly computer-oriented lifestyle. This extremely rapid transformation has largely eliminated the possibility of maintaining traditional lifestyles. Today's individual, who has transitioned from a mobile lifestyle to a mobilised life, is evolving into a structure that develops communication models based on the need for fast access in a universe where borders disappear. The new requirements brought about by this change and development pave the way for the integration of many technological innovations into the daily life of humanity.

In addition to sectors such as science, commerce, medicine, defence industry, automotive, textile, food, mineral processing, chemistry and communication, the construction sector, which is a pioneer in terms of monetary volume, can also be counted. Adaptation to technological developments for the construction sector is progressing more slowly than other sectors and is not at the desired level especially in our country. The reasons for not being at the desired level in our country include high initial investment and maintenance costs for digitalisation, low level of education of employees, insufficient digital training, resistance to adaptation to innovation, too many subcontractor companies, etc.

Technological applications for the construction sector include BIM technology, VR (Virtual Reality), AR (Augmented Reality), drone, artificial intelligence supported applications. Technological applications support the increase in productivity in the construction sector and contribute to the transformation into an innovative and competitive structure that benefits the sector in a sustainable sense.

Applications such as VR (Virtual Reality), AR (Augmented Reality), drone provide significant advantages in terms of time and cost with observations and measurements carried out in the field. In this study, AR technology application was integrated into a construction project. With the application made in the preliminary project phase, design quality, time and cost management were tried to be made more effective.

Within the scope of the study, a ground + 4 storey project was studied, and the application areas of AR technology were tried to be determined in the initial and application stages. The project image was drawn in three dimensions with Revit program and then visualised with augmented reality with Unity program. After the visualisation, revisions were completed with the feedback received and a decision was made for the final project. In the study, the building was analysed both as a whole and floor by floor. In addition, in order to make the stages such as monitoring and control of the construction more effective during the project implementation, the visualisation of the columns, beams and floors of the project was created and the scope of the project was tried to be determined.

Within the scope of the study, it has been tried to be shown that the factors that have a negative impact on the project in terms of time such as renovation project, renovation licence and reconstruction costs such as deck, roof, wall, window, door, plaster, paint can be prevented with AR application. When analysed in terms of the determination of reconstruction costs, the differences that will occur in approximately 875.000 USD of this investment with an investment cost of 1.000.000 USD were determined. In case the construction is completed, approximately 120.000 USD reconstruction cost will be prevented by identifying these differences. While this cost is approximately 14% of the initial construction cost for the part where the differences are detected, it constitutes 12% of the total construction cost. In terms of working days, it is seen that the reconstruction that will be affected by the construction activities in the 390-day part of this construction, which is calculated as 600 days in total, will take a total of 90 days, which corresponds to approximately 15% of the total construction process.

In addition to the findings obtained within the scope of the project preliminary studies, it is foreseen that augmented reality (AR) technology can provide maximum benefit at every stage from project initiation to completion and beyond. In the planning phase, thanks to the transfer of projects to the virtual environment, important decisions such as the placement of buildings on the parcel, evaluation of sustainability rates and increasing energy savings can be made more effectively. In the implementation phase, AR technology will provide important contributions in many critical processes such as optimising material choices, early detection and intervention of errors overlooked in project design. It is also considered that AR technology will play an effective role in protecting worker health and ensuring safe working environments. In addition, it will also support the reduction of time and resource waste due to paperwork and procedures. After the project is completed, it will be possible to detect and intervene quickly in maintenance and repair processes before damages grow. In line with one of the main objectives of a business, which is to generate profit, AR technology will facilitate marketing processes; it will contribute to increasing market share by enabling customers to be reached quickly and at low cost from anywhere in the world.

Recent studies reveal that virtual reality (VR) and augmented reality (AR) technologies will play a critical role in the future of construction management. It is predicted that the integration of these technologies into different areas of the construction industry will enable cost, time and energy savings, as well as increase productivity in the industry through positive contributions to occupational health and safety. Especially in the sales phase of construction projects, VR and AR technologies will be used as an effective communication tool, thus enabling more efficient use of time by eliminating the need to go to a physical location. In the coming years, mixed reality (MR) and extended reality (XR) applications are expected to pave the way for further technological transformations in the sector. All these findings show that technology has become an indispensable element for the construction industry. Although it has progressed more slowly in technology adaptation compared to other sectors, it is predicted that the construction industry will face digitalisation and technological innovations more intensively in the coming period.

References

Ahmed, S. (2018). A Review on Using Opportunities of Augmented Reality and Virtual Reality in Construction Project Management. 1839–1852.

Atahan, D. (2024). Inşaat Sektöründe Sanal Gerçeklik Uygulamalarinin Kullanimi. 104. info:eu-repo/semantics/openAccess

Azhar, S. (2011). Building Information Modeling (BIM): Trends, Benefits, Risks, and Challenges for the AEC Industry. Leadership and Management in Engineering, 11(3), 241–252.

Azuma, R. (1997). A Survey of Augmented Reality. Chaos, Solitons and Fractals, 42(3),

Behzadi, A. (2016). Using Augmented and Virtual Reality Technology in the Construction Industry. American Journal of Engineering Research, 512, 2320–2847. www.ajer.org

Erdik, M. Ve Gökuç T., Y. (2020) Türk Yapı Sektöründe Yapı Bilgi Modellemesinin Adaptasyonu, BAUN Fen Bil. Enst. Dergisi, 22(1), 159-171.

Genç, M. (2019) Sanal Gerçeklik Teknolojilerinin, İnşaat Endüstrisinde ve İnşaat Mühendisliğinde Kullanılabilirliği, Yüksek Lisans Tezi, Eskişehir Anadolu Üniversitesi ve Bilecik Şeyh Edebali Üniversitesi.

Gökçearslan, A. (2016). Artırılmış gerçeklik Uygulamaları Ve Grafik Tasarım Alanına Yansımaları. Turkish Studies, 11(19), 267–282

Hajirasouli, A., Banihashemi, S., Drogemuller, R., Fazeli, A., & Mohandes, S. R. (2022). Augmented reality in design and construction: thematic analysis and conceptual frameworks. Construction Innovation, 22(3), 412–443.

İçten, T., & Bal, G. (2017). Artırılmış gerçeklik üzerine son gelişmelerin ve uygulamaların incelenmesi. Gazi Üniversitesi Fen Bilimleri Dergisi Part C, 5(2), 111–136

Kıvrak, S., & Arslan, G. (2018). İnşaat Proje İmalatlarında Artırılmış Gerçeklik Teknolojisi Uygulamaları. Journal of Polytechnic, 0900(2), 379–385.

Koch, C., Neges, M., König, M., & Abramovici, M. (2014). Natural markers for augmented reality-based indoor navigation and facility maintenance. Automation in Construction, 48, 18–30.

Sevindik, T., Kamacioğlu, B., Binol, U. & Özer, B. Y. (2025). İnsan Bilgisayar Etkileşiminde Artırılmış Gerçeklik ve Sanal Gerçeklik Uygulamalarının Karşılaştırılması, Art7 Sanat ve İletişim Dergisi, 2(1), 27-39.

Tao, F., Zhang, H., Liu, A., & Nee, A. Y., (2018), Digital twin in industry: State-of-the-art. IEEE Transactions on industrial informatics, 15 (4), 2405-2415.

Volk, R., Stengel, J., & Schultmann, F. (2014). Building Information Modeling (BIM) for existing buildings—Literature review and future needs. Automation in Construction, 38, 109–127.

Whyte, J., Centre, I. S., & Campus, S. K. (2003). Industrail Applications Of Virtual Reality In Architecture and Construction. 8(May), 43–50.

Yenigün, İ., Yenigün, K., & Erdoğan, S. (2020). Sanal Gerçekliğe Ticari Uygulama Yaklaşımları; İnşaat Sektörü Örneği. 1, 1–11

Zheng, X., Lu, J., & Kiritsis, D. (2022). The emergence of cognitive digital twin: vision, challenges and opportunities. International Journal of Production Research, 60 (24), 7610-7632.

4th International Civil Engineering & Architecture Conference
17-19 May 2025, Trabzon, Türkiye

Exploring the feasibility of istanbul as an olympic host: lessons from previous hosts

Ayşe İ. Arasan[1], Mustafa F. Aşkın[1], Semra Çomu*[1]

[1] Boğaziçi University, Department of Civil Engineering, 34342 İstanbul, Türkiye

Abstract. Istanbul's long-standing goal of hosting the Olympic Games represents the city's desire to establish itself as a major center of innovation, sports, and culture worldwide. A symbolic candidate to host the Olympic Games, Istanbul is situated at the meeting point of Europe and Asia and is known for its vibrant metropolitan environment and rich cultural legacy. Achieving this aim, however, requires confronting significant problems in financial planning, infrastructure development, and social inclusion. This study evaluates Istanbul's capacity to host the 2036 Summer Olympic Games by analyzing insights from previous Olympics, doing economic assessments of budgets from former hosts since 2000, and examining the city's current circumstances. The research utilizes a multi-method approach, incorporating findings from a literature analysis, case studies of prior host towns, and economic assessments. Accordingly, this study aims to develop data-driven estimates specific to Istanbul by examining bid budgets and final accounts. Istanbul has considerable potential to serve as an Olympic host city, owing to its physical and cultural characteristics, established infrastructure, and enduring aspirations. However, hosting the games has significant obstacles, such as managing budget overruns, guaranteeing enduring legacy benefits, and addressing socio-economic repercussions. The analysis emphasizes the importance of realistic budgeting and implementing extreme cost control measures, leveraging existing resources and adopting sustainable practices to align with IOC (International Olympic Committee) priorities. As a result, Istanbul's aspiration to host the 2036 Summer Olympic Games may be viable, contingent upon the implementation of stringent cost control measures, sustainable planning, and efficient stakeholder collaboration.

Keywords: Istanbul; Olympics; Olympic hosting feasibility; Budget.

1. Introduction

Mega-events, especially the Olympic Games are considered prestigious yet challenging opportunities worldwide. The Olympics represent not only global visibility but also a testament to economic strength for aspiring cities. Cities all around the world compete for the chance to host the Olympic Games, aiming to showcase their cultural and economic vitality, stimulate urban development, and secure a prominent place on the global stage (Andranovich et al., 2001). As one of those cities, hosting the Olympics has been a long-standing aspiration for Istanbul, symbolizing the city's ambition to position itself as a global hub of culture, sports, and innovation.

Although the Olympics has a very long history, the first modern Olympics dated back to the 1896 Athens Games, and since then the perception of the Olympic Games has shifted. While the Games were merely a sporting event celebrating unity and progress once, they have become an extravagant event to showcase strength to the world, drifting away from the essence of sport, resulting in high costs with limited returns, leaving host cities burdened with debt and underutilized facilities (Koba et al., 2020). Kavetsos and Szymanski (2010) state that "In this 'beauty contest', the winner is frequently the bidder that offers the most lavish showcase for the event, usually a state-of-the-art sports facility of an impressive architectural conception and size." As a result, recent editions have drawn criticism for severe budget overruns, underutilized infrastructure, and long-term economic strain. In response to that, public opposition has grown, leading several cities like Boston and Hamburg to withdraw their bids in response to the local resistance (Baade & Matheson, 2016; Jin & Jeon, 2022; Lauermann, 2022). Recognizing those challenges, the IOC has attempted to reverse those trends through their strategic agendas promoting more sustainable and financially sound Olympic Games.

Despite that shifting priorities, Istanbul has been a persistent candidate to host the Olympics with a total of five bids. Even though none of those bids have been successfull, repeated candidacies have not only increased public awareness and institutional capacity but also resulted in substantial urban investments, especially in transportation and sports infrastructure for Istanbul's residents. Yet, challenges related to political considerations, financial

*Corresponding author, E-mail: semra.comu@bogazici.edu.tr

https://doi.org/10.31462/icearc2025_ce_mng_160

concerns, and planning capacity have remained persistent in Istanbul's case and this situation has emphasized the need for more realistic and economically sound strategies in future bids.

These recurring challenges highlight the need to assess one of the most decisive factors in Olympic bids: economic feasibility. Considering Istanbul's long-standing ambitions and the growing attention to the economic challenges of hosting, assessing financial feasibility has become increasingly relevant. This study aims to examine and analyze the budgets of the previous hosts to prepare a preliminary budget for Istanbul.

This paper is structured as follows to address that objective. Section 2, materials and methods, outlines the data sources and preparation process with the analytical approach used. Section 3 reviews the previous studies on the Olympic Games from multiple perspectives to highlight key considerations that inform strategic and financial planning. Section 4 presents the analyses performed and discussion on main outcomes and findings of the analyses with proposed budgets and key insights. Lastly, Section 5 is the conclusion that finalizes the paper by summarizing key insights and offering recommendations, and the paper closes with a brief discussion of its limitations.

2. Materials and methods

First, a temporal scope was set to define the boundaries of the study and ensure consistency in data collection to start. The scope was kept limited to the Summer Olympic Games held between 2000 and 2024, including host cities of Sydney, Athens, Beijing, London, Rio de Janeiro, Tokyo, and Paris. In addition to them, the awarded bids for the 2028 Los Angeles and 2032 Brisbane Games were included to incorporate long-term visions in Olympic budgeting and establish benchmarks. This timeframe was selected due to the availability of financial records and the growing economic complexity that has come to define recent Olympic Games.

Second, the data collection phase was carried out to gather the necessary figures for economic analyses and to examine the existing literature. A substantial body of literature has emerged analyzing the financial, social, and infrastructural consequences of hosting the Olympics as cities around the world have experienced both the benefits and disbenefits of hosting mega-events. These insights, ranging from budget overruns and legacy outcomes to public perception, have formed an important contextual foundation for the comparative approach adopted in this study. Nonetheless, the financial data has served as the main input for the analysis, and two different datasets were incorporated to provide a solid foundation.

The first dataset consists of OCOG (Organising Committee for the Olympic Games) budgets sourced from official bid files that were submitted to the IOC with the candidature file. Those budgets represent estimated operational costs and revenues, and are regarded as the most consistent and comparable financial elements across various Olympic Games editions by academic working on this subject. On the other hand, it is important to note that, non-OCOG budgets, which typically include long-term infrastructure investments and broader public spending, vary widely in scope, content, and reporting quality. Reliable and consistent data for non-OCOG components is lacking in many editions, making meaningful cross-city comparisons almost impossible. Therefore, this study excludes non-OCOG budgets, in line with established academic practice, which often focuses on OCOG budgets as the most analytically robust and accessible component of Olympic financial planning.

The second dataset utilized in the study was derived from the works of Preuss et al. (Preuss & Weitzmann, 2023; Preuss, Andreff, & Weitzmann, 2019). Their research on the financial aspects of the Olympics is widely recognized in the academic literature. This dataset includes figures of the Games held between 2000 and 2016, incorporating both bid-phase budgets and final post-games accounts to evaluate cost overruns and underruns. Even though Preuss et al.'s data also relies on official reports and official committees, what distinguishes his bid budget data from the first dataset is its focus on revised budgets prepared approximately four years prior to the event. These revised figures are considered by Preuss et al. to be the most reliable version of the budget, as they are developed with more grounded assumptions and updated economic expectations. That distinction is important, as it reflects how budget accuracy and reliability can vary depending on the timing of their preparation. Despite these differences, Preuss et al.'s dataset remains rooted in official sources, allowing it to serve as a useful comparative reference in this study.

Third, in order to enable accurate and consistent comparisons across different datasets with different currencies over time, all financial data used in this study were systematically standardized to 2024 values in US dollars. For the first dataset, the first step involved converting figures into local currencies using the average exchange rates applicable in the bid submission year, since data from the official bid file was originally expressed in US dollars in the bid years value. This step ensured that inflation adjustments could be performed based on country-specific figures rather than global estimates. Subsequently, inflation adjustments were calculated using the relevant GDP deflators for each host country, bringing all cost estimates in line with 2024 prices. After the inflation adjustment, the values were converted back into US dollars using 2024 exchange rates. This three-step preperation process produced comparable data for the analyses.

For the second dataset, a similar approach was adopted. Although Preuss et al.'s figures were already adjusted to the estimated price levels of the event year in their local currencies, they were just further standardized to 2024 values using GDP deflators in the respective local currencies. Those values were also converted to US dollars using 2024 exchange rates to ensure consistency and compatibility with the first dataset.

Fourth, two analyses were performed on standardized datasets to assess the economic feasibility of Istanbul's potential Olympic bid. Before starting, it is important to note that, due to differences in reporting structures across cities and years, the analysis focused exclusively on main budget categories. Subcategories were excluded, as they were often inconsistent in definition and reporting scope, making reliable comparisons difficult. This level of standardization aimed methodological consistency and enhanced the reliability of quantitative and percentage-based analyses done for this study. Also, particular attention was given to upcoming editions such as Tokyo 2020, Paris 2024 and Los Angeles 2028, as they reflect the IOC's strategic shift toward cost containment under Olympic Agenda 2020 and serve as forward-looking benchmarks relevant to Istanbul's planning context.

To begin with, a quantitative analysis of the figures was conducted to assess the absolute values of OCOG budget items across host cities and over time. The purpose of this analysis was to determine overall cost levels, highlight variations in spending patterns, and identify trends in budgets. Additionally, the comparison between initial bid-phase budgets and revised budgets from Preuss et al.'s dataset enabled an assessment of the reliability and realism of cost projections made at different planning stages compared with final accounts.

Subsequently, a percentage distribution analysis was carried out to examine how the total OCOG budgets were distributed among spending and revenue categories. This method allowed for the exploration of structural similarities and differences between cities and provided insights into changing budget priorities over time.

The combination of these two analyses provided a comprehensive foundation for evaluating Istanbul's proposed OCOG budget. By comparing both absolute figures and proportional allocations, it was possible to contextualize Istanbul's estimates within broader Olympic budgeting trends and assess their consistency with past and upcoming host cities. The projections were shaped by considering Istanbul's economic indicators, recent infrastructure developments, and historical bidding context, based on trends found in the data. This analysis helped estimate the likely costs of hosting while also identifying opportunities for cost-efficiency in alignment with the IOC's current emphasis on sustainability and the reuse of existing infrastructure.,

A preliminary budget was drafted for Istanbul's candidacy based on the analysis of figures and derived insights. Rather than applying a strict mathematical model, the study projected a realistic OCOG budget by focusing on trends within the dataset, rather than solely using median or average values. The estimations for each category were primarily drawn from the budget structures and spending levels of recent and upcoming Games that particularly reflect the IOC's evolving policy direction under Olympic Agenda 2020 and Agenda 2020+5.

Once an initial budget was drafted, percentage-based allocations were calculated and compared with historical patterns identified through the percentage distribution analysis, the second analysis performed on the datasets. This step was used to verify consistency and to benchmark Istanbul's distribution model against previous Olympic budgets. It also allowed for the identification of any disproportionate expenditures or underfunded areas. Finally, to improve the adaptabilitiy to different scenarios and provide flexibility on the proposed budget, three versions were created: a conservative base case, as described above, and two adjusted alternatives -optimistic and aggressive- each incorporating strategic percentage modifications in both revenues and expenditures. These scenarios provided the necessary flexible framework for assessing Istanbul's economic feasibility under different planning assumptions, despite the absence of a rigid computational model.

To sum up, this study has aimed to provide a standardized and comparative framework based on OCOG budgets from previous and upcoming Games, supported by data from Preuss et al.'s works. Through a multi-step process of data normalization, trend interpretation, and percentage-based validation, a tailored budget structure was produced for Istanbul's potential Olympic candidacy. The proposed scenarios aim to reflect a flexible approach and serve as the analytical foundation for the discussion of results in the following section.

3. Context and previous studies

Academic studies have repeatedly highlighted that the financial variability of the outcomes of Olympic Games, in relation to chronic budget overrun issues with underestimated expenditures and uncertainties surrounding long-term legacy outcomes. (Preuss & Weitzmann, 2023). These concerns are especially pronounced in developing economies, where public spending pressures are high and the promised benefits of mega-events are often delayed or unevenly distributed (Baade & Matheson, 2016). Empirical studies show pre-event estimates frequently and optimistically overestimate economic benefits, while post-event evaluations reveal more modest outcomes, particularly when infrastructure investments lack long-term use or are driven by prestige rather than practicality (Kasimati, 2003). Despite potential short-term gains such as increased tourism, global visibility or stock market reactions (Dick & Wang, 2008), long-term financial returns remains uncertain.

Beyond economic factors, social, political, and intangible factors also play a vital role in evaluating the overall feasibility of hosting the Olympic Games. Studies emphasize growing public skepticism driven by unmet expectations with limited local benefits (Lauermann, 2022). Beyond opposition, research also highlights intangible benefits such as national pride and social cohesion, which can generate significant public support. However, these effects tend to be concentrated in core urban areas and willingness to pay the Olympic bills diminish with distance (Atkinson et al., 2008). On the other hand, studies on legacy underscore the risks of underutilized infrastructures left to the locals as burdens after the games and stress the importance of post-event planning to ensure lasting value (Alm, 2016; Koba et al., 2021).

Recent IOC reforms, particularly those introduced under Olympic Agenda 2020 and reinforced by Agenda 2020+5, mark a significant shift in the Olympic hosting strategy, prioritizing sustainability, cost-efficiency, and the reuse of existing infrastructure (Schnitzer & Haizinger, 2019). Among past hosts, Los Angeles is often cited as the most financially successful model, especially the 1984 Games, which achieved profitability by leveraging pre-existing venues and avoiding excessive construction (Baade & Matheson, 2016). The upcoming 2028 Los Angeles Games intend to replicate this low-cost, reuse-oriented strategy, reinforcing the IOC's broader policy direction. These developments suggest that the era of glory is being replaced by financially responsible and context based approaches. In line with this trend, this study adopts a similar mindset: budget models and strategic recommendations are designed around the assumption that Istanbul's success as a host city would depend on embracing a comparable model focused on infrastructure reuse, realistic spending, and long-term legacy planning rather than spectacle-driven investments that prioritize short-term image over long-term impact.

4. Results and discussion

This section presents the analyses on previous hosts data and explains the results from Istanbul's perspective giving the drafted budget. Building on these, three adjusted scenarios are introduced for Istanbul, each reflecting different strategic planning assumption as previously mentioned. The analyses are structured around the main expenditure and revenue categories typically found in Olympic budget structures, as shown above in Table 1. These categories form the foundation for the analyses as well as the scenario modeling that follow.

To enable consistent comparison across both datasets, the set of expenditure and revenue categories was aligned by codes. Since the budget structure in Preuss et al.'s revised data differs slightly from the original bid file categorizations, most notably through broader groupings or the absence of certain new categories such as Ceremonies & Culture or People Management, several categories from Preuss et al.'s data were grouped to align with the bid file categories. This process aims to ensure methodological consistency maintaining analytical accuracy throughout the study. To achieve this, categories that were present in one dataset but missing in the other, such as People Management, were excluded from comparative evaluations and were examined only through the first dataset based on recent Olympic Games practices and evolving IOC budgeting trends.

By harmonizing the categories between datasets and accounting for structural differences, this approach aim to ensure a consistent analytical framework while accommodating the evolving nature of Olympic budgeting.

Table 1. Expenditure and revenue categories

Categories from Bid File	
Expenditure Categories	**Revenue Categories**
E1. Venue Infrastructure	R1. IOC Contribution
E2. Sport, Games Services & Operations	R2. TOP Programme
E3. Technology	R3. Domestic Sponsorship
E4. People Management	R4. Ticket Sales
E5. Ceremonies & Culture	R5. Licensing & Merchandising
E6. Communications, Marketing and Look	R6. Government Contribution
E7. Corporate Administration and Legacy	R7. Lotteries
E8. Other Expenses	R8. Other Revenues
E9. Contingency	
Categories from Preuss et al.'s Data	
Expenditure Categories	**Revenue Categories**
	R1. IOC Contribution
E1. Venues	R2. TOP Programme
E2. Workforce	R3. National Sponsorship
E2. Services	R4. Ticket Sales
E2. Marketing and Events	R5. Licensing
E3. Technology	R6. Subsidies
E7. Administration and Coordinations	R7. Lotteries
E8-9. Other	R8. Other
	R8. Disposal of Assest
	R8. Donations

4.1 Quantitative analysis of figures

This analysis focused on evaluating the absolute OCOG budget figures from selected Summer Olympics. This comparison utilized two datasets: the initial bid budgets submitted through official candidature files, shown in Table 2 below, and the final accounts compiled by Preuss et al., presented in Table 3 below. To provide clarity, each expenditure category is examined individually based on observed trends and final reported costs below.

E1 covers venue infrastructure which is the most overrun expense category across Olympic Games, with final costs frequently clustering around USD 1 billion. Despite efforts to limit costs, recent hosts like Paris and Los Angeles still approached or exceeded this level. Istanbul's E1 projection is set at USD 1.2 billion, allowing for inflation and necessary upgrades to meet international standards.

E2 covers Sport, Games Services & Operations and it is a category that has shown fluctuations across editions but has consistently exceeded initial projections since 2004. Final expenditures often exceeded USD 1 billion, so, Istanbul's projection is set at USD 1.2 billion, aligned with recent trends and considering historic overruns.

E3 covers technology, a growing category shaped by advances in broadcasting, data, and cybersecurity. Recent Games have shown rising budgets, overruns and figures are reaching up to USD 613 million. Istanbul's projection is set at USD 900 million, reflecting continued growth and alignment with recent IOC priorities.

E4 covers people management which is a recently added category reflecting staffing and volunteer-related costs. Since it appears only in the 2024, 2028, and 2032 budgets, historical comparisons are limited so, projection for E4 is set at USD 800 million, consistent with Los Angeles expecting similar staffing and coordination needs.

E5 covers ceremonies and cultural programs, a relatively small but symbolically important category. The historical average stands at approximately USD 140 million. Based on this trend and recent editions of the Games, Istanbul's E5 projection is set at USD 150 million. This figure is positioned between the average and Paris's allocation, aiming to deliver a compelling program while avoiding extravagance in line with recent IOC agendas.

E6 covers communications and marketing and is a consistent category yet shows overruns. The average is USD 140 million so, E6 projection is set at USD 200 million, slightly above average with in line with recent trends.

E7 covers corporate administration and legacy planning, a consistent category with a pattern of dramatic cost overruns. While the average for past Games ranged from USD 165 to 332 million, final accounts indicate upward revisions across all editions. Istanbul's E7 projection is set at USD 500 million, considering historical overruns.

E8 covers other expenses, a variable and often undefined category used differently across Games. Due to inconsistent content and frequent merging with contingency, past data offers no reliable basis for direct comparison. For Istanbul, no fixed amount is assigned; instead, a percentage of the total budget is allocated to this category in the next analysis.

E9 covers contingency, a category often inconsistently reported or merged with others in past budgets. Rather than assigning a fixed amount, contingency is traditionally calculated as a percentage of total costs based on the risk level of each budgeting scenario, and the same approach is applied for Istanbul in the next analysis.

Table 2. Analysis of initial bid budgets on expenditures *000, USD 2024

Games Edition	E1	E2	E3	E4	E5	E6	E7	E8	E9
2000	212.783	681.912	313.311	-	-	46.913	80.422	273.100*	
2004	184.915	957.802	-	-	156.376	195.470	185.045	366.767*	
2008	370.526	2.014.490	-	-	195.014	117.008	243.767	196.964*	
2012	699.422	642.934	460.119	-	94.489	94.489	261.898	167.409	107.840
2016	474.983	583.093	338.596	-	86.677	98.109	117.488	253.128*	
2020	601.185	561.233	250.541	-	59.135	122.971	23.054	217.216	162.212
2024	800.184	1.015.697	540.324	605.227	209.616	258.890	250.022	265.808	393.943
2028	1.385.700	1.158.000	613.800	800.400	227.100	226.500	332.600	884.800	567.400
2032	526.473	802.703	493.505	607.635	100.763	143.906	165.165	314.098	618.095

*E8+E9 given together in the respective editions

Table 3. Analysis on final accounts from Preuss et al.'s data on expenditures *000, USD 2024

Games Edition	E1	E2	E3	E7	E8-9
2000	716.231	945.534	460.305	151.584	420.539
2004	445.244	1.188.609	480.436	376.721	559.656
2008	1.102.049	1.826.491	851.125	519.314	132.540
2012	1.229.080	1.311.457	879.134	532.188	200.691
2016	N/A	N/A	N/A	N/A	N/A

Following the expenditure analysis, the same approach is applied to the revenue side to assess the structure and reliability of projected Olympic income. This evaluation uses data from the initial bid budgets, shown in Table 4 below, and final accounts from Preuss et al.'s, presented in Table 5 below. Each revenue category is examined to understand typical income patterns and inform Istanbul's projections as previous.

R1 covers the IOC Contribution, a core revenue source comes from the IOC's broadcast income share. While past Games have shown fluctuations, recent bids reflect a downward trend, with Paris, Los Angeles, and Brisbane budgeting between USD 750 and 855 million. Istanbul's R1 projection is set at USD 700 million, reflecting this decline and the need for conservative forecasting.

R2 covers revenue from the IOC's The Olympic Partner (TOP) Programme, a global sponsorship initiative that provides financial support to the host city and the broader Olympic Movement. While bid budgets show fluctuation and recent declines, final accounts in Preuss's data consistently exceed initial estimates. Based on this contrast, Istanbul's R2 projection is set at USD 400 million, balancing conservative bids and reliable historical returns.

R3 covers domestic sponsorships, often the largest revenue component in Olympic budgets and highly dependent on local market capacity. While bid data shows wide fluctuations which is expected since finding sponsors directly related to the city, final accounts consistently exceed initial projections. Projection for R3 is set USD 2 billion, reflecting strong national sponsorship potential due to high national pride of Turkish people and the country's proven track record of mobilizing private sector.

R4 covers ticket sales which is the largest non-IOC-dependent revenue stream and traditionally ranking second after domestic sponsorships. While figures vary, recent Games like Paris have seen record-breaking demand even though rising ticket prices, and upcoming host project continued growth driven by rising prices. Projection for R4 is set at USD 1.6 billion, based on the assumption of 8 million tickets sold at an average price of USD 200.

R5 covers licensing and merchandising which is a modest but consistent revenue category across Olympic budgets. Despite fluctuations, actual revenues have typically ranged below USD 150 million. Istanbul's R5 projection is set at USD 150 million, aligned with both historical averages and recent outcomes.

R6 covers government contributions. It is a minor item in most Olympic budgets and often excluded in initial plans. While avoiding public funding may seem ideal, historical data shows that even cities aiming for minimal support often report income from government subsidies post-Games. A contribution of USD 170 million is projected, acknowledging both precedent and the likelihood of partial state involvement despite initial intentions.

R7 covers lottery revenues which is a fluctuating item that has been excluded in some budgets but remains relevant in countries with strong public interest in games of chance. Given Türkiye's engagement with national lotteries and the successful example of 2004, R7 projection is set at USD 300 million, reflecting local potential.

R8 includes miscellaneous revenues including donations and asset disposal and often tailored to the specific strategies of each host city. Historical data shows that final revenues in this category frequently exceed initial estimates, especially in cities relying on temporary infrastructure. Given Türkiye's strong civic engagement and IOC's reuse-focused strategy, USD 500 million is projected for R8, reflecting local potential.

Table 4. Analysis of initial bid budgets on revenues *000, USD 2024

Games Edition	R1	R2	R3	R4	R5	R6	R7	R8
2000	817.624	150.791	346.820	232.889	85.448	-	-	
2004	777.970	144.648	371.393	260.627	100.341	-	306.236	132.920
2008	1.382.646	253.518	292.520	273.019	136.510	195.014	351.024	284.720
2012	616.231	308.115	744.612	481.687	94.489	73.948	-	181.788
2016	403.569	200.289	355.723	250.200	31.204	479.891	-	231.199
2020	469.874	199.251	554.225	461.756	83.134	-	-	268.314
2024	855.000	453.500	1.240.074	1.289.486	144.594	114.000	55.246	177.807
2028	855.000	453.500	2.246.500	1.788.100	262.400	11.600	8.100	570.900
2032	757.725	340.756	1.329.092	990.448	110.687	-	-	275.637

Table 5. Analysis on final accounts from Preuss et al.'s data on revenues *000, USD 2024

Games Edition	R1	R2	R3	R4	R5	R6	R7	R8
2000	1.282.464	776.729	-	687.795	81.683	34.894	-	254.227
2004	897.154	350.056	481.986	300.757	128.519	296.726	437.958	639.651
2008	1.403.165	566.250	1.916.080	290.415	307.774	-	-	160.559
2012	668.431	406.734	1.280.635	1.151.012	141.709	199.864	-	373.803
2016	N/A	N/A	N/A	N/A	N/A	N/A	N/A	N/A

4.2 Percentage distribution analysis

This section presents the second analysis that examines the proportional allocations within total OCOG budgets to highlight shifting priorities. Expenditure data is drawn from the initial bid budgets shown in Table 6 and the final accounts compiled by Preuss et al. presented in Table 7.

E1 ranged from 13% to 38% in bid budgets, with an average of 25%. Recent editions like Paris, Los Angeles, and Brisbane allocated 18%, 22%, and 14%, reflecting a decline probobaly due to re-use strategies. Final accounts confirm this shift, averaging around 24%. So, projection for Istanbul's is set at 20%, in line with this trend.

E2 ranged from 19% to 42% in bid budgets, but Sydney's 42% included ceremonies and cultural programs due to different budget structure. Excluding that, the range tightens to 19–37%. More recent Games show a decrease, 22% in Paris and 19% in LA, reflecting a trend aiming operational efficiency. Final accounts report 32–41% for a broader category including marketing and ceremonies; adjusting for these, the effective average drops to around 25%. Istanbul's share is set at 22%, aligned with recent Games and adjusted for structural changes in budgeting.

E3 ranged from 10% to 19% in bid budgets, averaging 15% while recent editions allocated closer to 12%, reflecting cost-efficiency strategies. Final accounts show a slightly higher range of 16–21%, with an average of 18%, likely due to broader definitions in earlier Games. Istanbul's allocation is set at 15%, balancing cost-efficiency trends with potential future technological demands.

E4 appears only in the 2024, 2028, and 2032 budgets since it is a newly introduced category, with allocations of 15%, 13%, and 16%, respectively. Due to limited historical data, no broader trend can be observed and Istanbul's allocation is set at 14%, matching the average.

E5 ranged from 3% to 7% in candidature budgets, with recent editions clustering around 5% and showing a declining trend. As this category is not reported separately in final accounts, no comparative analysis could be made. Istanbul's allocation is set at 3%, reflecting a more modest and sustainable approach emphasizing a commitment to efficiency and the avoidance of unnecessary extravagance in line with recent Olympic agendas.

E6 ranged from 3% to 9% in candidature budgets, averaging 5% with a median of 4%, showing a downward trend in recent editions. Since second dataset groups this category with Events, no direct comparison was possible. Istanbul's allocation is set at 4%, aiming cost-efficiency with effective communication and branding efforts.

E7 ranged from 4% to 10% in candidature budgets, averaging 7%, with a declining trend in recent editions. Preuss's final accounts show consistently higher allocations suggesting underestimation during planning. Istanbul allocates 7% to this category, balancing historical overruns also keeping the reclining trend in mind.

E8 is a flexible category for unforeseen or uncategorized costs, with inconsistent definitions across editions. It ranged from 7% to 14% in candidature budgets, averaging 5%, while final accounts show 11%. Istanbul allocates 10%, providing a buffer aligned with past trends.

E9 covers contingency, a risk management buffer often grouped with other expenses in earlier budgets. While it ranged from 4% to 16% in candidature budgets, with an average of 9%, it was not separately analyzed in final accounts. For Istanbul, E9 is set between 5-12%, adjusted according to the risk appetite of each budgeting scenario.

Table 6. Analysis of initial bid budgets on expenditures, %

Games Edition	E1	E2	E3	E4	E5	E6	E7	E8	E9
2000	13%	42%	19%	-	-	3%	5%	17%*	
2004	35%	19%	-	-	7%	9%	9%	18%*	
2008	38%	37%	-	-	6%	4%	8%	6%*	
2012	28%	25%	18%	-	4%	4%	10%	7%	4%
2016	24%	30%	17%	-	4%	5%	6%	13%*	
2020	30%	26%	12%	-	3%	3%	6%	12%	8%
2024	18%	22%	12%	15%	5%	6%	6%	6%	11%
2028	22%	19%	10%	13%	4%	4%	5%	14%	9%
2032	14%	21%	13%	16%	3%	4%	4%	8%	16%

*E8+E9 given together in the respective editions

Table 7. Analysis on Preuss et al.'s data on expenditures, %

Games Edition	E1	E2	E3	E7	E8-9
2000	27%	35%	3%	13%	19%
2004	15%	39%	3%	13%	23%
2008	25%	41%	7%	13%	21%
2012	30%	32%	4%	11%	16%
2016	24%	38%	12%	10%	16%

Following the expenditure analysis, the same methodology is applied to the revenue categories to evaluate the internal structure and distribution of projected Olympic income. This section examines how revenue streams have been historically distributed and how they have performed in actual financial outcomes. The analysis draws on initial bid budget data, as shown in Table 8, and final account figures compiled by Preuss et el., presented in Table 9. Each revenue stream is reviewed individually to identify recurring trends, assess the accuracy of past projections, and provide a sound basis for shaping Istanbul's revenue allocation strategy to cross check with previous analysis.

R1 shows a wide range across both bid budgets and final accounts but follows a clear and sharp downward trend over time. Final figures frequently fall short of projections, reflecting systematic overestimation and suggesting declining IOC revenue shares. To reflect this pattern and reduce reliance, Istanbul's share is conservatively set at 14%.

R2 ranged from 7% to 12% in bid budgets, averaging 9%, while final accounts remained within a stable 10% to 12%. Though historically dependable, this revenue also derives from IOC and given potential to mirror the decline in R1, Istanbul's share is cautiously set at 8%, trusting Games-driven efforts over external programmes.

R3 ranged from 9% to 36% in bid budgets, averaging 24% with recent editions showing sharp increases. Final accounts ranged from 14% to 41%, averaging 26%, often exceeding estimates. Given this pattern and Istanbul's strong local and international sponsorship potential, 30% is allocated, reflecting both upward trends and the city's mature business base.

R4 ranged from 9% to 29% in bid budgets and 9% to 27% in final accounts. Recent editions indicate a rise toward 30%, supported by high sales volumes like Paris's record-breaking ticket numbers. As the largest revenue stream not tied to the IOC, 26% is allocated for R4, balancing strong potential with caution due to incomplete recent data.

R5 ranged from 2% to 4% in bid budgets, averaging 3%, while final accounts showed an average of 4%. Although smaller in scale, this revenue often slightly outperforms projections. Istanbul's allocation is set at 4%, aligning with historical reliability and modest growth expectations.

R6 ranged from 1% to 25% in bid budgets, though most cases fall between 1% and 6% when that one outlier is excluded. Some cities initially budgeted zero but still received government support, as seen in final accounts ranging from 0% to 8%. To reflect moderate involvement without overdependence, 3% is allocated for R6.

R7 was included in few editions, with allocations from 1% to 15% in bid budgets and a single 12% share in final accounts (Athens 2004). Despite limited data, Türkiye's strong interest in lotteries and the need to diversify revenue justify a 4% allocation and it is considered as modest yet meaningful within Istanbul's case.

R8 ranged from 4% to 13% in bid budgets, averaging 9%, while final accounts range from 3% to 18%, averaging 10%. Istanbul's use of temporary infrastructure and donation potential further support this stream since it is the current strategy of IOC. A 10% allocation is set, balancing city-specific opportunities with historical norms alongside IOC agendas.

Table 8. Analysis of initial bid budgets on revenues, %

Games Edition	R1	R2	R3	R4	R5	R6	R7	R8
2000	50%	9%	21%	15%	5%	-	-	-
2004	37%	7%	18%	12%	5%	-	15%	6%
2008	44%	8%	9%	9%	4%	6%	11%	9%
2012	24%	12%	29%	19%	5%	3%	-	7%
2016	21%	10%	18%	13%	2%	25%	-	12%
2020	23%	10%	27%	23%	4%	-	-	13%
2024	21%	11%	28%	29%	3%	3%	1%	4%
2028	14%	7%	36%	29%	4%	0,2%	0,1%	9%
2032	20%	9%	35%	26%	3%	-	-	7%

Table 9. Analysis on Preuss et al.'s data on revenues, %

Games Edition	R1	R2	R3	R4	R5	R6	R7	R8
2000	41%	-	25%	22%	3%	-		9%
2004	25%	10%	14%	9%	4%	12%	0%	26%
2008	30%	12%	41%	6%	7%	0%	0%	3%
2012	16%	10%	30%	27%	3%	0%	0%	14%
2016	21%	10%	18%	13%	2%	0%	1%	35%

4.3 Comparison and key findings of analyses

This section brings the estimates together made on both the quantitative and percentage distribution analyses to assess their internal alignment. The first analysis focused on absolute figures and the evolution of budget categories over time. On the other hand , the second analysis highlighted the structural distribution of expenditures and revenues, offering broader insights into changing priorities. Table 10 presents Istanbul's estimated preliminary budget, derived from the figures analysis alongside with calculated percentage distributions, allowing for a direct comparison with the results of the percentage distribution analysis. This two layer approach aims to strengthen the reliability of the findings.

The comparisons show strong alignment between proposed figures and the proportional allocations identified in the second analysis. Even though there are deviations, they are minor and fall within an acceptable range for this sstudy. Categories with a history of overruns, such as venue infrastructure and sport operations, were intentionally estimated near the upper limits of the historical range in anticipation of potential financial pressures. On the revenue side, projections remain cautious, especially in areas such as IOC contributions and the TOP Programme, where historical trends indicate both overdependence and sharp recent declines.

The proposed plan reflects a modest shortfall of approximately USD 30 million despite efforts to ensure a balanced budget. This represents around 0.5 percent of the nearly USD 6 billion total. Although this gap is relatively small, closing it is essential to ensure the financial feasibility. Possible strategies may help mitigate this.

On the revenue side, both domestic and international sponsorship can be enhanced by leveraging Istanbul's unique strategic location and market appeal. Engaging Turkish corporations and global brands in a targeted manner may unlock additional funding opportunities. Furthermore, models like dynamic ticket pricing could increase revenue while maintaining accessibility. Although grants and donations from international organizations make up a small portion in the budget, minor increases in these areas also could provide meaningful support. If required, an increase in government funding could resolve the deficit.

On the expenditure side, scaling back non-essential components, simplifying ceremonies, and improving the efficiency of resource allocation could produce measurable savings without compromising overall quality. Moreover, prioritizing the use of existing and temporary venues could help reduce capital investment and long-term financial liabilities increasing potential revenues from asset disposals.

Overall, these findings confirms the internal alignment between two analyses and even though there is a shortfall in this baseline scenario, there are a number of actions that can make small yet meaningful changes to the outcome to ensure financial feasibility.

Table 10.Istanbul's estimated preliminary budget, USD 2024 and %

Expenditures

No	Item	Figures Analysis	%	Percentage Analysis
E1	Venue Infrastructure	1.200.000	21%	20%
E2	Sport, Games Services & Operations	1.200.000	21%	22%
E3	Technology	900.000	15%	15%
E4	People Management	800.000	14%	14%
E5	Ceremonies & Culture	150.000	3%	3%
E6	Communications, Marketing and Look	200.000	3%	4%
E7	Corporate Administration and Legacy	500.000	9%	7%
E8	Other Expenses	500.000	9%	10%
E9	Contingency	400.000	7%	5%
	Total Expense	5.850.000		

Revenues

No	Item	Figures Analysis	%	Percentage Analysis
R1	IOC Contribution	700.000	12%	15%
R2	Top Programme	400.000	7%	8%
R3	Domestic Sponsorship	2.000.000	34%	30%
R4	Ticket Sales	1.600.000	27%	26%
R5	Licensing & Merchandising	150.000	3%	4%
R6	Government contribution	170.000	3%	3%
R7	Lotteries	300.000	5%	4%
R8	Other Revenues	500.000	9%	10%
	Total Revenue	5.820.000		

4.4 Budget scenarios for Istanbul

To add further flexibility to the proposed figures, two more financial scenarios developed and all of them presented in this section. These scenarios are designated to reflect varying assumptions about revenue potential and cost control, providing another perspevtive to assess how Istanbul's budget performs under different planning conditions with different risk levels. The scenario that drafted under the light of the previous analyses (given in Table 10 above), emphasizes realistic revenues and expenditures and aim avoiding overestimation of income or underbudgeting of costs and thereby accepted as baseline in this section and labeled as conservative scenario.

Building on the conservative scenario, the optimistic model assumes stronger performance in sponsorship, ticketing, and merchandising, supported by increases in marketing and technology investments to achieve that revenue growth. The aggressive scenario aimes even further for maximum revenue generation while implementing strict cost controls, representing a high-risk, high-reward approach.

Table 11 given below presents the detailed percentage adjustments made across revenue and expenditure categories for each scenario, taking the conservative model as the baseline. The optimistic and aggressive scenarios reflect upward adjustments in revenue projections, particularly in domestic sponsorship (R1), ticketing (R2), and other commercial sources (R7, R8), based on potential market performance and strategic engagement. Cost reductions and targeted efficiency measures are applied in these scenarios in areas such as infrastructure (E1–E3), operations (E4), and technology (E6), while maintaining stable allocations for fixed-cost items like government contributions (R6). This approach aims to ensure a stable budget while allowing flexibility in areas responsive to planning strategies or market shifts.

Under the light of these projections, the conservative model presents a $30 million shortfall, about 0.5% of the total budget. The optimistic scenario offsets this with a $27 million cost reduction and a $100.5 million revenue increase, producing a $73.5 million surplus.By boosting revenues and cutting costs further, the aggressive model achieves a $140 million surplus. Though these figures are modest within an overall $6 billion budget, they highlight how strategic adjustments can transform a deficit into a surplus perfectly. While breaking even is typically the goal in OCOG budgeting, a surplus would enhance financial credibility and the Olympic legacy. Demonstrating profitability would boost Istanbul's image and affirm its capacity to host major events.

Table 11. Budget scenarios, *000, USD 2024 and %

Expenditures						
No	Conservative	%	Optimistic	% Change	Aggressive	% Change
E1	1.200.000	21%	1.176.000	-2%	1.164.000	-3%
E2	1.200.000	21%	1.188.000	-1%	1.176.000	-2%
E3	900.000	15%	891.000	-1%	882.000	-2%
E4	800.000	14%	808.000	1%	816.000	2%
E5	150.000	3%	150.000	0%	150.000	0%
E6	200.000	3%	202.000	1%	204.000	2%
E7	500.000	9%	500.000	0%	500.000	0%
E8	500.000	9%	500.000	0%	500.000	0%
E9	400.000	7%	408.000	2%	420.000	5%
Ttl	5.850.000	100%	5.823.000	0%	5.812.000	-1%
Revenues						
No	Conservative	%	Optimistic	% Change	Aggressive	% Change
R1	700.000	12%	707.000	1%	714.000	2%
R2	400.000	7%	404.000	1%	408.000	2%
R3	2.000.000	34%	2.040.000	2%	2.060.000	3%
R4	1.600.000	27%	1.632.000	2%	1.664.000	4%
R5	150.000	3%	151.500	1%	153.000	2%
R6	170.000	3%	170.000	0%	170.000	0%
R7	300.000	5%	306.000	2%	309.000	3%
R8	500.000	9%	510.000	2%	520.000	4%
Ttl	5.820.000	100%	5.920.500	2%	5.998.000	3%
Net Total (Revenues – Expenses)						
	Conservative		Optimistic		Aggressive	
	-30.000		97.500		186.000	

5. Conclusions

This study have explored the economic feasibility of Istanbul hosting the Olympic Games by examining past OCOG budgets, conducting comparative analyses, and developing budget scenarios for different risk levels tailored to the city's context. By analyzing both absolute budget figures and proportional allocations across multiple host cities, the research aimed to provide a grounded framework to inform Istanbul's potential Olympic planning for future.

An examination of past Olympics revealed a consistent challenge managing cost overruns, with notable differences between developed developing cities (Baade & Matheson, 2016). While cost overruns are a common issue of Olympic planning today, they are generally better contained in cities with mature infrastructure and greater economic capacity. In contrast, developing cities that pursue event-driven growth and rely heavily on public funding are more vulnerable to long-term financial and social burdens. These often include underutilized venues and growing levels of public debt (Koba, et al., 2020).

From a financial standpoint, the analyses conducted on past data in this study confirm that cost overruns have been a recurring issue, consistent with the findings of researches Holger Preuss (2023, 2019). However, these overruns are frequently accompanied by revenue overruns, revealing a structural tendency to underestimate budgets during the bidding phase (Preuss & Weitzmann, 2023). This pattern, influenced by the competitive nature of the candidature process, underscores the need for more realistic and data-informed financial projections in future Olympic planning.

These findings aim to provide a comprehensive understanding of the opportunities and challenges associated with hosting the Olympic Games. However, framed in the simplest terms, the central question this study seeks to answer was whether hosting the Olympic Games is financially feasible for Istanbul. Based on the conservative baseline scenario, the answer would unfortunately be no. However, the budgetary scenarios presented in this study demonstrate that, hosting the Games in a financially sustainable manner is within the realm of possibility. However even though hosting the Games in a financially feasible manner is achievable it is only achiavable with strategic planning. From managing cost overruns to ensuring long-term legacy benefits, success would require careful alignment of resources, priorities, and stakeholder collaboration since this study also highlights thses issues as the challenges associated with such an ambitious undertaking.

Beyond financial feasibility, the long-term legacy of the Olympic Games holds significant importance for Istanbul. Strategic investments in infrastructure, transportation, and public facilities should be aligned with the city's existing development goals to ensure lasting value beyond the event itself (Baade & Matheson, 2016). As a city that uniquely bridges continents, cultures, and histories, Istanbul carries symbolic significance that could elevate the Olympic narrative on a global stage. However, this distinctiveness also demands careful and context-sensitive planning to integrate Olympic preparations with urban realities and social dynamics. A well-designed legacy strategy would not only enhance public benefit but also strengthen Istanbul's international image and long-term development trajectory.

In the end, it is important to note that, while this study aims to provide a historically grounded perspective, it should be considered a preliminary assessment as a baseline. The projections are deliberately conservative and informed by past data, but the absence of real-time, city-specific inputs and formal stakeholder engagement limits the analysis to an illustrative level. A comprehensive feasibility study conducted by professional experts, integrating current data and insights from municipal and governmental bodies with stakeholder engagement would be essential for producing more precise and actionable results. Nonetheless, the approach adopted here, favoring realism over idealism, establishes a practical foundation for future, more detailed financial planning.

Limitations

This study offers a preliminary evaluation of Istanbul's feasibility as an Olympic host with publicly available data and historical trends. However, it is limited by the absence of access to internal financial records, real-time city inputs, and stakeholder involvement, which would be necessary for an accurate financial study. The budget models are simplified, based on generalized categories without detailed sub-itemization. Additionally, the study does not incorporate the time value of money or cash flow considerations due to uncertainty in economic forecasts. Finally, no formal risk analysis was conducted, leaving certain uncertainties unexamined. Despite these limitations, the findings serve as a data-informed starting point for more comprehensive feasibility studies.

Acknowledgements

This study benefited substantially from the data provided in *Cost and Revenue Overruns of the Olympic Games 2000–2018* by Holger Preuss, Wladimir Andreff, and Maike Weitzmann (2019), as well as the article *Changes of Costs, Expenditures, and Revenues Between Bidding and Staging the Olympic Games from Sydney 2000 to Tokyo 2020* by Holger Preuss and Maike Weitzmann (2023). The extensive empirical data and methodological clarity offered in these works greatly helped inform the direction of this study. Data from their works supported a historically grounded analysis of Olympic budgeting practices, without which the assessment performed in this study would not have been possible in its current form.

References

Alm, J., Solberg, H. A., Storm, R. K., & Jakobsenc, T. G. (2014). Hosting major sports events: The challenge of taming white elephants. *Leisure Studies*, *35*(5), 564–582. https://doi.org/10.1080/02614367.2014.994550

Andranovich, G., Burbank, M. J., & Heying, C. H. (2001). Olympic cities: Lessons learned from mega-event politics. *Journal of Urban Affairs*, *23*(2), 113–131. https://doi.org/10.1111/0735-2166.00079

Athens 2004 Olympic Bid Committee. (1996). *Athens 2004 candidate city.* Retrieved from https://library.olympics.com/Default/doc/SYRACUSE/53479/athens-2004-candidate-city-athens-2004-olympic-bid-committee

Atkinson, G., Mourato, S., Szymanski, S., & Ozdemiroglu, E. (2008). Are we willing to pay enough to "back the bid"?: Valuing the intangible impacts of London's bid to host the 2012 summer olympic games. *Urban Studies*, *45*(2), 419–444. https://doi.org/10.1177/0042098007085971

Australian Olympic Committee. (2021). *Brisbane Queensland : Aspiring to host the Olympic and Paralympic Games 2032.* Retrieved from https://library.olympics.com/Default/doc/SYRACUSE/733849/ioc-future-host-commission-questionnaire-response-final-submission-may-2021-brisbane-queensland-aspi

Baade, R. A., & Matheson, V. A. (2016). Going for the gold: The economics of the olympics. *Journal of Economic Perspectives*, *30*(2), 201–218. https://doi.org/10.1257/jep.30.2.201

Beijing 2008 Bid Committee. (2000). *Beijing 2008 Candidate City.* Retrieved from https://library.olympics.com/Default/doc/SYRACUSE/42147/beijing-2008-candidate-city-comite-pour-la-candidature-de-beijing-aux-jeux-olympiques-de-2008

Dick, C. D., & Wang, Q. (2010). The economic impact of the Olympic Games: Evidence from stock markets. *Applied Economics Letters*, *17*(9), 861–864. https://doi.org/10.1080/13504850802552291

Jin, C., & Jeon, B. (2022). *Opportunity or Burden? Evaluation of the Factors behind the Decision to Host the Olympic Games*. In Proceedings of the International Conference on Big Data Economy and Digital Management (BDEDM 2022) 720–724. https://doi.org/10.5220/0011238000003440

Kasimati, E. (2003). Economic aspects and the Summer Olympics: a review of related research. *International Journal of Tourism Research*, *5*(6), 433–444. https://doi.org/10.1002/jtr.449

Kavetsos, G., & Szymanski, S. (2010). National well-being and international sports events. *Journal of Economic Psychology*, *31*(2), 158–171. https://doi.org/10.1016/j.joep.2009.11.005

Koba, T., Gong, H., Ross, W. J., & Grady, J. (2021). Sustainable Olympic Development: A Proposed Benchmark for Managing Economic Outcomes. *Journal of Global Sport Management*, *6*(1), 49–69. https://doi.org/10.1080/24704067.2019.1565925

Lauermann, J. (2022). The declining appeal of mega-events in entrepreneurial cities: From Los Angeles 1984 to Los Angeles 2028. *Environment and Planning C: Politics and Space*, *40*(6), 1203–1218. https://doi.org/10.1177/23996544211066101

London 2012 Candidate City. (2004). *London 2012 Candidate City: Candidature file.* Retrieved from https://library.olympics.com/Default/doc/SYRACUSE/28313/london-2012-candidate-city-dossier-de-candidature-london-2012-candidate-city-candidature-file-comite

Los Angeles Olympic Games 2024. (2016). *Candidature file: Los Angeles Candidate City Olympic Games 2024*. Retrieved from https://library.olympics.com/Default/doc/SYRACUSE/171668/candidature-file-los-angeles-candidate-city-olympic-games-2024

Paris 2024 Candidate City. (2016). *Candidature file: Paris candidate city Olympic Games 2024*. Retrieved from https://library.olympics.com/Default/doc/SYRACUSE/171681/candidature-file-paris-candidate-city-olympic-games-2024

Preuss, H., & Weitzmann, M. (2023). Changes of costs, expendıtures, and revenues between bıddıng and stagıng the olympıc games from sydney 2000 to Tokyo 2020. *Event Management*, *27*(3), 455–476. https://doi.org/10.3727/152599522X16419948695297

Preuss, H., Andreff, W., & Weitzmann, M. (2019). *Cost and Revenue Overruns of the Olympic Games 2000-2018*. (p. 184). Springer Nature.

Rio 2016 Bid Committee. (2008). *Rio 2016 Candidate City: Candidature file*. Retrieved from https://library.olympics.com/Default/doc/SYRACUSE/38508/rio-2016-candidate-city-dossier-de-candidature-de-rio-de-janeiro-a-l-accueil-des-jeux-olympiques-et-

Schnitzer, M., & Haizinger, L. (2019). Does the Olympic Agenda 2020 have the power to create a New Olympic Heritage? An analysis for the 2026 Winter Olympic Games Bid. *Sustainability (Switzerland)*, *11*(2). https://doi.org/10.3390/su11020442

Sydney Olympics 2000 Bid Ltd. (1993). *Sydney 2000: Share the spirit*. Retrieved from https://library.olympics.com/Default/doc/SYRACUSE/37644/sydney-2000-share-the-spirit-sydney-olympics-2000-bid-ltd

Tokyo 2020 Olympic Games Bid Committee. (2013). *Tokyo 2020: Discover tomorrow.* Retrieved from https://library.olympics.com/Default/doc/SYRACUSE/70447/tokyo-2020-discover-tomorrow-tokyo-2020-olympic-games-bid-committee

Predicting the resolution time of disputes in public-private construction contracts using bayesian network analysis

Buse Un*[1], Ercan Erdis[2]

[1] Iskenderun Technical University, Department of Civil Engineering, 31200 İskenderun/Hatay, Türkiye
[2] Iskenderun Technical University, Department of Architecture, 31200 İskenderun/Hatay, Türkiye

Abstract. Construction projects typically involve numerous work items and organizations. Although mutual trust is fundamental to many projects, the parties need well-written contracts in order to have a legal basis. Due to the complex nature of the construction industry and poorly written contracts, disputes are common in this sector. The fact that each construction site in construction projects has its own unique conditions; that it often takes place in a wide and scattered area under natural climatic conditions, with different organizations using cheap labor and personnel and having a culture of working with traditional methods; the presence of unmanaged risks such as cost reduction, compromising on occupational health and safety and quality of work; as well as deficiencies in supervision and control, increases disputes. Although contracts are essential documents to consult in disputes, they are occasionally insufficient to resolve issues. Therefore, parties appeal to a resolution method in order to avoid wasting both time and cost and to reach an effective solution. The objective of the current study is to establish a predictive tool for assessing the duration of decision-making in construction disputes. This study analyzes a dataset comprising characteristics of disputes from public-private construction contracts in Türkiye. The analysis is conducted using IBM SPSS Modeler and the Bayesian Network method. The study's findings reveal that the Tree Augmented Naive Bayes (TAN) algorithm achieved a classification accuracy of 73%. The present study especially aids the disputant parties in making critical scheduling decisions. The findings of the present study contribute to project management and practitioners' decision-making by promoting amicable settling. In additionthe findings of the investigation have implications for subsequent studies on Bayesian approaches in construction disputes.

Keywords: Disputes, Decision-making, Predictive, SPSS modeler, Bayesian network

1. Introduction

Construction projects ordinarily include numerous work items and organizations. Owing to the complex structure of the construction sector, disputes are highly common in this sector. Although contracts are crucial documents for reference in disputes, they are not always adequate for the resolution of issues (Haugen & Singh, 2014; Zhang et al., 2021). Thus, parties appeal to a resolution method to prevent the expenditure of time and cost, and to reach an effective solution (Abwunza et al., 2021).Until the late 1980s, the primary methods of dispute resolution in the construction sector consisted of negotiation, mediation, arbitration and court proceedings. However, in recent years, alternative resolution methods have been developed for the settlement of disputes in this sector. There are 30 different dispute prevention and resolution methods in the literature (Bult, Halligan, Pray ve Zack, 2016: 347). Nonetheless, certain methods (e.g., litigation) can take a long time, affect parties' relationships, induce financial loss, and cause deviation from the aims of projects. Consequently, research utilizing information technology to resolve conflicts has been steadily increasing, with the aim of alleviating the adverse impacts of resolution strategies and providing foresight to the parties involved regarding disputes (Yılmaz 2020).

Researchers developing predictive models for construction disputes generally analyze historical project data to identify patterns and risk factors, aiming to facilitate early detection of potential conflicts and promote informed, proactive decision-making to avert their emergence. The researchers have generally focused on issues involving tendency conflict (Ayhan et al., 2021; J.-S. Chou et al., 2014; J. S. Chou et al., 2016), outcomes of disputes (Arditi et al., 1998; Arditi & Pulket, 2005, 2010; Bagherian-Marandi et al., 2021; Chaphalkar et al., 2015; Pulket & Arditi, 2009; Zheng et al., 2021), appropriate dispute resolution methods (Ayhan, 2019; J. Chou, 2012; Zheng et al., 2021), and cost and time claims (Yousefi et al., 2016). Despite the fact that there are different studies on these issues, no study has been found in the literature on the estimation of the decision duration of construction disputes.

*Corresponding author, E-mail: buseun.mfbe19@iste.edu.tr

https://doi.org/10.31462/icearc2025_ce_mng_168

Previous studies on disputes and risks have used the Bayesian network method, which yields robust results in situations where uncertainty is high. Shojaat et al (2025), in order to enhance the management of disputes in construction projects, the Decision Making Trial and Evaluation Laboratory (DEMATEL) and Bayesian Network methods were combined. This combination aimed to clarify the cause-and-effect relationships within disputes and to identify the key factors triggering them. The study by Chou and Lin (2013) assessed the efficacy of Bayesian methods for the early prediction of conflicts in public-private partnership (PPP) projects. Moreover, a scenario-based optimization model was developed in the study by Pourdoustmohammadi and Ansari (2024) to anticipate risks associated with high-rise building projects. Furthermore, the implementation of a Bayesian Network-based decision support system has been demonstrated to be an effective tool for the management of uncertainties. Notwithstanding these advancements, Hon et al. (2022) emphasized the necessity for further research to investigate the implementation of the Bayesian method in contract management.

This study uses Bayesian networks to predict the decision duration in disputes arising from construction contracts. The present study especially aimed to assist the disputant parties in making critical scheduling decisions. To this end, 45 arbitration decisions from the Supreme Board of Construction and Infrastructure, which employs an arbitration model for resolving disputes between the public and private sectors in Türkiye, were utilized to predict decision durations. The analyses were conducted using the Bayesian network method via the SPSS Modeler software package.

Unlike the previous ones, this study addresses the prediction of decision duration in construction disputes to address the gap in the literature. Furthermore, the present study employs the Bayesian network method, which has limited application in contract management in civil engineering, to develop a predictive model for contract-related disputes, thereby enhancing the literature both methodologically and contextually. The findings provide significant insights for project management and assist practitioners in making informed decisions by promoting amicable dispute resolution. Moreover, the results of the study suggest implications for future research regarding the application of Bayesian methodologies in construction disputes.

The remainder of this research is structured as follows: Section 2 contains the methodology, presenting the collection of data, the determination of attributes, and the methods of analysis used. Section 3 provides the results and discussion. Finally, evaluation of the model and conclusion exist in section 5.

2. Materials and methods

The present study employs a research methodology comprising three stages: (1) the development of a conceptual framework for predicting the duration of dispute resolutions through a comprehensive literature review, (2) the collection of data and the elimination of cases with incomplete information, and (3) the development of a predictive model for decision duration (Fig. 1).

The dataset employed in the present paper consists of the decisions made by the Supreme Board of Construction and Infrastructure, which utilizes the arbitration model for public construction projects in Türkiye and assesses and resolves conflicts between the administration and contractors. The data was obtained from the publication "2005-2020 Decisions and Opinions" available on the official website of the Supreme Board of Construction and Infrastructure (The Supreme Board of Construction and Infrastructure, 2020), and specific permission was secured from the board for data utilization. The data utilized in the study were manually extracted from the book, which contained case details spanning approximately four pages per case.

This study primarily focused on identifying critical attributes in construction disputes. To determine these attributes, relevant studies in the literature are examined. Subsequently, the dataset was analyzed by taking into account the significant attributes. Following this, cases with missing information on the attributes were eliminated from the dataset, and the final analysis was performed using the remaining 45 cases. The attributes of the model, along with their subcategories and statistical distributions, are displayed in Table 1.

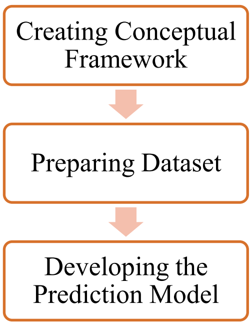

Fig 1.Research methodology

Table 1. Statistical distributions of attributes in the dataset

Attributes	Sub-categories	Frequencies	Percents
İnput Attributes			
Contract Types	Unit Price	36	80,0
	Lump-Sum	9	20,0
Work type	Construction	40	88,9
	Completion	4	8,9
	Renovation	1	2,2
Project Type	Building	25	55,6
	Social facilities	14	31,1
	Water facilities	2	4,4
	Industrial facilities	2	4,4
	Other	2	4,4
Phase of Occurrence	Build/payment	42	93,3
	Temporary acceptance	2	4,4
	Other	1	2,2
Decision	In favor of the contractor	14	31,1
	In favor of the administration	27	60,0
	To some extent in favor of the contractor	1	2,2
	Without clear decision	3	6,7
Output attribute			
Decision Duration	0–10 days	1	2,2
	11–20 days	12	26,7
	21–30 days	15	33,3
	More than 30 days	17	37,8

2.1.The Bayesian networks

The Bayes network (BN) is a probabilistic network in which the attributes are represented by nodes and the probabilistic dependency relationships between the attributes are indicated by directional arrows (Babacan & Karaduman, 2018; Pearl, 1988). This data mining method, frequently employed in classification problems, has been utilized in various domains, including molecular biology, engineering, and information technology (Hon et al., 2022; Wu et al., 2015). The Bayesian Network facilitates the construction of a probabilistic model by combining observed or recorded evidence with real-world commonsense reasoning to determine the probability of events based on seemingly unrelated attributes (*IBM SPSS Modeler 18.3 Applications Guide*, 2023, p. 183). When observed values are added to a network, the network is updated and changed. In other words, the probabilities predicted based on previous observations can be improved according to the results of new information and observations (Babacan & Karaduman, 2018; Sağır et al., 2018).

BN classifiers are standard probability-based classifiers. When all attributes are assumed to be independent, the resulting classifier is called Naive Bayes (NB) (Jiang et al., 2012). In an Bayesian network representation, a NB classifier features a simple structure where the classification node is connected to every other node with an arrow, while no connections exist between the other nodes (Madden, 2009). Tree Augmented Naive Bayes (TAN) is considered a natural extension to the NB classifier, and TAN outperforms NB in terms of accuracy. The TAN model has a structure in which each attribute links the class attribute and at most another attribute. The TAN model was utilized in this study due to its robust performance in data mining, despite its assumption of one-dependence among attributes (Wu et al., 2015). The structures of General BN, NB, and TAN are illustrated in Fig. 2 below.

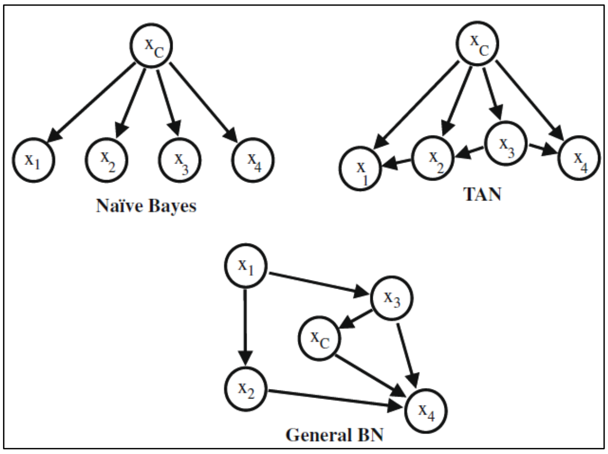

Fig. 2. Structure of Naïve Bayes, TAN, and general BN *(x_c: Class attributes $X_{1\text{-}4}$: attributes)* (Madden, 2009)

2.2.Tools
All analyses in this study were conducted using the IBM SPSS Modeler 18.3 software package and Microsoft Excel 2016. The data were initially organized and prepared utilizing Microsoft Excel 2016. Afterwards, classification analyses were conducted employing the Tree Augmented Naive Bayes (TAN) algorithm with IBM SPSS Modeler software. IBM SPSS Modeler is a data mining application that enables users to rapidly develop predictive models and integrate them into business operations to enhance decision-making. It provides a range of modeling techniques based on machine learning, artificial intelligence, and statistical methodologies (*IBM SPSS Modeler 18.3 Applications Guide*, 2023).

3. Results and discussion
Fig. 3 depicts the TAN analysis process within IBM SPSS Modeller for the categorisation of dispute decision durations.

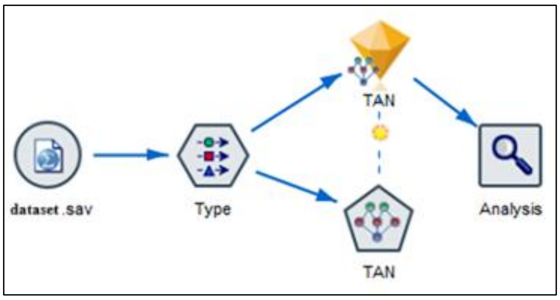

Fig. 3. TAN analysis process in IBM SPSS Modeler

The results indicate that 33 (73.33%) of the 45 data points were correctly classified by the TAN algorithm. However, the algorithm incorrectly classified 12 data points (Fig. 4). In consideration of the limited number of cases and the inconsistency of statistical distributions within the dataset, the achieved accuracy rate can be deemed acceptable (Bagherian-Marandi et al., 2021).

Correct	33	73.33%
Wrong	12	26.67%
Total	45	

Fig. 4. Results from IBM SPSS modeler

This study theoretically contributes to the literature by adapting Bayesian approaches to the field of dispute management in contracts, in response to previous research emphasizing the need for further studies on the application of Bayesian methods in contract management (Hon et al., 2022). Practically, the findings of this study can assist disputing parties in project planning by providing a probabilistic basis for estimating the duration of dispute resolution. The methodology and results presented in this study may also serve as a foundation for decision-time analyses in court and arbitration cases. Moreover, by highlighting the importance of dispute resolution durations, the study may encourage decision-makers to establish new procedures aimed at reducing decision-making times. Overall, this research not only fills an important gap in the theoretical discourse but also provides practical insights that could lead to more timely and cost-effective management of disputes in the construction and broader contract management sectors.

4. Conclusions
This study predicted the duration of decisions in disputes stemming from construction contracts through the application of Bayesian Networks. The main objective was to assist disputant parties in making essential scheduling decisions by offering probabilistic assessments of dispute resolution durations. To accomplish this, 45 arbitration decisions provided by the Supreme Board of Construction and Infrastructure, an organization tasked with adjudicating disputes between the public and private sectors in Türkiye, were examined. The Bayesian network methodology was implemented using the IBM SPSS Modeler software suite. The results show that 33 out of 45 cases (73.33%) were accurately classified using the Tree Augmented Naive Bayes (TAN) algorithm, illustrating the prospective efficacy of Bayesian methods in predicting dispute decision durations.

It is recommended that subsequent studies employ larger and more diverse datasets to enhance the model's robustness and generalizability. In addition to the fundamental-level analyses conducted in this study, comparative analyses using alternative machine learning methods could be performed to benchmark and enhance predictive performance. Incorporating additional variables such as project size, complexity, or the characteristics of the disputed issues could enhance the model's predictive performance. Ultimately, a more comprehensive and refined model could contribute significantly to both academic understanding and practical decision-making in the field of construction dispute management.

Acknowledgments

Thanks to The Scientific Technological Research Council of Türkiye (TUBITAK-2211/A General Domestic Ph.D. Scholarship Program) and The Council of Higher Education (100/2000 Ph.D. scholarship program) for B. UN.

References

Abwunza, A. A., Peter, T. K., & Muigua, K. (2021). Explaining the Effectiveness of Construction Arbitration: An Organizational Justice Perspective. *Journal of Legal Affairs and Dispute Resolution in Engineering and Construction*, *13*(3). https://doi.org/10.1061/(ASCE)LA.1943-4170.0000479

Arditi, D., Oksay, F. E., & Tokdemir, O. B. (1998). Predicting the outcome of construction litigation using neural networks. *Computer-Aided Civil and Infrastructure Engineering*, *13*(2), 75–81. https://doi.org/10.1111/0885-9507.00087

Arditi, D., & Pulket, T. (2005). Predicting the Outcome of Construction Litigation Using Boosted Decision Trees. *Journal of Computing in Civil Engineering*, *19*(4), 387–393. https://doi.org/10.1061/(asce)0887-3801(2005)19:4(387)

Arditi, D., & Pulket, T. (2010). Predicting the Outcome of Construction Litigation Using an Integrated Artificial Intelligence Model. *Journal of Computing in Civil Engineering*, *24*(1), 73–80. https://doi.org/10.1061/(asce)0887-3801(2010)24:1(73)

Ayhan, M. (2019). *Development of dispute prediction and resolution method selection models for construction disputes.* Middle East Technical University.

Ayhan, M., Dikmen, I., & Birgonul, M. T. (2021). Predicting the Occurrence of Construction Disputes Using Machine Learning Techniques. *Journal of Construction Engineering and Management*, *147*(4), 04021022. https://doi.org/10.1061/(asce)co.1943-7862.0002027

Babacan, E., & Karaduman, M. Ö. (2018). Bayes Ağları-K2 Algoritması Üzerine Bir Çalışma. *Karadeniz Fen Bilimleri Dergisi*, *8*(2), 24–38. https://doi.org/10.31466/kfbd.418862

Bagherian-Marandi, N., Ravanshadnia, M., & Akbarzadeh-T, M. R. (2021). Two-layered fuzzy logic-based model for predicting court decisions in construction contract disputes. In *Artificial Intelligence and Law* (Vol. 29, Issue 4). Springer Netherlands. https://doi.org/10.1007/s10506-021-09281-9

Bult, A. K., Halligan, D. W., Jonathan Pray, & Jr., J. G. Z. (2016). *Construction Contract Claims, Changes, and Dispute Resolution* (P. Levin (Ed.); Third Edit). American Society of Civil Engineers. https://doi.org/10.1061/9780784414293

Chaphalkar, N. B., Iyer, K. C., & Patil, S. K. (2015). Prediction of outcome of construction dispute claims using multilayer perceptron neural network model. *International Journal of Project Management*, *33*(8), 1827–1835. https://doi.org/10.1016/j.ijproman.2015.09.002

Chou, J.-S., Cheng, M.-Y., Wu, Y.-W., & Pham, A.-D. (2014). Optimizing parameters of support vector machine using fast messy genetic algorithm for dispute classification. *Expert Systems with Applications*, *41*(8), 3955–3964. https://doi.org/10.1016/j.eswa.2013.12.035

Chou, J.-S., & Lin, C. (2013). Predicting Disputes in Public-Private Partnership Projects: Classification and Ensemble Models. *Journal of Computing in Civil Engineering*, *27*(1), 51–60. https://doi.org/10.1061/(asce)cp.1943-5487.0000197

Chou, J. (2012). Comparison of multilabel classification models to forecast project dispute resolutions. *Expert Systems with Applications*, *39*(11), 10202–10211. https://doi.org/10.1016/j.eswa.2012.02.103

Chou, J. S., Hsu, S. C., Lin, C.-W., & Chang, Y.-C. (2016). Classifying influential for project information to discover rule sets for project disputes and possible resolutions. *International Journal of Project Management*, *34*(8), 1706–1716. https://doi.org/10.1016/j.ijproman.2016.10.001

Haugen, T., & Singh, A. (2014). *Dispute Resolution Strategy Selection*. *1992*. https://doi.org/10.1061/(ASCE)LA.1943-4170.0000160.

Hon, C. K. H., Sun, C., Xia, B., Jimmieson, N. L., Way, K. A., & Wu, P. P. Y. (2022). Applications of Bayesian approaches in construction management research: a systematic review. *Engineering, Construction and Architectural Management*, *29*(5), 2153–2182. https://doi.org/10.1108/ECAM-10-2020-0817

IBM SPSS Modeler 18.3 Applications Guide. (2023). IBM. https://www.ibm.com/docs/en/SS3RA7_18.3.0/pdf/ModelerApplications.pdf

Jiang, L., Cai, Z., Wang, D., & Zhang, H. (2012). Improving Tree augmented Naive Bayes for class probability estimation. *Knowledge-Based Systems*, *26*, 239–245. https://doi.org/10.1016/j.knosys.2011.08.010

Madden, M. G. (2009). On the classification performance of TAN and general Bayesian networks. *Knowledge-Based Systems*, *22*(7), 489–495. https://doi.org/10.1016/j.knosys.2008.10.006
Pearl, J. (1988). *Probabilistic Reasoning in Inteligent Systems: Networks of Plausible Inference*. Morgan Kaufmann.
Pourdoustmohammadi, S., & Ansari, R. (2024). Developing a Scenario-Based Optimization Model for Planning Risks in Construction Projects by Integrating a Decision Support System with Bayesian Belief Network Analysis Approach: A Case Study in High-Rise Buildings. *Iranian Journal of Science and Technology - Transactions of Civil Engineering*, *Rahman 2021*. https://doi.org/10.1007/s40996-024-01590-8
Pulket, T., & Arditi, D. (2009). *Construction litigation prediction system using ant colony optimization Construction litigation prediction system using ant colony optimization*. *6193*. https://doi.org/10.1080/01446190802714781
Sağır, M., Genç, O., & Coşkun, H. (2018). *İnşaat Sektöründe İş Kazası Üzerine Bir Araştırma*. 25–29.
Shojaat, M., Malekitabar, H., & Isfahani, H. H. (2025). *Navigating the Complexity of Dispute Management in Construction : A DEMATEL and Bayesian Network Approach*. *17*(1). https://doi.org/10.1061/JLADAH.LADR-1143
The Supreme Board of Construction and Infrastructure. (2020). *Decisions and Opinions 2005-2020 (Turkish)*. https://webdosya.csb.gov.tr/db/yfk/icerikler//kg-2005-2020-20210809125703.pdf
Wu, J., Wu, B., Pan, S., Wang, H., & Cai, Z. (2015). Locally weighted learning: How and when does it work in Bayesian networks? *International Journal of Computational Intelligence Systems*, *8*, 63–74. https://doi.org/10.1080/18756891.2015.1129579
Yılmaz, İ. C. (2020). *An Automation Model For Construction Dispute Documents In Turkish Public Projects*. 8–19.
Yousefi, V., Yakhchali, S. H., Khanzadi, M., Mehrabanfar, E., & Šaparauskas, J. (2016). Proposing a neural network model to predict time and cost claims in construction projects. *Journal of Civil Engineering and Management*, *22*(7), 967–978. https://doi.org/10.3846/13923730.2016.1205510
Zhang, L., Fu, Y., & Lu, W. (2021). Contract Enforcement for Claimants' Satisfaction with Construction Dispute Resolution: Moderating Role of Shadow of the Future, Fairness Perception, and Trust. *Journal of Construction Engineering and Management*, *147*(2), 04020168. https://doi.org/10.1061/(asce)co.1943-7862.0001981
Zheng, X., Liu, Y., Jiang, J., Thomas, L. M., & Su, N. (2021). Predicting the litigation outcome of ppp project disputes between public authority and private partner using an ensemble model. *Journal of Business Economics and Management*, *22*(2), 320–345. https://doi.org/10.3846/jbem.2021.13219

A literature review of digital twins (DT) in infrastructure projects: trends, challenges, and future directions

Elif G. Petek*[1], Onur B. Tokdemir[1]

[1] *Istanbul Technical University, Department of Civil Engineering, Istanbul 34469, Turkey*

Abstract. The purpose of this study is to review and analyze the literature comprehensively using a bibliometric approach to the implementation of Digital Twins (DT) in civil infrastructure projects by identifying the current state, recent technologies, key aspects, and challenges while providing insights and guidance to shape the future developments in this field. The application of DT in infrastructure projects is reviewed from the "Scopus" database, carefully analyzed, and appraised, and new ideas are generated for future research. DT technology in civil infrastructure projects enables construction progress monitoring, quality management, and real-time analysis. However, some crucial points in using DT, such as having accurate and consistent data, are crucial. DT is highly beneficial and significant when reliable data is available. Despite its growing importance, implementing DT in civil infrastructure projects remains a nascent field, lacking resources. Therefore, studies can be conducted and further developed in this field. This study includes a comprehensive literature review about implementing DT in civil infrastructure projects. It presents compelling arguments and feasible ideas for efficiently adopting DT in civil infrastructure projects.

Keywords: Digital twins (DT); Civil infrastructure; Bibliometric analysis; Innovation; Data

1. Introduction

The recent studies, rising prominence, and extensive applications of Digital Twins (DTs) have led researchers to diverse definitions. Callcut et al. (2021) interviewed in August 2020 and one of the questions was about the definition of DTs. Most interviewees agreed that DTs are a realistic digital representation of physical assets, processes, and systems; however, they stated that DTs do not have to be physical objects but real, and bi-directional connections are significant. Some organizations also define DT, but they are in their infancy. For instance, according to a study comprising literature research, survey, and interview findings, the Centre for Digital Built Britain (CDBB), which is the leading organization for the development of DTs in the United Kingdom (UK), should reconsider its definition of DT, a systematic approach should be created, uncertainties should be quantified, DT efforts should focus shorter timelines and high safety, investigating how DTs can be used to reduce operational energy, developing networks for secured accessible data, reaching digital maturity and establishing an organization to coordinate government-funded DT projects (Callcut et al., 2021). At a fundamental level, DTs are virtual replicas of physical assets that leverage dynamic, real-time data to enable predictive maintenance and informed decision-making. With the evolution of technology, DTs have been adopted significantly in various fields due to their considerable potential for accurately representing and managing real physical systems. As a result of utilizing DTs in various fields such as water management, transport systems, and traffic optimization, there is no standardization on how to develop DT. Standardization and using CEN/TC 442/WG 9 standards, integration with IoT, digital logbooks, and digital product passports are crucial for DT usage. DTs benefit from real-time monitoring and maintenance, reducing project costs, energy efficiency, sustainability, and public safety. For the full adoption of DTs, a standardized, unified educational framework should be built (Aragón et al., 2025).

In the construction industry, continuous innovation has driven the development of numerous methods and models, which have been researched, tested, and proposed for practical implementation. DTs enable civil engineers to conduct performance analysis that optimizes asset performance by visualizing assets along their service life and monitoring changes (Sanfilippo et al., 2022). However, despite these advancements, the widespread adoption of DT technologies in construction has not yet reached the desired level. Despite ongoing research and innovations in DTs in civil infrastructure systems, the practical applications are insufficient, and this has encouraged a growing body of research aimed at exploring the potential of DTs in complex and long-lived systems, particularly within

* Corresponding author, E-mail: peteke19@itu.edu.tr

https://doi.org/10.31462/icearc2025_ce_mng_179

golden light publishing

the infrastructure domain in the context of how benefit can be achieved by implementing DTs in the civil infrastructure projects.

Since 2020, the digital twin (DT) approach for infrastructures has gained a lot of interest and development (Li et al., 2025). The United States of America (USA) and the UK are the leading countries in developing DTs (Taherkhani et al., 2024). The importance of DT technologies has become increasingly pronounced within infrastructure projects due to the scale, complexity, and longevity of physical assets such as roads, bridges, pipelines, and utility networks. DTs facilitate proactive maintenance, lifecycle optimization, and stakeholder collaboration by providing a dynamic digital representation of physical infrastructure.

Infrastructure systems require continuous oversight and efficient coordination across their lifecycle stages, from design and construction to operation and maintenance. However, DTs are predominantly applied during construction projects' operation and maintenance phases, which is unsatisfactory. The projects should be monitored digitally by the stakeholders, such as the client, project manager, contractor, and consultant, starting from the beginning of the project, not just in the operation and maintenance stage. If DT implementation starts from the beginning of the project, the defects could be recognized earlier, allowing the stakeholders to save money and time. In light of this, the goal is to broaden DT utilization to encompass the design and construction stages. Automation and coordination in the design and construction stage will reduce project costs and delivery time (Callcut et al., 2021). By creating real-time digital models of physical infrastructure, DTs enable project stakeholders to monitor the performance conditions of the systems, forecast failures, and simulate alternative management strategies. This capability improves operational efficiency and supports enduring sustainability goals, especially in critical service continuity and safety environments. As infrastructure systems grow more interconnected and data-driven, integrating DTs offers a transformative approach to managing assets more intelligently and proactively.

While numerous studies have explored the concept and applications of DTs in the built environment, the literature still lacks a comprehensive and structured synthesis that critically examines current trends, recurring challenges, and emerging research priorities, particularly in the context of infrastructure projects. To close this gap, this paper aims to systematically review existing research on Digital Twin implementations in infrastructure with bibliometric analysis by classifying the findings into key thematic areas—such as current applications, methods, key challenges, and future technologies. This study maps the state of the art and highlights the barriers that hinder wider adoption. Furthermore, the paper outlines future research directions to support more effective and scalable DT applications in the infrastructure sector.

2. Materials and methods

A systematic approach was implemented to conduct a comprehensive literature review on implementing DTs in infrastructure projects. Scopus, a well-known, reputable database for scientific research, was used to conduct this study. The study has no publication date limit; however, recent studies were prioritized to learn and examine the recent trends, technologies, and innovations. The methodology of this study began with defining the scope, which is a comprehensive literature review of DT applications in civil infrastructure. A keyword search strategy was used by Boolean operators, combining the terms "digital twin" and "civil infrastructure." This initial query yielded a total of 64 records. A detailed literature review and bibliometric analysis were carried out to identify the research trends, innovations, knowledge gaps, challenges, key contributors, and future study directions. The research methodology can be found in Fig. 1.

2.1. Bibliometric analysis

Bibliometric metrics are crucial for assessing and capturing innovations in specialized disciplines (Van Raan, 2003). This study exported bibliographic data, including metadata such as authors, title, abstract, publication date, publisher, keywords, and citation counts, from Scopus in CSV format to carry out the analysis. A bibliometric analysis was applied to analyze and examine this data accurately. In this study, bibliometric analysis was conducted using Open Knowledge Maps, Bibliometrix, an R-based package, VOSviewer, and Biblioshiny tools.

2.2. Open knowledge maps

In this study, Open Knowledge Maps, an AI-based visual interface, was utilized as a complementary tool to support the literature review from a conceptual view shown in Fig. 2. While VOSviewer is used for conducting detailed literature reviews through bibliometric analysis, Open Knowledge Maps, on the other hand, is a tool that can visualize the topic to be researched and allows for a conceptual exploration of the literature. It enables a topical overview and provides the most relevant 100 documents based on the research topic by using the Artificial Intelligence (AI) pipeline. The pipeline utilizes natural language processing methods to collate and display publications according to similar topics. Visualizing the research topic is beneficial for taking a broad perspective on the research area. Upon entering the website, the research topic should be written first. Then, keywords related to the topic are visualized, and once one of them is clicked, the related articles are shown. In the tool, the details and links of each article can be accessed by clicking on the articles.

2.3. Bibliometrix and biblioshiny

Biblioshiny, which is the web interface of Bibliometrix, was used to review annual scientific production of DTs in infrastructure shown in Fig. 3 and three-field plot shown in Fig. 4.

2.4. VOSviewer

VOSviewer was used to create co-occurrence analysis maps, as shown in Figure 5. According to the co-occurrence analysis based on the author's keywords, the frequently used keywords are digital twin, civil infrastructure, Structural Health Monitoring (SHM), and Building Information Modelling (BIM). VOSviewer produced structured maps that reflected associations within the dataset.

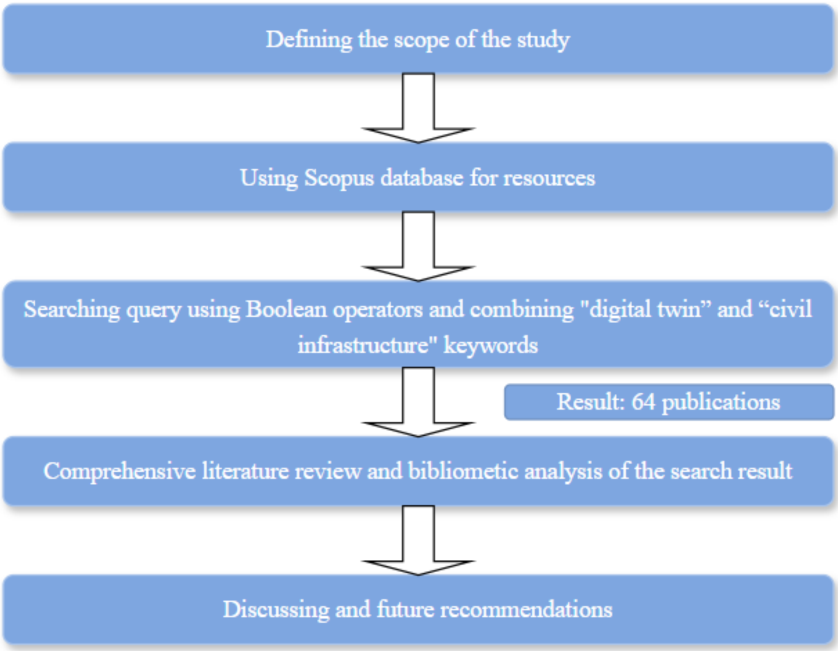

Fig. 1. Research Methodology

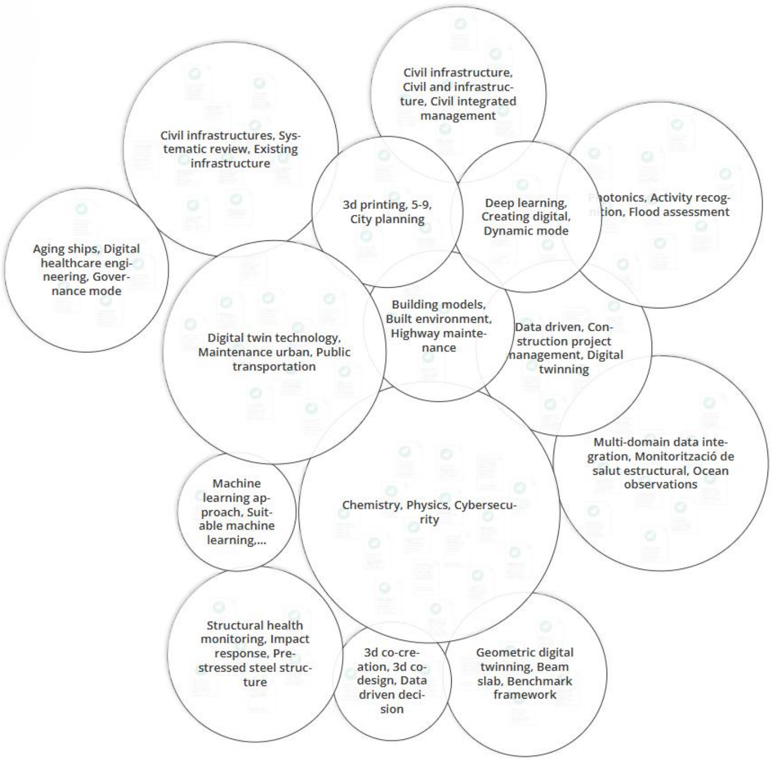

Fig. 2. Knowledge Map for research on digital twins in civil infrastructure (Open Knowledge Maps, 2025)

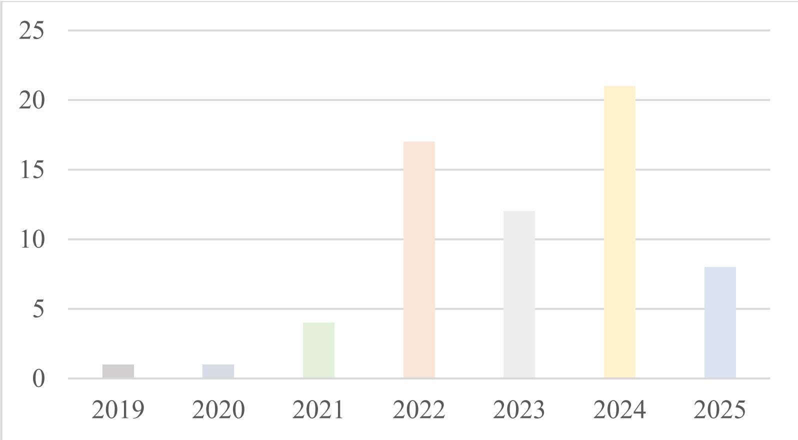

Fig. 3. Annual Scientific Production of DTs in Infrastructure

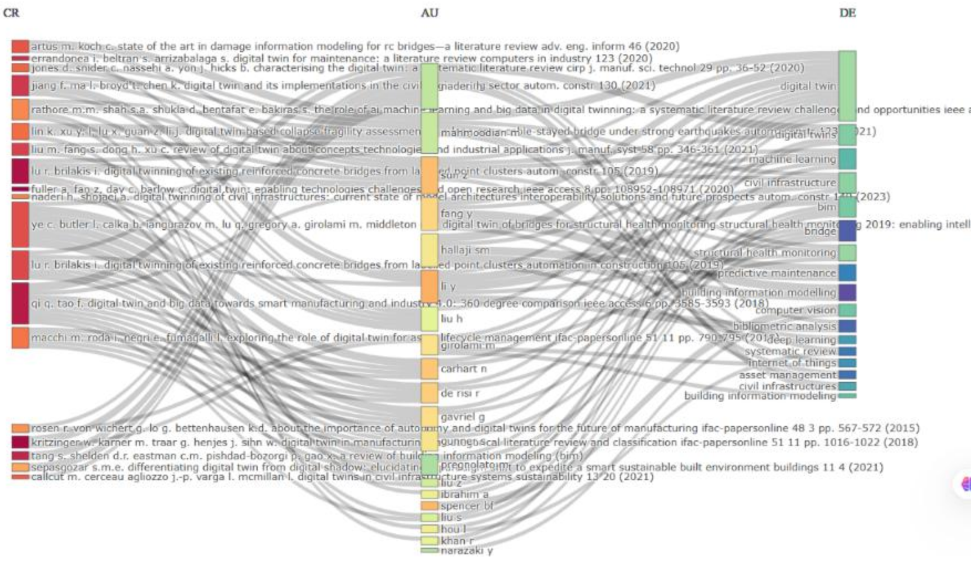

Fig. 4. Three-field plot (Bibliometrix, 2025)

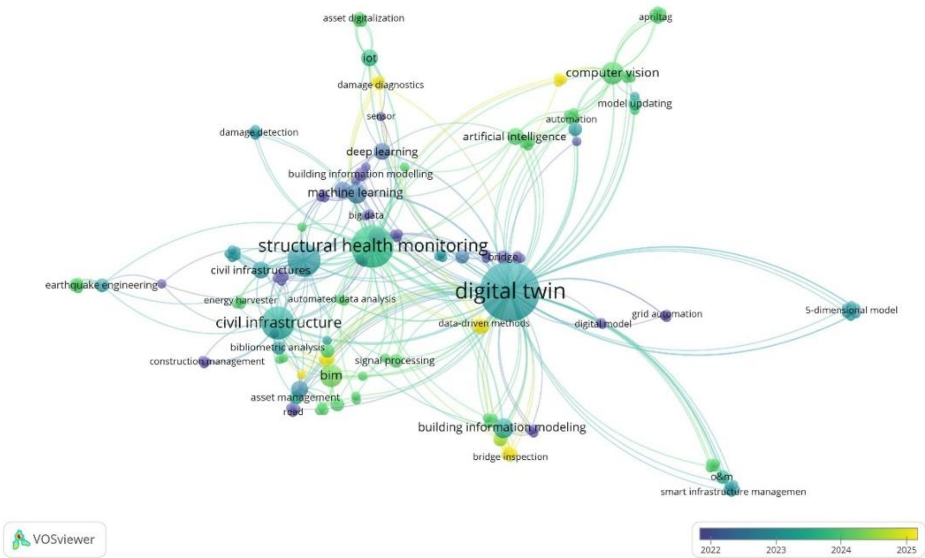

Fig. 5. Co-occurrence analysis of author keywords with no constraint

3. Results and discussion

3.1. Digital twins applications in civil infrastructures

Many studies have been conducted in various sectors about DT applications in civil infrastructure. The number of studies conducted on Digital Twin (DT) applications in the bridge sector is significantly higher than in other fields. A few studies have been conducted for tunnel and road domains. For the aviation and marine sectors, the implementation of DTs mainly focuses on operational management and security issues (Broo & Schooling, 2023). This study analyzes rail and road, transportation, bridge, water systems, waste management, energy systems, telecommunication systems, and tunnels infrastructure applications.

3.1.2. Rail and road infrastructure

DT studies on rail and road infrastructure networks are still lacking. They provide critical service to the public and face many challenges, such as increasing demand, territorial dispersion, a wide range of asset types, and investment backlogs. For this reason, utilizing DTs will help address these issues by providing efficient asset information. DT research in rail and road infrastructure is very recent and has increased at a minimum rate of 100% over the past four years, as indicated in the bibliometric analysis (Vieira et al., 2022).

According to Sanfilippo et al. (2022), DTs can be used in road infrastructure systems by representing them with 3D technology, and the related information can be used via a data management system. Data can be collected by blockchain techniques, automated devices such as mobile and fixed sensors, and multiple mobile robots. They concluded that a systematic design approach for using DTs in road infrastructure is missing in the literature. Therefore, they present this systematic approach by considering flexibility, integrability, and reliability. The Robot Operating System (ROS) and the Gazebo simulator execute the suggested framework. The bottom-up method consists of physical/virtual layer that interconnects physical and virtual road infrastructures. These sensors enable the collection of data such as accelerometers and vibrometers (more sensors means more precise data), carrier layer that will accumulate the important data, add-on layer which enables adding extra sensors, data acquisition layer that gets all raw data from not only the fixed sensors but also from the mobile sensors, annotation layer which enables manually adding information and storing historical data such as damages in the road traffic status and finally application layer (data interpretation) which analysis and examines the data reached and presents it to the users to make determinations, action plans.

Eighty articles were examined in a study that confirmed the advancement of DTs in road engineering. It focuses mainly on virtual geometry models and getting real-world data. It emphasizes that 5D DT implementations are not sufficient enough. Ground Penetrating Radar (GPR) and Internet of Things (IoT) technologies are used to monitor, maintain, and develop DTs. Existing studies examine the incorporation of related physical theories, mechanical rules, and behavioral codes, primarily to construct detailed and multi-level models. There are compelling challenges for data processing and connection-enabling technologies because of the complexity of pavement structures and the built-in inconsistency of materials. The use of DTs in road engineering primarily focuses on the Operational & Maintenance (O&M) stages. Conversely, DTs are less common in the design, construction, and reconstruction stages, especially noticeable in the demolition stage. There is no common understanding of specific application roadmaps and standardization. Further studies should be conducted on developing standardization, real-time interaction, innovative data analysis, expanded lifespan applications, and transformative DTs in road engineering (Yan et al., 2024).

3.1.3. Transportation infrastructure

DT technology has the potential to manage transportation infrastructure; however, the recent implementations are still in the early stages, especially in large urban systems. The studies mainly focused on traffic management and structural health monitoring, which misses a comprehensive full lifecycle approach. This study proposes a full lifecycle DT system from planning to maintenance that introduces a "4 horizontal + 4 Vertical + N" framework for urban transportation infrastructure. The horizontal layers are data, model, service, and application, and the vertical layers are planning/design, construction, operation, and optimization. Moreover, the "Form-Condition-Mechanism-Tendency" concept is analyzed, and it is a robust tool supporting efficient operation and sustainable development (Wu, 2025).

3.1.4. Bridge infrastructure

Data and Knowledge-Driven Digital Twin Modeling (DK-DTM) can be used in civil infrastructure, such as bridges, where there is insufficient data and high certainty. Spatial modeling of bridges can be done to establish correlations between bridge defects and explain the root causes of these structural health issues. Innıvative applications of advanced data processing techniques for SHM, such as YOLOv8, can be used for crack detection of 2D images, PointNet for 3D point cloud deformation analysis, and LTSM networks for sensors and early warnings (Sun et al., 2025).

A five-step framework can be developed for DTs' existing structures, including data and need acquisition, digital modeling, dynamic data transmission, data/model integration, and operation. The framework was applied as a case study to the Grade I listed Clifton Suspension Bridge (Bristol, UK) completed in 1864 and has no BIM data (Mitchell-Baker and Cullimore, 1988; Anderson, 2013). The management and maintenance of The Clifton Suspension Bridge are under the responsibility of The Clifton Suspension Bridge Trust (CSBT), and they have concerns about the operation of the tower saddles as their potential seizure, which may impair the bridge's safety. With the help of DTs, sensor information is taken periodically, enabling managers to see the risk factors, focus on operational needs, select the suitable one, and take safe and cost-effective actions (Pregnolato et al., 2023).

Another publication analyzed the Clifton Suspension Bridge (Bristol, UK) as a case study to show DTs in the Architecture, Engineering, and Construction (AEC) sector. It applies the five-step workflow process for utilizing DTs in the built environment. A Three Dimensional Finite Element Method (3D FEM) was developed, and Midas Gen (MA4) was chosen for initial FE modeling (Pregnolato et al., 2022).

According to another study conducted on a bridge called McKanes Falls Bridge located in NSW, Australia, the accuracy level of two-point clouds acquired based on UAV photogrammetry and Terrestrial Laser Scanning (TLS), TLS is very beneficial for bridge inspection and 3D model reconstruction; however, there are challenges such as expensive pieces of equipment and limited site access (Mohammadi et al., 2021).

3.1.5. Water systems

The structure of urban water systems is inherently intricate, and in case of a failure, it will be tough to repair. Hence, the necessary precautions should be taken before the failure. Supervisor control and data acquisition (SCADA) systems enable hydrological modeling to prevent failures arising from fluctuations in rainfall, population growth, infrastructure wear and tear, and resources. The subsequent step is to use DTs in the water distribution industry for dynamic processing. All types of water infrastructure, such as pipe networks, pumping stations, treatment facilities, and storage tanks, can benefit from and implement DTs (Callcut et al., 2021).

3.1.6. Waste management

Wide-ranging research is conducted in wastewater to improve control strategies and process monitoring systems (Therrien et al., 2020). Research conducted by Ghandar et al. (2021) recommends a decision support system called aquaponics to complement a novel urban farming framework. With the help of this technique, the transportation distance decreases between producers and consumers. However, because of the complex human activity in the system, DTs can be used to gather real-time data to minimize waste. Moreover, wastewater treatment plants (WWPTs) are very significant and critical civil infrastructure for protecting the environment. DT usage will be very beneficial in performing predictive maintenance (PdM) of pumps, critical assets in WWTPs. A DT framework can be created to broaden the scope of PdM by utilizing Building Information Modelling (BIM) and Deep Learning. (Hallaji S.M. et al., 2021). While integrating DTs in wastewater systems, the data types are also very significant. In other words, the data types used in Machine Learning are limited to vibration and flow, which may not be sufficient, especially for Waste Water Treatment Plants (WWTPs) for diagnosing the condition of pumps and their attributes, which can result in inaccurate predictions. To effectively integrate BIM into the digital twin framework, interoperability is needed between IoT and maintenance and operation databases. Deep learning techniques effectively process massive datasets; however, they rely on sensing that might be limited in older WWTP facilities, so this should be considered (Hallaji et al., 2022).

3.1.7. Energy systems

Failure of pipeline assets is a significant problem in the energy sector. Improved operation and maintenance strategies are being sought by oil and gas operators in order to lower downtime from costly planned or unplanned maintenance. For the subsea pipeline system, a conceptual DT with integrated sensors is proposed, which predicts future conditions, recognizes anomalies, and forecasts the remaining life span of the asset (Bhownik, 2019). Another research analysis is PetroChina's proposal of a top-level intelligent pipeline based on DT technology (Xiandong et al., 2020). For maintenance, a proposed DT-based system uses a Russian-made robotic system called Cablewalker and a DT for overhead transmission lines for predictive maintenance (Gitelman et al., 2019).

3.1.8. Telecommunication systems

DTs set a solid foundation for advancing telecommunication networks and aggregating data by harnessing vast datasets, data mining, and neural networks. Using DTs in telecommunication systems is beneficial, especially for emergency traffic monitoring (Seilov et al., 2021). Consolidated Digital Twin for Telecommunication Towers (cDTT) enables real-time analysis, multi-tenant coordination, maintenance, and public safety (Medeisis A. and Radis, 2022).

3.1.9. Tunnels

Civil infrastructures undergo a degradation process over time. A model is developed to predict tunnel performance deterioration using visual inspection data, classification systems, and predictive models. In the model, degradation assessment is first done by conducting visual inspections on tunnel walls and roofs determined from geological-geotechnical mapping. Defects such as cracks, infiltration, and spalling are classified into four degradation states from I to IV. Tunnel Serviceability Index (TSI), which ranges between 0 (worst) to 5 (best), which indicates defect severity, is used. Secondly, prediction modeling is done using an inverse exponential equation, and forecast curves determine intervention timeframes for maintenance target intervention time by a limit analysis of approximately 16 years. Finally, Rhinoceros 3D and EleFront plugins are used to build a 3D virtual tunnel model. Inspection Digital Twin (IDT) has enabled virtual inspection, condition tracking, and lifecycle management (Bellini Machado & Massao Futai, 2024).

3.2. Current technologies and research trends in digital twins-enabled infrastructure

3.2.1. Sensing and data integration

The key enabling techniques for DTs are mechanical modeling, geographic information systems (GIS), City Information Modelling (CIM), machine/deep learning, and extended reality (XR). (Chang et al., 2024). DTs are advancing through sensing technologies, finite element modeling, data analysis, and system identification methods. Load Identification (LID) and Response Reconstruction (RRE) are core techniques that enable the creation of DTs by predicting unmeasurable external forces and reconstructing unmeasured structural responses (Li et al., 2025).

3.2.2. Energy harvesting

Triboelectric Nanogenerators (TENGs) support the development of DTs in the context of Civil Engineering Infrastructure 4.0 by energy harvesting, real-time monitoring, and self-powered sensing. It converts mechanical energy such as vibration, pressure, wind, and raindrops into electrical energy, enables self-powered sensors for Structural Health Monitoring (SHM), and supports wireless communication and integration into IoT systems. It can be applied to smart buildings, roads, rail tracks, tunnels, and ports. TENG enables using materials such as concrete, paints, and wood for energy harvesting in smart structures. Cement-based composites are very effective in performance enhancement. Metamaterial concrete is used for advanced sensing and resilience. (Pang et al., 2024).

3.2.3. Modeling

The literature mainly focuses on visualization and physical modeling using CAD, GIS, and BIM in urban building and evaluation. However, semantic, planning-oriented features also should be used. A method called Fractalopolis, a Multiscaling Zoning system unique in explicitly modeling urban centralities, can be used to show urban structure across scales and allows planners to develop scenarios in coherence (Bonin & Frankhauser, 2025). Finite element-based methods, data-driven approaches, 3D model reconstruction using laser scanning methods, and 3-D model reconstruction using unmanned aerial vehicle (UAV) methods can be used to build DTs in civil infrastructures. (Liu et al., 2023) A graphics-based digital twin (GBDT) is created for civil infrastructure and suggests a method integrating photographic displacement measurements with finite element (FE) simulations through a graphics-based digital twin (GBDT) to improve structural models and assess degradation (Wang et al., 2023). Using mesoscale phase-field modeling and macroscale structural analysis within a unified framework allows the digital representation to show both local damage (pitting) and global structural effects. The two-stage Approximate Bayesian Computation (ABC) method enables continuous calibration, essential for self-adaptive DTs (Qian et al., 2024). An innovative BIM-enabled digital twin framework is created and tested by monitoring and visualizing the deformation of critical structural elements such as beams and columns by a structural frame prototype and laser displacement sensor measurements. The model was used to perform structural analysis to find optimal locations for sensors and guide the creation of a DT model for real-time structural behavior visualization (Hu et al., 2024).

3.2.4. Machine learning

Machine learning enables a new 5th-level damage type classification to be added to 4 level damage detection hierarchy, which includes detection, location, severity, and prognosis) (Malekloo et al., 2022) Physics-informed machine learning (PIML) incorporates past knowledge of the physical world and data-driven solutions. They are practical tools for modeling in DTs (Heidarian Radbakhsh et al., 2024).

3.3. Advanced technologies

Recent Infrastructure Digital Twins (IDTs) are based on BIM and the Internet of Things (IoT) and are mainly used in the Operation and Maintenance (O&M) phase of infrastructure projects. Technologies such as GIS, Point Cloud Data, Finite Element Models (FEM), and Machine Learning techniques are utilized by researchers in order to have a more complex Infrastructure Digital Twin (IDT) architecture. (Naderi and Shojaei, 2023). DTs have started to be implemented in various fields. For instance, prestressed steel structures in the O&M stage are analyzed by a prediction method created by DTs and an improved Back Propagation Neural Network (BP) optimized by the Levenberg-Marquardt (LM) algorithm, a machine learning method. The DT-based solution predicts the impact response of prestressed steel structures with an eight percent fluctuation, showing high accuracy (Liu et al., 2022). Moreover, Proactive Perceptive Road (PPR), which is an innovative DT-driven infrastructure model, can be used to monitor roads. The PPR enables the gathering of real-time, accurate data, comprehensive detection, and simulation of road condition data. It ensures precise mapping and shows the road's observable and internal conditions. It maximizes using sensors to detect explicit state information in the road domain, such as geometric dimensions, physical materials, and surface and structural conditions (e.g., cracks and potholes). Moreover, it utilizes simulation tools and Machine Learning (ML) algorithms to make the models work with high sensitivity and analyze implicit state information of performance, life span, and behavior that is hard to measure. (Han et al., 2025). Fast Bayesian (FFT) and Principal Component Analysis (PCA) can also be used for trend detection and early warnings (Li et al., 2024). Additionally, Proper Orthogonal Decomposition (POD) is used to create a digital twin model framework for real-time prediction of the stress response of tubular joints. Leave-one-out cross-validation (LOOCV) is used to optimize and select the modal order of the Reduced Order Model (ROM). The study confirms that the proposed Reduced-Order Model (ROM) achieves high prediction accuracy (avg. error: 5.16×10^{-7}%) and real-time performance, with 99.86% greater efficiency than the full-order model (FOM) (Leng J C. et al., 2025). Stochastic Subspace Identification with Covariances (SSI-COV) method using real sensor data can detect modal parameters without artificial excitation (Lozano-Allimant S. et al., 2025). A new approach utilizes Convolutional Neural Networks (CNN), Robotic Arms (ROIs), laser line scanners, and 3D LiDAR mapping for automatic crack detection and measurement (Ghadimzadeh Alamdari and Ebrahimkhanlou, 2024). A study collected 204 papers from the Web of Science about Advanced Information Technologies (AITs) used in civil infrastructure planning, construction, and maintenance stages between 2010 and 2020. Key technologies such as Wireless Sensor Networks (WSN), Building Information Modelling BIM), Fiber Optic Sensing (FOS), and Radio Frequency Identification (RFID) are reviewed (Li et al., 2022).

Taherkhani et al. (2024) examined 130 articles from the Scopus and Web of Science databases using VOSviewer. Their findings revealed a notable rise in publications on applying Digital Twins in infrastructure, indicating increasing scholarly interest and growing research momentum since 2018. However, they concluded that the number of studies focused on DT-enabled infrastructure remains insufficient. The co-authorship analysis showed that most contributions originated from the United States, the United Kingdom, and China. According to their citation analysis, the five most-cited articles applied Digital Twins to address wide-ranging challenges through real-time predictive insights and decision-making, with the primary obstacle being acquiring accurate data for their frameworks. Additionally, the keyword co-occurrence analysis revealed that terms such as AI, IoT, BIM, decision-making, structural health monitoring (SHM), visualization, and operation and maintenance are among the most frequently used in the literature.

3.4. DTs in the construction of smart cities

DT applications in the built environment can be classified into five major application areas: Smart cities, Design decision-making, product manufacturing, real-time construction progress monitoring, and facility management (Zribi et al., 2025). civil infrastructure innovations are integrated into real life by smart city applications. Smart Underground Grid Transformation, an Urban Futurability Project managed by ENEL São Paulo, is a great example of smart city applications. The project combines digital tools such as Ground Penetrating Radar (GPR) with civil infrastructure innovations. This case offers a blueprint for future smart cities (Simao et al., 2022).

The infrastructure management framework with the 5D smart city conceptual model in the UN Sustainable Development Goals can be used instead of traditional systems to improve smart cities. The 5D conceptual model integrates five core dimensions of infrastructure management: environmental, financial-economic, political-governance, social people, and technological (Chang et al., 2023).

3.5. Structural health monitoring (SHM) in civil infrastructure

DTs are beneficial for real-time structural health monitoring and are an alternative to non-destructive testing methods and traditional visual inspections. While creating the DTs, selecting suitable software is vital due to the effects of determining the boundary conditions with minimal discrepancies from reality. Moreover, the development platform is crucial as a central hub for data exchange and interpretation. DT designers have key responsibilities in addressing potential challenges early as these can affect the accuracy of the DTs (Sun et al., 2025).

The structural health and behavior should be understood by collecting data from the real-time simulation modeling to develop a DT for intelligent infrastructure maintenance. A case study is conducted on the conveyor jetty at the Dalrymple Bay Coal Terminal (DBCT) in Queensland, Australia. Tiltmeters, strain gauges, and vibrometers are used as sensors and installed on the structure to monitor real-time changes. The collected sensor data is integrated with Finite Element Model (FEM) developed by using ANYS, and data acquisition is made by Senscope, which is a RESENSYS platform that supports continuous monitoring. What-if scenarios are simulated in the digital environment before utilizing them in the physical asset to choose the safer, cost-effective, and evidence-based maintenance planning (Mahmoodian et al., 2022). Another study was conducted by installing a structural health monitoring (SHM) system on the precast concrete bridge, El Cacique Bridge, in the Dominican Republic (DR) to improve the state of knowledge and take information about the vibration characteristics of the structure. The parameters taken from SHM data are integrated with a computational structural model to develop a DT, and the DT is used to formulate a set of fragility curves for different damage limit states. The study presents a more accurate, data-driven method for mitigating seismic risks in critical infrastructure; therefore, the methodology can be adapted for other bridges or infrastructure systems (Rojas-Mercedes et al., 2022).

Despite these benefits, using DTs in Structural Health Monitoring has challenges and limitations, such as data privacy and security problems, data integration from various sources, model calibration and validation, computational complexity, resource requirements, and data quality (Parida and Moharana, 2024).

In order to establish suitable standards and protocols for DT-based Structural Health Monitoring (SHM), a deep understanding of the integration of emerging technologies such as the Internet of Things (IoT), Artificial Intelligence (AI), Augmented Reality (AR), Virtual Reality (VR), Big Data and other Industry 4.0 elements is necessary (Sakr & Sadhu, 2024).

4. Conclusion

Several studies were analyzed, and bibliometric analysis was conducted about DTs in civil infrastructure using Bibliometrix, Biblioshiny, VOSviewer, and Open Knowledge Maps tools. The Scopus database was chosen because of being a reliable source, and 64 articles were examined. According to the research, it has been seen that since 2020, DT applications have gained more importance and started to be studied and implemented in various fields such as rail and road, transportation, bridge, water systems, waste management, energy systems, telecommunication systems, and tunnel infrastructure. Many advanced technologies like BIM, IoT, SHM, GIS, GPR, FEM, AR, and VR can be integrated and utilized with DTs. There are attempts to utilize DTs in civil infrastructure; however, they are still insufficient and need to be improved. Moreover, the implementations are mainly limited by O&M stages of construction. However, DTs should be implemented in the design and construction phases so that action can be taken earlier in case of a defect. DTs are very beneficial for the civil infrastructure sector if they can be sensors that can collect standardized and accurate data. By SHM, the problems and defects in the systems can be recognized, and root cause analysis can be conducted to prevent future issues from happening, which will provide us with know-how. This comprehensive literature review contributes to the academic literature by conducting a detailed analysis using various tools, including reviews of case studies and previous literature reviews and their conclusions. Furthermore, this study is enhanced by reviewing the case studies. The research starts from the definition of DTs and continues with the bibliometric analysis of the publications, mainly focusing on the recent trends of using DTs in civil infrastructure, advanced technologies, and the relation of DTs with other technologies. Although the study has contributions to the literature, using only the Scopus database and publications written in English are the limitations. For future research, the databases used in the studies can be increased.

References

Anderson, D. (2013). *Maintenance of the Clifton Suspension Bridge: An historic and iconic Grade 1 listed structure*. In *ICSBOC (8th International Cable Supported Bridge Operators' Conference)*, Edinburgh, 3–5 June 2013. CRC Press. ISBN 9781482208450

Aragón, A., Arquier, M., Tokdemir, O. B., Enfedaque, A., Alberti, M. G., Lieval, F., & Yagüe, Á. (2025). Seeking a definition of digital twins for construction and infrastructure management. *Applied Sciences, 15*(3), 1557. https://doi.org/10.3390/app15031557

Bellini Machado, L., & Massao Futai, M. (2024). Tunnel performance prediction through degradation inspection and digital twin construction. *Tunnelling and Underground Space Technology, 144*, 105544. https://doi.org/10.1016/j.tust.2023.105544

Bhowmik, S. (2019, April). Digital twin of subsea pipelines: Conceptual design integrating IoT, machine learning and data analytics. In *Offshore Technology Conference* (Paper D011S010R004). OTC.

Bonin, O., & Frankhauser, P. (2025). Digital twins versus simulation models and planning concepts: Increasing the resemblance between a digital twin and the modeled territory to facilitate the construction and evaluation of urban scenarios. *Environment and Planning B: Urban Analytics and City Science*. https://doi.org/10.1177/23998083251318474

Broo, D. G., & Schooling, J. (2023). Digital twins in infrastructure: Definitions, current practices, challenges and strategies. *International Journal of Construction Management, 23*(7), 1254–1263. https://doi.org/10.1080/15623599.2021.1966980

Callcut, M., Cerceau Agliozzo, J.-P., Varga, L., & McMillan, L. (2021). Digital twins in civil infrastructure systems. *Sustainability (Switzerland), 13*(20), 11549. https://doi.org/10.3390/su132011549

Chang, C. M., Salinas, G. T., Gamero, T. S., Schroeder, S., Vélez Canchanya, M. A., & Mahnaz, S. L. (2023). An infrastructure management humanistic approach for smart cities development, evolution, and sustainability. *Infrastructures, 8*(9), 127. https://doi.org/10.3390/infrastructures8090127

Chang, X., Zhang, R., Mao, J., & Fu, Y. (2024). Digital twins in transportation infrastructure: An investigation of the key enabling technologies, applications, and challenges. *IEEE Transactions on Intelligent Transportation Systems, 25*(7), 6449–6471. https://doi.org/10.1109/TITS.2024.3401716

Ghadimzadeh Alamdari, A., & Ebrahimkhanlou, A. (2024). A multi-scale robotic approach for precise crack measurement in concrete structures. *Automation in Construction, 158*, 105215. https://doi.org/10.1016/j.autcon.2023.105215

Ghandar, A., Ahmed, A., Zulfiqar, S., Hua, Z., Hanai, M., & Theodoropoulos, G. (2021). A decision support system for urban agriculture using digital twin: A case study with aquaponics. *IEEE Access, 9*, 35691–35708. https://doi.org/10.1109/ACCESS.2021.3063203

Gitelman, L. D., Kozhevnikov, M. V., & Kaplin, D. D. (2020). Asset management in grid companies using integrated diagnostic devices. *Energy Resources and Policies for Sustainability, 211*, 1–9.

Hallaji, S. M., Fang, Y., & Winfrey, B. K. (2021). A digital twin framework for enhancing predictive maintenance of pumps in wastewater treatment plants. In *ISARC. Proceedings of the International Symposium on Automation and Robotics in Construction* (Vol. 38, pp. 88–93). IAARC Publications.

Hallaji, S. M., Fang, Y., & Winfrey, B. K. (2022). Predictive maintenance of pumps in civil infrastructure: State-of-the-art, challenges and future directions. *Automation in Construction, 134*, 104049. https://doi.org/10.1016/j.autcon.2021.104049

Han, T., Ma, T., & Xiao, J. (2025). Proactive perceptive road: A digital twin-driven intelligent road infrastructure towards proactive road state perception and deduction. *Smart Materials and Structures, 34*(2), 025030.

Heidarian Radbakhsh, S., Nik-Bakht, M., & Zandi, K. (2024). Model updating for structural digital twins through physics-informed data-driven models. In *Lecture Notes in Civil Engineering* (Vol. 497). https://doi.org/10.1007/978-3-031-62170-3_9

Hu, X., Olgun, G., & Assaad, R. H. (2024). An intelligent BIM-enabled digital twin framework for real-time structural health monitoring using wireless IoT sensing, digital signal processing, and structural analysis. *Expert Systems with Applications, 252*, 124204.

Li, C. Z., Guo, Z., Su, D., Xiao, B., & Tam, V. W. Y. (2022). The application of advanced information technologies in civil infrastructure construction and maintenance. *Sustainability (Switzerland), 14*(13), 7761. https://doi.org/10.3390/su14137761

Li, Y., Luo, L., Wang, X., Zhou, X., Sun, L., & Xia, Y. (2025). State-of-art review on load identification and response reconstruction to realize digital twin of infrastructures. *Advances in Structural Engineering.* https://doi.org/10.1177/13694332251321196

Liu, C., Zhang, P., & Xu, X. (2023). Literature review of digital twin technologies for civil infrastructure. *Journal of Infrastructure Intelligence and Resilience, 2*(3), 100050. https://doi.org/10.1016/j.iintel.2023.100050

Liu, Z., Yuan, C., Sun, Z., & Cao, C. (2022). Digital twins-based impact response prediction of prestressed steel structure. *Sensors, 22*(4), 1647. https://doi.org/10.3390/s22041647

Lozano-Allimant, S., Lopez, A., Gomez, M., Atencio, E., Lozano-Galant, J. A., & Fingerhuth, S. (2025). Structural health assessment of a reinforced concrete building in Valparaíso under seismic and environmental shaking: A foundation for IoT-driven digital twin systems. *Applied Sciences, 15*(3), 1202.

Mahmoodian, M., Shahrivar, F., Setunge, S., & Mazaheri, S. (2022). Development of digital twin for intelligent maintenance of civil infrastructure. *Sustainability (Switzerland), 14*(14), 8664. https://doi.org/10.3390/su14148664

Malekloo, A., Ozer, E., AlHamaydeh, M., & Girolami, M. (2022). Machine learning and structural health monitoring overview with emerging technology and high-dimensional data source highlights. *Structural Health Monitoring, 21*(4), 1906–1955. https://doi.org/10.1177/14759217211036880

Medeisis, A., & Radis, D. (2022). Design principles for consolidated digital twin of a telecommunication tower. *2022 IEEE Open Conference of Electrical, Electronic and Information Sciences (EStream 2022) –* Proceedings. https://doi.org/10.1109/eStream56157.2022.9781769

Mitchell-Baker, D., & Cullimore, M. S. G. (1988). Operation and maintenance of the Clifton Suspension Bridge. *Proceedings of the Institution of Civil Engineers, 1*(84), 291–308. https://doi.org/10.1680/iicep.1988.63

Mohammadi, M., Rashidi, M., Mousavi, V., Karami, A., Yu, Y., & Samali, B. (2021). Case study on accuracy comparison of digital twins developed for a heritage bridge via UAV photogrammetry and terrestrial laser scanning. *International Conference on Structural Health Monitoring of Intelligent Infrastructure: Transferring Research into Practice (SHMII 2021)*, June, 1713–1720.

Naderi, H., & Shojaei, A. (2023). Digital twinning of civil infrastructures: Current state of model architectures, interoperability solutions, and future prospects. *Automation in Construction, 149*, 104785. https://doi.org/10.1016/j.autcon.2023.104785

Pang, Y., He, T., Liu, S., Zhu, X., & Lee, C. (2024). Triboelectric nanogenerator-enabled digital twins in civil engineering infrastructure 4.0: A comprehensive review. *Advanced Science, 11*(20), 2306574. https://doi.org/10.1002/advs.202306574

Parida, L., & Moharana, S. (2024). Current status and future challenges of digital twins for structural health monitoring in civil infrastructures. *Engineering Research Express, 6*(2), 025004. https://doi.org/10.1088/2631-8695/ad4aea

Pregnolato, M., Gunner, S., Voyagaki, E., De Risi, R., Carhart, N., Gavriel, G., ... & Taylor, C. (2022). Towards Civil Engineering 4.0: Concept, workflow and application of digital twins for existing infrastructure. *Automation in Construction, 141*, 104421. https://doi.org/10.1016/j.autcon.2022.104421

Pregnolato, M., Gunner, S., Voyagaki, E., De Risi, R., Gavriel, G., Tully, P., & Taylor, C. (2023). Digital twins for civil infrastructure: A case study on the Clifton Suspension Bridge (Bristol, UK). In *Life-Cycle of Structures and Infrastructure Systems* (pp. 2219–2226). CRC Press.

Qian, G., Wu, Z., Hu, Z., & Todd, M. D. (2024). Pitting corrosion diagnostics and prognostics for miter gates using multiscale simulation and image inspection data. *Structural Health Monitoring*. https://doi.org/10.1177/14759217241264291

Rojas-Mercedes, N., Erazo, K., & di Sarno, L. (2022). Seismic fragility curves for a concrete bridge using structural health monitoring and digital twins. *Earthquake and Structures, 22*(5), 503–515. https://doi.org/10.12989/eas.2022.22.5.503

Sakr, M., & Sadhu, A. (2024). Recent progress and future outlook of digital twins in structural health monitoring of civil infrastructure. *Smart Materials and Structures, 33*(3). https://doi.org/10.1088/1361-665X/ad2bd7

Sanfilippo, F., Thorstensen, R. T., Jha, A., Jiang, Z., & Robbersmyr, K. G. (2022). A perspective review on digital twins for roads, bridges, and civil infrastructures. In *2022 International Conference on Electrical, Computer, Communications and Mechatronics Engineering (ICECCME)*. https://doi.org/10.1109/ICECCME55909.2022.9988693

Seilov, S. Z., Kuzbayev, A. T., Seilov, A. A., Shyngisov, D. S., Goikhman, V. Y., Levakov, A. K., ... & Zhursinbek, Y. S. (2021). The concept of building a network of digital twins to increase the efficiency of complex telecommunication systems. *Complexity, 2021*(1), 9480235. https://doi.org/10.1155/2021/9480235

Simao, M. S., Cardoso, B. B., Martins, M. A. I., & Junior, M. F. L. (2022). The automation and the use of innovative civil infrastructure in the construction of smart cities. In *2022 ASU International Conference in Emerging Technologies for Sustainability and Intelligent Systems (ICETSIS 2022)* (pp. 121–125). https://doi.org/10.1109/ICETSIS55481.2022.9888944

Sun, Z., Jayasinghe, S., Sidiq, A., Shahrivar, F., Mahmoodian, M., & Setunge, S. (2025). Approach towards the development of digital twin for structural health monitoring of civil infrastructure: A comprehensive review. *Sensors, 25*(1). https://doi.org/10.3390/s25010059

Sun, Z., Liang, B., Liu, S., & Liu, Z. (2025). Data and knowledge-driven bridge digital twin modeling for smart operation and maintenance. *Applied Sciences (Switzerland), 15*(1). https://doi.org/10.3390/app15010231

Taherkhani, R., Ashtari, M. A., & Aziminezhad, M. (2024). Digital twin-enabled infrastructures: A bibliometric analysis-based review. *Journal of Infrastructure Systems, 30*(1), 03123001. https://doi.org/10.1061/JITCFA.IJENG-12345

Therrien, J. D., Nicolaï, N., & Vanrolleghem, P. A. (2020). A critical review of the data pipeline: How wastewater system operation flows from data to intelligence. *Water Science and Technology, 82*(12), 2613–2634. https://doi.org/10.2166/wst.2020.542

Van Raan, A. (2003). The use of bibliometric analysis in research performance assessment and monitoring of interdisciplinary scientific developments. *TATuP – Zeitschrift für Technikfolgenabschätzung in Theorie und Praxis, 12*(1), 20–29.

Vieira, J., Martins, J. P., de Almeida, N. M., Patrício, H., & Morgado, J. G. (2022). Towards resilient and sustainable rail and road networks: A systematic literature review on digital twins. *Sustainability (Switzerland), 14*(12), 7060. https://doi.org/10.3390/su14127060

Wang, S., Rodgers, C., Fillmore, T., Welsh, B., Golecki, T., v. Shajihan, S. A., Eick, B. A., & Spencer, B. F. (2023). Vision-based model updating and evaluation of miter gates on inland waterways. *Engineering Structures, 280*, 115674. https://doi.org/10.1016/j.engstruct.2023.115674

Wu, D., Zheng, A., Yu, W., Cao, H., Ling, Q., Liu, J., & Zhou, D. (2025). Digital twin technology in transportation infrastructure: A comprehensive survey of current applications, challenges, and future directions. *Applied Sciences, 15*(4), 1911.

Xiangdong, X., Bo, L., & Jiannan, G. (2020). Asset management of oil and gas pipeline system based on digital twin. *IFAC-PapersOnLine, 53*(5), 715–719.

Yan, Y., Ni, L., Sun, L., Wang, Y., & Zhou, J. (2024). Digital twin enabling technologies for advancing road engineering and lifecycle applications. *Engineering*.

Zribi, H., Ben Abid, T., Elloumi, A., Hani, Y., Graba, B. B., & Elmhamedi, A. (2025). Industry 4.0: Digital twins characteristics, applications, and challenges in-built environments. *Production & Manufacturing Research, 13*(1), 2456277.

Clustering of construction business surveys: case of Türkiye

Serkan Aydınlı*[1]

[1] *Çukurova University, Department of Civil Engineering, 01250 Adana, Türkiye*

Abstract. The construction industry is a crucial locomotive industry for national economies. Business surveys in the construction industry are essential instruments for evaluating sectoral health and trends. They provide timely and organized data that serves many stakeholders, including policymakers, enterprises, analysts, and contractors. Since May 2011, TurkStat has begun the publication of construction business surveys to facilitate stakeholders to track sector trends. Some of the key indicators reflecting sectoral health and trends include construction confidence indicator, employment expectations, building activity development, and price expectations. This study aims to reveal the relationships and correlations between construction business surveys. To this end, construction business surveys published by Eurostat are obtained, and the data are clustered utilizing the Dynamic Time Warping (DTW) approach, a commonly used technique for clustering time series data. The clusters that were identified as a result of the analysis were interpreted and their contributions to sectoral trends were analyzed. The study enables the simplification of sectoral health indicators and enhances the understanding of them by sector stakeholders. The clusters also have the potential for forecasting important indicators such as the construction cost index and the construction production index.

Keywords: Business surveys; Dynamic time warping; Time series analysis; Construction industry.

1. Introduction

The construction sector plays an important role in national growth and serves as an engine for several sectors (Alaloul et al., 2021). It also significantly impacts employment, as it is a labor-intensive industry. Construction projects are complex activities that employ several laborers and technical staff. The extensive workforce involvement directly promotes employment rates (Ernst & Sarabia, 2015; Fendoglu & Polat, 2021). The employment in the construction industry directly contributes to economic growth, particularly in emerging nations. The industry also represents a substantial share of Gross Domestic Product (GDP) (Chiang et al., 2015; Qabaja & Tenekeci, 2023). Furthermore, infrastructures, including highways, dams, and bridges, which are essential projects in the sector, enhance economic development and stimulate higher investments (Rephann & Isserman, 1994; World Commission on Dams, 2000). Infrastructure investments boost urban development, leading to an increase in GDP per capita alongside population and investment growth. The industry promotes national economic indicators through various channels and serves as a crucial catalyst for growth, particularly in developing economies.

The construction sector is affected by many internal variables. For instance, restricted access to materials, machinery, labor and money, which are important inputs, can negatively affect production in the sector. Its dependency on financial resources and important inputs such as labor and materials requires close monitoring of economic developments in the construction sector (Hillebrandt, 2000). Tracking major economic developments such as employment expectation, sectoral confidence, and activity developments can be useful for accurate forecasts and guide investment decisions. The increase in production and employment expectations suggests that a positive climate will dominate the sector moving forward, fostering an encouraging atmosphere for investors. Economic expansion in the construction sector is evident in the sales of products utilized to equip real estate properties, and this correlates with an increase in bank loans for residential and commercial transactions. Consequently, advancements in the industry light the future of other sectors. Therefore, sector dynamics must be rigorously observed, and investment decisions should be based on developments.

In this study, cluster analysis of construction business surveys, which are significant indicators of sector dynamics, has been conducted using DTW. Thus, it was aimed to interpret the surveys more effectively. The article is organized as follows. The second section of the study presents data collection and analysis methodologies. The third section elucidates and examines the findings of the analysis. The final section summarizes the study's results and discusses possible implications.

* Corresponding author, E-mail: saydinli@cu.edu.tr

https://doi.org/10.31462/icearc2025_ce_mng_185

golden light publishing

2. Methodology

2.1 Data collection

The construction business surveys are available as open source on the EUROSTAT database (Eurostat, 2025). The monthly surveys regularly provided by Turkstat since May 2011 are listed below.

- Employment expectations over the next 3 months (EEON3)
- Building activity development over the past 3 months (BADOP3)
- Evolution of the current overall order books (ECOOB)
- Price expectations over the next 3 months (PEON3)
- Construction confidence indicator (CONFIN)
- Factors limiting building activity – none (FLBAN)
- Factors limiting building activity – insufficient demand (FLBAID)
- Factors limiting building activity – weather conditions (FLBAWC)
- Factors limiting building activity – shortage of labour (FLBASOL)
- Factors limiting building activity – shortage of material and/or equipment (FLBASME)
- Factors limiting building activity – other (FLBAO)
- Factors limiting building activity – financial constraints (FLBAFC)

The surveys are conducted by the statistical office directly to sector stakeholders. The survey questions include three response alternatives: positive, no change, and negative. Survey statistics are calculated as in Equation 1 (Eurostat, 2023).

$$Balance = \%\ Positive\ Responses - \%\ Negative\ Responses \tag{1}$$

EEON3 evaluates the expected short-term employment level in the industry. This variable can also be considered an indicator of the sectoral production volume. Another indicator that shows the sector's activity level and hence the production volume is BADOP3. PEON3 indicates whether there is an expectation of a change in construction costs in the near future. Price increases/decreases also significantly impact production and employment. CONFIN refers to the confidence in the sector. This confidence helps to assess the feasibility of investing in the sector in the current period. The final significant business survey category is "Factors Limiting Building Activities." Seven sub-indicators under this category are FLBAN, FLBAID, FLBAWC, FLBASOL, FLBASME, FLBAO, and FLBAFC. FLBAN indicates that there are no substantial barriers to building activities. A positive answer to this survey states that the industry is entirely appropriate for investment. FLBAID examines whether the level of demand in the sector is sufficient. The level of demand is an extremely crucial factor for the sector, directly affecting production and enterprises. FLBAWC is a seasonal indicator and explores whether the current weather conditions are an obstacle to production. FLBASOL and FLBASME reflect access limitations to labor, materials, and equipment, critical inputs for construction projects. FLBAO addresses variables other than the identified barriers, including political situations and legal impediments. Ultimately, FLBAFC relates to the availability of financial resources, including bank loans, during the construction phase. The positive values signify more difficulty in obtaining financing, and negative ones denote enhanced accessibility.

2.2 Dynamic time wraping (DTW) method

Dynamic Time Warping (DTW) is a technique designed to identify similarities in time series data. The method is employed for various purposes, such as time series clustering (Izakian et al., 2015; Wang et al., 2018), voice recognition (Bhadragiri Jagan Mohan & Ramesh Babu N., 2014; Pandey & Singh, 2017), and gesture recognition (Plouffe & Cretu, 2016; Ruan & Tian, 2015).

The first step of the technique is to determine the wraping distances between time series data on the wraping path using Euclidean Distance (Eq. 2).

$$DTW(X,Y) = \sqrt{\textstyle\sum_{(i,j)\in\pi} \left\| X_i - Y_j \right\|^2} \tag{2}$$

The second step of the approach is the clustering analysis. The study has employed "hierarchical clustering" to progressively unveil the associations between the series. In this approach, following the calculation of the distances between the series, the linkages are determined by Ward's method, and all the distances between the series and clusters are shown hierarchically on a dendrogram. The approach offers a straightforward computational framework that efficiently utilizes time series data to cluster them.

3. Results

In the study, twelve construction industry surveys were grouped using DTW, and series that demonstrated temporal alignment were hierarchically clustered. The distances between series are given in a heatmap matrix as given in Figure 1.

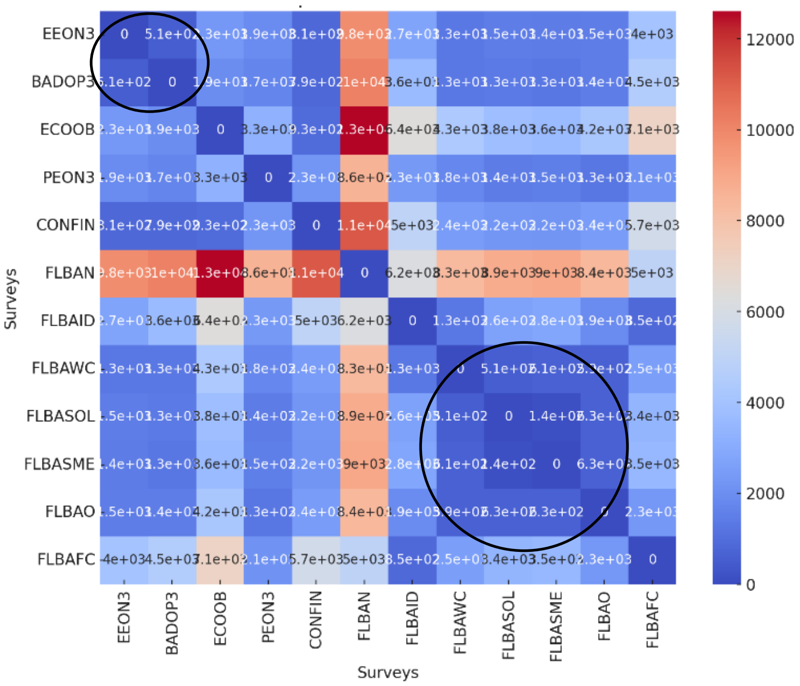

Fig. 1. DTW Distance Matrix

The first striking finding in the matrix is the similarity of the FBLA series with each other. Among these series, only the FBLAN is significantly incompatible with the others. This is entirely comprehensible. FLBAN suggests the absence of obstacles in the sector, fostering a favorable environment, while the other FLBA components indicate the presence of various barriers. On the other hand, the distance between EEON3 and BADOP3 is also relatively low. This points out that the expected increase in production in the industry also generates expectations for employment growth.

DTW grouped the twelve surveys into three clusters and showed them in Multi-Dimensional Scaling (MDS) projection (Fig. 2). MDS enables the visual representation of multidimensional distances in two or three dimensions.

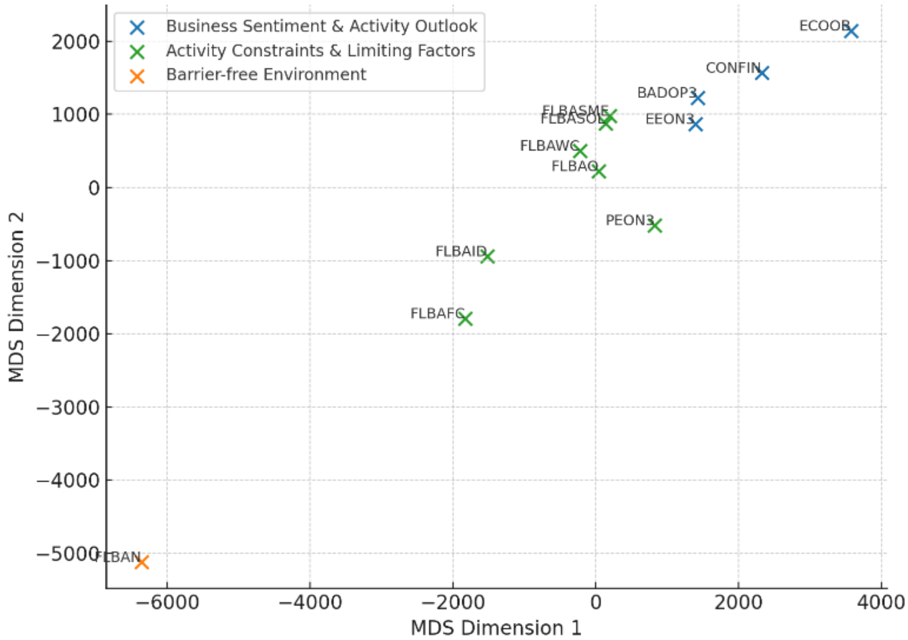

Fig. 2. MDS Projection of Surveys

The first cluster represents the sector's general economic outlook. Therefore, the cluster is labeled “Business Sentiment & Activity Outlook”. The second cluster mostly covers barriers to production. Therefore, the cluster is labeled “Activity Constraints & Limiting Factors”. Finally, FLBAN is labeled “Barrier-free Environment”. Thus, construction business surveys are categorized into 3 major groups. Fig. 3 shows the patterns of the groups over time. The graph indicates that the industry has faced no substantial impediments for an extended period; however, the “Business Sentiment & Activity Outlook” has been persistently negative. Particularly during the pandemic, substantial fluctuations in indices are noted.

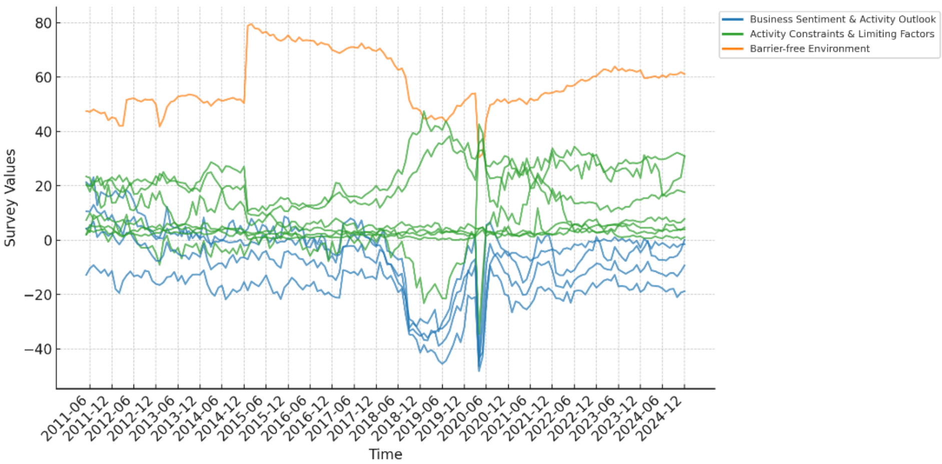

Fig. 3. Clustered Time Series of Business Surveys

The DTW dendrogram clearly illustrates the links among the series and the subsets constituting the three primary groups (Fig. 4). The connections in the graph outline the subgroups, whereas the Y-axis represents the distances between the series. Material, equipment (FLBASME), and labor (FLBASOL) shortages appear to be highly interrelated and trigger each other. Similarly, the proximity between employment expectations (EEON3) and production (BADOP3) is also evident in this graph. The graph shows that insufficient demand and financial constraints produce series close to each other. Financial constraints are a factor that deeply affects not only enterprises but also consumers. The difficulty in accessing financial resources is also reflected in sales, leading to a significant decline in real estate transactions. The graph demonstrates that, despite being in the same cluster, inadequate demand and limited access to financial resources are distinct from other barriers.

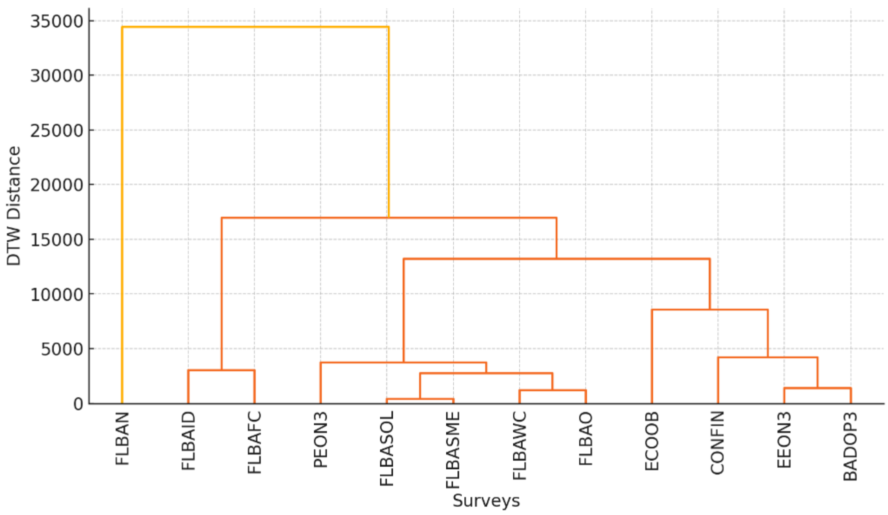

Fig. 4. Dendrogram of Business Surveys

4. Discussion

The study clearly reveals the interrelationship of construction sector business surveys. The initial significant finding of the study is the synchronization between EEON3 and BADOP3. These two variables are deeply interconnected. A recession in the economy initially leads to unemployment, subsequently diminishing production and, consequently, supply within the sector (Le, 2025). Another factor directly affecting employment and production is confidence in the sector. Reduced employment and production will lead to a decline in confidence in the sector. The status of existing orders is associated with these variables as an indicator of production volume.

The second cluster in the study contains the components that limit productivity. It is an unexpected discovery that PEON3 is classified as a factor that limits construction activities. The pessimistic prognosis for price expectations restricts activity, as do issues related to access to materials and equipment. The scarcity of resources results in higher prices, thereby increasing construction costs. Enterprises transfer the increase in costs onto pricing, resulting in price escalations (Guan & Cheung, 2023).

5. Conclusions

Statistical offices publish monthly industrial and consumer surveys. The surveys provide an outlook on the economic environment and are also conducted by sector. The study clustered business surveys of the construction sector, which is particularly critical for emerging economies, using DTW. Consequently, 12 monthly surveys were obtained from the Eurostat database and analyzed. As a result of the study, the questionnaires were categorized into three main groups which are "Business Sentiment & Activity Outlook", "Activity Constraints & Limiting Factors", and "Barrier-free Environment". Business Sentiment & Activity Outlook Business Sentiment & Activity Outlook includes the general outlook of the sector and forward-looking expectations. Activity Constraints & Limiting Factors cover challenges that adversely impact the sector, including inadequate supply and demand, resource scarcity, and obstacles to accessing financial resources. In contrast to the previous factor, Barrier-free Environment refers to the absence of any obstacles for production in the sector.

The study simplifies and clarifies the surveys and enables stakeholders to monitor the surveys more consciously. The results offer a useful categorization of surveys for possible future utilization in generating sectoral forecasts. The study has important implications for the prediction of parameters such as construction cost index and production index, which are of vital importance for the sector.

References

Alaloul, W. S., Musarat, M. A., Rabbani, M. B. A., Iqbal, Q., Maqsoom, A., & Farooq, W. (2021). Construction Sector Contribution to Economic Stability: Malaysian GDP Distribution. *Sustainability*, *13*(9), 5012. https://doi.org/10.3390/su13095012

Bhadragiri Jagan Mohan, & Ramesh Babu N. (2014). Speech recognition using MFCC and DTW. *2014 International Conference on Advances in Electrical Engineering (ICAEE)*, 1–4. https://doi.org/10.1109/ICAEE.2014.6838564

Chiang, Y. H., Tao, L., & Wong, F. K. W. (2015). Causal relationship between construction activities, employment and GDP: The case of Hong Kong. *Habitat International*, *46*, 1–12. https://doi.org/10.1016/j.habitatint.2014.10.016

Ernst, C., & Sarabia, M. (2015). *The role of construction as an employment provider: a world-wide input-output analysis* (No. 186; Employment Policy Department Employment).

Eurostat. (2023). *The Joint Harmonised EU Programme of Business and Consumer Surveys*. https://economy-finance.ec.europa.eu/system/files/2023-02/bcs_user_guide.pdf

Eurostat. (2025). *Construction Business Surveys*. Directorate-General for Economic and Financial Affairs (ECFIN). https://doi.org/https://doi.org/10.2908/EI_BSBU_M_R2

Fendoglu, E., & Polat, M. A. (2021). İnşaat Sektörünün Ekonomik Büyüme ve Finansal Piyasalar Üzerindeki Etkileri: Türkiye Örneği. *Business and Economics Research Journal*, *12*(3), 575–598. https://doi.org/10.20409/berj.2021.339

Guan, Y., & Cheung, K.-S. (2023). The Costs of Construction and Housing Prices: A Full-Cost Pricing or Tendering Theory? *Buildings*, *13*(7), 1877. https://doi.org/10.3390/buildings13071877

Hillebrandt, P. M. (2000). *Economic Theory and the Construction Industry*. Palgrave Macmillan UK. https://doi.org/10.1057/9780230372481

Izakian, H., Pedrycz, W., & Jamal, I. (2015). Fuzzy clustering of time series data using dynamic time warping distance. *Engineering Applications of Artificial Intelligence*, *39*, 235–244. https://doi.org/10.1016/j.engappai.2014.12.015

Le, T. (2025). The scarring of the Great Recession on construction labor and housing supply. *Real Estate Economics*. https://doi.org/10.1111/1540-6229.12526

Pandey, D., & Singh, K. K. (2017). Implementation of DTW algorithm for voice recognition using VHDL. *2017 International Conference on Inventive Systems and Control (ICISC)*, 1–4. https://doi.org/10.1109/ICISC.2017.8068638

Plouffe, G., & Cretu, A.-M. (2016). Static and Dynamic Hand Gesture Recognition in Depth Data Using Dynamic Time Warping. *IEEE Transactions on Instrumentation and Measurement*, *65*(2), 305–316. https://doi.org/10.1109/TIM.2015.2498560

Qabaja, M., & Tenekeci, G. (2023). Nexus between construction sector and economic indicators for Turkey and European Union evidenced by panel data analysis. *Engineering, Construction and Architectural*

Management, *30*(5), 1978–2007. https://doi.org/10.1108/ECAM-10-2021-0927
Rephann, T., & Isserman, A. (1994). New highways as economic development tools: An evaluation using quasi-experimental matching methods. *Regional Science and Urban Economics*, *24*(6), 723–751. https://doi.org/10.1016/0166-0462(94)90009-4
Ruan, X., & Tian, C. (2015). Dynamic gesture recognition based on improved DTW algorithm. *2015 IEEE International Conference on Mechatronics and Automation (ICMA)*, 2134–2138. https://doi.org/10.1109/ICMA.2015.7237816
Wang, W., Lyu, G., Shi, Y., & Liang, X. (2018). Time Series Clustering Based on Dynamic Time Warping. *2018 IEEE 9th International Conference on Software Engineering and Service Science (ICSESS)*, 487–490. https://doi.org/10.1109/ICSESS.2018.8663857
World Commission on Dams. (2000). *Dams and development: A new framework for decision-making: The report of the world commission on dams*. Earthscan.

4th International Civil Engineering & Architecture Conference
17-19 May 2025, Trabzon, Türkiye

Leveraging graph-based neural networks for enhancing early-stage screening of construction projects: GraphSAGE model

Fatemeh Mostofi*[1], Onur B. Tokdemir[2], Vedat Toğan[1]

[1] Karadeniz Technical University, Department of Civil Engineering, 61080 Trabzon, Türkiye
[2] Istanbul Technical University, Civil Engineering Department, 34469, Istanbul, Türkiye

Abstract. Selecting construction projects has long been a multifaceted challenge due to the complexity of variables such as cost, time, environmental impact, and strategic alignment. The critical problem identified is that existing methods in construction project selection are predominantly reliant on conventional machine learning (ML) models, which are unable to effectively capture relational dependencies among project attributes, especially for unseen or evolving data. Despite the popularity of graph convolutional networks (GCNs) in construction project management studies, these models are inherently transductive, requiring all nodes to be available during training, thereby restricting their flexibility in dynamic decision-making systems. To address these limitations, this study integrates GraphSAGE (Graph Sample and Aggregate), a state-of-the-art graph neural network (GNN) algorithm that supports inductive learning by aggregating neighborhood features, into a multi-criteria decision-making (MCDM) framework for project selection. Construction projects and investment records are represented as nodes in a graph, with edges formed based on shared regions or attributes, enabling the model to extract relational insights. Experimental evaluation on over 10,000 project investment records demonstrated that GraphSAGE achieves superior performance, with an accuracy of 92% and an F1 score of 90%, significantly outperforming GCN's accuracy of 57% and F1 score of 56%. This methodology enables enhanced decision-making by modeling project selection as a dynamic relational network, reducing decision uncertainty and improving investment strategies. The practical implications of this study include early-stage project screening, optimized resource allocation, and the development of scalable decision-support systems for construction firms, paving the way for data-driven investment in large-scale infrastructure.

Keywords: Multi-criteria decision-making (MCDM); Project value prediction; Construction investment decision; GraphSAGE; Machine learning (ML).

1. Introduction

Investment decisions have consistently influenced the long-term viability of construction endeavors (Egorov et al., 2018; Munir et al., 2022). Project selection, a pivotal dimension of these investment decisions, conventionally integrates financial analytics, risk profiling, and expert judgment to assess different prospectives within different proposals (Mahad et al., 2020). Nevertheless, selecting from multiple perspective investments remains inherently a multi-criteria decision-making (MCDM) challenge (Amiri, 2010; P. Li et al., 2022; Mehrez & Sinuany-Stern, 1983).

In contemporary practice, decision-makers often adopt structured frameworks, optimization, and decision-support systems to align individual project choices with overarching corporate mandates (Ghasemzadeh & Archer, 2000; Song et al., 2017). Here, MCDM approaches fundamentally addresses the trade-offs that arise when different, and sometimes conflicting, criteria must be assessed within a single decision-making framework. Its strength in examining various proposals has led to extensive applications across a wide spectrum of project environments (Mogbojuri & Olanrewaju, 2023; Pariz et al., 2022; Rouyendegh, 2012). Consequently, scholars have increasingly explored integrated methods, combining MCDM with technological methods like fuzzy logic (Kheyraie et al., 2021), GIS (Hashemizadeh & Ju, 2019; Rębiasz et al., 2014), and system dynamics (Bai et al., 2021). These hybrid approaches allowed more complex ways of accounting for uncertainties and interdependencies, from stochastic economic variables to geographic constraints.

Parallel to these developments, recently there has been an attempt on leveraging machine learning (ML) techniques to enhance project selection and portfolio management (Corsaro et al., 2022; Sezer et al., 2021). most ML research on project portfolio management has centered on numerical optimization (Corsaro et al., 2022) or

* Corresponding author, E-mail: fatemee.mostofi@gmail.com

https://doi.org/10.31462/icearc2025_ce_mng_198

post-hoc performance prediction, leaving a methodological gap concerning how ML could systematically derive preliminary evaluations (i.e., project value ratings) from unstructured or partially structured records. Consequently, there is a clear need to investigate how ML-driven models can be integrated with MCDM principles to improve early-stage project filtering. This gap is particularly salient in construction management, where decisions about whether a proposal is viable are made long before robust cost or engineering data are fully available. By blending ML with MCDM, the sector could realize a more reliable, data-enriched pathway for identifying and prioritizing construction projects likely to yield higher returns and stronger alignment with strategic goals.

In this context, conventional ML methods have also struggled to integrate relational information, thus constraining any complex relational approach like MCDM to construction project selection. Prior studies deployed ML in construction project management but were largely limited to standard models that do not natively capture MCDM factors in networked data, restricting how well they could use geographical or functional interdependencies. This gap has prompted inquiries into more advanced architectures, including graph neural networks (GNNs), which not only digest numeric features but also learn the relational or structural connections between projects and their associated attributes.

Acknowledged for their efficacy in deep learning, graph neural networks became the standard method for addressing relational and connected data (W.-Z. Li et al., 2023). Their functionality included aggregating and disseminating node-level features via defined connectivity mechanisms (Mostofi & Toğan, 2023; Scarselli et al., 2009; Ye et al., 2022). Studies such as those by (Yuan et al., 2021) and (Mostofi, Toğan, Başağa, et al., 2023) confirmed that GNNs, using spatial data, excelled over shallow models like random forests and SVMs (Chen, 2023). The GNN models investigated in construction project management mostly adopted transductive learning, whereby not generalize from the training data to unseen instances; instead, they make predictions based on specific examples that include unlabeled data during the training phase (Rossi et al., 2018).

Developed transductive MLs like graph convolutional network (GCN) (Gao et al., 2023; Mostofi et al., 2022) and graph attention network (GAT) (Mostofi, Toğan, & Tokdemir, 2023; Pan et al., 2022) leverage the relationships among the data points, which are often embodied in graph structures, to make predictions about new data points by inferring from the examples it has seen (Rossi et al., 2018). In contrast, in inductive learning GNN models the algorithm derives a general rule from specific examples within a training set, which then applies to unseen data to make predictions (Rossi et al., 2018). In practice, comprehensive GNN model leverage both inductive and transductive learning methodologies to process data represented in graph form. This is crucial for handling different types of construction projects that may not exactly match the training data but share similar characteristics.

Given that different GNN models are appropriate for different applications (Khemani et al., 2024), there exists a gap to investigate inductive GNN models like GraphSAGE (SAmple and aggreGatE) in context of construction project management. GraphSAGE (Hamilton et al., 2017), in particular, has garnered interest across disparate applications. (Hamilton et al., 2017) introduced it as an inductive system able to generate node embeddings in expansive, evolving graphs, thereby learning to generalize to unseen data points (Hamilton et al., 2017). (Sun et al., 2024) adopted GraphSAGE within a deep reinforcement learning framework to enhance financial portfolio optimization, enhanced the performance and robustness of the proximal policy optimization (PPO) agent on portfolio optimization. Considering graphs as a universal language for describing and modelling complex data structure, (Van Belle et al., 2022) investigated GraphSAGE for fraud detection in credit card networks. In another study (Abdullayeva & Suleymanzade, 2024) adopted GraphSAGE to detect cyberattacks in cloud computing networks, achieved a very high prediction accuracy and F1-scores. In another study, (Verma & Jadeja, 2023) explored GraphSAGE for classifying floor plans, while incorporating centrality metrics like betweenness centrality and clustering coefficients to improve the classification accuracy. Lastly, (Wang et al., 2022) utilized and improved GraphSAGE that accounts for both node and edge features during embedding to process node and edge features for semantic enrichment in BIM models, achieving improved accuracy and efficiency in room type classification tasks. Despite these diverse applications, GraphSAGE had not been fully investigated in construction project management contexts, where relational and temporal aspects can significantly influence a project's success or feasibility.

GraphSAGE as an inductive graph-based learning model is capable of subsampling and aggregating local neighborhood features (Oh et al., 2019). This study models construction projects and their associated investment records as nodes within a graph, connected by edges based on common geographical or regional attributes. This is expected to allow models to effectively handle diverse construction projects by applying learned rules and adapting to new, unseen project data, enriching the models' applicability and effectiveness across various scenarios.

2. Methodology

The methodology adopted in this study focused on integrating GraphSAGE into a multi-criteria decision-making framework for construction project selection. The approach systematically utilized relational graph modeling to evaluate construction projects, and their associated investments based on geographical and temporal attributes.

GraphSAGE was selected due to its inductive learning capability, which allowed embeddings for unseen projects without retraining the model, and its efficient neighborhood sampling, which made it particularly suited for large-scale, globally distributed construction datasets.

2.1 Data collection and preprocessing

Data for this study was sourced from records related to investments in diverse construction projects across various global regions. The dataset included both essential identifiers (e.g., project IDs and names) and a detailed range of features such as project stages, estimated values (in billion USD), timelines (announcement and construction phases), and location-based attributes. These records also captured contextual descriptors, such as business development ratings, geographical specifications, and types of construction work required.

To ensure data quality and relevance, an initial screening of construction projects was conducted based on primary selection criteria established by senior management experts. These criteria encompassed factors such as geographic proximity, alignment with core technological expertise, and historical success in similar projects. Each project was assigned a “project value” score on a scale of 1 to 5, where only projects rated 4 (“high value”) or 5 (“very high value”) were retained for further analysis. This refinement process reduced the dataset to approximately 30,000 entries, concentrating the analysis on projects with significant potential and strategic fit.

Further filtering was performed to focus specifically on energy-related projects, encompassing renewable and non-renewable energy infrastructure, reducing the dataset to 2,906 entries. Key features such as “project name,” “geographical region,” “construction timeline,” and “project scope” were standardized and consolidated into a single “Explanation” column to capture textual insights critical for accurate evaluations. This preprocessing ensured consistency and maximized the availability of relevant data for modelling.

2.2 Graph construction

The pre-processed dataset was transformed into a graph structure, where each construction project was represented as a node, and edges were created based on shared regional or contextual attributes. Specifically, nodes represented individual construction projects, while edges connected projects within the same geographical region to capture shared economic, political, and infrastructural contexts. For instance, projects in Asia were connected within a regional subgraph. A source target dataset was used instead of an adjacency matrix to define the connectivity among nodes, and a two-dimensional tensor (edge index) was created to specify edges in the PyTorch Geometric framework.

The resulting graph captured relational dependencies across 13,399 projects spanning eight global regions: Asia (3,514 projects), North America (2,918), Europe (2,706), MENA (741), Oceania (728), South America (526), Africa (398), and South and Central America (31). To preserve privacy, sensitive data such as specific city names were anonymized using generic mapped identifiers.

2.3 Feature engineering and input preparation

The graph model’s input features were standardized to ensure compatibility with the GraphSAGE architecture. Feature columns, excluding temporal attributes (construction start quarter) and class labels (project value), were normalized and converted into PyTorch tensors. Here, node features (**X**) were employed as a matrix where rows represented projects and columns corresponded to standardized attributes. The class labels (**Y**) was used as a vector indicating whether a project was categorized as high or very high value, encoded as binary labels (0 and 1, respectively). Uniform weights of 1.0 were assigned to edges to indicate basic connectivity. The data object was structured in the PyTorch Geometric format and loaded onto a GPU-enabled computing device for efficient processing. Rolling windows were introduced to simulate temporal dynamics, enabling the model to evaluate new projects based on past and ongoing data. Fig. 1 illustrate the input network and the number of each premium and high-value investment labels in utilized dataset.

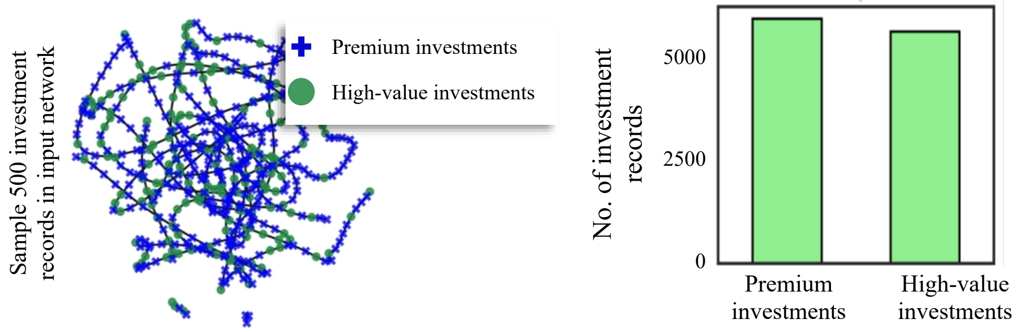

Fig. 1. Premium and high-value investment decision labels.

Temporal data, represented by the “construction start quarter” column, was transformed into a numeric scale to facilitate chronological slicing. The dataset was further segmented into training, validation, and testing sets, ensuring that the temporal ordering of projects was preserved. Fig. 2 displays the number of investment records across training, validation, and test sets.

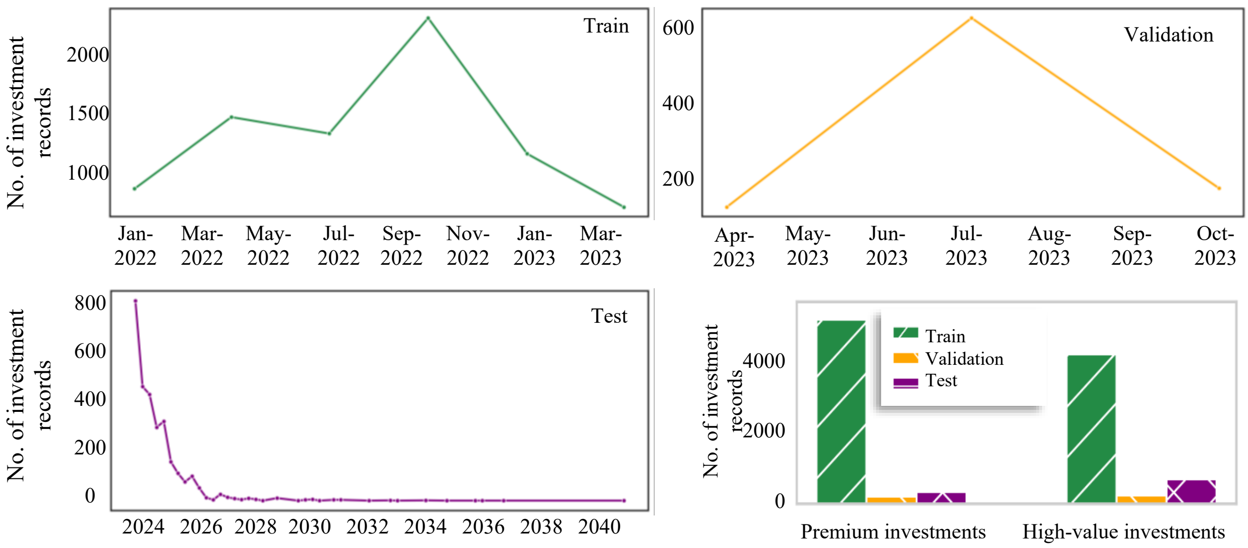

Fig. 2. Distribution of the investment records into training, validation, and test sets across construction start years.

2.4 Model training and evaluation

The GraphSAGE model was trained using a supervised learning approach applied to graph data. Initially, the input network was converted into a PyTorch Geometric Data object, incorporating node features, class labels, and edge indices. GraphSAGE utilized the feature information from neighboring nodes to generate embeddings, enabling relational learning.

The parameters of the GraphSAGE and benchmark GCN models were tuned iteratively with different learning rates, ranging from 0.1 to 0.0001, and dropout rates from 0.1 to 0.9. Both models were trained with a cross-entropy loss function, 64 neurons, 0.005 weight decay, and a 0.2 dropout rate. The most accurate GCN configuration was achieved with a batch size of 8 and a learning rate of 0.001, while GraphSAGE performed best with a batch size of 64 and a learning rate of 0.01. The models were evaluated using accuracy and F1 score metrics, showing GraphSAGE's superiority over the baseline GCN model.

3. Results and discussions

Fig. 3 the prediction performance of the GraphSAGE and GCN models across various parameter configurations (Fig. 3a), highlighting their respective best configurations (Fig. 3b). Both models were iteratively tuned using multiple parameter combinations, each assessed using accuracy and F1 score metrics.

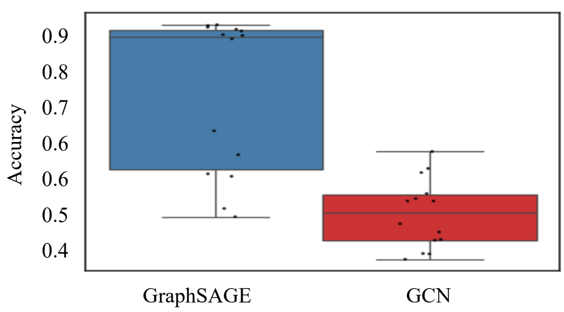

(a) Prediction performance across different model configurations.

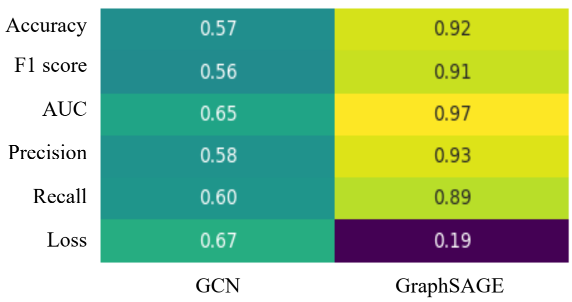

(b) Prediction performance of the most accurate configuration.

Fig. 3. Prediction performance of GraphSAGE and GCN models, (a) across various parameter configurations and (b) for their best-selected configurations.

As depicted in Fig. 3(a), the performance of both models varied across parameter configurations, but GraphSAGE consistently outperformed GCN. The most accurate configuration for GraphSAGE utilized a batch size of 64, a learning rate of 0.01, and a dropout rate of 0.2. Conversely, GCN performed best with a batch size of 8, a learning rate of 0.001, and the same dropout rate of 0.2.

Fig. 3(b) highlights the best configurations for each model, further illustrating the gap in their performances. The GraphSAGE model demonstrated superior predictive performance over the baseline GCN model across a variety of configurations, where results consistently favored GraphSAGE. Under the optimal settings, GraphSAGE achieved a prediction accuracy of 92% and an F1 score of 91%, outperforming the GCN model, which achieved an accuracy of 57% and an F1 score of 56%. Additionally, GraphSAGE showed more balanced performance across precision (93%) and recall (89%), whereas GCN's metrics were less consistent. The area under the curve (AUC) for GraphSAGE was 97%, significantly higher than GCN's AUC of 65%, reflecting GraphSAGE's superior ability to distinguish between premium and high-value investment decisions.

In terms of training duration, GraphSAGE achieved its best performance in 253 epochs, whereas GCN converged in 249 epochs. However, the training time for GraphSAGE was slightly faster at 3.31 seconds compared to GCN's 3.42 seconds, demonstrating its computational efficiency despite its superior performance.

Overall, GraphSAGE's ability to leverage relational features through neighborhood aggregation proved critical in delivering robust and consistent predictions. Its inductive learning capabilities allowed it to generalize better across unseen nodes compared to the transductive nature of GCN. This was particularly valuable given the graph structure's inherent sparsity and the heterogeneity of project attributes.

4. Conclusions

The selection of construction projects remains a complex challenge due to the interactions among cost, timelines, strategic objectives, and environmental factors. Existing GNN methods, like GCNs and GATs have limitations due to their transductive nature, which requires all nodes to be present during training, making them unsuitable for dynamic and evolving datasets. To address these gaps, this study proposed the use of GraphSAGE, an inductive graph neural network capable of learning from graph-based relationships and generalizing to unseen projects without retraining.

The methodology transformed construction project data into a graph structure, where nodes represented projects and edges captured shared regional or contextual attributes. The dataset was processed to include approximately 11,399 projects across eight global regions, with temporal attributes incorporated to simulate real-world scenarios. GraphSAGE was trained and evaluated using a rolling-window approach, ensuring that the model could adapt to new data while maintaining temporal integrity.

The results demonstrated the clear superiority of GraphSAGE over GCN in predictive performance. GraphSAGE achieved 92% accuracy and an F1 score of 91%, significantly outperforming GCN, which achieved only 57% accuracy and an F1 score of 56%. The AUC for GraphSAGE was 97%, compared to 65% for GCN, indicating its ability to reliably distinguish between high-value and low-value projects. GraphSAGE outperformed GCN significantly, delivering higher accuracy, precision, and recall. Its inductive learning capabilities and neighborhood aggregation approach provide a scalable and adaptable solution for complex and dynamic construction project datasets, marking a significant step forward in the field.

References

Abdullayeva, F., & Suleymanzade, S. (2024). Cyber security attack recognition on cloud computing networks based on graph convolutional neural network and GraphSAGE models. *Results in Control and Optimization, 15*, 100423. https://doi.org/10.1016/j.rico.2024.100423

Amiri, M. P. (2010). Project selection for oil-fields development by using the AHP and fuzzy TOPSIS methods. *Expert Systems with Applications, 37*(9), 6218–6224. https://doi.org/10.1016/j.eswa.2010.02.103

Bai, L., Han, X., Wang, H., Zhang, K., & Sun, Y. (2021). A method of network robustness under strategic goals for project portfolio selection. *Computers & Industrial Engineering, 161*, 107658. https://doi.org/10.1016/j.cie.2021.107658

Corsaro, S., De Simone, V., Marino, Z., & Scognamiglio, S. (2022). L1-regularization in portfolio selection with machine learning. *Mathematics, 10*(4), 540. https://doi.org/10.3390/math10040540

Egorov, A., Pilipchuk, N., Selskov, A., & Grabovyy, K. (2018). Optimization of managerial decisions during innovative-and-investment activities of construction company. *MATEC Web of Conferences, 193*, 05045. https://doi.org/10.1051/matecconf/201819305045

Gao, Y., Chen, R., Qin, W., Wei, L., & Zhou, C. (2023). Learning from explainable data-driven tunneling graphs: A spatio-temporal graph convolutional network for clogging detection. *Automation in Construction, 147*, 104741. https://doi.org/10.1016/j.autcon.2023.104741

Ghasemzadeh, F., & Archer, N. P. (2000). Project portfolio selection through decision support. *Decision Support Systems, 29*(1), 73–88. https://doi.org/10.1016/S0167-9236(00)00065-8

Hamilton, W. L., Ying, R., & Leskovec, J. (2017). Inductive representation learning on large graphs. *arXiv preprint*. https://arxiv.org/abs/1706.02216
Hashemizadeh, A., & Ju, Y. (2019). Project portfolio selection for construction contractors by MCDM–GIS approach. *International Journal of Environmental Science and Technology, 16*(12), 8283–8296. https://doi.org/10.1007/s13762-019-02248-z
Khemani, B., Patil, S., Kotecha, K., & Tanwar, S. (2024). A review of graph neural networks: Concepts, architectures, techniques, challenges, datasets, applications, and future directions. *Journal of Big Data, 11*(1), 18. https://doi.org/10.1186/s40537-023-00876-4
Kheyraie, H., Mirhosseini, S. M., & Zeyghami, E. A. (2021). Proposing a comprehensive portfolio management model for contractor companies in construction industry using multi-criteria decision-making techniques and fuzzy logic. *Information Technology in Industry, 9*(1), 569–580. https://doi.org/10.17762/itii.v9i1.172
Li, P., Liu, J., Wei, C., & Liu, J. (2022). A new EDAS method based on prospect theory for Pythagorean fuzzy set and its application in selecting investment projects for highway. *Kybernetes, 51*(8), 2636–2651. https://doi.org/10.1108/K-01-2021-0066
Li, W.-Z., Wang, C.-D., Xiong, H., & Lai, J.-H. (2023). GraphSHA: Synthesizing harder samples for class-imbalanced node classification. *arXiv preprint*. https://arxiv.org/abs/2306.09612
Mahad, N. F., Mohd Azli, N. A. S., Razalli, N. A. F., & Mohd Nor Azmi, N. N. (2020). Condorcet voting theory based on Analytical Hierarchy Process (AHP) for project selection problems. *ASM Science Journal*. https://doi.org/10.32802/asmscj.2020.sm26(2.7)
Mehrez, A., & Sinuany-Stern, Z. (1983). An interactive approach for project selection. *Journal of the Operational Research Society, 34*(7), 621–626. https://doi.org/10.1057/jors.1983.143
Mogbojuri, A. O., & Olanrewaju, O. A. (2023). Using the deterministic approach model for project portfolio selection problem (PPSP) solutions. *Heliyon, 9*(9), e19129. https://doi.org/10.1016/j.heliyon.2023.e19129
Mostofi, F., & Toğan, V. (2023). Construction safety predictions with multi-head attention graph and sparse accident networks. *Automation in Construction, 156*, 105102. https://doi.org/10.1016/j.autcon.2023.105102
Mostofi, F., Toğan, V., Ayözen, Y. E., & Tokdemir, O. B. (2022). Construction safety risk model with construction accident network: A graph convolutional network approach. *Sustainability, 14*(23), 15906. https://doi.org/10.3390/su142315906
Mostofi, F., Toğan, V., Başağa, H. B., Çıtıpıtıoğlu, A., & Tokdemir, O. B. (2023). Multiedge graph convolutional network for house price prediction. *Journal of Construction Engineering and Management, 149*(11). https://doi.org/10.1061/JCEMD4.COENG-13559
Mostofi, F., Toğan, V., & Tokdemir, O. B. (2023). Enhancing construction productivity prediction through variational autoencoders and graph attention network. *ICEARC 2023 Proceedings*. https://doi.org/10.31462/icearc.2023.cme227
Munir, W., Hui, J. K. S., & Abdullah, M. A. B. (2022). Impact of individuals saving and consumption behaviour towards investment as inflow of money in the economy of Pakistan: A case of salaried class. *International Journal of Asian Social Science, 12*(11), 477–508. https://doi.org/10.55493/5007.v12i11.4685
Oh, J., Cho, K., & Bruna, J. (2019). Advancing GraphSAGE with a data-driven node sampling. *arXiv preprint*. https://arxiv.org/abs/1906.01210
Pan, Y., Fu, X., & Zhang, L. (2022). Data-driven multi-output prediction for TBM performance during tunnel excavation: An attention-based graph convolutional network approach. *Automation in Construction, 141*, 104386. https://doi.org/10.1016/j.autcon.2022.104386
Pariz, M. C., Carvalho, C. M. F., Rebelo, P. C. A., & Colmenero, J. C. (2022). Treatment of the uncertainties in prioritization of information technology projects: A hybrid multicriteria approach. *Journal of Multi-Criteria Decision Analysis, 29*(5–6), 327–340. https://doi.org/10.1002/mcda.1777
Rębiasz, B., Skalna, I., & Gaweł, B. (2014). Hybrid framework for investment project portfolio selection. *IFAC Proceedings Volumes*, 47(3), 1117–1122. https://doi.org/10.15439/2014F347
Rossi, A., Tiezzi, M., Dimitri, G. M., Bianchini, M., Maggini, M., & Scarselli, F. (2018). Inductive–transductive learning with graph neural networks. In *Lecture Notes in Computer Science* (pp. 201–212). https://doi.org/10.1007/978-3-319-99978-4_16
Rouyendegh, B. D. (2012). Evaluating projects based on intuitionistic fuzzy group decision making. *Journal of Applied Mathematics, 2012*, 1–16. https://doi.org/10.1155/2012/824265
Scarselli, F., Gori, M., Tsoi, A. C., Hagenbuchner, M., & Monfardini, G. (2009). The graph neural network model. *IEEE Transactions on Neural Networks, 20*(1), 61–80. https://doi.org/10.1109/TNN.2008.2005605
Sezer, A. A., Thunberg, M., & Wernicke, B. (2021). Digitalization index: Developing a model for assessing the degree of digitalization of construction projects. *Journal of Construction Engineering and Management, 147*(10). https://doi.org/10.1061/(ASCE)CO.1943-7862.0002145
Song, Q., Liu, A., & Yang, S. Y. (2017). Stock portfolio selection using learning-to-rank algorithms with news sentiment. *Neurocomputing, 264*, 20–28. https://doi.org/10.1016/j.neucom.2017.02.097

Sun, Q., Wei, X., & Yang, X. (2024). GraphSAGE with deep reinforcement learning for financial portfolio optimization. *Expert Systems with Applications, 238*, 122027. https://doi.org/10.1016/j.eswa.2023.122027
Van Belle, R., Van Damme, C., Tytgat, H., & De Weerdt, J. (2022). Inductive graph representation learning for fraud detection. *Expert Systems with Applications, 193*, 116463. https://doi.org/10.1016/j.eswa.2021.116463
Verma, A. K., & Jadeja, M. (2023). CB-SAGE: A novel centrality based graph neural network for floor plan classification. *Engineering Applications of Artificial Intelligence, 126*, 107121. https://doi.org/10.1016/j.engappai.2023.107121
Wang, Z., Sacks, R., & Yeung, T. (2022). Exploring graph neural networks for semantic enrichment: Room type classification. *Automation in Construction, 134*, 104039. https://doi.org/10.1016/j.autcon.2021.104039
Ye, W., Huang, Z., Hong, Y., & Singh, A. (2022). Graph neural diffusion networks for semi-supervised learning. *arXiv preprint*. https://arxiv.org/abs/2201.09698
Yuan, Q., Szczypiński, F., & Jelfs, K. (2021). Explainable graph neural networks for organic cages. *ChemRxiv*. https://doi.org/10.26434/chemrxiv-2021-zhcb1

4th International Civil Engineering & Architecture Conference
17-19 May 2025, Trabzon, Türkiye

Cost estimation in early design stages using regression model-Kuwait case study

Khaled Alrasheed[1*], Ehab Soliman[1]

[1] Kuwait University, Department of Civil Engineering, 17067 Kuwait, Kuwait

Abstract. The project generally passes through many steps, and the cost estimate is supplemented in each step. The accuracy of the cost estimate is crucial to the construction project's success. In the design stage, the accurate cost estimate leads to good cost, resource allocation, value engineering, project feasibility study, and stakeholders' financial management procedures proposed. The design starts by identifying the schematic design and general design layouts with no detailed design. In that design stage, the cost estimate is highly different from the actual cost resulting after the design details or the construction phase. In this study, a regression model is proposed to assist stakeholders in predicting the project cost based on some of the general criteria that can be available in the stage of schematic design. The model takes into consideration criteria such as land area, gross area, excavation volume, and estimated concrete volume. The model will be built based on real gathered data from several construction projects in Kuwait. The model used a multi-regression technique. The model was verified through the root mean squared error. This model can be used as a primary estimator for anticipated construction project costs in its early stage of design.

Keywords: Cost estimate; Design; Multi-regression; Validation

1. Introduction

Estimating costs during the early phases of a construction project is both critical and challenging for all stakeholders involved. Accurately forecasting project expenses while minimizing deviations from actual costs remains a formidable task. Despite decades of research dedicated to enhancing cost estimation accuracy, significant challenges persist due to the influence of fluctuating raw material prices, labor costs, and equipment rates in an ever-volatile market. These uncertainties can have profound implications for a project's ultimate success.

The success of a construction project is a primary concern for both owners and contractors, as it hinges on effective budget allocation and resource management. Accurate cost estimation is vital to these processes and impacts decision-making throughout the project's lifecycle. However, the precision of cost estimates is influenced by numerous factors. A survey by Ibrahim and Elshwadfy (2021) categorizes these factors into three main groups:

- Consultants, Design Parameters, Information & Estimators: This category includes factors such as the clarity and level of detail in project documentation, the expertise of the estimator, and the availability of accurate cost data.
- External Factors: These include market-driven variables such as the cost and availability of materials and complexities related to the importing process.
- Contractor Characteristics: This category highlights the contractor's experience with similar projects, which significantly affects their ability to provide accurate estimates.

Various cost estimation techniques are used during the early stages of construction projects, ranging from simple approaches, like the square meter method, to advanced methodologies incorporating machine learning. These include Artificial Neural Networks (ANN), Fuzzy Logic, Genetic Algorithms (GA), Regression Analysis (RA), and Case-Based Reasoning (CBR), Kim et al, 2012. This research work has two objectives:

- Develop a multi-regression model to predict project budgets based on predefined factors using real data during the early design stages.
- Validate the accuracy and reliability of the proposed model.

[*] Corresponding author, E-mail: k.alrasheed@ku.edu.kw

https://doi.org/10.31462/icearc2025_ce_mng_254

2. Background

2.1. The importance of cost estimation in the construction industry

Cost estimation is a critical process in the construction industry, as it helps predict the time, costs, and resources needed to achieve a project's objectives. According to Dysert (2003), cost estimation involves systematically quantifying financial resources and setting a budget based on the project's scope and expected investment. Hatamleh et al, 2018 defined cost estimation as the process of determining the project's scope of work and identifying the financial resources required to meet the project's goals, from initiation to handover.

Hashemi et al 020 identified two main components in the final cost estimate of any construction project: project cost and markup. Layer et al 2002 further classified project costs into direct and indirect costs. Direct costs refer to expenses directly tied to the project, such as labor, materials, equipment, and subcontractor services. These costs can be accurately estimated if there is sufficient information about site conditions, required resources, and the construction methods to be employed. Despite its importance, cost estimation is not always straightforward, particularly during the early stages of a project, where limited information can complicate the process Hegazy, 2002.

2.2. Factors affecting accuracy in the cost estimation process

The accuracy of a cost estimate depends on several factors that influence the overall estimation process. Various researchers have identified different parameters and models to ensure accurate cost predictions. Hyari et al 2016 interviewed with senior engineers in Jordan, concluded that four main factors affect cost estimation accuracy:

- Project Type – the nature of the construction project, such as residential buildings, transportation infrastructure, or land development.
- Engineering Services – including design, construction, or integrated design and construction services.
- Project Location – the geographical context, which can impact costs due to local conditions or regulations.
- Project Costs – covering all expenses associated with the project site.

Conversely, Gunaydın et al 2004 identified other key factors impacting building project costs, including the total building area, floor area ratios, number of floors, floor types, slab types, foundation types, and structural system cost per square meter. Kim et al 2012 proposed additional factors for predicting building project costs, such as land area, building area, gross area, land-to-building area ratio, structural type (e.g., reinforced concrete, steel), and building type (e.g., residential, retail, cultural, educational).

In the context of residential buildings in Korea, Ji et al 2012 highlighted factors such as unit size, number of units per floor, building type, and stair-core design. These findings suggest that the factors influencing the cost estimation process can vary by location and are highly dependent on the specific engineering characteristics of the project.

2.3. Key determinants of cost estimation accuracy

The level of accuracy in cost estimation is influenced by several factors, some of which have been ranked by various researchers. Hatamleh et al 2018 identified the following factors as critical to the accuracy of cost estimates:

- Clear and detailed drawings and specifications
- Experience of the construction project personnel
- Equipment availability, cost, and performance
- Project complexity
- Clear scope definition
- Accuracy and reliability of cost data

Enshassi et al 2013 ranked the factors affecting cost estimation accuracy differently, placing particular emphasis on:

- Material prices, availability, supply, quality, and imports
- Border closures and trade blockades
- The experience of the project team with the specific type of construction
- The experience and skill level of the consultant
- Detailed project drawings and specifications
- Chimdi et al 2020 further expanded on these factors by adding variables such as material price volatility, accessibility, source, and quality; the consultant's expertise and ability; economic conditions in the country; and the financial stability of the client.

Ultimately, the accuracy of the cost estimation process depends on the quality of the available project information and the estimation techniques employed at the time.

2.4. Techniques used for cost estimation: prediction models

There are several techniques employed to predict the final cost of a construction project during the early stages of the tender phase. These techniques primarily fall into two categories: qualitative and quantitative approaches, both utilizing historical and technical data.

- Qualitative techniques rely on the estimator's experience and judgment, often using heuristics (rule-of-thumb methods) to make educated predictions based on similar past projects or expert opinion.
- Quantitative approaches, on the other hand, involve the collection and analysis of data from previous projects to establish cost predictions through various estimation models. The accuracy of these models depends on how accurately the data is gathered, the type of project for which the method is applied, and the specific input factors used in the estimation process.

Quantitative estimation methods can be broadly classified into three main categories: statistical models, analogous models, and analytical models (Figure 1).

Firstly, Statistical Models (also known as parametric models) rely on mathematical formulas and relationships to predict costs. These models typically follow a top-down approach, where the estimator establishes correlations between input factors (e.g., project size, materials, labor) and the final project cost. This approach aims to use known data to predict future costs with a reasonable degree of accuracy.

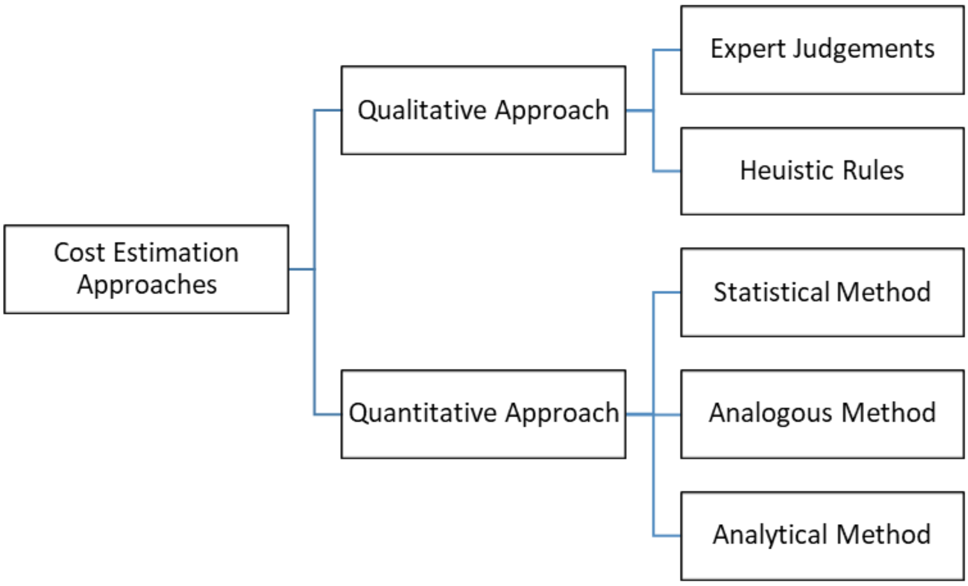

Fig. 1. Cost Estimation Approaches

Secondly, analogous models rely on data from previous projects that are similar in function, design, or other key characteristics such as size, capacity, location, and cost constraints. These projects serve as analogies for the new project. According to Rad 2001, the analogous model is one of the simplest cost estimation tools. It is commonly used in the early stages of a project, such as during the order of magnitude estimate, conceptual estimate, or ballpark estimate phases. These rough estimates help evaluate the feasibility of different project options and allow for the screening of alternatives based on high-level cost projections.

Finally, analytical models take a more detailed approach to cost estimation. They break down the project into its individual components and processes, estimating the cost of each factor and then using a bottom-up approach to sum these costs and determine the final project estimate. Hashemi et al 2020 noted that analytical models typically provide higher accuracy than both statistical and analogous models. However, they require extensive data collection and input from various processes to ensure the most accurate predictions. The accuracy of these models depends heavily on the quality and quantity of the data used.

2.5. Cost estimation in the design phase

Molcho et al 2014 emphasized that approximately 70% of the total project cost is determined during the early design stages, although designers often struggle to provide accurate cost estimates at this point. As the design evolves and more cost-related information becomes available, the cost model becomes progressively more precise. The design phase is typically divided into several stages: conceptual/schematic design, detailed design, construction documentation, bidding, and construction (Manfredonia et al, 2016).

Samphaongoen 2010 categorized cost estimates into three types: conceptual, semi-detailed, and detailed. Each type has its own level of accuracy, with conceptual estimates having an error margin of around 20%, semi-detailed estimates offering a moderate level of precision, and detailed estimates being the most accurate, with an error margin as low as 5%. These variations in accuracy reflect the increasing availability of detailed project information as the design progresses.

3. Methodology

To achieve the research objectives, the study followed these key steps:

- Literature Search: The first step involved conducting a thorough literature review. This was done through desk research, focusing on keywords relevant to the research objectives, such as "cost estimate factors," "cost estimate accuracy," "cost estimation in the design phase," and "techniques for cost estimation." The resulting research works were then analyzed to provide the necessary background and form the foundation for the literature review.
- Identification of Factors for Early Design Stages: The next step was to identify the factors available during the early design stages. In the conceptual or schematic design phase, only a limited number of criteria can be used to estimate costs accurately. The chosen factors for this study are:
  a. Land Area: Land area is typically known before the design phase begins. This area is crucial as it serves as the control area for the project and is measured in square meters (m^2).
  b. Gross Area: Gross area refers to the total built area of the project, which can be determined early in the design process. It can either be directly calculated from the design space program or be constrained by local regulations set by governmental agencies or municipalities. This area is also measured in square meters (m^2).
  c. Excavation Volume: Excavation volume is calculated once the foundation system is defined. After the space program and initial design layouts are approved, the proposed foundation system allows for the calculation of excavation volume, measured in cubic meters (m^3).
  d. Concrete Volume: Concrete volume can be estimated after the general architectural plans and layouts are approved. This volume is measured in cubic meters (m^3).

  These four variables—land area, gross area, excavation volume, and concrete volume—will serve as the independent variables in the multiple regression model used to predict the project budget.
- Data Collection for Real Projects: The next step was to collect data from real construction projects. This data was obtained by contacting several governmental agencies and consulting offices. The data collected were derived from a list of projects that had already completed the design and awarding phases. For each project, the following data points were collected:
  - Project Budget
  - Gross Area (in m^2)
  - Land Area (in m^2)
  - Excavation Volume (in m^3)
  - Concrete Volume (in m^3)

  The collected data spanned a variety of project types, functions, and ownership structures. A total of 22 projects were included in the study. The dataset included several types of projects:
  - Vertical Buildings (e.g., high-rise buildings)
  - Multi-building Projects (e.g., multiple small buildings under one contract)
  - Horizontal Buildings (e.g., low-rise buildings with large horizontal areas)

  The projects were also categorized by ownership type: governmental and private. Figure 2 illustrates the distribution of project types and ownership categories.

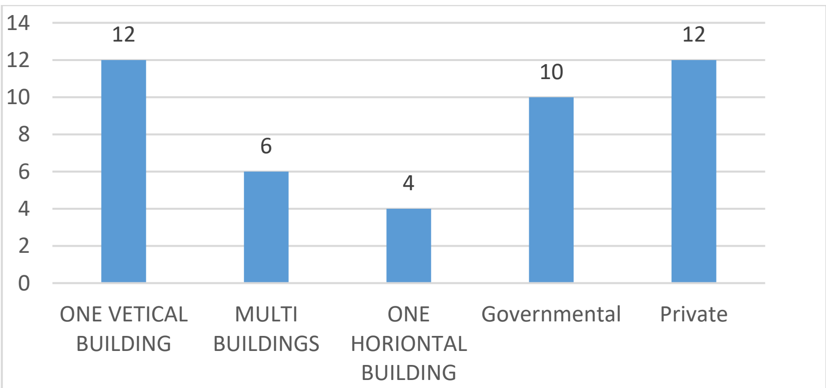

Fig. 2. Project demographic analysis

The collected data spans projects constructed over several years, from 2009 to 2015. Since the projects vary in their tendering periods, a baseline date of 2015 was chosen to standardize all project costs to a common reference point. This ensures consistency in cost comparisons across different years. To adjust the costs to the baseline year, the inflation rates published by the Central Bank of Kuwait were applied, allowing for the conversion of all project costs to 2015 values

- Development of the Multiple Regression Model: The first step in the methodology is to develop a multiple regression model using the collected data. The model will predict the project budget (in Kuwaiti Dinars (KWD), with 1 KWD approximately equal to 3.3 USD) based on four independent variables:
  - Land Area (m^2)
  - Gross Area (m^2)
  - Excavation Volume (m^3)
  - Concrete Volume (m^3)

  The project budget will serve as the dependent variable, while the above four factors will be the independent variables. Since the majority of the collected projects are high-rise buildings, a separate regression model will also be developed specifically for this subset of projects to account for any project-specific characteristics that might affect cost estimation.
- Model Validity Check: Once the regression models are developed, it is essential to check their validity and reliability. To assess the solidness of the models and their applicability for future use, the following steps will be taken:
  - Residual Analysis: The residuals (the differences between the observed and predicted values) will be calculated for each project. This will help assess the model's accuracy and whether the errors are randomly distributed, which is a key assumption in regression analysis.
  - Root Mean Squared Error (RMSE): The RMSE will be calculated to measure the model's prediction error. A lower RMSE indicates a more accurate model, while a higher RMSE suggests that the model's predictions deviate more from the actual values. This will provide an overall evaluation of the model's predictive power and reliability.

  These steps will ensure that the developed regression models are robust, applicable to different project types, and capable of providing reliable cost estimates for new projects based on the available input variables.

4. Analysis and discussion

4.1. Development of the multiple regression model

In this study, a multiple regression model was developed to predict the estimated project budget based on several key independent variables. The choice of these variables is grounded in the early design stages of a project, where they serve as primary factors influencing the overall cost estimation. Specifically, the independent variables used in the model include:

- Land Area (m^2): The total area of land on which the project will be built. This is typically known early in the design phase and serves as a key cost determinant.
- Gross Area (m^2): The total area of the building or structure, which can also be estimated during the conceptual design phase.
- Excavation Volume (m^3): The estimated volume of excavation required for the foundation, which is calculated after the preliminary design and structural system have been proposed.
- Concrete Volume (m^3): The estimated volume of concrete required for the project, which is also determined early on, once the architectural plans and layouts are approved.

These independent variables were chosen because they are among the first elements to be defined during the early design stages. Architectural sketches and plans are usually developed first, followed by the proposal of a structural system. From these early design steps, the excavation volume and concrete quantities are calculated, making them essential factors in estimating the final project budget.

The regression model was built using Microsoft Excel to analyze the collected data. The dependent variable, project budget (measured in Kuwaiti Dinars, KWD), was predicted based on these key independent variables. Figure 3 below presents the results of the multiple regression analysis.

SUMMARY OUTPUT

Regression Statistics	
Multiple R	0.992309172
R Square	0.984677492
Adjusted R Square	0.981072196
Standard Error	6996620.139
Observations	22

ANOVA

	df	*SS*	*MS*	*F*	*Significance F*
Regression	4	5.35E+16	1.34E+16	273.1197	3.52E-15
Residual	17	8.32E+14	4.9E+13		
Total	21	5.43E+16			

	Coefficients	*Standard Error*	*t Stat*	*P-value*
Intercept	-2340375.831	2271910	-1.03014	0.317381
X Variable 1	471.1013372	1273.907	0.369808	0.716092
X Variable 2	-1677.758895	966.8704	-1.73525	0.100787
X Variable 3	-142.7924662	242.1221	-0.58975	0.563113
X Variable 4	8511.036254	3433.646	2.478717	0.023968

Fig. 3. Multiple regression model for all samples

As shown in Figure 3, the Adjusted R-squared value is 98%, which indicates that the model explains 98% of the variance in the project budget based on the independent variables. This is a strong result, as an adjusted R-squared value above 95% typically suggests a good fit, meaning the model effectively represents the data from the sample and provides a reliable prediction of the project budget. Additionally, the Significance F value is almost zero, which is well below the 0.05 threshold. This indicates that the overall regression model is highly significant and that the relationships between the independent variables and the project budget are not due to random chance. In other words, the model is reliable, and its coefficients provide meaningful insights into the factors influencing the project budget. These results further reinforce the solidness of the regression model, confirming that it is a reliable tool for predicting construction project costs based on the key factors identified in the early design stages. This model equation can be written as in Equation 1:

$$\begin{aligned} \mathrm{EBC} = &-2340375.831 + 471.1013372 * \mathrm{LA} - 1677.758895 * \mathrm{GA} \\ &-142.792466227889 * \mathrm{EV} + 8511.036254 * \mathrm{CV} \end{aligned} \tag{1}$$

where, EBC: estimate budget cost, LA: land area (m^2), GA: gross area (m^2), EV: excavation volume (m^3), and CV: concrete volume.

As shown in Figure 3, the p-value is 0.023968 for the concrete volume, indicating that this variable is the most significant variable presented by the model.

4.2. The model for high-rise buildings

As mentioned in Figure 2, the maximum number of gathered samples was from one high-rise building project type, the samples of high-rise buildings have been chosen to build a separate multiple regression model. Figure 4 shows model properties as a result of Excel.

Regression Statistics	
Multiple R	0.995905
R Square	0.991827
Adjusted R Square	**0.987157**
Standard Error	2817261
Observations	12

ANOVA

	df	*SS*	*MS*	*F*	*Significance F*
Regression	4	6.74E+15	1.69E+15	212.3812	**2.21E-07**
Residual	7	5.56E+13	7.94E+12		
Total	11	6.8E+15			

	Coefficients	*Standard Error*	*t Stat*	*P-value*	*Lower 95%*	*Upper 95%*	*Lower 95.0%*	*U 9*
Intercept	**-1780727**	1864636	-0.955	0.371386	-6189890	2628437	-6189890	262
X Variable 1	**-3201.88**	2063.922	-1.55136	0.164755	-8082.28	1678.521	-8082.28	167
X Variable 2	**3872.875**	836.6877	4.628818	**0.002401**	1894.423	5851.327	1894.423	585
X Variable 3	**377.407**	218.0885	1.730522	0.127153	-138.29	893.1044	-138.29	893.
X Variable 4	**-12237.7**	3110.662	-3.93413	**0.005646**	-19593.3	-4882.2	-19593.3	-48

Fig. 4. Multiple Regression Model for High-Rise Building Samples

As shown in Figure 4, the Adjusted R-squared value is 98.7%, indicating that the model explains 98.7% of the variance in the project budget based on the independent variables. This is an excellent result, as an adjusted R-squared value above 95% typically suggests that the model fits the data very well, with minimal unexplained variance. Therefore, the model is highly effective in predicting the project budget and provides a strong representation of the surveyed data. Additionally, the Significance F value is almost zero, which is well below the critical threshold of 0.05. This signifies that the overall regression model is statistically significant, meaning the relationships between the independent variables (land area, gross area, excavation volume, and concrete volume) and the project budget are not due to random chance. This further reflects the reliability and validity of the model, confirming that it can be trusted for predicting project costs. Together, these statistical results demonstrate the solidness of the regression model, highlighting its robustness and its suitability for accurate cost estimation in construction projects based on the early design parameters. This model equation can be written as the following equation.

$$\mathrm{EBC} = \mathbf{-1780727} \ \mathbf{-3201.88} * \mathrm{LA} \ \mathbf{+3872.875} * \ \mathrm{GA} \ \mathbf{+377.407} * \ \mathrm{EV} - \mathbf{12237.7} * \mathrm{CV} \tag{2}$$

As shown in Figure 4, the p-value is **0.005646** for the concrete volume, **0.002401** for gross area**,** indicating that this variable is the most significant variable presented by the model values.

4.3. Model validation

To validate the developed multiple regression model for high-rise buildings, two methods were used: residual analysis and the calculation of the Root Mean Square Error (RMSE).

- Residual Analysis: Residuals are the differences between the actual project budget (surveyed value) and the predicted budget (value obtained from the regression model). By calculating the residuals, we can assess how accurately the model predicts the actual costs. If the residuals are small, this indicates that the model's predictions are close to the actual values, supporting its validity. The average residual percentage for the high-rise building projects was found to be 1.5%, which is relatively small. This suggests that the model provides highly accurate predictions, with minimal deviation from the actual project costs. A small residual percentage is a strong indication that the model is well-calibrated and reliable.
- Comparison of Actual vs. Predicted Values: Figure 5 compares the actual project budgets and the model-predicted budgets for the high-rise building projects. The close alignment between the two sets of values further confirms the solidness of the model. The visual comparison demonstrates that the model is capable

of predicting project costs with a high degree of accuracy, making it a reliable tool for cost estimation in the early design stages.

These validation methods—residual analysis and the comparison of actual versus predicted values—demonstrate that the model is both accurate and applicable for predicting project budgets in high-rise construction projects. The small residual percentage and the strong alignment between actual and predicted costs underscore the reliability and effectiveness of the model for use in practical cost estimation scenarios.

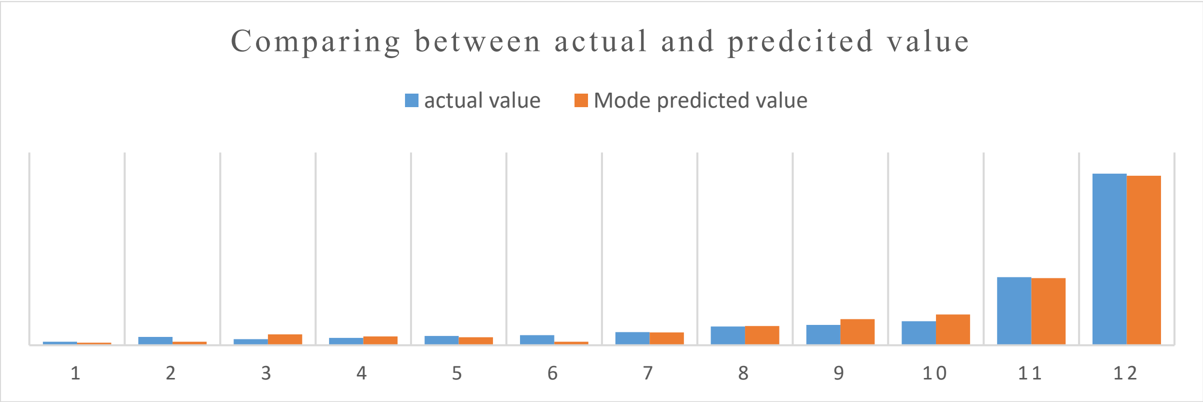

Fig. 5. Comparison between model prediction value and actual values

The model validation will use root mean squared error. This error measures the difference between the predicted value using the model and the actual value used. The root mean squared error can be calculated by the following Equation (3).

$$\text{RMSE} = \sqrt{\frac{\sum_i^n [P - A]2}{N}} \tag{3}$$

where P is the model prediction value, A is the actual value, and N is the total number of model samples used. The Root Mean Square Error (RMSE) for the developed multiple regression cost estimate model was calculated to be 754,235 KWD, which represents approximately 6% of the sample average project budget. This RMSE value is considered acceptable, especially during the early stages of a project, where more uncertainties and limited data are typically present.

According to the American Association of Cost Engineering (AACE) Recommended Practice and Standards (1990), a cost estimate is classified as definitive if the inaccuracy range falls between -5% and +15%. Since the RMSE value for this model is within this range (6%), it confirms that the model's predictions are consistent with the definitive range of cost estimates.

Therefore, the model's results can be classified as falling within the definitive category of cost estimates, indicating that it is a reliable tool for predicting project costs with an acceptable level of accuracy during the early design stages. The fact that the model's accuracy is within the standard industry guidelines further underscores its applicability and validity for use in construction cost estimation.

5. Conclusion

The success of the construction project depends on the level of the cost estimate accuracy, and this level begins in the design stage. Cost estimate in the design stage depends on some general data and information that can be ascertained later. The cost estimate in the design stage has many important aspects, such as feasibility study, bid or not to bid, financial structure preparation, and many other aspects. Two regression models have been proposed to estimate the anticipated project cost in early design stages through collected samples from the state of Kuwait. The first model used data from 22 construction projects, the second model was developed for a selected number of high-rise buildings. The model shows that 98.7% of samples are fitted well in the model parameters. The model results are validated by comparing actual values with model prediction values can be used in construction projects in Kuwait. The model validation will use root mean squared error (RMSE). The calculated RMSE value for this model was (6%), which confirms that the model's predictions are consistent with the definitive range of cost estimates.

Acknowledgement

The authors want to acknowledge Kuwait University- Research Section for funding this research under grant no EV04/23.

References

Chimdi, J., Girma, S., Mosisa, A., & Mitiku, D. (2020). Assessment of factors affecting accuracy of cost estimation in public building construction projects in Western Oromia Region, Ethiopia. *Journal of Civil Engineering, Science and Technology, 11*(2).

Dysert, L. R. (2003). Sharpen your cost estimating skills. *Cost Engineering, 45*(6), 22.

Enshassi, A., Sherif, M., & Munther, A. (2013). Factors affecting the accuracy of pre-tender cost estimates in the Gaza Strip. *Journal of Construction in Developing Countries, 18*(1), 73–94.

Gunaydın, H. M., & Doğan, S. Z. (2004). A neural network approach for early cost estimation of structural systems of buildings. *International Journal of Project Management, 22*(7), 595–602.

Hashemi, T. S., Ebadati, O. M., & Kaur, H. (2020). Cost estimation and prediction in construction projects: A systematic review on machine learning techniques. *SN Applied Sciences, 2*, 1–27.

Hatamleh, M. T., Hiyassat, M., Sweis, G. J., & Sweis, R. J. (2018). Factors affecting the accuracy of cost estimate: case of Jordan. *Engineering, Construction, and Architectural Management, 25*(1), 113–131.

Hegazy, T. (2002). *Computer-based construction project management*. Upper Saddle River, NJ: Prentice-Hall Inc.

Hyari, K. H., Al-Daraiseh, A., & El-Mashaleh, M. (2016). Conceptual cost estimation model for engineering services in public construction projects. *Journal of Management in Engineering, 32*(1), 04015021.

Ibrahim, A., & Elshwadfy, L. (2021). Factors affecting the accuracy of construction project cost estimation in Egypt. *Jordan Journal of Civil Engineering, 15*(3), 329.

Ji, S. H., Park, M., & Lee, H. S. (2012). Case adaptation method of case-based reasoning for construction cost estimation in Korea. *Journal of Construction Engineering and Management, 138*(1), 43–52.

Kim, H. J., Seo, Y. C., & Hyun, C. T. (2012). A hybrid conceptual cost estimating model for large building projects. *Automation in Construction, 25*, 72–81.

Layer, A., Brinke, E. T., Houten, F. V., Kals, H., & Haasis, S. (2002). Recent and future trends in cost estimation. *International Journal of Computer Integrated Manufacturing, 15*(6), 499–510.

Manfredonia, B., Calculations, C., Majewski, P., Consultants, C., Perryman, J., & Consultants, D. (2016). Cost estimating. *Whole Building Design Guide*, National Institute of Building Sciences, Washington, pp. 202–289.

Molcho, G., Asher, C., & Moshe, S. (2014). Part cost estimation at early design phase. *CIRP Annals, 63*(1), 153–156.

Rad, P. F. (2001). *Project estimating and cost management*. Berrett-Koehler Publishers.

Samphaongoen, P. (2010). *A visual approach to construction cost estimating*. Unpublished master's thesis, Marquette University, WI.

4th International Civil Engineering & Architecture Conference
17-19 May 2025, Trabzon, Türkiye

Work accident analysis with LLMs: Can LLMs identify liability classifications?

İpek N. Semercioğlu*[1], Mahdis Motamedi[1], Hasan B. Başağa[1,2]

[1] Karadeniz Technical University, Department of Civil Engineering, 61080 Trabzon, Türkiye
[2] Earthquake and Structural Health Application and Research Center, Karadeniz Technical University, 61080 Trabzon, Türkiye

Abstract. This study investigates the capability of four large language models (LLMs), ChatGPT, Perplexity, Grok, and DeepSeek, to perform accurate stakeholder liability classifications based on expert witness reports of work accidents in the construction sector. Three expert witness reports, originally written in Turkish, were analyzed to assess whether LLMs can accurately determine the responsible parties and assign appropriate liability levels: primary liable, secondary liable and non-liable. The findings reveal that while the LLMs consistently identified primary liable parties, particularly employers, their performance varied significantly in detecting specific roles and assigning detailed liability classifications. Notably, models frequently struggled with accurately attributing liability classifications and recognizing involved parties mentioned explicitly in expert reports. Additionally, certain models introduced entities not referenced in the original reports, raising concerns about potential inferential inaccuracies. Overall, the results suggest that current generation LLMs possess strengths for preliminary stakeholder identification and broad liability classification. However, their limitations underline the necessity of human oversight, indicating that LLMs should currently serve as complementary tools rather than replacements for expert analysis in high stakes occupational safety evaluations. Further research focusing on tailored fine-tuning and hybrid decision-making frameworks is recommended to enhance the accuracy and reliability of LLM assisted liability assessments.

Keywords: Work accident analysis; Large language models; Grok; ChatGPT; DeepSeek; Perplexity

1. Introduction

Artificial intelligence (AI) has recently gained significant prominence due to its ability to reduce labor and operational effort, thereby offering effective solutions to a wide range of problems across various disciplines. Techniques such as machine learning, deep learning, natural language processing (NLP), large language models (LLMs), image processing, and text-to-image generation are commonly associated with AI advancements. Among these, LLMs trained using NLP methods have become particularly popular following the global rise of ChatGPT in 2022. ChatGPT (2022) is an advanced language model developed by OpenAI that can generate coherent and contextually relevant text based on user prompts, making it capable of assisting in tasks ranging from writing and translation to reasoning and explanation across multiple domains.

Following ChatGPT's remarkable success, several alternative LLMs have also gained attention. DeepSeek (2023) is an open-source LLM developed to support multilingual and code-related tasks with high accuracy and transparency. Perplexity (2022) serves as an AI-powered search and reasoning engine that combines language modeling with real-time information retrieval. Grok (2023), developed by xAI, is designed to offer a conversational interface integrated with real-world data streams, emphasizing real-time assistance and personalization.

While LLMs can assist users in everyday tasks, they are increasingly being applied to more complex problems in fields such as medicine (e.g., analyzing medical records (Thirunavukarasu et al., 2023)), marketing (e.g., content generation and trend analysis (Arora et al., 2025)), law (e.g., case summarization and legal provision interpretation (Kim et al., 2024)), education (e.g., automated tutoring and content explanation (Kasneci et al., 2023)) and finance (e.g., financial statement analysis (Li et al., 2023)). In addition, there is growing interest in their potential use within the field of occupational health and safety, particularly in supporting incident investigations, risk assessment, and regulatory compliance (Sammour et al., 2024; Padovan et al., 2025; Tiikkaja et al., 2024). As

* Corresponding author, E-mail: ipeknaz@ktu.edu.tr

https://doi.org/10.31462/icearc2025_ce_mng_257

such, LLMs are envisioned to eventually take on a consultative role for occupational safety experts, offering preliminary analyses or hypothesis generation based on structured incident reports.

Based on this perspective, the present study investigates whether LLMs can accurately assess stakeholder responsibilities in work accident contexts. For this purpose, three expert witness reports on work accident were examined to explore the reasoning capacities of LLMs in evaluating involved parties' liability. Rather than focusing on a single model, the study comparatively assesses the performance of four different LLMs: ChatGPT, DeepSeek, Perplexity, and Grok. Each LLM was tasked with reading the expert reports and responding with liability classification to the involved parties. The liability classification labels responsed by the LLMs were then compared against the official conclusions presented in the expert reports. This approach allows the study to evaluate how closely the assessments made by LLMs match the official decisions, and how well these models can replicate the legal reasoning typically used in evaluating work accident cases.

2. Materials and methods

2.1. Materials

This study discusses three expert witness reports on work accidents in construction works. These expert reports were selected to reflect prevalent occupational hazards, as of fall from height and equipment failures, which pose significant risks in construction environments. Each report varies in its content but typically includes documents such as worker complaints, witness testimonies, employer statements, police records, inspection reports, and regulatory provisions, offering a robust dataset for assessing LLM performance in liability analysis. To uphold ethical standards, all identifying details in reports, including names, locations, and specific dates, were redacted. Additionally, the liability classification labels determined by the experts were extracted from the reports, while only general descriptions of the work accidents were taken into consideration.

All reports were originally written in the Turkish language. In each report, the responsibilities of the involved parties in the occurrence of the work accident are classified into three main categories. Since the reports are written in Turkish language, the original liability classification labels are also in Turkish: "*asli kusurlu"*, "*tali kusurlu"* and "*kusursuz"*. In this study, these labels are respectively interpreted as "*primary liable*", "*secondary liable*" and "*non-liable*". Detailed information extracted from the expert reports is presented in the remainder of this section.

Report 1: At a construction site operated by a private construction company (employer), during concrete pouring conducted by a concrete supplier (service provider private company), the hose of the concrete pump went out of control and struck two workers involved in the pouring process. As a result, one worker died and the other was injured. Following the examination of the documents included in the report, the individuals identified by the expert witnesses as bearing responsibility for the work accident were as follows: employer's representative, site manager, occupational health and safety (OHS) expert, representative of service provider private company, two pump operators, deceased worker, foreman and injured worker.

Report 2: During ongoing construction activities at a fish processing facility (employer), a worker lost his balance and fell from a height of approximately three meters.The incident resulted in a non-fatal injury, with no immediate threat to the worker's life. Following the examination of the documents included in the report, the individuals identified by the expert witnesses as bearing responsibility for the work accident were as follows: employer and injured worker.

Report 3: During transportation activities on the access road of a hydroelectric power plant construction site (employer), a road roller lost control and veered off toward the riverbank. The machine eventually came to a halt after colliding with a tree. The operator (worker) was ejected from the vehicle upon impact and was subsequently found deceased worker at the edge of the riverbed. Following the examination of the documents included in the report, the individuals identified by the expert witnesses as bearing responsibility for the work accident were as follows: employer's representative, site manager, OHS expert and deceased worker.

2.2. Methods

The study evaluates four LLMs, ChatGPT (2022), Perplexity (2022), Grok (2023), and DeepSeek (2023), to investigate their ability to act like expert witnesses in determining stakeholder liabilities in work accidents. These models were chosen for their advanced natural language processing capabilities and proven efficacy in domain-specific applications. Respectively, each LLM analyzed the three reports to determine involved parties' liability. To ensure a standardized and objective evaluation framework, each LLM in the study was prompted with an identical input. This approach was adopted to eliminate variability arising from prompt differences and to enable a fair comparison of the models' performance.

Given that the expert reports are written in Turkish, the prompts presented to the LLMs were also constructed in Turkish language. This decision is based on the assumption that consistency between the language of the reports and the input prompts would enhance the accuracy and reliability of the LLMs' liability assessments. While constructing the prompt text, careful attention was given to formulating a message that would be most effectively understood by the LLMs. To ensure harmony with the original language of this study, the finalized prompt was translated into English and is presented below:

"I have three expert witness reports related to work accidents. I will share these documents with you sequentially, and I would like you to act as an expert witness. Based on the content of each report, please identify the stakeholders involved in the occurrence of the accident and classify their level of liability according to the following categories: *primary liable*, *secondary liable* and *non-liable*. Conduct your analyses with a professional approach and present your findings in table format. Additionally, I kindly ask you to provide a brief explanation for the evaluation made in each report."

Finally, for each report, the outputs generated by each LLM were subjected to a cross-comparison to identify similarities, differences, and patterns in liability classification, and the findings were systematically presented.

3. Results and discussion

3.1. Report 1

The expert report assigns primary liability to the employer's representative, site manager, and OHS expert due to their failure to enforce compliance with occupational health and safety legislation, as well as construction specific safety directives. Secondary liability is attributed to the service provider company and the pump operators, citing deficiencies in worker training and non-compliance with established operational protocols. The deceased worker is also deemed secondarily liable for failing to utilize the personal protective equipment (PPE) that had been made available. Foreman and the injured worker are identified as non-liable involved parties. Table 1 presents a comparative overview of the liability classifications responsed by the four LLMs for this specific work accident scenario.

Table 1. Liability classifications responsed by LLMs for Report 1

Liability Classification	Expert Report	Perplexity	ChatGPT	Grok	DeepSeek
Primary liable	Employer's representative Site manager OHS expert	Employer	Employer Pump operators	Employer Pump operators	Employer Employer's representative
Secondary liable	Representative of service provider private company Pump operators Deceased worker	Pump operators Site manager Workers	OHS expert Pump operators	OHS expert Site manager Injured worker etc.	OHS expert Pump operators
Non-liable	Foreman Injured worker	OHS expert Assistant control worker	Foreman Deceased worker Injured worker	Administrative affairs officer Representative of service provider private company Witnesses	Deceased worker

In the analysis of the expert witness report, LLMs demonstrated varying levels of success in identifying involved parties and assigning appropriate liability classifications. While some key stakeholders such as the 'employer' and 'pump operators' were consistently recognized across models, more specific roles cited in the expert report, such as the 'employer's representative', 'foreman' and the 'representative of the service provider company', were often overlooked. Notably, only DeepSeek successfully identified the 'employer's representative', who held primary liability in the expert assessment, while other models either generalized this role as 'employer'.

In terms of liability classification accuracy, the LLMs frequently produced results that did not align with the classifications assigned by expert witnesses in the original reports. The 'OHS expert', for instance, was assigned as primary liable in the expert report, yet was classified as having secondary liability by three of the LLMs, while the remaining model assigned as non-liable. Conversely, the 'pump operators', classified as secondary liable in the expert report, were incorrectly elevated to primary liability by ChatGPT and Grok. These inconsistencies reveal a tendency among LLMs to either misjudge severity or adopt overly cautious classifications.

When comparing the outputs across models, DeepSeek demonstrated an ability to identify the 'employer's representative', showing closer alignment with the expert report. Similarly, although Grok misclassified the level of liability, it was able to identify the 'representative of the service provider private company' as an involved party.

On the other hand, ChatGPT demonstrated strong performance by correctly identifying the ‘foreman’ and the ‘injured worker’ as non-liable parties, in alignment with the expert report. Morover, it is worth noting that Grok and Perplexity introduced stakeholders not referenced in the expert report, which suggests a tendency toward over-interpretation and may have contributed to less accurate liability assessments.

3.2. Report 2

The expert report underscores a complete lack of occupational safety precautions, citing the absence of documented risk assessments, safety training, and the provision of PPE, including fall-prevention systems. As a result, the employer is assigned primary liability for the failure to implement mandatory safety protocols, constituting a violation of applicable health and safety regulations. The injured worker, on the other hand, is classified as non-liable, as the lack of training, PPE, and clearly defined work instructions impeded his ability to fulfill personal safety responsibilities. Table 2 presents a comparative overview of the liability classifications responsed by the four LLMs for this specific work accident scenario.

Table 2. Liability classifications responsed by LLMs for Report 2

Liability Classification	Expert Report	Perplexity	ChatGPT	Grok	DeepSeek
Primary liable	Employer	Employer	Employer	Employer	Employer
Secondary liable	-	Injured worker	Injured worker	Injured worker	Injured worker
Non-liable	Injured worker	-	-	Witnesses Others (OHS Expert, etc.)	-

When evaluating the LLMs’ outputs against the expert report, all four models correctly identified the ‘employer’ as bearing primary liability, indicating a strong alignment with the expert judgment. This consensus suggests that LLMs are capable of detecting direct employer responsibility, particularly when the report includes clear indicators of systemic negligence. However, in contrast to the expert report, all four LLMs attributed secondary liability to the ‘injured worker’, whereas the expert report explicitly classified the worker as non-liable. This observation has prompted the opinion that LLMs may inherently tend to attribute partial liability to directly involved parties.

When comparing the models, Perplexity, ChatGPT, and DeepSeek demonstrated similar behavior by limiting their outputs to the two main stakeholders. However, Grok introduced additional involved parties such as ‘witnesses’ and ‘OHS expert’ under the category of non-liable, which were not referenced in the expert report. This may indicate that, compared to the other LLMs, Grok is more inclined to identify a broader range of parties involved in the accident.

3.3. Report 3

The expert report assigns primary liability to the employer’s representative, site manager, OHS expert, and the deceased worker. The report specifically notes that the road roller was not equipped with a functional door or a seatbelt, and that the worker was not wearing any PPE at the time of the incident. Based on these observations, it can be concluded that the employer’s representative and the site manager failed to ensure proper equipment maintenance and enforce essential safety protocols, thereby violating applicable occupational health and safety regulations. The report also notes that the OHS expert failed to document existing risks or enforce necessary safety measures, and that the worker contributed to the accident by operating the defective machine without objecting to the unsafe working conditions. Table 3 presents a comparative overview of the liability classifications responsed by the four LLMs for this specific work accident scenario.

Table 3. Liability classifications responsed by LLMs for Report 3

Liability Classification	Expert Report	Perplexity	ChatGPT	Grok	DeepSeek
Primary liable	Employer's representative Site manager OHS expert Deceased worker	Employer	Employer Site manager	Employer OHS expert	Employer Site manager
Secondary liable	-	-	OHS expert Worker	Site Manager Worker	OHS expert Worker Joint Health and Safety Unit
Non-liable	-	-	-	Witnesses	Forensic medicine Gendarmerie

When comparing LLM outputs to the expert findings, all models identified the 'employer' as bearing primary liability, aligning with the broader institutional responsibility highlighted in the report. Beyond this, DeepSeek and ChatGPT performed well in identifying 'site manager' as an involved party and also succeeded in assigning the correct liability classification in accordance with the expert report. However, the 'deceased worker', who was explicitly assigned primary liability in the expert report, was entirely omitted from all four LLM outputs. This consistent omission may suggest that LLMs are hesitant to assign primary liability to a deceased individual, possibly due to inherent biases in their training data or ethical safeguards embedded in their response generation.

In terms of liability classification, models frequently reassigned roles with varying severity. For instance, 'OHS expert' was shifted between primary and secondary liability across ChatGPT, Grok, and DeepSeek. DeepSeek uniquely introduced external stakeholders such as 'joint health and safety unit', 'forensic medicine' and 'gendarmerie'.

Across the models, Grok and DeepSeek demonstrated greater stakeholder coverage but also a higher likelihood of introducing involved parties not referenced in the original report. Perplexity demonstrated the most limited perspective, identifying only the employer as an involved party and disregarding all other potentially responsible stakeholders. ChatGPT adopted a moderate approach by identifying relevant stakeholders, however, it failed to accurately assign their corresponding levels of liability.

Across all three expert reports, the models consistently identified the 'employer' as a primary liable involved party, aligning with the dominant attribution of responsibility in construction-related incidents. However, when it came to role-specific stakeholders such as the 'employer's representative', 'site manager', or 'OHS expert', performance varied widely. In future studies, increasing the number of expert witness reports analyzed may allow for more specific and nuanced observations.

4. Conclusions

This study explored the effectiveness of four LLMs -ChatGPT, Perplexity, Grok, and DeepSeek- in performing liability classifications from expert witness reports of construction related work accidents. The results indicate that while LLMs are successful in identifying the main parties involved and assigning general liability classifications, they often have difficulty with more detailed judgments such as determining the level of each involved party's responsibility and correctly identifying specific roles cited in the expert reports.

The consistent ability of models to assign primary liability to employers highlights their potential usefulness as preliminary tools for rapid identification of principal responsible parties. However, recurrent errors, such as the misclassification of non-liable injured workers or the omission of deceased individuals, underscore critical limitations, possibly influenced by inherent biases or ethical filters within model behavior. Given these insights, it can be concluded that although current generation LLMs may assist experts by providing initial assessments or supporting comparative analysis, they are not yet capable of independently delivering fully reliable or legally robust liability evaluations. Their role should therefore be considered complementary to expert judgment rather than a substitute for it. Future research may focus on adapting LLMs more closely to occupational safety and legal reasoning contexts through fine-tuning with domain specific datasets or developing hybrid frameworks that combine AI reasoning with human oversight.

References

Arora, N., Chakraborty, I., & Nishimura, Y. (2025). AI–Human Hybrids for Marketing Research: Leveraging Large Language Models (LLMs) as Collaborators. *Journal of Marketing, 89*(2), 43-70. https://doi.org/10.1177/00222429241276529

ChatGPT (2024). *ChatGPT* (Mar 14 version) [Large language model]. https://chat.openai.com/
DeepSeek. (2023). *DeepSeek* [Multimodal language model]. https://www.DeepSeek.com/
Grok xAI. (2023). *Grok* [Conversational AI model]. https://x.ai/
Kasneci, E., Seßler, K., Küchemann, S., Bannert, M., Dementieva, D., Fischer, F., ... & Kasneci, G. (2023). ChatGPT for good? On opportunities and challenges of large language models for education. *Learning and Individual Differences, 103*, 102274. https://doi.org/10.1016/j.lindif.2023.102274
Kim, Y., Shin, H., Choi, E., Oh, H., Kim, H., & Hwang, W. (2025). On the consideration of AI openness: Can good intent be abused? *Proceedings of the AAAI Conference on Artificial Intelligence, 39*(26), 27374–27382. https://doi.org/10.1609/aaai.v39i26.34948
Li, Y., Wang, S., Ding, H., & Chen, H. (2023). Large language models in finance: A survey. In *Proceedings of the fourth ACM international conference on AI in finance* (pp. 374-382). https://doi.org/10.1145/3604237.3626869
Padovan, M., Palla, A., Marino, R., Porciatti, F., Cosci, B., Carlucci, F., ... & Foddis, R. (2025). ChatGPT-4 vs. Google Bard: Which chatbot better understands the Italian Legislative framework for worker health and safety?. *Applied Sciences*, *15*(3).
Perplexity AI. (2022). *Perplexity* [AI search engine]. https://www.perplexity.ai/
Sammour, F., Xu, J., Wang, X., Hu, M., & Zhang, Z. (2024). Responsible AI in construction safety: Systematic evaluation of Large Language Models and prompt engineering. *arXiv preprint* arXiv:2411.08320
Thirunavukarasu, A. J., Ting, D.S.J., Elangovan, K., Gutierrez, L., Tan, T.F., & Ting, D.S.W. (2023). Large language models in medicine: Opportunities and challenges. *Nature Medicine, 29*(8), 1930–1940. https://doi.org/10.1038/s41591-023-02448-8
Tiikkaja, M., Kannisto, H., Nurmi, A., Puro, V., Heikkilä, T., Kivimäki, I., ... & Teperi, A.M. (2024). AI-supported safety management-analysing occupational safety data using machine learning within the framework of human factors. Available at *SSRN* 4879013.

4th International Civil Engineering & Architecture Conference
17-19 May 2025, Trabzon, Türkiye

Identification of gaps in civil engineering undergraduate education in Turkey

Ilker B. Alkan*[1], Hasan B. Basaga[1]

[1] Karadeniz Technical University, Department of Civil Engineering, 61080 Trabzon, Türkiye

Abstract. Civil Engineering undergraduate education is of even greater importance in countries like Turkey, which is located in an earthquake zone and has witnessed major disasters. This is because engineers who graduate with the right education can shape the industry and make cities prepared for earthquakes. In Turkey, the Chamber of Civil Engineers and some researchers have identified a number of shortcomings in undergraduate education. However, these findings are often one-sided and may not fully reflect all perspectives. To accurately identify the shortcomings in undergraduate education, the opinions of both academics and representatives from the private sector are necessary. Furthermore, the opinions of academics who have worked both in Turkey and in developed countries are also of great importance.In this study, in order to identify the shortcomings in civil engineering undergraduate education in Turkey, open-ended interviews were first conducted with private sector employees, and the responses were classified. The first survey was conducted in an open-ended manner to prevent participants from focusing on specific problems based on predefined views. Participants answered general questions such as, "What shortcomings do you think exist in civil engineering undergraduate education?" The new questions that emerged from the classification were then presented to academics who have worked both in Turkey and in developed countries. After conducting interviews with 8 experts, the shortcomings in undergraduate education in Turkey were identified. There were topics where the experts did not agree, as well as topics where all were in agreement. However, the vast majority of experts do not agree with the private sector on the inadequacy of university undergraduate education.

Keywords: Mechanics; Civil engineering education; Undergraduate education shortcomings; Turkiye; Private sector; Academic perspectives

1. Introduction

In Turkey, earthquakes with a magnitude of 7 or higher occur approximately every five years. In the most recent one—the Kahramanmaraş earthquake on February 6, 2023—39,000 buildings collapsed, 53,597 people lost their lives, and 107,213 were injured (Özmen & Varol, 2024). In a country where earthquakes have such devastating effects, it is essential to evaluate all processes related to the construction sector, identify deficiencies, and implement necessary improvements.

Undergraduate education in Civil Engineering is a critical area of research that warrants careful consideration, including the identification and resolution of any existing deficiencies. This is because graduates of this program will eventually hold managerial positions in various disciplines within the industry. Therefore, addressing shortcomings in their education will have positive impacts across all areas of the sector.

To date, numerous studies have been conducted to identify the deficiencies in undergraduate civil engineering education in Turkey. One of the most prominent among these is the study carried out by TMMOB (2024). According to this study, although the undergraduate civil engineering program was among the most popular fields at the beginning of the 2000s, it has rapidly lost both its popularity and significance. This decline in popularity is attributed not only to macro-level factors—such as the reduction of sectoral investments in parallel with economic fluctuations—but also to planning errors, which have negatively affected the programs and driven them into a state of crisis.

According to data from the Council of Higher Education (YOK, 2024), there were fewer than 40 undergraduate civil engineering programs in Turkey at the beginning of the 2000s. However, as of 2024, this number has increased to programs offered in 126 faculties. This rapid expansion in enrollment capacity has occurred not as a result of strategic planning, but rather as an outcome of populist approaches. Today, Turkey is producing more civil engineering graduates than are demanded by the industry.

*Corresponding author, E-mail: ilkerbakialkan@gmail.com

https://doi.org/10.31462/icearc2025_ce_mng_271

In the early 2000s, as in other developing countries, undergraduate civil engineering programs in Turkey gained significance due to extensive infrastructure investments. During this period, graduates had little difficulty finding employment, earned higher incomes compared to graduates of other engineering programs, and consequently, the profession's popularity increased. However, this high level of interest was transformed by decision-makers into an unplanned expansion of enrollment quotas.

Many new universities have launched Civil Engineering programs, and in existing faculties, enrollment capacities have been expanded without increasing the number of faculty members or improving laboratory facilities. In some universities, a second Civil Engineering program has even been established within different faculties. This situation has negatively impacted the quality of education and posed serious risks to the sustainability of the profession.

Since the 2010s, the number of civil engineers in Turkey has increased, while the demand for this profession has followed a downward trend. Particularly after 2018, infrastructure investments have shown a declining trend (Yıldız et al., 2023).

With the enrollment quotas reaching their highest level in 2018, graduates of civil engineering programs have struggled to find jobs or have had to work for low wages. This has led to what can be described as an "inflation of civil engineers" in the country. Due to difficult living conditions and the challenges of finding employment, the Civil Engineering undergraduate program has ceased to be a popular field and has gradually become one of the less preferred programs. At this point, a significant portion of the 126 Civil Engineering programs that have been established either cannot attract any students or are trying to continue with very low enrollment numbers (TMMOB, 2024).

The significant decline in the popularity of the undergraduate program has forced Civil Engineering programs to face an issue they had not encountered before: a student profile with low academic performance. The preference of students with lower achievement levels for this field has negatively impacted the quality of undergraduate education, particularly due to their deficiencies in mathematics and physics.

The study by Demirtürk & Tunç (2021) examined how many mathematics and physics questions students who chose the Civil Engineering program in the university entrance exam answered correctly. The findings clearly reveal a significant decline in the quality of undergraduate programs. For example, in 2018, students who were admitted to the Civil Engineering program at Fırat University were only able to correctly answer an average of 1.12 out of 14 questions requiring basic knowledge of physics.

In the early 2000s, Civil Engineering undergraduate programs were preferred by Turkey's most successful students. However, as a result of planning mistakes made over nearly a decade, these programs have turned into fields chosen by students who lack even basic knowledge of physics.

Another significant issue identified in the study conducted by TMMOB (2024) is the inability to adequately develop laboratory facilities and academic staff in parallel with the increase in enrollment quotas. The study emphasizes that many universities in Turkey lack the minimum laboratory infrastructure required for Civil Engineering undergraduate education. Additionally, due to the inability to meet the need for faculty members, it is noted that many lecturers from outside the department have been assigned to Civil Engineering programs.

In addition to the major problems that have led to a rapid and nationwide decline in the quality of Civil Engineering undergraduate programs, there are also additional issues threatening these programs.

Demirtürk & Tunç (2021) evaluated the civil engineering undergraduate education in Turkey from a curriculum perspective and identified several deficiencies by comparing the curricula of some Turkish universities with those of institutions in developed countries. While this study provides valuable initial insights, expanding its scope could yield more concrete results. In fact, regularly conducting such comparative studies and reviewing curricula annually against international standards would be important to ensure that programs remain up to date. This is especially crucial because curricula in Turkey are often not flexibly adapted to new problems and emerging topics of the modern era. Similarly, Bayram et al. (2015) conducted a study on the adequacy of technical courses in undergraduate education. However, their study focused more on enhancing the understanding of existing courses.

Other researchers who have studied the deficiencies in undergraduate civil engineering education have emphasized the lack of practical training. Karaçor et al. (2021)) noted that students learned more effectively through active learning methods during their internships and capstone projects, which better prepared them for their future professional lives. They also highlighted the need to extend the duration of internships.

Bayer Öztürk et al. (2022), emphasized that undergraduate education should include not only technical subjects but also courses on social issues. In their survey study, they found that 76.9% of the participating fourth-year civil engineering students had not taken a course on Engineering Ethics.

Aydinli et al. (2020) focused on students' readiness and questioned whether those who chose to study civil engineering at the undergraduate level made this decision consciously. Their study revealed that 13% of the students surveyed enrolled in the civil engineering program due to social pressure, despite not wanting to become civil engineers. Furthermore, 31% of the participants had not included civil engineering among their top five university choices, but registered in the program because they were not admitted to the departments they initially preferred.

Although some basic-level studies have been conducted to identify deficiencies in undergraduate civil engineering education in Turkey, a comprehensive assessment that detects and categorizes all deficiencies has not yet been carried out. Although Birinci & Koç (2007) provided a general evaluation compiling these deficiencies, the study is outdated—having been conducted in 2007—and its scope is limited as it relies solely on the opinions of the study group.

The aim of the study presented in this paper is to identify the deficiencies in undergraduate civil engineering education in Turkey. In doing so, the study will compile findings from all previous research conducted on the topic, and further expand its scope and depth through expert opinions.

2. Method

Undergraduate civil engineering programs in Turkey, when compared to those in other countries, unfortunately exhibit a low performance profile. Global rankings of civil engineering programs show that universities in Turkey are not listed among the top institutions. For example, in the 2024 QS World University Rankings, no Turkish university is ranked within the top 100 for civil engineering programs (QS, 2024). Similarly, in the 2024 Times Higher Education rankings, no civil engineering program from Turkey is included in the top 250 universities (THE, 2024). In contrast, programs from countries such as the United States and the United Kingdom rank much higher in these lists.

For Turkey to rank higher in these prestigious rankings, various improvements need to be made. These improvements can be identified by comparing Turkey's civil engineering undergraduate programs with those in developed countries and analyzing the differences between them. This will help pinpoint the specific shortcomings of Turkey's educational system, and strategic steps can be taken to address these deficiencies. Such research could present a significant opportunity to enhance Turkey's international academic prestige.

The most common approach in comparing undergraduate programs is the comparison of written materials and curricula. This method is widely preferred by many researchers and provides valuable data. However, written sources may not always fully reflect the realities of a program. For example, the curriculum of the Civil Technology two-year associate degree program at Gümüşhane University's Keşap Vocational School includes courses such as Statics and Strength, Structural Mechanics, Reinforced Concrete, and Soil Mechanics, which cover the challenging calculations found in Civil Engineering undergraduate programs(Giresun University, 2025). These courses offer similar content when compared to the leading Civil Engineering undergraduate programs in Turkey.

However, when student success profiles are taken into account, it cannot be expected that courses with similar curricula will be delivered with the same quality. This indicates that comparisons based solely on written sources and curricula may not fully reflect the quality of the programs. Therefore, attempting to identify the shortcomings of Civil Engineering undergraduate programs in Turkey solely based on written sources may lead to incomplete and misleading information. To evaluate the effectiveness and quality of the programs more accurately, more comprehensive analyses are required, including student performance, teaching methods, and industry alignment.

In order to identify the differences between Civil Engineering undergraduate programs in developed countries and those in Turkey, expert opinions that are familiar with the education systems and cultures of both countries are necessary. This is because the cultural structure of a program cannot be fully conveyed through written sources, and researchers unfamiliar with the culture may not notice these differences without significant effort. Therefore, identifying the areas in which Civil Engineering undergraduate programs in Turkey are lacking compared to developed countries can only be done by experts who have experience in the educational cultures of both countries.

The depth of the research has been enhanced by the opinions of experts who have either studied, worked, or taught in Civil Engineering programs in developed countries such as the UK, the US, and Japan, as well as in Civil Engineering programs in Turkey. The experts' opinions were gathered through interviews, not surveys, as face-to-face verbal communication is a much more effective method than written communication. At the beginning of the interview, the purpose and objectives of the study were explained to the experts, and their suggestions for future versions of the research were also gathered. To ensure that no information was lost, all interviews were recorded on video, and each interview was transcribed and analyzed individually.

In order for the interview to be conducted within specific boundaries, five different topics were addressed to the participants. These questions were formulated based on feedback received from the industry. The questions are as follows:

- Do you agree with the view that individuals graduating from undergraduate education in Turkey are insufficient in transferring theoretical knowledge to practical knowledge? If you agree, could you explain the reasons for this problem by highlighting the differences between your experiences in Turkey and those in the United States/United Kingdom/Japan?
- Do you think that internship processes in Turkey are not being carried out efficiently? If so, could you explain the reasons for this problem by highlighting the differences between your experiences in Turkey and those in the United States/United Kingdom/Japan?
- Do you think that universities and faculty members in Turkey are less advanced compared to developed countries in terms of collaboration with the industry, and that this negatively impacts undergraduate

education? If so, could you explain the reasons for this problem by highlighting the differences between your experiences in Turkey and those in the United States/United Kingdom/Japan?

- Do you think that students graduating from the civil engineering undergraduate program in Turkey enter their professional careers without sufficient knowledge in social areas such as communication, management, and hierarchical relationships? If so, could you explain the reasons for this problem by highlighting the differences between your experiences in Turkey and those in the United States/United Kingdom/Japan?
- What do you think are the most important shortcomings in civil engineering undergraduate education in Turkey? What needs to be changed or improved? Could you explain the reasons for these issues by highlighting the differences between your experiences in Turkey and those in the United States/United Kingdom/Japan?

The interview process was conducted with 8 experts who have experience in civil engineering undergraduate programs both abroad and in Turkey. Four of the experts have experience in the United States, three in the United Kingdom, and one in Japan. Since the areas of expertise in developed countries may vary, it was considered that their overseas experiences could be in more specific fields such as Construction Management rather than Civil Engineering. However, since these fields are considered within the scope of Civil Engineering in Turkey, experts with experience in these areas were also included in the interview process.

Some experts agreed with each question, while others disagreed. The reasons for agreement or disagreement were asked individually to each expert, and these reasons were taken into consideration in the evaluation. The experts' opinions sometimes contradicted each other, and these differing views were also analyzed. All opinions were compiled into a single text as a unified pool of responses. The process of transcribing the interviews was carried out entirely through the efforts of our research group. Since the experts only shared their own opinions, they are not responsible for any errors or flaws in the final product.

3. Findings and discussion

In this section, the responses provided by the experts are presented under separate headings for each question.

3.1. Criticism of the ınability to transfer theoretical knowledge to practical knowledge

This issue is a common criticism in Turkey. Experienced engineers in the country often express that recent graduates are lacking in applying theoretical knowledge in practice. Industry stakeholders, on the other hand, point out that newly graduated civil engineers are inexperienced in site applications and graduate without being prepared for the industry environment or the conditions of construction sites.

The first of the five questions we asked the experts during the interview addressed this issue. We asked the experts whether there is a gap in the teaching of practical knowledge in undergraduate education in Turkey. The responses provided valuable insights, allowing for a deeper analysis of the issue and enabling it to be viewed from different perspectives.

Out of the 8 participants, 4 disagreed with the criticisms from the industry regarding recent graduates and criticized these expectations. The experts emphasized that it is not the correct approach for universities to directly train engineers to meet industry expectations.

It was stated that the expectations from industry—such as recent graduates being proficient in commonly used software packages and having full command of all stages of site operations—are unrealistic. It was emphasized that engineers who are trained only to meet the current system's needs will lack the capacity to improve or transform that system. Such knowledge and skills were considered more appropriate for technician or technologist profiles. It was argued that engineers should be educated with a strong theoretical foundation to be able to solve future and yet undefined problems.

The experts also criticized the expectation from industry that recent graduates should fully adapt to work processes from the outset. It was emphasized that professional life should be seen as a continuous learning process, and that companies should offer educational and innovative working environments to support this. Otherwise, it was stated that such companies would struggle to compete with their rivals and in the global market. If a company performs the same tasks repeatedly without change or development, it was noted that such a company is likely in need of a technician who already knows the job from day one, rather than an engineer. The view was shared that Turkey should train engineers for innovative and forward-thinking companies that can compete globally. Moreover, expecting new engineers to already know the specific software used in a workplace was deemed an inappropriate approach. It was emphasized that it is unrealistic to teach all industry-specific software and operational procedures during undergraduate education, and that the responsibility to develop such skills lies with the employer.

Some experts pointed out that experienced engineers tend to evaluate recent graduates based on the conditions of their own education period. It was emphasized that access to information has changed significantly and that engineering codes and technical knowledge have become far more comprehensive than in the past. For example, while the Turkish Earthquake Code in force in 1975 was only 63 pages long, it has now expanded to 376 pages.

Therefore, while it may have been realistic for engineering students in the past to learn a 63-page regulation in its entirety, it is no longer realistic to expect students today to memorize every detail of a 376-page modern regulation. In this context, experts argued that rather than memorizing all information, it is more important for students to know how to access information when needed. They also emphasized that students with a strong technical foundation can learn practical skills relatively quickly once they enter the workforce.

Additionally, some experts noted that this issue should not be reduced solely to the structure of undergraduate education. It was stated that new graduates often experience a loss of motivation due to low wages and poor working conditions, and that industry stakeholders harshly criticize young engineers without giving them adequate time to demonstrate their potential. Therefore, criticisms targeting new graduates were described as part of a complex issue with social, cultural, and economic dimensions, making it difficult to resolve.

Four out of eight participants offered suggestions for improving the teaching of practical knowledge within undergraduate education in Turkey. Experts pointed out that such practices have been successfully implemented in developed countries and could also be adapted for Turkey.

Firstly, it was noted that engineering education in Turkey is excessively theoretical, and practical training remains insufficient. Most course content is designed for office-based work, although many engineering graduates end up working on construction sites. Currently, only a few courses cover site management, and experts argued that these are not sufficient to prepare graduates for managing the harsh conditions of construction sites. In contrast, developed countries offer dedicated undergraduate programs in "Construction Management" where students take hands-on courses in site supervision, planning, and project management. These programs also include opportunities for students to work on real-world projects, receive mentorship from industry professionals, and become directly prepared for the sector.

Experts also emphasized the need to improve assessment and evaluation methods. In developed countries, student performance is not measured solely through written exams but also through reports prepared using professional software and tools. This method allows students to demonstrate their knowledge more comprehensively and become better prepared for industry expectations. However, for such a system to be feasible in Turkey, it was noted that class sizes would need to be reduced; while this approach is effective in classrooms of 15–20 students, it poses challenges in large groups of 80–100 students, as is often the case in Turkey.

Finally, it was highlighted that in developed countries, students often begin working part-time in their field during their undergraduate studies. In particular, the high cost of education in these countries compels students to balance their studies with early work experience. This process helps students reinforce their theoretical knowledge through practical experience and better prepares them for professional life upon graduation.

3.2. Evaluation of internship efficiency

In Turkey, the short duration and inefficiency of internship programs are frequently criticized. One of the most significant issues is that some internships are not actually completed in practice but are merely shown as completed on paper. Moreover, in the majority of internships, students are not paid and are assigned passive observer roles, where they are expected to simply watch rather than actively participate. To identify whether such inefficient practices also occur in developed countries and, if so, how they are addressed, expert opinions were consulted. Some experts stated that they had not personally witnessed such ineffective internship examples in Turkey. However, all experts provided suggestions for improving the internship system, which are summarized below.

In Turkey, the internship process typically ends when the student submits their internship report to the university; during this process, neither the company nor the university is actively involved. In contrast, in developed countries, universities and companies jointly manage the internship programs, and internship committees conduct periodic on-site visits to monitor both the company conditions and the student's active participation. Furthermore, in these countries, it is highly unlikely for a company to allow a fake internship. Such behavior poses a reputational risk for the company and is also avoided due to the potential for legal sanctions.

In Turkey, the oversupply of engineering graduates leads companies to view interns as "additional labor" and therefore not value them sufficiently. Conversely, in developed countries, the limited number of engineers and interns fosters an understanding of interns as a strategic investment and potential future employees. In these countries, companies assign concrete responsibilities to interns, closely monitor their performance, and enhance motivation by offering compensation—thus making the internship process more efficient and effective. In Turkey, however, most interns work without pay. Companies that do not perceive any benefit from the process assign students passive observer roles and feel no obligation to pay them. This approach significantly undermines the internship experience and the professional development of students.

In developed countries, the high cost of higher education and living expenses places a substantial financial burden on students. Therefore, many students are compelled to seek paid internships or part-time jobs to support themselves during their studies. This reality increases students' motivation to demand paid internships and encourages companies to offer fair compensation. In Turkey, however, the absence of tuition fees and the fact that students' basic living expenses are largely covered by their families reduce the need to demand payment for internships. This contributes to the prevalence of unpaid internships and weakens students' bargaining power regarding their economic rights.

In Turkey, compulsory internships are usually limited to the summer months and do not exceed a few weeks. In some developed countries, however, an entire academic year may be allocated to internships, or through the "cooperative education" model, students undertake long-term internships during different periods of the year. These practices not only allow students to experience work processes in different seasons but also make internships more attractive and beneficial by providing income. Short and compulsory internships often fail to create effective learning environments, while long-term and flexible internship models enhance both students' professional experience and their motivation.

In developed countries, the rights of interns are clearly protected by law. Companies are obligated to pay interns, provide suitable working conditions, and document the process to ensure traceability. Moreover, internship supervisors regularly monitor the students' daily tasks and performance. In Turkey, due to both legal infrastructure deficiencies and a lack of enforcement of existing regulations, fake internships have become widespread. This situation decreases student motivation and leads companies to undervalue the process. While unpaid internships are prevented by labor laws and effective monitoring systems in developed countries, in Turkey, employing unpaid interns has become a normalized practice. Therefore, similar to the legal obligation to employ persons with disabilities, the regulations surrounding internship employment must be clarified by law and effectively monitored to protect interns' rights.

3.3. Criticism of industry-university collaboration

Some experts do not agree with the criticism that universities in Turkey do not have sufficient collaboration with industry, and they have evaluated the topic from different perspectives. On the other hand, some experts have pointed out that universities in Turkey have areas that need development in this field and have listed these points. Experts who do not agree with the criticism emphasize that the main responsibility for the weakness of university-industry collaboration in Turkey lies with the industrial sector. They argue that the insufficient development of R&D culture in Turkish companies, the lack of vision for developing innovative technologies and methods, and their failure to invest adequately in R&D are key barriers to collaboration. These experts have stated that while academics are willing to share knowledge and research results, companies are not as willing to allocate financial resources for these results. It has been suggested that government incentives could be effective in solving this problem. They reminded that, as in the defense industry example, public support has allowed companies to establish more effective collaborations with universities.

Furthermore, these experts emphasized that it is not correct for universities to become entirely focused on the private sector. They noted that the cultures of the private sector and universities are different, and universities should not be reduced to just training labor for the private sector or conducting R&D. While the private sector expects quick and direct results from research, universities must evaluate the impacts of scientific studies in detail. Therefore, it has been argued that if universities adopt the same cultural structure as the industry, it could weaken the university's originality and its ability to produce science. Experts holding this view have stressed that universities should protect their status and academic freedom; therefore, they did not consider it a deficiency for academics not to engage in industry-specific or mandatory collaborations.

On the other hand, some experts have pointed out that there are areas where Turkish universities need improvement to establish stronger relationships with industry. In Turkey, for a faculty member to be promoted, conducting scientific research is considered sufficient, while the quality of teaching and updating curricula are not taken into account as promotion criteria. This situation may cause faculty members to lack sufficient motivation to reflect industry collaborations in their undergraduate programs, update curricula, and offer innovative courses, even if they collaborate with industry.

In contrast, in developed countries, faculty contracts can be arranged with both research and education-focused terms, and faculty members can be promoted by updating curricula and developing course content. Moreover, in these countries, securing funding for projects and research is also an important criterion for promotion. It has been suggested that Turkish universities could make institutional arrangements to encourage and monitor faculty members in obtaining funding.

In developed countries, there are special units managing industry relations, which contact companies through databases and effectively coordinate processes such as internships and course contributions. Furthermore, these universities regularly meet with industry representatives to keep their curricula up to date and maintain this process in a dynamic and systematic manner. Although similar meetings are held periodically in some universities in Turkey, it has been stated that this process is more limited and irregular compared to developed countries.

Experts have also pointed out that professional chambers play an important role in industry-university collaboration. In developed countries, professional chambers closely follow the course processes in universities and make various suggestions. Universities update their curricula based on these suggestions, enabling them to better respond to industry expectations. In Turkey, while there is some relationship between professional chambers and universities, it is said to be weak and limited.

Additionally, it has been suggested that practices such as private sector managers giving seminars at universities and making better use of alumni networks could better prepare students for industry expectations. In developed countries, the rankings of universities in international rankings are of great importance for institutional prestige. Criteria such as graduate employment rates and employer opinions stand out in these rankings, which motivate universities to enhance the employability of their graduates and establish stronger relationships with the business world. Therefore, in developed countries, industry collaboration in universities has become a structural and sustainable priority.

Some experts have expressed the need to strengthen the R&D centers in universities and stated that companies could carry out research and development activities more efficiently and cost-effectively through these centers. It was highlighted that this process would bring significant benefits to the industry, as establishing in-house R&D systems in companies is a costly and labor-intensive process. In contrast, joint R&D centers to be established within universities and structured on a national scale would contribute to both universities and industrial organizations. Moreover, it has been suggested that increased participation from various sectors in organizations such as Teknofest would enhance the culture of industry-university collaboration.

3.4. Management and communication skills deficiencies

In this study, professionals with more than 10 years of industry experience in civil engineering were asked for their opinions on the shortcomings of undergraduate education. The participants noted that recent graduates particularly show deficiencies in areas such as management, communication, and handling relationships between subordinates and superiors, and stated that these deficiencies should be addressed during the undergraduate education process. The findings were presented to faculty members with academic experience in both Turkish universities and universities in developed countries for evaluation, and expert opinions are summarized below.

Some experts argued that communication problems seen in low-profile firms in Turkey lead to criticism of new graduates. Communication issues such as disrespect, gossip, and blind obedience to authority, commonly observed on construction sites, were mentioned as reasons why new graduates are seen as "incompatible." In this context, it was emphasized that not only universities but also workplaces need to adopt modern communication approaches.

On the other hand, some experts pointed out that Turkish universities need to improve in terms of equipping students with social skills. They noted that communication and leadership workshops, which are part of advanced education systems, help students develop skills such as effective listening, empathetic communication, and team management, and suggested that such practices could provide significant benefits if implemented in Turkish universities.

Experts also emphasized that the written exam-based assessment methods commonly used in Turkey highlight analytical skills but neglect social interaction. In contrast, in the educational models of developed countries, both technical and communication performance are evaluated through project assignments and report presentations, ensuring continuous faculty-student dialogue. These methods were stated to contribute to the development of students' coordination and public speaking skills outside the classroom.

Furthermore, it was mentioned that faculty-student interaction in Turkey is largely limited in crowded classrooms (80–100 students), while in developed countries, the one-on-one guidance, presentations, and feedback opportunities in 15–20 person classrooms help strengthen students' social skills. It was also emphasized that communication and leadership skills should not only be developed at the undergraduate level but must be foundational in primary, middle, and high school periods, and even within the family environment. The university should be considered as the final stage that reinforces and enhances these skills.

3.5. General options of experts

In this section, experts were asked an open-ended question: “In which areas do you observe shortcomings in education?” without adhering to a predefined framework regarding undergraduate education in Turkey. The participants were asked to freely describe the aspects of the program they found weak, and the opinions obtained in this way are summarized and presented below.

The dominant one-size-fits-all educational model in Turkish civil engineering undergraduate programs forces students to take courses from all main branches, even if only superficially. However, in universities in developed countries, after the first year, students choose a specialization, and it becomes possible to focus on specific fields, such as hydraulics or structural courses. The "everything for everyone" approach in Turkey, however, prevents the younger generation of engineers from specializing according to their personal interests and abilities.

Civil engineering undergraduate education in Turkey is still largely shaped within the framework of classical engineering understanding. While the curriculum heavily emphasizes traditional subjects like reinforced concrete calculations, it does not allocate enough space to modern necessities such as construction management, digital construction applications, and virtual laboratory technologies. Sustainability, climate change, and the social and environmental dimensions of engineering are offered only as elective courses in most programs, leading to a lack of sufficient awareness among students in these areas. However, classical civil engineering topics are largely solved problems today. While performing reinforced concrete calculations for a building may offer a satisfying learning process for students, these calculations can now be easily performed by advanced software. Leading universities in the world have largely abandoned investing in classical calculations. When determining their curricula, they consider the interests of scientific funding bodies and their investment priorities, enabling easier access to funding and keeping their education programs continuously updated. At the same time, by following the areas of focus of leading companies in the industry, curricula are shaped according to the needs of next-generation engineering. Today, large firms are still building skyscrapers, but universities no longer need basic knowledge based on fundamental calculations to design such structures. The pursuit of innovation in energy projects, sustainable urbanism, and digital construction makes universities attractive for collaboration. Instead of sticking to old curricula that revolve around solved problems, Turkish universities need to focus on training engineers who can solve the complex, multidisciplinary problems of the new world. It is clearly seen today that students who can see the big picture, think interdisciplinarily, and have the ability to develop solutions to the problems of the new world are more successful, not just those who are good at static and reinforced concrete calculations. Restructuring education programs in this direction has become a necessity, not just a choice.

It is argued that free higher education reduces the value placed on universities and knowledge, and since students do not financially invest in their learning process, their sense of ownership and responsibility remains low.

Quality assurance mechanisms and self-assessment processes in Turkish universities are extremely weak. Universities do not conduct curriculum, resource, and process evaluations internally or through external committees; accreditation processes generally remain formal rather than substantial. In contrast, in many developed education models, departmental committees conduct periodic audits, submit deficiency reports, and follow up with improvement plans.

The lack of institutional accountability is also reflected in the protective structure of state universities. Faculty members or administrative staff can serve for long periods without undergoing performance evaluations, and mistakes and inefficiencies can go unpunished. This "immunity" culture weakens both academic and administrative initiative.

4. Conclusions

In this section, the problems in Turkey's Civil Engineering undergraduate education are presented in bullet points based on the data obtained from interviews with experts and the results of previous studies. The identified problems are the conclusions drawn from the findings of our working group. The experts interviewed are not responsible for the errors or deficiencies found. The identified deficiencies are presented below:

- Every year, more Civil Engineers are graduated in Turkey than needed. The quotas are not created as a result of a proper planning process.
- The mathematics and physics foundations of Civil Engineering undergraduate students are insufficient.
- There is no determination of which laboratory facilities universities should have for Civil Engineering undergraduate education, and these facilities are not periodically inspected for their existence.
- No study has been conducted on which fields of expertise universities should have in their faculty for Civil Engineering undergraduate education, and the qualifications of the academic staff to deliver this education are not inspected.
- The assessment and evaluation system consists solely of written exams, which is insufficient to comprehensively assess all the knowledge students have acquired throughout the semester. Additionally, it does not contribute to preparing students for the workforce or developing their communication skills, as advanced educational systems do with reporting evaluation systems.
- Although the majority of graduates work on construction sites, the curriculum lacks courses focused on site management that students will need during their careers, and the course hours are insufficient.
- The curriculum does not include courses where students, like in advanced educational systems, can collaborate on real projects and perform tasks such as time scheduling and cost calculations, or establish cooperation with industry managers.
- Students cannot gain work experience during their undergraduate education. There is no opportunity for students to spend a year between their 3rd and 4th years in the industry, extending their undergraduate program for this purpose.
- Internships are solely managed by students. The internship process is not conducted in collaboration between universities and industry. University internship committees passively evaluate only the internship report, do not determine the internship placements, do not inspect the internship sites, and do not communicate with the industry during the internship. Furthermore, the committees do not monitor what competencies students should gain during the internship or track these competencies.
- The excess supply of engineers leads to industries viewing interns as a burden. Rather than actively seeking interns, industries accept interns through special requests, do not pay them, and instead of giving them active tasks, they want them to observe passively in the work environment.

- The rights of interns regarding payment are not adequately protected. An unjust environment is created where unpaid interns are employed.
- The inefficiency of internships, the non-payment of interns, and the lack of sufficient supervision by both universities and the Ministry of Labor lead to a widespread phenomenon where internships are reported as completed but are not actually performed.
- The lack of a research and development culture in the industry, and the absence of firms with a vision for leadership or innovation, prevents industries from collaborating with universities on R&D, which indirectly affects the quality of undergraduate education.
- Faculty members can only be promoted through academic research. Curriculum updates and the programming of innovative courses are not criteria for promotion. Unlike in advanced educational systems, faculty members cannot be promoted by producing course content or keeping teaching processes up to date. This results in a low motivation for updating curricula.
- There is no department within Turkish universities that tracks industry relations, keeps records of companies and relationships with managers, offers internship opportunities to students, or ensures industry contributions to courses.
- Turkish universities do not have a systematic curriculum update follow-up program that would allow them to learn about the needs of industry and update their curricula accordingly, or meet with industry and professional associations. While some universities hold such meetings, this process does not proceed continuously or systematically. Curricula that are completely shaped according to industry needs are not supported, and curricula that are outdated and created without listening to the legitimate demands of industry are seen as a problem.
- Undergraduate programs do not include workshops where students can develop their communication and social skills.
- A one-size-fits-all education model is applied in Civil Engineering undergraduate curricula. Students are required to take courses from all sub-disciplines, even if they are not interested in those areas, preventing them from specializing in the fields they wish to work in. This "one size fits all" approach hinders young engineers from specializing according to their personal interests and skills. This lack of specialization also manifests in internships and thesis work.
- The Civil Engineering undergraduate curricula focus on the classical engineering mindset, offering courses on solved problems that all students take, without providing courses that would equip students with the ability to solve new, complex problems or give them knowledge and awareness of future challenges they may face.
- Universities lack internal and external audit mechanisms to inspect their curricula, academic staff, educational conditions, and resources within the department, university, or by other universities.

Each deficiency identified in this study needs to be addressed individually, and valuable findings should be developed for improvements. In an area where so many problems have been identified, it is clear that existing academic work is insufficient. We invite researchers to work in this area for more efficient and effective undergraduate education.

Acknowledgments
We would like to thank Prof. Dr. Ayhan İrfanoğlu, Prof. Dr. İrem Dikmen, Prof. Dr. Ertuğrul Taciroğlu, Assistant Professor Fatih Sütçü, Associate Professor Abdulhakim Zeybek, Prof. Dr. Erkan İstanbulluoğlu, Dr. Zafer Yılmaz, and Dr. Vahaddin Alperen Baki for their valuable insights and contributions that helped us identify the issues and improve the process.

References

Aydinli, S., Tantekin Çelik, G., Bayram, S., & Oral, E. (2020). İnşaat mühendisliği öğrencilerinin mesleki beklentileri ve kariyer planları. *Yükseköğretim Dergisi, 10*(1), 38–50. https://doi.org/10.2399/YOD.19.012

Bayer Öztürk, Z., Tavşancı, Ö., Nur İster, Ş., Hacı Bektaş Veli Üniversitesi, N., & Malzeme Mühendisliği Bölümü, M. (2022). İnşaat mühendisliği eğitiminde mühendislik etiği uygulamaları ve etkileri. *International Journal of Engineering Research and Development, 14*(2), 777–783. https://doi.org/10.29137/UMAGD.1104015

Bayram, S., Çelik, G., & Oral, E. (2015). Mühendislik öğrencilerinin öğrenim yeterlilikleri ve mesleki yetkinlikleri: İnşaat mühendisliği öğrenci perspektifi. *Turkish Journal of Education, 4*(1), 4–18. https://doi.org/10.19128/TURJE.181092

Birinci, F., & Koç, V. (2007). Türkiye'de inşaat mühendisliği eğitiminin genel yapısı ve geliştirilmesi için yeni yaklaşımlar. *4th Construction Management Congress*.

Demirtürk, D., & Tunç, G. (2021). İnşaat mühendisliği eğitimi ve Türkiye'de inşaat sektörünün lisans eğitimine bakış açısı. *Engineering Sciences*. https://dergipark.org.tr/tr/pub/nwsaeng/issue/59904/811399

Giresun University. (2025). *Construction technology program*. https://kesapmyo.giresun.edu.tr/Files/ckFiles/kesapmyo-giresun-edu-tr/insaat%20tek..pdf

Karaçor, F., Yünkül, K., & Erdağ, A. (2021). İnşaat mühendisliği öğrencilerinin ana bilim dallarındaki yeterlilikleri üzerine bir araştırma: Mevcut durum, sorunlar ve çözüm önerileri. *European Journal of Science and Technology, 31*, 545–552. https://doi.org/10.31590/ejosat.1012610

Özmen, B., & Varol, N. (2024). 30 Ekim 2020 İzmir ve 6 Şubat 2023 Kahramanmaraş depremlerinin teknik ve yönetsel karşılaştırılması. *Afet ve Risk Dergisi, 7*(1), 319–328. https://doi.org/10.35341/afet.1448495

QS. (2024). *Subject rankings 2024 | Top Universities*. https://www.topuniversities.com/subject-rankings

THE. (2024). *World university rankings 2024: Methodology | Times Higher Education (THE)*. https://www.timeshighereducation.com/world-university-rankings/world-university-rankings-2024-methodology

TMMOB. (2024). İnşaat mühendisliği eğitiminde sorunlar ve çözüm önerileri. https://www.imo.org.tr/Eklenti/8617,tmh-517-webpdf.pdf?0&_tag1=CD4A0365C235BFE8140517C2980C396425E44291

Yıldız, F., Nur Kavak, Z., Nur Aktan, M., Kelimeler, A., Büyüme, E., Yatırım Harcamaları, K., & Analizi, A. (2023). The impact of public investment expenditures on economic growth in Turkey. *BILTURK Journal of Economics and Related Studies, 5*(3), 199–213. https://doi.org/10.47103/bilturk.1306908

YOK. (2024). *İnşaat mühendisliği programı bulunan tüm üniversiteler | YÖK Lisans Atlası*. https://yokatlas.yok.gov.tr/lisans-bolum.php?b=10110

Enhancing tunneling projects with digital twin technology: Applications and benefits across the tunnel lifespan

Abdolsattar Roudini[*1], Melek H. Beşer[1], Serkan İnal[1], Kerim Aydiner[1]

[1] *Karadeniz Technical University, Department of Mining Engineering, 61080 Trabzon, Türkiye*

Abstract. Tunnels are structures utilized across various fields of engineering, ranging from mining, where they serve as the main access points, to civil engineering, where they are used as road tunnels or subway tunnels or for water supply and drainage. Digital twin technology is increasingly being embraced in both mining and civil engineering sectors, as these fields utilize its potential to improve operational effectiveness, safety measures, and environmental sustainability. By generating virtual models of the entire tunnel lifespan, engineers can observe ongoing tunnelling operations in real time, replicate excavation techniques, and anticipate ground reactions. This enables proactive risk management and streamlined decision-making processes. The construction of a tunnel encompasses design, construction, and maintenance phases. For each phase, engineers need to have access to different data to make a decision. Digital twin will be a useful tool for engineers to have a full vision of the project and make an accurate decision. In this paper, the Scopus database is used to collect papers related to the different applications of digital twins in tunnelling projects to give a comprehensive view of digital twin applications in this field, find the gaps that should be filled and suggest future works. Despite substantial advancements, current research primarily emphasizes digital twin applications in the construction and maintenance phases, focusing on real-time data acquisition, risk management, and operational efficiency. By synthesizing the findings, this paper underscores the role of digital twin in streamlining decision-making across all project phases and suggests pathways for extending its application to underexplored areas.

Keywords: Digital twin; Tunneling projects; Tunnel lifespan; Operational effectiveness; Risk management

1. Introduction

Tunnel infrastructure is highly essential and often serves as the foundation upon which modern transportation systems and industrial operations depend. Tunnels also have an extra vital role to play for the mining industry by providing access to ore bodies, improving ventilation, and carrying out haulage operations. In hydropower development, diversion tunnels carry water from reservoirs to turbines, while utility tunnels are used for space wherever water, gas, and data had to be conveyed. Notwithstanding such, because of the strategic importance, such projects often bear upon themselves issues regarding complex designs, construction risks, safety, and large maintenance costs.

Digital twin (DT) technology involves creating a virtual replica of a physical system, which can be used for monitoring, analyzing, and optimizing the real-world counterpart. This technology is increasingly being applied in various sectors to enhance operational efficiency and safety. DT technology can be utilized in various stages of tunneling projects, delivering many benefits throughout the life cycle from design to maintenance. During the design process, DT facilitates the generation of precise virtual representations of tunnels for planning and detailed design verification, which can reveal possible problems before physical construction (Zhang et al., 2024; Zhao et al., 2024). DT also permits simulation of various construction scenarios to check adherence to safety regulations and streamline design decisions without physical trials(Diren & Althen, 2023).

During construction, DT aggregates data from various sources such as IoT sensors, GNSS technology, and 3D modeling to provide real-time monitoring and control, reducing on-site inspection and minimizing errors (Cheng et al., 2024; Xu et al., 2023). Additionally, DT maximizes safety management through continuous monitoring of unsafe habits, machinery status, and environmental conditions, improving overall on-site safety performance(Attar et al., 2024; Zou & Ma, 2023). In Tunnel Boring Machine (TBM) construction, DT applies intelligent geological awareness to predict and manage subsurface conditions, ensuring safer excavation and efficiency (Xu et al., 2023).

Throughout the operation and maintenance period, DT facilitates digital maintenance of tunnels through the integration of surveillance data to create a virtual model of the structure, enabling efficient traffic management,

[*] Corresponding author, E-mail: Roudini@ktu.edu.tr

https://doi.org/10.31462/icearc2025_ce_mng_306

golden light publishing

rapid accident response, and systematic facility maintenance (Wu et al., 2022). Further, DT architectures for rail tunnels integrate data flow and application processes to enhance the intelligence and efficiency of maintenance operations, including state perception, data analysis, and decision support (Zhao & Ma, 2024). By integrating data from all phases of the tunnel's lifecycle, from design and construction through to operation and maintenance, DT systems provide a comprehensive perspective to guide decision-making and optimize resource allocation (Maxwell & Grasmick, 2021;Wu et al., 2025).

Despite these advantages, full realization of DT in tunneling projects is hindered by challenges related to data integration and standardization among heterogeneous stages and systems, and the need for harmonized standards and improved data collection practices (Li et al., 2024; Zhang et al., 2024). Future research is therefore aimed at integrating emerging technologies such as 5G communications, artificial intelligence, and cloud computing to continue enhancing the functionality and scalability of DT in tunneling applications(Li et al., 2024; Xu et al., 2023).

In the this study, an effort is made to present a comprehensive review of existing applications and advantages of DT technology throughout the whole lifecycle of tunnel projects encompassing the design stage, construction process, operation process, and maintenance stage. The study also categorizes the real-life applications of DT, assesses real-time monitoring and risk reduction ability, and highlights current research trends. In doing so, it also identifies knowledge gaps that already exist, most significantly those related to data integration, interoperability, and lack of representation of DT applications in initial design or terminal maintenance. Finally, this paper provides future research directions by proposing directions for increasing the use of DT and the utilization of future digital technologies such as AI, 5G, and cloud computing in tunneling applications.

2. Research methodology

This research aims to identify current research trends in the application of digital twin technology in tunneling projects across their design, construction, operation, monitoring, and inspection phases. The objective is to gain a clearer understanding of the current state of adoption, the challenges encountered, and the potential future directions of digital twin integration in tunnel engineering. The main steps of the systematic literature review presented in this study include the formulation of research questions, development of the search protocol including query and database selection, definition of screening and inclusion/exclusion criteria, and synthesis and analysis of the retrieved information.

The review focuses on addressing the following research questions:

1- How and within which main phases (design, construction, operation, monitoring, and inspection) has digital twin technology been adopted in tunneling projects?
2- What are the main challenges and advantages reported when applying digital twin technology in tunneling?
3- How has the research and application of digital twins in tunneling evolved over time?

Research question 1 investigates the main lifecycle phases of tunnels where digital twin technology has been applied to better understand the focus areas of current research. Research question 2 aims to capture the main reported benefits and limitations encountered in practical and experimental applications of digital twins in tunneling projects. Research question 3 aims to synthesize the evolution of digital twin applications in tunneling over time and identify trends and gaps for future research.

The search was conducted for publications from the year 2012 up to April 15th, 2025, in the Scopus database, which was selected for its extensive coverage of peer-reviewed literature in engineering, construction, and technology disciplines. The search query used is presented below:

TITLE-ABS-KEY (("digital_twin") AND ("tunnel") AND ("design" OR "construction" OR "operation" OR "monitoring" OR "inspection")) AND (EXCLUDE (LANGUAGE, "Chinese") OR EXCLUDE (LANGUAGE, "German")) AND (EXCLUDE (EXACTKEYWORD, "Wind Stress") OR EXCLUDE (EXACTKEYWORD, "Wind-tunnel Testing") OR EXCLUDE (EXACTKEYWORD, "Air Navigation") OR EXCLUDE (EXACTKEYWORD , "Air Transportation") OR EXCLUDE (EXACTKEYWORD , "Aircraft Models") OR EXCLUDE (EXACTKEYWORD , "Wind Tunnels")

The search targeted articles that mention the digital twin concept explicitly linked to tunneling projects across different lifecycle stages, while excluding studies related to wind-tunnel testing, aviation, or aerodynamics that were irrelevant to the focus of this study.The search protocol consisted of the following sets:

- *Keywords for technology:* "digital twin"
- *Keywords for domain:* "tunnel"
- *Keywords for lifecycle phases:* "design", "construction", "operation", "monitoring", "inspection"

Each set was combined using the AND operator to ensure that papers contained at least one keyword from each conceptual group. Irrelevant topics and unrelated languages were filtered out through EXCLUDE operators.

By applying the defined search query and inclusion criteria, a total of 139 papers were retrieved from the Scopus database. Following a review of the titles and abstracts, 99 papers were identified as relevant and selected for detailed analysis of research areas and trends. The overall process of the literature search and selection is illustrated in Fig. 1.

3. Systematic review

3.1. Classification of literature

A total of 139 papers were retrieved based on the defined search query and inclusion criteria. After reviewing the titles and abstracts, 99 papers were identified as relevant for a detailed analysis of the research areas and trends, while 40 papers were deemed irrelevant and excluded. The distribution of relevant papers across different years is summarized in Fig. 2. A notable increase in the number of relevant publications was observed in recent years, particularly from 2020 onwards. The number of relevant papers progressively grew, with a significant rise in 2023 and 2024, reflecting a surge in research interest and advancements in digital twin technology applied to tunneling and related construction processes.

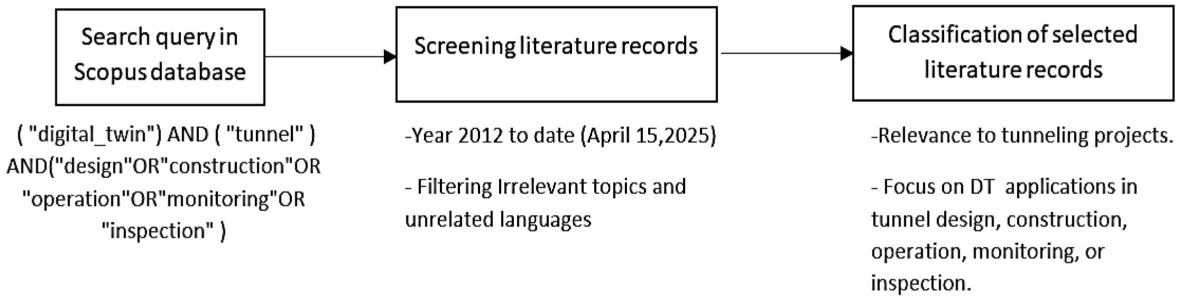

Fig. 1. Framework for literature retrieval and analysis

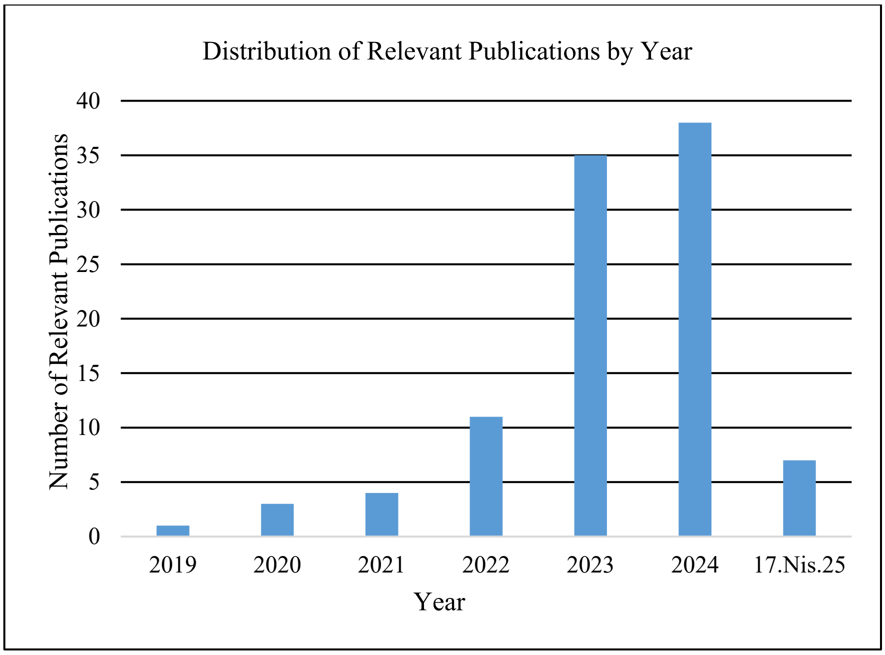

Fig. 2. Annual distribution of relevant publications related to the application of digital twin in tunneling projects

3.2. Keyword co-occurrence analysis

A keyword co-occurrence analysis was performed in order to identify the main research topics and relations between main topics in the selected literature. The visualization map, created using VOSviewer, displays several clusters demonstrating closely related research areas (Fig. 3).

- The keyword "digital twin" comes as the primary and prevailing term, reflecting its central significance along the whole period of the research. Around "digital twin," several significant clusters could be seen.
- An information and technology-based cluster (green) linking "technology," "infrastructure development," "challenge," and "research," indicating high interest in the development and application of digital twin technology for tunneling and infrastructure projects.

- A cluster of modeling and performance (red) linking "model," "efficiency," "performance," "problem," and "digital," indicating research aimed at developing digital twin models to enhance operational performance and efficiency.
- A cluster of project and information management (blue) centered on "project," "risk," "information," and "analysis," indicating a focus on the application of digital twins in project management, risk analysis, and information analysis.
- A small cluster concerning methodology and structure (yellow-green) indicates research founded upon the methodological frameworks employed in the application of digital twins in tunneling projects.

The complex interconnections among keywords echo the multidisciplinary character of digital twin solutions for tunneling, encompassing elements of engineering design, project management, technological development, and operational enhancement.

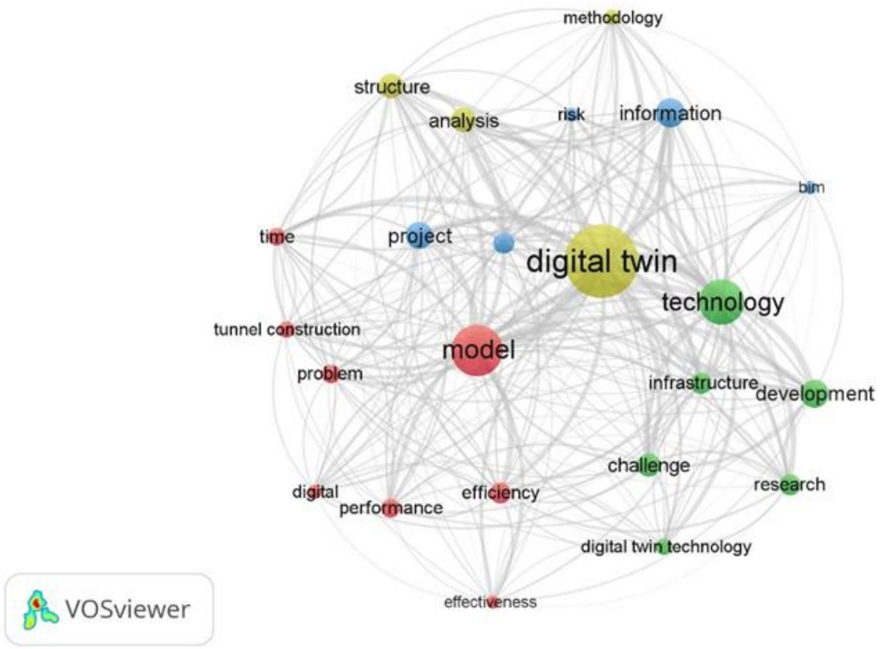

Fig. 3. Keyword co-occurrence network map of the selected literature, created using VOSviewer

4. Results and discussion

The distribution of applications according to the project phase is illustrated in Fig. 4. The most researched phase is construction, with 19 studies aimed at DT solution application in this phase. This is followed by applications during the entire lifecycle (14 studies), operation and maintenance (13 studies), and combined design and construction phases (9 studies). The quantity of studies exclusively on maintenance (7 studies) or just design (3 studies) was less.

This distribution illustrates that the construction phase continues to be the key area of ongoing DT research within tunneling construction projects. Such focus is perhaps expected in view of the pressing need for acquiring real-time data, monitoring, and decision-making processes during the process of excavation work. Still, the shifting interest towards lifecycle, operational, and maintenance phases signifies the greater realization of the value proposition of DTs as far as ensuring long-term asset management, predictive maintenance, and risk management measures are concerned. The lack of research particularly focusing on the design stage suggests a research gap, offering opportunities for future studies to examine how the integration of DT in the early stages can be used to improve project planning and lifecycle performance.

More detailed analysis identified ten research clusters with distinct differences between them, mirroring the diversity of DT applications to tunneling and underground infrastructure. The clusters, their key applications, and associated key authors are listed in Table 1. From Table 1, DT research on tunneling can be divided into some principal clusters. Visualization & Inspection explores 3D and VR-based systems for asset inspection and stakeholder communication. Maintenance & Asset Management deals with digital maintenance planning, O&M decision support, and lifecycle asset management. Safety & Risk Assessment uses DTs for safety risk prediction, deformation monitoring, and hazard simulation.

The results indicate that DT technology in tunneling projects is primarily applied in the construction phase, enhancing real-time monitoring, safety, and excavation efficiency. However, there is a clear trend toward integrating DT across the entire project lifecycle, especially in maintenance and asset management, where it improves decision-making and optimizes long-term operations. Despite these advancements, areas like Tunnel Boring Machine (TBM) applications and early design phase integration remain underexplored. Table 2 summarizes the application and benefits of DT across different phases of tunneling projects, highlighting its growing impact. Real-world projects, such as Crossrail and the Brenner Base Tunnel, demonstrate the practical benefits of DT, indicating its transformative potential in the industry.

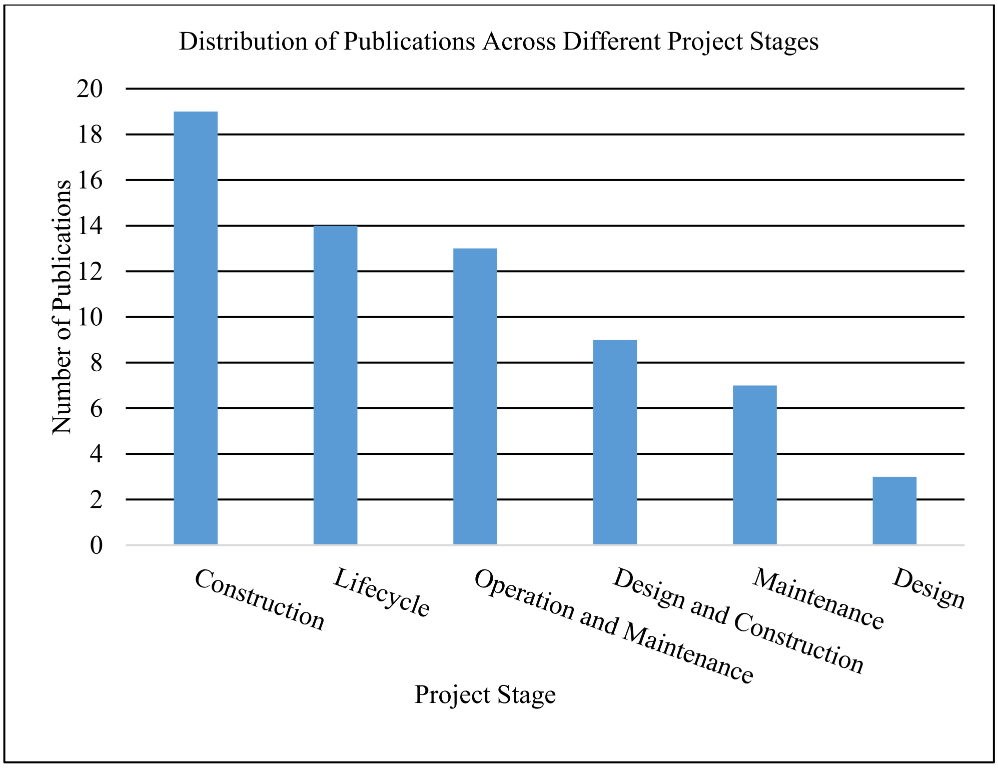

Fig. 4. Distribution of relevant publications across different stages of tunneling projects

Table 1. Detailed clusters on Digital Twin (DT) applications in tunneling, with core focuses and key authors

Cluster	Core Application(s)	Authors
Modeling & Simulation	High-fidelity modeling, scenario testing, maturity evaluation, ontology & graph-based modeling	(Liang et al., 2024), (Zhao et al., 2024), (Li, Rui, Zhao, et al., 2024), (Li, Rui, et al., 2024), (Li, Li, et al., 2024), (Beigel et al., 2024), (Wang et al., 2024), (Sakr & Sadhu, 2024)
Construction Monitoring & Control	Real-time monitoring, status update, excavation control, JIT design	(Fang et al., 2024), (Latif et al., 2023), (Zhang, et al., 2024), (Cheng et al., 2024), (Liu et al., 2024), (Li et al., 2023), (Chang et al., 2022), (Zendaki et al., 2024), (Hegemann et al., 2023)
Visualization & Inspection	3D/VR visualization, inspection, virtual-real fusion	(Wu et al., 2022), (McDonald et al., 2022), (Ding et al., 2024), (Traxler & Chmelina, 2023), (Li, et al., 2024)
Maintenance & Asset Management	Digital maintenance, O&M decision support, ventilation/lighting control, planning	(Yang et al., 2024), (Yu et al., 2023),(Zhou et al., 2024), (Tomar et al., 2019), (Spallarossa & Pasqualato, 2024), (Chen et al., 2023), (Sanfilippo et al., 2023), (Diren & Althen, 2023), (Rezakhani & Kim, 2023)

Table 2. Continued

Safety & Risk Assessment	Safety risk assessment, deformation prediction, hazard simulation	(Zhao et al., 2022), (Feng et al., 2024), (He et al., 2024), (Gu et al., 2023), (Fukuda et al., 2023)
Intelligent Geological & Rock Analysis	Geological perception, rock mass classification, advanced grouting	(Martens et al., 2022), (Song et al., 2023), (Wang et al., 2021), (Delport et al., 2023)
Specialized TBM & Robotic Systems	TBM tool-replacing, robotic simulation, performance learning	(Liu et al., 2023), (Gannouni et al., 2023)
Cybersecurity & Output Control	Attack simulation, belief rule base for operational control	(Masi et al., 2023), (Chang et al., 2022)
Multimodal Data Fusion & Feature Extraction	Sensor fusion, point cloud & imagery, feature extraction	(Lee et al., 2023), (Yang et al., 2024)
Concept & Platform Development	Interactive concept creation, holistic platforms	(Bauer & Lienhart, 2023), (Zhou et al., 2022), (Lu et al., 2024), (Petschen et al., 2023)

Table 3. Applications and benefits of Digital Twin technology across the lifecycle of tunneling projects

Lifecycle stage	Applications for digital twin	Benefits
Design	High-fidelity modeling, simulation, and scenario testing	Identifies potential issues early, optimizes design choices
Construction	Real-time monitoring, safety management, intelligent geological perception	Reduces on-site errors, enhances safety, ensures efficient excavation
Operation & maintenance	Digital maintenance, intelligent operation and maintenance, lifecycle data integration	Improves management efficiency, supports intelligent decision-making, provides comprehensive view

5. Applications of DT in some tunneling projects

5.1. Application of DT in hypertunnel innovative tunneling method

The application of DT technology in hyperTunnel's innovative tunneling method revolutionizes traditional underground construction by integrating advanced AI, swarm robotics, and real-time data. Unlike conventional methods where a hole is dug first, hyperTunnel 3D-prints the tunnel structure inside the ground, using a digital twin to guide the process(Fig. 5-a). A fleet of hyperBot robots, guided by the digital twin, operates in parallel along the tunnel path (Fig. 5-b), enhancing productivity and reducing construction time. These robots perform tasks such as drilling, cutting, and material deployment through a collaborative swarm method. The digital twin provides a rich, data-driven representation of the tunnel and surrounding geology, which supports real-time monitoring, virtual reality (VR) training, and predictive maintenance. This integrated system minimizes uncertainty, cuts costs, and ensures faster, safer, and more sustainable tunneling. By merging advanced technologies, hyperTunnel transforms how tunnels and underground structures are designed, built, and maintained, promising substantial efficiency gains over traditional methods (URL1).

5.2. Application of DT in Wuhan Metro Line 2 Phase I (China)

The application of Digital Twin (DT) technology in Wuhan Metro Line 2 Phase I represents a significant advancement in urban transportation management. The Smart Metro Service Platform (SMSP), as illustrated in Fig. 6 (Zhou et al., 2024), integrates physical tunnel data with virtual models and real-time sensor inputs to monitor key parameters such as settlement, convergence, leakage, and structural degradation of the metro tunnels. This system is crucial for assessing and managing the long-term structural performance of the metro's underground infrastructure, which spans 60.8 km with Phase I operational since 2012. By leveraging DT technology, the SMSP enhances operations and maintenance (O&M) capabilities by providing early warnings and predictive maintenance insights, thus improving the overall lifecycle management of the tunnels. This proactive approach ensures the safety and service quality of the metro system, effectively mitigating risks posed by geological and train-induced stresses. The integration of DT in the Wuhan Metro demonstrates its potential to optimize maintenance practices and extend the lifespan of critical urban infrastructure.

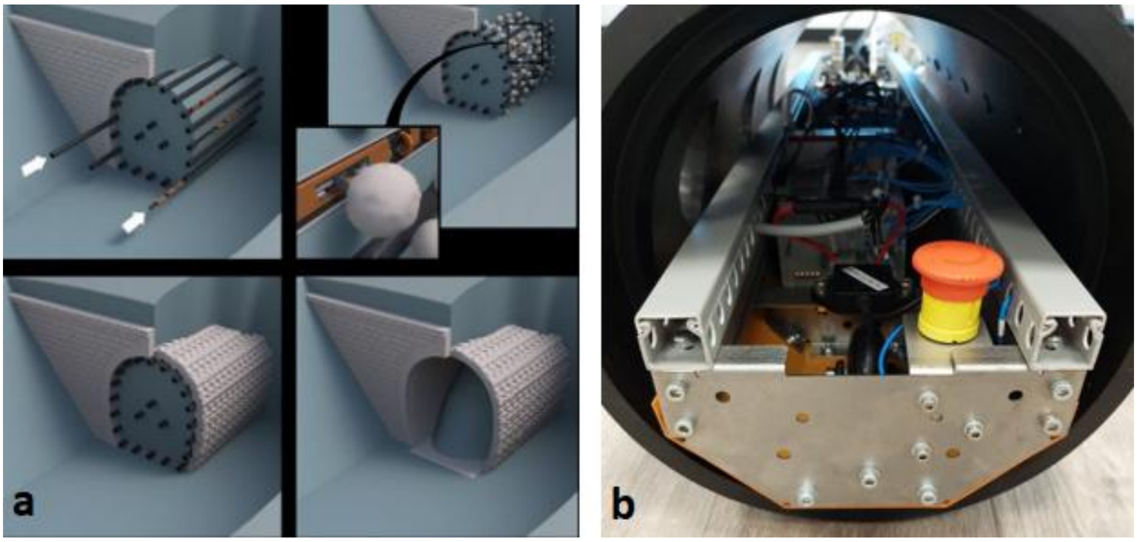

Fig. 5. a) HyperTunnel 3D-prints the structure inside the ground, working with a digital twin b) Using swarm construction methods according to a digital twin of the tunnel, a fleet of 'hyperBot' robots enters the ground via an arch of HDPE pipes (credit: hyperTunnel)

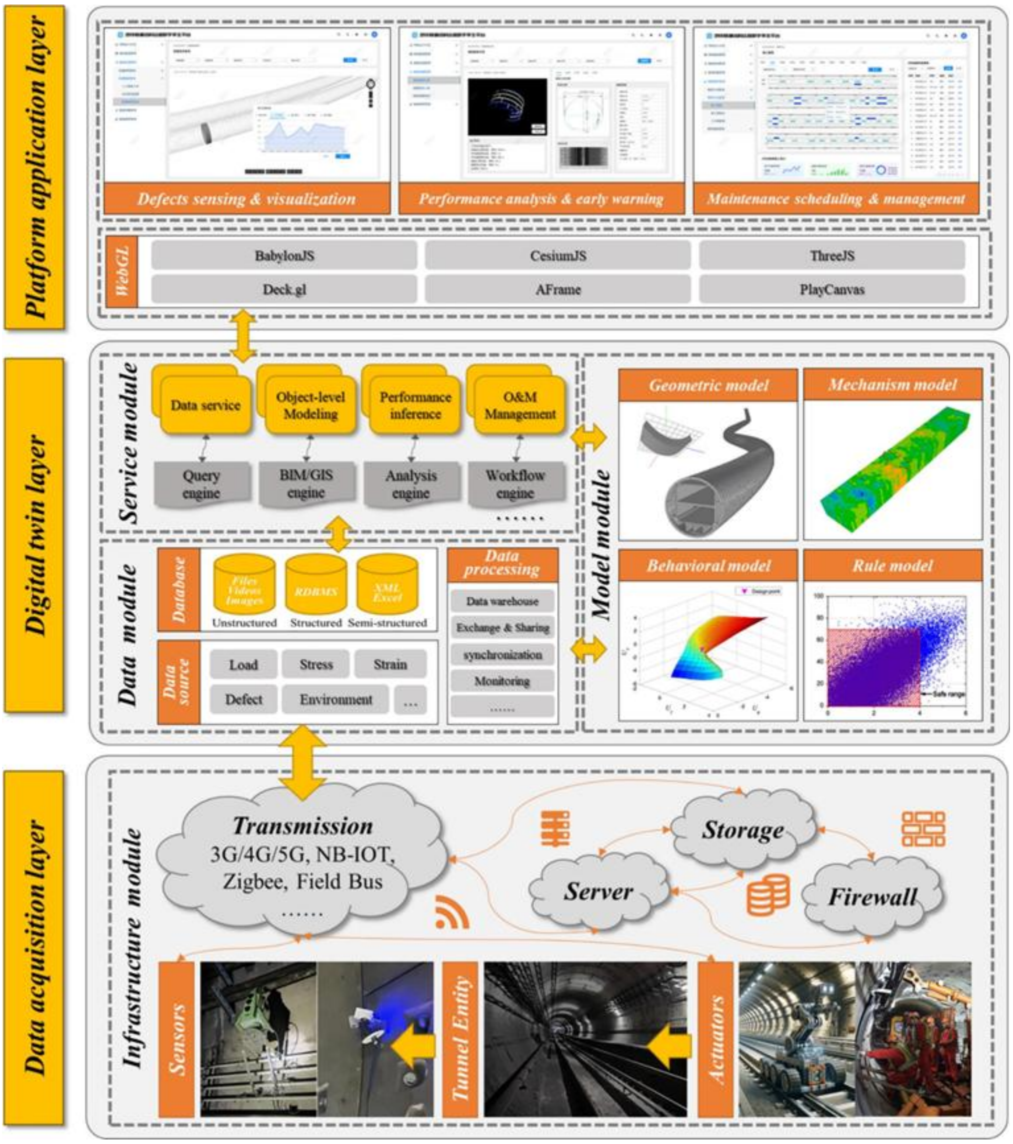

Fig. 6. Applied Smart metro service platform framework for Wuhan Metro Line 2 Phase I (Zhou et al., 2024)

Table 3 summarizes various tunneling projects that have implemented Digital Twin (DT) technology to enhance tunnel construction, operation, and maintenance. Notable examples include the Grand Canyon Tunnel in China, which uses DT for automatic rock grade identification and dynamic support (Zhu et al., 2021), and the Swalmen Tunnel in the Netherlands, where DT supports supervisory controller design during renovation (Van Hegelsom et al., 2021). Other applications span pavement performance prediction, remote inspection, automated excavation assessment, and intelligent asset management, with projects such as the Guizhou Tunnel and Altona Tunnel employing DT for lifecycle management and system integration (Fang et al., 2024; Diren & Althen, 2023). These implementations highlight DT's growing role in improving tunnel safety, efficiency, and maintenance across different regions and project phases.

Table 4. Summary of tunneling projects that have adopted Digital Twin (DT) technology

Tunnel Name	Application of Digital Twin (DT)	Author(s)
Grand Canyon Tunnel (Sichuan Ehan High-Speed Project, China)	Automatic identification of surrounding rock grade and digital dynamic support	URL2
Swalmen Tunnel (Netherlands)	Supervisory controller design support during renovation	Hegelsom et al., (2021).
Dalian Highway Tunnel (Shanghai, China)	Pavement performance prediction via MTSS for lifecycle management	Yu et al., (2020).
Wuxi Qingqi Tunnel (China)	Electromechanical DT system using IoT and BIM for 3D monitoring and remote inspection	China Jiangsu Net.
Guizhou Tunnel Project (China)	'Status' DT for automated over-and-under excavation assessment using BIM and point cloud data	Fang et al., (2024).
Zizhi Tunnel (Hangzhou) (China)	BIM-based construction system; groundwork for DT using 3D Tunnel Information Model	Wang et al., (2015).
Tunnel Laboratory 01 (TL 01) (Brazil)	Tunnel performance prediction and condition monitoring using visual inspection data to build a digital inspection twin	Machado & Futai, (2024).
Sipicciano & Collecervo Tunnels (Italy)	Digital twins created from ARCHITA multi-dimensional survey system for tunnel management planning and design	Foria et al., (2023).
Altona Tunnel (Germany)	Managed digital twin integrating BIM, asset and traffic management, and simulation	Diren & Althen, (2023).
Tunnel Schöneich (Zurich)	DT for improved operation and maintenance workflows using laser scanning and BIM	Sanfilippo et al., (2023).
Niu Tingling Tunnel (Lishui, Zhejiang) (China)	Intelligent O&M of electromechanical equipment using digital twin	Chen et al., (2023).

6. Conclusions

Based on the systematic literature review using the Scopus database, this study examined the applications and benefits of Digital Twin (DT) technology across the tunnel project lifecycle.

The review found a significant increase in publications on DT in tunneling, especially since 2020. Currently, the construction phase is the most researched area, reflecting its need for real-time monitoring and decision-making during excavation. However, there is a growing trend towards applying DT across the entire project lifecycle, particularly in operation and maintenance, for long-term asset and risk management. A research gap was identified specifically in the initial design and terminal maintenance stages.

Digital Twin technology offers substantial benefits throughout the tunnel lifespan. In design, it aids in planning and simulation to identify issues early and optimize choices. During construction, DT enables real-time monitoring, enhances safety, and improves excavation efficiency. For operation and maintenance, it supports efficient management and decision-making. These applications contribute to overall effectiveness, safety, and sustainability. Real-world examples demonstrate DT's practical benefits.

Despite these benefits, challenges, primarily related to data integration and standardization, hinder the full realization of DT's potential. Future research should focus on integrating emerging technologies like 5G, AI, and cloud computing and expanding DT applications into the underexplored design and terminal maintenance areas.

Acknowledgments
The research described in this paper was conducted without any financial support. No funding was received from any agency, foundation, or institute for the development of this work.

References

Attar, K.M., Abbasianjahromi, H., & Poshdar, M. (2024). Digital Twins for improving the construction safety: literature content analysis and gap spotting for future directions. *Iranian Journal of Science and Technology Transactions of Civil Engineering, 48*(4), 1887–1901 https://doi.org/10.1007/s40996-024-01495-6

Bauer, P., & Lienhart, W. (2022). 3D concept creation of permanent geodetic monitoring installations and the a priori assessment of systematic effects using Virtual Reality. *Journal of Applied Geodesy, 17*(1), 1–13. https://doi.org/10.1515/jag-2022-0020

BDigital_Admin, & BDigital_Admin. (2022, November 16). Digital twins will revolutionise tunnelling. Build in Digital. https://buildindigital.com/digital-twins-will-revolutionise-tunnelling/

Beigel, A., Strauss, A., Frangopol, D.M., & Cao, M. (2024). Limits of digital twin modelling. In: *CRC Press eBooks* (pp. 777–784) https://doi.org/10.1201/9781003483755-90

Chen, F., Zhang, Y., & Deng, M. (2023). Research on the Application of Digital Twin in the Operation and Maintenance of Electromechanical Equipment in Highway Tunnels. In: *2023 2nd International Conference on Artificial Intelligence and Intelligent Information Processing (AIIIP)*, Hangzhou, China, 2023 (pp. 310–315). https://doi.org/10.1109/aiiip61647.2023.00066

Cheng, W., Pan, Y., Ma, Z., Cai, Y., Li, Y., & Peng, T. (2024). Tunnel construction site monitoring and digital twin system. In: *2024 26th International Conference on Advanced Communications Technology (ICACT),* Pyeong Chang, Korea. https://doi.org/10.23919/icact60172.2024.10471763

Delport, T., McCosh, J., & Nowak, K. (2023). Geotechnical analysis of adapted permeation and compaction grouting techniques for detailed design and construction of underground structures. In: *CRC Press eBooks* (pp. 252–259). https://doi.org/10.1201/9781003348030-31

Ding, X., Chen, S., Duan, M., Shan, J., Liu, C., & Hu, C. (2024). Towards 3D reconstruction of Multi-Shaped tunnels utilizing mobile laser scanning data. *Remote Sensing, 16*(22), 4329 https://doi.org/10.3390/rs16224329

Diren, N., & Althen, S. (2023). Tunnel 4.0: Managed digital twin for tunnel operations. In: *CRC Press eBooks* (pp. 2635–2642) https://doi.org/10.1201/9781003348030-317

Fang, W., Chen, W., Love, P. E., Luo, H., Zhu, H., & Liu, J. (2024). A status digital twin approach for physically monitoring over-and-under excavation in large tunnels. *Advanced Engineering Informatics, 62*, 102648 https://doi.org/10.1016/j.aei.2024.102648

Feng, Z., Wang, J., Liu, W., Li, T., Wu, X., & Zhao, P. (2024). Data-driven deformation prediction and control for existing tunnels below shield tunneling. *Engineering Applications of Artificial Intelligence, 138*, 109379 https://doi.org/10.1016/j.engappai.2024.109379

Fukuda, T., Yoshikawa, S., Hosono, K., & Iwanaga, S. (2023). Development of a ground forecasting system based on the geological and groundwater conditions in mountain tunneling. In: *CRC Press eBooks* (pp. 2660–2669) https://doi.org/10.1201/9781003348030-320

Gannouni, A., Naqwi, A., Zhou, H.A., Abdelrazeq, A., Hees, F., & Schmitt, R.H. (2023). Experimental digital twin of a tunnel ring building erector. In: *IEEE EUROCON 2023-20th International Conference on Smart Technologies*, Torino, Italy, 2023 (pp. 60–65) https://doi.org/10.1109/eurocon56442.2023.10198935

Gu, Y., Zhang, L., Ai, Q., Jiang, X., & Yuan, Y. (2023). Digital twin-oriented maintenance: A hybrid finite element and surrogate model approach for predicting the excavation-induced tunnel displacement. In: *CRC Press eBooks* (pp. 600–607) https://doi.org/10.1201/9781003323020-72

He, Y., Ding, Y., Zhu, Q., Wu, H., Guo, Y., Wang, Q., & Zhou, R. (2024). Reliable simulation analysis for high-temperature inrush water hazard based on the digital twin model of tunnel geological environment. *Tunnelling and Underground Space Technology, 154*, 106110 https://doi.org/10.1016/j.tust.2024.106110

Hegemann, F., Stascheit, J., Maidl, U., Gangrade, R., & Kottke, P. (2023). Generating a digital twin for tunneling projects during the construction phase. In: *CRC Press eBooks* (pp. 2701–2709) https://doi.org/10.1201/9781003348030-325

Latif, K., Sharafat, A., & Seo, J. (2023). Digital Twin-Driven Framework for TBM Performance Prediction, Visualization, and Monitoring through Machine Learning. *Applied Sciences, 13*(20), 11435 https://doi.org/10.3390/app132011435

Lee, J., Lee, Y., Park, S., & Hong, C. (2023). Geospatial feature extraction based on multimodal image sensor by implementing a digital twin of underground utility tunnel. In: *2023 IEEE Smart World Congress (SWC),* Portsmouth, United Kingdom, 2023, (pp. 1–8) https://doi.org/10.1109/swc57546.2023.10448570

Li, T., Li, X., Rui, Y., Ling, J., Zhao, S., & Zhu, H. (2023). Digital twin for intelligent tunnel construction. *Automation in Construction, 158*, 105210. https://doi.org/10.1016/j.autcon.2023.105210

Li, T., Rui, Y., Zhao, S., Zhang, Y., Zhu, H., & Li, X. (2024). A quantitative digital twin maturity model for underground infrastructure based on D-ANP. *Tunnelling and Underground Space Technology, 146*, 105612 https://doi.org/10.1016/j.tust.2024.105612

Li, T., Rui, Y., Zhu, H., Lu, L., & Li, X. (2024). Comprehensive digital twin for infrastructure: A novel ontology and graph-based modelling paradigm. *Advanced Engineering Informatics, 62*, 102747 https://doi.org/10.1016/j.aei.2024.102747

Li, X., Tang, L., Ling, J., Chen, C., Shen, Y., & Zhu, H. (2023). Digital-twin-enabled JIT design of rock tunnel: Methodology and application. *Tunnelling and Underground Space Technology, 140*, 105307 https://doi.org/10.1016/j.tust.2023.105307

Li, Y., Xiao, Z., Li, J., & Shen, T. (2023). Integrating vision and laser point cloud data for shield tunnel digital twin modeling. *Automation in Construction, 157*, 105180 https://doi.org/10.1016/j.autcon.2023.105180

Liang, C., Zhu, J., Zhang, J., Zhu, Q., Lu, J., Lai, J., & Wu, J. (2024). A Knowledge-Guided Intelligent Analysis Method of Geographic Digital twin Models: A case study on the diagnosis of geometric deformation in tunnel excavation profiles. *International Journal of Geo-Information, 13*(3), 78 https://doi.org/10.3390/ijgi13030078

Liu, J., Yuan, J., Du, L., & Bao, S. (2023). Digital twin system for robotic tool-replacing in tunnel boring machine. *2021 IEEE International Conference on Robotics and Biomimetics (ROBIO)*, 1–6 https://doi.org/10.1109/robio58561.2023.10354924

Liu, Z., Fang, Q., Shen, Y., Ai, Q., Wang, H., Huang, X., & Yuan, Y. (2024). Two-stage surrogate modeling strategy for predicting foundation pit excavation-induced strata and tunnel deformation. *Tunnelling and Underground Space Technology, 151*, 105845 https://doi.org/10.1016/j.tust.2024.105845

Lu, H., Yu, H., Yan, S., & Li, S. (2024). Key Technologies study on Digital Twin Platform for Comprehensive Utility Tunnel. *2022 IEEE 5th Advanced Information Management, Communicates, Electronic and Automation Control Conference (IMCEC)*, 931–936 https://doi.org/10.1109/imcec59810.2024.10575808

Martens, J., Blut, T., & Blankenbach, J. (2022). Cross Domain Matching for Semantic Point Cloud Segmentation based on Convolutional Neural Networks. *29th International Workshop on Intelligent Computing in Engineering*, EG-ICE 2022 Aarhus, 186–195 https://doi.org/10.7146/aul.455.c209

Masi, M., Sellitto, G.P., Aranha, H., & Pavleska, T. (2023). Securing critical infrastructures with a cybersecurity digital twin. *Software & Systems Modeling, 22*(2), 689–707 https://doi.org/10.1007/s10270-022-01075-0

Maxwell, A., & Grasmick, J. (2021, June 13–16). Quantification of tangible and intangible benefits of digitalization in tunnel construction. In: *Proceedings of the Rapid Excavation and Tunneling Conference (RETC 2021),* (pp. 854–863). Las Vegas, NV

McDonald, T., Robinson, M., & Tian, G.Y. (2022). Developments in 3D visualisation of the rail tunnel subsurface for inspection and monitoring. *Applied Sciences, 12*(22), 11310 https://doi.org/10.3390/app122211310

Petschen, V., Brandt, R., Celebi, O., Wyss, R., & Elkuch, N. (2023). Tunnel Digitalization Center – Beyond BIM in underground construction. In: *CRC Press eBooks* (pp. 2861–2868) https://doi.org/10.1201/9781003348030-345

Rezakhani, M., & Kim, S. (2023). Utilizing Web Applications for Developing Digital Twin: Case study urban tunnel with kinetic roof. *eCAADe Proceedings, 2*, 791–800 https://doi.org/10.52842/conf.ecaade.2023.2.791

Sakr, M., & Sadhu, A. (2024). Recent progress and future outlook of digital twins in structural health monitoring of civil infrastructure. *Smart Materials and Structures, 33*(3), 033001 https://doi.org/10.1088/1361-665x/ad2bd7

Sanfilippo, R., Canini, P., Carrera, E., Neidhart, M., Eberle, R., & Wieland, M. (2023). The digitalization of the Tunnel Schöneich-Using a digital twin to improve operation and maintenance workflows of an existing road tunnel. In: *CRC Press eBooks* (pp. 2877–2884) https://doi.org/10.1201/9781003348030-347

Song, S., Xu, G., Bao, L., Xie, Y., Lu, W., Liu, H., & Wang, W. (2023). Classifying the surrounding rock of tunnel face using machine learning. *Frontiers in Earth Science, 10* https://doi.org/10.3389/feart.2022.1052117

Spallarossa, E., & Pasqualato, G. (2024). Digital Twin and Asset Management for Italian highways decision support towards scheduled maintenance, repair and rehab. *Procedia Structural Integrity, 62*, 241–249 https://doi.org/10.1016/j.prostr.2024.09.039

Tomar, R., Piesk, J., Sprengel, H., Isleyen, E., Duzgun, S., & Rostami, J. (2019). Digital twin of tunnel construction for safety and efficiency. In: *CRC Press eBooks* (pp. 3224–3234) https://doi.org/10.1201/9780429424441-341

Traxler, C., & Chmelina, K. (2023). Storytelling as collaboration support for 3D tunnel monitoring. In: *CRC Press eBooks* (pp. 2552–2559) https://doi.org/10.1201/9781003348030-307

URL1: BDigital_Admin. (2022, November 16). Digital twins will revolutionise tunnelling. Build in Digital. Retrieved April 29, 2025, from https://buildindigital.com/digital-twins-will-revolutionise-tunnelling/

Wang, J., Li, P., Li, X., & Zhu, H. (2021). Complex 3D geological modeling based on digital twin. *IOP Conference Series Earth and Environmental Science, 861*(7), 072046 https://doi.org/10.1088/1755-1315/861/7/072046

Wang, Y., Chen, Z., Zhang, C., Hu, H., Zhang, Z., & Zhu, M. (2024). Digital Twin-Driven Smart Transportation Infrastructure: Connotation, reference model, applications and research issues. *2022 IEEE International Conference on Industrial Technology (ICIT), 1*, 1–6 https://doi.org/10.1109/icit58233.2024.10540741

Wu, D., Zheng, A., Yu, W., Cao, H., Ling, Q., Liu, J., & Zhou, D. (2025). Digital Twin Technology in Transportation Infrastructure: A Comprehensive survey of current applications, challenges, and future directions. *Applied Sciences, 15*(4), 1911 https://doi.org/10.3390/app15041911

Wu, Z., Chang, Y., Li, Q., & Cai, R. (2022). A novel method for tunnel digital twin construction and Virtual-Real fusion application. *Electronics, 11*(9), 1413 https://doi.org/10.3390/electronics11091413

Xu, Z., Wang, Z., Zhang, J., Yu, D., Lin, P., Zhang, X., Pan, D., & Li, T. (2023). Geological Perception and Digital Twin of Rock and Machine for TBM Tunnelling: Methods-Research Status-Digital and Intelligent Development Direction. *Yingyong Jichu yu Gongcheng Kexue Xuebao/Journal of Basic Science and Engineering, 31*(6), 1361–1381 https://doi.org/10.16058/j.issn.1005-0930.2023.06.002

Yang, X., Yu, S., Wang, J., Chen, H., Huang, Y., Luo, Z., & Fu, L. (2024). Application of a digital twin for highway tunnels based on multi-sensor and information fusion. *Frontiers in Physics, 12*. https://doi.org/10.3389/fphy.2024.1335494

Yu, G., Lin, D., Wang, Y., Hu, M., Sugumaran, V., & Chen, J. (2023). Digital Twin-enabled and Knowledge-driven decision support for tunnel electromechanical equipment maintenance. *Tunnelling and Underground Space Technology, 140*, 105318 https://doi.org/10.1016/j.tust.2023.105318

Zendaki, Y., Cao, B., Stascheit, J., Alsahly, A., Freitag, S., Maidl, U., & Meschke, G. (2024). Coupling process controlling data and numerical simulation in mechanised tunnelling. *Geomechanics and Tunnelling, 17*(4), 324–331 https://doi.org/10.1002/geot.202400011

Zhang, L., Guo, J., Fu, X., Tiong, R.L.K., & Zhang, P. (2023). Digital twin enabled real-time advanced control of TBM operation using deep learning methods. *Automation in Construction, 158*, 105240 https://doi.org/10.1016/j.autcon.2023.105240

Zhao, P., & Ma, W. (2024). Key technologies and implementation method of intelligent operation and maintenance of railway tunnels based on digital twins. *Tunnel Construction, 44*(8), 1697–1712 https://doi.org/10.3973/j.issn.2096-4498.2024.08.017

Zhao, Y., Liu, Y., & Mu, E. (2024). A review of intelligent subway tunnels based on digital twin technology. *Buildings, 14*(8), 2452 https://doi.org/10.3390/buildings14082452

Zhao, Y., Wang, N., & Liu, Z. (2022). An established theory of digital twin model for tunnel construction safety assessment. *Applied Sciences, 12*(23), 12256 https://doi.org/10.3390/app122312256

Zhou, C., Qin, W., Luo, H., Yu, Q., Fan, B., & Zheng, Q. (2024). Digital twin for smart metro service platform: Evaluating long-term tunnel structural performance. *Automation in Construction, 167*, 105713 https://doi.org/10.1016/j.autcon.2024.105713

Zhou, S., Dumss, S., Nowak, R., Riegler, R., Kugu, O., Krammer, M., & Grafinger, M. (2022). A conceptual model-based digital twin platform for holistic large-scale railway infrastructure systems. *Procedia CIRP, 109*, 362–367 https://doi.org/10.1016/j.procir.2022.05.263

Zou, P.X.W., & Ma, S. (2023). Digital Twin technology for improving safety management in construction. In Lecture notes in operations research (pp. 40–56) https://doi.org/10.1007/978-981-99-3626-7_4

4th International Civil Engineering & Architecture Conference
17-19 May 2025, Trabzon, Türkiye

An analysis of course contents and educational materials in strengthening university-industry collaboration

Ediz Boz*[1], Vedat Toğan[2]

[1] Bayburt University, Aydıntepe Vocational School, Construction Technology Department, 69020 Bayburt, Türkiye
[2] Karadeniz Technical University, Department of Civil Engineering, 61080 Trabzon, Türkiye

Abstract. Rapidly evolving sector dynamics and technological advancements highlight the growing importance of university-industry collaboration. Incorporating stakeholder perspectives into students' education is crucial for institutions engaged in quality assurance and accreditation, such as the Higher Education Quality Council of Turkiye (YOKAK) and the Association for Evaluation and Accreditation of Engineering Programs (MUDEK). This study examines how civil engineering students relate their courses to practical applications, evaluate the adequacy of educational materials, and perceive their professional competence post-graduation. To achieve this, multiple-choice and semi-structured Likert-scale surveys were conducted, and the alignment of course content with industry needs was assessed. The findings reveal that courses like "Reinforced Concrete" and "Construction Management" are strongly linked to professional practice, yet traditional teaching methods in these courses are insufficient. Students recommended integrating advanced technologies such as virtual reality (VR) and augmented reality (AR) to improve educational effectiveness. Additionally, students reported difficulties in courses requiring three-dimensional thinking, such as "Steel Structures" and "Structural Analysis" and emphasized the value of modern technological integration. The results underscore the need for civil engineering programs to adapt to sectoral advancements and contribute to quality assurance processes. Updating course content and incorporating innovative technologies into education can better equip graduates for the workforce, strengthening the university-industry relationship and enhancing professional readiness.

Keywords: Civil engineering education; University-Industry collaboration; Construction management; Practical education

1. Introduction

In today's construction industry, continuous change and renewal are driven by technological advancements, sustainability requirements, and global competitive conditions. Training engineers who can adapt to this dynamic environment necessitates practice-oriented educational processes that go beyond the mere transmission of academic knowledge (Moezabadi, 2024). In this context, university-industry collaboration plays a pivotal role in civil engineering education. Such collaboration enables students to integrate theoretical knowledge with practical experience. While universities provide future engineers with a theoretical foundation in basic sciences, engineering principles, and design processes, industry partnerships offer opportunities to encounter real-world applications of this knowledge. This integration enhances students' professional competencies, contributing to their graduation as more prepared and qualified individuals who are ready to meet sectoral demands (Jonassen et al., 2006). Particularly, quality assurance and accreditation bodies such as the Higher Education Quality Council of Turkey (YOKAK) and the Association for Evaluation and Accreditation of Engineering Programs (MUDEK) define stakeholder involvement namely, the inclusion of industry representatives' perspectives and the subsequent updating of educational content accordingly as a key quality criterion (URL-1 & URL-2). In this regard, systematically reflecting current industry needs in engineering curricula not only increases the effectiveness of quality assurance processes but also strengthens the reputation of educational institutions within the sector.

In the field of civil engineering, gaining direct experience in areas such as site practices, construction management, project development, and engineering design significantly contributes to the development of students' problem-solving, decision-making, and leadership skills (Boz & Toğan, 2021). Moreover, internship programs, industry-led seminars, joint project collaborations, and simulation-based applications facilitated through university-industry partnerships enable students to enhance not only their technical knowledge but also essential professional competencies such as teamwork, communication, and ethical responsibility (Shah & Gillen, 2024).

* Corresponding author, E-mail: edizboz@bayburt.edu.tr

https://doi.org/10.31462/icearc2025_ce_mng_359

On the other hand, the industry benefits from these collaborations by actively contributing to the education of future engineers and supporting the development of a skilled workforce aligned with its needs (Murray, 2024). This mutual benefit necessitates the establishment of a sustainable collaboration model between universities and industry stakeholders. In civil engineering education, university-industry cooperation holds strategic importance not only in terms of individual student outcomes but also for the overall advancement of the sector, the prestige of the engineering profession, and broader societal development. Therefore, it is essential to promote the active involvement of industry partners in the design of educational programs, increase the availability of practice-oriented learning environments, and expose students to real-world problems at earlier stages of their education (Litzinger et al., 2011). Through such approaches, it becomes possible to cultivate innovative and responsible engineers who can effectively respond to the evolving needs of the construction industry.

Evaluating the extent to which undergraduate education meets industry expectations enables the anticipation of potential challenges graduates may encounter during their transition into professional life and allows for necessary improvements in educational programs. In this context, assessments based on students' self-perceptions provide valuable data for directly linking educational outcomes to industry needs. Similarly, gathering student feedback on which courses need to be better understood to meet industry expectations helps identify critical knowledge domains and prioritize course content. Such analyses are particularly useful in determining areas that should be prioritized for the development of applied engineering skills (Mukherji & Sisale, 2022). Moreover, questioning the adequacy and engagement level of traditional educational materials (chalkboards, textbooks, 2D slides) plays a significant role in enhancing course learnability and fostering the development of student-centered teaching approaches. Finally, identifying which courses should be supported by advanced educational technologies such as virtual reality (VR), augmented reality (AR), 3D modeling, and simulations offers concrete suggestions for the integration of next generation learning tools in engineering education (Suhail et al., 2024; de Carvalho, 2019). In this regard, the integration of technology into educational processes directly contributes to students' ability to concretize abstract concepts, visualize complex structural systems more effectively, and acquire the practical competencies demanded by the industry. Systematic analysis of these questions yields findings that can significantly contribute to the restructuring of civil engineering education programs in alignment with industry expectations, ultimately supporting efforts to train future engineers as more competent and well-equipped professionals.

The aim of this study is to analyze which courses civil engineering students associate with practical application in order to achieve success in professional practice, to evaluate the adequacy of current educational materials, and to assess students' self-confidence in performing their profession after graduation. In line with this objective, multiple choice and semi structured Likert type questionnaires were administered to students, and the alignment of course content with industry requirements was evaluated based on the collected data. Addressing the research questions within the scope of this study holds critical importance for both individual and institutional development in civil engineering education.

2. Method

There are certain limitations regarding the sample selected for this study. The participants consisted of senior students enrolled in the Department of Civil Engineering at Karadeniz Technical University (KTU). Senior students were chosen because they are nearing the completion of their education and have acquired at least one internship experience. Therefore, fourth-year civil engineering students were considered the most appropriate sample group to evaluate the contribution of course content and educational materials to the enhancement of university-industry collaboration. A total of 173 students participated in the study, of whom 136 were male and 37 were female. Among the participants, 132 were enrolled in the Turkish program and 41 in the English program. The age of the students ranged between 21 and 28 years. According to KTU's civil engineering internship regulations, students are required to complete a total of 60 days of internship. The research questionnaire was administered face to face during class hours with the permission of the course instructor. Students were given 10 minutes to complete the survey, and all participants submitted their responses within this timeframe.text.

In this study, a questionnaire developed for civil engineering students was used to address the following research questions:

- The adequacy of their undergraduate education in meeting industry expectations,
- The sufficiency and attractiveness of traditional educational materials,
- The courses most closely associated with the knowledge required during internship experiences,
- The courses that need to be better understood in order to meet industry expectations,
- The courses that should be supported with advanced educational technologies (virtual reality, augmented reality, 3D modeling, simulation, etc.) to enhance professional competencies.

Questions related to the adequacy of undergraduate education in meeting industry expectations and the sufficiency and attractiveness of traditional educational materials were presented in a Likert type format. For the remaining questions, students were asked to select the specific courses they considered relevant. The course options provided included: Reinforced Concrete, Steel Structures, Transportation, Construction Management, Occupational Safety, Water Resources, Foundations, Soil Mechanics, Structural Analysis, Construction Materials, Strength of Materials, and Other. The data obtained were analyzed using the SPSS 26 statistical software package.text.

3. Findings and discussions

Students' responses to the following questions are presented in Table 1:

Table 1. Students' perceptions of their education and traditional educational materials

Question	Likert Scale				
	Strongly Disagree (1)	Disagree (2)	Neutral (3)	Agree (4)	Strongly Agree (5)
Do you think the education you have received in the civil engineering department is sufficient to meet the expectations of the industry	%8 N=13	%15 N=26	%29 N=51	%39 N=67	%9 N=16
What is your opinion regarding the adequacy of traditional educational materials in terms of understanding, comprehension, and the ability to visualize the content presented during undergraduate education	%10 N=17	%24 N=42	%29 N=51	%31 N=53	%6 N=10
What is your opinion regarding the attractiveness of traditional educational materials in terms of stimulating interest in the course, motivation to learn, and willingness to conduct further research	%13 N=22	%33 N=57	%34 N=58	%16 N=29	%4 N=7

When examining students' responses to the statement "Do you think the education you have received in the civil engineering department is sufficient to meet the expectations of the industry" it is observed that 23% expressed a negative opinion, 29% remained neutral, and 48% responded positively. This suggests a level of uncertainty regarding how well the current education system prepares students for the demands of the industry, although the overall tendency appears to be positive.

In the literature, a gap between the competencies expected by employers and the skills provided by higher education is frequently emphasized (Kwan, 2016; Leong & Elleithy, 2016). A discrepancy seems to exist between the findings of this study and those reported in the literature. While a significant portion of students (48%) believe that their education sufficiently meets industry expectations, scholarly studies often underline a mismatch between higher education outcomes and sectoral needs. This discrepancy highlights the potential divergence between students' perceptions and the evaluations made by employers or academic researchers regarding the readiness of graduates for the workforce. Students tend to assess the relevance of their education based on their perceived gains in knowledge and skills. In contrast, employers evaluate graduates through their ability to solve real-world problems and apply knowledge in professional contexts. The survey results suggest that the theory–practice gap emphasized in the literature may not yet be fully perceived by students, as they have not been extensively exposed to the complexities of real-world professional environments. Consequently, while students may believe their education is adequate prior to graduation, this perception may shift once they enter the workforce and encounter practical challenges that reveal potential deficiencies in their training.

An analysis of responses to the statement "What is your opinion regarding the adequacy of traditional educational materials in terms of understanding, comprehension and the ability to visualize the content presented during undergraduate education" reveals that 34% of students expressed a negative opinion, 29% remained neutral, and 37% indicated a positive view. These results demonstrate a clear divide among students regarding the adequacy of traditional educational materials. While some participants consider these materials sufficient, an almost equal proportion believes they are inadequate. Furthermore, a discrepancy can be observed between students' perceptions and the findings reported in the literature. Li et al. (2018) emphasized that the effectiveness of instructional materials in contributing to the learning process is closely linked to the level of student interaction. Their study also suggests that active learning methods, such as XR (Extended Reality), VR (Virtual Reality), and AR (Augmented Reality), are more effective than traditional, passive teaching tools. One possible explanation for this discrepancy is the limited exposure of students to active learning experiences. In educational environments where such approaches are not widely implemented, students may perceive the current system as adequate.

However, research in the field of educational sciences consistently indicates that traditional methods, being rooted in passive knowledge transmission, limit student engagement and hinder long-term learning retention.

An examination of responses to the statement “What is your opinion regarding the attractiveness of traditional educational materials in terms of stimulating interest in the course, motivation to learn, and willingness to conduct further research” reveals that 46% of students expressed a negative opinion, 34% were undecided and only 20% responded positively. These findings indicate that a significantly higher proportion of students perceive traditional materials as unengaging compared to those who find them appealing. Moreover, the relatively high percentage of neutral responses suggests that many students lack a definitive stance on the matter; however, the dominant trend points toward a general perception of disengagement. This outcome implies that traditional educational tools may be considered insufficient in capturing and sustaining students’ interest during the learning process.

The responses of students to the question “Which courses do you think are more closely related to the knowledge you are expected to acquire during your internship?” are presented in Figure 1

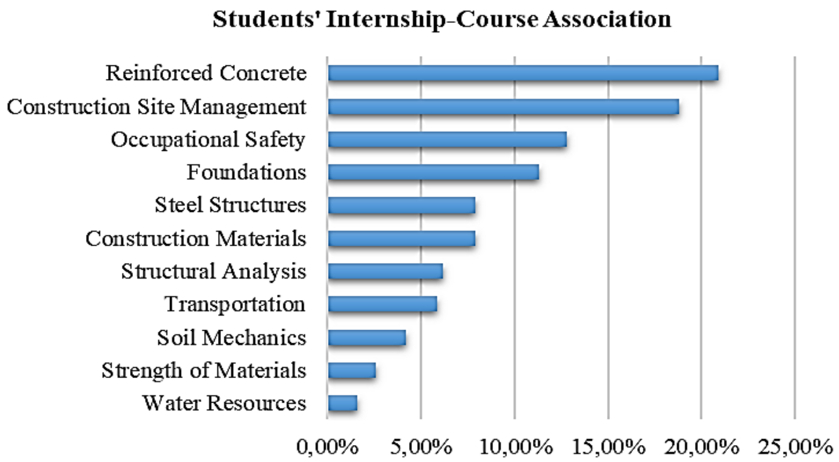

Fig. 1. Students’ internship-course association

As seen in Fig. 1, Reinforced Concrete Structures (20.90%) and Construction Site Management (18.80%) received the highest percentages. This indicates that students believe they need applied engineering knowledge and site management skills the most during their internships. Occupational Safety (12.80%) ranked third, suggesting that being aware of on-site risks and knowing the relevant safety precautions is considered a critical issue by students. In addition, more theoretical courses (Mechanics of Materials, Water Resources, Soil Mechanics) appear to be less emphasized during field experience. These results reflect civil engineering students’ perceptions, based on their internship experiences, of which courses are more directly related to practical applications in the field.

Fig. 2 presents the responses to the question: “Which courses do you think should be better understood during your undergraduate education in order to meet industry expectations?”

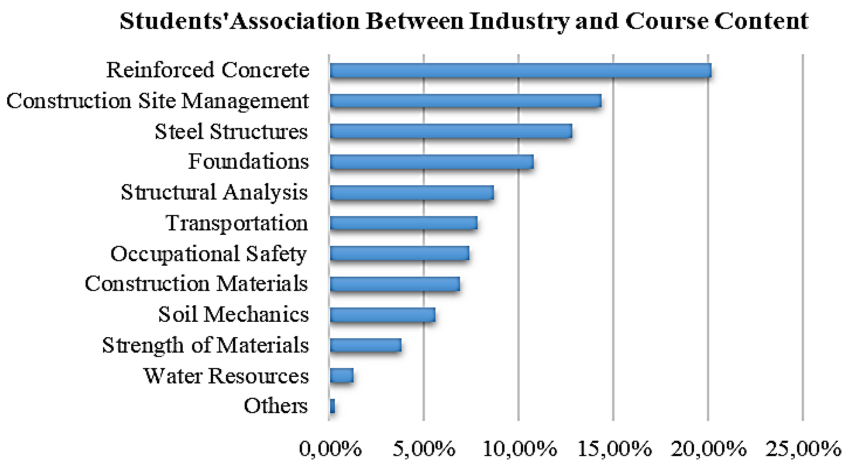

Fig. 2. Students’ association between ındustry and course content

As shown in Fig. 2, the courses “Reinforced Concrete” (20.20%) and “Construction Site Management” (14.40%) stand out with the highest proportions. This indicates that students believe they need a deeper understanding of structural design and site management. In particular, given the widespread use of reinforced concrete structures in the construction industry, students’ expectations to gain a better grasp of this course’s content can be considered a meaningful outcome. Similarly, the high preference for the Construction Site Management course suggests that topics such as project management, work planning, and site organization are perceived as critically important by students. The findings also show that the courses “Steel Structures” (12.80%) and “Foundations” (10.80%) are considered significant by students. This result implies that knowledge in load bearing system design and foundation engineering is viewed as essential for professional success. On the other hand, more theoretical courses such as “Mechanics of Materials” (3.80%), “Soil Mechanics” (5.60%), and “Water Resources” (1.30%) received relatively lower preferences. This suggests that students tend to value courses that have direct applications in the field more highly.

Students’ responses to the question, “Which courses in your undergraduate education should be supported with advanced educational materials (such as virtual reality, augmented reality, 3D modeling, animation, simulation, gamification, etc.) in order to improve your understanding of the profession?” are presented in Fig. 3.

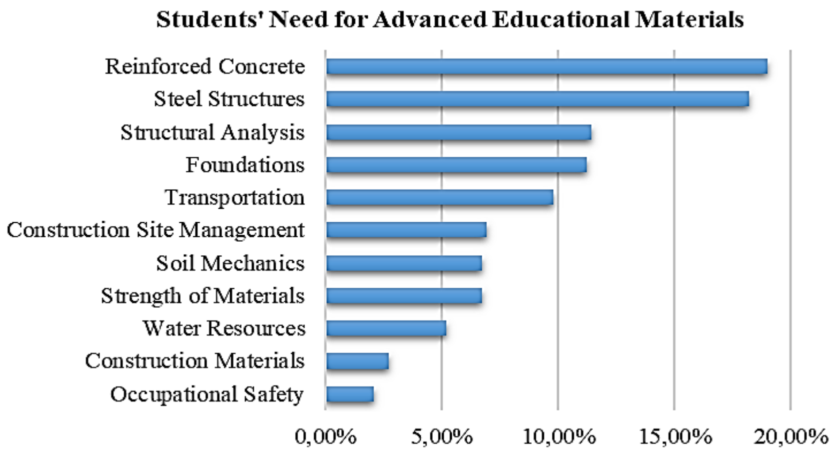

Fig. 3. Students’ Need for Advanced Educational Materials

As shown in Fig. 3, the courses “Reinforced Concrete” (19.00%) and “Steel Structures” (18.20%) received the highest percentages. This indicates that students particularly feel the need for advanced visualization and simulation techniques to better understand structural system design, structural analysis, and material behavior. The modeling of topics covered in Reinforced Concrete and Steel Structures courses often involving complex calculations and three-dimensional structural behavior in virtual environments is considered potentially beneficial for enhancing students’ professional learning. The relatively high preference for “Structural Analysis” (11.40%) and “Foundations” (11.20%) suggests that visual and interactive educational materials supporting the understanding of load bearing system behavior under loads and fundamental principles of foundation design could be valuable learning tools for students. In particular, simulations and interactive applications can be considered critical for improving comprehension of static and dynamic systems. The notable percentages for “Transportation” (9.80%) and “Construction Site Management” (6.90%) also reveal students’ support for teaching topics such as site organization, project planning, traffic engineering, and transportation infrastructure through virtual models. Virtual reality and simulations can enhance the acquisition of professional knowledge by providing students with immersive experiences that replicate real-world construction site conditions.aliqua.

4. Conclusions

This study aimed to reveal civil engineering undergraduate students’ perceptions of their education, its alignment with industry expectations, and their needs for advanced educational materials. The findings indicate that there may be significant differences between students’ perceptions and the findings reported in the literature when evaluating educational processes.

Approximately half of the students (48%) reported that they found their education sufficient in meeting industry expectations. However, existing literature frequently emphasizes a notable mismatch between higher education curricula and sectoral demands. This discrepancy may be attributed to the fact that students have not yet fully encountered the realities and dynamics of professional practice, leading them to assess the adequacy of their education primarily based on perceived knowledge and skill acquisition. In contrast, employers typically evaluate educational outcomes based on practical problem-solving abilities and application competence, which may explain the divergence between student perceptions and industry realities.

A similar divergence was observed regarding the adequacy and appeal of traditional educational materials. While a significant portion of students (34%) found traditional materials insufficient, another group (37%) expressed positive views, and a noteworthy percentage (29%) remained undecided. Furthermore, responses to the statement “Traditional educational materials are engaging” revealed that 46% of the participants disagreed, suggesting that traditional materials may fall short in maintaining student interest. These findings align with the literature, which asserts that conventional, passive teaching methods often limit student engagement and long-term learning retention.

Based on their internship experiences, students particularly highlighted that “Reinforced Concrete” (20.90%) and “Construction Site Management” (18.80%) are closely related to industry practices. The practice-oriented nature of these courses aligns well with students’ on-site experiences, reinforcing the importance of such courses in preparing them for the profession. Similarly, students identified “Reinforced Concrete” (20.20%) and “Construction Site Management” (14.40%) as the courses that require a deeper understanding to meet industry expectations. These results suggest that professional competencies such as structural system design, construction management, and project planning should be prioritized during undergraduate education.

Another key finding of the study was students’ strong demand for the integration of advanced educational technologies. In particular, they emphasized the need to support courses like “Reinforced Concrete” (19.00%) and “Steel Structures” (18.20%) with innovative tools such as virtual reality, augmented reality and simulation. These results indicate that abstract and complex engineering concepts can be more effectively learned through three-dimensional, visual, and interactive materials. Additionally, courses such as “Structural Analysis”, “Foundations”, “Transportation” and “Construction Site Management” were also identified as potentially benefiting from enhanced technological support.

In summary, students view practice-oriented courses as more critical for both professional development and preparation for the industry. Moreover, the limited interest in traditional educational materials and the expressed need for advanced technologies highlight the importance of adopting active learning strategies in engineering education. In this context, updating curricula, incorporating innovative teaching tools, and expanding hands-on learning environments are essential steps for universities to better respond to industry expectations.left.

References

Boz, E., & Toğan, V. (2021). Using audio visual materials for civil engineering students to gain field experience in schools: Stone wall example. *Journal of Education and New Approaches, 4*(1), 14–27.

De Carvalho, C. V. (2019, October). Virtual experiential learning in engineering education. In *2019 IEEE Frontiers in Education Conference (FIE)* (pp. 1–8). IEEE.

Jonassen, D., Strobel, J., & Lee, C. B. (2006). Everyday problem solving in engineering: Lessons for engineering educators. *Journal of Engineering Education, 95*(2), 139–151.

Kwan, C. (2016). Findings from the implementation of project-based learning in civil engineering education. *SHS Web of Conferences, 26*, 01016.

Leong, L., & Elleithy, W. (2016). Impact of past project on the educational experience of civil engineering students. In *The 3rd International Conference on Civil and Environmental Engineering for Sustainability* (p. 04010). Melaka, Malaysia.

Li, X., Yi, W., Chi, H. L., Wang, X., & Chan, A. P. C. (2018). A critical review of virtual and augmented reality (VR/AR) applications in construction safety. *Automation in Construction, 86*, 150–162.

Litzinger, T., Lattuca, L. R., Hadgraft, R., & Newstetter, W. (2011). Engineering education and the development of expertise. *Journal of Engineering Education, 100*(1), 123–150.

Moezabadi, D. M. (2024). *Enhancing competence in civil engineering: Assessment of international research experience* (Doctoral dissertation, Arizona State University).

Mukherji, P., & Sisale, V. (2022). Importance of students’ feedback for modifying course syllabus and revising curriculum of UG electronics and telecommunication engineering programme.

Murray, M. (2024). Civil engineering employers’ engagement in work-integrated learning. *Proceedings of the Institution of Civil Engineers - Management, Procurement and Law*, 1–13.

Shah, R., & Gillen, A. L. (2024). A systematic literature review of university-industry partnerships in engineering education. *European Journal of Engineering Education, 49*(3), 577–603.

Suhail, N., Bahroun, Z., & Ahmed, V. (2024). Augmented reality in engineering education: Enhancing learning and application. *Frontiers in Virtual Reality, 5*, 1461145.

Yükseköğretim Kalite Kurulu (YÖKAK). (2025, April 10). *Yükseköğretim Kalite Kurulu*. https://www.yokak.gov.tr/

Mühendislik Eğitim Programları Değerlendirme ve Akreditasyon Derneği (MÜDEK). (2025, April 10). *MÜDEK – İlkeler*. https://www.mudek.org.tr/tr/ana/ilk.shtm

ICEARC'25
4th International Civil Engineering & Architecture Conference
17-19 May 2025, Trabzon, Türkiye

A spreadsheet application for the heuristic solution of Time Cost Trade-off Problem

Ayşe Nur Şengül*[1], Önder H. Bettemir[1]

[1] İnönü University, Department of Civil Engineering, 44280 Malatya, Türkiye

Abstract. Time Cost Trade-Off Problem (TCTP) is an important problem in construction management since its optimum solution minimizes the total project cost. Although there are meta-heuristic and mathematical programming algorithms for the optimization of the problem, optimum or near-optimum solutions can also be obtained with heuristic methods with very few operations and computation. In this study, an spreadsheet application that automatically performs most of the operations and logical tests required for the solution of TCTP with heuristic methods was developed and TCTP was solved with minimal human effort. At the initial stage, the project diagram of the problem was drawn in Activity-On-Arrow type. The nodes of the networks and crashing alternatives are defined to the application. Since the application is coded to have the feature of determining the critical activity with the lowest crashing cost, it offers the most suitable crashing option to the user. If the number of critical paths is more than one, the critical activity with the unit cheapest crashing alternative is accelerated first, but the project duration does not change. However, the number of critical paths drops to one and the cheapest crashing alternative of the remaining critical path is suggested by the application. In this way, although the best solution cannot be guaranteed, the near-optimum solution can be obtained with very little human effort. As a result, the developed spreadsheet application offers a practical and accessible approach for the solution of TCTP by heuristic methods. The created spreadsheet application solves the entire problem again after shifting the crashing modes of the critical activities, which minimizes user mistakes, speeds up decision-making processes and enables projects to achieve cost and time targets more effectively. Although the best solution cannot be guaranteed, the proposed approach stands out as an effective and applicable alternative for engineers when considering the constraints and time pressure encountered in real life.

Keywords: Time-cost trade-off problem; Optimization; Heuristic algorithm; Project management.

---

1. Introduction

The time-cost trade-off problem aims to obtain the most suitable construction time and total construction cost by creating different construction alternatives for the work items that constitute a construction project. Meta-heuristic methods are widely used to solve this problem.

Ballesteros-Pérez et al. (2019) focused on a Genetic Algorithm (GA) that applies crashing and fast tracking separately and together for a 10-activity project. Anagnostopoulos and Kotsikas (2010) examined different annealing algorithm variants that address the problem of minimizing the total cost in activity networks when certain time and cost modes are allowed in the project activities. The most effective variant produces local optima very close to the global optimum and is the slowest algorithm, although it is time efficient (Anagnostopoulos and Kotsikas, 2010). Bettemir and Bulak (2022) aimed to develop an integrated method that includes the steps of preparing quantity take-off, determining activity durations and resource requirements, creating a work schedule, and determining the construction cost and duration with unit prices in the project management process. Optimum or near-optimum solutions were obtained by using the GA with Simulated Annealing which increases the convergence ability of the GA. Banihashemi and Mohammed (2022) proposed an optimization model by examining construction projects in four dimensions, namely time, cost, risk and quality, and considering real projects, and the NSGA-II meta-heuristic algorithm and goal programming approach were used to solve this model. The results showed that the NSGA-II algorithm provides results close to the optimal solution (Banihashemi and Mohammed, 2022). Jun and El-Rayes (2010) developed a multi-objective optimization model for scheduling multiple shifts in construction projects, and the developed model minimizes the negative effects on project performance by optimizing the distribution of limited labor resources between shifts. Bettemir and Yücel (2021) developed an application that enables the creation of construction alternatives with minimal human intervention.

* Corresponding author, E-mail: 36233621010@ogr.inonu.edu.tr

https://doi.org/10.31462/icearc2025_ce_mng_428

golden light publishing

Since the application works on a spreadsheet and is automated independently of human intervention, it ensures that results are obtained quickly. This application can help them achieve significant savings in construction costs.

Bettemir and Yücel (2023) proposed a framework to provide the optimal time-cost balance with minimum effort for construction projects. For this purpose, a spreadsheet application was developed to calculate the quantity extraction of construction materials with minimum data input from the user, and this application can provide significant cost and time savings in the planning process. Cheng and Tran (2015) demonstrate the effectiveness of the OMODE algorithm using numerical case studies on two construction projects. The OMODE algorithm resulted in shorter project duration and lower cost compared to other algorithms. Luong et al., (2021) used the Differential Evolution (DE) algorithm, one of the most popular evolutionary algorithms, to solve the DTCTP. In terms of time, all models exhibit similar time performance, while OMODE provides higher quality and lower cost. Agarwal et al., (2024) developed a model that increases the efficiency of construction projects and contributes to their successful management by facilitating the decision-making process by simultaneously optimizing project duration and cost. The effectiveness of the MOPSO approach demonstrates its potential to improve scheduling options in the construction industry and maximize project outcomes (Agarwal et al., 2024). Al-Shihabi and AlDurgam (2020) developed a mixed integer linear programming (MILP) model to balance the extension and acceleration processes of projects. This problem is called the "discrete time, cost, and credit trade-off problem" (DTCCTP). This model aims to meet budget and credit limit constraints while minimizing the project duration (Al-Shihabi and AlDurgam, 2020). Yilmaz and Dede (2023) examined the effectiveness and performance of the multi-objective Rao series optimization model, which was used for the first time in the field of construction management. The results show that the developed model is an outstanding alternative for solving the multi-objective time-cost trade-off optimization problem in construction management. Maravas and Pantouvakis (2012) developed a computer program that performs fuzzy calculations for activity durations and costs and displays the results in graphical and tabular form. Network Analysis Algorithm (NAA) searches for the optimum solution by accelerating the activities step by step. The algorithm has been tested in terms of finding the global optimum and fast convergence. The results show that the algorithm quickly reaches optimum or close solutions (Bettemir and Birgönül, 2017). Geem (2010) tested the HS model on two network examples and compared to other evolutionary algorithms, GA and ACO, it found Pareto solutions as good as or better than other applications in (Geem, 2009). For the solution of the seven-activity problem, HS found the global Pareto set faster than ACO, while GA could not show this success. For the eighteen-activity problem, HS obtained a better Pareto solution than ACO, while GA did not give certain results. Akkoyunlu and Engin (2011) examined HAA as a new algorithm that reaches satisfactory results within an acceptable time within the search space containing infinite number of solutions. Since the variables of optimization problems in daily life are more discrete, KHAA was emphasized. As a result of the examinations, it was determined that KHAA method would be an alternative method in solving optimization problems for discrete data. To optimize the traditional time-cost trade-off problem, a least-cost mathematical optimization model has been developed by associating CPM, mathematical programming and DCF techniques. This model allows projects to be used for all types of projects without being limited to certain techniques (Ammar, 2011). Cura (2008) optimized a nonlinear function with the Tabu search algorithm. The developed algorithm was tested on a seven-variable minimization problem and significant results were obtained. The TA algorithm has achieved successful results for this problem (Cura, 2008). The cited studies present successful results for the solution of TCTP but the construction sector cannot implement the sophisticated optimization methods. Therefore, the construction schedules are not optimized by considering construction cost and duration.

Besides meta-heuristic algorithms DTCTP was solved by heuristic methods. Bettemir and Birgönül implemented minimum cost slope based heuristic algorithm to determine the activities to be crashed. The proposed method obtained the optimum solution of 18-Activity project and obtained near optimum solution of 63 Activity project (Bettemir and Birgönül, 2017). The obtained near optimum solution is used to generate population and better solutions are obtained (Bettemir and Birgönül, 2025).

2. Method

In this study, a heuristic method for solving the time-cost trade-off problem of a construction project is coded into a spreadsheet application. In the solution process, critical activities are accelerated to shorten the total project duration and the relationship between the increase in direct costs and the decrease in indirect costs is evaluated. A network diagram is created as shown in Fig. 1 by considering the physical relationships between the activities.

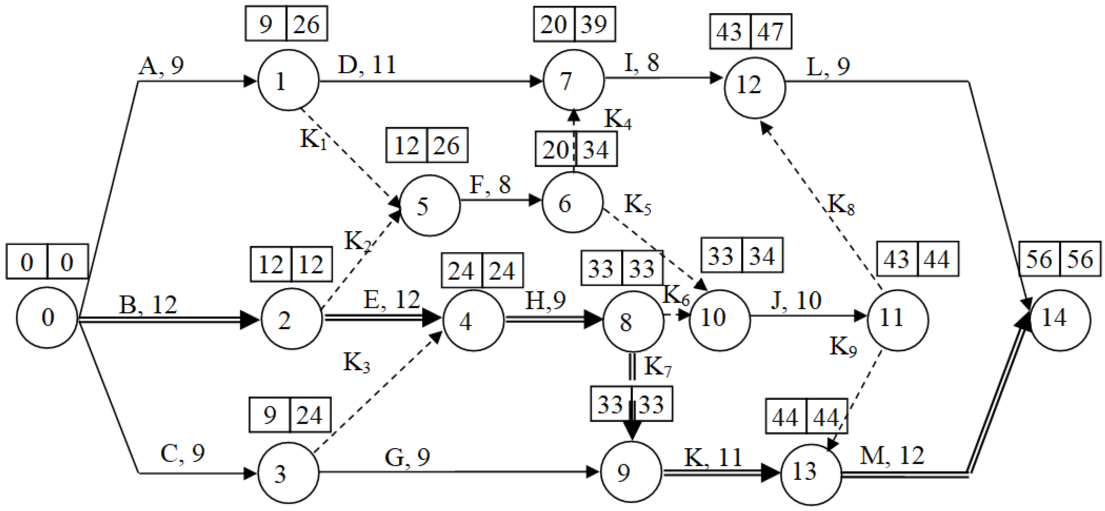

Fig. 1. Hypothetical thirteen activity project diagram

Different construction duration and construction cost options of the activities are entered to the spreadsheet application. To assist the selection of different construction alternatives the application computes the crashing costs of each activity. Early Event (EET) and Late Event times (LET) of the nodes are automatically calculated in a separate table which enables automatic computation of the activity start and finish time. The spreadsheet automatically assigns duration and cost values and recalculates the construction schedule. In this way, when a different alternative is selected for any activity, the project completion time is automatically updated. In order for the network drawn as an arrow diagram to be transferred to the spreadsheet application, it is necessary to define the activities connected to the nodes. The EET and GOZ calculations of the nodes are given in Fig. 2.

Here, the LET calculation of node number 2 is shown as a representation. Since the dummy activity is connected to node number 5 from the mentioned node point, C26, and since there is also activity E between it and node number 4, the smaller of the C25-D7 values are assigned as LET to this node point. The specified calculations are performed for all nodes and the network is introduced to the application. When the activity durations change, the network calculations are automatically updated.

Activity	Start	Finish	Duration	Cost	Selected Alternative
A	0	1	6	31875	3
B	0	2	8	25000	3
C	0	3	20	30350	1
D	1	7	12	17437,5	2
E	2	4	12	31500	3
F	5	6	10	43750	3
G	3	9	8	26312,5	3
H	4	8	6	22250	3
I	7	12	14	41000	3
J	10	11	6	18437,5	3
K	9	13	6	18750	3
L	12	14	10	22500	3
M	13	14	8	24750	3
				353913	Direct Cos
				42	353913
Node	EET	LET			
0	0	0			
1	6	6			
2	8	=MİN(C25-D7;C26)			
3	20	20			
4	20	20			
5	8	8			

Fig. 2. Preparation of Excel application for automatic calculation of activity start and end times.

The calculation of the acceleration cost of the activity to be accelerated is shown in Figure 3. The acceleration cost is calculated as presented in Eq 1.

$$CrashingCost = \frac{C_{next} - C_{current}}{D_{next} - D_{current}} \tag{1}$$

In Eq 1:
Cnext is the cost of the next selected construction alternative.
Ccurrent is the cost of the currently selected construction alternative.
Dnext is the duration of the next selected construction alternative.
Dcurrent is the duration of the currently selected construction alternative.

The formula entered into the spreadsheet application to apply Equation 1 is given in the expression below.
"=IF(AND(F3<G3;L3=0);(VLOOKUP(A3;$A$3:$S$15;F3*2+15;FALSE)-VLOOKUP (A3;$A$3:$S$15;F3*2+13;FALSE))/(VLOOKUP(A3;$A$3:$S$15;F3*2+12;FALSE)-VLOOKUP (A3;$A$3:$S$15;F3*2+14; FALSE)); 9999999999)"

The unit acceleration cost of the relevant activity in the project is calculated in TL/day and is used to select the activities that will increase the direct cost the least. If the activity is not a critical activity, acceleration of the activity will not provide an improvement in the project cost. The equation defined to eliminate non-critical activities assigns very high acceleration costs as shown in the equation defined in MS Excel.

Activity	Start	Finish	Duration	Cost	Selected Alternative	Alt. Number	EETi	LETi	EETj	LETj	Total Floa	Accelerat	Duration	Cost	Duration	Cost	Duration	Cost	Start	Finish
A	0	1	6	31875	3	3	0	0	6	6	0	=IF(AND(F3<G3,L3=0),(VLOOKUP(A3,$A$3:$S$15,F3*2+15,FALSE())-VLOOKUP(A3,$A$3:$S$15,F3*2+13,FALSE()))/(VLOOKUP(A3,$A$3:$S$15,F3*2+12,FALSE())-								
B	0	2	8	25000	3	3	0	0	8	8	0	VLOOKUP(A3,$A$3:$S$15,F3*2+14,FALSE())),9999999999)								
C	0	3	20	30350	1	3	0	0	20	20	0	758.75	20	30350	15	34143.75	10	37937.5	0	20
D	1	7	12	17437.5	2	3	6	6	18	18	0	484.375	16	15500	12	17437.5	8	19375	6	18
E	2	4	12	31500	3	3	8	8	20	20	0	1E+10	24	25200	18	28350	12	31500	8	20
F	5	6	10	43750	3	3	8	8	18	18	0	1E+10	20	35000	15	39375	10	43750	8	18
G	3	9	8	26312.5	3	3	20	20	28	28	0	1E+10	16	21050	12	23681.25	8	26312.5	20	28
H	4	8	6	22250	3	3	20	20	26	26	0	1E+10	12	17800	9	20025	6	22250	20	26
I	7	12	14	41000	3	3	18	18	32	32	0	1E+10	28	32800	21	36900	14	41000	18	32
J	10	11	6	18437.5	3	3	26	26	32	32	0	1E+10	12	14750	9	16593.75	6	18437.5	26	32
K	9	13	6	18750	3	3	28	28	34	34	0	1E+10	12	15000	9	16875	6	18750	28	34
L	12	14	10	22500	3	3	32	32	42	42	0	1E+10	20	18000	15	20250	10	22500	32	42
M	13	14	8	24750	3	3	34	34	42	42	0	1E+10	16	19800	12	22275	8	24750	34	42

Fig. 3. Calculation of acceleration costs of the activities

The spreadsheet recommends the most suitable activity for acceleration, as shown in Fig. 4. In making this recommendation, it considers the activities whose total float time is 0, that is, the activity that is on the critical path in the network and has the lowest acceleration cost. Activities on the critical path are prioritized. Since the critical path may change after each acceleration operation, the duration of an activity is recalculated each time it is updated. The total float time of the activities is calculated as in Equation 2.

$$TF = LFT - EST - Duration \tag{3}$$

Here TF is the total float time, LFT is the late finish time, and EST is the early start time. Also, LST is the latest start time and EFT is the earliest finish time. The time unit is days. The formula used in the spreadsheet application to show the recommended activity for acceleration is represented as

"=INDEX(A3:A15;MATCH(M18;M3:M15;0);1)". In the expression, cell M18 represents the lowest acceleration cost and the INDEX function finds the activity with the cheapest speedup cost.

	A	B	C	D	E	F	G	H	I	J	K	L	M	N	O	
1		Daily Ove	5000	TL										Alt.1 daytime		A
2	Activity	Start	Finish	Duration	Cost	Selected Alternative	Alt. Number	EETi	LETi	EETj	LETj	Total Floa	Acceleration	Duration	Cost	D
3	A	0	1	6	31875	3	3	0	0	6	6	0	9999999999	12	25500	
4	B	0	2	8	25000	3	3	0	0	8	8	0	9999999999	16	20000	
5	C	0	3	20	30350	1	3	0	0	20	20	0	758.75	20	30350	
6	D	1	7	12	17437.5	2	3	6	6	18	18	0	484.375	16	15500	
7	E	2	4	12	31500	3	3	8	8	20	20	0	9999999999	24	25200	
8	F	5	6	10	43750	3	3	8	8	18	18	0	9999999999	20	35000	
9	G	3	9	8	26312.5	3	3	20	20	28	28	0	9999999999	16	21050	
10	H	4	8	6	22250	3	3	20	20	26	26	0	9999999999	12	17800	
11	I	7	12	14	41000	3	3	18	18	32	32	0	9999999999	28	32800	
12	J	10	11	6	18437.5	3	3	26	26	32	32	0	9999999999	12	14750	
13	K	9	13	6	18750	3	3	28	28	34	34	0	9999999999	12	15000	
14	L	12	14	10	22500	3	3	32	32	42	42	0	9999999999	20	18000	
15	M	13	14	8	24750	3	3	34	34	42	42	0	9999999999	16	19800	
16																
17												Recomme	Unit Acceleration Cost			
18					353912.5	Direct Co	Indirect C	Total Cost				=INDEX(A3:A15,MATCH(M18,M3:M15,0),1)				

Fig. 4. Display of critical activities and automatic computation of available acceleration alternatives

The prepared spreadsheet identifies the critical activities and calculates the acceleration cost if there is any acceleration alternative for critical activities. The acceleration alternative with the minimum acceleration cost is suggested by the developed application. The scheduler can assign the activity to be accelerated by examining the suggested acceleration alternatives.

3. Case study

A network diagram showing the constraints between the activities is given in Figure 1. Different duration and construction alternatives for each activity are presented in Table 1. Alternative 1 is the daytime working option. The project is completed with standard working hours and has the lowest cost. However, the duration is the longest. Alternative 2 is the daytime working option with overtime. The duration is shortened by shortening the daytime by adding overtime, but the cost slightly increases since overtime payments are higher than normal payments. Alternative 3 is the night + day double shift option. The night + day shift alternative is implemented with the shortest duration but the highest cost. The costs increase due to acceleration. The cost unit is TL and the daily overhead for this schedule is 5000 TL.

The formed construction cost and duration alternatives are entered into the spreadsheet application as shown in Fig. 5.

Table 1. Construction duration and cost alternatives

Alt.1 (Day time work)		Alt.2 (Day time work with overtime)		Alt.3 (Day and night shifts)	
Duration	Cost	Duration	Cost	Duration	Cost
12	25500	9	28687.5	6	31875
16	20000	12	22500	8	25000
20	30350	15	34143.75	10	37937.5
16	15500	12	17437.5	8	19375
24	25200	18	28350	12	31500
20	35000	15	39375	10	43750
16	21050	12	23681.25	8	26312.5
12	17800	9	20025	6	22250
28	32800	21	36900	14	41000
12	14750	9	16593.75	6	18437.5
12	15000	9	16875	6	18750
20	18000	15	20250	10	22500
16	19800	12	22275	8	24750

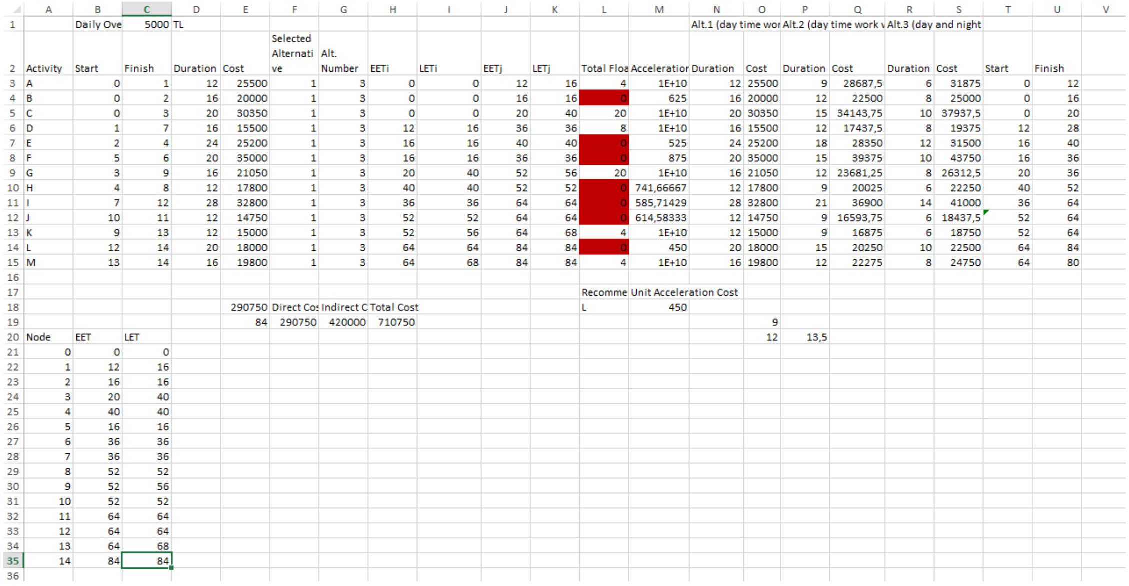

	A	B	C	D	E	F	G	H	I	J	K	L	M	N	O	P	Q	R	S	T	U	V
1		Daily Ove	5000	TL										Alt.1 (day time wor		Alt.2 (day time work v		Alt.3 (day and night				
2	Activity	Start	Finish	Duration	Cost	Selected Alternati ve	Alt. Number	EETi	LETi	EETj	LETj	Total Floa	Acceleratior	Duration	Cost	Duration	Cost	Duration	Cost	Start	Finish	
3	A	0	1	12	25500	1	3	0	0	12	16	4	1E+10	12	25500	9	28687,5	6	31875	0	12	
4	B	0	2	16	20000	1	3	0	0	16	16	0	625	16	20000	12	22500	8	25000	0	16	
5	C	0	3	20	30350	1	3	0	0	20	40	20	1E+10	20	30350	15	34143,75	10	37937,5	0	20	
6	D	1	7	16	15500	1	3	12	16	36	36	8	1E+10	16	15500	12	17437,5	8	19375	12	28	
7	E	2	4	24	25200	1	3	16	16	40	40	0	525	24	25200	18	28350	12	31500	16	40	
8	F	5	6	20	35000	1	3	16	16	36	36	0	875	20	35000	15	39375	10	43750	16	36	
9	G	3	9	16	21050	1	3	20	40	52	56	20	1E+10	16	21050	12	23681,25	8	26312,5	20	36	
10	H	4	8	12	17800	1	3	40	40	52	52	0	741,66667	12	17800	9	20025	6	22250	40	52	
11	I	7	12	28	32800	1	3	36	36	64	64	0	585,71429	28	32800	21	36900	14	41000	36	64	
12	J	10	11	12	14750	1	3	52	52	64	64	0	614,58333	12	14750	9	16593,75	6	18437,5	52	64	
13	K	9	13	12	15000	1	3	52	56	64	68	4	1E+10	12	15000	9	16875	6	18750	52	64	
14	L	12	14	20	18000	1	3	64	64	84	84	0	450	20	18000	15	20250	10	22500	64	84	
15	M	13	14	16	19800	1	3	64	68	84	84	4	1E+10	16	19800	12	22275	8	24750	64	80	
16																						
17												Recomme	Unit Acceleration Cost									
18					290750	Direct Cos	Indirect C	Total Cost				L	450									
19					84	290750	420000	710750							9							
20	Node	EET	LET												12	13,5						
21	0	0	0																			
22	1	12	16																			
23	2	16	16																			
24	3	20	40																			
25	4	40	40																			
26	5	16	16																			
27	6	36	36																			
28	7	36	36																			
29	8	52	52																			
30	9	52	56																			
31	10	52	52																			
32	11	64	64																			
33	12	64	64																			
34	13	64	68																			
35	14	84	84																			
36																						

Fig. 5. The early start schedule of the network.

The formed application highlights the activities B, E, F, H, J, and L since they are critical activities with feasible crashing modes. In column M the application proposes crashing activity L since it has the least unit crashing cost with 450 monetary units per day.

The activity L is crashed by changing the alternate mode from 1 to 2 as shown in cell F14 which is illustrated in Fig. 6. Similarly four crashing steps are implemented and the resulting schedule is shown in Fig. 7.

After the 4th acceleration, it is suggested to accelerate the activity J in the 5th step. However, since there are other critical paths besides the line where the activity J is located, the project duration did not shortened and the total cost increased. Therefore, the next suggested activity M was also accelerated in the 5th step and the schedule given in Fig. 8 was obtained.

	A	B	C	D	E	F	G	H	I	J	K	L	M	N	O	P	Q	R	S	T	U
1		Daily Ove	5000	TL										Alt.1 (day time wor		Alt.2 (day time work v		Alt.3 (day and night			
2	Activity	Start	Finish	Duration	Cost	Selected Alternati	Alt. Number	EETi	LETi	EETj	LETj	Total Floa	Acceleratior	Duration	Cost	Duration	Cost	Duration	Cost	Start	Finish
3	A	0	1	12	25500	1	3	0	0	12	17	5	1E+10	12	25500	9	28687,5	6	31875	0	12
4	B	0	2	16	20000	1	3	0	0	16	16	0	625	16	20000	12	22500	8	25000	0	16
5	C	0	3	20	30350	1	3	0	0	20	36	16	1E+10	20	30350	15	34143,75	10	37937,5	0	20
6	D	1	7	16	15500	1	3	12	17	36	37	9	1E+10	16	15500	12	17437,5	8	19375	12	28
7	E	2	4	24	25200	1	3	16	16	40	40	0	525	24	25200	18	28350	12	31500	16	40
8	F	5	6	20	35000	1	3	16	17	36	37	1	1E+10	20	35000	15	39375	10	43750	16	36
9	G	3	9	16	21050	1	3	20	36	52	52	16	1E+10	16	21050	12	23681,25	8	26312,5	20	36
10	H	4	8	12	17800	1	3	40	40	52	52	0	741,66667	12	17800	9	20025	6	22250	40	52
11	I	7	12	28	32800	1	3	36	37	64	65	1	1E+10	28	32800	21	36900	14	41000	36	64
12	J	10	11	12	14750	1	3	52	52	64	64	0	614,58333	12	14750	9	16593,75	6	18437,5	52	64
13	K	9	13	12	15000	1	3	52	52	64	64	0	625	12	15000	9	16875	6	18750	52	64
14	L	12	14	15	20250	2	3	64	65	80	80	1	1E+10	20	18000	15	20250	10	22500	64	79
15	M	13	14	16	19800	1	3	64	64	80	80	0	618,75	16	19800	12	22275	8	24750	64	80
16																					
17												Recomme	Unit Acceleration Cost								
18					293000	Direct Cos	Indirect C	Total Cost				E	525								
19					80	293000	400000	693000							9						
20	Node	EET	LET												12	13,5					
21	0	0	0					Accelerati	Act	Duration	Direct Cos	Indirect C	Total Cost								
22	1	12	17					0	--	84	290750	420000	710750								
23	2	16	16					1	L	80	293000	400000	693000								
24	3	20	36					2													
25	4	40	40					3													
26	5	16	17					4													
27	6	36	37					5													
28	7	36	37					6													
29	8	52	52					7													
30	9	52	52					8													
31	10	52	52					9													
32	11	64	64					10													
33	12	64	65					11													
34	13	64	64					12													
35	14	80	80					13													
36								14													

Fig. 6. The network formed after the 1st acceleration in the heuristic solution of DTCTP.

	A	B	C	D	E	F	G	H	I	J	K	L	M	N	O	P	Q	R	S	T	U
1		Daily Ove	5000	TL										Alt.1 (day time wor		Alt.2 (day time work v		Alt.3 (day and night			
2	Activity	Start	Finish	Duration	Cost	Selected Alternati ve	Alt. Number	EETi	LETi	EETj	LETj	Total Floa	Acceleratior	Duration	Cost	Duration	Cost	Duration	Cost	Start	Finish
3	A	0	1	12	25500	1	3	0	0	12	17	5	1E+10	12	25500	9	28687,5	6	31875	0	12
4	B	0	2	16	20000	1	3	0	0	16	16	0	625	16	20000	12	22500	8	25000	0	16
5	C	0	3	20	30350	1	3	0	0	20	24	4	1E+10	20	30350	15	34143,75	10	37937,5	0	20
6	D	1	7	16	15500	1	3	12	17	36	37	9	1E+10	16	15500	12	17437,5	8	19375	12	28
7	E	2	4	12	31500	3	3	16	16	28	28	0	1E+10	24	25200	18	28350	12	31500	16	28
8	F	5	6	20	35000	1	3	16	17	36	37	1	1E+10	20	35000	15	39375	10	43750	16	36
9	G	3	9	16	21050	1	3	20	24	40	40	4	1E+10	16	21050	12	23681,25	8	26312,5	20	36
10	H	4	8	12	17800	1	3	28	28	40	40	0	741,66667	12	17800	9	20025	6	22250	28	40
11	I	7	12	21	36900	2	3	36	37	57	58	1	1E+10	28	32800	21	36900	14	41000	36	57
12	J	10	11	9	16593,8	2	3	40	43	49	52	3	1E+10	12	14750	9	16593,75	6	18437,5	40	49
13	K	9	13	12	15000	1	3	40	40	52	52	0	625	12	15000	9	16875	6	18750	40	52
14	L	12	14	10	22500	3	3	57	58	68	68	1	1E+10	20	18000	15	20250	10	22500	57	67
15	M	13	14	16	19800	1	3	52	52	68	68	0	618,75	16	19800	12	22275	8	24750	52	68
16																					
17												Recomme	Unit Acceleration Cost								
18					307494	Direct Cos	Indirect C	Total Cost				M	618,75								
19					68	307494	340000	647494							9						
20	Node	EET	LET												12	13,5					
21	0	0	0					Accelerati	Act	Duration	Direct Cos	Indirect C	Total Cost								
22	1	12	17					0	--	84	290750	420000	710750								
23	2	16	16					1	L	80	293000	400000	693000								
24	3	20	24					2	E	79	296150	395000	691150								
25	4	28	28					3	L	74	298400	370000	668400								
26	5	16	17					4	E,I	68	305650	340000	645650								
27	6	36	37					5	J												
28	7	36	37					6													
29	8	40	40					7													
30	9	40	40					8													
31	10	40	43					9													
32	11	49	52					10													
33	12	57	58					11													
34	13	52	52					12													
35	14	68	68					13													
36								14													

Fig. 7. The schedule formed after the 4th acceleration of the heuristic solution of DTCTP.

	A	B	C	D	E	F	G	H	I	J	K	L	M	N	O	P	Q	R	S	T	U
1		Daily Over	5000	TL										Alt.1 (day time worl		Alt.2 (day time work wi		Alt.3 (day and night sl			
2	Activity	Start	Finish	Duration	Cost	Selected Alternative	Alt. Number	EETi	LETi	EETj	LETj	Total Float	Acceleration	Duration	Cost	Duration	Cost	Duration	Cost	Start	Finish
3	A	0	1	12	25500	1	3	0	0	12	16	4	1E+10	12	25500	9	28687,5	6	31875	0	12
4	B	0	2	16	20000	1	3	0	0	16	16	0	625	16	20000	12	22500	8	25000	0	16
5	C	0	3	20	30350	1	3	0	0	20	27	7	1E+10	20	30350	15	34143,75	10	37937,5	0	20
6	D	1	7	16	15500	1	3	12	16	36	36	8	1E+10	16	15500	12	17437,5	8	19375	12	28
7	E	2	4	12	31500	3	3	16	16	28	31	3	1E+10	24	25200	18	28350	12	31500	16	28
8	F	5	6	20	35000	1	3	16	16	36	36	0	875	20	35000	15	39375	10	43750	16	36
9	G	3	9	16	21050	1	3	20	27	40	43	7	1E+10	16	21050	12	23681,25	8	26312,5	20	36
10	H	4	8	12	17800	1	3	28	31	40	43	3	1E+10	12	17800	9	20025	6	22250	28	40
11	I	7	12	21	36900	2	3	36	36	57	57	0	585,71429	28	32800	21	36900	14	41000	36	57
12	J	10	11	9	16593,8	2	3	40	46	49	55	6	1E+10	12	14750	9	16593,75	6	18437,5	40	49
13	K	9	13	12	15000	1	3	40	43	52	55	3	1E+10	12	15000	9	16875	6	18750	40	52
14	L	12	14	10	22500	3	3	57	57	67	67	0	1E+10	20	18000	15	20250	10	22500	57	67
15	M	13	14	12	22275	2	3	52	55	67	67	3	1E+10	16	19800	12	22275	8	24750	52	64
16																					
17												Recomme	Unit Acceleration Cost								
18					309969	Direct Cost	Indirect Co	Total Cost				I	585,71429								
19					67	309969	335000	644969							9						
20	Node	EET	LET												12	13,5					
21	0	0	0					Acceleratio	Act	Duration	Direct Cost	Indirect Co	Total Cost								
22	1	12	16					0	--	84	290750	420000	710750								
23	2	16	16					1	L	80	293000	400000	693000								
24	3	20	27					2	E	79	296150	395000	691150								
25	4	28	31					3	L	74	298400	370000	668400								
26	5	16	16					4	E,I	68	305650	340000	645650								
27	6	36	36					5	J,M	67	309969	335000	644968,75								
28	7	36	36					6													
29	8	40	43					7													
30	9	40	43					8													
31	10	40	46					9													
32	11	49	55					10													
33	12	57	57					11													
34	13	52	55					12													
35	14	67	67					13													
36								14													

Fig. 8. The network formed after the 5th crashing of the heuristic DTCTP solution algorithm.

	A	B	C	D	E	F	G	H	I	J	K	L	M	N	O	P	Q	R	S	T	U
1		Daily Over	5000	TL										Alt.1 (day time worl		Alt.2 (day time work wi		Alt.3 (day and night sl			
2	Activity	Start	Finish	Duration	Cost	Selected Alternative	Alt. Number	EETi	LETi	EETj	LETj	Total Float	Acceleration	Duration	Cost	Duration	Cost	Duration	Cost	Start	Finish
3	A	0	1	12	25500	1	3	0	0	12	16	4	1E+10	12	25500	9	28687,5	6	31875	0	12
4	B	0	2	16	20000	1	3	0	0	16	16	0	625	16	20000	12	22500	8	25000	0	16
5	C	0	3	20	30350	1	3	0	0	20	27	7	1E+10	20	30350	15	34143,75	10	37937,5	0	20
6	D	1	7	16	15500	1	3	12	16	36	36	8	1E+10	16	15500	12	17437,5	8	19375	12	28
7	E	2	4	12	31500	3	3	16	16	28	31	3	1E+10	24	25200	18	28350	12	31500	16	28
8	F	5	6	20	35000	1	3	16	16	36	36	0	875	20	35000	15	39375	10	43750	16	36
9	G	3	9	16	21050	1	3	20	27	40	43	7	1E+10	16	21050	12	23681,25	8	26312,5	20	36
10	H	4	8	12	17800	1	3	28	31	40	43	3	1E+10	12	17800	9	20025	6	22250	28	40
11	I	7	12	21	36900	2	3	36	36	57	57	0	585,71429	28	32800	21	36900	14	41000	36	57
12	J	10	11	12	14750	1	3	40	43	52	55	3	1E+10	12	14750	9	16593,75	6	18437,5	40	52
13	K	9	13	12	15000	1	3	40	43	52	55	3	1E+10	12	15000	9	16875	6	18750	40	52
14	L	12	14	10	22500	3	3	57	57	67	67	0	1E+10	20	18000	15	20250	10	22500	57	67
15	M	13	14	12	22275	2	3	52	55	67	67	3	1E+10	16	19800	12	22275	8	24750	52	64
16																					
17												Recomme	Unit Acceleration Cost								
18					308125	Direct Cost	Indirect Co	Total Cost				I	585,71429								
19					67	308125	335000	643125							9						
20	Node	EET	LET												12	13,5					
21	0	0	0					Acceleratio	Act	Duration	Direct Cost	Indirect Co	Total Cost								
22	1	12	16					0	--	84	290750	420000	710750								
23	2	16	16					1	L	80	293000	400000	693000								
24	3	20	27					2	E	79	296150	395000	691150								
25	4	28	31					3	L	74	298400	370000	668400								
26	5	16	16					4	E,I	68	305650	340000	645650								
27	6	36	36					5	M	67	308125	335000	643125								
28	7	36	36					6													
29	8	40	43					7													
30	9	40	43					8													
31	10	40	43					9													
32	11	52	55					10													
33	12	57	57					11													
34	13	52	55					12													
35	14	67	67					13													

Fig. 9. Uncrashing activity J to the 1st alternative after the 5th acceleration of the heuristic DTCTP solution algorithm.

Activity J becomes noncritical activity after the acceleration of the activity M. Therefore, the activity J was uncrashed and was reversed to its previous state to prevent cost increase.

Crashing of Activity B was suggested in step 9, but crashing only the activity B was not enough to reduce the project duration and total cost alone because of the existence of the other critical paths.

In the 9th acceleration step, the next proposed activity, activity K, was also accelerated in addition to activity B. However, since there was another critical path, no decrease was observed in the project duration. On the other hand, total cost of the project in increased.

In the 9th acceleration step, the acceleration of activities B and K, which was suggested due to multi critical path, could not reduce the project duration and cost. As illustrated in Fig. 11 the application proposed acceleration of activity F. When the next suggested activity F was accelerated, the project duration decreased from 56 days to 53 days, and the total project cost decreased by 6250 TL to 592793.75 TL.

	A	B	C	D	E	F	G	H	I	J	K	L	M	N	O	P	Q	R	S	T	U
1		Daily Ove	5000	TL										Alt.1 daytime		Alt.2 (Daytime overti		Alt.3 (night+daytime			
2	Activity	Start	Finish	Duration	Cost	Selected Alternative	Alt. Number	EETi	LETi	EETj	LETj	Total Floa	Accelerat	Duration	Cost	Duration	Cost	Duration	Cost	Start	Finish
3	A	0	1	12	25500	1	3	0	0	12	12	0	1062,5	12	25500	9	28687,5	6	31875	0	12
4	B	0	2	8	25000	3	3	0	0	8	12	4	1E+10	16	20000	12	22500	8	25000	0	8
5	C	0	3	20	30350	1	3	0	0	20	20	0	758,75	20	30350	15	34143,75	10	37937,5	0	20
6	D	1	7	16	15500	1	3	12	12	32	32	4	1E+10	16	15500	12	17437,5	8	19375	12	28
7	E	2	4	12	31500	3	3	8	12	20	24	4	1E+10	24	25200	18	28350	12	31500	8	20
8	F	5	6	20	35000	1	3	12	12	32	32	0	875	20	35000	15	39375	10	43750	12	32
9	G	3	9	16	21050	1	3	20	20	36	36	0	657,8125	16	21050	12	23681,25	8	26312,5	20	36
10	H	4	8	12	17800	1	3	20	24	32	36	4	1E+10	12	17800	9	20025	6	22250	20	32
11	I	7	12	14	41000	3	3	32	32	46	46	0	1E+10	28	32800	21	36900	14	41000	32	46
12	J	10	11	9	16593,75	2	3	32	37	41	46	5	1E+10	12	14750	9	16593,75	6	18437,5	32	41
13	K	9	13	12	15000	1	3	36	36	48	48	0	625	12	15000	9	16875	6	18750	36	48
14	L	12	14	10	22500	3	3	46	46	56	56	0	1E+10	20	18000	15	20250	10	22500	46	56
15	M	13	14	8	24750	3	3	48	48	56	56	0	1E+10	16	19800	12	22275	8	24750	48	56
16																					
17												Recomme	Unit Acceleration Cost								
18					321543,8	Direct Cos	Indirect C	Total Cost				K	625								
19					56	321543,8	280000	601543,8							9						
20	Node	EET	LET												12	13,5					
21	0	0	0						Acceleration	Act	Duration	Direct Cos	Indirect C	Total Cost							
22	1	12	12						0	--	84	290750	420000	710750							
23	2	8	12						1	L	80	293000	400000	693000							
24	3	20	20						2	E	79	296150	395000	691150							
25	4	20	24						3	L	74	298400	370000	668400							
26	5	12	12						4	E,I	68	305650	340000	645650							
27	6	32	32						5	M	67	308125	335000	643125							
28	7	32	32						6	I	64	312225	320000	632225							
29	8	32	36						7	J,M	60	316543,8	300000	616543,75							
30	9	36	36						8	B	56	319043,8	280000	599043,75							
31	10	32	37						9	B											
32	11	41	46						10												
33	12	46	46						11												
34	13	48	48						12												
35	14	56	56						13												
36									14												

Fig. 10. Activity proposal for Acceleration Step 9 of the heuristic DTCTP solution algorithm

	A	B	C	D	E	F	G	H	I	J	K	L	M	N	O	P	Q	R	S	T	U
1		Daily Ove	5000	TL										Alt.1 daytime		Alt.2 (Daytime overti		Alt.3 (night+daytime			
2	Activity	Start	Finish	Duration	Cost	Selected Alternative	Alt. Number	EETi	LETi	EETj	LETj	Total Floa	Accelerat	Duration	Cost	Duration	Cost	Duration	Cost	Start	Finish
3	A	0	1	12	25500	1	3	0	0	12	12	0	1062,5	12	25500	9	28687,5	6	31875	0	12
4	B	0	2	8	25000	3	3	0	0	8	12	4	1E+10	16	20000	12	22500	8	25000	0	8
5	C	0	3	20	30350	1	3	0	0	20	23	3	1E+10	20	30350	15	34143,75	10	37937,5	0	20
6	D	1	7	16	15500	1	3	12	12	32	32	4	1E+10	16	15500	12	17437,5	8	19375	12	28
7	E	2	4	12	31500	3	3	8	12	20	25	5	1E+10	24	25200	18	28350	12	31500	8	20
8	F	5	6	20	35000	1	3	12	12	32	32	0	875	20	35000	15	39375	10	43750	12	32
9	G	3	9	16	21050	1	3	20	23	36	39	3	1E+10	16	21050	12	23681,25	8	26312,5	20	36
10	H	4	8	12	17800	1	3	20	25	32	37	5	1E+10	12	17800	9	20025	6	22250	20	32
11	I	7	12	14	41000	3	3	32	32	46	46	0	1E+10	28	32800	21	36900	14	41000	32	46
12	J	10	11	9	16593,75	2	3	32	37	41	46	5	1E+10	12	14750	9	16593,75	6	18437,5	32	41
13	K	9	13	9	16875	2	3	36	39	45	48	3	1E+10	12	15000	9	16875	6	18750	36	45
14	L	12	14	10	22500	3	3	46	46	56	56	0	1E+10	20	18000	15	20250	10	22500	46	56
15	M	13	14	8	24750	3	3	45	48	56	56	3	1E+10	16	19800	12	22275	8	24750	45	53
16																					
17												Recomme	Unit Acceleration Cost								
18					323418,8	Direct Cos	Indirect C	Total Cost				F	875								
19					56	323418,8	280000	603419							9						
20	Node	EET	LET												12	13,5					
21	0	0	0						Acceleration	Act	Duration	Direct Cos	Indirect C	Total Cost							
22	1	12	12						0	--	84	290750	420000	710750							
23	2	8	12						1	L	80	293000	400000	693000							
24	3	20	23						2	E	79	296150	395000	691150							
25	4	20	25						3	L	74	298400	370000	668400							
26	5	12	12						4	E,I	68	305650	340000	645650							
27	6	32	32						5	M	67	308125	335000	643125							
28	7	32	32						6	I	64	312225	320000	632225							
29	8	32	37						7	J,M	60	316543,8	300000	616543,75							
30	9	36	39						8	B	56	319043,8	280000	599043,75							
31	10	32	37						9	B,K											
32	11	41	46						10												
33	12	46	46						11												
34	13	45	48						12												
35	14	56	56						13												
36									14												

Fig. 11. At the 9th Acceleration step activity K is also accelerated during the heuristic solution of DTCTP

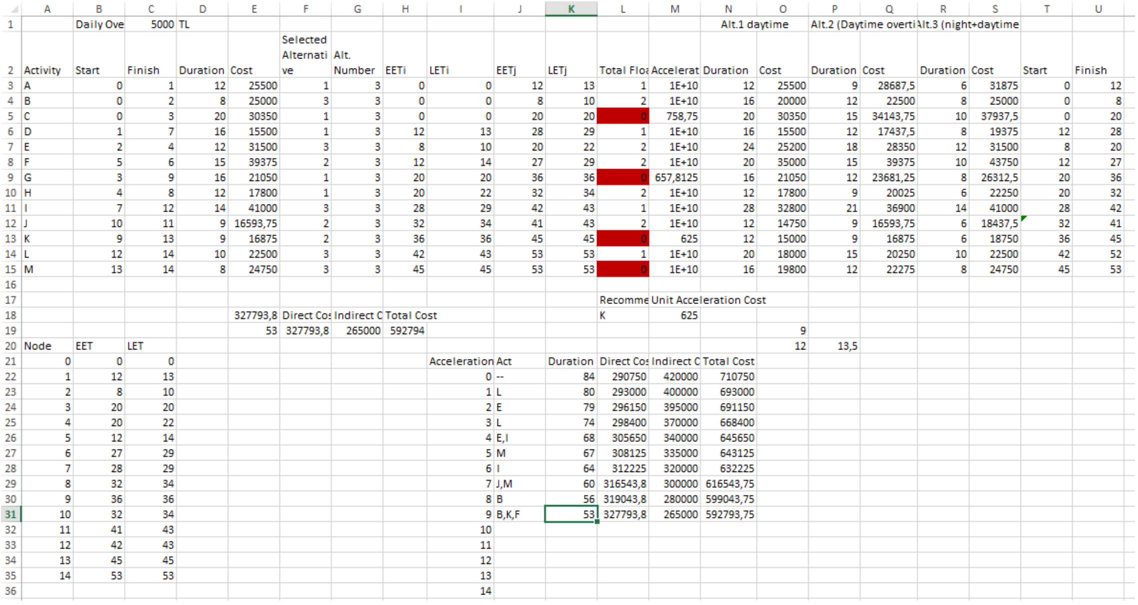

	A	B	C	D	E	F	G	H	I	J	K	L	M	N	O	P	Q	R	S	T	U
1		Daily Ove	5000	TL										Alt.1 daytime		Alt.2 (Daytime overti		Alt.3 (night+daytime			
2	Activity	Start	Finish	Duration	Cost	Selected Alternati ve	Alt. Number	EETi	LETi	EETj	LETj	Total Floa	Accelerat	Duration	Cost	Duration	Cost	Duration	Cost	Start	Finish
3	A	0	1	12	25500	1	3	0	0	12	13	1	1E+10	12	25500	9	28687,5	6	31875	0	12
4	B	0	2	8	25000	3	3	0	0	8	10	2	1E+10	16	20000	12	22500	8	25000	0	8
5	C	0	3	20	30350	1	3	0	0	20	20	0	758,75	20	30350	15	34143,75	10	37937,5	0	20
6	D	1	7	16	15500	1	3	12	13	28	29	1	1E+10	16	15500	12	17437,5	8	19375	12	28
7	E	2	4	12	31500	3	3	8	10	20	22	2	1E+10	24	25200	18	28350	12	31500	8	20
8	F	5	6	15	39375	2	3	12	14	27	29	2	1E+10	20	35000	15	39375	10	43750	12	27
9	G	3	9	16	21050	1	3	20	20	36	36	0	657,8125	16	21050	12	23681,25	8	26312,5	20	36
10	H	4	8	12	17800	1	3	20	22	32	34	2	1E+10	12	17800	9	20025	6	22250	20	32
11	I	7	12	14	41000	3	3	28	29	42	43	1	1E+10	28	32800	21	36900	14	41000	28	42
12	J	10	11	9	16593,75	2	3	32	34	41	43	2	1E+10	12	14750	9	16593,75	6	18437,5	32	41
13	K	9	13	9	16875	2	3	36	36	45	45	0	625	12	15000	9	16875	6	18750	36	45
14	L	12	14	10	22500	3	3	42	43	53	53	1	1E+10	20	18000	15	20250	10	22500	42	52
15	M	13	14	8	24750	3	3	45	45	53	53	0	1E+10	16	19800	12	22275	8	24750	45	53
16																					
17												Recomme	Unit Acceleration Cost								
18					327793,8	Direct Cos	Indirect C	Total Cost				K	625								
19					53	327793,8	265000	592794							9						
20	Node	EET	LET												12	13,5					
21	0	0	0						Acceleration	Act	Duration	Direct Cos	Indirect C	Total Cost							
22	1	12	13						0	--	84	290750	420000	710750							
23	2	8	10						1	L	80	293000	400000	693000							
24	3	20	20						2	E	79	296150	395000	691150							
25	4	20	22						3	L	74	298400	370000	668400							
26	5	12	14						4	E,I	68	305650	340000	645650							
27	6	27	29						5	M	67	308125	335000	643125							
28	7	28	29						6	I	64	312225	320000	632225							
29	8	32	34						7	J,M	60	316543,8	300000	616543,75							
30	9	36	36						8	B	56	319043,8	280000	599043,75							
31	10	32	34						9	B,K,F	53	327793,8	265000	592793,75							
32	11	41	43						10												
33	12	42	43						11												
34	13	45	45						12												
35	14	53	53						13												
36									14												

Fig. 12. Result of the 9th acceleration step.

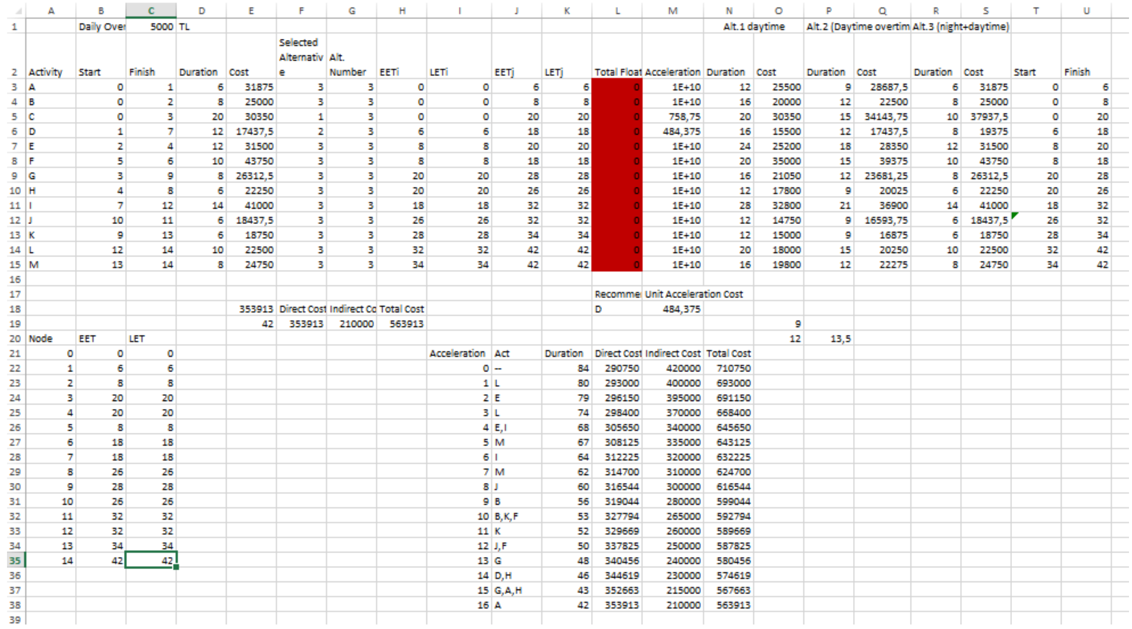

	A	B	C	D	E	F	G	H	I	J	K	L	M	N	O	P	Q	R	S	T	U
1		Daily Ove	5000	TL										Alt.1 daytime		Alt.2 (Daytime overtim		Alt.3 (night+daytime)			
2	Activity	Start	Finish	Duration	Cost	Selected Alternativ e	Alt. Number	EETi	LETi	EETj	LETj	Total Float	Acceleration	Duration	Cost	Duration	Cost	Duration	Cost	Start	Finish
3	A	0	1	6	31875	3	3	0	0	6	6	0	1E+10	12	25500	9	28687,5	6	31875	0	6
4	B	0	2	8	25000	3	3	0	0	8	8	0	1E+10	16	20000	12	22500	8	25000	0	8
5	C	0	3	20	30350	1	3	0	0	20	20	0	758,75	20	30350	15	34143,75	10	37937,5	0	20
6	D	1	7	12	17437,5	2	3	6	6	18	18	0	484,375	16	15500	12	17437,5	8	19375	6	18
7	E	2	4	12	31500	3	3	8	8	20	20	0	1E+10	24	25200	18	28350	12	31500	8	20
8	F	5	6	10	43750	3	3	8	8	18	18	0	1E+10	20	35000	15	39375	10	43750	8	18
9	G	3	9	8	26312,5	3	3	20	20	28	28	0	1E+10	16	21050	12	23681,25	8	26312,5	20	28
10	H	4	8	6	22250	3	3	20	20	26	26	0	1E+10	12	17800	9	20025	6	22250	20	26
11	I	7	12	14	41000	3	3	18	18	32	32	0	1E+10	28	32800	21	36900	14	41000	18	32
12	J	10	11	6	18437,5	3	3	26	26	32	32	0	1E+10	12	14750	9	16593,75	6	18437,5	26	32
13	K	9	13	6	18750	3	3	28	28	34	34	0	1E+10	12	15000	9	16875	6	18750	28	34
14	L	12	14	10	22500	3	3	32	32	42	42	0	1E+10	20	18000	15	20250	10	22500	32	42
15	M	13	14	8	24750	3	3	34	34	42	42	0	1E+10	16	19800	12	22275	8	24750	34	42
16																					
17												Recomme	Unit Acceleration Cost								
18					353913	Direct Cost	Indirect Co	Total Cost				D	484,375								
19					42	353913	210000	563913							9						
20	Node	EET	LET												12	13,5					
21	0	0	0						Acceleration	Act	Duration	Direct Cost	Indirect Cost	Total Cost							
22	1	6	6						0	--	84	290750	420000	710750							
23	2	8	8						1	L	80	293000	400000	693000							
24	3	20	20						2	E	79	296150	395000	691150							
25	4	20	20						3	L	74	298400	370000	668400							
26	5	8	8						4	E,I	68	305650	340000	645650							
27	6	18	18						5	M	67	308125	335000	643125							
28	7	18	18						6	I	64	312225	320000	632225							
29	8	26	26						7	M	62	314700	310000	624700							
30	9	28	28						8	J	60	316544	300000	616544							
31	10	26	26						9	B	56	319044	280000	599044							
32	11	32	32						10	B,K,F	53	327794	265000	592794							
33	12	32	32						11	K	52	329669	260000	589669							
34	13	34	34						12	J,F	50	337825	250000	587825							
35	14	42	42						13	G	48	340456	240000	580456							
36									14	D,H	46	344619	230000	574619							
37									15	G,A,H	43	352663	215000	567663							
38									16	A	42	353913	210000	563913							
39																					

Fig. 13. Optimum result achieved after 16 acceleration steps by the heuristic algorithm

After 16 acceleration steps, heuristic solution algorithm has reached the optimum result. The optimized project duration is 42 time units and the total project cost is 563912.5 TL. The short revision of the construction schedule provides a reduction of 40 time units and a saving of 146837.5 TL compared to the initial schedule obtained with the first construction modes of the activities.

Time-cost trade-off problem is solved by selecting proposed alternatives for the appropriate activities by the spreadsheet application. When the proposed activities are accelerated in order, the results presented in Table 2 are obtained. In Table 2, Cr A represents the crashed activity. Direct costs are the construction costs of each activity for the selected alternative. Indirect costs are obtained by multiplying the daily cost by the total project duration. In the later stages of the optimization process, the network has more than one critical path. In this case, more than one activity may need to be accelerated. In some table rows, the total project duration does not change even if a critical activity is accelerated. In this case, the accelerated critical path becomes non-critical and the remaining critical path prevents the project duration from being shortened. The project duration is 84 time units and the total cost is 710750 TL. The optimized project duration is 42 time units and the total project cost is 563912.5 TL. The short revision of the construction schedule provides a reduction of 40 time units and a saving of 146837.5 TL.

Table 2. Activity crashing sequence applied to solve the time-cost trade-off problem.

Step	Cr A	Project Duration	Direct Cost	Overhead Cost	Total Cost
0	YOK	84	290750	420000	710750
1	L	80	293000	400000	693000
2	E	79	296150	395000	691150
3	L	74	298400	370000	668400
4	E,I	68	305650	340000	645650
5	M	67	308125	335000	643125
6	I	64	312225	320000	632225
7	M	62	314700	310000	624700
8	J	60	316543.8	300000	616543.8
9	B	56	319043.8	280000	599043.8
10	B,K,F	53	327793.8	265000	592793.8
11	K	52	329668.8	260000	589668.8
12	J,F	50	337825	250000	587825
13	G	48	340456.3	240000	580456.3
14	D,H	46	344618.8	230000	574618.8
15	G,A,H	43	352662.5	215000	567662.5
16	A	42	353912.5	210000	563912.5

4. Conclusions

Construction sector is focused on the execution of the project scope on time and within budget. Therefore, utilization of sophisticated algorithms during the scheduling phase is not the priority of the construction firms. As a result of this, initial construction schedule is not improved and the contractors lose the opportunity of reductions in the total project cost. In this study time-cost trade-off problem is solved by a heuristic method which is based on minimum cost slope. The computations are formulated with parameters and the solution process is automated.

The developed application is used to solve 13-activity problem. The application proposed the most suitable critical activity to be crashed and the necessity computations of the crashing process is done. The spreadsheet application significantly reduces the computational burden and assists the scheduler to make deeper analysis and investigations as the scheduler only shifts the utilization mode of the alternative and the rest of the calculations are done by the developed application. The construction sector frequently utilizes spreadsheets for their scheduling tasks and therefore the proposed approach can be utilized by the construction companies.

Acknowledgments

This study is supported by the Scientific Research Project Coordination of İnönü University with grant number FYL-2025-3857.

References

Agarwal, A. K., Chauhan, S. S., Sharma, K., & Sethi, K. C. (2024). Development of time–cost trade-off optimization model for construction projects with MOPSO technique. *Asian Journal of Civil Engineering*, 1–11.

Akkoyunlu, M. C., & Engin, O. (2011). Kesikli Harmoni Arama Algoritması ile optimizasyon problemlerinin çözümü: Literatür araştırması. *Selçuk Üniversitesi Mühendislik, Bilim ve Teknoloji Dergisi*, 26(4), 140–148.

Al-Shihabi, S., & AlDurgam, M. M. (2020). The contractor time–cost–credit trade-off problem: Integer programming model, heuristic solution, and business insights. *International Transactions in Operational Research*, 27(6), 2841–2877.

Ammar, M. A. (2011). Optimization of project time-cost trade-off problem with discounted cash flows. *Journal of Construction Engineering and Management*, 137(1), 65–71.

Anagnostopoulos, K. P., & Kotsikas, L. (2010). Experimental evaluation of simulated annealing algorithms for the time–cost trade-off problem. *Applied Mathematics and Computation*, 217(1), 260–270.

Ballesteros-Pérez, P., Elamrousy, K. M., & González-Cruz, M. C. (2019). Non-linear time-cost trade-off models of activity crashing: Application to construction scheduling and project compression with fast-tracking. *Automation in Construction*, 97, 229–240.

Banihashemi, S. A., & Mohammad, M. (2022). Time-cost-quality-risk trade-off project scheduling problem in oil and gas construction projects: Fuzzy logic and genetic algorithm. *Jordan Journal of Civil Engineering*, 16(2).

Bettemir, Ö. H., & Bulak, Ö. (2022). İnşaat sürecinin iş çizelgelemesi, yönetimi ve optimizasyonu. *Teknik Dergi*, 33(6), 12945–12986.
Bettemir, Ö. H., & Yücel, T. (2021). Zaman maliyet ödünleşim probleminin en az insan müdahalesi ile oluşturulup çözülmesi. *Uludağ Üniversitesi Mühendislik Fakültesi Dergisi*, 26(2), 461–480.
Bettemir, Ö. H., & Yücel, T. (2023). Simplified solution of time-cost trade-off problem for building constructions by linear scheduling. *Jordan Journal of Civil Engineering*, 17(2).
Bettemir, Ö. H., & Birgönül, M. T. (2025). Solution of discrete time–cost trade-off problem with adaptive search domain. *Engineering, Construction and Architectural Management*, 32(2), 1032–1052.
Bettemir, Ö. H., & Talat Birgönül, M. (2017). Network analysis algorithm for the solution of discrete time-cost trade-off problem. *KSCE Journal of Civil Engineering*, 21, 1047–1058.
Cheng, M. Y., & Tran, D. H. (2015). Opposition-based multiple objective differential evolution (OMODE) for optimizing work shift schedules. *Automation in Construction*, 55, 1–14.
Cura, T. (2008). Doğrusal olmayan küresel optimizasyon problemleri için tabu arama algoritmasının kullanılması. *İstanbul Üniversitesi İşletme Fakültesi Dergisi*, 37(1), 22–38.
Geem, Z. W. (2010). Multiobjective optimization of time-cost trade-off using harmony search. *Journal of Construction Engineering and Management*, 136(6), 711–716.
Geem, Z. W. (Ed.). (2009). *Music-inspired harmony search algorithm: Theory and applications* (Vol. 191). Springer Science & Business Media.
Jun, D. H., & El-Rayes, K. (2010). Optimizing the utilization of multiple labor shifts in construction projects. *Automation in Construction*, 19(2), 109–119.
Luong, D. L., Tran, D. H., & Nguyen, P. T. (2021). Optimizing multi-mode time-cost-quality trade-off of construction project using opposition multiple objective differential evolution. *International Journal of Construction Management*, 21(3), 271–283.
Maravas, A., & Pantouvakis, J. P. (2012). Project cash flow analysis in the presence of uncertainty in activity duration and cost. *International Journal of Project Management*, 30(3), 374–384.
Yılmaz, M., & Dede, T. (2023, February). Multi-objective time–cost trade-off optimization for the construction scheduling with Rao algorithms. In *Structures* (Vol. 48, pp. 798–808). Elsevier.

4th International Civil Engineering & Architecture Conference
17-19 May 2025, Trabzon, Türkiye

Generating a Dynamo-based quantity takeoff from BIM models: A case study

Ümit Bahadır*[1], Vedat Toğan[1]

[1] Karadeniz Technical University, Department of Civil Engineering, 61080 Trabzon, Türkiye

Abstract. Nowadays, Building Information Modeling (BIM) tools offer significant opportunities for automation, integration, and data consistency in the design and management phases of construction projects. This study aims to generate comprehensive quantity takeoff for all critical project components by extracting the concrete and formwork quantities of structural elements—such as foundations, columns, beams, slabs, and staircases—as well as the quantities of walls, doors, and windows from 3D BIM models using Dynamo software. The developed algorithm will be tested on a sample project. Compared to traditional quantity surveying processes, the proposed method provides faster data processing and a reduced error rate, thereby making important contributions to project management and cost control. When integrated with on-site construction practices, the model-based data collection process facilitates decision-making based on up-to-date information. This study underscores the impact of effectively utilizing digital model data in the quantity estimation process, particularly for large-scale construction projects. The findings indicate that systematically integrating tools such as BIM and Dynamo can enhance efficiency throughout construction processes.

Keywords: Automated data processing; BIM; Dynamo; Quantity takeoff

1. Introduction

Quantity takeoff (QTO), a critical component of construction project management and cost control, traditionally involves manual calculations based on two-dimensional (2D) drawings. This process is labor-intensive, time-consuming, and prone to errors, primarily due to the varied interpretations of project details (Monteiro & Martins, 2013; Khosakitchalert et al., 2020). These inconsistencies can lead to significant discrepancies in project budgets and planning processes (Monteiro & Martins, 2013; Pham et al., 2024). Measurement errors in building components result in incorrect material orders and disruptions in scheduling, jeopardizing timely project completion and adherence to projected budgets (Tserng et al., 2006; Bahadır, 2025).

In recent years, Building Information Modeling (BIM) has significantly improved QTO processes by enabling automated data integration and providing higher accuracy compared to traditional methods (Bečvarovská & Matějka, 2014; Heigermoser et al., 2019). BIM-based methods allow the geometric and semantic information of building elements to be automatically extracted directly from digital models, substantially reducing errors and accelerating the QTO process (Sacks et al., 2018). For instance, BIM methods reportedly achieve up to 80% time savings and accuracy rates above 97% compared with traditional approaches (Olsen & Taylor, 2017). However, inaccuracies in BIM-based quantity takeoffs can still occur because of a low Level of Development (LOD) or incomplete modeling processes, resulting in lower-quality data (Smith, 2014; Le & Cong, 2023).

The current literature indicates that BIM models created during the design stages often lack the necessary detail required for accurate quantity extraction (Khosakitchalert et al., 2019; Sattineni & Bradford, 2011). Typically, these models focus on architectural visualizations and presentations, necessitating further refinement and adjustments for quantity calculations (Kensek & Noble , 2014). This issue limits the full potential of BIM-based QTO, adding extra time and cost (Franco et al., 2015; Bahadır, 2025). Additionally, incorrect modeling, such as geometric clashes or improperly modeled layered components, can lead to quantity overestimation, negatively impacting cost estimates (Khosakitchalert et al., 2018).

Recently, visual programming tools, such as Dynamo, have gained attention for automating the extraction of quantities from BIM models. Dynamo facilitates the rapid analysis of building elements, detection of overlapping areas, and accurate calculation of quantities, thus significantly speeding up the QTO process (Url-1, 2025; Cepni et al., 2020). The current study adopted this approach to automatically generate comprehensive quantity lists

* Corresponding author, E-mail: umitbahadir@ktu.edu.tr

https://doi.org/10.31462/icearc2025_ce_mng_429

covering a wide range of building elements, from structural components (foundations, columns, beams, slabs and walls) to architectural elements (walls, doors and windows).

The primary objective of this study is to develop a Dynamo-based method for comprehensive and automated quantity extraction from BIM models. This aims to enhance cost control and resource planning efficiency in construction projects. By addressing existing gaps in the literature, particularly errors arising from incomplete or incorrect BIM modeling, this study seeks to significantly improve the accuracy and reliability of BIM-based QTO processes.

2. Literature review

Traditional QTO has historically relied on manual methods using 2D drawings. Jadid & Idrees (2007) proposed an automated approach that recognizes structural elements from 2D CAD drawings, significantly enhancing accuracy and efficiency. Manrique et al. (2015) introduced a 3D CAD-based system that generates detailed material quantities for wood-framing walls, streamlining the shop-drawing production process. However, such solutions rely on consistent layer naming and drawing quality, which limits their broader applicability (Khosakitchalert et al., 2020).

The shift towards BIM has introduced advanced methods for QTO, significantly improving efficiency and accuracy. BIM-based approaches facilitate the direct extraction of geometric and semantic data from digital models, thereby reducing the manual errors inherent in traditional methods (Sacks et al., 2018). Bečvarovská & Matějka (2014) conducted comparative case studies demonstrating substantial reductions in both time and inaccuracies through a BIM-based QTO compared with conventional approaches.

However, several studies have highlighted the challenges associated with BIM-based methods, which are primarily linked to model quality and completeness. Smith (2014) emphasized that insufficient BIM model quality and validation methods limit their effectiveness for QTO. Firat et al. (2010) concluded that BIM models need clearer guidelines and standards to ensure their usability for accurate QTO. Olsen & Taylor (2017) identified that BIM models often contain only half of the required data for comprehensive quantity takeoffs, particularly lacking detail in areas like architectural finishes and temporary structures.

Researchers have proposed numerous innovative solutions to address these limitations. For example, Choi et al. (2015) developed a BIM-based system specifically designed for quantity extraction of structural elements at early design stages, including built-in quality checks to enhance reliability. Rajabi et al. (2015) proposed a logic-based approach to estimate the quantities of lighting and heating appliances typically omitted from BIM models, integrating additional calculations to fill the gaps in standard modeling processes.

Cho & Chun (2015) combined BIM-based quantity extraction with data prediction algorithms to accurately estimate the quantities of reinforced concrete structures, thereby addressing uncertainties in early stage modeling. Lim et al. (2016) introduced algorithms specifically tailored for automated rebar quantity extraction from 3D structural models, which significantly improved the precision of structural engineering projects. Kim et al. (2009) developed an automatic modeling system to generate interior wall finishes directly from room data, enhancing accuracy and reducing manual workload.

Moreover, Aram et al. (2014) proposed a knowledge-based system framework aimed at automating precast concrete QTO processes, leveraging detailed BIM data to improve precision and efficiency. Cheung et al. (2012) introduced a real-time cost estimation system based on gross floor areas extracted from early stage BIM models, enabling rapid and accurate preliminary cost assessments. In the domain of schedule-driven material planning, Khosakitchalert et al. (2018) computed zone-specific concrete and formwork volumes, whereas Cepni et al. (2020) employed Dynamo to calculate formwork for complex geometries and benchmarked automated outputs against manual take-off durations. However, these contributions typically concentrate on a single material category or structural subsystem, and few integrate architectural components, such as openings, doors, windows, and façade finishes, into a unified bill of quantities (BOQ).

The LOD of BIM models significantly influences QTO accuracy. Monteiro & Martins (2013) highlighted that LOD 300 is generally sufficient for QTO; however, compound elements require at least LOD 350 for accurate layer separation and detailed quantity extraction. According to Leite et al. (2011), transitioning from one LOD to another can substantially increase the modeling time and costs, creating a critical practical consideration for BIM-based QTO implementation.

The literature consistently supports the assertion that BIM-based QTO significantly enhances productivity, accuracy, and completeness of cost estimation compared to traditional methods (Alathamneh et al., 2024). Recent studies have provided empirical evidence and discussions highlighting the advantages of various digital tools and methods (Wardito & Husin, 2024; Wahab & Wang, 2022). Commonly proposed solutions involve the use of specialized software platforms such as Autodesk Revit, Navisworks (Shick Alshabab et al., 2020), Cubicost (Tamrin et al., 2024; Soon et al., 2024), and Allplan (Saputra et al., 2020). Alternative approaches include IFC-based BIM (Yang et al., 2024), ontological algorithms (Ergen & Bettemir, 2024), knowledge graph frameworks (Liu et al., 2022), and digital technologies like scan-to-BIM (Jamal et al., 2021) and virtual reality (Bademosi et al., 2019), each aimed at automating and improving QTO processes. However, many theoretical models lack validation through practical implementation (Nguyen et al., 2024). Despite this, advanced integrated frameworks incorporating automatic data extraction, precision checking modules, and interactive visualization dashboards, such as those utilizing Microsoft Power BI, demonstrate high-level automation capabilities and effectiveness in BIM-based QTO (Valinejadshoubi et al., 2024).

These studies collectively underscore the evolving nature of BIM-based QTO methodologies, emphasizing continuous improvements in automation, data integration, and model accuracy. This study proposes a Dynamo-based method that extracts concrete, formwork, and key architectural quantities from a single Revit model without additional modelling effort, thereby extending previous algorithmic approaches to a broader set of building components and delivery requirements.

3. Methodology

The research methodology was structured to demonstrate how a fully digital workflow, grounded in Autodesk Revit 2024 and Dynamo 2.19, can deliver a complete BOQs without additional manual modelling effort. Drawing on the goals established in the preceding sections, this study isolates three sequential phases. First, a project-specific BIM model was prepared with sufficient geometric and semantic details to support the quantity extraction. Second, Dynamo visual-programming scripts were developed to filter model objects, resolve overlaps, and compute material volumes and counts for both structural and architectural components. Third, the workflow was validated through a real-world case project in which automated outputs were benchmarked against conventional takeoff records and on-site measurements. The following subsections elaborate on these phases, highlighting the interplay between model preparation, script logic, and empirical verification.

3.1. Creation of the 3D BIM model

The reliability of the automated workflow depends on the rigorous modelling protocols applied in Autodesk Revit. Therefore, two fundamental constraints were imposed: (i) delimitation of the building elements to be analysed, and (ii) enforcement of a consistent naming scheme that enables unambiguous filtering by Dynamo scripts.

Scope of building elements: The model is limited to primary structural members—foundations, columns, beams, slabs, stairs, and shear walls—and to key architectural items such as walls, doors, and windows. Mechanical, electrical, plumbing, façade systems, and temporary works were excluded to avoid superfluous geometry and parameters that could compromise data integrity.

Element naming scheme: Because the Revit categories frequently host heterogeneous objects, a keyword-based convention was adopted to eliminate selection errors during script execution. In this study, the Type Name attribute of some object must include a distinguishing keyword— the term “Foundation” for structural foundation elements, “Floor” for slabs, “Structural” for shear walls, and “Wall” for all other architectural wall instances—thereby eliminating selection errors during script execution. No additional keywords are required for the remaining elements. Table 1 shows the elements and naming conventions used in this study.

The two constraints outlined above underpin the data integrity of subsequent methodological steps. Compliance ensures that the Dynamo scripts operate without misclassification and that the resulting QTO is both accurate and reproducible.

3.2. Development of Dynamo scripts

This study implements three dedicated Dynamo scripts—Parameter Creation (DYN-01), Formwork Calculation (DYN-02) and Quantity Schedule Generation (DYN-03)—that operate sequentially on the Autodesk Revit model. The cascade ensures that the output of each stage is passed directly to the next, thereby limiting user intervention and eliminating cumulative error throughout the workflow.

Table 1. Considered elements and naming conventions

Element	Category	Naming convention
Structural Foundation	Structural Foundations	Must include the “Foundation”.
Structural Column	Structural Columns	There is no rule.
Shear Wall	Walls	Must include the “Structural”.
Beam	Structural Framing	There is no rule.
Slab	Floors	Must include the “Floor”.
Stair	Stairs	There is no rule.
Architectural Wall	Walls	Must include the “Wall”.
Door	Doors	There is no rule.
Window	Windows	There is no rule.

3.2.1. Parameter creation script (DYN-01)

Because Revit lacks several fields required for the planned QTO, DYN-01 programmatically inserts three instance parameters: Total Formwork Quantity (Structural Foundations category), Volume (Stairs category) and Formwork Quantity (Generic Models category). Each parameter is defined through the Project Parameters API as a Number data type and assigned to the General group for ease of inspection. Table 2 summarizes their principal attributes, and an overall diagram of the parameter workflow is presented in Fig. 1.

3.2.2. Formwork and stair concrete volume calculation script (DYN-02)

The second Dynamo script automatically derives formwork areas and stair concrete volumes from the 3D BIM model through a three-stage procedure. In the first stage, stair elements are isolated and converted to solid geometry; their volumes are computed via the Solid.Volume node, converted to cubic meters, and written to the Volume instance parameter. The concrete requirement for all stairs is therefore stored directly at element level and can be referenced in later reporting without re-calculation. Fig. 2 shows the Dynamo script developed for calculating the stair concrete volume.

The second stage targets elements that require formwork: foundations, columns, beams, slabs, shear walls, and stairs. These objects were unioned into single solids (Solid.ByUnion), converted to polysurfaces (PolySurface.BySolid), and decomposed into individual faces (PolySurface.Surfaces), as shown in Fig. 3. Face normals were examined to classify surfaces as horizontal or vertical; the corresponding areas were converted to square meters and populated in the Formwork Quantity parameter. At this point, all formwork surfaces, except the underside of the stairs, were quantified.

The third stage addresses the stair soffit. Geometric and specification data already embedded in Revit—Desired Stair Height, Actual Tread Depth, Desired Number of Risers, and Minimum Run Width—are retrieved through Elements.GetParameterValueByName. Using the formulation implemented in Fig. 4, the soffit area is calculated and added to Formwork Quantity.

Table 2. Defined project parameters and key features

Parameter name	Parameter application type	Application category	Data type	Revit group
Total Formwork Quantity	Instance	Structural Foundations	Number	General
Formwork Quantity	Instance	Generic Models	Number	General
Volume	Instance	Stairs	Number	General

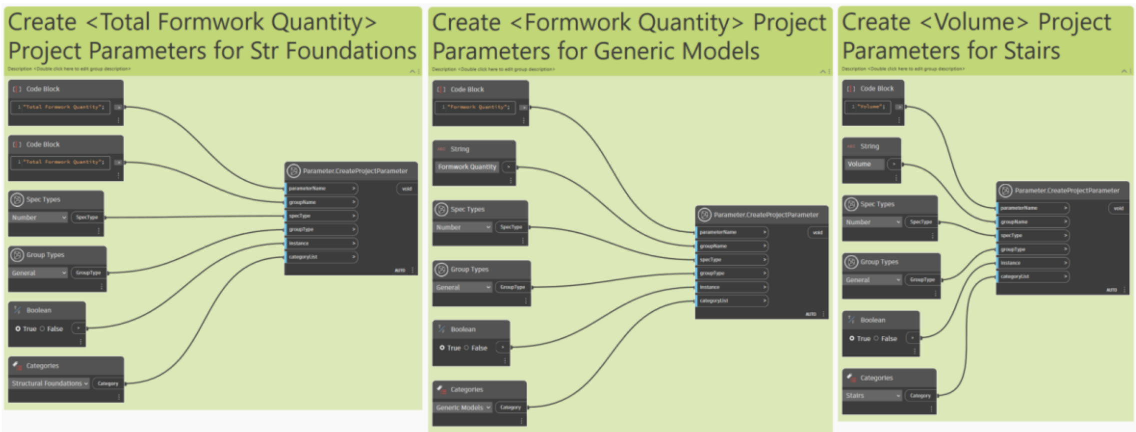

Fig. 1. Parameter creation script

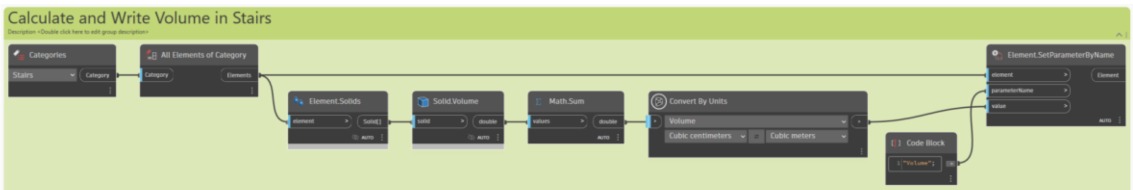

Fig. 2. Stair concrete volume script

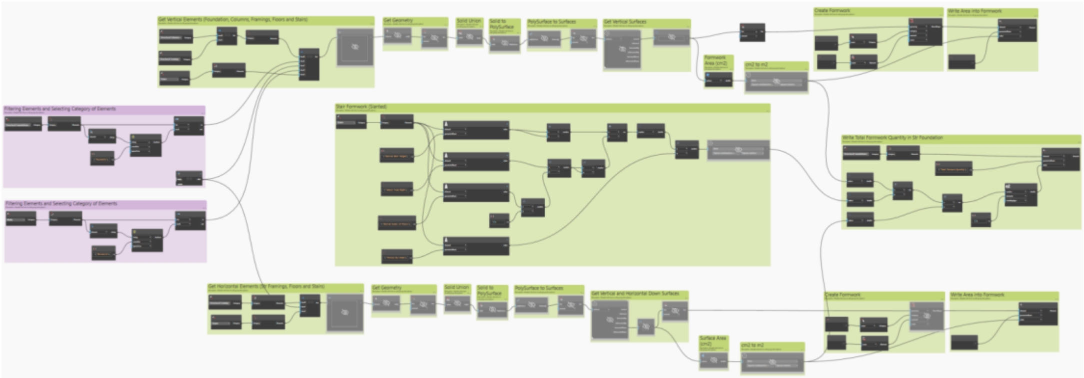

Fig. 3. Formwork calculation script

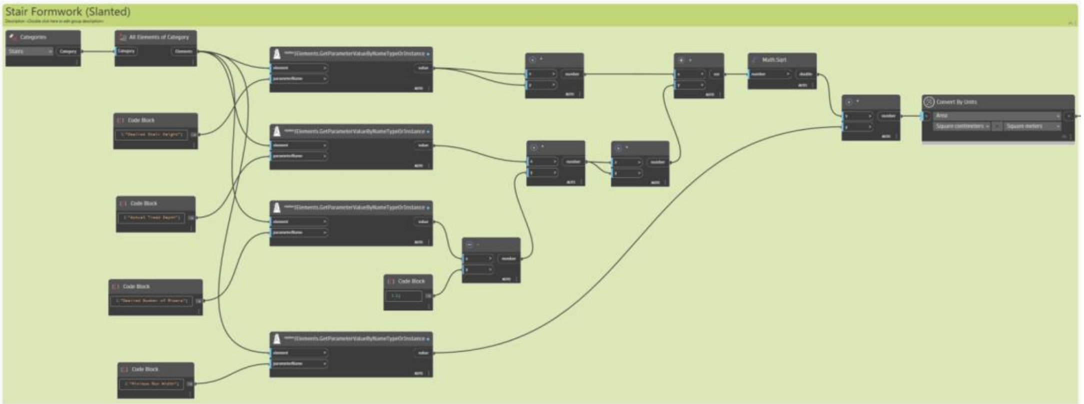

Fig. 4. Stair soffit formwork calculation script

Finally, the horizontal and vertical surface areas, together with the calculated stair soffit, were aggregated and assigned to the Total Formwork Quantity parameter (Fig. 3). This layered strategy ensures that the complete formwork requirement is consistently reported, even when Generic Model surfaces extend across multiple levels or cannot be directly attributed to a single building element.

3.2.3. Quantity schedule generation script (DYN-03)

The third Dynamo script automatically compiles quantitative data for the selected categories into Revit Schedule/Quantities tables, thereby unifying geometric metrics (e.g., volume, area, length) with the project-specific parameters created in earlier steps. The overall logic of the script is illustrated in Fig. 5.

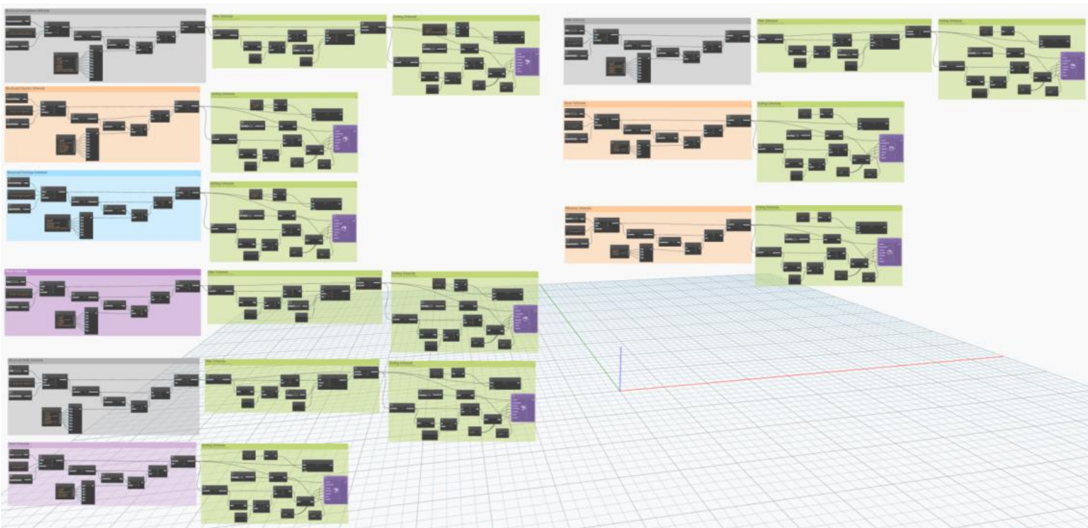

Fig. 5. Quantity schedule generation script

The script first defined the scope: foundations, columns, beams, slabs, shear walls, stairs, architectural walls, doors, and windows, and the set of fields to be displayed for each category. A schedule is then instantiated per category; rows are filtered by element name and level to retain only relevant items (Fig. 6), whereas an embedded Python node sorts the output in ascending order and appends automatic totals for selected fields (Fig. 7). This approach enables rapid verification of both native and user-defined parameters before exporting the data to external cost-control tools.

As shown in Figs. 5-7, DYN-03 enables users to obtain up-to-date, category-specific quantity reports within seconds, verify the values populated in earlier scripts, and export the results as a BOQs ready for cost-management applications.

3.3. Case study

To assess the proposed Dynamo-based QTO workflow, a single-family villa in Trabzon (Türkiye) was modelled as a case study. This project was modelled in Autodesk Revit 2024 and developed to LOD 300, corresponding to the detailed-design phase. All modelling guidelines specified in Section 3.1 were strictly followed, ensuring that every structural and architectural element required by the study—foundations, columns, beams, slabs, shear walls, stairs, walls, doors, and windows— were present and correctly named. Additionally, only those elements expressly required by the study were modelled, whereas finishes, such as floor and wall coverings or ceiling systems, were purposefully excluded to avoid extraneous complexity.

The villa consists of three storeys—basement, ground, and first—each with a uniform storey height of 3.0 m. Perspective views from the northwest and southeast, together with an overall structural view, are shown in Figs. 8, 9, and 10, respectively. The floor areas amount to 40 m² for the basement and 127 m² for both the ground and first floors.

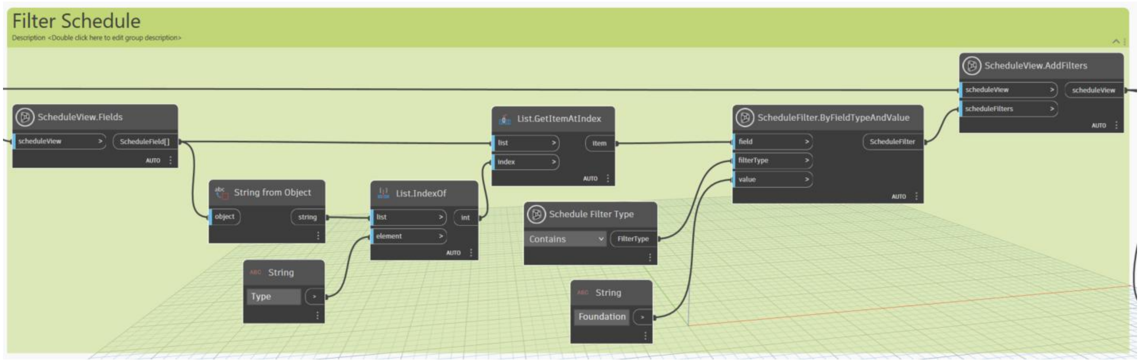

Fig. 6. Filtering of bill of quantities

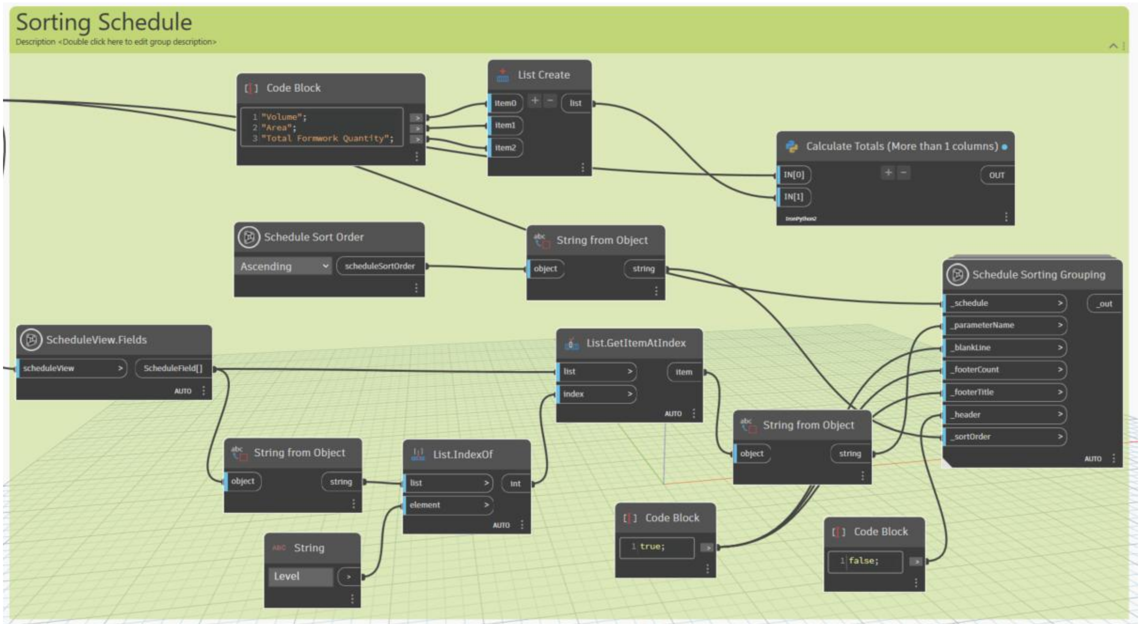

Fig. 7. Sorting of bill of quantities

Fig. 8. Northwest view of the 3D model

Fig. 9. Southeast view of the 3D model

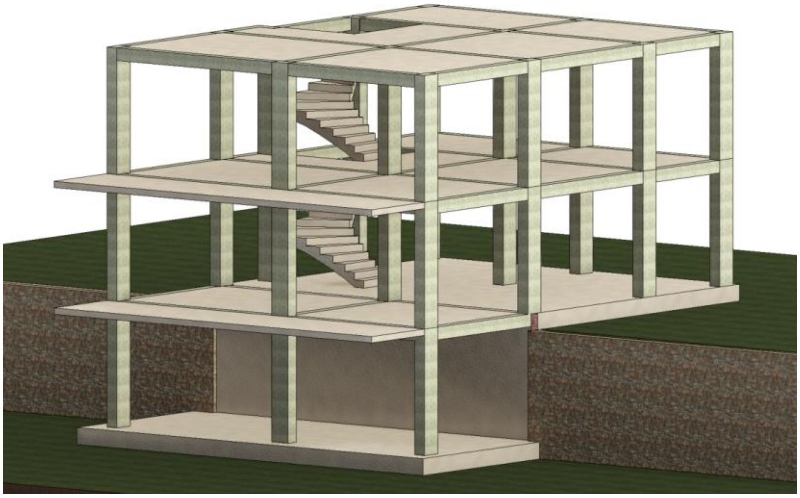

Fig. 10. Structural view of the 3D model

4. Results and discussion

The Dynamo-based automated QTO methodology was successfully validated through a real-world case study of a single-family villa project located in Trabzon, Türkiye. The practical implementation of the qualitatively studied Dynamo scripts (DYN-01, DYN-02, and DYN-03) demonstrated correct performance, efficiency, and reliability.

The Parameter Creation script (DYN-01) accurately adds the necessary parameters to the designated elements. Fig. 11 illustrates the successfully integrated parameters for the structural foundations and stairs within the Revit interface. These custom parameters provided the basis for subsequent quantity calculations, enabling precise and consistent data collection.

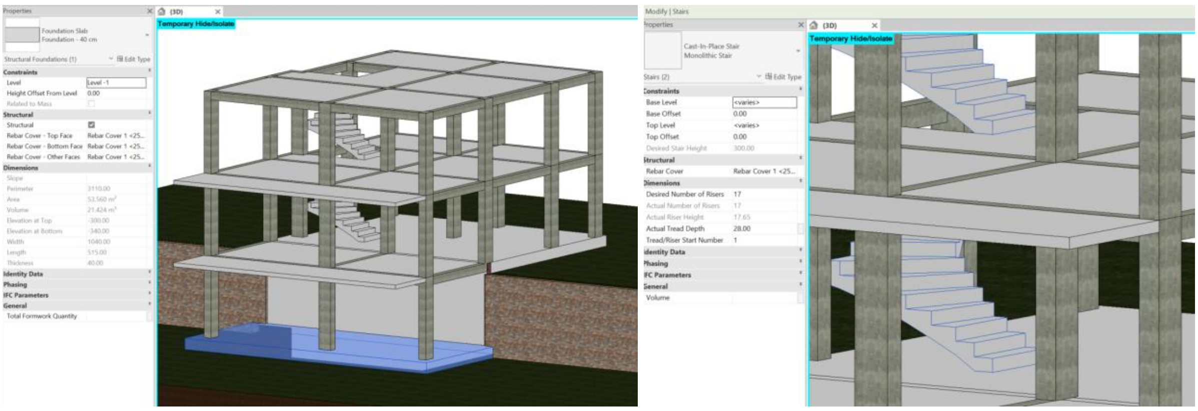

Fig. 11. Integrated parameters for foundation and stair elements in Revit

The Formwork Calculation script (DYN-02) effectively identified and quantified formwork surface areas and stair concrete volumes. Fig. 12 shows the automatically generated formwork surfaces in the Revit environment. From this visualization, it can be observed that specific scenarios, such as stair openings in slabs, correct formwork coverage of side surfaces, proper handling of connections between columns, beams, and slabs (without formwork at junctions), and accurate identification of formwork-exempt areas (e.g., upper and lower surfaces of foundations and columns), were effectively managed. Additionally, the calculated formwork areas were aligned closely with manual verifications, reinforcing the reliability and precision of the developed script in generating accurate project-specific quantities.

Further validation was conducted by examining the automatically generated Revit schedules using the Quantity Schedule Generation script (DYN-03). Fig. 13 demonstrates the detailed schedule of quantities produced for individual elements with examples of columns and architectural walls, confirming the accuracy and completeness of data extraction. This step critically verifies earlier script outcomes, facilitating error-free, rapid exportation of data for further cost management processes.

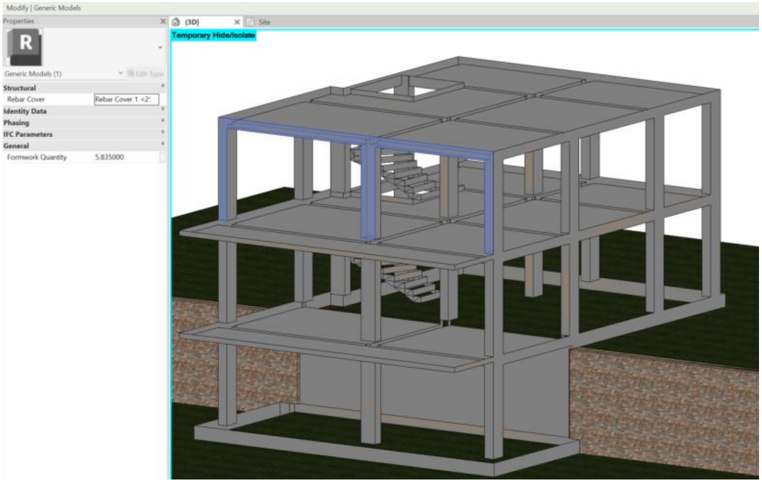

Fig. 12. Generated formwork surfaces visualization in Revit

<STRUCTURAL COLUMNS QUANTITY>

A	B	C	D	E	F	G	H	I
Count	Type	Family and Type	Volume	Top Offset	Base Offset	Top Level	Base Level	Length
1	30 x 50	M_Concrete-Rectan	0.45 m³	0	0	Level 1	Level -1	300
1	30 x 50	M_Concrete-Rectan	0.45 m³	0	0	Level 1	Level -1	300
1	30 x 50	M_Concrete-Rectan	0.45 m³	0	0	Level 1	Level -1	300
Level -1: 3			1.35 m³					
1	30 x 50	M_Concrete-Rectan	0.45 m³	0	0	Level 2	Level 1	300
1	30 x 50	M_Concrete-Rectan	0.45 m³	0	0	Level 2	Level 1	300
1	30 x 50	M_Concrete-Rectan	0.45 m³	0	0	Level 2	Level 1	300
1	30 x 50	M_Concrete-Rectan	0.45 m³	0	0	Level 2	Level 1	300
1	30 x 50	M_Concrete-Rectan	0.45 m³	0	0	Level 2	Level 1	300
1	30 x 50	M_Concrete-Rectan	0.45 m³	0	0	Level 2	Level 1	300
1	30 x 50	M_Concrete-Rectan	0.45 m³	0	0	Level 2	Level 1	300
1	30 x 50	M_Concrete-Rectan	0.45 m³	0	0	Level 2	Level 1	300
1	30 x 50	M_Concrete-Rectan	0.45 m³	0	0	Level 2	Level 1	300
1	30 x 50	M_Concrete-Rectan	0.45 m³	0	0	Level 2	Level 1	300
1	30 x 50	M_Concrete-Rectan	0.45 m³	0	0	Level 2	Level 1	300
1	30 x 50	M_Concrete-Rectan	0.45 m³	0	0	Level 2	Level 1	300
1	30 x 50	M_Concrete-Rectan	0.45 m³	0	0	Level 2	Level 1	300
Level 1: 13			5.85 m³					
1	30 x 50	M_Concrete-Rectan	0.45 m³	0	0	Level 3	Level 2	300
1	30 x 50	M_Concrete-Rectan	0.45 m³	0	0	Level 3	Level 2	300
1	30 x 50	M_Concrete-Rectan	0.45 m³	0	0	Level 3	Level 2	300
1	30 x 50	M_Concrete-Rectan	0.45 m³	0	0	Level 3	Level 2	300
1	30 x 50	M_Concrete-Rectan	0.45 m³	0	0	Level 3	Level 2	300
1	30 x 50	M_Concrete-Rectan	0.45 m³	0	0	Level 3	Level 2	300
1	30 x 50	M_Concrete-Rectan	0.45 m³	0	0	Level 3	Level 2	300
1	30 x 50	M_Concrete-Rectan	0.45 m³	0	0	Level 3	Level 2	300
1	30 x 50	M_Concrete-Rectan	0.45 m³	0	0	Level 3	Level 2	300
1	30 x 50	M_Concrete-Rectan	0.45 m³	0	0	Level 3	Level 2	300
1	30 x 50	M_Concrete-Rectan	0.45 m³	0	0	Level 3	Level 2	300
1	30 x 50	M_Concrete-Rectan	0.45 m³	0	0	Level 3	Level 2	300
1	30 x 50	M_Concrete-Rectan	0.45 m³	0	0	Level 3	Level 2	300
Level 2: 13			5.85 m³					
Grand total			13.05 m³					

a) Structural columns quantity

<WALLS QUANTITY>

A	B	C	D	E	F	G	H
Count	Type	Family and Type	Base Constraint	Width	Volume	Area	Length
1	Wall - 20 cm brick	Basic Wall: Wall - 2	Level -1	20	1.58 m^3	8 m^2	380
1	Wall - 20 cm brick	Basic Wall: Wall - 2	Level -1	20	1.64 m^3	8 m^2	465
1	Wall - 20 cm brick	Basic Wall: Wall - 2	Level -1	20	1.21 m^3	6 m^2	365
1	Wall - 20 cm brick	Basic Wall: Wall - 2	Level -1	20	1.87 m^3	10 m^2	365
1	Wall - 20 cm brick	Basic Wall: Wall - 2	Level -1	20	1.78 m^3	9 m^2	405
1	Wall - 10 cm brick	Basic Wall: Wall - 1	Level -1	10	0.38 m^3	4 m^2	148
1	Wall - 10 cm brick	Basic Wall: Wall - 1	Level -1	10	0.16 m^3	2 m^2	130
Level -1: 7						46 m^2	
1	Wall - 20 cm brick	Basic Wall: Wall - 2	Level 1	20	1.17 m^3	6 m^2	380
1	Wall - 20 cm brick	Basic Wall: Wall - 2	Level 1	20	1.63 m^3	8 m^2	465
1	Wall - 20 cm brick	Basic Wall: Wall - 2	Level 1	20	1.33 m^3	7 m^2	340
1	Wall - 20 cm brick	Basic Wall: Wall - 2	Level 1	20	0.73 m^3	4 m^2	135
1	Wall - 20 cm brick	Basic Wall: Wall - 2	Level 1	20	1.17 m^3	6 m^2	260
1	Wall - 20 cm brick	Basic Wall: Wall - 2	Level 1	20	1.35 m^3	7 m^2	250
1	Wall - 20 cm brick	Basic Wall: Wall - 2	Level 1	20	1.52 m^3	8 m^2	430
1	Wall - 20 cm brick	Basic Wall: Wall - 2	Level 1	20	2.11 m^3	11 m^2	390
1	Wall - 20 cm brick	Basic Wall: Wall - 2	Level 1	20	0.54 m^3	3 m^2	240
1	Wall - 20 cm brick	Basic Wall: Wall - 2	Level 1	20	1.32 m^3	7 m^2	385
1	Wall - 20 cm brick	Basic Wall: Wall - 2	Level 1	20	1.55 m^3	8 m^2	340
1	Wall - 10 cm brick	Basic Wall: Wall - 1	Level 1	10	1.05 m^3	11 m^2	390
1	Wall - 10 cm brick	Basic Wall: Wall - 1	Level 1	10	0.96 m^3	10 m^2	450
1	Wall - 10 cm brick	Basic Wall: Wall - 1	Level 1	10	0.84 m^3	8 m^2	385
1	Wall - 10 cm brick	Basic Wall: Wall - 1	Level 1	10	1.05 m^3	11 m^2	390
1	Wall - 10 cm brick	Basic Wall: Wall - 1	Level 1	10	0.45 m^3	4 m^2	240
1	Wall - 10 cm brick	Basic Wall: Wall - 1	Level 1	10	0.52 m^3	5 m^2	187
1	Wall - 10 cm brick	Basic Wall: Wall - 1	Level 1	10	0.69 m^3	7 m^2	315
Level 1: 18						128 m^2	
1	Wall - 20 cm brick	Basic Wall: Wall - 2	Level 2	20	1.17 m^3	6 m^2	380
1	Wall - 20 cm brick	Basic Wall: Wall - 2	Level 2	20	1.63 m^3	8 m^2	465
1	Wall - 20 cm brick	Basic Wall: Wall - 2	Level 2	20	1.33 m^3	7 m^2	340

b) Architectural walls quantity

Fig. 13. Sample of automatically generated quantity schedule in Revit

Table 3 summarizes the quantity results for all modeled structural and architectural components. This comprehensive overview clearly illustrates that the Dynamo-based automated methodology delivers precise and consistent outputs for each building element type, significantly reducing time and minimizing potential human errors, typical of traditional methods.

Overall, the Dynamo-based scripts streamlined the QTO process efficiently, ensuring data integrity, accuracy, and reproducibility. Empirical validation using the case study conclusively demonstrated the potential of this automated workflow to significantly enhance construction project management and cost control practices. Future studies could further expand this approach by incorporating additional elements and exploring its integration with other construction management tools.

Table 3. Summary of QTO results

Element Category	Quantity Metric	Calculated Quantity
Foundations	Volume (m^3)	49.445
Columns	Volume (m^3)	13.050
Beams	Volume (m^3)	10.830
Slabs	Volume (m^3)	36.303
Shear Walls	Volume (m^3)	7.033
Stairs	Volume (m^3)	2.937
Architectural Walls	Area (m^2)	331.104
Doors	Count (units)	19
Windows	Count (units)	18
Total Formwork	Area (m^2)	568.700

5. Conclusions

This study presented a comprehensive Dynamo-based automated QTO workflow integrated with Autodesk Revit to enhance the accuracy and efficiency of construction project management. The implemented scripts (DYN-01, DYN-02, and DYN-03) effectively streamlined the processes of parameter creation, formwork area calculation, stair volume determination, and comprehensive schedule generation. Practical application to a real-world project validated the reliability, accuracy, and efficiency of the scripts, highlighting their capability to eliminate manual errors and significantly accelerate data processing. The Dynamo-based methodology presented herein offers a robust and replicable framework for precise and efficient quantity management, positively contributing to cost control and project management practices. Future research should explore its applicability in large-scale projects, diverse construction elements, and integration with advanced project management platforms.

References

Alathamneh, S., Collins, W., & Azhar, S. (2024). BIM-based quantity takeoff: Current state and future opportunities. *Automation in Construction, 165*, 105549.

Aram, S., Eastman, C., & Sacks, R. (2014). A knowledge-based framework for quantity take-off and cost estimation in the AEC industry using BIM. In *Proceedings of the 31st International Symposium on Automation and Robotics in Construction (ISARC)* (pp. 434–442). Sydney, Australia.

Bahadır, Ü. (2025). *Development of four-dimensional models through automatically generated construction schedules based on Building Information Modeling and machine learning* (Doctoral dissertation, Karadeniz Technical University, Institute of Natural Sciences, Trabzon, Türkiye).

Bademosi, F., Tayeh, R. I., & Raja, R. A. (2019, June 17–19). An immersive approach to construction cost estimating. In *Proceedings of the ASCE International Conference on Computing in Civil Engineering 2019* (pp. 48–54). Atlanta, GA, United States.

Bečvarovská, R., & Matějka, P. (2014). Comparative analysis of creating traditional quantity take-off method and using a BIM tool. Paper presented at *Construction Maeconomics Conference 2014*.

Cepni, Y., Akcamete, A., & Klein, R. (2020, September 30–October 2). Automated BIM-based formwork quantity take-off. In *Proceedings of the 20th International Conference on Construction Applications of Virtual Reality (CAVR)*. Middlesbrough, United Kingdom.

Cheung, F. K. T., Rihan, J., Tah, J., Duce, D., & Kurul, E. (2012). Early stage multi-level cost estimation for schematic BIM models. *Automation in Construction, 27*, 67–77.

Cho, J., & Chun, J. (2015). Cost estimating methods for RC structures by quantity take-off and quantity prediction in the design development stage. *Journal of Asian Architecture and Building Engineering, 14*, 65–72.

Choi, J., Kim, H., & Kim, I. (2015). Open BIM-based quantity take-off system for schematic estimation of building frame in early design stage. *Journal of Computational Design and Engineering, 2*, 16–25.

Ergen, F., & Bettemir, Ö. H. (2024). Development of ontological algorithms for exact QTO of reinforced concrete construction items. *Structures, 60*, 105907.

Firat, C. E., Arditi, D., Hämäläinen, J. P., Stenstrand, J., & Kiiras, J. (2010). Quantity take-off in model-based systems. In *Proceedings of the 27th CIB W78 International Conference* (pp. 16–18). Cairo, Egypt.

Franco, J., Mahdi, F., & Abaza, H. (2015). Using building information modeling (BIM) for estimating and scheduling, adoption barriers. *Universal Journal of Management, 3*, 376–384.

Heigermoser, D., García de Soto, B., Abbott, E. L. S., & Chua, D. K. H. (2019). BIM-based Last Planner System tool for improving construction project management. *Automation in Construction, 104*, 246–254.

Jadid, M. N., & Idrees, M. M. (2007). Cost estimation of structural skeleton using an interactive automation algorithm: A conceptual approach. *Automation in Construction, 16*, 797–805.

Jamal, K. A. A., Ee, C. S., Khiyon, N. A., & Wahab, N. A. A. (2021). Scan-to-BIM approach towards producing quantity take-off of heritage buildings in Malaysia. *Journal of Engineering Science and Technology, 17*, 120–137.

Kensek, K. M., & Noble, D. E. (2014). *Building information modeling: BIM in current and future practice*. Wiley.

Khosakitchalert, C., Yabuki, N., & Fukuda, T. (2018). The accuracy enhancement of architectural walls quantity take-off for schematic BIM models. In *Proceedings of the 35th International Symposium on Automation and Robotics in Construction (ISARC)* (pp. 768–775). Berlin, Germany.

Khosakitchalert, C., Yabuki, N., & Fukuda, T. (2019). Improving the accuracy of BIM-based quantity take-off for compound elements. *Automation in Construction, 106*, 102891.

Khosakitchalert, C., Yabuki, N., & Fukuda, T. (2020). Automated modification of compound elements for accurate BIM-based quantity take-off. *Automation in Construction, 113*, 103142.

Kim, S. A., Chin, S., Yoon, S. W., Shin, T. H., & Kim, Y. S. (2009). Automated building information modeling system for building interior to improve productivity of BIM-based quantity take-off. In *Proceedings of the 26th International Symposium on Automation and Robotics in Construction (ISARC)* (pp. 492–496). Austin, TX, United States.

Le, T. H. T., & Cong, T. D. (2023). BIM-integrated system: A successful alternative for estimating cash flow in building projects. *ASEAN Engineering Journal, 13*, 103–112.
Leite, F., Akcamete, A., Akinci, B., Atasoy, G., & Kiziltas, S. (2011). Analysis of modeling effort and impact of different levels of detail in building information models. *Automation in Construction, 20*, 601–609.
Lim, C., Hong, W. K., Lee, D., & Kim, S. (2016). Automatic rebar estimation algorithms for integrated project delivery. *Journal of Asian Architecture and Building Engineering, 15*, 411–418.
Liu, H., Cheng, J. C. P., Gan, V. J. L., & Zhou, S. (2022). A novel data-driven framework based on BIM and knowledge graph for automatic model auditing and quantity take-off. *Advanced Engineering Informatics, 54*, 101757.
Manrique, J. D., Al-Hussein, M., Bouferguene, A., & Nasseri, R. (2015). Automated generation of shop drawings in residential construction. *Automation in Construction, 55*, 15–24.
Monteiro, A., & Poças Martins, J. (2013). A survey on modeling guidelines for quantity take-off oriented BIM-based design. *Automation in Construction, 35*, 238–253.
Nguyen, T.-Q., Lou, E. C. W., & Nguyen, B. N. (2024). A theoretical BIM-based framework for quantity take-off to facilitate progress payments: The case of high-rise building projects in Vietnam. *International Journal of Building Pathology and Adaptation, 42*(4), 704–728.
Olsen, D., & Taylor, J. M. (2017). Quantity take-off using building information modeling (BIM), and its limiting factors. *Procedia Engineering, 196*, 1098–1105.
Pham, V. H., Chen, P. H., Nguyen, Q., & Duong, D. T. (2024). BIM-based automatic extraction of daily concrete and formwork requirements for site work planning. *Buildings, 14*(12), 4021.
Rajabi, M., Bigga, T., & Bartl, M. A. (2015). Optimization of the quantity take-off (QTO) process for mechanical, electrical and plumbing (MEP) trades in tender estimation phase of construction projects. In *Proceedings of the 32nd International Symposium on Automation and Robotics in Construction (ISARC)* (pp. 1–8). Oulu, Finland.
Sacks, R., Eastman, C., Lee, G., & Teicholz, P. (2018). *BIM handbook: A guide to building information modeling for owners, designers, engineers, contractors, and facility managers* (3rd ed.). Wiley.
Saputra, H., Pratama, R., Tita, E. E., & Yusa, M. (2024). Comparative analysis of quantity take-off material between conventional method and BIM Nemetschek Allplan method on bridge. *Architecture, 12*, 2622–2633.
Sattineni, A., & Bradford, R. (2011). Estimating with BIM: A survey of U.S. construction companies. In *Proceedings of the 28th International Symposium on Automation and Robotics in Construction (ISARC)* (pp. 564–569). Seoul, South Korea.
Shick Alshabab, M., Vysotskiy, A., Petrichenko, M., & Khalil, T. (2020, November 19–20). BIM-based quantity take-off in Autodesk Revit and Navisworks Manage. In A. Belyaev, N. Vassilyev, & V. Savchenko (Eds.), *Proceedings of EECE 2019* (pp. 413–421). Springer International Publishing.
Smith, P. (2014). BIM & the 5D project cost manager. *Procedia – Social and Behavioral Sciences, 119*, 475–484.
Soon, L. T., Wong, L. S., Kamarazaly, M. A., Saar, C. C., & Ilmi, H. S. (2024). Comparison of BIM-based quantities take-off in quantity surveying profession. *Planning Malaysia, 22*(32), 150–164.
Tamrin, A. G., Sucipto, T. L. A., Noviansyah, W., Sukatiman, Rahmawati, A., & Mar'atussoleha, M. (2024). Investigating the benefit and challenges of implementing BIM-based quantity take-off in a grand mosque project. *AIP Conference Proceedings, 3145*, 020007.
Tserng, H. P., Yin, S. Y. L., & Li, S. (2006). Developing a resource supply chain planning system for construction projects. *Journal of Construction Engineering and Management, 132*, 393–407.
Url-1. (2025, April 15). Dynamo BIM. Retrieved from http://dynamobim.org/
Valinejadshoubi, M., Moselhi, O., Iordanova, I., Valdivieso, F., & Bagchi, A. (2024). Automated system for high-accuracy quantity take-off using BIM. *Automation in Construction, 157*, 105155.
Wahab, A., & Wang, J. (2022). Factors-driven comparison between BIM-based and traditional 2D quantity takeoff in construction cost estimation. *Engineering, Construction and Architectural Management, 29*(2), 702–715.
Wardito, E., & Husin, A. E. (2024). Increasing the value of jetty projects based on building information modelling 5D (BIM 5D). *AIP Conference Proceedings, 2710*, 090010.
Yang, F., Zhang, J., Chong, O. W., & Sexton, C. (2024, July 28–31). Introducing computing to construction management undergraduate students through automated quantity take-off from IFC-based BIM. In *Proceedings of the ASCE International Conference on Computing in Civil Engineering* (pp. 630–638). Pennsylvania, PA, United States.

Cost analysis of UWB and SLAM integrated building surveying technologies

Nezir Doğan[*1], Önder H. Bettemir[1]

[1] *İnönü University, Department of Civil Engineering, 44280 Malatya, Türkiye*

Abstract. Earthquake performance analyses of the damaged buildings which are classified as the medium damage level are carried out after the devastating earthquakes. Then the retrofit project is prepared by evaluating the earthquake performance analysis data and results, and the retrofit construction starts after the construction permit is obtained. Technical drawings of the structural and architectural elements are required to conduct earthquake performance analysis. However, it is quite common that buildings are constructed without completely complying with the approved static and architectural technical drawings or the aforementioned technical drawings might be lost long after their construction. For these reasons, a detailed building survey becomes mandatory. In this study, a cost analysis of the surveying of a building using UWB (ultra-wideband) indoor positioning sensors and SLAM (Simultaneous Localization and Mapping) based algorithms is performed. In the first phase of the study, 5 UWB sensors were placed in a suitable room of the building and positioning was performed using the multilateration method with these sensors. However, a SLAM-based tool was developed in the rooms where positioning accuracy deteriorated or position information could not be obtained in case of multipath effect and signal transmission failure due to obstacles such as furniture and walls in the building, and both positioning and mapping were performed with this tool. In addition, the effect of the placement pattern of the sensors on the cost and positioning accuracy was analyzed. The building survey was completed by considering the cost and technical feasibility of the implemented methods. The focus of the study is to examine in detail the cost of the survey work done with the integration of these two different technologies. Within the scope of the cost analysis, elements such as sensor and device purchases, equipment installations and software development were evaluated.

Keywords: Indoor positioning; Cost analysis; Multilateration; SLAM; Simulation.

1. Introduction

With the availability of the necessary sensors at affordable prices, the use of indoor positioning systems has become widespread. Indoor positioning systems can be used for different needs. Since system designs with different features and qualities specific to these applications are required, the selection of the indoor positioning system directly affects the system cost (Doğan & Bettemir 2024). Indoor location information increases efficiency in various construction applications such as control of the construction process, construction automation and the use of building information modeling (BIM) technology (Li et al., 2020).

Performance analyses of structures damaged after an earthquake are of great importance for the preparation and implementation of reinforcement projects. In order to perform the earthquake performance analysis, which is the first step of this process, the existing structure must have static and architectural projects. It is quite common for structures to be constructed without fully complying with the licensed static and architectural projects. In addition, it is quite common for projects belonging to buildings that have been built for a long time to be lost. For the reasons mentioned, it is mandatory to carry out a detailed survey study inside the buildings during the earthquake performance analysis process.

In this study, the additional cost that occurs when UWB and SLAM technologies are integrated and used in surveying studies is analyzed. UWB indoor positioning systems and SLAM-based algorithms are applied in an integrated manner in order to provide precision and efficiency in the surveying process. While UWB-based positioning systems provide location determination with the multilateration method, SLAM-based systems are activated in areas where location accuracy decreases due to reasons such as signal attenuation and multipath effects due to obstacles in the environment, location accuracy is improved and mapping is also performed. The effects of the sensor distribution used on cost and positioning accuracy are examined and equipment installation and software

[*] Corresponding author, E-mail: 36223621015@ogr.inonu.edu.tr

https://doi.org/10.31462/icearc2025_ce_mng_432

golden light publishing

development processes are evaluated economically. In this way, it is aimed to design a system that provides high accuracy and is also cost-effective in surveying studies.

2. Literature review

GPS signals do not provide accurate positioning indoors due to obstacles in the environment. There are different technologies that can position indoors such as infrared, WiFi, UWB, Bluetooth, inertial navigation and magnetic technologies. UWB, Wi-Fi, Bluetooth and Zigbee are short-range and low-power protocol standards. Bluetooth is a wireless personal area network (WPAN) standard designed for short-range and low-cost devices over IEEE 802.15.1. UWB is suitable for multimedia connections requiring high bandwidth over IEEE 802.15.3. Zigbee is designed for reliable wireless monitoring and control networks over IEEE 802.15.04. Wi-Fi is designed to replace the extension of wired networks for inter-computer connections over IEEE 802.11 (Lee et al., 2007). WiFi technology is widely available in many environments, has a low cost due to the prevalence of existing infrastructure, and is not affected by complex non-line-of-sight (NLOS) environments with obstacles. WiFi-based indoor positioning systems do not require additional equipment as they measure the quality of the signals they receive from devices within the coverage area. Therefore, it is an advantageous system in terms of cost (Liu et al., 2009; Mrindoko & Minga 2016).

Infrared (IR)-based systems, radio frequency (RF)-based systems, and ultrasound-based systems are among the most widely used network techniques and systems. One of the most important advantages of infrared is that it has a wide range of use, as many devices have infrared features. Since the infrastructure is simple, the installation and maintenance costs are also low. However, its inability to pass through obstacles and the need for line of sight make infrared technology inapplicable in complex indoor scenarios (Zhang et al., 2010).

Ultrasonic-based indoor positioning systems have the ability to position with high accuracy at the centimeter level. It is also a low-cost system compared to other indoor positioning systems. However, ultrasound-based systems have lower stability than infrared-based systems due to the reflection effect. In addition, the need to synchronize these systems by associating them with RF technologies increases the cost (Zhang et al., 2010; Ijaz et al., 2013).

Mrindoko and Minga (2016) comparatively examined the fingerprint techniques, angle of arrival (AoA) and time of arrival (ToA) techniques used in indoor positioning systems according to criteria such as accuracy, adaptability and cost. The angle of arrival (AoA) determines the location of the target according to the angle of arrival of the signal to the receiver sensor. Technologies using the AoA method increase the cost because they require antennas that can calculate the angle. Reflections, multipath reflections and non-line-of-sight (nLOS) reflections due to objects located indoors cause changes in the direction of arrival of the signal and affect positioning accuracy. In cases where the signal speed is known, the distance between the receiver and transmitter devices can be determined using the transmission time of the signal. It is necessary to know the start time of signal transmission and requires time synchronization in all devices used.

Radio frequency systems are divided into systems that can estimate location using features such as RSSI, UWB, and RFID. RSSI-based indoor positioning systems are affected by errors caused by multipath effects and reflection and diffraction. RFID systems provide low-cost positioning that can position in NLOS environments. VLC-based systems can perform low-cost positioning using lamps or LEDs located in buildings. The emitted lights are detected by cameras (Kunhoth et al., 2020; Ijaz et al., 2013). Dabove et al. (2018) conducted outdoor tests using low-cost Pozyx, a product series that provides a positioning and tracking technology. First, it was aimed to determine the maximum range between a tag and a fixed device. The maximum range was determined as 40 meters. Secondly, the information obtained from the sensors was examined to evaluate the internal capability of the system. The sensor information obtained from the Tag and the MicroStrain IMU fixed on a total station was compared. The total station was used as a reference. It was concluded that the IMU sensors on the tag card had the same accuracy values as the MicroStrain.

In the indoor room test, four anchors with different heights were placed in the corners of a 6.44 m x 4.91 m room and positioning was tested with two different algorithms. The average 3-dimensional accuracy value was 100 ± 25 mm. In the narrow corridor test, 4 stations were placed in a 1.8 m x 6.8 m corridor. The standard deviation value increased compared to the room test. The absolute average accuracy of the range measurement values was approximately 150 ± 50 mm. The three-dimensional positioning accuracy was approximately 60 ± 45 mm. UWB-based systems provide high-precision location determination at a lower cost compared to other technologies, and UWB sensors consume less power compared to other technologies (Alışkan and Şahin, 2023). The 802.15.4a standardization group was established by IEEE for low-data-rate communication, and UWB is an important technology for this standardization. Since the use of antenna arrays increases the cost of the positioning system, AOA-based approaches are not suitable for UWB localization. In addition, due to the high bandwidth, the possibility of multipath tracking of UWB signals may increase and it will be difficult to estimate the angle accurately due to scattering from objects in indoor spaces. Thanks to the high time resolution (wide bandwidth) of UWB signals, time-based approaches in UWB localization provide high-accuracy positioning and are less costly than AOA-based approaches (Gezici et al., 2005). On the other hand, detection of multipath effect can be a feasible alternative if one of the received signals followed multipath, but detection of the signals that followed multipath can be infeasible if two or more signals followed multipath (Doğan and Bettemir, 2025).

Low-cost sensors such as smartphones and wearable devices have become widespread thanks to micro-electro-mechanical systems (MEMS). Accelerometers and gyroscopes in these devices are used for continuous monitoring of human activities such as gait detection. Positioning technologies such as GNSS are not reliable in indoor areas or in areas where the satellite signal is blocked. For this reason, PDR methods that can track user movements without the need for external infrastructure have gained importance (Basso et al., 2017).

Ruiz et al. (2011) aimed to increase the accuracy of indoor pedestrian positioning systems by tightly combining IMU and RFID measurements. This method, proposed as a solution to the inadequacy of GPS in indoor spaces, offers a low-cost and portable system. The 1% drift error of IMU was reduced to 1.5 meters with the help of RFID. The algorithm provided consistent accuracy regardless of walking speed or direction. The optimum cost-accuracy balance was evaluated using different RFID tag densities. As the density of RFID tags increased, location accuracy also increased. However, a distribution rate of 30 m² per 1 RFID tag was suggested to achieve an optimum cost-accuracy balance. The algorithm produced consistent results in different walking scenarios such as slow walking, fast walking or backward movement. Zero speed (ZUPT) and zero angular velocity (ZARU) updates reduced IMU-induced drifts and provided high accuracy (Ruiz et al., 2011). Bahl and Padmanabhan (2000) provide a solution to the problem of determining and tracking the location of users inside buildings with RADAR, a radio frequency (RF) based system. The RADAR system provides an effective solution for indoor user location and tracking. The average error distance was calculated as 2-3 meters with the empirical method. The radio propagation model reduced the installation costs but increased the error rate to approximately 4.3 meters. These results show that RADAR enables the development of location-aware services operating on RF-based network infrastructures. In the future, it is aimed to further develop the system by integrating user movement profiles and sensitivity to environmental factors. Zhang et al. (2006) conducted 1D and 2D localization experiments. In the 1D experiment, the receiver is placed 3 m away from the transmitter and then moved 2 cm away in the same direction to provide a precise displacement in one dimension. According to the value read from the oscilloscope, a shift of 64ps was detected between the two peaks. According to the detected shift value, the result is 1.92 cm. This indicates a difference of 0.8 mm from the true value of 2 cm. Experimental results show that Zhang et al. (2006) developed a positioning system based on UWB principles for low-cost indoor applications with subcentimeter accuracy. Doğan and Bettemir (2025) analyzed the error distribution of locationing with triangulation by differential sensitivity analysis. The results stated that the magnitude of the locatioıning error varies with respect to the position. Minimum location error is expected to be obtained at the center of gravity of the station points.

Randell and Multer (2001) developed a low-cost indoor positioning system that provides 8x8m coverage using one RF transmitter and four ultrasonic transmitters. Ultrasonic systems offer low-cost solutions, but they have disadvantages such as signal loss and signal reflections due to obstacles in the environment and interference from high-frequency sounds. Companies such as Intersense and AT&T have produced systems that can minimize these disadvantages. The average cost of commercial systems such as these is around $15,000. The system developed by Randell and Multer (2001) costs approximately $150 and provides 10-25cm accuracy. Yaman et al. (2021) designed 3 "Location Transmitter Electronic Cards", 1 "Location Receiver Electronic Card" and 1 "Location Receiver-Transmitter Electronic Card" as shown in Table 1, and this system; It is more economical than the system using 4 ready-made electronic cards and 1 smart device, the system using 1 electronic device and 1 smart device, and the systems using 1 ready-made electronic card and 7 electronic cards. The error level of the designed system was compared with existing studies and it was stated that it exhibited similar performance.

Table 1: Cost analysis of indoor positioning systems compiled from the literature

	Duong & Dinh (2019)		Sato et al (2019)		Poulose & Han (2019)		Yaman et al (2021)	
Hardware Used	Component Name	Approximate Current Cost	Component Name	Approximate Current Cost	Component Name	Approximate Current Cost	Component Name	Approximate Current Cost
Smart Device	1xIphone SE	20000 ₺	1xLenovo Phab 2	12000₺	1xSamsung S6 Edge	18180₺	-	-
BLE Beacon	4xEstimote Beacon	7500 ₺	4xnRF51822	1850 ₺	-	-	-	-
IMU Sensor	-	-	-	-	7xBiscuit - WiFi 9 Axis Sensor	1800 ₺	-	-
Microcontroller	-	-	-	-	-	-	5xArduino Leonardo	1750₺

The components used and their costs for the system created by integrating UWB and SLAM technologies are given in Table 2.

Table 2: Cost of the developed system components

Components Used	Quantity	Unit Price
Arduino Uno	1	270 ₺
DWM1000 UWB Module	5	2597 ₺
Ultrasonic Distance Meter	4	50 ₺
L298 Motor Driver	1	77₺
Sensor Shield	1	80₺
HC-06 Bluetooth Module	1	184,5₺
6V 250 RPM Motor	4	50₺
Servo Motor	4	65₺

3. Method

3.1 Location estimation with multilateration

In indoor positioning, three distance measurements from known points are sufficient to determine the coordinates of an unknown point, while in the multilateration method, measurements are made from more points. The error values of the measurements are distributed with the least squares correction as shown in Equation 1 and the position is estimated.

$$\Delta\beta = (X^T X)^{-1} X^T \Delta Y \tag{1}$$

The vector expressed as ΔY in Equation 1 is the difference between the measured distance and the distances calculated for the estimated approximate location, as expressed in Equation 2. The explicit form of the X matrix for 2D positioning is expressed in Equation 3.

$$\Delta Y = \begin{bmatrix} d_1 \\ d_2 \\ d_3 \\ d_4 \\ d_5 \end{bmatrix} - \begin{bmatrix} \hat{d}_1 \\ \hat{d}_2 \\ \hat{d}_3 \\ \hat{d}_4 \\ \hat{d}_5 \end{bmatrix} \tag{2}$$

$$X = \begin{bmatrix} \frac{\partial \hat{d}_1}{\partial x} & \frac{\partial \hat{d}_1}{\partial y} \\ \frac{\partial \hat{d}_2}{\partial x} & \frac{\partial \hat{d}_2}{\partial y} \\ \frac{\partial \hat{d}_3}{\partial x} & \frac{\partial \hat{d}_3}{\partial y} \\ \frac{\partial \hat{d}_4}{\partial x} & \frac{\partial \hat{d}_4}{\partial y} \\ \frac{\partial \hat{d}_5}{\partial x} & \frac{\partial \hat{d}_5}{\partial y} \end{bmatrix} \tag{3}$$

The matrix X contains the partial derivatives of the distances with respect to the estimated position. The estimated distances are calculated as given in Equation 4.

$$\hat{d}_i = \sqrt{(\hat{x} - x_i)^2 + (\hat{y} - y_i)^2} \tag{4}$$

In Equation 4, $\hat{x}$ and $\hat{y}$ are the estimated coordinates of the point to be positioned and the index i represents the station points. The vector represented as Δβ contains the corrections to be made to the initial position values. In order to linearize the Euclidean distance equations, they are linearized with the first-order Taylor series expansion. The Taylor series expansion requires approximate initial position information. Initial position estimates are shown in Equation 5. The obtained Δβ vector is the correction made to the initial position estimate. The corrections are obtained after the least squares solution according to Equation 1. The corrections are added to the current solution obtained in the previous parameter estimation cycle as shown in Equation 6. The iteration continues until the correction values fall below the desired level.

$$\beta_0 = \begin{bmatrix} x_0 \\ y_0 \end{bmatrix} \tag{5}$$

$$\beta = \Delta\beta + \beta_0 \tag{6}$$

The approximate value is subtracted from the true value and the Euclidean distance of the obtained values is reported as the error value. The least squares adjustment will be applied 25 times for each point. The number of iterations is sufficient to ensure convergence.

3.2 Improving position accuracy with SLAM based algorithm

It is not possible to achieve continuous and high-accuracy positioning with indoor positioning systems. In order to prepare a high-accuracy and detailed interior survey, at least four distance meters as shown in Figure 1 will be placed on an autonomous vehicle. The vehicle will map the room by moving counterclockwise in the room, taking into account the distance defined as d3 distance, 50 cm from the wall, and making a full circle in the room. The location accuracy will be improved with the SLAM-based supporting algorithm as presented below.

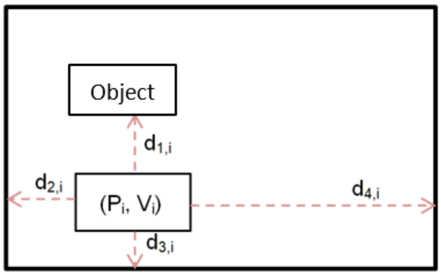

(a)

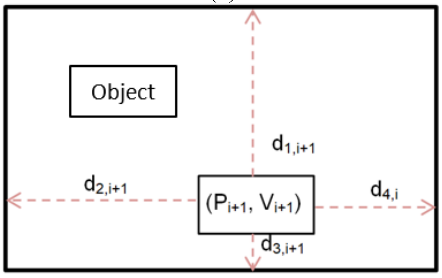

(b)

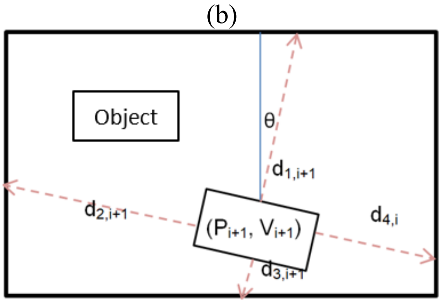

(c)

Fig. 1. Measurements of the vehicle at time labels i (a) and i+1 (b) in a simplified spatial environment

Pi is the position vector at the ith time tag, Vi is the speed vector at the ith time tag, d1,i, d2,i, d3,i and d4,i are the distance readings obtained from the ultrasound sensors placed on the vehicle as presented in Figure 1 at the ith time. The situation when the vehicle moves for a period of Δt and the time is i+1 is presented in Figure 1.b. The progress shown in Figure 1 is exaggerated to make generalizations, the time interval is planned to be 1 second and the expected progress is 5 cm. In the case when the time period is i+1, the location is determined by indoor positioning and after the iteration is stopped, if the residual values calculated with Equation 2 are more than the threshold value, at least one of the signals will be considered to have come by following a multipath and the location obtained by indoor positioning will be corrected as specified in Equation 7. In Equation 7, the position vector at the i+1 time is estimated using the position and position vectors at the ith time.

$$\hat{P}_{i+1} = P_i + V_i * \Delta t \tag{7}$$

The prediction vector presented in Equation 7 will be highly accurate if the vehicle's forward speed remains constant, but there will be a high probability that it will deviate from the forward direction as a result of being caught on objects such as carpets etc. Therefore, the forward angle will be calculated from the direction perpendicular to the forward direction as presented in Equation 8.

$$\theta_{i+1} = \arccos\left(\frac{d_i + v_i \sin\theta_i}{d_{i+1}}\right) \tag{8}$$

It is possible to encounter situations where the distance between the object and the object is measured at time i and the distance between the object and the wall at time i+1 as indicated in Figures 1a and 1b. In this case, measurements numbered 1 and 3 will be evaluated together. If abnormal changes are detected in both measurements, measurements numbered 4 and 2, which are the forward direction, will be evaluated.

$$\theta_{i+1} = \arccos\left(\frac{d_i - v_i \cos\theta_i}{d_{i+1}}\right) \tag{9}$$

The signs of the sine and cosine functions in Equations 8 and 9 will be determined by taking into account the direction of the distance measurement and the sign of the angle. The position vector will be determined by taking into account the d4 and d2 measurements that are in the same direction as the direction of advancement.

$$\Delta x_{i+1} = d_i \cos\theta_i - d_{i+1} \cos\theta_{i+1} \tag{10}$$

If a sudden change is observed in the d1 and d3 measurements perpendicular to the direction of advancement, there is a possibility of an item or column protrusion.

4. Case study

The positioning accuracy was investigated when the sensor distributions were placed at $(x_1, y_1) = (5, 0)$; $(x_2, y_2) = (7, 0)$; $(x_3, y_3) = (10, 7)$; $(x_4, y_4) = (4, 10)$, and $(x_5, y_5) = (0, 6)$ as shown in Figure 2. In the case of a 1.0m x 0.3m column at point (5,5) of the room, the positioning accuracy of the blind spots relative to the sensors was investigated.

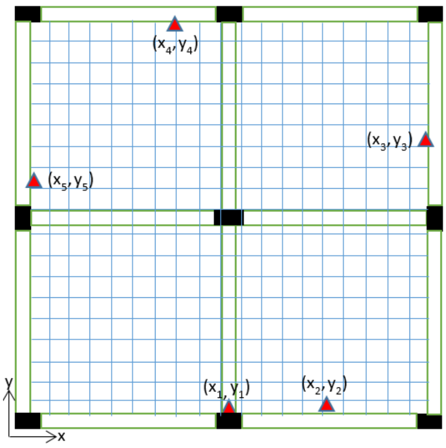

Fig. 2. Location of the columns and positions of the station points

The placement of sensors 1 and 2 on the same line and close to each other caused some points to be identified as blind spots by both sensors. Table 3 shows how many sensors identified a point as a blind spot for grid points created at 1 meter intervals.

Table 3. Number of distance measurements exposed to multipath

	0	1	2	3	4	5	6	7	8	9	10
0	0	0	0	1	0	0	0	0	0	0	0
1	0	0	0	1	0	0	0	0	0	0	0
2	0	0	0	0	1	0	0	0	0	0	1
3	0	0	0	0	1	0	0	0	1	1	1
4	0	0	0	0	0	0	1	1	1	1	2
5	1	1	1	1	1		2	1	1	1	1
6	1	1	1	1	0	1	0	0	0	0	1
7	1	0	0	0	0	0	0	0	0	0	0
8	0	0	0	0	1	0	0	0	0	0	0
9	0	0	0	0	1	0	0	0	0	0	0
10	0	0	0	0	1	0	0	0	0	0	0

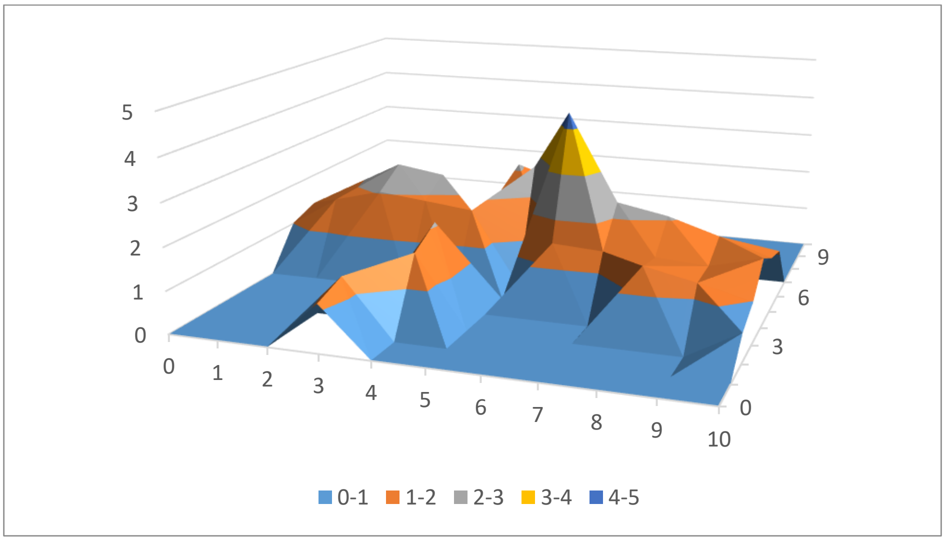

Fig 3. Positioning errors obtained as a result of simulation without considering the multipath effect

In order to determine the improvement provided by the proposed method, it is first assumed that the signals directly reach the receiving points and the distance values are computed accordingly when performing positioning with least squares adjustment. The error values of the positioning according to the position estimation without considering the multi-path tracking of the signals are visualized in Figure 3. The results are also tabulated in Table 4. The largest positioning error was 4.36m at (5,6) and the smallest positioning error was 0.00037m at (4,0).

Table 4. Tabular presentation of the positioning errors obtained as a result of simulation without considering the multipath effect

	0	1	2	3	4	5	6	7	8	9	10
0	0.0039	0.0114	0.0054	1.1218	0.0072	0.0048	0.0065	0.006	0.0075	0.0023	0.003
1	0.0051	0.005	0.0082	1.3749	0.0041	0.0025	0.0012	0.0069	0.0041	0.0034	0.0016
2	0.0035	0.0053	0.0034	0.0043	1.6965	0.0041	0.0037	0.0062	0.0065	0.0043	0.6939
3	0.0045	0.0043	0.0045	0.0009	2.0923	0.0052	0.0039	0.0039	1.546	1.2876	0.9893
4	0.00037	0.0075	0.0023	0.004	0.0036	0.0032	1.4994	1.4237	1.4019	1.3216	1.6253
5	1.0126	1.7393	2.0406	1.911	1.7748		4.3646	2.2957	2.069	1.6949	1.2932
6	1.2555	1.8749	2.4865	2.3066	0.0013	2.7071	0.0083	0.0029	0.0023	0.0025	1.1317
7	0.849	0.0037	0.0082	0.0039	0.0068	0.0047	0.0065	0.0025	0.002	0.0025	0.0024
8	0.0069	0.0058	0.0011	0.0047	2.1584	0.0022	0.0047	0.0029	0.0011	0.0042	0.0037
9	0.0017	0.0016	0.0006	0.0026	1.7419	0.0039	0.0094	0.0036	0.001	0.0076	0.0019
10	0.0032	0.0069	0.0042	0.002	1.4079	0.0097	0.0059	0.0033	0.0042	0.0077	0.0055

Signals cannot reach blind spots directly, they follow reflected paths and reach the receiver. For this reason, positioning based on the assumption that the signal reaches the receiver directly will be incorrect. At these points, the analysis should be made by taking into account the length of the path that the signal will follow. The positioning errors obtained by neglecting the case where the signal reaches the receiver by following multiple paths are shown in Figure 4. The largest positioning error is 4.58m at (5,6), which is defined as a blind spot with respect to sensors 1 and 2. The next largest error was 1.04m at (4,10), which is also defined as a blind spot by sensors 1 and 2. The minimum error was 0.00037m at (6,1), where signals could be received without following multiple paths.

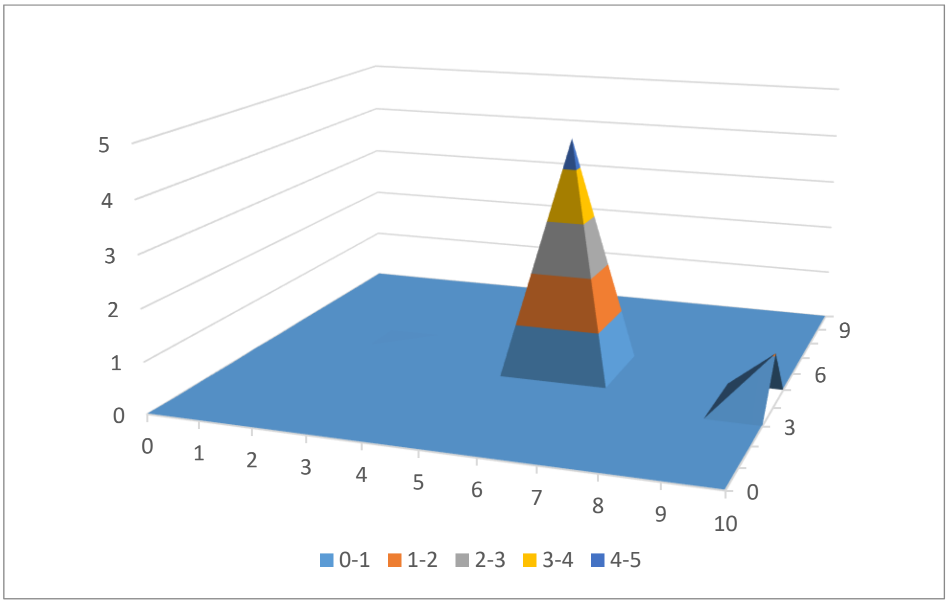

Fig. 4. Error values obtained after the implementation of the proposed algorithm

Table 5. Tabular representation of the error values obtained as a result of the analysis

	0	1	2	3	4	5	6	7	8	9	10
0	0.01142	0.00223	0.00099	0.00344	0.00525	0.00641	0.00262	0.00316	0.00882	0.00538	0.00649
1	0.00347	0.00091	0.0022	0.00538	0.00598	0.00285	0.00615	0.00496	0.00564	0.00511	0.00625
2	0.00704	0.00818	0.00268	0.00531	0.00703	0.00602	0.00638	0.00505	0.00586	0.00659	0.01059
3	0.00172	0.00392	0.00654	0.00475	0.0092	0.00236	0.00989	0.00635	0.00276	0.00816	0.00407
4	0.00926	0.00197	0.00308	0.00744	0.00752	0.00443	0.00517	0.00701	0.00565	0.00857	1.04765
5	0.00132	0.00605	0.00813	0.00105	0.00714		4.58519	0.01109	0.00493	0.00643	0.00118
6	0.00732	0.00037	0.00199	0.01087	0.00951	0.00589	0.00505	0.0096	0.01123	0.00425	0.00332
7	0.00553	0.00786	0.00561	0.00659	0.00906	0.00206	0.00214	0.0074	0.00376	0.0096	0.00734
8	0.00438	0.00118	0.00567	0.00309	0.00699	0.0019	0.00579	0.00668	0.00626	0.00778	0.00457
9	0.00292	0.00127	0.00235	0.00597	0.00399	0.00741	0.00747	0.00768	0.00436	0.0061	0.00459
10	0.00721	0.00184	0.00177	0.00524	0.00428	0.00551	0.00729	0.00404	0.00521	0.00603	0.00602

5. Conclusions

In this study, we focus on the cost analysis and positioning accuracy of the surveys of the buildings classified as medium damage level according to the locations of the sensors placed by using the integration of UWB sensor technology, indoor positioning methods and SLAM-based algorithms. High accuracy positioning is achieved at the points where the signals emitted from the UWB sensors can reach directly, but the positioning accuracy is reduced due to the multipath effect at the points where the signals cannot reach directly. In areas of the building where UWB signals are inadequate or do not reach at all, the SLAM algorithm is used to complete the missing areas in the measurements.

With the proposed algorithm, 31 out of 33 blind spots were successfully detected and positioning accuracies of the detected points are improved by implementing the proposed algorithm. Consequently, apart from the 2 unsuccessful points, important improvements were obtained in the analysis performed considering the multipath effect. Sensor placement has an impact on positioning accuracy, so the layout of the UWB sensors for high accuracy surveying was an important factor affecting the total hardware cost.

Acknowledgments

This study is supported by the Scientific Research Project Coordination of İnönü University by the grant number FYL-2024-3612.

References

Alışkan, İ., & Şahin, A. (2023). Ultra geniş bant teknolojisi ile kapalı alanlarda konum belirleme. *Karaelmas Fen ve Mühendislik Dergisi*, *13*(1), 179–190.

Bahl, P., & Padmanabhan, V. N. (2000, March). RADAR: An in-building RF-based user location and tracking system. In *Proceedings IEEE INFOCOM 2000. Conference on Computer Communications. Nineteenth Annual Joint Conference of the IEEE Computer and Communications Societies* (Vol. 2, pp. 775–784). IEEE.

Basso, M., Galanti, M., Innocenti, G., & Miceli, D. (2016). Pedestrian dead reckoning based on frequency self-synchronization and body kinematics. *IEEE Sensors Journal*, *17*(2), 534–545.

Dabove, P., Di Pietra, V., Piras, M., Jabbar, A. A., & Kazim, S. A. (2018, April). Indoor positioning using ultra-wide band (UWB) technologies: Positioning accuracies and sensors' performances. In *2018 IEEE/ION Position, Location and Navigation Symposium (PLANS)* (pp. 175–184). IEEE.

Doğan, N., & Bettemir, Ö. H. (2024, September). Examination of accuracy of interior positioning. In *2024 8th International Artificial Intelligence and Data Processing Symposium (IDAP)* (pp. 1–6). IEEE.

Doğan, N., & Bettemir, Ö. H. (2025). Determination of precision of triangulation by error propagation law. *Fırat Üniversitesi Mühendislik Bilimleri Dergisi, 37*(1), 93–110.

Doğan, N., & Bettemir, Ö. H. (2025). Assessment of Blind-Spots and Multi-Path Effects at Indoor Positioning by Multilateration. *The International Archives of the Photogrammetry, Remote Sensing and Spatial Information Sciences*, *48*, 337-344.

Duong, N. S., & Dinh, T. M. (2019, September). Indoor localization with lightweight RSS fingerprint using BLE iBeacon on iOS platform. In *2019 19th International Symposium on Communications and Information Technologies (ISCIT)* (pp. 91–95). IEEE.

Gezici, S., Tian, Z., Giannakis, G. B., Kobayashi, H., Molisch, A. F., Poor, H. V., & Sahinoglu, Z. (2005). Localization via ultra-wideband radios: A look at positioning aspects for future sensor networks. *IEEE Signal Processing Magazine*, *22*(4), 70–84.

Ijaz, F., Yang, H. K., Ahmad, A. W., & Lee, C. (2013, January). Indoor positioning: A review of indoor ultrasonic positioning systems. In *2013 15th International Conference on Advanced Communications Technology (ICACT)* (pp. 1146–1150). IEEE.

Kunhoth, J., Karkar, A., Al-Maadeed, S., & Al-Ali, A. (2020). Indoor positioning and wayfinding systems: A survey. *Human-centric Computing and Information Sciences*, *10*(1), 1–41.

Lee, J. S., Su, Y. W., & Shen, C. C. (2007, November). A comparative study of wireless protocols: Bluetooth, UWB, ZigBee, and Wi-Fi. In *IECON 2007 – 33rd Annual Conference of the IEEE Industrial Electronics Society* (pp. 46–51). IEEE.

Li, C. T., Cheng, J. C., & Chen, K. (2020). Top 10 technologies for indoor positioning on construction sites. *Automation in Construction*, 118, 103309.

Liu, F., Liu, J., Yin, Y., Wang, W., Hu, D., Chen, P., & Niu, Q. (2020). Survey on WiFi-based indoor positioning techniques. *IET Communications*, 14(9), 1372–1383.

Mrindoko, N. R., & Minga, L. M. (2016). A comparison review of indoor positioning techniques. *International Journal of Computer (IJC)*, *21*(1), 42–49.

Poulose, A., & Han, D. S. (2019). Hybrid indoor localization using IMU sensors and smartphone camera. *Sensors*, 19(23), 5084.

Randell, C., & Muller, H. (2001, September). Low cost indoor positioning system. In *International Conference on Ubiquitous Computing* (pp. 42–48). Springer Berlin Heidelberg.

Ruiz, A. R. J., Granja, F. S., Honorato, J. C. P., & Rosas, J. I. G. (2011). Accurate pedestrian indoor navigation by tightly coupling foot-mounted IMU and RFID measurements. *IEEE Transactions on Instrumentation and Measurement*, *61*(1), 178–189.

Sato, A., Nakajima, M., & Kohtake, N. (2019, September). Rapid BLE beacon localization with range-only EKF-SLAM using beacon interval constraint. In *2019 International Conference on Indoor Positioning and Indoor Navigation (IPIN)* (pp. 1–8). IEEE.

Yaman, Ş., Gündoğdu, K., & Çalhan, A. (2021). Yeni bir iç mekân konum bulma sistemi. *Düzce Üniversitesi Bilim ve Teknoloji Dergisi*, *9*(2), 636–645.

Zhang, C., Kuhn, M., Merkl, B., Fathy, A. E., & Mahfouz, M. (2006, October). Accurate UWB indoor localization system utilizing time difference of arrival approach. In *2006 IEEE Radio and Wireless Symposium* (pp. 515–518). IEEE.

Zhang, D., Xia, F., Yang, Z., Yao, L., & Zhao, W. (2010, May). Localization technologies for indoor human tracking. In *2010 5th International Conference on Future Information Technology* (pp. 1–6). IEEE.

4th International Civil Engineering & Architecture Conference
17-19 May 2025, Trabzon, Türkiye

Understanding the key drivers of construction labor productivity in bricklaying

Abdirisak M. Abdillahi[1], Savaş Bayram[*2]

[1] Erciyes University, Graduate School of Natural and Applied Sciences, 38280 Kayseri, Türkiye
[2] Erciyes University, Faculty of Engineering, Department of Civil Engineering, 38280 Kayseri, Türkiye.

Abstract. Labor productivity in construction is crucial for project success. Despite its significance, productivity growth in the construction industry remains generally static. The building sector in Somaliland is fundamental to economic recovery and development, particularly following the devastation caused by the civil war. Understanding labor productivity is essential for improving the sector's contribution to economic advancement. This research collected data from 52 projects across four major cities in Somaliland: Berbera, Borama, Burao, and Hargeisa. A dataset of 532 cases of bricklaying activity was analyzed using descriptive statistics and non-parametric tests. Spearman's Rank Correlation, Kruskal-Wallis H, Mann-Whitney U, and Chi-Square tests were employed to examine relationships between productivity and various factors. Findings highlight the significant impact of resource availability, workspace conditions, and minimizing disruptions on labor productivity. This research provides actionable insights to improve productivity in the construction industry.

Keywords: Labor productivity; Drivers; Construction; Somaliland; Bricklaying

1. Introduction

Construction labor productivity (CLP) remains a critical concern in the global construction industry, with persistent challenges obstructing progress despite numerous efforts to improve it. Studies show that productivity growth in construction has either stagnated or declined in many countries, lagging behind other sectors in terms of innovation and efficiency (Van Tam, 2024). This issue is especially pressing in developing regions, where the construction sector is vital in economic development and post-conflict recovery. In Somaliland, construction is one of the most active and impactful industries, driven by the urgent need to rebuild infrastructure that was destroyed during the civil conflict. Building projects, particularly in urban centers, have become the backbone of urban renewal and national reconstruction efforts (Omar et al., 2020).

In construction, productivity is most commonly understood as labor productivity, typically defined as the ratio of output to a single input, labor. This form of partial productivity is widely used due to its practicality for task-specific assessments (Cevikbas, 2022). Labor productivity is especially significant because labor costs often account for up to half of a project's total expenditure (Buchan et al., 2012; Kaming et al., 1997; Zakeri et al., 1997). Consequently, a thorough understanding of labor performance is crucial for managing project costs and schedules effectively. As Ulubeyli et al. (2014) note, decisions related to labor allocation influence the overall time and budget of construction projects. Labor productivity metrics thus serve as benchmarks for contractors and managers in planning workforce needs, determining schedules, and estimating costs.

In recent years, research on CLP has intensified globally, reflecting a growing recognition of its impact on project success. Scholars have examined factors influencing labor productivity from various angles, including those of workers (Edwin & Calistus, 2023), engineers (Abdillahi & Kazaz, 2021; Attar et al., 2012), and broader stakeholder groups comprising clients, consultants, contractors, and suppliers (Alyew et al., 2020). These studies reveal a wide array of influences, from material supply and site conditions to communication practices and environmental constraints. Moreover, literature reviews by Momade et al. (2023) and Lee et al. (2023) show regional disparities in research priorities. While studies in North America and Europe focus on optimization techniques and advanced resource management, those in developing countries often address more fundamental challenges, such as labor shortages, site logistics, and informal project organization.

In the African context, including Somaliland, construction practices are often shaped by cultural norms, informal systems, and limited institutional support. Formal project management frameworks are weak or inconsistently applied, and much of the work relies on locally adapted methods of organization, negotiation, and

[*] Corresponding author, E-mail: sbayram@erciyes.edu.tr

https://doi.org/10.31462/icearc2025_ce_mng_438

leadership (Abdi & Hareru, 2024; Abdillahi et al., 2024). Understanding CLP in such a setting requires contextualized investigation grounded in local data and realities. To address this need, the present study explores the key drivers of construction labor productivity in bricklaying, one of the most common and labor-intensive activities in Somaliland's building sector. By grounding its findings in real-world data, this study contributes to a more inclusive understanding of labor productivity and provides practical insights for improving site performance under similar conditions.

The remainder of this paper is organized as follows: the next section presents the materials and methods used for data collection and analysis. This is followed by the results and discussion. The paper concludes with a summary of the main insights, their implications for construction management, and suggestions for future research.

2. Materials and methods

This study is based on a dataset collected by the researchers to explore the key factors influencing labor productivity in bricklaying. Data was gathered from 52 construction projects spread across four major cities in Somaliland, Berbera, Borama, Burao, and Hargeisa, over a five months from June to October 2024. The projects represented a mix of residential and commercial projects, providing a diverse and realistic snapshot of labor performance under varying site conditions.

Table 1. Description of variables used in the study

No	Variable	Type	Descriptions	Coding
1	Material Availability (MA)	Qualitative	Availability of materials needed for the work on-site	1 = Low Quantity, 2 = Medium Quantity, 3 = High Quantity
2	Weather Conditions (WC)	Qualitative	Weather condition on site	1 = Poor, 2 = Moderate, 3 = Good
3	Communication among Workers (CW)	Qualitative	Communication among workers on-site	1 = Poor, 2 = Medium, 3 = Good
4	Availability of Tools/Equipment (AT)	Qualitative	Availability of tools and equipment needed for work	1 = Low Quantity, 2 = Medium Quantity, 3 = High Quantity
5	Working Space Conditions (WS)	Qualitative	Working site conditions in terms of space	1 = Cramped, 2 = Adequate, 3 = Spacious
6	Rework Frequency (RF)	Quantitative	Number of reworks done by the crew in a day	Scale (0, 1, 2, etc.)
7	Accident Frequency (AF)	Quantitative	Number of accidents involving the crew in a day	Scale (0, 1, 2, etc.)
8	Working Hours (WH)	Quantitative	Number of hours worked by the crew in a day	Scale (e.g., 5, 6, 7, 8)
9	Gang Size (GS)	Quantitative	Number of laborers in the crew	Scale (e.g., 2, 4, 8, etc.)
10	Productivity (P)	Quantitative (Target)	Amount of work done per day per laborer per hour	$\frac{\text{Ammount of work done per day}}{\text{Number of labor perday} * \text{Work hour}}$

A total of 532 observations were recorded, each representing a daily productivity entry for a labor crew engaged in bricklaying. The dataset comprises 10 variables, including both qualitative and quantitative types. The target variable is labor productivity, defined as the amount of work completed per day per laborer per hour. The independent variables include material availability, weather conditions, communication among workers, availability of tools and equipment, and workspace conditions, all recorded as ordinal categorical variables. Additionally, rework frequency, accident frequency, working hours, and gang size were measured as continuous variables. The complete list of variables, their types, descriptions, and coding schemes is provided in Table 1. Descriptive statistics summarizing the data distribution are presented in Table 2, offering insights into the central tendencies and variability of each variable.

Table 2. Descriptive statistics of bricklaying data

Statistic	MA	WC	CW	AT	WS	RF	AF	WH	GZ	P
Count	532	532	532	532	532	532	532	532	532	532
Mean	2.68	2.50	2.63	2.94	2.56	0.22	0.14	7.22	6.72	23.91
Std	0.59	0.73	0.68	0.30	0.63	0.48	0.40	0.96	3.60	4.35
Min	1.0	1.0	1.0	1.0	1.0	0.0	0.0	5.0	2.0	12.5
Max	3.0	3.0	3.0	3.0	3.0	2.0	2.0	8.0	13.0	35.0

The current dataset serves as the foundation for the statistical analyses carried out in this study, aimed at identifying significant relationships between the selected factors and labor productivity in the context of bricklaying operations.

3. Results and discussion

Several methods are available for assessing the normality of data, including the Shapiro-Wilk test, Kolmogorov-Smirnov test, skewness and kurtosis analysis, and visual tools such as histograms, boxplots, P-P plots, and Q-Q plots. The Shapiro-Wilk and Kolmogorov-Smirnov tests are the most commonly used methods. The Shapiro-Wilk test is generally applied to smaller sample sizes ($N < 50$), while the Kolmogorov-Smirnov test is more suitable for larger samples ($N \geq 50$) (Yalçın & Bayram, 2023). In this study, the Kolmogorov-Smirnov test was used to assess the normality of the data. The results revealed significant deviations from normality, with p-values of 0.000, indicating that the data do not follow a normal distribution. Consequently, non-parametric tests were employed for further analysis to ensure accurate conclusions under the assumption of non-normality.

3.1. Correlation between productivity and key variables

Spearman's Rank Correlation was used to examine the strength and direction of relationships between productivity and the other variables. As shown in Table 3, several significant associations emerged. Working space conditions ($rs = 0.276$, $p < 0.001$) and tools/equipment availability ($rs = 0.201$, $p < 0.001$) displayed the strongest positive correlations with productivity, suggesting that improved site conditions and resource provision significantly enhance labor efficiency. Material availability ($rs = 0.146$, $p = 0.001$) and communication among workers ($rs = 0.088$, $p = 0.043$) also showed weaker but statistically significant positive relationships.

Table 3. Spearman's rank correlation between labor productivity and influencing variables (N = 532).

No	Variables	Spearman Correlation	p-value
1	Material Availability	0.146	0.0010
2	Weather Conditions	-0.118	0.0070
3	Communication among Workers	0.088	0.0430
4	Availability of Tools/Equipment	0.201	0.0000
5	Working Space Conditions	0.276	0.0000
6	Rework Frequency	-0.266	0.0000
7	Accident Frequency	-0.279	0.0000
8	Working Hours	-0.393	0.0000
9	Gang size	-0.052	0.2330

On the other hand, accident frequency ($rs = -0.279$, $p < 0.001$), rework frequency ($rs = -0.266$, $p < 0.001$), and extended working hours ($rs = -0.393$, $p < 0.001$) were negatively associated with productivity, reflecting the disruptive impact of unsafe or inefficient working conditions. Weather conditions ($rs = -0.118$, $p = 0.007$) also had a small but significant inverse relationship. Notably, gang size did not show a significant relationship ($rs = -0.052$, $p = 0.233$), indicating that crew size alone does not guarantee better performance. These results underline the importance of improving working conditions and minimizing disruptions on-site. They also support prior findings in the literature that emphasize workspace quality and resource availability as key productivity drivers (Alyew et al., 2020; Ulubeyli et al., 2014).

Fig. 1 illustrates the strength and direction of the relationships between productivity and the examined variables using a heatmap of Spearman's Rank Correlation coefficients. Positive associations are shown in warmer tones, while negative associations are depicted in cooler tones. This visual reinforces the statistical results in Table 3, highlighting the strongest positive correlations for working space conditions and tool availability, and the strongest negative correlations for working hours, accident frequency, and rework frequency.

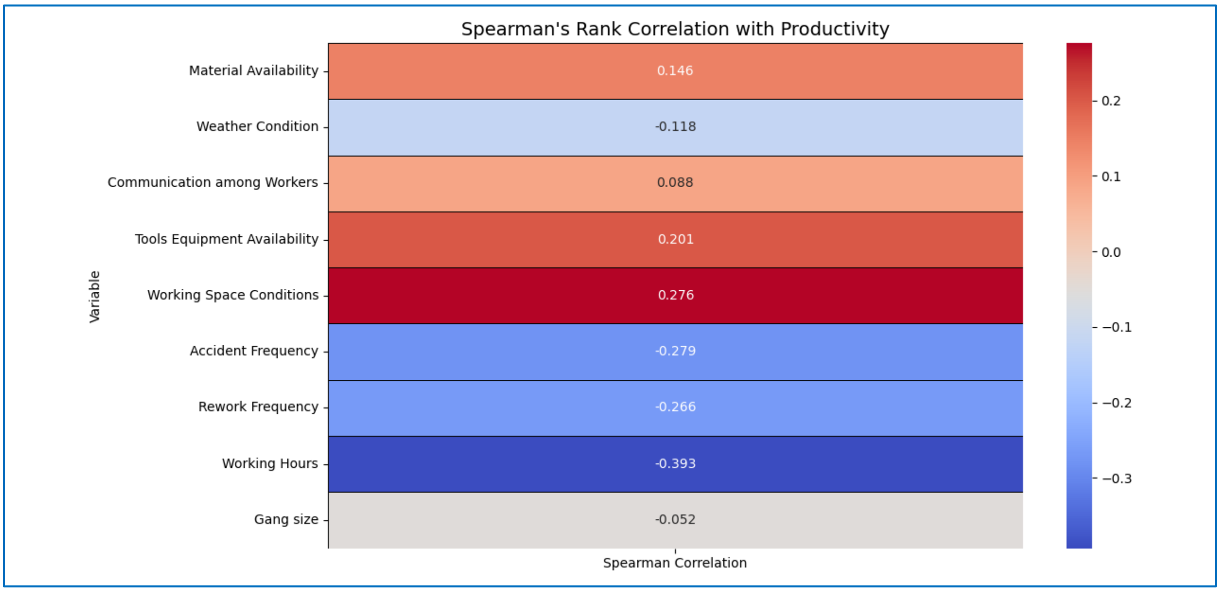

Fig. 1. Spearman correlation heatmap between productivity and influencing variables.

3.2. Group comparisons of categorical variables

To assess whether productivity significantly varied across different levels of key categorical variables, the Kruskal-Wallis H test was employed. As shown in Table 4, productivity differed greatly across all five variables tested. The strongest effect was observed for Working Space Conditions ($H = 43.011$, $p < 0.001$), indicating that laborers working in more spacious environments achieved considerably higher productivity than those in cramped or moderately sized spaces. Similarly, Tools Equipment Availability ($H = 25.161$, $p < 0.001$) and Material Availability ($H = 22.190$, $p < 0.001$) showed significant associations, which shows that access to necessary resources directly enhances work performance. Communication among Workers ($H = 23.724$, $p < 0.001$) was also a significant factor, reflecting the role of coordination and collaboration on-site. Lastly, Weather Condition ($H = 7.353$, $p = 0.025$) exhibited a smaller but statistically significant influence, indicating that productivity declines under poor weather conditions, a relevant concern in Somaliland's semi-arid climate, which presents frequent exposure to heat and dust, particularly on outdoor construction sites (Nelson et al., 2020). The influence of communication on productivity confirms Soekiman et al. (2011), who highlighted that poor communication on construction sites has a high effect on projects. These findings collectively underscore the importance of managing site environment, resource provision, and interpersonal dynamics to improve labor productivity.

Table 4. Kruskal-Wallis H test results

Variables	Kruskal-Wallis H	p-value
Material availability	22.190	0.0000
Weather condition	7.353	0.0253
Communication among workers	23.724	0.0000
Tools equipment availability	25.161	0.0000
Working space conditions	43.011	0.0000

3.3. Pairwise group comparisons

Following the Kruskal-Wallis results, Mann-Whitney U tests were conducted to compare productivity between the most contrasting groups (Level 1 vs Level 3) across selected categorical variables. These comparisons aimed to isolate the impact of moving from poor or limited site conditions to more favorable ones. As summarized in Table 5, all four variables demonstrated statistically significant differences in productivity between their lowest and highest levels.

Specifically, productivity was significantly higher under conditions of spacious working environments compared to cramped ones ($U = 3148.5$, $p < 0.001$), and when tools and equipment were highly available rather than scarce ($U = 262.5$, $p < 0.001$). Similarly, high material availability ($U = 3498.5$, $p < 0.001$) and good communication among workers ($U = 7939.5$, $p < 0.001$) were both associated with significantly higher productivity than their lowest categories. These results reinforce the importance of well-organized, well-equipped, and communicative work environments in maximizing labor output on construction sites.

Table 5. Mann-Whitney U test results for Level 1 vs Level 3 comparisons

Variable	Group Compared	Mann-Whitney U	p-value
Working space conditions	Cramped vs Spacious (1 vs 3)	3148.5	0.0000
Tools equipment availability	Low vs High (1 vs 3)	262.5	0.0000
Material availability	Low vs High (1 vs 3)	3498.5	0.0000
Communication among workers	Poor vs Good (1 vs 3)	7939.5	0.0000

3.4. Categorical associations

Chi-Square tests were conducted to explore potential associations between accident occurrence and key categorical variables, including resource availability, workspace conditions, communication, and rework. Given the practical and safety implications of accidents on construction sites, this analysis specifically examined accident frequency to categorical variables. Accidents are a critical barrier to productivity (Abdillahi & Kazaz, 2021). As shown in Table 6, only one statistically significant relationship was found. Weather Condition was significantly associated with accident frequency ($\chi^2 = 12.952$, $p = 0.0015$), indicating that poor weather may contribute to increased safety risks on construction sites.

No statistically significant associations were observed between accident frequency and other variables such as material availability, tool availability, working space conditions, communication among workers, or rework occurrence. While these factors are often considered influential in practice, the present data did not provide evidence of a strong statistical relationship. This may suggest that weather-related disruptions are the most immediate environmental concern for safety in the context of Somaliland's semi-arid construction sites.

Table 6. Chi-Square Test of Independence between Accident Frequency and Categorical Variables

Test	X^2 Value	Degrees of Freedom	p-value
Material vs Accident	0.986	2	0.6109
Weather vs Accident	12.952	2	0.0015
Communication vs Accident	0.446	2	0.8003
Tools and equipment vs Accident	1.162	2	0.5595
Space vs Accident	0.955	2	0.6204
Rework vs Accident	0.207	1	0.6489

4. Conclusion

This study investigates the key drivers of labor productivity in bricklaying within the construction sector of Somaliland, drawing on real-world data collected from 52 projects across four major cities. Using non-parametric statistical methods, the analysis revealed that factors such as working space conditions, availability of tools and materials, and communication among workers significantly enhance productivity. Conversely, disruptions, including frequent rework, extended working hours, and accidents, were found to negatively impact labor output.

The findings emphasize the central role of site conditions and resource availability in facilitating efficient labor performance. In particular, the consistent influence of workspace and tool access across multiple statistical tests underscores the need for construction managers to prioritize physical working conditions alongside technical planning. Notably, while many factors are assumed to affect safety and productivity, the data showed that only weather had a significant statistical association with accident frequency, highlighting the need for greater attention to environmental factors, particularly in semi-arid regions like Somaliland.

This study contributes to the growing body of productivity research by contextualizing findings in a post-conflict, low-infrastructure setting where formal project management frameworks are often absent. The practical implications are clear: improving basic site logistics, fostering team communication, and minimizing avoidable disruptions can yield measurable productivity gains even in resource-constrained environments.

The findings hold particular value for construction environments like Somaliland's, where informal labor structures and limited access to formal project management tools are the norm. By grounding the analysis in real-world conditions, this study demonstrates that meaningful productivity gains can be achieved not through high-tech solutions but through improvements in basic site organization, such as ensuring adequate workspace, maintaining tool availability, and promoting consistent crew communication. These are practical, low-cost interventions that local contractors and site supervisors can implement without systemic overhaul. Moreover, the results challenge assumptions common in highly industrialized settings, where factors like crew size and communication are typically strong predictors of productivity. In contrast, this study found that in Somaliland, these variables behaved differently, likely due to cultural norms, informal labor arrangements, and non-standardized communication practices on-site.

Future research should extend beyond bricklaying to explore productivity in other trades and across different project phases. Additionally, longitudinal studies tracking changes over time or intervention-based research testing specific productivity-enhancing strategies would further enrich understanding and application in the field.

References

Abdi, M. A., & Hareru, W. K. (2024). Assessment of Factors Affecting the Implementation of Occupational Health and Safety Measures in the Construction Industry in Somaliland. *Advances in Civil Engineering*, *2024*(1), 8324294. https://doi.org/10.1155/2024/8324294

Abdillahi, A. M., Biçer, Z. Ö. P., & Bayram, S. (2024). Assessment of Construction Site Management Practices: A Case Study of a Construction Project in Hargeisa. *Journal of Advanced Research in Natural and Applied Sciences*, *10*(1), 228–242.

Abdillahi, A. M., & Kazaz, A. (2021). Evaluating Factors Effecting Building Construction Labor Productivity in Somaliland. *Journal of Construction Engineering, Technology & Management*, *11*(2), 19–28. https://doi.org/10.37591/JoCETM

Alyew, A., Bassa, M., Reta, A., & Tora, M. (2020). A Study on Factors Affecting Labour Productivity on Construction Projects in Wolaita Zone, Ethiopia. *International Journal of Engineering Research and Technology*, *8*(12), 817–822.

Attar, A. A., Gupta, A. K., & Desai, D. B. (2012). A study of various factors affecting labour productivity and methods to improve it. *IOSR Journal of Mechanical and Civil Engineering (IOSR-JMCE)*, *1*(3), 11–14.

Buchan, R. D., Fleming, E., & Grant, F. (2012). *Estimating for Builders and Surveyors*. Routledge.

Cevikbas, M. (2022). Determining the Causes of Fluctuation in Productivity in Construction Projects. *Dicle Üniversitesi Mühendislik Fakültesi Mühendislik Dergisi*, *13*(3), Article 3. https://doi.org/10.24012/dumf.1074842

Edwin, A. A., & Calistus, A. (2023). Measurement and Analysis of Impact of Supervision on Construction Labour Productivity: A Case Study of North-Central Nigeria. *BIMA JOURNAL OF SCIENCE AND TECHNOLOGY (2536-6041)*, *7*(01).

Kaming, P. F., Olomolaiye, P. O., Holt, G. D., & Harris, F. C. (1997). Factors influencing craftsmen's productivity in Indonesia. *International Journal of Project Management*, *15*(1), 21–30.

Lee, T. Y., Ahmad, F., & Sarijari, M. A. (2023). Current Status and Future Research Trends of Construction Labor Productivity Monitoring: A Bibliometric Review. *Buildings*, *13*(6), 1479.

Momade, M. H., Shahid, S., Falah, G., Syamsunur, D., & Estrella, D. (2023). Review of construction labor productivity factors from a geographical standpoint. *International Journal of Construction Management*, *23*(4), 697–707. https://doi.org/10.1080/15623599.2021.1917285

Nelson, E. L., Khan, S. A., Thorve, S., & Greenough, P. G. (2020). Modeling pastoralist movement in response to environmental variables and conflict in Somaliland: Combining agent-based modeling and geospatial data. *Plos One*, *15*(12), e0244185.

Omar, M. A., Fashina, A. A., & Fakunle, F. F. (2020). The status quo of Somaliland construction industry: A development trend. *PM World Journal*, *IX*(V), 1–18.

Soekiman, A., Pribadi, K. S., Soemardi, B. W., & Wirahadikusumah, R. D. (2011). Factors relating to labor productivity affecting the project schedule performance in Indonesia. *Procedia Engineering*, *14*, 865–873.

Ulubeyli, S., Kazaz, A., & Er, B. (2014). Planning engineers' estimates on labor productivity: Theory and practice. *Procedia-Social and Behavioral Sciences*, *119*, 12–19.

Van Tam, N. (2024). Unveiling global research trends in construction productivity: A scientometric analysis of twenty-first century research. *Smart Construction and Sustainable Cities*, *2*(1), 2. https://doi.org/10.1007/s44268-024-00025-7

Yalçın, G., & Bayram, S. (2023). The effect of communication on construction project management processes during the covid-19 pandemic period: A case study in Türkiye. *International Advanced Researches and Engineering Journal*, *7*(2), 125–137.

Zakeri, M., Olomolaiye, P., Holt, G. D., & Harris, F. C. (1997). Factors affecting the motivation of Iranian construction operatives. *Building and Environment*, *32*(2), 161–166.

4th International Civil Engineering & Architecture Conference
17-19 May 2025, Trabzon, Türkiye

Developing a virtual reality-based safety training tool for undergraduate civil engineering students

Umutcan Kılıç[1], İlyas B. Altun[1], Semra Çomu[*1]

[1] *Boğaziçi University, Department of Civil Engineering, 34342 İstanbul, Türkiye*

Abstract. Construction sites present numerous hazards, particularly for inexperienced individuals such as undergraduate civil engineering students completing mandatory site internships. Without adequate safety training, students may struggle to effectively recognize and respond to high-risk conditions, increasing the likelihood of accidents. This study proposes the development of an immersive, AI-powered Virtual Reality (VR) safety training tool integrating Unity, Convai, a VR headset, and motion controllers—to enhance civil engineering students' hazard recognition skills prior to exposure to real-world construction environments. The training module focuses on two critical risk sources commonly encountered on construction sites: falling from height and being struck by a moving object. Throughout the training, the students are accompanied by a voice-interactive AI-powered Non-Playable Character (NPC) who provides information regarding safety procedures and responds to their questions. Through a realistic and interactive simulation, students can observe the consequences of safe and unsafe behaviors and engage directly with an AI-powered NPC to ask safety-related questions. The anticipated outcomes of this study include enhanced hazard recognition, improved situational awareness, increased confidence in identifying risks, and the development of a proactive safety mindset among students. By demonstrating the potential of integrating AI-powered VR-based training into the civil engineering curriculum, this study aims to contribute to the broader goal of enhancing worksite safety by better preparing future civil engineers to understand and manage the complexities of real-world construction sites.

Keywords: Virtual Reality (VR) training; Artificial Intelligence (AI)-powered Non-playable Characters (NPCs); Unity VR Development; Construction Safety; Civil Engineering Education

1. Introduction

With high rates of occupational accidents and fatalities, the construction industry consistently ranks among the most hazardous sectors worldwide (International Labour Organization [ILO], 2023). In developing countries such as Türkiye, this risk is further amplified due to limited regulatory enforcement. Undergraduate civil engineering students are a particularly vulnerable group to these hazards, as they are often required to participate in mandatory internships or site visits without sufficient prior safety training. Their lack of practical experience and hazard awareness compromises their ability to recognize and respond effectively to unsafe site conditions, which might increase the likelihood of accidents during their early professional exposure. For instance, according to data from the Turkish Social Security Institution (SGK), nearly 25% of workplace injuries involve workers with less than one year of experience, a category into which many students fall (SGK, 2022). These statistics, when considered alongside the construction industry's widely recognized reputation for being hazardous, underscore an urgent need for innovative educational approaches that effectively equip students with relevant hazard recognition skills and safety awareness before they enter dynamic construction environments.

Traditional safety training is primarily theoretical and classroom-based. This approach often relies on crowded lectures given by an occupational health and safety expert and textual materials to communicate complex and dynamic site hazards. While it may be sufficient for conveying basic concepts, number of research indicated that traditional approaches fail to replicate the sensory and situational aspects of a real construction site, causing students and workers to struggle to translate what they learn in a classroom into practical situational awareness when confronted with active construction environments (Zhang et al., 2023). Furthermore, the lack of interactivity and engagement, which are often associated with traditional methods, can limit knowledge retention and can reduce students' motivation to internalize safety principles (Casey et al., 2021). Consequently, students may enter construction sites with limited risk awareness and hazard recognition, which will lead them to depend heavily on their observations and trial-and-error methods rather than proactive safety practices.

[*] Corresponding author, E-mail: semra.comu@bogazici.edu.tr

https://doi.org/10.31462/icearc2025_ce_mng_527

VR technology offers a promising alternative to traditional safety education methods. By immersing users in simulated environments, VR enables workers and students to experience realistic construction scenarios without exposure to actual danger. It allows them to observe, assess, and respond to hazardous conditions in a fully controlled and repeatable setting (Comu et al. 2021). This immersive approach enhances engagement and encourages active learning by allowing students to make decisions, see the outcomes of their actions, and receive immediate feedback. VR also accommodates a range of learning styles by combining visual, auditory, and kinesthetic elements, making it more effective than static teaching materials (Jena, 2016). According to Man et al. (2024), VR is significantly more effective than traditional methods in construction safety training, especially for enhancing behavior, skills, and experience, with its impact influenced by training context and worker experience.

Although several past studies have demonstrated the potential of VR-based safety training, they mostly relied on deterministic scenarios and predefined interactions that limit user input and adaptive learning (Akindele et al., 2024). In addition, most research investigating the integration of health and safety education into civil engineering curriculum has primarily focused on adapting traditional training content to better suit students' needs rather than reimagining the training method itself (Neto & Amaral, 2024). This study addresses these gaps by developing and evaluating a VR-based safety training tool specifically designed for undergraduate civil engineering students that incorporates AI-powered NPCs that students can communicate with using natural voice commands. The AI-powered NPC allows students to ask context-specific questions during training, receive verbal responses, and simulate real-time dialogue with a site supervisor or coworker. Because of its ability to replicate complex environments, dynamic risk factors, and authentic human interaction, the integrated VR-AI training system can significantly improve hazard recognition, situational awareness, and overall readiness among civil engineering students. By engaging with realistic site scenarios, students are expected to improve their hazard perception and response strategies before entering actual construction sites. This approach contributes to civil engineering education by promoting a proactive safety mindset and preparing students for the complexities of real-world construction environments.

2. Materials and methods

We developed the VR-based training tool using Unity, a cross-platform game engine widely used for immersive simulation design (Unity, 2024). We chose Unity for its flexibility, ease of use, and hyper-realistic graphics, which enabled us to rapidly develop a realistic construction environment. We designed the application to run on a standalone VR headset (HTC Vive Pro 2) with motion controllers (HTC Vive Controller), enabling full interaction within a virtual construction site. The virtual site was rendered in real-time using Unity's real-time rendering engine that ensured smooth visual feedback as users moved through the virtual site, which made interactions feel natural and allowed an experience as close as possible to the real world. To further increase realism and engagement, the system includes an AI-powered NPC with whom students can communicate using voice inputs through a microphone. This interactive NPC is powered by Convai, a conversational AI system integrated with Unity that combines speech-to-text (STT), large language models (e.g., GPT-4 and Gemini Flash), dialogue management, and neural text-to-speech (TTS) synthesis to enable realistic, voice-driven interaction with virtual characters (Convai, 2025). This integration allows adaptive learning where students can engage with the NPC to freely ask any questions that they might have. The system also includes a question filtering system to make sure that only questions relevant to the safety training module are answered.

The developed training tool simulates two of the most commonly encountered construction site hazards: falling from heights and being struck by a moving object. These scenarios were selected based on their frequency and severity in real-world construction sites (Kim et al., 2023). Within an interactive virtual environment, students are exposed to realistic situations where they are informed about these hazards and related safety practices. Each scenario presents both safe and unsafe behaviors, allowing students to observe the consequences of different actions when incidents occur. Safety recommendations and critical errors are highlighted before and after each scenario to reinforce the learning process. This scenario-based structure is intended not only to enhance hazard perception through consequence-based learning but also to support effective decision-making under realistic construction site conditions.

The training environment includes detailed 3D models of scaffolding, construction machinery and vehicles, construction materials, other workers, and other elements typically found on real construction sites. Figure 1 presents a screenshot of the virtual training environment as viewed from an aerial perspective. Throughout the training session, participants are accompanied by the AI-powered NPC. Figure 2 displays the AI-powered NPC's appearance inside the VR simulation. The AI-powered NPC offers verbal guidance and reminders to encourage reflective thinking during each stage.

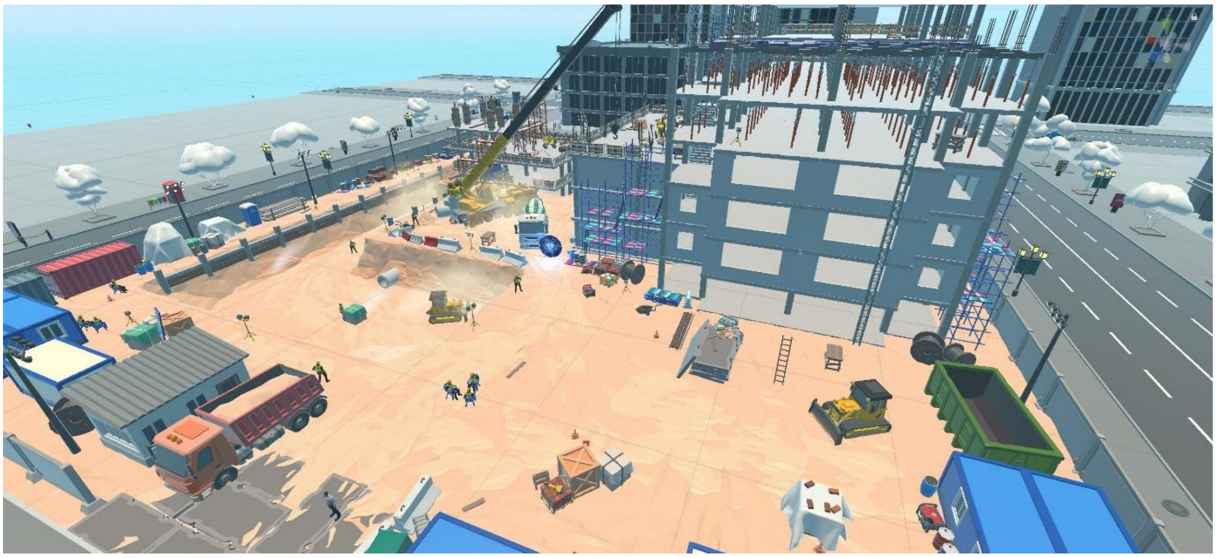

Fig. 1. Virtual training environment

Students can freely explore the virtual construction site and interact with various objects and workers. Hazards are integrated into the environment through scripted events developed in C# 8.0, while visual and audio cues enhance the sense of realism. The AI-powered NPC is designed to regularly prompt students to ask safety-related questions during the training. This immersive setup enables experiential learning by simulating real-world scenarios, reinforcing safe behaviors through observation and consequence-driven feedback, and encouraging active inquiry to deepen understanding.

The experiments were conducted with undergraduate civil engineering students who are in their freshman year and have not completed their mandatory site internships yet. Participation in the study was voluntary, and informed consent was obtained from all students prior to the experiment. A total of 7 students voluntarily participated in the study, and none of the students had prior experience in a real construction site. Following the VR training sessions, a survey was completed to evaluate the AI-powered VR-based safety training tool. Each session was conducted individually and lasted approximately 10 to 15 minutes per student. The overall goal of the experimental design was to measure the effectiveness of the AI-powered VR-based safety tool in improving construction safety competence of the students and also their opinion regarding the tool. The students were also instructed to ask at least one question related to the safety training and one unrelated question to evaluate the AI-powered NPC's response capabilities to different question types.

Fig. 2. AI-powered NPC guide

The survey was designed to capture quantitative feedback regarding the tool. The survey consisted of 12 close-ended statements rated on a five-point Likert scale (1 = Strongly Disagree, 2 = Disagree, 3 = Neutral/Uncertain, 4 = Agree, 5 = Strongly Agree). Table 1 demonstrates the Likert scale descriptions and corresponding intervals for analysis (Nyutu et al., 2020). Table 2 summarizes the 12 close-ended statements included in the survey, designed to assess students' perceptions of the VR-based safety training environment, including usability, engagement, realism, and perceived learning outcomes. The survey structure and content were informed by established practices in VR-based safety education and human-computer interaction design, as demonstrated in previous research (Abotaleb et al., 2022; Joshi et al., 2021; Xu & Zheng, 2020). In addition to the structured statements, participants were asked to provide qualitative feedback specifically regarding the AI-powered NPC, focusing on the relevance, clarity, and helpfulness of its responses to safety-related questions posed during the training. Survey responses were collected anonymously to ensure participant privacy and were used solely for research purposes. The collected data served to evaluate the overall effectiveness of the training tool and to identify specific areas requiring refinement, particularly in relation to the integration of AI-driven interaction and the realism of immersive training scenarios.

3. Results and discussion

Experiments were first conducted with seven first-year undergraduate students, who completed the AI-powered VR-based safety training session. Following the training, participants were asked to complete a survey consisting of 12 statements rated on a five-point Likert scale. The survey aimed to evaluate their perceptions of the training tool in terms of effectiveness, usability, realism, and educational value. Based on their context, the statements were categorized into three groups: (1) AI-powered VR-based Training Tool Related Statements, (2) Virtual Environment Related Statements, and (3) Learning Experience Related Statements.

Statements 1 through 6 comprise the first category of the post-training survey, focusing on participants' perceptions of the effectiveness, interactivity, and educational value of the AI-powered virtual reality (VR) training tool. Table 3 provides a summary of the descriptive statistics for each item. Based on the five-point Likert scale, which categorizes responses from "Strongly Disagree" (1.00–1.80) to "Strongly Agree" (4.21–5.00), the results reflect a generally positive evaluation of the training experience.

Among these six statements, only Statement 1, "The VR training improved my awareness of construction site hazards", received a mean score below 4.00 (M = 3.71, SD = 0.70), which falls within the "Agree" range (3.41–4.20). This suggests that, while students recognized the training's contribution to hazard awareness, their agreement was somewhat moderate. Similarly, Statement 3, "The AI NPC helped me better understand safety-related concepts", had a mean score of 4.14 (SD = 0.64), placing it near the upper boundary of the same range. These slightly lower ratings may reflect the current version of the training tool, which includes only two pre-defined scenarios: a fall-from-height incident and a being struck by a moving object incident. This limited scope likely reduced the diversity of hazardous events presented and restricted opportunities for meaningful dialogue and contextual learning with the AI-powered NPC.

Conversely, Statements 2, 4, 5, and 6 received mean ratings well within the "Strongly Agree" range. Notably, Statement 2, "The scenarios demonstrated clear consequences of unsafe behavior", achieved a high mean of 4.71 (SD = 0.45), indicating that the visual and narrative design of the scenarios effectively communicated the risks associated with unsafe practices. Statements 4 and 6 also performed strongly (both M = 4.57), suggesting that students found the AI NPC's responses to be both satisfactory and integral to the training's overall impact. Statement 5 received the highest mean score (M = 4.86, SD = 0.35), emphasizing that students overwhelmingly perceived voice-based interaction as a key factor in enhancing the naturalness and realism of the training environment.

These results highlight the value added by integrating conversational AI into immersive VR training settings. The strong agreement on interaction-related statements (4-6) suggests that students not only benefited from observing hazardous scenarios but also appreciated the opportunity to engage in a more personalized and responsive learning experience. This finding is consistent with previous research highlighting the positive role of AI-driven agents in improving user engagement and learning effectiveness across various educational domains (Lin et al., 2023).

Table 1. Five-point Likert scale descriptions and corresponding intervals

Likert-Scale Description	Likert-Scale	Likert Scale Interval
Strongly Disagree	1	1.00 – 1.80
Disagree	2	1.81 – 2.60
Neutral/Uncertain	3	2.61 – 3.40
Agree	4	3.41 – 4.20
Strongly Agree	5	4.21 – 5.00

Table 2. Survey content

ID	Statements
1	The VR training improved my awareness of construction site hazards.
2	The scenarios demonstrated clear consequences of unsafe behavior.
3	The AI-powered NPC helped me better understand safety-related concepts.
4	The AI-powered NPC's responses to my questions were adequate and satisfactory.
5	The voice interaction made the experience more natural and effective.
6	The training would have not been as effective if there was no AI NPC.
7	The training environment felt realistic.
8	I found it easy to navigate and interact within the virtual environment.
9	The scenarios reflected realistic construction site conditions.
10	I was able to focus and stay engaged throughout the session.
11	After completing the AI-powered VR training, I feel more confident about identifying hazards on a real construction site.
12	I would recommend this training tool to other civil engineering students.

In summary, while there is room to expand the scenario diversity to strengthen hazard awareness and conceptual learning, the current implementation of the AI-powered VR training tool was highly rated overall. The integration of natural voice interaction with a conversational agent appears to significantly enhance learner engagement, realism, and perceived training effectiveness, supporting the growing potential of such technologies in construction safety education.

The second category of the survey focuses on Statements 7 through 9, which assess students' perceptions of the virtual environment's realism, usability, and fidelity to actual construction site conditions. As shown in Table 4, the mean ratings for all three items fall within the "Agree" range (3.41–4.20), indicating a generally favorable reception of the virtual training environment.

Statement 7, "The training environment felt realistic", received a mean score of 3.43 (SD = 1.18), which, while indicating agreement, reflects the lowest mean in this category and shows considerable variation among responses. This variability may be influenced by students' differing levels of familiarity with immersive environments. Although the participants were first-year civil engineering students with no prior exposure to real construction sites, some may have had prior experience with VR technologies in other contexts (e.g., gaming or entertainment), which could have shaped their expectations and affected their perceptions of realism.

Statement 8, "I found it easy to navigate and interact within the virtual environment", achieved a higher mean score of 4.00 (SD = 0.76), indicating a consistent perception that the system was user-friendly and that the controls enabled seamless movement and interaction. This is a key aspect of effective VR-based training, as ease of use is essential for maintaining learner engagement and minimizing cognitive overload.

Statement 9, "The scenarios reflected realistic construction site conditions", received a mean score of 3.86 (SD = 0.99), suggesting that students generally found the training scenarios credible and aligned with what they imagine real site conditions to be. These perceptions are noteworthy given the students' lack of firsthand construction site experience and may again reflect the influence of prior exposure to digital or simulated environments. These findings are consistent with those reported by Xu and Zheng (2020), who observed that participants in their VR-based training, also developed with Unity, perceived the simulated environment as both usable and representative of real-world settings.

In sum, the results from this category suggest that the virtual environment effectively replicated core elements of a construction site, allowing students to engage in meaningful, risk-free safety training. Despite the absence of real-world experience, students were able to evaluate the tool's realism and usability, likely drawing on their prior familiarity with virtual platforms. This reinforces the value of immersive technologies in construction safety education, particularly for novices who have yet to access physical job sites.

Table 3. Survey results for AI-powered VR-based training tool related statements

Statement ID	Mean	Standard Deviation
1	3.71	0.70
2	4.71	0.45
3	4.14	0.64
4	4.57	0.73
5	4.86	0.35
6	4.57	1.05

Table 4. Survey results for virtual environment related statements

Statement ID	Mean	Standard Deviation
7	3.43	1.18
8	4.00	0.76
9	3.86	0.99

Table 5 presents the survey results for the third and final category of statements, which explores participants' overall learning experience. This category includes Statements 10 through 12, focusing on engagement, perceived learning outcomes, and students' willingness to recommend the training to peers.

Statement 10, "I was able to focus and stay engaged throughout the session", received a mean rating of 4.00 (SD = 1.07), indicating that students generally agreed that the training environment successfully maintained their attention. This finding is particularly important in the context of VR-based education, as previous studies have highlighted the risk of cognitive disengagement and sensory overload due to isolation in immersive settings (Abotaleb et al., 2022). The presence of an AI-powered NPC likely contributed to maintaining focus by fostering a more interactive and responsive learning environment, thus mitigating the typical shortcomings of VR training experiences.

Statement 11, "After completing the AI-powered VR training, I feel more confident about identifying hazards on a real construction site", also received a positive mean rating of 3.71 (SD = 0.16), indicating agreement among students, albeit with a narrow distribution of responses. Given that participants were first-year civil engineering students with no prior field experience, this result indicates the potential of immersive simulations to improve confidence and hazard recognition skills even among novices.

Statement 12, "I would recommend this training tool to other civil engineering students", received the highest mean rating in this category at 4.43 (SD = 0.49), falling within the "Strongly Agree" interval. This result strongly suggests a high level of satisfaction with the training experience and indicates students' belief in its value for their peers. Collectively, these findings reinforce the effectiveness of the developed AI-powered VR safety training tool in enhancing students' engagement, perceived preparedness, and peer endorsement.

Additionally, as part of the evaluation, students were instructed to interact with the AI NPC by asking at least one question relevant to the safety training and one unrelated question. All participants complied, asking exactly two questions each. For safety-related queries, all students reported receiving responses they deemed relevant and adequate. However, when it came to unrelated questions, the AI NPC responded to five out of seven inputs despite being designed to filter such content. It successfully identified only two unrelated questions and attempted to deflect them by humorously steering the conversation back toward safety training. While this behavior demonstrates some conversational flexibility, it also exposes a potential vulnerability in the system—namely, the risk of misinformation or unintended learning outcomes when off-topic dialogue is permitted.

This observation highlights the importance of implementing more robust content-filtering algorithms and topic-detection mechanisms in conversational AI agents, particularly in educational applications. Ensuring that the AI remains contextually aligned with training objectives is essential for maintaining educational integrity and avoiding distraction or confusion among learners. Overall, the results in this category affirm the pedagogical value of AI-integrated VR tools and highlight both their promise and the areas requiring further development to ensure safe, focused, and effective deployment in educational settings.

4. Conclusions

This study showcases the development and initial evaluation of an AI-powered VR-based safety training tool specifically designed for undergraduate civil engineering students. The developed tool addresses the limitations of traditional safety education, which often lacks interactivity, immersion, and practical applicability, by leveraging state-of-the-art technologies including Unity, VR headsets, motion controllers, and a conversational AI-based NPC. By simulating two of the most common construction hazards—falling from heights and being struck by a moving object in a virtual environment—the training tool aims to improve safety knowledge, hazard awareness, and proactive safety behavior among inexperienced civil engineering students before they enter real construction sites.

Table 5. Survey results for learning experience related statements

ID	Mean	Standard Deviation
10	4.00	1.07
11	3.71	0.16
12	4.43	0.49

Survey results collected from first-year civil engineering students indicate a high level of satisfaction with the training tool, its effectiveness, its usability, and its educational value. Notably, participants strongly agreed that the voice-interactive AI-powered NPC enhanced their safety training experience by making it more engaging and realistic. Moreover, the inclusion of consequence-based scenarios allowed students to internalize the importance of safe behaviors. Despite the limited number of scenarios included in the current version of the tool, the students expressed improved confidence in recognizing hazards and a willingness to recommend the tool to their peers, underlining its educational potential.

However, the study also identified a couple of areas for improvement. While the AI-powered NPC effectively responded to safety-related questions, its response filtering system requires further improvements to better identify and manage off-topic questions, preventing the risk of misinformation. This limitation is not only relevant to educational tools but should also be a key consideration for all applications integrating conversational AI to enhance user experience. Future iterations of the tool should incorporate a broader set of safety scenarios, more advanced AI filtering mechanisms, and a more diverse participant pool to strengthen its reliability, scalability, and generalizability.

In conclusion, the integration of VR and AI technologies in construction safety education showcases significant potential for transforming traditional methods. This study demonstrates that training tools, including not only virtual environments but also conversational AI agents, can play a critical role in equipping future civil engineers with the safety competencies necessary to navigate complex and hazardous construction sites. As civil engineering education continues to evolve in response to Industry 5.0 and Construction 5.0, tools like the one developed in this study will become essential components of modern civil engineering curricula.

References

Abotaleb, I., Hosny, O., Nassar, K., Bader, S., Elrifaee, M., Ibrahim, S., El Hakim, Y., & Sherif, M. (2022). An interactive virtual reality model for enhancing safety training in construction education. *Computer Applications in Engineering Education*, *31*(2), 324–345. https://doi.org/10.1002/cae.22585

Akindele, N., Taiwo, R., Sarvari, H., Oluleye, B. I., Awodele, I. A., & Olaniran, T. O. (2024). A state-of-the-art analysis of virtual reality applications in construction health and safety. *Results in Engineering*, *23*, 102382. https://doi.org/10.1016/j.rineng.2024.102382

Casey, T., Turner, N., Hu, X., & Bancroft, K. (2021). Making safety training stickier: A richer model of safety training engagement and transfer. *Journal of Safety Research*, *78*, 303–313. https://doi.org/10.1016/j.jsr.2021.06.004

Convai. (2025). Conversational AI for virtual worlds. Retrieved 2025 from https://www.convai.com/

Comu, S., Kazar, G. and Marwa, Z., 2021. Evaluating the attitudes of different trainee groups towards eye tracking enhanced safety training methods. Advanced Engineering Informatics, 49, p.101353. https://doi.org/10.1016/j.aei.2021.101353

Jena, R. K. (2016). Investigating the interrelation between attitudes, learning readiness, and learning styles under virtual learning environment: A study among Indian students. *Behaviour & Information Technology*, *35*(11), 946–957. https://doi.org/10.1080/0144929x.2016.1212930

Joshi, S., Hamilton, M., Warren, R., Faucett, D., Tian, W., Wang, Y., & Ma, J. (2021). Implementing Virtual Reality Technology for safety training in the precast/ prestressed concrete industry. *Applied Ergonomics*, *90*, 103286. https://doi.org/10.1016/j.apergo.2020.103286

Kim, K.-N., Kim, T.-H., & Lee, M.-J. (2023). Analysis of building construction jobsite accident scenarios based on Big Data Association analysis. *Buildings*, *13*(8), 2120. https://doi.org/10.3390/buildings13082120

Lin, C.-C., Huang, A. Y., & Yang, S. J. (2023). A review of AI-Driven Conversational Chatbots implementation methodologies and Challenges (1999–2022). Sustainability, 15(5), 4012. https://doi.org/10.3390/su15054012

Man, S.S., Wen, H. and So, B.C.L., 2024. Are virtual reality applications effective for construction safety training and education? A systematic review and meta-analysis. Journal of safety research, 88, pp.230-243. https://doi.org/10.1016/j.jsr.2023.11.011

Nearly 3 million people die of work-related accidents and diseases. International Labour Organization [ILO]. (2023, November 26). Retrieved 2025 from https://www.ilo.org/resource/news/nearly-3-million-people-die-work-related-accidents-and-diseases

Neto, I.R. and Amaral, F.G., 2024. Teaching occupational health and safety in engineering using active learning: A systematic review. Safety science, 171, p.106391. . https://doi.org/10.1016/j.ssci.2023.106391

Nyutu, E., Cobern, W. W., & Pleasants, B. A.-S. (2020). Correlational study of student perceptions of their undergraduate laboratory environment with respect to gender and major. International Journal of Education in Mathematics, Science and Technology, 9(1), 83–102. https://doi.org/10.46328/ijemst.1182

Sosyal Güvenlik Kurumu. (2023). 2022 Yılı - YILLIK BÖLÜM 3-1 İş Kazası ve Meslek Hastalığı İstatistikleri - (4a). Retrieved 2025 from https://www.sgk.gov.tr/Istatistik/Yillik/fcd5e59b-6af9-4d90-a451-ee7500eb1cb4/

Unity. (2024). Unity 2022.3.33. Retrieved 2025 from https://unity.com/releases/editor/whats-new/2022.3.33

Xu, Z., & Zheng, N. (2020). Incorporating Virtual Reality Technology in safety training solution for construction site of urban cities. *Sustainability*, *13*(1), 243. https://doi.org/10.3390/su13010243

Zhang, Z., Guo, B. H. W., Chang-Richards, A., Feng, Z., Jin, R., Zou, Y., & Miang Goh, Y. (2023). Digital Technology Enhanced Situation Awareness for Construction Safety: Systematic Review and future research directions. *Safety Science*, *167*, 106280. https://doi.org/10.1016/j.ssci.2023.106280

4th International Civil Engineering & Architecture Conference
17-19 May 2025, Trabzon, Türkiye

The cost impact of using high fire-resistance materials in building claddings

S. Alperen Koçak*[1], Asude Göç[1], Hasan B. Başağa[1,2]

[1] Karadeniz Technical University, Department of Civil Engineering, 61080 Trabzon, Türkiye
[2]Earhquake and Structual Health Application and Research Center, Karadeniz Technical University, Trabzon, Türkiye

Abstract. In this study, the impact of fire resistance of exterior cladding materials used in building construction on overall cost has been examined. Materials classified as A1, A2, B, and C were compared in terms of their fire resistance characteristics and associated costs. The primary objective was to determine whether the higher initial costs of fire-resistant materials are justified by their long-term benefits, particularly in terms of safety and reduced risk of damage in the event of a fire. The findings indicate that although fire-resistant materials—especially those in the A1 class—have higher initial costs, these are significantly outweighed by the long-term savings associated with reduced maintenance, repairs, and potential losses of life and property due to fire incidents. Furthermore, such materials offer additional value in critical infrastructures where fire safety is paramount, such as hospitals, schools, and other high-risk structures. The analysis also revealed that exterior cladding materials constitute a relatively small portion of the total building cost, making the selection of fire-resistant materials financially feasible without imposing a substantial burden on the project budget. In conclusion, it is recommended that materials with higher fire resistance be prioritized, particularly in densely populated areas and structures with elevated risk profiles. This approach not only ensures compliance with safety regulations but also helps protect human lives and property.

Keywords: Fire; Material; Cost; Cladding

1. Introduction

In recent years, large-scale fires have once again brought building safety to the forefront, especially in urban areas. These events have made fire safety an increasingly critical factor both in engineering design and in user awareness. Efforts to raise building standards and tighten regulations have led to fire resistance being considered one of the fundamental criteria in architectural design. While numerous factors influence a building's fire performance, one of the most impactful variables is the type of construction materials used. Specifically, during the onset and spread of a fire, the material type, its reaction, and its behavior play a decisive role.

Continuous developments in construction technologies have expanded the variety of materials used in building processes, thereby making it more feasible to meet safety criteria such as fire resistance. Today, thanks to innovative production techniques and advanced performance analysis tools, access to materials with high fire resistance or non-combustible properties has become more attainable. As a result, it is now easier to design buildings that comply with safety norms and sustainability principles alike.

In material selection, exterior cladding occupies a critical role in terms of fire safety. The spread of fire along a building's outer surface poses significant risks, especially in densely populated cities. Therefore, the fire resistance properties of exterior cladding materials have become an inseparable part of building safety. This importance is further underscored by real-world data, such as that from the Istanbul Fire Department's 2023 statistics, which report 6,456 residential fires, 290 factory fires, and 3,176 other building fires in that year alone. These figures clearly highlight the life-critical importance of using fire-resistant materials.

All these considerations demonstrate that material selection lies at the heart of fire safety strategies and directly impacts a structure's risk profile. Although fire safety standards and implementation principles vary from country to country, each nation has its own legal framework tailored to its specific conditions. In Turkey, the primary regulatory reference in this regard is the "Regulation on the Protection of Buildings from Fire." According to this regulation, exterior cladding materials must possess at least a Class C or higher fire resistance rating.

* Corresponding author, E-mail: alperenskocak@ktu.edu.tr

https://doi.org/10.31462/icearc2025_ce_mng_528

Despite their safety advantages, several economic and aesthetic challenges hinder the widespread adoption of highly fire-resistant materials. Especially when conducting cost-effectiveness analyses, decision-makers often opt for cheaper materials that offer less fire resistance. This situation necessitates a delicate balance between safety and economic sustainability. Consequently, material performance, in addition to cost, must be considered in fire safety-related decisions.

The literature addresses this issue from various perspectives. One group of researchers has argued that traditional construction materials do not provide sufficient fire safety for façades and thus called for the development of new-generation materials and application techniques. In this context, innovative solutions such as hybrid composite systems (Zhou, 2013) have gained prominence (Thevega et al., 2022). Another line of research experimentally analyzes the fire behavior of exterior cladding materials. These studies compare materials in laboratory settings in terms of ignition temperature, flame spread rate, and smoke production. The findings emphasize that, besides aesthetics and cost, fire performance should also be a key consideration in material selection (Hossain et al., 2021; McLaggan et al., 2021; Dréan et al., 2019).

A third approach involves retrospective analyses of fire incidents. Researchers adopting this method evaluate a building's fire performance based on post-event reports and on-site observations following large-scale fires. Such analyses offer concrete examples of risks posed by construction materials and often lead to questions about the adequacy of existing regulations (Yaman and Demirel, 2020; İnce, 2016).

Unlike previous studies, this research does not focus on a specific building typology. Instead, it addresses the relationship between fire safety and material cost from a broader economic perspective. Material unit prices are analyzed independently of building types, and in this context, the study explores how decisions can be made to ensure both fire safety and economic sustainability. The ultimate aim is to support decision-makers in selecting materials that are both fire-resistant and financially viable.

2. Aim of the study

This study analyzes the relationship between fire performance and cost based on the unit prices of façade cladding materials used in buildings. Fire safety, which has become a critical design component particularly in densely populated urban areas, is addressed in conjunction with economically sustainable solutions. In this context, the costs of materials with different fire reaction classifications are compared. The study aims to guide decision-makers in making optimal choices between fire safety and cost-effectiveness across various scales and types of construction projects. In this regard, it differentiates itself from the existing literature by offering a material-based and comprehensive economic assessment.

3. Methodology

This study was conducted to analyze the economic impact of façade cladding materials based on their fire resistance classifications and to evaluate the relationship between fire safety and cost-effectiveness.

The study was carried out in three main steps:

1. Identifying the fire classification categories to be considered within the scope of relevant regulations,
2. Selecting the façade materials corresponding to the identified fire classifications,
3. Conducting cost analyses of the selected materials.

3.1. Material fire classes

The fire resistance ratings of materials used in the construction sector are determined based on the classification system outlined in the Regulation on the Protection of Buildings from Fire. Each material is categorized according to this system, and its fire performance is evaluated accordingly. Under the relevant regulation, building materials are classified into seven categories—A1, A2, B, C, D, E, and F—based on their combustibility levels. In the scope of this study, only materials used in façade cladding that fall under the mandatory fire resistance classes A1, A2, B, and C were considered.

3.2. Material selection

A wide range of materials fall under the fire resistance classes considered in this study. During the selection process, both the fire resistance performance and the accessibility and common usage of materials in the industry were taken into account. The technical properties and application areas of the materials were examined in detail through literature review and market research. In this way, the material selection was carried out to reflect both the requirements of the regulations and the real-life conditions likely to be encountered in practice. The materials selected for the study and their corresponding fire resistance classes are presented in Table 1.

Table 1. Materials with classes

Material	A1	A2	B	C
Glass Mosaic Cladding	X			
Ceramic Cladding	X			
Seamless Natural Stone Cladding	X			
Jointed Natural Stone Cladding	X			
Aerated Concrete Cladding	X			
Stone Wool		X		
Cement-Based Cladding		X		
Aluminum Sheet With Stone Wool		X		
Electrostatic Powder-Coated Aluminum Sheet		X		
Silicon-Modified Acrylic-Based Colored Cladding			X	
Modified Acrylic-Based Colored Cladding			X	
XPS				X
EPS				X
Carbon-Based EPS				X

3.3. Final unit prices

This study examines the relationship between the fire performance and the cost of materials used in façade construction. In this context, the unit costs of selected materials were compared. However, to ensure a realistic comparison, the assessment was based on the completed state of façade applications. Therefore, for materials used solely as insulation, additional construction components such as plaster (item no 15.275.1111) and paint (item no 15.540.1601) were also included in the evaluation. Conversely, for materials used primarily as cladding, insulation applications—specifically stone wool (item no 15.341.3001)—were integrated into the cost analysis. The unit prices of the selected materials were obtained from the 2025 unit price lists published by public institutions, primarily the Ministry of Environment, Urbanization and Climate Change. The selected materials, their unit prices, and final unit costs are presented in Tables 2, 3, 4, and 5.

In this study, a representative building model was created to calculate the share of exterior cladding materials in the total building cost. In this model, a multi-story residential building with two apartments on each floor and a floor area of 25x20 m (500 m²) was considered. The total cost of this building was calculated based on the unit construction costs for the year 2025 published by the Ministry of Environment, Urbanization, and Climate Change of the Republic of Turkey. These costs were categorized into three different categories according to building height: less than 21.5 m, 21.5–30.5 m, and 30.5–51.5 m. Cost analyses for different building height scenarios were performed, considering these classifications.

In calculating the cost of the exterior cladding, the surface area of the building's façade was approximately determined. In this calculation, the building's perimeter was multiplied by the building height, and then a 15% reduction was made from the total surface area to account for openings such as windows and doors. This method was chosen as an approach that simplifies the area calculation but still allows for realistic results.

With this representative model, the share of exterior cladding material costs in the total building cost for various building heights was analyzed by comparing the unit prices of materials with different fire-resistance classes. The obtained data show that the total cost impact of fire-resistant cladding materials on the project is limited, and therefore, products providing high fire safety are economically feasible as well.

Table 2. A1-class materials

Material		Item No	Unit Price (TL)	Final Unit Price (TL)
Glass Mosaic Cladding		15.445.1001	886,10	886,10
Ceramic Cladding		15.445.1002	1034,16	1034,16
Seamless Natural Stone Cladding		15.445.1003	1336,10	1336,10
Jointed Natural Stone Cladding		15.445.1004	1433,29	1433,29
Aerated Concrete Cladding	5 cm	15.345.1001	894,60	1786,23
(For the final unit Price, the material price was supplemented with the cost of plaster (item no 15.275.1111; 601.88 TL) and paint (item no 15.540.1601; 289.75 TL).)	6 cm	15.345.1002	917,56	1809,19
	7 cm	15.345.1003	940,54	1832,17
	8 cm	15.345.1004	963,50	1855,13
	9 cm	15.345.1005	986,48	1878,11
	10 cm	15.345.1006	1009,44	1901,07
			Average	1575,16 TL

Table 3. A2-class materials

Material		Item No	Unit Price (TL)	Final Unit Price (TL)
Stone Wool	5 cm	15.341.3001	962,99	1854,62
(For the final unit Price, the material price was supplemented with the cost of plaster (item no 15.275.1111; 601.88 TL) and paint (item no 15.540.1601; 289.75 TL).)	6 cm	15.341.3002	997,76	1889,39
	8 cm	15.341.3003	1067,33	1958,96
	10 cm	15.341.3004	1139,14	2030,77
Cement-Based Cladding	1,5 mm	15.540.1427	372,99	1267,59
(For the final unit Price, the material price was supplemented with the cost of plaster (item no 15.275.1111; 601.88 TL) and paint (item no 15.540.1601; 289.75 TL).)	2 mm	15.540.1428	375,93	1270,53
	3 mm	15.540.1429	435,55	1327,15
Aluminum Sheet With Stone Wool	5 cm	77.105.1002	3303,40	3303,40
	6 cm	77.105.1003	3324,30	3324,30
	8 cm	77.105.1004	3366,13	3366,13
Electrostatic Powder-Coated Aluminum Sheet		77.105.1005	4375,00	4375,00
			Average	2360,71 TL

Table 4. B-class materials

Material		Item No	Unit Price (TL)	Final Unit Price (TL)
Silicon-Modified Acrylic-Based Colored Cladding	1,5 mm	15.540.1424	474,25	1437,24
	2 mm	15.540.1425	533,00	1495,99
(For the final unit price, the material price was supplemented with the cost of stone wool (item no 15.341.3001; 962.99 TL).)	3 mm	15.540.1426	621,66	1584,65
Modified Acrylic-Based Colored Cladding	1,5 mm	15.540.1421	455,00	1417,99
(For the final unit price, the material price was supplemented with the cost of stone wool (item no 15.341.3001; 962.99 TL).)	2 mm	15.540.1422	505,00	1467,99
	3 mm	15.540.1423	586,56	1549,55
			Average	1492,24 TL

Table 5. C-class materials

Material		Item No	Unit Price (TL)	Final Unit Price (TL)
6 cm thick XPS with 200 kPa compressive strength		15.341.2001	966,08	1857,71
Plaster		*15.275.1111*	*601,88*	
Paint		*15.540.1601*	*289,75*	
6 cm thick XPS with 400 kPa compressive strength		15.341.2002	1076,33	1967,96
Plaster		*15.275.1111*	*601,88*	
Paint		*15.540.1601*	*289,75*	
8 cm thick XPS with 200 kPa compressive strength		15.341.2003	1050,08	1941,71
Plaster		*15.275.1111*	*601,88*	
Paint		*15.540.1601*	*289,75*	
8 cm thick XPS with 400 kPa compressive strength		15.341.2004	1197,08	2088,71
Plaster		*15.275.1111*	*601,88*	
Paint		*15.540.1601*	*289,75*	
EPS	5 cm	15.341.1001	801,03	1692,66
(For the final unit Price, the material price was supplemented with the cost of plaster (item no 15.275.1111; 601.88 TL) and paint (item no 15.540.1601; 289.75 TL).)	6 cm	15.341.1002	818,43	1710,06
	8 cm	15.341.1003	853,20	1744,83
	10 cm	15.341.1004	887,99	1779,62
Carbon-Based EPS	5 cm	15.341.1021	817,11	1708,74
(For the final unit Price, the material price was supplemented with the cost of plaster (item no 15.275.1111; 601.88 TL) and paint (item no 15.540.1601; 289.75 TL).)	6 cm	15.341.1022	837,71	1729,34
	8 cm	15.341.1023	878,93	1770,56
	10 cm	15.341.1024	920,14	1811,77
			Average	1816,97 TL

5. Results and discussion

The ratio of the exterior cladding cost to the total building cost, based on building height and the exterior cladding, is provided in Table 6.

As the building height increases, the cost ratios of non-combustible materials generally decrease. This indicates that the use of non-combustible materials in taller buildings does not lead to a significant increase in cost. According to the data, the price difference between A1 and A2 class high fire-resistant materials and other materials decreases as the height increases. Specifically, in high-rise buildings, there is only a 0.20% difference between the most expensive materials chosen for aesthetic and safety purposes and the least expensive, widely preferred materials. Although there are materials with significantly different costs in the A2 class, economic solutions can still be found. This shows that the use of non-combustible materials, while necessary for safety in high-rise buildings, does not impose a substantial cost burden.

The selected materials, under the non-combustibility class categories, are presented in maximum, minimum, and average values in Fig. 1.

Table 6. The ratio of cladding costs to total building costs

Materials		>21,50 m	21,50-30,50 m	30,50-51,50 m
A1	Glass Mosaic Cladding	%2,23	%2,12	%1,89
	Ceramic Cladding	%2,61	%2,48	%2,21
	Seamless Natural Stone Cladding	%3,37	%3,20	%2,85
	Jointed Natural Stone Cladding	%3,61	%3,44	%3,06
	Aerated Concrete Cladding	%4,50	%4,28	%3,81
A2	Stone Wool	%4,68	%4,45	%3,96
	Cement-Based Cladding	%3,20	%3,04	%2,71
	Aluminum Sheet With Stone Wool	%8,33	%7,92	%7,05
	Electrostatic Powder-Coated Aluminum Sheet	%11,03	%10,49	%9,34
B	Silicon-Modified Acrylic-Based Colored Cladding	%3,62	%3,44	%3,07
	Modified Acrylic-Based Colored Cladding	%3,57	%3,40	%3,03
C	XPS	%4,69	%4,45	%3,97
	EPS	%4,27	%4,06	%3,61
	Carbon-Based EPS	%4,31	%4,10	%3,65

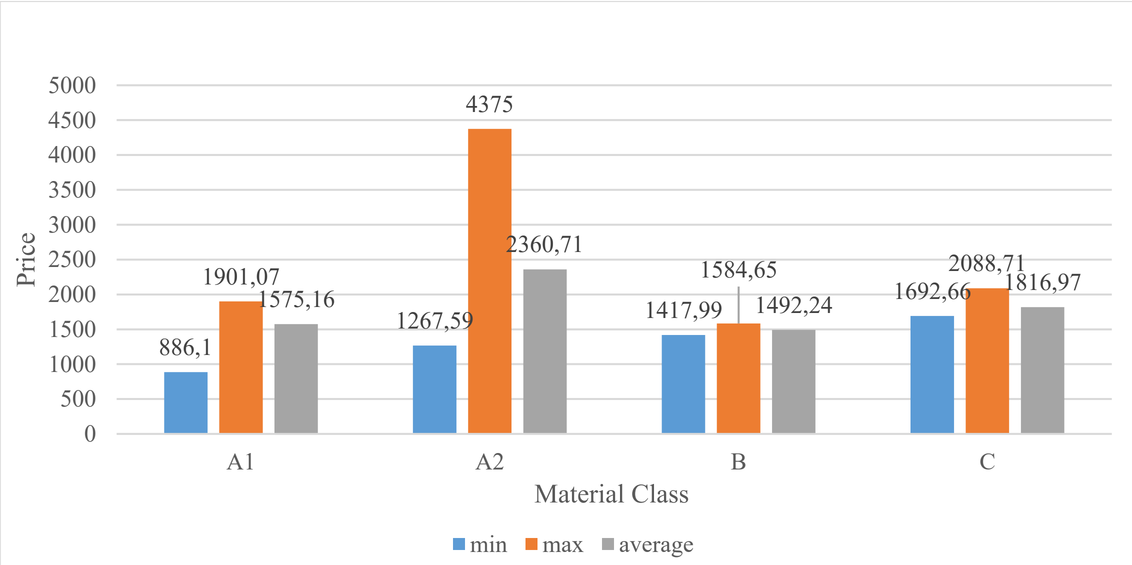

Fig. 1. Minimum, maximum, and average unit costs of cladding materials by class

When the selected façade cladding materials are examined according to their fire reaction classes, it is observed that the highest average cost is found in the A2 class, at 2,360.71 TL, followed by C (1,816.97 TL), A1 (1,575.16 TL), and B (1,492.24 TL) class materials. It is noteworthy that A1 class materials, which have the highest fire resistance, have a lower average cost compared to A2 and C class materials. This suggests that more fire-resistant materials are not always more expensive.

When the maximum and minimum cost ranges are examined, it is observed that the A2 class shows a wide distribution (4,375 TL – 1,267.59 TL), indicating variation in quality or production diversity within this class. In contrast, the B and C classes have narrower cost ranges, suggesting that the prices in these classes are more predictable.

According to the findings, high fire-resistant materials such as those in the A1 class have competitive average cost levels, and in some cases, are even more economical than lower-class materials. This result indicates that the impact of choosing superior materials for fire safety on the total project cost may be limited and could remain at an economically negligible level. Therefore, the selection of fire-resistant materials can be considered a reasonable choice not only in terms of safety but also in terms of sustainability. (Fig. 1)

A1 sınıfı malzemelerinin nihai birim fiyatları Fig. 2.'de gösterilmiştir.

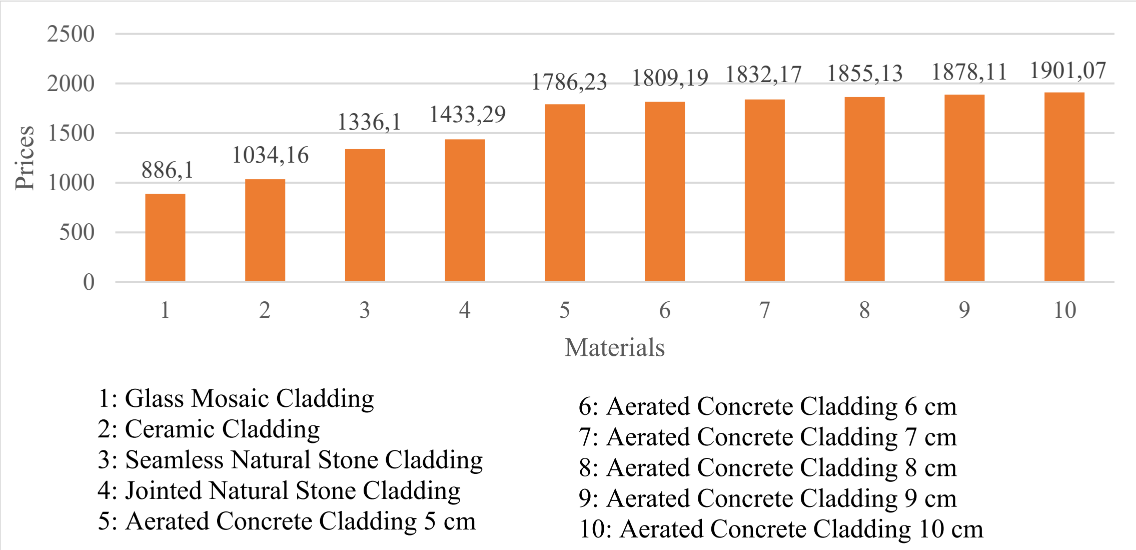

Fig. 2. A1-class materials

A1 class façade cladding materials include various building materials such as mineral-based products, natural stone, and ceramics. The unit costs range from 886.10 TL to 1,901.07 TL, with an average cost of 1,575.16 TL. This shows that A1 class materials, which offer the highest level of fire resistance, are available in a wide price range and can cater to different budgets.

When the data is examined, it is seen that the lowest-cost product is Glass Mosaic Cladding, at 886.10 TL, while the highest-cost product is Aerated Concrete Cladding (10 cm), at 1,901.07 TL. Decorative and aesthetically strong materials such as Ceramic Cladding and Natural Stone Cladding are priced at mid-range levels.

Overall, A1 class materials are notable not only for their fire resistance but also for their accessible cost structures. Thanks to the wide product range, a balance between aesthetics, technical performance, and budget can be achieved, making A1 class materials a rational choice for many projects. (Fig. 2)

The final unit prices of A2 class materials are shown in Fig. 3.

A2 class cladding materials have a very wide price range. The lowest cost is recorded as 1,267.59 TL for Cement-Based Cladding (1.5 mm), while the highest value is 4,375 TL for Electrostatic Powder-Coated Aluminum Sheet. The average unit cost of 2,360.71 TL indicates that this class generally falls into the medium-high cost group.

Stone Wool-based products (5–10 cm thickness) offer a balanced and performance-oriented option with prices ranging from 1,854.62 TL to 2,030.77 TL. As the thickness increases, the cost rise remains relatively limited, which indicates that the fire resistance can be increased while keeping costs under control in projects. On the other hand, Cement-Based Cladding products stand out with their low costs and emerge as an economic alternative within the A2 class.

However, materials developed with advanced technology and aesthetic concerns, such as Aluminum Sheet With Stone Wool and Electrostatic Powder-Coated Aluminum Sheet, show a rapid increase in cost. This observation demonstrates that the A2 class has a very wide product variety and that selections can significantly affect the cost based not only on fire performance but also on material type and design.

In conclusion, A2 class materials provide acceptable fire resistance performance, while their cost diversity offers flexible solutions for different projects (Fig. 3).

The final unit prices of B class materials are shown in Fig. 4.

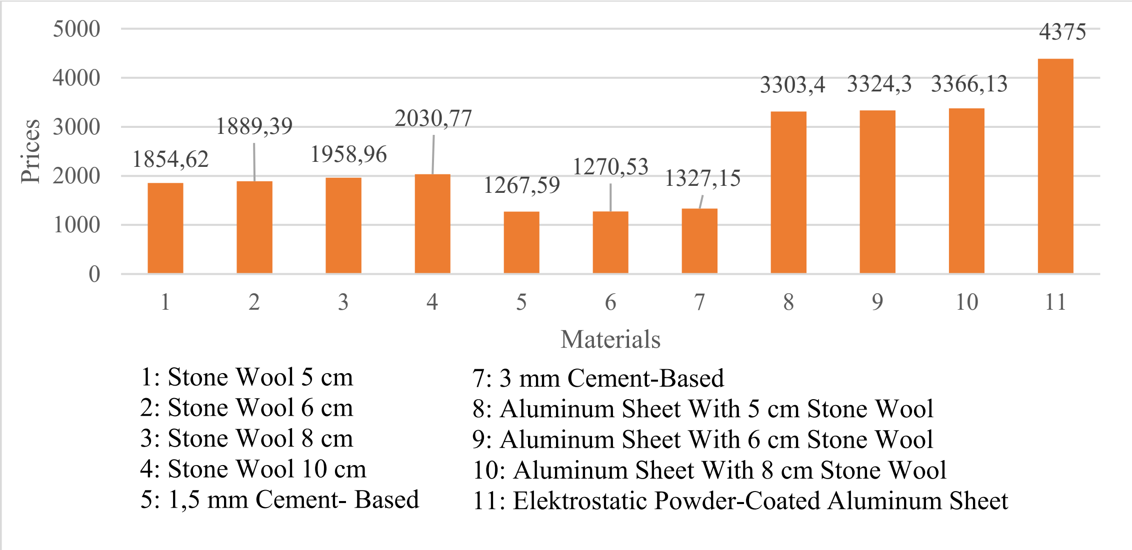

Fig. 3. A2-class materials

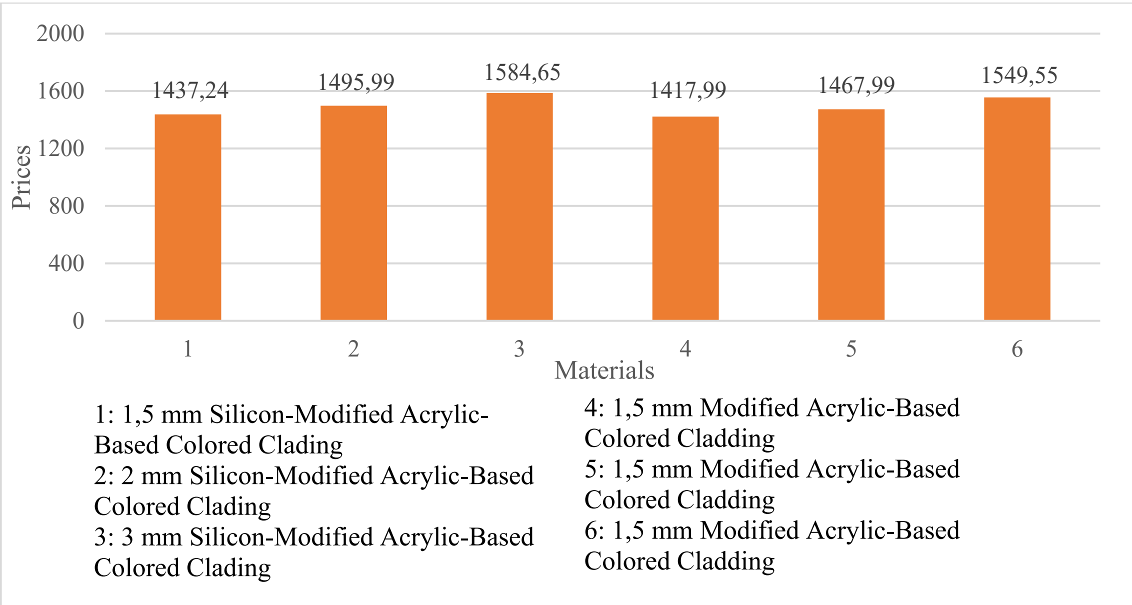

Fig. 4. B-class materials

B class cladding materials generally include acrylic-based and colored cladding solutions. The unit costs of materials in this class range from 1,417.99 TL to 1,584.65 TL, with an average value of 1,492.24 TL. This narrow price range indicates that the products are homogeneous both in terms of content and application, and that market prices have shaped within a certain balance.

According to the data, the lowest cost product is the 1.5 mm Modified Acrylic-Based Colored Cladding at 1,417.99 TL, and the highest cost product is the 3 mm Silicon-Modified Acrylic-Based Colored Cladding at 1,584.65 TL. As the thickness increases, the cost rises gradually, and it is also observed that silicon-modified products are sold at a higher price compared to standard acrylic coatings of the same thickness.

In conclusion, B class materials offer different technical specifications with limited cost differences and strike a balance between fire resistance and aesthetic expectations. However, in buildings where fire safety is a priority, the use of materials from this class should be carefully considered (Fig. 4).

The final unit price information for C class materials is shown in Fig. 5.

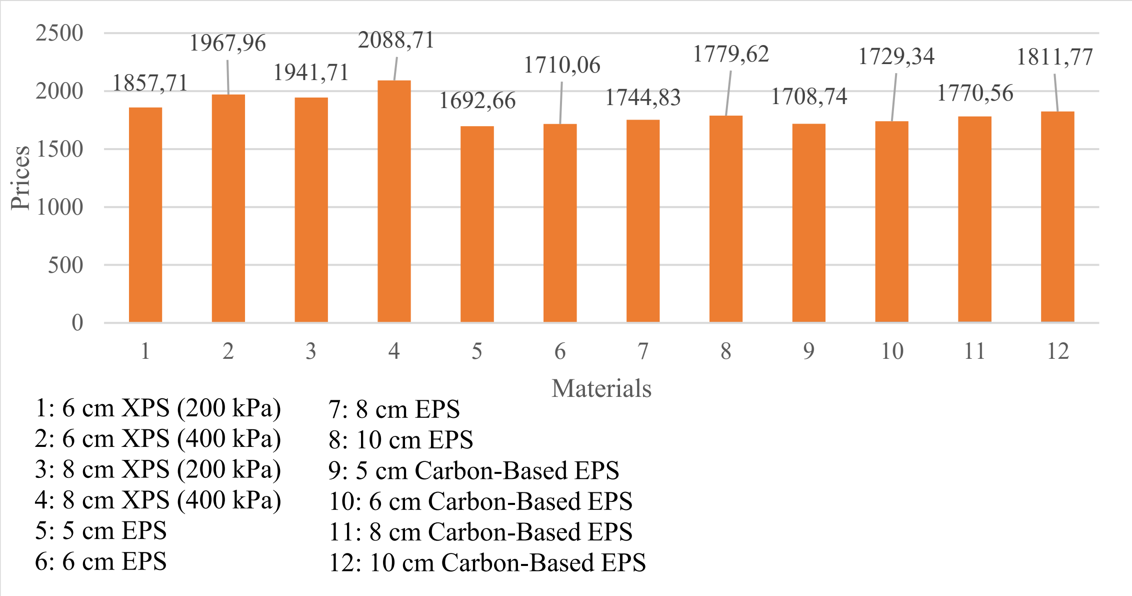

Fig. 5. C-class materials

C class cladding materials generally consist of low-density insulation products, particularly those based on XPS (Extruded Polystyrene) and EPS (Expanded Polystyrene). This class offers more limited performance in terms of fire resistance but is positioned in the mid-range in terms of cost. According to the data, the unit prices of the products range from 1,692.66 TL to 2,088.71 TL, with an average cost of 1,816.97 TL.

EPS and Carbon-Based EPS products typically offer low-cost options. Standard EPS with a thickness of 5 cm is priced at 1,692.66 TL, while the 10 cm thick version increases to 1,779.62 TL. Similarly, carbon-enhanced EPS prices rise with thickness, ranging from 1,708.74 TL to 1,811.77 TL.

On the other hand, XPS products, especially those with high pressure resistance, offer more costly solutions. A 6 cm thick XPS with a 200 kPa pressure resistance costs 1,857.71 TL, while the same thickness with a 400 kPa version is priced at 1,967.96 TL. When the thickness increases to 8 cm, the price reaches 2,088.71 TL.

In general, C class materials provide low-to-medium level fire performance, but their prices can approach those of some A1 class products. This presents a controversial situation in terms of fire safety, indicating that the cost-fire safety balance should be carefully reconsidered (Fig. 5).

6. Conclusions

This study compared cladding materials of different fire resistance classes and evaluated the effects of fire resistance levels on cost. The findings indicate that, although materials with high fire resistance appear to have higher initial investment costs, considering their contribution to building safety and human life, this cost difference is justified and necessary.

When building cost analyses are considered, it is evident that cladding materials have a small share of the total building cost. For example, there is only a 0.20% difference between the most expensive material of class A1 and the cheapest material of class C. Therefore, the choice of materials with higher fire resistance does not significantly impact the total project budget. This situation makes the use of higher-quality materials for fire safety also economically sustainable.

Additionally, while materials with lower fire resistance classes may offer cost advantages in the short term, they increase the total cost of ownership over time due to performance loss, maintenance, and repair needs. This creates risks for long-term building performance and user safety.

Especially in buildings with a high importance coefficient such as hospitals, schools, and public buildings, the use of class A1 fire-resistant materials should be preferred. In densely populated areas, these materials should become the standard. This approach not only ensures compliance with regulations but also fulfills the responsibility of protecting human life.

References

Yaman, M., Demirel, F. (2020). Cephelerde yangın güvenlik önlemleri ve mevzuatların karşılaştırmalı analizi. *Uluslararası Doğu Anadolu Fen Mühendislik ve Tasarım Dergisi, 2*(1), 88-108 (in Turkish).

McLaggan, B., Osorio, A.F., Heitzmann, M.T., Carrascal, J., Lange, D., Maluk, C. & Torero, J. L. (2021). Towards a better understanding of fire performance assessment of façade systems: Current situation and a proposed new

assessment framework. *Construction and Building Materials, 300*, 124301. https://doi.org/10.1016/j.conbuildmat.2021.124301
Zhou, N., Zhu, C. L., Bao, Y. T., Ji, G. Q., & Qian, X. Q. (2013). Simulated fire testing of a real building with eps exterior thermal ınsulation composite systems (ETICS) Including rock wool fire barrier. In *Applied Mechanics and Materials* (Vols. 368–370, pp. 868–872). Trans Tech Publications, Ltd. https://doi.org/10.4028/www.scientific.net/amm.368-370.868
Hossain, M.D., Hassan, M.K., Yuen, A.C.Y., He, Y., Saha, S., & Hittini, W. (2021). Flame behaviour, fire hazard and fire testing approach for lightweight composite claddings – A review. *Journal of Structural Fire Engineering, 12*(3), 257–292. https://doi.org/10.1108/JSFE-09-2020-0027
Dréan, V., Girardin, B., Guillaumel, E., & Fateh, T. (2019). Numerical simulation of the fire behaviour of facade equipped with aluminium composite material-based claddings-Model validation at large scale. *Fire and Materials, 43*(8), 981–1002. https://doi.org/10.1002/fam.2759
İnce, A. (2016). *Hastanelerde yangin güvenliği ve tahliye gerekleri üzerine bir irdeleme* (Master's thesis). Üsküdar University, İstanbul, Türkiye.
İstanbul İtfaiyesi. (2025 , April 25). https://itfaiye.ibb.gov.tr/
Binaların Yangından Korunması Hakkında Yönetmelik Kılavuzu. (2024). (in Turkish)

Estimation of construction material consumption with smart contract

Ali Uzunkaya*[1], Suat Topuz[1], Önder H. Bettemir[1]

[1] *İnönü University, Department of Civil Engineering, 44280 Malatya, Türkiye*

Abstract. Monitoring the remaining amount of the stocked material stored at the construction site is difficult and error prone when the intense and hurried work at the construction site is considered. Underestimating the construction wastes leads to ordering materials in short quantities while overestimating the wastes would lead to long term storage requirements of the material which may lead to deteriorate. In this study a smart contract based construction material quantity tracking frame system is proposed in order to prevent the aforementioned adverse consequences. The proposed system detects the required amounts of construction material from the quantity take-off data. The construction schedule is investigated to detect the time of the consumption requirement of the construction material. Proposed system determines the order time of the material to ensure the on time commencement of the construction activities. The waste amounts of the construction material are measured and the quantity of stock is updated by considering both the waste and the construction progress. The frame work detects any lack of construction material and updates the material order quantities and the corresponding payment amounts.

Keywords: Smart contract; Scheduling; Construction site management.

1. Introduction

Construction projects are complex processes that involve many dynamic factors from the planning to the completion stages and need to be continuously monitored. The material supply chain plays a key role in this process; the on time and within budget completion of the construction depends on the efficiency of suppliers and inventory management. It is very important that the required materials throughout the construction process are supplied at the appropriate time, in the right quantity and quality, and that these materials are stored and monitored properly. Incomplete, faulty or late delivery of materials to the construction site may cause delays in the construction process, while overstocked materials may cause contractors to make procurement payments earlier, and some of the materials that are stocked for a long time may be deteriorated due to the harsh environmental conditions and become unusable. Aforementioned situations may lead to an increase in costs. Therefore, proper procurement and inventory management is vital for the uninterrupted progress of the construction process.

Traditional procurement and inventory management methods are often based on manual data entry, human intervention and paper-based recording systems. Such processes are prone to errors and create many problems that reduce efficiency and slow down the process. Moreover, construction schedule may be updated according to the progress reports and the traditional methods require notification of the updated schedule to each department and any glitch may lead to the execution of the outdated construction schedule for procurement. Aforementioned event will lead to incorrect execution of the material procurement process and causing cost and time increases in the project. In this context, technology-based solutions, especially blockchain and smart contracts, contribute to the digitalization of procurement and stock tracking in the construction industry, creating a reliable and traceable material procurement and monitoring framework.

Smart contracts using blockchain technology offer powerful tools for the modernization of the supply chain in the construction industry (Li & Kassem, 2021). Smart contracts are reliable code snippets that can automatically initiate transactions under predefined conditions (Zheng et al., 2020). The entry or exit of a material into or out of a warehouse can be verified and recorded by smart contracts under these conditions. This structure allows transactions to take place securely and transparently, without the need for any human intervention. In addition, it accelerates decision-making processes and minimizes the margin of error by providing up-to-date and accurate information for all parties (Raffik et al., 2021).

In this study, the integration of an MS Excel-based inventory tracking system and blockchain-based smart contracts is analyzed. MS Excel offers flexible data processing and analysis solutions. With this feature, it is an

*Corresponding author, E-mail: 36223621016@ogr.inonu.edu.tr

https://doi.org/10.31462/icearc2025_ce_mng_579

golden light publishing

ideal tool for creating a user-friendly procurement and inventory tracking system. It can also be preferred as a cost-effective solution in small and medium-sized projects. With this infrastructure offered by MS Excel, manual data entry, stock control and reporting processes will be facilitated and material stock movements will be made traceable. In this study, it is aimed to create a detailed roadmap for automating material procurement and stock tracking in the construction process with blockchain-based smart contracts. In the next section of the paper, the literature review is presented, followed by the methodology section, which describes the creation of a spreadsheet application file that enables the tracking of material order and stock status with a smart contract. In the last section of the paper, the results are discussed.

2. Literature review

Carrying out accurate and fast inventory management of assets in warehouses is a critical factor in terms of operational efficiency and cost control. However, manual counting has disadvantages such as high labor requirement, time loss and error risks. A semi-automated system (SAS) combines the advantages of existing manual and automated systems used in inventory counting. SAS automates many processes in the counting process, while it does not make the process completely unmanned and it requires warehouse workers. Increasing operational efficiency by reducing inventory counting time with a semi-automated system is an important factor (Cidal et al., 2019) Manual inventory counting in warehouse management requires a lot of labor and time and increases error rates (Tong, 2023). Tong aimed to improve warehouse inventory management processes by designing an intelligent system that speeds up the counting process, increases accuracy and minimizes human errors by using automation technologies. The system provides accurate counting and positioning of products with sensors, Radio Frequency Identification (RFID) and barcode technologies used in the warehouse. It makes the warehouse inventory counting process more accurate, fast and cost-effective. With the semi-automatic system, this process is made more efficient with less labor usage. The study also aims to develop a flexible and intelligent system that can be used in different warehouse conditions (Tong, 2023)

Currently, warehouse inventory management is usually carried out by manual operations or partial automation, and these methods increase limited data access, cost and labor requirements. The main objective of the proposed system by (Grmek at el., 2011) is to optimize the inventory management process by using the advantages of cloud infrastructure such as centralized data access, flexibility, real-time tracking and low cost. The prototype provides great convenience to businesses by automatically monitoring warehouse inventory, increasing data accuracy and providing users with quick access to inventory information (Grmek at el., 2011). The automatic data collection system developed by (Montaser, 2023) offers significant advantages in terms of data accuracy and speed, resource management, real-time monitoring, ease of decision making, security and risk management. This system increases data accuracy by reducing manual errors, provides real-time access to information through automated processes and facilitates managers to evaluate the project in a timely manner. In resource management, it prevents unnecessary waste by ensuring efficient resource utilization, while saving costs by shortening manual data collection time (Montaser, 2013).

Material losses, misplacement and inventory imbalances can increase the costs of construction projects and prevent their timely completion. In this context, RFID technology has emerged as an effective solution for automated material tracking systems. Kasim et al. explained the integration of RFID technology for material tracking in construction projects and emphasized the contribution of these systems to business processes. They aimed to reduce costs and ensure project efficiency by increasing the effectiveness of these systems (Kasim at el., 2019). Traditional inventory management methods can be time consuming and prone to human error. By providing automation of warehouse inventory management processes, it is aimed to increase efficiency, reduce costs and minimize human errors. Automation in warehouse management increases overall efficiency by enabling processes to be performed faster and more accurately. The benefits of automated warehouse inventory management include increased efficiency, error reduction, cost reduction and improved monitoring and control. Automation speeds up business processes by enabling inventory to be updated quickly and reduces reliance on manpower, resulting in more efficient use of labor. In addition, human errors are minimized thanks to automated data collection systems. Barcode and RFID technologies increase the accuracy of inventory data and improve the reliability of the data. Automation, which also has a positive impact on costs, reduces labor costs, performs certain tasks with robotic systems and enables optimization of stock levels with better inventory management; this reduces costs by preventing unnecessary stock accumulation (Hajibabaei, 2024).

Material management in construction projects is critical to the success of the project. Material tracking applications play a major role in effectively managing and controlling material movements. Traditional methods are often limited to manual operations, which can lead to errors, time loss and cost increase (Liwan et al., 2013). The construction industry is turning to technological innovations to overcome the challenges faced in materials management and supply chain processes. Material tracking technologies increase the efficiency of construction projects, reduce costs and make business processes more effective by automating processes. Young evaluated the performance of automated material location and tracking technologies in the construction supply chain and identified the potential advantages that these technologies can provide (Young, 2009).

Supply chain management is a critical area to improve the competitiveness of modern businesses. Rapidly changing market conditions and customer demands have led to the need to optimize inventory control and supply chain processes. Industrial automation tools and industrial internet of things (IIoT) offer many advantages in terms of supply chain control and inventory management. Thanks to IIoT, businesses can make faster and more effective decisions by accessing real-time data at every stage of the supply chain, while automation processes enable faster adaptation to changing market conditions. In addition, automated systems help optimize stock levels, reducing inventory costs and thus giving businesses a competitive advantage. Continuous monitoring and analysis of data provides an advantage in risk management by identifying potential problems in advance. IIoT provides better communication between different departments by improving data flow throughout the supply chain (Raffik et al., 2021). Material management in construction projects is a critical process that directly affects project efficiency and success rate. Difficulties in material tracking can lead to time loss, cost increase and quality problems. Therefore, it is necessary to establish an effective material tracking system. Innovative tools such as RFID, barcode and IIoT increase the speed of operations by making material tracking processes more effective. In addition, the training that employees receive about the system ensures the effective use of material tracking systems. Systems created with the participation of stakeholders provide better communication and coordination between all parties, making material management processes efficient. These systems keep costs under control while minimizing risks in projects by reducing material loss and waste (Liwan, 2015).

In the construction industry, materials management is critical for cost control and project efficiency. Keeping track of materials on site, providing timely access and positioning them in the right place are critical to the success of projects. RFID (Radio Frequency Identification) technology is used to make material tracking processes more precise. It increases the accuracy of material location estimates through reference RFID tags (Razavi, 2011).
Supply chain management (SCM) is important for the realization of objectives such as cost reduction, efficient use of time and optimal allocation of resources in construction projects. The complex and multi-stakeholder nature of projects in the construction industry necessitates the effective management of supply chain processes. Studer and Mello (2021) analyzed the main elements required for successful supply chain management in the construction industry and their impact on the success of the project (Studer, 2021).

The construction industry is known for its large number of stakeholders, unpredictable timelines and fluctuating material demands. Effective SCM is critical to ensure that projects are completed on time, within established budgets and in accordance with the required quality standards. Optimization in construction supply chain management can increase efficiency, reduce costs and improve overall project output. Golpîr and Tirkolaee investigated key strategies for optimization in construction supply chain management, exploring areas ranging from demand forecasting to inventory management, procurement strategies to logistics (Golpîra & Tirkolaee, 2021). In the construction industry, inventory management plays a critical role in ensuring that project deadlines are not exceeded, costs are reduced and materials are available when needed. Since construction projects are intertwined with fluctuations in material demands and project-specific needs, traditional inventory systems cannot adequately cope with the dynamic and complex nature of construction projects. (Kumar et al., 2024) developed a machine learning (ML) based intelligent inventory system designed to optimize inventory management in the construction industry. The proposed system utilizes advanced ML algorithms for accurate demand forecasting, real-time inventory tracking and automatic stock replenishment (Kumar et al., 2024).

Although the construction sector is one of the key components of economic growth and development worldwide, it faces significant challenges in terms of environmental and social sustainability. This sector struggles with sustainability issues such as depletion of natural resources, environmental degradation and social injustice. Construction projects can involve large consumption of natural resources, energy expenditure and negative impacts on the environment. Moreover, the production, transport and use of construction materials lead to greenhouse gas emissions, water pollution and waste generation. In this context, the concept of sustainable supply chain management (SSCM) stands out as a critical tool for balancing environmental, economic and social objectives in the construction industry. Sustainable supply chain management has been developed as an approach that aims to organize supply processes in the industry in a more efficient, environmentally friendly and socially just manner (Mohammadnazari & Ghannadpour, 2021). The construction industry, with its increasing complexity and size, needs the integration of digital technologies to meet the requirements for effective supply chain management and inventory control. Supply chain and inventory systems managed by traditional methods can lead to negative consequences such as inefficiency, errors and cost increases. Digital technologies improve the efficiency of these processes, enhance communication between supply chain participants and optimize resource utilization. The rapid development of digital technologies in recent years offers the potential to make supply chain management in the construction industry more efficient, transparent and optimized. This integration contributes to the timely completion of projects, reducing costs and minimizing environmental impacts (Güngör & Leindecker, 2024).

Supply chain visibility can be defined as the timely and accurate monitoring and reporting of all elements. Visibility enables all participants in the supply chain to see each other's activities and processes, enabling early detection and rapid response to potential disruptions. Supply chain visibility in industrial construction projects can improve overall efficiency and sustainability, as well as increasing on-time and on-budget completion of projects (Dharmapalan et al., 2021).

The UK construction industry is characterized by large-scale and complex projects and effective materials inventory management is critical to ensure projects are completed on time and on budget. However, traditional materials management methods in the industry are often characterized by inefficiencies, excess material purchases, inventory errors and disruptions due to manual processes. Nwankwo addresses the current state of materials inventory management in the UK construction industry, discusses the challenges faced and suggests improved approaches that can be developed through digitalization, artificial intelligence and other innovative technologies to address these issues. Since effective material management is a factor that directly affects the cost-effectiveness, on-time completion and quality standard compliance of projects, improvements in this area will contribute to productivity growth and sustainability in the sector (Nwankwo, 2023).

The construction industry deals with large-scale and complex projects, and the effectiveness of material management plays a critical role in the successful completion of projects. Material management covers the processes of procuring, storing, transporting and consuming materials in the right way, and failures in these processes can lead to failure to complete projects on time, cost increases and quality losses. Effective materials management not only optimizes the materials procurement process, but also contributes to factors such as labor productivity, occupational safety and environmental sustainability. Therefore, improving materials management practices can improve the overall performance of construction projects, enabling projects to be completed on budget and ensuring high quality standards (Yıldız et al., 2024). Literature review demonstrates the importance of the stock monitoring and management of construction materials stored at construction sites. In this study, a material stock monitoring and management framework is proposed by taking into account the capabilities of smart contract and IoT.

3 Methodology

In this study, it is aimed to monitor the material procurement and construction processes required for the construction of structural elements at the foundation and floor levels of a construction project with a detailed schedule. For this purpose, firstly, the quantity quantities of the construction items are calculated, the construction schedule is prepared by creating logical relationships between the work items, the construction definitions of the construction items are created to determine the required materials and equipment to be used for each construction item. The time when the materials and equipment will be needed is determined by evaluating the construction schedule and the calculated material and equipment data, and finally, the ordering process of the material is managed within the scope of the smart contract. The construction items included in the scope of the study are reinforcement steel detailing of foundation, installation of foundation formwork, pouring of foundation concrete, installation of scaffoldings for the formwork and placement of floor reinforcement. For each work item, information such as the materials used, order and delivery times and total completion times of the process were recorded, and the basic stages were structured in order to manage the project process effectively. The flowchart of the proposed material management framework is given in Fig. 1.

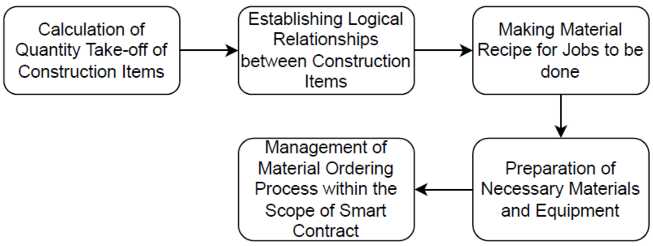

Fig. 1. Flowchart of the proposed material stock monitoring framework

Recent studies for accurate computation of quantity take-off of construction items exist in the literature (Ergen and Bettemir, 2022, Ergen & Bettemir, 2023, Ergen & Bettemir, 2024, Bettemir, 2018). With the correct establishment of semantic relationships including the dimensions and neighborhood of structural and architectural elements, the quantities of the work items are calculated and then the material requirement is calculated by multiplying the job definitions and their quantity take-off values. By defining the relationships between the activities, it is possible to prepare the construction schedule with the critical path method in MS Excel (Bettemir, 2018, Bettemir & Birgonul, 2023). In this way, when the materials are required is computed including the quantity of the corresponding material as presented in Figure 2.

	A	B	C	D	E	F	G	H	I	J	K	L
1	Activity	Material Name	Unit	Order Day	Delivery Date	Start date	Duration	Finish date	Input quantity	Quantity Used	Amount of required	Amount of lost
2	Rebar (Foundation)	Rebar	tonne	18.10.2024	23.10.2024	25.10.2024	4	29.10.2024	57,75	56,65	55	1,65

Fig. 2. Computation of quantities of material stock on MS Excel

The computations are conducted by defining the following equations defined in MS Excel.

Order Day = D1= F2 - 7

Delivery Date = E1 = F2 - 2

Required Reinforcement Amount is calculated by adding loss amounts to the quantity take-off value calculated in the beginning of the project. It is ensured that the material reaches the construction site before the start of the work by placing an order as many days before the required day defined in the construction schedule. The order amount is computed by considering 3% material waste. The total amount is calculated by the statement given below.

Amount of lost = 0.03* K2

Quantity Used = J1 = K2 + L2

Formwork board is a reusable building material. On the other hand, the formwork board brought to the construction site will suffer some loss during dismantling after use. The remaining material can be reused on the next floor. The use of formwork board based on the aforementioned situation is presented in Fig. 3.

	A	B	C	D	E	F	G	H	I	J	K	L
1	Activity	Material Name	Unit	Order Day	Delivery Date	Start date	Duration	Finish date	Input quantity	Quantity Used	Amount of required	Amount of lost
3	Formwork (Foundation)	Plywood	m2	23.10.2024	28.10.2024	30.10.2024	3	2.11.2024	154	154	140	14

Fig. 3. Calculation of the order time and amount of the formwork material

Material order date and the delivery date are determined by considering the start time of the corresponding activity which requires the relevant material. The formwork material is accepted to be wasted 10% at each usage.

Order Date = D1= F3 - 7

Delivery Date = E1 = F3 - 2

Amount of lost = 0.1* K3

Quantity Used = J1 = K3 + L3

Fresh concrete is not a material that can be stocked and cannot be produced at the construction site in accordance with the laws in force, but can only be purchased from the ready-mixed concrete plant. The fresh concrete material management table, which is created by taking into account the specified conditions, is presented in Fig. 4.

	A	B	C	D	E	F	G	H	I	J	K	L
1	Activity	Material Name	Unit	Order Day	Delivery Date	Start date	Duration	Finish date	Input quantity	Quantity Used	Amount of required	Amount of lost
4	Concreting (Foundation)	Concrete	m3	27.10.2024	3.11.2024	3.11.2024	3	6.11.2024	500	500	500	0

Fig. 4. Calculation of the order time and amount of the fresh concrete

The following statements are defined to the spreadsheet application. The waste amount is taken as zero since the waste of fresh concrete is a sign that the related work items such as formwork or scaffolding for the formwork or placement of the concrete is not done properly. The mentions issues are not expected to happen therefore the fresh concrete waste is taken as zero.

Order Day = D1= F4 - 7

Delivery Date = E1 = F4

Amount of lost = 0

Quantity Used = J1 = K4 + L4

The erection of scaffolding for the formwork is significantly similar to the manufacture of formwork. Since metal telescopic struts are commonly used in the erection of scaffolding for the formwork, the waste rate is lower than that of wooden formwork. The order of material quantity of formwork scaffolding is presented in Fig. 5.

	A	B	C	D	E	F	G	H	I	J	K	L
1	Activity	Material Name	Unit	Order Day	Delivery Date	Start date	Duration	Finish date	Input quantity	Quantity Used	Amount of required	Amount of lost
5	Scaffolding for the formwork (1.floor)	Scaffolding formwork	m2	31.10.2024	5.11.2024	7.11.2024	2	9.11.2024	2100	2100	2000	0

Fig. 5: Calculation of the order time and amount of the scaffolding for the formwork material

Order Day = D1= F5 - 7
Delivery Date = E1 = F5 - 2
Required Scaffolding Quantity
Amount of lost = K5* 0.03
Quantity Used = J1 = K5 + L5
The table created for tracking the order day of all work items is presented in Fig. 6.

	A	B	C	D	E	F	G	H	I	J	K	L
1	Activity	Material Name	Unit	Order Day	Delivery Date	Start date	Duration	Finish date	Input quantity	Quantity Used	Amount of required	Amount of lost
2	Rebar (Foundation)	Rebar	tonne	18.10.2024	23.10.2024	25.10.2024	4	29.10.2024	57,75	56,65	55	1,65
3	Formwork (Foundation)	Plywood	m2	23.10.2024	28.10.2024	30.10.2024	3	2.11.2024	154	154	140	14
4	Concreting (Foundation)	Concrete	m3	27.10.2024	3.11.2024	3.11.2024	3	6.11.2024	500	500	500	0
5	Scaffolding for the formwork (1.floor)	Scaffolding formwork	m2	31.10.2024	5.11.2024	7.11.2024	2	9.11.2024	2100	2100	2000	0
6	Rebar (1. Floor)	Rebar	tonne	3.11.2024	8.11.2024	10.11.2024	4	14.11.2024	23,1	22,66	22	0,66
7	Concreting (1.Floor)	Concrete	m3	8.11.2024	15.11.2024	15.11.2024	3	18.11.2024	150	150	150	0
8	Scaffolding for the formwork (2.floor)	Scaffolding formwork	m2	12.11.2024	17.11.2024	19.11.2024	2	21.11.2024	100	2100	2000	100
9	Rebar (2. Floor)	Rebar	ton	15.11.2024	20.11.2024	22.11.2024	4	26.11.2024	23,1	22,66	22	0,66
10	Concreting (2.Floor)	Concrete	m3	20.11.2024	27.11.2024	27.11.2024	3	30.11.2024	150	150	150	0
11	Scaffolding for the formwork (3.floor)	Scaffolding formwork	m2	24.11.2024	29.11.2024	1.12.2024	2	3.12.2024	100	2100	2000	100
12	Rebar (3. Floor)	Rebar	tonne	27.11.2024	2.12.2024	4.12.2024	4	8.12.2024	23,1	22,66	22	0,66
13	Concreting (3.Floor)	Concrete	m3	2.12.2024	9.12.2024	9.12.2024	3	12.12.2024	150	150	150	0
14	Scaffolding for the formwork (4.floor)	Scaffolding formwork	m2	6.12.2024	11.12.2024	13.12.2024	2	15.12.2024	100	2100	2000	100
15	Rebar (4 Floor)	Rebar	tonne	9.12.2024	14.12.2024	16.12.2024	4	20.12.2024	23,1	22,66	22	0,66
16	Concreting (4.Floor)	Concrete	m3	14.12.2024	21.12.2024	21.12.2024	3	24.12.2024	150	150	150	0
17	Scaffolding for the formwork (5.floor)	Scaffolding formwork	m2	18.12.2024	23.12.2024	25.12.2024	2	27.12.2024	100	2100	2000	100
18	Rebar (5. Floor)	Rebar	tonne	21.12.2024	26.12.2024	28.12.2024	4	1.01.2025	23,1	22,66	22	0,66
19	Concreting (5.Floor)	Concrete	m3	26.12.2024	2.01.2025	2.01.2025	3	5.01.2025	150	150	150	0

Fig. 6: List of order date, order amount and type of material created automatically from the construction schedule and BOQ

In this study, a comprehensive timeline has been developed for the construction process, detailing material procurement, delivery schedules, start and finish dates for each task required throughout the project. Each task's procurement, delivery, and execution phases have been carefully planned to facilitate a structured progression in the project timeline, aiming to minimize delays.The project focuses on core construction tasks, including foundation and floor slab installations, arranged in a logical sequence to ensure structural stability. Each stage has been detailed to ensure materials are procured, delivered, and utilized at the appropriate times. This approach establishes a series of systematic steps intended to support efficient, uninterrupted progression throughout the construction process.

Materials required for each task have been ordered and scheduled to arrive on-site in advance of each phase. A variety of materials have been used, from essential reinforcement and formwork boards to ready-mix concrete and scaffolding. Delivery timelines were organized by accounting for lead times between order and delivery dates to ensure materials are on-site before installation begins, minimizing disruptions due to material delays and keeping each stage on track.

Throughout the project, workflows have been organized with a flexible, structured timeline based on material delivery schedules. Task durations were assigned by considering the difficulty and labor requirements for each task, with start dates and completion times recorded. This data has facilitated the correct scheduling of parallel or sequential tasks as needed, ensuring a logical flow from foundational work to upper-floor installations. The orderly sequence has not only streamlined time management but also ensured completion within the planned timeframe.
The proposed framework executes project management and workflow monitoring tasks. Each task was integrated into project management processes, allowing close tracking of procurement and delivery times, along with task start and completion dates. This recording of workflows has enabled consistent monitoring and adjustments as needed. Each phase has been checked step-by-step, with necessary adjustments documented throughout the project. This systematic approach prevented delays in subsequent stages by allowing prompt adjustments if a task requires more time or materials than anticipated.

4. Conclusions

The developed framework improves the overall project process and efficiency. The sequential and systematic application of construction elements contributed to completing the project within the planned timeframe. Every task was organized to maximize the efficient use of both labor and materials, ensuring effective allocation of the resources. Timely material delivery and labor optimization enabled project completion within the scheduled period. Detailed planning was conducted at each stage, with alternate procurement sources or process adjustments applied as needed to maintain efficiency. This method minimized unexpected delays and interruptions in the construction process.

Within this framework, tasks in the project were executed in a sequential, organized, and efficient flow, with the goal of maintaining rigorous planning and meticulous oversight throughout all processes. This ensured that construction activities at each level contributed cohesively to the overall structural integrity and resulted in a high level of structural coherence.

Acknowledgments
This study is supported by the Scientific Research Projects Coordination of İnönü University by the Grant Number FYL-2024- 3641 and FYL-2024-3471.

References

Bettemir, Ö. H. (2018). Development of spreadsheet based quantity take-off and cost estimation application. *Journal of Construction Engineering, Management & Innovation*, *1*(3), 108–117.

Bettemir, Ö. H., & Birgonul, M. T. (2023). Solution of discrete time–cost trade-off problem with adaptive search domain. *Engineering, Construction and Architectural Management*.

Bettemir, Ö. H., & Bulak, Ö. F. (2022). Scheduling, management and optimization of construction process. *Teknik Dergi*, *33*(6), 12945–12986. https://doi.org/10.18400/tekderg.981601

Cidal, G. M., Cimbek, Y. A., Karahan, G., Böler, Ö. E., Özkardesler, Ö., & Üvet, H. (2019, April). A study on the development of semi automated warehouse stock counting system. In *2019 6th International Conference on Electrical and Electronics Engineering (ICEEE)* (pp. 323–326). IEEE.

Dharmapalan, V., O'Brien, W. J., & Morrice, D. J. (2021). Defining supply chain visibility for industrial construction projects. *Frontiers in Built Environment*, *7*, 651294.

Ergen, F., & Bettemir, Ö. H. (2022). Development of BIM software with quantity take-off and visualization capabilities. *Journal of Construction Engineering, Management & Innovation*, *5*(1), 1–14.

Ergen, F., & Bettemir, Ö. H. (2023). Development of BIM-based prototype software for the accurate quantity take-off calculation of rough construction items. *Gümüşhane Üniversitesi Fen Bilimleri Dergisi*, *13*(1), 86–105. https://doi.org/10.17714/gumusfenbil.1117848

Ergen, F., & Bettemir, Ö. H. (2024, February). Development of ontological algorithms for exact QTO of reinforced concrete construction items. In *Structures* (Vol. 60, p. 105907). Elsevier.

Golpîra, H., & Tirkolaee, E. B. (2021). Optimization for construction supply chain management. In *Application of Mathematics and Optimization in Construction Project Management* (pp. 165–183).

Grmek, R., Khmelevsky, Y., & Syrotovsky, D. (2011, July). Automated inventory tracking system prototype in cloud. In *2011 International Conference on High Performance Computing & Simulation* (pp. 435–441). IEEE.

Güngör, B., & Leindecker, G. (2024, May). Digital technologies for inventory and supply chain management in circular economy: A review study on construction industry. In *International Conference "Coordinating Engineering for Sustainability and Resilience"* (pp. 700–709). Cham: Springer Nature Switzerland.

Hajibabaei, N. (2024). *Automating warehouse inventory management* (Doctoral dissertation, University of Victoria).

Kasim, N., Sarpin, N., Noh, H. M., Zainal, R., Mohamed, S., Manap, N., & Yahya, M. Y. (2019). Automatic materials tracking practices through RFID implementation in construction projects. In *MATEC Web of Conferences* (Vol. 266, p. 05001). EDP Sciences.

Kumar, M. M., Rohith, D., Kumar, T. M., Rahul, R., & Koustub, B. K. (2023, July). A machine learning based intelligent inventory system for construction industry. In *International Conference on Interdisciplinary Approaches in Civil Engineering for Sustainable Development* (pp. 523–530). Singapore: Springer Nature Singapore.

Li, J., & Kassem, M. (2021). Applications of distributed ledger technology (DLT) and blockchain-enabled smart contracts in construction. *Automation in Construction*, *132*, 103955.

Liwan, S. R. (2015). *The framework of improving on-site materials tracking for inventory management process in construction projects* (Doctoral dissertation, Universiti Tun Hussein Onn Malaysia).

Liwan, S. R., Kasim, N., & Zainal, R. (2013). Materials tracking practices for inventory management in construction projects. Retrieved from http://eprints.uthm.edu.my/5779/1/2._Siti_Radziah_Liwan.pdf

Mohammadnazari, Z., & Ghannadpour, S. F. (2021). Sustainable construction supply chain management with the spotlight of inventory optimization under uncertainty. *Environment, Development and Sustainability*, *23*, 10937–10972.

Montaser, A. (2013). *Automated site data acquisition for effective project control* (Doctoral dissertation, Concordia University).

Nwankwo, D. C. (2023). *Improving approaches to material inventory management in construction industry in the UK* (Doctoral dissertation, University of Wales Trinity Saint David).

Raffik, R., Rakesh, D., Venkatesh, M., & Samvasan, P. (2021, October). Supply chain control and inventory tracking system using industrial automation tools and IIoT. In *2021 International Conference on Advancements in Electrical, Electronics, Communication, Computing and Automation (ICAECA)* (pp. 1–5). IEEE.

Razavi, S. N., & Haas, C. T. (2011). Using reference RFID tags for calibrating the estimated locations of construction materials. *Automation in Construction*, *20*(6), 677–685.
Studer, W. P., & De Brito Mello, L. C. B. (2021). Core elements underlying supply chain management in the construction industry: A systematic literature review. *Buildings*, *11*(12), 569.
Tong, C. (2023). An efficient intelligent semi-automated warehouse inventory stocktaking system. *arXiv preprint arXiv:2309.12365*.
Yıldız, S., Güneş, S., & Kıvrak, S. (2024). Examining the impact of material management practices on project performance in the construction industry. *Buildings*, *14*(7), 2076.
Young, D. (2009). *Modeling the impact of automated materials locating and tracking technology on the construction supply network* (Master's thesis, University of Waterloo).
Zheng, Z., Xie, S., Dai, H. N., Chen, W., Chen, X., Weng, J., & Imran, M. (2020). An overview on smart contracts: Challenges, advances and platforms. *Future Generation Computer Systems*, *105*, 475–491.

4th International Civil Engineering & Architecture Conference
17-19 May 2025, Trabzon, Türkiye

Measures of the central tendency for occupational accidents in the building industry

Özge Alboğa*[1] , Ercan Erdiş[2]

[1] *Department of Civil Engineering, Faculty of Engineering and Natural Sciences, Iskenderun Technical University, Hatay, Türkiye*
[2] *Department of Architecture, Faculty of Architecture, Iskenderun Technical University, Hatay, Türkiye*

Abstract. The construction industry is one of the sectors with the highest number of occupational accidents worldwide. These accidents negatively affect the health and safety of the workers and the stakeholders in the sector economically and socially, causing a decline in labor productivity. In this context, spreading occupational health and safety awareness among stakeholders is critical to prevent accidents and make the work environment safe. The objective of the present study was to ascertain the measures of central tendency concerning occupational accidents in the construction industry. The research process involved the administration of questionnaires to stakeholders, which yielded data on accident details. The research findings indicated that the predominant category of occupational accidents was that of falls from height, with a notable concentration of incidents occurring during the morning hours. Furthermore, it was established that the majority of accidents resulted in injury. It is thought that the findings obtained will contribute to a deeper understanding of accidents in the construction sector and the development of safety culture in the sector. Moreover, it is anticipated that these findings will enhance stakeholder awareness regarding occupational health and safety, thereby facilitating the formulation of strategies to mitigate the material and moral ramifications of accidents.

Keywords: Construction Industry; Occupational Accident; Type of Accident

1. Introduction

Construction activities are one of the priority intervention areas in terms of occupational health and safety due to their structural complexity and physical risks. When the frequency and consequences of occupational accidents in different sectors around the world are assessed, the construction sector has a higher risk profile (Eurostat, 2024). Variable working conditions, multidisciplinary production processes, and operational intensity on site make the occurrence of accidents in this sector both more likely and more devastating.

A significant number of accidents in the sector result in serious injury or death, making occupational health and safety a problem that needs to be addressed not only nationally but also globally (Ayduran & Olcay, 2022; Birhane et al., 2022; Mosquera & Ileana, 2024). Working at height, moving equipment, outdoor weather conditions, and the simultaneous activity of subcontractor networks are the main sources of risk in the field (Alboga et al., 2023). Furthermore, managerial factors such as time pressure and cost-oriented decision-making processes can lead to postponement or neglect of necessary precautions (Forteza et al., 2017).

Sectoral statistics published in Turkey also support this picture. As demonstrated by data from the Social Security Institution (SSI), the construction industry ranks among the top in terms of both the frequency and severity of accidents (Gözüak & Ceylan, 2021; SSI, 2025). The high rate of fatal accidents in this sector makes it imperative to address safety precautions not only at the individual level but also at the institutional and systematic levels.

National and international literature similarly describes the types of accidents frequently encountered in the sector. Incidents such as falls from heights, equipment-related injuries, material falls, and collisions are the types of accidents that are emphasized in almost all studies (Müngen, 2011; Olcay et al., 2021; Williams et al., 2017). Structural problems such as inadequate supervision, irregular site layout, and poor safety culture are often at the root of these accidents. Conversely, the treatment of accidents as a purely technical issue may result in the oversight of the social and managerial components. Therefore, accidents need to be addressed multidimensionally in terms of time, type, and consequences (Halabi et al., 2022; Tixier et al., 2016). Traditionally, the approach to accidents has been mostly reactive, i.e., focused on post-incident response. Today, however, the need to quickly identify

*Corresponding author,E-mail: oalboga.mfbe19@iste.edu.tr

https://doi.org/10.31462/icearc2025_ce_mng_608

risks and design preventive precautions brings the proactive safety management approach to the forefront (Awolusi et al., 2022; Xu et al., 2023).

The effects of occupational accidents are not limited to the individual level. The economic losses, decrease in labor productivity, deviation in project deadlines, and damage to the reputation of the company directly affect all stakeholders in the sector (Elsebaei et al., 2022; Junjia et al., 2024). In this context, it is important to systematically analyze the structural causes of accidents and the conditions under which they occur to ensure that the precautions to be taken are targeted and sustainable.

Research indicates that different statistical methods are used to determine the causes and common types of accidents in the construction industry (Birgönül et al., 2016; Duman & Hamzaoğlu, 2011; Gürcanli & Müngen, 2013; Kang & Ryu, 2019; Williams et al., 2017; Zhang et al., 2020). Some studies in the literature have revealed that a significant portion of these accidents occur in building constructions (Baradan et al., 2016; Halabi et al., 2022). On the other hand, studies focusing only on a specific type of accident or outcomes such as fatalities have investigated the causes of these accidents (Assaad & El-adaway, 2021; Halabi et al., 2022; Olcay et al., 2021; Ünal & Aykaç, 2010).

Nevertheless, a significant number of studies in the relevant literature frequently depend on official records and secondary data sources (Assaad & El-adaway, 2021; Zhang et al., 2020). Such data is often insufficient to understand the actual dynamics of accidents on the ground. In contrast, primary data based on direct field experiences allows for a more detailed analysis of the contextual characteristics of accidents. Such information, obtained through surveys and similar data collection tools, not only describes the current situation but also contributes to the development of more effective and targeted preventive strategies. The studies developed in this context help us understand past accidents and have the potential to pave the way for data-driven, proactive policies to prevent similar incidents in the future.

The present study analyzes the times, types, and consequences of accidents within the framework of measures of central tendency in building construction. This analysis is based on the responses of industry professionals who have directly experienced occupational accidents. The findings of the study are anticipated to contribute to the development of a safety culture in the sector, raising stakeholder awareness and shaping strategies for occupational health and safety in a more targeted manner, taking into account the frequent recurrence of accidents in building construction.

2. Materials and methods

The present study is designed as quantitative research that aims to describe the type, time, and outcome occupational accidents that occur in building construction in the construction industry. The data for the research was obtained from professionals who have either directly witnessed or been involved in occupational accidents in the sector.

A questionnaire was utilised as a data collection tool. The questionnaire was administered to a total of 236 people working in different professional roles, such as project managers, construction site supervisors, labor inspectors, experts, and occupational health and safety specialists. Responses that were incomplete, contradictory, or insufficient for analysis were eliminated, and analysis was conducted on 203 valid responses. All participants were experienced personnel who had either witnessed or been involved in at least one occupational accident in their working lives.

The questionnaire form included questions on demographic information of participants and workers (including age, occupation and years of experience), time of the accident, accident type and outcome, and environmental conditions (including temperature). The questions were prepared in multiple-choice and ordinal scale format; the content was developed in line with expert opinions and simplified through the pre-test process.

The analysis process involved the utilisation of descriptive statistical methods, encompassing the calculation of measures of central tendency (mean, median, mode), standard deviation, and minimum and maximum values for both continuous and ordinal variables. Frequency and percentage distributions were presented for the categorical variables. A comparative analysis of accident types was conducted through graphical representation, with the variables of age, experience, and temperature taken into account. Additionally, an evaluation of accident frequency was undertaken, utilising a descriptive analysis across hourly time periods. The analysis was conducted utilising the Python programming language, and the findings were presented with graphical support.

3. Results and discussion

This section presents the main statistical findings on the type, timing, and outcome of accidents, as derived from the data obtained through the questionnaire. The analyses are based on measures of central tendency and descriptive statistical methods.

An analysis of the demographic profile of the respondents indicates that the majority possess a bachelor's degree, and that their professional experience is predominantly concentrated within the range of 0-10 years. A substantial proportion of the participants are construction site supervisors and occupational safety specialists. Table 1 presents the demographic information of the participants.

Table 1. Demographic information of the participants

		n	%
	Bachelor's Degree	149	73.40
Education Status	Master's Degree	50	24.63
	Doctorate (PhD)	4	1.97
	Site Supervisor	114	56.16
	Occupational Safety Specialist	37	18.23
Occupation	Project Manager	26	12.81
	Labor Inspector	15	7.39
	Expert	11	5.42
	0-10	159	78.71
	11-20	24	11.88
Experience (Year)	21-30	11	5.45
	31-40	7	3.47
	41-50	1	0.50

The results of the analysis of the distribution of accidents by time period demonstrate the presence of a pattern of concentration, particularly in the 10:01-12:00 and 14:01-16:00 periods (Fig. 1). These periods correspond to times of increased workload in the field and periods of reduced attention. The findings support studies in the literature suggesting that accidents occur more frequently in the middle hours of the working day (Akboğa, 2014; Ayhan & Tokdemir, 2020; Halabi et al., 2022). The result raises the need to reconsider preventive strategies such as work scheduling and the timing of breaks.

The analysis of accident types revealed that falling from a height was the most common type. Such accidents occur frequently in areas where temporary safety precautions are inadequate in building construction. Accidents such as falls of materials and equipment, as well as cuts and punctures, follow falls from height (Fig. 2). This distribution is in line with the patterns reported in national and international literature (Liu et al., 2020; Olcay et al., 2021; Williams et al., 2017). On the other hand, elevator falls, poisoning and explosions were the least frequently observed accidents in the study.The frequency of falls from height suggests that both the physical safety infrastructure on site and worker behavior should be more closely evaluated. Despite increased awareness and regulations, the persistence of fall-related accidents indicates possible gaps in enforcement, design adaptation, or training persistence.

Fig. 3 shows the distribution of occupational accidents by outcome, with each outcome category represented by descriptive abbreviations. According to the data, the most common accident outcome is minor injuries requiring treatment (MIN), with 58 cases, the highest frequency among all groups. This is followed by the group of 49 cases resulting in severe injury, occupational disease or permanent disability (Severe Injury - SEV). These two categories reveal that a significant proportion of accidents result in mild or serious health consequences. On the other hand, accidents requiring only first aid with no lost working days (First Aid, No Day Loss - FA1) and accidents requiring first aid with no lost working hours (First Aid, No Hour Loss - FA2) are less frequent with 35 and 27 cases respectively. This suggests that some accidents are survived with relatively less serious consequences. Fatality accidents (FAT) stand out as an important category with serious consequences with 35 cases. This distribution shows that although minor injuries are more frequent, severe consequences are also considerable and therefore preventive strategies for all types of accidents need to take a multidimensional approach.

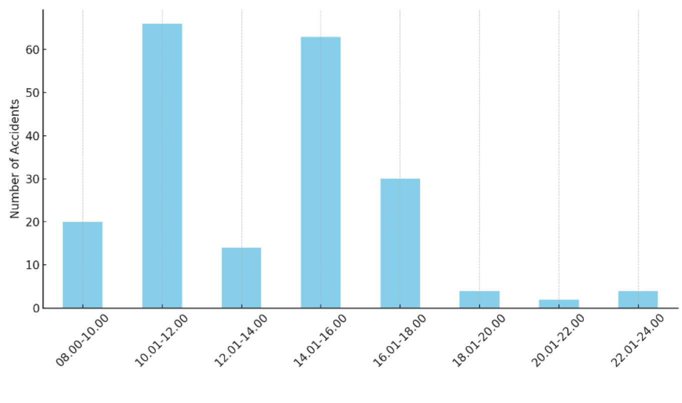

Fig.1. Distribution of Accidents by Time Interval

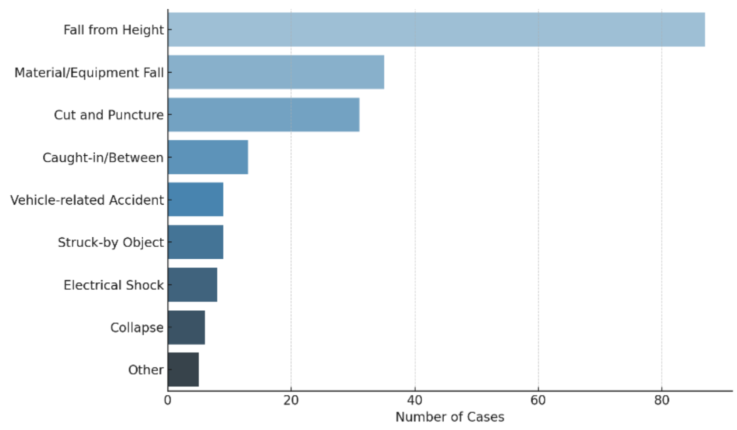

Fig. 2. Distribution of Accident Types

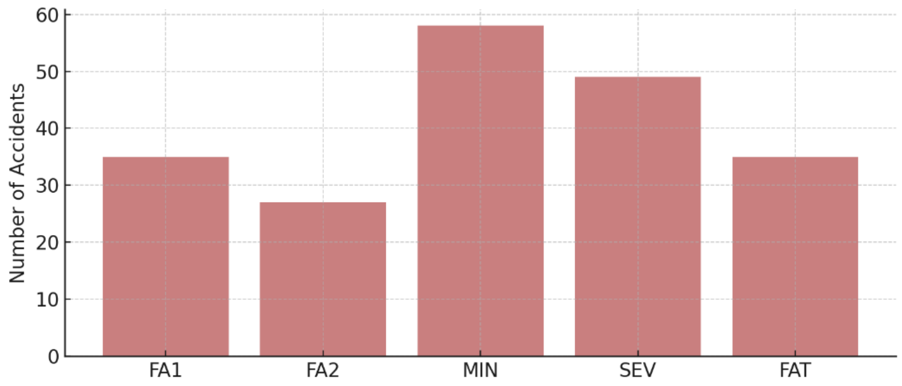

Fig. 3. Distribution of Accident Outcome

In the box graph showing the age distribution according to accident types, there are significant differences between age groups, especially in the "struck-by object" and "collapse" types. While the median age is 51 for "struck-by-object" accidents, it is 25 for "collapse-type" accidents. This difference indicates a concentration of certain accident types within either younger or older labor force groups. For common accidents such as "falling from height," the age distribution is more balanced, with a median of 39 and an average of around 38. These findings suggest that the age difference by accident type is an important variable to be taken into account in safety strategies. Similarly, it is also stated in the literature that types of accidents vary according to age groups (Kang & Ryu, 2019; Nai'em et al., 2021). In practical terms, age-sensitive safety training may help reduce incident rates in high-risk groups. This distribution is presented in Fig. 4.

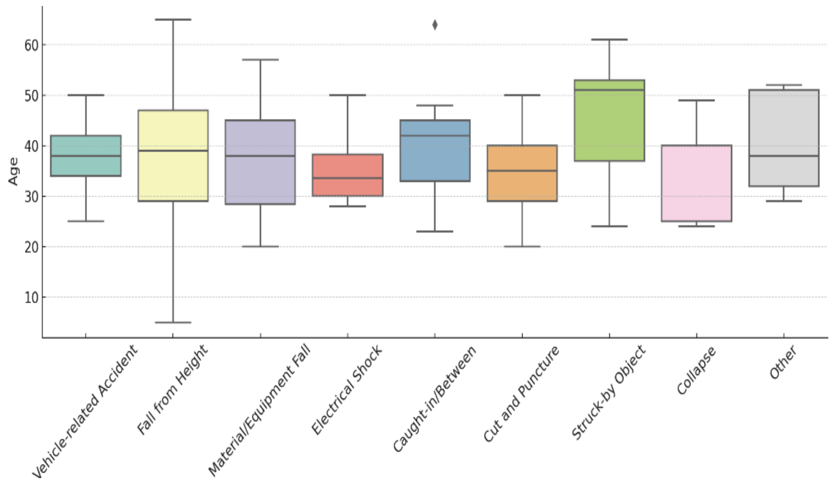

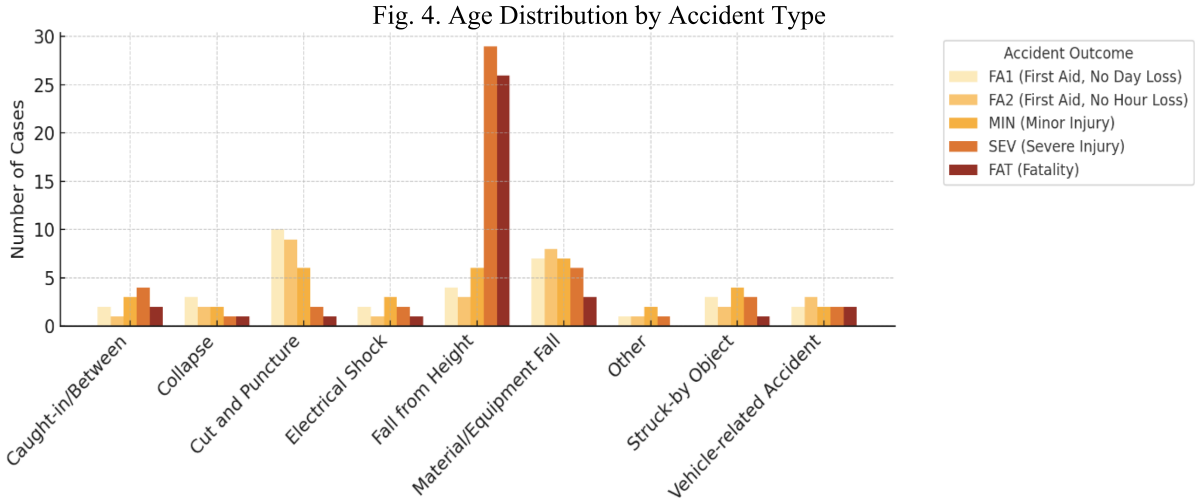

Fig. 5. Distribution of Accident Outcomes by Accident Type

Table 2. Statistics of Temperature by Type of Accident

Accident Type	**Mean Temp (°C)**	**Std. Deviation**	**Min Temp**	**Max Temp**
Collapse	26.00	9.06	16	39
Vehicle-Related Accidents	25.71	5.68	17	33
Material/Equipment Fall	25.45	9.74	2	39
Fall From Height	22.54	9.77	-2	40
Struck-By Object	22.33	7.65	11	34
Cut and Puncture	21.45	10.44	1	37
Caught-In/Between	21.38	10.94	0	34
Electric Shock	21.00	11.49	0	32
Other	19.60	10.33	7	33

Analysis of outcome distribution by accident type reveals that "fall from height" incidents are more prone to cause severe injuries and fatalities than other categories (Akboğa & Baradan, 2015; Halabi et al., 2022). Conversely, some accident types, such as "cut and puncture" and "caught-in/between," are limited to milder outcomes. This difference indicates that certain types of work are inherently higher risk and points to the need to diversify occupational safety measures according to the type of accident. This distribution is presented in Fig. 5.

An analysis of temperature distribution by accident type reveals that collapses and vehicle-related incidents predominantly occurred under high-temperature circumstances (mean >25°C). Conversely, "fall from height" accidents occurred in lower temperature conditions, with a minimum recorded temperature of -2°C. This finding suggests that low temperatures may increase the risk of falls by causing distraction, slippery surfaces, and difficulties in using equipment. These findings indicate that environmental conditions can also have an impact on the types of accidents and suggest that weather conditions should be taken more into account in safety planning processes (Kang & Ryu, 2019). The statistics on temperature distribution are presented in Table 2.

Fig. 6 illustrates the temporal distribution of occupational accidents within the construction sector, categorized by kind of accident. To facilitate a comprehensive observation and precise analysis of temporal patterns, the three most frequent time periods (mode values) for each accident type are determined and depicted as distinct bars in the display. The data indicates that specific categories of accidents are prevalent during particular periods of the day. Specifically, incidents including "Falls from Height," "Material/Equipment Falls," and "Cuts and Punctures" occur more frequently throughout the morning (10:01-12:00) and afternoon (14:01-16:00). This suggests that the likelihood of accidents escalates during periods of heightened physical exertion, while worker vigilance may diminish owing to exhaustion. Consequently, for certain categories of accidents, interventions (e.g. brief rest intervals, work rotations, enhanced field inspections, safety briefings prior to critical moments) can be more successfully formulated during high-risk intervals.

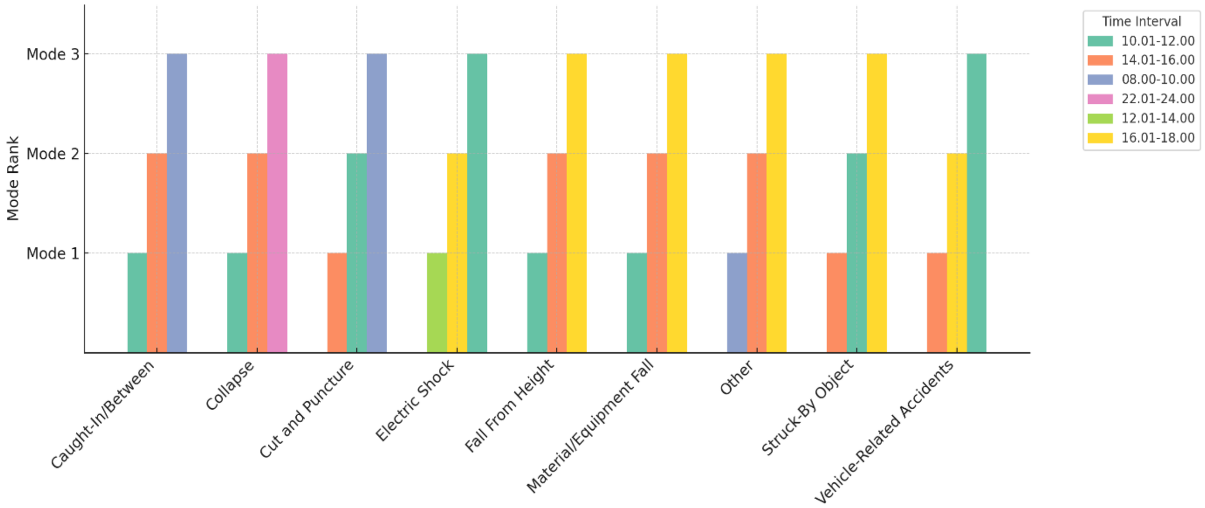

Fig. 6. Distribution of the Top 3 Most Frequent Time Periods by Accident Type

The results show that a significant number of incidents are associated with “falls from height”, with a notable concentration occurring in the morning hours. Analysis of the distribution of accident effects reveals that “minor injury” is the most common outcome, but there is also a significant frequency of major injuries and fatalities. Analysis of the age factor by type of accident revealed that certain types are associated with younger workers. In particular, accidents such as “collapse” are associated with younger workers, while accidents such as “struck by an object” are more prominent in older and more experienced groups. Mode-based analysis by time periods shows that occupational accidents are concentrated in specific time periods, allowing for the development of time-based preventive strategies. Taken together, these results emphasize the need for a multidimensional approach to safety planning that includes not only technical and environmental risk factors, but also demographic and task complexity considerations.

4. Conclusion

This study contributes to a deeper understanding of accident trends and high-risk conditions in the construction industry by providing a detailed analysis of occupational accidents in terms of time, type, and outcome. The findings, obtained through data based on direct field experiences, both shed light on the challenges faced in practice and generate concrete recommendations for improving safety culture. In particular, the concentration of certain types of accidents, such as “falls from height” in the morning hours reveals the importance of time management and on-the-job safety practices. Although most of the accidents result in minor injuries, serious injuries and fatalities are also prominent in certain circumstances.

The observed differences in age and experience based on accident type suggest that safety strategies need to be tailored to the employee profile. The increased vulnerability of young and less experienced workers to certain types of accidents highlights the importance of targeted training and mentoring programs. On the other hand, the exposure of experienced worker to more serious accidents in complex tasks shows that experience alone is not a protective factor; other factors such as equipment, organizational structure, and work planning should also be managed effectively. Moreover, it was observed that different types of accidents differed significantly in terms of severity of consequences. In particular, serious injury and death rates are higher in types such as falls from height, which suggests that accidents should be evaluated not only according to their frequency but also according to the severity of their consequences. This finding emphasizes the importance of developing accident type based preventive strategies.

The present study provides a multidimensional assessment of the types of accidents specific to the construction industry and how these accidents are shaped in environmental, temporal, and individual contexts and paves the way for proactive management of risks. The findings are expected to contribute to the development of occupational safety policies, improvement of practices, and data-based decision-making processes at the sectoral level. This research also demonstrates the effectiveness of analyses based on direct field experiences in better explaining the contextual dimensions of accidents. In this respect, the study serves as a reference for further research in both methodological and contextual terms. The findings suggest that types of accidents can be associated not only with individual or managerial factors but also with environmental conditions

However, some limitations of the study should also be considered. The sample may not be representative of all construction workforce groups, as it consists only of professionals with a certain sectoral experience. Future studies should recommend broader comparisons with data from different geographical regions and project types at different scales. In addition, the development of holistic modeling, including psychosocial and managerial factors regarding the causes of occupational accidents, will contribute more to the institutionalization of safety culture in the sector.

Acknowledgments
The authors would like to thank the Scientific and Technical Research Council of Turkey (TÜBİTAK- 2211-C Domestic Priority Areas PhD Scholarship Program) and the Council of Higher Education for the 100/2000 Doctoral Fellowship Program (Özge Alboğa).

References

Akboğa, Ö. (2014). *İnşaat İş Kazalarında Lojistik Regresyon İle Kaza Şiddetinin Modellenmesi*. Ege Üniversitesi.

Akboğa, Ö., & Baradan, S. (2015). İnşaat Sektöründeki Ölümlü İş Kazalarının Karakteristiklerinin İncelenmesi: İzmir Alan Çalışması. In İnşaat Mühendisleri Odası (Ed.), *5.İş Sağlığı ve Güvenliği Sempozyumu* (pp. 215–224).

Alboga, Ö., Çelik Tantekin, G., Aydinli, S., Un, B., Budak, A., & Erdis, E. (2023). İnşaat Sektöründe İş Kazalarının Nedenleri ve Türleri Üzerine Bir İnceleme. *II. International XI. National Congress on Occupational Health and Safety*, *November*, 437–443.

Assaad, R., & El-adaway, I. H. (2021). Determining Critical Combinations of Safety Fatality Causes Using Spectral Clustering and Computational Data Mining Algorithms. *Journal of Construction Engineering and Management*, *147*(5), 1–21. https://doi.org/10.1061/(ASCE)CO.1943-7862.0002040

Awolusi, I., Marks, E., Hainen, A., & Alzarrad, A. (2022). *Incident Analysis and Prediction of Safety Performance on Construction Sites*. *3*, 669–686.

Ayduran, A. C., & Olcay, Z. F. (2022). Investigation of The Effects of Construction Sector Employees on The Occupational Health and Safety Culture Levels and Safe Behaviors. *Ergonomi*. https://doi.org/10.33439/ergonomi.1112393

Ayhan, B. U., & Tokdemir, O. B. (2020). Accident Analysis for Construction Safety Using Latent Class Clustering and Artificial Neural Networks. *Journal of Construction Engineering and Management*, *146*(3). https://doi.org/10.1061/(ASCE)CO.1943-7862.0001762

Baradan, S., Akboğa, Ö., Üstmen, M., & Çetinkaya, U. (2016). Ege Bölgesindeki İnşaat İş Kazalarının Sıklık ve Çapraz Tablolama Analizleri. *Teknik Dergi*, *27*(1,7345-7370), 7345–7370.

Birgönül, M. T., Dikmen, I., Budayan, C., & Demirel, T. (2016). An expert system for the quantification of fault rates in construction fall accidents. *International Journal of Occupational Safety and Ergonomics*, *22*(1), 20–33. https://doi.org/10.1080/10803548.2015.1123516

Birhane, G. E., Yang, L., Geng, J., & Zhu, J. (2022). Causes of construction injuries: a review. *International Journal of Occupational Safety and Ergonomics*, *28*(1), 343–353. https://doi.org/10.1080/10803548.2020.1761678

Duman, E., & Hamzaoğlu, O. (2011). İstanbul'da Bir Şantiyede Çalışanların İş Kazalarının İzlemi. *Türk Tabipler Birliği Mesleki Sağlık ve Güvenlik Dergisi*, 35–42.

Elsebaei, M., Elnawawy, O., Ahmed, A., & Othman, E. (2022). Causes and impacts of site accidents in the Egyptian construction industry. *International Journal of Construction Management*, *22*(14), 2659–2670. https://doi.org/10.1080/15623599.2020.1819523

Eurostat. (2024). *Accidents at work statistics*. An Official Website of the European Union. https://ec.europa.eu/eurostat/statistics-explained/index.php?title=Accidents_at_work_statistics

Forteza, F. J., Carretero-Gómez, J. M., & Sesé, A. (2017). Occupational risks, accidents on sites and economic performance of construction firms. *Safety Science*, *94*, 61–76. https://doi.org/10.1016/j.ssci.2017.01.003

Gözüak, M. H., & Ceylan, H. (2021). Türkiye'de inşaat sektöründe meydana gelen iş kazalarının iş sağlığı ve güvenliği bağlamında analizi : Güncel eğilimlere genel bir bakış. *Sağlık Akademisyenleri Dergisi*, *8*(2), 133–143.

Gürcanli, G. E., & Müngen, U. (2013). Analysis of construction accidents in Turkey and responsible parties. *Industrial Health*, *51*(6), 581–595. https://doi.org/10.2486/indhealth.2012-0139

Halabi, Y., Xu, H., Long, D., Chen, Y., Yu, Z., Alhaek, F., & Alhaddad, W. (2022). Causal factors and risk assessment of fall accidents in the U.S. construction industry: A comprehensive data analysis (2000–2020). *Safety Science*, *146*, 105537. https://doi.org/10.1016/j.ssci.2021.105537

Junjia, Y., Alias, A. H., Haron, N. A., & Abu Bakar, N. (2024). Identification and analysis of hoisting safety risk factors for IBS construction based on the AcciMap and cases study. *Heliyon*, *10*(1), e23587. https://doi.org/10.1016/j.heliyon.2023.e23587

Kang, K., & Ryu, H. (2019). Predicting types of occupational accidents at construction sites in Korea using random forest model. *Safety Science*, *120*, 226–236. https://doi.org/10.1016/j.ssci.2019.06.034

Liu, R., Mou, X., & Liu, H.-C. (2020). Occupational Health and Safety Risk Assessment based on Combination Weighting and Uncertain Linguistic Information: Method Development and Application to a Construction

Project. *IISE Transactions on Occupational Ergonomics and Human Factors*, *8*(4), 175–186. https://doi.org/10.1080/24725838.2021.1875519

Mosquera, R., & Ileana, G. P. (2024). A model based on PDCA and data mining approach for the prevention of occupational accidents in the plumbing activity in the construction sector. *WORK: A Journal of Prevention, Assessment & Rehabilitation*, *78*, 399–410. https://doi.org/10.3233/WOR-230112

Müngen, U. (2011). İnşaat Sektörümüzdeki Başlıca İş Kazası Tipleri. *Türkiye Mühendislik Haberleri Dergisi*, *469*, 32–39.

Nai'em, M. F., Darwis, A. M., & Maksun, S. S. (2021). Trend analysis and projection of work accidents cases based on work shifts, workers age, and accident types. *Gaceta Sanitaria*, *35*, 94–97. https://doi.org/10.1016/j.gaceta.2020.12.026

Olcay, Z. F., Sakallı, A. E., Temur, S., & Yazıcı, A. (2021). A study of the shift in fatal construction work- related accidents during 2012 – 2019 in Turkey. *International Journal of Occupational Safety and ErgonomicsErgonomics*, *28*(3). https://doi.org/10.1080/10803548.2021.1900503

Öztürk, T. (2019). *İŞ KAZALARINA ETKİ EDEN FAKTÖRLERİN ÇOK DEĞİŞKENLİ İSTATİSTİKSEL YÖNTEMLERLE DEĞERLENDİRİLMESİ*. İstanbul Aydın Üniversitesi.

SSI. (2025). *Social Security Institution Statistics*. https://www.sgk.gov.tr/Istatistik/Yillik/fcd5e59b-6af9-4d90-a451-ee7500eb1cb4

Tixier, A. J.-P., Hallowell, M. R., Rajagopalan, B., & Bowman, D. (2016). Application of machine learning to construction injury prediction. *Automation in Construction*, *69*, 102–114. https://doi.org/10.1016/j.autcon.2016.05.016

Ünal, M. . Ö., & Aykaç, B. (2010). Yapı İşlerinde Asansör Kazaları ve Güvenlik Önlemleri. *International Journal of Engineering Research and Development*, *2*(2), 13–19.

Williams, O. S., Hamid Abdul, R., & Misnan, M. S. (2017). Analysis of Fatal Building Construction Accidents : Cases and Causes. *Journal of Multidisciplinary Engineering Science and Technology*, *4*(8), 8030–8040.

Xu, J., Cheung, C., Manu, P., Ejohwomu, O., & Too, J. (2023). Implementing safety leading indicators in construction : Toward a proactive approach to safety management. *Safety Science*, *157*(March 2022), 105929. https://doi.org/10.1016/j.ssci.2022.105929

Zhang, J., Zi, L., Hou, Y., Deng, D., Jiang, W., & Wang, M. (2020). A C-BiLSTM approach to classify construction accident reports. *Applied Sciences (Switzerland)*, *10*(17). https://doi.org/10.3390/APP10175754

4th International Civil Engineering & Architecture Conference
17-19 May 2025, Trabzon, Türkiye

Comparative analysis of AI platforms developed in the AEC Industry

Mahdis Motamedi*[1], İpek N. Semercioğlu[1], Hasan B. Başağa[1,2]

[1] Karadeniz Technical University, Department of Civil Engineering, 61080 Trabzon, Türkiye
[2] Earthquake and Structural Health Application and Research Center, Karadeniz Technical University, 61080 Trabzon, Türkiye

Abstract. This study aims to provide a detailed comparative analysis of six AI platforms in the Architecture, Engineering, and Construction (AEC) Industry: Civils.ai, Kwant.ai, ArchiLabs, Nicky AI, Buildots, and Karmen. These AI platforms provide a variety of features, from project automation and construction site monitoring to resource optimization and AI-driven design. Their efficacy in tackling industry issues, including data processing, project efficiency, and workflow integration, will be assessed, and their specific advantages and possible overlaps will be identified. Key parameters, including launch year, supported file types, integration with programs, automation capabilities (functions/features), and price for users, are the focus of a qualitative comparison approach. Based on these key parameters, the analysis offers insights into how these AI platforms are used in the real world. The outcomes indicate notable differences in their functionalities; some concentrate on design automation, project collaboration, or predictive analytics, while others specialize in construction site management and real-time progress tracking. The study also identifies important areas for improvement, such as AI customization and interoperability, which may influence future developments in AI for AEC. This study conveys a systematic comparison of cutting-edge AI platforms, offering useful advice for corporate professionals looking to improve workflows and boost productivity with AI-driven solutions.

Keywords: AEC industry; AI platforms; Construction technology; Design automation; Workflow optimization

1. Introduction

The Architecture, Engineering, and Construction (AEC) industry has undergone a profound transformation, evolving from manual, labor-intensive practices to highly digital and intelligent systems. In the early 20th century, construction projects were predominantly managed through hand-drawn blueprints, physical models, and paper-based documentation, which often led to coordination errors, time inefficiencies, and increased costs(Eastman et al., 2011). The 1960s marked a pivotal turning point with the advent of computer-aided design (CAD), allowing for more precise and efficient drafting (Sacks et al., 2018). At the turn of the millennium, Building Information Modeling (BIM) revolutionized the industry by integrating 3D modeling with data-driven project management capabilities, thereby facilitating collaboration across disciplines and improving lifecycle coordination(Autodesk, 2024).

The emergence of Industry 4.0 further accelerated the digitalization of construction practices, introducing cyber-physical systems, Internet of Things (IoT) technologies, and cloud-based data exchange platforms(Oztemel & Gursev, 2020). These advancements transformed static digital models into dynamic, interoperable systems that support real-time decision-making. Most recently, artificial intelligence (AI) has emerged as a key technological enabler in the AEC industry, expanding the scope of digital transformation beyond automation toward intelligent decision support (Dattaa et al., 2021). AI applications are now being leveraged to enhance design generation, monitor construction progress, assess risks, and optimize resource allocation.

This technological evolution has given rise to a new generation of AI-driven platforms specifically tailored to the complex demands of construction environments. These platforms aim to improve productivity, increase safety, enable real-time collaboration, and provide greater transparency throughout the project lifecycle. Many platforms promote comprehensive solutions through their actual capabilities and applicability in diverse construction contexts. Despite their growing adoption, however, there remains a critical need for systematic evaluations of these emerging tools.

* Corresponding author, E-mail: motamedi.mahdis@gmail.com

https://doi.org/10.31462/icearc2025_ce_mng_651

This study conducts a comparative analysis of six prominent AI platforms developed for the AEC industry: Civils.ai (2022), Kwant.ai (2018), ArchiLabs (2024), Nicky AI (2023), Buildots (2018), and Karmen (2024). The analysis is structured around key parameters including launch year, supported file types, integration with programs, automation features, and pricing models. By identifying each AI platform's features, this study provides valuable insights for AEC industry professionals and researchers aiming to leverage AI technologies for improved efficiency, coordination, and decision-making in construction projects.

2. Methodology

In this study, which examines AI platforms currently utilized in the AEC industry, Civils.ai, Kwant.ai, ArchiLabs, Nicky AI, Buildots, and Karmen were selected for analysis, respectively, as shown in Fig. 1. These AI platforms support the AEC industry's digital transformation by automating processes such as project design, project management, site monitoring, etc. With this context, the mentioned platforms were evaluated based on key parameters identified as launch year, supported file types, integration with programs, automation capabilities (functions/features), and pricing for users. When defining these parameters, the supported file types category refers to the typical file formats that the platforms can import and export. The integration with programs parameter denotes the software applications with which the platforms can interoperate during data exchange. It should be acknowledged that, as these platforms are continually updated and refined, the specific items listed under each parameter are subject to change.

This evaluation was structured to emphasize the AI platforms' technical features and contributions to the AEC industry. This approach aims to elucidate the current impact and future potential of AI platforms in the AEC industry. In the remainder of the study, each platform is discussed in sequence, and the information compiled for each platform is presented in table form. Data were compiled from official platform resources such as their own websites, LinkedIn accounts, and YouTube Channels.

a) Civils.ai b) Kwant.ai c) Archilabs d) Nicky AI e) Buildots f) Karmen

Fig. 1. AI platforms

3. Findings and discussions

3.1. Civils.ai

Civils.ai is an AI-powered platform designed to streamline data management in the construction industry, particularly for handling complex technical documents. Its primary purpose is to eliminate time-consuming manual tasks, such as searching through disorganized files and completing repetitive paperwork, while ensuring compliance and risk mitigation. It targets civil engineers, project managers, architects, and geoscientists who need to process large volumes of geotechnical and construction data efficiently (Civils-ai Construction AI, 2025). Table 1 presents the detailed features of the Civils.ai platform based on the specified key parameters.

Table 1. Detailing Civils.ai according to key parameters

Launch Year	Supported File Types	Program Integration	Functions/Features	Price
2022 (January)	PDF files Excel files AGS files Word files	Autodesk Procore SharePoint Power BI Microsoft Office	Data extraction (OCR/NLP) Generative design Predictive modeling Real-time monitoring Workflow automation Chat interface for automation	Basic: \$49/user/month Advanced: \$83/user/month

Civils.ai was launched in January 2022. It is designed to streamline data-intensive tasks, The platform employs advanced Optical Character Recognition (OCR) and Natural Language Processing (NLP) to extract structured information from diverse sources, including PDF borehole logs, geotechnical reports, CAD drawings, and site investigation documents. Civils.ai supports output generation in formats such as Excel, AGS, Word, and Power

BI dashboards, and integrates effectively with commonly used tools like Autodesk, Procore, SharePoint, and Microsoft Office—thereby embedding itself within standard AEC digital workflows. Technically, Civils.ai offers a range of functions spanning data extraction, generative design (generates design alternatives for structural optimization), predictive modeling (simulates soil behavior and assesses geotechnical risks), real-time monitoring (integrates with IoT for geotechnical data analysis), and workflow automation. This allows engineering teams to reduce manual labor, automate compliance checks, and simulate geotechnical behavior for informed decision-making. The platform emphasizes accessibility through its no-code workflow builder, enabling non-technical users to leverage AI capabilities without programming expertise (Civils-ai Construction AI, 2023). Additional features such as interactive mapping from location-tagged data, intelligent document search, and automated categorization of project files enhance productivity and reduce human error. Civils.ai is competitively priced, with a basic plan at $49/user/month (10 users with 12 month license period and 50 GB file storage) and an advanced plan at $83/user/month (10 users with 12 month license period and 100 GB file storage-2000 advanced AI workflow runs). Its adoption across multiple regions, including the United States, Hong Kong, Singapore, the European Union, the United Kingdom, Australia, New Zealand, and South Africa, demonstrates its global applicability and compliance adaptability in varied regulatory environments.

3.2. Kwant.ai

Kwant.ai is an AI-driven construction management platform designed to enhance workforce efficiency, improve on-site safety, and streamline compliance monitoring processes. Kwant.ai aims to overcome challenges such as manual reporting and delayed risk detection by delivering real-time site intelligence through integrated IoT devices and AI-driven analytics. It is designed for general contractors, project owners, insurance carriers, and brokers seeking to enhance productivity and safety on construction sites (Kwant, 2023). Table 2 presents the detailed features of the Kwant.ai platform based on the specified key parameters.

Table 2. Detailing Kwant.ai according to specified parameters

Launch Year	Supported File Types	Program Integration	Functions/Features	Price
2018	3D-BIM models Image files Excel files PDF files Files from the IoT sensor data	Procore Autodesk BIM 360 Autodesk Construction Cloud CMIC Checkr Primavera P6 Power BI Microsoft	Asset tracking Predictive analytics Real-time dashboards Workforce management Safety monitoring Fatigue management Heatmaps Fall detection Daily reports Chat interface for automation	*Pricing not publicly disclosed

Kwant.ai is introduced in 2018. By integrating IoT smart badges, environmental sensors, and 5D-BIM models, the platform enables continuous tracking of worker locations, activity levels, fatigue, and safety conditions while automating administrative tasks like timesheets, onboarding, and certification monitoring. A distinguishing feature of Kwant.ai is its fusion of real-time site intelligence with predictive analytics and multilingual LLM-based querying. Users can interact with the system in multiple languages through a built-in AI question interface, powered by OpenAI models and AWS integration, to generate instant reports, insights, and even customized data outputs. In addition, Kwant.ai's privacy-by-design approach ensures that no personally identifiable information is exposed during data collection or analysis, an essential feature for compliance-conscious organizations. Functionally, Kwant.ai supports predictive risk scoring, automated compliance monitoring, safety alert systems (e.g., fall detection, SOS), and asset tracking via IoT data. Its seamless integration with major AEC platforms such as Procore, Autodesk BIM 360, Primavera P6, and Power BI enables construction firms to embed Kwant.ai into their existing digital workflows without significant adaptation costs. The platform also contributes to productivity gains by reducing manual reporting time by an estimated 8–10 hours per week per site. While specific pricing is not publicly disclosed, Kwant.ai operates under a scalable subscription model based on peak workforce size, allowing firms to adapt usage to project demands. Having been deployed across major construction sites in the United States, Canada, and select regions in Asia and Africa, Kwant.ai demonstrates both technical robustness and global adaptability.

3.3. Archilabs

Archilabs is an AI assistant developed to revolutionize architectural design and planning by automating CAD/BIM tasks. Its purpose is to simplify complex workflows, allowing architects to focus on creativity rather than repetitive tasks, using natural language processing to translate commands into actionable outputs. It is intended for architects, designers, and planners working with BIM tools like Revit and SketchUp (Archi Lab, 2023). Table 3 shows the detailed features of the Archilabs platform based on the specified key parameters.

Table 3. Detailing Archilabs according to specified parameters

Launch Year	Supported File Types	Program Integration	Functions/Features	Price
2024 (April)	CAD/BIM models 2D sketches Excel files TXT files Render files Python scripts	Autodesk Revit Autodesk BIM 360 Autodesk Construction Cloud Rhino SketchUp ArchiCAD Vectorworks Dynamo Grasshopper	AI-based generation with Python Generative design Visualization Compliance checking Automating repetitive tasks Chat interface for automation	Ideation: Free Architecture/Design: $1,000/idea Development: Custom pricing AI Toolset: $2,500/month

Archilabs, launched in April 2024, is developed with a focus on eliminating inefficiencies in traditional design tools like Autodesk Revit. Archilabs allows users to interact with complex CAD/BIM environments using plain English prompts, automatically converting these into executable Python scripts. This AI-driven approach facilitates rapid modeling, compliance verification, data conversion, and visualization, considerably reducing the time and expertise required for manual tasks. At the core of Archilabs is its AI Co-Pilot, which interprets natural language inputs such as “add windows to the north wall” or “check building code compliance” and translates them into actionable commands within Revit, Rhino, SketchUp, or ArchiCAD. The platform also features a Python Generator for automating API-based operations, an AI-enhanced editor for Excel/CSV/TXT files, and generative design capabilities that propose optimized layouts. Distinct from many other platforms, Archilabs also includes an AI-powered Revit tutorial generator, enabling users to receive customized, step-by-step learning guides tailored to their project context, thereby supporting both task execution and continuous professional development. The system architecture ensures a scalable and responsive user experience that accommodates evolving project demands. Archilabs supports a wide range of input and output formats, including CAD/BIM files, 2D sketches, project specs, and structured data files (Excel, CSV, TXT), enhancing interoperability across different design and project documentation tools. Output capabilities include annotated floor plans, model updates, compliance reports, and interactive dashboards, all accessible via web and mobile interfaces. Integration with platforms such as Autodesk BIM 360, ArchiCAD, Dynamo, and Grasshopper positions Archilabs as a powerful automation layer within existing BIM ecosystems. Pricing is structured flexibly, offering a free plan for ideation, a $1,000 one-time project fee for architecture and planning use cases, a custom pricing model for development, and a $2,500/month full-access plan for firms seeking enterprise-level AI toolsets. Although currently based in the United States, Archilabs is designed for global scalability and is accessible worldwide via cloud applications.

3.4. Nicky AI

Nicky AI, proposed in 2023, is an AI-powered administrative assistant developed specifically for construction project teams seeking to streamline communication, document management, and routine workflow administration. Unlike other AI platforms, Nicky AI is tailored to the needs of construction professionals, addressing common challenges such as submittal tracking, request for information (RFI) management, and email handling through intelligent automation and voice-activated interaction. It intends to reduce administrative workload, enabling faster project coordination and fewer errors (Sibay, 2024). Table 4 demonstrates the detailed features of the Nicky AI platform based on the specified key parameters.

Table 4. Detailing Nicky AI according to specified parameters

Launch Year	Supported File Types	Program Integration	Functions/Features	Price
2023	Emails Text messages PDF files Excel files Voice commands	Gmail Outlook Procore Microsoft Excel	Voice-enabled AI for tasks Workflow automation Email management Document control Real-time updates RFI management	*Pricing not publicly disclosed

The platform ingests unstructured data from multiple sources, including emails, text messages, PDF documents, submittals, RFIs, and even spoken commands, and transforms them into structured outputs such as automated cover sheets, workflow reports, email responses, project updates, and Excel exports. These functionalities are accessible via Nicky AI's web and mobile applications, making it a highly portable and responsive tool for on-site and remote users alike. A standout feature of Nicky AI is its voice enabled interface, which allows users to issue natural language commands (e.g., "Show me the approved electrical panel") to instantly retrieve documents or project information. This capability significantly reduces search time, particularly in fast-paced site environments. Moreover, its email automation feature enables users to draft and send context-aware communications through integrations with Gmail and Outlook, thereby enhancing professional correspondence while reducing manual workload. In terms of workflow efficiency, Nicky AI automates the generation of submittal cover sheets, maintains task lists, and delivers real-time notifications for pending actions or project changes. It also provides document control functionality, organizing information extracted from unstructured files such as PDFs and submittals into integrated platforms like Procore and Excel. These tools collectively yield substantial time savings, estimated at over three hours per day per user, by eliminating repetitive administrative labor and enabling professionals to refocus on higher-value activities such as project coordination and field supervision. While the pricing structure for Nicky AI is not publicly disclosed, it follows a subscription-based model that is likely customized based on team size and project complexity. Headquartered in New York City, the platform is primarily focused on the U.S. construction market, though its cloud-based architecture ensures broader accessibility.

3.5. Buildots

Another AI-driven platform, Buildots, launched in 2018, is a computer vision-powered construction management platform that revolutionizes site monitoring through full integration with BIM models, project schedules, and AI analytics. Developed to bridge the gap between digital plans and on-site execution, Buildots enables real-time, objective oversight of construction progress by combining 360-degree imagery, automated data processing, and predictive insights. It targets contractors, project managers, and site supervisors managing large-scale construction projects (Buildots, 2025). Table 5 demonstrates the detailed features of the Buildots platform based on the specified key parameters.

Table 5. Detailing Buildots according to specified parameters

Launch Year	Supported File Types	Program Integration	Functions/Features	Price
2018	360-degree camera footage BIM models BCF files	Autodesk BIM 360 Autodesk Construction Cloud Procore Revizto Navisworks MS Project Primavera P6 Power Project	AI-powered progress tracking Predictive Analytics Issue Management Delay Reduction Gap analysis Gantt view powered by AI Digital twin-based visualization	*Pricing not publicly disclosed

At the core of the platform is a helmet-mounted 360-degree camera system, which captures site conditions passively during routine site walks. The captured footage is automatically synchronized with BIM models and construction schedules to generate an as-built 4D timeline of project execution. This allows for AI-powered progress tracking, in which computer vision algorithms compare current site conditions against planned milestones to detect deviations, identify misalignments or missing installations, and generate visual, actionable reports. The result is a continually updated model of project reality, providing a clear, verifiable basis for informed decision making. Buildots' automated gap analysis feature enhances quality control by flagging discrepancies between planned and actual progress, significantly reducing the need for manual inspections. Its predictive analytics engine offers early warnings about potential delays and bottlenecks, enabling project teams to take preemptive action before minor issues escalate. All identified issues are exported in BCF (BIM Collaboration Format), with precise BIM location tagging and linked visual evidence, ensuring seamless issue tracking and resolution in platforms such as Autodesk BIM 360, Procore, and Revizto. Accessible via web and mobile interfaces, the Buildots Control Center also empowers field personnel to view task-specific dashboards, receive real-time notifications, and manually update progress when needed. This mobile access enhances collaboration between office-based teams and on-site staff, further streamlining the construction management workflow. Buildots supports input formats such as 360-degree video, BIM models, and project timelines, and generates outputs including predictive reports, gap analyses, and actionable metrics. It integrates seamlessly with a wide range of AEC software platforms, including Autodesk Construction Cloud, Procore, Navisworks, MS Project, and Primavera P6. While pricing is not publicly disclosed, the platform is offered as a customized subscription based on project scale and configuration.

3.6. Karmen

Karmen is a specialized AI automation assistant designed to reduce the administrative burden of data entry, document handling, and communication tracking in construction projects. By minimizing manual data entry and reducing administrative errors, Karmen ensures timely project updates and enhances cost control. The platform is tailored for use by project managers, administrative staff, and subcontractors involved in construction projects (Karmen, 2025). Table 6 presents the detailed features of the Karmen platform based on the specified key parameters.

Table 6. Detailing Karmen according to specified parameters

Launch Year	Supported File Types	Program Integration	Functions/Features	Price
2024 (August)	Emails Text messages Invoices PDF files Excel files	Microsoft Suite Outlook Procore Excel SAP CMIC Oracle Autodesk	Data entry automation Project matching Real-time updates Invoice processing RFI management	*Pricing not publicly disclosed

Geared toward project managers, coordinators, and administrative staff, Karmen leverages AI to extract structured information from unstructured sources, including emails, text messages, invoices, PDFs, and purchase orders. Automatically enters this data into project management and enterprise resource planning (ERP) systems such as Procore, Excel, SAP, CMIC, and Oracle. A central feature of Karmen is its project-matching engine, which intelligently associates incoming communications with specific subcontractors or projects. This automated categorization streamlines documentation workflows and ensures traceability across a wide range of project inputs. By integrating with tools from the Microsoft Suite, Outlook, Procore, and Autodesk, Karmen creates a unified interface where teams can process and review information efficiently without switching between platforms. Karmen's real-time update functionality enables proactive management by notifying users of emerging risks such as potential change orders that could affect schedule or budget, thus allowing timely decision making. In addition, the platform automates invoice processing to reduce the likelihood of approval errors and supports RFI and change order management to improve visibility into contract modifications. Users can access a centralized dashboard to control or confirm extracted data before final submission, reinforcing accuracy and compliance. While Karmen's availability outside the U.S. has not been explicitly confirmed, its compatibility with globally adopted platforms and standard file formats suggests high adaptability for international construction teams. Finally, pricing details are not publicly disclosed.

4. Discussions

A comparative analysis of six AI platforms including Civils.ai, Kwant.ai, Archilabs, Nicky AI, Buildots, and Karmen reveals that the benefits of artificial intelligence tools have increased across various functions in the AEC industry. While each platform shares the common objective of improving productivity, minimizing manual effort, and enhancing decision-making accuracy, they cater to diverse operational phases and user needs across the projects.

A key similarity across all platforms is their strategic use of AI to automate repetitive, time-consuming tasks. From extracting structured data from unorganized files (Civils.ai, Karmen), to automating administrative workflows (Nicky AI), and tracking site progress via computer vision (Buildots), these platforms together demonstrate how construction management is evolving toward digital workflows and real-time decision-making.

However, significant functional and domain-based differences also emerge. Civils.ai, Archilabs, and Buildots primarily support technical design and analysis processes. While Civils.ai focuses on geotechnical data extraction and modeling, Archilabs emphasizes natural language–based BIM interaction and generative design for architectural planning. These tools are tailored for engineers, architects, and planners operating at the early stages of a project. Buildots offers a unique solution through AI-driven 4D progress tracking, combining helmet-mounted 360-degree camera data with BIM models and schedules. This approach enables precise detection of deviations, improving scheduling accuracy and issue resolution.

In contrast, platforms such as Kwant.ai, Nicky AI, and Karmen are more aligned with site-level operations and administrative management. Kwant.ai integrates AI and IoT devices to enable real-time worker monitoring and predictive risk analytics. Nicky AI serves as a digital administrative assistant with voice-enabled interaction for email and document management. Karmen supports document automation and ERP integration, especially for financial documents like invoices and change orders.

5. Conclusions

In this study, which examines AI platforms used in the AEC industry, the analysis shows that AI tools in this industry are becoming more specialized and technically advanced. Instead of providing general-purpose solutions, today's platforms are designed to support specific tasks by integrating AI into areas such as design, project administration, safety checks, and tracking construction progress. While common themes such as automation, integration, and time savings are evident across all six platforms, their diversity underscores the need for contextual platform selection. Firms must assess their technological maturity, project scale, and operational priorities when adopting these tools. Platforms like Civils.ai and Archilabs are ideal for design-centric organizations, whereas Nicky AI and Karmen are more suited to administrative optimization. For large-scale construction projects with tight deadlines, platforms like Buildots and Kwant.ai offer valuable real-time tracking and risk prediction capabilities. As AI technologies continue to develop, future platforms will likely become more compatible with each other, able to understand and combine different types of data such as text, voice, images, and sensor readings, and offer smarter predictions.

References

Abioye, S.O., Oyedele, L.O., Akanbi, L., Ajayi, A., Delgado, J.M.D., Bilal, M., Akinade, O.O., & Ahmed, A. (2021). Artificial intelligence in the construction industry: A review of present status, opportunities and future challenges. *Journal of Building Engineering*, *44*, 103299. https://doi.org/10.1016/j.jobe.2021.103299

Archilabs. (2024). Retrieved from https://www.archilabs.ai/

Archi Lab. (2023, October 12). *AI Rendering in SketchUp with Archilab AI 1.0 BETA! #ai #architecture.* Retrieved from https://www.youtube.com/watch?v=wcbc77cKUaA

Autodesk. (2024). *What is BIM? Building Information Modeling*. Retrieved from https://www.autodesk.com/solutions/bim

Azhar, S. (2011). Building Information Modeling (BIM): Trends, benefits, risks, and challenges for the AEC industry. *Leadership and Management in Engineering*, *11*(3), 241–252. https://doi.org/10.1061/(asce)lm.1943-5630.0000127

Buildots. (2018). Retrieved from https://buildots.com/

Buildots. (2025, April 15). *Buildots' work ready areas.* Retrieved from https://www.youtube.com/watch?v=P4Ft1mu38YQ

Chen, K., & Zhou, X., Bao, Z., & Skibniewski, M. J., & Fang, W.(2025). Artificial intelligence in infrastructure construction: A critical review. *Frontiers of Engineering Management*, 12, 635–657. https://doi.org/10.1007/s42524-024-3128-5

Civils.ai. (2022). Retrieved from https://civils.ai/

Civils-ai Construction AI. (2023, July 15). *How Civils.ai are using AI in Geotechnical Engineering.* Retrieved from https://www.youtube.com/watch?v=EZZOMXjERAI

Civils-ai Construction AI. (2025, March 12). *How to review construction contracts using Civils.ai.* Retrieved from https://www.youtube.com/watch?v=xGYWSp_iurA

Datta, S. D., Islam, M., Sobuz, M.H.R., Ahmed, S., & Kar, M. (2024). Artificial intelligence and machine learning applications in the project lifecycle of the construction industry: A comprehensive review. *Heliyon*, *10*(5), e26888. https://doi.org/10.1016/j.heliyon.2024.e26888

Eastman, C., Teicholz, P., Sacks, R., & Liston, K. (2011). *BIM handbook: A guide to Building Information Modeling for owners, managers, designers, engineers, and contractors* (2nd ed.). Wiley.

Karmen. (2024). Retrieved from https://www.karmenai.com/

Karmen. (2025). *AI Assistant for Construction Project Managers | Y Combinator*. Retrieved from https://www.ycombinator.com/companies/karmen

Kwant.ai. (2018). Retrieved from https://kwant.ai/

Kwant. (2023, April 27). *Welcome to Kwant.* Retrieved from https://www.youtube.com/watch?v=8NCUCL0vaWY

Nicky AI. (2023). Retrieved from https://www.heynicky.com/

Oztemel, E., & Gursev, S. (2020). Literature review of Industry 4.0 and related technologies. *Journal of Intelligent Manufacturing*, *31*(1), 127–182. https://doi.org/10.1007/s10845-018-1433-8

Sibay, E.M. (2024, November 4). *Nicky AI — AI Assistant for Construction Teams | Esat M. Sibay.* Retrieved from https://www.linkedin.com/posts/esatsibay_ai-powered-construction-management-activity-7259252211891757058-jSG6?utm_source=share&utm_medium=member_desktop&rcm=ACoAAAvWSKoBujiNh5pu416BRT8f5T5LKF_ekHc

4th International Civil Engineering & Architecture Conference
17-19 May 2025, Trabzon, Türkiye

Implementing IDS-based information validation in BIM: A practical application

Bayram A. Temel*[1]

[1] Karadeniz Technical University, Department of Civil Engineering, 61080 Trabzon, Türkiye

Abstract. This study presents an application scenario developed to demonstrate the applicability of the Information Delivery Specification (IDS) standard in automating information validation processes within Building Information Modeling (BIM) projects. In this example, the fire resistance ratings (FireRating) of wall and door elements in a BIM model were validated using IDS-based rules. The validation process was structured in three main stages. First, an IDS file was created using Solibri IDS Editor, defining information requirements related to the selected elements. Second, this file was imported into Solibri Office, where the relevant elements were automatically filtered and verified using classification-based methods. Third, the detected data inconsistencies were reported to stakeholders using the BIM Collaboration Format (BCF) to facilitate feedback. The findings indicate that the use of IDS enables the early identification of data deficiencies and may offer advantages in terms of time efficiency and systematic control compared to manual validation processes. This study provides a practical example of how IDS can be implemented and aims to serve as an introductory reference for users unfamiliar with its use in BIM workflows.

Keywords: Information delivery specification (IDS); Building information modeling (BIM); Information validation; Exchange information requirements (EIR); BIM collaboration format (BCF)

1. Introduction

Building Information Modeling (BIM) has brought significant transformations to project processes within the architecture, engineering, and construction (AEC) industries by enabling the digitalization of design coordination, project management, and facility operations (Pauwels et al., 2017). At its core, BIM represents the physical and functional characteristics of building elements in a structured and accurate digital environment (Eastman et al., 2011). This structured information enhances decision-making efficiency throughout the project lifecycle and plays a critical role in applications such as design validation, clash detection, energy efficiency analysis, and maintenance management (Volk et al., 2014).

However, manually checking the accuracy and completeness of information in BIM models can lead to significant time losses, human errors, and information inconsistencies, especially in large-scale projects (Succar, 2009). Moreover, the use of different software platforms and multidisciplinary teams in projects often results in non-standard data exchanges (buildingSMART International, 2024). Such issues can cause quality losses and increased costs in project delivery processes.

To address these challenges, the Information Delivery Specification (IDS) was developed by buildingSMART International. IDS enables the automatic, transparent, and standardized validation of BIM data by transforming project information requirements (Exchange Information Requirements - EIR) into a machine-readable format. Designed in alignment with the ISO 19650 series, IDS enhances efficiency in information management processes and supports cross-platform interoperability within the openBIM framework (ISO 19650-1, 2018).

In this study, the concept of Information Delivery Specification (IDS) is examined in detail, and its role and significance in structured BIM data validation are explained. Furthermore, the contributions of IDS to information management processes in the AEC sector are evaluated, and its potential applications within BIM workflows are discussed. In this context, a practical application using the Solibri IDS Editor is presented in the following sections to demonstrate the practical use of IDS.

*Corresponding author, E-mail: bayramali.temel@ktu.edu.tr

https://doi.org/10.31462/icearc2025_ce_mng_661

2. Information Delivery Specification (IDS)

The construction industry is undergoing a significant transformation driven by digitalization. At the center of this transformation, BIM not only enables the digital representation of physical designs but also facilitates the management of information required throughout the entire lifecycle of buildings (Eastman et al., 2011).

However, in BIM applications, the absence of required information or the provision of incorrect data can lead to major disruptions and increased project costs. As a result, clearly, understandably, and verifiably defining which information should be present on which elements has become a critical necessity in modern projects (Pauwels et al., 2017).

In response to this need, the IDS was developed. IDS explicitly defines the information that must be present in BIM models and allows the automatic validation of this information through software tools (buildingSMART International, 2024).

IDS is a standard that specifies, in a machine-readable and human-understandable format, the information that must be associated with specific model elements. In simple terms, IDS enables automated checks for questions such as:

- "Does this door have fire resistance information?"
- "Is the thermal transmittance of this wall correctly defined?"

Summarizing this structure, IDS systematically answers the following three fundamental questions:

- What? → Which elements will be checked?
- For what? → Which information is required?
- How? → According to which rules will it be evaluated?

Traditionally, information requirements in BIM projects have been specified through lengthy textual documents, contract appendices, and technical specifications. However, this approach has introduced several challenges, as summarized in Table 1.

Table 1. Common problems in traditional information requirement definitions

Problem	Description
Ambiguity	The required information was not clearly defined.
Interpretation Differences	Each team could interpret the textual requirements differently.
Manual Validation	Information validation was performed manually, resulting in time consumption and human errors.

For instance, if a contract merely states, "Doors must be fire-resistant," this phrase leaves significant ambiguity:

- Which doors?
- According to which fire-resistance standard?
- Based on which testing methods?

IDS addresses such ambiguities by defining information requirements in a clear, measurable, and machine-verifiable manner. When rephrased using IDS principles, the statement becomes objective, unambiguous, and instantly verifiable across different software environments.

An example of an IDS definition is given Table 2.

Table 2. Example of an IDS requirement definition

Element	Property	Requirement
IfcDoor	FireRating	≥ EI60 standard

An IDS file organizes information requirements within a clearly structured framework. The core components of this framework are illustrated in Fig. 1. This systematic structure standardizes information demands, facilitates interoperability between different platforms, and ensures objective measurement of information accuracy.

The Entity facet specifies the type of IFC entity to which the IDS rule applies, ensuring that validation checks are only performed on relevant elements. For example, a rule regarding thermal transmittance would apply specifically to IfcWall and IfcWindow entities.

The Attribute facet refers to fundamental metadata associated with an IFC entity, such as its GlobalId and Name.

The Classification facet enables validation based on standardized classification systems such as OmniClass, Uniclass, or COBie. This approach ensures structured data organization within the BIM model. For instance, a classification rule may require that all structural beams are correctly categorized under a predefined standard.

The Property facet concerns measurable or definable attributes assigned to an element. These properties align with IFC schemas and BIM project requirements. For instance, an IfcDoor could have a Width property that must be at least 900 mm to meet accessibility standards.

The Material facet verifies whether elements have the correct material definitions, which is critical for sustainability assessments, structural integrity evaluations, and compliance with environmental regulations. An IDS rule might, for example, ensure that IfcSlab elements utilize C30/37 concrete for structural strength.

The PartOf facet defines the relationships between elements, ensuring that grouped components meet specific requirements. For instance, a IfcDoor located within a fire compartment (IfcSpace) must have a fire rating that matches the safety classification of that compartment.

Fig. 1. Facets of IDS (Dias, 2024)

The IDS validation process operates in two main stages: Applicability and Requirements. In the Applicability stage, the specific elements to be checked are defined (e.g., "Only external walls will be checked."). In the Requirements stage, the attributes or properties that the selected elements must possess are specified (e.g., "Each external wall must have a ThermalTransmittance value of ≤ 0.30 W/m²K."). In essence, IDS translates information requirements into a machine-readable language and enables automated model validation according to these defined rules.

The concept of IDS aims to standardize the definition of information requirements within BIM workflows. However, integrating the IDS framework into real-world sectoral practices poses challenges due to technical limitations within the current software ecosystem.

Currently, the number of software tools capable of generating and utilizing IDS files remains limited. Solibri IDS Editor, supported by buildingSMART International, and some solutions offered by ACCA Software, allow for the creation of IDS rules. Nevertheless, most of these tools serve only specific functions and may not adequately support integrated data management in large-scale, multidisciplinary projects.

Moreover, widely used design platforms such as Autodesk Revit and Graphisoft ArchiCAD are not currently capable of directly producing or validating IDS files within their native environments. This limitation primarily stems from the restricted alignment of these platforms' data modeling approaches with open data standards like IFC. Specifically, proprietary platforms such as Revit require users to export data for subsequent processing, which introduces additional steps to ensure compatibility with IDS rules (Volk et al., 2014).

Currently, the use of IDS in BIM projects typically involves a two-stage workflow. In the first stage, BIM models are exported using open data standards such as IFC. In the second stage, the exported models are validated against IDS rules using verification tools like Solibri Office.

While this two-stage approach offers certain advantages in terms of data integrity, it also introduces additional coordination and time management challenges during project execution. Particularly in large-scale and international projects, the integration of data from various platforms into the IDS validation process requires meticulous planning and effective data management strategies.

In conclusion, for IDS to achieve broader adoption across the industry, design authoring tools must evolve to natively support IDS-compliant data generation. Accordingly, buildingSMART International and various software developers are actively working to enhance IDS compatibility in future software releases.

3. IDS setup and implementation using Solibri solutions

In this study, Solibri's IDS Editor platform was used to define IDS rules, while Solibri Office software was employed to perform information validation on the BIM model. The Solibri IDS Editor is an online platform that enables the creation of IDS specifications, whereas Solibri Office is a robust verification tool designed for quality control and data validation in building information models. Both tools operate in full compliance with the Industry Foundation Classes (IFC) standard (Solibri, 2024).

As part of the study, an information validation procedure was carried out to identify critical data deficiencies related to fire safety within wall and door elements of the BIM model. In particular, the FireRating property, which represents a building component's resistance to fire, plays a vital role in ensuring both design accuracy and building safety.

The validation process consists of three main stages:

1- *Definition of IDS Rules:* Separate IDS specifications were created for each element group (walls and doors) using the Solibri IDS Editor (2024). At this stage, the element type to be validated (IfcWall, IfcDoor), relevant classifications (e.g., Fire Compartment, Fire Doors), and the property to be checked (FireRating) were defined.

2- *Importing into Solibri Office and Automated Validation:* The defined IDS file was imported into Solibri Office, and the BIM model was validated against the rules. All relevant elements in the model were scanned to verify compliance with the IDS criteria.

3- *Error Detection, Issue Creation via BCF, and Feedback:* For entries that failed to meet the validation criteria, issues were created within Solibri Office using the BIM Collaboration Format (BCF). These issues were then communicated to responsible stakeholders (e.g., architects), enabling correction of erroneous data in the authoring software and contributing to overall data quality improvement.

This case study clearly demonstrates how the IDS approach can be effectively utilized in project information management processes and how it contributes to enhancing the quality of BIM model data.

3.1. Fire safety check

In this case study, the aim is to verify whether the fire compartment walls contain the FireRating property. To apply the IDS rules correctly—targeting only fire compartment walls—the walls were classified within Solibri as either belonging to a fire compartment or not, as illustrated in Fig. 2.

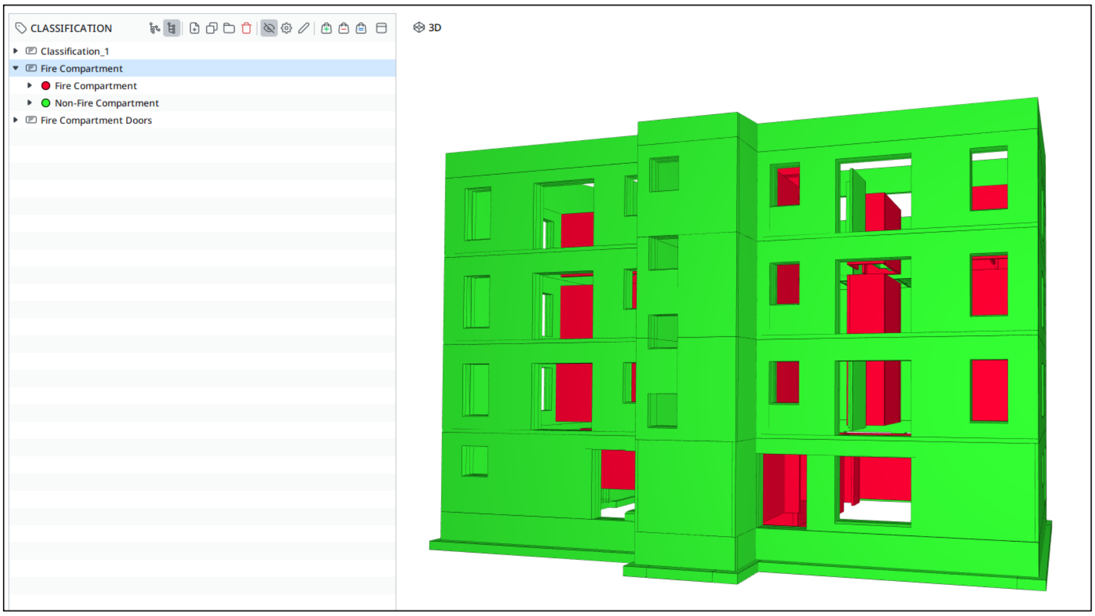

Fig. 2. Classification of walls based on fire compartment status within Solibri

Then, the creation of the IDS was initiated using the Solibri IDS Editor (Solibri, 2024). Initially, it was intended to verify whether the fire compartment walls include the FireRating value. As shown in Fig. 3, the IFC schema selected for IDS creation is IFC4. In the applicability section, the Entity facet of IDS was used, with its value set to IfcWall, this filters all wall elements from the model. Since the goal is to check only the walls that are part of the fire compartment, a classification was applied as a second applicability condition, and its value was defined based on the previously created classification within Solibri.

In the requirement section, the Property facet was used, and the value was set to FireRating, as this is the property to be checked. The data type was automatically assigned according to the IFC schema. Additionally, under the requirement section, a list of acceptable values for the FireRating property such as EI90, EI60, and EI120, was defined. This ensures that during validation, only these specific values are accepted; any deviation from them will be flagged as an error.

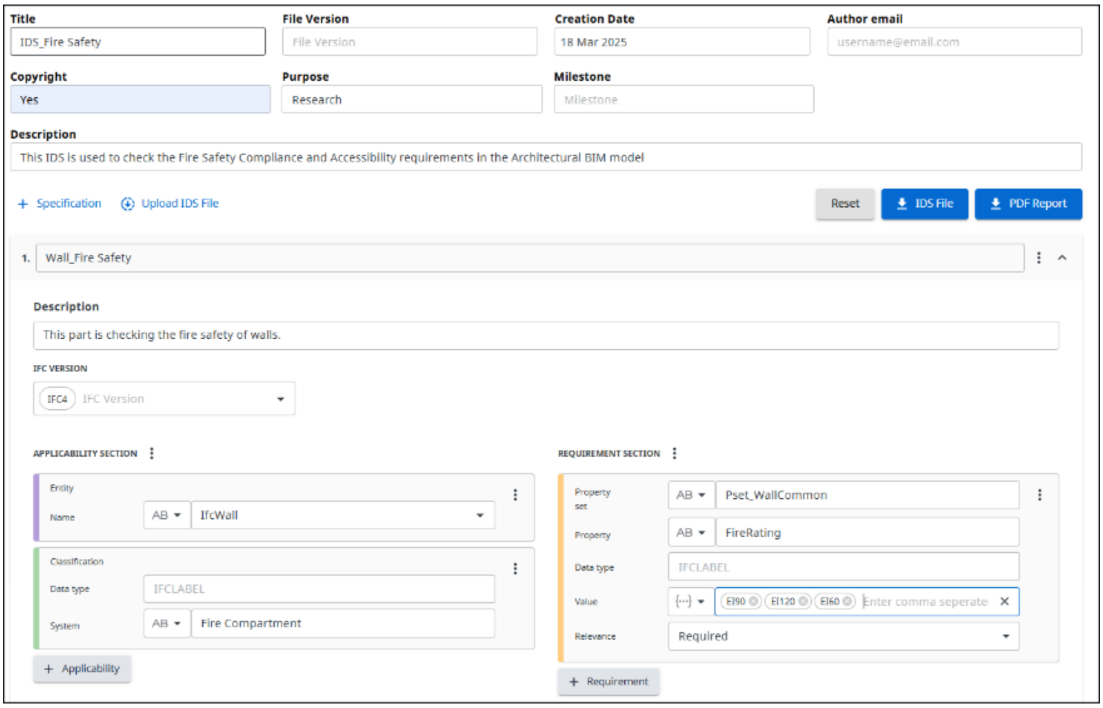

Fig. 3. IDS configuration for fire safety validation of walls using the Solibri IDS Editor

After creating the specification for the fire safety of walls, the next step is to define the requirements for the fire safety check of doors. As shown in Fig. 4, like the approach used for walls, the doors were first classified within Solibri as Fire Doors and Non-Fire Doors.

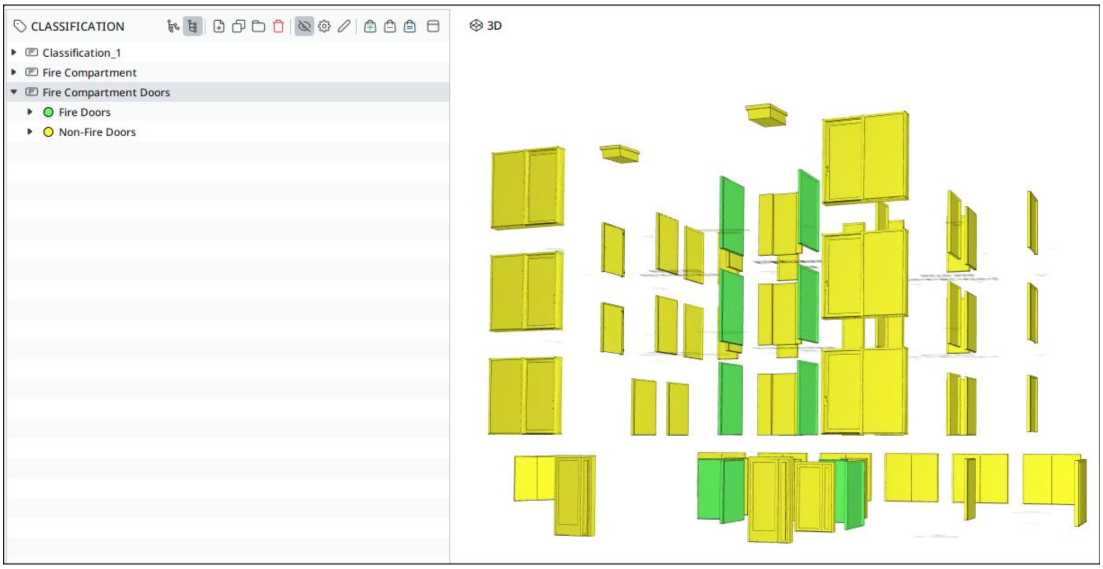

Fig. 4. Classification of doors based on fire safety criteria within Solibri

As shown in Fig. 5, another specification was added within the Solibri IDS Editor to perform the fire safety check for doors. The IFC schema selected for validation is IFC4, as the BIM model conforms to this schema. In the applicability section, the Entity facet was used, and its value was set to IfcDoor, thereby filtering all door elements from the model. Since the goal is to check only the doors that are part of the fire compartment, a classification was applied as a second applicability condition, and its value was defined based on the previously created classification within Solibri.

In the requirement section, the Property facet was selected, and the value was set to FireRating, since this is the property to be validated. The data type was automatically assigned based on the IFC schema. A list of acceptable values for the FireRating property such as EI30 and EI60 was defined so that during validation, only these values are accepted. Any deviation from the predefined list will result in an error.

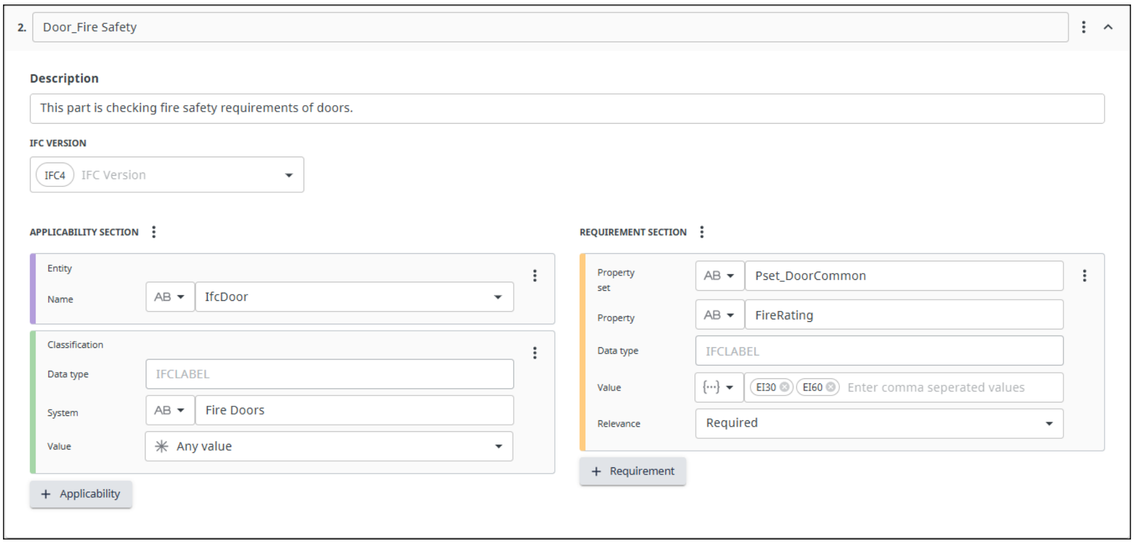

Fig. 5. IDS configuration for fire safety validation of doors using the Solibri IDS Editor

After creating the IDS using the Solibri IDS Editor online service, the resulting IDS file was downloaded. The specifications defined for the fire safety of walls and doors are summarized as follows:

```
<?xml version="1.0" encoding="UTF-8"?>
<!-- Generated by the Solibri IDS editor at https://idseditor.solibri.com | v1.2.1 | 1742723948460 -->
<ids:ids xmlns:ids="http://standards.buildingsmart.org/IDS"
xmlns:xs="http://www.w3.org/2001/XMLSchema" xmlns:xsi="http://www.w3.org/2001/XMLSchema-
instance" xsi:schemaLocation="http://standards.buildingsmart.org/IDS
http://standards.buildingsmart.org/IDS/1.0/ids.xsd">
  <ids:info>
    <ids:title>IDS_Fire Safety</ids:title>
    <ids:description>This IDS is used to check the Fire Safety Compliance and Accessibility requirements
in the Architectural BIM model</ids:description>
    <ids:date>2025-03-18</ids:date>
    <ids:copyright>Yes</ids:copyright>
    <ids:purpose>Research</ids:purpose>
  </ids:info>
  <ids:specifications>
    <ids:specification name="Wall_Fire Safety" ifcVersion="IFC4" description="This part is checking the
fire safety of walls.">
      <ids:applicability minOccurs="1" maxOccurs="unbounded">
        <ids:entity>
          <ids:name>
            <ids:simpleValue>IFCWALL</ids:simpleValue>
          </ids:name>
        </ids:entity>
        <ids:classification>
          <ids:system>
            <ids:simpleValue>Fire Compartment</ids:simpleValue>
          </ids:system>
```

```
      </ids:classification>
    </ids:applicability>
    <ids:requirements>
      <ids:property cardinality="required" dataType="IFCLABEL">
        <ids:propertySet>
          <ids:simpleValue>Pset_WallCommon</ids:simpleValue>
        </ids:propertySet>
        <ids:baseName>
          <ids:simpleValue>FireRating</ids:simpleValue>
        </ids:baseName>
        <ids:value>
          <xs:restriction base="xs:string">
            <xs:enumeration value="EI120"/>
            <xs:enumeration value="EI60"/>
            <xs:enumeration value="EI90"/>
          </xs:restriction>
        </ids:value>
      </ids:property>
    </ids:requirements>
  </ids:specification>
  <ids:specification name="Door_Fire Safety" ifcVersion="IFC4" description="This part is checking fire
safety requirements of doors.">
    <ids:applicability minOccurs="1" maxOccurs="unbounded">
      <ids:entity>
        <ids:name>
          <ids:simpleValue>IFCDOOR</ids:simpleValue>
        </ids:name>
      </ids:entity>
      <ids:classification>
        <ids:system>
          <ids:simpleValue>Fire Doors</ids:simpleValue>
        </ids:system>
      </ids:classification>
    </ids:applicability>
    <ids:requirements>
      <ids:property cardinality="required" dataType="IFCLABEL">
        <ids:propertySet>
          <ids:simpleValue>Pset_DoorCommon</ids:simpleValue>
        </ids:propertySet>
        <ids:baseName>
          <ids:simpleValue>FireRating</ids:simpleValue>
        </ids:baseName>
        <ids:value>
          <xs:restriction base="xs:string">
            <xs:enumeration value="EI30"/>
            <xs:enumeration value="EI60"/>
          </xs:restriction>
        </ids:value>
      </ids:property>
    </ids:requirements>
  </ids:specification>
 </ids:specifications>
</ids:ids>
```

After downloading the IDS file from the Solibri IDS Editor online service, it was uploaded into Solibri Office to validate the information content of the BIM model against the defined IDS requirements.

As shown in Fig. 6, the fire safety check for the doors was successfully completed, with no errors detected during validation.

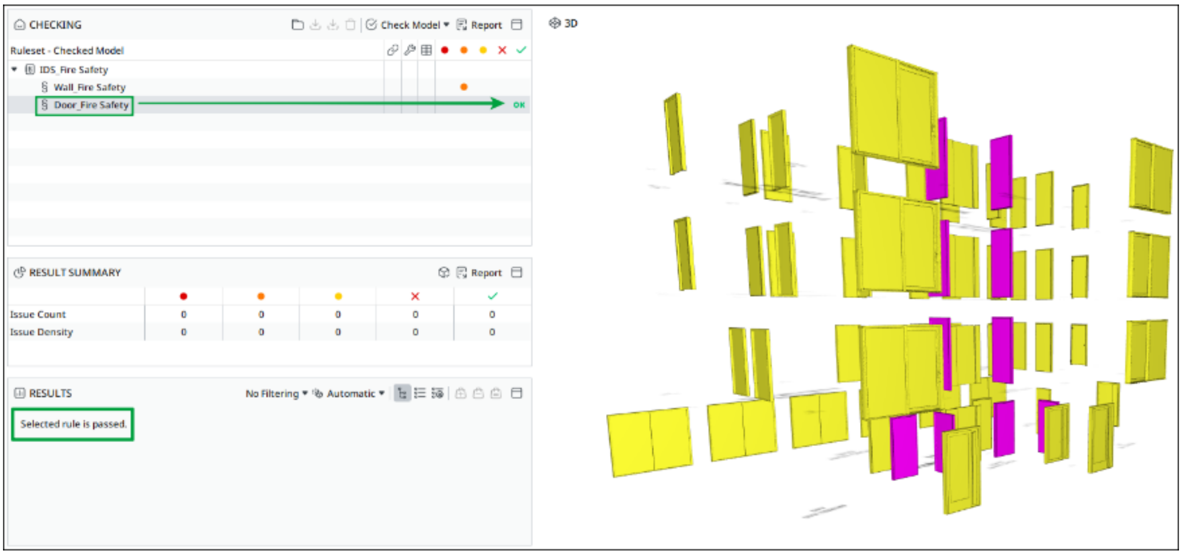

Fig. 6. Validation results of door fire safety requirements against IDS in Solibri Office

On the other hand, as shown in Fig. 7, Solibri Office identified errors related to the fire safety of certain walls during the IDS-based validation process. Specifically, two errors were detected, both resulting from the use of values that do not match the predefined acceptable values specified in the IDS.

Two issues related to the data entry errors were created in Solibri Office and exported in BCF in Figs. 7 and 8. Thess issues were then forwarded to the architect to correct the erroneous values for the relevant elements, allowing the architect to update the information in the BIM authoring tool with the appropriate values.

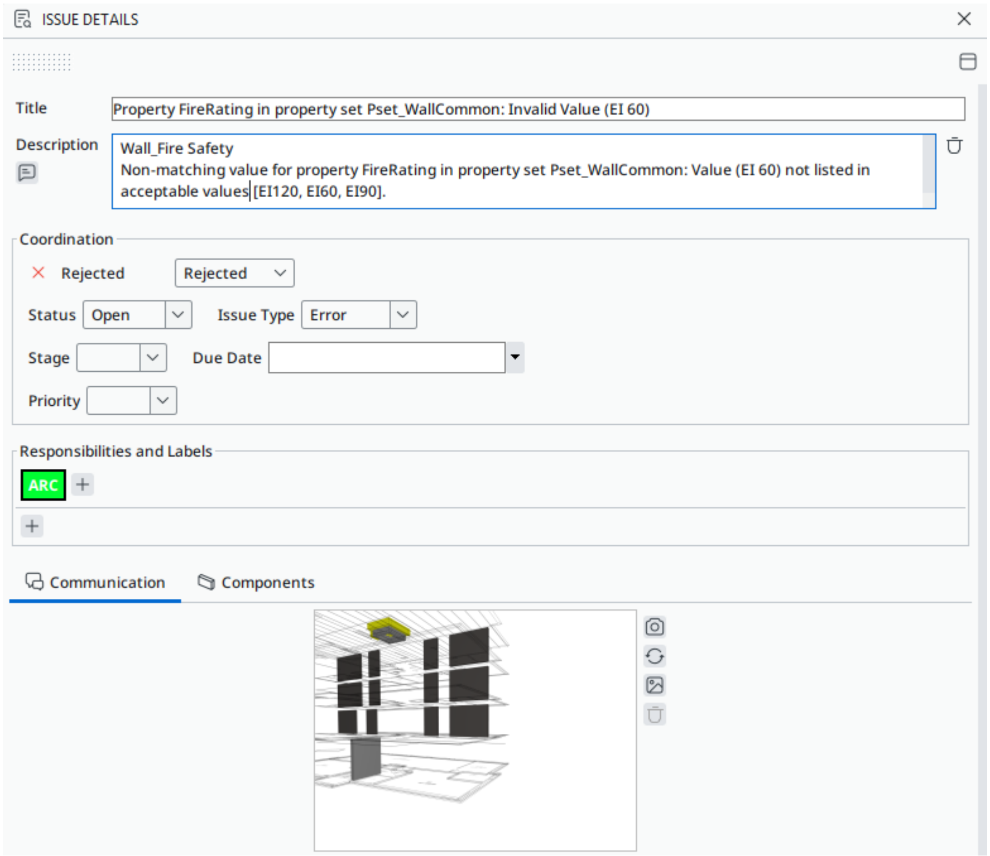

Fig. 7. Creating an issue in Solibri Office for inaccurate fire rating data (e.g., EI 60) using the BCF format

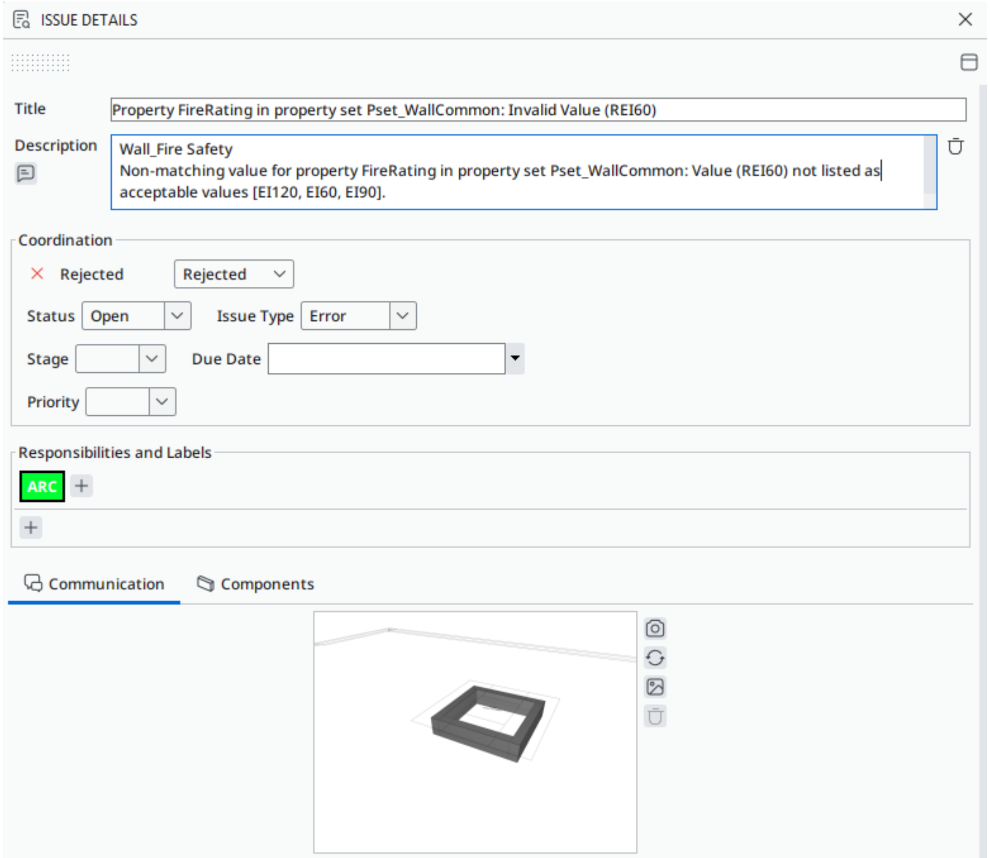

Fig. 8. Creating an issue in Solibri Office for inaccurate fire rating data (REI60) using the BCF format

4. Conclusions

This study presented an example scenario illustrating the application of the IDS approach, which was developed to ensure information accuracy in BIM projects. The increasing complexity of information management and model coordination in contemporary projects necessitates systematic and standards-based data validation. In this context, IDS provides significant support to project information workflows by enabling the automatic verification of defined information requirements across model elements.

To demonstrate this applicability, a scenario was developed in which the FireRating properties of wall and door elements in a BIM model were validated. IDS rules were defined using the online Solibri IDS Editor, and the generated IDS file was imported into Solibri Office to conduct the automated validation process. Detected inconsistencies were reported to stakeholders using the BIM Collaboration Format (BCF), enabling an effective feedback mechanism. The findings suggest that the use of IDS allows for the early identification of data deficiencies and may provide advantages in terms of time efficiency during the validation process. This application demonstrated that IDS has the potential not only to ensure data integrity but also to support risk mitigation, improve design decision-making, and enhance interdisciplinary coordination.

The ability to define information requirements in a standardized format and to validate them automatically is becoming essential for achieving the digital transformation goals of the AEC industry. This study offers a practical scenario to demonstrate how IDS can be applied, providing a clear and accessible example for users who may be unfamiliar with the concept.

References

buildingSMART International. (2024). *Information Delivery Specification (IDS)*. Retrieved from https://www.buildingsmart.org/standards/ids/

Dias, C. (2024). Retrieved from https://www.linkedin.com/posts/carlos-dias-6a293868_buildingsmartinternational-buildingsmartinternational-activity-7109134129908097024-yAl9/

Eastman, C., Teicholz, P., Sacks, R., & Liston, K. (2011). *BIM Handbook: A Guide to Building Information Modeling for Owners, Managers, Designers, Engineers, and Contractors* (2nd ed.). Wiley.

ISO 19650-1. (2018). International Organization for Standardization. Organization and digitization of information about buildings and civil engineering works, including building information modelling (BIM) – Information management using building information modelling – Part 1: Concepts and principles.

Pauwels, P., Zhang, S., & Lee, Y.C. (2017). Semantic web technologies in AEC industry: A literature overview. *Automation in Construction, 73*, 145–165

Solibri. (2024). Retrieved from https://www.solibri.com/

Solibri IDS Editor. (2024). *Solibri IDS Editor – User Guide.* Retrieved from https://idseditor.solibri.com/

Succar, B. (2009). Building information modelling framework: A research and delivery foundation for industry stakeholders. *Automation in Construction*, *18*(3), 357–375

Volk, R., Stengel, J., & Schultmann, F. (2014). Building Information Modeling (BIM) for existing buildings - Literature review and future needs. *Automation in Construction*, *38*, 109–127

4th International Civil Engineering & Architecture Conference
17-19 May 2025, Trabzon, Türkiye

From courts to boards: Comparative legal analysis of early-stage dispute management in public construction disputes

Mahmut Sarı*[1], Savaş Bayram[2]

[1] *Kırşehir Ahi Evran University, Department of Construction, 41100, Kırşehir, Türkiye*
[2] *Erciyes University, Department of Civil Engineering, 38039, Kayseri, Türkiye*

Abstract. Disputes occurring in the construction industry cause quantifiable damages, like delays in project timelines, cost increases, quality degradation, and incalculable effects, like loss of trust among concerned stakeholders and deteriorated business relationships. Resolving conflicts at the initial phase is instrumental in maintaining project continuity and reducing temporal and monetary losses. The legislative change enacted in 2020, which gave contractors the discretion of submitting applications to the Directorate of High Technics Board (DHTB) directly, afforded a significant administrative framework for the speedy resolution of disputes in public works projects. The present research conducts a comparative analysis of the efficiency of the modified application to the DHTB used by contractors and that of the judicial process of the Court of Cassation. The results are that both the Court of Cassation and the DHTB have the same approach in solving disputes, except that the DHTB provides a faster and less expensive means of dispute resolution. The significant limitation of this research is that the analysis is conducted based on two case studies alone. It is recommended that future research explore the impact of DHTB decisions on dispute resolution practices using larger population samples and both quantitative and qualitative approaches.

Keywords: Construction disputes; Dispute resolution mechanisms; Early-stage dispute management; Comparative legal analysis; Public construction projects

1. Introduction

Construction disputes have been technically referred to as legal and technical disagreements that develop between parties through the process of project delivery, construction, and design. These disputes are essentially caused by defective or insufficient realization of contractual duties, differing interpretation of contract conditions, or unforeseen circumstances (Fenn et al., 1997; Sarı et al., 2021). The construction industry, with its numerous stakeholders, prolonged project durations, and intricate technical specifications, is prone to result in the occurrence of disputes (Kumaraswamy, 1997; Sarı et al., 2024). Additionally, communication inefficiencies, scope changes in the project, and ambiguous contractual terms greatly enhance the likelihood of disputes in mega-projects (Mitkus & Mitkus, 2014).

Disputes arising in construction projects cause delayed timelines, cost overruns, and a decline in quality, thereby inflicting real economic damages on the industry (Assaf & Al-Hejji, 2006). Especially in large projects, such delays put added financial strains on contractors and employers, dramatically heightening the duration required for the fulfillment of a project (Koushki et al., 2005). Likewise, research in Jordan found that disputes result in higher project costs, major variations in completion schedules, and dissatisfaction experienced by both employers and contractors (Sweis et al., 2008).

Early resolution of construction disputes is known to be a crucial way to avoid the possible escalation of conflicts that could adversely affect project goals. Alternative Dispute Resolution (ADR) techniques like negotiation, mediation, adjudication, and arbitration enable prompt and cost-effective resolution of conflicts in the construction industry while emphasizing the importance of maintaining interpersonal relationships (Cheung et al., 2002). Signing detailed and unambiguous contractual terms at the beginning of a project and maintaining effective communication channels minimizes the possibility of conflict and improves the continuity of the project (Yates & Epstein, 2006). Currently, in addition to conventional methods, emerging technologies such as Building Information Modeling (BIM), blockchain, and smart contracts are also essential tools for the early identification and resolution of conflict (Kalogeraki & Antoniou, 2024). These technologies accelerate data exchange between the parties, enhance transparency, and contribute to faster advancement in resolution procedures.

* Corresponding author, E-mail: mahmutsari@ahievran.edu.tr

https://doi.org/10.31462/icearc2025_ce_mng_670

In Turkiye, judicial and administrative bodies have important roles in the resolution of disputes arising from construction projects during their execution phases. In this context, the Court of Cassation and the Directorate of High Technics Board (DHTB) under the Ministry of Environment, Urbanization, and Climate Change are noted as two main bodies in resolving technical and contractual disputes occurring in the course of project execution. The Court of Cassation is the supreme judicial body for the settlement of legal disputes stemming from construction contracts, including developing case law on contractual provision interpretation, contractor-employer performance relations, determination of construction defects, consideration of time extension and variation claims, payment of progress payments, return of performance bonds, and contract termination (Sarı et al., 2025). The decisions of the Court of Cassation define the rights and duties that govern subcontractors, employers, and contractors, thus promoting legal certainty within the sector.

Conversely, DHTB functions as a distinct administrative entity tasked with the resolution of technical and contractual conflicts arising within public construction initiatives. The technical assessments and contractual interpretations provided by DHTB serve an advisory role and lack legal enforceability for judicial bodies and involved parties; however, its decisions regarding unit prices hold binding authority following applicable regulations.

In 2020, there was a regulatory change that permitted contractors to approach the DHTB directly, hoping to settle disagreements at the preliminary phases through the application of technical expertise. This has been a great boost for DHTB in resolving disputes. DHTB is now a neutral technical authority to be accessed not only by administrative authorities but even contractors, thus acquiring a more central position in the resolution of technical and contractual disputes in public works contracts. In particular, in technically complex disputes, DHTB provides fast and impartial opinions, opening up the possibility of settlement between the parties before their escalation to judicial proceedings. Nonetheless, since DHTB's decisions are mostly non-binding, they do preserve the parties' freedom of action but also possibly limit the finality of dispute resolution. Therefore, DHTB's increased role must be maintained in delicate equilibrium with the principles of the rule of law.

The current state of research literature available on construction dispute resolution is predominantly concentrated on ADR techniques, judicial proceedings, and the incorporation of technology. Research investigating the use of institutional systems to enable early-stage dispute resolution is significantly lacking. The 2020 amendment, under which contractors could submit directly to DHTB, has created a mechanism akin to conventional ADR methods (e.g., mediation and arbitration), whereby parties can seek solutions from an administrative technical authority before the courts. This innovation is a significant alternative for the early resolution of disputes in public construction projects. Yet, no systematic research on the impact of this regulatory reform on sectoral practice, early resolution of disputes, and settlement promotion between parties can be found in the literature, indicating a broad research gap.

This research aimsto assess the efficiency of allowing contractors to make direct applications to the DHTB in comparison with the conventional judicial resolution mechanism as determined by the Court of Cassation. Despite the wealth of in-depth studies on other ADR approaches, there is a notable lack of studies that investigate comparative roles of administrative technical organs and judicial bodies in terms of dispute resolution effectiveness. The research aims to uncover the real-world contributions of DHTB's expertise-based early-stage dispute settlement mechanisms compared to the Court of Cassation's dispute settlement results in terms of time, expenses, and settlement dynamics. In this way, it hopes to make an original contribution to academic literature and supply practitioners with a comparative assessment of the procedural efficiency of DHTB and the Court of Cassation.

2. Materials and methods

Case study analysis is a qualitative research method that enables an in-depth examination of a particular event, phenomenon, or decision-making process within its contextual framework. This method is widely utilized across disciplines such as psychology, anthropology, sociology, political science, education, clinical sciences, social work, and administrative sciences (Baron & McNeal, 2019; Miles-Keogh, 2015). In the fields of construction law and dispute resolution, case study methodology is employed to thoroughly understand the procedures adopted by decision-making bodies and the reasoning logic underpinning their rulings. Particularly in the prediction and resolution of construction disputes, previous studies have utilized case analysis to perform detailed evaluations of each case and identify key factors influencing the decisions of judges or arbitrators (Arditi et al., 1998; Arditi & Tokdemir, 1999; Chaphalkar et al., 2015; Mahfouz & Kandil, 2012).

Case study methodology, especially within the framework of interpretivist qualitative research paradigms, aims to achieve a deep understanding of the context and dynamics of specific events. In this study as well, this specific qualitative approach was preferred, considering the objective of analyzing each decision within its unique contextual features. Case study analysis provides an effective methodology for comprehensively understanding the dispute resolution processes and the legal and technical reasoning underlying decisions in the field of construction law (Hemanth Sai Kalyan et al., 2022). Similarly, studies predicting the outcomes of disputes in Public-Private Partnership (PPP) projects between public authorities and private sector participants have demonstrated that case study methodology serves as an effective tool for data collection and evaluation (Zheng, 2021).

Given the significant importance of the unique circumstances surrounding each case in construction law disputes, case study analysis is considered a superior method compared to other qualitative approaches for revealing the reasoning patterns and decision-making mechanisms across different cases.In this context, the case study method will be employed to conduct an in-depth examination of the decisions rendered by two different institutions (the 15th Civil Chamber of the Court of Cassation and DHTB) in terms of both procedural and substantive aspects. In this study, each decision will be analyzed separately as a case under the following thematic headings:

- Subject of the Dispute
- Procedural Rules Applied
- Evaluation Criteria and Use of Evidence
- Legal and Technical Grounds Underpinning the Final Decision

Through this framework, case study analysis will offer a detailed examination not only of the textual content of the decisions but also of the logical structures underlying the decision-making processes.

3. Results and discussion

In this study, two construction dispute cases arising from public works contracts based on lump-sum turnkey agreements in Türkiye have been examined. In each case, the contractors sought additional payments from the contracting authority for some items of work they alleged were not included within the contractual scope. An analysis of the judicial and administrative decisions related to these disputes shows that, despite the structural and authoritative differences between the Court of Cassation and the Directorate of High Technics Board (DHTB), there are significant similarities in their interpretive approaches (Table 1). Surprisingly, both were found to heavily depend on expert testimony from technical experts and utilized the same reasoning strategies when deciding whether the contested works fell under the original contract. These findings suggest a convergence between judicial and administrative systems' decision-making reasoning for the resolution processes of public works disputes in Türkiye.

To begin with, both rulings expressly declare the nature and extent of the agreements. The Court of Cassation expressly declares:

"*... a contract was executed between the parties on 18.07.2011 for the construction of the District Police Headquarters and Lodging Building at a fixed lump sum of 2,124,000.00 TL + VAT...*", thus affirming the lump-sum contractual structure. Similarly, DHTB notes:

"*... a construction work contracted under a lump-sum turnkey contract on 08.05.2017 under the Public Procurement Law No. 4734 and the Public Procurement Contracts Law No. 4735...*", confirming the same contractual framework.

In both cases, the contractors made similar claims. In the case before the Court of Cassation, the contractor requested payment for the fitting of a generator that was allegedly not covered by the contractual agreement, with the decision stating:

"*...regarding the purchase of a 150 KW generator, the technical specifications did not define the generator's features, it was absent from the room lists, and no payment was foreseen in the bill of quantities, thereby seeking to recover the generator's cost outside the contractual scope...*". In the Directorate's decision, the contractor claimed:

"*...in a petition dated 18.09.2017, the contractor summarized that for Poz Y.16.062/09 works of the Ministry of Environment and Urbanisation, debris generated from borehole drilling was transported over 12 km whereas the contract assumed up to 60 meters; hence, an additional transport cost was sought for the distance exceeding 60 meters...*".

Both decision texts strongly emphasise the binding nature of project documents and contractual annexes. The Court of Cassation underlined that:

"*...the contract was based on a lump-sum turnkey price, and Article 8 of the contract listed the annexes, with the implementation projects qualifying as part of the contract documents. Since the 150 KW generator was included within the implementation project, it cannot be considered as an extra work item. Thus, the trial court's ruling in favour of the claim was erroneous...*".

Similarly, the Directorate's assessment stated:

"*...Article 6 of the contract stipulates that 'this is a lump-sum turnkey contract based on the implementation projects and room lists included in the tender documents, and the total contract price offered by the contractor covers the entire work.' Furthermore, Article 39 of the General Specifications for Construction Works prescribes that 'for lump-sum turnkey contracts, payments are made based on progress percentages as foreseen in the tender documents, under the principles outlined in the contract and its annexes'...*".

Table 1. Comparison of Court of Cassation and DHTB Decisions on construction disputes

No	Criterion	Court of Cassation Decision	Excerpt (Court of Cassation)	DHTB Opinion	Excerpt (DHTB)	Similarity / Difference
1	Type and Nature of Contract	Lump-sum turn-key contract; annexed documents are essential	"...a lump-sum turn-key contract of 2,124,000 TL + VAT was signed..."	Lump-sum turn-key; based on technical specifications and item lists	"...this is a lump-sum turn-key contract as defined..."	Similarity
2	Subject of Dispute	Whether generator work was contractually included	"...claimed payment for generator work excluded from the original scope..."	Whether hauling of pile waste was within contractual scope	"...a dispute arose as the contractor requested payment for hauling over 60 meters for surplus material (pasa)..."	Similarity
3	Project Documentation and Annexes	Implementation drawings and quantity lists are integral parts of the contract	"...since the 150 KW generator was part of the implementation project..."	Technical specs and project definitions are binding	"...the contract includes all works defined in the project and specification..."	Similarity
4	Normative Legal Basis	Art. 355 et seq. of the Turkish Code of Obligations; Articles 22–23 of the GSC	"...Articles 355 et seq. establish the work contract; Articles 22–23 of the GSC apply..."	General Specification Article 39	"...payments are made according to Article 39 of the General Specifications..."	Similarity
5	Outcome and Legal Effect	Court ruling reversed; retrial to be conducted	"...the decision was REVERSED in favor of the defendant..."	Advisory technical opinion given to administration, not binding	"...the Board unanimously issued this non-binding opinion..."	Difference

Consequently, both parties founded their arguments on the General Specifications for Construction Works, though citing different articles: the Court of Cassation relied on provisions related to the price of additional works, whereas the Directorate put forward payment procedures in the event of lump-sum contracts. Both approaches, however, refer to mutual dependence on the same normative framework, indicating an integrated legal framework for the adjudication of technical disputes.

The fundamental structural difference between the two judgments is in their binding effects. The Court of Cassation, holding that there was both a failure of proof in the expert report and a grave error of law on the part of the trial court, ruled that the judgment at first instance be annulled:

"*...since the implementation project envisaged the construction of a 150 KW generator, this work cannot be classified as extra. Therefore, the court's acceptance of the claim was incorrect. Accordingly, the appeal of the defendant is upheld, and the judgment is REVERSED in favour of the appellant...*".

This implies that the Court not only evaluated the expert evidence but also addressed the substantive questions directly, thus rendering a binding judicial decision that calls for a retrial. On the other hand, the decision of the Directorate is a non-binding technical view addressed to the administrative authority. As stipulated clearly:

"*...regarding the additional claims for the 'Annex Building Construction Work,' it was concluded that the transport of debris beyond 60 meters falls within the contract price. According to Article 16 of Decree Law No. 644 on the Organization and Duties of the Ministry of Environment and Urbanisation, this evaluation was adopted unanimously in the meeting held on 11.01.2018...*".

This explains that the conclusions of the Directorate, while having force, do not carry the force of a judicial ruling, and therefore, the contracting authority is afforded discretion to implement the recommendations.

One of the important points of convergence observed in both institutions' rulings is how they deal with the normative value of contract documents. Important also is the acknowledgment by the Court of Cassation and the DHTB of execution drawings, technical specifications, and bills of quantities as basic and defining components of the contract to indicate that dispute resolution is concerned not just with the work's completion itself but with addressing whether the scope defined has been exceeded. This statement illustrates the significance attached to the principles of foreseeability and contract discipline.

In the same vein, the perspective regarding the General Specifications for Construction Works also strengthens inter-institutional coherence. Both institutions view the Specification as not merely a guide to be followed, but as a binding requirement that incorporates the terms of the contract and delineates the roles of the contracting parties. This method is designed to provide both legal certainty and uniform application by demanding a systematic interpretation of the documents in case of technical disputes. Besides, ascertainment of dispute between the contracting parties is founded not merely on technical proof but also adherence to contractual agreements and general system coherence; in this case, the assessment process is done on the grounds of 'legitimate demand' and not merely on 'work done'. This practice enhances the doctrine of contractual fidelity between the administrative organization and the contractor. Both decisions dismissed the claim against the project description of the work on technical grounds, i.e., while the Court of Cassation decision states that 'if there is a generator in the application project, this work is within the scope of the contract', the DHTB decision states that 'material transported in the works described in the bored piling exposure is covered in the contract price'. When assessing the contractor's requests, both institutions consider not only the fact of completion of the work but also its conformity with the requirements established in the contract and technical documentation; moreover, they give contextual and document-based explanations for the rejection of requests outside the contractual agreement.

This methodology holds significant importance for safeguarding both legal integrity and technical rigor. Despite their specific natures, it can be claimed that the Court of Cassation and DHTB judgments share a common framework, especially concerning contractual interpretation, conformity with technical documentation, and enforcing normative texts; such a framework is fundamental to ensuring the consistency of the legal and technical framework in public projects. This common knowledge works towards a more equitable resolution of disputes and an explicit definition of the boundaries regarding the rights and responsibilities of stakeholders in the industry.

DHTB is a specialized organization that has been in operation since 1927 and has a high level of institutional experience in the settlement of technical disputes regarding public works. The Board's evolution over time reveals that, drawing on its expertise developed over the years, it has transcended its original role of providing technical advice to contracting authorities. Remarkably, the addition of Article 2 to the Public Procurement Contracts Law No. 4735 by Article 31 of Law No. 7221, which entered into force on February 14, 2020, paved the way for both the contracting authority and the contractors to make applications to the DHTB. This amendment has reshaped the DHTB, shaping it from a traditional administrative advisory committee into an efficient first-instance mechanism for dispute resolution, facilitating the impartial, technical, and speedy resolution of disputes occurring in construction works. The ability to conduct examinations within a considerably shorter time and at a lesser expense than the judicial process enhances the possibility of the DHTB to get involved at an early phase, thereby safeguarding public administrations and contractors from lengthy and expensive litigation. In this regard, the DHTB is a solutions platform that balances the stakeholders, is founded on technical competency, and aligns with the legal framework.

In the present research, the case analysis approach has been applied in order to examine critically the contextual variables, rational reasoning, and decision-making processes that support the judgments of the Court of Cassation and DHTB. Due to the ability of case analysis to allow an in-depth exploration of each case in its specific context, it has been possible to conduct a comprehensive comparison of decision texts with both procedural and substantive elements. Yet, while the case analysis approach is beneficial insofar as it affords detailed qualitative data, it is worth noting that the research findings may be restricted in terms of their generalizability. Thus, conclusions drawn will be regarded as applicable to specific contexts, and interpretations arrived at will be envisioned in terms of applicability only to the qualities of the two judgments examined and to analogous controversies involving construction contracts. This limitation is embraced within the methodological rigor of the study, in light of a recognition that findings are not directly applicable to more comprehensive judicial processes.

4. Conclusions

The current study aimed to make a comparative examination of the interpretative approaches taken by the Court of Cassation and DHTB in two construction dispute cases arising out of public works contracts that were lump-sum turnkey agreement-based in Türkiye. The present study makes a new contribution in examining the impacts of the 2020 amendment of the regulations that allowed contractors to apply directly to the DHTB as a right, on dispute resolution processes.

The results indicated that despite variations in institutional and jurisdictional frameworks, the two institutions employed the same interpretative approaches in addressing technical disputes. The convergence witnessed is a sign of harmonization among the rational frameworks employed in judicial and administrative decision-making in public building disputes in Türkiye. Specifically, following the establishment of the contractor's right to make direct applications, the DHTB has begun to work as an effective alternative dispute settlement process at the early stages. As such, DHTB provides a technically viable solution platform for the speedy, economic, and preservation-of-continuity resolution of disputes without resorting to formal judicial process. In addition, the DHTB process eliminates the lengthy timetables, cumbersome bureaucratic red tape, and prohibitive expense usually involved in litigation before the Court of Cassation, and thus presents disputing parties with an alternative method that is more feasible and accessible for conflict resolution.

Further research is suggested to enhance the examination of DHTB decisions using larger samples and both quantitative and qualitative methods. Further research is also needed to quantify the effect of contractor applications on settlement rates, the decrease in litigation frequency, and the overall effect of DHTB decisions on dispute resolution culture in the construction sector.

Acknowledgements

This work was supported by the Scientific and Technological Research Council of Turkiye (TUBITAK) through 1002 - B Emergency Support Module under grant 224K720.

Data availability

Data will be made available on reasonable request.

References

Arditi, D., Oksay, F.E., & Tokdemir, O.B. (1998). Predicting the outcome of construction litigation using Neural Networks. *Computer-Aided Civil and Infrastructure Engineering, 13*(2), 75-81. https://doi.org/10.1111/0885-9507.00087

Arditi, D., & Tokdemir, O.B. (1999). Using case-based reasoning to predict the outcome of construction litigation. *Computer-Aided Civil and Infrastructure Engineering, 14*(6), 385-393. https://doi.org/10.1111/0885-9507.00157

Assaf, S.A., & Al-Hejji, S. (2006). Causes of delay in large construction projects. *International Journal of Project Management, 24*(4), 349-357. https://doi.org/10.1016/j.ijproman.2005.11.010

Baron, A., & McNeal, K. (2019). *Case study methodology in higher education*. Information Science Reference.

Chaphalkar, N.B., Iyer, K.C., & Patil, S.K. (2015). Prediction of outcome of construction dispute claims using multilayer perceptron neural network model. *International Journal of Project Management, 33*(8), 1827-1835. https://doi.org/10.1016/j.ijproman.2015.09.002

Cheung, S.-O., Suen, H.C. H., & Lam, T.-I. (2002). Fundamentals of alternative dispute resolution processes in construction. *Journal of Construction Engineering and Management, 128*(5), 409-417. https://doi.org/10.1061/(ASCE)0733-9364(2002)128:5(409)

Fenn, P., Lowe, D., & Speck, C. (1997). Conflict and dispute in construction. *Construction Management and Economics, 15*(6), 513-518. https://doi.org/10.1080/014461997372719

Hemanth Sai Kalyan, B., Sekar, A., Sindhu Nachiar, S., & Ravichandran, P.T. (2022). Discerning recurrent factors in construction disputes through judicial case studies—An Indian perspective. *Buildings, 12*(12), 2229. https://www.mdpi.com/2075-5309/12/12/2229

Kalogeraki, M., & Antoniou, F. (2024). *Claim Management and Dispute Resolution in the Construction Industry: Current Research Trends Using Novel Technologies*. https://doi.org/10.20944/preprints202401.1195.v1

Koushki, P.A., Al-Rashid, K., & Kartam, N. (2005). Delays and cost increases in the construction of private residential projects in Kuwait. *Construction Management and Economics, 23*(3), 285-294. https://doi.org/10.1080/0144619042000326710

Kumaraswamy, M.M. (1997). Conflicts, claims and disputes in construction. *Engineering, Construction and Architectural Management, 4*(2), 95-111. https://doi.org/10.1108/eb021042

Mahfouz, T., & Kandil, A. (2012). Litigation outcome prediction of differing site condition disputes through machine learning models. *Journal of Computing in Civil Engineering, 26*, 298-308. https://doi.org/10.1061/(ASCE)CP.1943-5487.0000148

Miles-Keogh, R. (2015). Complexity, representation and practice: Case study as method and methodology. *Issues in Educational Research, 25*.

Mitkus, S., & Mitkus, T. (2014). Causes of conflicts in a construction industry: A communicational approach. *Procedia - Social and Behavioral Sciences, 110*, 777-786. https://doi.org/10.1016/j.sbspro.2013.12.922

Sarı, M., Bayram, S., & Aydemir, E. (2025). When defendants speak: Quantifying the predictive value of defence arguments in construction litigation. *Journal of Construction Engineering, Management & Innovation (JCEMI), 8*(1), 64-88. https://doi.org/10.31462/jcemi.2025.01064088

Sarı, M., Bayram, S., & Aydemir, E. (2024). Construction-related disputes: A comprehensive bibliometric investigation. In: *Proceedings of 8th International Project and Construction Management Conference (IPCMC 2024),* İstanbul.

Sarı, M., Sayın, B., & Akçay, C. (2021, 08/19). Classification and resolution procedure for disputes in public construction projects. *Revista de la Construcción. Journal of Construction, 20*(2), 259-276. https://doi.org/10.7764/RDLC.20.2.259

Sweis, G., Sweis, R., Abu Hammad, A., & Shboul, A. (2008). Delays in construction projects: The case of Jordan. *International Journal of Project Management, 26*(6), 665-674. https://doi.org/10.1016/j.ijproman.2007.09.009

Yates, J.K., & Epstein, A. (2006). Avoiding and minimizing construction delay claim disputes in relational contracting. *Journal of Professional Issues in Engineering Education and Practice, 132*(2), 168-179. https://doi.org/10.1061/(ASCE)1052-3928(2006)132:2(168)

Zheng, X., Liu, Y., Jiang, J., Thomas, L.M., Su, N. (2021). Predicting the litigation outcome of PPP project disputes between public authority and private partner using an ensemble model. *Journal of Business Economics and Management, 22*, 320-345. https://doi.org/10.3846/jbem.2021.13219

4th International Civil Engineering & Architecture Conference
17-19 May 2025, Trabzon, Türkiye

Different stakeholders in construction and public works knowledge of Building Information Modeling for construction in Morocco

F. Jehhad[*1], F. El Khannoussi[1], B. El Yamouni[3], L. Bounab[1]

[1*] *Research team AMSCG, Laboratory ICST, National School of Applied Sciences at Tetouan, Abdelmalek Essaadi University, Tetouan, Morocco*
[3] *Research team 3M, Laboratory ICST, National School of Applied Sciences at Tetouan, Abdelmalek Essaadi University Tetouan, Morocco*

Abstract. In developing countries, the construction industry plays a crucial role in economic growth but faces significant challenges, including inefficiency, poor working conditions, low quality, and frequent accidents. In recent years, Building Information Modeling (BIM) has emerged as a powerful tool to improve efficiency, productivity, and coordination in construction projects. Despite its proven benefits and widespread adoption in developed nations, the uptake of BIM in Morocco has been limited, primarily restricted to specific stages like design and surveying in a few major projects. This study aims to explore the current state of BIM adoption in the Moroccan construction industry by examining the knowledge, experiences, and attitudes of various stakeholders, including architects, engineers, project managers, and technicians. A comprehensive survey was conducted using Google Forms, targeting a diverse group of professionals across different age groups and professional backgrounds. The findings reveal a mixed level of familiarity with BIM, with a significant portion of respondents acknowledging its potential benefits but also highlighting challenges such as resistance to change, lack of awareness, and high implementation costs. The study identifies key barriers to BIM adoption and underscores the need for targeted education, training, and investment to foster wider acceptance of BIM practices. By addressing these challenges, the Moroccan construction industry can leverage BIM to enhance project management, reduce costs, and improve overall quality and safety in construction projects. The insights from this study provide guidance for policymakers, educators, and industry leaders to promote BIM integration and maximize its benefits in the Moroccan context.

Keywords: Building information modeling (BIM), Civil engineering; Construction industry; Morocco; Project management efficiency

1. Introduction

According to the World Bank, there are 135 middle- and low-income economies classified as developing countries. These nations experience significant knowledge gaps and are marked by infrequent and limited technological innovation. Within these developing countries, the construction industry remains labor-intensive (World Bank, 2015a; 2015b; 2015c). Various challenges in construction within developing countries result in delays, substandard site environments, poor working conditions, low quality, and frequent accidents. The inefficiency in this sector highlights a significant opportunity for development. As construction can optimize the use of human and material resources, it is often regarded as a key driver for economic growth and achieving development objectives (Latiffi et al., 2013) and (Giang & Pheng, 2011).

Similar to other industries, construction companies leverage a variety of information and communication technology (ICT) solutions to enhance project delivery. Research indicates that the integration of ICT applications can significantly increase the efficiency and productivity of construction projects (Latiffi et al., 2013). One notable ICT application is Building Information Modeling (BIM). Invented in the 1970s by Professor Charles M. Eastman, BIM is based on a procedure that organizes all task information. It has become a practice, and even a requirement, in many countries across different continents. BIM is a strategy in construction aimed at improving productivity and profitability through the use of various collaborative tools. It provides a universal platform for working consistently and collaboratively (Idrissi Gartoumi et al., 2021). Traditionally, checking, controlling, and rectifying

[*] Corresponding author, E-mail: fahd.jehhad@etu.uae.ac.ma

https://doi.org/10.31462/icearc2025_ce_mng_700

discrepancies has been a time-consuming process. BIM addresses this by offering an information-rich design in the form of mock-ups that can be automatically updated (Czmoch & Pękala, 2014). It begins at the design phase and serves as a foundational information resource throughout construction and project supervision, encompassing time, budget, facility management, and environmental considerations (Montiel-Santiagoet al., 2020) and (Cheng et al., 2016). Although originally developed for the building industry, BIM has successfully penetrated various sectors of the construction industry, making a positive impact throughout the life cycle of infrastructure projects. BIM has gained significant traction, proving its value on numerous real-world projects. During the COVID-19 pandemic, BIM played an important role in global efforts to enhance hospital infrastructure. However, its adoption in Morocco remains limited. In practice, the implementation of BIM in Morocco has been slow. BIM is primarily used in a few major projects and is often confined to specific stages like design and surveying. Therefore, the aim of this study is to explore the knowledge and adoption of BIM among different stakeholders in construction and public works in Morocco. The perspectives and experiences of various professionals will be examined, including architects, BIM managers, project managers, construction directors, construction engineers, civil engineers, and technicians, across different age groups. This study seeks to understand the current state of BIM implementation, identify barriers, and highlight opportunities for enhancing BIM adoption in the Moroccan construction industry.

2. Materials and methods

To investigate the knowledge and adoption of Building Information Modeling among various stakeholders in the Moroccan construction industry, a comprehensive questionnaire was developed and administered via Google Forms. This approach facilitates efficient data collection while leveraging modern technological solutions. The questionnaire is structured into six sections, each designed to capture insights from professionals in the field, including engineers, architects, surveyors, and other relevant roles. Below is a detailed description of each section: Section 1 concerned demographics, aiming to gather basic demographic information to contextualize the responses. It includes gender to understand gender representation among respondents, age to analyze trends and attitudes across different age groups, profession to identify the professional backgrounds of participants, allowing for a comparative analysis of BIM knowledge and adoption among different roles. Sections 2-5 concerned respectively the knowledge of BIM to assesses the familiarity and experience of respondents with BIM in section 2, project management practices in section 3 to explore the effectiveness of project management within the Moroccan construction sector, Section 4 examines perceptions of BIM's potential benefits, it also addresses barriers and potential benefits associated with BIM implementation and the last section is for open-ended comments allowing respondents to share any further thoughts or insights not captured in previous sections, providing qualitative data that enriches our analysis (Table. 1).

Table 1. Overview of each section and its corresponding subsections, along with their purposes

Section	Subsection	Description
Demographics	Gender	Collecting information on the gender of respondents to analyze representation.
	Age	Gathering age data to explore trends and attitudes across different age groups.
	Profession	Identifying professional backgrounds to compare BIM knowledge among various roles.
Knowledge of Building Information Modeling	Familiarity	Assessing how familiar respondents are with BIM on a scale.
	Experience	Determining if participants have worked on projects utilizing BIM.
Project management practices	Effectiveness	Evaluating the effectiveness of project management practices in the Moroccan construction sector.
	Use of digital tools	Investigating the frequency of digital tool usage in construction projects.
Optimization of coordination and communication with BIM	Coordination	Assessing beliefs about BIM's ability to enhance project coordination.
	Communication	Exploring how BIM can improve communication among project stakeholders.
	Challenges	Identifying key challenges faced regarding BIM adoption in the construction industry.
	Opportunities	Highlighting perceived opportunities that BIM offers for the industry.
Additional Comments		Providing an open-ended space for respondents to share further insights or thoughts.

3. Results

To account for the diversity in construction professionals, the questionnaire included an assessment of the distribution of respondents by both their professional profiles (Table. 2) and gender (Fig. 1). There was a noticeable gender imbalance among participants, with 74.3% being male and 26.7% female. This disparity reflects the ongoing gender imbalance in the Moroccan engineering sector, where approximately 42% of engineers are women and 58% are men. The age range of participants varied significantly, from 20 to 66 years old, with an average age of 30.6 years. Upon examining the demographic characteristics of the participants, also their familiarity with BIM technology was analyzed, as shown in Table. 1 of the Materials and Methods section. The findings indicate varying levels of familiarity with BIM among respondents: 40% reported being very familiar with using BIM in the context of construction projects, 20% were somewhat familiar, 11.4% were quite unfamiliar, and 5.7% were very unfamiliar, with the remaining respondents expressing a neutral stance. Additionally, 62.9% of the participants used BIM in at least one construction project, while 37.1% had not, underscoring the growing need for wider adoption of this technology in the industry (Fig. 2). These results highlight an increasing trend in the adoption of BIM across different construction project profiles, as depicted in Fig. 2. The data suggest that while there is a significant portion of professionals who are well-versed in BIM, a substantial number still lack familiarity, indicating an opportunity for further education and training to enhance the effective implementation of BIM practices across the Moroccan construction sector.

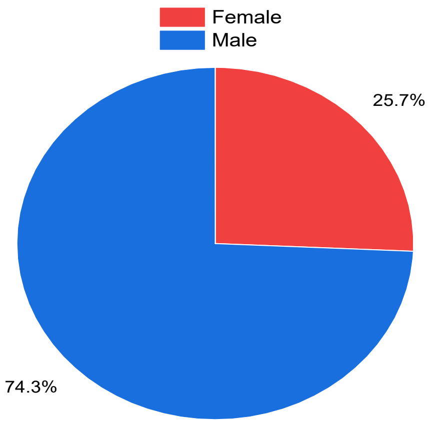

Fig 1. Sexe distribution of this study's participants in Morocco

Table 2. Different professions of participants in the present study

Profession	Count	Percentage (%)
Technician	5	14.29
Civil Engineer	10	28.57
Architecture	8	22.86
Topographical engineer	5	14.29
Project director	7	20%

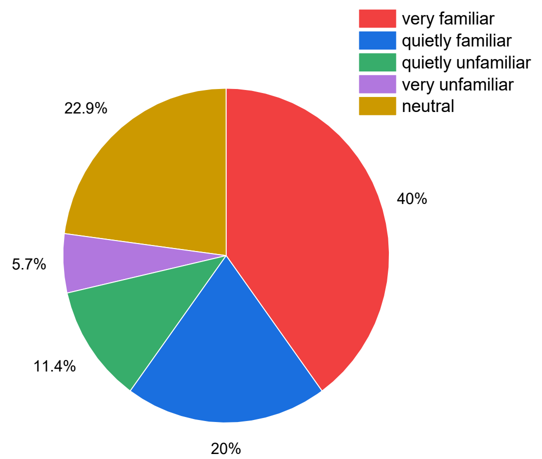

Fig 2. Familiarity rate distribution of BIM knowledge across different age, sex and profiles

To evaluate the extent of BIM management practices in the Moroccan construction industry, a question designed to determine the perceived effectiveness of BIM's usage was included. The responses indicated that approximately 74.3% of participants were satisfied, reporting that BIM was either "very effective" or "effective" in enhancing their overall project outcomes. In contrast, the remaining participants were either neutral, lacking sufficient knowledge to judge its effectiveness, or considered it ineffective. These results are further supported by the fact that over 70% of respondents reported using digital tools, such as project management software and applications, within their construction projects, whereas the rest relied solely on conventional methods. Even among those with limited knowledge of BIM, there was a consensus that BIM could significantly optimize the coordination process in project planning. Specifically, 51% of respondents highlighted that the most critical role of BIM in project management is facilitating real-time collaboration among various project stakeholders. Additionally, 26% identified the centralization on information as the primary benefit of BIM, while the remaining respondents believed that BIM tools greatly enhance the visualization and tracking of a project's status. When assessing the challenges associated with implementing BIM for project management and optimization, the survey revealed that 46% of participants were primarily concerned about the resistance to transitioning from traditional methods to newer, more optimized approaches. Meanwhile, 29% pointed out a significant lack of awareness regarding the importance of BIM in the Moroccan context. The remaining respondents expressed concerns about technical difficulties and the high costs associated with implementing BIM technology (Table. 3). These findings suggest that while there is a growing recognition of the benefits of BIM in improving project management practices, there are also notable barriers to its widespread adoption, including cultural resistance, inadequate knowledge, and financial constraints. Addressing these challenges through targeted education, training, and strategic investment could further enhance the adoption and effectiveness of BIM in the Moroccan construction industry.

Table 3. BIM effectiveness in optimizing and managing construction projects: insights from different profiles

Parameter	Response	Percentage
Perceived effectiveness of BIM	Very effective/effective	74.3%
	Neutral/No knowledge Not effective	25.7%
Use of digital tools versus conventional methods	Digital tools	70%
	Conventional tools	30%
Perception of BIM benefits	Real time collaboration	51%
	Centralization on information	26%
	Enhancement of visualization and tracking	23%
Challenges in BIM adoption	Resistance to change	46%
	Lack of awareness of BIM benefits	29%
	Technical and implementation costs	25%

4. Discussion

BIM offers more than just improved building modeling, it also enhances the design of infrastructure compared to traditional methods, which were limited to simple lines without detailed properties. With BIM, each element in the design has parameterizable values and interacts with other elements, allowing us to identify and address potential issues before project execution, something that was not possible with conventional approaches (Latiffi et al., 2013). Interoperability and automated electronic data delivery are crucial for maximizing the effectiveness of BIM in project management. Interoperability ensures that different software platforms and tools used across various stages of a project can seamlessly exchange and interpret data. This capability is essential in a BIM environment, where multiple stakeholders, from architects and engineers to contractors and facility managers, need to collaborate and share information in real-time. Automated electronic data delivery further enhances this process by streamlining the flow of information, reducing the likelihood of errors, and ensuring that all team members have access to the most up-to-date data. Together, these features significantly improve coordination, increase efficiency, and help prevent costly mistakes and delays in construction projects (Montiel-Santiago et al., 2020). In the present study, a section of additional comments was added at the end to establish more insights: BIM fundamentally transforms the way construction projects are managed and executed. It offers a centralized model where all project data is stored, facilitating easy access and retrieval of information. This centralized approach allows for better project tracking, enabling early detection of potential issues, which is a significant improvement over traditional methods that lacked this level of integration and detail. The enhanced data management capabilities of BIM are crucial for efficient project execution and are particularly beneficial in managing the complexities of modern construction projects. In addition to better data management, BIM supports project management by providing tools for controlling all technical aspects across different phases of a project's lifecycle. This includes design, construction, and maintenance, ensuring that each phase is well-coordinated and executed efficiently. The integration of BIM into project management practices enables improved planning, resource allocation, and risk management, ultimately leading to projects that are completed on time and within budget. However, the implementation of BIM in Morocco faces several challenges. One significant hurdle is the resistance to upgrading existing workflows and methodologies. This resistance is often rooted in the need for a cultural shift within construction companies, which may be accustomed to traditional, often informal, ways of working. The construction sector in Morocco, still largely characterized by artisanal and informal practices, may find it challenging to adopt the digitalization and organizational changes required for effective BIM implementation. Furthermore, the lack of highly qualified professionals in BIM is another barrier that could hinder its widespread adoption. Without a skilled workforce, the effective use of BIM could be compromised, potentially damaging its reputation and leading to a lack of confidence among senior management in its benefits. This emphasizes the need for comprehensive training and education programs to build the necessary competencies within the industry. Despite these challenges, there are substantial opportunities for BIM to revolutionize the construction industry in Morocco. The introduction of BIM could significantly enhance collaboration among various stakeholders, such as architects, engineers, contractors, and project managers. By facilitating better communication and coordination, BIM reduces errors that often arise from misinterpretations of traditional plans, leading to more efficient and effective project execution. BIM also offers significant advantages in cost and schedule management. Its ability to provide three-dimensional visualization of projects enables early detection of design conflicts and quick resolution of issues, thereby avoiding costly delays and optimizing resource management. This not only improves project timelines but also contributes to cost savings, making projects more economically viable. Furthermore, the adoption of BIM could encourage the standardization of construction processes in Morocco. By promoting common standards for modeling and information exchange, BIM could lead to more consistent and high-quality project outcomes, even when multiple companies are involved. This standardization could be a significant step towards modernizing the Moroccan construction industry.

5. Conclusion

While the adoption of BIM in Morocco presents certain challenges, particularly related to cultural resistance and the need for skilled professionals, the potential benefits are significant. By addressing these challenges through strategic initiatives in training, technology integration, regulatory development, and government support, BIM can lead to more efficient, sustainable, and economically viable construction projects.

To fully leverage the benefits of BIM in Morocco, several strategic actions are recommended. Training and awareness initiatives must be prioritized, investing in comprehensive programs to equip engineers, architects, and project managers with the necessary skills. Furthermore, the integration of BIM with emerging technologies such as the Internet of Things (IoT) and Artificial Intelligence (AI) offers opportunities to enhance project management through real-time monitoring and predictive analytics.

It is equally crucial to establish a regulatory framework that defines specific standards for BIM implementation, ensuring data security, quality consistency, and alignment with international practices. Additionally, promoting the long-term benefits of BIM, such as improved asset lifecycle management, easier maintenance, and greater sustainability, that will foster a deeper and more enduring adoption.

Finally, government involvement is fundamental. By establishing clear legal frameworks and policies, inspired by successful models in Anglo-Saxon countries, public authorities can stimulate the modernization and digitalization of the Moroccan construction sector.

The successful adoption of BIM could thus transform the Moroccan construction industry, aligning it with global standards and practices, and ensuring its competitiveness in the international market.

References

Cheng, J. C., Lu, Q., & Deng, Y. (2016). Analytical review and evaluation of civil information modeling. Automation in Construction, 72, 97–106.

Czmoch, I., & Pękala, A. (2014). Traditional design versus BIM-based design. Procedia Engineering, 91, 210–215.

Giang, D. T., & Pheng, L. S. (2011). Role of construction in economic development: Review of key concepts in the past 40 years. Habitat International, 35(1), 118–125.

Idrissi Gartoumi, K., Aboussaleh, M., & Zaki, S. (2021). Building Information Modelling in Morocco: Quo vadis? [Unpublished manuscript].

Latiffi, A. A., Mohd, S., Kasim, N., & Fathi, M. S. (2013). Building Information Modeling (BIM) application in Malaysian construction industry. International Journal of Construction Engineering and Management, 2(1), 1–6.

Montiel-Santiago, F. J., Hermoso-Orzáez, M. J., & Terrados-Cepeda, J. (2020). Sustainability and energy efficiency: BIM 6D. Study of the BIM methodology applied to hospital buildings. Value of interior lighting and daylight in energy simulation. Sustainability, 12(14), 1–29.

World Bank. (2015a). About development. Retrieved December 15, 2015, from http://web.worldbank.org/WBSITE/EXTERNAL/EXTSITETOOLS/0,,contentMDK:20147486menuPK:344190pagePK:98400piPK:98424theSitePK:95474,00.html

World Bank. (2015b). Country and lending groups. Retrieved December 15, 2015, from http://data.worldbank.org/about/country-and-lending-groups

World Bank. (2015c). How does the World Bank classify countries? Retrieved December 15, 2015, from https://datahelpdesk.worldbank.org/knowledgebase/articles/378834-how-does-the-world-bank-classify-countries

4th International Civil Engineering & Architecture Conference
17-19 May 2025, Trabzon, Türkiye

Sustainability under disaster threat: A LEED-based assessment of Istanbul University Hasdal Campus

Mahmut SARI[*1], Cemil AKÇAY[2]

[1] *Kırşehir Ahi Evran University, Department of Construction, 41100 Kırşehir, Türkiye*
[2] *Istanbu University, Department Of Architecture, 34100 Istanbul, Türkiye*

Abstract. LEED (Leadership in Energy and Environmental Design) certification is a worldwide rating system for green buildings. LEED certification is essential in the architectural design of buildings that aim to reduce environmental impacts and promote energy conservation. LEED-certified buildings benefit the environment and occupants by saving energy. Additionally, green buildings have the answer to issues like global climate change and depletion of energy resources. Therefore, LEED certification has environmental, economic, and social benefits. The application of energy-saving measures at Istanbul University Hasdal Campus is a good example of sustainable construction with increased energy efficiency. Not only do they help the university attain its sustainability objectives, but they also contribute to the development of an environmental awareness in a wider population. The main objective of this study is to examine the compatibility of the energy and sustainability strategies implemented in Istanbul University Hasdal Campus with LEED certification, and to explore how a healthcare campus can be designed in a high-risk seismic city through the lenses of sustainability, energy efficiency, and resilience. More specifically, the study aims to measure the conformity of energy efficiency procedures to LEED requirements. To this end, this research seeks to generate implications for planning more efficient energy management and conservation measures in university campuses. In future research, a more holistic evaluation of sustainability is recommended by incorporating components such as water efficiency, material circularity, and waste management. Comparative analyses involving different certification systems—such as LEED, BREEAM, and WELL—applied to the same healthcare project can reveal their methodological distinctions and practical implications. Additionally, long-term modeling of the environmental and economic impacts of energy infrastructures in public investments, particularly in high-risk urban areas, may support the development of more resilient, inclusive, and cost-effective planning strategies.

Keywords: LEED certification, Energy efficiency, Sustainable buildings, Energy conservation, Disaster-resilient buildings.

---

1. Introduction

Istanbul is situated at the western terminus of the North Anatolian Fault Line and is considered one of the world's megacities with the greatest seismic risk. The city's geographical setting, geological conditions, fast demographic expansion, and unplanned urbanization amplify the threat of earthquake-induced damage (Eraybar et al., 2010). In Parsons (2004) study, the probability of the occurrence of an earthquake of magnitude 7.0 or larger in Istanbul region and the Marmara Sea during 2004-2034 was calculated as 38% based on a time-independent model, whereas the time-dependent model incorporating the effect of stress transfer provided the probability as 53 ± 18%. For Istanbul specifically, this probability was calculated as 41 ± 14% (Parsons, 2004).

Istanbul University is the oldest institution of higher learning in Turkey, dating back to the Sahn-ı Seman Madrasahs established following Mehmed II's conquest of Istanbul in 1453 (Günergün & Kadıoğlu, 2006). The contemporary university creation process was finalized with the founding of Darülfünun in 1900 and the subsequent University Reform of 1933. The university has played a pioneering role in the development of higher medical education and health care in Turkey, and, above all, in the health sector, represented by institutions such as the Istanbul Faculty of Medicine. The current building stock of the university is comprised of a combination of historically significant structures as well as educational and healthcare facilities that were built in the mid-20th century. Earlier research attests that a high proportion of the cultural heritage structures in Istanbul have considerable seismic-related hazards (D'Ayala & Ansal, 2012; D'Ayala et al., 2008). As a result, harmonizing the physical structure of Istanbul University with modern seismic codes has become a vital need for protecting cultural

* Corresponding author, E-mail: mahmutsari@ahievran.edu.tr

https://doi.org/10.31462/icearc2025_ce_mng_702

heritage as well as maintaining institutional services' provision on a continuous basis. The geographical location of the Hasdal Campus of Istanbul University is endowed with serious strategic and locational advantages.
Hasdal is situated on the European side of Istanbul city, close to the TEM Motorway (O-2) corridor, and has a good link to the city center. The developed transport system in the region is a factor that supports the accessibility of the campus in terms of emergency management and logistics activities following disasters. It is reported to have a closed solid waste landfill in the Hasdal region previously, and the region has been subjected to large-scale rehabilitation activities since then (Ozcan et al., 2007). Research has indicated that there has been soil stability in the region and environmental hazards have been significantly reduced. Moreover, the adverse environmental effects have been mitigated through sustainable practices, such as controlled methane gas extraction and energy generation. The mentioned characteristics have played a major role in selecting the Hasdal region as a green and resilient campus area for Istanbul University's education and health services.

The Hasdal site is located on the European side of Istanbul, the northwestern region of the city, and is characterised by having geologically stable ground conditions (Kundak & Handan, 2005). Based on high-resolution seismic hazard studies carried out all over Istanbul, it is explained that the stiffness of the ground is greater in the northern parts - among them Hasdal - than in the southern coastal parts near the Marmara Sea, and thus earthquake waves will be less amplified (Kalkan & Gülkan, 2023). The results indicate that, in comparison to Istanbul's high-risk coastal zones, the Hasdal region demonstrates superior seismic performance characteristics.

Istanbul University Hasdal Campus has been master-planned as part of a strategy to revitalize the current vulnerable building stock and reinforce healthcare infrastructure to mitigate the impact of future catastrophes. Situated in the Hasdal area in the northwestern sector of Istanbul, the campus is known for being close to key roadways, stable ground conditions, and far from active fault lines. It encompasses a series of healthcare facilities, schools, laboratories, emergency response and disaster management spaces, parking, and central energy systems. The project has been designed using a modular and staged planning approach, with the inclusion of sustainable energy technologies like photovoltaic panels and trigeneration system. The main goal of this research is to investigate the campus plan of a medical facility based in a city with severe seismic hazards, with a specific reference to the case of Istanbul University Hasdal Campus. The study will adhere to sustainability, energy efficiency, and resilience guidelines, as well as to confirm the degree to which it conforms to the conditions set by the LEED (Leadership in Energy and Environmental Design) certification scheme.

2. A case study: Istanbul University Hasdal Campus

Istanbul University Hasdal Campus was planned through a phased settlement and construction process (Table 1). The planning of the campus was staged in three principal phases to facilitate uninterrupted healthcare services, enhance operational capacity following a disaster, and to systematically organize the different medical specialties.

- **Blocks A, A1, A2:** Operating theaters, intensive care units, emergency services, and outpatient clinics
- **Block B:** Clinical specialties such as pediatric surgery, ENT, ophthalmology, and general surgery
- **Block C:** Faculty building
- **Blocks H1, H2, and H:** Technical elements, mechanical areas, and medical storage units.
- **Block H Utility Gallery:** Mechanical and electrical infrastructure systems
- **Block I:** Technical and clinical support units
- **Block G:** Main block at a later stage of construction

The next phase includes the opening of more clinical centers specialized in different fields, such as pediatrics, infectious diseases, cardiology, internal medicine, and oncology.

- **Block D:** Infectious Diseases and Childhood Health
- **Block F:** Pulmonary disease, cardiology, internal medicine, oncology
- **Block E:** Faculty building
- **Block J:** Newly established clinical units

Phase three includes state-of-the-art treatment and research centers:

- **Cardiovascular Center:** Evaluation, management, and recovery services for cardiovascular conditions.
- **Oncology Institute:** Research and education in oncology
- **Chronic Diseases and Treatment Center:** Diagnosis and rehabilitation of chronic conditions
- **Proton Therapy Center:** Proton radiation therapy
- **Faculty of Dentistry:** Dental education and clinical practice
- **Nuclear Medicine Unit:** Treatment and diagnostic imaging unit

Table 1. Istanbul University Hasdal Campus Phases, blocks and functional distribution

Phases	Blocks	Functions
PHASE I	**Block A**	Operating Rooms, Intensive Care Units, Laboratories, Emergency Service Units
	Block A1	Outpatient Services, Patient Examination Areas
	Block A2	Outpatient Services, Patient Examination Areas
	Block B	Pediatric Surgery, Otorhinolaryngology (ENT), Ophthalmology, Audiology, General Surgery, Urology, Orthopedics, Thoracic Surgery, Cardiovascular Surgery, Dermatology
	Block C	Faculty Building
	Block H1	Technical Units, Mechanical Areas
	Block H2	Technical Units, Mechanical Areas
	Block H	Medical Storage, Technical Support Areas
	Block H Utility Gallery	Mechanical and Electrical Infrastructure Gallery
	Block I	Clinical Support and Technical Areas
PHASE II	**Block G**	Main Block Under Advanced Construction
	Block D	Pediatric Health, Infectious Diseases, Neurology
	Block F	Pulmonology, Cardiology, Internal Medicine, Oncology, Dermatology, Nephrology
	Block E	Faculty Building
	Block J	New Clinical Units
PHASE III	**Cardiovascular Center**	Cardiovascular Diagnosis, Treatment, and Rehabilitation Center
	Oncology Institute	Oncology Research, Treatment, and Training Center
	Chronic Diseases and Treatment Center	Diagnosis and Rehabilitation Center for Chronic Diseases
	Proton Therapy Center	Proton Therapy Treatment Center
	Faculty of Dentistry	Faculty of Dentistry – Education and Clinical Application Center
	Nuclear Medicine Unit	Diagnostic Imaging and Therapeutic Unit

The first phase covers the main health services units and support infrastructures:

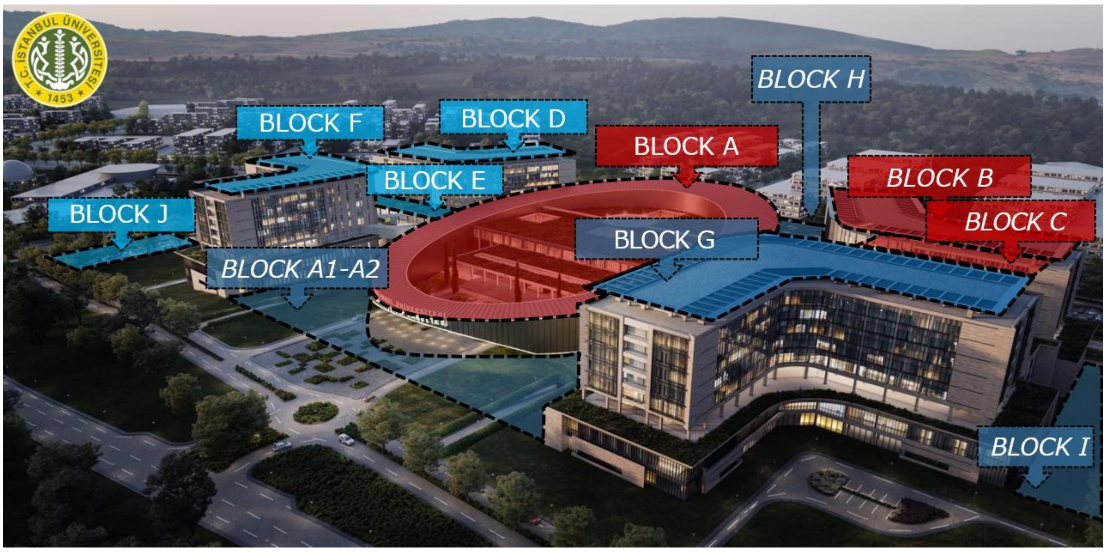

Fig. 1. Layout of Istanbul University Hasdal Campus Blocks

Table 2. Energy infrastructure and project specifications

Category	Description
General Project Information	**Total Area – Phase I:** 451.167 m² **Total Area – Phase II:** 202.344 m² **Total Approximate Area:** 653.511 m² **Total Bed Capacity:** 1.678 beds **Number of Operating Rooms:** 50 **Number of Outpatient Clinics:** 117 **Parking Capacity:** 2.129 vehicles
Photovoltaic Panel Application	A rooftop photovoltaic system with an approximate capacity of 480 kW will be installed on Blocks B, G, F, and D. Each roof will accommodate 210–230 panels, ensuring a minimum production of 120 kW per block. Panels will be south-oriented for optimal solar gain, and no energy storage system is planned. The payback period for the system is estimated at approximately 4.5–5 years.
Trigeneration System	Trigeneration system will be installed in Block H4, supplying electricity, heating, and cooling across the entire campus. The system aims to achieve 30–40% higher energy efficiency compared to conventional systems.
Integrated Energy Strategies	The integrated use of photovoltaic panels and the trigeneration system will reduce carbon emissions and improve energy efficiency across the campus.

This phased and functional structure of the campus reflects Istanbul University's goals of sustainability in health services, expertise-based organisation and high resilience after disasters.

The campus structure aligns with the objectives of healthcare sustainability, organizational structure based on specialization, and high post-disaster resilience by Istanbul University. Istanbul University's Hasdal Campus has been planned with dual consideration for seismic resilience and as a pioneering concept that integrates innovative design principles for sustainability, energy efficiency, and continuity of functioning. This campus goes beyond the traditional campus scheme by aiming to operate as an edifice complex that can facilitate rapid recovery during disasters, acquire a level of energy autonomy, and integrate green technologies for the environment. As a component of the project energy policy, it includes the simultaneous production of electricity, heat, and cold by a trigeneration system, and electricity from solar energy by photovoltaic panels. Project features and campus energy infrastructure are described in Table 2. The campus is built on a total area of 653,511 m² and comprises 1,678 inpatient beds, 50 operating rooms, 117 outpatient clinics, along with parking for 2,129 vehicles (Figure 2).

Fig. 2. Istanbul University Hasdal Campus Construction Site

Fig. 3. Photovoltaic panels and trigeneration system in Istanbul University Hasdal Campus

In accordance with sustainable energy goals, it is suggested that photovoltaic panels be mounted on Blocks B, G, F, and D to a total installed capacity of approximately 480 kW (Figure 3). The installation would comprise around 210-230 panels per block in order to produce a minimum electric output of 120 kW per block. The system is meant to satisfy a major part of the daily electricity requirement directly using the energy from the sun. The solar panels face the south direction to absorb more solar radiation and increase the output energy. The system has no energy storage capacity since the power that will be produced will be used instantly. The payback period for the installation has been estimated at around 4.5 to 5 years. This project is supposed to enhance the environmental sustainability objectives of the campus through carbon emission reduction and additional contribution to energy security during cases of post-disaster scenarios.

With a view to developing energy efficiency and continuous energy supply during crisis periods, trigeneration system is going to be installed in Block H4 (Figure 3). The system will be designed to produce electricity, heat, and cold at the same time. Implementation of trigeneration systems in hospitals results in significant energy conservation and carbon emission savings because of the constant need for electricity, heating, and cooling throughout the year (Ziher & Poredos, 2006). When compared to traditional methods of separate production of energy, trigeneration systems decrease primary energy consumption by a great extent and enhance operational energy efficiency in hospitals. Besides, by providing a solution to the cooling issue, the systems meet the energy profile of the facility throughout the year. Within this system, trigeneration is central to providing energy supply security in the case of emergencies. During normal operations, the system is able to fulfill a significant proportion of campus electricity and HVAC requirements, while during the occurrence of a disaster, it will offer extended energy support for maintaining the provision of health services. Consequently, the trigeneration system will assist Hasdal Campus in realizing its vision of establishing a disaster-resilient campus framework in addition to supporting environmental sustainability by reducing carbon emissions.

3. Discussion

LEED (Leadership in Energy and Environmental Design) is a globally recognized green building certification system that evaluates and rates the design, construction, operation, and maintenance of sustainable buildings(Cole, 2005). The LEED system assesses a building's performance across environmental, social, and economic sustainability metrics under various categories: Sustainable Sites, Water Efficiency, Energy and Atmosphere, Materials and Resources, Indoor Environmental Quality, Innovation, and Regional Priority. Projects earn certification levels based on the number of points achieved in these categories: Certified (40–49 points), Silver (50–59 points), Gold (60–79 points), and Platinum (80+ points). Achieving LEED certification allows buildings to increase energy efficiency, reduce operational costs, minimize environmental impacts, and improve occupant health. Moreover, LEED-certified buildings have been shown to provide economic benefits, including increased market value and higher occupancy rates (Bond & Devine, 2016).

The design and implementation processes of the Istanbul University Hasdal Campus demonstrate strong alignment with the LEED certification framework due to their focus on environmental sustainability and energy efficiency. The strategic development of the campus as a disaster-resilient facility, combined with the integration of a trigeneration system and photovoltaic panels in the energy infrastructure, significantly enhances its potential to score highly in the "Energy and Atmosphere" and "Sustainable Sites" categories.

The geographic location and soil characteristics of the Hasdal region offer advantages in minimizing environmental risk, contributing positively to the "Sustainable Sites" category in LEED evaluations. The campus's modular building system and phased planning strategy support credit acquisition in the "Regional Priority" and "Innovation" categories. Additionally, the design of operational continuity in emergency scenarios—particularly crucial for healthcare services—aligns with LEED's environmental management and resilience criteria.

The photovoltaic panel application directly contributes to the "Energy and Atmosphere" category. With approximately 480 kW of installed capacity and south-facing orientation, these panels are expected to meet a significant portion of the campus's daily energy demand using renewable sources. The planned trigeneration system at the Istanbul University Hasdal Campus also significantly contributes to energy efficiency. It has the potential to substantially reduce primary energy consumption compared to standalone electricity production and separate HVAC systems (Ziher & Poredos, 2006). This energy efficiency supports direct credit acquisition under the "Optimize Energy Performance" and "Fundamental Commissioning and Verification" criteria within the "Energy and Atmosphere" category. Improvements in total energy consumption and operational efficiency are key parameters that can earn high scores under LEED. However, the LEED credits for "Renewable Energy Production" and "Green Power and Carbon Offsets" are specifically tied to the use of fully renewable energy sources. Nonetheless, improvements in energy production efficiency, reductions in carbon emissions, and enhanced energy autonomy at the campus support continued indirect point acquisition under the LEED framework. The trigeneration system offers significant advantages for LEED certification due to its high energy efficiency, reduced carbon emissions, and uninterrupted energy supply during emergencies.

4. Conclusions

The aim of this research was to investigate the use of a healthcare campus plan in a city having high-risk characteristics, specifically the case of the Istanbul University Hasdal Campus. The research sought to align this plan with the concepts of sustainability, energy efficiency, and resilience, as well as how well it adheres to the standards set by the LEED rating system. Case study methodology was used to examine the geographic location of the campus, earthquake-resistant design objectives, phased planning process, and energy systems infrastructure, with the project features assessed based on the benchmarks stipulated by LEED standards.

The results show that Hasdal Campus has a high degree of compliance with the LEED system, specifically in the "Energy and Atmosphere," "Sustainable Sites," and "Innovation" categories. The use of photovoltaic panels, supported by a very efficient trigeneration system, increases the campus's energy efficiency, while the modular planning approach allows for ease in maintaining flexibility and ensuring continuity of operations in the event of post-disaster situations.

Future studies need to strive for in-depth analyses of health care facilities in urban high-risk areas, especially with regard to sustainability criteria; make comparative analyses of various green building rating systems, i.e., LEED, BREEAM, and WELL, applied to the same projects; and simulate long-term environmental and economic effects of energy infrastructure. Furthermore, incorporating sustainability strategies into decision support systems for major public investments with cost-benefit analyses will lead to the further evolution of more inclusive and resilient planning strategies.

5. Acknowledgements

We would like to thank Istanbul University Department of Building Works for their support in obtaining the data used in this study.

References

Bond, S. A., & Devine, A. (2016). Certification matters: Is green talk cheap talk? *The Journal of Real Estate Finance and Economics, 52*(2), 117–140. https://doi.org/10.1007/s11146-015-9499-y

Cole, R. J. (2005). Building environmental assessment methods: Redefining intentions and roles. *Building Research & Information, 33*(5), 455–467. https://doi.org/10.1080/09613210500219063

D'Ayala, D., & Ansal, A. (2012). Non linear push over assessment of heritage buildings in Istanbul to define seismic risk. *Bulletin of Earthquake Engineering, 10*(1), 285–306. https://doi.org/10.1007/s10518-011-9311-1

D'Ayala, D., Carriero, A., Sabbadini, F., Fanciullacci, D., Ozelik, P., Akdogan, M., & Kaya, Y. (2008). Seismic vulnerability and risk assessment of cultural heritage buildings in Istanbul, Turkey. In *14th World Conference on Earthquake Engineering (14th WCEE)*, Beijing.

Eraybar, K., Okazaki, K., & Ilki, A. (2010). An exploratory study on perceptions of seismic risk and mitigation in two districts of Istanbul. *Disasters, 34*(1), 71–92. https://doi.org/10.1111/j.1467-7717.2009.01115.x

Günergün, F., & Kadıoğlu, S. (2006). İstanbul Üniversitesi'nin yerleşim tarihçesi üzerine notlar [Historical notes on Istanbul University and its main campus]. *Osmanlı Bilimi Araştırmaları, 8*(1), 135–163. https://dergipark.org.tr/tr/pub/iuoba/issue/1207/14206

Kalkan, E., & Gülkan, P. (2023). Assessing seismic risk in the built environment of Istanbul: High-resolution hazard mapping and ground motion analysis in the Sea of Marmara region. *Building Engineering, 1*(1), 403–403.

Kundak, S., & Handan, T. (2005). Assessment of seismic risk in Istanbul.

Ozcan, H. K., Nemlioglu, S., Demir, G., Ozbas, E. E., & Borat, M. (2007). Methane emission in landfill gas at two closed waste disposal sites in Istanbul, Turkey.

Parsons, T. (2004). Recalculated probability of M ≥ 7 earthquakes beneath the Sea of Marmara, Turkey. *Journal of Geophysical Research: Solid Earth, 109*(B5). https://doi.org/10.1029/2003JB002667

Ziher, D., & Poredos, A. (2006). Economics of a trigeneration system in a hospital. *Applied Thermal Engineering, 26*(7), 680–687. https://doi.org/10.1016/j.applthermaleng.2005.09.007

4th International Civil Engineering & Architecture Conference
17-19 May 2025, Trabzon, Türkiye

Sketch-to-BIM: A comparative analysis for automated truss design in Dynamo

Feyzullah Yavan*[1], Reza Maalek[1], Atefeh Aali[1]

[1] *Institute of Technology and Management in Construction (TMB), Department of Digital Engineering and Construction (DEC), Gotthard-Franz-Straße 3, 76131 Karlsruhe, Germany*

Abstract. The advent of digital technologies and artificial intelligence has transformed designers' capability and allowed them to reveal their potential to achieve optimal designs. However, in the initial design explorations, many designers, similar to artists, rely on freehand sketches, which must then be converted to digital designs for information modeling, structural analysis, and engineering optimization. Such a fragmented approach results in time inefficiencies, compatibility errors, and a lack of opportunity for design explorations. Thus, to address these challenges, this paper presents an integrated workflow for converting hand-sketched truss designs into digital structural models within building information modeling (BIM)-based software environments, referred to as Sketch-to-BIM (StB). This unified framework employs Dynamo's visual programming capabilities and involves several interconnected stages: (i) exploring different methods available in the open literature (e.g., Harris corner detection, Skeletonization method, Heat map technique, and Deep Learning (DL) techniques) for geometry extraction, which includes node and element recognition from sketches; (ii) converting the identified nodes and elements into parametric designs in Dynamo; and (iii) testing and comparing these sourced methods on the proposed workflow. The results showed that the proposed methodology is successful in solving test problems, and each feature extraction method provides different trade-offs in both execution time and accuracy. Overall, the current manuscript created a valuable foundation for upcoming studies on StB workflow, and the findings can be utilized to discuss and determine the most effective approach based on the use case.

Keywords: Computer vision; Deep learning; Dynamo; Feature extraction; Image processing

1. Introduction

Current industry practices typically involve: (i) manual creation of structural models in Computer-Aided Design (CAD) software; (ii) separate optimization tools, which are usually coded as part of the research, for sizing, shape, and topology optimization; (iii) Finite Element Method (FEM) analysis software like Robot Structural Analysis (RSA) for final validation; and (iv) iterative refinement through multiple software platforms. Multiple research studies were proposed to enhance this workflow. In this regards, scholars have developed a parametric modeling framework through Dynamo and RSA for FEM analysis within Visual Programming (VP) environment for model creation and optimization to enhance structural design and optimization workflow. This line of research was also followed with employing Python libraries and RSA Application Programming Interface (API) for FEM analysis to further enhance proposed workflow with different constraint conditions such as reliability of structure and different Metaheuristic Algorithms (MAs) (Yavan, Maalek, & Maalek, 2024; Yavan, Maalek, & Toğan, 2024; Yavan & Maalek, 2025). However, while these methods improved the engineering design process compared to textual programming (e.g., Python, C#, etc.) and manual methods, parametric modeling in a VP environment is very demanding in terms of technical expertise and possesses a steep learning curve. In this respect, while VP tools such as Dynamo can enhance and ease the engineering design process by automating structural model complexities, the designer must obtain strong programming skills in addition to their civil engineering background in order to effectively employ them (Kossakowski, 2023). On the other hand, the integration of automation to find the optimal design rather than a good enough option is essential to create cost-effective and structurally efficient models (Kubicki et al., 2018). In response to these challenges, this study focuses on developing the structural model from hand-drawn sketches. This approach eliminates the necessity for parametric modeling in VP, textual programming-based modeling, and even manual modeling, which is time-consuming and prone to error (Joffe et al., 2024). Recent studies have focused on innovative methods to convert hand-drawn sketches into structurally analysed models. In the referenced study (Joffe et al., 2024), a computer vision-based framework that enables the

* Corresponding author, E-mail: feyzullah.yavan@kit.edu

https://doi.org/10.31462/icearc2025_ce_mng_736

automatic conversion of hand-drawn beam diagram sketches was introduced. In their study, the YOLOv5 (You Only Look Once) (Redmon et al., 2016) was used to detect objects such as beams, supports, and the loads with 99.1% mean average precision. The numerical values were determined using a Deep Learning (DL) model with 99.0% accuracy, and after determining the relationships between the elements with Multi Layer Perceptrons (MLPs) (Rosenblatt, 1957) with 95.1% to 99.5% accuracy, the structural analysis was performed using OpenSees (Mckenna et al., 2010). Their system could correctly analyse 45% of test images entirely and 55% partially.

In a separate study, (Hutchinson et al., 2007) introduced 2DSketchFEA, an innovative sketch-based tool for two-dimensional Finite Element Analysis (FEA). This system enabled users to draw structural models by using conventional engineering symbols directly. Their system integrates sketch recognition, geometric meshing, FEA, and result visualization within a single sketch-based interface, without the need to use traditional command-line or menu-driven modeling environments, and is easy to use by those with minimal CAD or FEA experience. In a similar study, (Jeong et al., 2024) proposed a way to automate the conversion of sketch-based architectural data to BIM models using ResUnet (Z. Zhang et al., 2018), which is a DL-based sketch recognition model to distinguish architectural sketches from redundant data. This data was eventually converted to a BIM model using Autodesk Revit and Dynamo for automated model creation. In another study, (Peschel & Hammond, 2008) introduced STRAT (A Sketched-Truss Recognition and Analysis Tool), which could find all the unknown forces in a truss and avoid the complexity and time-consuming process of performing manual calculations or using CAD-based software for structural analysis. In their study, full truss recognition was done with an accuracy of 70%. Other scholars have also worked on the interpretation and conversion of sketches into digital representations (Ahmed et al., 2014; Aoki et al., 1996; de Klerk et al., 2019; C. Li et al., 2022; Weber et al., 2010).

Despite the previous work on the structural analysis of models converted from sketch to digital model, there is still a need to extend this approach to other systems, such as trusses. For this purpose, this paper performs a comparative analysis of the success rates of 4 different methods, namely the Harris corner detection algorithm (Harris & Stephens, 1998), Skeletonization method (T. Y. Zhang & Suen, 1984), Heat map technique (Cheng & Schwartzman, 2017), and DL techniques with YOLO (Redmon et al., 2016), in sketch recognition and digital model conversion. Numerous industries have made extensive use of these techniques for various objectives. Harris corner detection finds corners and feature points in a sketch by detecting variations in intensity. In the literature, this method has been applied for tasks such as image restoration in occluded environments (Dong & Liu, 2013) and human activity recognition (Babiker et al., 2017). In the skeletonization process, binary shapes are converted into simplified lines, or so-called skeletons. This technique has been applied in a variety of fields, including skeleton-based morphing between sketching images (Tan, 2010) and the retrieval of 3D objects from sketch inputs (X. Zhao et al., 2019). The Heat map approach is used in computer vision to determine the possible location or a part of an object. This technique has been applied in the literature for doing tasks like analyzing the accuracy of human sketches (Thibhodee & Viyanon, 2021) and even in the medical sciences to evaluate the fidelity of compressed Computed Tomography (CT) scans (Lee et al., 2011). YOLO is a DL method to analyse and extract structural relationships in images. Scholars have employed different versions of YOLOs for tasks such as image and color recognition (X. Zhang et al., 2018), facial mask detection during COVID-19 (Loey et al., 2021), and multivehicle detection (Diwan et al., 2023; X. Li et al., 2018). To achieve better outcomes, several researchers have also combined some of these techniques. For instance, (Wang et al., 2022) combined Harris corner detection method and an improved version of YOLO, namely YOLOX (Ge et al., 2021), for camera calibration.

The significance of this study lies in providing a comparative analysis of the methods available in open literature for feature extraction and addressing the gap in the current structural design workflow by suggesting a fully integrated pipeline that is capable of converting hand-sketched truss designs to digital models in a BIM environment. This approach eliminates the necessity for manual and parametric modeling and advanced technical knowledge on software platforms. It also makes the traditional time-consuming design and analysis workflow more efficient with Dynamo; hence, this study not only enhances automated geometry extraction but also provides a scalable and intuitive framework that can improve creativity and productivity in architectural and structural engineering designs.

2. Methodology

For the present study, a Dynamo workflow presented in
Fig. 1 was prepared, and a comparative analysis of different feature extraction methodologies, namely Harris corner detection, Skeletonization method, Heat map technique, and DL technique, was performed for the Sketch-to-BIM (StB) concept. The problem was approached through two different methods: (i) generating more artistic sketches without any pre-specification and letting the algorithms understand the connection points for Group 1 examples; (ii) marking the nodes in sketches to ease feature extraction for Group 2 examples shown in Fig. 2. For this purpose, two different test examples were prepared, as one group was identical to the other, with connection points specified by round ball-like drawings, as presented in the Experimental Design section.

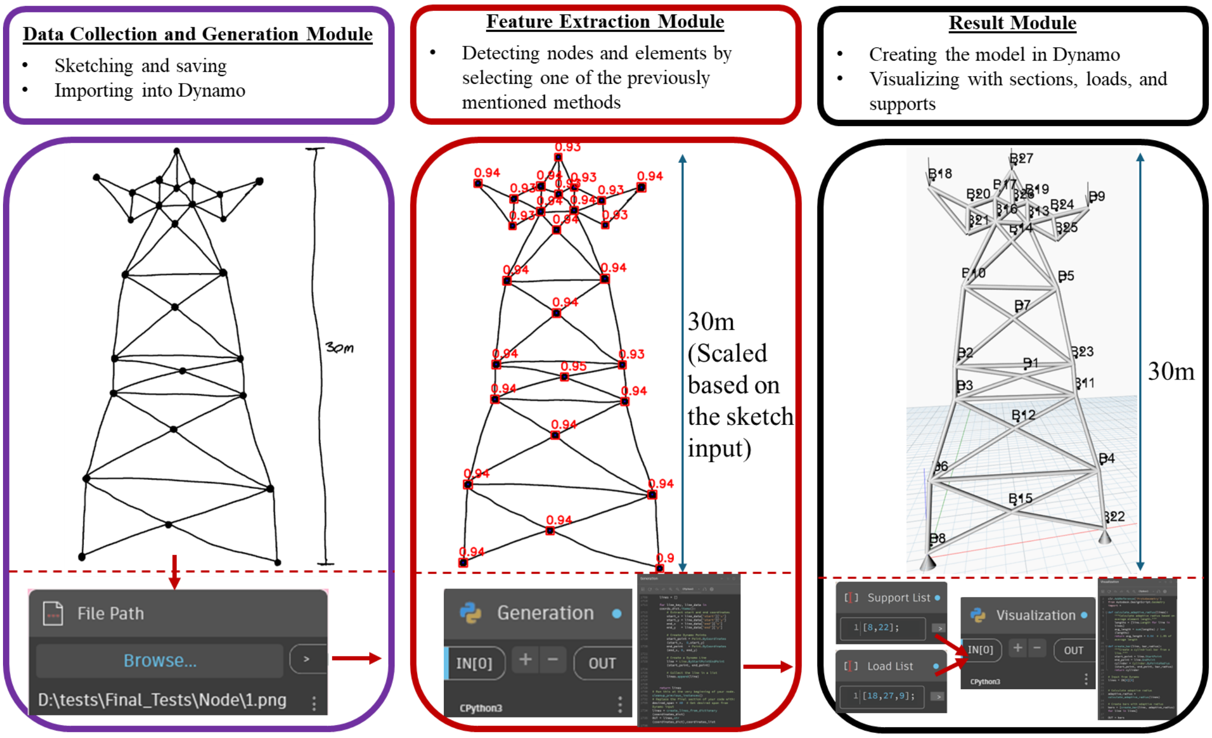

Fig. 1. The Sketch-to-BIM process is divided into sections as importing hand-drawn sketches to Dynamo, extracting geometric features, and displaying visualization outcomes.

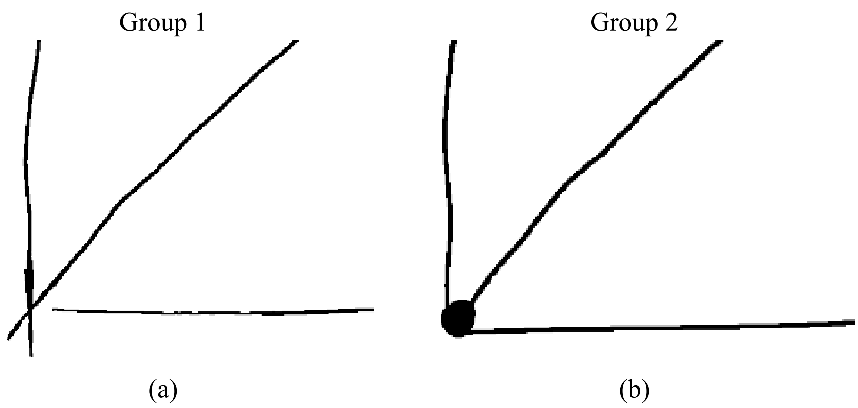

Fig. 2. The two different test examples: (a) Test example without node specification (example from Group 1); (b) Test example with node specification (example from Group 2).

2.1. Feature extraction

In the proposed method, the connection points, i.e., nodes in the present truss example, were first extracted from sketches. To achieve this, previously mentioned 4 different methods were employed, and the outcomes were presented in the Results section. For feature extraction, a common first step is to convert the input image into grayscale and then into a binary image. In our use case, this translates into the truss elements, drawn as lines, separating from a contrasting background. This preprocessing stage includes: (i) convolving the image with a kernel that gives more weight to central pixels, effectively blurring the image slightly to diminish noise (Mafi et al., 2019); (ii) median filter which uses a 5x5 window size utilized for removing salt-and-pepper noise (Justusson, 2006); (iii) enhancing the contrast through adaptive histogram equalization; and (iv) image binarization using the global Otsu's thresholding method (Otsu, 1979) for small object removal, which is basically based on labeling the components and then discarding those whose area (pixel count) is below a given threshold (Haralick & Shapiro, 1985), and morphological operations such as dilation and closing (Soille, 1999). Following image preprocessing, the subsequent steps included node detection, which will be explained thoroughly in the upcoming section, and clustering. Given that multiple connection points may be identified due to drawing artifacts, such as discontinuity, a process to segment these connection points into one node was necessary. To this end, the unsupervised clustering method, Density-Based Spatial Clustering of Applications with Noise (DBSCAN), was employed, which does not require specifying the number of clusters in advance, can find clusters of arbitrary shapes, is robust to noise, and can identify outliers (Schubert et al., 2017). The clustering process took place with epsilon (eps): 50 parameters. Then, cluster centers using the mean position of points within each cluster were computed, and cluster weights based on the number of points in each cluster were determined.

2.1.1. Harris corner detection

The first considered method for feature extraction is the classical Harris corner detection, which is implemented using the OpenCV library (OpenCV: Harris Corner Detection; Ye et al., 2009) and "cv2.goodFeaturesToTrack" function. It is used to locate potential corners based on parameters such as quality level, minimum distance, block size, etc. The script marks each detected corner on a copy of the original image for visualization. Next, circles representing nodes are drawn around each cluster center, with the radius scaled by the cluster weight to emphasize clusters with more detections, as presented in
Fig. 3b.

2.1.2. Skeletonization method

This method is mainly designed for the Group 1 examples shown in Fig. 2a to be able to detect the nodes, even though the node in the sketch is not clear. To detect nodes and lines from the hand sketch image, the skeletonization technique from "scikit-image" was employed by converting the image to a one-pixel-wide representation while preserving the overall structure of the drawing, and then analyzing the local connectivity of each pixel in that skeleton. Specifically, a small neighbor kernel is convolved over the skeleton, yielding a numerical score that indicates how many neighboring pixels are also part of the skeleton. Pixels with a connectivity value exceeding a certain threshold are labeled as branch points, and those with a specific connectivity count are labeled as endpoints, similar to the referenced study (Aastrup Olsen et al., 2011), in which the same method was employed for detecting end and intersection points in vascular/vein images . This combined skeleton-based approach gives closely spaced branch/endpoints as a single "node," shown in
Fig. 3c.

2.1.3. Heat map detection

The third method is a simpler version of the second approach, where skeletonization is not needed while using similar principles with the Harris method, and is specifically designed for Group 2 examples, where nodes are specified with round drawings that clearly state where the nodes are. This approach utilizes pixel density analysis and peak detection, as presented in
Fig. 3e, to identify regions of high pixel concentration in images, and the methodology employs the same principles explained in (Zhao et al., 2022) by using density map generation and peak detection. For density map generation, a zero-initialized array matching the input image dimensions is created, and binary pixels of interest are mapped to value one in their corresponding positions. Then, Gaussian smoothing is applied with a controllable sigma parameter. The smoothing operation creates a continuous density field around pixel clusters. Consequently, the density map is normalized to the range [0,1] using min-max normalization, which ensures consistent interpretation of density values across different images. The final stage involves identifying and visualizing regions of high pixel density by detecting the local maxima, using the "peak_local_max" algorithm from the "skimage.feature" library with parameters such as minimum distance between peaks, absolute threshold, etc. For visualization, the original image was displayed alongside the density heatmap and detected peaks marked with blue circles. The methodology provides a robust approach for identifying regions of high pixel concentration, which are nodes in this scenario.

2.1.4. Deep learning technique

This method combines DL based node detection techniques to analyze and extract structural relationships (nodes) in images. The system employs a YOLOv8n DL model for initial node detection, implementing a sliding window with 416×416 pixels and a 75% overlapping ratio between adjacent windows, showing the detections with over 50% confidence, which can be found in
Fig. 3d. Since creating annotated datasets for computer vision tasks typically involves extensive manual effort, for training the model, a synthetic dataset generator of graph-like structures with varying visual styles, presented in
Fig. 3d, was created. The step-by-step process includes: (i) initialization by setting parameters such as image size and node box size; (ii) shape generation by automatically creating predefined shapes (regular, X, T, V, star); (iii) node validation by computing intersection angles and annotating valid nodes; (iv) realism enhancement by applying waviness, noise, and thickness variations to the lines; (v) annotation by converting node positions into YOLO annotations, then saving images and labels; and (vi) visualization by randomly selecting samples for visual quality assurance. The system implements a multi-style generation approach with configurable parameters for visual variation and structural diversity. The generated data has 416×416 pixels for image resolution and consists of PNG images. Each image contains 4 to 8 nodes, placed using a grid-based distribution with a minimum separation of 80% of the cell size and margins preserved at twice the maximum node size. Connectivity is

guaranteed through the generation of a spanning tree, with additional random edges added to meet a minimum of four connections per image. Node placement is validated based on distance to prevent overlap. Post-processing steps include style-specific adjustments such as adding random noise and applying a Gaussian blur with style-dependent sigma values to enhance the natural appearance of the images. Also, the most common connection types, such as K, X, T, V, etc., were separately created and added to the sample group to ease the detection process, as presented in
Fig. 3d. In total, 21,000 images with corresponding annotations in YOLO format were generated to train the DL model.

2.2. Path analysis and line extraction

The system implements a path-finding and analysis approach by identifying intersection points between skeleton lines and cluster boundaries found by the previously mentioned methods. Then the algorithm traces skeleton paths and labels connected regions in the skeletonized image, presented in
Fig. 3a, where pixels are connected to clusters while validating paths for intersection with other clusters and preventing redundant path detection between cluster pairs. Each labeled component represents a continuous path between node clusters, specifying a linear element of structure as shown in
Fig. 3a. Subsequently, the “Generation” node shown in
Fig. 1 integrates computer vision, DL, geometry processing, and user-driven scaling to create an interactive, end-to-end pipeline for extracting and adjusting structural components from a hand-sketched image. First, it attempts to automatically read a dimension line from the source image and numeric annotation by employing Artificial Intelligence (AI). If the script successfully identifies this dimension line from the sketched image shown in
Fig. 1, it calculates a scale factor by comparing pixel distance to the real measurement, thus automatically converting the structure’s pixel geometry into real-world units. If automatic scaling is not viable, due to user preference, the code switches to a manual mode and launches a PyQt-based Graphical User Interface (GUI) shown in
Fig. 4. Within this interface, a user can pick reference connections or a known span to define the structure’s scaling. The GUI provides real-time visual feedback, displaying node position and element lengths, and a calculated scale factor. Subsequently, the user’s chosen scale factor is applied to all relevant coordinates. Finally, the script integrates with Dynamo (through the clr reference to ProtoGeometry) by converting the scaled coordinates into Dynamo-native geometry objects for further parametric modeling. The visualization module, shown in
Fig. 1, was prepared to number the nodes, create sections for structure, and provide the supports and force representation on the Dynamo. The result is a flexible framework that adapts to varying quality of source images while maintaining precise control over final geometry.

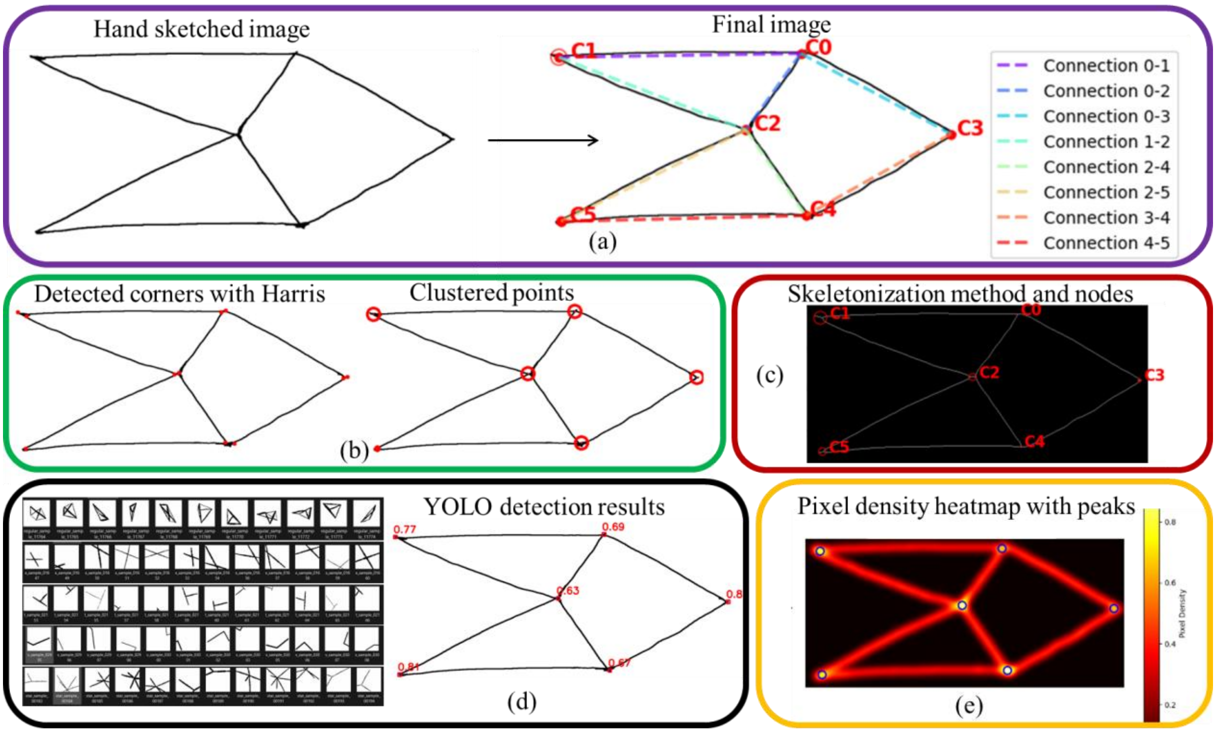

Fig. 3. Overall representation of employed methods: (a) showing the objective of the workflow and path finding; (b) Harris corner detection process (c) image skeletonization and cluster results; (d) synthetic data created to train the YOLO and the results gathered with trained model along with confidence levels; (e) Heat map technique with detected nodes

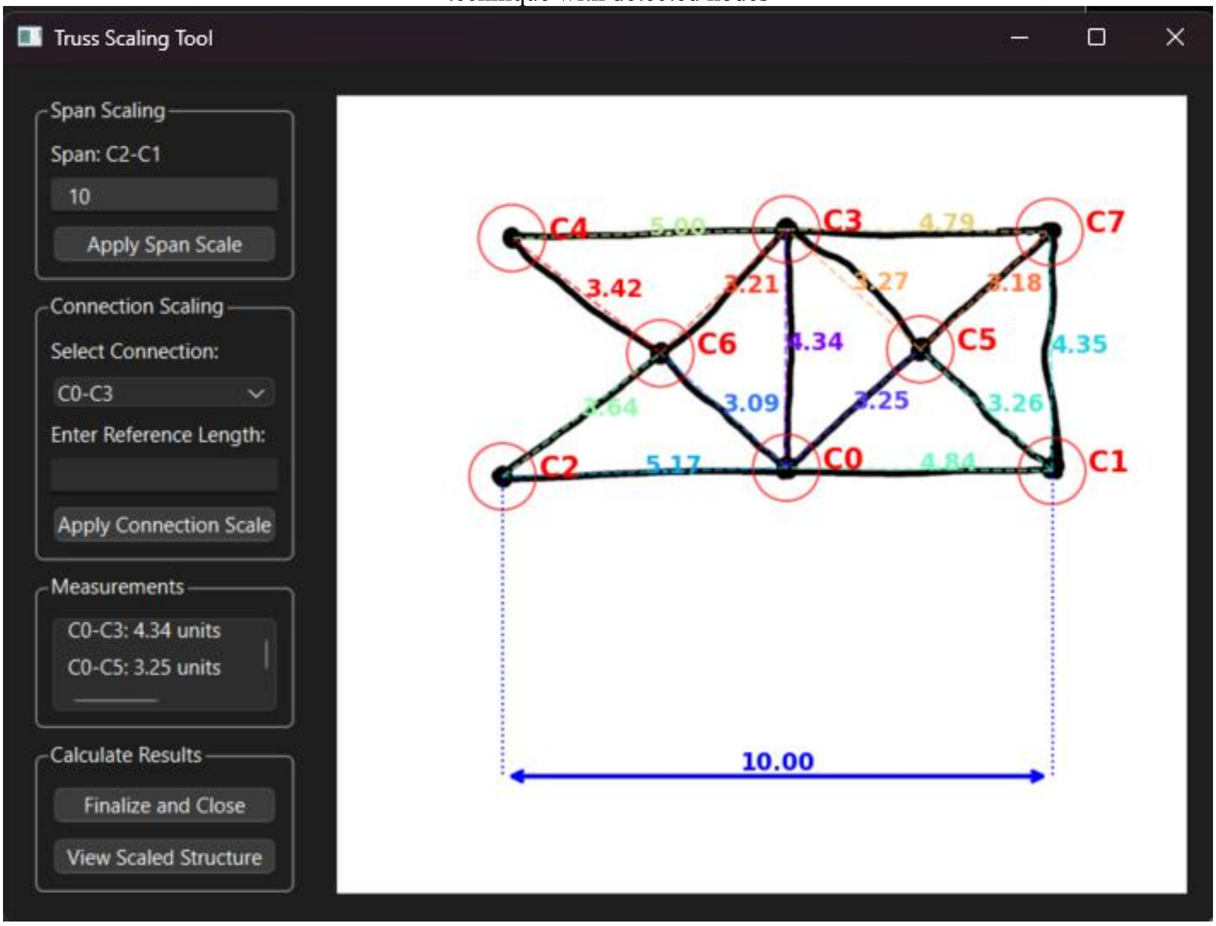

Fig. 4. Truss Scaling Tool GUI. The left-hand panel lets the user scale a hand-sketched truss in two ways: by specifying a span length (here C2 – C1 = 10 units, shown with blue dashed guides) or by entering a reference length for any single member. Detected nodes are marked with red circles, and the automatically calculated member lengths appear alongside each bar. After the desired scale is applied, the Finalize and Close or View Scaled Structure buttons generate a dimension-consistent digital model.

3. Experimental design

As discussed in the methodology section, the most important step for this methodology is detecting the connection points (nodes) for the structure. As such, the effectiveness of four methods—namely, Harris corner detection, Skeletonization method, Heat map technique, and DL technique—was tested on 10 different hand-sketched truss examples presented in Table 1. For comparison, each example was implemented in the previously mentioned workflow, and the results, such as any missing nodes, connections, or false-positive nodes, were counted as errors along with each specific algorithm's runtime. To provide extensive and robust experimental results, different drawing styles were implemented with varying line thicknesses. For instance, example 4 from Group 1 was created to challenge the algorithms with drawings that are misconnected, not connected at all, or overly connected. Example 3 represents small, imperfect drawings with varying line thicknesses within the same sketch. Example 9 was created to test curved drawings, while Example 6 tests both curved and unattached node connections. Example 7 evaluates the detection of more rounded L-shaped connections, and example 10 tests sketches with many node connections at varying distances, specifically challenging for the clustering algorithm. Initially, a fifth feature extraction method using Large Language Models (LLMs) was considered; however, during the experimental design, models such as ChatGPT 4o, o3 mini, o3 mini high, Claude 3.5, and Gemini 2.0 failed to produce meaningful results. Thus, the comparison of future and advanced LLMs remains as a topic for future study.

Table 1. Test examples

No	Group 1	Group 2
1	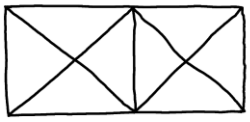	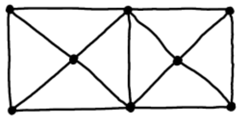
2	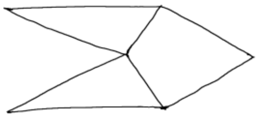	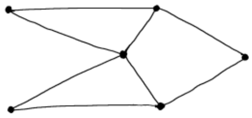
3	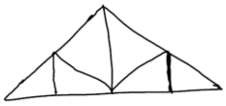	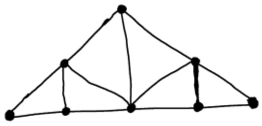
4	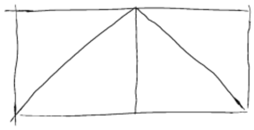	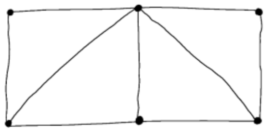
5	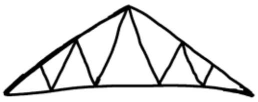	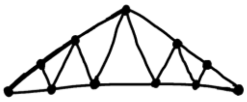
6	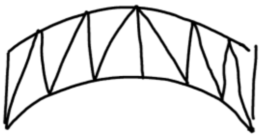	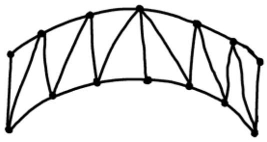
7	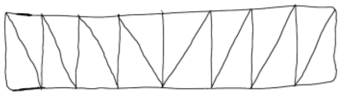	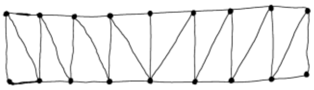
8	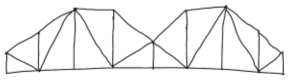	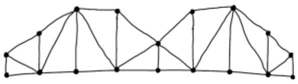
9	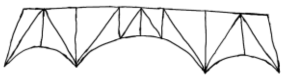	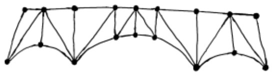
10	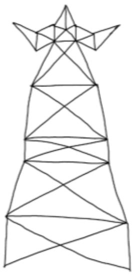	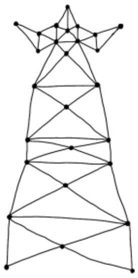

4. Results

As summarized in Table 2 and

Fig. 5, each feature extraction method provided different trade-offs in both execution time and accuracy. Notably, all methods performed worse with Group 1 examples, except the Skeleton method, with average error rates approximately 79% higher than Group 2 examples when the Heat map detection technique was excluded. Moreover, Table 3 provides visual comparisons of the four methods across 4 different structural examples selected during the tests. The overall execution time from sketching to optimized FEM model took approximately 500 seconds which is promising for future studies to enhance design workflow and add optimization step to this process. These findings demonstrate that a hybrid approach combining multiple detection methods or training more comprehensive DL model, since it maintained the most consistent performance for most of the cases despite the short training and data creation time spent on the technique, for fixing all weaknesses with current model could further enhance both reliability and speed, thereby improving the overall automation process for converting sketches into structurally valid models.

Table 2. Feature extraction methodology comparison results

No	Group	Harris corner detection		Heat map detection		DL detection		Skeleton Method	
		Error	Execution Time (sec)	Error	Execution Time (sec)	Error	Execution Time (sec)	Error	Execution Time (sec)
1	Gr. 1	0	0.031	0	0.187	0	1.583	0	0.106
	Gr. 2	0	0.024	0	0.170	0	1.772	0	0.120
2	Gr. 1	0	0.024	3	0.049	1	0.248	0	0.092
	Gr. 2	0	0.011	0	0.049	0	0.264	0	0.101
3	Gr. 1	3	0.007	7	0.053	1	0.286	1	0.099
	Gr. 2	2	0.021	0	0.080	0	0.721	0	0.165
4	Gr. 1	0	0.014	2	0.057	2	0.57	0	0.110
	Gr. 2	0	0.011	1	0.061	0	0.241	2	0.097
5	Gr. 1	2	0.014	3	0.078	0	0.425	1	0.122
	Gr. 2	1	0.009	0	0.069	0	0.243	1	0.081
6	Gr. 1	2	0.019	4	0.091	1	1.238	1	0.166
	Gr. 2	0	0.016	0	0.101	2	0.884	2	0.159
7	Gr. 1	2	0.019	14	0.088	3	0.820	2	0.170
	Gr. 2	1	0.022	0	0.095	0	1.458	2	0.212
8	Gr. 1	1	0.025	11	0.090	2	1.520	1	0.186
	Gr. 2	2	0.019	0	0.096	0	1.393	2	0.208
9	Gr. 1	2	0.015	13	0.070	3	0.522	2	0.235
	Gr. 2	1	0.016	5	0.081	0	0.583	2	0.140
10	Gr. 1	4	0.018	14	0.063	5	0.795	1	0.113
	Gr. 2	3	0.034	0	0.144	0	2.275	1	0.300

Table 3. Visual comparison of employed methods with selected examples

Harris corner detection	Heat map detection	DL detection	Skeleton Method

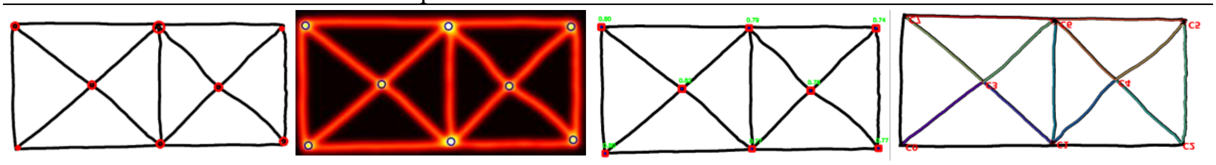

Group 1, Example no 1

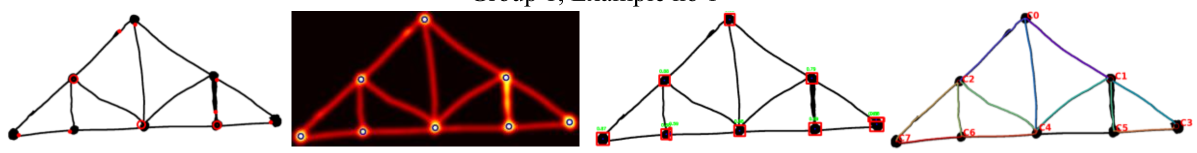

Group 2, Example no 3

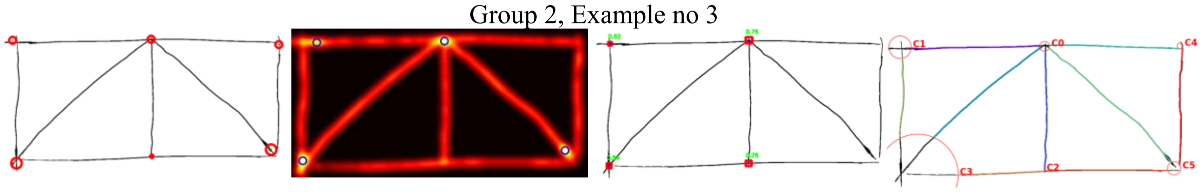

Group 1, Example no 4

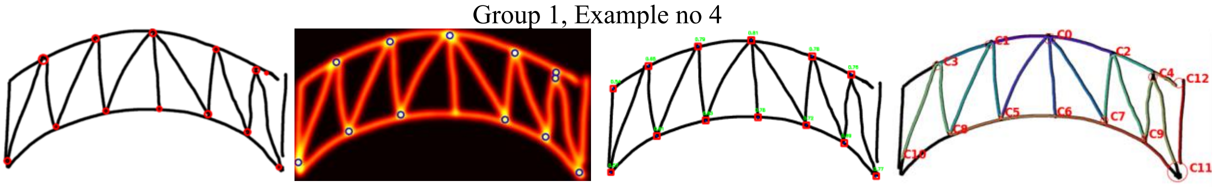

Group 1, Example no 6

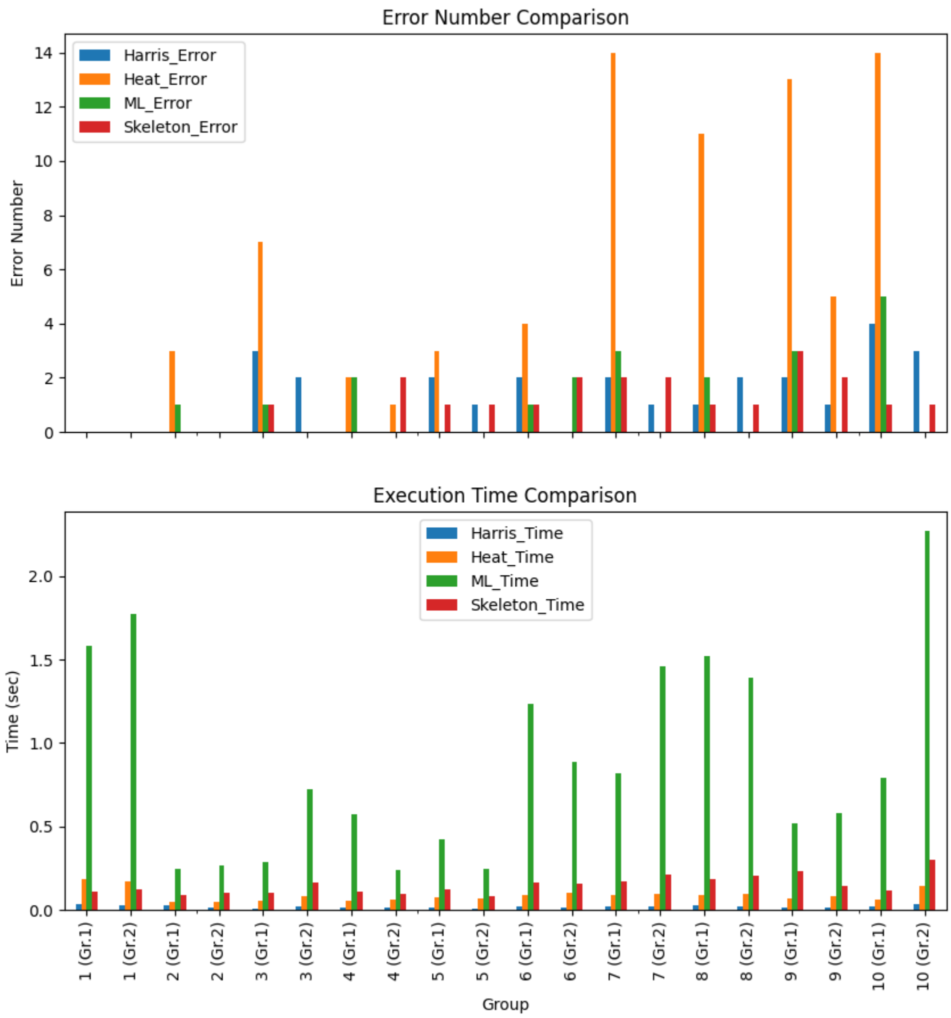

Fig. 5. Graphical comparison of the results

5. Conclusions and discussion

The present study focuses on the development of a hybrid workflow that converts hand-drawn truss designs into digital models on a BIM platform while assessing the ability of different methods, namely Harris corner detection, Skeletonization, Heat map analysis, and Deep learning-based YOLO detection, to extract features. During the process, features such as AI-based dimension specification using image inputs and an advanced GUI have been added to the workflow. These achievements are the starting point for a larger Augmented Reality (AR)-based project where users define structures in a real-world environment, similar to scenes in science fiction movies, by using Virtual Reality (VR) glasses, voice commands, and sketches, which results in a streamlined design and optimization workflow. The findings of this study demonstrated that the Sketch-to-BIM (StB) framework significantly enhanced and sped up the design process. From an accuracy standpoint, Heat map detection had low error rates for Group 2's well-defined nodes, yet provided by far the highest error rates for Group 1 examples. Deep learning detection, despite its higher computational demand, maintained its detection accuracy across both groups, providing the best performance for Group 2 examples. These findings provide valuable insights for the authors regarding the future direction to enhance the methodology by incorporating AI-based optimization, speech-to-structure techniques, more robust feature extraction, and enhanced capabilities with sketches, such as load and support definitions. The workflow can also be further improved by merging several feature extraction methods to complement their strengths and bypass their weaknesses or by training more advanced machine learning models to improve feature detection precision. Adding a systematic error detection mechanism would make the detection of nodes more robust, and expanding the dataset to include a greater variety of hand-drawn samples would make the proposed approach more broadly applicable. Overall, the present study performs a comparative analysis among four different methods by converting hand-drawn sketches into digital models. The results outline the strengths and limitations of each approach and exhibit their potential for reducing the design time, increasing accuracy, and bridging the gap between digital modeling and hand sketching, which lays out the foundation for prospective future studies on the StB workflow.

Acknowledgments
The authors wish to acknowledge the generous endowment provided by GOLDBECK GmbH to the Karlsruhe Institute of Technology (KIT) to establish the Chair for Digital Engineering and Construction (DEC) at the Institute for Technology and Management in Construction (TMB).

References

Aastrup Olsen, M., Hartung, D., Busch, C., & Larsen, R. (2011). Convolution approach for feature detection in topological skeletons obtained from vascular patterns.In *2011 IEEE Workshop on Computational Intelligence in Biometrics and Identity Management (CIBIM)*, 163–167. https://doi.org/10.1109/CIBIM.2011.5949223

Ahmed, S., Weber, M., Liwicki, M., Langenhan, C., Dengel, A., & Petzold, F. (2014). Automatic analysis and sketch-based retrieval of architectural floor plans. *Pattern Recognition Letters, 35*(1), 91–100. https://doi.org/10.1016/j.patrec.2013.04.005

Aoki, Y., Shio, A., Arai, H., & Odaka, K. (1996). A prototype system for interpreting hand-sketched floor plans. In *Proceedings of 13th International Conference on Pattern Recognition*, 747–751 vol.3. https://doi.org/10.1109/ICPR.1996.547268

Babiker, M., khalifa, O.O., Kyaw Htike, K., Hassan, A., & Zaharadeen, M. (2017). *Measurement and Applications (ICSIMA) 28*, 1–5. https://doi.org/10.1109/ICSIMA.2017.8312025

Cheng, D., & Schwartzman, A. (2017). Multiple testing of local maxima for detection of peaks in random fields. *The Annals of Statistics, 45*(2). https://doi.org/10.1214/16-AOS1458

de Klerk, R., Duarte, A.M., Medeiros, D.P., Duarte, J.P., Jorge, J., & Lopes, D.S. (2019). Usability studies on building early stage architectural models in virtual reality. *Automation in Construction, 103*, 104–116. https://doi.org/10.1016/j.autcon.2019.03.009

Diwan, T., Anirudh, G., & Tembhurne, J.V. (2023). Object detection using YOLO: challenges, architectural successors, datasets and applications. *Multimedia Tools and Applications, 82*(6), 9243–9275. https://doi.org/10.1007/s11042-022-13644-y

Dong, A.S., & Liu, X. (2013). The depth image restoring based on Harris corner detection. *Advanced Materials Research, 791–793*, 852–856. https://doi.org/10.4028/www.scientific.net/amr.791-793.852

Ge, Z., Liu, S., Wang, F., Li, Z., & Sun, J. (2021). YOLOX: Exceeding YOLO Series in 2021 (Vol. 5, p. 12). *arXiv preprint arXiv:2107.08430*.

Haralick, R.M., & Shapiro, L.G. (1985). Image segmentation techniques. *Computer Vision, Graphics, and Image Processing, 29*(1), 100–132. https://doi.org/10.1016/S0734-189X(85)90153-7

Harris, C., & Stephens, M. (1988). A combined corner and edge detector. In C. J. Taylor (Ed.), *Proceedings of the Alvey Vision Conference* (pp. 23.1–23.6). Alvety Vision Club. https://doi.org/10.5244/C.2.23

Hutchinson, T.C., Kuester, F., & Phair, M.E. (2007). Sketching finite-element models within a unified two-dimensional framework. https://doi.org/10.1061/(ASCE)0887-3801(2007)21:3(175)

Jeong, W.S., Kong, B.C., Adhikari, M.D., & Yum, S.G. (2024). The development of a framework for the automated translation of sketch-based data into BIM models. *Buildings, 14*(4), 916. https://doi.org/10.3390/buildings14040916

Joffe, I., Qian, Y., Talebi-Kalaleh, M., & Mei, Q. (2024). A computer vision framework for structural analysis of hand-drawn engineering sketches. *Sensors, 24*(9), 2923. https://doi.org/10.3390/s24092923

Justusson, B.I. (2006). Median filtering: Statistical properties. In *Two-Dimensional Digital Signal Processing II: Transforms and Median Filters* (pp. 161–196).

Kossakowski, P.G. (2023). Visual programming as modern and effective structural design technology—Analysis of opportunities, challenges, and future developments based on the use of Dynamo. *Applied Sciences, 13*(16), 9298. https://doi.org/10.3390/app13169298

Kubicki, S., Mukkavaara, J., & Sandberg, M. (2018). A master model approach for design and analysis of roof trusses. In J. Teizer (Ed.), *Proceedings of the 35th International Symposium on Automation and Robotics in Construction (ISARC)* (pp. 2413–5844). International Association for Automation and Robotics in Construction (IAARC). https://doi.org/10.22260/isarc2018/0046

Lee, H., Kim, B., Kim, K.J., Seo, J., Park, S., Shin, Y.G., & Lee, K.H. (2011). Introduction of heat map to fidelity assessment of compressed CT images. *Medical Physics, 38*(8), 4667–4671. https://doi.org/10.1118/1.3611046

Li, C., Pan, H., Bousseau, A., & Mitra, N.J. (2022). Free2CAD: Parsing freehand drawings into CAD commands. *ACM Transactions on Graphics, 41*(4). https://doi.org/10.1145/3528223.3530133

Li, X., Liu, Y., Zhao, Z., Zhang, Y., & He, L. (2018). A deep learning approach of vehicle multitarget detection from traffic video. *Journal of Advanced Transportation.* https://doi.org/10.1155/2018/7075814

Loey, M., Manogaran, G., Taha, M.H.N., & Khalifa, N.E.M. (2021). Fighting against COVID-19: A novel deep learning model based on YOLO-v2 with ResNet-50 for medical face mask detection. *Sustainable Cities and Society, 65*. https://doi.org/10.1016/j.scs.2020.102600

Mafi, M., Martin, H., Cabrerizo, M., Andrian, J., Barreto, A., & Adjouadi, M. (2019). A comprehensive survey on impulse and Gaussian denoising filters for digital images. *Signal Processing, 157*, 236–260. https://doi.org/10.1016/j.sigpro.2018.12.006

McKenna, F., Scott, M.H., & Fenves, G.L. (2010). Nonlinear finite-element analysis software architecture using object composition. *Journal of Computing in Civil Engineering, 24*(1), 95–107. https://doi.org/10.1061/(ASCE)CP.1943-5487.0000002

OpenCV: Harris corner detection. (2025, January 23). Retrieved from https://docs.opencv.org/3.4/dc/d0d/tutorial_py_features_harris.html

Otsu, N. (1979). A threshold selection method from gray-level histograms. *IEEE Transactions on Systems, Man, and Cybernetics, 9*(1), 62–66. https://doi.org/10.1109/TSMC.1979.4310076

Peschel, J.M., & Hammond, T.A. (2008). STRAT: A sketched-truss recognition and analysis tool. *International Workshop on Visual Languages and Computing*, 282–287.

Redmon, J., Divvala, S., Girshick, R., & Farhadi, A. (2016, June). You only look once: Unified, real-time object detection. In *Proceedings of the IEEE Conference on Computer Vision and Pattern Recognition (CVPR)*.

Rosenblatt, F. (1957). The perceptron, a perceiving and recognizing automaton. *Project Para*. Cornell Aeronautical Laboratory.

Schubert, E., Sander, J., Ester, M., Kriegel, H.P., & Xu, X. (2017). DBSCAN revisited, revisited. *ACM Transactions on Database Systems, 42*(3), 1–21. https://doi.org/10.1145/3068335

Soille, P. (1999). *Morphological image analysis* (Vol. 2, No. 3). Springer Berlin Heidelberg. https://doi.org/10.1007/978-3-662-05088-0

Thibhodee, S., & Viyanon, W. (2021). An application of evaluation of human sketches using deep learning technique. In *Proceedings of the 12th International Conference on Advances in Information Technology*, 1–7. https://doi.org/10.1145/3468784.3469852

Wang, G., Zheng, H., & Zhang, X. (2022). A robust checkerboard corner detection method for camera calibration based on improved YOLOX. *Frontiers in Physics, 9*. https://doi.org/10.3389/fphy.2021.819019

Wang, H. (2010). Skeleton-based morphing between sketching images. In *3rd International Congress on Image and Signal Processing*, 2665–2668. https://doi.org/10.1109/CISP.2010.5648112

Weber, M., Liwicki, M., & Dengel, A. (2010). a.SCAtch - A sketch-based retrieval for architectural floor plans. In *Proceedings - 12th International Conference on Frontiers in Handwriting Recognition (ICFHR 2010)*, 289–294. https://doi.org/10.1109/ICFHR.2010.122

Yavan, F., & Maalek, R. (2025). Reliability-constrained structural design optimization using visual programming in Building Information Modeling (BIM) projects. *Applied Sciences, 15*(3), 1025. https://doi.org/10.3390/app15031025

Yavan, F., Maalek, R., & Maalek, S. (2024). Enhancing spatial truss designs by integrating metaheuristic optimization techniques via visual programming in BIM-based projects. In P. Block, G. Boller, C. DeWolf, J. Pauli, & W. Kaufmann (Eds.), *Redefining the Art of Structural Design. Proceedings of the IASS 2024 Symposium*.

Yavan, F., Maalek, R., & Toğan, V. (2024). Structural optimization of trusses in Building Information Modeling (BIM) projects using visual programming, evolutionary algorithms, and life cycle assessment (LCA) tools. *Buildings, 14*(6), 1532. https://doi.org/10.3390/buildings14061532

Ye, Z., Pei, Y., & Shi, J. (2009). An improved algorithm for Harris corner detection. *2009 2nd International Congress on Image and Signal Processing*, 1–4. https://doi.org/10.1109/CISP.2009.5304635

Zhang, T.Y., & Suen, C.Y. (1984). A fast parallel algorithm for thinning digital patterns. *Communications of the ACM, 27*(3), 236–239.

Zhang, X., Qiu, Z., Huang, P., Hu, J., & Luo, J. (2018). Application research of YOLO v2 combined with color identification. In *Proceedings - 2018 International Conference on Cyber-Enabled Distributed Computing and Knowledge Discovery (CyberC 2018)*, 138–141. https://doi.org/10.1109/CyberC.2018.00036

Zhang, Z., Liu, Q., & Wang, Y. (2018). Road extraction by deep residual U-Net. *IEEE Geoscience and Remote Sensing Letters, 15*(5), 749–753. https://doi.org/10.1109/LGRS.2018.2802944

Zhao, L., Bao, Z., Xie, Z., Huang, G., & Rehman, Z.U. (2022). A point and density map hybrid network for crowd counting and localization based on unmanned aerial vehicles. *Connection Science, 34*(1), 2481–2499. https://doi.org/10.1080/09540091.2022.2130878

Zhao, X., Shi, X., Yang, B., Gao, Q., Yu, Z., Liu, J.K., Tian, Y., & Huang, T. (2019). Skeleton-based 3D object retrieval using retina-like feature descriptor. *IEEE Access, 7*, 157341–157352. https://doi.org/10.1109/ACCESS.2019.2944307

4th International Civil Engineering & Architecture Conference
17-19 May 2025, Trabzon, Türkiye

Türkiye's climate change mitigation efforts: Evaluating the role of GBCs in the construction sector

Zulfiqar Ali*[1], Gözde Tantekin-Çelik[1]

[1] *Cukurova University, Engineering Faculty, Department of Civil Engineering, 01250 Adana, Türkiye*

Abstract. Climate change is a pressing global issue demanding immediate action to minimize its harmful effects. Türkiye, identified as the 14th largest CO_2 emitter worldwide (EDGAR, 2024), urgently requires sustainable urban development strategies. This study explores how Türkiye's construction sector can reduce carbon emissions by adopting green building certifications (GBCs). A review of global climate policies reveals that Türkiye's current efforts fall short of addressing this challenge stating, "critically insufficient". To bridge this gap, the study proposes prioritizing Green Building Ratings as a key tool to combat climate change. Successful implementation of this approach could position Türkiye as a meaningful contributor to global climate action. By evaluating Türkiye's existing, green-certified buildings, the research demonstrates that adopting advanced construction practices would not only reduce emissions but also accelerate progress toward Sustainable Development Goal 11 (SDG-11), which focuses on sustainable cities. The study enhances awareness among policymakers, construction experts, and stakeholders, emphasizing that eco-friendly buildings serve as long-term and effective solutions in combating climate change. Ultimately, integrating GBCs into national strategies can drastically lower the sector's carbon footprint, aligning Türkiye's climate objectives with international sustainability targets.

Keywords: Türkiye; Climate crisis; Construction sector; Green building certification systems

1. Introduction

Emissions from the building sector, including both direct and indirect sources, account for approximately one-third of global greenhouse gas emissions (IEA, 2024). To mitigate the environmental impact of emissions from the building and construction sector, sustainable frameworks such as Green Building Rating Systems (GBRS) have emerged. These include Leadership in Energy and Environmental Design (LEED), EDGE, Building Research Establishment Environmental Assessment Methodology (BREEAM), DGNB, HQE, Green Star, and several others. These rating systems aim to achieve net-zero emissions by promoting sustainability within the construction industry. Building certification systems predominantly adopt conventional production approaches and regulatory frameworks tailored to specific geographic regions within the construction sector to enhance resource efficiency in new developments, achieve net-zero emissions during operations, and ensure indoor air quality surpasses regulatory (Kokatnur et al., 2025; Leite Ribeiro et al., 2025).

To align with the global sustainability goals for 2030 and 2050, the construction industry plays a crucial role as it is one of the largest consumers of natural resources and energy. Addressing the climate crisis and energy challenges, Green Building Rating Systems (GBRS) serve as an effective solution to improve energy efficiency in the building sector while reducing carbon emissions and enhancing indoor environmental comfort (Ribeiro et al., 2025). The building sector must prioritize energy efficiency and shift from conventional to renewable energy sources. Liu (2022) analyzed energy consumption statistics alongside economic growth and population trends to advocate for increased renewable energy use. The study found that a 1% rise in renewable energy consumption could lead to a 0.144% reduction in carbon emissions. However, a 1% increase in population and economic growth would result in carbon emissions rising by 1.51% and 0.961%, respectively (Liu et al., 2022).

Each country has established its own Green Building Council under the World Green Building Council (WGBC) to promote sustainable development and advance sustainability in the construction industry (WGBC, 2024a). Türkiye, situated at the crossroads of Asia and Europe, is implementing climate change policies to reduce emissions by 41% by 2030. The country is advancing its energy transition by shifting to renewable energy sources (Gül et al., 2025).

The analysis of retrospective studies highlights the existing research gap concerning the role of GBRS at both regional and national level (Anyanya et al., 2025; Eminel & Salgın, 2025). This study focuses on evaluating the

* Corresponding author, E-mail: 2021913104@ogr.cu.edu.tr

https://doi.org/10.31462/icearc2025_ce_mng_768

influence of Green Building Rating Systems (GBRS) around the world, particularly in developing regions. The primary emphasis is on Türkiye, aiming to explore how GBRS can help address the challenges of climate change. The central research question explores how carbon emissions in the construction sector can be mitigated through the adoption of GBRS.

2. Materials and methods

This study examines Türkiye's greenhouse gas emissions in comparison with those of other countries, emphasizing emissions from the construction sector and highlighting the role of buildings in climate change. It also addresses the application of green building certifications in Türkiye. Furthermore, the study analyzes the implications of measures starting at the building scale and extending to the national scale through an exemplary scenario. Details of the databases used and the analyses conducted are presented below.

1. Global Emissions Dynamics. In this study, to examine global emission dynamics, data from the Emissions Database for Global Atmospheric Research (EDGAR), a widely utilized source in scientific research (EDGAR, 2024) has been used to enable cross-country comparisons of emission trends, identify decoupling patterns between emissions and GDP/population growth, and determine high-impact sectors.

Within the scope of this study, CO_2 emissions of year 2023 have been analyzed at both the national and sectoral levels, with a particular focus on the building sector. Emissions per capita, Gross Domestic Product (GDP) by country, and population-based emissions have been examined accordingly. The results of Global Emission Dynamics are depicted in sections 3.1 and 3.2.

2. Climate Policy Compliance Assessment. Using progress reports from the UNFCCC and Nationally Determined Contributions (NDCs), quantitative metrics track national adherence to net-zero commitments (UNFCCC, 2024). Indicators include emission reduction rates, policy implementation timelines, and sectoral decarbonization targets, benchmarked against global climate goals by employing the Global Climate Action Portal (Global Climate Action) and Climate Action Tracker Portal (Climate Action Tracker, 2025). Climate Policy Compliance Assessment results are mentioned in section 3.3.
3. Energy Performance of Green Buildings in Türkiye. An inventory of 802 certified sustainable buildings in Türkiye spanning LEED, BREEAM, DGNB, EDGE, YES-TR and BEST certifications is analyzed to evaluate energy efficiency outcomes (B.E.S.T | ÇEDBİK; BREEAM Projects; EDGE Buildings; LEED; YES-TR). Metrics include energy consumption intensity (kWh/m²), renewable energy integration rates, and certification-specific benchmarks. Moreover, the results are described in sections 3.4 and 3.5.
4. Türkiye's Progress toward SDGs. To evaluate the progress of countries in achieving the Sustainable Development Goals (SDGs), an OECD tool is applied specifically to Türkiye's regions and cities. This tool measures how far they are from achieving the 17 SDGs outlined in the United Nations' 2030 Agenda (OECD, 2025). Results are mentioned in section 3.6.
5. Scenarios for reduction in GHGs.Opting the literature supported options how to reduce the GHGs emissions from building and construction sector mainly in the perspective of Türkiye to support the adoptability of GBRS, a data of Edge rating system is used along with the data of energy consumption in a residential household of 100m^2 for 4 persons in Türkiye and the findings are mentioned in section 3.7.

The reason for focusing on EDGE rating system is access to data. Because EDGE provides data on energy saving, emissions savings and water consumption of every building. While other rating systems don't give access to data except giving details like category of buildings.

The methodology computes the macro-scale emission of countries specifically Türkiye with micro-scale built-environment emissions, while embedding Türkiye NDCs to reveal actionable insights. By triangulating EDGAR's global data, Türkiye's building-specific metrics, and UNFCCC compliance reports, the study promotes a comprehensive approach to adopting green building certifications as a strategic measure for addressing climate change.

3. Results and discussion

This section presents a detailed analysis of global GHGs emissions and from building sector, renewable energy integration and Türkiye's mapping with SDGs. Moreover, discusses the research findings while systematically evaluating the outcomes to align with the study's aims and objectives.

3.1. Global comparison of CO_2 emissions & climate action ratings

The analysis of global CO_2-equivalent emissions has identified the top 27 highest-emitting countries based on 2023 greenhouse gas (GHG) emission statistics, as illustrated in Fig. 1 and Table 1 (EDGAR, 2024). Notably, Table 1 serves as a key reference, providing an in-depth breakdown of emissions from the building sector, per capita emissions, and GDP-based emissions. Additionally, it presents demographic insights, including total population figures and urbanization trends, both current and projected.

Additionally, the research is focused on the Eurasian country of Türkiye. Türkiye became a member of the Kyoto Protocol in 2009 and approved the Paris Agreement in 2015 to act against global climate change. According to the 2023 greenhouse gas (GHG) emission statistics, Türkiye is ranked 14th globally for total emissions. When looking at emissions per capita, Türkiye is ranked 7th in the world, which is most alarming and concerning climatic situation. However, when emissions are measured based on the country's total land area, Türkiye records 773.60 tons of CO_2 equivalent per square kilometer (tCO_2e/km^2). With this value, Türkiye is not among the top 50 countries in terms of emissions per land area (EDGAR, 2024).

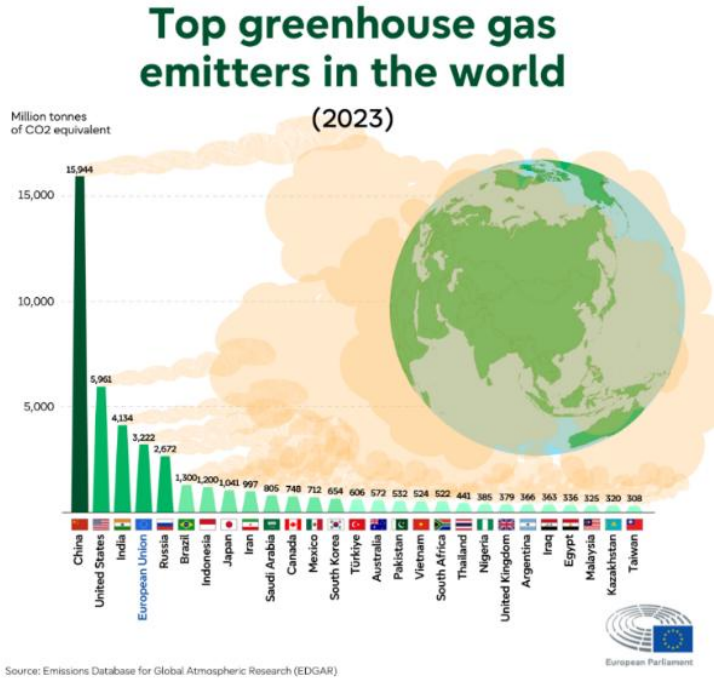

Fig. 1. Global top GHGs emitter 26 & EU27 countries

3.2. Emissions from the building sector

Analyzing sectoral CO_2-equivalent emissions, the Building Sector emerges as a key contributor, with China leading the emissions chart, followed by the USA, Russia, and India. Türkiye ranks 9th in this sector, as illustrated in Fig. 2 (EDGAR, 2024). In terms of global population statistics for 2023, Türkiye holds the 14th position, maintaining the same emission levels. However, when considering urban population dynamics, the country's ranking shifted from 14th to 13th due to a 5% increase between 2023 and 2024. This ranking is expected to remain unchanged in the near future (EDGAR, 2024; Urbanization, 2024). Projections by the World Bank indicate that Türkiye's urban population will rise to 80.25% by 2030 and further to 86% by 2050 as shown in Fig. 3.

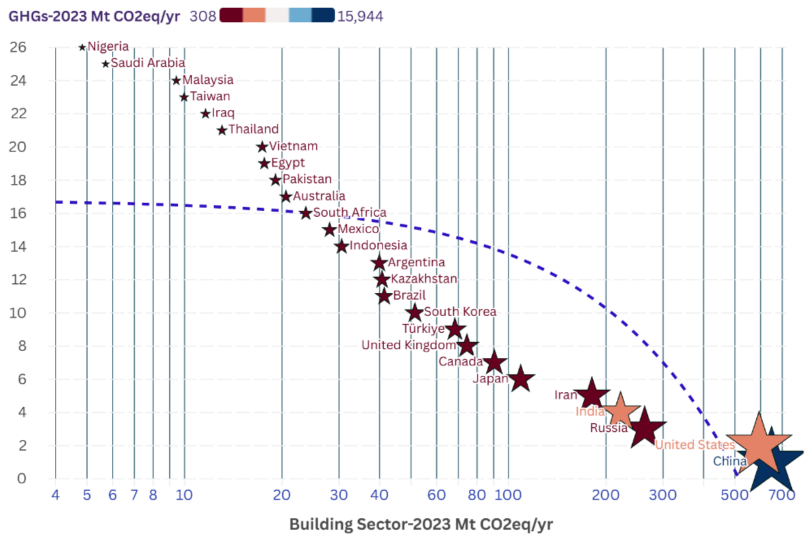

Fig. 2. Global emissions from the building sector

Table 1. Globally highest GHGs emitting countries and statistics

Countries	GHGs-2023 Mt CO_2e/yr	Building Sector-2023 Mt CO_2eq/yr	Population-2023	GDP by Country tCO_2eq/kUSD/yr	Per Capita tCO_2eq/cap/yr	Urban Population (%age)			
						2023	2024	2030	2050
China	15,944	648.631127	1,422,584,937	0.5106	11.1133	56.53	65.54	70.63	80.03
United States	5,961	593.486741	343,477,332	0.2417	17.6082	85.79	83.52	84.86	89.16
India	4,134	221.759053	1,438,069,597	0.3155	2.9004	37.49	36.87	40.14	52.84
Russia	2,672	263.189639	145,440,504	0.4594	18.6589	78.12	75.55	77.08	83.33
Brazil	1,300	41.3407372	211,140,731	0.3238	5.9658	89.16	88.02	89.28	92.43
Indonesia	1,200	30.5628225	281,190,068	0.30729	4.2874	52.43	59.20	62.84	72.81
Japan	1,041	109.051849	124,370,947	0.18069	8.3109	71.73	92.13	92.70	94.71
Iran	997	180.948497	90,608,708	0.69195	11.64309	75.77	77.70	80.13	85.98
Saudi Arabia	805	5.70807064	33,264,288	0.43965	22.1739	85.57	85.17	86.48	90.35
Canada	748	90.4156819	39,299,099	0.33405	19.3915	84.67	81.98	82.88	87.29
Mexico	712	28.0446642	129,739,764	0.24785	5.14812	82.06	81.86	83.50	88.21
South Korea	654	51.4201885	51,748,744	0.25002	12.5836	86.34	81.50	82.05	86.44
Türkiye	*606*	*68.317866*	*87,270,503*	*0.20652*	*7.1007*	*73.36*	*77.89*	*80.25*	*85.95*
Australia	572	20.5616735	26,451,125	0.36105	21.7537	91.18	86.75	87.62	90.96
Pakistan	532	19.0879776	247,504,504	0.39536	2.4252	43.69	38.37	40.68	52.20
Vietnam	524	17.3735644	100,352,189	0.38712	5.1851	38.37	40.20	44.46	57.33
South Africa	522	23.6848379	63,212,386	0.60502	8.6142	68.46	69.30	72.07	79.80
Thailand	441	13.0552301	71,702,438	0.29078	6.3312	41.58	54.32	58.42	69.46
Nigeria	385	4.83375501	227,882,949	0.30216	1.7321	57.83	55.03	59.19	69.92
United Kingdom	379	74.3996947	68,682,965	0.10253	5.5452	89.40	84.88	86.29	90.22
Argentina	366	39.9278243	45,538,402	0.29615	7.82934	94.48	92.58	93.25	95.18
Iraq	363	11.6103897	45,074,055	0.63319	8.08434	72.30	71.85	73.56	80.45
Egypt	336	17.6304745	114,535,772	0.17573	3.10745	51.38	43.26	43.26	55.61
Malaysia	325	9.43250238	35,126,295	0.28250	9.53403	76.78	79.20	81.79	87.33
Kazakhstan	320	40.7176689	20,330,106	0.45406	16.60103	66.40	58.38	60.02	69.11
Taiwan	308	9.97077506	23,317,145	0.19291	12.85049	80.39	80.42	82.41	87.47
EU 27	3,222	428.991712	745,083,823	0.13326	7.26410	75.30	75.60	77.60	85.20
Global Total	24,002,52	3,413.53273		0.31973	6.59414				

Fig. 3. Urban population statistics

3.2.1. Role of building sector in greenhouse gas emissions
The buildings and construction sector stands one of the biggest contributors to global greenhouse gas emissions, accounting for an astonishing 34% of total emissions. The environmental impact is further exacerbated by the production and utilization of energy-intensive materials such as cement, steel, and aluminium, each leaving a substantial carbon footprint (UNEP & GABC, 2024). Furthermore, an in-depth assessment of embodied carbon emissions in the construction sector, based on the International Energy Agency (IEA) report (IEA, 2023) reveals the embodied emissions from construction subsectors like residential, non-residential and industry as illustrated in Table 2.

Table 2. Embodied carbon emissions from the construction sector

Sectorial Emissions	Embodied Emissions (%)
Residential (direct)	5
Residential (indirect)	10
Non-residential (direct)	2
Non-residential (indirect)	8
Buildings construction industry	6
Building Construction other materials	2
Other construction industry	5
Other	63
Total	100

However, Operational Carbon emissions which stem from heating, cooling, and lighting, constitute a significant portion of a building's total environmental impact. Projections indicate that these emissions currently account for 75% of total building-related emissions, with expectations to decline to 50% in the coming decades through enhanced energy efficiency measures and technological advancements. Moreover, according to Energy Performance of Buildings directive building materials can be classified into three primary categories (non-renewable, transitional and renewable materials) based on their decarbonization potential (European Commission, 2025). By prioritizing the use of renewable and transitional materials, alongside innovative design and sustainable green building construction practices, the built environment can significantly reduce its carbon footprint and contribute to a climate-resilient future. Strategic policies, coupled with advancements in green building technologies, will be essential in accelerating the shift towards sustainable and energy-efficient buildings worldwide.

3.3. Energy use in the building sector & renewable energy trends
At this stage, the total final energy consumption of the country will be evaluated, with a focus on usage trends for renewable energy. The analysis will primarily target the residential and construction sectors. mainly associated with the residential and construction sector.

3.3.1. Total Final Consumption (TFC) in residential sector

In most countries, heating and cooling account for the largest portion of residential energy consumption (UNFCCC, 2024). While air conditioners, appliances, and lighting predominantly rely on electricity, heating and cooking still depend heavily on combustible fuels such as natural gas, oil, coal, and biomass. Transitioning these energy intensive applications to electricity particularly by replacing conventional fossil fuel-based heating systems with advanced energy efficient systems is a critical step toward reducing CO_2 emissions (Sghiri et al., 2025; Tang et al., 2025).

In the case of Türkiye, the building sector remains heavily reliant on natural gas, which constitutes 59% of the country's total final energy consumption (TFC), as illustrated in Fig. 4 (UNFCCC, 2024). This significant dependence underscores the urgent need for strategic electrification and energy-efficient solutions to enhance sustainability and mitigate environmental impact.

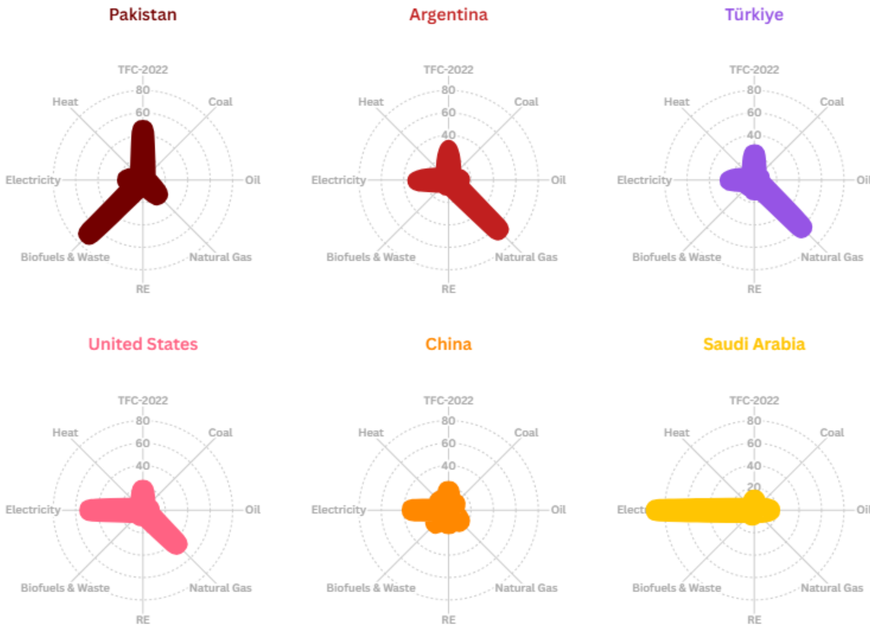

Fig. 4. Total final consumption in building sector

3.3.2. Role of modern renewables

As nations strive to lower CO_2 emissions and reduce reliance on imported fossil fuels, renewable energy is emerging as a crucial component of the global energy transition. While renewables are predominantly utilized for electricity generation, their applications extend to residential and commercial heating. Additionally, biofuels are increasingly being explored as a viable solution to decarbonize sectors of transportation that are otherwise difficult to electrify. It is important to distinguish modern renewable energy sources from traditional biomass usage, such as burning wood, agricultural residues, or dung for cooking and heating practices that have significant health and environmental consequences. Unlike these conventional methods, modern renewables contribute to a cleaner and more sustainable energy mix.

According to Sustainable Development Goal-7.2, the share of modern renewables in final energy consumption has been analysed over the period from 2000 to 2021. Fig. 5 highlights trends in renewable energy consumption across the world’s 27 highest-emitting countries. Notably, Argentina, Pakistan, Egypt, Kazakhstan, and Türkiye have experienced declines of approximately -1%, -6%, -13%, -20%, and -30%, respectively. Furthermore, the adoption of modern renewable energy in the residential sector is examined (IRENA, 2025). As illustrated in Fig. 6, Türkiye ranks 10th among the highest-emitting countries, with the share of renewable energy usage in the residential sector's total energy consumption being approximately 12%. It is evident that Türkiye needs to increase its investments in renewable energy.

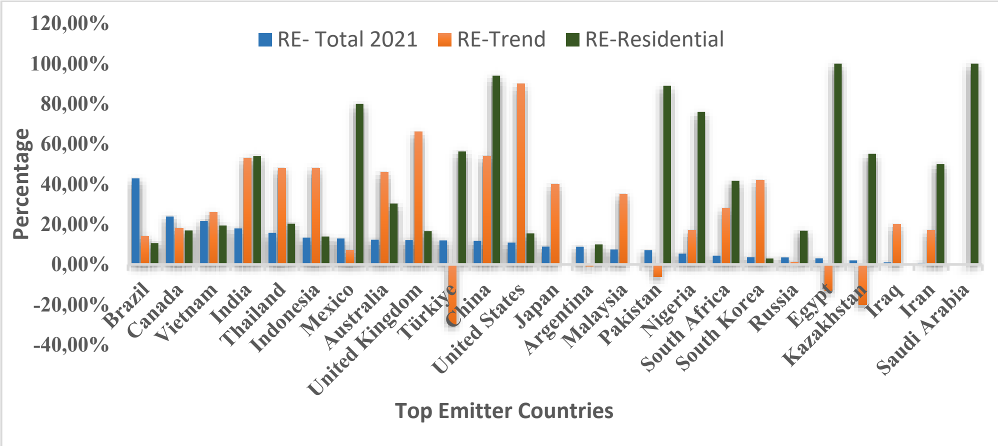

Fig. 5. Share of renewable energy in TFC 2021 statistics and country-wise trend

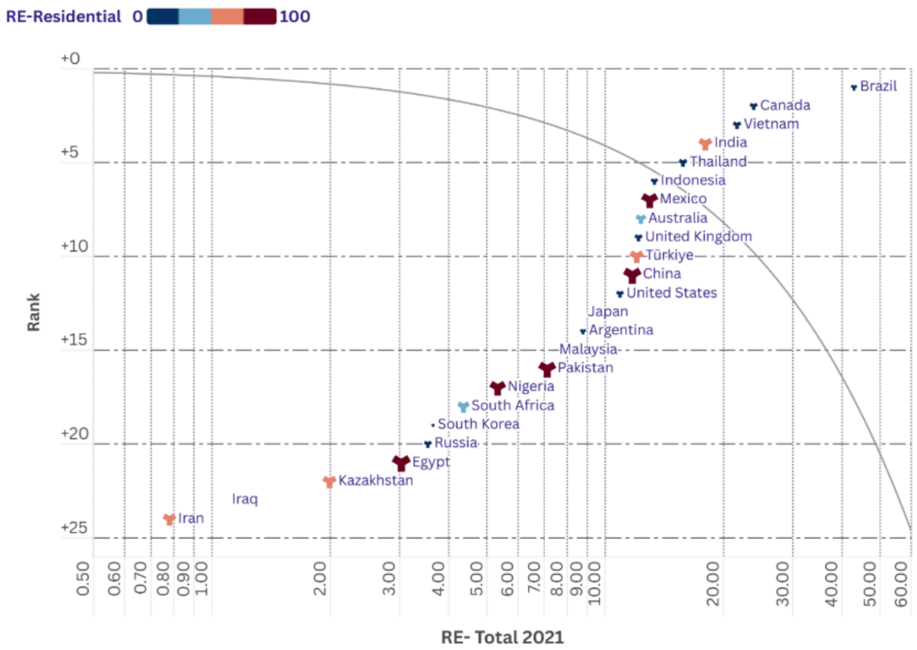

Fig. 6. Percentage of renewable energy in residential sector

3.4. Role of green building certifications in reducing emissions

Under the framework of the World Green Building Council (WGBC), each country operates its own Green Building Council, striving to advance sustainability in the built environment. Complementing these efforts, various rating systems are employed globally to assess buildings based on their climate resilience and sustainability performance, as illustrated in Fig. 7. A critical aspect of sustainable building practices involves evaluating the role of Green Building Regulations (GBRs) concerning energy efficiency, consumption patterns, and renovation strategies, particularly in mitigating greenhouse gas (GHG) emissions from the construction industry. According to the Energy Performance of Buildings Directive (EPBD), approximately 75% of buildings in the European Union are classified as energy inefficient. Furthermore, as per 2022 statistics, the annual building renovation rate remains alarmingly low at just 1% (European Commission, 2025).

However, GBRS drive carbon reduction by significantly improving energy efficiency. These systems establish rigorous criteria that prioritize enhancing energy efficiency, encouraging low-carbon materials, water and waste reduction, enhancing indoor environmental quality (IEQ) and passive design and lifecycle carbon accounting and net-zero pathways (European Commission, 2025; Xian et al., 2025). By adopting these measures, buildings can reduce their operational carbon footprint by up to 50%, significantly cutting emissions over time (WGBC, 2024b).

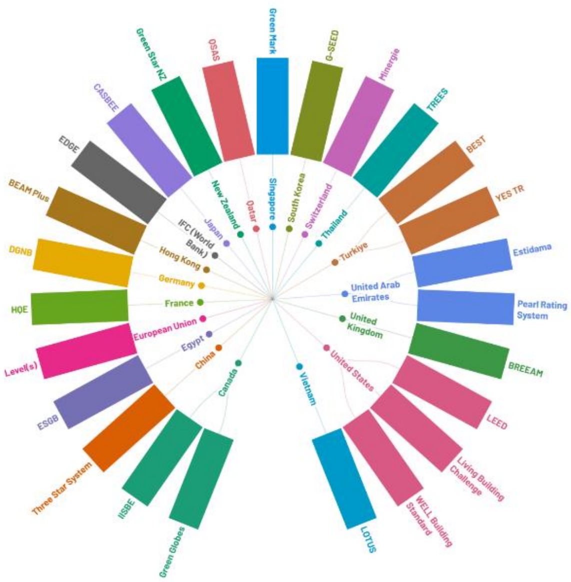

Fig. 7: Green building certification systems

Türkiye, like many other countries, has developed its own building certification systems YES-TR and BEST (B.E.S.T; YES-TR) as illustrated in Fig. 7. These systems aim to reduce the environmental impact of the built environment by addressing local needs, conditions, and regulations. While they share similarities with other international certification systems, they are specifically tailored to Türkiye's unique local context (YeS-TR).

3.5. Türkiye's status

Analysing Türkiye's climate action policies, as illustrated in Fig. 8, reveals a multifaceted scenario encompassing progress and challenges. While Türkiye has made strides in certain areas, there is a pressing need to accelerate the adoption of renewable energy sources to meet its 2035 targets. However, Türkiye's Nationally Determined Contribution (NDC) falls behind its existing policies and demonstrates insufficient progress in aligning with the Paris Agreement's 1.5°C temperature target. The Climate Action Tracker (CAT) classifies Türkiye's climate policies, targets, and financial commitments as "Critically Insufficient," indicating that its efforts remain far from the necessary benchmarks to curb emissions effectively (Climate Action Tracker, 2025).

At COP29, Türkiye introduced its Long-Term Strategy (LTS) (Ministry of Climate Change, 2025), reaffirming its previously declared goal of achieving net-zero emissions by 2053. The action plan for the Building and Services sector emphasizes the integration of Green Building Ratings (GBRs) as a key adaptation measure to combat climate change. If Türkiye successfully implements this strategy, it will mark a significant contribution to the global fight against climate change.

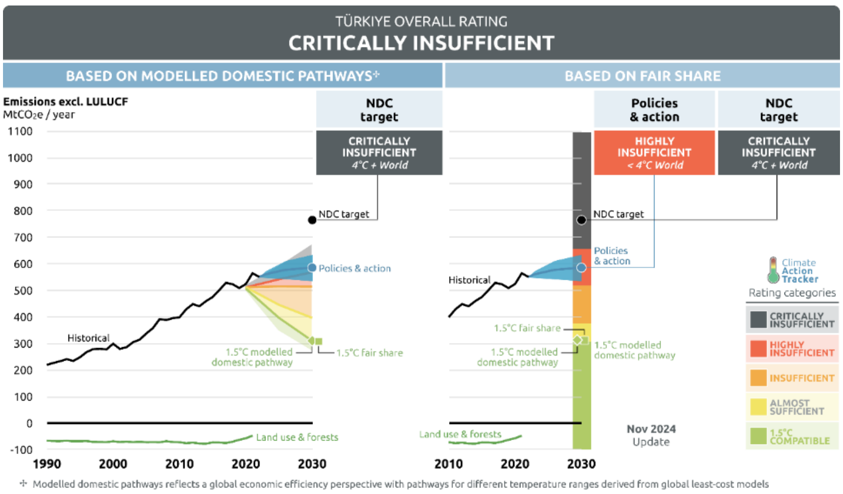

Fig. 8: Climate action tracker – Türkiye statistics

3.5.1. Türkiye's construction sector and green building certifications

About the Türkiye's construction sector, Statista reported the fluctuating trend of construction permits from 2002 to 2024 and residential building developments from 2015 to 2023 respectively. The industry peaked in 2017 with 139.555 new residential buildings, while in 2023, 120.113 new buildings were constructed (Statista-Türkiye, 2025). According to Turkish Statistical Institute, from 2002 to 2024, Türkiye issued 7.528 million construction permits, distributed as Buildings: 2.5 million (33.33%), Residential Buildings: 2.14 million (28.51%), and Two-and-Dwelling Buildings: 1.49 million (19.85%). Despite these numbers, the proportion of green-certified buildings is still quite small (TURKSTAT, 2025b). In the Turkish construction and building sector, several international and national green building rating systems are in use. These include LEED, BREEAM, DGNB, EDGE, WELL, BEST, and YES-Tr. However, due to limited availability of data from some of these systems, this section only includes information about buildings certified under LEED, BREEAM, EDGE, BEST and YES-TR. There are 802 certified buildings in total (B.E.S.T; BREEAM; EDGE Buildings; LEED; YES-TR) as illustrated in Table 3, with the majority (35.54%) being newly constructed buildings and certified residential buildings constitute merely 8.23%, as shown in Fig. 9.

Table 3: Green building certifications in the Turkish construction sector

Certification	Type	Number of Units	%
LEED	International	600	74.82
BREEM	International	72	8.97
EDGE	International	3	0.37
WELL	International	0	0
DGNB	International	0	0
BEST	National	23	2.87
YES-TR	National	104	12.97
Total		802	100

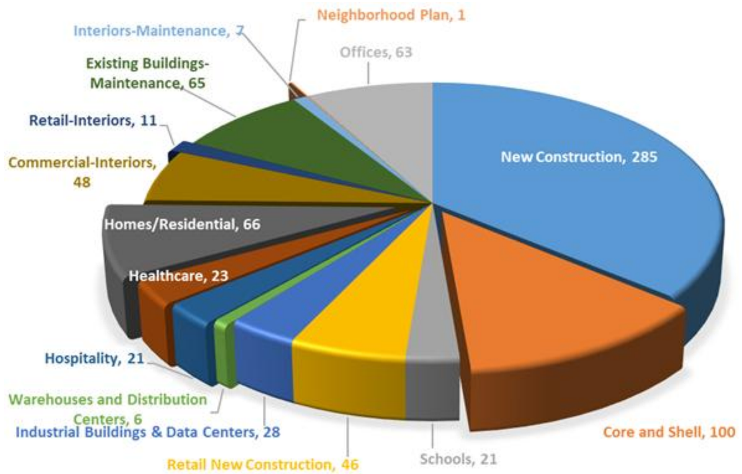

Fig. 9: Classification of Türkiye certified buildings

To assess Türkiye's performance in green building standards, LEED scoring system about Türkiye, scores highest in Energy & Atmosphere, alongside notable ratings in Indoor Environmental Quality (IEQ), Water Efficiency, Material Resources, and Sustainable Sites (LEED). These scores emphasize Türkiye's potential to enhance its sustainability credentials through focused policy and investment in green buildings. Furthermore, an analysis of the EDGE rating system quantifies potential reductions in emissions through green building certifications. Per square meter of construction, EDGE-certified buildings can achieve 0.15% saving in energy consumption, 0.17% saving in water consumption, 0.25% reduction in embodied energy material usage and 0.95% annual reduction in CO_2 emissions (tons) (EDGE Buildings, 2025). Moreover, BREEAM framework offers the sustainability solutions by making built environment resilient towards net zero emissions through life cycle analysis (LCA). In regional perspective of Türkiye, BREEAM can be effective to achieve net zero emissions from the built environment by making it more sustainable and resilient for people. The national certification system mainly YES-TR and B.E.S.T focus on less energy usage including eco-friendly materials and offer healthier indoor spaces. B.E.S.T standards can help compare local building performance with European practices. YES-TR can also focus on building energy efficiency; water use and innovation to improve the health and comfort of people inside buildings.

If Türkiye adopts a Green Building Rating System (GBRS) like YES-TR, B.E.S.T or other internationally recognized certifications in the construction sector, it could significantly lower greenhouse gas emissions. Over the past two decades, Türkiye has issued 7.528 million construction permits, yet only 802 buildings have received green certification as the illustrated in Table 5 and Fig. 10. In 2023 alone, 120,113 residential buildings were built, but just 55 were certified highlighting the urgent need for a strategic shift toward sustainable construction practices.

3.6. Türkiye's progress toward SDGs

Organisation for Economic Co-operation and Development (OECD) is working with more than 100 countries around the globe to help in the shaping of regional public policies and innovation in the societies against the 2030 agenda by comparing the performances of countries.

Eurasian country Türkiye is a member of OECD which is further comprised of multiple regions including Ankara, Central Anatolia-East, Central Anatolia-Middle, Central Anatolia-West & South, E Anatolia-E, E Anatolia-W, Eastern Black Sea, Eastern Marmara-North, Eastern Marmara-South, Istanbul, Izmir, Mediterranean-E, Mediterranean region-Middle, Mediterranean region-West, Middle Black Sea, N.E. Anatolia-E, N.E. Anatolia-W, Northen Aegean, S. Aegean, S.E. Anatolia-E, S.E. Anatolia-W, Southeastern Anatolia-Middle, Southern Marmara-West, Thrace, W. Black Sea-ME and Western Black Sea-West within the boundary. To assess Türkiye's regional progress towards SDGs, an OECD Tool has been utilized to enable subnational governments to evaluate current standing concerning the 2030 Agenda. The OECD tool which comprises more than 100 indicators working in approximately 600 regions and 600 cities to measure the distance from SDGs (OECD, 2025).

As depicted in Fig. 10, Türkiye's national score for SDG-11 (Sustainable Cities and Communities) stands at 66, with regional variations: Middle Black Sea leads with a score of 76, Ankara follows at 70, while Southeast Anatolia East lags at 50, indicating a critical need for urban sustainability interventions. In contrast, for SDG-7 (Affordable and Clean Energy), Türkiye scores 34 out of 100, with Izmir leading at 51, Ankara at 34, and the Western Black Sea registering zero, a concerning indicator for energy sustainability efforts.

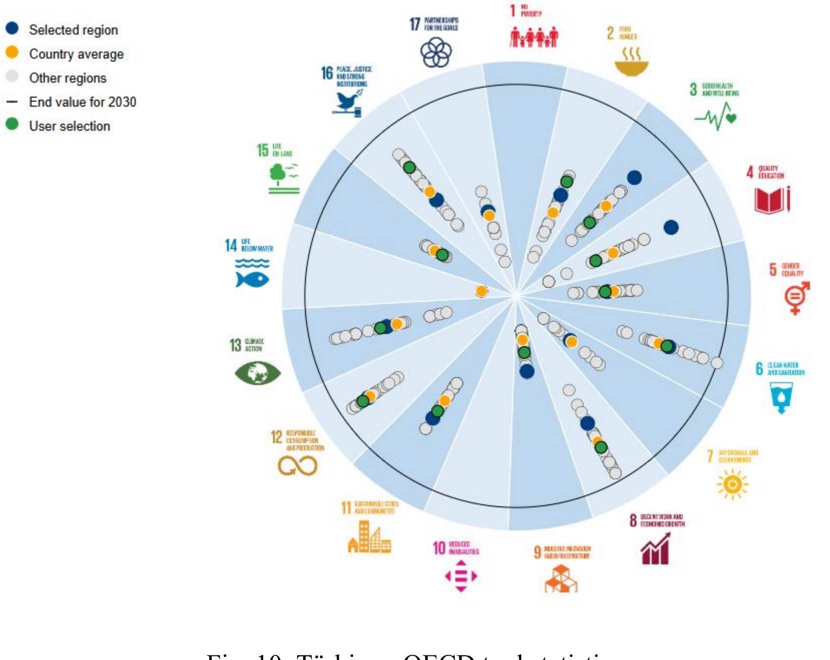

Fig. 10: Türkiye - OECD tool statistics

3.7. Analysis of the scenario for reducing greenhouse gas emissions

Türkiye's energy consumption patterns highlight critical challenges in reducing its carbon footprint. Consumer right association in Türkiye reported that an average four-member household having a net area of 100m^2 in Türkiye consumes 1,500 m^3 of natural gas annually, with monthly averages of 125 m^3, increasing to 250 m^3 in winter. Additionally, the average monthly electricity consumption for a four-member household stands at 230 kWh (Tüketici Hakları Derneği, 2025). However, natural gas accounts for 59% of energy consumption, signalling an urgent need to transition towards renewable energy sources in the residential sector. But alarmingly, the trend of renewable energy use in the building sector is insufficient, undermining efforts to meet the 2030 sustainability goals as depicted in Fig. 6.

To estimate the impact of GBRS in regional context of Türkiye, two approaches are formulated using data enlisted in Table 4 to estimate the emissions reduction. The Approach-I is about to calculate savings per m^2 by using the EDGAR emissions data and the Approach-II is to calculate the saving in emissions by using the Türkiye population and the EDGAR emissions data comprised of methodologies enlisted in Table 5.

Table 4: Emissions reduction by using GBRS

Data	Value	Unit	Reference
Total Population	85,664,944		(TURKSTAT-2025a)
a 4-person household of area	100	m^2	(Tüketici Hakları Derneği-2025)
Annual emission per person	7.01	ton CO_2eq/yr	(EDGAR - 2024)
Emissions Saving	0.95	% per m^2	(EDGE Buildings-2025)
Energy Consumption	0.15	% per m^2	(EDGE Buildings-2025)

Table 5: Key methodologies

Step	Methodology	Purpose
Residential Area	Per Capita Scaling	Total built environment based on Population data
Energy Consumption	Sectoral Energy Demand Modeling	Quantify natural gas and electricity use.
Emissions calculations	Emission Factor Approach according to IPCC guidelines	Convert energy to CO_2 emissions. - 1.9 kg CO_2/m^3 for natural gas, - 0.4 kg CO_2/kWh for electricity
Green Certification Savings	Efficiency Improvement Modelling + Energy Consumption Savings	Model direct and energy-related savings. - Edge Data
Total Savings	Integrated Emissions Reduction Framework - direct and indirect savings	Aggregate impacts for policy/climate strategy.

3.7.1. Approach-I

Baseline for Building: for a 4-person household of area 100-m^2

a. Annual Emission per Person: $Ep = 7.01 - \text{ton } CO_2eq/yr$
b. Annual Emission – Building: $Eb = 4 \text{ x } Ep = 28.04 - \text{ton } CO_2eq/yr$
c. Emission Intensity (per m^2): $I = Eb/100m2 = 0.2804 - \text{ton } CO_2eq/m2/yr$
   Maximizing Savings with EDGE Green Certification System
d. Emissions: 0.95% per m^2
e. Energy Consumption: 0.15% per m^2
f. Saving per m^2 = $0.95\% \text{ x } I = 0.0026638 - \text{ton } CO_2eq/m2/yr$
g. Total saving for 100 m^2 building: $Semission = 100 \text{ x } 0.0026638 = 0.26638 - \text{ton } CO_2eq/m2/yr$
h. Energy (related emission) savings: $Senergy = 0.15\% \text{ x } Eb = 0.04206 - \text{ton } CO_2eq/yr$
i. Total Saving per Building: $Stotal = Semission = 0.26638 - \text{ton } CO_2eq/yr$
j. P_{total} = 85,664,944 (assuming 4 people in 100 m^2 building)
k. $N_{buildings}$: $Nb = \frac{Ptotal}{4} = 21{,}415{,}236.00$ (assuming every building will be green-certified)
l. $S_{national}$: $Sn = Nb \text{ x } Stotal = 5{,}704{,}856.9 \text{ ton} - CO_2eq/yr$
m. $EnergyS_{national}$: $ESn = Nb \text{ x } Senergy = 900{,}766.1 \text{ ton} - CO_2eq/yr$

By opting the green building certification, around 5.704 Mtons-CO_2eq can be saved per annum.

3.7.2. Approach II

a. Population: 85,664,944
b. Average area per person: 25 m^2 (from 100 m^2 for 4 people)
c. Total residential area: $TRarea = 85664944x25 = 2{,}141{,}623{,}600 \text{ m2}$
d. Total households: $Thouses = \frac{85664944}{4} = 21416236$
e. Total Consumption Natural gas $= 21416236x1500 = 32.12 \text{ billion m3/yr}$
   Electricity $= 21416236x2760 = 59.11 \text{ billion kWh/yr}$
f. Emission factors:
   Natural Gas = 1.9 kg CO_2/m^3
   Electricity = 0.4 kg CO_2/kWh
g. Total Emissions: Natural gas $= 1.9\, kg \frac{CO2}{m3} x32.12 billion \frac{m3}{yr} = 61.028\, MtonsCO2/yr$

$$\text{Electricity} = 0.4\, kg \frac{CO2}{kWh} x59.11\ billion \frac{kWh}{y} = 23.64\, MtonsCO2/yr$$

h. Total residential emissions: Electricity + Natural Gas = $84.668\ \text{MtonsCO2/yr}$

i. Opting Green building certification

Emission-Savings: 0.95% /m^2. $Savings = 0.95\%\ x\ 84.668 \frac{MtonsCO2}{yr} = 804{,}346 \frac{tonsCO2}{yr}$

Energy Consumption Savings:

$$\text{Natural Gas} = 32.12\ \text{billion m3}\ x\ 0.15\% = 48.18\ \text{million m3}$$
$$\text{Electricity} = 59.11\ \text{billion kWh}\ x\ 0.15\% = 88.665\ \text{million kWh}$$

Emissions Savings:

$$\text{Natural Gas} = 48.18\ \text{million m3 x 1.9kg/m3} = 91{,}542\ \text{tons CO2/yr}$$
$$\text{Electricity} = 88.665\ \text{million kWh x 0.4kg/kWh} = 35{,}466\ \text{tons CO2/yr}$$

Total Energy (related) savings = 127,008 tons CO_2/yr

By utilizing the green building certification in Türkiye might save the 804,346 tons of CO_2 annually or might save the 127,008 tons of CO_2 per annum from energy consumption in residential sector to support national climate goals.

4. Conclusions

Türkiye's climate action trajectory presents a blend of achievements and critical gaps, requiring a concerted effort to accelerate progress toward sustainability. While policy frameworks, international collaborations, and strategic initiatives offer a foundation, the nation must enhance its renewable energy adoption, green building certifications, and emissions reduction strategies to align with global climate objectives.

One important step toward sustainable development in Türkiye is using local and international green building certification systems. As of 2025, the limited number of buildings with green building certification have been identified, and it has been observed that the proportion is very low. The long-term importance of green buildings in the fight against climate change and to progress to achieve the 2030 UN SDGs which should be understood by all stakeholders and property owners, and it is recommended that practices be encouraged through government support which can help developers to design buildings with less energy consumption, eco-friendly materials, and healthier indoor spaces.

The strategic adoption of these global sustainability frameworks holds significant potential for Türkiye. By fostering sustainable urbanization, the country can establish a robust foundation for reducing its environmental footprint to achieve the 2030 climate targets. Aligning Türkiye's national policies and regulations with these internationally recognized certification systems will enable continuous innovation and improvement in the construction sector, reinforcing its commitment to climate action.

In the future, Türkiye's success in sustainable urban development will depend on how well it can improve its policies, increase financial support, and strengthen its laws and regulations by embedding sustainability into its core development strategies, Türkiye can drive long-term economic, environmental, and social benefits, contributing meaningfully to the global climate agenda and setting a precedent for responsible urban growth.

Acknowledgments

This study has been conducted as part of the first author's PhD thesis research. With deep gratitude, the author acknowledges YTB (Yurtdışı Türkler ve Akraba Topluluklar Başkanlığı - Presidency for Turks Abroad and Related Communities) for generously providing a scholarship, which has enabled the continuation of doctoral studies at Çukurova University in Adana, Türkiye.

References

Anyanya, D., Paulillo, A., Fiorini, S., & Lettieri, P. (2025). Evaluating sustainable building assessment systems: A comparative analysis of GBRS and WBLCA. *Frontiers in Built Environment, 11*. Frontiers Media SA. https://doi.org/10.3389/fbuil.2025.1550733

B.E.S.T | ÇEDBİK. (2025). https://www.cedbik.org/best

Climate Action Tracker. (2025). https://climateactiontracker.org/countries/

EDGE Buildings. (2025). *Project studies.* https://edgebuildings.com/project-studies/

EDGAR-The Emissions Database for Global Atmospheric Research. (2024, November 16). Retrieved from https://edgar.jrc.ec.europa.eu/

Eminel, K.N., & Salgın, B. (2025). An evaluation of the topics relating to construction & demolition waste management in green building certification systems. *Erciyes Akademi, 39*, 206–227. https://doi.org/10.48070/erciyesakademi.1590710

European Commission. (2025). *Energy performance of buildings directive*. https://energy.ec.europa.eu/topics/energy-efficiency/energy-efficient-buildings/energy-performance-buildings-directive_en

BREEAM (2025). *Explore the data behind BREEAM projects*. https://tools.breeam.com/projects/explore/map.jsp

Gül, H.H.M., Ercan, H., Akınoğlu, B., & Açıkgöz, Ş. (2025). A retrospective assessment of Türkiye's recent energy policy in terms of energy security and climate change mitigation. *Energies, 18*. https://doi.org/10.3390/en18040951
IEA. (2023). Global CO_2 emissions from buildings, including embodied emissions from new construction, 2022. https://www.iea.org/data-and-statistics/charts/global-co2-emissions-from-buildings-including-embodied-emissions-from-new-construction-2022
IEA. (2024). *Buildings – Energy system*. https://www.iea.org/energy-system/buildings
International Renewable Energy Agency (IRENA). (2025). https://www.irena.org/
Kokatnur, T., Faris, F., Gunay, B., O'Brien, W., & Azar, E. (2025). The WELL Building Standard: A literature review and bibliometric analysis of a nascent field. *Journal of Building Engineering, 103*. https://doi.org/10.1016/j.jobe.2025.112121
Leite Ribeiro, L.M., Piccinini Scolaro, T., & Ghisi, E. (2025). LEED certification in building energy efficiency: A review of its performance efficacy and global applicability. *Sustainability (Switzerland), 17*. https://doi.org/10.3390/su17051876
Liu, S., Durani, F., Syed, Q.R., Haseeb, M., Shamim, J., & Li, Z. (2022). Exploring the dynamic relationship between energy efficiency, trade, economic growth, and CO_2 emissions: Evidence from novel Fourier ARDL approach. *Frontiers in Environmental Science, 10*. https://doi.org/10.3389/fenvs.2022.945091
Ministry of Climate Change. (2025). İklim Değişikliği Başkanlığı. https://iklim.gov.tr/ (in Turkish)
OECD. (2025). *OECD local SDGs.* https://www.oecd.org/en/data/tools/oecd-local-sdgs.html
Ribeiro, F.P., Oladimeji, O., de Mendonça, M.B., Boer, D., Maqbool, R., Haddad, A.N., & Najjar, M.K. (2025). BIM-based parametric energy analysis of green building components for the roofs and facades. *Next Sustainability, 5*, 100078. https://doi.org/10.1016/j.nxsust.2024.100078
Sghiri, A., Gallab, M., Merzouk, S., & Assoul, S. (2025). Leveraging digital twins for enhancing building energy efficiency: A literature review of applications, technologies, and challenges. *Buildings, 15*. https://doi.org/10.3390/buildings15030498
Statista-Türkiye. (2025). *Turkey: Residential building construction 2023*. https://www.statista.com/statistics/1374876/turkey-residential-building-contruction/
Tang, J., Sha, L., Sun, H., & Zhang, W. (2025). Optimizing energy efficiency in buildings' cold water systems: A differential pressure control-based global approach. *Energy and Buildings, 327*. https://doi.org/10.1016/j.enbuild.2024.115108
Tasarım, E. (2025). *YeS TR yeşil sertifika*. https://yestr.org/ (in Turkish)
Tüketici Hakları Derneği. (2025). https://www.tuketicihaklari.org.tr/haberler/basinaciklamalari.html (in Turkish)
Turkish Statistical Institute (TURKSTAT). (2025a, April 12). *The results of address based population registration system, 2024*. Retrieved from https://data.tuik.gov.tr/Bulten/Index?p=The-Results-of-Address-Based-Population-Registration-System-2024-53783&dil=2
Turkish Statistical Institute (TURKSTAT). (2025b). *Statistical themes*. Retrieved from https://www.tuik.gov.tr/
UNFCCC. (2024, January 24). Retrieved from https://unfccc.int/
United Nations Environment Programme, & Global Alliance for Buildings and Construction. (2025). *Not just another brick in the wall: The solutions exist – Scaling them will build on progress and cut emissions fast. Global Status Report for Buildings and Construction 2024/2025*. https://wedocs.unep.org/20.500.11822/47214
Urbanization (2024, September 29). *Our World in Data*. Retrieved from https://ourworldindata.org/urbanization#number-of-people-living-in-urban-areas
USGBC. (2025). https://www.usgbc.org/projects?country=%5B%22Turkey%22%5D
World Green Building Council (WGBC). (2024a). Retrieved January 31, 2024, from https://worldgbc.org/
World Green Building Council (WGBC). (2024b, January 30). *ANZ Status Report 2023—Page 2*. Retrieved from https://viewer.ipaper.io/worldgbc/wgbc-anz-status-report-2023/?page=2
Xian, Y., Wang, H., Zhang, Z., Yang, Y., & Zhong, Y. (2025). Driving factors and reduction paths dynamic simulation optimization of carbon dioxide emissions in China's construction industry under the perspective of dual carbon targets. *Environmental Impact Assessment Review, 112*. https://doi.org/10.1016/j.eiar.2024.107789
Yeşil Bina Sertifikasyonları LEED ve YeS-TR'nin Karşılaştırmalı Özellikleri. (2025). https://www.ituvakif.org.tr/leed-ve-yes-tr-nin-karsilastirmasi (in Turkish)

Proposal of a framework for data acquisition for Digital Twin of building façade

Merve Kaya*[1], Önder H. Bettemir[1]

[1] İnönü University, Department of Civil Engineering, 44280 Malatya, Türkiye

Abstract. The construction sector is one of the cornerstones of developing economies and it has great importance for economic development. However, traditional construction methods pose serious limitations in terms of efficiency and quality. Therefore, the sector needs to be aligned with technological advances in order to increase efficiencies of construction and management processes. These developments provide benefits to the sector in terms of minimizing personnel mistakes, while increasing construction speed and ensures occupational safety. Technological developments also assisted process monitoring and detection of unanticipated mistakes. Earthquakes are important events that affect the structural integrity as well as proper functioning of roof and building façade which interferes with the energy consumption dynamics of buildings. Even if the building is in service after the earthquake, failures of infrastructure system such as heating, electricity, water and communication networks may occur. In addition windows, doors and roofs, especially those in contact with the building façade, are likely to be affected by the earthquake, worsening thermal insulation and increasing heat losses. Therefore, it is necessary to inspect such buildings at frequent intervals. In this study, a framework system including an autonomous ground vehicle algorithms and software that performs non-destructive testing and collects data on the building exterior is proposed to reduce building inspection costs and guarantee the integrity and accuracy of the collected data. The vehicle will be capable of navigating autonomously around the building with a maze algorithm based algorithm and maps the building exterior. The vehicle will be equipped with an optical camera, thermal camera, ultrasonic distance sensors, servo motors for vertical and horizontal scanning from different angles, 2D laser scanner, 9 dof IMU and GPS receiver and Radio Frequency transmitter for real-time data sharing. At night, exterior of the building will be monitored with thermal camera at regular intervals so that early detection of possible heat losses and installation failures will be possible. The developed system will detect the condition of the building infrastructures in a short time with minimum human labor and will accelerate the necessary measures to ensure the effective operation of the heating systems, thus energy will be used effectively.

Keywords: Digital twin; Building monitoring; Building service life; Cyber-physical systems

1. Introduction

Digital transformation is the realization of fundamental changes by integrating digital technologies into business models, processes, organizational structures and systems. Digitalization involves changing socio-technical structures using digital technology and affects the social and technical aspects of structures (Yoo et al., 2010; Fichman et al., 2014). Digital transformation, digitalization and digital innovation are interconnected and enable organizations or industries to make major changes in the way they do business (Fichman et al., 2014). Organizations make the decision to engage in digital transformation by combining their internal needs with external factors such as the proliferation of digital technologies and increased competition. Changing ways of doing business and the evolution of customer expectations make it imperative for organizations to move towards digitalization. This change provides significant advantages, such as maintaining competitive advantage in the sector, increasing efficiency, reducing costs, mitigating risks and engaging with the market. Many different sectors such as industry, health, education and construction have embarked on digital transformation. The construction industry faces chronic problems such as long project durations, high costs, inefficiency, lack of information and communication gaps. The integration of digital technologies is crucial to overcome these problems and create a sustainable, efficient and collaborative building production process for stakeholders. At this point, digital twin technology stands out as one of the building blocks of digital transformation in the construction industry.

The construction industry is one of the most information-intensive sectors where information must be readily available, accurate, complete and in an understandable format. A huge amount of data is generated from a

* Corresponding author, E-mail: 36233621008@ogr.inonu.edu.tr

https://doi.org/10.31462/icearc2025_ce_mng_773

construction project throughout its lifecycle, and the success of the project depends on the insights gained through effective management and analysis of this data. Research emphasizes that knowledge management is an integral part of construction projects and the importance of the processes by which knowledge is generated, communicated and interpreted. However, the literature has mostly focused on the design and construction phases, which account for only 30-40% of the total project cost. The major cost, which is 60-80% of the total cost, is incurred during the operation and utilization phase (El jazzar et al., 2020). The design and management tools used in construction projects have evolved over time from paper drawings to CAD, Building Information Modeling (BIM) and Geographic Information Systems (GIS) (Hasan et al. 2022). In recent years, important steps have been taken in information management thanks to BIM. BIM has transformed the construction industry from 2D-based systems to 3D-object-based systems, making the information needed throughout the project lifecycle more accessible. However, the BIM cannot fully capture the data generated during the operation and utilization phase. To address this shortcoming, Digital Twin technology, one of the key elements of Industry 4.0, comes to the fore.

In the context of the digital twin, the earliest mention of the 'twin' concept is in aerospace. Its general philosophy dates back to NASA's Apollo project in the 1960s (Shafto et al. 2010; Negri et al. 2017; Boschert et al. 2018). However, at that time, the 'twin' was a physical system (Zhuang et al., 2018). The digital side was not included in the title of 'twin' in this period. The term digital twin was first coined by Grieves in 2003 during a lecture on product lifecycle management (PLM) (Grieves, 2014). The first Digital Twin application was implemented by NASA in the Apollo program in 2010 to reflect the state of the spacecraft. The definition of the Digital Twin has evolved over time, focusing on three main components: physical environment, virtual environment, and the data that connects these two environment. Based on the work of Kritzinger et al. (2018), the level of integration of these components is classified as Digital Model (manual data flow), Digital Shadow (automatic one-way data flow), and fully integrated Digital Twin (two-way data flow). Existing BIM applications in the construction industry generally fall into the Digital Shadow subcategory and changes to the digital models do not affect the physical environment. A fully integrated Digital Twin should be able to enable bidirectional data exchange between both physical and virtual environments.

2. Materials and methods

Maze solving algorithms aim to solve a maze autonomously without external intervention. Various algorithms have been developed in this regard, depending on the type of maze. Left/right hand rule, depth-first search, width-first search, Dijkstra's algorithm and A* search algorithm are some of them. The left-hand or right-hand rule, also known as the wall-following algorithm, is widely used in maze solving. In this algorithm, the robot starts by placing its hand on a wall and then proceeds by always following the wall in that direction. It is suitable for simply-connected mazes, where all walls are connected to each other or to an external boundary. If there are loops in the maze, the robot may return to the same place or may not reach the exit. In the left hand rule, the robot moves forward by placing its hand on the left wall and prioritizes turning left at the junctions. In a maze using this method, the robot can encounter eight basic situations: left turn only, right turn only, right or left turn, straight ahead and left or right turn, straight ahead or left turn, straight ahead or left turn, straight ahead or right turn, straight ahead or right turn, reaching the end of the maze and dead end.

Suthar and Shukla (2023) designed, implemented and analyzed the performance of a robot that autonomously solves loop-free mazes using infrared (IR) sensors and the Left-Hand-Wall Algorithm. The developed robot is equipped with an Arduino Uno microcontroller, L298N motor driver, two DC motors, three IR sensors and a 7.4V Li-ion rechargeable battery. The IR sensors enabled the robot to be steered by detecting the contrast between the black maze lines and the white background. The motor driver and Arduino Uno processed the data from the sensors to determine the robot's movements and direction changes. As a result of the experiments, it was observed that the robot completed the maze with 70% success.

Suryanarayana and Akhila (2021), developed a Maze Solving Robot that uses the wall following algorithm (left hand rule) by measuring distance with ultrasonic sensors. In the study, 6 path detection sensors were used. Two sensors act as path sensors and detect the robot's deviations, helping to keep it on track. Two sensors allow the robot to turn left or right. One sensor is used for forward direction detection, while one sensor is used to determine when the end of the maze has been reached. As the robot moves forward, it exhibits the following behaviors: Finds the next intersection by following the line, detects the type of intersection and changes direction at the intersection. These processes continue cyclically until the end of the maze. Using the data from its sensor, the Arduino determines the direction of movement according to a specific algorithm. First it checks the left path, if there is no left path, it evaluates the forward direction. If there is no forward path, it checks the right path. If there is no right path, it makes a 'U' turn and continues to try possibilities until it is determined that all sensors are on the black surface. When all IR (Infrared) sensors of the robot are on the black surface, it stops the movement. IR sensors work by detecting the color of the surface. When the sensor is on a dark surface, the surface absorbs the rays and the IR receiver does not receive any rays. This sends an active high signal to the Arduino. On light-colored surfaces, most of the reflected rays are detected by the IR receiver because these surfaces reflect the beam. This is how IR sensors detect the black path.

Khaleel and Oleiwi (2024), developed a decision-making algorithm for autonomous mobile robots to move through a maze without hitting walls. Ultrasonic sensors are used to avoid obstacles and the robot moves flexibly according to the measured distances. The algorithm starts with determining the starting point, activating the ultrasonic sensor, servo motor and DC motors. When the robot starts, the ultrasonic sensor measures the distance and this sensor scans its surroundings by rotating between 0 and 180 degrees through the micro servo motor. To make the measurements more stable, the robot waits three seconds before moving. If the distance is 20 cm or less, the robot stops the right DC motor and turns to the left. If the distance is more than 20 cm, the left DC motor is stopped and the robot turns to the right. The distance of 20 cm was chosen because it is compatible with the robot's height. To complete the 300 cm long maze, the robot stopped 10 times and checked its surroundings with an ultrasonic sensor moving between 0-180 degrees. If it encounters an obstacle, it continues on its way in an unobstructed direction. If there is no obstacle, the robot stops and reaches the target point. The central control of the system is provided by the Arduino Uno microcontroller. The movement of the robot is provided by two DC motors controlled by an L298N motor driver. The robot reached the target point in 60 seconds by moving at a speed of 5 cm/sec. It is stated that the developed algorithm is highly suitable for autonomous mobile robots to avoid collisions with wooden walls and offers the fastest solution compared to similar studies.

Pandian et al. (2012) developed a maze solving robot (MSR). The robot consists of three subsystems: the drive system, the sensor system consisting of various sensors and the control system. The developed robot aims to find the shortest route in the maze using an algorithm called LSRB. In the LSRB algorithm, the robot reaches the target from the starting point in two stages. Four basic motion decisions are defined here: L (left), S (straight), R (right) and B (return). In the search phase, at each intersection, the robot evaluates these movements in a certain priority order and records them in the decision book. In the journey phase, this sequence of decisions is optimized to obtain a shorter and more efficient path. For example, while solving the maze, the decision sequence is “LBLLBSR”, this sequence is optimized and reduced to “SRR”. Thus, the robot efficiently determines the shortest path to reach the goal.

In this study, it is aimed to create an algorithm which can loop around a building without any help from a human. The algorithm will run on an unmanned ground vehicle equipped with distance sensors and LIDAR devices that will autonomously navigate around a building and create a database for digital twin creation by laser scanning. The robot will navigate with certain functions based on the maze algorithm. The vehicle will move counterclockwise and follow the walls with the left hand algorithm. In areas where the building walls or columns protrude and there are stones, sand piles or any other obstacles in the direction of the vehicle, the vehicle will activate the 'obstacle avoidance algorithm to overcome this situation and continue on its way. In cases where the building has a indendated architectural elements, the 'exit from the recess' algorithm will work. In cases where the walls continue straight and the robot's hand can move forward without touching the left wall for a while, the straight ahead algorithm will be active. The general flowchart and the specific algorithms that the vehicle will use while moving will be explained separately.

2.1. Explanation of algorithms

In the first step of the algorithm, before the vehicle starts looping, it requests the initial values to be assigned to the sensors. Once the data entry is complete, the mapping process will begin. At the beginning, the vehicle proceeds with the straight forward function and checks whether there are any obstacles, wall indentation or wall protrusions. As shown in Fig. 1, if the answer to the question “Are there any obstacle in the way?” is yes, the obstacle avoidance function is started in order to avoid the obstacle and continue the movement. After the obstacle is successfully overcome, the robot continues its path by activating the straight forward function again. It moves forward again by checking whether there is an obstacle, wall indentation or wall protrusion in front of it. The check whether there is a wall indentation or not is done with the question “Is there an indentation in the way?”. If the answer to this question is “Yes”, the robot moves to the relevant area and initiates the indentation escape function. This function will allow the vehicle to enter the indentation, scan the area inside and then return to the main route. After the indentation is completed, the vehicle moves forward again with the straight forward function. When each progress step is completed, it will ask the question “Is the building tour complete?”. If the tour around the building is complete, the mapping process is successfully completed, otherwise, the algorithm reverts back to the beginning and the steps are performed again. The flowchart presented in Fig. 1 shows the logical basis of the autonomous progression process based on the robot's environmental awareness and situation-based decision-making capabilities.

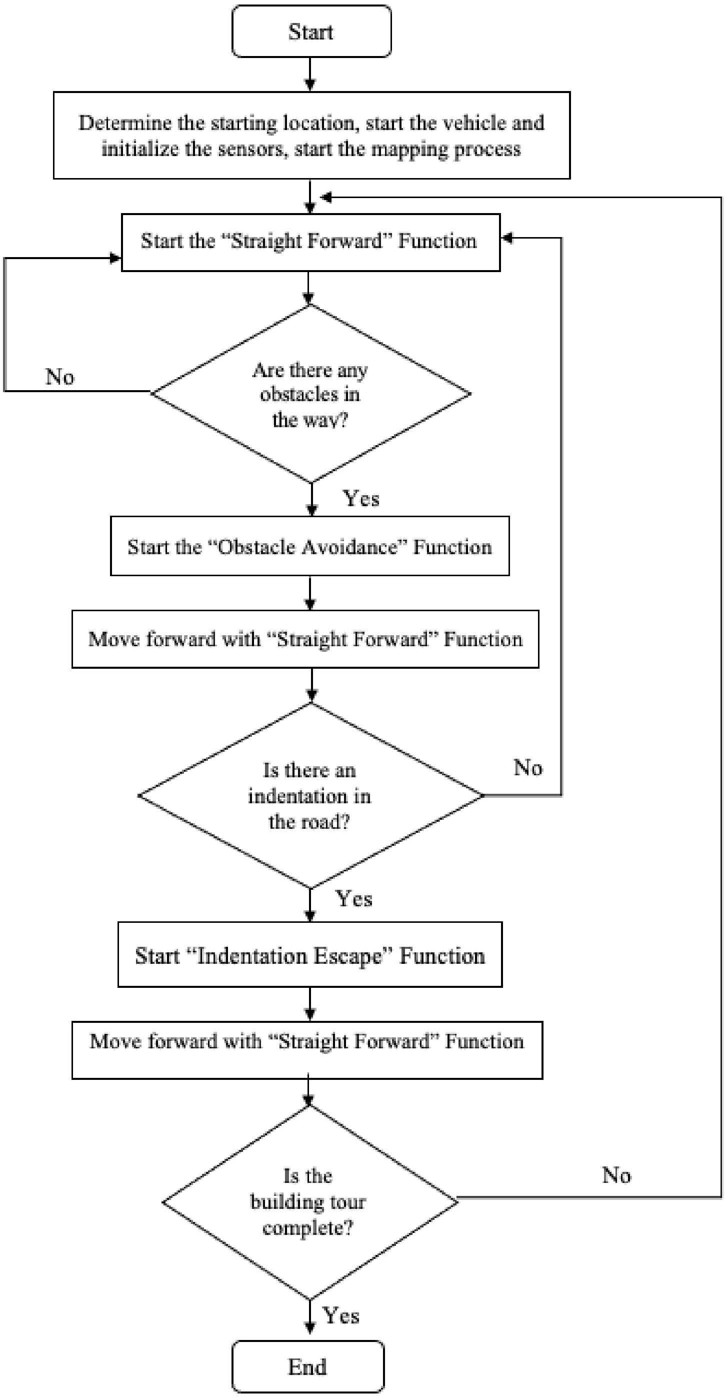

Fig. 1. Flowchart of the proposed algorithm

2.1.1. Straight forward function

In the "Straight Forward" function, the process starts by measuring the distance between the vehicle and the wall via the ultrasonic sensor. The vehicle then advances 5 cm, stops and scans its surroundings. During the scan, it checks whether the distance between its current position and the wall. If this distance is more than 50 cm, the vehicle rotates 5 degrees to the left to correct this deviation, assuming that the vehicle is moving away from the reference wall. Otherwise, if the distance is less than 50 cm, it is assumed that the robot is getting too close to the wall and the vehicle it rotates 5 degrees to the right to adjust the heading. After orientation, the vehicle is moved forward again and the process is repeated iteratively. Thanks to this approach, the robot can move in a linear and controlled manner, keeping the distance from the wall as close as possible to 50 cm. The flowchart of the straight forward function is as shown in Fig. 2.

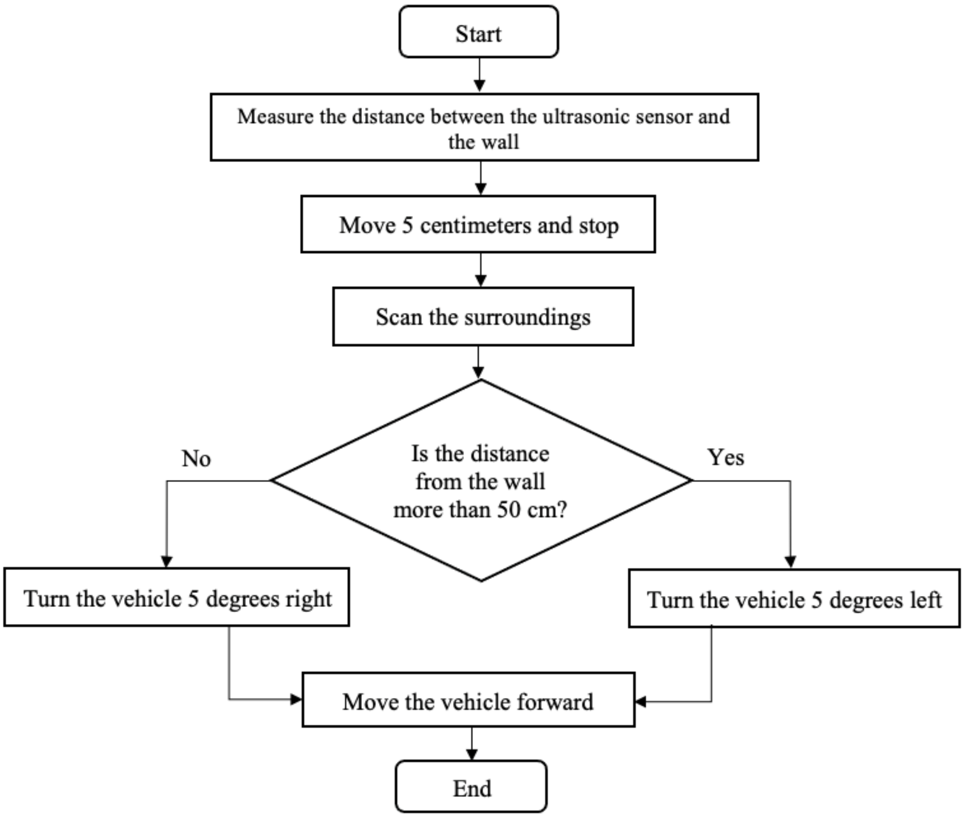

Fig. 2. Flowchart of the forward motion algorithm

2.1.2. Obstacle avoidance algorithm

If there is an obstacle in front of the vehicle, the "Obstacle Avoidance" function is activated and determines whether there is an obstacle on the road based on the distance between the front sensor and the wall or obstacle. If the distance measured by the front sensor is less than 50 cm, it will be assumed that there is an obstacle in front of the vehicle and the vehicle will turn 90 degrees to the right and start the obstacle avoidance maneuver. As the vehicle travels, the distance between the left sensor and the wall is continuously monitored and at the same time it is queried whether the distance increase is more than 1 meter. If the increase between consecutive distance measurement values is more than 1 meter, the vehicle has completed the obstacle avoidance maneuver. Since it moves away from the front face of the obstacle, it turns 90 degrees to the left in order to prevent losing its route and continues to move straight ahead by approaching the wall line again. While moving forward, the vehicle's left sensor distance increase will be queried again and if it is more than 1 meter, the vehicle will turn ninety degrees to the left and continue straight ahead. Finally, the front sensor distance is monitored and if the distance value decreases to 50 cm, the vehicle turns to the right and continues moving forward, thus overcoming the obstacle in front of it. This algorithm aims to realize a safe progress by enabling the vehicle to react autonomously to environmental obstacles. The flowchart of the algorithm is presented in Fig. 3.

2.1.3. Wall indentation exploration algorithm

In cases where the vehicle needs to enter narrow areas or inside a wall indentation, the "Indentation Escape" function is activated to scan the recessed area and exit the area correctly and safely. In this algorithm, firstly, the distance between the left sensor of the vehicle and the wall is monitored and the distance increase is queried and if the increase is more than 1 meter, the vehicle will turn 90 degrees to the left and the decision is made to proceed straight. This progress continues until the front sensor distance is 50 cm. When 50 cm is reached, the vehicle turns 90 degrees to the right and drives straight ahead. While moving forward, the front sensor distance is queried at every 5 cm step interval and when it drops to 50 cm again, the vehicle will once again turn 90 degrees to the right and move forward. Finally, the left sensor distance will be evaluated again and the distance increase will be checked and if the difference between 2 consecutive distance measurement values is more than 1 meter, the vehicle will turn 90 degrees to the left and continue with the straight ahead function and the process of exiting the recess will be completed. The flowchart of the algorithm is presented in Fig. 4.

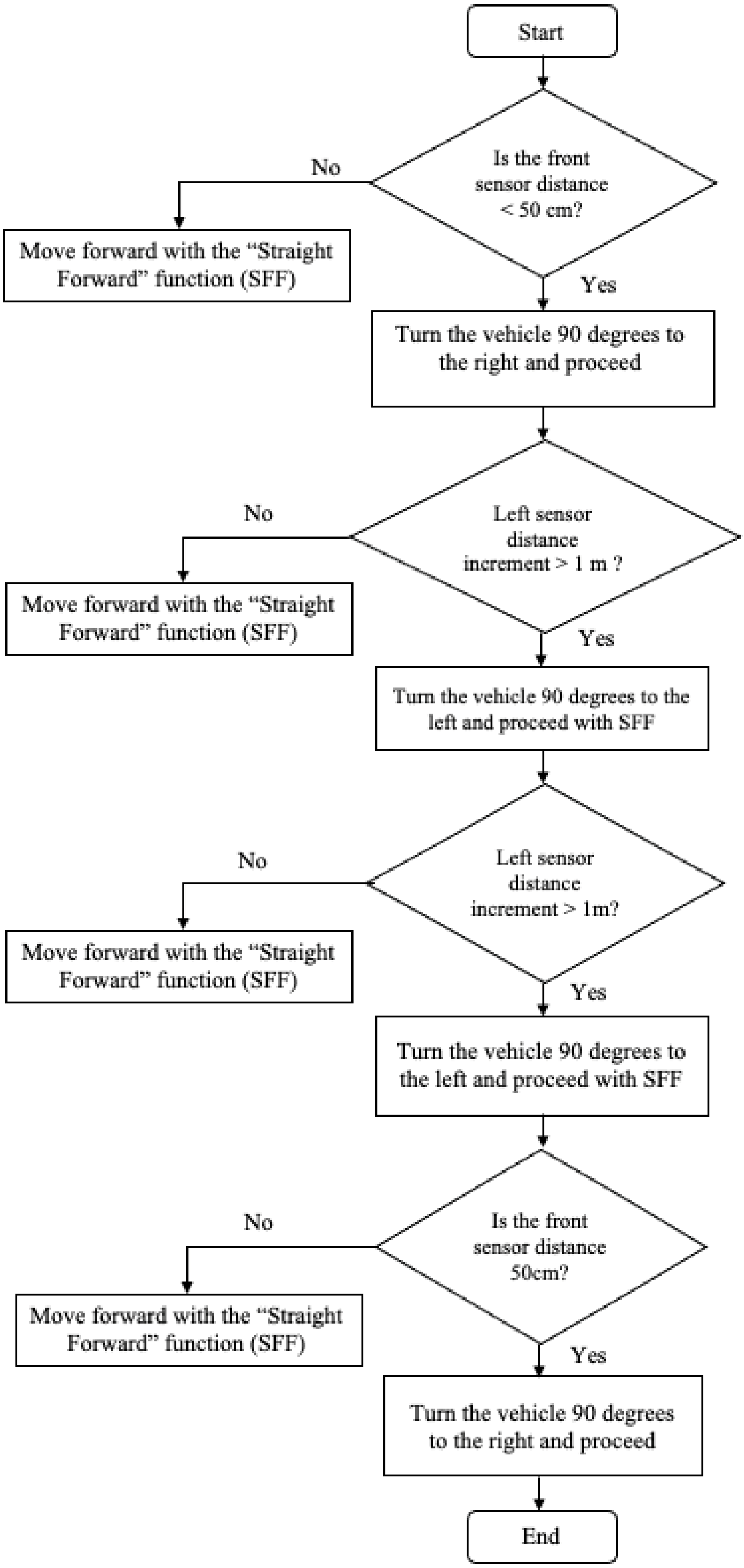

Fig. 3. Flowchart of the obstacle avoidance algorithm

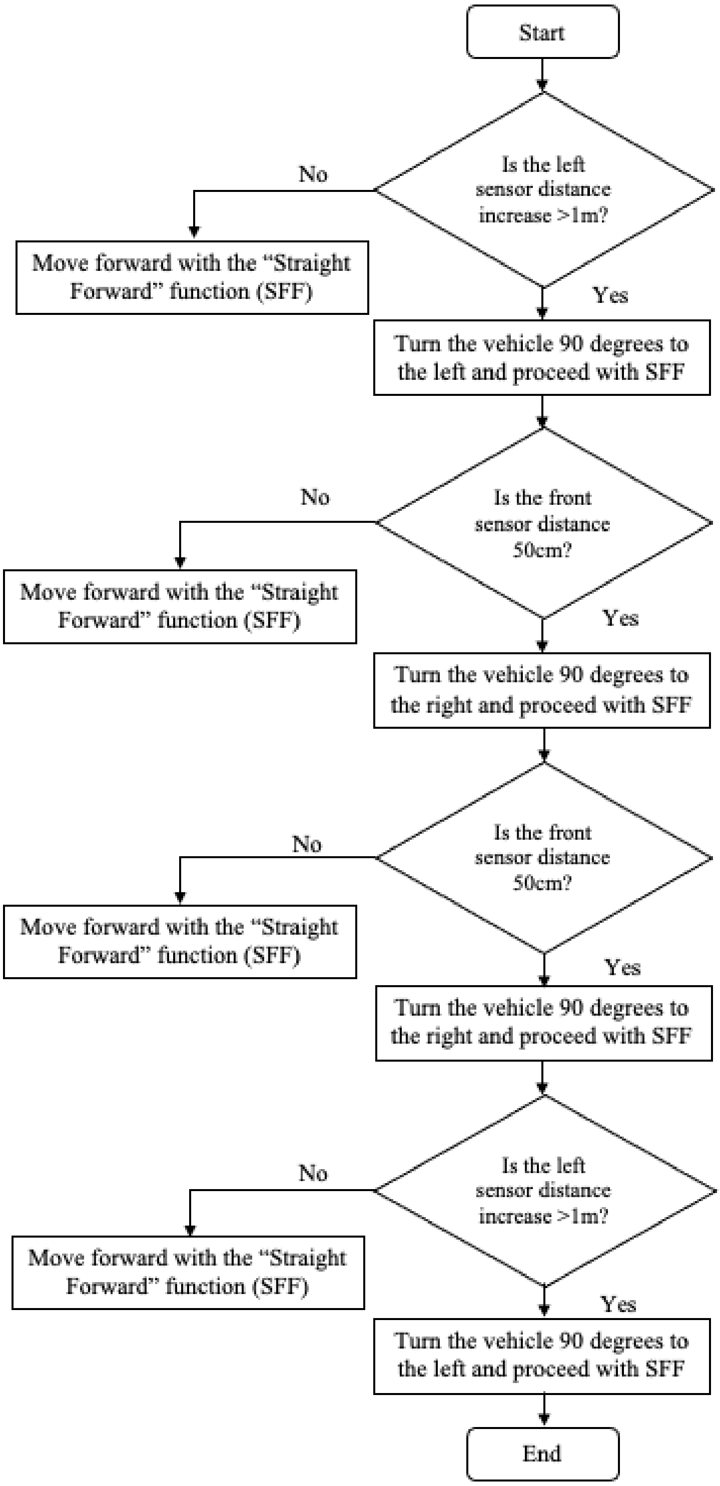

Fig. 4. Flowchart of the wall indentation exploration algorithm

3. Case study

The study, in which a sample environment model is created and the algorithm mentioned above is applied in a simulation environment, is described in detail in this section.

3.1. Facade modeling and design for autonomous vehicle integration

In the first phase of the study, a building façade was modeled for the vehicle to navigate around and extract its digital twin. This was done using the SketchUp program, which allows three-dimensional (3D) modeling. In this context, an environment presented in Fig. 5 was designed with various obstacle situations that the vehicle may encounter as it travels. In this building environment model, the building is assumed to have straight walls with protruding and indentationed architectural areas. These regions are considered separately and algorithms are generated for each situation in order for the vehicle to navigate autonomously. In particular, the model includes a combination of facade surfaces enriched with indentations and protrusions, and building components that run straight. This diversity was chosen in order to test the vehicle in different situations. The geometry of the building façade is detailed to be suitable for sensor detection, taking into account volumetric differences, depths and edge lines that can be read by Lidar sensors and cameras. Indentations and protrusions are added to the model to enable the vehicle's sensor systems to detect the boundaries and form of the structure more effectively. These architectural elements have the potential to serve as reference points in the robot's pose estimation, distance measurement and environment mapping processes. Sections of the model with flat surfaces are important areas for evaluating the vehicle's ability to move without deviating from a certain direction. These surfaces can also be preferred as reference planes when creating a digital twin of the building.

3.2. Creation of simulation environment and implementation of autonomous navigation algorithms

In the second phase of the study, a simulation environment was designed to display the building façade in three dimensions and allow an autonomous ground vehicle to navigate around the building. The main goal of the simulation is to enable the vehicle to develop environmental awareness based on the building geometry, detect the façade and determine its route accordingly. This digital environment allows testing algorithms, evaluating vehicle-building interaction and testing data collection processes.

The environment used in the simulation is based on a three-dimensional model of the building facade modeled in SketchUp software. The model is adjusted to reflect the real environment conditions in terms of surface details and change of direction points that the autonomous vehicle will interact with. Geometric variations on the façade, such as indentations, recesses, flat surface transitions and corner points, are crucial for the vehicle to analyze sensor data and map its surroundings. In the simulation, the algorithm detailed above, which is based on the wall tracking method used in maze solving, was used. The algorithm allows the vehicle to change direction at each decision point by evaluating the obstacles in front and to the sides.

This simulation environment was a useful test platform for developing the data collection infrastructure for the digital twin formation process. The data acquired by the autonomous vehicle will be integrated into the digital twin model of the building and will form the basis for the reconstruction of the building envelope under real environmental conditions. At the same time, this environment will increase the applicability of the system by enabling the algorithms to be tested on different building typologies and facade geometries.

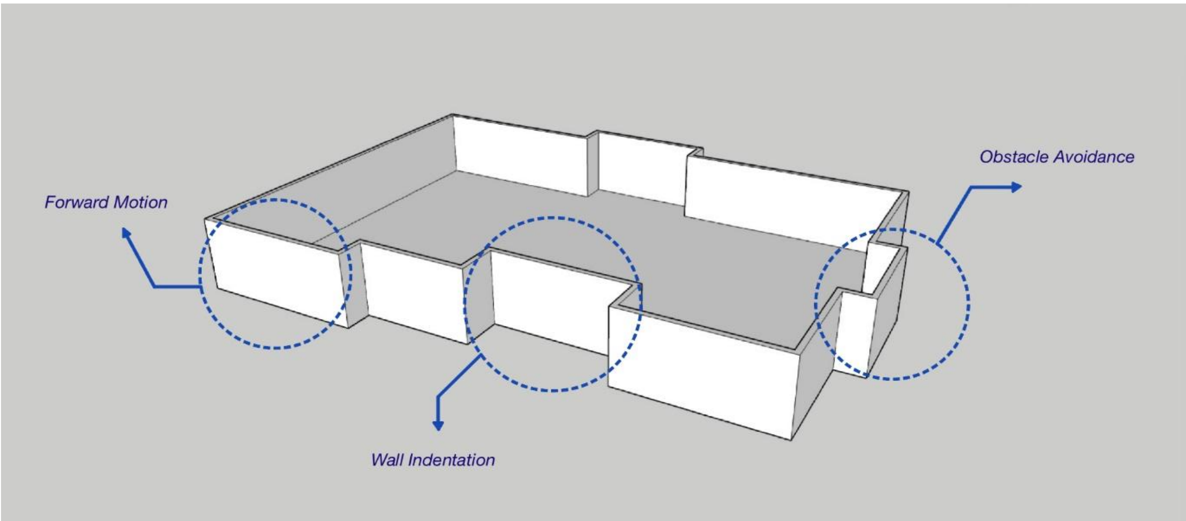

Fig. 5. Fictitious building façade

3.3 Simulation outputs

3.3.1. Forward motion example

By applying the forward motion function in the simulation environment, the images in Figure 6 are generated. The vehicle starts its movement at the starting point of a straight wall (Fig. 6a). While moving forward, the vehicle also tracks the distance between the left sensor and the wall and when it detects that it is more than 50 cm away from the wall, it changes its heading angle by 5 degrees to the left and continues its movement (Fig. 6b). When the vehicle is closer than 50 cm to the wall, as shown in Figure 6c, it turns 5 degrees to the right, moves away from the wall and continues its movement straight ahead again at a distance of 50 cm (Fig. 6d-e).

3.3.2. Obstacle avoidance example
Fig. 7 shows the results of testing the obstacle escape function in the simulation. The vehicle detects that there is an obstacle in front of it when the front sensor distance, which it monitors continuously, reaches 50 cm (Fig. 7a). In order to go around the obstacle, it turns 90 degrees to the right and continues moving forward (Figure 7b). At the same time, the vehicle also monitors the left sensor distance and when it detects a value of more than 1m, it turns 90 degrees to the left and starts moving parallel to the wall again (Fig. 7c-d-e). When it reaches the end of the wall, it detects a high value for the left sensor distance and moves 90 degrees to the left (Fig. 7f-g). It analyzes the front sensor values again and when it reaches 50 cm, it detects the presence of a wall in front of it and continues its movement by turning 90 degrees to the right and thus successfully overcomes the obstacle (Fig. 7h- i- j).

3.3.3. Example of escape from an indentation
While moving forward, the vehicle scans the building facade with the LIDAR device on the vehicle and exhibits the behavior shown in Fig. 8 when it encounters an indentation. The vehicle detects that it will enter an indentation when the left sensor distance is more than 1 meter and initiates the exit function (Fig. 8a-b). It first turns left and moves into the recess, and when the front sensor distance is 50 cm, it detects that there is a wall in front of it and which prevents it to move further. Therefore it continues its movement by turning 90 degrees to the right (Fig. 8c-d-e). It continues until the front sensor distance is 50 cm again, at which point it turns right once more and exits the recess (Fig. 8f-g). Finally, in order not to move away from the wall but to follow it, it continues its movement by turning left when the left sensor distance is greater than 1 m (Fig. 8 h-i-j).

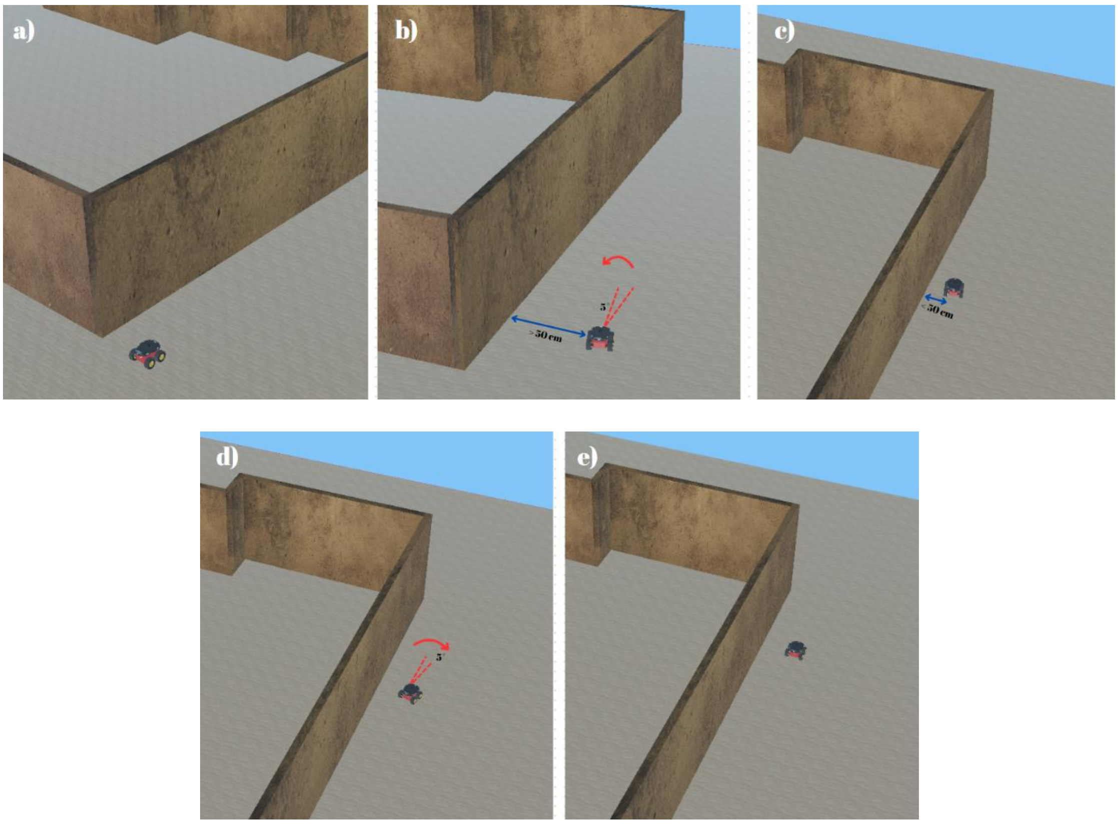

Fig. 6. Simulation outputs of the forward motion algorithm

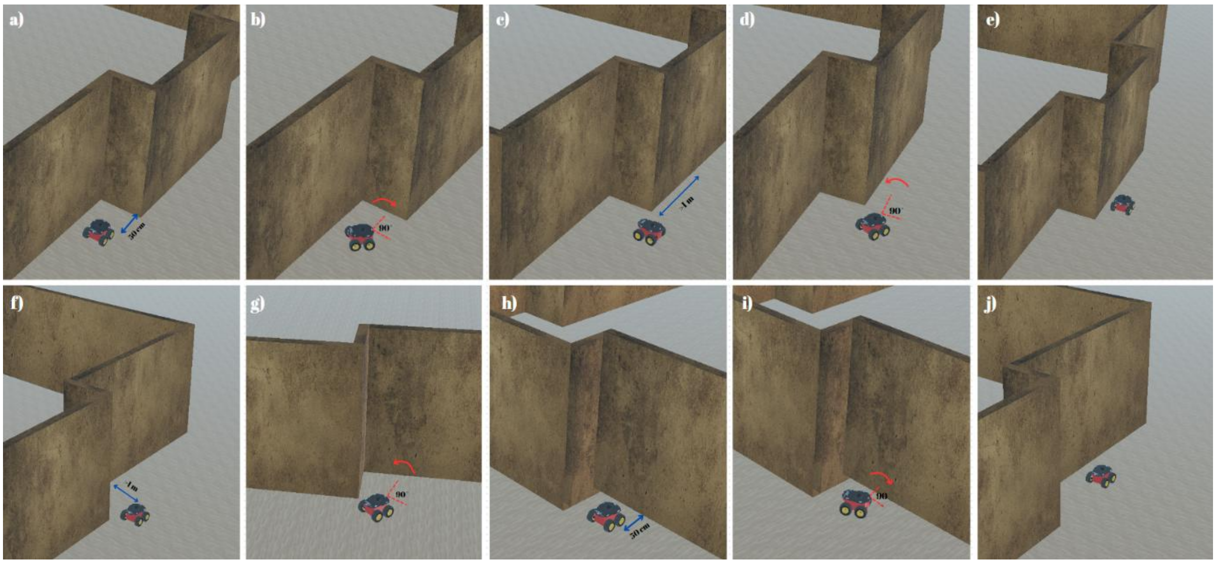

Fig. 7. Simulation outputs of the obstacle avoidance algorithm

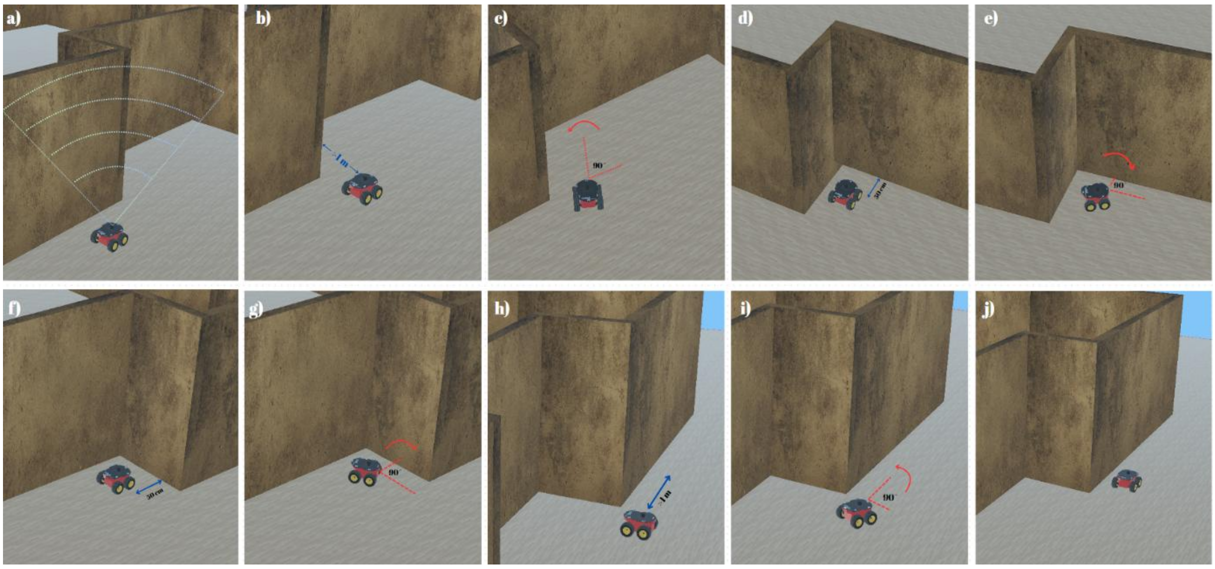

Fig. 8. Simulation outputs of the wall indentation exploration algorithm

4. Results and discussion

As a result of simulation experiments, it was observed that the developed algorithms worked successfully against complex geometries such as recesses and protrusions on the building facade. Thanks to the wall-following algorithm based on the left-hand rule, the vehicle followed a route around the structure at a certain distance and was able to follow the exterior facade line without deviating. The fact that the vehicle continued without deviating from the route at corner points and narrow recesses that required sudden changes of direction, which have the potential to cause complexity, shows that the developed algorithm can correctly analyze the architectural form of the structure.

The vehicle is equipped with various distance sensors and data is collected from these sensors continuously. On the other hand, the algorithm that forms the vehicle's orientation mechanism consists of many "if" loops in order to make the right decisions and ensure continuous progress. When all these are taken into consideration, it is seen that the size of the collected data and the computational complexity of the algorithm allow it to be processed on the Arduino Mega microcontroller card, the memory and processing power of the Arduino Mega are compatible with the selected algorithms and can successfully perform real-time location calculations. This situation shows that the system can be applied with low-cost hardware.

In addition, within the scope of the study, an easy but functional mapping algorithm and a cost-effective tool in terms of hardware were developed by considering the cost. The sensors and routing algorithm used ensured the implementation of environmental mapping with minimum hardware requirements. Simplicity of the algorithm increased the accessibility of the system for both academic studies and field applications.

When all these results are brought together, it was seen that the developed system is sufficient to be used in real applications. The positive evaluations made in terms of simulation tests, sensor performance, hardware compatibility and software stability show the applicability of the system in terms of digital twin production. In this respect, the study contributes to digitalization in the construction sector by developing a low-cost and integrable solution.

5. Conclusions

Traditional methods in today's construction sector take time due to the complexity and difficulty of application and create certain restrictions on efficiency. For such reasons, the need to adapt to digitalization is increasing day by day. At this point, digital twin technology is an important tool in terms of making the design, operation and maintenance processes of buildings more efficient, cost-effective, sustainable and smart. However, data collection, which is one of the basic steps of the digital twin creation process, is a significant challenge in this process due to high hardware costs, manual operations requiring expertise, and time-intensive resource consumption. The maze-based, left-hand rule-based autonomous navigation algorithm developed in this study has automated the data collection process and made it more efficient in terms of both time and cost. Mapping the building geometry through environmental scanning by an autonomous ground vehicle has reduced the workload in the process by minimizing human intervention and enabled the automatic collection of the data needed for the formation of digital twin.

The fact that the developed system can work seamlessly with low-cost hardware has increased the accessibility and applicability of the method. Tests conducted in a simulation environment have shown that the algorithm provides reliable results on building facades with structural recesses and protrusions. However, testing the system on more complex building geometries will provide a clearer understanding of the potential deficiencies and limitations that the algorithm may encounter. In this way, it will be possible to adapt it to more flexible usage scenarios in digital twin formation processes.

References

Yoo, Y., Lyytinen, K.J., Boland, R.J., & Berente, N. (2010). The next wave of digital innovation: Opportunities and challenges. A report on the research workshop: 'Digital Challenges in Innovation Research'.

Fichman, R.G., Dos Santos, B.L., & Zheng, Z. (2014). Digital innovation as a fundamental and powerful concept in the information systems curriculum. *MIS Quarterly, 38*(2), 329-A15

El Jazzar, M., Piskernik, M., & Nassereddine, H. (2020). Digital twin in construction: An empirical analysis. In: *Proceedings of EG-ICE 2020 Workshop on Intelligent Computing in Engineering,* 501-510

Hasan, S.M., Lee, K., Moon, D., Kwon, S., Jinwoo, S., & Lee, S. (2022). Augmented reality and digital twin system for interaction with construction machinery. *Journal of Asian Architecture and Building Engineering, 21*(2), 564-574

Shafto, M., Conroy, M., Doyle, R., Glaessgen, E., Kemp, C., LeMoigne, J., & Wang, L. (2010). Draft modeling, simulation, information technology & processing roadmap. *Technology Area, 11*, 1-32

Negri, E., Fumagalli, L., & Macchi, M. (2017). A review of the roles of digital twin in CPS-based production systems. *Procedia Manufacturing, 11*, 939-948

Boschert, S., Heinrich, C., & Rosen, R. (2018). Next generation digital twin. In: *Proc. TMCE*, 2018, 7-11. Las Palmas de Gran Canaria, Spain

Zhuang, C., Miao, T., Liu, J., & Xiong, H. (2021). The connotation of digital twin, and the construction and application method of shop-floor digital twin. *Robotics and Computer-Integrated Manufacturing, 68*, 102075

Grieves, M. (2014). Digital twin: manufacturing excellence through virtual factory replication. *White Paper, 1*(2014), 1-7

Kritzinger, W., Karner, M., Traar, G., Henjes, J., & Sihn, W. (2018). Digital Twin in manufacturing: A categorical literature review and classification. *Ifac-PapersOnline, 51*(11), 1016-1022

Suthar, S., & Shukla, V. (2023). Intelligent non-looped maze solving robot: IR sensor-driven autonomous navigation. In: *Proc. 2023 IEEE Technology & Engineering Management Conference-Asia Pacific (TEMSCON-ASPAC)*, 1-5

Suryanarayana, S., & Akhila, V. (2021). Autonomous maze solving robot using arduino. *Technology (IJARET), 12*(3), 595-603

Khaleel, H.Z., & Oleiwi, B.K. (2024). Ultrasonic sensor decision-making algorithm for mobile robot motion in maze environment. *Bulletin of Electrical Engineering and Informatics, 13*(1), 109-116

Pandian, J.A., Karthick, R., & Karthikeyan, B. (2012). Maze solving robot using freeduino and LSRB algorithm. *International Journal of Modern Engineering Research, 56*, 92-100

4th International Civil Engineering & Architecture Conference
17-19 May 2025, Trabzon, Türkiye

Analyzing causal factors of workflow variability in construction projects: An exploratory factor analysis

Rajaa Abuelaish*[1], Ümit Bahadır[1], Vedat Toğan[1]

[1] Karadeniz Technical University, Department of Civil Engineering, 61080 Trabzon, Türkiye

Abstract. Construction projects are characterized by complexity and high levels of variability, which often lead to reduced performance, cost overruns, and inefficiencies in planning. Recognizing workflow variability as a critical challenge in the construction industry, this study aims to systematically identify and categorize its key causes. A quantitative approach was employed, utilizing a structured questionnaire informed by an extensive literature review, which identified 38 potential causes. The data were analyzed using exploratory factor analysis (EFA), resulting in the retention of 21 causes, grouped into four principal factors: resources, management and planning, material, and prerequisite. The study provides empirical insights into the primary sources of workflow variability in Turkish construction projects, an area with limited prior research. By organizing the causes into clear and actionable categories, the findings offer practical guidance for minimizing variability and enhancing project performance. In particular, the results highlight the critical role of resource management in achieving workflow stability. This research contributes to both academic knowledge and industry practice by presenting a structured framework for understanding and addressing workflow variability in construction.

Keywords: Workflow variability; Turkish construction projects; Factor analysis

1. Introduction

Workflow variability remains a persistent and significant challenge in construction projects, often leading to budget overruns and delays (Han & Park, 2011). The construction industry's inherent complexity arises from the dynamic interaction among multiple variables and activities, resulting in unpredictable workflows and disruptions (Abbasian-Hosseini et al., 2018; Abusalem, 2020). Prior studies emphasize that ineffective variability management significantly impacts project performance, extending durations and increasing costs (Jaśkowski et al., 2021; Salhab et al., 2022).

For example, research by Ballesteros-Pérez et al. (2020) noted variability levels as high as 60% in activity durations, profoundly influencing overall project schedules. Furthermore, reducing variability in critical activities substantially improves project completion probabilities and reduces waiting times (Salhab et al., 2022). Despite this understanding, limited empirical research has investigated the root causes of workflow variability, particularly in developing countries. To address this gap, the present study employs exploratory factor analysis (EFA) through a questionnaire survey to systematically identify and analyze critical factors causing workflow variability in construction projects.

2. Literature review

Workflow variability in production systems primarily results from two interconnected factors: variability sources and delayed flow between upstream and downstream activities (Garcia-Lopez & Fischer, 2024; Wambeke et al., 2011). These factors are interdependent, as variability sources often lead to activity delays, subsequently causing late delivery of downstream workflows (Garcia-Lopez & Fischer, 2024).

Prerequisite work significantly contributes to workflow variability through delayed interactions between upstream and downstream activities (Garrido Martins et al., 2023). Construction processes typically involve interconnected sequences of predecessor (upstream) and successor (downstream) activities, where delays in upstream tasks propagate downstream, creating cumulative disruptions (Su et al., 2024; Wambeke et al., 2011). Consequently, delays in prerequisite activities can trigger rework, extend subsequent task durations, and intensify workflow variability across the project (Salhab et al., 2022; Ye et al., 2015).

Design-related workflow variability mainly results from errors, omissions, and inadequate details in project drawings, causing rework and delays due to frequent changes and incomplete information (Ballesteros-Pérez et

* Corresponding author, E-mail: rabuelaish@hotmail.com

https://doi.org/10.31462/icearc2025_ce_mng_774

al., 2020; Shehab et al., 2023). Resource-related variability, particularly regarding material and equipment availability, critically affects workflow continuity (Umar et al., 2020). Delays or incorrect specifications in material deliveries frequently disrupt tasks, leading to idle time, increased costs, and reduced productivity (Arbulu et al., 2005; Wambeke, 2011; Yap et al., 2018).

Labor-related issues, including absenteeism, skill shortages, low productivity, and inadequate training significantly increase workflow variability (Javanmardi et al., 2016; Lindhard et al., 2019). Unplanned absenteeism and ineffective site management create disruptions, reducing worker morale and performance, particularly in developing countries (Handayani et al., 2021; Radjawane & Darmawan, 2022). Equipment management also plays a vital role, with breakdowns, insufficient availability, or inadequate maintenance practices directly impacting worker efficiency and causing project delays (Ballesteros-Pérez et al., 2020).

Additionally, site congestion and poor workspace layouts lead to overcrowding, safety hazards, and reduced productivity, further exacerbating workflow variability (Salhab et al., 2022; Umar et al., 2020). Finally, ineffective management practices, delayed payments, unclear contract administration, and inadequate communication among project stakeholders significantly intensify workflow disruptions, negatively affecting overall project performance (Ballesteros-Pérez et al., 2020; Peters et al., 2019; Sümer & Arditi, 2022).

The pertinent causes of workflow variability that potentially affect the project performance were explored by conducting a systematic background review. A comprehensive review of 20 relevant studies led to the identification of 61 distinct factors contributing to workflow variability in construction projects. The frequency of each factor, based on its occurrence across the reviewed literature, ranged from one to eight.

3. Methodology

Initially, a literature review was carried out to provide a comprehensive list of common workflow variability causes that could be examined in construction projects. The questionnaire was then designed based on the list of workflow variability causes extracted from the literature review. In the context of construction management studies, a questionnaire survey has been widely used to rank relevant variables (Garrido Martins et al., 2023; Jaśkowski et al., 2021; Shehab et al., 2023). This study employs a quantitative method, as shown in Fig. 1, to explore workflow variability causes and aims to evaluate them by conducting EFA.

Factor analysis is widely recognized as a statistical technique for data reduction and the identification of underlying patterns among interrelated variables (Hair et al., 2019). In this study, 61 causes of workflow variability were initially compiled from the literature and structured into a preliminary questionnaire. The questionnaire was refined through an extensive literature review and expert consultations. Face validity was applied to ensure the clarity and relevance of item wording, while expert feedback was used to modify existing items and suggest new ones (Broder et al., 2007). Based on this assessment, necessary adjustments were made to enhance content accuracy. A pilot study was subsequently conducted to evaluate the questionnaire's structure and usability in preparation for full-scale data collection (Dikko, 2016).

Incorporating feedback from the pilot study, the final version of the questionnaire comprised two sections: Section A collected respondents' general information (3 items), while Section B asked respondents to rate the identified workflow variability causes across 38 items using a five-point Likert scale (1 = not significant; 5 = extremely significant). The survey was distributed both electronically and face-to-face to Turkish construction professionals, including contractors, clients, and consultants. Out of 300 distributed questionnaires, 201 fully completed responses were received, yielding a response rate of 67%, considered high compared to similar studies (Culfik et al., 2014; KV & Bhat, 2019; Umar et al., 2020).

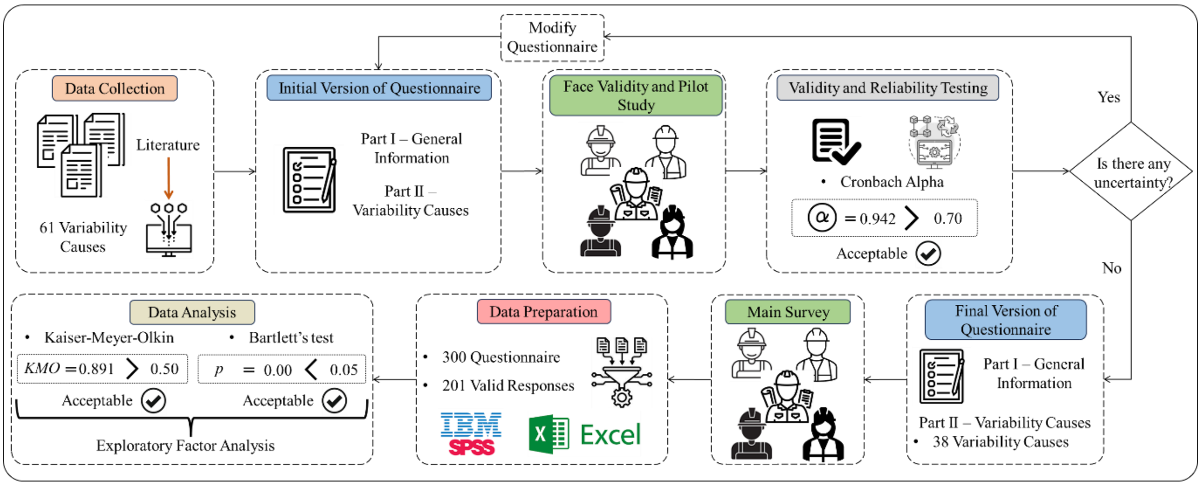

Fig. 1. Research methodology

Table 1 summarizes the professional profiles of survey respondents, highlighting diverse job roles and extensive experience. Approximately half possessed over 10 years of experience in construction, with 79.6% holding administrative positions across various specializations, predominantly within contracting firms. This respondent profile is appropriate and sufficiently representative for conducting exploratory research.

To identify underlying factors causing workflow variability in construction projects, EFA was conducted on the identified variability causes, consistent with established practices in construction management research (Umar et al., 2020; Yap et al., 2018). Prior to analysis, assumptions such as data suitability, correlation adequacy, and rotation effectiveness were verified (Taherdoost et al., 2014). EFA effectively clusters correlated variables into fewer interpretable underlying factors, facilitating a clearer understanding of relationships among variables (Hair et al., 2019; Yap et al., 2018). This analytical approach uncovers hidden data structures and provides reliable constructs useful for subsequent scale development (Jadidoleslami et al., 2018). IBM SPSS Statistics (version 27) was utilized to perform the EFA and categorize workflow variability causes systematically.

4. Results and discussion

Prior to performing EFA, a correlation test was conducted to assess relationships among the workflow variability items. Principal component analysis (PCA) was applied to identify and extract initial factors (Taherdoost et al., 2014). Items with factor loadings lower than 0.50 or those exhibiting significant cross-loadings were excluded (Hooper, 2012). Factors were extracted based on eigenvalues greater than one (Suhr, 2006), and their internal consistency was verified using Cronbach's alpha, with values above 0.70 indicating acceptable reliability (Bolarinwa, 2019). The overall Cronbach's alpha for the 38 items before rotation was 0.942, indicating excellent internal consistency. To achieve clearer and more interpretable factor structures, this study uses PCA varimax rotation, the most commonly applied method for easier interpretation of the extracted factors (Umar et al., 2020; Yap et al., 2018).

EFA examines correlations and variances to uncover the underlying structure of data and identify common factors among variables (Hair et al., 2019). It also assesses item alignment with factors, facilitating the removal of irrelevant or overlapping items to enhance scale clarity and reliability (Ye et al., 2015). Prior to conducting EFA, tests such as the Kaiser-Meyer-Olkin (KMO) measure and Bartlett's test of sphericity are required to assess data suitability. A KMO value above 0.5 indicates adequate sampling and the presence of shared variance (Howard, 2016), while a significant Bartlett's test ($p < 0.05$) confirms that the correlation matrix is appropriate for factor extraction (Ayarkwa et al., 2012). In this study, the KMO value was 0.891, well above the threshold, confirming sampling adequacy. Bartlett's test of sphericity was also significant ($p = 0.000$), supporting the feasibility of factor analysis. These results validate the suitability of the dataset for extracting meaningful underlying factors using EFA.

Factor analysis assesses the proportion of a variable's variance that is shared with other variables, referred to as communality (Field, 2005). Table 2 presents the communalities of each cause, indicating the extent to which their variances are explained by the underlying latent factors. Communality values typically range between 0.4 and 0.7 (Taherdoost et al., 2014). To enhance interpretability, the extracted factors were subjected to varimax rotation (Umar et al., 2020). Items with factor loadings below 0.50 or those exhibiting cross-loadings across multiple components (Costello & Osborne, 2019) were deleted. In each rotation cycle, non-significant or cross-loading items were removed, and the analysis was repeated. Based on these criteria, seventeen items were excluded to ensure the clarity and reliability of the final factor structure.

The rotated component matrix resulted in 21 causes with factor loadings between 0.570 and 0.873, grouped into four factors, as presented in Table 2. These factors collectively explained 60.58% of the total variance, exceeding the 60% threshold considered sufficient for construct validity. The scree plot supported this outcome, showing a clear inflection after the fourth factor. Factor labels were assigned based on dominant factor loadings and conceptual relevance (Yap et al., 2018). The extracted factors were: (1) Resources, (2) Management & Planning, (3) Material, and (4) Prerequisite factors. Items were distributed as follows: seven in factors 1 and 2, four in factor 3, and three in factor 4. Cronbach's alpha values for each factor exceeded 0.70, confirming internal consistency (Bolarinwa, 2019). These validated factors represent the final categorization of key workflow variability causes in construction project.

The extracted EFA factors offer a clear framework for understanding and managing workflow variability in construction projects. By consolidating 21 key causes into four core factors, this classification enables targeted, proactive interventions. High factor loadings underscore the importance of these domains in addressing variability at its source. Categorizing the causes facilitates early identification of potential disruptions, supporting more effective planning and execution. These factors form a robust foundation for developing practical tools to enhance workflow stability and overall project performance. The underlying factors of workflow variability causes, as shown in Fig. 2 are discussed below.

Table 1. Respondent's profile

General information	Categories	Frequency	Percent%
Profession area	Administrative position	160	79.6
	Operational position	41	20.4
Nature of the workplace	Consultant	22	10.9
	Government	49	24.4
	Owner	23	11.4
	Contractor	77	38.3
	Subcontractor	30	14.9
Years of experience	Less than 5 years	44	21.9
	From 5 to less than 10 years	58	28.9
	10 years and more	99	49.3

Table 2. Component labels, factor loadings, criteria, and communality in the final rotation of EFA

Factors	Factor loading	Eigen Value	Variance %	Cronbach's Alpha	Communality
Factor 1: Resources	-	7.70	18.70	0.87	-
Lack of worker/crew skills/experience to perform the task	0.718	-	-	-	0.600
Poor productivity	0.720	-	-	-	0.622
People arriving late and/or leaving early because of illness, injury, family or personal reason	0.702	-	-	-	0.557
Low morale and/or lack of motivation	0.698	-	-	-	0.583
Crew size is inadequate	0.659	-	-	-	0.607
Lack of equipment related technical training	0.628	-	-	-	0.504
Equipment allocation problem	0.640	-	-	-	0.518
Factor 2: Management and planning	-	2.06	18.29	0.86	-
Poor contract management	0.700	-	-	-	0.547
Irregular financing and payment for completed works	0.703	-	-	-	0.654
Cultural resistance to change	0.676	-	-	-	0.503
Coordination between different trades	0.686	-	-	-	0.610
Not flexible or unrealistic work schedule	0.748	-	-	-	0.640
Change in scope of work	0.685	-	-	-	0.514
Poor or miscommunication between project stakeholders (project manager, foreman, workers, etc.)	0.570	-	-	-	0.537
Factor 3: Material	-	1.564	14.409	0.86	-
Excess time of the material procurement	0.646	-	-	-	
Problems in material inventories (Accumulation or damaged material)	0.748	-	-	-	0.703
Error in material size	0.873	-	-	-	0.838
Error in material type	0.852	-	-	-	0.796
Factor 4: Prerequisite	-	1.397	9.176	0.70	-
Obtaining required permits for the work to begin	0.789	-	-	-	0.648
Sequencing of planned activities	0.789	-	-	-	0.644
Inspections for previously completed work (for example: quality test)	0.752	-	-	-	0.595

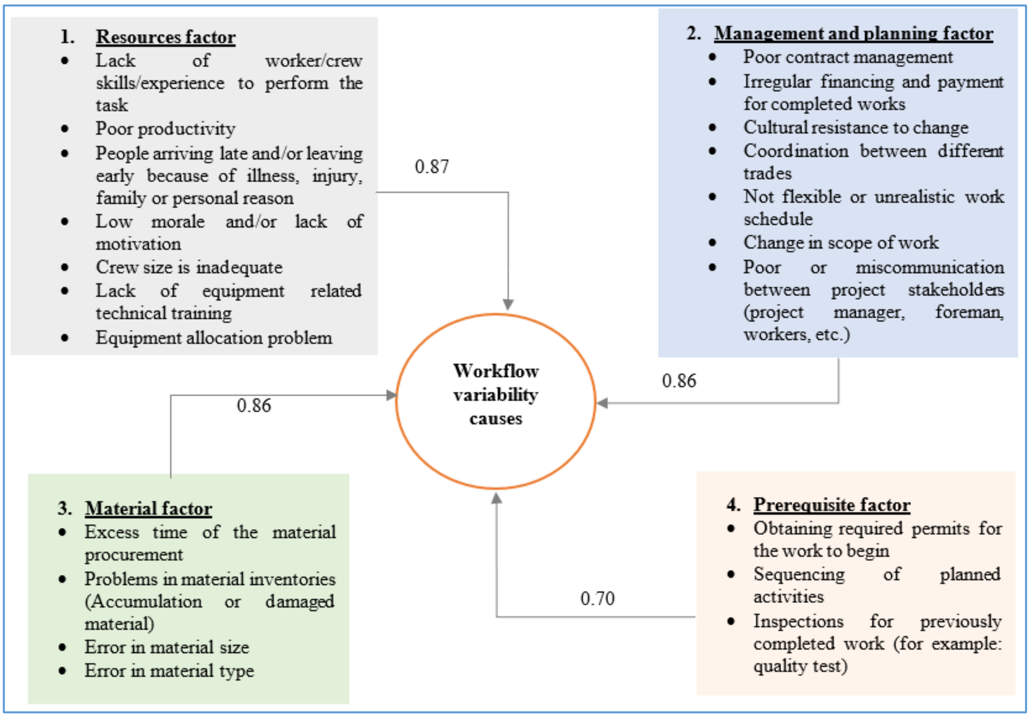

Fig. 2. Components diagram of workflow variability causes

Prior studies have consistently linked poor resource coordination to delays and inefficiencies (Christodoulou, 2017). To mitigate such impacts, it is essential to ensure that labor and equipment are reliably allocated in the right quantities, at the right time and place (Abbasian-Hosseini et al., 2018).

4.2. Management and planning factor

The management and planning factor accounts for 18.3% of the total variance, making it the second most influential factor contributing to workflow variability in construction projects. This factor includes seven key causes, with factor loadings ranging from 0.57 to 0.75, encompassing issues such as contract administration, financing, coordination, communication, workload scheduling, and scope changes. These findings highlight that addressing workflow variability requires a holistic approach to improving planning and managerial practices (Wambeke et al., 2011).

Ineffective communication, poor planning, and cultural resistance to change are widely recognized as internal drivers of variability (Kimpland, 2009). Clear documentation and regular stakeholder communication are essential for preventing misunderstandings and maintaining workflow continuity (Latilo et al., 2024; Sigalov et al., 2021). Disruptions often arise when trades prioritize individual productivity over coordinated progress, leading to delays in downstream activities and misuse of project buffers (Lindhard & Wandahl, 2014).

Contract-related issues, such as delayed payments and lack of transparency, further contribute to workflow instability by disrupting cash flow and lowering productivity (Sigalov et al., 2021). Timely and structured financial management enables efficient resource allocation and supports smoother project execution (Francis et al., 2016). Moreover, unrealistic scheduling and frequent scope changes imposed by clients intensify workflow interruptions, increase error risks, and compromise overall project performance (Assaad et al., 2020; Love & Smith, 2018). Effective planning and contract management are therefore vital to reducing workflow variability and ensuring reliable construction performance.

4.3. Material factor

The material factor, comprising four key factors with loadings between 0.697 and 0.792, accounts for 9.80% of the total variance, making it the third most influential contributor to workflow variability. This factor emphasizes the strategic importance of proper material selection, timely delivery, and maintaining sufficient inventory levels on-site to support uninterrupted workflows. Disruptions related to material issues often result in rework, delays, and inefficiencies (Arbulu et al., 2005; Wambeke et al., 2011; Zhang et al., 2015).

Client-driven changes, incorrect specifications, and late deliveries frequently lead to idle labor and task interruptions, impacting downstream activities (Hwang et al., 2019; Yap et al., 2018). Furthermore, material management is often isolated from production planning, causing misalignments that exacerbate workflow disruptions. Common challenges include shortages, delivery errors, and excessive on-site inventory, all of which contribute to schedule unreliability and are considered forms of waste (Arbulu et al., 2005).

Material-related errors, particularly those unnoticed until installation, can significantly delay progress and reduce productivity. Therefore, implementing integrated and proactive material control strategies is essential for minimizing variability and ensuring reliable, continuous construction workflows (Wang et al., 2019).

4.4. Prerequisite factor

The prerequisite factor accounts for 9.2% of the total variance and includes three critical factors, permits, inspections, and activity sequencing, with factor loadings ranging from 0.75 to 0.79. This factor highlights the essential role of prerequisite conditions in maintaining workflow continuity and minimizing variability in construction projects.

These factors are directly linked to the delayed release of flows between upstream and downstream activities, a primary source of workflow variability (Hamzeh, 2009). Construction processes function as interdependent systems, where disruptions in upstream task completion adversely affect the performance of successor activities, increasing waiting times and variability-related waste (Salhab et al., 2022).

Effective management of prerequisite flows, such as ensuring permits and inspections are completed and that work is properly sequenced, is critical for reducing variability. This involves assessing the readiness of tasks and ensuring constraints are removed before execution (Garcia-Lopez, 2017). Approaches like the make-ready process in the Last Planner System reinforce the importance of executing only work that is free of constraints, thereby improving planning reliability and enhancing workflow stability in complex construction environments (Lindhard & Wandahl, 2014; Montalbán-Domingo et al., 2024).

5. Conclusions

Addressing workflow variability is essential for improving the performance and reliability of construction projects, as it has a direct impact on productivity, scheduling efficiency, and overall project outcomes. Given the persistent nature of workflow variability in the construction industry, this study aimed to investigate its fundamental causes and contribute to a deeper understanding of their origins. Through EFA, the study identified and categorized 21 key causes into four core factors: resources, management and planning, material, and prerequisite factors. These categories offer a structured framework for recognizing and addressing the primary sources of variability. The findings provide valuable insights for project managers during the planning and preparation phases, supporting the development of targeted strategies to minimize variability and enhance project performance.

This study emphasizes the need for improved management of resources, particularly labor and equipment, to ensure workflow reliability. It also highlights the importance of effective material planning and timely delivery in minimizing disruptions and maintaining workflow continuity. Addressing these factors during the planning phase can significantly reduce workflow-related variability and project disruptions. Early attention to workflow issues enhances project clarity and performance. The findings offer a basis for developing a comprehensive framework for managing workflow variability and contribute to improving current practices in construction project management. As this study focuses on identifying the root causes of workflow variability, future research is encouraged to develop and test workflow management strategies tailored to these causes, enabling more targeted and effective approaches for improving construction project performance.

Acknowledgments

The authors would like to thank questionnaire respondents for their remarkable contributions to this study.

References

Abbasian-Hosseini, S. A., Liu, M., & Howell, G. (2018). Investigating the cost-benefit trade-off of additional planning using parade game simulation. *Journal of Management in Engineering*, *34*(2), 04017066.

Abusalem, O. (2020). Towards last planner system implementation in Gaza Strip, Palestine. *International Journal of Construction Management*, *20*(5), 367-384.

Arbulu, R. , Koerckel, A. & Espana, F. (2005). Linking Production-Level Workflow With Materials Supply. *Proceedings of the 13th Annual Conference of the International Group for Lean Construction (IGLC)*, Sydney, Australia, 199-206.

Assaad, R., Elsayegh, A., Ali, G., Abdul Nabi, M., & El-Adaway, I. H. (2020). Back-to-back relationship under standard subcontract agreements: Comparative study. *Journal of legal affairs and dispute resolution in engineering and construction*, *12*(3), 04520020.

Ayarkwa, J., Agyekum, K., & Acheampong, A. (2012). Factors affecting the performance of contractors on building construction projects in Ghana. *Journal of Construction Project Management and Innovation, 2*(1), 294-313.

Ballesteros-Pérez, P., Sanz-Ablanedo, E., Soetanto, R., González-Cruz, M. C., Larsen, G. D., & Cerezo-Narváez, A. (2020). Duration and cost variability of construction activities: An empirical study. *Journal of Construction Engineering and Management*, *146*(1), 04019093.

Bolarinwa, O. A. (2019). Principles and methods of validity and reliability testing of questionnaires used in social and health science researches. *Nigerian Postgraduate Medical Journal, 26*(4), 195-201.

Broder, H. L., McGrath, C., & Cisneros, G. J. (2007). Questionnaire development: Face validity and item impact testing of the Child Oral Health Impact Profile. *Community Dentistry and Oral Epidemiology, 35*(1), 8-19.

Christodoulou, S. E. (2017). Entropy-based heuristic for resource-constrained project scheduling. *Journal of Computing in Civil Engineering*, *31*(3), 04016068.

Costello, A. B., & Osborne, J. (2019). Best practices in exploratory factor analysis: Four recommendations for getting the most from your analysis. *Practical assessment, research, and evaluation*, *10*(1), 7.

Culfik, M., Birgonul, M. T., & Dikmen, I. (2014). Analysis of delay causes in Turkish construction projects: A contractor perspective. *International Journal of Project Management, 32*(3), 524-535.

Dikko, M. (2016). Establishing Construct Validity and Reliability: Pilot Testing of a Qualitative Interview for Research in Takaful (Islamic Insurance). *The Qualitative Report, 21*(3), 521-528.

Field, A. (2005). Factor analysis using SPSS. London: SAGE Publications Ltd.

Francis, M., Ramachandra, T., & Rotimi, J. O. B. (2016). Strategies to minimise the effects of delayed payments. *Proceedings of the Institution of Civil Engineers-Management, Procurement and Law*, *169*(5), 199-207.

Garcia-Lopez, N. P. (2017). *An activity and flow-based construction model for managing on-site work* .Doctoral dissertation, Stanford University.

Garcia-Lopez, N. P., & Fischer, M. (2024). Managing On-Site Production Using an Activity and Flow–Based Construction Model. *Journal of Construction Engineering and Management*, *150*(1), 04023144.

Garrido Martins, C., Bogus, S. M., & Valentin, V. (2023). Perceptions of construction risks due to fast-track activity overlapping. *Eng*, *4*(4), 2879-2895.

Hair, J. F., Black, W. C., Babin, B. J., & Anderson, R. E. (2019). *Multivariate Data Analysis* (8th ed.). Cengage Learning.

Hamzeh, F. R. (2009). *Improving construction workflow-The role of production planning and control*. University of California, Doctoral dissertation, Berkeley.

Han, S. & Park, M.. (2011). Interactive parade game: Impact of managerial reactions to workflow variability. *Electronic Journal of Information Technology in Construction. 16*. 104-117.

Handayani, B., N. S. Wisnujati, Budiono, D. Darmawan & Y. Kurniawan. (2021). Environmental Management and Law Enforcement, *Studi Ilmu Sosial Indonesia, 1*(1), 65-76.

Hooper, D. (2012). *Exploratory factor analysis.* In M. P. Spector, D. Ifenthaler, D. Sampson, & P. Isaias (Eds.), *The Routledge Companion to Research in Education* (pp. 167-178). Routledge.

Horman, M. J., & Thomas, H. R. (2005). Role of inventory buffers in construction labor performance. *Journal of Construction Engineering and Management*, *131*(7), 834-843.

Howard, M. C. (2016). A review of exploratory factor analysis decisions and overview of current practices: What we are doing and how can we improve? *International Journal of Human-Computer Interaction, 32*(1), 51-62.

Hwang, B. G., Zhao, X., & Yang, K. W. (2019). Effect of BIM on rework in construction projects in Singapore: Status quo, magnitude, impact, and strategies. *Journal of construction engineering and management*, *145*(2), 04018125.

Jadidoleslami, S., Saghatforoush, E., & Zare Ravasan, A. (2021). Constructability obstacles: an exploratory factor analysis approach. *International Journal of Construction Management*, *21*(3), 312-325.

Jaśkowski, P., Biruk, S., & Krzemiński, M. (2021). Proactive scheduling of repetitive construction processes to reduce crews idle times and delays. *Archives of Civil Engineering*, *67*(4).

Javanmardi, A., Abbasian-Hosseini, S. A., Liu, M., & Hsiang, S. M. (2016). Analysis of workflow variability's impacts on trade and project performance. *Procedia Engineering*, *145*, 281-287.

Kimpland, S. L. (2009). 2009 Contractor productivity survey results, FMI Corp., Raleigh, NC.

KV, P., V, V., & Bhat, N. (2019). Analysis of causes of delay in Indian construction projects and mitigation measures. *Journal of Financial Management of Property and Construction*, *24*(1), 58-78.

Latilo, A., Uzougbo, N. S., MC, U., & Oduro, P. (2024). Role and effectiveness of advance payment guarantees in construction contracts. *World Journal of Advanced Science and Technology*, *6*(01), 088-102.

Lindhard, S. M., Hamzeh, F., Gonzalez, V. A., Wandahl, S., & Ussing, L. F. (2019). Impact of activity sequencing on reducing variability. *Journal of Construction Engineering and Management*, *145*(3), 04019001.

Lindhard, S., & Wandahl, S. (2014). Scheduling of large, complex, and constrained construction projects–an exploration of LPS application. *International Journal of Project Organisation and Management*, *6*(3), 237-253.

Love, P., & Smith, J. (2018). Unpacking the ambiguity of rework in construction: Making sense of the literature. *Civil engineering and environmental systems*, *35*(1-4), 180-203.

Montalbán-Domingo, L., Casas-Rico, J., Alarcón, L. F. and Pellicer, E. (2024). Influence of the experience of the project manager and the foreman on project management's success in the context of LPS implementation. *Ain Shams Engineering Journal, 15*(1), 102324.

Peters, E., Subar, K., & Martin, H. (2019). Late payment and nonpayment within the construction industry: Causes, effects, and solutions. *Journal of Legal Affairs and Dispute Resolution in Engineering and Construction*, *11*(3), 04519013.

Radjawane, L. E., & Darmawan, D. (2022). Construction Project Worker Satisfaction Reviewing from the Role of the Work Environment and Leadership. *International Journal of Service Science, Management, Engineering, and Technology, 1*(3), 36-40.

Salhab, D., Møller, D. E., Lindhard, S. M., Hamzeh, F., Randrup, M., & Pilgaard, A. (2022). Accounting for variability: identifying critical activities as a supplement to the critical path. *Journal of Construction Engineering and Management*, *148*(5), 04022019.

Shehab, L., Al Hattab, M., Khalife, S., El Samad, G., Abbas, Y., & Hamzeh, F. (2023). Last Planner System Framework to Assess Planning Reliability in Architectural Design. *Buildings*, *13*(11), 2684.

Sigalov, K., Ye, X., König, M., Hagedorn, P., Blum, F., Severin, B., ... & Groß, D. (2021). Automated payment and contract management in the construction industry by integrating building information modeling and blockchain-based smart contracts. *Applied sciences*, *11*(16), 7653.

Su, Y., Lucko, G., & Isaac, S. (2024). Cruciality: Role of Network Topology in Schedule Resilience to Delay Propagation. *Construction Research Congress 2024*, 228-237.

Suhr, D. D. (2006). *Exploratory or confirmatory factor analysis?* Proceedings of the Thirty-first Annual SAS® Users Group International Conference, Cary, NC: SAS Institute Inc. Available at: https://support.sas.com/resources/papers/proceedings/proceedings/sugi31/200-31.pdf

Sümer, L. & Arditi, D. (2022). Turkish building construction contracts vs. FIDIC contracts. *Journal of Construction Engineering, Management & Innovation, 5* (2), 107-118.

Taherdoost, H., Sahibuddin, S., & Jalaliyoon, N. (2014). *Exploratory Factor Analysis; Concepts and Theory*. In *Advances in Applied and Pure Mathematics* (pp. 375-382). WSEAS Press.

Umar, A. A., Rizeiqi, R. K. A., & Badr, A. (2020). Major causes assessment of construction delays. *J. Eng. Proj. Prod. Manag*, *10*(3).

Wambeke, B. W. (2011). *Identifying, prioritizing, and reducing variation of construction related tasks*. North Carolina State University.

Wambeke, B. W., Hsiang, S. M. and Liu, M. (2011). Causes of variation in construction project task starting times and duration. *Journal of Construction Engineering and Management, 137*(9), 663-677.

Wang, C., Yap, J. B. H., Wood, L. C., & Abdul-Rahman, H. (2019). Knowledge modelling for contract disputes and change control. *Production planning & control*, *30*(8), 650-664.

Yap, J. B. H., Abdul-Rahman, H., Wang, C., & Skitmore, M. (2018). Exploring the underlying factors inducing design changes during building production. *Production Planning & Control*, *29*(7), 586-601.

Ye, G., Jin, Z., Xia, B., & Skitmore, M. (2015). Analyzing causes for reworks in construction projects in China. *Journal of management in engineering*, *31*(6), 04014097.

Zarghami, S. A., Gunawan, I., Corral de Zubielqui, G., & Baroudi, B. (2020). Incorporation of resource reliability into critical chain project management buffer sizing. *International Journal of Production Research*, *58*(20), 6130-6144.

Zhang, J., Song, X., Chen, H., & Shi, R. (2015). Optimisation of critical chain sequencing based on activities' information flow interactions. *International Journal of Production Research*, *53*(20), 6231-6241.

4th International Civil Engineering & Architecture Conference
17-19 May 2025, Trabzon, Türkiye

Identification of criteria influencing suitable site selection for highway construction projects

Gonca Kamber Yılmaz*[1], Hasan Basri Başağa[2,3]

[1] Karadeniz Technical University, Faculty of Technology, Department of Civil Engineering, Trabzon, Türkiye.
[2] Karadeniz Technical University, Department of Civil Engineering, Trabzon, Türkiye
[3]Earthquake and Structural Health Application and Research Center, Karadeniz Technical University, Trabzon, Türkiye

Abstract. In highway construction projects, the location selection of site layout is a critical process in terms of project efficiency, cost and time management. This selection is a complex process that requires consideration of many factors. In this study, a survey is conducted for the problem of selecting a suitable construction site location along the route and a multi-criteria evaluation is performed with the AHP (Analytic Hierarchy Process) method. Literature review results and interviews with experts in the field are effective in determining the factors that are effective in site selection. In order to determine the importance levels of the factors, interviews and questionnaires are conducted with experts in the field. In the application phase of the questionnaire; the participants are asked to evaluate the relative importance of the factors under the main and sub-criteria through pairwise comparisons. The collected data are analyzed with the AHP method. AHP is a method that evaluates the criteria numerically by considering complex decision-making processes in a hierarchical structure. With this method, it is aimed to express the priority ranking of the factors related to the selection of construction site locations problem numerically and consequently to support the decision with mathematical data.

Keywords: Site layout; Location selection; AHP; Multi-criteria evaluation; Decision-making

1. Introduction

Highway construction projects are among the high cost investments that spread over large areas. In these projects, the effectiveness of the planning and implementation processes directly affects the success of the project. Determining the appropriate construction site location provides both economic and environmental benefits by ensuring that labor, equipment and material logistics are managed at an optimal level. The decision of the construction site location is one of the strategic and critical decisions that significantly affect both the construction time and costs. This process of selection and evaluation is a complex one that requires many factors to be taken into account. The complex evaluation processes that decision makers often encounter can be made more systematic and objective with multi-criteria decision making (MCDM) techniques. The Analytical Hierarchy Process (AHP) is one of the most widely used approaches among these techniques. AHP is a powerful method in which both quantitative and qualitative criteria can be evaluated together, which can convert the preferences of the Decider into numerical data in a structured manner.

The AHP method used in site selection analyses finds application in a wide range of areas, from the selection of the most suitable location for solid waste warehouses (Siddiqui et al., 1996) to the selection of industrial zones (Eldrandaly et al., 2003). In the literature, there are many studies conducted using AHP.

Kodali and Routroy (2006) studied the location problems of potential facilities in the supply chain using the AHP method. In a study conducted by Başkaya and Akar (2005), they tried to decide which of the fabric alternatives should be produced by using the Analytical Hierarchy Process, which is a decision-making method that takes subjective evaluations into account in the selection of production alternatives. Kalan (2024) determined the importance ranking of the station locations by using the AHP method in the location selection of the stations to be built on the Mersin-Gaziantep HSR (high speed rail)line. Tzeng et al.(2002) used AHP method in restaurant location selection in Taipei. Hwang et al. (2005) evaluated the supplier selection and planning model using AHP, a multi-criteria decision method. Yang and Lee (1997) used AHP to find a solution for location selection. Burdurlu and Ejder (2003) decided on the site location of the furniture sector by using AHP method. In his study, Zahir

* Corresponding author, E-mail: goncakamber@ktu.edu.tr

https://doi.org/10.31462/icearc2025_ce_mng_795

(1991) eliminated the uncertainties related to the decision of location by ranking them according to their priorities with AHP.

In this study, the AHP method, which is one of the multi-criteria decision-making methods in the selection of construction site locations required for highway construction projects, was used to determine the criteria weights. The criteria needed and to be taken into consideration in the region where the construction site facility will be established are determined and a decision hierarchy is formed according to the weights and importance levels of these criteria. The decider's preference values were determined by making pairwise comparisons of all criteria that make up this hierarchical structure.

2. Materials and methods

When there are two or more quantitative and qualitative criteria and objectives in decision problems, such decision-making situations are considered as Multi-Criteria Decision Making (MCDM) problems. MCDM methods are analytical methods that allow simultaneous evaluation of measurable and immeasurable strategic and operational factors and can involve multiple people in the decision-making process.

In this study, the problem of selecting a suitable site location along the route for highway construction sites is considered as a MCDM problem. In the solution of the problem, the AHP method, which is one of the MCDM methods, is used. As a result of interviews with experts in the field and literature research, criteria that are considered to be effective in site selection are determined. Interviews and surveys are conducted with experts in the field to determine the importance of the criteria. In the application phase of the questionnaire, deciders are asked to determine the importance values of the criteria through pairwise comparisons. The data collected in the evaluation phase of the questionnaire are analyzed with the AHP method.

2.1. Analytical Hierarchy Process

AHP was first proposed by Myers and Alpert in 1968. It is one of the very important decision-making techniques developed by Thomas L. Saaty in 1977 to help decider in the decision-making process (Yaralıoğlu,2001). Since the day it was developed, AHP has found application opportunities in many fields. Some of these application areas are soil analysis (Min, 1994), resource allocation (Cheng & Li, 2001), marketing (Davies, 2001), energy (Kim & Min, 2004), education (Saaty, 1991), risk analysis (Millet & Wedley, 2002), environmental impact assessment (Ramanathan, 2001) and land suitability analysis (BanaiKashani, 1989). The increase in the number of uses of applications over time has enabled the development of the method.

AHP is a multi-criteria decision-making method that can evaluate quantitative and qualitative criteria in decision making, incorporate the preferences, experiences, intuitions, knowledge, judgments and thoughts of the group or individual into the decision process, and solve complex problems in a hierarchical structure. The decision maker can include both objective and subjective considerations in the decision process. Therefore, this situation provides the decision-maker with the opportunity to recognize their own decision-making mechanisms.

In AHP, the hierarchy is organized in at least three levels. At the top level of the hierarchy is the objective. There are main criteria at a lower level, and sub-criteria below the main criteria, if any. For pairwise comparisons to be consistent, the number of criteria should be determined correctly and each criterion should be defined correctly. Criteria should be classified according to their common characteristics. It is a very good method for group decision-making. Thanks to consistency analysis it is possible to analyze the flexibility of the result. Since the construction of the hierarchy and pairwise comparison matrices is subjective, experienced and specialized experts are needed. The algorithmic steps of the AHP method are as follows:

Step 1. Identification of the problem
Step 2. Establishing the Hierarchical Structure
Step 3. Construction of pairwise comparison matrices
Step 4. Normalizing pairwise comparison matrices
Step 5. Calculation of the priority vector
Step 6. Calculation of the consistency ratio
Step 7. Ranking of decision options

AHP is basically based on the comparison of the criteria that are effective in solving the problem according to their degree of importance. After the purpose, factor and sub-factors are determined, pairwise comparison decision matrices are created to determine the importance of factors and sub-factors among themselves. The importance scale of 1-9 proposed by Saaty is used in the creation of these matrices and is given in Table 1. A score of one represents equal importance between two criteria, while a score of nine indicates that one criterion is extremely important compared to the other (Saaty, 2008). If the decision to be made at the end of the study will affect many people, pairwise comparison decision matrices are formed by combining the judgments of different people. In this merging process, many researchers recommend the use of the geometric mean method to obtain consistent pairwise comparison matrices (Saaty, 2000; Tam&Tummala, 2001).

Table 1. Pairwise comparison scale for AHP (Saaty, 2008)

Importance Scale	Definition	Explanation
1	Equal importance	Two activities contribute equally to the objective
3	Moderate importance	Experience and judgement slightly favour one activity over another
5	Strong importance	Experience and judgement strongly favour one activity over another
7	Very strong importance	An activity is favoured very strongly over another
9	Extreme importance	The evidence favouring one activity over another is of the highest possible order of affirmation
2,4,6,8	Intermediate values	Values between two consecutive judgments to be used when compromise is needed

2.1.1. Identification of the problem

The first step in AHP analysis is to define the decision problem. At this stage, the purpose of the problem, that is, the decision to be made, should be determined. The purpose of this study is to be able to choose the most suitable location for highway construction sites along the route.

2.1.2. Establishing the hierarchical structure

In the step of creating the hierarchical structure, the main goal to be achieved is at the top. Once the main objective is set, there are main criteria at a lower level and sub-criteria below the main criteria. The number of stages of the hierarchy depends on the complexity and level of detail of the problem. It is very important to correctly identify the criteria in the hierarchical structure of the decision model. While determining the criteria, surveys, literature review, opinions of experts and practitioners operating in the field related to the decision problem are utilized. As given in Table 2, the criteria affecting the selection of the highway construction site location are listed to consist of the main and sub-criteria. Distance and terrain characteristics are expressed as the main criteria.

Distance criterion consists of sub-criteria of proximity to the center of the work area, residential areas, raw material sources, fuel stations and support construction sites.

The land characteristics criterion consists of three sub-criteria: land structure (land height, slope, ground type), infrastructure supply (drinking water, electricity, telephone, natural gas, sewerage) and land use.

Table 2. Hierarchical structure of criteria

Determination of the most suitable location for highway construction sites	
The Main Criteria	The Sub-Criteria
Distance	Proximity to the center of the work site
	Proximity to the residential areas
	Proximity to raw material sources
	Proximity to fuel stations
	Proximity to support construction sites
Land characteristics	Land structure
	Infrastructure supply
	Land use

2.1.3. Construction of pairwise comparison matrices

The pairwise comparison matrix is created by comparing the criteria at the same level in the hierarchical structure in pairs, and by comparing the sub-criteria within the criteria they are connected to. The comparison matrix is created in accordance with the comparison scale in Table 1 proposed by Thomas L. Saaty. The elements above the diagonal are the “aij” value obtained as a result of the comparison of the i-th criterion with the j-th criterion. The “aji” value obtained by comparing the j-th criterion and the i-th criterion in the matrix is equal to the “1/aij” value due to the correspondence property. The pairwise comparison matrix obtained as a result of the comparison is presented in Table 3. Since the elements on the diagonal of the matrix are self-comparisons of the criteria, the value of these elements is “1”.

Table 3. Pairwise comparison matrices ($A=[a_{ij}]$)

Criteria	Criteria 1	Criteria 2	Criteria 3	…	Criteria n
Criteria 1	1	a_{12}	a_{13}	…	a_{1n}
Criteria 2	$a_{21}=1/a_{12}$	1	a_{23}	…	a_{2n}
Criteria 3	$a_{31}=1/a_{13}$	$a_{32}=1/a_{23}$	1	…	a_{3n}
…	…	…	…	1	…
Criteria n	an1=1/a1n	$a_{n2}=1/a_{2n}$	$a_{n3}=1/a_{3n}$	…	1

2.1.4. Normalizing pairwise comparison matrices
Each element in the matrix is normalized by dividing it by its own column total. The sum of each column value in the normalized matrix is "1". Its formula is given in Equality 1.

$$a'_{ij} = \frac{a_{ij}}{\sum_{i=1}^{n} a_{ij}} \quad (1)$$

2.1.5. Calculation of the priority vector
The formula given in Equation 2 is used to calculate the priority vector. The sum of each row values of the normalized matrix is averaged by dividing by the size of the matrix. Therefore, the weight of the criterion in that row is obtained. These values are the importance weights calculated for each criterion.

$$W_i = \frac{\sum_{j=1}^{n} a'_{ij}}{n} \quad (2)$$

2.1.6. Calculation of the consistency ratio
First, the comparison matrix A is multiplied by the column vector W and the column vector D is obtained in Equality 3. The elements of the column vector X and the column vector W are mutually divided in Equality 4 and the arithmetic average is taken in Equality 5. So λ is calculated.

$$A \times W = |a_{ij}| \times |w_i| = |x_i| \quad (3)$$

$$d_i = \frac{x_i}{w_i} \quad (4)$$

$$\lambda_{max} = \frac{\sum_{i=1}^{n} d_i}{n} \quad (5)$$

After λ is calculated, the Consistency Index (CI) is calculated in Equality 6. CR is obtained by dividing the CI value by the Random Index (RI) value given in Table 4. The CR formula is given in Equality 7.

$$CI = \frac{\lambda_{max} - n}{n-1} \quad (6)$$

$$CR = {}^{CI}/_{RI} \quad (7)$$

Table 4. Random Index (Saaty, 1980)

n	1	2	3	4	5	6	7	8	9	10	11	12	13	14	15
RI	0.00	0.00	0.58	0.90	1.12	1.24	1.32	1.41	1.45	1.49	1.51	1.53	1.56	1.57	1.59

If CR ≤ 0.10, the comparisons are consistent. If CR > 0.10 the results obtained are inconsistent.

2.1.7. Ranking of decision options
The decision option with the highest weight is determined as the decision option that should be preferred for the solution of the problem.

3. Results and discussion

In this study, the site selection problem required for highway construction projects is discussed. In the solution of the problem, AHP method is preferred from multi criteria decision making (MCDM) methods. The criteria that may be effective in the construction site location selection process are determined as a result of literature review and interviews with experts in the field. Surveys and interviews with civil engineering experts are conducted to determine the importance of these criteria. The basis of the AHP method is the mutual comparison of criteria according to the importance performance suggested by Saaty. A survey was prepared in accordance with this importance scale and civil engineers who are experts in this field were asked to evaluate the criteria. The results of the surveys conducted with 11 civil engineers are evaluated in the MS Excel program. In the MS Excel program, the geometric mean of the expert opinions is taken and the weights of the criteria are determined by creating pairwise comparison matrices. The obtained criterion weights are given in Table 5.

Table 5. Weights of main and sub-criteria

The Main Criteria		The Sub-Criteria		Common weights	% weights	Consistency ratio
Criteria	Weights	Criteria	Weights			
Distance	0.66667	Proximity to the center of the work site	0.40043	0.267	26.7	λ_{max} =5.26324 CI=0.06581 RI=1.12 CR=0.05876≤ 0.10 The comparisons are consistent.
		Proximity to the residential areas	0.13394	0.089	8.9	
		Proximity to raw material sources	0.12393	0.083	8.3	
		Proximity to fuel stations	0.07173	0.048	4.8	
		Proximity to support construction sites	0.26996	0.180	18	

The table continues below

Land characteristics	0.33333	Land structure	0.62322	0.208	20.8	λ_{max} =3.01834
		Infrastructure supply	0.23949	0.079	7.9	CI=0.00917
						RI=0.58
		Land use	0.13729	0.046	4.6	CR=0.01581≤ 0.10 The comparisons are consistent.
TOTAL	1.00000	TOTAL		1.000	100	

4. Conclusions

Site selection problems are encountered both in the service sector and in the production sector. There are many examples of site loacation problems such as construction sites, factories, warehouses, universities, and airport locations. In this study, the problem of site location is addressed.The AHP method, which evaluates qualitative and quantitative data together, is often used in appropriate site location analyses. In the AHP method, expert opinions are taken to determine the extent to which the criteria affect the site location. Criteria weights are calculated by creating pairwise comparison matrices. The consistency of the transactions is tested by calculating the consistency ratio. In this study, a questionnaire was conducted and 11 opinions of civil engineers who are experts in this field were evaluated in the MS Excel program.

The weights of distance and land characteristics criteria and the sub-criteria of these criteria are calculated and given in Table 5. The importance weights and consistency ratios found for the main and sub-criteria are shown in Table 5.

- When the results are analyzed, it is seen that the consistency ratios of all pairwise comparison decision matrices are less than 0.10.
- Based on this, it is concluded that the pairwise comparison decision matrices are consistent.
- As a result of the analyses conducted, the distance main criterion was determined as the most important criterion in the ranking of criteria with a priority value of 0.6667 for choosing a highway construction site location.
- Land features are the second criterion in the ranking of the main criteria with a priority value of 0.3333.
- As a result of the evaluation of the sub-criteria, the most important of the criteria were determined as proximity to the center of the work site, land structure, proximity to support construction sites, respectively.

The construction site location criteria determined by using expert opinions and literature will form the basis of the following studies.

References

BanaiKashani, R. (1989). A New Method for Site Suitability Analysis: The Analytic Hierarchy Process. *Environmental Management*, 13(6), 685-693.

Başkaya, Z. & Akar, C. (2005). Ürün Alternatifi Seçiminde Analitik Hiyerarşi Süreci: Tekstil İşletmesi Örneği. *Anadolu Üniversitesi*, *Sosyal Bilimler Dergisi*, 2005(1), 273-286 (in Turkish).

Burdurlu, E. & Ejder, E. (2003). Location Choice For Furniture Industry Firms By Using Analytic Hierarchy Process (AHP) Method, *Gazi Üniversitesi, Fen Bilimleri Enstitüsü Dergisi*, 16(2), 369-373.

Cheng, E.W.L. & Li, H. (2001). Information Prioritysetting for Better Resource Allocation Using Analytic Hierarchy Process. *Information Management and Computer Security*, 9(2), 61–70.

Davies, M. (2001). Adaptive AHP: A Review of Marketing Applications with Extensions. *European Journal of Marketing*, 35 (7/8), 872–893.

Eldrandaly, K., Eldin, N. & Sui, D. (2003). A COM-based Spatial Decision Support System for Industrial Site Selection. *Journal of Geographic Information and Decision Analysis*, 7(2), 72-92.

Hwang, H.S., Moon, C., Chuang, C.L. & Goan, M.J. (2005). Supplier Selection Planning Model Using AHP. *International Journal of the Information Systems for Logistics and Management*, 1(1), 47-53.

Kalan, O. (2024). Analitik Hiyerarşi Prosesi ile Mersin-Gaziantep Yüksek Hızlı Tren Hattı için İstasyon Yeri Seçimi. *Çukurova Üniversitesi, Mühendislik Fakültesi Dergisi,* 39(1), 31-45 (in Turkish).

Kim, S.C. & Min, K.J. (2004). Determining Multicriteria Priorities in the Planning of Electric Power Generation: The Development of an Analytic Hierarchy Process for Using the Opinions of Experts. *International Journal of Management,* 21, (2), 186–193.

Kodali, R. & Routroy, S. (2006). Decision Framework for Selection of Facilities Location in Competitive Supply Chain. *Journal of Advanced Manufacturing Systems*, 5(1), 89-110.

Millet, I. & Wedley, W.C. (2002). Modelling Risk and Uncertainty with the Analytic Hierarchy Process. *Journal of Multicriteria Decision Analysis*, 11(2), 97–107.

Min, H. (1994). Location Analysis of International Consolidation Terminals Using the Analytic Hierarchy Process. *Journal of Business Logistics*, 15(2), 25–44.

Ramanathan, R. (2001). A Note on the Use of the Analytic Hierarchy Process for Environmental Impact Assessment. *Journal of Environmental Management*, 63, 2735.
Saaty, T.L. (1980). The Analytical Hierarchy Process, Planning, Priority, Resource Allocation. RWS Publications, USA.
Saaty, T.L. (1991). Modelling the Graduate Business School Admission Process. SocioEconomic Planning Science, 25, 155–162.
Saaty, T.L. (2000). Fundamentals of Decision Making and Priority Theory. RWS Publications, Pittsburgh, USA.
Saaty, T.L.(2008). Decision Making with the Analytic Hierarchy Process. *International Journal of Services Sciences*, 1(1), 83-98.
Siddiqui, M.Z., Everett, J .W. & Vieux, B.E. (1996). Landfill Siting Using Geographic Information Systems: A Demonstration. *Journal of Environmental Enginering*, ASCE, 122(6).
Tam, M.C.Y. & Tummala, V.M.R. (2001). An Application of The AHP in Vendor Selection of a Telecommunications System. *The International Journal of Management Science*, 29(2), 171-182.
Tzeng, G.H., Teng, M.H., Chen, J.J. & Opricovic, S. (2002). Multicriteria Selection for a Restaurant Location in Taipei. *International Journal of Hospitality Management*, 21(2), 171-187.
Uzun, S. & Kazan, H. (2016). Comparing MCDM Methods of AHP, TOPSIS and PROMETHEE: A Study on the Selection of Ship Main Engine System. *Journal of Transportation and Logistics*, 1(1), 99-113.
Yang, J. & Lee, H. (1997). An AHP Decision Model for Facility Location Selection. Facilities, 15(9-10), 241-254.
Yaralıoğlu, K. (2001). Performans Değerlendirmede Analitik Hiyerarşi Prosesi. *Dokuz Eylül Üniversitesi İ.İ.B.F. Dergisi*, 129-142 (in Turkish).
Zahir, M.S. (1991). Incorporating The Uncertainty of Decision Judgements in The Analytic Hierarchy Process. *European Journal of Operational Research*, 53, (2), 206-216.

4th International Civil Engineering & Architecture Conference
17-19 May 2025, Trabzon, Türkiye

Prioritization of design risks in construction projects

Aynur Kazaz[1], Gökçen Arslan*[1]

[1] Akdeniz University, Department of Civil Engineering, 07070 Antalya, Türkiye

Abstract. The complex and unique structure of construction projects inherently contains numerous risks that may prevent their successful completion. Multiple studies conducted by various researchers on risk assessment in construction projects have identified design risks, along with financial and construction risks, as the most significant factors affecting construction projects. This study aims to identify and prioritize design risks that may impact construction projects. To this end, 11 design risks potentially affecting construction projects were identified and prioritized according to their likelihood of occurrence and their impact on project success. In prioritizing design risks, expert opinions from designers with a minimum of 20 years of experience in Turkey were solicited, and the obtained data were prioritized using the Fuzzy AHP technique. The study results indicate that the most significant design risks are the client's revision requests, faulty design, and incompatibility between design projects. The findings of this study are expected to contribute to the existing literature on risk and risk management in construction projects. Furthermore, it is anticipated that the results obtained can guide the industry in determining priority areas for developing strategies to mitigate design risks in construction projects.

Keywords: Construction projects; Design risks; Fuzzy AHP; MCDM; Risk management

1. Introduction

Construction projects represent highly intricate systems that necessitate extensive interdisciplinary coordination and are inherently influenced by long-term uncertainties. These projects are dynamic and multifaceted structures where financial, political, legal, technical, design, and environmental risks intersect, posing substantial challenges to cost efficiency, schedule adherence, quality assurance, sustainability objectives, and occupational safety protocols. This study aims to systematically identify and prioritize design-related risks inherent in construction projects. In pursuit of this objective, an extensive literature review was undertaken, and the identified risk factors were meticulously assessed through expert evaluations, and the data obtained from these assessments were processed using the Fuzzy Analytical Hierarchy Process (Fuzzy AHP) methodology to establish a structured prioritization model.

The results of this study are anticipated to refine risk perception in the Turkish construction industry and facilitate the development of structured risk mitigation strategies. Prospective research directions may encompass a more integrative approach by incorporating proactive and reactive risk management strategies, culminating in the formulation of an adaptive and scalable decision-support model tailored to the diverse nature of construction projects, thereby offering substantive contributions to the academic and professional discourse in the field.

2. Literature review

The construction industry is a critical sector on a global scale in terms of its economic contribution to Gross Domestic Product (GDP), employment creation potential and value production (Schoonwinkel & Fourie, 2016; Urbański et al., 2019; Boateng et al., 2022). However, the long-term, financially intensive and multi-stakeholder nature of construction projects causes the projects to be exposed to various risk factors. If risks cannot be managed, failure scenarios such as serious cost overruns, time losses and failure to meet quality standards may occur in projects. The complex, variable and risk-prone nature of construction projects increasingly increases the importance of risk management practices within the sector; In this context, academic research also focuses on sector-specific risk management strategies and offers comprehensive reviews on the subject. A substantial body of research has focused on the identification and prioritization of risks in construction projects. Within this domain, design risks have been widely recognized by scholars as one of the most critical risks influencing construction project outcomes (Table 1).

*Corresponding author, E-mail: gokcenarslan@akdeniz.edu.tr

https://doi.org/10.31462/icearc2025_ce_mng_882

Table 1. Critical risks in construction projects

Year	Researcher	Risk Groups
2010	Zou & Li	Economic and Financial Risks, Planning Risks, Contractual and Legal Risks, Design Risks, Geological Risks, Construction Risks
2011	Nieto-Morote & Ruz-Vila	Project Management Risk, Design Risk, Construction Risk, Supplier Risk
2012	Abdul-rahman et. al.	Financial, Managerial, Construction, Design, Operational, Occupational Health and Safety
2013	Kuo &Lu	Engineering Design, Natural Hazards, Construction Safety-Related, Social and Economic, Construction Management
2014	Choudhry et. al.	Health and Safety Risks, Contract Risks, Financial Risks, Design Risks, Management Risks, Construction Risks, External Risks
2015	Enshassi &Mosa	Legal, Physical, Design, Political, Environmental, Logistics, Management, Construction
2016	Sastoque et. al.	Political, Macroeconomic, Legal, Social, Natural, Project Selection, Financial, Design, Construction, Business, Relationship
2017	Dehdasht et. al.	Technical, Financial, Environmental, Design and Construction, Contract, Political
2018	Forcael et. al.	Contractor Risks, Project Design Risks, Owner Risks, Labor Risks, Material and Equipment Risks, Project Risks, External Risks
2019	Adeleke et. al.	Political Risks, Economic Risks, Technology Risks, Management Risks, Material Risks, Design Risks, Financial Risks, Labor and Equipment Risks
2020	Darko et. al.	Planning and Design Risk, Manufacturing Risks, Logistics Risks, On-Site Assembly Risks, Multi-Phase Risks, Universal Risks
2021	Lin &Chen	Customer Risks, Design Risks, Contractor Risks, Subcontracting Risks, External Risks
2022	Shelake et. al.	Geological characteristics, Site Condition, Groundwater, Actual construction, Administration, Design, Management, Faults in contracting, Resource Monitoring, Miscellaneous

Design-related risks are inherently prevalent in construction projects; moreover, inadequate management of these risks can initiate a chain reaction of secondary risks, potentially jeopardizing the project's success throughout the tendering, procurement, and construction phases. Therefore, conducting a comprehensive analysis of potential design-related risks at the early stage of construction projects and implementing necessary precautionary measures are crucial for ensuring the successful completion of the projects.

Although the literature provides extensive coverage of the identification and prioritization of general risks in construction projects, research specifically focusing on the prioritization and management of design-related risks remains remarkably scarce. However, as illustrated in Table 2, the limited existing studies have identified several critical risk factors that may compromise project success. These include requests for design modifications, delays in the employer's approval process, design solutions unsuitable for on-site implementation, communication deficiencies within the design team, and changes in project scope (Liu et.al., 2017; Gashaw and Jilcha 2023; Wuni et.al. , 2023; Erlita et al., 2023).

Table 2. Design risk factors from different studies

Research and its scope	Design Risk Factors
Subramanyan et.al (2012) Research Scope: Investigation of project risk assesment in Indian construction industry	Insufficient data collection and survey before design Complex/nonexecutable design Delay in performing inspection and testing by consultant Unclear and inadequate details in drawings Non use of advanced engineering design software
Liu et.al. (2017) Research Scope: To identify the design risk factors and interrelationships between these factors in design build projects	Inaccurate, missing, vague, or illegal information in employer's requirements Unduly long period of design review required by employer or employer's deferred design review Employer's requirement for design changes A communication gap or misinterpretation on exchange information between employer and designers Delayed information from suppliers Insufficient geological investigation or unknown geological conditions Poor morale among designers Churn among core designers Inadequate communication or coordination between designers Designers' incompetency Designers' unfamiliarity with local requirements of human rights, religion, cultural customs, and lifestyle Difference between designers' work habits and local practice Inadequate checks on design input Inadequate checks on design drawings Unproven design solutions adopted Inadequate design standard/specification adopted Overdesign due to conservatism Employer's excessive right to design review or employer's misuse of right to design review Inaccurate information from suppliers Inaccurate parameters of interfaces between matching equipment Information loss or misconception during design conversion Employer's disagreement on source of main equipment or materials Infringement of design scheme on someone else's intellectual property
Gashaw and Jilcha (2023) Research Scope: Determining design risks in railway projects	Change in scope of work by the client Incomplete design Cost underestimation Design changes Inadequate site investigations Design errors Misunderstanding of client's requirements Contractor's experience Design delay Lack of coordination Schedule pressure Client's lack of experience Poor labor productivity Change in government regulation and law Unsafe project location

Table 2 continued

Research and its scope	Design Risk Factors
Wuni et.al. (2023) Research Scope: To conduct a knowledge-based evaluation and ranking of the design risk factors (DRFs) for modular integrated construction projects.	Inaccurate information, defective design and change order Unable to freeze design early Late involvement of suppliers, fabricators and contractors Lack of bespoke MiC design codes, guidelines and standards Supply chain information gap and inconsistency Design complexity Dimensional and geometric tolerance errors Design information gap between the designer and fabricator Inadequate design planning Inefficiency in design approval Design rework Unsuitability of the design for the MiC method
Erlita et al. (2023) Research Scope: To identify risk factors that cause delays in the preliminary design, design, procurement and construction processes of a factory building project	Building permit data is different from site conditions Lack of open spaces on site Changes in development regulations Issuance of purchase order and late progress payments In-depth feasibility study Incomplete as built drawing Design idea changes Consultant presentation The process of tendering and the implementation of new site Differences in idealism with foreign consultants Design errors The machine plan has not been fixed Delay in production of drawings and tender documents Late progress payment from owner Late of design approval from owner Changes from owner Waiting for owner's decision Coordination meetings between consultants Poor communication and coordination with other parties Drawing information is in PDF format Use of different software Differences between local and foreign regulations Unclear scope of work

The objective of this study is to determine the critical design risk factors that could influence construction projects in Türkiye from the perspective of designers. Using the Fuzzy AHP technique, risks were evaluated and prioritized according to their probability of occurrence and their degree of impact on project success. The anticipated results aim to enrich the existing body of research on design risks. Furthermore, by drawing attention to these risks and suggesting mitigation strategies, the study aspires to support the effective management of design-phase risks, which, if left unaddressed, could lead to project failures in later stages.

3. Methodology

The primary objective of this study is to prioritize design risks in the Turkish construction industry. To achieve this, design risk factors that may influence project success were identified through a comprehensive literature review. The probability of occurrence and impact levels of these risks were assessed based on insights gathered from expert designers via focus group discussions. As a widely recognized qualitative research method, focus groups serve as a validation technique that enables data collection through structured and interactive discussions moderated by an expert, typically involving five to ten participants (Chan et al., 2012; Aladağ & Işık, 2019). In this study, ten experienced designers participated in focus group discussions. The demographic details of the experts who contributed their opinions to this study are summarized in Table 3.

Table 3. Demographic information of participants

Expertise (Profession)	Civil Engineer (2) Mechanical Engineer (2) Electrical/Electronics Engineer (1) Architect (3) Interior Designer (1)
Role	Designer (10)
Annual project budget (USD$/year)	1 - 10 Million (2) 10 - 100 Milyon (8)
Experience in the Construction Industry (years)	10 -20 (2) 20 -30 (4) > 30 (4)
Education Level	Bachelor's degree (7) Master's degree (3)

The Fuzzy Analytic Hierarchy Process technique was subsequently applied to prioritize the data obtained from these discussions. The Fuzzy Analytic Hierarchy Process (FAHP) was developed by incorporating fuzzy logic into the conventional AHP methodology to improve decision-making in environments characterized by uncertainty. This approach employs fuzzy numbers, which are more effective in representing linguistic variables. Various FAHP techniques have been introduced in the academic literature, among which Chang's method (Chang, 1996) is particularly notable. Chang proposed the fuzzy extent analysis technique, which utilizes triangular fuzzy numbers. The following section outlines the key steps involved in the Fuzzy Analytic Hierarchy Process (FAHP) methodology.

Step 1: Model Development and Problem Structuring – Through a comprehensive literature review, 11 design risk factors listed in Table 4, were identified as potentially critical to the success of construction projects.

Table 4. Design risk factors

Risk Code	Design Risk Factors
DR01	Incompatibility between design projects
DR02	Change of regulations and standards
DR03	Faulty design
DR04	Missing details in project drawings
DR05	Design delay
DR06	Failure to analyze the needs and customer demands required for design correctly
DR07	Poor performance of the design team
DR08	Failure to provide optimized design for construction
DR09	Employer's design revision request
DR10	Inadequate site/ geological investigations
DR11	Inefficiency in design approval

Step 2: Construction of Pairwise Comparison Matrices Using Fuzzy Judgments with Triangular Fuzzy Numbers – Experts were asked to perform a pairwise evaluation of the identified indicators. To determine the relative preferences between two components within the fuzzy AHP matrix, the Triangular Fuzzy Scale (Table 5) was utilized.

Table 5. Triangle fuzzy scale (Chang 1996)

Preferences expressed in linguistic variables	Numeric variables	Triangle fuzzy scale	Triangle fuzzy reciprocal scale
Just Equal	1	(1, 1, 1)	(1, 1, 1)
Equally Important/preferred	2	(1/2, 1, 3/2)	(2/3, 1, 2)
Weakly Important/preferred	3	(1, 3/2, 2)	(1/2, 2/3, 1)
Strongly More Important/preferred	4	(3/2, 2, 5/2)	(2/5, 1/2, 2/3)
Very Strongly More Important/preferred	5	(2, 5/2, 3)	(1/3, 2/5, 1/2)
Absolutely More Important/preferred	6	(5/2, 3, 7/2)	(2/7, 1/3, 2/5)

Step 3: Implementation of Chang's Extent Analysis Method – After constructing the pairwise comparison matrix using fuzzy numbers, Chang's Extent Analysis Method was employed to eliminate the uncertainty present. Developed by Chang (1996), this method offers a structured framework for converting fuzzy data into crisp mathematical representations. In this context, let X = (x1, x2, x3, ..., xn) represent the object set, and U = (u1, u2, u3, ..., um) denote the goal set. According to Chang's Extent Analysis Method, each object is individually analyzed for each goal, gi, respectively. Initially, the fuzzy synthetic extent value is calculated using equations (1) to (4):

$$S_i = \sum_{j=1}^{m} M_{gi}^{j} \; x \left[\sum_{j=1}^{n}\sum_{j=1}^{m} M_{gi}^{j}\right]^{-1} \tag{1}$$

$$\sum_{j=1}^{m} \left(\sum_{j}^{m} l_j, \sum_{j=1}^{m} m_j, \sum_{j=1}^{m} u_j\right) \tag{2}$$

$$\left[\sum_{j=1}^{n}\sum_{j=1}^{m} M_{gi}^{j}\right] = \left(\sum_{j}^{m} l_j, \sum_{j=1}^{m} m_j, \sum_{j=1}^{m} u_j\right) \tag{3}$$

$$\left[\sum_{j=1}^{n}\sum_{j=1}^{m} M_{gi}^{j}\right]^{-1} = \left(\frac{1}{\sum_{j=1}^{n} u_i}, \frac{1}{\sum_{j=1}^{n} m_i}, \frac{1}{\sum_{j=1}^{n} l_i}\right) \tag{4}$$

Then, degree of possibility was obtained using the value of fuzzy synthetic extent. Probability values were calculated using using equations (5, 6). Here, the possibility of choosing one criterion out of the other criterion was obtained. The weights vector was then obtained with the help of the possibilities. The normalized weights vector was used to select the best alternative. The degree of possibility of M2=(l2, m2, u2)≥ M2=(l2, m2, u2) is defined as:

$$V\,(M_2 \geq M_1) = sup_{y\geq x}[\min\,(\mu_{M1}(x), \mu_{M2}(y))] \tag{5}$$

The probability degree of triangular fuzzy numbers $M1$=($l1$,$m1$,$u1$) and $M2$=($l2$,$m2$,$u2$) can also be defined as follows;

$$V\,(M_2 \geq M_1) = hgt(M_1 \cap M_2) = \mu_{M2}(d) = \begin{cases} 1 & m_2 \geq m_1 \\ 0 & l_1 \geq u_2 \\ \frac{l_1 - u_2}{(m_2-u_2)-(m_1-l_1)} & otherwise \end{cases} \tag{6}$$

The expression $V(M2 \geq M1)$ here expresses the membership function value of the intersection point of triangular (convex) fuzzy numbers $M1$ and $M2$. Additionally, to compare $M1$ and $M2$, both values of $V(M2 \geq M1)$ and $V(M1 \geq M2)$ must be found. The degree of probability of convex fuzzy number M being greater than k convex fuzzy numbers Mi, i=1,2,…,k can be defined as follows:

$$V(M \geq M_1, M_2, \dots, M_k = V[(M \geq M_1), (M \geq M_2), \dots, (M \geq M_k)] = minV(M \geq M_i), \tag{7}$$

$$i = 1, 2, 3, \dots, k$$

Taking $i \neq k$ for k=1,2,…,n and $d(A$i)= min $V(S$i≥Sk), the weight vector for the criteria can be given as follows:

$$W' = (d'(A_1), d'(A_2), \dots., d'(A_n))^{T} \tag{8}$$

The weight vector obtained in the previous step is normalized to obtain the following vector.

$$W = (d(A_1), d(A_2), \ldots, d(A_n))^T \quad (9)$$

Step 4: Calculation of the Fuzzy Eigenvalue – After constructing the pairwise comparison matrix and applying Chang's Extent Analysis Method to mitigate uncertainty, the Eigenvalue was computed to evaluate the consistency of the matrix. Saaty (1980) introduced the Consistency Index (C.I.) and Consistency Ratio (C.R.) as measures to verify the reliability of comparison matrices. The Consistency Index of a matrix is determined using Equations (10) and (11).

$$CI = \frac{(\lambda_{max} - n)}{(n-1)} \quad (10)$$

$$CR = \frac{CI}{RI} \quad (11)$$

where: λ_{max} is the largest Eigen value of the comparison matrix, n is the dimension of the matrix, and RI(n) is a random index, that depends on n, as shown in Table 6.

Table 6. Consistency index, R.I., of random matrices (Golden and Wang, 1989)

Number of Criteria	1	2	3	4	5	6	7	8	9	10	11
RI	0.00	0.00	0.58	0.90	1.12	1.24	1.32	1.41	1.45	1.49	1.51

In accordance with the scale ranging from zero to one, the overall inconsistency ought to be approximately 10%. However, if the judgments provided by the experts demonstrate inconsistency, as stated by Büyüközkan and Çifçi (2012) and Yasmin et al. (2013), the decision maker is required to undertake the process of repeating the pairwise comparison matrix. To defuzzify a triangular fuzzy number, denoted as M = (l, m, u), and convert it into a crisp number, one can utilize Eqn (12) (Kwong and Bai, 2003).

$$M - Crisp = \frac{4 * m + l + u}{6} \quad (12)$$

In this research, a fuzzy decision support system was developed using Microsoft Excel to solve FAHP matrices. The Excel spreadsheets incorporated Chang's Extent Analysis Method as the primary procedure for processing these matrices. All components of the study, including the initial matrix configuration, problem definition, input matrices, FAHP matrix solutions, consistency ratio calculations, and weighted values (W), were systematically executed within the Microsoft Excel environment.

4. Findings and discussion

The successful completion of construction projects is strongly linked to the effectiveness of risk management strategies. While extensive research has been conducted on risk management in construction projects, studies specifically addressing design-related risks remain relatively scarce. It is believed that implementing effective risk management strategies during the early stages of a project, particularly in the design phase, can significantly enhance the likelihood of project success by mitigating risks that may emerge in later phases. This study aims to prioritize design risk factors relevant to the Turkish construction sector. As a result of the FAHP-based analysis of data obtained from the interview, Table 7 presents key findings, including risk occurrence probabilities, their impact on project success, consistency ratios, and final weightings.

The consistency rates for the pairwise comparison matrices constructed to evaluate the probability of occurrence of the identified risk factors and their impact on project success were 0.024 and 0.025, respectively. Both values fall within the acceptable threshold of 0.10, ensuring the reliability of the comparisons. Based on the probability of occurrence, the top five ranked risk factors are as follows: missing details in project drawings, employer-initiated design revisions, inconsistencies between design projects, delays in the design phase, and inefficiencies in the design approval process. The five most significant risk factors with the potential to jeopardize project success are as follows: design defects, employer-requested design modifications, misinterpretation of design requirements and client expectations, inconsistencies across design projects, and poor performance of the design team. In the final ranking, derived from the arithmetic average of the risk factor weights based on both their probability of occurrence and their impact on project success, the most influential risk factor was identified as the employer's revision request. This factor accounted for approximately 15% of the total weight among the 11 assessed factors. Ranked second was faulty design, with an importance weight of 13%, followed by design project incompatibility in third place, with an approximate weight of 11%. The failure to accurately analyze the employer's requirements and design needs (10.60%) and insufficient field and geological investigations (9.20%) were ranked fourth and fifth, respectively.

Table 7. Design risk factors ranking

Risk Code	Design Risk Factors	Weights regarding the prob. of occur.	Rank regarding the prob. of occur.	Weights regarding the impact on project success	Rank regarding the impact on project success	Final Weight	Final Rank
DR01	Incompatibility between design projects	12.31%	3	9.18%	4	10.75%	3
DR02	Change of regulations and standards	0.11%	11	7.24%	6	3.68%	11
DR03	Faulty design	10.29%	6	16.33%	1	13.31%	2
DR04	Missing details in project drawings	14.85%	1	1.59%	10	8.22%	8
DR05	Design delay	11.79%	4	5.02%	8	8.40%	7
DR06	Failure to analyze the needs and customer demands required for design correctly	9.88%	7	11.32%	3	10.60%	4
DR07	Poor performance of the design team	9.54%	8	8.14%	5	8.84%	6
DR08	Failure to provide optimized design for construction	3.66%	9	6.05%	7	4.86%	10
DR09	Employer's design revision request	14.50%	2	15.69%	2	15.09%	1
DR10	Inadequate site/ geological investigations	2.07%	10	16.33%	1	9.20%	5
DR11	Inefficiency in design approval	11.01%	5	3.11%	9	7.06%	9
CR (Consistency ratio):		0.024		0.025			

The research findings indicate that inadequate analysis of client demands and design requirements, along with employer-initiated revision requests, can significantly hinder project success. Similarly, a separate study conducted to identify critical risks and their impacts in Build-Operate-Transfer (BOT) projects has highlighted that design risks originating from the employer are among the most influential factors contributing to cost overruns and schedule delays (Aladağ & Işık, 2019). In a different study, it was also emphasized by Gashaw and Jilcha (2023) that design changes, scope changes and coordination deficiencies are the most effective design risk factors in construction project time and cost overruns. A study on risk analysis in tunnel construction highlighted that design modifications pose a critical challenge to project success. Extensive research has highlighted that design alterations represent a major impediment to project success. Accordingly, scholars have recommended the implementation of contractual constraints on employer-driven design revisions to minimize their disruptive effects (Subramanyan et al., 2012; Satıcı and Satıcı, 2024). Different research on employer-related risks in the design phase of construction projects has identified scope changes and design defects as critical risk factors, following employer inexperience, poor coordination, and rigid project schedules. Moreover, these risks have been shown to extend project durations by up to 6%. The same study suggests that implementing quality control systems, involving an independent consultant for design review, and establishing a coordination unit are the most effective strategies for mitigating these risks. Notably, the implementation of these strategies has been found to reduce project schedule overruns by 28% (Albogamy and Dawood, 2015). Another empirical study examining critical risk factors in construction projects and their implications for project duration and cost performance identified organizational, construction, financial, design, and political risks as the most influential. The study reported that these risks could extend project timelines by 21% and increase costs by 42%. However, it was highlighted that with the implementation of targeted risk mitigation strategies, these adverse effects could be mitigated by 57% in terms of time delays and 67% in cost overruns. (Kazaz and Arslan, 2024). In addition to cost overruns, Bachayo et al. (2022) emphasized that frequent design changes, last-minute employer demands, and design flaws significantly contribute to the increase in construction waste. Erlita et al. (2023) investigated the primary contributors to time overruns in factory construction projects and found that employer-induced delays in design approval and insufficient coordination among designers exert a substantial influence on project timelines. Their findings highlight the necessity of expediting employer decision-making in both the design and construction phases and mitigating coordination inefficiencies to achieve timely project completion.

Another critical factor influencing project success is the lack of coordination among designers. Given that inadequate communication within the design team can lead to design delays and increase the risk of design flaws, addressing collaboration issues becomes even more essential. Also, Erlita et al. (2023) too highlighted the imperative of streamlining employer decision-making processes during the design and construction phases and strengthening coordination mechanisms within the design team to ensure that construction projects adhere to their intended schedules. Liu et al. (2017) emphasized that establishing a well-structured and proficient design team, along with ensuring team stability, is a crucial strategy for minimizing design-related risks. The adoption of digital technologies, such as Building Information Modeling (BIM), is frequently recommended as a key strategy for mitigating integration challenges among stakeholders throughout both the design and construction phases (Othman and Alamoudy, 2021; Moshtaghian and Noorzai, 2022; Sun et al., 2023; Tabarroki et.al., 2024). A study on the selection of optimal risk strategies in construction projects has also demonstrated that the integration of BIM-based project management and artificial intelligence-supported decision support mechanisms constitutes the most effective risk mitigation measures in project risk management (Kazaz & Arslan, 2023).

In summary, the most critical risks affecting the success of construction projects were identified as employer-driven design modifications, design errors, inconsistencies between design projects, inadequate analysis of design requirements, and insufficient field and geological investigations. To mitigate the impact of employer-initiated design changes, organizing detailed stakeholder meetings and workshops between the employer and the design team during the preliminary and detailed design stages, conducting a comprehensive analysis of needs and requirements, and incorporating change management procedures into contracts—such as legally documenting additional costs and time adjustments related to change requests, limiting revisions, and clearly defining responsibilities arising from design modifications—are proposed as effective solution strategies. To minimize inconsistencies between design teams and design projects, increased adoption of BIM, the preference for integrated project delivery methods, and the utilization of interoperable software tools are recommended. Furthermore, ensuring effective design control through independent design consultants and standardizing design processes are suggested strategies to mitigate the risk of design errors. In addition to comprehensive geotechnical investigations, detailed site exploration before the design phase and the use of design guidelines that consider site-specific and environmental conditions can help mitigate the adverse impacts associated with design risks.

Beyond these measures, technological solutions such as the implementation of smart contracts to regulate employer-driven revision requests, the integration of artificial intelligence-powered quality control systems for design verification, the application of virtual and augmented reality tools along with digital twin technology to minimize revision requests and expedite design approval processes, and the deployment of unmanned aerial vehicles (drones) and robotic systems to gather precise and comprehensive field data to prevent inadequate site and geological assessments are also proposed as effective strategies for the efficient management of design risks.

5. Conclusion

The objective of this research was to identify design risk factors that hold critical importance in the success of construction projects. To achieve this, data obtained from expert designers through interviews were analyzed using the Fuzzy AHP technique. The findings revealed that the most influential risk factors were design revisions, faulty designs, and inconsistencies among design teams and projects. To mitigate these risks, solution strategies such as increasing the adoption of digital tools like BIM, limiting revision requests through contractual provisions, and standardizing design and control processes were proposed.

It is anticipated that the findings of this study will contribute to the existing body of knowledge on design risks in construction projects and that the identified critical risk factors will support the development of effective risk management strategies during both the design and construction phases. However, several limitations should be noted. The study did not conduct a separate impact analysis of design risks in relation to fundamental project goals, including cost, time, quality, sustainability, and safety. Additionally, while risk factors were prioritized, no specific ranking was provided for the suggested mitigation strategies. Moreover, the research was confined to qualitative risk analysis. Future studies should aim to overcome these limitations by broadening the scope of research and validating the findings through case studies.

References

Abdul-Rahman, H., Loo, S. C., & Wang, C. (2012). Risk identification and mitigation for architectural, engineering, and construction firms operating in the Gulf region. *Canadian Journal of Civil Engineering*, *39*(1), 55-71.

Adeleke, A. Q., Bahaudin, A. Y., Kamaruddeen, A. M., Bamgbade, J. A., & Ali, M. W. (2019). An empirical analysis of organizational external factors on construction risk management. *International Journal of Supply Chain Management*, *8*(1), 932-940.

Aladağ, H., & Işık, Z. (2019). Design and construction risks in BOT type mega transportation projects. *Engineering, Construction and Architectural Management*, *26*(10), 2223-2242.

Albogamy, A., & Dawood, N. (2015). Development of a client-based risk management methodology for the early design stage of construction processes: applied to the KSA. *Engineering, Construction and Architectural Management*, *22*(5), 493-515.
Bachayo, A., Memon, A. H., Hussain, M., Rahman, I. A., & Ahmed, S. J. (2022). Risk Level of Design and Procurement Factors Causing Construction Waste Generation. *Journal of Applied Engineering Sciences*, *12*(1).
Boateng, A., Ameyaw, C., & Mensah, S. (2022). Assessment of systematic risk management practices on building construction projects in Ghana. *International journal of construction management*, *22*(16), 3128-3136.
Büyüközkan, G., & Çifçi, G. (2012). A novel hybrid MCDM approach based on fuzzy DEMATEL, fuzzy ANP and fuzzy TOPSIS to evaluate green suppliers. *Expert Systems with Applications*, *39*(3), 3000-3011.
Chan, I. Y. S., Leung, M. Y., & Yu, S. S. W. (2012). Managing the stress of Hong Kong expatriate construction professionals in Mainland China: Focus group study exploring individual coping strategies and organizational support. *Journal of Construction Engineering and Management*, *138*(10), 1150-1160.
Chang, D. Y. (1996). Applications of the extent analysis method on fuzzy AHP. *European journal of operational research*, *95*(3), 649-655.
Choudhry, R. M., Aslam, M. A., Hinze, J. W., & Arain, F. M. (2014). Cost and schedule risk analysis of bridge construction in Pakistan: Establishing risk guidelines. *Journal of Construction Engineering and Management*, *140*(7), 04014020.
Darko, A., Chan, A. P., Yang, Y., & Tetteh, M. O. (2020). Building information modeling (BIM)-based modular integrated construction risk management–Critical survey and future needs. *Computers in Industry*, *123*, 103327.
Dehdasht, G., Mohamad Zin, R., Ferwati, M. S., Mohammed Abdullahi, M. A., Keyvanfar, A., & McCaffer, R. (2017). DEMATEL-ANP risk assessment in oil and gas construction projects. *Sustainability*, *9*(8), 1420.
Enshassi, A., & Mosa, J. A. (2015). Risk management in building projects: owners' perspective. *IUG Journal of Natural Studies*, *16*(1).
Erlita, A., Amin, M., & Bintoro, B. P. K. (2023). Multiphase Project Risk Management on Food Factory Building Construction: Consultant Perspective. *Journal of Construction in Developing Countries*, *28*(1), 1-17.
Forcael, E., Morales, H., Agdas, D., Rodríguez, C., & León, C. (2018). Risk identification in the Chilean tunneling industry. *Engineering Management Journal*, *30*(3), 203-215.
Gashaw, T., & Jilcha, K. (2023). Design risk modeling and analysis for railway construction projects. *International Journal of Construction Management*, *23*(14), 2488-2498.
Golden, B. L., & Wang, Q. (1989). An alternate measure of consistency. *The analytic hierarchy process: Applications and studies*, 68-81.
Kazaz, A., & Arslan, G. (2023). A Multi-Criteria Decision Support Model for the Management of Construction Project Risks. *J. Constr. Eng. Manag. Innov. (Online)*, *6*, 57-69.
Kazaz, A., & Arslan, G. (2024). An Assessment of Risk Impact on Time and Cost Performance of Construction Projects. *Proceedings of the Creative Construction Conference (2024) (Online), 6, 84*
Kuo, Y. C., & Lu, S. T. (2013). Using fuzzy multiple criteria decision making approach to enhance risk assessment for metropolitan construction projects. *International journal of project management*, *31*(4), 602-614.
Kwong, C. K., & Bai, H. (2003). Determining the importance weights for the customer requirements in QFD using a fuzzy AHP with an extent analysis approach. *Iie transactions*, *35*(7), 619-626.
Lin, C. L., & Chen, B. K. (2021). Research for risk management of construction projects in Taiwan. *Sustainability*, *13*(4), 2034.
Liu, J., Xie, Q., Xia, B., & Bridge, A. J. (2017). Impact of design risk on the performance of design-build projects. *Journal of Construction Engineering and Management*, *143*(6), 04017010.
Moshtaghian, F., & Noorzai, E. (2023). Integration of risk management within the building information modeling (BIM) framework. *Engineering, Construction and Architectural Management*, *30*(5), 1951-1977.
Nieto-Morote, A., & Ruz-Vila, F. (2011). A fuzzy approach to construction project risk assessment. *International journal of project management*, *29*(2), 220-231.
Othman, A. A. E., & Alamoudy, F. O. (2021). Optimising building performance through integrating risk management and building information modelling during the design process. *Journal of Engineering, Design and Technology*, *19*(6), 1233-1267.
Sastoque, L. M., Arboleda, C. A., & Ponz, J. L. (2016). A proposal for risk allocation in social infrastructure projects applying PPP in Colombia. *Procedia Engineering*, *145*, 1354-1361.
Satici, O., & Satici, E. (2024). Theoretical semi-quantitative risk assessment methodology for tunnel design and construction processes. *International Journal of System Assurance Engineering and Management*, *15*(7), 3385-3405.
Schoonwinkel, S., & Fourie, C. J. (2016). A risk and cost management analysis for changes during the construction phase of a project. *Journal of the South African Institution of Civil Engineering*, *58*(4), 21-28.
Shelake, A. G., Gogate, N. G., & Rajhans, N. R. (2022). An integrated approach for identification and prioritization of risk factors in tunnel construction. *Materials Today: Proceedings*, *65*, 1805-1812.

Subramanyan, H., Sawant, P. H., & Bhatt, V. (2012). Construction project risk assessment: development of model based on investigation of opinion of construction project experts from India. *Journal of construction engineering and management*, *138*(3), 409-421.
Sun, R., Geng, X., Zhao, L., Wang, Y., & Guo, R. (2023). Research on the Risk-Inducing Factors of Prefabricated Building Design Change Based on Improved DEMATEL-ISM. *Buildings*, *13*(12), 3036.
Tabarroki, S., Nazari, A., & Banihashemi, S. (2024). Risk stages and factors in architectural design-A structural equation modelling. *Architectural Engineering and Design Management*, *20*(1), 79-101.
Urbański, M., Haque, A. U., & Oino, I. (2019). The moderating role of risk management in project planning and project success: Evidence from construction businesses of Pakistan and the UK. *Engineering Management in Production and Services*, *11*(1), 23-35.
Wuni, I. Y., Shen, G. Q., & Antwi-Afari, M. F. (2023). Exploring the design risk factors for modular integrated construction projects. *Construction Innovation*, *23*(1), 213-228.
Yasmin, F., Kumar, A., & Kumar, A. (2013). Fuzzy theory concept applied in analytic network process. *International Journal of Advanced Research in Computer Science and Software Engineering*, *3*(5), 832-837.
Zou, P. X., & Li, J. (2010). Risk identification and assessment in subway projects: case study of Nanjing Subway Line 2. *Construction Management and Economics*, *28*(12), 1219-1238.

Input scenario-based modeling of office building energy consumption with ensemble algorithms

Merve Kuru Erdem[1], Osman Gökalp[2], Gulben Calış[*3]

[1] Ph.D. Ege University, Faculty of Engineering, Department of Civil Engineering, Izmir, Türkiye
[2] Assistant Professor, Izmir Institute of Technology, Department of Computer Engineering, Izmir, Türkiye
[3] Associate Professor, Ege University, Faculty of Engineering, Department of Civil Engineering, Izmir, Türkiye

Abstract. In the last decade, advancements in computer science and Artificial Intelligence (AI), particularly Machine Learning (ML), have significantly impacted energy consumption modeling. ML, with its ability to solve complex, non-linear problems, is widely used in building energy consumption studies. The accuracy of these models depends heavily on the selection of algorithms and input features. This study aims to demonstrate how different algorithms and input features affect the accuracy of building energy consumption predictions. A publicly available dataset, including outdoor air variables, HVAC energy consumption data, time, and occupant-related factors from an office building in California, was used for this study. The HVAC energy consumption was modeled using four ensemble learning algorithms: Random Forest, Adaboost, Bagging, and Gradient Boosting across three scenarios. Scenario (1) used only weather variables; Scenario (2) combined weather and time-related variables; and Scenario (3) included weather, time-related, and occupant-related variables.. Performance metrics were used to evaluate the results, which showed Random Forest performed best in all scenarios. Its accuracy increased from 0.19 in scenario (1) to 0.81 in scenario (3), highlighting the importance of time-related and occupant-related variables in energy consumption. These findings provide valuable insights for building managers aiming to improve energy efficiency in office buildings.

Keywords: Energy consumption modelling; Advanced ensemble algorithms; Machine learning; Office building

1. Introduction

Recently, there has been more focus on energy efficiency in the building sector because of environmental concerns and higher building operation costs. Among the various systems in buildings, Heating, Ventilation, and Air Conditioning (HVAC) systems account for a substantial portion of energy consumption, especially in commercial buildings (Simpeh et al., 2022). Accurate prediction of HVAC energy usage is therefore vital for developing effective energy management and control strategies.

With the rapid advancement of computational power and Artificial Intelligence (AI), particularly Machine Learning (ML), researchers have increasingly turned to data-driven methods to model and predict building energy consumption. ML techniques have shown great promise in handling the complex, non-linear relationships between various factors affecting energy use, such as weather conditions, time patterns, and occupant behavior (Das et al., 2024; Zhou et al., 2024; Hosamo & Mazzetto, 2025; Sharma, 2022). Compared to traditional physics-based models, ML-based approaches offer faster computation, adaptability, and higher accuracy in many scenarios (Wu & He, 2023; Alawi et al., 2024; Liu et al., 2019). Ensemble learning, a subfield of machine learning, combines the predictions of multiple models to improve robustness and accuracy. Algorithms such as Random Forest, Bagging, AdaBoost, and Gradient Boosting have been widely used in various prediction tasks due to their ability to reduce overfitting and capture complex patterns in data.

Despite the increasing adoption of ensemble models in the field, the influence of different input features — such as weather variables, time-related and occupant-related variables — on model performance has not been comprehensively analyzed in a unified framework. This gap becomes more critical when modeling HVAC energy consumption, which is highly sensitive to both external environmental changes and internal occupancy behaviors (Müller, 2021; Mo & Zhao, 2021; Zhang & Wen, 2019).

This study aims to address this gap by evaluating the performance of four ensemble regression algorithms — Random Forest, AdaBoost, Bagging, and Gradient Boosting — in predicting HVAC energy consumption using different combinations of input features. A real-world, open source dataset from an office building in California

[*] Corresponding author, E-mail: gulben.calis@ege.edu.tr

https://doi.org/10.31462/icearc2025_ce_mng_888

was utilized, including outdoor air parameters, HVAC energy use, time attributes, and occupancy-related parameters. The study was structured around three scenarios to examine the incremental impact of input features. Scenario 1 involved using only weather variables as model inputs. In Scenario 2, time-related variables were added to the weather variables to enhance the input set. Finally, Scenario 3 further expanded the input set by incorporating occupant-related variables, resulting in a comprehensive combination of weather, time, and occupancy features.

2. Data and method

In this study, an open dataset from the years 2018-2020 obtained from an office building located in Berkeley, California, was utilized (Luo et al., 2022). The building from which the dataset was obtained is a medium-sized office building located on the Lawrence Berkeley National Laboratory campus in Berkeley, California (Building 59 or Wang Hall).

The building is divided into two wings, north and south, and is segmented into a total of 57 thermal zones. Thermal zones that have exterior walls and windows are classified as exterior zones, while the others are classified as interior zones. Heating and cooling for the offices are provided by a underfloor air distribution system. The system utilizes 4 Roof Top Units (RTUs) located on the roof with water-cooled direct expansion coils to supply cold air to the underfloor plenums. Each RTU, serves the offices on the third and fourth floors between specific vertical lines of the building, although the service areas are not separated by internal wall partitions. Detailed information about the building and the RTU systems can be accessed from (Luo et al., 2022). Due to the fact that each RTU controls different sections of the building and the number of occupants in these sections differs, the historical building automation data values vary. Therefore, in this study, . the focus was on predicting energy consumption of RTU1, which operates 14 thermal zones located in the north wing of the building.

The distributions of 30-minute interval data, collected between February 22, 2018 and February 22, 2020, which include the weather variables — outdoor air temperature, relative humidity, dew point, and solar radiation — as well as the energy consumption of RTU1, are presented in Fig. 1.

The weather variable data mentioned above were preprocessed for use in the study. In this process, if any data point for a given variable was missing at a particular timestamp, the corresponding data points for all other variables at that timestamp were also excluded. Furthermore, due to changes in the operating principles of the HVAC system caused by a wildfire near the building location between 11/12/2018 and 11/20/2018, the data from this period were also removed from the dataset. Subsequently, an outlier analysis was conducted on the remaining data, and identified outliers were eliminated. The boxplots illustrating the results of the outlier analysis for each variable are presented in Fig. 2.

The relationships between the preprocessed weather variables and HVAC energy consumption are illustrated in Fig. 3.

In addition to weather variables, the time-related variables were defined as year, month, day, and hour, while the occupant-related variables were defined based on occupants' working and non-working days and hours in this study. These variables were encoded using the Label Encoding method. The encoded labels are presented in Table 1. As a result, a dataset consisting of 11 columns and 22,136 rows was constructed for predicting RTU energy consumption.

As observed from the relationships in Fig. 3, the association between RTU energy consumption and the variables is non-linear. Therefore, in this study, ensemble learning algorithms were preferred for the prediction of energy load. In this context, four regression algorithms — Random Forest, AdaBoost, Bagging, and Gradient Boosting — from the sklearn.ensemble library in Python were implemented.

Random Forest is an ensemble learning method based on decision trees. It operates by constructing a large number of decision trees during training and outputting the average of their predictions in regression tasks. Each tree is trained on a randomly selected subset of the data with randomly selected features, which increases diversity and reduces overfitting (Zhang & Suganthan, 2014). The model improves prediction accuracy and robustness by aggregating the results of many weak learners (Lin et al., 2017).

Bagging Regression trains multiple instances of a base learner (commonly decision trees) on different bootstrap samples drawn from the training set. Each learner is trained independently, and the final prediction is made by averaging the outputs. This parallel structure helps reduce variance and prevents overfitting (Ghojogh & Crowley, 2019). Bagging is especially effective when the base model is prone to high variance (Grandvalet, 2004).

AdaBoost Regression combines several weak learners in a sequential manner. Initially, all data points are given equal weights. After each iteration, the weights of incorrectly predicted samples are increased, so that the next learner focuses more on these hard-to-predict cases. The final prediction is a weighted sum of the outputs from each model. In regression, AdaBoost minimizes the weighted absolute error, making the model more attentive to difficult samples (Shanmugasunda et al., 2021).

Gradient Boosting Regreesion also builds models sequentially, but unlike AdaBoost, it uses gradient descent to minimize a specific loss function. At each step, a new weak learner is trained to predict the residual errors of the combined previous learners. This process continues until a predefined number of learners is reached or the error no longer improves. Gradient Boosting is known for its high accuracy, but it requires careful tuning to avoid overfitting (Bentéjac et al., 2021).

In this study, the performance of the algorithms was evaluated using Mean Absolute Error (MAE), Root Mean Square Error (RMSE), Coefficient of Variation of the Root Mean Square Error (CV-RMSE), and the coefficient of determination (R^2). The corresponding formulas are presented in Equations 1–4. MAE and RMSE are scale-dependent metrics that reflect the magnitude of errors in relation to the building's energy consumption data. CV-RMSE and R^2 indicate the degree of deviation between predicted and actual values. The closer the R^2 value is to 1, the more similar the trend between predicted and actual values. The CV-RMSE for computer-based prediction models performing hourly-level forecasts should be between 10% and 30% according to ASHRAE Guideline 14–2014.

$$\begin{gathered} MAE = \frac{1}{n}\sum_{i=1}^{n}|(y_i - \hat{y}_i)| \\ RMSE = \sqrt{\frac{1}{n}\sum_{i=1}^{n}(\hat{y}_i - y_i)^2} \\ CV - RMSE = \frac{\sqrt{\frac{1}{n}\sum_{i=1}^{n}(\hat{y}_i - y_i)^2}}{\bar{y}} \\ R^2 = \frac{\sum_i(\hat{y}_i - y_i)^2}{\sum_i(\bar{y}_i - y_i)^2} \end{gathered} \qquad (1)$$

where y_i represents the actual value of observation i, , $\hat{y}_i$ denotes the predicted value by the model, $\bar{y}$ is the mean of the observed values, and n refers to the number of samples.

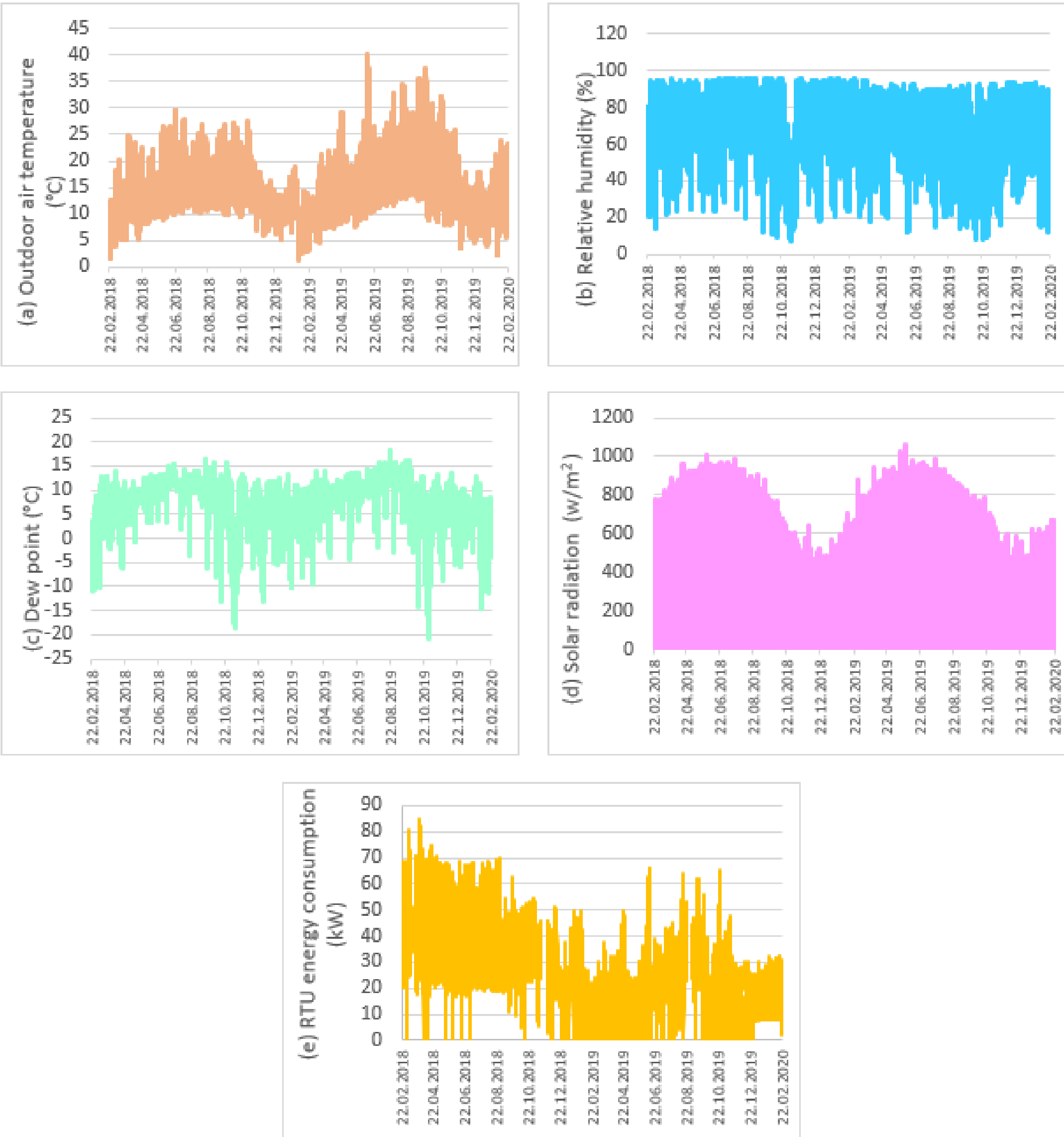

Fig. 1. (a) outdoor air temperature; (b) relative humidity; (c) dew point; (d) solar radiation; (e) RTU energy consumption vs time

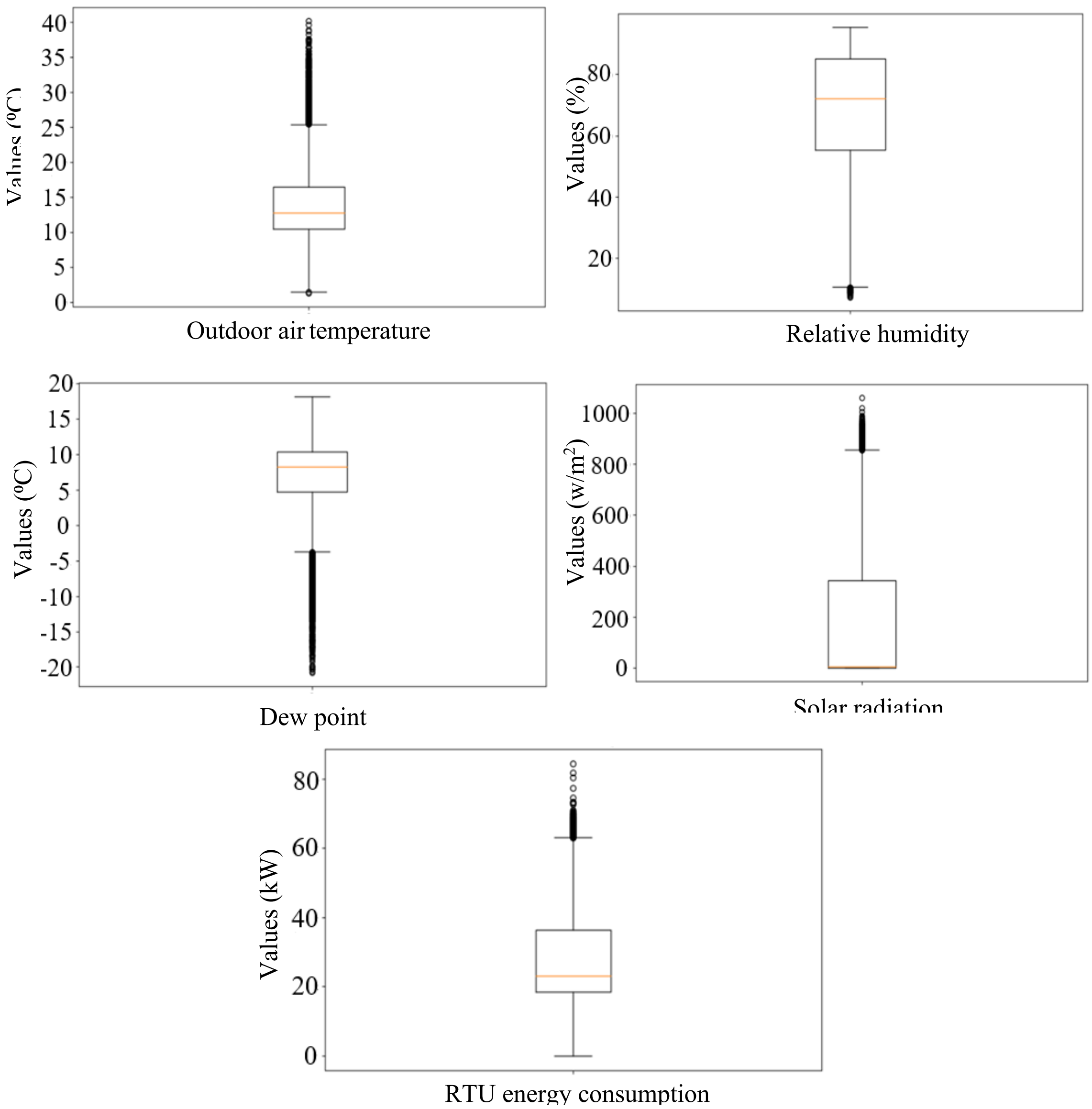

Fig. 2. Box plots of outdoor air temperature, relative humidity, dew point, solar radiation and RTU energy consumption

Table 1. Labels of time-related and occupant-related variables

Variable	Unit
Time-related	
hour	0, 1, 2, …, 46
day	0, 1, 2, …, 6
month	0, 1, 2, …., 11
year	0, 1, 2
Occupancy-related	
it is a weekday or not	0, 1
it is a working hour or not	0, 1

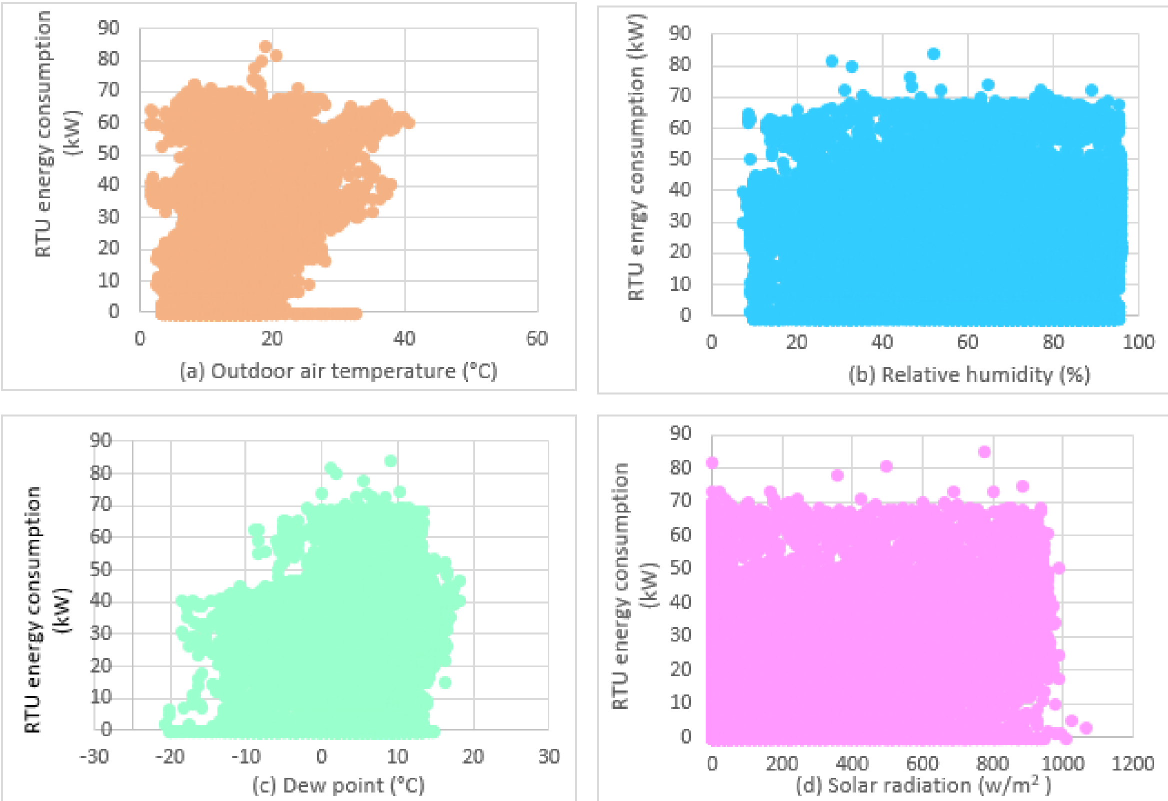

Fig. 3. RTU energy consumption vs (a) outdoor air temperature; (b) relative humidity; (c) dew point; (d) solar radiation

3. Findings and discussion

In the study, the energy consumption prediction model of the RTU was created with four different ensemble learning algorithms using different input features in three different scenarios. The performance metrics of the prediction models in which only weather variables were used as input parameters for Scenario 1 are presented in Fig. 4. It is observed that all algorithms yielded relatively low R^2 values, indicating poor predictive performance. Random Forest achieved the highest R^2 (0.19) among the four algorithms, followed by Gradient Boosting (0.16), Bagging (0.12), and Adaboost (0.12). Similarly, Random Forest exhibited the lowest MAE and RMSE values within this scenario, suggesting a slight edge over the other models when only weather data were available. Nevertheless, the overall predictive accuracy remained limited due to the restricted input features.

The performance metrics of the prediction models in Scenario 2, that is, in which time-related variables are used as input features in addition to weather variables, are presented in Fig. 5. Random Forest again demonstrated superior performance, achieving an R^2 of 0.67, a MAE of 2.35, and a RMSE of 7.02, indicating a notable enhancement compared to Scenario 1. Bagging followed closely behind with an R^2 of 0.65. On the other hand, Adaboost and Gradient Boosting still lagged behind, with relatively lower R^2 values (0.42 and 0.54, respectively) and higher MAE and RMSE values compared to Random Forest and Bagging. The overall results highlight that the inclusion of time-related variables significantly contributes to improving model accuracy, particularly for ensemble-based models like Random Forest and Bagging.

The performance metrics of the prediction models in Scenario 3, that is, where weather, time-related and occupant-related features are all used as input features, are presented in Fig. 6. Random Forest achieved the best results across all metrics, with an R^2 of 0.81, MAE of 1.94, and RMSE of 5.78, outperforming all other algorithms across the three scenarios. Bagging also showed a significant improvement, reaching an R^2 of 0.78. Although Adaboost and Gradient Boosting demonstrated slight enhancements compared to Scenario 2, their performances remained inferior to those of Random Forest and Bagging, reaffirming their relatively lower adaptability to the problem structure. Furthermore, the overall decrease in CV-RMSE values from Scenario 1 to Scenario 3 indicates a progressive enhancement in predictive reliability as additional input features were incorporated.

Considering the results across all scenarios, it is evident that the selection of input features critically influences model performance. Using only weather variables led to limited predictive capabilities, whereas the addition of time-related features notably enhanced model accuracy. The further inclusion of occupant-related variables resulted in the most substantial improvements, suggesting that the operational characteristics of the building, such as occupancy patterns, play a significant role in energy consumption dynamics. This observation aligns with previous research emphasizing that occupant behavior and occupancy schedules are critical factors affecting HVAC system performance and overall building energy use (Hong et al., 2016; Uddin et al., 2021; Li et al., 2021; Ebuy et al., 2023). Among the algorithms, Random Forest consistently demonstrated superior adaptability and predictive performance across different input settings, highlighting its robustness and effectiveness in modeling complex building energy behaviors. This finding is also consistent with previous studies that have similarly reported the strong predictive capability and stability of Random Forest in building energy modeling applications (Liu et al., 2021; Wang et al., 2018; Deng et al., 2018; Pham et al., 2020).

These findings underscore the importance of integrating operational variables, such as occupancy patterns, alongside weather and time-related data when modeling building energy consumption. While weather conditions are undeniably influential, they alone are insufficient to fully capture the variability in HVAC system behavior. The addition of time-related variables improved the models by capturing periodic and seasonal effects, while the incorporation of occupant-related variables further enhanced the models by accounting for human-driven fluctuations in system operation. Particularly, the notable improvements observed in Random Forest and Bagging performances highlight the advantages of ensemble methods in handling complex, multi-dimensional input spaces.

The consistently superior performance of Random Forest, followed closely by Bagging, across all scenarios can be attributed to their inherent characteristics. Random Forest benefits from aggregating multiple decision trees trained on bootstrapped datasets with random feature selection, which enhances its generalization ability and reduces overfitting, particularly when dealing with noisy, multi-variable data such as weather, time, and occupancy patterns (Faisal et al, 2025). Bagging, while similar in leveraging multiple models, lacks the random feature selection step, which may explain why its performance, although strong, remained slightly behind that of Random Forest (Strobl et al., 2009). The robustness of these two ensemble approaches indicates their effectiveness in capturing non-linear relationships and complex interactions among input features, which are prevalent in building energy consumption data.

Furthermore, considering the CV-RMSE values obtained across all scenarios, it can be observed that the predictive models meet acceptable accuracy standards. According to ASHRAE Standard 14–2014, computer-based prediction models performing hourly-level forecasts should exhibit a CV-RMSE between 10% and 30%. In Scenario 1, despite the limited input set, all models achieved CV-RMSE values within this acceptable range, although their R^2 scores indicated weak explanatory power. With the addition of time-related and occupant-related variables in Scenarios 2 and 3, not only did the R^2 values substantially improve, but the CV-RMSE values also decreased, especially for Random Forest and Bagging, reaching approximately 11.6% and 11.8% respectively in Scenario 3. These results confirm that the models are well-calibrated and validate the effectiveness of incorporating richer input sets to enhance predictive accuracy and reliability for practical applications.

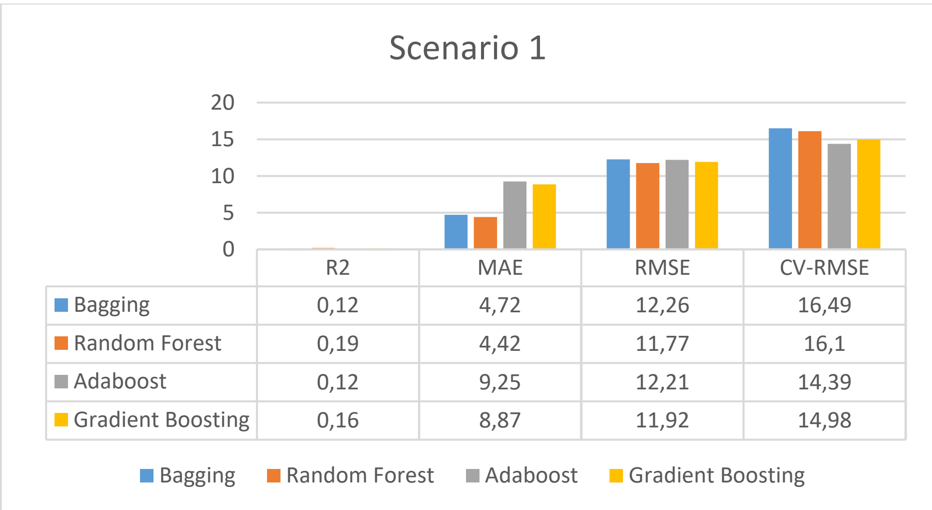

Fig. 4. Performance metrics for Scenario 1

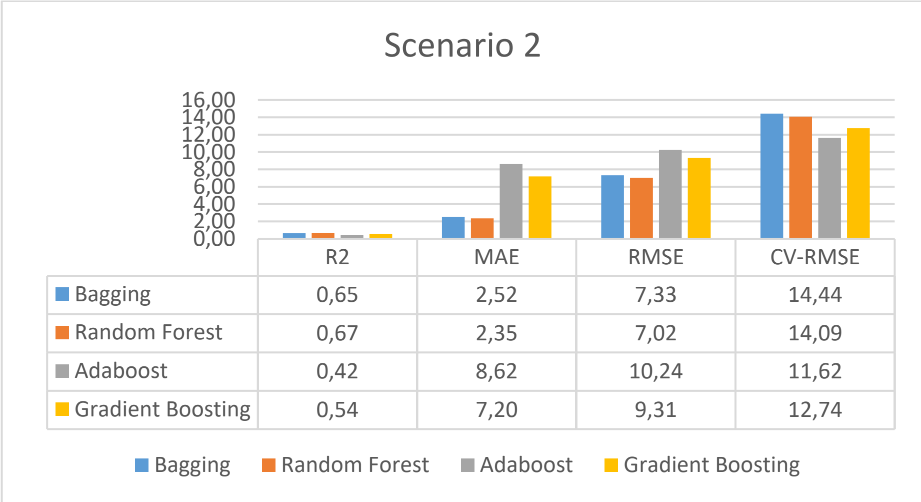

Fig. 5. Performance metrics for Scenario 2

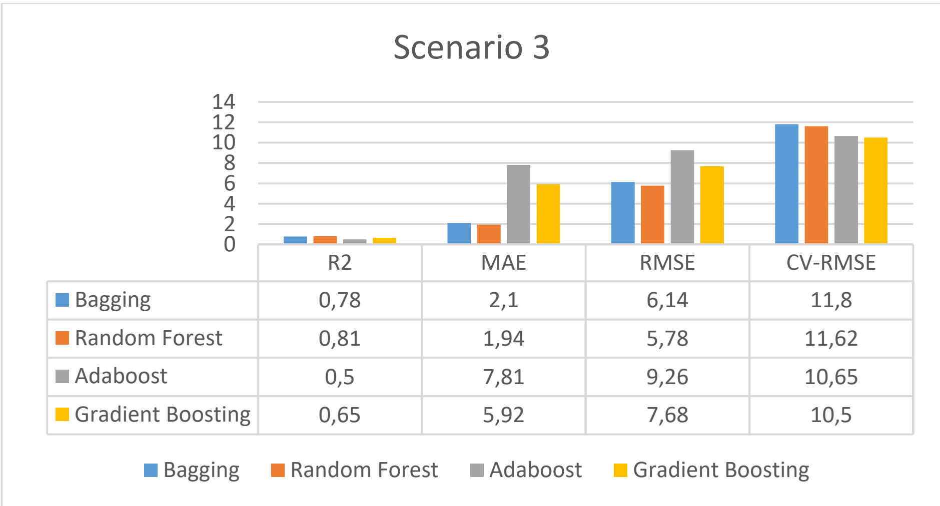

Fig. 6. Performance metrics for Scenario 3

4. Conclusion

This study investigated the modeling of office building energy consumption using various advanced ensemble algorithms under different input faetures scenarios. Specifically, three scenarios were developed based on the inclusion of weather variables alone, the addition of time-related variables, and the further incorporation of occupant-related variables. The predictive performances of Bagging, Random Forest, Adaboost, and Gradient Boosting algorithms were evaluated based on R^2, MAE, RMSE, and CV-RMSE metrics.

The key findings of the study are summarized as follows:

- The selection of input features critically influenced model performance. Using only weather variables resulted in limited predictive accuracy.
- The addition of time-related variables significantly enhanced model performance, capturing periodic and seasonal effects in energy consumption patterns.
- The further inclusion of occupant-related variables led to the most substantial improvements, highlighting the importance of operational characteristics such as workday and working hour status.
- Among the algorithms tested, Random Forest consistently demonstrated superior adaptability and predictive accuracy across all scenarios, followed closely by Bagging.
- The CV-RMSE values obtained for the models across all scenarios were within the acceptable range specified by ASHRAE Guideline 14–2014 (10–30%), with the best-performing models achieving CV-RMSE values close to 11%, indicating strong predictive reliability.

This study provides valuable insights into the importance of careful input feature selection for energy consumption modeling and the effectiveness of ensemble learning approaches, particularly Random Forest and Bagging, in handling complex building energy dynamics. The findings are particularly beneficial for building energy managers, HVAC system designers, and researchers aiming to enhance energy efficiency through data-driven modeling strategies.

For future work, expanding the input feature set to include real-time occupancy detection data, HVAC operational parameters, and indoor environmental quality measurements could further improve model performance. Additionally, exploring deep learning approaches or hybrid ensemble techniques may yield even more robust and accurate prediction models for building energy management applications.

References

Alawi, O. A., Kamar, H. M., & Yaseen, Z. M. (2024). Optimizing building energy performance predictions: A comparative study of artificial intelligence models. *Journal of Building Engineering*, *88*, 109247.

American Society of Heating, Refrigerating and Air-Conditioning Engineers. (2014). *ASHRAE Guideline 14-2014: Measurement of Energy, Demand, and Water Savings*. ASHRAE.

Bentéjac, C., Csörgő, A., & Martínez-Muñoz, G. (2021). A comparative analysis of gradient boosting algorithms. *Artificial Intelligence Review*, *54*, 1937-1967.

Das, H. P., Lin, Y. W., Agwan, U., Spangher, L., Devonport, A., Yang, Y., ... & Spanos, C. J. (2024). Machine learning for smart and energy-efficient buildings. *Environmental Data Science*, *3*, e1.

Deng, H., Fannon, D., & Eckelman, M. J. (2018). Predictive modeling for US commercial building energy use: A comparison of existing statistical and machine learning algorithms using CBECS microdata. *Energy and Buildings*, *163*, 34-43.

Ebuy, H. T., Bril El Haouzi, H., Benelmir, R., & Pannequin, R. (2023). Occupant behavior impact on building sustainability performance: A literature review. *Sustainability*, *15*(3), 2440.

Faisal, A., Jhanjhi, N. Z., Ashraf, H., Ray, S. K., & Ashfaq, F. (2025). A Comprehensive Review of Machine Learning Models: Principles, Applications, and Optimal Model Selection. *Authorea Preprints*.

Ghojogh, B., & Crowley, M. (2019). The theory behind overfitting, cross validation, regularization, bagging, and boosting: tutorial. *arXiv preprint arXiv:1905.12787*.

Grandvalet, Y. (2004). Bagging equalizes influence. Machine Learning, 55, 251-270.

Hong, T., Taylor-Lange, S. C., D'Oca, S., Yan, D., & Corgnati, S. P. (2016). Advances in research and applications of energy-related occupant behavior in buildings. *Energy and buildings*, *116*, 694-702.

Hosamo, H., & Mazzetto, S. (2024). Performance Evaluation of Machine Learning Models for Predicting Energy Consumption and Occupant Dissatisfaction in Buildings. *Buildings*, *15*(1), 39.

Li, H., Wang, Z., & Hong, T. (2021). Occupant-Centric key performance indicators to inform building design and operations. *Journal of Building Performance Simulation*, *14*(6), 814-842.

Lin, L., Wang, F., Xie, X., & Zhong, S. (2017). Random forests-based extreme learning machine ensemble for multi-regime time series prediction. *Expert Systems with Applications*, *83*, 164-176.

Liu, Y., Chen, H., Zhang, L., & Feng, Z. (2021). Enhancing building energy efficiency using a random forest model: A hybrid prediction approach. *Energy Reports*, *7*, 5003-5012.

Liu, Z., Wu, D., Liu, Y., Han, Z., Lun, L., Gao, J., ... & Cao, G. (2019). Accuracy analyses and model comparison of machine learning adopted in building energy consumption prediction. *Energy Exploration & Exploitation*, *37*(4), 1426-1451.

Luo, N., Wang, Z., Blum, D., Weyandt, C., Bourassa, N., Piette, M. A., & Hong, T. (2022). A three-year dataset supporting research on building energy management and occupancy analytics. *Scientific Data*, *9*(1), 156.

Mo, Y., & Zhao, D. (2021). Effective factors for residential building energy modeling using feature engineering. *Journal of Building Engineering*, *44*, 102891.

Müller, I. M. (2021). Feature selection for energy system modeling: Identification of relevant time series information. *Energy and AI*, *4*, 100057.

Pham, A. D., Ngo, N. T., Truong, T. T. H., Huynh, N. T., & Truong, N. S. (2020). Predicting energy consumption in multiple buildings using machine learning for improving energy efficiency and sustainability. *Journal of Cleaner Production*, *260*, 121082.

Shanmugasundar, G., Vanitha, M., Čep, R., Kumar, V., Kalita, K., & Ramachandran, M. (2021). A comparative study of linear, random forest and adaboost regressions for modeling non-traditional machining. *Processes*, *9*(11), 2015.

Sharma, V. (2022). Exploring the Predictive Power of Machine Learning for Energy Consumption in Buildings. *Journal of Technological Innovations*, *3*(1).

Simpeh, E. K., Pillay, J. P. G., Ndihokubwayo, R., & Nalumu, D. J. (2022). Improving energy efficiency of HVAC systems in buildings: a review of best practices. *International Journal of Building Pathology and Adaptation*, *40*(2), 165-182.

Strobl, C., Malley, J., & Tutz, G. (2009). An introduction to recursive partitioning: rationale, application, and characteristics of classification and regression trees, bagging, and random forests. *Psychological methods*, *14*(4), 323.

Uddin, M. N., Wei, H. H., Chi, H. L., & Ni, M. (2021). Influence of occupant behavior for building energy conservation: A systematic review study of diverse modeling and simulation approach. *Buildings*, *11*(2), 41.
Wang, Z., Wang, Y., Zeng, R., Srinivasan, R. S., & Ahrentzen, S. (2018). Random Forest based hourly building energy prediction. *Energy and Buildings*, *171*, 11-25.
Wu, Z., & He, H. (2023). Traditional Machine Learning Models for Building Energy Performance Prediction: A Comparative Research. *Machine Learning Research*, *8*(1), 1-8.
Zhang, L., & Suganthan, P. N. (2014). Random forests with ensemble of feature spaces. *Pattern Recognition*, *47*(10), 3429-3437.
Zhang, L., & Wen, J. (2019). A systematic feature selection procedure for short-term data-driven building energy forecasting model development. *Energy and Buildings*, *183*, 428-442.
Zhou, X., Du, H., Xue, S., & Ma, Z. (2024). Recent advances in data mining and machine learning for enhanced building energy management. *Energy*, 132636.

4th International Civil Engineering & Architecture Conference
17-19 May 2025, Trabzon, Türkiye

A review of technology trends for off-site construction

Handan Kunkcu*[1], Idil Calik[2], Kerim Koc[3], Asli P. Gurgun[3]

[1] Eskisehir Technical University, Department of Civil Engineering, 26555 Eskisehir, Türkiye
[2] Istanbul Bilgi University, Department of Civil Engineering, 34060 Istanbul, Türkiye
[3] Yildiz Technical University, Department of Civil Engineering, 34220 Istanbul, Türkiye

Abstract. Off-site construction (e.g., prefabricated construction and modular construction) is among the most modern industrial techniques for construction. Most recently, the use of technological means in off-site construction processes has attracted considerable attention as it offers many advantages in terms of productivity, health and safety, production quality, and sustainability within the construction industry. This study aims to develop a comprehensive framework to identify technologies and explore their impacts on construction production. In order to achieve the study objective, a systematic literature review was conducted to identify the relevant technologies in the first stage. Then, the identified 46 studies that were published between 2022 and 2025 were analyzed to reveal the benefits and advantages brought by them. The results indicate that building information modeling (BIM), tracking tools, and machine learning methods were the most frequently adopted technological tools/methods. These technologies can facilitate information and data sharing, visualization, and constructability issues in construction projects. Meanwhile, this study focuses on different applications of technologies implemented in various countries. Overall, this study is expected to help project practitioners evaluate the applicability of the proposed technologies in construction projects in many countries. The results would contribute to a better understanding of the potentials of emerging technologies and develop more effective ways of managing, controlling, coordinating, and operating the projects.

Keywords: Modular construction; Digitalization; Prefabricated construction; Literature review; Construction industry

1. Introduction

Off-site construction is an alternative traditional construction method used to minimize project cost and shorten the on-site construction duration (Lei et al., 2023). Prefabricated construction, modular construction, industrialized construction, and assembly construction methods can be indicated as off-site construction practices (Cheng et al., 2023; Junjia et al., 2025; Lei et al., 2023). These construction practices can reduce carbon emissions, waste generation, noise and risks faced, while also playing a significant role in increasing productivity, production quality, and occupational health and safety (Junjia et al., 2025; Y. Wang et al., 2024; Zhan et al., 2024). The off-site construction process consists of project planning, design, manufacturing, transportation, and on-site installation/assembly (Lei et al., 2023).

In this context, integrating advanced technologies within these processes presents better performance outcomes (Cheng et al., 2023). In the literature, various technological tools are used to obtain digital data, achieve automation and ensure digital connectivity in the work environment (Bhatia & Diaz-Elsayed, 2023). Some of the adopted technological tools/methods are: building information modeling (BIM), blockchain, smart contract, machine learning methods, sensors, and digital twin (Chen et al., 2022; Cheng et al., 2023) and each of them offers specific advantages. Although past studies have focused on the integration of technology and off-site construction, there is a gap in the literature in providing a general view on the applicability of technologies.

This study aims to develop a comprehensive framework for identifying the technologies used in off-site construction and analysing their usage purposes and benefits to the construction process. To achieve this objective, a systematic literature review was conducted to address the technologies adopted, and the selected studies were classified based on the construction techniques and technologies. Furthermore, the different methodologies applied in the utilization of these technologies in the off-site construction and countries covered in each research are also assessed. The findings of this study would be beneficial to explore the potential of technological improvements for enhancement construction practices.

*Corresponding author, E-mail: handan424@eskisehir.edu.tr

https://doi.org/10.31462/icearc2025_ce_mng_933

2. Methodology

The research methodology applied in this study is shown in Fig. 1. A systematic literature review was conducted to identify technologies/methods adopted for off-site applications by using search engine Scopus. Scopus for this study was preffered because of its wider coverage, broad usage, and fast indexing capability (Kazmi & Sodangi, 2022; Koc & Gurgun, 2021; Rathnayake et al., 2022). The keywords chosen for search strings of Scopus are listed in Fig. 1. In "Title, Abstract, and Keywords" sections, the first search string had keywords that related to off-site construction and its alternatives, the second string comprised of keywords relating to technology, and the third string was related to "construction industry". This search resulted in 730 documents. Then, the search results were limited by the following criteria: (1) the articles written in English, (2) only journal papers, (3) document type chosen as article, and (4) results between 2022-2025. A total of 193 papers were identified and each was investigated on the abstract level. At the end of the abstract and full text screening, 46 research papers were found suitable to this study.

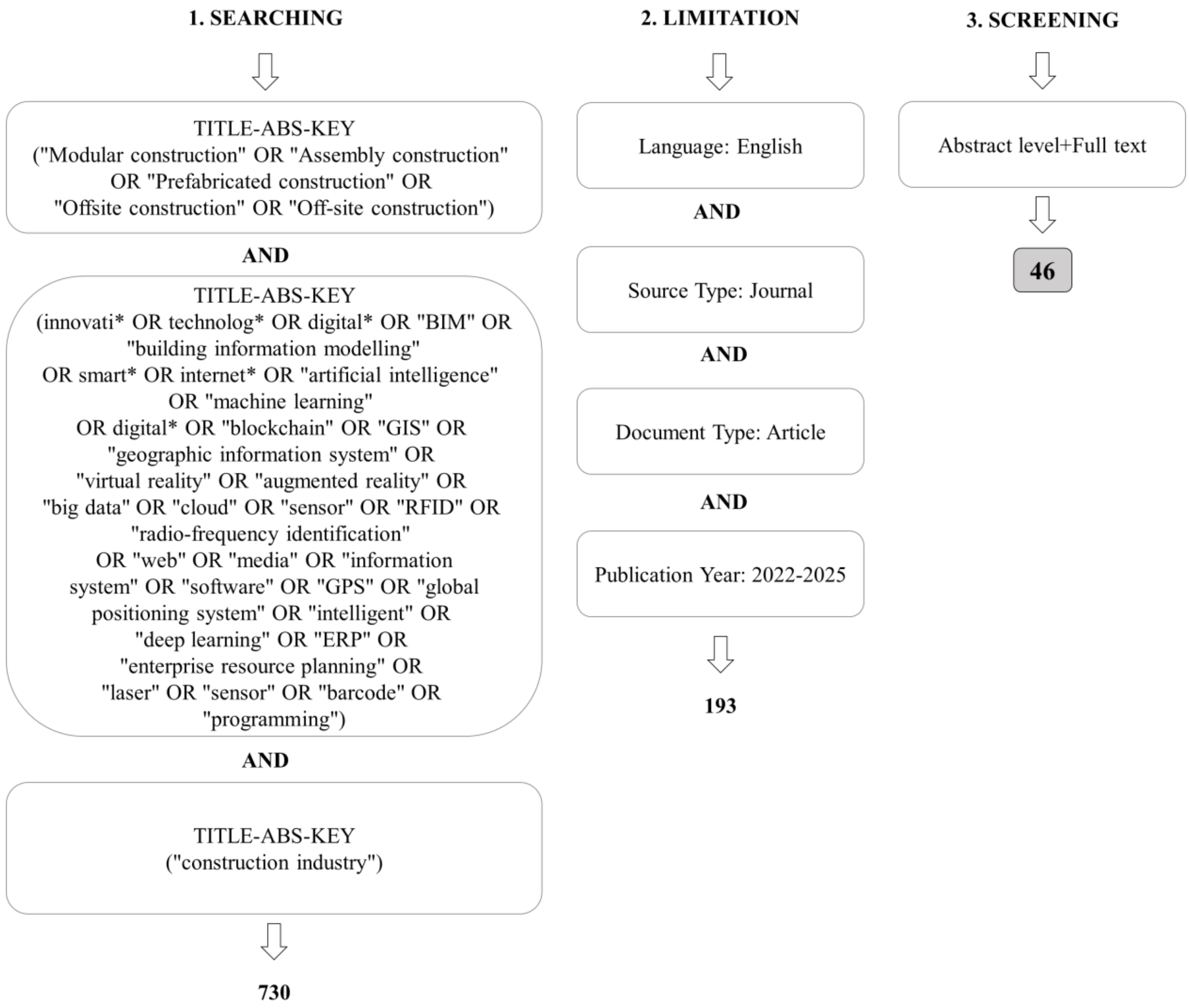

Fig. 1. Research flow

3. Results and discussion

The articles were categorized based on off-site construction techniques. The findings show that 17, 15, and 14 of the studies addressed off-site construction, modular construction, and prefabricated construction contexts, respectively. The yearly distribution of the articles indicated that 12 studies had been published in 2021, 10 studies in 2023, 23 studies in 2024, and 1 study in 2025. The findings illustrate that diverse technological tools and techniques (such as BIM, sensors, and machine learning methods) were implemented in the selected studies. Besides, it was observed that various methodologies were applied in the reviewed articles such as case study, questionnaire study, interviews, and multi-criteria decision making (MCDM) methods, and most of the studies were conducted in the different countries. To identify publications according to the region, the data source country was addressed. When the region was not explicitly mentioned in the studies, the country of the corresponding author was considered (Gurgun et al., 2024). Technologies used, qualitative and/or quantitative analyses, and countries implemented in studies are shown in Figure 2 for modular construction, in Figure 3 for prefabricated construction, and in Figure 4 for off-site construction. The findings show that researchers extensively adopted BIM, machine learning/deep learning tools, and internet-supported tools. Since case study can be regarded as a powerful method that reveal existing gaps between current literature and practice (Zhao et al., 2022), it was found to be the most frequently used method in the selected articles, even adopting in nearly all technology applications. Furthermore, the majority of the selected studies conducted research in China, Australia, and South Korea, while one study included a comparative analysis of off-site construction measurement level in Singapore, United Kingdom, Hong Kong, Malaysia, and China (Im et al., 2024).

In terms of modular construction, most of the articles adopted BIM (8 publications), machine learning/deep learning methods (2 publications), and circular economy (2 publications) (Fig. 2). These tools were mainly related to improvement in scheduling requirements, reducing waste generation and energy consumption, increasing project quality and construction safety, and offering design alternative options (Dewagoda et al., 2024; Liu et al., 2022; Mayouf et al., 2024; Wei et al., 2022).

Fig. 2. Technologies used in modular construction

Regarding prefabricated construction, BIM (9 publications) was the most frequently addressed technology (Fig. 3) with a particular focus on used data formats (such as 2D drawings, 3D model, and 4D BIM model), its practical benefits (such as enhancing management efficiency, shortening construction duration, and promoting quality development), and visual simulation (Xiang et al., 2024; Y. Xiao & Bhola, 2022; Zhang et al., 2024; Zou & Feng, 2023). On the other hand, utilizing for progress/location monitoring, obtaining more details, and providing time and resource efficiency were among the mainly addressed benefits of tracking tools (such as Internet of Things (IoT), sensors, and laser scanning) (Katiyar & Kumar, 2022; M. Wang et al., 2024; Y. Wang et al., 2024).

In terms of off-site construction, most of the selected articles widely adopted BIM (7 publications) as well as machine learning/deep learning algorithms (5 publications) (Fig. 4). At this point, using machine learning algorithms can help management process of projects enhancing the usability of the workflow, reducing constraint violations, and enabling quality inspection systems (Bae et al., 2024; Lee et al., 2022). On the other hand, blockchain applications for off-site construction context were indicated in 2 of the examined studies (Fig. 4). In this context, researchers emphasized that increased visibility and transparency contribute to the decision-making process (Bakhtiarizadeh et al., 2022; Kim et al., 2023).

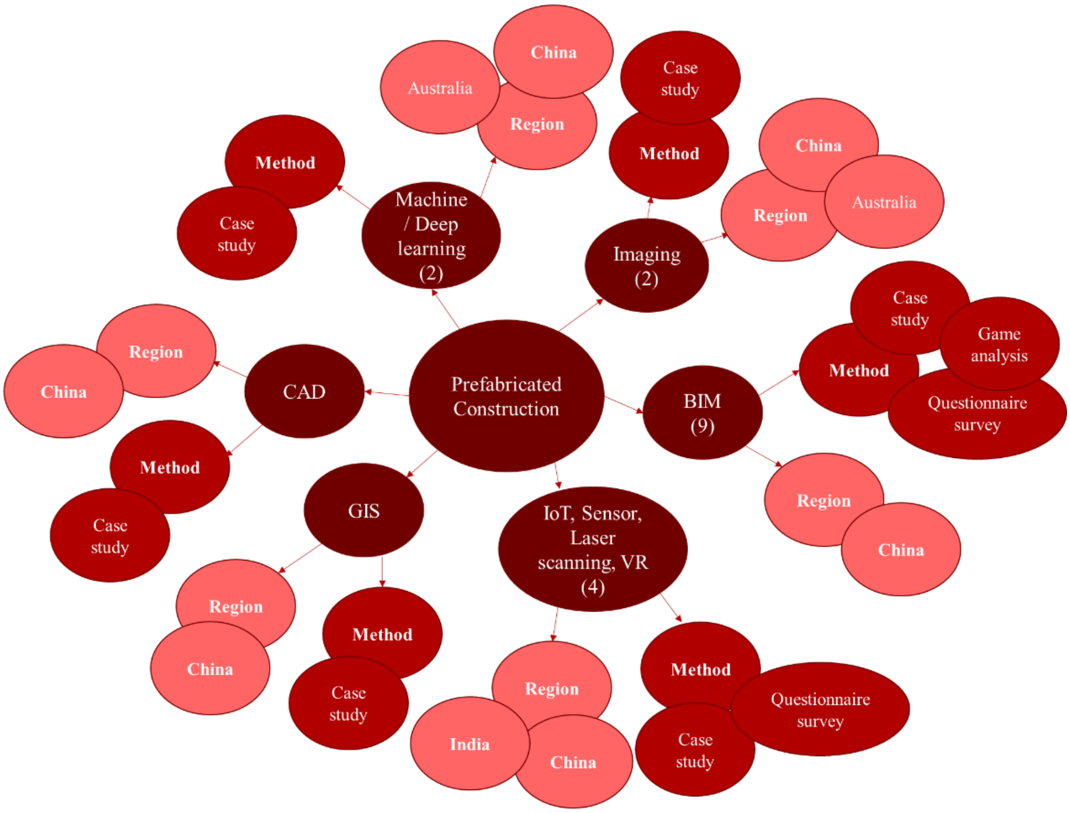

Fig. 3. Technologies used in prefabricated construction

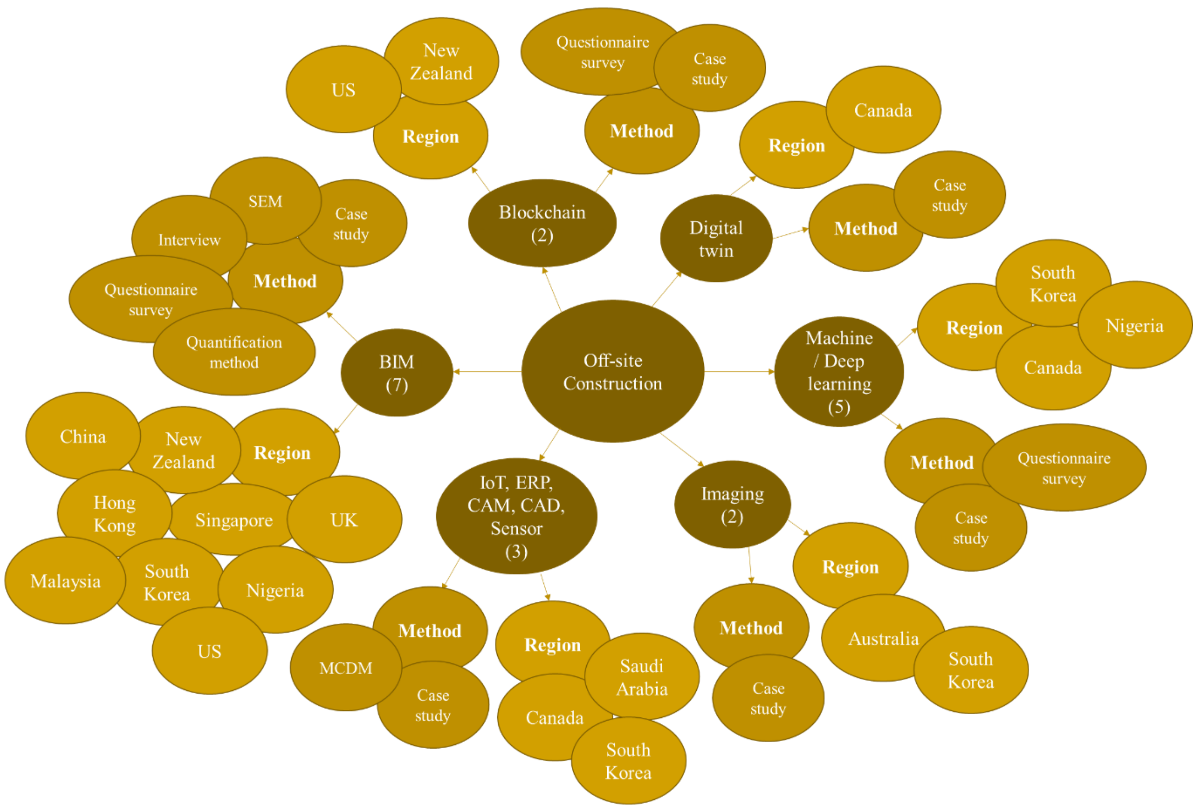

Fig. 4. Technologies used in off-site construction

As explained in Figure 5, technological tools/methods have been used widely for diverse purposes and discovered many benefits and advantages brought by them. It is apparent from the findings that purposes of BIM application in off-site construction are higher compared with other tools. BIM-enabled applications could greatly improve construction process, facilitate information and data flow, reduce constructability issues, and increase communication among different disciplines (Kordestani Ghalenoei et al., 2024; Kordestani et al., 2024). Moreover, a plethora of studies emphasized the benefits of using other technologies (e.g., (Lee et al., 2022; Lei et al., 2023; Xi, 2023; J. Xiao et al., 2024), as shown in Figure 5. On the other hand, hybrid use of some of these tools was also observed in some of the studies. For instance, Katiyar & Kumar (2022) used BIM and IoT to track project stages automatically; Gao et al. (2024) integrated BIM and Geographic Information System (GIS) to quantify greenhouse gas emissions from prefabricated elements; Tan et al. (2024) developed automated quality control approach via BIM and Light Detection and Ranging (LiDAR); and J. Xiao et al. (2024) used digital twin to evaluate virtual and real world concurrently, and the digital twin system was supported by blockchain for efficient data sharing among users. Overall, Figure 5 provides a practical contribution to the technologies to maintain their functions and roles in off-site construction practices.

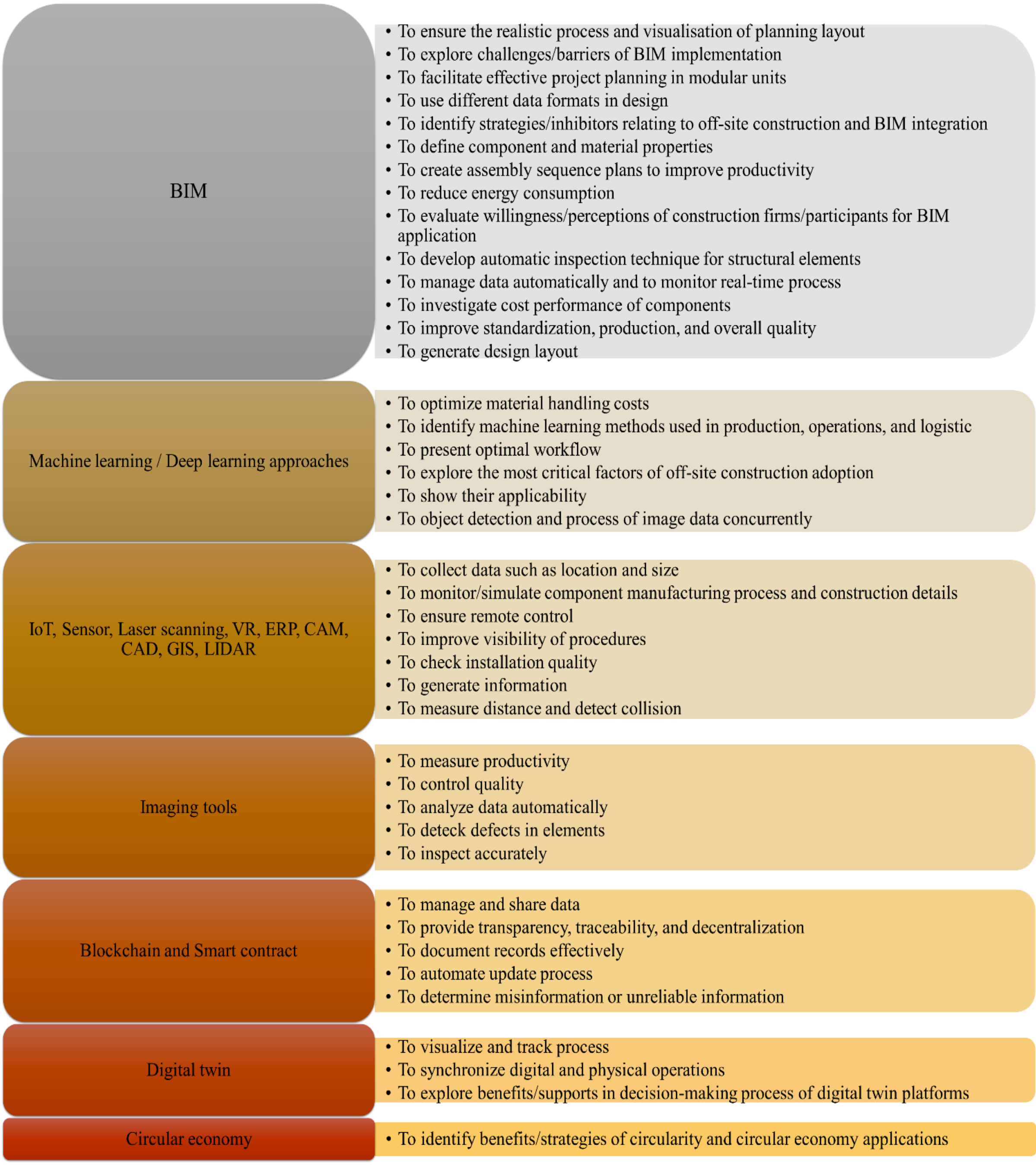

Fig. 5. Usage purposes and benefits of technological tools/methods in the selected articles

4. Conclusions

Off-site construction can be considered as a practical solution that provides high efficiency and low cost ways. In the literature, many studies have promoted to improve traditional construction practices by adopting innovative technologies. For investigating the applicability of technologies, various methodologies have been used in many countries. This study offers a review of the use of technologies in off-site construction techniques by focusing on research articles published between 2022 and 2025. BIM was found to be the most widely used technology to improve and facilitate the process in modular, prefabricated, and off-site construction contexts. In addition, case study and questionnaire survey were also frequently utilized, and studies relating to technology integrated off-site construction were conducted in many countries such as China, Australia, and South Korea. It was also observed that the integration of different technological tools can be an effective option as an innovative construction method.

- This study provides a deep understanding of the technologies adopted in each country for off-site applications and the methods applied to examine these technological applications in the selected studies.
- This study can inform both practitioners and researchers for effective implementation of off-site construction.
- The findings can be used as a guideline to the technology usage in each technique of off-site construction by indicating the potential benefits of technologies for construction practices.

References

Bae, S., Cha, H., & Jiang, S. (2024). Building an Information Modeling-Based System for Automatically Generating the Assembly Sequence of Precast Concrete Components Using a Genetic Algorithm. *Applied Sciences (Switzerland)*, *14*(4), 1358. https://doi.org/10.3390/app14041358

Bakhtiarizadeh, E., Shahzad, W. M., Poshdar, M., & Rotimi, J. O. B. (2022). Blockchain technology applicability in New Zealand's prefabricated construction industry. *Engineering Management in Production and Services*, *14*(1), 103–112. https://doi.org/10.2478/emj-2022-0009

Bhatia, P., & Diaz-Elsayed, N. (2023). Facilitating decision-making for the adoption of smart manufacturing technologies by SMEs via fuzzy TOPSIS. *International Journal of Production Economics*, *257*, 108762. https://doi.org/10.1016/j.ijpe.2022.108762

Chen, G., Li, H., Liu, M., Hsiang, S. M., & Jarvamardi, A. (2022). Knowing what is going on—a smart contract for modular construction. *Canadian Journal of Civil Engineering*, *50*(3), 210–223. https://doi.org/10.1139/cjce-2021-0649

Cheng, Z., Tang, S., Liu, H., & Lei, Z. (2023). Digital Technologies in Offsite and Prefabricated Construction: Theories and Applications. *Buildings*, *13*(1), 163. https://doi.org/10.3390/buildings13010163

Dewagoda, K. G., Ng, S. T., Kumaraswamy, M. M., & Chen, J. (2024). Design for Circular Manufacturing and Assembly (DfCMA): Synergising Circularity and Modularity in the Building Construction Industry. *Sustainability (Switzerland)*, *16*(21), 9192. https://doi.org/10.3390/su16219192

Gao, Y., Wang, J., & Yiu, T. W. (2024). Multi-information integration-based life cycle analysis of greenhouse gas emissions for prefabricated construction: A case study of Shenzhen. *Environmental Impact Assessment Review*, *104*, 107330. https://doi.org/10.1016/j.eiar.2023.107330

Gurgun, A. P., Koc, K., & Kunkcu, H. (2024). Exploring the adoption of technology against delays in construction projects. *Engineering, Construction and Architectural Management*, *31*(3), 1222–1253. https://doi.org/10.1108/ECAM-06-2022-0566

Im, C., Kim, J.-I., Kim, I., & Yu, J. (2024). Comparison of OSC (Off-Site Construction) Level Measurement Methods. *Buildings*, *14*(5), 1281. https://doi.org/10.3390/buildings14051281

Junjia, Y., Alias, A. H., Haron, N. A., & Abu Bakar, N. (2025). Deep learning for safety risk management in modular construction: Status, strengths, challenges, and future directions. *Automation in Construction*, *169*, 105894. https://doi.org/10.1016/j.autcon.2024.105894

Katiyar, A., & Kumar, P. (2022). Automated Construction Progress Monitoring of Prefabricated Concrete Structures using Building Information Modeling and Internet of Things. *International Journal on Recent and Innovation Trends in Computing and Communication*, *10*(7), 14–18. https://doi.org/10.17762/ijritcc.v10i7.5560

Kazmi, Z. A., & Sodangi, M. (2022). Modeling the Constraints to the Utilization of the Internet of Things in Managing Supply Chains of Off-Site Construction: An Approach toward Sustainable Construction. *Buildings*, *12*(3), 388. https://doi.org/10.3390/buildings12030388

Kim, M., Zhao, X., Kim, Y. W., & Rhee, B. D. (2023). Blockchain-enabled supply chain coordination for off-site construction using Bayesian theory for plan reliability. *Automation in Construction*, *155*, 105061. https://doi.org/10.1016/j.autcon.2023.105061

Koc, K., & Gurgun, A. P. (2021). Stakeholder-Associated Life Cycle Risks in Construction Supply Chain. *Journal of Management in Engineering*, *37*(1), 04020107. https://doi.org/10.1061/(asce)me.1943-5479.0000881

Kordestani Ghalenoei, N., Babaeian Jelodar, M., Paes, D., & Sutrisna, M. (2024). Challenges of offsite construction and BIM implementation: providing a framework for integration in New Zealand. *Smart and*

Sustainable Built Environment, *13*(4), 780–808. https://doi.org/10.1108/SASBE-07-2022-0139

Kordestani, N., Babaeian Jelodar, M., Paes, D., Sutrisna, M., & Rahmani, D. (2024). A comprehensive evaluation of factors influencing offsite construction and BIM integration in the construction industry. *Engineering, Construction and Architectural Management*. https://doi.org/10.1108/ECAM-12-2023-1278

Lee, S., Jeong, M., Cho, C. S., Park, J., & Kwon, S. (2022). Deep Learning-Based PC Member Crack Detection and Quality Inspection Support Technology for the Precise Construction of OSC Projects. *Applied Sciences (Switzerland)*, *12*(19), 9810. https://doi.org/10.3390/app12199810

Lei, Z., Sadiq Altaf, M., Cheng, Z., Liu, H., & Tang, S. (2023). Measurement of Information Loss and Transfer Impacts of Technology Systems in Offsite Construction Processes. *Journal of Construction Engineering and Management*, *149*(9), 05023011. https://doi.org/10.1061/jcemd4.coeng-13637

Liu, C., M.E. Sepasgozar, S., Shirowzhan, S., & Mohammadi, G. (2022). Applications of object detection in modular construction based on a comparative evaluation of deep learning algorithms. *Construction Innovation*, *22*(1), 141–159. https://doi.org/10.1108/CI-02-2020-0017

Mayouf, M., Jones, J., Elghaish, F., Emam, H., Ekanayake, E. M. A. C., & Ashayeri, I. (2024). Revolutionising the 4D BIM Process to Support Scheduling Requirements in Modular Construction. *Sustainability (Switzerland)*, *16*(2), 476. https://doi.org/10.3390/su16020476

Rathnayake, I., Wedawatta, G., & Tezel, A. (2022). Smart Contracts in the Construction Industry: A Systematic Review. *Buildings*, *12*(12), 2082. https://doi.org/10.3390/buildings12122082

Tan, Y., Chen, L., Huang, M., Li, J., & Zhang, G. (2024). Automated geometric quality inspection for modular boxes using BIM and LiDAR. *Automation in Construction*, *164*, 105474. https://doi.org/10.1016/j.autcon.2024.105474

Wang, M., Wang, C. C., Zlatanova, S., Shen, X., & Brilakis, I. (2024). A Streamlined Laser Scanning Verticality Check Method for Installation of Prefabricated Wall Panels. *Journal of Construction Engineering and Management*, *150*(11), 04024159. https://doi.org/10.1061/jcemd4.coeng-14989

Wang, Y., Li, Y., & Zhuang, J. (2024). Research on the green development path of prefabricated building industry based on intelligent technology. *Engineering, Construction and Architectural Management*. https://doi.org/10.1108/ECAM-11-2023-1139

Wei, Y., Choi, H., & Lei, Z. (2022). A generative design approach for modular construction in congested urban areas. *Smart and Sustainable Built Environment*, *11*(4), 1163–1181. https://doi.org/10.1108/SASBE-04-2021-0068

Xi, R. (2023). Construction and Application of Prefabricated Architectural Design Teaching Platform Based on CAD Technology. *Computer-Aided Design and Applications*, *20*(S4), 56–66. https://doi.org/10.14733/cadaps.2023.S4.56-66

Xiang, Y., Mahamadu, A. M., & Florez-Perez, L. (2024). Engineering information format utilisation across building design stages: An exploration of BIM applicability in China. *Journal of Building Engineering*, *95*, 110030. https://doi.org/10.1016/j.jobe.2024.110030

Xiao, J., Ma, S., Wang, S., & Huang, G. Q. (2024). Fine-grained digital twin sharing framework for smart construction through an incentive mechanism. *International Journal of Production Economics*, *276*, 109382. https://doi.org/10.1016/j.ijpe.2024.109382

Xiao, Y., & Bhola, J. (2022). Design and optimization of prefabricated building system based on BIM technology. *International Journal of System Assurance Engineering and Management*, *13*(s1), 111–120. https://doi.org/10.1007/s13198-021-01288-4

Zhan, W., Pan, W., Law, W., & Shen, H. (2024). Stakeholders' Knowledge, Attitudes, and Intentions of Adopting Modular Integrated Construction for Sustainable Development in Hong Kong. *Journal of Management in Engineering*, *40*(2), 04023070. https://doi.org/10.1061/jmenea.meeng-5642

Zhang, C., He, K., Zhang, W., Jin, T., & Ao, Y. (2024). Game evolution analysis of BIM application willingness of prefabricated construction parties. *Engineering, Construction and Architectural Management*, *72171028*. https://doi.org/10.1108/ECAM-11-2022-1063

Zhao, F., Kuang, X., Hao, H., & Liu, Z. (2022). Selection of Emerging Technologies: A Case Study in Technology Strategies of Intelligent Vehicles. *EMJ - Engineering Management Journal*, *34*(1), 37–49. https://doi.org/10.1080/10429247.2020.1839844

Zou, Y. F., & Feng, W. H. (2023). Cost optimization in the construction of prefabricated buildings by using BIM and finite element simulation. *Soft Computing*, *27*(14), 10107–10119. https://doi.org/10.1007/s00500-023-08239-0

4th International Civil Engineering & Architecture Conference
17-19 May 2025, Trabzon, Türkiye

Thermal insulation optimization for energy efficient buildings in Antalya: Multi-criteria decision making approach

Aynur Kazaz[1], Ender Yetim[*1]

[1] Akdeniz University, Department of Civil Engineering, 07058 Antalya, Türkiye

Abstract. The rapid growth of the world's population and increasing demand for housing have significantly increased energy consumption, exacerbating environmental challenges. By ratifying the Paris Climate Agreement in 2021, Türkiye has committed to improving energy efficiency and reducing greenhouse gas emissions. These commitments highlight the need for energy-efficient building design, especially given Türkiye's extensive building stock and high energy consumption in the construction sector. Heating, which accounts for a significant portion of building energy consumption, underscores the critical role of thermal insulation. This study investigates the optimal insulation thicknesses for various building envelope components in Antalya, located in the 1st degree day zone of Türkiye. The analysis includes different building elements (masonry wall-block bims, hollow brick, aerated concrete-, reinforced concrete wall, roof flooring, earth contact flooring), two different fuel types (natural gas, electricity), and four insulation materials (XPS, EPS, glass wool, and rock wool). Using Life Cycle Cost Analysis (LCCA) and Heating Degree Days (HDD) and Cooling Degree Days (CDD) data, the study calculates optimal insulation thicknesses, energy savings, payback periods, and environmental impacts using a static method. The results were evaluated using Multi-Criteria Decision Making (MCDM) methods including Analytical Hierarchy Process (AHP) and Technique for Ranking Preference by Similarity to Ideal Solution (TOPSIS) and a holistic thermal insulation optimization was provided for Antalya. This study differs from other studies by using electrical energy for heating in optimum thermal insulation calculations, performing a holistic optimisation for the building envelope and using MCDM analysis. The study's focus on sustainable energy and its exploration of the relationship between energy efficient design practices and costs are expected to benefit municipalities, academia, and the construction industry.

Keywords: Thermal insulation thickness; Life-cycle cost analysis; AHP; TOPSİS; Multi-criteria decision making

1. Introduction

The rapid growth of the global population has led to increased housing demand, resulting in higher energy consumption and the accelerated depletion of limited natural resources (Arslan & Oral, 2023). This trend has exacerbated climate change and raised energy costs, turning energy efficiency into a critical global issue (Ertürk, 2021; Sloggy et al., 2021). The building sector accounts for approximately 40% of global energy consumption and 35% of greenhouse gas emissions (Zamorano, 2022). In the European Union (EU), 35% of the building stock is over 50 years old and 75% is energy inefficient (Eurostat, 2024). Without effective measures, building energy consumption and associated emissions are projected to double by 2050 (Canbolat & Albak, 2024; Celik et al., 2025; Mohkam et al., 2023). In response, the European Commission's "Fit for 55" package aims to reduce emissions by 55% by 2030 and increase energy efficiency by 32.5% (Wilson, 2021). Similarly, the International Energy Agency projects that $4 trillion in annual clean energy investments will be necessary by 2030 to achieve net-zero emissions by 2050 (IEA, 2021).

Türkiye, as a signatory to the Paris Agreement, has committed to a 21% reduction in greenhouse gas emissions by 2030 and to promoting energy-efficient building practices (Resmi Gazete, 2021). In alignment with these targets, the first and second National Energy Efficiency Action Plans (NEEAP) aim to achieve significant cumulative energy savings and emissions reductions through targeted investments (Ministry of Energy and Natural Resources, 2024). In residential buildings, space heating constitutes a major share of energy consumption: 64% in the EU (Eurostat, 2024) and 65% in Türkiye (TÜİK, 2024), with natural gas being the predominant energy source in both regions.

Building envelope design plays a critical role in improving energy efficiency, offering potential energy savings of up to 50–60% with appropriate interventions (Shehadi, 2018). Specifically, effective thermal insulation can

[*] Corresponding author, E-mail: ender-ytm@hotmail.com

https://doi.org/10.31462/icearc2025_ce_mng_945

reduce fuel consumption by 25–50%, minimizing both heating and cooling loads (Altun et al., 2020; Özturan & Seyhan, 2024). Thus, improving the thermal performance of building envelopes remains a key strategy for reducing energy consumption and supporting climate goals.

In the literature, many studies have determined optimum insulation thickness through Life Cycle Cost Analysis (LCCA) using various building elements, insulation materials, and fuel types across different climatic zones (Akan, 2021; Akan & Akan, 2022; Akbulut, 2024; Aktemur et al., 2021; Kon & Caner, 2023; Uçar, 2024). However, these studies often focus primarily on economic optimization through cost minimization, with limited integration of user preferences and environmental impacts. Addressing this gap, the present study evaluates outputs such as insulation thickness, insulation material cost, fuel cost, total cost, energy savings, payback period, and emission value using the Analytic Hierarchy Process (AHP) and the Technique for Order Preference by Similarity to Ideal Solution (TOPSIS). By incorporating multi-criteria decision-making, this study offers a user-centered and sustainability-oriented framework, contributing to the literature by promoting a holistic evaluation approach that integrates technical, economic, and environmental considerations.

2. Materials and methods

This study analyzes external thermal insulation for residential buildings in Antalya, representing Türkiye's Mediterranean Climate Zone. Three external wall types (three row-hole hollow block, hollow brick, aerated concrete), reinforced concrete wall, roof flooring and earth contact flooring were assessed. Natural gas and electricity were considered as heating sources to evaluate their influence on optimum insulation design. Four common insulation materials (XPS, EPS, glass wool, rock wool) were analyzed. Using the static method and LCCA, optimum insulation thicknesses, annual energy savings, payback periods, and CO_2 emissions were calculated. Results were weighted by the AHP and ranked using the TOPSIS method within a multi-criteria decision-making framework.

2.1.Structure of building envelope

2.1.1. External wall layers

In this study, external insulation was preferred to minimize thermal bridges and effectively reduce heat losses through exterior walls. The wall section configurations are presented in Fig. 1, while the physical properties and cost details of the insulation materials are provided in Table 1.

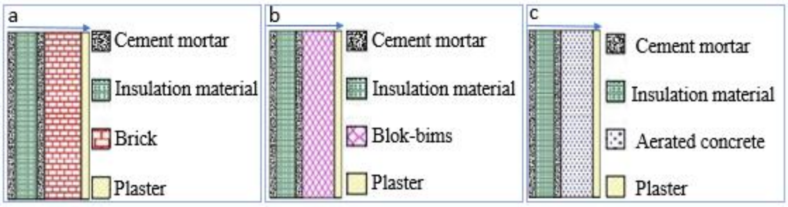

Fig. 1. External wall layers (a) Brick wall, (b) Hollow block wall, (c) Aerated concrete wall

Table 1. Unit price and thermal conductivity value of exterior wall materials

Wall material	Dimension (WxLxH[a])(mm)	Thermal conductivity coefficient (W/m.K)	Total wall thermal conductivity R(m²K/W)	Unit price ($/m³)
Three row-hole hollow block	190x390x180	0.20	1.19	30.21
Hollow brick	250x200x235	0.22	1.38	17.94
Aerated concrete	150x250x600	0.19	1.03	65.09

[a]W:width; L: length; H: height

2.1.2. External reinforced concrete envelope layers

In the study, the insulation material and optimum insulation thickness in the concrete wall (with outdoor air contact), roof flooring and earth contact flooring that make up the facade, ceiling and base surfaces. In the study, the total resistance of thermal conductor R(m²K/W) values of the outer reinforced concrete envelope layers were obtained as 0.34 for concrete wall, 0.32 for roof flooring and 0.44 for earth contact flooring. Section configurations are shown in Figure 2. In this study, four insulation materials were evaluated: Extruded polystyrene (XPS), expanded polystyrene (EPS), glass wool, and rock wool. Their thermal conductivity coefficients were determined as 0.035 W/mK, 0.032 W/mK, 0.031 W/mK, and 0.037 W/mK, respectively. The corresponding unit costs were 66.89 $/m³ for XPS, 43.51 $/m³ for EPS, 71.76 $/m³ for Glass Wool, and 79.72 $/m³ for Rock Wool.

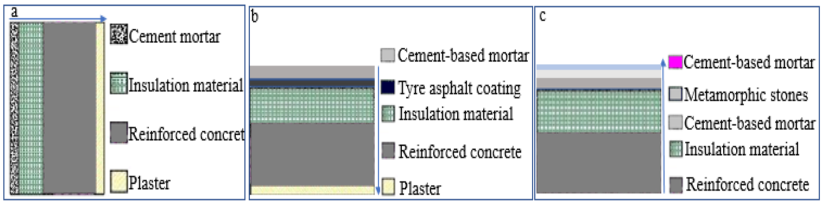

Fig. 2. Building concrete envelope structure (a) Concrete wall, (b) Roof flooring, (c) Earth contact flooring

2.2. Calculation for heating and cooling loads of building envelope

In the calculations, heating degree-days (HDD) were considered for temperatures ≤15°C and cooling degree-days (CDD) for temperatures >22°C, and the corresponding heat losses and energy demands were determined. For Türkiye's 1st climate zone, average HDD and CDD values were calculated as 711 and 751, respectively, based on 2010–2020 data. Heat loss and gain per unit surface of exterior walls were calculated using Eq. 1 (Ucar & Balo, 2010).

$$q = U \cdot \Delta T \tag{1}$$

In these equations, U represents the total heat transfer coefficient and ΔT the temperature difference between the exterior and the constant interior environment. Annual heat loss ($q_{year,h}$) and heat gain ($q_{year,c}$) per unit surface are calculated using Eqs. 2 and 3, based on U, the heating degree-days (HDD), and cooling degree-days (CDD). The U-value for a typical wall is determined using Eq. 4 (Kon, 2018).

$$q_{year,h} = 86400 \cdot HDD \cdot U \tag{2}$$

$$q_{year,c} = 86400 \cdot CDD \cdot U \tag{3}$$

$$U = \frac{1}{R_i + R_{wall} + R_{ins} + R_o} \tag{4}$$

In Eq. 4, R_i and R_o represent the convective heat resistances of the interior and exterior environments, respectively, while R_{wall} denotes the conduction resistance of the uninsulated wall layers. The thermal resistance of the insulation material (R_{ins}) is calculated using Eq. 5, where x is the insulation thickness and k is the thermal conductivity (Rosti et al., 2020). The total resistance of the non-insulated wall ($R_{w,t}$) is determined by Eq. 6 (Alsayed & Tayeh, 2019), and the overall heat transfer coefficient (U) is calculated using Eq. 7 (Vincelas & Ghislain, 2017).

$$\mathrm{R_{ins}} = \frac{\mathrm{x}}{\mathrm{k}} \tag{5}$$

$$\mathrm{R_{w,t}} = \mathrm{R_I} + \mathrm{R_{wall}} + \mathrm{R_o} \tag{6}$$

$$\mathrm{U} = \frac{1}{\mathrm{R_{w,t}} + \mathrm{R_{ins}}} \tag{7}$$

$E_{year,h}$ value is the annual energy need required for heating and $E_{year,c}$ value is the annual energy need required for cooling. They are calculated by Eq. 8 and Eq. 9 (Koru et al., 2022). The fuels used in the study and their properties are presented in Table 3.

$$\mathrm{E_{year,h}} = \frac{86400 \cdot \mathrm{HDD}}{(\mathrm{R_{w,t}} + \mathrm{R_{ins}}) \cdot \eta} \tag{8}$$

$$\mathrm{E_{year,c}} = \frac{86400 \cdot \mathrm{CDD}}{(\mathrm{R_{w,t}} + \mathrm{R_{ins}}) \cdot \mathrm{COP}} \tag{9}$$

Table 3. Properties of fuels used for heating (Çay & Gürel, 2013; Koru et al., 2022)

Fuel	Price	Lower calorific value (Hu)	Efficiency ($\eta_{H,S}$)
Natural gas	0.28 $/m³	34.285x10⁶ J/m³	0.93
Electricity	0.08 $/kWh	3.599x10⁶ j/kWh	0.99

2.3. Cost analysis and determination of optimum thickness for insulation material

Applying insulation to exterior walls can significantly reduce heat losses and gains; however, a cost analysis is necessary to determine the optimum insulation thickness. The annual energy cost per unit surface for heating ($C_{year,h}$) and cooling ($C_{year,c}$) is calculated using Eqs. 10 and 11, respectively (Canbolat et al., 2020).

$$\mathrm{C_{year,h}} = \frac{86400 \cdot \mathrm{U} \cdot \mathrm{HDD} \cdot \mathrm{C_{fuel}}}{\mathrm{Hu} \cdot \eta} \tag{10}$$

$$\mathrm{C_{year,c}} = \frac{86400 \cdot \mathrm{U} \cdot \mathrm{CDD} \cdot \mathrm{C_e}}{\mathrm{COP}} \tag{11}$$

In Eqs. 10 and 11, C_{fuel} denotes the unit price of fuel, Hu the lower calorific value, η the thermal efficiency of the combustion system, Ce the electricity unit price, and COP (assumed as 3) the cooling system efficiency. The life-cycle cost analysis method was used to determine the optimum insulation thickness, with annual energy costs calculated based on the Present Value Factor (PVF) and the defined life cycle. PVF varies depending on inflation (g) and interest (i) rates. The actual interest rate (r) is calculated using Eq. 12 when i > g, Eq. 13 when g > i, and PVF is subsequently computed using Eq. 14. If i = g, PVF is determined through Eq. 15 (Aydın & Bıyıkoğlu, 2020).

$$\mathrm{r} = \frac{\mathrm{i} - \mathrm{g}}{1 + \mathrm{g}} \tag{12}$$

$$\mathrm{r} = \frac{\mathrm{g} - \mathrm{i}}{1 + \mathrm{i}} \tag{13}$$

$$\mathrm{PVF} = \frac{(1 + R)^N - 1}{r \cdot (1 + r)^N} \tag{14}$$

$$\mathrm{PVF} = \frac{N}{1 + i} \tag{15}$$

The Present Value Factor (PVF) was calculated as 7.95 using 2021-January economic data from the Central Bank of the Republic of Turkey (10-year life cycle, 19.60% interest rate, and 14.60% inflation). Insulation cost is determined by Eq. 16, where Cy represents the unit cost of insulation. The total heating and cooling costs for an insulated building are calculated using Eqs. 17 and 18, respectively. For buildings insulated for both heating and cooling, the total cost is calculated using Eq. 19 (Koru et al., 2022).

$$\mathrm{C_{ins}} = \mathrm{C_y} \cdot \mathrm{x} \tag{16}$$

$$\mathrm{C_{ins,t,h}} = \mathrm{C_{year,h}} \cdot \mathrm{PVF} + \mathrm{C_y} \cdot \mathrm{x} \tag{17}$$

$$\mathrm{C_{ins,t,c}} = \mathrm{C_{year,c}} \cdot \mathrm{PVF} + \mathrm{C_y} \cdot \mathrm{x} \tag{18}$$

$$\mathrm{C_{ins,t,h,c}} = \mathrm{C_{year,h}} \cdot \mathrm{PVF} + \mathrm{C_{year,c}} \cdot \mathrm{PVF} + \mathrm{C_y} \cdot \mathrm{x} \tag{19}$$

The optimum insulation thickness minimizing the total heating cost is calculated using Eq. 20, while that minimizing the total cooling cost is determined by Eq. 21 (Bolattürk, 2008). The optimum thickness minimizing both heating and cooling costs is obtained through Eq. 22 (Aydın & Bıyıkoğlu, 2020).

$$\mathrm{X_{opt,h}} = 293{,}94 \cdot \left(\frac{\mathrm{HDD} \cdot \mathrm{C_{fuel}} \cdot \mathrm{PVF} \cdot \mathrm{k}}{\mathrm{Hu} \cdot \mathrm{C_{ins}} \cdot \eta}\right)^{\frac{1}{2}} - \mathrm{k} \cdot \mathrm{R_{w,t}} \tag{20}$$

$$\mathrm{X_{opt,c}} = 293{,}94 \cdot \left(\frac{\mathrm{CDD} \cdot \mathrm{C_e} \cdot \mathrm{PVF} \cdot \mathrm{k}}{\mathrm{C_{ins}} \cdot \mathrm{COP}}\right)^{\frac{1}{2}} - \mathrm{k} \cdot \mathrm{R_{w,t}} \tag{21}$$

$$\mathrm{X_{opt,c}} = 293{,}94 \cdot \left(\frac{\mathrm{CDD} \cdot \mathrm{C_e} \cdot \mathrm{PVF} \cdot \mathrm{k}}{\mathrm{C_{ins}} \cdot \mathrm{COP}}\right)^{\frac{1}{2}} - \mathrm{k} \cdot \mathrm{R_{w,t}} \tag{22}$$

2.4. Payback period method

The total annual net savings for buildings with heating-only insulation are calculated using Eq. 23, while those with both heating and cooling insulation are determined by Eq. 24. In these equations, C_h and $C_{h,c}$ represent the 10-year heating and heating-cooling energy costs of uninsulated buildings. The payback periods of insulation investments are calculated using Eq. 25 and Eq. 26, respectively (Kurekci, 2016).

$$\mathrm{A_{year,h}} = \mathrm{C_h} - \mathrm{C_{ins,t,h}} \tag{23}$$

$$A_{year,h,c} = C_{h,c} - C_{ins,t,h,c} \tag{24}$$

$$PP_h = \frac{C_{ins}}{Ayear,_h} \tag{25}$$

$$PP_{h,c} = \frac{C_{ins}}{A_{year,h,c}} \tag{26}$$

2.5. Environmental analysis

In the study, emission values depending on different insulation materials and thickness of insulation materials were calculated according to the use of natural gas and electrical energy. The amount of CO_2 emission per unit surface according to the annual fuel consumption is calculated by Eq. 27 and Eq. 28 (Çay & Gürel, 2013).

$$\mathrm{M_{CO_2}} = \frac{\mathrm{x} \cdot \mathrm{M_{CO_2}}}{\mathrm{M_{fuel}}}\ (\mathrm{kg\ CO_2/kg\ fuel}) \tag{27}$$

$$\mathrm{M_{CO_2}} = \frac{44\mathrm{x}}{\mathrm{M_{fuel}}}\ \mathrm{E_A}\ (\mathrm{kg\ CO_2\ /m^2 - year}) \tag{28}$$

2.6. Selecting the optimal insulation material

In this study, economic optimization parameters were defined as criteria and insulation materials as alternatives. The Analytic Hierarchy Process (AHP) was used to prioritize the criteria, while the Technique for Order Preference by Similarity to Ideal Solution (TOPSIS) was applied for selecting the optimal insulation material. AHP, developed by Saaty (1977), is based on pairwise comparisons to determine the relative importance of multiple criteria (Kazaz & Arslan, 2023). The method involves three main phases: (i) structuring the decision hierarchy, (ii) collecting expert judgments using a 1–9 scale to construct a pairwise comparison matrix, and (iii) calculating the Consistency Index (CI) and Consistency Ratio (CR) to assess the reliability of the comparisons, which should be below 0.10 (Saaty, 2004; Senan et al., 2023). The equations given below are used to calculate the consistency index and consistency ratio (Eqs. 29-30) (Saaty, 2004).

$$CI = \frac{\lambda_{\max} - n}{\mathrm{n} - 1} \tag{29}$$

$$CI = \frac{CI}{\mathrm{RI}} \tag{30}$$

The most suitable insulation material was selected using the Multi-Criteria Decision Making (MCDM) approach, based on the performance values determined for building envelope alternatives. Given the defined insulation options and evaluation based on seven criteria, the TOPSIS method was deemed appropriate for this study. Developed by Yoon and Hwang (1980), TOPSIS ranks alternatives based on their relative closeness to the ideal solution. The MCDM process involves defining the problem, generating alternatives and criteria, weighting criteria, evaluating options, selecting the appropriate method, and ranking alternatives (Erikci Çelik & Zorer Gedik). The TOPSIS procedure includes six steps: constructing the Decision Matrix (A), Standard Decision Matrix (R), Weighted Standard Decision Matrix (V), determining Ideal (A*) and Negative Ideal (A^-) solutions, calculating Discrimination Measures (Si*, Si^-), and computing the Relative Closeness (Ci*) to the ideal solution. Based on these analyses, the optimal insulation material was identified. In the decision matrix, the rows contain the decision points whose superiority is desired to be listed, and the columns contain the evaluation factors to be used in decision making (Saaty, 2004). In Eq. 31, m gives the number of decision points and n the number of evaluation factors in the Aij matrix. The Standard Decision Matrix is calculated using the elements of matrix A and using Eq. 32 (de Lima Silva & de Almeida Filho, 2020; Wang et al., 2022).

$$\mathrm{A_{ij}} = \begin{bmatrix} \mathrm{a_{11}} & \cdots & \mathrm{a_{1n}} \\ \vdots & \ddots & \vdots \\ \mathrm{a_{m1}} & \cdots & \mathrm{a_{mn}} \end{bmatrix} \tag{31}$$

$$\mathrm{r_{ij}} = \frac{\mathrm{a_{ij}}}{\sqrt{\sum_{k=1}^{m} a_{kj}^2}} \tag{32}$$

After the decision matrix is created, the normalization process (r_{ij}) is performed. In this step, the goal is to convert the criteria numeric values into comparable numeric values between 0 and 1. This transformation is carried out with the help of Eq. 33. Then, the weight values (w_i) of the evaluation factors are determined with the help of Eq. 34 (Li et al., 2022).

$$\mathrm{R_{ij}} = \begin{bmatrix} \mathrm{r_{11}} & \cdots & \mathrm{r_{1n}} \\ \vdots & \ddots & \vdots \\ \mathrm{r_{m1}} & \cdots & \mathrm{r_{mn}} \end{bmatrix} \tag{33}$$

$$\sum_{i=1}^{n} w_i = 1 \tag{34}$$

The elements of each column in the normalized decision matrix (R) are multiplied by their respective criterion weights to form the weighted normalized matrix (V) (Eq. 35) (Chakraborty, 2022). In the V matrix, the maximum and minimum values for each criterion are identified to establish the ideal and negative ideal solutions (Eqs. 36–41) (Abdel-Basset & Mohamed, 2020; Chen, 2021; Rafiei-Sardooi et al., 2021).

$$V_{ij} = \begin{bmatrix} w_1 r_{11} & w_2 r_{12} & w_{13} r_{13} & \dots & w_n r_{1n} \\ w_1 r_{21} & w_2 r_{22} & w_3 r_{23} & \ddots & w_n r_{2n} \\ & & & & \vdots \\ w_1 r_{m1} & w_2 r_{m2} & w_3 r_{3m3} & \cdots & w_n r_{mn} \end{bmatrix} \tag{35}$$

$$A^* = \{(max_i v_{ij} | j \in J), (min_i v_{ij} | j \in J'\} \tag{36}$$

$$A^* = \{(max_i v_{ij}\} \tag{37}$$

$$A^* = \{v_1^*, v_2^*, \dots, v_n^*\} \tag{38}$$

$$A^- = \{(min_i v_{ij} | j \in J), (max_i v_{ij} | j \in J'\} \tag{39}$$

$$A^- = \{(min_i v_{ij}\} \quad (40)$$

$$A^- = \{v_1^-, v_2^-, \ldots, v_n^-\} \quad (41)$$

In both Eq. 36 and Eq. 39, benefit (maximization) and loss (minimization) values are indicated. In the TOPSIS method, the Euclidean Distance Approach is applied to determine the deviations of each decision point from the ideal and negative ideal solution sets (Eqs. 42–43). In Eq. 42, Si* denotes the Ideal Discrimination Measure, where Vij represents the maximum value in the ideal set and vj the corresponding value in the weighted decision matrix (Chen, 2019; Yu & Pan, 2021). Similarly, Si⁻ denotes the Negative Ideal Discrimination Measure, where Vij refers to the minimum value in the negative ideal set. These discrimination measures are subsequently used to calculate the relative closeness (Ci*) of each decision point to the ideal solution (Eq. 44) (Çelikbilek & Tüysüz, 2020; Yu & Pan, 2021).

$$S_i^* = \sqrt{\sum_{j=1}^{n} (v_{ij} - v_i^*)^2} \quad (42)$$

$$S_i^- = \sqrt{\sum_{j=1}^{n} (v_{ij} - v_i^-)^2} \quad (43)$$

$$C_i^* = \frac{S_i^-}{S_i^- + S_i^*} \quad (44)$$

In Eq. 32, the Ci* value ranges between 0 and 1, where Ci* = 1 indicates absolute closeness to the ideal solution, and Ci* = 0 indicates closeness to the negative ideal solution. For each building envelope element, the Decision Matrix (A), Standard Decision Matrix (R), Weighted Standard Decision Matrix (V), Ideal (A*) and Negative Ideal Solutions (A⁻), Discrimination Measures (Si*, Si⁻), and Relative Closeness to Ideal Solution (Ci*) were calculated using the AHP and TOPSIS methods and presented in the tables.

3. Results and discussion

Optimum thickness of insulation materials is calculated on the exterior walls for both heating and cooling energy by using three different wall elements (Three-row-hole hollow block, brick, aerated concrete), two different fuel types (natural gas, electricity) and four different insulation materials (xps, eps, glass wool, rock wool) in buildings located in the Mediterranean Climate Zone. The cost calculation based on the optimum thickness of insulation materials used in buildings has been made by taking two situations as reference, according to the type of energy used. The first situation: In the building, natural gas is used for heating and electrical energy is used for cooling. The second situation: electrical energy is used for both heating and cooling in the building. Optimum insulation material thicknesses depending on different insulation materials in Three-row-hole hollow block, hollow brick, aerated concrete, concrete wall, earth contact flooring and roof flooring are presented in Table 4 and cost calculations are presented in Table 5. The amount of CO_2 emission after energy consumption depending on the optimum insulation thickness is presented in Figures (3-8) respectively. In the figures, a) shows the emission values from heating the building, and (b) shows the emission values from heating and cooling the building.

Table 4. Optimum insulation material thickness

Envelope Element		Fuel Type	Insulation Material			
			XPS	EPS	Glass Wool	Rock Wool
			$X_{opt,h,c}$	$X_{opt,h,c}$	$X_{opt,h,c}$	$X_{opt,h,c}$
Wall	Tree row-hole hollow block	Natural gas	0.040	0.059	0.038	0.033
		Electricity	0.061	0.083	0.056	0.052
	Hollow brick	Natural gas	0.034	0.053	0.032	0.026
		Electricity	0.054	0.078	0.051	0.046
	Aerated concret	Natural gas	0.046	0.064	0.043	0.039
		Electricity	0.067	0.089	0.061	0.059
Concrete wall		Natural gas	0.070	0.086	0.064	0.065
		Electricity	0.091	0.111	0.083	0.065
Earth contact flooring		Natural gas	0.043	0.055	0.039	0.039
		Electricity	0.057	0.072	0.052	0.052
Roof flooring		Natural gas	0.071	0.087	0.065	0.065
		Electricity	0.091	0.111	0.083	0.085

Table 5. Heating and cooling cost analysis based on optimal insulation thickness for structure envelope elements

Envelope Element		Fuel Type		Amount of Fuel Consumed (natural gas m³/m², electricity kWh/m²)				Cost of Fuel ($/m²-year)				Insulation Material Cost ($/m²-year)				Total Cost ($/m²-year)			
				XPS	EPS	Glass wool	Rock wool	XPS	EPS	Glass wool	Rock wool	XPS	EPS	Glass wool	Rock wool	XPS	EPS	Glass wool	Rock wool
Wall	Tree row-hole hollow block	Heating	Natural gas	1.44	1.12	1.39	1.61	0.05	0.31	0.38	0.44	0.34	0.74	0.43	0.00	0.73	1.05	0.81	0.44
			Electricity	7.75	5.98	7.63	8.71	0.09	0.50	0.64	0.73	2.41	2.35	2.37	2.31	3.06	2.85	3.01	3.04
		Cooling	Electricity	6.80	5.24	6.59	7.60	0.08	0.44	0.55	0.64	1.67	1.78	1.72	1.51	2.24	2.22	2.27	2.15
	Hollow brick	Heating	Natural gas	1.40	1.10	1.40	1.40	0.05	0.30	0.39	0.39	0.00	0.52	0.00	0.00	0.39	0.83	0.39	0.39
			Electricity	7.82	5.99	7.56	8.75	0.09	0.50	0.63	0.73	1.94	2.09	2.01	1.75	2.59	2.59	2.64	2.49
		Cooling	Electricity	6.76	5.19	6.63	7.63	0.08	0.44	0.56	0.64	1.27	1.57	1.29	0.96	1.84	2.00	1.85	1.60
	Aerated concret	Heating	Natural gas	1.43	1.10	1.39	1.62	0.05	0.30	0.38	0.45	0.74	1.00	0.79	0.48	1.13	1.30	1.17	0.92
			Electricity	7.83	6.00	7.54	8.73	0.09	0.50	0.63	0.73	2.74	2.57	2.80	2.79	3.40	3.07	3.43	3.52
		Cooling	Electricity	6.78	5.20	6.60	7.61	0.08	0.44	0.55	0.64	2.07	2.04	2.08	1.99	2.64	2.48	2.63	2.63
Concrete wall		Heating	Natural gas	0.72	0.55	0.70	0.80	0.03	0.15	0.19	0.22	2.34	1.96	2.30	2.55	2.54	2.11	2.49	2.77
			Electricity	3.87	3.00	3.79	4.39	0.04	0.25	0.32	0.37	4.41	3.52	4.31	4.78	4.74	3.78	4.62	5.15
		Cooling	Electricity	6.79	5.20	6.54	7.55	0.08	0.44	0.55	0.63	3.68	3.00	3.66	4.07	4.25	3.44	4.21	4.70
Earth contact flooring		Heating	Natural gas	1.01	0.79	0.98	1.15	0.04	0.22	0.27	0.32	1.20	1.09	1.22	1.20	1.48	1.31	1.49	1.51
			Electricity	5.46	4.25	5.40	6.24	0.06	0.36	0.45	0.52	2.68	2.22	2.58	2.79	3.13	2.58	3.04	3.31
		Cooling	Electricity	4.81	3.71	4.62	5.32	0.05	0.31	0.39	0.45	2.14	1.83	2.15	2.31	2.54	2.14	2.54	2.76
Roof flooring		Heating	Natural gas	1.43	1.12	1.39	1.62	0.05	0.31	0.38	0.45	2.41	1.96	2.37	2.55	2.80	2.27	2.75	3.00
			Electricity	7.81	5.98	7.64	8.75	0.09	0.50	0.64	0.73	4.42	3.57	4.31	4.86	5.07	4.07	4.95	5.60
		Cooling	Electricity	6.75	5.24	6.60	7.64	0.08	0.44	0.55	0.64	3.74	3.00	3.66	4.07	4.31	3.44	4.21	4.71

https://doi.org/10.31462/icearc2025_ce_mng_945

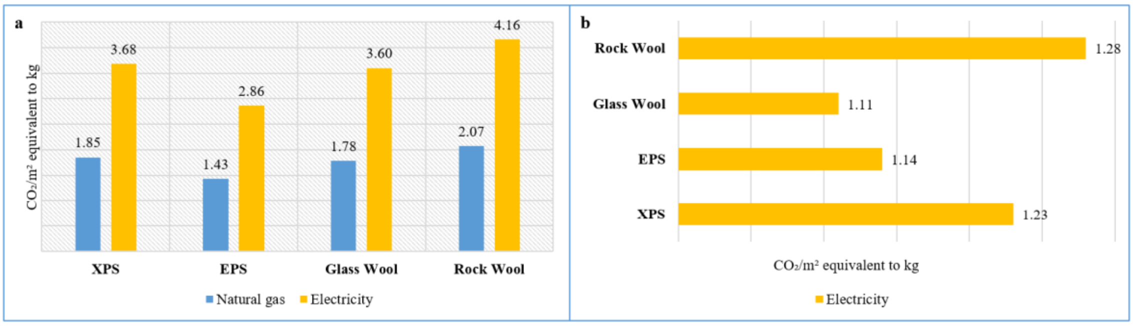

Fig. 3. Amount of CO_2 emission values (kg CO_2-eq./m^2) for three-row-hole hollow block walls

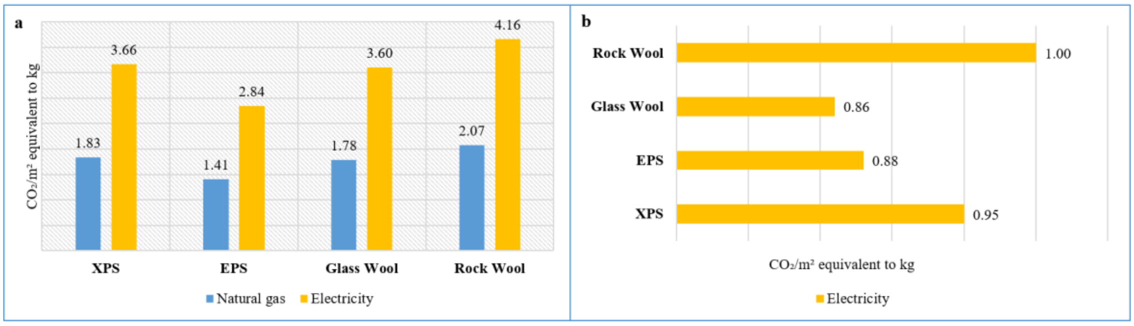

Fig. 4. Amount of CO_2 emission values (kg CO_2-eq./m^2) for hollow brick walls

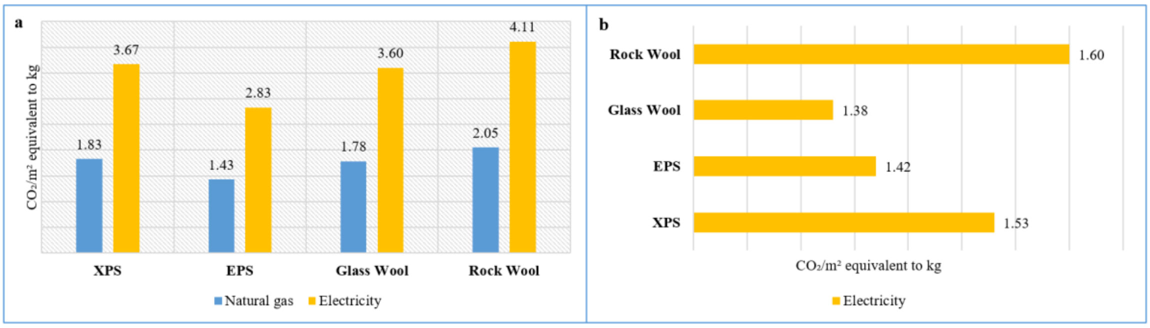

Fig. 5. Amount of CO_2 emission values (kg CO_2-eq./m^2) for aerated concrete walls

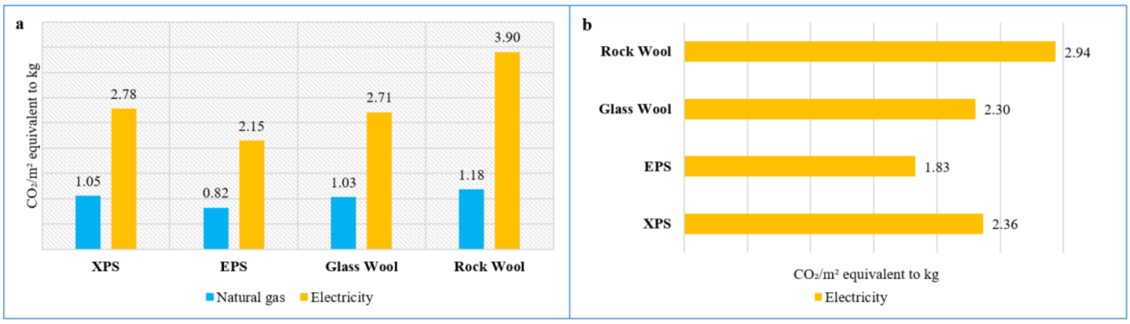

Fig. 6. Amount of CO_2 emission values (kg CO_2-eq./m^2) for concrete walls

https://doi.org/10.31462/icearc2025_ce_mng_945

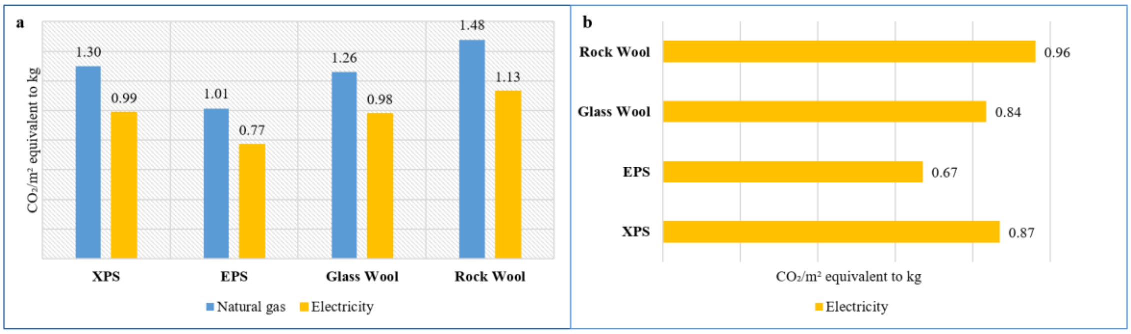

Fig. 7. Amount of CO_2 emission values (kg CO_2-eq./m^2) for earth contact flooring

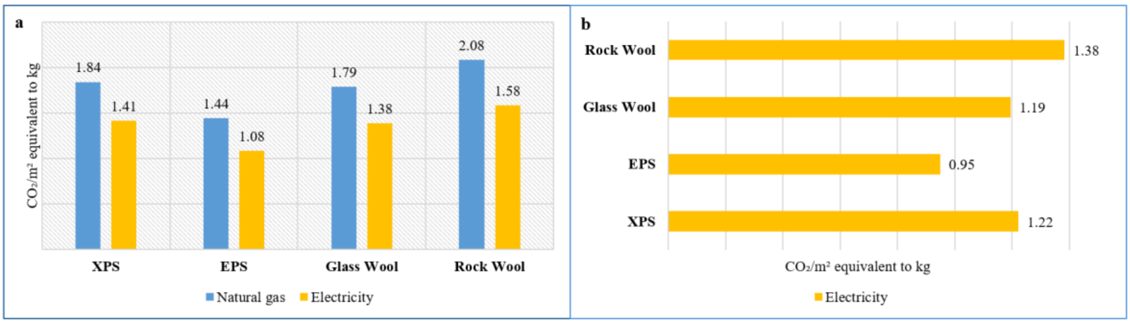

Fig. 8. Amount of CO_2 emission values (kg CO_2-eq./m^2) for roof flooring

After the economic optimization, a survey was conducted with experts who have experience in the field of insulation in the construction industry, and the criteria weights of insulation thickness, insulation cost, fuel cost, energy savings, payback period and emission amount were determined by the AHP method. The demographic information of the experts participating in the survey is presented in Table 6, the criteria descriptions in Table 7, and the pairwise comparison scale used to prioritize the criteria in Table 8. Comparison matrix, normalized matrix and criterion weights used for weighting insulation material criteria are shown in Table 9 and Table 10.

Table 6. Profile of respondents

Category		Number
Proficiency	Civil Engineer	3
	Mechanical Engineering	5
	Architecture	2
Role	Designer	10
Experience in construction sector (year)	≤10	6
	10 -20	2
	20 -30	1
	≥ 30	1
Education level	Bachelor	8
	MSc or PhD	2

With the AHP method, criterion weights were obtained with a consistency index (CI) of 0.09 and a consistency ratio (CR) of 0.01. Then, the TOPSIS method is applied to the three-row-hole hollow block, hollow brick, aerated concrete, concrete wall, earth contact flooring, roof flooring elements, which form the entire building envelope, separately, according to the type of energy used in heating, and Decision matrix(A) Standard Decision Matrix(R), Weighted Standard Decision Matrix(V), Ideal(A*) and Negative Ideal Solutions(A-), Discrimination Measures(Si*, Si-) and Relative Closeness to Ideal Solution(Ci*) calculations are made and presented in tables (Table 11-12)

Table 7. Criteria classification and explanations

Classification	Explanations
Insulation Thickness	The thickness of the insulation material to be applied in the envelope element. (m)
Insulation Material Cost	The annual cost of the insulation material to be applied to the envelope element, calculated with the Net Present Value. ($/m²-year)
Cost of Fuel	The cost of the annual energy consumed in the building by the application of the insulation material. ($/m²-year)
Total Cost	The total cost of the energy consumed annually in the building by using the insulation material and the annual cost of the insulation material calculated with the Net Present Value. ($/m²-year)
Energy Saving	Reduced energy consumption cost with the use of insulation material compared to the non-insulated situation. ($/m²-year)
Payback Period	The time it takes for the energy savings provided by the application of the insulation material to cover the cost of the insulation material. (year)
Emission Value	The amount of emission caused by the energy consumed in the building by the use of insulation material. (kg CO_2-eq./m²)

Table 8. Pairwise comparison scale (Saaty, 2004)

Importance level	Value Definitions	Description
1	Description	Each activity contributes equally.
3	Less important	As a result of experience and evaluations, an activity is a little more preferred than the other.
5	Quite important	As a result of experience and evaluations, one activity is much more preferred than the other.
7	Very important	An activity is preferred very strongly compared to the other.
9	Highly important	An activity is preferred as the highest possible degree compared to the other.
2,4,6,8	Intermediate values	If words are insufficient to make an assessment, a value in the middle of numerical values is given.

Table 9. The comparison matrix of the priority of the insulation material criteria

	Insulation Thickness	Insulation Material Cost	Cost of Fuel	Total Cost	Energy Saving	Payback Period	Emission Value
Insulation Thickness	1.00	0.21	0.18	0.17	0.13	0.20	0.20
Insulation Material Cost	4.65	1.00	0.80	0.80	0.20	0.68	0.26
Cost of Fuel	5.53	1.25	1.00	1.25	0.34	1.25	0.40
Total Cost	5.80	1.25	0.80	1.00	0.27	0.76	0.23
Energy Saving	7.67	5.04	2.94	3.74	1.00	3.65	2.69
Payback Period	4.94	1.46	0.80	1.31	0.27	1.00	0.57
Emission Value	5.09	3.84	2.48	0.51	0.37	1.74	1.00

Table 10. Normalized comparison matrix and criterion weights of the insulation material criteria

	Insulation Thickness	Insulation Material Cost	Cost of Fuel	Total Cost	Energy Saving	Payback Period	Emission Value	Weight	Ranking
Insulation Thickness	0.03	0.02	0.02	0.02	0.05	0.02	0.04	0.03	7
Insulation Material Cost	0.13	0.07	0.09	0.09	0.08	0.07	0.05	0.08	6
Cost of Fuel	0.16	0.09	0.11	0.14	0.13	0.13	0.08	0.12	3
Total Cost	0.17	0.09	0.09	0.11	0.10	0.08	0.04	0.10	5
Energy Saving	0.22	0.36	0.33	0.43	0.39	0.39	0.50	0.37	1
Payback Period	0.14	0.10	0.09	0.15	0.11	0.11	0.11	0.12	4
Emission Value	0.15	0.27	0.28	0.06	0.14	0.19	0.19	0.18	2

.

Table 11. Weighted normalized decision matrix, ıdeal and negative ıdeal solutions, distinction measurements, and relative closeness to the ıdeal solution for situation 1

Envelope Element		Alternatives	Insulation Thickness	Insulation Material Cost	Cost of Fuel	Total Cost	Energy Saving	Payback Period	Emission Value	Si*	Si⁻	Ci*	Ranking
Weight			0.03	0.08	0.12	0.10	0.37	0.12	0.18				
Wall	Tree row-hole hollow block	XPS	0.014	0.04	0.06	0.05	0.17	0.06	0.09	0.090	0.046	0.340	3
		EPS	0.020	0.04	0.05	0.04	0.25	0.04	0.08	0.009	0.136	0.938	1
		Glasswool	0.013	0.04	0.06	0.05	0.17	0.06	0.09	0.085	0.051	0.375	2
		Rock wool	0.011	0.04	0.07	0.05	0.13	0.08	0.10	0.135	0.009	0.063	4
		A^*	0.011	0.039	0.048	0.043	0.251	0.036	0.077				
		A^-	0.020	0.041	0.069	0.055	0.127	0.078	0.101				
	Hollow brick	XPS	0.014	0.04	0.06	0.05	0.16	0.06	0.09	0.118	0.056	0.320	3
		EPS	0.021	0.04	0.05	0.04	0.27	0.03	0.08	0.012	0.173	0.934	1
		Glasswool	0.013	0.04	0.06	0.05	0.17	0.06	0.09	0.108	0.066	0.379	2
		Rock wool	0.010	0.04	0.07	0.05	0.11	0.08	0.10	0.173	0.012	0.066	4
		A^*	0.010	0.037	0.048	0.043	0.270	0.034	0.076				
		A^-	0.021	0.042	0.069	0.054	0.108	0.081	0.102				
	Aerated concret	XPS	0.014	0.04	0.06	0.05	0.17	0.06	0.09	0.070	0.036	0.339	3
		EPS	0.020	0.04	0.05	0.04	0.24	0.04	0.08	0.008	0.106	0.933	1
		Glasswool	0.013	0.04	0.06	0.05	0.18	0.06	0.09	0.065	0.042	0.395	2
		Rock wool	0.012	0.04	0.07	0.06	0.14	0.07	0.10	0.106	0.008	0.067	4
		A^*	0.012	0.037	0.048	0.042	0.236	0.040	0.078				
		A^-	0.020	0.041	0.069	0.055	0.142	0.074	0.101				
Concrete wall		XPS	0.015	0.04	0.06	0.05	0.18	0.06	0.09	0.035	0.021	0.378	3
		EPS	0.018	0.03	0.05	0.04	0.20	0.05	0.07	0.005	0.056	0.924	1
		Glasswool	0.013	0.04	0.06	0.05	0.18	0.06	0.09	0.032	0.024	0.430	2
		Rock wool	0.014	0.05	0.07	0.06	0.18	0.07	0.10	0.056	0.004	0.073	4
		A^*	0.013	0.033	0.048	0.040	0.197	0.046	0.071				
		A^-	0.018	0.045	0.069	0.057	0.175	0.073	0.103				
Earth contact flooring		XPS	0.014	0.04	0.06	0.05	0.18	0.06	0.09	0.045	0.024	0.346	3
		EPS	0.019	0.03	0.05	0.04	0.21	0.04	0.07	0.005	0.068	0.927	1
		Glasswool	0.013	0.04	0.06	0.05	0.18	0.06	0.09	0.039	0.030	0.428	2
		Rock wool	0.013	0.04	0.07	0.06	0.16	0.07	0.10	0.068	0.005	0.073	4
		A^*	0.013	0.034	0.048	0.041	0.210	0.044	0.072				
		A^-	0.019	0.044	0.068	0.056	0.164	0.072	0.104				
Roof flooring		XPS	0.014	0.04	0.06	0.05	0.18	0.06	0.09	0.036	0.019	0.346	3
		EPS	0.019	0.04	0.04	0.04	0.20	0.05	0.07	0.006	0.054	0.895	1
		Glasswool	0.013	0.04	0.06	0.05	0.18	0.06	0.09	0.031	0.024	0.439	2
		Rock wool	0.013	0.04	0.07	0.06	0.18	0.07	0.10	0.054	0.006	0.105	4
		A^*	0.013	0.036	0.043	0.040	0.196	0.049	0.072				
		A^-	0.019	0.044	0.070	0.057	0.176	0.068	0.104				

https://doi.org/10.31462/icearc2025_ce_mng_945

Table 12. Weighted normalized decision matrix, ıdeal and negative ıdeal solutions, distinction measurements, and relative closeness to the ıdeal solution for situation 2

Envelope Element		Alternatives	Insulation Thickness	Insulation Material Cost	Cost of Fuel	Total Cost	Energy Saving	Payback Period	Emission Value	Si*	Si^-	Ci*	Ranking
Weight			0.03	0.08	0.12	0.10	0.37	0.12	0.18				
Wall	Tree row-hole hollow block	XPS	0.014	0.04	0.06	0.05	0.16	0.06	0.09	0.105	0.047	0.311	3
		EPS	0.019	0.04	0.05	0.04	0.26	0.03	0.07	0.007	0.151	0.954	1
		Glasswool	0.013	0.04	0.06	0.05	0.18	0.06	0.09	0.089	0.063	0.415	2
		Rock wool	0.012	0.04	0.07	0.06	0.12	0.08	0.10	0.151	0.007	0.046	4
		A^*	0.012	0.036	0.048	0.042	0.257	0.031	0.071				
		A^-	0.019	0.042	0.069	0.056	0.120	0.081	0.103				
	Hollow brick	XPS	0.014	0.04	0.06	0.05	0.15	0.05	0.09	0.137	0.086	0.385	3
		EPS	0.020	0.04	0.05	0.04	0.28	0.02	0.07	0.008	0.220	0.964	1
		Glasswool	0.013	0.04	0.06	0.05	0.16	0.05	0.09	0.128	0.095	0.427	2
		Rock wool	0.012	0.04	0.07	0.06	0.08	0.09	0.10	0.220	0.008	0.036	4
		A^*	0.012	0.038	0.048	0.042	0.284	0.024	0.071				
		A^-	0.020	0.041	0.069	0.056	0.081	0.095	0.104				
	Aerated concret	XPS	0.014	0.04	0.06	0.01	0.17	0.06	0.09	0.076	0.093	0.552	2
		EPS	0.019	0.04	0.05	0.01	0.24	0.04	0.07	0.006	0.145	0.958	1
		Glasswool	0.013	0.04	0.06	0.10	0.18	0.05	0.09	0.108	0.053	0.332	4
		Rock wool	0.013	0.04	0.07	0.01	0.14	0.08	0.10	0.117	0.083	0.415	3
		A^*	0.013	0.035	0.048	0.011	0.238	0.036	0.072				
		A^-	0.019	0.043	0.069	0.097	0.137	0.080	0.103				
Concrete wall		XPS	0.015	0.04	0.06	0.05	0.18	0.06	0.08	0.032	0.042	0.567	3
		EPS	0.019	0.03	0.04	0.04	0.19	0.05	0.07	0.008	0.071	0.902	1
		Glasswool	0.014	0.04	0.06	0.05	0.18	0.06	0.08	0.029	0.046	0.610	2
		Rock wool	0.011	0.04	0.08	0.06	0.18	0.06	0.12	0.069	0.012	0.147	4
		A^*	0.011	0.035	0.044	0.040	0.195	0.052	0.066				
		A^-	0.019	0.044	0.079	0.058	0.176	0.065	0.119				
Earth contact flooring		XPS	0.015	0.04	0.06	0.05	0.18	0.06	0.10	0.041	0.020	0.325	3
		EPS	0.018	0.03	0.05	0.04	0.20	0.05	0.08	0.005	0.057	0.918	1
		Glasswool	0.013	0.04	0.06	0.05	0.18	0.06	0.10	0.037	0.023	0.380	2
		Rock wool	0.013	0.04	0.07	0.06	0.17	0.07	0.09	0.054	0.010	0.160	4
		A^*	0.013	0.034	0.047	0.041	0.204	0.046	0.075				
		A^-	0.018	0.045	0.069	0.057	0.169	0.071	0.098				
Roof flooring		XPS	0.015	0.04	0.06	0.05	0.18	0.06	0.09	0.036	0.018	0.325	3
		EPS	0.018	0.03	0.05	0.04	0.19	0.04	0.07	0.005	0.053	0.922	1
		Glasswool	0.013	0.04	0.06	0.05	0.18	0.06	0.09	0.030	0.024	0.440	2
		Rock wool	0.014	0.05	0.07	0.06	0.18	0.07	0.10	0.053	0.004	0.073	4
		A^*	0.013	0.032	0.048	0.040	0.194	0.045	0.071				

A^-	0.018	0.046	0.069	0.057	0.178	0.070	0.103

As a result of the AHP and TOPSIS methods, it has been seen that the optimum insulation material is EPS for all the elements that make up the building envelope. In this study, in the process of determining the optimum thermal insulation thickness, the technical and economic outputs obtained based on static life cycle cost analysis were re-evaluated with the AHP-TOPSIS multi-criteria decision making method. Criterion weights were determined with AHP and then the most appropriate insulation strategies were determined by ranking the alternatives with TOPSIS method.

In the AHP analysis carried out by taking expert and user opinions through questionnaires, "Energy Saving" was determined as the criterion with the highest importance among the criteria and this criterion ranked first in the total decision weight. This result reveals that energy efficiency policies and sustainable building targets have gained significant awareness among users and sector professionals. "Emission Value" ranked second, which shows that energy efficient building applications are evaluated not only in terms of economic but also environmental sustainability. The third ranked "Fuel Cost" criterion reflects the short and medium term cost sensitivity of the users. The fact that "Payback Period" ranks fourth and "Total Cost" ranks fifth indicates that users prioritise energy and environmental performance over investment cost. The fact that total cost, which is usually the main decision criterion in traditional approaches, is left behind in this ranking is one of the unique aspects of the study. In this context, it is understood that users tend towards environmental and energy-oriented strategies beyond economic optimisation. The sixth ranked "Insulation Material Cost" and seventh ranked "Insulation Thickness" criteria are considered as secondary priorities for decision makers. This result shows that result-oriented outputs (savings, environmental impact) are valued more than technical design variables.

4. Conclusions

This study comprehensively examined the optimization of thermal insulation thickness for residential buildings located in Antalya, representing Türkiye's Mediterranean climate zone. Various building envelope elements, fuel types, and insulation materials were analyzed through a static Life Cycle Cost Analysis (LCCA), and further evaluated using multi-criteria decision-making (MCDM) methods, namely the Analytical Hierarchy Process (AHP) and the Technique for Order Preference by Similarity to Ideal Solution (TOPSIS). Heating and cooling energy loads were calculated based on Heating Degree Days (HDD) and Cooling Degree Days (CDD), and corresponding optimum insulation thicknesses, energy savings, payback periods, and environmental impacts were determined for multiple scenarios involving both natural gas and electricity as energy sources.

Initially, the optimum insulation thicknesses were determined using the static LCCA method, focusing primarily on economic parameters such as insulation cost, energy savings, and payback period. However, when these outputs were re-evaluated through AHP-TOPSIS methods that incorporated environmental impacts and user preferences, a significant shift in prioritization was observed. While the static LCCA approach generally suggested lower insulation thicknesses favoring quicker payback and lower investment costs, the AHP-TOPSIS evaluations tended to favor slightly thicker insulation, optimizing not only for economic benefits but also for maximum energy savings and reduced CO_2 emissions. This comparison highlights that although traditional static methods are effective for pure cost optimization, multi-criteria approaches offer a more holistic evaluation by balancing economic, environmental, and user-centered factors.

The results further indicated that the optimum insulation thickness varied considerably based on wall type, insulation material, and energy source. Specifically, thicker insulation was required when electricity was used as the heating source compared to natural gas, due to electricity's lower efficiency and higher operational cost. Among the evaluated insulation materials, Expanded Polystyrene (EPS) consistently emerged as the most optimal alternative according to AHP-TOPSIS results. Notably, the prioritization of "Energy Saving" and "Emission Value" criteria over traditional cost metrics such as "Total Cost" reflects a paradigm shift towards sustainability-oriented building practices.

The integration of AHP and TOPSIS methods in the insulation optimization process has enabled a user-centered, multi-dimensional decision-making approach, moving beyond conventional economic analyses. By incorporating expert judgments and user expectations into the weighting of evaluation criteria, this study presents a more realistic and comprehensive framework for insulation material and thickness selection. It demonstrates that while initial investment costs remain important, long-term energy savings, environmental benefits, and user-driven considerations must also be pivotal in designing energy-efficient building envelopes.

In conclusion, the proposed methodology provides valuable insights for policymakers, designers, and construction industry stakeholders aiming to enhance building energy performance, particularly in Mediterranean climates. Furthermore, the approach can be adapted to other climatic regions and extended to broader sustainability assessments. Future studies are recommended to integrate dynamic thermal simulations, account for hourly climatic variations, and incorporate real-time occupancy data to further refine and validate the proposed optimization model.

https://doi.org/10.31462/icearc2025_ce_mng_945

References

Abdel-Basset, M., & Mohamed, R. (2020). A novel plithogenic TOPSIS-CRITIC model for sustainable supply chain risk management. *Journal of Cleaner Production, 247*, 119586.

Akan, A. E. (2021). Determination and modeling of optimum insulation thickness for thermal insulation of buildings in all city centers of Turkey. *International Journal of Thermophysics, 42*(4), 49.

Akan, A. P., & Akan, A. E. (2022). Modeling of CO_2 emissions via optimum insulation thickness of residential buildings. *Clean Technologies and Environmental Policy*, *24*, 949–967.

Akbulut, U. (2024). Entransy-based environmental and life cycle cost analysis to determine optimum insulation thickness: Effect of the fuel sources. *Journal of the Faculty of Engineering and Architecture of Gazi University, 39*(2), 869–882.

Aktemur, C., Bilgin, F., & Tunçkol, S. (2021). Optimisation on the thermal insulation layer thickness in buildings with environmental analysis: An updated comprehensive study for Turkey's all provinces. *Journal of Thermal Engineering, 7*(5), 1239–1256.

Alsayed, M. F., & Tayeh, R. A. (2019). Life cycle cost analysis for determining optimal insulation thickness in Palestinian buildings. *Journal of Building Engineering, 22*, 101–112.

Altun, M., Akgül, Ç., & Akçamete, A. (2020). Effect of envelope insulation on building heating energy requirement, cost and carbon footprint from a life-cycle perspective. *Journal of the Faculty of Engineering and Architecture of Gazi University, 35*(1), 147-163.

Arslan, H., & Oral, G. (2023). Sensitivity analysis of facade design parameters in residential buildings in the context of climatic design. *Journal of the Faculty of Engineering and Architecture of Gazi University, 38*(3), 1769-1780.

Aydın, N., & Bıyıkoğlu, A. (2020). The effect of coolıng load on optımum insulatıon thickness in residentıial buildings. *J. of Thermal Science and Technolog, 40*(2), 281–291.

Bolattürk, A. (2008). Optimum insulation thicknesses for building walls with respect to cooling and heating degree-hours in the warmest zone of Turkey. *Building and Environment, 43*(6), 1055–1064.

Canbolat, A. S., & Albak, E. İ. (2024). Multi-objective optimization of building design parameters for cost reduction and CO_2 emission control using four different algorithms. *Applied Sciences, 14*(17), 7668.

Canbolat, A. S., Bademlioğlu, A. H., Saka, K., & Kaynaklı, O. (2020). Investigation of parameters affecting the optimum thermal insulation thickness for buildings in hot and cold climates. *Thermal Science, 24*(5A), 2891–2903.

Çay, Y., & Gürel, A. E. (2013). Determination of optimum insulation thickness, energy savings, and environmental impact for different climatic regions of Turkey. *Environmental Progress & Sustainable Energy, 32*(2), 365-372.

Çelik, A., Manay, E., & Şahin, B. (2025). Comparison of the energy and economic performance of a LEED certified educational building located in a cold climate region with the national standard. *Journal of the Faculty of Engineering and Architecture of Gazi University, 40*(2), 777-788.

Çelikbilek, Y., & Tüysüz, F. (2020). An in-depth review of theory of the TOPSIS method: An experimental analysis. *Journal of Management Analytics, 7*(2), 281–300.

Chakraborty, S. (2022). TOPSIS and modified TOPSIS: A comparative analysis. *Decision Analytics Journal, 2*, 100021.

Chen, P. (2019). Effects of normalization on the entropy-based TOPSIS method. *Expert Systems with Applications, 136*, 33–41.

Chen, P. (2021). Effects of the entropy weight on TOPSIS. *Expert Systems with Applications, 168*, 114186.

de Lima Silva, D. F., & de Almeida Filho, A. T. (2020). Sorting with TOPSIS through boundary and characteristic profiles. *Computers & Industrial Engineering, 141*, 106328.

Erikci Çelik, S. N., & Zorer Gedik, G. (2019). Evaluation of building shell performance in the scope of an innovative design: Modular hybrid wall example with surface heating cooling system—İstanbul. *Megaron, 14*(4), 495–506.

Ertürk, M. (2021). Calculation amount of carbon dioxide and sulfur dioxide per capita area, per unit area for the heating period: Example of Izmir. *Journal of the Faculty of Engineering and Architecture of Gazi University*, *36*(1), 319-332.

Eurostat. (2024). *Energy consumption in households*. Retrieved from https://ec.europa.eu/eurostat/statistics-explained/index.php?title=Energy_consumption_in_households#Energy_products_used_in_the_residential_sector

IEA. (2021). *Energy Efficiency 2021*. International Energy Agency. Retrieved from https://www.iea.org/reports/energy-efficiency-2021

Kazaz, A., & Arslan, G. (2023). A multi-criteria decision support model for the management of construction project risks. *Journal of Construction Engineering Management Innovation, 6*(1), 57–69.

Kon, O. (2018). Calculation of fuel consumption and emissions in buildings based on external walls and windows using economic optimization. Journal of the Faculty of Engineering and Architecture of Gazi University *33*(1), 101-113.

Kon, O., & Caner, İ. (2023). Calculation of insulation thickness depending on the coolest and hottest climate conditions for different flat roof types of buildings. *Black Sea Journal of Engineering and Science, 6*(1), 1–9.

Koru, M., Korkmaz, E., & Kan, M. (2022). Determination of the effect of the change in the thermal conductivity coefficient of EPS depending on the density and temperature on the optimum insulation thickness. *International Journal of Thermophysics, 43*(9), 143.

Kurekci, N. A. (2016). Determination of optimum insulation thickness for building walls by using heating and cooling degree-day values of all Turkey's provincial centers. *Energy and Buildings, 118*, 197–213.

Li, Z., Luo, Z., Wang, Y., Fan, G., & Zhang, J. (2022). Suitability evaluation system for the shallow geothermal energy implementation in region by Entropy Weight Method and TOPSIS method. *Renewable Energy, 184*, 564–576.

Ministry of Energy and Natural Resources. (2024). *Energy Efficiency 2030 Strategy and 2nd National Energy Efficiency Action Plan (2024–2030)*. Retrieved from https://enerji.gov.tr//Media/Dizin/EVCED/tr/EnerjiVerimlili%C4%9Fi/UlusalEnerjiVerimlili%C4%9FiEylemPlan%C4%B1/Belgeler/EnerEffi2030Str2ndNatEnerEffiActPlan2024-2030.pdf

Mohkam, M., Mohammadi, S. H., Arababadia, R., & Jahanshahi Javaran, E. (2023). Impacts of phase change materials on performance of operational peak load shifting strategies in a sample building in hot-arid climate. *Environmental Progress & Sustainable Energy, 42*(1), e13961.

Özturan, M. K., & Seyhan, A. K. (2024). Determination of optimum insulation thickness of building walls according to four main directions by accounting for solar radiation: A case study of Erzincan, Türkiye. *Energy and Buildings, 304*, 113871.

Rafiei-Sardooi, E., Azareh, A., Choubin, B., Mosavi, A. H., & Clague, J. J. (2021). Evaluating urban flood risk using hybrid method of TOPSIS and machine learning. *International Journal of Disaster Risk Reduction, 66*, 102614.

Rosti, B., Omidvar, A., & Monghasemi, N. (2020). Optimal insulation thickness of common classic and modern exterior walls in different climate zones of Iran. *Journal of Building Engineering, 27*, 100954.

Saaty, T. L. (2004). Decision making—the analytic hierarchy and network processes (AHP/ANP). *Journal of Systems Science and Systems Engineering, 13*, 1–35.

Senan, C. P., Ajin, R., Danumah, J. H., Costache, R., Arabameri, A., Rajaneesh, A., Sajinkumar, K., & Kuriakose, S. L. (2023). Flood vulnerability of a few areas in the foothills of the Western Ghats: A comparison of AHP and F-AHP models. *Stochastic Environmental Research and Risk Assessment, 37*(2), 527–556.

Shehadi, M. (2018). Energy consumption optimization measures for buildings in the Midwest regions of USA. *Buildings, 8*(12), 170.

Sloggy, M. R., Suter, J. F., Rad, M. R., Manning, D. T., & Goemans, C. (2021). Changing climate, changing minds? The effects of natural disasters on public perceptions of climate change. *Climatic Change, 168*, 1–26.

Uçar, A. (2024). The annual CO_2 emissions and energy costs of different exterior wall structures in residential buildings in Türkiye. *Isı Bilimi ve Tekniği Dergisi, 44*(1), 1–17.

Ucar, A., & Balo, F. (2010). Determination of the energy savings and the optimum insulation thickness in the four different insulated exterior walls. *Renewable Energy, 35*(1), 88–94.

Vincelas, F. F. C., & Ghislain, T. (2017). The determination of the most economical combination between external wall and the optimum insulation material in Cameroonian's buildings. *Journal of Building Engineering, 9*, 155–163.

Wang, Y., Liu, P., & Yao, Y. (2022). BMW-TOPSIS: A generalized TOPSIS model based on three-way decision. *Information Sciences, 607*, 799–818.

Wilson, A. B. (2021). Revising the Energy Efficiency Directive: Fit for 55 package. *European Energy Policy Review Service*. Retrieved from https://coilink.org/20.500.12592/dzmnv4

Yu, D., & Pan, T. (2021). Tracing knowledge diffusion of TOPSIS: A historical perspective from citation network. *Expert Systems with Applications, 168*, 114238.

Zamorano, M. (2022). Recent advances in energy efficiency of buildings. *Applied Sciences, 12*(13), 6669.

Investigation of the usage of technology in the civil engineering education with bibliometric analysis

Meryem F. Görhan[1], Gökhan Kürklü[2], Gökhan Görhan[*2]

[1] *Huriye Aşkar Secondary School, ICT Teacher, 03200 Afyonkarahisar, Türkiye*
[2] *Afyon Kocatepe University, Department of Civil Engineering, 03200 Afyonkarahisar, Türkiye*

Abstract. In recent years, it is thought that the use of technology in engineering education will increase student motivation, support learning and personalized learning. In this study, it is aimed to quantitatively address the existing studies on the base of increasing technology use in civil engineering education and to reveal the areas of study needed on the subject. In this direction, the concepts of "civil engineering education" and "technology" in the Web of Science database were analyzed by bibliometric analysis method by considering 134 scientific literatures published between 1991 and 2024. VOSviewer was used for the related technique. Four different analyses were applied using VOSviewer software; (I) country network from co-authorship analysis, (II) country network from citation analysis, (III) keyword network from co-occurrence analysis, and (IV) words in abstract network. According to the results of the analysis, it was seen that the countries where the most studies were conducted were USA, England and the People's Republic of China. According to the data obtained, it was determined that the related keywords were engineering education, virtual reality, civil engineering and building information modeling (BIM). However, in the summary sections of the scientific literature, the terms industry and building information modeling (BIM) were found to be prominent. Therefore, considering the concept of technology in civil engineering education, it was concluded that there are few studies on game-based learning, visualization and augmented reality and there is a need for studies on this subject.

Keywords: Civil engineering education, Technology, Bibliometric analysis, VOSviewer

1. Introduction

The term engineer is defined by the Turkish Language Association as "a person who develops technology or systems with the highest level of efficiency and safety in order to meet the needs of humanity within the framework of basic sciences with good aesthetic design". Civil engineering is the branch of engineering that investigates the construction and demolition conditions of facilities to be created by humans in order for living beings to continue their lives in harmony with nature and to build civilization, makes calculations to ensure that they will last for a certain period of time in harmony with nature and economically, and carries out material selection and scientific research (Birinci, 2016).

The qualities of a good civil engineer should have are shaped by the developing technology and the needs of the companies. These qualities are stated by Ohio University as communication skills, decision-making skills, leadership skills, problem-solving skills and organizational skills (Ohio University, 2025). Similarly, the qualifications required for a good engineer are listed by Harvard Business School as technology and computer science skills, leadership, communication, problem-solving, management, research and critical thinking, business operations (Harvard Business School, 2025). In the study conducted by Ramadhan et al., (2023), the qualities that future civil engineers should have are expressed as communication, professionalism, technical, team work, problem-solving, collaboration and sustainability. In the study conducted by Özbaşaran, et al. (2024), 1374 job advertisements for civil engineers were examined. It has been observed that the qualifications sought in civil engineering job advertisements include the ability to use office programs, computer-aided design and project management programs. These qualifications needed by the business world can be provided with computer-aided education and technology education (Demirtürk ve Tunç, 2021). The types of software used in civil engineering are; computer-aided building operation systems (service management series etc.), computer-aided cost systems (bidworx etc.), computer-aided engineering systems (finite element analysis etc.), computer-aided design and visualization systems (AutoCAD etc.), business and information management systems (sap

[*] Corresponding author, E-mail: ggorhan@aku.edu.tr

https://doi.org/10.31462/icearc2025_ce_mng_948

software etc.), planning and project management systems (Microsoft project etc.) and building information modeling (coordinate-based computer software etc.) (Demirtürk and Tunç, 2021).

In this study, civil engineering education refers to the education provided in the field of civil engineering at universities. In civil engineering education, basic science courses (Chemistry, physics, mathematics, etc.), social and human courses (Occupational safety, foreign language, etc.) and specialized field courses (Building materials, etc.) are given. The use of technology in civil engineering education is grouped under two headings as design and calculation and has a multidisciplinary structure (Bayhan & Karaca, 2020). When current studies are examined, it can be seen that the use of technology in civil engineering education has positive effects.. An experimental study was conducted by Hanna and Barber (2001) examining the effect of technology-aided design programs. It was observed that concept building, visual quality, and presentation techniques skills improved. In the study conducted by Blashki et al. (2007), it was concluded that the use of virtual games and forums in engineering education developed risk-taking attitude and creativity. By using technology in engineering education, the efficiency of education is increased, more senses are included in the learning process, and different learning methods are supported (Hernandez-de-Menendez & Morales-Menendez, 2019).

The purpose of this study is to examine the existing studies published in Web of Science (WOS) on the use of technology in civil engineering education using bibliometric analysis. For this purpose, the following research questions guided this study:

1. How are published articles on the use of technology in engineering education distributed by year?
2. Which countries show more interest in the use of technology in engineering education?
3. Which countries receive more citations on the use of technology in engineering education?
4. Which common words reflect the use of technology in engineering education?

2. Materials and methods

In the bibliometric examination of technology use in civil engineering education, a search was conducted in the Web of Science database using the words "civil engineering education" and "technology". The search results were limited to articles and 134 articles were examined. The following steps were followed in this study:

1. Data collection stage: Relevant search results were obtained from the WOS database.
2. The data analysis phase was performed using the VOSviewer tool.
3. The analysis results were examined according to the research questions.

With bibliometric analysis, existing studies are examined mathematically according to specified criteria. With this analysis, the studies conducted in a subject area are evaluated quantitatively. Data on the network between the author, institution, country, words used, citations, etc. are obtained. It reveals a general picture for a specific subject. With biometric analysis, clues can be obtained for revealing the more or less studied topics and the connections and networks between them (Umut Zan, 2012; Yılmaz, 2021).

In this study, VOSviewer 1.6.20 was used as a bibliometric analysis tool. VOSviewer is a tool for constructing and visualizing bibliometric networks, such as co-authorship networks, citation networks, and co-occurrence networks (VOSviewer, 2025). Co-authorship, Co-occurrence, Citation-countries analyses were performed using this tool in this study.

3. Results and discussion

In the bibliometric examination of technology use in civil engineering education, the concepts of "civil engineering education" and "technology" were searched in the Web of Science database. Accordingly, as seen in Fig. 1, according to the research date range, the oldest publication belongs to 1991. In the following years, there were either no publications or only one. In 1999, there was a jump in the number of publications and although it was not continuous, there was an increase in the number of publications for the years. In 2024, the number of publications reached 18. There were 134 publications and 774 citations in total.

VOSviewer software version 1.6.20 was used to access bibliometric analyses and visualize the data. Fig. 2 shows the countries that published and received citations according to the results obtained in this analysis. Accordingly, a total of 41 countries have published on this subject. When the countries with the most publications are examined, the USA ranks first with 44 publications, the PRC ranks second with 24 publications, and Portugal ranks third with 11 publications. While the first place in the citations is unchanged with 244, Portugal ranks second with 233 and the PRC ranks third with 218. Only 13 of these 41 countries have published three or more publications. Publications in 12 countries were not cited at all.. However, Türkiye has two publications and 33 citations on this subject.

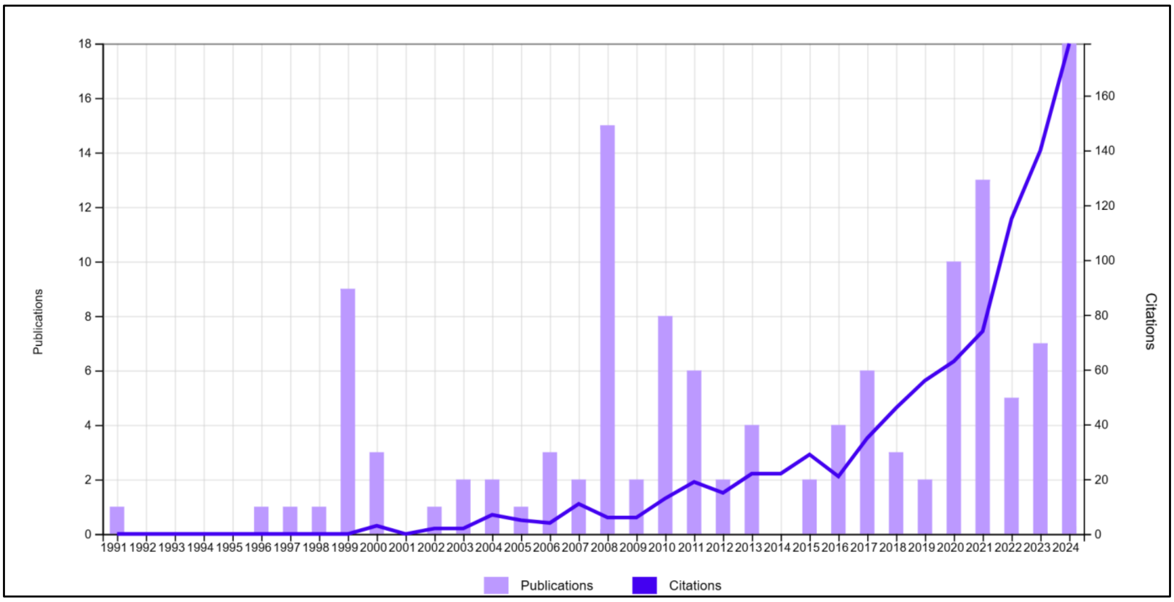

Fig. 1. Distribution of publishing by year

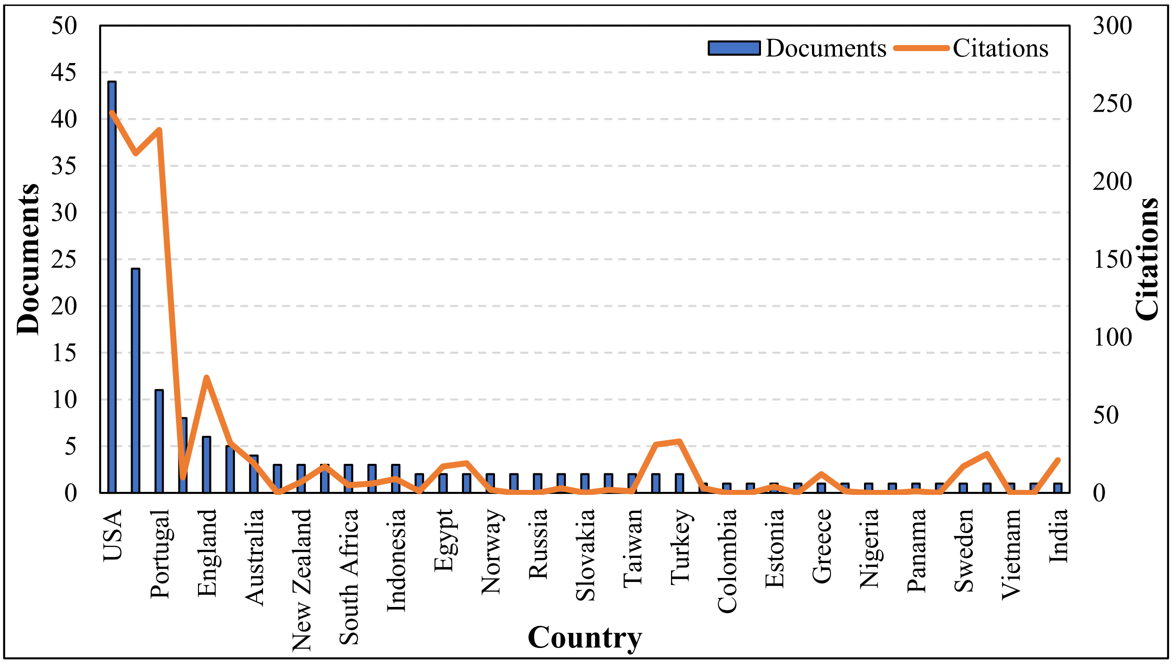

Fig. 2. Documents and citations score of the countries with the most studies

The network visualization map of the studies conducted by these countries through joint authorship is given in Fig. 3 and the density map is given in Fig. 4. Accordingly, a multi-faceted country network is formed in countries with a high number of publications, while a one-sided relationship is observed in countries with a limited number of publications. Although there is no obvious clustering in the density map, the USA stands out. While the number of countries with total link strength of seven and above is 9, the remaining countries are between three and zero and remain local in size.

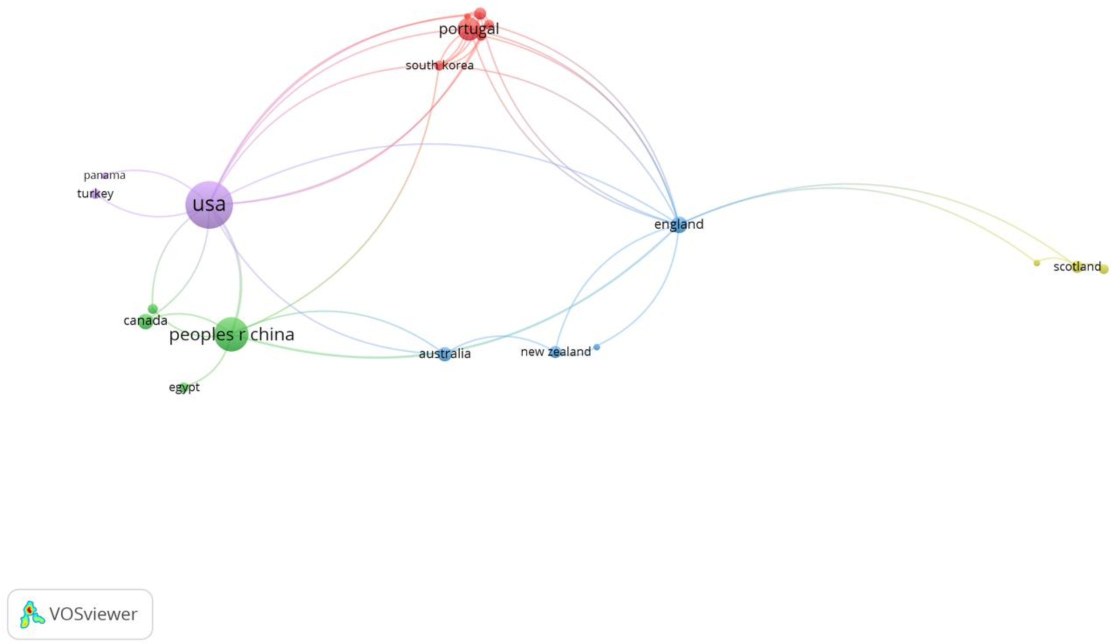

Fig. 3. Co-authorship network of the countries with the most studies

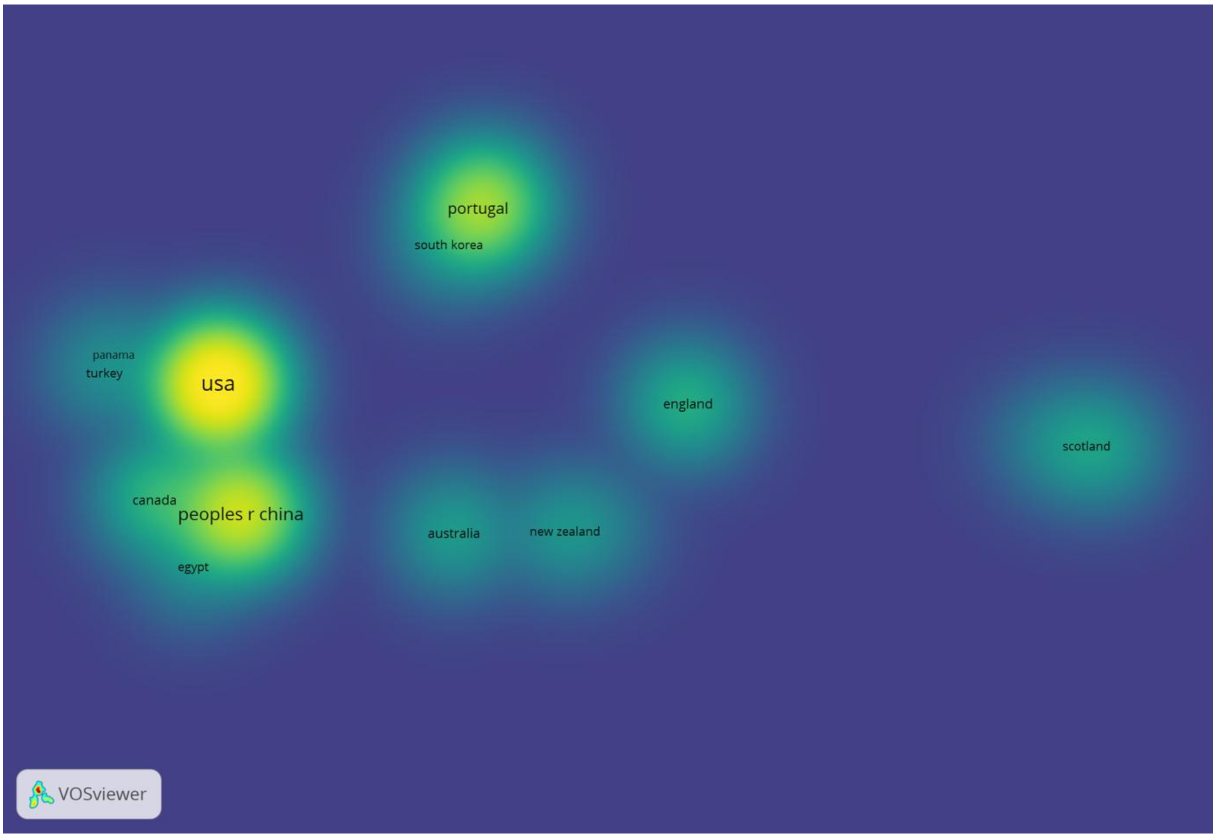

Fig. 4. Co-authorship visualization of the countries with the most studies

Citation was selected as the analysis type, country was selected as the unit, and the results obtained from the analysis without defining a lower limit are given in Figures 5 and 6. Although the USA comes to the fore in citation, when looking at the connection forces, it was seen that the regional ties of the countries also have an effect.

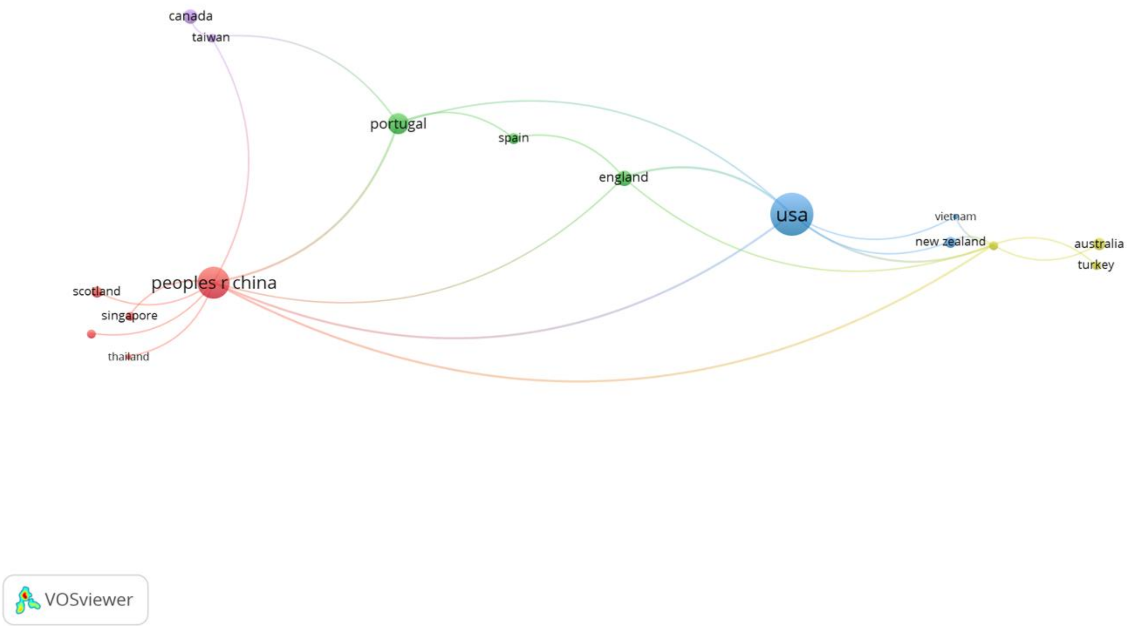

Fig. 5. Citation network of the countries with the most studies

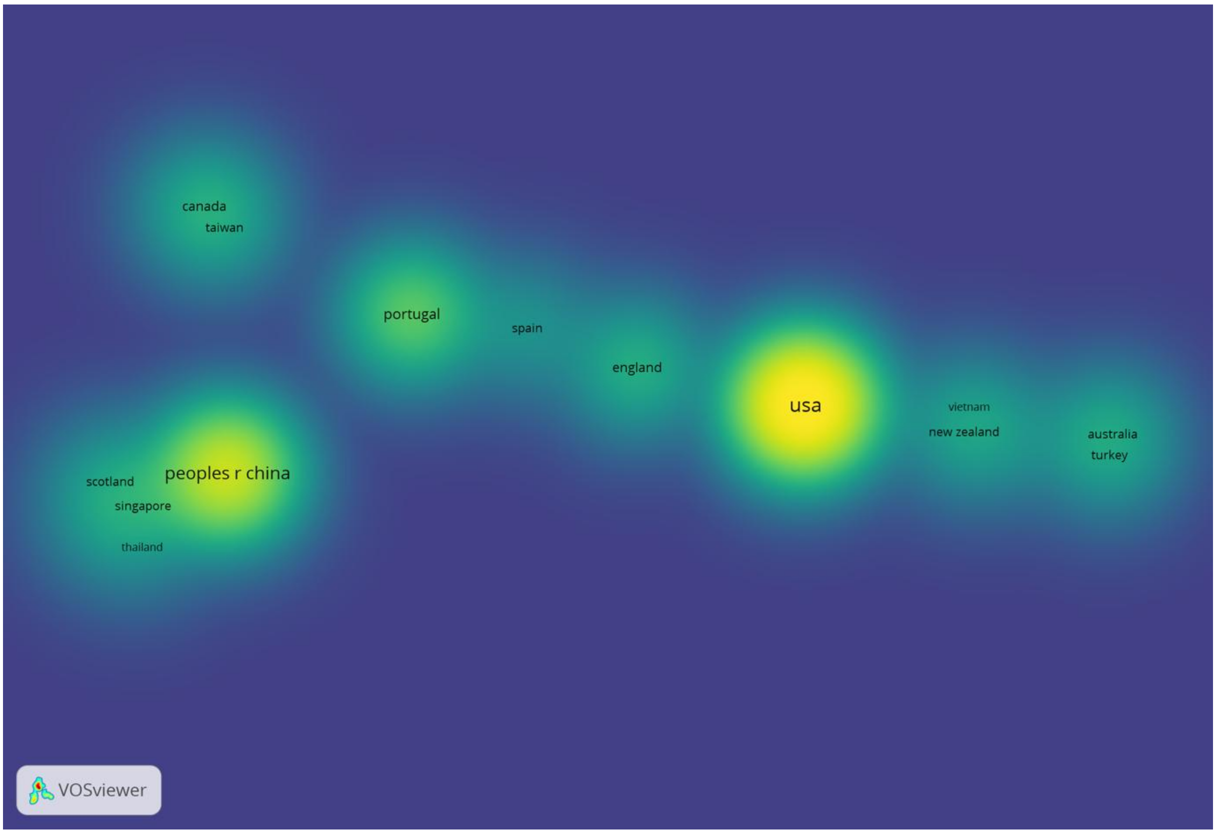

Fig. 6. Citation visualization of the countries with the most studies

In the section where the most frequently used keywords were analyzed in the studies, the selected analysis type was “Co-occurrence” and the unit was “Authors keywords”. Restriction criteria were applied to obtain more meaningful results; in this context, it was required that a keyword be repeated at least three times (Fig. 7).

Accordingly, “engineering education” was used 17 times. If we evaluate the expressions “civil engineering” and “civil engineering education” as close to the expression “engineering education”, it can be said that it was used 41 times in total. Following these, “virtual reality” was used 13 times and “building information modeling (BIM)” was used seven times. The connections between the keywords given in the network map in Fig. 8 are seen. The density distribution is as in Fig. 9. “Virtual reality” is seen densely at the common point of other dense keywords. “Building information modeling (BIM)” is located in a separate position from this word and with less density.

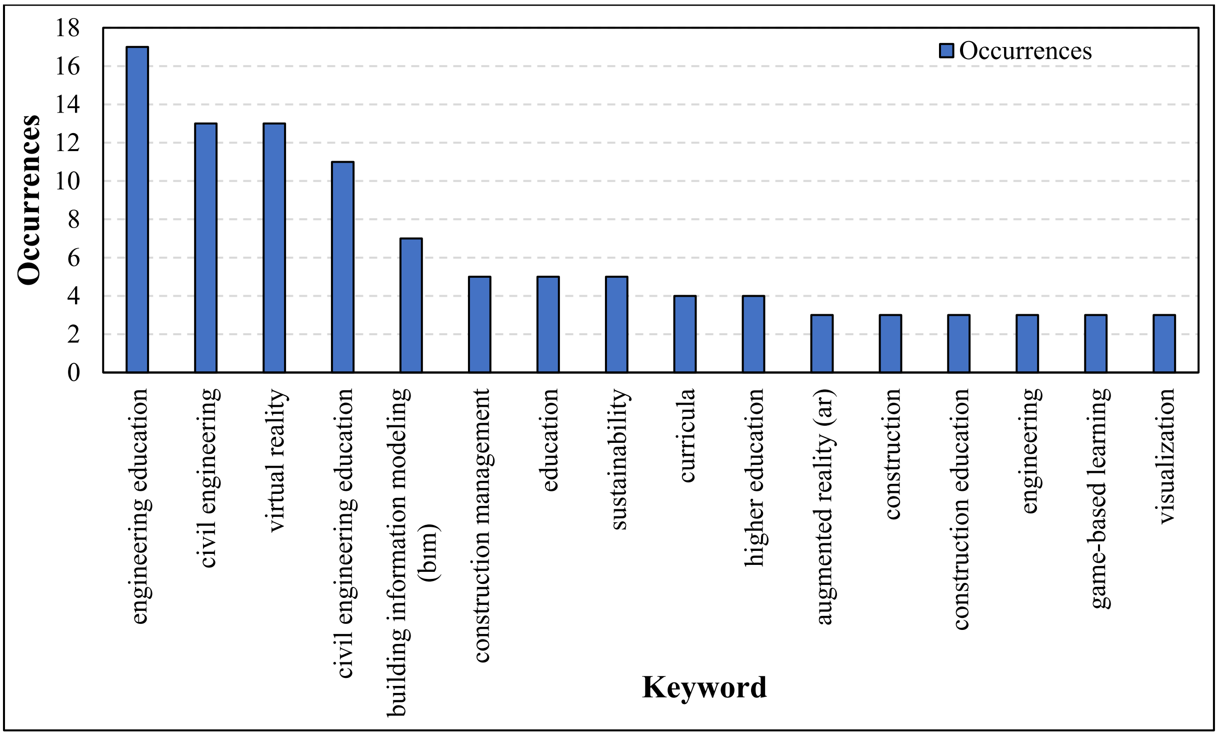

Fig. 7. Occurrence score of most frequently take part keywords

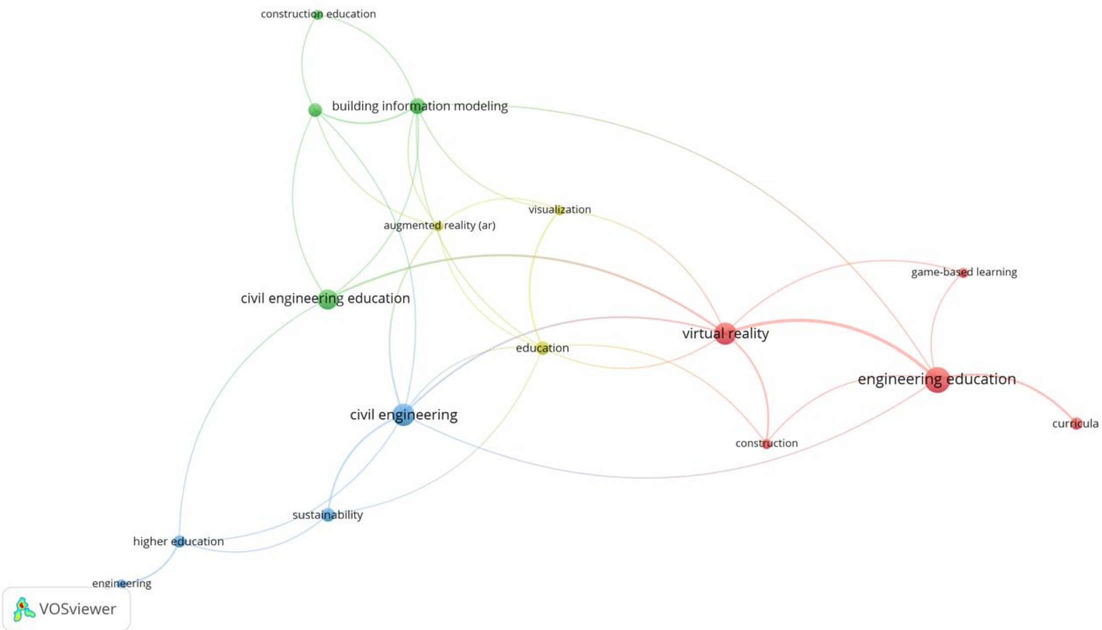

Fig. 8. Co-occurrence network of most frequently take part keywords

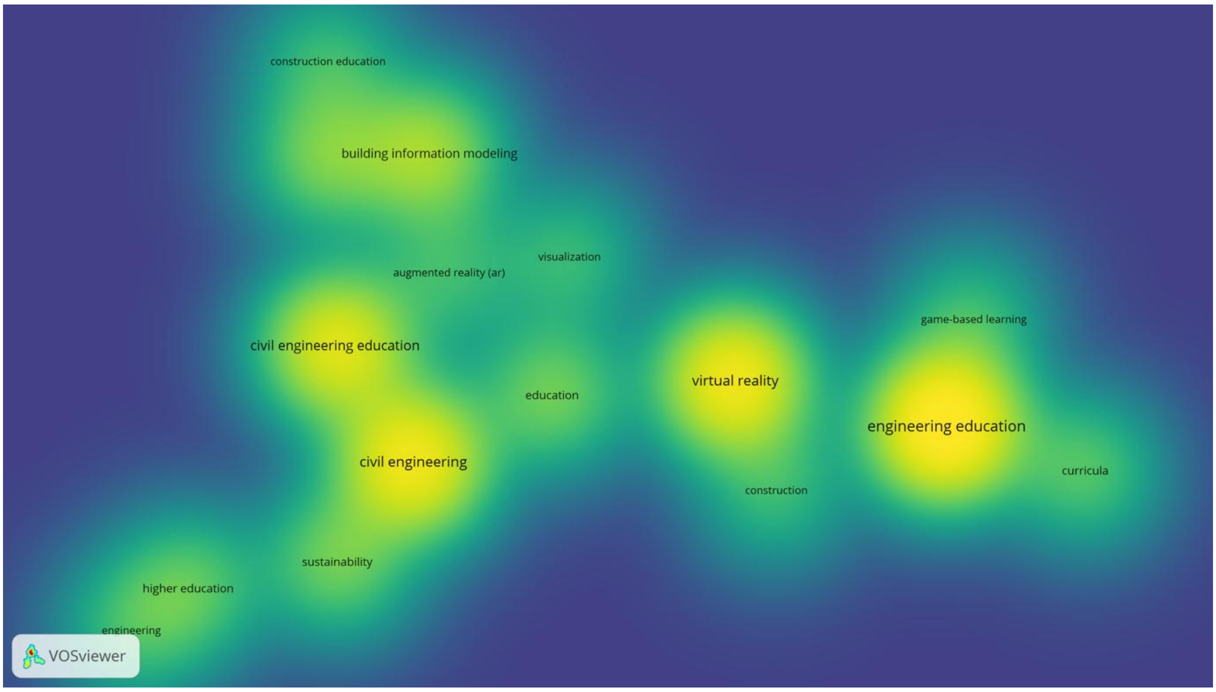

Fig. 9. Visualization of most frequently takes part keywords

By reading the data from the bibliographic database files, a map based on the text data was created and the "Abstract field" of the articles was examined and the minimum occurrence number of a term was considered as five as the boundary condition. Accordingly, the condition of 227 words out of 3550 words was met and 136 words were selected. The occurrence and relevance score values given in Fig. 10 are given. Due to the large number of words in Fig. 10, the graphs in Fig. 11 and Fig. 12 were created by taking into account the words in the first 22. The highest words in occurrences are "industry", "bim" and "work". The most specific word related to the research topic among these three words is seen as "bim". The concepts of "teaching mode" and "fundamental concept" that stand out differently from all other words in relevance score.

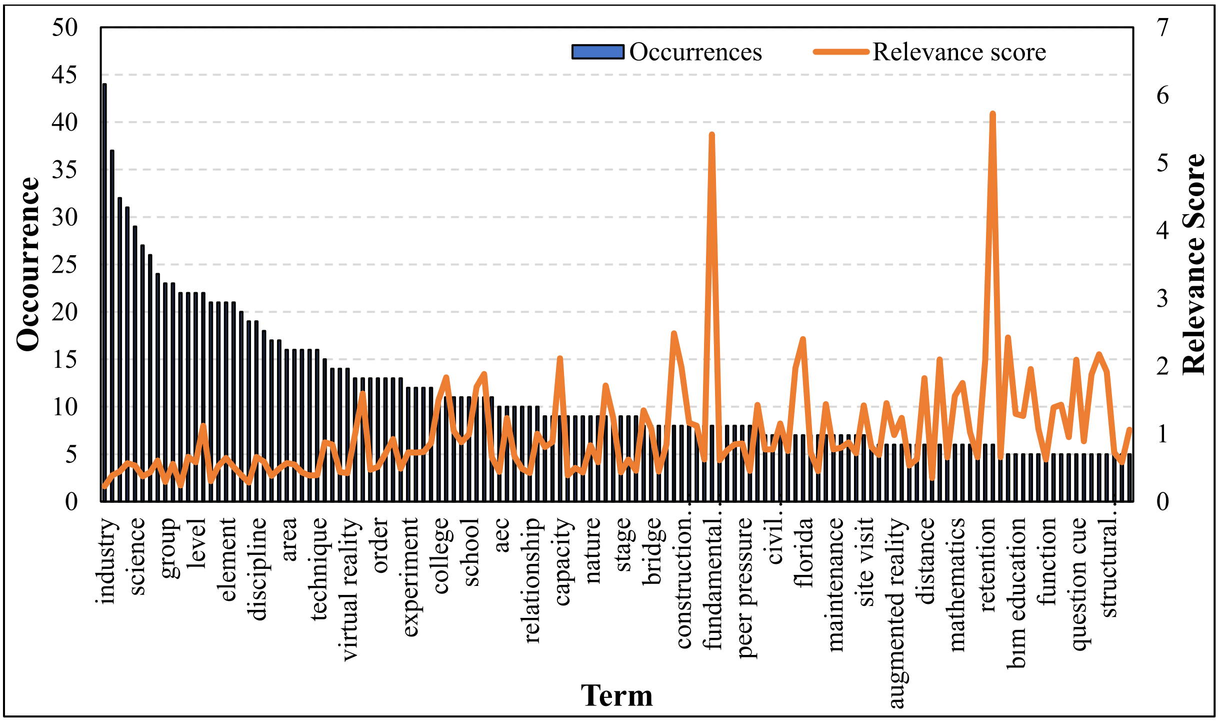

Fig. 10. Occurrence and relevance score of most frequently take part words in the abstract

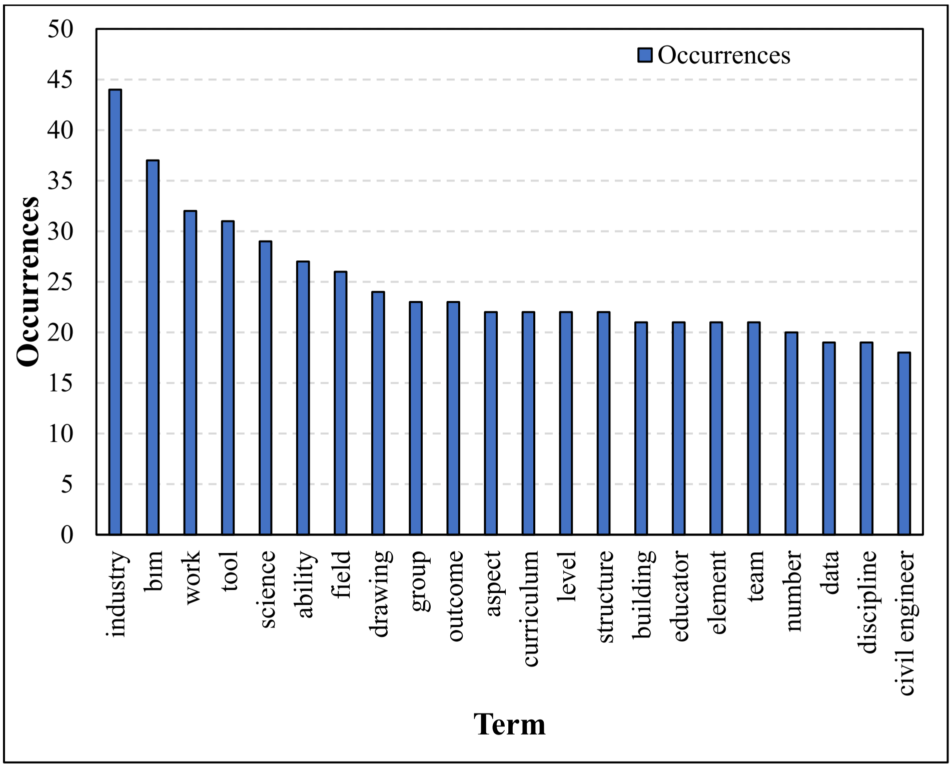

Fig. 11. Occurrences score of most frequently take part words in the abstract

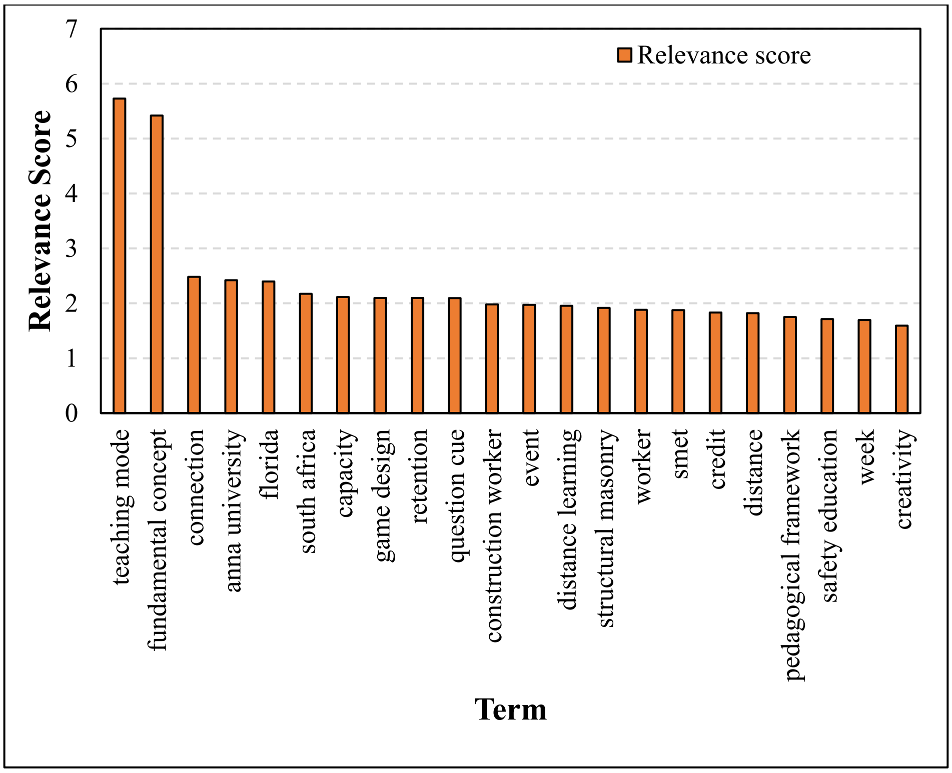

Fig. 12. Relevance score of most frequently take part words in the abstract

Fig. 13 shows the visual mapping of the words used in the “Abstract field” and Fig. 14 shows the density distribution. The connections between the words can be seen through the color distribution. On the density map, the words industry, work, bim, curriculum, strategy, ability, group and tool stand out.

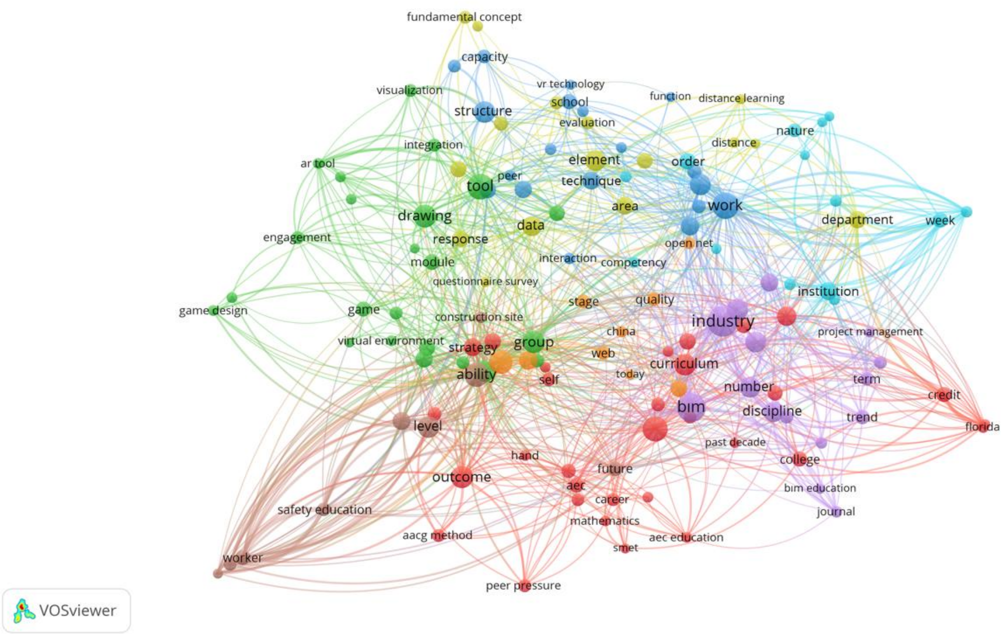

Fig. 13. Network of most frequently take part words in the abstract

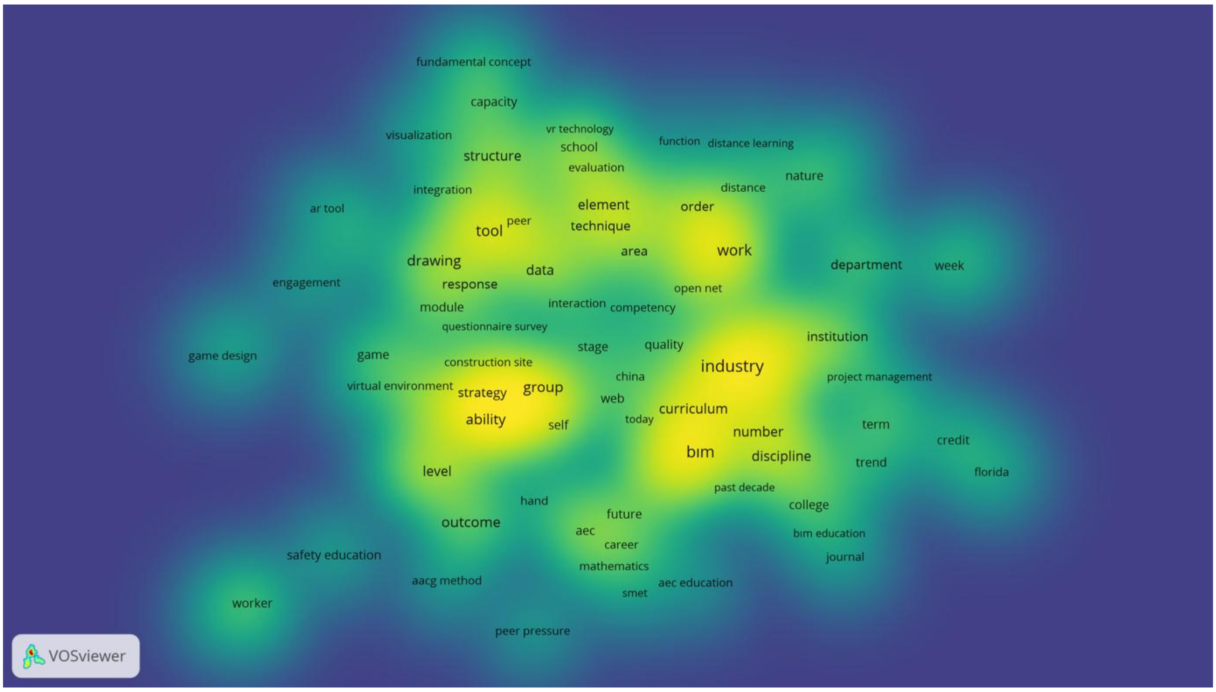

Fig. 14. Visualization of most frequently takes part words in the abstract

4. Conclusions

In this study, studies on the use of technology in engineering education were examined. The results are listed below:

- Current studies begin in 1991.
- When the studies are examined, there is a significant increase in 1999 and 2008. However, there has been an increase in the number of published publications in recent years..
- The countries with the most publications are listed as USA, Portugal and PRC according to the number of citations.
- The most commonly used keywords appear to be civil engineering education, virtual reality and building information modeling (BIM).

- The most frequently used words in the abstract section are industry, work, bim, curriculum, strategy, ability, group and tool.

References

Bayhan, H. G., & Karaca, E. (2020). Technological innovation in architecture and engineering education-an investigation on three generations from Turkey. *International Journal of Educational Technology in Higher Education, 17*, 1-22.

Blashki, K., Nichol, S., Jia, D., & Prompramote, S. (2007). 'The future is old': Immersive learning with generation Y engineering students. *European Journal of Engineering Education, 32*(4), 409–420.

Birinci, F. (2016). İnşaat Mühendisliği ve İnşaat Mühendisi'nin Türkçe Tanımlanması. TMMOB İnşaat Mühendisleri Odası, 3. İnşaat Mühendisliği Eğitimi Sempozyumu, 22-26.

Demirtürk, D., & Tunç, G. (2021). İnşaat mühendisliği eğitimi ve Türkiye'de inşaat sektörünün lisans eğitimine bakış açısı. *Engineering Sciences, 16*(1), 15-38.

Hanna, R., & Barber, T. (2001). An inquiry into computers in design: Attitudes before–attitudes after. *Design Studies, 22*(3), 255–281.

Harvard Business School, (2025, April 2), 6 Business skills every engineer needs. Retrieved from https://online.hbs.edu/blog/post/business-skills-for-engineers

Hernandez-de-Menendez, M. & Morales-Menendez R. (2019). Technological Innovations and Practices in Engineering Education: A Review. *International Journal on Interactive Design and Manufacturing (IJIDeM), 13*, 713-728.

Ohio University (2025, April 2). Essential civil engineering skills. Retrieved from: https://www.ohio.edu/engineering/civil/academics/graduate-programs/master-science-civil-engineering-online/resources/essential-civil-engineering-skills

Özbaşaran, H., Taşcı, G., Tuna, M., Karataş, İ., Çelik, A., Gümüş, M., & Birşen, M. İnşaat Mühendisleri için Açılan İş İlanlarının Metin Madenciliği ile Değerlendirilmesi. *Afyon Kocatepe Üniversitesi Fen ve Mühendislik Bilimleri Dergisi, 24*(3), 685-693.

Ramadhan, M. A., Sutarto, S. W., & Anisa, N. (2023). Skills for prospective civil engineers: mastery of current and future situations. *Journal of Hunan University Natural Sciences, 50*(1).

Umut-Zan, B. (2012). Türkiye'de bilim dallarında karşılaştırmalı bibliyometrik analiz çalışması (Doktora Tezi). Ankara Üniversitesi Sosyal Bilimler Enstitüsü, Ankara.

VOSviewer, (2025, April 10). Highlights. Retrieved from https://www.vosviewer.com/features/highlights

Yılmaz, K. (2021). Sosyal bilimlerde ve eğitim bilimlerinde sistematik derleme, meta değerlendirme ve bibliyometrik analizler. *Manas Sosyal Araştırmalar Dergisi, 10*(2), 1457-1490.

4th International Civil Engineering & Architecture Conference
17-19 May 2025, Trabzon, Türkiye

Enhancing mega-infrastructure project performance in South Africa through critical construction management factors: Insights from confirmatory factor analysis

Dillip Kumar Das*[1], Ayodeji Olatunji Aiyeatn[2]

[1] *University of KwaZulu-Natal, Discipline of Civil Engineering, Howard College Campus, Glenwood, Durban, 4041 South Africa*
[2] *Durban University of Technology, Department of Construction Management and Quantity Surveying, Steve Biko Campus, Durban, 4000, South Africa*

Abstract. Mega-infrastructure projects play a critical role in driving sustainable development in emerging economies like South Africa, fostering inclusive growth, improving service delivery, and promoting regional integration. However, despite their transformative potential, these projects often face significant challenges such as delays, cost overruns, and inefficiencies, particularly during construction. Based on data from a structured stakeholder survey and Confirmatory Factor Analysis (CFA), this study explores the construction-related factors influencing the successful delivery of mega-infrastructure projects in South Africa. The research identifies five interdependent latent constructs that impact project performance: Plant and Technological Resources, Stakeholder Engagement and Communication, Construction Management, Labour and Workforce Organisation, and Material and Logistics Management. Key factors for success include reliable plant and machinery, effective maintenance, strong stakeholder coordination, clear communication, adaptive construction practices, disciplined workforce deployment, and efficient logistics for quality materials. The study suggests several critical strategies to improve project outcomes: (1) ensuring the availability of competent personnel and quality plant for maintenance, (2) adopting transparent stakeholder engagement and advanced communication systems, (3) implementing adaptive construction practices, (4) fostering workforce engagement and discipline, and (5) securing a steady supply of quality materials. Prioritising these strategies is crucial for reducing delays, controlling costs, and achieving project objectives.

Keywords: Communication system; Construction management; Infrastructure; Mega-projects; Supervision and monitoring, Stakeholder engagement

1. Introduction

Sustainable development has emerged as a global imperative, requiring nations to balance economic advancement with social equity and environmental responsibility. In this context, mega-infrastructure projects are seen as critical drivers of long-term transformation—particularly in developing countries such as South Africa—where large-scale public investments are intended to stimulate inclusive economic growth, enhance service delivery, and promote regional integration (Cohen, 2006; Zeybek & Kaynak, 2006; Human Development Report, 2011). These projects span diverse sectors, including transportation, energy, water, communication, health, and education, and typically demand substantial financial investment, institutional coordination, and political commitment (Field & Ofori, 1988; Khan, 2008; Mthalane et al., 2007; Othman, 2012, 2013).

In South Africa, flagship national strategies such as the National Development Plan (NDP) and Strategic Infrastructure Projects (SIPs)—operationalised through the Infrastructure Development Act—reflect the government's ambition to harness megaprojects as engines of sustainable development. Prominent examples include the Gautrain rapid rail system, Kusile and Medupi power stations, Mthombo oil refinery, and the Transnet multiproduct pipeline. Typically valued at over USD 2 billion, these projects are designed to generate employment, stimulate local economies, address historical infrastructure deficits, and enhance national competitiveness.

Despite these aspirational goals, megaproject implementation in South Africa has been marred by chronic underperformance. Approximately 65% of such projects suffer from cost overruns, schedule delays, or failure to meet planned objectives (Deloitte, 2013; Khatleli, 2016; Mashegoana & Khatleli, 2019). These persistent issues highlight deeper systemic problems within the construction delivery phase, where resource limitations, skills

*Corresponding author, E-mail: dasd@ukzbn.ac.za

https://doi.org/10.31462/icearc2025_ce_mng_958

shortages, governance deficiencies, and outdated project management practices exacerbate execution complexities. Challenges such as inadequate supervision, fragmented communication, underperforming contractors, and limited technological integration continue to undermine project efficiency.

Globally, recent literature underscores the importance of identifying and understanding Critical Success Factors (CSFs) for megaproject construction, particularly in emerging economies. Key factors contributing to project success include the availability of financial, human, and technological resources; effective stakeholder engagement; robust communication; and adaptive planning mechanisms (Wang et al., 2021, 2022; Malek & Bhatt, 2023). However, the practical realisation of these factors is often hindered by institutional inefficiencies, regulatory bottlenecks, and capacity constraints within implementing agencies. Delays in contractor payments, weak inter-agency coordination, and rigid planning processes frequently result in misalignment between project objectives and actual outcomes.

Mega-infrastructure projects are inherently complex socio-technical systems characterised by uncertainty, diverse stakeholder interests, and intricate interdependencies among resources, personnel, and processes (Flyvbjerg, 2014; Shore & Cross, 2005; Erol et al., 2018). Traditional, linear project management models have proven inadequate in navigating these challenges. Consequently, scholars increasingly advocate for more agile, innovative approaches, such as proactive risk mitigation, stakeholder engagement strategies, digital project management tools, smart construction technologies, and data-informed decision-making (Al Ani, 2024; Caldas & Gupta, 2017; Wu et al., 2018; Zaman et al., 2022).

However, the adoption of advanced construction management systems in South Africa remains limited. Many projects continue to rely on legacy systems and rigid workflows ill-suited to the dynamic nature of megaproject environments. This has resulted in reduced responsiveness to change, poor resource utilisation on construction sites, and an erosion of public trust in large-scale infrastructure initiatives. Additional complications stem from political interference, limited community involvement, and hierarchical organisational structures, all of which further impede project delivery and sustainability (Aiyetan & Das, 2022; Wtaermeyer, 2013).

While macro-level studies have examined financing models, policy frameworks, and institutional arrangements (Ref), there remains a significant gap in empirical research on micro-level construction practices, especially at the site level in Global South contexts. Understanding these granular dynamics—including plant utilisation, labour discipline, stakeholder coordination, material logistics, and on-site supervision—provides valuable insight into the root causes of performance bottlenecks. Moreover, it supports the development of context-sensitive, practically grounded strategies to enhance delivery outcomes. Although existing literature identifies broad success factors such as financial models and governance structures, there is insufficient exploration of micro-level, construction-related factors and their systemic interactions. Given megaprojects' complex, socio-technical nature, a systems-based perspective is essential—one that integrates construction methodologies, stakeholder dynamics, workforce organisation, and logistical management within a coherent performance framework.

This study addresses this gap by examining the factors influencing the successful delivery of megaprojects in South Africa, using empirical analysis from Confirmatory Factor Analysis (CFA). The study focuses on five key latent constructs—Plant and Technological Resources, Stakeholder Engagement and Communication, Construction Management, Labour and Workforce Organisation, and Material and Logistics Management—as core subsystems that underpin construction performance. Accordingly, the objectives of the study are:

- To identify and validate the critical construction-related factors influencing the successful delivery of mega-infrastructure projects in South Africa.
- To examine the role of key subsystems—plant and technological resources, stakeholder engagement and communication, construction management practices, workforce organisation, and material and logistics management—in shaping project outcomes.
- To explore a systems-oriented framework that reflects the interdependence of construction management domains in complex megaproject environments.

For this purpose, the study investigates the following research questions (RQs):

RQ1: What are the key micro-level construction management factors that significantly affect the performance of mega-infrastructure projects in South Africa?

RQ2: How do plant and technological resources, stakeholder engagement, construction management practices, workforce organisation, and material logistics each contribute to project success?

RQ3: How do interactions among technical, organisational, and human subsystems as an integrated system shape megaproject delivery within a systems-oriented framework?

2. Mega infrastructure projects in South Africa

Mega infrastructure projects are large-scale, capital-intensive ventures that span extended durations and require coordination among multiple stakeholders. These include transportation corridors, energy plants, rail systems, and public utilities—all of which are foundational to national development by facilitating economic growth, enhancing regional integration, and improving service delivery. In South Africa, such projects are envisioned as engines of socio-economic transformation, job creation, and industrialisation (Burger & Hawkesworth, 2011).

Despite their strategic significance, many mega projects in South Africa have experienced chronic underperformance. High-profile examples—such as the Gautrain rapid rail link, Eskom's Medupi and Kusile power stations, and the stadiums for the 2010 FIFA World Cup—have been plagued by delays, cost overruns, and quality deficiencies (Fourie, 2008). The Medupi project, for instance, escalated from an initial R69 billion budget to over R150 billion, with completion delayed by nearly a decade (Eberhard & Godinho, 2017).

These challenges are compounded by systemic issues within the South African construction industry, including skills shortages, volatile demand, regulatory hurdles, fragmented value chains, and weak institutional capacity (CIDB, 2016). Moreover, governance inefficiencies, stakeholder misalignment, and corruption exacerbate project risks (Aiyean & Das, 2022; Watermeyer, 2013).

In response, the government has introduced reforms such as the National Infrastructure Plan (NIP) and the establishment of Infrastructure South Africa (ISA) to enhance project readiness and execution capacity (RSA, 2020). Nonetheless, the recurring underperformance of mega infrastructure projects calls for a systematic investigation to identify the factors that influence the success of mega projects and explore strategies from a systems-oriented strategic perspective to improve the success of such projects.

3. Literature review

3.1. Critical factors affecting mega project performance

Mega projects inherently involve high uncertainty, risk, and multiple interfaces, making them susceptible to inefficiencies in key performance metrics. The "iron triangle" of time, cost, and quality remains a foundational framework for evaluating project outcomes, yet achieving an optimal balance is often elusive due to challenges such as regulatory delays, shifting political priorities, financing issues, and complex procurement processes. In South Africa, delays are often attributed to late approvals, contractor underperformance, and coordination failures, while cost overruns are linked to poor planning, inflation, and scope changes (Windapo & Cattell, 2013; Mbachu & Nkado, 2007).

Effective project planning and proactive risk management are consistently identified as critical success factors. However, issues such as optimistic bias and strategic misrepresentation often result in unrealistic estimates and misalignment of scope. In South Africa, the lack of rigorous feasibility assessments and early stakeholder involvement undermines the credibility and efficiency of project execution (Flyvbjerg et al., 2003; CIDB, 2016).

Governance and leadership are also key, with weak accountability and political interference frequently reducing transparency and hindering performance monitoring. South African mega projects often suffer from diffuse accountability, political interference, and institutional weaknesses, which diminish effective oversight and adaptive decision-making (Aiyeatn & Das, 2022; Watermeyer, 2013).

Furthermore, poor stakeholder engagement and communication can lead to community resistance, legal disputes, and project stoppages. Strategic engagement and effective communication frameworks are crucial for aligning diverse interests and minimising risks (Aaltonen & Kujala, 2010; Olander & Landin, 2008).

Resource availability, including skilled labour shortages and logistical delays, continues to disrupt project timelines. South Africa faces critical skilled labour shortages, compounded by industrial disputes and weak safety standards (Holt, 2001; CIDB, 2016). Logistical inefficiencies and fragmented supply chains, especially in rural or underdeveloped regions, are significant barriers to timely project completion (Olawale & Sun, 2015).

3.2. Role of key subsystems in mega project delivery

The performance of mega projects is highly dependent on the coordination of subsystems such as plant and technological resources, stakeholder engagement, construction management, labour and workforce organisation, and material and logistics management. The availability, suitability, and operational efficiency of construction equipment significantly impact project productivity and cost. Technological tools such as Building Information Modelling (BIM), drones, and ICT platforms can enhance planning, monitoring, and execution. However, adoption remains limited in South Africa due to high initial investment, lack of technical capacity, and cultural resistance to innovation (Gamil & Rahman, 2020; Windapo, 2016).

Effective stakeholder engagement frameworks ensure inclusive decision-making, risk-sharing, and dispute minimisation. Miscommunication can derail project timelines, particularly in cross-cultural and politically sensitive contexts. Strategic communication and trust-building are essential for aligning diverse interests (Freeman, 1984; Aaltonen & Kujala, 2010; Olander & Landin, 2008).

Sound construction management practices—such as accurate scheduling, cost control, and project governance—are fundamental to project success. Adopting formal methodologies like PMBOK and PRINCE2 enables systematic monitoring and accountability. In South Africa, poor site management, inconsistent oversight, and leadership gaps have been flagged as recurring issues (PMI, 2017; Windapo & Cattell, 2013).

Labour productivity, skill availability, and organisational cohesion are decisive factors in construction outcomes. South Africa continues to face critical skilled labour shortages, compounded by industrial disputes and weak safety standards. Structured workforce management and improved training programs are necessary to bridge performance gaps (Holt, 2001; CIDB, 2016).

Material availability, procurement efficiency, and logistics planning directly influence construction timelines and budgets. The use of digital tools and just-in-time delivery models can reduce waste and improve responsiveness. In South Africa, logistical inefficiencies and fragmented supply chains remain significant barriers, particularly in rural or underdeveloped regions (Cheng & Kumar, 2014; Olawale & Sun, 2015).

The literature reveals that the successful delivery of mega infrastructure projects depends on an integrated understanding of multiple performance dimensions and subsystem interactions. Traditional project management approaches must be supplemented by frameworks that accommodate complexity, dynamic interdependencies, and contextual realities.

3. Research methodology

This study adopted a quantitative, cross-sectional research design aimed at validating the latent structure of factors influencing the successful delivery of mega infrastructure projects. Confirmatory Factor Analysis (CFA) was employed to assess the factorial validity of a hypothesised five-factor measurement model.

3.1. Data collection

Due to the lack of structured statistical data related to construction site factors, primary data were collected through a structured stakeholder survey. The study targeted professionals directly or indirectly engaged in mega infrastructure projects across three South African provinces—KwaZulu-Natal, Gauteng, and Western Cape—where such projects are most concentrated.

Participants were selected based on professional roles, qualifications, and experience in areas such as project planning, design, management, or site-level decision-making. Out of 225 stakeholders contacted via email, telephone, and in-person invitations, 189 agreed to participate, yielding a strong response rate of 84%, which was considered sufficient for exploratory factor analysis.

The sample included a diverse mix of contractors, project managers, engineers, quantity surveyors, site agents, designers, and academics. A structured questionnaire was developed based on a comprehensive literature review and expert consultations. Respondents were asked to rate the influence of various site-related factors on project performance using a five-point Likert scale (1 = Very Low to 5 = Very High).

The survey was administered both online and face-to-face. To ensure inclusivity and eliminate bias, no restrictions were applied regarding race, gender, age, or nationality. The collected data were cleaned and assessed for missing values, multivariate outliers, normality, and reliability before being analysed using CFA to ensure suitability for statistical examination.

3.2. Data analysis

Confirmatory Factor Analysis (CFA) was used to examine whether observed variables reliably reflect a smaller number of latent constructs. As a theory-driven method based on the common factor model, CFA assumes that the correlations among observed variables can be explained by their loadings on latent constructs and measurement error (Brown, 2015). Fig. 1 presents the CFA model with the factor loadings.

The basic CFA equation is given in Equation 1:

$$X = \Lambda\xi + \delta \tag{1}$$

where x is a vector of observed variables, Λ is the matrix of factor loadings, ξ is the vector of latent variables (factors), δ is the vector of measurement errors

The covariance matrix of observed variables is represented by Equation 2:

$$\Sigma = \Lambda\Phi\Lambda^{T} + \Theta\delta \tag{2}$$

where: Σ is the model-implied covariance matrix, Φ is the covariance matrix of latent variables, $\Theta\delta$ is the diagonal matrix of error variances

3.2.1. Measurement model specification

The hypothesised model consisted of five first-order latent constructs: Plant and Technological Resource, Stakeholder Engagement and Communication, Construction Management, Labour and Workforce Organisation, and Material and Logistics Management.

Each construct was measured using multiple observed indicators derived from empirical literature. Indicators were restricted to load on a single factor, and error terms were assumed to be uncorrelated unless theoretically justified.

3.2.2. CFA estimation and model fit evaluation

CFA was conducted using the Maximum Likelihood Estimation (MLE) approach, which provides robust parameter estimates under the assumption of multivariate normality. The MLE objective function is expressed in Equation 3:

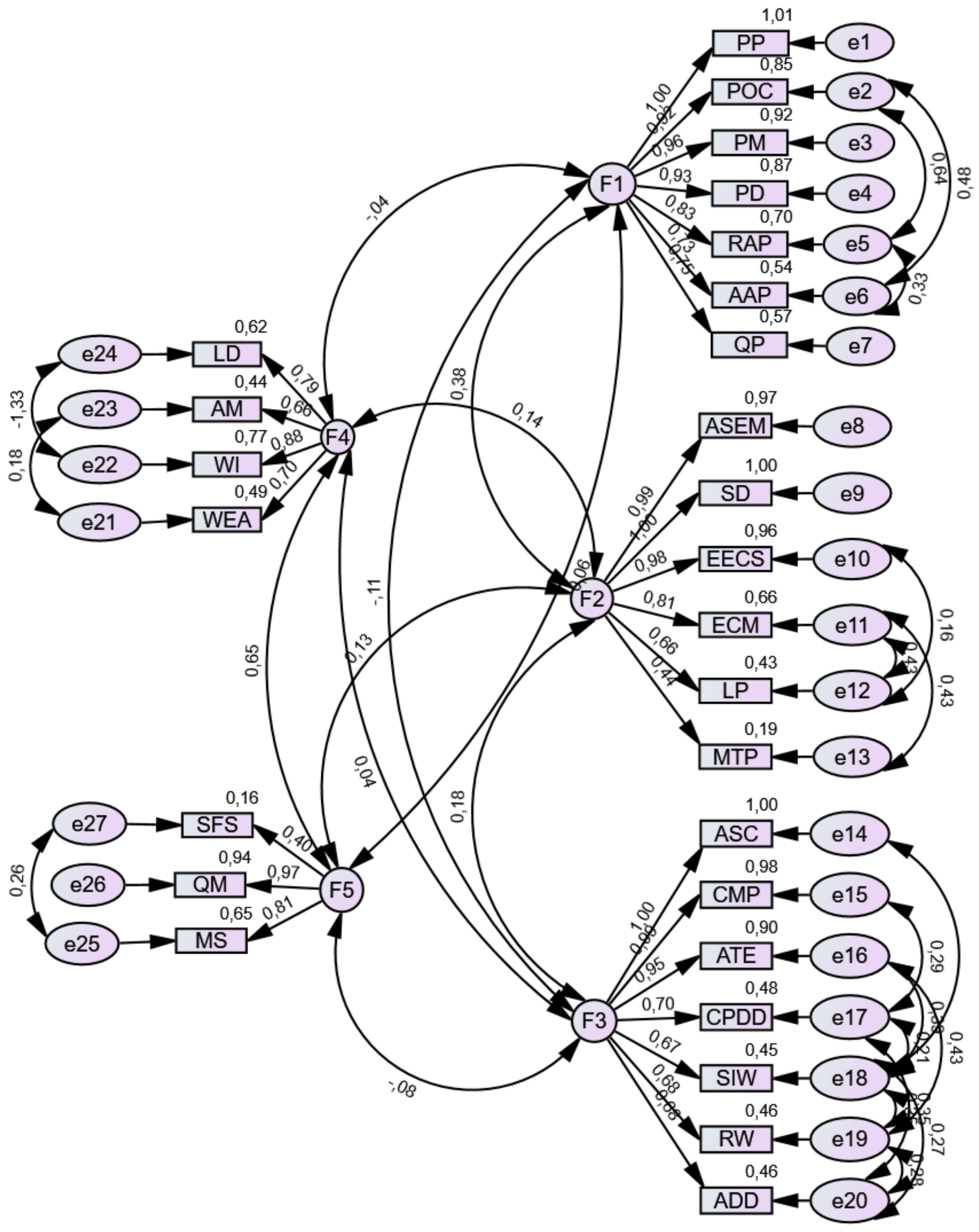

Fig. 1. Confirmatory factor analysis model results (Factor loadings)

$$FML = log|\Sigma| + tr(S\Sigma^{-1}) - log|S| - p \tag{3}$$

where tr is the trace operator, |·| denotes the determinant, S is the sample covariance matrix, p is the number of observed variables

Model fit was evaluated using several indices such as Chi-square (χ^2) and normed chi-square (χ^2/df), with χ^2/df < 3.0 considered acceptable; Comparative Fit Index (CFI) and Tucker-Lewis Index (TLI), with values ≥ 0.90 indicating good fit; Root Mean Square Error of Approximation (RMSEA), with RMSEA < 0.08 deemed acceptable; Standardised Root Mean Square Residual (SRMR), with values < 0.08 reflecting good fit (Kline, 2016).

3.2.3. Assessment of validity and reliability

Convergent validity was assessed through standardised factor loadings (≥ 0.70), and items with slightly lower loadings were retained if theoretically significant (Hair et al., 2019). Average Variance Extracted (AVE) was calculated using Equation 4:

$$AVE = \frac{\sum \lambda i^2}{(\sum \lambda i^2 + \sum \theta_i)} \tag{4}$$

An AVE ≥ 0.50 was considered acceptable. Construct Reliability (CR) was calculated to ensure internal consistency (Equation 5):

$$CR = \frac{(\sum \lambda i)^2}{((\sum \lambda i)^2 + (\sum \theta_i))} \tag{5}$$

A CR ≥ 0.70 was deemed acceptable. Discriminant validity was assessed using the Fornell-Larcker criterion, ensuring that the square root of AVE for each construct exceeded its correlation with other constructs (Fornell & Larcker, 1981).

3.2.4. Model specification and misspecification treatment

The initial CFA model was structured based on theoretical insights and stakeholder input. Each observed variable was specified to load onto only one latent construct with uncorrelated residuals unless empirical diagnostics indicated otherwise.

In cases of model misfit, such as Heywood cases (e.g., loadings > 1.0 or negative error variances), modification indices were examined. Adjustments such as correlating residuals or removing problematic indicators were considered, but only applied when theoretically defensible.

All statistical analyses were performed using IBM SPSS AMOS version 30. The final model integrates theoretical relevance and statistical robustness, offering a valid measurement framework for analysing the interdependencies of construction-related factors in the delivery of mega infrastructure projects.

4. Results and discussion

4.1. Reliability and normality analysis

To ensure the internal consistency of the measurement scale, Cronbach's alpha was calculated. The result yielded a Cronbach's alpha coefficient of 0.88 (Table 1), indicating a high level of internal reliability (George & Mallery, 2003; Nunnally, 1978). To assess the suitability of the data for CFA, skewness and kurtosis statistics were examined to evaluate the assumption of normality. Skewness values ranged between -0.233 and 1.145, indicating that the data distribution is approximately symmetric and within the acceptable range of ±2 (George & Mallery, 2010). Similarly, the kurtosis values ranged between -0.260 and 2.333, also falling within the acceptable limits of ±7 recommended by Byrne (2010), suggesting no significant issues with the peakedness of the distribution (Table 1). These results indicate that the data do not deviate significantly from normality and are therefore considered suitable for CFA and other parametric statistical analyses.

Table 1**.** Summary of reliability and normality statistics

Measure	Value/Range	Acceptable Range	Interpretation
Cronbach's Alpha	0.88	≥ 0.70	High internal consistency-reliable
Skewness (range of values from all items)	-0.233-1.145	±2	Within normal range (acceptable)
Kurtosis (range of values from all items)	-0.260-2.333	±7	Within normal range (acceptable)

4.2. Model fit information

The model fit information of the Confirmatory Factor Analysis (CFA) offers evidence that the five-factor measurement model exhibits an acceptable fit to the observed data. The model fit information is presented in Table 2. The model produced a statistically significant chi-square value (χ^2 = 647.942, df = 298, p < 0.001).

Table 2. The model fit information

Fit Index	Value	Recommended Threshold	Interpretation
Chi-square (χ^2)	647.942	—	Significant (expected in large samples)
Degrees of Freedom (df)	298	—	—
Normed Chi-Square (χ^2/df)	2.174	< 3.0 (acceptable)	Acceptable
Root Mean Square Error of Approximation (RMSEA)	0.078	< 0.08 (acceptable)	Acceptable
Goodness-of-Fit Index (GFI)	0.818	≥ 0.90 (good)	Slightly lower but acceptable
Comparative Fit Index (CFI)	0.945	≥ 0.90 (acceptable)	Excellent
Tucker-Lewis Index (TLI)	0.935	≥ 0.90 (acceptable)	Excellent
Normed Fit Index (NFI)	0.903	≥ 0.90 (acceptable)	Acceptable
Standardised Root Mean Square Residual (SRMR)	0.057	< 0.08 (acceptable)	Acceptable
RMSEA 90% Confidence Interval	0.071–0.087	0.05-0.10	Within an acceptable range

However, given the well-documented sensitivity of the chi-square statistic to sample size, the normed chi-square (χ^2/df) is considered a more appropriate indicator of model fit. The normed chi-square value (χ^2/df = 2.174) is found to be within the acceptable range ($1 \leq \chi^2/\text{df} \leq 3.00$). Also, the Complementary fit indices further support the model's adequacy. The Comparative Fit Index (CFI) was 0.945, and the Tucker-Lewis Index (TLI) was 0.35, exceeding the recommended threshold of 0.90. The Root Mean Square Error of Approximation (RMSEA) was 0.078, with a 90% confidence interval ranging from 0.071 to 0.87, indicating a moderate yet acceptable level of fit. The Standardised Root Mean Square Residual (SRMR) was also 0.057, well below the conventional cut-off value of 0.08, suggesting a good correspondence between the model and the observed data.

Furthermore, most standardised factor loadings were statistically significant ($p < 0.001$) and surpassed the recommended threshold of 0.70 (Table 3), indicating strong relationships between the latent constructs and their observed indicators. Thus, the model demonstrates a good fit and is deemed suitable for subsequent analysis.

4.3. Factors influencing the success of mega projects

The standardised factor loadings from the Confirmatory Factor Analysis (CFA) are presented in Table 3. The results of CFA identified five key latent constructs that significantly influence the successful delivery of mega projects. The latent constructs are (1) Plant and Technological Resources, (2) Stakeholder Engagement and Communication, (3) Construction Management, (4) Labour and Workforce Organisation, and (5) Material and Logistics Management. Each construct is supported by statistically significant factor loadings, affirming both their empirical relevance and theoretical robustness (Table 3).

4.3.1. Plant and technological resources (F1)

This construct emerged as a critical driver of project performance, evidenced by high standardised loadings for indicators such as Plant maintenance (0.957), Plant downtime (0.934), Plant operators and competence (0.924), Robotics and automation of plant (0.835), Quality of plant (0.754) and Availability of advanced plant (0.734). These findings underscore the importance of operational efficiency, equipment reliability, skilled personnel, and advanced automation technologies in maintaining productivity and ensuring continuity in large-scale infrastructure projects.

4.3.2. Stakeholder engagement and communication (F2)

Strong loadings were observed for stakeholder delineation (0.999), ensuring effective communication among stakeholders (0.977), advanced stakeholder engagement methods (0.987), and effective communication methods (0.811), reflecting the centrality of transparent and structured stakeholder interactions. Although leadership (0.656) and monitoring of team performance (0.439) had lower loadings, they remain relevant, indicating that leadership dynamics and performance oversight also contribute to effective stakeholder coordination. Overall, this construct highlights the need for participatory engagement strategies, clear role definitions, and open communication channels to reduce uncertainty and align stakeholder interests.

4.3.3. Construction management (F3)

This dimension is anchored by strong loadings for construction methods and process (0.992), and availability of tools and equipment (0.947), with moderate contributions from change in plan design and drawings (0.696), rework (0.678), availability of detailed drawings(0.676) and supervision and inspection of work (0.670). These results emphasise the importance of systematic planning, adaptive construction methodologies, and robust oversight mechanisms for ensuring quality and timely project execution.

4.3.4. Labour and workforce organisation (F4)

The factor is characterised by high loadings of workforce involvement(0.876) and labour discipline (0.786), as well as moderate loadings of work and equipment allocation (0.698) and availability of manpower (0.663), which contribute meaningfully to the construct. This highlights the role of engaged, disciplined labour forces and strategic human resource allocation in facilitating smooth project implementation.

4.3.5. Material and logistics management (F5)

This construct was validated by strong loadings for quality of material(0.967) and material supply (0.805). However, storage facilities on site (0.397) exhibited a lower loading, possibly reflecting contextual variability. These findings affirm the significance of timely and organised material delivery and stringent quality control processes for effective infrastructure project execution.

Together, the five constructs provide a robust, evidence-based foundation for analysing the complex variables that impact megaproject success. The findings highlight the critical need for cohesive planning that spans technical systems, organisational structures, and stakeholder involvement. Prioritising strategic alignment in areas such as plant readiness, stakeholder collaboration, adaptable construction processes, workforce organisation, and logistical resource planning is crucial for meeting cost, schedule, and quality objectives.

Table 3. Standardised factor loadings

Latent Factor	Observed Variable	Standardised Loading
F1: Plant and Technological Resources	Plant maintenance	0.957
	Plant downtime	0.935
	Plant operators and competence	0.924
	Robotics and automation of the plant	0.835
	Availability of advanced plant	0.734
	Quality of the plant	0.754
	Plant productivity	1.003
F2: Stakeholder Engagement	Stakeholders delineation	0.999
	Advanced stakeholder engagement methods	0.987
	Ensuring effective communication among the stakeholders	0.977
	Effective communication methods	0.811
	Leadership	0.656
	Monitoring of team performance	0.439
F3: Construction Management	Accessibility and site conditions	1.001
	Construction methods and processes	0.992
	Availability of tools and equipment	0.947
	Change in plan design and drawings	0.696
	Supervision and inspection of work	0.670
	Rework	0.678
	Availability of detailed drawings	0.676
F4: Labor and Workforce Organization	Workforce involvement	0.876
	Labour discipline	0.786
	Work and equipment allocation	0.698
	Availability of manpower	0.663
F5: Material and Logistics Management	Quality of material	0.967
	Material supply	0.805
	Storage facilities on site	0.397

5. Discussion and systems framework

5.1. Discussion

Mega-infrastructure projects are increasingly positioned as transformative instruments for sustainable development in emerging economies (Zeybek & Kaynak, 2006; Human Development Report, 2011). South Africa's strategic orientation—reflected in initiatives such as the National Development Plan (NDP) and Strategic Infrastructure Projects (SIPs)—demonstrates an explicit ambition to deploy large-scale investments for economic redress, regional integration, and long-term growth (Field & Ofori, 1988; Khan, 2008; Othman, 2012). However, despite these ambitions, the chronic underperformance of megaprojects—manifesting in cost overruns, schedule slippages, and quality shortfalls—points to deeper systemic inefficiencies (Deloitte, 2013; Mashegoana & Khatleli, 2019).

Critically, the literature attributes many of these failures to the rigid application of traditional project management paradigms in contexts defined by uncertainty, political complexity, and resource asymmetry (Flyvbjerg, 2014; Erol et al., 2018). While the project management "iron triangle"—time, cost, and quality—remains conceptually central (Atkinson, 1999), its practical utility in mega-infrastructure projects is limited without adaptive, context-sensitive approaches (Windapo & Cattell, 2013; Mbachu & Nkado, 2007). For example, governance breakdowns and weak oversight mechanisms in South African projects are symptomatic of deeper institutional fragility (Aiyetan & Das, 2022; Watermeyer, 2013), where fragmented communication and contractor underperformance derail project continuity.

From a systems theory perspective, megaprojects are not merely technical ventures but complex socio-technical systems, requiring the orchestration of interdependent subsystems (Shore & Cross, 2005; Caldas & Gupta, 2017). The study’s identification of five latent constructs through Confirmatory Factor Analysis (CFA)—namely Plant and Technological Resources, Stakeholder Engagement and Communication, Construction Management, Labour and Workforce Organisation, and Material and Logistics Management—resonates with current scholarly emphasis on integrated and multivariate frameworks for infrastructure delivery (Wang et al., 2021; Malek & Bhatt, 2023; Zaman et al., 2022).

Plant and Technological Resources, with strong CFA loadings, highlight the underexplored link between plant efficiency, automation, and project productivity. In contexts such as South Africa, where outdated machinery and poor maintenance are prevalent, this construct aligns with Gamil and Rahman’s (2020) emphasis on Building Information Modelling (BIM) and smart construction technologies as levers for performance optimisation. However, the low adoption of such tools—due to cultural inertia, high upfront costs, and skills deficits—continues to inhibit technological modernisation (Windapo, 2016).

The second construct, Stakeholder Engagement and Communication, affirms the proposition by Freeman (1984) and Aaltonen & Kujala (2010) that stakeholder alignment is central to project resilience. In practice, South African megaprojects often fail to harmonise divergent interests due to top-down governance and exclusionary decision-making, resulting in community resistance and legal entanglements (Olander & Landin, 2008). Here, the empirical validation of stakeholder delineation and communication effectiveness (CFA loadings near 0.999 and 0.977, respectively) reinforces the need for participatory frameworks and trust-building mechanisms.

Construction Management practices, particularly those related to supervision, method choice, and flexibility in responding to design changes, form another cornerstone of successful delivery. While global frameworks such as PMBOK and PRINCE2 advocate for standardised project governance (PMI, 2017), empirical studies in South Africa repeatedly note deficiencies in these areas, often stemming from weak project leadership and inconsistent oversight (Windapo & Cattell, 2013; CIDB, 2016). The CFA findings support this, showing strong loadings for construction methods and tool availability, underscoring the importance of structured yet adaptable execution strategies.

The Labour and Workforce Organisation construct also warrants attention, particularly in light of South Africa’s persistent labour-market challenges. Holt (2001) and Hwang & Ng (2013) have stressed that skilled labour shortages, poor labour discipline, and weak safety regimes are significant sources of inefficiency. The high CFA loading for workforce involvement (0.876) suggests that meaningful engagement and discipline are pivotal to labour productivity. However, systemic issues like inadequate training and politicised union dynamics undermine project execution (CIDB, 2016).

Finally, Material and Logistics Management remains a persistent bottleneck in infrastructure delivery, especially in rural or under-resourced areas. The CFA-confirmed relevance of material quality and supply corroborates findings by Cheng & Kumar (2014) and Olawale & Sun (2015), who argue that fragmented supply chains, poor storage facilities, and last-mile delivery failures often derail otherwise well-conceived projects.

Importantly, the empirical model presented in this study substantiates the need for a systems-oriented performance framework that recognises the interdependence of technical, human, and organisational factors. As Flyvbjerg et al. (2003) argue, optimism bias and strategic misrepresentation often cloud feasibility assessments; thus, integrating micro-level construction practices into performance analysis can ground strategic planning in operational realities. This is particularly vital for the Global South, where systemic risks—such as institutional weakness, socio-political volatility, and regulatory ambiguity—compound project complexity (Ofori, 2015).

Moreover, the CFA-based model supports a paradigm shift away from deterministic, linear planning towards adaptive governance and agile construction management. As suggested by Wu et al. (2018) and Al Ani (2024), digital platforms, proactive risk tools, and dynamic feedback loops are essential in navigating uncertainty and achieving performance resilience.

5.6. Toward a systems-oriented framework for mega project delivery

Collectively, the findings reinforce the conception of mega projects as complex socio-technical systems—an idea advanced in the work of Shore and Cross (2005) and Erol et al. (2018). Each latent construct identified through CFA represents a vital subsystem, whose interactions fundamentally shape project outcomes. This systems perspective complements the emerging literature advocating for non-linear, integrated project management models (Zaman et al., 2022; Al Ani, 2024). The empirical robustness of the five constructs underscores the need for coordinated planning across technical, organisational, and human dimensions, rather than siloed interventions.

From a policy and managerial standpoint, this implies that performance optimisation cannot be achieved through isolated reform (e.g., improving procurement efficiency without addressing labour practices or stakeholder engagement). Instead, systems-based interventions—focusing on synchronising subsystems, reducing interface friction, and embedding continuous feedback loops—are more likely to yield sustained improvements in megaproject outcomes.

6. Conclusion

This study examined the critical construction-related factors that influence the successful delivery of mega infrastructure projects in South Africa, where such initiatives are pivotal to national development yet often plagued by delays, cost overruns, and quality shortfalls. A key challenge addressed was the limited understanding of micro-level operational issues within the construction phase—issues such as inefficient plant utilisation, poor stakeholder coordination, labour unrest, inadequate logistics, and weak construction management practices.

Through a confirmatory factor analysis, the study confirmed five interdependent domains—Plant and Technological Resources, Stakeholder Engagement and Communication, Construction Management, Labour and Workforce Organisation, and Material and Logistics Management—as core contributors to project performance. Among these, technical efficiency, participatory governance, robust management processes, effective human capital utilisation, streamlined logistics, technological readiness, stakeholder collaboration, and effective site-level management emerged as dominant success drivers. The findings highlight that systemic inefficiencies at the construction delivery level—rather than only at the strategic or policy level—often underlie project failures.

This study contributes to the growing body of knowledge on mega infrastructure project performance by empirically identifying and validating five critical subsystems—Plant and Technological Resources, Stakeholder Engagement and Communication, Construction Management, Labour and Workforce Organisation, and Material and Logistics Management—that significantly influence project outcomes in the South African context. Through the application of Confirmatory Factor Analysis (CFA), the findings substantiate project delivery's multidimensional and interdependent nature, underscoring the necessity for a systems-oriented approach in policy and practice.

Thus, successful megaproject delivery demands more than financial resources or high-level policy alignment—it requires a holistic, adaptive, and context-sensitive management paradigm that links systemic thinking with operational excellence. Future research could further explore causal relationships among these subsystems and develop dynamic performance models that account for temporal and contextual variability in project environments across the Global South.

References

Aaltonen, K., & Kujala, J. (2010). A project lifecycle perspective on stakeholder influence strategies in global projects. *Scandinavian Journal of Management, 26*(4), 381–397

Aiyetan, A.O., & Das, D.K. (2022). Factors and strategies for improving construction management on sites in mega-projects in South Africa: An explorative survey. *Infrastructures, 7*, 19. https://doi.org/10.3390/infrastructures7020019

Al Ani, S.N.H. (2024). Utilising project management techniques to model critical success factors in large-scale construction projects. *American Journal of Economics and Business Management, 7*(8), 468–483. https://doi.org/10.31150/ajebm.v7i8.2901

Atkinson, R. (1999). Project management: Cost, time and quality, two best guesses and a phenomenon, it's time to accept other success criteria. *International Journal of Project Management, 17*(6), 337–342

Brown, T.A. (2015). *Confirmatory factor analysis for applied research* (2nd ed.). Guilford Press.

Burger, P., & Hawkesworth, I. (2011). How to attain value for money: Comparing PPP and traditional infrastructure public procurement. *OECD Journal on Budgeting, 11*(1), 91–146

Byrne, B.M. (2010). *Structural equation modelling with AMOS: Basic concepts, applications, and programming* (2nd ed.). New York: Taylor and Francis Group.

Caldas, C.H., & Gupta, A. (2017). Critical factors impacting the performance of mega-projects. *Engineering, Construction and Architectural Management, 24*(6), 920–934. https://doi.org/10.1108/ECAM-05-2016-0117

Cheng, J.C.P., & Kumar, S. (2014). A BIM-based framework for material logistics planning. *Automation in Construction, 37*, 87–97

CIDB. (2016). *Skills development and capacity building report*. Construction Industry Development Board, South Africa.
Cohen, B. (2006). Urbanisation in developing countries, current trends, future. *Deloitte on Africa African Construction Trends Report*. Retrieved from https://www.icafrica.org/fileadmin/documents/Knowledge/Deloitte_Construction_Trends_Report.pdf
Deloitte. (2013). *Deloitte on Africa African Construction Trends Report 2013*. Retrieved from https://www2.deloitte.com/content/dam/Deloitte/fpc/Documents/secteurs/immobilier/deloitte_etude_african-construction-trends-report-2013.PDF
Eberhard, A., & Godinho, C. (2017). *A review and exploration of the status, context and political economy of power sector reforms in Sub-Saharan Africa*. University of Cape Town: Graduate School of Business.
Erol, H., Dikmen, I., Atasoy, G., & Birgonul, M.T. (2018). Contemporary issues in mega construction projects. In: *Proceedings of the 5th International Project and Construction Management Conference (IPCMC 2018)*, Nicosia, Cyprus, 16–18 November 2018 (pp. 1022–1035)
Field, B., & Ofori, G. (1988). Construction and economic development—A case study. *Third World Planning Review, 10*, 41–50
Flyvbjerg, B. (2014). What you should know about megaprojects and why: An overview. *Project Management Journal, 45*(2), 6–19
Flyvbjerg, B., Holm, M.K.S., & Buhl, S.L. (2003). How common and how large are cost overruns in transport infrastructure projects? *Transport Reviews, 23*(1), 71–88
Fornell, C., & Larcker, D.F. (1981). Evaluating structural equation models with unobservable variables and measurement error. *Journal of Marketing Research, 18*(1), 39–50. https://doi.org/10.2307/3151312
Fourie, J. (2008). The South African 2010 FIFA World Cup: A case study of mega event impacts. *South African Journal of Economics, 76*(s1), S69–S86
Freeman, R.E. (1984). *Strategic management: A stakeholder approach*. Boston: Pitman.
Gamil, Y., & Rahman, I.A. (2020). Technology adoption in the construction industry: Literature review. *Engineering, Technology & Applied Science Research, 10*(1), 5265–5269
George, D., & Mallery, P. (2003). *SPSS for Windows step by step: A simple guide and reference* (4th ed.). Allyn & Bacon.
George, D., & Mallery, P. (2010). *SPSS for Windows step by step: A simple guide and reference* (10th ed.). Pearson.
Hair, J.F., Black, W.C., Babin, B.J., & Anderson, R.E. (2019). *Multivariate data analysis* (8th ed.). Pearson.
Holt, G.D. (2001). Skilled labour availability: Key challenges facing the construction industry. *Construction Management and Economics, 19*(7), 713–720
Hwang, B.G., & Ng, W.J. (2013). Project management knowledge and skills for green construction: Overcoming challenges. *International Journal of Project Management, 31*(2), 272–284
Khan, R.A. (2008). Role of construction sector in economic growth: Empirical evidence from Pakistan economy. In *Proceedings of the First International Conference on Construction in Developing Countries (ICCIDC)* (pp. 279–290). Karachi, Pakistan.
Khatleli, N. (2016). The impediments to efficient megaproject implementation in South Africa. In: *Proceedings of the 32nd Annual ARCOM Conference*, Manchester, UK (pp. 803–812).
Kline, R.B. (2016). *Principles and practice of structural equation modelling* (4th ed.). Guilford Press.
Malek, M., & Bhatt, V. (2023). Investigating the effect of risk reduction strategies on the construction of mega infrastructure project (MIP) success: A SEM-ANN approach. *Engineering, Construction and Architectural Management*. https://doi.org/10.1108/ecam-12-2022-1166
Mashegoana, G., & Khatleli, N. (2019). Mega construction projects in South Africa: Cultural complexity. In: *Proceedings of the 11th Annual SACQSP International Conference*, Johannesburg, South Africa.
Mbachu, J., & Nkado, R. (2007). Factors constraining successful building project implementation in South Africa. *Construction Management and Economics, 25*(1), 39–54
Nunnally, J.C. (1978). *Psychometric theory* (2nd ed.). McGraw-Hill.
Ofori, G. (2015). Nature of the construction industry, its needs and its development: A review of four decades of research. *Journal of Construction in Developing Countries, 20*(2), 115–135
Olander, S., & Landin, A. (2008). A comparative study of factors affecting the external stakeholder management process. *Construction Management and Economics, 26*(6), 553–561
Olawale, Y.A., & Sun, M. (2015). Construction project control in the UK: Current practice, existing problems and recommendations for future improvement. *International Journal of Project Management, 33*(3), 623–637
Othman, A.A.E. (2012). A study of the causes and effects of contractors' non-compliance with the health and safety regulations in the South African construction industry. *Journal of Architectural Engineering and Design Management, 8*, 180–191
Othman, A.A.E. (2013). Challenges of mega construction projects in developing countries. *Organization, Technology and Management in Construction: An International Journal, 5*, 730–746

Project Management Institute (PMI). (2017). *A guide to the project management body of knowledge (PMBOK® Guide)* (6th ed.).
Republic of South Africa (RSA). (2020). *National Infrastructure Plan 2050: Phase 1*. Department of Public Works and Infrastructure.
Shore, B., & Cross, B.J. (2005). Exploring the role of national culture in the management of large-scale international science projects. *International Journal of Project Management, 23*, 55–64
Wang, T., Wang, T., Chan, A.P.C., & He, Q. (2021). Identification of critical factors for construction megaprojects success (CMS). In: *Proceedings* (pp. 83–88). Springer Nature. https://doi.org/10.1007/978-3-030-48465-1_14
Wang, T., Xu, J., He, Q., Chan, A.P.C., & Owusu, E.K. (2022). Studies on the success criteria and critical success factors for mega infrastructure construction projects: A literature review. *Engineering, Construction and Architectural Management, 30*(5), 1809–1834. https://doi.org/10.1108/ecam-12-2020-1042
Watermeyer, R. (2013). Unpacking corruption, its causes and how to combat it. *Civil Engineering: Magazine of the South African Institution of Civil Engineering, 21*(5), 43–49
Windapo, A.O. (2016). Relationship between degree of risk, cost and project procurement systems in South African construction projects. *Construction Economics and Building, 16*(3), 20–36
Windapo, A.O., & Cattell, K.S. (2013). The South African construction industry: Perceptions of key challenges facing its performance, development and growth. *Journal of Construction in Developing Countries, 18*(2), 65–79
Wu, C., Chen, D., & Huang, S. (2018). Complexity of construction mega infrastructure project. *Complexity,* Article ID 7382083. https://doi.org/10.1155/2018/7382083
Zaman, U., Florez-Perez, L.A., Abbasi, S., Nawaz, S., Ferreira Farias, P.F., & Pradana, M. (2022). A stitch in time saves nine: Nexus between critical delay factors, leadership self-efficacy, and transnational mega construction project success. *Sustainability, 14*(4), 2091. https://doi.org/10.3390/su14042091
Zeybek, H., & Kaynak, M. (2008). Role of mega projects in sustainable urban transport in developing countries: The case of Istanbul Marmaray Project. In *Proceedings of the Codatu xIII*, Ho Chi Minh City, Vietnam. Retrieved from http://www.codatu.org/english/conferences/codatu13/CodatuxIII-CDrom/codCD-Zeybek.pdf

4th International Civil Engineering & Architecture Conference
17-19 May 2025, Trabzon, Türkiye

A new type shear connector for lipped channel section cold formed steel-concrete composite beams

Fatih Cebir*[1], Hussein E. Soalih[2], Ayşegül Durmuş Demir[1], Serhat Demir[1]

[1] Karadeniz Technical University, Department of Civil Engineering, 61080, Trabzon, Türkiye
[2] Karadeniz Technical University, Graduate School of Natural and Applied Science, 61080, Trabzon, Türkiye.

Abstract. In steel–concrete composite beams, shear connectors play a critical role in effectively utilizing the tensile strength of the steel profile and the compressive strength of the concrete. Traditionally, shear connectors are attached to the beam flange. While this method is suitable for heavy steel profiles, it leads to damage concentration in the beam flange rather than the shear connector due to the very thin web in cold-formed steel beams. In this study, for the first time in the literature, an innovative shear connector was designed where the connection element is attached to the web of the beam instead of the flange, and its performance was experimentally evaluated. Additionally, the shear connector was partially isolated from the concrete to allow it to bend freely. The experimental study involved full-scale push-out tests, and the results were compared with commonly used bolted shear connectors in practice. The push-out test results revealed that all the damage was concentrated in the proposed shear connector, and no damage was observed in the cold-formed steel beam.

Keywords: Cold formed steel; Concrete; Composite beam; Shear connector; Push-out test

1. Introduction

In recent years, technological advancements have contributed significantly to time and cost savings in the construction industry while also promoting the development of environmentally friendly solutions. In this context, due to their low weight, high strength-to-weight ratios, and environmental benefits, cold-formed steel structures have emerged as a significant alternative in modern construction practices. Particularly since the 1990s, the use of cold-formed steel components has increased markedly and found widespread application, especially in residential and commercial buildings (Hancock, 2003). Compared to hot-rolled steel sections, cold-formed steel sections reduce structural weight and provide substantial savings in transportation and assembly costs (Zeynalian, 2015). The reduction in structural weight also improves the seismic performance of buildings, making such systems attractive in regions with high seismic risk (Karamanoğlu & Ulay, 2017). These developments have increased the demand for durable and efficient structural systems that combine the advantages of different materials. Accordingly, composite systems integrating steel and concrete have long been used due to their durability, rapid installation, and economic benefits (Pavlović et al., 2013). While these systems initially employed hot-rolled steel sections, there has been a growing trend toward using cold-formed steel sections, particularly in low-rise residential and commercial structures. The use of cold-formed steel sections contributes to sustainable construction by reducing both structural weight and material consumption (Wehbe et al., 2013).

Composite systems formed by combining cold-formed steel beams with concrete slabs significantly enhance load-bearing capacity and stiffness. The combination of concrete's high compressive strength and steel's tensile strength leads to improved structural performance (Jianguo et al., 1999). Moreover, the lateral stability provided by the concrete slab reduces the risk of buckling in cold-formed steel components (Zeynalian et al., 2013). However, existing design standards do not adequately address the specific requirements of cold-formed steel–concrete composite systems, necessitating comprehensive research.

Shear connectors, which ensure the transfer of shear forces between steel and concrete, play a critical role in the performance of these systems (Hosseinpour et al., 2018). While welded headed studs are commonly used in traditional hot-rolled steel–concrete systems, the deformation sensitivity of cold-formed steel profiles has led to the exploration of alternative connection methods (Hanaor, 2000). Consequently, the use of mechanical connectors is recommended in cold-formed steel–concrete composite applications (Alhajri et al., 2016).

Irwan et al. (2009) demonstrated that triangular-shaped bent projections can provide 91% to 135% higher shear capacity. Irwan et al. (2011) reported that triangular connectors increased flexural capacity by 18% and that the

* Corresponding author, E-mail: fatihcebir@ktu.edu.tr

https://doi.org/10.31462/icearc2025_ce_sme_006

profile thickness significantly influenced the damage modes. Bamaga et al. (2019) investigated the performance of angle and plate-type connectors developed for cold-formed steel–concrete composite beams and found that hot-rolled steel plates offered high strength and ductility. Hosseinpour et al. (2021) examined the performance variation of U-shaped connectors depending on screw diameter and steel thickness, showing that screw diameter can increase load capacity by 25–40%. In another study conducted the same year, push-out tests were used to determine the ultimate load and failure modes of cold-formed steel sections with varying thicknesses. Numerical analyses by Hosseinpour et al. (2022) revealed that the embedment depth of the bolt within the concrete slab had a positive impact on shear capacity.

Findings in the literature indicate that current shear connectors are fully embedded within the concrete slab, which limits their deformation capacity and may lead to damage in both the beam and slab components. This study aims to enhance the performance of cold-formed steel–concrete composite systems by designing and experimentally evaluating a novel mechanical shear connector that is partially isolated from the concrete slab.

2. Partially isolated shear connector

In composite beam systems, various shear connectors have been developed to enable load transfer between the reinforced concrete slab and the steel beam. The primary objectives in these designs have been to improve ease of application and/or enhance structural performance. The literature shows that connectors with different geometric configurations have been developed to increase ductility—thereby reducing or delaying damage—and simultaneously improve load-bearing capacity. However, the complete embedment of shear connectors within the concrete slab restricts their ability to deform freely under loading, preventing the intended structural behavior from being fully achieved during the design phase. To overcome this limitation, a design approach that allows the connector to deform independently by partially isolating it from the concrete slab must be adopted.

In this study, a novel shear connector partially isolated from the reinforced concrete slab has been designed (Fig. 1). The proposed system consists of a continuous steel plate placed between two cold-formed C-shaped steel beams that are connected through their webs. The portion of the connector embedded within the concrete slab consists of steel strips arranged in a grid-like form to promote flexural behavior. To achieve this, trapezoidal gaps are created between the strips, preventing direct contact with the surrounding concrete. Load transfer is achieved via reinforcing bars that pass through holes drilled into the upper sections of the strips. Due to the relative displacements that occur between the concrete slab and the cold-formed steel beam, the partially isolated steel strips are able to bend freely. Furthermore, since the connector is welded to the web of the cold-formed steel beam, shear forces developed at the interface can be transferred directly to the beam web, offering a significant structural advantage over conventional connector systems.

In the structural behavior of the connector, the height and width dimensions of the steel strips embedded within the reinforced concrete slab emerge as two key parameters. Due to the limited thickness of the slab, the free length of the steel strips was set at 30 mm, while the width was determined as 5 mm to enhance displacement ductility.

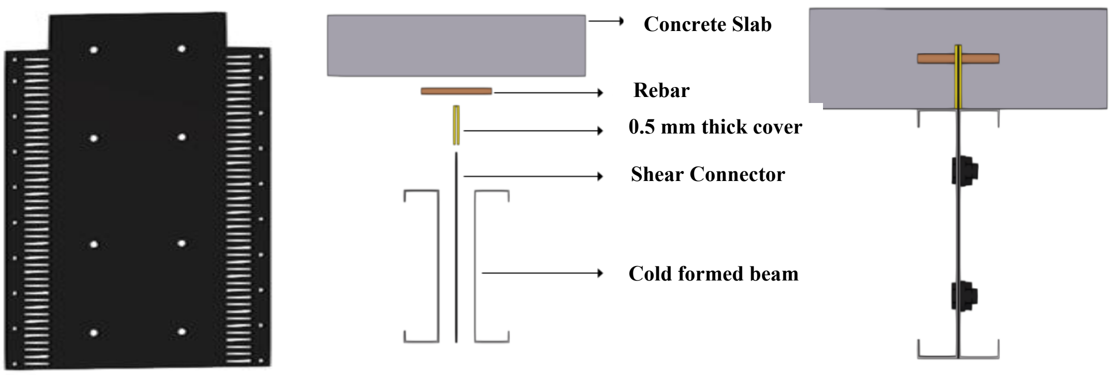

Fig. 1. New shear connector assembly in the composite beam

3. Experimental program

3.1. Test specimens and fabrication

Within the scope of the static push-out tests, a total of five specimens were prepared (Cebir,2024). Three of these specimens were equipped with bolted shear connectors of different diameters, while the remaining two were equipped with the partially isolated shear connectors proposed in this study. Bolted shear connectors, which are commonly used in composite beams, were considered as reference specimens in this study. The specimens labeled PO-B-8, PO-B-10, and PO-B-12 were equipped with M8, M10, and M12 diameter bolted shear connectors, respectively. The longitudinal spacing between the centers of adjacent bolts was set at 200 mm, satisfying both the minimum (six times the bolt diameter) and maximum (914 mm) spacing requirements specified in AISC 360-16. The bolts were arranged in double rows along the beam flanges, with a transverse spacing of 60 mm between the centers of two adjacent bolts. This distance meets the "minimum four times the bolt diameter" requirement stated in AISC 360-16. According to the AISC 360-16 standard, the bolt length must be at least four times the bolt diameter. Accordingly, in the PO-B series specimens, the length of the connectors measured from the top surface of the beam flange was designed as 60 mm (Fig. 2). Additionally, reinforced concrete slabs with a thickness of 80 mm were placed on both flanges of the cold-formed steel beam (Fig. 2), providing a 20 mm concrete cover above the bolted shear connectors (AISC 360-16, 2016).

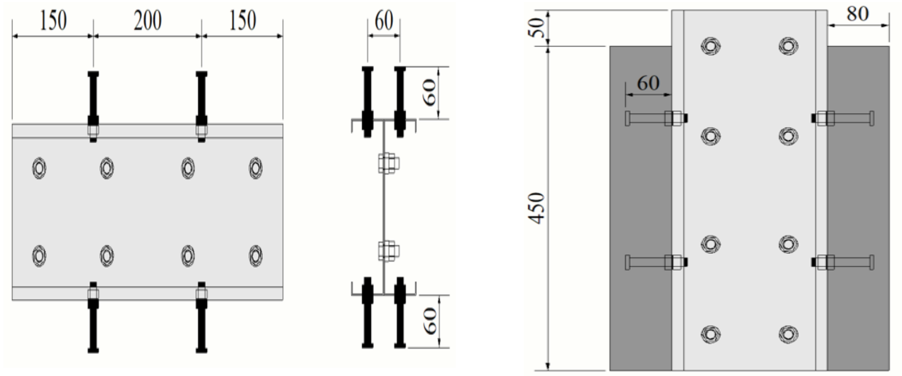

Fig. 2. Bolted shear connector–beam connection detail in PO-B series specimens

In the PO-PL-ISO and PO-PL specimens, shear connectors formed using 3 mm thick steel plates were placed between cold-formed C-shaped steel profiles joined at their webs and were fixed to the profiles using M10 bolts. The width of the connectors was designed to extend 50 mm beyond both sides of the top and bottom flanges of the C-shaped profile to ensure effective composite action with the reinforced concrete slab (Fig. 3). Additionally, mechanical interaction with the reinforced concrete slab was achieved through reinforcing bars passing through 9 mm diameter holes spaced at 50 mm intervals along the free edges of the connectors. The primary difference between these two specimens lies in the insulation condition of the connector portion embedded within the concrete slab. In the PO-PL-ISO specimen, the 50 mm long section of the connector embedded in the concrete was partially insulated by covering it with a 0.5 mm thick U-shaped steel sheet (Fig. 3(a)), whereas in the PO-PL specimen, the connector was embedded directly into the concrete without any insulation (Fig. 3(b)). This difference between the two specimens was comparatively evaluated in terms of the deformation capacity of the connectors under loading and their interaction behavior with the reinforced concrete slab.

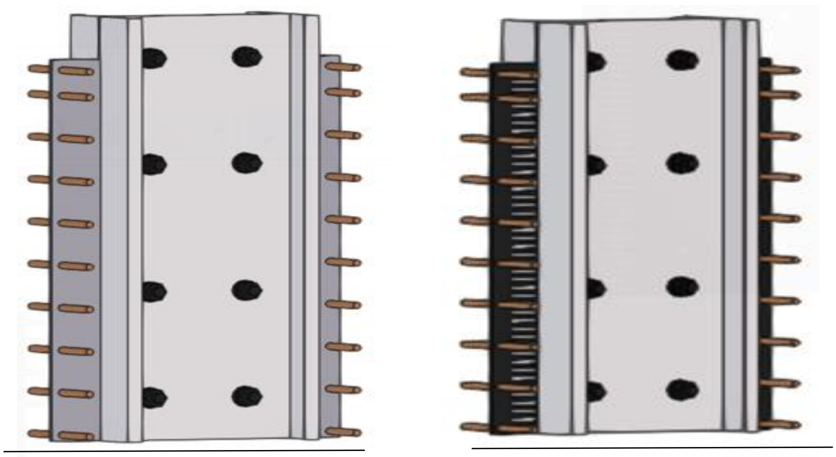

(a) **(b)**

Fig. 3. Beam-to-plate connection detail in PO-PL-ISO and PO-PL test specimens

3.2. Material properties

The steel profile specimens used in the experiments were fabricated from galvanized steel sheets produced by the hot-dip method, classified as S320GD+Z grade according to TS EN 10346 (2015), with a minimum yield strength of 320 MPa and a thickness of 1.5 mm. To determine the mechanical properties of the steel sheets, coupon specimens were prepared according to the dimensions specified in TS EN ISO 6892-1 (2016). Tensile tests were then conducted on these specimens in accordance with the same standard. The average values obtained from the tests are presented in Table 1.

Table 1. Average results obtained from the monotonic tensile test (Öztürk, 2021)

Yield Strength (MPa)	Tensile Strength (MPa)	Elongation at Break (%)	Elastic Modulus (GPa)
334	443	28.7	184.03

In the experimental studies, two types of connectors were used: bolts and plates. For the bolted connectors, Grade 8.8 bolts with a yield strength of 640 MPa and a tensile strength of 800 MPa were selected. The plates were fabricated from S235JRH (1.0039) grade steel sheets with a minimum yield strength of 235 MPa and a thickness of 3.0 mm, in accordance with the EN 1993-1-1 (2014) standard.

According to the Turkish Building Earthquake Code 2018(67), a minimum concrete class of C30/37 is required for precast reinforced concrete elements. In line with this requirement, the concrete slabs of the test specimens were produced with C30/37 quality concrete. Six cylindrical concrete samples were cast and cured in a standard curing tank for 28 days. At the end of the curing period, compressive strength tests were performed on the specimens (Fig. 4). Based on the results of these tests, the average compressive strength of the concrete material was determined to be 38.8 MPa, confirming that the target values were achieved.

Fig. 4. Uniaxial compression test

3.3. Test setup and loading program

The static push-out tests were conducted using a loading frame. The test specimens were placed freely onto the yellow-colored steel supports, as shown in Fig. 5(a), through the reinforced concrete slabs located at both flanges of the cold-formed C-shaped steel beams. The specimens maintained their vertical stability through the reinforced concrete slabs attached to the flanges. The cold-formed C-shaped steel beam was subjected to a push-out load from its top using a hydraulic jack with a capacity of 1000 kN, inducing relative vertical displacement with respect to the concrete slabs. To prevent potential local damages during load transfer, the upper end of the steel beam, where the load was applied, was clamped from both sides with 8 mm thick steel plates. Similarly, the spacing between the yellow-colored steel supports beneath the reinforced concrete slabs was designed to allow free vertical movement of the beams. During the experiments, a load cell with a capacity of 600 kN was placed at the tip of the hydraulic jack for load measurements, and displacement measurements were taken using a linear potentiometric displacement transducer (LPDT). All data obtained during the tests were transferred and recorded in a computer environment. The loading protocol presented in Fig. 5(b) was applied during the static push-out tests.

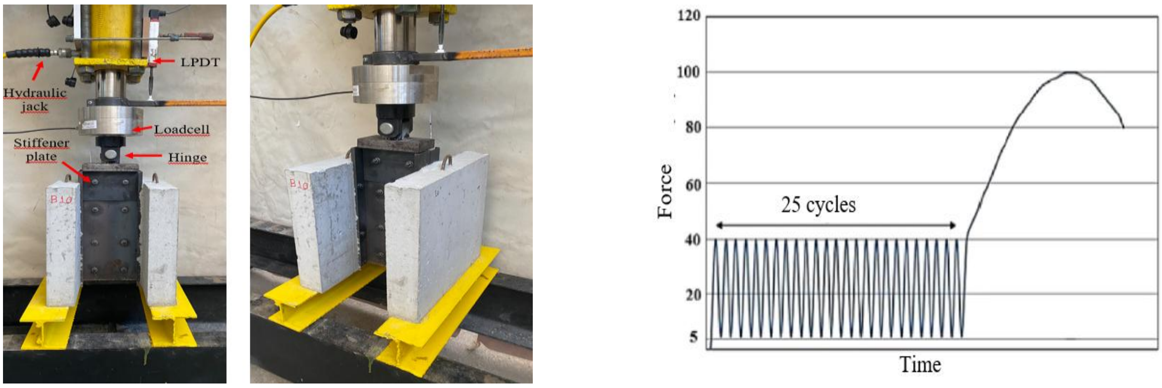

(a) **(b)**

Fig. 5. Push-out test setup and loading protocol (Eurocode 4, 2004)

4. Results and discussions

A total of five specimens were tested within the scope of the push-out experiments. The loading protocol shown in Fig. 5(b) was applied; initially, load-controlled cycles were performed, followed by displacement-controlled loading until a 20% reduction from the maximum load was observed. Since reinforced concrete slabs were present on both flanges of the beams, the obtained push-out load values were divided by two for presentation. The push-out load–slip relationships are presented in Fig. 6.

In the PO-B-8, PO-B-10, and PO-B-12 specimens equipped with bolted shear connectors, the maximum push-out loads and the corresponding slip values were found to be relatively close to each other, and only limited differences in load-carrying capacities were observed. However, no direct correlation was identified between the bolt diameter and the load-carrying capacity; the damages were predominantly concentrated in the flanges of the cold-formed steel beams.

In contrast, the PO-PL-ISO and PO-PL specimens with plate-type shear connectors exhibited a distinct yielding plateau, and a ductile behavior was observed in the system response. In the PO-PL specimen, where the steel strips were fully embedded in the concrete, the yield strength was approximately twice that of the PO-PL-ISO specimen, although their ultimate load capacities remained at similar levels. In terms of displacement capacity, the PO-PL-ISO specimen demonstrated superior performance compared to the PO-PL specimen. Overall, the plate-type shear connectors showed a clear superiority over the bolted connectors in both load-carrying and displacement capacities.

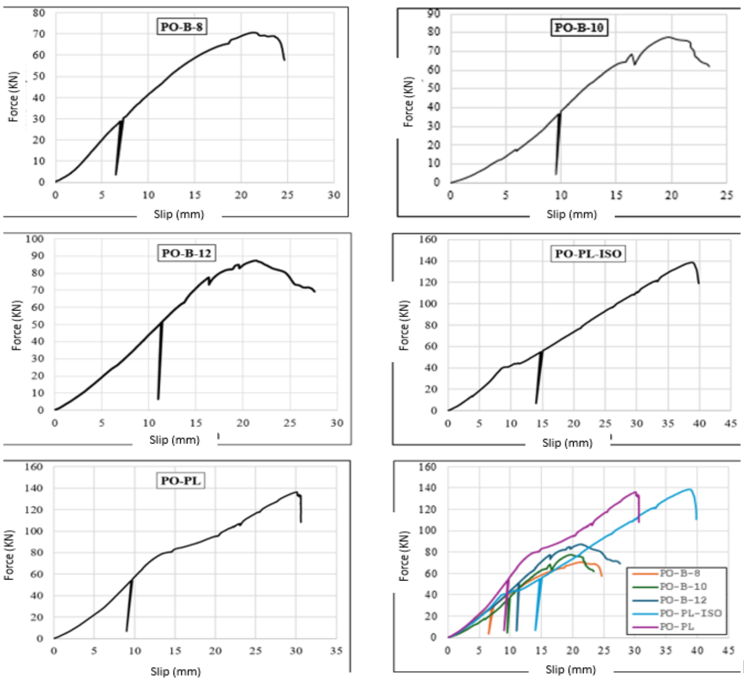

Fig. 6. Load vs. slip displacements curves

4.1. Failure mode

During and after the push-out tests, the types and distributions of damage observed in the specimens were examined. Observations revealed that the damage mechanisms varied significantly depending on the type of shear connector used.

In the PO-B-8 specimen, bending deformations in the bolts and bearing deformations around the bolt holes were observed at the beginning of the test. With increasing load, the bending deformations progressed, leading to bolt failures and tearing in the flange of the cold-formed steel beam. This process resulted in the loss of connection between the bolted connectors and the beam, causing the reinforced concrete slab to separate from the beam flange and terminating the test (Fig. 7(a)). Similarly, in the PO-B-10 specimen, bearing deformations around the bolt holes were observed; however, significant bending deformations in the bolts were not detected. As the load and slip increased, the bearing deformations around the holes progressed, leading to tearing in the beam flange. At the end of the test, damage was observed in both the beam flange and the bolts, along with cracking in the reinforced concrete slab (Fig. 7(b)). In the PO-B-12 specimen, the initial stages of the test showed only bearing deformations at the bolt holes. As the load increased, these bearing deformations intensified, leading to tearing in the beam flange. In this specimen, no significant bending deformation occurred in the bolts during the test; instead, the damage was primarily concentrated in the beam flange. The test was completed when the reinforced concrete slab separated from the beam flange (Fig. 7(c)).

(a) **(b)** **(c)**

Fig. 7. Damages observed during the test on the PO-B-8, PO-B-10 and PO-B-12 specimens

In the PO-PL specimen with a plate-type shear connector, no damage was observed until the yield strength was reached. Due to the full embedment of the steel strips within the concrete, hairline cracks parallel to the shear direction appeared in the reinforced concrete slab immediately after yielding. The size and width of these cracks increased with higher load and slip levels. At the final stage, no damage was observed in the cold-formed steel beam; however, the test was terminated due to the sudden fragmentation of the reinforced concrete slab (Fig. 8(a)). Similarly, in the PO-PL-ISO specimen, which had a partially isolated shear connector, no damage occurred until the yield strength was reached. As the maximum load capacity was approached, cracks formed in the reinforced concrete slab and propagated with increasing load. At the end of the test, no damage was observed in the cold-formed steel beam; the test concluded with the sudden collapse of the reinforced concrete slab (Fig. 8(b)). In both specimens, the connection plate was subjected to bending until the complete failure of the concrete slab. However, in the PO-PL-ISO specimen, the partial isolation of the steel strips from the concrete effectively delayed significant damage in the slab up to the maximum load capacity. Additionally, in both specimens, since the shear connectors were mounted to the web of the cold-formed steel beams instead of the flange, no damage was observed in the beams themselves.

(a) **(b)**

Fig. 8. Damages observed during the test on the PO-PL and PO-PL-ISO specimens

5. Conclusion

In this study, a novel mechanical shear connector was designed for cold-formed steel–concrete composite beam systems, and its performance was experimentally evaluated. The behavior of the developed connector was comparatively assessed against bolted shear connectors commonly used in practice. The main findings obtained from the study are summarized below:

- In specimens with 8 mm diameter bolted shear connectors, initial damage occurred as bending deformation in the connectors. In later stages, bearing deformations and tearing around the bolt holes in the flanges of the cold-formed steel beams were observed, and the test was ultimately terminated by the collapse of the beam flange.
- In specimens with bolted shear connectors larger than 8 mm in diameter, damage was concentrated directly in the flanges of the cold-formed steel beams, and no significant damage was detected in the connectors themselves. Since the flange plates governed the structural behavior, no substantial differences were observed among specimens with different bolt diameters in terms of push-out load, slip, and stiffness values. Therefore, no direct relationship could be established between bolt diameter and load-carrying capacity.
- The proposed shear connector significantly increased both the push-out load capacity and the ductility of the system compared to the bolted shear connectors.
- Mounting the connector directly to the web of the cold-formed steel beam instead of the flanges prevented damage to the steel beam during the push-out tests, concentrating all damage within the connector itself.
- The load–slip curves of the specimens with the proposed shear connector exhibited a distinct yielding plateau, indicating a ductile system behavior.
- The partial isolation of the connector from the reinforced concrete slab delayed crack formation and enhanced the system's ductility; however, it did not result in a significant increase in the push-out load capacity.
- In specimens with bolted connectors, load-carrying capacity was reached through tearing of the beam flanges, whereas in specimens with the proposed shear connectors, it was reached through the fragmentation of the reinforced concrete slab.

References

Alhajri, T.M., Tahir, M.M., Azimi, M., Mirza, J., Lawan, M.M., Alenezi, K.K., & Ragaee, M.B. (2016). Behavior of pre-cast U-shaped composite beam integrating cold-formed steel with ferro-cement slab. *Thin-Walled Structures, 102*, 18–29

American Institute of Steel Construction. (2016). ANSI/AISC 360-16: Specification for Structural Steel Buildings. Chicago, IL.

Bamaga, S.O., Zafar, A., Kim, B., & Nguyen, K.T. (2019). Push-out tests on three innovative shear connectors for composite cold-formed steel concrete beams. *Journal of Constructional Steel Research*, *161*, 110–123

Cebir, F. (2024). *Design and Experimental Investigation of Partially Isolated Shear Connectors for Cold-Formed Steel-Concrete Composite Beams* (Master's thesis, Karadeniz Technical University, Faculty of Engineering, Trabzon).

European Committee for Standardization. (2014). EN 1993-1-1:2014 Eurocode 3 - Design of Steel Structures - Part 1-1: General Rules and Rules for Buildings. Brussels.

Öztürk, F. (2021). Sigma Kesitli Hafif Çelik Profillerin Eksenel ve Eksantrik Yükleme Altındaki Davranışlarının Deneysel ve Sayısal Olarak İncelenmesi (Doctoral dissertation, Karadeniz Technical University, Faculty of Engineering, Trabzon).

Hancock, G. J. (2003). Cold-formed steel structures. *Journal of Constructional Steel Research, 59*(4), 473–487

Hanaor, A. (2000). Tests of composite beams with cold-formed sections. *Journal of Constructional Steel Research*, *54*(1), 57–89

Hosseinpour, E., & Abbasnia, R. (2018). Push-out test on the web opening shear connectors in composite beam: Experimental and analytical study. *Journal of Constructional Steel Research*, *144*, 221–236

Hosseinpour, M., Zeynalian, M., Ataei, A., & Daei, M. (2021). Push-out tests on bolted shear connectors in composite cold-formed steel beams. *Thin-Walled Structures*, *164*, 107831

Hosseinpour, M., Zeynalian, M., Daei, M., & Ataei, A. (2022). Numerical study on behavior of bolted shear connector used in composite cold-formed steel beams. *Thin-Walled Structures*, *177*, 109377

Irwan, J.M., Hanizah, A.H., & Azmi, I. (2009). Test of shear transfer enhancement in symmetric cold-formed steel–concrete composite beams. *Journal of Constructional Steel Research*, *65*(12), 2087–2098

Irwan, J.M., Hanizah, A.H., Azmi, I., & Koh, H.B. (2011). Large-scale test of symmetric cold-formed steel (CFS)–concrete composite beams with BTTST enhancement. *Journal of Constructional Steel Research, 67*(5), 720–726

Jianguo, N., & Zhiwu, Y. (1999). Research and practice of composite steel-concrete beams in China. *China Civil Engineering Journal*, *32*(2), 3–8

Karamanoğlu, M., & Ulay, G. (2017). Deprem riski yüksek bölgelerde iç mekân düzenlemelerinin incelenmesi (Tosya örneği). *Journal of Forestry Faculty, 17*(1), 186–193

Pavlović, M., Marković, Z., Veljković, M., & Buđevac, D. (2013). Bolted shear connectors vs. headed studs behaviour in push-out tests. *Journal of Constructional Steel Research*, *88*, 134–149

TS EN 10346. (2016). Sıcak daldırmayla sürekli olarak kaplanmış çelik yassı mamuller–Teknik teslim şartları.

TS EN ISO 6892-1. (2016). Metalik malzemeler–Çekme deneyi–Bölüm 1: Ortam sıcaklığında deney metodu.

Türkiye Bina Deprem Yönetmeliği (TBDY). (2018). Afet ve Acil Durum Yönetimi Başkanlığı, Ankara.

Wehbe, N., Bahmani, P., & Wehbe, A. (2013). Behavior of concrete/cold-formed steel composite beams: Experimental development of a novel structural system. *International Journal of Concrete Structures and Materials*, *7*(1), 51–59

Zeynalian, M. (2015). Numerical study on seismic performance of cold-formed steel sheathed shear walls. *Advances in Structural Engineering, 18*(11), 1819–1828

A higher-order finite element for buckling analysis of functionally graded sandwich beams

Muhittin Turan*[1], Mahmut İlter Hacıoğlu[1]

[1] *Bayburt University, Department of Civil Engineering, 69000 Bayburt, Türkiye*

Abstract. Functionally graded (FG) materials have been developed to meet the material requirements of engineering fields due to their various superior properties, such as durability, lightness, and sound insulation. Due to their superior properties, FG materials are widely used in modelling structural elements in the field of Civil and Mechanical Engineering. Therefore, the behaviour of structural elements made of FG materials must be thoroughly analysed. This study proposes a higher-order finite element for the buckling analysis of FG sandwich beams. The proposed finite element has 16 degrees of freedom. The finite element analysis considers two types of FG sandwich beams. In addition to the finite element solution, studies were performed using the Ansys Mechanical APDL program. This problem is modelled using the SHELL 281 element in the Ansys Mechanical APDL program. Critical buckling loads of two different types of FG sandwich beams are obtained by considering different boundary conditions. The results obtained are presented in a dimensionless form and compared with those of the literature. Upon examining the results, it is observed that the data agree well with the literature, confirming the accuracy of the finite element.

Keywords: FG sandwich beam; Buckling analysis; A higher-order finite element; Ansys Mechanical APDL

1. Introduction

With the rapid advancement of technology, materials science has continuously evolved. Technological developments in various fields such as engineering, medicine, and aerospace have led to the demand for materials that simultaneously exhibit multiple superior properties, such as high thermal resistance and strength. In response to these demands, researchers have developed laminated composites to meet high temperature and strength performance requirements. Laminated composites are produced by stacking or layering at least two different materials. However, due to the abrupt changes in material properties between the layers, stress concentrations may occur at the interfaces, forming stress cracks. Researchers have developed functionally graded (FG) materials to overcome this disadvantage of laminated composites, in which the material properties vary gradually according to a specific function.

In civil engineering, structural elements have increasingly been designed using functionally graded (FG) materials to withstand mechanical and thermal loads simultaneously. Accurate prediction of the mechanical behavior of FG material-based structural components is essential before their application. For this reason, numerous studies in the literature have focused on the static, free vibration, and buckling analyses of structural elements such as FG shells, plates, and beams.

A new finite element has been proposed for the free vibration and buckling analysis of sandwich functionally graded (FG) beams based on the Higher-Order Shear Deformation Theory (HSDT) (Vo et al., 2014). A finite element has been proposed for the free vibration and buckling analyses of functionally graded (FG) sandwich beams. The equations of motion for the FG beam were derived using Hamilton's principle(Vo et al., 2015). The effects of porosity on the free vibration, buckling, and static behavior of porous functionally graded (FG) beams have been investigated using the Euler-Bernoulli beam theory (Fouda et al., 2017). A finite element model has been proposed for the free vibration and buckling analyses of functionally graded (FG) beams based on the First-Order Shear Deformation Theory (FSDT). The developed finite element has five nodes and ten degrees of freedom. The equations of motion for the FG beam were derived using the Lagrangian formulation (Kahya & Turan, 2017). Using the First-Order Shear Deformation Theory (FSDT), a finite element has been proposed for the static, buckling, and free vibration analyses of laminated composite and functionally graded (FG) beams. The accuracy of the proposed finite element was validated by comparing the obtained results with those available in the literature (Turan, 2018).

* Corresponding author, E-mail: mturan@bayburt.edu.tr

https://doi.org/10.31462/icearc2025_ce_sme_007

golden light publishing

The free vibration and buckling analyses of sandwich beams and laminated composites have been conducted using a finite element model with 9N+7 degrees of freedom (Kahya & Turan, 2018). The buckling behavior of sandwich functionally graded (FG) beams has been investigated using the finite element method in Ansys software. The Taguchi orthogonal array technique was employed to examine and optimize the layer positions and levels of the FG beams (Evran, 2019). Using the finite element method, a new semi-analytical solution has been proposed for the buckling analysis of sandwich functionally graded (FG) beams (Liu et al., 2021). A new finite element has been proposed for the static, free vibration, and buckling analyses of nano functionally graded (FG) beams. The displacement field was obtained using Hermite interpolation. In addition to the proposed finite element solution, a comparison was made by solving the problem using the differential quadrature method (Bian et al., 2022). A finite element has been proposed for the buckling and free vibration analyses of bidirectional functionally graded (FG) porous beams based on the Higher-Order Shear Deformation Theory (HSDT). The proposed finite element has twelve degrees of freedom. Three different types of porosity and various boundary conditions were considered in the study (Turan & Adiyaman, 2023).

This study analyzes the buckling behavior of functionally graded (FG) sandwich beams using a high-order finite element that accounts for shear deformation effects. The finite element has five nodes and sixteen degrees of freedom. The FG material properties vary according to a power law through the beam thickness. The equilibrium equations were derived using the Lagrangian formulation. The analyses considered different boundary conditions, power law index, and slenderness. The results were compared with the results of the literature and the Ansys Apdl package program. It was demonstrated that the results are in excellent agreement.

2. Material method

2.1. Material properties

In this study, two different types of sandwich beams are considered, referred to as Type-1 and Type-2. The material properties of the beams vary in the thickness direction according to Hooke's law, as given in equation (1).

$$P(z) = (P_c - P_m)V_c(z) + P_m \tag{1}$$

P_m and P_s represent the properties of metal and ceramic, respectively. The volumetric fraction function of the ceramic material, V_c, is provided separately for Type-1 and Type-2.

The core of the Type-1 FG sandwich beam is made of homogeneous ceramic material, while the upper and lower layers are composed of FG material, as shown in Fig. 1. The volumetric fraction function of the ceramic material for the Type-1 FG beam is given in equation (2).

The core of the Type-2 FG sandwich beam consists of an FG material layer, with the lower layer made of homogeneous metal material and the upper layer made of homogeneous ceramic material. The volumetric fraction function of the Type-2 FG sandwich beam, V_c, is given in equation (3).

$$\begin{aligned} V_c^{(1)}(z) &= \left(\frac{z-h_0}{h_1-h_2}\right)^p, & h_0 \le z \le h_1 \ (\textit{FG bottom surface}) \\ V_c^{(2)}(z) &= 1, & h_1 \le z \le h_2 \ (\textit{Ceramic core}) \\ V_c^{(3)}(z) &= \left(\frac{z-h_3}{h_2-h_3}\right)^p, & h_2 \le z \le h_3 \ (\textit{FG top surface}) \end{aligned} \tag{2}$$

$$\begin{aligned} V_c^{(1)}(z) &= 0, & h_0 \le z \le h_1 \ (\textit{Metal bottom surface}) \\ V_c^{(2)}(z) &= \left(\frac{z-h_3}{h_2-h_3}\right)^p, & h_1 \le z \le h_2 \ (\textit{FG core}) \\ V_c^{(3)}(z) &= 1, & h_2 \le z \le h_3 \ (\textit{Ceramic top surface}) \end{aligned} \tag{3}$$

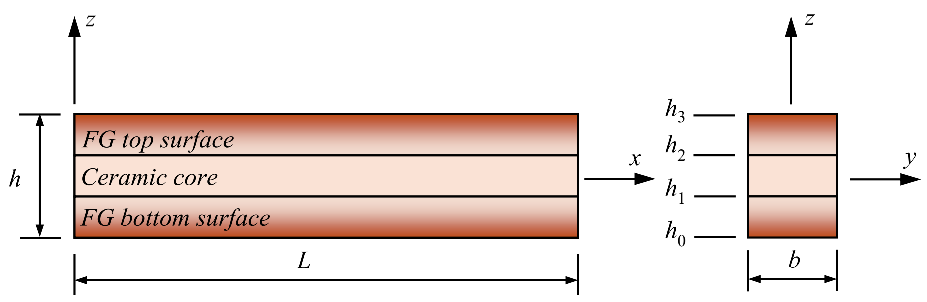

Fig. 1. Type-1 FG sandwich beam

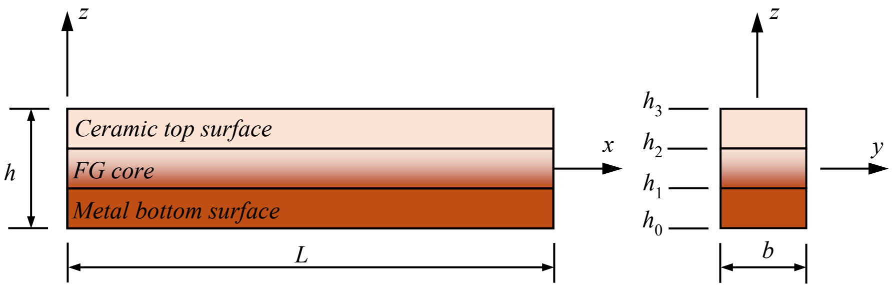

Fig. 2. Type-2 FG sandwich beam

2.2. Solution using the finite element method

In this study, a high-order finite element that accounts for shear deformation effects has been proposed. The finite element has five nodes and sixteen degrees of freedom, as shown in Fig. 3. The displacement vector of the finite element nodes is given in equation (4). The horizontal and vertical displacements, respectively, u and w while the rotations are expressed by ϕ. β_{1i} and β_{2i} the terms represent the higher-order terms derived from the Taylor series expansion.

$$\mathbf{u} = \left(u_i \quad w_j \quad \phi_i \quad \beta_{1i} \quad \beta_{2i} \right), \qquad i=1,2,3 \qquad j=1,2,3,4 \tag{4}$$

The displacement expressions at any point of the FG beam according to the high-order shear deformation theory (HSDT) are given by U and W in equation (5).

$$\begin{aligned} U(x,z,t) &= u(x,t) - z\,\phi(x,t) - z^2 \beta_1(x,t) - z^3 \beta_2(x,t), \\ W(x,z,t) &= w(x,t) \end{aligned} \tag{5}$$

Here, t represents time. The unit shape and displacement expressions of the FG beam are given in equation (6).

$$\varepsilon_{xx} = \frac{\partial U}{\partial x} = u_{,x} - z\phi_{,x} - z^2 \beta_{1,x} - z^3 \beta_{2,x} \quad , \quad \gamma_{xz} = \frac{\partial U}{\partial z} + \frac{\partial W}{\partial x} = w_{,x} - \phi - 2z\beta_1 - 3z^2 \beta_2 \tag{6}$$

Here, $\square_{,x}$ It represents the derivative with respect to x. The normal and shear stresses of the FG beam are given in equation (7). Here, E and G represent the Young's modulus and the shear modulus, respectively.

$$\sigma_{xx} = E(z)\,\varepsilon_{xx} \quad , \quad \tau_{xz} = G(z)\,\gamma_{xz} \tag{7}$$

The expressions used in the solution of the problem, u, w, ϕ, β_1 and β_2 are clearly given in equation (8).

$$\begin{aligned} &u(x,t) = \sum_{i=1}^{3} \varphi_i(x)\, u_i(t) \;, \quad w(x,t) = \sum_{j=1}^{4} \psi_j(x)\, w_j(t) \;, \quad \phi(x,t) = \sum_{i=1}^{3} \varphi_i(x)\, \phi_i(t) \;, \\ &\beta_1(x,t) = \sum_{i=1}^{3} \varphi_i(x)\, \beta_{1i}(t) \;, \quad \beta_2(x,t) = \sum_{i=1}^{3} \varphi_i(x)\, \beta_{2i}(t) \end{aligned} \tag{8}$$

Here, $u_i(t)$, $\phi_i(t)$, $\beta_{1i}(t)$ and $\beta_{2i}(t)$ the terms represent the generalized displacements. $\varphi_i(x)$ and $\psi_i(x)$ the terms represent the shape functions. The equations of motion for the FG beam were derived using the Lagrangian formulation and are given in equation (9).

$$\frac{d}{dt}\left(\frac{\partial \Pi}{\partial \dot{q}_i} \right) - \frac{\partial \Pi}{\partial q_i} = 0 \tag{9}$$

Here, $\dot{q}_i$ and qi represents the independent variables. The Lagrangian equation is expressed in equation

$$\Pi = T - (U^* + V) \tag{10}$$

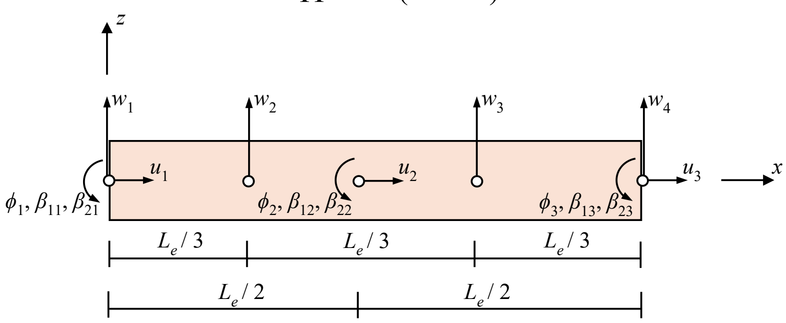

Fig. 3. Proposed finite element

The strain energy of the FG beam is explicitly given in equation (11).

$$
\begin{aligned}
U^{*} &= \frac{1}{2}\int_0^{L_e}\int_A (\sigma_{xx}\varepsilon_{xx}+\tau_{xz}\gamma_{xz})dAdx \\
&= \frac{1}{2}\int_0^{L_e}\Big\{X_0(u_{,x})^2-2X_1u_{,x}\phi_{,x}+X_2\left((\phi_{,x})^2-2u_{,x}\beta_{1,x}\right)+2X_3\left(\phi_{,x}\beta_{1,x}-u_{,x}\beta_{2,x}\right)+ \\
&\quad X_4\left(\beta_{1,x}^2+2\phi_{,x}\beta_{2,x}\right)+2X_5\beta_{1,x}\beta_{2,x}+X_6\beta_{2,x}^2+Y_0\left((\phi)^2-2\phi w_{,x}+\left(w_{,x}\right)^2\right)+ \\
&\quad 4Y_1\beta_1\left(\phi-w_{,x}\right)+2Y_2\left(2\beta_1^2+3\phi\beta_2-3\beta_2w_{,x}\right)+12Y_3\beta_1\beta_2+9Y_4\beta_2^2\Big\}dx
\end{aligned}
\tag{11}
$$

Here, X_a and Y_b express the material coefficients, which are explicitly stated in (12).

$$
X_a=\int_A E(z)z^a dA \ , \ Y_b=G(z)z^b dA \ , \ (a=0,1,...,6; \quad b=0,1,...,4) \tag{12}
$$

The kinetic energy expression of the FG beam is given in equation (13).

$$
\begin{aligned}
T &= \int_0^{L_e}\int_A \rho(z)\left(\dot{U}^2+\dot{W}^2\right)dAdx \\
&= \frac{1}{2}\int_0^{L_e}\Big\{I_0(\dot{u})^2-2I_1\dot{u}\dot{\phi}+I_2\left((\dot{\phi})^2-2\dot{u}\dot{\beta}_1\right)+2I_3\left(\dot{\phi}\dot{\beta}_1-\dot{u}\dot{\beta}_2\right) \\
&\quad +I_4\left(\dot{\beta}_1^2+2\dot{\phi}\dot{\beta}_2\right)+2I_5\dot{\beta}_1\dot{\beta}_2+I_6\dot{\beta}_2^2+I_0(\dot{w})^2\Big\}dx
\end{aligned}
\tag{13}
$$

In this expression, I_c is a coefficient dependent on the material constants, and it is given in equation (14).

$$
I_c=\int_A \rho(z)z^c dA \ , \ (c=0,1,...,6) \tag{14}
$$

For the buckling analysis of the FG beam, a compressive force P_0 is applied at the beam's endpoints. The work done by this force is expressed in equation (15).

$$
V=\frac{1}{2}\int_0^{L_e} P_0\left(w_{,x}\right)^2 dx \tag{15}
$$

By substituting the solutions from equation (8) and considering equations (11), (13), and (15), and taking the derivatives in the Lagrangian expression from equation (10), the equation of motion for the FG beam is obtained as shown in equation (16).

$$
\mathbf{m}\ddot{\mathbf{u}}+\left(\mathbf{k_e}-P_0\mathbf{k_g}\right)\mathbf{u}=\mathbf{f} \tag{16}
$$

Here, $\mathbf{f}$ represents the external force vector. $\mathbf{m}$, $\mathbf{k_e}$ and $\mathbf{k_g}$ represent the element mass, element stiffness, and element geometric matrices, respectively. In the buckling analysis of sandwich FG beams with length L considered in this study, the equation of motion used is derived using the finite element method, as shown in equation (17).

$$
\mathbf{M}\ddot{\mathbf{X}}+\left(\mathbf{K}-P_0\mathbf{K}_g\right)\mathbf{X}=\mathbf{F} \tag{17}
$$

Here, **M**, **K** and $\mathbf{K_g}$ represent the global mass, global stiffness, and global geometric stiffness matrices, respectively. The critical buckling load is denoted by $P_0=(P_0)_{cr}$, and if **M**=0 and **F**=0 are assumed, the equation of motion is obtained as shown in equation (18).

$$
\left(\mathbf{K}-P_0\mathbf{K}_g\right)\mathbf{u}=0 \tag{18}
$$

The obtained equation of motion is an eigenvalue problem, and the values of P_0 that make the coefficient matrices of this equation zero represent the critical buckling loads of the FG beam.

2.3. Solution with ansys mechanical apdl

In this section, the buckling analyses of Type-1 and Type-2 FG sandwich beams are conducted using the Ansys Mechanical APDL software, considering different boundary conditions, slenderness ratios (L/h), and material exponential variation coefficients. The Shell 281 element available in the program is selected for the analyses. After selecting the element, the elastic modulus and density (ρ) values of the FG material are obtained using the MATLAB program and defined in the Ansys software. After defining the material properties, the geometric properties of the FG sandwich beams are specified, with a beam length L and a rectangular cross-section of $b\times h$. After the modeling of the FG sandwich beams was completed, separate convergence studies were conducted for each beam type to determine the sufficient number of finite elements. In the convergence study, for the Type-1 sandwich beam, the homogeneous ceramic layer was not divided, and only the FG surface layers were divided into 20 layers each, resulting in a total of 41 layers. For the Type-2 sandwich FG beam, the FG core was divided into 40 layers, resulting in a total of 42 layers. The mesh generation was performed, and the sandwich FG beams were discretized into finite elements. For the buckling analysis, an axial load of 1 N was applied at the beam ends, and separate analyses were conducted for different boundary conditions, slenderness ratios, and FG material variation coefficients. The obtained results were presented in a dimensionless form in the next section.

3. Results and discussion

In this section, buckling analyses of the sandwich FG beams have been conducted using the proposed finite element method and the Ansys APDL package program, utilizing the material properties provided in Table 1.

The obtained results have been nondimensionalized using equation (19). The nondimensional results are presented in comparison with the literature data.

$$\bar{\lambda} = \frac{12\left(P_0\right)_{cr} L^2}{E_m h^3} \tag{19}$$

3.1. The critical buckling loads of the Type-1 sandwich FG beam

The nondimensional critical buckling loads of the Type-1 FG sandwich beams, obtained through the convergence study using the proposed finite element method and Ansys APDL, are presented in Tables 2 and 3, respectively. Upon examining the data in the tables, the sufficient number of layers for the finite element method was determined to be 14, and for Ansys APDL, it was determined to be 41.

In Table 4, the variation of non-dimensional critical buckling loads with respect to p for different boundary conditions and layer thicknesses is presented, considering L/h=5. The results are compared with literature data. When examining the table, it can be observed that increasing the thickness of the homogeneous ceramic core layer increases the stiffness of the FG beam. As a result, the non-dimensional critical buckling loads increase. The highest non-dimensional critical buckling load was obtained under the clamped boundary condition with a layer thickness of 1-8-1. Furthermore, as the value of p increases, the material property of the FG beam tends to resemble that of metal, leading to a decrease in the non-dimensional critical buckling loads.

In Figure 4, the variation of non-dimensional critical buckling loads with slenderness ratios is comparatively presented for different boundary conditions and various p values, using both the proposed finite element and Ansys APDL, for the case where the layer thicknesses are (1-1-1). Upon examining the obtained results, it is observed that the non-dimensional critical buckling loads increase up to a certain slenderness ratio and then converge. Furthermore, due to the reduction in the stiffness of the FG beam with increasing p values, a decrease in the non-dimensional critical buckling loads is observed.

Table 1. Material properties

Metal	E_m (GPa)	ρ_m (kg/m^3)	v	Ceramic	E_c (GPa)	ρ_c (kg/m^3)	v
Aluminum (Al)	70	2702	0.30	Aluminum oxide (Al_2O_3)	380	3960	0.30

Table 2. Variation of non-dimensional critical buckling loads with finite element number for Type-1 FG beam with different boundary conditions, p=1 and L/h=5 (1-1-1)

Boundary Conditions	Number of Elements							
	4	8	10	12	14	16	18	20
C-C	84.2516	83.7803	83.7600	83.7526	83.7496	83.7481	83.7473	83.7469
S-S	24.5625	24.5515	24.5509	24.5508	24.5508	24.5509	24.5507	24.5506
C-F	6.4152	6.4145	6.4150	6.4148	6.4150	6.4150	6.4167	6.4150

Table 3. Variation of non-dimensional critical buckling loads with number of layers for Type-1 sandwich FG beams calculated with Ansys, p=1 and L/h=5 (1-1-1)

Boundary Conditions	Present Study	Number of Layers							
		3	*e(%)*	5	*e(%)*	21	*e(%)*	41	*e(%)*
		Dimensionless Critical Buckling Loads							
C-C	83.7469	75.6171	10.75	80.9957	3.40	83.2029	0.65	84.0771	0.38
S-S	24.5506	21.6339	13.48	23.3824	5.00	24.0073	2.26	24.2974	1.04
C-F	6.4150	5.6323	13.90	6.1063	5.05	6.2640	2.41	6.3424	1.14

Table 4. Variation of dimensionless critical buckling load of Type-1 sandwich FD beam with p for L/h=5

Beam	p	Theory	1-0-1	2-1-2	2-1-1	1-1-1	2-2-1	1-2-1	1-8-1
S-S	0	Present Study	48.5962	48.5961	48.5966	48.5079	48.5961	48.5959	48.5961
		Turan (2018) [(1)]	48.5905	48.3339	48.2775	48.1523	48.1306	47.9691	48.0132
		Vo et al. (2014) [(2)]	48.5959	48.5959	48.5959	48.5959	48.5959	48.5959	48.5959
	0.5	Present Study	27.8535	30.0270	31.0681	31.8177	33.2516	34.7630	41.9852
		Turan (2018) [(1)]	27.6787	29.7869	30.7992	31.5671	32.9245	34.3605	41.5890
		Vo et al. (2014) [(2)]	27.8574	30.0301	31.0728	31.8784	33.2536	34.7653	41.9897
	1	Present Study	19.6390	22.2017	23.5112	24.5508	26.3552	28.4391	38.7732
		Turan (2018) [(1)]	19.4857	22.0171	23.3039	24.3266	26.1083	28.1421	38.4631
		Vo et al. (2014) [(2)]	19.6525	22.2108	23.5246	24.5596	26.3611	28.4447	38.7838
	2	Present Study	13.5398	15.8865	17.2863	18.3088	20.3571	22.7753	35.6735
		Turan (2018) [(1)]	13.4369	15.7626	17.1449	18.1906	20.1868	22.5714	35.4435
		Vo et al. (2014) [(2)]	13.5801	15.9152	17.3249	18.3587	20.3750	22.7863	35.6914
	5	Present Study	10.0365	11.5710	12.9011	13.6375	15.6653	18.0632	32.7465
		Turan (2018)[(1)]	10.0122	11.5171	12.8395	13.5836	15.5726	17.9412	32.5909
		Vo et al. (2014) [(2)]	10.1460	11.6676	13.0270	13.7212	15.7307	18.0914	32.7725
	10	Present Study	9.3206	10.3771	11.6315	12.1371	14.0856	16.3321	31.4966
		Turan (2018)[(1)]	9.3292	10.3549	11.6069	12.1121	14.0279	16.2440	31.3722
		Vo et al. (2014) [(2)]	9.4515	10.5348	11.8370	12.2605	14.1995	16.3783	31.5265
C-C	0	Present Study	152.1461	152.1454	152.1453	151.9288	152.1452	152.1451	152.1456
		Turan (2018) [(1)]	151.9426	149.5367	148.9976	147.8945	147.6590	146.2149	146.4849
		Vo et al. (2014) [(2)]	152.1470	152.1470	152.1470	152.1470	152.1470	152.1470	152.1470
	0.5	Present Study	92.8135	99.9435	102.8596	105.4994	109.5831	114.1570	134.2639
		Turan (2018) [(1)]	90.8635	97.3130	99.9504	102.3356	106.0949	109.9390	130.2102
		Vo et al. (2014) [(2)]	92.8833	99.9860	102.9120	105.6790	109.6030	114.1710	134.2870
	1	Present Study	67.3087	76.1440	80.0135	83.7496	89.1445	95.6776	125.3068
		Turan (2018) [(1)]	65.5503	74.0105	77.6545	81.1635	86.3848	92.3982	122.0472
		Vo et al. (2014) [(2)]	67.4983	76.2634	80.1670	83.8177	89.2208	95.7287	125.3860
	2	Present Study	47.1816	55.8380	60.1464	64.1218	70.5397	78.4356	116.4989
		Turan (2018) [(1)]	45.9691	54.3375	58.4671	62.3940	68.5304	76.0661	114.0148
		Vo et al. (2014) [(2)]	47.7010	56.2057	60.6056	64.4229	70.7563	78.5608	116.6580
	5	Present Study	34.2337	40.7826	44.8791	48.4533	55.0285	63.4268	108.0455
		Turan (2018)[(1)]	33.9501	40.1136	44.1224	47.5431	53.8895	61.9478	106.3066
		Vo et al. (2014) [(2)]	35.5493	42.0033	46.3743	49.2763	55.8271	63.7824	108.2970
	10	Present Study	30.8183	36.0401	39.8069	42.9892	49.3561	57.6569	104.3966
		Turan (2018)[(1)]	30.9059	35.7615	39.4849	42.4612	48.6357	56.5736	102.9857
		Vo et al. (2014) [(2)]	32.3019	37.9944	42.1935	44.3374	50.7315	58.2461	104.6920
C-F	0	Present Study	13.0603	13.0589	13.0601	13.0356	13.0614	13.0555	13.0595
		Turan (2018) [(1)]	13.0597	13.0395	13.0372	13.0262	13.0254	13.0154	13.0172
		Vo et al. (2014) [(2)]	13.0594	13.0594	13.0594	13.0594	13.0594	13.0594	13.0594
	0.5	Present Study	7.3315	7.9070	8.1949	8.3885	8.7835	9.1944	11.2018
		Turan (2018) [(1)]	7.3184	7.8898	8.1762	8.3831	8.7594	9.1645	11.1776
		Vo et al. (2014) [(2)]	7.3314	7.9068	8.1951	8.4051	8.7839	9.1940	11.2021
	1	Present Study	5.1243	5.7917	6.1479	6.4150	6.9029	7.4611	10.3085
		Turan (2018) [(1)]	5.1126	5.7791	6.1335	6.4005	6.8875	7.4456	10.2865
		Vo et al. (2014) [(2)]	5.1245	5.7921	6.1490	6.4166	6.9050	7.4639	10.3093
	2	Present Study	3.515	4.1137	4.4902	4.7460	5.2940	5.9346	9.4510
		Turan (2018) [(1)]	3.5078	4.1051	4.4805	4.7449	5.2823	5.9179	9.4342
		Vo et al. (2014) [(2)]	3.5173	4.1156	4.4927	4.7564	5.2952	5.9348	9.4531
	5	Present Study	2.6224	2.9940	3.3523	3.5202	4.0576	4.6788	8.6477
		Turan (2018)[(1)]	2.6210	2.9904	3.3481	3.5217	4.0513	4.6705	8.6368
		Vo et al. (2014) [(2)]	2.6298	3.0004	3.3609	3.5310	4.0620	4.6806	8.6493
	10	Present Study	2.4594	2.6972	3.0387	3.1361	3.6518	4.2235	8.3061
		Turan (2018)[(1)]	2.4602	2.6957	3.0370	3.1390	3.6477	4.2177	8.2968
		Vo et al. (2014) [(2)]	2.4683	2.7077	3.0527	3.1488	3.6595	4.2267	8.3073

[(1)] Finite element solution according to FSDT, [(2)] Finite element solution according to HSDT

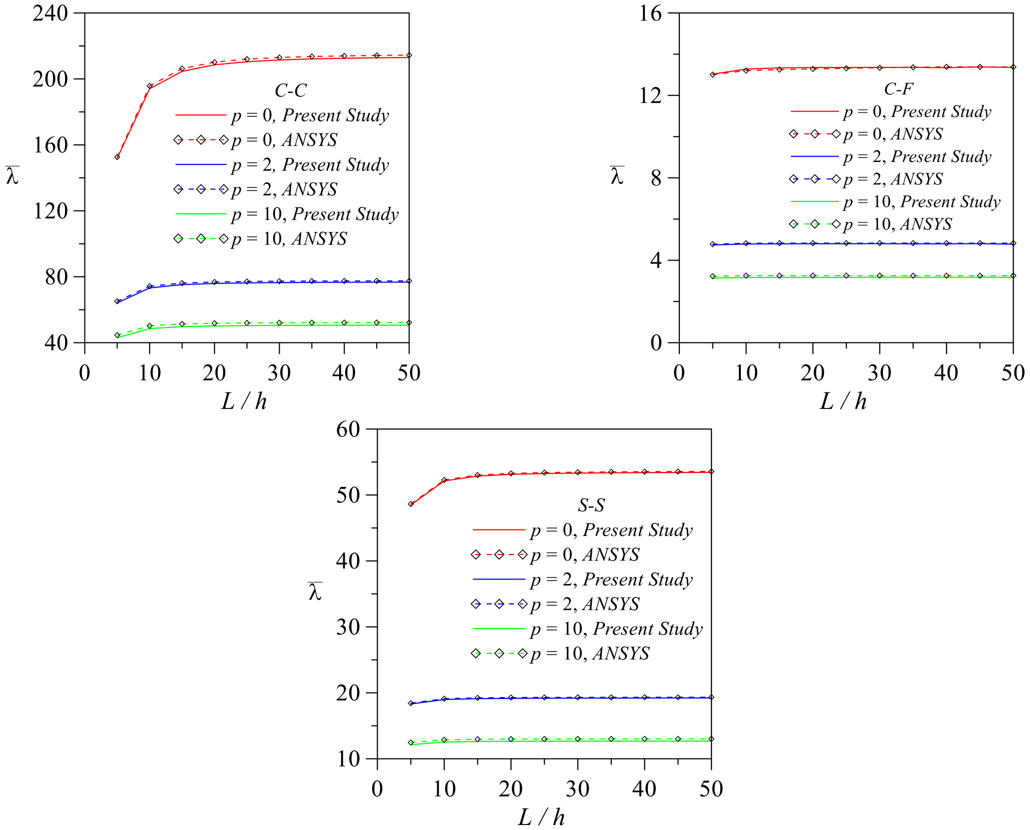

Fig. 4. The variation of dimensionless critical buckling loads of Type-2 sandwich FD beams, calculated using the proposed finite element method and Ansys, depending on the *L*/*h* ratio.

3.2. Critical buckling loads of the Type-2 sandwich FG beam

The data from the convergence studies conducted to determine the sufficient number of layers required for the dimensionless buckling analysis of the Type-2 sandwich FG beam are presented in Table 5 for the proposed finite element and in Table 6 for Ansys. Upon examining the tables, the sufficient number of layers was determined to be 14 for the proposed finite element and 42 for Ansys.

Table 7 presents the dimensionless critical buckling loads obtained using the proposed finite element for *L*/*h*=5, considering different layer thicknesses, boundary conditions, and values of the power-law index *p*. Upon examining the table, it is observed that the dimensionless critical buckling loads decrease with increasing values of *p*. The highest dimensionless critical buckling load is obtained under clamped–clamped boundary conditions with a layer thickness configuration of 1-8-1.

Table 5. Variation of the dimensionless critical buckling loads with the number of finite elements for Type-2 sandwich FG beams with different boundary conditions at *p*=1and *L*/*h*=5 (1-1-1 Layer Configuration)

Boundary Conditions	Number of Elements							
	4	8	10	12	14	16	18	20
C-C	65.9541	65.5984	65.5831	65.5774	5.2140	65.5739	65.5733	65.5731
S-S	19.7751	19.7662	19.7659	19.7658	65.5751	19.7657	19.7658	19.7656
C-F	5.2143	5.2140	5.2141	5.2141	19.7657	5.2141	5.2143	5.2142

Table 6. Variation of the dimensionless critical buckling loads of Type-2 sandwich FG beams calculated with Ansys according to the number of layers for *p*=1and *L*/*h*=5 (1-1-1)

Boundary Conditions	Present Study	Number of Layers									
		7	*e(%)*	12	*e(%)*	22	*e(%)*	32	*e(%)*	42	*e(%)*
		Dimensionless Critical Buckling Loads									
C-C	65.5751	66.1757	0.91	66.5143	1.41	67.3714	2.67	67.4871	2.83	67.0371	2.18
S-S	19.7657	19.6131	0.78	19.7559	0.05	19.8771	0.56	19.9046	0.70	19.8814	0.58
C-F	5.2140	5.1411	1.42	5.1836	0.59	5.2046	0.18	5.2114	0.05	5.2144	0.01

Table 7. Variation of dimensionless critical buckling loads of Type-2 FG sandwich beam with p (L/h=5)

Beam	p	Theory	2-1-2	2-1-1	1-1-1	2-2-1	1-2-1	1-8-1
S-S	0	Present Study	21.2645	18.7884	23.7053	21.2643	27.8183	38.6275
		Turan (2018)(1)	21.2291	18.7563	23.5900	21.1692	27.6656	38.3737
		Turan (2018)(2)	21.3699	19.1654	23.7148	21.3699	27.7461	38.5911
	0.5	Present Study	19.9074	18.0592	21.0464	19.3008	22.9466	27.7113
		Turan (2018)(1)	19.8649	18.0339	20.9100	19.2095	22.7526	27.4410
		Turan (2018)(2)	20.0470	18.4822	21.0835	19.4744	22.8938	28.3499
	1	Present Study	19.2239	17.68	19.7657	18.3834	20.6986	22.8992
		Turan (2018)(1)	19.2050	17.6981	19.6630	18.3549	20.5447	22.6885
		Turan (2018)(2)	19.4283	18.1871	19.8887	18.6768	20.7435	23.7567
	2	Present Study	18.5605	17.3006	18.6015	17.5726	18.7937	19.1534
		Turan (2018)(1)	18.5796	17.3786	18.5601	17.6378	18.7238	19.0629
		Turan (2018)(2)	18.8764	17.9463	18.8857	18.0642	19.0354	20.1265
	5	Present Study	17.9543	16.9394	17.6487	16.9136	17.4263	16.8513
		Turan (2018)(1)	17.9844	17.0238	17.6396	17.0061	17.4249	16.9226
		Turan (2018)(2)	18.4351	17.7714	18.1915	17.6708	18.0096	18.0550
	10	Present Study	17.7087	16.7804	17.3084	16.6486	17.0046	16.1259
		Turan (2018)(1)	17.6998	16.7983	17.2481	16.6525	16.9499	16.1736
		Turan (2018)(2)	18.2849	17.7080	18.0052	17.5322	17.7910	17.6642
C-C	0	Present Study	71.2915	60.9902	80.0143	71.2914	93.3014	124.8213
		Turan (2018)(1)	70.8756	60.6352	79.0492	70.2264	91.6131	122.1338
		Turan (2018)(2)	72.2987	64.6370	79.9061	72.2987	92.4621	124.3371
	0.5	Present Study	66.2868	57.4591	70.6564	63.3621	76.9985	90.8917
		Turan (2018)(1)	65.7765	57.1383	69.4120	62.3172	74.8685	88.0078
		Turan (2018)(2)	67.6097	61.4707	70.8644	65.0160	76.3548	90.1544
	1	Present Study	63.4206	55.2152	65.5751	58.9346	68.6933	74.9852
		Turan (2018)(1)	63.1401	55.2830	64.6610	58.5010	66.9950	72.7239
		Turan (2018)(2)	65.3830	59.9610	66.6816	61.7282	69.0673	74.9501
	2	Present Study	60.3017	52.6267	60.326	54.2943	60.671	61.2303
		Turan (2018)(1)	60.3811	53.2040	60.0015	54.7110	59.8317	60.2058
		Turan (2018)(2)	63.3411	58.5465	63.0289	58.8599	62.9927	62.8509
	5	Present Study	57.0256	49.8314	55.1254	49.7069	53.3251	50.329
		Turan (2018)(1)	57.1944	50.4255	55.0921	50.3268	53.1471	50.7920
		Turan (2018)(2)	61.6022	57.2370	60.2083	56.4205	58.7149	54.8107
	10	Present Study	55.5182	48.5323	52.8559	47.7104	50.3351	46.2654
		Turan (2018)(1)	55.3363	48.5782	52.3961	47.6271	49.7574	46.5152
		Turan (2018)(2)	60.9478	56.6546	59.2618	55.3392	57.3692	51.7361
C-F	0	Present Study	5.5900	4.998	6.2153	5.59	7.3073	10.2701
		Turan (2018)(1)	5.5876	4.9957	6.1991	5.5838	7.2966	10.2521
		Turan (2018)(2)	5.5976	5.0251	6.2197	5.5976	7.3022	10.2677
	0.5	Present Study	5.2462	4.8363	5.529	5.1098	6.0272	7.3311
		Turan (2018)(1)	5.2437	4.8348	5.5123	5.1035	6.0141	7.3128
		Turan (2018)(2)	5.2562	4.8672	5.5338	5.1223	6.0236	7.5075
	1	Present Study	5.0827	4.7658	5.214	4.9068	5.4578	6.0623
		Turan (2018)(1)	5.0814	4.7672	5.2001	4.9053	5.4472	6.0475
		Turan (2018)(2)	5.0974	4.8029	5.2243	4.9282	5.4608	6.2778
	2	Present Study	4.7078	4.9467	4.7525	5.0037	5.113	4.7078
		Turan (2018)(1)	4.9355	4.7139	4.9375	4.7575	4.9987	5.1066
		Turan (2018)(2)	4.9571	4.7554	4.9680	4.7885	5.0209	5.3176
	5	Present Study	4.6669	4.7578	4.6593	4.7302	4.61	4.6669
		Turan (2018)(1)	4.8150	4.6736	4.7515	4.6665	4.7307	4.6155
		Turan (2018)(2)	4.8476	4.7289	4.7981	4.7157	4.7732	4.7948
	10	Present Study	4.7698	4.6529	4.7054	4.6298	4.6739	4.4788
		Turan (2018)(1)	4.7691	4.6544	4.6952	4.6309	4.6700	4.4829
		Turan (2018)(2)	4.8118	4.7225	4.7574	4.6969	4.7322	4.7158

(1) Finite element solution according to FSDT, (2) Analytics solution according to FSDT

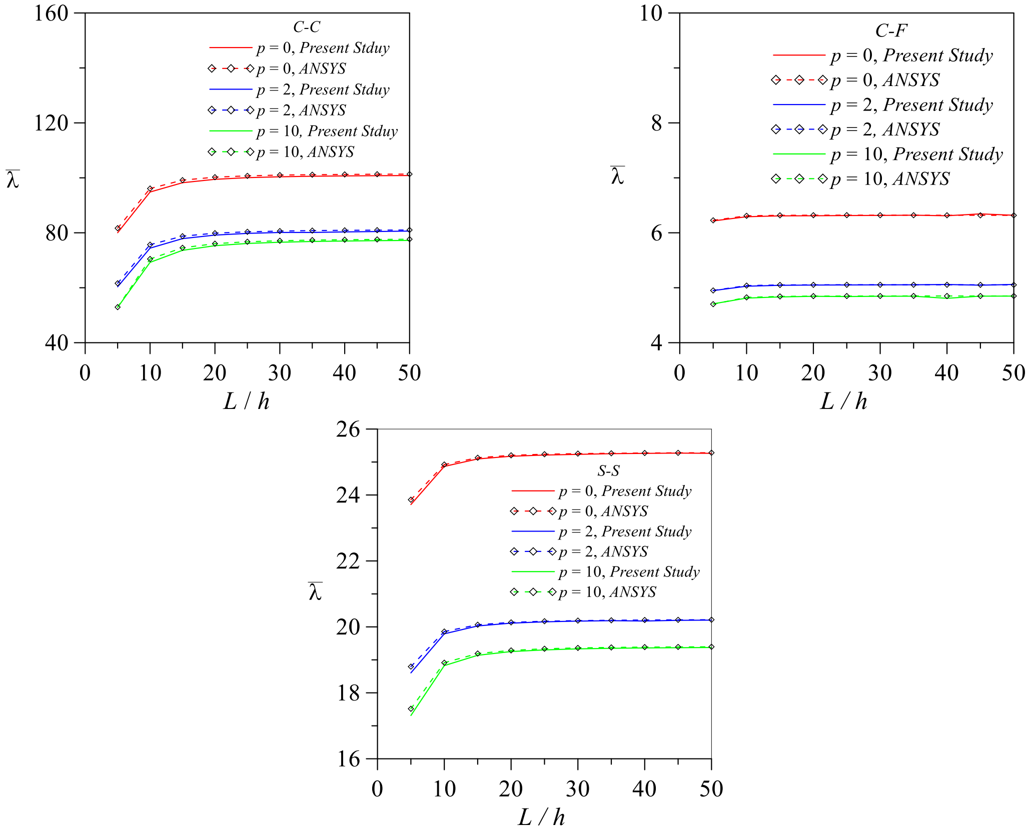

Figure 5. The variation of dimensionless critical buckling loads of Type-2 sandwich FD beams, calculated using the proposed finite element method and Ansys, depending on the L/h ratio.

4. Conclusions

This study proposes a finite element with sixteen degrees of freedom, accounting for higher-order shear deformation effects, for the buckling analysis of sandwich FG beams. The same analyses were solved with the Ansys APDL software to validate the accuracy of the results obtained from the buckling analysis of FG sandwich beams using the proposed finite element. The analyses considered different slenderness ratios, boundary conditions, and FG material variation coefficients. The results obtained by both methods are presented, and the comparisons between them are made with the literature data, showing that the results are highly consistent.

Based on the results obtained from the analyses, the following conclusions can be drawn:

- As the slenderness ratio increases, the dimensionless critical buckling loads decrease.
- For the Type-1 sandwich FG beam, the dimensionless critical buckling loads increase as the core thickness increases.
- When the material property of the Type-2 sandwich FG beam is more metal-dominant, the dimensionless critical buckling loads decrease.

References

ANSYS Mechanical APDL, Swanson Analysis Systems Inc., Houston, PA, USA, 2023.

Bian, P. L., Qing, H., & Yu, T. (2022). A new finite element method framework for axially functionally-graded nanobeam with stress-driven two-phase nonlocal integral model. *Composite Structures*, *295*(2022), 115769. https://doi.org/10.1016/j.compstruct.2022.115769

Evran, S. (2019). Investigation of Effects of Layer Positions on Mechanical Buckling Behavior of Axially Layered Functionally Graded Beams. *Pamukkale University Journal of Engineering Sciences*, *25*(1), 20–26. https://doi.org/10.5505/pajes.2018.00243

Fouda, N., El-midany, T., & Sadoun, A. M. (2017). Bending, buckling and vibration of a functionally graded porous beam using finite elements. *Journal of Applied and Computational Mechanics*, *3*(4), 274–282. https://doi.org/10.22055/jacm.2017.21924.1121

Kahya, V., & Turan, M. (2017). Finite element model for vibration and buckling of functionally graded beams based on the first-order shear deformation theory. *Composites Part B: Engineering*, *109*, 108–115. https://doi.org/10.1016/j.compositesb.2016.10.039

Kahya, V., & Turan, M. (2018). Vibration and buckling of laminated beams by a multi-layer finite element model. *Steel and Composite Structures*, *28*(4), 415–426. https://doi.org/10.12989/scs.2018.28.4.415
Liu, J., He, B., Ye, W., & Yang, F. (2021). High performance model for buckling of functionally graded sandwich beams using a new semi-analytical method. *Composite Structures*, *262*(January), 113614. https://doi.org/10.1016/j.compstruct.2021.113614
Turan, M. (2018). *Tabakalı kirişlerin statik, serbest titreşim ve burkulma analizleri için bir sonlu eleman modeli*. Karadeniz Teknik Üniversitesi.
Turan, M., & Adiyaman, G. (2023). Free Vibration and Buckling Analysis of Porous Two-Directional Functionally Graded Beams Using a Higher-Order Finite Element Model. *Journal of Vibration Engineering and Technologies*, *0123456789*. https://doi.org/10.1007/s42417-023-00898-5
Vo, T. P., Thai, H. T., Nguyen, T. K., Inam, F., & Lee, J. (2015). A quasi-3D theory for vibration and buckling of functionally graded sandwich beams. *Composite Structures*, *119*, 1–12. https://doi.org/10.1016/j.compstruct.2014.08.006
Vo, T. P., Thai, H. T., Nguyen, T. K., Maheri, A., & Lee, J. (2014). Finite element model for vibration and buckling of functionally graded sandwich beams based on a refined shear deformation theory. *Engineering Structures*, *64*, 12–22. https://doi.org/10.1016/j.engstruct.2014.01.029

The Degradation of mechanical characteristics in GFRP composite under real maritime conditions for civil building application

Djaber Bouhafara*[1], Younes Menail[2], Farouk Mesrafet[2], Mohammed İslem Aissaoui[1]

[1] National Higher School of Technology and Engineering, Laboratory of Energy Systems Technologies (LTSE), 23005 Annaba, Algeria.
[2] BadjiMokhtar University, Department of Mechanical Engineering, LR3MI,Box 12, 23052SidiAmmar Annaba, Algeria

Abstract. The composite materials have created their own importance in all areas of technology with special attention to design materials for civil engineering applications like GRP bars. Spicily, glass fibers are being used as reinforcement of polymeric composite in many industries.To meet the challenges in overcoming the difficulties in mechanical properties, erosion behavior, instant cracking, and thermal resistance, composite materials are developed to solve these difficulties. The present article reveals the effects of degradation conditions like seawater and distilled water in applications of composite materials in the areas related to civil engineering. The article explains the effects of these marine environments on the damage of polyester/glass composites. The idea of composite materials in various applications may explore a new window in modern civil engineering. An investigation was carried out to compare the energy absorption capability of glass/polyester composites in 2 months in salt water and distilled water. The injection molding techniques were used to fabricate the specimens with a 60% glass fiber weight fraction. The Charpy impact test was performed on composite specimens, and the results showed that the glass/polyester composite in distilled water after 1 month and 2 months has the highest energy absorption, compared with the composite degrading in seawater, but it's not that big of a difference, so it's pretty close. In addition, the scanning electron microscopy was assessed to demonstrate the different failure in fracture surfaces. It was found that the glass/polyester composite after aging in marine condition failed by fiber fracture and fracture through the matrix.

Keywords: Mechanical properties; Fibre glass; GRP bars; Seawater; Distilled water

1.Introduction

Glass fiber reinforced polymer composites are used in many marine and water transport industries(Deniz & Karakuzu, 2012; Liao, Gu, Liu, et al., 2024; Liao, Gu, Yan, et al., 2024; Sebaey, 2022), construction of bridges(Jiang, Kolstein, & Bijlaard, 2013) and GFRP bars(Hosen, Johnson Alengaram, Jumaat, Ramli Sulong, & Darain, 2017; Pan & Yan, 2021; Xian, Bai, et al., 2024; Xian, Zhou, et al., 2024)**,** It replaces ordinary steel bars with bars made of composite materials such as Fig. 1, which have corrosion-resistant properties in various aquatic environments and are cheaper in import and manufacturing costs, and the first choice in various applications; it has good mechanical properties and improves the hardness of offshore structures. In this case, composite materials are subjected to mechanical loads and harsh environmental conditions which lead to damage and corrosion over time.

However a decrease in the mechanical properties of polymer matrix composites occurs upon exposure to moisture in distille-water and seawater environments due to the plasticization, hydrolysis of polymer resin and the effect of salts in the water on its properties(Cabral-Fonseca, Correia, Rodrigues, & Branco, 2012; Cerbu, 2010; Fang et al., 2017; Heshmati, Haghani, & Al-Emrani, 2017; Mansouri, Djebbar, Khatir, & Abdel Wahab, 2019),Researches focused on the performance of FRP materials at elevated temperatures (Hawileh & Rasheed, 2017), Because most important factor in the progression and hastening of the degradation on the mechanical characteristics in composite materials is the rise and fall of temperature.More recently, the integration of fiber-reinforced polymer laminates is recognised as an expanded material for the bridge structures owing to its higher

*Corresponding author, E-mail: d.bouhafara@etu.ensti-annaba.dz

https://doi.org/10.31462/icearc2025_ce_sme_014
golden light publishing

strength rating(Heshmati, Haghani, & Al-Emrani, 2016; Jiang, Kolstein, Bijlaard, & Qiang, 2014; Jiang et al., 2013), therefore, bars made of composite materials are used as an alternative to steel due to their excellent properties, or they are used as an addition to steel and are called hybrid bars, or repairing steel bridges as they give additions to the properties of steel and give more durability and resistance over time. (G. Feng et al., 2024; Li et al., 2022; Xu, Du, Guo, Pan, & Zhu, 2025)studied the decrease in the mechanical properties of BFRP bars embedding inside the SSC concrete after the exposure in seawater; the maritime environment diminishes dynamic tensile strength and failure strain, while exerting a negligible influence on the elastic modulus(Li et al., 2022) .
Therefore from the literature, it is evident that the FRP composite has been widely used for the beams in construction marine, so, the main goal of the current study is to investigate the structural strength, focusing on the ability to maintain mechanical properties, energy absorption capacities of the specimens and damage characteristics of GFRP composites reinforced with E glass, after exposed to accelerate environmental aging in seawater & distille water.

Fig. 1. GFRP bars(Hosen et al., 2017)

2. Experimental

2.1. Materials and preparations of composites
A standard unsaturated polyester resin and woven fiberglass (mats & toils) and gel cota resin; the materials was provided by local company. An Infusion molding method was used in the fabrication of the composites laminates.

The matrix material was prepared from the unsaturated polyester resin and the catalyst. The catalyst was added to the polyester and the batch was stirred before pour into a mold. Fiber glasses were arranged inside the mold. Four fiberglass's (mats) and four (toils) with nominal size 1m^2 used in each layer plus layer of gel cota, Composite maritime constructions have been protected by a terminal layer of gel coat that shields them from water. Then, the polyester matrix was pour onto the fiberglass in a mold.

The size of the mold was the 1 m^2. And was swept by the wax and covered with the steel frame for easy removal and good surface finishing of the laminates specimen. The specimen preparation process was shown in Fig. 2 Finally, the specimen was removed from the mold and cured for 24 hours at room temperature to ensure the specimen was hard and dry enough for the cutting process.

Fig. 2. Preparation of fiberglass reinforced polyester (Infusion molding).

2.2. Immersion process

The composite laminate samples were immersed in distilled water and seawaters solutions in sealed containers at laboratory conditions (23°C) for 2 month. During the environmental ageing process, the samples were taken out every week and weighed to analyses the weight change of the specimens, the absorption of the composites after different solutions immersion was determined by the weight gain relative to the oven dry weight. For the analysis of weight gain, 5 samples were weighed for each composite type.

2.3.Absorption testing

The absorption in weight percentage (W %) was calculated from Eq. below:

$$w(\%) = \frac{w_t - w_0}{w_t} \times 100 \quad (1)$$

where W_t and W_0 denotes weight of wet composite at time t and the weight of dry specimen, respectively , the process was shown in Fig .3**,** All the coupons were weighed dry and measured with±0.1 mm accuracy. And subdivided into 3 groups according the type of marine environments (dry, seawater, distille water)

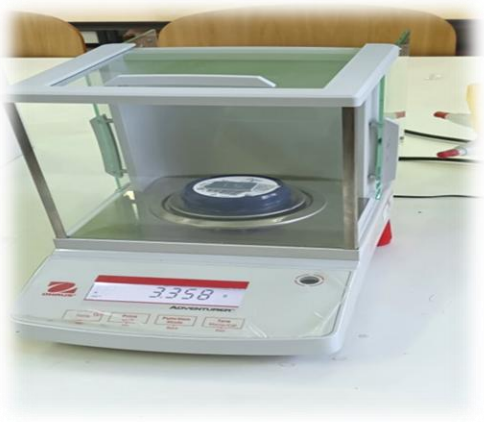

Fig. 3. Weight of specimens

2.4. Charpy testing

Fifths specimens of composite were fabricated for each condition marine, Standard ISO 179 Charpy notched specimens (ISO, 2010), 78 mm × 10 mm × 5,5 mm was cut from the composite plate and tested with energy 50 Joule , Utilizing a cutting machine, the specimens were meticulously cut and refined from the composite to the precise dimensions. The notches were created with a radius of curvature using a motorized notch Vis in the center, in accordance with the norm. The charpy impact tests were conducted by using a universal testing machine Zwick-Roell, the figure 4 shows the specimens before & after breaking.

Fig. 4. Specimen of charpy impact.

3. Result and Discussion

3.1.Absorption Properties

Fig. 5 illustrates the weight gain behavior of the composite as a function of immersion duration in two different aqueous environments: seawater and distilled water. The weight gain, expressed as a percentage, increases progressively with time for both media, indicating the absorption by this material. At initially, especially in the first 14 days, a fast uptake is seen, which might be ascribed to capillary action and surface diffusion into micro-voids and fiber-matrix interfaces. We also saw that salt water absorbed more slowly than distilled water.

These findings support earlier studies (Mansouri et al., 2019), which indicated that the glass/polyester lost less weight under saltwater exposure than under distilled water exposure. and this is due to the ratio of salts in both solutions and the overlap of salts in the voids, so the percentage of salt water absorbed decreases.Subsequently, the absorption rate then decreases and eventually reaches a plateau when balance is neared. However, the glass/polyester composite submerged in distilled water exhibits a little higher weight gain compared to seawater, especially after 35 days. The variation may be attributed to the lower ionic concentration in distilled water and the absence of large amounts of salts, which may enhance the diffusion gradient and make water faster .Conversely, the presence of salts in seawater probably causes osmotic effects and might lower the rate of water diffusion because of interactions with the composite matrix or partial pore blockage.

And these findings imply that the environmental medium greatly affects the moisture absorption properties of the composite, which can affect its mechanical propritie and durability performance under maritime service settings, (Mansouri et al., 2019) Noted that mixed short and woven fibre glass reinforced polyester composite exhibited quick moisture absorption at first, then 20 days stabilised thus Consequently, over prolonged peeriods of periods , the composites will stabilise or slightly decrease in distille water and saltwater.

Fig. 6 shows the weight gain (%) of the composite after 1 and 2 months of immersion in two different environments At 1 Month in Distilled water and seawater the composite show similar absorption (~0,65–0,7% weight gain) ,distilled water appears slightly higher, but within error margins — so the difference might not be statistically significant. and At 2 Months Both groups show a decrease in weight gain compared to 1 month ,so the samples in Distilled-water retain slightly more weight gain (~0,45–0,5%) compared to Seawater (~0,4%). In the initial phases, water ions rapidly penetrate the polyester matrix, filling micro-voids by diffusion-driven mechanisms, Subsequent to the initial saturation; the material may experience structural relaxation. Certain tiny molecules such as those from polyester may be leached out into the solution, resulting in a net weight loss that counteracts additional water absorption.

The polymer chains may reorganize, reducing the free volume and impeding more water absorption our Salts in seawater can reduce the chemical potential of water molecules, slowing their diffusion into the composite, Furthermore, salt ions might create a surface barrier restricting water entrance—a process known as salting-out effect.

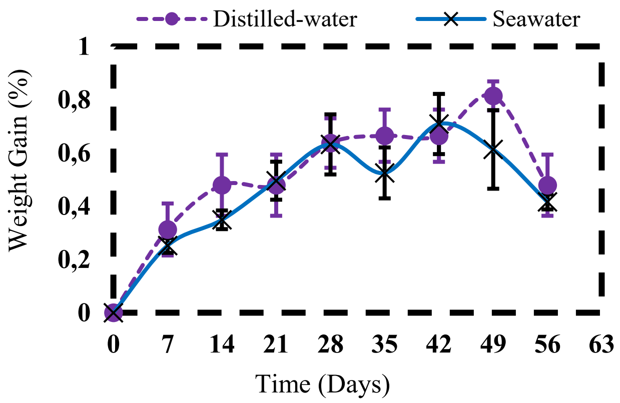

Fig. 5. Weight gain as a function of duration of immersion per day of composite

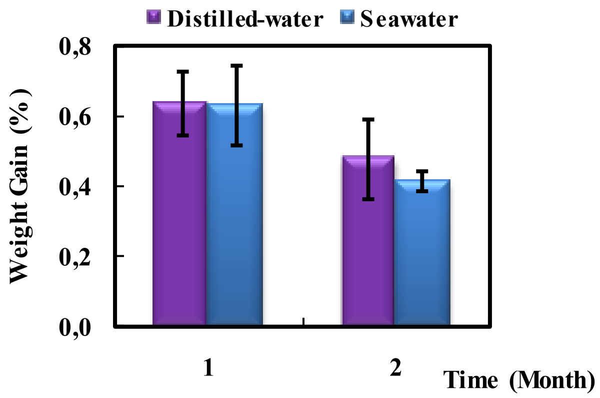

Fig. 6. Weight gain of glass/polyester composite after 1& 2 months of immersion in environments

3.2 Charpy Properties

Fig. 7 shows first State of the Both samples before immersion have a great ability for energy absorption, 195,89 (kJ/m2), this is the baseline impact strength of the virgin composite material. After one month immertion in solutions, there is a notable reduction in the energy absorbed by the glass/polyester composite in both settings; in distille water the value decreases to around 156,54 (kJ/m2), and in seawater the value decreases little to around 150,78 (kJ/m2), this signifies a decrease of around 18-23% from the original value, reflecting a deterioration in toughness or impact resistance during one month of immersion.the decline is slightly more pronounced in the marine environment.

The main cause of the notable decline in impact energy after one month is the negative consequences of water in polyester Matrix Plasticization; the sea and distille waters serve as plasticizers, thereby lowering energy absorption before fracture under impact. Two months later Curiously, the energy absorption capacity for both environments shows a little rise over the one month mark In distilled water, it recovers to around 168 (kJ/m2); in saltwater it recovers to about 162 (kJ/m2); Although there is some recovery, the numbers are still much lower by 13-16% than the first impact strength recorded at firste time.

The sample in distilled water exhibits somewhat greater re covery than the one in saltwater, the little rise in impact energy noted between 1 and 2 months is less common than the early deterioration but may occur under specific situations, such as Saturation Effect, Stress Relaxation/Redistribution, or Plasticization Dominance. Although interfacial weakening and hydrolysis diminish toughness, the plasticization effect may marginally enhance the material's ductility in some instances.

The persistent plasticization enables the compromised material to absorb slightly more energy prior to total failure compared to its condition after one month. This impact is often subordinate to the general deterioration or the experimental variability.

The data presented in Fig. 8 shows the comparative Impact strength of samples exposed to distilled water and seawater environments over 1 and 2 months. At 1 month, composite immersed in distilled water and seawater energy absorption are close, but the composite after distilled water aging is slightly higher and At 2 months, both composite show slightly increased of Impact strength compared to 1 month, with distilled water again a bit higher.When composites are submerged in water (either distilled or seawater), water molecules infiltrate the matrix via diffusion, therefore functioning as a plasticizer inside the polymer matrix.

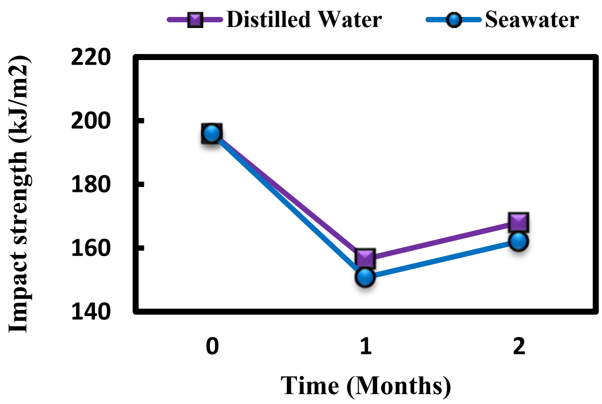

Fig. 7. The energy absorbed by Glass/polyester composite in each environment.

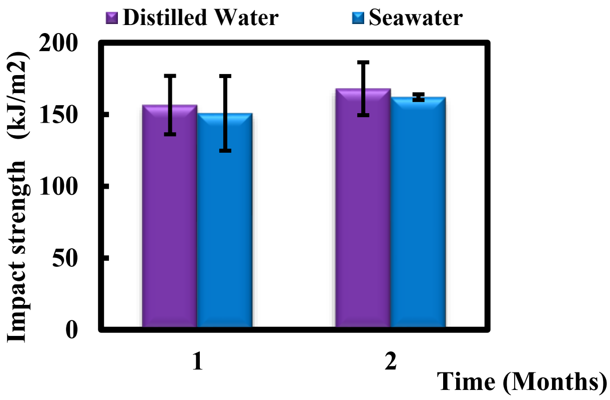

Fig. 8. The Impact strength of Glass/polyester composite in each environment.

This process lowers internal stresses and may temporarily augment impact strength by increasing the ductility of the matrix. Distilled water facilitates pure plasticization without the introduction of salts or ions, whereas saltwater contributes salt ions that can induce micro-cracks and expedite matrix breakdown.Due to the absence of salts, distilled water primarily causes plasticization without significant chemical degradation in the polyester.

Thus, a slight increase in toughness is observed and for the Seawater introduces additional factors like ionic attack and salt crystallization, which can initiate micro-cracks within the matrix of polyester. This reduces impact resistance compared to distilled water.Initially, water ingress improves the ductility. However, if the immersion continued much longer (beyond 2 months), we would expect a decline in impact strength due to long-term hydrolytic degradation.but clearly, the mechanical properties like tensile and flexural strength of aged glass/polyester composite specimens after every time fall in comparison to virgin specimens.

The variations in this mechanical feature, however, seem to lack any obvious pattern. Similar behavior was seen by (Fang et al., 2017; P. Feng, Wang, Wang, Loughery, & Niu, 2014)

3.3 SEM micrographs

Fig. 9 represent the micrograph on the surface befour the immersion, The morphology of the control glass/polyester composite specimen exhibits a robust adhesion between the fiber and the matrix.in Fig. 10 and Fig. 11 represent the SEM micrographs on the surfaces of polyester/glass composite after 4th months of sewater and distille water immersion. humidity aging is Widely recognized as a main cause of the long-term deterioration of an polymers matrix exposed to the environment or in contact with watery solutions like distille water our seawater, Seawater penetration to the surface of the composite coupons and absorption by the resin of polyester over the course of four months led to created voids in the polyester resin and produced a direct effect on mechanical properties. The mechanism of this effects needs deeper analysis and research.

However, in the context of distille water and the effect on the microscopic properties of composite materials, we observe almost the same effect as for seawater.Based on the morphology achieved, composite immersion in seawater and distille water faileds by :dilamination between the layape of composite,change in the surface of polyester matrix with crack propagations through the matrix , and debonding occurs between the fiber and matrix these modes of failure correspond rather well to the measured impact damage by (Fang et al., 2017), Clearly, moisture induces resin hydrolysis and debonding at the interface, which are the main deteriorating factors.

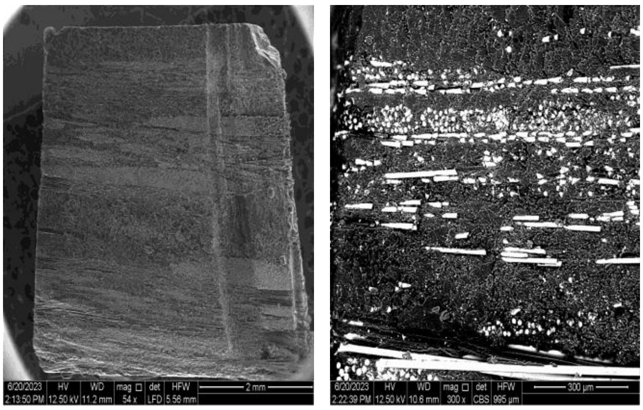

Fig.9. SEM micrograph of polyester/glass composite before immersion

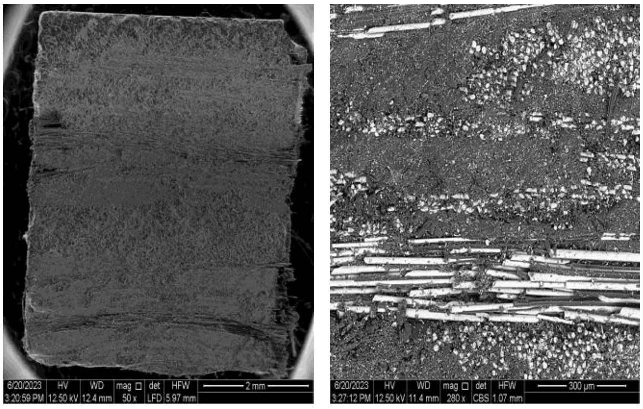

Fig.10. SEM micrograph of polyester/glass composite after 4 months of immersion in seawater

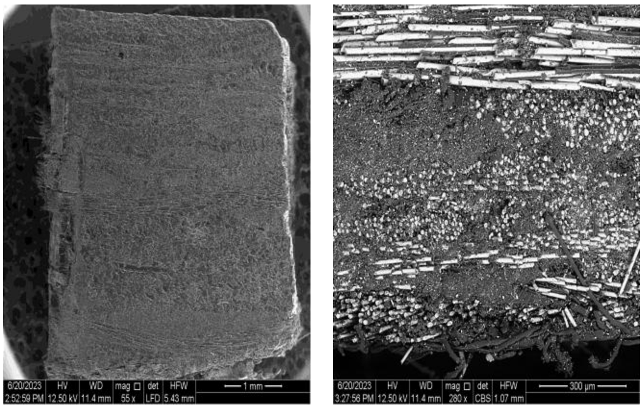

Fig.11**.** SEM micrograph of polyester/glass composite after 4 months of immersion in distille water

4.Conclusion

Current investigation focuses on the influence of seawater & distille water absorptions on glass fiber reinforcement polyester composites and effects of ageing process in impact strength and the absorbed energy values,the following inferences are drawn.

- The glass/polyester composites absorbed more moisture initially, which reduced after 2 months and Distilled water caused slightly higher moisture uptake than seawater.
- Short-term immersion (1–2 months) generally improves impact strength due to plasticization, and Distilled water effect is almoste same aggressive compared to seawater, leading to better preservation of impact properties.
- Almost the same between effects of distile water and seawater in The microscopic properties of glass/polyester surface
- The findings of the research indicate the importance of Change in salt ratio in environmental degradation of impact properties and energy absorption of composite materials in the marine environment, The main goal of this research remains the development of a reliable predictive numerical model of the charpy impacts behavior of glass/polyester materials exposed to real marine environment, which would represent a basic tool to assess the durability of composite marine structures during their exploitation.

Acknowledgments

The authors declare that they have no known competing financial interests or personal relationships that could have appeared to influence the work reported in this paper.

References

Cabral-Fonseca, S., Correia, J. R., Rodrigues, M. P., & Branco, F. A. (2012). Artificial accelerated ageing of GFRP pultruded profiles made of polyester and vinylester resins: Characterisation of physical-chemical and mechanical damage. *Strain*, *48*(2), 162–173.

Cerbu, C. (2010). Effects of the Long-Time Immersion on the Mechanical Behaviour in Case of Some E-glass / Resin Composite Materials. *Woven Fabric Engineering*.

Deniz, M. E., & Karakuzu, R. (2012). Seawater effect on impact behavior of glass-epoxy composite pipes. *Composites Part B: Engineering*, *43*(3), 1130–1138. Elsevier Ltd. Retrieved from http://dx.doi.org/10.1016/j.compositesb.2011.11.006

Fang, Y., Wang, K., Hui, D., Xu, F., Liu, W., Yang, S., & Wang, L. (2017). Monitoring of seawater immersion degradation in glass fibre reinforced polymer composites using quantum dots. *Composites Part B: Engineering*, *112*, 93–102. Elsevier Ltd. Retrieved from http://dx.doi.org/10.1016/j.compositesb.2016.12.043

Feng, G., Guo, S., Zhou, L., Luo, W., Guo, X., Jin, Z., & Zhu, D. (2024). Effects of surface characteristics and alkalinity on the deterioration of BFRP bars and BFRP-SSC interface in seawater environment. *Composites Part B: Engineering*, *268*(May 2023).

Feng, P., Wang, J., Wang, Y., Loughery, D., & Niu, D. (2014). Effects of corrosive environments on properties of pultruded GFRP plates. *Composites Part B: Engineering*, *67*, 427–433. Elsevier Ltd. Retrieved from http://dx.doi.org/10.1016/j.compositesb.2014.08.021

Hawileh, R. A., & Rasheed, H. A. (2017). Thermal analysis of GFRP-reinforced continuous concrete decks subjected to top fire. *International Journal of Advanced Structural Engineering*, *9*(4), 315–323. Springer Berlin Heidelberg.

Heshmati, M., Haghani, R., & Al-Emrani, M. (2016). Effects of moisture on the long-term performance of adhesively bonded FRP/steel joints used in bridges. *Composites Part B: Engineering*, *92*, 447–462. Elsevier Ltd. Retrieved from http://dx.doi.org/10.1016/j.compositesb.2016.02.021

Heshmati, M., Haghani, R., & Al-Emrani, M. (2017). Durability of bonded FRP-to-steel jointsEffects of moisture, de-icing salt solution, temperature and FRP type. *Composites Part B: Engineering*, *119*, 153–167. Elsevier Ltd. Retrieved from http://dx.doi.org/10.1016/j.compositesb.2017.03.049

Hosen, M. A., Johnson Alengaram, U., Jumaat, M. Z., Ramli Sulong, N. H., & Darain, K. M. U. (2017). Glass Fiber Reinforced Polymer (GFRP) Bars for Enhancing the Flexural Performance of RC Beams Using Side-NSM Technique. *Polymers*, *9*(5).

ISO. (2010). ISO 179-1, Plastics - Determination of Charpy impact properties. *ISO - International Standards Organization*, *2010*(1110), 1–11.

Jiang, X., Kolstein, H., Bijlaard, F., & Qiang, X. (2014). Effects of hygrothermal aging on glass-fibre reinforced polymer laminates and adhesive of FRP composite bridge: Moisture diffusion characteristics. *Composites Part A: Applied Science and Manufacturing*, *57*, 49–58. Elsevier Ltd. Retrieved from http://dx.doi.org/10.1016/j.compositesa.2013.11.002

Jiang, X., Kolstein, H., & Bijlaard, F. S. K. (2013). Moisture diffusion in glass-fiber-reinforced polymer composite bridge under hot/wet environment. *Composites Part B: Engineering*, *45*(1), 407–416. Elsevier Ltd. Retrieved from http://dx.doi.org/10.1016/j.compositesb.2012.04.067

Li, S., Zhu, D., Guo, S., Xi, H., Rahman, M. Z., Yi, Y., Fu, B., et al. (2022). Static and dynamic tensile behaviors of BFRP bars embedded in seawater sea sand concrete under marine environment. Composites Part B: *Engineering*, *242*(February).

Liao, D., Gu, T., Liu, J., Chen, S., Zhao, F., Len, S., Dou, J., et al. (2024). Degradation behavior and ageing mechanism of E-glass fiber reinforced epoxy resin composite pipes under accelerated thermal ageing conditions. *Composites Part B: Engineering*, *270*(December 2023).

Liao, D., Gu, T., Yan, J., Yu, Z., Dou, J., Hu, M., Zhao, F., et al. (2024). Study on the effect of multi-factor compound action on long-term tensile performance of GFRP composite pipe and life prediction analysis. *Composite Structures*, *348*(July).

Mansouri, L., Djebbar, A., Khatir, S., & Abdel Wahab, M. (2019). Effect of hygrothermal aging in distilled and saline water on the mechanical behaviour of mixed short fibre/woven composites. *Composite Structures*, *207*(September 2018), 816–825.

Pan, Y., & Yan, D. (2021). Study on the durability of GFRP bars and carbon/glass hybrid fiber reinforced polymer (HFRP) bars aged in alkaline solution. *Composite Structures*, *261*(September 2020).

Sebaey, T. A. (2022). Crashworthiness of GFRP composite tubes after aggressive environmental aging in seawater and soil. *Composite Structures*, *284*(October 2021), 115105. Elsevier Ltd. Retrieved from https://doi.org/10.1016/j.compstruct.2021.115105

Xian, G., Bai, Y., Zhou, P., Wang, J., Li, C., Dong, S., Guo, R., et al. (2024). Long-term properties evolution and life prediction of glass fiber reinforced thermoplastic bending bars exposed in concrete alkaline environment. *Journal of Building Engineering*, *91*(May).

Xian, G., Zhou, P., Bai, Y., Wang, J., Li, C., Dong, S., Guo, R., et al. (2024). Design, preparation and mechanical properties of novel glass fiber reinforced polypropylene bending bars. *Construction and Building Materials*, *429*(May).

Xu, A., Du, Y., Guo, A., Pan, W., & Zhu, D. (2025). Durability and long-term life prediction of hybrid FRP bars embedded in SSC under seawater environment. *Composites Part B: Engineering*, *292*(July 2024).

4th International Civil Engineering & Architecture Conference
17-19 May 2025, Trabzon, Türkiye

FEM and X-FEM analyses of a reinforced concrete flat slab under sudden dynamic impact loading

Ibrahim N. Yahya*[1], Berat F. Soysal[2]

[1]Master student, Çankaya University, Department of Civil Engineering, Ankara, Türkiye
[2]Asst. Prof. Dr., Çankaya University, Department of Civil Engineering, Ankara, Türkiye

Abstract
Civil engineering structures are usually designed to withstand static and earthquake loads. However, the structural elements also need to resist dynamic impact loading as they could be affected by falling objects, causing shock loads. Slabs, in particular, play a vital role in buildings since they transfer loads to other structural elements. This study investigates the nonlinear behavior of a reinforced concrete flat slab under sudden dynamic impact loading. The slab was previously tested in a laboratory using a cylindrical drop hammer, and the experiment was also simulated numerically using the finite element method. In this study, the nonlinear behavior of the reinforced concrete flat slab subjected to impact loading was investigated using both the finite element method (FEM) and the extended finite element method (XFEM). To the best of the author's knowledge, there is no previous research on studying the effect of sudden impact loading on reinforced concrete flat slabs using X-FEM. To this end, a parametric study, together with a mesh sensitivity study, was conducted using both methods. The effect of material properties on the maximum displacement, and failure behavior of the slab was determined. The effect of finite element size was also investigated to address the reliability of numerical models. The FEM and X-FEM results were compared in terms of damage indices and failure modes.

Keywords: Impact Loading; Finite element method; Reinforced concrete flat slab; Extended finite element method

---

1. Introduction
Recently, there has been an increase in interest in designing reinforced concrete structures under the influence of various dynamic loads such as earthquake loads, explosions and shock loads. There has been an increased focus on the impact of shock load on reinforced concrete structures, especially the load resulting from accidental shocks, which can occur due to intentional or unintentional human errors which can lead to a disaster in the targeted structure. Reinforced concrete slabs represent an important part of concrete structures. They are the largest part directly exposed to dead, live and other load types, and one of their main functions is to transfer these loads to other structural elements. Although slabs are among the largest components of a concrete structure in terms of area, they generally have a relatively small thickness; thus, they are considered thinner concrete elements in comparison to columns and beams. Hence, these features make slabs vulnerable to flexural and shear loads, or both, if they are exposed to accidental impact loads directly. Many methods are used to study the effect of shock load on reinforced concrete slabs, some of which are impractical and others very expensive because they require laboratories equipped with multi-purpose measuring devices. The great development in the last three decades, especially in simulation software, has made numerical techniques play a significant role in studying the effect of dynamic loads on the elements of reinforced concrete structures. There has been great interest by researchers in conducting numerical studies of reinforced concrete slabs under the influence of impact loads, mainly using the finite element method, such as Zineddin (2002), Anil et al. (2015), Kumar et al. (2018) and Trivedi & Singh (2013). However, estimating the nonlinear behavior of reinforced concrete slabs under the effect of shock loads is challenging. This study utilizes numerical methods to predict the structural response of reinforced concrete slabs that were tested by Zineddin & Krauthhammer (2007) in a laboratory using a cylindrical drop hammer, when they are subjected to impact loads by using two different approaches; first of the two uses the dynamic/explicit finite element method (FEM) simulation to predict the behavior of the reinforced concrete slabs under the effect of impact load, and the second uses the dynamic/implicit extended finite element method (XFEM) to do the same mission.

* Corresponding author, E-mail: ibraheem200tt@gmail.com

https://doi.org/10.31462/icearc2025_ce_sme_022

2. Theoretical backround

This section discusses fundamental concepts related to impact loading that were adopted in this study. It includes the use of the Finite Element Method (FEM) and the Extended Finite Element Method (XFEM) to simulate reinforced concrete slabs under the effect of impact loads, as well as the Constitutive Model of Concrete.

2.1. Finite element method

Impact analysis on reinforced concrete slabs can be performed using a variety of numerical methodologies. The finite element method (FEM) is one of the most widely used numerical approaches for analyzing engineering problems. Its advancement has enabled the modeling and analysis of a wide range of problems across numerous engineering disciplines. In this study, the FEM program ABAQUS is used. The dynamic equilibrium equations are solved with the ABAQUS/Explicit Solver, which is computationally efficient for studying large models with dynamic responses, as well as for investigating highly discontinuous events or processes. Although the explicit integration rule is simple to solve, it does not provide the same computing efficiency as the implicit dynamics technique (ABAQUS, 2016). In this investigation, the FEM ABAQUS/Explicit code is used to simulate impact loading on reinforced concrete slabs. From the single degree of freedom system shown in Fig. 1, a fundamental dynamics equation can be established. The mass is m, the spring stiffness constant is k, and the damping is denoted by c_v.

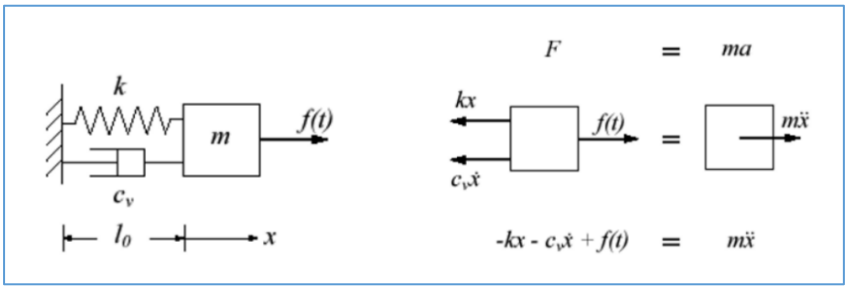

Fig. 1. Single degree of freedom system under dynamic loading (Rehman, 2017)

The equation of motion for this system can be described in Equation (1) by employing the equilibrium of forces and Newton's second law of motion:

$$m\ddot{x}(t) + c_v\dot{x}(t) + kx(t) = f(t) \tag{1}$$

The displacement is expressed as $x = x(t)$. The general governing equation for structural dynamics uses a three-dimensional example to illustrate the same concept. The governing equation for a three-dimensional problem can be derived using the following principle: for any virtual displacement (any small motion that meets the compatibility and essential boundary conditions), the external work done by the applied loads equals the work absorbed by inertial, dissipative, and internal forces. The work balance for an element with volume V and surface area S can be expressed as in Equation (2) (Rehman, 2017):

$$\int_V \delta u^T F dV + \int_V \delta u^T \Phi dS + \sum_{i=1}^{np} \delta u_i^T p_i = \int_V (\delta u^T \rho \ddot{u} + \delta u^T c\dot{u} + \delta\varepsilon^T \sigma)\, dV \tag{2}$$

where F and Φ refer to the surface traction and body forces, respectively, p_i and δu_i represent the concentrated forces and their virtual displacement at np number of points. ρ is the mass density and c is the damping parameter. $\delta\varepsilon$ represents the corresponding strains and δu represents the virtual displacement. This second order differential equation can be solved in ABAQUS using two different methods: the explicit and the implicit procedures. The impact phenomena includes massive deformations, nonlinear material response, and contact boundary conditions, making the implicit approach unattractive and expensive due to the costly inversion of the stiffness matrix, especially in large models, despite its accuracy in dynamic impact loading problem's solutions. However, identical events can be handled more successfully by the explicit technique, which uses the explicit central-difference time integration algorithm in addition to mass matrices with lumped parts. The explicit technique eliminates the requirement for iterations and inversion of tangent stiffness matrix (Rehman, 2017).

2.2. Extended finite element method

The extended finite element method (XFEM) is an expansion of the traditional finite element method that considers discontinuities like cracks as enriched features. It is based on the partition of unity notion. It enables the presence of discontinuities in an element by extending degrees of freedom using particular displacement functions. It does not need the mesh to match the geometry of the discontinuities. It is a very appealing and successful method for simulating the start and propagation of a discrete fracture along an arbitrary, solution-dependent route without the need for remeshing in bulk materials (ABAQUS, 2016). Belytschko et al. (2009) were the first to introduce the extended finite element approach. Based on Melenk & Babuska's (1996) idea of unit partitioning, it is an expansion of the traditional finite element method that makes it simple to include local enrichment functions in the finite element approximation (Belytschko et al., 2009). The extended finite element technique (XFEM) addresses the issues involved with meshing crack surfaces. The presence of discontinuities is ensured by unique enriched functions combined with additional degrees of freedom. However, the finite element framework and its features, such as sparsity and symmetry, are preserved. It allows for the interaction of contact between cracked element surfaces with a small-sliding formulation, facilitates the application of distributed pressure loads to those surfaces, provides outputs for certain surface variables on cracked elements, and incorporates both material and geometric nonlinearity. The XFEM is applicable to first-order stress/displacement solid continuum elements, first-order displacement/pore pressure solid continuum elements, and second-order stress/displacement tetrahedral elements (ABAQUS, 2016).

2.3. Concrete constitutive model

Reinforced concrete is recognized for its non-linear behavior, which originates from the non-linear stress-strain relationship of ordinary concrete. Concrete numerical modeling is classified into two categories: elasticity and plasticity-based models. Elasticity-based models assume that total stress varies with total strain or with loading or reloading stress histories. Plasticity theory was developed to explain the behavior of ductile materials such as metals. A conventional plasticity model has three basic conditions: a yield surface, a hardening rule, and a flow rule (Tahmasebinia, 2011). In ABAQUS software, three forms of cracking models exist to account for nonlinear behavior of concrete. Smeared Crack Concrete Model is the first of them. This technique is intended for use in circumstances where small confinement pressures cause concrete to undergo mostly monotonic strain. It has a distinct crack detection method in addition to an isotropic hardening yield surface. The second model is the Brittle Crack Concrete Model. Although concrete is quasi-brittle, it is frequently classified as brittle for simplicity. The brittle crack concrete model is a theoretical and computational framework for investigating concrete structures under stress, with a focus on fracture generation and propagation. The third model is Concrete Damage Plasticity Model, CDP. It is the most widely used and precise criterion for studying nonlinear behavior of concrete. This model assumes two basic failure mechanisms: tensile cracking and compressive crushing (ABAQUS, 2016). In this study, Concrete Damage Plasticity model is employed.

2.3.1 Concrete damage plasticity model (CDP)

The concrete damage plasticity material model (CDP) is a constitutive model that is based on both plasticity theory and damage mechanics theory. CDP is developed at the VTT Technical Research Center of Finland (Rehman, 2017). This material model is frequently used to solve geotechnical problems because it precisely describes the mechanical behavior of concrete (Rakić et al., 2021). Concrete damage plasticity (CDP) provides a fundamental technique to describe concrete in various kinds of structural elements, including slabs, beams, shells, and trusses. It is a continuum damage model for concrete that employs plasticity to represent the inelastic behavior of concrete. It use isotropic damaged elasticity alongside with isotropic tensile and compressive plasticity. It considers concrete failures in two ways: tension-based cracking and compression-based crushing. Although it can be used for plain concrete analysis, its major function is to analyze reinforced concrete structures. When modeling concrete, it can be used to simulate dynamic, cyclic, and/or monotonic loads with low confining pressure (Esfahani et al., 2017). As shown in Fig. 2(a), under uniaxial compression, the material is linearly elastic until it hits the initial yielding point, σ_{c0}. After then, the material undergoes strain hardening until it reaches its ultimate limit σ_{cu}, where strain softening occurs. The damage variable, d_c, is a function of plastic stresses and includes the deterioration of the material's stiffness in the stress softening zone. If the material is unloaded in the stress softening zone, the unloading slope decreases as it exceeds the maximum stress since the damage variable d_c rises up from zero (undamaged material) to a maximum value of one (fully damaged material). ε_c^{el} and $\tilde{\varepsilon}_c^{pl}$ represent equivalent elastic and plastic strain in compression, respectively. In uniaxial tension (Fig. 2b), the stress-strain relationship is linear elastic until it reaches the maximum stress σ_{t0}. This failure stress indicates the beginning of cracking in the material. After this point, the material softens, resulting in the production of microcracks. The damage variable, d_t, represents deterioration in tensile stiffness. ε_t^{el} and $\tilde{\varepsilon}_t^{pl}$ are elastic and equivalent plastic strains in tension, respectively (ABAQUS, 2016).

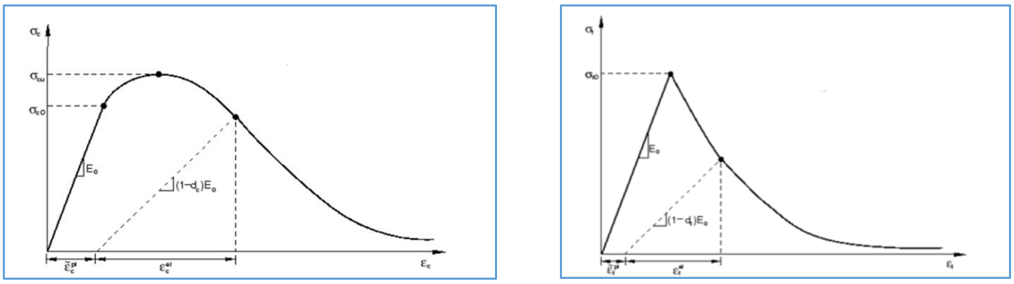

(a) (b)

Fig. 2. Concrete Response in uniaxial loading in compression (a) and tension (b) (ABAQUS, 2016)

The CDP model is defined in ABAQUS by specifying three material parameters and characterizing the inelastic compressive and tensile behavior as a collection of point pairs. Inelastic compressive behavior is characterized by a stress-strain pair of points. However, tensile behavior can also be characterized as a stress-fracture energy or stress-cracking displacement relationship in the form of point data. These parameters are presented briefly in the next section.

2.3.1.1 Concrete damage plasticity parameters

A set of required parameters are specified in order to use the Concrete Damage Plasticity (CDP) Model in ABAQUS. The CDP parameters include three main parameters. First of them are plasticity flow parameters which include: dilation angle, eccentricity, ratio of initial equi-biaxial compressive yield stress to initial uni-axial compressive yield stress and ratio of the second stress invariant on the tensile meridian. Compressive behavior parameters include compressive yield stress, compressive inelastic strain, and compressive damage parameter. Tensile behavior parameters are tensile yield stress, tensile cracking strain, and tensile damage parameter (ABAQUS, 2016).

Plasticity flow parameters are typically determined and calibrated experimentally. The dilation angle, ψ, is defined as the ratio of volume strain to shear strain. The dilation angle for concrete is typically 20 to 40 (Esfahani et al., 2017) or 30 to 40 (Sledziewski, 2017), affecting its ductility. It has been determined that the ideal dilation angle for characterizing concrete behavior in both compression and tension situations is ψ = 31° (ABAQUS, 2016). The eccentricity parameter, ε, is defined as the ratio of tensile strength to compressive strength. The recommended value for the CDP model is ε = 0.1 (Sledziewski, 2017). fb_0/fc_0 parameter is the initial equi-biaxial compressive yield stress, fb_0, divided by the initial uniaxial compressive yield stress, fc_0. The default value equals 1.16 (ABAQUS, 2016). K_c is the ratio of the second stress invariant on the tensile meridian. This parameter is generally set between 0.667 and 1, with some academics suggesting a maximum value of 0.8. The default value in ABAQUS is 0.667 (ABAQUS, 2016). In ABAQUS/Standard and Explicit analyses, the viscosity parameter is employed to regularize the concrete constitutive equations using visco-plasticity. This parameter is ignored in ABAQUS/Explicit. Hence, the default value is zero (ABAQUS, 2016). The inelastic hardening strain in compression is calculated as follows (Equation 3):

$$\varepsilon_{ic} = \varepsilon_c - \frac{\sigma_c}{E_c} \tag{3}$$

where ε_{ic} is inelastic concrete compressive strain, ε_c is nominal concrete compressive strain, σ_c is nominal concrete compressive strength, and E_c is the elasticity modulus of concrete.

The cracking strain is expressed by Equation (4).

$$\varepsilon_{it} = \varepsilon_t - \frac{\sigma_t}{E_c} \tag{4}$$

where ε_{it} is concrete cracking strain, ε_t is nominal concrete tensile strain, σ_t is nominal concrete tensile strength, and E_c is the elasticity modulus of concrete.

The unloading curve slope in the compressive region (Fig. 1a) is determined by the inelastic hardening strain during compression (d_c) (Esfahani et al., 2017). The compressive damage parameter is expressed by the following equation (Equation 5):

$$d_c = 1 - \frac{\sigma_c}{f_c'} \tag{5}$$

where d_c is compressive damage parameter, σ_c is nominal concrete compressive strength, and f_c' is compressive strength of concrete.

The tensile damage parameter (d_t) is expressed by Equation (6):

$$d_t = 1 - \frac{\sigma_t}{f_t} \tag{6}$$

where d_t is tensile damage parameter, σ_t is nominal concrete tensile strength and f_t is concrete tensile strength.

Table 1 shows computed concrete damaged plasticity parameters of the concrete material of compressive strength equals to 35 MPa.

Table 1. CDP Parameters for concrete with 35 MPa compressive strength

Compressive Stress (MPa)	Compressive Strain	Inelastic Compressive Strain	Compressive Damage Parameter
17.5	0.00059	0	0
22.5	0.00080	0.00005	0
27.5	0.00107	0.00010	0
32.5	0.00147	0.00030	0
35	0.002	0.00103	0
33	0.00248	0.00129	0.05714
31	0.00268	0.00156	0.11429
29	0.00282	0.00185	0.17143
27	0.00296	0.00199	0.22857
25	0.00307	0.00217	0.28571
23	0.00317	0.00234	0.34286
21	0.00326	0.00251	0.40000
19	0.00335	0.00267	0.45714
17	0.00343	0.00282	0.51429
15	0.00351	0.00297	0.57143
13	0.00359	0.00312	0.62857
11	0.00366	0.00326	0.68571
9	0.00372	0.00340	0.74286
7	0.00379	0.00354	0.80000
Tensile Stress (MPa)	Tensile Strain	Cracking Strain	Tensile Damage Parameter
3.313	0.00012	0	0.00000
2.208666667	0.00036	0.00028	0.33333
1.242375	0.00069	0.00064	0.62500
0.552166667	0.00125	0.00123	0.83333

3. Nonlinear behavior of reinforced concrete slab under impact loading

This section presents the numerical investigation of the nonlinear behavior of reinforced concrete slabs under the effect of impact loadings. The experimental study conducted by Zineddin & Krauthammer (2007) was simulated using both the FEM-Explicit and XFEM-Implicit codes available in ABAQUS software. The simulation results were compared to the experimental results by means of the displacement of the midpoint of the slab bottom, as well as identifying the failure modes.

3.1 Reinforced concrete slab and impact system description

Zineddin & Krauthammer (2007) used a drop hammer with a weight of 2608kg and a diameter of 250mm to strike RC slabs measuring 3.353m by 1.524m and 90mm thick. The hammer was dropped at predetermined heights of 152mm, 305mm, and 610mm in the center of the slab. Reinforcing bars with a diameter of 10mm were placed 152mm apart throughout both spans. The position of the reinforcement mesh within the slab varied. In the experiment, three slabs were reinforced with two steel meshes located 25mm from both faces, whereas the remaining three had a single steel mesh located in the slab center, 45mm from both faces. Fig. 3 depicts the slab's reinforcing system.

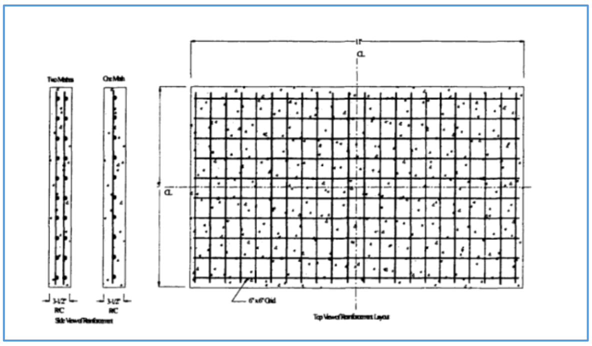

Fig. 3. Reinforcement Arrangement (Zineddin, 2002)

Zineddin & Krauthammer (2007) mentioned that the slab support can best be described as somewhere between simple and fixed support. The slab was connected on all four sides with two rows of 25 mm bolts through steel channels and a strong test frame supported by steel stands as shown in Fig. 4(a). Therefore, the unsupported slab area measured 914 x 2,743mm (**Hata! Başvuru kaynağı bulunamadı.**b).

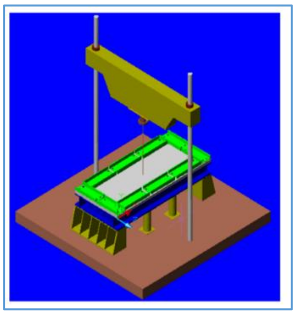

(a)

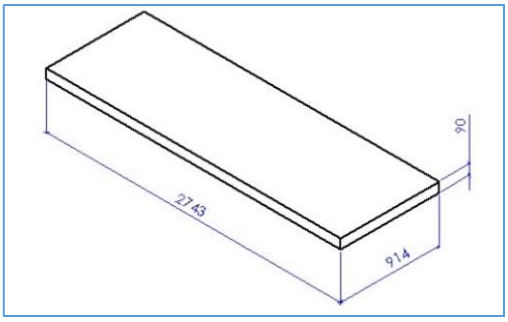

(b)

Fig. 4. (a) Experimental impact systems (Zineddin & Krauthammer 2007), (b) the unsupported slab area

3.2 Numerical impact loading setup in ABAQUS

The numerical impact loading system consists of three main components. First, a 3D deformable extruded solid is created to represent the concrete slab, which has dimensions of 2743 mm x 914 mm x 90 mm. Second, two reinforcing steel meshes, each with a square pattern of 152 mm x 152 mm, are included. These meshes contain both long and short reinforcing steel elements with a diameter of 10 mm, and each mesh is positioned beneath a concrete cover of 25 mm on both sides of the slab. The steel reinforcement elements are modeled in ABAQUS as 3D deformable wire structures. Finally, a rigid hemispherical shell with a diameter of 250 mm is used to simulate the falling body, positioned at the midpoint of the slab. **Hata! Başvuru kaynağı bulunamadı.** shows the assembled impact loading system.

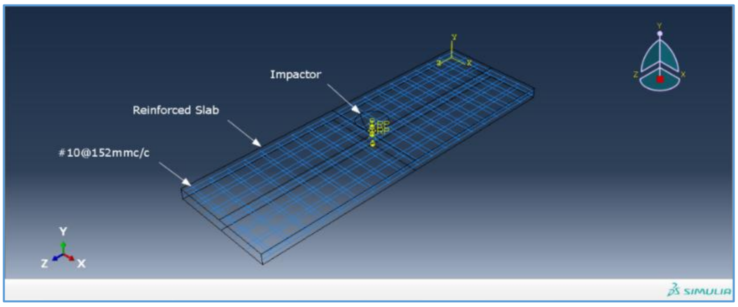

Fig. 5. Numerical impact loading setup

The elastic material properties of concrete and steel employed in the experimental investigation of Zineddin & Krauthammer (2007), as cited by Trivedi & Singh (2013), are as follows: concrete Poisson's ratio (v) equals to 0.17, concrete density equals to 2400 kg/m³, concrete cracking strain equals to 0.002, steel Poisson's ratio (v) equals to 0.33, steel density equals to 7850 kg/m³, steel modulus of elasticity equals to 200 GPa and steel yield strength equals to 500 MPa. As will be explained later, the concrete compressive strength was assumed as 35, 45, 55, and 65MPa. Accordingly, the elasticity modulus and tensile strength were calculated based on the assumed concrete compressive strength using the relationships per ACI318M-14 building design code. Accordingly, the parameters in the CDP model were modified based on the assumed concrete compressive strength.

The slab is assumed to be a fixed supported slab, as can be seen in **Hata! Başvuru kaynağı bulunamadı.**. The impactor considered striking the slab vertically at the slab's upper mid-point as a free-falling body of 2608 kg from a vertical distance of 152mm.

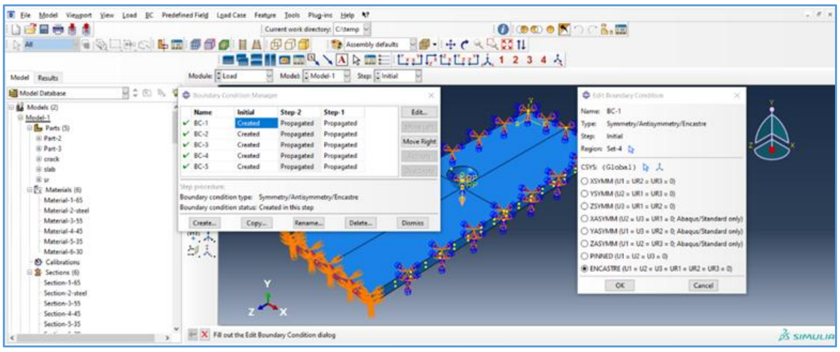

Fig. 6. Fixed supported RC slab

The interaction between the embedded reinforcement and the concrete slab is defined using embedded region constraint property available in ABAQUS. This characteristic enables the steel mesh to behave as reinforcement for the concrete slab. The slab element type is defined as an 8-node linear brick, reduced integration with hourglass control C3D8R available in ABAQUS element library. Steel reinforcement is specified as T3D2, a 2-node linear 3-D truss element type employed for defining rebar. For the rigid impactor, the element type is R3D4, which is a 4-node 3-D bilinear rigid quadrilateral.

To simulate the reinforced concrete slab under the effect of impact loading using the XFEM, the dynamic/implicit code, which is available in ABAQUS/STANDARD, has been used. The same reinforced concrete slab that was used in the FEM-Dynamic/Explicit simulation is utilized. The Dynamic/Implicit-XFEM simulation was implemented by creating an extruded deformable shell part with dimension of 50x25mm, as shown in **Hata! Başvuru kaynağı bulunamadı.**(a)**Hata! Başvuru kaynağı bulunamadı.** below. This part represents the crack that will propagate through the targeted reinforced concrete slab. The crack is embedded in the upper concrete cover of the reinforced concrete slab near the support, as shown in Fig. 7(b).

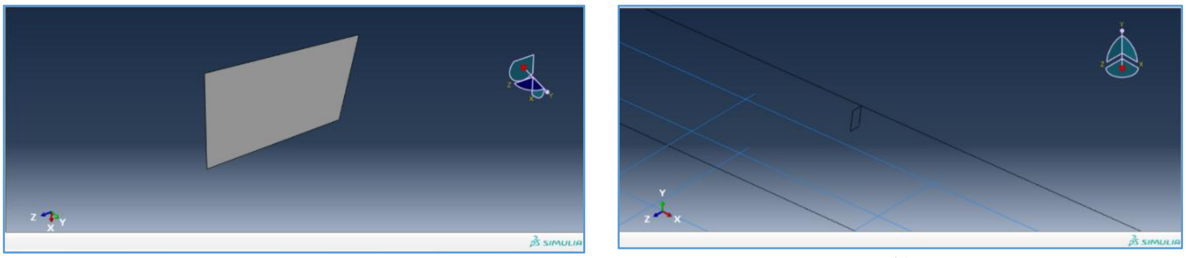

(a) (b)

Fig. 7. (a) Crack model, (b) Crack location inside the slab

After identifying the cracks, parametric and mesh sensitivity studies utilizing XFEM were conducted, similar to the parametric and mesh sensitivity studies of FEM. The displacement results obtained from these studies were compared with both the experimental data and the FEM results.

3.3 Parametric and mesh sensitivity studies using fEM

The concrete compressive strength used in the experimental study of Zineddin & Krauthammer (2007) was not known because they could not accurately determine the compressive strength of the concrete. However, they mentioned that it was either 28MPa or 41MPa. In contrast, the value of compressive strength adopted by Trivedi & Singh (2013) was 37.5MPa. Due to the range of reported compressive strengths, a parametric study has been conducted, assuming concrete compressive strengths of 35, 45, 55, and 65MPa. Accordingly, the elasticity modulus, tensile strengths and the parameters in the CDP model were modified based on the assumed concrete compressive strength.

As is well known in the finite element analysis approach, the mesh sizes play a vital role in the simulation results. Therefore, a mesh sensitivity study was also conducted to study the influence of changes in mesh sizes on the displacement values. To this end, three different models with mesh sizes of 15x15x15mm, 18x18x18mm and 22.5x22.5x22.5mm were created. For each model, concrete compressive strengths varied from 35MPa to 65MPa, as mentioned above. Hence, in total, 12 nonlinear dynamic simulations were conducted. All simulations were run up to 30 milliseconds, which is the impact test time period adopted by Zineddin (2002) in his numerical study.

The results of the slab displacement at the center are shown in Table 2. The table also includes the relative percent difference ($\frac{Disp_{Exp}-Disp_{FEM}}{Disp_{Exp}} \times 100$) compared to the experimental value of 42 mm. Therefore, the negative values in the table indicate that the displacements are overestimated, and vice versa. It is noted from the table that the displacement values ranged from 41.6 mm to 42.5 mm, indicating that FEM simulations estimated the results within 1% of the experimental results. The displacement results obtained using concrete with a compressive strength of 45MPa were closer to the experimental displacement results than those obtained using concrete with compressive strengths of 35,55 and 65MPa. The relative difference across the mesh sizes was low. For the coarsest mesh, the displacements were overestimated, and with the decrease in the element size, displacements were estimated closer to the experimental value. Therefore, it can be deduced that the chosen mesh sizes are appropriate for simulation and the results are not dependent on the element size. It can be concluded from the parametric and mesh sensitivity studies that the FEM simulations can be used for obtaining the displacement values, as they estimated the values within -0.24 to 0.71% of the experimental results for $f_c' = 45\ MPa$.

Table 2. Displacement results of parametric and mesh sensitivity studies of FEM simulations

Concrete f_c'*	Mesh Size (mm)	Displacement (mm)	Relative Difference (%)
	15x15x15	41.6	0.95
$f_c' = 35\ MPa$	18x18x18	41.8	0.48
	22.5x22.5x22.5	42.3	-0.71
	15x15x15	41.7	0.71
$f_c' = 45\ MPa$	18x18x18	41.8	0.48
	22.5x22.5x22.5	42.1	-0.24
	15x15x15	41.8	0.48
$f_c' = 55\ MPa$	18x18x18	41.7	0.71
	22.5x22.5x22.5	42.3	-0.71
	15x15x15	41.8	0.48
$f_c' = 65\ MPa$	18x18x18	41.9	0.24
	22.5x22.5x22.5	42.5	-1.19

*f_c': Concrete Compressive Strength

Fig. 8 shows the maximum displacement time histories resulting from the impact test of the slab with a compressive strength of 45MPa for the three mesh sizes. It clearly shows how varying mesh sizes affect displacement results. The displacement time history curves of the slab with all three mesh sizes are almost the same until 30 milliseconds, which represents the maximum time period of the impact test adopted by Zineddin (2002). After this time, it is clear that the displacements increased with time for all mesh sizes, until the displacement curve remained constant over a certain time. For example, for the slab with a mesh size of 22.5x22.5x22.5 mm, the displacement curve began to remain constant at 0.3 second, but the displacement curves began to remain constant at 0.34 and 0.4 seconds for the slabs with mesh sizes of 18x18x18 and 15x15x15 mm, respectively.

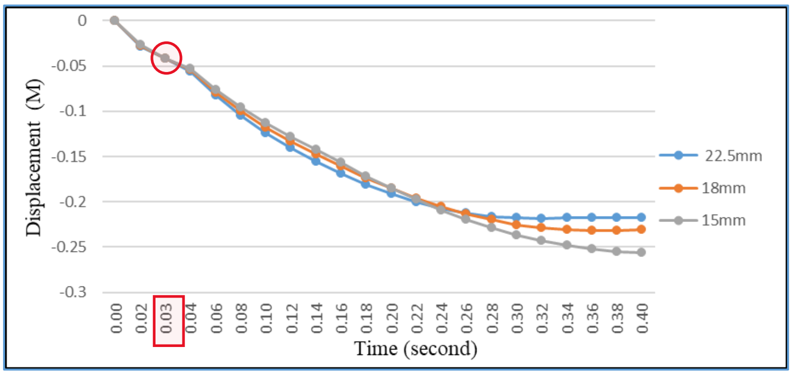

Fig. 8. Maximum displacement time history of the slab with fc'= 45MPa

Hata! Başvuru kaynağı bulunamadı.(a) and (b) represent the compression and tension damage, respectively, resulted from the impact loading to the RC slab with a 15mm element size and a compressive strength of 45 MPa. Accordingly, localized compression damage was observed at the center of the slab (**Hata! Başvuru kaynağı bulunamadı.**a). In contrast, damage in tension was distributed, with additional damage observed at the supports (**Hata! Başvuru kaynağı bulunamadı.**b).

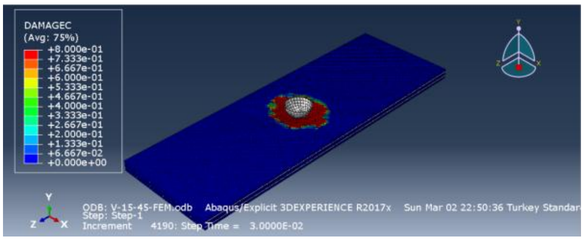

(a) Compression damage

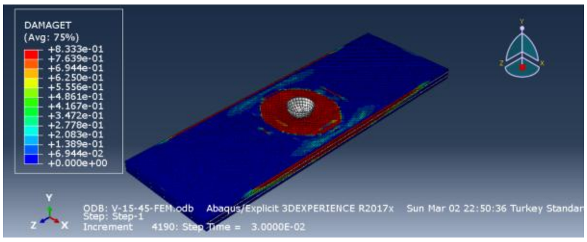

(b) Tension damage

Fig. 9. Compression and tension damage of the RC slab

The punching shear failure mode, resulting from the numerical impact loading simulation of the slab with a 15 mm mesh size and a compressive strength of 45 MPa, is illustrated in **Hata! Başvuru kaynağı bulunamadı.**(b). **Hata! Başvuru kaynağı bulunamadı.**(c) presents the results for the 22.5 mm mesh size. When these are compared to **Hata! Başvuru kaynağı bulunamadı.**(a), which shows the punching failure of the reinforced concrete slab from the experiment conducted by Zineddin & Krauthammer (2007), similarities can be observed in the punching shear failure across these scenarios. Notably, it appears that a smaller mesh size in the reinforced concrete slab leads to a closer resemblance in the shape of the punching failure. Additionally, scabbing of the reinforced concrete slab is evident in **Hata! Başvuru kaynağı bulunamadı.**(b) and 10(c). **Hata! Başvuru kaynağı bulunamadı.**(d) highlights that steel yielding occurred in the impact zone beneath the center of the reinforced concrete slab. This steel yielding shows similarities when compared to the experimental results depicted in Fig. 10(a). Thus, it can be concluded that the finite element method (FEM) simulation effectively captured the punching shear failure mode, scabbing, and steel yielding of the reinforced concrete slab.


(a) Experimental result
(Zineddin & Krauthammer, 2007)

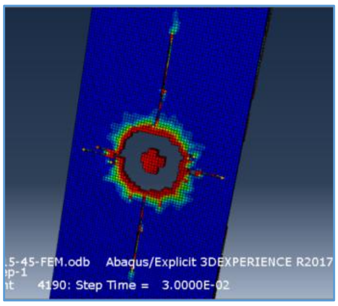
(b) Punching shear failure mode and scabbing, 15mm mesh size

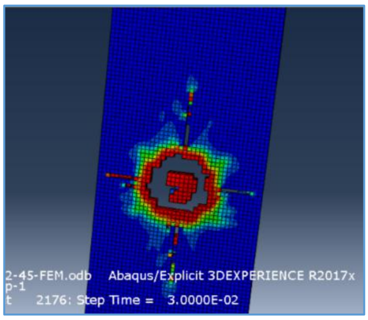
(c) Punching shear failure mode and scabbing, 22.5mm mesh size

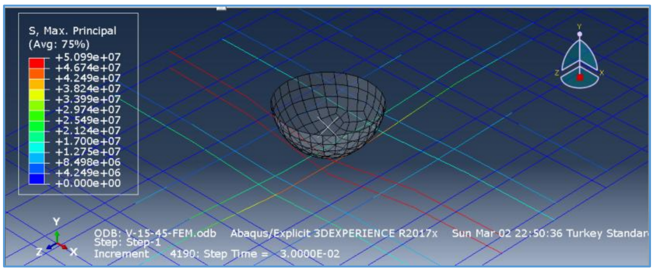

(d) Steel yielding, 15mm mesh size

Fig. 10. Experimental result, punching, scabbing and steel yielding failure mode

3.4 Parametric and mesh sensitivity studies using XFEM

For parametric and mesh sensitivity studies using XFEM, three different mesh sizes were employed for the reinforced concrete slab: 15x15x15mm, 18x18x18mm and 22.5x22.5x22.5mm. The compressive strengths of the concrete were assumed to be 35,45,55 and 65 MPa, for the parametric simulations. In total, 12 nonlinear dynamic simulations were carried out, and the displacement results were compared with the experimental displacement result, which was equal to 42mm, to validate the effectiveness of XFEM for the impact simulation (Table 3). Additionally, the XFEM results were compared to the FEM results in the same table. The relative percent differences with respect to the experiment and FEM were computed with $\frac{Disp_{Exp}-Disp_{XFEM}}{Disp_{Exp}} \times 100$ and $\frac{Disp_{FEM}-Disp_{XFEM}}{Disp_{FEM}} \times 100$, respectively. Hence, the negative values in the table indicate that the displacements are overestimated, and vice versa.

The data presented in the table shows that displacement values ranged from 41.3 mm to 43 mm. This indicates that the XFEM simulations estimated results within a range of 1.67% to -2.38% compared to the experimental results. In alignment with the FEM solution, the displacement results from concrete with a compressive strength of 45 MPa were closer to the experimental values than those derived from concrete with compressive strengths of 35, 55, and 65 MPa. In this case, for the finest mesh, the relative difference compared to the experiment was only 0.24%. In general, as the element size decreased, the estimated displacements were more aligned with the experimental observation. Coarse meshes tended to overestimate the displacements, while finer meshes provided estimates much closer to the experimental result. Overall, the XFEM results were conservative, showing higher displacements than those obtained through FEM, with a greater deviation in XFEM compared to FEM. Nonetheless, the parametric and mesh sensitivity studies indicate that XFEM effectively simulated the experimental results, particularly for concrete with a compressive strength of 45 MPa.

Table 3. Displacement results of parametric and mesh sensitivity studies of XFEM simulations

Concrete f_c'*	Mesh Size (mm)	Displacement (mm)	Relative Difference (%)	Relative Difference Wrt FEM(%)
$f_c' = 35\ MPa$	15x15x15	41.3	1.67	0.72
	18x18x18	41.7	0.71	0.24
	22.5x22.5x22.5	42.9	-2.14	-1.42
$f_c' = 45\ MPa$	15x15x15	41.9	0.24	-0.48
	18x18x18	42.3	-0.71	-1.20
	22.5x22.5x22.5	42.6	-1.43	-1.19
$f_c' = 55\ MPa$	15x15x15	42.6	-1.43	-1.91
	18x18x18	42.7	-1.67	-2.40
	22.5x22.5x22.5	42.7	-1.67	-.095
$f_c' = 65\ MPa$	15x15x15	42.8	-1.9	-2.39
	18x18x18	43	-2.38	-2.63
	22.5x22.5x22.5	42.8	-1.9	-0.71

Fig. 11 shows the maximum displacement time history resulting from the impact test of the slab with a compressive strength of 45 MPa. Similar to the FEM results, the impact of varying mesh sizes on the displacement results up to 30 miliseconds was minimal.

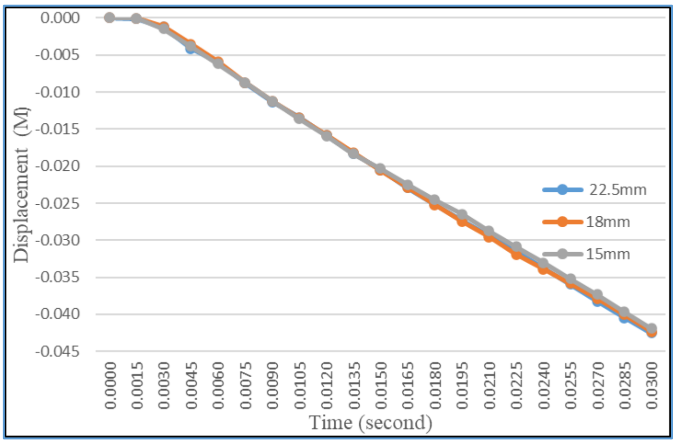

Fig. 11. Maximum displacement time history of a slab with fc'= 45MPa and a mesh size of 15x15x15mm

Fig. 12. Failure modes of XFEM simulation
shows the compression and tension damages, perforation and steel yielding modes resulted from conducting XFEM impact loading simulation on the reinforced concrete slab with a 15x15x15mm mesh size and a compressive strength of 45MPa.

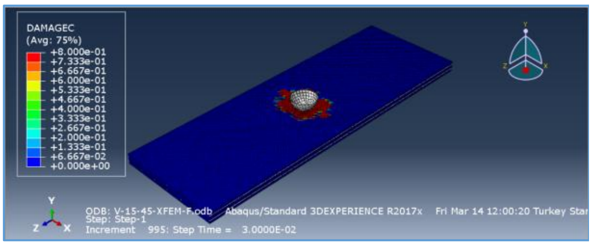

(a) Compression damage

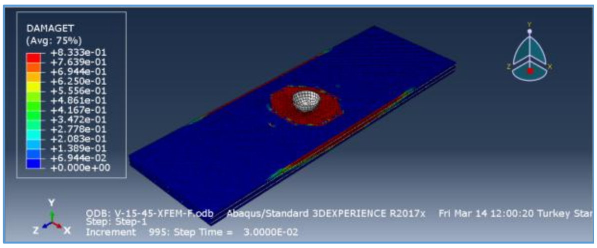

(b) Tension damage

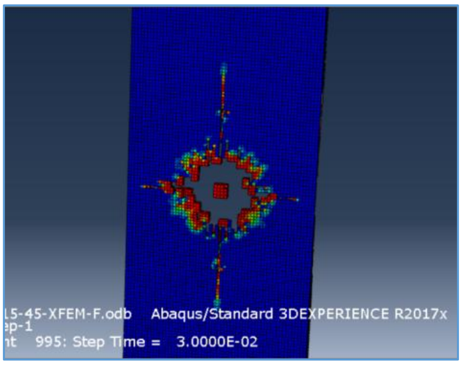

(c) Perforation failure mode

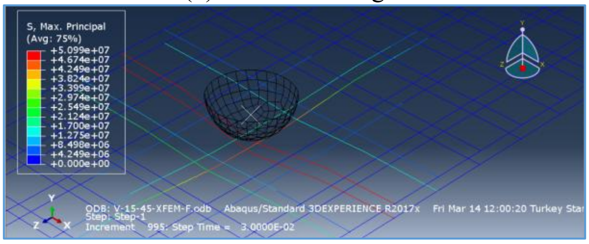

(d) Steel yielding mode

Fig. 12. Failure modes of XFEM simulation

Comparing Figs. 9(a) and 12(a), it is clear that there is no significant difference between the compression damage failure modes resulting from FEM and XFEM simulations. However, the comparison between **Hata! Başvuru kaynağı bulunamadı.**(b) and 12(b) reveal a noticeable difference in the tensile damage mode observed in the targeted area, as well as the damage at the supports. The XFEM results provided a more realistic depiction of the tensile damage mode; on the other hand, in the FEM simulation, the tensile damage was smeared. From Fig. 12. Failure modes of XFEM simulation
(c), it can be noticed that the perforation failure mode obtained by implementing dynamic implicit XFEM impact loading is somewhat similar to the perforation failure obtained by performing dynamic explicit FEM shown in Fig. 10(b), except for the slight difference in the scabbed concrete. The steel yielding modes were similar for FEM (**Hata! Başvuru kaynağı bulunamadı.**d) and XFEM simulations (Fig. 12. Failure modes of XFEM simulation
d).

5. Conclusion

The nonlinear behavior of reinforced concrete slabs under impact loading was investigated by modeling the reinforced concrete slab from the experimental study conducted by Zineddin & Krauthammer (2007) using ABAQUS/CAE 2017. Three different mesh sizes (15x15x15 mm, 18x18x18 mm, and 22.5x22.5x22.5 mm) and four different concrete compressive strengths of 35, 45, 55, and 65 MPa were employed to conduct mesh sensitivity and parametric studies, respectively. This was achieved using both the Dynamic/Explicit-FEM and Dynamic/Implicit-XFEM codes available in ABAQUS. The results were evaluated in terms of maximum displacement, compression, tension, perforation failure modes, and steel yielding.

The following conclusions were drawn from this study:

- The simulation results indicated that the Dynamic/Explicit FEM approximated the displacement obtained experimentally with an error of 0.71%. In contrast, the displacement value estimated using Dynamic/Implicit-XFEM showed an error of only 0.24%. Therefore, the XFEM solution provided results that were closer to the experimental measurements.
- The perforation failure mode and steel yielding modes were approximately similar for Dynamic/Explicit-FEM and the Dynamic/Implicit-XFEM. Furthermore, the deformation and punching failure modes of the reinforced concrete slab in both numerical methods were similar to the punching failure mode obtained

from the experimental study. The compression damage was identical in both FEM and XFEM. However, while the tensile damage was smeared in the FEM simulation, the XFEM result provided a more realistic representation of tensile damage.

- Close agreements were found in the failure modes when comparing the results of the two numerical studies with the experimental study. Additionally, the displacement results differed by less than 1% from the experimental observations, indicating a strong alignment between the numerical and experimental studies. When examining the tensile damage modes, the XFEM model demonstrated an advantage by producing less smeared tensile damage compared to the results from the FEM model.

References

ABAQUS. (2016). *ABAQUS/CAE User's Guide,* Retrieved from http://130.149.89.49:2080/v2016/books/key/default.htm?startat=ch03abk31.html

Anil, Ö., Kantar, E. & Yılmaz, M.C. (2015). Low velocity impact behavior of RC slabs with different support types. *Construction and Building Materials*, *93*, 1078-1088, Retrieved from https: doi.org/10.1016/j.conbuildmat.2015.05.039.

ACI Committee 318. (2015). *Building Code Requirements for Structural Concrete: (ACI318M-14); and Commentary (ACI318RM-14),* American Concrete Institute.

Belytschko, T., Gracie, R. & Ventura, G. (2009). A Review of Extended/Generalized Finite Element Methods for Material Modelling. *Modelling and Simulation In Materials Science and Engineering*, *17*, 043001.

Esfahani, M.H., Vaghei, R., Hejazi, F., & Karimzadah, K. (2017). Simplified Damage Plasticity Model for Concrete. *Structural Engineering International*, *27*(1), 68-78.

Kumar, V., Iqbal, M.A & Mittal, A.K. (2018). Study of induced prestress on deformation and energy absorption characteristics of concrete slabs under drop impact loading, *Construction and Building Materials, 188*, 656-675.

Rakić, D.M, Bodić, A.S, Milivojević, N.J., Dunić, V.L. & Živković, M.M. (2021). Concrete Damage Plasticity Material Model Parameters Identification. *Journal of the Serbian Society for Computational Mechanics,15*(2), 111-122.

Rehman, S.U. (2017). *Finite Element Analysis of Impact-perforated Reinforced Concrete Slabs*, (Master Thesis), Aalto University Department of Civil Engineering, Espoo, Finland.

Sledziewski, K. (2017). Selection of appropriate concrete model in numerical calculation, *ITM Web of Conferences, 15,* 1-9, Lublin.

Tahmasebinia, F. (2011). *Reinforced Concrete Slabs Under Impact Loading*, (Master's Thesis), Faculty of Engineering, University of Wollongong.

Trivedi, N. & Singh, R.K. (2013). Prediction of impact induced failure modes in reinforced concrete slabs through nonlinear transient dynamic finite element simulation. *Annals of Nuclear Energy*, *56*, 109-121.

Zineddin, M. & Krauthammer, T. (2007). Dynamic response and behavior of reinforced concrete slabs under impact loading. *International Journal of Impact Engineering, 34*(9), 1517-1534.

Zineddin, M. (2002). *Behavior of Structural Concrete Slabs under Localized Impact,* (Master Thesis), Civil and Environmental Engineering Department, The Pennsylvania State University, Pennsylvania.

4th International Civil Engineering & Architecture Conference
17-19 May 2025, Trabzon, Türkiye

The distelled water absorption behavior of two types of resin polymers used in the manufacturing of structures

Mohammed I. Aissaoui*[1], Djaber Bouhafara[1], Younes Menail[2], Farouk Mesrafet[2]

[1] National Higher School of Technology and Engineering, Laboratory of Energy Systems Technologies (LTSE), 23005 Annaba, Algeria.
[2] BadjiMokhtar University, Department of Mechanical Engineering, LR3MI,Box 12, 23052SidiAmmar Annaba, Algeria

Abstract. The civil industry is using many types of alternative Polymer materials in the manufacture of bulding structure.However,during application polyester are exposed to marine environments In various constructions used in rivers and lakes Which leads to a change in mechanical properties. Here, the mechanical properties of polyester in composite materials and the changes in distillid water absorption over time due to exposure to this environments were studied This exposure is simulated by diving under controlled laboratory conditions in ambient temperatures. The organization of this paper is as follows: Firstly, the phenomenon of water ageings and absorption ,this section discussed how the marine environment affects the polymers and the absorption phenomenon in composites, Secondly, the effect of water conditions on the mechanical properties of different types of polymers is discussed .Two types of resin, polyester and c-orthocryl, were exposed to water (distilled water) in this study. Specimens were immersed in this environment at room temperature for one month in order to perform an absorption test. Two polymers' absorption of water was recorded and contrasted.Although the polyester's weight gain from absorption was minimal, it differed from that of the other C-orthocryl The mechanical properties of the composites were reduced by the absorption of simulated water.Because of the notable differences in absorption between the polyester and C-orthocryl resins, it may not be feasible to use C-orthocryl as a replacement for polyester in the naval structure sector.

Keywords: distelled water; Absorption ; Composites ; civil structure ; Polymer.

1.Introduction

The utilisation of resin-based polymers in structural contexts has markedly increased owing to their lightweight characteristics, superior strength-to-weight ratios, and corrosion resistance. Thermosetting resins, including c-orthocryl and unsaturated polyester, are often utilised in the production of structural components throughout aerospace, marine, and civil engineering sectors. Nonetheless, a pivotal aspect influencing the long-term efficacy and resilience of these polymers is their interaction with moisture, namely through the absorption of distilled water in humid or submerged environments (Cabral-Fonseca, Correia, Rodrigues, & Branco, 2012; Cerbu, 2010; Fang et al., 2017; Heshmati, Haghani, & Al-Emrani, 2017; Mansouri, Djebbar, Khatir, & Abdel Wahab, 2019).

Water absorption in polymeric materials can result in plasticization, hydrolysis, and microcracking, eventually undermining mechanical and dimensional stability (Sarkar & Young, 2001). The degree and manner of water absorption are affected by the resin's chemical composition, crosslink density, and level of hydrophilicity (Ghasemi et al., 2012). Epoxy resins, recognised for their superior adhesive and mechanical qualities, can absorb greater moisture than polyester resins owing to the presence of polar hydroxyl and ether groups (Wang et al., 2006).

Several research have looked at how these resins absorb moisture. Though variations can happen during extended exposures or at higher temperatures, Kinloch et al. (1983) found that at early stages water diffusion into epoxy systems is usually Fickian. By contrast, while less hydrophilic, polyester resins show hydrolytic breakdown during long-term immersion, especially when not well cured (Djazeb et al., 2017).

Environmental durability is crucial in structural applications; hence, knowing the distilled water absorption behaviour of resin systems is vital for guaranteeing material dependability. This work compares the water

*Corresponding author E-mail: m.aissaoui@etu.ensti-annaba.dz

https://doi.org/10.31462/icearc2025_ce_sme_034

absorption properties of two commonly used resins—epoxy and polyester—when submerged in distilled water, examining the rate, saturation point, and consequent material deterioration.

2. Experimental

2.1. Materials and Preparations of composites

A standard unsaturated polyester and c-orthocryl resins; the materials was provided by local company. An Infusion molding method was used in the fabrication of the polymers laminates. The material was prepared from the unsaturated polyester resin and c-orthocryl resin. The catalyst was added to the polymer and the batch was stirred before pour into a mold with nominal size 1m^2 used . Then, the polymers matrix was pour onto the mold.the specimen was removed from the mold and cured for 24 hours at room temperature to ensure the specimen was hard and dry enough for the cutting process.

2.2. Immersion process

The polyester and c-orthocryl laminates samples were immersed in distilled water in sealed containers at tempirature 23°C for 1 month. During the environmental ageing process, the samples were taken out every week and weighed to analyses the weight change of the specimens, the absorption of the polyester and c-orthocryl after immersion was determined by the weight gain relative to the oven dry weight For the analysis of weight gain, 5 samples were weighed.

3. Result and discussion

Absorption Properties

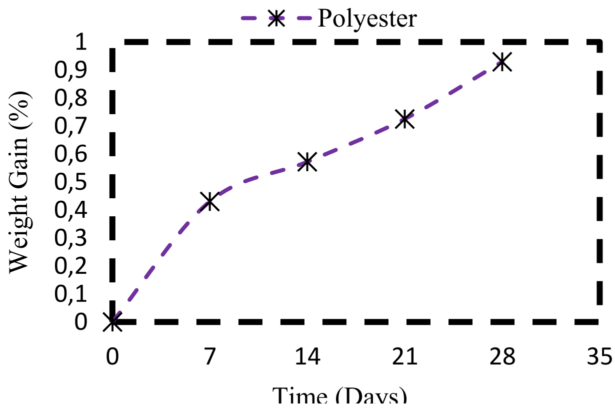

Fig. 1. Weight gain as a function of duration of immersion per day of polyester in distille water.

The graph illustrates the percentage of weight gain in polyester over a period of days, presumably attributable to moisture absorption or chemical interactions with its surroundings. From Day 0 to Day 7, there is an initial rapid uptake. Polyester, as a semi-crystalline polymer, may absorb a limited quantity of water or chemicals, particularly through its amorphous regions.The rapid increase initially indicates that the surface or near-surface absorption sites reach saturation swiftly.Hydrophobic polymers exhibit characteristic behaviour by absorbing a restricted quantity of moisture, predominantly during the initial phase.

From Day 7 to Day 28, there is a gradual long-term absorption.Following initial saturation, the diffusion process decelerates as deeper layers require more time to absorb moisture.The configuration of polyester, characterised by the dense arrangement of polymer chains and little polarity, inhibits extensive infiltration of water or chemicals.The plateauing effect is prevalent in diffusion-controlled systems. and Minimal Final Gain (~0.9%) This corresponds with polyester's established low moisture absorption.The gradual, persistent rise over time may suggest continuous, sluggish diffusion into less accessible areas or chemical interactions resulting in bound water formation.

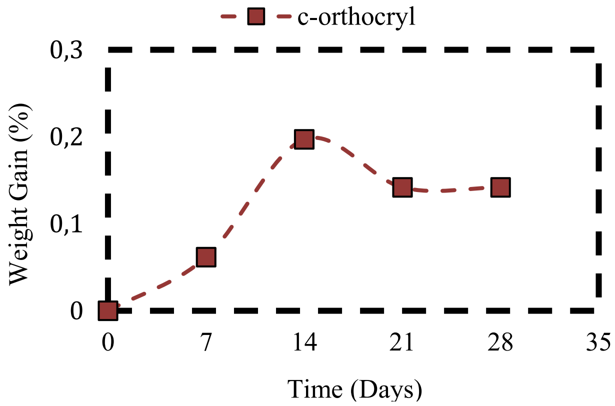

Fig. 2. Weight gain as a function of duration of immersion per day of c-orthocryl in distille water.

The graph depicts the weight gain percentage of a substance designated as "c-orthocryl" over a span of 35 days. During the first phase from Day 0 to Day 7, there is a marginal rise in weight gain, rising from roughly 0% to about 0.07%. This indicates that c-orthocryl commences moisture or substance absorption shortly after exposure, albeit at a gradual pace initially. Initial absorption may be superficial.

During this Mid Phase from Day 7 to Day 14 A more pronounced increase is noted, with weight gain reaching a maximum of around 0.2%. This phase presumably signifies the onset of the material's saturation curve, which begins to ascend rapidly as internal absorption commences. The diffusion into the material matrix may be most vigorous during this phase.

Stabilisation Phase from Day 14 to Day 35 Post Day 14, the curve stabilises, with weight increase maintaining a range of 0.13%–0.15%, indicating a quasi-equilibrium condition of the material. It no longer absorbs a substantial amount of moisture, perhaps due to having achieved its absorption capacity or the stabilisation of environmental variables, such as humidity.

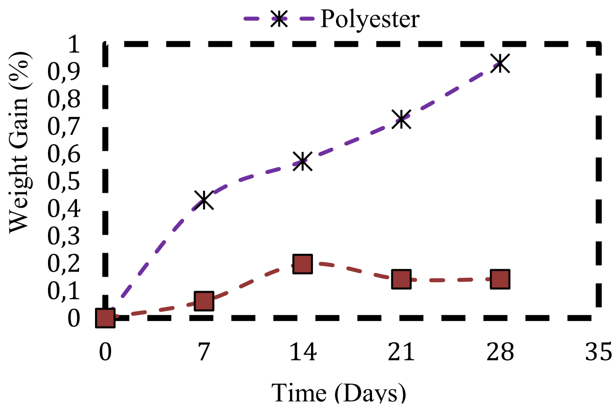

Fig. 3. Weight gain as a function of duration of immersion per day of c-orthocryl & polyester in distille water.

Starting at about 0.05% at Day 0, polyester shows a constant weight rise over time, rising quickly to about 0.4% by Day 7 and then steadily increasing to about 0.9% by Day 28. This implies polyester is reacting with the environment or absorbing moisture over time, therefore generating a noticeable weight increase.
C-orthocryl Starts low too, at ~0.05% at Day 0, Shows a little rise, peaking at about Day 14 with ~0.2% weight growth, Plateaus or slightly declines after that (~0.15% by Day 28), Suggests far less and more constrained contact with the surroundings than polyester.

The significant disparity in weight increase indicates that polyester possesses a greater propensity for absorbing the surrounding medium, possibly attributable to its hydrophilic functional groups (such as ester groups that may interact with water) or its amorphous areas that facilitate molecular diffusion.The alternative material is perhaps more hydrophobic or chemically resistant, maybe a polymer such as polypropylene or polyethylene, recognised for their little moisture absorption.

4. Conclusion

The current investigation focuses on the influence of distille water absorptions on glass polyester & c-orthocryl and effects of ageing process,the following inferences are drawn.

- Polyester shows significantly higher weight gain over time, indicating higher moisture absorption or chemical interaction.
- c-orthocryl material is more resistant, making it more suitable for applications where dimensional stability and moisture resistance are critical.
- Therefore, material choice should depend on the intended environmental exposure ,Use polyester where absorption or permeability is needed (e.g., filtration, controlled-release).
- Use c-orthocryl material (likely a hydrophobic polymer) where durability and moisture resistance are key (e.g., outdoor, packaging, electronics).

Acknowledgments
The authors declare that they have no known competing financial interests or personal relationships that could have appeared to influence the work reported in this paper.

References

Cabral-Fonseca, S., Correia, J. R., Rodrigues, M. P., & Branco, F. A. (2012). Artificial accelerated ageing of GFRP pultruded profiles made of polyester and vinylester resins: Characterisation of physical-chemical and mechanical damage. *Strain*, 48(2), 162–173. https://doi.org/10.1111/j.1475-1305.2011.00826.x

Cerbu, C. (2010). Effects of the long-time immersion on the mechanical behaviour in case of some E-glass/resin composite materials. *Woven Fabric Engineering*. InTech. https://doi.org/10.5772/9992

Fang, Y., Wang, K., Hui, D., Xu, F., Liu, W., Yang, S., & Wang, L. (2017). Monitoring of seawater immersion degradation in glass fibre reinforced polymer composites using quantum dots. *Composites Part B: Engineering*, 112, 93–102. https://doi.org/10.1016/j.compositesb.2016.12.043

Heshmati, M., Haghani, R., & Al-Emrani, M. (2017). Durability of bonded FRP-to-steel joints: Effects of moisture, de-icing salt solution, temperature and FRP type. *Composites Part B: Engineering*, 119, 153–167. https://doi.org/10.1016/j.compositesb.2017.03.049

Mansouri, L., Djebbar, A., Khatir, S., & Abdel Wahab, M. (2019). Effect of hygrothermal aging in distilled and saline water on the mechanical behaviour of mixed short fibre/woven composites. *Composite Structures*, 207, 816–825. https://doi.org/10.1016/j.compstruct.2018.09.056

Sarkar, P., & Young, R. J. (2001). Influence of moisture on the interfacial strength of glass fibre/epoxy composites. *Composites Part A: Applied Science and Manufacturing*, 32(3–4), 411–417. https://doi.org/10.1016/S1359-835X(00)00115-2

Ghasemi, A. R., Morshedian, J., & Azizi, H. (2012). Effects of water absorption on mechanical properties of unsaturated polyester composites. *Polymer-Plastics Technology and Engineering*, 51(4), 391–395. https://doi.org/10.1080/03602559.2011.652423

Wang, X., Zhang, X., & Li, Z. (2006). Moisture absorption and mechanical degradation of epoxy composite with different curing agents. *Composites Science and Technology*, 66(13), 1741–1746. https://doi.org/10.1016/j.compscitech.2005.12.014

Kinloch, A. J., Little, M. S. G., & Watts, J. F. (1983). The role of water in the degradation of epoxy adhesives. *Journal of Materials Science*, 18, 1087–1098. https://doi.org/10.1007/BF00552041

Djazeb, D., Mansouri, M., & Laghlimi, M. (2017). Water absorption and its effect on mechanical properties of polyester-based composites. *Materials Today: Proceedings*, 4(7), 7352–7359. https://doi.org/10.1016/j.matpr.2017.07.071

4th International Civil Engineering & Architecture Conference
17-19 May 2025, Trabzon, Türkiye

High-temperature performance of FRP systems for structural strengthening applications

Yunus E. Akbulut*[1], Sertaç A. Koçak[1], Asude Göç[1], Ayça Çalık[1], Ahmet C. Altunışık[1,2]

[1] *Karadeniz Technical University, Department of Civil Engineering, 61080 Trabzon, Türkiye*
[2] *Earthquake and Structural Health Application and Research Center, Karadeniz Technical University, 61080 Trabzon, Türkiye*

Abstract. Fiber-reinforced polymer (FRP) systems are widely used in modern structural engineering for strengthening and rehabilitating structures, owing to advantages such as high strength, low weight, corrosion resistance, and ease of application. However, the structural contribution of FRP systems—comprising various fiber types embedded in polymer matrices—can be significantly diminished when exposed to environmental conditions such as high temperature. In particular, as the polymer matrix approaches its glass transition temperature (T_g), structural integrity begins to deteriorate, leading to reduced load-carrying capacity. This study aims to evaluate the high-temperature performance of FRP systems and examine the influence of thermal effects on their structural contribution. A comprehensive experimental program was designed considering four key parameters: fiber type, number of wrapping layers, temperature level, and exposure duration. Wrapped and unwrapped standard cylindrical concrete specimens were subjected to designated thermal scenarios, followed by compressive strength testing. FRP system performance was assessed based on numerical data (surface temperature and compressive strength) and visual indicators (color changes, resin degradation, and failure modes). The findings show that FRP effectiveness depends not only on composite type and wrapping configuration but also on the level and duration of temperature exposure. As the epoxy matrix approached its T_g, reductions in bonding capacity were initiated, leading to weakened fiber–matrix interactions and a gradual shift in failure behavior with increasing temperature. These results emphasize the necessity of incorporating thermal considerations into the design process and supporting FRP systems with appropriate insulation strategies for reliable performance under high temperature.

Keywords: Concrete; Strengthening; FRP; High temperature; Glass transition

1. Introduction

Fiber-reinforced polymer (FRP) composites have become increasingly preferred materials in the field of civil engineering due to their advantages such as high strength-to-weight ratio, corrosion resistance, design flexibility, and rapid applicability. Particularly in applications such as the strengthening of reinforced concrete structural elements, enhancement of load-carrying capacity, improvement of seismic performance, and repair of damaged regions, FRP systems offer effective and economical solutions. Their lightweight nature, which prevents additional loading on the structural system, their ability to reduce labor time, and their ease of application to different geometries distinguish these systems among modern strengthening techniques. FRP reinforcements are applied by external wrapping or surface bonding to reinforced concrete elements, thereby increasing both the load-bearing capacity and ductility of the structural members.

Nevertheless, despite all these advantages, the sensitivity of FRP systems to high temperature is considered a significant drawback in terms of structural safety. Engineering structures are exposed not only to static and dynamic loads but also to various environmental and thermal effects. Structures may be subjected to different levels of thermal influence in scenarios such as fires, secondary fires following earthquakes, high-temperature accidents in industrial facilities, vehicle fires, or heat accumulation around heat-emitting equipment such as electrical panels, exhaust ducts, and generators. In such cases, the thermal sensitivity of FRP components can lead to a reduction in the load-carrying contribution of the system and cause unexpected performance losses in the strengthened structural elements.

In particular, as the resin matrix approaches its glass transition temperature (T_g), the material undergoes a phase change from a rigid–brittle state to a viscous–soft phase. This transformation weakens the fiber–matrix interaction and leads to a loss of adhesion between the FRP and the concrete surface. Such bond degradation can severely

* Corresponding author, E-mail: emrahan@ktu.edu.tr

https://doi.org/10.31462/icearc2025_ce_sme_041

limit the load-carrying function of the system and cause unexpected reductions in structural performance. The influence of temperature is not limited to the resin alone; the fiber reinforcements used in the system may also experience structural degradation, such as microscopic separation, embrittlement, oxidation, and reductions in mechanical capacity within specific temperature ranges.

These types of thermal degradation processes lead to the development of critical damage modes in FRP-strengthened structural members, such as delamination, fiber separation, bond failure, and brittle fracture. In particular, under fire scenarios that produce extreme temperatures, preserving structural integrity becomes highly challenging. Therefore, understanding the behavior of FRP systems under high temperature conditions is of great importance for ensuring their safe and durable use in load-bearing structural elements.

In the literature, the behavior of FRP-strengthened reinforced concrete elements under high temperatures is largely attributed to the thermomechanical degradation process that begins as the resin matrix approaches its T_g. Saafi (2002) defined this process in two stages: in the first stage, a significant reduction in stress transfer occurs due to resin softening around T_g; in the second stage, when the fibers reach their decomposition temperature, the load-bearing function is entirely lost. Firmo et al. (2015) reported that the T_g of resin matrices generally ranges between 50–120 °C and emphasized that mechanical degradation begins even before reaching Tg. Furthermore, it was noted that complete degradation of the resin matrix and loss of fiber–matrix interaction occur at temperatures above 300–400 °C. It has also been stated that at 500–700 °C, the load-bearing capacity provided by FRP materials is almost entirely lost. Bazli and Abolfazli (2020) indicated that the T_g typically ranges between 65–120 °C, and that complete thermal degradation (T_d) of the resin occurs between 300–500 °C, resulting in the breakdown of fiber–resin bonds and the near-total loss of structural contribution. The same study defined a critical temperature (T_c) as the temperature at which the FRP material loses 50% of its load-carrying capacity. This threshold was reported to be between 250–330 °C for carbon fiber-based FRP (CFRP) and between 300–350 °C for glass fiber-based FRP (GFRP). Overall, while GFRP systems demonstrated better thermal resistance than CFRP, the latter exhibited superior mechanical strength. Ahmed and Kodur (2011) observed that in uninsulated reinforced concrete beams, the bond between CFRP and concrete weakened at around $T_g \approx 82$ °C, and sudden increases in deflection were recorded beyond this point. Their findings revealed that exceeding T_g does not necessarily result in structural failure and that insulation efficiency is a determining factor in maintaining the performance of FRP. Al-Salloum et al. (2011) reported that such performance losses became more pronounced when T_g (≈88 °C) was exceeded and that CFRP-wrapped specimens were more sensitive to high-temperature effects compared to GFRP-wrapped ones. Gamage et al. (2005) experimentally showed that when epoxy temperatures exceeded 60 °C, there was a sharp decline in bond strength at the FRP–concrete interface and peel-off type failures occurred.

Cleary et al. (2003) reported that increasing temperature also leads to a shift in failure modes; while hoop-splitting mechanisms were predominant at lower temperatures, the failure behavior transformed into seam debonding at higher temperatures. The same study emphasized that T_g should not be considered as a singular failure threshold, noting that permanent bond deterioration and changes in failure modes began at temperatures approximately 30 °C above the matrix's T_g (121 °C). El-Gamal et al. (2015) evaluated the color changes observed in FRP layers as an indicator of thermal degradation, and sudden fiber rupture as a sign of embrittlement behavior in FRP systems. Li et al. (2017) demonstrated that with increasing temperature, both the FRP and adhesive materials exhibited gradual reductions in mechanical properties, accompanied by the formation of micro-cracks at the interface. Moreover, they found that fracture energy was more sensitive to changes in temperature than to the duration of exposure. Lau et al. (2016) stated that epoxy resins begin to soften between 65 °C and 150 °C, and undergo thermal decomposition at temperatures exceeding 400 °C. This degradation, driven by evaporation and dissociation mechanisms, resulted in the complete loss of the load-carrying capacity of the FRP systems. Maraveas et al. (2012) reported that especially for epoxy-based adhesives, bond strength decreased by an average of 40% in the 100–200 °C temperature range, and dropped below 20% above 200 °C. In terms of tensile strength, FRP materials were shown to suffer 60–80% strength losses between 200–400 °C, and almost complete loss of structural capacity above 400 °C. Elsanadedy et al. (2017) observed that even under exposures up to 300 °C, FRP reinforcement continued to enhance the axial load-carrying capacity of reinforced concrete columns. However, this benefit decreased significantly at approximately 345 °C, the decomposition temperature of the epoxy matrix. Green et al. (2006) stated that FRP systems rapidly reached T_g during fire tests, and in the absence of fire insulation, they ignited and became ineffective within minutes. Sobia et al. (2022) emphasized the critical role of insulation applications in maintaining the matrix temperature below T_g in CFRP-strengthened concrete members exposed to fire. They concluded that the duration for which insulation effectively prevents the matrix from exceeding T_g plays a key role in ensuring the residual performance of the system.

As evidenced by the detailed literature review, a wide range of studies have examined the thermal performance of FRP-strengthened concrete members, particularly focusing on the degradation of mechanical properties with increasing temperature and the critical role of the matrix's T_g. However, many of these investigations were limited in scope, either by isolating a narrow set of experimental parameters or by evaluating only specific material configurations under thermal exposure. In contrast, the present study aims to comprehensively assess the behavior of FRP systems under high temperatures by simultaneously considering multiple critical parameters—including fiber type, number of wrapping layers, temperature level, and exposure duration—within a single experimental framework. By integrating both quantitative and qualitative evaluation methods, this research provides a broader understanding of the load-bearing efficiency and failure characteristics of FRP-strengthened concrete elements exposed to high-temperature conditions. The findings are expected to contribute significantly to the development of more robust design strategies that ensure structural safety and long-term performance under thermal effects.

2. Material and methods

In this experimental study, a comprehensive dataset was developed by systematically considering four key parameters: composite fabric type (carbon and glass fiber), number of wrapping layers (1, 2, and 3 layers), temperature level (80 °C, 150 °C, and 250 °C), and exposure duration (90 and 180 minutes). The experimental program commenced with the casting of standard cylindrical concrete specimens (150 × 300 mm). Following curing, the specimens were grouped in accordance with the planned testing matrix (Figure 1). Specimens assigned to the strengthening group were externally wrapped with FRP composites based on predefined configurations of fabric type and number of layers.

Subsequently, to evaluate the extent to which FRP systems retained their functionality under high temperature exposure, the specimens were subjected sequentially to thermal exposure followed by compressive strength testing. The effects of the considered parameters on the performance of the FRP composites were assessed in an integrated manner. This evaluation was based on three primary sources of data: (1) surface temperature measurements conducted during the thermal exposure stage, (2) compressive strength values obtained from mechanical tests, and (3) visual inspections performed throughout both testing phases, including observations of color changes in the composite layers and the identification of fracture mechanisms.

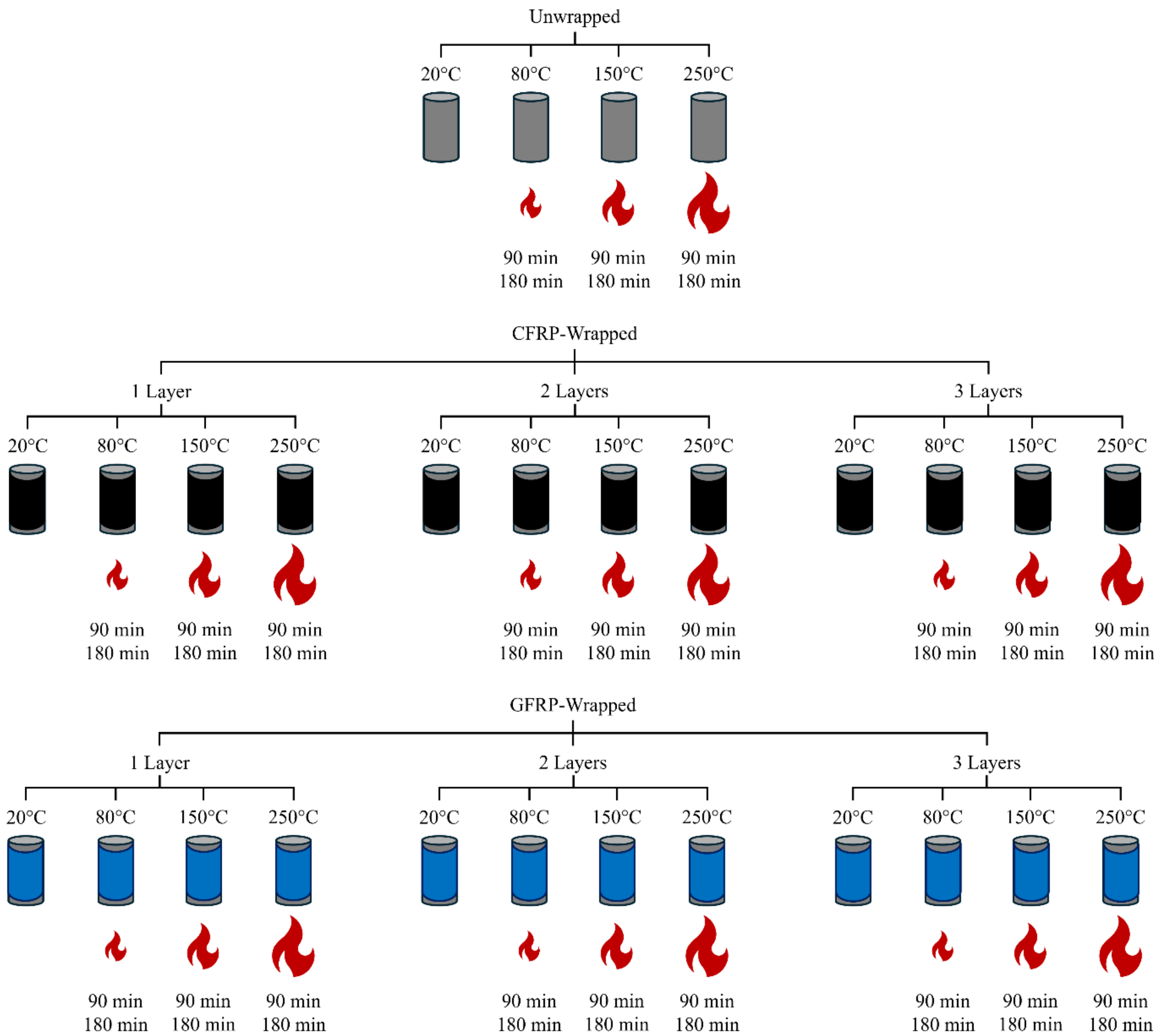

Fig. 1. Test matrix

2.1. Specimen preparation

As shown in Fig. 1, a total of 49 different cases were identified based on variations in the parameters considered within the scope of this study. To increase the reliability of the results and ensure more accurate evaluations through meaningful data, two specimens were prepared for each case, resulting in a total of 98 concrete specimens.

A concrete mixer with an effective mixing capacity of up to 45 liters was used during the production process. The mixed concrete was transferred to a wheelbarrow using shovels and then poured into plastic cylindrical molds placed on a vibrating table. The molds were filled in two stages: the first vibration was applied after filling the molds halfway, and the second vibration was applied once they were completely filled. The exposed top surfaces of the specimens were leveled using a trowel. After a 24-hour resting period, the specimens were demolded and placed in a curing tank. Following a 28-day curing period, they were removed from the tank. This production procedure was repeated 14 times to meet the required number of specimens (Fig. 2). Each concrete mix (for 45 liters) included 46.41 kg of coarse aggregate, 37.65 kg of fine aggregate, 15.75 kg of CEM I 42.5R cement, 7.09 kg of water, 0.4 kg of saturated surface dry water, and approximately 130 g of chemical admixture. The water-to-cement ratio was 0.45.

Fig. 2. Specimen production process

2.2. Strengthening applications

Following the completion of specimen production, preparations for the strengthening applications were initiated. FRP fabrics and epoxy-based adhesives were used for strengthening. Prior to application, both carbon and glass fiber fabrics were cut to appropriate dimensions to ensure a standard overlap length of 20 cm for each of the 1, 2, and 3-layer configurations. It was aimed to achieve an approximate balance between the weight of the fabric and the amount of epoxy adhesive used during wrapping. To this end, the weight of each cut fabric piece was measured using a high-precision electronic scale. The carbon fiber fabrics used in this study had a tensile modulus of 230 GPa, a tensile strength of 4900 MPa, and an elongation at break of 2.1%. For the glass fiber fabrics, these values were 65 GPa, 1300 MPa, and 2.5%, respectively. While the carbon fabrics were unidirectional, the glass fiber fabrics featured a bidirectional open-weave structure, commonly used with cementitious matrices to enhance the compressive strength and ductility of concrete and masonry elements (Trapko, 2013; Ameli et al., 2022).

The strengthening procedure began with the cleaning of the specimen surfaces to remove dust and other contaminants, followed by the application of a primer epoxy layer to the lateral surfaces where wrapping would occur. After a 24-hour waiting period, the wrapping process was carried out using the prepared FRP fabrics and an epoxy adhesive mixture. Both the primer and the adhesive mixture were prepared according to manufacturer specifications by mixing the components in a metal container with a mechanical mixer. The amount of adhesive used during wrapping was monitored by measuring the reduction in the epoxy's weight in the container. The epoxy adhesive used had a T_g of 71 °C, with flash points of its components at 93 °C and 110 °C. During CFRP applications, the amount of epoxy used for 1, 2, and 3 layers was 67.9 g, 104 g, and 140.8 g, respectively. For GFRP, the corresponding amounts were 60.4 g, 80.3 g, and 110.2 g. The specimens were then left to cure under laboratory conditions for 7 days to ensure complete hardening of the epoxy adhesive. Illustrative images of the strengthening process are presented in Fig. 3.

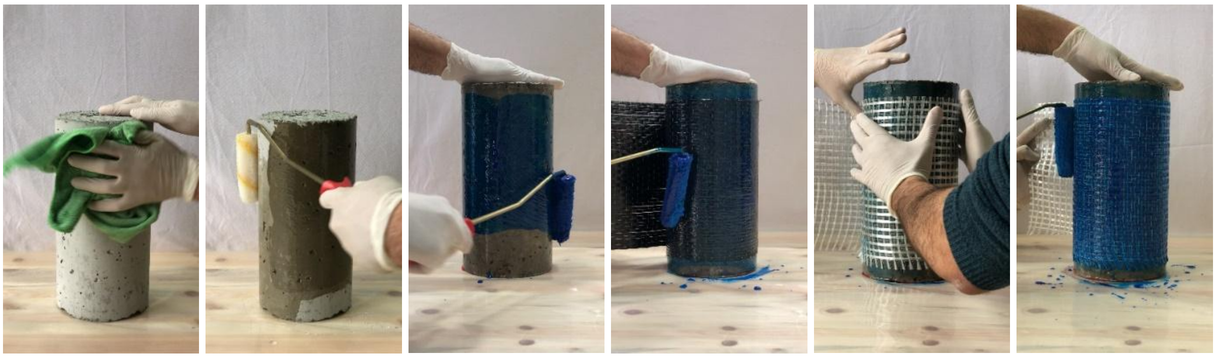

Fig. 3. Strengthening applications on specimens

2.3. Thermal exposure tests

After the completion of the curing process of the strengthened specimens, thermal exposure tests were conducted. For these tests, a trolley-based electric furnace was used. The furnace, powered by electricity and offering a usable volume of 6 m³ (2.0 × 1.5 × 2.0 m), was capable of reaching temperatures up to 1120 °C. Additionally, K-type thermocouples integrated into the system allowed for continuous monitoring of the internal furnace temperature during testing.

Throughout the tests, a constant heating rate of 5 °C/min was applied until the furnace reached the target temperatures defined in the experimental program (80 °C, 150 °C, and 250 °C). Once the target temperature was reached, the specimens were held at that temperature for either 90 or 180 minutes, depending on the designated exposure duration in each scenario. A total of six different thermal exposure tests were carried out based on the combinations of temperature level and exposure time considered in the study (Fig. 4).

Fig. 4. Temperature tests conducted under different heating regimes

Immediately after the completion of each thermal exposure, the furnace door was opened and the surface temperatures of the specimens were measured using an AST TI 1500 model dual-laser portable pyrometer. Subsequently, the furnace trolley was rolled out to extract the specimens, which were visually inspected for any changes in their FRP components and then allowed to cool under laboratory conditions.

2.4. Compressive strength tests

Following the thermal exposure phase and subsequent cooling of the specimens under ambient laboratory conditions, compressive strength tests were conducted in accordance with the BS EN 12390-3 (2019) standard. These tests were performed using a hydraulic compression testing machine with a maximum capacity of 3000 kN. All specimens were loaded under a constant rate of 0.6 MPa/s until failure.

The compressive strength results obtained from each specimen were used as the primary numerical data for assessing the mechanical performance of the FRP systems under high temperature conditions. In addition, immediately after the completion of each test, the failure modes of the specimens were visually inspected and documented to evaluate the influence of temperature on the structural behavior and damage characteristics of the FRP-reinforced concrete elements.

Representative post-test images of specimens strengthened with CFRP and GFRP systems are presented in Fig. 5. These visual observations provided supplementary insights into failure patterns such as delamination, fiber rupture, surface peeling, and debonding, which are critical indicators of thermally induced degradation in FRP composites.

Fig. 5. Post-compression failure mechanisms of FRP-strengthened specimens

3. Results and discussion

This section presents the data obtained from the temperature and compression tests, along with visual inspections conducted after testing, and discusses the findings in detail.

Surface temperature data collected before and after the thermal tests using a pyrometer are presented in Table 1. Visual inspections following the temperature exposure indicated no observable deterioration in the epoxy resin of the strengthened specimens used in Tests 1 and 2. In contrast, specimens used in Tests 3 and 4 showed significant softening in the resin due to exceeding T_g. In the tests conducted at the target temperature of 80 °C, the epoxy surface largely retained its gloss, whereas a matte appearance became noticeable after the 150 °C exposure. For the tests conducted at 250 °C, particularly after the 90-minute exposure in Test 6, partial burning and charring marks were observed on the resin surface, and in some areas, the fibers were fully exposed due to thermal degradation of the matrix.

Table 1. Surface temperature measurements

Test no	Target temperature (°C)	Exposure duration (min)	Surface temperature (°C)		
			Pre-test	Post-test	
				FRP	Concrete
1	80	60	26.2	53.5	69.8
2	80	90	27.1	63.1	77.1
3	150	60	27.0	97.1	130.2
4	150	90	27.1	109.2	134.7
5	250	60	26.8	154.1	211.1
6	250	90	29.3	179.7	229.5

Although average compressive strength results are summarized in Table 2, the general behavioral trends can be outlined as follows: Unwrapped concrete specimens tested at 80 °C exhibited a 6–8% increase in strength compared to ambient conditions; at 150 °C, a short-duration exposure led to a 2% increase, whereas longer exposure resulted in up to a 4% loss. At 250 °C, strength reductions of 6–7% were recorded. CFRP wrapping enhanced compressive strength by 55%, 109%, and 168% for one, two, and three layers, respectively, while GFRP contributed improvements ranging between 14% and 31% for the same configurations. In the 80 °C tests where the T_g was not exceeded, CFRP specimens retained 92–107% of their initial strength, while GFRP specimens retained 85–116%, with values exceeding 100% reflecting temporary strength gains from drying and partial hardening of the concrete core. These results indicate that strength loss begins as FRP–concrete bond degradation starts approaching T_g. At 150 °C, within the epoxy's viscoelastic softening region, residual strength ratios decreased to 88–98% for CFRP and 73–94% for GFRP, indicating a faster deterioration of the glass fiber–epoxy bond compared to the carbon fiber–epoxy bond. At 250 °C, where pyrolytic degradation initiates, GFRP specimens dropped to 67–81%, whereas CFRP specimens maintained 50–100% higher strength than unwrapped concrete even with one or two layers. Extending the exposure duration from 90 to 180 minutes caused an additional 2–11% strength loss at 80 °C and 150 °C, with time sensitivity more pronounced in GFRP systems, while some specimens showed slight strength gains (approximately 5–15%) at 250 °C. These findings confirm that early strength increases due to drying and hardening of the concrete may mask the percentage contribution of FRP, yet softening above T_g and degradation at high temperatures progressively reduce the confinement effectiveness of FRP systems with increasing temperature and exposure time.

Table 2. Average compressive strength values (MPa) obtained from the compression tests

Target temperature (°C)	Exposure duration (min)	Unwrapped	Number of FRP wrapping layers					
			CFRP			GFRP		
			1	2	3	1	2	3
20	---	28.65	44.28	59.84	76.65	32.58	35.22	37.67
80	90	30.97	47.51	60.09	79.09	33.14	40.88	33.27
	180	30.51	46.66	59.26	70.63	31.58	32.21	32.07
150	90	29.24	43.20	56.83	68.50	30.51	30.47	30.36
	180	27.35	41.28	52.88	68.43	28.05	27.56	27.32
250	90	26.53	40.46	52.25	61.38	26.24	23.44	27.31
	180	26.96	42.74	54.84	59.11	25.54	26.85	27.48

4. Conclusions

The findings obtained in this study reveal that the strengthening contribution provided by FRP systems primarily depends on the type of composite material used and the number of wrapping layers. However, the performance of these systems was also found to be sensitive to temperature level and exposure duration. Based on the experimental findings that reveal the behavior of FRP systems under high temperature conditions, the key conclusions are presented below:

- Regardless of temperature effects, FRP strengthening systems provided a significant increase in compressive strength to the concrete specimens. This contribution increased with the number of applied wraps. CFRP systems offered a higher strength gain compared to GFRP systems. Even under thermal exposure, CFRP systems maintained their confinement effectiveness more efficiently. Although GFRP systems provided strength enhancement at low and moderate temperatures, their effectiveness remained limited compared to CFRP. These outcomes are directly associated with the mechanical and thermal properties of the fiber fabrics used in strengthening applications, as well as their compatibility with the resin matrix.
- The strength increase observed in unwrapped concrete specimens at 80 °C and 150 °C was attributed to a temporary drying–stiffening effect due to moisture loss. In some cases, this phenomenon may lead to an overestimation of the actual contribution of FRP systems. Therefore, when evaluating the performance of FRP systems, it is essential to consider the influence of such temporary strength increases and isolate their effects in the analysis.
- Epoxy softening and pyrolytic degradation processes, which became more pronounced above T_g, gradually reduced the confinement effectiveness of the FRP systems with increasing temperature and exposure duration. These reductions initiated as the matrix approached its T_g and became more evident once T_g was exceeded, leading to softening of the epoxy and a decline in bond strength. The findings suggest that bond losses at the FRP–concrete interface begin not only after T_g is exceeded but already as it is approached.
- It was also observed that the failure mechanisms of FRP systems varied significantly depending on temperature and exposure time. While the fiber–matrix integrity was maintained at low temperatures,

increasing temperature led to matrix softening, resulting in delamination, fiber–matrix separation, debonding, and interlayer peeling. At 250 °C, decomposition of the epoxy matrix exposed the fibers, causing brittle fractures and fiber ruptures in these regions. This clearly indicates a substantial reduction in the structural contribution of FRP systems with increasing thermal exposure. After the 250 °C tests, the strength contribution of GFRP systems was entirely lost, whereas CFRP systems, despite a significant reduction, retained some structural functionality.

- These findings clearly demonstrate the vulnerability of FRP composite materials to high temperature. Therefore, the use of such systems must be considered in conjunction with appropriate insulation and fire protection measures to ensure safety and long-term performance.

Acknowledgments

The research presented in this paper was financially supported by the Scientific and Technological Research Council of Türkiye (TÜBİTAK) under the grant number [1919B012209899], as part of the 2209-A Research Project Support Programme for Undergraduate Students.

References

Ahmed, A., & Kodur, V. (2011). The experimental behavior of FRP-strengthened RC beams subjected to design fire exposure. *Engineering Structures*, *33*(7), 2201-2211

Al-Salloum, Y.A., Elsanadedy, H.M., & Abadel, A.A. (2011). Behavior of FRP-confined concrete after high temperature exposure. *Construction and Building Materials*, *25*(2), 838-850

Bazli, M., & Abolfazli, M. (2020). Mechanical properties of fibre reinforced polymers under elevated temperatures: An overview. *Polymers*, *12*(11), 2600

BS EN 12390-3. (2019). Testing hardened concrete, Part 3: Compressive strength of test specimens. *British Standards Institution,* London, UK

Cleary, D.B., Cassino, C.D., Tortorice, R., Newell, J.A., & Tyers, B.W. (2003). Effect of elevated temperatures on a fiber composite used to strengthen concrete columns. *Journal of Reinforced Plastics and Composites*, *22*(10), 881-895

El-Gamal, S., Al-Jabri, K., Al-Mahri, A., & Al-Mahrouqi, S. (2015). Effects of Elevated Temperatures on the Compressive Strength Capacity of Concrete Cylinders Confined with FRP Sheets: An Experimental Investigation. *International Journal of Polymer Science*, *2015*, 549187

Elsanadedy, H., Almusallam, T., Al-Salloum, Y., & Iqbal, R. (2017). Effect of high temperature on structural response of reinforced concrete circular columns strengthened with fiber reinforced polymer composites. *Journal of Composite Materials*, *51*(3), 333-355

Firmo, J.P., Correia, J.R., & Bisby, L.A. (2015). Fire behaviour of FRP-strengthened reinforced concrete structural elements: A state-of-the-art review. *Composites Part B: Engineering*, *80*, 198-216.

Gamage, J.C.P.H., Wong, M.B., & Al-Mahadi, R. (2005). Performance of CFRP strengthened concrete members under elevated temperatures. In *Proceeding of the International Sysposium on Bond Behaviour of FRP in Structures (BBFS 2005)*, 113-118

Green, M.F., Bisby, L.A., Fam, A.Z., & Kodur, V.K.R. (2006). FRP confined concrete columns: Behaviour under extreme conditions. *Cement and Concrete Composites*, *28*(10), 928-937

Lau, D., Qiu, Q., Zhou, A., & Chow, C.L. (2016). Long term performance and fire safety aspect of FRP composites used in building structures. *Construction and Building Materials*. *126*, 573-585

Li, Y., Liu, X., & Wu, M. (2017). Mechanical properties of FRP-strengthened concrete at elevated temperature. *Construction and Building Materials*, *134*, 424-432

Maraveas, C., Miamis, K., & Vrakas, A.A. (2012). Fiber-reinforced polymer-strengthened/reinforced concrete structures exposed to fire: A review. *Structural Engineering International: Journal of the International Association for Bridge and Structural Engineering (IABSE)*, *22*(4), 500-513

Saafi, M. (2002). Effect of fire on FRP reinforced concrete members. *Composite Structures*, *58*(1), 11–20

Sobia, A.Q., Afifudin, H., Hamidah, M.S., & Azmi, I. (2022). Thermo-mechanical behavior of fire insulated fiber-reinforced polymer (FRP) strengthened reinforced concrete square column. *Asian Journal of Civil Engineering*, *23*(4), 573-583

4th International Civil Engineering & Architecture Conference
17-19 May 2025, Trabzon, Türkiye

Wind speed simulation techniques for dynamic structural analysis and design

Cavit Serhatoğlu*[1], Ramazan Livaoğlu[1,2]

[1] *Bursa Uludağ University, Department of Civil Engineering, 16059 Bursa, Turkey*
[2] *RL ProjeDestek Consulting Company, Bursa, Turkey*

Abstract. Conventional design methodologies for wind loads frequently depend on static analyses, which may inadequately represent the dynamic behavior of certain structures, such as tall buildings or wind turbines.In such instances, time-domain analysis is more suitable for accurately capturing the wind-induced effects.Time-dependent wind loads for design purposes are typically derived from wind tunnel tests. However, conducting such tests during the preliminary design stages is often impractical due to cost constraints and the potential for iterative design changes. This study proposes a methodology for generating multivariate wind speed fields to be used in the calculation of time-dependent wind loads on structures and in applications such as energy production.The proposed methodology is based on the modeling of the spectrum of atmospheric surface-layer turbulence according to basic wind velocities. It enables the simulation of one-, two-, or three-dimensional fields with one, two, or three components of wind velocity fluctuations (u, v, w). The simulation of these velocity fields is conducted with the models characterized as gaussian random processes dependent on the parameters t and $\mathbf{x}$ position within a finite spatial domain. As a demonstrative application, this study presents a regular 2D vertical grid oriented perpendicularly to the flow, incorporating the longitudinal mean wind velocity and the longitudinal, lateral, and vertical atmospheric turbulence components. This approach can offer a cost-effective and versatile solution for wind analysis, enhancing preliminary design processes and broadening applications in structural and energy-related fields.

Keywords: Mean wind velocity; Velocity of turbulence components; Time domain; Random process

1. Introduction

One of the most critical design considerations for many special structures is their response to wind. On the other hand, A proper selection and design of a building's structural system depend on the accurate identification of the loads acting on the structure and the selection of appropriate analysis methods. Although building codes specify the minimum forces that a structure must withstand, they typically do not impose requirements related to other specific performance criteria. For instance, in the case of tall buildings, inter-story shear forces and occupant comfort are often key design constraints from a serviceability perspective. However, the minimum wind forces prescribed in most codes do not adequately account for the potential dynamic response of tall structures, and therefore may significantly underestimate the actual demand levels. Therefore, wind tunnel studies are often suitable for better characterizing the wind response of the special structures. Very few countries or local authorities have established guidelines for when such testing is required, and the decision is typically left to the discretion of the design professional. Another method for estimating the loads acting on a structure is Computational Fluid Dynamics (CFD) analysis. The results from both methods are commonly translated into an equivalent static load, incorporating an approximation of the structure's dynamic response. In the case of wind tunnel testing, the equivalent static load is calculated by considering the fundamental period of the structure, while contributions from higher modes are typically neglected. This simplification is also inherent in most national standards and building codes. However, such an approach may, in some cases, fail to capture the actual dynamic behavior of the structure. Time-domain analyses methods offer a more appropriate method to incorporate the effects of higher modes, which cannot be accounted for in equivalent static load procedures. However; unlike earthquakes, wind lacks a well-defined time history database, and the temporal variation of wind effects depends on a wide range of factors such as structural geometry, regional characteristics, wind profile, and building height. Consequently, wind represents a highly complex and variable load, and no design code currently prescribes time-domain dynamic load procedures for wind.

* Corresponding author, E-mail: cserhatoglu@uludag.edu.tr

https://doi.org/10.31462/icearc2025_ce_sme_061

Many wind design codes guide towards strength-based design and allow only elastic behavior in the design. However, wind loads acting on special structures such as tall buildings may exceed seismic demands in some cases and have the potential to induce nonlinear structural responses. In recent years, researchers have become increasingly aware of these limitations in both design practices and building codes. As a result, the concept of Performance-Based Wind Design (PBWD)—which allows inelastic behavior under strong wind loading—has been introduced specifically for the design of such structures. Unlike Performance-Based Seismic Design (PBSD), there is a notable lack of guidelines and research addressing inelastic wind design. In PBWD, time-history wind loads are typically derived from surface pressure data obtained through wind tunnel testing. However, for preliminary design phases, conducting wind tunnel experiments is often impractical due to design modifications, the need to evaluate multiple performance levels, and associated costs.

In this context, there is a need to develop a procedure for the generation of synthetic data as a more practical means of determining time-dependent wind loads. This need has served as the primary motivation for this study. To achieve this, it is necessary to obtain either time-dependent pressure coefficients or wind velocity records at the specific location on the structure. In this context, this study proposes a methodology for generating multivariate wind speed fields to be used in the calculation of time-dependent wind loads on structures and in applications such as energy production.The proposed methodology is based on the modeling of the spectrum of atmospheric surface-layer turbulence according to basic wind velocities. For the simulation, a software was developed in the MATLAB language, which can offer different design spectrum options and enables the calculation of height- and time-dependent wind speeds using the conventional spectrum-based method. It enables the simulation of one-, two-, or three-dimensional fields with one, two, or three components of wind velocity fluctuations (*u, v, w*). The simulation of these velocity fields is conducted with the model characterized as gaussian random processes dependent on the parameters t and $\mathbf{x}$ position within a finite spatial domain. A sample application has been provided to demonstrate the methodology developed in the scope of this study.

2. Materials and methods

Studies focusing on the simulation of atmospheric wind velocities are notably limited in number. Moreover, existing research often restricts the user's flexibility in selecting different spectra and parameters, or allows for the generation of wind records at only a single spatial point (e.g., Kwon et al., 2011; Branlard, 2017; Wang et. al., 2018; Cheynet, 2020). Although limited in number, these studies have emphasized the necessity of addressing the gap in the literature and have thus provided both a conceptual basis and a source of motivation for the present study.

Before describing the framework used for wind velocity generation, it is beneficial to first understand the concept of time-dependent data generation. This generation can fundamentally be examnied to two parts: the first involves generating a vector-valued synthetic record at a single coordinate point, while the second involves producing specially distributed data for multiple coordinate points and various vector components.

The first part is particularly useful for understanding the fundamental principles of random data generation. Some of the methods commonly used for this purpose include the Complex Amplitude of White Noise Spectrum (CAWS) Method (Goto and Toki, 1969), the Weighted Amplitude Wave Superposition (WAWS) Method (Shinozuka, 1985), and the Auto-Regressive (AR) Filtering Approach.

In the second part, the process becomes more complex in terms of both methodology and computation. This complexity arises from the fact that the locations within the data set to be generated may lie in one-, two-, or three-dimensional spatial coordinate systems, and each location may possess between one and three vector components. Consequently, the generation of multivariate random data requires the definition of correlation both among different vector components at the same location and among identical vector components across different locations. To characterize these correlations, it is necessary to employ either cross power spectral density functions incorporating coherence functions or covariance functions. Furthermore, spatial (three-dimensional) matrix formulations and solutions are required. In the second part, some of the simulation schemes can used for this purpose include Discrete Frequency Function with FFT (Wittig and Sinha, 1975), Schur Decomposition Approach with AR (Di Paola 1998, Di Paola and Gullo, 2001), Ergodic Spectral Representation Method (Deodatis, 1996; Ding et al. 2006), Conventional Spectral Representation Method (Shinozuka and Deodatis,1991). In this study, the Conventional Spectral Representation Method was adopted for the simulation of three-dimensional (3D) multivariate Gaussian wind velocity fields.

2.1. Theoretical backgrounds

Simulated wind velocity fields are generated depending on time t and of the position $\mathbf{x}= [x, y, z]^T$ in a finite spatial domain. The orthogonal reference system *(x, y, z)* has origin on the ground and the axis z is vertical and directed upwards.

The wind velocity is idealized as the sum of two terms: (1) the mean wind velocity $\overline{U}(\mathbf{x})$ or $U_{mean}(\mathbf{x})$, function of the position $\mathbf{x}$, and oriented in the whole domain along the positive direction of the axis *x*; (2) the random function **u**(**x**, t), function of space and time, whose Cartesian components *u, v, w* along *x, y,* and *z,* respectively, represent the longitudinal, lateral and vertical atmospheric turbulence components.

2.1.1. Design mean wind speed profile models
The mean wind speed profile in each standard is defined either by a Power Law or a Logarithmic Law. The AS/NZ, EU, and ISO standards adopt the Logarithmic Law, while the others primarily use the Power Law. If the basic wind speed at 10 meters height is not known, but the mean wind speed measured at a reference point is available, it is still possible to determine the mean wind speed at the desired height by applying either the logarithmic law or the power law. In the developed software, the calculation of the mean wind speed profile has been made possible through three different options.

The Power Law is defined as follows:

$$\bar{U}(z) = b\left(\frac{z}{10}\right)^{\alpha} U_b \tag{1}$$

Here, α (the exponent of the mean wind speed profile) and *b* are terrain-dependent parameters, z is the height of interest, and U_b is the basic wind speed.

The Logarithmic Law is defined as follows:

$$\begin{aligned} \bar{U}(z) &= \frac{u*}{\kappa} In\left(\frac{z}{z_0}\right) U_b \qquad & z > z_{min} \\ \bar{U}(z) &= \bar{U}(z_{min}) \qquad & z \le z_{min} \end{aligned} \tag{2}$$

u∗ is the friction velocity (also referred to as the shear velocity), z_0 is the surface roughness length, and κ is the von Kármán constant.

Calculation according to the mean wind speed measured at a reference point:

$$\bar{U}(z) = \bar{U}(z_{ref}) \frac{In\left(\frac{z}{z_0}\right)}{In\left(\frac{z}{z_{ref}}\right)} \tag{3}$$

$$\bar{U}(z) = \bar{U}(z_{ref}) \left(\frac{z}{z_{ref}}\right)^{\alpha} \quad eksponent : \alpha = \left(\frac{1}{In(z_{ref} / z_0)}\right) \tag{4}$$

2.1.2. Models for turbulence components
The fluctuating components of the wind velocity are modelled as a Gaussian random process.

Power Spectral Density (PSD) function:

Kailmal Power Spectral Density (PSD) function of the turbulence component ε = *u, v, w* in the point **x** of the finite spatial domain is defined as follows:

$$\frac{fS_u(\mathbf{x}, f)}{u_*^2} = \frac{200 f_{mc}}{[1 + 50 f_{mc}]^{5/3}} \tag{5}$$

$$\frac{fS_v(\mathbf{x}, f)}{u_*^2} = \frac{17 f_{mc}}{[1 + 9.5 f_{mc}]^{5/3}} \tag{6}$$

$$\frac{fS_w(\mathbf{x}, f)}{u_*^2} = \frac{2 f_{mc}}{[1 + 5.3 f_{mc}]^{5/3}} \tag{7}$$

$$f_{mc} = \frac{f.z}{\bar{U}(z)} \tag{8}$$

f: frequency,f_{mc}: Monin coordinate,$S_\varepsilon(\mathbf{x},f)$: represents the power spectral density of the turbulence velocity component in the point **x** of finite spatial domain

Computation of Coherence and Cross Power Spectral Density

Coherence is a function that characterizes the degree of correlation between signals (records) at different spatial locations. In this study, the coherence between two different points for the same vector component is modeled using the function proposed by Davenport (1967). In future developments, alternative coherence models and computational methods may be incorporated into the software to enhance its flexibility and applicability.

$$Coh_{\varepsilon\varepsilon}(\mathbf{x}_j,\mathbf{x}_k;f)=\exp\left(-\frac{2f\sqrt{C_{x\varepsilon}^2\left|x_j-x_k\right|^2+C_{y\varepsilon}^2\left|y_j-y_k\right|^2+C_{z\varepsilon}^2\left|z_j-z_k\right|^2}}{\bar{U}(z_j)+\bar{U}(z_k)}\right) \tag{9}$$

Here, the values of $C_{\mathbf{x}\varepsilon}$ represent exponential decay coefficients, which are determined empirically. Depending on whether the coherence function is defined in a one-, two-, or three-dimensional coordinate system, both the exponential decay coefficients and the spatial location parameters can be simplified. As a result, the formulation allows for one-dimensional, two-dimensional, and three-dimensional solution options.

The exponential decay coefficients have been determined as the average of numerous experiments, as reported by Solari and Piccardo (2001). In their study, the values of $C_{\mathbf{x}\varepsilon}$ were established based on data collected from approximately 40 different researches.

$$\begin{array}{lll} C_{xu}=3.0 & C_{xv}=3.0 & C_{xw}=0.5 \\ C_{yu}=10.0 & C_{yv}=6.5 & C_{yw}=6.5 \\ C_{zu}=10.0 & C_{zv}=6.5 & C_{zw}=3.0 \end{array}$$

The cross power spectral density (CPSD) of two continuous turbulence records is a measure of the degree of correlation between the two signals. In the developed program, CPSD is computed using the following equations:

$$S_{\varepsilon\varepsilon}(\mathbf{x}_j,\mathbf{x}_k;f)=\sqrt{S_{\varepsilon\varepsilon}(\mathbf{x}_j,f)S_{\varepsilon\varepsilon}(\mathbf{x}_k,f)}coh_{\varepsilon\varepsilon}(\mathbf{x}_j,\mathbf{x}_k;f) \tag{10}$$

$$S_{\varepsilon\eta}(\mathbf{x}_j,\mathbf{x}_k;f)=\sqrt{S_{\varepsilon}(\mathbf{x}_j,f)S_{\eta}(\mathbf{x}_k,f)}coh_{\varepsilon\eta}(\mathbf{x}_j,\mathbf{x}_k;f) \qquad \varepsilon,\eta=u,v,w \tag{11}$$

2.1.3. Simulation algorithm

The simulation of the turbulence field is carried out by the spectral-representation algorithm. The procedure is organized as follows:

1- The PSD matrix **S** of the turbulence component ε selected for the simulation is obtained evaluating Eqs. (12) for every pair of simulation points $\mathbf{x}_j$ and $\mathbf{x}_k$ ($j,k=1,\ldots,N_m$) in the simulation domain (Fig. 1).

$$\left[\mathbf{S}(f)\right]_{jk}=S_{\varepsilon\varepsilon}(\mathbf{x}_j,\mathbf{x}_k;f)\ \ (j,k=1,..,N_m) \tag{12}$$

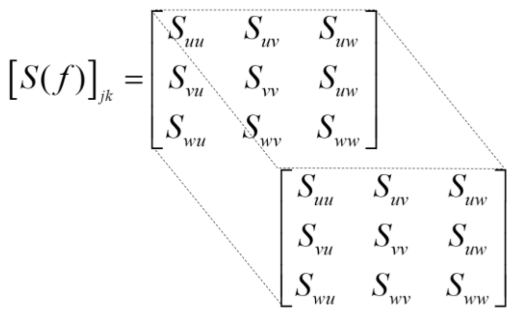

Fig. 1. Solution main matrix

2- Frequency can be discretized using either a linear or logarithmic scale. In this study, the computation is carried out based on a linear frequency scale. Before performing the frequency discretization, it is essential to define the sampling vector parameters used in the analysis. Specifically, the sampling frequency (f_s) and the number of samples (N) should be specified as user-defined input parameters, which would enhance the flexibility and applicability of the analysis process.

Time step, *dt (s):*

$$dt=1/\ f_s \tag{13}$$

Maximum simulation time, T_{max} *(s):*

$$t_{mak}=dt*N \tag{14}$$

Time vector, *t (s)*:

$$t = (0 : N - 1) * dt \tag{15}$$

Minimum resolvable frequency, f_0 (Hz):

$$f_0 = 1 / t_{mak} \tag{16}$$

Nyquist frequency, f_c *(Hz):*

$$f_c = f_s / 2 \tag{17}$$

Frequency vector, f *(Hz):*

$$f = \left[f_0 : f_0 : f_c \right] \tag{18}$$

Therefore, if the frequency vector is to be expressed on a linear scale, it is defined as f_h *(Hz)::*

$$f_h = h\Delta f \qquad (h=1,...,N_{freq}) \tag{19}$$

Here, $\Delta f=f_0$ represents the frequency resolution, and $N_{freq}=N/2$ corresponds to the number of frequency components considered in the simulation.

3- The CPSD matrix, denoted as **S**, is factorized into its eigenvalues and eigenvectors for each frequency value defined by either a logarithmic or linear frequency scale. For this decomposition, either the Cholesky decomposition or the LDL^T decomposition method can be employed. In this study, the LDL^T decomposition technique has been utilized.

$$\mathbf{S}(f_h) = \mathbf{\Theta}(f_h)^T \mathbf{\Gamma}(f_h) \mathbf{\Theta}(f_h) \qquad (h = 1, ..., N_{freq}) \tag{20}$$

Here, $\mathbf{\Gamma}$ and $\mathbf{\Theta}$ denote the matrices containing the eigenvalues and eigenvectors of the CPSD matrix **S**, respectively. The decomposition process defined in the above equation is repeated N_{freq} times ($h = 1{:}N_{freq}$). Subsequently, the core spectral matrix **A** is computed using the eigenvalues, eigenvectors, and uniformly distributed random phase angles**.**

4- The spectral core matrix **A**, composed of a combination of real and complex-valued components, is used to construct the matrix U, which is then transformed using the Inverse Fast Fourier Transform (*IFFT*) algorithm. As a result of this procedure, the time-domain turbulence wind velocities at specified locations are obtained. These data can subsequently be used for the computation of wind-induced forces in the transverse direction or for evaluating base moments.

5- *Power Spectral Density Estimation and Comparison:* To assess the spectral consistency of the generated turbulence velocity records, the generated velocities were converted back to frequency-based power spectral density (PSD) using either the Welch Method (Welch, 1967) or the Multitaper Spectral Estimation Method (Thomson, 1982; Percival and Walden, 1993). The resulting PSD estimates were then compared with the original PSD functions used during the generation of the records. This approach allowed for evaluating the spectral compatibility of the simulated data with the target spectra.

2.2. Case study information

The mesh grid specifications of the example for wind velocity computation and the selected parameters for time-dependent wind velocity calculation, are presented in Table 1. Eurocode (2010) standard was referenced for the parameter values. According to the standard, Terrain Category III represents suburban terrain. The basic wind speed is the velocity calculated from recordings taken over 10-minute averages in the region.

Table 1. Case study information

Wind-exposed a regular 2D vertical mesh grid	Terrain category (Eurocode-2010)	Surface roughness length (z_0)	Friction velocity (u*)	Basic wind speed (U_b)	Sampling frequency (f_s)	Number of samples (N)	Time step *(dt)*	Total time
H=200 m (20 location) B=30 m (4 location)	III	0.3	0.086	30 m/s	20 Hz	16384	0.05 s	820 s

3. Results and discussion

The simulation results of the selected example are summarized under this section. The coordinates of the points where the atmospheric wind velocities are to be computed are presented as a regular 2D vertical grid oriented perpendicularly to the flow in Fig. 2. The Power Spectral Density (PSD) of the turbulence wind velocity component $\varepsilon = u, v, w$ graph computed for a selected point is presented in Figure 3.

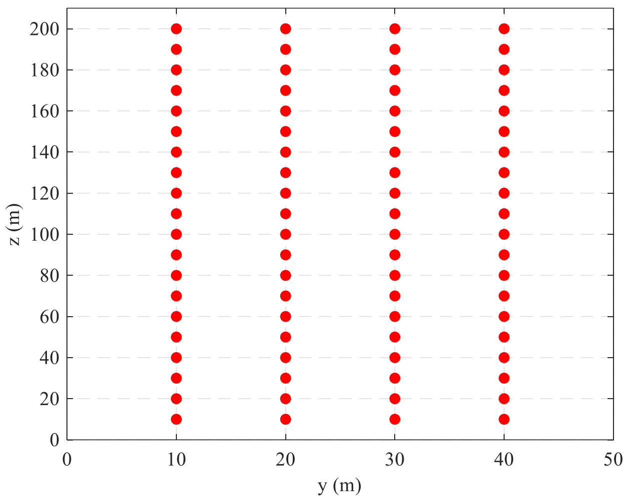

Fig. 2. The spatial coordinates of the points used for the example

As seen in Fig. 3, the PSD characteristics of the turbulence components differ from one another. While the PSD values of the three components are similar in the frequency range between 0.1 Hz and 10 Hz, the longitudinal component becomes significantly dominant at frequencies below 0.1 Hz

It can be stated that the frequencies corresponding to the maximum PSD values obtained for the selected reference wind speed and height are generally far from the fundamental frequency of the structures. Therefore, it can be concluded that the along-wind forces generated by the maximum wind speed data obtained for this example will not have a significant effect on the dynamic response of the structure.

The mean wind velocity in the prevailing wind direction; the time-dependent longitudinal, lateral and vertical atmospheric turbulence velocity components and longitudinal total velocity were calculated for 80 points with specified coordinates (Figs. 4-5). As observed in Fig. 4, the maximum turbulence velocity components (u, v, w) generated are consistent with the PSD used, indicating coherent results. Accordingly, the absolute maximum velocity components $|(u, v, w)|_{max}$ are 35.11, 18.67, and 13.47 m/s, respectively.

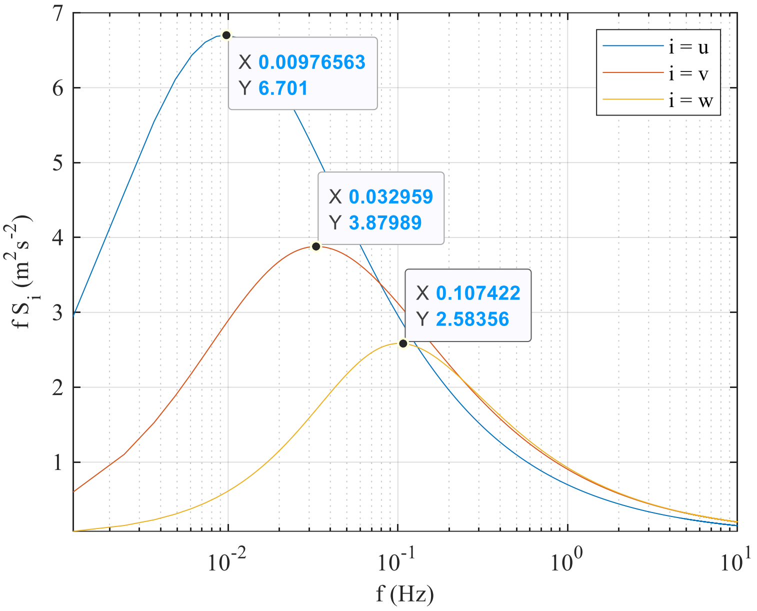

Fig. 3. A sample Kaimal PSD used for the generation of turbulence velocity components
(Heigt of the point=200 m)

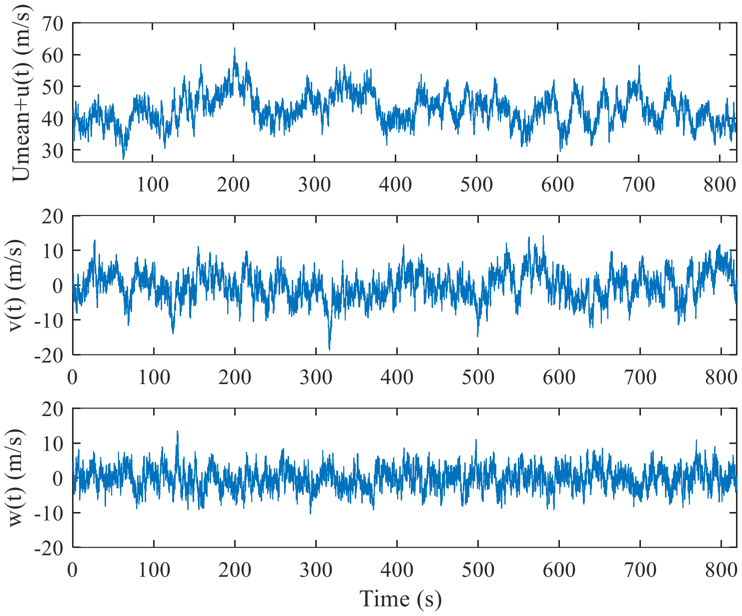

Fig. 4. Wind velocity–time series computed at a point (Height 200 m)

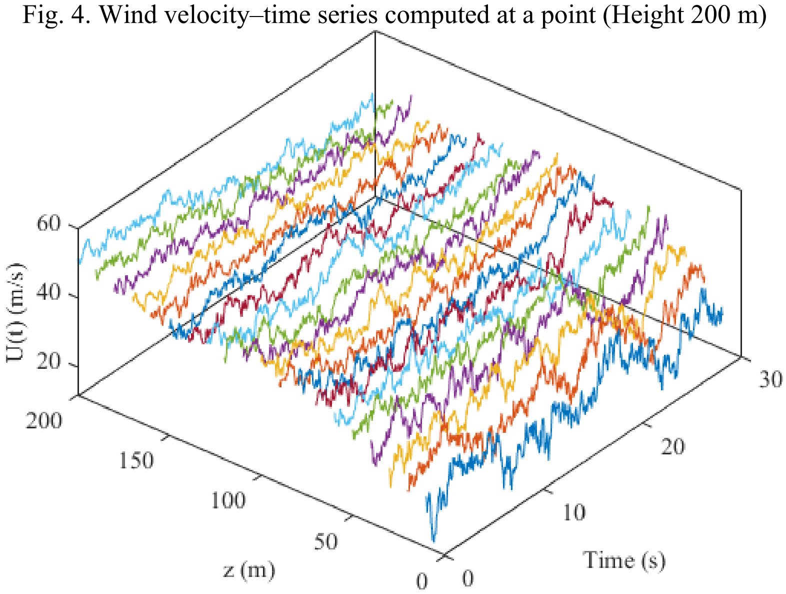

Fig. 5. Longitudinal total velocity, *U(t)*–time series calculated at various elevations

In the subsequent part of the study, the agreement between the mean values calculated from the longitudinal wind velocity time series obtained and the initial mean wind speed was examined at different heights ;and the maximum and minimum wind speeds were compared (Fig. 6). It was observed that the calculated mean wind speeds are very close to the target mean values. Accordingly, it can be stated that the resulting turbulence components have approximately zero-mean, which is generally a desirable condition in turbulence modelling.

It has been observed that the maximum wind speed generally increases with height, and the shape of the resulting maximum wind speed profile is consistent with the mean wind velocity in Figure 6. This is a desirable behavior for the generated wind records. On the other hand, deviations from this trend have been observed at certain points. These deviations are attributed to the influence of the coherence function and the random process (Serhatoğlu, 2025). This behavior closely resembles real atmospheric wind characteristic.

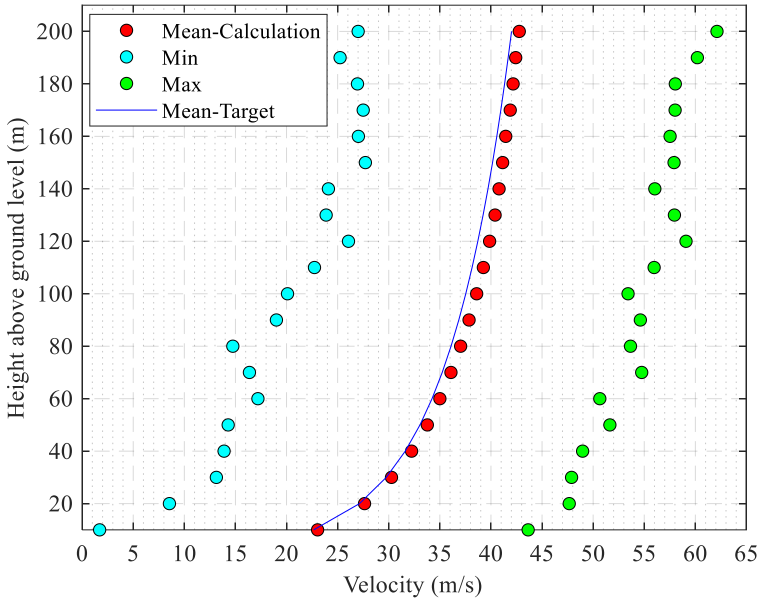

Fig. 6. Mean and maximum/minimum wind velocities calculated from longitudinal velocity *U(t)*–time series at different heights

In the final part of the study, the estimated PSD derived from the generated wind velocity data was evaluated for its consistency with the reference PSD used in the calculations (Fig. 7). Based on the comparison results, it can be stated that the generated records exhibit an acceptable level of agreement with the reference PSD.

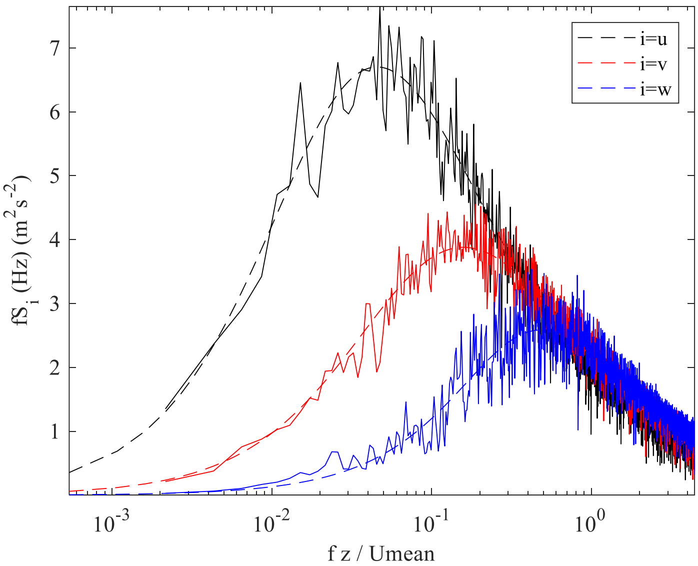

Fig. 7. Comparison of the PSD estimates obtained from generated wind velocities with the reference Spectrum for a sample point (Height 200 m)

4. Conclusions

This study proposes a methodology for generating multivariate wind speed fields to be used in the calculation of time-dependent wind loads on structures and in applications such as energy production. Therefore, a specialized software was developed using the MATLAB language to enable the practical simulation of time-dependent wind velocity components.

To verify whether the developed software produces realistic results, a simulation was conducted on the multi-point example. The results were observed to resemble real atmospheric wind velocity behavior.

Based on the obtained time-dependent wind velocity components, it is possible to compute the corresponding pressure and force distributions over a specific area or all of the structure surfaces. The software is intended to be further enhanced by incorporating various turbulence parameters, PSD and coherence functions and new methodologies to establish a more comprehensive simulation framework.

This approach can offer a cost-effective and versatile solution for wind analysis, enhancing preliminary design processes and broadening applications in structural and energy-related fields.

References

Branlard, E. (2017). Wind turbine aerodynamics and vorticity-based methods: Fundamentals and recent applications. *Springer International Publishing (ebook).* doi: 10.1007/978-3-319-55164-7

Cheynet, E. (2020). Wind field simulation (text-based input). *Zenodo*. Retrieved from https://zenodo.org/record/3823864

Deodatis, G. (1996). Simulation of ergodic multivariate stochastic processes. *Journal of engineering mechanics*, *122*(8), 778-787.

Davenport, A. G. (1967). *The dependence of wind loads on meteorological parameters.* International Research Seminar Wınd Effects On Buıldıngs And Structures. Ottawa, Canada.

Di Paola, M. (1998). Digital simulation of wind field velocity. *Journal of Wind Engineering and Industrial Aerodynamics*, *74*, 91-109

Ding, Q., Zhu, L., and Xiang, H. (2006). Simulation of stationary Gaussian stochastic wind velocity field. *Wind and Structure, 9(3)*, 231-243.

European Committee for Standardization (2011). *Eurocode 1: Actions on structures – Part 1–4: General actions – wind actions. EN 1991-1-4:2005/ AC:2010 (E). Europe: European Standard (Eurocode),* EU.

Goto, H., & Toki, K. (1969, January). Structural response to nonstationary random excitation. In *Proc. 4th World Conf. on Earthquake Engrg., Santiago, Chile* (Vol. 1, pp. 130-144).

Kwon, D. K., Carassale, L., and Kareem, A. (2011). "VORTEX-Winds on-line wind simulator (VOWS) : on-line simulation of Gaussian three-dimensional multivariate wind fields." *NatHaz Modeling Laboratory Report*, Univ. of Notre Dame.

Percival, D. B., & Walden, A. T. (1993). *Spectral analysis for physical applications: Multitaper and Conventional Univariate Techniques.* Cambridge; New York, NY, USA: Cambridge University Press.

Serhatoğlu, C. (2025). *Investigation of Wind Performance of Tall Buildings in Time Domain* (Doctoral thesis, Bursa Uludağ University, Turkey)

Shinozuka, M. (1985). Lecture at CISM Course on stochastic methods in Struct, Engrg. Int. *Center for Mech. Sci., August*, 28-30.

Shinozuka, M and Deodatis, G. (1991). Simulation of stochastic processes by spectral representation. *Applied Mechanics Reviews, 44(4),* 191–204.

Solari, G., & Piccardo, G. (2001). Probabilistic 3-D turbulence modeling for gust buffeting of structures. *Probabilistic Engineering Mechanics, 16(1),* 73-86.

Thomson, D. J. (1982). *Spectrum estimation and harmonic analysis*. Proceedings of the IEEE 70, no. 9:1055–96.

Wang, J., Cheynet, E., Snæbjörnsson, J. Þ., & Jakobsen, J. B. (2018). Coupled aerodynamic and hydrodynamic response of a long span bridge suspended from floating towers. *Journal of Wind Engineering and Industrial Aerodynamics*, *177*, 19-31.

Welch, P. (1967). The use of fast Fourier transform for the estimation of power spectra: a method based on time averaging over short, modified periodograms. *IEEE Transactions on audio and electroacoustics*, *15*(2), 70-73.

Wittig, L. E. and Sinha, A. K. (1975). Simulation of multicorrelated random processes using the FFT algorithm. *The Journal of the Acoustical Society of America, 58(3)*, 630–633.

4th International Civil Engineering & Architecture Conference
17-19 May 2025, Trabzon, Türkiye

Dynamic characterization of polycarbonate: A constitutive model capturing temperature and strain rate effects

Cem İ. Kapcı*[1], Merve Z. Tekin[1], Aiman Tarıq[1], Babür Deliktas[1], Mustafa Ö. Yaylı[1]

[1] *Bursa Uludag University, Faculty of Engineering, Department of Civil Engineering, Artificial Intelligence and Computational Mechanics Laboratory, 16059, Bursa, Turkey*

Abstract. Polycarbonate (PC) is a widely used material known for its impact resistance, transparency and thermal properties. However, there are challenges in capturing its behavior under different temperatures and strain rates. The stress drop after yielding and subsequent plastic flow behavior are examples of the major challenges that classical hardening models cannot represent. In this work, a robust constitutive model is developed to accurately describe the mechanical response of PC. The model is based on experimental data from tensile and compression tests performed at various temperatures and strain rates. First, a validation study was carried out for the use of the developed model in a finite element program. The developed model was then implemented in Abaqus/Explicit for impact simulations, allowing realistic predictions of failure modes, crack propagation and fracture behavior. The simulation results were confirmed to show improved accuracy in capturing the temperature and strain rate dependent response of the PC. This research advances predictive modeling for PC, making it highly valuable for applications in protective structures in civil engineering, automotive crashworthiness and impact resistant materials.

Keywords: Polycarbonate (PC); Constitutive model; Strain rate; Temperature dependence; Impact simulation

1. Introduction

Engineering thermoplastics are widely used in the automotive, aerospace and defense industries due to their high impact strength, light weight and ease of production. Plastic components in these industries need to withstand external factors structurally and aesthetically. Especially exterior automotive parts play a crucial role in terms of functionality and safety. Polycarbonate (PC), known for its high impact resistance, optical transparency and thermal stability, is widely used in applications such as headlight covers and protective elements.

The mechanical behavior of PC under impact loading is complex due to its sensitivity to temperature and strain rate. Wei et al. (2024) modeled the deformation behavior of PC under varying temperatures and loading rates using experimental and numerical methods. Husain et al. (2024) evaluated post-impact deformations through Dynamic Enhancement Factor (DEF) obtained from quasi-static and dynamic tests. Mullaoglu et al. (2024) investigated the impact response of PC panels under high velocity steel projectile impacts and analyzed the effects of impact angle and position.

Ma et al. (2024) investigated the effect of fabric weave patterns on the energy absorption of PC-based composites. Ćwiklak et al. (2024) demonstrated the importance of accurate material parameter definitions for PC-based glass and panel systems under bird impact simulations. Kholoosi and Nia (2024) compared glass, PC and TPU layer systems and showed that PC significantly increases impact resistance.

Bozkurt (2025) analyzed how curvature and core thickness affect ballistic performance in honeycomb structures. Long et al. (2025) emphasized that combining shear thickening fluids (STF) with PC increases energy absorption under impact. Li, Nie, and Wu (2025) developed a hybrid model combining SPH and FEM to analyze damage in transparent armor systems composed of sapphire, glass and PC layers.

Lance et al. (2025) studied the high strain rate behavior of polymers, emphasizing viscoelastic and shock absorbing properties. Aziukovskyi et al. (2024) proposed a nonlinear modeling approach for external ballistic problems. Li et al. (2024) established a mathematical correlation between ballistic resistance and mechanical properties of armor steel based on the Johnson-Cook model. Ongaro et al. (2024) investigated computational and lumped parameter models for internal ballistic processes and evaluated their strengths and limitations.

An et al. (2024) applied machine learning techniques to model the relationships between mechanical properties and ballistic performance and identified key optimization strategies.

* Corresponding author, E-mail: cemibrahimkapci@gmail.com

https://doi.org/10.31462/icearc2025_ce_sme_071

The existing literature is predominantly simulation studies, which are limited for temperature and strain rate sensitive materials. In this study, the effects of temperature and strain rate dependent variations in material parameters for PC impact analysis are comprehensively investigated for a polycarbonate lens.

2. Material model used for PC

Finite element method (FEM) modeling of amorphous thermoplastic polymers such as polycarbonate presents significant challenges due to the complex mechanical properties of the material. In addition to exhibiting viscoelastic and viscoplastic behavior, this material is notable for its sensitivity to temperature and strain rate. Therefore, advanced material models are required to accurately represent the nonlinear, time-dependent and temperature-dependent behavior. In this context, it is inevitable to develop parametrically optimized material models calibrated with experimental data in order to obtain reliable results in multi-axis loading situations. Furthermore, in dynamic analyses under high strain rate, the integration of appropriate constitutive (relative) relations is required for the material model to adequately reflect time-dependent effects.

In this study, to overcome these problems, the Modified Liu-Subhash model is preferred to characterize the nonlinear mechanical behavior of PC (Wei, 2024). The expression is as follows:

$$\sigma(\varepsilon_p,\ \dot{\varepsilon}\,, T) = \ (1 - m_1 T^{*m_2})[A(e^{\alpha\varepsilon_p + \eta_1} - 1) + \mu e^{B}(e^{\gamma\varepsilon_p + \eta_2} - 1)](1 + C(ln\,\dot{\varepsilon}\,^{*})^{p}\,) \quad (1)$$

Here, A, B, α, β and γ are undetermined parameters and ε is the total strain of the specimen. A is associated with the yield stress and governs the stress level of the flow platform. The variables α and β determine the modulus of the elastic phase and the transition phase of the curve, respectively. Parameters β and γ primarily govern the plastic phase of the curve and changing their values can change the starting point and upward slope of the material strengthening phase. Here ε_p is the plastic strain, η_1 is the product of α and ε_p, and η_2 is the product of γ and ε_p . Moreover, the fluctuation of the ambient temperature and the loaded strain rate has a significant influence on the yield stress of the PC specimen, and its law is the same as the development trend of the temperature function and strain rate function of the J-C model. m_1 and m_2 are unspecified parameters. T^* represents the dimensionless temperature and is defined as $T^*= (T-T_r) / (T_g - T_r)$. T represents the ambient temperature in the experiment. T_r represents the room temperature, which is 298K. The glass transition temperature (T_g) of PC is 413K. Since the strain rate strengthening effect of PC at high strain rates is more significant than at low strain rates, p is used as a correction factor. $\dot{\varepsilon}^* = \dot{\varepsilon} / \dot{\varepsilon}_0$ .where $\dot{\varepsilon}_0$ represents the reference strain rate, typically ranging from 0.001 s^{-1} to 1 s^{-1}

2.1. VUHARD implementation in abaqus

In order to integrate this unique material model into finite element analysis, the user-defined hardening subroutine VUHARD, which is compatible with the Abaqus Explicit solver, was used. VUHARD allows to describe the complex hardening behavior of the material during plasticization, especially in cases where standard material definitions are insufficient. In this study, the evolution of the yield stress in the developed material model depending on variables such as equivalent plastic strain and temperature was integrated into the Abaqus environment through the VUHARD subroutine written in Fortran. Thus, the accuracy of the developed model in numerical analyses could be tested and compared with experimental findings.

3. **Validation of constitutive model**

The Liu-Subhash constitutive model parameters suitable for the stress-strain relationship of polycarbonate (PC) are given in Table 1. With these parameters, a three-dimensional, quasi-static tensile specimen model was created in ABAQUS software. The dimensions of the model are taken from Wang et al. (2019) and the experimental data are taken from Wei et al. (2024). The length of the specimen is 450 mm, the gauge is 25 mm and the thickness is 4 mm. Other values are given in Fig. 1(a). A fine mesh was used in the center of the neck region of the specimen, with element dimensions of 0.8 mm × 0.8 mm × 0.8 mm × 0.8 mm × 0.8 mm (Fig. 1(b)). As we proceeded along the length of the specimen, the mesh size was gradually increased. The element type used is C3D8R.

The results of the tests performed at various speeds and temperatures were repeated exactly and which tests were performed at which speeds and temperatures are given in Table 2.

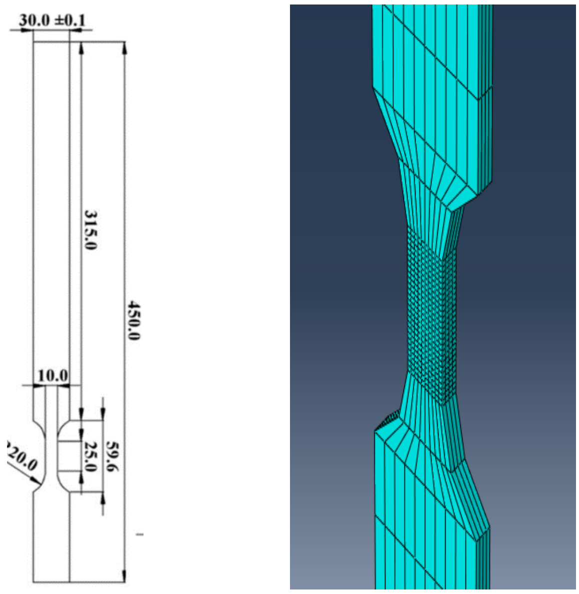

a) Abaqus model b) Meshing of tensile test

Fig. 1. Finite element model

Table 1. Values for parameters of the constitutive equation

Parameters	Values
A	-62.70 MPa
B	-1.62
μ	2.46 MPa
α	-30.99
γ	4.54
η_1	-1.86
η_2	0.27
m_1	0.63
m_2	1.00
C	0.002
p	2.7

Table 2. Variables of Simulation

Serial Number	Strain rate / s^{-1}	Ambient temperature / K
1	200	298
2	200	348
3	200	398
4	4	298
5	20	298

4. Finite element analysis

In the finite element model in this study, a ballistic impact simulation is performed to evaluate the accuracy of the modified Liu-Subhash model in the field of impact dynamics.

4.1 Finite Element Model Description

In this study, the outer lens of a car headlight, which is known to be made of polycarbonate material, was used for representation. It is shown in Fig. 2. The width of the lens, modeled as the outer lens of an average car headlight, is 570 mm at its widest point. Fig. 3 shows how it was modeled in Abaqus

The projectile is described as cylindrical with a diameter of 12.9 mm and a length of 25 mm. The projectile was created as a solid object with no defined material. The mass of the projectile is 25 grams. The projectile is defined as 60 m/s. The contact between the projectile and the target plate is set to surface-to-surface contact. The contact property option set a sliding friction coefficient of 0.1 for the contact surface of the projectile with the target plate and defined the usual contact behavior as hard contact

Fig. 2 Car headlight and exterior lens

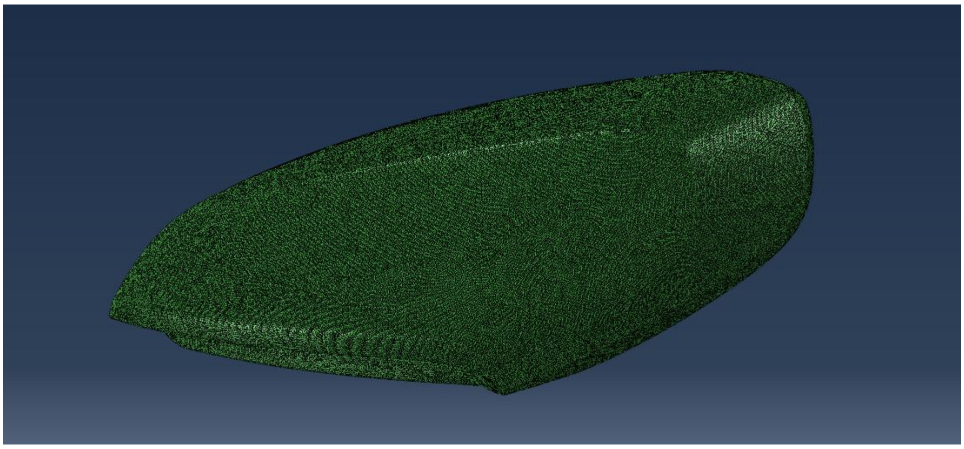

Fig. 3 Abaqus model

4.2 Finite element model result

At the end of the simulation, the behavior of the lens against impact is modeled and compared with the results of the simulation with the Johnson-Cook model. The two models were given an inlet velocity of 60 m/s and their behavior as residual velocity was compared. Both models gave similar results. Graphs for the 2 models are shown in Fig. 4.

5.Conclusions

Although the modified Liu-Subhash model gave comparable results to the Johnson-Cook model, it showed significant differences in behaviour under impact loading of the polycarbonate lens. These differences were particularly evident in the post-yield regime and at varying strain rates, with the Liu-Subhash model more accurately representing the viscoplastic properties of the material. This indicates that although both models produce numerically similar results in some scenarios, their predictive capacities differ in reflecting the actual mechanical response of the polycarbonate lens under dynamic loading.

Therefore, diversification of experimental data and evaluation of multiple shots in model validation studies will make important contributions to increase the reliability of simulation results and to compare the performance of material models more accurately.

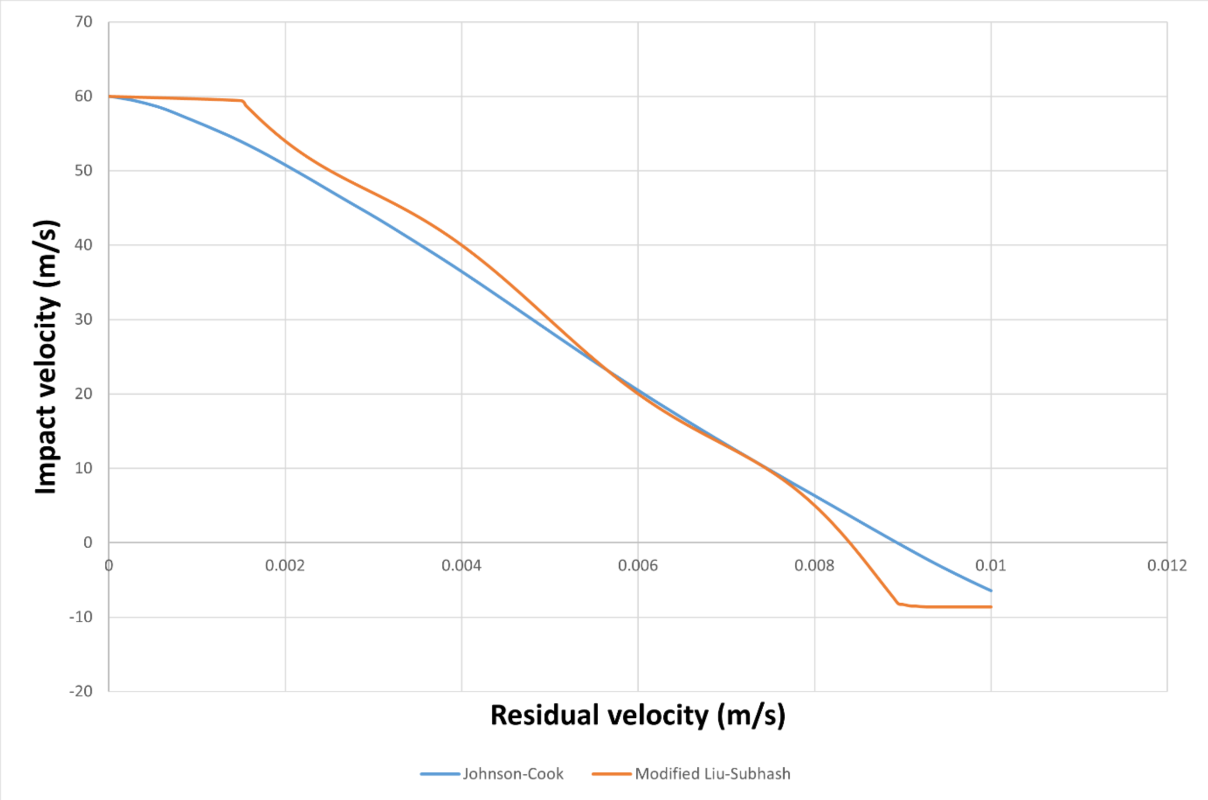

Fig. 4 Impact Velocity-Residual Velocity

References

An, R., Wang, Y., Bao, J., Jiang, B., Cheng, H., Cheng, X., & Wang, F. (2024). Predicting ballistic resistance based on the mechanical properties of armored ceramics. *Journal of Materials Research and Technology, 32*, 2370–2385.

Aziukovskyi, O., Gristchak, V., Hryshchak, D., Ziborov, K., Fedoriachenko, S., & Harkavenko, D. (2024). Determining the parameters of the functioning for a nonlinear ballistic system in a real external environment. *Naukovyi Visnyk Natsionalnoho Hirnychoho Universytetu, (2)*, 140–144.

Bozkurt, I. (2025). Effect of curvature angle and structural configurations on dynamic performance of honeycomb sandwich structures. *Mechanics of Advanced Materials and Structures*, 1–22.

Ćwiklak, J., Gołda, P., Goś, A., Kobiałka, E., & Krasuski, K. (2024). Experimental and numerical investigations on polycarbonate samples and rotorcraft windshield for bird model impacts. *Archives of Transport, 70*(2), 79–96.

Husain, A., Khan, S. H., Mourad, A. H. I., & Ansari, R. (2024). Ballistic performance of polycarbonate plate subjected to truncated cone projectile. *Diffusion Foundations and Materials Applications, 36*, 67–73.

Kholoosi, F., & Nia, A. A. (2024). Experimental and numerical investigation of the behavior of multi-layer windshield consisting of glass and polycarbonate against bird strike. *International Journal of Impact Engineering, 194*, 105092.

Lance, P., Ortellado, L., & Gómez, L. R. (2025). Functional polymers for impact absorption. In *Soft materials for functional applications* (pp. 381–414). Singapore: Springer Nature Singapore.

Li, D., Huang, F., Ren, B., Zhang, W., Xiong, J., Zhou, B., & Guo, X. (2024). Ballistic analysis of high-performance armor steel by numerical simulation. *Scientific Reports, 14*(1), 11466.

Li, J., Nie, H., & Wu, J. (2025). Structure design optimization of sapphire transparent armor through numerical simulation of ballistic impact response. *Materials Today Communications, 42*, 111404.

Long, S., Chen, H., Yao, X., & Liu, T. (2025). Response of shear thickening fluids to high velocity ballistic impact. *International Journal of Impact Engineering*, 105248.

Ma, Y., Li, X., Zhang, B., Tan, H., Huo, S., Liu, X., ... & Sun, J. (2024). Influence of fabric structure of aramid-reinforced polycarbonate composites on its ballistic resistance verified by experiment and simulation. *Journal of Materials Engineering and Performance*, 1–12.

Mullaoglu, F., Usta, F., & Turkmen, H. S. (2024). The impact-induced deformation characteristics of polycarbonate panels. *Polymer Engineering & Science, 64*(6), 2579–2593.

Ongaro, F., Robbe, C., Papy, A., Stirbu, B., & Chabotier, A. (2024). Modelling of internal ballistics of gun systems: A review. *Defence Technology*.

Wang, H., Deng, X., Wu, H., Pi, A., Li, J., & Huang, F. (2019). Investigating the dynamic mechanical behaviors of polyurea through experimentation and modeling. In P. Lance, L. Ortellado, & L. R. Gómez (Eds.), *Soft materials for functional applications* (pp. 875–884). Singapore: Springer Nature Singapore.

Wei, G., Wang, J., Zhang, H., & Hu, J. (2024). Analysis and methods for studying the mechanical properties of polycarbonate subjected to dynamic loading situations. *Mechanics of Advanced Materials and Structures*, 1–19.

4th International Civil Engineering & Architecture Conference
17-19 May 2025, Trabzon, Türkiye

Post-earthquake damage status and numerical analysis of a historical masonry building

Kağan Çanakçı*[1], Muhammet Karaton[1]

[1] Fırat University, Department of Civil Engineering, 23119 Elazığ, Türkiye

Abstract. Turkey, due to its geographical location, possesses a rich stock of historical structures inherited from the Roman, Byzantine, Seljuk, and Ottoman periods. These historical buildings have a variety of sizes, shapes and materials that reflect the technical and aesthetic features of their periods. While preserving and strengthening these structures and passing them on to future generations makes an important contribution to preserving our cultural heritage, the fact that most of these historical structures are masonry structures and are generally designed to carry vertical loads makes them of special importance in strengthening works. Because the resistance of historical masonry structures to dynamic lateral loads such as earthquakes is quite low. In particular, the Kahramanmaraş earthquakes that occurred in 2023 have once again revealed the requirement of evaluating the dynamic performance of historical artifacts. For this reason, determining the performance of historical structures under external loads and increasing the resistance of structures with inadequate performance with appropriate retrofitting methods emerges as a critical engineering problem. In this study, the damage status of a historical masonry building after the 2023 Elbistan-Kahramanmaraş earthquake was examined and the causes of damage were examined in detail. In this context, the finite element model of the structure was created with the macro modeling technique and dynamic analyzes were performed. The analyzes were performed with the nonlinear analysis method in the time history using the SAP2000 finite element software. As a result of the numerical analyzes performed using the Malatya records of the 2023 Elbistan-Kahramanmaraş earthquake (Mw = 7.7), the post-earthquake damage status of the building was compared with the numerical model.

Keywords: Masonry building; Macro modelling; Dynamic analysis; Time history analysis

1. Introduction

Turkey is a country with high seismic activity and hosts numerous historical structures that bear the traces of different civilizations throughout history. A significant portion of these historical structures were constructed using the masonry construction technique. In masonry structures, the majority of static and dynamic loads are carried by the walls. Earthquakes are among the external factors that cause the most damage to these walls. Earthquake forces create tensile and shear stresses in the walls, causing cracks to form, wall elements to separate, and ultimately, structures to partially or completely collapse. Therefore, determining the performance of historical structures under external loads and increasing the resistance levels of structures that are found to be inadequate in terms of performance with appropriate reinforcement methods emerge as an important engineering problem.

In this context, there are many studies in the literature. In a study conducted in 2021 [1] (Nochebuena-Mora et al., 2021), a macro-model of a 49 meter high historic masonry bell tower was developed, and performance analyses under different loading conditions were carried out. The static and dynamic effects of the bell mass were incorporated into the model. To evaluate the tower's performance, modal analysis, nonlinear static pushover analysis, and nonlinear time-history dynamic analysis were performed and compared. Seismic forces were applied in both directions to determine the possible crack patterns in the structure, and it was calculated that the crack widths ranged between 1 and 5 mm under the maximum displacement scenario.

It was observed that the structure remained within linear behavior limits in all three methods. Despite the high computational demand and long analysis times, the nonlinear dynamic analysis was identified as the most accurate method. In another study, four different finite element models were developed for a U-shaped masonry prototype composed of stone units, and nonlinear dynamic analyses were conducted (Maccarini et al., 2018). Three of these models were created using a macro-modeling approach, while one was developed using a simplified micro-modeling technique. It was determined that the macro-modeling approach reduced the number of degrees of freedom and computation times by 90%. In the next step, analyses were carried out on a rectangular-shaped

* Corresponding author, E-mail: canakcikagan@gmail.com

https://doi.org/10.31462/icearc2025_ce_sme_085

structure, and the results were compared with those from the first stage. Through this comparison, the influence of building geometry on strength and ductility was evaluated. In order to the seismic performance of the historic masonry structure known as Arge-Tabriz, a numerical model was developed using a macro-modeling approach (Hoveidae et al., 2021). Nonlinear time-history dynamic analysis and static pushover analysis were performed on this model. For the dynamic analysis, four different earthquake records with magnitudes ranging from 6.5 to 7.7 were utilized. Field surveys were conducted to identify existing crack patterns in the structure, and these were compared with the cracks obtained from the analysis results. The comparisons revealed that the finite element model showed a high level of agreement with the actual condition of the structure. It was concluded that, due to the inherently low seismic resistance of masonry structures, the primary cause of the observed damage over the years has been the occurrence of earthquakes. A finite element model was developed to investigate the structural behavior, assess the seismic performance, and identify potential damage mechanisms of a section of the Tabriz Bazaar, recognized as the world's oldest bazaar (Aghabeigi & Farahmand-Tabar, 2021). The finite element model was developed using a macro-modeling approach. Mechanical tests were conducted to determine the material properties of the structure. Static analysis, modal analysis, and nonlinear time-history dynamic analysis were performed to evaluate the structural performance. Despite the structure demonstrated adequate strength under its self-weight, certain sections became unsafe under seismic loading when yield criteria were considered. The results indicated that the most critical part of the structure was the main dome, which necessitated strengthening interventions. Carbon fiber reinforcement was proposed for the dome and the walls. After the strengthening, performance analyses showed that the lateral load-bearing capacity of the walls increased by approximately 575%.

A three-dimensional finite element model was created using macro elements to determine the performance of a historical masonry building that experienced large displacements on its front facade as a result of the earthquakes that occurred in Italy (Barbieri et al., 2013). Nonlinear time-history dynamic analyses were conducted on the model. The building has a rectangular plan with dimensions of 67 × 16 meters and a height of 22 meters. A total of 465,490 solid finite elements were generated for the model. Consistent with the observed damage, dynamic analysis results indicated that the façade walls experienced significant damage within the first seconds of seismic loading. It was concluded that the building's seismic performance was insufficient, and necessary retrofitting measures were recommended. The study revealed that numerical simulations are very important for evaluating the seismic performance of historical structures.

A finite element model was created using the macro modeling method to determine the seismic performance of a masonry educational building damaged in the earthquake that occurred in Croatia in 2020 after reinforcement (Moreti et al., 2022). Three different numerical models were created by selecting three different reinforcement methods. The first of these models was strengthened with carbon fiber, the second with reinforced concrete, and the third with both carbon fiber and reinforced concrete. Nonlinear pushover analysis was applied to the models and the performance analyses of the strengthened buildings were compared. The strengthening methods were compared in terms of earthquake performance capacity, cost and environmental impact. It was concluded that the reinforced concrete strengthening method was the best method in terms of capacity, but the carbon fiber method was a better method in terms of environmental impact. In their study, Jasieńko et al. (2021) aimed to identify the causes of structural damage in a historic masonry structure resulting from various loading combinations. The building consists of a dome, drum, buttresses, arches, and columns. To model this complex structural system, plastic material models were employed within the finite element method. The connection between the dome and the buttresses was modeled using three-dimensional solid elements, and a diameter-to-thickness ratio was proposed for the dome geometry. Nonlinear pushover analyses were performed on the building model to assess its performance, and crack patterns consistent with the historically observed damages were obtained, thus validating the accuracy of the numerical model.

2.Historical house

In this study, a historical building located in Malatya province was studied. The historical building was located in Malatya, Turkiye, at coordinates 38.2817° North, 38.2606° East. The location of the building on the Turkish Earthquake Hazard Map is shown in Fig. 1. The masonry walls on the ground floor of the building are built entirely of rubble stone, but the first floor consists of different masonry material properties called stone and adobe. The average floor height is 3.15 meters, and the total construction area is 252 m^2. The façade view of the building is given in Fig. 2. The plans and façade views of the building are given in Fig. 3. The building was determined to be heavily damaged as a result of the February 6 Kahramanmaraş earthquakes.

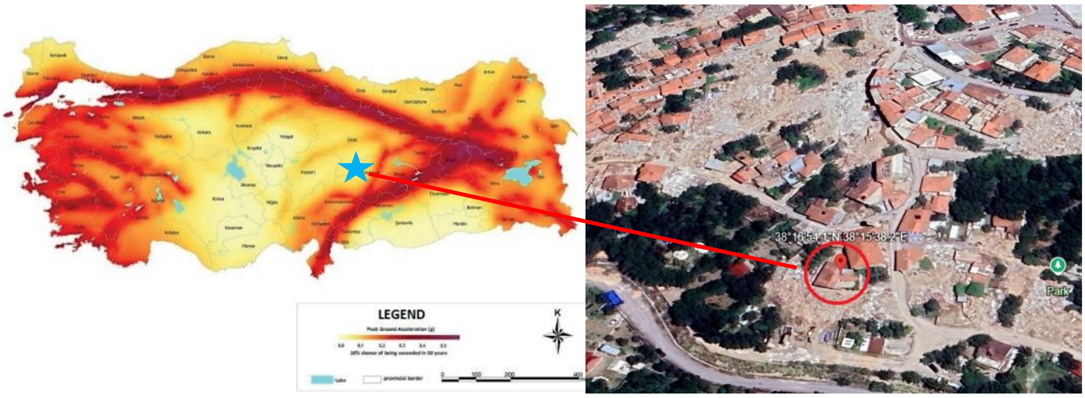

Fig. 1. The location of the building on the Turkish Seismic Hazard Map (TSHM, 2018)

Fig. 2. Façade of the building

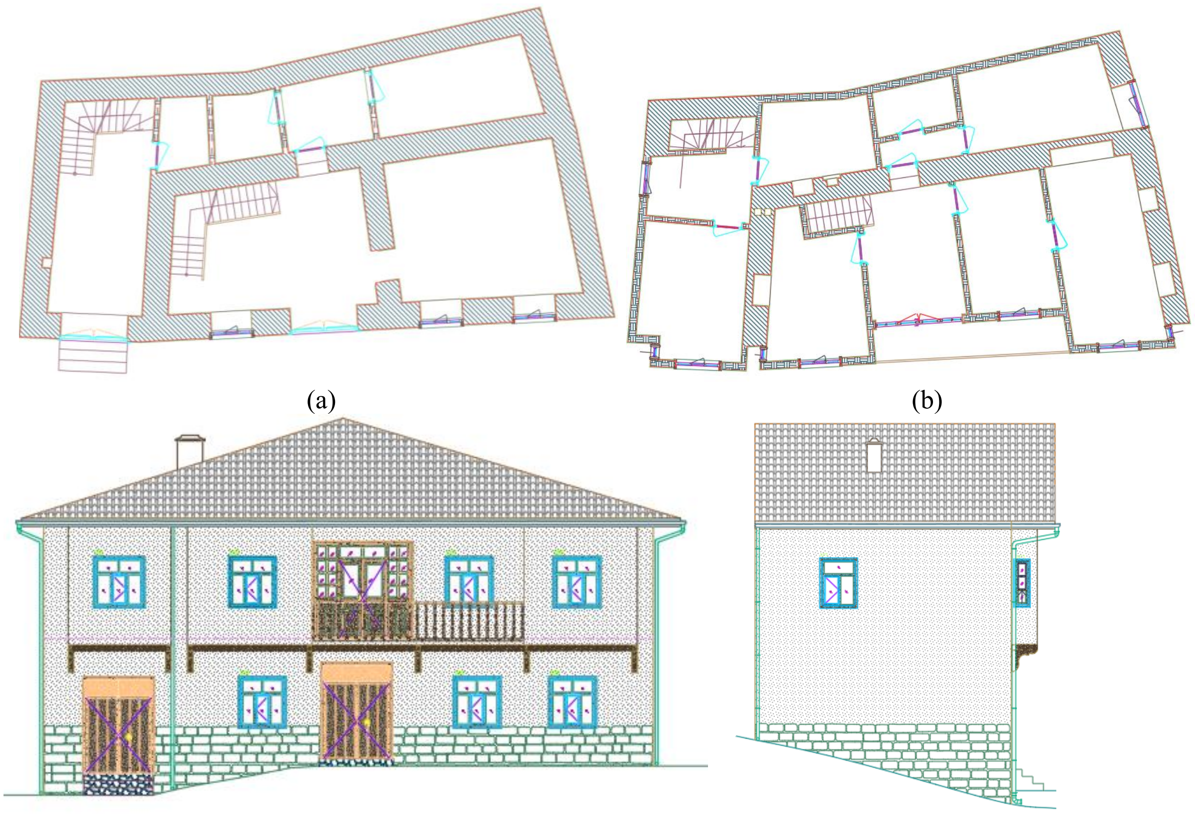

Fig. 3. Building (a) Ground floor plan, (b) 1st floor plan, (c) front façade, (d) side façade

3. Damage status of the structure

After the 2023 Elbistan-Kahramanmaraş earthquakes, the damage status of the structure was examined in order to compare it with the numerical analyzes of the structure. In the examinations, it was determined that the masonry walls on the ground floor of the structure were constructed as rubble stone, but the first floor was composed of different masonry material properties called stone and adobe. It was observed that the adobe and stone materials on the first floor of the structure had different strengths. For this reason, separations were observed at the wall joints. It is thought that the significant damages in the structure occurred due to the different strengths of these materials. Due to the materials used in the structure inadequate compressive and tensile strength, shear cracks was observed on the edges of the windows as a result of seismic loading. The areas where the most damages occurred are shown in Fig. 5, and sample photographs of the damages in the structure are shown in Fig. 6. In addition, there was shedding in the materials and plasters of all walls.

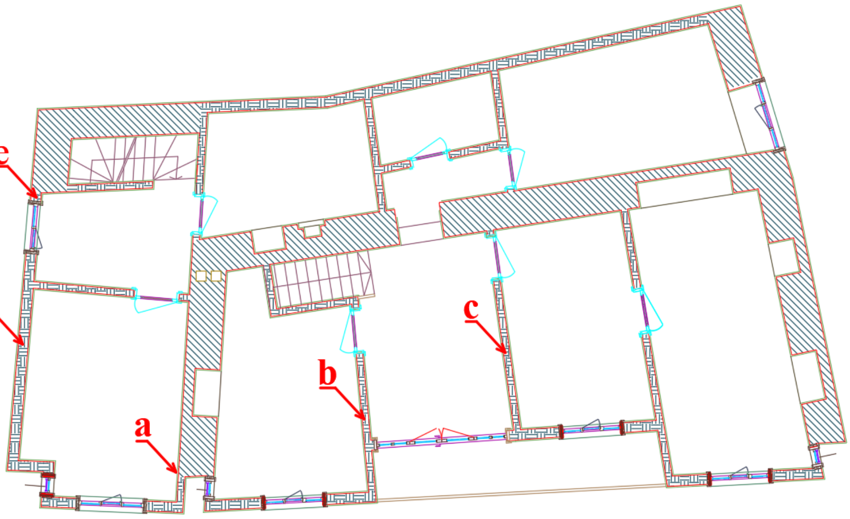

Fig. 5. The regions where most damage occurs.

(a) (b) (c)

(d) (e)

Fig. 6. Example photos of the damages.

4. Numerical solution

In this section, the stability analyzes of the current status of the structure under static and dynamic loads are examined. The finite element method was used to perform these analyses, with solutions obtained using the SAP2000 finite element software. The finite element model, created using the macro-modeling approach, consists of a total of 5.934 nodes and 3.046 solid elements. The finite element model of the historical structure is shown in Fig. 7. The foundation-soil interaction of the structure is defined as fixed support. Two different materials, stone and adobe, were defined for the masonry walls. The material properties of the stone and adobe walls are given in Table 1 and the this material properties were obtained according to the composite material theory. The linear analysis method in the time history was applied to the building using the records of the 2023 Pazarcık-Kahramanmaraş earthquake (Mw = 7.7) (Fig. 8). The dynamic response of the building was evaluated.

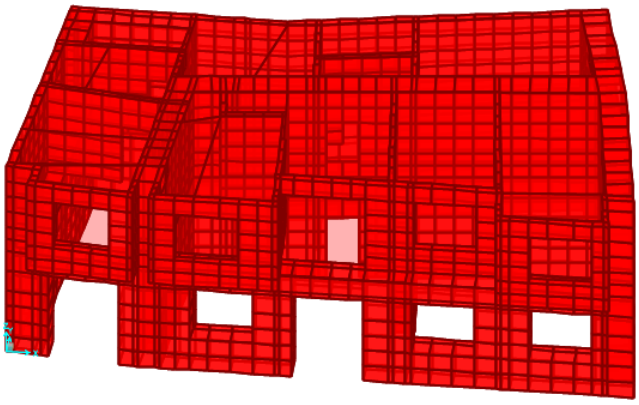

Fig. 7. Finite element model of historical structure.

Table 1. Masonry wall material properties (Mpa)

Wall	Young Modulus	Compressive strength	Tensile strength	Poisson ratio
Stone	21276	15.95	1.69	0.28
Adobe	136.5	1.4	0.14	0.25

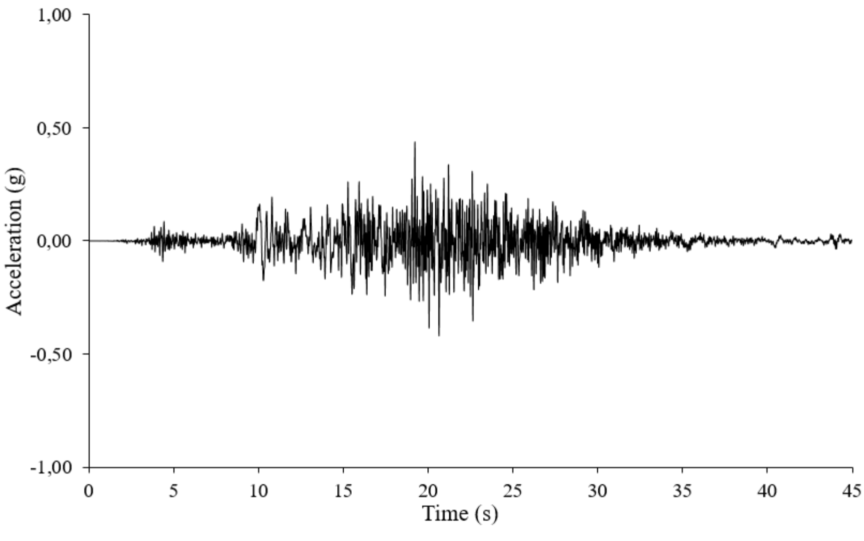

Fig. 8. 2023 Acceleration record of the Elbistan-Kahramanmaraş earthquake

The time history graph of the displacement values in the x direction for node 5056, which is the top point of the structure, under the combined effect of static and seismic loads, is shown in Fig. 9. It can be observed that the maximum displacement occurs at 10.31 seconds. As seen in Fig. 9, the maximum and minimum displacement values were recorded as -0.555 mm at 10.31 seconds and 0.513 mm at 9.87 seconds, respectively. The corresponding maximum and minimum principal stress-strain curves for these moments are presented in Fig. 10. A detailed examination of the obtained results revealed that the maximum principal stress, minimum principal stress, and shear stress were found to be 0.266 N/mm², -0.321 N/mm², and 0.299 N/mm², respectively.

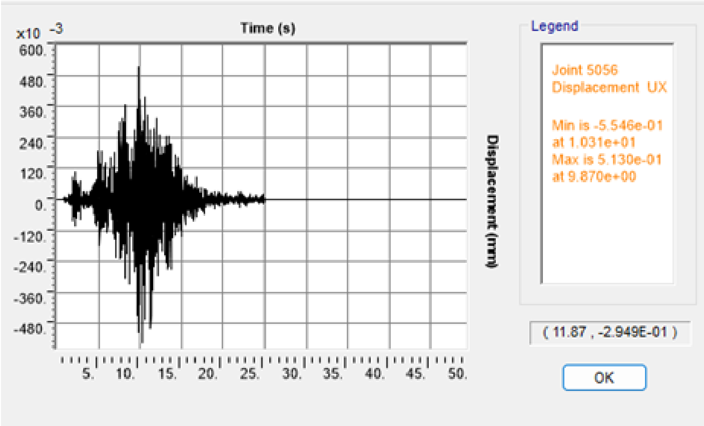

Fig. 9. Graph of the change in x direction with time of node 5056 under earthquake loading.

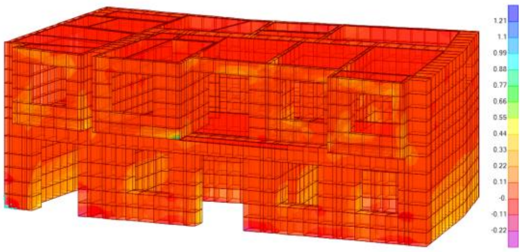

(a)

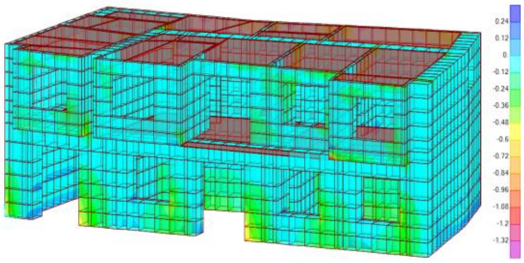

(b)

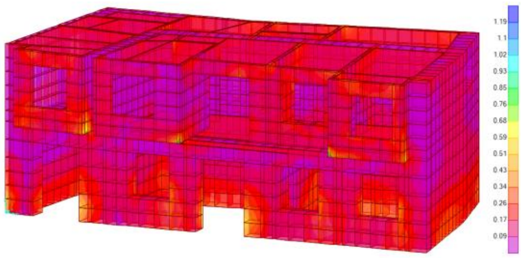

(c)

Fig. 10. (a) maximum, (b) minimum, (c) shear stress curves of the structure for the moment t=10.31 s under earthquake loading.

4. Conclusions

In this study, the damage status of a historical masonry building after the 2023 Elbistan-Kahramanmaraş earthquake was examined and the causes of damage were examined in detail. In this context, the finite element model of the structure was created with the macro modeling technique and dynamic analyzes were performed. The analyzes were performed with the nonlinear analysis method in the time history using the SAP2000 finite element software. As a result of the numerical analyzes performed using the Malatya records of the 2023 Elbistan-

Kahramanmaraş earthquake (Mw = 7.7), the post-earthquake damage status of the building was compared with the numerical model.

According to the study results:

- It was observed that the adobe and stone materials on the first floor of the structure had different strengths. For this reason, separations were observed at the wall joints.
- Shear cracks was observed on the edges of the windows as a result of seismic loading.
- Since the materials used in the structure inadequate compressive and tensile strength, damage occurred to the structure due to the effects of earthquake loads.
- As a result of numerical analysis, the maximum and minimum displacement values were obtained as -0.555 mm at 10.31 s and 0.0513 mm at 9.87 s, respectively.
- As a result of numerical analysis, maximum, minimum principal stress and shear stresses were found to be 0.266, -0.321 and 0.299 N/mm2, respectively. The stress values obtained from the numerical results exceeded the stress values of the existing material.
- Due to the low resistance of masonry structures to seismic forces, it is recommended that retrofitting measures be implemented for masonry buildings.

5. References

Aghabeigi, P., & Farahmand-Tabar, S. (2021). Seismic vulnerability assessment and retrofitting of historic masonry building of Malek Timche in Tabriz Grand Bazaar. *Engineering Structures*, *240*(June 2020), 112418. https://doi.org/10.1016/j.engstruct.2021.112418

Barbieri, G., Biolzi, L., Bocciarelli, M., Fregonese, L., & Frigeri, A. (2013). Assessing the seismic vulnerability of a historical building. *Engineering Structures*, *57*, 523–535. https://doi.org/10.1016/j.engstruct.2013.09.045

Hoveidae, N., Fathi, A., & Karimzadeh, S. (2021). Seismic damage assessment of a historic masonry building under simulated scenario earthquakes: A case study for Arge-Tabriz. *Soil Dynamics and Earthquake Engineering*, *147*(December 2020), 106732. https://doi.org/10.1016/j.soildyn.2021.106732

Jasieńko, J., Raszczuk, K., Kleszcz, K., & Frąckiewicz, P. (2021). Numerical analysis of historical masonry domes: A study of St. Peter's Basilica dome. *Structures*, *31*(February), 80–86. https://doi.org/10.1016/j.istruc.2021.01.082

Maccarini, H., Vasconcelos, G., Rodrigues, H., Ortega, J., & Lourenço, P. B. (2018). Out-of-plane behavior of stone masonry walls: Experimental and numerical analysis. *Construction and Building Materials*, *179*, 430–452. https://doi.org/10.1016/j.conbuildmat.2018.05.216

Moreti, A., Stepinac, M., & Lourenço, P. B. (2022). *Case Studies in Construction Materials Seismic upgrading of cultural heritage – A case study using an educational building in Croatia from the historicism style*. *17*(March). https://doi.org/10.1016/j.cscm.2022.e01183

Nochebuena-Mora, E., Mendes, N., Lourenço, P. B., & Greco, F. (2021). Dynamic behavior of a masonry bell tower subjected to actions caused by bell swinging. *Structures*, *34*(September), 1798–1810. https://doi.org/10.1016/j.istruc.2021.08.066

TSHM (2018) Turkish Seismic Hazard Map.

4th International Civil Engineering & Architecture Conference
17-19 May 2025, Trabzon, Türkiye

Free vibration analysis of FG-CNTRCs with arbitrary CNT distribution based on higher-order shear deformation theory

Serhan Koç*[1], Gökhan Adıyaman[1]

[1] Karadeniz Technical University, Department of Civil Engineering, 61080 Trabzon, Türkiye

Abstract. This paper introduces a finite element (FE) model, featuring three nodes and four degrees of freedom per node, to conduct free vibration analysis of carbon nanotube reinforced composite (CNTRC) beams. The free vibration behaviour of single-walled carbon nanotube (SWCNT) reinforced nanocomposite beams under various boundary conditions is investigated using the higher-order shear deformation theory (HSDT). CNTRC beams featuring arbitrary distributions of CNTs are examined. The consideration of arbitrary CNT distribution, representing potential defects or specific design configurations, ensures a realistic depiction of composite beam behaviour during free vibration analysis. For diverse end supports, including simply supported, clamped, and free conditions, the energy formulas, with varying coefficients, are solved by employing Hamilton equations to derive the governing differential equations. The material properties of functionally graded CNTRC (FG-CNTRC) beams are assumed to vary gradually along the thickness direction and are predicted using the extended rule of mixture. The free vibration analysis is conducted for the CNTRC beam in order to interpret the influence of different CNT volume fractions, distribution profiles, boundary conditions, and beam-slenderness ratios. The numerical values obtained are subsequently compared with those associated with a normal CNT distribution.

Keywords: Free vibration; Arbitrary distribution; Frequency; HSDT

1. Introduction

Mankind consistently pursues engineering materials that offer reliability, economic advantages, and environmental sustainability. Among these promising materials, carbon nanotubes (CNTs), initially introduced by Iijima in 1991 (Iijima,1991), have emerged prominently due to their remarkable physical and mechanical properties. Extensive research efforts utilizing analytical, experimental, and numerical methods have demonstrated that CNTs possess superior strength-to-weight ratios and multifunctional attributes such as electrical conductivity, making them highly favorable as reinforcing elements within polymer composites (Shirazi et al.,2011).

Composite materials reinforced with CNTs have gained widespread popularity due to their distinct advantages compared to traditional engineering materials. Notably stronger and harder than steel, CNTs also have significantly lower densities, positioning these composites ideally for advanced applications in aerospace, automotive, and electronics sectors. Additionally, their impressive corrosion resistance and extended fatigue life make CNT-reinforced composites particularly suited for challenging operational environments.

In CNTRC beams, the introduction of CNTs modifies the dynamic response, producing measurable shifts in natural frequencies and alterations in mode shapes. These effects are governed by the overall CNT volume fraction, the chosen gradation profile, and the imposed boundary conditions, underscoring the need for comprehensive numerical modeling to capture the resulting vibrational behavior.

Numerous studies have advanced the understanding of free vibration characteristics in CNTRC beams. Shen et al. (2017) compared various higher-order shear deformation theories to predict dynamic responses of CNTRC beams, highlighting the critical impact theory selection has on vibration analysis accuracy. Ansari et al. (2020) comprehensively investigated the vibration responses of functionally graded CNTRC beams, emphasizing the effects of different boundary conditions, CNT distributions, and volume fractions on the beams' dynamic characteristics. More recently, El-Ashmawy and Xu (2021) developed a finite element model based on Timoshenko beam theory, thoroughly exploring the combined impacts of CNT orientation and functional gradation on both static and free vibration behaviors of CNTRC beams. Their findings underscore the potential to tailor mechanical properties effectively by manipulating CNT orientations and grading indices without increasing structural mass.Investigation into the free vibration characteristics of CNT-reinforced beams remains ongoing

* Corresponding author, E-mail: serhan.61@hotmail.com

https://doi.org/10.31462/icearc2025_ce_sme_092

however, the notable advancements achieved in recent years have facilitated the design of novel and optimized CNT-reinforced beam configurations with a broad spectrum of potential applications.

This study investigates the free-vibration response of CNT-reinforced beams utilizing a three-node finite element formulated within the context of Higher-Order Shear Deformation Theory (HSDT), featuring twelve degrees of freedom per element. To enable the examination of responses within specific regions of the beam's cross-section, an arbitrary cross-sectional geometry was considered. For the numerical implementation along the beam's length, the beam was divided into equal segments along the z-axis. The fundamental governing relations were derived from HSDT principles. Effective material properties were determined using the extended rule of mixtures. Hamilton's principles were employed to derive the equations of motion, which were subsequently solved numerically to obtain dimensionless natural frequency values. The results, covering various support conditions, CNT volume fractions, and slenderness ratios, are presented.

2. Materials and methods for modeling cntrc beams

The uniform distribution (UD) and three functionally graded distributions (FGA, FGX) for a CNTRC beam of thickness h are illustrated in Fig. 1. The beam's length, width, and height are denoted by L_t, b, and h, respectively.

Fig. 2 illustrates the beam's geometric properties and coordinate system, with displacement in the y-direction assumed zero. The carbon nanotube volume fractions are then defined as functions of the thickness coordinate as follows:

The distribution of CNTs as a function of the z coordinate is given as follows:

UD-CNT $$V_{cnt}(z) = V_{tcnt} \quad (\frac{-h}{2} \le z \le \frac{h}{2}) \tag{1a}$$

FGA-CNT $$V_{cnt}(z) = (1 - \frac{2z}{h})V_{tcnt} \quad (\frac{-h}{2} \le z \le \frac{h}{2}) \tag{1b}$$

FGX-CNT $$V_{cnt}(z) = \frac{4z}{h}V_{tcnt} \quad (0 \le z \le \frac{h}{2}),\ V_{cnt}(z) = -\frac{4z}{h}V_{cnt} \ (-\frac{h}{2} \le z \le 0) \tag{1c}$$

The parameters V_{cnt} and V_{tcnt} denote the volume fraction of carbon nanotubes and the total volume fraction, respectively. Composite mechanical properties are governed by the relative proportions of reinforcement and matrix. Effective Young's and shear moduli for CNT-reinforced beams are obtained by calibrating molecular dynamics simulation outcomes to the extended rule of mixtures (Ashmawy and Xu,2021).

The elastic behavior of the CNT-reinforced composite is described by its longitudinal and transverse Young's moduli, E_{11} and E_{22}, and by its shear moduli, G_{12}, G_{13}, and G_{23}. These composite moduli are obtained from the constituent phase properties: E_{11}^{cnt},E_{22}^{cnt}, and G_{12}^{cnt} for the nanotube phase, E^m and G^m for the polymer matrix. Load-transfer efficiency between phases is characterized by the parameters η_1, η_2, and η_3. Poisson's ratio of the composite, $\nu(z)$, is similarly phase-specific, with values ν_{12}^{cnt} and ν^m for the nanotubes and matrix, respectively. Finally, the mass densities of the two phases are denoted ρ^{cnt} and ρ^m.

$$E_{11}(z) = \eta_1 V_{cnt}(z)E_{11}^{cnt} + V_m(z)E^m \tag{2a}$$

$$\frac{\eta_2}{E_{22}(z)} = \frac{V_{cnt}(z)}{E_{22}^{cnt}} + \frac{V_m(z)}{E^m} \tag{2b}$$

$$\frac{\eta_3}{G_{12}(z)} = \frac{V_{cnt}(z)}{G_{12}^{cnt}} + \frac{V_m(z)}{G^m} \tag{2c}$$

$$\nu(z) = V_{cnt}(z)\nu_{12}^{cnt} + V_m(z)\nu^m \tag{2d}$$

$$\rho(z) = V_{cnt}(z)\rho^{cnt} + V_m(z)\rho^m \tag{2e}$$

$$V_m(z) = 1 - V_{cnt}(z) \tag{2f}$$

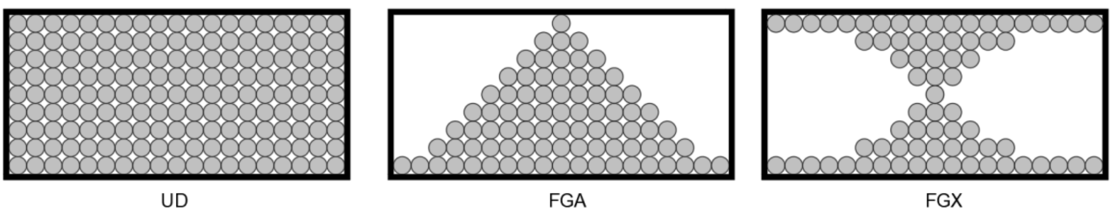

Fig. 1. SWCNT patterns in a CNTRC beams UD, FGA and FGX

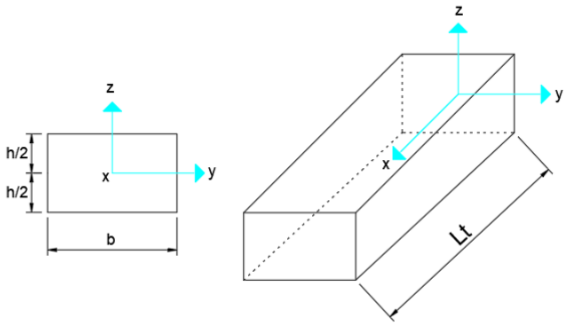

Fig. 2. Geometric properties and coordinate system of the beam

The associated nodal displacement vector for this element is defined as follows:

$$u_0 = N_1 u_1 + N_2 u_2 + N_3 u_3 \tag{3a}$$

$$w_0 = M_1 w_1 + M_2 w_2 + M_3 w_3 + M_4 \phi_1 + M_5 \phi_2 + M_6 \phi_3 \tag{3b}$$

$$\beta_0 = N_1 \beta_1 + N_2 \beta_2 + N_3 \beta_3 \tag{3c}$$

$$\phi_0 = \frac{\partial w_0}{\partial x} \tag{3d}$$

According to the HSDT, the axial displacement of the bar is given by:

$$u = u_0(x) - z\phi(x) + f(z)\beta(x) \tag{4a}$$

$$w = w_0(x) \tag{4b}$$

In this formulation, u and w denote transverse and axial displacement components (along the x- and z-axes) at any beam point. The mid-plane displacements along the x and z-axes are represented by u_0 and w_0, respectively, while ϕ corresponds to the section's rotation. The shear deformation shape function f(z) is adopted from Reddy's higher-order theory (Reddy,2003).

$$f(z) = z - \frac{4z^3}{3h^2} \tag{5}$$

According to the theory of elasticity, the shape-displacement relations are given as follows.

$$\varepsilon_{xx} = \frac{\partial u}{\partial x} = \frac{\partial u_0}{\partial x} - z\frac{\partial \phi_x}{\partial x} + f(z)\frac{\partial \beta_x}{\partial x} \tag{6a}$$

$$\varepsilon_{xz} = \frac{\partial u}{\partial z} + \frac{\partial w}{\partial x} = -\phi(x) + f(z)\beta_x + \frac{\partial w_0}{\partial x} \tag{6b}$$

Fig. 3 depicts the finite-element model comprising three nodes and twelve degrees of freedom. Under plane stress assumptions, the transverse normal stress component was set to zero, and the associated stiffness contribution was omitted from the analysis.

$$\begin{Bmatrix} \sigma_1 \\ \sigma_2 \\ \sigma_3 \\ \sigma_4 \\ \sigma_5 \\ \sigma_6 \end{Bmatrix} = \begin{bmatrix} Q_{11} & Q_{12} & Q_{13} & 0 & 0 & 0 \\ Q_{12} & Q_{22} & Q_{23} & 0 & 0 & 0 \\ Q_{13} & Q_{23} & Q_{33} & 0 & 0 & 0 \\ 0 & 0 & 0 & Q_{44} & 0 & 0 \\ 0 & 0 & 0 & 0 & Q_{55} & 0 \\ Q_{16} & Q_{26} & Q_{36} & 0 & 0 & Q_{66} \end{bmatrix} \begin{Bmatrix} \varepsilon_1 \\ \varepsilon_2 \\ \varepsilon_3 \\ \varepsilon_4 \\ \varepsilon_5 \\ \varepsilon_6 \end{Bmatrix} \tag{7}$$

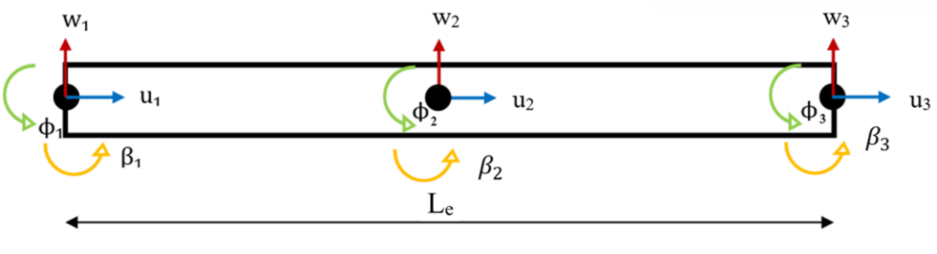

Fig 3. Finite Element Model

Here, σ and ε denote the stress and strain tensors, respectively, whose components define the mechanical behavior of the CNT-reinforced beams

$$Q_{11} = \frac{E_{11}(z)}{1-\nu^2}, Q_{12} = \frac{\nu_{12}(z)E_{22}(z)}{1-\nu^2}, \mathrm{Q}_{22} = \frac{E_{22}(z)}{1-\nu^2} \tag{8a}$$

$$Q_{44} = G_{23}(z), Q_{55} = G_{13}(z), Q_{66} = G_{12}(z) \tag{8b}$$

By accounting for the CNT orientation, the constitutive stress–strain relations are mapped from the principal material axes (1, 2, and 3) to the global Cartesian coordinate system (x, y, and z), yielding

$$\begin{Bmatrix} \sigma_{xx} \\ \sigma_{yy} \\ \sigma_{yz} \\ \sigma_{xz} \\ \sigma_{xy} \end{Bmatrix} = \begin{bmatrix} \bar{Q}_{11} & \bar{Q}_{12} & 0 & 0 & \bar{Q}_{16} \\ \bar{Q}_{12} & \bar{Q}_{22} & 0 & 0 & \bar{Q}_{26} \\ 0 & 0 & \bar{Q}_{44} & \bar{Q}_{45} & 0 \\ 0 & 0 & \bar{Q}_{45} & \bar{Q}_{55} & 0 \\ \bar{Q}_{16} & \bar{Q}_{26} & 0 & 0 & \bar{Q}_{66} \end{bmatrix} \begin{Bmatrix} \varepsilon_{xx} \\ \varepsilon_{yy} \\ \varepsilon_{yz} \\ \varepsilon_{xz} \\ \varepsilon_{xy} \end{Bmatrix} \tag{9}$$

Under the plane-strain hypothesis, the out-of-plane strain component is taken as zero. Consequently, the following stress and shear-strain components vanish: [$\sigma_{yy} = \sigma_{yz} = \sigma_{yy} = \varepsilon_{yz} = \varepsilon_{xy} = 0$ ve $\varepsilon_{yy} \neq 0$]

$$\begin{Bmatrix} \sigma_{xx} \\ \sigma_{xz} \end{Bmatrix} = \begin{bmatrix} \tilde{Q}_{11} & 0 \\ 0 & \tilde{Q}_{55} \end{bmatrix} \begin{Bmatrix} \varepsilon_{xx} \\ \varepsilon_{xz} \end{Bmatrix} \tag{10a}$$

$$\tilde{Q}_{11} = \bar{Q}_{11} - \frac{(\bar{Q}_{12})^2}{\bar{Q}_{22}}, \tilde{Q}_{55} = \bar{Q}_{55} \tag{10b}$$

The governing equations of motion are obtained using Hamilton's Principle, stated as (Nejati,2016)

$$\delta\Pi \;=\; \delta(U-T) \;=\; 0 \tag{11}$$

where δU represents the variation of the potential energy and δT is the variation of the kinetic energy. The relevant integrals defining U and T for the element are given by

$$U = \frac{1}{2}\int_0^{L_e}\int_A [\sigma_x \frac{\partial \delta u}{\partial x} + \sigma_{xz}(\frac{\partial \delta u}{\partial z} + \frac{\partial \delta w}{\partial x})] \tag{12a}$$

$$T = \frac{1}{2}\int_0^{L_e}\int_A \left\{\rho[(\frac{\partial \delta u}{\partial t})^2 + (\frac{\partial \delta w}{\partial t})^2]\right\} \tag{12b}$$

Since b=1, the width does not affect the area integral, so a one-dimensional through-thickness integration is performed instead of a full two-dimensional procedure. The total height h is divided into N horizontal layers of thickness (see Fig. 4).

$$\Delta z = h/h_n \tag{13}$$

Within the i_{th} layer, the sampling points for the CNT distribution function g(z) are defined as

$$z_i^- \;= -\frac{h}{2} + (i-1)\Delta z \tag{14a}$$

$$z_i^0 \;= z_i^- + \frac{\Delta z}{2} \tag{14b}$$

$$z_i^+ = z_i^- + \Delta z \tag{14c}$$

The integral of g(z) over the layer is then approximated by Simpson’s one-third rule

$$\int_{z_i^-}^{z_i^+} g\,(z)dz \;\approx\; \frac{\Delta z}{6}[g(z_i^-) \;+\; 4g(z_i^0) \;+\; g(z_i^+)]. \tag{14d}$$

All expressions (Eqs. 14a–14d) are evaluated in succession for each layer to construct the overall through-thickness integral.

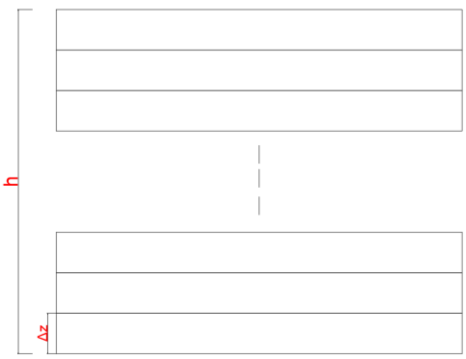

Fig 4. Illustration of the beam cross-section discretized arbitrarily into uniform layers of thickness Δz

The layer-wise contributions are cumulatively summed from the beam's base to any specified elevation z, yielding a highly accurate estimate of the CNT influence at that height. Comparison with a reference analytical profile shows that the composite Simpson's rule implementation reproduces the known results with negligible error.

Finally, by using the variation approach, the governing equations of the FGCNT beam are obtained.

$$\delta u = 0 \;\Rightarrow\; \frac{\partial \sigma_x}{\partial x} + \frac{\partial \sigma_{xz}}{\partial z} = \rho \frac{\partial^2 u}{\partial t^2} \tag{15a}$$

$$\delta w = 0 \;\Rightarrow\; \frac{\partial \sigma_z}{\partial z} + \frac{\partial \sigma_{xz}}{\partial x} = \rho \frac{\partial^2 w}{\partial t^2} \tag{15b}$$

Neglecting the inertial forces in Eqs. (14a) and (14b), the governing equations for free-vibration analysis of the FG-CNT beam are derived, enabling the determination of its natural frequencies.

3. Numerical results

In numerical analyses (10,10) a matrix called PMMA reinforced with seat type single-walled CNTs is used. Assuming a room temperature of 300 K, the material properties of the poly methyl methacrylate matrix called PMMA are ν^m=0.3, ρ^m=1190 kg/m^3, E^m=2.5 GPa. Material properties of armchair type CNTRC reinforcement;ν_{12}^{cnt}=0.19, G_{12}^{cnt}=17.2 GPa, E_{11}^{cnt}=600 GPa, E_{22}^{cnt}=10 GPa and ρ^{cnt}=1400kg/m^3. Table 1 presents the total CNT volume fractions together with their corresponding efficiency parameters.

Table 1. Total volume fractions and efficiency parameters of CNTs

V_{tcnt}	$\boldsymbol{\eta_1}$	$\boldsymbol{\eta_2}$	$\boldsymbol{\eta_3}$
0.12	1.2833	1.0556	1.0556
0.17	1.3414	1.7101	1.7101
0.28	1.3238	1.7380	1.7380

The following section presents an investigation of the dimensionless free-vibration characteristics of a finite-element beam configured with a variety of boundary conditions (clamped–clamped, clamped–simply supported, simply supported–simply supported, and clamped–free) using the classical beam theory. A convergence study was conducted, and h_n=25 was used to verify calculation accuracy. For the two-distribution combinations, h_n=20 was adopted. The resulting dimensionless natural frequency, ϖ, for each boundary case is determined from the relation

$$\varpi = \omega L_t \sqrt{\frac{I_0^m}{A_{11}^m}} \tag{16}$$

I_0^m and A_{11}^m are given below

$$I_0^m = \int_{-h}^{h} \rho^m (1 - (\upsilon^m)^2) dz \;\text{ and }\; A_{11}^m = \int_{-h}^{h} E^m dz \tag{17}$$

Fig. 5 shows that ϖ decreases as L_t/h increases for all distribution types and V_{tcnt}, reflecting the lower natural frequencies of more slender beams in free vibration. At a given slenderness ratio, FGX produces the highest ϖ, FGA yields intermediate values, and UD the lowest, demonstrating how gradation enhances vibrational performance.

Table 2 presents the first three dimensionless natural frequencies ϖ of CNTRC beams under simply supported conditions for various CNT distribution types and V_{tcnt}. Results are compared with Yas and Samadi (2012), who used Hamilton's principle and Timoshenko beam theory for free-vibration analysis, confirming the accuracy and convergence of the arbitrary cross-section model. The FGX distribution yields the highest ϖ, FGA is intermediate, and UD the lowest. The maximum relative deviation for FGX at V_{tcnt}=0.28.

Table 3 and Table 4 present the first dimensionless natural frequency ϖ of CNTRC beams for all pairwise mixtures of two CNT distribution types at slenderness ratios of 5 and 20 (θ=0), under various boundary conditions and volume fractions V_{tcnt}.

The data demonstrate that exchanging the order of two distributions (UD & FGX) produces identical ϖ values. Mixtures involving the surface-graded FGX distribution consistently deliver higher natural frequencies than those employing FGA or UD, with the largest gains observed under the most constrained boundary (C–C). Increasing V_{tcnt} from 0.12 to 0.28 raises ϖ in all cases, reflecting the stiffening effect of greater CNT content.

The UD & FGA mixture yields a lower natural frequency than the UD distribution alone. In contrast, the FGA & UD combination produces higher frequencies than either UD or FGA individually. The UD & FGX pairing gives an intermediate result exceeding UD but falling short of FGX. Likewise, the FGA & FGX mixture elevates frequencies above both single distributions, whereas the FGX & FGA arrangement reduces the frequency relative to either FGX or FGA alone.

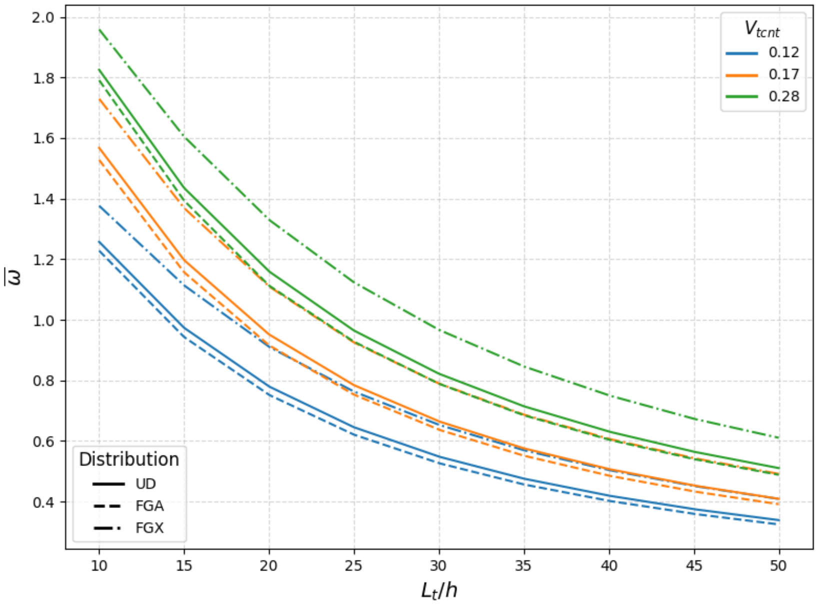

Fig 5. Slenderness-ratio comparison of ϖ for different CNT distributions and V_{tcnt} (S-S, $\theta = 0$, h_n=25)

Table 2. First three ϖ of a CNTRC beam under different volume fraction (S-S, L_t/h =15, θ = 0, h_n=25)

V_{tcnt}	Mode		UD	FGA	FGX
0.12	1	Present	0.9736	0.9432	1.1137
		Yas and Samadi (2012)	0.9753	0.9453	1.1150
	2	Present	2.8787	2.6431	3.0985
		Yas and Samadi (2012)	2.8728	2.6424	3.0814
	3	Present	4.9275	4.7093	5.1656
		Yas and Samadi (2012)	4.8704	4.6675	5.0695
0.17	1	Present	1.1971	1.1570	1.3741
		Yas and Samadi (2012)	1.1999	1.1609	1.3830
	2	Present	3.6269	3.2993	3.9061
		Yas and Samadi (2012)	3.6276	3.3084	3.9293
	3	Present	6.2827	5.9695	6.5657
		Yas and Samadi (2012)	6.2363	5.9498	6.5447
0.28	1	Present	1.4352	1.3922	1.6096
		Yas and Samadi (2012)	1.4401	1.4027	1.6493
	2	Present	4.1327	3.8287	4.3226
		Yas and Samadi (2012)	4.1362	3.8639	4.4752
	3	Present	6.9927	6.7438	7.1230
		Yas and Samadi (2012)	6.9245	6.7618	7.3068

Table 3. First natural frequency (ϖ) of CNTRC beams under various boundary conditions and V_{tcnt} for mixtures of two CNT distributions (L_t/h =5, θ = 0, h_n=20)

Boundary Condition	V_{tcnt}	UD & FGA	FGA & UD	UD & FGX	FGX & UD	FGA & FGX	FGX & FGA
CC	0.12	1.919	2.1721	2.1163	2.1163	2.2063	1.9729
	0.17	1.5036	1.7217	1.6900	1.6900	1.7525	1.5890
	0.28	1.6651	1.9103	1.8687	1.8687	1.9456	1.7206
SS	0.12	0.6549	0.8225	0.8052	0.8052	0.8523	0.6919
	0.17	2.4361	2.7813	2.6948	2.6948	2.8156	2.5028
	0.28	1.9022	2.2088	2.1526	2.1526	2.2443	2.0094
CS	0.12	2.1129	2.4480	2.3802	2.3802	2.4869	2.1776
	0.17	0.8125	1.0397	1.0129	1.0129	1.0779	0.8590
	0.28	2.6862	3.1284	2.9752	2.9752	3.1482	2.7403
CF	0.12	2.1292	2.4723	2.3656	2.3656	2.4872	2.1225
	0.17	2.3448	2.7477	2.6203	2.6203	2.7692	2.3939
	0.28	0.9448	1.1932	1.1450	1.1450	1.2229	0.9868

Table 4. First natural frequency ($\bar{\omega}$) of CNTRC beams under various boundary conditions and V_{tcnt} for mixtures of two CNT distributions (L_t/h =20, θ = 0, h_n=20)

Boundary Condition	V_{tcnt}	UD & FGA	FGA & UD	UD & FGX	FGX & UD	FGA & FGX	FGX & FGA
CC	0.12	1.1307	1.4625	1.4327	1.4327	1.5260	1.2023
	0.17	0.6329	0.8795	0.8497	0.8497	0.9381	0.7178
	0.28	0.8524	1.1623	1.1367	1.1367	1.2296	0.9160
SS	0.12	0.2184	0.3286	0.3199	0.3199	0.3585	0.2389
	0.17	1.3942	1.8396	1.7938	1.7938	1.9222	1.4845
	0.28	0.7676	1.0771	1.0388	1.0388	1.1507	0.8727
CS	0.12	1.0416	1.4455	1.4089	1.4089	1.5324	1.1208
	0.17	0.2631	0.3989	0.3883	0.3883	0.4358	0.2879
	0.28	1.6423	2.1283	2.0481	2.0481	2.1966	1.7277
CF	0.12	0.9431	1.3057	1.2552	1.2552	1.3849	1.0636
	0.17	1.2523	1.7055	1.6468	1.6468	1.7876	1.3546
	0.28	0.3269	0.4913	0.4778	0.4778	0.5342	0.3567

Table 4 shows that the UD & FGA combination consistently underperforms both UD and FGA alone, while FGA & UD exceed each single-distribution case. The UD & FGX pairing improves the response relative to UD but remains below the single FGX distribution, and although FGA & FGX raises the frequency above both individual distributions, the FGX & FGA sequence yields lower results than either FGX or FGA by itself.

4. Conclusions

The finite-element framework, which employs layered through-thickness discretization and Simpson's rule, reproduces reference free-vibration frequencies of CNTRC beams with negligible error. The dimensionless fundamental frequency decreases as the slenderness ratio increases and increases with higher CNT volume fraction. Among single-distribution configurations, the surface-concentrated FGX pattern yields the highest frequencies, the FGA pattern produces intermediate values, and the uniform UD distribution gives the lowest.
In mixed-distribution cases, the sequence of gradation dictates the outcome:

- UD & FGA reduces the frequency below either UD or FGA alone.
- FGA & UD raises the frequency above both single distributions.
- UD & FGX yields a value between UD and FGX.
- FGA & FGX elevate the frequency beyond both parent patterns.
- FGX & FGA produces a lower frequency than either FGX or FGA alone.
- These sequence-dependent effects persist across slenderness ratios of 5 and 20, zero angular orientation, all boundary conditions, and various volume fractions.
- The findings provide clear guidance for optimizing CNTRC beam vibrational performance through informed selection of CNT gradation pattern, volume fraction, and mixture order.

References

Ansari, R., Shojaei, M. F., Mohammadi, V., Gholami, R., & Sadeghi, F. (2014). Nonlinear forced vibration analysis of functionally graded carbon nanotube-reinforced composite Timoshenko beams. *Composite Structures, 113*, 316–327.

Balasubramanian, K., & Burghard, M. (2005). Chemically functionalized carbon nanotubes. *Small, 1*(2), 180–192.

Bathe, K. J. (2019). *Finite element procedures* (2nd ed.). Massachusetts, United States of America.

Belarbi, M.-O., Salami, S. J., Garg, A., Daikh, A.-A., Houari, M.-S.-A., Dimitri, R., & Tornabene, F. (2023). Mechanical behavior analysis of FG-CNT-reinforced polymer composite beams via a hyperbolic shear deformation theory. *Continuum Mechanics and Thermodynamics, 35*(2), 497–520.

El-Ashmawy, A. M., & Xu, Y. (2021). Combined effect of carbon nanotubes distribution and orientation on functionally graded nanocomposite beams using finite element analysis. *Materials Research Express, 8*(1), 015012.

Han, Y., & Elliott, J. (2007). Molecular dynamics simulations of the elastic properties of polymer/carbon nanotube composites. *Computational Materials Science, 39*(2), 315–323.

Iijima, S. (1991). Helical microtubules of graphitic carbon. *Nature, 354*(6348), 56–58.

Kiani, Y. (2016). Free vibration of FG-CNT reinforced composite skew plates. *Aerospace Science and Technology, 58*, 178–188.

Kumar, P., & Srinivas, J. (2017). Free vibration, bending and buckling of a FG-CNT reinforced composite beam: Comparative analysis with hybrid laminated composite beam. *Multidiscipline Modeling in Materials and Structures, 13*(4), 590–611.

Nejati, M., Eslampanah, A., & Najafizadeh, M. (2016). Buckling and vibration analysis of functionally graded carbon nanotube-reinforced beam under axial load. *International Journal of Applied Mechanics, 8*(1), 1650008.
Reddy, J. N. (2003). *Mechanics of laminated composite plates and shells: Theory and analysis*. CRC Press.
Shen, H. S., & Xiang, Y. (2013). Nonlinear analysis of nanotube-reinforced composite beams resting on elastic foundations in thermal environments. *Engineering Structures, 56*, 698–708.
Shirazi, Y., Tofighy, M. A., Mohammadi, T., & Pak, A. (2011). Effects of different carbon precursors on synthesis of multiwall carbon nanotubes: Purification and functionalization. *Applied Surface Science, 257*(16), 7359–7367.
Thostenson, E. T., Ren, Z., & Chou, T.-W. (2001). Advances in the science and technology of carbon nanotubes and their composites: A review. *Composites Science and Technology, 61*(13), 1899–1912.
Yas, M. H., & Samadi, N. (2012). Free vibrations and buckling analysis of carbon nanotube-reinforced composite Timoshenko beams on elastic foundation. *International Journal of Pressure Vessels and Piping, 98*, 119–128.

4th International Civil Engineering & Architecture Conference
15-17 May 2025, Trabzon, Türkiye

Nonlinear time history and pushover analysis of a multi-storey reinforced concrete building

Ozan İnce*[1], Burak Çakıl[1], Ömer F. Taş[1], Ömer F. Osmanlı[1], Muhammet Karaton[1], Erkut Sayın[1]

[1] *Fırat University, Department of Civil Engineering, 23119 Elazığ, Türkiye*

Abstract. An earthquake is a natural disaster that critically tests the resilience of structures. The 2023 Kahramanmaraş earthquakes, with their significant magnitude and destructiveness, have once again raised concerns about the seismic performance of the building stock in our country. Accurately modeling the loads caused by earthquakes and predicting the behavior of structures are crucial in engineering practices. Nonlinear analysis methods are frequently used to assess structural performance. The pushover analysis determines the capacity curve of a structure, revealing its general resilience level, while time history analysis provides a detailed evaluation of seismic behavior. Both methods offer valuable insights for earthquake engineering, but their results may differ in interpretation. In this study, nonlinear analysis methods, namely pushover and time history analysis, were applied on a 6-storey multi-storey building model. In the time history analysis, the ground motion record obtained from 4406 station during the February 6, 2023 Elbistan earthquake (M_w: 7.6) was used. The results of both methods were compared and the differences they provided in terms of evaluating the seismic behavior of the structures were examined.

Keywords: Reinforced concrete structure; Time history analysis; Pushover analysis

1. Introduction

Earthquakes are natural disasters that causing loss of life and property with their devastating effects. Many countries in the world are affected by this disaster; earthquakes are an inevitable fact of daily life and construction in countries located on active fault zones. Türkiye has active fault zones (North Anatolian Fault, East Anatolian Fault and West Anatolian Fault zones) that cause devastating earthquakes. The 2023 Kahramanmaraş earthquakes (Pazarcık Mw: 7.7 and Elbistan Mw: 7.6) that occurred on the Eastern Anatolian fault line showed the destructive effects of earthquakes (Dema, 2023). In the literature studies conducted after the earthquake, the deficiencies in the existing building stock and the causes of damage to the buildings were given in detail (Avcıl, 2024; Işık, 2024; İnce, 2024; Yetkin, 2024).

For earthquake-resistant design, engineering approaches and methods have a big importance. The behavior of buildings under earthquake effects should be accurately modeled and analyzed. There are different methods for modelling the nonlinear behaviour of buildings. Among these methods, pushover analysis and time history analysis are widely used, especially in the performance evaluation of existing structures. Some studies in the literature have questioned the effectiveness of these two methods. In the study conducted by Korkmaz and Düzgün (2006), four reinforced concrete frame structures (3, 5, 8 and 15 floors) were considered and nonlinear static pushover analyses were performed for these frame structures under rectangular, triangular and parabolic load effects. Static pushover analyses were compared with the results of time history dynamic analyses performed with 50 different earthquake data. In the study conducted by Çapa (2020), linear and nonlinear calculation methods were applied on three, five and seven-story buildings according to TBDY 2018. In order to evaluate the earthquake performance with the static pushover method and the nonlinear analysis method in the time history, parameters such as maximum plastic rotation values of the plasticized sections, base shear forces, peak displacement values and damage amounts in the structural system were analyzed and compared. In the study conducted by Toplu and Kırtel (2021), three different seismic base isolated structure models were designed and comparisons were made with different analysis methods in these models. Nonlinear behaviors and collapse mechanisms of structures were analyzed using static pushover analysis with time history analysis method based on real earthquake records. As a result of the study, it was observed that the data obtained in the time history were compatible with the pushover analysis results.

*Corresponding author, E-mail: o.ince@firat.edu.tr

https://doi.org/10.31462/icearc2025_ce_sme_093

In this study, it is aimed to compare two nonlinear analysis methods used in reinforced concrete buildings. For this purpose, a reinforced concrete building with a 6-storey frame system was designed. Nonlinear time history analyses of the designed building were performed using an acceleration record of the 2023 Elbistan earthquake. The damage to the building as a result of these two methods was compared. TBEC-2018 was taken into consideration in the analyses and evaluations made within the scope of the study.

2. Material and metod

TBEC-2018 was taken into consideration in the analyses and evaluations made within the scope of the study. In numerical analysis, SAP2000 finite element program was used. The fiber element method was used for consider the nonlinear behavior of reinforced concrete elements. It is a widely used method for nonlinear behaviour of reinforced concrete structures and provides successful results (Karaton et al., 2021; Karaton et al., 2023).

In static pushover analysis, increasing horizontal forces are applied to the building exposed to vertical loads. The capacity curve is obtained by recording the displacement values corresponding to the increasing horizontal load. Horizontal loads are increased until the building collapses. Then, the target displacement value is calculated using the building's capacity curve and the damage conditions at this point are evaluated. In the time history analyses, earthquake records are applied to the buildings. Acceleration records can be used directly or scaled with the design earthquake. The damages occurring in the building during the earthquake are obtained.

3. Numerical analysis

In this study, nonlinear analysis of a 6-storey reinforced concrete building was performed with different methods. Fig. 1 shows the model of the designed building. The damage status of this building was compared by performing static pushover and time history analyses. In the building design, concrete with a compressive strength of 30 MPa and reinforcement with a yield strength of 420 MPa were used. All floor heights are equal and designed as 3 m. Column dimensions are designed as 50x50 cm and beam dimensions are designed as 30x50 cm. In the modeling of the building, slabs were not included in the model and rigid diaphragms were defined at each floor level. Floor and wall loads were applied on the beams. Plastic hinges are defined at the end regions of columns and beams. The first two periods of this building occurred as T_1: 0.85 s and T_2: 0.85 s with a mass participation ratio of 82%.

The fiber element method was used to reflect the nonlinear behavior of the reinforced concrete building. Plastic hinges were defined at the end regions of each column and beam element. In modeling the concrete material, the stress and strain graphs of confined and unconfined concrete were taken into account with the Mander model. Damage limits of confined concrete, unconfined concrete and reinforcement were calculated taking into account TBDY-2018 and defined in SAP2000 program. Table 1 shows the damage limits of these material.

Table 1. Damage limits of materials

Damage limits	Unconfined concrete	Confined concrete	Steel
Limited damage	0.0025	0.0025	0.0075
Controlled damage	0.0026	0.0133	0.024
Collapse prevention	0.0035	0.0177	0.032

In the static pushover analysis of a reinforced concrete building, the building is first subjected to vertical loads. Then, increasing horizontal forces are applied to the building and the horizontal load-displacement graph is obtained (Fig. 2). As a result of the analysis, the target displacement of the building is determined and the damage status at this displacement value is evaluated. The target displacement of this building was calculated as 0.132 m, taking into account TBDY-2018.

Nonlinear time history analyses of the designed reinforced concrete building were performed. In this analysis, the acceleration record of station number 4406 from the 2023 Elbistan earthquake was used (Fig. 3). Although the original record is longer, only the 35-second interval where the ground motion is most effective was used. In the time history analyses, the maximum peak displacement was obtained as 0.163 m. The damage states obtained as a result of the static pushover analysis and time history analysis of the 6-storey reinforced concrete building are given in Table 2.

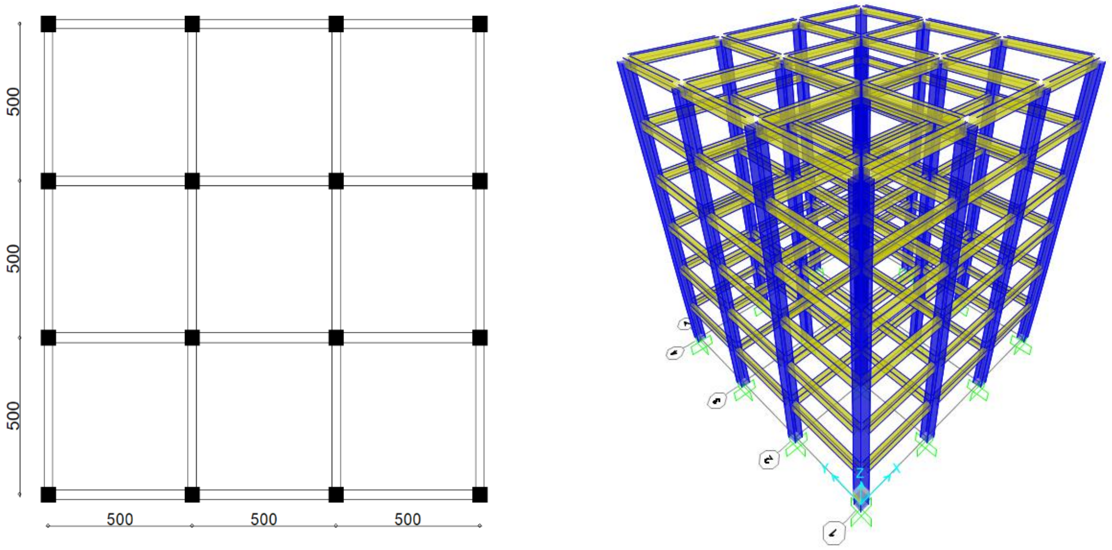

(a) (b)

Fig. 1. (a) Floor plan (cm) (b) Three-dimensional finite element model

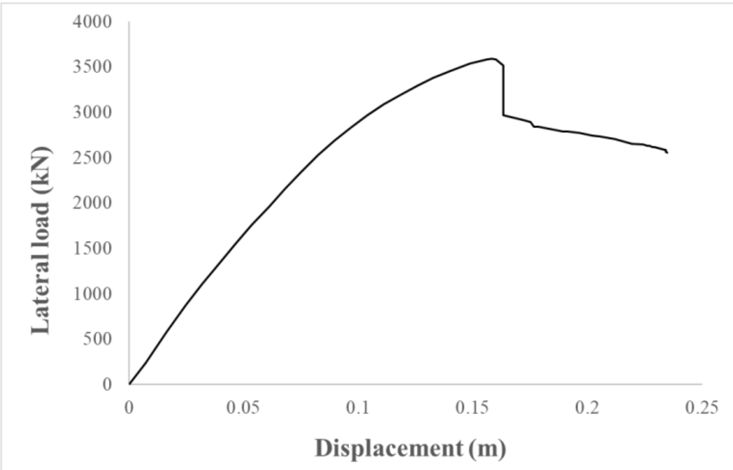

Fig. 2. Lateral load – displacement graph of the building

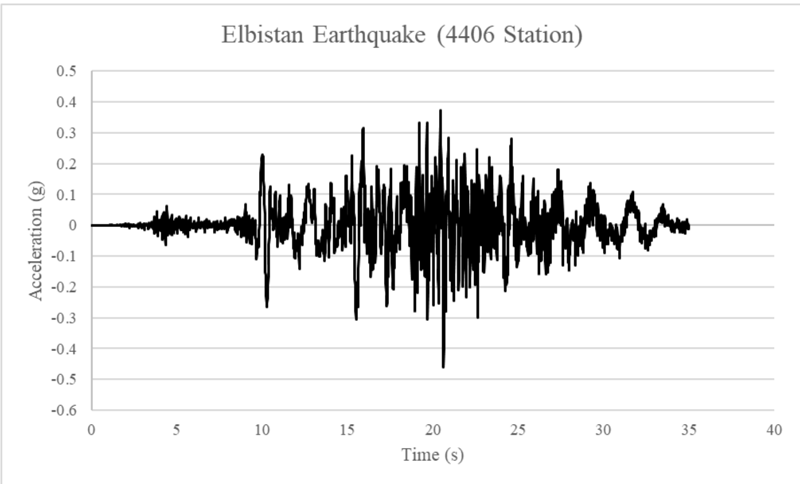

Fig. 3. Elbistan earthquake, scaled acceleration-time graph of 4406 station

Table 2. Damage status obtained by nonlinear analysis

		Static pushover analysis			Time history analysis		
		Immediate occupancy	Life safety	Collapse prevention	Immediate occupancy	Life safety	Collapse prevention
Ground floor	Column	4	12	-	-	16	-
	Beam	-	12	-	-	12	-
1	Column	2	-	-	12	-	-
	Beam	-	12	-	-	12	-
2	Column	4	-	-	10	-	-
	Beam	10	2	-	-	12	-
3	Column	4	-	-	12	-	-
	Beam	2	-	-	10	2	-
4	Column	-	-	-	10	-	-
	Beam	-	-	-	-	-	-
5	Column	-	-	-	2	-	-
	Beam	-	-	-	-	-	-

Conclusion

There are different methods for determining the nonlinear performance of reinforced concrete buildings. The methods used may have advantages over each other in terms of practicality and accuracy. The appropriate method should be selected according to the characteristics of the building to be analyzed. Within the scope of this study, the static pushover and nonlinear time history analyses of a reinforced concrete building consisting of a 6-storey frame system were performed and their damage conditions were compared. The results obtained from the analyses are summarized below:

- A symmetrical, 6-storey building consisting of frame elements was designed for numerical analysis. The first two periods of this building occurred as T_1: 0.85 s and T_2: 0.85 s with a mass participation rate of 82%.
- In static pushover analyses, the demand displacement of the building was calculated as 0.132 m according to TBDY-2018 and the damages at this displacement value were taken into account.
- In the nonlinear time history analyses, the acceleration records recorded at 4406 stations of the Elbistan earthquake were scaled according to the design earthquake and analyzed. As a result of the analysis, the maximum top displacement of the building was obtained as 0.163 m.
- The damage states obtained from nonlinear static pushover and time history analyses were compared. It was observed that there was a significant difference in the damages occurring in the structural elements. These results were obtained in a building that was symmetrical and had no structural irregularities. In future studies, it is necessary to evaluate which buildings static pushover analysis can be effectively applied, considering different floors and irregularities.

References

Avcil, F., Işık, E., İzol, R., Büyüksaraç, A., Arkan, E., Arslan, M. H., & Harirchian, E. (2024). Effects of the February 6, 2023, Kahramanmaraş earthquake on structures in Kahramanmaraş city. *Natural Hazards, 120*(3), 2953–2991. https://doi.org/10.1007/s11069-023-06314-1

Çapa, Y. U. (2020). *Kat adetleri farklı betonarme binaların deprem performanslarının incelenmesi* (Master's thesis, Fatih Sultan Mehmet Vakıf Üniversitesi, Lisansüstü Eğitim Enstitüsü).

DEMA. (2023). *06 February 2023 Pazarcık–Elbistan (Kahramanmaraş) Mw: 7.7 – Mw: 7.6 earthquakes report*. Disaster and Emergency Management Presidency.

Işık, E., Avcil, F., İzol, R., Büyüksaraç, A., Bilgin, H., Harirchian, E., & Arkan, E. (2024). Field reconnaissance and earthquake vulnerability of the RC buildings in Adıyaman during 2023 Türkiye earthquakes. *Applied Sciences, 14*(7), 2860. https://doi.org/10.3390/app14072860

İnce, O. (2024). Structural damage assessment of reinforced concrete buildings in Adıyaman after Kahramanmaraş (Türkiye) earthquakes on 6 February 2023. *Engineering Failure Analysis, 156*, 107799. https://doi.org/10.1016/j.engfailanal.2023.107799

Karaton, M., Osmanlı, Ö. F., & Awla, H. A. (2023). Comparison of ACI-318 and TS-500 codes for nonlinear seismic analysis of RC structures using force-based fiber element approach. *Structures, 57*, 105291. https://doi.org/10.1016/j.istruc.2023.105291

Karaton, M., Osmanlı, Ö. F., & Gülşan, M. E. (2021). Numerical simulation of reinforced concrete shear walls using force-based fiber element method: Effect of damping type and damping ratio. *Bulletin of Earthquake Engineering, 19*(14), 6129–6156. https://doi.org/10.1007/s10518-021-01221-x

Korkmaz, K. A., & Düzgün, M. (2006). Statik artımsal itme analizinde kullanılan yük dağılımlarının değerlendirilmesi. *Teknik Dergi, 17*(82), 3873–3878.

TBEC. (2018). *Türkiye Bina Deprem Yönetmeliği (TBEC-2018)*. Disaster and Emergency Management Authority, Ankara, Türkiye.

Toplu, E., & Kırtel, O. (2021). Sismik taban yalıtımlı yapılarda zaman tanım alanında analiz ve artımsal tek modlu itme yöntemlerinin karşılaştırılması. *Türk Doğa ve Fen Dergisi, 10*(2), 123–131. https://doi.org/10.46810/tdfd.897951

Yetkin, M., Dedeoğlu, I. Ö., & Tunç, G. (2024). February 6, 2023, Kahramanmaraş twin earthquakes: Evaluation of ground motions and seismic performance of buildings for Elazığ, southeast of Türkiye. *Soil Dynamics and Earthquake Engineering, 181*, 108678. https://doi.org/10.1016/j.soildyn.2024.108678

4th International Civil Engineering & Architecture Conference
17-19 May 2025, Trabzon, Türkiye

Buckling and load capacity of thin-walled variable cross-section columns: Influence of fiber orientation and weld lines

Gökçen Kurt*[1], Ayşe Polat[1], Mustafa Özgür Yaylı[1], Murat Yazıcı[2], Babür Deliktaş[1]

[1] *Bursa Uludag University, Department of Civil Engineering, Artificial Intelligence and Computational Mechanics Laboratory, 16059, Bursa, Turkey,*
[2] *Bursa Uludag University, Department of Automotive Engineering, Applied Mechanics and Advanced Materials Research Group Lab.16059, Bursa, Turkey,*

Abstract. The construction, automotive, and aerospace industries all make extensive use of short fiber-reinforced thermoplastic composites because of its remarkable mechanical qualities, lightweight nature, and ability to be recycled. However, anisotropic effects from injection molding, like fiber orientation and weld lines, make it difficult to anticipate their structural performance, especially under buckling stresses. To account for manufacturing-induced anisotropy in finite element calculations, this study offers an integrated computational framework that combines Moldex3D, Digimat RP, and ABAQUS. The framework assesses the buckling and nonlinear anisotropic behavior of hollow square cross-section columns made of Polyamide 6 reinforced with 40% glass fiber (PA6-GF40). J2 plasticity models the behavior of the elastoplastic matrix, whereas the Mori-Tanaka technique forecasts effective material properties. The findings provide a solid methodology for creating high-performance composite structures under challenging loading circumstances, emphasizing the important influence of fiber orientation and weld lines on structural stability.

Keywords: Finite element analysis (FEA); Mold flow simulation; Plastic injection; Buckling; Thermoplastic composites.

1. Introduction

Fiber-reinforced composites, a type of load- bearing component used in the aerospace, civil and automotive industries (Rozylo & Debski, 2024), have gained popularity due to their superior mechanical properties and light weight (Fu et al., 2009). However, these structures are particularly vulnerable to buckling failure modes (Kroon et al., 2024). There has been little research considering random fiber distributions to study the buckling behavior of fiber reinforced polymer plates (Schreiber et al., 2020). Conventional methods used to improve buckling stability include finite element method (Li & Kapania, 2018), finite difference method, boundary element method (Paiva, 2018) and finite integral transformation method.

Injection-molded short-fiber composites are ideal for large-scale applications due to their high mechanical qualities (Zhou et al., 2013), wear resistance (Chen et al., 2007), and recyclability. However, the complicated anisotropic behavior caused by local variations in microstructural properties during the injection molding process makes it difficult to correctly predict their performance and failure (Saraçoğlu & Uzun, 2020). In spite of advances in simulation tools, current approaches based on failure onset criteria are still not enough to accurately predict the failure of injection molded short fiber composites. To alleviate this constraint, numerical Finite Element Analysis (FEA) methods that explicitly account for the anisotropic and elastoplastic properties of these materials are required (Tseng et al., 2017). A comprehensive computational modeling technique for the full plastic injection molding process of fiber-reinforced thermoplastic composites is currently unavailable, and it must account for the anisotropic elastoplastic behavior caused by fiber orientations and weld lines (Polat et al., 2024).

In this study, Moldex3D, Digimat RP and ABAQUS software are used to provide a framework for complex simulation to integrate basic manufacturing data into finite element models. The study focuses on the buckling and nonlinear anisotropic behavior of columns with hollow square sections under different injection molding configurations, which improves the prediction reliability and contributes to the design and optimization of lightweight, high-performance composite structures for load demanding applications.

* Corresponding author, E-mail: gokcenkurtj@gmail.com

https://doi.org/10.31462/icearc2025_ce_sme_097

2. Method

Numerical analyses often use the homogenization method, which assumes a component to be isotropic. However, this method can lead to significant discrepancies between numerical predictions and actual parts due to the component's inherent anisotropic nature. In contrast, models incorporating mold flow information exhibit non-homogeneous distributions, with fiber orientation and content varying spatially. The recommended method closely replicates real-life material behavior, enhancing the specificity and accuracy of simulations for fiber-reinforced composites.

Optimization techniques are not included in this workflow, as it emphasizes the integration of material data and manufacturing parameters for precise initial simulations. The process involves several essential stages: collecting manufacturing data, collecting structural data, using Digimat MX, combining production data with material properties, and using a finite element analysis application like ABAQUS.

The manufacturing data involves collecting critical production process parameters, such as manufacturing mesh, fiber orientation, and weld lines, which significantly influence material properties. Structural data, including material characteristics, loading conditions, and assembly details, can be continuously modified and updated based on simulation outcomes, enabling iterative improvements and optimization of component designs.

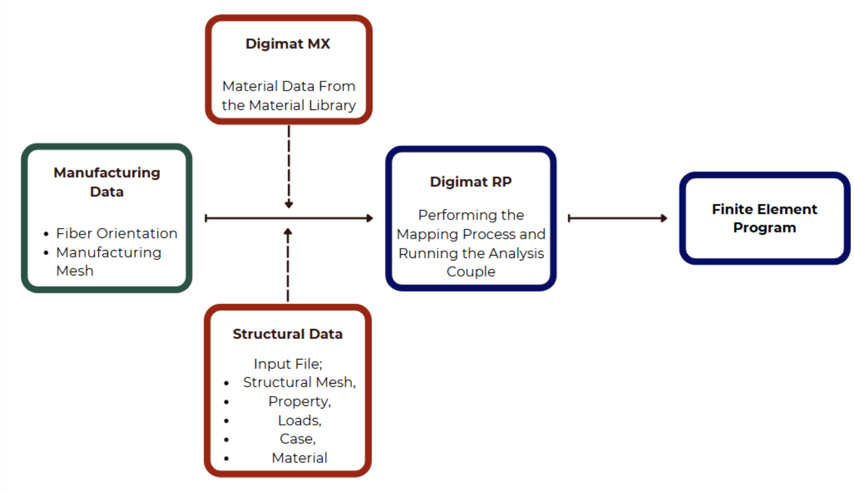

Fig. 1. Digimat RP working principle

2.1. Mori-Tanaka Method to fiber reinforced composite with elastoplastic matrix

A micromechanical method that independently assesses the mechanical characteristics of the matrix and fiber phases in order to forecast the effective properties of the heterogeneous material is used to study the mechanical behavior of short fiber reinforced composites. Digimat software—more especially, the MF and MX modules—was used to create the material model used in this investigation.

To determine the macroscopic properties of composite materials, Digimat MF, the software's homogenization tool, models each phase separately. It takes into account important microstructural information such as fiber volume fraction, aspect ratio and orientation to properly represent the microstructure of the material. Digimat offers two homogenization techniques: mean field homogenization (MFH) and direct finite element analysis of a representative volume element (RVE) at the microscale.

Two approaches are provided by the MFH framework: The Mori-Tanaka Method is commonly employed in most situations and provides accurate estimations for composites with acceptable fiber mass fractions (Mori & Tanaka, 1973). The Double Inclusion Method improves accuracy for composites with very high fiber mass fractions.

Anisotropic measurements and associated material models are comprehensively stored in the Digimat MX module. Elastic, plastic, elastic-plastic, elastic-viscoplastic, and viscoelastic-viscoplastic models are among the various mechanical behaviors and levels of complexity it supports. Because of its adaptability, materials' responses to various loads can be accurately depicted.

In this study, the Digimat MX tool was used, which is the library of the Digimat program provided by the manufacturers. The Mori-Tanaka method combined with a plasticity model was used to characterize the nonlinear behavior of short fiber reinforced composites, in particular PA6-GF40. The complex relationships between the polyamide matrix (PA6) and the glass fibers (GF40) are well captured by this method, allowing a comprehensive study of the behavior of the material under various loading scenarios.

The Mori-Tanaka method is particularly suitable for this type of analysis as it takes into account the anisotropic and heterogeneous properties of the composite. Thanks to the integration of these properties, the approach provides more precise predictions of the mechanical properties of the material, leading to a strong understanding of its behavior.

The goal of homogenization is to compute the instantaneous effective stiffness tensor (Ceff) at the macro level, using the mechanical properties of the microstructural components.

$$\dot{\boldsymbol{\sigma}} = \mathbf{C}_{eff}\colon \dot{\boldsymbol{\varepsilon}} \tag{1}$$

In this equation, $\dot{\boldsymbol{\sigma}}$ is the macroscopic stress rate tensor, $\dot{\boldsymbol{\varepsilon}}$ is the macroscopic strain rate tensor, and $\mathbf{C}_{eff}$ is the elastic stiffness tensor to be calculated.

The Mori-Tanaka (MT) method accepts that the interactions between various types of inhomogeneities with finite volume concentrations are approximated by embedding the inhomogeneities in a medium with effective thermomechanical properties.

The following formula is used by the MT method to determine the effective properties of composites (Jain, 2019):

$$\boldsymbol{C}_{eff} = \boldsymbol{C}_m + v_f\left(\boldsymbol{C}_f - \boldsymbol{C}_m\right)\boldsymbol{A}_f \tag{2}$$

In this case, $\boldsymbol{C}_m$; represents the matrix's stiffness tensor, $\boldsymbol{C}_f$; represents the fiber's stiffness tensor, and v_f; represents the fiber volume fraction. An expression for the instantaneous stress concentration factor is:

$$\mathbf{A}_f = \left[\mathbf{I} + \mathbf{S}\,(\mathbf{C}_{\boldsymbol{m}})^{-1}\,(\mathbf{C}_{\boldsymbol{f}} - \mathbf{C}_{\boldsymbol{m}})\right]^{-1} \tag{3}$$

In this case, $\boldsymbol{S}$ stands for the Eshelby tensor and $\boldsymbol{I}$ for the identity tensor. The shape, aspect ratios, and orientation of the fibers used in composite materials all affect the Eshelby tensor.

$$S_{ijkl} = \mathrm{f}(v_m, \text{aspect ratios, orientation of fibers}) \tag{4}$$

For a generic anisotropic material the Eshelby tensor is given by the following surface integral

$$S_{ijkl} = \frac{1}{8\pi}\boldsymbol{C}_{m_{pqkl}}\int_{-1}^{1} d\zeta_3 \int_0^{2\pi}\left\{G_{iqjp}(\bar{\xi}) + G_{jqip}(\bar{\xi})\right\}dw \tag{5}$$

where

$$\begin{gathered} G_{ijkl}(\bar{\xi}) = \bar{\xi}_k\bar{\xi}_l N_{ij}(\bar{\xi})/D(\bar{\xi}) \\ \bar{\xi}_i = \frac{\zeta_i}{a_i} \\ \zeta_1 = (1-\zeta_3^2)^{1/2}\ \cos w, \\ \zeta_2 = (1-\zeta_3^2)^{1/2}\ \sin w \\ D(\bar{\xi}) = \epsilon_{mnl}K_{ml}K_{n2}K_{l3} \\ N_{ij}(\bar{\xi}) = \frac{1}{2}\epsilon_{ikl}\epsilon_{jmn}K_{km}K_{ln} \\ K_{ik} = C_{m_{ijkl}}\bar{\xi}_j\bar{\xi}_l \end{gathered} \tag{6}$$

The tensor of permutations is represented by ϵ_{ikl}. The formula for a_i for spherical inculison is $(a_1 = a_2 = a_3)$. The impact of fiber orientations on the effective mechanical behavior of composites is taken into consideration by combining the orientation distribution tensor $\mathbf{\Theta}$ with the Eshelby tensor S_{ijkl}. The effective properties are calculated as an average across all possible fiber orientations when working with composites that contain randomly oriented fibers. This averaging is made possible by the orientation distribution tensor, $\mathbf{\Theta}$. When the orientation distribution tensor $\mathbf{\Theta}$ is incorporated into the micromechanical framework using the Eshelby tensor, the orientation-averaged Eshelby tensor that results is as follows:

$$\bar{S}_{ijkl} = \int S_{ijkl}\,(\boldsymbol{n}) \cdot f(\boldsymbol{n})d\Omega \tag{7}$$

The Eshelby tensor for a specific fiber orientation is denoted as $S_{ijkl}(\boldsymbol{n})$. $d\Omega$ is the differential solid angle over the unit sphere, and $\boldsymbol{n}$. $f(\boldsymbol{n})$ is the orientation distribution function (ODF) that characterizes the probability density of fibers being oriented in direction $\boldsymbol{n}$. The orientation distribution tensor can also be used to express the orientation-averaged Eshelby tensor:

$$\bar{S}_{ijkl} = \langle S_{ijkl}(\boldsymbol{n})\rangle = \int S_{ijkl}\, n_i n_j n_k n_l f(\boldsymbol{n})d\Omega \tag{8}$$

The orientation distribution tensor, $\mathbf{\Theta}$ is given as

$$\Theta_{ijkl} = \langle n_i n_j n_k n_l\rangle = \int n_i n_j n_k n_l\, f(\boldsymbol{n})d\Omega \tag{9}$$

Here $\boldsymbol{n}$ is the unit vector that defines the microscopic orientation of the fiber.

Digimat is a tool that efficiently integrates fiber orientation using symmetry and numerical optimization techniques. Advani and Tucker's formulation uses the orientation distribution tensor O (or more generally, a_{ij} and

a_{ijkl}), representing the average fiber orientation for randomly oriented fibers. The Mori-Tanaka method directly influences the stiffness matrix components, affecting the B coefficients used in the Advani-Tucker formulation (Advani & Tucker III, 1987). For randomly oriented fibers, O is included in the stiffness tensor computation (C_{ijkl}).

$$C_{ijkl} = B_1 a_{ijkl} + B_2(a_{ij}\delta_{kl} + a_{kl}\delta_{ij}) + B_3(a_{ik}\delta_{jl} + a_{il}\delta_{jk} + a_{jl}\delta_{ik} + a_{jk}\delta_{il}) + B_4(\delta_{ij}\delta_{kl}) + B_5(\delta_{ik}\delta_{jl} + \delta_{il}\delta_{jk}) \tag{10}$$

Short fiber reinforced composites are modeled using second order unit tensor components, δ_{ij}, and fourth order and second order fiber orientation tensor components, a_{ijkl} and a_{ij}. The coefficients B are related to the components of the stiffness matrix of a transversely isotropic unidirectional composite (Jong et al., 2018).

The matrix phase behaves elastoplastically, while the fiber phase is assumed elastic. The average concentration factors of the matrix phase are influenced by internal state variables such as damage, kinematic hardening and isotropic hardening as well as stress state variables. The following equations are used to describe the increasing elastoplastic response of the matrix phase:

$$\begin{gathered}
\dot{\boldsymbol{\sigma}} = \boldsymbol{C}:(\dot{\boldsymbol{\varepsilon}} - \dot{\boldsymbol{\varepsilon}}^p) \\
\dot{\boldsymbol{\varepsilon}}^p = \dot{\lambda}\frac{\partial f}{\partial \boldsymbol{\sigma}} \\
\dot{R} = [k(1+mp) - m(R - R_\infty)]\dot{p} \\
\dot{p} = \dot{\lambda} \\
\dot{f} = \frac{\partial f}{\partial \boldsymbol{\sigma}}\dot{\boldsymbol{\sigma}} + \frac{\partial f}{\partial R}\dot{R} = 0 \\
f = J_2(\boldsymbol{\sigma}) - R(p) - \sigma_{yp} \\
R(p) = kp + R_\infty[1 - \exp(-mp)]
\end{gathered} \tag{11}$$

The nonlinear isotropic hardening is modeled using a linear and exponential law, with material yield strength (σ_{yp}) and material-dependent constants (k , m, and R_∞). This approach helps optimize the mechanical behavior of short fiber-reinforced composites. However, the validity and applicability of these theories depend on precise determination of parameters like fiber orientation, elastic modulus, yield properties, and hardening behavior. Software tools like Digimat RP and Moldex3D provide essential capabilities for modeling these parameters, enabling more accurate simulations of composite materials.

Therefore, in order to guarantee accurate results in predicting the mechanical performance of composite materials, it is essential for advanced analyses to carefully evaluate fiber orientation, material parameters, and plasticity behavior. Using the values obtained from the Digimat material, the stress and strain curves for the PA6 GF40 material are displayed in Fig. 2.

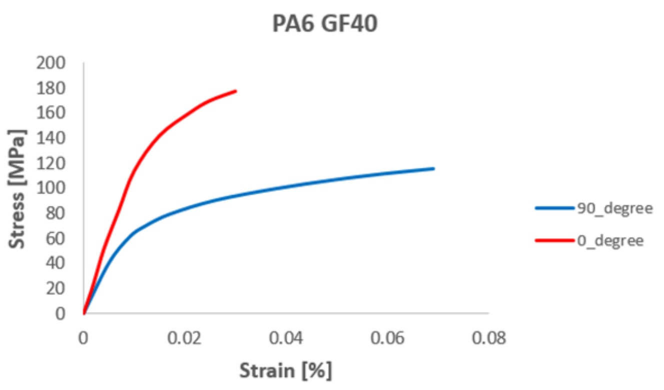

Fig. 2. Under tensile testing, the stress-strain curves of 40% glass fiber-reinforced PA6 were examined both in the fiber direction and perpendicular to it.

3. Finite element buckling analysis

The PA6-GF40 material was routinely modeled using Poisson's ratio and a single elastic modulus. Injection molding simulations were performed across four configurations to evaluate the impact of weld lines and fiber orientation on the critical buckling load and load-carrying capability. For the purpose of calculating critical buckling loads, the fiber orientation, distribution, and weld line data obtained from these simulations were imported into ABAQUS with Digimat RP. The load-carrying capacity of the columns were then compared using nonlinear anisotropic analysis.

3.1. Finite element buckling analyses of the conventional model

ABAQUS was used to examine a hollow square cross-section column with a consistent wall thickness of 4 mm. According to Fig. 3, the column's base cross-section measured 60 x 60 mm, decreasing to 30 x 30 mm at the top. Its overall length was 200 mm.

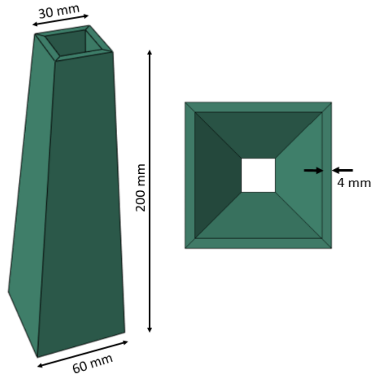

Fig. 3. Variable cross-section column geometry with thin walls

In accordance with the material parameters of the finite model, the 40% glass fiber reinforced polyamide's modulus of elasticity and Poisson's ratio were found to be 12.6 GPa and 0.35, respectively. While there are no restrictions on movement along the load axis, there are (DOF 1, 2) on other axes of motion at the upper side of the specimen. At the bottom, motion is restricted in all directions (DOF 1, 2, 3). Buckle analysis was performed to determine the critical buckling load after applying 1 N load to the column.

3.2.Finite element buckling analyses using the model integrating real material data

3.2.1.Mold flow simulation

A thin-walled variable cross-section column was simulated in four configurations using Moldex3D software with 40% glass fiber reinforced polyamide 6 material. The configurations varied the number and placement of injection gates in Moldex3D. (Filling began at the top or bottom, and two gates were positioned at corners or edges.) Fig 4.

The filling analysis was conducted at a melt temperature of 260°C and a mold temperature of 85°C, with a maximum mold pressure of 155 MPa. The melt storage times and cycle times for all fillings are as follows: For the two corners on top (A) filling type, the filling time is 2.18 seconds, and the cycle time is 19.58 seconds. For the two edges on top (B) filling type, the filling time is 2.17 seconds, and the cycle time is 19.56 seconds. For the two corners on bottom (C) filling type, the filling time is 2.20 seconds, and the cycle time is 18.90 seconds. For the two edges on bottom (D) filling type, the filling time is 2.19 seconds, and the cycle time is 19.59 seconds.

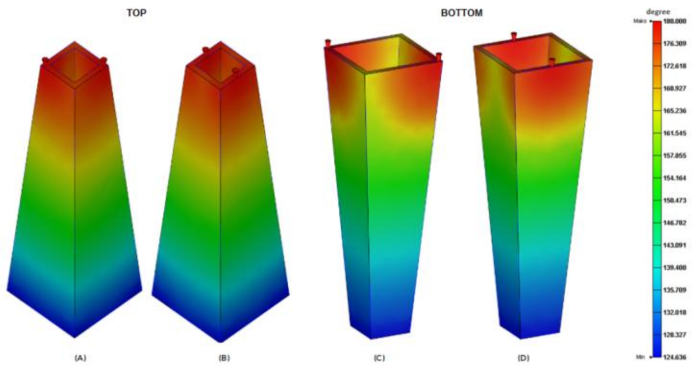

Fig. 4. Models made for mold flow simulation (A) two corners on top, (B) two edges on top, (C) two corners on bottom, (D) two edges on bottom.

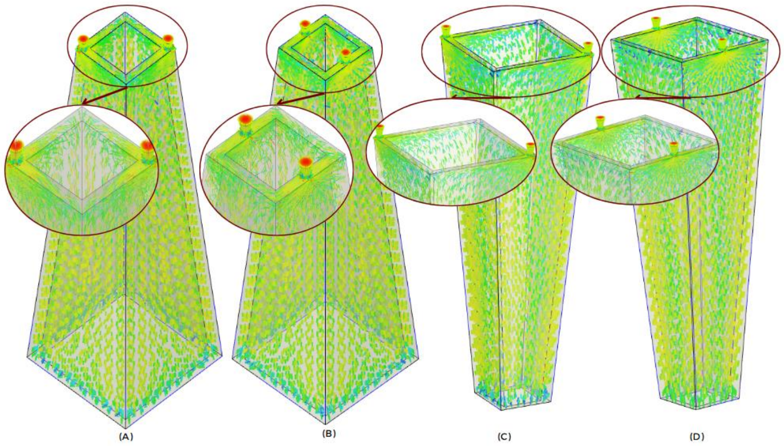

Fig. 5. Fiber orientation information according to filling type (A) two corners on top, (B) two edges on top, (C) two corners on bottom, (D) two edges on bottom.

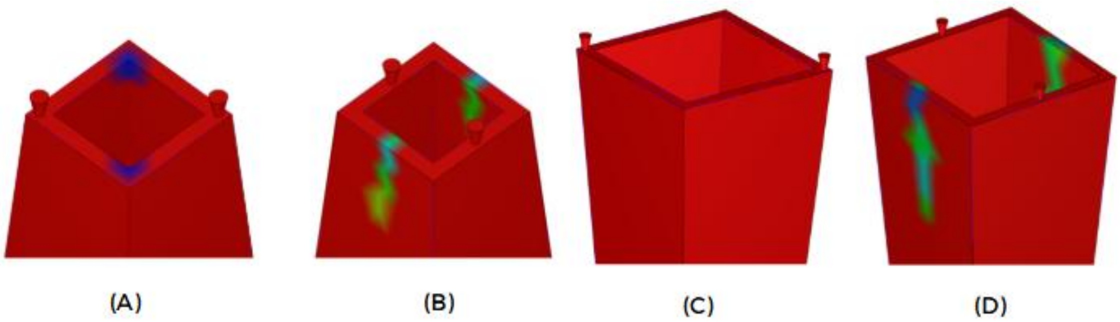

Fig. 6. Weldline information according to filling type (A) two corners on top, (B) two edges on top, (C) two corners on bottom, (D) two edges on bottom.

The simulation results provide crucial data for Digimat software, aiming to investigate the impact of altering fiber orientation (Fig. 5) and weld line regions (Fig. 6) on mechanical performance.

3.2.2. Transferring Real Material Data to the Finite Element Program
The Digimat RP software was used to import the structural mesh information (.inp file from Abaqus) of a thin-walled variable cross-section column. The properties of PA6 GF40 material were extracted using the Digimat MX tool. The production mesh was used for Digimat RP's mapping process, followed by matching fiber orientation and weldline data from the Moldex3D simulation. The plastic injection molding procedure for fiber-reinforced thermoplastic composites is depicted in Fig. 7.

Fig. 7. Process steps of transferring real material data (fiber orientation & weldline) to the finite element program with Digimat RP

4. Results & discussion

4.1. Conventinal model buckling analysis results
The CM simulation results in Table 1 showing the buckling modes of the column, with critical buckling loads calculated as 242 kN, 252 kN, and 295 kN in the first, second, and third modes, respectively.
Table 1. Conventional model column buckling analysis modes

	Mode 1	Mode 2	Mode 3
Conventional Model	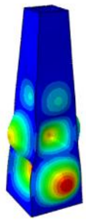	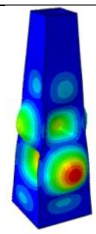	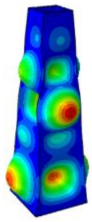

4.2. Column buckling analysis by transferring mold flow simulation data to finite element program
In the study, DIGIMAT RP was used to import the structural network, production network, fiber orientation, weld line data from mold flow simulation and PA6 GF40 material data from DIGIMAT MX. The mold flow simulation data was integrated into the structural mesh during the mapping procedure. The anisotropic material data were imported into the finite element model and the buckling analysis was repeated under the same boundary and loading conditions. The buckling modes of the column were obtained by integrating the results obtained from the MC simulation. As can be seen in Table 2, the first, second and third critical buckling loads obtained from the buckling analysis vary according to the gate location and number. In the models with mold flow data, the first mode values vary between 144-150 kN, the second between 152-158 kN and the third between 182-186 kN.

Table 2. Buckling modes and critical buckling loads in the first, second and third modes according to the filling type of the column for which the real material data model is integrated.

	Critical Bucklig Load (N)		
Filling Type	**Mode 1**	**Mode 2**	**Mode 3**
Two corners on top (A)	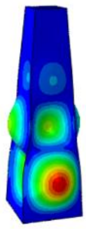 144.123 N	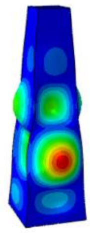 152.691 N	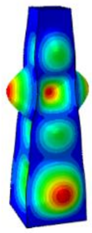 182.739 N
Two edges on top (B)	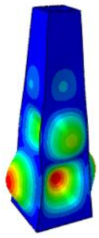 143.897 N	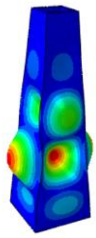 152.510 N	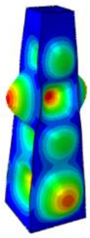 182.162 N
Two corners on bottom (C)	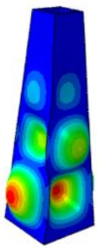 149.559 N	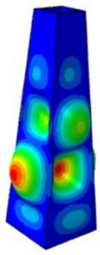 157.343 N	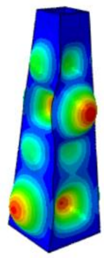 185.115 N

Table 2. Continued

Two edges on bottom (D)	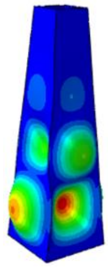 145.209 N	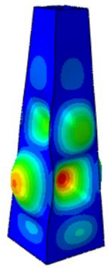 155.314 N	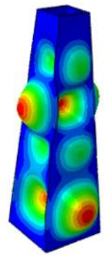 179.81

4.3. Load carrying capacity analysis of thin walled variable cross-section column

The study analyzed the critical buckling loads for the first three modes of four different models, which integrated both conventional model and mold flow data. Variations in the number of gates and melt injection regions led to changes in fiber orientation and weldline data across each analysis. Nonlinear analyses were conducted to determine and compare the load-carrying capacity of these models. The columns were subjected to a compressive load of 295 kN. Additionally, arrangements were made to obtain 'Node fill' data in the .inp file for each buckling analysis. Stability was ensured through the use of 'Node fill' data, which illustrates how loads and deformations are distributed at nodes, facilitating a more stable progression of the solution. Convergence criteria were employed to maintain stability, and incremental load application helped prevent sudden large deformations that could lead to instability. Material modeling played a critical role in accurately defining the transition between elastic and plastic behavior, ensuring proper prediction of plastic deformation areas. The stability of the solution was ensured through careful load distribution, mesh refinement, and accurate material modeling. The comparison of results shows which areas of the material underwent plastic deformation during column loading and at which points these deformations occurred.

Load Proportionality Factor (LPF) and displacement (U) graphs are important for understanding a structure's load-bearing capacity and behavior, particularly in nonlinear analyses (Chai vd., 2023). The maximum load-bearing capacity is indicated by the peak of the LPF, which compares the applied load to a reference load level. The maximum load-bearing capacity is attained at higher displacement values in models that incorporate real material data, indicating lower resistance to deformation. Because there is more fiber concentrated in the top region of bottom-filled models, the critical buckling region in the narrower top section is strengthened, increasing the maximum load-bearing capacity. The significance of these tools in structural analysis was demonstrated by comparing the obtained LPF and U graphs with conventional models. Load proportionality factor (LPF) and displacement (U) graphs were acquired, and Fig. 8 shows a comparison between the conventional model and the model that incorporated real material data.

Table 3. Plastic deformation zones in models where conventional model and mold flow data are integrated

	Plastic deformation zone	
Conventional model	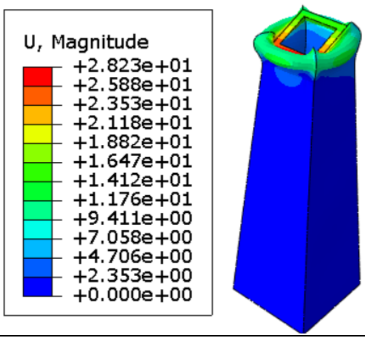	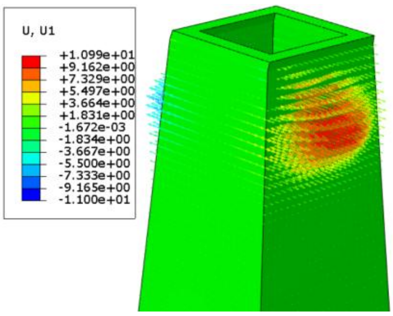

Table 3. Continued

<table>
<tr><td>Two corners on top (A)</td><td>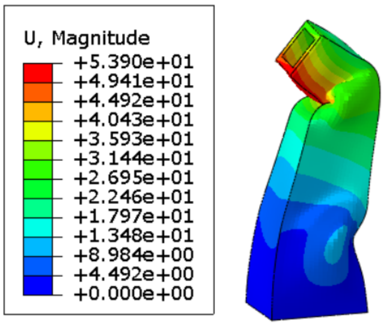</td><td>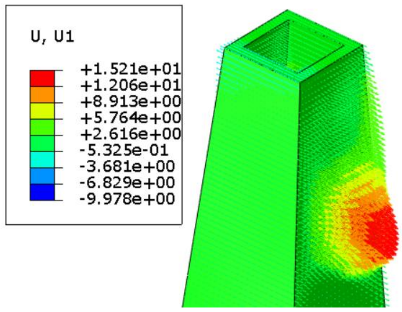</td></tr>
<tr><td>Two edges on top (B)</td><td>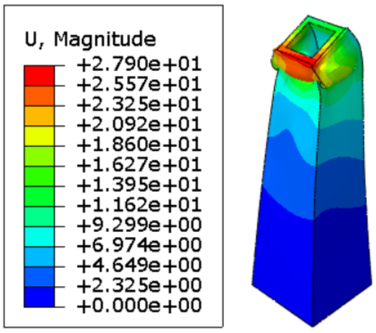</td><td>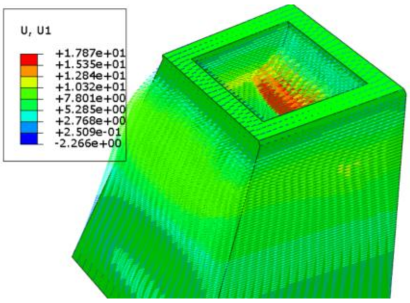</td></tr>
<tr><td>Two corners on bottom (C)</td><td>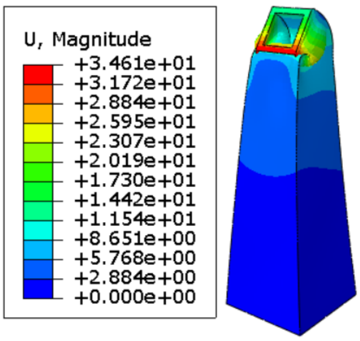</td><td>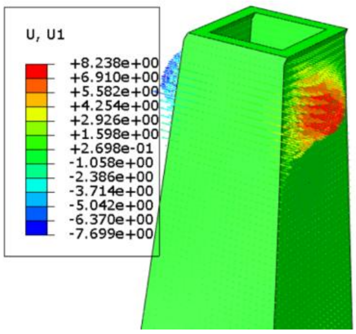</td></tr>
<tr><td>Two edges on bottom (D)</td><td>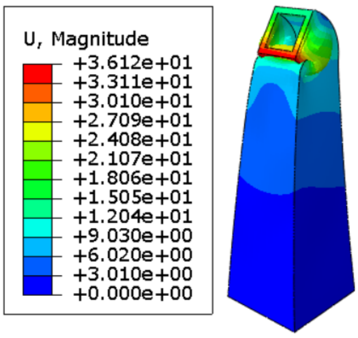</td><td>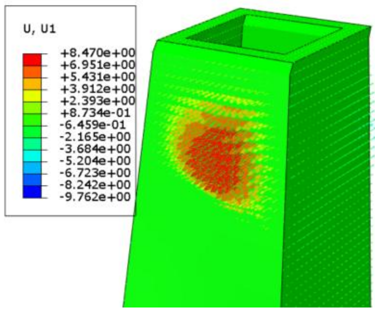</td></tr>
</table>

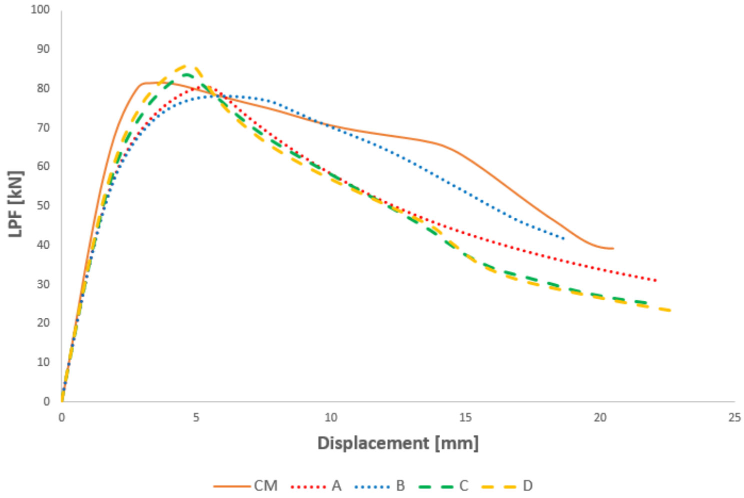

Fig. 8. Load proportionality factor (LPF) and displacement (U) graphs of models with conventional (CM) and real material data (A, B, C, D)

5. Conclusions

The study investigates the buckling behavior of PA6-GF40 columns, as well as the effects of manufacturing parameters such as fiber orientation and weld lines on mechanical performance. Initially, a conventional model was used to calculate critical buckling loads and modes. However, integrating fiber orientation and weld line data from Moldex3D simulations into ABAQUS using Digimat RP was a significant step forward. The real material data increased the load-bearing capacity of the columns, resulting in decreased deformation resistance. The placement of injection gates also had an impact on fiber orientation. Models filled from the bottom had a greater load-carrying capacity.

In conclusion, this study emphasizes the importance of taking into account real material data and injection molding parameters, demonstrating that their integration is critical in the design of fiber-reinforced thermoplastic components. It outlines strategies for improving the manufacturing process, allowing for the creation of more durable and efficient parts.

Acknowledgments

We would like to thank The Scientific and Technological Research Council of Turkey (TÜBİTAK) for providing the scholarship to the first author under the Cornet Project (Project No: 123N452). We also express our sincere gratitude to TÜBİTAK for supporting the second author with the scholarship under 2244 - Industry Doctorate Program (Project No: 119C089). Their invaluable support has greatly contributed to the successful completion of this research.

References

Advani, S. G., & Tucker III, C. L. (1987). The use of tensors to describe and predict fiber orientation in short fiber composites. *Journal of Rheology, 31*(8), 751–784.

Chai, J. H., Zhong, J. P., Xu, B., Zhang, Z. J., Shen, Z., Zhang, X. L., & Shen, J. M. (2023). Finite element analysis and experimental validation of the failure characteristic of pressurized cylinder. International Journal of Structural *Integrity, 14*(6), 874–890.

Chen, Z., Liu, X., Lü, R., & Li, T. (2007). Friction and wear mechanisms of PA66/PPS blend reinforced with carbon fiber. *Journal of Applied Polymer Science, 105*(2), 602–608.

Fu, S.-Y., Lauke, B., & Mai, Y.-M. (2009). *Science and engineering of short fibre reinforced polymer composites*. Woodhead Publishing Limited.

Jain, A. (2019). Micro and mesomechanics of fibre reinforced composites using mean field homogenization formulations: A review. *Materials Today Communications, 21*, 100552.

Jong, W. R., Hwang, S. S., Wu, C. C., Kao, C. H., Huang, Y. M., & Tsai, M. C. (2018). Using a visualization mold to discuss the influence of gas counter pressure and mold temperature on the fountain flow effect. *International Polymer Processing, 33*(2), 255–267.

Kroon, M., Andreasson, E., Petersson, V., & Jutemar, E. P. (2024). Numerical and experimental analysis of inelastic and rate-dependent buckling of thin injection-moulded high-density polyethylene structure. *International Journal of Solids and Structures, 290*, 112673.

Li, T., & Kapania, R. K. (2018). On the formulation of a high-order discontinuous finite element method based on orthogonal polynomials for laminated plate structures. *International Journal of Mechanical Sciences, 149*, 530–548.

Mori, T., & Tanaka, K. (1973). Average stress in matrix and average elastic energy of materials with misfitting inclusions. *Acta Metallurgica, 21*(5), 571–574.

Paiva, J. B. (2018). Corner restrictions and their application to bending plate analyses by the boundary element method. *Engineering Analysis with Boundary Elements, 95*, 1–11.

Polat, A., Deliktaş, B., Yazıcı, M., & Voyiadjis, G. Z. (2024). Computational modeling of weld-line impacts on mechanical behaviour of fiber-reinforced thermoplastics. *European Journal of Mechanics - A/Solids*, 105485.

Rozylo, P., & Debski, H. (2024). Stability and load carrying capacity of thin-walled composite columns with square cross-section under axial compression. *Composite Structures, 329*, 117795.

Saraçaoğlu, M. H., & Uzun, S. (2020). Stability analysis of columns with variable cross-sections. *Journal of Structural Engineering & Applied Mechanics, 3*, 169–179.

Schreiber, P., Mittelstedt, C., & Beerhorst, M. (2020). Buckling of shear-deformable orthotropic laminated plates with elastic restraints. *Thin-Walled Structures, 157*, 107071.

Tseng, H. C., Chang, R. Y., & Hsu, C. H. (2017). Numerical prediction of fiber orientation and mechanical performance for short/long glass and carbon fiber-reinforced composites. *Composites Science and Technology, 144*, 51–56.

Zhou, S., Zhang, Q., Wu, C., & Huang, J. (2013). Effect of carbon fiber reinforcement on the mechanical and tribological properties of polyamide6/polyphenylene sulfide composites. *Materials & Design, 44*, 493–499.

4th International Civil Engineering & Architecture Conference
17-19 May 2025, Trabzon, Türkiye

Effect of hybrid steel fiber effect on concrete mechanical properties

Merve Arpacıktaş*[1], Fatih Altun[2]

[1] Nuh Naci Yazgan University, Vocational Schools, Construction Technology Program, Kayseri, Türkiye
[2] Erciyes University, Faculty of Engineering, Department of Civil Engineering, Kayseri, Türkiye

Abstract. The use of fibers to increase the mechanical properties of concrete has been a common practice for a long time. Although various materials can be used as fibers, steel fibers are preferred in applications where higher performance is required due to their superior mechanical properties. The effects of the length, aspect ratios, amount, and strength of steel fibers on concrete have been investigated by many researchers. In this study, steel fibers with different aspect ratio, were added to concrete at dosages of 0 kg/m³, 30 kg/m³, and 60 kg/m³. The fibers added to the concrete were obtained by adding a single type of fiber, and hybrid steel fiber-reinforced concrete samples were also produced by adding two steel fibers in equal amounts. In order to investigate the effect of hybrid steel fiber additive on the mechanical properties of concrete, compressive strength, splitting tensile, and flexural tensile strength tests were conducted on the samples. As a result of the experimental studies, it was observed that the use of steel fibers did not provide a significant contribution to improving the compressive strength of concrete. When the splitting tensile strength test results were examined, the highest increase in tensile strength was obtained in hybrid steel-reinforced concrete where the fiber dosage was 60 kg/m³. This increase was calculated to be 55% compared to the reference samples. When the consumed energy obtained from the load-CMOD curve as a result of the bending tensile tests was compared, the energy consumed by the hybrid steel fiber samples where the fiber dosage was 60 kg/m³ was 2.72 times the energy consumed by the hybrid steel fiber effect where the dosage was 30 kg/m³. As a result of the study, it was observed that the hybrid steel fiber additive had positive effects on the tensile strengths, which are among the mechanical properties of concrete.

Keywords: Concrete;Steel fiber; Hybrid steel fiber; Mechanical properties

1. Introduction

Concrete has inherently low tensile strength and ductility. To improve these deficiencies, various types of additives with different properties are incorporated into concrete. Among the most commonly used of these are steel fibers. Steel fiber reinforced concrete (SFRC) is a composite material produced by adding steel fibers to conventional concrete components such as aggregate, cement, and water, as well as mineral and/or chemical admixtures. Steel fibers are used to enhance the performance of both plain and reinforced concrete elements. Their inclusion improves the energy absorption capacity, increases ductility at the moment of fracture, and reduces the risk of cracking. Owing to these advantages, SFRC is widely used in applications such as highways, tunnel linings, industrial flooring, slope stabilization, dam structures, port construction and repair, fire protection, concrete pipes, and reinforced concrete frames (Köksal, 2004),(Mohod,2012), (Altun & Aktaş, 2011).

In concrete reinforced with a single type of fiber, the multi-scale and progressive failure mechanisms of concrete limit the effectiveness of the fiber to a specific range, resulting in suboptimal overall performance. To address this issue, it has been suggested that combining fibers of different sizes, functions, and structural responses can enhance the utilization of concrete's material properties and improve the mechanical performance of structural elements. Hybrid fiber reinforced concretes are defined as novel cement-based composite materials produced by incorporating more than one type and size of fiber, instead of relying on a single fiber type. The main purpose of using hybrid fibers is to achieve more controlled and ductile behavior in concrete by taking advantage of the complementary effects of different fiber types. This approach enables better control over crack initiation and propagation. While many previous studies have investigated the effects of various fiber combinations and hybrid fiber usage, research specifically focusing on steel–steel hybrid fiber reinforced concretes where both fibers are of the same type but with different geometries remains limited (Rossi, 2000) ,(Türk & Kına, 2017),(Ganesan et al., 2014), (Issa et al., 2011).

*Corresponding author, E-mail: marpaciktas@nny.edu.tr

https://doi.org/10.31462/icearc2025_ce_sme_105

This study experimentally investigates the influence of hybrid steel fiber reinforcement, consisting of fibers with different aspect ratios, on the mechanical behavior of concrete.

2. Materials and methods

To investigate the effect of hybrid steel fiber reinforcement on the mechanical properties of concrete, experimental studies were conducted on both cylindrical and prismatic concrete specimens.Compressive strength and splitting tensile strength tests were performed on the cylindrical specimens, while the flexural behavior of steel fiber reinforced concrete was evaluated using prismatic beam specimens.

2.1. Steel fiber

In this study, two types of steel fibers with different aspect ratios, KMX 80/60 BG and KMX 65/60 BG, were added to concrete designed to achieve C30 strength class, at dosages of 0 kg/m³ (reference), 30 kg/m³, and 60 kg/m³. The fibers were incorporated into the concrete either as a single fiber type or as a hybrid combination, in which equal proportions of both fiber types were used. The steel fibers used in the study were hooked-end fibers bonded together in bundles using adhesive. The physical and mechanical properties of the fibers are presented in Table 1., and their general appearance is shown in Fig. 1.

Table 1. Steel fiber properties

Steel Fiber	Length,l (mm)	Diameter,d (mm)	Aspect Ratio (l/d)	Tensile Strength (N/mm^2)
KMX 65/60 BG	60	0,9	65	1150 N/mm^2
KMX 80/60 BG	60	0,75	80	1200 N/mm^2

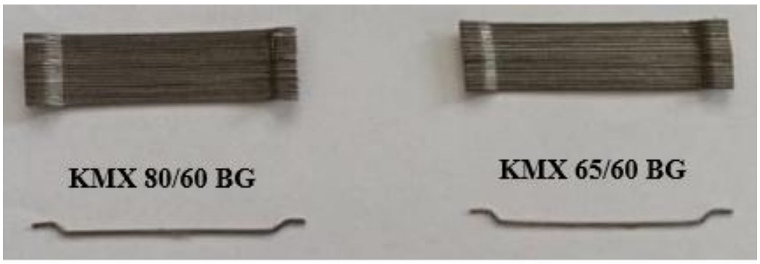

Fig. 1. Steel fibers

2.2. Experimental program

Within the scope of the study, two specimens were taken from each concrete mixture. Accordingly, a total of 28 cylindrical specimens were obtained 14 for compressive strength and 14 for splitting tensile strength tests. The cylindrical specimens had dimensions of Ø150×300 mm. Compressive strength tests were performed in accordance with TS EN 12390-3, and splitting tensile strength tests were carried out according to TS EN 12390-6.For the flexural tensile strength tests, 14 prismatic concrete beams with dimensions of 150 × 150 × 600 mm were produced, and the tests were conducted in accordance with TS EN 14651+A1. Notches with a depth of 25 mm were cut at the mid-span of the specimens. At the end of the tests, which were carried out up to a deflection of 4 mm, load–CMOD (Crack Mouth Opening Displacement) curves were obtained, and energy consumption was calculated.

The concrete mixtures used in this study were systematically named based on the type of steel fiber and the fiber dosage.In the sample codes, the expression "SF" denotes the presence of steel fiber reinforcement, the numerical value indicates the fiber dosage in kg/m³, and the term "Type" refers to the classification according to fiber type.All sample codes and their corresponding contents are presented in Table 2.

Table 2. Specimen codes and fiber compositions

Sample Code	Fiber Dosage (kg/m³)	Description
Ref	0	Reference concrete (no fiber)
SF30-Type65	30	Single-type fiber (100% KMX 65/60 BG)
SF30-Hybrid	30	Hybrid fiber (50% KMX 65/60 + 50% KMX 80/60)
SF30-Type80	30	Single-type fiber (100% KMX 80/60 BG)
SF60-Type65	60	Single-type fiber (100% KMX 65/60 BG)
SF60-Hybrid	60	Hybrid fiber (50% KMX 65/60 + 50% KMX 80/60)
SF60-Type80	60	Single-type fiber (100% KMX 80/60 BG)

3. Results and discussion

The test results were presented based on the average values of two specimens from each concrete mixture group.

The compressive strength results obtained from cylindrical concrete specimens are shown in Fig. 2. When the results are examined, it is observed that the compressive strength of SF30-Type65 specimens increased by approximately 7% compared to the reference group. However, a 15% decrease was observed in the SF30-Hybrid specimens. The SF30-Type80 group showed a 10% increase, while the SF60-Type80 group exhibited a 20% decrease in compressive strength. The SF60-Hybrid specimens experienced a 7% reduction, and SF60-Type80 showed a more significant decrease of approximately 16%. Overall, it was concluded that the addition of steel fibers did not consistently improve compressive strength. In some mixtures, the inclusion of fibers—particularly in hybrid combinations—resulted in a decrease in compressive strength.According to the experimental results, the use of steel fibers does not make a significant contribution to enhancing the compressive strength of concrete.

The average splitting tensile strength values of the cylindrical concrete specimens are presented in Fig. 4. When the results are examined, the splitting tensile strength of SF30-Type65 specimens increased by approximately 18% compared to the reference samples. A 6% decrease was observed in the SF30-Hybrid group, while SF30-Type80 showed a 13% increase. For SF60-Type65, the increase was approximately 15%, whereas the highest improvement was recorded in SF60-Hybrid specimens, with an increase of about 55%. In contrast, the increase in SF60-Type80 specimens was limited to around 5%. Overall, the test results indicate that the addition of steel fibers generally enhances the splitting tensile strength of concrete.The most significant improvement was achieved in the SF60-Hybrid group, where a fiber dosage of 60 kg/m³ and the use of hybrid steel fibers provided the highest contribution. These results suggest that steel fiber reinforcement is more effective in enhancing tensile strength compared to compressive strength. In particular, hybrid fiber combinations at higher dosages (60 kg/m³) significantly improve the tensile performance of concrete.

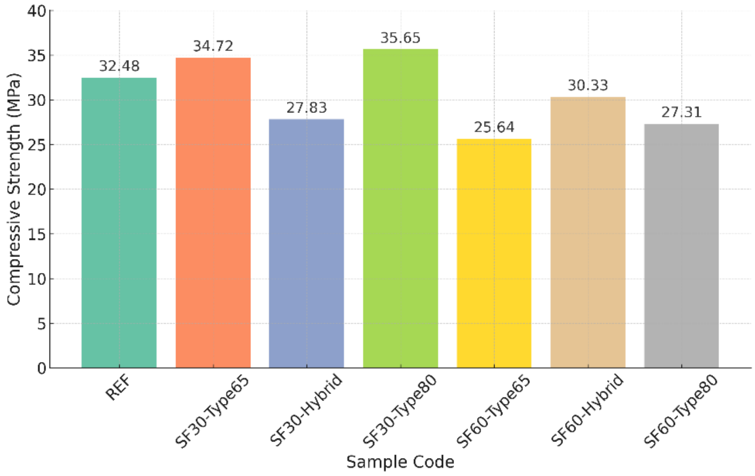

Fig. 3 Compressive strength of samples

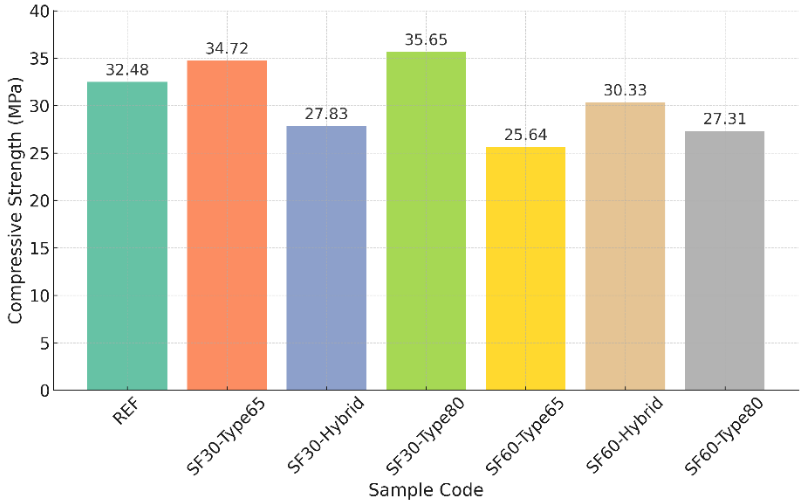

Fig. 4. Splitting tensile strength of samples

The load–CMOD curves obtained from the prismatic concrete beam tests are presented in Fig. 5.When the load–CMOD curves of the specimens are examined, SF60-Hybrid specimens are observed to carry the highest loads.The SF60-Type65, SF60-Hybrid, and SF60-Type80 specimens exhibited increasing load resistance with displacement up to the first crack, and after cracking, they maintained their load-carrying capacity due to the fiber–matrix interaction, without a sudden drop.In contrast, SF30-Type65, SF30-Hybrid, and SF30-Type80 specimens showed a noticeable decrease in load after the first crack, attributed to a lower fiber phase, but continued to dissipate energy.As expected, the reference beams, which contained no fibers, exhibited brittle failure and their energy consumption remained significantly lower compared to fiber-reinforced concretes.

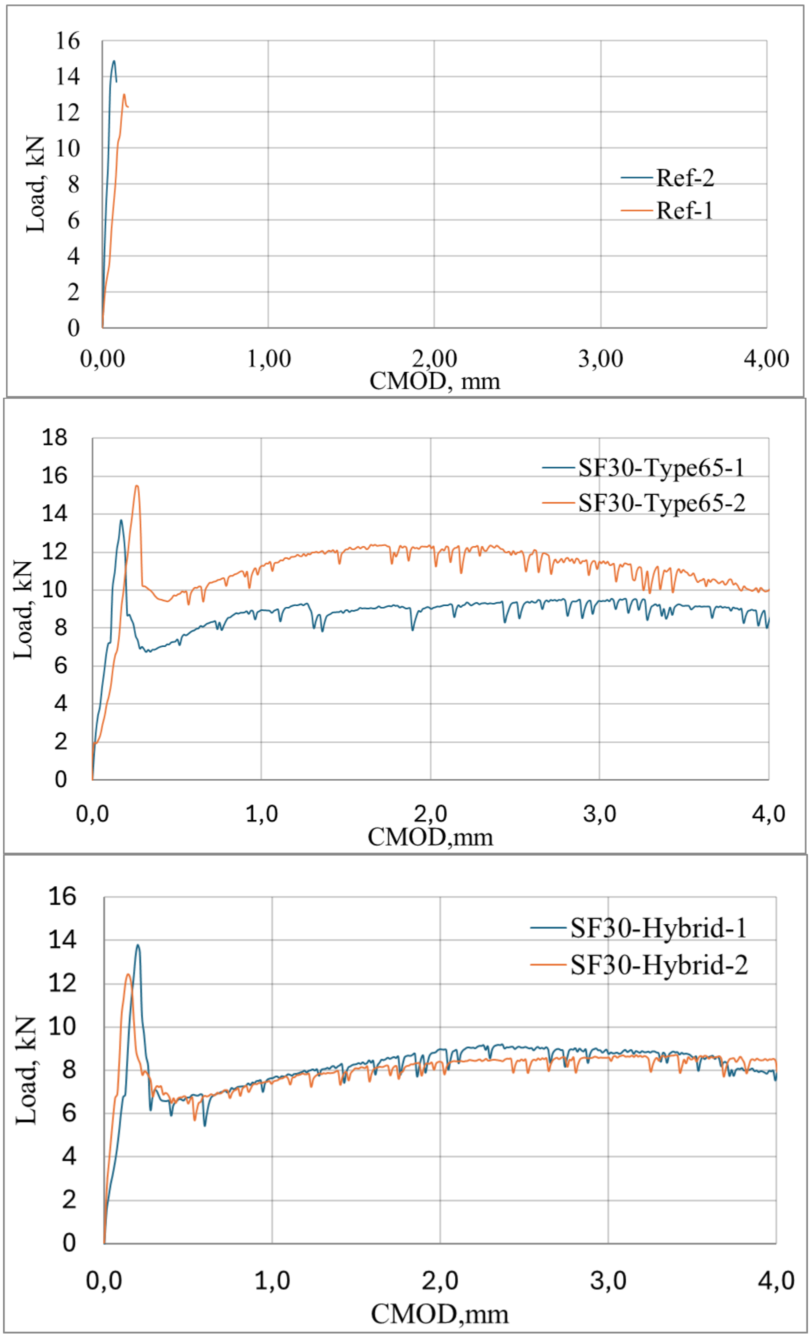

Fig. 5. Load- CMOD deflection

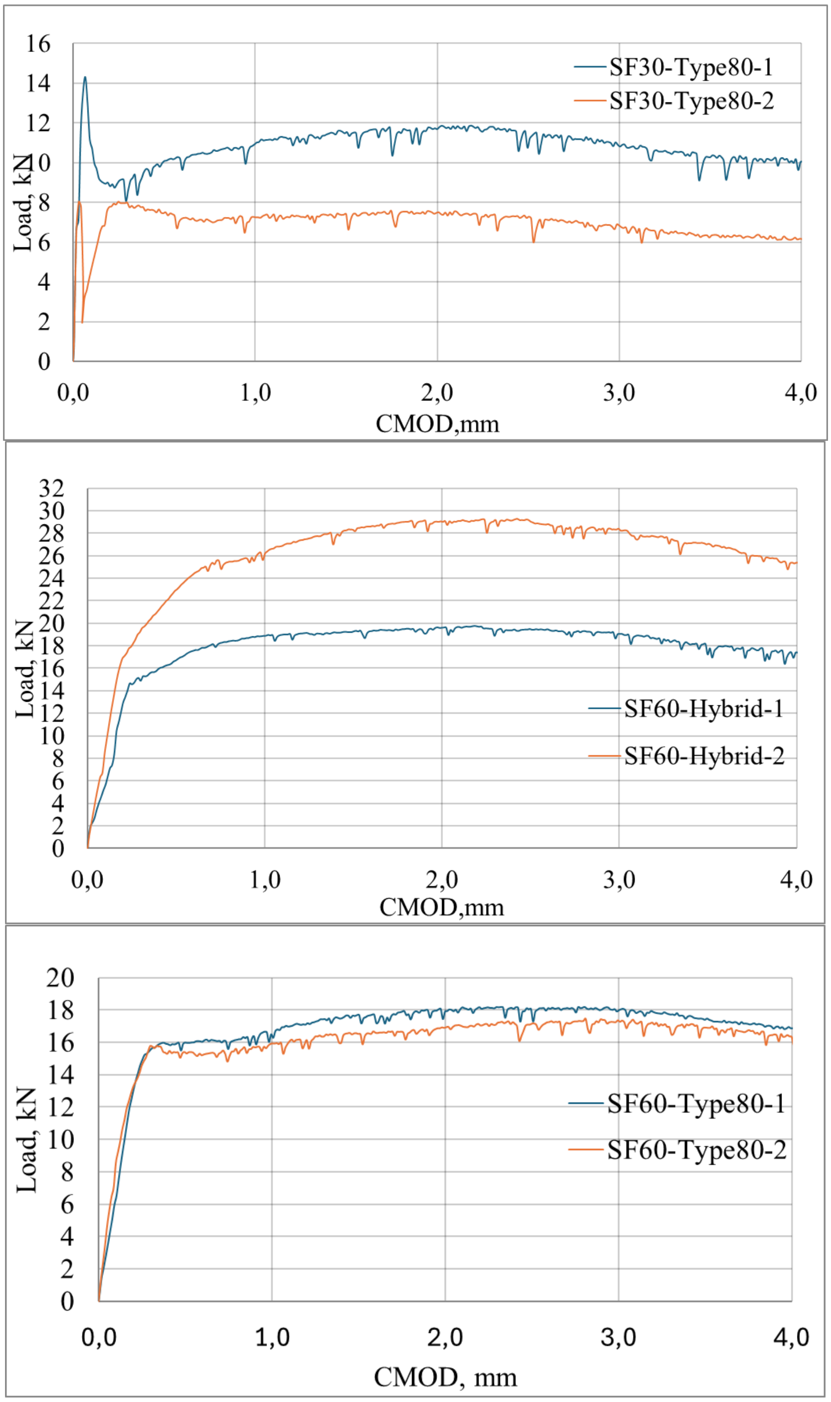

Fig. 5. Continued

The energy consumption of the prismatic concrete specimens is presented in Fig. 6. As shown in Fig. 6., the reference specimens, which did not contain steel fibers, failed abruptly at the first crack load and exhibited no energy consumption.A significant increase in energy consumption was observed in the specimens with a fiber dosage of 60 kg/m³.The highest increase was recorded in the SF60-Hybrid specimens, which incorporated hybrid fibers at this dosage.It was observed that doubling the fiber dosage approximately doubled the energy consumption.Specifically, the energy consumed in the SF60-Hybrid specimens was 2.72 times greater than that of the SF30-Hybrid specimens, indicating the pronounced effect of hybrid steel fibers at higher dosages.

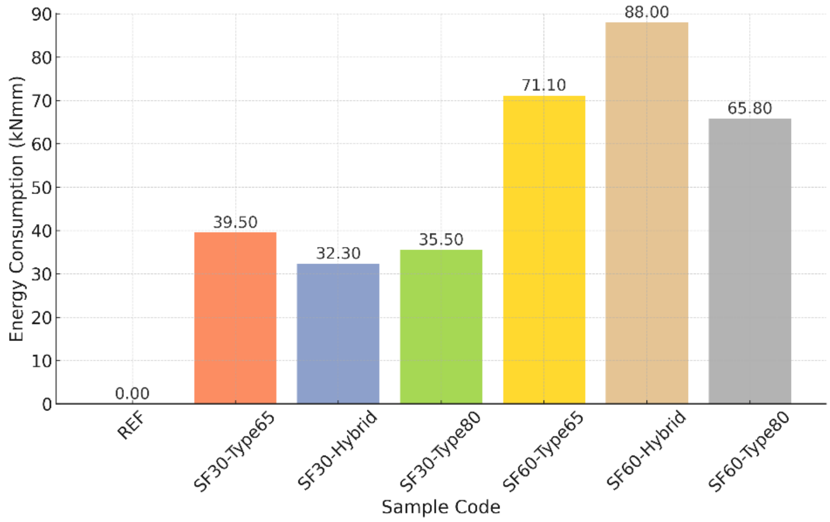

Fig. 6. Energy consumption of prismatic concrete

4. Conclusions

In this study, the effect of hybrid steel fiber reinforcement on the mechanical properties of concrete was investigated. Based on the results obtained, the following conclusions were drawn:

- It was concluded that the compressive strength of concrete did not increase with the addition of steel fibers. In fact, a reduction in compressive strength was observed at certain fiber dosages, including in mixtures with hybrid fibers. According to the test results, the use of steel fibers does not provide a significant contribution to improving the compressive strength of concrete.
- When the splitting tensile strength results were evaluated, it was found that the inclusion of steel fibers generally enhanced tensile strength. The most significant improvement—an increase of approximately 55% compared to the reference—was observed in the SF60-Hybrid specimens. This indicates that steel fiber reinforcement is more effective in improving tensile strength than compressive strength. In particular, a fiber dosage of 60 kg/m³ and the use of hybrid steel fibers significantly increased the tensile performance of concrete.
- When the load–CMOD curves of prismatic concrete specimens were examined, a sudden decrease in post-crack load-bearing capacity was observed at lower fiber dosages. However, with increasing fiber content, the specimens were able to sustain and transfer load more effectively after cracking. This behavior—attributed to the contribution of the steel fiber phase—was most evident in hybrid fiber-reinforced specimens with a dosage of 60 kg/m³. In addition to the improvement in strength, the energy consumption of SF60-Hybrid specimens was found to be 2.72 times higher than that of SF30-Hybrid, demonstrating the significant effect of higher hybrid fiber content on energy dissipation capacity.

Acknowledgments

This study was supported by Erciyes University Scientific Research Projects Unit with the project code FYL-2019-8833.

References

Altun, F., & Aktaş, B. (2011). Çelik tel katkılı hafif betonun eğilme tokluğunun incelenmesi. *Kahramanmaraş Sütçü İmam Üniversitesi Mühendislik Bilimleri Dergisi, 14*(2), 27–33. (in Turkish)

Arpacıktaş, M. (2020). *Hibrit çelik lif katkılı ankastre mesnetli betonarme kiriş davranışının deneysel incelenmesi* (Master's thesis, Erciyes Üniversitesi, Fen Bilimleri Enstitüsü, Kayseri, Türkiye). (in Turkish)

Ganesan, N., Indira, P. V., & Sabeena, M. V. (2014). Behaviour of hybrid fibre reinforced concrete beam–column joints under reverse cyclic loads. *Materials and Design, 54*, 686–693.

Issa, M., Metwally, I., & Elzeiny, S. M. (2011). Influence of fibers on flexural behavior and ductility of concrete beams reinforced with GFRP rebars. *Engineering Structures, 33*(5), 1754–1763.

Köksal, F. (2004). *Çelik tel donatılı betonların mekanik davranışı ve optimum tasarımı* (Doctoral dissertation, İstanbul Teknik Üniversitesi, Fen Bilimleri Enstitüsü, İstanbul, Türkiye). (in Turkish)

Mohod, M. V. (2015). Performance of steel fiber reinforced concrete. *International Journal of Engineering and Technology, 3*(2), 121–124.

Rossi, P. (2000, September). Ultra-high performance fibre reinforced concretes (UHPFRC): An overview. In *Fifth RILEM Symposium on Fibre-Reinforced Concretes (FRC)* (pp. 87–100). Lyon, France.

Türk, K., & Kına, C. (2017). Çimento esaslı kompozitlerde karma lif kullanımı. *Pamukkale University Journal of Engineering Sciences, 23*(6), 671–678. (in Turkish)

Türk Standardları Enstitüsü. (2002). *TS EN 12390-6 Beton – Sertleşmiş beton deneyleri – Bölüm 6: Deney numunelerinin yarmada çekme dayanımının tayini*. Ankara, Türkiye. (in Turkish)

Türk Standardları Enstitüsü. (2003). *TS EN 12390-3 Beton – Sertleşmiş beton deneyleri – Bölüm 3: Deney numunelerinde basınç dayanımının tayini*. Ankara, Türkiye. (in Turkish)

Türk Standardları Enstitüsü. (2008). *TS EN 14651 + A1 Metal lifli beton – Deney yöntemi – Eğilmede çekme dayanımının tayini (Kalıcı orantısal sınır (LOP))*. Ankara, Türkiye. (in Turkish)

4th International Civil Engineering & Architecture Conference
17-19 May 2025, Trabzon, Türkiye

Development of demountable steel-timber-concrete composite floors: literature review and connection challenges

Lara Kachouh*[1], Chaimaa Jaafari[1], Sébastien Durif[1], Abdelhamid Bouchair[1]

[1] *Université Clermont Auvergne, INP Clermont Auvergne, CNRS, Institut Pascal, F-63000 Clermont-Ferrand, France.*

Abstract. Mixed structures combining steel, wood and concrete represent a promising solution for sustainable construction, thanks to their ability to combine lightness, rigidity and durability. These systems exploit the complementary properties of materials: concrete offers exceptional rigidity and stability, wood provides lightness and flexibility, while steel guarantees high mechanical strength. By combining these advantages, these structures optimize performance while meeting today's ecological challenges. However, current solutions have two major limitations: they are essentially non-dismantlable, as concrete is often poured on site, and they lack suitable connections that would enable all three materials to work simultaneously. While wood-concrete and steel-wood connections have been extensively explored in literature, dismountable and efficient connections for steel-wood-concrete structures remain non-existent, posing a significant technical challenge. This study provides a detailed examination of existing research on composite structures, highlighting the mechanical performance and limitations of timber-concrete and steel-timber connections. In addition to this analysis, numerical models were developed on Abaqus to assess the behavior of three demountable composite floors combining steel, timber, and concrete connected using different types of connections in order to compare their performance.

Keywords: Hybrid structures; steel-timber-concrete systems; mechanical performance; demountable floor systems; sustainable design.

1. Introduction

Integrating several materials into a single structure optimizes their mechanical performance while meeting the challenges of sustainability and reducing environmental footprints. Among the most studied combinations in civil engineering, wood-concrete and steel-wood hybrid systems have been the focus of much research aimed at improving their structural efficiency and durability (Okutu et al., 2017), (Djoubissié Denouwe, 2018)

Integrating concrete, wood and steel in the same composite structure could offer significant advantages by combining the rigidity and durability of concrete, the lightness and flexibility of wood, and the mechanical strength of steel. However, this combination poses a number of challenges, not the least being the development of suitable connections that can be dismantled and ensure effective composite action between the three materials.

Connections play a key role in the mechanical behavior of hybrid structures. There are several existing wood-concrete connection types in the literature, , such as fastener-type connectors, longitudinal connectors or notches or glue connections, that enable efficient transmission of shear forces (Lecours, 2022). Steel-wood connections, on the other hand, use solutions such as bolts, screws or steel plates to guarantee structural stability (Loss et al., 2016a). While these connections have been extensively studied separately, there is little research on assemblies that simultaneously integrate steel, wood and concrete in a non-dismantling system (Winter et al., 2016), (Tavoussi et al., 2018), (Tavoussi et al., 2019).

One of the main technical challenges lies in the development of efficient connections, capable of ensuring optimum stress transfer between materials, while allowing components to be dismantled and reused. Indeed, the differences in stiffness, mechanical behavior and failure modes between concrete, wood and steel make designing a suitable connection a complex task. An optimal connection must therefore guarantee good mechanical resistance, limit the effects of slippage and enable simplified installation.

In order to better understand these interactions, this study uses a numerical approach to analyze the behavior of steel-wood-concrete demountable composite floors. Three types of connections, identified from the literature, were numerically modeled in order to assess their performance and ability to ensure effective composite action.

* Corresponding author, E-mail: Lara.KACHOUH@doctorant.uca.fr

https://doi.org/10.31462/icearc2025_ce_sme_126

This article is structured into two main parts. The first section provides a review of the different connection solutions for timber-concrete and steel-timber composite structures found in the literature. The second section presents the numerical models developed in order to compare the performance of composite steel-timber-concrete structures for 3 different connection configuration systems.

2. State of the art on connections in composite floors

Connections between materials in wood-concrete, steel-wood and steel-wood-concrete composite structures are a subject of intense study, aimed at optimizing the stiffness, strength and demountability of assemblies. Connection systems are generally evaluated by means of large-scale shear (push-out) and bending tests, to analyze their mechanical behavior and determine their load-bearing capacity.

One of the main challenges lies in designing connections that are both high-performing and demountable, capable of withstanding mechanical loads while allowing for quick assembly and disassembly without damaging the materials. Mechanical fasteners such as screws, bolts, and perforated plates are generally preferred over epoxy adhesives, as they offer greater potential for component reuse. However, material compatibility, accessibility to fasteners, and durability after multiple assembly-disassembly cycles remain critical issues that are still insufficiently explored.

For wood-concrete connections, common systems include notches, bolts, screws and sometimes epoxy resins. Notches are particularly appreciated for their ability to transmit shear forces effectively through mechanical locking, but they do exhibit a certain fragility under heavy loading. Push-out tests show good initial rigidity with limited plastic deformation before failure, often at wood level. Bolts and screws provide a certain ductility and better removability, but their stiffness is lower than that of notches. Mixed bolt-notch connections show an interesting performance in terms of stiffness-strength compromise, but the question of their demountability remains little studied.

In terms of notch geometry, several studies show that conventional rectangular notches have high initial stiffness but are prone to brittle shear failure, mainly in the wood according to (Fragiacomo et al., 2008). Shear tests indicate that an increase in notch depth improves stiffness, but may also increase the brittleness of the system according to (Xu et al., 2023). Inclined or dovetail-shaped notches offer greater force transmission capacity, while improving assembly stability thanks to an increased mechanical locking effect. However, these geometries are less common, as they complicate the manufacturing process and may limit the system's demountability, according to the thesis by (Boccadoro, 2016).

The addition of bolts or screws to the notches is a common method of improving the rigidity and load-bearing capacity of the assembly. In effect, bolts or screws act as reinforcing devices that increase the sliding resistance between wood and concrete, (Boccadoro et al., 2017). Push-out tests generally show that this combination increases the overall system stiffness and improves its ultimate capacity compared to notches alone, according to (Xu et al., 2023). However, the use of screws or bolts can limit the demountability of the system, especially when combined with glue or sealed in concrete pockets.

Specific wood-concrete connections also include innovative systems such as perforated plates (Miotto & Dias, 2012), concrete shell (Auclair et al., 2016), connecting plywood plate with steel reinforcing (Daňková et al., 2019) , inclined full-thread screws and bonded reinforcing bars and dowels (Djoubissie et al., 2018) and (Fragiacomo et al., 2018). These methods provide better stress distribution, increased stiffness and higher load-bearing capacity than traditional connections. Perforated plates embedded in concrete show a good shear strength. Systems using inclined screws show a notable improvement in load-bearing capacity and stiffness, but their demountability remains limited when combined with epoxy adhesives or resins.

Steel-wood connections have evolved with the development of several systems aimed at improving rigidity, strength and, to a lesser extent, demountability. The most common methods include the use of self-tapping screws, Gang Nail Plates, bolts inserted in concrete pockets or epoxy resins, as well as devices combining several techniques to achieve better mechanical performance.

Self-tapping screws, particularly those with inclined full threads, are widely used for their ability to provide high rigidity and good ultimate strength due to their deep anchorage in wood. Shear tests show that these screws can offer significantly higher slip resistance than traditional connectors. However, these systems are generally non-removable when combined with epoxy glue, or when the screws are sealed in cement pockets (Loss et al., 2016).

Nail-on plates, although considered economical solutions, offer limited performance in terms of rigidity and strength, (Okutu et al., 2017). However, they do have the advantage of being removable if not combined with permanent adhesives.

Bolts inserted into concrete pockets or fixed with epoxy resins provide good load-bearing capacity but render the connection non-dismantlable (Hassanieh et al., 2017). However, the use of bolts alone (without chemical sealing) could allow some demountability, although this may reduce the overall stiffness of the system.

Combination systems incorporating screws, nailing plates and bolts are currently being explored to improve overall mechanical performance while seeking to maintain a certain degree of demountability. However, few studies specifically address the issue of demountability of steel-wood connections, which is a major gap in the current literature.

Steel-wood-concrete connections are still little explored in the literature. Researchers tackling this subject focus mainly on systems where concrete is poured in situ, often using perforated metal plates, screws or notches made in the wood. However, the experimental tests carried out to date are mainly push-out tests performed separately to evaluate steel-wood connections (perforated plates, inclined screws, bolts) on the one hand, and wood-concrete connections (notches, screws, perforated plates) on the other hand (Winter et al., 2016), (Tavoussi et al., 2018).

Very few studies combine all three materials steel, wood, and concrete into a single hybrid assembly subjected to shear or bending tests, which represents a major gap in the current research. Most existing work focuses on improving stiffness and strength through permanent joining methods, with little to no consideration for demountability. However, bending tests on systems that simultaneously combine steel, wood, and concrete are crucial to better understanding fatigue phenomena, the effects of repeated loading, and long-term deformations in such systems. The development of these types of connections requires optimization of connector geometry, selection of compatible materials, and a design strategy focused on reversibility and durability, in line with the principles of the circular economy.

Fig. 1 illustrates the shear force versus relative slip relationship obtained for different connection types using pushout tests.

This literature review highlights the diversity of connection types explored for composite floors, as well as the trade-offs between stiffness, strength, and demountability. Notched connections provide good stiffness but tend to be brittle and offer limited reversibility. Screws and bolts, on the other hand, allow for better demountability, often at the cost of lower stiffness. The use of epoxy adhesives improves bonding performance but significantly limits the potential for disassembly. Finally, hybrid solutions, such as perforated plates, appear promising, although they have been studied little in the context of demountable configurations.

In the first phase of our experimental work, we selected three types of connections: bolts alone, notched connections, and a combination of bots, in order to evaluate their mechanical performance and potential for disassembly. Depending on the results obtained, other configurations such as perforated plates or hybrid systems may be considered to refine the balance between stiffness, strength, and demountability. This progressive approach will help identify the most relevant solutions for the development of demountable, durable structures in line with circular economic principles.

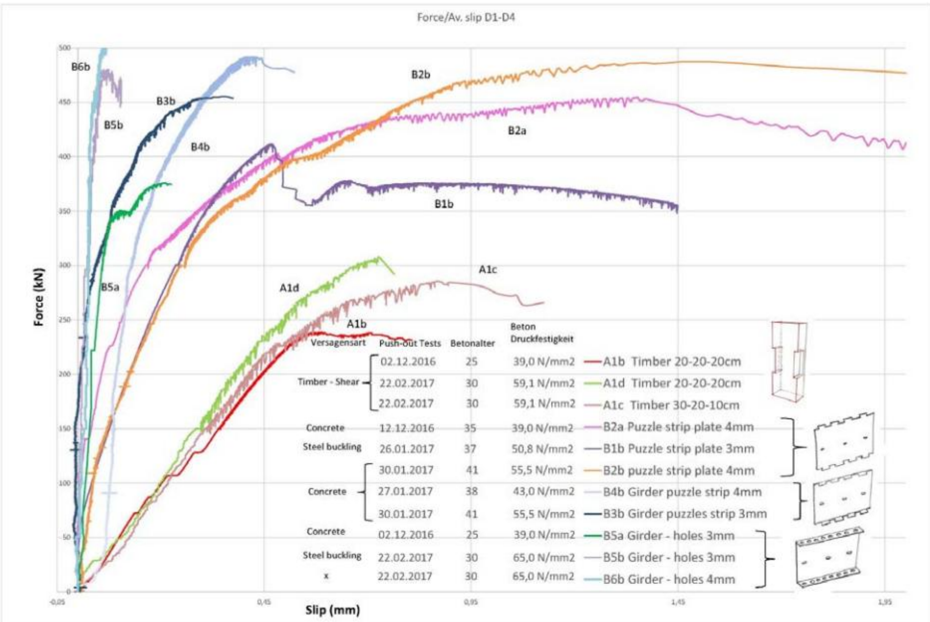

Fig. 1. Push-out test results for all specimens: Relationship between shear force and relative slip, (Tavoussi et al., 2018)

3. Numerical model and results

Once the literature review was achieved, a preliminary selection of connection configurations was made for numerical testing using the Abaqus finite element analysis software. The objective is to identify the most promising configurations for experimental validation.

In this study, five configurations of dismountable composite beams made of steel, wood, and concrete were analyzed. Three of them involve mechanical connection systems designed for disassembly: bolts only, notches only, and a combination of both. Two additional boundary cases were also introduced: one with perfect contact between the materials, simulating a fully rigid connection, and another without any mechanical linkage, where only frictional contact is modeled between interfaces.

This comparative analysis aims to evaluate the influence of connection systems on load transfer, global stiffness, and the disassembly potential of the structure.

3.1 Geometry and mechanical properties

Figure 3 illustrates the geometry of the demountable composite beams combining steel, timber, and concrete under study. Each configuration studied consists of a concrete block measuring 3000 mm in length and 1000 mm in width, connected to a cross-laminated timber (CLT) panel of the same dimensions. This CLT panel is composed of three spruce layers, with two longitudinal layers in C18 grade, 30 mm thick each and one transverse layer in C24 grade, 20 mm thick. The assembly is achieved using an HEA 160 steel profile, ensuring the transfer of forces between materials and guaranteeing the overall stiffness of the structure.

Three demountable connection configurations were studied to assess their mechanical efficiency. The first configuration relies exclusively on 32 M16 bolts to connect the materials. The second implementation features only rectangular notches of 200 mm in length and 20 mm in thickness between concrete and timber to exploit the mechanical interlock effect. The third configuration combines bolts and notches, aiming to optimize both the stiffness of the assembly and the disassembly capacity of the system.

This approach allowed us to compare the performance of the different connections in terms of force transfer and stiffness, while maintaining a consistent geometry for the comparative analysis of numerical results.

The mechanical properties used in this study are based on previous experimental results to best approximate the actual characteristics of the materials, (Kachouh et al., 2024).

Steel is considered homogeneous and isotropic. According to Eurocode 3 (AFNOR, 2005), it has a density of 7850 kg/m³, an elastic modulus of 210 GPa, and a Poisson's ratio of 0.3. To characterize its elasto-plastic behavior, a tensile test was conducted on a sample taken from the HEA 160 profile in order to get its stress-strain curve. Tensile tests were also performed on M16 bolts to determine their yield strength and ultimate tensile strength, considering the average value of the results obtained.

To ensure a more realistic modeling, the experimental values were corrected by applying the classical formulas for true strain and true stress. The true strain is defined by equation (1) and the true stress by equation (2), as described in **"Mechanical Behavior of Materials"** (E. Dowling, 2012) as shown in Fig. 2 (a) and (b).

$$\ln\left(\varepsilon_{exp} + 1\right) \tag{1}$$

$$\sigma_{exp} \times (1 + \varepsilon_{exp}) \tag{2}$$

Poisson's ratio adopted for concrete is equal to 0.2. Concrete blocks used have an average compressive strength of 35.46 MPa with a standard deviation of 1.23 MPa based on five compression tests. The behavior of concrete under load is simulated using the damage plasticity model available in Abaqus, allowing the representation of cracking and progressive degradation of the material (Abaqus 6.14 Documentation, 2014). This model is based on two main mechanisms: plasticity, which represents irreversible deformation, and damage, which reflects the progressive loss of stiffness and strength due to the formation of cracks. The evolution of damage is tracked through a degradation variable that reduces the concrete's load-bearing capacity as the applied loads increase. The required parameters were estimated from the Model Code and incorporated into the numerical simulation shown in Fig. 3 (Telford, 1993).

The CLT wood used exhibits anisotropic behavior, influencing its mechanical properties depending on the orientation of the layers. The average modulus of elasticity is 9000 MPa (C18) and 11,000 MPa (C24) in the direction parallel to the wood grain, while it is significantly lower in the perpendicular direction (300 to 370 MPa) according to the Hexapli technical approval (Hexapli, 2012). Poisson's ratios are equal to 0.48 in the principal directions and 0.22 in shear.

The Hill criterion was used to model the anisotropic plastic behavior of wood, with Hill's equivalent stress being equal to 31.17 MPa and 36.37 MPa for C18 and C24, respectively (Nowak et al., 2013).

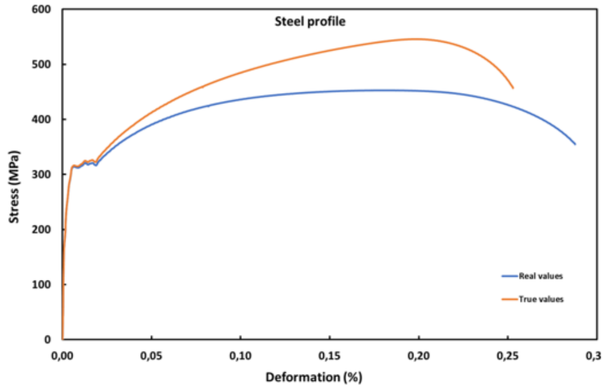

Fig. 2.a

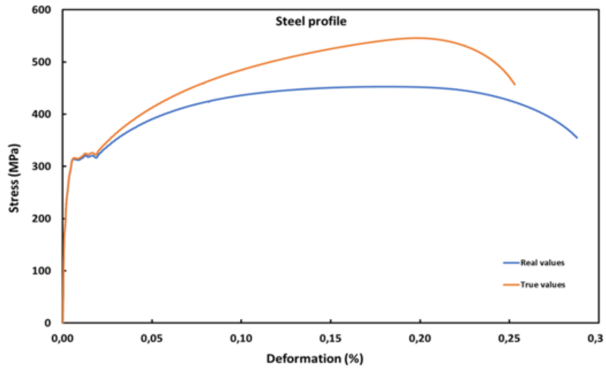

Fig. 2.b

Fig. 2. Comparison between nominal and true stress–strain curves: (a) steel profile; (b) bolts

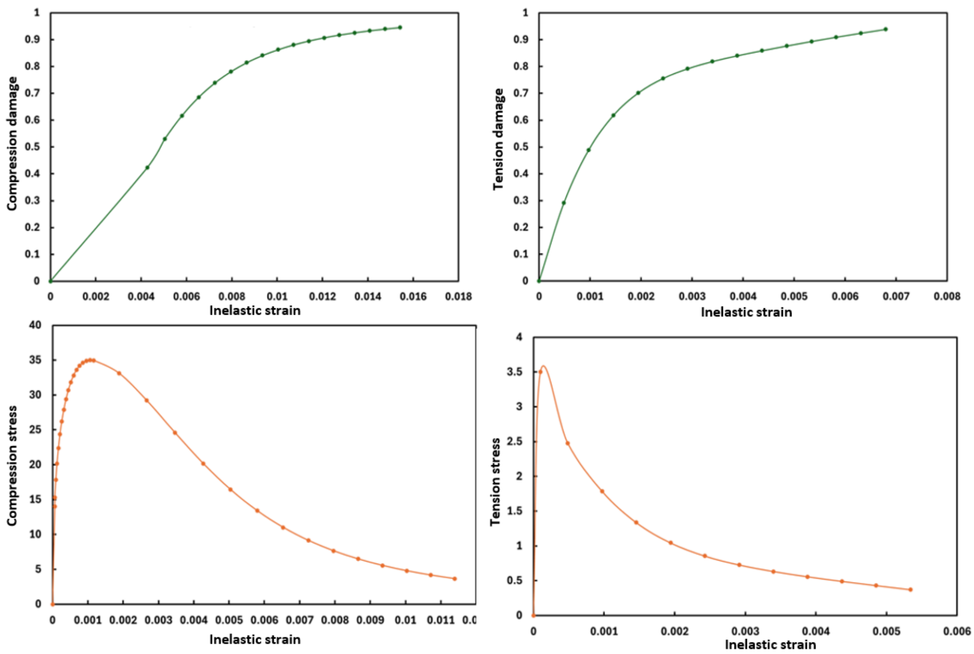

Fig. 3. Constitutive behavior of concrete under compression and tension

3.2 Numerical modelling assumptions

The 3D meshing of the steel profiles and CLT panels was performed using linear hexahedral solid elements (C3D8R). To reduce computation time, only a fraction of the structure, corresponding to a quarter of the model,

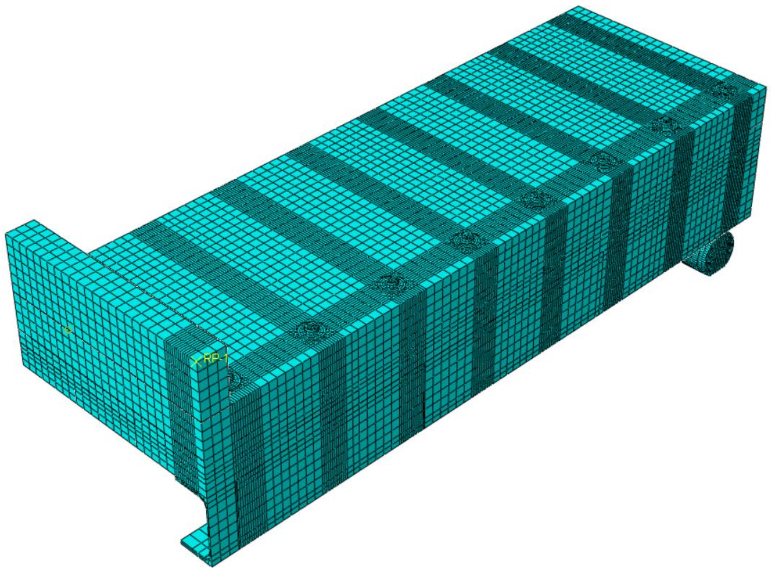

Fig. 4. Mesh adopted for the three-point bending test

was considered due to double symmetry. Unlike a homogenized modeling of wood, each individual lamella of the CLT was explicitly discretized.

The primary mesh size adopted is 20 mm. However, a parametric study showed that a local mesh refinement, ranging from 6 to 8 mm around the connections, was necessary to ensure optimal regularity and better representation of the interactions. Fig. 4 illustrates the final mesh configuration adopted.

Interactions between the CLT lamellae were modeled by incorporating frictional contact as well as cohesive contact between the different layers. Additionally, interactions between the steel profiles and the CLT, as well as between the CLT and concrete, were simulated using frictional contact with a friction coefficient of $\mu = 0.1$.

In addition to the three mechanical configurations, two limiting cases were also modeled to frame the performance range of the dismountable solutions. A perfect contact case was simulated using the tie constraint in Abaqus, enforcing a fully rigid connection between interface surfaces, with no relative slip or separation. Conversely, a no-connection case was considered. Such case relied solely on surface-to-surface frictional contact with the aforementioned coefficient, without any mechanical fasteners or interlocking elements.

3.3 Numerical results

The numerical results allowed evaluating the influence of the connection type on the global flexural behavior of the steel–timber–concrete composite beams. The five dismantlable configurations studied reveal significant differences depending on the nature of the connection system. Among the three configurations incorporating mechanical connectors (bolts only, notches only, and a combination of both), the configuration combining both bolts and notches appears to be the most effective, with an initial stiffness of 13.76 kN/mm and a maximum load of 329.65 kN. This performance results from the complementarity between two mechanisms: notches provide geometric interlock to limit longitudinal slip, while bolts ensure vertical force transfer and stabilize the assembly. The numerical values of the initial stiffness and maximum load of each configuration are summarized in Table 1.

The bolted configuration exhibits higher stiffness than the one using notches (10.74 kN/mm versus 8.35 kN/mm), along with greater load-bearing capacity 262.46 kN versus 187.13 kN. However, stress concentrations appear around the bolt holes, which may lead to localized damage over time. In the case of notches, concrete damage is more pronounced, especially at the ends of the recesses, limiting the structure's ability to carry load. The load–displacement curves in Fig. 5 confirm these observations: a lower initial slope and a more ductile behavior are observed for the notched connection, whereas the bolted and mixed configurations show a more linear and stiffer response.

To further assess the role of connections in activating composite behavior, two limit cases were modeled. The first, based on frictional contact only ($\mu = 0.1$), simulates a scenario without any mechanical linkage. The lack of force transfer between layers results in very low stiffness of 8.11 kN/mm and a limited maximum load of 165.62 kN, clearly reflecting the absence of composite action. The second case, modeled using a tie constraint, imposes perfect continuity of displacements at the interface, reproducing an ideal monolithic behavior. Although such a configuration is not feasible in practice, it serves as a theoretical upper bound. The stiffness obtained equal to 25.24 kN/mm is the highest, and the maximum load reaches 448.91 kN.

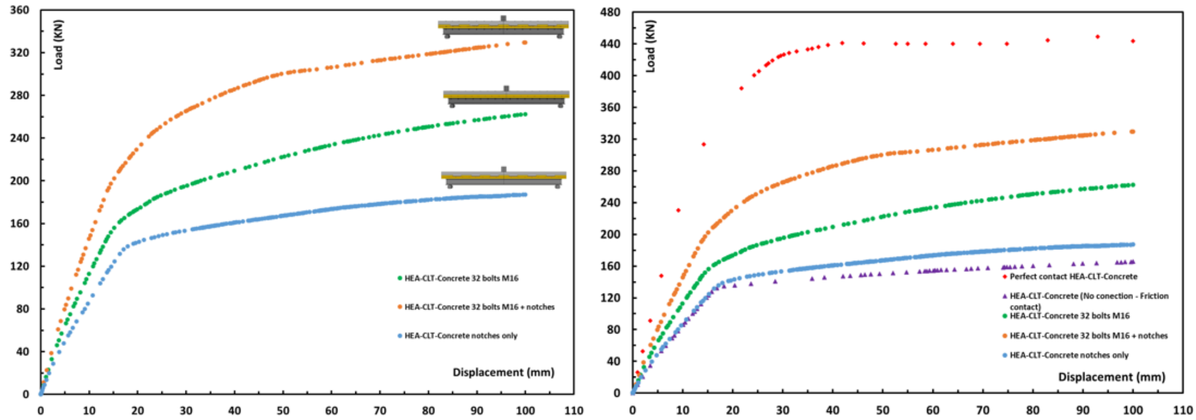

Fig. 5. Results of the three-point bending test on the composite beam: load-vertical displacement curve measured at mid-span

Table 1. Comparison of initial stiffness and maximum load for each connection configuration with the perfect contact case

Connection type	K(kN/mm)	Comparison between various cases and the perfect contact case	Maximum load (kN)	Comparison between various cases and the perfect contact case
With 6 notches	8.35	67%	187.13	58%
With 32 M16 bolts	10.74	57%	262.46	42%
With 32 M16 bolts + 6 notches	13.76	45%	329.65	27%
No connection – Friction contact	8.11	68%	165.62	63%

By comparison, the configuration combining bolts and notches develops a maximum load approximately 45% lower than that of the ideal case, while retaining nearly 73% of its initial stiffness. This demonstrates that a well-designed dismantlable system can closely approach the stiffness performance of a perfectly rigid assembly. The load-bearing capacity of the system can also be improved if an appropriate connection system is used. These results highlight the crucial role of connections in enabling composite behavior and emphasize the trade-offs to consider between strength, stiffness, and dismantlability.

4. Conclusions

This study provided a comprehensive review of connection systems used in composite floors combining timber, concrete, and steel. Timber-concrete and steel-timber connections have been widely studied, with solutions such as notches, bolts, and screws offering good mechanical performance. In contrast, assemblies combining all three materials simultaneously remain scarcely documented in the literature, particularly regarding their global flexural behavior.

To better understand these complex assemblies, a numerical study was conducted on five configurations, including three dismantlable connection systems and two theoretical limit cases: a perfect contact case and a frictional contact only case. These reference cases allowed quantifying the performance losses induced by using mechanical connections. Results highlight the crucial role of connections in enabling composite action. They also show that well-designed dismantlable systems can approach the stiffness of a monolithic structure while maintaining the potential for reversibility.

Results show that the mixed configuration (bolts + notches) offers the best overall compromise.

The perspectives of this work focus on the development of innovative connection solutions, aimed at improving composite interaction between materials and bringing the system's behavior closer to the ideal case simulated by perfect contact. These efforts include detailed analysis of stress and strain distributions within the different configurations, as well as the exploration of more efficient joining strategies. Full-scale prototypes will be developed to experimentally validate the performance observed in numerical simulations. Flexural tests on complete beams and instrumented push-out tests (with displacement sensors, accelerometers, and strain gauges) will allow a precise characterization of the mechanical behavior and dismantling potential. Finally, special attention will be given to the vibrational performance of this type of demountable composite floor system, with the aim of improving both comfort and long-term durability.

References

AFNOR. (2005). *NF EN 1993-1-1: Eurocode 3 – Calcul des structures en acier – Partie 1-1: Règles générales et règles pour les bâtiments*. Retrieved from https://viewerbdc-afnor-org.ezproxy.uca.fr/pdf/viewer/N3qnWsE4mDE1?proxy=true

Al Rahim, A., Heng, P., Lepourry, C., Somja, H., & Palas, F. (2023). A 3D ductile-notched connection for timber-concrete composite beam: Experimental investigation. *Engineering Structures and Technologies, 15*(2), 134–145.

Auclair, S. C., Sorelli, L., & Salenikovich, A. (2016). A new composite connector for timber-concrete composite structures. *Construction and Building Materials, 112*, 84–92.

Boccadoro, L. (2016). *Timber-concrete composite slabs made of beech laminated veneer lumber with notched connection* [Doctoral dissertation, ETH Zürich].

Boccadoro, L., Zweidler, S., Steiger, R., & Frangi, A. (2017). Bending tests on timber-concrete composite members made of beech laminated veneer lumber with notched connection. *Engineering Structures, 132*, 14–28.

CSTB. (2012). *Hexapli – Document technique d'application*. Retrieved from https://www.cstb.fr/pdf/atec/GS03-D/AD318958_V1.pdf

Daňková, J., Mec, P., & Šafrata, J. (2019). Experimental investigation and performance of timber-concrete composite floor structure with non-metallic connection system. *Engineering Structures, 193*, 207–218.

Dassault Systèmes. *Abaqus 6.14 documentation*. Retrieved from http://62.108.178.35:2080/v6.14/index.html

Djoubissie, D. D., Messan, A., Fournely, E., & Bouchaïr, A. (2018). Experimental study of the mechanical behavior of timber-concrete shear connections with threaded reinforcing bars. *Engineering Structures, 172*, 997–1010.

Djoubissie, D. D., Messan, A., Fournely, E., & Bouchaïr, A. (2018). Influence of interlayer in timber-concrete composite structures with threaded rebar as shear connector: Experimental study. *Engineering Structures, 173*, 1010–1021.

Dowling, N. E. (2012). *Mechanical behavior of materials: Engineering methods* (4th ed.).

Fragiacomo, M., Aldi, P., Mazzilli, M., & Kuhlmann, U. (2008). Performance of notched coach screw connection for timber-concrete composite floor system. In *Proceedings of the 10th World Conference on Timber Engineering (WCTE 2008)* (pp. 1–8). Miyazaki, Japan.

Fragiacomo, M., Gregori, A., Xue, J., Demartino, C., & Toso, M. (2018). Timber-concrete composite bridges: Three case studies. *Journal of Traffic and Transportation Engineering (English Edition), 5*(6), 429–438.

Hassanieh, A., Valipour, H. R., & Bradford, M. A. (2017). Composite connections between CLT slab and steel beam: Experiments and empirical models. *Journal of Constructional Steel Research, 138*, 823–836.

Kachouh, L., Jaafari, C., Durif, S., & Bouchair, A. (2024). Effect of concrete inter-blocks spacing on the mechanical behavior of demountable steel-concrete floors under flexure. *Academic Journal of Civil Engineering, 42*(1), Article 1.

Lecours, S. (2022). *Optimisation multicritère des planchers préfabriqués en bois-béton pour les bâtiments multiétages en considérant la méthode constructive* [Master's thesis, Université Laval]. Retrieved from https://corpus.ulaval.ca/jspui/handle/20.500.11794/71772

Loss, C., Piazza, M., & Zandonini, R. (2016a). Connections for steel–timber hybrid prefabricated buildings. Part I: Experimental tests. *Construction and Building Materials, 122*, 781–795.

Loss, C., Piazza, M., & Zandonini, R. (2016b). Connections for steel–timber hybrid prefabricated buildings. Part II: Innovative modular structures. *Construction and Building Materials, 122*, 796–808.

Miotto, J. L., & Dias, A. A. (2012). Evaluation of perforated steel plates as connection in glulam–concrete composite structures. *Construction and Building Materials, 28*(1), 216–223.

Nowak, T. P., Jasieńko, J., & Czepiżak, D. (2013). Experimental tests and numerical analysis of historic bent timber elements reinforced with CFRP strips. *Construction and Building Materials, 40*, 197–206.

Okutu, K., Davison, B., & Carr, J. (2017). CLT-steel composite slimfloor construction: An investigation of mechanical behaviour using finite element software. *International Journal of Civil Engineering and Technology, 8*(4), 245–255.

Tavoussi, K., Fadai, A., & Riola-Parada, F. (2019). Prefabricated timber-steel-concrete ribbed decks – Development and experimental studies. In J. M. Branco, E. Poletti, & H. S. Sousa (Eds.), *Proceedings of the 5th International Conference on Structural Health Assessment of Timber Structures (SHATiS 2019)* (p. 10). Universidade do Minho, Departamento de Engenharia Civil.

Tavoussi, K., Winter, W., Riola-Parada, F., Fadai, A., Lopatič, J., & Prašnjak, I. (2018). Prefabricated timber-steel-concrete ribbed decks: Experimental study. In *Proceedings of the World Conference on Timber Engineering (WCTE 2018)*. Seoul, South Korea.

Thomas Telford. (1993). *CEB-FIP model code 1990*. Retrieved from http://www.tocasa.es/zona2/CEB_FIP_model_code_1990_ing.pdf
Winter, W., Tavoussi, K., Fadai, A., Riola Parada, F., & Prašnjak, I. (2016). Development of prefabricated timber-steel-concrete ribbed decks. Retrieved from https://www.researchgate.net/publication/331355210_Development_of_Prefabricated_Timber-Steel-Concrete_Ribbed_Decks
Winter, W., Tavoussi, K., Fadai, A., Riola Parada, F., & Prašnjak, I. (2016). *Development of prefabricated timber-steel-concrete ribbed decks* [Research report]. Vienna University of Technology.

4th International Civil Engineering & Architecture Conference
17-19 May 2025, Trabzon, Türkiye

Decrease of the radius of gyration of the I-beam column due to long–term corrosion

Jurijus Tretjakovas*[1], Jolanta Pileckienė[2a]

[1] Vilniaus Kolegija, Higher Education Institution, Department of Mechnical Engineering, LT119651314 Vilnius, Lithuania
[2] Vilniaus Kolegija, Higher Education Institution, Department of Electrical and Electronics Engineering, LT119651314 Vilnius, Lithuania

Abstract. The buckling in axially loaded members is a critically important issue in structural engineering design. Long-term corrosion progressively reduces the geometrical characteristics of a column's cross-section, thereby increasing the risk of structural instability and failure. The key geometrical properties of columns include length, second moment of area, and radius of gyration. The radius of gyration depends on the moment of inertia and the cross-sectional area; thus, a reduction in either of these parameters directly affects it.

The decrease in area and moment of inertia is influenced by the corrosion rate and can be mathematically described as an average rate of material loss across different surfaces of the cross-section. The corrosion process gradually removes material from the column, leading to a yearly reduction in the radius of gyration. The corrosion rate is determined by various factors such as surface coating, environmental conditions, and the presence of localized corrosion sites. In this study, the corrosion effect is modeled based on annual corrosion intensity and projected over a period of up to 50 years. The degradation of steel columns is inevitably associated with the reduction of cross-sectional area and moment of inertia. It was concluded that special attention should be paid to columns after 20 to 30 years of service to prevent the development of critical corrosion zones.

Keywords: Buckling; Critical load; Radius of Gyration; Corossion, I-beam.

1. Introduction

When the internal stress state within a vertical structural member changes abruptly in response to gradually increasing axial loading, a sudden and unexpected structural failure may occur. In the case of a slender rod subjected to axial compressive forces, the member initially experiences uniform compression, and its longitudinal axis remains straight and stable, as illustrated in Fig. 1. However, if the applied compressive load exceeds a critical threshold - a value that depends on the rod's effective length, cross-sectional geometry, and boundary conditions - the structural behavior of the member may change significantly. At this point, the rod may become laterally unstable and experience a sudden lateral deflection, indicating the onset of buckling. This lateral deflection introduces additional internal forces in the form of bending moments, which in turn generate secondary stresses within the material. These combined stresses can accelerate structural failure even in the absence of material yielding.

As noted by Barry (2022), "the stability of slender members is often governed more by geometry and loading conditions than by the strength of the material itself," which emphasizes the importance of structural configuration in resisting instability.

This phenomenon is referred to as buckling, a mode of instability that is especially critical in slender, axially loaded elements. Buckling-induced failures are considered particularly hazardous in engineering practice because they often occur without significant prior deformation or visible warning, posing serious risks to structural safety.

The critical elastic stress corresponding to the critical force devided by cross section area in the column just before buckles defined as follows (Hibbeler, 2023).

$$\sigma_{cr} = \frac{\pi^2 \cdot E}{\left(L/i_{min}\right)^2} \tag{1}$$

where
E – modulus of elasticity of the material;
L – unsupported length of the column;

*Corresponding author, E-mail: j.tretjakovas@tef.viko.lt

https://doi.org/10.31462/icearc2025_ce_sme_142

i_{min}– smallest radius of gyration of the column.

Fig. 1. Columns of the building

The slenderness ratio serves classify columns as long, intermediate and short. This geometrical parameter is a measure of the vertical rod flexibility and known as ratio

$$\lambda = \frac{\mu \cdot l}{i_{min}} \tag{2}$$

where
μ–effective length factor;
l – supported length of the column;
i_{min}– smallest radius of gyration of the column.

The radius of gyration determined from ratio

$$i_{min} = \sqrt{\frac{I_{min}}{A}} \tag{3}$$

where
I_{min}– smallest second moment of area (moment of inertia) of the cross section of the column;
A – area of the cross section of the column;

The service life of steel structures, including I-beams, is closely linked to corrosion effects. Long-term corrosion not only reduces material thickness but also causes significant geometric changes in structural elements, affecting their mechanical properties (Crespi at al., 2022; Gonzalez at al., 2018). This article examines the reduction of the gyroscopic radius of an I-beam column due to long-term corrosion, analyzes the main causes of corrosion, and evaluates its impact on structural stability. Metal structures are often affected by corrosion, which can significantly impact their strength and stability. I-beams are widely used in construction and infrastructure projects; however, their performance deteriorates over time due to corrosion.

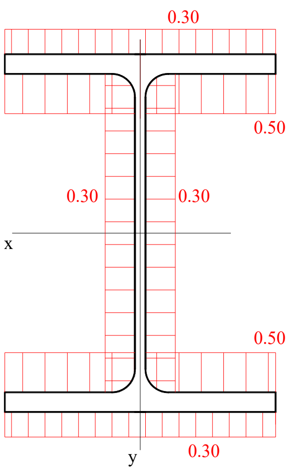

Fig. 2. Cross section of the IPE column and corrosion rates

Corrosion is a critical factor affecting the long-term stability and load-bearing capacity of steel structures. In axially loaded members, such as columns, long-term corrosion progressively reduces the cross-sectional area and moment of inertia, leading to a decrease in the radius of gyration. This deterioration weakens the structural integrity and increases the risk of buckling, a major concern in engineering design.

The aim of the work is to describe the decrease in radius of gyration of cross section in Fig. 2 of the IPE column due to long-term corrosion by mathematical expression.

Tasks for the achievement of the goal:

- To describe the influence of the corrosion over a period of one year and up to 40 years;
- To make an analytical model of the radius of gyration of the cross-section of the I-column;
- To model the influence of corrosion rusts on the radius of gyration.

The columns of a building usually have a rational cross-sectional shape, which is is close to the I-beam. Therefore, this paper investigates a computational model of cross section of the I-Beam column depending on a variable. The corrosion is modelled as degradation and loss of material in a long term process, in terms of corrosion intensity over one year and intensity up to 40 years.

The analytical model of corrosion describes the reduction of the cross-sectional area over a long period of time and its influence on the radius of gyration of the cross-section. It was found that radius of gyration don't depend on decrease of the area of cross section of the column. On the other hand special attention should be paid to the columns after the first 20 ... 30 years in order to stop the corrosion focal points.

2. The model of corrosion rate

The corrosion rate is influenced by various factors, including environmental conditions, protective coatings, and localized corrosion spots caused by external factors. Over time, material loss due to corrosion significantly impacts the geometric properties of a column.. Research indicates that after 20 to 30 years, intensified corrosion prevention measures should be implemented to mitigate further structural degradation (Akduman et al., 2024, Simoncelli at al., 2023). Modeling corrosion effects over periods of up to 50 years highlights the necessity of proactive monitoring and maintenance strategies to enhance the longevity and safety of steel columns.

2.1. The Effect of Corrosion on I-Beam Columns

Corrosion is an electrochemical process that leads to the formation of rust on the steel surface, reducing the effective cross-section of the structure. The main factors influencing the corrosion of I-beam columns include:

- Atmospheric humidity (>60%), which promotes electrochemical reactions (Bradford, 2015);
- Pollutants such as chlorides and sulfur oxides, which accelerate metal oxidation;
- Mechanical damage, leading to the wear of protective coatings.

Corrosion not only reduces metal thickness but also alters geometric parameters, including the gyroscopic radius.

2.2. Analysis of Gyroscopic Radius Reduction

Due to long-term corrosion, the flanges and web of the I-beam become thinner, decreasing their moment of inertia (I) and consequently reducing the radiuso f guyration (Wu, B. et al., 2017).

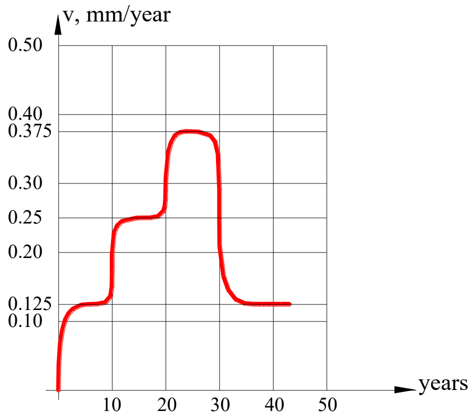

Fig. 3. Corrosion rate graph in 40 years

When modeling the corrosion rate, it is assumed that corrosion focuses appear in the structural element already in the first year, and the rate for the first 10 years is equal to 1/4 of the maximum rate, from 10 to 20 years the value is 1/2 of the maximum rate, from 20 years the rate can be 3/4 of the maximum rate described in the literature (Šulčius, 2006). After 30 years the rate of corrosion drop till 1/4 of the maximum rate. All this is illustrated in Fig. 4 as a graph of the change in rate over the time.

Surfaces of IPE with corrosion rates less than 0.50 mm/m will also maintain lower and proportional corrosion rates from the start throughout the modelling start.

3. The variation of the radius of gyration in mathematical model

3.1. The areas of rust in cross section

For analysis the IPE 500 according DIN 1025-5:1994-03 (Euronorm 19-57) was choosen. The mathematical model describes the radiuses of gyration about the x-axis and the y-axis. Rusts are modelled as a variable parameter in the model and are described as a time function. The rust zones are modeled as perfect rectangles are shown in Fig. 3 (figures from 1 to 7). They are marked with thick brown lines. Here we see the thickness t and the width l of each of the three corrosion zones, because areas from 4 to 7 are symetrical zones.

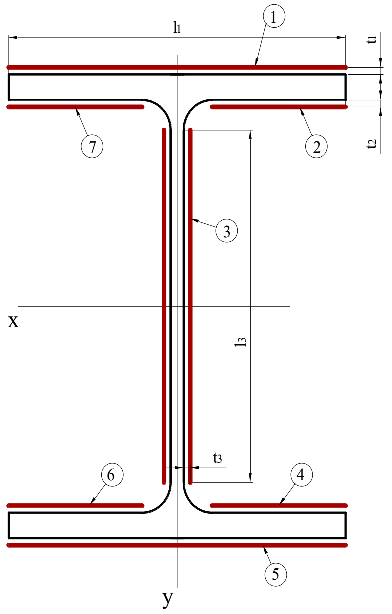

Fig. 4. Corosssion areas in cross section

The variable of the geometrical parameters during long-term corrosion is modeled as the elimination of corroded areas from the equations of the moments of inertia and eliminations of corroded area from primary area.

3.2. Influence of rusts to radius of gyration

The mathematical model of corrosion describes the reduction of these loss areas (Fig. 3) over time and their influence on the radius af gyration and moments of inertia of the entire cross-section.

Radius of gyration about x axis

$$i_x = \sqrt{\frac{I_x - \sum_{i=1}^{7}(I_{xci} + A_i \cdot y_{ci}^2)}{A - \sum_{i=1}^{7} A_i}} \tag{4}$$

where

I_{xci} – moment of inertia of area of rust about horizontal x-axis;

y_{ci} – distance from rust area center to x axis.

Geometrical characteristics about y axis are solved by the same algorithm.

3.3. Modellling results

The results of the modelling during 40 years of the IPE 500 geometrical parameters are presented in Table 1: the changes in the cross-sectional area A, moment of inertia I_x and I_y and radiuses of gyration i_x and i_y.

It should be noted that moment of inertia of the cross section dramatically after 20 years. The decrease of the radiuses of gyrations (Table 1) ir practicaly negligible, therefore we should note that slenderness ratio of column not depend on rusts.

Table 1. Area, moments of inertia and radiuses of gyration

Years	A, cm^2	Ix, cm^4	ix, cm	Iy, cm^4	iy, cm
0	115.5	48199	20.43	2142	4.306
10	114.2	47680	20.44	2115	4.304
20	111.6	46650	20.45	2062	4.300
30	72.3	31330	20.81	1266	4.184
40	71.1	30810	20.83	1240	4.178

Mathematical simulations were performed based on the described methodology, and the results are presented as graphs in this section. The change in moment of inertia about centroidal over time is shown in Figure 5.

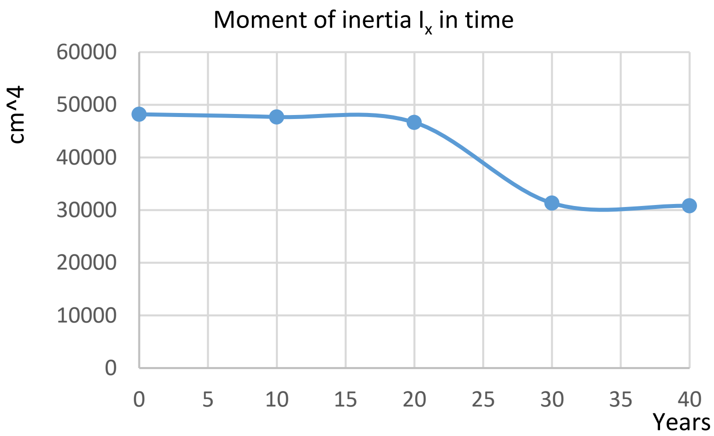

Fig. 5. Decrease of moment of inertia

The data obtained (Fig. 5) illustrate that for given corrosion rate moment of inertia of cross section in beginning of column exploatation is almost constant and after 20 years this geometrical parmeter decrease.

4. Conclusions and remarks

On the basis of the analytical modelling results obtained in the present investigation the following conclusions have been drawn.

- The study showed that special attention should be paid to columns from the first year in order to prevent the formation of corrosion focuses.
- The rusts surfaces are described as areas of corrosion that continuously increase over time, with the area decreasing by 1 % in the first 10 years, by 3,4 % between 10 and 20 years, by 37 % between 20 and 30 years, and by 40 years only 38 % of the total area remaining.
- The geometric parameter – moment of inertia - decreases by 1% during the first 10 years, from 10 to 20 years the decrease reaches 3,2%, from 20 to 30 years the decrease 35 %, and after 40 years - more 36%.
- The of the radiuses of gyrations in time are practicaly constants;
- To mitigate corossion effect, the following preventive measures are recommended: regular inspections – to identify early corrosion signs and apply protective measures, anti-corrosion coatings and galvanization – to slow down the corrosion rate, environmental control – to reduce humidity and pollutant concentration in the operational environment, systematic maintenance and repairs – reinforcement or replacement of damaged structures.

References

Akduman, S., & Öztürk, H. (2024). Effect of reinforcement corrosion on structural behavior in reinforced concrete structures according to initiation and propagation periods. *Buildings, 14*(12), 4026.

Barry, D. (2022). *Strength of materials for engineering technology* (23rd ed.).

Bradford, S. A. (2015). Formation of water films on the iron oxide surface. In *Surface chemistry of aqueous corrosion processes*.

Crespi, P., Zucca, M., Valente, M., & Longarini, N. (2022). Influence of corrosion effects on the seismic capacity of existing RC bridges. *Engineering Failure Analysis, 140*.

Gonzalez, J. M., & Lira, J. M. (2018). Corrosion effects on steel in coastal environments.

Hibbeler, R. C. (2023). *Mechanics of materials*. Prentice Hall.

Simoncelli, M., Aloisio, A., Zucca, M., Venturi, G., & Alaggio, R. (2023). Intensity and location of corrosion on the reliability of a steel bridge. *Journal of Constructional Steel Research, 206*.

Wu, B., Cao, J., & Kang, L. (2017). Influence of local corrosion on behavior of steel I-beams subjected to end patch loading: Experiments. *Journal of Constructional Steel Research*, 150–161.

Šulčius, A. (2006). *Metalų korozija ir sauga* (p. 242). Kaunas: Technologija.

4th International Civil Engineering & Architecture Conference
17-19 May 2025, Trabzon, Türkiye

Deformable spring effects on axial vibration of Rayleigh bars reinforced with short fibers

Gökhan Güçlü*[1], Büşra Uzun[2], Uğur Kafkas[3], Mustafa Özgür Yaylı[2]

[1] *Engineering Faculty, Department of Civil Engineering, Kutahya Dumlupınar University, Kütahya, Türkiye*
[2] *Engineering Faculty, Department of Civil Engineering, Bursa Uludag University, Bursa, Türkiye*
[3] *Kutahya Voc. School of Technical Sciences, Kütahya Dumlupınar University, Kütahya, Türkiye*

Abstract. This study investigates the effect of deformable springs on the axial vibration of Rayleigh bars reinforced with short fibers. The Rayleigh bar is reinforced with randomly distributed short fibers, and springs that can be deformed in the axial direction are added to both ends of the bar to determine the axial displacement effects. The Halpin-Tsai model is used to calculate the effective stiffness of the Rayleigh bar, and the mixture rule is used to calculate the effective mass density. In this study, where the axial displacement is considered a Fourier sine series, the Stokes' transformation is applied to obtain the solutions of the boundary conditions (rigid, semi-rigid, free) in the most general sense. An eigenvalue problem formulation, including the stiffnesses of the springs at both ends of the Rayleigh bars reinforced with short fibers, is obtained. In this eigenvalue problem, the eigenvalues that make the determinant of the coefficient matrix zero give the axial vibration frequencies of the Rayleigh bars. The effect of parameters such as fiber properties and stiffness of deformable springs on the axial vibration frequencies of Rayleigh bars is determined by solving the eigenvalue problem. In addition, the frequencies of the classical bar theory are also mentioned. Various examples are given to compare the axial vibration frequencies of classical and Rayleigh bars. Thus, the differences between the two bar theories mentioned are clearly shown.

Keywords: Rayleigh bar; Short-fiber-reinforced material; Deformable springs; Stokes' transform

1. Introduction

Composite materials are engineering materials formed by combining two or more materials, exhibiting superior properties that the components do not possess individually (Leite & da Rocha, 2024; Mohammed et al., 2015; Singh et al., 2024). These materials are replacing traditional materials in many fields such as aerospace, automotive, marine, and civil engineering (Civalek et al., 2022a). Short fiber reinforced composites (SFRCs) are created by embedding short fibers, cut to specific lengths, into a matrix in various arrangements (Hamza et al., 2017). They possess advantages such as ease of manufacturing processes, low costs, and suitability for manufacturing parts with complex geometries (Arumugam et al., 2022). The random or specific directional distribution of fibers within the matrix affects the macroscopic behavior of the material (Baniya & Tsegai, 2022)

Determining the dynamic and vibration characteristics of composite materials is necessary for identifying the resonance frequencies, estimating the fatigue life, and understanding the damping capacity of systems using these materials (Bonopera, 2023; Kalusuraman et al., 2023; Mortazavian & Fatemi, 2015; Wu et al., 2023). Determining the axial natural frequencies and mode shapes of such elements is important for avoiding resonance conditions, evaluating dynamic stability, and ensuring structural integrity (Lelkes et al., 2024).

The generally random distribution of short fibers within the matrix, although making the material appear homogeneous at the macroscopic level, harbors significant heterogeneity and anisotropy at the microscopic scale (Hao et al., 2020). This situation necessitates the use of micromechanical models, such as the Halpin-Tsai model (Zhou et al., 2024) or the rule of mixtures (Sotomayor & Pancho, 2024), to predict the effective (average) mechanical properties of the composite.

When considering axial vibrations, the most fundamental approach is the classical rod theory. This theory is based on the assumption that only axial deformations are considered, neglecting transverse movements and their associated inertia effects. This approach yields adequate results, especially for the low-frequency axial vibrations of slender (long and thin) rods (Han et al., 2014). However, when the cross-sectional dimensions of the rod are not negligible compared to its length, or when high-frequency vibrations are examined, the necessity arises to consider the lateral movements occurring during axial motion and their associated inertia effects. More advanced rod

* Corresponding author, E-mail: gokhan.guclu@dpu.edu.tr

https://doi.org/10.31462/icearc2025_ce_sme_178

theories have been proposed to model these effects (Fedotov et al., 2016; Leamy, 2014). Rayleigh rod theory accounts for the lateral inertia effect and the effect of the material's Poisson's ratio in axial vibration analysis (Ananthapuvirajah, 2019).

In the dynamic analysis of structural elements, using elastic boundary conditions (modeling supports with springs) instead of classical end conditions (clamped, simply supported, and free) offers a more realistic approach (Fernández-Sáez et al., 2017). Beyond offering a more realistic approach, elastic end conditions allow the use of spring stiffnesses as a design variable (Civalek et al., 2022b). For example, if resonance at specific frequencies is undesirable for a structure, or if a specific dynamic response is targeted, the stiffnesses of the springs at the support points can be adjusted to achieve these goals (M. Kamal & İnel, 2021). This offers potential for applications such as passive vibration control or vibration isolation. Furthermore, elastic boundary conditions encompass classical boundary conditions as special cases (Yaylı et al., 2014).

The mechanical and dynamic behaviors of short fiber reinforced composites, particularly their vibration characteristics, have been investigated in numerous studies (Akpınar et al., 2024; Amsalu et al., 2024; Geethamma et al., 2005; Y. Huang et al., 2023; Kalusuraman et al., 2023; A. M. Kamal & Taha, 2010; Kumar & Kumar, 2024; Nciri et al., 2017; Nurazzi et al., 2021). The effect of lateral inertia and Poisson's ratio on axial vibration has been emphasized in many studies (Bordiga et al., 2019; Chang et al., 2010; Farshbaf Zinati et al., 2020; Ghayesh & Balar, 2008; X. F. Li et al., 2013; Yaylı, 2020; Zhu & Chung, 2019). The effect of elastic boundary conditions on vibration behavior has been examined using various analytical and numerical methods (Ding et al., 2024; Lee & Lin, 1996; Lv et al., 2015; Ratazzi et al., 2013; L. Wang et al., 2022; Y.-R. Wang & Fang, 2015; Yang & Yang, 2017). Fourier series and Stokes' transformation (Jeong & Lee, 1996; Kadıoğlu & Yaylı, 2017; Khalili et al., 2005; W. L. Li & Xu, 2009), the differential quadrature method (X. Huang et al., 2024; Jena & Chakraverty, 2018; Laura & Gutierrez, 1993; Liu et al., 2022), and the finite element method (Belabed et al., 2024; Friswell et al., 2007; Hien et al., 2023; Z. Huang et al., 2019; Wen & Yi, 2014) are some of the approaches used to solve such problems.

In this study, an analytical approach has been adopted for the axial vibration analysis of a Rayleigh rod reinforced with short fibers and supported by axially deformable springs at both ends. The effective elasticity modulus of the rod is determined using the Halpin-Tsai model and the effective mass density is determined using the rule of mixtures. The equation of motion is obtained using Hamilton's principle. The axial displacement function is expressed as a Fourier sine series. Stokes' transformation is applied to systematically address the elastic boundary conditions at the ends of the rod. Stokes' transformation allows the derivatives of the Fourier series to be expressed in terms of the series itself and the boundary values, enabling the incorporation of boundary conditions into the equation of motion and providing an analytical framework even for non-homogeneous boundary conditions. Axial natural vibration frequencies are obtained from the solution of the eigenvalue problem. The vibration frequencies obtained for the Rayleigh rod are compared with the frequencies obtained according to the classical rod theory. The developed model comprehensively reveals the effects of fundamental parameters such as fiber properties (volume fraction, aspect ratio), rod geometry, and spring stiffnesses on the axial natural vibration frequencies.

Upon reviewing the existing literature, a lack of analytical studies addressing the combination of three topics – (1) short fiber reinforced composite material, (2) Rayleigh rod model including lateral inertia effects for axial vibration, and (3) elastic boundary conditions – has been identified. The presented analytical solution and frequency equation offer the possibility to analytically evaluate the effect of different material and boundary condition parameters on the system's dynamic behavior without the need for complex numerical simulations. This formulation provides a valuable fundamental and practical solution capability for the preliminary design, optimization, and more accurate dynamic analysis of similar structural elements. Furthermore, thanks to the approach combining Fourier series with Stokes' transformation, an analytical solution has been obtained for the boundary value problem that could not be solved with classical methods.

In Section 2, the mathematical modeling for the axial vibration of the short fiber reinforced Rayleigh bar is detailed, the calculation of effective material properties is explained, and the eigenvalue problem formulation using Fourier series and Stokes' transformation is derived. In Section 3, the obtained frequency equation is solved numerically, the effects of various parameters on the axial natural frequencies are comprehensively examined, and the results are presented through graphs. This section also includes comparisons between the Rayleigh theory and the classical theory. Finally, in Section 4, the main findings obtained from the study are summarized, and the conclusions reached are discussed.

2. Definition and solution of the problem

This chapter deals with the axial vibration behavior of short fiber reinforced Rayleigh bars in an analytical framework. First, the transformation of micromechanical scale heterogeneity caused by randomly oriented fiber reinforcement into macro-scale effective elastic parameters is described. Then, the equation of motion derived using a variational approach based on Hamilton's principle is reduced to an eigenvalue problem using Fourier sine series and Stokes' transformation. Thus, the effects of design variables such as fiber property and volume fraction on the natural frequencies are revealed through closed formulas.

2.1. Material properties

In this section, the effective modulus of elasticity and bulk density are presented in closed form to provide input for the axial vibration analysis of rod-type elements reinforced with short fibers and modeled by the Rayleigh approach. As given in Fig. 1, the fibers are assumed to be completely randomly oriented. Hence, the macroscopic behavior of the composite is represented by isotropic singular parameters.

Parameters such as length/diameter ratio and volume fraction of short fibers directly affect the overall mechanical behavior of the composite material. In this study, the widely used Halpin-Tsai equations are used to predict the modulus of elasticity of short fiber reinforced materials (Agarwal et al., 2006) . Halpin-Tsai equations, which are widely used to estimate Young's moduli of short fiber reinforced composites, allow both longitudinal and transverse stiffnesses to be calculated analytically by taking into account the effect of fibers in the matrix phase (Agarwal et al., 2006). With this approach, the longitudinal and transverse Young's moduli are expressed by as follows (Agarwal et al., 2006):

$$E_l = E_m \left[\frac{1+2(l/d)V_f\left(\frac{(E_f/E_m)-1}{(E_f/E_m)+2(l/d)}\right)}{1-V_f\left(\frac{(E_f/E_m)-1}{(E_f/E_m)+2(l/d)}\right)} \right] \tag{1}$$

$$E_t = E_m \left[\frac{1+2V_f\left(\frac{(E_f/E_m)-1}{(E_f/E_m)+2}\right)}{1-V_f\left(\frac{(E_f/E_m)-1}{(E_f/E_m)+2}\right)} \right] \tag{2}$$

Where E_l, E_t, E_m and E_f are the longitudinal Young's modulus of the composite, transverse Young's modulus of the composite, Young's modulus of the matrix, and Young's modulus of the short-fiber, l/d is the short-fiber length/diameter ratio, and V_f is the short-fiber volume distribution, respectively.

Using Equations (1) and (2), the Young's modulus (E_{RSF}) and shear modulus (G_{RSF}) of the composite material reinforced with randomly oriented short fibers can be calculated as follows (Agarwal et al., 2006):

$$E_{RSF} = \frac{3}{8}E_l + \frac{5}{8}E_t \tag{3}$$

$$G_{RSF} = \frac{1}{8}E_l + \frac{1}{4}E_t \tag{4}$$

The Poisson's ratio of a reinforced with randomly aligned short fibers composite (ν_{RSF}) can be calculated using E_{RSF} and G_{RSF} as follows (Agarwal et al., 2006):

$$\nu_{RSF} = \frac{E_{RSF}}{2G_{RSF}} - 1 \tag{5}$$

With the matrix density (ρ_m) and short-fiber density (ρ_f), the density (ρ_{RSF}) of randomly distributed short-fiber reinforced composite material can be calculated as follows (Pan, 1993):

$$\rho_{RSF} = \rho_m(1 - V_f) + \rho_f V_f \tag{6}$$

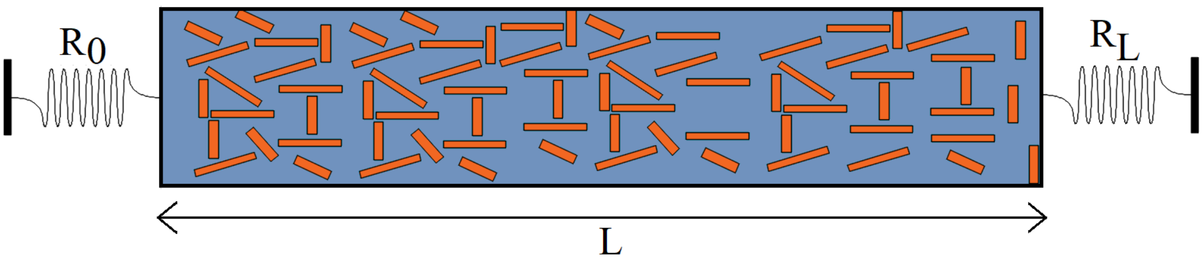

Fig. 1. Axially restrained short fiber reinforced Rayleigh bar

2.2. Rayleigh model

This subsection details the kinematic definitions, energy functionals, equation of motion and boundary conditions derived based on Rayleigh rod theory to describe the axial vibration of randomly oriented short fiber reinforced rod-type elements.

In the Rayleigh approach, the section planes remain flat without rotation relative to their initial position, but inertia effects are taken into account at points far from the axial axis. The displacement field is defined as (Yayli, 2020):

$$w = w(z, t) \tag{7}$$

$$u = -\nu \frac{\partial w}{\partial z} x \tag{8}$$

$$v = -\nu \frac{\partial w}{\partial z} y \tag{9}$$

Where w represents the axial displacement along the bar axis, u and v represent the axial-plane shrinkage in the x and y directions, respectively. ν represents Poisson's ratio.

Since the Rayleigh model includes the section rotational inertia, the total kinetic energy can be expressed as follows:

$$T = \frac{1}{2}\int_0^L \int_A \rho\left[\left(\frac{\partial u}{\partial t}\right)^2 + \left(\frac{\partial v}{\partial t}\right)^2 + \left(\frac{\partial w}{\partial t}\right)^2\right] dA dz = \int_0^L \left[A\left(\frac{\partial w}{\partial t}\right)^2 + v^2 I\left(\frac{\partial^2 w}{\partial z \partial t}\right)^2\right] dz \tag{10}$$

Where A is the cross-sectional area, t is the time, I is the polar moment of inertia of the cross-section, and I is calculated as follows:

$$I = \int_A (x^2 + y^2)\, dA \tag{11}$$

The longitudinal load (N) can be represented as follows:

$$N = \int_A \sigma_z\, dA = EA\frac{\partial w}{\partial z} \tag{12}$$

The axial derivative of N can be given as follows:

$$\frac{\partial N}{\partial z} = \rho A\frac{\partial^2 w}{\partial t^2} \tag{13}$$

By applying the variational form of Hamilton's principle, the following partial differential equation can be obtained (Li et al., 2017):

$$\rho A\frac{\partial^2 w}{\partial t^2} - \rho I v^2\frac{\partial^4 w}{\partial z^2 \partial t^2} - EA\frac{\partial^2 w}{\partial z^2} = 0 \tag{14}$$

This equation is the equation valid along the bar. For the supports at the two endpoints of the bar, the differential equation can be given in the following form:

$$\left[\rho I v^2\frac{\partial^3 w}{\partial z \partial t^2} + EA\frac{\partial w}{\partial z}\right]\delta w = 0 \tag{15}$$

For a rod-type element reinforced with randomly oriented short fibers, the equations of motion can be written as follows:

$$\rho_{RSF} A\frac{\partial^2 w}{\partial t^2} - \rho_{RSF} I v_{RSF}^2\frac{\partial^4 w}{\partial z^2 \partial t^2} - E_{RSF} A\frac{\partial^2 w}{\partial z^2} = 0, \quad 0 < z < L \tag{16}$$

$$\left[\rho_{RSF} I v_{RSF}^2\frac{\partial^3 w}{\partial z \partial t^2} + E_{RSF} A\frac{\partial w}{\partial z}\right]\delta w = 0, \quad z = 0, z = L \tag{17}$$

2.3. Solution procedure

When the displacement for free vibration is assumed as$w(z,t) = \phi(z)\, cos[\,\omega t]$, the equation of motion can be given as follows:

$$\rho_{RSF} I v_{RSF}^2 \omega^2\frac{d^2\phi}{dz^2} - E_{RSF} A\frac{d^2\phi}{dz^2} - \rho_{RSF} A\omega^2\phi = 0, \quad 0 < z < L \tag{18}$$

Where ω is the natural frequency, the force boundary conditions can be written as follows:

$$E_{RSF} A\frac{d\phi}{dz} - \rho_{RSF} I v_{RSF}^2 \omega^2\frac{d\phi}{dz} = \Gamma_0, \quad z = 0 \tag{19}$$

$$E_{RSF} A\frac{d\phi}{dz} - \rho_{RSF} I v_{RSF}^2 \omega^2\frac{d\phi}{dz} = -\Gamma_L, \quad z = L \tag{20}$$

In this context, Γ_0 and Γ_L represent the axial forces acting at both ends of the bar. The relevant relations can be rewritten using the axial spring stiffnesses at the end points (R_0 and R_L) and the axial displacements at those points:

$$R_0\phi_0 = E_{RSF} A\frac{d\phi}{dz} - \rho_{RSF} I v_{RSF}^2 \omega^2\frac{d\phi}{dz}, z = 0 \tag{21}$$

$$-R_L\phi_L = E_{RSF} A\frac{d\phi}{dz} - \rho_{RSF} I v_{RSF}^2 \omega^2\frac{d\phi}{dz}, z = L \tag{22}$$

2.4. Solution procedure

The axial displacement function in Eq. (18) can be defined as follows (Uzun et al., 2020):

$$\phi(z) = \begin{bmatrix} \phi_0 & z = 0 \\ \phi_L & z = L \\ \sum_{n=1}^{\infty} A_n\, sin(\frac{n\pi z}{L}) & 0 < z < L \end{bmatrix} \tag{23}$$

In the context of this study using the Stokes transformation, the coefficient (A_n) in Eq. (23) can be represented as follows:

$$A_n = \frac{2}{L}\int_0^L \phi\,(z)\, sin(\frac{n\pi z}{L})dz \tag{24}$$

The derivative of Eq. (23) with respect to z is as follows:

$$\phi'(z) = \sum_{n=1}^{\infty}\frac{n\pi}{L} A_n\, cos(\frac{n\pi z}{L}) \tag{25}$$

Eq. (25) is expressed as a Fourier cosine series:

$$\phi'(z) = \frac{f_0}{L} + \sum_{n=1}^{\infty} f_n\, cos(\frac{n\pi z}{L}) \tag{26}$$

here,

$$f_0 = \frac{2}{L}\int_0^L \phi'(z)dz = \frac{2}{L}[\phi(L) - \phi(0)] \tag{27}$$

$$f_n = \frac{2}{L}\int_0^L \phi'(z)\, cos(\frac{n\pi z}{L})dz \quad (n = 1,2,\ldots) \tag{28}$$

If Eq. (28) is integrated according to the integral by parts rule (Uzun et al., 2020):

$$f_n = \frac{2}{L}[\phi(z)\,cos(\frac{n\pi z}{L})]_0^L + \frac{2}{L}\left[\frac{n\pi}{L}\int_0^L \phi\,(z)\,sin(\frac{n\pi z}{L})dz\right] \tag{29}$$

$$f_n = \frac{2}{L}[(-1)^n\phi(L) - \phi(0)] + \frac{n\pi}{L}A_n \tag{30}$$

Using the equations obtained, higher-order derivatives can be calculated as follows:

$$\frac{d\phi(z)}{dz} = \frac{\phi_L - \phi_0}{L} + \sum_{n=1}^{\infty}\frac{n\pi}{L}cos(\frac{n\pi z}{L})\left[\frac{2}{L}((-1)^n\phi_L - \phi_0) + \frac{n\pi}{L}A_n\right] \tag{31}$$

$$\frac{d^2\phi(z)}{dz^2} = -\sum_{n=1}^{\infty}\frac{n\pi}{L}sin(\frac{n\pi z}{L})\left[\frac{2}{L}((-1)^n\phi_L - \phi_0) + \frac{n\pi}{L}A_n\right] \tag{32}$$

Substituting Eqs. (23) and (32) into Eq. (18) allows the coefficient A_n and the angular rotation field $\phi(z,t)$ to be reformulated in terms of ϕ_0 and ϕ_L as follows:

$$A_n = \frac{2n\pi(E_{RSF}A - \rho_{RSF}Iv_{RSF}^2\omega^2)(-\phi_0 + (-1)^n\phi_L)}{-E_{RSF}An^2\pi^2 + AL^2\rho_{RSF}\omega^2 + n^2\pi^2\rho_{RSF}Iv_{RSF}^2\omega^2} \tag{33}$$

Using the above relation, the axial deflection function can be defined as follows:

$$\phi(z) = \sum_{n=1}^{\infty}\frac{2n\pi(E_{RSF}A - \rho_{RSF}Iv_{RSF}^2\omega^2)(-\phi_0 + (-1)^n\phi_L)}{-E_{RSF}An^2\pi^2 + AL^2\rho_{RSF}\omega^2 + n^2\pi^2\rho_{RSF}Iv_{RSF}^2\omega^2}sin(\frac{n\pi z}{L}) \tag{34}$$

Then, based on the force boundary conditions and A_n, the following equation sets are written:

$$\left(-R_0 - \frac{E_{RSF}A - \rho_{RSF}Iv_{RSF}^2\omega^2}{L} - \sum_{n=1}^{\infty}\frac{2AL\rho\omega^2(E_{RSF}A - \rho_{RSF}Iv_{RSF}^2\omega^2)}{-E_{RSF}An^2\pi^2 + AL^2\rho_{RSF}\omega^2 + n^2\pi^2\rho_{RSF}Iv_{RSF}^2\omega^2}\right)\phi_0$$
$$+\left(\frac{E_{RSF}A - \rho_{RSF}Iv_{RSF}^2\omega^2}{L} + \sum_{n=1}^{\infty}\frac{2(-1)^nAL\rho\omega^2(E_{RSF}A - \rho_{RSF}Iv_{RSF}^2\omega^2)}{-E_{RSF}An^2\pi^2 + AL^2\rho_{RSF}\omega^2 + n^2\pi^2\rho_{RSF}Iv_{RSF}^2\omega^2}\right)\phi_L = 0 \tag{35}$$

$$\left(\frac{E_{RSF}A - \rho_{RSF}Iv_{RSF}^2\omega^2}{L} + \sum_{n=1}^{\infty}\frac{2(-1)^nAL\rho\omega^2(E_{RSF}A - \rho_{RSF}Iv_{RSF}^2\omega^2)}{-E_{RSF}An^2\pi^2 + AL^2\rho_{RSF}\omega^2 + n^2\pi^2\rho_{RSF}Iv_{RSF}^2\omega^2}\right)\phi_0$$
$$+\left(-R_L - \frac{E_{RSF}A - \rho_{RSF}Iv_{RSF}^2\omega^2}{L} - \sum_{n=1}^{\infty}\frac{2AL\rho\omega^2(E_{RSF}A - \rho_{RSF}Iv_{RSF}^2\omega^2)}{-E_{RSF}An^2\pi^2 + AL^2\rho_{RSF}\omega^2 + n^2\pi^2\rho_{RSF}Iv_{RSF}^2\omega^2}\right)\phi_L = 0 \tag{36}$$

By writing this set of equations in matrix form, the following equation is obtained:

$$\begin{bmatrix} H_{11} & H_{12} \\ H_{21} & H_{22} \end{bmatrix}\begin{bmatrix} \phi_0 \\ \phi_L \end{bmatrix} = 0 \tag{37}$$

In the above expression, axial vibration frequencies are obtained by setting the determinant of the coefficients matrix equal to zero and the elements of this coefficients matrix are as follows:

$$H_{11} = -R_0 - \frac{E_{RSF}A - \rho_{RSF}Iv_{RSF}^2\omega^2}{L} - \sum_{n=1}^{\infty}\frac{2AL\rho\omega^2(E_{RSF}A - \rho_{RSF}Iv_{RSF}^2\omega^2)}{-E_{RSF}An^2\pi^2 + AL^2\rho_{RSF}\omega^2 + n^2\pi^2\rho_{RSF}Iv_{RSF}^2\omega^2} \tag{38}$$

$$H_{12} = H_{21} = \frac{E_{RSF}A - \rho_{RSF}Iv_{RSF}^2\omega^2}{L} + \sum_{n=1}^{\infty}\frac{2(-1)^nAL\rho\omega^2(E_{RSF}A - \rho_{RSF}Iv_{RSF}^2\omega^2)}{-E_{RSF}An^2\pi^2 + AL^2\rho_{RSF}\omega^2 + n^2\pi^2\rho_{RSF}Iv_{RSF}^2\omega^2} \tag{39}$$

$$H_{22} = -R_L - \frac{E_{RSF}A - \rho_{RSF}Iv_{RSF}^2\omega^2}{L} - \sum_{n=1}^{\infty}\frac{2AL\rho\omega^2(E_{RSF}A - \rho_{RSF}Iv_{RSF}^2\omega^2)}{-E_{RSF}An^2\pi^2 + AL^2\rho_{RSF}\omega^2 + n^2\pi^2\rho_{RSF}Iv_{RSF}^2\omega^2} \tag{40}$$

3. Numerical results

In this part of the study, the effects of important parameters for short fiber reinforced Rayleigh bars are investigated. These are E_f/E_m, ρ_f/ρ_m, V_f, l/d and spring stiffnesses. In this study, the analyses are carried out with the following parameters considered constant unless otherwise stated: Bar radius $r = 0.2\ m.$, bar length $L = 40r\ m.$, $d = r/10, l/d = 5, V_f = 0.2, E_f/E_f = 5, \rho_f/\rho_m = 2, n = 60$. In the study, the stiffnesses of the springs at both ends of the bar are considered equal to each other and are included in the analysis in the following dimensionless forms:

$$\overline{R_0} = \frac{R_0L}{E_mA} \tag{41}$$

$$\overline{R_L} = \frac{R_LL}{E_mA} \tag{42}$$

Here, $\overline{R_0}$ and $\overline{R_L}$ are the non-dimensional spring stiffnesses at the ends of bar. The study deals with first mode frequencies except for the last figure. In addition, the study shows the dimensionless frequencies ($\overline{\omega}$) as output and the calculation of the dimensionless frequencies is realized with the following equation:

$$\overline{\omega} = \omega L\sqrt{\frac{\rho_m}{E_m}} \tag{43}$$

All the graphs presented in the study include different parameters against $\overline{R_0} = \overline{R_L}$ values ranging from 200 to 1200. In Fig. 2 the effect of varying E_f/E_m ratios from 5 to 25 is investigated. E_f/E_m increases the dimensionless axial vibration frequencies of the Rayleigh bar reinforced with short fibers. Although the E_f/E_m ratios increase regularly at intervals of 5, the change in frequencies is not regular. The increase at higher values of E_f/E_m plays less role in the increase of frequencies. It is clear from this and other graphs that the increase in spring stiffnesses increases $\overline{\omega}$. This increase is more pronounced at lower values of spring stiffness and the increase in stiffness affects $\overline{\omega}$ much less. This is because as the spring stiffnesses increase, the Rayleigh bar limits are very close to the full stiffness and the change in frequencies is no longer noticeable.

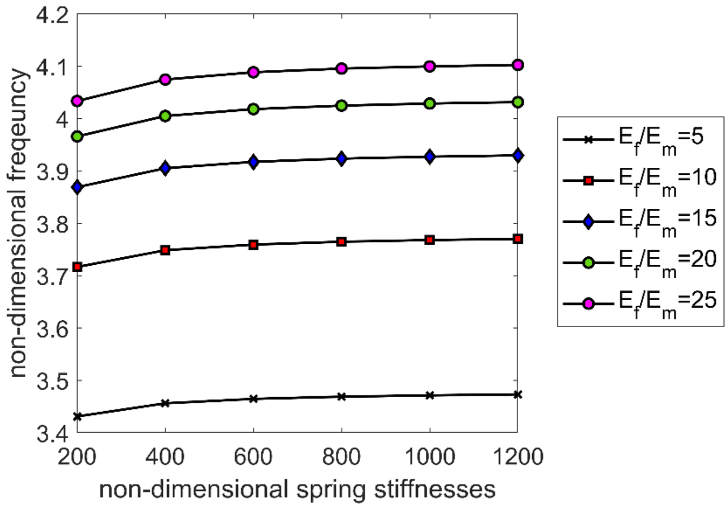

Fig. 2. Effect of E_f/E_m on non-dimensional frequencies

In Fig. 3, the effect of the ρ_f/ρ_m ratio considered in five different values from 2 to 10 is analyzed. The increase in the ρ_f/ρ_m ratio decreases the axial vibration frequencies. This can be explained by the increasing effective mass density of the bar. It is expected that the frequencies decrease when the effective mass density increases. Similar to the previous example, the increase in the ρ_f/ρ_m ratio starts to decrease at higher values.

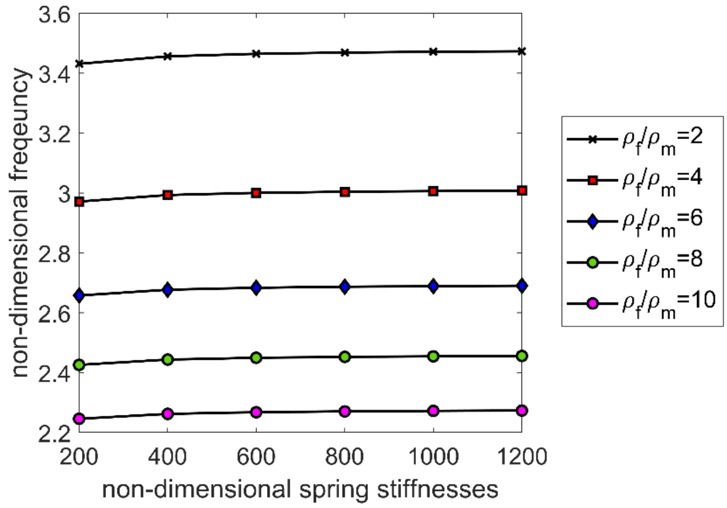

Fig. 3. Effect of ρ_f/ρ_m on non-dimensional frequencies

Fig. 4 focuses on the effect of fiber volume fraction on axial vibration frequencies. For this analysis, fiber volume fraction ranges from 0.2 to 0.4 are considered. The increase in $\bar{\omega}$ with increasing fiber volume fraction is clearly seen. The reason for this increase can be explained by the increasing stiffness of the bar with increasing V_f. As can be predicted, increasing V_f increases both the effective modulus of elasticity and the effective mass density. However, it is clear from this that the effective modulus of elasticity of the bar increases at a higher rate, leading to higher frequencies. Also, another conclusion from this analysis is that the spring stiffnesses have a greater effect on the frequencies at higher values of V_f.

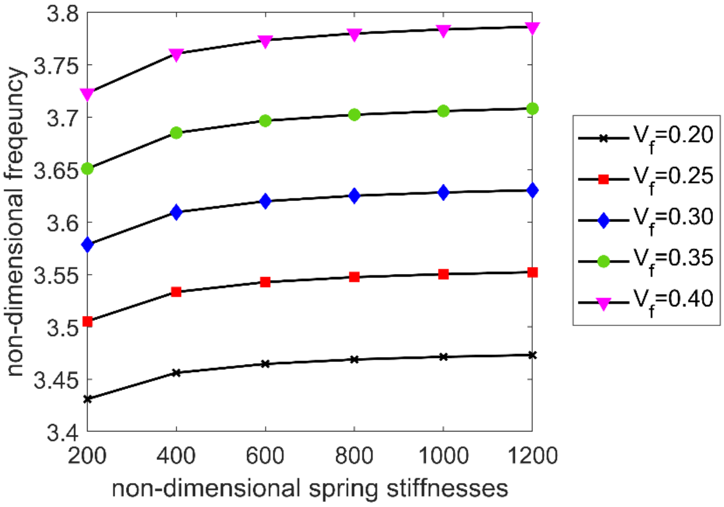

Fig. 4. Effect of V_f on non-dimensional frequencies

The Halpin-Tsai model is an approach that takes into account the geometric properties of short fibers. In this model, the length and diameter values of short fibers contribute to the effective modulus of elasticity. For this reason, axial vibration frequencies for five different l/d values ranging from 5 to 9 are analyzed in Fig. 5. Since the increase in the l/d ratio of the fibers provides a more rigid form of the bar, it also causes an increase in $\overline{\omega}$.

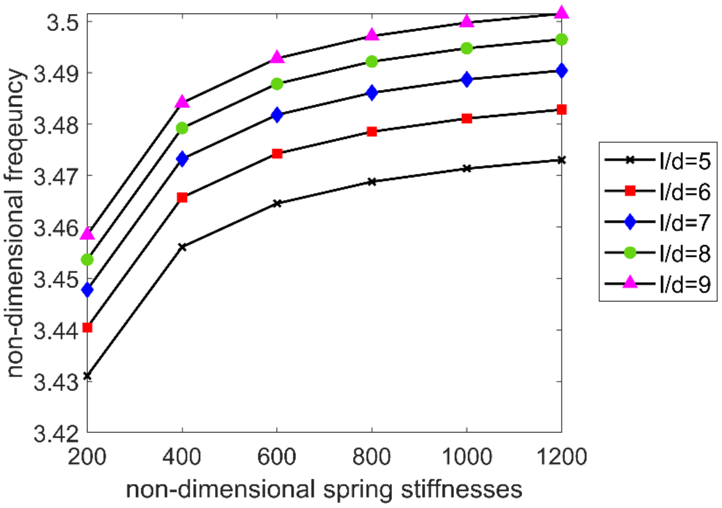

Fig. 5. Effect of $\mathrm{l/d}$ on non-dimensional frequencies

Finally, frequency ratios against non-dimensional spring stiffnesses are presented for the first three modes. The frequency ratios given in this graph are calculated as the ratio of the Rayleigh theory frequencies to the frequencies based on the classical theory for the relevant mode. Since the values of the frequency ratios are less than 1, it is easily understood that the classical theory calculates the frequencies higher. The decrease in frequency ratios as the mode number increases is explained by the fact that Rayleigh rod theory is more effective at higher ratios. In addition, while the frequency ratios for mode 1 remain constant despite the change in spring stiffness, the frequency ratios change in higher modes. The second and third mode frequency ratios decrease as the spring stiffnesses increase. The conclusion to be drawn from this is that rigid boundary conditions are more important in the use of Rayleigh theory.

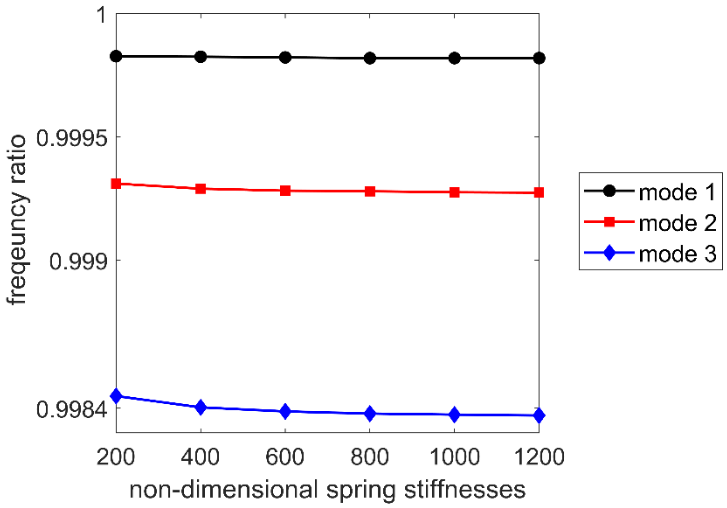

Fig. 6. Effect of theory ($l/d = 10$)

4. Conclusions

The aim of this study is to investigate the axial vibration frequencies of short fiber reinforced Rayleigh bars under deformable boundary conditions. For this purpose, short fiber reinforced Rayleigh bars are modeled as deformable axial springs at both ends. The study is finally based on an eigenvalue solution, which is derived in a form that allows to analyze the effects of arbitrary (both rigid and deformable) boundary conditions. The matrix of coefficients whose solution gives the axial vibration frequencies of short fiber reinforced Rayleigh bars includes the axial spring stiffnesses at both ends. These spring stiffnesses can be set arbitrarily and give rigid boundary conditions at their specific values. Following this effective eigenvalue solution, the effect of a number of parameters important for short fiber reinforced Rayleigh bars is investigated. These parameters are E_f/E_m, ρ_f/ρ_m, V_f, l/d, spring stiffnesses and lateral inertia effect. As a result of the analyzes, the following conclusions are reached: Increases in E_f/E_m, V_f and l/d make the structure of the Rayleigh bar more rigid and thus increase the axial vibration frequencies. The increase of ρ_f/ρ_m increases the effective mass density and causes the frequencies to decrease. The increase in the stiffness of the springs at both ends of the bar makes the boundary conditions stiffer, leading to an increase in axial vibration frequencies. Finally, the lateral inertia effect causes the axial frequencies to decrease slightly.

References

Agarwal, B. D., Broutman, L. J., Agarwal, B. D., & Broutman, L. J. (2006). Analysis and performance of fiber composites (Third edition). John Wiley & Sons.

Akpınar, M., Uzun, B., & Yaylı, M. Ö. (2024). On the thermo-mechanical vibration of an embedded short-fiber-reinforced nanobeam. *Advances in Nano Research*, *17*(3), 197–211.

Amsalu, C., Negasa, D., & Merga, A. (2024). Numerical analysis of fiber reinforced composite material for structural component application. *Heliyon*, *10*(18)

Ananthapuvirajah, A. (2019). *Free vibration and flutter behaviour of metallic and composite aircraft using DSM and developments of dynamic stiffness matrices for structural elements with applications* [Doctoral thesis]. City, University of London.

Arumugam, S., Kandasamy, J., Venkatesan, S., Murugan, R., Narayanan, V. L., Sultan, M. T. H., Shahar, F. S., Shah, A. U. M., Khan, T., & Sebaey, T. A. (2022). A Review on the Effect of Fabric Reinforcement on Strength Enhancement of Natural Fiber Composites. *Materials*, *15*(9).

Baniya, J., & Tsegai, S. B. (2022). *Modelling of crack initiation in fibre-reinforced injection moulded parts* [Master Thesis]. Oslo Metropolitan University.

Belabed, Z., Tounsi, A., Bousahla, A. A., Tounsi, A., Bourada, M., & Al-Osta, M. A. (2024). Free vibration analysis of Bi-Directional Functionally Graded Beams using a simple and efficient finite element model. *Structural Engineering and Mechanics*, *90*(3), 233–252.

Bonopera, M. (2023). Stress Evaluation in Axially Loaded Members of Masonry Buildings and Space Structures: From Traditional Methods to Combinations with Artificial Intelligence Approaches. *Buildings*, *13*(8).

Bordiga, G., Cabras, L., Bigoni, D., & Piccolroaz, A. (2019). Free and forced wave propagation in a Rayleigh-beam grid: Flat bands, Dirac cones, and vibration localization vs isotropization. *International Journal of Solids and Structures*, *161*, 64–81.

Chang, J.-R., Lin, W.-J., Huang, C.-J., & Choi, S.-T. (2010). Vibration and stability of an axially moving Rayleigh beam. *Applied Mathematical Modelling*, *34*(6), 1482–1497.

Civalek, Ö., Uzun, B., & Yaylı, M. Ö. (2022a). Nonlocal Free Vibration of Embedded Short-Fiber-Reinforced Nano-/Micro-Rods with Deformable Boundary Conditions. *Materials*, *15*(19).

Civalek, Ö., Uzun, B., & Yaylı, M. Ö. (2022b). Torsional and longitudinal vibration analysis of a porous nanorod with arbitrary boundaries. *Physica B: Condensed Matter*, *633*.

Ding, Z., Tang, Z., Zhang, B., & Ding, Z. (2024). Vibration Response of Metal Plate and Shell Structure under Multi-Source Excitation with Welding and Bolt Connection. *Agriculture (Switzerland)*, *14*(6).

Farshbaf Zinati, R., Rezaee, M., & Lotfan, S. (2020). Nonlinear Vibration and Stability Analysis of Viscoelastic Rayleigh Beams Axially Moving on a Flexible Intermediate Support. *Iranian Journal of Science and Technology - Transactions of Mechanical Engineering*, *44*(4), 865–879.

Fernández-Sáez, J., Morassi, A., & Rubio, L. (2017). Crack identification in elastically restrained vibrating rods. *International Journal of Non-Linear Mechanics*, *94*, 257–267.

Friswell, M. I., Adhikari, S., & Lei, Y. (2007). Vibration analysis of beams with non-local foundations using the finite element method. *International Journal for Numerical Methods in Engineering*, *71*(11), 1365–1386.

Geethamma, V. G., Kalaprasad, G., Groeninckx, G., & Thomas, S. (2005). Dynamic mechanical behavior of short coir fiber reinforced natural rubber composites. *Composites Part A: Applied Science and Manufacturing*, *36*(11), 1499–1506.

Ghayesh, M. H., & Balar, S. (2008). Non-linear parametric vibration and stability of axially moving visco-elastic Rayleigh beams. *International Journal of Solids and Structures*, *45*(25–26), 6451–6467.

Hamza, K. S., Shash, A. Y., & Abdrabou, M. (2017). Application of short fibers reinforced composites in power transmission coupling. *Latin American Journal of Solids and Structures*, *14*(10), 1789–1803.

Han, J.-B., Hong, S.-Y., Song, J.-H., & Kwon, H.-W. (2014). Vibrational energy flow models for the Rayleigh-Love and Rayleigh-Bishop rods. *Journal of Sound and Vibration*, *333*(2), 520–540.

Hao, X., Zhou, H., Mu, B., Chen, L., Guo, Q., Yi, X., Sun, L., Wang, Q., & Ou, R. (2020). Effects of fiber geometry and orientation distribution on the anisotropy of mechanical properties, creep behavior, and thermal expansion of natural fiber/HDPE composites. *Composites Part B: Engineering*, *185*.

Hien, T. D., Diem, N. D., Van Tan, G., Van Hiep, V., & Van Thuan, N. (2023). Stochastic Higher-order Finite Element Model for the Free Vibration of a Continuous Beam resting on Elastic Support with Uncertain Elastic Modulus. *Engineering, Technology and Applied Science Research*, *13*(1), 9985–9990.

Huang, X., Zhang, L., Cui, H., & Hu, G. (2024). Dynamic Characteristics of Functionally Graded Timoshenko Beams by Improved Differential Quadrature Method. *CMES - Computer Modeling in Engineering and Sciences*, *140*(2), 1647–1668.

Huang, Y., EShun, F. T., Hu, J., Zhang, X., Zhao, J., Zhang, S., Qian, R., Chen, Z., & Chen, D. (2023). Research on Low-Velocity Impact Response of Novel Short-Fiber-Reinforced Composite Laminates. *Polymers*, *15*(4).

Huang, Z., Wang, X., Wu, N., Chu, F., & Luo, J. (2019). A finite element model for the vibration analysis of sandwich beam with frequency-dependent viscoelastic material core. *Materials*, *12*(20).

Jena, S. K., & Chakraverty, S. (2018). Free vibration analysis of variable cross-section single-layered graphene nano-ribbons (slgnrs) using differential quadrature method. *Frontiers in Built Environment*, *4*.

Jeong, K.-H., & Lee, S.-C. (1996). Fourier series expansion method for free vibration analysis of either a partially liquid-filled or a partially liquid-surrounded circular cylindrical shell. *Computers and Structures*, *58*(5), 937–946.

Kadıoğlu, H., & Yaylı, M. Ö. (2017). Buckling analysis of non-local Timoshenko beams by using Fourier series. *International Journal of Engineering and Applied Sciences*, *9*(4), 89–99.

Kalusuraman, G., Kumaran, S. T., Balamurugan, K., Sivashanmugam, N., Sivaprakasam, P., Kurniawan, R., & Ezhilmaran, V. (2023). Vibration Studies on Fiber Reinforced Composites–a Review. *Journal of Natural Fibers*, *20*(1).

Kamal, A. M., & Taha, I. (2010). Vibration damping behavior of fiber reinforced composites: A review. In *Key Engineering Materials* (Vol. 425).

Kamal, M., & İnel, M. (2021). Orta yükseklikteki betonarme binalarda çekiçlemenin deplasman talepleri üzerindeki etkileri. *Pamukkale Üniversitesi Mühendislik Bilimleri Dergisi*, *27*(6).

Khalili, M. R., Malekzadeh, K., & Mittal, R. K. (2005). A new approach to static and dynamic analysis of composite plates with different boundary conditions. *Composite Structures*, *69*(2), 149–155.

Kumar, M., & Kumar, S. (2024). Short Literature Survey on Fiber-Reinforced Hybrid Composites. *Mechanics of Advanced Composite Structures*, *11*(2), 425–452.

Laura, P. A. A., & Gutierrez, R. H. (1993). Analysis of vibrating timoshenko beams using the method of differential quadrature. *Shock and Vibration*, *1*(1), 89–93.

Lee, S. Y., & Lin, S. M. (1996). Dynamic analysis of nonuniform beams with time-dependent elastic boundary conditions. *Journal of Applied Mechanics, Transactions ASME*, *63*(2), 474–478.

Leite, L. F. P., & da Rocha, F. C. (2024). Rayleigh-Ritz method applied to high-order zigzag theory for static analysis of laminated composite beams with different boundary conditions. *Revista Sergipana de Matemática e Educação Matemática*, *9*(2), 73–88.

Lelkes, J., Bak, B. D., & Kalmár-Nagy, T. (2024). Vibrations and energy distribution in inhomogeneous rods with elastic and viscous boundary conditions. *Scientific Reports*, *14*(1).

Li, W. L., & Xu, H. (2009). An exact Fourier series method for the vibration analysis of multispan beam systems. *Journal of Computational and Nonlinear Dynamics*, *4*(2), 1–9.

Li, X. F., Tang, A. Y., & Xi, L. Y. (2013). Vibration of a Rayleigh cantilever beam with axial force and tip mass. *Journal of Constructional Steel Research*, *80*, 15–22.

Li, X.-F., Shen, Z.-B., & Lee, K. Y. (2017). Axial wave propagation and vibration of nonlocal nanorods with radial deformation and inertia. ZAMM - Journal of Applied Mathematics and Mechanics / Zeitschrift Für Angewandte Mathematik Und Mechanik, 97(5), 602–616

Liu, T., Ding, J. Y., & Xu, X. Y. (2022). Differential quadrature method for partial differential dynamic equations of beam–ring structure. *AIAA Journal*, *60*(4), 2542–2554.

Lv, B., Li, W., & Ouyang, H. (2015). Moving force-induced vibration of a rotating beam with elastic boundary conditions. *International Journal of Structural Stability and Dynamics*, *15*(1).

Mohammed, L., Ansari, M. N. M., Pua, G., Jawaid, M., & Islam, M. S. (2015). A Review on Natural Fiber Reinforced Polymer Composite and Its Applications. *International Journal of Polymer Science*, *2015*.

Mortazavian, S., & Fatemi, A. (2015). Fatigue behavior and modeling of short fiber reinforced polymer composites: A literature review. *International Journal of Fatigue*, *70*, 297–321.

Nciri, M., Notta-Cuvier, D., Lauro, F., Chaari, F., Maalej, Y., & Zouari, B. (2017). Modelling and characterisation of dynamic behaviour of short-fibre-reinforced composites. *Composite Structures*, *160*, 516–528.

Nurazzi, N. M., Asyraf, M. R. M., Fatimah Athiyah, S., Shazleen, S. S., Rafiqah, S. A., Harussani, M. M., Kamarudin, S. H., Razman, M. R., Rahmah, M., Zainudin, E. S., Sapuan, S. M., & Khalina, A. (2021). A review on mechanical performance of hybrid natural fiber polymer composites for structural applications. *Polymers*, *13*(13).

Ratazzi, A. R., Bambill, D. V, & Rossit, C. A. (2013). Free vibrations of beam system structures with elastic boundary conditions and an internal elastic hinge. *Chinese Journal of Engineering*, *2013*(1), 624658.

Singh, S., Kamble, Z., & Neje, G. (2024). Textile-reinforced composite structural-health monitoring systems. *Textile Progress*, *56*(4), 415–516.

Sotomayor, O., & Pancho, A. (2024). Comparison of Micromechanical Models for Predicting the Young's Modulus of Fiber-Reinforced Epoxy | Comparación de Modelos Micromecánicos para Predecir el Módulo de Young en resinas Epoxi reforzadas con fibras. *Revista Politecnica*, *54*(2), 47–55.

Uzun, B., Kafkas, U., & Yaylı, M. Ö. (2020). Axial dynamic analysis of a Bishop nanorod with arbitrary boundary conditions. ZAMM - Journal of Applied Mathematics and Mechanics / Zeitschrift Für Angewandte Mathematik Und Mechanik, 100(12), e202000039.

Wang, L., Su, Z., & Wang, L. (2022). Flutter analysis of rotating beams with elastic restraints. *Applied Mathematics and Mechanics (English Edition)*, *43*(5), 761–776.

Wang, Y.-R., & Fang, Z.-W. (2015). Vibrations in an elastic beam with nonlinear supports at both ends. *Journal of Applied Mechanics and Technical Physics*, *56*(2), 337–346.

Wen, J.-J., & Yi, L. Y. (2014). Analyze on a coupled beam vibration system by FEM (I): Theory. In *Advanced Materials Research* (Vol. 933).

Wu, H., Shen, A., Ren, G., Ma, Q., Wang, Z., Cheng, Q., & Li, Y. (2023). Dynamic mechanical properties of fiber-reinforced concrete: A review. *Construction and Building Materials*, *366*.

Yang, S., & Yang, Q. (2017). Geometrically Nonlinear Transient Response of Laminated Plates with Nonlinear Elastic Restraints. *Shock and Vibration*, *2017*.

Yaylı, M. Ö. (2020). Axial vibration analysis of a Rayleigh nanorod with deformable boundaries. *Microsystem Technologies*, *26*(8), 2661–2671.

Yaylı, M. Ö., Aras, M., & Aksoy, S. (2014). An efficient analytical method for vibration analysis of a beam on elastic foundation with elastically restrained ends. *Shock and Vibration*, *2014*.

Zhou, D., Tong, X., Liu, H., Lv, S., Srivatsan, T. S., & Gao, X. (2024). A modified Halpin-Tsai model for predicting the elastic modulus of composite materials. *AIP Advances*, *14*(1).

Zhu, K., & Chung, J. (2019). Vibration and stability analysis of a simply-supported Rayleigh beam with spinning and axial motions. *Applied Mathematical Modelling*, *66*, 362–382.

4th International Civil Engineering & Architecture Conference
17-19 May 2025, Trabzon, Türkiye

A study on methods to increase ductility of timber beams

Gokhan Sakar*[1], Huseyin Kursat Celik[1,2]

[1] *Department of Civil Engineering, Dokuz Eylul University, 35300, Türkiye*
[2] *Department of Civil Engineering, Izmir University of Economics, 35300, Türkiye*

Abstract. Timber has many advantages in its nature like high strength over density ratio. Due to this, timber is getting more common in construction works in general, especially in seismic regions. However, there are some concerns about its ductility. Although it behaves ductile under compression, brittle failure occurs under tension. Literature knowledge on this topic is also limited with a few results. To clarify this, the ductility of timber beam was studied by means of material, elemental and structural ductility. Methods to increase the ductility of timber beams were evaluated, and effectiveness of the methods was investigated using complete nonlinear moment-curvature analysis. As a result of the study, various conclusion was highlighted regarding the methods to increase ductility of timber beams and recommendations were made.

Keywords: Timber beam; Ductility; Moment-curvature; Nonlinear; Strengthening

1. Introduction

Timber is a natural composite material widely used in construction. It possesses several advantageous properties for this purpose. Timber is easily shaped to form structural elements, it is a sustainable material, and it has a high strength-to-weight ratio. This last property is particularly important in seismic design, as it results in lower seismic forces acting on the structure due to the material's lightweight. However, timber structures also have certain disadvantages when it comes to seismic design. In brief, a building should be designed to possess sufficient stiffness, ductility, and strength (Turkish Building Seismic Code, 2018). As a material, timber has limitations in terms of both stiffness and ductility, which present challenges in seismic design.

From a material perspective, timber is an anisotropic material, meaning its strength properties vary depending on the direction (Fig. 1). Specifically, the longitudinal direction exhibits higher strength parameters compared to the transverse direction. However, the behaviour of timber is more influenced by the type of stress than by the load direction. Under compression, timber can undergo plastic deformation without experiencing a reduction in strength. In contrast, under tension, timber fails in a brittle manner. From a design perspective, the required stiffness can be achieved through structural configurations such as relatively high sectional dimensions or the use of braces or shear walls. However, controlling the behaviour of timber under different stress conditions is a more complex issue. If failure occurs due to tensile stress, it will be brittle, which is an undesirable condition during seismic excitation. This has led to increased attention on studies regarding the ductility of timber.

Several pioneering studies proposed in the literature. Jorissen A. et al. (2011) critiqued the ductility of timber structures from a design perspective, demonstrating that a ductile design can be achieved through the use of steel connectors. This idea has been further supported by several subsequent studies (Brühl et al., 2011; Ottenhaus et al., 2021; Rebouças et al., 2022). Another research area focuses on enhancing the performance of timber elements by incorporating materials such as steel and fibre-reinforced polymers (FRP). It should be noted that this approach has primarily been studied for strengthening purposes, rather than specifically targeting the enhancement of ductility or the improvement of the behaviour of timber elements.

Based on the current literature, several key points should be highlighted. Steel connectors have gained attention as ductile details; however, their role as the ductile reserve of a structure can be questioned, as their primary function is to hold elements together, ensuring the continuity of the structure. To achieve ductile behaviour, timber members should not fail while the connections undergo plastic rotation. In this context, timber members may not perform effectively, as they will not be subjected to the capacity loads required to yield the steel connectors. Furthermore, the plastic deformation of the timber elements will not be utilized. On the other and, from a general perspective, the goal is for the structural members to undergo yielding while the connections are designed to accommodate the plastic rotation of the elements. Another option for enhancing ductility involves using external materials such as steel or FRP. However, there is limited research on enhancing ductility using these materials.

* Corresponding author, E-mail: gokhan.sakar@deu.edu.tr

https://doi.org/10.31462/icearc2025_ce_sme_210

Therefore, to explore alternative solutions, this study is proposed by the authors. The primary objective of this study is to utilize the existing plastic behaviour of timber. Since timber can undergo plastic deformation under compression, the failure of timber elements can be controlled to prevent tensile failure. As timber, by itself, is prone to failure under tension, its tensile strength needs to be enhanced. To achieve this, in line with existing literature, steel, FRP, or other materials with higher tensile strength can be employed. For the study of ductility, timber beams were selected as the focus, as plastic rotation is directly related to bending behaviour. To analyse this, moment-curvature analysis (or sectional analysis) was chosen. A reference timber beam was considered, and several strengthening options were evaluated. Conclusions were drawn regarding the effectiveness of these methods.

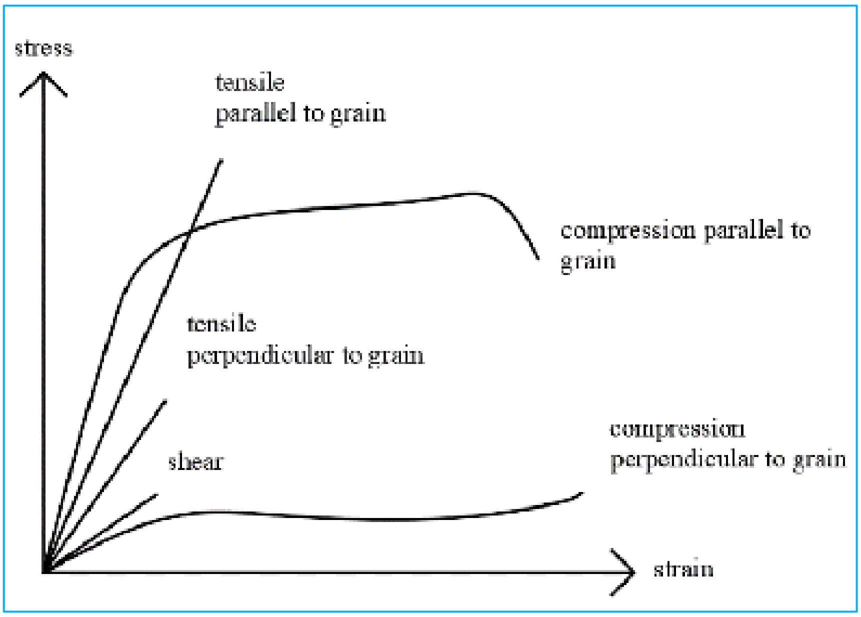

Fig. 1. Stress-strain relationship of timber in different loading directions

2. Material and method

In this study, a simply supported beam and three-point bending scheme was used as the reference. Timber of grade was selected as C16 (Regulation on the Design, Analysis and Construction of Timber Buildings, 2024). Steel plates with a thickness of 2 mm and FRP bonding were regarded as strengthening. For the steel, S235 grade was assumed, and CFRP was selected for the FRP material. The loading scheme is shown in Fig. 2, the material properties are given in Table 1.

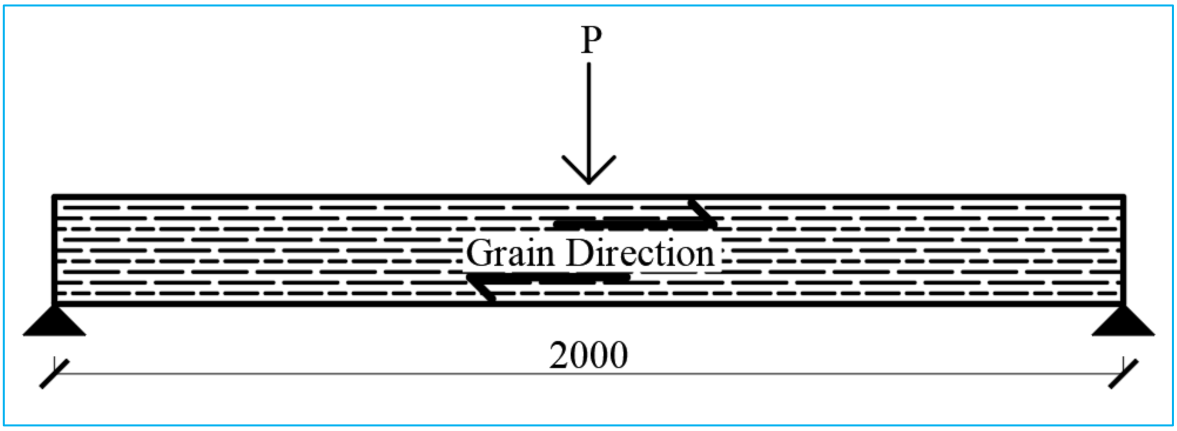

Fig. 2. Loading scheme

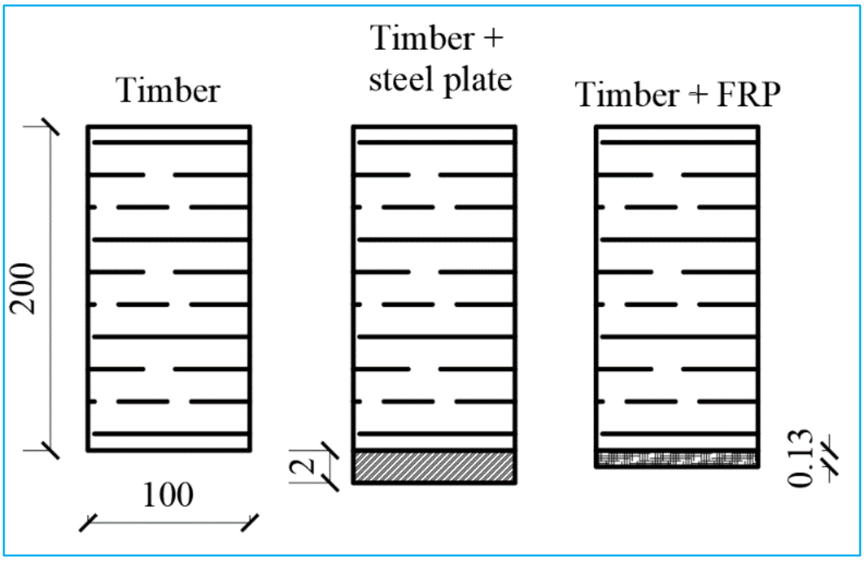

Fig. 3. Strengthening configurations

Table 1. Material properties

Properties	Timber	Steel	FRP
Width (mm)	100	100	100
Height (mm)	200	2	0.13
Elastic Modulus (MPa)	8000	210000	231000
Yield Compressive Strength (MPa)	16	-	-
Yield Compressive Strain	0.002	-	-
Compressive Strength, Ultimate (MPa)	16	-	-
Compressive Strain, Ultimate	0.01	-	-
Yield Tensile Strength (MPa)	-	235	-
Yield Tensile Strain	-	0.0012	-
Ultimate Tensile Strength (MPa)	8	235	4100
Ultimate Tensile Strain	0.001	0.15	0.016

3. Analytical method

To capture the full load-displacement curve of a beam, section analysis can be employed, rather than directly calculating the ultimate states. This requires the material constitutive laws, section properties, and the loading scheme. Based on these factors and Euler beam theory, the load-displacement curve can be obtained using the moment (M) - curvature ($\emptyset$) relationship, as shown in Equation 1. Additionally, strain (ε) can be defined using Equation 2, which relates strain to curvature and the height of the layer (y). If the section is discretized by fibres, the strain distribution along the height of the section can be computed. By using the strain values and material models, stresses (σ) along the section can be obtained, as shown in Equation 3. The forces (F) can then be defined as components along the fibres, as expressed in Equation 4. By taking the moments of these forces, the moment at a given curvature can be captured, as shown in Equation 5. For a three-point bending scheme, the corresponding load (P) can be calculated using Equation 6, and the displacement (δ) can be determined by Equation 7. Using Equations 1-7, the complete load-displacement curve can be constructed. The material models for timber, steel, and FRP are provided in Equations 8 to 11, respectively.

Several assumptions made during the analysis should be stated. Timber is assumed to behave as elastic-perfectly plastic in compression and elastic-brittle in tension, as outlined in Eurocode 5 (1995). For steel, an elastic-perfectly plastic model was adopted. FRP was assumed to behave in a linear elastic manner up to failure. Full composite action was assumed, and the plane section assumption, as in general beam theory, was applied, meaning that the plane section remains plane during deformation. Since the study focuses on exploring potential, the debonding of the FRP and steel plates was disregarded during the analysis, and the ultimate strain was considered without any reduction. The slip between timber, steel, and FRP was neglected. Curves were constructed up to the point of reaching the ultimate strain of the materials. After the complete construction of these curves, ductility was determined as the ratio between the ultimate and yielding displacements.

$$\emptyset = \frac{M}{E * I_{eff}} \tag{1}$$

$$\varepsilon(y) = \emptyset * y \tag{2}$$

$$\sigma(y) = f\big(\varepsilon(y)\big) \tag{3}$$

$$F_{i.fiber} = \sigma_{i.fiber} * b * d_y \tag{4}$$

$$M = \sum F_i * y_i \tag{5}$$

$$P = \frac{4M}{L} \tag{6}$$

$$\delta = \frac{\emptyset * (L)^2}{8} \tag{7}$$

$$\sigma_{timber,tension} = \begin{cases} E * \varepsilon, & \varepsilon \leq \dfrac{f_t}{E} \\ 0, & \varepsilon > \dfrac{f_t}{E} \end{cases} \tag{8}$$

$$\sigma_{timber,compression} = \begin{cases} E * \varepsilon, & \varepsilon \leq \dfrac{f_c}{E} \\ f_c, & \varepsilon > \dfrac{f_c}{E} \end{cases} \tag{9}$$

$$\sigma_{FRP} = \begin{cases} E * \varepsilon, & \varepsilon \leq \dfrac{f_f}{E} \\ 0, & \varepsilon > \dfrac{f_f}{E} \end{cases} \tag{10}$$

$$\sigma_{steel} = \begin{cases} E * \varepsilon, & \varepsilon \leq \dfrac{f_s}{E} \\ f_{yield}, & \varepsilon > \dfrac{f_s}{E} \end{cases} \tag{11}$$

4. Results and discussion

According to the study results, the timber beam failed when the stress reached the tensile strength. Since the tensile strength is lower than the compressive strength, the beam did not exhibit any plastic deformation. In the case of steel strengthening, the timber beam initially cracked when it reached its tensile strength. With the addition of steel, the beam was able to bear a higher load and exhibit plastic deformation. Furthermore, steel strengthening increased the beam's initial stiffness. The FRP-strengthened beam showed a similar initial load-displacement curve to the unstrengthened timber beam, as there was a limited increase in stiffness. However, the FRP-strengthened beam was able to undergo plastic deformation up to the point of timber crushing. The load-displacement curves of the beams are presented in Fig. 4. The failure load, displacement, and ductility ratio of the beams are summarised in Table 2.

Table 2. Results

Beam	Failure Load (kN)	Yield Displacement (mm)	Ultimate Displacement (mm)	Ductility
Timber	18	-	9.5	Brittle
Timber + Steel	32	20	50	2.5
Timber + FRP	23	20	50	2.5

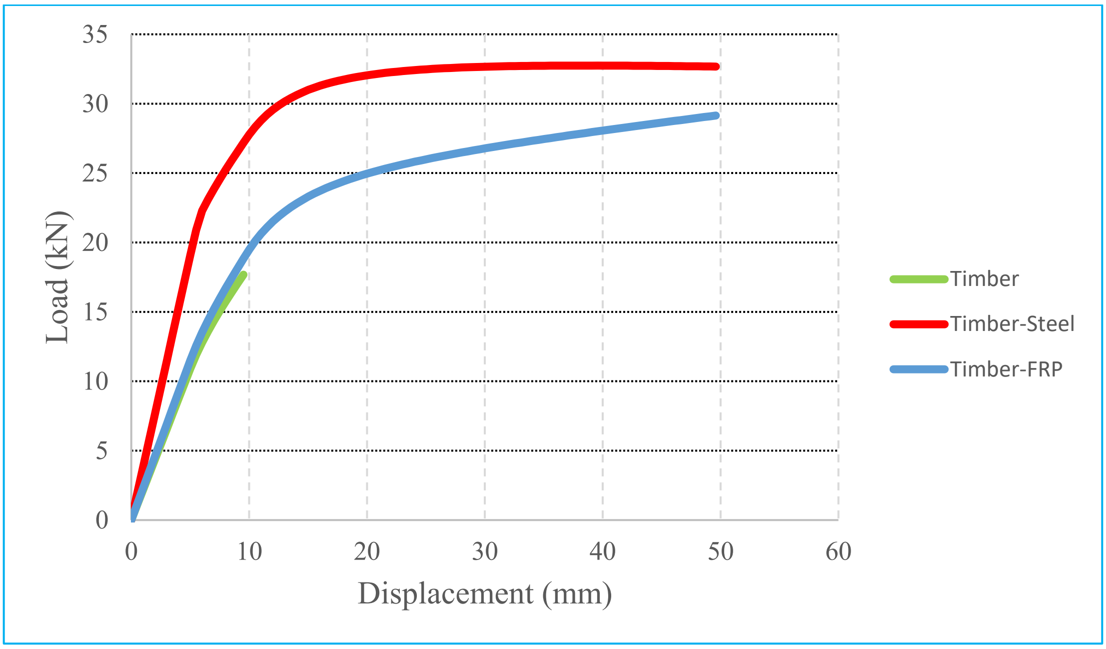

Fig. 4. Load-displacement curves of the beams

5. Conclusion

In this study, the ductility of timber structures is briefly discussed. The ductile potential of timber beams, particularly based on their compressive behaviour, is critically examined. To assess the ductility, section analysis was employed. To construct the load-displacement curve, the moment-curvature relationship, incorporating nonlinear material behaviour and fibre section idealisation, was utilised. Initially, a reference beam made of C16 grade timber was considered. Then, steel plate and FRP strengthening options were analysed. According to the study results, strengthened beams were able to undergo plastic deformation. The steel plate strengthening option also increased the initial stiffness of the beam. Based on these findings, the ductility of timber beams can be enhanced through strengthening methods. Although FRP is brittle, the plastic behaviour of timber contributes to the overall ductility of the beam. Further studies should investigate cyclic behaviour and the semi-composite interaction between the strengthening materials and timber. This study demonstrated that strengthened timber beams possess significant ductility potential. Additionally, structural details that ensure and enhance ductility should be further improved.

Acknowledgements

The authors declare that there is no conflict of interest to disclose.

References

Brühl, F., Kuhlmann, U., & Jorissen, A. (2011). Consideration of plasticity within the design of timber structures due to connection ductility. *Engineering Structures, 33*(11), 3007–3017.

European Committee for Standardization. (2004). *EN 1995-1-1: Eurocode 5 – Design of timber structures – Part 1-1: General – Common rules and rules for buildings*. CEN.

Jorissen, A., & Fragiacomo, M. (2011). General notes on ductility in timber structures. *Engineering Structures, 33*(11), 2987–2997.

Ministry of Environment, Urbanization and Climate Change. (2018). *Turkish building earthquake code (TBDY-18)*. Türkiye.

Ministry of Environment, Urbanization and Climate Change. (2024). *Regulation on the principles of design, analysis and construction of timber buildings*. Türkiye.

Ottenhaus, L. M., Jockwer, R., van Drimmelen, D., & Crews, K. (2021). Designing timber connections for ductility – A review and discussion. *Construction and Building Materials, 304*, 124621. https://doi.org/10.1016/j.conbuildmat.2021.124621

Rebouças, A. S., Mehdipour, Z., Branco, J. M., & Lourenço, P. B. (2022). Ductile moment-resisting timber connections: A review. *Buildings, 12*(2), 240.

ICEARC'25

4th International Civil Engineering & Architecture Conference
15-17 May 2025, Trabzon, Türkiye

Comparative analysis of ribbed and solid slabs in enhancing progressive collapse resistance of rc buildings following multiple column loss

Muneeb Jadallah*[1], Adem Doğangün[1]

[1] *Bursa Uludağ University, Faculty of Engineering, Department of Civil Engineering, Turkey*

Abstract. This study examines the influence of slab types on the progressive collapse resistance of reinforced concrete (RC) buildings, with a specific focus on comparing one-way ribbed slabs and solid slabs under multiple-column removal scenarios. The models 3- and 5-story RC buildings were designed following the 2018 Turkish Building Earthquake Code and analyzed using 3D nonlinear dynamic simulations via the Applied Element Method (AEM) in Extreme Loading for Structures (ELS) software. Two distinct column removal scenarios were considered to evaluate the performance of each slab type.The analysis revealed that buildings with ribbed slabs exhibit significantly greater resistance to progressive collapse than those with solid slabs. Ribbed slab systems showed lower vertical deformations (≤ 60 mm) and plastic rotations (≤ 0.01 rad), remaining within the acceptable limits defined by the Unified Facilities Criteria (UFC). In contrast, buildings with solid slabs often exceeded UFC thresholds, leading to partial or total collapse. The superior performance of ribbed slabs is attributed to their ability to engage both membrane and flexural actions, facilitating effective load redistribution during failure.Although ribbed slabs are generally considered less favorable in seismic design due to increased drift and resulting limitations on story height, their behavior under progressive collapse differs substantially. These findings underscore the potential of ribbed slabs to enhance the resilience of RC buildings under extreme loading. The study advocates for further research on ribbed slab systems to refine design strategies and improve structural safety against progressive collapse.

Keywords: Progressive Collapse; Reinforced concrete; Ribbed slab; Solid slab; Applied element method (AEM)

1. Introduction

The Unified Facilities Criteria (UFC) defines progressive collapse as "a chain reaction of failure of building members to an extent disproportionate to the original localized damage." Such failures can result in the collapse of upper floors onto lower ones. Various factors can lead to column loss in reinforced concrete (RC) structures, including vehicle impacts, earthquakes, and explosive blasts. Several notable progressive collapse incidents have occurred globally, such as the Ronan Point apartment collapse in the UK (1968), the Alfred P. Murrah Federal Building in Oklahoma City (1995), and the World Trade Center in New York City (2001). These events have prompted structural engineers to develop and improve design methodologies aimed at preventing or minimizing the effects of progressive collapse.

Design guidelines such as UFC (2009) and GSA (2003) have been established to address progressive collapse mechanisms. In this study, the UFC 2009 guidelines are employed to assess the response of RC buildings under simultaneous removal of multiple columns, including corner and interior columns. Numerical models were developed using the Applied Element Method (AEM) in the Extreme Loading for Structures (ELS) software (ASI, 2004), and structural designs were based on the Turkish Building Earthquake Code (TBEC-2018).

Previous studies investigating progressive collapse mechanisms include both experimental testing and numerical modeling approaches. With increasing threats such as war, strong earthquakes, and terrorist attacks, scenarios involving the loss of more than one column are becoming more relevant. Such scenarios often lead to the failure of a large portion or the entirety of a building. This paper investigates the potential of RC slab systems, particularly ribbed versus solid slabs, in enhancing progressive collapse resistance. The analysis is conducted using the Alternative Path Method, a widely adopted direct design approach.

* Corresponding author, E-mail: m.jad@cst.ps

https://doi.org/10.31462/icearc2025_ce_sme_217

golden light publishing

Pachenari et al. (2013) modeled a multistory RC building using nonlinear static and dynamic analysis and found that static analysis tends to overestimate shear forces compared to dynamic analysis. Kim and Kim (2009) studied 2D steel moment frames and concluded that an increased number of stories tends to reduce the progressive collapse potential. Gamaniouk (2014) analyzed 2D steel frames of various heights and observed that taller structures developed fewer plastic hinges, and the use of bracing was ineffective due to a lack of continuity in the models.

Kim et al. (2011) examined eight different bracing configurations in 2D steel frames using FEM analysis and found that inverted V-bracing exhibited the best ductile behavior under progressive collapse. Nassir et al. (2019) studied a multi-story building under single and multiple column removal scenarios, finding that dual column loss, especially at corner and edge locations, was more critical. Bhatta (2023) demonstrated experimentally that infill walls significantly improve resistance to progressive collapse.

Yi et al. (2008) tested a one-third scale RC frame under quasi-static loading and found failure at a displacement of 43.6 cm and rotation of 10.3°, with a capacity exceeding the plastic limit state by 1.4 times. Sasani et al. (2008) highlighted the importance of beam reinforcement in resisting collapse after interior column loss. Su (2009) studied 12 RC beam-column specimens under quasi-static loading and showed that beams with higher span-to-depth ratios or longitudinal reinforcement ratios exhibit greater load resistance due to enhanced catenary action (CAA).

Farhang Vesali et al. (2013) assessed the influence of longitudinal and transverse reinforcement and found that stirrups have a minor effect on CAA. Yu and Tan (2013) investigated seismic detailing and span-depth ratios and concluded that higher ratios lead to faster engagement of catenary action. Alogla et al. (2016) showed that adding mid-layer longitudinal reinforcement improves beam ductility. Dmitriev and Lalin (2021) compared different analysis methods and confirmed that nonlinear dynamic analysis, such as that used in AEM, is more accurate and consistent with experimental results.

As highlighted in the literature review, most existing studies on progressive collapse primarily focus on single-column removal scenarios in buildings with solid or flat slabs. However, research on the behavior of ribbed slab systems, particularly under multiple-column removal conditions, remains limited. This gap emphasizes the need for further investigation into the performance of ribbed slabs and a comparative assessment with solid slabs to evaluate their effectiveness in enhancing the progressive collapse resistance of RC structures.

2. Model analysis

This study follows the guidelines provided by the Unified Facilities Criteria (UFC) (2009), which outlines two main approaches for progressive collapse analysis: the direct design method and the indirect design method. Among the direct methods, the Alternative Path Method (APM) is the most widely used by researchers. APM allows the load from a failed column to be redistributed to adjacent columns through connecting beams.

Following UFC 2009, the applied load depends on the selected analysis type, static or dynamic. In this study, nonlinear dynamic analysis is adopted, and the load combination used is 1.2DL + 0.5LL, where *DL* represents the dead load and *LL* the live load. UFC guidelines assume that the failure of a primary structural element (e.g., a column) occurs suddenly, simulating an extreme event.

To simulate the behavior of the RC buildings under progressive collapse, the Applied Element Method (AEM) is utilized in this research. While most previous studies have used the Finite Element Method (FEM), AEM offers a more comprehensive approach, as it models the entire structural response from the initial loading phase through to complete failure. AEM uniquely combines the strengths of both FEM (before element separation) and the Discrete Element Method (DEM) (after separation occurs).

In AEM, each structural component is divided into a mesh of small elements interconnected by springs representing material stiffness and interaction forces, as shown in Fig. 1. These springs simulate the stress–strain relationship between adjacent elements and can fail under extreme loading, allowing for realistic modeling of structural separation. Each element possesses six degrees of freedom, three translational and three rotational, as depicted in Fig. 2.

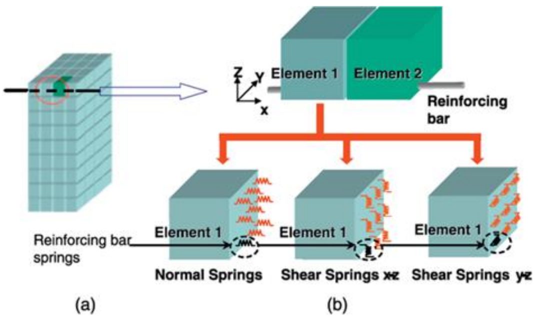

Fig.1 Element of structure modeled by AEM

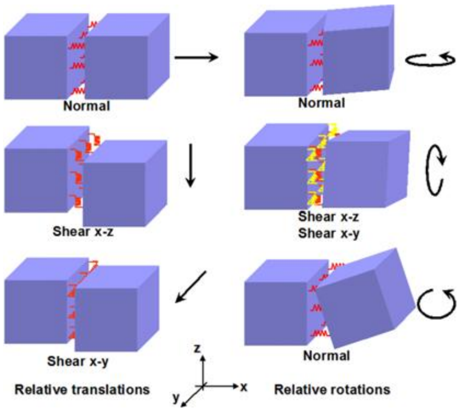

Fig. 2 Element degrees of freedom

3. Methodology of work

The primary objective of this study is to evaluate the progressive collapse resistance of 3-story and 5-story reinforced concrete (RC) buildings, designed following TBEC-2018, under scenarios involving the removal of two external columns. The investigation compares the structural performance of two slab systems, solid slabs and ribbed slabs, in resisting progressive collapse. Various scenarios of removing multiple columns will be studied in this paper using the extreme loading element program (ELS).

3.1. Description of the model

A 3 and 5-story RC 3D structure with solid slab and ribbed slab, as shown in Fig. 3, is analyzed considering various scenarios of removing columns using ELS software. Table 1 shows the general properties of the RC structure elements; Table 2 shows the designed dimensions of the RC structures.

Table 1: General properties and dimensions of RC structure

No.	Description	Value
1.	Concrete Grade	C30
2.	Steel Grade	F420
3.	Story height	3.2m
4.	Span distance between columns – Center to Center –	6.0m
5.	Live load	0.20 ton/m^2
6.	Dead Load (covering material + equivalent partition load)	0.362 ton/m^2
7.	Analysis type	Nonlinear Dynamics Analysis

Table 2: Design of RC structure

<table>
<tr><td colspan="7">Solid Slab</td></tr>
<tr><td colspan="2" rowspan="2">Story No.</td><td colspan="2">Column</td><td rowspan="2">Shear Wall</td><td rowspan="2">Beam mm</td><td rowspan="2">Slab Thickness mm</td></tr>
<tr><td>External Column Dimension(mm)</td><td>Internal Column Dimension(mm)</td></tr>
<tr><td>3-Story</td><td>1st.—3th.</td><td>400x400</td><td>450x450</td><td>2000x300</td><td>250x500</td><td rowspan="2">150</td></tr>
<tr><td>5-Story</td><td>1st.—5th.</td><td>450x450</td><td>500x500</td><td>2500x300</td><td>250x500</td></tr>
<tr><td colspan="7">Ribbed Slab</td></tr>
<tr><td colspan="2" rowspan="2">Story No.</td><td colspan="2">Column</td><td rowspan="2">Shear Wall</td><td rowspan="2">Beam mm</td><td rowspan="2">Slab Thickness mm</td></tr>
<tr><td>External Column Dimension(mm)</td><td>Internal Column Dimension(mm)</td></tr>
<tr><td>3-Story</td><td>1st.—3th.</td><td>400x400</td><td>450x450</td><td>2000x300</td><td>600x300
400x300</td><td rowspan="2">300</td></tr>
<tr><td>5-Story</td><td>1st.—5th.</td><td>450x450</td><td>500x500</td><td>2500x300</td><td>600x300
400x300</td></tr>
</table>

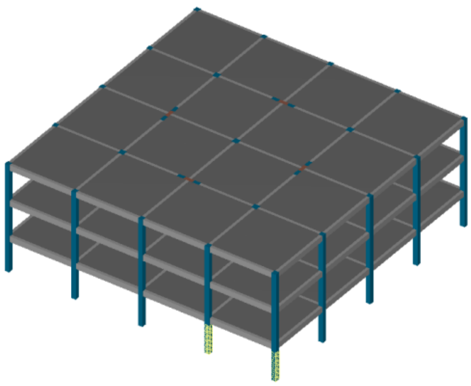

3-Floors – Solid Slab

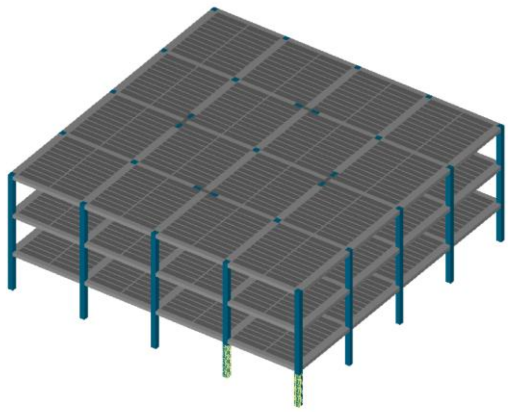

3-Floors – Ribbed Slab

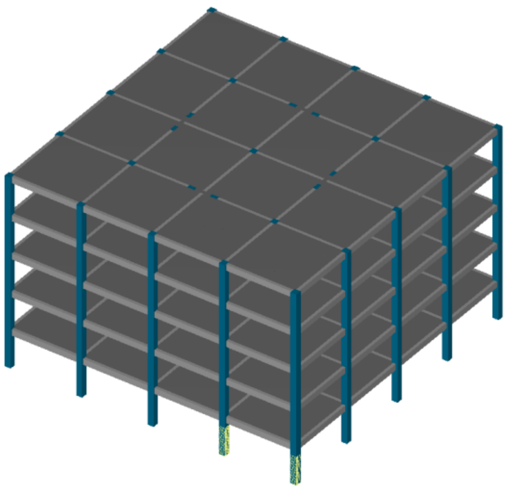

5-Floors – Solid Slab

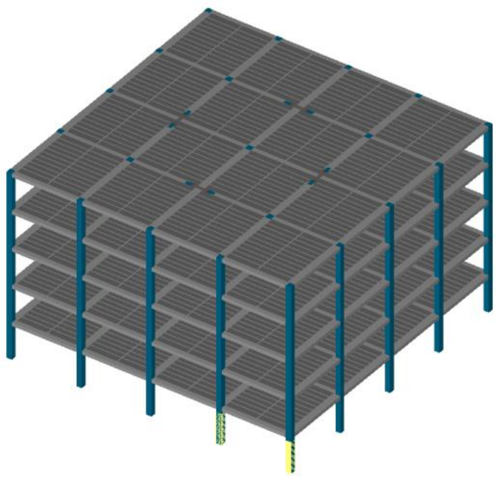

5-Floors – Ribbed Slab

Fig.3. 3D RC structure for 3 and 5-story

In this study, multiple-column removal scenarios were considered by simultaneously removing two columns, one located at the corner and the other at the preultimate position, as illustrated in Fig. 3. This approach was applied to both 3-story and 5-story RC building models with solid and ribbed slab systems.

4. Results and discussion

The progressive collapse analysis of reinforced concrete (RC) frame structures with shear walls was performed using the *Extreme Loading for Structures* (ELS) software. A simulation duration of one second was used for all column removal scenarios, which was sufficient to capture the peak vertical displacement or to observe the full cycle of vertical motion at the point of column removal. This duration proved effective for evaluating structural behavior under progressive collapse conditions for both solid and ribbed slab systems across all scenarios.

Fig. 4 presents the vertical displacement results for the 3-story and 5-story models under the removal of two ground-floor columns, one at the corner and one at the preultimate position. The analysis revealed substantial differences in the structural response based on the slab type.

Solid slab systems exhibited a more brittle behavior under column loss, where a large portion of the structure experienced partial failure. The inability of solid slabs to effectively redistribute loads following sudden column loss led to excessive deformation and local collapse, highlighting their vulnerability in progressive collapse scenarios involving multiple column removals.

In contrast, ribbed slab systems showed significantly improved performance. Both the 3-story and 5-story ribbed slab models remained stable throughout the analysis period, with no signs of collapse or excessive damage. The 5-story ribbed slab model demonstrated a maximum vertical displacement below 60 mm, and all observed plastic rotations remained under 0.0035 radians (as illustrated in Fig. 5), which is well below the UFC's permissible limit of 0.063 radians. This confirms that ribbed slab systems have superior energy absorption and load redistribution capacity under extreme loading conditions, making them more resilient against progressive collapse.

These findings clearly underscore the importance of slab type in the structural integrity of RC buildings during column removal events. Ribbed slabs not only performed within safe UFC-defined limits but also maintained overall structural stability, whereas solid slabs failed to do so under similar conditions.

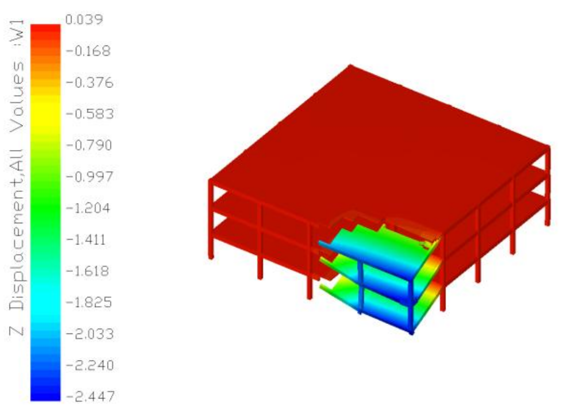

Vertical displacements (m) 3-Floors – Solid Slab

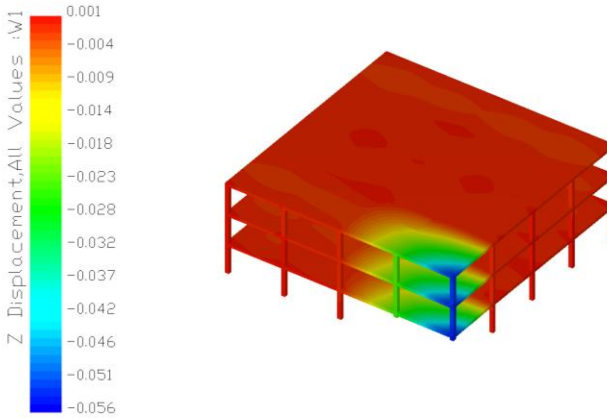

Vertical displacements (m) 3-Floors – Ribbed Slab

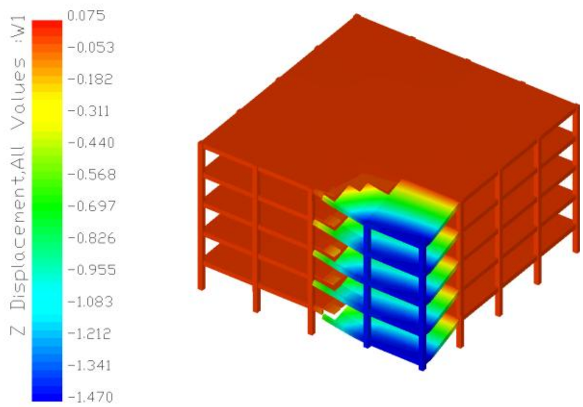

Vertical displacements (m) 5-Floors – Solid Slab

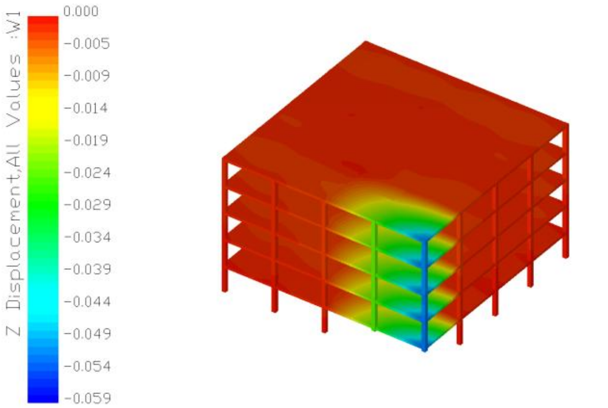

Vertical displacements (m) 5-Floors – Ribbed Slab

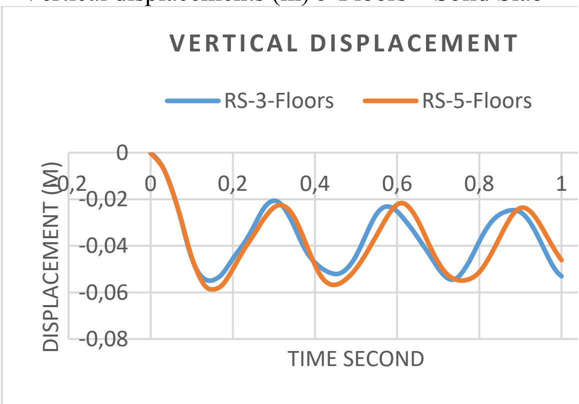

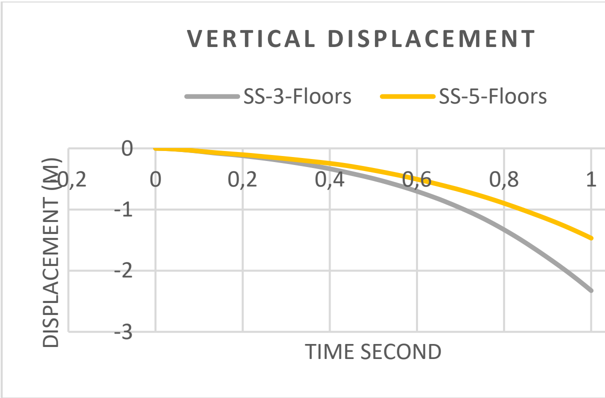

Fig. 4 Vertical displacements (m) for both solid slab and ribbed slab in the case of multiple column removal scenarios on the ground floor.

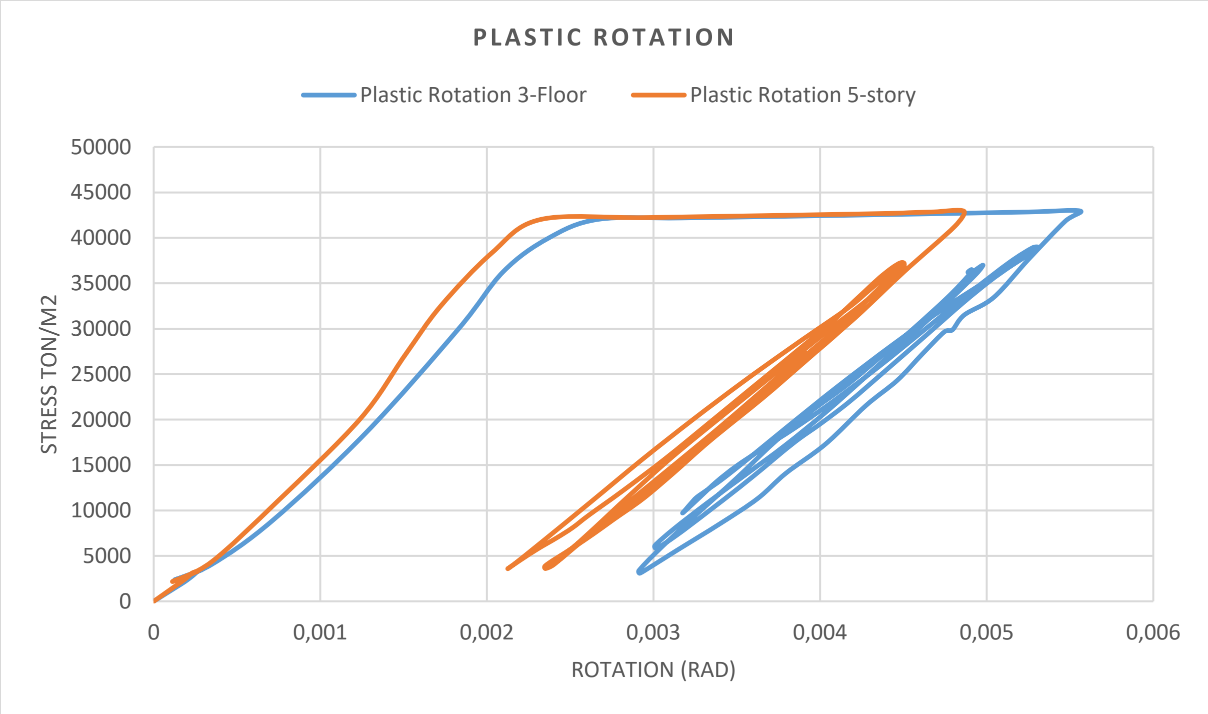

Fig. 5. Plastic rotation for ribbed slab in the case of multiple column removal scenarios on the ground floor.

5. Conclusion

This study investigated the progressive collapse behavior of reinforced concrete (RC) buildings designed in accordance with the Turkish Building Earthquake Code (TBEC-2018), focusing on two different slab systems, solid and ribbed slabs, under scenarios involving the sudden removal of two ground-floor columns. The analyses were performed using the Alternative Path Method (APM) in the Extreme Loading for Structures (ELS) software, with a dynamic load combination as recommended by UFC guidelines.

The key findings of this study can be summarized as follows:

- Slab type plays a critical role in progressive collapse resistance. Buildings with ribbed slabs exhibited superior performance compared to those with solid slabs when subjected to multiple column removal scenarios.
- Solid slab systems showed vulnerability to local collapse, where the structure was unable to redistribute loads effectively after the sudden loss of support elements. This led to large displacements and partial structural failure.
- Ribbed slab systems maintained structural integrity under all tested scenarios. In the 3-story and 5-story building models, maximum vertical displacements remained below 60 mm, and plastic rotations were significantly lower than the UFC limit of 0.063 radians, demonstrating the ribbed slabs' ability to dissipate energy and redistribute internal forces more effectively.
- The use of AEM in this study provided valuable insights into both the global and local failure mechanisms, offering an advantage over conventional FEM approaches in capturing progressive collapse phenomena.

In conclusion, ribbed slab systems offer enhanced robustness against progressive collapse in RC buildings, especially under multiple column removal scenarios. These results highlight the need to consider slab configuration as a key design parameter in the assessment and mitigation of progressive collapse risks, particularly for mid-rise structures designed under TBEC-2018.

Acknowledgments

We gratefully acknowledge the support provided by the Bursa Uludağ University's BAP project number FDK-2025-2169

We express our deep appreciation to Applied Science International, LLC (ASI) for their valuable contributions.

References

Alogla, K., Weekes, L., & Augusthus-Nelson, L. (2016). A new mitigation scheme to resist progressive collapse of RC structures. *Construction and Building Materials, 125*, 533–545.

Applied Science International, LLC. (2004). *Applied Science International, ASI*. https://www.appliedscienceint.com/ [Accessed 2024].

Bhatta, S. Y. (2023). Numerical modelling of structural behavior of RC frames with and without infill walls subjected to progressive collapse. *Journal of Civil Engineering and Construction, 12*(3), 111–123.

Dmitriev, A. N., & Lalin, V. V. (2021). Comparison of different procedures for progressive collapse analysis of RC flat slab structures under corner column loss scenario. *Buildings, 11*(9), 405.

FarhangVesali, N. V. (2013). Development of arching action in longitudinally-restrained reinforced concrete beams. *Construction and Building Materials, 47*, 7–19.

Gamaniouk, T. (2014). *Parametric analysis of progressive collapse in high-rise buildings* (Doctoral dissertation, Massachusetts Institute of Technology).

General Services Administration (GSA). (2003). *Progressive collapse analysis and design guidelines for new federal office buildings and major modernization projects*. U.S. Government, Washington, DC.

Kim, J., & Kim, T. (2009). Assessment of progressive collapse-resisting capacity of steel moment frames. *Journal of Constructional Steel Research, 63*(1), 169–179.

Kim, J., Lee, Y., & Choi, H. (2011). Progressive collapse resisting capacity of braced frames. *The Structural Design of Tall and Special Buildings, 20*(2), 237–270.

Nassir, M., Yang, J., Nyunn, S., Azim, I., & Wang, F. L. (2019). Progressive collapse analysis of multi-story building under the scenario of multi-column removal. *E3S Web of Conferences, 136*, 04030. EDP Sciences.

Pachenari, A., Keramati, A., & Pachenari, Z. (2013). Investigation of progressive collapse in intermediate RC frame structures. *The Structural Design of Tall and Special Buildings, 22*(2), 116–123.

Sasani, M. (2008). Progressive collapse analysis of an RC structure. *The Structural Design of Tall and Special Buildings, 17*(4), 737–771.

Su, Y. T. (2009). Progressive collapse resistance of axially-restrained frame beams. *ACI Structural Journal, 106*(3).

TBEC. (2018). *Turkish Building Earthquake Code*. Ankara, Turkey.

UFC 4-023-03. (2009). *Unified Facilities Criteria: Design of buildings to resist progressive collapse*. Department of Defense, USA.

Yi, W. J., He, Q. F., Xiao, Y., & Kunnath, S. K. (2008). Experimental study on progressive collapse-resistant behavior of reinforced concrete frame structures. *ACI Structural Journal, 103*(4), 433–442.

Yu, J., & Tan, K. H. (2013). Structural behavior of RC beam-column subassemblages under a middle column removal scenario. *Journal of Structural Engineering, 139*(2), 233–250.

Nonlinear analysis of flush end-plate beam-to-column connections under cyclic loading

Alper Demir*[1], Cüneyt Vatansever[1]

[1] *Istanbul Technical University, Department of Civil Engineering, Istanbul, Türkiye*

Abstract. This study numerically investigates the nonlinear cyclic behavior of flush end-plate beam-to-column connections, which are widely used as semi-rigid structural connections. Two configurations, a two-bolt and a four-bolt semi-rigid partial-strength connection, were modeled using ABAQUS software to examine their moment-rotation behavior under cyclic loading. To validate the finite element modeling methodology, experimental data from a previously tested two-bolt flush end-plate connection were utilized. The numerical model accurately replicated the cyclic behavior observed experimentally, with deviations of 1.30% and 6.1% in moment capacity and initial stiffness, respectively. Following validation, finite element analyses were conducted to evaluate the nonlinear cyclic performance of both configurations. The moment capacities of the connections were calculated using the yield line method specified in AISC 341-16 and the component method outlined in Eurocode 1993-1-8. The initial stiffness values were also determined using the component method. Comparative analyses showed that the yield line method underestimated moment capacities by 13.6%, 20.8%, and 52.8% for the two-bolt and four-bolt configurations, respectively, relative to finite element results. Similarly, the component method underestimated moment capacities by 11%, 17.7%, and 31%. Conversely, initial stiffness predictions by the component method exceeded finite element results by 20%, 26%, and 37% for the respective configurations. These findings highlight the conservative nature of both the yield line and component methods in estimating connection performance and emphasize the need for refined analytical approaches to accurately predict the cyclic behavior of flush end-plate connections.

Keywords: Steel connections; Finite element analysis; Cyclic loading; Nonlinear analysis

1. Introduction

Flush end-plate beam-to-column connections are widely used in gravity load frames due to their simplicity, economy, and ease of fabrication with a wide design range to satisfy different structural demands. These connections, typically classified as semi-rigid and partial-strength, offer a favorable balance between stiffness and ductility while enabling energy dissipation during seismic events. Unlike fully rigid joints, semi-rigid connections may be used to provide plastic deformations that can enhance global structural performance by delaying plastic hinge formation in beams and reducing force demands on adjacent members.

This study investigates the nonlinear cyclic behavior of two semi-rigid flush end-plate connections designed using a thin-plate design philosophy. The aim is to dissipate seismic energy through plastic deformation caused by yielding of the end-plate while keeping bolt stresses below their tensile capacity under prying forces. Two different configurations, a two-bolt and a four-bolt connection, were analyzed numerically using ABAQUS finite element software under cyclic loading protocols consistent with AISC 341-16.

A nonlinear material model based on true stress-strain behavior was adopted for S275 structural steel and grade 10.9 high-strength bolts. The numerical model was validated using experimental data for a two-bolt flush end-plate connection. Subsequently, the validated models were used to analyze the moment-rotation behavior and assess the effectiveness of Eurocode's component method and AISC's yield line theory in predicting moment capacity and initial stiffness. The results provide insights into the conservative nature of current design methodologies and their implications for performance-based seismic design.

2. Materials and methods

The investigated connections employ a thin end-plate intended to yield before bolt fracture. This design philosophy aims to localize plastic deformation in the end-plate, effectively forming a plastic hinge at the connection zone and enhancing the seismic energy dissipation capacity of the joint. Two configurations were studied: FEB-2B, two-

* Corresponding author, E-mail: alper.demir@itu.edu.tr

https://doi.org/10.31462/icearc2025_ce_sme_223

golden light publishing

bolt flush end-plate connection, and FEP-4B, four-bolt flush end-plate connection. Both connections are aimed to be classified as semi-rigid partial-strength, as their rotational stiffness and moment capacity are less than those of the connected beams, thereby conforming to Eurocode 1993-1-8 classification.

The finite element analysis was conducted using ABAQUS/Standard, with a focus on capturing the complex cyclic behavior of the connections. The model includes detailed geometry of the beam, column, end-plate, bolts, and welds. Solid elements (C3D8R) were used for all components. Contact interactions between end-plates and column flanges, including nut, hole edge, bolt head and bolt shank, as well as bolt pretension, were explicitly modeled.

2.1. Connection design

The connections investigated in this study are aimed to display thin-plate behaviour, where the end-plate yielding governs the connection strength. The two flush end-plate connections used in this study are shown in Fig. 1.

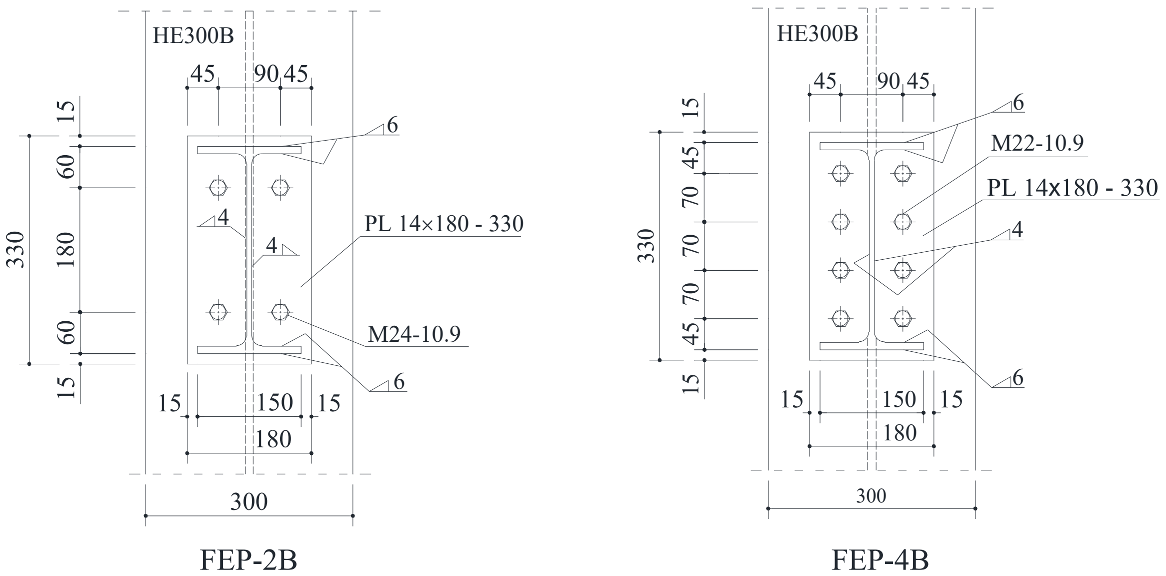

Fig. 1. Flush end-plate configurations

The column ends are assumed to be pinned, restricting displacements and axial torsion. Beam displacement is applied with out-of-plane displacement restricted.

2.2. Material models

The engineering stress-strain values are determined using the tri-linear material models (Baei et al., 2012) shown in Fig. 2. Young's Modulus and Poisson's Ratio are assumed as E = 200 GPa and v = 0.3 respectively. Yielding and ultimate strength of steel are assumed as 1.3×275=357.5 MPa, while F_y=900 MPa and F_u=1000 MPa are taken for bolts.

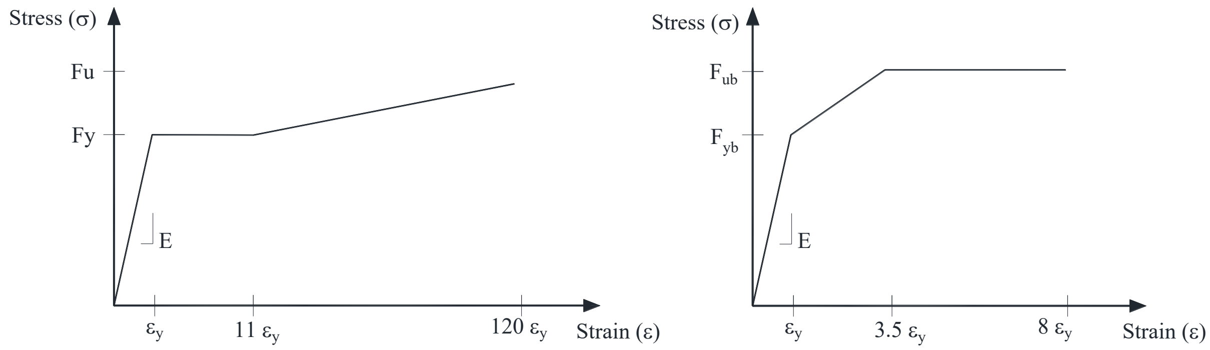

Fig. 2. Engineering stress-strain material models

After determining the engineering stress-strain curves, Equation 1 is used to obtain the true stress-strain values of both the bolt and steel material.

$$\sigma_{true} = \sigma_{eng}(1 + \varepsilon_{true}) \qquad \varepsilon_{true} = \ln(1 + \varepsilon_{eng}) \tag{1}$$

Based on the yield and ultimate stress-strain values obtained from Equation 1, the nonlinear material behavior is modeled using the relationship $\sigma = K\varepsilon^n$, as described by Kaufmann et. al. (2001). In this approach, appropriate values for the material constants K and n are determined to accurately match the nonlinear stress-strain curve. The plastic stress-strain values, observed after the yield point, are taken to use in ABAQUS as shown in Fig. 3.

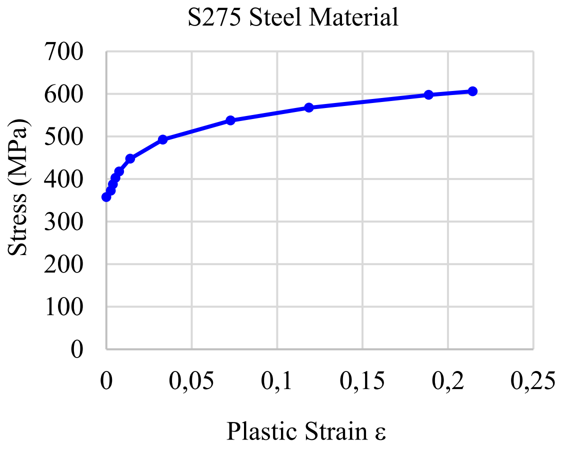

Fig. 3. Plastic stress-strain curves used in FE models

2.3. Loading history and bolt pre-tensioning

The loading history, illustrated in Fig. 4, followed the AISC 341-16 recommendations for qualification testing of beam-to-column moment connections. A symmetric cyclic displacement-controlled protocol was applied to the beam tip, incrementally increasing the amplitude of rotations until strength degradation was observed.

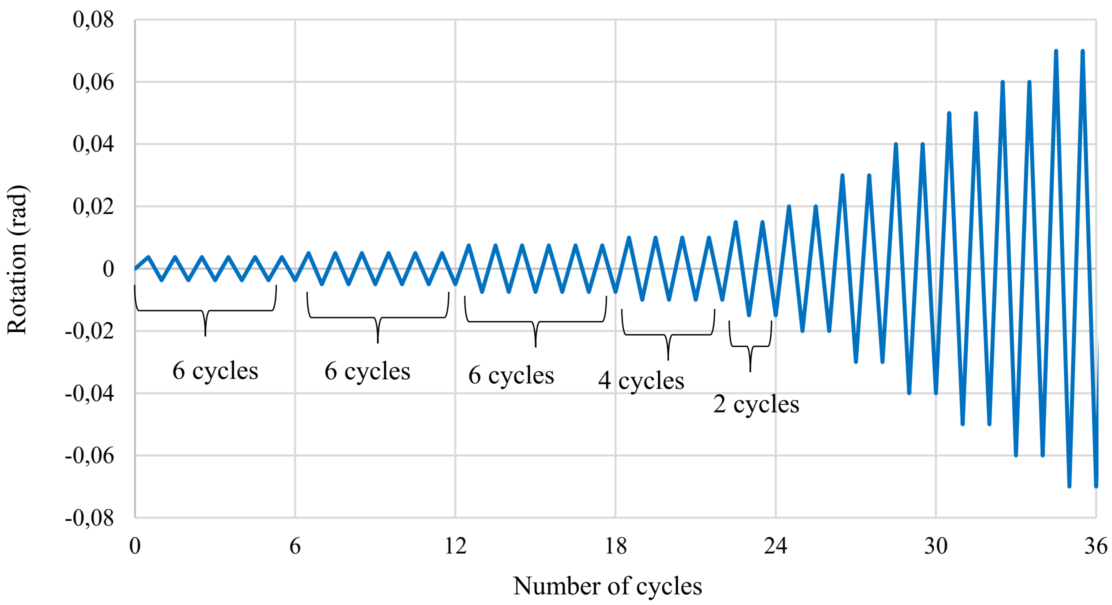

Fig. 4. Cyclic loading protocol

The cyclic loading protocol was continued until drift ratios of approximately 0.06 radians and 0.08 radians were reached for the FEP-2B and FEP-4B connections, respectively. These target drift values were selected to ensure the development of significant inelastic behavior and to assess the full cyclic performance of the connections up to the point of notable strength degradation.

Bolt pretension was simulated using ABAQUS's pre-tension section method to accurately reflect bolt clamping forces. For the M22 and M24 10.9 grade bolts, 212 kN and 247 kN bolt pre-tension force was applied to each bolt respectiely, as recomended by TCDCSS (2018).

2.4. Meshing of elements

A refined meshing approach was employed to capture localized stress concentrations and plastic deformation accurately, particularly in regions expected to undergo significant yielding. Smaller mesh sizes were applied to bolt components and end-plates, where high stress gradients were anticipated due to contact and bearing interactions. Fig. 5 illustrates the meshing scheme adopted for the end-plate and bolts, highlighting the enhanced resolution in critical areas to ensure convergence and result accuracy in nonlinear cyclic simulations.

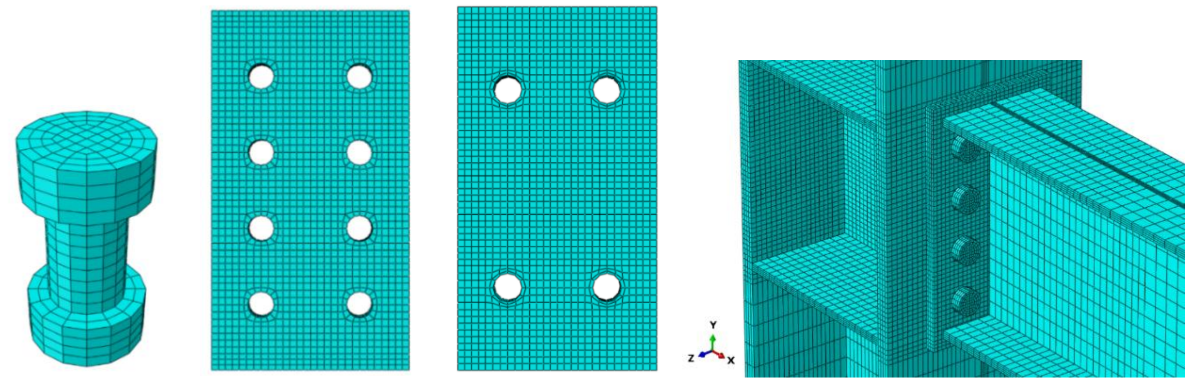

Fig. 5. Mesh sizes used in models

2.5. Surface interactions

Accurate definition of surface-to-surface contact is essential in finite element analysis, as the interaction between different connection components significantly influences the moment-rotation response of the joint. In this study, individual contact interactions were explicitly defined for critical interfaces, including:

- Between the bolt head and the end-plate
- Between the nut and the column flange
- Between the bolt shank and bolt hole edge
- Between the end-plate and the column flange

Normal contact behavior was modeled using the penalty formulation, allowing limited interpenetration with appropriate contact stiffness to simulate compressive behavior. Tangential contact behavior was modeled using the penalty method with a friction coefficient of 0.3 applied to all interfaces. This friction value was selected based on typical steel-to-steel contact conditions, ensuring realistic representation of sliding resistance and load transfer mechanisms within the joint.

2.6. Finite Element Model Validation with Experimental Data

The finite element model was validated against experimental results of a previously tested two-bolt flush end-plate connection. Comparisons were made in terms of moment capacity, initial rotational stiffness and hysteretic response. Test set-up is shown in Fig. 6.

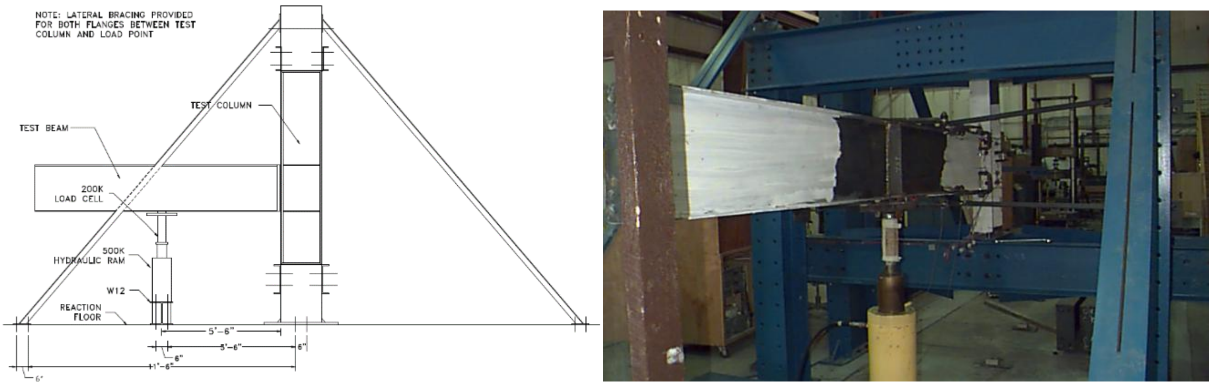

Fig. 6. Experimental setup (Boorse, 1999)

The connection detail is illustrated in Fig. 7. The connecion is named F1-3/4-3/8-16 indicating the bolt diameter (3/4 inches, or 19.05 mm), end-plate thickness (3/8 inches, or 9.525 mm) and beam depth (16 inches, or 406.4mm).

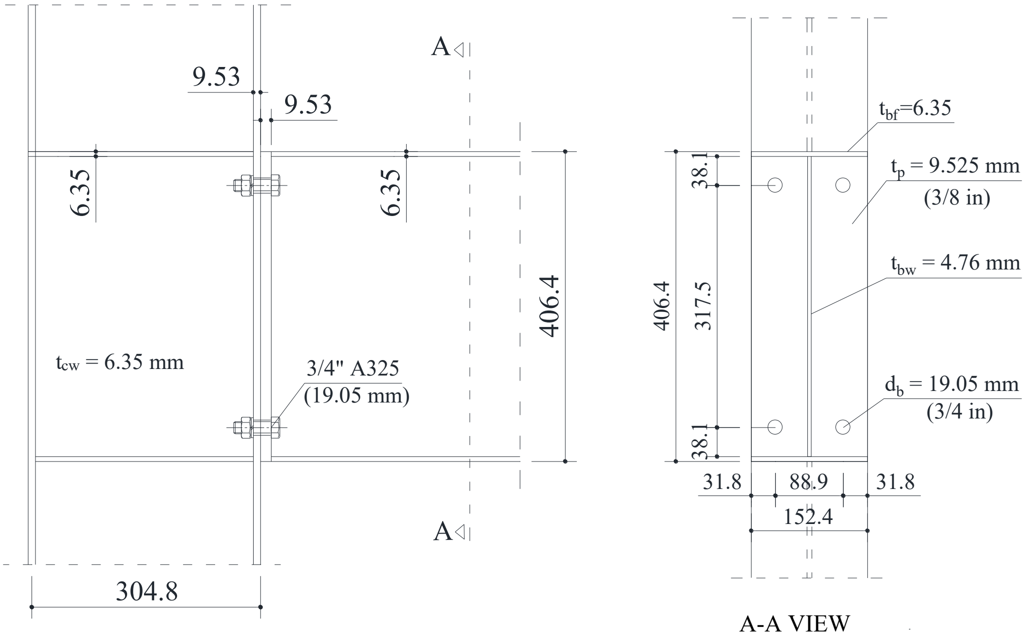

Fig. 7. Connection detail

Grade 50 steel is used for all components, while the yield and tensile strength values obtained from coupon tests are used to identify detailed stress-strain behaviour of the connection elements, using the same material model shown in Fig. 1. Bolt pretension force of 137kN is applied to the middle section of bolts.

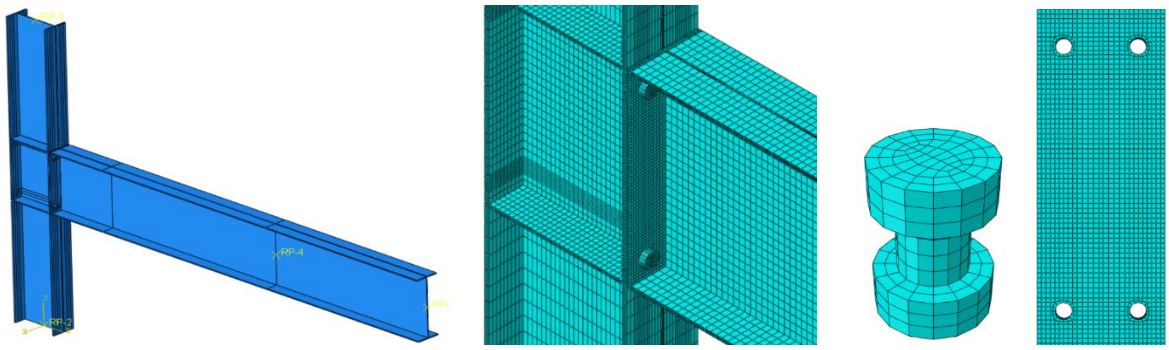

Fig. 8. Finite element model and meshing of the elements involved in the connection

Moment-rotation curves obtained from the experimental work is compared with the FEA results obtained in this study as shown in Fig. 9.

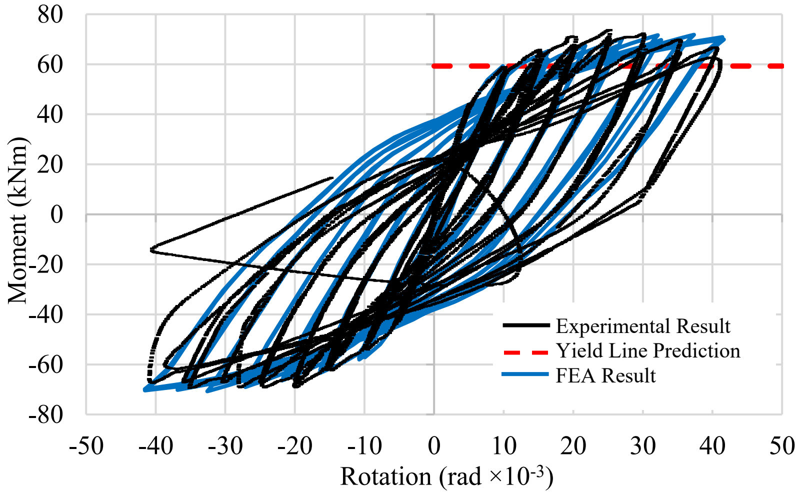

Fig. 9. Moment-rotation curve comparison between FEA and experimental results

The FE model accurately captured the experimental behavior, with only 0.6% difference in moment capacity and 3.5% difference in initial stiffness, confirming the reliability of the modeling methodology.

While the FEA result accurately reflects the initial stiffness and maximum moment capacity, the unloading stiffness is differing close to last cycles, most likely due to the material properties. Since the detailed material properties are not explained in the experimental work such as modulus of elasticity and curve.

3. Analytical methods for comparison

Two analytical methods were used to estimate the performance of the connections: AISC Yield Line Theory (AISC 341-16) which provides a simplified analytical estimation of plastic moment capacity based on yield mechanisms in the end-plate and Eurocode component method (EN 1993-1-8) used to estimate both moment capacity and initial stiffness by modeling the joint as an assembly of individual mechanical components (e.g., bolts in tension, end-plate in bending, column flange in compression). These methods were compared against finite element analysis to assess their accuracy and conservatism. The maximum end-plate yielding strength ($\phi_b M_{pl}$) is calculated by using Equation 2.

$$\phi M_n = \phi_b M_{pl} = \phi_b F_y t_p^2 Y_p \tag{2}$$

Where Y_p stands for yield line parameter dependant on the geometry and F_y and t_p represent end-plate's yield stress and thickness. Equations 3 and 4 are used to obtain the yield line parameter Y_p for the 2-bolted and 4-bolted connections respectively.

$$Y_p = \frac{b_p}{2}\left[h_1\left(\frac{1}{p_{fi}}+\frac{1}{s}\right)\right]+\frac{2}{g}\left[h_1\left(p_{fi}+s\right)\right] \tag{3}$$

$$Y_p = \frac{b_p}{2}\left[h_1\left(\frac{1}{p_{fi}}\right)+h_2\left(\frac{1}{s}\right)\right]+\frac{2}{g}\left[h_1\left(p_{fi}+0.75p_b\right)+h_2\left(s+0.25p_b\right)\right]+\frac{g}{2} \tag{4}$$

The parameters h_1 and h_2 are the moment arms for first and second bolt group, g is the bolt gauge and b_p is the width of the plate. Equation 5 is used to calculate the geometric paremeter s.

$$s = \frac{1}{2}\sqrt{b_p g} \tag{5}$$

As another limit state, the bolt rupture strength is calculated considering the prying forces in action for the thin-plate design. Equation 6 is used to determine the connection strength in this case.

$$\phi M_n = \phi_r M_q = \phi_r \sum \alpha_i P_{qi} n_i h_i \tag{6}$$

Each horizontal bolt group are considered seperately to reduce the tensile strength with maximum possible prying forces. The number of bolts in the bolt group, n_i, is taken as 2 for both 2-bolted and 4-bolted connections. The moment arm h_i is the distance between the bolt axis to the center of the compression flange of the beam. The moment capacities calculated for end-plate yielding and bolt rupture considering the prying forces are shown in Table 1.

Table. 1. Moment capacity predictions based on the yield line theory

Connection	End-plate yielding (kNm)	Bolt rupture with prying action (kNm)
F1-3/4-3/8-16	63.18	71.51
FEP-2B	85.08	96.52
FEP-4B	110.96	150.60

End-plate yielding governs the flexural strength for all the connections as seen in Table 1. The initial stiffnesses calculated using component method are shown in Table 2. In order to classify the connections as semi-rigid, the initial stiffness of the connections should be at least 25% of the beam's stiffness.

Table. 2. Initial stiffness and moment capacity predictions calculated using component method

Connection	Calculated initial stiffness $S_{j,ini}$ (kNm/rad)	Initial stiffness of the beam S_b (kNm/rad)	$S_{j,ini}/S_b$	Connection flexural strength calculated M_j (kNm)	Beam flexural strength M_b (kNm)	M_j/M_b
F1-3/4-3/8-16	11578.40	5809.64	1.99	64.67	262.97	0.25
FEP-2B	13690.53	5570.67	2.46	87.35	269.41	0.32
FEP-4B	17305.91		3.11	129.29		0.48

As it can be seen from Table 2, all connections satisfy the partial strength and semi-rigid classifications, which aligns well with the dissipative connection approach aimed.

4. Results and discussion

Both connection configurations exhibited stable cyclic performance with distinct hysteretic loops. The moment-rotation curves obtained from the finite element analyses are shown in Fig. 10. Predictions based on the yield line theory are also compared with the FEA results, which shows the conservative strength predictions.

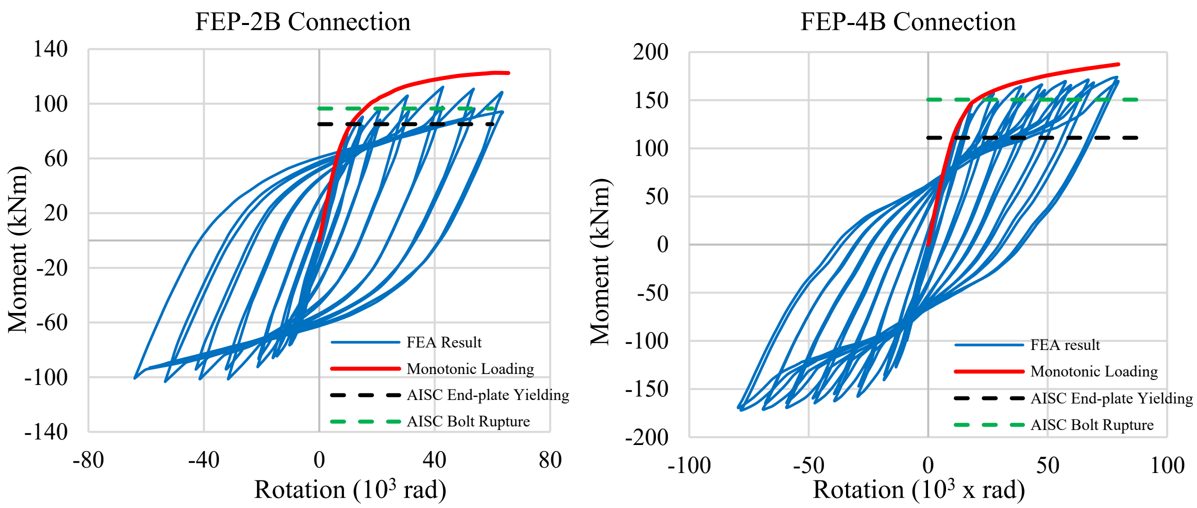

Fig. 10. Moment-rotation curves obtained from FEA

The green line represents bolt rupture with prying action while dashed black line represents end-plate yielding strength in Fig. 10. according to AISC. Monotonic moment-rotation curves are shown in red, with a close agreement to the backbone curve of the cyclic loading, which is shown in blue.

The finite element analysis results can be summarized as follows:

- Configuration FEP-2B (2-bolt): This configuration demonstrated a ductile response, characterized by substantial plastic deformation concentrated in the end-plate. The unloading stiffness was observed to be higher than that of the 4-bolt configuration. Ultimate strength was attained when the end-plate underwent full plasticization.
- Configuration FEE-4B (4-bolt): This configuration also exhibited a ductile behavior; however, it achieved higher initial stiffness and greater energy dissipation capacity compared to the 2-bolt configuration.

The hysteresis loops indicated stable and symmetric energy dissipation, verifying the effectiveness of the thin-plate design in achieving controlled plastic hinge formation.

4.1. Moment-rotation behavior

The moment-rotation curves demonstrated nonlinear behavior characterized by; an initial elastic region, a gradual transition into plasticity, a peak moment capacity followed by slight strength degradation.

The validated FE model closely matched the experimental moment-rotation behavior. For the four-bolt configuration, the moment capacity increased by approximately 35% compared to the two-bolt configuration, primarily due to improved force transfer and reduced local yielding.

4.2. Moment capacity comparison

The moment capacities derived from the finite element model were compared to predictions by the yield line and component methods. The results are summarized below in Table 3.

Table. 3. Moment capacity comparisons

Connection	Experimental moment capacity (kNm)	FEA moment capacity (ABAQUS, kNm)	Yield line theory (AISC, kNm)	Component method (Eurocode, kNm)
F1-3/4-3/8-16	72.73	71.80	63.18	64.67
FEP-2B	-	102.82	85.08	87.35
FEP-4B	-	169.52	110.96	129.29

The results confirm that both analytical methods underestimate the moment capacity compared to FE analysis, with deviations up to 52% and 31% for the yield line theory and component method respectively. The conservative nature of these methods is due to simplified assumptions, such as rigid body mechanisms and neglect of strain hardening effects.

4.3. Initial stiffness comparison

Initial stiffness values from finite element results were also compared with those predicted by the Eurocode component method in Table 4.

Table. 4. Initial Stiffness comparisons

Connection	Experiment result (kNm/rad)	Component method ($S_{i,CM}$) (kNm/rad)	FEA result ($S_{i,FEM}$) (kNm/rad)	$S_{i,CM}$ /$S_{i,FEM}$
F1-3/4-3/8-16	10235	11578.40	9647	1.20
FEP-2B	-	13690.53	10851	1.26
FEP-4B	-	17305.91	12562	1.37

The component method consistently overestimates the initial stiffness, likely due to idealized assumptions of component rigidity and lack of consideration for bolt slippage and localized deformation in plates.

5. Conclusions

This study presented a detailed numerical investigation of two semi-rigid flush end-plate connections subjected to cyclic loading. The main conclusions are:

- Thin-plate design philosophy, which promotes yielding of the end-plate while preventing bolt failure, effectively facilitates plastic hinge formation and energy dissipation.
- Finite element models in ABAQUS, using nonlinear true stress-strain relationships, accurately captured the cyclic behavior of the connections, as validated against experimental results.
- Yield line theory and the component method significantly underestimated the moment capacity of the connections by up to 52%, underscoring their conservative nature.
- The Eurocode component method overestimated initial stiffness by up to 37% due to simplified assumptions and exclusion of deformation mechanisms.

These findings emphasize the conservative nature of current analytical methods. While such conservatism ensures safety, it may lead to overdesign or underutilization of joint capacity. Finite element modeling, although computationally intensive, offers a more accurate assessment of connection performance under realistic loading conditions.

The thin-plate design philosophy proves effective in ensuring ductile behavior and predictable plastic hinge formation. However, the disparity between analytical and numerical predictions highlights the need for refined analytical tools that incorporate nonlinear effects, material hardening, and prying action more realistically.

There is a clear need for enhanced analytical methods that can accurately predict the nonlinear cyclic behavior of semi-rigid connections for performance-based seismic design.

Future work will include parametric studies to evaluate the influence of bolt diameter, end-plate thickness, and beam/column size on connection performance, as well as potential development of modified analytical expressions based on calibrated finite element models.

References

ABAQUS. (2019). *Abaqus/CAE User's Guide*. Dassault Systèmes Simulia Corp., Providence, RI, USA.

AISC 341-16. (2016). *Seismic provisions for structural steel buildings (ANSI/AISC 341-16)*. American Institute of Steel Construction, Chicago, IL.

Baei, M., Ghassemieh, M., & Goudarzi, A. (2012). Numerical modelling of end-plate moment connection subjected to bending and axial forces. *The Journal of Mathematics and Computer Science*, 4(3), 463–472.

Boorse, M. R. (1999). *Evaluation of the inelastic rotation capability of flush end-plate moment connections* (Master's thesis). Department of Civil Engineering, Virginia Polytechnic Institute and State University.

EN 1993-1-8. (2005). *Eurocode 3: Design of steel structures – Part 1-8: Design of joints*. European Committee for Standardization, Brussels, Belgium.

Faella, C., Piluso, V., & Rizanno, G. (2000). *Structural steel semirigid connections: Design and software*. Boca Raton, FL: CRC Press LLC.

Kaufmann, E. J., Metrovich, B., & Pense, A. W. (2001). *Characterization of cyclic inelastic strain behavior on properties of A572 Gr. 50 and A913 Gr.50 rolled sections* (ATLSS Report No. 01-13). Lehigh University.

TCDCSS. (2018). *Turkish Code for Design and Construction of Steel Structures*. Republic of Turkey Ministry of Environment and Urbanization, Ankara, Türkiye.

4th International Civil Engineering & Architecture Conference
17-19 May 2025, Trabzon, Türkiye

Structural health monitoring through vibration-based feature extraction and machine learning: a comparative study of AR, VAR, and SVD methods

Mohamad Alhasan*[1], Volkan Kahya[1], Kemal Hacıefendioğlu[1], Sebahat Şimşek[1]

[1] Karadeniz Technical University, Department of Civil Engineering, 61080 Trabzon, Türkiye

Abstract. Ensuring the durability and safety of infrastructure relies heavily on SHM, which facilitates the prompt identification of structural damage.This study introduces a vision-based approach that utilizes ambient vibration measurements extracted from high-speed video recordings. Optical flow techniques are employed to track structural displacements, providing a non-contact method for vibration analysis. Three feature extraction methods Autoregressive (AR), Vector Autoregressive (VAR) and Singular Value Decomposition (SVD) are assessed for their effectiveness in identifying structural damage. Residual errors derived from these methods are used as input features for a Support Vector Machine (SVM) classifier to differentiate between healthy and damaged states. The findings reveal that AR offers the best future extraction method for ambient vibration, SVD exhibits high sensitivity in SVM but is prone to noise induced variations, and VAR captures system interactions with relatively lower sensitivity than AR. The SVM classifier demonstrates high accuracy in damage detection, highlighting the potential of video-based ambient vibration analysis combined with machine learning for reliable structural health assessment.

Keywords: Structural Health Monitoring (SHM); Support Vector Machine (SVM); Autoregressive (AR); Vector Autoregresive (VAR), Singular Value Decomposition (SVD)

---

1. Introduction

Structural Health Monitoring (SHM) plays a crucial role in ensuring the safety, functionality, and longevity of civil infrastructure. As structures age and environmental challenges increase, the demand for advanced SHM methods capable of detecting and diagnosing structural damage in real-time has intensified (Farrar et al., 2025). Traditional SHM approaches have relied on manual inspections and physics-based models that utilize sensor-collected dynamic responses to assess structural conditions (Malekloo et al., 2022). While these methods provide valuable insights, they are often labor-intensive, costly, and less effective in capturing early-stage damage (Tahat et al., 2022).

To address these limitations, modern SHM systems integrate various sensor technologies for enhanced data acquisition. Piezoelectric energy harvesters convert mechanical vibrations into electrical energy, enabling self-powered SHM in wind turbines. They are lightweight and flexible, making them ideal for dynamic environments, but their low power output restricts broader applications (Kullukçu et al., 2022). Similarly, Surface Acoustic Wave (SAW) sensors provide wireless, battery-free strain and temperature monitoring in reinforced concrete, offering localized, long-term durability but suffering from signal interference and limited range (Jeltiri et al., 2023). Radio Frequency (RF) energy-powered sensor nodes (RF-SNs) further support wireless SHM by harvesting RF energy for sustainable, maintenance-free monitoring, though signal attenuation and low power efficiency remain challenges (Luo et al., 2023).

With advancements in IoT and edge computing, smart SHM systems leverage wireless sensors, cloud computing, and AI for real-time monitoring. IoT-enabled SHM solutions provide cost-effective, remote data collection, yet cybersecurity risks and network reliability issues persist (Bhatta & Dang, 2024). MEMS-based wireless sensor networks (WSNs) offer scalable, low-cost earthquake monitoring, but power consumption and unstable data transmission limit their reliability (López-Castro et al., 2022). Similarly, MEMS accelerometers and geophone sensors, when paired with Raspberry Pi-based data loggers, enable affordable, real-time structural vibration monitoring, but their noise levels and time drift issues affect long-term accuracy (Özdemir & Kömeç Mutlu, 2024).

---

*Corresponding author, M.Sc. Student, E-mail: alhsn.mohamad1@gmail.com

https://doi.org/10.31462/icearc2025_ce_sme_226

Beyond traditional sensors, advanced SHM technologies have emerged to enhance damage detection accuracy. Field programmable gate arrays-based SHM systems, using torsional ultrasonic guided waves, allow real-time defect localization in pipelines while maintaining low power consumption. However, hardware limitations and the need for FPGA expertise restrict adoption (Patil et al., 2024). Infrared (IR) cameras detect thermal variations that indicate hidden fatigue damage and subsurface cracks, proving effective in harsh environments, though environmental fluctuations can impact accuracy (He et al., 2020). Laser vibrometers provide non-contact, high-precision vibration monitoring, but lighting conditions and airborne particles may degrade accuracy (Klun et al., 2019). Fiber optic sensors, particularly Fiber Bragg Gratings (FBGs), offer high sensitivity to strain and temperature with immunity to electromagnetic interference, yet installation complexity remains a barrier (Kinet et al., 2014; Mohapatra et al., 2022; Qiu et al., 2013). For large-scale SHM, wireless sensor networks (WSNs) support real-time, multi-node data acquisition with event-triggered sensing and edge computing, but scalability and power efficiency challenges persist (Yu et al., 2024).

While these advanced sensing techniques have significantly improved data collection, the challenge now lies in effectively interpreting the vast and complex datasets a challenge that Machine Learning (ML) methods are well positioned to address Machine Learning (ML) and Artificial Intelligence (AI) have advanced traditional Structural Health Monitoring (SHM), enhancing its capabilities in damage detection and structural anomaly classification. However, a critical challenge in ML-driven SHM arises: the selection of a suitable damage detection method. In recent years Support Vector Machines (SVMs) and Random Forests (RFs) have been widely used in structural health monitoring (SHM) for damage classification. These models excel in detecting structural anomalies based on sensor data, with Random Forests particularly effective in capturing complex vibration patterns, achieving high classification accuracy (Vélez et al., 2024). Autoencoder-based models, such as the Mechanics-Informed Autoencoder (MIAE), have shown significant improvements in structural damage detection. Li et al. (2024) introduced this model, which relies on passive sensor data to learn from the undamaged state of a structure, enhancing its ability to detect and localize unforeseen damage without requiring extensive labeled datasets. A probabilistic approach to SHM was proposed by Torzoni et al. (2024), who developed a Bayesian model updating framework combined with deep learning-based feature extraction. This method employs learnable mappings to improve damage sensitivity while reducing computational costs, making it particularly effective for long-term monitoring. Transformer-based foundation models have also emerged as powerful tools in SHM. According to Benfenati et al. (2024), these models leverage self-supervised learning to extract generalizable structural representations, significantly outperforming traditional methods in anomaly detection and traffic load estimation tasks. Reinforcement learning (RL) is another promising technique for optimizing SHM strategies. Plevris & Papazafeiropoulos (2024) demonstrated that RL models can dynamically adjust monitoring parameters, improving both detection efficiency and cost-effectiveness by learning from past decisions. These advancements highlight the versatility of machine learning in SHM, ranging from classification models to self-learning frameworks that adapt to evolving structural conditions, ultimately enabling proactive maintenance and increased infrastructure safety.

Against this backdrop, the present study aims to develop a vision-based, data-driven framework for structural diagnosis and anomaly detection by integrating optical flow techniques, advanced feature extraction methods, and Support Vector Machines (SVMs). Unlike traditional SHM methods that depend on direct sensor contact, this approach leverages high-speed video recordings to capture ambient vibrations, offering a non-contact, precise, and scalable monitoring solution. Vibration data is extracted using optical flow algorithms, specifically the Lucas-Kanade method, which tracks pixel displacement in successive video frames to estimate structural motion. This method enables high-precision displacement measurements without the need for physical sensors. In our setup, four high-resolution cameras are used to monitor predefined measurement points (MPs) marked with QR codes, ensuring accurate tracking of even minute structural displacements. To analyze the extracted displacement signals, three feature extraction techniques are evaluated for their ability to capture damage-sensitive patterns: Autoregressive (AR) model, Vector Autoregressive (VAR) model, and Singular Value Decomposition (SVD). The residual errors from these methods serve as input features for an SVM classifier, which distinguishes between healthy and damaged states. A comprehensive benchmarking process compares the sensitivity and reliability of each feature extraction method, ensuring the optimal selection for SHM applications.

By integrating vision-based sensing with advanced ML techniques, this study presents a scalable, non-invasive, and accurate framework for real-time structural monitoring. The proposed system reduces the dependence on manual inspections also enhances early-stage damage detection in critical infrastructures across civil and mechanical engineering applications.

2. Methodological framework

Machine learning techniques provide a robust framework for data mining, as illustrated in Fig. 1. In the context of SHM, the structural diagnosis process generally consists of three main stages: (a) data acquisition and preprocessing; (b) feature extraction; and (c) model training and development using support vector machines.

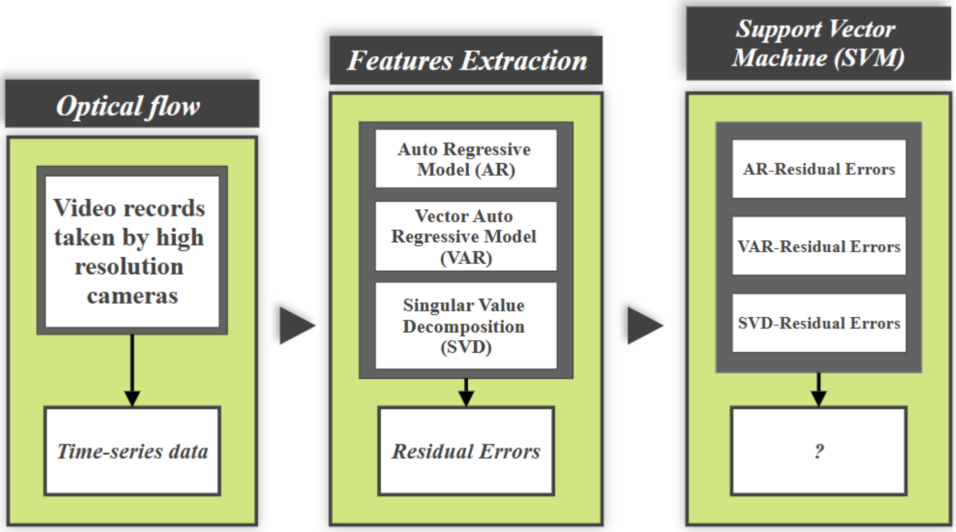

Fig. 1. Workflow of structural health monitoring using optical flow,
feature extraction, and SVM classification

Data-driven SHM involves acquiring and preprocessing data to remove noise and standardize inputs. Features such as (AR), (VAR), and (SVD) are extracted to highlight structural anomalies. Residual errors (REs) are particularly sensitive indicators, providing valuable insights into damage. Machine learning models like support vector machines (SVMs) are then trained on these features to classify structural health states with high accuracy.

2.1. Optical flow (Lucas-Kanade Method)

To precisely quantify the temporal movement of different structural components, An optical flow-based displacement measurement approach is employed.. In this method, each frame of a high-speed video captures the structural state at a specific moment. A Region of Interest (ROI), representing a small subset of pixels corresponding to a structural feature, is identified in the initial reference frame to establish a fixed reference point. As subsequent frames are processed, the Lucas-Kanade method is utilized to track the ROI's position, enabling the detection of pixel-level displacements across frames. This frame-by-frame tracking of ROIs generates a continuous time series of displacements, serving as the foundational dataset for subsequent causal analysis. Fig. 2 illustrates this concept, showing how a chosen ROI is tracked from the reference frame to subsequent frames, how pixel coordinate displacements are computed, and how these displacements are converted into physical units using a known scaling factor.

The Lucas-Kanade algorithm assumes brightness constancy, spatial coherence, and temporal persistence. It computes the local displacement of image features by solving a set of equations derived from intensity gradients(Kanade & Lucas, 1981). In essence, it finds the pixel shift between the initial ROI and its position in the next frame that best explains how the image intensities have changed. Once the algorithm determines the new pixel coordinates of the ROI in the jth frame, the pixel-level displacement $(X_{p,i}, Y_{p,i})$ is obtained by subtracting the original (reference) coordinates $(x_{p,1}, y_{p,1})$ as follows:

$$(X_{p,i}\,, Y_{p,i}) = (x_{p,i}\,, y_{p,i}) - (x_{p,1}\,, y_{p,1}) \tag{1}$$

This calculation yields displacement in pixel units. To convert pixel displacement to a physical displacement measure (e.g., millimeters), a scaling factor (SF) is introduced. This factor is determined by known geometric relationships between the image and the actual structure (such as calibration targets, known dimensions, or camera parameters). Multiplying the pixel displacement by the scaling factor provides the physical displacement as

$$(X_{p,i}\,, Y_{p,i}) = SF \times (x_{p,i}\,, y_{p,i}) \tag{2}$$

where SF is expressed in mm/pixel (or another suitable unit ratio).

By integrating the Lucas-Kanade optical flow technique with ROI tracking and scaling procedures, an accurate, non-contact measurement of structural displacements over time is achieved. This approach utilizes standard camera footage to systematically capture frame-by-frame structural movements, ultimately producing precise physical displacement data suitable for SHM and damage detection analyses.

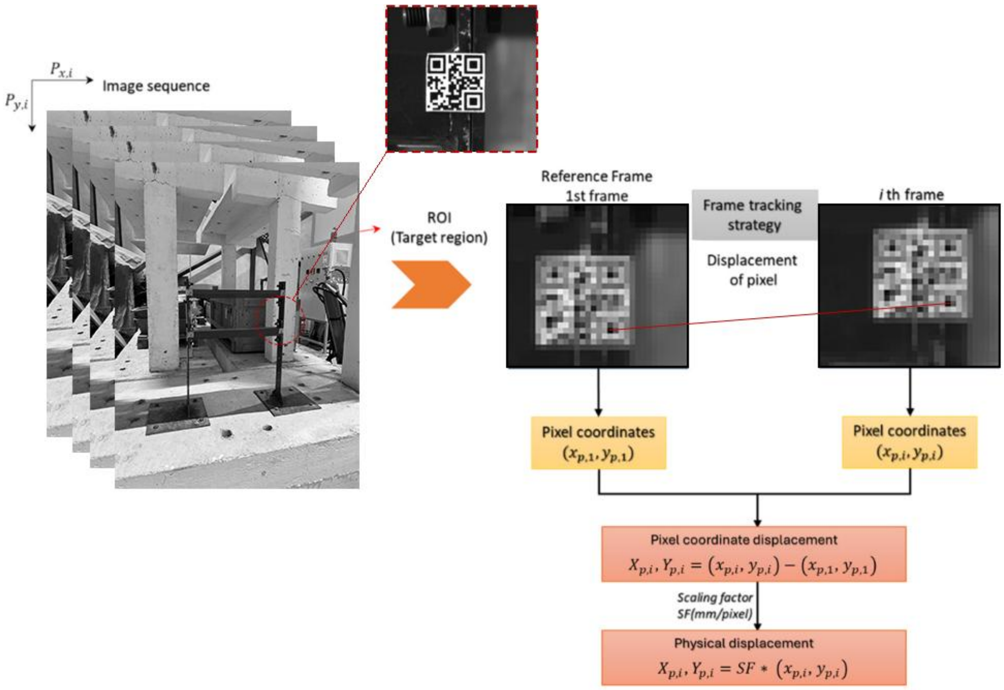

Fig. 2. A QR-code-based displacement tracking schemati

2.2. Features Extraction

2.2.1. Autoregresive (AR)

The AR model is a fundamental time-series analysis technique that predicts the current value of a signal based on a linear combination of its previous values (see Fig 3). Mathematically, the AR model of order p is expressed as:

$$x_i = \sum_{j=1}^{p} \phi_j \, x_{i-j} + e_i \tag{3}$$

where x_i represents the time-series data at time i, ϕ_j are the AR coefficients to be determined, and $e_i$is the error term (residual).

The selection of the model order p is critical for accurately capturing the temporal dependencies in the data The Akaike Information Criterion (AIC) was used to identify the optimal AR model order. AIC evaluates the trade-off between model complexity and goodness of fit. It is mathematically defined as:

$$AIC(p) = N \cdot ln(\hat{\sigma}^2) + 2p \tag{4}$$

where N is the number of data points, $\hat{\sigma}^2$ is the residual variance of the AR model of order p and p is the number of parameters in the model. The model with the smallest AIC value is considered optimal, effectively balancing model accuracy with simplicity.

AR enhances damage detection by emphasizing point-level sensitivity. Its reliance on past values from the same sensor allows it to build a highly personalized prediction model for each measurement point. When structural behavior shifts due to damage, even minor inconsistencies trigger a noticeable increase in residuals. This method is especially effective for detecting early-stage or highly localized faults that may not yet affect the broader system (Zhang et al., 2024).

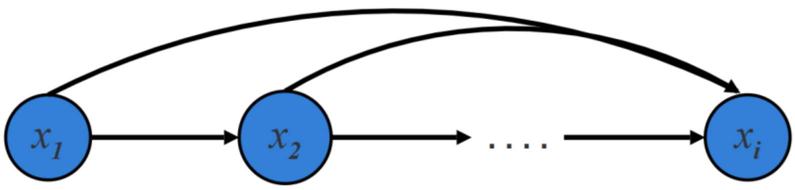

Fig. 3. Representation of the AR process

2.2.2.Vector autoregressive (VAR)

The VAR model is a multivariate time-series analysis technique designed to capture the temporal dependencies among multiple variables. In the VAR(p) model, each variable is represented as a linear combination of its own past values and the past values of other variables in the system (see Fig 4).

Mathematically, the VAR(p) model is expressed as:

$$y_t = a_0 + \sum_{j=1}^{p} A_j y_{t-j} + e_t \tag{5}$$

where y_t is an $M \times 1$ vector of M data acquisition sensors at time t, a_0 is an $M \times 1$ intercept vector, A_j are $M \times 1$ coefficient matrices, and e_t is an $M \times 1$ vector of errors, assumed to follow a zero-mean Gaussian distribution with covariance $\sum$.

Choosing the appropriate lag order p is vital for capturing the system's dynamics. The Akaike Information Criterion (AIC) was employed to determine the optimal p. AIC evaluates the balance between model complexity and goodness of fit, and for the VAR(p) model is defined as:

$$AIC(p) = 2 \cdot dof - 2 \cdot ln(L) \tag{6}$$

where $dof = K \cdot M$ denotes the number of parameters (K is the number of regressors per variable and M is the number of variables), and L is the log-likelihood of the model.

VAR contributes by modeling the interdependencies between multiple measurement points. Instead of treating each point in isolation, it accounts for how vibrations at one location influence others over time. This allows the method to uncover system-level anomalies, such as coordinated or cascading structural changes. It's particularly useful for identifying damage that alters the dynamic relationship between different regions of the structure (Liu et al., 2019).

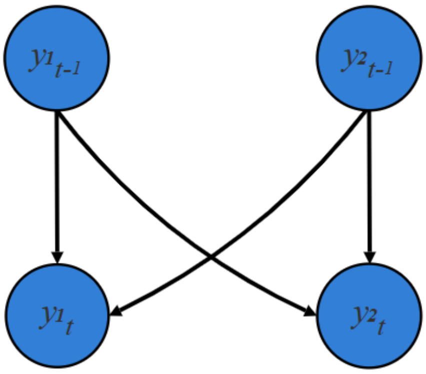

Fig. 4. Representation of the VAR process

2.2.3. Singular value decomposition (SVD)

The singular value decomposition (SVD) is a robust matrix factorization technique applied to time-series signals in structural health monitoring. By transforming the signal into a Hankel matrix, SVD decomposes it into its singular components, isolating the dominant dynamic patterns and facilitating damage detection. The SVD of a matrix H is expressed as:

$$H = USV^T \tag{7}$$

In this formulation, U is an $m \times m$ orthonormal matrix of left singular vectors, S is an $m \times n$ diagonal matrix containing the singular values $\sigma_1, \sigma_2, \cdots, \sigma_n$ and V is an $n \times n$ matrix of right singular vectors (see Fig 5). The singular values $\sigma_1, \sigma_2, \cdots, \sigma_n$ are arranged in descending order ($\sigma_1 \geq \sigma_2 \geq \cdots \geq \sigma_n \geq 0$). The dominant singular vectors, associated with the largest singular values, define a reduced subspace that encapsulates the most significant information in the original signal.

The SVD enables a subspace-based representation of H. Assuming $\gamma \leq N$, where γ is the number of dominant variables in the data, the decomposition can be written as:

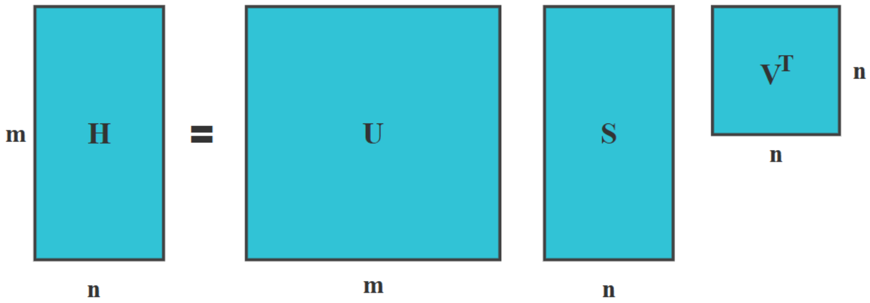

Fig. 5. Decomposition of matrix H into singular value components using SVD.

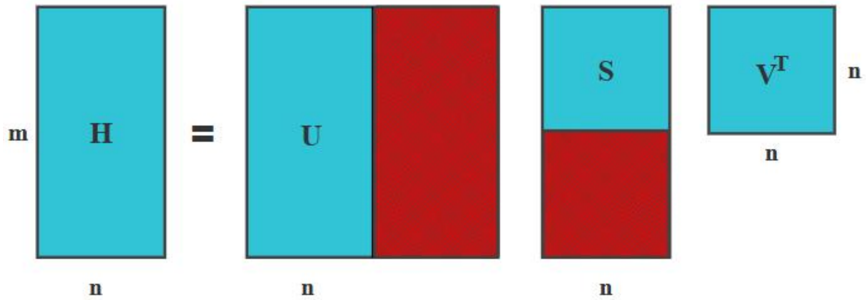

Fig. 6. Representation of SVD in the dominant subspace

$$H = USV^T = \begin{bmatrix} U_\gamma & U_\gamma^\perp \end{bmatrix} \begin{bmatrix} S_\gamma & 0 \\ 0 & 0 \end{bmatrix} \begin{bmatrix} V_\gamma^T \\ (V_\gamma^\perp)^T \end{bmatrix} \tag{8}$$

Here, $U_\gamma$and $U_\gamma^\perp$ are the dominant and complementary left singular vectors, respectively, while V_γ and $V_\gamma^\perp$ are the dominant and complementary right singular vectors. The diagonal matrix $S_\gamma = diag(\sigma_1, \ldots, \sigma_\gamma)$ contains the dominant singular values, which represent the most significant dynamic patterns in the system .

The complementary subspaces and the corresponding smaller singular values are assumed to represent noise or less relevant variations. These components are discarded, and their influence is effectively reduced to zero in the decomposition (see Fig 5).

The singular vectors $\mu_i$or v_i are regarded as the dominant singular vectors. For the signal X , the number of dominant orthonormal dimensions can be determined based on the Frobenius norm as:

$$\| H \|_F = \sum_{i=1}^{m} \sum_{j=1}^{n} H_{ij}^2 = \| S \|_F = \sigma_1^2 + \sigma_2^2 + \cdots + \sigma_n^2 \tag{9}$$

The energy of the data is preserved within the singular value spectrum σ_i. For noise-corrupted signals, the denoising process can be regarded as removing certain minimal σ_i. values. In the general decomposition process, the signal is first reshaped into a Hankel matrix.

SVD is then applied to decompose the Hankel matrix, determine the number of selected singular values , and subsequently reconstruct the denoised signal and noise components as:

$$X = X_0 + X_{noise} \tag{10}$$

where X_0 represents the first row of $H_{\{X_0\}}$, and X_{noise} corresponds to the residual of the denoised signal.

The SVD aids in damage detection by transforming vibration signals into a set of orthogonal modes based on energy content. This decomposition filters out noise and isolates the most structurally meaningful behaviors. When damage occurs, the energy distribution among these modes changes subtly but detectably. SVD’s strength lies in identifying global structural changes and maintaining accuracy even under complex, ambient vibration conditions (Tomassini et al., 2024).

2.2.4.Residual errors

To evaluate the performance of the AR, VAR, and SVD models, the residual errors were computed by comparing the measured signal $x_i$with the predicted signal $\hat{x}_i$. the residual error e_i^D is calculated as:

$$e_i^D = x_i - \hat{x}_i \tag{11}$$

Following this, damage detection is performed by defining thresholds based on the healthy (undamaged) condition. Specifically, the maximum and minimum thresholds $T_{\_max}$ and T_{min} , are obtained from the residuals of the undamaged state e^{UD}, as:

$$T_{\max} = \max(e^{UD}), T_{\min} = \min(e^{UD}) \tag{12}$$

A total of sixteen statistical features were extracted from the residual errors, following the methodologies summarized in Table 1. These features serve as damage-sensitive indicators for structural health monitoring applications (Boldt et al., 2013; Sharma et al., 2016).

Table 1. Definition of statistical features

Feature	Description	Formulation
RE1	Maximum value of the residual error	$\max(e_i)$
RE2	Minimum value of the residual error	$min\ (e_i)$
RE3	Mean of the residual error	$\mu = \frac{1}{N}\sum_{j=1}^{N} e_i$
RE4	The peak-to-peak value of the residual error	$\max(e_i) - \min(e_i)$
RE5	Mean of the absolute residual error	$\frac{1}{N}\sum_{j=1}^{N} \lvert e_i \rvert$
RE6	The standard deviation of the residual error	$\sigma = \sqrt{\sum_{j=1}^{N} \frac{(e_i - \bar{e}_i)}{N}}$
RE7	Skewness of the residual error	$\sqrt{\frac{1}{6N}\sum_{j=1}^{N}\left(\frac{e_i - \mu}{\sigma}\right)^3}$
RE8	Kurtosis of the residual error	$\sqrt{\frac{N}{24}\left[\frac{1}{N}\sum_{j=1}^{N} -3\right]}$
RE9	Root mean square of the residual error	$rms = \sqrt{\frac{1}{N}\sum_{j=1}^{N} e_i^2}$
RE10	Form factor	$\frac{rms}{\frac{1}{N}\sum_{j=1}^{N}\lvert e_i \rvert}$
RE11	Crest factor	$\frac{\max(e_i) - \min(e_i)}{rms}$
RE12	Kurtosis factor	$\frac{\sum_{i=11}^{N} e_i^4}{\sqrt{\sum_{i=1}^{N} e_i^2}}$
RE13	Pulse factor	$\frac{\max(e_i) - \min(e_i)}{\frac{1}{N}\sum_{j=1}^{N}\lvert e_i \rvert}$
RE14	Margin factor	$\frac{\max(e_i) - \min(e_i)}{\left[\frac{1}{N}\sum_{j=1}^{N}\lvert e_i \rvert\right]^2}$
RE15	Upper control limit	$UCL = \mu + 3\frac{\sigma}{\sqrt{n}}$
RE16	Lower control limit	$lCL = \mu - 3\frac{\sigma}{\sqrt{n}}$

2.2.5. Support vector machine (SVM)

Support Vector Machine (SVM) is a supervised learning algorithm widely used in classification problems due to its robust generalization capabilities. In the context of Structural Health Monitoring (SHM), SVM has gained significant traction because of its ability to effectively distinguish between healthy and damaged structural states. The core idea behind SVM is to find a decision boundary or hyperplanethat maximizes the margin between two classes of data points . This is formulated in the binary classification setting as:

$$f(X) = W^T X_i + b \tag{13}$$

where W is the weight vector , X_i is the feature vector of the i-th sampl, and b is the bias.

For damage detection tasks involving only one class (typically healthy data), One-Class Support Vector Machines (OC-SVM) are applied as reported by Pollastro et al. (2023). The OC-SVM seeks to estimate a function that returns positive values for most training data and negative values for anomalies. The optimization objective for the OC-SVM is:

$$\min_{W,b} \frac{1}{2} \|W\|^2 + \frac{1}{\upsilon N} \sum_{i=1}^{N} \xi_i - \rho \tag{14}$$

here, ξ_i is the slack variables allowing for outlires, And ρ defines the margin threshold

3.Case study

3.1. Testbed structure

The study's lab model is a steel frame consisting of two vertical bars supported by bolted base plates, connected by horizontal bars to create a stable and rigid configuration (Fig. 7). Assembled with adjustable bolts, it allows for flexible configurations suited to various testing needs. The material properties are Young's modulus $E = 2 \times 10^{11}$ N/m^2, Poisson's ratio $\upsilon = 0.30$, and density $\rho = 7850$ kg/m^3. The robust construction and stable alignment of the model provide a reliable setup for accurately tracking its responses under different conditions.

Using four high-resolution cameras the data collection process was conducted as shown in Fig. 8, each aimed at a specific QR code attached to the corners of the model, as detailed in Fig. 9, which also shows the damage scenarios considered. The cameras were strategically positioned to capture the vibrations and movements of the QR codes, providing precise time series data.

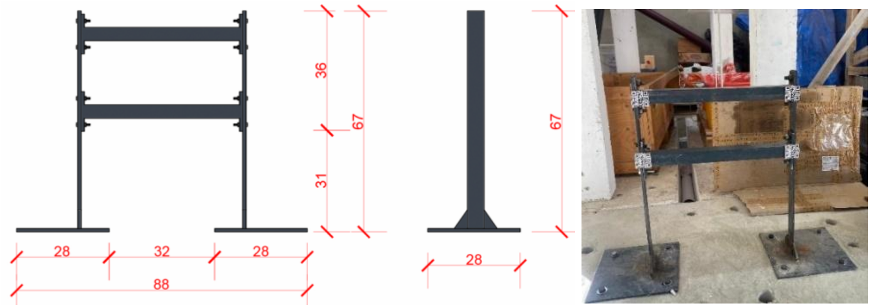

Fig. 7. Laboratory model (Units in cm)

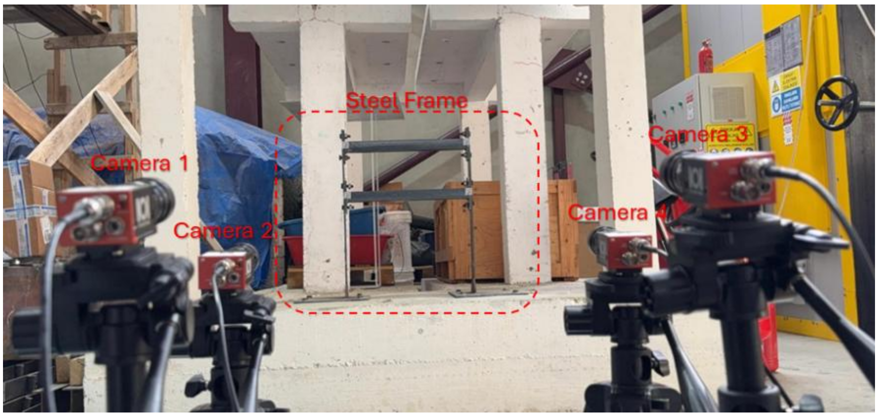

Fig 8. Camera setup

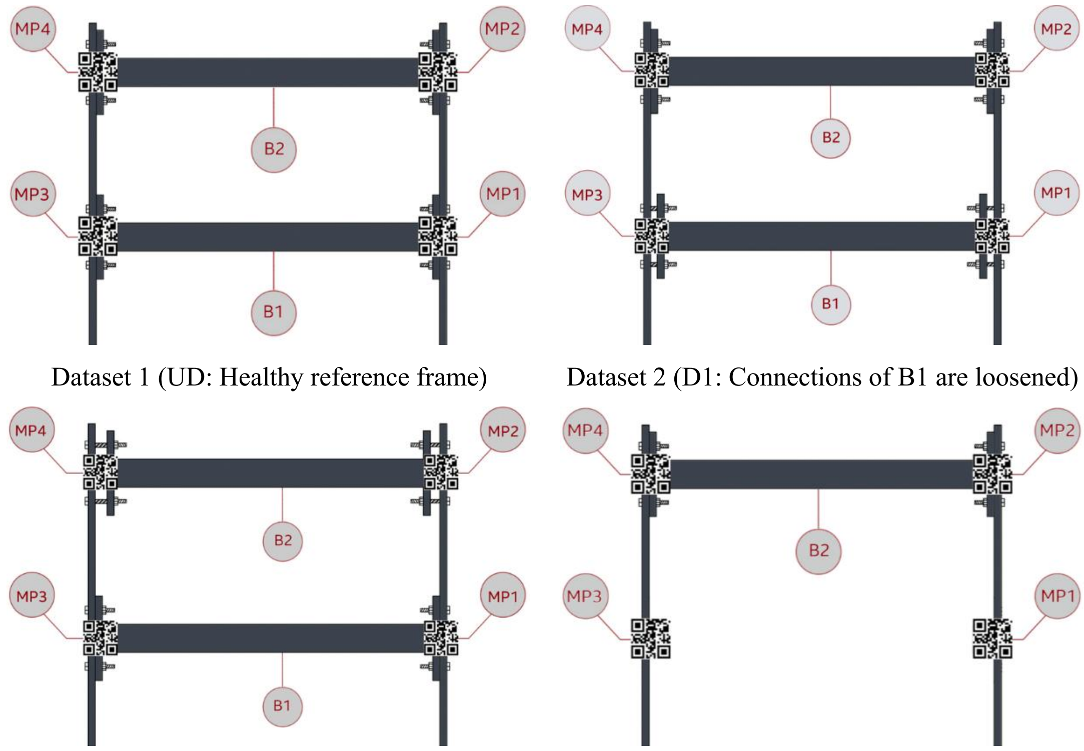

Dataset 1 (UD: Healthy reference frame) Dataset 2 (D1: Connections of B1 are loosened)

Dataset 3 (D2: Connections of B2 are loosened) Dataset 4 (D3: B1 is removed)

Fig. 9. Baseline and damaged conditions for SHM dataset with QR code placement

3.2. Data acquisition system

To capture ambient vibration data from the laboratory steel frame model, a vision-based measurement system composed of four high-speed cameras and corresponding optical lenses was employed (see Fig. 10). The integrated hardware system comprising four high-speed CMOS cameras, each with its precision lens, and a versatile CoaXPress video recorder, supported by a capable computing unit provided a robust platform for capturing, recording, and analyzing the ambient vibrations of the steel frame model. This configuration ensured that the collected image data met the temporal resolution and clarity demands necessary for accurate displacement tracking and reliable analysis.

Video signals from the four cameras were streamed to an IO Industries DVR Express Core 2 CoaXPress (CORE2CX) video recorder. This recorder supported multiple CoaXPress link configurations (CXP–1, CXP–2, and CXP–3) and adhered to CoaXPress v1.1 and GenICam Rev. 2.4 standards. Furthermore, it accommodated various video formats—8/10/12/14/16-bit monochrome and Bayer or RGB modes—ensuring that the recorded image data maintained the fidelity required for subsequent data analysis.

Data processing and analysis were performed on a computing unit (HP Victus 16-d1006nt) equipped with a 12th Gen Intel® Core™ i5-12500H processor running at 2.50 GHz, 16 GB of RAM, and a 512 GB SSD.

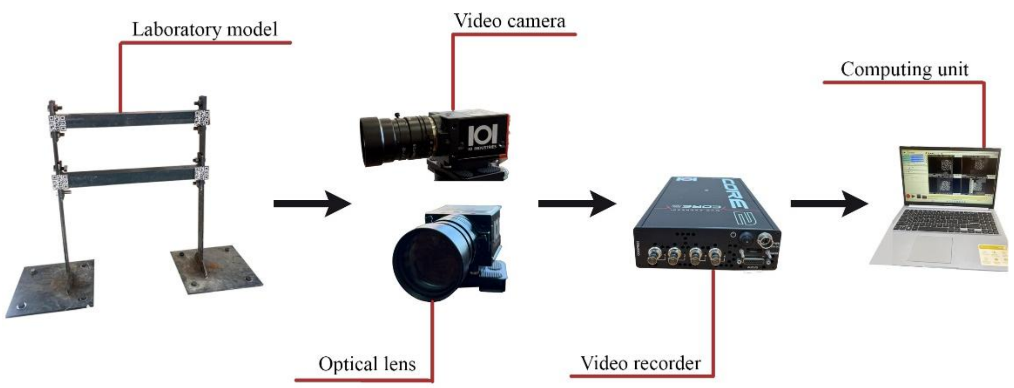

Fig. 10. Monitoring system

4.Results

In the experiment, vibration data were recorded along both the x-axis and y-axis. However, the primary focus was placed on horizontal (x-axis) displacement, as it provided a clear, one-dimensional representation of the movement of each measurement point over time. While structural vibrations can occur in multiple directions, selecting a single principal axis in this case, the x-axis simplifies data acquisition and processing while still capturing the dominant motion relevant to damage detection objectives. Tracking x-axis displacement enabled the generation of straightforward time series inputs for the causal analysis framework, ensuring clarity and consistency in sensor behavior comparisons across different damage scenarios. In Figs 11 and 12, the time series data for healthy and D2 cases obtained by the optical flow approach at the relevant MPs are, respectively, shown.

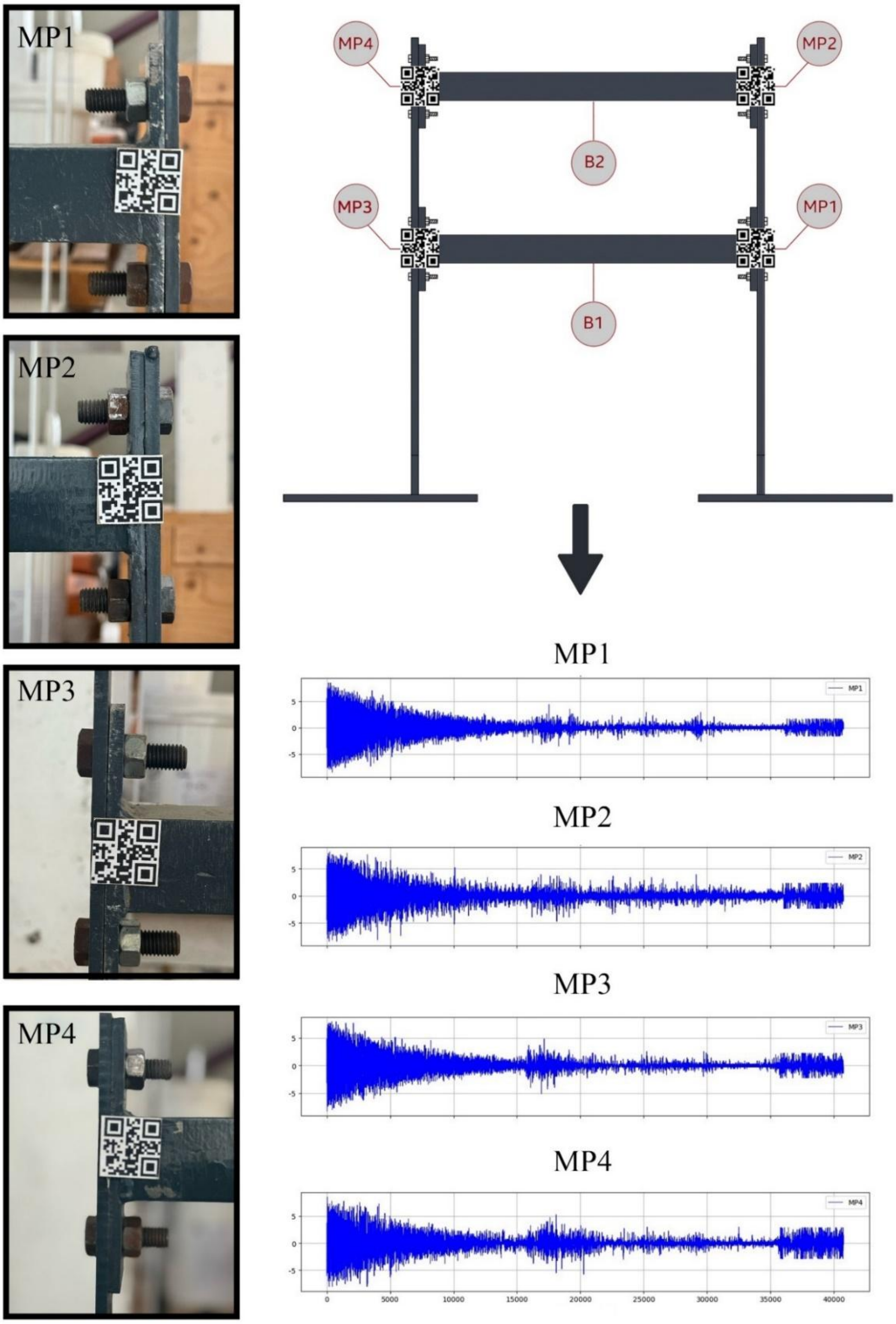

Fig. 11. Displacement time series data for the healthy condition

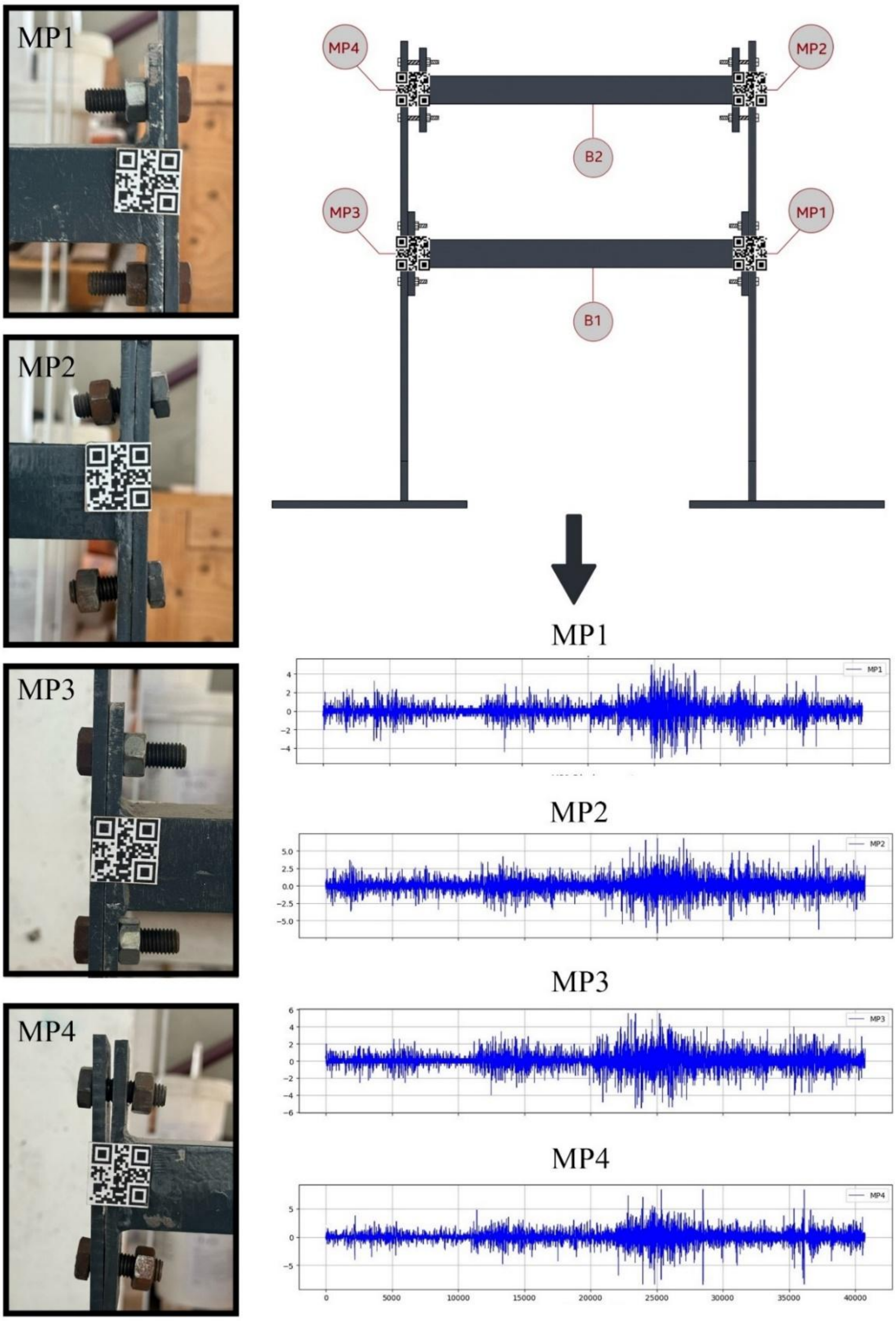

Fig. 12. Displacement time series data for the damaged condition D2

Feature extraction methods were evaluated using residuals from AR, VAR, and SVD, as stated in Eq. (X), to assess their effectiveness in distinguishing between undamaged and damaged states. The results showed differences in each model's ability to detect structural anomalies under ambient vibration conditions.

Figs 13–15 present the computed data from AR, VAR, and SVD models. The red dashed lines indicate the threshold range of healthy structural behavior, defined by Eq. (12). When the computed time series exceed these thresholds, the structure is identified as damaged. Blue segments correspond to the UD dataset, while purple segments represent the damaged cases (D1, D2, D3). Each MP (MP1–MP4) is displayed side by side across the scenarios to allow direct comparison between the normal behavior in the UD data and deviations observed in the damaged datasets.

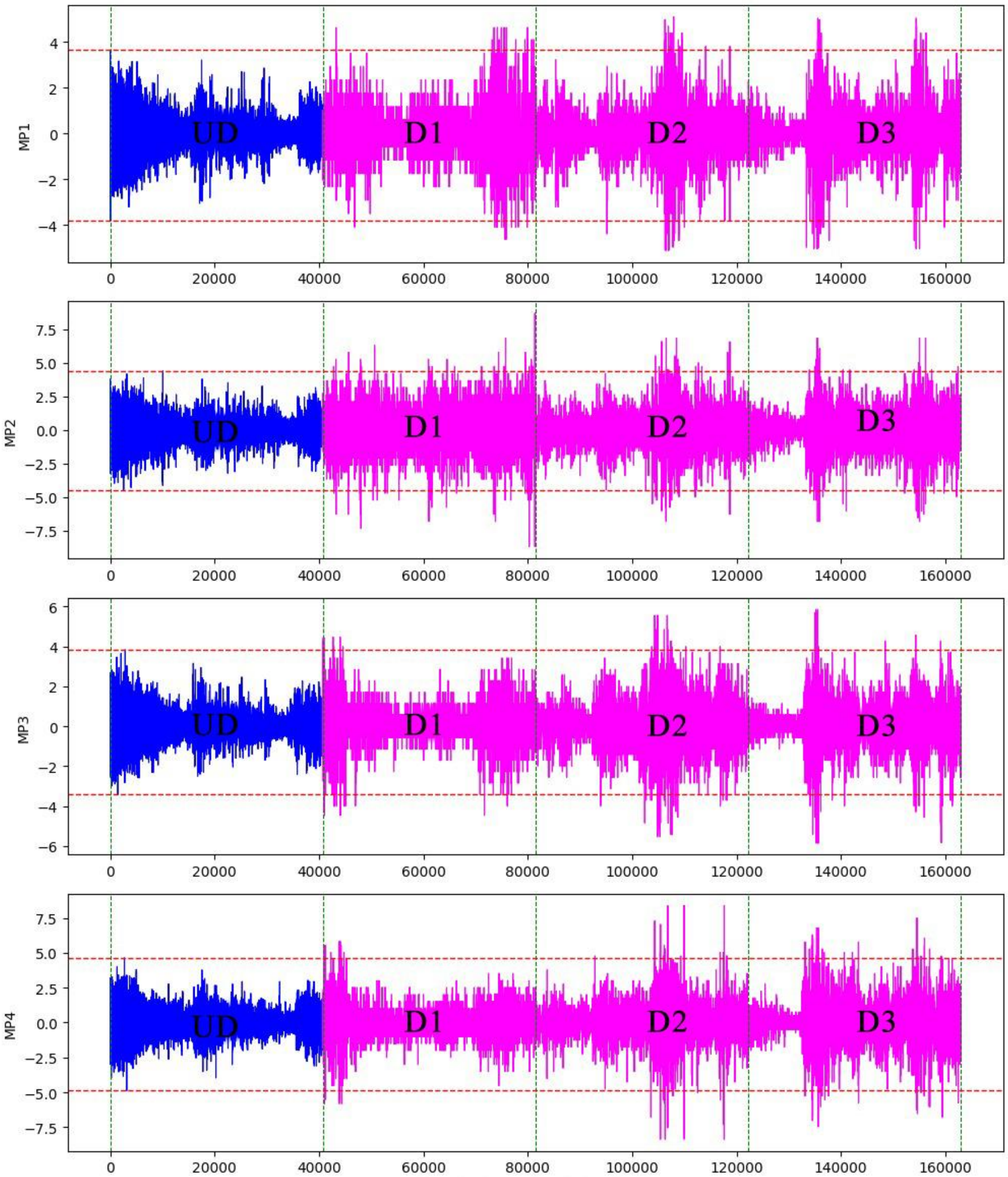

Fig. 13. AR model features .

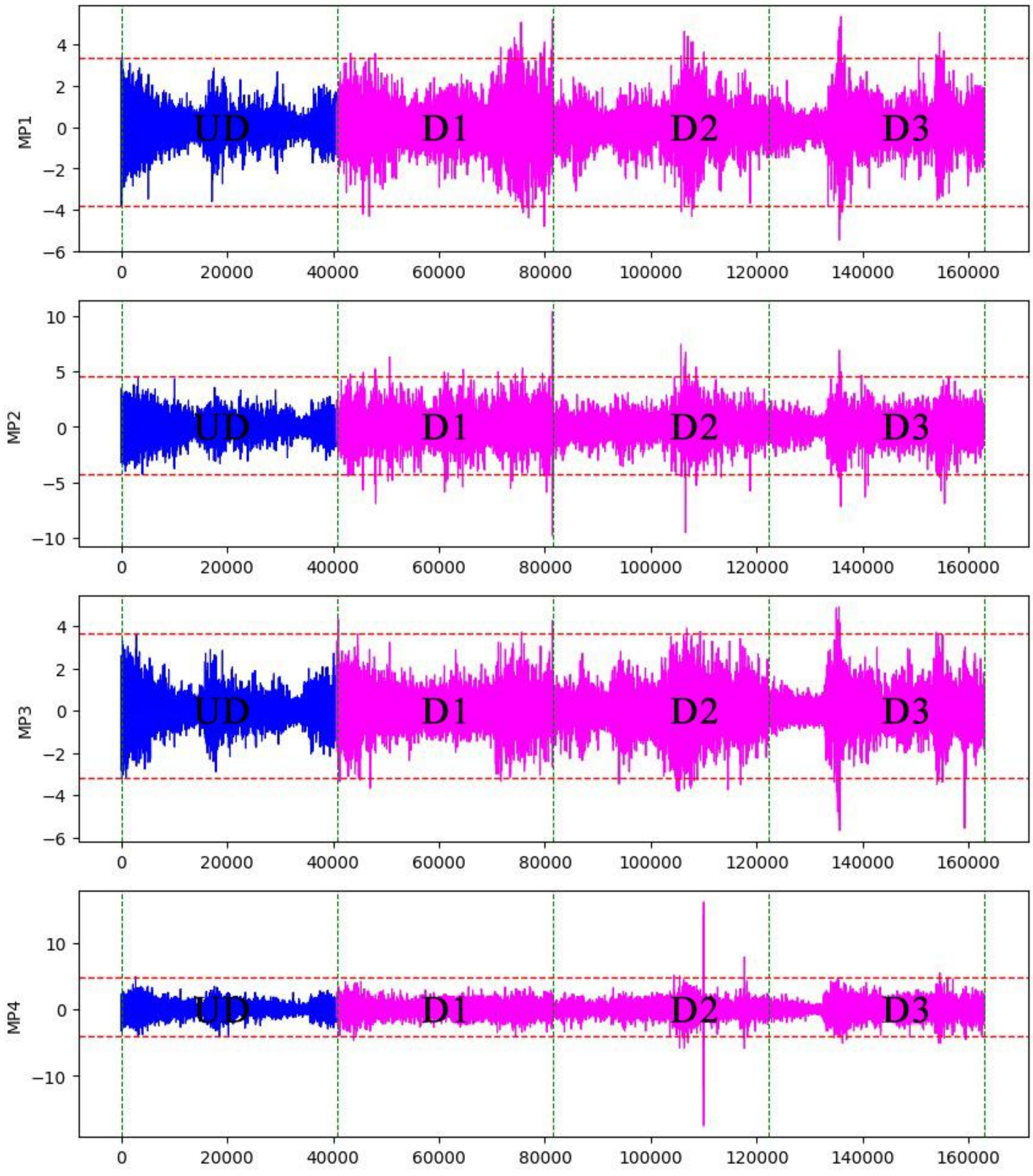

Fig. 14. VAR model features

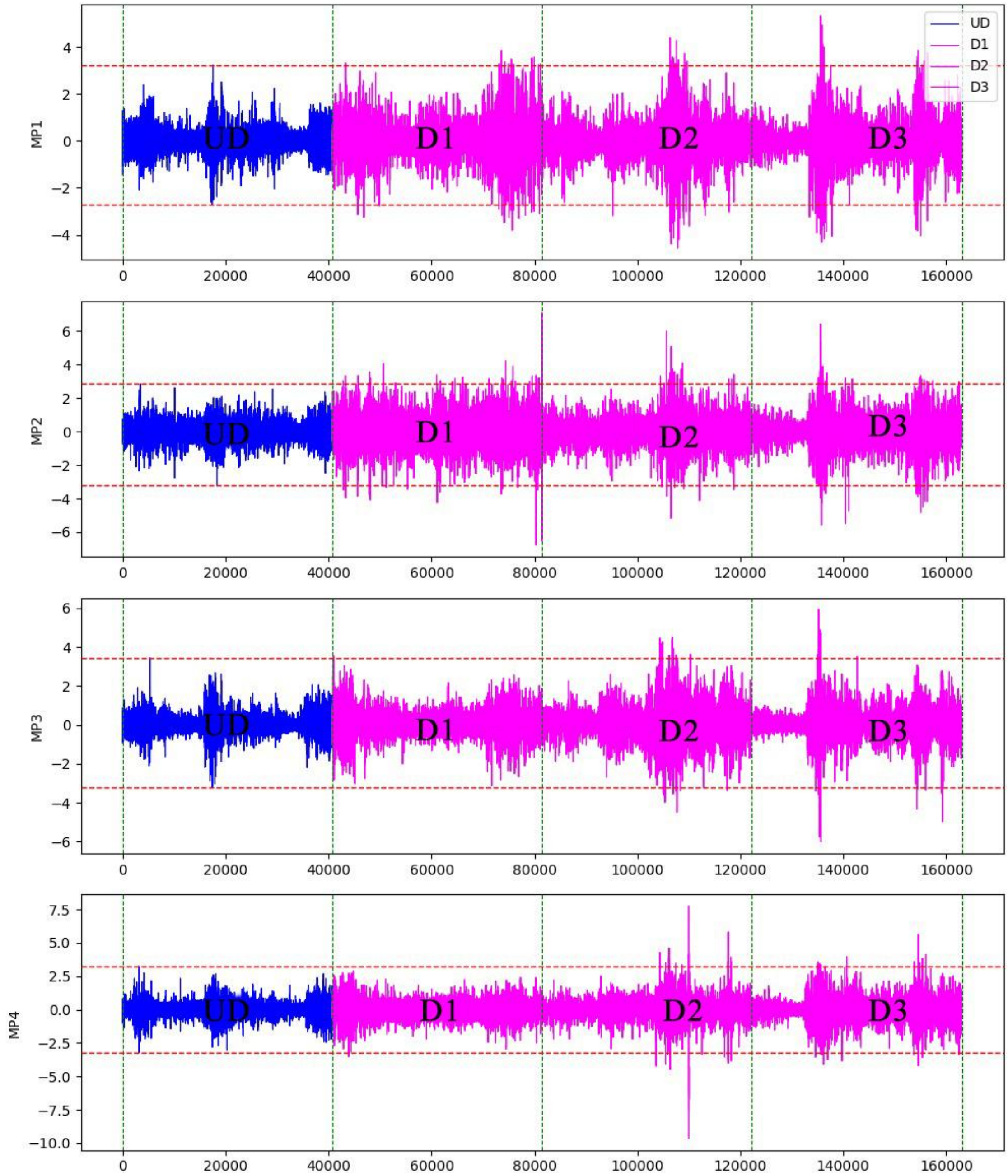

Fig. 15. SVD model features

While all three methods AR, VAR, and SVD performed satisfactorily overall, AR-based features demonstrated superior effectiveness in detecting structural damage. This advantage is clearly illustrated in Fig. 16, particularly for MP3, where the AR model distinctly captured deviation patterns under both D1 and D2 conditions. Fig. 17 further underscores the robustness of the AR model in MP4, as it successfully identified all three damage scenarios (D1, D2, D3) with residuals exceeding the defined thresholds.

The strength of the AR model lies in its reliance on the temporal history of a single measurement point, as described in Eq. (3). This formulation enables the model to establish a highly accurate baseline for each point individually. When applied to damaged data, any deviation from the learned healthy behavior produces pronounced residuals, enhancing its capability to detect localized anomalies.

In contrast, the VAR model defined in Eq. (5) accounts for interactions across multiple measurement points, capturing broader system dynamics. While this multivariate approach is valuable for understanding global behavior, it may reduce sensitivity to localized damage. Similarly, the SVD method reconstructs structural behavior by decomposing vibration signals into dominant oscillatory components and retaining those with the highest energy, as shown in Eq. (8). Although effective in capturing global trends, this method may be less responsive to subtle changes induced by ambient vibrations

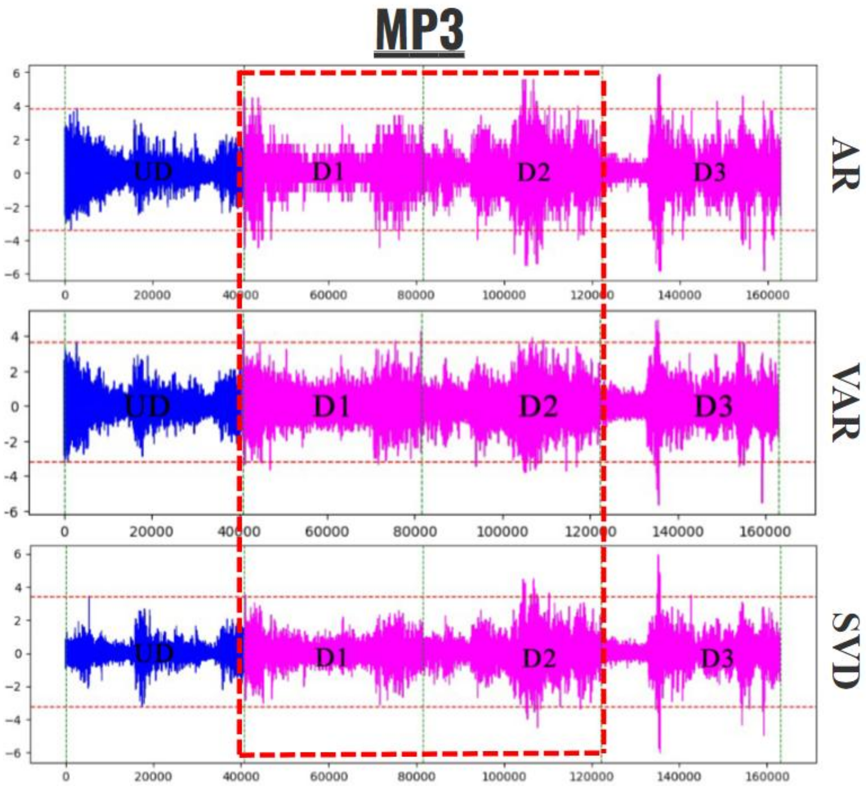

Fig. 16. Comparison of AR, VAR, and SVD Performance
in Damage Detection at MP3

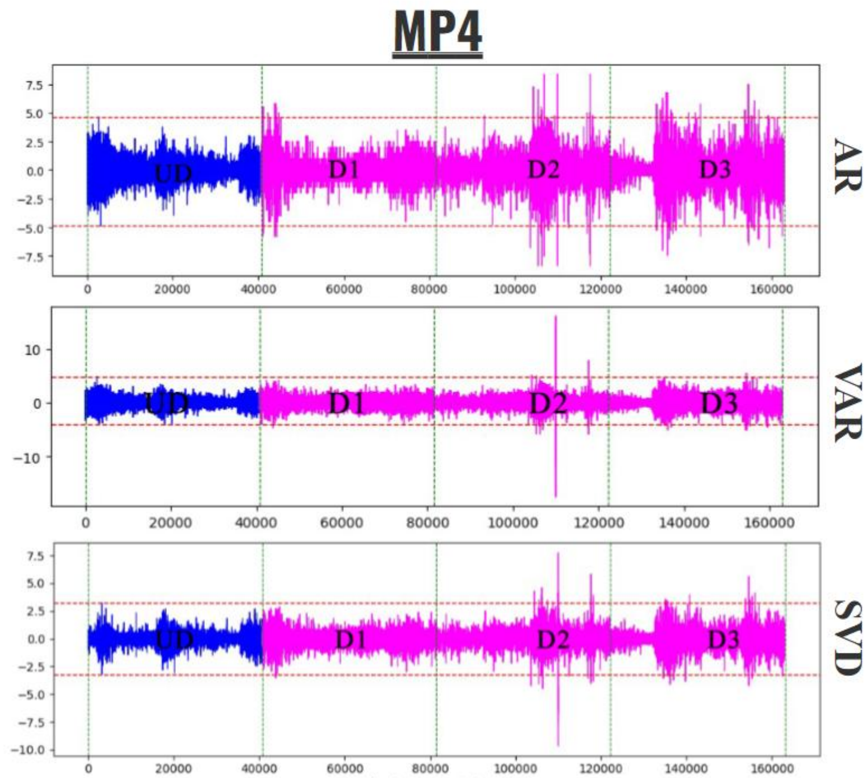

Fig 17. Comparison of AR, VAR, and SVD Performance
in Damage Detection at MP4

The primary goal of SHM is to detect even subtle indications of structural damage at an early stage. By analyzing how residual errors vary between the undamaged (UD) and damaged (D1–D3) states, the proposed model effectively achieves this objective.

Figs 18 to 20 depict the distribution of 16 statistical features (RE1–RE16) extracted from the residuals produced by the AR, VAR, and SVD methods, respectively, as summarized in Table 1. Each data point in these plots represents a specific feature (e.g., maximum, mean, RMS, kurtosis) calculated for a given measurement point (MP). The structural condition is indicated through color coding: blue for D1, green for D2, red for D3, and yellow for UD.

The observed spread and separation in feature values across the different conditions highlight underlying structural differences. Notably, the damaged datasets (D1–D3) exhibit increased variability and outliers in several statistical features, while the UD data remains tightly clustered. This divergence in feature distributions underscores the presence of distinct residual patterns across structural states, offering strong discriminatory potential. Consequently, the model can accurately classify the data into healthy or damaged categories, minimizing the risk of false negatives—i.e., cases where damage might otherwise go undetected.

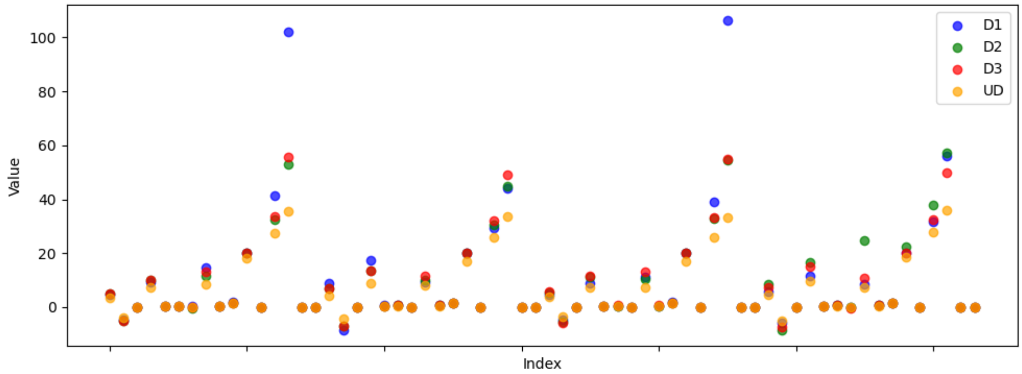

Fig. 18. Distribution of AR statistical features

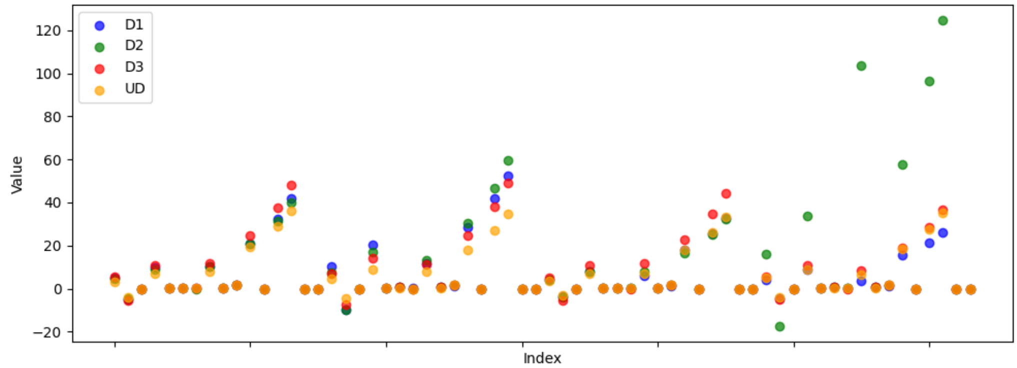

Fig. 19. Distribution of VAR statistical features

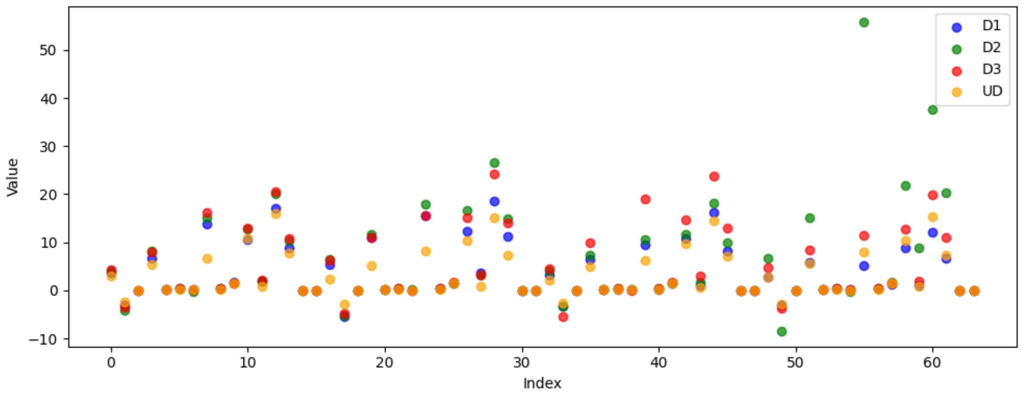

Fig. 20. Distribution of SVD statistical features

Fig. 21 presents the confusion matrix based on the AR-derived statistical features (RE1–RE16). The AR residuals demonstrate excellent overall performance, with no missed damaged cases (i.e., zero false negatives) and an accuracy of approximately 93%. Specifically, 19 undamaged samples are correctly classified, 7 are incorrectly flagged as damaged, and all 77 damaged samples are accurately identified.

Fig. 22 displays the confusion matrix using statistical features extracted from the VAR residuals. Similar to the AR-based results, the VAR model achieves strong performance, with 18 undamaged samples correctly classified, 8 misclassified as damaged, and all 77 damaged samples correctly detected. This results in an overall accuracy of 92%, further confirming the effectiveness of VAR residuals in distinguishing between UD (labeled as 0) and damaged states (labeled as 1).

Fig. 23 shows the confusion matrix for the SVD-based statistical features. The classifier maintains perfect recall by correctly identifying all 77 damaged samples, while also improving classification of the undamaged class: 21 UD samples are correctly labeled, with only 5 false positives. This yields the highest accuracy among the three methods approximately 95%—highlighting the strong classification capability of the SVD-based approach.

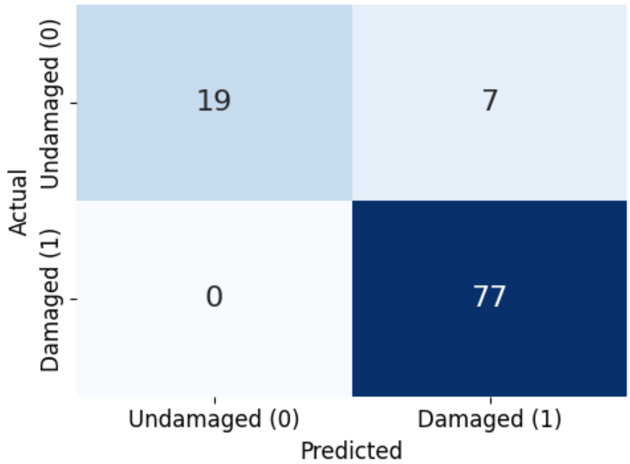

Fig. 21. Confusion matrix for AR residual

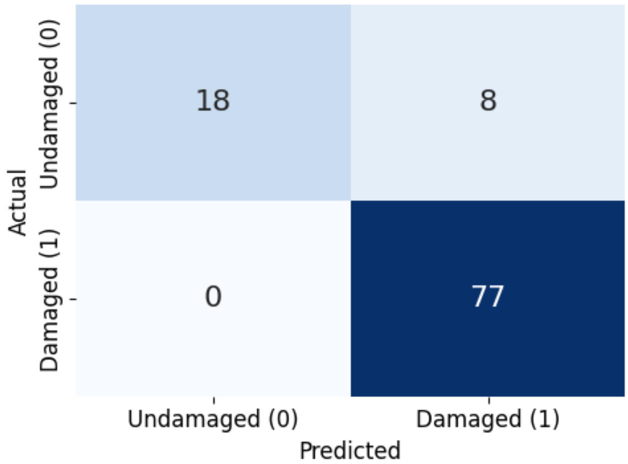

Fig. 22. Confusion matrix for VAR residual

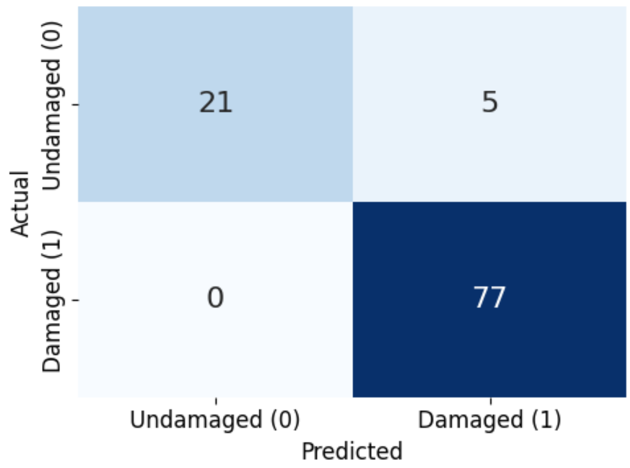

Fig. 23. Confusion matrix for SVD residual

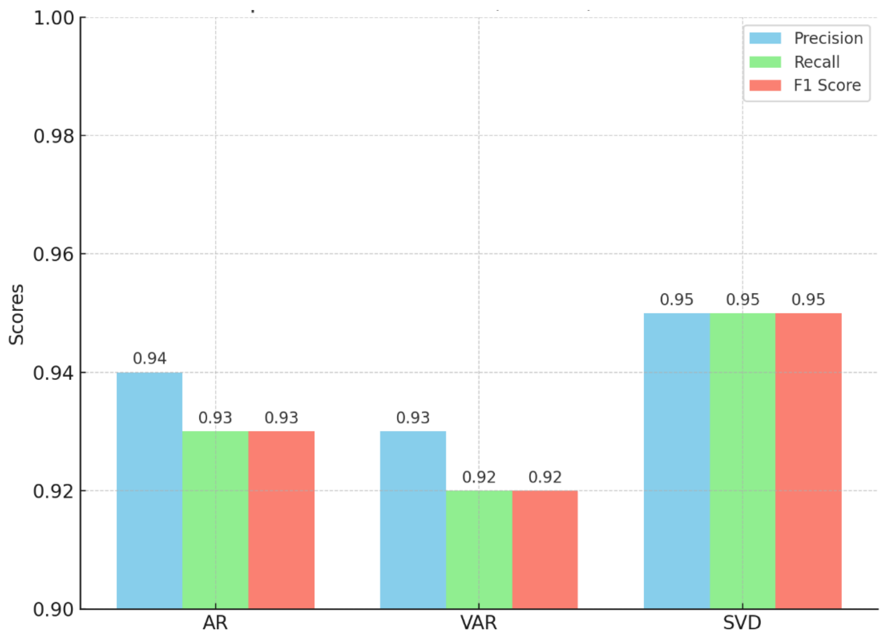

Fig. 24. Performance comparison of precision (Blue), recall (Green), and F1 score (Red) for AR, VAR, and SVD

Despite minor variations in false positive rates, all three methods AR, VAR, and SVD xhibit strong damage detection performance, underscoring the effectiveness of residual error-based classification in distinguishing between healthy and damaged structural states. Notably, the statistical feature distributions shown in Figs 18–20 reveal that SVD provides the most distinct separation across the UD, D1, D2, and D3 conditions. This enhanced separability contributes to superior classification performance, with the SVD-based model achieving 95% precision, recall, and F1-score, as illustrated in Fig. 24.

5.Conclusions

This thesis presents a vision-based Structural Health Monitoring (SHM) framework that integrates high-speed imaging, optical flow analysis, and machine learning to detect damage in a steel frame structure. Displacement time-series data were extracted non-contactly from QR-coded Regions of Interest (ROIs) using the Lucas-Kanade optical flow technique.

A key limitation of the proposed system is its reduced effectiveness under ambient vibration conditions, which introduced noise and made it difficult for VAR and SVD models to capture subtle interactions. This limitation contributed to their lower performance compared to the AR model.

Three main feature extraction techniques—Autoregressive (AR), Vector Autoregressive (VAR), and Singular Value Decomposition (SVD)—were used to generate residual signals, later transformed into 16 statistical features and classified via Support Vector Machine (SVM). The key findings are:

- AR model effectively captured localized temporal deviations with high sensitivity, achieving 93% accuracy. It is particularly suitable for passive monitoring under ambient vibrations due to its responsiveness to subtle signal changes.
- VAR model showed moderate performance under ambient conditions, with a classification accuracy of around 92%. Its dependency on cross-sensor interactions makes it more appropriate for setups involving forced excitation.
- SVD model delivered the best classification results, with a precision, recall, and F1-score of 0.95. It excels in detecting dominant oscillatory patterns but may overlook minor amplitude variations linked to early-stage damage.

These results confirm the potential of the proposed framework for practical SHM applications, offering reliable damage detection

Refences

Benfenati, L., Pagliari, D. J., Zanatta, L., Velez, Y. A. B., Acquaviva, A., Poncino, M., Macii, E., Benini, L., & Burrello, A. (2024). Foundation Models for Structural Health Monitoring. http://arxiv.org/abs/2404.02944

Bhatta, S., & Dang, J. (2024). Use of IoT for structural health monitoring of civil engineering structures: a state-of-the-art review. Urban Lifeline, 2(1), 17. https://doi.org/10.1007/s44285-024-00031-2

Farrar, C. R., Dervilis, N., & Worden, K. (2025). The Past, Present and Future of Structural Health Monitoring: An Overview of Three Ages. In Strain (Vol. 61, Issue 1). John Wiley and Sons Inc. https://doi.org/10.1111/str.12495

He, J. H., Liu, D. P., Chung, C. H., & Huang, H. H. (2020). Infrared thermography measurement for vibration-based structural health monitoring in low-visibility harsh environments. Sensors (Switzerland), 20(24), 1–15. https://doi.org/10.3390/s20247067

Jeltiri, P., Al-Mahmoud, F., Boissière, R., Paulmier, B., Makdissy, T., Elmazria, O., Nicolay, P., & Hage-Ali, S. (2023). Wireless strain and temperature monitoring in reinforced concrete using Surface Acoustic Wave (SAW) sensors. *IEEE Sensors Letters*, 7(10), 1–4. https://doi.org/10.1109/LSENS.2023.3315219

Kanade, T., & Lucas, B. D. (1981). An Iterative Image Registration Technique with an Application to Stereo Vision (IJCAI) An Iterative Image Registration Technique with an Application to Stereo Vision. https://www.researchgate.net/publication/215458777

Kinet, D., Mégret, P., Goossen, K. W., Qiu, L., Heider, D., & Caucheteur, C. (2014). Fiber Bragg grating sensors toward structural health monitoring in composite materials: Challenges and solutions. In Sensors (Switzerland) (Vol. 14, Issue 4, pp. 7394–7419). MDPI AG. https://doi.org/10.3390/s140407394

Klun, M., Zupan, D., Lopatič, J., & Kryžanowski, A. (2019). On the application of laser vibrometry to perform structural health monitoring in non-stationary conditions of a hydropower dam. Sensors (Switzerland), 19(17). https://doi.org/10.3390/s19173811

Kullukçu, B., Bathaei, M., Awais, M., Mirzajani, H., & Beker, L. (2022). Piezoelectric PVDF-TrFE/ PET Energy Harvesters for Structural Health Monitoring (SHM) Applications. http://arxiv.org/abs/2210.13217

Li, X., Bolandi, H., Masmoudi, M., Salem, T., Lajnef, N., & Boddeti, V. N. (2024). Mechanics-Informed Autoencoder Enables Automated Detection and Localization of Unforeseen Structural Damage. http://arxiv.org/abs/2402.15492

Liu, A., Wang, L., Bornn, L., & Farrar, C. (2019). Robust structural health monitoring under environmental and operational uncertainty with switching state-space autoregressive models. Structural Health Monitoring, 18(2), 435–453. https://doi.org/10.1177/1475921718757721

López-Castro, B., Haro-Baez, A. G., Arcos-Aviles, D., Barreno-Riera, M., & Landázuri-Avilés, B. (2022). A Systematic Review of Structural Health Monitoring Systems to Strengthen Post-Earthquake Assessment Procedures. In Sensors (Vol. 22, Issue 23). MDPI. https://doi.org/10.3390/s22239206

Luo, Y., Pu, L., Wang, J., & Howard, I. (2023). Enhancing In-Situ Structural Health Monitoring through RF Energy-Powered Sensor Nodes and Mobile Platform. https://doi.org/10.1109/TMC.2024.3491574

Malekloo, A., Ozer, E., AlHamaydeh, M., & Girolami, M. (2022). Machine learning and structural health monitoring overview with emerging technology and high-dimensional data source highlights. In Structural Health Monitoring (Vol. 21, Issue 4, pp. 1906–1955). SAGE Publications Ltd. https://doi.org/10.1177/14759217211036880

Mohapatra, A. G., Talukdar, J., Mishra, T. C., Anand, S., Jaiswal, A., Khanna, A., & Gupta, D. (2022). Fiber Bragg grating sensors driven structural health monitoring by using multimedia-enabled iot and big data technology. Multimedia Tools and Applications, 81(24), 34573–34593. https://doi.org/10.1007/s11042-021-11565-w

Özdemir, K., & Kömeç Mutlu, A. (2024). Cost-Effective Data Acquisition Systems for Advanced Structural Health Monitoring. Sensors, 24(13). https://doi.org/10.3390/s24134269

Patil, S., Banerjee, S., & Tallur, S. (2024). Smart structural health monitoring (SHM) system for on-board localization of defects in pipes using torsional ultrasonic guided waves. Scientific Reports, *14*(1), 24455. https://doi.org/10.1038/s41598-024-76236-w

Plevris, V., & Papazafeiropoulos, G. (2024). AI in Structural Health Monitoring for Infrastructure Maintenance and Safety. In Infrastructures (Vol. 9, Issue 12). Multidisciplinary Digital Publishing Institute (MDPI). https://doi.org/10.3390/infrastructures9120225

Pollastro, A., Testa, G., Bilotta, A., & Prevete, R. (2023). Semi-Supervised Detection of Structural Damage Using Variational Autoencoder and a One-Class Support Vector Machine. IEEE Access, 11, 67098–67112. https://doi.org/10.1109/ACCESS.2023.3291674

Qiu, Y., Wang, Q. B., Zhao, H. T., Chen, J. A., & Wang, Y. Y. (2013). Review on composite structural health monitoring based on fiber Bragg grating sensing principle. Journal of Shanghai Jiaotong University (Science), 18(2), 129–139. https://doi.org/10.1007/s12204-013-1375-4

Tahat, A., Al-Zaben, A., El-Deen, L. S., Abbad, S., & Talhi, C. (2022). An Evaluation of Machine Learning Algorithms in an Experimental Structural Health Monitoring System Incorporating LoRa IoT Connectivity. Conference Record - IEEE Instrumentation and Measurement Technology Conference. https://doi.org/10.1109/I2MTC48687.2022.9806560

Tomassini, E., García-Macías, E., & Ubertini, F. (2024). Fast Stochastic Subspace Identification of Densely Instrumented Bridges Using Randomized SVD. http://arxiv.org/abs/2411.05510

Torzoni, M., Manzoni, A., & Mariani, S. (2024). Enhancing Bayesian model updating in structural health monitoring via learnable mappings. http://arxiv.org/abs/2405.13648

Vélez, A. P., Muñiz, M. Z. F., & Martínez, J. L. F. (2024). Enhancing structural health monitoring with machine learning for accurate prediction of retrofitting effects. AIMS Mathematics, *9*(11), 30493–30514. https://doi.org/10.3934/math.20241472

Yu, X., Fu, Y., Li, J., Mao, J., Hoang, T., & Wang, H. (2024). Recent advances in wireless sensor networks for structural health monitoring of civil infrastructure. In Journal of Infrastructure Intelligence and Resilience (Vol. 3, Issue 1). Elsevier B.V. https://doi.org/10.1016/j.iintel.2023.100066

Zhang, X., Li, L., & Qu, G. (2024). Data-Driven Structural Health Monitoring: Leveraging Amplitude-Aware Permutation Entropy of Time Series Model Residuals for Nonlinear Damage Diagnosis. Sensors, *24*(2). https://doi.org/10.3390/s24020505

4th International Civil Engineering & Architecture Conference
17-19 May 2025, Trabzon, Türkiye

Numerical investigation on the out-of-plane behavior of unreinforced masonry walls with and without opening

Ahmet Yıldırım*[1], Bilge Doran[1], Sema Alacalı[1], Zeynep Ünsal Aslan[2]

[1] Yildiz Technical University, Department of Civil Engineering, 34220 İstanbul, Türkiye
[2] Batman University, Department of Civil Engineering, 72000 Batman, Türkiye

Abstract. Masonry walls are highly vulnerable to out-of-plane (OOP) effects, especially in the case of lateral loadings such as seismic loads. Observations after strong earthquakes show that the main reason for the collapse of masonry walls is the OOP impacts. Therefore, many researchers have investigated to understand and model the actual behavior of masonry walls in this type of loading. This paper aims to examine the behavior of unreinforced masonry walls (URM) with and without openings under OOP loading using the macro-modeling technique. For this purpose, a three-dimensional (3D) nonlinear finite element analysis (NLFEA) was conducted using ANSYS software, utilizing the Extended Drucker-Prager (EDP) plasticity model. The model was validated by comparison with one-way OOP-loaded walls from the literature. The results of the NLFEA exhibited high accuracy in terms of OOP strength capacities and the initial stiffness of the load-displacement relationship. The numerical investigations indicate that the model has the potential to realistically simulate the out-of-plane behavior of URM walls for practical engineering applications.

Keywords: Out-of-plane; Unreinforced masonry wall; Opening; Finite element method; Extended drucker-prager

1. Introduction

Masonry structures, whose most important feature is their simple construction, are among the oldest structural systems in the world (Lourenço, 1996). This type of structure constitutes a high percentage of the building inventory worldwide. For instance, the percentage of unreinforced masonry (URM) buildings among all structures is 93% in Pakistan, 73.2% in Peru, and 52.9% in Australia, based on data from 1998, 2007, and 2000, respectively (Frankie, 2013). A similar situation is observed in Türkiye, where a building census conducted in 2002 revealed that masonry structures accounted for 44.43% of residential buildings and 6.72% of other types, totaling 51.15% of the overall building stock (Özer Ay & Eroğlu Azak, 2021). The masonry building stock highlights the importance of understanding their behavior and developing numerical techniques to simulate it effectively.

In the context of understanding structural behavior, URM walls serve as the primary load-bearing components in buildings. URM walls are particularly vulnerable to earthquake loads due to their nonhomogeneous and complex nature. Despite its critical importance, the out-of-plane (OOP) behavior of URM walls remains less explored. Research on URM walls has predominantly focused on their in-plane performance because it is the main load path in the load transfer mechanism (Noor-E-Khuda et al., 2016); however, there is a limited amount of research available to fully understand the OOP behavior. In this regard, the OOP behavior of URM walls has been investigated both experimentally and numerically by some researchers (Vaculik, 2012; Graziotti, Tomassetti, Sharma, Grottoli, & Magenes, 2019; Messali, Ravenshorst, Esposito, & Rots, 2017). It is vital to highlight that the OOP strength of URM walls with openings, also known as perforated URM walls, decreases when compared to solid walls (Graziotti et al., 2019; Messali et al., 2017; Chong, 1993; Singh & Munjal, 2020; Kahya et al., 2024). Eventually, experiments are necessary to understand the OOP mechanism and also to model the OOP behavior of URM walls (Graziotti et al., 2019). On the other hand, it is highly important to study numerical simulations of the URM walls because the experimental programs are costly and time-consuming (Noor-E-Khuda et al., 2016). Chang, Rots, and Esposito (2022) conducted a numerical study to obtain the two-way bending capacity of unreinforced masonry walls. They used three distinct modeling techniques for the S1 wall (Vaculik, 2012) studied in this paper, namely macro, simplified micro, and micro modeling techniques. They found that the macro-modeling technique is a very computationally cost-effective method to simulate the OOP behavior of the URM walls; to exemplify, it is nearly four times faster than the simplified and micro-modeling techniques, respectively. They have also shown that calibrating the elastic modulus and other related parameters in the numerical model

*Corresponding author, E-mail: ahmet.yildirim@yildiz.edu.tr

https://doi.org/10.31462/icearc2025_ce_sme_248

leads to good agreement with experimental results, particularly in estimating the OOP strength and displacement capacity. Noor-E-Khuda et al. (2016) formulated an explicit finite element (EFE) model, which considers masonry as a macro-homogenized material. They also calibrated the EFE macro-model parameters using the trial and error method based on wall test data (Vaculik, 2012) and found that the numerical results were well consistent with the experimental results.

This study aims to examine the OOP behavior of URM walls with and without openings under constant vertical loads and OOP loading, using the NLFEA macro-modeling technique. In this context, the EDP plasticity model was used in ANSYS software (Mechanical APDL Enterprise Academic Research, Release 23.2). The numerical model results were calibrated with the experimental findings of the S1 Solid Wall Test (Vaculik, 2012).

2. Constitutive modeling

In the macro modeling technique, masonry units and mortar are modelled as a single material. In this chapter, the constitutive model and material properties used in the model will be explained in detail.

The Extended Drucker-Prager (EDP) criterion is used as a constitutive model. This criterion was first developed by Drucker and Prager (Drucker & Prager, 1952) as a pressure-dependent 3D model (Alejano & Bobet, 2012) based on a close approximation to the Mohr-Coulomb yield criterion (De Souza Neto & Perić, 2008). The original form of the Drucker-Prager criterion proposed that if the hydrostatic stress, p, and the invariant of the deviatoric stress, $J_2(s)$, take the value of the critical combination, $\bar{c}$, this is the onset of the plastic yielding (De Souza Neto et al., 2008), as expressed:

$$\sqrt{J_2(s)} + \eta p = \bar{c} \tag{1}$$

In the approximation of the Drucker-Prager criterion to the Mohr-Coulomb criterion, the yield function can be expressed as (De Souza Neto et al., 2008):

$$\sqrt{J_2(s(\sigma))} + \eta p(\sigma) - \xi c = 0 \tag{2}$$

Here, c is defined as the cohesion, while the parameters η and ξ can be named as the parameters determined as the necessary approximation of the Drucker-Prager to the Mohr-Coulomb criterion (De Souza Neto et al., 2008). In the analysis of solid materials like concrete and, as in this study, masonry, it is convenient to use the biaxial fit approximation of the Drucker-Prager to the Mohr-Coulomb criterion in the principal stress axis, as seen in Fig. 1. This is because masonry exhibits a very high compressive-to-tensile strength ratio, and using the uniaxial fit can significantly overestimate the OOP strength or the limit load (De Souza Neto et al., 2008). The biaxial fit parameters η and ξ can be defined as (De Souza Neto et al., 2008):

$$\eta = \frac{3sin\phi}{2\sqrt{3}} \tag{3}$$

$$\xi = \frac{2cos\phi}{\sqrt{3}} \tag{4}$$

According to Ansys® Material Reference Guide, the EDP criterion is an extension of the linear Drucker-Prager yield criterion, allowing the definition of both yield surface and the flow potential as linear, hyperbolic, or power law independently, and thus results in either an associated or nonassociated flow rule. The EDP linear yield criterion form in the ANSYS Software could be defined as (Release 25.1):

$$f(\sigma, \sigma_y) = \sigma_e + \alpha \frac{1}{3} tr(\sigma) - \sigma_y = 0 \tag{5}$$

The α and σ_y parameters in Eq. (5) correspond to the properties of “pressure sensitivity” and “uniaxial yield stress”, respectively. These two parameters can be expressed as in Eqs. (8) and (9) after defining the Eqs. (6) and (7) (De Souza Neto et al., 2008; Ansys® Material Reference Guide):

$$\sigma_e = \sqrt{3J_2(s)} \tag{6}$$

$$\frac{1}{3} tr(\sigma) = p(\sigma) \tag{7}$$

$$\alpha = \eta\sqrt{3} \tag{8}$$

$$\sigma_y = \xi c\sqrt{3} \tag{9}$$

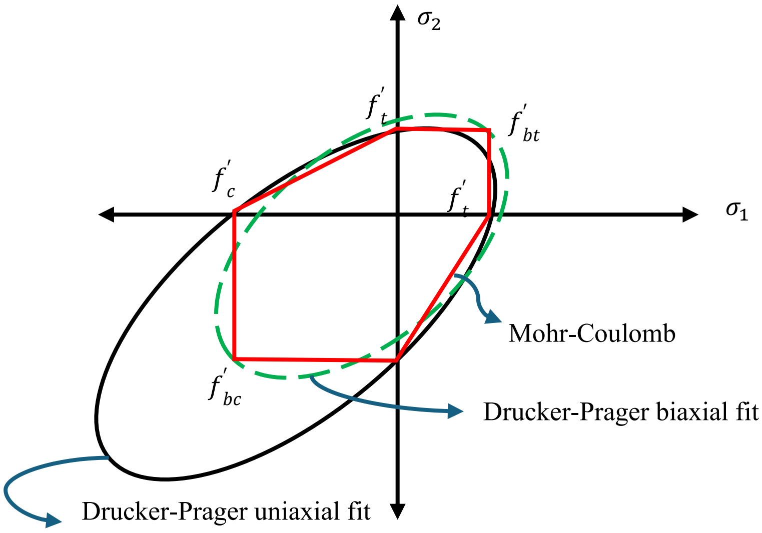

Fig. 1. EDP biaxial fit used in the model (De Souza Neto et al., 2008)

To determine the parameters α and σ_y according to Eqs. (8) and (9), ϕ and c must be known to determine η and ξ parameters given in Eqs. (3) and (4), respectively. Then, the following equations are used to define ϕ and c using compressive strength (f_c) and tensile strength (f_t) of the masonry (De Souza Neto et al., 2008):

$$\phi = sin^{-1}\left(\frac{f_c - f_t}{f_c + f_t}\right) \tag{10}$$

$$c = \frac{f_c f_t}{f_c - f_t} tan\phi \tag{11}$$

Eventually, the parameters α and σ_y can be expressed based on Eqs. (12) and (13) as follows:

$$\alpha = \frac{3sin\phi}{2} \tag{12}$$

$$\sigma_y = 2ccos\phi \tag{13}$$

Moreover, it should also be noted here that the plastic flow potentials are defined by the plasticity model as associative instead of non-associative for the sake of simplicity. The evolution of plastic strain is controlled by the flow rules: When the associative flow is used, plastic strain increases proportionally to the stress increment of the material (Ansys® Material Reference Guide). Obviously, this results in dilation (expansion) of the volume of the material with plastic deformations. In the space of stresses, the plastic strain rate is normal to the yield surface when an associative flow model is used (De Souza Neto et al., 2008). To define the plasticity model as associative in ANSYS Software, associativity is selected as the linear form (Ansys® Material Reference Guide):

$$Q(\sigma, \sigma_y) = \sigma_e + \bar{\alpha}\frac{1}{3}tr(\sigma) \tag{14}$$

The parameter $\bar{\alpha}$, defined as flow potential pressure sensitivity, was taken equal to α as defined in Eq. (12) in order to realize associative flow.

After the constituting material model, the study was conducted to calibrate the elastic and plastic parameters in the S1 wall. The calibration process for the material properties of the model is executed using four key parameters: Elastic Modulus, Poisson's ratio, compressive strength (f_c), and tensile strength (f_t). The value of compressive strength is taken from the experiment (Vaculik, 2012) as 17.6 MPa. Poisson's ratio is assumed as 0.2, generally preferred in the masonry materials (Graziotti et al., 2019; Noor-E-Khuda et al., 2016; Singh et al., 2020). The Elastic Modulus is calibrated to reflect the experimental behavior of the wall accurately; specifically, it is selected as a value of 7000 MPa, as reported in the literature (Chang et al., 2022). The tensile strength is established at 0.15 MPa with the trial-and-error method, reflecting the low tensile capacity typically associated with masonry materials. Table 1 shows the summary of the material parameters used in this study.

Table 1. Material parameters

Elastic Parameters	Modulus of Elasticity (MPa)	Poisson's Ratio	Compressive Strength (MPa)	Tensile Strength (MPa)
	7000	0.2	17.6	0.15
Plastic Parameters	Pressure Sensitivity	Uniaxial Yield Stress (MPa)	Flow Potential Pressure Sensitivity	
	1.4746	0.2975	1.4746	

3. Numerical simulation

The increasing emphasis on preserving historic structures and buildings has increased the need for advanced numerical methods for structural analysis (Koksal et al., 2016). The main objective in numerical analysis is to simulate the actual behavior of structural elements using computerized methods. One of them is the finite element (FE) method, which discretizes structural parts into smaller finite elements with certain properties like degree of freedom and shape to create a mathematical model. FE analysis for masonry is generally achieved by the macro-modeling approach, in which masonry is taken as a homogenous continuum. The reason for using the macro-modeling technique is the efficiency, computational cost, and analysis time (Doran, Karslioglu, Unsal Aslan, & Vatansever, 2023).

In the numerical simulation, the model is constructed utilizing the experimental data presented by Vaculik (Vaculik, 2012). The analysis focuses on the solid S1 and S3 walls with a window opening, initially subjected to a precompression of 0.1 MPa. Upon the complete application of this load, a unidirectional lateral pressure to the main wall is imposed via airbags, inducing compression in the return walls. This one-way loading test is designed to evaluate the ultimate load-bearing capacity of the wall.

For numerical model calibration, the EDP model was used to accurately capture the nonlinear behavior of the wall in the finite element analysis software ANSYS Mechanical APDL. The boundary conditions, mesh, and the exerted loads are shown in Fig. 2. It is highly important to mention that SOLID186, a 3D 20-node solid element, is used as a finite element type (Ansys® Element Reference Guide, Release 25.1). The mesh size of 55 mm is selected after a sensitivity analysis by considering accuracy and efficiency. The boundary conditions were selected so that the sides of the walls behave like fixed supports (F), the upper and lower parts of the wall are simply supported (SS), and the base is supported vertically. These boundary conditions are also illustrated in the bottom-right sections of Figs. 3 and 4, adapted from the literature (Vaculik, 2012). The dimensions are in “mm” in these Figs.

The pre-compression load of 0.1 MPa is applied during the first time step over both the return walls and the main wall, as shown in Fig. 2. It should be noted that, there is a window opening at the middle left for the S3 wall, shown in the bottom-right section of Fig. 4. In the second time step, the OOP pressure load is applied uniformly and monotonically to push the main face of the wall to simulate the airbag pressure load.

It is noteworthy to mention that nonlinearity in the model is introduced through the material scale, and geometric nonlinearity is not considered within the model framework. It should also be noted that including geometric nonlinearity and prestress effects can lead to a reduction in OOP strength by approximately 1% to 5%. However, this effect is often considered negligible in the macro-modeling of such structures, allowing for simplification of the analysis. The experimental data were evaluated by examining the relationship between the applied pressure and the midpoint displacement of the wall (Vaculik, 2012). The total OOP support force versus the maximum OOP displacement of the midpoint graph was obtained. The total OOP support force is calculated by the applied pressure times the area of the wall, and the OOP displacement of the midpoint is taken as given in the literature (Vaculik, 2012). Then, the results of the numerical model are compared with the experimental results. The displacement is limited to approximately 16 mm, considering near-collapse conditions (Beyer, Araya, & Saloustros, 2022).

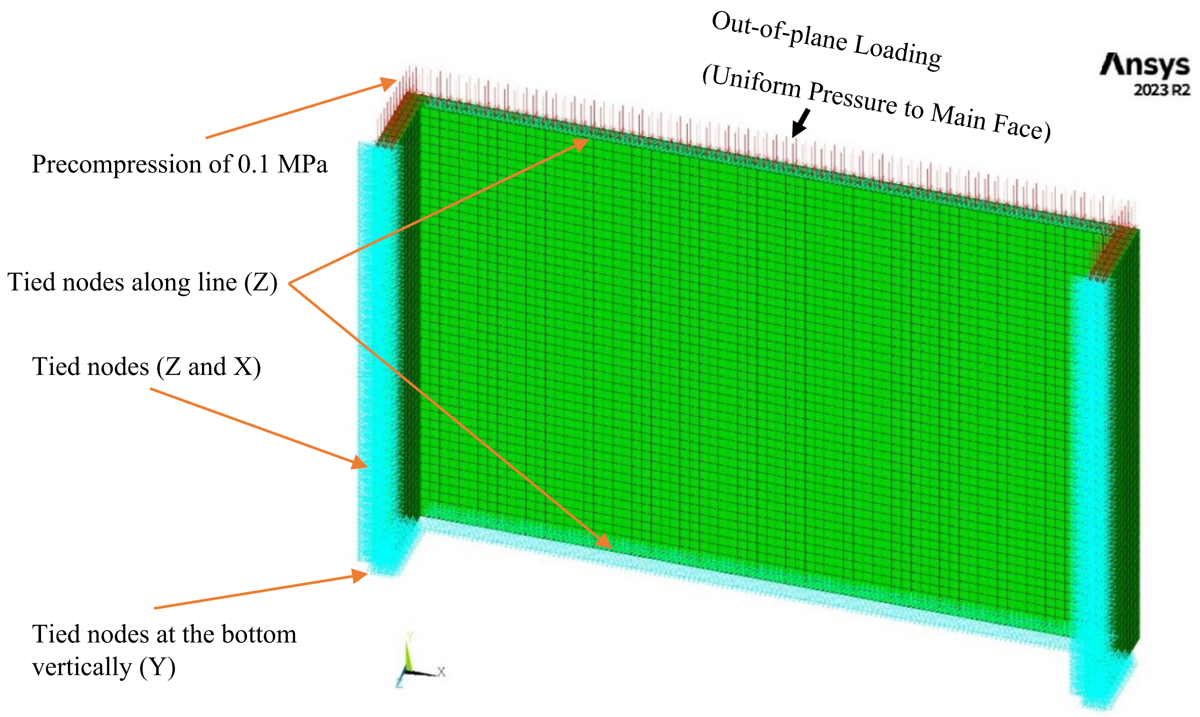

Fig. 2. FE mesh with boundary and loading conditions

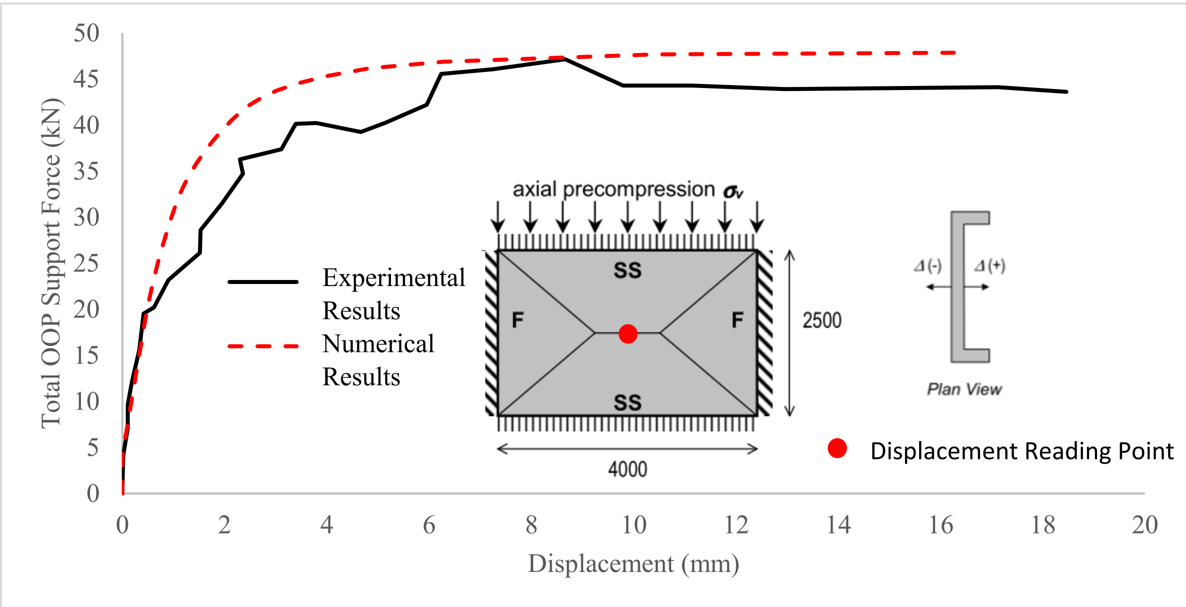

Fig. 3. Out-of-plane load – displacement response of S1 wall

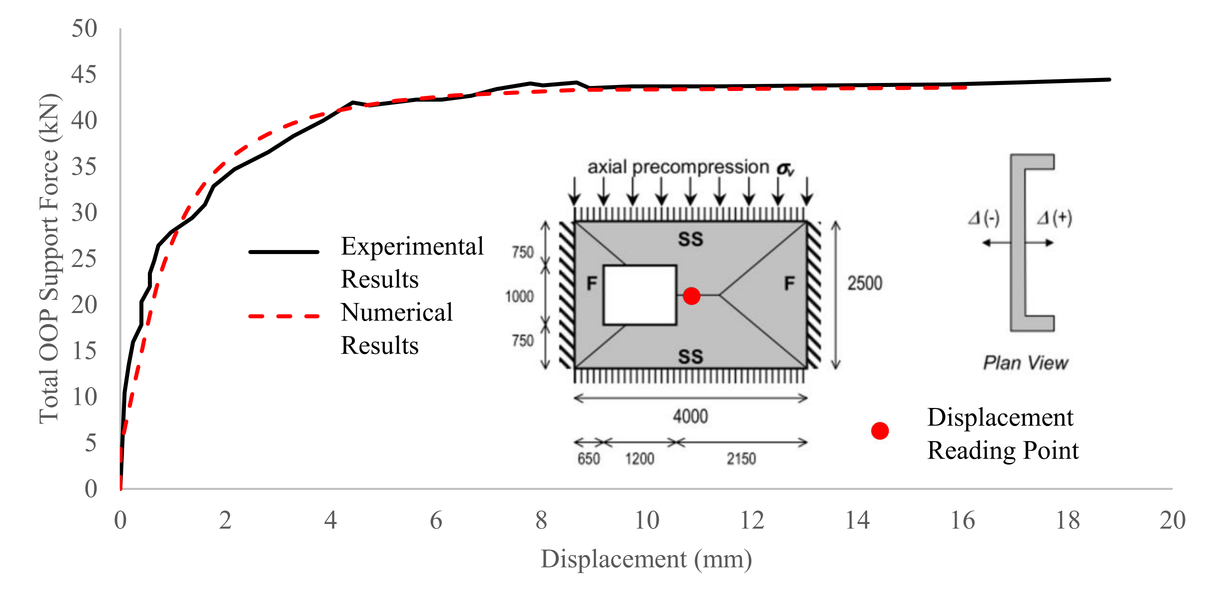

Fig. 4. Out-of-plane load – displacement response of S3 wall

Table 2. Comparison of model and experimental results

		S1 Wall	S3 Wall
OOP Strength (kN)	Experiment	47.14	44.12
	Model	47.85	43.57

It can be seen from the numerical results and Table 2 that the model proposed in this study accurately captures the OOP strength of the walls and initial stiffness to some degree. In Table 2, it is clear that the OOP strength decreases when an opening exists in the solid wall, as expected. In Figs. 3 and 4, OOP responses of the experimental results and numerical results also demonstrate a strong correlation with the overall load-displacement relation.

Finally, it is important to mention computational cost, which can be defined as the total amount of time required for an analysis. Maximum analysis time can be mentioned as 20 minutes for an analysis studied in this paper with the processor of the employed desktop of Intel(R) Core(TM) i5-10400 CPU @ 2.90GHz. This suggests that the numerical strategy is computationally efficient when compared to other studies, for instance, Chang et al. (2022).

4. Conclusions

Masonry structures, maintaining their existence from the beginning of humanity, will continue to play a significant role in our built environment. The efforts to understand the behavior of these structures are highly important to ensure their presence for both historic and new buildings. Based on the evaluations conducted on solid walls and those with openings, using a macro-modeling approach and the EDP criterion, the following conclusions can be drawn:

- The proposed macro-modeling strategy provides a computationally efficient alternative by requiring few parameters and less computational cost for capturing the nonlinear behavior of masonry walls under out-of-plane loading.
- Sensitivity to material parameters, such as compressive and tensile strength, was observed to significantly influence the predicted capacity, highlighting the importance of accurate material calibration.
- The inclusion of an opening in URM walls was found to reduce their OOP strength when compared to solid walls.
- The initial stiffness of the wall could be correctly determined with the calibration of the elasticity modulus while still in line with the overall load-displacement response.

References

Alejano, L.R., & Bobet, A. (2012). Drucker-Prager criterion. *Rock Mechanics and Rock Engineering*, *45*(6), 995–999. https://doi.org/10.1007/s00603-012-0278-2

Ansys® Academic Research Mechanical, Release 25.1, Help System, Element Reference Guide, ANSYS, Inc.

Ansys® Academic Research Mechanical, Release 25.1, Help System, Material Reference Guide, ANSYS, Inc.

Ansys® Mechanical APDL Enterprise Academic Research, Release 23.2
Beyer K., Araya E.A.I., Saloustros S. (2022). Drift capacity models for the new masonry chapter of eurocode 8 part 1-2. *Springer Proceedings in Earth and Environmental Sciences*, 398–416. https://doi.org/10.1007/978-3-031-15104-0_24
Chang, L.Z., Rots, J.G., & Esposito, R. (2022). Influence of openings on two-way bending capacity of unreinforced masonry walls. *Journal of Building Engineering, 51*(January), 104222. https://doi.org/10.1016/j.jobe.2022.104222
Chong, V.L. (1993). *The behavior of laterally loaded masonry panels with openings* (Doctoral dissertation). University of Plymouth, University of Plymouth Pearl. https://pearl.plymouth.ac.uk/secam-theses/271
De Souza Neto, E.A., Perić, D., & Owen, D.R.J. (2008). Computational Methods for Plasticity: Theory and Applications. John Wiley & Sons Ltd. https://doi.org/10.1002/9780470694626
Doran, B., Karslioglu, M., Unsal Aslan, Z., & Vatansever, C. (2023). Experimental and numerical investigation of unreinforced masonry walls with and without opening. *International Journal of Architectural Heritage*, *17*(11), 1833–1854. https://doi.org/10.1080/15583058.2022.2080611
Drucker, D.C., & Prager, W. (1952) Soil mechanics and plastic analysis or limit design. *Quarterly of Applied Mathematics, 10*(2), 157-165. Retrieved from https://jstor.org/stable/43633942
Frankie, T.M., Gencturk, B., & Elnashai, A.S. (2013). Simulation-Based Fragility Relationships for Unreinforced Masonry Buildings. *Journal of Structural Engineering*, *139*(3), 400–410. https://doi.org/10.1061/(asce)st.1943-541x.0000648
Graziotti, F., Tomassetti, U., Sharma, S., Grottoli, L., & Magenes, G. (2019). Experimental response of URM single leaf and cavity walls in out-of-plane two-way bending generated by seismic excitation. *Construction and Building Materials*, *195*, 650–670. doi.org/10.1016/j.conbuildmat.2018.10.076
Kahya, V., Genç, A.F., Sunca, F., Roudane, B., Altunişik, A.C., Yilmaz, S., Günaydin, M., Dok, G., Kirtel, O., Demir, A., Aykanat, B., Arslan, M.E., Saribiyik, A., Aydin, F., Aslan, B., Sezdirmez, T., Tatar, T., Emiroğlu, M., Atmaca, B., … Akgül, T. (2024). Evaluation of earthquake-related damages on masonry structures due to the 6 February 2023 Kahramanmaraş-Türkiye earthquakes: A case study for Hatay Governorship Building. *Engineering Failure Analysis*, *156*(December 2023). https://doi.org/10.1016/j.engfailanal.2023.107855
Koksal, H.O., Doran, B., Kuruscu, A.O., & Kocak, A. (2016). Elastoplastic finite element analysis of masonry shear walls. *KSCE Journal of Civil Engineering*, *20*(2), 784–791. https://doi.org/10.1007/s12205-015-0393-1
Lourenço , P.B. (1996). *Computational strategies for masonry structures* (Doctoral dissertation). Delft University of Technology, TU Delft Repository. https://resolver.tudelft.nl/uuid:4f5a2c6c-d5b7-4043-9d06-8c0b7b9f1f6f
Messali, F., Ravenshorst, G., & Esposito, R. (2017). *Large-Scale Testing Program for the Seismic Characterization of Large-Scale Testing Program for the Seismic*. *January*.
Noor-E-Khuda, S., Dhanasekar, M., & Thambiratnam, D.P. (2016). An explicit finite element modelling method for masonry walls under out-of-plane loading. *Engineering Structures*, *113*, 103–120. https://doi.org/10.1016/j.engstruct.2016.01.026
Özer Ay, B., & Eroğlu Azak, T. (2021). A comparative investigation of changing building characteristics in Turkey. *Cukurova University Journal of the Faculty of Engineering*, *36*(4), 1111–1126 (in Turkish). https://doi.org/10.21605/cukurovaumfd.1048380
Singh, S.B., & Munjal, P. (2020). Out-of-plane response of ECC strengthened masonry wallets with openings. *KSCE Journal of Civil Engineering*, *24*(7), 2078–2087. https://doi.org/10.1007/s12205-020-1346-x
Vaculik, J. (2012). *Unreinforced masonry walls subjected to out-of-plane seismic actions* (Doctoral dissertation). University of Adelaide, University of Adelaide Digital Library. http://hdl.handle.net/2440/77089

ICEARC'25
4th International Civil Engineering & Architecture Conference
17-19 May 2025, Trabzon, Türkiye

Effects of different basement wall configurations on structural seismic behavior of the buildings

Burak Çakıl*[1], Ömer F. Osmanlı[1], Ömer F. Taş[1], Ozan İnce[1], Erkut Sayın[1], Muhammet Karaton[1]

[1] *Fırat University, Department of Civil Engineering, 23119 Elazığ, Türkiye*

Abstract. Earthquakes are one of the most significant natural disasters that cause ground shaking and challenge the durability and rigidity capacities of structures. Particularly, high-magnitude earthquakes can lead to the collapse of poorly engineered or substandard structures, resulting in substantial loss of life and property. To minimize such devastating effects, earthquake-resistant building design is important. One of the significant structural elements used in the earthquake resistance of structures is basement walls. These walls increase the lateral stiffness and strength of structures, limit the inter-story drifts and reduce the torsional effects. In this study, the effects of different basement wall configurations on seismic performance of structures were investigated. For this purpose, four different building models were generated with SAP2000 software for numerical analyses. The first model represents a regular system with basement walls at all four sides of the building. In the second model there are basement walls at three sides of the building, while third one includes at two sides. In the fourth model, a single basement wall was present. The January 24, 2020 Elazığ earthquake (Mw: 6.8) was used in time history analyses. As a result of the dynamic analyses, it was revealed that the placement of basement walls significantly affects the behavior of buildings during earthquakes.

Keywords: Reinfoced concrete buildings; Basement wall; Dynamic analysis

1. Introduction

Earthquakes have caused significant loss of life and demonstrated that the design and construction of the building are among the most critical issues. Especially last earthqauekes occurred in Pazarcık-Kahramanmaraş (M_w=7.8) and Elbistan-Kahramanmaraş (M_w=7.5) have exhibited that the design of reinforced concrete (RC) buildings, which constitute the majority of the building stock, is of critical importance in terms of both reducing loss of life and preventing damage (İnce, 2024; Özmen et al., 2024). Understanding the specific damage mechanisms and the factors that influence the response of RC buildings to seismic loads is essential for improving their resilience. The seismic behavior of the RC structures is strengthened by using the structural elements that have more shear force capacity, especially for the basement level. Although the basement walls provide a significant advantages for the RC buildings, the unusual deisgn and different location configuration of these structural elements may cause negative effects under earthquake loading.

The behavior of the RC basement walls was investigated in the literature based on several parameters that effective on the buildings that are designed with basement walls. The number of stories that constructed with basement walls was investigated for 7, 20, and 40 floor RC buildings in 2018 (Kılıç Erdim, 2018). In the study, the basement wall stories was changed by 3, 5, and 7 floor for the building models and compared with the buildings that has no basement walls. The behavior, stiffness and period of the building was investigated. By increasing the stiffness, the period of the building with basement walls decreases between 6% and 25% depending on the building floor plans. In the low-rise frame building, the base shear forces of buildings with basement walls increased by 1%-16%, and the base shear forces of high-rise rigid buildings increased by 1%-13% compared to the base shear forces of buildings with non-basement wall buildings. Gökçeoğlu investigated the nonlinear behavior of a 26-storey RC building based on the Türkiye Building Earthquake Code 2018 (TBEC 2018) considering basement wall placement (Gökçeoğlu, 2020). Performance criterias were determined with the approaches specified in TBDY 2018, and the Collapse Prevention criteria level was achieved. Perform3D software was used for nonlinear analyses. The RC structural elements were modeled by taking into account of nonlinear behavior of the elements. In the study, the design of the building was changed; a shear wall was added to one axis of the building, the height

*Corresponding author, E-mail: burakk.cakill@gmail.com

https://doi.org/10.31462/icearc2025_ce_sme_258

golden light publishing

was changed, and the design method was re-evaluated. The effects of the changes were investigated by comparing the new design with the previous design. Based on the results of the study, no significant base shear force or amount of reinforcement differences are observed throughout the buildings. The reason for this situation can be explained by a lot of reinforced concrete shear walls in the second building and the limited number of shear walls added to the first designed building. Öztemel et al. were analysed the building models with and without basement walls in order to investigate the effects of the placement of shear walls in the plan on the structural behavior in RC buildings (Öztemel et al. 2022). 6 numerical models with different shear wall placements were produced with the İdeCad software. In the analyses, parameters such as vibration period, base shear force, horizontal displacement, torsion coefficient, relative story drift and cost were evaluated. As a result, it was determined that the earthquake effects were decrased in the model where the basement floor was completely surrounded by shear walls, but the cost increased, and that the use of additional shear walls was required in the model that designed with only RC frame system. Özcan was compared the 9-story two type of RC building with and without basement wall by using ETABS software (Özcan, 2024). The comparisons were achieved for two different solution method by considering the base shear forces, maximum floor displacements, irregularities available in TBEC 2018, and relative floor displacements.

In this study, the effects of different basement wall configurations on structural seismic behavior of the buildings was investigated. Four different building model was constituted in SAP2000 software for the time-history analyses. The basement walls was located on all around the building basement, third side, two adjesent side, and only single side of the basement for the 1st , 2nd , 3rd and the 4th building models respectively. Elazığ 2020 earthquake record was applied to the buildings for x, y, and the z directions. the comparisons was achieved in terms of story displacements, rotation angle, angular velocity, and angular acceleration values.

2. Materials and methods

In this study, four different structural models were generated to investigate the effects of RC basement walls, on the structural dynamics of RC buildings. The buildings consist of a basement, a ground storey, and four typical storey (B+G+4), with identical cross-sectional properties for all structural elements.

- **Model 1**: The basement is entirely enclosed by RC walls.
- **Model 2**: The basement has RC walls on three sides.
- **Model 3**: The basement has RC walls on two sides.
- **Model 4**: The basement has an RC wall on only one side.

The basement storey plans and the corresponding three-dimensional structural models are presented in Fig. 1–4.

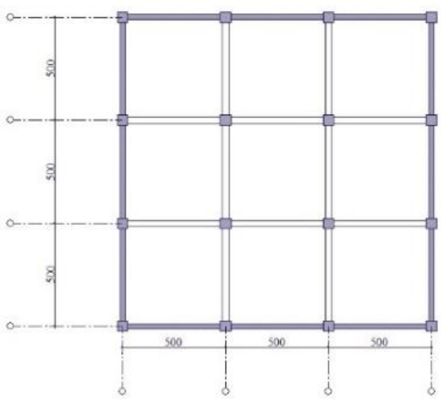

(a)

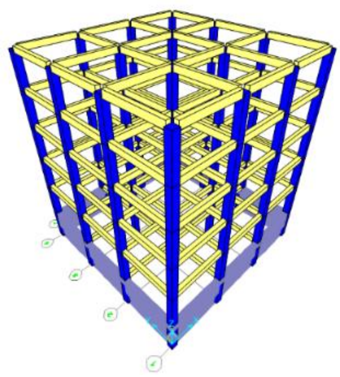

(b)

Fig. 1. Model 1 (a) basement storey plan (cm) (b) three-dimensional finite element model

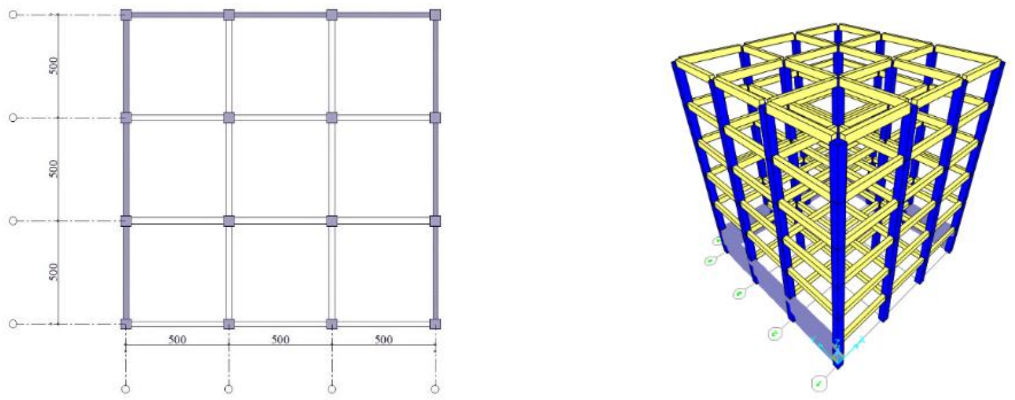

(a) (b)

Fig. 2. Model 2 (a) Basement storey plan (cm) (b) Three-dimensional finite element model

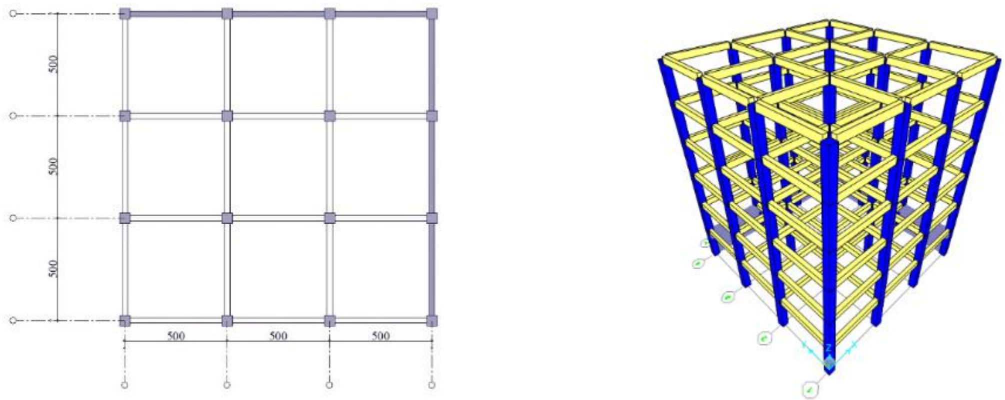

(a) (b)

Fig. 3. Model 3 (a) Basement storey plan (cm) (b) Three-dimensional finite element model

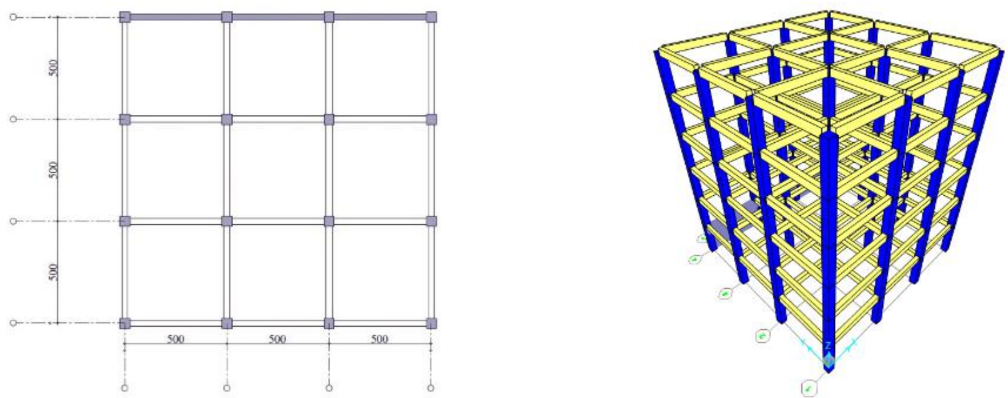

(a) (b)

Fig. 4. Model 4 (a) Basement storey plan (cm) (b) Three-dimensional finite element model

In the design of the RC buildings, C25/30 concrete grade and B420C reinforcing steel were considered. The columns were designed with cross-sections of 50×50 cm, while the beams had cross-sections of 30×50 cm. The analyses accounted for the effective section stiffness of the structural elements. To improve the realistic representation of the basement, spring stiffness values derived from the subgrade modulus were incorporated into the foundation system. The subgrade modulus was assumed to be approximately 17000 kN/m³, corresponding to an average foundation excavation on ZD-type soil in Elazığ. Based on this value, the spring stiffness was calculated as 1050 kN/m and integrated into the model. The spring elements are illustrated in Fig. 5.

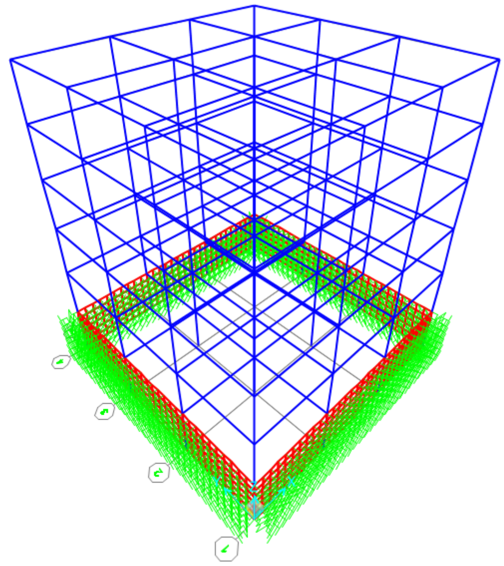

Fig. 5. Ground spring model

To investigate the seismic behavior of the buildings, linear time-history analysis was performed. In this study, the buildings were assumed to be located in Elazığ, and accordingly, the original ground motion records from the 24 January 2020 Elazığ Earthquake (Mw 6.8) were used. The earthquake data were obtained from AFAD's Station No. 2308 [AFAD]. The acceleration-time histories of the earthquake in the East-West (E-W), North-South (N-S), and Up directions are presented in Fig. 6–8, respectively. The seismic records were applied to the structure as follows: E-W component in the x-direction, N-S component in the y-direction, and Up component in the z-direction for the analyses. As a result of the analysis, the displacement values of the structures in the x, y and z directions as well as the rotation angle, angular velocity and angular acceleration values in the z direction were examined.

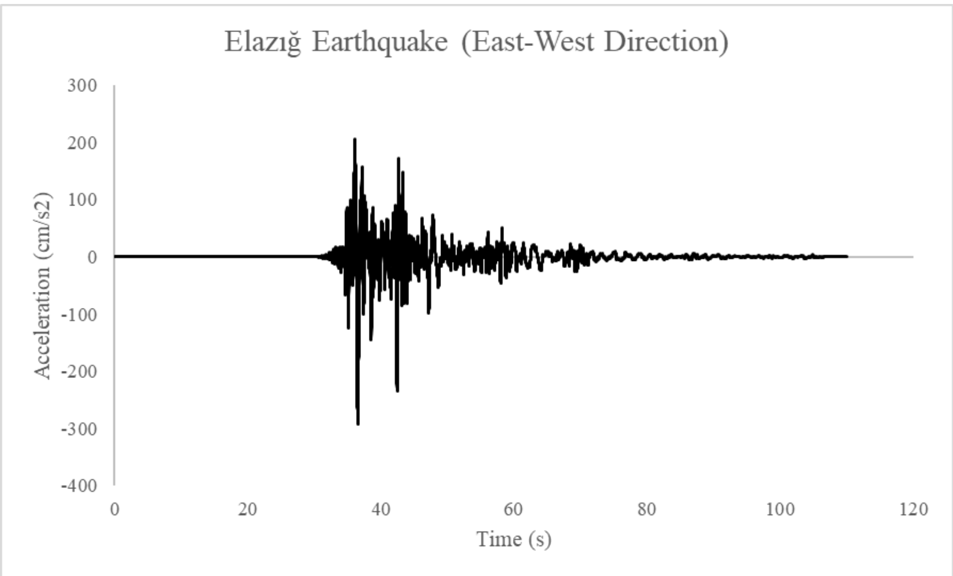

Fig. 6. Acceleration-time graph of the earthquake in the E-W direction

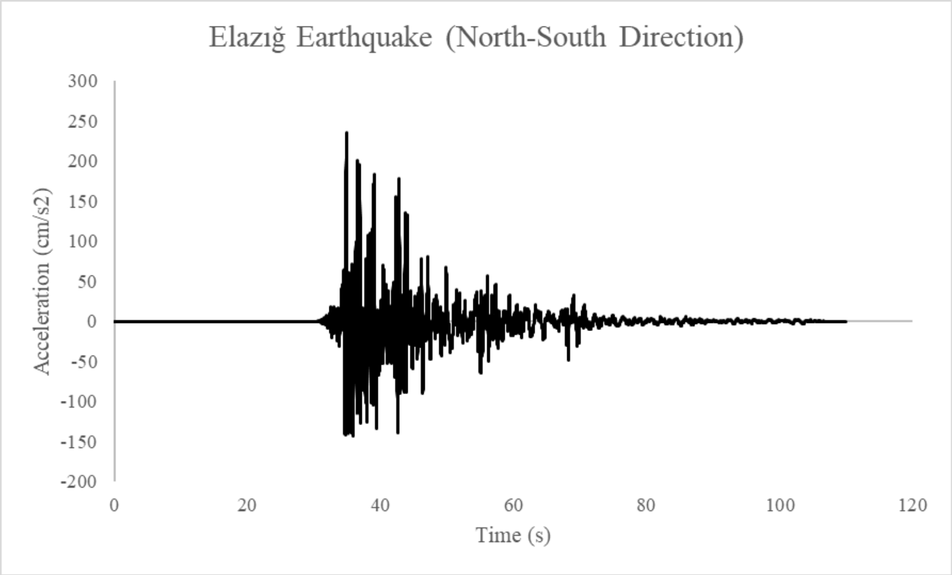

Fig. 7. Acceleration-time graph of the earthquake in the N-S direction

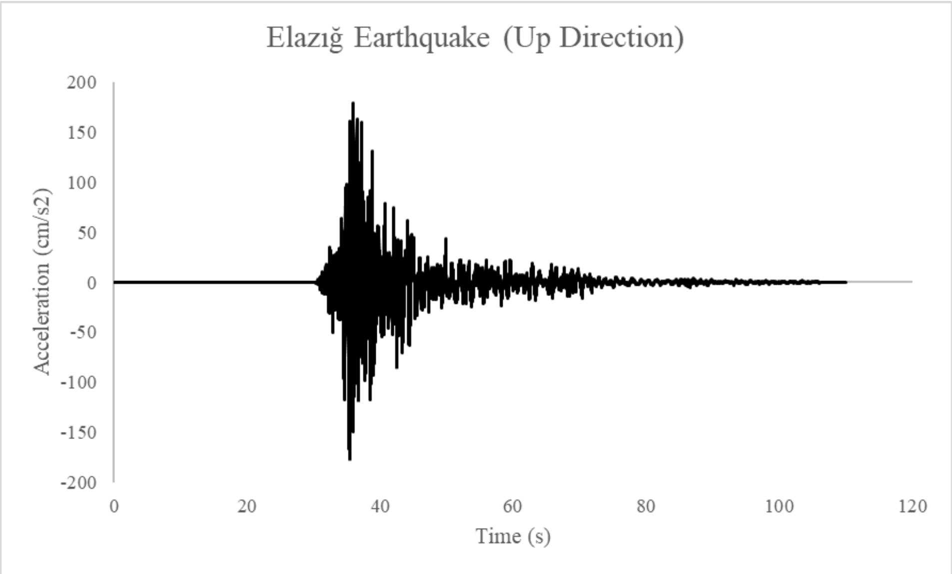

Fig. 8. Acceleration-time graph of the earthquake in the Up direction

3. Results and discussion

This section presents and discusses the results of the analyses conducted to evaluate the effect of basement walls on the torsional behavior of the structure. The assessment is based on displacement, rotation angle, angular velocity, and angular acceleration values obtained at different storey levels for the four structural models with varying basement wall configurations. According to the analysis results, displacement values in the x, y, and z directions are presented in Table 1, Table 2, and Table 3, respectively. The results indicate that displacements in the x and y directions increase significantly as the number of basement walls decreases (Fig. 9–10). In Model 1, where the structure is fully enclosed by basement walls, the lowest displacement values are observed. In contrast, Model 4, with only one basement wall, exhibits notably higher displacements, particularly at the upper storey levels. For instance, at the fourth storey, the displacement in the x direction increases from 0.1397 m in Model 1 to 0.2024 m in Model 4. Similarly, displacements in the y direction also show a clear increase from Model 1 to Model 4. This finding highlights the significant contribution of basement walls to the overall stiffness of the structural system. However, when examining the displacement values in the z direction, the variation appears to be quite limited (Fig. 11). While there is no significant difference between Model 1 and Model 2, slight increases are observed in Models 3 and 4. This suggests that as stiffness decreases from the ground level upward, greater movement occurs in the upper stories.

Table 1. Displacement results in the x direction

Storey level	Displacement (m)			
	Model 1	Model 2	Model 3	Model 4
Foundation (-2)	0	0	0	0
Basement (-1)	0.000419	0.001578	0.015228	0.026747
Ground (0)	0.025324	0.027761	0.044894	0.07213
1. Storey (1)	0.063542	0.066713	0.07982	0.117964
2. Storey (2)	0.098506	0.101987	0.113111	0.156644
3. Storey (3)	0.124101	0.127715	0.13853	0.184712
4. Storey (4)	0.139727	0.143427	0.154798	0.202446

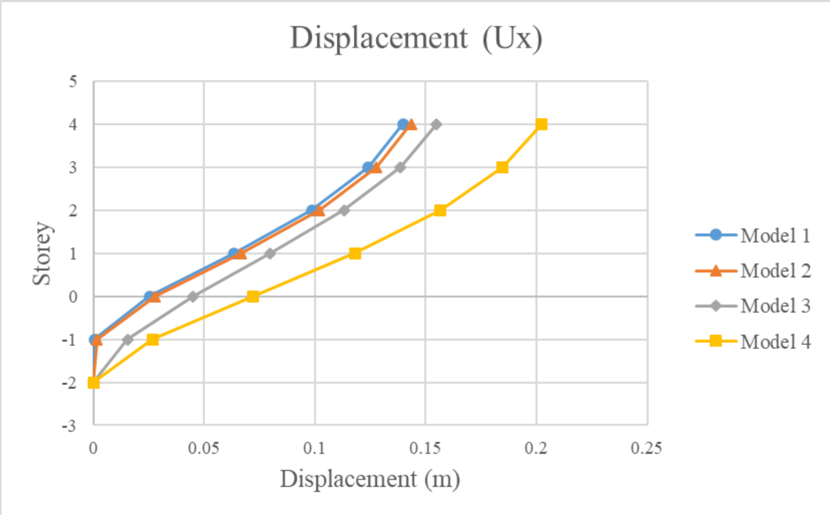

Fig. 9. Storey-displacement graph in x direction

Table 2. Displacement results in the y direction

Storey level	Displacement (m)			
	Model 1	Model 2	Model 3	Model 4
Foundation (-2)	0	0	0	0
Basement (-1)	0.0002	0.00043	0.015181	0.017451
Ground (0)	0.011756	0.012192	0.041332	0.042923
1. Storey (1)	0.029186	0.030024	0.068895	0.066103
2. Storey (2)	0.045416	0.046636	0.094148	0.084924
3. Storey (3)	0.057504	0.058983	0.115442	0.09965
4. Storey (4)	0.065075	0.066754	0.130473	0.109548

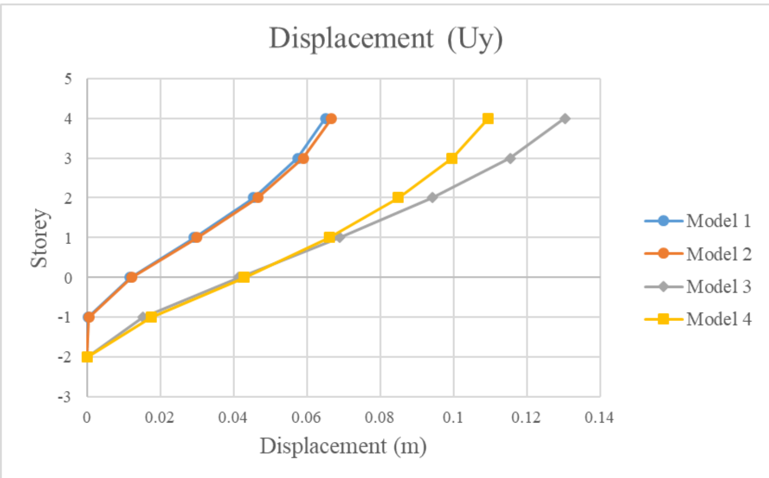

Fig. 10. Storey-displacement graph in y direction

Table 3. Displacement results in the z direction

Storey level	Displacement (m)			
	Model 1	Model 2	Model 3	Model 4
Foundation (-2)	0	0	0	0
Basement (-1)	0.000834	0.000843	0.000935	0.000999
Ground (0)	0.001631	0.001639	0.001877	0.002022
1. Storey (1)	0.002447	0.002464	0.002725	0.002911
2. Storey (2)	0.003185	0.003204	0.003356	0.003558
3. Storey (3)	0.003667	0.003686	0.003742	0.003948
4. Storey (4)	0.003882	0.003901	0.003913	0.004119

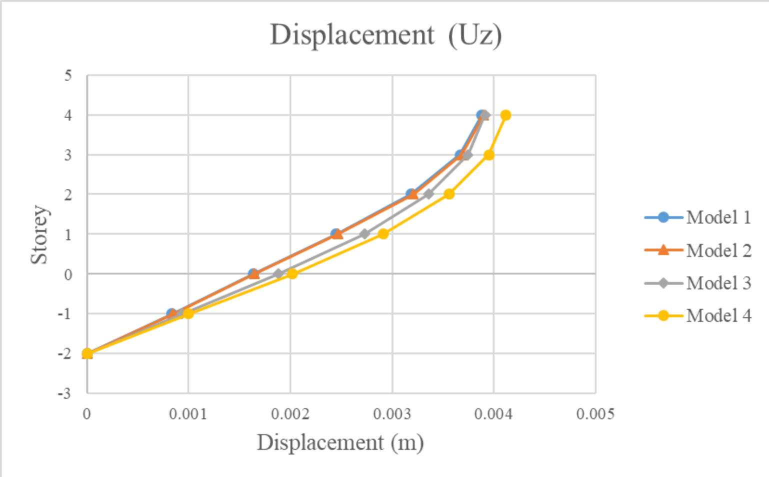

Fig. 11. Storey-displacement graph in z direction

When examining the rotation angle values calculated in the z direction, it is observed that the torsional effect increases as the number of basement walls decreases (Table 4, Fig. 12). For instance, at the fourth storey, the rotation angle in Model 1 is 0.0000079 rad, whereas in Model 4, this value increases to 0.0112 rad. This indicates that the reduction in basement walls leads to a decrease in structural stiffness, resulting in an increased torsional effect at storey levels.

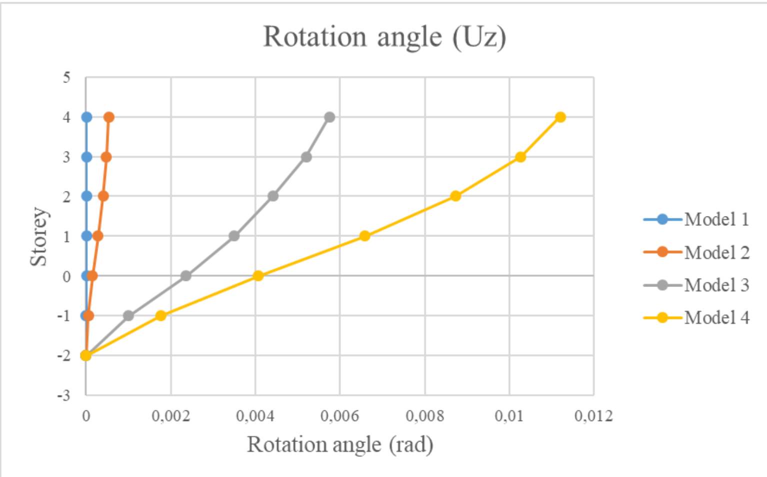

Fig. 12. Storey-rotation angle graph in the z direction

Table 4. Results of rotation angle in z direction

Storey level	Rotation angle (rad)			
	Model 1	Model 2	Model 3	Model 4
Foundation (-2)	0	0	0	0
Basement (-1)	0.000000053	0.000052	0.001008	0.001762
Ground (0)	0.000007072	0.000156	0.00236	0.004066
1. Storey (1)	0.000011	0.000287	0.003499	0.006588
2. Storey (2)	0.000009391	0.000399	0.004407	0.00872
3. Storey (3)	0.000005955	0.00048	0.005198	0.010268
4. Storey (4)	0.000007946	0.000532	0.00575	0.011199

The angular velocity results exhibit a similar trend. While the angular velocity values remain low in Models 1 and 2, a significant increase is observed in Model 3, and especially in Model 4, due to torsional effects (Table 5, Fig. 13). For instance, at the fourth storey, the angular velocity increases from 0.000165 rad/s in Model 1 to 0.083 rad/s in Model 4.

Table 5. Angular velocity results in the z direction

Storey level	Angular velocity (rad/s)			
	Model 1	Model 2	Model 3	Model 4
Foundation (-2)	0	0	0	0
Basement (-1)	0.000002218	0.0004409	0.00727	0.012
Ground (0)	0.0001158	0.001482	0.016	0.031
1. Storey (1)	0.0001251	0.00228	0.026	0.048
2. Storey (2)	0.0001057	0.00322	0.033	0.065
3. Storey (3)	0.0001011	0.003953	0.04	0.075
4. Storey (4)	0.0001652	0.004367	0.044	0.083

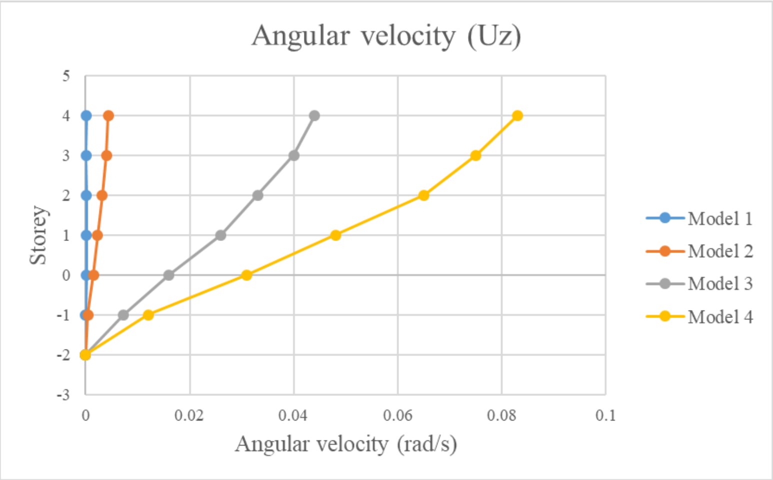

Fig. 13. Storey-angular velocity graph in the z direction

A similar trend is observed in the angular acceleration values, with the highest values recorded in Model 4 (Table 6, Fig. 14). For instance, at the fourth storey, the angular acceleration increases from 0.0049 rad/s² in Model 1 to 0.704 rad/s² in Model 4.

Table 6. Angular acceleration results in the z direction

Storey level	Angular acceleration (rad/s^2)			
	Model 1	Model 2	Model 3	Model 4
Foundation (-2)	0	0	0	0
Basement (-1)	0.0001864	0.018	0.121	0.249
Ground (0)	0.007466	0.031	0.227	0.277
1. Storey (1)	0.005675	0.034	0.26	0.427
2. Storey (2)	0.005833	0.047	0.302	0.603
3. Storey (3)	0.007152	0.056	0.335	0.697
4. Storey (4)	0.004909	0.045	0.385	0.704

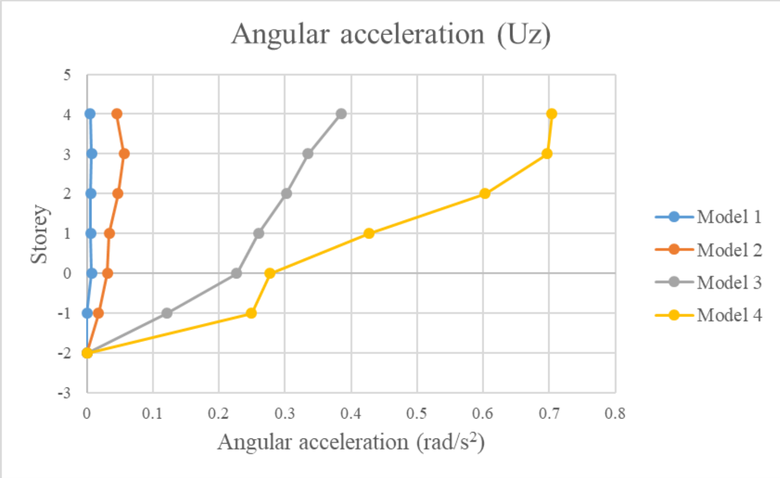

Fig. 14. Storey-angular acceleration graph in the z direction

4. Conclusions

The analysis results indicate that basement walls directly influence the structural rigidity and significantly reduce torsional effects. Model 1, which includes basement walls on all four sides, exhibits the lowest displacement, rotation angle, and angular velocity values. In contrast, Model 4, with only one basement wall, shows the highest values for these parameters.

Based on these findings, it is concluded that basement walls play a critical role in the torsional rigidity of a structure, and the absence of such walls negatively impacts structural performance. In particular, for buildings with irregular basement walls, it is recommended to implement stiffness-enhancing measures to mitigate torsional effects. Additionally, the obtained results support the definitions related to A3 irregularity in the TBEC 2018.

In summary, the lack of basement walls increases torsional effects at storey levels, adversely affecting the seismic performance of the building. Therefore, the inclusion of basement walls should be carefully considered, especially in the design of structures susceptible to high torsional effects. Furthermore, it is recommended that the performance of structures exhibiting torsional irregularities be analyzed in greater detail and, if necessary, that stiffness-enhancing measures be implemented.

References

AFAD (2024), Republic of Türkiye Ministry of Interior Disaster and Emergency Management Presidency. https://tadas.afad.gov.tr/

Gökçeoğlu, U. (2020). *Betonarme bir yüksek binanın 2018 Türkiye Bina Deprem Yönetmeliği'ne göre performans esaslı tasarımı ve bodrum perde duvar yerleşiminin tasarıma etkisi* (Master's thesis). İstanbul Technical University, Institute of Science and Technology.

İnce, O. (2024). Structural damage assessment of reinforced concrete buildings in Adıyaman after Kahramanmaraş (Türkiye) Earthquakes on 6 February 2023. *Engineering Failure Analysis, 156*, 107799. https://doi.org/10.1016/j.engfailanal.2023.107799

Kılıç Erdim, Y. (2018). *Betonarme binalarda rijit bodrum kat sayısının yapısal davranışa etkisi* (Master's thesis). İstanbul Gelişim University, Institute of Science and Technology.

Özcan, G. (2024). *Bodrum perdeli ve bodrum perdesiz betonarme binanın eşdeğer deprem yükü yöntemi ile kıyaslanması* (Master's thesis). İstanbul Arel University, Institute of Graduate Programs.

Özmen, A., İnce, O., Taş, Ö. F., Atar, M., Ozbulut, O. E., & Sayın, E. (2024). Seismic performance assessment of structures in Malatya Province after 6 February 2023 Turkey earthquake sequences. *Natural Hazards*, 1-34. https://doi.org/10.1007/s11069-024-07017-x

Republic of Türkiye Ministry of Interior Disaster and Emergency Management Authority. (2018). *Türkiye Building Earthquake Code (TBEC-2018)*. Ankara, Türkiye.

SAP2000 V.24.0.0, Computers and Structures, Inc., http://www.csiberkeley.com, 1995 University Avenue Berkeley, California 94704 USA,. 1978-2010

Estimation of the frequency value of masonry arches by classical regression analysis

Muhammed M. Öztürk*[1], Sinan Nacar[1], Yunus E. Akbulut[2], Ahmet C. Altunışık[2,3]

[1] *Tokat Gaziosmanpaşa University, Department of Civil Engineering, 60010 Tokat, Türkiye*
[2] *Karadeniz Technical University, Department of Civil Engineering, 61080 Trabzon, Türkiye*
[3] *Earthquake and Structural Health Application and Research Center, Karadeniz Technical University, 61080 Trabzon, Türkiye*

Abstract. This study estimated the first frequency values of masonry stone arches subjected to high-temperature effects by classical regression analysis (CRA). Within the scope of the study, 450 heat transfer and 5850 modal analysis results of masonry stone arches with different dimensions and temperature histories were used. The first mode frequencies of the arch members were obtained with 6300 finite element analysis. Then, the first mode frequencies of the arch members were estimated by CRA using the geometrical parameters of the arch member (span, height, width, thickness) and the temperature history condition (0, 15, 30, 45, 60, 75, 90, 105, 120, 135, 150, 165, 180 min) to which the arch members were exposed. In the CRA method, four different functions, namely linear function (LF), power function (PF), exponential function (EF), and quadratic function (QF), were applied, and the coefficients of these functions were calculated. While developing the prediction models, %70 of the data was used for training and the remaining %30 for testing the models. Various performance statistics (square root of mean squared error, mean absolute error, scatter index, and Nash Sutcliffe (NS) efficiency coefficient) were used to evaluate the prediction performance of the developed models. The NS performances of the models developed using LF, PF, EF, and QF functions in the CRA method are calculated as 0.448, 0.923, 0.975, and 0.772 for the training data set and 0.449, 0.922, 0.975, and 0.722 for the test data set, respectively. When the performance statistics obtained are compared, it is seen that the most successful prediction results are obtained from EF. The performance statistics obtained from the modeling studies showed that the first mode frequency values of masonry stone arches with different dimensions and temperature histories could quickly be predicted with high performance, with less model and cost.

Keywords: Masonry stone arch; Heat transfer analysis; Modal analysis; Classical regression analysis

1. Introduction

It is seen that arch elements are used in many buildings (mosques, bridges, churches, water channels, etc.), especially in historical buildings. Arches are curved structural elements that transfer the loads onto the load-bearing vertical elements and allow the openings between these elements to be passed (Morgan, 1970). These arches, mainly used in the structural system of historical masonry structures, are used to transform small volumes into a more extensive form and pass large openings.

During their service life, structural damages may occur in arches that may be exposed to different dynamic effects (earthquake, wind, fire, explosion, traffic load, etc.). These damages can be determined by analyzing the changes in the element's dynamic characteristics (natural frequency, mode shape, and damping ratio) or stiffness. Experimental and numerical methods can be used to obtain dynamic characteristics (Bovo et al., 2015; Albuerne et al., 2019; Altunışık et al., 2024). Altunışık et al. (2024) in their study, investigated the changes in the dynamic behavior of masonry stone arches subjected to high-temperature effects using experimental and numerical methods. Within the scope of the study, finite element models were used to determine the dynamic characteristics of arch models with different spans, heights, widths, and thicknesses for different temperature history conditions. Subsequently, formulations and graphs/plots based on these results were obtained.

In recent years, it has been seen that many modeling-based studies have been carried out to solve engineering problems with the developing computer technology (Deifalla, 2021; Cho et al., 2022; Saxena et al., 2024). When the studies in the literature are examined, it is seen that the frequency and mode shape parameters of masonry structures can be estimated using different methods Diaferio et al., 2018; Onat, 2020). Moser & Moaveni (2011),

* Corresponding author, E-mail: mmustafa.ozturk@gop.edu.tr

https://doi.org/10.31462/icearc2025_ce_sme_278

investigated the effect of environmental factors such as temperature, humidity, and vibration amplitude on dynamic modal parameters using the results of a continuous monitoring system installed on the Dowling Hall Pedestrian Bridge at Tufts University. In the study, a significant variability in the natural frequencies of the bridge was observed, and these changes were found to be strongly related to temperature. Several non-linear models were proposed to model the relationship between natural frequencies and temperature. The final model was validated with independent data sets, and confidence intervals were estimated for natural frequencies as a function of temperature. Serhatoğlu & Livaoğlu (2019) in their study, investigated the dynamic and structural properties of eighteen Ottoman minarets in Bursa using experimental and numerical techniques. They developed empirical formula to estimate the initial periods of historical Ottoman minarets. They stated that the obtained formulae can be used as a practical and valuable method for determining the first periods of historical minarets.

Although masonry structures have survived to the present day by showing resistance against various disasters throughout history, most of them have been damaged or destroyed due to earthquakes, fires, wars, and environmental impacts. The behavior of arches plays a vital role in determining the damaged conditions of these structures. For this purpose, the first mode frequencies of masonry stone arches with different dimensions (span, height, width, thickness) and temperature history were obtained by finite element analysis. Then, the first mode frequencies of the arch elements were estimated using the classical regression analysis (CRA) method using the geometrical parameters of the arch element and the independent variables of the temperature history condition to which the arch elements were exposed. Four different functions, namely linear (LF), exponential (UF), exponential (EF), and quadratic (KF), were applied in the KRA method, and the coefficients of these functions were calculated. While developing the prediction models, %70 of the data was used for training and the remaining %30 for testing the models. The results obtained were compared by using different performance statistics, and the functions and coefficients of these functions that gave the closest values to the experimental results were determined.

2. Finite element analysis of arches

The first mode frequency (f_{FE}) values of masonry arch elements with different cross-sectional dimensions subjected to high-temperature effects are taken from our previous study (Altunışık et al., 2024). Within the scope of the study, 450 heat transfer and 4850 modal analyses were performed using the finite element (FE) method to determine f_{FE}. Due to the variable parameters considered, many numerical analyses were performed, and a data pool was created based on the results obtained.

The FE analyses first generated 450 FE models of arch elements with different section properties listed in Table 1. In order to determine the temperature distributions along the cross-sections of these arch elements under high-temperature effect, heat transfer analyses were performed on the FE models considering the transient regime. Then, depending on the results of these analyses, 4850 modal analyses were performed for exposure times of 0, 15, 30, 45, 60, 75, 90, 105, 120, 135, 150, 165, and 180 minutes of ISO 834 standard temperature-time graph. The same FE model was used in both analyses performed using the ABAQUS package program. Detailed information on FE analyses (FE models, thermal and mechanical material properties, etc.) can be found in (Altunışık et al., 2024).

Table 1. Arch dimensions considered in FE analyses

Group	Arch dimension (m)										
	Span (s)	Height (h)		Width (w)			Thickness (t)				
1	1-3						0.2	0.3	0.4	0.5	0.6
2	4-7	$\frac{s}{2}$	$\frac{s}{2}x0.8$	0.5	1.0	1.5	0.4	0.5	0.6	0.7	0.8
3	8-11						0.6	0.7	0.8	0.9	1.0
4	12-15						0.8	0.9	1.0	1.1	1.2

3. Classical regression analysis (CRA)

Regression is a statistical method used to estimate the relationship between a dependent variable and two or more independent variables. Regression equations are mathematical expressions showing these variables' relationship (Bayazıt & Yeğen, 2005). Four different regression functions, namely LF, PF, EF and QF were used in this study. The functions used are given in Equations 1-4:

$$y_{LF} = w_0 + w_1 x_1 + w_2 x_2 + w_3 x_3 + \cdots + w_n x_n \tag{1}$$

$$y_{PF} = w_0 x_1^{w_1} x_2^{w_2} x_3^{w_3} \ldots x_n^{w_n} \tag{2}$$

$$y_{EF} = w_0 + \exp\left(w_1 + w_2 x_1 + w_3 x_2 + \cdots + w_{n-1} x_n\right) \tag{3}$$

$$y_{QF} = w_0 + w_1x_1 + w_2x_2 + \cdots + w_6x_1x_2 + w_7x_1x_3 + \cdots + w_{15}x_1^2 + w_{16}x_2^2 \ldots + w_{20}x_5^2 \quad (4)$$

In the given equations, w's represent the regression coefficients, x's represent the independent variables, and y's represent the frequency values of the first modes of the arches, which are the dependent variables. Determining the regression equation that best predicts the value of the dependent variable is called regression analysis (Bayazıt, 1981).

3.1. Modelling

In the modeling studies, the geometrical parameters of the arch elements (span, height, width, thickness) and the temperature history condition (0, 15, 30, 45, 60, 75, 90, 105, 120, 135, 150, 165, 180 min) to which the arch elements were exposed were used as independent variables, and the first mode frequencies (f_{FE}) of the arches were used as the dependent variable. In the model prepared by using 5315 data in total, 3985 data were allocated for training, and 1330 data were allocated for testing. While dividing the data into training and test sets, care was taken to ensure that both sets had values that could represent the entire data group. The models with the highest performance for the training data set were also evaluated using the test data set. Table 2 shows the minimum, maximum, mean, and standard deviation fundamental statistical values for training, test, and all data.

Since the value ranges of the dependent and independent variables in the data set are different, modeling may become difficult. For this reason, a normalization process was applied to the data in order to obtain the solution faster and easier. As a result of this process, the data of the dependent and independent variables in the data set were normalized between 0.1 and 0.9. The formulation used in this process is given in Equation 5 (Bayram et al., 2015)

$$Normalized\ value = \left[\frac{Raw\ value - Minimum\ Value}{Maximum\ value - Minimum\ Value}\right] x(0.8) + 0.1 \quad (5)$$

Table 2. Basic statistics of the variables in the modeling

Data Set	Variable	Unit	The smallest	Average	The biggest	Standard Deviation
All of them	Span	m	1.000	8.468	15.00	4.220
	Height	m	0.400	3.809	7.500	1.958
	Width	m	0.500	0.961	1.500	0.403
	Thickness	m	0.200	0.758	1.200	0.238
	Temperature	℃	0.000	98.96	180.0	56.12
	f_{FE}	Hz	0.430	10.72	130.3	19.92
Training	Span	m	1.000	8.468	15.00	4.220
	Height	m	0.400	3.808	7.500	1.958
	Width	m	0.500	0.961	1.500	0.403
	Thickness	m	0.200	0.758	1.200	0.238
	Temperature	℃	0.000	89.93	180.0	56.12
	f_{FE}	Hz	0.440	10.73	130.3	19.99
Testing	Span	m	1.000	8.468	15.00	4.223
	Height	m	0.400	3.811	7.500	1.960
	Width	m	0.500	0.959	1.500	0.403
	Thickness	m	0.200	0.759	1.200	0.238
	Temperature	℃	0.000	90.03	180.0	56.12
	f_{FE}	Hz	0.430	10.65	121.6	19.70

3.2. Evaluation of modeling results

As a result of CRA modeling studies, the coefficient values in Table 3 were obtained for LF, PF, EF, and QF functions as a result of the application of CRA methods, training, and test data sets were generated by substituting the coefficients of the functions in the equations.

Table 3. Coefficients of LF, PF, EF, and QF functions obtained from regression analysis

Coefficients obtained from regression analysis	Model functions			
	LF	PF	EF	QF
w_0	0.327	0.064	0.113	0.637
w_1	-0.295	-0.658	0.721	6.655
w_2	-0.048	-0.328	-2.602	-8.985
w_3	0.060	0.192	-11.13	0.286
w_4	-0.003	-0.040	0.823	-0.134
w_5	-0.022	-0.076	-0.871	-0.109
w_6			-0.342	-454.1
w_7				-0.220
w_8				0.211
w_9				0.074
w_{10}				-0.029
w_{11}				0.001
w_{12}				0.015
w_{13}				-0.098
w_{14}				0.003
w_{15}				0.041
w_{16}				199.91
w_{17}				256.11
w_{18}				-0.030
w_{19}				0.024
w_{20}				0.018

3.3. Evaluation of model performance

Root mean square error (RMSE), mean absolute error (MAE), and Nash Sutcliffe efficiency coefficient (NS) performance statistics were used to compare the forecasting performance of the models. The formulae used are given in Equations 6-8:

$$RMSE = \left[\frac{1}{n}\sum_{i=1}^{n}(t_i - td_i)^2\right]^{1/2} \tag{6}$$

$$MAE = \frac{1}{n}\sum_{i=1}^{n}|(t_i - td_i)| \tag{7}$$

$$NS = 1 - \frac{\sum_{i=1}^{n}(t_i - td_i)^2}{\sum_{i=1}^{n}(t_i - \bar{t})^2} \tag{8}$$

In the given equations, t_i indicates measurement values, td_i indicates prediction values, $\bar{t}$ indicates the mean of measurement values, and n indicates the number of data. NS value is between -∞ and 1. NS=1 indicates that the method used is perfect (Moriasi et. Al., 2007) proposed a range for NS, as shown in Table 4.

The performance statistics calculated between the prediction and measurement values of f_{FE} training and test data sets are given in Table 5. When Table 5 is analyzed, it is determined that EF is the function type that gives the lowest RMSE and MAE and the highest NS values for both training and testing. As can be seen in Table 5, the EF function predicted an 'excellent' level according to the NS performance statistic for training (Moriasi et al., 2007). Fig. 1 shows the scatter plots of the prediction and measurement values of the training and test data obtained with the EF function for f_{FE}.

The distribution of the data on the diagonal in the scatter plots shows that the prediction values are very close to the measurement values. In other words, it means that the RMSE and MAE values of the points on the diagonal are zero (Bayram & Kankal, 2015; Nacar et al., 2020). Fig. 1 shows that the majority of the training and test data of f_{FE} are distributed on the diagonal. This indicates that the prediction data are close to the FE data. Fig. 2 and Fig. 3 shows the comparison of the training and test data estimated with the EF function, which performs the best in the CRA method, with the FE data as a time series. When the figure is analyzed, the results are close to the FE data.

Table 4. NS value range

Parameter	Very good	Good	Adequate	Inadequate
NS	0.75-1.00	0.65-0.75	0.50-0.65	<0.50

Table 5. RMSE, MAE, and NS values of training and test data for f_{FE}

Data Set	Training				Testing			
Model functions	LF	PF	EF	QF	LF	PF	EF	QF
RMSE	14.85	5.554	**3.155**	9.555	14.62	5.512	**3.112**	9.411
MAE	9.945	4.499	**2.129**	6.892	9.891	4.479	**2.114**	6.845
NS	0.448	0.923	**0.975**	0.772	0.449	0.922	**0.975**	0.772

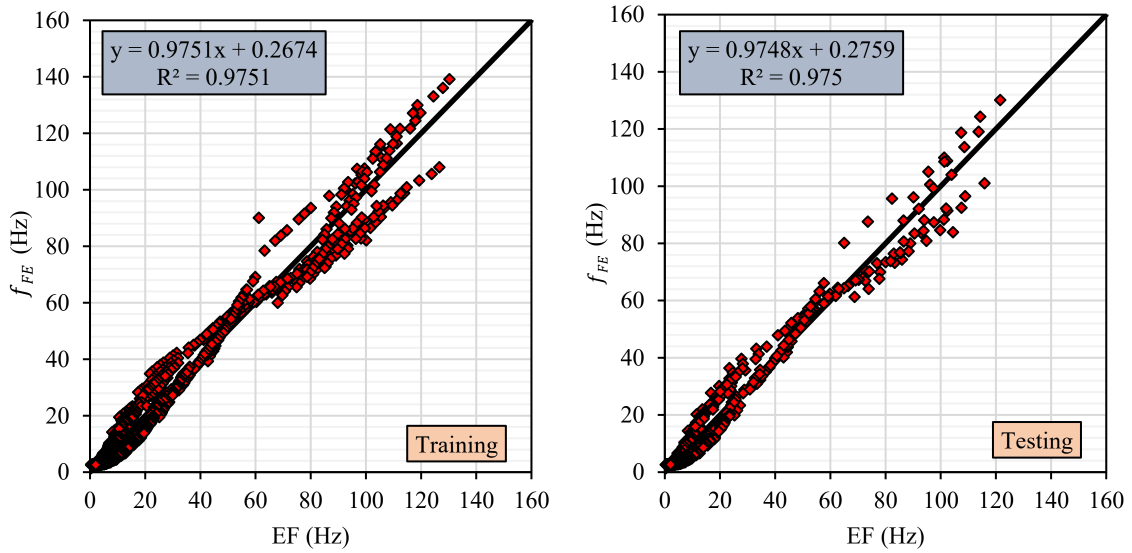

Fig. 1. Training and test data sets obtained with the EF function (comparison of f_{FE} estimation results with measurement values)

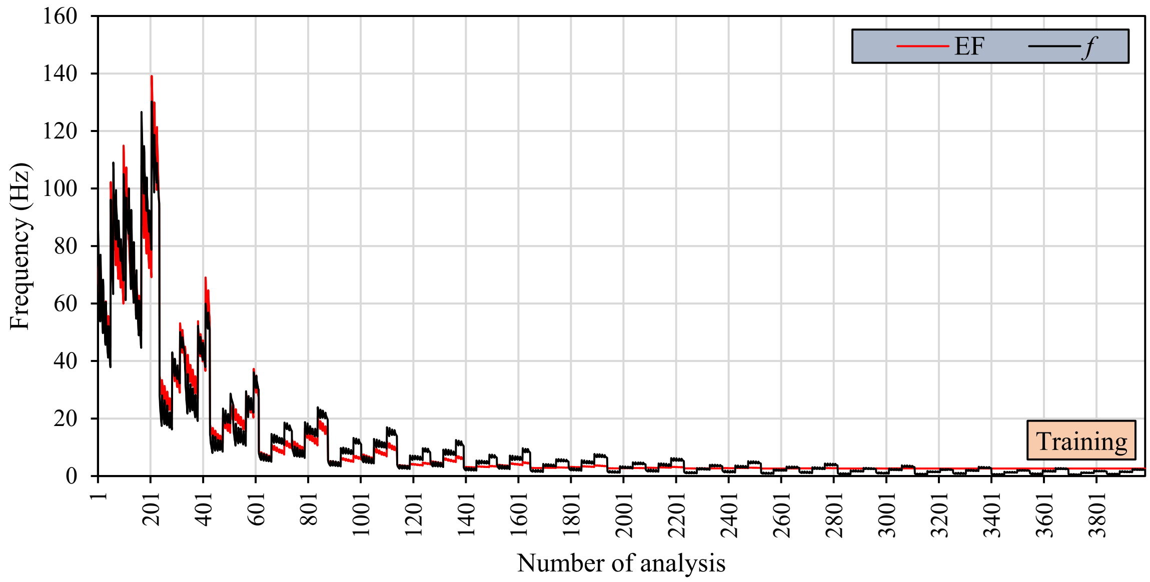

Fig. 2. Comparison of FE-predictive values of training datasets for f_{FE}

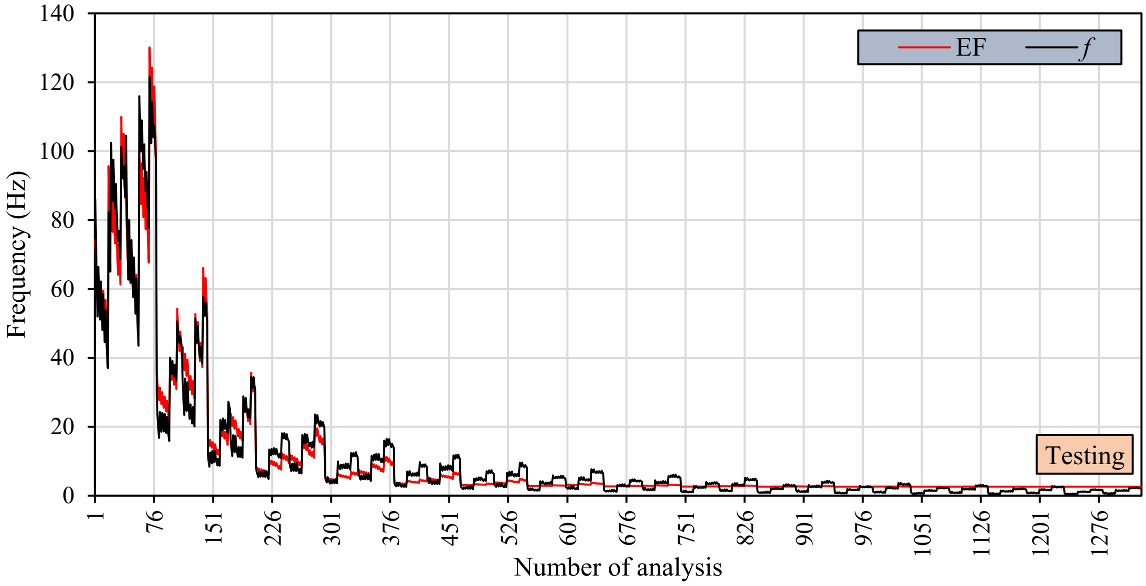

Fig. 3. Comparison of FE-predictive values of testing datasets for f_{FE}

4. Conclusions

In this study, the first frequency values of masonry stone arches subjected to high-temperature effects are estimated by classical regression analysis (CRA) using numerical methods. Within the scope of the study, 6300 FE analysis results of masonry stone arches with different geometries and temperature histories were used. As a result of the analyses, a data set was created with the first mode frequencies of 5315 arch elements. Then, CRA was performed using geometrical parameters such as span, height, width, thickness of the arch element, and the temperature history condition (0, 15, 30, 30, 45, 60, 75, 90, 105, 120, 135, 150, 165, 180 min) to which the arch elements were exposed. As a result of this analysis, the first mode frequencies of the arch members were estimated. Four different functions, namely linear function (LF), power function (PF), exponential function (EF), and quadratic function (QF), were used in the CRA method, and the coefficients of these functions were calculated. While developing the prediction models, 70% of the data was used for training and the remaining 30% for testing the models. Finally, performance statistics such as the square root of the mean squared error, the mean absolute error, and the Nash Sutcliffe (NS) efficiency coefficient were used to evaluate the prediction performance of the developed models. The results obtained from the study are summarised below;

- It was found that the FE parameter can be estimated with high accuracy by CRA functions from the dynamic characteristics of masonry stone arches with different geometries and temperature histories.
- The NS performances of the models developed using LF, PF, EF, and QF functions in the CRA method are calculated as 0.448, 0.923, 0.975, and 0.772 for the training data set and 0.449, 0.922, 0.975, and 0.722 for the test data set, respectively.
- Considering the performance statistics obtained from CRA models, it is seen that the closest prediction values to the f_{FE} data obtained by FE analysis are obtained from EF.
- FE analyses to determine the f_{FE} parameter can be tiring and time-consuming. The models proposed in this study show that f_{FE} can be determined with less data, less time, and high accuracy.

Dynamic characteristics of structures play a vital role in determining their behavior. It is known that the dynamic behavior of structures does not only depend on the frequency of the first mode. It depends on many parameters, such as mode shape, frequency value, and damping ratio. Therefore, in future studies, the dynamic behavior of structures can be predicted by using methods such as fuzzy logic, genetic programming, and different types of regression analysis by considering different criteria.

Acknowledgments

This study was supported by the Scientific and Technological Research Council of Turkey (TÜBİTAK) under grant number 117M819 and Karadeniz Technical University under project number FBA-2018-7292.

References

Albuerne, A., Pappas, A., Williams, M., & D'Ayala, D. (2019). Experimental and numerical study of the dynamic behaviour of masonry circular arches with non-negligible tensile capacity. *Journal of Mechanics of Materials and Structures, 14*(5), 621-644

Altunişik, A.C., Öztürk, M.M., Genc, A.F., Günaydin, M., Kaya, A., Akbulut, Y.E., & Sunca, F. (2024). Dynamic characteristics changes of masonry arches exposed to elevated temperature. *Construction and Building Materials, 418*, 135423

Altunişik, A.C., Öztürk, M.M., Genç, A.F., Kaya, A., Akbulut, Y.E., Sunca, F., & Günaydin, M. (2024). Estimating fundamental frequency of masonry arches under elevated temperature: numerical analysis and validation using ambient vibration tests. *Archives of Civil and Mechanical Engineering, 25*(1), 23

Bayazıt, M., & Yeğen Oğuz, E.B. (2005). Mühendisler İçin İstatistik. İstanbul, Türkiye: Birsen Yayınevi

Bayazıt, M. (1981). Hidrolojide istatistik yöntemler. Gümüşsuyu, İstanbul: İTÜ Yayınevi

Bayram, A., Uzlu, E., Kankal, M., & Dede, T. (2015). Modeling stream dissolved oxygen concentration using teaching–learning based optimization algorithm. *Environmental Earth Sciences*, 73, 6565-6576

Bayram, A., & Kankal, M. (2015). Artificial Neural Network Modeling of Dissolved Oxygen Concentration in a Turkish Watershed. *Polish Journal of Environmental Studies, 24*(4)

Bovo, M., Mazzotti, C., & Savoia, M. (2015). Structural behaviour of historical stone arches and vaults: Experimental tests and numerical analyses. *Key Engineering Materials, 628*, 43-48

Cho, Y., Khosravikia, F., & Rathje, E.M. (2022). A comparison of artificial neural network and classical regression models for earthquake-induced slope displacements. *Soil Dynamics and Earthquake Engineering, 152*, 107024

Deifalla, A. (2021). Refining the torsion design of fibered concrete beams reinforced with FRP using multi-variable non-linear regression analysis for experimental results. *Engineering Structures, 226*, 111394

Diaferio, M., Foti, D., & Potenza, F. (2018). Prediction of the fundamental frequencies and modal shapes of historic masonry towers by empirical equations based on experimental data. *Engineering Structures, 156*, 433-442

Moser, P., & Moaveni, B. (2011). Environmental effects on the identified natural frequencies of the Dowling Hall Footbridge. *Mechanical Systems and Signal Processing,* 25(7), 2336-2357

Morgan, W. (1970). The Elements of Structure an Introduction to the principles of Building and Structural Engineering. New York, USD: Pitman Publishing

Moriasi, D.N., Arnold, J.G., Van Liew, M.W., Bingner, R.L., Harmel, R.D., & Veith, T.L. (2007). Model evaluation guidelines for systematic quantification of accuracy in watershed simulations. *Transactions of the ASABE, 50*(3), 885-900

Nacar, S., Mete, B., & Bayram, A. (2020). Günlük çözünmüş oksijen konsantrasyonunun çok değişkenli uyarlanabilir regresyon eğrileri ile tahmin edilmesi. *Uludağ Üniversitesi Mühendislik Fakültesi Dergisi, 25*(3), 1479-1498

Onat, O. (2020). Impact of mechanical properties of historical masonry bridges on fundamental vibration frequency. *In Structures, 27*, 1011-1028

Saxena, A., Sabillon-Orellana, C., & Prozzi, J. (2024). Prediction of compressive strength in sustainable concrete using regression analysis. *Journal of Material Cycles and Waste Management, 26*(5), 2896-2909

Serhatoğlu, C., & Livaoğlu, R. (2019). A fast and practical approximations for fundamental period of historical Ottoman minarets. *Soil Dynamics and Earthquake Engineering, 120*, 320-331

Finite element homogenization of octet-truss-based lattice structures with periodic boundary conditions

Soheil Gholibeygi [1], Bahar Ayhan[2], Hale Ergün [*2]

[1] Istanbul Technical University, Graduate School, Civil Engineering Department, 34469, Istanbul, Turkiye
[2] Istanbul Technical University, Civil Engineering Faculty, Civil Engineering Department, 34469, Istanbul, Turkiye

Abstract. The use of numerical homogenization methods has become essential for accurately estimating the mechanical properties of composites and lattice structures. These techniques help minimize the reliance on expensive and time-consuming experiments while providing reliable predictions of material behavior. At the core of numerical homogenization lies the concept of a representative volume element (RVE), which encapsulates the necessary microstructural details within a smaller, computationally efficient domain. Proper boundary conditions applied to the RVE enable effective evaluation of the overall structural properties. This research explores the application of finite element (FE) homogenization methods for analyzing lattice structures. The FE approach is well-regarded for its straightforward implementation, capacity to model complex microstructures, and accuracy in determining effective material properties. Lattice structures, valued for their superior strength-to-weight ratios, energy absorption capabilities, and porosity, are widely used in aerospace, automotive, and medical applications. Enhancing their performance requires careful consideration of topology choices (such as octet-truss, honeycomb, and foam), unit cell configurations, and material characteristics. In this study, the mechanical properties of the octet-truss unit cell are examined alongside combinations with other unit cells, including simple cubic (SC), cross struts, and body-centered cubic (BCC). Simulations are conducted using the finite element software ABAQUS, incorporating periodic boundary conditions (PBC) to ensure accurate homogenization. By analyzing the effects of varying relative densities and unit cell arrangements, this work provides valuable insights for optimizing lattice structures in advanced engineering applications.

Keywords: Homogenization; Lattice structures; Octet-truss; Periodic boundary conditions; Representative volume element

1. Introduction

Cellular structure is a type of a porous structure which is naturally found in the nature, such as corals, leaves and bones. Artificial cellular structures have been manufactured and structured based on these natural designs. Such materials are classified into two categories based on the structures, the stochastic and the periodic (Gibson & Ashby, 1997). Periodic cellular solids with three-dimensional spatial architectures of unit cells are called lattice structures. These extraordinary materials derive properties that are unique because of their unique structural design. With a low density, these materials can certainly be used as lightweight structural components (Tancogne-Dejean et al., 2018). The characteristic plateau behavior under compression generates enhanced energy absorption capacity (Qiu et al., 2022). Furthermore, due to their unique flow characteristics, lattice structures find uses as sound absorbers and thermal exchangers (Dixit et al., 2021). Thus, these structures find applications in many fields, including aerospace, defense, biomedical engineering, automotive design, and sports equipment manufacturing.

Unit cells of the lattice structures can be strut-based (composed of struts and nodes) or TPMS-based (Triply Periodic Minimal Surfaces). The mechanical behavior of strut-based lattice structures is categorized as bending or stretch-dominated according to the Maxwell number $M = b - 3j + 6$, where b and j are the numbers of struts and joints in unit cell, respectively (Deshpande et al., 2001). When $M < 0$, struts primarily experience bending. In cases where $M = 0$, the structure is statically determinate and deformation is dominated by tension or compression and when $M > 0$, excess stiffness leads to stretch-dominated behavior. Stretch-dominated structures typically exhibit higher stiffness and initial collapse strength compared to bending-dominated structures. This characteristic makes stretch-dominated lattices particularly suitable for lightweight, load-bearing applications. In contrast, bending-dominated structures are characterized by greater compliance and a prolonged flat plateau in the post-

[*]Corresponding author, E-mail: ergunh@itu.edu.tr

https://doi.org/10.31462/icearc2025_ce_sme_318

golden light publishing

yield regime, which makes them highly advantageous for applications where energy absorption is the primary focus (Habib et al., 2018).

The structural behavior of lattice structures can be fine-tuned by adjusting factors such as cell topology, strut shape, cell size and base material (Morrish et al., 2017; Qi et al., 2019). Several attempts have been made to optimize and improve the mechanical properties of lattice structures. For example, in Body-centered (BC) unit cell, stress concentrations have been occurred at the joints. In order to reduce that, the nodal regions were modified by considering fillets causes increase in stiffness by 55% (Wang et al., 2021). Also, by changing the strut shape of unit cell, the mechanical properties can be improved. Tancogne-Dejean et al. (2016) simulated octet-truss (OT) unit cell with cylindrical and tapered struts, which have circular cross-section. Tapered strut ends are cylindrical shape over a length of twice the radius of strut (R), and the strut radius changes gradually reaching its maximum value of αR at the center. They showed that in the unit cells with strongly tapered struts $(\alpha \leq 0.6)$ increases the stability of the microstructure, and the ones with $\alpha = 0.8$ have higher strength and specific energy absorption (SEA). Also, Tancogne-Dejean & Mohr (2018) simulated the BC unit cell with tapered beams and they found that the effective Young's modulus and SEA increased up to 70% and 45%, respectively. In another attempt, the cross-section of struts has been altered. For example, Zhao et al. (2023) created a BC unit cell with bamboo-inspired struts which were tapered and hollow. They found that the mentioned parameters changed the deformation behavior from bending to stretch-dominated under uniaxial compression. Also, they showed that by modeling bamboo-inspired BC, elastic modulus can be increased by $271.24 - 1335\%$. Another approach is changing the cell configuration by inserting additional struts. Smith et al. (2013) designed BC-Z unit cell by inserting an additional vertical strut. The deformation behavior was changed from bending-dominated to stretch-dominated and the stiffness was significantly increased due to the existence of the vertical strut in BC.

At the microscopic scale, the fundamental unit cell of a lattice structure, referred to as the Representative Volume Element (RVE), exhibits a heterogeneous nature, with varying material properties across its structure. However, when considered at the macroscopic level, the RVE can be approximated as homogenous, anisotropic continuum. To simplify the analysis and design of lattice structures, a homogenization approach is commonly employed. This technique replaces the complex, detailed geometry of the RVE with an equivalent homogenous material at the macroscopic scale. The mechanical properties of this equivalent material are characterized by effective material parameters, which are derived from the microscale geometry. Although the base material of the lattice is isotropic, the overall mechanical response of homogenized structure can become fully anisotropic. This occurs because the effective elastic properties are strongly influenced by the geometry and orientation of the RVE at the microscale (De Pasquale et al., 2018). In literature, there are several homogenization methods including, average stress method, mathematical homogenization method and asymptotic homogenization. During the homogenization process on the RVE, three types of boundary conditions are applied including displacement-type, force-type and periodic boundary conditions (PBC). As it stands, the use of homogeneous displacement boundary conditions has been proved to yield upper bounds on the effective mechanical properties, and the lower bound brought about by using homogeneous traction boundary conditions in comparison to those obtained using PBCs. Also, it was proven that during analysis of a periodic RVE, PBCs is the best boundary condition type (Yu, 2016).

The octet truss unit cell (OT) is considered as the base RVE in this study. Homogenization process will be done by finite element analysis software (ABAQUS, 2022) using average stress method. Due to the periodicity of the RVE, periodic boundary conditions (PBCs) will be used. By this procedure, the effective material properties of OT will be extracted. Also, by combining the body-centered (BC), simple cubic (SC) and cross rods (C) with the OT, new three configurations are developed to investigate how these combinations affect the homogenized material properties of the OT unit cell. The struts of all unit cells are cylindrical with circular cross-section. Whole models exhibit cubic symmetry. These simulations are done by different relative densities varying from 0.05 to 0.4. Spatial dependence of homogenized material properties is presented graphically. The change of anisotropy of each material constant is also given for the combinations of OT.

2. Materials and methods

In this section, first the geometry of unit cells and the bulk material properties are presented in section 2.1 and then the methodology of the homogenization process is given in section 2.2.

2.1. Geometry and material

In this study, the side length of each unit cell was considered as $L_{uc} = 6mm$. A unit cell of the octet truss with relative density of $\bar{\rho} = 0.2$ is sketched in Fig. 1 and clearly shows its face-centered nature. It is composed by an octahedron at the center of unit cell, which is shown with red color, and eight tetrahedrons, which are attached to the eight faces of the octahedron. The new configurations are modeled by inserting Cross, SC and BC unit cells inside the OT. These new unit cells are named as OT+C, OT+SC and OT+BC, respectively and shown in Fig. 2 for the same relative density of $\bar{\rho} = 0.2$. In Fig. 2, the OT was shown by yellow color and the inserted unit cell was depicted by blue color.

The relative density of a lattice material $\bar{\rho}$ is defined as the ratio of the density of the cellular material and the density of the bulk material. Relative density of OT unit cell is already given with Equation.1 for cylindrical struts by Tancogne-Dejean et al. (2016).

$$\bar{\rho} = 6\pi\sqrt{2}\left(\frac{R}{l}\right)^2 - \frac{32}{2-\sqrt{2}}\left(\frac{R}{l}\right)^3 \tag{1}$$

Here, R and l is the radius and the length of each strut, respectively. The second term in this equation is the correction term in order to consider the complex geometry of the joints. Equation.1 was solved for different relative densities varying from 0.05 to 0.40, and the corresponded radius of strut were calculated for the OT unit cell. Also, the relative densities and radius of new configurations were calculated by Python scripting in ABAQUS/CAE. In order to make a comparison between the unit cells with different configurations, the relative density is kept constant and the required radius values of the struts were calculated and tabulated in Table 1.

In all simulations, the isotropic linear elastic material, Nylon-12 (PA-12) is used as the bulk material. This material has elastic modulus of $E = 969.52\ MPa$ and Poisson's ratio of $\upsilon = 0.33$.

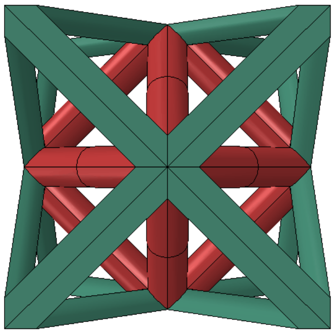

Fig. 1. Geometry of the OT unit cell with relative density of $\bar{\rho} = 0.2$

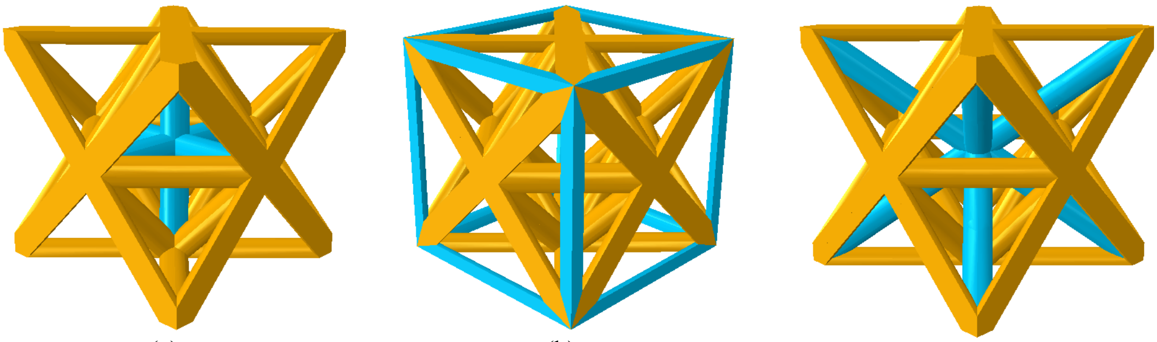

(a) (b) (c)

Fig. 2. Geometry of the new configurations (a) OT+C, (b) OT+SC and (c) OT+BC with relative density of $\bar{\rho} = 0.2$

Table 1. Required strut radius R values for each relative density

Unit Cell	$\bar{\rho} = 0.05$	0.10	0.15	0.20	0.25	0.30	0.35	0.40
OT	0.19296	0.27939	0.34903	0.41041	0.46686	0.52013	0.57132	0.62119
OT+C	0.17814	0.25814	0.32273	0.37977	0.43236	0.48210	0.53004	0.57690
OT+SC	0.17758	0.25689	0.32065	0.37672	0.42816	0.47657	0.52294	0.56796
OT+BC	0.16177	0.23358	0.29106	0.34137	0.38732	0.43034	0.47131	0.51083

2.2. RVE homogenization process using finite element analysis

In this study, as it was mentioned, average stress method is used by implying the PBCs on the RVE. ABAQUS/CAE software is used for the simulations. The homogenization process involves applying uniform strain conditions. These conditions are presented in Fig. 4 for OT+BC with relative density of $\bar{\rho} = 0.4$. In the software, there is not any predefined boundary condition for implying PBCs. These PBCs are implemented using EasyPBC plugin which is written in Python scripts using the commands of ABAQUS (Omairey et al., 2019). By using this plug-in, the uniform strains are imposed on the RVE to calculate the homogenized elastic properties. Also, the constrained equations and displacement boundary conditions are automatically applied to keep the periodicity of the RVE. It generates node sets for each side, edge and corner of the RVE and by utilizing the derived constraint equations, each node is linked with its corresponding node on the other side to maintain the periodicity of the deformation. During the process, some reference points are constructed automatically to imply the required displacement boundary condition for each homogenized property. Then, the reaction force data are requested from the reference points. This reaction force is divided by the affected surface area to calculate the stress value and then Young's modulus is determined by dividing the stress value to the applied strain. Also, the same output is used to obtain the Poisson's ratio in the two transverse directions by dividing the transverse strain by applied axial strain. Shear moduli are calculated by the ratio of shear stress to shear strain in the corresponding directions.

This plug-in calculates all homogenized elastic moduli, shear moduli and Poisson's ratios. For each unit cell, a stiffness matrix is constructed using Equation.2. The subsequent calculation of anisotropy and examination of spatial variation of Young's moduli, shear moduli and Poisson's ratios for the unit cells is performed using ELATE, which is an open-source online tool for analyzing and visualizing elastic tensors (Gaillac et al., 2016).

In all simulations, Hexagonal linear element type C3D8R, that is available in ABAQUS library, is used with mesh seed size of $0.2\ mm$. Mesh of OT, OT+BC, OT+SC and OT+C unit cells are presented for relative density of $\bar{\rho} = 0.2$ in Fig. 3.

$$\begin{bmatrix} E_1(v_{23}v_{32}-1)/D & -E_1(v_{21}+v_{23}v_{31})/D & -E_1(v_{31}+v_{21}v_{32})/D & 0 & 0 & 0 \\ -E_2(v_{12}+v_{13}v_{32})/D & E_2(v_{13}v_{31}-1)/D & -E_2(v_{12}v_{31}+v_{32})/D & 0 & 0 & 0 \\ -E_3(v_{13}+v_{12}v_{23})/D & -E_3(v_{13}v_{21}+v_{23})/D & E_3(v_{12}v_{21}-1)/D & 0 & 0 & 0 \\ 0 & 0 & 0 & G_{23} & 0 & 0 \\ 0 & 0 & 0 & 0 & G_{13} & 0 \\ 0 & 0 & 0 & 0 & 0 & G_{12} \end{bmatrix} \quad (2)$$

$$D = v_{12}(v_{21}+v_{23}v_{31}) + v_{23}v_{32} + v_{13}(v_{31}+v_{21}v_{32}) - 1$$

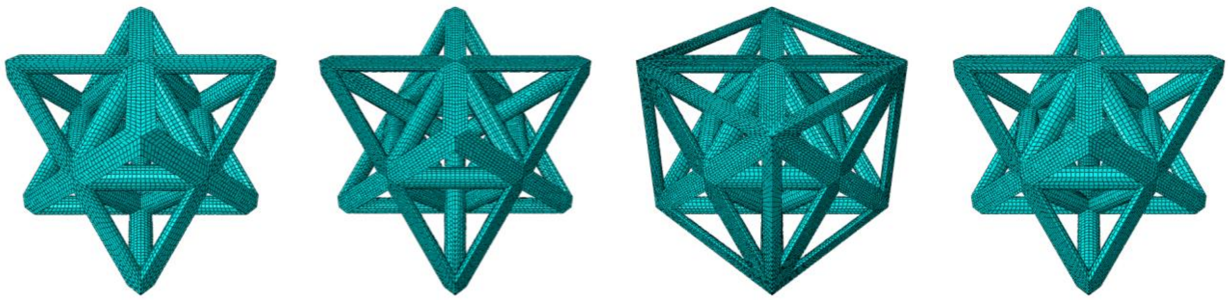

(a) (b) (c) (d)

Fig. 3. Mesh of (a) OT, (b) OT+BC, (c) OT+SC and (d) OT+C unit cells with constant relative density of $\bar{\rho} = 0.2$

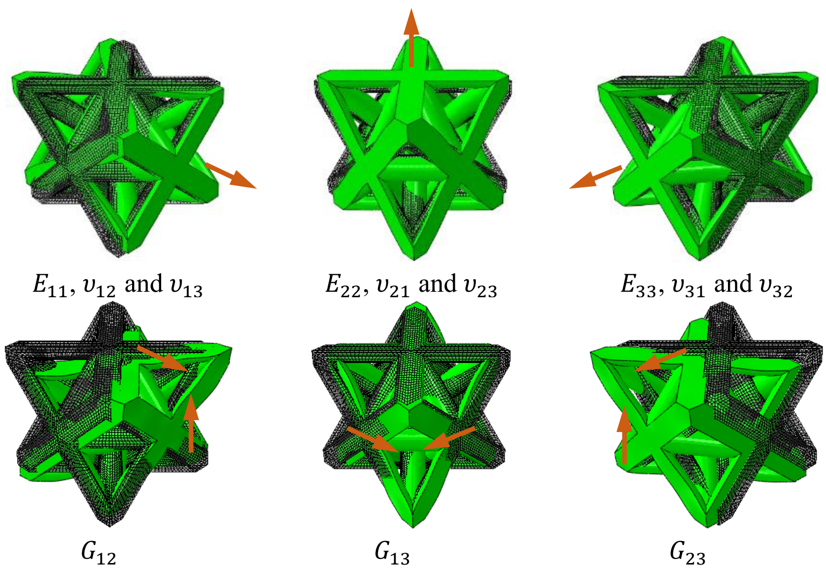

Fig. 4. Displacement loading used to determine the effective elastic properties of an RVE

3. Results and discussion

The unit cells considered in this study have cubic symmetry which has three independent material constants. Three dimentional plot of material constants of OT is shown in Fig. 5 for $\bar{\rho} = 0.05$. This figure is obtained from open source online tool Elate (Gaillac et al., 2016). The material constants have minimum and maximum values in different directions. For example elastic modulus has minimum value E_{min} in [100] direction and maximum value E_{max} in [111] direction. Shear modulus has minimum value G_{min} in [110] direction and maximum value G_{max} in [100] direction. Variation of elastic and shear modulus on xy plane is shown in Fig. 6. The homogenized values found in this study belong to [100] direction, those are E_{min} and G_{max}. Transformation matrix operations can be applied to the stiffness matrix obtained from homogenization process to find the variation of moduli in other directions, as it is done by the open source online tool Elate, and E_{max} and G_{min} can be determined.

Anisotropy of a material constant is described by the ratio of maximum to minimum values of this material constant (Gaillac et al., 2016). Minimum and maximum elastic modulus values of Octet-Truss unit cell are plotted with solid lines in Fig. 7. On the same figure, anisotropy of all unit cells are also presented on the secondary vertical axis. As a general rule, elastic anisotropy decreases with increasing relative density, in other words, material approaches to isotropy. In order to inspect the contribution of Cross, SC and BC unit cells one by one in the OT unit cell, they are presented in the same figure. Recall that the combined unit cell dimensions are not changed but the radius of struts are changed to provide the same relative volume density of OT alone for proper comparison in this study. Change in E_{min} and E_{max} are calculated by $(E_{comb} - E_{OT})/E_{OT}$ and elastic anisotropy are tabulated in Table 2.

Introduction of Cross or SC unit cells have approximately the same effect on the material properties, but Cross unit cell has slightly better contribution compared to SC unit cell. Since the struts of Cross and SC unit cells are parallel to the [100], [010], [001] directions, they increase E_{min} which is in the same directions, but decrease E_{max} which is in [111] direction. The maximum contribution to elastic modulus is 35.2% with Cross UC for $\bar{\rho} = 0.05$ and the contribution decreases to 19.6% for $\bar{\rho} = 0.40$. On the contrary, the struts of BC unit cell are in [111] direction, its presence decreases E_{min} of OT seriously with 30.4% for $\bar{\rho} = 0.4$. Besides this, contribution of BC unit cell on E_{max} is very small.

Minimum and maximum shear modulus values of OT unit cell and its combinations are plotted in Fig. 8. Change in G_{min} and G_{max} are calculated with the same manner as for elastic modulus and tabulated in Table 3.

Addition of Cross or SC unit cells have approximately the same effect on the shear modulus of OT. Their presence increases G_{min} which is in [110] direction around 20-40%, but decreases G_{max} which is in [100] direction around 11-16%. Presence of BC unit cell decreases G_{min} seriously around 29-32%, but does not have any significant increase on G_{max}.

In order to observe the effect of relative density on OT unit cell and its combinations, x-y plane projection plots showing the variation of elastic and shear modulus of OT and its combinations for $\bar{\rho} = 0.05 - 0.4$ are tabulated in Table 4 and Table 5. Poisson Ratio of OT and its combinations are plotted on xy plane in Table 6. These figures are obtained from open source tool ELATE. Blue curves represent the maximum positive, green curves shows minimum positive and red curves are for minimum negative values (Gaillac et al., 2016). The Poisson anisotropy of OT was 22.24 for $\bar{\rho} = 0.05$, by the combinations of Cross and SC unit cells, it decreases significantly down to 1.48 and 1.46, respectively. It is shown from the last row of Table 6 that by adding BC unit cell, the material experiences negative Poissons ratio values. For low values of relative density unit cell becomes highly auxetic material and negative Poisson ratio value decreases by increasing relative density.

Finally, it is observed that, addition of BC unit cell which have the similar strut directions with the OT unit cell, did not have favorable improvement on the material properties. On the contrary, contribution of Cross and SC unit cells, those have struts in other directions than the struts of OT unit cell, its material constants are improved.

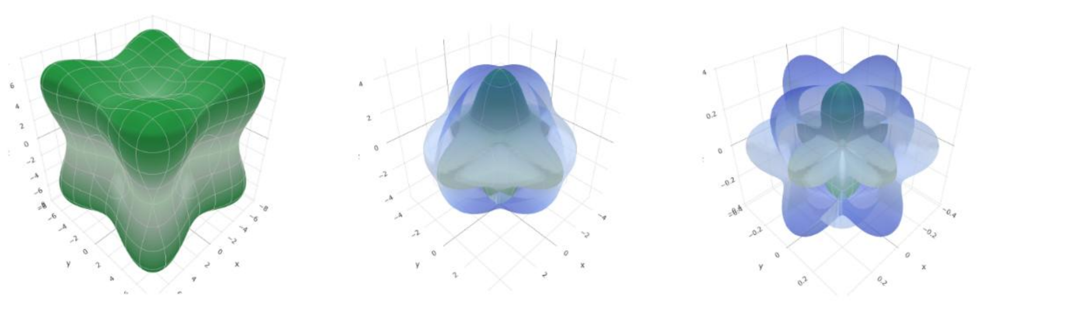

(a) (b) (c)

Fig. 5. Three dimentional spherical plots of (a) Elastic Modulus, (b) Shear Modulus, (c) Poisson's Ratio obtained from Elate for OT unit cell for $\bar{\rho} = 0.05$

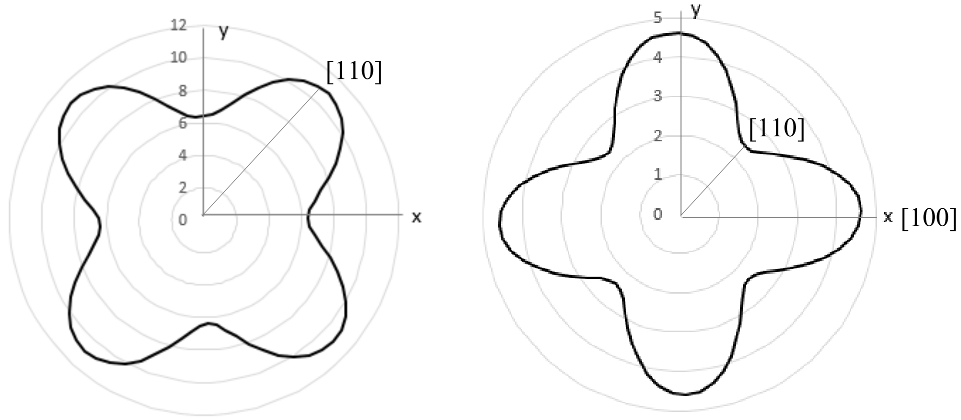

(a)

(b)

Fig. 6. (a) Elastic and (b) Shear modulus (MPa) of OT projected on xy-plane for $\bar{\rho} = 0.05$

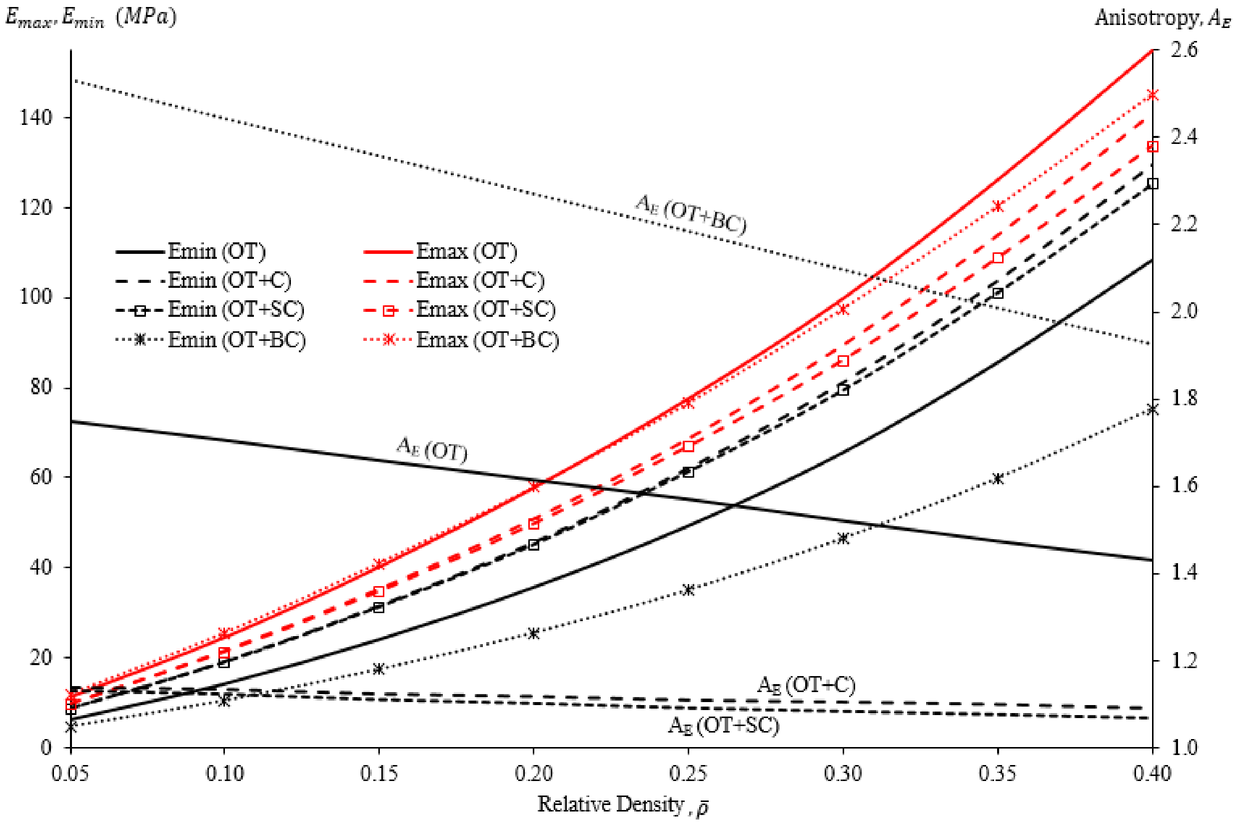

Fig. 7. E_{min}, E_{max} and elastic anisotropy A_E of OT and its combinations with respect to relative density $\bar{\rho}$

Table 2. Effect of Cross, SC and BC unit cells to the Elastic modulus values of OT and elastic anisotropy

	Change in E_{min} (%)			Change in E_{max} (%)			Elastic anisotropy, A_E			
$\bar{\rho}$	OT+C	OT+SC	OT+BC	OT+C	OT+SC	OT+BC	OT	OT+C	OT+SC	OT+BC
0.05	35.2	34.7	-26.9	-12.0	-12.7	5.8	1.75	1.14	1.13	2.53
0.10	33.0	32.2	-27.3	-11.7	-12.9	4.1	1.71	1.13	1.12	2.44
0.15	30.0	29.3	-28.1	-12.1	-13.4	2.2	1.66	1.12	1.11	2.36
0.20	27.4	26.3	-28.7	-11.9	-13.8	0.3	1.61	1.12	1.10	2.27
0.25	25.5	24.3	-29.0	-11.4	-13.7	-1.3	1.57	1.11	1.09	2.18
0.30	23.6	21.2	-29.1	-10.3	-13.7	-2.2	1.52	1.10	1.08	2.10
0.35	21.2	18.4	-30.0	-9.7	-13.7	-4.6	1.47	1.10	1.08	2.01
0.40	19.6	15.8	-30.4	-9.0	-13.7	-6.2	1.43	1.09	1.07	1.93

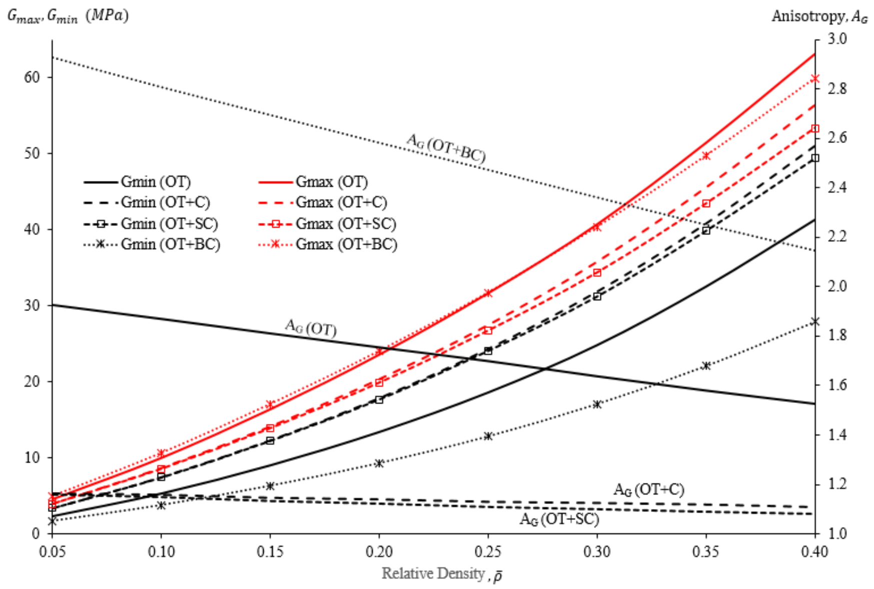

Fig. 8. G_{min}, G_{max} and shear anisotropy A_G of OT and its combinations with respect to relative density $\bar{\rho}$

Table 3. Contribution of added unit cells to shear modulus of OT and shear anisotropy

	Change in G_{min} (%)			Change in G_{max} (%)			Shear anisotropy, A_G			
$\bar{\rho}$	OT+C	OT+SC	OT+BC	OT+C	OT+SC	OT+BC	OT	OT+C	OT+SC	OT+BC
0.05	41.42	40.93	-29.14	-14..4	-15.13	7.77	1.93	1.17	1.16	2.93
0.10	38.76	37.97	-29.53	-13.90	-15.18	5.87	1.87	1.16	1.15	2.81
0.15	35.41	34.72	-30.27	-14.23	-15.68	3.82	1.81	1.15	1.13	2.70
0.20	32.43	31.37	-30.87	-13.94	-15.95	1.80	1.75	1.14	1.12	2.58
0.25	30.78	29.08	-31.21	-13.38	-15.77	0.15	1.70	1.13	1.11	2.47
0.30	27.89	25.56	-31.29	-12.19	-15.72	-0.90	1.64	1.12	1.10	2.36
0.35	25.12	22.43	-32.15	-11.50	-15.64	-3.33	1.58	1.12	1.09	2.25
0.40	23.19	19.47	-32.49	-10.70	-15.50	-5.05	1.53	1.11	1.08	2.15

Table 4. Effect of added unit cells on the material constants of OT plotted on xy plane for relative density values of 0.05, 0.2 and 0.4

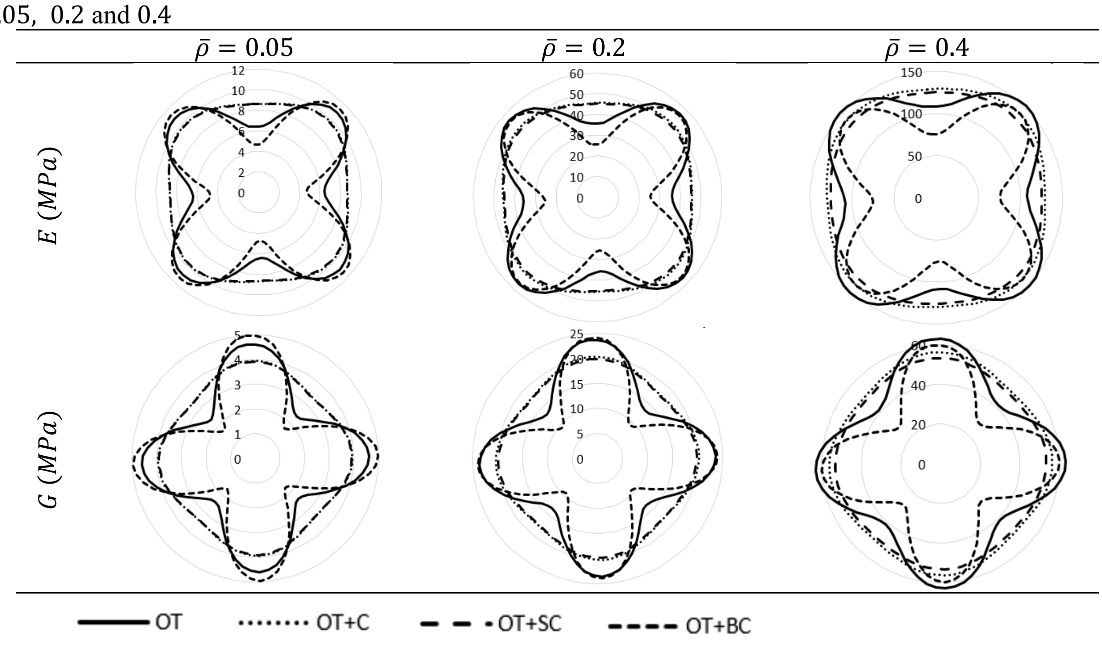

Table 5. Effect of relative density on the material constants of OT and its combinations plotted on xy plane

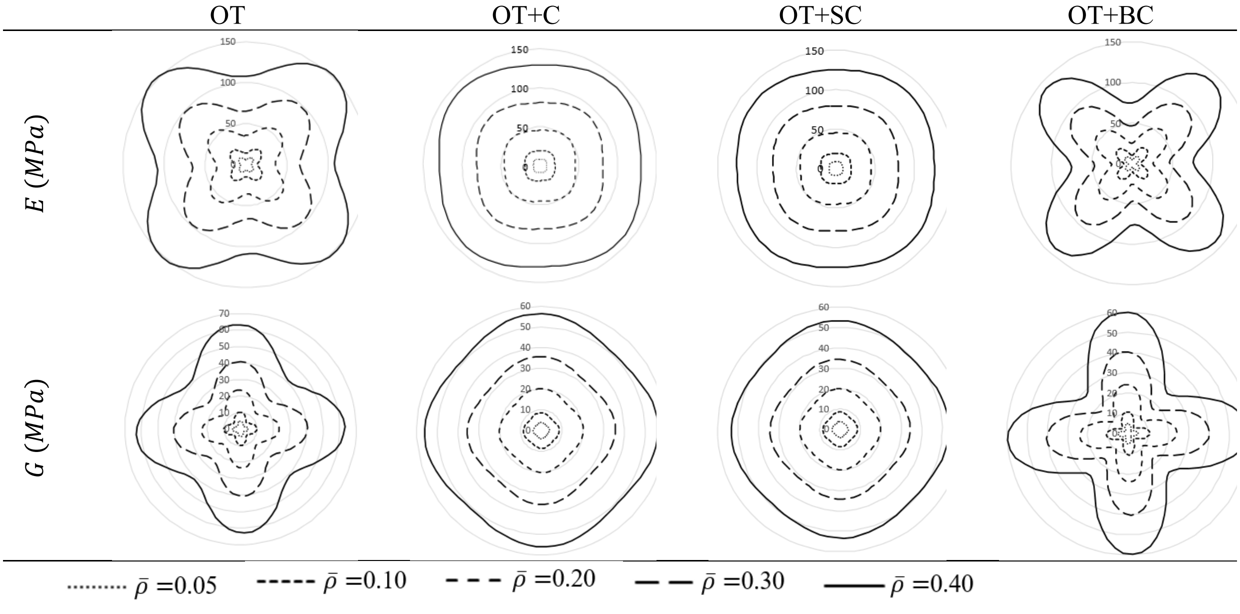

Table 6. Poisson Ratio of OT and its combinations plotted on xy plane. Blue: maximum positive, green: minimum positive, red: minimum negative (Gaillac et al., 2016)

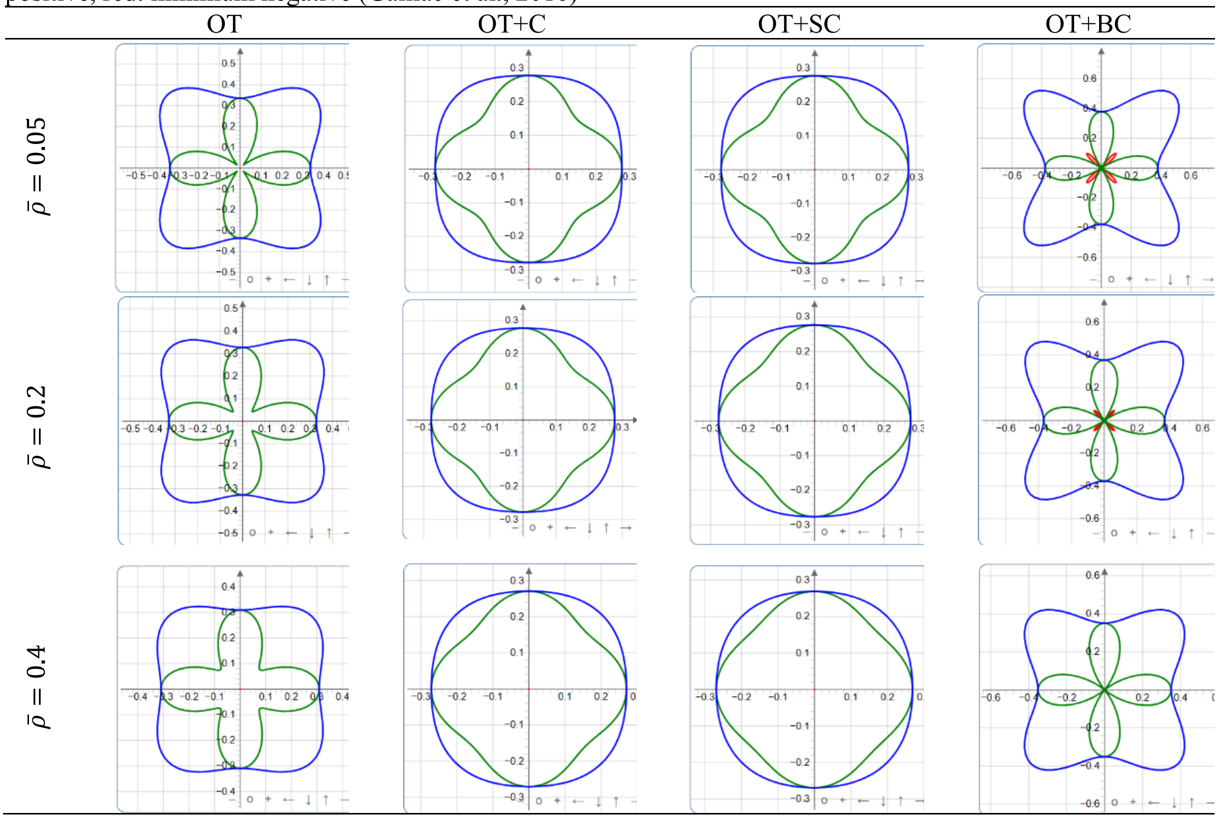

4. Conclusions

- It is verified that the anisotropy of lattice material constants decreases with the increase of relative volume density as expected. In other words, lattice material deviates from isotropy when relative density is decreased.
- OT unit cell and its combinations with Cross, SC, BC unit cells are compared in this study, provided that they have the same relative density. In order to accomplish this, required radius of the struts are calculated and used in the homogenization simulations.
- With the addition of Cross, SC, BC unit cells, the change in elastic and shear modulus are presented with tables and figures.

- Combination of Cross or SC unit cells to OT have approximately the same effect on its material properties, but Cross unit cell has slightly better contribution compared to SC unit cell.
- Cross and SC unit cells presence increases E_{min}, but decreases E_{max}. The maximum contribution to elastic modulus is 35.2% with Cross UC for $\bar{\rho} = 0.05$. On the contrary, BC unit cell's presence decreases E_{min} of OT seriously with 30.4% for $\bar{\rho} = 0.4$. Besides this, contribution of BC unit cell on E_{max} is very small.
- Addition of Cross or SC unit cells increases G_{min} around 20-40%, but decreases G_{max} around 11-16%. Presence of BC unit cell decreases G_{min} seriously around 29-32%, but does not have significant increase on G_{max}.
- Addition of Cross and SC unit cells, decreased the Poisson anisotropy of OT from 22.24 to 1.4-1.5 for $\bar{\rho} = 0.05$. Addition of BC unit cell to OT unit cell yielded an auxetic material.
- It is concluded that, addition of BC unit cell which have the similar strut directions with the OT unit cell, did not have favorable improvement on the material properties. On the contrary, contribution of Cross and SC unit cells , those have struts in other directions than the struts of OT unit cell, material constants are improved.

Acknowledgements
The research described in this paper was financially supported by the Scientific Research Projects Coordination Unit, BAP (Bilimsel Araştırma Projeleri Koordinasyon Birimi) at Istanbul Technical University, Turkiye under the grant number [MDK-2022-43793] during the PhD study of the first author.

References

Abaqus/CAE (2022), Simulia. http://www.3ds.com/products/simulia/portfolio/abaqus.

De Pasquale, G., Montemurro, M., Catapano, A., Bertolino, G., & Revelli, L. (2018). Cellular structures from additive processes: Design, homogenization and experimental validation. *Procedia Structural Integrity*, *8*, 75–82. https://doi.org/10.1016/j.prostr.2017.12.009

Deshpande, V. S., Fleck, N. A., & Ashby, M. F. (2001). Effective properties of the octet-truss lattice material. In *Journal of the Mechanics and Physics of Solids* (Vol. 49). www.elsevier.com/locate/jmps

Dixit, T., Nithiarasu, P., & Kumar, S. (2021). Numerical evaluation of additively manufactured lattice architectures for heat sink applications. *International Journal of Thermal Sciences*, *159*. https://doi.org/10.1016/j.ijthermalsci.2020.106607

Gaillac, R., Pullumbi, P., & Coudert, F. X. (2016). ELATE: An open-source online application for analysis and visualization of elastic tensors. *Journal of Physics Condensed Matter*, *28*(27). https://doi.org/10.1088/0953-8984/28/27/275201

Gibson, L., & Ashby, M. (1997). Cellular Solids: Structure and Properties (2nd ed.). Cambridge, UK: Cambridge Solid State Science Series; *Cambridge University Press.*

Habib, F. N., Iovenitti, P., Masood, S. H., & Nikzad, M. (2018). Fabrication of polymeric lattice structures for optimum energy absorption using Multi Jet Fusion technology. *Materials and Design*, *155*, 86–98. https://doi.org/10.1016/j.matdes.2018.05.059

Morrish, S. J. N., Pedersen, M., Wong, K. F. W., Todd, I., & Goodall, R. (2017). Size effects in compression in Electron Beam Melted Ti6Al4V diamond structure lattices. *Materials Letters*, *190*, 138–142. https://doi.org/10.1016/j.matlet.2016.12.130

Omairey, S. L., Dunning, P. D., & Sriramula, S. (2019). Development of an ABAQUS plugin tool for periodic RVE homogenisation. *Engineering with Computers*, *35*(2), 567–577. https://doi.org/10.1007/s00366-018-0616-4

Qi, D., Yu, H., Liu, M., Huang, H., Xu, S., Xia, Y., Qian, G., & Wu, W. (2019). Mechanical behaviors of SLM additive manufactured octet-truss and truncated-octahedron lattice structures with uniform and taper beams. *International Journal of Mechanical Sciences*, *163*. https://doi.org/10.1016/j.ijmecsci.2019.105091

Qiu, N., Zhang, J., Yuan, F., Jin, Z., Zhang, Y., & Fang, J. (2022). Mechanical performance of triply periodic minimal surface structures with a novel hybrid gradient fabricated by selective laser melting. *Engineering Structures*, *263*. https://doi.org/10.1016/j.engstruct.2022.114377

Smith, M., Guan, Z., & Cantwell, W. J. (2013). Finite element modelling of the compressive response of lattice structures manufactured using the selective laser melting technique. *International Journal of Mechanical Sciences*, *67*, 28–41. https://doi.org/10.1016/j.ijmecsci.2012.12.004

Tancogne-Dejean, T., Diamantopoulou, M., Gorji, M. B., Bonatti, C., & Mohr, D. (2018). 3D Plate-Lattices: An Emerging Class of Low-Density Metamaterial Exhibiting Optimal Isotropic Stiffness. *Advanced Materials*, *30*(45). https://doi.org/10.1002/adma.201803334

Tancogne-Dejean, T., & Mohr, D. (2018). Stiffness and specific energy absorption of additively-manufactured metallic BCC metamaterials composed of tapered beams. *International Journal of Mechanical Sciences*, *141*, 101–116. https://doi.org/10.1016/j.ijmecsci.2018.03.027

Tancogne-Dejean, T., Spierings, A. B., & Mohr, D. (2016). Additively-manufactured metallic micro-lattice materials for high specific energy absorption under static and dynamic loading. *Acta Materialia*, *116*, 14–28. https://doi.org/10.1016/j.actamat.2016.05.054

Wang, X., Zhu, L., Sun, L., & Li, N. (2021). Optimization of graded filleted lattice structures subject to yield and buckling constraints. *Materials and Design*, *206*. https://doi.org/10.1016/j.matdes.2021.109746

Yu, W. (2016). An Introduction to Micromechanics. *Applied Mechanics and Materials*, *828*, 3–24. https://doi.org/10.4028/www.scientific.net/amm.828.3

Zhao, M., Li, X., Zhang, D. Z., & Zhai, W. (2023). Geometry effect on mechanical properties and elastic isotropy optimization of bamboo-inspired lattice structures. *Additive Manufacturing*, *64*. https://doi.org/10.1016/j.addma.2023.103438

4th International Civil Engineering & Architecture Conference
17-19 May 2025, Trabzon, Türkiye

Finite element analysis and experimental investigation of load capacities of cold formed steel columns

Nefya Soysal*[1], Zeynep Fırat Alemdar[2]

[1] *Yıldız Technical University, Graduate School of Science and Engineering, 34220 Istanbul, Türkiye*
[2] *Yıldız Technical University, Department of Civil Engineering, 34220 Istanbul, Türkiye*

Abstract. Cold-formed steel structural members have distinct advantages over reinforced concrete and structural steel members. These include fast manufacturing in roll-forming machines indoors for 12 months of the year, light weight, and easy construction on site. A comparative analysis of cold-formed steel structures with other building systems reveals their superiority across the entire construction period, from initiation to completion. Cold-formed steel structures have been demonstrated to conserve natural resources due to the low level of waste generation and the recyclability of the structures during the production process. Following two significant seismic events measuring Mw 7.7 and Mw 7.6, respectively, which occurred in our nation on 6 February 2023, with epicenters located in Pazarcık (Kahramanmaraş) and Elbistan (Kahramanmaraş), the significance of cold-formed steel structures has been accentuated. In the context of this study, cold-formed steel stud (column) members were conceptualised in five distinct configurations, and their load-bearing capacities under compression were examined through a combination of finite element method (FEM) simulations and experimental methodologies.The tensile stress-strain values of the material in question are derived from the experimental data collected from the steel samples utilised in the tensile tests. The material properties under investigation were defined within the ABAQUS program, and the studs were modelled and analysed. Load-displacement results were obtained and then compared with the results of the experimentally tested columns. Furthermore, an investigation was conducted into the buckling conditions of the studs.

Keywords: Cold-formed steel stud; Load carrying capacity; Abaqus; Material behavior, Buckling

1. Introduction

Schafer et al. (2018) conducted experimental research into the phenomenon of buckling and collapse in built-up columns. A total of 32 test specimens with different cross-sections, thicknesses and joints were created for the purpose of the study. This study demonstrated that the displacements of elements connected with screws were greater than those of elements without joints, i.e. elements without screws.

Sang vd. (2022) conducted an investigation into the buckling behaviour of columns formed by three sections, with a particular focus on corner joints in light-weight steel structures. A total of 54 experimental studies were conducted. The experimental studies were modelled in the CUFSM Program and the results compared. The experimental specimens were prepared by altering the lengths, screw spacings, thicknesses, and head widths of the columns formed from C and U profiles that were contacted into each other. The screws utilised in the study were identified as ST 4.8 self-drilling screws. The findings of the study indicated that the effect of screw spacing was minimal in L and D type joints. However, an increase in screw spacing from 300 mm to 1000 mm in G-type columns resulted in a 11.71% decrease in ultimate load-bearing capacity. This decrease reduced the ultimate load-bearing capacity to 14.54%.Schafer et al. (2018) conducted experimental studies on the buckling and collapse of built-up columns. A total of 32 test specimens with different cross-sections, thicknesses and joints were created for the purpose of the study. This study demonstrated that the displacements of elements connected with screws were greater than those of elements without joints, i.e. elements without screws.

Mohan et al. (2022) conducted a study in which they tested 36 built-up specimens of varying dimensions. The test specimens were analysed numerically using the Abaqus programme. Consequently, the load-displacement graphs yielded divergent results. It was observed that the buckling conditions obtained from the experimental study occurred in similar locations to those obtained from the numerical study.

2. Material and method

The objective of this study is to investigate and compare the load-carrying capacities of five 2-metre-long constructed columns under pressure using a combination of experimental and numerical methods. In this study,

* Corresponding author, E-mail: nefyasoysal@gmail.com

https://doi.org/10.31462/icearc2025_ce_sme_327

the C140x35x10x1.5 and U144x24x1.5 profiles will be used. As shown in Fig. 1, the net dimensions of the sections were calculated using the CUFSM programs.

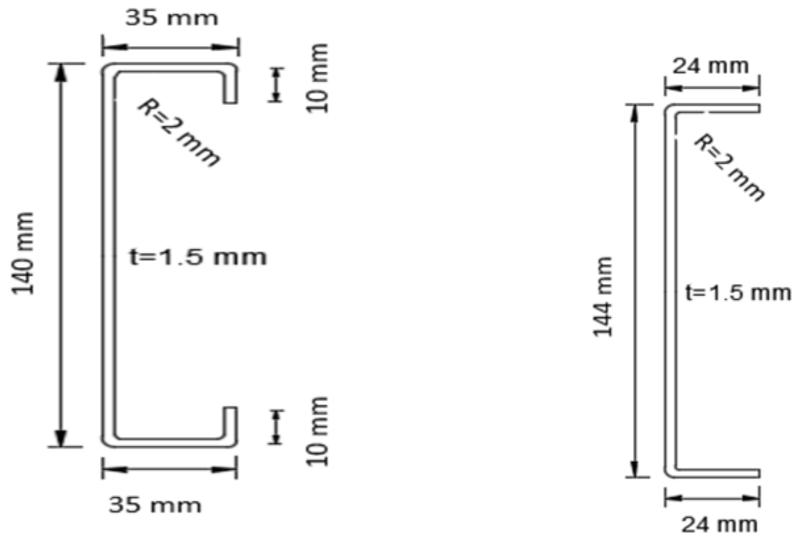

Fig. 1. Cross-sectional dimensions of the C140x35x10x1.5 and U144x24x1.5 profiles used

2.1 Cross-sectional properties of the profiles used

The profiles to be used are defined in the CUFSM program, and the cross-section properties obtained are given below. It is evident that the cross-sections are also defined in the Sap2000 program, and a comparison is made between the properties of these cross-sections as defined in the two programs. The findings indicate a high degree of similarity between the results. Fig. 2 and Fig. 3 show the results of the cross-sectional properties of the profiles in the CUFSM program.

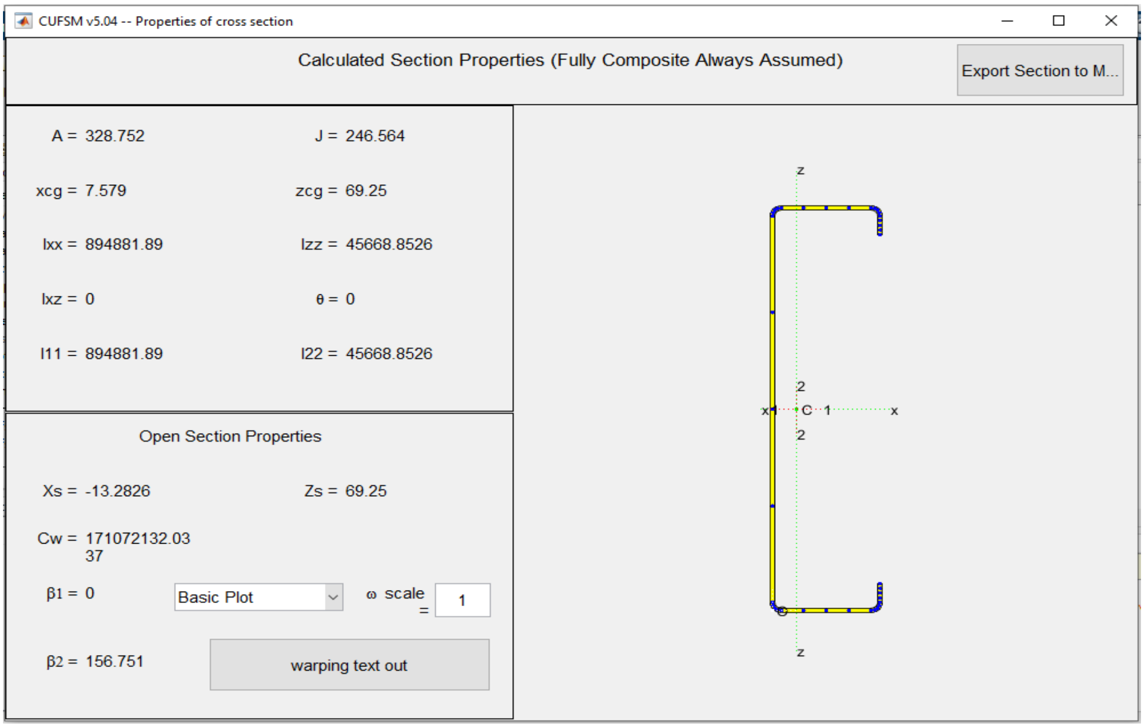

Fig. 2. Cross-sectional properties of C140x35x10x1.5 section

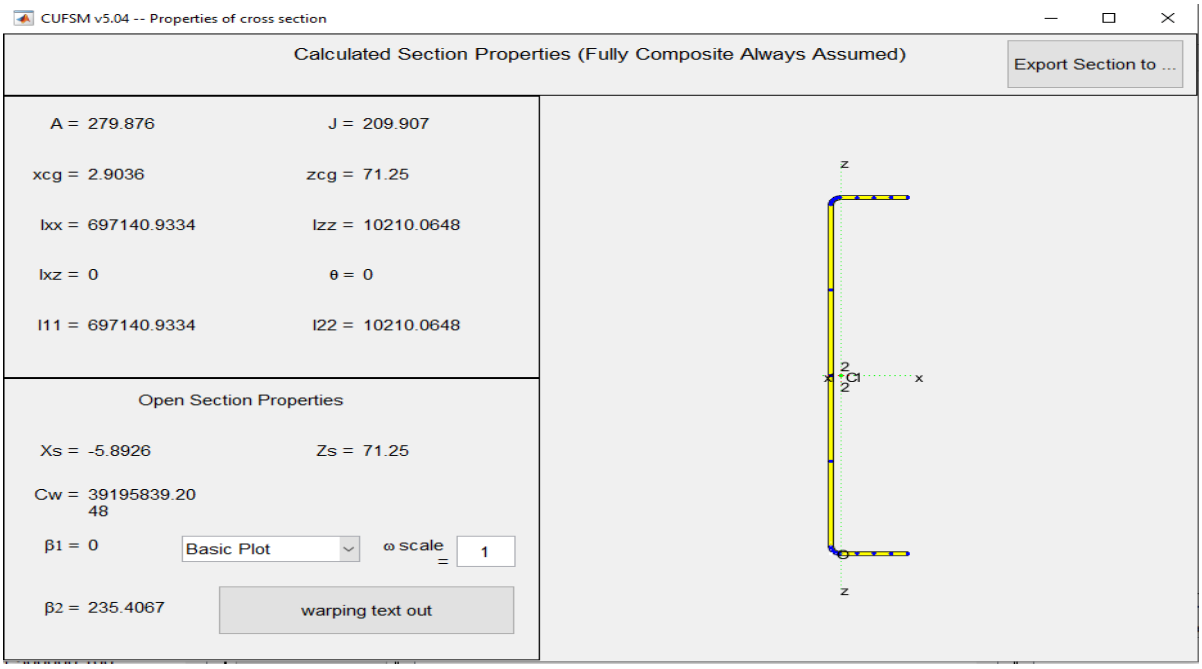

Fig. 3. The following cross-sectional details of U144x24x1.5 section

2.2 Experimental setup system

The 3D model of the test setup where the test specimens will be tested is given below. During the test, 25 mm thick elements shown with black plates were used to avoid out-of-plane behavior. The same plate is mounted on the load cell in the upper section. No out-of-plane behavior was detected during the test. Fig.4 shows the experimental setup and 3D images.

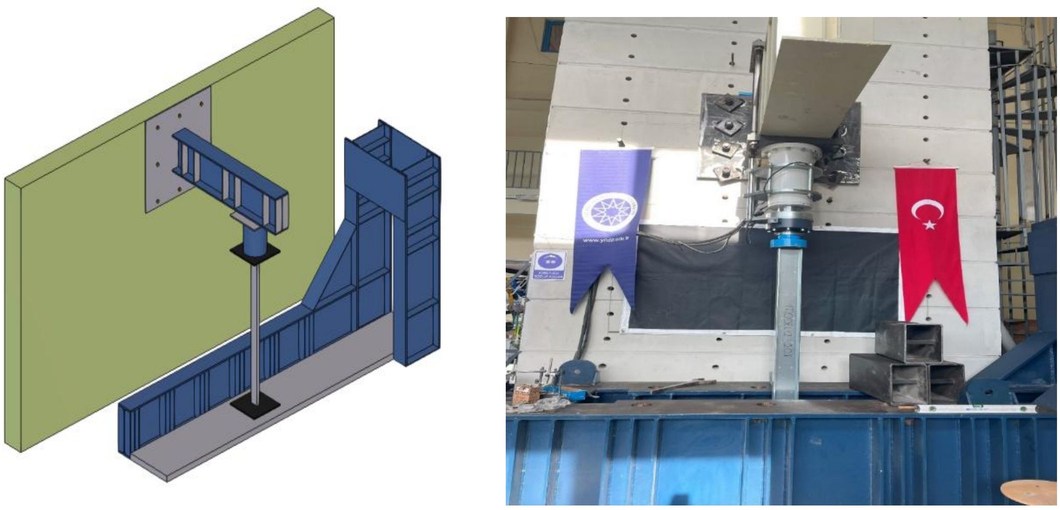

Fig. 4. The 3D design of the experimental setup

2.3 Material properties

In the experimental study, four samples were tested in accordance with BS EN ISO 6892-1. Tensile tests were performed on samples made from galvanized sheet metal. Four samples were taken from the profiles, consisting of two main bodies and one side panel, and tensile tests were conducted at Yıldız Technical University. As a result, the material was identified as S355GD. Using these values, nonlinear analysis data were defined for the models in Abaqus analyses. Fig. 5 shows the images of the materials before and after the tensile test and Fig. 6 shows the stress strain graphs obtained as a result of the experiment

Fig. 5. Test specimens used in tensile testing

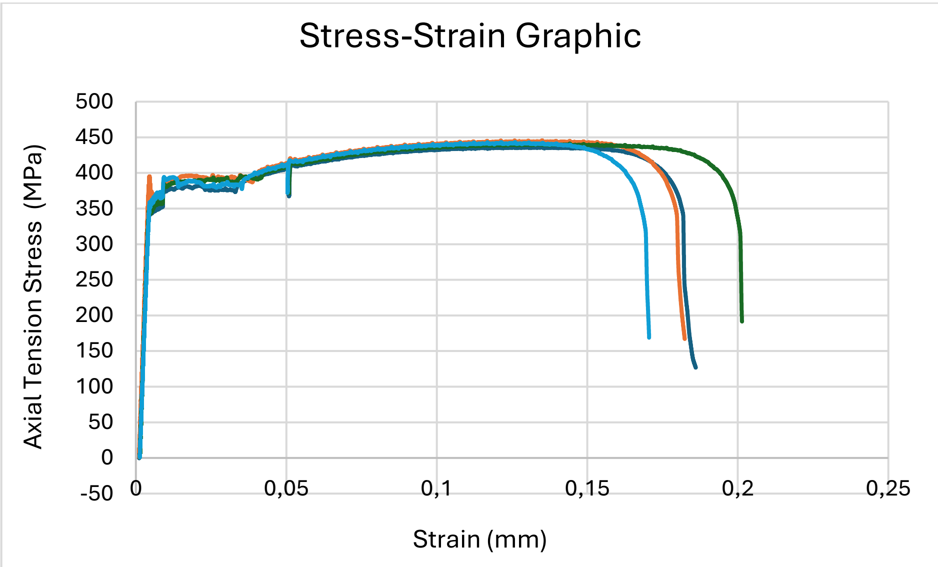

Fig. 6. Stress – strain curved

2.4 Experimental studies

Within the scope of experimental studies, 2 m long studs were fabricated and analysed. The cross-sectional views of the column studs are presented in the Fig. 7. The construction of the specimens involved the utilisation of screws with a diameter of 3.9 mm, which were employed to facilitate the connection of the built-up columns at 20 cm intervals. In the Model-3 and Model-4 designs, the connection of the studs was achieved through the use of 2 mm thick plates, with dimensions of 10x5 cm. The studs were positioned in a flat configuration, with a 25 cm thick plate acting as a foundation before being inserted into the test specimen. During the experiment, the specimens were positioned between these plates, thereby restricting their movement. It was observed that no shear occurred in the connection parts of the specimens after the experiment.

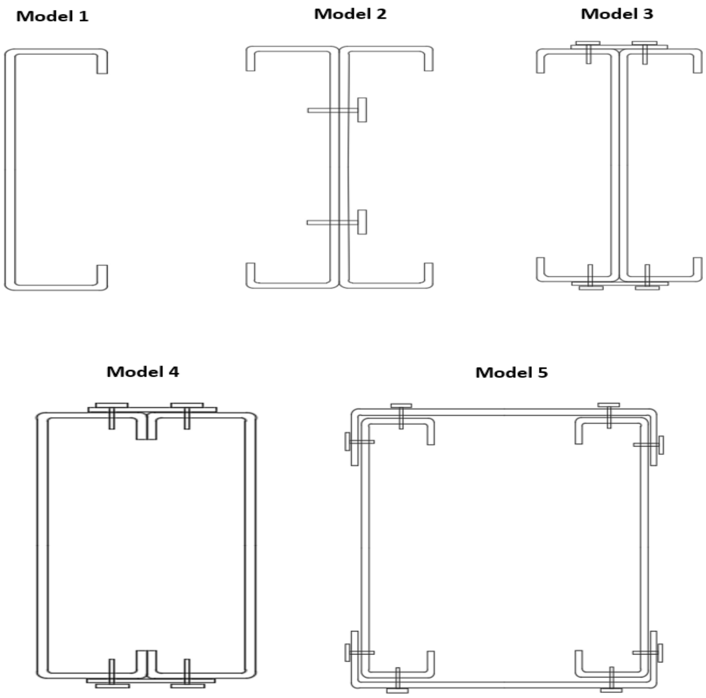

Fig. 7. The cross-sectional views of the columns.

2.5 Numerical studies

The numerical solutions were analyzed by defining initial imperfection in the Abaqus program. In Fig. 8, the boundary conditions of the load and support related to model 1 in the abaqus program are given.The sections in the models were defined as Shell element. The mesh intervals selected in the models were changed and it was decided that the most appropriate one should be defined as 10 mm meshing initial imperfection were selected in the range specified in the studies of Schafer and Peköz(1998) and defined by buckle analysis to the models as seen in the Fig. 9. Fig. 10 shows the Abaqus models of the 5 columns studied.

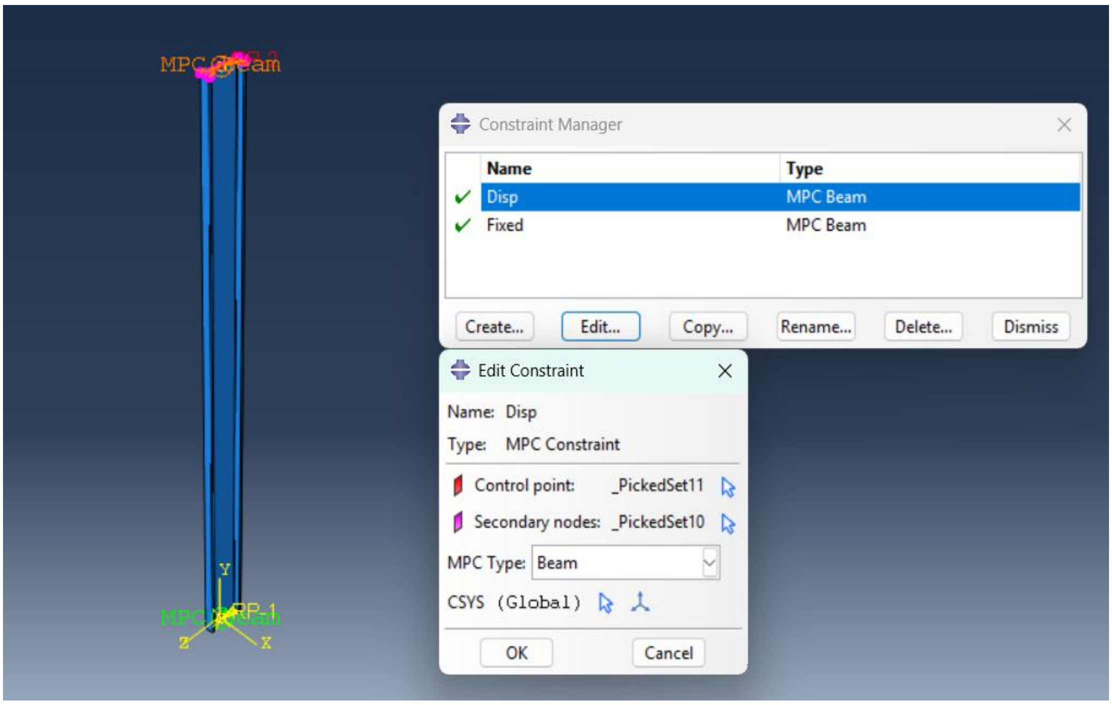

Fig. 8 Column 1 support conditions

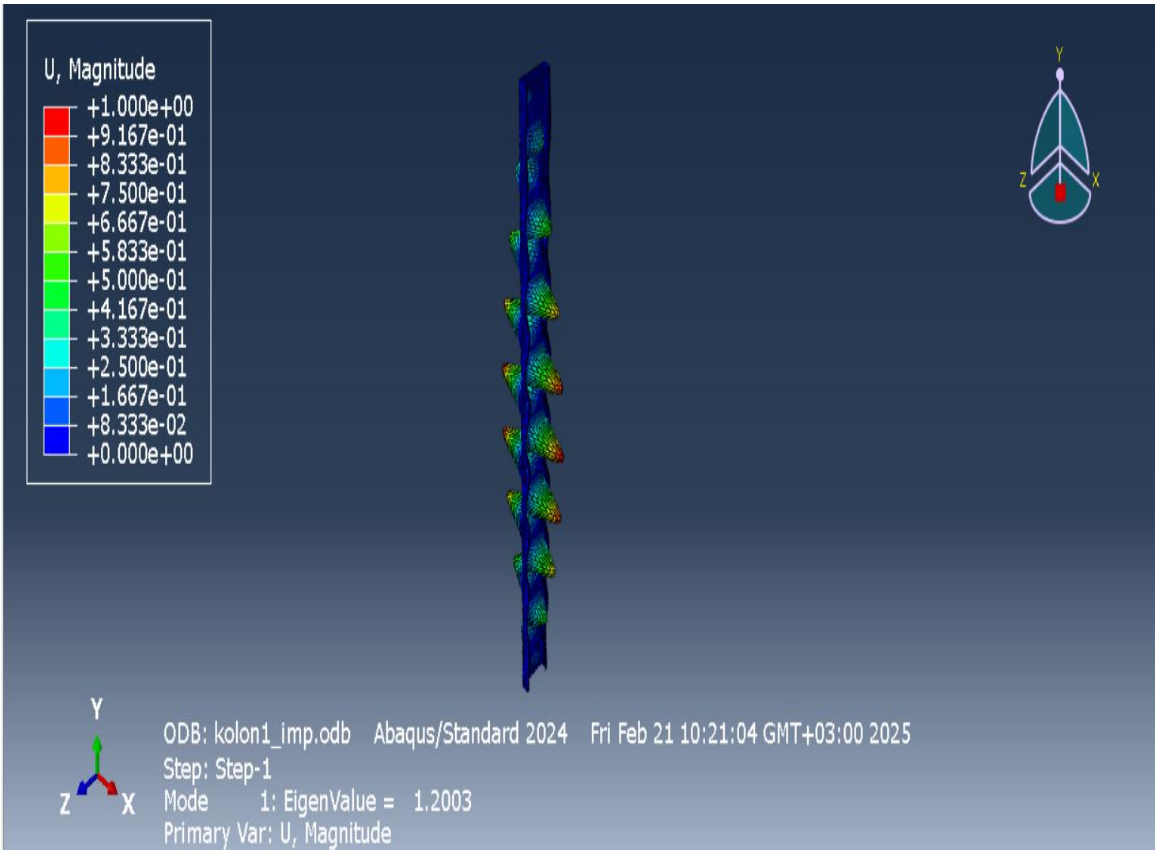

Fig. 9. Deformation occurring in the model after buckling analysis

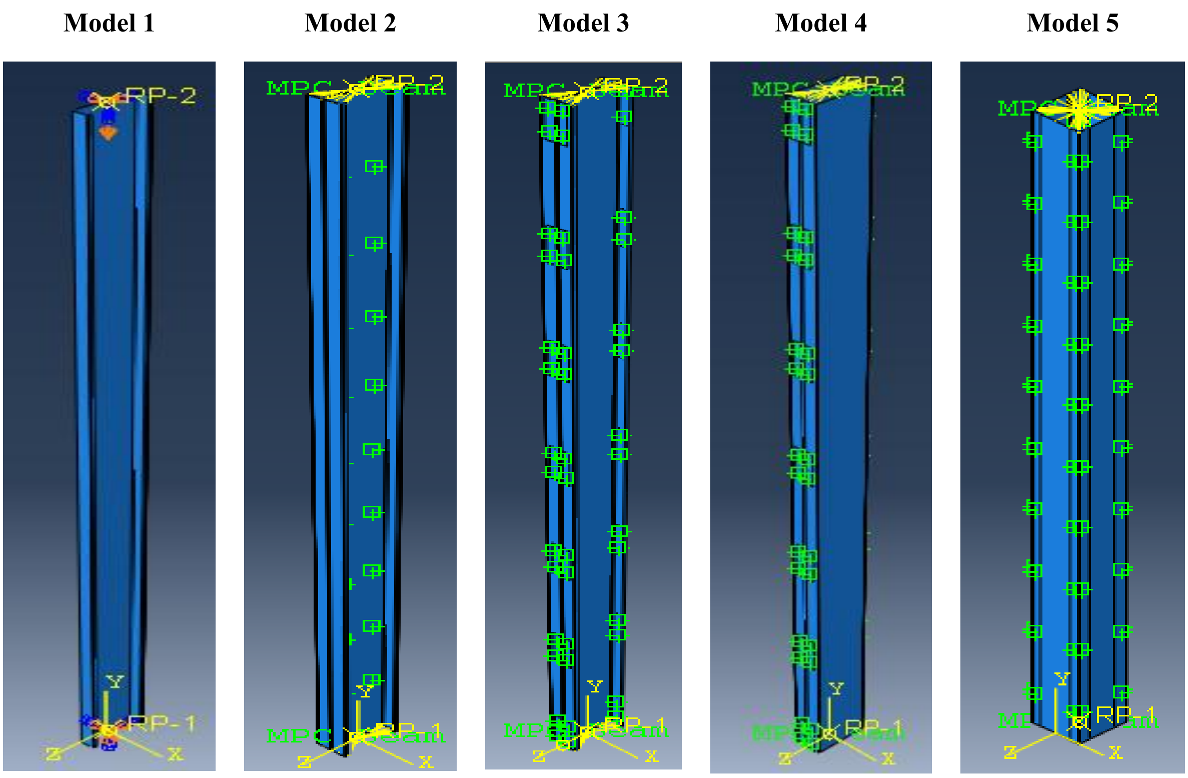

Fig 10. Models created in the Abaqus

3. Short column test

Within the study's parameters, an 80-centimetre short column test was conducted, as can be seen in the Fig.11 accompanying image. The C140x35x10x1.5 profile, which exhibited equivalent cross-section and material properties to those of the stud, was utilised as the primary profile. Fig.12 shows the load-displacement graph obtained as a result of the experiment. The experiment yielded a maximum load-bearing capacity of 67.65 kN.

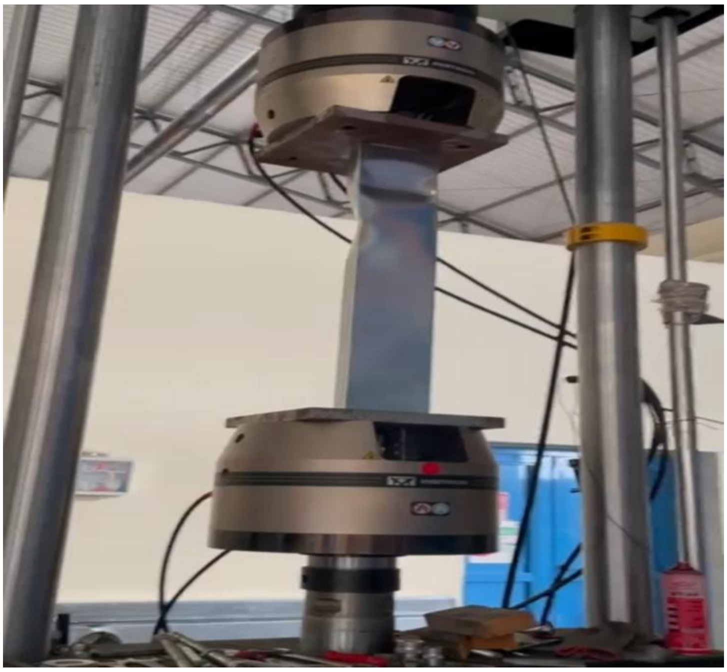

Fig. 11. The deformation of the column during the test

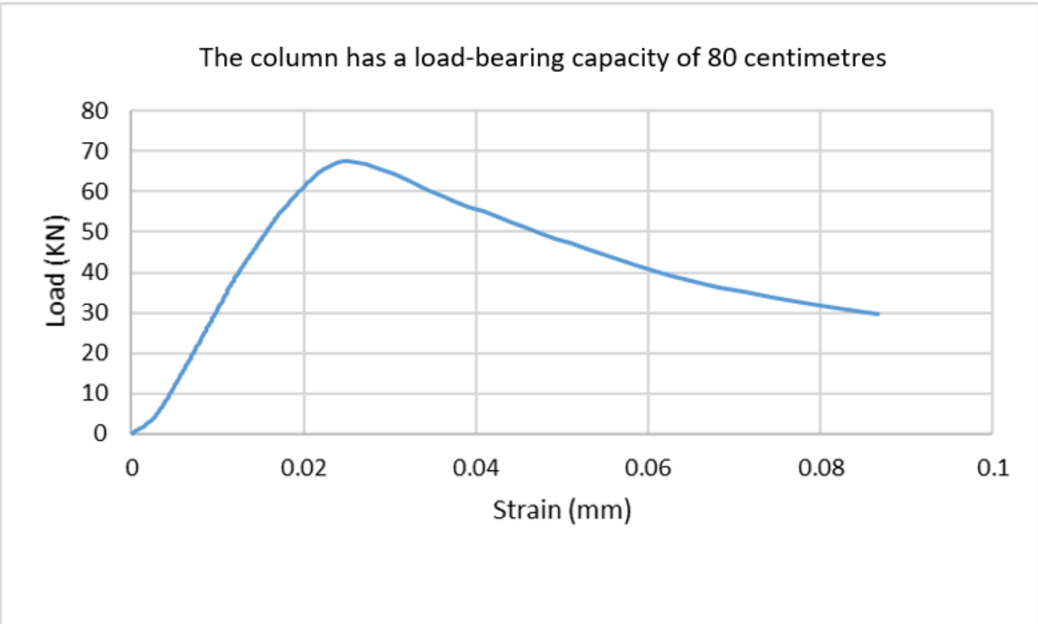

Fig. 12. The column load carrying capacity graph is 80 centimetres in length

4. Results

In the studies conducted in the literature on studs, Phan D. (2022) and Yilmaz. Y (2024) obtained similar load-displacement curves with this study. It is reason for the observed difference in value that the material quality of the profile employed is believed to be the cause, variations in the profile's cross-sectional dimensions, differences in thickness, and variations in connection types. In Tab.1, numerical analysis results and experimental results are compared with each other.

Table 1. Comparison of Experimental and Abaqus Analysis Results for Columns

<table>
<tr><th colspan="3">Comparison of Experimental and Abaqus Analysis Results for Column 1</th></tr>
<tr>
<td></td>
<td>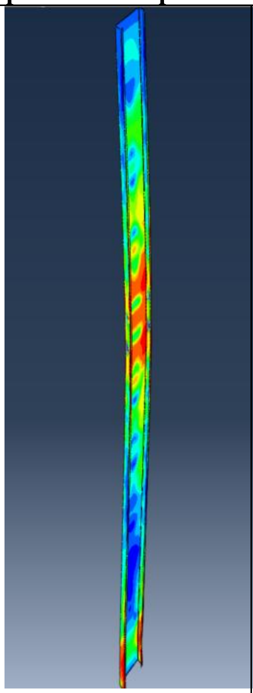</td>
<td>

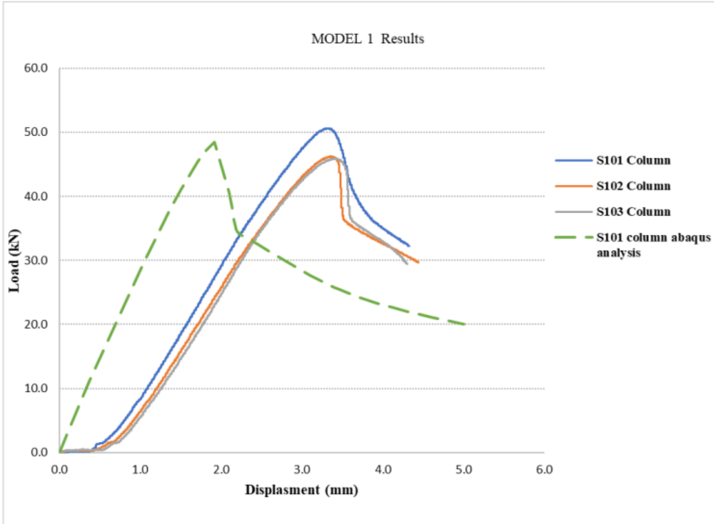

The maximum load value of the S101 test sample is as follows:50,62 kN
The maximum load value of the S102 test sample is as follows:46,24 kN
The maximum load value of the S103 test sample is as follows:45,9 kN
Maximum load value of the S101 Abaqus model: 48,43 kN

</td>
</tr>
<tr><td colspan="3"></td></tr>
<tr><th colspan="3">Comparison of Experimental and Abaqus Analysis Results for Column 2</th></tr>
<tr>
<td></td>
<td>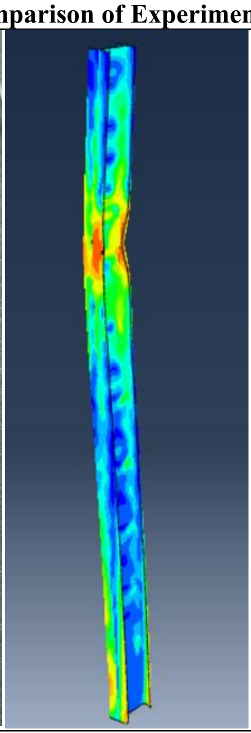</td>
<td>

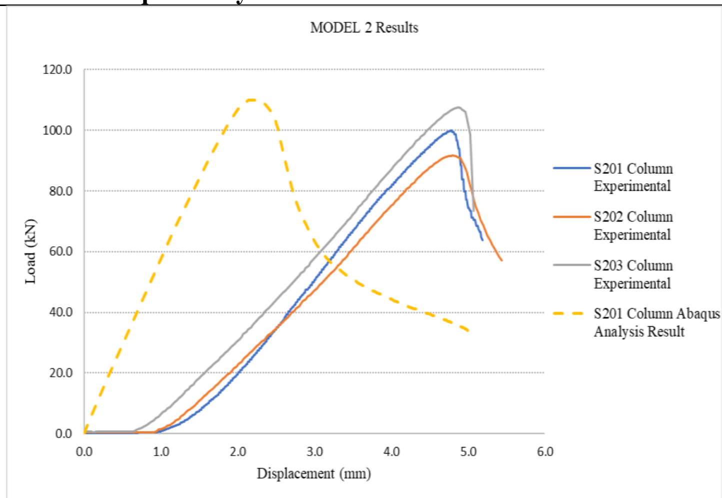

The maximum load value of the S201 test sample is as follows: 99,9 kN
The maximum load value of the S202 test sample is as follows: 91,7 kN
The maximum load value of the S203 test sample is as follows: 107,48 kN
Maximum load value of the S201 Abaqus model: 110 kN

</td>
</tr>
</table>

Table 1 continued

Comparison of Experimental and Abaqus Analysis Results for Column 3

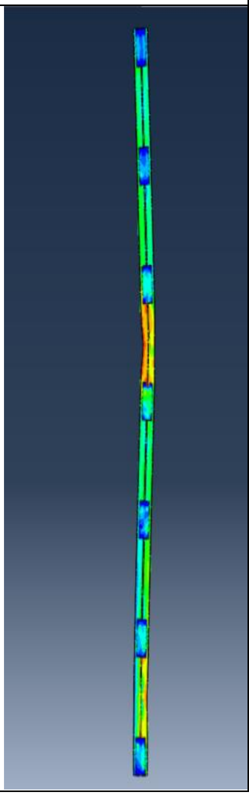

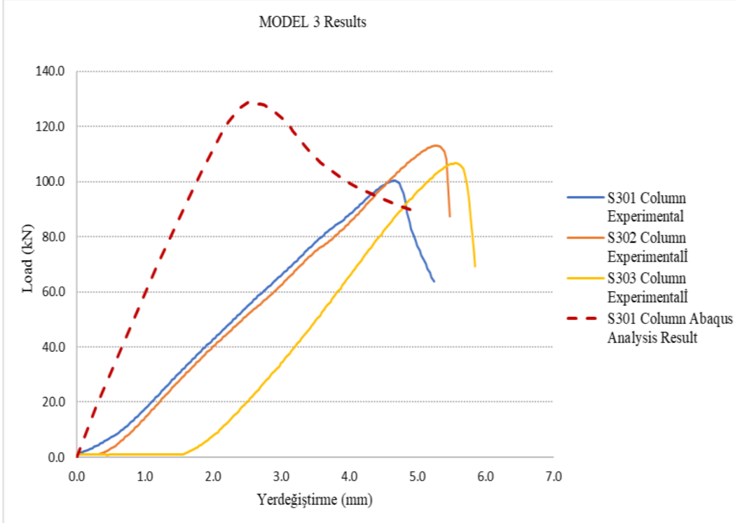

The maximum load value of the S301 test sample is as follows: 113.13 kN
The maximum load value of the S302 test sample is as follows: 100.28 kN
The maximum load value of the S303 test sample is as follows: 106.59 kN
Maximum load value of the S301 Abaqus model: 128.2 kN

Comparison of Experimental and Abaqus Analysis Results for Column 4

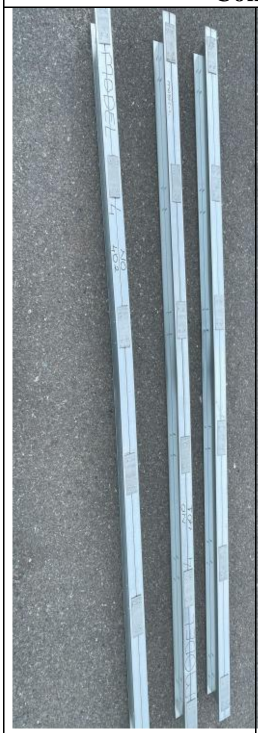

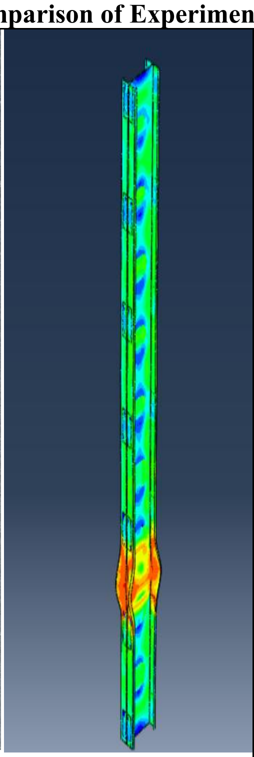

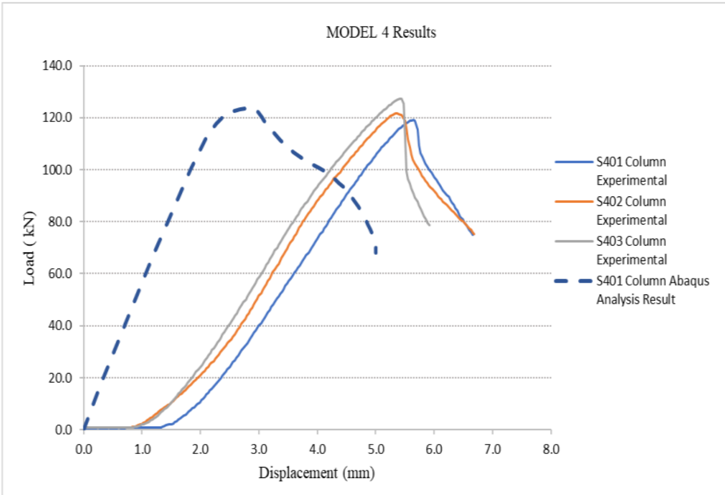

The maximum load value of the S401 test sample is as follows: 119 kN
The maximum load value of the S402 test sample is as follows: 121.5 kN
The maximum load value of the S403 test sample is as follows: 127.6 kN
Maximum load value of the S401 Abaqus model: 123.55 kN

Table 1 continued

<table>
<tr><th colspan="3">Comparison of Experimental and Abaqus Analysis Results for Column 5</th></tr>
<tr>
<td></td>
<td>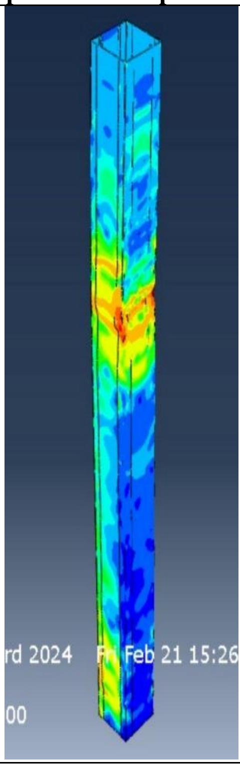
</td>
<td>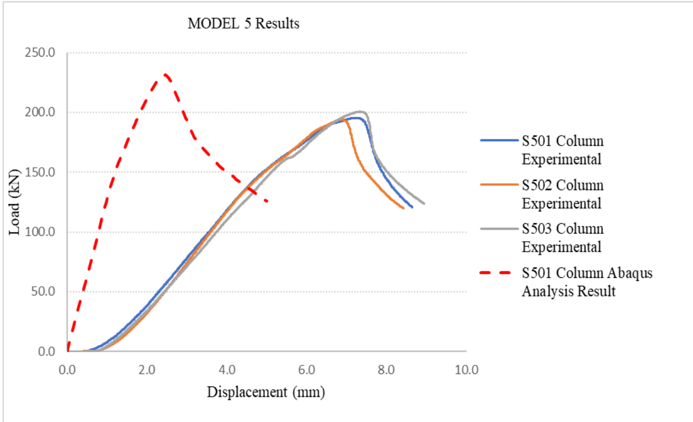

The maximum load value of the S501 test sample is as follows: 195,5 kN
The maximum load value of the S502 test sample is as follows: 194,18 kN
The maximum load value of the S503 test sample is as follows: 200,63 kN
Maximum load value of the S501 Abaqus model : 231,48 kN</td>
</tr>
</table>

5. Conclusion

Within the course of this project, load-displacement graphs were obtained for five different columns. Consequently, it was observed that the load-bearing capacity of the column designated Column 5 was the highest. In Columns 2, 3, and 4, the loads were found to be in close proximity to each other. The column with the lowest capacity was identified as Column 1. It was thus determined that the utilization of built-up (fabricated) columns within the system results in a significantly increased capacity of lightweight steel elements.

It has been observed that the most stress under load occurs on the sides and corners of the profiles. In each sample, buckling was found to occur in different areas rather than in the same areas. It was evident that the maximum stress was observed at the covers and studs, where the panels are attached to the floor.

Consequently, it was determined that the local buckling behaviour exhibited by cold formed steel elements under load affects the overall buckling behaviour of the system. Consequently, when designing lightweight steel elements, connections that prevent local buckling must be incorporated. The calculation of the behaviour of the thickness of the profiles under load should be conducted using programs such as CUFSM or CFS. Furthermore, the behaviour of the profile under pressure and bending effects should be determined prior to design. The selection of profiles is to be made on the basis of their buckling modes.

Acknowledgments

The authors gratefully acknowledge the support of the Scientific and Technological Research Council of Turkey (TUBITAK) ARDEB 1002 Grant No 223M448. The assistance and support of Prof. Dr. Serkan Bekiroglu, Assoc. Prof. Dr. Fatih Alemdar, and the entire staff of the Structural Laboratory at the Yildiz Technical University are also gratefully acknowledged.

References

Al-Gaadi, F. M. A. (n.d.). *Experimental Study of Earthquake Simulator for Cold-Formed Lightweight Steel Sturctures*. Yıldız Technical University, İstanbul. (2020)

Schafer, B. W., & Peköz, T. (1998). Computational modeling of cold-formed steel: characterizing geometric imperfections and residual stresses. *Journal of constructional steel research*, *47*(3), 193-210.

Alıca, H. Ç.. *Lateral Load Behavior of Cold-Formed Steel Wall Panels* (Issue March). Atılım University. (2013)

Cai, Y., & Young, B.. Structural behavior of cold-formed stainless steel bolted connections. *Thin-Walled Structures*, *83*, 147–156. (2014)

Ishaq D. M. G. A. *Assessment of performance to new turkish earthquake code of a light steel construction.* Süleyman Demirel Üniversitesi. (2019)

Fang, Z., Roy, K., Lakshmanan, D., Pranomrum, P., Li, F., Lau, H. H., & Lim, J. B. P. Structural behaviour of back-to-back cold-formed steel channel sections with web openings under axial compression at elevated temperatures. *Journal of Building Engineering*, *54*(May), 104512. (2022).
Fratamico, D. C., Torabian, S., Zhao, X., Rasmussen, K. J. R., & Schafer, B. W. Experiments on the global buckling and collapse of built-up cold-formed steel columns. *Journal of Constructional Steel Research*, *144*, 65–80. (2018).
Güneş, S. A., & Çeribaşı, S.. Approaches for design of lightweight steel structures, current controlling conditions, and the issues recommended to be emphasized in a prospective lightweight steel building code. *Pamukkale University Journal of Engineering Sciences*, *24*(3), 362–375. (2018)
Hasanali, M., Mojtabaei, S. M., Clifton, G. C., Hajirasouliha, I., Torabian, S., & Lim, J. B. P. . Capacity and design of cold-formed steel warping-restrained beam-column elements. *Journal of Constructional Steel Research*, *190*(October 2021),
Karabulut, B. (2016). *Analytical and Experimental Studies of Cold-Formed Steel Shear Panels*. Boğaziçi Üniversitesi.
Maali, M., Sagiroglu, M., & Semih Solak, M. Experimental behavior of screwed beam-to-column connections in cold-formed steel frames. *Arabian Journal of Geosciences*, *11*(9) (2018)
Mohan, M., Ramachandran, A., & Amran, M.. *Determination of Buckling Behavior of Web-Stiffened*. (2022)
Öztürk, F. *Experimental and numerical investigation of cold formed sigma profiles behaviour under axial and eccentric loading. Karadeniz Technical University*. (2021)
Phan, D. K., Rasmussen, K. J. R., & Schafer, B. W. Numerical investigation of the strength and design of cold-formed steel built-up columns. *Journal of Constructional Steel Research*, *193*(April), 107276. (2022).
Sang, L., Zhou, T., Zhang, L., Chen, B., & Wang, S. (2022). Experimental investigation on the axial compression behavior of cold-formed steel triple-limbs built-up columns with half open section. *Thin-Walled Structures*, *172*(June 2021)
Solak, M. S. *Experimental behavior of screwed beam-to-column connections in cold-formed steel frames*. Erzurum Technical University (2019).
Tavlaşlıoğlu, M. E.. *Experimental behavior of the cold-formed steel beam-to-column screw connections under cycle loads.* Erzurum Technical University,. (2022)
Topçuoğlugil, Y.. Numerical Modeling of Cold-Formed Steel Sheathed Shear Walls Under Lateral Loading. Middle East Technical University, Ankara. (2019)
T.H. Miller, T. Pekoz, Load-eccentricity effects on cold-formed steel lipped-channel columns, J. Struct. Eng. 120 (3) (1994) 805–823.
Yılmaz, Y. C *Investigation of the behavior of C-section cold-formed steelprofiles under axial and eccentric loading* Karadeniz Technical University, Trabzon, Türkiye. (2024)

4th International Civil Engineering & Architecture Conference
17-19 May 2025, Trabzon, Türkiye

Contact analysis loaded with a block on a functionally graded layer

Ezgi Ayhan[1], Berivan Y. Polat[*2], Jitendra Khatti[3]

[1] Munzur University, Department of Civil Engineering, 62000, Tunceli, Türkiye
[2] Munzur University, Disaster and Emergency Management, 62000, Tunceli, Türkiye
[3] Rajasthan Technical University, Department of Civil Engineering, Rajasthan, India

Abstract. In this study, the analysis of the continuous contact problem of a functionally graded material was realized by the finite element method (FEM). The problem consists of a functionally graded plate resting between two semi-infinite elastic planes and loaded with a rigid block. A rigid block transmits the external load (P) to the slab. It is supposed that there is no friction on the surfaces. The finite element model of the functionally graded layer was created using the ANSYS package program, and a two-dimensional analysis of the problem was performed.

Keywords: Functionally graded material; Stress analysis; Contact pressure; Finite element method; Homogenous layer

---

1. Introduction

The contact problem has become a subject studied in many engineering fields. İn most mechanical systems, the elements are in contact, and this causes some problems. Because when two or more components come into contact, stresses and displacement behaviors occur in these areas. Contact problems cause damage to the structure and elements as a result of stress and displacement behaviors. For engineers, knowing the nature of the contact occurring in these systems, their lengths, and the stress distributions in the contact areas provides great convenience in the design and production of the material.Since the contact problem causes much damage to the structure and elements, it has been studied in many engineering fields from the past to the present. Hertz first studied classical contact mechanics at the University of Berlin in 1882. Hertz studied the equilibrium of two elastic bodies in contact, assuming the contact region to be elliptical, and developed formulations for contact stress and deformations (Hertz, Heinric*h*, 1882). After Hertz's inspiring research, many researchers have conducted various studies on the contact problem. The contact problem remains a subject of study in many engineering fields. In layered systems where contact problems occur, sudden changes in material properties can also cause systemic deterioration. As a solution to this problem, with the advancement of technology, it has become clear that the structure of materials can change along their homogeneity or continuously. Functionally graded materials (FGM) are specially structured materials whose components' mechanical and thermal properties are continuously changing (Alagöz et al., 2004). In other words, materials with a composition or structure that varies throughout the volume of the material are defined as Functionally Grade Materials (Alagöz et al., 2004). Due to their ability to reduce surface stress, FGMs have found applications in a wide range of fields since their emergence, including aerospace, electronics, energy, chemical engineering, optical materials, and biomedical engineering. Functionally graded materials have a wide range of applications in the aerospace, automotive, and biomedical industries due to their lightweight, high strength, thermal resistance properties, and resistance to corrosion and wear (Alagöz et al., 2004). The first steps of functionally graded materials were taken during the studies of spacecraft and aircraft at a university in Japan in 1984-1985. In 1987, researchers who worked on FGM were brought together for a large project with the support of the Japanese Ministry of Education and Science. Later, many researchers conducted studies on FGM. Koizumi (1997) has studied these materials. The author examined this material's properties, usage areas, and advantages. Ke and Wang (2006) studied the contact problem that occurs when a single force from an elastic punch and friction forces perpendicular to the force acting on an elastic half-plane covered with a thin layer. Polat (Polat, 2021) examined the continuous contact problem in a functionally graded (FGM) layer loaded with an FG flat punch sitting on an elastic semi-infinite plane using the finite element method (FEM). Balci and Dag (Balci & Dag, 2020) examined the problem of moving contact on functionally graded coating loaded with a rigid

---

[*] Corresponding author, E-mail: bpolat@munzur.edu.tr

https://doi.org/10.31462/icearc2025_ce_sme_342

punch. Further, this study is the first to examine the effect of FGM punch on the FGM layer.Yan and Mi (Yan & Mi, 2019) performed contact analysis for an elastic sheet strengthened with a functionally graded coating and pressed into a half-plane.At the end of this study, the results were compared using analytical and finite element methods.This study investigated the effects of the material changing parameters such as punch speed, friction coefficient, material homogeneity, and coating thickness on the contact stress distributions and stress density. Polat (2019) analyzed the continuous contact problem of a homogeneous layer of constant thickness, perfectly bonded to a rigid support on its lower surface and loaded with a rigid stamp, using the finite element method (FEM). He also examined the contact length and contact stress between the rigid block and the homogeneous layer. Çömez et al. (2020) in their work, they investigated the problem of frictional sliding double contact, including an advancing contact region between a rigid cylindrical block and a stepped sheet and a receding contact region between the stepped sheet and a homogeneous sheet bonded to a homogeneous half-plane. Liu et al. (2016) studied the axisymmetric pair contact problems of a functionally graded plate with a rigid cylindrical block and a rigid spherical block loaded. The numerical results analyzed that the stiffness ratio and gradient index greatly influence the contact area and contact pressure. Yan and Mi (2019) analyzed in detail the frictionless contact problem of an elastic structure consisting of an elastic layer and an elastic half-plane loaded with two rigid punches having circular and parabolic profiles. Apatay et al. (2010) analyzed subsurface contact stresses caused by the frictional rigid punch effect in functionally graded coatings. The effects of punch width, punch position, friction coefficient, and material parameters on the stress distributions throughout the coating depth are investigated. Chidlow and Teodorescu (2013) investigated the frictionless two-dimensional contact problem of an inhomogeneous material loaded with a rigid punch. The study investigates the effects of material homogeneity and coating thickness on the cylindrical block. It was stated that the thickness and mechanical properties of the layer significantly affect the maximum stress. Çömez (2013) studied the contact problem in a functionally graded layer supported by the Winkler foundation using linear elasticity theory. The researcher analyzed the effects of material inhomogeneity, the Winkler Foundation's inhomogeneity, and the punch's size on contact stress, contact distance, and normal stresses. Adıyaman et al. (2015) analyzed the split contact problem for a punch resting on two quadrants and an elastic plane loaded with a distributed load using analytical and finite element methods. Contact lengths and contact stresses are solved for different loadings for both solutions. As a consequence of the study, it is analyzed that the values acquired by the finite element method are close to the values obtained by the analytical method. Su et al. (2015) investigated the two-dimensional wear contact problem of a piezoelectric half-plane loaded with a cylindrical punch using analytical methods. As a consequence of the study, they observed that the piezoelectric effect causes the coupling of normal contact pressure and tangential tension, which can significantly affect wear contact damage. Fu et al. (2024) investigated the elastic vibration analysis of the two-dimensional moving contact problem in a functionally graded layer with arbitrarily varying thermoelastic properties. In their study, they stated that increases in friction coefficient and motion speed can cause a decrease in the elastic jolt limit, and the elastic jolt limit can be improved significantly by adjusting the shear modulus and yield stress distribution gradients appropriately. Polat and Kaya (2022) analyzed the contact problem in two functionally graded layers loaded with two rigid blocks, the upper and lower surfaces of which are metal and ceramic, using the finite element method. In this study, the effects of different properties of functionally graded layers on the normal stresses between layers and between rigid blocks and the upper surface of the layer are investigated. In addition, the normal and shear stresses are investigated along the depth at the separation point under the influence of the different properties of the layers. It is noticed in the literature that the solution of this study is not found analytically and positive results are obtained in a short time with the finite element method. Kaya and Polat (2023) carried out the contact analysis of the functionally graded layer resting on the elastic two quadrants using the finite element method. In the functionally graded (FG) layer, the change in material properties along the depth is functionally defined. The changes in the FG layer initial separation distances and contact stresses and stress under the block were investigated for different values of the stiffness parameters β (Elasticity), different values of the load (P) on the block, and different block width values. İf for (FG) layer the change parameter β is very close to zero, the layer will exhibit homogeneous behavior. Analysis was also performed with the values where the FG layer showed homogeneous behavior and was added to the solution part.

2. Definition of the problem

The variation functions of a functionally graded plate located between two semi-infinite elastic planes and loaded with a rigid block are as follows.

$$\mu_2(y) = \mu_0 e^{\beta y},\ \rho_2(y) = \rho_0 e^{\gamma y} \tag{1}$$

μ and ρ state the shear modulus and density. The layer extends in the range (-∞, +∞). This system assumes the block is rigid and the contact stresses transfer only compressive stresses. Therefore, separation occurs between the elastic layers and the (FG) plane when the critical load is exceeded. The problem assumes that all surfaces are frictionless and the thickness in the z-axis direction is unity. The geometry of the problem is shown in Fig. 1.

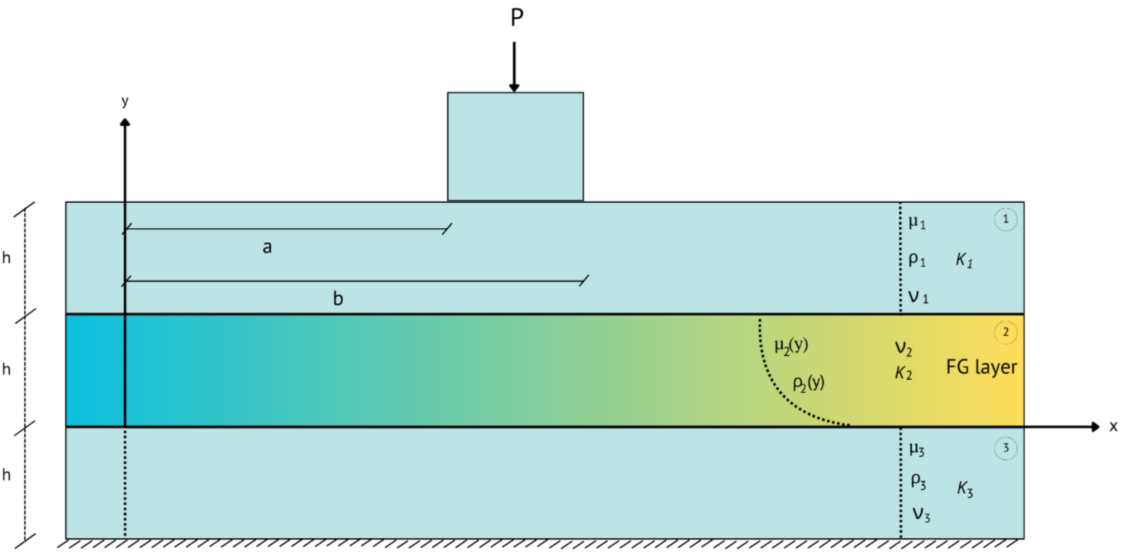

Fig. 1. Geometry of the problem loaded with a block

2.1. Analysis with finite element method

With the development of technology, analytical solutions consisting of long and complex expressions have been replaced by solution methods that can provide effective results quickly. SEM, which seeks a solution by simplifying a complex engineering problem, has become a frequently preferred method in recent years. This method relies on the basis that the solution can be divided into many finite parts. The problem is simplified. Although creating many meshes is important in approaching the complete solution, it can be seen as a disadvantage due to the increase in solution time. The use of SEM-based computer programs is quite common today. The finite element model and analysis of this solvable problem includes the ANSYS (2019) package program. All operations related to blocks and homogeneous planes were done with standard ANSYS menus. The FG layer's material storage and finite element division process was done with a program-specific macro. With the development, the code starts by defining the problem code, such as geometry and material properties, with the *set command. Depending on the simple geometry of the problem, a two-dimensional (2D) aeronautical geometric model is used for FG sheets and homogeneous elastic wings and is divided into sections with RECTNG cuts. The material properties of homogeneous elastic semi-infinite planes and blocks are selected as linear, elastic-isotropic. Defining the element type is important to obtain correct results when solving the problem. In this study, 8-node PLANE183 was used as the element type for static and 2-dimensional flight problems. Each node of this element has degrees of freedom in x and y accuracy. This element has no rotational freedom. ANSYS models of the problem are given in Figs. 2, 3, 4, and 5.

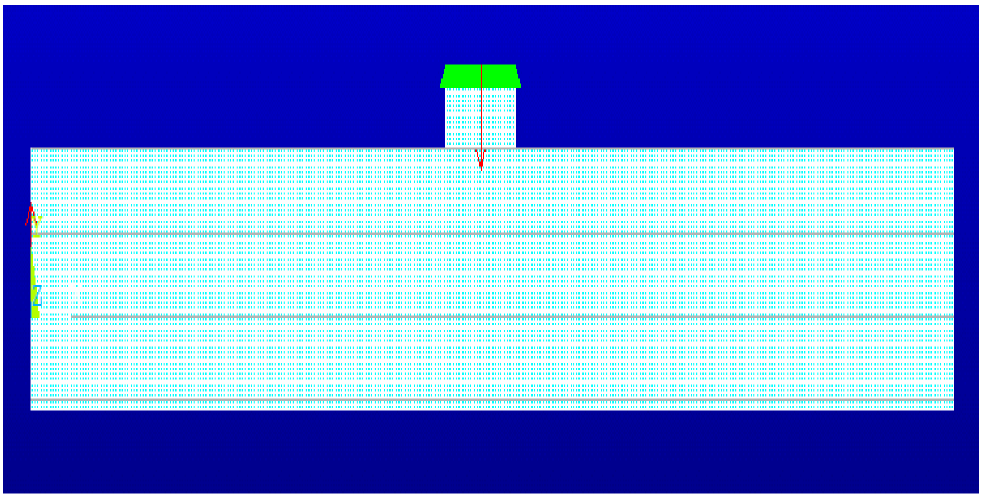

Fig. 2. Finite element model of the problem loaded with block

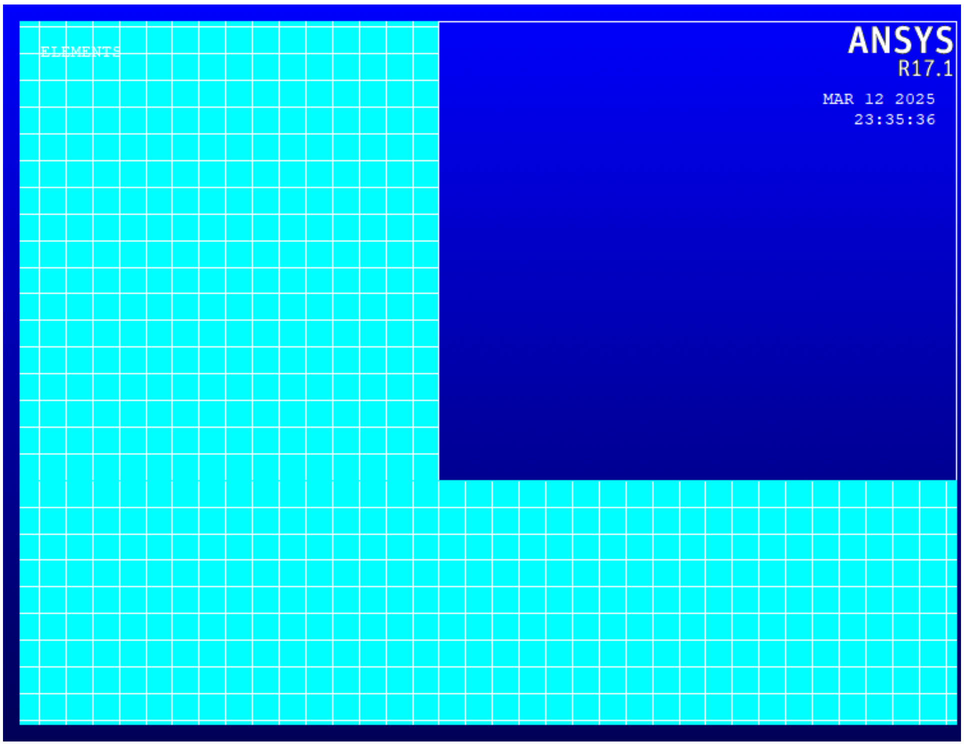

Fig. 3. Free quadrilateral mesh

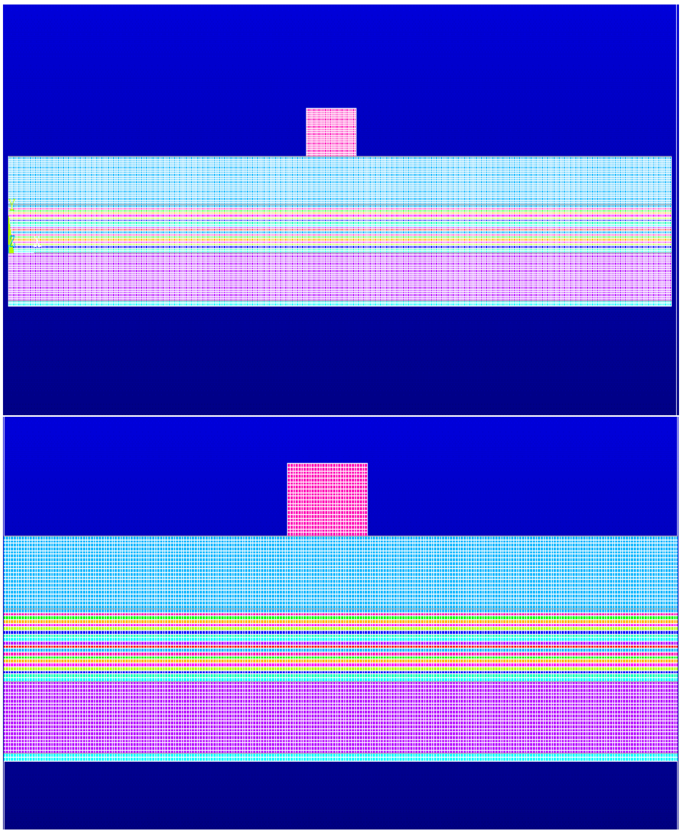

Fig. 4. Assignment of material of the problem loaded with block

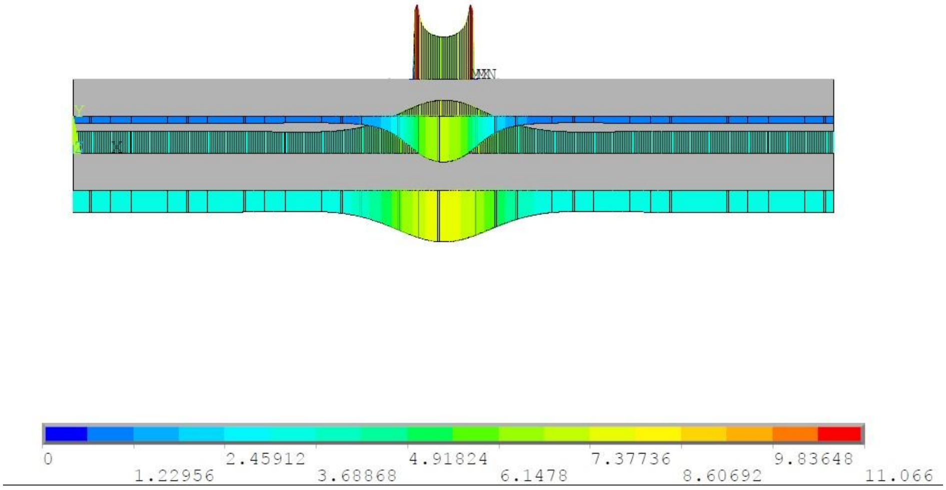

Fig. 5. ANSYS display of the status in contact with continuous contact

At this stage the recorded material is selected according to the program where only the layers graded in the factory and macro are changed exponentially to create the network.The macro used to program the material properties according to exponential change is as follows.

```
!!Material Top
*set, E_t, 100000
*set, nu_t, 0.25
*set,dens_t,1
*set,B,1.3864
*set,A,0.00001
*set,G,-0.6931
*create, mat_fgm_pol
/nopr
y_coord = arg1
E_fgm=E_t*EXP(B*y_coord) !!B=Beta
nu_fgm=nu_t*EXP(A*y_coord) !!A=Alfa
den_fgm=dens_t*EXP(G*y_coord) !!G=Gama
/gopr
*end !mat_fgm_pol
```
(2)

İn formula, the *create command is used to create a macro for the layer consisting of functionally graded material and sets a variable named y_coord = arg1. The mesh section has been moved on to. An additional macro has been added to mesh the FG layer. All geometry has been subjected to the Free Quadrilateral Mesh more frequently in contact areas. The macron for meshing the FG layer is as follows.

```
*do, j, 1, ele_numb_y, 1
y_coord = length_e_y*(j)
*use, mat_fgm_pol,y_coord
mp, ex, cntr,E_fgm
mp, prxy, cntr,nu_fgm
mp, dens, cntr,den_fgm
esel,r,cent,x,0,lngt_lyr
emodif, all, mat, counter
esel, all
```
(3)

In addition, surface-to-surface contact pairs are defined between the block-layer and layer-elastic plane. These pairs are divided into two contact and target elements. The contact is selected as CONTA172, and the target is selected as TARGE169 elements. Selecting more rigid elements than the contact element as the target element would be appropriate. In addition, the mathematical method that will provide the appropriate contact conditions is also decided while selecting the formulation to be used in the contact region. There are various contact algorithms in ANSYS, depending on the problem type. The Augmented Lagrangian Method, which provides fast results using the total potential energy theorem, was preferred as the contact algorithm.

3. Results and discussion

It is observed that as Bh increases, the initial separation distance between the FG layer and the upper homogeneous layer decreases and the initial separation load increases. It was also observed that as the load (P) acting on the Block increases, the initial separation distance does not change and the initial separation load decreases.The results are shown in Table 1.

It was observed that as Bh increased, the initial separation distance and initial separation load between the FG layer and the under homogeneous layer increased. It was also observed that as the load (P) acting on the Block increased, the initial separation distance did not change and the initial separation load decreased.The results are shown in Tables 2.

It was observed that as Bh increased, the initial separation distance and initial separation load between the under homogeneous layer and ground increased. It was also observed that as the load (P) acting on the Block increased, the initial separation distance did not change and the initial separation load decreased.The results are shown in Tables 3.

It was observed that as βh increases, the stresses between the FG layer and the upper homogeneous layer increase, while as βh decreases, the stresses decrease.The results are presented in Fig. 7.

It was observed that as βh increases, the stresses between the FG layer and the under homogeneous layer increase, while as βh decreases, the stresses decrease The results are presented in Fig. 8.

Table 1. According to the increase of the shear modulus change parameter (β) between the FG layer and the upper homogeneous layer

	P=10		P=20		P=30	
βh	$Xcr_{sağ}$	λ_{cr}	$Xcr_{sağ}$	λ_{cr}	$Xcr_{sağ}$	λ_{cr}
-0.6931	13.35	127.16	13.35	96.4	13.35	65.7
0.0001	13.3	180.1	13.3	112.94	13.3	74.1
0.6931	13.25	257.2	13.25	140.42	13.25	94.138

* Xcr= initial separation distance and λcr= initial separation load change

Table 2. According to the increase of the shear modulus change parameter (β) between the FG layer and the under homogeneous layer

	P=10		P=20		P=30	
βh	$Xcr_{sağ}$	λ_{cr}	$Xcr_{sağ}$	λ_{cr}	$Xcr_{sağ}$	λ_{cr}
-0.6931	13.9	141.16	13.9	107.208	13.9	73.3
0.0001	13.95	252.48	13.95	134.96	13.95	96.12
0.6931	14	331.41	14	234.6	14	138.96

* Xcr= initial separation distance and λcr= initial separation load change

Table 3. According to the increase of the shear modulus change parameter (β) between the under homogeneous layer and ground

	P=10		P=20		P=30	
βh	$Xcr_{sağ}$	λ_{cr}	$Xcr_{sağ}$	λ_{cr}	$Xcr_{sağ}$	λ_{cr}
-0.6931	13.4	129.12	13.4	97.94	13.4	66.78
0.0001	13.45	228.98	13.45	122.48	13.45	83.64
0.6931	13.5	301.626	13.5	213.3	13.5	127.974

*Xcr= initial separation distance and λcr= initial separation load change

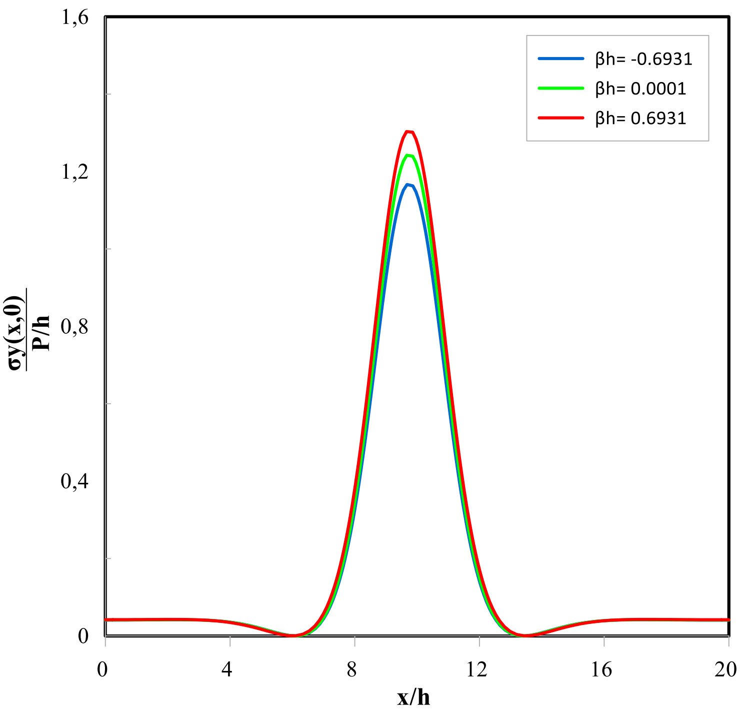

Fig. 7. Contact stress distributions between FG layer and upper homogeneous layer according to the layer stiffness parameter (βh) (a/h=9, (b-a)/h=1.5, μ0=1, K1= K 2=2, y=h, h=1, μ-h=1)

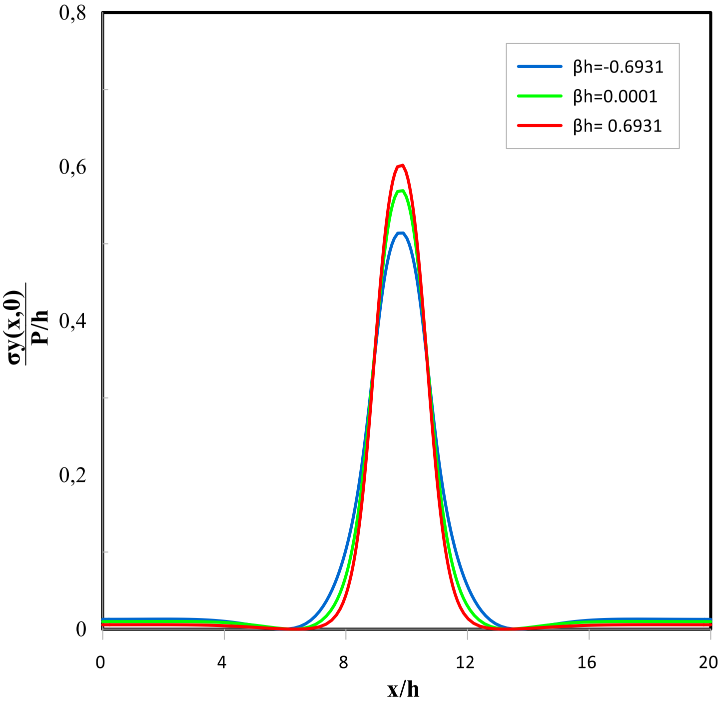

Fig. 8. Contact stress distributions between FG layer and under homogeneous layer according to the layer stiffness parameter (βh) (a/h=9, (b-a)/h=1.5, μ0=1, K2= K3=2, y=h, h=1, μ-h=1)

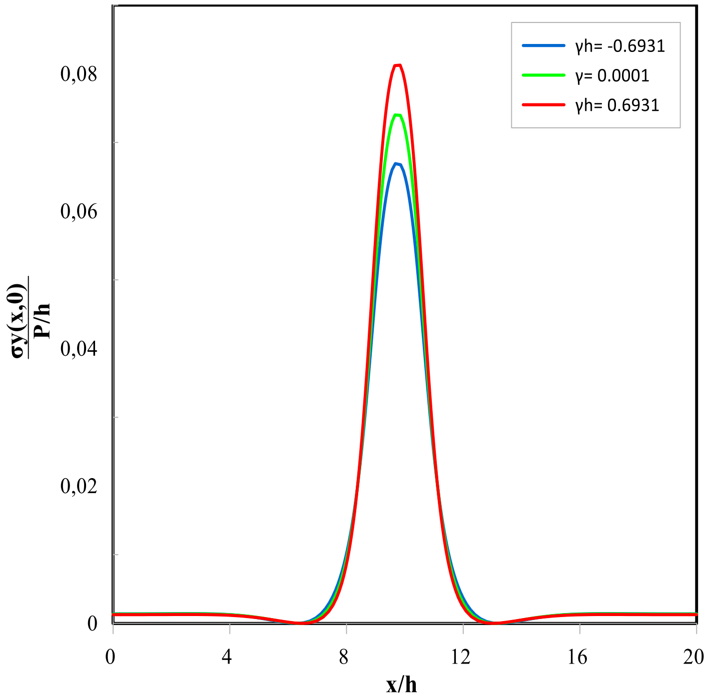

Fig. 9. Contact stress distributions between FG layer and upper homogeneous layer according to the layer stiffness parameter (γh) (a/h=9, (b-a)/h=1.5, μ0=1, K1= K2=2, y=h, h=1, μ-h=1)

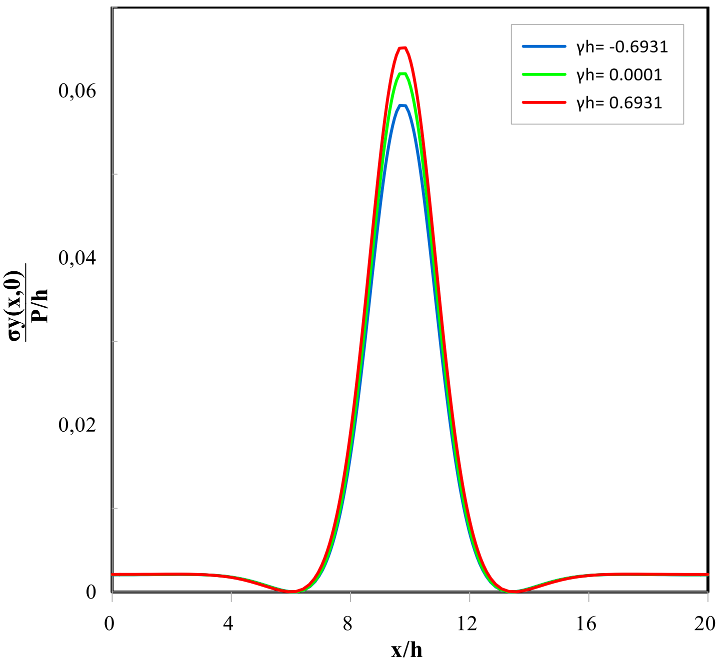

Fig. 10. Contact stress distributions between FG layer and under homogeneous layer according to the layer stiffness parameter (γh) (a/h=9, (b-a)/h=1.5, μ0=1, K2= K3=2, y=h, h=1, μ-h=1)

It was observed that the increase in the γh value led to higher stresses between the FG layer and the upper homogeneous layer, while the decrease in the γh value was associated with the decrease of these stresses. The results are presented in Fig. 9.

It was observed that the increase in the γh value led to higher stresses between the FG layer and the under homogeneous layer, while the decrease in the γh value was associated with the decrease of these stresses. The results are presented in Fig. 10.

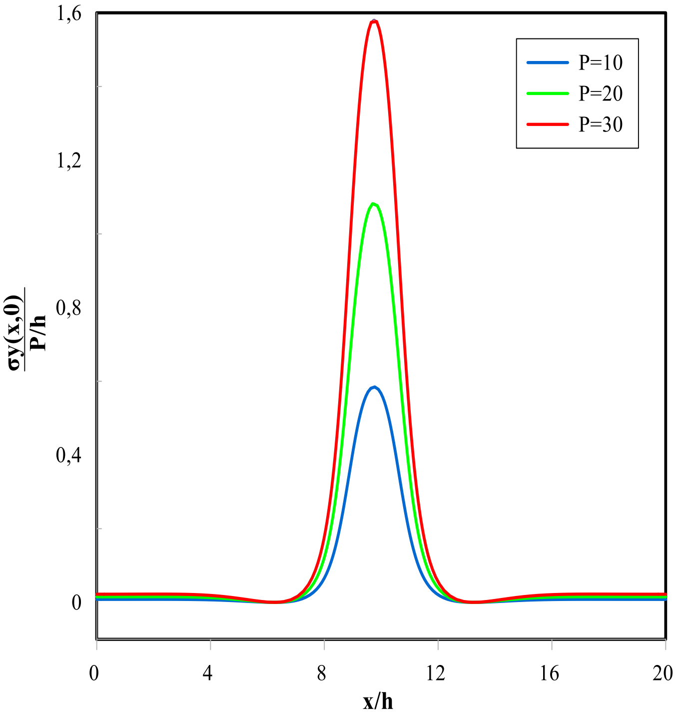

Fig. 11. Contact stress distributions between FG layer and upper homogeneous layer according to of change load(P) on the block (βh=0,693147) (a/h=9, (b-a)/h=1.5, μ0=1, K1= K2=2, y=h, h=1, μ-h=1)

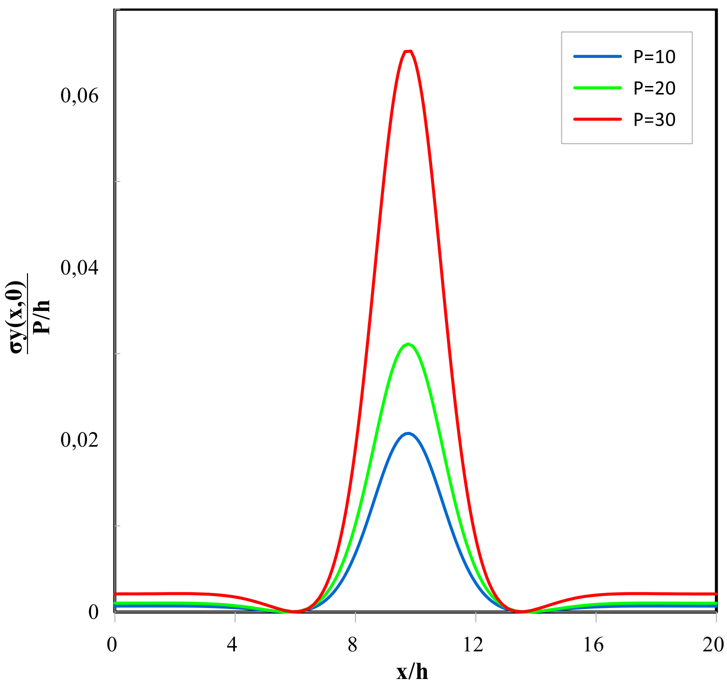

Fig. 12. Contact stress distributions between FG layer and underr homogeneous layer according to of change load(P) on the block (βh=0,693147) (a/h=9, (b-a)/h=1.5, μ0=1, K_2= K_3=2, y=h, h=1, μ-h=1)

It was observed that the increase in the load (P) applied to the block caused an increase in the contact stress values between the FG layer and the upper homogeneous layer.The results are presented in Fig. 11.

It was observed that the increase in the load (P) applied to the block caused an increase in the contact stress values between the FG layer and the under homogeneous layer. The results are presented in Fig. 12.

4. Conclusions

The aim of this study is to investigate the contact stresses in a functionally graded layer loaded with a block according to different variables such as βh, γh and load(P). These investigations have led us to the following conclusions.

- It was observed that the change in βh caused a change in the initial separation distance ($Xcr_{sağ}$) and initial separation load (λ_{cr}). It was observed that different load values did not cause a change in the initial separation distances ($Xcr_{sağ}$) but caused a change in the initial separation loads (λ_{cr}).
- It was observed that βh, γh and load(P) changes caused changes in contact stresses.

References

ANSYS (2019), Swanson Analysis Systems Inc., Canonsburg, PA, USA.

Adiyaman, G., Yaylaci, M., & Birinci, A. (2015). Analytical and finite element solution of a receding contact problem. *Structural Engineering and Mechanics*, *54*(1), 69–85. https://doi.org/10.12989/SEM.2015.54.1.069

Alagöz, H., Güleç, M., & Konez, A. (2004). Fonksyionel derecelendirilmiş malzemeler ve kullanim alanları. *Mühendis ve Makina*, *45*(5), 25–32. http://dx.doi.org/10.1016/j.compscitech.2017.08.007%0A

Apatay, T., Dağ, S., Güler, M.A., & Gülgeç, M. (2010). Subsurface contact stresses in functionally graded coatings loaded by a frictional flat stamp. *Journal of the Faculty of Engineering and Architecture of Gazi University, 25*(3), 611–623 (in Turkish).

Balci, M.N., & Dag, S. (2020). Moving contact problems involving a rigid punch and a functionally graded coating. *Applied Mathematical Modelling*, *81*, 855–886. https://doi.org/10.1016/J.APM.2020.01.004

Chidlow, S.J., & Teodorescu, M. (2013). Two-dimensional contact mechanics problems involving inhomogeneously elastic solids split into three distinct layers. *International Journal of Engineering Science*, *70*, 102–123. https://doi.org/10.1016/J.IJENGSCI.2013.05.004

Çömez, I. (2013). Contact problem of a functionally graded layer resting on a Winkler foundation. *Acta Mechanica*, *224*(11), 2833–2843. https://doi.org/10.1007/S00707-013-0903-5

Çömez, I., El-Borgi, S., & Yildirim, B. (2020). Frictional receding contact problem of a functionally graded layer resting on a homogeneous coated half-plane. *Archive of Applied Mechanics*, *90*(9), 2113–2131. https://doi.org/10.1007/S00419-020-01712-4

Fu, P., Zhao, J., Zhang, X., Miao, H., Wen, Z., Wang, P., Kang, G., & Kan, Q. (2024). Elasto-plastic partial slip contact modeling of graded layers. *International Journal of Mechanical Sciences*, *264*, 108823. https://doi.org/10.1016/J.IJMECSCI.2023.108823

Hertz, Heinrich. (1882). https://onlinebooks.library.upenn.edu/webbin/book/lookupname?key=Hertz%2C Heinrich%2C 1857-1894

Kaya, F., & Polat, A. (2023). Stress analysis of the contact problem in a functionally graded layer loaded with a distributed load and two rigid circular punches resting on an elastic two quarter planes. *Forces in Mechanics*, *11*, 100203. https://doi.org/10.1016/J.FINMEC.2023.100203

Ke, L.L., & Wang, Y.S. (2006). Two-dimensional contact mechanics of functionally graded materials with arbitrary spatial variations of material properties. *International Journal of Solids and Structures, 43*(18–19), 5779–5798. https://doi.org/10.1016/J.IJSOLSTR.2005.06.081

Koizumi, M. (1997). FGM activities in Japan. *Composites Part B: Engineering*, *28*(1–2), 1–4. https://doi.org/10.1016/S1359-8368(96)00016-9

Liu, T.J., Zhang, C., Wang, Y.S., & Xing, Y.M. (2016). The axisymmetric stress analysis of double contact problem for functionally graded materials layer with arbitrary graded materials properties. *International Journal of Solids and Structures*, *96*, 229–239. https://doi.org/10.1016/J.IJSOLSTR.2016.06.006

Polat, A. (2019). Investigation of the frictionless contact problem in a rigidly supported homogeneous layer by using FEM. *Gümüşhane Üniversitesi Fen Bilimleri Enstitüsü Dergisi*, *9*, 797–807. https://doi.org/10.17714/gumusfenbil.569047

Polat, A. (2021). Examination of contact problem between functionally graded punch and functionally graded layer resting on elastic plane. *Structural Engineering and Mechanics*, *78*(2), 135–143. https://doi.org/10.12989/SEM.2021.78.2.135

Polat, A., & Kaya, Y. (2022). Analysis of discontinuous contact problem in two functionally graded layers resting on a rigid plane by using finite element method. *Computers and Concrete*, *29*(4), 247–253. https://doi.org/10.12989/CAC.2022.29.4.247

Su, J., Ke, L.L., & Wang, Y.S. (2015). Two-dimensional fretting contact analysis of piezoelectric materials. *International Journal of Solids and Structures*, *73–74*, 41–54. https://doi.org/10.1016/J.IJSOLSTR.2015.07.026

Yan, J., & Mi, C. (2019). A receding contact analysis for an elastic layer reinforced with a functionally graded coating and pressed against a half-plane. *Journal of Mechanical Science and Technology*, *33*(9), 4331–4344. https://doi.org/10.1007/S12206-019-0829-5

4th International Civil Engineering & Architecture Conference
17-19 May 2025, Trabzon, Türkiye

A parametric study of rectangular plates under large deflection by a quadrilateral finite element

Abdulrahman M. Al-Nadhari*[1], Djamal Hamadi[1], Salah E. Hamadi[2], Maria Legouirah[1]

[1]*Larghyde Laboratory, Civil Engineering and Hydraulics Department, Biskra University, B.P145.RP.07000, Biskra, Algeria*
[2]*Yıldız Technical University, Department of Civil Engineering, İstanbul, Türkiye*

Abstract. This study investigates the performance of the geometrical nonlinear analysis of thin and thick plates under large deflections and small rotations. A parametric study was performed on rectangular plates with different boundary conditions, thicknesses and applied loadings. The numerical analysis is performed on the coupled isoparametric quadrilateral plate finite element baptized "QC4", which incorporates five degrees of freedom, deduced from the plate bending element Q4 with 3DOF/ node (W, θ_x,θ_y) and the membrane element Q4 with 2DOF/node (U, V), to engender the membrane forces induced from large deflexion. The stiffness matrices are calculated according to the Mindlin's thick plate theory and the nonlinear equilibrium equations are solved by the Newton-Raphson iterative algorithm. A MATLAB program is elaborated to compute the related stiffness matrices; the linear stiffness matrix (K_0), the large deflection stiffness matrix (K_L) and the geometric stiffness matrix ($K\sigma$). To validate the proposed approach and element; the ABAQUS software is used to validate the deflections obtained. Additionally, an experimental results of a rectangular plate subjected to a concentrated load is used to evaluate the efficiency of the formulated plate bending element"QC4". The results obtained demonstrate that the computed displacements are in strong agreement with the analytical solution and the experimental results. Moreover, validation tests confirmed the accuracy and effeciency of the QC4 element in performing the geometrical nonlinear analysis for both thin and thick plate structures.

Keywords: Quadrilateral isoparametric element; Geometrical nonlinear analysis; Thick and thin plates; Large deflections; ABAQUS software

1. Introduction

Nonlinear analysis plays a critical role in engineering, particularly in civil engineering, as it enables a precise determination of a structure's behavior. In contrast to linear analysis, which fails to provide accurate predictions, nonlinear analysis offers a more realistic representation of structural performance (Al-Nadhari et al., 2024). Numerous studies have employed various nonlinear analysis techniques to investigate the behavior of plates.Wood and Hinto(Pica et al., 1980) employ finite element analysis (FEA) based on the Mindlin plate formulation to investigate the nonlinear behavior of plates. Their study conducts a comparative evaluation of four distinct element types: linear, serendipity, Lagrangian, and Heterosis elements, under varying loading conditions. Zhang and Kim (Zhang et al., 2006) developed two displacement-based 4-node quadrilateral elements, RDKQ-NL20 and RDKQ-NL24 for nonlinear analysis of laminated composite plates. The elements are based on first-order shear deformation theory (FSDT) and von-Karman's large deflection theory, using the total Lagrangian approach.Chau-Dinh et al. (Chau-Dinh et al., 2024) presented a triangular flat shell formulation with three nodes, tailored for examining geometric nonlinearities in plates and shells. Their approach integrates Allman-type interpolation and the MITC strategy to effectively address shear locking phenomena. Rezaiee-Pajand et al. (Rezaiee-Pajand et al., 2019) introduce an advanced six-node triangular element based on a locking-free, mixed finite element methodology, designed to improve the accuracy of displacement and stress evaluations in linear as well as nonlinear structural simulations. Atnaik et al. (Patnaik et al., 2020) developed a finite element for to tackle the geometrically nonlinear analysis in plate structures, employing a fractional-order continuum framework. The two-dimensional nonlinear model, grounded in a frame-invariant and thermodynamically sound fractional theory, captures nonlocal softening effects through both Mindlin and Kirchhoff plate formulations.

* Corresponding author, E-mail: a.alnadhari@univ-biskra.dz

https://doi.org/10.31462/icearc2025_ce_sme_349

In this paper, a coupled isoparametric quadrilateral plate finite element baptized "QC4", which incorporates five degrees of freedom, deduced from the plate bending element Q4 with 3DOF/ node (W, θ_x,θ_y) and the membrane element Q4 with 2DOF/node (U, V), to engender the membrane forces induced from large deflexion is used. In addition to the ABAQUS S4R element and Q4 element that developed by Patil and Kolukula(A. Patil et al., 2016) to carry out a parametric study of the plates under large deflection including the effect of boundary conditions and the effect of the thickness ratio (**Fig.1)**. The results obtained are compared with the experimental results as a reference solution and with the analytical solution.

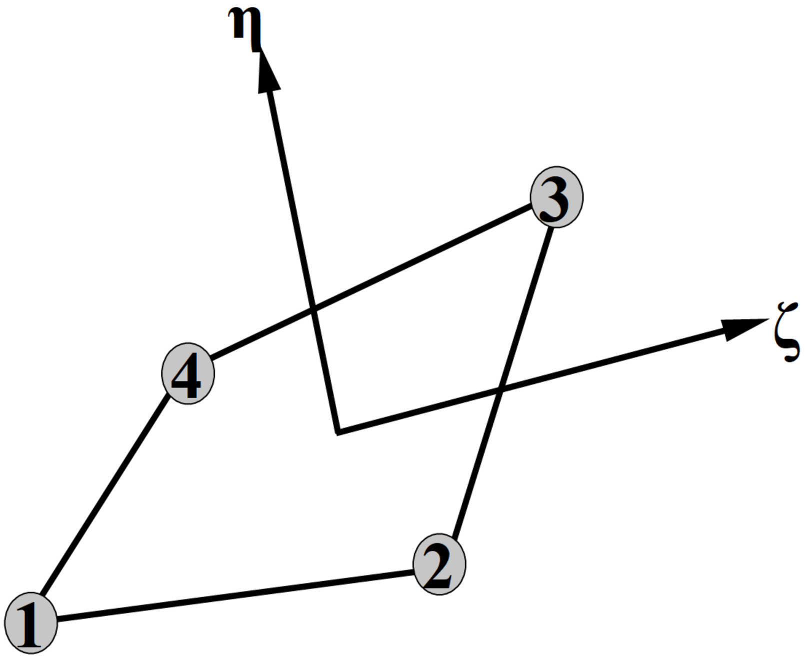

Fig. 1 Coupled isoparametric quadrilateral plate finite element "QC4"

2. Formulation of nonlinear matrices

The Green strain vector ε characterizes the primary measurement of deformation at a specific location situated a distance z from the mid-plane of a plate, as formulated in the equation below(Ganaba, 1985).

$$\{\varepsilon\} = \left\{ \begin{array}{c} \dfrac{\partial u}{\partial x} + \dfrac{1}{2}\left[\left(\dfrac{\partial u}{\partial x}\right)^2 + \left(\dfrac{\partial v}{\partial x}\right)^2 + \left(\dfrac{\partial w}{\partial x}\right)^2\right] \\ \dfrac{\partial v}{\partial y} + \dfrac{1}{2}\left[\left(\dfrac{\partial u}{\partial y}\right)^2 + \left(\dfrac{\partial v}{\partial y}\right)^2 + \left(\dfrac{\partial w}{\partial y}\right)^2\right] \\ \dfrac{\partial u}{\partial y} + \dfrac{\partial v}{\partial x} + \dfrac{\partial u}{\partial x}\dfrac{\partial u}{\partial y} + \dfrac{\partial v}{\partial x}\dfrac{\partial v}{\partial y} + \dfrac{\partial w}{\partial x}\dfrac{\partial w}{\partial y} \\ \dfrac{\partial u}{\partial z} + \dfrac{\partial w}{\partial x} + \dfrac{\partial u}{\partial x}\dfrac{\partial u}{\partial z} + \dfrac{\partial v}{\partial x}\dfrac{\partial v}{\partial z} + \dfrac{\partial w}{\partial x}\dfrac{\partial w}{\partial z} \\ \dfrac{\partial v}{\partial z} + \dfrac{\partial w}{\partial y} + \dfrac{\partial u}{\partial y}\dfrac{\partial u}{\partial z} + \dfrac{\partial v}{\partial y}\dfrac{\partial v}{\partial z} + \dfrac{\partial w}{\partial y}\dfrac{\partial w}{\partial z} \end{array} \right\} \tag{1}$$

The above equation can be written as follows:

$$\varepsilon = \begin{Bmatrix} \varepsilon_x \\ \varepsilon_y \\ \gamma_{xy} \\ \gamma_{xz} \\ \gamma_{yz} \end{Bmatrix} = \begin{Bmatrix} \varepsilon_m \\ 0 \end{Bmatrix} + \begin{Bmatrix} z\kappa \\ \gamma_s \end{Bmatrix} + \begin{Bmatrix} \varepsilon_{NL} \\ 0 \end{Bmatrix} \tag{2}$$

Where ε_m, zκ, γ_s, and ε_{NL} denote, respectively, the linear membrane strain components, the linear bending-induced strain terms, the linear transverse shear strain measures, and the nonlinear in-plane deformation contributions as outlined in reference(Ganaba, 1985).

$$\varepsilon_m = \begin{Bmatrix} \varepsilon_x \\ \varepsilon_y \\ \gamma_{xy} \end{Bmatrix} = \begin{Bmatrix} \frac{\partial u}{\partial x} \\ \frac{\partial v}{\partial y} \\ \frac{\partial u}{\partial y} + \frac{\partial v}{\partial x} \end{Bmatrix}, \kappa = z \begin{Bmatrix} \frac{\partial^2 w}{\partial^2 x} \\ \frac{\partial^2 w}{\partial^2 y} \\ \frac{\theta_x}{\partial y} + \frac{\theta_y}{\partial x} \end{Bmatrix}, \text{and } \gamma_s = \begin{Bmatrix} \frac{\partial w}{\partial x} - \theta_x \\ \frac{\partial w}{\partial y} - \theta_y \end{Bmatrix}, \varepsilon_{NL} = \frac{1}{2} \begin{Bmatrix} \left(\frac{\partial w}{\partial x}\right)^2 \\ \left(\frac{\partial w}{\partial y}\right)^2 \\ \frac{\partial w}{\partial x}\frac{\partial w}{\partial y} \end{Bmatrix} \tag{3}$$

The displacement components (u, v, w) at a spatial position (x, y, z) are described as functions of the mid-surface translational displacements (u_0, v_0, w_0), along with the independent rotations θ_x and θ_y about the xz and yz planes, respectively, as formulated in the framework of Mindlin plate theory (Ganaba, 1985).

$$\begin{aligned} u &= u_0(x,y) - z\beta_x(x,y) \\ v &= v_0(x,y) - z\beta_y(x,y) \\ w &= w_0(x,y) \end{aligned} \tag{4}$$

The stiffness matrix can be obtained by using the principle of virtual work as given in reference (Ojeda et al., 2007) expressed as:

$$\int_A [\bar{B}]\{\sigma\} dA = P \tag{5}$$

the above equation can be written as:

$$[K_T]\{d\delta_i\} = \{P\} - [K_s]\{\delta_{i-1}\} \tag{6}$$

Where K_T, K_S, $d\delta_i$, and P are tangent stiffness matrix, secant stiffness matrix and nodal displacement respectively as given in references (Ganaba, 1985; Ojeda et al., 2007).

$$[K_T] = [K_0] + [K_L] + [K_\sigma]$$

$$[K_L] = \int_A [B_L]^T[D][B_{NL}]dA + \int_A [B_{NL}]^T[D][B_L]dA + \int_A [B_{NL}]^T[D][B_{NL}]dA$$

$$[K_\sigma] = \int_A [G]^T[S][G]\, dA \tag{7}$$

$$[K_0] = \int_A [B_L]^T[D][B_L]dA + \int_A [B_s]^T[D_s][B_s]dA$$

$$[K_s] = \int_A [B_L]^T[D][B_L]dA + \frac{1}{2}\int_A [B_L]^T[D][B_{NL}]dA + \int_A [B_{NL}]^T[D][B_L]dA + \frac{1}{2}\int_A [B_{NL}]^T[D][B_{NL}]dA$$

3. Applications

3.1. Clamped square plate

The clamped square plate shown in Fig.2 is analysis with the following paramaters, the parameter load $P_0 = q_0a^4/Eh^4$, the thickness ratio is taken as L/h = 100 and the Poisson's ratio v=0.316. The results obtained by the "QC4" and S4R elements are compared with the analytical solution and with those obtained by another method as presented in Table 1.

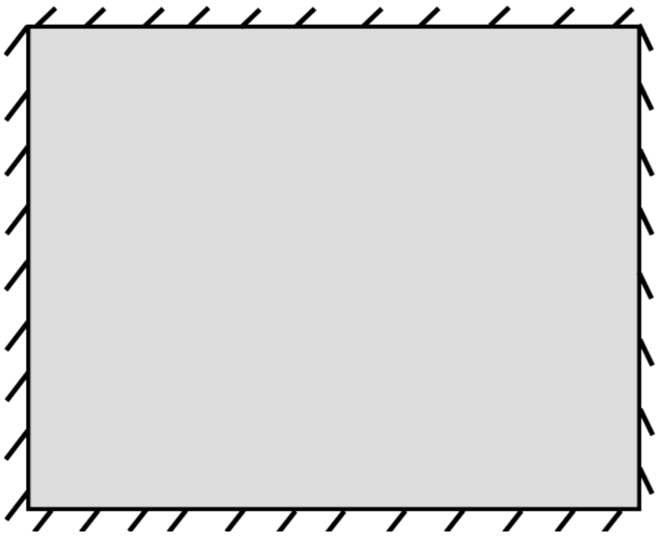

Fig.2 Clamped square plate

Table 1 Comparison of the central dimensionless deflection (w/h)

P_0	Analytical Levy(Levy et al., 1942)	"QC4"	S4R	MXFEM (Urthaler et al., 2008)	NURBSKR (Kapoor et al., 2012)
17.8	0.237	0.2356	0.2380	0.239	0.233
38.3	0.471	0.4699	0.4750	0.474	0.464
63.4	0.695	0.6957	0.7024	0.697	0.685
95	0.912	0.91273	0.9223	0.909	0.899
134.9	1.121	1.1220	1.1340	1.113	1.105
184	1.323	1.32216	1.3360	1.308	1.302
245	1.521	1.51902	1.5350	1.501	1.497
318	1.714	1.70916	1.7280	1.688	1.686
402	1.902	1.8896	1.9130	1.866	1.865

From the results shown in Table 1, it is clear that both element "QC4" and S4R provide almost similar deflections (w/h) that very cloose to the analytical Levy solution across all load levels. This confirming the effeciency of the formulate element"QC4". The "QC4" element consistently yields values nearly identical to the analytical ones, with minimal error even as the load increases, indicating strong numerical stability and precision. The S4R element, while also accurate, tends to produce slightly higher deflections at larger loads, such as at (P_0 = 402), where it predicts 1.9130 compared to 1.902 from the analytical solution and 1.8896 from "QC4" compared to the more advanced methods —MXFEM and NURBSKR—. Both "QC4" and S4R elements show better agreement with the analytical reference, with MXFEM occasionally overestimating and NURBSKR generally underestimating the response. However, the differences are minor, and both elements demonstrate high accuracy, with QC4 showing superior consistency and S4R offering slightly more sensitivity to nonlinearity.

3.2. Square plate with two clamped edges and two free edges

A square plate is subjected to concentrated load with two clamped edges and the other are free (Fig.2). The mechanical and geometrical properties of the plate are: E = 2.15×10^4 kg/mm², ν=0.3, and h= 1.98 mm. The load is applied in point N and the deflections at point A are calculated and ploted as shown in Fig.3. The results obtained from the S4R and "QC4" elements are compared with the experimental results (Kawai et al., 1969) and those found from the nonlinear theory (Kawai et al., 1969) and natural mode (Argyris et al., 1994) elements.

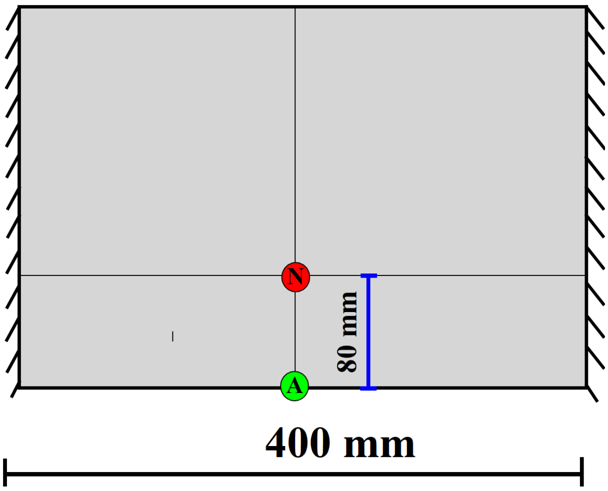

Fig. 2 Square plate with two edges clamped

The results obtained from the nonlinear analysis using "QC4" and S4R elements were compared with those derived from nonlinear theory, natural mode analysis, and experimental results are presented in (Fig. 3). Among all methods, the S4R element showed the closest agreement with the experimental and theoretical results across the entire load range, indicating its high accuracy in predicting the plate's nonlinear response. The "QC4" element, while following the general trend, consistently overestimated deflections, particularly at higher loads, showing a noticeable deviation from the reference data. The natural mode and nonlinear theory solutions remained in close proximity to the experimental values, with slightly conservative predictions. Overall, the comparison highlights that the S4R element produced results most consistent with the validated benchmarks, while the Q4 element exhibited a greater margin of error in capturing the plate's deflection under nonlinear conditions.

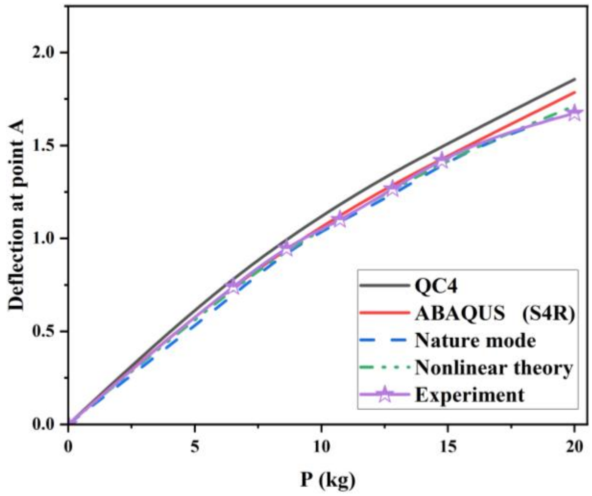

Fig.3 Comparison of the deflection at point A

3.3. Simply supported square plate

In this application, a parametric study will be conducted on the same previuos example in order to investigate the influence of boundary conditions and plate thickness on its nonlinear behavior. Initially, the existing constraints will be modified to simple supports and their impact on the plate's response. The results of this analysis are plotted in Fig. 4 and compared to the results obtained with the original constraint configuration. It is well observed that boundary conditions of a plate have a significant impact on its structural behavior, particularly in terms of stiffness and deformation. Also, clamped edges provide both translational and rotational restraints, resulting in higher stiffness and lower deflection, whereas simply supported edges allow rotation, making the plate more flexible. This reduction in constraint led to consistently higher mode or response values in the simply supported (SFSF) plate compared to the clamped-free (CFCF) case, as seen in the numerical results using both S4R and "QC4" elements. It is clear that the "QC4" element showed slightly higher values than S4R, which may be due to differences in stiffness formulation and integration schemes. Overall, the results confirm that altering boundary conditions significantly influences the plate's response, with the SFSF condition producing greater deformation and higher modal, aligning well with theoretical expectations.

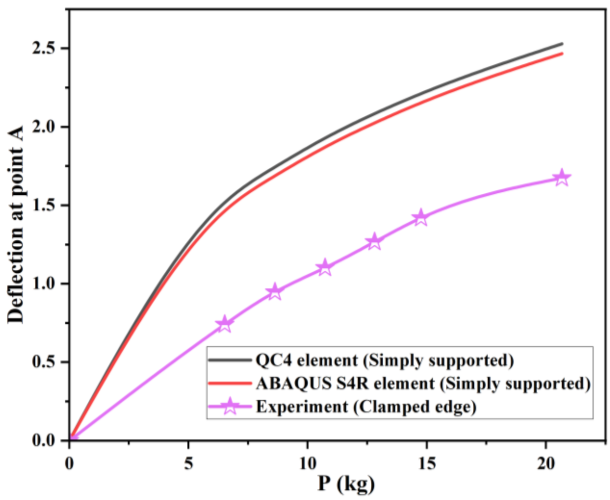

Fig. 4 Deflection of two simply supported edge

3.4. Clamped square plate

In this example, the effect of plate thickness on the nonlinear behavior of a square plate is investigated. Experimental results were obtained for a plate with a thickness of 1.98 mm (Kawai et al., 1969) and compared with numerical simulations, using "QC4" and S4R elements ith the following thickness values: 2.5 mm, 3 mm, 3.5 mm and 4 mm. Obvuiousely, as the thickness increases, the plate becomes stiffer, which leads to important reduction in nonlinearity behavior through the consistent decrease in the response values across all thicknesses and load levels as shown in (Fig. 5). This trend is observed in both QC4 and S4R element analyses, with QC4 generally predicting slightly higher values than S4R, likely due to differences in element formulation and sensitivity to bending. The reduction in response with increasing thickness indicates that thicker plates exhibit more linear behavior, as they are less sensitive to geometric nonlinearity and large deflections under the same loading conditions. The comparison with experimental data for the thinnest plate (h = 1.98 mm) confirms the validity of the numerical model and highlights how thickness plays a crucial role in controlling the degree of nonlinearity behavior in plate structures.

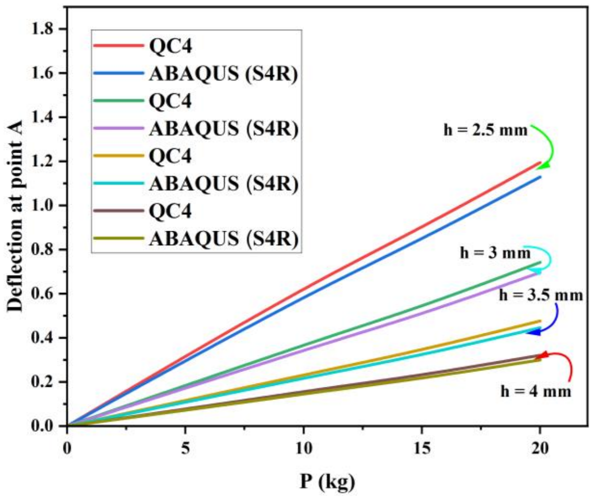

Fig. 5 Comparison of deflection at point A with different thickness

As the plate thickness increases, the displacement decreases significantly, with reductions reaching up to 81%. This highlights the stiffening effect of thickness in reducing nonlinearity behavior. In contrast, changing the boundary condition from clamped to simply supported results in an increase in displacement of up to 51%, indicating greater flexibility and enhanced nonlinear response. Fig. 6 shows the percentage increase in displacement when changing the boundary conditions. It also shows the percentage decrease in displacement as the thickness increases.

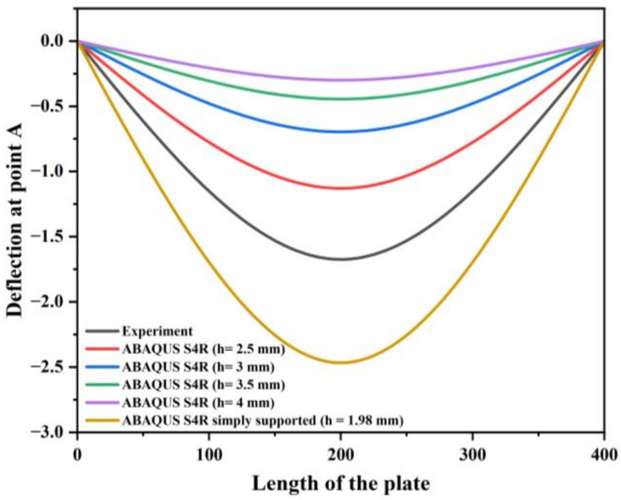

Fig. 6 Effect of the boundary condition and the thickness ratio

4. Conclusion

The nonlinear analysis of square plates using "QC4" and ABAQUS S4R elements confirm the efficiency and performance of both elements with "QC4" . It is notes that a strong alignment with analytical solutions observed with QC4, while S4R element show good agreement with experimental results, particularly at higher load levels. The parametric study highlights the significant influence of boundary conditions and plate thickness on nonlinear behavior. Clamped boundary conditions enhance stiffness and reduce deflections, while simply supported configurations increase structural flexibility and nonlinear response. Moreover, increasing plate thickness reduces deflections as thick plates exhibit more linear behavior under the same loading conditions (small deflection). These results confirm the effeciency of the formulated finite element QC4 in nonlinear analysis of plates and provide valuable engineering applications.

References

A. Patil, & S. S. Kolukula. (2016). *FEM MATLAB Code for Linear and Nonlinear Bending Analysis of Plates*. doi: m-matlab-code-for-linear-and-nonlinear-bending-analysis-of-plates

Al-Nadhari, A. M., Abderrahmani, S., Hamadi, D., & Legouirah, M. (2024). The efficient geometrical nonlinear analysis method for civil engineering structures. *Asian Journal of Civil Engineering 2024*, 1–9.

Argyris, J., & Tenek, L. (1994). Linear and geometrically nonlinear bending of isotropic and multilayered composite plates by the natural mode method. *Computer Methods in Applied Mechanics and Engineering*, *113*(3–4), 207–251.

Chau-Dinh, T., Tran-Chi, N., Nguyen, V. H., & Nguyen, T. K. (2024). Geometrically nonlinear analysis of plates and shells by a cell-based smoothed CS-MITC18+ flat shell element with drilling degrees of freedom. *Thin-Walled Structures*, *203*, 112254.

Ganaba, T. H. (1985). *Nonlinear finite element analysis of plates and slabs* [Doctoral Thesis, The University of Warwick]. Retrieved from https://wrap.warwick.ac.uk/34590/1/WRAP_THESIS_Ganaba_1985.pdf

Kapoor, H., & Kapania, R. K. (2012). Geometrically nonlinear NURBS isogeometric finite element analysis of laminated composite plates. *Composite Structures*, *94*(12), 3434–3447.

Kawai, T., & Yoshimura, N. (1969). Analysis of large deflection of plates by the finite element method. *International Journal for Numerical Methods in Engineering*, *1*(1), 123–133.

Levy, S., & Chiarito, P. (1942). *Square plate with clamped edges under normal pressure producing large deflections*. Retrieved from https://books.google.com/books?hl=en&lr=&id=_3xDAQAAIAAJ&oi=fnd&pg=PA209&dq=Levy+S.+Square+plate+with+clamped+edges+under+normal+pressure+producing+large+deflections.+NACA+Report+1942.&ots=tJDg3hYZNs&sig=k6k_hTugei46Xy3aYYIdQDnwTOs

Ojeda, R., Gangadhara Prusty, B., Lawrence, N., & Thomas, G. (2007). A new approach for the large deflection finite element analysis of isotropic and composite plates with arbitrary orientated stiffeners. *Finite Elements in Analysis and Design*, *43*(13), 989–1002.

Patnaik, S., Sidhardh, S., & Semperlotti, F. (2020). Geometrically nonlinear analysis of nonlocal plates using fractional calculus. *International Journal of Mechanical Sciences*, *179*, 105710.

Pica, A., Wood, R. D., & Hinton, E. (1980). Finite element analysis of geometrically nonlinear plate behaviour using a mindlin formulation. *Computers & Structures*, *11*(3), 203–215.

Rezaiee-Pajand, M., Rajabzadeh-Safaei, N., & Masoodi, A. R. (2019). Linear and geometrically nonlinear analysis of plane structures by using a new locking free triangular element. *Engineering Structures*, *196*, 109312.

Urthaler, Y., & Reddy, J. N. (2008). A Mixed Finite Element for the Nonlinear Bending Analysis of Laminated Composite Plates Based on FSDT. *Mechanics of Advanced Materials and Structures*, *15*(5), 335–354.

Zhang, Y. X., & Kim, K. S. (2006). Geometrically nonlinear analysis of laminated composite plates by two new displacement-based quadrilateral plate elements. *Composite Structures*, *72*(3), 301–310.

ICEARC'25

4th International Civil Engineering & Architecture Conference
17-19 May 2025, Trabzon, Türkiye

Geometry effects on rock fracture toughness under combined tension-shear loading

Majid R. Ayatollahi*[1], Morteza Rashidi-Moghaddam[1]

[1] *Fatigue and Fracture Lab., Centre of Excellence in Experimental Solid Mechanic and Dynamics, School of Mechanical Engineering, Iran University of Science and Technology, Narmak, 16846, Tehran, Iran*

Abstract. Fracture toughness and crack growth resistance are important material properties which describe the critical states of stresses or energy near the crack tip required for the initiation of brittle fracture. Fracture toughness can be used to determine the critical applied load required for the initiation of crack growth under static loading in cracked components and structures and can be employed as a useful tool to solve various rock engineering problems such as rock excavation, tunneling, rock cutting processes, hydraulic fracturing, rock blasting and rock slope stability analysis. The conventional fracture criteria like the maximum tangential stress (MTS) criterion and the minimum strain energy density (SED) criterion sometimes underestimate or overestimate the experimentally obtained fracture toughness in rocks particularly under combined tension-shear (or mixed mode I and II) loading conditions. In addition, the conventional fracture criteria assume that fracture resistance is not influenced by the geometry and loading conditions. In this paper, an improved approach is suggested for predicting mode I, mode II and mixed mode I/II fracture behavior of rocks using the averaged strain energy density (ASED) criterion. The Generalized ASED (GASED) criterion takes into account the effect of T-stress in addition to the singular terms of stresses/strains of William's series expansion in order to provide more accurate estimates for fracture toughness of rocks. The experimental results obtained from fracture tests performed on a British limestone using the Brazilian disk (BD) and Semi-circular bend (SCB) specimens are used to show the validity of the GASED criterion.

Keywords: Rock fracture mechanics; Tension-shear fracture; Limestone; Geometry effects; Strain energy density criterion

1. Introduction

Rock burst and rock fragmentation are considered as a process of crack initiation and propagation in rock masses. Fracture toughness and crack growth resistance are important material properties which describe the critical states of stresses or energy near the crack tip required for the initiation of brittle fracture (Ba et al., 2021 and Mehraban et al, 2023). Fracture toughness can be used to determine the critical applied load required for the initiation of crack growth under static loading in cracked components and structures and can be employed as a useful tool to solve various rock engineering problems such as rock excavation, tunneling, rock cutting processes, hydraulic fracturing, rock blasting and rock slope stability analysis. Because of the wide applications of fracture toughness in rock engineering; its determination is an important subject for engineers and researchers.

Several researchers have suggested a wide range of specimens for determination of the fracture toughness in rocks. Among these specimens, the centrally cracked Brazilian disk (BD) specimen subjected to diametral compressive load and the edge cracked semi-circular bend (SCB) specimen subjected to three-point bending (see Fig. 1) have been recognized as favorite test specimens for investigating mode I, mode II and mixed mode I/II fracture behavior in rock materials (Khan & Al-Shayea, 2000, Chang et al., 2002, Akbardoost et.al 2014).

Previous studies have shown that the conventional fracture criteria like the maximum tangential stress (MTS) criterion and the minimum strain energy density (SED) criterion sometimes underestimate or overestimate the experimentally obtained mixed mode I/II fracture toughness in rocks. In addition, the conventional fracture criteria assume that the mode I fracture resistance (K_{If}^{I}) is not influenced by the geometry and loading conditions. In this paper, an improved approach is suggested for predicting mode I, mode II and mixed mode I/II fracture behavior of rocks using the averaged strain energy density (ASED) criterion. The Generalized ASED (GASED) criterion takes into account the effect of T-stress in addition to the singular terms of stresses/strains of William's series expansion in order to provide more accurate estimates for fracture toughness of rocks.

* Corresponding author, Email: m.ayat@iust.ac.ir

https://doi.org/10.31462/icearc2025_ce_sme_359

golden light publishing

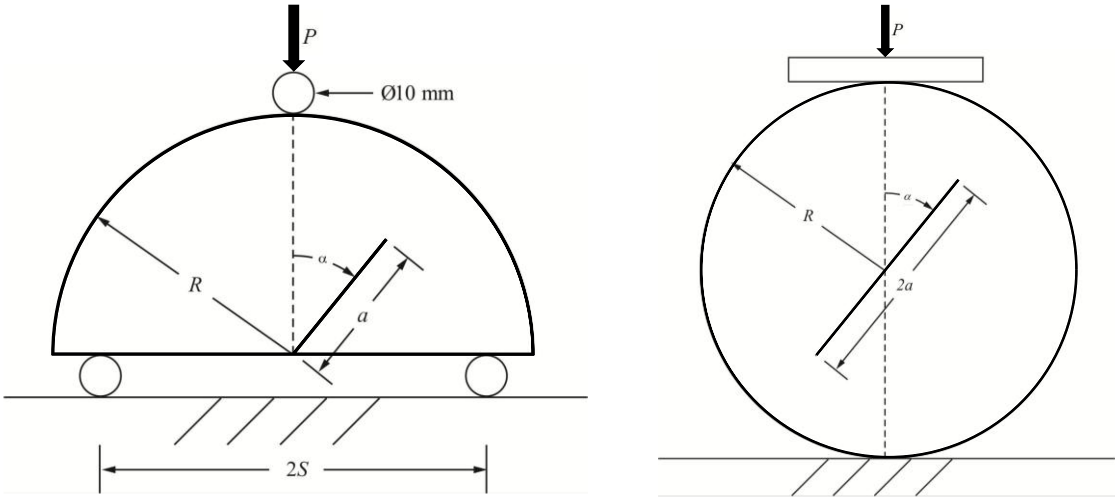

a b

Fig. 1. The edge cracked semi-circular bend (SCB) specimen subjected to three-point bending (a) and the centrally cracked Brazilian disk (BD) specimen subjected to diametral compressive load (b)

2. Fracture model

Lazzarin & Zambardi (2001) suggested the averaged strain energy density (ASED) criterion which uses the values of strain energy density averaged in a localized damage zone of radius r_c (called control volume) to estimate the fracture load for cracked and notched specimens. They determined the ASED values directly from finite element analysis.

As an alternative approach, one can calculate the strain energy density using the equations of stresses/strains written based on the well-known Williams' series expansions. The GASED criterion accounts for the effect of *T*-stress as a key parameter in calculating the strain energy density factor around the crack tip. Based on this approach, a general equation for mixed mode fracture is obtained

$$K_{Ic}^2 = [K_{If}^2 + \frac{9-8\upsilon}{5-8\upsilon} K_{IIf}^2 + \frac{16(8-20\nu)}{15\pi(5-8\nu)} K_{If} K_{eff}(B\alpha) + \frac{4-4\upsilon}{2(5-8\upsilon)} K_{eff}^2 (B\alpha)^2] \tag{1}$$

where K_{Ic} is called mode-I fracture toughness, which should be obtained experimentally using a cracked specimen in which the *T*-stress is zero or negligible. K_{If} and K_{IIf} are the critical stress intensity factor and T_f is the critical T-stress corresponding to the fracture load. The dimensionless parameters B and α are defined as

$$B = \frac{T_f\sqrt{\pi a}}{K_{eff}} = \frac{T_f\sqrt{\pi a}}{\sqrt{K_{If}^2 + K_{IIf}^2}}, \quad \alpha = \sqrt{\frac{2r_c}{a}} \tag{2}$$

For pure mode-I loading, when $K_{IIf} = 0$, Eq. (1) is simplified to

$$K_{Ic} = K_{If}^I \sqrt{[1 + \frac{16(8-20\nu)}{15\pi(5-8\nu)}(B\alpha) + \frac{4-4\upsilon}{2(5-8\upsilon)}(B\alpha)^2]} \tag{3}$$

For pure mode-II loading, when $K_{If} = 0$, Eq. (1) is simplified to

$$K_{Ic}^2 = K_{IIf}^2 [\frac{9-8\upsilon}{5-8\nu} + \frac{4-4\upsilon}{2(5-8\upsilon)}(B\alpha)^2] \tag{4}$$

3. Results

The theoretical predictions of the mode I fracture resistance based on the GASED criterion together with the experimental data reported by Akbardoost et al (2014) for a British limestone are plotted in Fig. 2. The proposed modified criteria provide very good estimates of the mode I fracture resistance for this wide range of data. A comparison between the mode I fracture resistance predicted using the GASED criterion (Eq. (3)) and the test data shows that the GASED criterion provides very good estimates for the experimental results reported for the British limestone.

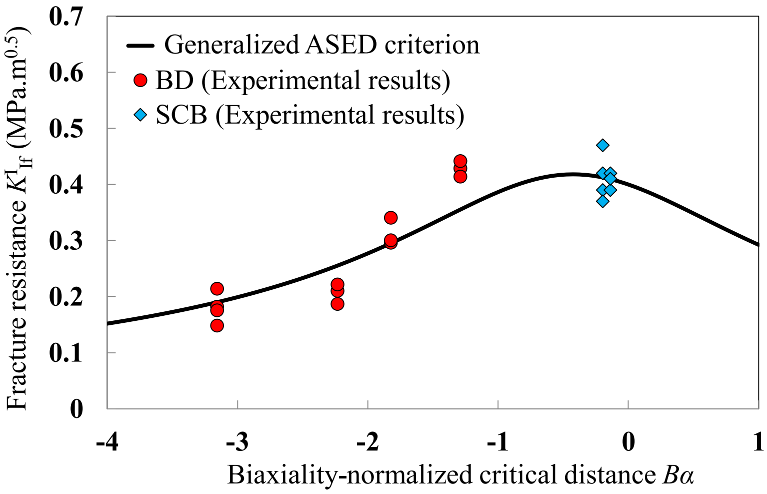

Fig. 2. Variation of mode I fracture resistance versus Bα for the British limestone extracted from the test performed by Akbardoost et al, (2014) on BD and SCB specimens

Mixed mode fracture tests were also performed on a British limestone using BD and SCB specimens by Akbardoost and his co-researchers (2014). The GASED criterion based on the critical stress intensity factors K_{If} and K_{IIf} together with the T-stress (Eq.(1)) was then used for fracture load predications in both specimens. It is seen from Figs. 3 and 4 that the GASED criterion provides significantly better predictions for the experimental results compared to the conventional ASED criterion. The improved predictions of generalized ASED criterion suggests that the increase and decrease in fracture toughness of the rock samples tested by the BD and SCB specimens were mainly due to the effect of T-stress which is ignored in the conventional criterion.

It is finally noted that the geometry dependency of fracture resistance under mixed mode loading is an important issue because engineers have to correlate the experimental results which are obtained in the laboratory conditions to practical problems where a crack is found in the field rock masses. For this purpose, the application of GASED criterion can be very useful as it considers the effects of geometry of cracked rock samples for better predictions of crack behaviour in real engineering projects related to rock mechanics.

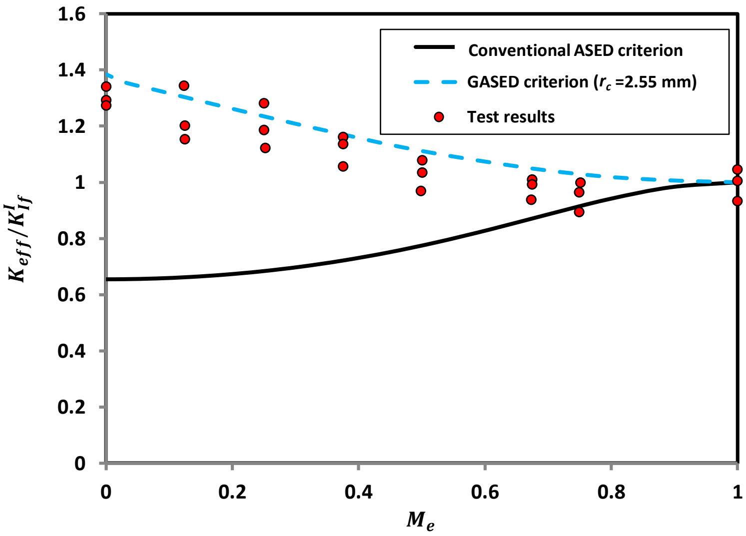

Fig. 3. Predictions of GASED criterion for mixed mode fracture toughness of a British limestone tested by Akbardoost et al, (2014) using the BD specimen

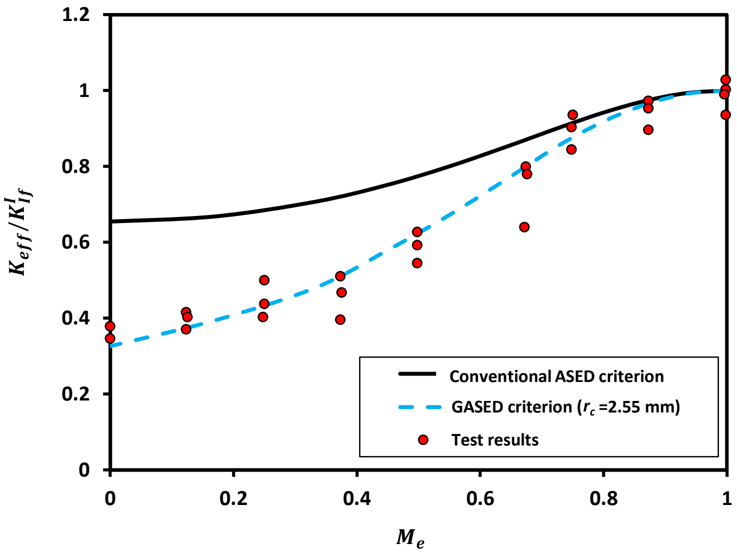

Fig. 4. Predictions of GASED criterion for mixed mode fracture toughness of a British limestone tested by Akbardoost et al, (2014) using the SCB specimen

3. Conclusions

Fracture toughness is an important parameter in rock fracture mechanics both for mode I fracture and for mixed mode I-II fracture. It was shown in this paper that the value of this parameter depends on the geometry and loading conditions in the rock samples. The effects of specimen geometry on the mixed mode fracture resistance of a British limestone were investigated using SCB and BD disk type specimens. The generalized ASED (GASED) criterion was employed to estimate the variation of the mixed mode fracture resistance with specimen geometry. The GASED criterion takes into account the effects of second term of stress field around the crack tip (*T*-stress) in addition to the conventional stress intensity factors K_{If} and K_{IIf}. It was shown that there is very good agreement between the theoretical predictions and the experimental results reported for the BD (with negative *T*-stress) and SCB (with positive *T*-stress) specimens when the modified energy-based criterion is employed.

References

Akbardoost, J., Ayatollahi, M.R., Aliha, M.R.M., Pavier, M.J., & Smith, D.J. (2014). Size-dependent fracture behaviour of Guiting limestone under mixed mode loading. *International Journal of Rock Mechanics and Mining Sciences*, *71*, 369–380

Ba, Z.P., Le, J.L., & Salviato, M. (2021). Quasibrittle fracture mechanics and size effect: A first course. Oxford, UK, Oxford University Press.

Chang, S.H., Lee, C.I., & Jeon, S. (2002). Measurement of rock fracture toughness under modes I and II and mixed-mode conditions by using disk-type specimen. *Engineering Geology*, *66*, 79-97

Khan, K., & Al-Shayea, N.A. (2000). Effect of specimen geometry and testing method on mixed I–II fracture toughness of a limestone rock from Saudi Arabia. *Rock Mechanics and Rock Engineering*, *33*(3), 179–206

Lazzarin, P., & Zambardi, R. (2001). A finite-volume-energy based approach to predict the static and fatigue behavior of components with sharp V-shaped notches. *International Journal of Fracture*, *112*(3), 275–298

Mehraban, M.R., Bahrami, B., Ayatollahi, M.R., & Nejati, M. (2023). A non-local XFEM-based methodology for modeling mixed-mode fracturing of anisotropic rocks. *Rock Mechanics and Rock Engineering, 56*(2), 895-909

ICEARC'25
4th International Civil Engineering & Architecture Conference
17-19 May 2025, Trabzon, Türkiye

Comparison of integrated force method and displacement method for metaheuristic optimization of civil structural systems

Ibrahim Torunoglu[1], Ayse T. Daloglu[*1]

[1] *Karadeniz Technical University, Department of Civil Engineering, 61080 Trabzon, Türkiye*

Abstract. In the optimization process where metaheuristic methods are used, large number of structural analysis is needed due to the nature of the methods. The most popular method used in structural analysis in civil engineering is the finite element displacement method. In the displacement method, after the global stiffness matrix is created, first the nodal displacements and then the internal forces of the elements are calculated. And these steps are repeated in each iteration, depending on the optimization method used, and naturally requires longer time for the analysis. Especially in structural systems with large number of elements, reducing analysis times can be an advantageous. In order to benefit from this advantage, choosing different structural analysis methods appears as an alternative. In this context, the performance of metaheuristic optimization methods combined with Integrated Force Method for structural analysis have been investigated. In the Integrated Force Method, first the internal forces of the elements and then the displacements of the nodes are calculated. Displacement method and Integrated Force Method are compared in terms of section optimization based on Harmony Search Algorithm and Teaching Learning Based Optimization. The obtained data show that the CPU times spent in the optimization processes using Integrated Force Method are shorter than the times spent in the case of Displacement Method.

Keywords: Finite Element Analysis; Integrated Force Method; Displacement Method; Metaheuristic Optimization

1. Introduction

From a structural engineering perspective, structural design can be considered as two stages. The first stage can be described as structural analysis and the second stage as structural design. Both stages are intertwined with each other. Pre-design is needed to perform structural analyses, and structural analysis results are needed to perform design.

In parallel with the ever-increasing vital needs of mankind, the developing engineering science has developed and continues to develop new methods for the structural analysis of increasingly complex physical models. Analytical methods, which began to be inadequate in solving complex structural models, began to give way to numerical methods as of the second half of the 20th century with the development of computer technology. The leading numerical method is the finite element method. The finite element method is divided into two separate methods. The first of these is the finite element displacement method, which is actively used in the analysis of today's engineering models, and the second is the finite element force method, which has remained in the background compared to the first. In both methods, the structural model, which is a continuum, is addressed by discretizing it into finite parts, and is analyzed under external loads by taking into account the equilibrium, boundary and compatibility conditions. The fundamental difference between the two methods is the assumption of unknowns. In the displacement method, the main unknowns are the displacements and rotations at the nodes. The internal forces occurring in the discrete elements are obtained with secondary calculations. In the force method, the main unknowns are the internal forces occurring in the elements (axial, shear, moment etc.). In this case, the displacements and rotations occurring at the nodes of the discrete elements are obtained by secondary calculations.

Increasing construction costs on a global scale, decrease in raw materials, and aesthetic concerns due to architectural reasons force the selection of cross sections to be minimized. However, earthquakes and wind loads, which have a significant effect especially on steel structures, force the designer to increase the section. The most important design criterions that comes out of this are; aesthetics, cost, sufficient strength, rigidity and ductility. Considering the factors that force the cross section selection in the minimum and maximum direction, reaching the optimum has become inevitable. This type of cross section optimization can be done manually by trial and

[*] Corresponding author, E-mail: aysed@ktu.edu.tr

https://doi.org/10.31462/icearc2025_ce_sme_363

golden light publishing

error and in a limited number of times. With the development of computer technology, cross section optimizations have now reached programmable levels simultaneously with structural analysis and design. Structural engineers have to design structures with minimum weight in order to choose the optimum one among the applicable designs (Artar, 2015). Considering steel structure optimization only in terms of bearing capacity and servisibilty constraints is insufficient in practice. Secondary constraints are regulations, specifications, standards, manufacturability and usable material section types that may vary from country to country. In this case, a very wide solution space appears for the optimization of steel structures. In this case, optimization methods that use mathematical programming techniques may not be reliable in terms of optimal convergence in such solution spaces (Hasançebi & Saka, 2010). Naturally, meta-heuristic methods have begun to be used to obtain optimum solutions in such wide solution spaces (Artar & Daloğlu, 2018). In case meta-heuristic methods are preferred, sometimes hundreds or even tens of thousands of structural analyzes need to be performed even on the smallest structural models. This circumstance results in a time constraint for the designer. In order to compare the length of the central processing unit (CPU) operating time in the case of using metaheuristic methods in the structural analysis and dimensioning process, the finite element displacement method (DM) and the finite element integrated force method (IFM) were compared. Harmony Search Algorithm (HSA) and Teaching-Learning Based Optimization (TLBO) methods were preferred as optimization techniques.

2. Integrated force method

The integrated force method was first proposed by Patnaik (1973). IFM, as in the finite element displacement method (DM), is based on the discretization of the continuum of the structural model into finite parts. Unlike DM, the force equilibriums on the nodes are taken into account. It consists of the solution of the linear equation system obtained by creating the equilibrium equations of the internal forces (moment, shear, axial, etc.) and external loads belonging to the elements which connected at the nodes. The "mxn" dimensional "B" matrix shown in Equation (1) represents the equilibrium matrix. The "nx1" dimensional "F" vector represents the internal forces belonging to the elements, and the "mx1" dimensional "P" vector represents the external forces acting on the nodes. The "m" value in the equation represents the total number of equilibrium equations, and "n" represents the number of unknown internal forces. If "m=n", the system is defined as statically determined, and if "m<n", it is defined as statically undetermined (Patnaik, 1973).

$$[B]_{mxn}|F|_{nx1}=|P|_{mx1} \tag{1}$$

Instead of creating the equilibrium equations for each node one by one, calculating the local equilibrium matrices of the elements provides convenience in terms of numerical operations (Topçu, 2017). By calculating the local equilibrium matrix "$\hat{B}$" separately for each element, the global equilibrium matrix "B_e" of the element and the global equilibrium matrix "B" of the system can be calculated with the help of the transformation matrix. For example, in Fig. 1, the local end forces at the ends "i" and "j" of a plane truss "k."th element are shown, and in Fig. 2, the global end forces at the ends "i" and "j" are shown.

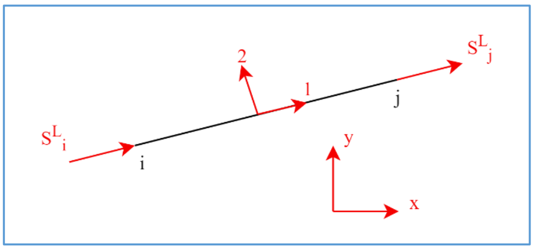

Fig. 1. Local internal forces of a plane truss element

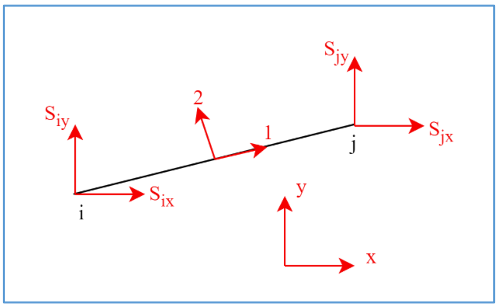

Fig. 2. Global internal forces of a plane truss element

The steps of calculating the local and global equilibrium matrices of the "k."th element in Fig. 1 and Fig. 2 are shown in eq. (2). In plane truss elements, only the axial internal force "F" occurs. The local and global end forces of the truss element can be expressed in matrix form in terms of the axial internal force.

$$S_j^L = F_k \Rightarrow \underbrace{\begin{vmatrix} \hat{S}_i^L \\ \hat{S}_j^L \end{vmatrix}}_{\hat{S}} = \underbrace{\begin{vmatrix} -1 \\ 1 \end{vmatrix}}_{\hat{B}} F_k$$

$$\underbrace{\begin{vmatrix} S_{ix} \\ S_{iy} \\ S_{jx} \\ S_{jy} \end{vmatrix}}_{S} = \underbrace{\begin{bmatrix} c & 0 \\ s & 0 \\ 0 & c \\ 0 & s \end{bmatrix}}_{T^T} \underbrace{\begin{vmatrix} \hat{S}_i^L \\ \hat{S}_j^L \end{vmatrix}}_{\hat{S}} \quad \text{(T; transformation matrix)}$$

$$\underbrace{\begin{vmatrix} S_{ix} \\ S_{iy} \\ S_{jx} \\ S_{jy} \end{vmatrix}}_{S} = \underbrace{\begin{bmatrix} c & 0 \\ s & 0 \\ 0 & c \\ 0 & s \end{bmatrix}}_{T^T} \underbrace{\begin{vmatrix} -1 \\ 1 \end{vmatrix}}_{\hat{B}} F_k \tag{2}$$

$$\underbrace{\begin{vmatrix} S_{ix} \\ S_{iy} \\ S_{jx} \\ S_{jy} \end{vmatrix}}_{S} = \underbrace{\begin{vmatrix} -c \\ -s \\ c \\ s \end{vmatrix}}_{B_e} F_k$$

In case the structural system is statically determined (m=n), eq. (1) can be solved by direct methods. In case the structural system is statically undetermined (n>m), (r=n-m) additional equations are needed. "r" represents the degree of hyperstaticity of the system. Additional equations are obtained by equating the work of the internal and external forces (eq. (3)). In eq. (3), "β" and "U" vectors represent the deformation vector of the elements and displacement vector of the nodes, respectively.

$$\frac{1}{2}\left|F^T\right|\left|\beta\right| = \frac{1}{2}\left|P^T\right|\left|U\right| \tag{3}$$

If the expression in eq. (1) is substituted into eq. (3), the expression in eq. (4) is obtained (Deformation-Displacement Relationship, DDR). Thus, with the help of eq. (4), "n" number of deformations are expressed with "m" number of displacements.

$$\left|\beta\right| = \left[B\right]^T \left|U\right| \tag{4}$$

If the displacements are expressed in terms of deformations, eq. (5) is obtained. In this expression, the matrix "C" is the "rxn" dimensional compatibility condition (CC). CC can be obtained by the SVD method.

$$\left[C\right]\left|\beta\right| = \left|0\right| \tag{5}$$

If the deformation expression in eq. (5) is expressed in terms of internal forces for each element and written in matrix form, eq. (6) which expressing the Force-Deformation Relationship (FDR) is obtained.

$$\beta_k = \underbrace{\frac{l}{AE}}_{G_k} F_k \Rightarrow \begin{vmatrix} \beta_1 \\ \beta_2 \\ \vdots \\ \beta_n \end{vmatrix} = \underbrace{\begin{bmatrix} G_1 & 0 & 0 \\ 0 & \ddots & 0 \\ 0 & 0 & G_n \end{bmatrix}}_{G} \begin{vmatrix} F_1 \\ F_2 \\ \vdots \\ F_n \end{vmatrix} \tag{6}$$

The "G" matrix expressed in eq. (6) is the concatenated flexibility matrix of the structure. If eq. (6) is substituted into eq. (5), eq. (7) is obtained. Eq. (7) has the dimension "rxn" and the unknown vector is expressed in terms of internal forces. In this case, eq. (1) and (7) can be combined into a single equation system.

$$\left[C\right]\left[G\right]\left|F\right| = \left|0\right| \tag{7}$$

$$\begin{bmatrix} & \left[B\right] & \\ \left[C\right] & & \left[G\right] \end{bmatrix} \left|F\right| = \begin{vmatrix} P \\ 0 \end{vmatrix} \Leftrightarrow \quad \left[S\right]\left|F\right| = \left|P\right|^* \tag{8}$$

The coefficient matrix "S" in eq (8) is "nxn" dimension and the internal forces "F" can be obtained by direct methods. Nodal displacements are calculated with the help of eq. (9).

$$|U| = [J][G]|F| \tag{9}$$

The "J" matrix witch expressed in eq. (9) is;

$$[J] = m\,rows\,of\left[[S]^{-1}\right]^{T} \tag{10}$$

3. Optimization techniques used in this study

In this study TLBO and HSA methods are used to compare the integrated force method and the displacement method in aspect of CPU time. Before giving theoretical information about the methods to be used, the objective function and penalty coefficients used in almost every structural optimization process will be briefly stated.

Considering that the main purpose of structural optimization is to reduce the structural weight, it is inevitable to adopt the structural weight as the objective function.The objective function to be minimized for these methods is expressed in eq. (11).

$$\min.W = \sum_{k=1}^{ng} A_k \sum_{i=1}^{nk} \rho_i L_i \tag{11}$$

The penalty coefficient calculation method used for element cross sections and node displacements is taken into account as shown in eq. (12). The expression "C" is the penalty coefficient of the entire system, which includes the sum of the element and node penalty coefficients.

$$c_j = \frac{\sigma_j - \sigma_{u/l}}{\sigma_{u/l}},\ c_i = \frac{\delta_i - \delta_{u/l}}{\delta_{u/l}},\ C = \sum_{j=1}^{m} c_j + \sum_{i=1}^{n} c_i \tag{12}$$

The penalized objective function expresses the circumstance where the objective function is increased by the penalty coefficient. The expression "ε" in eq. (13) is the positive valued penalty multiplier and is taken into account as "2" in the current study.

$$\psi(x) = W(x)(1+C)^{\varepsilon} \tag{13}$$

3.1. Teaching learning based optimization

Like many metaheuristic optimization methods, TLBO is also a population-based optimization method and consists of populations of candidate solution sets to obtain the optimum solution (Rao et al., 2011). TLBO method is based on the principle that a good teacher will positively affect the grades (design variables) of students in the class (solution set). Similarly, the interaction of students with each other (information exchange) will positively affect their grades (Rao et al., 2011).

The TLBO method consists of two stages. The first stage is the teacher, and the second stage is the student stage (Rao et al., 2011). At the teacher stage, the student with the best level of knowledge (the individual with the best objective function) in the class (population) increases the average knowledge of the class by transferring his knowledge to the whole class (Rao et al., 2011). In the second stage, each student interacts with other students, exchanges information with each other and increases their knowledge levels (Rao et al., 2011).

Since TLBO is a population-based optimization method, firstly each student in the population is created with randomly selected values from the solution space. As can be seen from the relation in eq. (14), each student represents a solution set and the number of elements of the set (X^i) is equal to the number of design variables (D).

$$\begin{gathered} X^i = \left[x_1^i\ x_2^i\ x_3^i\ \ldots x_j^i\right] \\ i \in (1,2,3,\ldots NP) \\ j \in (1,2,3,\ldots D) \end{gathered} \tag{14}$$

The students of the class ($X^{1,2,\ldots,NP}$) and their current knowledge levels ($\psi(x^{1,2,\ldots,NP})$) are shown in eq. (15).

$$\text{class} = \begin{bmatrix} x_1^1 & x_2^1 & \cdots & x_D^1 \\ x_1^2 & x_2^2 & \cdots & x_D^2 \\ \vdots & \vdots & \ddots & \vdots \\ x_1^{NP} & x_2^{NP} & \cdots & x_D^{NP} \end{bmatrix} \begin{matrix} \rightarrow \psi(x^1) \\ \rightarrow \psi(x^2) \\ \rightarrow \quad \vdots \\ \rightarrow \psi(x^{NP}) \end{matrix} \tag{15}$$

In the teacher phase, the class average and the student with the best knowledge level (the student with the best objective function) are determined. Each student is allowed to communicate with the teacher using the eq. (16).

$$X^{new,i} = X^i + r(X_{teacher} - T_f X_{mean}) \tag{16}$$

The parameter "r" expressed in eq. (16) is a row vector consisting of random numbers ranging from 0 to 1, and its length is equal to the number of design variables. "T_f" is the teaching coefficient and is considered as one of the randomly selected values of 1 or 2. At the end of the teacher phase, it is checked whether the obtained $\psi(x^{new,i})$ value of i.th student is a more appropriate solution than the $\psi(x^i)$ value. If the new calculated value is more suitable than the old one, $\psi(x^{new,i})$ replaces $\psi(x^i)$. Similarly, the solution vector $X^{new,i}$ replaces the solution vector X^i.

In the student phase, each student in the population must exchange information with other students at least once (Rao et al., 2011). In this case, the i.th student selected from the population interacts with the k.th student (i≠k). Using eq. (17), each student is enabled to interact with other students.

$$\begin{aligned} \psi(X^i) < \psi(X^k) \Rightarrow X^{new,i} = X^i + r(X^i - X^k) \\ \psi(X^i) > \psi(X^k) \Rightarrow X^{new,i} = X^i - r(X^i - X^k) \end{aligned} \tag{17}$$

Similarly, if the new calculated value is more suitable than the old one, $\psi(x^{new,i})$ replaces $\psi(x^i)$. Similarly, the solution vector $X^{new,i}$ replaces the solution vector X^i.

Deb's heuristic constraint handling method (Deb, 2000) is used to compare the objective functions calculated at the teacher and student stages with the old objective function (Rao et al., 2011). This comparison takes into account the following 3 rules:

- If a solution (objective function) is a feasible solution (penalty coefficient C=0) and the other solution is an infeasible solution (penalty coefficient C>0), the feasible solution is preferred.
- If both solutions are feasible (penalty coefficient C=0), the solution with the most feasible objective function value is preferred.
- If neither solution is a feasible solution (penalty coefficient C>0), the solution with the lowest penalty coefficient is preferred.

At the end of the accepted iteration (T_{max}), the student who gives the most appropriate objective function is accepted as the solution set and the process is terminated.

3.2. Harmony search algorithm

HSA can be defined as an optimization method obtained by developing a better harmony finding method in musical performance (Geem et al., 2001). Musical harmony is an aesthetic combination of sounds coming out of instruments (design variable) (Geem et al., 2001). In HSA method, each of the solution sets is called a harmony. In eq. (18), i.th harmony (X^i) and design variables are seen.

$$\begin{aligned} & X^i = \left[x_1^i \; x_2^i \; x_3^i \; \ldots x_j^i \right] \\ & i \in \left(1,2,3,\ldots \text{HMS}\right) \\ & j \in \left(1,2,3,\ldots \text{D}\right) \end{aligned} \tag{18}$$

In order to make melodies aesthetic, each musical instrument tries to find the most aesthetic melody by producing different sounds with different notes. The notes in the melody are either taken from the note pool or the sounds in the existing harmonies are used. The sounds in the existing harmonies are subjected to pitch if necessary (Lee & Geem, 2004). Firstly, a certain number of harmonies come together to create the harmony memory (HM) (Eq. (19)) and the aesthetic performance of each melody is calculated (objective function).

$$\text{HM} = \begin{bmatrix} x_1^1 & x_2^1 & \cdots & x_D^1 \\ x_1^2 & x_2^2 & \cdots & x_D^2 \\ \vdots & \vdots & \ddots & \vdots \\ x_1^{HMS} & x_2^{HMS} & \cdots & x_D^{HMS} \end{bmatrix} \tag{19}$$

In the second stage, a new harmony is created (Eq. (20)).

$$X^{new} = \left[x_1^{new}, x_2^{new}, \ldots, x_D^{new} \right] \tag{20}$$

The calculation of the design variable of the new harmony depends on three different possibilities. In the first possibility, a random “rand-1” value between 0 and 1 is selected. The condition that the “rand-1” value is greater or less than the Harmony Memory Consideration Ratio (HMCR) is examined (Eq. (21)). If “rand-1” is greater than HMRC, the design variable is selected randomly from the solution space. In the second possibility, if the “rand-1” value is less than or equal to HMRC, the design variable is selected randomly from the melodies in the relevant column in the current HM.

$$x_j^{new} \leftarrow \begin{cases} x_j^{new} \in \left\{ x_j^1, x_j^2, \ldots x_j^{HMS} \right\} \Rightarrow \text{rand1} \le \text{HMCR} \\ x_j^{new} \in X \Rightarrow \text{rand1} \ge \text{HMCR} \end{cases} \tag{21}$$

In the third possibility, the “rand-2” value randomly selected between 0 and 1 is compared with the pitch adjustment ratio (PAR). If “rand-2” is greater than the PAR value, no change is made to the X_j^{new} value. Otherwise, the pitch adjustment is made to the newly selected design variable as specified in eq. (22). It is rounded to the nearest notes. The amount of rounding is measured by the bandwidth coefficient “b_w”.

$$x_j^{new} \leftarrow \begin{cases} = x_j^{new} + b_w * u(-1,1) \Rightarrow \text{random} \le \text{HMCR} \\ = x_j^{new} \Rightarrow \text{random} \ge \text{PAR} \end{cases} \tag{22}$$

The value of u(-1,1) shown in eq (22) represents the random number chosen between -1 and 1. The larger the selected bandwidth, the more the notes ahead or behind are rounded. The aesthetic performance of the newly formed melody is calculated $\psi(x^{new})$ and replaced with the melody with the worst performance in the HM. The calculation step mentioned above is repeated for a predetermined number of iterations.

4. Benchmark studies

In cross-section optimizations using metaheuristic methods, cross-section checks are performed for structural elements after each structural analysis. In addition, if necessary, displacement constraints at nodal points are checked. In such optimizations, while the structural geometry remains constant, element cross-sections can change at each stage. In case of using the finite element Displacement Method (DM), local and global stiffness matrices of the bar elements are calculated and the global stiffness matrix of the system is created at each structural analysis stage. In case of using the Integrated Force Method (IFM), the only expression that needs to be recalculated is the concatenated flexibility matrix seen in eq. (8). The “B” and “C” matrices depend on the structural system geometry and are independent of the element cross-section. For this reason, it is not necessary to calculate them repeatedly at each analysis stage. In order to compare the performance of both analysis methods, examples obtained from the literature containing metaheuristic methods were used. The selected examples belong to plane truss systems. HSA, TLBO, DM and IFM codes are prepared in Python programming language using object-oriented programming (OOP).

4.1. 10 bar plane truss

The plane truss system with 6 nodes and 10 bar elements defined in the X-Z plane is shown in
Fig. 3. The elasticity modulus of the material is 10000 ksi and the density of the material is 0.1 lb/in^3. The allowable stress limit for all elements is ±25 ksi, and the displacement limit for the nodes is considered to be ±2 in. Each of the elements will be sized independently. There are a total of 10 design dariables. A force of 100 kips acts on the nodes 2 and 4 in the direction seen in the figure. The structure will be optimized for both continuous and discrete variable sections, and the sections to be used for the discrete value design are shown in Table 1. Continued

10	0.100	0.100	0.100	0.100	0.100	0.100	0.100
Weight (lb)	5057.88	5061.42	5060.97	5064.24	5079.44	5061.13	5061.26
Iteration	20000	-	-	50000.000	50000.000	200	200
Population	-	-	-	-	-	70	70
Harmony	20	20	-	25	25	-	-
HMCR	0.8	0.9	-	0.95	0.95	-	-
PAR	0.3	~	-	0.5	0.5	-	-
bw	-	~	-	0.1	0.1	-	-
CPU (sec.)	-	-	-	157.0625	31.4125	85.6406	23.5625

Table 2.

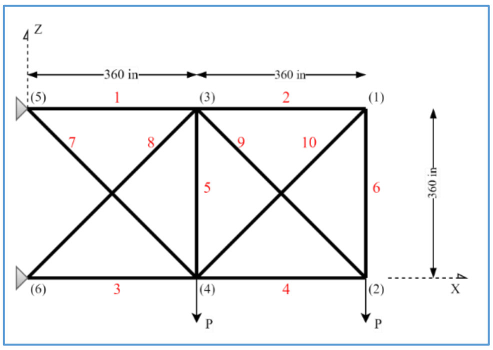

Fig. 3. 10 bar plane truss model

Table 1. Optimization results that containing continuous variables for a 10 bar element truss model

Design variables (in^2)	Lee & Geem (2004)	Değertekin (2012)	Farshchin & Camp (2014)	Current Study (DM)	Current Study (IFM)	Current Study (DM)	Current Study (IFM)
Element	HSA	SAHS	TLBO	HSA	HSA	TLBO	TLBO
1	30.150	30.394	30.668	30.377	30.333	30.725	30.509
2	0.102	0.100	0.100	0.100	0.100	0.100	0.100
3	22.710	23.098	23.158	24.327	23.805	23.253	23.479
4	15.270	15.491	15.223	14.724	14.739	15.260	15.227
5	0.102	0.100	0.100	0.100	0.100	0.100	0.100
6	0.544	0.529	0.542	0.628	0.100	0.571	0.574
7	7.541	7.488	7.465	7.324	8.586	7.443	7.437
8	21.560	21.189	21.026	20.653	20.491	20.854	20.941
9	21.450	21.342	21.466	21.718	21.679	21.510	21.446
Table 1. Continued							
10	0.100	0.100	0.100	0.100	0.100	0.100	0.100
Weight (lb)	5057.88	5061.42	5060.97	5064.24	5079.44	5061.13	5061.26
Iteration	20000	-	-	50000.000	50000.000	200	200
Population	-	-	-	-	-	70	70
Harmony	20	20	-	25	25	-	-
HMCR	0.8	0.9	-	0.95	0.95	-	-
PAR	0.3	~	-	0.5	0.5	-	-
bw	-	~	-	0.1	0.1	-	-
CPU (sec.)	-	-	-	157.0625	31.4125	85.6406	23.5625

Table 2. Discrete variable cross section areas for 10 bar truss

NO	in^2	NO	in^2	NO	in^2
1	1.62	15	3.63	29	11.50
2	1.80	16	3.84	30	13.50
3	1.99	17	3.87	31	13.90
4	2.13	18	3.88	32	14.20
5	2.38	19	4.18	33	15.50
6	2.62	20	4.22	34	16.00
7	2.63	21	4.49	35	16.90
8	2.88	22	4.59	36	18.80
9	2.93	23	4.80	37	19.90
10	3.09	24	4.97	38	22.00
11	3.13	25	5.12	39	22.90
12	3.38	26	5.74	40	26.50
13	3.47	27	7.22	41	30.00
14	3.55	28	7.97	42	33.50

Table 3. Optimization results that containing discreate variables for a 10 bar element truss model

Design Variable (in^2)	Li et al. (2009)	Farshchin & Camp (2014)	Dede (2014)	Current Study (DM)	Current Study (IFM)	Current Study (DM)	Current Study (IFM)
Element	HPSO	TLBO	TLBO	HSA	HSA	TLBO	TLBO
1	30.00	33.50	33.50	33.50	33.50	33.50	33.50
2	1.62	1.62	1.62	1.62	1.62	1.62	1.62
3	22.90	22.90	22.90	22.90	22.90	22.90	22.90
4	13.50	14.20	14.20	14.20	14.20	14.20	14.20
5	1.62	1.62	1.62	1.62	1.62	1.62	1.62

6	1.62	1.62	1.62	1.62	1.62	1.62	1.62
7	7.97	7.97	7.97	7.97	7.97	7.97	7.97
8	26.50	22.90	22.90	22.90	22.90	22.90	22.90
9	22.00	22.00	22.00	22.00	22.00	22.00	22.00
10	1.80	1.62	1.62	1.62	1.62	1.62	1.62
Weight (lb)	5531.98	5490.74	5490.74	5490.74	5490.74	5490.74	5490.74
Iteration	1000	-	50	50000	50000	200	200
Population	50	-	20	-	-	70	70
Harmony	20	20	-	25	25	-	-
HMCR	0.8	0.9	-	0.95	0.95	-	-
PAR	0.3	~	-	0.5	0.5	-	-
CPU (sec.)	-	-	-	156.3281	47.5625	85.0938	26.9063

4.2. 15 bar plane truss

The plane truss system with 8 nodes consisting of 15 bar elements defined in the X-Z plane is shown in Fig. 4. The elasticity modulus of the material is 200000 MPa and the density of the material is 7860 kg/m^3. The allowable stress limit for all elements is ±120 MPa and the displacement limit for the nodes is considered to be ±10 mm. Each of the elements will be sized independently and there are 15 design variables in total. A force of 35 kN acts on the nodes 4, 6 and 8 in the direction seen in the figure. The truss system will be optimized for discrete variable sections. The sections to be used in the design are shown in Table 4.

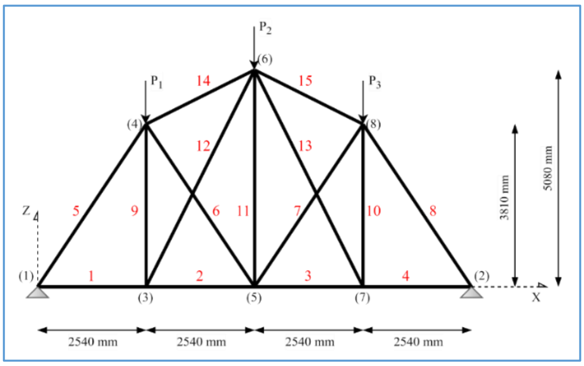

Fig. 4. 15 bar plane truss model

Table 4. Discrete variable cross section areas for 15 bar truss

NO	mm^2	NO	mm^2
1	113.2	9	308.6
2	143.2	10	334.3
3	145.9	11	338.2
4	174.9	12	497.8
5	185.9	13	507.6
6	235.9	14	736.7
7	265.9	15	791.2
8	297.1	16	1063.7

Table 5. Optimization results that containing discreate variables for a 15 bar plane truss system

Design Variable (in^2)	Dede (2014)	Current Study (DM)	Current Study (BKM)	Current Study (DM)	Current Study (BKM)
Element	TLBO	HSA	HSA	TLBO	TLBO
1	113.20	113.20	113.20	113.20	113.20
2	113.20	143.20	113.20	113.20	113.20
3	113.20	113.20	113.20	113.20	113.20

4	113.20	113.20	113.20	113.20	113.20
5	736.70	736.70	736.70	736.70	736.70
6	113.20	113.20	113.20	113.20	113.20
7	113.20	113.20	113.20	113.20	113.20
8	736.70	736.70	736.70	736.70	736.70
9	113.20	113.20	113.20	113.20	113.20
10	113.20	113.20	113.20	113.20	113.20
11	113.20	113.20	113.20	113.20	113.20
12	113.20	113.20	113.20	113.20	113.20
13	113.20	113.20	113.20	113.20	113.20
14	334.30	338.20	338.20	334.30	334.30
15	334.30	338.20	334.30	334.30	334.30
Weight (kg)	105.735	106.50	105.82	105.735	105.735
Iteration	50	50000	50000	50	50

Tablo 5. Continued

Population	30	-	-	30	30
Harmony	-	30	30	-	-
HMCR	-	0.95	0.95	-	-
PAR	-	0.5	0.5	-	-
CPU (sec.)	-	253.0625	61.5938	13.8438	2.9375

Table 6. Discrete variable cross section areas for 52 bar truss

NO	mm^2	NO	mm^2	NO	mm^2	NO	mm^2
1	71.613	17	1008.385	33	2477.414	49	7419.34
2	90.968	18	1045.159	34	2496.769	50	8709.66
3	126.451	19	1161.288	35	2503.221	51	8967.72
4	161.290	20	1283.868	36	2696.769	52	9161.27
5	198.064	21	1374.191	37	2722.575	53	9999.98
6	252.258	22	1535.481	38	2896.768	54	10322.56
7	285.161	23	1690.319	39	2961.284	55	10903.20
8	363.225	24	1696.771	40	3096.768	56	12129.01
9	388.386	25	1858.061	41	3206.445	57	12838.68
10	494.193	26	1890.319	42	3303.219	58	14193.52
11	506.451	27	1993.544	43	3703.218	59	14774.16
12	641.289	28	729.031	44	4658.055	60	15806.42
13	645.160	29	2180.641	45	5141.925	61	17096.74
14	792.256	30	2238.705	46	5503.215	62	18064.48
15	816.773	31	2290.318	47	5999.988	63	19354.80
16	939.998	32	2341.931	48	6999.986	64	21612.86

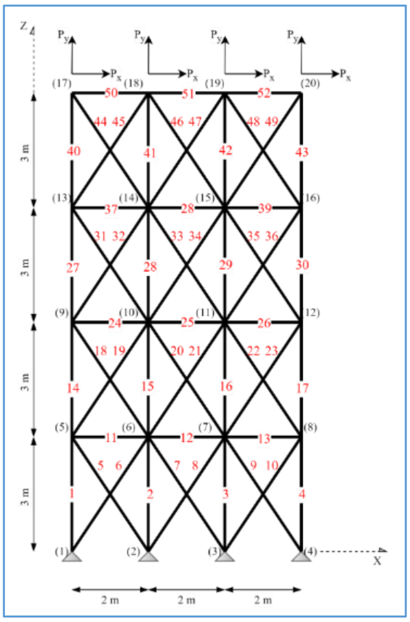

Fig. 5. 52 bar plane truss model

4.3.52 bar plane truss

The plane truss system with 20 nodes consisting of 52 bar elements defined in the X-Z plane is shown in Fig. 5. The elasticity modulus of the material is 207000 MPa and the material density is 7860 kg/m^3. The allowable stress limit for all elements is ±180 MPa, and there is no displacement limit for nodes. It will be sized in groups and there are 12 design variables in total. The nodes numbered 17, 18, 19 and 20 are subject to a force of 100 kN in the X direction and 200 kN in the Z direction. The carrier system will be optimized for discrete variable sections. The sections to be used for the discrete value design are shown in Table 6.

Table 7. Optimization results that containing discreate variables for a 52 bar element truss model

Design Variable (in^2)		Lee et al. (2005)	Dede (2014)	Current Study (DM)	Current Study (BKM)	Current Study (DM)	Current Study (BKM)
Group	Element	HS	TLBO	HSA	HSA	TLBO	TLBO
1	1-4	4658.055	4658.055	4658.055	4658.055	4658.055	4658.055
2	5-10	1161.288	1161.288	1161.288	1161.288	1161.288	1161.288
3	11-13	506.451	494.193	388.386	388.386	494.193	494.193
4	14-17	3303.219	3303.219	3303.219	3303.219	3303.219	3303.219
5	18-23	939.998	939.998	939.998	939.998	939.998	939.998
6	24-26	494.193	494.193	729.031	506.451	494.193	494.193
7	27-30	2290.318	2238.705	2238.705	2238.705	2238.705	2238.705
8	31-36	1008.385	1008.385	1008.385	1008.385	1008.385	1008.385
9	37-39	2290.318	494.193	388.386	363.225	494.193	494.193
10	40-43	1535.481	1283.868	1283.868	1283.868	1283.868	1283.868
11	44-49	1045.159	1161.285	1161.288	1161.288	1161.285	1161.285
12	50-52	506.451	494.193	494.193	729.031	494.193	494.193
Weight (kg)		1906.760	1902.605	1903.710	1903.102	1902.605	1902.605
Iteration		30000	100	50000	50000	120	120
Population		-	60	-	-	60	60
Harmony		20	-	30	30	-	-
HMCR		0.9	-	0.95	0.95	-	-
PAR		0.45	-	0.5	0.5	-	-
CPU (sec.)		-	-	775.8125	140.125	216.0625	36.0938

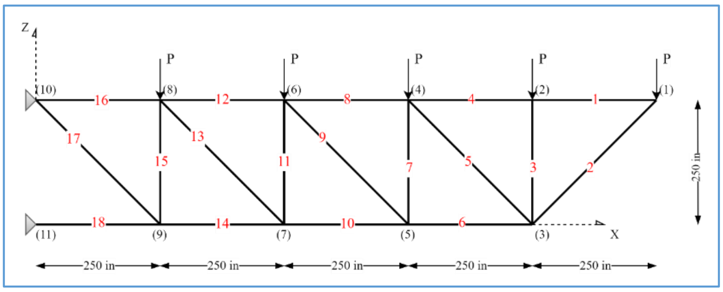

Fig. 6. 18 bar plane truss model

Table 8. Optimization results that containing continuous variables for a 18 bar element truss model

Design Variable (in^2)		Lee & Geem (2004)	Current Study (DM)	Current Study (BKM)	Current Study (DM)	Current Study (BKM)
Group	Element	HS	HSA	HSA	TLBO	TLBO
1	1, 4, 8, 12, 16	9.980	10.000	10.000	10.000	10.000
2	2, 6, 10, 14, 18	21.630	21.651	21.651	21.651	21.651
3	3, 7, 11, 15	12.490	12.500	12.500	12.500	12.500
4	5, 9, 13, 17	7.057	7.072	7.072	7.072	7.072
Weight (kg)		6421.880	6430.969	6430.969	6430.913	6430.521
Iteration		2000	20000	20000	100	100
Population		-	-	-	20	20
Harmony		20	20	20	-	-
HMCR		0.8	0.95	0.95	-	-
PAR		0.3	0.3	0.3	-	-
bw		-	0.1	0.1	-	-
CPU (sec.)		-	105.5469	17.4844	20.4375	3.1406

Tablo 8. Continued

4.4.18 bar plane truss

The plane truss system with 11 nodes consisting of 18 rod elements defined in the X-Z plane is shown in Fig. 6. The elasticity modulus of the material is 10000 ksi, and the material density is 0.1 lb/in^3. The allowable stress limit for all elements is ±20 ksi, and there is no displacement limit for the nodes. In addition to the given stress limit, Euler buckling stress $\left(\sigma_b^i = -4EA_i/L_i^2\right)$ will be taken into account for rod elements under compression. The system will be dimensioned in groups and there are 4 design variables in total. A force of -20 kips acts in the Z direction as seen in the figure from the nodes 1, 2, 4, 6 and 8. The system will be optimized for continuously variable cross-sections.

5. Results and discussion

Under the headings 4.1, 4.2, 4.3 and 4.4, plane truss models were examined by considering continuous and discrete design variables. When the obtained results were compared with the benchmark studies, it was concluded that the prepared structural analysis and optimization codes provided sufficiently accurate data.

In terms of optimization data input parameters, the required user data input parameters for the TLBO method are the population number and the iteration number. The required parameters in the HSA method are the harmony number, iteration number, HMCR and PAR values. The TLBO method offers simplicity in terms of user data input. In the HSA method, it should be taken into account that the HMCR and PAR parameters may vary depending on the structural model. Since there is no single acceptance for these values, it is necessary to check and verify them over different values even in the same structural model.

When the data obtained in terms of analysis times are compared, it is determined that structural analysis performed with IFM are 6-8 times faster than DM. The reason for this circumstances is that, as mentioned before, in fixed geometry section optimizations, when IFM is used, the only expression that changes is the concatenated flexibility matrix. It should be noted that the analysis times obtained in this study may vary from computer to computer depending on the hardware performance. Even in such a case, it will not change the fact that the CPU time rates of both analysis methods are at the same levels.

6. Conclusion

In this study, IFM and DM were compared in terms of CPU time under iterative structural analysis. Since the most intensive use of iterative analysis is metaheuristic optimization methods, two metaheuristic optimization methods were selected and cross section optimizations were performed on plane truss models. The results obtained were compared with the results in the literature. As a result of the comparisons made, it was concluded that the expected goals were achieved and IFM was more efficient in terms of CPU times compared to DM in iterative processes.

It should be noted that the obtained results are valid for fixed geometry plane truss systems. Because, it should not be forgotten that in case of geometry optimizations, the equilibrium and compatibility matrices must be recalculated at each stage.

References

Artar, M. (2015). *Optimization of steel frames with composite beams using genetic algorithm* [Doctoral dissertation, Karadeniz Technical University].

Artar, M., & Daloğlu, A. T. (2018). Optimum weight design of steel space frames with semi-rigid connections using harmony search and genetic algorithms. *Neural Computing and Applications, 29*(11), 1089–1100.

Camp, C. V., & Farshchin, M. (2014). Design of space trusses using modified teaching–learning-based optimization. *Engineering Structures, 62–63*, 87–97.

Deb, K. (2000). An efficient constraint handling method for genetic algorithm. *Computer Methods in Applied Mechanics and Engineering, 186*, 311–338.

Degertekin, S. O. (2012). Improved harmony search algorithms for sizing optimization of truss structures. *Computers and Structures, 92–93*, 229–241.

Dede, T. (2014). Application of teaching-learning-based-optimization algorithm for the discrete optimization of truss structures. *KSCE Journal of Civil Engineering, 18*(6), 1759–1767.

Geem, Z. W., Kim, J. H., & Loganathan, G. V. (2001). A new heuristic optimization algorithm: Harmony search. *Simulation, 76*(2), 60–68.

Hasançebi, O., & Saka, M. P. (2010). Optimum design of three dimensional steel structural systems using stochastic optimization methods and its application to structural engineering in our country. Retrieved from https://open.metu.edu.tr/bitstream/handle/11511/50065/TVRBNU9UTXo.pdf

Lee, K. S., & Geem, Z. O. (2004). A new structural optimization method based on the harmony search algorithm. *Computers and Structures, 82*, 781–798.

Lee, K. S., & Geem, Z. O. (2005). A new meta-heuristic algorithm for continuous engineering optimization: Harmony search theory and practice. *Computer Methods in Applied Mechanics and Engineering, 194*, 3902–3933.

Lee, K. S., Geem, Z. O., Lee, S. H., & Bae, K. W. (2005). The harmony search heuristic algorithm for discrete structural optimization. *Engineering Optimization, 37*(7), 663–684.

Li, L. J., Huang, Z. B., & Liu, F. A. (2009). A meta-heuristic particle swarm optimization method for truss structures with discrete variables. *Computers and Structures, 87*, 435–443.

Patnaik, N. S. (1973). An integrated force method for discrete analysis. *International Journal for Numerical Methods in Engineering, 6*, 237–251.

Rao, R. A., Savsani, V. J., & Vakharia, D. P. (2011). Teaching–learning-based optimization: A novel method for constrained mechanical design optimization problems. *Computer-Aided Design, 43*, 303–315.

Topçu, A. (2017). Element types and matrices part 22. Retrieved from https://atopcu.osmanmuratkaya.com/index_dosyalar/Dersler/SonluElemanlarMetodu/SEM22_KUVVET%20METODU_ElemanMatrisleri.pdf

4th International Civil Engineering & Architecture Conference
17-19 May 2025, Trabzon, Türkiye

Comparative analysis of vision-based vibration identification techniques using digital camera imaging

Selenay Gençcelep*[1], Volkan Kahya[2], Kemal Hacıefendioğlu[2], Sebahat Şimşek[2]
Tunahan Aslan[2]

[1] Avrasya University, Department of Civil Engineering, 61080 Trabzon, Türkiye
[2] Karadeniz Technical University, Department of Civil Engineering, 61080 Trabzon, Türkiye

Abstract: With the rapid advancement of technology, Structural Health Monitoring (SHM) has increasingly embraced innovative computer vision techniques, offering real-time, non-contact monitoring that significantly enhances structural integrity assessment. These methods provide efficient and cost-effective alternatives to traditional techniques, making them highly attractive for practical applications. This study aims to determine the most effective computer vision-based SHM method by comparing four optical flow algorithms—Lucas-Kanade, Farnebäck, Horn-Schunck, and Phase-based—in terms of accuracy, computational efficiency, and adaptability to varying structural conditions. Optical flow algorithms analyze pixel intensity changes between successive images to detect structural movements. Lucas-Kanade calculates displacements by tracking distinct image points, while Farnebäck estimates dense optical flow capable of capturing complex movements. Horn-Schunck incorporates a smoothness constraint, enhancing robustness against noise, whereas the Phase-based method identifies movements through phase differences derived from Fourier transforms. Displacement graphs generated from laboratory videos capturing structural vibrations were analyzed using these algorithms. Subsequently, the Fast Fourier Transform (FFT), a powerful technique converting time-domain signals into frequency-domain data, was applied to these displacement signals to accurately determine structural vibration characteristics and modal parameters. By evaluating the accuracy of anomaly detection and robustness of each method, this research provides valuable insights into their respective strengths and limitations, thereby contributing to developing reliable, scalable, and economically feasible SHM systems to enhance critical infrastructure safety and sustainability.

Keywords: Structural health monitoring (SHM); Computer vision-based methods; Optical flow algorithm; Lucas-Kanade; Farnebäck; Horn-Schunck; Phase-based

1. Introduction

With the rapid advancement of technology, Structural Health Monitoring (SHM) has increasingly incorporated innovative techniques to ensure the long-term performance, safety, and integrity of engineering structures. Traditional SHM methods typically rely on contact-based sensors such as accelerometers, displacement transducers, and strain gauges. However, in recent years, interest in non-contact measurement techniques has grown due to the challenges and costs associated with implementing these conventional sensors (Cha et al., 2017; Feng & Feng, 2018). Among non-contact approaches, computer vision-based techniques offer significant advantages as they do not impose additional loads on the structure during measurement and are capable of providing remote and real-time data (Lydon et al., 2019; Yang et al., 2020). These methods can effectively detect structural vibrations, deformations, and displacements using camera systems and image processing algorithms.
The primary objective of this study is to comprehensively evaluate the performance of computer vision-based SHM methods in terms of accuracy and computational efficiency, and to identify the most suitable technique for SHM applications. To this end, four optical flow algorithms that are widely used in the literature and have demonstrated success in various applications were examined: Lucas-Kanade (Lucas & Kanade, 1981; Baker & Matthews, 2004), Farnebäck (Farnebäck, 2003), Horn-Schunck (Horn & Schunck, 1981), and Phase-based methods (Fleet & Jepson, 1990; Gautama & Van Hulle, 2002).

Optical flow algorithms aim to precisely determine movements and displacements in the two-dimensional image plane by analyzing the temporal variations in pixel intensities between successive image frames (Barron et al., 1994; Sun et al., 2014). The Lucas-Kanade algorithm tracks motion by computing optical flow vectors at salient points in the image, offering advantages such as fast computation and high accuracy, particularly with high-

* Corresponding author, E-mail: selenay.pembeoglu@avrasya.edu.tr

https://doi.org/10.31462/icearc2025_ce_sme_386

resolution imagery (Bouguet, 2001; Brox & Malik, 2011). The Farnebäck algorithm, based on polynomial expansion, estimates dense optical flow and is particularly effective at capturing small, complex, and continuous motions in the images (Farnebäck, 2003). The Horn-Schunck algorithm incorporates a smoothness constraint into the optical flow estimation process, which enhances consistency and reliability in noisy environments. As such, it yields effective results even with low-quality images (Horn & Schunck, 1981; Pérez et al., 2013). Phase-based methods, on the other hand, analyze phase variations in the Fourier domain of images, making them especially advantageous for detecting fine and small-amplitude movements at the micrometer scale (Fleet & Jepson, 1990; Wadhwa et al., 2013).

In this study, the effectiveness of the four different computer vision-based methods was evaluated through experimental tests conducted on a steel structure model in a laboratory environment. During the experiments, structural vibrations were induced by applying controlled impacts from below, and the entire process was recorded in video format using a fixed camera. The recorded videos were then processed using a custom-developed graphical user interface (GUI)-based analysis software. This software, designed with a user-friendly interface, enables the application of the Lucas-Kanade, Farnebäck, Horn-Schunck, and Phase-based optical flow algorithms and performs displacement analysis within the user-defined regions of interest (ROIs) on the structure for each method. Time-series displacement graphs representing the vibrational motions of the structure were generated for each algorithm, and the frequency content of these signals was analyzed using the Fast Fourier Transform (FFT) method. FFT is a powerful mathematical tool that transforms time-domain vibration signals into the frequency domain, allowing for the precise determination of modal parameters such as natural frequencies and mode shapes (Antoni & Randall, 2006).Through this integrated methodological approach, each optical flow algorithm's capability to accurately and consistently detect structural vibrations was comparatively assessed in terms of both temporal resolution and frequency-domain performance. The findings derived from these analyses will contribute to the development of scalable, reliable, and cost-effective SHM systems by enabling more effective utilization of computer vision techniques for the safety and sustainability of critical infrastructure.

2.Theory

Optical flow is a technique that enables the quantitative estimation of pixel displacements over time between consecutive frames in an image sequence. This approach is widely employed in applications such as analyzing the dynamics of moving objects and monitoring structural vibrations. Its fundamental assumptions include brightness constancy and the continuity of motion across neighboring pixels (Lucas & Kanade, 1981). Brightness constancy is mathematically expressed as

$$I(x,t) = I(x+\delta x, t+\delta t) \tag{1}$$

where I denotes the image intensity, x the spatial coordinate (or pixel location), t the time (frame index), δx the small spatial displacement vector, and δt the corresponding time increment. The optical flow constraint equation obtained through the Taylor series expansion of the above equation is as follows:

$$\nabla I(x,t) \cdot u + I_t(x,t) = 0 \tag{2}$$

were, ∇I denotes the spatial gradient of the image intensity, I_t denotes the temporal gradient, and $u = (u_x, u_y)$ is the optical flow vector. Since it is a single equation with two unknowns, the Lucas-Kanade method minimizes this error using the least squares approach:

$$E(u) = \sum_{(x,y)\in W} (\nabla I \cdot u + I_t)^2 \;\; \Rightarrow \;\; Au = b$$
$$A = \sum \begin{pmatrix} {I_x}^2 & I_x I_y \\ I_x I_y & {I_y}^2 \end{pmatrix}, \quad b = -\sum \begin{pmatrix} I_x I_t \\ I_y I_t \end{pmatrix} \tag{3}$$

In the implemented code, the parameter *winSize* = (25,25) defines a 25×25 pixel region, while *maxLevel=2* enables a two-level image pyramid (half and quarter resolutions), allowing for coarse-to-fine motion estimation. Consequently, for each primitive ROI, optical flow is estimated at feature points using the Lucas-Kanade (LK) method. New feature points are re-detected every 20 frames, and the iteration continues until either 20 iterations are completed or the update falls below 0.03 pixels. These settings provide a well-balanced trade-off between computational efficiency and accuracy.

In the Farnebäck method, each local image patch is modeled as a second-order polynomial surface

$$f(x) \approx x^T A x + b^T x + c \tag{4}$$

where $x = (x,y)^T$ denotes the spatial coordinate within the patch, A is a symmetric $2x2$ matrix of quadratic coefficients, b is a $2x1$ vector of linear coefficients, c and is a constant term. When this polynomial approximation is computed independently in two consecutive frames—yielding (A_1, b_1, c_1) and (A_2, b_2, c_2)—the inter-frame displacement d that best aligns the two surfaces can be obtained in closed form as

$$d = -\frac{1}{2}(A_1 + A_2)^{-1}(b_2 - b_1) \tag{5}$$

This analytic solution allows Farnebäck's algorithm to compute a dense flow field efficiently by directly estimating the sub-pixel shift of each patch (Farnebäck, 2003).

The Horn–Schunck method enforces both the brightness constancy constraint and the smoothness of the flow by minimizing a global energy function (Horn & Schunck, 1981). The energy function is given by

$$E(u,v) = \iint (I_x u + I_y v + I_t)^2 + \alpha^2(\|\nabla u\|^2 + \|\nabla v\|^2)\ dx\,dy \tag{6}$$

Here, α serves to balance data fidelity and flow smoothness. The iterative update derived from the associated Euler–Lagrange equations is:

$$u^{(n+1)} = \bar{u}^{(n)} - \frac{I_x \left(I_x \bar{u}^{(n)} + I_y \bar{v}^{(n)} + I_t\right)}{a^2 + {I_x}^2 + {I_y}^2}$$

$$v^{(n+1)} = \bar{v}^{(n)} - \frac{I_y (I_x \bar{u}^{(n)} + I_y \bar{v}^{(n)} + I_t)}{a^2 + {I_x}^2 + {I_y}^2} \tag{7}$$

where, $\bar{u}$ and $\bar{v}$ represent local averages from the previous iteration, computed using a kernel. In the implemented code, the parameters define the regularization weight, the number of iterations, and the convergence threshold, respectively. Initially, image noise is reduced using a Gaussian blur, followed by the computation of image gradients using simple difference kernels. Due to its global formulation, the estimated flow is smooth and robust across the entire frame, although it may smooth out sharp motion boundaries.

Phase correlation leverages the Fourier-shift theorem: a pure translation between two images manifests as a linear phase difference in the frequency domain (Kuglin & Hines, 1975). Concretely, given two windows f and g, one computes

$$F = \mathcal{F}\{f\},\quad G = \mathcal{F}\{g\},\quad R = \frac{F\bar{G}}{|F\bar{G}|},\quad r = \mathcal{F}^{-1}\{R\} \tag{8}$$

where the peak of the cross-correlation r gives the sub-pixel shift $(\Delta x, \Delta y)$. In OpenCV this is wrapped by *cv2.phaseCorrelate(prev, curr)*, which returns *(dx,dy)* directly along with a confidence *response*. Converting the images to *float32* format enhances numerical precision. The Phase-based method is robust against illumination changes and, since it provides a single displacement vector per ROI, it serves as a strong complement to gradient-based methods.

3. Methodology

The application developed in this study performs video-based optical-flow analysis and enables a comparative assessment of four algorithms—Lucas–Kanade, Farnebäck, Horn–Schunck, and Phase-based optical flow. Implemented in Python, it relies chiefly on the OpenCV, NumPy, SciPy, Pillow (PIL), Matplotlib, and Tkinter libraries. Consequently, users can (i) select a video file, (ii) define regions of interest (ROIs), (iii) determine a scale factor, and (iv) detect motion using the aforementioned optical-flow methods.

A graphical user interface (GUI) was created with Tkinter and organized into multiple function-specific frames. Within the main window, separate menu items provide core controls (play, pause, rewind, fast-forward), file handling, method selection, ROI selection, scale-factor computation, and visualisation of analysis results. When a user initiates a task, the interface switches to the relevant frame (e.g., the ROI-selection or analysis panel), ensuring that all operations remain distinct yet mutually compatible.

Video processing begins with OpenCV's *VideoCapture*, which retrieves the frame count, frames-per-second (FPS), and other basic parameters of the selected file. Each frame is resized to suit the display area with Pillow and rendered in a Tkinter Label. During playback, a slider supplies real-time feedback on the frame index, FPS, and elapsed duration.

Optical-flow analysis is conducted on the user-defined ROIs. With the Lucas–Kanade method, corner points are detected in the first frame and their subsequent positions are tracked via *calcOpticalFlowPyrLK*, after which the mean displacement vector is computed for each ROI. Farnebäck produces dense motion fields, whereas Horn–Schunck calculates spatial and temporal derivatives (using Gaussian blurring and Sobel kernels) and iteratively refines the flow field. In the Phase-based approach, consecutive frames undergo a Fourier transform to extract phase components; phase differences are unwrapped, and mean gradient values (obtained with a Sobel filter) yield the motion information. Employing multiple algorithms in this manner facilitates a rigorous comparison of their accuracy and suitability for diverse motion scenarios.

ROI selection and scale-factor estimation are fully interactive. Users delineate arbitrary regions with the mouse; these ROIs are highlighted on a Tkinter Canvas and previewed as thumbnails in real time. For scale calibration, two points are marked, the corresponding pixel distance and true physical distance are entered, and the pixel-to-length conversion factor is calculated automatically. This factor is subsequently applied to convert optical-flow displacements into meaningful physical units.

The analysis routine executes in a background thread, preventing the GUI from becoming unresponsive. A progress bar continuously displays the elapsed time and percentage completion. For every frame, x- and y-direction displacements within each ROI are aggregated, and average motion vectors are recorded. The resulting time-series data are visualised with Matplotlib; dominant frequency components are identified via a fast Fourier transform (FFT) and annotated on the plots. All graphs can be exported in PNG or PDF format. Figure 1 illustrates the application's flowchart, detailing the sequence of operations and interactions among key modules.

In conclusion, the methodological framework integrates multiple optical-flow algorithms with an intuitive interface, providing a comprehensive platform for video-based motion analysis, interactive ROI selection, and scale calibration. The application enables detailed examination of motion data in both the time and frequency domains, supports direct comparison of algorithmic performance, and yields physically interpretable results through precise unit conversion.

4. Experimental study

The experimental studies were conducted at the Earthquake and Structural Health Monitoring Laboratory of Karadeniz Technical University, utilizing a previously developed high-speed video monitoring system designed for structural health monitoring and modal parameter identification (Hacıefendioğlu et al., 2024). The portable and non-contact monitoring system comprises a CoaXPress VICTOREM high-speed industrial camera, a DVR Express Core 2 CoaXPress recording device for data storage, and a computer (Table 1). Powered by mains electricity and supported by a portable generator for field applications, the system enables the acquisition of high-resolution images and their analysis using customized software tools. The system components are connected via HDMI and USB cables, while a single CoaXPress cable is used for both power supply and data transmission (Fig. 2). The recording device supports up to four cameras simultaneously; however, an increase in the number of cameras leads to larger data sizes and reduced recording durations. Provided that the system capacity is not exceeded, there is no need to adjust the frame rate (FPS).

The test model is a rectangular steel bar with a length of 550 mm, a width of 4.42 mm, and a thickness of 3.2 mm. To ensure accurate displacement measurements based on optical flow, six square tracking points were placed at equal intervals along the length of the model. This configuration enabled the precise detection of time-dependent vibration modes and facilitated highly accurate frequency analysis.

During the experiment, the model was clamped to a rigid concrete block using a vise, leaving a 5 cm support distance at one end. The distance between the camera and the test specimen was set to 8.5 meters. This setup allowed the entire model to be captured within a single frame using one camera, thereby minimizing potential measurement errors. After configuring the camera settings, an impulsive load was applied to the lower part of the concrete block to initiate experimental vibration, ensuring that the block itself remained stationary. Video recordings were conducted at a resolution of 1552×1544 pixels, for a duration of 2 minutes, and at a frame rate of 80 FPS. This experimental setup contributed to the reduction of measurement errors, while the stable lighting conditions in the laboratory ensured consistent image quality throughout the analysis. Fig. 3 illustrates the spatial configuration of the camera and the model.

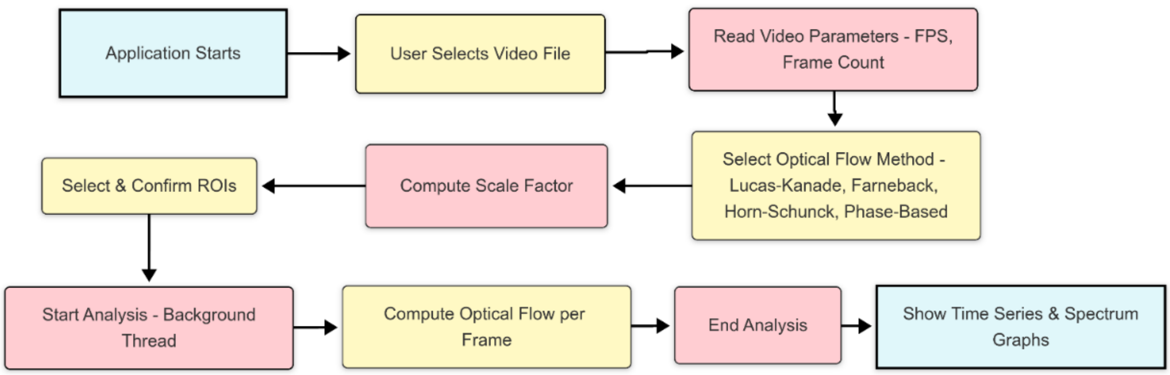

Fig. 1. Flow chart of prepared code

Fig. 2. The connection diagram of the video camera-based monitoring system

Fig. 3. Camera and composite material positioning

Table 1. Video camera-based monitoring system hardware components

Components	Model	Technicial Specifications
Video Camera-2	IO Industries CoaxPress VICTOREM 32B216MCX	Maximum Resolution: 2064 x 1544 Number of Frames: 216 FPS Pixel size: 3,45×3,45 μm²
Video Recorder	IO Industries DVR Express Core 2 CoaXPress	Video Format: 8/10/12/14/16-bit Monochrome 24-bit RGB
Computer	HP Victus 16d1006nt	12th Gen Intel(R) Core (TM) i5-12500H 2.50 GHz

5. Results and discussion

In this section, the outcomes obtained from the code developed in a GUI-based environment are presented. All analyses were performed on a Lenovo Ideapad L340-15IRH Gaming laptop equipped with an Intel® Core™ i5-9300H processor, 8 GB of RAM, and a 250 GB SSD. In prior work, computer vision and optical flow methods were employed to compare experimental and numerical results in structural vibration analysis; the observed agreement validated the chosen algorithms (Hacıefendioğlu et al., 2024). Consequently, here we compare only the displacement and frequency data derived from our four optical flow algorithms via code execution.

Frequency analyses were conducted by applying the Fast Fourier Transform (FFT) to each displacement time series. During the experimental phase, videos were recorded at 80 FPS to capture the full model dimensions, resulting in only the primary (fundamental) frequency component appearing in the spectrum. Table 2 summarizes the computation times and fundamental frequencies for each optical flow method, facilitating direct comparison. Displacements along the X and Y axes are shown in Fig. 4, 6, 8, and 10. and the corresponding frequency spectra in Fig. 5, 7, 9, and 11. Since no significant Y-axis vibrations were detected, the analyses focus exclusively on the X-component. The fundamental vibration frequency was consistently observed at 10.16 Hz for all methods.

In terms of computation time, the Phase-based algorithm completed analysis in 2.28 s, making it the fastest; Lucas–Kanade (2.32 s) and Farnebäck (2.40 s) exhibited similar performance. The Horn–Schunck method required 4.53 s, representing the highest computational load and potentially limiting its applicability in real-time scenarios. The Lucas–Kanade method (Figs. 4 and 5) produced sharp, high-amplitude vibration peaks along the X-axis and low-amplitude noise on the Y-axis. FFT analysis revealed a dominant frequency of 10.16 Hz in both components. Corner-based feature tracking successfully balanced high frequency resolution with modest processing times.

The Farnebäck algorithm (Figs. 6 and 7) generated lower-amplitude vibrations by averaging dense flow vectors. Its FFT spectrum also indicated secondary frequency components around 30.55 Hz in the Y-axis, while maintaining a computation time comparable to Lucas–Kanade and offering broader flow-field coherence.

The Horn–Schunck approach (Figs. 8 and 9) yielded a smooth displacement profile through iterative averaging but exhibited a dominant 10.16 Hz peak on the X-axis and a 37.66 Hz secondary component on the Y-axis. However, its 4.53 s processing time may constrain its use in time-critical applications.

Table 2. Comparison of computation time and fundamental frequency for optical flow methods

Method	Computation Time (s)	Fundamental Frequency (Hz)
Lucas-Kanade	2.32	10.16
Farnebäck	2.40	10.16
Horn–Schunck	4.53	10.16
Phase-based	2.28	10.16

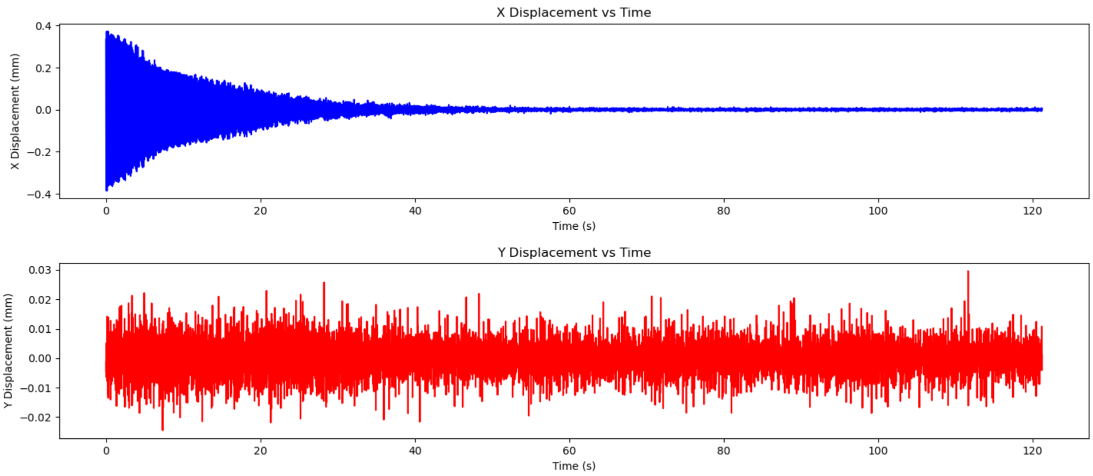

Fig. 4. X- and Y-axis displacement time series obtained using the Lucas–Kanade optical flow method

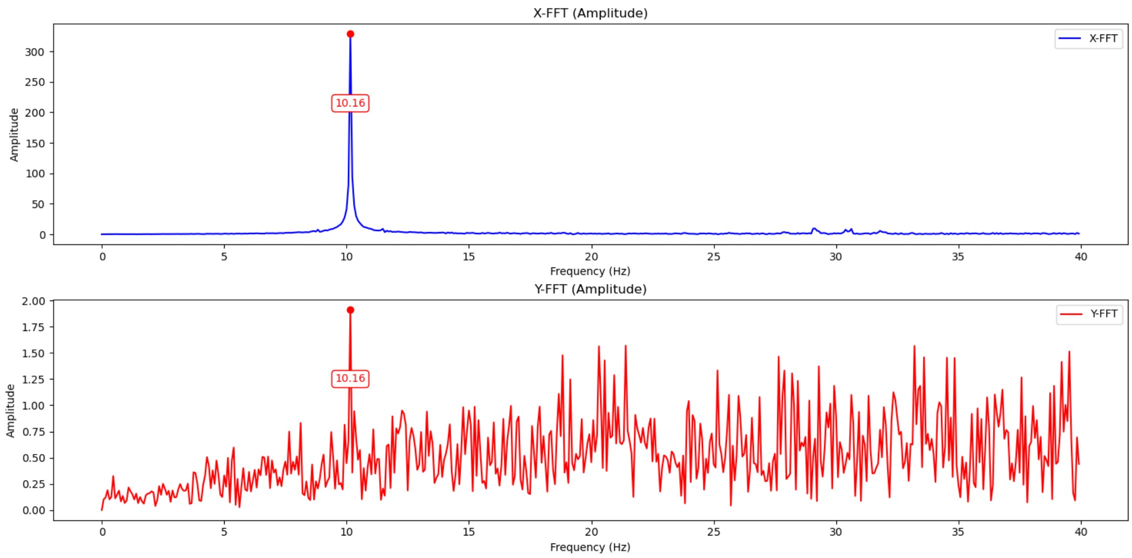

Fig. 5. Frequency spectra obtained using the Lucas–Kanade optical flow method

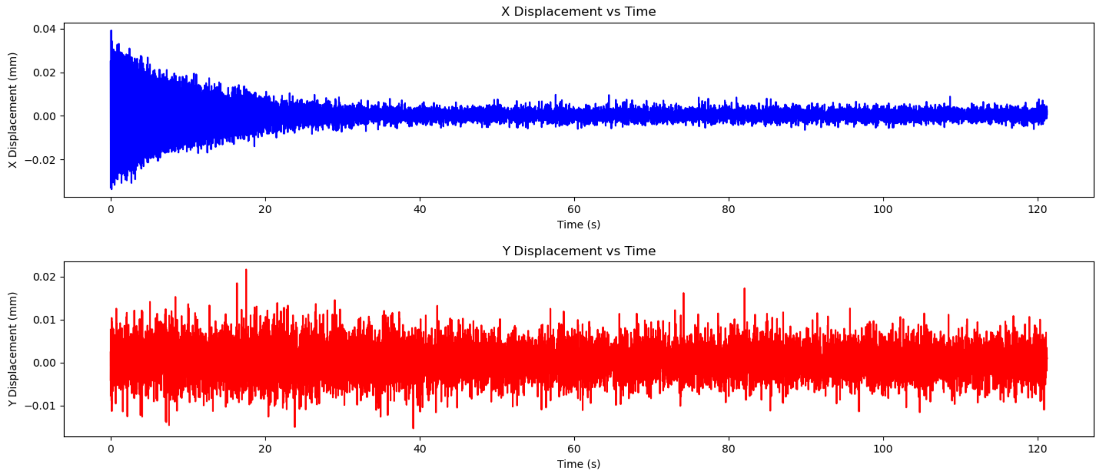

Fig. 6. X- and Y-axis displacement time series obtained using the Farnebäck optical flow method

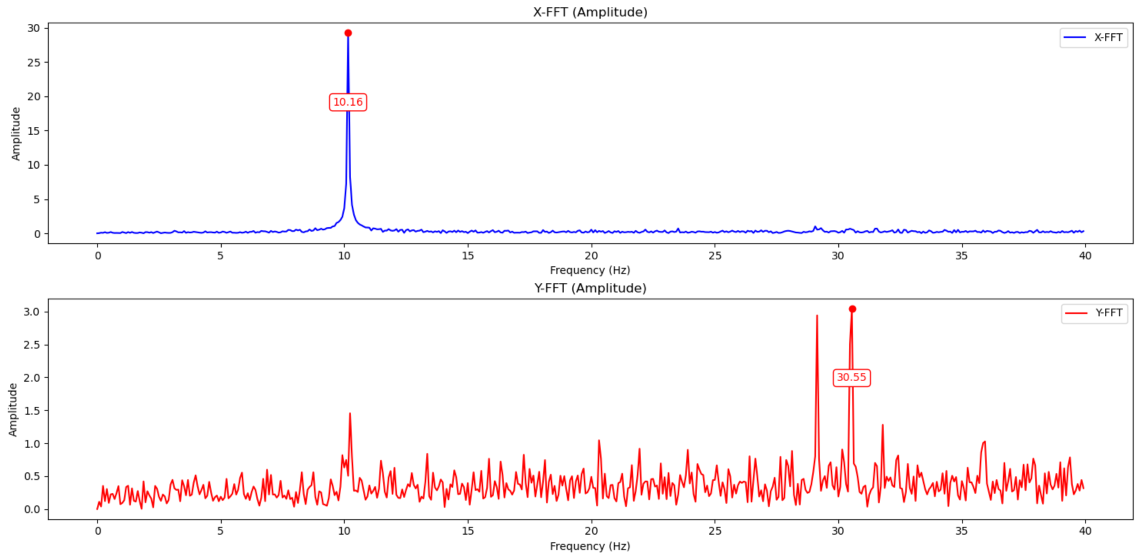

Fig. 7. Frequency spectra obtained using the Farnebäck optical flow method

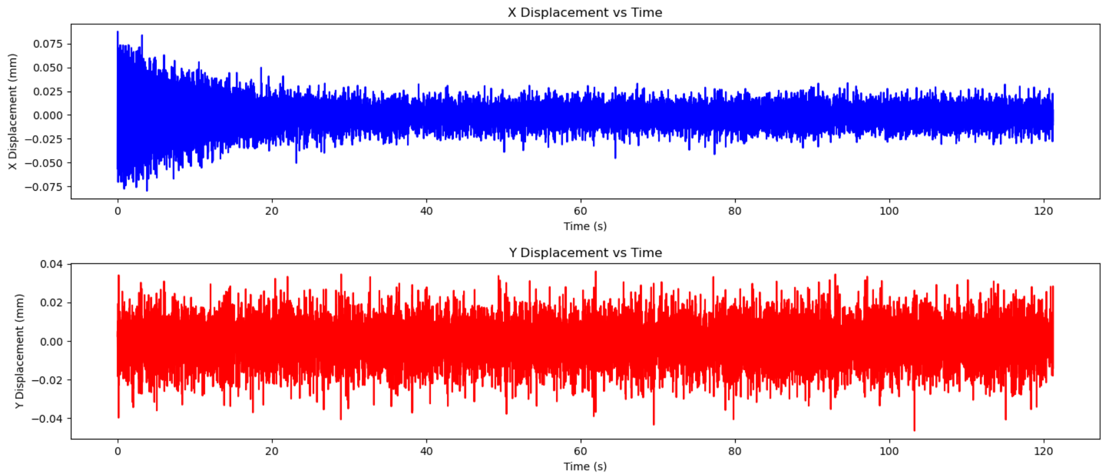

Fig. 8. X- and Y-axis displacement time series obtained using the Horn–Schunck optical flow method

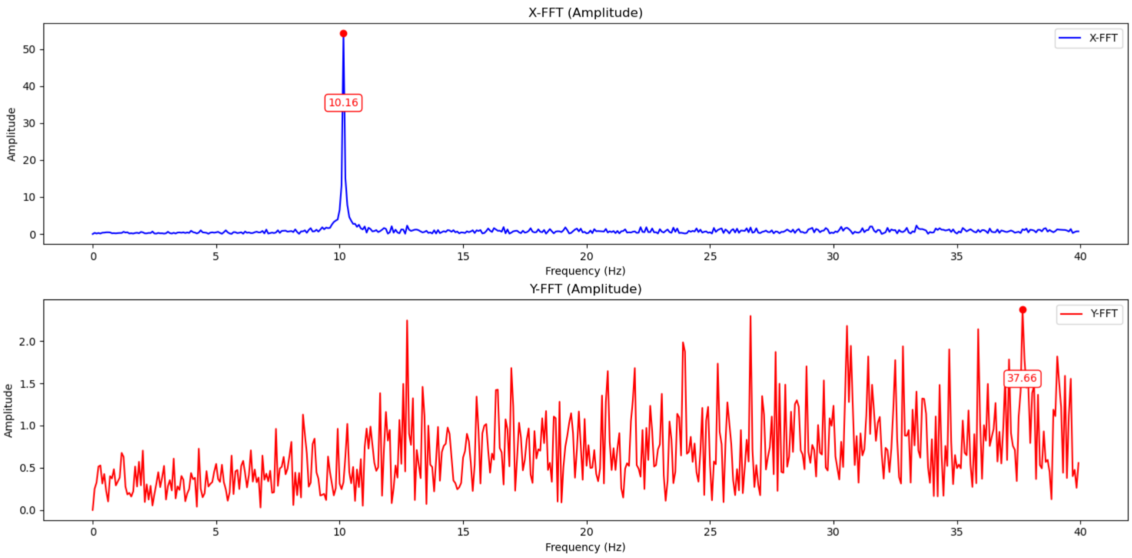

Fig. 9. Frequency spectra obtained using the Horn–Schunck optical flow method

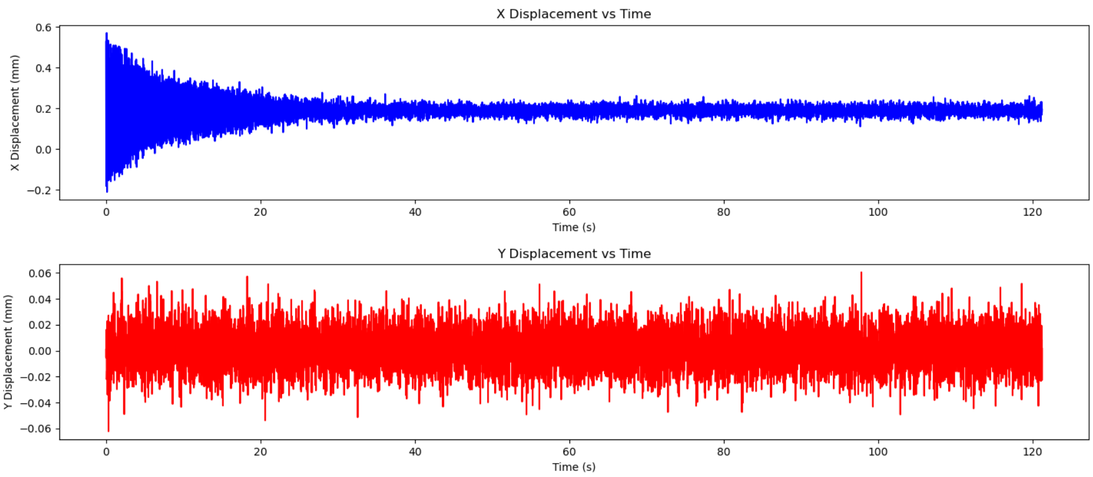

Fig. 10. X- and Y-axis displacement time series obtained using the Phase-based optical flow method

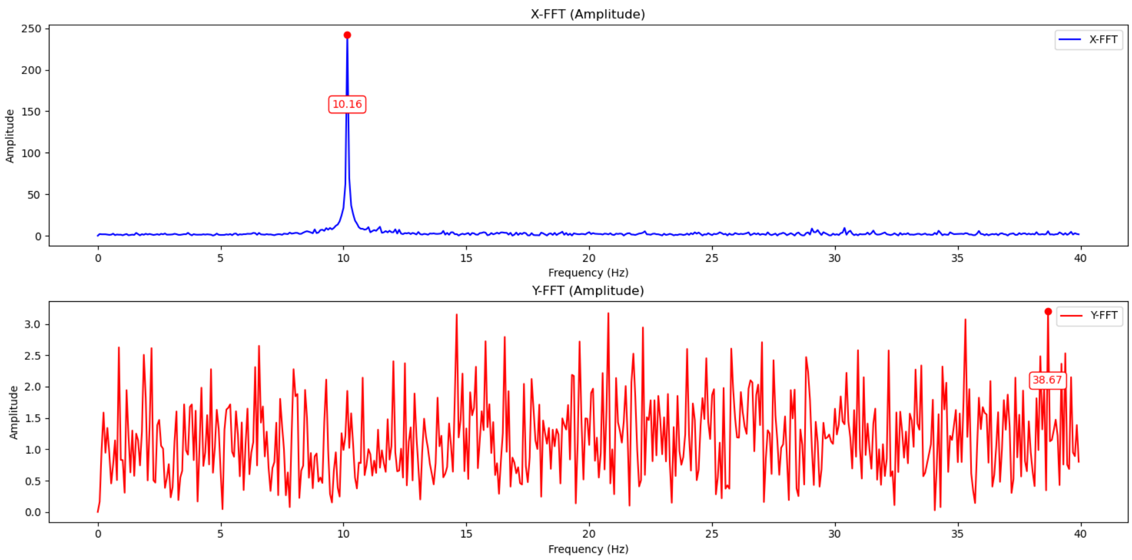

Fig. 11. Frequency spectra obtained using the Phase-based optical flow method

The Phase-based algorithm (Figs. 10 and 11) employed Fourier-domain phase correlation to capture robust, singular peaks at 10.16 Hz in both X and Y components. Its 2.28 s execution time makes it particularly attractive for applications demanding both speed and spectral accuracy.

According to the present study, the Phase-based and Lucas–Kanade methods achieved an optimal balance of speed and spectral clarity; Farnebäck provided enhanced flow-field integrity; and Horn–Schunck offered iterative smoothness. Depending on specific application requirements, the Phase-based approach is recommended for high-speed analyses; Lucas–Kanade for precise frequency studies; Farnebäck for detailed flow-map generation; and Horn–Schunck for scenarios requiring uniform displacement profiling.

6. Conclusion

In this study, a Python-based GUI application was developed to apply four optical flow algorithms to high-speed video for non-contact structural vibration analysis, featuring interactive ROI selection, scale calibration, and FFT-based frequency extraction. Benchmarking on 80 FPS data revealed that the phase-based and Lucas–Kanade methods achieve the optimal balance of speed and spectral accuracy; Farnebäck provides enhanced spatial coherence at a modest runtime increase; and Horn–Schunck yields the smoothest displacement profiles with a longer processing time. This versatile platform establishes an efficient foundation for camera-based SHM, with future work aimed at validating video-derived measurements against traditional sensors, optimizing the GUI for field use, and extending the methodology to more complex structural scenarios.

References

Antoni, J., & Randall, R. B. (2006). The spectral kurtosis: Application to the vibratory surveillance and diagnostics of rotating machines. Mechanical Systems and Signal Processing, 20(2), 308–331. https://doi.org/10.1016/j.ymssp.2004.09.002

Baker, S., & Matthews, I. (2004). Lucas–Kanade 20 years on: A unifying framework. *International Journal of Computer Vision, 56*(3), 221–255. https://doi.org/10.1023/B:VISI.0000011205.11775.fd

Barron, J. L., Fleet, D. J., & Beauchemin, S. S. (1994). Performance of optical-flow techniques. *International Journal of Computer Vision, 12*(1), 43–77. https://doi.org/10.1007/BF01420984

Bouguet, J. Y. (2001). *Pyramidal implementation of the Lucas-Kanade feature tracker* (Tech. Rep.). Intel Corporation, Microprocessor Research Labs.

Brox, T., & Malik, J. (2011). Large-displacement optical flow: Descriptor matching in variational motion estimation. *IEEE Transactions on Pattern Analysis and Machine Intelligence, 33*(3), 500–513.

Cha, Y. J., Choi, W., & Büyüköztürk, O. (2017). Deep learning-based crack-damage detection using convolutional neural networks. *Computer-Aided Civil and Infrastructure Engineering, 32*(5), 361–378. https://doi.org/10.1111/mice.12263

Farnebäck, G. (2003). Two-frame motion estimation based on polynomial expansion. In *Proceedings of the 13th Scandinavian Conference on Image Analysis* (pp. 363–370). Springer.

Feng, D., & Feng, M. Q. (2018). Computer vision for SHM of civil infrastructure: From dynamic response measurement to damage detection – A review. *Engineering Structures, 156*, 105–117. https://doi.org/10.1016/j.engstruct.2017.11.018

Fleet, D. J., & Jepson, A. D. (1990). Computation of component image velocity from local phase information. *International Journal of Computer Vision, 5*(1), 77–104. https://doi.org/10.1007/BF00056772

Gautama, T., & Van Hulle, M. M. (2002). A phase-based approach to the estimation of the optical-flow field using spatial filtering. *IEEE Transactions on Neural Networks, 13*(5), 1127–1136.

Hacıefendioğlu, K., Kahya, V., Limongelli, M. G., Okur, F. Y., Altunışık, A. C., Aslan, T., Pembeoğlu, S., Duman, C., Bostan, A., & Aleit, H. (2024). Applications of optical flow methods and computer vision in structural health monitoring for enhanced modal identification. *Structures*, *69*, 107414. https://doi.org/10.1016/J.ISTRUC.2024.107414

Horn, B. K. P., & Schunck, B. G. (1981). Determining optical flow. *Artificial Intelligence, 17*(1–3), 185–203. https://doi.org/10.1016/0004-3702(81)90024-2

Kuglin, C. D., & Hines, D. C. (1975). The phase correlation image alignment method. Proceedings of the IEEE International Conference on Cybernetics and Society, 163–165.

Lucas, B. D., & Kanade, T. (1981). An iterative image-registration technique with an application to stereo vision. In *Proceedings of the 7th International Joint Conference on Artificial Intelligence* (pp. 674–679).

Lydon, D., Lydon, M., Taylor, S., Del Rincon, J. M., & Hester, D. (2019). Development and field testing of a vision-based displacement system using a low-cost wireless action camera. *Mechanical Systems and Signal Processing, 121*, 343–358.

Pérez, J. S., Meinhardt, E., & Kondermann, D. (2013). Horn–Schunck optical flow with a multi-scale strategy. *Image Processing On Line, 3*, 151–172. https://doi.org/10.5201/ipol.2013.20

Sun, D., Roth, S., & Black, M. J. (2014). A quantitative analysis of current practices in optical-flow estimation and the principles behind them. *International Journal of Computer Vision, 106*(2), 115–137. https://doi.org/10.1007/s11263-013-0644-x

Wadhwa, N., Rubinstein, M., Durand, F., & Freeman, W. T. (2013). Phase-based video-motion processing. *ACM Transactions on Graphics, 32*(4), Article 80. https://doi.org/10.1145/2461912.2461966

Yang, J., Zhang, L., Chen, C., Li, Y., Li, R., Wang, G., Jiang, S., & Zeng, Z. (2020). A hierarchical deep convolutional neural network and gated recurrent unit framework for structural-damage detection. *arXiv* Preprint arXiv:2006.01045. https://doi.org/10.48550/arXiv.2006.01045

4th International Civil Engineering & Architecture Conference
17-19 May 2025, Trabzon, Türkiye

Delamination study when drilling on a carbon c-orthocryl composite used in civil structural strengthening

Farouk Mesrafet*[1], Younes Menail[1], Djaber Bouhafara[2]

[1] *Badji Mokhtar University, Department of Mechanical Engineering,LR3MI, Box 12, 23052 Sidi Ammar Annaba, Algeria*
[2] *National Higher School of Technology and Engineering, Laboratory of Energy Systems Technologies (LTSE), 23005 Annaba, Algeria.*

Abstract. Gaining Carbon composites are popularity in Civil construction applications due to their excellent strength-to-weight ratio and environmental compatibility. These materials are widely utilized to reinforce, retrofit, and rehabilitate concrete structures , and other civil structures, enhancing Building strength and overall quality of life. However, the long-term performance and durability of carbon composites against machining settings remain inadequately understood, especially at the microscopic level. The microscopic degradation of carbon composites in civil structures is a complex issue influenced by factors such as mechanical properties, environmental conditions, and manufacturing parameters. understanding the damage mechanisms is essential for ensuring the reliability and safety of articulations throughout their intended lifespan. Consequently, there is an urgent need for a comprehensive investigation into the microscopic degradation of carbon composites in civil applications. This research aims to fill this critical knowledge gap by thoroughly examining the microscopic degradation processes, particularly focusing on delamination. By utilizing advanced analytical techniques like scanning electron microscopy, we intend to reveal the morphological and mechanical changes occurring at the microscale, including delamination and decohesion. Furthermore, this study will assess the impact of various mechanical and environmental factors on the degradation behavior of carbon composites, offering valuable insights into their long-term performance in civil applications.

Keywords: Carbon; C-orthocryl; Delamination; Drilling; SEM; CFRP

1. Introduction

Because of their remarkable strength-to-weight ratio, corrosion resistance, and versatility when mixed with several matrices, carbon fiber reinforced polymer (CFRP) composites have drawn great interest in several application areas. Recent studies offer several angles on both the inherent qualities of carbon composites and the many techniques for its integration into sophisticated engineering uses. focusing on civil engineering, we combine developments in carbon-c orthocryl resin research in this paper, manufacturing processes, functional applications such reinforce, repair, and rehabilitate concrete buildings, and innovative material improvements using nanotechnology, carbon composites are being used more and more in civil engineering for structural strengthening and repair. Important processes to reduce bond deterioration were found by(Borrie, Al-saadi, Zhao, Singh Raman, & Bai, 2021), who also offered an in-depth analysis on bonded carbon-composite/steel systems. This is absolutely vital for the lifetime of strengthened structures.

Alongside this,(Pawlak, Górny, Dopierała, & Paczos, 2022) and(J. Wang, Su, & Gao, 2025) looked at pragmatic uses of composites advancements in fortifying both new and retrofitted buildings. Researches on the repair and rehabilitation of masonry structures (Fagone & Ranocchiai, 2017) and steel components (Kalavagunta, Naganathan, & Mustapha, 2014) underline even more the function of carbon composites in prolonging service lives and satisfying more load requirements. These findings highlight that carbon-epoxy is absolutely necessary for modern civil engineering infrastructure since its lifetime and fatigue resistance (Alam, Mamalis, Robert, Floreani, & Ó Brádaigh, 2019). In fields including fire safety improvements, composites have also developed into multifunctional materials. (Dagdag & Kim, 2024) also combined developments in via unique flame-retardant techniques, hence extending the application possibility of these composites in safety-critical settings. Particularly in the aerospace and automotive industries, where accuracy and low damage are vital, developments in manufacturing technology and processing techniques have greatly affected CFRP's use. Described by (Z. Wang et

---

* Corresponding author, E-mail: farouk.mesrafet@univ-annaba.dz

https://doi.org/10.31462/icearc2025_ce_sme_387

al., 2023) and (Zheng, Wu, Yu, Wang, & Ma, 2024), laser processing methods offer non-contact, high-quality machining options that address typical problems including delamination
and burr generation. (Ge, J., Zhang, J., Xu, M., Wu, M., Yao, Z., Fu, G., & Sun, 2025) also underlined smart machining techniques such as data-driven prediction and optimization, therefore demonstrating the changing power of combining machine learning with conventional production methods. essential for aerospace component manufacture and other high-value industrial applications, these methods allow improved surface quality and higher production. Recent research on material improvement has concentrated on adding nanoparticles to raise the interfacial characteristics of carbon composites. (Luo et al., 2024) examined how the inclusion of metal nanomaterial's, silicon-based, and carbon-based nanoparticles can greatly increase mechanical characteristics, impact resistance, and fiber-matrix adhesion. at the same time, (Liu, Du, & Liu, 2023) offered a methodical summary of microscopic characterization techniques—including SEM, TEM, and AFM—that are absolutely vital for interpreting the intricate interfacial interactions in these nano modified composites. these developments open the door for next-generation composites with customized qualities for particular uses by improving the structural integrity at the micro-scale.

Long-term performance and safety are still much dependent on inspection and quality assurance of carbon composites components. presented by (B. Wang et al., 2022), ultrasonic testing methods allow thorough flaw detection and offer a foundation for smart nondestructive evaluation tools. ultrasonic wave propagation in CFRP composites exposes vital information on internal delamination and other damage types, hence enabling a strong framework for maintenance plans and lifecycle management. tool geometry has also been highlighted as a key factor where traditional twist drills may produce too much thrust, causing more delamination in comparison to specially designed tools like tapered drill-reamers or drills with optimized point angles (Su, Wang, Yuan, & Cheng, 2015)(Feito, Diaz-Álvarez, López-Puente, & Miguelez, 2016)(Kamaruzaman, Hassan, & Razali, 2022). though with differing success as various mechanisms like chip evacuation and heat buildup become important during drilling operations, these sophisticated geometries aid to lower the critical axial force, hence controlling the beginning of delamination (Zhang, Hu, Wang, Wang, & Luo, 2024). creative drilling techniques including ultrasonic vibration-assisted drilling have also been presented as hopeful ways to further lower mechanical loads and thermal consequences supporting delamination. by encouraging a decrease in chip adhesion and local heating, these methods improve the integrity of the drilled holes. our research is founded on the application of the SEM to examine the various degradation facies of the samples. we aim to identify the several degradations and their influence on the life of the material examined by means of several micrographs at suitable magnifications.

2. Materials and methodes

The fabrication of carbon- c-orthocryl plate to reinforce concrete beams such as the one used prevesiouly by (Abdel-Jaber, Al-Nsour, Almahameed, & Ashteyat, 2025) Fig.1 even when finishing the molding process the final plates requires a machining for assembly purpose, we used in this study were conducted based on 2*2 twill weave carbon fiber Weave 245gr/m , and for the matrix we used a special c-orthocryl resin designated for carbon fiber tissue and with hardener (112P33), one unidirectional plate 100*50 cm were made by infusion molding under
0.8 Bar pressure Fig.2, 8 layers of the fabrics the obtained thickness of the laminates was h=3 mm , the laminates were cured at room temperature for 24 hours, then at 60 c° ,For 6 hours.

Fig. 1. Carbon reinforeced beams (Abdel-Jaber et al., 2025)

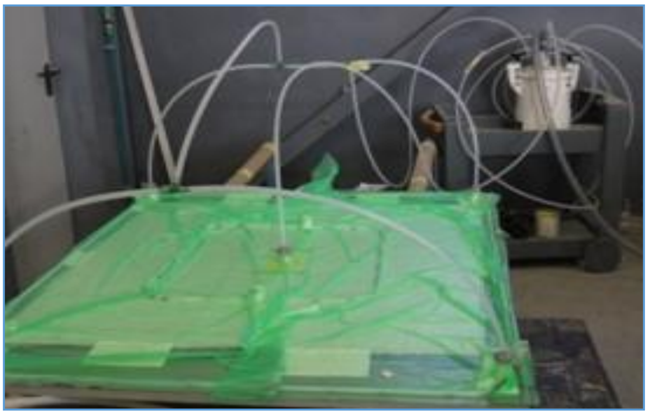

Fig. 2. Infusion moulding

2.1. Protocol

After polymerization, the plates were cut into parallelepipedic specimens of 220x30x2 mm3 and drilling process is conducted usig HSS twist drill-bit with a constant speed and feed rate v=900 rpm delamination happens at the entrance, exit, and even inside the hole Fig.3 , making the drilling process more prone to several kinds of defects (Quan & Sun, 2010). The major defects is directly related to the cutting tool's initial impact against the fiber-matrix interface causes delamination to start at the hole entrance. At the exit, however, the sudden loss of support causes fiber pull-out and crack propagation, therefore causing major damage(Hamamoto, Hirogaki, Aoyama, Fujiwara, & Taketani, 2023)(Shyha, Soo, Aspinwall, & Bradley, 2011) , Table 1 summurazie material used charactersitics .

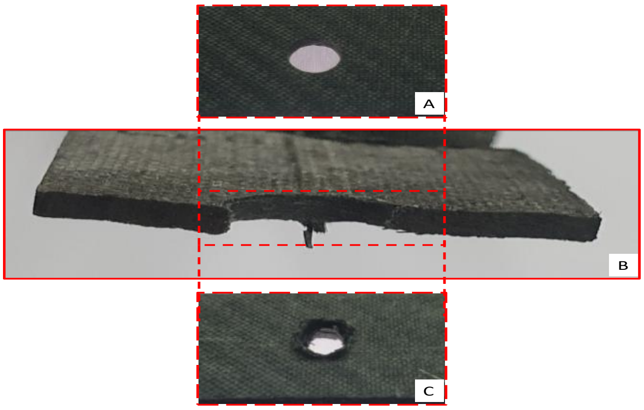

Figure 3 : Drilled specimen A: entry of the hole (peel-up) ,B: inside hole , C: exit of the hole (push-down)

Table 1. Material characteristics

Fiber	weaving	Surface density [g/m^2]	Mass fraction [%]	Supplier
Carbon	taffeta	300	35	Otto bock Germany
Resin	Layer	Weight [g]	Dimensions [mm^3]	
Epoxy c-orthocryl	3	12	220x30x2	

2.2 Microscopy

For absolute understanding of delamination when drilling this composite SEM analysis with assistance (Machine MEB), specimens were cut carefully from the drilled area of all holes with an HSS twist drill to ensure minimum marks were generated during the cutting process for a clear imaging surface. or image acquisition, a Quanta 250 In Fig. 4, SEM images were acquired in black scattered electron, the SEM images were treated using TrackerLab, the images were converted to grayscale, and the ellipse mask was applied to the region of interest.

We cut the control specimen in the longitudinal, transverse and frontal directions, Fig. 5. this cutting allows us to know the internal structure of the material and to detect possible moulding defects and fiber-resin compatibility.

Fig.4 SEM electronic mecroscopic Quanta 250

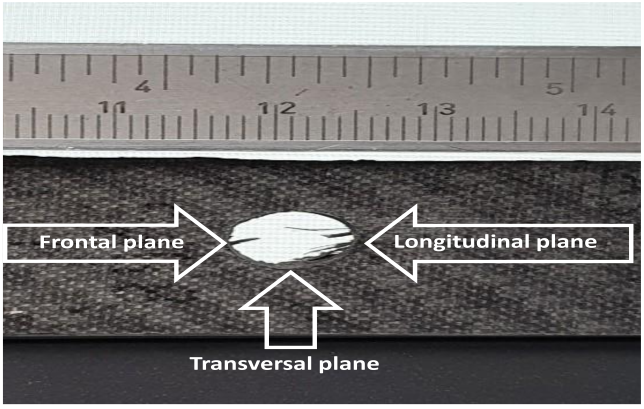

Fig.5 Different Plane according to the cross-sectional planes of the drilled hole

3. Results and discussion

3.1 Delamination in the different planes

3.1.1.Frontale plane

The obtained SEM images illustrate the different damages occuring in carbon-c-orthocryl composite in multiple locations during the drilling, highlighting intralaminar delamination and matrix tearing occurrences.Fig.6 magnified at 160x, displays considerable intralaminar delamination on the fracture surface inside hole.

The differences between separate laminates is apparent, marked by the visibility of aligned fiber bundles and the disruption of matrix homogeneity. the delamination seems to align with the fiber direction, indicating that the matrix distribution between the plies or inside the matrix was weakened under drilling process .the significant fiber pull-out and the existence of the hole fibers suggest that fracture propagation was mainly observed along the weak interlaminar planes, which is characteristic of multilayer composites subjected to out-of-plane or interlaminar loading. furthermore, matrix tearing occurs at various regions surrounding the fiber bundles.

These zones display a damaged and fractured appearance, indicating that the resin matrix failed to keep its cohesiveness during the crack propagation. the c-orthocryl resin brittle characteristics are indicated by the act of the fracture direction caused by the drill bit. Fig.7 taken at a lower magnification (56x), presents a wider perspective of the composite structure at the level of the hole entry. larger-scale delamination at the this , characterized by the separations and damages aligned with the fiber orientation. This macro-level damage corresponds with standard intralaminar delamination failure modes, where crack propagation is influenced by the anisotropic characteristics of the composite (Kamaruzaman et al., 2022) confirmed this is related to thrust force applied during the drilling , also the matrix regions exhibit increased degradation, characterized by matrix cracking and longitudinal tearing, understanding that the brittle fracture characteristic of the matrix under stress. the smooth portions between fiber-resin areas shows a good cohesion between the plies, while Fig.8 displays delamination ant the exit it appears noticeable , indicating the separation of the bottom nost layers, collectively these SEM pictures illustrate the initiation and propagation of intralaminar delamination along weak planes inside the composite, by matrix tearing, which acts as a mechanism for energy distribution but ultimately results in a catastrophic loss of structural integrity when drilling.

The observations align with failure scenarios in fiber-reinforced composites under high-stress or impact loading circumstances, where matrix-dominated failures against fiber failure.

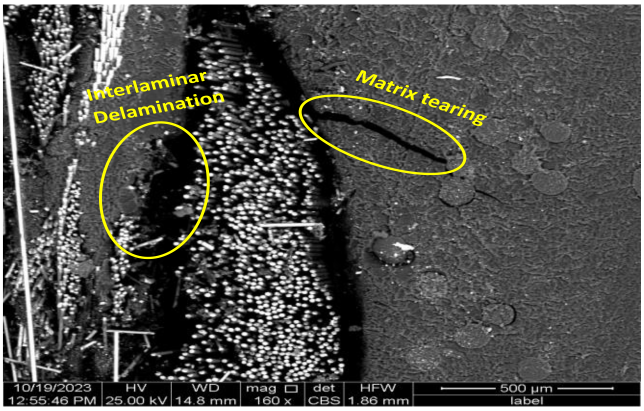

Figure 6 : SEM Image for frontal plane inside hole at 160X

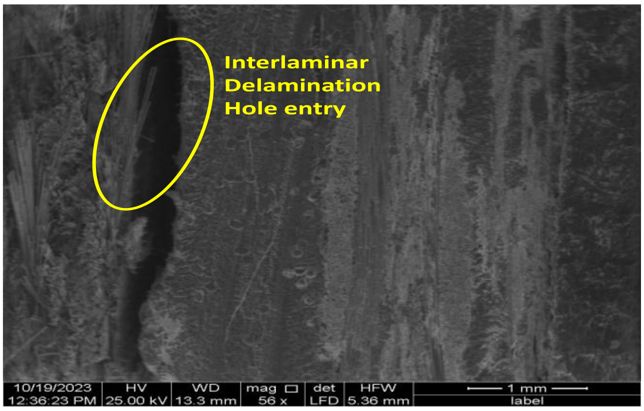

Figure 7 : SEM Image for frontal plane hole entry at 56 X

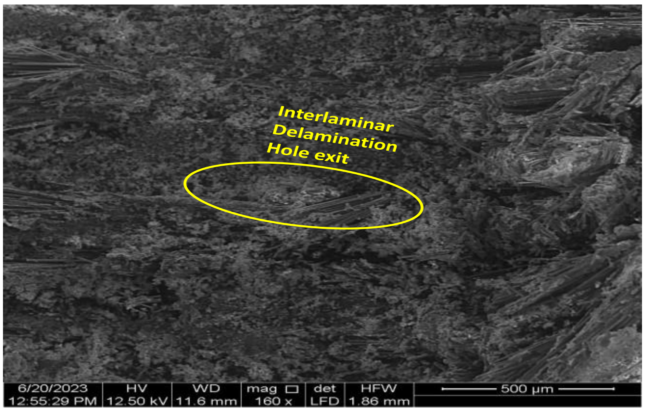

Figure 8 : SEM Image for frontal plane hole exit at 160 X

3.1.2 Longitudinal plane

The longitudinal plane micrographs shows an intralaminar delamination as a critical damage in carbon- c orthocryl composite throughout all the images. an intermediate stage of delamination, where several fiber layers are separated but still partially connected by broken fibers inside hole, is shown in Fig. 9 (120×).

While Fig. 11 taken at a higher magnification (300×) offers a detailed view of the crack network and exposed fibers at the exit of the hole, emphasizing the microstructural roughness caused by progressive damage, Fig. 9 (60×) shows the large scale of intralaminar delamination and the general fiber tearing morphology at the level inside hole .large fractures between inside fiber layers in Fig.9 and Fig.11 point to separation inside the laminate rather than complete interfacial fiber-matrix debonding. when the matrix toughness is too poor to resist fracture beginning and propagation under mechanical stress, a common feature is the separation seeming to propagate along the weak matrix-rich interlaminar regions.

The widespread, random voids point to slow delamination, due to the beginning with matrix microcracking and accelerating under greater thrust force (Sobri et al., 2020) explained this due to stress concentration generated by the drill bit . Fig.9, which shows a lesser magnification, clearly shows a weakened overall integrity of the laminate as it exposes multiple delamination planes producing a broken look. Fig.8 and Fig.10 reveal fiber ripping where bundles of fibers are damaged and pushed out at the hole exit. the fibers suggest they were under significant shear stress before collapse since they are ragged rather than smooth fiber breakage. this suggests that the fiber-matrix contact initially resisted debonding, directly transferring weight to the fibers until they tore rather than causing brittle fracture.the broken fibers in Fig.9, which project unevenly from the delaminated areas, underline that the load-bearing ability of the fibers contributed to the fracture resistance up to the point of failure.Fig.11 also shows some fibre ends exposed along the fracture paths, therefore supporting the idea of fibre rupture occurring parallel to matrix cracking and delamination.

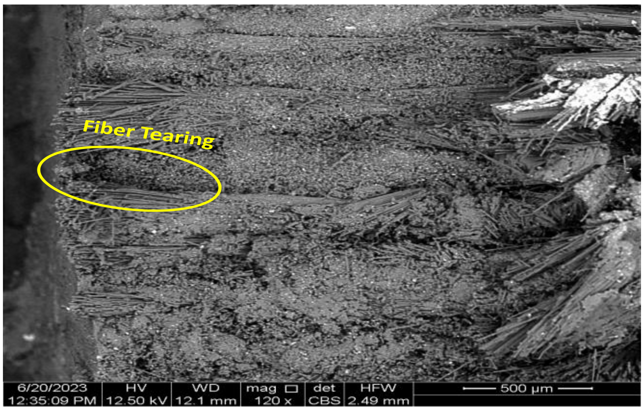

Figure 9 : SEM Image for Longitidunal plane inside hole at 120 X

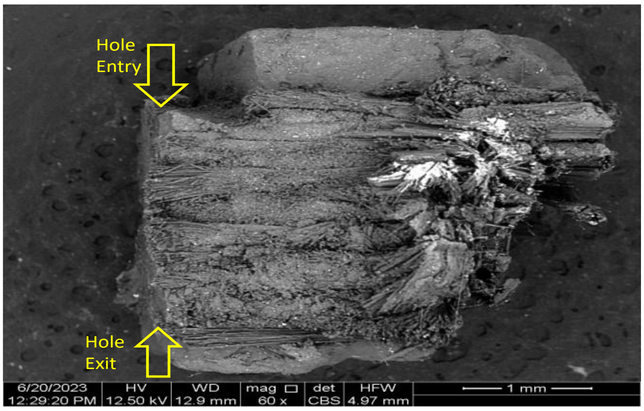

Figure 10 : SEM Image for Longitidunal plane at 60 X

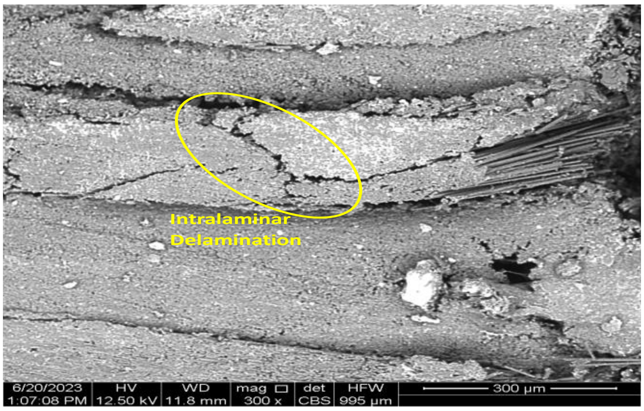

Figure 11 : SEM imagefor Longitudinal Plane hole exit at 300 X

3.1.3 Tranversal plane

Clear signs of translaminar delamination are seen in Fig. 12 and Fig. 13 at the hole enry and inside hole, unlike intralaminar delamination, which follows the plane between layers, on anther hand translaminar delamination cuts through both the matrix and the fiber bundles, usually perpendicular or at angles to the principal laminate planes and drilling direction. With delamination planes comprise across the thickness of the composite, several fiber bundles seem to have been displaced and split under 80× magnification in Fig. 12 the sharp boundaries between fiber-rich and matrix-rich regions imply that the fracture ran over the whole composite structure, cutting through the fiber and matrix phases both. where fiber bundles exhibit obvious symptoms of vertical cracking across their thickness, Fig. 13 (200× magnification) offers a closer view of the broken cross-section.

This translaminar cracking suggests that the crack energy was significant enough to fracture not only the matrix but also enter into the fiber tows, hence fostering deep-seated delamination routes, Fig.13 and Fig.14 show clear matrix decohesion. especially around the damaged fiber bundles at the interface inside and at the hole exit , notable voids and rough matrix surface areas are seen in Fig. 14 (200x magnification).

This structure shows matrix cracking and decohesion a failure mode in which excessive stress concentration or bad adhesion causes the c-orthocryl resin separates from the supporting fibers. (Haldar, Herráez, Naya, González, & Lopes, 2019) highlighted this during the fiber pull-up the due to energy dissipation generated by the drilling while (Bullegas, Pinho, & Pimenta, 2016) on the other hand demonstrated that the traslaminar delamination at pull-out in thin ply composites occurs crucially when the drill bit exit the last ply, fairly flat matrix surfaces and fiber imprints left behind verify that adhesive failure at the fiber-matrix contact have place. moreover, places where the matrix seems to have cracked or separated from fibers show the low energy absorption capacity of the matrix under drilling stress, leading to the beginning of decohesion.

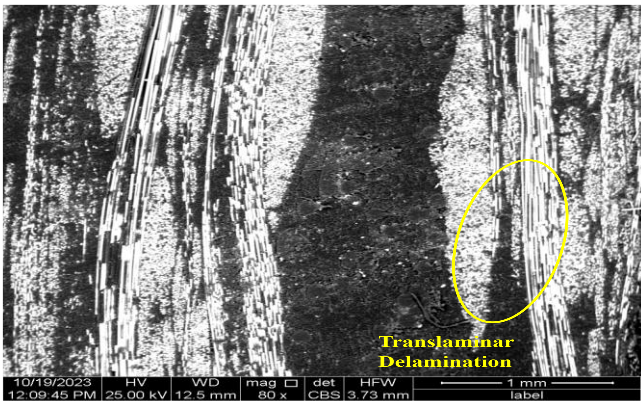

Figure 12 : SEM image for tranversal plane hole entry at 80 X

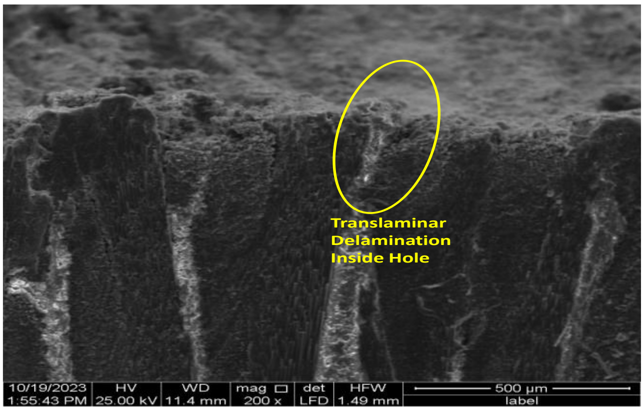

Figure 13 : SEM image for tranversal plane inside hole at 200 X

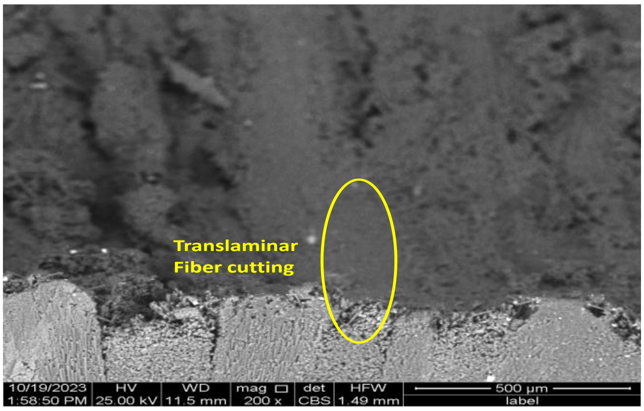

Figure 14 : SEM image for tranversal plane hole exit at 200 X

4. Conclusions

Drilling-related stresses mostly produce microdamages observed in the SEM analysis of the carbon-C-orthocryl composite across the frontale, longitudinal, and transversal planes.

- On the frontale plane Large interlaminar delamination in line with fiber orientations and significant matrix tearing in the frontale plane reveal the carbon-c orthocryl composite sensitivity to the drilling operation inside the hole and a the exit, straining the brittle matrix due to drilling induced thrust and shear force.
- the longitudinal plane micrographs draw attention to intralaminar delamination even more, so implying that inadequate matrix toughness generated slow but wide damage spread by means of progressive fiber tearing and matrix cracking.
- In the transverse plane, translaminar delamination predominated; cracks spreading across matrix regions and fiber bundles indicated that the fracture energy from drilling operation was sufficient to permeate both phases of the material. Moreover, the results indicate that matrix-dominated failures via matrix tearing, decohesion, and fiber ripping are quite significant for the overall drop in structural integrity during drilling operations in carbon-c-orthocryl composites.

Acknowledgments

We would like to express our gratitude to our colleagues (Dr. Menail Younes , Dr. Bouhafara Djaber) for their assistance and dedication in the preparation of the test plates and the SEM microscopy. It is important to note that the material utilized in this study was not funded by the University of Annaba. We would also like to express our gratitude to the individuals responsible for the operation and the manipulators of the SEM at the ENSMM (Ecole Nationale Supérieure des Mines et Métallurgie d'Annaba).

References

Abdel-Jaber, M., Al-Nsour, R., Almahameed, A., & Ashteyat, A. (2025). Comparative analysis of shear behavior in continuous low-strength RC beams strengthened with BFRP and CFRP: An experimental and numerical investigation. *Composites Part C: Open Access*, *16*(February), 100575. Elsevier B.V. Retrieved from

https://doi.org/10.1016/j.jcomc.2025.100575
Alam, P., Mamalis, D., Robert, C., Floreani, C., & Ó Brádaigh, C. M. (2019). The fatigue of carbon fibre reinforced plastics - A review. *Composites Part B: Engineering*, *166*, 555–579.
Borrie, D., Al-saadi, S., Zhao, X. L., Singh Raman, R. K., & Bai, Y. (2021). Bonded cfrp/steel systems, remedies of bond degradation and behaviour of CFRP repaired steel: An overview. *Polymers*, *13*(9).
Bullegas, G., Pinho, S. T., & Pimenta, S. (2016). Engineering the translaminar fracture behaviour of thin-ply composites. *Composites Science and Technology*, *131*, 110–122.
Dagdag, O., & Kim, H. (2024). Recent Advances in Fire Safety of Carbon Fiber-Reinforced Epoxy Composites for High-Pressure Hydrogen Storage Tanks. *Polymers*, *16(23)*(3343).
Fagone, M., & Ranocchiai, G. (2017). An experimental analysis of the mechanical behaviour of anchored CFRP-to-masonry reinforcements loaded by out-of-plane actions. *Key Engineering Materials*, *747 KEM*, 204–211.
Feito, N., Diaz-Álvarez, J., López-Puente, J., & Miguelez, M. H. (2016). Numerical analysis of the influence of tool wear and special cutting geometry when drilling woven CFRPs. *Composite Structures*, *138*, 285–294.
Ge, J., Zhang, J., Xu, M., Wu, M., Yao, Z., Fu, G., & Sun, D. (2025). Intelligent machining of cfrp composites via data-driven prediction and optimization: advances, challenges and future prospects. *Advances*, *challenges*.
Haldar, S., Herráez, M., Naya, F., González, C., & Lopes, C. S. (2019). Relations between intralaminar micromechanisms and translaminar fracture behavior of unidirectional FRP supported by experimental micromechanics. *Composites Part B: Engineering*, *174*.
Hamamoto, S., Hirogaki, T., Aoyama, E., Fujiwara, K., & Taketani, M. (2023). Drilling Holes in Cfrp for Aircraft Using Cbn Electroplated Ball End Mill Using Helical Interpolation Motion. *Proceedings of the ASME Design Engineering Technical Conference*, *5*.
Kalavagunta, S., Naganathan, S., & Mustapha, K. N. Bin. (2014). Axially loaded steel columns strengthened with CFRP. *Jordan Journal of Civil Engineering*, *8*(1), 58–69.
Kamaruzaman, M. F. S., Hassan, M. H., & Razali, M. F. (2022). Hole Quality Assessment of Drilled Carbon Fiber Reinforced Polymer (CFRP) Panel Using Various Custom Twist Drill Geometries. *Pertanika Journal of Science and Technology*, *30*(4), 2603–2612.
Liu, L., Du, M., & Liu, F. (2023). Recent advances in interface microscopic characterization of carbon fiber-reinforced polymer composites. *Frontiers in Materials*, *10*.
Luo, Y., Shi, Z., Qiao, S., Tong, A., Liao, X., Zhang, T., Bai, J., et al. (2024). Advances in nanomaterials as exceptional fillers to reinforce carbon fiber-reinforced polymers composites and their emerging applications. *Polymer Composites*.
Pawlak, A. M., Górny, T., Dopierała, Ł., & Paczos, P. (2022). The Use of CFRP for Structural Reinforcement—Literature Review. *Metals*, *12*(9).
Quan, Y., & Sun, L. (2010). Investigation on drilling-induced delamination of CFRP with infiltration method. *Advanced Materials Research*, *139–141*, 55–58.
Shyha, I. S., Soo, S. L., Aspinwall, D. K., & Bradley, S. (2011). The effect of peel ply layer on hole integrity when drilling carbon fibre-reinforced plastic. *Proceedings of the Institution of Mechanical Engineers, Part B: Journal of Engineering Manufacture*, *225*(7), 1217–1223.
Sobri, S. A., Whitehead, D., Mohamed, M., Mohamed, J. J., Amini, M. H. M., Hermawan, A., Rasat, M. S. M., et al. (2020). Augmentation of the delamination factor in drilling of carbon fibre-reinforced polymer composites (CFRP). *Polymers*, *12*(11), 1–14.
Su, F., Wang, Z., Yuan, J., & Cheng, Y. (2015). Study of thrust forces and delamination in drilling carbon-reinforced plastics (CFRPs) using a tapered drill-reamer. *International Journal of Advanced Manufacturing Technology*, *80*(5–8), 1457–1469.
Wang, B., He, P., Kang, Y., Jia, J., Liu, X., & Li, N. (2022). Ultrasonic Testing of Carbon Fiber-Reinforced Polymer Composites. *Journal of Sensors*, *2022*.
Wang, J., Su, X., & Gao, Q. (2025). A Review of the Applications of CFRP Reinforcements in Civil Engineering. *E3S Web of Conferences*, *617*.
Wang, Z., Ma, Y., Yuan, B., Wu, C., Li, C., & Sun, S. (2023). Development of Laser Processing Carbon-Fiber-Reinforced Plastic. *Sensors*, *23*(7).
Zhang, Y., Hu, Z., Wang, G., Wang, L., & Luo, Q. (2024). Establishment of CFRP drilling simulation model considering heat accumulation effect and study on its delamination damage. *International Journal of Advanced Manufacturing Technology*, *134*(3–4), 1699–1710.
Zheng, Z., Wu, C., Yu, X., Wang, Z., & Ma, Y. (2024). Research progress on laser processing of carbon fiber-reinforced composites. *International Journal of Advanced Manufacturing Technology*.

4th International Civil Engineering & Architecture Conference
17-19 May 2025, Trabzon, Türkiye

Measurement of residual stiffness of cracked segmental girder using multi-reference impact testing

Arka Mandal[1], J. M. Chandra Kishen[*1]

[1] *Indian Institute of Science, Department of Civil Engineering, 560012 Bangalore, India*

Abstract. Cracking is one of the most observed defects in reinforced concrete structures. This is due to the low tensile strength of concrete. Many of the infrastructures such as bridges, viaducts, etc suffer from severe cracking at the construction stages itself due to accidental loadings. In this work, the residual stiffness of a cracked segment of a metro viaduct under construction is determined using the dynamical characteristics through multi-reference impact testing. Cracked and uncracked segments are subjected to impact loading using an instrumented hammer. Accelerometers are mounted on these segments to measure their vibration parameters. The time histories are converted into frequency domain to determine their natural frequency. Important conclusions regarding the factor of safety and the effect of cracks on the stiffness parameters are obtained which are used to classify the cracks as structural or non-structural.

Keywords: Impact testing; Stiffness; Structural health monitoring; Natural frequency

1. Introduction

Cracking in concrete structures is the most unwanted and unavoidable feature that might cause some undesirable effects on the serviceability of the structure. Agents like fatigue, creep and corrosion adversely affect the structure in such a way as the design loads of the structures that they are fully capable of bearing without any sign of distress, can cause observable deterioration (Larosche, 2009). Under such weakening mechanisms, the load resisting stiffness reduces, which implies the lowering of the load bearing capacity. Another source of cracking is the work progress loads, where the structure is not yet ready for service (Mandal et al., 2023). Under this category most of the cracks occur and since these cracks are during the early stages of the construction, repair must be done quickly to continue with the further work without compromising the safety (Buitrago et al., 2020).

Therefore, these structures need to be monitored quite regularly and thus the methods adopted must be very feasible and efficient at the same time. Among the several techniques available like acoustic emission testing, ultrasonic testing and impact based vibration testing, the last one is supposedly the most versatile one.

The conventional nondestructive methods need a long term evaluation period which may not be available or be feasible for the regular monitoring of important structures like bridges, flyovers, etc. This issue is not faced in the case of vibration based techniques, as the structural condition is interpreted in terms of the stiffness calculated from the measured vibration response to an excitation (Saidin et al., 2023). Evaluating the structural stiffness form the natural frequency is one of the efficient yet effective methods for experimental modal analysis (Ewins, 2000). However, there are cracks that do not affect structural stiffness significantly, and such cracks are termed as the non-structural cracks, while the cracks that affect stiffness are known as the structural cracks (Kwak et al., 2006). Classifying these cracks are of utmost importance as spending a lot of time in excessive retrofitting which is not at all efficient for the development and consumes resources as well. These cracks usually do not form due to service loads, but due to early age shrinkage, exothermal concrete hydration or due to accidental loads during the construction stage (Qu et al., 2024). The fundamental operational principle by assessing the structure in the Fourier domain is explained in the upcoming section.

2. Basics of operational modal analysis

To understand the basics of the working principle of the impulse hammer test, a single degree of freedom system is considered with m, c and k representing the mass, damping and stiffness respectively with zero initial conditions.

$$m\ddot{x} + c\dot{x} + kx = f(t), x(0) = 0, \dot{x}(0) = 0 \tag{1}$$

[*] Corresponding author, E-mail: chandrak@iisc.ac.in

https://doi.org/10.31462/icearc2025_ce_sme_396

The response to the applied force *f(t)* is evaluated by the Duhamel's principle as:

$$x(t) = \int_0^t h(t-\tau)f(\tau)d\tau = \int_{-\infty}^{\infty} h(t-\tau)f(\tau)d\tau, f(\tau) = 0\ \forall\ \tau < 0, h(t-\tau) = 0\ \forall\ \tau > t \tag{2}$$

Where, *h(t)* is the impulse response function and the system is considered to be causal so there is no response until the force *f(t)* is applied. The response x(t) is in the time domain, Fourier transform of which will change the domain from time to frequency as:

$$X(\omega) = \int_{-\infty}^{\infty} x(t)e^{-i\omega t}dt \leftrightarrow x(t) = \frac{1}{2\pi}\int_{-\infty}^{\infty} X(\omega)e^{i\omega t}d\,\omega \tag{3}$$

Where, *X(ω)* is the Fourier domain response of the same quantity *x(t)* and similarly two more Fourier pairs are constructed as:

$$H(\omega) = \int_{-\infty}^{\infty} h(t)e^{-i\omega t}dt \tag{4}$$

$$F(\omega) = \int_{-\infty}^{\infty} f(t)e^{-i\omega t}dt \tag{5}$$

From the convolution operation of the Duhamel's integral given in Equation 2, the Fourier equivalent operation becomes:

$$X(\omega) = H(\omega)F(\omega) \tag{6}$$

To find the value of the transfer function *H(ω)* in Equation 6, the governing differential equation of motion in Equation 1 is converted into the Fourier domain with the following components:

$$\dot{x}(t) = \frac{1}{2\pi}\int_{-\infty}^{\infty} i\omega X(\omega)e^{i\omega t}\,d\omega \tag{7}$$

$$\ddot{x}(t) = \frac{1}{2\pi}\int_{-\infty}^{\infty} -\omega^2 X(\omega)e^{i\omega t}\,d\omega \tag{8}$$

Finally, the governing equation of motion becomes:

$$\int_{-\infty}^{\infty} [(-m\omega^2 + i\omega c + k)X(\omega) - F(\omega)]e^{i\omega t}d\omega = 0 \tag{9}$$

Since the integral is zero for all values of *ω*, the integrand must me zero, with the exponential part as non-zero as usual. The expression for the transfer function *H(ω)* in Equation 6 becomes:

$$X(\omega) = \left[\frac{1}{-m\omega^2 + i\omega c + k}\right]F(\omega) \tag{10}$$

As discussed earlier, for the impact hammer test, basically the structure is excited using a sledge hammer, which basically implies that the forcing function *f(t)* is an impulse, but here just for simplicity the magnitude is assumed to be unity. The forcing function becomes:

$$\int_{\infty}^{\infty} \delta(t)e^{-i\omega t}dt = 1, f(t) = \delta(t) \tag{11}$$

where, *δ(t)* is the Dirac's delta operator. Therefore, the final expression for the displacement function becomes:

$$X(\omega) = H(\omega) = \frac{1}{-m\omega^2 + i\omega c + k} \tag{12}$$

The amplitude of the complex function H(ω) is given as:

$$|H(\omega)| = \left|\frac{1}{-m\omega^2 + i\omega c + k}\right| = \frac{1}{|-m\omega^2 + i\omega c + k|} = \frac{1}{\sqrt{(k - m\omega^2)^2 + (\omega c)^2}} \tag{13}$$

This expression of the amplitude of the complex transfer function *H(ω)* plays the pivotal role in the entire operational modal analysis subject. As it can be seen in Equation 13, the denominator under the root contains sum of two squared quantities, and for the *H(ω)* to be maximum, the quantity under the root has to be minimum. The second term cannot be zero but the first one can. The value of the frequency *ω* at which the first bracket term of Equation 13 goes to zero is the natural frequency of the structure. This is why the responses in the time domain is measured and then the peak of the Fourier transform is computed. One point to observe is that, the accelerations are measured using accelerometers instead of the displacement and their Fourier transforms are computed. This can be explained as, we know for a single degree of freedom system with zero initial conditions, the impulse response has the form:

$$x(t) = e^{-\eta\omega t}\,sin(\omega_d t), \omega_d = \omega\sqrt{1-\eta^2}, \eta = \frac{c}{2\sqrt{km}} \tag{14}$$

Double differentiating x(t) with respect to time gives:

$$\ddot{x}(t) = e^{-\eta\omega t}sin\left(\omega_d t - \tan^{-1}\left(\frac{2\eta\omega\omega_d}{(\eta\omega)^2 - (\omega_d)^2}\right)\right)\left[\sqrt{(-\omega_d^2 + \eta^2\omega^2)^2 + (2\eta\omega\omega_d)^2}\right] \tag{15}$$

Equation 15 reveals that, the displacement and the acceleration both have the same frequency, but the amplitudes and phases are different, which does not alter the position of the maxima of their respective transfer functions. Now it is understood that the location of the peak of frequency spectrum of the acceleration response gives the natural frequency of vibration. In reality most of the structures continuous systems which are approximated as multi degree of freedom systems. In such cases, there will be multiple spikes, but the peak will represent the first mode of vibration, which is the frequency of primary interest.

The acceleration response is measured using accelerometers which are usually accompanied with bandpass filter which sets a lower and upper bounds for the frequencies captured by the data acquisition system, which is why most of the times the zero frequency measurements are neglected as it may be erroneous, or else the zero value would have given the static stiffness, evident from Equation 12.

3. Methodology implemented

To classify the cracks as non-structural and structural, the first intuitive idea is to check for the loss of stiffness due to the formation of cracks. As mentioned in the preceding section, most of the real-life structures are continuous in nature with complicated geometries. Therefore, for this section, the discussion shall include a cantilever beam with a notch at some strategic location so as to check its effect. The governing differential equation of a beam in terms of its length *L*, density *ρ*, area of cross section *A* and flexural rigidity *EI*, is given as:

$$\frac{\partial^4 v}{\partial x^4} + \frac{\rho A}{EI} \cdot \frac{\partial^2 v}{\partial t^2} = 0 \tag{16}$$

where, *v(x,t)* is the deflection at abscissae *x* at a time instant *t*. This equation is derived from the Lagrangian *H* of the elemental strips of the beam given as:

$$H = \frac{1}{2}\int_0^L \left[\rho A \left(\frac{\partial v}{\partial t}\right)^2 - EI\left(\frac{\partial^2 v}{\partial x^2}\right)^2\right] dx \tag{17}$$

Equation 17 reveals that, the origin of the governing differential Equation 16 is dependent upon the deflection of the individual elemental strips. This gives an idea that, for the strips whose effective deflection is zero or negligible, the effect on the differential equation would not be significant and hence the natural frequency will not be affected (Gillich & Praisach, 2014). The general solution to Equation 16 is assumed to have the variable separable form:

$$v(x,t) = \phi(x)e^{i\omega t} \tag{18}$$

The new form of the governing equation after substitution becomes an eigen value problem as:

$$\frac{d^4\phi(x)}{dx^4} - \lambda\phi(x) = 0, \lambda^4 = \left(\frac{\omega^2 \rho A}{EI}\right) \tag{19}$$

The mode shape function *ϕ(x)* has the general solution as:

$$\phi(x) = c_1 \sin(\lambda x) + c_2 \cos(\lambda x) + c_3 \sinh(\lambda x) + c_4 \cosh(\lambda x) \tag{20}$$

where, the constants c_1, c_2, c_3 and c_4 depends upon the boundary conditions, and for a cantilever beam they are:

$$\phi(x)|_{x=0} = \left.\frac{d\phi(x)}{dx}\right|_{x=0} = \left.\frac{d^2\phi(x)}{dx^2}\right|_{x=L} = \left.\frac{d^3\phi(x)}{dx^3}\right|_{x=L} = 0 \tag{21}$$

The null space solution of Equation 20 evaluates to:

$$\cos(\lambda L)\cosh(\lambda L) + 1 = 0 \tag{22}$$

The solutions to the above trigonometric equation for the first three modes are:

$$\lambda_1 L = 1.875,\ \ \lambda_2 L = 4.694,\ \ \lambda_3 L = 7.855$$

and the natural frequency *f* in cycles per second for the mode number *n* is given by:

$$f_n = \frac{(\lambda_n L)^2}{2\pi L^2}\sqrt{\frac{EI}{\rho A}} \tag{23}$$

The mode shape for number n is given as:

$$\phi_n(x) = c_2\left[\cos(\lambda_n x) - \cosh(\lambda_n x) + \frac{\sin(\lambda_n L) - \sinh(\lambda_n L)}{\cos(\lambda_n L) + \cosh(\lambda_n L)}\{\sin(\lambda_n x) - \sinh(\lambda_n x)\}\right] \tag{24}$$

For the second mode, there exists a node where the mode shape function of Equation 24 goes to zero at *x = 0.783L*. Since it is a node, then there is no displacement and hence a notch should not affect much. To check this, a model is constructed in ABAQUS with the following specifications and appropriate units as given in Table 1.

Table 1. Specifications of the beam modelled in ABAQUS.

Length	Width	Depth	Modulus of Elasticity	Density	Poisson's ratio
mm	mm	mm	N/mm^2	tonne/mm^3	

500	50	20	210×10^3	7.8×10^{-9}	0.28

Theoretically, the value of the natural frequency for the first mode of vibration is 67 *Hz*, and the ABAQUS model with tetrahedral elements with the beam modelled as a deformable solid with one face encased gave 67.21 *Hz*.

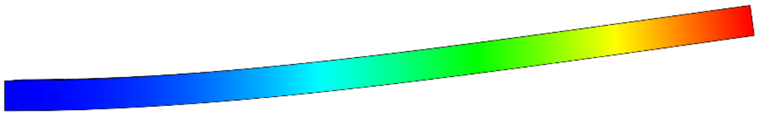

Fig. 1. Deformed shape of uncracked cantilever beam

Fig. 1 shows the deformed shape of the beam and for a later case to study the effect of a notch at the node, which in this case is starts at an abscissa of 391.5 *mm* and ends at 392.5 *mm*. The height of the notch is 15 *mm* and it produced a natural frequency of 66.92 *Hz*.

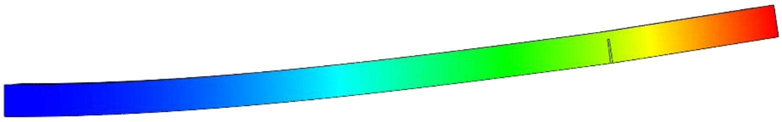

Fig. 2. Introduction of a notch at the node of mode number 1

The notch in this case is introduced by reducing the area of cross section by the area of the notch. The percentage loss of stiffness assuming that the change in mass is neglected, is *0.88%* roughly. Now, a notch of exactly same dimension is placed at a distance of 70 *mm* from the encased fixed boundary. Now the deformed beam is shown in Fig. 3.

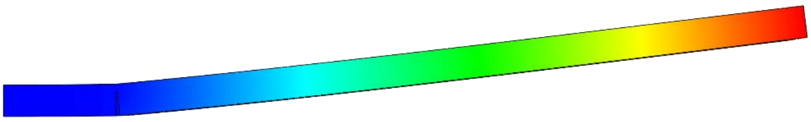

Fig. 3. Notch near the fixed end

Due to the introduction of this notch, there is a drastic loss of the natural frequency. The new natural frequency is 37.018 *Hz*, which means there is a loss

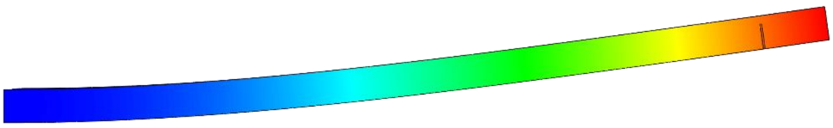

Fig. 4. Notch near the free end

Another notched case is considered where the notch is placed very close to the free end is shown in Fig 4., at a distance of 40 *mm* from the free end, so as to ensure that the notch at the mode one has the least effect. The natural frequency for this case is very close to the discussed case, but is lower. The natural frequency is 66.54 *Hz*. This shows that the node is the safest point in the cantilever beam, since the natural frequency of interest is the first one. Since the node is for the second mode, the natural frequency of vibration was about 419 *Hz*, exactly same as that of the uncracked beam. With this idea, a box girder was assessed using the vibration test.

4. Instrumentation and test program

A concrete box girder segment was reported to have some observable cracks near the joint between the flange and the web. Usually, cracks in these locations are not structural because they are in the compression side of the beam, and this is concept is kept in mind while designing the beam for loads acting downwards, like the gravity load. When these girders are lifted and placed on the bearings of the columns, sometimes due to some eccentricity or due to fast pulling of the crane shaft, there might be a vertical force acting on the joint that might cause tensile stresses in the zone which is expected to resist compressive loads. Under static cases, these cracks are dormant, but these types of girders are used for the metro system, they carry heavy and fast moving trains. Under the action of the wheel loads, there might be stress reversals, that may allow the crack to extend. Therefore, to check for the activeness of the cracks, dynamic tests are the most ideal ones.

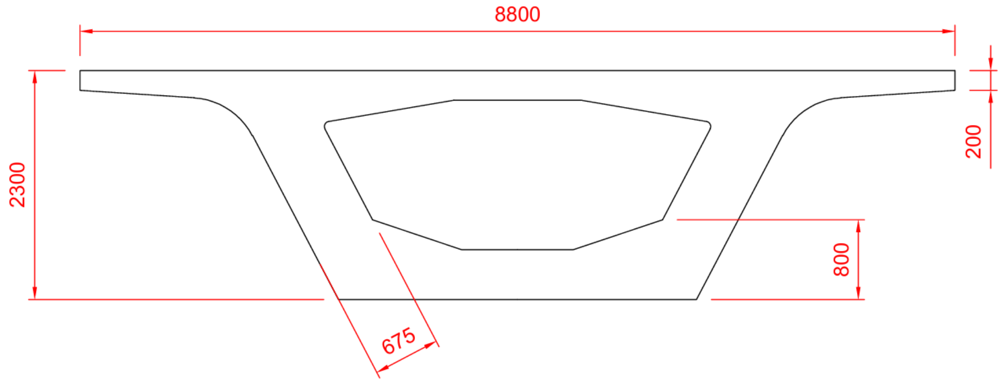

Fig. 5. Geometry of the box girder segment of length 3000 *mm* (All dimensions in *mm*)

An instrumented hammer was utilized to set the structure into vibration and accelerometers were placed on the cantilever flanges, so as to measure the vibrations (Kishen et al., 2013). Two accelerometers were utilized for this study, so as to ensure that the crack has not propagated, by the Maxwell-Betti's theorem.

First the hammer was struck near accelerometer one, and the responses of both the accelerometers were recorded, then the hammer was hit near the accelerometer two and the responses were recorded. If there were a significant amount of crack, there will be a difference in the cross responses of the two accelerometers (Raghavendrachar & Aktan, 1992). A 64-channel data acquisition system manufactured by M/s DEWETRON was used to capture the data continuously from the pair of accelerometers. First the acquisition was turned on and after that the hammer was hit and the data was recorded till the acceleration decayed significantly. An input from the hammer is shown in Fig. 6.

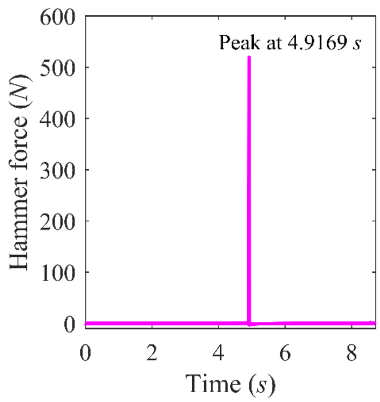

Fig. 6. Impulse input to the system when hammer is struck near accelerometer one

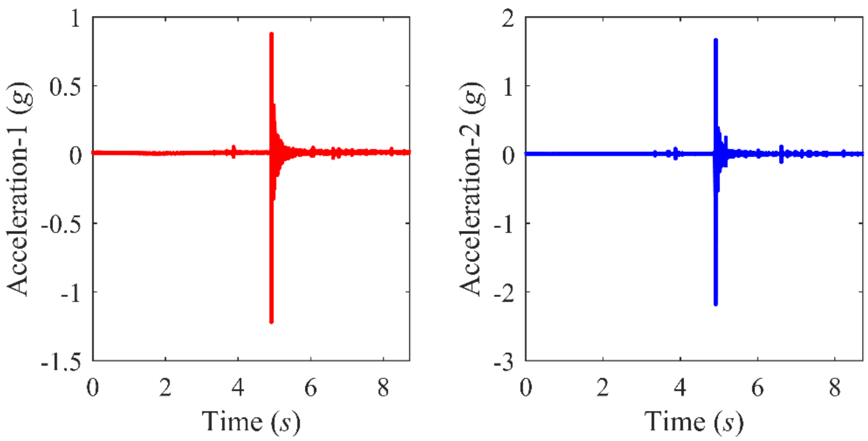

Fig. 7. Accelerometer responses to the excitation by the hammer strike near accelerometer one

Fig. 7 shows the responses of the accelerometers when the hammer is struck near the accelerometer one. Similarly, this process is further repeated once again near the accelerometer two, but sufficient time was given each time in between tests so that residual vibrations are decayed. Every time the accelerometers were calibrated using the calibrator and the surfaces on which they are supposed to be mounted by silicon grease were finely sanded so as to ensure adequate contact. The hammer tip made of rubber used for all the tests were the stiffest available and was calibrated using the hung mass technique so as to get the conversion factors from millivolts to Newtons. Also, the vibrations prior to the hammer strike were minimized so as to minimize the errors.

5. Results and discussions

The natural frequency was obtained by the Fast Fourier Transform (FFT) technique using MATLAB. The FFT was applied on the last few seconds of the signal after hammer hit, as this constituted the free vibration of the structure. The key step while computing the FFT is the sampling frequency. As per the Nyquist-Shannon sampling theorem, the sampling frequency must be at least twice the highest frequency present in the signal, and for this case it was taken care of by generating the frequency spectrum till the value which is half of the actual data acquisition frequency. The results for the hit shown in Fig. 6 are shown in Fig. 8.

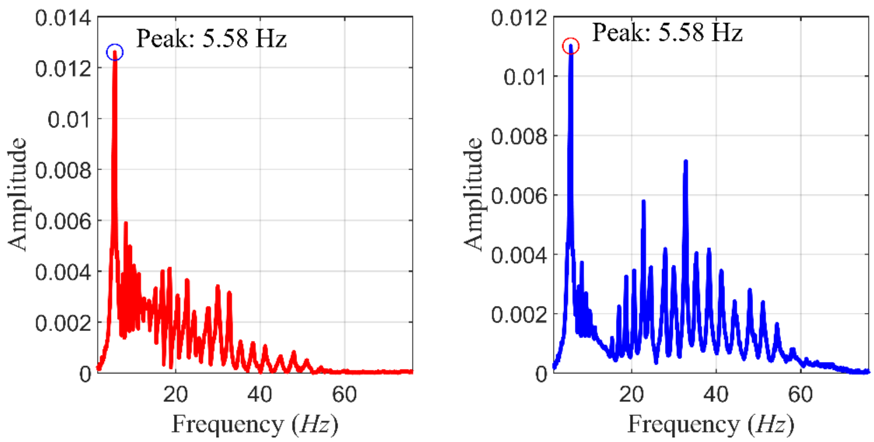

Fig. 8. Acceleration spectra in Fourier domain when hammer is struck near accelerometer one

The first observable feature is that the frequencies are same for both the accelerometers indicating that there are not enough micro-cracks that might contribute to damping and essentially lower the recorded frequency. However, to ensure that the stiffness is intact, the responses have to be considered when the hammer was struck near the second accelerometer.

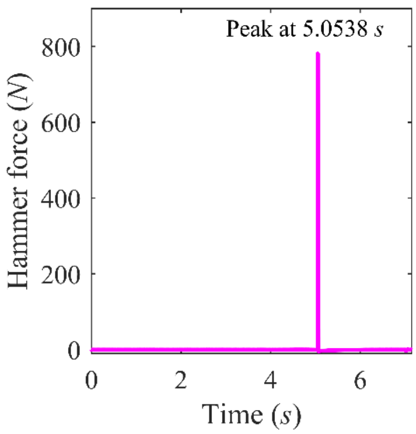

Fig. 9. Impulse input to the system when hammer is struck near accelerometer two

Due to the input of Fig. 9, the time domain responses of the accelerometers are shown in Fig. 10. The natural frequencies are obtained using the FFT technique, and the results are shown in Fig. 11.

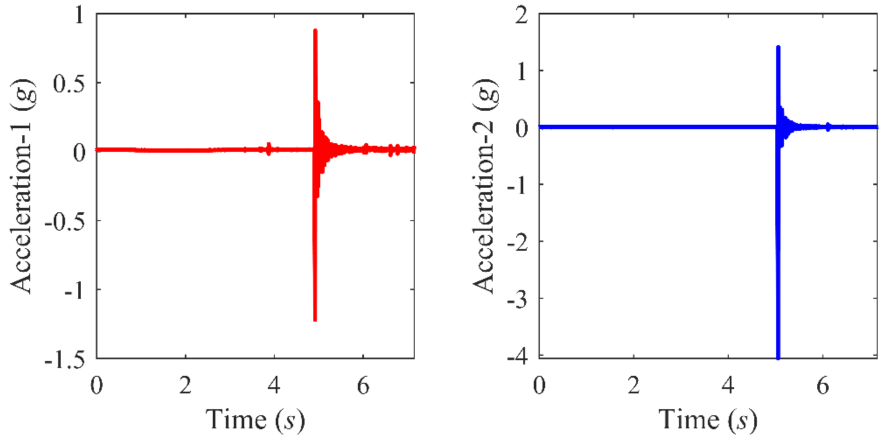

Fig. 10. Accelerometer responses to the excitation by the hammer strike near accelerometer two

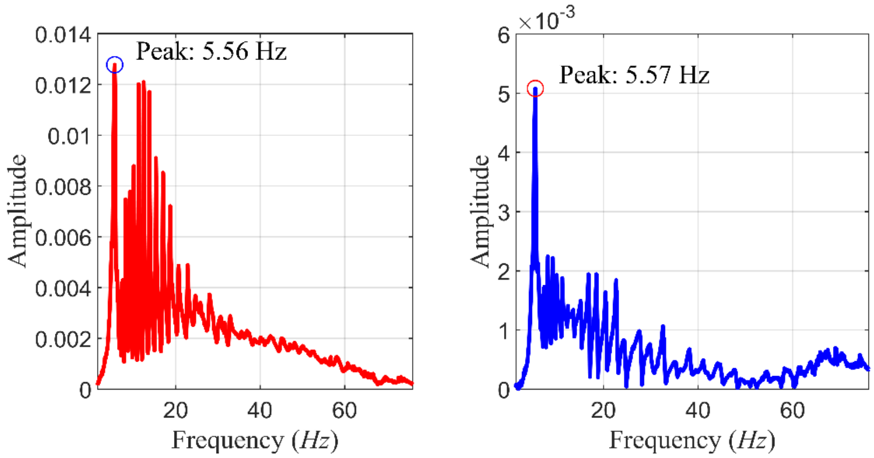

Fig. 11. Acceleration spectra in Fourier domain when hammer is struck near accelerometer two

The frequency is nearabout the same for the alternate cases, which ensures the reliability of the readings. To check whether the crack is really dormant, a model was prepared in ABAQUS with the specified geometry as shown in Fig. 5. The mode shapes indicate that the region of interest is always within the nodal zone.

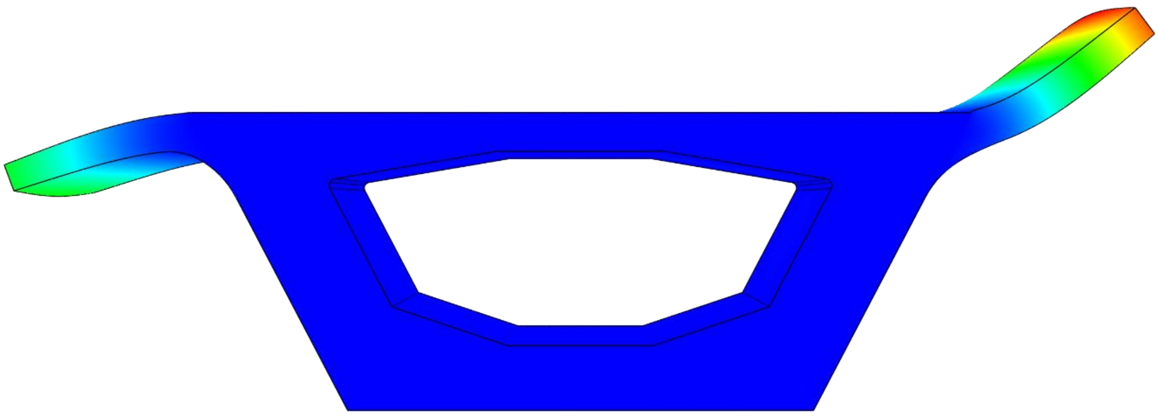
Fig.12. First mode shape of the girder

In fact, this remains in the nodal zone even for the second mode as shown in Fig. 13.

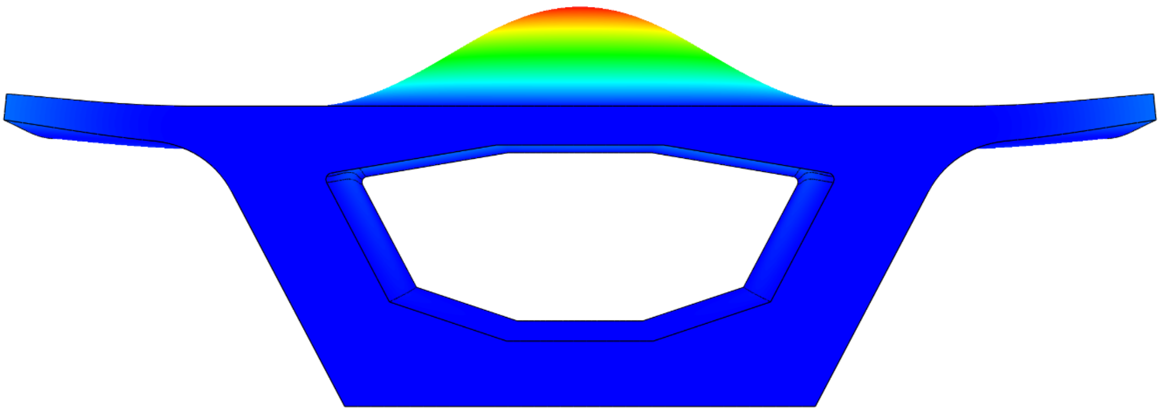

Fig. 13. Second mode shape of the girder

This natural frequency computed from the numerical model in ABAQUS was 5.73 *Hz*, which is very close to the obtained frequencies from the FFT of the time domain signals obtained. Therefore, it can be concluded that the cracks occurring in the nodal regions do not impose a sever threat to the structure, but still there is a reduction in the natural frequency. This loss can however be regained easily with minimal retrofits, and moreover all these types of girders used for metro will have railway tracks laid on them. Those steel tracks will enhance the stiffness to a huge extent and ultimately after the construction the differences would not be evident.

6. Conclusions

The results as obtained from the vibration test using the impact hammer, show that the cracks caused in the region of joint of the cantilever flanges with the web of the girder do not impose a serious issue to the structure. Even though they are dormant, due to corrosion of the reinforcements, or due to fatigue action, these cracks may propagate so it is better to take at least the minimum prescribed or the necessary retrofits. In this study, there was indeed a change in the natural frequency, but was not significant so the crack can be classified as a non-structural one.

In fact, if test reports are available for the intact girders, and if any crack appears in the future, the vibration tests on the affected segment can be used to classify the cracks as structural or non-structural based on the percentage change in the natural frequency of vibration and also the importance of the structure.

- The vibration tests are capable of assessing the structure within a very short span of time, and that too with adequate reliability.
- For this study, two accelerometers were used in order to check the modal reciprocity which is also a very good test regarding the increase in damping due to presence of micro-cracks, that may not be evident from the change in the natural frequency.
- The natural frequency obtained from the tests were very close to the one obtained from the numerical model, thus showing that the crack in the joint in between the flange and the web is an inactive zone.

As a future scope, these preliminary conclusions need to be investigated further by involving the transfer matrix approach to estimate the actual modal mass and the modal stiffness. Also, to reinforce this idea, modal acceptance criteria on more number of tests will be imposed so as to minimize the chances of instrumentation and experimental errors.

References

Buitrago, M., Sagaseta, J., & Adam, J. M. (2020). Avoiding failures during building construction using structural fuses as load limiters on temporary shoring structures. *Engineering Structures*, *204*, 109906. https://doi.org/10.1016/j.engstruct.2019.109906

Ewins, D. J. (2000). Basics and state-of-the-art of modal testing. *Sadhana*, *25*(3), 207–220. https://doi.org/10.1007/BF02703540

Gillich, G. R., & Praisach, Z. I. (2014). Modal identification and damage detection in beam-like structures using the power spectrum and time-frequency analysis. *Signal Processing*, *96*(PART A), 29–44. https://doi.org/10.1016/j.sigpro.2013.04.027

Kishen, J. M. C., Ramaswamy, A., & Manohar, C. S. (2013). Safety Assessment of a Masonry Arch Bridge: Field Testing and Simulations. *Journal of Bridge Engineering*, *18*(2), 162–171. https://doi.org/10.1061/(ASCE)BE.1943-5592.0000338

Kwak, H.-G., Ha, S.-J., & Kim, J.-K. (2006). Non-structural cracking in RC walls. *Cement and Concrete Research*, *36*(4), 749–760. https://doi.org/10.1016/j.cemconres.2005.12.001

Larosche, C. J. (2009). Types and causes of cracking in concrete structures. In *Failure, Distress and Repair of Concrete Structures* (pp. 57–83). Elsevier. https://doi.org/10.1533/9781845697037.1.57

Mandal, A., Samanta, A. K., & Ghosh, S. (2023). *A Deep Insight into the Design Methodology of T-Beam Bridge Girders as Per the Guidelines of IRC: 112–2020 Compared to the Conventional Method* (pp. 197–210). https://doi.org/10.1007/978-981-19-4040-8_17

Qu, Z., Zhang, Y., Liu, Z., Si, R., & Wu, J. (2024). A review on early-age cracking of concrete: Causes and control. *Case Studies in Construction Materials*, *21*, e03848. https://doi.org/10.1016/j.cscm.2024.e03848

Raghavendrachar, M., & Aktan, A. E. (1992). Flexibility by Multireference Impact Testing for Bridge Diagnostics. *Journal of Structural Engineering*, *118*(8), 2186–2203. https://doi.org/10.1061/(ASCE)0733-9445(1992)118:8(2186)

Saidin, S. S., Kudus, S. A., Jamadin, A., Anuar, M. A., Amin, N. M., Ya, A. B. Z., & Sugiura, K. (2023). Vibration-based approach for structural health monitoring of ultra-high-performance concrete bridge. *Case Studies in Construction Materials*, *18*. https://doi.org/10.1016/j.cscm.2022.e01752

4th International Civil Engineering & Architecture Conference
17-19 May 2025, Trabzon, Türkiye

Automated structural crack detection using a deep learning-based YOLO algorithm and robotic dog

Ayşecan Bostan*[1], Kemal Hacıefendioğlu[1]

[1] Karadeniz Technical University, Department of Civil Engineering, 61080 Trabzon, Türkiye

Abstract. This study aims to automatically detect cracks in structural elements using the YOLO object detection algorithm, based on Deep Learning techniques, integrated with robotic dog technology. This approach seeks to enhance both the accuracy and efficiency of structural health monitoring processes. The study begins with the selection of appropriate datasets via the Roboflow platform, where a dataset consisting of 2,600 annotated crack images was utilized for model training. Training was conducted in the Google Colab environment, resulting in the development of an object detection model. Additionally, a segmentation model was created using the same dataset to ensure more precise crack boundary delineation. The performance of the trained models was evaluated through real-time tests using images captured by cameras mounted on the Unitree Go2 Edu Plus robotic dog. These tests were conducted on a reinforced concrete frame with induced cracks at the Structural Health Monitoring Laboratory of Karadeniz Technical University. The images were processed in real-time using YOLO models, enabling immediate crack detection. The findings demonstrate that the robotic system, combined with the YOLO algorithm, effectively detects cracks in real-time with high accuracy. This study highlights the potential of integrating Deep Learning and robotic technologies for structural health monitoring, offering a reliable and efficient solution for damage assessment in civil engineering applications. The results validate the proposed approach as a practical and dependable method for automated structural crack monitoring.

Keywords: Crack detection; Robotic dog; YOLO models; Deep Learning; Object detection

1. Introduction

Earthquakes are natural disasters that cause extensive physical destruction and significant loss of life on a large scale. In the aftermath of such catastrophic events, the rapid and reliable assessment of the structural integrity of buildings is of critical importance. Traditional damage detection methods primarily rely on manual inspections, which are often time-consuming, labor-intensive, and susceptible to human error. These limitations underline the necessity of developing innovative and automated approaches that can deliver fast and accurate evaluations of structural conditions (Qayoumi et al., 2025; Jia & Ye, 2023).

Recent advancements in robotics and artificial intelligence (AI) offer promising opportunities to revolutionize post-disaster structural assessments (Zhai et al., 2024; Ye et al., 2022). In this context, the primary aim of this study is to develop an integrated system that utilizes robotic technologies and deep learning-based methods for the rapid and automated detection of structural damages. The project involves the integration of the Unitree Go2 robotic dog platform with the YOLOv8 deep learning model to enable real-time detection of cracks, deformations, and other structural damages on building surfaces.

The robotic dog is designed to move safely and efficiently even in challenging terrain conditions. It is equipped with advanced sensors and reinforced with artificial intelligence algorithms, allowing it to autonomously explore and inspect areas that are difficult or dangerous for human access. Through the use of a deep learning model capable of processing environmental images, the system can accurately identify and classify structural damages without the need for human intervention (Morfidis et al., 2023; Ilmak et al., 2024).

Another significant feature of the developed system is its ability to process data in real time, providing operators with instant information and comprehensive reporting during inspections. This capability ensures that critical decisions can be made rapidly, which is particularly vital in the immediate aftermath of earthquakes when timely interventions can save lives and prevent further structural failures.

By combining robotic mobility, advanced sensing technologies, and AI-driven damage detection, this study aims to offer a fast, reliable, and efficient solution for post-earthquake structural assessments. The proposed system

*Corresponding author, E-mail: aysecanbostan61@gmail.com

https://doi.org/10.31462/icearc2025_ce_sme_419

represents a significant step forward in enhancing the effectiveness of disaster response efforts and minimizing the risks associated with manual inspection methods.

2. Materials and methods

The following section provides a comprehensive overview of the key components utilized in the study, including the robotic dog platform, the YOLO algorithm, the dataset employed for training and testing, and the testing model. These elements are essential for understanding the methodology and the process of damage detection that forms the basis of this research.

2.1. Unitree Go2 Robotic Dog

The Unitree Go2 is a next-generation robotic dog model developed by the Chinese robotics company, Unitree Robotics. It features a quadrupedal structure resembling that of a cat or dog. The Go2 builds upon the experience gained from previous models such as the A1, Go1, and AlienGo. Designed for both industrial and individual use cases, it offers advanced performance, agility, and enhanced artificial intelligence (AI) capabilities.

One of the most prominent features of the Go2 is its advanced mobility. Thanks to its quadrupedal design, it is capable of maintaining balance even in rugged terrains. The robot can easily navigate difficult environments, including stairs and obstacles, making it versatile in various scenarios. Compared to earlier models, the Go2's maximum speed has been increased, and its acceleration has been significantly improved, enhancing its overall performance.

In terms of artificial intelligence and sensing capabilities, the Go2 is equipped with a range of sensors, including depth cameras and LiDAR, enabling it to perceive its surroundings in three dimensions. The robot can perform functions such as object recognition, obstacle detection, and path planning with high accuracy. The combination of a powerful processor and AI algorithms further boosts the robot's ability to process data in real-time, enhancing its responsiveness to environmental changes.

Additionally, the durability and portability of the Go2 are noteworthy. Constructed with lightweight yet robust materials, its body is resistant to impacts and falls, ensuring longevity even in challenging environments. The robot's rechargeable battery allows for extended periods of continuous operation, and different battery options may be available depending on the application. Furthermore, its foldable or easily portable design makes it convenient to transport from one location to another, offering practicality for various use cases. The Unitree Go2 robot dog and its equipment are shown in Fig. 1.

Fig. 1. Unitree Go2 robotic dog and equipment

2.2.YOLO (You Only Look Once) algorithm

YOLO (You Only Look Once) is a computer vision model introduced by Joseph Redmon, Santosh Divvala, Ross Girshick, and Ali Farhadi at the CVPR conference in 2016, where it gained significant attention. Winning OpenCV's "People's Choice" awards, YOLO is a single-stage detector that performs object detection and classification through a single network pass (Nelson, 2025).

Among single-stage detection models, YOLO remains one of the most well-known and widely used frameworks. However, it is not the only example of such models; for instance, MobileNetSSDv2 is another popular single-stage detector. Nonetheless, YOLO often demonstrates superior performance compared to other models in terms of both speed and accuracy.

YOLO models approach the object detection task through a single-shot regression method that predicts the bounding boxes of objects directly. This approach provides high processing speed and a compact network structure. These characteristics make YOLO not only an efficient tool for accelerating the training process but also highly suitable for deployment on edge devices with limited computational resources.

An example illustrating the working principle of YOLO is presented in Fig. 2 below. The visual representation clearly demonstrates the process of detecting and classifying objects by identifying their bounding boxes.

Thanks to these advantages, YOLO has become a highly preferred model in a wide variety of practical applications. Its ability to balance accuracy and speed has led to its widespread adoption across both academic research and industry sectors. Furthermore, the model's efficiency in resource-constrained environments makes it a practical choice for real-world deployments where computational power may be limited.

YOLO models appeal to a wide range of developers due to their ability to be trained on a single GPU. Machine learning practitioners can deploy these models at a low cost, either on edge devices or in cloud environments. The speed offered by YOLO is particularly advantageous in scenarios that require real-time object detection.

Before the emergence of YOLO, R-CNNs were commonly used for object detection; however, their slow processing speeds made them unsuitable for real-time applications. In contrast, YOLO greatly facilitates rapid inference tasks in applications such as vehicle detection, animal recognition, and security surveillance, where fast and accurate detection is critical.

YOLOv8 represents a state-of-the-art advancement in computer vision, developed by Ultralytics, the organization behind the widely adopted YOLOv5 model. Designed to address a variety of tasks—including object detection, image classification, and instance segmentation—YOLOv8 combines cutting-edge performance with developer accessibility through an intuitive command-line interface (CLI) and a well-structured python package. This dual interface approach significantly lowers the barrier to entry for both novice and experienced practitioners, promoting widespread adoption across research and industry.

A major innovation distinguishing YOLOv8 from its predecessors is its anchor-free architecture. Unlike traditional models that rely on predefined anchor boxes to estimate object locations, YOLOv8 directly predicts object centers. This design shift results in enhanced localization accuracy, reduced computational complexity, and improved inference speed, making the model particularly well-suited for real-time applications on both high-performance and resource-constrained devices.

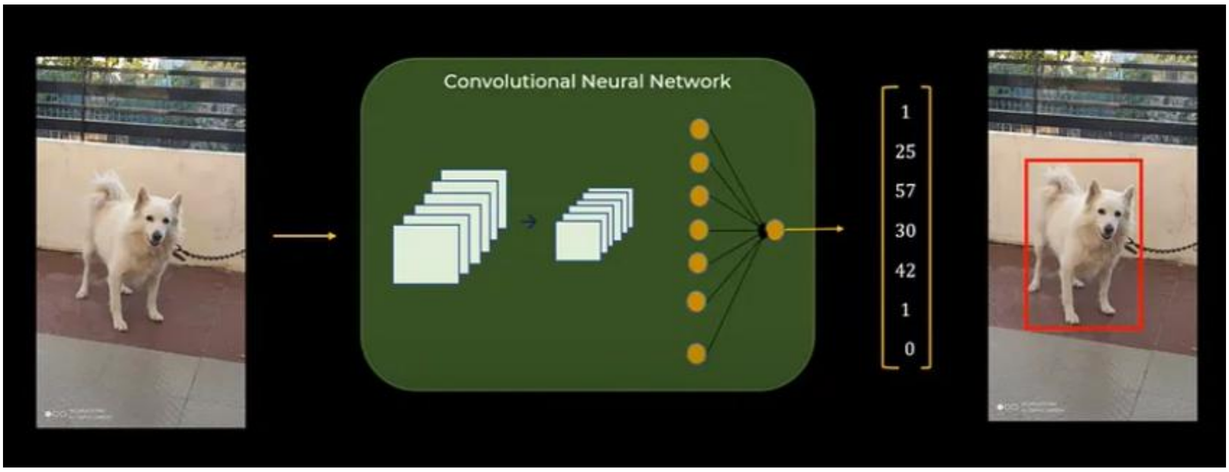

Fig. 2. General working mechanism of YOLO (Kumar, 2022)

Table 1. YOLOv8 detection models comparison (Ultralytics, 2025)

Model	Size (pixels)	mAPval (50-95)	Speed CPU (ms)	Speed T4 GPU (ms)	Params (M)	FLOPs (B)
YOLOv8n	640	37.3	-	-	3.2	8.7
YOLOv8s	640	44.9	-	-	11.2	28.6
YOLOv8m	640	50.2	-	-	25.9	78.9
YOLOv8l	640	52.9	-	-	43.7	165.2
YOLOv8x	640	53.9	-	-	68.2	257.8

In this study, the YOLOv8n model, whose features are presented in Table 1, has been selected. YOLOv8n operates with a 640x640 pixel input size and achieves a mAP (50-95) value of 37.3%. The model has only 3.2 million parameters (M) and 8.7 billion FLOPs (floating point operations). Due to its lightweight structure and low computational cost, it is particularly suitable for resource-constrained systems.

2.3. Characteristics of the dataset used

The dataset used in this study was obtained from the Roboflow platform. Roboflow is a comprehensive platform that provides all the necessary tools for creating, developing, and deploying computer vision models. The platform offers flexible usage by enabling integration at any step of the pipeline through APIs and SDKs. Additionally, it provides end-to-end interface support to automate the image processing workflow from start to finish.

Roboflow Annotate is an online annotation tool specifically designed for labeling images in tasks such as object detection, classification, and segmentation. This tool facilitates the accurate and rapid annotation of images, streamlining the dataset preparation process. These features significantly enhance the quality of the dataset used in this study, making a substantial contribution to the computer vision model development process. A visual taken from the Roboflow homepage is presented in Fig. 3.

The dataset used in this study consists of a total of 3,255 crack images. All these images have been carefully labed to precisely indicate the locations of the cracks. The dataset is divided into three groups for model training and evaluation: "training," "validation," and "test."

- Training Group: The largest group used for model training, consisting of 2,658 annotated images.
- Validation Group: This group, containing 300 annotated images, is used to evaluate the accuracy of the model during the training process.
- Test Group: This group, consisting of 297 annotated images, is reserved to independently assess the model’s performance.

The meticulous preparation of this dataset significantly contributes to achieving high accuracy and reliability during the model training and evaluation processes. The labeling process ensured that the data was processed in a clear and consistent manner, positively impacting the model’s performance.

Example excerpts from the image and label files in the dataset are presented in Fig. 4 and 5 below. These excerpts provide a clearer visual understanding of the dataset structure and the annotation format used.

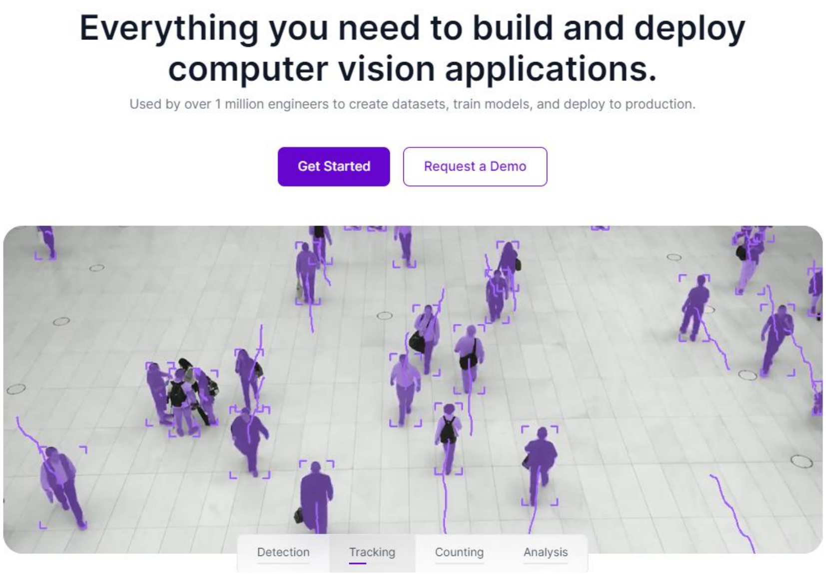

Fig. 3. Roboflow homepage (Roboflow, 2025)

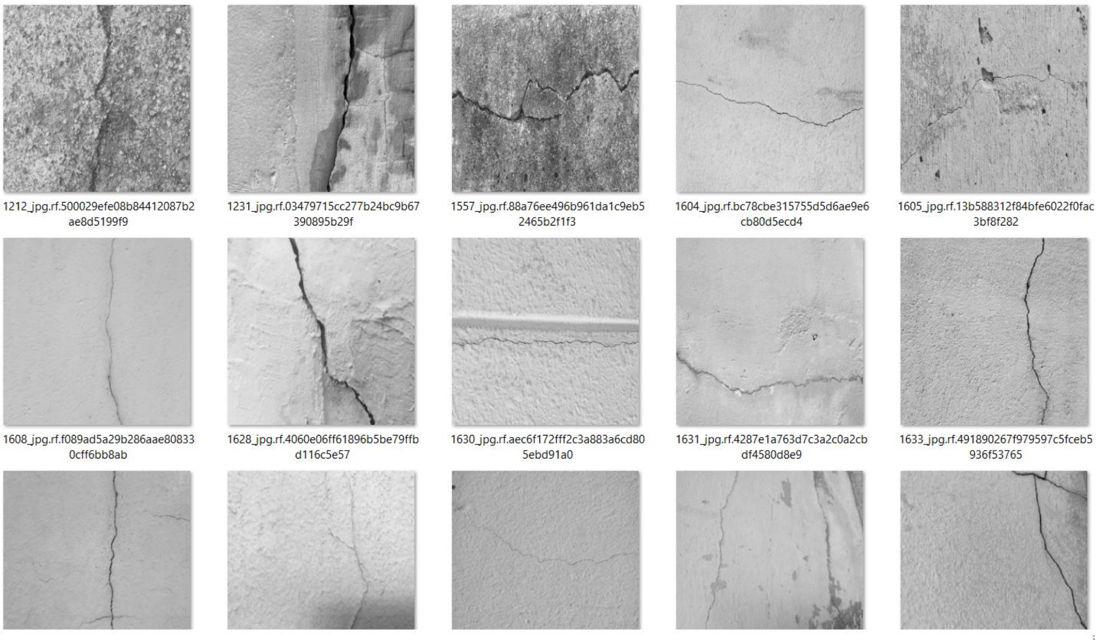

Fig. 4. Sample images from the dataset

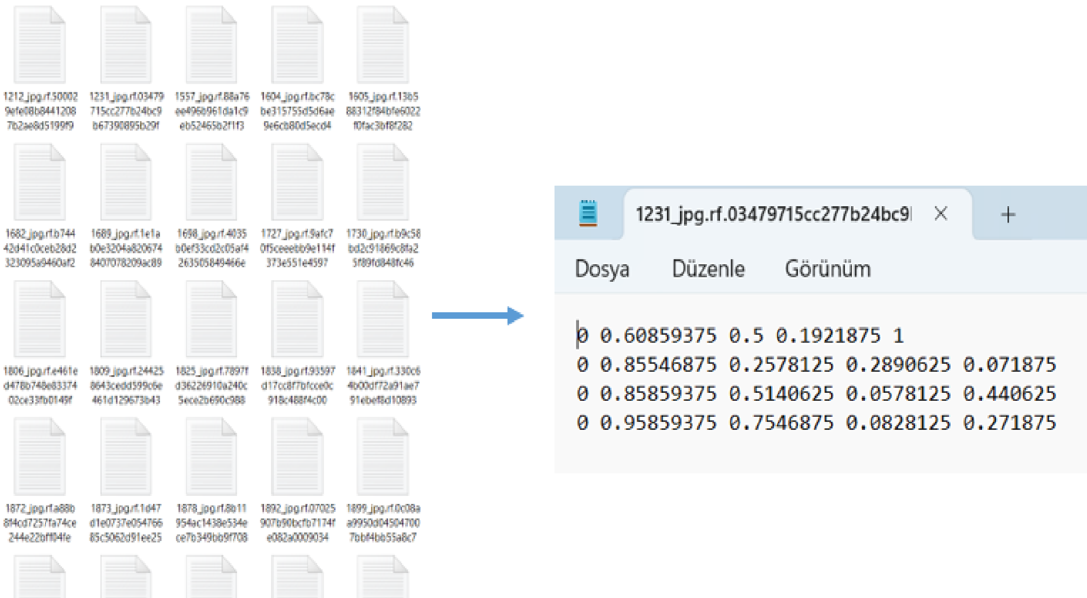

Fig. 5. Label files

The text file presented in Figure 5 is an annotation file in YOLO format, used to provide training data for an object detection model. Such files contain annotations that are essential for enabling the model to acquire object detection capabilities. Each line in the file represents an object and provides the following information: the class ID, the center coordinates of the bounding box, and the width and height of the box. All these values are normalized with respect to the dimensions of the corresponding image. This format helps the model learn the locations and sizes of objects within the images. Once the training process is completed, the model can detect and correctly classify similar objects in new data. The YOLO annotation structure plays a critical role in developing fast and efficient object detection models.

The object detection results for the first two lines provide detailed information about the identified objects, including their class, position, and bounding box dimensions in normalized coordinates. In Line 1, the object is assigned a Class ID of 0, with the center of its bounding box located at 60.86% of the image width and 50% of the image height. The bounding box spans 19.22% of the image width and covers the full height of the image, indicating a vertically elongated object occupying a significant portion of the image's vertical axis. In Line 2, another object with the same Class ID (0) is detected, with its bounding box center positioned at 85.55% of the image width and 25.78% of the image height. The corresponding bounding box dimensions are 28.91% of the image width and 7.19% of the image height, suggesting a more compact and horizontally wider object. Lines 3 and 4 follow the same format, representing additional detected objects using normalized center coordinates and relative dimensions.

2.4. Training process and code block used

The code block required to initiate the training process was obtained from the official page of the "Ultralytics YOLOv8" application and is presented in Fig. 6. Various modifications were made to the code to align it with the specific requirements of the project, and subsequently, the training process was initiated. The training was configured to run for a total of 100 epochs and took approximately 2.293 hours to complete. Throughout the training phase, the model parameters were optimized with the aim of achieving high accuracy. This stage played a critical role in enhancing the overall performance of the model and ensuring successful results in real-world applications.

The command shown in Fig. 7 is a terminal or Python code line used to train a YOLOv8 model on a dataset. Below is an explanation of each part of the command:

- !yolo detect train: Used to train the YOLOv8 model for an object detection task. This command indicates that the model will be run in training mode.
- data=/content/drive/MyDrive/object_detection2/config.yaml: The path to the configuration file of the dataset to be used for training. This file includes the dataset path, number of classes, and other relevant settings.
- model=yolov8n.pt: The pre-trained weight file of the YOLOv8 model to be used for training. (yolov8n.pt refers to the "nano" version of YOLOv8, which is lightweight and fast.)
- epochs=100: Indicates that the model will be trained for 100 epochs. An epoch means the entire training dataset is passed through the model once.
- imgsz=640: The resolution to which the images will be resized during training. Here, all images are resized to 640x640 pixels.
- workers=8: The number of CPU cores to be used for data loading. More workers can speed up the data loading process.
- batch=8: The number of images to be processed in each iteration during training. Larger batch sizes require more memory.
- device=0: Specifies which device will be used for the training process. (0: training will be performed on GPU. If training is to be performed on CPU, this should be set as device=cpu.)
- name=yolov8_crack_detection2: The name under which the trained model file will be saved. This will also be the name of the folder where training output files are stored.

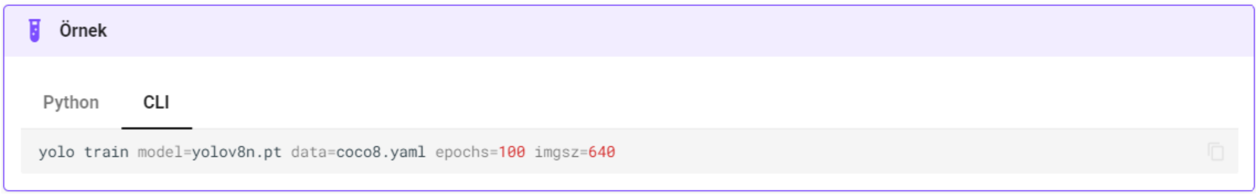

Fig. 6. Sample code block (Ultralytics, 2025)

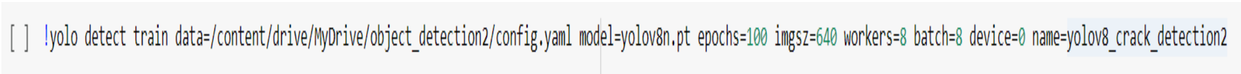

Fig. 7. Education code tailored to requirements

```
      Epoch    GPU_mem   box_loss   cls_loss   dfl_loss  Instances       Size
     98/100      1.18G     0.9092     0.7805      1.153          2        640: 100% 333/333 [01:11<00:00,  4.63it/s]
                 Class     Images  Instances      Box(P          R      mAP50  mAP50-95): 100% 19/19 [00:05<00:00,  3.38it/s]
                   all        300        367      0.839      0.826      0.857      0.611

      Epoch    GPU_mem   box_loss   cls_loss   dfl_loss  Instances       Size
     99/100      1.18G     0.9002     0.7743      1.151          2        640: 100% 333/333 [01:18<00:00,  4.24it/s]
                 Class     Images  Instances      Box(P          R      mAP50  mAP50-95): 100% 19/19 [00:03<00:00,  5.52it/s]
                   all        300        367      0.825      0.842      0.861      0.607

      Epoch    GPU_mem   box_loss   cls_loss   dfl_loss  Instances       Size
    100/100      1.17G      0.904     0.7676      1.156          2        640: 100% 333/333 [01:13<00:00,  4.52it/s]
                 Class     Images  Instances      Box(P          R      mAP50  mAP50-95): 100% 19/19 [00:03<00:00,  5.47it/s]
                   all        300        367      0.843      0.822       0.86      0.606

100 epochs completed in 2.293 hours.
Optimizer stripped from runs/detect/yolov8_crack_detection2/weights/last.pt, 6.3MB
Optimizer stripped from runs/detect/yolov8_crack_detection2/weights/best.pt, 6.3MB

Validating runs/detect/yolov8_crack_detection2/weights/best.pt...
Ultralytics YOLOv8.2.93 🚀 Python-3.10.12 torch-2.4.0+cu121 CUDA:0 (Tesla T4, 15102MiB)
Model summary (fused): 168 layers, 3,005,843 parameters, 0 gradients, 8.1 GFLOPs
                 Class     Images  Instances      Box(P          R      mAP50  mAP50-95): 100% 19/19 [00:09<00:00,  2.09it/s]
                   all        300        367      0.846      0.826      0.867      0.613
Speed: 1.1ms preprocess, 4.3ms inference, 0.0ms loss, 6.1ms postprocess per image
Results saved to runs/detect/yolov8_crack_detection2
```

Fig. 8. Training

As illustrated in Fig. 8, the training process was successfully completed, and the resulting data were analyzed to assess the model's performance in terms of both accuracy and speed. The YOLOv8 model was trained over a total of 100 epochs, with the entire training phase taking approximately 2.293 hours. Thanks to the carefully prepared dataset and the selection of appropriate hyperparameters, the model was able to learn efficiently and achieve a high level of generalization. Upon completion of the training, two optimized weight files were generated: *last.pt*, representing the model's weights at the end of the training, and *best.pt*, corresponding to the model's best performance during training. Both files were designed to be lightweight, each with a file size of just 6.3 MB, making them suitable for real-time applications.

The model's performance was rigorously evaluated using a validation dataset. It achieved a precision of 84.6%, indicating its ability to correctly classify detected objects, and a recall of 82.6%, reflecting its effectiveness in identifying all relevant objects. The mean Average Precision at a 50% Intersection over Union (mAP@50) was recorded at 86.7%, demonstrating the model's strong object detection capability. Furthermore, the model achieved a mAP@50-95 score of 61.3%, which assesses overall accuracy across a broader range of IoU thresholds, confirming its robustness in more complex evaluation settings.

In addition to accuracy, the model also performed efficiently in terms of speed. During validation, the average preprocessing time per image was measured at 1.1 milliseconds, the inference time at 4.3 milliseconds, and the post-processing time at 6.1 milliseconds. These results highlight the model's suitability for real-time detection tasks where both high accuracy and low latency are critical.

These results show that the YOLOv8 model can perform object detection tasks with high accuracy and sensitivity. A mAP@50 value of 86.7% proves that the model achieved a strong learning capacity during training and could effectively detect objects in the dataset. Additionally, the lightweight optimized weight files and fast processing times indicate that the model is also suitable for deployment in environments with limited computational resources.

2.5. Training and validation results

The figure shown in Fig. 9 illustrates the losses and performance metrics obtained during the training process of the YOLOv8 model. Each of these graphs is used to understand how the model progresses throughout the training and how its performance changes during validation. A detailed interpretation of the graphs is presented below:

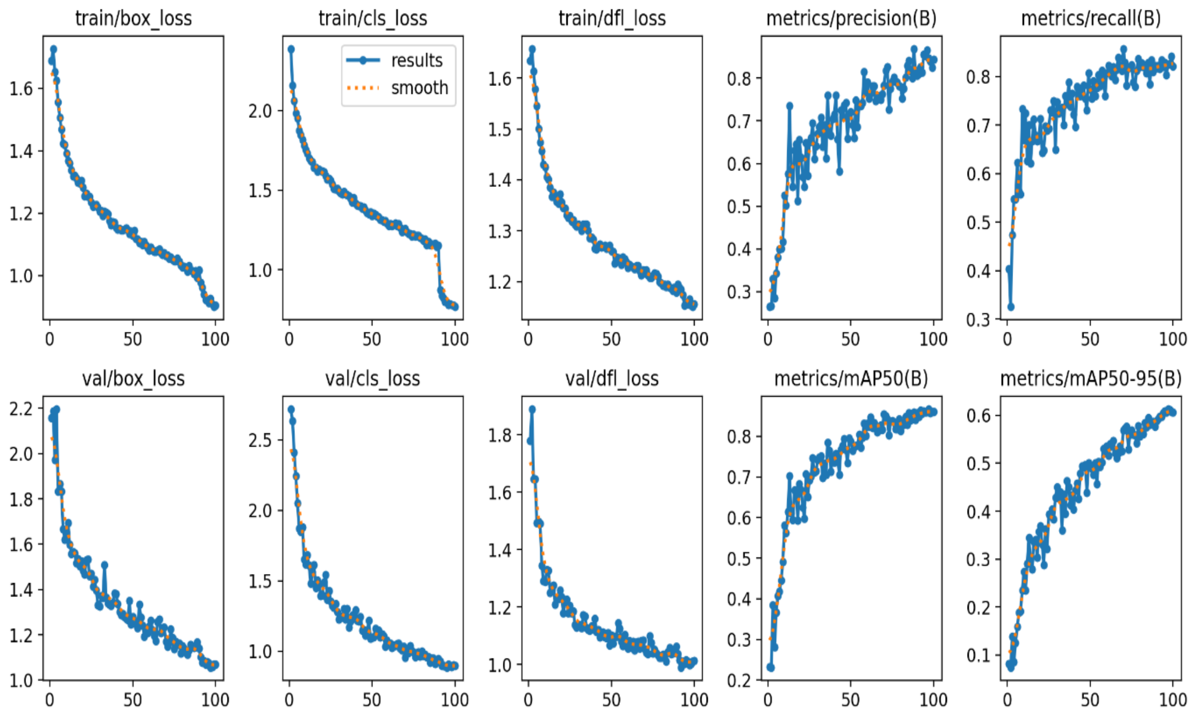

Fig. 9. Results

The evaluation of the training process included a detailed analysis of loss functions and performance metrics, which provided insights into the model's learning behavior and accuracy. The training losses, including box loss (*train/box_loss*), classification loss (*train/cls_loss*), and distribution focal loss (*train/dfl_loss*), consistently decreased over time. The reduction in box loss indicates that the model increasingly improved its accuracy in predicting bounding box locations. Similarly, the decrease in classification loss reflects enhanced accuracy in object classification, while the declining distribution focal loss shows progress in the precise localization of bounding boxes. Correspondingly, the validation losses—*val/box_loss*, *val/cls_loss*, and *val/dfl_loss*—also demonstrated a parallel downward trend. This consistency between training and validation losses suggests that the model achieved generalizable performance without significant overfitting.

In terms of performance metrics, the model showed continuous improvement across all key indicators. Precision steadily increased with each epoch, eventually reaching approximately 85%, indicating a high rate of correctly classified detected objects. Recall also showed a gradual upward trend, achieving around 82%, which confirms the model's ability to detect most objects present in the dataset. The mean Average Precision at an IoU threshold of 50% (*mAP@50*) reached about 86%, reflecting strong object detection accuracy. Moreover, the more comprehensive *mAP@50-95* metric, which evaluates performance across multiple IoU thresholds, achieved a value of approximately 61%. This result highlights the model's robustness and effectiveness in varying detection scenarios, confirming its suitability for practical applications in real-world environments.

Throughout the training process, a consistent reduction in both training and validation losses was observed, indicating that the model successfully learned the underlying distributions of the training data. The continuous improvement in performance metrics (precision, recall, and mAP) suggests that the model progressively became better at making predictions. Moreover, the parallel decrease in training and validation losses confirms that the model has strong generalization capabilities and that overfitting did not occur.

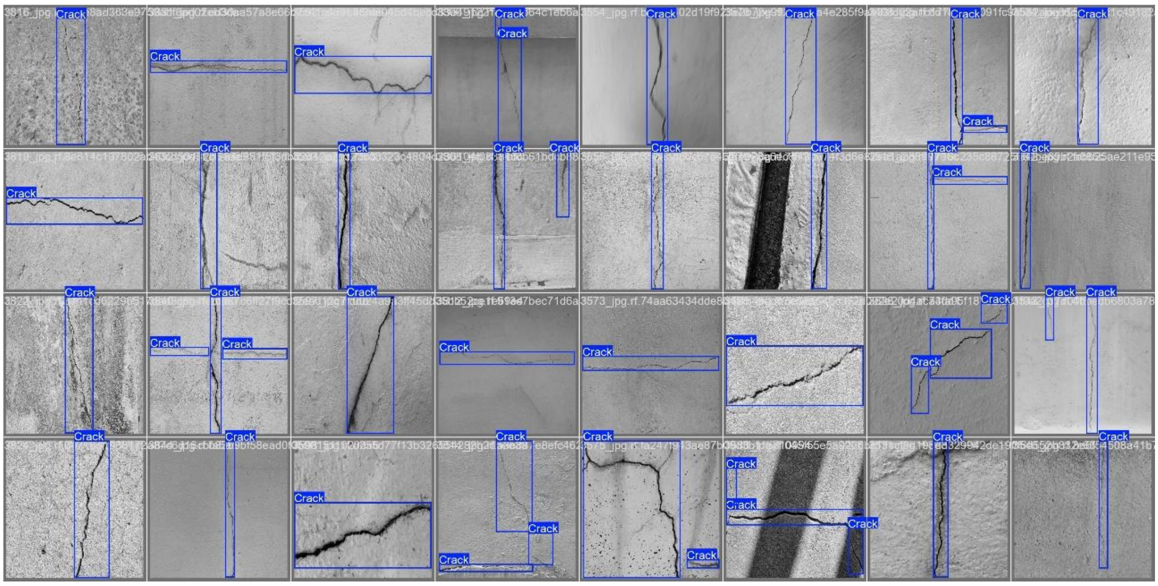

Fig. 10. Validation data set

The image presented in Fig. 10 shows the crack detection results performed by the model on the validation dataset. In the image, each detected crack is labeled with blue bounding boxes, indicating that the model has accurately identified each crack area. Such images are highly useful for evaluating how well the model has performed during training and for assessing its accuracy in object detection tasks.

Each blue bounding box represents a crack that the model has correctly detected. Observing that the objects in the image are correctly classified and the bounding boxes are properly placed demonstrates that the model operates with high accuracy and successfully performs the object detection task. Furthermore, the presence of cracks of different sizes and at various locations within the image reflects the model's ability to effectively detect various types of cracks. These kinds of outputs confirm that the model has processed the examples encountered during training correctly and has developed a strong generalization capability.

3. Testing process and analysis results

In this study, a YOLOv8 crack detection model was developed, and a comprehensive testing process was conducted to evaluate the model's accuracy. To assess the model's applicability, a successful connection was established between the robot and the YOLOv8 model, allowing the monitoring of the model's performance through this integration. The testing environment was set at the Structural Health Monitoring Laboratory of Karadeniz Technical University, where real-world measurements were conducted to assess the model's success under practical conditions. The use of a reinforced concrete steel frame structure for testing was deemed an appropriate choice to achieve highly accurate results in crack detection tasks.

The technical specifications of the tested reinforced concrete model in Fig. 11. were carefully defined. The concrete strength class was set at C25/30, a standard that ensures sufficient strength and durability of the material. The steel reinforcement strength was selected as B420C, guaranteeing high structural resilience. The physical dimensions of the reinforced concrete model were also an important criterion: the model measured 550 × 1700 × 300 mm (width × length × height) with a total height of 1850 mm (Çolakoğlu et al., 2024). These dimensions provided sufficient structural elements and an adequate testing area, enabling the development of a model suitable for crack detection studies.

This well-structured model increased the diversity of the data used during the training phase and allowed for broader testing of the model's capabilities.Tests conducted on the structure aimed to determine the effectiveness of the YOLOv8 model in crack detection. During these tests, the model's accuracy was compared against real-time data, and the results showed that the model performed with high accuracy not only in the training environment but also in real-world applications. This process demonstrated that the YOLOv8 model is a reliable and effective tool for crack detection in reinforced concrete structures. Moreover, integrating the model with robot technology proved to be an important innovation in the field of structural health monitoring.

The measurement process was meticulously carried out, and all stages were carefully monitored. The activated robot dog, as shown in Fig. 12, was remotely controlled via a remote control, enabling it to reach every point within the testing area. The camera mounted on the robot recorded real-time images and transmitted them to the computer screen, allowing for a detailed inspection of the entire reinforced concrete model through these images. Each surface of the model was observed via the camera footage, and potential cracks were carefully identified.

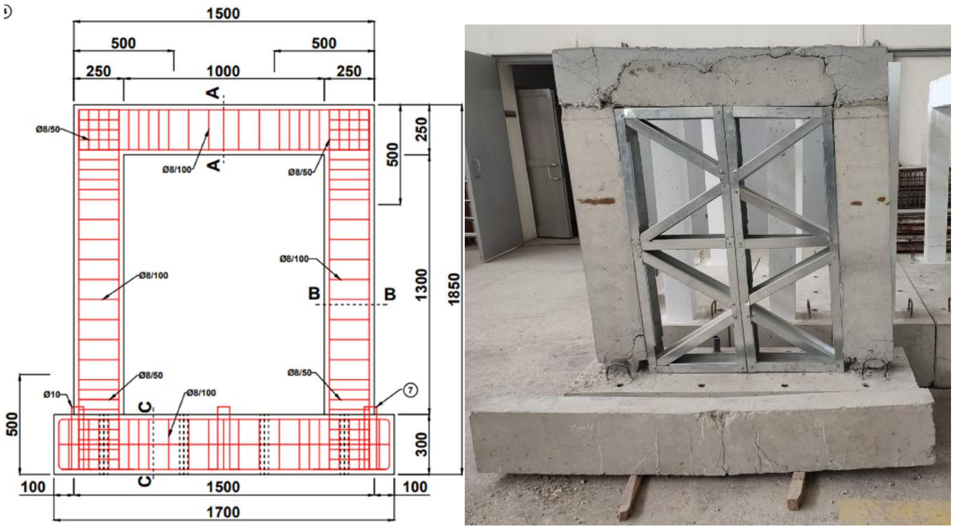

Fig. 11. Test model

Fig. 12. Images of the measurement process

A portion of the Python code that establishes the connection between the YOLOv8 model and the Unitree Go2 robot dog, enabling real-time analysis of the images captured by the robot's onboard camera, is presented in Fig. 13. This code processes the images obtained from the robot's camera, allowing the model to accurately detect cracks and simultaneously evaluate these detections with the model.

The Python script ensures that the images captured by the camera are converted into a format suitable for the model, allows the YOLOv8 model to make predictions on these images, and displays the results in real time on the screen. In this way, the system provides instant crack detection results to the user.

Additionally, the code is designed to operate in synchronization with the robot dog's movements. The images captured from different angles are accurately analyzed, and classification results are generated for each frame. This structure plays a crucial role in both testing the model's accuracy and enhancing the robot dog's effectiveness in field applications.

```python
import imutils
import cv2
import time
import random
import numpy as np
import sys
from ultralytics import YOLO
from unitree_sdk2py.core.channel import ChannelFactoryInitialize
from unitree_sdk2py.go2.video.video_client import VideoClient

# Predefined variables
confidence_score = 0.5
text_color_b = (0, 0, 0)  # Black
text_color_w = (255, 255, 255)  # White
background_color = (0, 255, 0)
font = cv2.FONT_HERSHEY_SIMPLEX

# Load YOLO model
model = YOLO("/home/kemalheo/Desktop/YOLO/models/yolov8n_büyük_veri_setli.pt")  # Model path
labels = model.names
colors = [[random.randint(0, 255) for _ in range(3)] for _ in labels]

# Initialize Unitree Go2 video client
if len(sys.argv) > 1:
    ChannelFactoryInitialize(0, sys.argv[1])
else:
    ChannelFactoryInitialize(0)

client = VideoClient()  # Create a video client
client.SetTimeout(3.0)
client.Init()
```

Fig. 13. A portion of the Python code

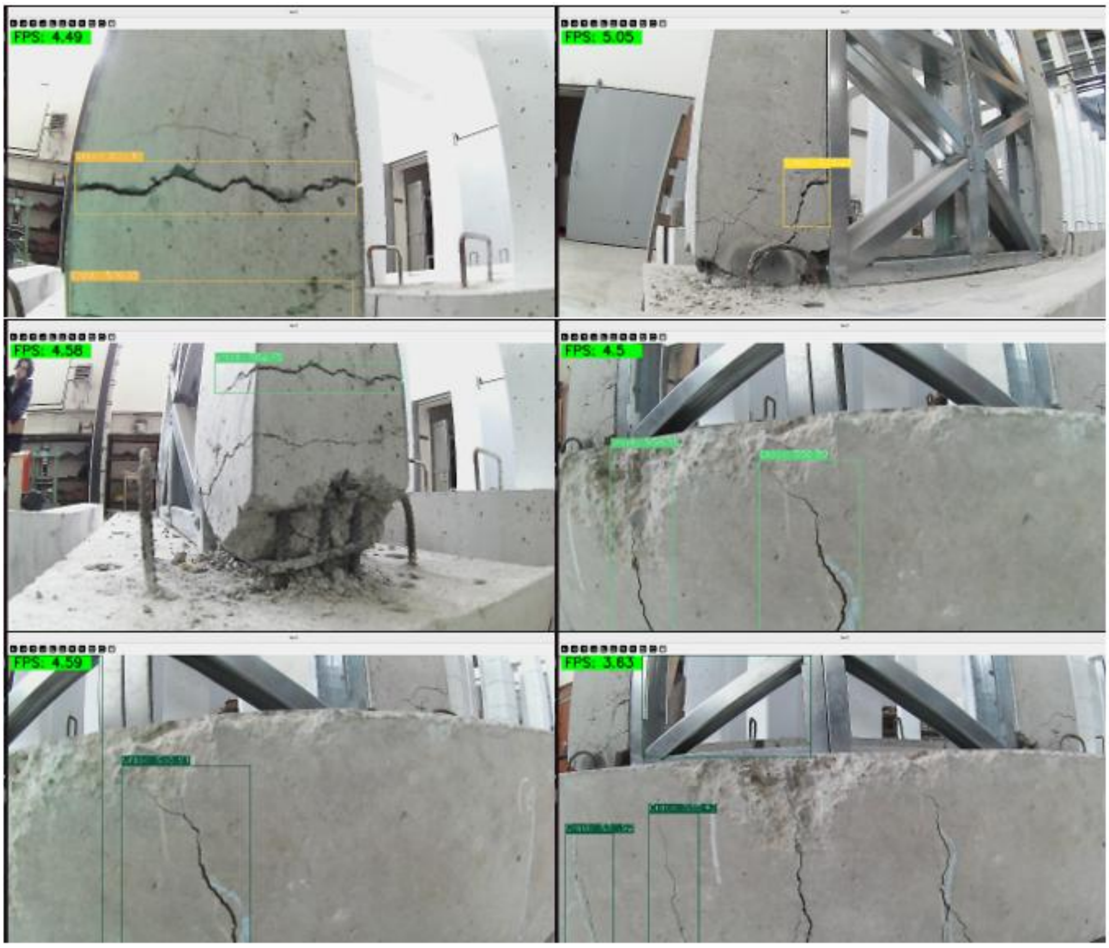

Fig. 14. Analysis results

During the testing phase, the YOLOv8-based crack detection model achieved highly successful results, particularly in accurately identifying and classifying cracks in structural elements. Analyses conducted on the captured images demonstrated that the model precisely detected cracks and accurately assigned them to the correct categories.

As shown in Fig. 14, the bounding boxes generated by the model were accurately placed over the regions containing cracks, and the locations of these cracks were determined with high precision. This level of accuracy indicates that the developed YOLOv8 model is capable of effectively detecting various types of cracks, including both micro-cracks and more visible structural damages. Moreover, the model's ability to maintain high detection performance across cracks of different sizes and locations highlights its robustness and versatility under varying conditions.

The results obtained during the tests confirmed that the model performs reliably not only on training datasets but also under real-world application conditions. Comprehensive measurements and evaluations demonstrated that the YOLOv8 model can be effectively utilized in the field of Structural Health Monitoring (SHM), offering significant advantages for on-site inspections.

Additionally, during this process, the integration between the robot dog's image processing capabilities and the YOLOv8 model was successfully achieved, enabling real-time crack detection. Through the analysis of images captured from multiple angles, the system exhibited considerable potential for advanced applications such as large-scale area scanning and automated defect detection.

In conclusion, this study successfully validated the reliability and efficiency of the developed YOLOv8 crack detection model under both laboratory and real-world conditions, confirming its applicability for critical structural health monitoring tasks.

4. Conclusions

In this study, a robust and efficient crack detection system was developed by integrating a state-of-the-art YOLOv8 deep learning model with the Unitree Go2 quadruped robot, aiming to enable autonomous, real-time structural inspection. The primary goal was to evaluate the feasibility and effectiveness of combining advanced object detection algorithms with mobile robotic platforms to facilitate the automated monitoring of structural integrity, particularly for reinforced concrete systems. The system was extensively tested in a controlled experimental environment at the Structural Health Monitoring Laboratory of Karadeniz Technical University. These tests were designed to simulate realistic inspection scenarios and assess the model's performance under practical conditions, including variable lighting, surface textures, and crack orientations.

Performance evaluation of the model revealed promising results. The normalized confusion matrix showed that the YOLOv8 model achieved a high crack detection accuracy of 89%, while demonstrating perfect classification (100%) for background regions. Although 11% of crack instances were incorrectly classified as background, the overall performance highlights the model's strong generalization capability and ability to reliably distinguish structural anomalies from non-defective areas. Moreover, the F1-Confidence Curve analysis indicated that the model achieved its peak F1-score of 0.84 at a confidence threshold of 0.531. This suggests that fine-tuning the confidence threshold can further optimize the model's detection performance, especially in safety-critical applications where false negatives must be minimized.

For the experimental validation, a full-scale reinforced concrete frame specimen was prepared using C25/30 concrete and B420C steel reinforcement. The specimen had dimensions of 550 mm × 1700 mm × 300 mm and a total height of 1850 mm, providing a realistic and sufficiently large surface for evaluating the model's ability to detect various types and sizes of cracks. The Unitree Go2 robot, equipped with a high-resolution onboard camera, was remotely navigated around the test specimen. As it moved, the robot continuously captured images of the concrete surface, which were processed in real time by the YOLOv8 model. This enabled the system to autonomously detect and localize cracks from different angles and distances, showcasing its adaptability to varying viewpoints.

Visual inspection results, supported by representative examples such as those presented in Fig. 10 and 14, confirmed the system's high localization accuracy. The model successfully identified and outlined crack regions with precise bounding boxes, even in complex surface conditions. This demonstrates the system's capability to perform detailed and reliable inspections without the need for manual intervention. The seamless integration of the YOLOv8 model with the Unitree Go2 robot resulted in a fully automated inspection workflow, capable of navigating, capturing, and analyzing structural data in real time.

In conclusion, the developed robotic inspection system has proven to be accurate, reliable, and efficient for detecting surface cracks in reinforced concrete structures. Its performance indicates strong potential for deployment in real-world Structural Health Monitoring (SHM) applications, particularly in scenarios where manual inspection is difficult, hazardous, or time-consuming. Future research will focus on improving the model's classification accuracy through advanced data augmentation, expanding the training dataset, and evaluating its performance across diverse structural materials and environmental conditions. Additionally, incorporating 3D mapping and path-planning algorithms may further enhance the robot's autonomy and inspection coverage in complex environments.

References

Çolakoğlu, H. E., Hüsem, M., Demir, S., Akbulut, Y. E., & Yılmaz, Y. (2024). The behavior of reinforced concrete frames exposed to high temperature under cyclic load effect. *Structures*, *63*, 106446. Retrieved from https://doi.org/10.1016/j.istruc.2024.106446 .

Ilmak, D., Iban, M. C., & Şeker, D. Z. (2024). Deep learning-based scene classification of very high-resolution satellite imagery for post-earthquake damage assessment: A case study of the 2023 Kahramanmaraş earthquakes. *The International Archives of the Photogrammetry, Remote Sensing and Spatial Information Sciences*, 249–256. Retrieved from https://doi.org/10.5194/isprs-archives-XLVIII-4-W9-2024-249-2024 .

Jia, J., Ye, W. (2023). Deep learning for earthquake disaster assessment: Objects, data, models, stages, challenges, and opportunities. *Remote Sensing* , 11. Retrieved from https://doi.org/10.3390/rs15164098.

Kumar, R. S. (2022 Dec 6). *Object detection with YOLO theory*. Retrieved from Object Detection with YOLO Theory .

Morfidis, K., Stefanidou, S., & Markogiannaki, O. (2023). A rapid seismic damage assessment (RASDA) tool for RC buildings based on an artificial intelligence algorithm. *Applied Sciences*, 3. Retrieved from https://doi.org/10.3390/app13085100.

Nelson, J. (2025, Jan 9). *What is YOLO? The ultimate guide*. Retrieved from What is YOLO? The Ultimate Guide [2025].

Ultralytics, (2025). *Ultralytics YOLOv8'i keşfedin.* Retrieved from Ultralytics YOLOv8 'i Keşfedin - Ultralytics YOLO Dokümanları .

Roboflow, (2025). *Everything you need to build and deploy computer vision applications*. Retrieved from Roboflow: Computer vision tools for developers and enterprises .

Qayoumi, A. S., Shalizi, H., & Dhankot, M. A. (2025). Review on artificial intelligence application in structural earthquake engineering. *International Journal of Science and Research Archive, 14*(01), 083-092. Retrieved from https://doi.org/10.30574/ijsra.2025.14.1.2659 .

Ye, X. W., Liu, Z. X., Ding, Y., & others. (2022). Post-earthquake damage recognition and condition assessment of bridges using UAV integrated with deep learning approach. *Structural Control & Health Monitoring,* 26. Retrieved from https://doi.org/10.1002/stc.3128.

Zhai, G., Xu, Y., & Spencer, B. F. (2024). Bidirectional graphics-based digital twin framework for quantifying seismic damage of structures using deep learning networks. *Structural Health Monitoring—An International Journal, 24.* Retrieved from https://doi.org/10.1177/14759217241231299.

4th International Civil Engineering & Architecture Conference
17-19 May 2025, Trabzon, Türkiye

Dynamic spatio-temporal modeling for fire-induced damage prediction in suspension bridges: an RNN-GCN approach

Sara Mostofi*[1], Fatih Y. Okur[1,2,3], Ahmet C. Altunışık[1,2,3]

[1] *Karadeniz Technical University, Department of Civil Engineering, 61080 Trabzon, Türkiye*
[2] *Karadeniz Technical University, Earthquake and Structural Health Monitoring Research Center, 61080 Trabzon, Türkiye*
[3] *Dynamic Academy Software, Construction Ind. Trade. Co., Ltd., Şti., Trabzon, Türkiye*

Abstract. The post-fire evaluation of structural damage in bridge elements has become increasingly critical within the context of modern infrastructure safety and resilience planning. The numerical evaluation of bridge fire exposure is generally relied heavily on Computational Fluid Dynamics (CFD) simulations, most notably the Fire Dynamics Simulator (FDS), to model flame propagation, smoke behavior, and thermal responses of structural elements. Among the key outputs of FDS, the Adiabatic Surface Temperature (AST) serves as a crucial thermal metric, providing surface-level temperature data essential for assessing instantaneous heat transfer and predicting post-fire conditions of exposed structural components. While FDS-based simulations offer crucial insights, their computational complexity and runtime constraints limit their practicality for real-time decision-making or iterative design workflows. To address this limitation, the present study proposes the use of Dynamic Spatio-Temporal Models (DSTMs) that integrate Recurrent Neural Networks (RNNs) for temporal modeling with Graph Convolutional Networks (GCNs) for spatial learning. A hybrid RNN-GCN architecture was developed and trained on FDS-generated bridge fire data from multiple vehicle fire scenarios initiating on suspension bridge deck. The model captures the evolution of fire exposure across time and its spatial propagation along the suspension bridge tower, predicting the damage condition of the tower at different heights. The proposed hybrid model demonstrated strong predictive performance, achieving a test accuracy of 88.6%, precision of 87%, and a ROC AUC score of 0.94, indicating high reliability in distinguishing between intact and damaged structural states. These results confirm the model's ability to generalize across varying fire intensities and spatial configurations. The integration of DSTMs into the structural fire engineering domain represents a significant shift from static simulations toward more adaptive and computationally efficient forecasting frameworks. By enabling rapid assessments of fire-induced damage, the approach supports enhanced operational readiness, real-time monitoring, and more resilient bridge design and management strategies.

Keywords: Computational fluid dynamics; Fire dynamics dimulator; Adiabatic surface temperature; Recurrent neural networks; Graph convolutional networks

1. Introduction

Fire presents a critical hazard to the structural integrity of bridges, with high-intensity fire incidents possessing the potential to cause significant structural damage or even total collapse. Vehicle fires occurring on bridge decks, ranging from standard passenger vehicles to heavy fuel tankers, can rapidly elevate temperatures in structural elements, severely compromising their mechanical properties (Mostofi et al., 2024). Notably, steel components such as cables and towers exhibit substantial strength degradation at elevated temperatures; empirical studies indicate that steel loses more than 50% of its tensile strength at approximately 500 °C (Q. Li et al., 2022), thereby rendering intense fire events particularly catastrophic for suspension bridges.

Assessment methodologies for bridge fire predominantly rely on physics-based simulation tools such as the Fire Dynamics Simulator (FDS) in conjunction with post-incident inspection protocols to quantify and evaluate fire-induced damage (Mostofi & Altunişik, 2024a). While these approaches provide valuable insights, they are time consuming and lack real-time predictive capabilities. As the frequency and intensity of fire incidents escalate, particularly in urban bridge environments, there is an urgent demand for the development and implementation of intelligent, predictive tools capable of delivering real-time evaluations during fire events. Recent advancements in

* Corresponding author, E-mail: saramostofi.4e@gmail.com

https://doi.org/10.31462/icearc2025_ce_sme_456

machine learning (ML) have significantly transformed bridge fire evaluation (Franchini et al., 2024). Conventional numerical techniques, although informative, are often limited by high computational costs. ML techniques offer an alternative by learning patterns from simulation data.

Dynamic Spatio-Temporal Models (DSTMs), a class of advanced machine learning frameworks, constitute an advanced class of deep learning architectures engineered to extract and learn underlying patterns that evolve simultaneously over both spatial and temporal dimensions. Unlike conventional neural networks that might treat data as independent (ignoring temporal order or spatial relations), DSTMs incorporate sequential time dependencies and spatial interconnections directly into their architecture. This dual capability renders them particularly effective for modeling complex systems such as critical infrastructure subjected to evolving loads, including fire events. Two of the key building blocks in DSTMs are recurrent neural networks (RNNs) and graph convolutional networks (GCNs), which can be combined into hybrid frameworks. These architectures can be integrated into hybrid spatio-temporal frameworks to provide comprehensive modeling of time-evolving systems with spatial heterogeneity.

- RNNs, including advanced variants such as Long Short-Term Memory (LSTM) networks and Gated Recurrent Units (GRUs), are adept at capturing long-range temporal dependencies within sequential data (Liu et al., 2023). These models maintain a dynamic internal state that evolves at each time step, allowing the network to encode both short-term fluctuations and long-term trends. Empirical evaluations have consistently demonstrated the efficacy of RNN-based architecture in long-horizon forecasting tasks, particularly where continuous monitoring data are available over extended periods. However, a vanilla RNN does not inherently understand spatial relationships among multiple input locations.
- GCNs are designed to model data defined on graphs, capturing spatial relationships in complex systems. In infrastructure modeling, each node in the graph may represent a physical element, while edges denote mechanical, physical, or communicative relationships. GCNs perform convolution-like operations that allow each node to update its feature representation by aggregating the states of its neighboring nodes. This approach enables the network to learn how spatially distributed phenomena—such as heat conduction, load redistribution, or structural degradation—propagate through interconnected elements. As a result, GCNs are particularly effective for modeling systems where spatial dependencies are critical to behavior prediction (X. Li et al., 2023). They overcome the limitations of traditional 1D Convolutional Neural Networks (CNNs) and RNNs, which often fail to adequately capture structural spatial dependencies in complex physical systems.
- By combining GCNs with temporal models like RNNs, one can capture both space and time dynamics. In such configurations, the GCN component is responsible for encoding the spatial state of the system at each discrete time step, effectively transforming the graph-based sensor or structural data into an enriched feature vector. This vector is then passed to an RNN layer, which propagates the information temporally, allowing the model to forecast future states of the system. prior studies in other domains have found that combining graph convolution with recurrent units significantly improves forecasting in complex, time-dependent systems. This dual-capability model structure is ideally suited for forecasting the evolution of fire-induced damage in large-scale structures such as suspension bridges.

The recent application of deep learning models has significantly advanced the damage assessment of structures. Techniques such as Bi-GRUs have been successfully integrated with attention mechanisms to capture dynamic dependencies across time (Dibiantara et al., 2025), while graph-based methods like GNNs and Graph Attention Networks (GATs) capture inter-sensor spatial correlations, significantly improving sensitivity to distributed damage patterns (Dang et al., 2022; Dang & Pham, 2023). Hybrid architectures, such as CLG-BHM and MPCA-biGRU-AM, show that combining temporal and spatial learning components enhances robustness in damage detection, even in the presence of sensor noise or missing data (Dang & Pham, 2023; Dibiantara et al., 2025). These frameworks are also capable of reducing detection delays and outperforming conventional CNN-based approaches in modeling long-range dependencies. By moving beyond purely temporal or spatial representations, spatio-temporal models support comprehensive understanding of damage propagation mechanisms, thereby offering new capabilities for digital twins, probabilistic assessment, and real-time structural integrity forecasting. Despite these advancements, relatively few studies have applied spatio-temporal deep learning specifically to bridge fire scenarios.

Numerical fire evaluation of bridges generally relies on coupled physics simulations: a fire model, using Computational fluid dynamics (CFD) such as Fire Dynamic Simulator (FDS) to provide thermal loads, and a structural model computes the response of the bridge to those loads. While accurate, this process is computationally intensive and impractical for real-time assessment. As an alternative, DSTMs offer a data-driven solution by learning from simulation outputs and directly mapping fire exposure patterns to structural damage predictions.

This study explores the use of DSTMs in the context of structural fire engineering, with a specific emphasis on suspension bridges. These models are uniquely designed to capture both spatial and temporal dependencies within dynamic systems, offering substantial advantages over static approaches. In particular, this research focuses on a hybrid Recurrent Neural Network–Graph Convolutional Network (RNN-GCN) architecture, which combines sequence modeling and graph-based learning to assimilate complex fire simulation data for predictive damage assessment. The study applied this hybrid framework to diverse vehicular fire scenarios, each representing varying fire sizes and intensities, to evaluate their impact on suspension bridge tower. The RNN component effectively captures the time evolution of thermal exposure, while the GCN component models the spatial relationships between structural nodes, allowing the architecture to forecast localized damage over time. The primary objective is to replace computationally intensive coupled physics simulations with a trained data-driven surrogate model capable of rapid and accurate post-fire assessment. To this end, a high-fidelity bridge fire dataset was synthetically generated using PyroSim (*PyroSim | Thunderhead Engineering*, n.d.), a graphical interface for the Fire Dynamics Simulator (FDS), simulating detailed thermal load distributions resulting from multiple vehicle fire scenarios on the Bosphorus Suspension Bridge.

Three distinct vehicle types were considered to represent varying fire intensities and durations: a standard passenger sedan, a full-sized passenger bus, and a large fuel-carrying truck. Each vehicle was positioned on lane 1 of the Bosphorus Bridge to simulate real-world urban fire risks and their localized thermal impact. The developed dataset was subsequently used as inputs to train a hybrid RNN-GCN model. Readings from temperature sensors were used as node-level features, representing localized thermal states at different heights of the bridge tower. Spatial relationships between these nodes were defined using the devices that recorded the adiabatic surface temperature (AST) as the edge column. AST defines the theoretical temperature a surface attains when exposed to convective and radiative heat transfer without conductive energy dissipation. AST provides a more accurate assessment of the thermal load on a structure, making it an important parameter for evaluating fire-induced damage (Mostofi & Altunişik, 2024b). The RNN component modeled the temporal evolution of fire exposure using sequential temperature data, while the GCN component captured spatial dependencies via graph convolutions at each time step. Once trained, the hybrid RNN-GCN model predicted damage condition at various heights of the tower. The developed DSTM can rapidly predict fire-induced damage – far faster than running detailed simulations – and can incorporate real-time data, making it valuable for both design assessment (e.g. evaluating many what-if scenarios of vehicle fires on a bridge) and active fire incident management.

2. Materials and methods

This study employed a hybrid RNN-GCN deep learning framework for predicting fire-induced damage conditions in a suspension bridge structure. The dataset employed in this study was synthetically generated using PyroSim and consists of fire simulation data representing various vehicle fire scenarios on the Bosphorus Suspension Bridge. The dataset comprised a total of 113,949 records, each corresponding to time-dependent thermal measurements from various points along the bridge tower. The data included seven key columns: Time, AST device, AST Value, Vehicle, Gas temperature device, Temp Value, and Damage Condition.

The input data was restructured to match the requirements of a spatio-temporal learning framework. Each temperature sensor reading was treated as a node feature, encoding the localized thermal condition of a specific point along the bridge tower. The AST device field defined graph edges and constructed the spatial topology GCN processing. Temporal modeling was enabled by organizing data into rolling windows with clearly defined durations for training, validation, and testing. Each window contained a time-series of node features representing thermal evolution under fire exposure, mapped to corresponding damage states.

The RNN component was constructed using a multi-layer recurrent network, which processes time-series thermal features from thermocouple sensors. The input features were first reshaped to include a sequence dimension and passed through two stacked RNN layers. The spatial learning component comprises a single-layer GCN implemented using the GCNConv function from the PyTorch Geometric library. It took the temporally processed features and performed graph convolutions using the bridge's spatial connectivity matrix (edge_index), defined by the AST device. The GCN propagates node features across adjacent nodes, effectively modeling the thermal interdependence among spatial regions of the bridge.

To prevent overfitting and enhance model generalization, a dropout layer of 0.3 was introduced between the RNN and GCN layers. The final output was passed through a ReLU activation followed by a log_softmax layer, producing class probability distributions over the target categories (Intact/Safe and Damaged). The model parameters, including input_dim, hidden_dim, and output_dim, were tuned for optimal classification performance. The training was conducted using a cross-entropy loss function. The training was executed over 500 epochs, with an early stopping patience of 25 epochs to prevent unnecessary computation once the validation performance plateaued. Data was processed using a batch size of 32, and training was conducted across multiple rolling time windows. Each rolling window included defined training, validation, and test masks, supporting spatio-temporal generalization. For each window, input data were preprocessed into PyTorch Geometric Data objects containing node features (x), edge indices (edge_index), and target labels (y), and were passed into customized DataLoaders. Model weights were updated for each window to improve generalizability across different phases of the fire.

At the start and end of the training block, timestamps, memory usage, and GPU statistics were recorded to compute elapsed wall-clock time, CPU user and system time, change in memory usage. These profiling results offer insights into the computational cost of deploying such deep models in real-time bridge monitoring systems.

3. Results and Discussion

The proposed model was trained using a dynamic spatio-temporal learning approach and evaluated across several performance metrics. The performance of the proposed model was evaluated using five standard classification metrics: accuracy, precision, recall, F1 score, and ROC-AUC. These metrics provide a comprehensive view of model behavior in correctly identifying damaged and intact structural states. Accuracy measures the overall correctness of the predictions by calculating the ratio of correctly predicted instances to the total instances evaluated. Precision assesses the model's ability to correctly identify only the relevant class (e.g., correctly labeling damage where damage exists). Recall (or sensitivity) quantifies the model's capability to capture all relevant cases, such as detecting all actual damaged regions. F1 Score provides a harmonic means of precision and recall, offering a balanced measure that accounts for both false positives and false negatives. ROC-AUC (Receiver Operating Characteristic – Area Under Curve) is used to evaluate the model's ability to distinguish between the two classes (intact vs. damaged).

During training, convergence was observed at Epoch 162, where the model achieved a training loss of 0.0533 and a corresponding training accuracy of 96.06%. On the validation set, the model attained a validation loss of 0.1586 and a validation accuracy of 86.93%, indicating good generalization to unseen temporal-spatial patterns in the bridge fire simulation data. The resulst yielded on the independent test set are shown in Table 1. The confusin matrix presented in Fig. 1 further interpret the classification behavior of the model.

Table 1. Performance evaluation of the model

Test loss	Test accuracy	Precision	Recall	F1 Score	AUC
0.18	88.6%	0.87	0.60	0.63	0.94

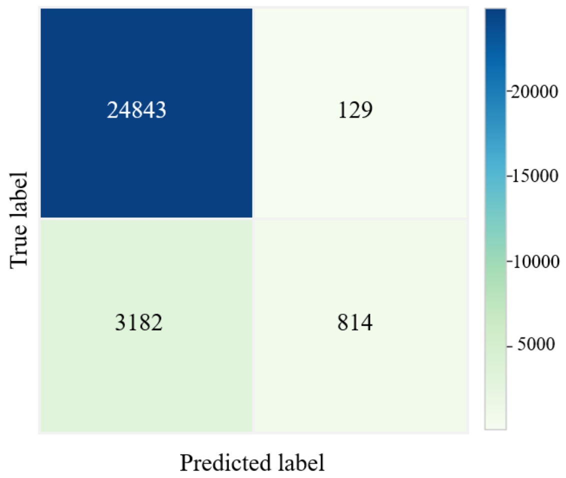

Fig. 1. The confusin matrix

From Fig. 1, it is clear that the model performs very well in predicting intact regions, correctly identifying 24,843 out of 24,972 intact cases (true negatives), with only 129 false positives. However, performance on the damaged class is more constrained, correctly identifying 814 out of 3,996 damaged nodes (true positives) but misclassifying 3,182 as intact (false negatives). Given that the dataset includes time-sequenced thermal exposures and spatial connectivity, the model's design is particularly suited to identify patterns that manifest over time and space. The high test accuracy and strong AUC confirm that the model effectively exploits both sequential temperature trends and structural adjacency patterns. This proves the suitability of hybrid architectures in capturing complex thermo-mechanical behaviors in real-world fire scenarios.

4. Conclusions

Structural fires represent a critical threat to steel components of bridges. Conventional fire evaluation techniques, primarily based on coupled physics simulations and post-event inspections, are often computationally intensive, time-consuming, and unsuitable for real-time deployment. This research addressed the need for rapid, and scalable alternatives by proposing a hybrid Recurrent Neural Network–Graph Convolutional Network (RNN-GCN) model tailored for dynamic spatio-temporal prediction of fire-induced damage in suspension bridge structures.

The primary objective of the study was to develop a data-driven surrogate capable of learning from simulation-derived thermal exposure profiles and accurately predicting post-fire condition of steel tower of suspension bridges. To achieve this, a novel methodology was adopted, integrating RNNs to model the temporal evolution of fire exposure and GCNs to capture spatial dependencies among temperature measurement nodes distributed along the vertical axis of a suspension bridge tower. The dataset used for model training and evaluation was derived from high-fidelity PyroSim-generated fire scenarios involving three vehicle types positioned on lane 1 of the simulated bridge.

The results demonstrate that the RNN-GCN model achieved high classification accuracy (88.6%), indicating excellent discriminative capability. The relatively moderate recall and F1 score, however, reveal an area for improvement in detecting damaged state.

Future research should focus on incorporating real-time sensor data from full-scale fire experiments or in-service bridge monitoring systems to enhance model realism and adaptability. Moreover, the architecture could be expanded to integrate attention mechanisms, temporal convolutions, or Transformer-based modules for improved temporal reasoning. Finally, embedding the model within a decision-support dashboard could facilitate real-time structural health evaluations for infrastructure stakeholders, contributing to safer and more resilient urban transportation systems.

References

Dang, V. H., & Pham, H. A. (2023). Vibration-based building health monitoring using spatio-temporal learning model. *Engineering Applications of Artificial Intelligence, 126*, 106858.

Dang, V. H., Vu, T. C., Nguyen, B. D., Nguyen, Q. H., & Nguyen, T. D. (2022). Structural damage detection framework based on graph convolutional network directly using vibration data. *Structures, 38*, 40–51.

Dibiantara, D. P., Adha, A., Darmawan, M. S., Imjai, T., Russell, J., & Laory, I. (2025). Spatio–temporal enhanced anomaly detection in FRP bridge monitoring using MPCA, biGRU, and attention mechanisms. *Journal of Civil Structural Health Monitoring*, 1–19.

Firdaus, M., Singh, G. V., Ekbal, A., & Bhattacharyya, P. (2023). Affect-GCN: a multimodal graph convolutional network for multi-emotion with intensity recognition and sentiment analysis in dialogues. *Multimedia Tools and Applications, 82*(28), 43251–43272.

Franchini, A., Barake, B., Galasso, C., Moreyra Garlock, M. E., Mulligan, J., Quiel, S., & Torero, J. L. (2024). Integrating fire safety into bridge design is essential for resilient infrastructure. *Nature Communications, 15*(1), 1–12.

Li, Q., Guo, H., Zhou, J., & Wang, M. (2022). Bridge Fire Vulnerability Hierarchy Assessment Based on the Weighted Topsis Method. *Sustainability, 14*(21), 14174.

Li, X., Xu, L., Guo, H., & Yang, L. (2023). Application of Graph Convolutional Neural Networks Combined with Single-Model Decision-Making Fusion Neural Networks in Structural Damage Recognition. *Sensors 23*(23), 9327.

Liu, K., Zhang, X., Wang, Y., Guo, F., Cui, Z., Zhang, J., Noh, G., & Park, H. J. (2023). ADSTGCN: A Dynamic Adaptive Deeper Spatio-Temporal Graph Convolutional Network for Multi-Step Traffic Forecasting. *Sensors 23*(15), 6950.

Mostofi, S., & Altunişik, A. C. (2024a). Recent Advances in CFD-based Bridge Fire Evaluations: A Brief Review. *Civil Engineering Research Journal, 14*(4).

Mostofi, S., & Altunişik, A. C. (2024b). Surrogate Model-Driven Estimation of Adiabatic Surface Temperature of Fire Exposed Suspension Bridge Towers. *Fire Technology*.

Mostofi, S., Altunişik, A. C., Akbulut, Y. E., & Okur, F. Y. (2024). A Simulation-Based Investigation on Thermal Responses of Suspension Bridge Tower Under Different Fire Scenarios. *Arabian Journal for Science and Engineering*.

PyroSim Thunderhead Engineering. Retrieved March 11, 2022, from https://www.thunderheadeng.com/pyrosim/

Zhu, H., Xie, Y., He, W., Sun, C., Zhu, K., Zhou, G., & Ma, N. (2020). A Novel Traffic Flow Forecasting Method Based on RNN-GCN and BRB. *Journal of Advanced Transportation, 2020*(1), 7586154.

4th International Civil Engineering & Architecture Conference
17-19 May 2025, Trabzon, Türkiye

Solving structural optimization problems using marathon runner algorithm

Kamil E. Arslan[1], Ali Mortazavi[*1]

[1] *Izmir Democracy University, Department of Civil Engineering, Izmir, Turkey*

Abstract. The structural optimization process aims to enhance performance of the structural system while minimizing weight and/or cost, considering some additional constraints to find feasible solutions. In this study, the recently developed optimization technique, the so-called Marathon Runner Algorithm (MRA) which is a metaheuristic approach inspired by endurance strategies, is tested on solving structural optimization problems. This method uses a special concept called region point to consider all data collected by the by the population in each step and by this approach, it prevents to waste any acquired data during the optimization process. This behavior helps the algorithm to search the domain more precisely while decreasing the likelihood of trapping into local minima. Also, this method models there, individual interactions between competitors in the real computation to perform a precise local search in each iteration. So, the MRA applies both exploration and exploitation search behavior in each iteration. The algorithm's performance is evaluated using a predefined performance index, considering factors such as convergence speed, solution accuracy, and computational efficiency. The results demonstrate that MRA offers superior solution accuracy and robustness, efficiently handling various problem complexities while maintaining stability. Overall, the MRA proves to be a promising optimization method, striking a balance between exploration and exploitation, making it a proper optimization technique for handling structural optimization problems.

Keywords: Marathon runner algorithm; Structural optimization; Metaheuristic techniques; Performance index; Engineering design

1. Introduction

In today's world, along with the rapid advancement of technology and constraints of natural resources, there is a growing demand for the construction of structures providing design requirements that are suitable for the conditions of the region where they are located all while minimizing costs. This advancement, leads to Structural optimization problems (Talatahari et al., 2013). Most of the time solutions of Structural optimization involve complex problems. Methods utilized in solutions to these optimization problems are generally categorized as deterministic and non-deterministic approaches. Deterministic methods operate within mathematical limitations such as gradient information of the objective function. These methods have rapid convergence. Gradient based deterministic methods may limit deterministic methods in many engineering problems. Moreover, these methods are very dependent on the starting point. Therefore, it may be insufficient to reach the optimum global solution in complex design spaces (Mortazavi, 2019).

Due to these reasons and the development of computer technologies, non-deterministic methods have come to the fore in solving structural optimization problems. Metaheuristic approaches are important subsets of non-deterministic methods. Thus, in the last decades metaheuristic approaches have been among methods widely explored and effectively employed. These approaches are easier to implement, and global searching capacity is better than deterministic methods. When examining the searching strategy of metaheuristic approaches, their search strategies often yield efficient solutions for complex optimization problems. These algorithms generally include randomness to reach a global solution and aim to balance various exploration and exploitation mechanisms in the search process (Gandomi et al., 2011). Metaheuristic approaches inspired by natural phenomena can be examined under four main headings: (i) Physical System and Simulation-based Algorithms, (ii) Swarm and Colony Algorithms, (iii) Evolutionary Algorithms and (iv) Human-based Algorithms. These categories and representative examples are examined below.

Physical System and Simulation-based Algorithms: These algorithms are inspired by physical and chemical processes in nature. (HTS) models the heat transfer mechanism in different environments (Patel & Savsani, 2015).

[*] Corresponding author, E-mail: ali.mortazavi@idu.edu.tr

https://doi.org/10.31462/icearc2025_ce_sme_485

Water Wave Optimization (WWO) mimics the water waves behavior (Zheng, 2015). The Ion Motion Algorithm (IMO) simulates the movement of ions such as anions and cations according to their energy in a physical space, aiming to reach more stable (lower energy) states (Javidy et al., 2015). and golden ratio optimization method (GROM) which based on principle of the golden ratio, is known as aesthetic ratio and found in growing plants and animals (Nematollahi et al., 2019).

Swarm and Colony Algorithms: Swarm and Colony Algorithms are inspired by the collective behavior of living organisms and communities in nature. Particle swarm optimizer (PSO) mimics the collective movement of swarms, such as bird or fish swarms (Kennedy & Eberhart, 1995). Butterfly Optimization Algorithm (BOA) models of Butterfly's food search mechanism (Arora & Singh, 2019). Drosophila food-Search Optimization (DSO) that simulates insects' food search mechanism (Das & Singh, 2014). Firefly Algorithm (FA) mimics fireflies' light emission behavior (Yang, 2009). Symbiotic organisms search (SOS) mimics symbiotic collaboration relationship of organisms (Cheng & Prayogo, 2014). Virus optimization algorithm (VOA) inspired by the mechanisms by which viruses spread and multiply in host cells (Liang & Cuevas Juarez, 2016).

Evolutionary Algorithms: Evolutionary Algorithms are inspired by natural evolution process such as natural selection, mutation and crossover. Genetic algorithm (GA), a search strategy that models the mechanisms of genetic evolution (Holland, 1984).

Human-based Algorithms: These algorithms are inspired by the way humans solve problems, learn, collaborate, and develop strategies. Teaching and Learning Based Optimization (TLBO) models the knowledge teach and learn process in the classroom (Rao et al., 2011). Tabu search (TS) algorithm limits the feasible neighborhood candidates by involving them in a list (Glover, 1989) and ship rescue optimization (SRO) mimics the ship maneuvering motion in operation of ship rescue process (Chu et al., 2024).

2. Materials and methods

2.1. Marathon Runner Algorithm (MRA)

Marathon Runner Algorithm (MRA), including in the literature as a next generation metaheuristic algorithm inspired by human behavior. The difference between MRA and conventional elitist algorithms is that MRA employs a guidance strategy based on the quality of the entire population, instead of Being guided only by the position of the best solution.

The development of the Marathon Runner Algorithm was inspired by the competitive behavior of marathon runners. These behaviors are modeled as two main components, namely ambitious movement and associated movement. The most distinctive difference between Marathon Runner Algorithm and conventional elitist algorithms is: Instead of the concept of 'best individual' utilized by elitist algorithms, MRA uses a weighted guide point known as the 'vision point (VP)'. Vision Point represents a weighted average considering the entire population. The directions of each agent are determined by the population's Vision Point. Thanks to the Vision Point (VP) approach, the algorithm reduces the risk of getting trapped in local minimum and protects the diversity of the population throughout the optimization process.

In Marathon Runner Algorithm the population is updated through three vectors. These vectors are the Distance Desired to be Decreased (DDD) vector, which represents the effort to reduce the distance between each agent's solution and its nearest agent. The second one is the Distance Desired to be Increased (DDI) vector, which represents the effort to increase that distance, and the last one is vision point (VP) vector. Also, if the relevant agent is in a bad situation according to VP, there will be an attractive effect; otherwise, the opposite is the case, there will be a repulsion effect. In both cases, the sign function (sgn) is utilized to determine the direction of the effect. Considering all these characteristics, the MRA exhibits a well-balanced structure that incorporates both exploration and exploitation capabilities.

$$X^W = \sum_{i=1}^{n} \bar{c}_i^{\,w} X_i \tag{1}$$

In which, X^W is weighted agent, X_i is i^{th} agent, $\bar{c}_i^{\,w}$ weighted coefficient of the i^{th} agent, calculated as:

$$\bar{c}_i^{\,w} = (\hat{c}_i^{\,w} / \sum_{i=1}^{n} \hat{c}_i^{\,w}) \tag{2}$$

$$\hat{c}_i^{\,w} = \frac{max_{1\le k\le n}(f(X_k)) - f(X_i)}{max_{1\le k\le n}(f(X_k)) - min_{1\le k\le n}(f(X_k)) + \varepsilon}, i = 1,2,\ldots,n \tag{3}$$

n is population size, $f(X_i)$ objective function value of the i^{th} agent and $f(X_k)$ is objective function value of k^{th} agent, $max(f(X_k)) - min(f(X_k))$: maximum and minimum objective function values of agents, a small positive number (e.g., 0.0001) to avoid division by zero condition.

$${}^{t+1}X_i = {}^{t}X_i + r_1 \odot ({}^{t}X_{i-1} - {}^{t}X_i) + r_2 \odot ({}^{t}X_i - {}^{t}X_{i+1}) + 2.\alpha.r_3 \odot ({}^{t}X^{w} - {}^{t}X_i) \tag{4}$$

where

$$\alpha = sgn(f({}^{t}X_i) - f(X^w)) \tag{5}$$

where ${}^{t}X_i$ is represents the i^{th} agent at the t^{th} iteration (current candidate solution), ${}^{t+1}X_i$ is denotes i^{th} agent at the $t+1^{th}$ iteration, ${}^{t}X^{w}$ is represents weighted agent at the t^{th} iteration, ${}^{t}X_{i-1}$ is refers to $i-1^{th}$ agent at the t^{th} iteration (better candidate), ${}^{t}X_{i+1}$ is represents the $i+1^{th}$ agent at the t^{th} iteration (worst candidate), r_1, r_2 and r_3 are uniform random values in the range [0,1], $\odot$ is Hadamard (elementwise) product, sgn(.): Sign function and returns +1, if the X^w is in the better location than current agent (${}^{t}X_i$), and otherwise it returns -1.

2.2. Structural optimization

In the structural design process, reducing the costs while remaining design constraints is the crucial point. Therefore, one of the crucial factors is minimizing total weight of structural components. Violation of constraints is significant to obtain feasible and practical design. Incorporating constraints violations into the objective function through a penalty mechanism is a common approach in literature. Total weight of structure represents objective function for feasible solutions to providing all constraints. Penalized objective function increase with violation ratio for Solutions with constraint violation. This process provides applicable solutions and leads to the optimum solution. In this study, analysis performed on 25 bar spatial truss and 72 bar spatial truss systems which are extensively cited in the literature. Minimizing the total weight process in this article is formulated below.

$$minimize\ W = \sum_{i=1}^{nm} \rho_i\, L_i A_i \tag{6}$$

In which ρ is the density of materials, L is length of each member, A is the cross-section area of each member and nm is the number of the members of the truss structures. The constraints that integrate the penalized objective function must be normalized and normalized stress and displacement constraints given as below:

$$g_i\,(x) = \frac{\sigma_i(x)}{\sigma_a} - 1\ \leq 0\ \ i = 1,2, \dots, nm \tag{7}$$

$$g_j\,(x) = \frac{\delta_j(x)}{\delta_a} - 1\ \leq 0\ \ j = 1, 2, 3, \dots, nd \tag{8}$$

In this formulation, ${g_i}^{\sigma}$ represents the normalized stress constraint, with σ_i is calculated stress for i^{th} structural member, σ_a is allowable stress limit. Meanwhile, ${g_j}^{\delta}$ denotes normalized displacement constraints, δ_j is calculated displacement in j^{th} node of system, δ_a is allowable displacement limit and "nd" is the number of nodes whose displacement is restricted. Penalty function is given as below,

$$C = \sum_{i=1}^{m} c_i\ ,\ \begin{cases} c_i = g_i(x) & ,if\ g(x)_i > 0 \\ c_i = 0\ , & otherwise \end{cases} \tag{9}$$

where, m represents number of constraints, c_i is the value of each constraint and this term can be calculated as,

The formulation of the penalized objective function is as follows:

if $C = 0$ then

$$F_i = \sum_{i=1}^{nm} W_i \tag{10}$$

if $C > 0$ then

$$F_i = (1 + \varepsilon_1 . C)^{\varepsilon_2} \sum_{i=1}^{nm} W_i \tag{11}$$

where, F_i is objective function value of each agent, ε_1 is a constant parameter and its value is 1, ε_2 is a constant parameter and its value is 2, C represents the sum of the constraints and W_i denotes sum of the weight of each agent in population.

3. Results and discussion

3.1. Numerical examples

In the current section, two benchmark problems are solved to evaluate the performance of the MRA algorithm on the handling the structural optimization problems. In this regard, A 25-bar and A 72-bar spatial truss systems are selected.

3.1.1. 25 Bar spatial truss system

25 Bar spatial truss system has 25 elements and 10 node numbers. Size, geometry, axes and node numbers of structure are shown in Fig. 1. Material properties, discrete cross-sectional areas and constraints of structure represent in Table 1. The node numbers to which each element is connected and the group numbers of the elements used in the grouping process for reaching the optimum solution are shown in Table 2. Load information about the 25-Bar spatial truss system defined in Table 3. Furthermore, this system has 18 degrees of freedom. Also, elements of this structure are divided into 8 groups. Thus, population dimension is defined as 8 in solution process.

Table 1. Material properties and constraints data of the 25-bar space truss system

Property (Unit)	Value
E, modulus of elasticity (ksi)	10^4
ρ, material density (lb/in^3)	0.1
Discrete area set for design variables (in^2)	0.1, 0.2, 0.3, 0.4, 0.5, 0.6, 0.7, 0.8, 0.9, 1.0, 1.1, 1.2, 1.3, 1.4, 1.5, 1.6, 1.7, 1.8, 1.9, 2.0, 2.1, 2.2, 2.3, 2.4, 2.5, 2.6, 2.8, 3.0, 3.2, 3.4
Constraints data	
Stress constraints	-40 ksi $\leq (\sigma)_i \leq$ 40 ksi i = 1, ...,25
Displacement constraints	$(\delta)_j$ ≤0.35in. in x and y directions j=1,2

Table 2. Grouping details of the 25-bar space truss system

Element no. (i)	Node (i,1)	Node (i,2).	Group no.	Element no.(i)	Node (i,1)	Node (i,2).	Group no.
1	1	2	1	14	3	10	6
2	1	4	2	15	6	7	6
3	2	3	2	16	4	9	6
4	1	5	2	17	5	8	6
5	2	6	2	18	4	7	7
6	2	4	3	19	3	8	7
7	2	5	3	20	5	10	7
8	1	3	3	21	6	9	7
9	1	6	3	22	6	10	8
10	6	3	4	23	3	7	8
11	4	5	4	24	4	8	8
12	3	4	5	25	5	9	8
13	6	5	5				

Table 3. Load information about the 25-bar space truss system

Node	X (kips)	Y (kips)	Z (kips)
1	1	-10	-10
2	0	-10	-10
3	0.5	0	0
6	0.6	0	0

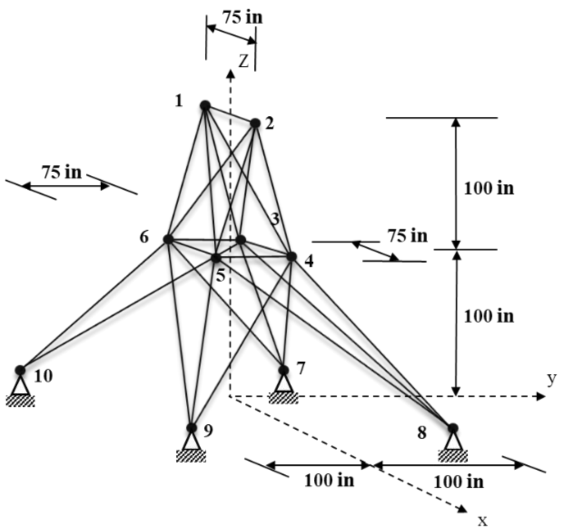

Fig. 1. A 25-Bar spatial truss system

3.1.2. 72 Bar spatial truss system

72 Bar spatial truss system has 72 elements and 18 degrees of freedom. This system's size, shape geometry, axes and node numbers of structure represent in Fig. 2. This system is a structure frequently studied in literature. Material properties, discrete cross-sectional areas and constraints of 72 Bar spatial truss system denoted in Table 4. The group numbers of the elements used in the grouping process for reaching the optimum solution are shown

in Table 5. Load information and cases are indicated in Table 6. Also, this structure's elements are divided into 16 groups. Therefore, population dimension is defined as 16 in solution process.

Table 4. Material properties and constraints data of the 72-bar space truss system

Property (Unit)	Value
E, modulus of elasticity (ksi)	10^4
ρ, material density (lb/in^3)	0.1
Discrete area set for design variables (in^2)	0.174, 0.220, 0.225, 0.270, 0.287, 0.350, 0.414, 0.431, 0.477, 0.508, 0.587, 0.600, 0.694, 0.667, 0.744, 0.882, 0.908, 0.978, 1.017, 1.071, 1.277, 1.349, 1.400, 1.457, 1.566, 1.705, 1.783, 1.845, 1.907, 2.046, 2.186, 2.217
Constraints data	
Stress constraints	-25 ksi $\leq (\sigma)_i \leq 25$ ksi $i = 1, ..., 72$
Displacement constraints	$(\delta)_j \leq 0.25$in. in x and y directions j = 17, 18, 19, 20

Table 5. Grouping information of 72-bar space truss system

Group no.	Group members	Group no.	Group members
A_1	1, 2, 3, 4	A_9	37, 38, 39, 40
A_2	5, 6, 7, 8, 9, 10, 11, 12	A_{10}	41, 42, 43, 44, 45, 46, 47, 48
A_3	13, 14, 15, 16	A_{11}	49, 50, 51, 52
A_4	17, 18	A_{12}	53, 54
A_5	19, 20, 21, 22	A_{13}	55, 56, 57, 58
A_6	23, 24, 25, 26, 27, 28, 29, 30	A_{14}	59, 60, 61, 62, 63, 64, 65, 66
A_7	31, 32, 33, 34	A_{15}	67, 68, 69, 70
A_8	35, 36	A_{16}	71, 72

Table 6. Load information and cases about the 72-bar space truss system

Load Case	Node	X (kips)	Y (kips)	Z (kips)
1	17	5	5	-5
2	17	0	0	-5
	18	0	0	-5
	19	0	0	-5
	20	0	0	-5

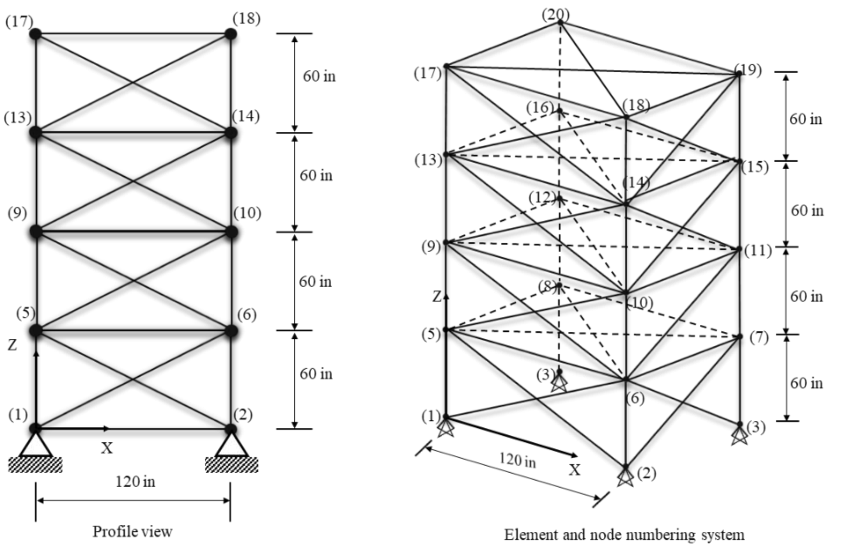

Fig. 2. A 72-bar spatial truss system

3.2. Optimum results for 25 and 72 bar spatial truss system

In this section the attained optimal results for selected problems are given and compared with those which are found with other methods.

Table 7. Optimum results for 25 bar spatial truss system

Design variable (area in^2)	(L.J. Li et al. 2009)		(T. Nguyen-Thoi et al. 2016)		(Mahdi Azizi et al. 2022)	(Mortazavi et al. 2017)	This Study
	PSO	HPSO	DE	aeDE	MGA	iPSO	MRA
A_1	0.4	0.1	0.1	0.1	0.1	0.1	0.1
A_2	0.6	0.3	0.3	0.3	0.3	0.3	0.3
A_3	3.5	3.4	3.4	3.4	3.4	3.4	3.4
A_4	0.1	0.1	0.1	0.1	0.1	0.1	0.1
A_5	1.7	2.1	2.1	2.1	2.1	2.1	2.1
A_6	1	1	1.0	1.0	1	1	1
A_7	0.3	0.5	0.5	0.5	0.5	0.5	0.5
A_8	3.4	3.4	3.4	3.4	3.4	3.4	3.4
W(lb)	486.54	484.85	484.854	484.854	484.8542	484.85	484.85
Std.	1.04208	0.02664	0.131	0.273	1.7437	2.023	1.88
OFE	25000	25000	3736	1678	2000	4980	1580

*PSO: Particle Swarm Optimization; HPSO: Heuristic Particle Swarm Optimization; DE: Differential Evolution; aeDE: Adaptive Elitist Differential Evolution; MGA: Material Generation Algorithm; ABC: Artificial Bee Colony Algorithm; CBO: Colliding Bodies Optimization; ECBO: Enhanced Colliding Bodies Optimization; iPSO: Integrated Particle Swarm Optimizer

Table 8. Optimum results for 72 bar spatial truss system

Design variable (area in^2)	(Erbatur et al. 2000)		(Lee et al. 2004)	(Talaslıoglu. 2009)	(Perez & Jansen. 2011)	(Dede et al. 2011)	This Study	
	GAOS2	GAOS3	HS	BGAwEIS	ALPSO	GA	MRA	
A_1	0.155	0.161	1.790	0.156	0.157	2.046	2.046	0.157
A_2	0.535	0.544	0.521	0.555	0.546	0.477	0.508	0.546
A_3	0.480	0.379	0.100	0.370	0.405	0.174	0.174	0.405
A_4	0.520	0.521	0.100	0.510	0.566	0.174	0.174	0.566
A_5	0.460	0.535	1.229	0.620	0.520	1.457	1.349	0.520
A_6	0.530	0.535	0.522	0.530	0.518	0.508	0.508	0.518
A_7	0.120	0.103	0.100	0.100	0.100	0.174	0.174	0.100
A_8	0.165	0.111	0.100	0.100	0.100	0.287	0.174	0.100
A_9	1.155	1.310	0.517	1.250	1.258	0.431	0.508	1.258
A_{10}	0.585	0.498	0.504	0.523	0.513	0.508	0.508	0.513
A_{11}	0.100	0.110	0.100	0.101	0.100	0.220	0.174	0.100
A_{12}	0.100	0.103	0.101	0.105	0.100	0.220	0.174	0.100
A_{13}	1.755	1.910	0.156	1.860	1.898	0.174	0.174	1.898
A_{14}	0.505	0.525	0.547	0.513	0513	0.587	0.508	0513
A_{15}	0.105	0.122	0.442	0.100	0.100	0.431	0.414	0.100
A_{16}	0.155	0.103	0.590	0.100	0.100	0.431	0.600	0.100
W(lb)	385.76	383.12	379.27	380.784	379.61	407.37	398.96	379.61
Std	-	-	-	409.814	-	-	11.25	8.25
OFE	-	-	20000	300000	25000	19100	2520	2140

*GAOS: Genetic Algorithm Based Optimum Structural Design; HS: Harmony Search Algorithm; BGAwEIS: Bipopulation-Based Genetic Algorithm with Enhanced Interval Search; GA: Genetic Algorithm; ALPSO: Augmented Lagrangian Particle Swarm Optimization Algorithm

4. Conclusions

In this study, the performance of a recently developed optimization technique, the Marathon Runner Algorithm (MRA), a metaheuristic approach inspired by endurance strategies, is evaluated for solving structural optimization problems with discrete variables. The algorithm is applied to weight minimization problems in two structures: a 25-bar spatial truss and a 72-bar spatial truss. The results obtained can be summarized as follows:

- The numerical results obtained for the selected problems indicate that the algorithm performs well in terms of accuracy.
- Statistical tests (measured by standard deviation) show that the MRA demonstrates a high level of stability in handling the selected problems.
- The number of required objective function evaluations (OFEs) suggests that the MRA demands comparatively lower computational cost to find the optimal solution.
- These improvements can be attributed to the Marathon Runner Algorithm's use of weighted agents, unlike many other metaheuristic algorithms that rely solely on the best agent during the population update phase.

By utilizing all stored information within the population, the weighted agent preventing data loss makes a better application of the gathered information and increases the efficiency of the search process.

According to these conclusions, generally, MRA shows promising optimization algorithm for structural optimization problems. Based on this fact, in the future works, it is planned to utilize Marathon Runner Algorithm on more complicated structural engineering problems.

References

Arora, S., & Singh, S. (2019). Butterfly optimization algorithm: A novel approach for global optimization. *Soft Computing, 23*(3), 715–734. https://doi.org/10.1007/s00500-018-3102-4

Ayvaz, Y., & Aydin, Z., (2000). Optimum design of trusses using a genetic algorithm. In *5th International Conference on Computational Structures Technology/2nd International Conference on Engineering Computational Technology* (pp.159-168). Leuven, Belgium.

Azizi, M., Baghalzadeh Shishehgar, M., & Basiri, M. (2022). Optimum design of truss structures by Material Generation Algorithm with discrete variables. *Decision Analytics Journal, 3*, 100043. https://doi.org/10.1016/j.dajour.2022.100043

Cheng, M.-Y., & Prayogo, D. (2014). Symbiotic organisms search: A new metaheuristic optimization algorithm. *Computers and Structures, 139*, 98–112. https://doi.org/10.1016/j.compstruc.2014.03.007

Chu, S.-C., Wang, T.-T., Yildiz, A.R., & Pan, J.-S. (2024). Ship rescue optimization: A new metaheuristic algorithm for solving engineering problems. *Journal of Internet Technology, 25*(1), 61–78. https://doi.org/10.53106/160792642024012501006.

Das, K.N., & Singh, T.K. (2014). Drosophila food-search optimization. *Applied Mathematics and Computation, 231*, 566–580. https://doi.org/10.1016/j.amc.2014.01.040

Dede, T., Bekiroğlu, S., & Ayvaz, Y. (2011). Weight minimization of trusses with genetic algorithm. *Applied Soft Computing, 11*(2), 2565–2575. https://doi.org/10.1016/j.asoc.2010.10.006

Erbatur, F., Hasançebi, O., Tütüncü, İ., & Kılıç, H. (2000). Optimal design of planar and space structures with genetic algorithms. *Computers and Structures, 75*(2), 209–224. https://doi.org/10.1016/S0045-7949(99)00084-X

Gandomi, A.H., Yang, X.-S., & Alavi, A.H. (2011). Mixed variable structural optimization using Firefly Algorithm. *Computers and Structures, 89*(23–24), 2325–2336. https://doi.org/10.1016/j.compstruc.2011.08.002

Glover, F. (1989). Tabu search– Part I. *ORSA Journal on Computing, 1*(3), 190–206. https://doi.org/10.1287/ijoc.1.3.190

Holland, J.H. (1984). Genetic algorithms and adaptation. In O.G. Selfridge, E.L. Rissland, & M.A. Arbib (Eds.), *Adaptive control of ill-defined systems* (pp. 317–333). Springer US.

Ho-Huu, V., Nguyen-Thoi, T., Vo-Duy, T., & Nguyen-Trang, T. (2016). An adaptive elitist differential evolution for optimization of truss structures with discrete design variables. *Computers and Structures, 165*, 59–75. https://doi.org/10.1016/j.compstruc.2015.11.014

Jansen, P.W., & Perez, R.E. (2011). Constrained structural design optimization via a parallel augmented Lagrangian particle swarm optimization approach. *Computers & Structures, 89*(13-14), 1352–1366. https://doi.org/10.1016/j.compstruc.2011.03.011

Javidy, B., Hatamlou, A., & Mirjalili, S. (2015). Ions motion algorithm for solving optimization problems. *Applied Soft Computing, 32*, 72–79. https://doi.org/10.1016/j.asoc.2015.03.035

Kennedy, J., & Eberhart, R. (1995). Particle swarm optimization. In *Neural Networks, 1995 Proceedings, IEEE International Conference* (Vol. 4, pp. 1942–1948). IEEE Xplore. https://doi.org/10.1109/ICNN.1995.488968

Lee, K.S., & Geem, Z.W. (2004). A new structural optimization method based on the harmony search algorithm. *Computers and Structures, 82*(9–10), 781–798. https://doi.org/10.1016/j.compstruc.2004.01.002

Li, L.J., Huang, Z.B., & Liu, F. (2009). A heuristic particle swarm optimization method for truss structures with discrete variables. *Computers and Structures, 87*(5-6), 435–443. https://doi.org/10.1016/j.compstruc.2009.01.004

Liang, Y.-C., & Cuevas Juarez, J.R. (2016). A novel metaheuristic for continuous optimization problems: Virus optimization algorithm. *Engineering Optimization, 48*(1), 73–93. https://doi.org/10.1080/0305215X.2014.994868

Mortazavi, A. (2019). Comparative assessment of five metaheuristic methods on distinct problems. *DUJE (Dicle University Journal of Engineering), 10*(3), 879–898. https://doi.org/10.24012/dumf.585790

Mortazavi, A., Toğan, V., & Nuhoğlu, A. (2017). Weight minimization of truss structures with sizing and layout variables using integrated particle swarm optimizer. *Journal of Civil Engineering and Management, 23*(8), 985–1001. https://doi.org/10.3846/13923730.2017.1348982

Nematollahi, A.F., Rahiminejad, A., & Vahidi, B. (2019). A novel metaheuristic optimization method based on golden ratio in nature. *Soft Computing, 24*, 1117–1151. https://doi.org/10.1007/s00500-019-03949-w

Patel, V.K., & Savsani, V.J. (2015). Heat transfer search (HTS): A novel optimization algorithm. *Information Sciences, 324*, 217–246. https://doi.org/10.1016/j.ins.2015.06.044

Rao, R.V., Savsani, V.J., & Vakharia, D.P. (2011). Teaching–learning-based optimization: A novel method for constrained mechanical design optimization problems. *Computer-Aided Design, 43*(3), 303–315. https://doi.org/10.1016/j.cad.2010.12.015

Talaslioglu, T. (2009). A new genetic algorithm methodology for design optimization of truss structures: Bipopulation-based genetic algorithm with enhanced interval search. *Modelling and Simulation in Engineering,* Article ID 615162, 28 pages. https://doi.org/10.1155/2009/615162

Talatahari, S., Kheirollahi, M., Farahmandpour, C., & Gandomi, A.H. (2013). A multi-stage particle swarm for optimum design of truss structures. *Neural Computing and Applications, 23*(5), 1297–1309. https://doi.org/10.1007/s00521-012-1072-5

Yang, X.S. (2009, October). Firefly algorithms for multimodal optimization. In International symposium on stochastic algorithms (pp. 169-178). Berlin, Heidelberg: Springer Berlin Heidelberg.

Zheng, Y.-J. (2015). Water wave optimization: A new nature-inspired metaheuristic. *Computers & Operations Research, 55*, 1–11. https://doi.org/10.1016/j.cor.2014.10.008

4th International Civil Engineering & Architecture Conference
17-19 May 2025, Trabzon, Türkiye

Geometrically nonlinear analysis of composite beams via mixed FEM

Elif Koc[1], Umit N. Aribas*[1], Merve Ermis[2], Mehmet H. Omurtag[1]

[1] *Istanbul Medipol University, School of Engineering and Natural Sciences, Department of Civil Engineering, 34810, Istanbul, Türkiye*
[2] *Kirklareli University, Faculty of Engineering, Department of Civil Engineering, 39000, Kirklareli, Türkiye*

Abstract. Geometrically nonlinear analysis of composite beams composed of transversely-isotropic layers is performed via the mixed finite element method under the influence of distributed forces along its length in this study. The classical beam stress-free surface conditions are satisfied on the three-dimensional constitutive equations of a transversely-isotropic body based on Von Kármán nonlinear strains. The virtual work theorem and the first variation of the Hellinger-Reissner functional are employed to derive the nonlinear equations of the mixed finite element formulation. The two-noded mixed finite elements have twenty-four degrees of freedom in total such as three displacements, three section rotations, three forces, two bending moments, and one torsional moment at each node. The finite element mesh convergence analysis is performed both for the mixed finite elements and the 3D brick finite elements (ANSYS SOLID186 elements). Quite satisfactory geometrically nonlinear displacements of composite beams having transversely isotropic layers are obtained via the two-noded mixed finite elements by using lesser degrees of freedom compared to the results of ANSYS SOLID186 elements. As benchmark examples, the moderately large deflections of composite beams subjected to the distributed forces are investigated and the results are compared to the linear deflections as the span ratio decreases and/or the thickness of stiffener increases.

Keywords: Geometrically nonlinear analysis; Composite beams; Transversely-isotropic material; Mixed finite elements

1. Introduction

Laminated composite structures are widely used in engineering due to their high strength, stiffness, and lightweight properties. These structures consist of fiber-reinforced layers, typically transversely isotropic, allowing engineers to optimize performance by adjusting fiber type, orientation, and matrix composition. Compared to metals, laminated composites offer superior weight reduction and mechanical efficiency, making them ideal for aerospace, automotive, and marine applications (Hwu, 2024).

A specialized type, sandwich structures, consists of stiff outer facings and a lightweight core (foam, honeycomb, or corrugated materials), enhancing impact resistance and reducing weight. Their excellent mechanical properties make them crucial in strength-sensitive applications (Sandeep & Srinivasa, 2020).

Composite structures exhibit nonlinear behavior under increased loading. Initially, load-displacement remains linear, but beyond a critical threshold, nonlinearity emerges due to material effects (plasticity, damage, matrix cracking) and geometric effects (large deformations altering stiffness). Understanding these nonlinearities enables the design of more efficient and durable structures (Drosopoulos & Stavroulakis, 2022).

Sayyad and Ghugal (2017) reviewed bending, buckling, and vibration analyses of laminated and sandwich beams, emphasizing the need for further nonlinear studies. Their study focused on equivalent single-layer, layerwise, and zig-zag theories, as well as exact elasticity solutions. They examined various analytical and numerical methods based on classical and refined beam theories. While linear analysis is well-explored (Baziyar Hamzehkhani et al., 2024; Ma, 2020; Pietro et al., 2019; Sorrenti et al., 2025; Yan et al., 2018), nonlinear analysis remains underdeveloped.

Given its crucial role in predicting structural behavior under large deformations, this study focuses on geometrically nonlinear analysis. The following section reviews recent research conducted over the past five years on this topic. Ascione and Gherlone (2020) developed a nonlinear formulation using Refined Zigzag Theory (RZT) to analyze the buckling and nonlinear static response of multilayered composite and sandwich beams with

* Corresponding author, E-mail: umit.aribas@medipol.edu.tr

https://doi.org/10.31462/icearc2025_ce_sme_497

geometric imperfections. Their numerical simulations examined three sandwich beams with different core materials and slenderness ratios under simply supported and cantilever boundary conditions. The analysis employed C_0-beam finite elements based on RZT and Timoshenko Beam Theory (TBT), with initial imperfections approximated using quadratic Lagrange polynomials. The results from RZT and TBT were validated against high-fidelity commercial software, such as Abaqus and Nastran.

Wei et al. (2020) introduced an extended high-order sandwich panel theory (EHSAPT) to evaluate the static response of sandwich panels while incorporating both geometrical and material nonlinearities. Geometrical nonlinearity was accounted for using Green–Lagrange strain expressions for the face sheets and core, while material nonlinearity was modeled through a piecewise function derived from experimental stress–strain data fitted with a polynomial approach. The governing equations were solved using the Ritz method, demonstrating the model's effectiveness in capturing the stress stiffening effect in geometric nonlinear analysis.

Wei and Wu (2023) developed a theoretical framework for analyzing the transient response of elastoplastic sandwich beams subjected to underwater blasts. They introduced two fully coupled fluid-structure interaction (FSI) models to study blast wave propagation, energy dissipation, and optimal sandwich structure design for enhanced blast resistance. Using nonlinear dynamic high-order sandwich panel theory (EHSAPT), they modified the governing equation by incorporating a rarefaction-wave-related term into the structural damping matrix. This reformulated the underwater blast analysis as a dynamic response problem under incident and reflected waves in a vacuum. Additionally, they derived a simplified governing equation to obtain an analytical solution for the impulse transferred to the structure, considering displacement and core rigidity assumptions.

Chen and Chen (2024) formulated finite element models based on higher-order refined zigzag theory (HRZT) to investigate the linear static bending, geometric nonlinearity, and buckling behavior of sandwich composite beams. HRZT extends RZT by incorporating higher-order terms related to average shear strain and zigzag-induced rotation. For linear static bending, both C_0 and C_1 finite elements were formulated, with an additional node introduced in the C_0 element to reduce shear locking. In the geometric nonlinear analysis, a two-node C_0 element was used to evaluate the bending response under lateral loading and buckling behavior. Numerical results were validated against 2D exact solutions, analytical solutions from HRZT, and commercial software models. Comparisons were also made with various beam theories, including first-order shear deformation theory (FSDT), higher-order shear deformation theory (HSDT), RZT, and other higher-order zigzag theories.

In this study, the moderately large deflections of composite beams having transversely-isotropic layers are investigated via the geometrically nonlinear mixed finite element formulation. The constitutive equations are derived via satisfying the classical beam stress-free surface conditions on the three-dimensional constitutive equations of transversely-isotropic bodies considering Von Kármán nonlinear strains. The nonlinear equations of the mixed finite element formulation are based on the first variation of the Hellinger-Reissner functional. The two-noded mixed finite elements have twelve degrees of freedom at each node.

2. Mathematical formulation

The constitutive relations of a transversely-isotropic body are given in Jones (2018) based on the Hooke's law as $\boldsymbol{\sigma} = \mathbf{E}\boldsymbol{\varepsilon}$, where $\boldsymbol{\sigma}$ and $\boldsymbol{\varepsilon}$ are the three-dimensional stress and strain vectors, respectively and $\mathbf{E}$ is the elasticity matrix. The constitutive relations of layered composite beams which are derived via satisfying the classical beam stress-free surface conditions on the three-dimensional constitutive relations are given in Aribas et al. (2019) as,

$$\begin{Bmatrix} \sigma_x \\ \tau_{zx} \\ \tau_{xy} \end{Bmatrix}_L = \boldsymbol{\beta}_L \begin{Bmatrix} \varepsilon_x \\ \gamma_{zx} \\ \gamma_{xy} \end{Bmatrix}_L \tag{1}$$

where the subscript L is the layer partition and $\boldsymbol{\beta}_L$ is a 3×3 matrix. The displacement field of the layered beam is stated as,

$$\begin{aligned} u_x^* &= u_x + z\,\Omega_y - y\,\Omega_z \\ u_y^* &= u_y - z\,\Omega_x \\ u_z^* &= u_z + y\,\Omega_x \end{aligned} \tag{2}$$

where, u_x, u_y, u_z and $\Omega_x, \Omega_y, \Omega_z$ are the displacements and the rotations on the beam axis, respectively. Von Kármán nonlinear strains are obtained based on the displacement field as,

$$
\begin{aligned}
\varepsilon_x^* &= u_{x,x}^* + \tfrac{1}{2}\left[\left(u_{x,x}^*\right)^2 + \left(u_{y,x}^*\right)^2 + \left(u_{z,x}^*\right)^2\right] \\
\varepsilon_{xy}^* &= \tfrac{1}{2}\left[u_{x,y}^* + u_{y,x}^* + u_{x,x}^*\, u_{x,y}^* + u_{y,x}^* u_{y,y}^* + u_{z,x}^* u_{z,y}^*\right] \\
\varepsilon_{zx}^* &= \tfrac{1}{2}\left[u_{x,z}^* + u_{z,x}^* + u_{x,x}^*\, u_{x,z}^* + u_{y,x}^*\, u_{y,z}^* + u_{z,x}^* u_{z,z}^*\right]
\end{aligned}
\tag{3}
$$

where, the partial derivations are denoted by the commas in the subscripts. The forces F_x, F_y, F_z and the moments M_x, M_y, M_z are obtained via the integration of stresses through the thickness (Aribas et al., 2022). Finally, the explicit form of the equilibrium equations is,

$$
\begin{aligned}
&-F_{x,x} - \left(F_x\, u_{x,x}\right)_{,x} - \left(M_y \Omega_{y,x}\right)_{,x} - \left(M_z \Omega_{z,x}\right)_{,x} + \left(T_y \Omega_z\right)_{,x} - \left(T_z \Omega_y\right)_{,x} - q_x = 0 \\
&-T_{y,x} - \left(T_x\, u_{y,x}\right)_{,x} + \left(M_y \Omega_{x,x}\right)_{,x} + \left(T_z \Omega_x\right)_{,x} - q_y = 0 \\
&-T_{z,x} - \left(T_x\, u_{z,x}\right)_{,x} + \left(M_z \Omega_{x,x}\right)_{,x} - \left(T_y \Omega_x\right)_{,x} - q_z = 0 \\
&-M_{x,x} + \left(M_y u_{y,x}\right)_{,x} + \left(M_z u_{z,x}\right)_{,x} + T_y u_{z,x} - T_z u_{y,x} - M_{x,x} - m_x = 0 \\
&-M_{y,x} + T_z - \left(M_y u_{x,x}\right)_{,x} - \left(M_x \Omega_z\right)_{,x} + T_z u_{x,x} - M_x \Omega_{z,x} - m_y = 0 \\
&-M_{z,x} - T_y - \left(M_z u_{x,x}\right)_{,x} - T_y u_{x,x} + M_x \Omega_{y,x} + \left(M_x \Omega_y\right)_{,x} - m_z = 0
\end{aligned}
\tag{4}
$$

where, the external distributed forces and moments are q_x, q_y, q_z and m_x, m_y, m_z, respectively. Based on the field equations and boundary conditions $-\mathbf{u} + \hat{\mathbf{u}} = \mathbf{0}$, $-\mathbf{\Omega} + \hat{\mathbf{\Omega}} = \mathbf{0}$, $\mathbf{F} - \hat{\mathbf{F}} = \mathbf{0}$ and $\mathbf{M} - \hat{\mathbf{M}} = \mathbf{0}$ where, the displacement, cross-sectional rotation, force and moment vectors are given by $\mathbf{u}(u_x, u_y, u_z)$, $\mathbf{\Omega}(\Omega_x, \Omega_y, \Omega_z)$, $\mathbf{F}(F_x, F_y, F_z)$ and $\mathbf{M}(M_x, M_y, M_z)$, respectively, and the terms with a hat are the known boundary values, the first variation of Hellinger-Reissner functional (Aksoylar, 2010) is derived via,

$$
\delta \Pi_{HR} = \int_V \left(\boldsymbol{\varepsilon}^{\mathrm{u}} - \boldsymbol{\varepsilon}^{\sigma}\right)^T \delta\boldsymbol{\sigma}^{\sigma} \mathrm{d}V + \int_V \left(\left(\boldsymbol{\sigma}^{\sigma}\right)^T \delta\boldsymbol{\varepsilon}^{\mathrm{u}} - \mathbf{q}^T \delta\mathbf{u}\right) \mathrm{d}V - \int_\Gamma \hat{\mathbf{t}}^T \delta\mathbf{u}\, \mathrm{d}\Gamma = 0 \tag{5}
$$

where, $\hat{\mathbf{t}}$ is the traction vector at the boundary Γ, the components in terms of the forces and displacements are denoted by the superscripts σ and ε, respectively. The variational equations in the mixed form are,

$$
\begin{aligned}
&\int_L \left[u_{x,x} + \tfrac{1}{2}u_{x,x}^2 + \tfrac{1}{2}u_{y,x}^2 + \tfrac{1}{2}u_{z,x}^2\right]\delta F_x\, \mathrm{d}x + \int_L \left[-C_{11}F_x - C_{12}F_y - C_{14}M_x - C_{15}M_y\right]\delta F_x\, \mathrm{d}x - \int_L \delta u_x q_x \mathrm{d}x \\
&+\int_L \left[\left(u_{y,x} - \Omega_z\right) - u_{x,x}\Omega_z + u_{z,x}\Omega_x\right]\delta F_y\, \mathrm{d}x + \int_L \left[-C_{12}F_x - C_{22}F_y - C_{24}M_x - C_{25}M_y\right]\delta F_y\, \mathrm{d}x - \int_L \delta u_y q_y \mathrm{d}x \\
&+\int_L \left[\left(u_{z,x} + \Omega_y\right) + u_{x,x}\Omega_y - u_{y,x}\Omega_x\right]\delta F_z\, \mathrm{d}x + \int_L \left[-C_{33}F_z\right]\delta F_z\, \mathrm{d}x + \int_L \left[\Omega_{x,x} + \Omega_{y,x}\Omega_z\right]\delta M_x\, \mathrm{d}x - \int_L \delta u_z q_z \mathrm{d}x \\
&+\int_L \left[-C_{14}F_x - C_{24}F_y - C_{44}M_x - C_{45}M_y\right]\delta M_x\, \mathrm{d}x + \int_L \left[\Omega_{y,x} + u_{x,x}\Omega_{y,x} - u_{y,x}\Omega_{x,x}\right]\delta M_y\, \mathrm{d}x - \int_L \delta\Omega_x m_x \mathrm{d}x \\
&+\int_L \left[-C_{15}F_x - C_{25}F_y - C_{45}M_x - C_{55}M_y\right]\delta M_y\, \mathrm{d}x + \int_L \left[\Omega_{z,x} + u_{x,x}\Omega_{z,x} - u_{z,x}\Omega_{x,x}\right]\delta M_z\, \mathrm{d}x - \int_L \delta\Omega_y m_y \mathrm{d}x \\
&+\int_L \left[-C_{66}M_z\right]\delta M_z\, \mathrm{d}x - \int_L \delta\Omega_z m_z \mathrm{d}x + \int_L \left[F_x + F_x\, u_{x,x} + M_y \Omega_{y,x} + M_z \Omega_{z,x} - F_y\Omega_z + F_z\Omega_y\right]\delta u_{x,x}\mathrm{d}x \\
&+\int_L \left[F_y + F_x\, u_{y,x} - M_y \Omega_{x,x} - F_z\Omega_x\right]\delta u_{y,x}\mathrm{d}x + \int_L \left[F_z + F_x\, u_{z,x} - M_z \Omega_{x,x} + F_y\Omega_x\right]\delta u_{z,x}\mathrm{d}x \\
&+\int_L \left[F_y u_{z,x} - F_z u_{y,x}\right]\delta\Omega_x \mathrm{d}x + \int_L \left[M_x - M_y u_{y,x} - M_z u_{z,x}\right]\delta\Omega_{x,x}\mathrm{d}x + \int_L \left[F_z + F_z u_{x,x}\right]\delta\Omega_y \mathrm{d}x \\
&+\int_L \left[M_y + M_y u_{x,x} + M_x\Omega_z\right]\delta\Omega_{y,x}\mathrm{d}x + \int_L \left[-F_y - F_y u_{x,x} + M_x\Omega_{y,x}\right]\delta\Omega_z \mathrm{d}x + \int_L \left[M_z + M_z u_{x,x}\right]\delta\Omega_{z,x}\mathrm{d}x \\
&-\Big\langle \left(\left(u_x - \hat{u}_x\right), F_x\right) + \left(\left(u_y - \hat{u}_y\right), F_y\right) + \left(\left(u_z - \hat{u}_z\right), F_z\right) + \left(\left(\Omega_x - \hat{\Omega}_x\right), M_x\right) + \left(\left(\Omega_y - \hat{\Omega}_y\right), M_y\right) \\
&+\left(\left(\Omega_z - \hat{\Omega}_z\right), M_z\right)\Big\rangle_{\varepsilon} - \Big\langle \left(\hat{F}_x, u_x\right) + \left(\hat{F}_y, u_y\right) + \left(\hat{F}_z, u_z\right) + \left(\hat{M}_x, \Omega_x\right) + \left(\hat{M}_y, \Omega_y\right) + \left(\hat{M}_z, \Omega_z\right)\Big\rangle_{\sigma}
\end{aligned}
\tag{6}
$$

where, $C_{11}, C_{12}, C_{14}, C_{15}, C_{22}, C_{24}, C_{25}, C_{33}, C_{44}, C_{45}, C_{55}, C_{66}$ are the components of the compliance matrix which is given in Aribas et al. (2024). The nonlinear equations are linearized (Basar & Krätzig, 2013; Doğruoğlu & Omurtag, 2000) and the functional is obtained. The two-noded mixed finite element formulation has twelve degrees of freedom at each node as three displacements, three rotations, one axial force, two shear forces, one torsional moment, and two bending moments (Aribas et al., 2024; Eratli et al., 2016; Omurtag & Aköz, 1992). The Newton-Raphson algorithm is employed for the iterative solution approach (Aksoylar, 2010).

3. Numerical examples

3.1. Convergence analysis

In this example, a finite element mesh convergence analysis is performed for the geometrically nonlinear deformations of a cantilever sandwich beam subjected to the distributed loading along its length via the mixed finite elements (MFEs) and SOLID186 brick finite elements of ANSYS. The length of the cantilever sandwich beam is L = 4m. The width and total thickness of the sandwich cross-section are w = 0.3m and h = 0.03m, respectively. The stiffeners have equal thicknesses, and the total thickness of the stiffeners is h_s = 0.05m. The core is made of Kevlar 49-Epoxy and its elasticity moduli are E_x = 76GPa, $E_y = E_z$ = 5.56GPa, Poisson's ratios are $\nu_{xy} = \nu_{xz} = 0.34$, $\nu_{yz} = 0.718$, and the shear moduli are $G_{xy} = G_{zx}$ = 2.3GPa, G_{yz} = 1.618GPa, respectively. The stiffeners are made of Boron Epoxy and its elasticity moduli are E_x = 241.5GPa, $E_y = E_z$ = 18.89GPa, Poisson's ratios are $\nu_{xy} = \nu_{xz} = 0.24$, $\nu_{yz} = 0.25$, and the shear moduli are $G_{xy} = G_{zx}$ = 5.18GPa, G_{yz} = 3.45GPa, respectively. The cantilever sandwich beam is subjected to the uniformly distributed load q_z = 184N/m along its length (Fig. 1). First, the displacement at the tip u_z of the cantilever sandwich beam is obtained via 10, 20, 30, 40 and 50 mixed finite elements (corresponding to 132, 252, 372, 492, 612 degrees of freedom, respectively) and the results are given in Table 1. It is obtained that 132 DOFs provide quite satisfactory convergence for the mixed finite elements. Next, the displacement at the tip u_z of the sandwich beam is obtained via SOLID186 brick finite elements with 801 – 775341 DOFs (Table 2). The percentage difference of the results with respect to the result of 775341 DOFs becomes less than 1% for the 15210 DOFs. The percentage difference of the results of MFEs having 132 DOFs with respect to the results of SOLID186 elements having 15210 DOFs is -0.93%.

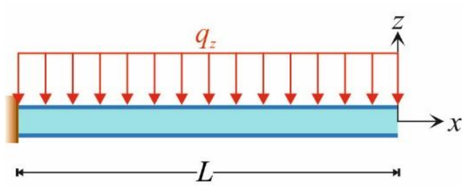

Fig. 1. The cantilever sandwich beam with transversely-isotropic layers subjected to a uniformly distributed load.

Table 1. The tip displacements of sandwich beam obtained via the geometrically-nonlinear mixed finite elements

MFEs	DOFs*	u_z (m)	Diff.%*
10	132	0.117377	0.48
20	252	0.116920	0.08
30	372	0.116850	0.02
40	492	0.116831	0.01
50	612	0.116822	

*DOFs: Degrees of freedom; Diff.%: The percentage difference with respect to the results of 612 DOFs.

Table 2. The tip displacements of sandwich beam obtained via the SOLID186 brick finite elements of ANSYS

DOFs*	u_z (m)	Diff.%*
801	-0.123280	4.05
972	-0.122710	3.57
2502	-0.121000	2.13
6012	-0.120650	1.83
8757	-0.120220	1.47
15210	-0.119180	0.59
32607	-0.118960	0.41
149649	-0.118640	0.14
775341	-0.118480	

*DOFs: Degrees of freedom; Diff.%: The percentage difference with respect to the results of 612 DOFs.

3.2. Parametric analysis

In this example, a parametric analysis is performed for the geometrically nonlinear deformations of a sandwich beam subjected to uniformly distributed loads along its length as the span ratio and/or the ratio of total thickness of stiffeners to cross-section decreases. The length of the sandwich beam is set to L = 4m, 6m and 8m, respectively while keeping the width and total thickness of the cross-section constant as w = 0.3m and h = 0.03m, respectively. The stiffeners have equal thickness and the ratio of total thickness of stiffeners to cross-section is set to λ_h = 0.100, 0.133 and 0.167, respectively. The core is made of Kevlar 49-Epoxy and the stiffeners are made of Boron Epoxy. The material properties of Kevlar 49-Epoxy and Boron Epoxy are given in Section 3.1. First, the displacement at the tip of a cantilever sandwich beam related to the increase in the magnitude of the distributed load q_z is given in Table 3 for each case. The percentage differences of the tip displacements obtained via the geometrically nonlinear analysis with respect to the linear analysis are illustrated in Fig. 2. Next, the midspan displacements of a sandwich beam having pinned support at both ends are obtained via the linear and geometrically nonlinear analyses for L = 4m (Table 4). Similarly, the percentage differences of the midspan displacements obtained via the geometrically nonlinear analysis with respect to the linear analysis are illustrated in Fig. 3.

Table 3. The tip displacement of the cantilever sandwich beam related to the increase in q_z

	L = 4m			L = 6m			L = 8m		
λ_h	q_z (N/m)	u_z (mm)	$\bar{u}_z$ (mm)	q_z (N/m)	u_z (mm)	$\bar{u}_z$ (mm)	q_z (N/m)	u_z (mm)	$\bar{u}_z$ (mm)
0.100	75.95	30.00	30.00	15.01	30.00	30.00	4.75	30.00	30.00
	151.89	60.00	59.98	30.02	60.00	59.99	9.50	60.00	59.99
	227.84	90.00	89.92	45.03	90.00	89.97	14.25	90.00	89.98
	303.78	120.00	119.82	60.04	120.00	119.92	19.00	120.00	119.95
	379.73	150.00	149.65	75.05	150.00	149.84	23.75	150.00	149.91
	455.68	180.00	179.40	90.06	180.00	179.73	28.50	180.00	179.85
	607.57	240.00	238.58	120.08	240.00	239.36	38.00	240.00	239.64
	759.46	300.00	297.24	150.10	300.00	298.76	47.50	300.00	299.30
0.133	84.06	30.00	30.00	16.61	30.00	30.00	5.26	30.00	30.00
	168.11	60.00	59.98	33.23	60.00	59.99	10.52	60.00	59.99
	252.17	90.00	89.92	49.84	90.00	89.97	15.77	90.00	89.98
	336.22	120.00	119.82	66.46	120.00	119.92	21.03	120.00	119.95
	420.28	150.00	149.65	83.07	150.00	149.84	26.29	150.00	149.91
	504.34	180.00	179.40	99.68	180.00	179.73	31.55	180.00	179.85
	672.45	240.00	238.58	132.91	240.00	239.36	42.06	240.00	239.64
	840.56	300.00	297.24	166.14	300.00	298.76	52.58	300.00	299.30
0.167	91.57	30.00	30.00	18.10	30.00	30.00	5.73	30.00	30.00
	183.13	60.00	59.98	36.20	60.00	59.99	11.46	60.00	59.99
	274.70	90.00	89.92	54.30	90.00	89.97	17.18	90.00	89.98
	366.26	120.00	119.82	72.40	120.00	119.92	22.91	120.00	119.95
	457.83	150.00	149.65	90.50	150.00	149.84	28.64	150.00	149.91
	549.39	180.00	179.40	108.59	180.00	179.73	34.37	180.00	179.85
	732.53	240.00	238.58	144.79	240.00	239.36	45.82	240.00	239.64
	915.66	300.00	297.24	180.99	300.00	298.76	57.28	300.00	299.30

* u_z and $\bar{u}_z$: Displacements of linear and geometrically nonlinear analyses, respectively.

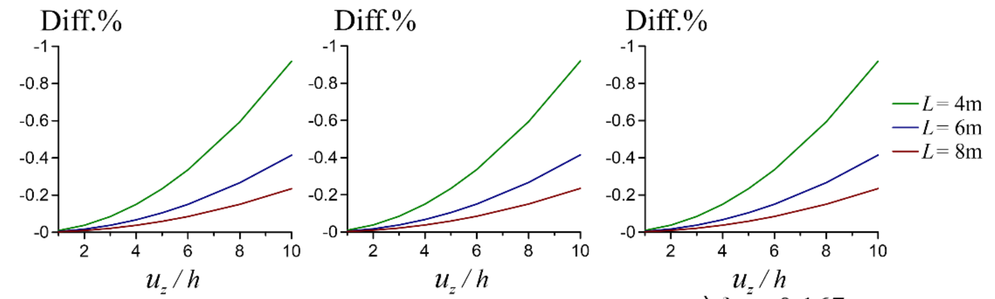

a) $\lambda_h = 0.100$ b) $\lambda_h = 0.133$ c) $\lambda_h = 0.167$

Fig. 2. The percentage differences of geometrically nonlinear displacements to linear displacements at the tip

Table 4. The midspan displacements of the sandwich beam with pinned supports as q_z increases (L = 4m)

$\lambda_h = 0.100$			$\lambda_h = 0.133$			$\lambda_h = 0.167$		
q_z (N/m)	u_z (mm)	$\bar{u}_z$ (mm)	q_z (N/m)	u_z (mm)	$\bar{u}_z$ (mm)	q_z (N/m)	u_z (mm)	$\bar{u}_z$ (mm)
14.51	0.60	0.60	14.51	0.60	0.60	17.49	0.60	0.60
29.03	1.20	1.20	29.03	1.20	1.20	34.99	1.20	1.20
43.54	1.80	1.79	43.54	1.80	1.79	52.48	1.80	1.79
58.05	2.40	2.37	58.05	2.40	2.37	69.98	2.40	2.37
72.56	3.00	2.93	72.56	3.00	2.94	87.47	3.00	2.94
87.08	3.60	3.49	87.08	3.60	3.49	104.97	3.60	3.50
116.10	4.80	4.56	116.10	4.80	4.56	139.95	4.80	4.57
145.13	6.00	5.56	145.13	6.00	5.57	174.94	6.00	5.58

* u_z and $\bar{u}_z$: Displacements of linear and geometrically nonlinear analyses, respectively.

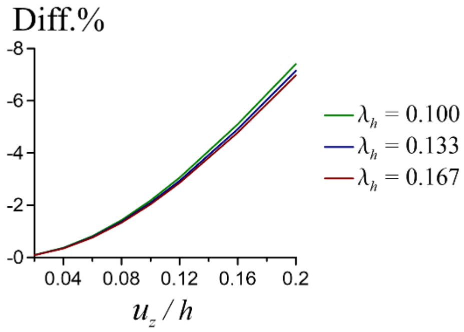

Fig. 3. The percentage differences of geometrically nonlinear midspan displacements to linear results

It is obtained that the absolute percentage differences of geometrically nonlinear tip displacements with respect to the linear displacements increase more as the span ratio of the cantilever sandwich beam decreases (Fig. 2). Similarly, the absolute percentage differences increase as the ratio of total thicknesses of stiffeners to cross-section decreases. It is more obvious as the span ratio decreases, for example, the percentage differences are -0.9197%, -0.9198% and -0.9200% for λ_h = 0.167, 0.133 and 0.100, respectively in the case of u_z / h =10 and L = 4m. However, the influence of the geometrically nonlinear deformation becomes greater within the scope of the pinned boundary conditions compared to the cantilever boundary conditions (Fig. 3). The percentage differences become -6.97%, -7.15% and -7.41% as u_z / h increases to 0.2 for λ_h = 0.167, 0.133 and 0.100, respectively in the case of L = 4m.

4. Conclusions

This study presents a geometrically nonlinear analysis of sandwich beams composed of transversely-isotropic layers, using the mixed finite element method under distributed loading along the beam's length. The analysis is grounded in satisfying the classical beam stress-free surface conditions on the three-dimensional constitutive equations specific to transversely isotropic materials, and it incorporates Von Kármán-type nonlinear strain assumptions. To derive the nonlinear governing equations, the virtual work principle and the first variation of the Hellinger-Reissner functional are applied. The two-noded mixed finite elements having twelve degrees of freedom at each node are used in this study. The convergence analyses show that the mixed FEM achieves accurate geometrically nonlinear displacement results while using fewer degrees of freedom than the high-resolution ANSYS 3D model, demonstrating the efficiency and robustness of the proposed approach. The study concludes that:

- Geometric nonlinearity becomes more significant as the span ratio decreases, leading to greater differences between nonlinear and linear tip displacements in cantilever sandwich beams.
- These percentage differences also increase as the thickness of stiffeners decreases, highlighting the sensitivity of beam behavior to cross-sectional composition.
- The effect of geometric nonlinearity is more pronounced under pinned boundary conditions than under cantilever conditions.
- For pinned beams, the nonlinear effects become greater with increasing u_z / h ratio, reaching differences over 7% in some cases, emphasizing the need for nonlinear analysis in such configurations.

References

Aksoylar, C. (2010). *Anlık Basınç Yükü Etkisindeki Kompozit Plakların Doğrusal Olmayan Dinamik Davranışının Sonlu Elemanlarla Çözümü* (Doctoral dissertation). İstanbul Technical University (in Turkish). https://polen.itu.edu.tr/bitstreams/3bce256c-a28b-4e62-8a96-2cf8860852a7/download

Aribas, U.N., Atalay, M., & Omurtag, M.H. (2024). Warping included mixed finite elements for bending and stresses of functionally graded exact curved beams. *Mechanics of Advanced Materials and Structures*, *31*(20), 5040-5056. https://doi.org/10.1080/15376494.2023.2211075

Aribas, U.N., Ermis, M., Eratli, N., & Omurtag, M.H. (2019). The static and dynamic analyses of warping included composite exact conical helix by mixed FEM. *Composites Part B: Engineering*, *160*, 285-297. https://doi.org/10.1016/j.compositesb.2018.10.018

Aribas, U.N., Ermis, M., Kutlu, A., Eratli, N., & Omurtag, M.H. (2022). Forced vibration analysis of composite-geometrically exact elliptical cone helices via mixed FEM. *Mechanics of Advanced Materials and Structures*, *29*(10), 1456-1474. https://doi.org/10.1080/15376494.2020.1824048

Ascione, A., & Gherlone, M. (2020). Nonlinear static response analysis of sandwich beams using the Refined Zigzag Theory. *Journal of Sandwich Structures & Materials*, *22*(7), 2250-2286. https://doi.org/10.1177/1099636218795381

Basar, Y., & Krätzig, W.B. (2013). *Mechanik der Flächentragwerke: Theorie, Berechnungsmethoden, Anwendungsbeispiele*. Springer-Verlag.

Baziyar Hamzehkhani, M., Zare, A., Gholami, M., & Gorji Azandariani, M. (2024). Analysis of bending vibrations of a three-layered pre-twisted sandwich beam with an exact dynamic stiffness matrix. *Composites Part C: Open Access*, *14*, 100473. https://doi.org/10.1016/j.jcomc.2024.100473

Chen, Y.H., & Chen, C.D. (2024). Linear static, geometric nonlinear static and buckling analyses of sandwich composite beams based on higher-order refined zigzag theory. *Composite Structures*, *339*, 118131. https://doi.org/10.1016/j.compstruct.2024.118131

Doğruoğlu, A.N., & Omurtag, M.H. (2000). Stability analysis of composite-plate foundation interaction by mixed FEM. *Journal of Engineering Mechanics*, *126*(9), 928-936. https://doi.org/10.1061/(ASCE)0733-9399(2000)126:9(928)

Drosopoulos, G.A., & Stavroulakis, G.E. (2022). *Nonlinear Mechanics for Composite Heterogeneous Structures*. CRC Press. https://doi.org/10.1201/9781003017240

Eratli, N., Yilmaz, M., Darilmaz, K., & Omurtag, M.H. (2016). Dynamic analysis of helicoidal bars with non-circular cross-sections via mixed FEM. *Structural Engineering and Mechanics*, *57*(2), 221-238. https://doi.org/10/f8pd8q

Hwu, C. (2024). *Mechanics of Laminated Composite Structures*. CRC Press.

Jones, R.M. (2018). *Mechanics of Composite Materials* (2. bs). CRC Press https://doi.org/10.1201/9781498711067

Ma, H. (2020). Rational approach for higher-order shear deformation beam theories. *Composite Structures*, *251*, 112599. https://doi.org/10.1016/j.compstruct.2020.112599

Omurtag, M.H., & Aköz, A.Y. (1992). The mixed finite element solution of helical beams with variable cross-section under arbitrary loading. *Computers and Structures*, *43*(2), 325-331. https://doi.org/10/b644p8

Pietro, G.D., Giunta, G., Belouettar, S., & Carrera, E. (2019). A static analysis of three-dimensional sandwich beam structures by hierarchical finite elements modelling. *Journal of Sandwich Structures & Materials*, *21*(7), 2382-2410. https://doi.org/10.1177/1099636217732907

Sandeep, S.H., & Srinivasa, C.V. (2020). Hybrid sandwich panels: A review. *International Journal of Applied Mechanics and Engineering*, *25*(3), 64-85

Sayyad, A.S., & Ghugal, Y.M. (2017). Bending, buckling and free vibration of laminated composite and sandwich beams: A critical review of literature. *Composite Structures*, *171*, 486-504. https://doi.org/10.1016/j.compstruct.2017.03.053

Sorrenti, M., Turon, F., Otero, F., Martinez, X., & Gherlone, M. (2025). Advanced finite element approaches for the 2D analysis of multilayered composite and sandwich beams. *European Journal of Mechanics - A/Solids*, *111*, 105606. https://doi.org/10.1016/j.euromechsol.2025.105606

Wei, G., Jin, Y., & Wu, L. (2020). Geometric and material nonlinearities of sandwich beams under static loads. *Acta Mechanica Sinica*, *36*(1), 97-106. https://doi.org/10.1007/s10409-019-00899-2

Wei, G., & Wu, L. (2023). Nonlinear transient response of elastoplastic sandwich beam in underwater blast and the fluid-structure interaction. *International Journal of Impact Engineering*, *172*, 104399. https://doi.org/10.1016/j.ijimpeng.2022.104399

Yan, Y., Pagani, A., Carrera, E., & Ren, Q. (2018). Exact solutions for the macro-, meso- and micro-scale analysis of composite laminates and sandwich structures. *Journal of Composite Materials*, *52*(22), 3109-3124. https://doi.org/10.1177/0021998318761785

Postfire response of GFRP-reinforced concrete beams with cement-based and intumescent paint fireproofing systems

Mohammed Al Dawood[1] , Salem Khalaf[1] , Farid Abed[*1]

[1] *American University of Sharjah, Department of Civil Engineering, Sharjah, United Arab Emirates*

Abstract. The fire safety considerations for Glass Fiber Reinforced Polymer (GFRP) bars, an alternative to traditional steel reinforcement in concrete structures, are being increasingly studied. This research addresses a critical gap by examining the postfire response of GFRP-reinforced concrete (RC) beams coated with different fireproofing systems. A total of six beams were tested, including two control beams without fire exposure, two fire-exposed beams without insulation, and two fire-exposed beams coated with either a cement-based mortar (Sikacrete 213F) or intumescent paint. The fire tests were conducted for a duration of 3 hours and followed the ASTM E119 fire curve. Post-fire flexural tests were performed to evaluate residual structural capacity. The results reveal significant differences in thermal and mechanical performance among the fireproofing systems. The Sikacrete-coated beam exhibited significant thermal resistance, maintaining lower internal temperatures and minimal surface damage compared to the intumescent paint-coated beam. Furthermore, the residual flexural capacity of the Sikacrete-coated beam was 147% higher than that of the intumescent paint-coated beam.

Keywords: Fire performance; GFRP-reinforced beams; Cement-based fireproofing; Intumescent paint; Flexural capacity

1. Introduction

Fiber reinforced polymers (FRP) are increasingly recognized as sustainable alternatives to conventional steel reinforcement, gaining widespread acceptance in modern construction. FRP materials commonly incorporate fibers such as basalt, carbon, and glass, with glass fiber reinforced polymer (GFRP) rebars emerging prominently due to their advantageous characteristics that include enhanced corrosion resistance, long-term durability, and high tensile strength. These features make GFRP particularly suitable for applications in aggressive environments, including hydraulic infrastructure like offshore structures and bridge decks (Al-Thairy et al., 2020). However, concerns regarding the deterioration of mechanical properties and the bond strength between GFRP bars and concrete at elevated temperatures have limited their adoption in fire-prone structural applications (Gooranorimi et al., 2018). To address these concerns, protective coatings such as cement-based mortars (e.g., Sikacrete 213F) or intumescent paints have been proposed to mitigate heat damage and preserve structural integrity (El-Kurdi et al., 2024). With the increasing interest in utilizing GFRP in various structural applications, it is essential to experimentally evaluate not only their thermal performance during fire but also their residual structural performance following fire exposure, to get keen insights on how GFRP reinforced concrete beams behave after cooling following fire exposure.

Abed et al. (2023) investigated the performance of GFRP bars under elevated temperatures up to 150°C. The results revealed a linear degradation in elastic modulus, with up to 87% strength loss occurring at 150°C—exceeding the glass transition temperature of the resin. These findings emphasize the susceptibility of GFRP bars to thermal damage even before reaching their decomposition.

Several authors also examined the postfire response of FRP reinforced concrete beams. Gooranorimi et al. (2018) exposed two simply-supported concrete slab strips that were reinforced with GFRP bars to fire for 2 hours. During fire exposure, the slabs were subjected to a sustained service load applied as a point load at midspan. The authors mentioned that the maximum recorded temperature was 1000˚C. However, the maximum recorded temperature on the internal bars was 115˚C. After exposure, the slabs were cooled for 24 hours and then tested using a three-point bending test. Results showed that, because the temperature of the bars only reached its approximate glass transitioning temperature, the beams exhibited load capacities greater than the theoretically calculated capacities and the load capacity of the control slab. The authors emphasized the need for high concrete

[*] Corresponding author, E-mail: fabed@aus.edu

https://doi.org/10.31462/icearc2025_ce_sme_517

covers to help insulate the GFRP bars from increased fire temperature, since the decomposition temperature is crucial for the flexural capacity of the bars.

Jafarzadeh and Nematzadeh (2022) studied concrete beams (150×200 mm cross-section, 1200 mm span) reinforced with two longitudinal GFRP bars. The beams were exposed to high temperatures in a furnace to simulate fire damage, and three target exposure levels of 200 °C, 400 °C, and 600 °C were applied to different beams. The flexural capacity of the beams was then evaluated and compared using four-point bending tests after cooling. The maximum temperature readings for the GFRP bars were approximately 200˚C and 400˚C for the beams exposed to 400˚C and 600˚C maximum temperatures, respectively. Results show that the flexural capacity of the beams that were exposed to a maximum temperature of 600˚C decreased by approximately 70% of the flexural capacity of the beams that were exposed to a maximum temperature of 400˚C. The authors attribute this decrease to the decompisiton temperature that the GFRP bars experienced (~400 °C). Additionally, the 400˚C exposed beams experienced an improved flexural capacity, approximately 14% more than the control beam, aligning with the results obtained by Gooranorimi et-al (2017). The authors essentially attribute this increase to the post-curing of the GFRP resin and enhanced bond conditions from microcrack resin infiltration, which improves its postfire performance, in opposite of the study performed by Abed et al. (2023).

Other authors verify the weakness of FRP reinforced concrete structures when temperatures exceed 600˚C Ghazal Aswad et al. (2025) evaluated the flexural performance of BFRP-reinforced beams exposed to temperatures up to 700°C. The study reported that BFRP beams retained around 34% of their capacity at 700°C, suggesting a vulnerability similar to GFRP at elevated temperatures.

These results underscore the necessity of effective fireproofing systems for FRP-reinforced concrete members. Khalaf et al. (2024) investigated the post-fire performance of GFRP-RC columns when insulating the columns and found that while non-insulated columns exhibited significant thermal degradation, insulated specimens—particularly those coated with cement-based systems like Sikacrete 213F—retained up to 60% of their axial capacity. This aligns with the findings in this study, where Sikacrete coating preserved the flexural performance of GFRP beams post-fire exposure

This paper aims to evaluate the post-fire flexural performance of 2.5-meter GFRP-reinforced concrete beams that were previously exposed to fire in a large-scale furnace following ASTM E119 standards. The main investigated parameter is the type of fireproofing system used: a cement-based mortar (Sikacrete 213F) and a single-component intumescent paint. By comparing the residual structural capacities of the beams, the study seeks to identify the more effective protection strategy for preserving the mechanical integrity of GFRP-RC members after fire exposure. This research addresses a critical gap in current ACI design provisions by providing experimental data on the behavior of fire-exposed GFRP-reinforced beams under flexural loading.

2. Materials and methods

2.1. Test matrix

All beams are 2.5 meters in length and share identical cross-section and reinforcement details. B1 and B2 were not exposed to fire to serve as control beams for the fire exposed beams. The other beams were exposed, as shown in Table 1. Additionally, B5 and B6 were coated with different fireproofing systems, namely Sikacrete 213F and intumescent paint, to evaluate their impact on the post-fire flexural performance of the beams.

Table 1. Test matrix

Beam ID	Fire Exposure	Coating
B1	Not exposed	None
B2	Not exposed	None
B3	Exposed	None
B4	Exposed	None
B5	Exposed	Intumescent pain
B6	Exposed	Sikacrete 213F

2.2. Beam fabrication

The GFRP-reinforced beams were designed to fail in flexure according to the guidelines provided in ACI 440.11-22 (2022). In compliance with the ACI 318-19 (2019) building code, which mandates a minimum concrete clear cover of 40 mm for protection against environmental exposure, a 40 mm cover was used. The beam dimensions were set at 300 mm in width and 400 mm in depth. The beams were reinforced with four 13 mm bottom GFRP bars and two 13 mm top GFRP bars. To ensure flexural failure during testing, 12 mm GFRP stirrups were placed at 150 mm intervals along the entire beam length. The typical dimensions and reinforcement details of the beams are displayed in Fig. 1. Prior to casting, *k*-type thermocouples were strategically positioned within the formwork—at the top and bottom reinforcement layers and around the stirrups. These thermocouples were used to monitor and record the temperature readings at the reinforcement, to provide explanation for the behavior of failure. After placement, the beams were cast and cured for 6 months before the fire test.

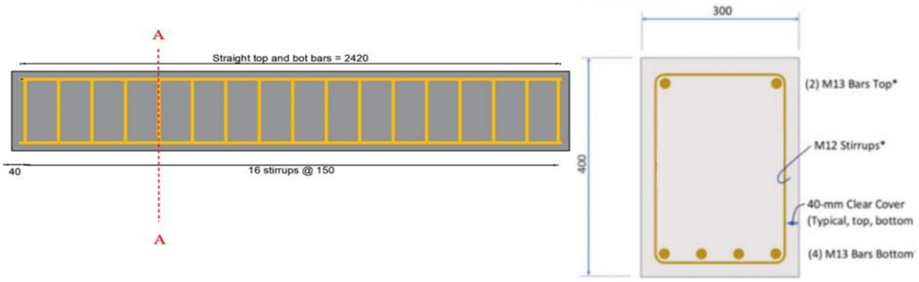

Fig. 1. Beam cross-sections

2.3. Material properties

In addition to casting the beams, a total of three cylinders, three cubes, and three prisms were cast to evaluate the compressive and flexural strength of the concrete. The cube tests yielded an average compressive strength of 47.623 MPa, while the cylinders recorded an average of 40.157 MPa. Flexural strength, determined from the prisms, averaged 5.278 MPa. The reinforcement used consisted of sand-coated M13 GFRP bars, which have a glass transition temperature of 110°C and a matrix decomposition range between 280°C and 445°C (Yousef et al., 2021). These bars possess an ultimate tensile strength of 850 MPa and a modulus of elasticity of 52 GPa.

For fire protection, two fireproofing systems were applied. Intumescent paint, known for expanding significantly under heat while maintaining low density, was applied in five layers to beam B5. This expansion forms an insulating char layer that restricts oxygen access and slows heat transfer to the underlying material (Khaneghagi et al., 2018). Sikacrete 213F, a high-performance, cement-based fire-resistant mortar, was also used as a protective layer. This non-shrink dry-mix mortar contains phyllosilicate and provides a compressive strength of 2.0 MPa with a thermal conductivity of 0.23 W/m·K at 10°C. Notably, Sikacrete offers up to four hours of fire resistance, making it well-suited for applications demanding strong thermal protection.

2.4. Fire and flexural testing

All beams underwent fire exposure in a large-scale furnace (5m x 4x x 2.5m) for a duration of 180 minutes. The furnace temperature was controlled to follow the ASTM E119-20 (2020) standard fire curve throughout the test. Thermocouples, connected to the laboratory data acquisition system, recorded temperature readings at 30-second intervals. With an operating range spanning from -270°C to 1260°C, the thermocouples provided accurate and consistent monitoring of temperature variations within the furnace. Essentially, the beams were not subjected to any mechanical loading during the fire exposure.

After cooling, the four fire-exposed beams (B3–B6) were tested alongside the two unexposed control beams (B1 and B2) using a three-point bending setup to evaluate their flexural performance. Each beam was simply supported at both ends, and a single concentrated load was applied at mid-span through the loading cell at a constant rate of 2 mm/min, as illustrated in Fig. 2. Testing continued until failure, which was identified by a substantial reduction in the beam's load-carrying capacity.

Fig. 2. Test setup

3. Results and discussions

3.1. GFRP temperatures

The maximum temperatures experienced by the GFRP bars for all of the fire exposed beams are presented in Table 2. It is shown that for B3 and B4, the maximum temperatures were the same, considering both beams were not insulated. B5 had a maximum GFRP temperature reading of 455 ˚C, indicating a minor but not sufficient decrease from the uninsulated beams. All three mentioned beams exceeded the typical decomposition temperature of GFRP bars. On the other hand, B6 had a maximum GFRP temperature of 147˚C, slightly higher than the typical glass transitioning temperature of 110˚C. Based on these results, Sikacrete 213F successfully insultated the GFRP bars from attaining temperature values up to decomposition temperature, whereas intumescent paint failed in doing so.

Table 2. Temperature readings for GFRP bottom bars

Beam ID	GFRP bottom bars temperature
B3	510˚C
B4	510˚C
B5	455˚C
B6	147˚C

3.2. Flexural test results

The post-fire flexural behavior of the beams varied significantly depending on their exposure conditions and fireproofing systems applied. The failure mode of all six beams are displayed in Fig. 3. The control beams, B1 and B2, which were not exposed to fire, exhibited classic flexural cracking patterns with vertical cracks forming near mid-span. In contrast, beams B3 and B4, which were exposed to fire without any insulation, experienced severe surface spalling and discoloration. The crack patterns in these beams were irregular and more dispersed, likely caused by the degradation of the GFRP bars due to high internal temperatures.

(a) B1

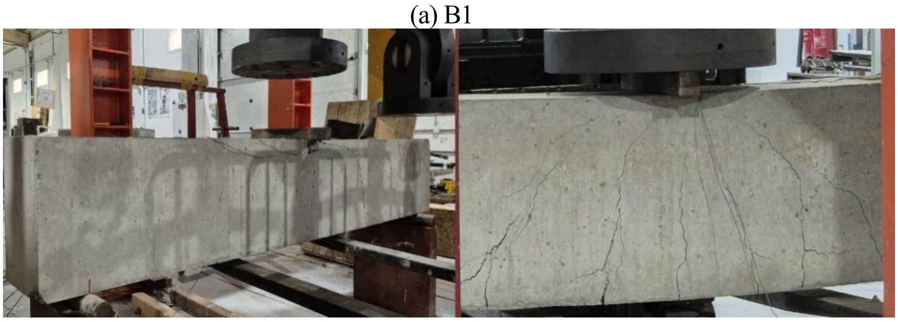

(b) B2

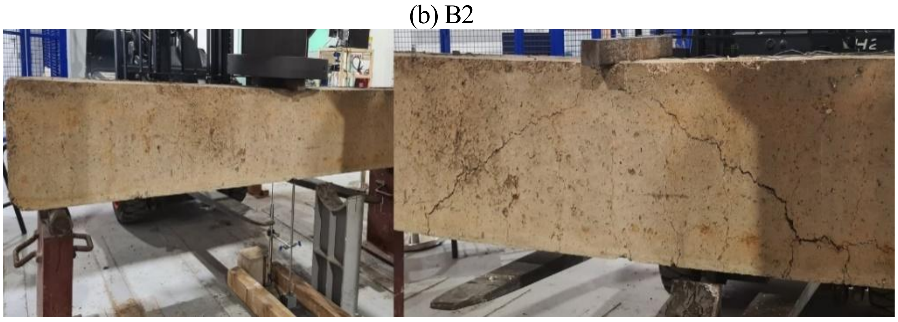

(c) B3

(d) B4

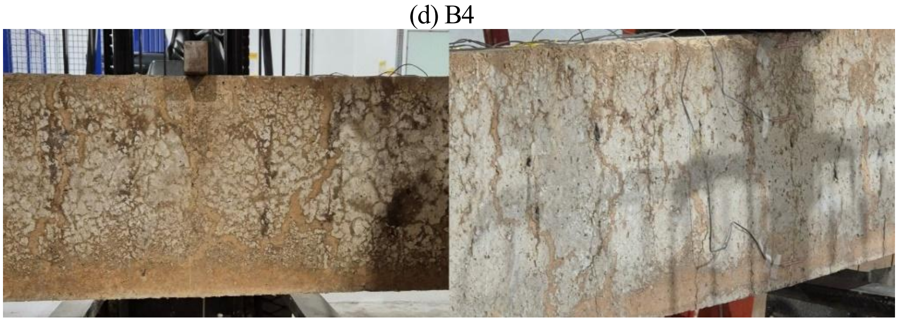

(e) B5

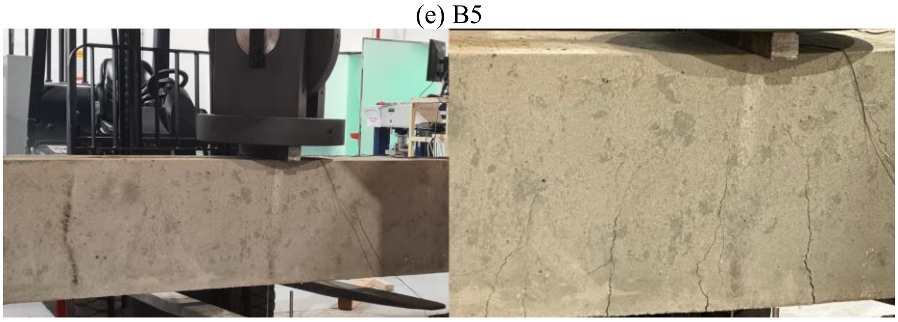

(f) B6

Fig. 3. All beams before and after flexural test

Beam B5, which was insulated with intumescent paint, displayed a charred surface with evidence of paint expansion, consistent with the material's response to heat. While the cracking pattern showed partial resemblance to flexural behavior, the damage suggested some thermal penetration and reduced structural performance. Beam B6, protected with Sikacrete 213F, showed the least surface damage and exhibited a well-defined flexural cracking pattern similar to the control beams.

Table 3 presents the maximum moments of each beam, as well as their residual capacities, calculated based on the average moments of B1 and B2. B3 and B4, the fire exposed beams without fire coating, have an average capacity of 50% of the control beams. This shows that the decomposition temperature experienced by the GFRP bars cause them to significantly deteriorate in strength. Additionally, B5, the beam coated with intumescent paint, retained a capacity of 44%, approximately similar to that of the uninsulated fire exposed beams. This shows that intumescent paint did not adequately provide proper insulation to the beam. On the other hand, and in alignment to the studies conducted by Gooranorimi et-al (2017) and Jafarzadeh and Nematzadeh (2022), B6, the beam exposed to fire and insulated with Sikacrete 213F, exhibited a higher maximum moment than B1 and B2, resulting in a residual capacity of 109%. As mentioned previously, the temperature of the bar was 147˚C, slightly above its typical glass transitioning temperature. In accordance with Jafarzadeh and Nematzadeh (2022), this caused the bars to undergo a process called post-curing, where additional polymer cross-linking occurred. This addition improved the bond performance of the GFRP bar, which in turn increased its moment capacity relative to its normal state.

Table 3. Maximum moment (kN-m) and residual capacity of the beams (%)

Beam ID	Moment capacity (kN-m)	Residual capacity (%)
B1	108.47	-
B2	117.30	-
B3	66.624	59
B4	45.73	40
B5	50.2	44
B6	123.92	109

4. Conclusions

This study presents the post-fire performance of four beams, two of which were coated with two different fireproofing systems : intumescent paint and Sikacrete 213F. The results of this study are as follows:

- Beams without insulation (B3 and B4) experienced significant thermal degradation, with GFRP bar temperatures exceeding 500 °C, resulting in a residual flexural capacity averaging only 50% of the unexposed control beams and a significantly less stiffness.
- The beam protected with intumescent paint (B5) exhibited similar performance to the uninsulated fire-exposed beams, with a GFRP bar temperature of 455 °C and a residual capacity of 44%. This indicates that the intumescent paint was ineffective in preventing thermal degradation of the reinforcement.
- In contrast, the beam insulated with Sikacrete 213F (B6) maintained a GFRP bar temperature well below the decomposition threshold (147 °C), resulting in minimal thermal damage. This beam exceeded the flexural capacity of the unexposed control beams, achieving a residual capacity of 109%.
- The enhanced performance of the Sikacrete coated beam is attributed to the post-curing effect, where thermal exposure near the glass transition temperature led to additional polymer cross-linking within the GFRP bars, hence improving their mechanical properties.

Acknowledgments

The research described in this paper was financially supported by the American University of Sharjah under grant number [FRG23-C-E04].

References

Abed, F., Elnassar, Z., Abuzaid, W., & Alhoubi, Y. (2023). Response of GFRP bars at different temperatures. In *Advanced Topics in Mechanics of Materials, Structures and Construction - AToMech1-2023* (pp. 1–6). Materials Research Forum LLC. https://doi.org/10.21741/9781644902592-1

Al-Thairy, H., & Al-Hasnawi, N. H. (2020). Behavior and failure mode of GFRP bars RC beams under elevated temperature. *IOP Conference Series: Materials Science and Engineering, 888*(1), Article 012012. https://doi.org/10.1088/1757-899X/888/1/012012

American Concrete Institute. (2019). *Building code requirements for structural concrete (ACI 318-19) and commentary (ACI 318R-19).* American Concrete Institute.

American Concrete Institute. (2022). *Building Code Requirements for Structural Concrete Reinforced with Glass Fiber-Reinforced Polymer (GFRP) Bars—Code and Commentary (ACI 440.11-22).* American Concrete Institute.

ASTM International. (2019). *Standard test methods for fire tests of building construction and materials (ASTM E119).* ASTM International.

Aswad, N.G., Al Dawood, M., Abed, F., & El Refai, A. (2025). Experimental study of BFRP-RC beams exposed to elevated temperatures. *Materials Research Proceedings, 48*, 86-92. https://doi.org/10.21741/9781644903414-10

El-Kurdi, A., Eldarwish, A., Khalifa, A., & Morsy, A. (2024, April). Thermal endurance of insulated R.C. columns strengthened with CFRP. Paper presented at the Asia-Pacific Conference on FRP in Structures.

Jafarzadeh, H., & Nematzadeh, M. (2022). Flexural strengthening of fire-damaged GFRP-reinforced concrete beams using CFRP sheet: Experimental and analytical study. *Composite Structures*, 115378. https://doi.org/10.1016/j.compstruct.2022.115378

Khaneghahi, M.H., Najafabadi, E.P., Shoaei, P., & Oskouei, A.V. (2018). Effect of intumescent paint coating on mechanical properties of FRP bars at elevated temperature. *Polymer Testing, 71*, 72–86. https://doi.org/10.1016/j.polymertesting.2018.08.020

Khalaf, S., Abed, F., Roshan, N., & Hajiloo, H. (2024). Post-fire performance of hybrid GFRP-steel reinforced concrete columns. *Construction and Building Materials, 450*, 138655. https://doi.org/10.1016/j.conbuildmat.2024.138655

Gooranorimi, O., Claure, G., De Caso, F., Suaris, W., & Nanni, A. (2018). Post-fire behavior of GFRP bars and GFRP-RC slabs. *Journal of Materials in Civil Engineering, 30*(3), 04017296. https://doi.org/10.1061/(ASCE)MT.1943-5533.0002168

Yousef, S., Eimontas, J., Striūgas, N., Subadra, S.P., & Abdelnaby, M.A. (2021). Thermal degradation and pyrolysis kinetic behaviour of glass fibre-reinforced thermoplastic resin by TG-FTIR, Py-GC/MS, linear and nonlinear methods.

ICEARC'25
4th International Civil Engineering & Architecture Conference
17-19 May 2025, Trabzon, Türkiye

Mixed finite element formulation for functionally graded beams resting on elastic foundation using HSDT

Doğan Kanığ*[1,2], Yonca Bab[1], Akif Kutlu[1], Mehmet H. Omurtag[3]

[1]Istanbul Technical University, Faculty of Civil Engineering, Department of Civil Engineering, Istanbul, Türkiye
[2]Altinbas University, Faculty of Engineering and Architecture, Department of Civil Engineering, Istanbul, Türkiye
[3]Istanbul Medipol University, Faculty of Engineering, Department of Civil Engineering, Istanbul, Türkiye

Abstract: This study presents a mixed finite element formulation for analyzing the behavior of functionally graded beams (FGBs) resting on an elastic foundation using the Higher-Order Shear Deformation Theory (HSDT). Functionally graded materials (FGMs) are characterized by continuous variations in material properties, enabling superior performance under complex loading conditions. The formulation is based on the Hellinger-Reissner variational principle, which incorporates both displacement and stress components as primary variables, ensuring improved accuracy and convergence. The functionally graded beam is modeled using a mixed approach that combines the displacement field and stress components as primary variables, ensuring higher accuracy and convergence rates. The elastic foundation is represented using Winkler and a two-parameter Pasternak model to account for shear interactions and foundation stiffness. The formulation is validated through benchmark problems, comparing results with existing solutions in the literature by utilizing different shear functions. Also, outcomes are obtained for various values of material gradation factor. Moreover, numeric studies are conducted to investigate the effects of length to thickness ratio, boundary conditions, foundation stiffness, and geometric parameters on the flexural responses of the FG beam. The results demonstrate the efficiency and accuracy of the mixed finite element formulation in capturing the complex interactions between the FGM beam and the elastic foundation. This study provides a robust tool for the design and analysis of FGBs in advanced engineering applications.

Keywords: Mixed finite element formulation; Hellinger-reissner principle, HSDT; Elastic foundation; Functionally Graded Beams

1. Introduction

Functionally graded materials (FGMs) are innovative materials increasingly utilized across industries such as aerospace, nuclear, automotive, civil, biomechanical, mechanical, electronic, chemical, and shipbuilding. Since their emergence in the 1980s, FGMs have been extensively researched, developed, and successfully applied in various industrial sectors. These materials exhibit microscopic inhomogeneity and spatial variation in composition, typically consisting of a blend of two distinct materials, such as ceramics and metals. Several studies have been performed to analyze the mechanical responses of FG structures. Abdelaziz et al. (Abdelaziz et al., 2011) proposed a novel high-order shear deformation theory with only four unknowns for analyzing the static response of functionally graded sandwich plates, deriving variationally consistent governing equations and validating its accuracy through comparisons with existing theories. Şimşek et al. (Şimşek & Kocatürk, 2009) examined the free and forced vibration behavior of a functionally graded Euler–Bernoulli beam subjected to a moving harmonic load. Turan and Hacıoğlu (2023) proposed a higher-order finite element model based on the Higher-Order Shear Deformation Theory (HSDT) for the static and free vibration analysis of Functionally Graded Beams (FGBs). They utilized five-node elements with 16 degrees of freedom to effectively capture transverse shear effects and prevent shear locking. Kafkas (2023) examined the influence of different homogenization techniques—particularly the power-law distribution—on the bending response of FGBs. The study used classical and refined beam theories combined with analytical methods to evaluate the effects of gradation on structural behavior. Wang et al. (2023) developed a model for axially graded microbeams based on the reformulated strain gradient elasticity theory. Using this approach, they analyzed both static bending and wave propagation, addressing material inhomogeneity and size effects inherent in micro-scale structures. Ghazwani (2023) introduced an enriched finite element formulation for porous functionally graded beams resting on elastic foundations. The study applied the First-Order Shear Deformation Theory (FSDT) and employed a polynomial shape function within a finite element framework for

* Corresponding author, E-mail: dogankanig@gmail.com

https://doi.org/10.31462/icearc2025_ce_sme_531

the static bending analysis. Hadji, Plevris, and Madan (2023) carried out a comprehensive study on the static and free vibration behavior of porous FGBs using a newly proposed HSDT. Their method incorporated variable porosity models and micromechanical considerations, providing enhanced accuracy for sandwich and layered beam structures. In another recent published by Ozman and Ozhan (2025), researchers employed the Euler–Bernoulli beam theory and verified their finite element simulations with experimental data obtained from 3D-printed FGB specimens, confirming the robustness of theoretical predictions. Li et al. (2025) proposed a force-based beam finite element model grounded in a modified HSDT, enhancing the accuracy of static analysis for FGBs by considering true transverse shear stress distribution. Eshaghi et al. (2025) explored various Scientific Machine Learning approaches, including Physics-Informed Neural Networks (PINNs), for analyzing functionally graded porous beams, demonstrating the potential of data-driven methods in structural analysis. Tran-Duc et al. (2025) developed a multiscale patch scheme for studying the system-level characteristics of heterogeneous FGBs in 3D, enhancing the predictive capabilities of computational models. Adiyaman (2024) proposed a higher-order shear deformation theory (HSDT) for the free vibration analysis of porous 2D FGBs. The study utilized a two-node finite element model with eight degrees of freedom, effectively capturing shear effects without the need for shear correction factors. Material properties were described by an exponential function, incorporating porosity effects, and the results were validated through convergence analysis. Mesbah et al. (2024) developed a new quasi-3D finite element model based on an accurate shear and normal deformation beam theory to evaluate the free vibration and stability behaviors of thick FGBs. The model employed a hyperbolic warping function for transverse shear deformation and stress, ensuring traction-free boundary conditions without shear correction factors. Comparative studies demonstrated the model's effectiveness in capturing the mechanical behavior of FGBs. Wu et al. (2023) presented a nonlinear free vibration analysis of FGBs using a mixed finite element method and a comparative artificial neural network. The study addressed the nonlinearities in FGBs and compared the results obtained from the finite element method with those predicted by the artificial neural network, demonstrating the potential of machine learning techniques in structural analysis. Huang et al. (2024) applied the differential quadrature method to investigate the free vibrations of bi-directional FGBs. The study considered various boundary conditions and material gradation profiles, providing insights into the dynamic characteristics of FGBs under different loading and boundary scenarios

When reviewing the literature, various types of analyses and beam theories for functionally graded beams can be found. In this study, however, the static behavior of functionally graded beams will be investigated using a mixed finite element method. The inclusion of higher-order shear theory and the effects of Winkler and Pasternak soil interactions make this study unique.

2. Formulation

Let us consider a functionally graded beam shown in Figure 1a, which is subjected to loading in the xz-plane. The centroidal axis of the beam lies along the x-axis, and the cross-section is defined with respect to the yz-axes. The material distribution equation of the functionally graded beam is given in the Numerical Examples section. Under a distributed load p(x) acting along the z-direction, the axial and transverse displacement fields of the beam can be defined according to the Higher-Order Beam Theory as follows:

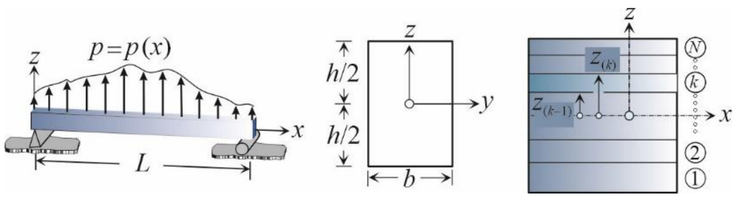

Fig. 1. Functionally graded beam a) Beam axes b) Cross-section dimensions c) Lamination

2.1. Field equations and formulation

$$\begin{aligned} u^* &= -z\, w_{,x} + f(z)\theta_x \\ w^* &= w \end{aligned} \tag{1}$$

w(x) is the transverse displacement along the x-axis, q(x) defines the rotation of the cross-section about the y-axis, and f(z) is the shear function, which in this study is taken as Reddy's shear function:

$$f(z) = z\left(1 - \frac{4z^2}{3h^2}\right) \tag{2}$$

Here, h denotes the beam height (see Figure 1b). The strain components throughout the beam cross-section, based on the displacement field given above, are expressed as:

$$\varepsilon_{xx} = u^*_{,x} = -zw_{,xx} + f\theta_{x,x}$$
$$\gamma_{xz} = u^*_{,z} + w^*_{,x} = f'\theta_x \tag{3}$$

The strain measures in Equation (3) can be expressed as follows:

$$\kappa_0 = -w_{,xx}$$
$$\kappa_1 = \theta_{x,x} \tag{4}$$
$$\varepsilon_s = \theta_x$$

The strain-stress relationship in the k-th layer of the laminated composite beam, as shown in Figure 1c, can be written using Hooke's Law as:

$$\begin{Bmatrix} \sigma_{xx} \\ \sigma_{xz} \end{Bmatrix}^{(k)} = \begin{bmatrix} \bar{Q}_{11} & 0 \\ 0 & \bar{Q}_{55} \end{bmatrix}^{(k)} \begin{Bmatrix} \varepsilon_{xx} \\ \gamma_{xz} \end{Bmatrix}^{(k)} \tag{5}$$

The first variation of the functional for the elastic system according to the Hellinger-Reissner principle is given by:

$$\delta\Pi_{HR} = \int_V \left(\boldsymbol{\varepsilon}^{\mathbf{u}} - \boldsymbol{\varepsilon}^{\sigma}\right)^T \delta\boldsymbol{\sigma}^{\sigma}\mathrm{d}V + \int_V \left(\left(\boldsymbol{\sigma}^{\sigma}\right)^T \delta\boldsymbol{\varepsilon}^{\mathbf{u}} - \mathbf{q}^T\delta\mathbf{u}\right)\mathrm{d}V - \int_\Gamma \hat{\mathbf{t}}^T\delta\mathbf{u}\mathrm{d}\Gamma = 0 \tag{6}$$

In this equation, the first integral corresponds to the weak form of the compatibility conditions of the strain field, while the second represents the weak form of the equilibrium equations under external loading. The last integral accounts for the work done by the boundary tractions. Here, the variation operator is denoted by δ. For beam problems, the 3D formulation in Equation (6) is reduced by integrating through the cross-section, resulting in stress components and strain measures.

$$\delta\Pi_{HR} = \int_L \left(\mathbf{e}^{\mathbf{u}} - \mathbf{e}^{\mathbf{P}}\right)^T \delta\,\mathbf{P}\,\mathrm{d}L + \int_L \left(\mathbf{P}^T\delta\,\mathbf{e}^{\mathbf{u}} - \mathbf{p}^T\delta\,\mathbf{u}\right)\mathrm{d}L - \int_\Gamma \hat{\mathbf{t}}^T\delta\mathbf{u}\mathrm{d}\Gamma = 0 \tag{7}$$

Here, the strain measures are defined kinematically by $\mathbf{e}^{\mathbf{u}T} = [\kappa_0 \quad \kappa_1 \quad \varepsilon_s]^T$, while they are also expressed in terms of stress resultants $\mathbf{P}^T = [M_{xx} \quad M^f_{xx} \quad Q_{xz}]$. The distributed load acting on the laminated composite beam is denoted by $\mathbf{p}$, where M_{xx}, M^f_{xx}, and Q_{xz} represent the bending moment, higher-order bending moment, and shear force, respectively.

$$\left(M_{xx}, M^f_{xx}, Q_{xz}\right) = b\sum_{k=1}^{N}\int_{z_{(k-1)}}^{z_{(k)}} \left(z\sigma^{(k)}_{xx},\, f(z)\sigma^{(k)}_{xx},\, (\mathrm{d}f(z)/\mathrm{d}z)\sigma^{(k)}_{xz}\right)\mathrm{d}z \tag{8}$$

Here, *b* is the beam width (see Figure 1b), and *N* is the total number of layers in the cross-section. Substituting the constitutive relations from Equation (5) into Equation (8), the relationship between strain measures and stress resultants is obtained as follows:

$$\mathbf{P} = \mathbf{E}\mathbf{e}^{\mathbf{u}} \quad or \quad \begin{Bmatrix} M_{xx} \\ M^f_{xx} \\ Q_{xz} \end{Bmatrix} = \begin{bmatrix} D_{11} & F_{11} & 0 \\ F_{11} & H_{11} & 0 \\ 0 & 0 & A^s \end{bmatrix} \begin{Bmatrix} \kappa_0 \\ \kappa_1 \\ \varepsilon_s \end{Bmatrix} \tag{9}$$

Here, the terms in the section stiffness matrix are computed as follows:

$$\left(D_{11} \quad F_{11} \quad H_{11}\right) = b\sum_{k=1}^{N}\int_{z_{(k-1)}}^{z_{(k)}} \bar{Q}^{(k)}_{11}\left(z^2 \quad zf(z) \quad f(z)^2\right)\mathrm{d}z \tag{10}$$

$$A^s = b\sum_{k=1}^{N}\int_{z_{(k-1)}}^{z_{(k)}} \bar{Q}^{(k)}_{55}\left(f'(z)\right)^2\mathrm{d}z \tag{11}$$

By defining the compliance matrix $\mathbf{S} = \mathbf{E}^{-1}$, Equation (9) is reformulated for use in Equation (7).

$$\mathbf{e}^{\mathbf{P}} = \mathbf{S}\mathbf{P} \quad or \quad \begin{Bmatrix} \kappa_0 \\ \kappa_1 \\ \varepsilon_s \end{Bmatrix} = \begin{bmatrix} D'_{11} & F'_{11} & 0 \\ F'_{11} & H'_{11} & 0 \\ 0 & 0 & A^s \end{bmatrix} \begin{Bmatrix} M_{xx} \\ M^f_{xx} \\ Q_{xz} \end{Bmatrix} \tag{12}$$

The Pasternak elastic foundation model (Kutlu & Omurtag, 2019) defines the interaction force intensity transmitted between the soil and the structure, based on the vertical displacement of the structure interacting with the soil, by the following expression:

$$p_f = K_w w - K_s w_{,xx} \tag{13}$$

Here, K_w is the Winkler foundation parameter, acting like a spring constant that relates the local settlement to the interaction force intensity. K_s is the shear parameter of the foundation, introducing a shear interaction between adjacent springs as defined in Winkler's foundation model. Considering the Pasternak foundation interaction, the beam equilibrium equations can be derived according to the Higher-Order Shear Deformation Theory (HSDT) as follows:

$$\begin{gathered} M_{xx,xx} + p - \overline{K_w} w + \overline{K_s} w_{,xx} = 0 \\ M^f_{xx,x} - Q_{xz} = 0 \end{gathered} \tag{14}$$

In Equation (14), the definitions of $\overline{K_w} = bK_w$ and $\overline{K_s} = bK_s$ enable the loading condition to be expressed as a line load along the beam axis. Ultimately, by substituting the equilibrium equations given in Equation (14) and the compatibility conditions from Equation (12) into the expression (7), and applying partial integration to the second-order derivative term related to the foundation, the stationary condition of the Hellinger-Reissner functional for a laminated composite beam resting on a Pasternak foundation and described by the Higher-Order Shear Deformation Theory (HSDT) is obtained as follows:

$$\begin{aligned} \delta\Pi_{HR} = {} & \int_L \left[w_{,x}\delta M_{xx,x} - \left(\bar{D}_{11}M_{xx} + \bar{F}_{11}M^f_{xx}\right)\delta M_{xx} \right] \mathrm{d}L \\ & + \int_L \left[\theta_{x,x} - \left(\bar{F}_{11}M_{xx} + \bar{H}_{11}M^f_{xx}\right) \right] \delta M^f_{xx}\mathrm{d}L + \int_L \left[\theta_x - \left(\bar{A}^s Q_{xz}\right) \right] \delta Q_{xz}\mathrm{d}L - \int_L \delta w p \mathrm{d}L \\ & + \int_L \left(M_{xx,x}\,\delta w_{,x} + M^f_{xx}\delta\theta_{x,x} + V_{xz}\delta\theta_x + \overline{K_w} w\delta w + \overline{K_s} w_{,x}\delta w_{,x} \right) \mathrm{d}L - \int_\Gamma \hat{\mathbf{t}}^T \delta\mathbf{u}\,\mathrm{d}\Gamma = 0 \end{aligned} \tag{15}$$

The stationary condition of the system described by Equation (15) will be used to derive the finite element system matrices. Since the highest derivative order in this expression is first-order, the beam domain will be discretized using linear elements, which involve linear shape functions possessing C0 continuity. The shape functions ensuring C0 continuity, the matrix of unknowns at the nodes, and the stress evaluation are described in detail by Bab and Kutlu (2023).

3. Numerical examples

In this study, a variety of solutions are carried out for functionally graded beams to validate the presented formulation and the generated numerical solution method. Convergence and comparison analyses are conducted, considering beams resting on elastic foundations with different thicknesses ($L/h = 5$ *and* $L/h = 20$) and subjected to sinusoidal loads. The results are obtained for simply supported boundary conditions.

All beams, which are used in this study, have same material properties. Those properties can be written as:

$$E_m = E_{al} = 70\ GPa,\ v_m = v_{Al} = 0.3,\ E_c = E_{Al_2 0_3} = 380\,GPa,\ v_c = 0.3$$

Here, $\boldsymbol{E_m}$ represents the young modulus of metalic phase and $\boldsymbol{E_c}$ denotes for ceramic one. The distribution of material property is given below as:

$$E(z) = (E_c - E_m)\left(\frac{z}{h} + 0.5\right)^n + E_m \tag{16}$$

Here, n corresponds for the exponential factor where it is used in the performed examples as $n = 0, 1, 5, 10$. Also, results of the mid-span deflection and axial stress are obtained by utiziling the following nondimensional formula (Hadji et al., 2023):

$$\bar{w} = 100\frac{E_m h^3}{q_0 L^4} w\left(\frac{L}{2}\right), \quad \overline{\sigma_x} = \frac{h}{q_0 L}\sigma_x\left(\frac{L}{2}, \frac{h}{2}\right) \tag{17}$$

Also, the results obtaine from the analysis for different slenderrness ratios and variable Ks & Kw factors for different exponential factors, and compared with the study of Sayyad and Ghugal (Sayyad & Ghugal, 2018), are given in Table 1 and Table 2.

Table 1. The results of FG beam under sinusoidal load resting on elastic foundation where $\rho = 5$ for various exponential factor

n	K_s	K_w	$\rho = 5$					
			w	*(w)expected*	*Error (%)*	S_x	*(Sx)expected*	*Error (%)*
0	0	0	2.497	2.502	0.18%	3.089	3.091	0.08%
	0.1	0	2.351	2.355	-0.17%	2.907	2.909	-0.07%
	0.1	0.1	1.487	1.489	-0.14%	1.839	1.841	-0.001
1	0	0	4.936	4.944	0.16%	4.749	4.944	3.95%
	0.1	0	4.394	4.402	-0.17%	4.227	4.350	-2.82%
	0.1	0.1	2.107	2.110	-0.13%	2.027	2.110	-3.92%
5	0	0	7.758	7.772	0.17%	6.384	6.605	3.35%
	0.1	0	6.498	6.507	-0.14%	5.347	5.530	-3.32%
	0.1	0.1	2.495	2.497	-0.11%	2.053	2.122	-3.29%
10	0	0	8.635	8.653	0.20%	7.398	7.907	6.43%
	0.1	0	7.102	7.115	-0.18%	6.085	6.501	-6.40%
	0.1	0.1	2.579	2.582	-0.12%	2.209	2.359	-6.36%

Table 2. The results of FG beam under sinusoidal load resting on elastic foundation where $\rho = 20$ for various exponential factor

n	Ks	Kw	$\rho = 20$					
			w	*(w)expected*	*Error (%)*	*Sx*	*(Sx)expected*	*Error (%)*
0	0	0	2.280	2.284	0.18%	12.160	12.171	0.09%
	0.1	0	1.192	1.194	-0.09%	6.360	6.361	-0.004%
	0.1	0.1	0.209	0.209	-0.11%	1.114	1.114	-0.001%
1	0	0	4.569	4.577	0.19%	18.668	18.814	0.77%
	0.1	0	1.616	1.617	-0.07%	6.603	6.646	-0.65%
	0.1	0.1	0.219	0.219	-0.09%	0.894	0.900	-0.67%
5	0	0	6.942	6.954	0.18%	24.927	25.794	3.36%
	0.1	0	1.838	1.839	-0.05%	6.600	6.821	-3.24%
	0.1	0.1	0.222	0.223	-0.07%	0.799	0.826	-3.27%
10	0	0	7.626	7.642	0.21%	28.929	30.923	6.45%
	0.1	0	1.883	1.884	-0.05%	7.142	7.622	-6.30%
	0.1	0.1	0.223	0.223	-0.10%	0.846	0.904	-6.34%

Table 1 summarizes the results for FG beams with a slenderness ratio of $\rho = 5$. The deflection predictions exhibit remarkable accuracy, with errors consistently below 0.2% across all gradation exponents and foundation stiffness parameters. For homogeneous beams $(n = 0)$, stress (S_x) errors remain minimal (≤0.08%), validating the formulation's capability for uniform materials. However, as the exponental factor (n) increases, stress errors escalate significantly, reaching 6.43% for $n = 10$, when $K_s = 0.1$ and $K_w = 0.1$. This trend underscores the challenge of modeling stress fields in beams with steep material gradation, particularly when coupled with foundation interactions. The systematic underestimation of S_x for $n \geq 1$ suggests that the current formulation may oversimplify stress redistribution mechanisms in graded materials, especially under combined elastic foundation effects.

Table 2 focuses on slender beams (and reveals similar deflection accuracy (errors <0.21%) but highlights amplified stress magnitudes compared to Table 1. Despite the increased slenderness, stress errors for $n \geq 1$ follow comparable trends, peaking at 6.45% for $n = 10$ with active foundation parameters. Notably, introducing K_s and K_w exacerbates discrepancies in S_x, even as deflection remains unaffected. This reinforces the hypothesis that stress inaccuracies stem primarily from material gradation complexity rather than geometric factors. The persistent underestimation of stress in high n cases, regardless of ρ, points to a fundamental limitation in capturing localized stress gradients under nonlinear material-foundation coupling.

Comparing both tables, the formulation demonstrates consistent deflection accuracy across slenderness ratios, confirming its reliability in predicting global stiffness. However, stress predictions degrade sharply with increasing nn, irrespective of ρ highlighting a critical gap in modeling functionally graded materials. The amplified errors in slender beams (Table 2) suggest that geometric slenderness compounds stress prediction challenges, likely due to heightened sensitivity to shear and foundation interactions. These results emphasize the need for advanced modeling techniques—such as enriched displacement fields or adaptive meshing—to address stress inaccuracies in high-n FG beams, particularly for applications requiring precise stress analysis in aerospace or civil engineering structures.

4. Conclusion

The present work advances the analysis of functionally graded beams (FGBs) on elastic foundations through a novel mixed finite element framework grounded in the Hellinger-Reissner variational principle and Higher-Order Shear Deformation Theory (HSDT). The methodology's efficacy is emphasized by its ability to maintain deflection accuracy within negligible margins (<0.21%) for diverse material gradations and foundation interactions, solidifying its utility in scenarios demanding reliable global deformation predictions. A critical insight from this investigation is the pronounced divergence in stress fidelity as material inhomogeneity intensifies. High gradation exponents induce stress prediction discrepancies exceeding 6%, attributed to inherent complexities in resolving steep property gradients and nonlinear interactions between foundation parameters and graded material behavior.

Notably, this study pioneers a versatile computational tool that harmonizes accuracy with efficiency, leveraging the mixed formulation to bypass shear correction factors while accommodating complex foundation interactions—a significant advancement over conventional approaches. The framework's adaptability to varying boundary conditions, material distributions, and slenderness ratios positions it as a valuable asset for preliminary design phases in aerospace, civil, and mechanical engineering. By rigorously validating results against established benchmarks and integrating higher-order kinematics, the work sets a robust foundation for future extensions into dynamic, nonlinear, or multi-physical analyses of FGBs. To bridge these gaps, future efforts should explore multi-scale modeling approaches, integrating microstructural gradation effects with macroscopic beam behavior. Additionally, coupling the formulation with optimization algorithms or probabilistic frameworks could enhance predictive reliability for extreme gradation and foundation conditions. By addressing these computational and theoretical frontiers, the proposed framework can evolve into a comprehensive tool for next-generation FGB design, balancing precision with adaptability in advanced engineering systems.

References

Abdelaziz, H. H., Atmane, H. A., Mechab, I., Boumia, L., Tounsi, A., & Abbas, A. B. E. (2011). Static Analysis of Functionally Graded Sandwich Plates Using an Efficient and Simple Refined Theory. *Chinese Journal of Aeronautics*, *24*(4), 434–448. https://doi.org/10.1016/S1000-9361(11)60051-4

Adiyaman, G. (2024). Free Vibration Analysis of a Porous 2D Functionally Graded Beam Using a High-Order Shear Deformation Theory. *Journal of Vibration Engineering & Technologies*, *12*(2), 2499–2516. https://doi.org/10.1007/s42417-023-00996-4

Bab, Y., & Kutlu, A. (2023). Stress analysis of laminated HSDT beams considering bending extension coupling. *Turkish Journal of Civil Engineering*, *34*(1), 1–23. https://doi.org/10.18400/tjce.1206777

Eshaghi, M. S., Bamdad, M., Anitescu, C., Wang, Y., Zhuang, X., & Rabczuk, T. (2025). Applications of Scientific Machine Learning for the Analysis of Functionally Graded Porous Beams. *Neurocomputing*, *619*, 129119. https://doi.org/10.1016/j.neucom.2024.129119

Ghazwani, M. H. (2023). New Enriched Beam Element for Static Bending Analysis of Functionally Graded Porous Beams Resting on Elastic Foundations. *Mechanics of Solids*, *58*(5), 1878–1893. https://doi.org/10.3103/S0025654423600885

Hadji, L., Bernard, F., & Zouatnia, N. (2023). Bending and Free Vibration Analysis of Porous-Functionally-Graded (PFG) Beams Resting on Elastic Foundations. *Fluid Dynamics & Materials Processing*, *19*(4), 1043–1054. https://doi.org/10.32604/fdmp.2022.022327

Huang, X., Zhang, L., & Ge, R. (2024). Investigation of the free vibrations of bi-directional functionally graded material beams using differential quadrature method. *Journal of Vibration and Control*, *30*(21–22), 4828–4851. https://doi.org/10.1177/10775463231214314

Kafkas, U. (2023). Fonksiyonel Derecelendirilmiş Kiriş Yapıların Eğilme Analizinde Homojenleştirme Modellerinin Etkisi. *Proceeding Book of 2nd International Conference on Frontiers in Academic Research ICFAR 2023*. 2nd International Conference on Frontiers in Academic Research ICFAR 2023. https://doi.org/10.59287/as-proceedings.479

Kutlu, A., & Omurtag, M. H. (2019). Elastik zeminle etkileşen nispeten kalın plağın karışık sonlu elemanlarla burkulma analizi. *Ulusal Mekanik Kongresi*, 774–780.

Li, W., Chen, H., Chen, S., & Liu, Z. (2025). A force-based beam element model based on the modified higher-order shear deformation theory for accurate analysis of FG beams. *Structures*, *71*, 107991. https://doi.org/10.1016/j.istruc.2024.107991

Mesbah, A., Belabed, Z., Tounsi, A., Ghazwani, M. H., Alnujaie, A., & Aldosari, S. M. (2024). Assessment of New Quasi-3D Finite Element Model for Free Vibration and Stability Behaviors of Thick Functionally Graded Beams. *Journal of Vibration Engineering & Technologies*, *12*(2), 2231–2247. https://doi.org/10.1007/s42417-023-00976-8

Özmen, U., & Özhan, B. B. (2025). Mechanics of functionally graded beams: Analytical, computational, and experimental analyses. *International Journal of Mechanics and Materials in Design*. https://doi.org/10.1007/s10999-025-09750-y

Sayyad, A. S., & Ghugal, Y. M. (2018). Analytical solutions for bending, buckling, and vibration analyses of exponential functionally graded higher order beams. *Asian Journal of Civil Engineering*, *19*(5), 607–623. https://doi.org/10.1007/s42107-018-0046-z

Şimşek, M., & Kocatürk, T. (2009). Free and forced vibration of a functionally graded beam subjected to a concentrated moving harmonic load. *Composite Structures*, *90*(4), 465–473. https://doi.org/10.1016/j.compstruct.2009.04.024

Tran-Duc, T., Bunder, J. E., & Roberts, A. J. (2025). Efficient prediction of static and dynamical responses of functional graded beams using sparse multiscale patches. *Computational Mechanics*. https://doi.org/10.1007/s00466-025-02614-4

Turan, M., & Hacioğlu, M. İ. (2023). Yüksek mertebe sonlu eleman modeliyle fonksiyonel derecelendirilmiş kirişlerin serbest titreşim ve statik analizi. *Gümüşhane Üniversitesi Fen Bilimleri Enstitüsü Dergisi*. https://doi.org/10.17714/gumusfenbil.1185301

Wang, S., Hong, J., Wei, D., & Zhang, G. (2023). Bending and wave propagation analysis of axially functionally graded beams based on a reformulated strain gradient elasticity theory. *Applied Mathematics and Mechanics*, *44*(10), 1803–1820. https://doi.org/10.1007/s10483-023-3042-6

Wu, C.-P., Yeh, S.-T., & Liu, J.-H. (2023). A Nonlinear Free Vibration Analysis of Functionally Graded Beams Using a Mixed Finite Element Method and a Comparative Artificial Neural Network. *Journal of Composites Science*, *7*(6), 229. https://doi.org/10.3390/jcs7060229

4th International Civil Engineering & Architecture Conference
17-19 May 2025, Trabzon, Türkiye

Performance of Ch-SAMP-Rao algorithm on RC slab bridge superstructure CO_2 emission optimization

Hasan Tahsin Öztürk *[1], Nurcan Öztürk[1]

[1] *Karadeniz Technical University, Faculty of Technology, Department of Civil Engineering, 61830, Trabzon, Türkiye*

Abstract. In this study, Rao1, Rao2, Rao3, SAMP-Rao1, SAMP-Rao2, SAMP-Rao3, and Ch-SAMP-Rao algorithms developed using a chaotic switching strategy were used in the optimum designs of single-span reinforced concrete slab bridge superstructures with minimum CO_2 emissions. The main purpose of the study is to examine the performance of the developed Ch-SAMP-Rao algorithm compared to other Rao algorithm versions. In the developed chaotic SAMP-Rao algorithm, switching was performed between the search equations used in the SAMP-Rao1, SAMP-Rao2, and SAMP-Rao3 algorithms with chaotic maps. Thus, it was thought that these three algorithms, which show different performance in different problems, could show a more stable performance. For this purpose, a problem suite consisting of two different reinforced concrete slab bridge problems was created by considering the AASHTO-LRFD Bridge Code. There was a total of 13 design variables in the problem. These were deck thickness, main rebar diameter in the interior and edge strip, distribution rebar diameter in the interior and edge strip, shrinkage and temperature rebar diameter, concrete grade, steel rebar grade, main rebar spacing in the interior and edge strip, distribution rebar spacing in the interior and edge strip, and shrinkage and temperature rebar spacing. The findings obtained as a result of the independent simulations were evaluated with box plot graphics and the Friedman test, which is a non-parametric statistical test. The findings showed that the performance of the proposed Ch-SAMP-RAO algorithm is better than the others.

Keywords: Slab Bridge; Superstructure; Optimization, CO_2 emission; Ch-SAMP-Rao

1. Introduction

Traditional design methods in structural engineering often rely on empirical knowledge and iterative trial-and-error approaches. While these methods ensure compliance with strength and durability regulations, they typically do not prioritize cost efficiency or material optimization. In the context of diminishing natural resources and increasing environmental concerns, there is a growing need for designs that minimize both economic costs and carbon emissions. This necessity has led to the widespread adoption of optimization techniques in structural engineering, particularly metaheuristic algorithms, due to their adaptability and effectiveness in solving complex real-world problems.

Numerous studies have explored the optimization of bridge structures using various metaheuristic approaches. For instance, Rana et al. (2010) and Ahsan et al. (2012) applied the Evolutionary Operation (EVOP) algorithm to optimize the cost of post-tensioned I-girder bridges, while Ghodoosi et al. (2018) employed Genetic Algorithms (GA) to minimize maintenance costs in reinforced concrete girder bridges. Other researchers, such as Martí et al. (2015) and Bruno et al. (2016), focused on optimizing prestressed and arch bridge configurations using memetic and iterative algorithms, respectively. Multi-objective optimization has also gained attention, with studies like those by Martinez-Martin et al. (2012) and García-Segura & Yepes (2016) incorporating cost, reinforcement density, and CO_2 emissions as key objectives.

Recent advancements have introduced hybrid and improved metaheuristic techniques, such as the Enhanced Colliding Bodies Optimization (ECBO) and Water Strider Algorithm (WSA), to enhance optimization efficiency (Kaveh et al., 2022). Additionally, sustainability-driven optimizations, including those by Yepes-Bellver et al. (2022) and Martínez-Muñoz et al. (2022), have emphasized reducing carbon footprints alongside cost. Despite these developments, further research is needed to refine optimization criteria, improve computational efficiency, and integrate emerging algorithms for more sustainable and economical bridge designs.

The SAMP-Rao and Rao algorithms are noteworthy as meta-heuristics that yield effective results in real-world optimization problems. However, the efficacy of variants 1, 2, and 3 of these algorithms varies in different problem

*Corresponding author, E-mail: htozturk@ktu.edu.tr

https://doi.org/10.31462/icearc2025_ce_sme_566

types. Specifically, while Rao-1 demonstrates efficacy in low-dimensional problems with its simple and fast convergence, the more complex search mechanisms of Rao-2 and Rao-3 can yield superior results in multimodal and high-dimensional optimization problems. In a similar vein, although the adaptive parameter structure of SAMP-Rao provides flexibility in engineering problems with uncertainty, performance fluctuations can be observed in some cases due to excessive parameter sensitivity. This finding indicates that the configuration of the problem should be considered when selecting the algorithm.

This study presents a new Chaotic SAMP-Rao (Ch-SAMP-Rao) algorithm by combining the convergence equations of the SAMP-RAO algorithm using chaotic mapping reference signals. Thus, it is thought that by selecting a problem-specific signal, an algorithm with higher performance than the variants of the SAMP-Rao and Rao algorithms can be developed. For this purpose, performance tests were performed on the optimization problem of reinforced concrete slab bridge deck with the same span and two different widths. The results obtained are compared with those obtained from the variants of SAMP-Rao and Rao algorithms by various statistical tests.

The structure of this study is as follows: The first section discusses the motivation and goal of the present study. The second section describes the formulation of the optimization problem, constraints, algorithm settings, and proposed Ch-SAMP-Rao algorithm. Findings and investigations are presented in the third section. Finally, the conclusions obtained from the study are summarized in the fourth section and some suggestions for future studies are made.

2. Method

2.1. Design variables, parameters, and objective function

The optimum design of the slab bridge deck shown in Fig. 1 was performed according to the AASHTO-LRFD bridge regulation with minimum CO_2 emission (Öztürk, 2024). The design variables used were shown on the bridge cross-section in Fig. 2. The lower and upper bounds of the design variables are presented in Table 1. and the design parameters of the problem are presented in Table 2.

The objective function of the optimization problem consists of the sum of the concrete and reinforcement costs of the bridge deck. Where V_c is the volume of concrete, W_s is the total weight of reinforcement, Cs and Cc are the unit costs of steel and concrete respectively, the objective function is calculated as in Eq. 1.

$$f(x) = V_c C_c + W_s C_s \tag{1}$$

Unit emission values for concrete and steel grades are given in Table 3.

In the study, two problem cases were analyzed as design 1 and design 2. In both problems, the bridge span is fixed and is 10 m. In design 1, the bridge width is 5.60 m with two traffic lanes and in design 2, the bridge width is 9.2 m with three traffic lanes.

2.2. Constraints

The first constraint concerns the minimum thickness control of the bridge deck. The first constraint is given in Eq.2, where h_{min} is the minimum thickness calculated according to AASHTO-LRFD bridge specifications.

$$g_1(x) = \frac{h_{min}}{X_1} - 1 \leq 0 \tag{2}$$

In this study, the longitudinal strip method presented in the AASHTO-LRFD regulation is used for the design of the bridge. In order to use this method, the span length must be greater than 4600 mm. This requirement is controlled by the constraint given in Eq. 3.

$$g_2(x) = \frac{4600}{L} - 1 \leq 0 \tag{3}$$

The third and fourth constraints are related to the crack control for the interior and edge strips of the deck. In this inspection, firstly, it should be checked whether there is cracking in the tensile region of the section. For this purpose, concrete is cracked if the maximum tensile stress f_t occurring in critical sections is greater than 80% of the modulus of rupture (f_r) of the section. If the section is not cracked, no cracking check will be performed. If the section is cracked, the tensile stress in the main reinforcement must satisfy the condition $f_{ss} \leq 0.60 \cdot f_y$ for the crack to be under control. The crack control constraint in Eq. 4 is checked separately for the interior and edge strips.

$$g_{3-4}(x) = \frac{f_{ss}}{0{,}60 \cdot f_y} - 1 \leq 0 \tag{4}$$

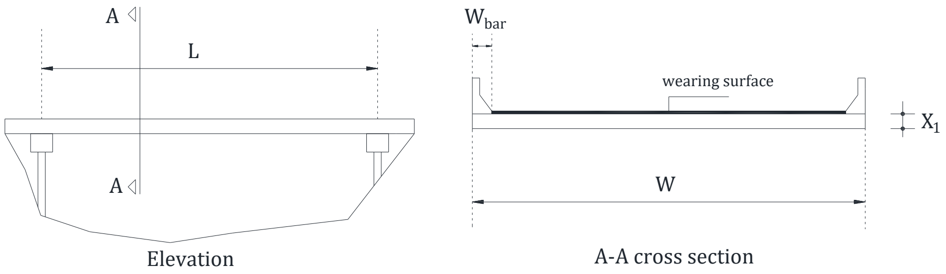

Fig. 1. Slab bridge elevation and cross section of superstructure

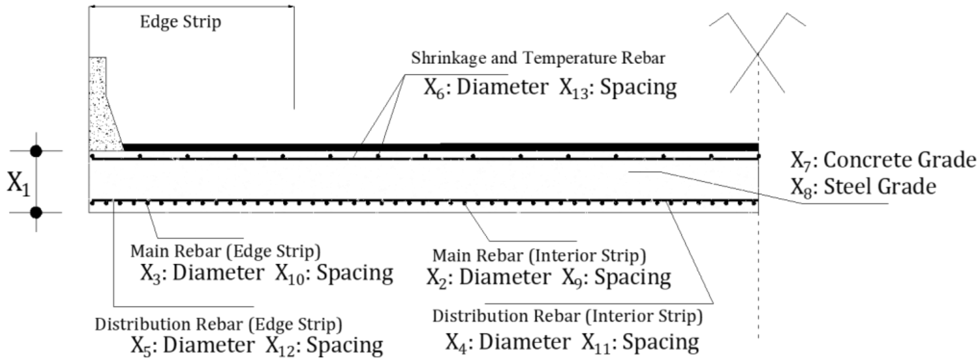

Fig. 2. Design variables in cross-section

Table 1. Upper, lower bounds and increments of design variables

Variable	Definition	Lower Bound	Upper Bound	Increment	Number of possible values
X_1	Deck thickness	300 mm	1200 mm	10 mm	91
X_2	Main rebar diameter in the interior strip	{6 8 10 12 14 16 20 25 28 32} mm			10
X_3	Main rebar diameter in the edge strip	{6 8 10 12 14 16 20 25 28 32} mm			10
X_4	Distribution rebar diameter in the interior strip	{6 8 10 12 14 16 20 25 28 32} mm			10
X_5	Distribution rebar diameter in the edge strip	{6 8 10 12 14 16 20 25 28 32} mm			10
X_6	Shrinkage and temperature rebar diameter	{6 8 10 12 14 16 20 25 28 32} mm			10
X_7	Concrete grade (fc')	{25, 30, 35, 40, 45, 50} MPa			6
X_8	Steel rebar grade (fy)	{400, 500} MPa			2
X_9	Main rebar spacing in the interior strip	50 mm	450 mm	10 mm	41
X_{10}	Main rebar spacing in the edge strip	50 mm	450 mm	10 mm	41
X_{11}	Distribution rebar spacing in the interior strip	50 mm	450 mm	10 mm	41
X_{12}	Distribution rebar spacing in the edge strip	50 mm	450 mm	10 mm	41
X_{13}	Shrinkage and temperature rebar spacing	50 mm	450 mm	10 mm	41

Table 2. Design parameters of slab bridge problem

Description and unit	**Value**
Width of traffic barriers (mm)	530
Load modifier (η)	1
Exposure factor (γ_e)	1
Wearing surface thickness (mm)	80
Impact factor	0.33
Impact factor (for fatigue)	0.15
Density of reinforced concrete (kN/m^3)	25
Density of wearing surface (kN/m^3)	22
Cross-sectional area of traffic barriers (mm^2)	0.24
Clear concrete cover for bottom of slab (mm)	25
Clear concrete cover for slab surface (mm)	60

Table 3. Unit emissions for concrete and reinforcement (Yepes et al., 2012)

Material	Unit CO_2 emission
Steel Rebar (400 MPa)	2.82 kg/kg
Steel Rebar (500 MPa)	3.02 kg/kg
Concrete (25 MPa)	224.34 kg/ m^3
Concrete (30 MPa)	224.94 kg/ m^3
Concrete (35 MPa)	265.28 kg/ m^3
Concrete (40 MPa)	265.28 kg/ m^3
Concrete (45 MPa)	265.91 kg/ m^3
Concrete (50 MPa)	265.95 kg/ m^3

The fifth and sixth constraints given in Eq. 5 are related to the crack control of the deck section. The expression in the denominator of the constraint is the maximum limit of the reinforcement spacing. Cracks are assumed to be under control if the principal reinforcement spacing in the interior and edge strips is below this maximum limit.

$$g_{5-6}(x) = \frac{s}{\frac{123000 \cdot \gamma_e}{\beta_s \cdot f_{ss}} - 2 \cdot d_c} - 1 \leq 0 \tag{5}$$

Where γ_e is the exposure factor and β_s is a factor, f_{ss} is the tensile stress in reinforcement at the service limit state, d_c is the concrete cover measured from the extreme tension fiber to the center of the closest flexural reinforcement.

The constraint given in Eq. 6 is used for deflection control where Δ_{LL+IM} is the deflection under live load and Δ_{LL+IM}^{allow} is the allowable deflection. The allowable deflection is considered as 1/800 of the span length.

$$g_7(x) = \frac{\Delta_{LL+IM}}{\Delta_{LL+IM}^{allow}} - 1 \leq 0 \tag{6}$$

For fatigue control, the condition $f_f < (\Delta F)_{TH}$ must be satisfied. Where $(\Delta F)_{TH}$ is the stress range limit for fatigue control and f_f is the stress amplitude. This condition is controlled by the constraint given in Eq. 7.

$$g_8(x) = \frac{f_f}{(\Delta F)_{TH}} - 1 \leq 0 \tag{7}$$

The moment capacity of the bridge deck must be greater than the design moment ($M_r \geq M_u$) in both the edge and interior strips. For this check, the ninth and tenth constraints for the interior and edge strips are used.

$$g_{9-10}(x) = \frac{M_u}{M_r} - 1 \leq 0 \tag{8}$$

In the constraint given in Eq. 9, where M_{cr} is the cracking moment and M_u is the design moment, the minimum reinforcement ratio limit is controlled by the eleventh and twelfth constraints in the interior and edge strips.

$$g_{11-12}(x) = \frac{\min\begin{cases}1{,}2 \cdot M_{cr} \\ 1{,}33 \cdot M_u\end{cases}}{M_r} - 1 \leq 0 \tag{9}$$

The distribution reinforcement control is realized by the thirteenth and fourteenth constraints given in Eq. 10 for the interior and edge strips. Where $A_d^{required}$ is the amount of transverse distribution reinforcement required and A_d is the amount of transverse distribution reinforcement placed in the section.

$$g_{13-14}(x) = \frac{A_d^{required}}{A_d} - 1 \leq 0 \tag{10}$$

The amount of shrinkage and temperature change reinforcement to be placed in both directions is $\text{Temp } A_s^{required}$ and the placed reinforcement $\text{Temp } A_s$, the amount of this reinforcement is controlled by the fifteenth constraint, and the spacing condition is controlled by the sixteenth constraint.

$$g_{15}(x) = \frac{\text{Temp } A_s^{required}}{\text{Temp } A_s} - 1 \leq 0 \tag{11}$$

$$g_{16}(x) = \frac{s_{TEMP}}{\min\begin{cases}3 \cdot h \\ 450 \text{ mm}\end{cases}} - 1 \leq 0 \tag{12}$$

2.3. Proposed Ch-SAMP-Rao algorithm

The difference of the Chaotic SAMP-Rao (Ch-SAMP-Rao) algorithm proposed here from the SAMP-Rao 1, SAMP-Rao 2 and SAMP-Rao 3 algorithms is presented below in Table 4. in the green colored lines. The difference between SAMP-Rao 1, SAMP-Rao 2 and SAMP-Rao 3 algorithms is the convergence equations used in the update mechanisms. The Ch-SAMP-Rao algorithm proposed in this study uses one of these three convergence equations according to a reference signal generated from chaotic maps according to the number of function evaluations.

Therefore, the algorithm uses SAMP-Rao 1, SAMP-Rao 2 and SAMP-Rao 3 convergence equations in a chaotic manner in its life cycle.

3. Results of simulation studies

3.1. Simulation environment and algorithm settings

The characteristics of the simulation environment are summarized in Table 5. The same equipment was used in all experiments to ensure a fair comparison.

In addition to the Ch-SAMP-Rao algorithm proposed in this study, Rao1, Rao2, Rao3, SAMP-Rao1, SAMP-Rao2, SAMP-Rao3 were used in the study and statistical performance comparisons were made. For the tested algorithms, the settings recommended in the literature were used as a standard procedure. The algorithms tested on the slab bridge problems investigated in this study, the reference works of the algorithms and the settings recommended in the reference works are presented in Table 6.

Table 4. General steps in Ch-SAMP-Rao Algorithm

Algorithm 1. General steps in Ch-SAMP-Rao

Begin
    Set parameters
    Generate the random initial candidate solutions
        for *i*=1: *N* (Population size)
            Evaluate the fitness values of the *i*th solution candidate
        end for
while (*FEs<MaxFEs*)
    Divide the entire population into ‘s’ number of groups based on the quality of the solutions (initially s = 2 is considered).
    Update best(t), and worst(t)
        for i=1:*s*
            for *j*=1: *SN* (Size of sub-population)
                Identify the best and worst solution
                switch *(reference_signal)*
                case *reference_signal<1/3*
                    $x_{new} = x_{old} + rand_1(x_{best} - x_{worst})$
                case *reference_signal≥1/3 & reference_signal<2/3*
                    $x_{new} = x_{old} + rand_1(x_{best} - x_{worst}) + rand_2(|x_{old}\ or\ x_{rand}| - |x_{rand}\ or\ x_{old}|)$
                case *reference_signal≥2/3*
                    $x_{new} = x_{old} + rand_1(x_{best} - |x_{worst}|) + rand_2(|x_{old}\ or\ x_{rand}| - |x_{rand}\ or\ x_{old}|)$
                end switch
            Update process: Apply an elitist strategy to select best solution.
            end for
        end for
end while
end

Table 5. The characteristics of the simulation environment

	Component	Description
Hardware	CPU and Frequency	Intel(R) Core(TM) i5-9400F CPU @ 2.90GHz
	RAM	8,00 GB
	Hard Drive	500 GB solid state drive
Software	Operating System	Windows 10 Pro 64 bit
	Language	MATLAB R2022b

Tablo 6. Settings of the tested algorithms

Algorithm	Reference	Parameters
Ch-SAMP-Rao	*In this study*	Population size = 50
Rao1	(R. V. Rao, 2020)	Population size = 50
Rao2	(R. V. Rao, 2020)	Population size = 50
Rao3	(R. V. Rao, 2020)	Population size = 50
SAMP-Rao1	(R. V. Rao & Pawar, 2020)	Population size = 50
SAMP-Rao2	(R. V. Rao & Pawar, 2020)	Population size = 50
SAMP-Rao3	(R. V. Rao & Pawar, 2020)	Population size = 50

3.2. Optimum design of problems

Details of the optimum designs of the 5.6m wide (Design 1) and 9.2m wide (Design 2) slab bridges are presented in Table 7.

Table 7. shows that as the bridge width increases, the amount of primary reinforcement, distribution reinforcement and shrinkage and temperature change reinforcement increases. When the bridge span is constant, an increase of 64% in the width causes an increase of approximately 45% in the prime reinforcement, 47% in the distribution reinforcement, 65% in the shrinkage and temperature change reinforcement, and 91% in the amount of concrete. In this context, it is understood that the increase in the width of the bridge causes the highest proportional increase in the amount of concrete and the highest increase in the amount of distributing reinforcement among the reinforcements.

When the CO_2 emissions are compared, it is seen that while the bridge span is constant, an increase of 64% in width increases concrete emissions by 62% and reinforcement emissions by 47%. The total emission decreased by 0.59%. This is due to the increase in the volume of concrete used as a result of the increase in width.

Another finding that should be noted is that the emissions per unit deck area decreased with an increase in bridge width by 64%. As the bridge width increases, the total emission value per unit area of the bridge decreases by 3%.

Tablo 7. Optimal design details

		Design 1	Design 2
	Span (m)	10	10
	Width (m)	5.6	9.2
Design variables	X_1 (mm)	1030	1200
	X_2 (mm)	32	14
	X_3 (mm)	32	14
	X_4 (mm)	14	10
	X_5 (mm)	14	14
	X_6 (mm)	6	6
	X_7 (MPa)	50	30
	X_8 (Mpa)	500	500
	X_9 (mm)	370	80
	X_{10} (mm)	370	80
	X_{11} (mm)	400	230
	X_{12} (mm)	400	450
	X_{13} (mm)	450	450
	Constraint Violation	0	0
Total	Main Bar Weight (kg)	950.76	1382.73
	Distribution Bar Weight (kg)	166.16	244.08
	Shrinkage and Temp. Bar Weight (kg)	54.86	90.28
	Total Bar Weight (kg)	1171.77	1717.09
	Total Concrete Amount (m^3)	57.68	110.40
	CO_2 Emission of Reinforcement (kg)	3304.39	4842.20
	CO_2 Emission of Concrete (kg)	15340.00	24833.38
	Total CO_2 Emission (kg)	18644.39	29675.58
Per slab area	CO_2 Emission of Reinforcement per Slab Area(kg)	59.01	52.63
	CO_2 Emission of Concrete per Slab Area (kg)	273.93	269.93
	Total CO_2 Emission per Slab Area	332.94	322.56

3.3. Statistical performance tests

In order to compare the proposed Ch-SAMP-Rao algorithm with the SAMP-Rao and Rao algorithms, three different statistical performance evaluations were performed. The first performance evaluation involves examining the mean solutions and their standard deviations of the results obtained from independent runs of the algorithms. In order to perform this evaluation, Table 8. presents the mean emission values and their standard deviations from the independent runs of the algorithms for both designs. In order to better evaluate these statistical findings visually, box-plot plots have been prepared and are presented in Fig. 3.

The algorithms in Table 8. are ranked from smallest to largest according to the average emission value. When the average emission values and standard deviations of the emissions given in Table 8. are analyzed, it is seen that the Ch-SAMP-Rao algorithm has the smallest average emission value for both problems. In addition, the proposed Ch-SAMP-Rao algorithm has the lowest standard deviation in both problems. This shows that Ch-SAMP-Rao is statistically the most successful algorithm among the competing algorithms. The algorithm with the second smallest mean in Design 1 is SAMP-Rao3, while the algorithm with the second smallest mean in Design 2 is SAMP-Rao1. This shows that the performances of Rao and SAMP-Rao algorithms are extremely sensitive to the problem.

Similarly, examination of the box-plot graphs presented in Fig. 3 shows that the Ch-SAMP-Rao algorithm achieved the lowest mean and standard deviation. Moreover, it is clear from both Table 8. and the box-plots that the SAMP-Rao algorithm variants using the sub-population separation method are more successful than the Rao variants.

The second performance comparison was performed with the Friedman Test (Friedman, 1940). With this test, the scores of the algorithms were determined and the performance ranking of the algorithms on the problems was given according to the scores. In addition, the average scores were calculated, and a ranking was also performed according to the average score. These rankings can be found in Table 9.

Table 8. Mean and standard deviation of algorithms

Design 1		Design 2	
Ch-SAMP-Rao	18644.39 (3.73 10^{-12})	Ch-SAMP-Rao	29680.79 (21.00)
SAMP-Rao3	18649.65 (14.04)	SAMP-Rao1	29755.98 (103.25)
SAMP-Rao1	18655.48 (15.39)	SAMP-Rao2	29706.06 (123.13)
Rao1	18657.79 (20.41)	SAMP-Rao3	29810.42 (130.02)
SAMP-Rao2	18666.13 (23.83)	Rao3	29811.74 (121.41)
Rao3	18930.63 (709.46)	Rao1	29870.96 (179.24)
Rao2	19259.77 (981.28)	Rao2	29889.03 (256.85)

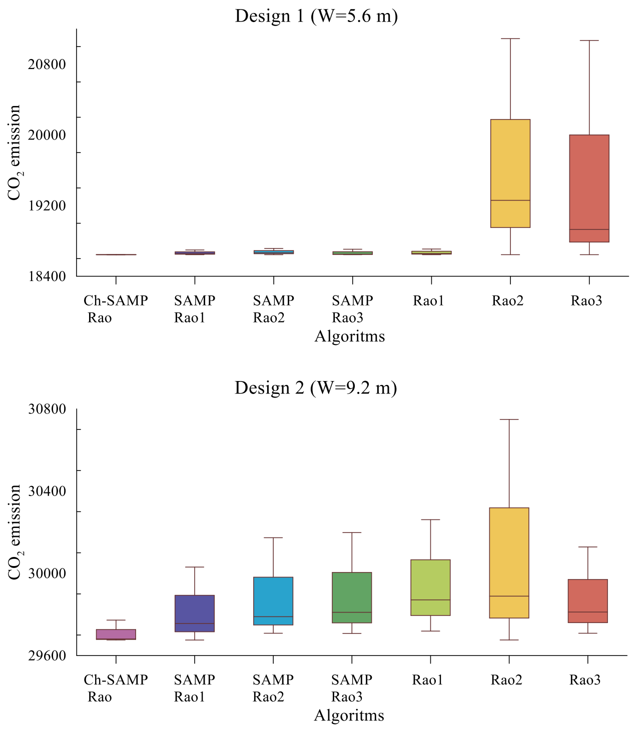

Fig. 3. Box plots of Ch-SAMP-Rao, SAMP-Rao and Rao variants for slab bridge problem

Table 9. Friedman scores of Ch-SAMP-Rao, SAMP-Rao and Rao variants for slab bridge problem

Friedman Scores and Rankings					
Design 1		Design 2		Mean Score	
Ch-SAMP-Rao	1.95	Ch-SAMP-Rao	1.43	Ch-SAMP-Rao	1.69
SAMP-Rao3	2.81	SAMP-Rao1	3.00	SAMP-Rao1	3.32
SAMP-Rao1	3.64	SAMP-Rao2	4.40	SAMP-Rao3	3.75
Rao1	3.71	Rao2	4.69	Rao1	4.39
SAMP-Rao2	4.40	SAMP-Rao3	4.69	SAMP-Rao2	4.40
Rao2	5.45	Rao3	4.71	Rao2	5.07
Rao3	6.02	Rao1	5.07	Rao3	5.37

According to the Friedman scores presented in Table 9, the proposed Ch-SAMP-Rao algorithm is ranked first in both designs. The second-ranked algorithms were SAMP-Rao3 in Design 1 and SAMP-Rao1 in Design 2. Friedman's tests further corroborate the hypothesis that SAMP-Rao algorithms may exhibit divergent performance, even when confronted with problems of a similar nature. According to the mean score, the proposed Ch-SAMP-Rao algorithm demonstrates the highest level of performance.

The third and final comparison was executed using the Wilcoxon test (Wilcoxon, 1945), which facilitates paired comparisons of the Ch-SAMP-Rao algorithm, which was ascertained to be in the leading position by the Friedman test, with other competitors. The Wilcoxon test results are presented in Table 10. The three scores assigned to each cell indicate the number of problems in which the competitor algorithm performs better, similar, or worse, respectively, compared to the Ch-SAMP-Rao algorithm.

The results of the Wilcoxon test, as presented in Table 10, indicate the superiority of the Ch-SAMP-Rao algorithm over all variants of the Samp-Rao and Rao algorithms in both problems.

In summary, the statistical evaluations indicate that the Ch-SAMP-Rao algorithm significantly outperforms the SAMP-Rao and Rao algorithm variants in the context of designing reinforced concrete slab bridges with minimal carbon dioxide emissions.

4. Conclusions

In this study, a novel metaheuristic algorithm, Chaotic SAMP-Rao (Ch-SAMP-Rao), was proposed for the optimum design of reinforced concrete slab bridges, targeting environmental sustainability and cost efficiency. The developed algorithm dynamically integrates the convergence equations of three variants of the SAMP-Rao family using chaotic maps, thereby offering a flexible and robust optimization mechanism that adapts to the structure of the problem.

Simulations were carried out on two different bridge design problems with widths of 5.6 m and 9.2 m. The performance of the proposed algorithm was compared with established variants of the Rao and SAMP-Rao algorithms from the literature. The results demonstrated that Ch-SAMP-Rao produced the lowest average CO_2 emission values in both problems and achieved the smallest standard deviations, indicating strong solution stability.

Statistical analyses using the Friedman and Wilcoxon tests further confirmed the superiority of the Ch-SAMP-Rao algorithm over its competitors. Notably, while the performance of traditional algorithms varied with problem structure, the proposed algorithm consistently exhibited high adaptability and success across different scenarios.

In conclusion, the Ch-SAMP-Rao algorithm provides an effective optimization approach for reducing environmental impacts and enhancing efficiency in structural engineering design. Future research may focus on applying the algorithm to different bridge types and infrastructure systems, testing it in multi-objective optimization scenarios, and developing hybrid enhancements to further improve computational efficiency.

Table 10. Wilcoxon test results of Ch-SAMP-Rao, SAMP-Rao and Rao variants for slab bridge problem

Ch-SAMP-Rao vs.	Design 1	Design 2
SAMP-Rao1	0 / 0 / 1	0 / 0 / 1
SAMP-Rao2	0 / 0 / 1	0 / 0 / 1
SAMP-Rao3	0 / 0 / 1	0 / 0 / 1
Rao1	0 / 0 / 1	0 / 0 / 1
Rao2	0 / 0 / 1	0 / 0 / 1
Rao3	0 / 0 / 1	0 / 0 / 1

References

Ahsan, R., Rana, S., & Ghani, S. N. (2012). Cost Optimum Design of Posttensioned I-Girder Bridge Using Global Optimization Algorithm. *Journal of Structural Engineering*, *138*(2), 273–284.

Bruno, D., Lonetti, P., & Pascuzzo, A. (2016). An optimization model for the design of network arch bridges. *Computers and Structures*, *170*, 13–25.

Friedman, M. (1940). A Comparison of Alternative Tests of Significance for the Problem of m Rankings. *The Annals of Mathematical Statistics*, *11*(1), 88–92.

García-Segura, T., & Yepes, V. (2016). Multiobjective optimization of post-tensioned concrete box-girder road bridges considering cost, CO2 emissions, and safety. *Engineering Structures*, *125*, 325–336.

Ghodoosi, F., Abu-Samra, S., Zeynalian, M., & Zayed, T. (2018). Maintenance cost optimization for bridge structures using system reliability analysis and genetic algorithms. *Journal of Construction Engineering and Management*, *144*(2), 1–10.

Kaveh, A., Mottaghi, L., & Izadifard, R. A. (2022). Optimal design of a non-prismatic reinforced concrete box girder bridge with three meta-heuristic algorithms. *Scientia Iranica*, *29*(3), 1154–1167.

Martí, J. V., Yepes, V., & González-Vidosa, F. (2015). Memetic algorithm approach to designing precast-prestressed concrete road bridges with steel fiber reinforcement. *Journal of Structural Engineering (United States)*, *141*(2), 1–9.
Martinez-Martin, F. J., Gonzalez-Vidosa, F., Hospitaler, A., & Yepes, V. (2012). Multi-objective optimization design of bridge piers with hybrid heuristic algorithms. *Journal of Zhejiang University: Science A*, *13*(6), 420–432.
Martínez-Muñoz, D., García, J., Martí, J. V., & Yepes, V. (2022). Discrete swarm intelligence optimization algorithms applied to steel–concrete composite bridges. *Engineering Structures*, *266*.
Öztürk, H. T. (2024). The effectiveness of metaheuristic algorithms modified with Fitness Distance Balance (FDB) method on RC slab bridge superstructure optimization. *Iranian Journal of Science and Technology, Transactions of Civil Engineering*, *48*(6), 4423–4442.
Rana, S., Ahsan, R., & Ghani, S. N. (2010). Design of prestressed concrete I-girder bridge superstructure using optimization algorithm. *Joint Conference on Advances in Bridge Engineering-II*, 978–984.
Rao, R. V. (2020). Rao algorithms: Three metaphor-less simple algorithms for solving optimization problems. *International Journal of Industrial Engineering Computations*, *11*(1), 107–130.
Rao, R. V., & Pawar, R. B. (2020). Self-adaptive Multi-population Rao Algorithms for Engineering Design Optimization. *Applied Artificial Intelligence*, *34*(3), 187–250.
Wilcoxon, F. (1945). Individual Comparisons by Ranking Methods. *Biometrics Bulletin*, *1*(6), 80–83.
Yepes, V., Gonzalez-Vidosa, F., Alcala, J., & Villalba, P. (2012). CO2-Optimization Design of Reinforced Concrete Retaining Walls Based on a VNS-Threshold Acceptance Strategy. *Journal of Computing in Civil Engineering*, *26*(3), 378–386.
Yepes-Bellver, L., Brun-Izquierdo, A., Alcalá, J., & Yepes, V. (2022). CO2-Optimization of Post-Tensioned Concrete Slab-Bridge Decks Using Surrogate Modeling. *Materials*, *15*(14).

4th International Civil Engineering & Architecture Conference
17-19 May 2025, Trabzon, Türkiye

Quality processes for bridge analysis models

Serhan Guner*[1]

[1] *University of Toledo, Department of Civil and Environmental Engineering, 2801 W. Bancroft St., MS 307, Toledo, Ohio 43606, USA*

Abstract. The design of bridges often involves the use of structural analysis models of varying degrees of complexity. Superstructure design models vary from approximate one-dimensional line girder analysis models to complex two- and three-dimensional finite element analysis models. Substructure and foundation models often consider soil-structure interaction, second-order effects, dynamic response for seismic analysis, and interaction with the superstructure. A variety of analysis methods and associated software are used to create and analyze these models and obtain the analysis output. This process can be quite complex with a large number of input parameters and significant amounts of output data. A study was recently conducted in the United States to identify and document state departments of transportation (DOT) practices related to the quality processes for bridge structural analysis models. The study documents the written and informal processes for identifying appropriately qualified staff including in-house personnel and consultants; choosing an appropriate analysis method and software; validating the analysis software; modeling a bridge structure with proper approaches and assumptions; verifying the analysis results; and reconciling discrepancies between independent models. Information was gathered through a literature review, a survey of all DOTs, and follow-up interviews with five selected agencies as case examples. The survey was completed by 51 DOTs, including 50 states and the District of Columbia, yielding an overall response rate of 100%. This paper aims to summarize the main findings and refer readers to the relevant references. In addition, commonly misunderstood concepts and processes, such as verification, validation, uncertainty, error, and calibration, are clarified.

Keywords: Bridge analysis; Consultant projects; In-house projects; Quality assurance; Quality control.

1. Introduction

The design of bridges often involves the use of structural analysis models of varying degrees of complexity. Superstructure design models vary from approximate one-dimensional line girder analysis models to sophisticated two- and three-dimensional finite element analysis models. Substructure and foundation models often consider soil-structure interaction, second-order effects, dynamic response for seismic analysis, and interaction with the superstructure. A variety of analysis methods and software can be used to create and analyze these models. This process can be quite complex with a large number of input parameters and significant amounts of output data.

The engineer must understand the limitations of the analysis method and software, possess experience in developing analysis models with proper approaches and assumptions, and correctly interpret the results. An appropriate understanding of the expected behavior of the structure is also required to assess if the predicted behavior represents the actual performance of the structure. A simple check of the program input values is not an adequate way of ensuring the accuracy and validity of these models. Quality assurance (QA) and quality control (QC) are two essential processes for the quality management of analysis models. Verification and validation (V&V) play a critical role in the QA/QC process.

A study was recently conducted in the United States to identify and document state Departments of Transportation (DOT) practices related to the quality processes for bridge structural analysis models. The study documents the written and informal processes for identifying appropriately qualified staff, including in-house personnel and consultants; choosing an appropriate analysis method and software; validating the analysis software; modeling a bridge structure with proper approaches and assumptions; verifying the analysis results; and reconciling discrepancies between independent models. In addition, the study identified gaps that could be addressed to enable state DOTs to benefit more effectively from the quality processes for bridge analysis models.

This paper aims to summarize the main findings and refer readers to the relevant references for the complete study details. In addition, commonly misunderstood concepts and processes are clarified.

*Corresponding author, Associate Professor, E-mail: Serhan.Guner@UToledo.edu

https://doi.org/10.31462/icearc2025_ce_sme_587

2. Commonly misunderstood concepts and processes

Quality assurance and quality control are two essential aspects of quality management. While some quality assurance and quality control activities are interrelated, they are defined differently. QA activities and responsibilities cover virtually all of the quality system in one fashion or another, while QC is a subset of the QA activities (American Society for Quality, 2023) (Fig. 1). Elements in the quality system might not be specifically covered by QA/QC activities and responsibilities but may involve QA and QC (Technical Committee ISO/TC 176, 2015).

Verification and validation (V&V) are indispensable components of QA/QC processes in computational modeling of bridge structures. V&V are the processes by which evidence is gathered to determine the accuracy of the computer model for specified conditions. These accuracy results, along with uncertainty quantification, contribute to the determination of the credibility of the model for the conditions of its intended use (ASME V&V 10-2019, 2020).

While the terms verification and validation are often used interchangeably in casual conversations in bridge engineering practice, they have, in fact, quite different meanings. Stated succinctly, verification deals with 'mathematics' while validation deals with 'physics' (Patrick J. Roache, 1998). Verification assesses the numerical accuracy of a computational model regardless of the physics being modeled, while validation assesses the degree to which the computational model is an accurate representation of the physics being modeled (ASME V&V 10-2019, 2020). Verification uses comparison of computational solutions with highly accurate (analytical or numerical) benchmark solutions whereas validation compares the numerical solution with the experimental results. In verification, the relationship of the simulation to the real world is *not* an issue. In validation, the relationship between computation and the real world *is* the issue (Oberkampf, Hirsch, & Trucano, 2003). The relationships between V&V activities involved are schematically presented in Fig. 2 (Kwaśniewski, 2009).

Verification is defined as 'the process of determining that a computational model accurately represents the underlying mathematical model and its solution' (ASME V&V 10-2019, 2020). Verification has also been described as *'solving the equations right'* (Van Hees, 2013). The fundamental strategy of verification is to identify, quantify, and reduce errors in the computational model and its numerical solution (Oberkampf et al., 2003).

Validation is defined as 'the process of determining the degree to which the model is an accurate representation of corresponding physical experiments from the perspective of the intended uses of the model' (ASME V&V 10-2019, 2020). Validation has also been described as *'solving the right equations'* (Van Hees, 2013). The fundamental strategy of validation involves identifying and quantifying errors and uncertainty through comparison of simulation results with experimental data.

At this point, it is useful to define uncertainty and error. *Uncertainty* is a potential deficiency in any phase or activity of the modeling process that is due to the lack of knowledge, while *error* is a recognizable deficiency in any phase or activity of modeling and simulation that is not due to lack of knowledge (AIAAG-077-1998, 2002). The key phrase differentiating the definitions of uncertainty and error is 'lack of knowledge.' The key word in the definition of uncertainty is 'potential,' which indicates that deficiencies may or may not exist. The definition of error implies that the deficiency is identifiable upon examination (Van Hees, 2013).

One approach for determining the level of uncertainty and its effect on an analysis is to perform a sensitivity analysis (AIAAG-077-1998, 2002). *Sensitivity analysis* is the general process of discovering the effects of model input parameters on the response quantities of interest using techniques such as analysis of variance (Mason, Gunst, & Hess, 2003). When performed after the computational model is verified but before it is validated, a sensitivity analysis can provide important insight into the characteristics of that computational model (ASME V&V 10-2019, 2020).

It is also important to define calibration and put it in perspective. One simple definition of *calibration* is to employ explicit tuning or updating of model parameters associated with an engineering code to achieve improved agreement with existing validation experiments (Oberkampf, Trucano, & Hirsch, 2004; Trucano, Swiler, Igusa, Oberkampf, & Pilch, 2006). As another definition, calibration is a procedure where, through repeated calculations with modified input parameters, the engineer tries to find an 'optimal' set of input data which can provide the model's response closest to the actual experimental data (Kwasniewski & Bojanowski, 2015). The process allows the most common sources of modeling (and experimental) difficulties to be represented as simple mechanical models and calibrated so that the global response of the computational model agrees with the experimental results (ASME V&V 10-2019, 2020). Calibration of the model should be performed only after both code verification and calculation verification have been performed (ASME V&V 10-2019, 2020).

Parametric model calibration determines only the model's fitting ability, not its predictive capability. A model calibrated to experimental results may not yield accurate predictions over the range of its intended use. It is possible that, due to superimposing of errors, the engineer can get good correlation between the experimental and numerical results for a wrong model, defined by incorrect input parameters. Such a situation is often detected when the model is used for a different case with changed input conditions. Furthermore, a complex model with only some of the input parameters 'correctly' calibrated should give a response different from the experimental data due to the indeterminacy of other parameters. (Oberkampf et al., 2004).

As another important definition, *a benchmark* is a choice of information that is believed to be accurate or true for use in verification, validation, or calibration. The fundamental purpose of benchmarks is to draw specific conclusions from their comparison with calculations. In the case of verification, this purpose is to assess the mathematical accuracy of numerical solutions. For validation, this purpose is to assess the physical fidelity for a stated application of the mathematical equations solved in the code. For calibration, the purpose is to choose parameter values that improve the agreement of the code calculations with the chosen benchmarks, in the belief that such tuned accuracy improvement will increase the believed credibility of the code – a goal commonly consider to be incorrect. The choice of benchmarks must vary depending on the purpose of the comparisons (Trucano et al., 2006).

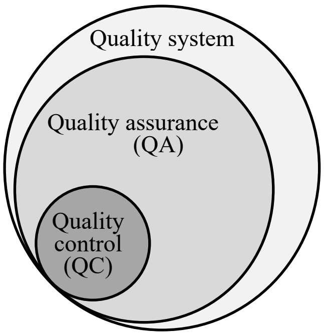

Fig. 1. Relationship between the quality system, quality assurance, and quality control.

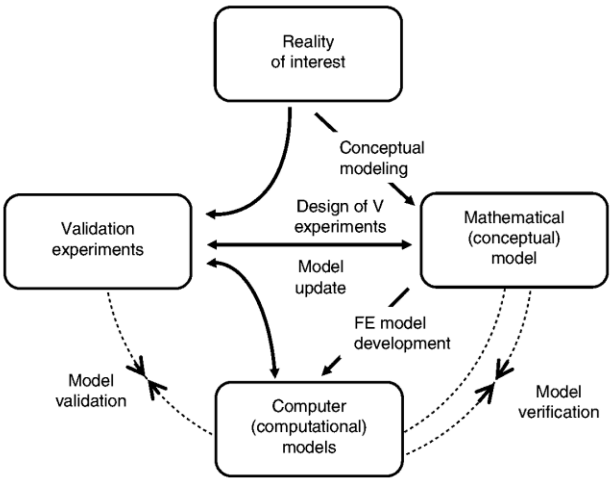

Fig. 2. Relationships between modeling, verification, and validation.

3. State of practice in the United States

To collect the most current information, an online survey was distributed to each DOT's voting member in the AASHTO Committee on Bridges and Structures. The survey included 25 questions grouped in three sections: quantities of the bridge design and evaluation projects undertaken; bridge designs completed by consultants; and bridge designs completed in-house by agencies. The survey was completed by 51 DOTs, including 50 states and the District of Columbia, giving an overall response rate of 100%. In addition, specific information was collected from five selected state DOTs—California, Colorado, Iowa, Louisiana, and New York— as case studies to expand on their quality processes related to bridge structural analysis models. The following section presents a summary of the results obtained from the survey and case studies under four headings.

3.1 Quantity of the Bridge Design and Evaluation Projects Undertaken

The survey asked respondents about the total number of bridge engineers employed by their agencies. As shown in Fig. 3, there is a large variation across the nation. The most represented range is 20 to 40 engineers as selected by 17 DOTs (33%) while the least represented range is less than 10 engineers as selected by 5 DOTs (10%).

Fig. 4 compares the responses from two questions related to the percentage of new bridge design and existing bridge analysis work assigned to consultants. The analysis of responses indicates that the average percentage of new bridge and bridge replacement designs assigned to consultants is 59% while the existing bridge analyses, including load ratings, assigned to consultants is 47%. The complete set of questions and results may be found in Guner (2024).

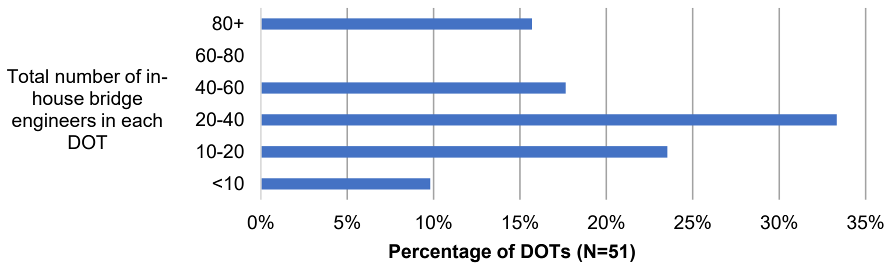

Fig. 3. Number of bridge engineers currently working in each DOT.

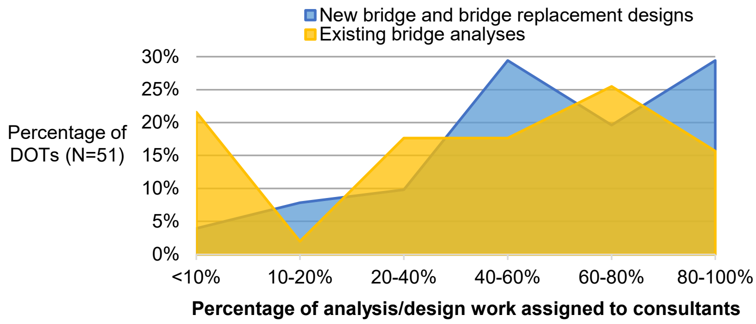

Fig. 4. Comparative DOT responses for new bridge design and existing bridge analysis assigned to consultants.

3.2 Quality processes for the bridge design projects undertaken by consultants

Three questions asked respondents about the presence of processes for certain consultant-related bridge design activities. As shown in Fig. 5, the most common written process, selected by 31 DOTs (61%), is for 'identifying appropriately qualified consultants.' This process also has the least amount of no process responses as only selected by 4 DOTs (8%). The least common written process, selected only by 8 DOTs (16%), is for 'verifying the analysis results obtained from consultants.' 6 DOTs (12%) indicated that this process may be undertaken as defined in the proposal of the consultant.

The respondents were asked how they select appropriately qualified consultants for bridge design projects. They were given three response options. The most common process, as selected by 46 DOTs (90%) is 'proposal evaluation,' while the least common process is 'interview' as selected by 18 DOTs (35%). The geographical distribution of two processes for selecting appropriately qualified consultants is presented in Fig. 6.

The survey asked a follow-up question to 36 respondents whose agencies have pre-qualification requirements, with four response options. As shown in Fig. 7, the most common requirement, selected by 30 DOTs (83%), was "minimum number of similar project experience," while the least common requirement, selected by only five DOTs (14%), was "structural engineer credentials."

The 15 DOTs (29%) which track what methods of analysis are used by their consultants were asked what methods of analysis are used for bridges analyzed by their consultants. As shown in Fig. 8, the most frequently used analysis method is "one-dimensional line girder analysis," while the least frequently used method is "nonlinear finite element method."

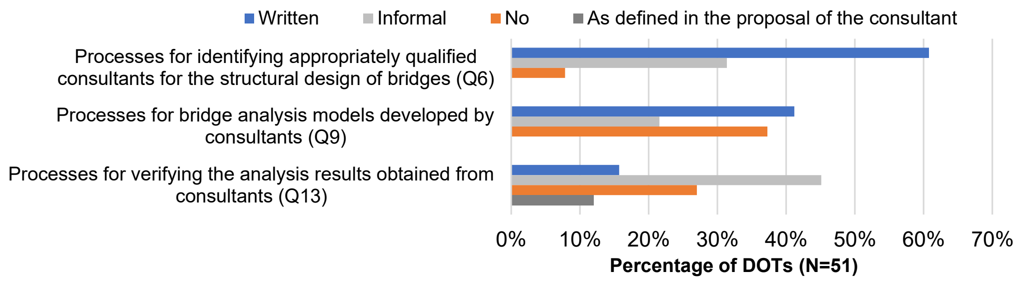

Fig. 5. Comparative DOT responses to three questions on consultant processes.

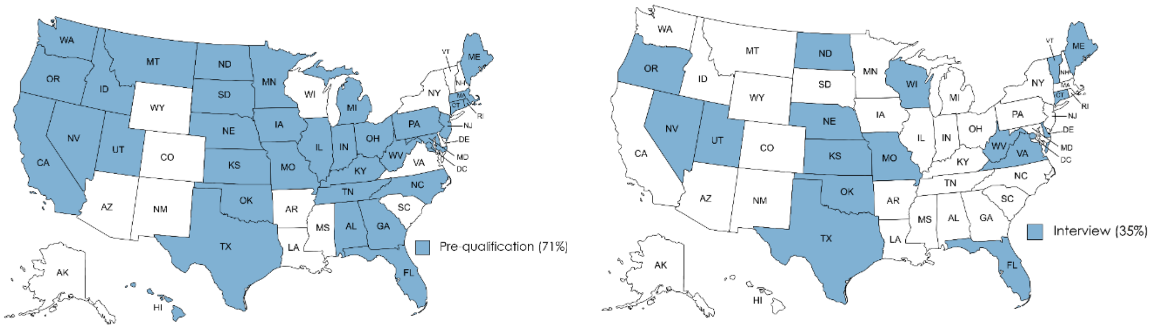

Fig. 6. DOTs with pre-qualification and interview requirements for selecting appropriately qualified consultants.

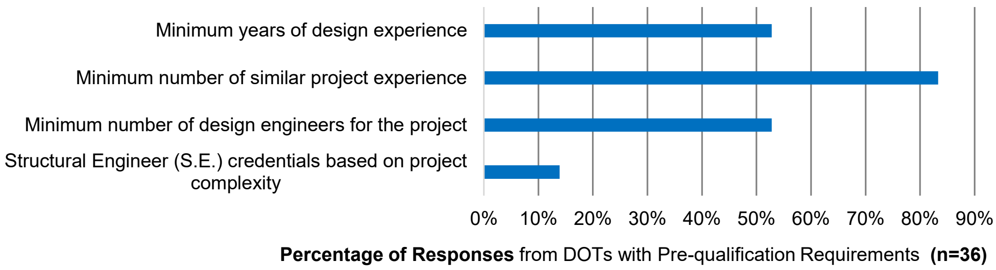

Fig. 7. DOT requirements for the pre-qualification process. Check-all-that-apply type of question.

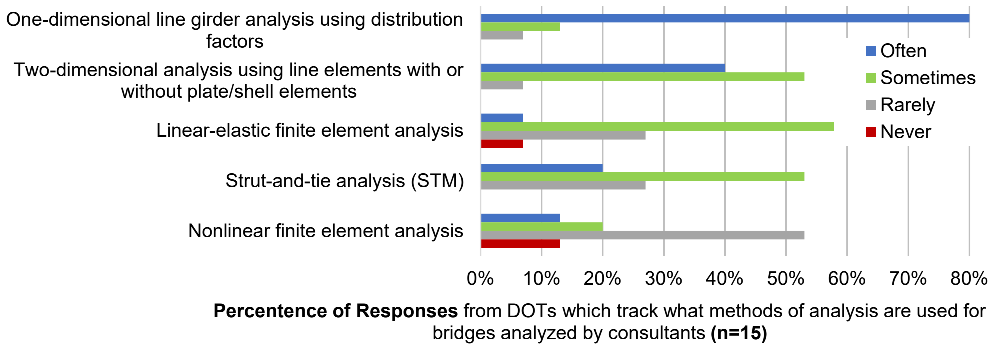

Fig. 8. Methods of analysis used for bridges analyzed by consultants.

3.3 Quantity of the bridge design projects performed in-house by agencies

The respondents were asked six questions on the presence of processes for certain in-house bridge design activities. As shown in Fig. 9, the largest number of DOTs with a written in-house process (for modeling a bridge) is 16 (31%), while the largest number of DOTs with a written consultant process (for identifying appropriately qualified consultants) is 31 (61%).

The respondents were asked what methods of analysis are used for bridges analyzed in-house by their agencies. Fig. 10 compares the percentage of responses from DOTs for the analysis methods used by consultants and DOTs for the "often" frequency. This comparison indicates that consultants use more refined analysis methods.

Fig. 11 shows the responses obtained from 7 DOTs which have written processes for validating the analysis software. The most common response for the "often" frequency, selected by five DOTs (71%), was "analysis engineer decides how to validate." The most common response option for the "sometimes" frequency, selected by four DOTs (57%), was "hiring external consultants."

The respondents were asked whether their agencies have any written or informal processes for verifying in-house analysis results. Fig. 12 shows the responses obtained from 13 DOTs which have written processes for verifying their in-house analysis results. The most common response for the "often" frequency, selected by eight DOTs (62%), was "checking of input variables." "Another team of engineers uses a different method or software" and "analysis engineer decides how to verify" were the other common responses for the "often" frequency.

The respondents were asked whether their agencies have any written or informal processes for reconciling discrepancies between independent models. Fig. 13 shows the responses obtained from eight DOTs that have written processes. The most common response for the "often" frequency was "the same team of engineers works to resolve the discrepancies," selected by five DOTs (63%), followed by "analysis engineers decide how to reconcile," selected by four DOTs (50%). The least common response was "data from field tests and sensor deployment are used," followed by "an external consultant is involved to perform independent checks."

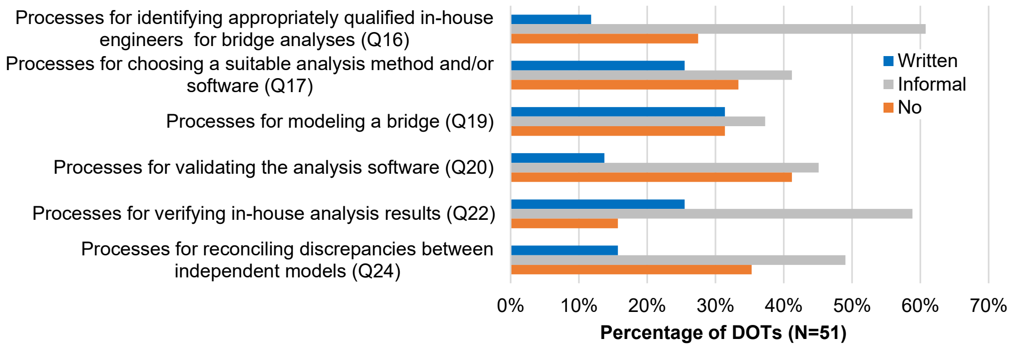

Fig. 9. Comparative DOT responses to six questions on in-house processes.

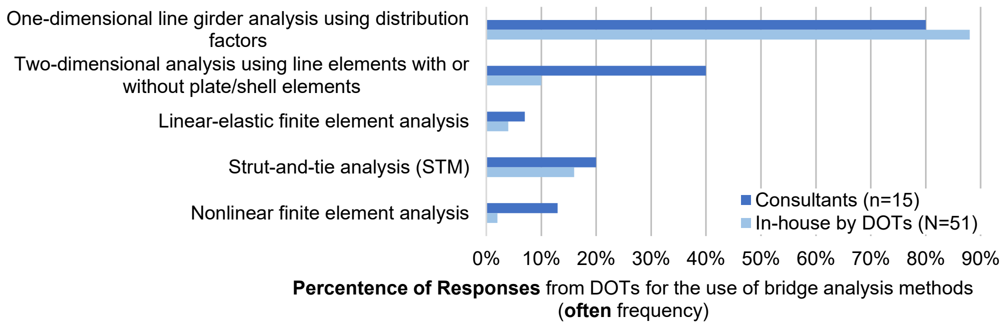

Fig. 10. Comparative DOT responses for methods of analysis used by consultants and DOTs ('often' frequency).

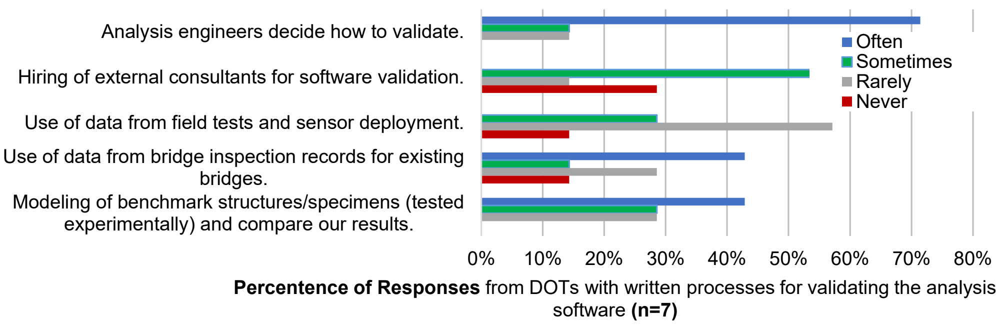

Fig. 11. Methods of validation of analysis software for medium- to high-complexity bridges and substructures that require 2D or 3D analysis models (DOTs with written processes).

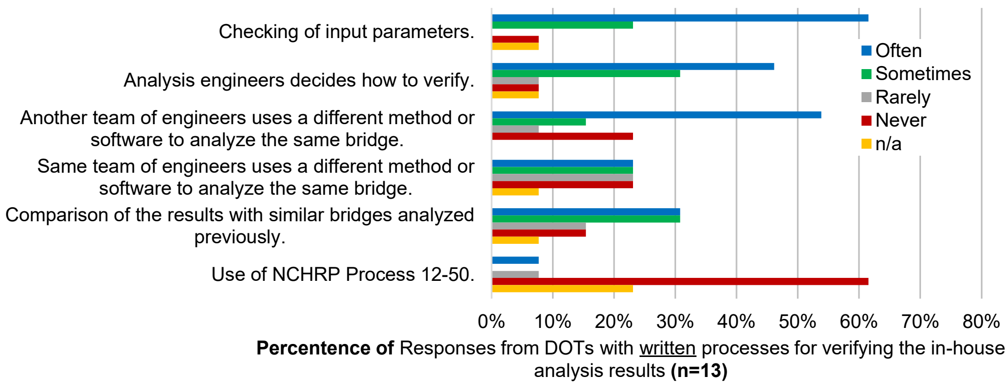

Fig. 12. Methods of verification of in-house analysis results for medium- to high complexity bridges and substructures that require 2D or 3D analysis models (DOTs with written processes).

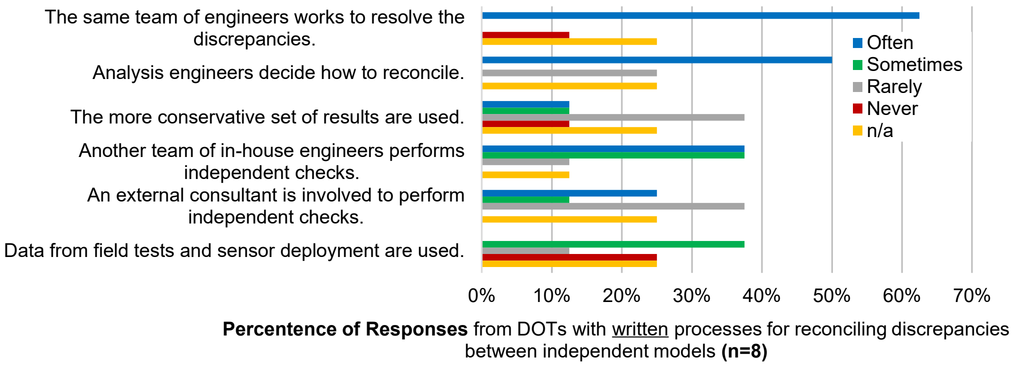

Fig. 13. Methods for reconciling discrepancies between independent models (DOTs with written processes).

3.4 Case examples

Five state DOTs were selected as case examples based on a set of criteria described in Guner (2024). The selected DOTs are as follows: California and Colorado from the West (Pacific and Mountain regions), Louisiana from the South, Iowa from the Midwest, and New York from the Northeast. Some of the findings obtained from these case studies are described below.

The case example agencies use two types of consultant selection processes: project-specific and/or statewide on-call. These agencies require consultants to either submit their QA/QC plans or follow the agency's specific QA/QC plans. As two examples, the Louisiana DOT has a well-defined evaluation and scoring criteria for consultant QA/QC plans while the New York State DOT (NYSDOT) has specific QA/QC plans that the consultants must follow.

All five case example agencies have informal processes that rely on a manager, supervisor, or unit leader to select appropriately qualified engineers based on their experience and availability. This decision also considers professional development needs, including training less experienced engineers or challenging more experienced engineers with unique or interesting projects.

All five case example agencies most frequently use 'one-dimensional line girder analysis.' While all case example agencies rely on the analysis (or design) team to select the most appropriate method(s), NYSDOT provides written guidance on when to use refined analysis methods.

All five case example agencies require a checker to independently verify the accuracy of design engineer's models, calculations, and results. For complex bridges, California DOT (Caltrans) requires project-specific design criteria, a peer review panel, and an independent check conducted by an engineer not associated with the group who has completed the original analysis. Both Caltrans and NYSDOT require the use of different software in the independent check.

To overcome the challenges with finding appropriately qualified engineers in district offices, Caltrans established the seismic and special analysis branch, which is only focused on structural modeling and analysis, while NYSDOT established the Main Office Structures group with sixty-five design staff who only perform structural analysis and final design.

For training engineering staff, Caltrans established a six-week 'bridge design academy' while NYSDOT has a 24-session 'Bridge 101' training series. Iowa DOT indicated the benefits of designer-checker pairing and a dedicated training budget for the professional development of engineering staff.

4. Conclusions

A selection from the major findings are summarized below.

- The majority of DOTs assign more than half (59%) of their new bridge and bridge replacement designs to consultants while they assign almost half (47%) of their existing bridge analyses, including load ratings, to consultants.
- The survey asked three questions on the presence of consultant quality processes. The most common written consultant process, as selected by 61% of DOTs, is 'identifying appropriately qualified consultants,' while the least common written process, selected by only 16% of DOTs, is 'verifying the analysis results obtained from consultants.' The most common 'no process' response, as selected by 37% of DOTs, is the 'bridge analysis models developed by consultants.'
- The survey asked six questions on the presence of in-house quality processes. The most common written in-house process, as selected by 31% of DOTs, is 'modeling a bridge'. The least common written process, as selected by 12% of DOTs, is 'identifying appropriately qualified in-house engineers.' This result is in sharp contrast with the consultant processes where 'identifying appropriately qualified consultants' was the most common written process. The most common 'no process' response, as selected by 41%, is 'validating the analysis software.'

- State DOTs and their consultants most frequently use the 'one-dimensional line girder analysis.' The least frequently used method is the 'nonlinear finite element method.'
- The skills acquired in undergraduate university education may not be sufficient for a competent application of the finite element and strut-and-tie methods and the interpretation of the analysis results obtained from these methods. A qualified training system with standardized requirements could be developed for bridge engineers performing these types of analyses.
- Future research could develop guidance to help state DOTs assess the effectiveness and quality of their QA/QC processes.
- Future research is suggested to develop a nationwide repository for sharing finite element and strut-and-tie models between DOTs.
- Future research could develop guidance and bridge-specific guidance on the development and verification of the finite element and strut-and-tie models.
- New training courses and seminars could be developed to cast light on commonly misunderstood concepts such as verification, validation, uncertainty, error, and calibration, and train bridge engineers on how to effectively perform these activities.

The full details of the studies conducted and the conclusions reached may be found in Guner (2024).

Acknowledgments
The research described in this paper was financially supported by the Transportation Research Board of The National Academies, Washington, DC, USA.

References

AIAAG-077-1998. (2002). Guide: Guide for the Verification and Validation of Computational Fluid Dynamics Simulations (AIAA G-077-1998(2002)). In *Guide: Guide for the Verification and Validation of Computational Fluid Dynamics Simulations (AIAA G-077-1998(2002))*. Washington, DC: American Institute of Aeronautics and Astronautics, Inc. https://doi.org/10.2514/4.472855.001

American Society for Quality. (2023). Quality Assurance and Quality Control. Retrieved from https://asq.org/quality-resources/quality-assurance-vs-control

ASME V&V 10-2019. (2020). *ASME V&V 10-2019: Standard for Verification and Validation in Computational Solid Mechanics*. New York, NY: Reprinted by permission of The American Society of Mechanical Engineers. All rights reserved. No further copies can be made without written permission from ASME. Permission is for this edition only.

Guner, S. (2024). *Quality Processes for Bridge Analysis Models*. Washington, D.C.: National Academies of Sciences, Engineering, and Medicine. The National Academies Press. https://doi.org/10.17226/27747

Kwaśniewski, L. (2009). On practical problems with verification and validation of computational models. *Archives of Civil Engineering*, *55*(3), 323–346.

Kwasniewski, L., & Bojanowski, C. (2015). Principles of verification and validation. *Journal of Structural Fire Engineering*, *6*(1), 29–40. https://doi.org/10.1260/2040-2317.6.1.29

Mason, R. L., Gunst, R. F., & Hess, J. L. (2003). *Statistical Design and Analysis of Experiments*. Hoboken, NJ, USA: John Wiley & Sons, Inc. https://doi.org/10.1002/0471458503

Oberkampf, W. L., Hirsch, C., & Trucano, T. (2003). *Verification, validation, and predictive capability in computational engineering and physics.* Albuquerque, NM, and Livermore, CA (United States). https://doi.org/10.2172/918370

Oberkampf, W. L., Trucano, T. G., & Hirsch, C. (2004). Verification, validation, and predictive capability in computational engineering and physics. *Applied Mechanics Reviews*, *57*(5), 345–384. https://doi.org/10.1115/1.1767847

Patrick J. Roache. (1998). *Verification and Validation in Computational Science and Engineering*. *Verification and Validation in Computational Science and Engineering*. Hermosa Publishers. Retrieved from http://pages.swcp.com/~hermosa/html/books.html#VVCSE

Technical Committee ISO/TC 176, Q. management and quality assurance, S. S. 1, C. and terminology. (2015). Quality management systems-Fundamentals and vocabulary ISO 9000:2015 (ISO 9000:2015(E). *ISO Standard*.

Trucano, T. G., Swiler, L. P., Igusa, T., Oberkampf, W. L., & Pilch, M. (2006). Calibration, validation, and sensitivity analysis: What's what. *Reliability Engineering and System Safety*, *91*(10–11), 1331–1357. https://doi.org/10.1016/j.ress.2005.11.031

Van Hees, P. (2013). Validation and verification of fire models for fire safety engineering. *Procedia Engineering*, *62*, 154–168. https://doi.org/10.1016/j.proeng.2013.08.052

4th International Civil Engineering & Architecture Conference
17-19 May 2025, Trabzon, Türkiye

Seismic performance evaluation of monopole billboard regarding connection stiffness

Huseyin K. Celik[*1,2], Gokhan Sakar[2]

[1] *Izmir University of Economics, Department of Civil Engineering, 35330 Izmir, Türkiye*
[2] *Dokuz Eylul University, Department of Civil Engineering, 35390, Izmir, Türkiye*

Abstract. Billboard structures are typically constructed with a single post and a panel installed over the monopole. Due to its nature, it does not have much redundancy. The structural stability mainly depends on the stiffness of the monopole i.e., its connection behaviour significantly affects the structural performance. Furthermore, there is no direct regulation on monopole billboards and it is generally treated as a product rather than a structure. However, many papers have already highlighted the importance of the billboard's structural safety concern, but not much effort has been made about its general design principles. Therefore, to investigate the seismic behaviour of monopole billboard structures, the study is proposed by the authors. An example monopole billboard was taken and static pushover analyses were performed for the flexibility of the post foundation and post panel connection. Base shear and peak displacement were compared. Important conclusions about the behavior of monopole billboard were proposed.

Keywords: Billboard; Monopole; Semi-rigid; Pushover; Sign post

1. Introduction

Billboards are one of most common non-building type of construction. Billboards are generally designed so that highlight an information like advertising or banner. For this purpose, billboards generally constructed with a single pole which will carry a panel where illustrations will be shown around its space. Panel is generally installed at a high level, like top of a monopole. Depending on the maintain and usage condition, billboards are generally subjected lateral (seismic, wind) and vertical (dead load) loads. For construction material, steel is preferred generally due to billboards slender nature (Jones B., 1998). An illustration of structural system is given in Fig. 1.

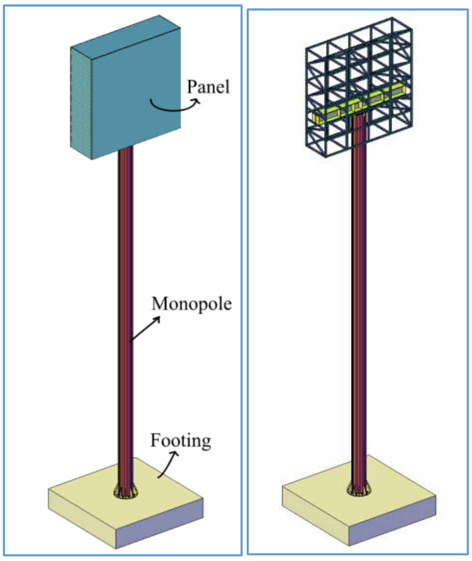

Fig. 1. Illustration of a monopole billboard or signpost and its structural system

* Corresponding author, E-mail: hkursadcelik@gmail.com

https://doi.org/10.31462/icearc2025_ce_sme_608

Being as a monopole construction, billboards have lack of redundancy. Its stiffness solely comes from the stiffness of the pole. Due to this, structural stiffness will be strongly affected by connections. In practice, idealization of connections is assumed as being perfectly rigid or hinged as illustrated in Fig. 2. This assumption states that rigid joint cannot rotate under moment while pinned joints can freely rotate under moments. However, in reality, most of the connections behaves like semi-rigid joints, which is fall into two ideal states. Due to this, connection will behave with an initial stiffness rather than totally rigid and hence, it can result decrease in structural stiffness. Same is valid for panel connection too. Panel is carried by monopole and its stiffness is strongly affected by connection behavior (Celik and Sakar, 2022).

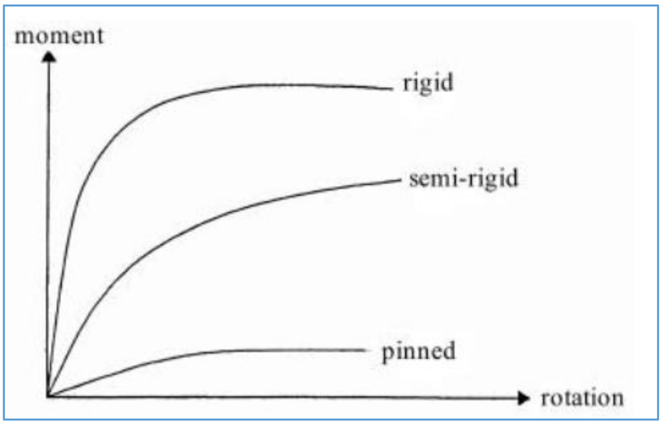

Fig. 2. Typical moment-rotation relationship of connections

Within this scope, design perspectives of monopole billboard regarding seismic actions should be examined. According to Turkish Building Seismic Design Code (2018), a building should have enough stiffness, ductility and robustness. Even if billboards differ from buildings, it's still valid for structural safety. On the other hand, there is no direct reference for design billboards.

Current seismic design regulation has some criteria to satisfy seismic safety of the building. With respect to limit state design; section of structural elements, story drifts, base shear etc. are regulated for a demand ductility. However, there is a few regulations can be highlighted in this scope. For example, Minimum Design Loads for Building and Other Structures (ASCE 7, 2022) has a mention about monopoles and its ductile demands is relatively low comparing building type construction. Due to lack of redundancy, after failing a component of structural system will lead sudden collapse of the system. Similar to this outcome, many example of sudden collapse is reported around the world, based on vulnerability of lateral loads

Current literature showed many reasons for failure of a signpost. In brief; corrosion, overloading due to wind and seismic excitation, inadequate structural detailing, accidental loads like car crash etc. leads to global collapse of a billboard. Beside the reason of it, failure mechanism in collapses is failure of base plate or foundation and buckling of the pile at base region (Herrera et al., 1995; Hosseini, 2005; Sha and Malinov, 2014; Carabollo and Ernesto, 2018; Wen and Xie, 2020).

Many studies showed that base connection is the most vulnerable component of a signpost. However, there is limited study exist about the connection behavior and impact of it on the sign post. Hence, this study presented by the authors to investigate seismic performance of monopole sign post under the effects of connection flexbility. An example sign post structure was taken and nonlinear static analysis was performed, with respect to rigid assumption and semi-rigid behavior. Base shear and peak displacement were compared and important conclusions were made.

2. Material and method

The model of the present study is given in Fig. 3. The signpost consists of a pole and panel. For the pole, circular hollow section (CHS406.4x12) was chosen. For panel truss, square hollow section (SHS40x4) was chosen. For all materials, S235 steel was selected. As joint, bolted connections were selected. For base joint, circular base plate with stiffeners were taken. For panel, a HEA300 beam was placed on the pole and connected with a plate with stiffeners. Panel components were assumed to be welded. So, only bolted connection was used in base and panel to pole joints. In total, panel height is 14 m while panel size was 3x3 m.

For global analyses, SAP2000 (2025) were used. SAP2000, a well-known structural analysis software which able to perform static and dynamic analysis of structure with regarding material and geometrical nonlinearities. However, analysis of connection is required to determine flexibilities of the connection. For this purpose, Idea Statica (2025) were used. Idea Statica is another software used in steel construction. Main purpose of the software is designing connection. The software is able to perform advanced analysis and it uses finite element method

(FEM) for modelling. The software can classify connection behavior according to Eurocode 3 (1993) or United States regulations (ASCE-AISC, 2022).

To model signpost, frame element was used. For modelling semi-rigid behavior of connection, several methods can be used. In this study, rotational sprigs were chosen. Even if the whole behavior of connection is nonlinear, only the initial stiffness was taken into account for the sake of calculation. Finally, signpost was pushed at center of the panel up to failure, with rigid assumption and semi-rigid behavior.

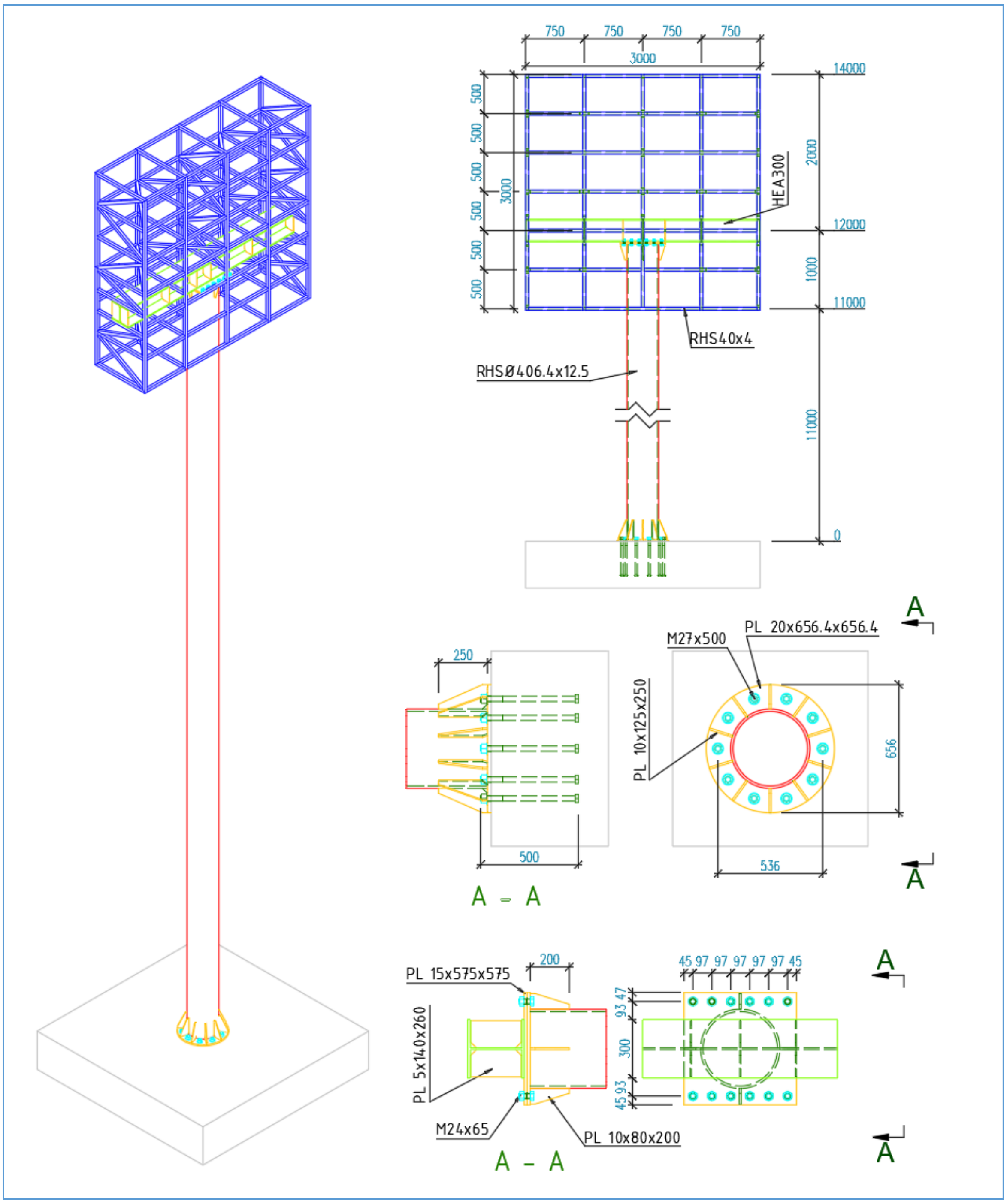

Fig. 3. Detail of the billboard

3. Analysis results

FEM analyses of two connection details showed that they fall into semi-rigid behavior, according to their initial stiffness. And, 140000 kNm/rad and 7000 kNm/rad of connection stiffness were found for base plate and seated connection, respectively. FEM models were given in Fig. 4. Moment-rotation curves of the connections were given in Fig. 5.

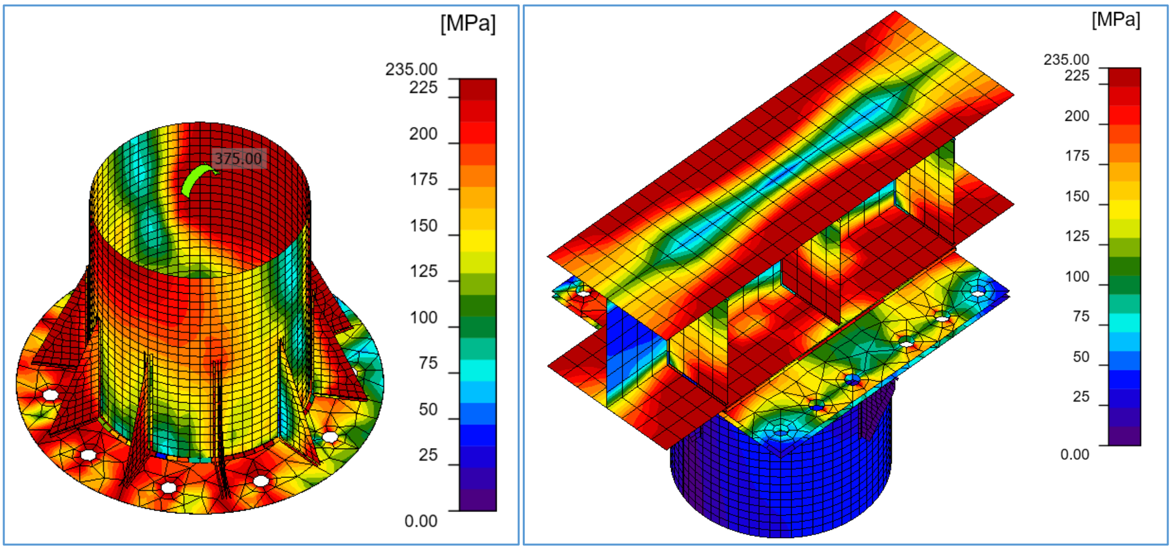

Fig. 4. FEM results of connection details

Analyses were performed in two steps. First, connections were assumed to rigid and pushover curve obtained. Then initial stiffness of the connections was adopted and second curve was obtained. Analysis model are given in Fig. 6. And, pushover curves are given in Fig 7.

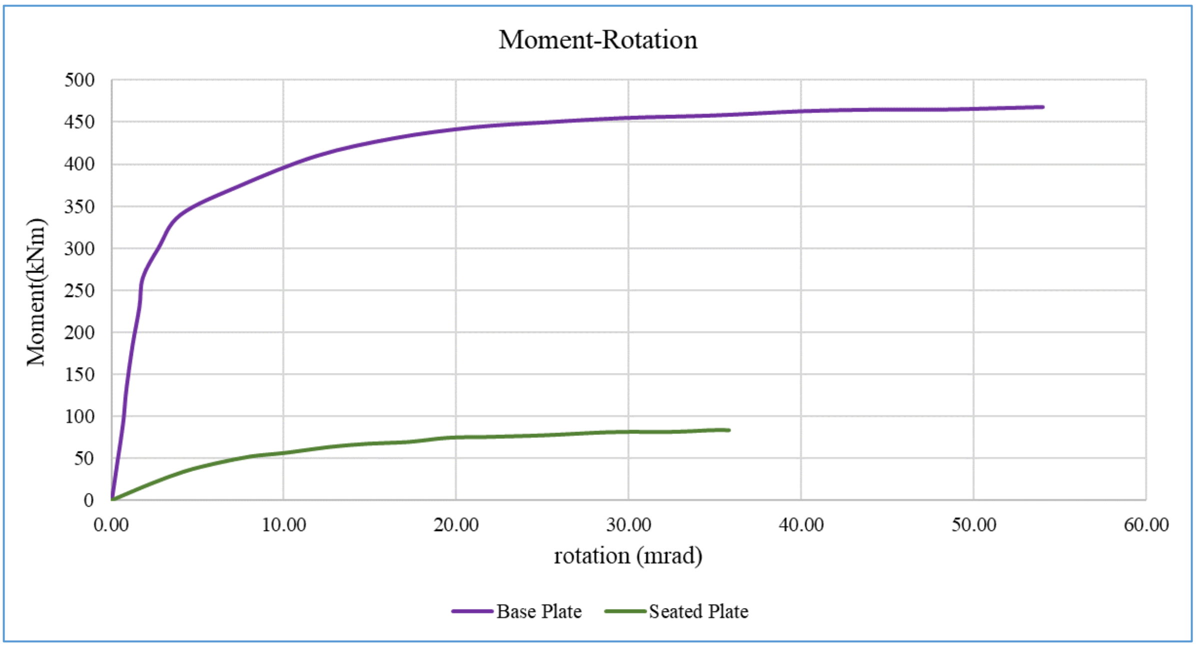

Fig. 5. Moment-rotation curves of connections

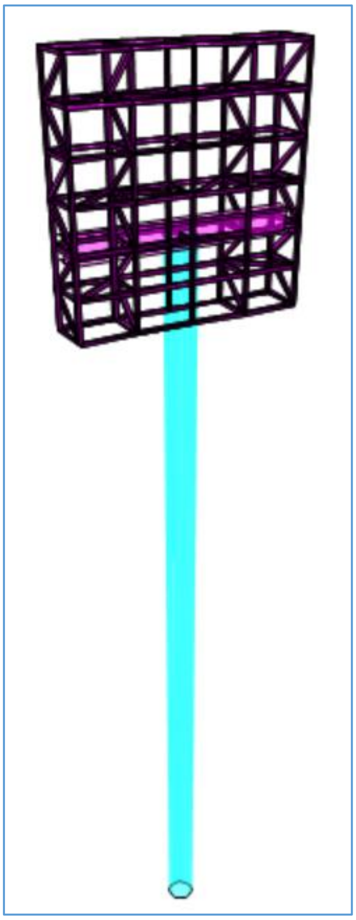

Fig. 6. Analysis model

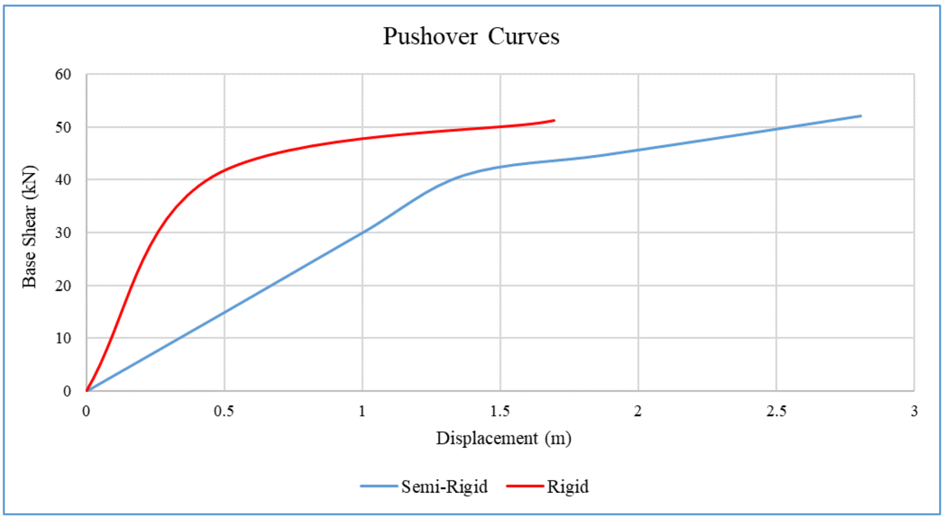

Fig. 7. Pushover curves of rigid and semi-rigid models

According to study result, base plate was found stiffer than seated joint, similar to previous studies (Celik and Sakar, 2024). For rigid assumption, signpost went strong drift after the plastic hinge formed at the bottom of the pole. After the signpost reached 10% story drift, it lost load bearing ability. For semi-rigid analysis, lateral stiffness of the pole decreased strongly due to flexible joint. Thus, drift ratio was increased under the same base shear. In contrast to this, both of the analyses went yielding at the same base shear. In both analyses, plastic hinge formed at the bottom of the pole. However, drift was affected by seated joint stiffness, rather than base shear. As a result of it, peak displacement was found higher than rigid assumption, even if the base shear was same for the both analyses.

4. Conclusions

In this study, seismic performance of monopole signpost was examined. A signpost detailed and then nonlinear static analyses were performed (pushover), with regarding connection stiffness. Models were created with frame elements while connection flexibilities were taken as rotational springs at the end of the frame. In brief:

- Connection stiffness has a strong impact on the stiffness of the structure.
- Rigid assumption may not valid; in other word, stiffness of the connection may differ from the assumption.
- Since the signposts are lack of redundancy, lateral stiffness of the monopole showed major impact of the pushover curves.
- In every case, plastic hinge was formed at the bottom of the pole. However, base shear at yielding didn't change. Further, connection stiffness mostly affects displacement of the structure.
- Semi-rigid connection reached higher displacement at same base shear; however, it should not be evaluated as higher ductility since stiffness of the pole is decreased.
- Even if the hinge formed at the bottom, seated joint stiffness mostly affect the behavior.
- Seated joint showed semi-rigid behavior at pinned limit, (similar to previous studies of the authors (Sakar and Celik, 2024).
- Connection stiffness should be taken into account in place of rigid assumption, especially for seated connection.

As a general outcome, several point should be highlighted for the design of the signpost:

- Base connection should be designed to bear plastic rotation of the pole under seismic demand.
- Flexibility of seated joint should be limited to satisfy drift ratio, since it contributes lateral displacements significantly.
- Drift limit and ductile demand may change for the place of construction. If human activities is dense at construction zone, harder limit may be taken into account for ductile design.
- Since stiffness of pole and panel is very different, stability of the panel throughout the loading should be covered with ensuring plastic rotation capacities of the seated joint.

Like stated previously, current design codes have lack of information about the design of signpost which is very slender and vulnerable for lateral loading. Thus, may be local regulation should be improvement especially region for high wind speed and high seismic hazard. Rather than an advertising product, signpost should be treated as an engineering structure.

Acknowledgments

Authors states that there is no conflict of interest to disclosure.

References

American Institute of Steel Construction. (2022). *Specification for structural steel buildings (ANSI/AISC 360-22)*.

American Society of Civil Engineers. (2022). *Minimum design loads and associated criteria for buildings and other structures (ASCE/SEI 7-22)*.

CEN. (2005). *EN 1993-1-1: Eurocode 3—Design of steel structures – Part 1-1: General rules and rules for buildings*. European Committee for Standardization.

Computers and Structures Inc. (2022). *SAP2000* (Version 24.2.0) [Computer software]. https://www.csiamerica.com

Çelik, H. K., & Şakar, G. (2022). Semi-rigid connections in steel structures: State-of-the-art report on modelling, analysis and design. *Steel and Composite Structures, 45*(1), 1–17.

Herrera, J. M., Spencer, P. R., Tarin, P. M., & Stafford, S. W. (1995). A failure analysis case study: Structural steel sign post collapse. *Materials Characterization, 34*(1), 57–61.

Hosseini, M. (2005). Behavior of nonstructural elements in the 2003 Bam, Iran, earthquake. *Earthquake Spectra, 21*(1_suppl), 439–453. https://doi.org/10.1193/1.2098946

Idea Statica. (2024). *Idea Statica* (Version 24.1.2.1513) [Computer software]. https://www.ideastatica.com/

Jones, B. (1998). *Engineering sign structures: An introduction to analysis and design*. ST Publications. https://books.google.com.tr/books/about/Engineering_Sign_Structures.html?id=zioCAAAACAAJ

Ministry of Environment, Urbanization and Climate Change. (2018). *Turkish building earthquake code (TBDY-18)*. Türkiye.

Santiago Caraballo, E. J. (2018). *Analysis of billboards signs collapse due to intensive wind of Hurricane Maria* [Master's thesis, Puerto Rico Research Repository]. https://prcrepository.org/xmlui/handle/20.500.12475/320

Sha, W., & Malinov, S. (2014). Cantilever steel post damaged by wind. *Case Studies in Engineering Failure Analysis, 2*(2), 162–168.

Şakar, G., & Çelik, H. K. (2024). Çelik yapıların birleşim rijitliğine geometrinin etkisi. In *DEU FBE 3rd International Symposium on Graduate Research*, İzmir. https://www.deuisgr24.org/

Wen, J., & Xie, Q. (2020). Field investigation and structural analysis of wind-induced collapse of outdoor single-post billboards. *Engineering Failure Analysis, 117*, 104810.

4th International Civil Engineering & Architecture Conference
17-19 May 2025, Trabzon, Türkiye

Contact stress analysis of layers loaded with two elastic punches

Ezgi Ayhan[1], Alper Polat[*2], Berivan Y. Polat[2]

[1] *Munzur University, Department of Civil Engineering, 62000, Tunceli, Türkiye*
[2] *Munzur University, Disaster and Emergency Management, 62000, Tunceli, Türkiye*

Abstract. In this study, the analysis of the continuous contact problem of a functionally graded material is carried out by the finite element method (FEM). The problem consists of a functionally graded plate resting between two semi-infinite elastic planes and loaded by two elastic blocks. The external loads P and Q are transmitted to the plate by means of two elastic blocks. It is assumed that there is no friction on the surfaces. The finite element model of the functionally graded plate is created using the ANSYS package program and the two-dimensional analysis of the problem is carried out.

Keywords: Functionally graded material; Stress analysis; Contact pressure; Finite element method; Homogenous layer

1. Introduction

Most mechanical systems and structures have elements that rub against each other, that is, in contact. This creates the contact problem. The term contact problem examines changes in structural behavior and mechanical properties due to friction and wear within the elements. In particular, structural elements and mechanical systems often come into contact with friction. Contact problems are widely used in various areas of engineering today. Examples include foundations, railways, grain elevators, fuel tanks, cylindrical shafts and shafts. With the development of technology, a non-homogeneous, gradual or continuously changing structure is required in the materials used to meet the needs of new types of systems and elements.

The lack of a material that provides high strength and thermal resistance, especially for space vehicles, has led scientists to new research. As a result of these studies, functionally graded materials have emerged that reduce thermal stresses caused by different thermal expansion coefficients between two substances that have different physical and chemical properties and minimize the disadvantages that may arise due to physical and chemical changes between the two substances. These materials are used in space, defense, medicine, electronics, energy and many other industries. They are widely preferred due to their high thermal resistance and durability. Functionally graded materials (FGMs) are a special class of dissimilar materials whose mechanical properties vary continuously from one point to another. FGM structures, made from two materials mixed in specific volume ratios, provide a solution for situations where composite materials cannot technically react.

These materials offer additional functionality in addition to the properties of traditional materials and are often the product of advanced technologies. The historical process of functionally graded materials began with people's interest in developing and customizing materials according to their functions. Even in the early periods of human history, the selection and processing of materials for specific purposes was a common practice. However, the development and use of modern functional materials emerged with more advanced science, technology and engineering developments. The World War II era was a major turning point for the development of functionally graded materials. During the war, the demand for special materials for military applications increased. For example, research and production of materials such as microwave absorber materials for the development of radar systems and special alloys for nuclear energy applications accelerated. In the early 20th century, research on understanding and controlling the physical, chemical and mechanical properties of materials accelerated. During this period, it was discovered that some metal alloys had special properties and began to be used for industrial applications. For example, nickel-based superalloys were used in areas such as aircraft engines due to their resistance to high temperatures and pressures. In recent years, the use of functionally graded materials has become more widespread, with factors such as sustainability and energy efficiency coming to the forefront. It is often used

[*]Corresponding author, E-mail: alperpolat@munzur.edu.tr

https://doi.org/10.31462/icearc2025_ce_sme_623

in fields such as civil engineering to increase the durability of materials, optimize energy efficiency and reduce environmental impact.

Today, thanks to advanced research and production methods, the use of functionally graded materials is rapidly increasing. Advances in materials science and engineering have made it possible to design and produce materials with previously unimaginable properties and functions. This increases the potential for more innovative and sustainable solutions in civil engineering and other industries. The use of these materials ensures the longevity of structures and is an important tool in the construction industry to build safer, more efficient and more environmentally friendly structures. Hertz's 1882 work, which inspired many researchers, is known to be the foundation of the field of contact problems (Johnson, 1985). Weitsman performed contact analysis on the elastic plate and elastic plane to investigate the distance of the contact area formed between the elastic plate and the sheet (Weitsman, 1969). Conway investigated the frictional contact analysis of the plate loaded with cylinder blocks. In his study, he investigated the effect of friction on the contact stress and found that this effect was very small (Conway, 1971). Erdoğan and Ratwani, İn their study performed the contact analysis of the elastic layer resting on the double elastic layer. Using the analytical method, they showed that the contact area does not change with the effect of the load but depends on the distance of the load.

Taking into account different load cases, the problem was reduced to a generalized Cauchy singular integral equation and presented the numerical results (Erdogan & Ratwani, 1974). Adams investigated the contact analysis of an elastic layer under a single load, lying on an elastic semi-infinite plane and showing a constant inclination. He observed the effect of different material changes by examining the complex problem in his work according to the Fredholm integral method (Adams, 1978). In their work, Keer and Miller investigated the contact problem of curved blocks and circular plates placed on simple or indented supports at the edges (Keer & Miller, 1983). Adams and Zeid investigated the effect of a fixed elastic block on an elastic plane. In their study, the stress distribution, sliding velocities and friction coefficients along the contact surface for various material combinations were discussed using the theory of elasticity (Adams & Zeid, 1984). Geçit and Gökpınar examined the contact analysis of an elastic plate with a rigid circular block. They did not take friction into account in the contact areas, and only the compressive stress was transmitted. With a uniformly acting force, the stress distributions in the contact area for blocks of different geometries and the contact distances were investigated (Gökpınar & Geçit, 1985). Nowell and Hills investigated the frictional and frictionless analysis of elastic plates that are acted upon by cylinder blocks. In the analysis part of the study, contact stresses were analyzed with a hybrid method (Nowell & Hills, 1988). Sabin and Kaloni in their study, solved the contact problem of a rigid body rotating about a vertical axis in an elastic half-plane using the theory of elasticity by including friction (Sabin and Kaloni, 1989).

Dempsey et al. in their study, investigated the contact analysis of elastic, homogeneous and isotropic layers based on the Winkler basis. In their study, the load was applied to both the rigid block and the cylinder and the results were observed (Dempsey et al., 1990). Wozniak et al. solved the symmetrically generated contact analysis loaded by spheres or cylinders. It was assumed that this layer was filled with material properties whose structure changed under the influence. This material was modeled in the Winkler environment and the Hankel integral transform technique was used in the solution (Wóniak et al., 2002). Rekik et al. analyzed the cracking effect in a functionally graded layer connected to a homogeneous semi-infinite plane by analytical method. In this analysis, cracks were also examined by finite element method and the data were compared with analytical solutions (Rekik et al., 2010).

Ellumi and his colleagues observed the contact situation between the half-layer, whose material properties varied from place to place, and the arbitrarily shaped block under vertical loading. It was stated that the graded medium observed in this analysis was materials with different properties, which belonged to constant Poisson ratios with shear modulus varying depending on a certain function (Elloumi et al., 2010). Kaman and Cetisli investigated the crack analysis in a cylinder coated with functional grade materials. In the analysis, the tensile strength was investigated for the crack length with different values of radii with different materials by processing in the Ansys program (Kaman & Çetişli, 2011). Abhilash and Murthy analyzed the contact of a semi-infinite plane covered by a functionally classified material and loaded with a block using the finite element method. Initially, the blocks were assumed to be rigid and the results were verified using solutions available in the literature. Then, the analysis was performed by including the blocks in the process where they were elastic (Abhilash & Murthy, 2014). Adıyaman et al. performed the separation contact analysis for a block resting on a double quadrant plane and an elastic layer loaded with a distributed load using analytical and finite element methods. For both solutions, contact lengths and contact pressures were examined for different load conditions and dimensionless quantities. In the research results, it was observed that the data obtained with the finite element method were consistent with the analytical results (Adiyaman et al., 2015). Kulchytsky et al. studied the contact analysis of a half-plane loaded with a functionally graded coating loaded with a distributed load.

As a result of the study, they observed that the Poisson value of the functionally graded coating did not change, while the shear modulus changed proportionally with the height (Kulchytsky-Zhyhailo & Bajkowski, 2015). Adıyaman et al. investigated the separation contact problem between a functionally graded layer and two homogeneous quarter planes in their study. They investigated the effect of material inhomogeneity parameter on the contact pressure and separation contact length (Adıyaman et al., 2016). Öner, in his study, analytically performed continuous and discontinuous contact analysis in functionally graded pavement loaded with a rigid punch and seated on an elastic half-layer. Two different solutions were made as rigid block circular and flat. In the study, contact stresses, normal stresses and shear stresses occurring under the punch in case of continuous contact, first separation loads and first separation distances occurred between functionally graded pavement and elastic half-layer were obtained. He stated that contact stresses decreased in case of flat punch as the punch width increased, in case of circular punch as the punch radius increased, the half-contact length between the functionally graded layer and the punch increased, and the half-contact length decreased as the load ratio increased. He also observed that as the rigidity parameter (βh) value increased in case of circular punch, the contact distance between the FG layer and the punch increased, and as the ratio of the rigidity of the lower surface of the FG layer to the rigidity of the elastic half-layer increased, the half-contact length increased (Öner et al., 2022) . Polat et al. analyzed the continuous contact condition in functionally graded coating using the finite element method. The data obtained in the case where the material properties do not change from one point to another were compared with the observed data in the case where the effect of the parameters that cause the properties of the material in the functionally graded coating to change from one point to another did not change at all.

In addition, the interaction of different Poisson values in the functionally graded coating was observed in the analysis (Polat et al., 2018). In their study, Demirbaş and Çakır obtained trained models using Artificial Neural Network to determine the equivalent stress levels of one-dimensional functionally graded rectangular plates. They obtained results close to the real values with 99% efficiency of the equivalent stress prediction value in the plates and the minimum number of cycles (Demirbaş & Çakır, 2019). In his study, Polat solved the continuous and discontinuous contact situation in the functionally graded layer where the load is transferred by rigid blocks on the elastic semi-infinite plane in two ways, namely the finite element method and analytically. He examined the effect of different stiffness and density parameters of the FD layer on the distances between the blocks, different geometries of the blocks and under different loads, and compared the values found with the analytical method with the results obtained with the finite element method (Polat, 2019).

Polat et al. investigated the contact problem for a partially functionally graded layer using the finite element method. The analysis for the partial FGM layer was compared with the fully FGM layer analysis in figures and tables, and as a result, they predicted that partial FGM could be used for static problems and could have practical applications in the industry (Polat et al., 2019). Balci and Dağ performed a moving contact analysis involving functionally graded coating where loads are transferred by means of a rigid punch. They analyzed the effects of punch speed, friction coefficient, material inhomogeneity and coating thickness on contact stress distributions and stress intensity factors (Balci & Dag, 2020).

Karabulut and Çömez analyzed the contact problem in an orthotropic functionally graded layer loaded with a rigid punch using analytical and finite element methods. They observed that the separation zone increased when the load and inhomogeneity parameters increased (Karabulut & Çömez, 2023). Kaya and Polat performed the contact analysis of the functionally graded layer resting on two elastic layers using the finite element method. In the study, the effects of external load, stiffness parameter (βh), density parameter (γh) and distributed load change on the resulting stresses were investigated. They observed that when the stiffness increased, the resulting stress values increased but the contact lengths decreased. They also examined that when the radius increased, the stresses formed in the edge region of the punches increased but the stresses formed in the middle region of the punches decreased (Kaya & Polat, 2023)

2. Definition of the problem

Material properties of functionally graded layer;

$$\mu_2(y) = \mu_0 e^{\beta y},\ \rho_2(y) = \rho_0 e^{\gamma y},\ v_2(y) = v_0 e^{\alpha y} \tag{1}$$

μ is the shear modulus, ρ is the density and v is the Poisson's ratio.

The layer extends in the range (-∞, +∞). In this system, the blocks are assumed to be elastic and the contact stresses transfer only compressive stresses. Therefore, when the critical load is exceeded, separation occurs between the elastic layers and the (FG) plane. In the problem, all surfaces are assumed to be frictionless and the thickness in the z-axis direction is uniform. The geometry of the problem is shown in Fig. 1.

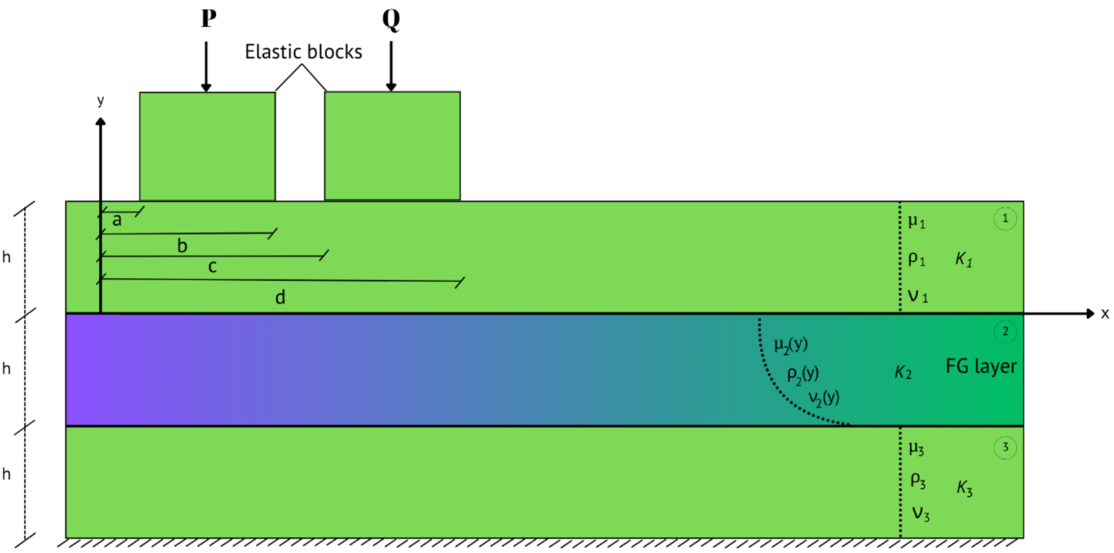

Fig. 1 Geometry of problems

2.1. Analysis with finite element method

The Finite Element Method, to put it briefly, is to solve a complex problem by simplifying it. The finite element method analyzes the behavior of each element by dividing a structure into small pieces (elements) and analyzes the entire structure by modeling it by combining the results. Thanks to this method, the behavior of complex structures can be calculated more easily and accurately. In the mesh process, instead of analyzing the problem as a single piece and as a whole, a large number of small pieces are created and a more precise solution is made with these pieces, and the problem is analyzed in more detail and with high accuracy. While the large number of these small pieces provides benefits for more accurate results in the analysis, it is a disadvantage in terms of time as it increases the solution time of the problem. The use of Finite Element Model-based computer programs has become quite widespread today.

The finite element model and analysis of this solvable problem includes the ANSYS (2019) package program. All operations related to blocks and homogeneous planes were done with standard ANSYS menus. The material storage and finite element division process of the FG layer was done with a program-specific macro. With the development, the code starts by defining the problem code such as geometry and material properties with the *set command. Depending on the simple geometry of the problem, a two-dimensional (2D) aeronautical geometric model is used for FG sheet and homogeneous elastic wings and is divided into sections with RECTNG cuts. The material properties of homogeneous elastic semi-infinite planes and blocks are selected as linear, elastic-isotropic. Defining the element type is important in terms to obtain correct results in solving the problem. In this study, 8-node PLANE183 was used as the element type for static and 2-dimensional flight problems. Each node of this element has degrees of freedom in x and y accuracy. This element has no rotational freedom. This element has no rotational freedom. ANSYS models of the problem are given in Figs. 2, 3, 4 and 5.

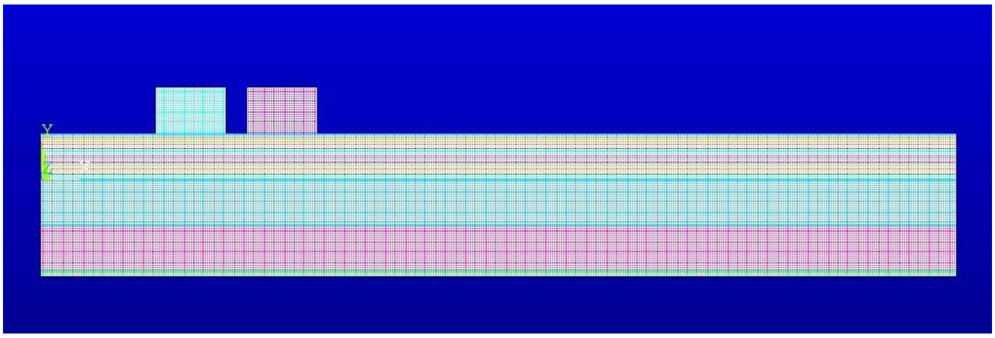

Fig. 2. Finite element model of the problem loaded with blocks

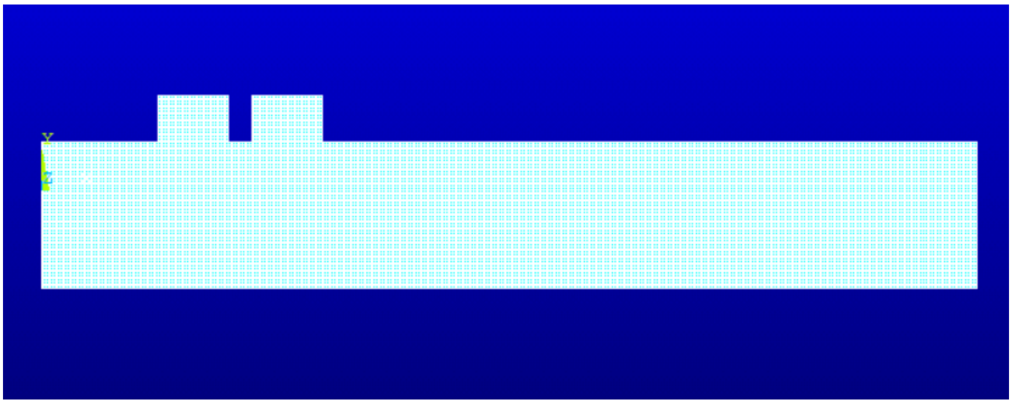

Fig. 3. Assignment of material of the problem loaded with blocks

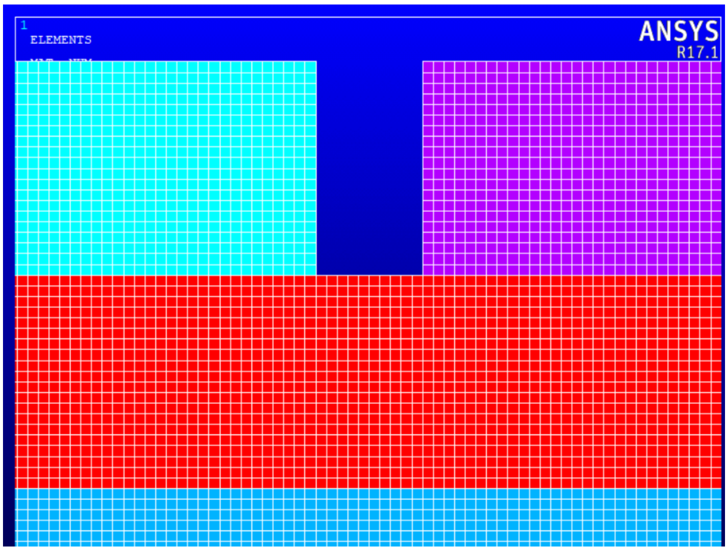

Fig. 4. Free quadrilateral mesh

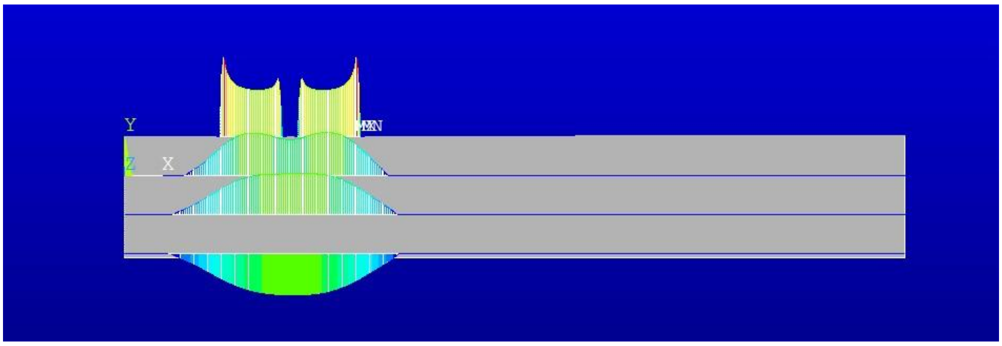

Fig. 5. ANSYS display of the status in contact with continuous contact

At this stage the recorded material is selected according to the program where only the layers graded in the factory and macro are changed exponentially to create the network.The macro used to program the material properties according to exponential change is as follows.

```
!!Material Top
*set, E_t, 100000
*set, nu_t, 0.25
*set,dens_t,1
*set,B,1.3864
*set,A,0.00001
*set,G,-0.6931
*create, mat_fgm_pol                                                    (2)
/nopr
y_coord = arg1
E_fgm=E_t*EXP(B*y_coord) !!B=Beta
nu_fgm=nu_t*EXP(A*y_coord) !!A=Alfa
den_fgm=dens_t*EXP(G*y_coord) !!G=Gama
/gopr
*end !mat_fgm_pol
```

In formula, the *create command is used to create a macro for the layer consisting of functionally graded material and sets a variable named y_coord = arg1

The mesh section has been moved on to. An additional macro has been added for meshing the FG layer. All geometry has been subjected to the Free Quadrilateral Mesh, more frequently in contact areas. The macron for meshing the FG layer is as follows.

```
*do, j, 1, ele_numb_y, 1
y_coord = length_e_y*(j)
*use, mat_fgm_pol,y_coord
mp, ex, cntr,E_fgm
mp, prxy, cntr,nu_fgm                                                   (3)
mp, dens, cntr,den_fgm
esel,r,cent,x,0,lngt_lyr
emodif, all, mat, counter
esel, all
```

In addition, surface to surface contact pairs are defined between the block-layer and layer-elastic plane. These pairs are divided into two as contact and target elements. The contact is selected as CONTA172, and the target is selected as TARGE169 elements. It would be appropriate to select more rigid elements than the contact element as the target element. In addition, while selecting the formulation to be used in the contact region, the mathematical method that will provide the appropriate contact conditions is also decided. There are various contact algorithms in ANSYS depending on the problem type. The Augmented Lagrangian Method, which provides fast results using the total potential energy theorem, was preferred as the contact algorithm.

3. Results and discussion

It was observed that the increase in the distance between the blocks (c-b) led to a decrease in the contact stress between the FG layer and the upper homogeneous layer.The results are presented in Fig. 6.

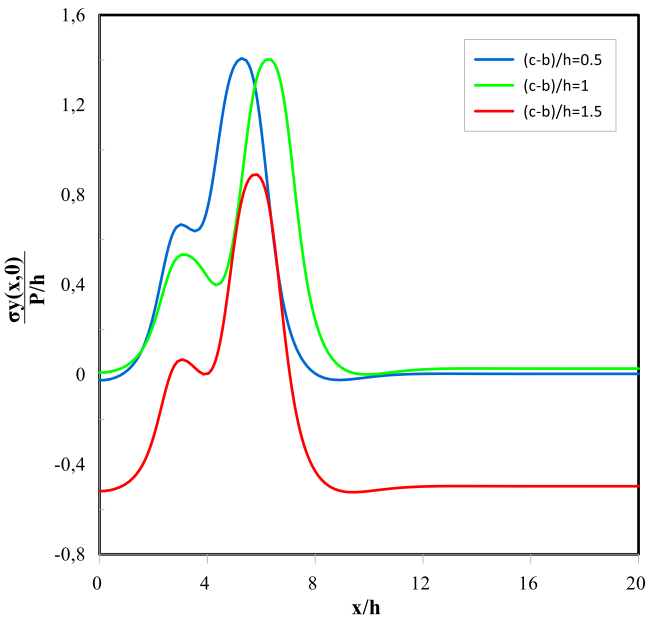

Fig. 6. Contact stress distributions between the FG layer and the upper homogeneous layer, depending on the distance between the blocks (a/h=2.5, μ0=1, K_1=K_2=2, y=h, h=1, μ-h=*1*)

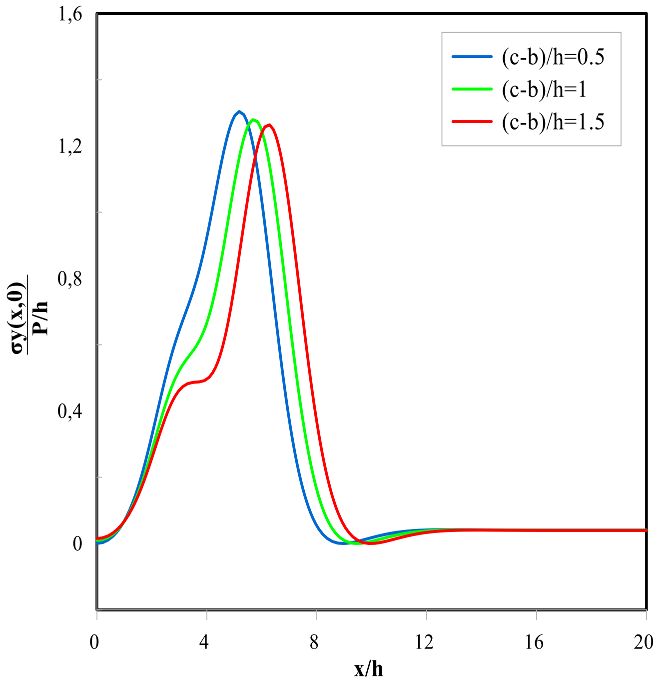

Fig. 7. Contact stress distributions between the FG layer and the under homogeneous layer, depending on the distance between the blocks (a/h=2.5, μ0=1, K_2= K_3=2, y=h, h=1, μ-h=1)

It was observed that the increase in the distance between the blocks (c-b) led to a decrease in the contact stress between the FG layer and the under homogeneous layer.The results are presented in Fig. 7.

The results showed that the increase in the load (Q) applied to the block caused an increase in the contact stress between the FG layer and the upper homogeneous layer.The results are presented in Fig. 8.

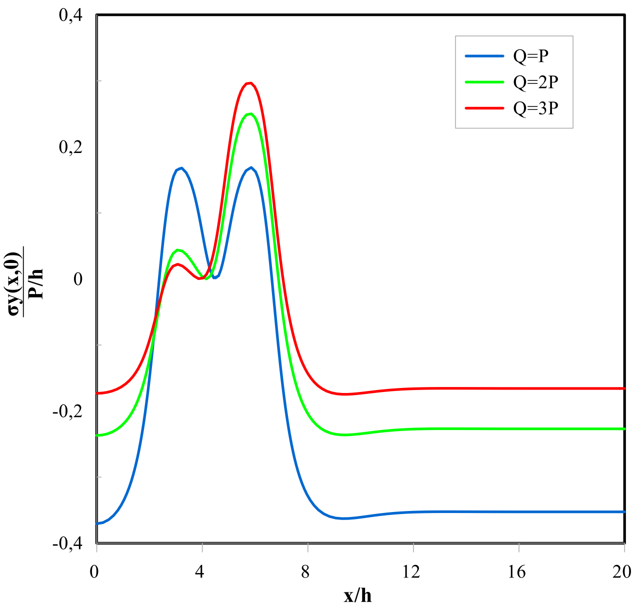

Fig. 8. Contact stress distributions between the FG layer and the upper homogeneous layer, according to the load (Q) change (a/h=2.5, (b-a)/h=1.5 μ0=1, $\kappa_1 = \kappa_2 = 2$, y=h, h=1, μ-h=1)

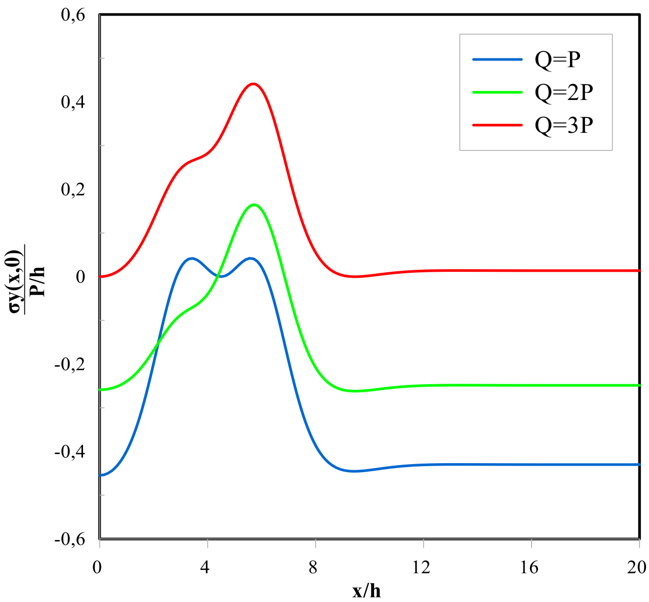

Fig. 9. Contact stress distributions between the FG layer and the under homogeneous layer, according to the load (Q) change (a/h=2.5, (b-a)/h=1.5 μ0=1, $\kappa_2 = \kappa_3 = 2$ y=h, h=1, μ-h=1)

The results showed that the increase in the load (Q) applied to the block caused an increase in the contact stress between the FG layer and the under homogeneous layer.The results are presented in Fig. 9.

It was found that the decrease in the stiffness of the blocks caused an increase in the contact stress between the FG layer and the upper homogeneous layer.The results are presented in Fig. 10.

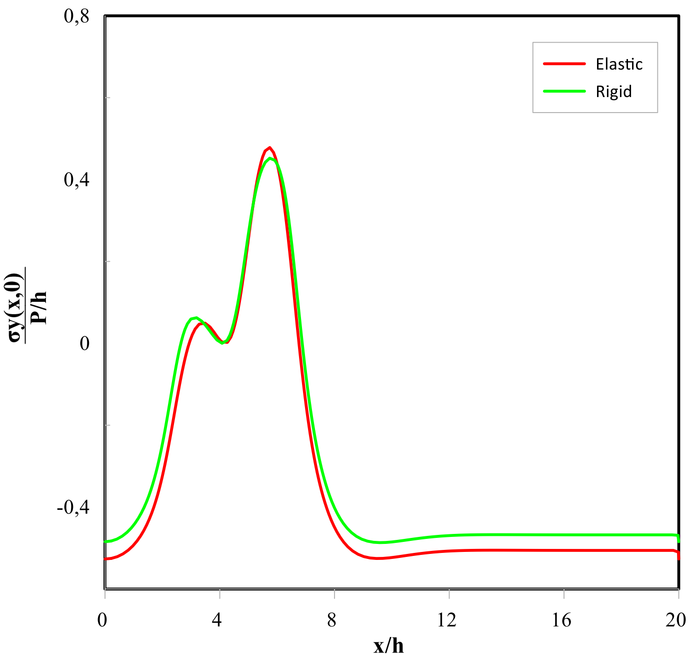

Fig. 10. Contact stress distributions between the FG layer and the upper homogeneous layer, according to the elasticity state of the blocks (a/h=2.5, μ0=1, K_1= K_2=2, y=h, h=1, μ-h=1)

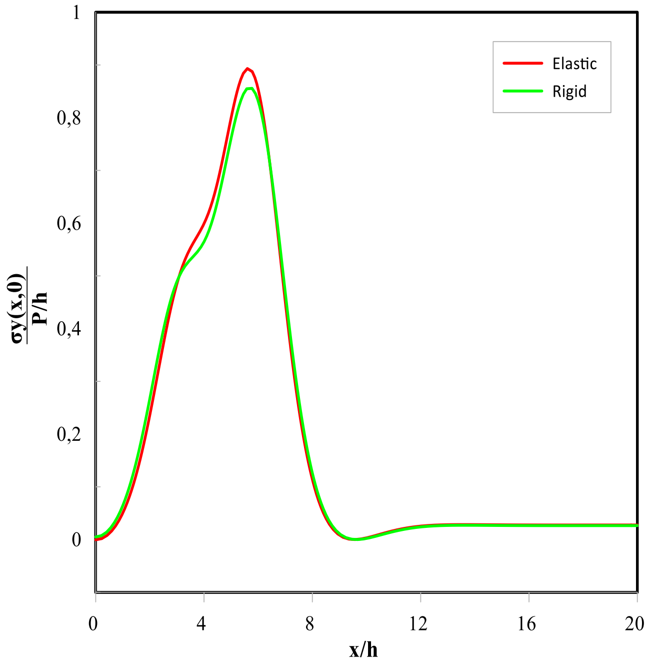

Fig. 11. Contact stress distributions between the FG layer and the under homogeneous layer, according to the elasticity state of the blocks (a/h=2.5, μ0=1, K_2= K_3=2, y=h, h=1, μ-h=1)

In the configuration where the first block is elastic and the second block is rigid, the increase in the rigidity of the upper homogeneous layer causes the first block to decrease. The results are presented in Fig. 12.

In the configuration where the first block is elastic and the second block is rigid, the increase in the rigidity of the upperr homogeneous layer causes the first block to decrease.The results are presented in Fig. 13.

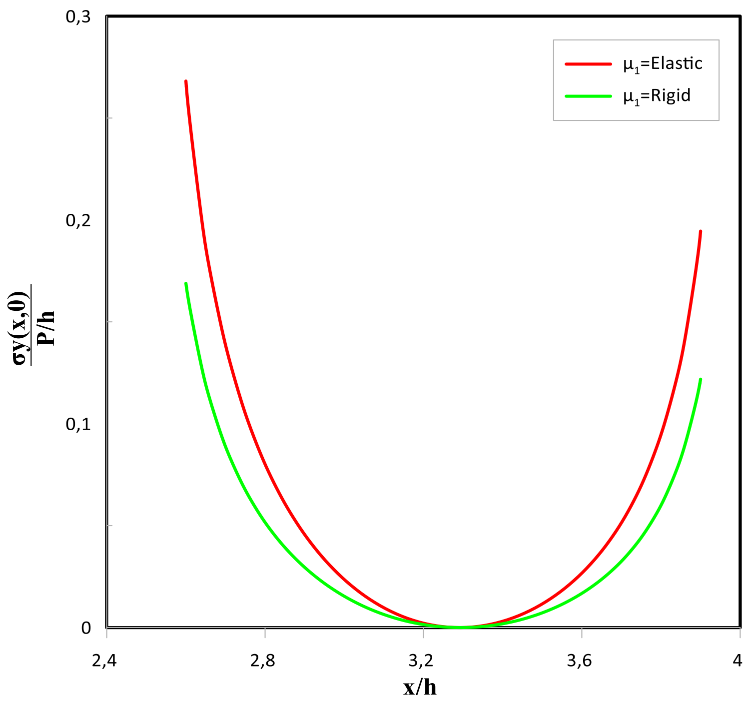

Fig. 12. According to the case where the 1st block is elastic and the 2nd block is rigid, the stress under the 1st block (μ_1= shear stress of the upper homogeneous layer) (a/h=2.5, μ0=1, K_1= K_2=2, y=h, h=1, μ-h=1)

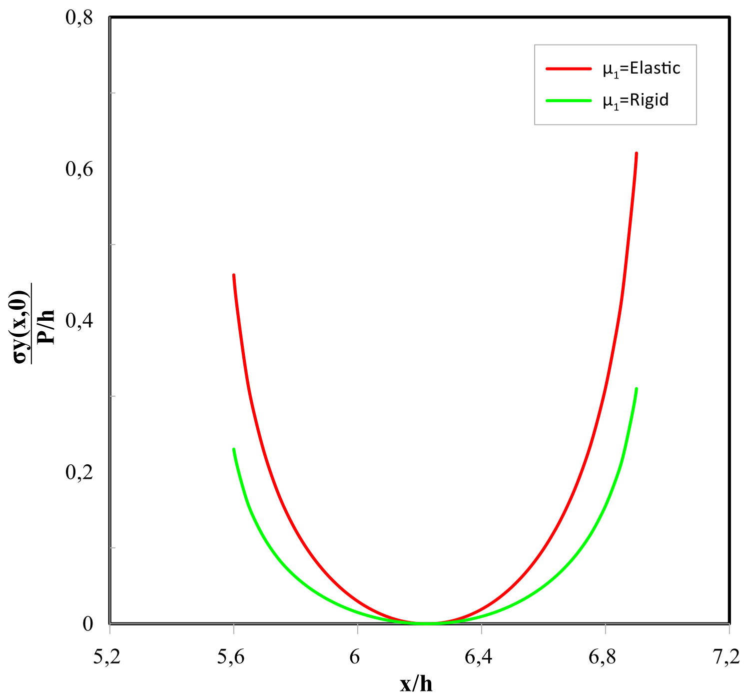

Fig. 13. According to the case where the 1st block is elastic and the 2nd block is rigid, the stress under the 2nd block (μ_1= shear stress of the upper homogeneous layer) (a/h=2.5, μ0=1, K_2= K_3=2, y=h, h=1, μ-h=1)

4. Conclusions

The aim of this study is to investigate the contact stresses in a functionally graded layered system loaded with two elastic blocks according to different variables such as the distance between the blocks and the stiffness of the blocks. These investigations led us to the following conclusions.

- t was observed that changes in different variables such as the distance between the blocks, the stiffness of the blocks, and the stiffness of the homogeneous layers lead to a change in the contact stresses.

- It was observed that the stiffness of the blocks and the stiffness of the homogeneous layers caused a change in the stresses under the blocks.

Reference

ANSYS (2019), Swanson Analysis Systems Inc., Canonsburg, PA, USA

Abhilash, M.N., & Murthy, H. (2014). Finite element analysis of 2-D elastic contacts involving FGMs. *International Journal for Computational Methods in Engineering Science and Mechanics, 15*(3), 253–257. https://doi.org/10.1080/15502287.2014.882445

Adams, G.G. (1978). An elastic strip pressed against an elastic half plane by a steadily moving force. *Journal of Applied Mechanics*, *45*(1), 89–94. https://doi.org/10.1115/1.3424279

Adams, G.G., & Zeid, I. (1984). An elastic punch moving across the surface of a semi-infinite solid. *Journal of Applied Mechanics*, *51*(3), 622–629. https://doi.org/10.1115/1.3167683

Adiyaman, G., Yaylaci, M., Birinci, A., Adiyaman, G., Yaylaci, M., & Birinci, A. (2015). Structural engineering and mechanics. *Structural Engineering and Mechanics*, *54*(1), 69. https://doi.org/10.12989/SEM.2015.54.1.069

Adıyaman, G., Birinci, A., Öner, E., & Yaylacı, M. (2016). A receding contact problem between a functionally graded layer and two homogeneous quarter planes. *Acta Mechanica*, *227*(6), 1753–1766. https://doi.org/10.1007/S00707-016-1580-Y/METRICS

Balci, M.N., & Dag, S. (2020). Moving contact problems involving a rigid punch and a functionally graded coating. *Applied Mathematical Modelling*, *81*, 855–886. https://doi.org/10.1016/J.APM.2020.01.004

Conway, H.D. (1971). The Effects of Friction on Normal Contact Stresses. *Journal of Applied Mechanics*, *38*(4), 1094–1095. https://doi.org/10.1115/1.3408932

Demirbaş, M.D., & Çakır, D. (2019). Thermal stress analysis in two-directional functionally graded plates with artificial neural network training algorithms. *Uluslararası Muhendislik Arastirma ve Gelistirme Dergisi*, *11*, 442–450. https://doi.org/10.29137/UMAGD.485604

Dempsey, J.P., Zhao, Z.G., Minnetyan, L., & Li, H. (1990). Plane contact of an elastic layer supported by a winkler foundation. *Journal of Applied Mechanics*, *57*(4), 974–980. https://doi.org/10.1115/1.2897670

Elloumi, R., Kallel-Kamoun, I., & El-Borgi, S. (2010). A fully coupled partial slip contact problem in a graded half-plane. *Mechanics of Materials*, *42*(4), 417–428. https://doi.org/10.1016/J.MECHMAT.2010.01.002

Erdogan, F., & Ratwani, M. (1974). The contract problem for an elastic layer supported by two elastic quarter planes. *Journal of Applied Mechanics*, *41*(3), 673–678. https://doi.org/10.1115/1.3423369

Gökpınar, S., & Geçit, M.R. (1985). *Frictionless contact between an elastic layer and a rigid rounded support*. http://masder.kfnl.gov.sa/Dspace/handle/123456789/4667

Johnson, K.L. (1985). *Contact Mechanics*. https://doi.org/10.1017/CBO9781139171731

Kaman, M.O., & Çetişli, F. (2011). *Fonksiyonel Derecelendirilmiş Malzeme ile Kaplı Silindirde Çatlak Problemi Request PDF*. https://www.researchgate.net/publication/269689814_Fonksiyonel_Derecelendirilmis_
Malzeme_ile_Kapli_Silindirde_Catlak_Problemi

Karabulut, P.M., & Çömez, İ. (2023). Continuous and discontinuous contact problem of a functionally graded orthotropic layer indented by a rigid cylindrical punch: Analytical and finite element approaches. *ZAMM Zeitschrift Fur Angewandte Mathematik Und Mechanik*, *103*(6). https://doi.org/10.1002/ZAMM.202200427

Kaya, F., & Polat, A. (2023). Stress analysis of the contact problem in a functionally graded layer loaded with a distributed load and two rigid circular punches resting on an elastic two quarter planes. *Forces in Mechanics*, *11*. https://doi.org/10.1016/J.FINMEC.2023.100203

Keer, L.M., & Miller, G.R. (1983). Contact between an elastically supported circular plate and a rigid indenter. *International Journal of Engineering Science*, *21*(6), 681–690. https://doi.org/10.1016/0020-7225(83)90113-1

Kulchytsky-Zhyhailo, R., & Bajkowski, A.S. (2015). Three-dimensional analytical elasticity solution for loaded functionally graded coated half-space. *Mechanics Research Communications*, *65*, 43–50. https://doi.org/10.1016/J.MECHRESCOM.2015.03.001

Nowell, D., & Hills, D.A. (1988). Contact problems incorporating elastic layers. *International Journal of Solids and Structures*, *24*(1), 105–115. https://doi.org/10.1016/0020-7683(88)90102-3

Öner, E., Şengül Şabano, B., Uzun Yaylacı, E., Adıyaman, G., Yaylacı, M., & Birinci, A. (2022). On the plane receding contact between two functionally graded layers using computational, finite element and artificial neural network methods. *Zamm-Zeitschrift Fur Angewandte Mathematik Und Mechanik*, *102*(2). https://doi.org/10.1002/ZAMM.202100287

Polat, A. (2019). *Elastik yarım düzleme oturan ve iki rijit blok aracılığıyla yüklenmiş fonksiyonel derecelendirilmiş tabakanın temas problemi* (Doctoral dissertation). Karadeniz Technical University, Trabzon, Türkiye.

Polat, A., Kaya, Y., Bora, P., Bendine, K., & Özşahin, T.Ş. (2019). Investigation of the contact problem for a partial functionally graded layer by using finite element method. *Journal of Structural Engineering Applied Mechanics*, *1*(4), 185–193. https://doi.org/10.31462/JSEAM.2019.01185193

Polat, A., Kaya, Y., & Özşahin, T.Ş. (2018). Analytical solution to continuous contact problem for a functionally graded layer loaded through two dissimilar rigid punches. *Meccanica*, *53*(14), 3565–3577. https://doi.org/10.1007/S11012-018-0902-7

Rekik, M., Neifar, M., & El-Borgi, S. (2010). An axisymmetric problem of an embedded crack in a graded layer bonded to a homogeneous half-space. *International Journal of Solids and Structures*, *47*(16), 2043–2055. https://doi.org/10.1016/J.IJSOLSTR.2010.04.006

Weitsman, Y. (1969). On the unbonded contact between plates and an elastic half space. *Journal of Applied Mechanics*, *36*(2), 198–202. https://doi.org/10.1115/1.3564607

Wóniak, M., Hummel, A., & Pauk, V.J. (2002). Axisymmetric contact problems for an elastic layer resting on a rigid base with a Winkler type excavitation. *International Journal of Solids and Structures*, *39*(15), 4117–4131. https://doi.org/10.1016/S0020-7683(02)00229-9

Advanced connection topology optimization in steel space frames using metaheuristic algorithms

Jay Prakash*[1], Ayşe T. Daloğlu[1]

[1] *Karadeniz Technical University, Department of Civil Engineering, 61080 Trabzon, Türkiye*

Abstract. This research paper elucidates an optimization process that utilizes two metaheuristic algorithm to achieve minimum weight by selecting beam-column connection types and structural sections as design variables. In connection topology optimization, connection topologies are classified into two principal categories: connection topology (1) and connection topology (2). Connection topology (1) encompasses rigid, semi-rigid (top and seat angles), and pinned connections. Conversely, connection topology (2) consists of rigid, semi-rigid (end plate with column stiffeners), and pinned connections. The design optimization incorporates the stress constraints established by the AISC-LRFD (American Institute of Steel Construction - Load and Resistance Factor Design) and considers displacement, inter-story, and geometric constraints. Initially, optimal designs for two distinct space frames drawn from existing literature are developed without factoring in the connection topology approach. Subsequently, the results are compared to those in the literature. Thereafter, the same optimization procedures are repeated for the case involving space frames with connection topology approaches. All optimization methods utilize C# version 17.10.5, designed for integration with version 22 of SAP2000-OAPI (Open Application Programming Interface) for two-way data flow. The results obtained in the study indicate that considering the arrangement of beam-column connections leads to heavier steel weights but results in more economical designs in terms of stiffness.

Keywords: Metaheuristic algorithms; Semi-rigid connection; Connection Topology Optimization; SAP2000-OAPI; AISC-LRFD

1. Introduction

Steel moment frameworks achieve their highest lateral stiffness when entire connections are firmly rigid. This situation allows designers to refine the dimensions of each beam and column to create the lightest and, in terms of material weight, the most cost-effective design. In comparison to pinned connections, rigid connections entail significantly higher costs due to the requirements for fabrication, welding, inspection, and other related processes (Alberdi, Murren, & Khandelwal, 2015). Although a fully rigid frame may produce the lightest structure, it is often not the most cost-effective design, considering the associated connection costs. For instance, Carter et al. (2000) noted that material expenses can account for just a 1/4th of the overall cost of a steel frame. In contrast, Evers and Maatje (2000) highlighted that nearly half of the expenses are linked solely to connections. Given the significant costs associated with rigid connections, more efficient designs can be achieved by concurrently adjusting member sections and the stiffness of connections, including the utilization of semi-rigid configurations.

The optimal arrangement of pinned, semi-rigid, and rigid connections, referred to as connection topology, along with effective member sizing, has the potential to produce designs that minimize costs. The incorporation of semi-rigid connections into the connection topology optimization process represents a more realistic design strategy, enhancing the practicality of steel frame optimization for engineering applications. Moreover, this approach provides engineers with the opportunity to strategically distribute frame stiffness, thereby facilitating the pursuit of more economical structural solutions.

In earlier studies, Xu (2002), Ali et al. (2009), and Degertekin and Hayalioglu (2010) explored the advantages of balancing the affordability of pinned connections with the overall lateral stiffness provided by moment and semi-rigid connections. However, some researchers, such as Hall (2006), Hagishita and Ohsaki (2008), Kripakaran et al. (2011), Tovar and Khandelwal (2013), Kaveh et al. (2017), and Rahami et al. (2017), have applied connection topology optimization techniques to two-dimensional steel frames.

This research presents the optimization of connection topology for steel space frames, employing metaheuristic methods to adjust connection types, including semi-rigid connections and member section profiles, to achieve

* Corresponding author, E-mail: jaypee@outlook.in

https://doi.org/10.31462/icearc2025_ce_sme_669

golden light publishing

optimum design in terms of stiffness. Two metaheuristic algorithms, Teaching-Learning-Based Optimization (TLBO) and Particle Swarm Optimization (PSO), are utilized to accomplish this.

2. Metaheuristic algorithms

2.1. Teaching-learning-based optimization (TLBO)

The TLBO algorithm was developed by Rao et al. (2011). This algorithm imitates the interactions of teaching and learning that ensue between instructors and students in a conventional classroom setting. The student with the most incredible level of knowledge in the class is chosen to act as the instructor. The class leader then shares their knowledge with the other students. These procedures offer practical strategies for optimizing steel frames. The essential elements of this innovative approach are teaching and learning. The initial step begins randomly generating values for the starting population in a matrix format during the teaching phase, as demonstrated in Eq. 1.

$$\text{Population} = \begin{bmatrix} x_1^1 & x_2^1 & \cdots & x_{ndv-1}^1 & x_{ndv}^1 \\ x_1^2 & x_2^2 & \cdots & x_{ndv-1}^2 & x_{ndv}^2 \\ \vdots & \vdots & \vdots & \vdots & \vdots \\ x_1^{ps-1} & x_2^{ps-1} & \cdots & x_{ndv-1}^{ps-1} & x_{ndv}^{ps-1} \\ x_1^{ps} & x_2^{ps} & \cdots & x_{ndv-1}^{ps} & x_{ndv}^{ps} \end{bmatrix} \begin{matrix} \rightarrow \\ \rightarrow \\ \rightarrow \\ \rightarrow \\ \rightarrow \end{matrix} \begin{matrix} f(x^1) \\ f(x^2) \\ \vdots \\ f(x^{ps-1}) \\ f(x^{ps}) \end{matrix} \tag{1}$$

Each row in the matrix corresponds to a student and presents a design solution. ps denotes the population size, indicating the total count of students. ndv signifies the digit of design variables. The function $f(x^{1,2,\dots,ps})$ symbolizes the unconfined objective for every student in the group. The objective function identifies an optimal value from the available solutions. The student with a profound understanding will become the class instructor. The instructor aids in redrafting the optimal amount of knowledge for the students in the class in accordance with Eq. 2.

$$x^{new,i} = x^i + r(x_{instructor} - T_F x_{mean}) \tag{2}$$

In the provided equations, r stands a number chosen within the range of [0, 1], T_F (teaching factor) typically equals 1 or 2, the new student is denoted as $x^{new,i}$, while the current student is represented as x^i. Defined as $x_{mean} = (mean(x_1^1)\dots mean(x_1^{ps}))$, this represents the average of the class. If the new student possesses preferential information ($f(x^{new,i})$), they will replace the current student. Knowledge is exchanged during the second phase, known as the learning phase. This phase is analogous to the first one. A new student will take the place of an existing student if they provide superior information. The updating of student information within the class is carried out according to Eq. 3.

$$\begin{gathered} if\ f(x^i) < f(x^j) \Rightarrow x^{new,i} = x^i + r(x^i - x^j), \\ \text{Otherwise} \Rightarrow x^{new,i} = x^i + r(x^j - x^i). \end{gathered} \tag{3}$$

Comprehensive details regarding the TLBO algorithm can be found in the works of Togan (2012), Artar (2016), and Zou et al. (2019).

2.2. Particle Swarm Optimization (PSO)

The PSO algorithm was initially conceived by Kennedy and Eberhart in 1995. Subsequent advancements to this algorithm were introduced by Pedersen and Chipperfield in 2010. PSO represents a stochastic search methodology that employs a population-based strategy for effectively exploring intricate solution spaces. The active foraging behavior of animal species, as they seek out food sources, serves as a basic concept for understanding this technique. This food-seeking behavior encompasses the formation of groups shaped by social influences that rely on the collective memory of each member and the data collected by the swarm.

The approach begins with random solutions and then progressively modifies the velocity and location of particles through iteration. Every particle is characterized by its position x_i^m and velocity v_i^m. The initial position x_i^0 is randomly scattered and taken from the given solution. The initial velocity v_i^0 is presumed to be zero. The initial parameters can be obtained from Eqs. 4-5.

$$x_i^0 = x_{min} + r(x_{max} - x_{min}) \tag{4}$$

$$v_i^0 = 0 \tag{5}$$

In the provided equations, x_{min} and x_{max} signify the lower and top limit of the design parameters, respectively.

This particle velocity reflects the extent of change, while particle positions denote possible solutions for optimal design challenges. Each particle is updated based on two optimal values during every iteration of its movement. The first optimal value is called $p_{best,i}^m$, which signifies the best position attained by the i^{th} particle. The second optimal value, p_{gbest}^m, indicates the best position among all particles at time m. The position and velocity of the i^{th} particle for the m iteration are adjusted according to Eqs. 6-7.

$$v_i^{m+1} = w^m v_i^m + c_1 r_1 (p_{best,i}^m - x_i^m) + c_2 r_2 (p_{gbest}^m - x_i^m) \tag{6}$$

$$x_i^{m+1} = x_i^m + v_i^{m+1} \tag{7}$$

In the formulas mentioned above, r_1 and r_2 serve as arbitrary values ranging from 0 to 1. The particle's inertia, denoted as w^m,influences the algorithm's exploration characteristics. The trust parameters c_1 and c_2 represent the coefficients for individual and collective learning, respectively. For further information on the PSO algorithm, one can refer to various sources, including Kennedy and Eberhart (1995), Saka and Geem (2013), and Gad (2022).

3. Integration of semi-rigid connections within connection topology optimization

The behavior of connections in steel frames is vital for structural performance and cost-effectiveness. Steel frames are typically designed with either fully rigid or pinned connections. Fully rigid connections improve lateral stiffness and can lead to lighter designs, but they often incur higher costs in fabrication, welding, inspection, and erection (Carter, Murray, & Thornton, 2000; Evers & Maatje, 2000). Thus, rigid connections may yield a lighter structure, but they are not always the most economical option when considering all related expenses (Kripakaran, Hall, & Gupta, 2011). To address this issue, each beam is considered a design variable that introduces the connection topology approach. As a result, nine specific beam types will be defined, which is depicted in Fig. 1:

- Type-1 is completely rigid-connected.
- Type-2 is fully semirigid-connected.
- Type-3 is fully pinned-connected.
- Type-4 features a rigid left-end connection and a semirigid right-end connection.
- Type-5 features a rigid left-end connection and a pinned right-end connection.
- Type-6 features a semirigid left-end connection and a rigid right-end connection.
- Type-7 features a semirigid left-end connection and a pinned right-end connection.
- Type-8 features a pinned left-end connection and a rigid right-end connection.
- Type-9 features a pinned left-end connection and a semirigid right-end connection.

Semi-rigid connections emerge as a vital intermediate solution between rigid and pinned behaviors within this optimization process. Semi-rigid connections possess partial rotational stiffness, offering a practical compromise that enhances frame stability without incurring the complete cost associated with rigid connections (Chen & Kishi, 1989; Degertekin & Hayalioglu, 2010). In alignment with this objective, specific types of semi-rigid connections are incorporated into the optimization framework. Based on the classifications by Hayalioglu and Degertekin (2004), six types of semi-rigid connections have been identified, with their moment-rotation characteristics illustrated in Fig. 2. For this study, two semi-rigid connection types are selected: top and seat angles and end plates with column stiffeners to balance cost and stiffness effectively. As shown in Fig. 3, these connections exhibit rotational stiffness values of 8.47×10^7 kNmm/rad and 3.39×10^8 kNmm/rad, respectively.

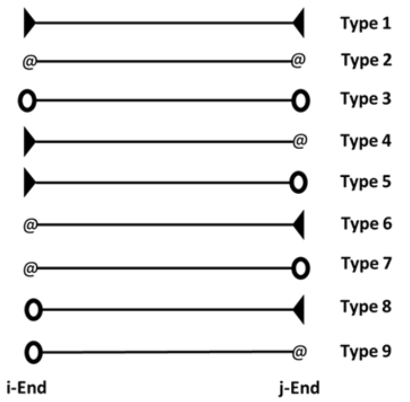

Fig. 1. Beam types incorporated in connection topology

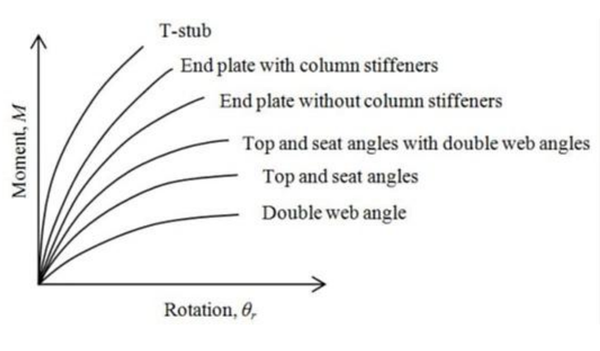

Fig. 2. The moment-rotation curves for semi-rigid connections (Hayalioglu & Degertekin, 2004)

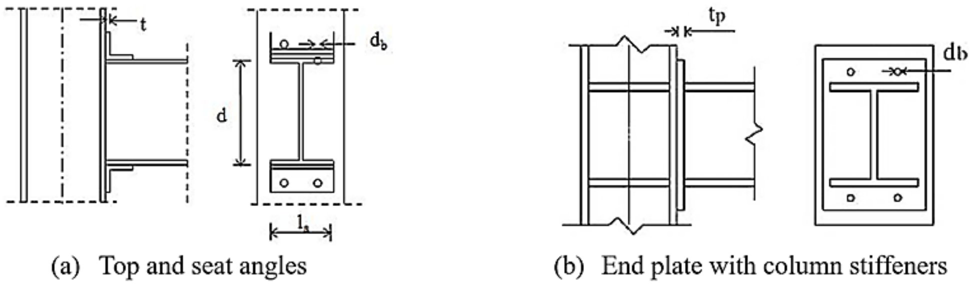

Fig. 3. Types of semi-rigid connections used in the connection topology optimization

4. Mathematical formulation of optimal structural design

In discrete optimization problems, the lowest weight of 3-dimensional steel frame is treated as the unconstrained objective function. The formulations for the objective and penalized functions are provided in Eqs. 8-11 (Daloglu, Artar, Özgan, & Karakas, 2016).

$$Min\ W_{sf} = \sum_{f=1}^{ng} A_f \sum_{i=1}^{nf} \rho_i L_i \tag{8}$$

$$\mathrm{g_i}(x) > 0 \rightarrow c_{vi} = \mathrm{g_i}(x) \tag{9}$$

$$\mathrm{g_i}(x) < 0 \rightarrow c_{vi} = 0 \tag{10}$$

$$\varphi_{sf}(x) = W_{sf}(x)\left(1 + P\sum_{i=1}^{m} c_{vi}\right) \tag{11}$$

In this context, the variable W_{sf} represents the total weight of the 3-dimensional steel frame, while A_f denotes the cross-sectional area of element group f. The symbols ρ_i and L_i refer to the density and length of the steel members. The variable ng indicates the total number of groups, and nf signifies the number of members within group f. The function $\varphi_{sf}(x)$ is called the penalized objective function, and P represents the penalty constant. The variable c_{vi} corresponds to constraint violations, and $\mathrm{g}_i(x)$ designates the constraints applicable to the design.

This study considers various limitations based on Prakash et al. (2024), which are expressed as follows:

The displacement constraints are delineated in Eq. 12.

$$\mathrm{g}_{jl}(x) = \frac{\delta_{jl}}{\delta_{ju}} - 1.0 \leq 0 \qquad \begin{matrix} j = 1, \ldots, cd \\ l = 1, \ldots, nl \end{matrix} \tag{12}$$

In this context, δ_{jl} represents the displacement associated with the j^{th} degree of freedom for the specified load case l. Additionally, δ_{ju} indicates the established upper limit, while cd signifies the total count of constrained displacements. Lastly, nl refers to the overall number of loading scenarios considered.

Inter-storey drift constraints are delineated in Eq. 13.

$$\mathrm{g}_{jil}(x) = \frac{\Delta_{jil}}{\Delta_{ju}} - 1.0 \leq 0, \qquad i = 1, \ldots, nsc, j = 1, \ldots, ns, l = 1, \ldots, nl \tag{13}$$

In this context, Δ_{jil} denotes the inter-storey drift of the i^{th} column in the j^{th} storey during load case l. The symbol Δ_{ju} indicates the permissible limit value, ns refers to the total number of stories, and nsc signifies the count of columns within a storey.

Column-to-column geometric constraints are delineated in Eq. 14.

$$\mathrm{g}_n(x) = \frac{D_{un}}{D_{ln}} - 1.0 \leq 0 \qquad n = 2, \ldots, ns. \tag{14}$$

In this context, D_{un} and D_{ln} signify the depths of the upper and lower floors, respectively.

Beam-to-column geometric constraints are delineated in Eq. 15.

$$\mathrm{g}_{bb,i}(x) = \frac{b_{fbk,i}}{b_{fck,i}} - 1.0 \leq 0 \qquad i = 1, \ldots, n_{bf}. \tag{15}$$

In this context, n_{bf} denotes the joint number where the beam is attached to the column's flange, while $b_{fbk,i}$ and $b_{fck,i}$ signify the flange widths of the beam and column elements, respectively.

According to AISC-LRFD (2010), the stress limits are presented in Eq. 16.

$$\mathrm{g}_{jl}(x) = \begin{cases} \left(\frac{P_u}{\phi P_n}\right)_{jl} + \frac{8}{9}\left(\frac{M_{ux}}{\phi_b M_{nx}} + \frac{M_{uy}}{\phi_b M_{ny}}\right)_{jl} - 1.0 \leq 0 & if\ \frac{P_u}{\phi P_n} \geq 0.2 \\ \left(\frac{P_u}{2\phi P_n}\right)_{jl} + \left(\frac{M_{ux}}{\phi_b M_{nx}} + \frac{M_{uy}}{\phi_b M_{ny}}\right)_{jl} - 1.0 \leq 0 & if\ \frac{P_u}{\phi P_n} < 0.2 \end{cases} \quad \begin{matrix} j=1,\ldots\ldots\ldots,nm \\ l=1,\ldots\ldots\ldots,nl \end{matrix} \tag{16}$$

In this context, the symbol ϕ signifies the resistance factor, which is defined as ϕ_c for compression (0.85), ϕ_t for tension (0.90), and ϕ_b for flexural (0.90). P_n and P_u denote the nominal strength and required axial strength, respectively. M_{nx} and M_{ny} indicate the nominal flexural strength of the major and minor axes, respectively. M_{ux} and M_{uy} represent the necessary flexural strength around the major and minor axes. The integers nm and nl denote the total number of members and the loading conditions, respectively.

5. Implementation and results

This research aims to identify the most effective configuration of pinned, semi-rigid, and rigid connections using a connection topology-based method. This study divides connection topology into two categories: Connection topology (1) and connection topology (2). In connection topology (1), rigid connections, top and seat angles used as semi-rigid connections, and pinned connections are included. On the other hand, in connection topology (2), rigid connections, end plates with column stiffeners as semi-rigid connections, and pinned connections are included. Two reference examples from the current literature illustrate the importance of comparison. The appropriate cross-sections for the frame components are chosen from 64 W-section profiles. The steel material is assumed to have an elastic modulus of $200\,\mathrm{GPa}$, a yield strength of $250\,\mathrm{MPa}$, and a density of $7.85\,\mathrm{t/m^3}$. Additionally, particular beam types for the connection topologies are chosen from a list of nine beam types, as shown in Fig. 1. For both benchmark examples, the population size is established at 20.

5.1. Case study-1: 2-storey, 21-member space frame design

The case study showcases an optimization of an asymmetrical steel space frame with two stories and 21 members, as reviewed by Artar and Daloğlu (2020). The current study emphasizes the use of a connection topology approach for the analysis of steel space frames. The components of the space frame have been systematically divided into five separate groups, consisting of two beams and three columns, to optimize their dimensions, as shown in Fig. 4 (a). The beams of the steel space frame are classified into eleven groups for the purpose of optimizing the connection topology, as illustrated in Fig. 4 (b). Fig 4 depicts the spatial arrangement of the major and minor axes of the columns and beams. In Fig. 4, vertical loads of $20\,\mathrm{kN/m}$ are applied to each beam, along with a wind load of $50\,\mathrm{kN}$. The maximum displacement and inter-storey drift limitations are established at 4.0 cm and 1.02 cm, respectively.

Table 1 presents the optimum results for rigid frames as reported by Artar and Daloğlu (2020). It also showcases the best outcomes for different connection topologies in steel space frames utilizing the TLBO and PSO algorithms. Figs. 5 and 6 illustrates the optimal arrangement of beam-to-column connections for connection topology (1) and (2) achieved by the TLBO and PSO algorithms, respectively. Fig. 7 display the design histories for each scenario, reflecting the optimal population design for every iteration. The example provided is implemented in five separate simulations.

Table 1 demonstrates that the optimal values for steel space frameworks identified in this study are in close agreement with the results published by Artar and Daloğlu (2020). It can also observed in Table 1 for TLBO solutions, the minimum weights of frames with connection topologies (1) and (2) are 9.90 and 1.05 percent greater than the lowest weight of 51.665 kN, respectively. The maximum displacement remains significantly lower than the established limit across all instances. However, the highest inter-storey drift approaches the maximum allowable threshold. Figs. 5 and 6 illustrate that each beam is assigned a connection type from a predetermined set comprising rigid, semi-rigid, and pinned connections. The connection layout demonstrates a strategic distribution of connection stiffness throughout the frame, aiming to minimize the overall structural cost while maintaining adequate stiffness and stability.

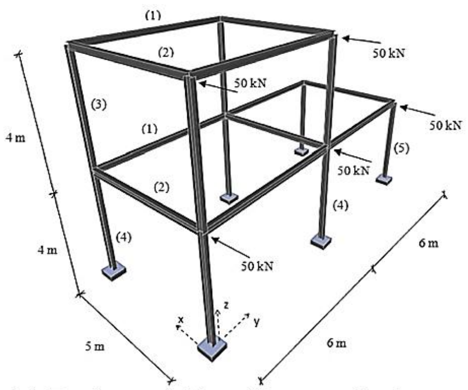

(a) Design variables of beam and columns for size optimization

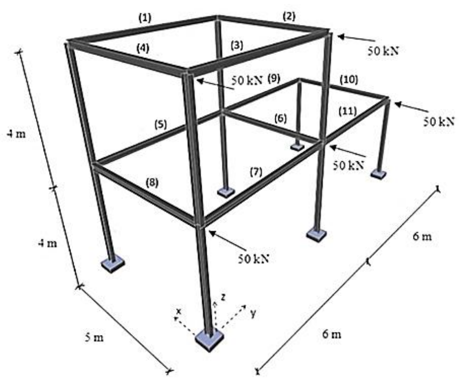

(b) Design variables of beams for connection topology optimization

Fig. 4. A 2-storey, 21-member space frame

Table 1. Optimum design of 2-storey, 21-member space frame

Element Group	With rigid connections			With variable connections			
	Artar and Daloğlu (2020)	Present study		Present study			
				Connection topology (1)		Connection topology (2)	
	JAYA	TLBO	PSO	TLBO	PSO	TLBO	PSO
1	W16×26	W16×26	W16×31	W16×31	W12×26	W12×26	W12×26
2	W18×40	W18×35	W18×40	W18×35	W14×26	W18×35	W18×40
3	W18×40	W18×40	W16×36	W18×35	W21×50	W18×40	W14×43
4	W18×40	W21×50	W21×50	W24×68	W27×94	W21×50	W14×61
5	W12×30	W18×35	W12×26	W14×30	W8×28	W18×40	W8×28
Min. weight (kN)	50.65	51.665	54.113	56.780	60.111	52.207	55.838
Max. top storey drift (cm)	1.96	1.793	1.763	1.582	1.501	1.797	1.939
Max. inter-storey drift (cm)	1.1011	0.992	1.003	1.016	1.017	0.993	0.994

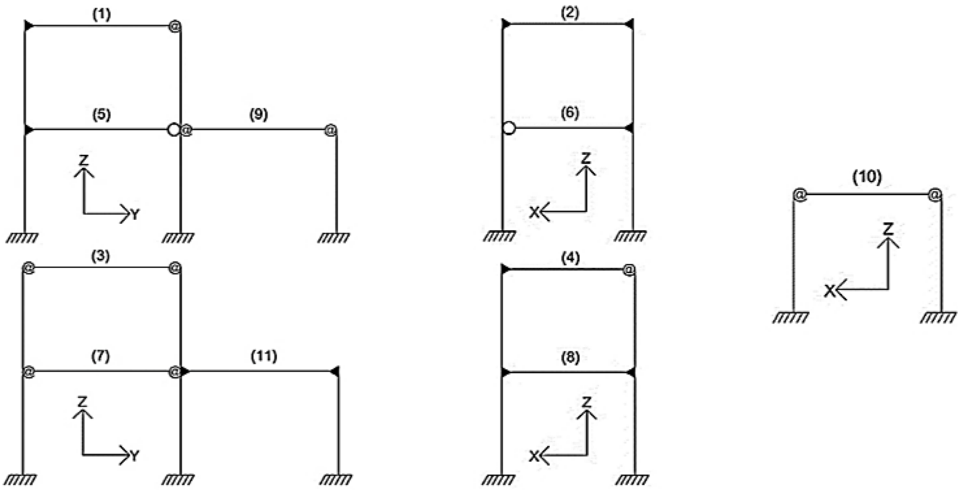

(a) TLBO solution

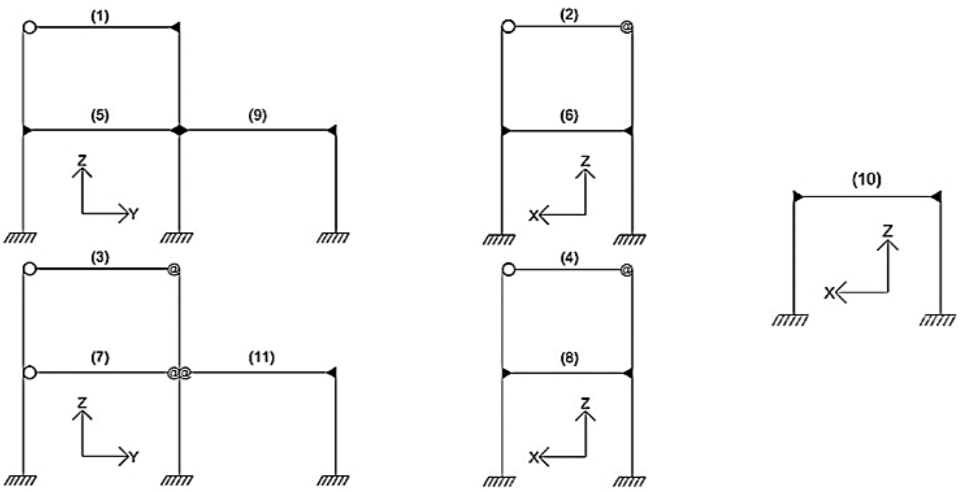

(b) PSO solution

Fig. 5. Optimum connection topology (1) of two-storey frame obtained by TLBO and PSO

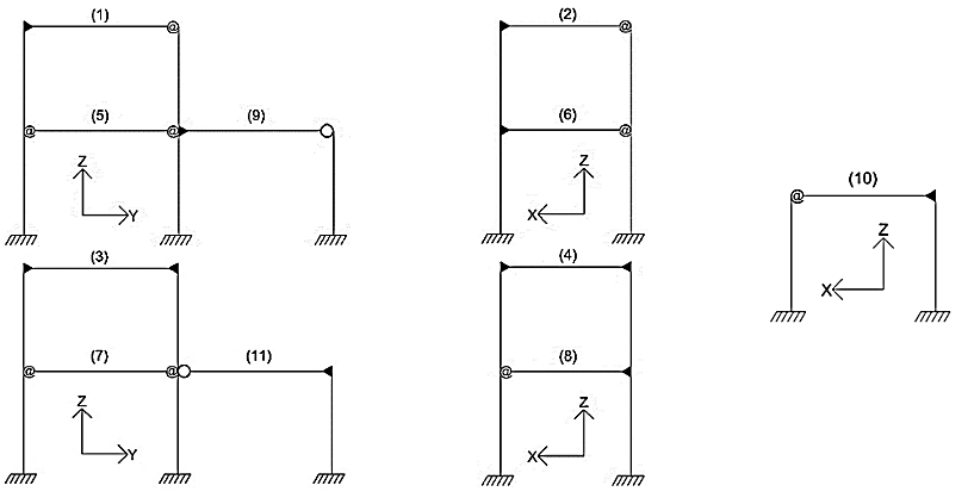

(a) TLBO solution

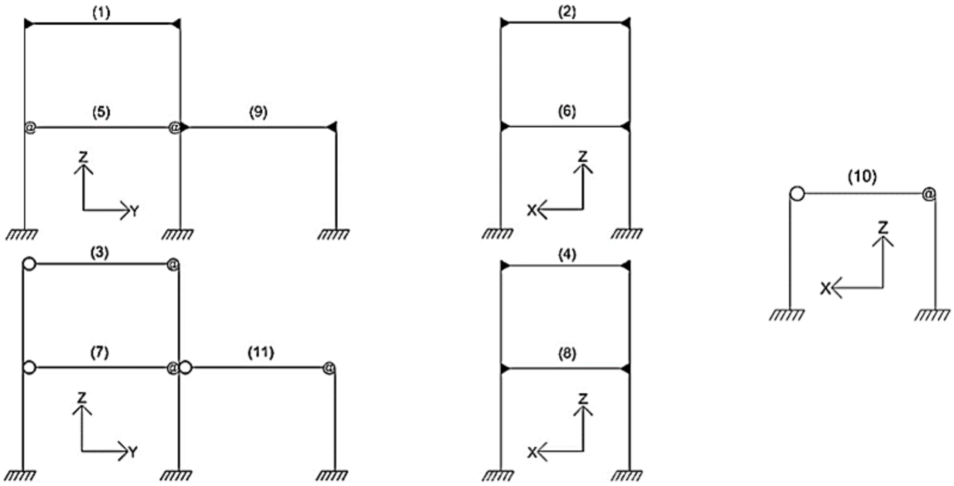

(b) PSO solution

Fig. 6. Optimum connection topology (2) of two-storey frame obtained by TLBO and PSO

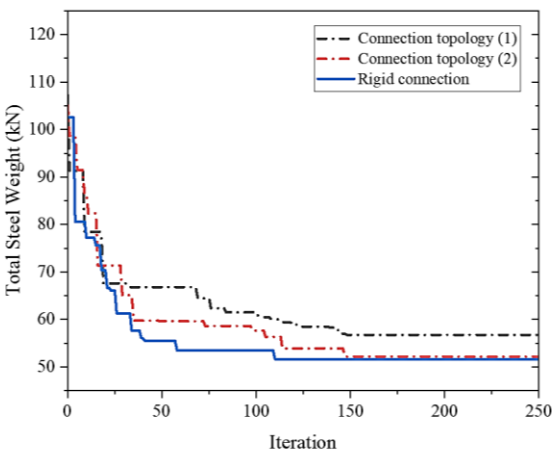

(a) TLBO solutions

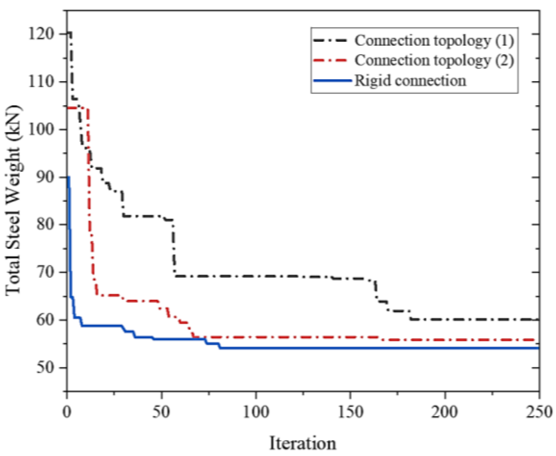

(b) PSO solutions

Fig. 7. Design histories of two-storey frame obtained by TLBO and PSO

It can be observed from these configurations that rigid connections are primarily located at joints requiring higher moment resistance and stiffness; semi-rigid connections are effectively employed in locations where a balance between stiffness and cost-efficiency is desirable; and pinned connections are assigned to areas where moment resistance is less critical, thereby contributing to reductions in fabrication and welding costs. This arrangement highlights the metaheuristic algorithm's capability to intelligently assign varying connection types, optimizing both structural performance and economic efficiency. Furthermore, Fig. 7 indicates that the minimum structural weight increases slightly when connection topology is considered. The results obtained from the Particle Swarm Optimization (PSO) algorithm closely match those of the Teaching-Learning-Based Optimization (TLBO) method, demonstrating a strong consistency between the two approaches.

5.2. Case study-2: 4-storey, 84-member space frame design

The current case study discusses optimizing the symmetrical steel space frame consisting of four stories and 84 members, as depicted in Fig. 8, previously examined by Artar and Daloğlu (2020). This study implements a connection topology method for analyzing steel space frames. The 84 frame members are divided into ten categories. The first category includes the external beams found on the fourth floor. The second category consists of the external beams on the third, second, and first floors. The inner beams on the fourth floor make up the third category. The fourth category contains the inner horizontal beams located on the third, second, and first floors. The fifth category consists of the corner columns on the fourth floor. The sixth category includes corner columns on the third, second, and first floors. The seventh category is made up of external columns positioned on the fourth floor. The eighth category covers external columns on the third, second, and first floors. The ninth category comprises internal columns on the fourth floor. Finally, the tenth category includes internal columns on the third, second, and first floors.

The maximum permitted lateral movement and inter-storey drift are 3.50 cm and 1.17 cm, respectively. The steel space frame is subjected to several loads: wind pressure ($p_w = C_e C_q q_s I_w$), live load ($L_l = 2.40\ \mathrm{kN/m^2}$), dead load ($D_l = 3.84\ \mathrm{kN/m^2}$), and nominal roof live load ($L_r = 2.40\ \mathrm{kN/m^2}$). In this regard, p_w stands for the design wind pressure, C_e denotes the exposure and guest factor coefficient along with the combined height, C_q is the pressure coefficient, which equals 0.8 for windward faces and 0.5 for leeward faces, q_s represents the wind stagnation pressure, quantified at $0.785\ \mathrm{kN/m^2}$, and I_w signifies the wind importance factor. The structure experiences wind loads in the X-direction. For each scenario, the following load combination is applied: $1.2D_l + 1.3W_l + 0.5L_r + 0.5L_l$, where W_l refers to the wind load.

Table 2 showcases the optimal results for rigid frames, as reported by Artar and Daloğlu (2020). It also highlights the best outcomes for various connection topologies in steel space frames using the TLBO and PSO algorithms. Figs. 9 and 10 illustrate the ideal configurations of beam-to-column connections for connection topology (1) and (2), respectively, achieved through the TLBO and PSO algorithms. Fig. 11 presents the design histories for each scenario, reflecting the optimal population design for each iteration.

Similar independent trials are conducted, similar to the previous example. Table 2 illustrates that the optimal values for steel space frameworks found in this research closely align with the findings reported by Artar and Daloğlu (2020). It can also be seen in Table 2 regarding TLBO solutions that the minimum weights for frames with connection topologies (1) and (2) exceed the lowest weight of 177.20 kN by 7.62 and 2.87 percent, respectively. The lateral displacement remains significantly below the established limit in all instances. Conversely, the inter-storey drift approaches the upper limit.

Figs. 9 and 10 illustrate a strategic distribution of connection stiffness throughout the frame to minimize overall structural costs while ensuring adequate stiffness and stability. This arrangement underscores the capabilities of the metaheuristic algorithm in intelligently assigning various connection types, thereby optimizing structural performance and economic efficiency. Additionally, Fig. 11 indicates a slight increase in the minimum structural weight when connection topology is considered.

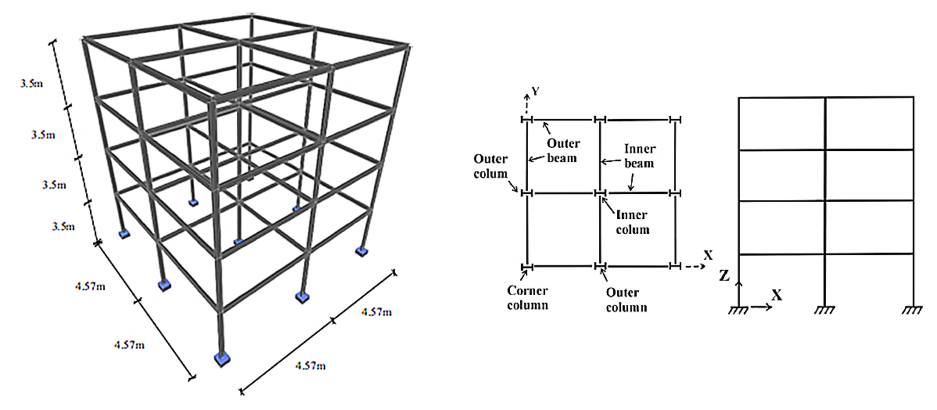

(a) 3D view (b) Plan and side view

Fig. 8. A 4-storey, 84-member space frame

Table 2. Optimum design of 4-storey, 84-member space frame

Element Group	With rigid connections			With variable connections			
	Artar and Daloğlu (2020)	Present study		Present study			
				Connection topology (1)		Connection topology (2)	
	JAYA	TLBO	PSO	TLBO	PSO	TLBO	PSO
1	W10×26	W14×43	W14×30	W18×35	W8×15	W8×21	W18×35
2	W10×26	W12×19	W14×26	W8×15	W18×35	W16×26	W8×15
3	W12×19	W18×35	W8×15	W8×15	W8×15	W12×19	W8×15
4	W16×26	W16×31	W8×15	W8×15	W8×15	W10×15	W8×15
5	W10×26	W14×68	W10×54	W12×35	W14×43	W14×61	W14×30
6	W14×30	W21×50	W16×40	W16×26	W18×35	W16×31	W16×26
7	W12×26	W12×53	W12×72	W18×50	W12×72	W18×76	W16×40
8	W30×108	W18×35	W12×72	W40×149	W12×96	W21×62	W40×149
9	W14×26	W14×48	W14×82	W14×43	W8×15	W16×26	W8×15
10	W18×35	W14×68	W16×36	W16×31	W14×26	W40×167	W8×21
Min. weight (kN)	183.21	177.20	178.05	190.71	188.80	182.28	184.72
Max. top storey drift (cm)	3.31	3.42	3.36	3.50	2.82	3.29	3.50
Max. inter-storey drift (cm)	0.94	1.09	1.00	1.17	1.14	1.09	1.17

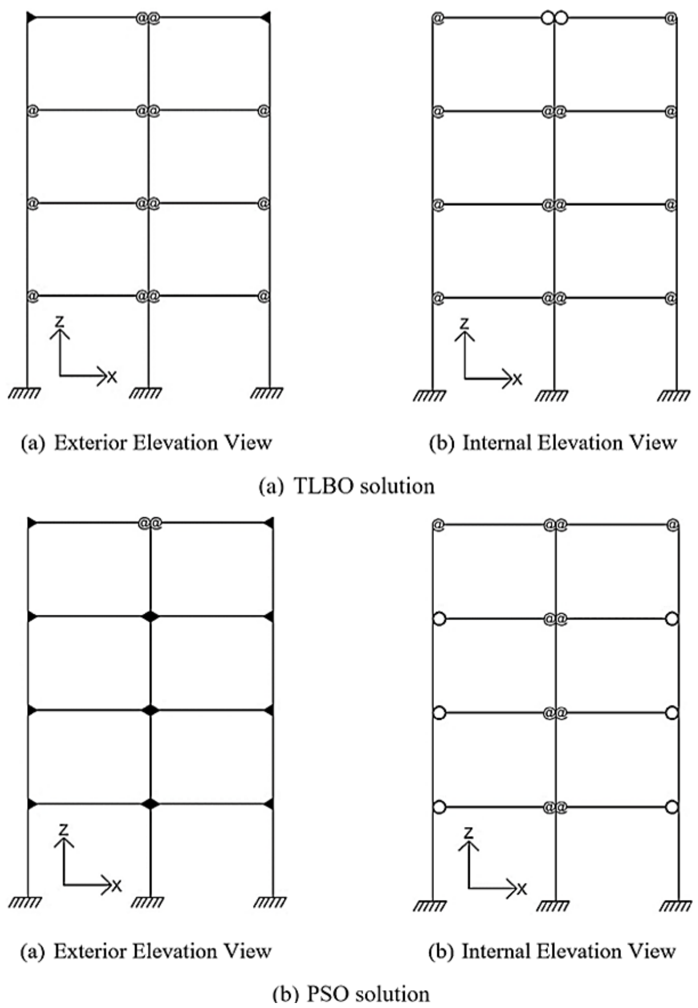

Fig. 9. Optimum connection topology (1) of four-storey frame obtained by TLBO and PSO

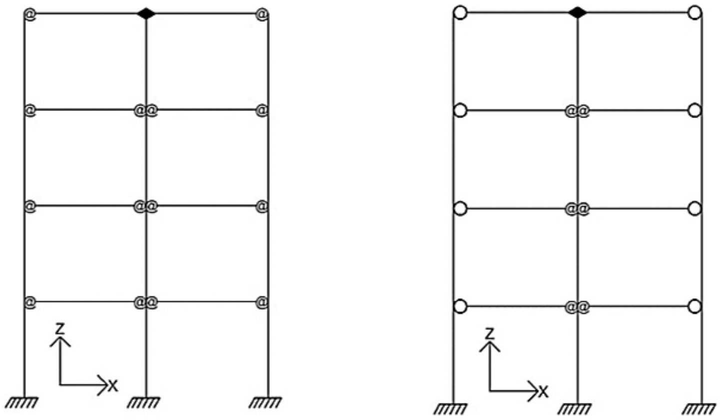

(a) Exterior Elevation View (b) Internal Elevation View

(a) TLBO solution

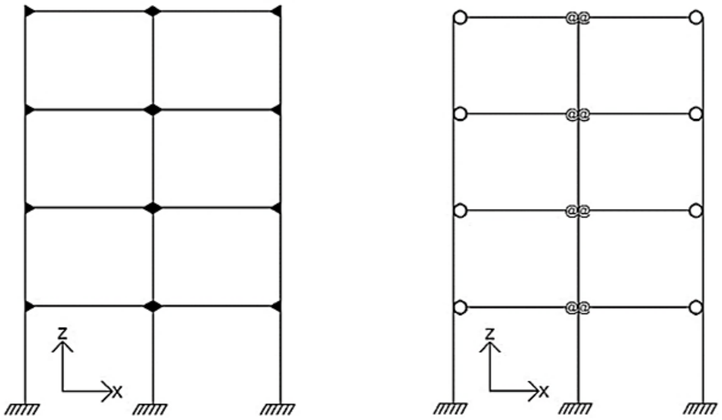

(a) Exterior Elevation View (b) Internal Elevation View

(b) PSO solution

Fig. 10. Optimum connection topology (2) of four-storey frame obtained by TLBO and PSO

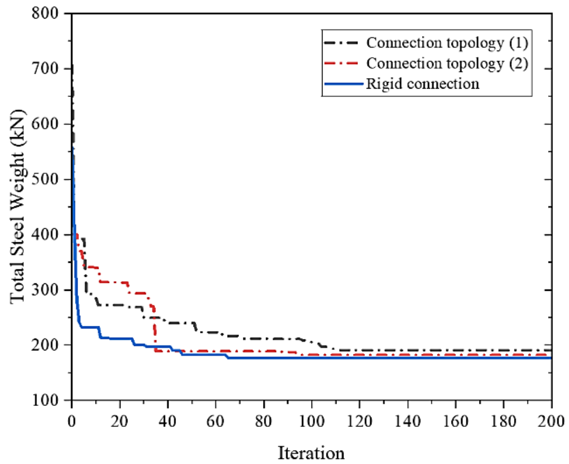

(a) TLBO solutions

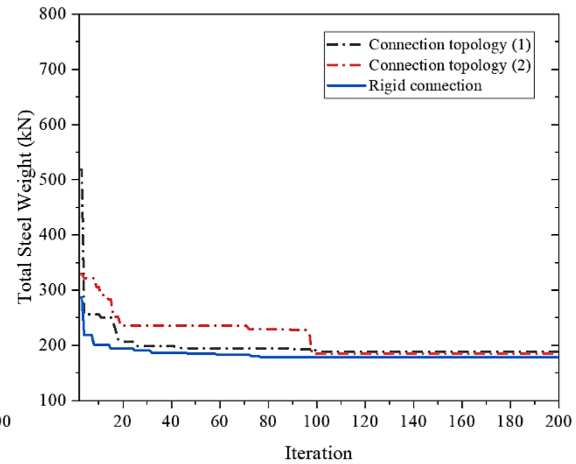

(b) PSO solutions

Fig. 11. Design histories of four-storey frame obtained by TLBO and PSO

The results derived from the Particle Swarm Optimization (PSO) algorithm show a high degree of consistency with those obtained from the Teaching-Learning-Based Optimization (TLBO) method, further validating the reliability of both approaches.

6. Conclusion

The primary aim of this study is to evaluate how randomly positioned beam-to-column connections influence the optimal design of steel space frames. TLBO and PSO are utilized to accomplish this goal. The effects of randomly positioned beam-to-column connections on steel frames are analyzed through connection topology optimization. The steel space frames are subject to various constraints, including geometry (beam-to-column and column-to-column), top and inter-story drift, and the stress requirements of LRFD-AISC. The total weight of the steel frame serves as the objective function in the analyses. The types of beams for connection topology optimization and the structural members for size optimization are identified as design variables.

Below are the comprehensive conclusions regarding the optimal design achieved through the C#-SAP2000 OAPI:

- Incorporating the effects of connection topologies into the optimization process for steel space frames slightly extends the time required to identify the most effective solution.
- In the conclusion of the first example, when the TLBO algorithm is used, it shows that the minimum weights of frames with connection topologies (1) and (2) are 9.90 and 1.05 percent greater than the lowest weight of 51.665 kN, respectively. Moreover, in the second example's conclusion, when the TLBO algorithm is used, it shows that the minimum weights for frames with connection topologies (1) and (2) exceed the lowest weight of 177.20 kN by 7.62 and 2.87 percent, respectively. These results indicate a slight increase in the minimum structural weight when connection topology is considered.
- The research indicates that inter-story drift and maximum lateral displacement limits are essential in determining the best design for the space frame.
- The connection layout demonstrates a strategic distribution of connection stiffness throughout the frame, aiming to minimize the overall structural cost while maintaining adequate stiffness and stability.
- The results indicate that the TLBO algorithm produces lighter frames than the PSO algorithm.

References

AISC-LRFD. (2010). *Manual of steel construction-load and resistance factor design.* Chicago, IL, USA: American Institute of Steel Construction.

Alberdi, R., Murren, P., & Khandelwal, K. (2015). Connection topology optimization of steel moment frames using metaheuristic algorithms. *Engineering Structures, 100*, 276–292.

Ali, N. B., Sellami, M., Cutting-Decelle, A. F., & Mangin, J. C. (2009). Multi-stage production cost optimization of semi-rigid steel frames using genetic algorithms. *Engineering Structures, 31*(11), 2766–2778.

Artar, M. (2016). Optimum design of braced steel frames via teaching learning based optimization. *Steel and Composite Structures, 22*, 733–744.

Artar, M., & Daloğlu, A. T. (2020). A research on optimum designs of steel frames including soil effects or semi rigid supports using Jaya algorithm. *Structural Engineering and Mechanics, An Int'l Journal, 73*(2), 153–165.

Carter, C. J., Murray, T. M., & Thornton, W. A. (2000). Economy in steel. *Modern Steel Construction, 40*(4), 39–48.

Chen, W.-F., & Kishi, N. J. (1989). Semirigid steel beam-to-column connections: Data base and modeling. *Journal of Structural Engineering, 115*, 105–119.

Daloglu, A. T., Artar, M., Özgan, K., & Karakas, A. İ. (2016). Optimum design of steel space frames including soil-structure interaction. *Structural and Multidisciplinary Optimization, 54*, 117–131.

Degertekin, S. O., & Hayalioglu, M. S. (2010). Harmony search algorithm for minimum cost design of steel frames with semi-rigid connections and column bases. *Structural and Multidisciplinary Optimization, 42*, 755–768.

Evers, H. G., & Maatje, I. R. (2000). Cost based engineering and production of steel constructions. *Steel Design Codes—Fourth International Workshop on Connections in Steel Structures*, (pp. 14–22).

Gad, A. G. (2022). Particle swarm optimization algorithm and its applications: a systematic review. *Archives of Computational Methods in Engineering, 29*, 2531–2561.

Hagishita, T., & Ohsaki, M. (2008). Optimal placement of braces for steel frames with semi-rigid joints by scatter search. *Computers & Structures, 86*(21-22), 1983–1993.

Hall, B. S., & others. (2006). *GA-Based Optimization of Steel Moment Frames: A Case Study.* Master's Thesis, North Carolina State University, North Carolina.

Hayalioglu, M. S., & Degertekin, S. O. (2004). Design of non-linear steel frames for stress and displacement constraints with semi-rigid connections via genetic optimization. *Structural and Multidisciplinary Optimization, 27*, 259–271.

Kaveh, A., Ghafari, M. H., & Gholipour, Y. (2017). Optimum seismic design of steel frames considering the connection types. *Journal of Constructional Steel Research, 130*, 79–87.

Kennedy, J., & Eberhart, R. (1995). Particle swarm optimization. *Proceedings of ICNN'95-International Conference on Neural Networks*, *4*, pp. 1942–1948.

Kripakaran, P., Hall, B., & Gupta, A. (2011). A genetic algorithm for design of moment-resisting steel frames. *Structural and Multidisciplinary Optimization, 44*, 559–574.

Prakash, J., DALOĞLU, A. Y., & Özgan, K. (2024). An optimal design approach for steel space frames with T-stub semi-rigid connections considering soil-structure interaction. *Journal of Structural Engineering & Applied Mechanics (Online), 7*(2), 104-122.
Rahami, H., Mohebian, P., & Mousavi, M. (2017). Performance-based connection topology optimization of unbraced and X-braced steel frames. *Int J Optim Civil Eng, 7*(3), 451–468.
Rao, R. V., Savsani, V. J., & Vakharia, D. P. (2011). Teaching–learning-based optimization: a novel method for constrained mechanical design optimization problems. *Computer-Aided Design, 43*(3), 303–315.
Saka, M. P., & Geem, Z. W. (2013). Mathematical and metaheuristic applications in design optimization of steel frame structures: an extensive review. *Mathematical Problems in Engineering, 2013*, 271031.
Toğan, V. (2012). Design of planar steel frames using teaching–learning based optimization. *Engineering Structures, 34*, 225–232.
Tovar, A., & Khandelwal, K. (2013). Topology optimization for minimum compliance using a control strategy. *Engineering Structures, 48*, 674–682.
Xu, L. (2002). Design and optimization of semi-rigid framed structures. *Recent Advances in Optimal Structural Design, 147*, 134–150.
Zou, F., Chen, D., & Xu, Q. (2019). A survey of teaching–learning-based optimization. *Neurocomputing, 335*, 366–383.

4th International Civil Engineering & Architecture Conference
17-19 May 2025, Trabzon, Türkiye

Progressive collapse simulation of a multi-storey building constructed using carbon steel and stainless steel under fire conditions

Athraa M. Nuhair[1,3*], Murat Günaydın[1], Sameer Alabsi[1], Emre Özyurt[2], Ahmet C. Altunışık[1], Yunus E. Akbulut[1]

[1] *Karadeniz Technical University, Department of Civil Engineering, 61080 Trabzon, Türkiye*
[2] *Gümüshane University, Department of Civil Engineering, 29100 Gümüşhane, Türkiye*
[3] *Wasit University, 52001 Wasit, Iraq*

Abstract. The objective of this study is to investigate the progressive collapse behavior of multi-storey buildings under fire conditions, considering the use of carbon steel and stainless steel materials. To achieve this, a series of nonlinear dynamic explicit analyses were carried out using Abaqus software. In the study, the validation procedure for the collapse simulation of a building under fire conditions was first carried out. The validated model was subsequently employed to simulate the progressive collapse behavior of carbon steel and stainless steel building under fire exposure. Finally, both cases were compared in terms of the results obtained under fire exposure, including progressive collapse cases, displacements, and stress outcomes.

Keywords: Elevated temperature; Nonlinear dynamic explicit analysis; Progressive collapse simulation

1. Introduction

The structural integrity of buildings under extreme conditions, such as fire, is a significant concern in modern civil engineering. Progressive collapse - defined as sequential failure in structural components as a result of localized damage - reflects a significant risk of life security and property. The outbreak of a fire in a particulary steel structure, if the structure is not at least partially protected from heat exposure, can result in a considerable decline in the material's strength and stiffness, potentially leading to significant loss of life and property. This is due to the fact that steel's physical properties are dependent on temperature.

Traditional carbon steel is widely used in modern structural engineering due to its exceptional strength, durability, and versatility. Today, it plays a vital role in the construction of skyscrapers, bridges, industrial buildings, and residential frameworks. Its high strength-to-weight ratio allows for taller and more open structures without compromising stability. Additionally, steel is recyclable, making it an environmentally responsible choice in sustainable building practices. With advancements in fabrication and design technologies, steel continues to be a cornerstone material in the development of safe, efficient, and innovative structures around the world. While steel is a strong and reliable material in construction, it is highly susceptible to damage at high temperatures. In the event of a fire, steel can lose up to 50% of its strength at around 550°C, which can compromise the structural integrity of a building. Therefore, it is essential to protect steel structures with fire-resistant materials. Common fire protection methods include applying fire-retardant coatings, such as intumescent paint that expands when exposed to heat, as well as encasing steel elements in fireproof boards or concrete. These protective systems help maintain the structural performance of steel during a fire, giving occupants more time to evacuate and emergency services more time to respond.

Stainless steel offers improved fire resistance compared to many other building materials due to its ability to retain strength at elevated temperatures. Unlike carbon steel, certain grades of stainless steel, such as austenitic types, maintain their structural integrity longer during a fire, making them a safer choice for critical components in buildings. Additionally, stainless steel does not burn, produce toxic fumes, or contribute to the spread of flames. These properties make it a preferred material in environments where fire safety is a high priority, such as in transportation hubs, high-rise buildings, and industrial facilities (Rossi, 2014; Karabulut et al., 2018; Molkens et al., 2021).

[1*]Corresponding author, E-mail: anuhair@uowasit.edu.iq

https://doi.org/10.31462/icearc2025_ce_sme_697

Stainless steel is widely recognized for its excellent corrosion resistance, structural flexibility, and ability to retain mechanical properties at elevated temperatures, making it a strong candidate for high-altitude and performance-critical structures. However, despite its increasing use in architectural and industrial applications, research on its behavior under fire-induced thermal loading remains limited (Gardner and Baddoo, 2006; Gardner, 2007; Wang et al., 2020; Segura et al., 2021). Most existing studies focus primarily on carbon steel frames (Jiang et al., 2014; Qin, 2016; Shan & Li, 2021; Shakeri et al., 2023), resulting in a significant knowledge gap regarding the response of stainless steel structures to localized fire exposure and their associated collapse mechanisms. This study aims to address this gap by investigating the collapse behavior of stainless steel frames subjected to realistic fire scenarios. The main objectives are twofold: (1) to monitor and analyze the structural performance of stainless steel during fire events, and (2) to explore the evolution of load-bearing capacity, progressive failure mechanisms, and structural hierarchy under fire conditions.

2. Case study

The case study presented in this research is based on the framework developed by Shan & Li (2021), with the bare frame configuration modeled and further analyzed in the current study. The study numerically investigates the impact of infill walls on the collapse performance of three-dimensional steel frames exposed to fire using nonlinear dynamic analysis. Two eight-story composite steel frames-one bare and one with infill walls—are analyzed under single-compartment and traveling fire scenarios, considering parameters such as load ratio, opening percentage, and number of infill walls. A preliminary analytical method is also proposed to predict collapse modes under traveling fire conditions.

In the present study, a multi-storey building without infill walls (Fig. 1a) subjected to single-compartment fire scenarios (Fig. 1b), as detailed by Shan & Li (2021), was modeled to simulate progressive collapse using carbon steel under fire conditions. Additionally, the same configuration was analyzed using stainless steel to enable a comparative assessment of the collapse behavior between the two materials. The fire analysis of the building using carbon and stainless steel was carried out against a corner compartment fire.

The modeled building, designed as a small shopping mall, is situated on Type II soil. The structural design accounts for a roof dead load of 3.5 kN/m² and 1.5 kN/m² for the typical floors, excluding the self-weight of slabs and framing members. Live loads are defined as 2.0 kN/m² on the roof and 3.5 kN/m² on all other floors. The structure consists of H-shaped steel members, composite concrete slabs, and reinforcing bars. Table 1 presents the cross-sections of frame members adopted in building. The first story of the building has a height of 4.2 m, while each of the remaining stories is 3.3 m tall. See the study by Shan & Li (2021) for detailed information on the building and its material characteristic.

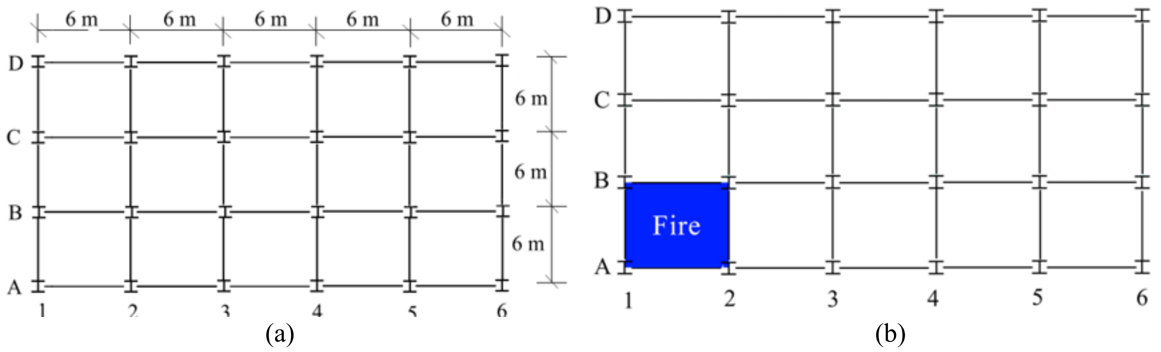

Fig. 1. View of the building (a) plan view, (b) single-compartment fire scenario

Table 1. Cross sections of the frame members used in the building

Structural member	Story		
	1	2-3	4-6
Corner column	HW250×250×9×14	HW250×250×9×14	HW250×250×9×14
Edge column	HW350×350×12×19	HW350×350×12×19	HW300×300×10×15
Interior column	HW400×400×13×21	HW350×350×12×19	HW300×300×10×15
Edge beam	HN 298×149×5.5×8	HN 298×149×5.5×8	HN 298×149×5.5×8
Interior beam	HN399×199×7×11	HN399×199×7×11	HN350×175×7×11

Note: the first to the fourth number represent the section height, section width, thickness of web and flange, respectively

3. Validation study

Before conducting the main numerical study, several validation analyses were performed to ensure the accuracy and reliability of the simulation results. These validation studies involved comparing the numerical model against experimental or numerical data and established benchmarks to confirm that the structural behavior under fire conditions was realistically captured. In this step, the numerical models were developed for selected case studies from the literature, and the simulation results were compared with the published findings to further validate the accuracy and robustness of the modeling approach.

Two specific studies were used to validate a line-element modeling approach. The first involved frames tested by Rubert and Schaumann (1986), known as the EHR (span x height, 1.24 m x 1.17 m) and ZSR (span x height, 1.20 m x 1.18 m) frames, which are given in Fig.2. The frames (IPE80 I-section) were uniformly heated using ISO-834 standard fire curve (Fig. 3) under the applied loads. The numerical analysis was carried using Abaqus softwarte (Abaqus, 2022). The mid-span deflections of the columns and beams in the EHR frame, as well as the lateral displacements of the ZSR frame, were evaluated and compared with both the simulation results obtained in this study and the corresponding data previously reported in the literature (Fig. 4). As can be seen in Fig. 4, the displacement–temperature curves of the validation models (current study in graphic) showed good agreement with other studies reported in the literature.

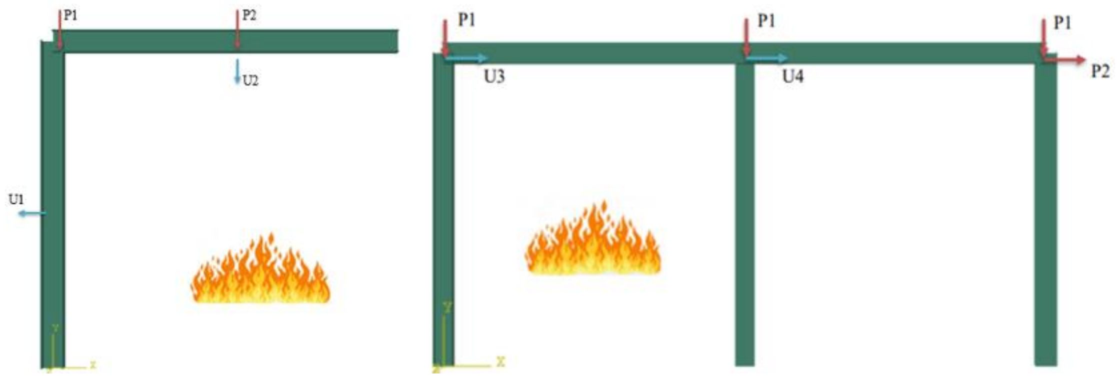

(a) (b)

Fig. 2. Validate frame tested by Rubert and Schauman (1986); (a) EHR, (b) ZSR

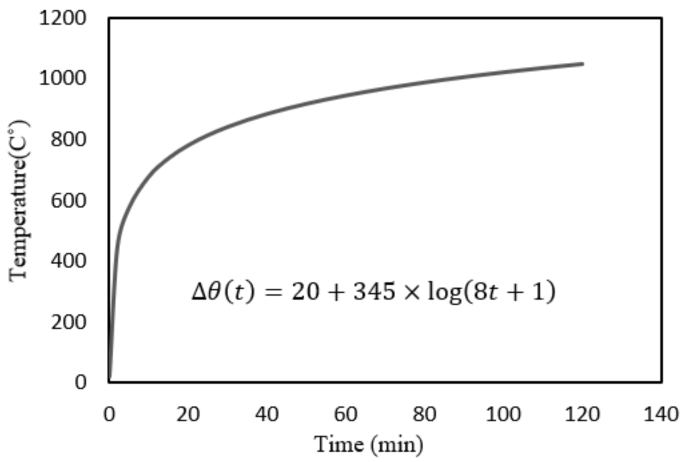

Fig.3. ISO-834 standard fire curve and relavant equation

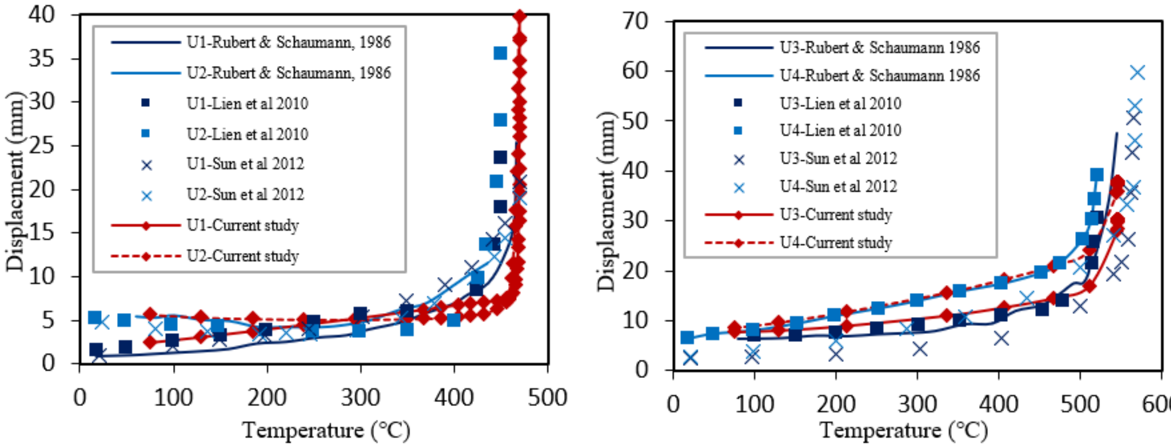

Fig.4. Displacement–temperature curves of the validation models and previously reported data

The second case study involved a five-by-three-bay, six-story steel frame tested by Shan & Li (2021). The same model was used to analyse further. The Finite Element (FE) model (Fig. 5) of the building was created using Abaqus softwarte (Abaqus, 2022). An explicit nonlinear analysis procedure was in place for the collapse simulation. In the numerical model, beams and columns were modeled using 2-node wire beam elements (B31), while floor slabs were represented with 4-node shell elements (S4R). Reinforcing bars within the slabs were included as embedded rebar layers within the shell elements. All beam-column connections were assumed to be rigid, which is a common simplification in the seismic analysis of steel frame structures. Secondary beams were excluded from the model. To represent the interaction between steel beams and concrete slabs, tie constraints were employed. A damping ratio of ξ = 0.05 was used for the steel frame.

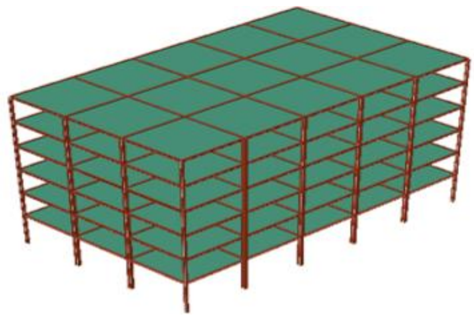

Fig. 5. FE model of the building

The building was exposed to corner compartment fire scenario, as illustrated in Fig. 1b. The simulation follows a two-phase loading protocol to realistically capture the structural response under fire conditions. In the first phase, gravity-induced loading is applied to the structure. This load is determined using the GSA-recommended combination of 1.2 times the dead load (DL) plus 0.5 times the live load (LL), as specified in GSA (2013). The gravitational load is gradually introduced over a period of 3 seconds to avoid sudden dynamic effects. Once the full load is applied, it is held constant for an additional 2 seconds to allow any transient structural responses to dissipate before the fire exposure begins. After the initial stabilization phase, thermal loading is introduced. The frame members exposed to fire, are heated in accordance with the parametric fire curve of Eurocode 1 (Fig. 6) (Eurocode 1- EN 1991-1-2), while the gravitational load applied earlier remains constant throughout this phase. To ensure the structural response remains quasi-static and is not influenced by excessive dynamic effects, the model's kinetic energy is continuously monitored. This monitoring helps verify that any failure of fire-exposed columns is captured accurately, ensuring that the simulation reflects realistic structural behavior under fire-induced material degradation. See the study by Shan & Li (2021) for detailed information on the paramaters of fire curve such as fire load density, an opening factor, thermal inertia value. Fig. 7 shows the variation of axial force and vertical displacement with increasing temperature for the columns located along the A1 and B1 axes. These relationships were systematically examined and compared with established results from the literature given by Shan & Li (2021). The close agreement between our findings and previously published data confirms the accuracy of the numerical model. This strong consistency validates the computational approach used in this study and demonstrates that the model is sufficiently robust to accurately capture the structural behavior under various conditions, including different fire scenarios considered in the collapse simulation.

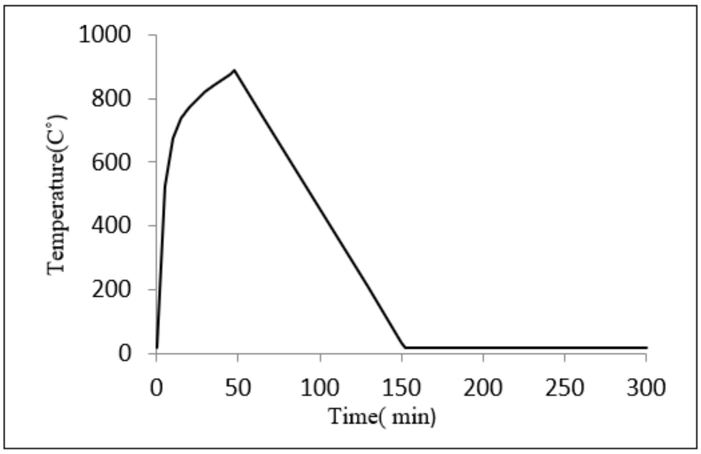

Fig.6. Eurocode fire curve and relavant equation

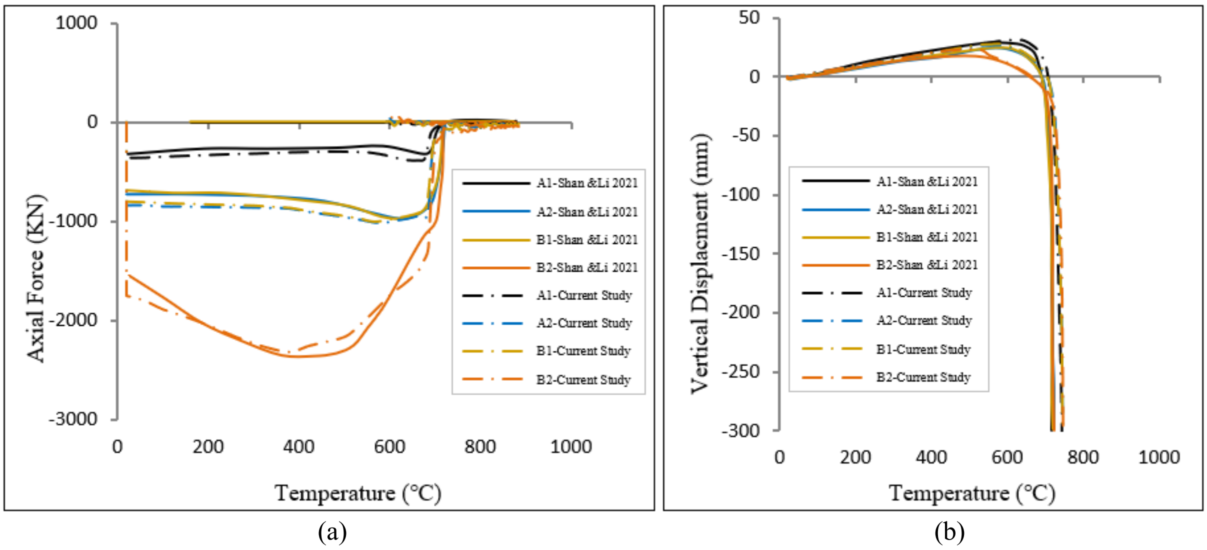

Fig.7. Variation of axial force (a) and vertical displacement (b) with increasing temperature of the validation model and previously reported data

4. Further analyses for staninless steel

In this section, the progressive collapse analysis and corresponding results of the multi-storey building-previously validated-are presented. The building, modeled with stainless steel (colums and beams), was subjected to the corner compartment fire scenario illustrated in Fig. 1b. The same scenario had been previously applied to a carbon steel building, allowing for a direct comparison of structural performance. The analysis focuses on the fire-induced behavior and progressive collapse mechanisms of the stainless steel structure, highlighting differences in thermal response and structural resilience between the two material types.

The elevated temperature material properties for both carbon steel and stainless steel were adopted from Eurocode 1 and Eurocode 3, respectively. For carbon steel, the yield strength and elastic modulus were taken as 235 MPa and 2.06×10^5 MPa. For stainless steel, specifically the austenitic grade 1.4301 as defined in Eurocode 3 (EN 1993-1-4), the yield strength was set to 230 MPa and the elastic modulus to 1.9798×10^5 MPa.

The reduction in strength and stiffness of structural materials at elevated temperatures is a critical consideration in fire-resistant design. Stainless steel, owing to its alloying elements, exhibits better high-temperature performance than carbon steel. As illustrated in Fig. 8a, grade 1.4301 (304) austenitic stainless steel exhibits significantly better strength retention than carbon steel at elevated temperatures, particularly beyond 500 °C-a critical range for fire-resistant design. While carbon steel retains nearly 100% of its strength up to approximately 450 °C, it experiences a rapid decline afterward, maintaining only about 10% of its strength at 800 °C. In contrast, stainless steel maintains around 90% of its strength at 200 °C and still retains approximately 75% at 500 °C. These values are represented by the strength reduction factor $k_{y,\Theta}$ which is defined as the ratio of the material's strength at elevated temperature (based on 2% total strain) to its 0.2% proof strength at room temperature. As shown in Fig. 8b, stainless steel exhibits superior stiffness retention at elevated temperatures compared to carbon steel. At

700 °C, stainless steel retains approximately 70% of its initial stiffness, while carbon steel drops sharply to about 13%. This indicates a more gradual degradation in stainless steel, which is beneficial for maintaining structural stability under fire conditions. Both materials, however, approach near-zero stiffness as the temperature nears 1200 °C. The stiffness reduction factor $k_{E,\Theta}$ represents the ratio of the tangent modulus at elevated temperature to that at room temperature.

These differences further highlight the advantages of stainless steel in fire-resistant design, particularly under severe conditions where temperatures exceed 700 °C-such as in standard 30-minute fire exposure scenarios. To support this analysis, the stress–strain relationships at various elevated temperatures were calculated for both materials and are illustrated in Fig. 9. These calculations are based on Eurocode 1 for carbon steel and Eurocode 3 for stainless steel of grade 1.4301.

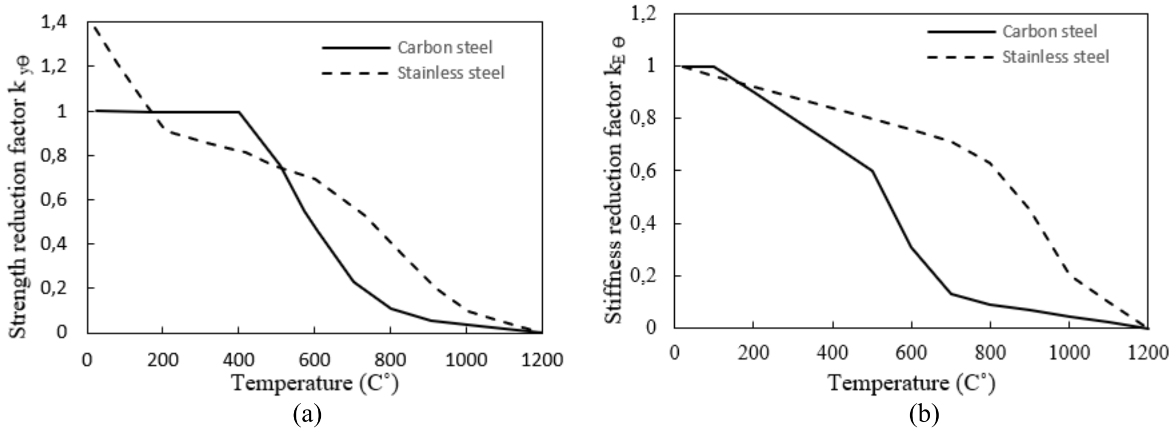

Fig. 8. Strength reduction (a) and stiffness reduction (b) of carbon steel and stainless steel at elevated temperatures

Figure 9 clearly illustrates the different thermal-mechanical behaviors of carbon steel and stainless steel (grade 1.4301) under elevated temperatures. According to Eurocode 1 for carbon steel and Eurocode 3 for stainless steel, the stress–strain relationships at elevated temperatures were derived and compared to assess their suitability for fire-exposed structures. Carbon steel (Fig. 9a) shows a sharp decline in mechanical strength beyond 500 °C, with a well-defined yield plateau at lower temperatures that disappears as the temperature rises. This degradation is particularly critical around 700 °C, where carbon steel loses most of its load-carrying capacity and becomes highly susceptible to sudden failure. Such behavior limits its effectiveness in maintaining structural integrity during prolonged fire exposure, even within standard fire durations (e.g., 30-60 minutes), where internal temperatures can exceed 700 °C. Conversely, stainless steel (Fig. 9b) demonstrates more gradual degradation. It exhibits no clear yield plateau but maintains ductile behavior with continuous strain hardening. Even at temperatures of 700 °C and beyond, the material retains significant stress capacity and deformation potential. This is consistent with previous findings that highlight the superior high-temperature stability of stainless steels due to their alloy composition, particularly the presence of nickel and chromium, which contribute to delayed strength and stiffness loss under thermal loading.

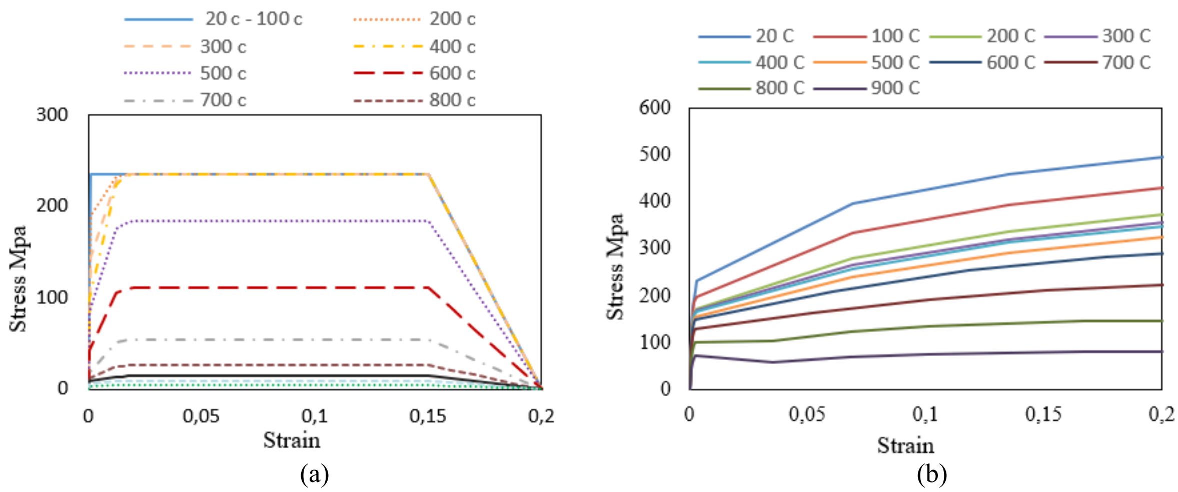

Fig. 9. Stress–strain curves of carbon steel (a) and stainless steel (b) at elevated temperatures

All metals expand when heated; however, in structural systems with continuity and localized fire exposure, this thermal expansion can be partially restrained, leading to additional internal forces and deformations. Fig. 10 illustrates the thermal elongation behavior of carbon steel and stainless steel used in this study. As can be seen, stainless steel undergoes greater thermal expansion-up to 50% more than carbon steel at high temperatures-highlighting the need to consider thermal strain effects carefully in fire-resistant design.

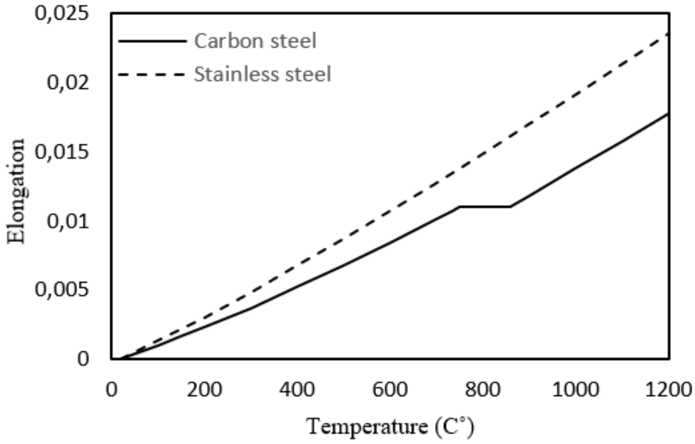

Fig. 10. Thermal elongation of carbon steel vs. stainless steel at elevated temperatures

Emissivity is defined as the ratio of a material's thermal radiation to that of a black body at the same temperature, ranging from 0 to 1 ($0 \leq \varepsilon \leq 1$) according to Eurocode 3. For carbon steel, emissivity increases with temperature due to the formation of an oxidized surface layer above 300 °C. This oxidation increases surface roughness and enhances heat absorption. In contrast, stainless steel forms a passive chromium-rich oxide layer even at room temperature. This layer remains stable at elevated temperatures and inhibits further oxidation, resulting in lower surface roughness and reduced emissivity. According to Eurocode 3, the recommended emissivity values are 0.7 for carbon steel and 0.4 for stainless steel.

The thermal conductivity of stainless steel and carbon steel exhibits distinct behavior as temperature increases, as illustrated in Fig.11a. Carbon steel begins with a relatively high conductivity of approximately 53 W/m·K at room temperature, which decreases steadily to around 27 W/m·K by 800 °C. This reduction stabilizes due to phase transformations occurring at elevated temperatures. In contrast, stainless steel does not undergo phase changes and shows an opposite trend: its thermal conductivity increases with temperature, rising from about 15 W/m·K at room temperature to nearly 30 W/m·K at 1200 °C. Below 1000 °C, stainless steel generally maintains lower conductivity than carbon steel, resulting in more localized heating. However, this difference in conductivity has a relatively limited impact on the overall fire performance of structural elements.

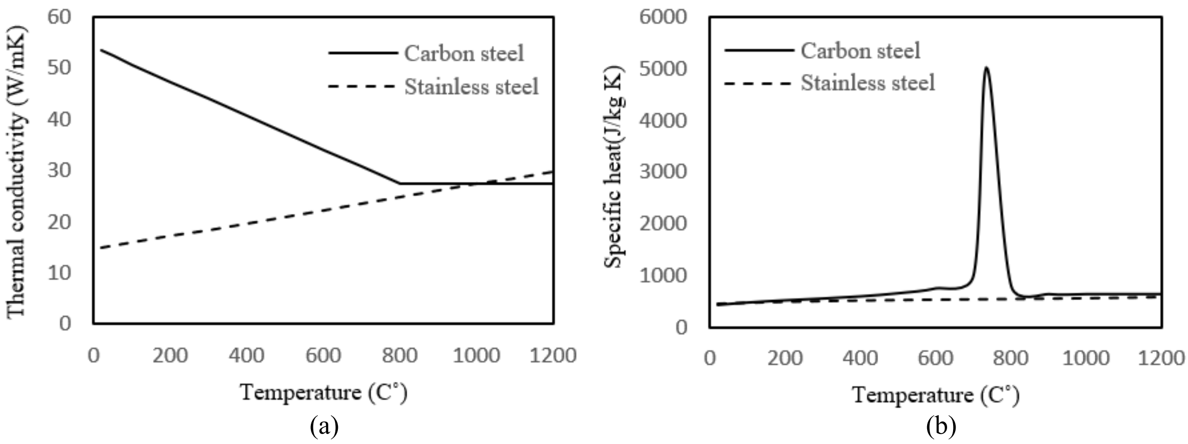

Fig. 11. Distribution of (a) thermal conductivity and (b) specific heat for carbon steel and stainless steel at elevated temperature

Specific heat is a key thermal property that affects how quickly a material heats up under thermal exposure. In this study, specific heat was incorporated into the simulation / numerical analyses for both carbon steel and stainless steel, as shown in Fig. 11b. Stainless steel exhibits a smooth and continuous increase in specific heat with rising temperature, due to the absence of phase transformations. In contrast, carbon steel shows a slightly higher average specific heat-approximately 600 J/kg·K compared to 550 J/kg·K for stainless steel-and features a pronounced peak near 735 °C, which corresponds to a phase transition. Materials with higher specific heat absorb more energy before experiencing a temperature rise, meaning they heat up more slowly when exposed to fire. This property plays an important role in determining the thermal response and fire resistance of structural components.

The numerical simulation assumed a compressive strength of 32.8 MPa for the concrete slab. The Concrete Damage Plasticity (CDP) parameters were estimated using the Kent and Park parabolic constitutive model (Kent & Park, 1971; Park & Paulay, 1991), as shown in Fig. 12. This model provided estimates for damage-related parameters in both compression and tension, as well as definitions for crack and inelastic strain behavior. The calculation of concrete compression damage parameters and inelastic strain values was based on the methodology proposed by Hafezolghorani et al. (2017). A summary of the adopted CDP parameters is presented in Table 2.

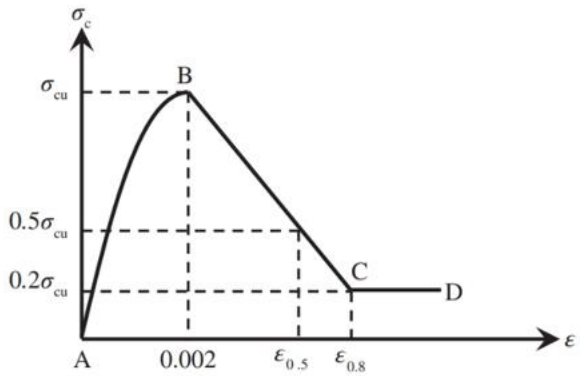

Fig. 12 Kent and Park parabolic constitutive model

Table 2. Concrete Damage Plasticity (CDP)

Dilation angle,ψ	Eccentricity,e	fb0/fc0	K	Viscosity parameter, μ
38	0.1	1.156	0.667	0.261

5. Results and discussion

For buildings constructed of carbon steel and stainless steel, an explicit non-linear analysis procedure was carried out at elevated temperatures. Fig. 13 presents the axial force and vertical displacement response of carbon steel and stainless steel components under elevated temperatures. The results reveal distinct differences in thermal-structural behavior between the two materials. The axial force–temperature curves indicate that stainless steel elements experience a more gradual reduction in axial force, maintaining load-carrying capacity up to approximately 600 °C. In contrast, carbon steel elements show a sharper and more sudden decline beyond this temperature, with some specimens (e.g., A2-Carbon, B2-Carbon) exhibiting abrupt force drops, likely due to local instability or phase transformation effects. This behavior aligns with the material's known loss of strength and stiffness at elevated temperatures (Fig. 13a). In addtion, the vertical displacement–temperature curves, as can be seen in Fig. 13b, further support these observations. Stainless steel components demonstrate controlled and stable displacement patterns, even at temperatures approaching 800 °C (approximately 55mm). Carbon steel elements, however, experience significant vertical displacement increases beyond 600 °C (approximately 300mm), including sudden drops indicative of structural collapse or progressive failure.

These findings confirm that stainless steel provides superior fire resistance by preserving both axial strength and deformation stability under elevated temperatures. This performance advantage is particularly relevant for critical load-bearing members in fire-exposed structures, where delayed collapse and maintained integrity are essential for occupant safety and structural performance.

Moreover, the deformation of the building for the carbon steel and stainless steel and the Mises stress contour with collapse sequence are given in Fig. 14. It is obvious that the building built stianless steel withstands the collapse during corner compartment fire. The stainless steel building displays much smaller displacements, with a peak value around 50 mm. The displacement is more evenly distributed, indicating higher stiffness retention and better structural integrity under thermal loading. However, fort he building built using carbon steel, the displacement field shows a significant concentration of deformation at the lower levels, especially around the fire-exposed region. The peak displacement reaches 300 mm, indicating severe vertical and lateral deformation and possible onset of progressive collapse (Fig. 14a). As can be seen in Fig. 14b, high stress concentrations are observed at the heated levels, exceeding 2.5×10^8 Pa, which likely exceed the yield strength of the material at elevated temperatures. This suggests a high potential for plastic deformation or local failure. Also, stress levels are more moderate and better distributed for the stainless steel. The highest stress values reach approximately 2.1×10^8 Pa, but do not localize as critically as in the carbon steel.

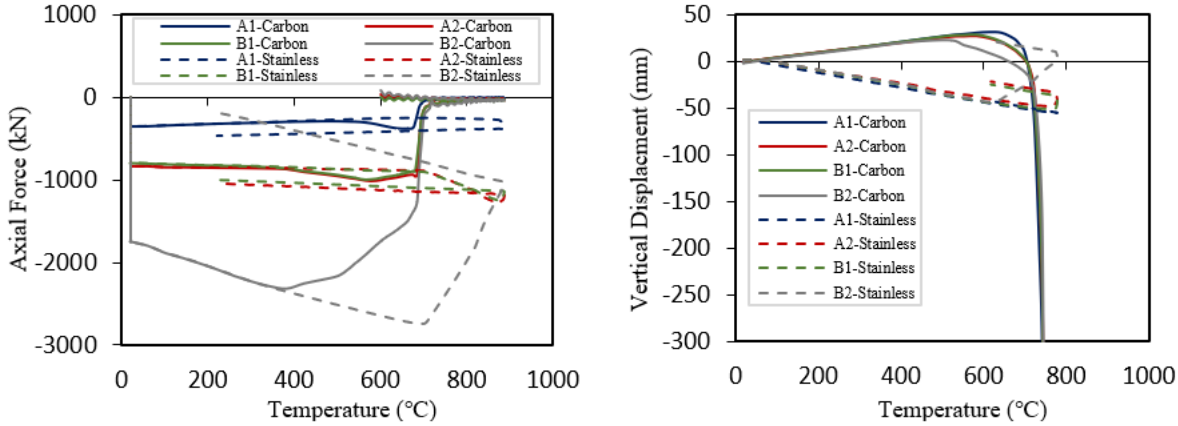

(a) (b)

Fig. 13. Axial force (a) and vertical displacement (b) response of carbon steel and stainless steel components under elevated temperatures

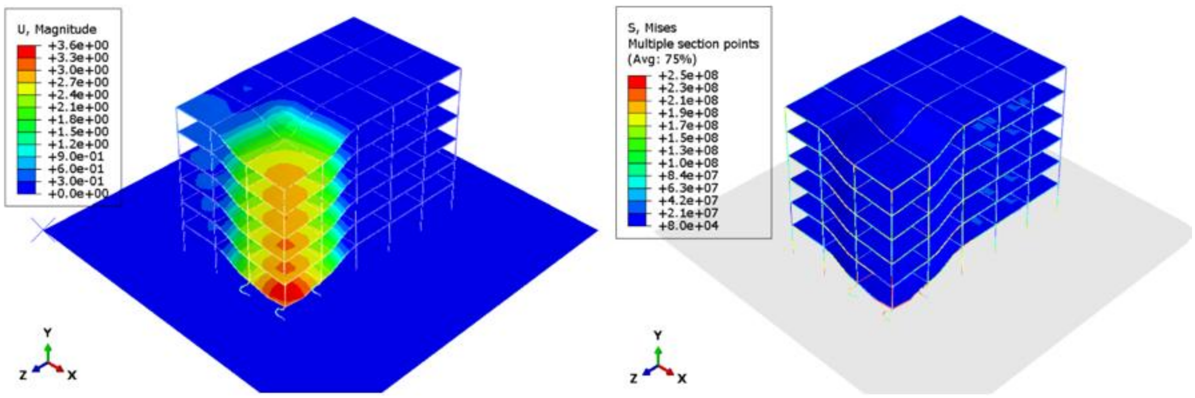

(a)

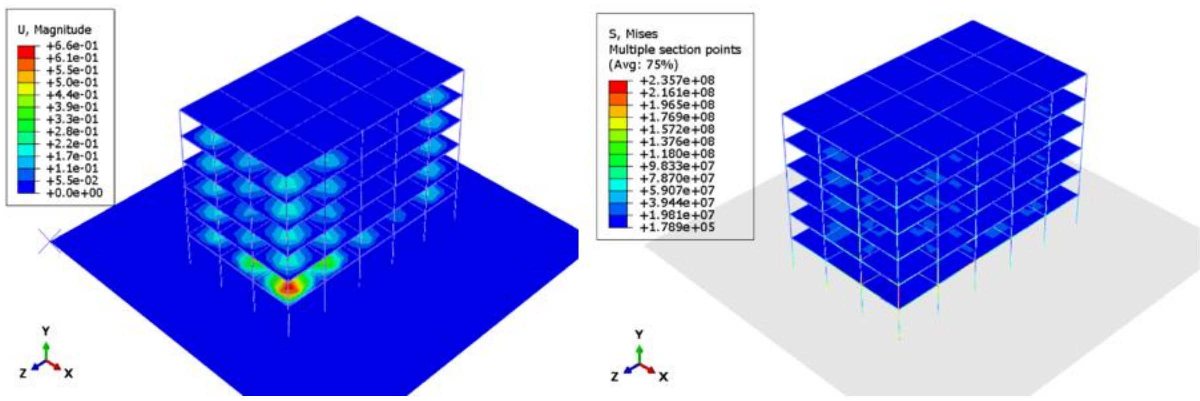

(b)

Fig. 14. Deformation of the building for the (a) carbon steel building and (b) stainless steel building and the Mises stress contour with collapse sequence

5. Conlusion

This study presented a comprehensive numerical investigation of multi-storey steel-building exposed to fire, focusing on the comparative performance of carbon steel and stainless steel. The evaluation was carried out through temperature-dependent material properties, structural response parameters, and damage accumulation under fire scenarios. The results consistently indicate that stainless steel outperforms carbon steel in fire-exposed conditions in terms of both strength retention and deformation control:

- Material properties such as strength, stiffness, and thermal conductivity showed that stainless steel retains its mechanical characteristics more effectively at elevated temperatures. Specifically, stainless steel preserved up to 75% of its strength at 500 °C, while carbon steel dropped sharply beyond 450 °C.
- In terms of thermal expansion and specific heat, stainless steel demonstrated smoother and more stable behavior due to the absence of phase transitions which contributes to greater predictability in structural fire response.
- The load–temperature and displacement–temperature relationships revealed that carbon steel members experienced earlier and more severe stiffness loss and vertical displacement, indicating a higher susceptibility to collapse.
- Carbon steel building exhibited large displacement concentrations and severe stress localization near the heated regions, whereas stainless steel building maintained more uniform stress distribution and reduced deformation.

These findings support the conclusion that stainless steel is a more robust and fire-resistant material for critical structural components in buildings exposed to elevated temperatures. Although its initial cost may be higher than that of carbon steel, its performance advantages under fire conditions are substantial. Stainless steel demonstrates a progressive and ductile failure behavior, retaining both strength and stiffness across a wider temperature range. This enhances overall structural resilience, delays collapse mechanisms, and provides a greater window for safe evacuation and emergency response. Its ability to maintain load-bearing capacity and reduce post-fire damage also contributes to lower repair demands, making stainless steel a technically and economically viable alternative for fire-prone or high-risk structures.

References

Abaqus (2022). Dassault Systèmes. RI, USA.

Eurocode 1. EN 1991-1-2. (2021). Actions on Structures: Part 1-2. General Actions. Actions on Structures Exposed to Fire. British Standards Institution.

Eurocode 3. EN 1991-1-4. (2006). Design of steel structures - Part 1-4: General rules - Supplementary rules for stainless steels, (Authority: The European Union Per Regulation 305/2011, Directive 98/34/EC, Directive 2004/18/EC).

Gardner, L. & Baddoo, N.R. (2006). Fire testing and design of stainless steel structures, *Journal of Constructional Steel Research,* 62, 532–543

Gardner, L. (2007). Stainless steel structures in fire. Proceedings of the Institution of Civil Engineers - Structures and Buildings. 160(3), 129-138.

GSA. (2013). Alternate path analysis & design guidelines for progressive collapse resistance. *General Services Administration.*

Hafezolghorani, M., Hejazi, F., Vaghei, R., Jaafar, M. S. Bin, & Karimzade, K. (2017). Simplified damage plasticity model for concrete. *Structural Engineering International*, *27*(1), 68–78.

Jiang, J., Li, G., & Usmani, A. (2014). Influence of fire scenarios on progressive collapse mechanisms of steel framed structures. *Steel Construction,* 7(3), 169–172.

Karabulut, B., Lombaert, G., Debruyne, D., & Rossi, B. (2018). Optimized design and life cycle cost analysis of a duplex welded girder bridge. Ghent.

Kent, D.C., & Park, R. (1971). Flexural members with confined concrete. *Journal of the Structural Division*, *97*(7), 1969-1990.

Lien, K.H., Chiou, Y.J., Wang, R.Z., & Hsiao, P.A. (2010). Vector form intrinsic finite element analysis of nonlinear behavior of steel structures exposed to fire. *Engineering Structures*, 32(1), 80–92.

Malkens, T., Cashell K.A., Malaska, M., Alanen, M. & Rossi, B. (2021). Performance of structural stainless steel following a fire, *Engineering Structures,* 235-112001

Qin, C. (2016). Collapse simulations of steel buildings under fire, For the Degree of Master of Science, Colorado State University Fort Collins, Colorado

Park, R., & Paulay, T. (1991). *Reinforced concrete structures*. John Wiley & Sons.

Rossi, B. (2014). Discussion on the us of stainless steel in constructions in view of sustainability. *Thin-Walled Struct*, 83:182-9

Rubert, A., & Schaumann, P. (1986). Structural Steel and Plane Frame Assemblies under Fire Action. *In Fire Safety Journal*, 10(3), 173-184.

Sun, R., Huang, Z., & Burgess, I.W. (2012). Progressive collapse analysis of steel structures under fire conditions. *Engineering Structures*, 34, 400–413. https://doi.org/10.1016/j.engstruct.2011.10.009

Segura, G., Pournaghshband, A., Afshan, S., & Mirambell, E. (2021). Numerical simulation and analysis of stainless steel frames at high temperature. *Engineering Structures*, *227*, 111446

Shakeri, K., Miryousefi Aval, S.M., Akrami, V., & Khansoltani, E. (2023). Progressive collapse analysis of intermediate moment-resisting steel frame under fire-induced column failure, *Journal of Performance of Constructed Facilities*, 37(4), 04023034

Shan, S., & Li, S. (2021). Collapse performances of steel frames against fire considering effect of infill walls. *Journal of Constructional Steel Research*, 182, 106691

Wang, J., Uy, B., Li, D., & Song, Y. (2020). Progressive collapse analysis of stainless steel composite frames with beam-to-column endplate connections. *Steel and Composite Structures*, 36(4), 427-446

4th International Civil Engineering & Architecture Conference
17-19 May 2025, Trabzon, Türkiye

Effect of cracks on dynamic behavior of stepped beams with general boundary conditions

Ezgi Sevilmiş*[1], Volkan Kahya[1], Sebahat Şimşek[1]

[1] Karadeniz Technical University, Department of Civil Engineering, 61080 Trabzon, Türkiye

Abstract. This study investigates the effects of cracks on the dynamic characteristics of structures, particularly in terms of natural frequencies and mode shapes. A stepped beam is considered as the primary structure, and cracks with varying depths are modeled at arbitrary locations on the beam. These cracks are represented as massless rotational springs to account for stiffness loss at the cross-sections. General boundary conditions are considered for the beams.The transfer matrix method is employed for the analytical solution of the problem. Using this method, analytical equations are developed to relate the beam segments separated by cracks. The resulting analytical model provides the capability to determine the mode shapes and natural frequencies of damaged beams. In the analyses, crack locations and depths, physical parameters of the beam and the effects of boundary conditions on vibration characteristics are examined.This study provides an analytical basis for artificial intelligence-based inverse analyses (damage detection) and enables the development of a training database that can be used for estimating parameters such as crack depth and location in beams with known frequencies.

Keywords: Stepped beam; Transfer matrix method; Crack; Vibration; Damage detection

1. Introduction

When mechanical structural members are subjected to static and dynamic loading, they undergo stress and deformation. These stresses and deformations can induce damage within the structure, thereby shortening its service life; as a result, both the safety margin against collapse and the overall reliability of the system decrease. Accordingly, evaluating the load-carrying capacity of damaged members is of critical importance. Structural vibrations arising from external loads generate cyclic stresses, which are regarded as primary precursors to crack initiation. Hence, damage detection can be carried out by analysing the vibration characteristics of the structure in both its intact and damaged states. Beams are among the elements most susceptible to cracking due to their dynamic behaviour; consequently, extensive research has been devoted to modelling and formulating cracks in beams and investigating their influence on structural performance.

Dimarogonas (Dimarogonas, 1996) proposed the local flexibility concept—derived from stress-intensity factors in fracture mechanics for modelling an open-edge crack. Under the most general loading, local flexibility can be represented by a 6×6 matrix (Papadopoulos,1987). The coefficients of this matrix depend on the crack size and the geometry of the crack plane. According to the theory, the local compliance introduced at the crack site is idealised as a massless rotational spring.

Research on the vibration behaviour of cracked beams that employs the local flexibility concept under general loading generally falls into two main categories:Direct problem – Investigation of how single or multiple cracks influence structural dynamic properties such as the natural frequencies and mode shapes of damaged beams.Inverse problem.- Estimation of crack location and size from measured dynamic data of the damaged beam system.

The Euler–Bernoulli beam theory has been extensively adopted in numerous investigations of cracked beams subjected to various boundary conditions. Narkis and Elmalah (Narkis,1996) analysed the vibration of a simply-supported cracked beam by modelling the crack as a massless rotational spring and partitioning the beam into two sub-beams. Zheng and Fan (Papadopoulos,1987) studied hollow beams with rectangular and circular cross-sections, while Lele and Maiti (Lele,2002) proposed a novel crack-identification method based on Timoshenko beam theory. Loya et al. (Loya et al., 2006) further examined the influence of cracks on the natural frequencies of a simply-supported Timoshenko beam.

Research carried out roughly two decades ago was largely confined to beams containing only one, or at most two, cracks. Chang and Bert (Jang et al, 1989) investigated the free vibration of stepped beams with various boundary conditions, and Naguleswaran (Naguleswaran, 2003) explored the vibrational behaviour of a stepped

*Corresponding author, E-mail: ezgisevilmiss@gmail.com

https://doi.org/10.31462/icearc2025_ce_sme_709

beam subjected to an axial load. Nandwana and Maiti introduced a crack-detection scheme for stepped cantilever beams, whereas Shifrin and Ruotolo (Shifrin et al., 1999) proposed a technique for analysing the dynamic characteristics of beams with multiple cracks; however, their approach was applicable only to beams with a limited number of cracks.

The present study aims, building upon previous research, to investigate the free-vibration behaviour of a stepped beam containing an arbitrary number of transverse open cracks under general boundary conditions; to quantify the influence of multiple cracks on the beam's dynamic characteristics; and to devise a methodology that will supply input data for future diagnostic systems by exploiting the differences between the intact and damaged states.

In the proposed model, the general boundary conditions are represented by concentrated masses attached to both beam ends, each supported by linear (K_1, K_2) and rotational (K_{R_1}, K_{R_2}) springs. The local flexibility introduced by each crack is idealised as a massless rotational spring. Differential-equation solutions obtained for every cracked sub-segment are assembled consecutively—linking the beam's tip to its root—to construct a transfer matrix. Coupling this transfer matrix with the boundary conditions yields the characteristic equation, which is solved analytically to determine the natural frequencies of the beam.

2. Theoretical background

Consider an intact steped beam with N cracks and a uniform area. The beam is assumed to be connected by massless rotational springs at cracked section as shown in Fig1 The differential equation that an elastic Euler–Bernoulli beam can be expressed as

$$EI\frac{d^4y(x,t)}{dx^4} + \rho A\frac{d^2y(x,t)}{dt^2} = 0 \tag{1}$$

where $Y_i(x,t)$ is the deflection function, EI is the flexural rigidity ρ is the mass density, A is the cross-sectional area of the beam

$$y(x,t) = Y(x)\,T(t) \tag{2}$$

$$\frac{d^4Y(x)}{dx^4} - \beta^4 Y(x) = 0 \tag{3}$$

$$\frac{d^2T(t)}{dt^2} - \omega^2 T(t) = 0 \tag{4}$$

where $\beta^4 = \omega^2(\rho A/EI)$ and ω is the natural frequency of the entire uniform beam. The solution of the Eq. 3 can be expressed ain Eq. 5

$$Y(x) = B_1\cos(\beta x) + B_2\sin(\beta x) + B_3\cosh(\beta x) + B_4\cos(\beta x) \tag{5}$$

in which $B_1 - B_4$are unkown constant.

As shown in Fig. 1 a section of uniform beam with an open edge crack is divided into two beam segments and the crack position is assumed as the separation point. If we write the sections in Eq. 5 obtaining a matrix form for each section as Eq. 6 – 7.

$$\begin{Bmatrix} Y_i(x) \\ \theta_i(x) \\ M_i(x) \\ V_i(x) \end{Bmatrix} = [T] * \begin{Bmatrix} Y_{1,i}(x) \\ \theta_{1,i}(x) \\ M_{1,i}(x) \\ V_{1,i}(x) \end{Bmatrix} \tag{6}$$

$$\begin{Bmatrix} Y_{i+1}(x) \\ \theta_{i+1}(x) \\ M_{i+1}(x) \\ V_{i+1}(x) \end{Bmatrix} = [T] * \begin{Bmatrix} Y_{1,i+1}(x) \\ \theta_{1,i+1}(x) \\ M_{1,i+1}(x) \\ V_{1,i+1}(x) \end{Bmatrix} \tag{7}$$

where;

$$[S(x)] = \begin{bmatrix} \cos(\beta x) & \sin(\beta x) & \cosh(\beta x) & \sinh(\beta x) \\ -\beta\sin(\beta x) & \beta\cos(\beta x) & \beta\sinh(\beta x) & \beta\cosh(\beta x) \\ -\mathrm{EI}\beta^2\cos(\beta x) & -\mathrm{EI}\beta^2\sin(\beta x) & \mathrm{EI}\beta^2\cosh(\beta x) & \mathrm{EI}\beta^2\sinh(\beta x) \\ \mathrm{EI}\beta^3\sin(\beta x) & -\mathrm{EI}\beta^3\cos(\beta x) & \mathrm{EI}\beta^3\sinh(\beta x) & \mathrm{EI}\beta^3\cosh(\beta x) \end{bmatrix} \tag{8}$$

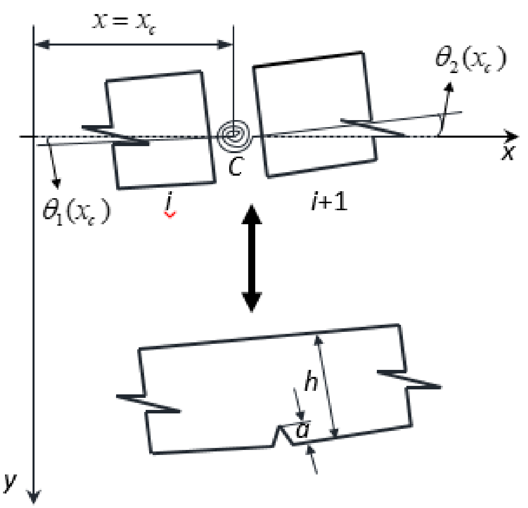

Fig. 1. Equivalent massless rotational spring and discontinuity of slope at crack position

Expressing the general equality more concisely given in Eq. 9.

$$Q_{i,j} = [S(x)_i] * \{B_{i,j}\} \tag{9}$$

There is continuity among the deflection, bending moment and shear force at the crack position for segments i and i+1. But there is a discontinuity between slopes which is revealed by the bending moment and rotation of the spring representing the crack. These boundary conditions at crack position given in the Eqn. 10-13.

$$Y_i(x_c) = Y_{i+1}(x_c) \tag{10}$$

$$M_i(x_c) = M_{i+1}(x_c) \tag{11}$$

$$V(x_c) = V_{i+1}(x_c) \tag{12}$$

$$\theta_{i+1}(x_c) - \theta_i(x_c) = C\, M_i(x_c) \tag{13}$$

Where C is obtained by Zheng(Zheng,2003). Written in matrix form in Eqn. 14

$$\begin{Bmatrix} Y_{i+1}(xc) \\ \theta_{i+1}(xc) \\ M_{i+1}(xc) \\ V_{i+1}(xc) \end{Bmatrix} = \begin{bmatrix} 1 & 0 & 0 & 0 \\ 0 & 1 & C & 0 \\ 0 & 0 & 1 & 0 \\ 0 & 0 & 0 & 1 \end{bmatrix} * \begin{Bmatrix} Y_{1,i+1}(xc) \\ \theta_{1,i+1}(xc) \\ M_{1,i+1}(xc) \\ V_{1,i+1}(xc) \end{Bmatrix} \tag{14}$$

Now consider a multi-stepped beam with an arbitrary cracks as shown in Fig.2. It consist of n uniform beam steps and the length of its step is L_i , the moment of inertia is I_i and the number of cracks in each step is N_i. These cracks located at points $x_{(i,j)}$ with size $a_{(i,j)}$. The model is created with general boundary conditions the both edge carry lumped masses (m is the mass , e is the eccentricity and J is the rotary inertia) and both side supported by linear springs (K) and the rotational springs (K_R) as shown in Fig 2 . For instance, springs stiffness coefficients for five common end conditions are listed in Table 1.

In the stepped-beam model, two types of continuity (connection) conditions are considered. The first concerns the internal connection within a segment; Eqn. 14 specifies how successive segments i and i+1 are linked. When segments i and i+1 are connected in accordance with the constraint this analytics process has been done in detail by Attar.2012.The Q matrix at the end of a segment can be related to the Q matrix at the beginning of the same segment give in the Eqn. 15-16. As a second concern, two steps should be connected to each other. Based on this principle, the formula for connecting the last point of the beam to the first point is given in Eqn. 17-18-19.

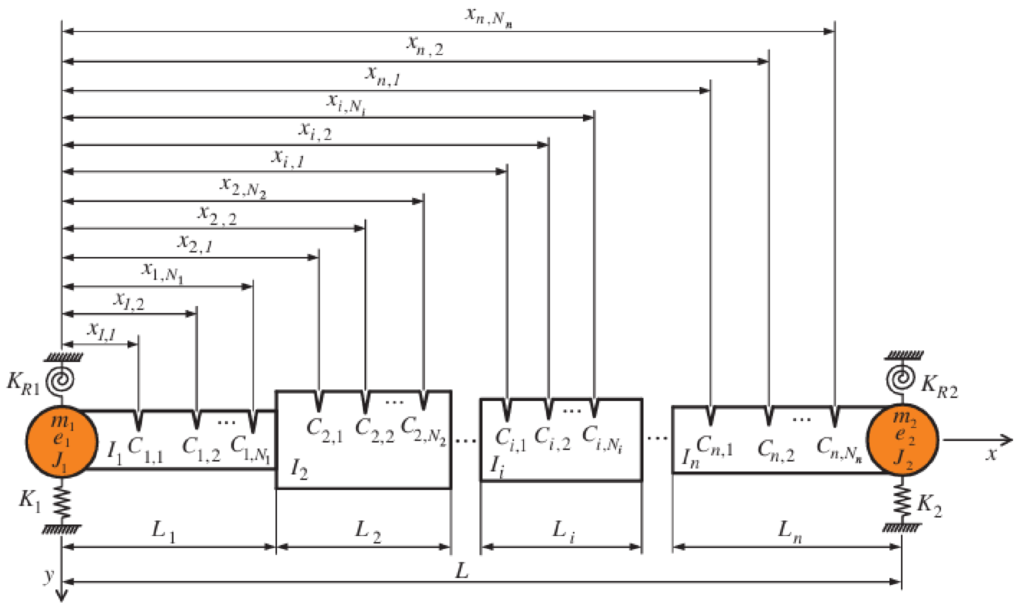

Fig. 2. A multi-stepped free-free beam with N edge open cracks composed of uniform beam segments and carrying lumped masses, linear and rotational springs at both ends

Table 1. Common boundary conditions modelled by appropriate value of stiffness of springs

Boundary conditions	Linear and rotational stiffness of springs $m_1=m_2=e_1=e_2=J_1=J_2=0$			
	K_1	K_{R1}	K_2	K_{R2}
Clamped-free	∞	∞	0	0
Pined-pined	∞	0	∞	0
Clamped-pined	∞	∞	∞	0
Clamped-clamped	∞	∞	∞	∞
Free-free	0	0	0	0

$$Q_{j,(N_n+1)}(x_{j,(N_n+1)}) = T_{i,j} * TC_{i,j-1} * TC_{i,j-2} * \dots\dots * TC_{i,1} * Q_{j,0}(x_{j,0}) \tag{15}$$

$$[T]_i = T_{i,j} * TC_{i,j-1} * TC_{i,j-2} * \dots\dots * TC_{i,1} \tag{16}$$

$$Q_{j,(N_n+1)}(x_{j,(N_n+1)}) = [T]_{N_n} * [T]_{N_{n-1}} * \dots\dots * [T]_i * \dots\dots * [T]_2 * [T]_1 * Q_{0,0}(x_{0,0}) \tag{17}$$

$$[T] = [T]_{N_n} * [T]_{N_{n-1}} * \dots\dots * [T]_i * \dots\dots * [T]_2 * [T]_1 \tag{18}$$

$$Q_{j,(N_n+1)}(x_{j,(N_n+1)}) = [T] * Q_{1,0}(x_{1,0}) \tag{19}$$

Matrix [T] has a general form given in Eqn. 20.

$$\begin{Bmatrix} Y_{n,N_{n+1}}(L) \\ \theta_{n,N_{n+1}}(L) \\ M_{n,N_{n+1}}(L) \\ V_{n,N_{n+1}}(L) \end{Bmatrix} = \begin{pmatrix} T_{11} & T_{12} & T_{13} & T_{14} \\ T_{21} & T_{22} & T_{23} & T_{24} \\ T_{31} & T_{32} & T_{33} & T_{34} \\ T_{41} & T_{42} & T_{43} & T_{44} \end{pmatrix} * \begin{Bmatrix} Y_{1,1}(0) \\ \theta_{1,1}(0 \\ M_{1,1}(0) \\ V_{1,1}(0 \end{Bmatrix} \tag{20}$$

The boundry conditions of general form given in Eqns 21-24

$$M(0) = -e_1 m_1 \omega^2 Y(0) + K_{R_1}\theta(0) - (J_1 + m_1 e_1^2)\omega^2\theta(0) \tag{21}$$

$$V(0) = -K_1 Y(0) + m_1\omega^2 Y(0) + e_1 m_1 \omega^2 \theta(0) \tag{22}$$

$$M(L) = e_2 m_2 \omega^2 Y(L) - K_{R_2}\theta(L) + (J_2 + m_2 e_2^2)\omega^2\theta(L) \tag{23}$$

$$V(L) = K_2 Y(L) - m_2\omega^2 Y(L) - e_2 m_2 \omega^2 \theta(L) \tag{24}$$

Substitutting Eqns . 21-24. into 20. From there Eqns 25 obtainin Eqns. 26-27.

$$\begin{Bmatrix} Y_{n,N_{n+1}}(L) \\ \theta_{n,N_{n+1}}(L) \\ e_2 m_2 \omega^2 Y(L) - K_{R_2}\theta(L) + (J_2 + m_2 e_2^2)\omega^2\theta(L) \\ K_2 Y(L) - m_2\omega^2 Y(L) - e_2 m_2 \omega^2 \theta(L) \end{Bmatrix} = [T]\begin{Bmatrix} Y_{1,1}(0) \\ \theta_{1,1}(0) \\ -e_1 m_1 \omega^2 Y(0) + K_{R_1}\theta(0) - (J_1 + m_1 e_1^2)\omega^2\theta(0) \\ -K_1 Y(0) + m_1\omega^2 Y(0) + e_1 m_1 \omega^2 \theta(0) \end{Bmatrix} \tag{25}$$

$$\begin{Bmatrix} Y_{n,N_{n+1}}(L) \\ \theta_{n,N_{n+1}}(L) \end{Bmatrix} = \begin{Bmatrix} T_{11} - e_1 m_1\omega^2 T_{13} + (m_1\omega^2 - K_1)T_{14} & T_{12} + \left(K_{R_1} - (J_1 + m_1 e_1^2)\omega^2\right)T_{13} + e_1 m_1 \omega^2 T_{14} \\ T_{21} - e_1 m_1\omega^2 T_{23} + (m_1\omega^2 - K_1)T_{24} & T_{22} + \left(K_{R_1} - (J_1 + m_1 e_1^2)\omega^2\right)T_{23} + e_1 m_1 \omega^2 T_{24} \end{Bmatrix}\begin{Bmatrix} Y_{1,1}(0) \\ \theta_{1,1}(0) \end{Bmatrix} \tag{26}$$

$$\begin{bmatrix} e_2 m_2 \omega^2 & -K_{R_2}(J_2 + m_2 e_2^2)\omega^2 \\ K_2 - m_2\omega^2 & -e_2 m_2 \omega^2 \end{bmatrix}\begin{Bmatrix} Y_{n,N_{n+1}}(L) \\ \theta_{n,N_{n+1}}(L) \end{Bmatrix} = \begin{Bmatrix} T_{31} - e_1 m_1\omega^2 T_{33} + (m_1\omega^2 - K_1)T_{34} & T_{32} + \left(K_{R_1} - (J_1 + m_1 e_1^2)\omega^2\right)T_{33} + e_1 m_1 \omega^2 T_{34} \\ T_{41} - e_1 m_1\omega^2 T_{43} + (m_1\omega^2 - K_1)T_{44} & T_{42} + \left(K_{R_1} - (J_1 + m_1 e_1^2)\omega^2\right)T_{43} + e_1 m_1 \omega^2 T_{44} \end{Bmatrix}\begin{Bmatrix} Y_{1,1}(0) \\ \theta_{1,1}(0) \end{Bmatrix} \tag{27}$$

Subtutiting Eqn. 26 into Eqn. 27 gives the general form of frequency equation for cracked beam in Eqn. 28.

$$F = f_1 f_4 - f_2 f_3 \tag{28}$$

As a result, the free vibration analysis of the cracked multi-stepped beam under general boundary conditions is found with $F = 0$.

3.Results

In this section, the developed solution methodology will be validated for accuracy by comparing it against various alternative approaches.Model 1. Free vibration of square-sectional cantilever beam having three cracks Fig 3. shows a square sectional cantilever beam with three open cracks. The material parameters for beam are, E=2,06×10^{11} N/m^2, ρ = 7800 kg/m^3 L = 900 mm and dimensions are 1cm x 3cm (h x b) . For this model, experimental (Karaca, 2016) and two-dimensional SEM analyses (Attar,2012) were compared with the results of the present study, and the corresponding values are provided in Table 2.

Model 2. Free Vibration of a stepped beam having three cracksFig 4. shows a square sectional cantilever beam with three open cracks. The material parameters for beam are . E= 210 Gps. ρ = 7860 kg/m^3 . L = 0.3 . $L_1 = L_2 = L_3$= 0.1 m dimensions are h_1 . h_3= 0.0075 m . h_2 =0.009375 m. For this model. Finite element model (ANSYS) analyses (Attar, 2012) were compared with the results of the present study. and the corresponding values are provided in Table 3.

Model 3. Free Vibration of a stepped beam having one cracks with the positional variationIn this example. the free-vibration response of a beam as a function of the positional variation of a single crack investigating using the configuration depicted in Fig. 3 of the preceding example. The material parameters for beam are . E=2.06×10^{11} N/m^2. ρ = 7800 kg/m^3 . L = 900 mm and dimensions are 1cm x 3cm (h x b). $x_{1.1}$=0.225. $x_{1.2}$=0.45. $x_{1.3}$= 0.675.values are provided in Table 4.

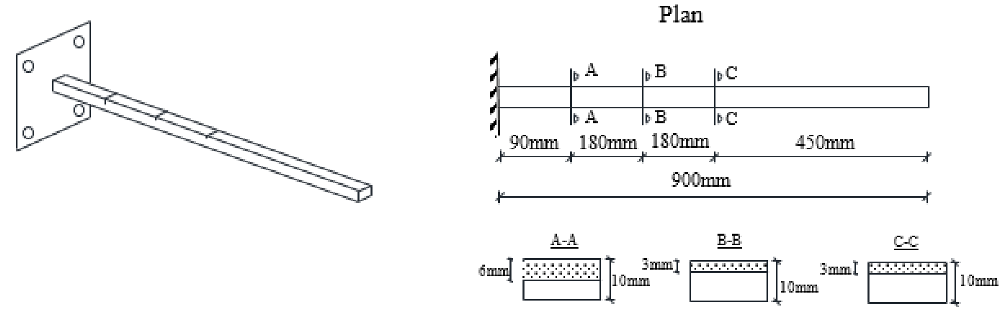

Fig 3. Free vibration of square-sectional cantilever beam having three cracks

Table 2. Free vibration of square-sectional cantilever beam having three cracks

Method	Case	Natural frequencies (Hz)				
		ω_1	ω_2	ω_3	ω_4	ω_5
Experimental Measurements	Intact	9.926	62.53	175.3	342.1	562
	Cracked	8.926	59.96	172.8	338.3	552.1
2B SEM	Intact	10.250	64.197	179.59	351.45	579.96
	Cracked	9.2823	61.509	177.09	346.92	573.45
Present Study	Intact	10.2495	64.2255	179.8438	352.4362	581.2467
	Cracked	9.2518	61.4485	177.174	347.66	575.96

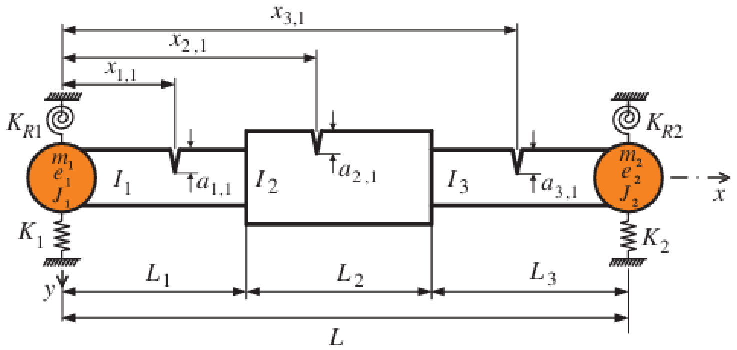

Fig. 4. Stepped beam having three cracks with general boundary conditions

Table 3. Free Vibration of a stepped beam having three cracks with clamped-free boundary conditions

Method	Normalized crack sizes			Natural frequencies (rad/s)		
	$a_{1,1}$ / h_1	$a_{2,1}$ / h_2	$a_{3,1}$ / h_3	ω_1	ω_2	ω_3
Finite Element Model	0	0	0	445.805	3054.130	7930.62
	0.2	0.2	0.2	439.880	3012.60	7804.32
ATTAR	0	0	0	446.497	3075.83	8004.68
	0.2	0.2	0.2	440.664	3034.30	7904.25
Present Study	0	0	0	449.412	3068.782	7983.875
	0.2	0.2	0.2	443.473	3027.752	7873.855

Table 4. Free Vibration of a stepped beam having one cracks with the positional variation

Normalized crack sizes			Natural frequencies (Hz)		
$a_{1,1}$ / h_1	$a_{2,1}$ / h_2	$a_{3,1}$ / h_3	ω_1	ω_2	ω_3
0	0	0	10.249	64.225	179.845
0.3	0	0	10.161	64.201	178.609
0	0.3	0	10.220	63.562	179.843
0	0	0.3	10.249	64.004	177.912

4.References

Attar, M. (2012). A transfer matrix method for free vibration analysis and crack identification of stepped beams with multiple edge cracks and different boundary conditions. *International Journal of Mechanical Sciences, 57*, 19–33.

Dimarogonas, A. D. (1996). Vibration of cracked structures: A state of the art review. *Engineering Fracture Mechanics, 55*(5), 831–857.

Jang, S. K., & Bert, C. W. (1989). Free vibration of stepped beams: Higher mode frequencies and effects of steps on frequency. *Journal of Sound and Vibration, 132*, 164–168.

Karaca, S. (2016). *Çatlaklı elastik kirişlerin dinamik davranışlarının analitik, sayısal ve deneysel yöntemlerle incelenmesi* (Master's thesis, Karadeniz Technical University, Graduate School of Natural and Applied Sciences, Trabzon). [In Turkish]

Lele, S. P., & Maiti, S. K. (2002). Modeling of transverse vibration of short beams for crack detection and measurement of crack extension. *Journal of Sound and Vibration, 257*, 559–583.

Loya, J. A., Rubio, L., & Fernandez-Saez, J. (2006). Natural frequencies for bending vibrations of Timoshenko cracked beams. *Journal of Sound and Vibration, 290*, 640–653.
Naguleswaran, S. (2003). Vibration and stability of an Euler–Bernoulli beam with up to three-step changes in cross-section and in axial force. *International Journal of Mechanical Sciences, 45*, 1563–1579.
Narkis, Y. (1996). Crack identification in a cantilever beam under uncertain end conditions. *International Journal of Mechanical Sciences, 38*(6), 499–507.
Papadopoulos, C. A., & Dimarogonas, A. D. (1987). Coupled longitudinal and bending vibrations of a rotating shaft with an open crack. *Journal of Sound and Vibration, 117*(1), 81–93.
Shifrin, E. I., & Ruotolo, R. (1999). Natural frequencies of a beam with an arbitrary number of cracks. *Journal of Sound and Vibration, 222*, 409–423.
Zheng, D. Y., & Fan, S. C. (2003). Vibration and stability of cracked hollow-sectional beams. *Journal of Sound and Vibration, 267*(4), 933–954.

4th International Civil Engineering & Architecture Conference
17-19 May 2025, Trabzon, Türkiye

A novel equivalent continuous beam model for seismic performance evaluation of multi-story buildings

Hacer Çolak*[1], Hakan T. Türker[2], Hilmi Coşkun[3]

[1] Kilis 7 Aralık University, Department of Civil Engineering, 79000 Kilis, Türkiye
[2] Bursa Uludağ University, Department of Civil Engineering, 16240 Bursa, Türkiye
[3] Iskenderun Technical University, Department of Civil Engineering, 31200 Hatay, Türkiye

Abstract. The inter-story drift ratio is a critical parameter strongly associated with building damage, particularly under earthquake ground motions. Therefore, seismic codes in various countries impose limitations on this parameter to ensure safe design of earthquake resistant structures. This study introduces an innovative continuous model approach to approximate the inter-story drift ratio, its variation along building height, and the location of its maximum value. This model represents an equivalent continuous beam composed of a combination of a shear beam and a flexural beam. In solving the continuous model, the rotational boundary condition at the base is expressed in terms of the first-story inter story drift, and closed-form solutions for the equation of motion of the model are derived. Two dimensionless parameters are required for solving the continuous model: i) the lateral stiffness ratio (α), which controls the structural behavior, and ii) the location of the first-story (θ). Here, the parameter α is defined through a simplified mathematical expression as a function of the number of stories (N) and the stiffness ratio between the beams and columns (ρ). Dynamic analyses were conducted using the response spectrum for low-rise and high-rise building models with various structural characteristics. Structural responses, including lateral displacements and inter story drift ratios, were investigated. The finite element model results obtained from the SAP2000 program were compared with the analytical solution results, revealing good agreement between the two sets of results.

Keywords: Continuous model; Lateral stiffness ratio; First-story location; Blume coefficient (index); Interstory drift ratio

1. Introduction

In the field of structural engineering, the accurate estimation of structural responses under earthquake loads is an important issue, particularly given the direct correlation between seismic-induced deformations and building damage. Among the various response parameters, the inter-story drift ratio has been consistently recognized as a key indicator of structural and non-structural damage during earthquakes (Miranda & Akkar, 2006; Neam & Taghikhany, 2016; Eroğlu Azak, 2013; Qu & Pan, 2022; Morfidis et al., 2023). Consequently, a considerable number of seismic design codes worldwide impose limitations on drift ratios. These limitations are implemented to ensure the safety and serviceability of buildings (FEMA 356, 2000; TBEC-2018, 2018).

Given the significance of drift demands, a range of analytical and numerical methodologies have been developed to estimate lateral displacements and inter-story drift distributions in buildings subjected to seismic loading. Among these, continuous beam models have gained increasing attention for their efficiency and simplicity in approximating the dynamic behavior of multi-story buildings, particularly in preliminary design and seismic assessment studies (Heidebrecht & Stafford Smith, 1973; Iwan, 1997; Miranda, 1999; Miranda & Taghavi, 2005; Miranda & Akkar, 2006; Khaloo & Khosravi, 2008; Wiebe & Christopoulos, 2015; Alonso-Rodríguez & Miranda, 2016, 2018; Alonso-Rodríguez & Tsavdaridis, 2021; Veladi et al., 2020). These models provide a representation of structural systems by idealizing the building as a continuous shear, flexural, or shear–flexural beam, enabling closed-form or semi-analytical solutions under various boundary conditions.

The coupling beam concept was subsequently enhanced by Heidebrecht and Stafford Smith (1973) and by Miranda (1999). Miranda (1999) introduced the coupling beam concept as a basis framework for modeling the seismic behavior of buildings. Building upon this research, Miranda and Reyes (2002) analyzed the effects of such stiffness variations and concluded that they do not significantly alter structural response unless the changes are abrupt and considerable. Expanding on this, Taghavi and Miranda (2005), Miranda and Taghavi (2005) and

*Corresponding author, E-mail: hacercolak@kilis.edu.tr

https://doi.org/10.31462/icearc2025_ce_sme_715

Reinoso and Miranda (2005) examined floor acceleration demands by using a continuous shear–flexural beam model, applying it to buildings of different heights and incorporating nonuniform stiffness distributions. In further elaboration on this subject, Miranda and Akkar (2006) developed a generalized spectrum for inter-story drifts in buildings subjected to earthquake-induced ground motions.

However, despite their widespread use, most existing continuous beam models adopt assumptions at the base, such as a zero-rotation boundary condition, which does not adequately reflect the inter-story drift at the first-story (Miranda & Akkar, 2006; Khaloo & Khosravi, 2008; Alonso-Rodríguez & Tsavdaridis, 2021). Given that maximum drift does not occur uniformly along the height, but is influenced by structural properties and boundary effects (Khaloo & Khosravi, 2008), accurate representation of boundary conditions becomes essential in determining both the magnitude and location of critical responses. Çolak et al. (2023) proposed a novel equivalent continuous beam model by improving the continuous shear-flexural beam model by including a rotation boundary condition at the base. Çolak (2024) investigated the higher mode effects using this novel equivalent continuous beam model and also pointed out that the solution of this model can be improved for buildings with different first-story heights.

In addressing these limitations, this study introduces a novel equivalent continuous beam model for the seismic performance evaluation of multistory buildings. This model incorporates a rotational boundary condition at the base, expressed in terms of the first-story drift. By considering a combination of shear and flexural deformation behavior, the model allows for a more realistic representation of structural dynamics and drift demand distribution. Closed-form solutions for lateral displacements and inter-story drift ratios are derived based on two key dimensionless parameters: the lateral stiffness ratio (α), and the first-story location (θ). The stiffness ratio α, which significantly influences the overall structural behavior, is defined as a function of the number of stories and the stiffness ratio between beams and columns.

The proposed model is distinct from previous studies (Heidebrecht & Stafford Smith, 1973; Iwan, 1997; Miranda, 1999; Miranda & Taghavi, 2005) in that it captures the influence of first-story drift on overall building response and enables more accurate estimation of maximum drift demands. Furthermore, a simplified mathematical expression for the lateral stiffness ratio is introduced, incorporating both geometric and material properties of the building through the beam-to-column stiffness ratio (ρ) and the number of stories (N). This formulation facilitates practical implementation while preserving analytical rigor. To evaluate the accuracy and robustness of the proposed method, dynamic analyses were conducted for a range of low-rise and high-rise structural configurations using response spectrum analysis. The analytical results derived from the continuous model were compared with detailed finite element simulations conducted in SAP2000. The comparisons demonstrated a high degree of agreement, thereby validating the proposed model's capability to effectively approximate structural responses under seismic loads.

2. A Novel equivalent continuous beam model

Continuous models are commonly employed in the literature as approximate methods for predicting structural responses, serving as alternatives to multi-degree-of-freedom systems. These models typically idealize the structure as a continuous cantilever beam with uniform mass and stiffness distributions and assume zero displacement and rotation at the base. However, this a simplification that overlooks the efficient of base rotation to drift. Addressing this limitation, the present study proposes a closed-form solution that incorporates a rotational boundary condition at the base, aiming to enhance the accuracy of structural response predictions. In this study, a novel equivalent continuous beam model for the seismic performance evaluation of multistory buildings is presented. The model was improved to continuous shear-flexural beam model proposed in Miranda and Taghavi (2005) by including a rotation boundary condition at the base.

Under the effect of a horizontal ground acceleration $\ddot{u}_g(t)$ applied at the base, the undamped dynamic behavior of the continuous beam model is governed by a partial differential equation, as presented in Eq. (1).

$$\frac{m}{EI}\frac{\partial^2 u(\zeta,t)}{\partial t^2}+\frac{1}{H^4}\frac{\partial^4 u(\zeta,t)}{\partial \zeta^4}-\frac{\alpha^2}{H^4}\frac{\partial^4 u(\zeta,t)}{\partial \zeta^4}=-\frac{m}{EI}\frac{\partial^2 u_g(t)}{\partial t^2} \tag{1}$$

In this context;
m ; the mass per unit length,
H ; the total height of the building,
$u(\zeta,t)$; the lateral displacement at a dimensionless height ζ at time t,
EI ; the flexural rigidity of the beam,
α ; the lateral stiffness ratio

Here, α is a dimensionless parameter that governs the relative contribution of flexural and shear deformations in the continuous model, thereby influencing the lateral displacement profile. The model reduces to an Euler–

Bernoulli beam when α = 0 and approaches a shear beam as α tends to infinity, with intermediate values capturing the combined behavior typical of multistory structures Miranda and Taghavi (2005).

$$\alpha = H\sqrt{\frac{GA}{EI}} \tag{2}$$

GA represents the shear rigidity of the continuous beam. According to Miranda and Reyes (2002), the stiffness ratio α varies with structural system type: it ranges from 0–2 for shear wall systems, 1.5–6 for dual systems, and 5–20 for moment-resisting frames, while values exceeding 30 indicate shear-dominated behavior. Taghavi and Miranda (2005) proposed representative α values of 3.125 for dual systems and 12.5 for moment-resisting frames.

The dynamic response of a linear elastic continuous system can be represented as a linear superposition of all modes, yielding the displacement u(ζ,t) as a function of dimensionless height (ζ) and time (t). With classical damping assumptions, modal expressions for lateral displacement ($u_i(\zeta,t)$) and inter-story drift ratio ($IDR_i(\zeta,t)$) can be derived to quantify each mode's contribution to the structural response.

$$u_i(\zeta,t) = \Gamma_i \phi_i(\zeta) D_i(t) \tag{3}$$

$$IDR_i(\zeta,t) = \frac{1}{H}\Gamma_i \phi_i'(\zeta) D_i(t) \tag{4}$$

The modal participation factor (Γ_i) corresponding to the continuous system with a uniform mass distribution, is expressed as follows:

$$\Gamma_i = \frac{\int_0^1 \phi_i(\zeta)d\zeta}{\int_0^1 \phi_i^2(\zeta)d\zeta} \tag{5}$$

Substituting Eq. (3) into Eq. (1) and applying the separation of variables technique for the free vibration case yields two decoupled equations: one spatially dependent ($\phi_i(\zeta)$) and the other time dependent($D_i(t)$). The mode shape function ($\phi_i(\zeta)$) is derived as the general solution to the differential equation governing the spatial behavior.

$$\phi_i(\zeta) = B_1 \sin(\gamma_i \zeta) + B_2 \cos(\gamma_i \zeta) + B_3 \sinh(\beta_i \zeta) + B_4 \cosh(\beta_i \zeta) \tag{6}$$

Here $\beta=\sqrt{\gamma_i^2+\alpha^2}$, where B_1 to B_4 denote the integration constants determined by the imposed boundary conditions.

The eigenvalue (γ_i) is determined by solving for the circular frequencies (ω_i) as described in Eq. (7).

$$\omega_i^2 = \frac{EI}{mH^4}\gamma_i^2(\gamma_i^2 + \alpha^2) \tag{7}$$

Accurate dynamic properties and predictions require selecting the correct α value Miranda (1999), because of the mode shape ($\phi(\zeta)$), drift mode shape ($\phi'(\zeta)$), modal participation factor (Γ_i), and circular frequencies (ω_i) depend on the lateral stiffness ratio α (Miranda & Taghavi, 2005; Miranda & Akkar, 2006).

2.1 Application of Boundary Conditions

In the continuous model with a fixed base, the boundary conditions enforce both zero displacement and rotation at the base. However, in the proposed model, while the displacement at the base remains zero (Eq. 8), the rotational boundary condition is defined in terms of the first-story inter-story drift, which is non-zero (Eq. 9). The following equations represent these conditions:

$$\phi_i(\zeta)_{\zeta=0} = 0 \tag{8}$$

$$\left.\frac{d\phi_i(\zeta)}{d\zeta}\right|_{\zeta=0} = \frac{\phi_i(h_1/H)}{h_1/H} \tag{9}$$

Here, h_1/H is the ratio of the first-story height (h_1) to the total building height (H). This ratio is defined as the '*first-story location*', hereafter referred to as θ, through the normalized building height (ζ) . In this case, θ is defined as follows:

$$\theta = \frac{h_1}{H} = \frac{h_1}{h_1 + (N-1)h_j} \tag{10}$$

In the case where all stories are assumed to have equal heights (i.e., $h_1=h_j$), the first-story location θ becomes equal to "*1/N*", where *N* is the total number of stories. In this study, equal story heights are considered for all stories unless stated otherwise. Notably, the special case of $\theta=0$, which corresponds to a zero rotational boundary condition at the base, yields results identical to those presented by Miranda and Taghavi (2005).

Correspondingly, in the continuous model, the boundary condition at the normalized height (ζ=1) (representing the free end) yields zero moment and shear force:

$$\left.\frac{d^2\phi_i(\zeta)}{d\zeta^2}\right|_{\zeta=1} = 0 \tag{11}$$

$$\left.\left(\frac{d^3\phi_i(\zeta)}{d\zeta^3} - \alpha^2 \frac{d\phi_i(\zeta)}{d\zeta}\right)\right|_{\zeta=1} = 0 \tag{12}$$

The following integration constants are obtained through the application of the boundary conditions:

$$\begin{gathered} B_2 = \left(-\frac{\beta_i \gamma_i^2 \theta \sin(\gamma_i) + \beta_i^2 \gamma_i \theta \sinh(\beta_i) - 2\beta_i^2 \sin(\gamma_i \theta)\sinh(\beta_i) - 2\gamma_i^2 \sin(\gamma_i)\sinh(\beta_i \theta)}{\left(\gamma_i^2 \cos(\gamma_i) + \beta_i^2 \cosh(\beta_i)\right)\left(\beta_i \theta - 2\sinh(\beta_i \theta)\right)} \right) B_1 \\ B_3 = \left(-\frac{\gamma_i \theta - 2\sin(\gamma_i \theta)}{\beta_i \theta - 2\sinh(\beta_i \theta)} \right) B_1 \\ B_4 = -B_2 \end{gathered} \tag{13}$$

The integration constants B_1 through B_4, defined in Equations (8)–(11), are employed to insert the mode shape function (Eq. 6) into the boundary condition (Eq. 12), leading to the formulation of the characteristic Eq. (14).

$$\left(\begin{gathered} -2\gamma_i \beta_i^3 \left(\gamma_i \theta - \sin(\gamma_i \theta)\right) + 2\gamma_i^2 \beta_i^2 \sinh(\beta_i \theta) - \sin(\gamma_i)\sinh(\beta_i)\left(\beta_i^2 \left(\alpha^2 \gamma i \theta - 2\beta_i^2 \sin(\gamma_i \theta)\right) + 2\gamma_i^3 \beta_i \sinh(\beta_i \theta)\right) + \\ \cos(\gamma_i)\cosh(\beta_i)\left(\beta_i \left(-\left(\left(\alpha^4 + 2\gamma_i^2 \beta_i^2\right)\theta\right) + 2\gamma_i^3 \sin(\gamma_i \theta)\right) + 2\beta_i^4 \sinh(\beta_i \theta)\right) \end{gathered} \right) = 0 \tag{14}$$

The eigenvalues (γi) are determined by solving the characteristic equation (Eq. (14)) as a function of α and θ. In the novel equivalent continuous beam model, presented in this study, with uniform mass and stiffness, mode shapes, period ratios, and participation factors are governed by the first-story location (θ) and lateral stiffness ratio (α). Base rotation is defined by the first-story drift. While the lateral stiffness ratio must be known, the literature offers only approximate values based on structural systems, without a definitive method. Although, this study proposes a simple empirical equation to improve response predictions, as well.

2.2 Formulation and identification of the lateral stiffness ratio

The lateral displacement of buildings under horizontal loads primarily results from column bending and the rotation of beams at column ends, both influenced by their relative stiffness. Blume (1968) showed that the structural and dynamic characteristics of frame systems depend on the stiffness ratio between beams and columns, defined as Blume coefficient (ρ), which reflects combined deformation behavior. ρ is a key structural parameter indicating relative joint rotations and is given by Eq. (15), assuming equal elastic modulus for beams and columns (Blume, 1968). It characterizes the contribution of flexural and shear deformations: ρ=0 represents a flexural system, ρ=∞ a shear system, and intermediate values indicate combined behavior (Miranda, 1999).

$$\rho = \frac{\sum_{beams} \left({I_b}/{l_b} \right)}{\sum_{columns} \left({I_c}/{h_c} \right)} \tag{15}$$

where I_b and I_c are the beam and column moments of inertia, and l_b and h_c are their respective lengths.

Additionally, ρ influences the natural period and mode shapes, providing insight into the dynamic response of moment-resisting frames (Chopra, 2012; Akkar et al., 2005). Unlike the dimensionless parameter α used in continuous models, ρ is independent of building height. In this study, the number of stories (N) is used instead of building height, relating the estimation of α to both ρ and N.

To determine this relationship, discrete frame models were used to estimate the lateral stiffness ratio (α) in the continuous beam model. Ten sets of moment-resisting frames with varying Blume coefficients (ρ), ranging from flexural to shear behavior values, were analyzed, each including buildings with low-rise to high-rise story buildings. The models were based on a six-span layout with 5 m beam lengths and 3 m story heights. The beam-to-column stiffness ratio (ρ) for building models, calculated via Eq. (15) . Dynamic analyses were performed by the response spectrum. Detailed information on the models can be found in Çolak et al. (2023) study.

To assess the efficacy of the proposed model in predicting structural responses, analyses were conducted on a range of sample building models that have been defined above. These structures, varying from 5 to 20 stories, were modeled and analyzed using SAP2000 software. The analysis results were then employed to generate predictions based on the proposed rotational base condition concept (θ=1/N) and the lateral stiffness ratio (α), as expressed by the relevant equations. An iterative trial-and-error procedure was employed to determine the optimal α value that provides the most accurate estimation of structural behavior. The main objective was to identify the α value that results in the best alignment between the predicted and actual structural responses. Specifically, this involved comparing the mode shape profiles obtained from the SAP2000 (FEM) analyses with those derived from the proposed model and iteratively adjusting α to achieve the closest match.

Closed-form analytical expressions of the continuous shear–flexural beam models' (lateral displacements, inter-story drift ratios, and mode shapes) were solved using MATHEMATICA in the calculations. Subsequently, these results were compared against dynamic responses from SAP2000, which was applied UBC97 response spectrum analysis by finite element model. This is treated here as the reference solution. Assuming a uniform mass distribution, the lateral displacement, as depicted in Eq. 3, is dictated by the parameters α and θ. The parameter θ, denoting the location of the first story, is delineated by Eq. 10. In the present study, θ was regarded as 1/N. Consequently, a comparison was conducted between the normalized displacement profile from SAP2000 and the mode shape (ϕ) and its derivative (ϕ′) from the continuous model. In this comparison, the parameter α was calibrated through iterative refinements to achieve maximum proximity to the target value. Furthermore, an evaluation of the SAP2000 models displacements was conducted in relation to the modal mode shape (Γϕ), while a comparison of the corresponding modal drift ratios with Γϕ′ was also undertaken.

However, in this section of the study compares the maximum inter-story drift ratios (IDR_{max}) of the proposed model (*θ=1/N*) and the fixed-base case (*θ=0*), as shown in Fig. 1. Lateral deformation profiles derived using Miranda's recommended average value (*α=12.5, θ=0*) were evaluated against those obtained using the estimated α values for the proposed condition (*θ=1/N*). These comparisons were carried out for sample building models in each group, and the results were benchmarked against FEM outputs. In Fig. 1, circular markers labeled A indicate results from Miranda's approach, while star-shaped markers labeled B represent outcomes from the proposed method. In all cases, the continuous model predictions slightly overestimated the FEM results.

The analytical results obtained with the proposed model demonstrated a marked enhancement in comparison to the fixed-base cases, particularly in the context of low-rise models. However, this improvement decreased with increasing story number, as first-story location value tends toward zero with higher N, approximating the fixed-end condition. Although continuous models are more suited to tall buildings, it was shown that incorporating base rotational condition extends to model their applicability to low-rise structures as well.

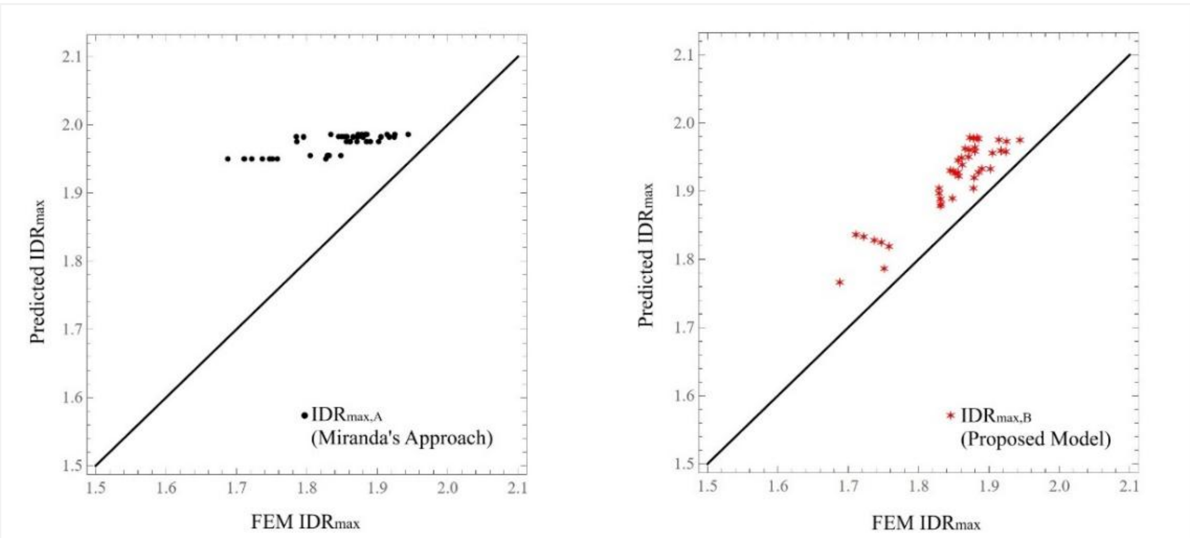

Fig. 1. Comparison of IDR_{max} for sample buildings

2.3. A New approach for lateral stiffness ratio (α)

In the previous section, the lateral stiffness ratios (α) were obtained through iterative procedures for structural models with varying numbers of stories and Blume coefficients (ρ). In light of these results, Çolak et al. (2023) showed how α evolves in conjunction with both the number of stories (N) and ρ, emphasizing their inherent interdependence.

The parameter ρ, defined for discrete systems, significantly affects structural displacements, as does α for continuous beams. As the parameter ρ increases, the lateral displacements show a significant increase, especially in the 0.0-0.125 range. At this point, the behavior of the system undergoes a transition from flexural to a combined flexural-shear mode. Beyond this threshold, the displacement variations become more gradual. A similar trend is observed in the inter-story drift patterns, with the maximum drift shifting to lower floors. Systems with ρ = 0.0

exhibit flexural-dominated behavior, while those with ρ = ∞ exhibit shear-dominated responses, with drift concentrated in the upper and lower floors (Akkar et al., 2005; Çolak et al., 2023).

To model the nonlinear relationship between α, ρ, and N, Çolak et al. (2023) proposed a piecewise regression approach. Assuming that ρ and N are independent variables, two equations were derived: one expressing the transition from flexural to mixed behavior (Eq. 16) and another expressing the transition to shear-dominated behavior (Eq. 17). These equations provide a more accurate and efficient means of estimating α, facilitating its application in structural analysis and design.

$$\alpha_{fc}(\rho, N) = a_1 N^{b_1} \rho^{c_1} \tag{16}$$

$$\alpha_e(\rho, N) = a_2 + b_2 N + c_2 \rho \tag{17}$$

The corresponding equation constants were; "$a_1 = 2.672$, $b_1 = 0.851$, $c_1 = 0.401$" for $0.0<\rho<0.125$ and "$a_2 = 0.0946$, $b_2 = 0.877$, $c_2 = 2.722$" for $\rho \geq 0.125$.

3. Accuracy and applicability of the proposed model

To verify the proposed model, one moment-resisting frame building model was consisted as detailed characteristics of this frame is provided below. The dynamic properties are obtained through eigenvalue analysis of comprehensive finite element model and compared with those derived from the simplified method developed in this study. In addition, response spectrum analysis is performed to evaluate the lateral deformation profiles and inter-story drift ratios, and results from the simplified model are compared. The model was constructed as two-dimensional linear elements using SAP2000, with the eigenvalue-based FEM results considered as the benchmark.

Example building model is consisted of five-story moment-resisting frame model. The beam–column rigidity ratio (ρ) was 0.53, the spans and story heights were equal, measuring 5 m and 3 m, respectively. The floor weights in the frame were uniformly distributed, with each floor weighing 907 kN. The first-mode period of vibration was 0.48 s. Dynamic analysis was performed using the response spectrum. The lateral deformation responses and the maximum inter-story drift ratio estimations along the building height for the fundamental mode were compared between the continuous beam model and FEM; the results are shown as graphically in Fig. 2 and Fig.3, respectively. The parameter α for this model was calculated via Eq. (17) for use in the proposed method.

Using the proposed method ($\phi_B(\alpha=5.93, \theta=1/5)$), the maximum inter-story drift ratio differed by only 3.4% from the finite element model results, with the peak value occurring at the same height level in the SAP2000 model. In contrast, applying Miranda's method ($\phi_A(\alpha_{ort}=12.5, \theta=0)$) resulted in a 10.0% difference. This indicates an improvement of about 6.5% in accuracy for the proposed model. The results confirm that a proper definition of α leads to more precise estimations of structural behavior along the height of the building.

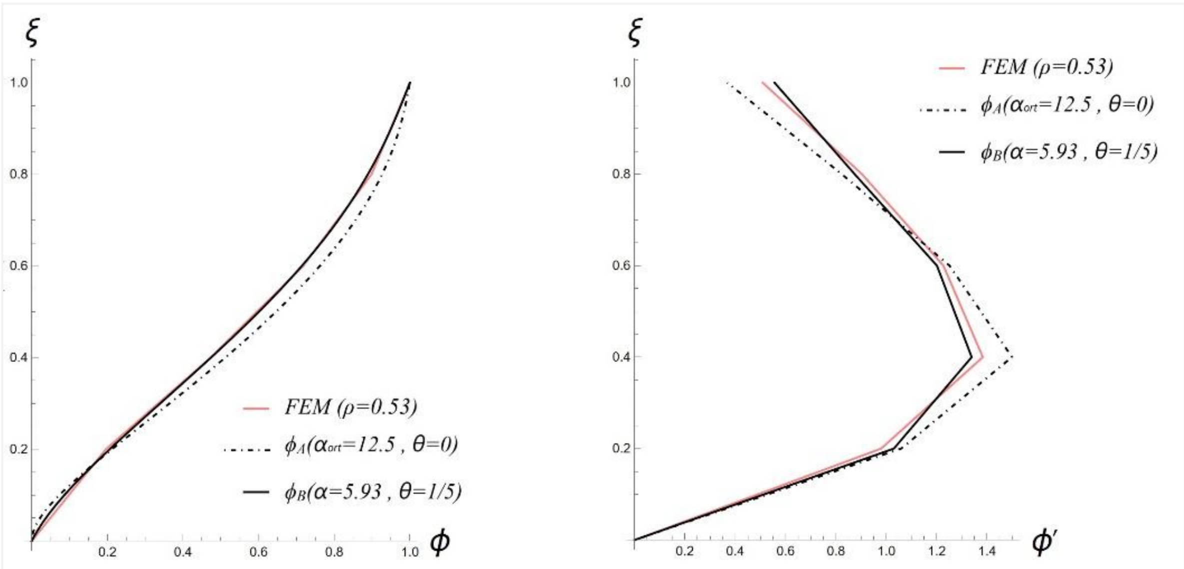

Fig. 2. Mod shapes (ϕ *and* ϕ') of FEM and continuous beam models

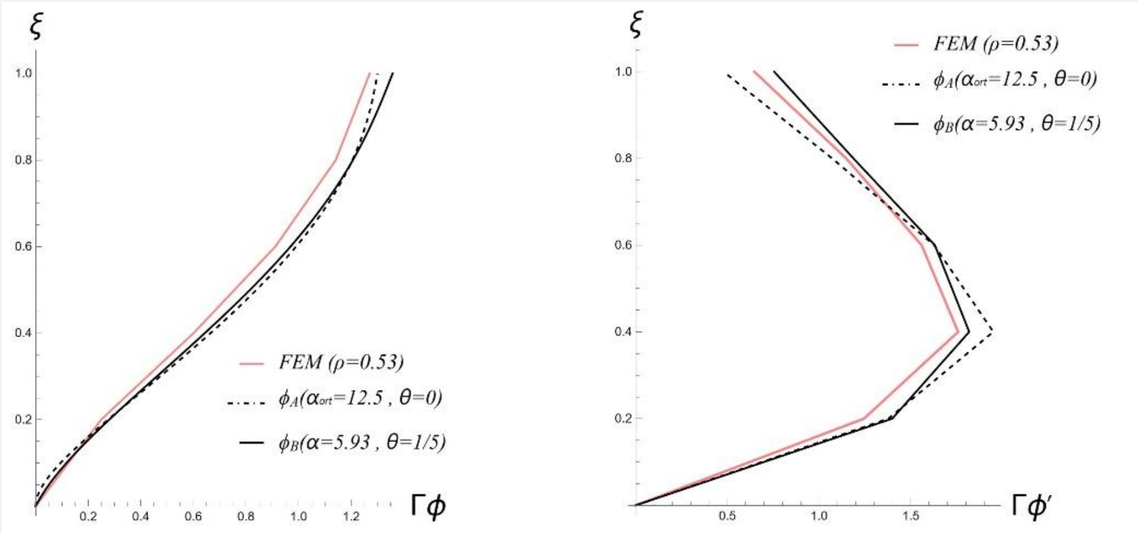

Fig. 3. Modal displacement and Modal IDR profiles ($\Gamma\phi$ *and* $\Gamma\phi'$) of FEM and continuous beam models

4. Conclusions

This study presented a novel equivalent continuous beam model for evaluating the seismic performance of multi-story buildings, with a particular focus on estimating inter-story drift ratios—an essential parameter in earthquake-resistant design. The model combines shear and flexural behavior to represent the overall structural response and enables closed-form analytical solutions.

By introducing a rotational boundary condition at the base expressed in terms of the first-story drift, the model simplifies the equation of motion and requires only two dimensionless parameters: the lateral stiffness ratio (α) and the location of the first story (θ). It was also observed that the expression α developed as a function of the number of storeys (N) and the stiffness ratio between beams and columns (ρ) contributed to more accurate prediction of the results.

Comparative dynamic analyses using the SAP2000 software confirmed that the proposed model provides reliable predictions of displacement profiles and maximum inter-story drift ratios across various structural configurations. The proposed model has also demonstrated its effectiveness in approximating the inter-story drift ratio, its variation along the building height, and the location of its maximum value. The results demonstrate that the method is both accurate and computationally efficient.

In conclusion, the continuous beam model proposed in this research offers a valuable tool for preliminary seismic design and assessment, particularly in identifying critical drift demands along the building height. Its simplicity, generality, and compatibility with code-based design criteria make it a strong candidate for both academic and engineering applications.

References

Akkar, S., Yazgan, U., & Gülkan, P. (2005). Drift estimates in frame buildings subjected to near-fault ground motions. *Journal of Structural Engineering*, *131*(7), 1014–1024. https://doi.org/10.1061/(ASCE)0733-9445(2005)131:7(1014)

Alonso-Rodríguez, A., & Miranda, E. (2016). Dynamic behavior of buildings with nonuniform stiffness along their height assessed through coupled flexural and shear beams. *Bulletin of Earthquake Engineering*, *14*, 3463–3483. https://doi.org/10.1007/s10518-016-0009-2

Alonso-Rodríguez, A., & Miranda, E. (2018). Assessment of effects of reductions of lateral stiffness along height on buildings modeled as elastic cantilever shear beams. *Journal of Earthquake Engineering*, *22*, 553–568. https://doi.org/10.1080/13632469.2016.1244132

Alonso-Rodríguez, A., & Tsavdaridis, K. D. (2021). Effect of rotational inertia on building response to earthquakes via a closed-form solution. *Mechanics Based Design of Structures and Machines*, *51*, 1842–1855. https://doi.org/10.1080/15397734.2021.1880329

Blume, J. A. (1968). Dynamic characteristics of multi-story buildings. *Journal of the Structural Division*, *94*, 377–402. https://doi.org/10.1061/jsdeag.0001880

Chopra, A. K. (2012). *Dynamics of structures: Theory and applications to earthquake engineering* (4th ed.). Pearson.

Cruz, E. F., & Chopra, A. K. (1986). Simplified procedures for earthquake analysis of buildings. *Journal of Structural Engineering*, *112*, 461–480. https://doi.org/10.1061/(ASCE)0733-9445(1986)112:3(461)

Çolak, H. (2024). *Deprem etkisi altındaki çok katlı bina tipi yapıların sürekli model yaklaşımı ile dinamik analizi* (Ph.D. thesis). Iskenderun Technical University (ISTE), Hatay, Turkey.

Çolak, H., Türker, H. T., & Coşkun, H. (2023). Accurate estimation of inter-story drift ratio in multistory framed buildings using a novel continuous beam model. *Applied Sciences*, *13*(13), 7819. https://doi.org/10.3390/app13137819

Eroğlu Azak, T. (2013). *A predictive model for maximum interstory drift ratio (MIDR) and its implementation in probability-based design and performance assessment procedures* (Ph.D. thesis). Middle East Technical University (METU), Ankara, Turkey.

FEMA. (2000). *FEMA 356 Prestandard and commentary for the seismic rehabilitation of buildings*. U.S. Federal Emergency Management Agency.

Heidebrecht, A., & Stafford Smith, B. (1973). Approximate analysis of tall wall-frame structures. *Journal of the Structural Division*, *99*, 199–221.

Iwan, W. D. (1997). Drift spectrum: Measure of demand for earthquake ground motions. *Journal of Structural Engineering*, *123*(4), 397–404. https://doi.org/10.1061/(ASCE)0733-9445(1997)123:4(397)

Khaloo, A. R., & Khosravi, H. (2008). Multi-mode response of shear and flexural buildings to pulse-type ground motions in near-field earthquakes. *Journal of Earthquake Engineering*, *12*, 616–630. https://doi.org/10.1080/13632460701513132

Miranda, E. (1999). Approximate seismic lateral deformation demands in multi-story buildings. *Journal of Structural Engineering*, *125*(4), 417–425. https://doi.org/10.1061/(ASCE)0733-9445(1999)125:4(417)

Miranda, E., & Akkar, S. D. (2006). Generalized interstory drift spectrum. *Journal of Structural Engineering*, *132*(6), 840–852. https://doi.org/10.1061/(ASCE)0733-9445(2006)132:6(840)

Miranda, E., & Reyes, C. J. (2002). Approximate lateral drift demands in multi-story buildings with nonuniform stiffness. *Journal of Structural Engineering*, *128*, 840–849. https://doi.org/10.1061/(ASCE)0733-9445(2002)128:7(840)

Miranda, E., & Taghavi, S. (2005). Approximate floor acceleration demands in multi-story buildings. I: Formulation. *Journal of Structural Engineering*, *131*(2), 203–211. https://doi.org/10.1061/(ASCE)0733-9445(2005)131:2(203)

Morfidis, K., Stefanidou, S., & Markogiannaki, O. (2023). A Rapid Seismic Damage Assessment (RASDA) Tool for RC Buildings Based on an Artificial Intelligence Algorithm. *Applied Sciences*, *13*(8). https://doi.org/10.3390/app13085100

Neam, A. S., & Taghikhany, T. (2016). Prediction equations for generalized interstory drift spectrum considering near-fault ground motions. *Natural Hazards*, *80*(3), 1443–1473. https://doi.org/10.1007/s11069-015-2029-7

Qu, J., & Pan, C. (2022). Incremental Dynamic Analysis Considering Main Aftershock of Structures Based on the Correlation of Maximum and Residual Inter-Story Drift Ratios. *Applied Sciences*, *12*(4). https://doi.org/10.3390/app12042042

Reinoso, E., & Miranda, E. (2005). Estimation of floor acceleration demands in high-rise buildings during earthquakes. *The Structural Design of Tall and Special Buildings*, *14*, 107–130. https://doi.org/10.1002/tal.272

Taghavi, S., & Miranda, E. (2005). Approximate Floor Acceleration Demands in Multistory Buildings. II: Applications. *Journal of Structural Engineering*, *131*(2), 212–220. https://doi.org/10.1061/(ASCE)0733-9445(2005)131:2(212)

Turkish Ministry of Environment and Urbanization. (2018). *Turkish Building Earthquake Code (TBEC-2018)*. Official Gazette No. 30364, Ankara, Turkey.

Veladi, H., Farahmand Azar, B., & Rahimi Gendeshmin, S. (2020). Quantifying higher mode effects in rocking systems considering shear-flexural behavior. *Structures*, *27*, 542–558.

Wiebe, L., & Christopoulos, C. (2015). A cantilever beam analogy for quantifying higher mode effects in multistorey buildings. *Earthquake Engineering & Structural Dynamics*, *44*, 1697–1716. https://doi.org/10.1002/eqe.2549

4th International Civil Engineering & Architecture Conference
17-19 May 2025, Trabzon, Türkiye

Chaotic Rao (Ch-Rao) algorithm for optimization of RC symmetric spread footings

Hasan Tahsin Öztürk[*1]

[1] Karadeniz Technical University, Faculty of Technology, Department of Civil Engineering, 61830, Trabzon, Türkiye

Abstract. The main objective of this study is to assess the efficacy of the recently developed and proposed chaotic Rao (Ch-Rao) algorithm in the optimization of the design of a symmetric reinforced concrete spread footing with minimum cost. The Ch-Rao algorithm was formulated by interchanging the convergence equations of the Rao1, Rao2, and Rao3 algorithms with chaotic maps, with a view to enhancing the variable performance of these three algorithms. The effectiveness of the developed algorithm was tested on a spread reinforced concrete foundation problem suite. For this purpose, a problem suite was created consisting of six different problems with only axial loading and combined bending in one and two directions. The Turkish Reinforced Concrete Standard (TS500) was used in the designs. In the optimisation problems, the objective function consists of reinforcement and concrete costs. Design variables include the thickness of the foundation, the dimensions of the foundation in the plan, and the diameters and numbers of the main reinforcements to be placed in two directions. The problems with a total of seven design variables were designed as discrete optimization problems, and the optimum solutions obtained from independent simulations performed on this problem suite were statistically evaluated. The performance of the developed Ch-Rao algorithm was compared with the original Rao algorithms using statistical data, the Friedman test, and Wilcoxon paired comparison tests. By evaluating the optimum solutions obtained from the problems for different bending moment levels, it was revealed how the optimum designs and costs change at different levels. The results showed that the Ch-Rao algorithm performs better than the original Rao algorithms.

Keywords: Reinforced concrete; Spread footing; Minimum cost; Optimization; Ch-Rao algorithm

1. Introduction

Optimal design in engineering problems is known to be a powerful tool for ensuring sustainability in engineering designs. Due to the difficulties in applying classical optimization methods to real-world problems, metaheuristic search algorithms have been increasingly used in the optimization of engineering problems. In this context, optimization with metaheuristic search algorithms has become a frequently used optimization tool in the field of civil engineering.

The optimum design of reinforced concrete spread footings at minimum cost is of critical importance in the building design process in terms of both economic and building performance. This is because foundations with larger capacity than necessary will increase the cost of concrete and steel consumption in the production of the structure and unnecessarily increase the project cost. On the other hand, foundations designed with insufficient capacity may endanger the stability of the structure and cause high repair and strengthening costs in the long term. For this reason, optimum design of spread footings with minimum cost by taking into account the loads acting on them and the soil conditions will not only ensure economical foundation designs, but will also guarantee safe designs.

A review of the extant literature reveals a notable interest among researchers in the optimization of spread footing with metaheuristic algorithms, a subject that is the focus of this study. A review of recent studies reveals that optimization studies on spread footings are performed for footings subjected to axial load (Arabali et al., 2022; Camp & Assadollahi, 2013; Islam & Rokonuzzaman, 2018), one uniaxial combined bending (Chaudhuri & Maity, 2020; Kashani et al., 2020; Khajehzadeh et al., 2012, 2013; Khajehzadeh, Iraji, et al., 2022; Öztürk, 2018) and biaxial combined bending (Nigdeli et al., 2018). The predominant focus of these studies is on spread footings subjected to uniaxial combined bending. The majority of the studies aim to minimize the cost, and a few studies aim to minimize carbon dioxide emissions (Arabali et al., 2022; Camp & Assadollahi, 2013; Khajehzadeh et al., 2013). However, it is seen that almost all of the studies in the literature use American reinforced concrete standards,

[*] Corresponding author, E-mail: htozturk@ktu.edu.tr

https://doi.org/10.31462/icearc2025_ce_sme_716

one study uses the Indian standard (Chaudhuri & Maity, 2020) and one study uses the Turkish reinforced concrete standard (Öztürk, 2018). In the reviewed studies; Gravitational Search Algorithm (GSA) (Khajehzadeh et al., 2012), Genetic Algorithm (GA) (Chaudhuri & Maity, 2020; Islam & Rokonuzzaman, 2018; Kashani et al., 2020; Khajehzadeh et al., 2012), Sequential Quadratic Programming (FaSQP) hybridized with Firefly algorithm (Khajehzadeh et al., 2013), Big Bang-Big Crunch Algorithm (Camp & Assadollahi, 2013), Differential Evolution (DE) Algorithm (Kashani et al., 2020; Nigdeli et al., 2018), Particle Swarm Optimization (PSO), Harmony Search (HS) and Flower Pollination (FPA) Teaching-Learning Based Optimization (TLBO) algorithms (Nigdeli et al., 2018), Teaching-Learning Based Optimization (TLBO) algorithm (Nigdeli et al., 2018; Öztürk, 2018), Artificial Bee Colony (ABC) and Cuckoo Search (CS) algorithms (Öztürk, 2018), Unified Particle Swarm Optimization (UPSO) (Chaudhuri & Maity, 2020), Evolution Strategy (ES), Biogeography-Based Optimization (BBO), Improved Differential Evolution (IDE), Weighted Differential Evolution (WDE), Linear Population Size Reduction Adaptive Differential Evolution Based on Success History (LSHADE) and Covariance Matrix-Based Migration with Biogeography-Based optimization algorithms (CMM-BBO) (Kashani et al., 2020), Adaptive Tunicate Swarm Algorithm (ATSA) and Tunicate Swarm Algorithm (TSA) (Arabali et al., 2022), Modified Rat Swarm Optimization and Rat Swarm Optimization Algorithms (MRSO and RSO) (Khajehzadeh, Keawsawasvong, et al., 2022).

This study presents a new Caotic Rao (Ch-Rao) algorithm by combining the convergence equations of the RAO algorithm using chaotic mapping reference signals. Thus, it is thought that by selecting a problem-specific signal, it is possible to create an algorithm that shows higher performance in variants of Rao algorithms. For this purpose, performance tests were performed on single foundation problems subjected to axial load, combined bending in one direction and combined bending in two directions at different bending moment levels. The results obtained are compared with those obtained from the variants of Rao algorithms by various statistical tests.

The structure of this study is as follows: The first section discusses the motivation and goal of the present study. The second section describes the formulation of the optimization problem, constraints, algorithm settings, and propoesed Ch-Rao algorithm. Findings and investigations are presented in the third section. The conclusions of the study are presented in the last section.

2. Method

2.1. Problem definition

2.1.1. Objective function and design variables

The objective function to be used in the optimization of the spread footing is represented by a relation expressing the cost of the footing, taking into account the cost of concrete and reinforcement.

$$f(\mathrm{x}) = \mathrm{V_c C_c} + \mathrm{W_s C_s} \tag{1}$$

Where $\mathrm{V_c}$ is the volume of concrete, $\mathrm{W_s}$ is the weight of reinforcement, $\mathrm{C_c}$ and $\mathrm{C_s}$ are the unit costs of concrete and reinforcement respectively. Unit costs will be taken from the catalog of construction and installation unit prices for 2024 of the Ministry of Environment, Urbanization and Climate Change. In the optimization problem, constraints will be defined to achieve a design that meets the desired conditions in terms of strength, durability and geometry. If these constraints are violated, the violation value is added to the objective function using a fixed penalty coefficient, thus creating a penalized objective function. In this case, the penalized objective function is given in Eq. 2, where CK denotes the penalty coefficient and g(x) denotes the constraint violations.

$$\Phi(\mathrm{x}) = \mathrm{f(x)} + \mathrm{CK} \cdot \sum \mathrm{g(x)} \tag{2}$$

Here, the objective function and constraint functions can be expressed as functions depending on the design variables. The penalty coefficient is taken as 10^8 in this study. The design variables are denoted by x.

In this study, the designed foooting was planned to be symmetrical, but it was enabled to be designed as a rectangular foooting. The design variables for this case are given in Fig. 1. According to this figure, design variables x_1 indicates the foundation thickness, x_2 indicates the length of the foundation cantilever in x direction, x_3 indicates the length of the foundation cantilever in y direction, x_4 indicates the diameter of the reinforcement in x direction, x_5 indicates the diameter of the reinforcement in y direction, x_6 indicates the number of reinforcements in x direction, x_7 indicates the number of reinforcements in y direction. There are 7 design variables in total in this problem. The lower and upper limits of the design variables of the spread footing problem to be created are given in Table 1.

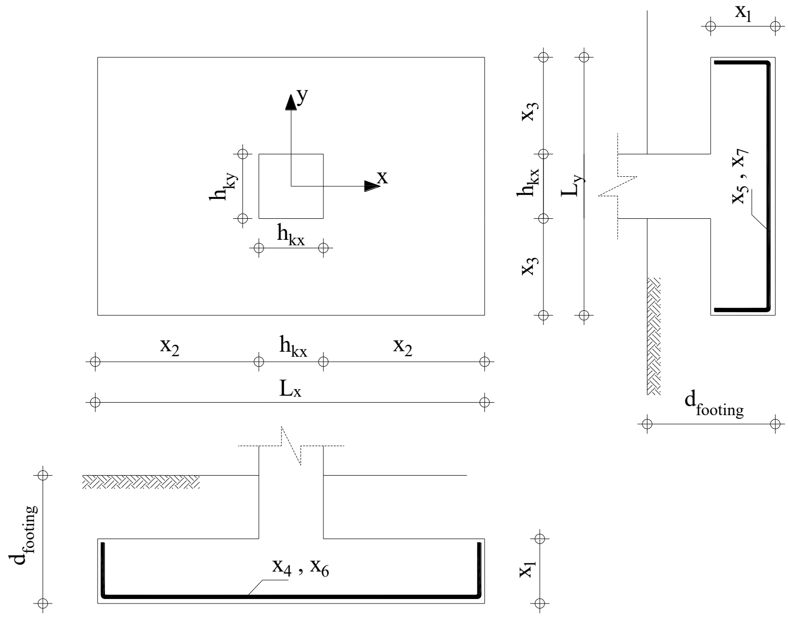

Fig. 1. Design variables for symmetric rectangular spread footing

Table 1. Lower and upper limits and increments of design variables for applications

Design Variables		Lower Bound	Upper Bound	Increment
x_1	Foundation thickness	250 mm	1000 mm	250 mm
x_2	Length of the foundation cantilever in x direction	300 mm	5000 mm	300 mm
x_3	Length of the foundation cantilever in y direction	300 mm	5000 mm	10 mm
x_4	Diameter of the reinforcement in x direction	{14 16 18 20 22 24 26 28} mm		
x_5	Diameter of the reinforcement in y direction	{14 16 18 20 22 24 26 28} mm		
x_6	Number of reinforcements in x direction	#1	#100	1
x_7	Number of reinforcements in y direction	#1	#100	1

2.1.2. Constraints

While searching for the minimum cost solution of the optimization problem, some constraints must be defined in order for the resulting design to meet the strength, durability and geometric conformity conditions. These constraints are listed below:

The maximum stress (q_{max}) under the foundation must be greater than the net strength of the soil ($q_{t,net}$). This condition is checked by Eq. 3 below.

$$g_1(x) = \frac{q_{max}}{q_{t,net}} - 1 \leq 0 \quad (3)$$

It is note that tensile stress should not occur under the foundation. Therefore, the minimum stress, (q_{min}), under the foundation must be greater than zero. The condition for this is specified in Eq.4.

$$g_2(x) = -\frac{q_{min}}{100} \leq 0 \quad (4)$$

The value 100 in this constraint is used to scale the constraint. The foundation thickness should be greater than 250 mm and one quarter of the cantilever overhangs. This condition will be checked for both directions.

$$g_{3-4}(x) = \frac{\text{Cantilever overhang (x or y dir.)}/4}{h_t} - 1 \leq 0 \quad (5)$$

Where h_t is the thickness of the footing. In this study, the condition that the footing thickness should be greater than 250 mm was achieved by taking the smallest value of 250 mm in the footing thickness data pool. On the other hand, according to TS500, the footing width should be at least 0.70 m. This condition was met with the upper and lower limits of the cantilever section selected in the data pool. Another condition, that the base area should be greater than 1 m^2 , is controlled by the constraint given in Eq.6.

$$g_5(x) = \frac{1}{L_x L_y} - 1 \leq 0 \quad (6)$$

The control of the punching strength of the footing is realized by the constraint given in Eq.7, where V_{pd} is the design punching force of the footing and V_{pr} is the punching strength of the footing.

$$g_6(x) = \frac{V_{pd}}{V_{pr}} - 1 \leq 0 \quad (7)$$

In shear control of the footing, the design shear force (V_d) acting on the cross section of the cantilever projections of the footing at the column face must be less than the shear crack strength (V_{cr}) of the footing. This condition is checked by Eq.8 in both directions.

$$g_{7-8}(x) = \frac{V_d}{V_{cr}} - 1 \leq 0 \quad (8)$$

In order to check the bending moment bearing capacity, the bending moment bearing capacity (M_{rx} or M_{ry}) at the critical sections in both directions, calculated according to the reinforcement placed in the section, should be greater than the design moment (M_d) at the column face of the footing.

$$g_{9-10}(x) = \frac{M_d}{M_{rx} \text{ or } M_{ry}} - 1 \leq 0 \quad (9)$$

In addition, the ratio of main reinforcement placed in both directions in the section must be greater than the minimum reinforcement ratio (ρ_{min}=0.002). This control is done with Eq.10 where ρx is the ratio of main reinforcement in x direction and ρy is the ratio of main reinforcement in y direction.

$$g_{11-12}(x) = \frac{\rho_{min}}{\rho_x \text{ or } \rho_y} - 1 \leq 0 \quad (10)$$

In addition, to guarantee adequate ductility, the reinforcement ratios in the x and y directions should be limited to a maximum reinforcement ratio no greater than 0.85 times the balanced reinforcement ratio.

$$g_{13-14}(x) = \frac{\rho_x \text{ or } \rho_y}{\rho_{max}} - 1 \leq 0 \quad (11)$$

The requirement that the distance between reinforcements is less than 250 mm is controlled by the following constraint in both directions, where s_x and s_y denote the spacing of the main reinforcements in the x and y directions respectively.

$$g_{15-16}(x) = \frac{s_x \text{ or } s_y}{250} - 1 \leq 0 \quad (12)$$

On the other hand, the net spacing between reinforcements should be at least 25 mm, less than the reinforcement diameter and 4/3 of the aggregate size. For this purpose, the constraint presented in Eq.13 is used, where s_{min} is the largest of these boundary conditions and s_{xnet} and s_{ynet} are the net spacing of the main reinforcements in the x and y directions, respectively.

$$g_{17-18}(x) = \frac{s_{min}}{s_{xnet} \text{ or } s_{ynet}} - 1 \leq 0 \quad (13)$$

2.1.3. Problems for parametric studies

In this study, the problem cases given in Table 2. below were created in order to examine the changes in minimum costs with the optimum designs of spreead footing under axial load, uniaxial and biaxial combined bending at different bending moment levels and to compare the minimum cost designs. In the table, Problem 1 corresponds to the axially loaded case, Problem 2 corresponds to the case subjected to uniaxial bending, Problem 3-6 corresponds to the case subjected to biaxial bending at various bending moment levels.

In all problems, concrete grade is C25/30 and reinforcement grade is B420C. Foundation depth is 1.50 m, foundation soil unit weight is 18 kN/m3, column size is 500 x 500 mm, net concrete cover is 50 mm, concrete unit weight is 25 kN/m3, reinforcement unit weight is 7850 kg/m3, maximum aggregate grain size is 16 mm, minimum reinforcement ratio is 0.002. Concrete and reinforcement unit costs are considered as 33511.95 ₺/kg and 2605.30 ₺/m3 respectively.

2.2. Proposed Ch-Rao algorithm

The difference of the proposed Chaotic Rao (Ch-Rao) algorithm from the Rao algorithms is presented in the green colored lines in Table 3. below. Rao 1, Rao 2 and Rao 3 algorithms each use different convergence equations in their update mechanisms. The proposed Ch-Rao algorithm switches between the convergence equations used by Rao 1, Rao 2 and Rao 3 algorithms according to a reference signal generated from chaotic maps according to the number of function evaluations. Therefore, the algorithm uses Rao 1, Rao 2 and Rao 3 convergence equations in a chaotic manner in its life cycle.

Table 2. Problem cases for axial load, uniaxial and biaxial combined bending

N= 2400 kN, q_t= 300 kN/m^2	M_{xx} =	0	0.2 x N	0.2 x N	0.2 x N	0.2 x N	0.2 x N
	M_{yy} =	0	0	0.1 x N	0.2 x N	0.3 x N	0.4 x N
	Problem No #	# 1	# 2	# 3	# 4	# 5	# 6

Table 3. Proposed Ch-Rao Algorithm pseudo code

General steps in Ch-Rao
Begin
Set parameters
Generate the random initial candidate solutions
for *i*=1: *N* (Population size)
Evaluate the fitness values of the *i*th solution candidate
end for
while (*FEs<MaxFEs*)
Update best(t) and worst(t)
for *j*=1: *N* (Size of population)
Identify the best and worst solution
switch *(reference_signal)*
case *reference_signal<1/3*
$x_{new} = x_{old} + rand_1(x_{best} - x_{worst})$
case *reference_signal≥1/3 & reference_signal<2/3*
$x_{new} = x_{old} + rand_1(x_{best} - x_{worst}) + rand_2(\lvert x_{old}\ or\ x_{rand}\rvert - \lvert x_{rand}\ or\ x_{old}\rvert)$
case *reference_signal≥2/3*
$x_{new} = x_{old} + rand_1(x_{best} - \lvert x_{worst}\rvert) + rand_2(\lvert x_{old}\ or\ x_{rand}\rvert - \lvert x_{rand}\ or\ x_{old}\rvert)$
end switch
Update process: Apply an elitist strategy to select best solution.
end for
end while
end

3. Results of simulation studies

3.1. Simulation environment and algorithm settings

The characteristics of the simulation environment are summarized in Table 4. The same equipment was used in all experiments to ensure a fair comparison.

In addition to the Ch-Rao algorithm proposed in this study, Rao1, Rao2, Rao3, were used in the study and statistical performance comparisons were made. For the tested algorithms, the settings recommended in the literature were used as a standard procedure. The algorithms tested on the symmetric spread footing problems investigated in this study, the reference works of the algorithms and the settings recommended in the reference works are presented in Table 5.

3.2. Optimum designs of problems

The details of the best solutions obtained from the optimum designs are presented in Table 6. With the help of the data in this table, the graph of the changes in the amount of main reinforcement in the problems is presented in Fig. 2, and the graph of the changes in concrete and reinforcement costs is presented in Fig. 3.

Table 4. The characteristics of the simulation environment

	Component	Description
Hardware	CPU and Frequency	Intel(R) Core(TM) i5-9400F CPU @ 2.90GHz
	RAM	8,00 GB
	Hard Drive	500 GB solid state drive
Software	Operating System	Windows 10 Pro 64 bit
	Language	MATLAB R2022b

Tablo 5. Settings of the tested algorithms

Algorithm	Reference	Parameters
Ch-Rao	*In this study*	Population size = 50
Rao1	(Rao, 2020)	Population size = 50
Rao2	(Rao, 2020)	Population size = 50
Rao3	(Rao, 2020)	Population size = 50

Tablo 6. The details of the best solutions

		Problem No					
		# 1	# 2	# 3	# 4	# 5	# 6
	M_{xx} =	0	0.2xN	0.2xN	0.2xN	0.2xN	0.2xN
	M_{yy} =	0	0	0.1xN	0.2xN	0.3xN	0.4xN
Foundation width in x direction	mm	3020	3420	3760	4120	4100	4380
Foundation width in y direction	mm	3100	3640	3700	3680	3980	3980
Foundation thickness	mm	560	590	600	610	630	650
Soil Stresses							
Subsoil Net Bearing Capacity	kN/m^2	256.71	256.42	256.32	256.22	256.03	255.83
q_{max}	kN/m^2	256.36	256.35	255.99	256.02	255.99	254.62
q_{min}	kN/m^2	256.36	129.23	89.03	60.57	38.16	20.73
Material Quantities							
Total Concrete Volume	m^3	5.24	7.34	8.35	9.25	10.28	11.33
Reinforcement Weight parallel to X direction	kg	106.73	135.1	180.2	237.53	244.58	292.56
Reinforcement Weight parallel to Y direction	kg	116.62	195.41	198.9	193.37	217.08	211.03
Total Reinforcement Weight	kg	223.35	330.52	379.09	430.9	461.66	503.59
Costs							
Total Concrete Cost	₺	13658.86	19135.39	21746.96	24095.32	26783.37	29520.81
Total Cost of Reinforcement	₺	7484.76	11076.22	12704.17	14440.17	15471.16	16876.18
Total Cost	₺	21143.62	30211.61	34451.13	38535.48	42254.53	46396.99

An analysis of the design details presented in Table 6. reveals that the base dimensions of axially loaded foundations are nearly square. However, as the moment level increases, one side of the foundation becomes longer than the other. Similarly, foundation thickness increases in parallel with the moment level. In optimum designs, the maximum base pressure approaches the net bearing capacity of the foundation soil. As the moment level rises, the difference between the minimum and maximum base pressures also increases.

The graph showing the variation of steel weight in Fig. 2 indicates that the total amount of reinforcement increases with the moment level. The reinforcement weight in the X-direction increases with the rise in M_{yy} moment, whereas the reinforcement in the Y-direction remains nearly constant after the second case. This is due to the fact that the M_{xx} moment remains constant in these cases.

As shown in Fig. 3, the cost of concrete, reinforcement, and total construction increases with the moment level. A 40% increase in the M_{yy} moment leads to an approximate 54% increase in concrete cost and a 52% increase in steel cost.

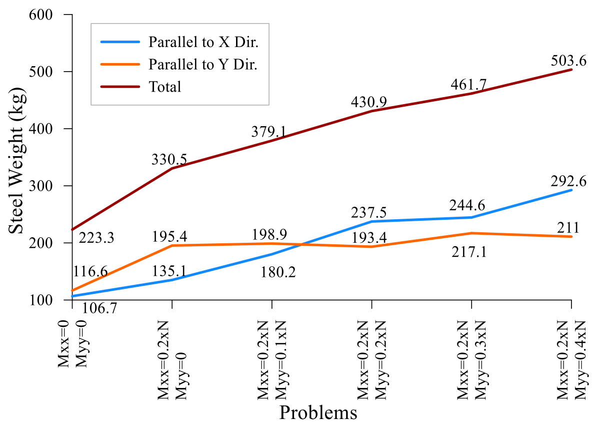

Fig. 2. Graph of the changes in the amount of main reinforcement in the problems

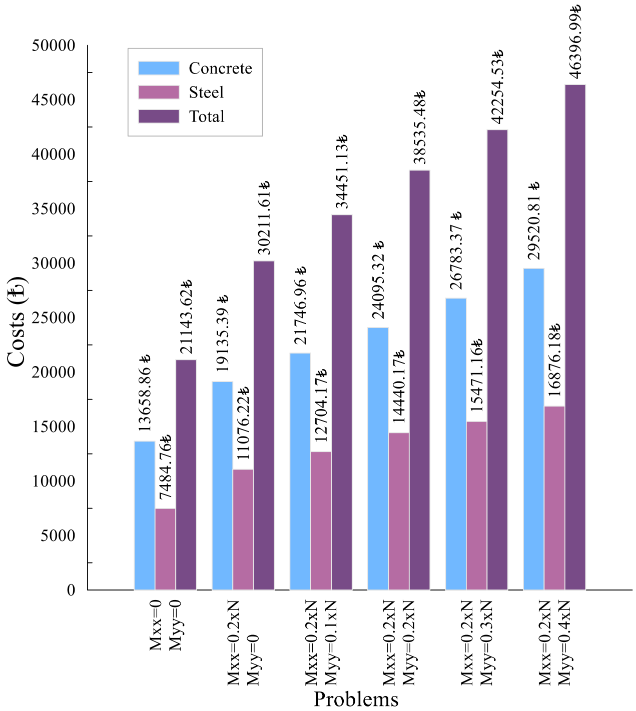

Fig. 3. Graph of the changes in concrete and reinforcement costs

3.3. Statistical performance tests

For the comparison of the proposed Ch-Rao algorithm with the Rao algorithms, two different statistical investigations were performed. The first performance evaluation is performed by comparing the mean solutions obtained from independent runs of the algorithms and their standard deviations. For this evaluation, Table 7. presents the mean costs and their standard deviations obtained from independent runs of the algorithms on six different problems. In order to better visually evaluate these statistical findings, box-plot plots have been prepared and are presented in Fig. 4.

When the mean costs and standard deviations of the costs obtained by the algorithms given in Table 7 are analyzed, it is seen that the Ch-Rao algorithm has the smallest mean cost value for all 6 different problems analyzed. However, the Ch-Rao algorithm achieved the lowest standard deviation in all problems except the fifth problem. This shows that Ch--Rao is statistically the most successful algorithm among the competing algorithms.

Similarly, examination of the box-plot graphs presented in Fig. 4 shows that the Ch-- Rao algorithm achieved the lowest means and the lowest standard deviation in all problems except the fifth problem. However, when an evaluation is made between the Rao algorithm variants, it is seen that Rao2 algorithm has lower mean and standard deviation in some problems and Rao3 algorithm in others. This proves that the Rao algorithm variants do not have a stable performance in these problems. When the performance of the proposed Ch-Rao algorithm is evaluated in this respect, it can be said that the Ch-Rao algorithm shows a much more stable performance than the Rao algorithm variants

Table 7. Mean and standard deviation of algorithms

Problem	Algorithms			
No #	Ch-Rao	Rao1	Rao2	Rao3
1	21152.24 (10.96)	21161.31 (10.52)	21160.71 (9.44)	21165.02 (13.14)
2	30211.61 ($3.73\ 10^{-12}$)	30244.48 (48.73)	30214.79 (14.58)	30212.35 (3.38)
3	34453.16 (9.27)	34510.47 (72.12)	34469.94 (35.25)	34463.45 (35.53)
4	38538.49 (8.99)	38582.85 (80.78)	38544.25 (32.50)	38574.90 (78.17)
5	42311.87 (49.96)	42388.04 (112.00)	42344.93 (45.01)	42329.89 (20.38)
6	46316.98 (14.18)	46355.06 (67.03)	46339.98 (53.94)	46321.09 (31.13)

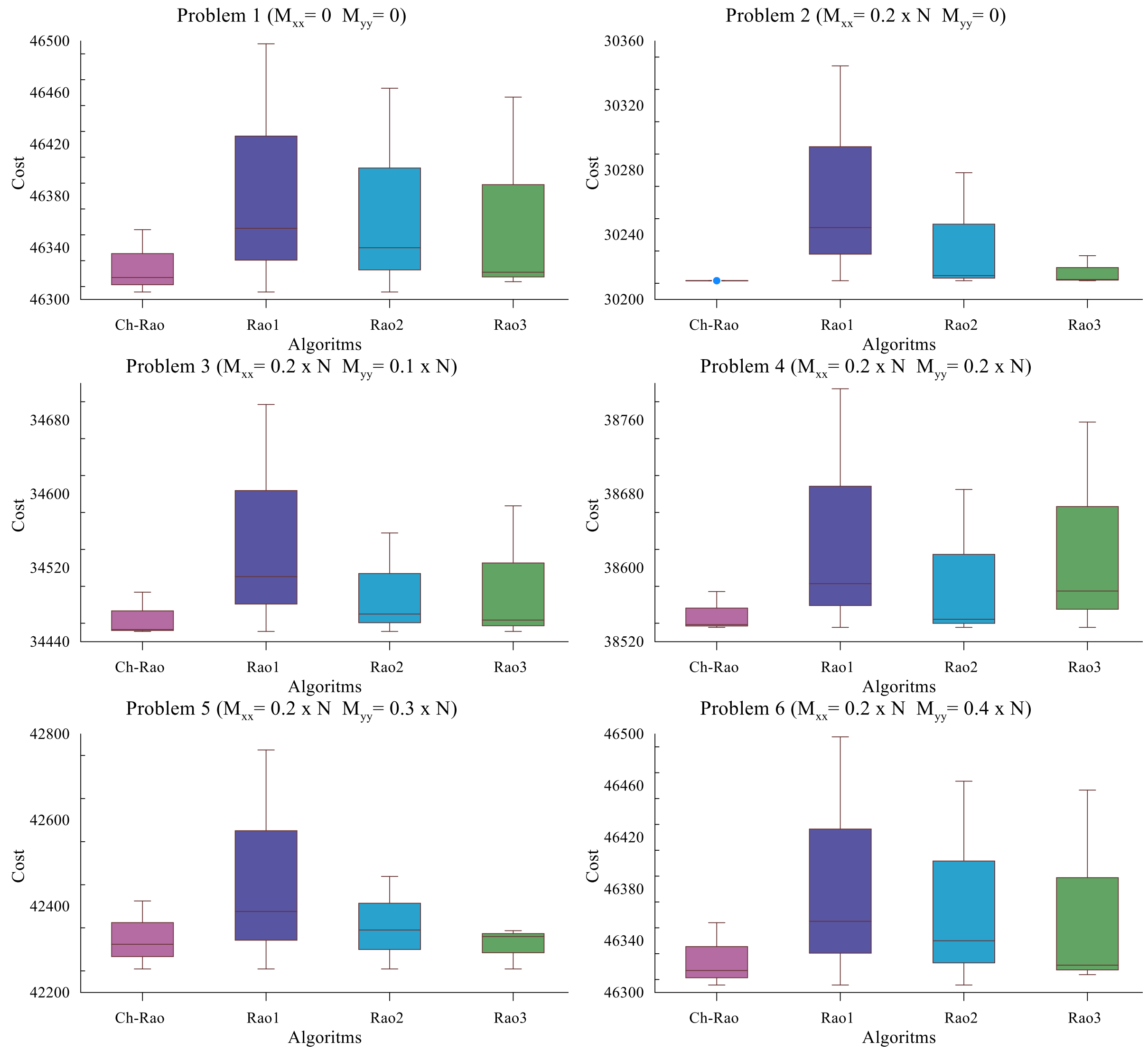

Fig. 4. Spread footing plans for the obtained best solutions

Table 8. Friedman scores of algorithms

	Friedman Scores						
Problem No #	1	2	3	4	5	6	
M_{xx} =	0	0.2xN	0.2xN	0.2xN	0.2xN	0.2xN	Mean
M_{yy} =	0	0	0.1xN	0.2xN	0.3xN	0.4xN	Score
Ch-Rao	1.79	2.26	1.98	2.07	2.24	2.12	2.08
Rao1	2.81	3.05	3.14	3.17	3.10	2.86	3.02
Rao2	2.60	2.33	2.50	2.24	2.24	2.60	2.42
Rao3	2.81	2.36	2.38	2.52	2.43	2.43	2.49

The second performance comparison was performed using the Friedman Test (Friedman, 1940). With this test, the scores of the algorithms on all problems are determined and presented in Table 8. Also, the mean score is calculated and given in the last column of Table 8.When Table 8. is analyzed, it is seen that the Ch-Rao algorithm ranked first in five problems. However, Ch-Rao algorithm and Rao2 algorithm share the first place in one problem. When the mean scores of all problems in the last column of Table 8. are analyzed, it is seen that Ch-Rao algorithm ranks first, Rao2 algorithm ranks second, followed by Rao3 and Rao1 algorithms respectively.

In summary, when all statistical investigations are evaluated together, it is understood that the proposed Ch-Rao algorithm is more successful than the Rao algorithms in this problem set where the optimum design of symmetric foundations subjected to axial load, one-axis combined bending and two-axis combined bending is performed.

4. Conclusions

In this study, a novel Chaotic Rao (Ch-Rao) algorithm was proposed to address the cost-optimal design of reinforced concrete spread footings subjected to axial load, uniaxial bending, and biaxial bending moments. The Ch-Rao algorithm enhances the original Rao family by incorporating chaotic reference signals to dynamically switch between different update equations, thereby improving exploration and exploitation capabilities during the optimization process.

The performance of the proposed algorithm was evaluated through a series of simulation studies on six parametric foundation design problems. These problems considered varying levels of moment and axial loading to reflect realistic structural demands. The optimization aimed to minimize total cost by balancing concrete volume and reinforcement quantity while satisfying structural, geometrical, and code-based constraints.

Results demonstrated that as the bending moment increased, the footing geometry and reinforcement demand changed accordingly, leading to increased foundation dimensions, thickness, and cost. The Ch-Rao algorithm consistently produced lower mean cost values than the original Rao algorithms (Rao1, Rao2, Rao3) in all problem cases, and achieved the lowest standard deviation in five out of six problems, indicating both accuracy and stability. Statistical analyses, including the Friedman test, further confirmed the superior performance of the Ch-Rao algorithm in terms of ranking and consistency.

Overall, the findings highlight that the Ch-Rao algorithm is an effective and robust optimization tool for the cost-efficient design of reinforced concrete spread footings under complex loading conditions. Its enhanced adaptability through chaotic switching mechanisms provides a promising direction for future research in structural optimization, particularly for real-world civil engineering applications where multiple objectives and constraints are involved.

References

Arabali, A., Khajehzadeh, M., Keawsawasvong, S., Mohammed, A. H., & Khan, B. (2022). An Adaptive Tunicate Swarm Algorithm for Optimization of Shallow Foundation. *IEEE Access*, *10*, 39204–39219.

Camp, C. V., & Assadollahi, A. (2013). CO2 and cost optimization of reinforced concrete footings using a hybrid big bang-big crunch algorithm. *Structural and Multidisciplinary Optimization*, *48*(2), 411–426.

Chaudhuri, P., & Maity, D. (2020). Cost optimization of rectangular RC footing using GA and UPSO. *Soft Computing*, *24*(2), 709–721.

Friedman, M. (1940). A Comparison of Alternative Tests of Significance for the Problem of m Rankings. *The Annals of Mathematical Statistics*, *11*(1), 88–92.

Islam, M. S., & Rokonuzzaman, M. (2018). Optimized design of foundations: an application of genetic algorithms. *Australian Journal of Civil Engineering*, *16*(1), 46–52.

Kashani, A. R., Gandomi, M., Camp, C. V., & Gandomi, A. H. (2020). Optimum design of shallow foundation using evolutionary algorithms. *Soft Computing*, *24*(9), 6809–6833.

Khajehzadeh, M., Iraji, A., Majdi, A., Keawsawasvong, S., & Nehdi, M. L. (2022). Adaptive Salp Swarm Algorithm for Optimization of Geotechnical Structures. *Applied Sciences (Switzerland)*, *12*(13).

Khajehzadeh, M., Keawsawasvong, S., & Nehdi, M. L. (2022). Effective Hybrid Soft Computing Approach for Optimum Design of Shallow Foundations. *Sustainability (Switzerland)*, *14*(3).

Khajehzadeh, M., Raihan Taha, M., El-Shafie, A., & Eslami, M. (2012). Optimization of Shallow Foundation Using Gravitational Search Algorithm. *Research Journal of Applied Sciences Engineering and Technology*, *4*(9), 1124–1130.

Khajehzadeh, M., Taha, M. R., & Eslami, M. (2013). A new hybrid firefly algorithm for foundation optimization. *National Academy Science Letters*, *36*(3), 279–288.

Nigdeli, S. M., Bekdaş, G., & Yang, X. S. (2018). Metaheuristic Optimization of Reinforced Concrete Footings. *KSCE Journal of Civil Engineering*, *22*(11), 4555–4563.

Öztürk, H. T. (2018). Cost optimum design of spread footing under uniaxial combined bending according to TS500 via various metaheuristic algorithms. *Pamukkale University Journal of Engineering Sciences*, *24*(6), 1030–1036.

Rao, R. V. (2020). Rao algorithms: Three metaphor-less simple algorithms for solving optimization problems. *International Journal of Industrial Engineering Computations*, *11*(1), 107–130.

4th International Civil Engineering & Architecture Conference
17-19 May 2025, Trabzon, Türkiye

Parametric analysis for axially functionally graded beams developed using different micromechanical models

Sarah S. M. A. Sayed[1], Merve Ermis[*1], Nihal Eratli[2]

[1] Kırklareli University, Department of Civil Engineering, 39000 Kırklareli, Türkiye
[2] Istanbul Technical University, Department of Civil Engineering, 34467 Istanbul, Türkiye

Abstract. The increased use of functionally graded beams in many applications due to their attractive properties in strength, stiffness, and lightness has resulted in a growing demand for such mechanical, civil, mechatronics, and aerospace engineering in the design of structures (such as bridges, railways, and aircraft). The scope of this study is to investigate the static analysis behavior of axially functionally graded straight beams developed using different micromechanical models, utilizing the mixed finite element method. The two-noded mixed finite element formulation is based on the Timoshenko beam theory, and each node has twelve degrees of freedom, namely three translations, three rotations, two shear forces, one axial force, two bending moments, and one torque. The functionally graded material consists of metal-matrix and ceramic-particle materials. The volume fraction ratios of ceramic and metal materials vary along the beam axis. Effective material properties (modulus of elasticity and Poisson's ratio) have been described through three different micromechanical models (Voigt, Mori-Tanaka, and Reuss). Numerical solutions are performed to analyze the static behavior of axially functionally graded straight beams. The results obtained using the mixed finite element method are compared with those from the displacement-based finite element method (ANSYS BEAM188). In the benchmark example, the effect of different micromechanical models has been investigated through a parametric study on the static analysis behavior (displacements, forces, and moments) of axially functionally graded straight beams. In this parametric study, static analysis results for different material gradient parameters, ceramic material content, and boundary conditions have been discussed in detail.

Keywords: Axially functionally graded beam; Micromechanics model; Finite element method; Timoshenko beam theory; Static analysis

1. Introduction

The utilization of composite materials is prevalent in sectors such as the defense/space industry, mechanical and civil engineering (Saleh et al., 2020). Composite materials offer advantages over homogeneous isotropic materials in scenarios involving sudden temperature/load fluctuations or corrosion due to their inherent properties, such as high strength, light weight, and adaptability to environmental factors (Sofiyev, 2019). In traditional composite materials (e.g., laminated composites), sudden temperature changes and various loads can lead to delamination or cracks between layers. In recent years, advancements in material production technologies have facilitated the development of functionally graded (FG) materials, which possess excellent mechanical and chemical properties, such as low thermal conductivity, low friction coefficient, high hardness, and resistance to wear. FG materials are two-phase composite materials characterized by a continuously varying function in the desired directions. This continuous variation in material properties, or functional grading, enhances the durability of these materials under sudden temperature changes or impact loads (Kır et al., 2021).

The primary objective of material mechanics is to predict the behavior of materials. Known as homogenization, this method estimates the effective mechanical properties of a material composed of different components (Karami et al., 2019). In the absence of precise information regarding the size, shape, and distribution of the components of an FG material, the effective elasticity modulus of the graded microstructure should be determined based on the volume fractions of the relevant components and the approximate shape of the dispersed phase. Over the years, various micromechanical models have been developed to determine the effective mechanical properties of macroscopically homogeneous composites and graded composite materials like FG materials (Srividhya et al., 2018). Among these micromechanical models, the most widely recognized and utilized model is the rule of mix-

*Corresponding author, E-mail: mermis@klu.edu.tr

https://doi.org/10.31462/icearc2025_ce_sme_721

tures (Voigt, 1889). Other notable micromechanical models include the Hashin-Shtrikman bounds (Mishnaevsky, 2007), Mori-Tanaka homogenization scheme (Benveniste, 1987; Mori & Tanaka 1973), Reuss model (Reuss, 1929), Tamura model (Tamura, 1973; Zuicker, 1995), and the local cubic representative volume element (Gasik & Lilius 1994). Within this scope, numerous studies in the literature employ various micromechanical models to determine the effective material properties, such as elastic modulus and Poisson's ratio, of functionally graded (FG) materials. These studies examine the static, dynamic, and buckling behaviors of plates and beams (Akbarzadeh et al., 2015; Alshabatat et al., 2016; Ebrahimi & Barati, 2017; Fan et al., 2020; Gupta & Talha, 2017; Kiani & Eslami, 2015; Loja et al., 2012; Sahmani & Safaei, 2020; Shahsavari & Karami, 2022; Shen & Wang, 2012; Wang & Wu, 2016; Yadav et al., 2021; Yuan et al., 2020a and 2020b; Zhang & Wang, 2019).

Regarding studies investigating the structural behavior of axially FG beams; Aydogdu (2008) analyzes the free vibration and buckling behavior of axially FG simply supported beams using the Euler–Bernoulli beam theory and the semi-inverse method. Based on the Euler- Bernoulli beam theory, the linear dynamic behavior of axially FG simply supported beams under moving harmonic loads, has been investigated in (Şimşek et al., 2019). The elasticity modulus and density of the beam vary exponentially along its axis. The equations of motion are derived using Lagrange's equations. The unknown functions representing the transverse displacements of the axially FG beam are expressed in a modal framework, and the Newmark method is employed to determine its dynamic behavior. Babilio (2013) investigates the time-dependent dynamic behavior of axially FG simply supported beams under axial loading. In (Calim, 2016), the free and forced vibration behavior of axially FG Timoshenko beams resting on a two-parameter viscoelastic foundation is investigated. The complementary function method is applied in the Laplace domain for the forced vibration analysis, where differential equations are computed to obtain solutions. Subsequently, the solutions in the Laplace domain are transformed into the time domain using the Durbin method. Shafiei et al. (2016) investigate the size-dependent nonlinear vibration behavior of axially FG microbeams with variable cross-sections. The microbeam is modeled using the modified couple stress theory, incorporating the Euler–Bernoulli beam theory and von Kármán’s geometric nonlinearity. The study examines three distinct boundary conditions: clamped-clamped, simply supported, and clamped-fixed. The equations of motion and boundary conditions are derived using Hamilton’s principle. Subsequently, the constitutive relations are solved using the generalized differential quadrature method and the direct iterative approach. Wang and Wu 2016 investigate the dynamic behavior of axially FG beams subjected to temperature variations and moving harmonic loads, employing both the classical beam theory and the Timoshenko beam theory. The equations governing the thermal buckling of the functionally graded beam are derived using Lagrange's method. Subsequently, the critical buckling temperature is incorporated as a parameter in the Newmark method to characterize the dynamic response of the axially FG beam under thermal effects. Azimi et al. (2017) investigate the in-plane nonlinear free vibration behavior of rotating axially FG Timoshenko beams under thermal loading. The equation of motion for the nanobeam is derived using Hamilton’s principle, incorporating Eringen’s nonlocal elasticity theory to account for nanoscale effects in the axially FG beam. Subsequently, the constitutive relations are solved using the generalized differential quadrature method. Ghayesh (2018) examines the nonlinear free vibration behavior of axially FG beams with variable cross-sections under harmonic loading. The equations of motion for the axially FG beam are derived using Hamilton’s energy principle based on the third-order shear deformation theory. The forced vibration behavior of axially FG beams has been investigated in (Ermis et al., 2019) using the mixed finite element method. Aribas et al. (2019) analyze the damped forced vibration behavior of axially FG beams using the mixed finite element method. Sharma et al. (2020) investigate the modal analysis of axially FG beams under humidity and thermal effects using the finite element method. Wang et al. (2020) examine the structural behavior of axially FG microbeams subjected to moving mass effects under thermal and humidity influences. The microbeam model is developed based on the first-order shear deformation theory, incorporating the modified couple stress theory and a closed-form solution method that accounts for size effects. Ebrahimi-Mamaghani et al. (2022) investigate the thermo-mechanical behavior of axially FG fluid-conveying pipes under fluid interaction. The equations of motion are derived using Rayleigh beam theory, incorporating both linear and nonlinear temperature-stress relationships. To solve these equations, the stability region is determined using the Galerkin discretization method and eigenvalue analysis. Using the interpolation matrix method, Ge et al. (2022) determine the critical buckling load of axially FG Timoshenko beams with variable cross-sections. Wadi et al. (2022) present the static displacement solution of an axially FG cantilever beam, formulated based on Euler–Bernoulli beam theory, through the application of the Rayleigh method and the finite element method. Elyasi et al. (2023) determine the vibration behavior of axially FG beams with variable cross-sections and damping under axial loading using the Galerkin method and the state-space formulation. Yadeem et al. (2024) investigate the free vibration behavior of simply supported axially functionally graded beams using the Rayleigh method, incorporating a power-law material distribution model, and demonstrate its accuracy and effectiveness in capturing the influence of power-law index, modulus-ratio, and density-ratio on natural frequencies and mode shapes.

This study investigates the static behavior of axially FG straight beams using different micromechanical models within a mixed finite element framework. The formulation is based on Timoshenko beam theory. It employs a two-node element with twelve degrees of freedom per node, including displacements, sectional rotations, internal forces, bending moments, and a torsional moment. A parametric analysis is presented on the influence of micromechanical model selection, material gradation parameters, and boundary conditions on maximum displacements, shear forces, and bending moments by using the outcomes of Sayed (2023).

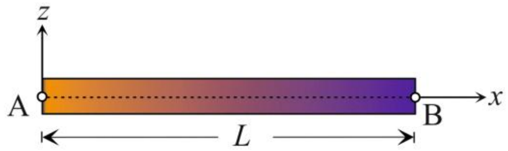

Fig.1 Axially functional graded (AFG) straight beam (Sayed, 2023)

2. Formulation for axially functionally graded straight beam

Functionally graded (FG) materials are derived by combining two different substances—one with a matrix and the other with particles or inclusions—in specified volume ratios. The volume fractions $(V_m$ and $V_i)$ of the matrix and particulate constituents within the functionally graded straight axis beams along the beam axis (x) direction can be defined through the following exponential function along the beam axis:

$$V_i\left(x\right)=V_{\mathrm{A}}+\left(V_B-V_{\mathrm{A}}\right)\left(\frac{x}{L}\right)^{n_h}, \quad 0\le x\le L \tag{1}$$

$$V_i\left(x\right)+V_m\left(x\right)=1 \tag{2}$$

The subscripts "i" and "m" represent the inclusions and the matrix, respectively. n_h is the non-homogeneity index $(n_h\ge 0)$. L is the total length of the beam. V_{A} and V_{B} are the volume fractions of the inclusions at the initial point A $(x=0)$ and the end point B ($x=L$) of the straight beam (Fig. 1). In this study, at the initial of the beam (point A, $V_{\mathrm{A}}=1$), the material is assumed to be composed of %100 ceramic, whereas at the end of the beam (point B, $V_{\mathrm{B}}=0$), it is assumed to be composed of %100 metal (Sayed, 2023).

2.1. Micromechanical material models

In this study, the micromechanical models used to determine the effective material properties (E_{eff}, υ_{eff}, ρ_{eff}) of functionally graded materials include the Voigt model, the lower bound of the Hashin-Shtrikman model (Mori-Tanaka), and the Reuss model (Benveniste, 1987; Mishnaevsky, 2007; Mori & Tanaka, 1973; Reuss, 1929; Voigt, 1889). The manner in which these micromechanical models (using the volume fractions V_m and V_i defined in Eqs. (1) and (2)) characterize the effective material constants is presented below, respectively.

Voigt model: The effective elasticity modulus, and Poisson's ratio can be obtained as follows:

$$P_{\mathrm{eff}}=P_iV_i+P_mV_m=\left(P_i-P_m\right)V_i+P_m \tag{3}$$

where P represents elasticity modulus and Poisson's ratio of the material.

Mori-Tanaka model: In this micromechanical model, also known as the lower bound of the Hashin-Shtrikman model, the effective bulk modulus and shear modulus can be given as follows:

$$K_{\mathrm{eff}}=K_m+\frac{V_i}{\dfrac{1}{K_i-K_m}+\dfrac{3\left(1-V_i\right)}{3K_m+4G_m}}, \quad G_{\mathrm{eff}}=G_m+\frac{V_i}{\dfrac{1}{G_i-G_m}+\dfrac{6\left(K_m+2G_m\right)\left(1-V_i\right)}{5G_m\left(3K_m+4G_m\right)}} \quad \left(i\ne m\right) \tag{4}$$

The effective elasticity modulus and Poisson's ratio are obtained using Eq. (4)

$$E_{\mathrm{eff}}=\frac{9K_{\mathrm{eff}}G_{\mathrm{eff}}}{\left(3K_{\mathrm{eff}}+G_{\mathrm{eff}}\right)}, \quad \upsilon_{\mathrm{eff}}=\frac{3K_{\mathrm{eff}}-2G_{\mathrm{eff}}}{2\left(3K_{\mathrm{eff}}+G_{\mathrm{eff}}\right)} \tag{5}$$

Reuss model: According to this model, the effective material properties are:

$$P_{\mathrm{eff}}=\frac{P_iP_m}{\left(P_m-P_i\right)V_i+P_i} \tag{6}$$

where P represents elasticity modulus and Poisson's ratio of the material. The effective density of material can be obtained by Voigt homogenization scheme for all considered micromechanical models.

$$\rho_{\mathrm{eff}}=\left(\rho_i-\rho_m\right)V_i+\rho_m \tag{7}$$

In this study, aluminum (Al) has been selected as the metal material, and zirconia (ZrO_2), silicon carbide (SiC), and alumina (Al_2O_3) as ceramic materials. The material constants are defined as follows: the modulus of elasticity is 70 GPa for aluminium (Al), 200 GPa for zirconia (ZrO_2), 302 GPa for silicon carbide (SiC), and 380 GPa for alumina (Al_2O_3). The corresponding Poisson's ratios are 0.30 for Al, 0.30 for ZrO_2, 0.17 for SiC, and 0.30 for Al_2O_3. The variation of the effective elastic modulus values obtained using the Voigt micromechanical model with respect to the normalized beam length (x/L) for the ceramic inclusions (Al_2O_3 , SiC , ZrO_2) and different material gradient parameter values $(n_h = 0.5, 1, 1.5, 2, 3 \text{ and } 5)$ is presented in Fig. 2. The variation of the effective elasticity modulus obtained using different micromechanical models (Voigt, Mori-Tanaka, Reuss) with respect to the normalized beam length (x/L) is also presented in Fig. 3 for the selected ceramic material (Al_2O_3) and the variation parameter $(n_h = 1)$.

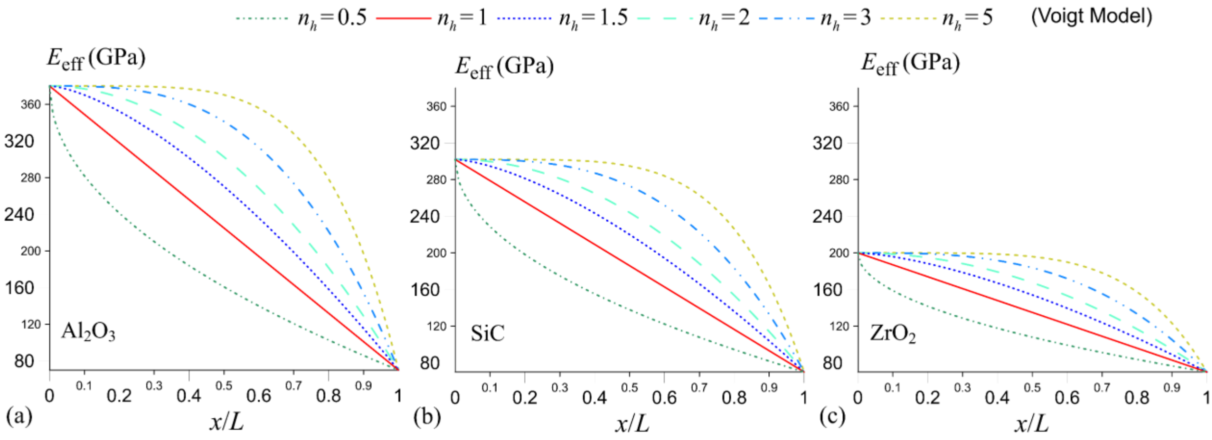

Fig. 2. Variation of the effective elastic modulus of the axially functionally graded straight beam with respect to the normalized AFG beam length (x / L) (Voigt model) (Sayed, 2023)

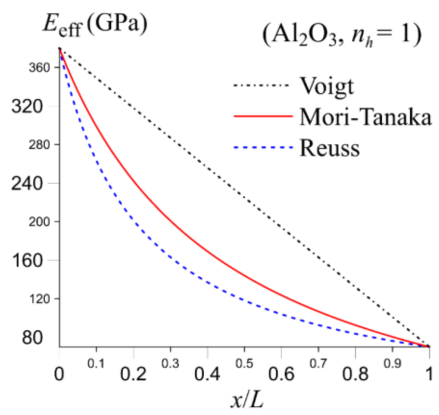

Fig. 3. Variation of the effective elastic modulus of the AFG straight beam with respect to the normalized beam length (x / L) for different micromechanical models (Al_2O_3 and $n_h = 1$) (Sayed, 2023)

2.2. Field equations

The field equations in Frenet coordinates (t, n, b) for isotropic spatial Timoshenko beams (Omurtag & Aköz, 1992) are extended to AFG straight beam in Fig. 1 and given as follows:

$$\left.\begin{aligned} -T_{x,x} + \rho_{\text{eff}} A\ddot{u}_x - q_x &= 0 \\ -T_{y,x} + \rho_{\text{eff}} A\ddot{u}_y - q_y &= 0 \\ -T_{z,x} + \rho_{\text{eff}} A\ddot{u}_z - q_z &= 0 \\ -M_{x,x} + \rho_{\text{eff}} I_x \ddot{\Omega}_x - m_x &= 0 \\ -M_{y,x} + T_z + \rho_{\text{eff}} I_y \ddot{\Omega}_y - m_y &= 0 \\ -M_{z,x} - T_y + \rho_{\text{eff}} I_z \ddot{\Omega}_z - m_z &= 0 \end{aligned}\right\} \quad \text{equations of motion} \qquad (8)$$

$$\left.\begin{aligned} u_{x,x}-T_x/E_{\text{eff}}A=0 \\ u_{y,x}-\varOmega_z-2\left(1+\upsilon_{\text{eff}}\right)k_y' T_y/E_{\text{eff}}A=0 \\ u_{z,x}+\varOmega_y-2\left(1+\upsilon_{\text{eff}}\right)k_z' T_z/E_{\text{eff}}A=0 \\ \varOmega_{x,x}-M_x/G(x)I_x=0 \\ \varOmega_{y,x}-M_y/E_{\text{eff}}I_y=0 \\ \varOmega_{z,x}-M_z/E_{\text{eff}}I_z=0 \end{aligned}\right\}\quad \text{constitutive equations} \tag{9}$$

where u, $\varOmega$, T and M are the displacement, the cross sections' rotation, the force and the moment, respectively. $\ddot{u}$ and $\ddot{\varOmega}$ are the acceleration of the displacement and rotation, respectively. A is the area of the cross section, I is the moment of inertia. ρ_{eff}, E_{eff} and υ_{eff} are the effective material density, elasticity modulus and Poisson's ratio, respectively. $G(x)I_x$ demonstrates the torsional rigidity by considering the warping effect in non-circular cross-sections (Ermis et al., 2022). Timoshenko beam theory is taken into consideration with the constant shear correction factor $k=5/6$, and $k'=k_y'=k_z'=1/k$. q and m are the distributed external force and moment, respectively.

2.3. Funtional

By employing the field equations expressed in Eqs. (8) and (9) the functional of an axially straight beam is derived using Gâteaux differential and the potential operator concept (Oden & Reddy 1976). The acceleration terms are $\ddot{u}$ and $\ddot{\varOmega}=0$ for static analysis.

$$\begin{aligned} I(y)=&-\left[T_{x,x},u_x\right]-\left[T_{y,x},u_y\right]-\left[T_{z,x},u_z\right]-\left[M_{x,x},\varOmega_x\right]-\left[M_{y,x},\varOmega_y\right]-\left[M_{z,x},\varOmega_z\right]-\left[\varOmega_z,T_y\right]+\left[\varOmega_y,T_z\right] \\ &-\tfrac{1}{2GI_x}\left[M_x,M_x\right]-\tfrac{1}{2E_{\text{eff}}I_y}\left[M_y,M_y\right]-\tfrac{1}{2E_{\text{eff}}I_b}\left[M_z,M_z\right]-\tfrac{1}{2E_{\text{eff}}A}\left[T_x,T_x\right]-\tfrac{(1+\upsilon_{\text{eff}})k_y'}{E_{\text{eff}}A}\left[T_y,T_y\right]-\tfrac{(1+\upsilon_{\text{eff}})k_z'}{E_{\text{eff}}A}\left[T_z,T_z\right] \\ &-\left[q_x,u_x\right]-\left[q_y,u_y\right]-\left[q_z,u_z\right]-\left[m_x,\varOmega_x\right]-\left[m_y,\varOmega_y\right]-\left[m_z,\varOmega_z\right]+\Big\langle\left(\left(T_x-\hat{T}_x\right),u_x\right)+\left(\left(T_y-\hat{T}_y\right),u_y\right) \\ &+\left(\left(T_z-\hat{T}_z\right),u_z\right)+\left(\left(M_x-\hat{M}_x\right),\varOmega_x\right)+\left(\left(M_y-\hat{M}_y\right),\varOmega_y\right)+\left(\left(M_z-\hat{M}_z\right),\varOmega_z\right)\Big\rangle_{\sigma} \\ &+\Big\langle\left(T_x,\hat{u}_x\right)+\left(T_y,\hat{u}_y\right)+\left(T_z,\hat{u}_z\right)+\left(M_x,\hat{\varOmega}_x\right)+\left(M_y,\hat{\varOmega}_y\right)+\left(M_z,\hat{\varOmega}_z\right)\Big\rangle_{\varepsilon} \end{aligned} \tag{10}$$

where the square brackets indicate the inner product, the terms with hats are known values on the boundary, and the subscripts ε and σ represent the geometric and dynamic boundary conditions, respectively (Eq. (10)).

2.4. Mixed finite element

A two-noded curved element based on Timoshenko beam theory is used in the construction of mixed finite element (MFE) matrices. Dimensionless coordinates (ξ) are used in the FE derivation and the linear shape functions are used as $\phi_i=1-\xi$ and $\phi_j=\xi$, where $\xi=(x-x_i)/\Delta L$, $0<\xi<1$ and $\Delta L=(x_j-x_i)$. The subscripts *i* and *j* is the local node number of start and end point for the element, respectively. The mixed type field variables at each node are

$$u_x,\ u_y,\ u_z,\ \varOmega_x,\ \varOmega_y,\ \varOmega_z,\ T_x,\ T_y,\ T_z,\ M_x,\ M_y,\ M_z \tag{11}$$

where u, $\varOmega$, T and M are the displacement, the cross sections' rotation, the force and the moment, respectively. Hence, the total DOF of the straight element are 24. The details of the mixed FE formulation and axially FG beam exist in (Omurtag & Aköz, 1992; Ermis et al., 2022; Oden & Reddy, 1976; Eratlı et al., 2016; Sayed, 2023).

3. Numerical examples

3.1. Convergence study – Mixed FEM and ANSYS analyses

A convergence test for mixed FEM and ANSYS-BEAM188 is carried out for the static analysis of axially FG straight beams subjected to uniformly distributed loaded, using Voigt micromechanics model. Parameters of the problem are: Ceramic material is Alumina (Al_2O_3), the non-homogeneity index is $n_h=1$, the length, width and height of the beam are $L=12\text{m}$, $w=0.5\text{m}$ and $h=0.4\text{m}$, respectively. The intensity of the uniform loading is taken $q_z=10$ N/m. The boundary condition is clamped-clamped. The convergence test for axially FG straight beams using Voigt micromechanics model is performed for the number of elements $n_e=10,20,30,40,60,80$ over mixed FEM and ANSYS-BEAM188. The results (the maximum displacement $u_z^{\max}$, the shear forces T_z^{A} and T_z^{B}, the moments M_y^{A} and M_y^{B} at the fix ends) are plotted in Fig. 4. Taking into account all micromechanical models

(Sayed, 2023), the maximum absolute percentage differences are 0.32% for the mixed finite element method and 0.04% for the displacement-type finite element method (BEAM188), respectively. In the following examples for axially FG straight beams, $n_e = 80$ is used.

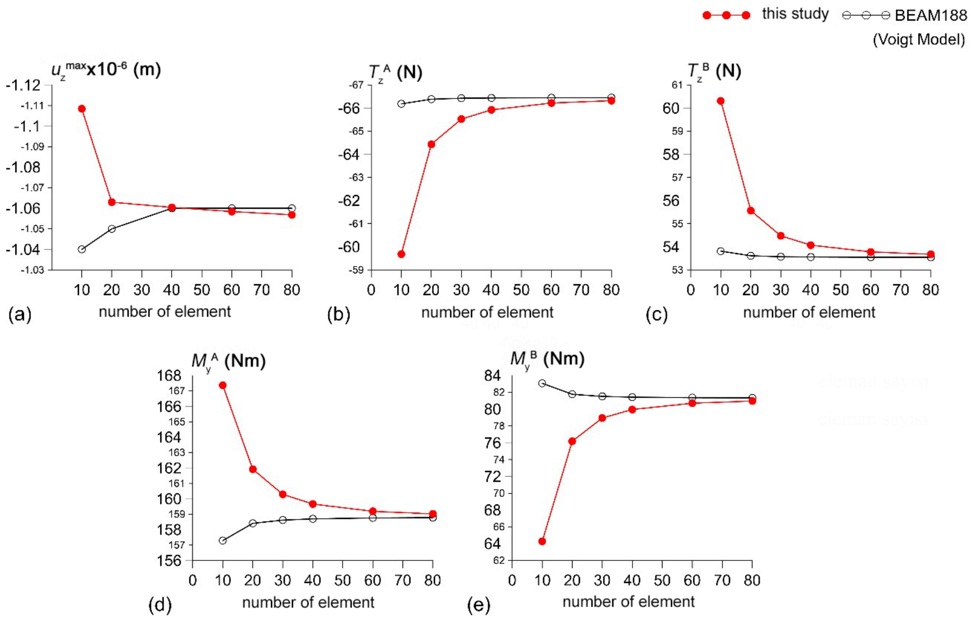

Fig. 4. Convergence analysis of the static analysis results (u_z^{max}, T_z^A, T_z^B, M_y^A, M_y^B) for the axially FG straight beam (Voigt model and clamped-clamped boundary condition)

3.2. Parametric analysis

This section examines the static behavior of axially FG straight beams developed through different micromechanical models under the effect of uniformly distributed loads. The investigation focuses on the maximum displacements, the shear forces, and bending moments through the beam domain. The effects of ceramic material, material variation parameter, and boundary conditions are analyzed comprehensively. The geometry and cross-sectional properties of the beam are the same as those presented in Section 3.1. The material and boundary condition information related to the problem under consideration is provided as follow: The ceramic inclusions are Al_2O_3, SiC and ZrO_2, respectively. Three different boundary conditions are considered: clamped-free, clamped-pinned, and clamped-clamped. The maximum displacements for all boundary conditions are plotted against the material gradient parameter in Fig. 5. The maximum shear forces and bending moments for the clamped-clamped and clamped-pinned boundary conditions are plotted against the material gradient parameter in Figs. 6 and 7, respectively.

3.2.1 The maximum vertical displacements

As the material gradient index increases from 0.5 to 5, the maximum vertical displacement decreases across all boundary conditions and micromechanical models. This reduction in displacement implies that a higher gradient index corresponds to a stiffer beam, as the increase in n_h makes the beam richer in ceramic material, thereby diminishing the displacement under the same load. The reduction in the vertical displacements is calculated by using the $\text{diff}^{n_h}.\% = \left|\Theta_{n_h=0.5} - \Theta_{n_h=5}\right| \times 100 \big/ \left|\Theta_{n_h=0.5}\right|$.

The maximum reduction of clamped-clamped boundary conditions are as follows:

- In case Al_2O_3, the percent differences are 54.4%, 52.0%, and 43.1% for the Reuss, Mori-Tanaka, and Voigt models, respectively.
- In case SiC, the percent differences are 49.0%, 46.5%, and 39.5% for the Reuss, Mori-Tanaka, and Voigt models, respectively.
- In case ZrO_2, the percent differences are 37.5%, 35.6%, and 31.6% for the Reuss, Mori-Tanaka, and Voigt models, respectively.

The maximum reduction of clamped-pinned boundary conditions are as follows:

- In case Al_2O_3, the percent differences are 59.5%, 58.1%, and 49.8% for the Reuss, Mori-Tanaka, and Voigt models, respectively.

- In case SiC , the percent differences are 54.4%, 52.8%, and 46.1% for the Reuss, Mori-Tanaka, and Voigt models, respectively.
- In case ZrO_2 , the percent differences are 43.1%, 41.6%, and 37.6% for the Reuss, Mori-Tanaka, and Voigt models, respectively.

The maximum reduction of clamped-free boundary conditions are as follows:

- In case Al_2O_3 , the percent differences are 63.0%, 56.2%, and 36.6% for the Reuss, Mori-Tanaka, and Voigt models, respectively.
- In case SiC , the percent differences are 56.2%, 49.5%, and 34.1% for the Reuss, Mori-Tanaka, and Voigt models, respectively.
- In case ZrO_2 , the percent differences are 42.1%, 37.1%, and 28.1% for the Reuss, Mori-Tanaka, and Voigt models, respectively.

Among the three ceramic inclusions, Al_2O_3 - based FG beams exhibit the lowest vertical displacement due to their higher stiffness, while ZrO_2 - based beams demonstrate the highest displacement owing to their relative flexibility. The increase in the vertical displacements is calculated by using the $\text{diff}^c.\% = \left|\Theta_{\mathrm{Al_2O_3}} - \Theta_{c=i}\right| \times 100 \big/ \left|\Theta_{\mathrm{Al_2O_3}}\right|$ where i=SiC and ZrO_2 .

The increase in vertical displacements of clamped-clamped boundary condition are as follows:

- In case SiC , the percent differences for n_h=0.5~5 vary between 3.6%~15.9%, 5.6%~17.7, and 14.1%~21.4% for the Reuss, Mori-Tanaka, and Voigt models, respectively.
- In case ZrO_2 , the percent differences for n_h=0.5~5 range between 12.3%~53.9%, 19.1%~59.8, and 42.5%~71.4% for the Reuss, Mori-Tanaka, and Voigt models, respectively.

The increase in vertical displacements of clamped-pinned boundary condition are as follows:

- In case SiC , the percent differences for n_h=0.5~5 lie within the range of 3.9%~17.0%, 6.1%~19.6, and 16.2%~24.8% for the Reuss, Mori-Tanaka, and Voigt models, respectively.
- In case ZrO_2 , the percent differences for n_h=0.5~5 vary between 13.4%~59.2%, 21.1%~68.9, and 49.0%~85.4% for the Reuss, Mori-Tanaka, and Voigt models, respectively.

The increase in vertical displacements of clamped-free boundary condition are as follows:

- In case SiC , the percent differences for n_h=0.5~5 range between 5.5%~24.7%, 8.6%~25.2, and 20.9%~25.8% for the Reuss, Mori-Tanaka, and Voigt models, respectively.
- In case ZrO_2 , the percent differences for n_h=0.5~5 change between 19.1%~86.2%, 30.7%~87.8, and 67.2%~89.7% for the Reuss, Mori-Tanaka, and Voigt models, respectively.

Also, the presented figures clearly demonstrate the effect of boundary conditions on the vertical displacement. The clamped-clamped configuration exhibits the lowest vertical displacement, indicating the highest stiffness among the three boundary conditions (see Figs.5 (a)-(c)). The clamped-pinned configuration shows a higher displacement compared to the clamped-clamped case (Figs. 5 (a)-(c)), indicating a reduction in stiffness due to the pinned end (Figs. 5 (d)-(f)). Furthermore, the influence of increasing material gradient index is more pronounced in this configuration, highlighting its more flexible response. Notably, the reduction in displacement with increasing material gradient index is more significant in the clamped-free configuration (Figs.5 (g)-(i)) compared to the other boundary conditions.

3.2.2 The maximum shear forces and bending moments

The Mori-Tanaka and Reuss models yield similar trends, both providing higher shear force and bending moment magnitudes compared to the Voigt model for higher values on the material gradient index for both boundary conditions (Figs, 6 and 7). In the clamped-clamped boundary condition (Figs.6 (a)-(c)), as the material gradient index (n_h) increases from 0.5 to approximately 1.5, the shear force values increase for both the Mori-Tanaka and Reuss models. However, when the gradient index continues to rise from 1.5 to 5, the shear forces decrease. In contrast, for the Voigt model, the shear force values increase up to $n_h = 1$, but then start to decrease as the gradient index increases beyond 1. For the Mori-Tanaka and Reuss models, the bending moment behavior (Figs. 6(d)-(f)) is similar to that of the shear force. As the material gradient index (n_h) increases from 0.5 to approximately 1.5, the bending moment values increase and then decrease as n_h continues to rise from 1.5 to 5. However, in the case of the Voigt model, the maximum bending moment value consistently decreases as n_h increases, indicating a distinct behavior compared to the other two models (Mori-Tanaka and Reuss). For both clamped-pinned (Fig.7) and clamped-clamped boundary conditions, the behavior of shear forces and bending moments exhibits a similar trend.

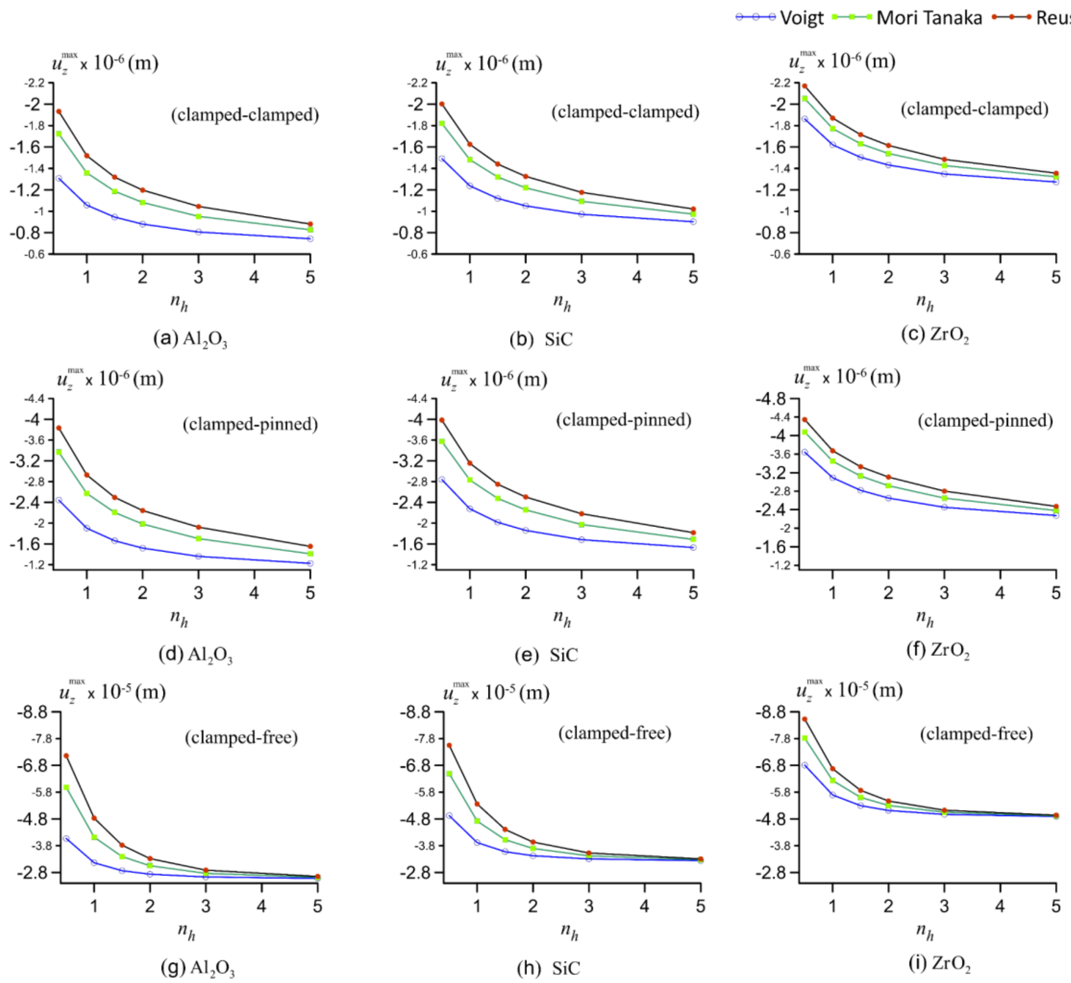

Fig.5 The maximum vertical displacements for different micromechanical models, ceramic constituents and boundary conditions.

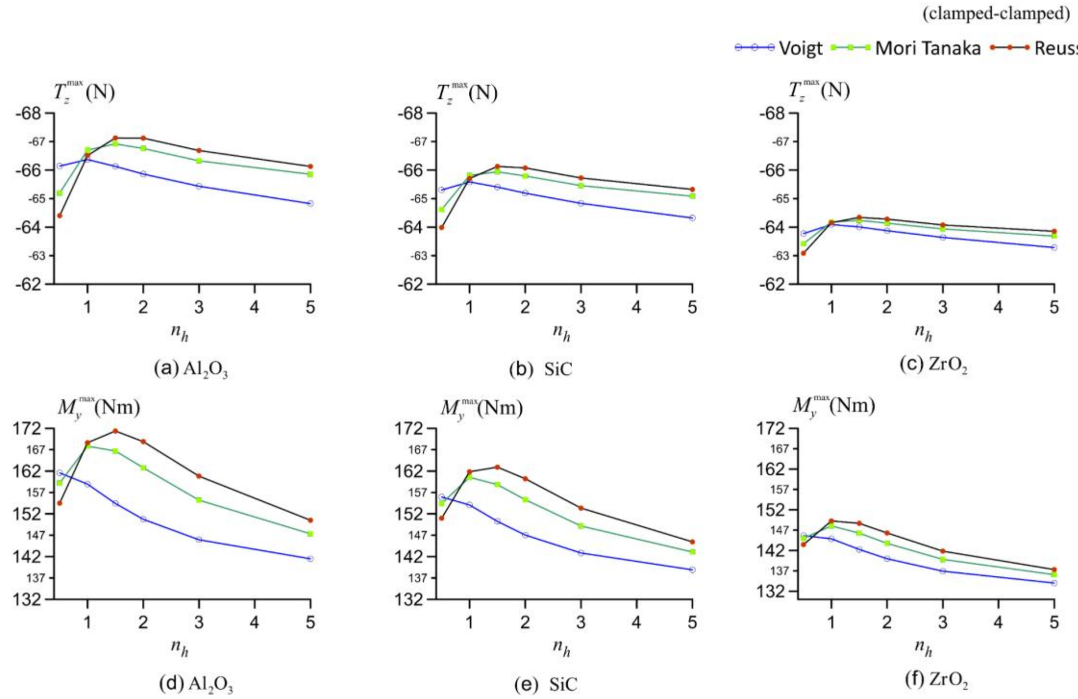

Fig.6 The maximum forces and moments of clamped-clamped boundary condition for different micromechanical models and ceramic constituents.

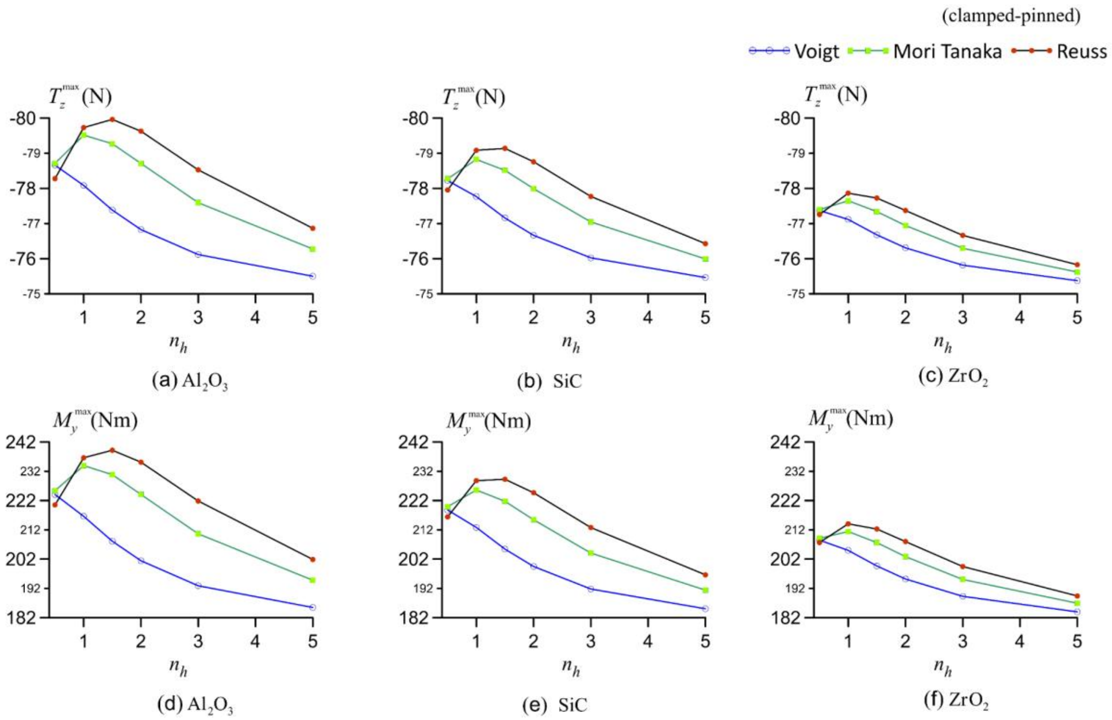

Fig.7 The maximum forces and moments of clamped-pinned boundary condition for different micromechanical models and ceramic constituents.

4. Conclusions

The static analysis behavior of axially FG straight beams under uniformly distributed loads has been investigated using the mixed finite element method with different micromechanical models. A mixed finite element formulation has been developed based on the Timoshenko beam theory, utilizing a two-node finite element. The results obtained from the mixed finite element method have been compared with those derived using the displacement-based finite element BEAM188 in ANSYS. It has been observed that the results from both methods are in good agreement (see Section 3.1). As part of the parametric analysis (Section 3.2), the influence of different micromechanical outcomes—such as displacements, shear forces and bending moments—has been examined in detail. The FG material consists of a metal matrix and ceramic models on the static analysis particle components, with the volume fractions of ceramic and metal materials varying along the beam axis. The effective material properties, including the elastisity modulus and Poisson's ratio, have been defined using three different micromechanical models: Voigt, Mori-Tanaka, and Reuss. The parametric analysis conducted within this study has thoroughly investigated the effects of varying ceramic content, material gradation parameters, and boundary conditions. The results of the parametric analysis are as follows:

- For each micromechanical model considered (Voigt, Mori-Tanaka, and Reuss), across different ceramic material (Al_2O_3 , SiC , ZrO_2) and boundary conditions (clamped-clamped, clamped-fixed, clamped-free), the maximum displacement u_z^{max} values reach their highest absolute magnitude at a material variation parameter of $(n_h = 0.5)$, while their lowest absolute magnitude is observed at $(n_h = 5)$.
- For each ceramic material, boundary condition, and material variation parameter considered $(n_h = 0.5, 1, 1.5, 2, 3 \text{ and } 5)$, the maximum displacement u_z^{max} values reach their highest absolute magnitude in the Reuss material model, while their lowest is observed in the Voigt material model.
- For an axially FG straight beam having clamped-clamped and clamped-pinned boundary conditions, the maximum shear force T_z^{max} and bending moments M_y^{max} initially increase as the material variation parameter rises, but then decrease. This behavior follows a continuous decreasing trend in the Voigt material model.

References

Akbarzadeh, A. H., Abedini, A., & Chen, Z. T. (2015). Effect of micromechanical models on structural responses of functionally graded plates. *Composite Structures, 119*, 598–609.

Alshabatat, N. T., Myers, K., & Naghshineh, K. (2016). Design of in-plane functionally graded material plates for optimal vibration performance. *Noise Control Engineering Journal, 64*(2), 268–278.

ANSYS Inc. (2016). *ANSYS® Academic Research Mechanical, Release 17.1* [Computer software]. Canonsburg, PA: ANSYS Inc.

Aribas, U. N., Ermis, M., Kutlu, A., Eratli, N., & Omurtag, M. H. (2019). Elastically damped transient response of axially FG straight beams. *International Journal of Theoretical and Applied Mechanics, 4*, 19–25.

Aydogdu, M. (2008). Semi-inverse method for vibration and buckling of axially functionally graded beams. *Journal of Reinforced Plastics and Composites, 27*(7), 683–691. https://doi.org/10.1177/0731684407081369

Azimi, M., Mirjavadi, S. S., Shafiei, N., & Hamouda, A. M. S. (2017). Thermo-mechanical vibration of rotating axially functionally graded nonlocal Timoshenko beam. *Applied Physics A, 123*(1), 104. https://doi.org/10.1007/s00339-016-0712-5

Babilio, E. (2013). Dynamics of an axially functionally graded beam under axial load. *The European Physical Journal Special Topics, 222*(7), 1519–1539. https://doi.org/10.1140/epjst/e2013-01942-8

Benveniste, Y. (1987). A new approach to the application of Mori–Tanaka's theory of composite materials. *Mechanics of Materials, 6*, 147–157.

Calim, F. F. (2016). Free and forced vibration analysis of axially functionally graded Timoshenko beams on two-parameter viscoelastic foundation. *Composites Part B: Engineering, 103*, 98–112. https://doi.org/10.1016/j.compositesb.2016.08.008

Ebrahimi, F., & Barati, M. R. (2017). Size-dependent dynamic modeling of inhomogeneous curved nanobeams embedded in elastic medium based on nonlocal strain gradient theory. *Proceedings of the Institution of Mechanical Engineers, Part C: Journal of Mechanical Engineering Science, 231*(23), 4457–4469.

Ebrahimi-Mamaghani, A., Sotudeh-Gharebagh, R., Zarghami, R., & Mostoufi, N. (2022). Thermo-mechanical stability of axially graded Rayleigh pipes. *Mechanics Based Design of Structures and Machines, 50*, 412–441. https://doi.org/10.1080/15397734.2020.1717967

Elyasi, P., Neya, B. N., & Firoozjaee, A. R. (2023). Free vibration of viscoelastic nonlocally damped tapered axially functionally graded beams using the state-space formulation. *Engineering Structures, 288*, 116183.

Eratlı, N., Yılmaz, M., Darılmaz, K., & Omurtag, M. H. (2016). Dynamic analysis of helicoidal bars with non-circular cross-sections via mixed FEM. *Structural Engineering and Mechanics, 57*(2), 221–238. https://doi.org/10.12989/sem.2016.57.2.221

Ermis, M., Aribas, U. N., Kutlu, A., Eratlı, N., & Omurtag, M. H. (2019). Forced vibration analysis of axially FG straight beams by mixed FEM. In *IV. Eurasian Conference on Civil and Environmental Engineering* (pp. 894–899). İstanbul, Türkiye.

Ermis, M., Kutlu, A., Eratlı, N., & Omurtag, M. H. (2022). Free vibration of axially FG curved beam on orthotropic Pasternak foundation via mixed FEM. *Journal of the Brazilian Society of Mechanical Sciences and Engineering, 44*(12), 597. https://doi.org/10.1007/s40430-022-03797-6

Fan, F., Lei, B., Sahmani, S., & Safaei, B. (2020). On the surface elastic-based shear buckling characteristics of functionally graded composite skew nanoplates. *Thin-Walled Structures, 154*, 106841.

Gasik, M. M., & Lilius, R. R. (1994). Evaluation of properties of W/Cu functional gradient materials by micromechanical model. *Computational Materials Science, 3*(1), 41–49.

Ge, R., Liu, F., Wang, C., Ma, L., & Wang, J. (2022). Calculation of critical load of axially functionally graded and variable cross-section Timoshenko beams by using interpolating matrix method. *Mathematics, 10*(13). https://doi.org/10.3390/math10132350

Ghayesh, M. H. (2018). Nonlinear vibration analysis of axially functionally graded shear-deformable tapered beams. *Applied Mathematical Modelling, 59*, 583–596. https://doi.org/10.1016/j.apm.2018.02.017

Gupta, A., & Talha, M. (2017). Large amplitude free flexural vibration analysis of finite element modeled FGM plates using new hyperbolic shear and normal deformation theory. *Aerospace Science and Technology, 67*, 287–308.

Karami, B., Shahsavari, D., Janghorban, M., & Li, L. (2019). Influence of homogenization schemes on vibration of functionally graded curved microbeams. *Composite Structures, 216*, 67–79. https://doi.org/10.1016/j.compstruct.2019.02.089

Kiani, Y., & Eslami, M. R. (2015). Thermal post buckling of imperfect circular functionally graded material plates: Examination of Voigt, Mori–Tanaka, and self-consistent schemes. *Journal of Pressure Vessel Technology, 137*(2).

Kır, O., Aydoğan, G., & Ermis, M. (2021). Free vibration analysis of metal matrix composite circular helical springs. In *3rd International Defense Industry Symposium (IDEFIS2021)*, Kırıkkale, Türkiye (in Turkish).

Loja, M. A. R., Barbosa, J. I., & Soares, C. M. (2012). A study on the modeling of sandwich functionally graded particulate composites. *Composite Structures, 94*(7), 2209–2217.

Mishnaevsky, L., Jr. (2007). *Computational mesomechanics of composites*. John Wiley.

Mori, T., & Tanaka, K. (1973). Average stress in matrix and average elastic energy of materials with misfitting inclusions. *Acta Metallurgica, 21*, 571–574.

Oden, J. T., & Reddy, J. N. (1976). *An introduction to the mathematical theory of finite elements*. New York, NY: John Wiley & Sons.

Omurtag, M. H., & Aköz, A. Y. (1992). The mixed finite element solution of helical beams with variable cross-section under arbitrary loading. *Computers & Structures, 43*(2), 325–331. https://doi.org/10.1016/0045-7949(92)90149-T
Reuss, A. (1929). Berechnung der Fließgrenze von Mischkristallen auf Grund der Plastizitätsbedingung für Einkristalle. *ZAMM - Zeitschrift für Angewandte Mathematik und Mechanik, 9*(1), 49–58.
Sahmani, S., & Safaei, B. (2020). Influence of homogenization models on size-dependent nonlinear bending and postbuckling of bi-directional functionally graded micro/nano-beams. *Applied Mathematical Modelling, 82*, 336–358.
Saleh, B., Jiang, J., Fathi, R., Al-hababi, T., Xu, Q., Wang, L., Song, D., & Ma, A. (2020). 30 years of functionally graded materials: An overview of manufacturing methods, applications and future challenges. *Composites Part B: Engineering, 201*, 108376.
Sayed, S. S. M. A. (2023). *Static analysis of axially functionally graded straight beams developed using different micromechanical models* (Master's thesis, in Turkish). Kirklareli University, Institute of Science and Technology.
Shafiei, N., Kazemi, M., & Ghadiri, M. (2016). Nonlinear vibration of axially functionally graded tapered microbeams. *International Journal of Engineering Science, 102*, 12–26. https://doi.org/10.1016/j.ijengsci.2016.02.007
Shahsavari, D., & Karami, B. (2022). Assessment of Reuss, Tamura, and LRVE models for vibration analysis of functionally graded nanoplates. *Archives of Civil and Mechanical Engineering, 22*(2), 1–13.
Sharma, P., Singh, R., & Hussain, M. (2020). On modal analysis of axially functionally graded material beam under hygrothermal effect. *Proceedings of the Institution of Mechanical Engineers, Part C: Journal of Mechanical Engineering Science, 234*, 1085–1101. https://doi.org/10.1177/0954406219888234
Shen, H. S., & Wang, Z. X. (2012). Assessment of Voigt and Mori–Tanaka models for vibration analysis of functionally graded plates. *Composite Structures, 94*(7), 2197–2208.
Şimşek, M., Kocatürk, T., & Akbaş, Ş. D. (2012). Dynamic behavior of an axially functionally graded beam under action of a moving harmonic load. *Composite Structures, 94*(8), 2358–2364. https://doi.org/10.1016/j.compstruct.2012.03.020
Sofiyev, A. H. (2019). Review of research on the vibration and buckling of the FGM conical shells. *Composite Structures, 211*, 301–317. https://doi.org/10.1016/j.compstruct.2018.12.047
Srividhya, S., Basant, K., Gupta, R. K., Rajagopal, A., & Reddy, J. (2018). Influence of the homogenization scheme on the bending response of functionally graded plates. *Acta Mechanica, 229*(10), 4071–4089.
Tamura, I. (1973). Strength and ductility of Fe–Ni–C alloys composed of austenite and martensite with various strength. In *Proceedings of the Third International Conference on Strength of Metals and Alloys* (pp. 611–615). Cambridge: Institute of Metals.
Voigt, W. (1889). Über die Beziehung zwischen den beiden Elastizitätskonstanten isotroper Körper. *Annalen der Physik, 38*, 573–587.
Wadi, K. J., Yadeem, J. M., Mustafa Khazaal, S., Al-Ansari, L. S., & Abdulsamad, H. J. (2022). Static deflection calculation for axially FG cantilever beam under uniformly distributed and transverse tip loads. *Results in Engineering, 14*(1), 100395.
Wang, Y., Ren, H., Fu, T., & Shi, C. (2020). Hygrothermal mechanical behaviors of axially functionally graded microbeams using a refined first order shear deformation theory. *Acta Astronautica, 166*, 306–316. https://doi.org/10.1016/j.actaastro.2019.10.036
Wang, Y., & Wu, D. (2016). Thermal effect on the dynamic response of axially functionally graded beam subjected to a moving harmonic load. *Acta Astronautica, 127*, 171–181. https://doi.org/10.1016/j.actaastro.2016.05.030
Yadav, A., Amabili, M., Panda, S. K., Dey, T., & Kumar, R. (2021). Nonlinear damped vibrations of three-phase CNT-FRC circular cylindrical shell. *Composite Structures, 255*, 112939.
Yadeem, J. M., Wadia, K. J., Abdulsamad, H. J., & Alansari, L. S. (2024). Free vibration analysis of a simply supported axial functionally graded beam using the Rayleigh method. *Mathematical Modelling of Engineering Problems, 11*(9), 2447.
Yuan, Y., Zhao, K., Han, Y., Sahmani, S., & Safaei, B. (2020a). Nonlinear oscillations of composite conical microshells with in-plane heterogeneity based upon a couple stress-based shell model. *Thin-Walled Structures, 154*, 106857.
Yuan, Y., Zhao, K., Sahmani, S., & Safaei, B. (2020b). Size-dependent shear buckling response of FGM skew nanoplates modeled via different homogenization schemes. *Applied Mathematics and Mechanics, 41*(4), 587–604.
Zhang, C., & Wang, Q. (2019). Free vibration analysis of elastically restrained functionally graded curved beams based on the Mori–Tanaka scheme. *Mechanics of Advanced Materials and Structures, 26*(21), 1821–1831.
Zuicker, J. R. (1995). Functionally graded materials: Choice of micromechanics model and limitations in property variation. *Composite Engineering, 5*(7), 807–819.

4th International Civil Engineering & Architecture Conference
17-19 May 2025, Trabzon, Türkiye

Comparison of FRP and RC Jacketing methods on the behaviour of old buildings

Esra İnan[1], Havva N. Canbazoğlu[1], Mehmet Palanci*[1], İlker Subaşı[1]

[1] Istanbul Arel University, Department of Civil Engineering, 34537 Istanbul, Türkiye

Abstract. In this study, a typical reinforced concrete building constructed according to the 1975 Turkish Earthquake Code (TEC) is analyzed in accordance with today's earthquake codes. For this purpose, the general building characteristics of the region were considered, and low- and mid-rise reinforced concrete buildings were considered. Buildings were first designed according to TEC-1975, and they were subject to static pushover analysis to determine the load and displacement capacity of the building by using the Turkish Building Earthquake (TBEC) 2018 code. Using this TBEC-2018, the performance levels of the buildings were also determined. Later, these buildings were strengthened with various strengthening methods such as Fiber Reinforced Polymer (FRP) and reinforced concrete (RC) jacketing methods separately. The behavior of strengthened buildings was also determined by static-pushover analysis. After determining the load and deformation capacity of the buildings, the effects of both methods on the structural behavior are investigated using the load-displacement behavior of existing and strengthened buildings. Displacement demands of both (as-built and strengthened) were determined by code-compatible elastic spectrum, and performance of the buildings were also obtained. Consequently, the behavior of strengthened and existing buildings was evaluated to determine the effectiveness of the methods for building frames considered.

Keywords: Reinforced concrete buildings; FRP; RC jacketing; Strengthening

1. Introduction

The severe earthquakes that occurred in recent years have caused loss of life and property. Especially, the Kahramanmaraş earthquakes affected a wide area, such as Kahramanmaraş, Hatay, Gaziantep, Adıyaman, Malatya, Kilis, Adana, Diyarbakır, Osmaniye, and Şanlıurfa. They caused many structures to be seriously damaged or collapsed (Kocakaplan Sezgin et al., 2024). These earthquakes showed the inadequacy of the building stock. Especially, RC columns with non-seismic detailing cannot provide principles and rules dictated by codes in terms of concrete quality, transverse and longitudinal reinforcement ratios (Orman Subaşi et al., 2024). Reconstruction of RC structures with such deficiencies is a process that requires time and cost. Another method for improving the performance of RC structures in terms of earthquake behavior is strengthening. In this way, time, cost, and material usage can be efficiently organized (Habib et al., 2020;Raza et al., 2019;Caglar et al., 2017).

RC jacketing, which has been used for many years in the reinforcement of RC structures, is widely used among the reinforcement methods (Aykaç & Can, 2008; Bousias et al., 2004). RC jacket is based on the casting of higher-strength concrete together with longitudinal and transverse reinforcement by expanding the cross-sectional area of the existing column on the RC structure (Minafò, 2015). The increase in the cross-sectional area increases the strength, stiffness, ductility, and earthquake performance of the RC columns, thus extending the service life of the structure. It is also a fact that this method may be a disadvantage from an architectural perspective. Another method widely used in the reinforcement of existing RC columns in recent years is the use of Fiber Reinforced Polymers (FRP). The main reasons for preferring the FRP jacketing technique are that it is easy to apply to the structural element, does not require special equipment, increases the axial load-carrying capacity and lateral displacement capacity of the columns, does not affect the architectural design, and can be applied to all types of building topologies (Pham & Hadi, 2014).

Goksu et al., (2006) investigated the changing seismic behavior of an RC building with inadequate seismic performance as a result of reinforcing RC jacketing and CFRP jacketing. The transfer of the reinforcing effect to the structure was done using finite element modeling. The ductility of the structure increased in both techniques. In addition, a slight increase in strength was observed in the case of CFRP jacketing. RC jacketing, the structure showed a much more significant increase in rigidity and strength. As a result, it was observed that the CFRP

* Corresponding author, E-mail: mehmetpalanci@arel.edu.tr

https://doi.org/10.31462/icearc2025_ce_sme_730

jacketing technique was preferable when it came to meeting the lateral displacement demand, but there was no increase in the seismic demand of the structure. Kalogeropoulos et al., (2019) compared the CFRP and RC jacketing methods with experimental studies on RC columns. The seismic performance of the RC column sample with low concrete compressive strength and plain reinforcement was improved by RC jacketing, especially in terms of rigidity and strength, while CFRP jacketing improved in terms of ductility. Latifi & Rouhi (2020) conducted a study in which they reinforced a two-story building with techniques such as FRP jacketing, RC jacketing, and the addition of shear walls to the structure, and they comparatively examined the results. It was shown that adding shear walls to the RC structure was the most effective way to reduce maximum roof displacements and the building foundation period. RC jacketing and adding shear walls to the structure caused a significant increase in the capacity curves. Although reinforcing with FRP caused an increase in ductility, it showed similar behavior to the existing structure. Mumtaz et al., (2021) studied the feasibility of using FRP in Afghanistan. While the RC jacketing method was found to be more efficient in terms of cost and strength, the FRP jacketing method was found to be more efficient in terms of time and lower CO_2 emissions.

In this study, two regular RC structures, a 5-story and a 7-story, were designed according to the 1975 earthquake regulations (TEC, 1975). Due to their regularity, buildings were modeled from the middle axes selected from the RC structures, and these frames were subjected to pushover analysis, and the building behavior of the buildings were determined. These buildings were then subjected to strengthening using RC and CFRP jacketing, considering only RC columns. During the strengthening of these buildings, special attention was paid to costs, and it was aimed at both methods being approximately equal. RC and CFRP jacketing were applied to all column sections, and moment-curvature analyses were obtained. As a result, the effects of different reinforcing techniques on RC structures with approximately equal costs were investigated.

2. Materials and methods

In this study, two reinforced concrete buildings that reflect existing building stock of Türkiye was considered. These models consist of five- and seven-story reinforced concrete residential structures, and they were designed according to TEC-1975. However, lateral confinement of columns was poorly considered to reflect existing building stock. In both structures, the floor height was determined to be 3 meters, and the horizontal and vertical axis distances were determined as 4.5 meters. Buildings were designed according to frame behavior consisting of column-beam connections. The 3D plot of the 5-story reinforced concrete residential structure is shown in Fig. 1.

In the five-story structure, the beam sections were 30×60cm, and the column sections were 40×40cm. In the seven-story structure, beam sections were considered as 30×70cm, and the column sections were generally determined as 45×45 cm, and the dimensions of the middle column was 50×50 cm.

The compressive strength of concrete was C16, and reinforcement steel was considered as S220. Since the buildings were planned regularly, the middle axis of both buildings was considered, and the necessary definitions (moment capacity, plastic rotations, etc.) for the analysis. In the final stage, static pushover analyses were performed for 5- and 7-story buildings in accordance with the first natural vibration mode, and the roof displacement of the structures were plotted against the base shear capacity of the buildings. In Fig. 2, the reinforcement details of the column and beam reinforcement details are given. Lateral spacing of confinement of all columns were taken as 200 mm for both buildings.

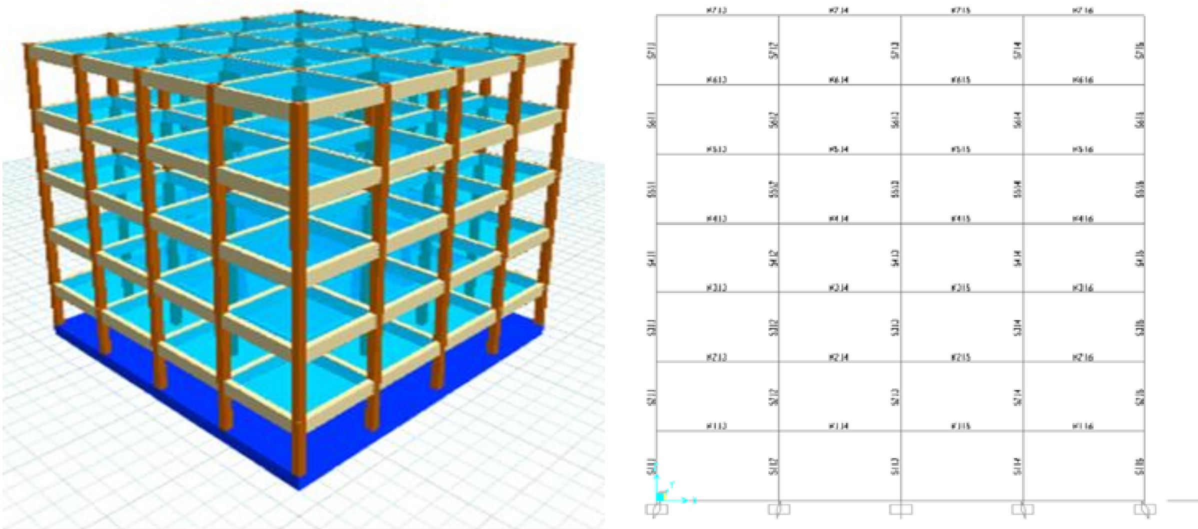

Fig. 1. 3D and 2D representation of typical RC building considered

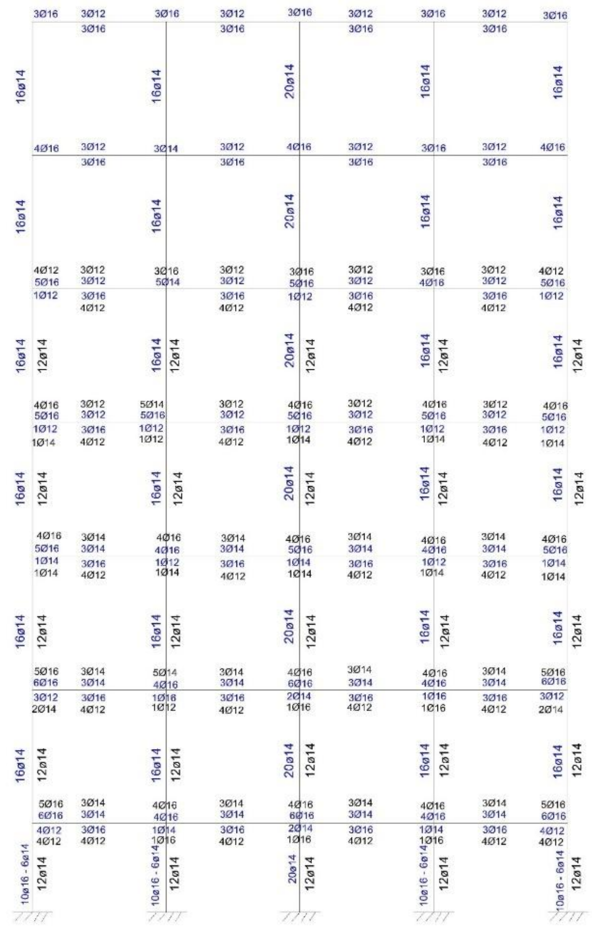

Fig. 2. Longitudinal reinforcement details of considered RC buildings (Blue color represents the 7-story building)

A large portion of the reinforced concrete building stock in Turkey built according to the 1975 Earthquake Code (TEC, 1975) does not meet the structural system and strength criteria of the earthquake codes in force today. Considering possible earthquakes, these building stocks pose a significant risk. For this reason, retrofitting applications to increase the strength of the existing building stock have become an important option to prepare buildings against earthquakes instead of demolishing and rebuilding buildings, considering the cost and time spent.

In this study, it is aimed to retrofit two different five- and seven-story reinforced concrete residential buildings designed according to the 1975 code. Accordingly, two different strengthening methods, FRP wrapping and the reinforced concrete jacketing method, were applied for both structures. In this way, the effects of both methods on both economic and structural performance were evaluated comparatively.

2.1. Damage limits for structural members

Damage limits of members are determined according to TBEC-2018. In the code, damage limits of members are determined in terms of concrete and steel strain limits, and moment-curvature analyses were performed, and limits are checked in each step. Later curvature responses are converted to rotation based on the TBEC equations. Damage limits and threshold values for these limits are shown in Fig. 3 for a typical RC member.

It can be seen from Fig. 3 that the unconfined concrete strain limit of MDL is constant at 0.0025 for concrete and 0.0075 for tensile reinforcement. Confined concrete strain limits of extensive damage limit (EDL) and collapse damage limit (CDL) are defined in terms of the ratio of mechanical transverse reinforcement ratio (w_{we}) and the MDL limit is calculated as 0.75 times the CDL. ε_{su} is the ultimate tensile strain, and it was taken as 0.08 for plain longitudinal bars as suggested in TBEC.

Material type	Damage limit	Strain values
Concrete strain limit	ε_{MDL}	0.0025
	ε_{EDL}	$0.75\varepsilon_{CDL}$
	ε_{CDL}	$0.0035 + 0.04\sqrt{w_{we}} \leq 0.0180$
Tensile reinforcement limit	ε_{MDL}	0.0075
	ε_{EDL}	$0.75\varepsilon_{CDL}$
	ε_{CDL}	$0.40\varepsilon_{su}$

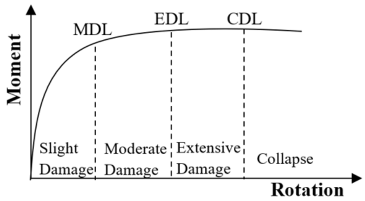

Fig. 3. Typical moment-rotation curve and damage limits definitions in TBEC-2018

2.2. Fiber reinforced polymer (FRP)

Fiber-reinforced polymer (FRP) composites are increasingly used in the reinforcement of reinforced concrete structures due to their high tensile strength, low specific gravity, corrosion resistance, and easy application (Hollaway & Leeming, 1999). These systems are applied to the surface of structural elements by means of epoxy-based adhesives. This application not only increases the axial and shear strengths of the element but also improves its ductility capacity and energy absorption ability (Seible et al., 1997; Teng et al., 2002).

All columns of the selected structures were wrapped with CFRP. The material behavior of CFRP developed by Palanci and Subasi (2024) based on Lam & Teng, 2003a and Lam & Teng, 2003b, was used to obtain the stress-strain relationship of concrete. The elastic stress at rupture was taken at 3530 MPa, and rupture strain was taken at 1.5%. It was assumed that the CFRP material is wrapped 0.5mm in two directions. Strain reduction factor (k_ε) was considered as 0.586 for carbon FRP material. Corner radius (r_c) was assumed 25 mm in all CFRP-wrapped RC sections.

In the model developed by Palanci and Subasi (2024), the compressive strength of FRP-wrapped concrete (f'_{cu}) is determined using Equation 1. ρ_j, E_j, f_{ju} and f'_c are volumetric ratio, tensile modulus, and strength of the FRP jacket and compressive strength of the unconfined concrete, ε_{co} is accepted as 0.002, b and h are the width and depth of the member section, respectively. Additionally, the ultimate unit strain (ε_{cu}) of FRP-confined concrete is determined by Equation 2. The coefficients a_2 and b_2 given in Equation 2 represent the coefficients that vary depending on the FRP volumetric ratio (ρ_j). The FRP volumetric ratio (ρ_j) is calculated by Equation 3. t_f is the thickness of CFRP.

$$\frac{f'_{cu}}{f'_c} = \left((48\left(\frac{k_\varepsilon}{0.4}\right)\left(\frac{f_{ju}}{700}\right)\left(\frac{1}{f'_c}\right)\left(\frac{h}{b}\right)^{-2.3}(r_c)^{0.37})\rho_j + 1\right) \tag{1}$$

$$\frac{\varepsilon_{cu}}{2\varepsilon_{co}} = \left(a_2 {\rho_j}^{b_2}\right) \tag{2}$$

$$\rho_j = \frac{2t_f(b+h)}{bh} \tag{3}$$

2.3. RC jacketing

Reinforced concrete (RC) jacketing is one of the common and effective retrofitting methods based on the principle of covering the existing structural system elements with a new layer of concrete by wrapping them with reinforcement. This method is frequently preferred to increase the performance of columns and beams with insufficient cross-sectional dimensions and low-strength materials against earthquake effects.

During the application, transverse and longitudinal reinforcement is placed around the existing element, then high-strength concrete is used to increase the strength capacity. As a result, the axial, flexural and shear strength of the element is significantly improved. According to TBEC (2018), RC jacketing thickness is recommended not to be less than 100 mm. Göksu (2004) emphasized that the thickness should not be less than 100 mm in case of single stirrups and 150 mm in case of double stirrups. In this study, the thickness was determined as 150 mm for easy settlement of reinforcement and concrete. Lateral and longitudinal reinforcement of jacket was considered as S420. The compressive quality of concrete was taken C40 and lateral spacing of jacketing was taken as 100 mm. In the 5-storey building, longitudinal reinforcement was used as 16ϕ20 in all columns. In the 7-storey building, longitudinal reinforcement was used as 18ϕ22 in the center column and 16ϕ22 in the other columns. The behavior of the RC jacketing model was reflected in the analysis with the concrete model developed by Campione et al., (2014). In the model, the concrete compressive strength of the concrete (f'_{cc}) is calculated via Equation 4. f_l is the effective confinement pressure and the ultimate unit strain (ε_{cu}) of reinforced concrete is calculated using Equation 5.

$$f'_{cc} = f'_c\left[2.254\sqrt{1+\frac{7.94f_l}{f'_c}}-2\frac{f_l}{f'_c}-1.254\right] \tag{4}$$

$$\varepsilon_{cu} = 0.004+\frac{1.4}{f'_{cc}}\left[\frac{f_{yc}\varepsilon_{suc}A_{sc}}{(b-c_c)s_c}+\frac{f_{yj}\varepsilon_{suj}A_{sj}}{(B-\delta)s_j}\right] \tag{5}$$

f_{yc}, A_{sc}, ε_{suc}, b, c_c, s_c are yield strength of longitudinal steel, area of longitudinal steel bars, ultimate strain of longitudinal steel, section width, cover, and pitch of stirrups in the core section, respectively. f_{yj}, A_{sj}, $\varepsilon_{suj}, B, \delta, s_j$ are yield strength of longitudinal steel, area of longitudinal steel bars, ultimate strain of longitudinal steel, section width, jacket thickness, and pitch of stirrups in the external jacket, respectively.

2.4. Cost analysis for retrofitting

In this study, two alternative strengthening methods were examined. As a result of the structural analysis, the elements where the damage was concentrated were identified, and retrofitting was applied for these elements. For this purpose, firstly, the reinforced concrete retrofitting cost was calculated by applying the RC jacketing method. Then, the FRP jacketing method was evaluated as an alternative solution. In the study, it was especially taken into consideration that the costs of both methods were approximately equal. Thus, the effect of retrofitting methods with similar costs on the behavior was examined. Cost calculations were based on the current unit price lists published by the Ministry of Culture and Tourism (2025) and the Ministry of Environment, Urbanization, and Climate Change (2025). Retrofitting operations were analyzed using both existing reinforced concrete buildings. During the calculation, both material and labor costs were considered.

Improving the performance of the existing building stock in areas with high earthquake risk is of great importance in terms of ensuring building safety. In this context, RC and FRP jacketing systems are prominent among the methods applied for retrofitting structures. However, it should be noted that structural conditions, damage distribution, architectural conditions, etc. are also important factors in the selection of retrofitting methods.

In Table 1 and Table 2, total costs of both methods are given in terms of Turkish Lira (TL). It can be seen from the tables that retrofitting costs of 5- story buildings are almost 1 million TL for 5-story buildings, while this cost is close to 2 million TL for 7-story buildings. The absolute difference between the costs is also given in the tables. It can be observed that the costs of both methods are very close in 5-story buildings, and the difference between the methods was calculated as 5%. This difference is observed as 7.5% in 7-story buildings. Although the percentage of difference seems higher, the difference in the costs between the methods is around 117 thousand TL, which can be considered minimal in terms of TL. Accordingly, it was assumed that the cost of both methods was approximately equal.

Table 1. Determination of RC and FRP jacketing costs for 5- story building

Method	Labor costs (TL)	Material costs (TL)	Total (TL)	Abs. difference (%)
RC jacketing	372326.78	575621.08	947947.86	5
FRP jacketing	765777.60	232830.72	998608.32	

Table 2. Determination of RC and FRP jacketing costs for 7- story building

Method	Labor costs (TL)	Material costs (TL)	Total (TL)	Abs. difference (%)
RC jacketing	565608.87	884935.39	1450544.26	7.5
FRP jacketing	1232901.94	334985.73	1567887.67	

3. Analysis results

Based on the material quality and quantities, moment-curvature, and hence the moment-rotation capacity of structural elements, were calculated using TBEC-2018. Later, buildings were applied lateral load according to their first mode shape. Finally, damage distribution of the building was determined according to target displacement determined according to the TBEC uniform hazard spectrum for DD-2. In the first case, as-built buildings are evaluated, and the damage distribution of the building at target displacements are shown in Fig. 4.

It can seen from the figure that due to lack of lateral confimement and strong column-weak beam behaviour both buildings were severely damaged at the base story. For both buildings, damages were most accumalated at the top and bottom of the columns due to lack of strength capacity. The lack of adequate confinement details also increased the damage distributions in both buildings. The damage at the beams are minimal and they were mostly around immediate occupancy (IO) or Life Safety (LS) damage levels. Pushover curve of existing buildings are also plotted in Fig. 5. It can be seen from the figure that displacement of both buildings is low and determined as around 6 cm and 8.2 cm at the roof story, for 5- and 7-story buildings, respectively. These values correspond to around 0.4% drift ratio (roof displacement/building height) for both buildings.

In the second case, the behaviour of buildings after retrofitting of CFRP is evaluated. Damage distribution of building at target displacement are plotted in Fig. 7. Target displacements for 5- and 7-story buildings were calculated as as 9.4 cm and 10.6 cm, respectvely.

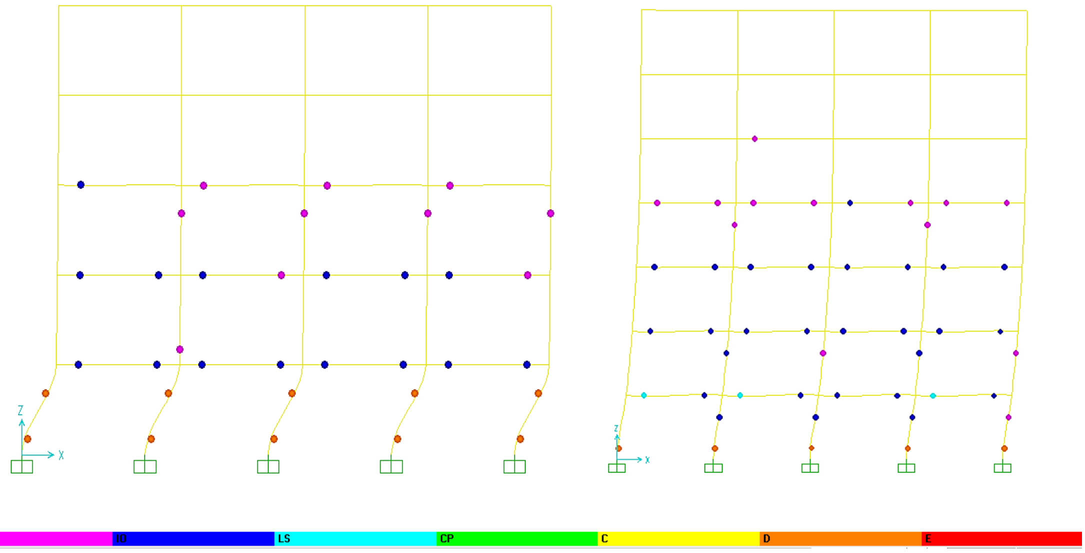

Fig. 4. Damage distribution of 5- and 7-story existing buildings at target displacement demand

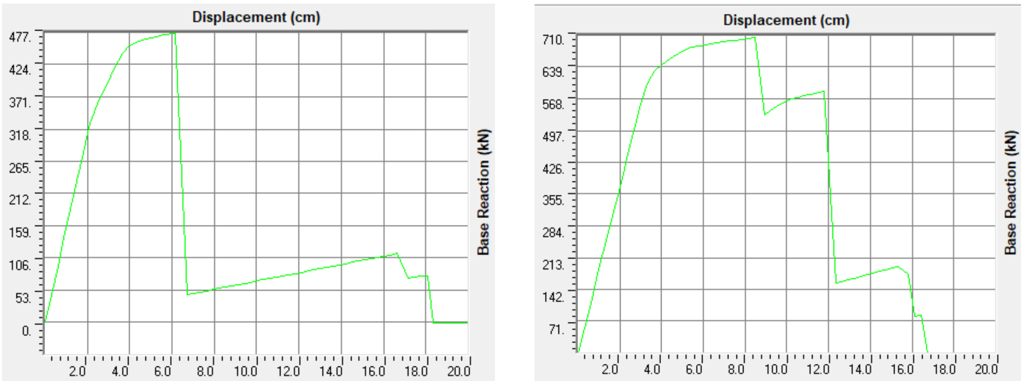

Fig. 5. Pushover curve of 5- and 7-story existing buildings

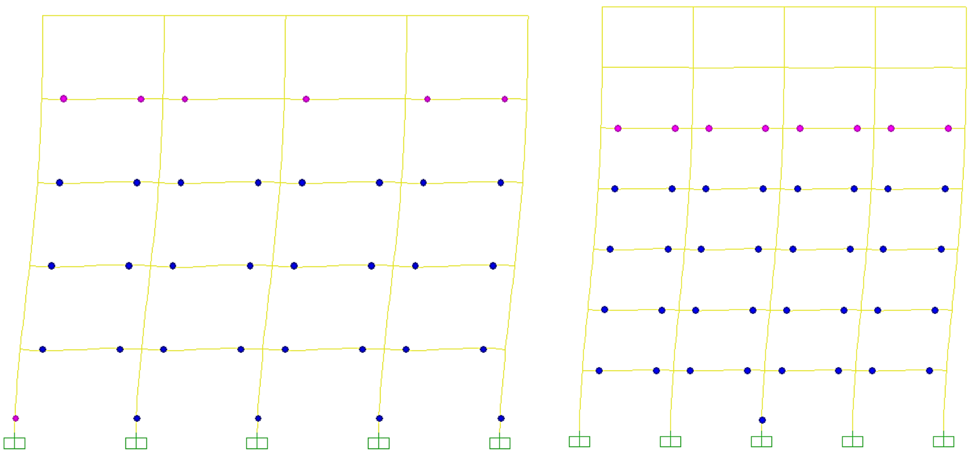

Fig. 6. Damage distribution of 5- and 7-story existing buildings at target displacement demand for CFRP retrofitting

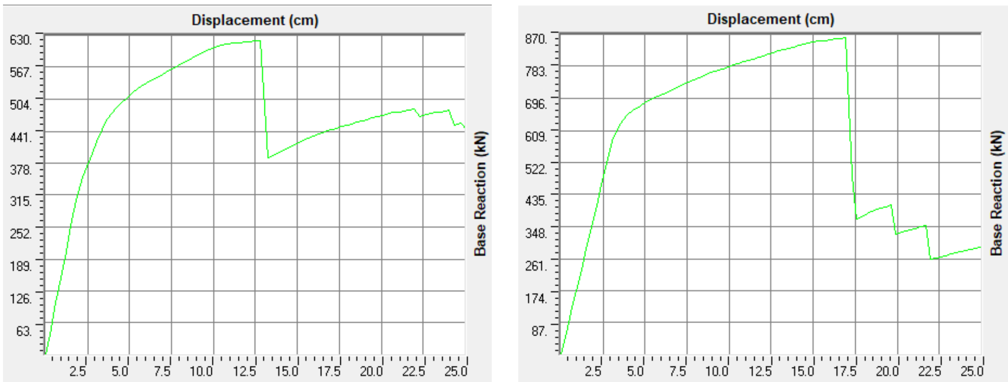

Fig. 7. Pushover curve of 5- and 7-story existing buildings for CFRP retrofitting

It can be seen from Fig. 6 that the damage distribution of buildings is dramatically changed when compared to the as-built case. In both buildings, both columns and beams were mostly in yield or IO level. In addition, the damage ratio of columns was dramatically reduced. For 5-story buildings, all columns were nearly yielding damage while columns at the middle of the frame were slightly damaged after the application of CFRP. When the pushover curve of buildings was observed (Fig. 7), it can be said that the lateral strength capacity of buildings was slightly increased. On the other hand, the displacement capacity of buildings was significantly increased. The application of two-directional FRP wrapping increased both capacities, but a more pronounced effect was observed for displacement capacity.

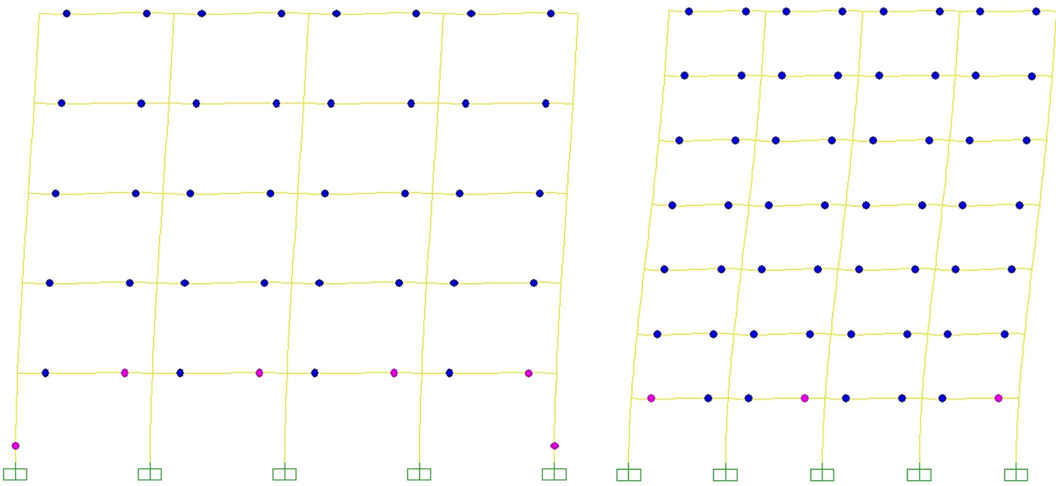

Fig. 8. Damage distribution of 5- and 7-story existing buildings at target displacement demand for RC jacketing retrofitting

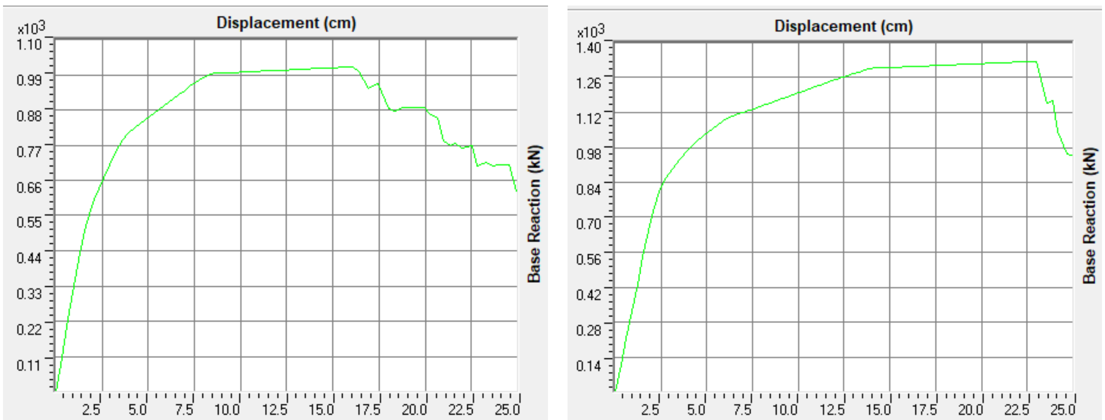

Fig. 9. Pushover curve of 5- and 7-story existing buildings for RC jacketing retrofitting

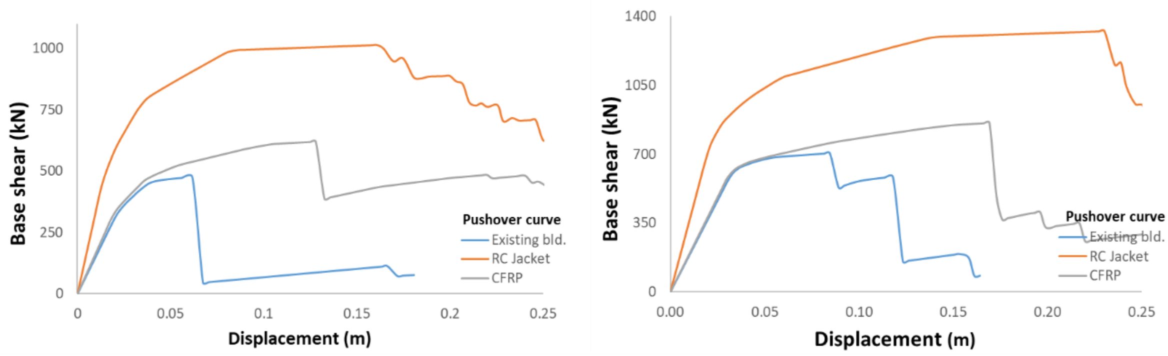

Fig. 10. Comparsion of Pushover curve of 5- and 7-story existing buildings for all three cases

In the third case, damage distributions at target displacement are plotted in Fig. 8 after retrofitting of RC jacketing. Target displacements for 5- and 7-story buildings were calculated as 7.73 cm and 9.24 cm, respectively.

It can be seen from Fig. 8 that the damage distribution of buildings are very close to the CFRP retrofitting case. In both buildings, all beams were mostly in yield or IO level. Furthermore, no column damage was observed. When the pushover curve of buildings was compared (Fig. 9), it can be said both the lateral strength and displacement capacity of buildings were dramatically increased compared to both the CFRP and as-built cases.

To make an overall comparison, pushover curves of all cases are plotted in a single figure to illustrate the change in building behavior and the results are plotted in Fig. 10. FRP was applied in both directions (transverse and longitudinal). FRP sheets in the longitudinal direction increased the moment capacity, while transverse sheets increased the shear strength and hence the ductility by enhancing the confinement effect. In the application, an equal amount of jacketing was applied in both directions. Thanks to this bidirectional application, both flexural and shear strengths of the structural elements were increased. It is worth mentioning that by changing the direction of the jacketing amount, the section behavior can be changed. However, this topic is not considered in this study.

As seen in Fig. 10, the FRP application showed a limited increase in initial stiffness in the 5-story building, while it seems not affected the 7-story building. Nevertheless, it provided a significant improvement in the strength and ductility for both structures. On the other hand, the capacity curve of both structures retrofitted by RC jacketing showed a significant increase in both initial stiffness and lateral strength capacity. The main reason for this increase can be attributed to the increase in the section dimensions because of RC jacketing. In addition, the ultimate displacement capacity has been postponed, and the ductile behavior of the system has become more pronounced. Considering the capacity curves of both reinforced concrete structures strengthened by taking into account the equivalent cost, it can be said that both methods increase the capacity and improve the performance significantly.

3. Conclusions

In this study, the structural behavior of the 5- and 7-story frame buildings designed according to TEC 1975 was investigated using RC and CFRP jacketing methods at approximately equal cost. The results can be listed as follows.

- In both structures, significant improvement in terms of strength, stiffness, and ductility was observed by RC jacketing.
- Although CFRP wrapping slightly increased stiffness in the 5-story structure, stiffness in the 7-story structure almost remained the same.
- CFRP wrapping increased the ultimate displacement value by about 2.1 for both structures.
- In both reinforcing methods, the strong column-weak beam mechanism is enhanced due to the strength in the structural member, and the damage mechanism was transferred to the beams.
- To increase the strength or ductility capacity of the member, the amounts of longitudinal and transverse FRP wrapping can be changed by assigning weighting ratios. In this study, equal (i.e., weights) amounts of transverse and longitudinal wrapping were applied, and the results were evaluated accordingly.

References

Aykaç, B., & Can, H. (2008). The applicability of the jacketing method in reinforced concrete columns of rectangular geometry. *Journal of the Faculty of Engineering and Architecture of Gazi University*, *23*(1), 223–229 (in Turkish).

Bousias, S., Spathis, A., & Fardis, M. (2004). Seismic retrofitting of columns with lap-splices through CFRP jackets. In *Proceedings of the 13th World Conference on Earthquake Engineering*. Vancouver, BC, Canada.

Caglar, N., Olabi, M.N., Koroglu, N., Subasi, I., & Serdar, A.H. (2017). Beton dayaniminin güçlendirilmiş betonarme kolonlarin davranişina etkisi. In *5th International Symposium on Innovative Technologies in Engineering and Science*, 1739–1745. Baku, Azerbaijan.

Campione, G., Fossetti, M., Giacchino, C., & Minafò, G. (2014). RC columns externally strengthened with RC jackets. *Materials and Structures*, *47*(10), 1715–1728. https://doi.org/10.1617/S11527-013-0146-X

Goksu, C., Demir, C., Darilmaz, K., & Ilki, A. (2006). Static nonlinear analysis of a retrofitted typical reinforced concrete building in Turkey. In *8th US National Conference on Earthquake Engineering*. California, USA.

Göksu, Ç. (2004). *The determination of principles for the retrofitting or strengthening of reinforced concrete structures with poor concrete strength* (Master's thesis). Trakya University, Edirne, Türkiye (in Turkish).

Habib, A., Yildirim, U., & Eren, O. (2020). Column repair and strengthening using RC jacketing: A brief state-of-the-art review. *Innovative Infrastructure Solutions*, *5*(3), 1–11. https://doi.org/10.1007/S41062-020-00329-4

Hollaway, L.C, & Leeming, M. (1999). *Strengthening of reinforced concrete structures: Using externally-bonded FRP composites in structural and civil engineering*. Elsevier.

İnşaat ve Tesisat Birim Fiyatları (2025). Ministry Of Environment, Urbanization And Climate Change.

Kalogeropoulos, G.I., Tsonos, A.-D.G., Konstantinidis, D., & Iakovidis, P.E. (2019). Earthquake-resistant rehabilitation of existing RC structures using high-strength steel fiber-reinforced concrete jackets. *Earthquakes and Structures*, *17*(1), 115. https://doi.org/10.12989/EAS.2019.17.1.115

Kocakaplan Sezgin, S., Sakcalı, G.B., Özen, S., Yıldırım, E., Avcı, E., Bayhan, B., & Çağlar, N. (2024). Reconnaissance report on damage caused by the February 6, 2023, Kahramanmaraş Earthquakes in reinforced-concrete structures. *Journal of Building Engineering*, *89*, 109200. https://doi.org/10.1016/J.JOBE.2024.109200

Kültür ve Turizm Bakanlığı Birim Fiyat Eki Listesi (2025).Ministry of Culture and Tourism.

Lam, L., & Teng, J. G. (2003a). Design-Oriented Stress-Strain Model for FRP-Confined Concrete in Rectangular Columns. *Journal of Reinforced Plastics and Composites*, *22*(13), 1149–1186. https://doi.org/10.1177/0731684403035429

Lam, L., & Teng, J.G. (2003b). Design-oriented stress–strain model for FRP-confined concrete. *Construction and Building Materials*, *17*(6–7), 471–489. https://doi.org/10.1016/S0950-0618(03)00045-X

Latifi, R., & Rouhi, R. (2020). Seismic assessment and retrofitting of existing RC structures: Seismostruct and seismobuild implementation. *Civil Engineering and Architecture*, *8*(2), 84–93. https://doi.org/10.13189/CEA.2020.080206

Minafò, G. (2015). A practical approach for the strength evaluation of RC columns reinforced with RC jackets. *Engineering Structures*, *85*, 162–169. https://doi.org/10.1016/J.ENGSTRUCT.2014.12.025

Mumtaz, Y., Nasiri, A., & Tetsuhiro, S. (2021). A comparative study on retrofitting concrete column by FRP-Wrapping and RC-Jacketing methods: A feasibility study for Afghanistan. *Indian Journal of Science and Technology*, *14*(7), 652–664. https://doi.org/10.17485/IJST/V14I7.141

Orman Subaşi, R., Çağlar, N., Dok, G., Öztürk, H., Arslan, M.E., Biçici, E., Uysal, M., & Olabi, M.N. (2024). Geopolimer beton ile güçlendirilmiş güncel deprem yönetmelikleri gereksinimlerini sağlamayan betonarme kolonlarin davranişinin deneysel ve sayisal olarak incelenmesi. In *9. Yapı Mekaniği Laboratuvarları Çalıştayı,* Düzce, Türkiye.

Palanci, M., & Subasi, I. (2024). Practical equations for constitutive model of design-oriented FRP-confined concrete rectangular members. *Journal of Building Engineering*, *92*, 109676. https://doi.org/10.1016/J.JOBE.2024.109676

Pham, T., & Hadi, M. (2014). Stress prediction model for FRP confined rectangular concrete columns with rounded corners. *Journal of Composites for Construction,* *18*(1), 04013019. https://doi.org/10.1061/(ASCE)CC.1943-5614.0000407

Raza, S., Khan, M.K.I., Menegon, S.J., Tsang, H.H., & Wilson, J.L. (2019). Strengthening and repair of reinforced concrete columns by jacketing: State-of-the-art review. *Sustainability*, *11*(11), 3208. https://doi.org/10.3390/SU11113208

Saatcioglu, M., & Yalcin, C. (2003). External prestressing concrete columns for improved seismic shear resistance. *Journal of Structural Engineering*, *129*(8), 1057–1070. https://doi.org/10.1061/(ASCE)0733-9445(2003)129:8(1057)

Seible, F., Priestley, M.J.N., Hegemier, G.A., & Innamorato, D. (1997). Seismic retrofit of RC columns with continuous carbon fiber jackets. *Journal of Composites for Construction*, *1*(2), 52–62. https://doi.org/10.1061/(ASCE)1090-0268(1997)1:2(52)

Teng, J., Chen, J., Smith, S., & Lam, L. (2002). *FRP: strengthened RC structures*. Wiley.

TBEC. (2018). Türkiye Building Earthquake Code:TBEC 2018. *Disaster and Emergency Management Presidency (AFAD), Ministry of Public Works and Settlement, Ankara, Türkiye*.

TEC. (1975). Turkish Earthquake Code:TEC1975. *Ministry of Public Works and Settlement, Ankara, Türkiye*.

Pounding effects on seismic behaviour and damage pattern of rc buildings

Sinem Ören*[1], Fezayil Sunca[2,3] Ahmet C. Altunışık[3,4]

[1] *Karadeniz Technical University, Department of Civil Engineering, Of Technology Faculty, Trabzon, Türkiye*
[2] *Karadeniz Technical University, Department of Construction Technologies, 61080 Trabzon, Türkiye*
[3] *Karadeniz Technical University, Earthquake and Structural Health Monitoring Research Center, 61080 Trabzon, Türkiye*
[4] *Karadeniz Technical University, Department of Civil Engineering, 61080 Trabzon, Türkiye*

Abstract. During an earthquake, due to differences in the dynamic characteristics of adjacent buildings and insufficient separation distances, a phenomenon commonly referred to as "pounding" occurs as the buildings vibrate out of phase with one another. In this study, the seismic behavior and damage mechanisms of a RC building that sustained severe damage during the 2023 Kahramanmaraş earthquakes are investigated using nonlinear time-history analysis. During the earthquakes, pounding occurred between the selected building and its surrounding wall, resulting in significant damage to the impacted column. The finite element model of the building was developed using the SAP2000 software, and pounding effects were represented by a nonlinear elastic spring (Hertz model). In the analyses, real ground motion records obtained from a station located near the building during the 2023 Kahramanmaraş earthquakes were used. The analyses were carried out in two stages, with and without the pounding effect taken into account. Interstory displacements, floor accelerations, plastic hinge formations, and damage states were examined in detail. The results clearly demonstrate that the pounding effect significantly influences structural responses and should not be neglected in seismic design practices.

Keywords: RC building; Pounding; Nonlinear analysis; Kahramanmaraş earthquakes; FEM

1. Introduction

The rapid increase in housing demand driven by population growth has led to the widespread adoption of adjacent building construction, particularly in urban areas of major cities. This trend, combined with limited land availability, inadequate urban planning practices, and aesthetic-architectural considerations, has resulted in buildings being constructed in very close proximity to one another (Çetinkaya, 2011; Gökdemir, 2019; Sunca, 2023). However, one of the most critical damage mechanisms observed during the past earthquakes was the pounding effect between adjacent buildings.

In the literature, studies investigating the pounding effects between adjacent buildings have typically employed simplified and idealized building models. In the study conducted by Anagnostopoulos and Spiliopoulos (1992), the pounding effect between adjacent structures with different story heights, masses, and periods during earthquakes was investigated using multi-degree-of-freedom (MDOF) and nonlinear models. Rajaram and Ramancharla (2014) investigated the three-dimensional pounding effects between adjacent RC buildings with different story heights, mass distributions, and setback distances using nonlinear time-history analyses. Akköse and Sunca (2016) investigated the pounding effect between two adjacent RC buildings with different plan configurations using near-fault and far-fault ground motions. Tekin and Pala (2016) investigated the structural response of adjacent RC buildings with vertical discontinuity in load-bearing systems under seismic pounding. In the study conducted by Sak and Beyen (2017), the impact of seismic pounding on the structural performance of adjacent RC buildings with different story heights was investigated through nonlinear time-history analyses. They revealed that providing adequate seismic joints significantly improves structural performance, whereas insufficient separation distances prevent the structure from achieving the targeted performance levels. Miari and Jankowski (2022) investigated the pounding effect between two steel structure models with different dynamic characteristics placed on various soil types through shaking table experiments. Sunca et al. (2024) conducted shake table experiments on three half-scale, two-story RC building models to investigate the floor-to-floor pounding effect between adjacent buildings with different story heights.

*Corresponding author, E-mail: sinemoren@ktu.edu.tr

https://doi.org/10.31462/icearc2025_ce_sme_748

The aim of this study is to investigate the seismic behavior of a RC building severely damaged by collision during the 2023 Kahramanmaraş earthquakes. During the earthquake, pounding occurred between the building and its surrounding wall, leading to severe damage, particularly in one column. In the first phase of the study, the seismic response of the structure was obtained without considering the pounding effect. Subsequently, nonlinear analyses were performed by accounting for the interaction between the building and the surrounding wall, and the results were compared accordingly.

2. Description of selected building

Within the scope of this study, a building that did not collapse but sustained severe damage during the February 6, 2023 Kahramanmaraş earthquakes was selected. Figure 1 shows the undamaged and damaged conditions of the selected building 2023 Kahramanmaraş earthquakes.

The building, constructed in 2014, was designed in accordance with Turkish Earthquake Code-2007 (TEC, 2007). The basement floor height is 3.0 meters, the ground floor height is 3.3 meters, and each of the remaining four normal floors has a height of 3.0 meters. The concrete used in the construction was classified as C25 (f_{ck} = 25 MPa), and the reinforcement bar was S420 (f_{yk} = 420 MPa). The general properties of the selected building are summarized in Table 1.

Fig 1. Undamaged and damaged conditions of the selected building

Table 1. General properties of selected building

General information about selected building	
Purpose of usage	Commercial+Residental
Area of storey	Basement and ground floor: 242 m^2 Normal floor: 296 m^2
Building height	18.3m
Story heights	Basement and normal floor: 3.00m Ground floor: 3.30m
Slab System	Ribbed Slab System
Properties of structural elements	
Column section	30×70cm,35×70cm,30×50cm,45×35cm 40×70cm,70×30cm,70×35cm
Beam section	50×30 cm, 25×50cm,
Slab thickness	7cm
Material and soil properties	
Concrete	C25 (f_{ck} = 25MPa)
Reinforcement	S420 (f_{yk} = 420MPa)
Soil classification	Z2 (according to TEC-2007)
Considered loads	
Slab dead loads	3.0 kN/m^2
Slab live loads	Rooms: 2.0 kN/m^2 Stairs: 3.5 kN/m^2 Balconies: 5.0 kN/m^2
Infill wall	
Wall type	Brick wall

3.Finite element (FE) model of building

Within the scope of the study, two different FE models were developed using SAP2000 software in order to investigate the structural response under pounding effects. Collision effects were not taken into account in Model-1. In Model-2, the building and the surrounding wall were modeled and the collision effects between them were taken into account. The gap between the building and the wall was considered as 0.5 cm. Figure 2 presents both the three-dimensional and plan views of the FE model of the selected building. In the FE models, columns and beams were modeled as frame elements, shear walls and slabs were modeled using shell elements.

During the load assignment stage, the infill weight of the ribbed slab and the weight of the rib beams were calculated and applied as additional dead load (DL) on top of the self-weight of the slab. For live loads (LL), 2 kN/m² was applied to typical floor slabs and 5 kN/m² to balcony slabs based on architectural usage. Wall loads acting on beams were calculated as 6.75 kN/m for 10 cm thick walls and 8.64 kN/m for 20 cm thick walls. For the roof level, a live load of 1.5 kN/m² was considered, and wall loads on the beams were excluded.

To represent the nonlinear material behavior in the analyses, the concrete model developed by Mander et al. (1988) was adopted. According to the Turkish Building Earthquake Code (TBEC-2018), the nonlinear behavior of structural members can be idealized using either lumped plasticity or distributed plasticity models (Köse Sunca, 2019). In this study, the distributed plasticity model was used, which assumes plastic deformations occur continuously along the section. In this model, the cross-sections of structural elements are divided into fiber elements that allow independent tracking of the behavior of core concrete, cover concrete, and reinforcement. This modeling approach enables the consideration of nonlinear behavior both within the section and along the length of the element, allowing for a more detailed and accurate representation of the mechanical behavior of structural components (Yön and Calayır, 2013).

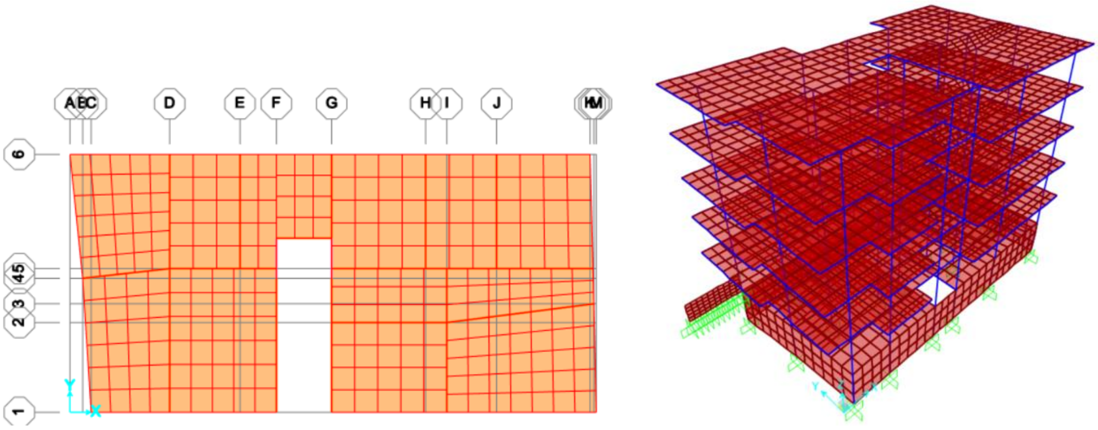

a) Plan view b) Three-dimensional

Fig 2. Plan and three-dimensional view of the building

In the FE model, various models are used to represent the impact behavior between adjacent structures. In this study, the nonlinear elastic spring model, known as the Hertz model, shown in Fig. 3, is employed to simulate the pounding effect.

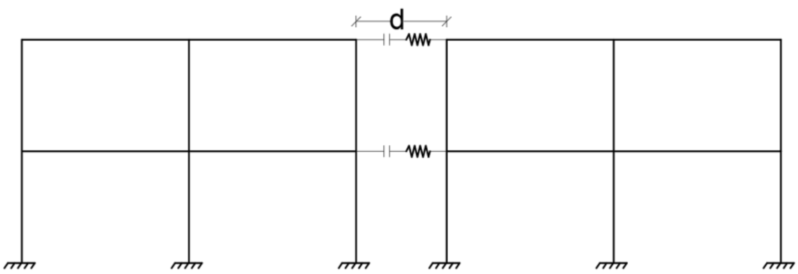

Fig. 3. Pounding model between buildings(Akköse et.al,2016)

This modeling approach simulates the dynamic interaction between structures through gap elements that are activated only at the contact. The force–deformation relationship of the gap element can be defined by the following equation:

$$f_G(t) = \begin{cases} k_g[u(t) - d]^{3/2}, & u(t) > d \\ 0, & u(t) \leq d \end{cases} \tag{1}$$

In the equation above k_g is the nonlinear spring stiffness of the gap element. $u(t)$ is defined as $u(t)_i - u(t)_j$, and d denotes the initial gap between the buildings at the beginning of the analysis. $u(t)_i$ and $u(t)_j$ represent the displacements of the adjacent structures in the same direction of the earthquake. The relationship between displacement and impact force in the Hertz model is illustrated in Figure 4.

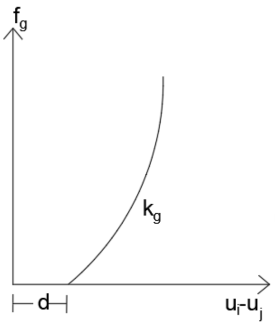

Fig 4. Pounding force-displacement relationship in the Hertz spring model (Muthukumar et al,2006)

4. Ground motion selection

The Turkish Strong Motion Database and Analysis System (AFAD-TADAS) of the Disaster and Emergency Management Authority (AFAD) was used to determine the ground motion to be applied to the structure. During the selection of earthquake records, data from the accelerograph stations closest to the location of the residential building were first examined. During the Kahramanmaraş-Pazarcık earthquake, five stations, ranging from 536 meters to 29 kilometers from the building, failed to record for the full duration of the earthquake. To evaluate the damage mechanism of the structure, it was necessary to select appropriate ground motion records. Therefore, the distances between the building and the epicenters of the earthquakes were calculated. The distance to the Pazarcık epicenter was approximately 120 km. To identify suitable ground motions, stations within a radius of 120 km were listed. Stations not representative of the local soil conditions of the building were eliminated. As a result, for the Pazarcık earthquake, the record from Station No. 6304, located 130.27 km from the epicenter, was selected. Figure 5 presents the acceleration records and the corresponding response spectra generated for a 5% damping ratio of the selected record.

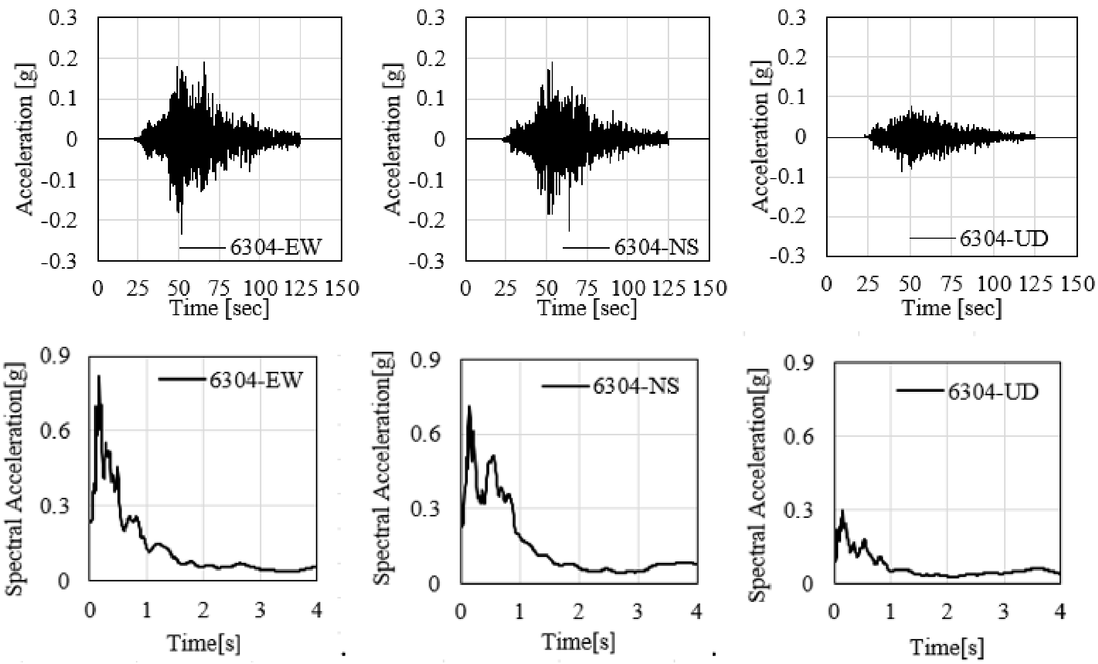

Fig 5. Acceleration-time and response spectrum graphs of the selected records

5.Result and discussion

In this section, the results obtained from the nonlinear time-history analyses of the selected building are presented. These results are comparatively evaluated for both pounding and non-pounding cases in terms of interstory displacements, acceleration, shear forces in the colliding column, pounding force, and the distribution of plastic hinges.

5.1. Accelerations and pounding forces

Collision effects between adjacent buildings cause sudden changes in velocity. This causes sudden spikes in acceleration responses. In the selected building, collisions occurred between the ground floor column and the surrounding wall during the 2023 Kahramanmaras earthquakes and significant damage occurred to the colliding column. The increases in acceleration due to the collision on the floor where the collision occurred are given in Figure 7. This twofold increase indicates that pounding significantly amplifies the seismic demands on the structure and raises the potential level of damage.

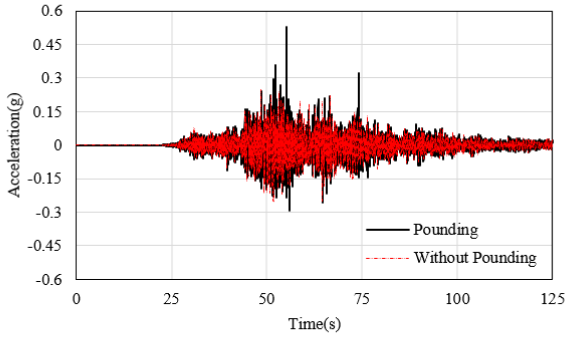

Fig 6. Increases in storey acceleration responses due to pounding

The maximum pounding force resulting from the pounding between the building and the surrounding wall was obtained as 420.9 kN. A comparative evaluation of Figures 6 and 7 shows that the time interval during which the pounding force reaches its peak coincides with the maximum acceleration. This indicates that the impact forces generated by pounding significantly increase the structural responses of the structure.

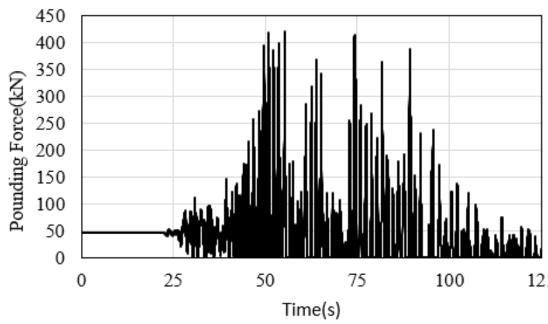

Fig 7. The time-histories of pounding forces at the ground floor

5.2.Storey displacements

When interaction occurs between two buildings due to insufficient gap, the displacement demands of the structures are affected in two different ways. In the direction where the collision occurs, a decrease in displacement responses is expected. However, due to the energy transferred in the free direction where there is no interaction, higher displacement demands can be observed, similar to accelerations. This is directly affected by the pounding forces and structural characteristics. The storey displacements obtained from the analysis with and without pounding cases are presented in Figure 8. It is observed that the displacements at each floor increase significantly in the impact case. As can be seen, displacement responses in the interaction direction decrease due to the collision, while displacements in the free direction increase.

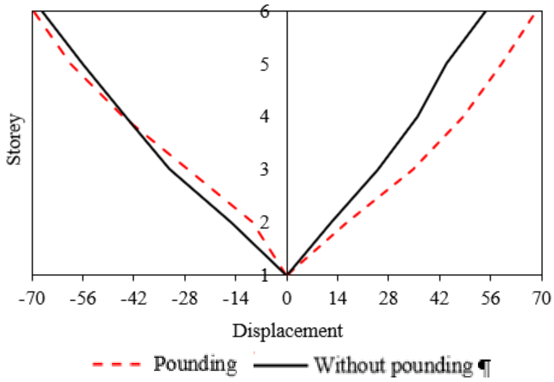

Fig 8. Changes in storey displacements responses due to pounding

5.3. Performance level of load-bearing elements

As a result of the analyses, the plastic hinge formations in the structural elements are presented in Figure 9. According to this distribution, it is seen that almost all of the structural system elements are at Immediate Occupancy (IO) performance level in the analyses where collision effects are neglected. However, in the analyses where collision effects are taken into account, it is clearly seen that plastic deformations increase at the storey where the collision occurs. On the other hand, it was observed that the column where the pounding occurred collapsed as observed in the 2023 Kahramanmaraş earthquakes.

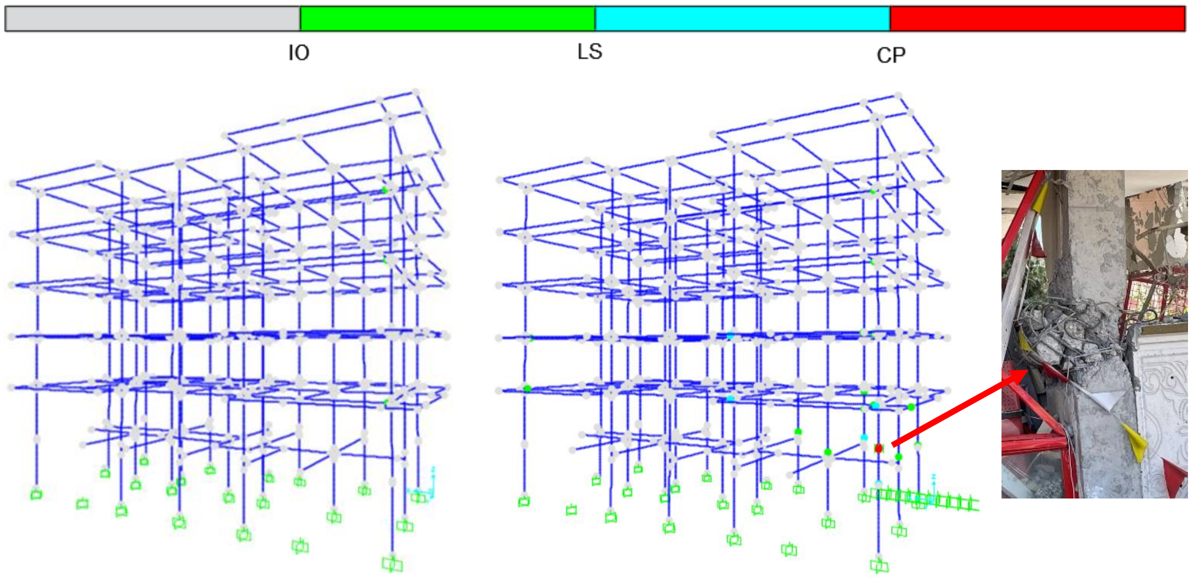

a. without pounding b. with pounding

Fig 9. Comparisons of performance level of load-bearing elements

5. Conclusion

In this study, the seismic behavior and damage mechanisms of a RC building that sustained severe damage during the 2023 Kahramanmaraş earthquakes are investigated using nonlinear time-history analysis. During the earthquakes, pounding occurred between the selected building and its surrounding wall, resulting in significant damage to the impacted column. The finite element model of the building was developed using the SAP2000 software, and pounding effects were represented by a nonlinear elastic spring (Hertz model). In the analyses, real ground motion records obtained from a station located near the building during the 2023 Kahramanmaraş earthquakes were used. The analyses were carried out in two stages, with and without the pounding effect taken into account. As a result of the analysis, it is seen that the structural responses are significantly affected by the pounding. It is also observed that the collisions cause significant damage to the structural elements where the interaction occurs. This situation clearly reveals that pounding effects neglected during design can have devastating effects.

References

AFAD-TADAS (Türkiye Afet ve Acil Durum Yönetimi Başkanlığı Kuvvetli Yer Hareketi Veritabanı),(2025, March 1), Retrieved from https://tadas.afad.gov.tr

Anagnostopoulos, S. A., & Spiliopoulos, K. V. (1992). An investigation of earthquake induced pounding between adjacent buildings.*Earthquake engineering & structural dynamics,21*(4), 289-302.

Akköse, M., Sunca, F. (2016). Effects of near-fault ground motions on earthquake-induced pounding response of RC buildings with plan irregularity. In *Insights and Innovations in Structural Engineering, Mechanics and Computation*, 320-325.

Çetinkaya, G., 2011. Deprem Yer Hareketine Maruz Komşu Binaların Çarpışma Analizi, Yüksek Lisans Tezi, Karadeniz Teknik Üniversitesi, Fen Bilimleri Enstitüsü, Trabzon.

Çatal, H. H. (2019). Deprem nedeniyle binalarda oluşan hasarlar. *In SETSCI-Conference Proceedings*, 4, .310-315.

Doğangün, A. (2004). Performance of reinforced concrete buildings during the May 1, 2003 Bingöl Earthquake in Turkey.*Engineering Structures*,*26*(6), 841-856.

Gökdemir, H. (2019). Failure of horizontal support system to adjacent buildings during reconstruction in Eskisehir.*Engineering Failure Analysis*,*103*, 82-94.

Google Earth. (2025). Google Earth (Version 7.x) [Computer software]. Google LLC. https://earth.google.com/

Google Maps. (2025). *Google Maps* (Version 11.x) [Computer software]. Google LLC. https://maps.google.com

Köse Sunca, G. Ç., 2019. Farklı Oran Ve Düzendeki Dolgu Duvarlara Sahip Betonarme Yapıların Sismik Performanslarının Belirlenmesi. Yüksek Lisans Tezi, Gümüşhane Üniversitesi Fen Bilimleri Enstitüsü, Gümüşhane, 137.

Mander, J. B., Priestley, M. J., & Park, R. (1988). Theoretical stress-strain model for confined concrete. *Journal of structural engineering, 114(8)*, 1804-1826.

Miari, M., & Jankowski, R. (2022). Shaking table experimental study on pounding between adjacent structures founded on different soil types. In*Structures*, 44, 851-879).

Muthukumar S, DesRoches R., (2006). A hertz contact model with non-linear damping for pounding simulation. *Earthquake Engineering and Structural Dynamics,35*,811-828.

Rajaram, C.,Ramancharla, P. K. (2014). Three dimensional analysis of pounding between adjacent buildings.*Journal of Structural Engineering*,*41*(2), 1-11.

Sak, Ö. F., Beyen, K. bitişik nizam betonarme yapilarda çarpişma etkisi ve zaman-frekans alaninda performans analizleri, 4. Uluslararası Deprem Mühendisliği ve Sismoloji Konferansı.

SAP2000, Integrated Software For Structural Analysis and Design, Computers and Structures,Version 25.1, Berkeley, California, USA.

Sunca, F., 2023. Betonarme Binalarda Çarpışma Etkisinin Sarsma Masası Deneyleri ile İncelenmesi ve Deneysel Yöntemlere Dayalı Hasar Tespiti. Yüksek Lisans Tezi, Karadeniz Teknik Üniversitesi Fen Bilimleri Enstitüsü, Trabzon, 1.

Sunca, F., Altunişik, A. C., Kaya, A., Genç, A. F., Şahin, M. C., & Karahasan, A. K. (2024). Shake table tests on story-to-story pounding between adjacent RC buildings. In *Structures*,Vol. 69, 107544

TBEC. (2018), TBEC Türkiye building earthquake code,Ankara, Turkey

Tekin, Ö. F., Pala, M. (2016). Taşıyıcı Sistemde Düşey Eleman süreksizliğinin sismik çarpışma anında yapı üzerine etkisi. In *4th International Symposium on Innovative Technologies in Engineering and Science (ISITES2016).*

TS 498. (1997), Turkish Standards Institution ,Ankara,Turkey.

Yön, B., & Calayır, Y. (2013). Betonarme Binalarda Sargı Donatısı Etkisinin Yayılı Plastik Mafsal Modeliyle İncelenmesi", 2.Türkiye Deprem Mühendisliği ve Sismoloji Konferansı, 25-27.

4th International Civil Engineering & Architecture Conference
17-19 May 2025, Trabzon, Türkiye

Optimal design of steel frames with semi-rigid connections and column bases using particle swarm optimization

Jay Prakash*[1], Ayşe T. Daloğlu[1]

[1] *Karadeniz Technical University, Department of Civil Engineering, 61080 Trabzon, Türkiye*

Abstract. The particle swarm optimization (PSO) method is utilized for two-dimensional steel frames featuring semi-rigid connections between beams and columns, as well as between columns and bases. The metaheuristic algorithm generates optimized steel frames by selecting suitable sections from a predetermined collection of standard steel sections. The standard steel sections, which include wide-flange profiles (W), are supplied by the American Institute of Steel Construction (AISC). The initial example is subject to displacement, inter-storey drift, and stress constraints, as outlined by the AISC Load and Resistance Factor Design (LRFD) regulations. In the last examples, the displacement, geometric, and stress constraints of the AISC Allowable Stress Design (ASD) standard are implemented. In the course of the optimization process, three distinct steel frames are examined, including configurations both with and without semi-rigid connections between the beams and columns, as well as between the columns and bases. All optimization techniques are implemented using the high-level programming language C# version 17.10.5, which is designed to integrate with version 22 of SAP2000's Open Application Programming Interface (OAPI). The results of the analysis indicate that the rigidity of the connections serves as a critical parameter in the optimization of weight for steel frames.

Keywords: Particle swarm optimization (PSO); Semi-rigid connection; Optimization of steel frames; SAP2000-OAPI; Column bases

1. Introduction

The process of optimizing steel frames structures begin with choosing steel profiles for the structural elements from a specific collection of available steel profile tables. This method reduces the steel frame's weight by considering various constraints, such as material properties, displacement, deflection, and dimensions (Prakash & Daloglu, 2023). The field of computer-aided optimization advanced significantly in the 1970s (Pincus, 1970; Talbi, 2009; Rao, 2019). Then, in the early 1990s, heuristic search techniques developed as a response to engineers and designers' requirements for cost-effective designs and improved optimization strategies (Jenkins, 1991; Tang & Yao, 2008; Yang, 2010).

In recent years, significant progress has been made in the development of innovative stochastic search methods within the field of structural optimization. These techniques, which are inspired by natural processes, effectively address the inconsistencies commonly associated with traditional mathematical programming-based optimization approaches. Typically, meta-heuristic algorithms aim to identify feasible solutions to optimization problems through a systematic 'trial and error' process within a reasonable computational timeframe (Arafa, Khalifa, & Alqedra, 2015). Numerous researchers have recently formulated and implemented diverse meta-heuristic strategies specifically designed for steel structures, accommodating both fully rigid and semi-rigid connections (Kameshki & Saka, 2003; Hayalioglu & Degertekin, 2004; Hayalioglu & Degertekin, 2005; Degertekin, Hayalioglu, & Gorgun, 2009; Rafiee, Talatahari, & Hadidi, 2013; Hadidi & Rafiee, 2014; Artar & Daloglu, 2015).

A thorough examination of the existing literature reveals a significant deficiency in studies utilizing metaheuristic algorithms for the optimal design of steel frames, specifically those incorporating semi-rigid connections and column bases. Among metaheuristic algorithms, the Particle Swarm Optimization (PSO) algorithm is well-regarded for its simplicity, computational efficiency, and ease of implementation. Unlike other methods that rely heavily on user-defined parameters, the PSO algorithm features a straightforward numerical structure governed by only a few control parameters: inertia weight (w), cognitive acceleration coefficient (c_1), and social acceleration coefficient (c_2). These parameters define the exploration-exploitation behavior of the swarm and can often be standardized for structural optimization problems (Clerc, 2010; Sengupta, Basak, & Peters, 2018). Moreover, PSO leverages these general parameters and does not require algorithm-specific operations such

* Corresponding author, E-mail: jaypee@outlook.in

https://doi.org/10.31462/icearc2025_ce_sme_780

as crossover or pheromone update schemes, reducing implementation complexity (Papazoglou & Biskas, 2023; Adeyiga, Sotonwa, & Adenibuyan, 2022). In comparison, Genetic Algorithms (GA) require the specification of crossover probability, mutation rate, and selection method. Ant Colony Optimization (ACO) involves configuring four parameters and an extra parameter for search-space reduction in multiphase applications. Harmony Search (HS) necessitates the harmony memory consideration and pitch adjusting rate (Kennedy & Eberhart, 1995). The reduced parametric complexity of Particle Swarm Optimization (PSO) lessens its vulnerability to subjective tuning biases, enabling more robust convergence in complex design spaces (Clerc & Kennedy, 2002; Perez & Behdinan, 2007).

Consequently, the PSO technique can be utilized to enhance the design of steel frames featuring semi-rigid connections and column bases. By employing the PSO method, the optimal design for steel frames has been evaluated and compared to prior studies. Three particular case studies are examined for this analysis. The first case study originates from Değertekin (2008), while the other two are based on the work of Artar and Daloğlu (2015). The findings indicate that the PSO method performs effectively and is viable for addressing structural challenges.

2. Particle swarm optimization (PSO)

The PSO algorithm was initially conceived by Kennedy and Eberhart in 1995. Subsequent advancements to this algorithm were introduced by Pedersen and Chipperfield in 2010. PSO represents a stochastic search methodology that employs a population-based strategy for effectively exploring intricate solution spaces. The active foraging behavior of animal species, as they seek out food sources, serves as a basic concept for understanding this technique. This food-seeking behavior encompasses the formation of groups shaped by social influences that rely on the collective memory of each member and the data collected by the swarm.

The approach begins with random solutions and then progressively modifies the velocity and location of particles through iteration. Every particle is characterized by its position x_i^m and velocity v_i^m. The initial position x_i^0 is randomly scattered and taken from the given solution. The initial velocity v_i^0 is presumed to be zero. The initial parameters can be obtained from Eqs. 1-2.

$$x_i^0 = x_{min} + r(x_{max} - x_{min}) \tag{1}$$

$$v_i^0 = 0 \tag{2}$$

In the provided equations, r denotes a random integer that can take a value between 0 and 1. At the same time, x_{min} and x_{max} signify the lower and top limit of the design parameters, respectively.

This particle velocity reflects the extent of change, while particle positions denote possible solutions for optimal design challenges. Each particle is updated based on two optimal values during every iteration of its movement. The first optimal value is called $p_{best,i}^m$, which signifies the best position attained by the i^{th} particle. The second optimal value, p_{gbest}^m, indicates the best position among all particles at time m. The position and velocity of the i^{th} particle for the m iteration are adjusted according to Eqs. 3-4.

$$v_i^{m+1} = w^m v_i^m + c_1 r_1 \left(p_{best,i}^m - x_i^m\right) + c_2 r_2 (p_{gbest}^m - x_i^m) \tag{3}$$

$$x_i^{m+1} = x_i^m + v_i^{m+1} \tag{4}$$

In the formulas mentioned above, r_1 and r_2 serve as arbitrary values ranging from 0 to 1. The particle's inertia, denoted as w^m,influences the algorithm's exploration characteristics. The trust parameters c_1 and c_2 represent the coefficients for individual and collective learning, respectively. For further information on the PSO algorithm, one can refer to various sources, including Kennedy and Eberhart (1995), Saka and Geem (2013), and Gad (2022).

3. Two-dimensional steel frame modeling with semi-rigid connections

The analysis of the frame is based on the assumption that the connection between the column and beam is entirely rigid, facilitating straightforward calculations. However, experimental findings indicate that most connections exhibit moment-rotation behavior that lies between pinned and rigid connections. As a result, these connections can be classified as semi-rigid. In the context of simple models, Simoes (1996) presented a linear model for the analysis of semi-rigid frameworks. Furthermore, Soares Filho et al. (2004) employed a linear technique in examining a 20-storey steel frame employing linear static analysis. Nevertheless, it is important to note that the actual behavior of the connections across all moment-rotation curves is nonlinear (Artar & Daloglu, 2015). As a result, this paper acknowledges the moment-rotation relationship of the connection as being nonlinear.

In numerous published studies, it is often assumed that connections between beams and columns or between columns and their bases are entirely rigid (Toğan, 2012; Artar, 2016). Nonetheless, semi-rigid connections can range from being fully pinned to completely rigid, depending on their specific type. When analyzing the bending moment (M) at these connections, it is crucial to consider semi-rigid connections, as they can cause rotational movement (θ_r) (Artar & Daloglu, 2015). Figs. 1 and 2 depict moment-rotation curves and the types of connections, respectively (Hayalioglu & Degertekin, 2004).

In the present study, a polynomial model proposed by Frye and Morris (1975) is utilized. The subsequent equations, denoted as Eq. 5, pertaining to odd-power polynomials, elucidate this model:

$$\theta_r = C_1(\kappa M)^1 + C_2(\kappa M)^3 + C_3(\kappa M)^5 \tag{5}$$

In this context, κ is defined as the standardization constant, contingent upon the geometrical variables and the characteristics of the connections. The constants C_1, C_2, and C_3 serve as the coefficients employed for the purpose of curve fitting.

In the analysis of the steel frames, as mentioned in Fig. 2, two semi-rigid connections are applied in this study. Table 1 provides these two connections' curve fitting and standardization constants (Faella, Piluso, & Rizzano, 1999). The values for rotational stiffness are 2.26×10^8 kNmm/rad for end plates lacking column stiffeners and 3.39×10^8 kNmm\rad for end plates including column stiffeners (Hayalioglu & Degertekin, 2004). Additionally, the semi-rigid connection for the column base utilized by Hayaloglu and Degertekin (2004) is incorporated, as depicted in Fig. 3.

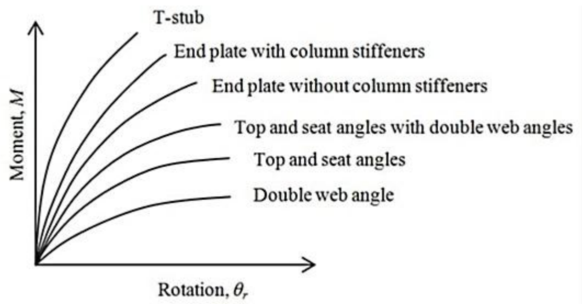

Fig. 1. The moment-rotation curves for semi-rigid connections (Hayalioglu & Degertekin, 2004)

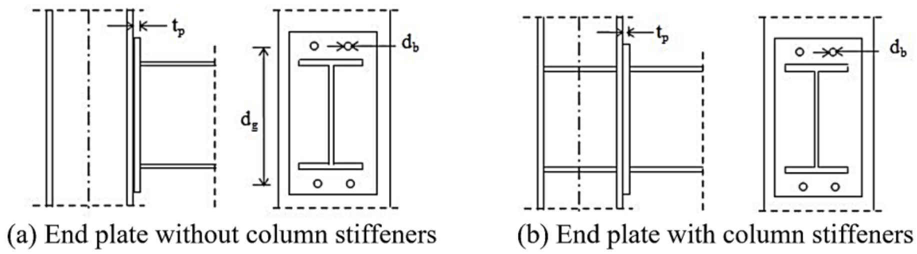

Fig. 2. Types of semi-rigid connections used in the study

Table 1. The details of semi-rigid connections used in the study

Connection Types	Curve fitting constants	Standardization constants
End plate without column stiffeners	$C_1 = 1.83 \times 10^{-3}$ $C_2 = 1.04 \times 10^{-4}$ $C_3 = 6.38 \times 10^{-6}$	$\kappa = d_g^{-2.4} t_p^{-0.4} d_b^{-1.5}$
End plate with column stiffeners	$C_1 = 1.79 \times 10^{-3}$ $C_2 = 1.76 \times 10^{-4}$ $C_3 = 2.04 \times 10^{-4}$	$\kappa = d_g^{-2.4} t_p^{-0.6}$

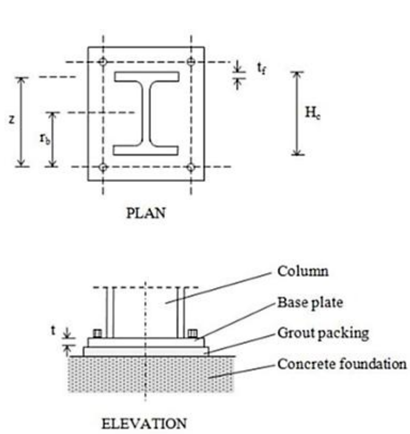

Fig. 3. Type of semi-rigid connection for column bases (Hayalioglu & Degertekin, 2004)

4. Mathematical formulation of optimal structural design

The lowest weight of unbraced steel structures is treated as the unconstrained objective function in discrete optimization problems. The formulations for the objective function and the penalized functions are provided in Eqs. 6-9 (Daloglu & Armutçu, 1998).

$$Min\ W_{sf} = \sum_{f=1}^{ng} A_f \sum_{i=1}^{nf} \rho_i L_i \tag{6}$$

$$\mathrm{g_i}(x) > 0 \rightarrow c_{vi} = \mathrm{g_i}(x) \tag{7}$$

$$\mathrm{g_i}(x) < 0 \rightarrow c_{vi} = 0 \tag{8}$$

$$\varphi_{sf}(x) = W_{sf}(x)\left(1 + P\sum_{i=1}^{m} c_{vi}\right) \tag{9}$$

In this context, the variable W_{sf} represents the total weight of the unbraced steel frame, while A_f denotes the cross-sectional area of element group f. The symbols ρ_i and L_i refer to the density and length of the steel members. The variable ng indicates the total number of groups, and nf signifies the total number of members within group f. The function $\varphi_{sf}(x)$ is referred to as the penalized objective function, and P representing the penalty constant. The variable c_{vi} corresponds to constraint violations, and $\mathrm{g_i}(x)$ designates the constraints applicable to the design.

This study considers various limitations based on Prakash and Daloglu (2023), which are expressed as follows:

The stress limits according to AISC-LRFD (2010) are presented in Eq. 10.

$$\mathrm{g_i}(x) = \begin{cases} \dfrac{P_u}{\phi P_n} + \dfrac{8}{9}\left(\dfrac{M_{ux}}{\phi_b M_{nx}} + \dfrac{M_{uy}}{\phi_b M_{ny}}\right) - 1.0 \le 0 & if\ \dfrac{P_u}{\phi P_n} \ge 0.2 \\ \dfrac{P_u}{2\phi P_n} + \left(\dfrac{M_{ux}}{\phi_b M_{nx}} + \dfrac{M_{uy}}{\phi_b M_{ny}}\right) - 1.0 \le 0 & if\ \dfrac{P_u}{\phi P_n} \le 0.2 \end{cases} \tag{10}$$

In this context, the symbol ϕ signifies the resistance factor, which is defined as ϕ_c for compression (0.85), ϕ_t for tension (0.90), and ϕ_b for flexural (0.90). P_n and P_u denote the nominal strength and required axial strength, respectively. M_{nx} and M_{ny} indicate the nominal flexural strength about the major and minor axes, respectively. M_{ux} and M_{uy} represent the necessary flexural strength around the major and minor axes, respectively, with the understanding that for a two-dimensional frame, M_{uy} is equal to zero.

The stress limits according to AISC-ASD (1989) are presented in Eqs. 11-12.

$$\mathrm{g_i}(x) = \left[\frac{f_a}{F_a} + \frac{C_{mx} f_{bx}}{\left(1 - \frac{f_a}{F'_{ex}} F_{bx}\right)}\right] - 1.0 \le 0 \qquad i = 1, 2, \dots, nc \tag{11}$$

$$\mathrm{g_i}(x) = \left[\frac{f_a}{0.60F_y} + \frac{f_{bx}}{F_{bx}}\right] - 1.0 \le 0 \qquad i = 1, 2, \dots, nc \tag{12}$$

If $\frac{f_a}{F_a}$ is less than or equal to 0.15, then Eq. 13 is used for calculations instead of Eqs. 11 and 12.

$$\mathrm{g_i}(x) = \left[\frac{f_a}{F_a} + \frac{f_{bx}}{F_{bx}}\right] - 1.0 \le 0 \qquad i = 1, 2, \dots, nc \tag{13}$$

In this context, The variable nc represents the total number of members, and C_{mx} is a factor typically assumed to be 0.85 for unbraced frame members. The terms F_{bx} and f_{bx} correspond to the allowable compressive bending stresses and the computed bending stresses about the major axis, respectively. Furthermore, F'_{ex} indicates the Euler stresses, and F_y refers to the yield stress of steel. f_a denotes the computed axial stress, while F_a signifies the allowable axial stress under axial compression, which is determined by the elastic or inelastic buckling characteristics of the member depending on its slenderness ratio, influenced by the effective length factor (K).

According to Dumonteil (1992), the effective length factor K is defined in Eq. 14.

$$K = \sqrt{\frac{1.6G_A G_B + 4.0(G_A + G_B) + 7.50}{G_A + G_B + 7.50}} \tag{14}$$

In this context, G_A and G_B denote the stiffness factors corresponding to the A^{th} and B^{th} ends of the columns, which can be determined using the equations provided in Eq. 15.

$$G = \left(\frac{\sum I_c/L_c}{\sum \alpha_{uf}(I_g/L_g)}\right) \tag{15}$$

In this context, I_c denotes the moment of inertia related to the column section that aligns with the buckling plane, while L_c signifies the column length. I_g refers to the moment of inertia associated with the beam section pertinent to the bending plane, and L_g represents the length of the beam. The coefficient α_{uf} reflects the connection state, equal to 1 for rigid connections. Semi-rigid connections are determined using Eq. 16 (Doğan, 2010).

$$\alpha_{uf} = \frac{1}{\left(1+\frac{6EI_g}{L_g K'}\right)} \tag{16}$$

Where, K' indicates the rotational spring stiffness at the member's end, expressed as M/θ_r.

The displacement constraints are delineated in Eq. 17.

$$g_{jl}(x) = \frac{\delta_{jl}}{\delta_{ju}} - 1.0 \leq 0 \qquad \begin{array}{l} j = 1, \dots, cd \\ l = 1, \dots, nl \end{array} \tag{17}$$

In this context, δ_{jl} represents the displacement associated with the j^{th} degree of freedom for the specified load case l. Additionally, δ_{ju} indicates the established upper limit, while cd signifies the total count of constrained displacements. Lastly, nl refers to the overall number of loading scenarios considered.

Inter-storey drift constraints are delineated in Eq. 18.

$$g_{jil}(x) = \frac{\Delta_{jil}}{\Delta_{ju}} - 1.0 \leq 0, \quad i = 1, \dots, nsc, j = 1, \dots, ns, l = 1, \dots, nl \tag{18}$$

In this context, Δ_{jil} denotes the inter-storey drift of the i^{th} column in the j^{th} storey during load case l. The symbol Δ_{ju} indicates the permissible limit value, ns refers to the total number of stories, and nsc signifies the count of columns within a storey.

Column-to-column geometric constraints are delineated in Eq. 19.

$$g_n(x) = \frac{D_{un}}{D_{ln}} - 1.0 \leq 0 \qquad n = 2, \dots, ns. \tag{19}$$

In this context, D_{un} and D_{ln} signify the depths of the upper and lower floors, respectively.

Beam-to-column geometric constraints are delineated in Eq. 20.

$$g_{bb,i}(x) = \frac{b_{fbk,i}}{b_{fck,i}} - 1.0 \leq 0 \qquad i = 1, \dots, n_{bf}. \tag{20}$$

In this context, $b_{fbk,i}$ and $b_{fck,i}$ signify the flange widths of the beam and column elements, respectively.

5. Implementation and results

Three particular unbraced steel frames are examined in this study to explore the impact of semi-rigid connections between beams and columns, as well as between columns and bases, utilizing the PSO optimization algorithm. The first example has been analyzed by several researchers (Pezeshk, Camp, & Chen, 2000; Camp, Bichon, & Stovall, 2005; Degertekin S. O., 2008), while the last two examples were investigated by Hayalioglu and Degertekin (2004) and Artar and Daloglu (2015). In this study, the permissible lateral displacement is limited to $H/250$, with H representing the overall height of the steel frame in centimeters, and the maximum inter-storey drift is constrained to $h_r/300$, where h_r denotes the height of the storey in centimeters. The rotational stiffness for the semi-rigid column-to-base connection in all frames is set at 1.13×10^8 kNmm/rad. The frame members are assumed to be made of steel with a Young's modulus of $E_s = 200$ GPa, a yield stress of $f_y = 248.2$ MPa, and a material density of $\rho_i = 7.85$ ton/m^3.

5.1. Case study-1: 2-bay, 3-storey frame design

A 2-bay, 3-story, 2-dimensional frame is depicted in Fig. 4, comprised of 15 members. Various researchers have assessed the steel frame, such as Pezeshk et al. (2000), Camp et al. (2005), Degertekin (2008). In this study, the steel frame is optimized with and without semi-rigid connections using particle swarm optimization in a hybrid SAP2000 and C# programming language approach. The stress limitations of AISC-LRFD, displacement limits, and inter-story constraints are applied to both the fully rigid and semi-rigid frames. The maximum lateral deflection and inter-story drift are constrained to 3.658 cm and 1.016 cm, respectively.

The frame components are categorized into two groups: the first group includes beam components, while the second group comprises column components. For the design, beam components are chosen from a selection of 276-W profiles, and column components are chosen from 38-W profiles. Dumonteil (1992) approximation equation is applied to determine the effective length factor regarding the major axis (K_x). The effective length factor concerning the minor axis K_y is assumed to be 1.0 for all column components and is considered to be 1/6th of the span length for each beam component.

The optimal outcomes for the rigid frame are presented in Table 2 for comparison with existing solutions in the literature. The ideal cross-sections for the semi-rigid structure, featuring both end plates without column stiffeners and those with stiffeners at the connections, are also shown in Table 2. Fig. 5 illustrates the design history of total steel weight through iterations for both the rigid and semi-rigid frames.

According to the PSO solution presented in Table 2, which pertains to the rigid frame, the weight of the 2-dimensional frame aligns with the minimum optimal design established in previous studies. The minimum weight of 8165 kg obtained in this study is roughly 4.4%, 4.4%, and 1.6% lighter than the lowest weights reported by Pezeshk et al. (2000), Camp et al. (2005), and Değertekin (2008), respectively.

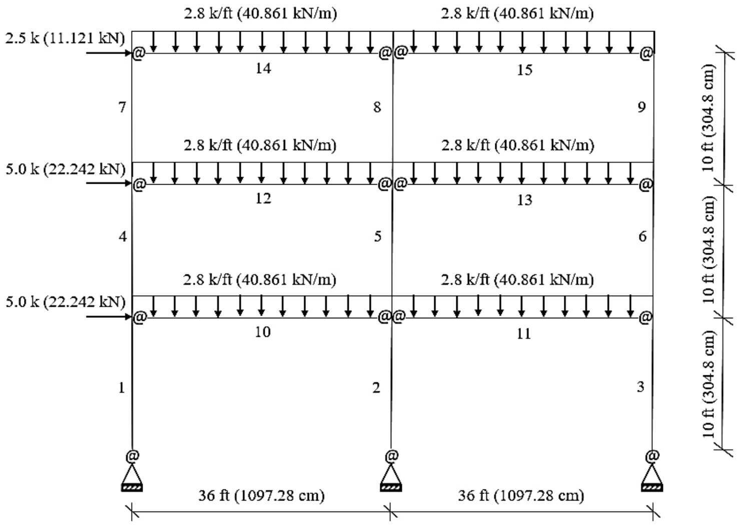

Fig. 4. A 2-bay, 3-storey steel frame

Table 2. Optimum design of 2-bay, 3-storey frame

Element Group	Member	Rigid frame				Semi-rigid frame	
						Present study	
		Pezeshk et al. (2000)	Camp et al. (2005)	Değertekin (2008)	Present study	End plate without column stiffeners	End plate with column stiffeners
		GA	ACO	HS	PSO	PSO	PSO
1 (Beam)	10-15	24 × 62	24 × 62	21 × 62	21 × 55	18 × 60	18 × 55
2 (Column)	1-9	10 × 60	10 × 60	10 × 54	10 × 68	10 × 68	10 × 77
Minimum weight (kg)		8524	8524	8297	8165	8655	8532
Maximum displacement (cm)		-	-	-	1.3947	1.6071	1.5433
Maximum inter-storey drift (cm)		-	-	-	0.8509	0.9571	0.8814

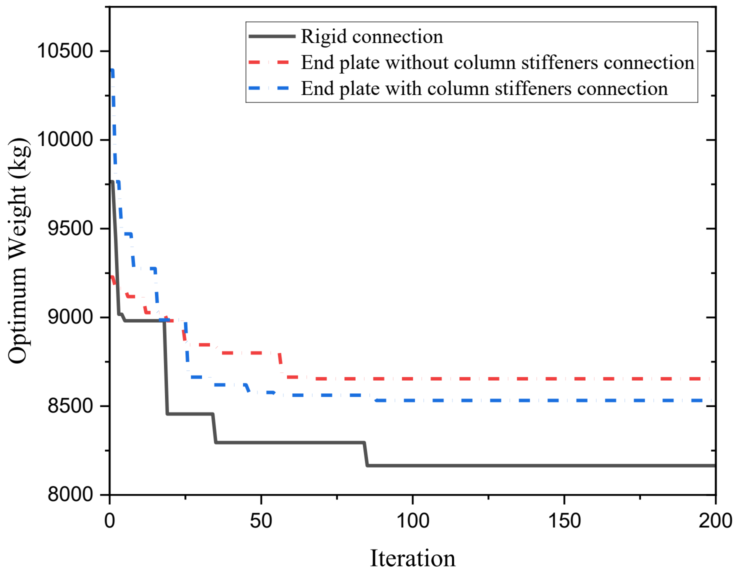

Fig. 5. Design histories of a 2-bay, 3-storey steel frame

Additionally, this research demonstrates a lower minimum weight than previous literature due to random initialization, stochastic search, and convergence criteria. The maximum top drift and inter-story drift are recorded at 1.3947 cm and 0.8509 cm, respectively. These values for top and inter-story drifts are significantly below the acceptable limits. Furthermore, as indicated in Table 2, the minimum weights for the semi-rigid frame with the end plate without column stiffeners and the end plate with column stiffeners are 6.0% and 4.5% heavier than the minimum weight of the rigid frame structure, respectively.

The optimal design of the steel frame is generated through the PSO algorithm after 200 iterations with a population of 20, resulting in an evaluation of 4000 frames. Additionally, a decrease in the rotational stiffness of the connection between the beam and the column leads to a considerable increase in the minimum weight. However, this research's findings are more cost-efficient than those of earlier studies.

5.2. Case study-2: 2-bay, 5-storey frame design

A 2-bay, 5-storey, 2-dimensional frame is depicted in Fig. 6, consisting of 25 elements. Hayaloglu and Degertekin (2004) and Artar and Daloglu (2015) employed a genetic algorithm to analyze the steel frame. This research optimizes the steel frame with and without semi-rigid connections using particle swarm optimization.

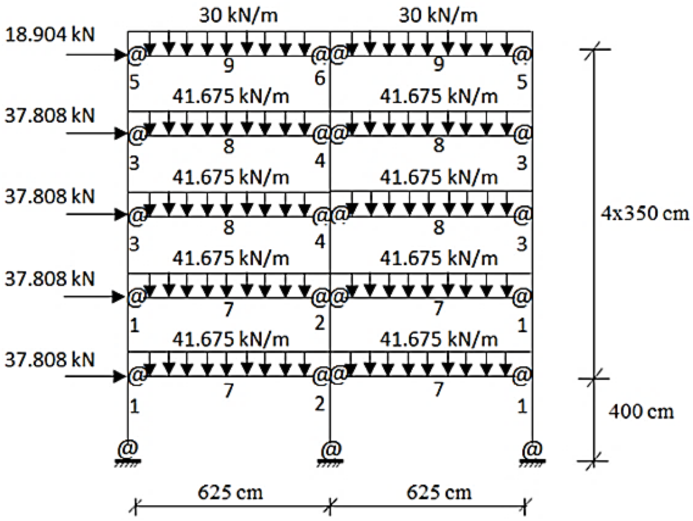

Fig. 6. A 2-bay, 5-storey steel frame

Table 3. Optimum design of 2-bay, 5-storey frame

Element Group	Rigid frame			Semi-rigid frame	
				Present study	
	Hayalioglu and Degertekin (2004)	Artar and Daloğlu (2015)	Present study	End plate without column stiffeners	End plate with column stiffeners
	GA	GA	PSO	PSO	PSO
1	18 × 55	21 × 68	16 × 36	12 × 120	21 × 55
2	18 × 65	16 × 100	24 × 146	21 × 73	21 × 68
3	14 × 61	16 × 45	12 × 53	10 × 60	18 × 71
4	14 × 43	1 × x50	21 × 101	16 × 67	14 × 193
5	14 × 43	12 × 26	8 × 10	8 × 10	8 × 10
6	8 × 31	8 × 24	16 × 89	8 × 10	8 × 18
7	18 × 50	24 × 55	18 × 46	14 × 43	16 × 40
8	14 × 43	24 × 55	8 × 48	12 × 53	21 × 50
9	21 × 50	18 × 35	8 × 10	8 × 10	8 × 10
Minimum weight (kg)	8888	9255	8840	9355	9208
Maximum displacement (cm)	3.68	2.17	5.10	6.74	4.97
Maximum inter-storey drift (cm)	-	-	1.254	1.822	1.395

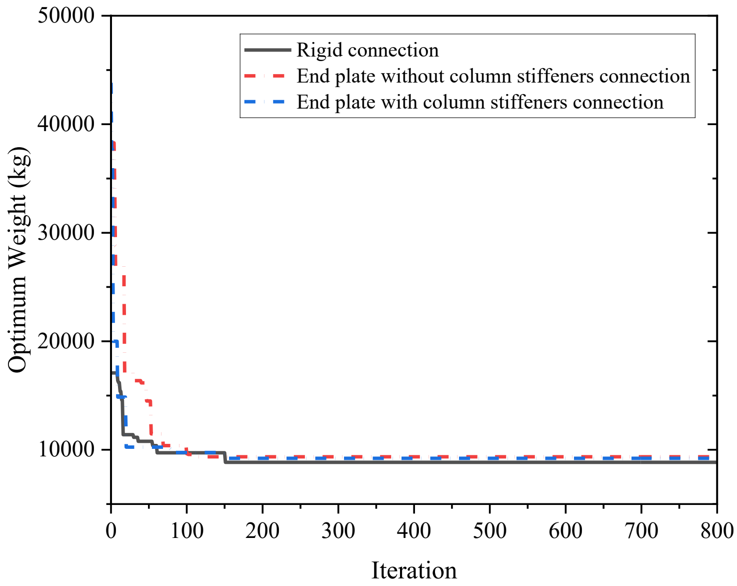

Fig. 7. Design histories of a 2-bay, 5-storey steel frame

The present study applies AISC-ASD stress limitations, restrictions on lateral displacement, and size constraints for column-to-column and beam-to-column connections to fully rigid and semi-rigid frames. The maximum allowable lateral displacement and inter-story drift are capped at 7.2 cm and 2.96 cm, respectively.

In the procedure, the cross-sections of the frame components are selected from a collection of 174-W sections provided by the American Institute of Steel Construction (AISC). Table 3 presents the optimal solutions identified for the completely rigid and semi-rigid frame based on solutions found in existing literature. Fig. 7 depicts the history of total steel weight design with iterations for both the rigid and semi-rigid frames.

Table 3 indicates that the optimal design outcomes from this research closely match the findings of earlier studies. According to the optimal design results for a fully rigid frame, the minimum weight achieved in this study is 8840 kg, which is about 0.5% and 4.5% lighter than the minimum weights reported by Hayaloglu and Degertekin (2004) and Artar and Daloglu (2015), respectively. This observation similarly applies to the optimal designs of semi-rigid frames (End Plate without Column Stiffeners and End Plate with Column Stiffeners connections, as detailed in Table 3). Furthermore, the weight of 8840 kg is roughly 5.5% and 4.0% below the minimum weights of 9355 kg and 9208 kg obtained from the optimal designs of the two semi-rigid frames, respectively. The maximum top and inter-story drifts are significantly below the allowable limits. As a result, stress and size constraints are crucial in achieving the best designs for fully and semi-rigid frames.

The PSO algorithm creates the optimal steel frame design after 800 iterations with a population of 20, resulting in the analysis of 16000 frames. Additionally, reducing the rotational stiffness value of the connection between the beam and column leads to a considerable increase in the minimum weight. Nonetheless, this study's findings are more cost-effective than earlier research's.

5.3. Case study-3: one-bay, 10-storey frame design

Fig. 8 depicts a one-bay, 10-storey 2-dimensional steel frame comprising 30 elements. Hayaloglu and Degertekin (2004) and Artar and Daloglu (2015) employed a genetic algorithm to examine the steel frame. The study optimizes the steel frame with and without semi-rigid connections using particle swarm optimization. This current study applies the same constraints as the earlier frame. The maximum lateral displacement and inter-story drift limits are set at 12 cm and 2.54 cm, respectively.

The cross-sectional dimensions of the frame components in the design are selected from 276-W sections as specified by the American Institute of Steel Construction (AISC). Table 4 summarizes the optimal solutions identified for the completely rigid and semi-rigid frames based on existing literature. Fig. 9 shows the total steel weight design histories with iterations for the rigid and semi-rigid frames.

Table 4 indicates that the optimal design results obtained from this study are very similar to the solutions found in existing literature. According to the optimal design for a fully rigid frame, the minimum weight of 12977 kg is approximately 7.3% heavier than the minimum weight reported by Hayaloglu and Degertekin (2004) and 7.0% lighter than the minimum weight noted by Artar and Daloglu (2015). This observation is also accurate for the optimal designs of semi-rigid frames (End Plate without Column Stiffeners and End Plate with Column Stiffeners connections, as shown in Table 4). Furthermore, the weight of 12977 kg is roughly 4.9% and 0.6% lighter than the minimum weights of 13646 kg and 13054 kg obtained from the optimal designs of the two semi-rigid frames, respectively. The top and inter-story drift measurements are significantly below the allowable limits.

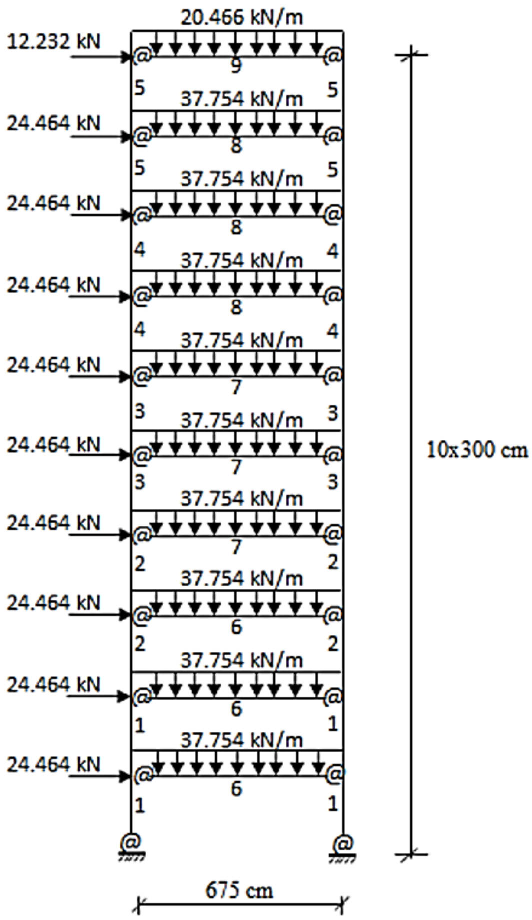

Fig. 8. A one-bay, 10-storey steel frame

Table 4. Optimum design of a one-bay, 10-storey frame

Element Group	Rigid frame			Semi-rigid frame	
				Present study	
	Hayalioglu and Degertekin (2004)	Artar and Daloğlu (2015)	Present study	End plate without column stiffeners	End plate with column stiffeners
	GA	GA	PSO	PSO	PSO
1	14 × 109	24 × 117	30 × 108	30 × 90	30 × 99
2	14 × 90	24 × 117	27 × 94	30 × 90	30 × 90
3	14 × 90	24 × 68	27 × 84	27 × 84	27 × 102
4	14 × 90	16 × 57	27 × 84	27 × 84	27 × 94
5	12 × 79	12 × 40	24 × 76	24 × 104	16 × 40
6	16 × 77	27 × 94	21 × 50	24 × 55	21 × 48
7	21 × 62	21 × 68	21 × 50	21 × 48	24 × 76
8	14 × 53	24 × 55	21 × 48	21 × 44	21 × 44
9	14 × 48	16 × 26	24 × 55	27 × 114	18 × 40
Minimum weight (kg)	12098	13951	12977	13646	13054
Maximum displacement (cm)	8.73	5.57	7.59	10.09	8.98
Maximum inter-storey drift (cm)	-	-	1.110	1.349	1.360

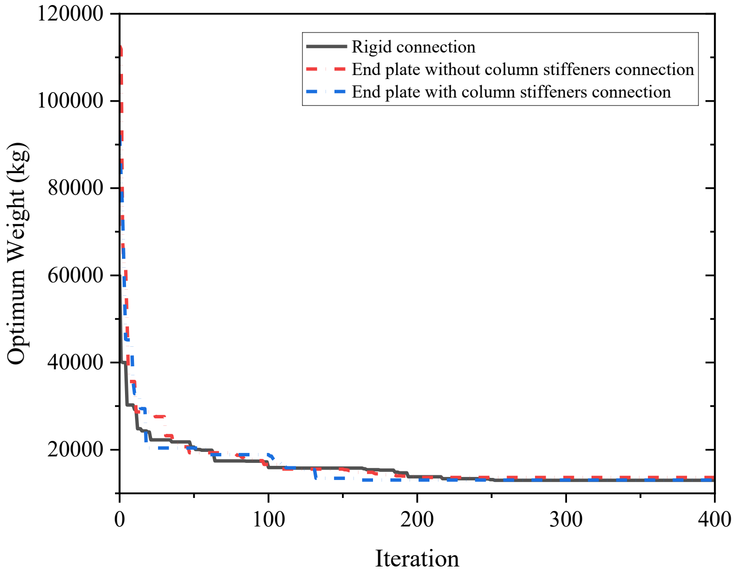

Fig. 9. Design histories of a one-bay, 10-storey steel frame

The PSO algorithm has yielded the most efficient steel frame design after conducting 400 iterations with a population of 40, resulting in an analysis of 16000 frames. In addition, reducing the rotational stiffness of the joint between the column and beam improves the minimum weight. Nevertheless, this research's findings are more economical than those from earlier studies.

6. Conclusion

The primary objective of this research is to utilize particle swarm optimization (PSO) for 2-dimensional frames featuring semi-rigid connections and column bases, aiming to determine the optimal weight of these steel frames. The high-level programming language C# implements the optimization technique to integrate with SAP2000 version 22 Open Application Programming Interface (OAPI). Stress constraints based on AISC-LRFD, along with displacement constraints and inter-story drift constraints, are applied in the first example. The subsequent two examples incorporate stress constraints based on AISC-ASD, displacement constraints, inter-story drift constraints, and geometric (dimension) constraints. The analysis results are presented in both tabular and graphical formats.

Key findings from the study are summarized below:

- The research outcomes across all three examples indicate that semi-rigid connections positively affect lateral displacements, leading to the selection of larger column profiles.
- Due to the influence of the rotational stiffness value, the minimum weight of the semi-rigid frames is greater than that of the fully rigidly connected frames.
- Analyzing the design histories of the 2-dimensional frames indicates that the third example was finalized after 400 iterations, whereas the first and second examples had 200 iterations and 800 iterations, respectively.
- Comparative analysis shows that the current study results are less weighted than previous works for the first two examples. However, for the third example, the current findings exhibit less weight than those of Artar and Daloglu (2015) yet greater weight than those of Hayalioglu and Degertekin (2004).

References

Adeyiga, J. A., Sotonwa, K. A., & Adenibuyan, M. T. (2022). Comparison of genetic algorithm and particle swarm optimization techniques in intelligent parking system. *Journal of Advanced Materials Science and Engineering, 2*(1), 1–10.

AISC-ASD. (1989). *Manual of steel construction: allowable stress design.* Chicago, IL, USA: American Institute of Steel Construction.

AISC-LRFD. (2010). *Manual of steel construction-load and resistance factor design.* Chicago, IL, USA: American Institute of Steel Construction.

Arafa, M., Khalifa, A., & Alqedra, M. (2015). Design optimization of semi-rigidly connected steel frames using harmony search algorithm. *Journal of engineering research and technology, 2*(2), 95-104.

Artar, M. (2016). Optimum design of braced steel frames via teaching learning based optimization. *Steel and Composite Structures, 22*(4), 733–744.

Artar, M., & Daloglu, A. T. (2015). Optimum design of composite steel frames with semi-rigid connections and column bases via genetic algorithm. *Steel and Composite Structures, 19*(4), 1035–1053.

Camp, C. V., Bichon, B. J., & Stovall, S. P. (2005). Design of steel frames using ant colony optimization. *Journal of structural engineering, 131*(3), 369–379.

Clerc, M. (2010). *Particle swarm optimization* (Vol. 93). Hoboken, NJ, USA: John Wiley & Sons.

Clerc, M., & Kennedy, J. (2002). The particle swarm-explosion, stability, and convergence in a multidimensional complex space. *IEEE transactions on Evolutionary Computation, 6*(1), 58–73.

Daloglu, A., & Armutçu, M. (1998). Optimum design of steel plane frames using genetic algorithm. *Tek dergi, 9*, 483–487.

Degertekin, S. O. (2008). Optimum design of steel frames using harmony search algorithm. *Structural and multidisciplinary optimization, 36*(4), 393–401.

Degertekin, S. O., Hayalioglu, M. S., & Gorgun, H. (2009). Optimum design of geometrically non-linear steel frames with semi-rigid connections using a harmony search algorithm. *Steel and Composite Structures, An International Journal, 9*(6), 535–555.

Doğan, E. (2010). *Optimum design of rigid and semi-rigid steel sway frames including soil-structure interaction.* Ph.D. dissertation, Middle East Technical University (Turkey).

Dumonteil, P. (1992). Simple equations for effective length factors. *Engineering Journal, 29*(3), 111–115.

Faella, C., Piluso, V., & Rizzano, G. (1999). *Structural steel semirigid connections: theory, design, and software* (Vol. 21). CRC press.

Frye, M. J., & Morris, G. A. (1975). Analysis of flexibly connected steel frames. *Canadian journal of civil engineering, 2*(3), 280–291.

Gad, A. G. (2022). Particle swarm optimization algorithm and its applications: a systematic review. *Archives of computational methods in engineering, 29*, 2531–2561.

Hadidi, A., & Rafiee, A. (2014). Harmony search based, improved particle swarm optimizer for minimum cost design of semi-rigid steel frames. *Structural engineering and mechanics: An international journal, 50*(3), 323–347.

Hayalioglu, M. S., & Degertekin, S. O. (2004). Design of non-linear steel frames for stress and displacement constraints with semi-rigid connections via genetic optimization. *Structural and Multidisciplinary Optimization, 27*(4), 259–271.

Hayalioglu, M. S., & Degertekin, S. O. (2005). Minimum cost design of steel frames with semi-rigid connections and column bases via genetic optimization. *Computers & structures, 83*(21-22), 1849–1863.

Jenkins, W. (1991). Towards structural optimization via the genetic algorithm. *Computers & Structures, 40*(5), 1321-1327.

Kameshki, E. S., & Saka, M. P. (2003, January). Genetic algorithm based optimum design of nonlinear planar steel frames with various semi-rigid connections. *Journal of Constructional Steel Research, 59*(1), 109–134. doi:10.1016/s0143-974x(02)00021-4

Kennedy, J., & Eberhart, R. (1995). Particle swarm optimization. *Proceedings of ICNN'95-international conference on neural networks*, *4*, pp. 1942–1948.

Papazoglou, G., & Biskas, P. (2023). Review and comparison of genetic algorithm and particle swarm optimization in the optimal power flow problem. *Energies 2023, 16*, 1152.

Perez, R. E., & Behdinan, K. (2007). Particle swarm approach for structural design optimization. *Computers & Structures, 85*(19-20), 1579–1588.

Pezeshk, S., Camp, C. V., & Chen, D. (2000). Design of nonlinear framed structures using genetic optimization. *Journal of structural engineering, 126*(3), 382–388.

Pincus, M. (1970). A Monte Carlo method for the approximate solution of certain types of constrained optimization problems. *Operations research, 18*(6), 1225-1228.

Prakash, J., & Daloglu, A. T. (2023). Teaching-learning-based optimization of unbraced steel frames with semi-rigid connections and column bases. *Journal of Structural Engineering & Applied Mechanics, 6*(1), 27-44.

Rafiee, A., Talatahari, S., & Hadidi, A. (2013). Optimum design of steel frames with semi-rigid connections using Big Bang-Big Crunch method. *Steel and Composite Structures, an International Journal, 14*(5), 431–451.

Rao, S. S. (2019). *Engineering optimization: theory and practice.* Hoboken, NJ, USA: John Wiley & Sons.

Saka, M. P., & Geem, Z. W. (2013). Mathematical and metaheuristic applications in design optimization of steel frame structures: an extensive review. *Mathematical problems in engineering, 2013*, 271031.

Sengupta, S., Basak, S., & Peters, R. A. (2018). Particle Swarm Optimization: A survey of historical and recent developments with hybridization perspectives. *Machine Learning and Knowledge Extraction, 1*(1), 157–191.

Simoes, L. M. (1996). Optimization of frames with semi-rigid connections. *Computers & structures, 60*(4), 531–539.

Soares Filho, M., Guimarães, M. J., Sahlit, C. L., & Brito, J. L. (2004). Wind pressures in framed structures with semi-rigid connections. *Journal of the Brazilian Society of Mechanical Sciences and Engineering, 26*, 180–189.

Talbi, E.-G. (2009). *Metaheuristics: from design to implementation.* Hoboken, NJ, USA: John Wiley & Sons.
Tang, K., & Yao, X. (2008). Special issue on" nature inspired problem-solving". *Information Sciences—Informatics and Computer Science, Intelligent Systems, Applications: An International Journal, 178*(5), 2983–2984.
Toğan, V. (2012). Design of planar steel frames using teaching–learning based optimization. *Engineering Structures, 34*, 225–232.
Yang, X.-S. (2010). *Nature-inspired metaheuristic algorithms.* Frome, UK: Luniver press.

4th International Civil Engineering & Architecture Conference
17-19 May 2025, Trabzon, Türkiye

An experimental investigation on internal temperature monitoring of RC beams cast-in-winter

Burak Gedik*[1], Dilek Okuyucu[1] ,İlker Kazaz[1], Ahmet F. Bingöl[2], Muhammet Şahin[1] , Burak Şahin[1]

[1] ErzurumTechnical University, Department of Civil Engineering, 25100 Erzurum, Türkiye
[2] Atatürk University, Department of Civil Engineering, 25240 Erzurum, Türkiye

Abstract. According to national and international construction standards, concrete casting under cold weather conditions—typically defined as temperatures below 5°C—is permissible only if specific precautions are taken. Although these regulations mandate protective measures, they often lack detailed guidance, leaving implementation decisions to practitioners. In regions with a harsh continental climate, such as Erzurum, construction activities involving significant concrete work are largely suspended during the long, cold winters. This seasonal inactivity negatively impacts the local economy. Key reasons include uncertainty about appropriate precautions, concerns over costs, and skepticism regarding the reliability of cold-weather concreting. To address these issues, a research project supported by the Scientific and Technological Research Council of Türkiye (TÜBİTAK) under grant number 1001-219M403 was conducted. The project titled *"Experimental Investigation of the Flexural Behavior of Reinforced Concrete Beams Cast-in Cold Weather"* involved casting full-scale beams during both summer and winter seasons. Various protection strategies—such as greenhouse plastic insulation, use of set-accelerating admixtures, and external heating—were applied in different combinations. Temperature sensors placed within the most densely reinforced beam recorded internal concrete temperatures for 72 hours post-casting. These data were used to estimate the 3-day axial compressive strength. Temperature-time factor values were calculated with the internal concrete temperature data and an attempt was made to relate them to the 3-day axial compressive strength, but it was observed that there was a more powerful relationship between the internal concrete temperature measured at the end of 72 hours and the 3-day axial compressive strength.

Keywords: RC manufacturing in winter; Temperature monitoring, Thermocouple, Temperature-time factor; Compressive strength

1. Introduction

Modern concrete, which has completely transformed construction technique preferences worldwide since its discovery, has emerged as a building material that requires meticulous attention at every stage—from mix design to production, from formwork to curing—due to its sensitivity to the atmospheric conditions of the environment in which it is produced. During the production of a simple concrete flowerpot, the observed weakness of concrete under tensile stress led to the idea of reinforcing it with steel, which gave birth to the technique of reinforced concrete. Today, this method has become the most preferred construction technique in Türkiye. It can also be stated that the reinforced concrete construction method is favored due to its relatively economical solutions for the construction of large-scale and multi-story buildings.

Fresh concrete is sensitive to ambient temperature due to the water component it contains. Although this sensitivity is more evident during the first three phases of hydration—generally described in five stages—the volume of the concrete cast also significantly influences this effect. For instance, the extent to which concrete is affected by atmospheric temperatures differs between a mass concrete of a dam body and a beam in a residential project. Neville (1997) defines hydration as a series of irreversible chemical reactions between cement and water. The hydration process begins the moment cement comes into contact with water. During hydration, the cement-water paste sets and hardens. Cement particles gradually and partially dissolve, and the dissolved compounds react at different rates. These reactions release heat and produce new compounds known as hydration products. These products form a solid structure, allowing the plastic cement paste to harden, bond with aggregates in the concrete mixture, and create a strong, dense matrix. The measurable heat released during hydration does not drop to zero for several days, as the reactions slow down over time. Hydration can continue for years as long as water and

* Corresponding author, E-mail: burak.gedik@erzurum.edu.tr

https://doi.org/10.31462/icearc2025_ce_sme_783

unreacted cement remain in the concrete. This ongoing process contributes to continued strength gain and the development of desirable properties such as low permeability. A general understanding of hydration reactions helps prevent or resolve concrete-related issues and ensures that the mixture performs as designed. Hydration is commonly accepted to occur in five main stages: mixing, dormant (sleep), hardening, cooling, and densification. The mixing phase is when cement and water first come into contact; cement particles begin to dissolve, forming a thin layer of reaction product on their surface. Hydration reactions are initiated at this point. In the dormant phase, reactions slow down and the concrete remains workable. This stage allows time for placing and shaping the mixture in the formwork, with minimal heat release. At the end of this phase, the hardening stage begins; reaction rates increase, heat generation intensifies, new hydration products form, and concrete starts gaining strength rapidly. Setting and early strength development occur during this stage. In the subsequent cooling phase, chemical reactions become less active, though strength development continues. In the long-term densification stage, remaining cement and water continue to react slowly. Voids within the concrete microstructure reduce, making the material denser, stronger, and less permeable. This process can last for years.

The influence of environmental parameters—such as ambient temperature, humidity, and wind—on concrete development during the mixing, dormant, and hardening phases of the exothermic chemical process known as hydration has highlighted the necessity for standards regulating concrete casting parameters under varying atmospheric conditions. Moreover, concrete is not alone in reinforced concrete applications. Once placed into formwork, the temperature of the surrounding steel reinforcement cage and even the formwork itself becomes crucial for the performance of reinforced concrete, particularly in achieving full bond between steel and concrete. In Türkiye, two national standards are in effect that regulate concrete casting conditions according to atmospheric conditions. These standards assume that full bond between concrete and reinforcement is achieved when their guidelines are followed. The first of these is TS 1247 (2018), which governs concrete placement under normal weather conditions. According to this standard, normal weather conditions are defined as ambient temperatures not falling below +5 °C or exceeding +30 °C at any hour over three consecutive days after casting. In other words, ideal casting requires the ambient temperature to remain between +5 °C and +30 °C during placement and for at least the following 72 hours. This temperature range is critical for the healthy progression of the hydration process and for the development of mechanical strength. Atmospheric conditions outside of this specified range are considered abnormal, and concrete placement under such conditions is governed by a separate Turkish standard, TS 1248 (2017).

According to TS 1248 (2017), extreme cold weather is defined as conditions where the average air temperature remains below +5°C for three consecutive days following concrete placement, while extreme hot weather is defined as conditions where the average air temperature exceeds +30°C for three consecutive days after placement. The authors' interest in reinforced concrete production under cold weather conditions led them to focus on the section of the standard that addresses cold weather. Both the American ACI PRC-306 (2016) and the Canadian CSA A23.1/A23.2 (2019) codes define the same conditions for cold weather, while the Japanese JSCE (2007) standard adopts a lower temperature threshold of +4°C for cold weather. All of the mentioned regulations allow concrete casting-in cold weather with precautions, but they leave the decision on specific measures to practitioners, providing no clear guidance on the actions to be taken. The only explicit criterion emphasized is that the fresh concrete temperature during placement should not fall below 10°C, a condition specified in TS 1248 (2017).

The casting of concrete under extreme cold weather conditions, as defined in TS 1248 (2017)**,** remains a preferred option in Türkiye's regions exposed to continental climate. In contrast, countries with vast territories, such as Canada and the Russian Federation, which have regions affected by extreme cold weather for most of the year, must carry out concrete-related constructions as a necessity. An analysis of the climate map for the Russian Federation reveals that extreme cold weather conditions prevail across more than half of the country, regardless of the season, as shown in Fig. 1. This figure also provides a visual example of reinforced concrete construction under such conditions, where the use of nylon protection is clearly observed in practice.

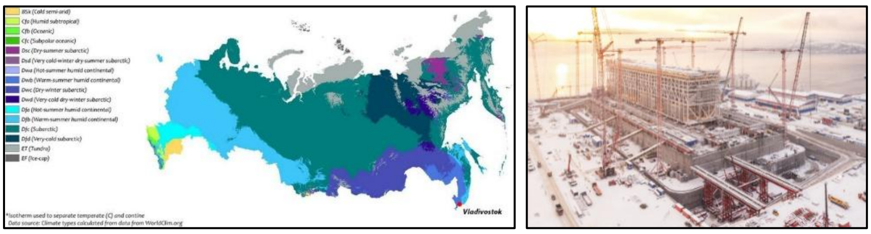

Fig. 1. Climate map of the Russian Federation, Khasikov (2020) and image of a reinforced concrete construction in the Murmansk Region, Novatek (2025)

More than half of Türkiye's land is dominated by a continental climate, with long and cold winters. As one moves eastward, the altitude from sea level increases, and the climatic conditions become more severe. According to data from the MGM (2019), the average monthly temperatures measured between 2012 and 2018 in Erzurum province were below +5°C in November, December, January, February, and March. The same source also indicates that the lowest temperatures, including those in May and June, fell below +5°C, while values as low as -30°C were measured during winter months such as January and February. Many settlements in regions with a continental climate, like Erzurum, experience similar harsh conditions, leading to a halt in the construction sector during the winter months. Studies by Koç et al. (2017) and KUDAKA (2014) emphasize that the suspension of the construction sector, which is the locomotive industry of the region, negatively impacts nearly 200 sub-sectors and causes significant economic and social problems. Although there is no legal barrier to concrete casting or reinforced concrete production during winter, the lack of clear data on the effectiveness and cost of the necessary precautions has prevented practitioners in the country from undertaking winter construction, even in cases of necessity. To address this issue and investigate the mechanical performance of reinforced concrete production in winter, the authors have conducted studies. The study by Gedik (2020) which examines the bond strength-shear behavior of reinforced concrete elements which were produced in winter, led to a comprehensive research project conducted by Okuyucu et al. (2023) and funded by he Scientific and Technological Research Council of Türkiye (TÜBİTAK), which investigates the mechanical behavior of full-scale reinforced concrete beams produced in winter.

Although there are studies in the accessible literature addressing concrete casting in winter, it has been observed that these studies are generally conducted on plain concretes without reinforcement, and the effects of various protective measures on the mechanical properties of concrete have not been sufficiently explored. It can also be stated that there is a greater focus on investigating the effects of chemical admixtures on the compressive strength and early-age behavior of concretes produced under cold weather conditions. Early works in this field, such as Karhonen (1990) and Karhonen (1992), conducted experimental research on the curing conditions, hydration process, and thermal behavior of concrete under cold weather. In Nmai (1998) study, the effects of chemical admixtures on the setting time and strength development of concrete at low temperatures were evaluated. In the works of Suk et al. (2012) and Nassif et al. (2013), the effects of antifreeze admixtures on fresh and hardened concrete properties were analyzed, and comparative results from field and laboratory environments were presented. The study conducted by Zhang et al. (2020) investigated the behavior of fresh concrete produced using the C-S-H (calcium silicate hydrate) seeding method under winter conditions and highlighted the significant potential of nanotechnological admixtures in enhancing early-age strength and optimizing the hardening process. As one of the recent studies, Pushpalal et al. (2022), conducted in Mongolia’s harsh winter conditions, evaluated the effects of various mineral admixtures on concrete performance, providing a comprehensive analysis of their impact on concrete durability and long-term performance.

This text presents information about the maturity index and internal temperature values calculated from the 3-day internal temperature tracking data taken from reinforced concrete beams cast under both summer (normal weather) and winter (abnormal weather) conditions, as part of the TÜBİTAK1001-219M403 project, which investigates the mechanical behavior of full-scale reinforced concrete beams produced in winter. In the winter production, set accelerator additive, greenhouse nylon protection and heating applications were applied in different configurations, and the mechanical test results carried out on concrete samples were examined and evaluations regarding the effectiveness of the protection measures were included. The study includes an investigation of axial compressive strength prediction using temperature-time factor, a type of maturity index, and concrete internal temperature values.

2. Materials and methods

The studies presented in this text, funded by the research grant from the TÜBİTAK1001-219M403 project, were conducted on the campus area of Erzurum Technical University. All sample productions carried out in summer and winter were made under real seasonal conditions. In practice, the mixture content was aimed at producing C30/37 class concrete based on the concrete recipe provided in Table 1.

Table 1. C30/37 class concrete mixture recipe, Okuyucu et al. (2023)

Material	Volume (dm^3)	Weight (kg)
Cement (CEMII - PC42.5-R)	133	400
Water	214	214
Air	10	-
Sand (0-3 mm)	193	421
Fine gravel (5-12 mm)	450	1134
Coarse gravel	-	-
Total	1000	2163

Table 2. Sample production schedule

Specimen	Relevant Standard	Defined Atmospheric Temperature at the Time of Casting (ºC)	Manufacturing Date	Average Atmospheric Temperature Measured at the Time of Casting (ºC)
Winter-2 Plain Concrete	TS1248(2017)	(+5) - (-15)	February 26, 2021	-13.9
*Winter-2 Concrete with SAA**	TS1248(2017)	(+5) - (-15)	March 4, 2021	-7.9
*Winter-1 Concrete with SAA**	TS1248(2017)	Below (-15)	March 12 , 2021	-19.0
Summer Plain Concrete	*TS1247(2018)*	*(+5) and above*	*June 29, 2021*	*20.3*
Winter-1 Plain Concrete	TS1248(2017)	Below (-15)	January 14, 2022	-17.3

* SAA: Setting Accelerator Admixture

Concrete casting was carried out in three seasonal periods.These periods are referred to as Summer, Winter-1, and Winter-2, with explanatory information provided in Table 2.

In the Summer group, defined in Table 2, the concrete casting under normal weather conditions was performed in the open air, and the samples were kept moist by being watered at specific intervals for 72 hours. After 72 hours, the samples removed from the molds were wetted with water until the 7th day, depending on the air temperature. For the Winter group productions, wooden-frame, greenhouse plastic-covered maintenance tents with the smallest volume, capable of holding three full-scale reinforced concrete beams (0.3x0.5x4.5 m), were used. Since covering the casting area with plastic is a widely preferred method globally, it was chosen for this project as well; however, greenhouse plastic was used in practice. The reason for this choice is the relatively high number of sunny days in Erzurum during the winter. A total of two maintenance tents covered with greenhouse plastic were used, one of which was heated with a thermostat-controlled heater for 72 hours to ensure the temperature inside did not drop below +5°C. The section with heating was referred to as the heated tent, while the section without heating was called the unheated tent. A general view of the heated and unheated tents used in the winter concrete casting works is presented in Fig. 2.

In this study, the temperature measurements of the beam sample designed as a doubly reinforced section were taken from the center of the section using K-type thermocouple sensors. The volume of the steel reinforcement within the full-scale reinforced concrete beam measuring 0.3x0.5x4.5 m corresponds to 1.99% of the total beam volume. After the sensors were connected to the system, the data collection software was programmed to measure and record temperatures in °C at 10-minute intervals. To prevent power outages and data loss, the system was supported by an external power supply. A visual representation of the concrete internal temperature measurement setup is shown in Fig. 3.

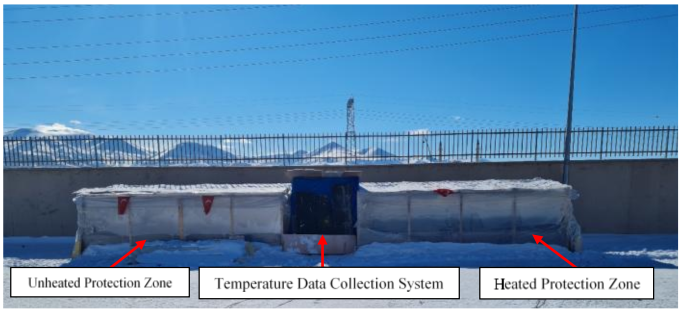

Fig. 2. Heated and unheated curing tents

Fig. 3. Thermocouple type sensor and data acquisition system used for reinforced concrete beam temperature monitoring

One of the objectives of measuring the internal temperature of concrete is to calculate a maturity index known as the temperature-time factor. TS13508 (2012) defines the maturity index as a value that indicates the maturity of a cement-based mixture, based on the temperature history of the material, using the maturity function. The calculated index is an indicator of maturity, assuming that sufficient water is provided for the pozzolanic reaction or hydration of cement-based materials during the calculation period. The two most commonly used maturity indices are the temperature-time factor and the equivalent age. In this study, the temperature-time factor is calculated as the maturity index. The formula presented in Equation 1 of TS13508 (2012) is used for the calculation of the temperature-time factor:

$$M(t) \; = \; \Sigma(T_a - T_o).\Delta t \tag{1}$$

In Equation 1:

M(t): temperature-time factor (degree-days or degree-hours) at age t,

Δt: Time interval (days or hours,

T_a: *Average temperature of concrete during Δt (ºC),*

T_o**:** Datum temperature (ºC).

The mathematical expression presented in Equation 1 essentially numerically calculates the area under the concrete’s internal temperature versus time graph, above the initial/datum temperature. The datum temperature used here is the lowest internal temperature at which the concrete can begin to gain strength or develop strength, and it will vary for each concrete mix. According to the ASTM C1074-19e1 (2019) standard, the datum temperature is a theoretical temperature value assumed to represent the point at which the hydration of concrete completely stops in the maturity method. In other words, this temperature is the threshold below which concrete gains no strength, and in the ASTM C1074-19e1 (2019) standard, it is generally accepted as -10°C. In the study by Elaty et al. (2017), experimental determination of the datum temperature was conducted for concretes made with different types and dosages of cement. In the examined study, for a mix close to the unmodified concrete used in this research, the datum temperature was determined to be -2.2°C, based on the type and dosage of cement. However, according to TS13508 (2012), the datum temperature is a parameter that needs to be determined experimentally. The datum temperature depends on the type of cement, the types and amounts of chemical or other admixtures that may affect the hydration rate, and the temperature range the concrete will be exposed to while hardening. In this study, an experimental procedure detailed in TS13508 (2012) for determining the datum temperature was not conducted. In cases where experimental studies cannot be carried out, TS13508 (2012) recommends using 0°C as the datum temperature value for concrete mixes made with unmodified CEM I cement and exposed to curing temperatures between 0°C and 40°C. For all the concrete mixtures produced in the project, CEM I type cement was used, and all the summer and winter samples were exposed to curing temperatures between 0°C and 40°C for the first 72 hours. Therefore, in this study, the datum temperature was taken as 0°C, and using the concrete internal temperature tracking data, the temperature-time factor values developed during the first 72 hours for all concrete groups were calculated.

As presented in Table 2, the use of setting accelerator additives is considered a parameter for winter group productions. In both the winter and summer concrete pours, concrete was supplied by Memişoğlu Erzurum Beton A.Ş., a company active in Erzurum. This company is the only facility in the region capable of producing concrete in winter due to its ability to adjust the temperature of mixing water, in addition to having a closed material loading area for its concrete mixer. In the application, the relationship between the freshly mixed concrete and the cold weather was interrupted by nylon protection, under which the concrete was placed in the mold. As experienced in Gedik (2020), where it was observed that fresh concrete can experience an abrupt temperature drop of 10-15°C when exposed to cold air in winter, this approach was adopted to prevent such drastic temperature reductions. The fresh concrete temperature under the nylon cover was kept above +10°C, in accordance with TS1248(2017). During the pouring, the fresh concrete temperatures were measured using probe thermometers and recorded. After 72 hours, the specimens were removed from the molds, the protection measures were terminated, and all samples were exposed to atmospheric conditions until the 28th day. Cube samples measuring 15x15x15 cm were taken for determining the axial compressive strength during both summer and winter concrete pours. General images related to the summer pour are shown in Fig. 4, and general images related to the winter pour are shown in Fig. 5.

Fig. 4. Images from the summer casting

Fig. 5. Images from the winter casting

Axial compressive strength tests were performed on the concrete samples in accordance with the TS EN 12390-3 (2019) Turkish standard. The experimental studies were conducted using a universal testing machine available at the Structural Materials and Structural Mechanics Laboratory, Department of Civil Engineering, Faculty of Engineering and Architecture, Erzurum Technical University.

3. Results and discussions

The results obtained from the experimental study are collectively presented in Table 3.

Upon examination of the data presented in Table 3, it is observed that the lowest fresh concrete temperature at the time of casting was measured as 10.4 °C for the Winter-1 group with admixture. Although the concrete was cast under greenhouse sheet protection, the ambient temperature of -19.0 °C at the start of casting is considered the primary reason for this low value.

Table 3. Experimental results

Specimen	Average Atmospheric Temperature at Casting Time (°C)	Fresh Concrete Temperature at the Time of Casting (°C)	Internal Temperature of Concrete Just Before Removal from Mold After 72 Hours (°C)		At the end of 72 hours: Uniaxial Compressive Strength (MPa)		At the end of 72 hours: Temperature-Time Factor (°C.Hours)	
Summer Plain Concrete	20.3	26.5	29.5		19		2474	
			Unheated	Heated	Unheated	Heated	Unheated	Heated
Winter-2 Plain Concrete	*-13.9*	*15.7*	*15.5*	*16.1*	*29*	*30*	*1653*	*2039*
*Winter-2 Concrete with SAA**	*-7.9*	*13.5*	*15.6*	*16.7*	*30*	*29*	*1706*	*1793*
Winter-1 Plain Concrete	-17.3	12.2	5.7	13.8	22	25	1173	1604
*Winter-1 Concrete with SAA**	-19.0	10.4	22.4	19.6	31	31	1484	1543

Table 3. Continued

Explanations Regarding Coloring					
#3 Protection Measures	Greenhouse Nylon Protection	+	Setting Accelerator Admixture	+	Heating
#2 Protection Measures	Greenhouse Nylon Protection	+	Setting Accelerator Admixture		
#2 Protection Measures	Greenhouse Nylon Protection	+	Heating		
#1 Protection Measure	Greenhouse Nylon Protection				

** SAA: Setting Accelerator Admixture*

Table 4. Axial compressive strength gain percentages of the samples (%)

Specimen	Heated	Unheated
Summer Plain Concrete	-	*51*
Winter-2 Plain Concrete	81	78
Winter-2 Concrete with SAA	78	81
Winter-1 Plain Concrete	*68*	*59*
Winter-1 Concrete with SAA	84	84

The fresh concrete temperature was measured as 12.2 °C for the Winter-1 group without admixture, 13.5 °C for the Winter-2 group with admixture, and 15.7 °C for the Winter-2 group without admixture. In all winter casting groups, the fresh concrete temperature exceeded the minimum threshold of 10 °C specified in the TS 1248 (2017) standard. For the summer group specimens, the fresh concrete temperature at the time of casting was recorded as 26.5 °C. According to TS EN 206+A2 (2021), the minimum fresh concrete temperature at the time of delivery should be +5 °C. However, it is not recommended for the temperature to fall below +10 °C, as it may prolong the setting time and negatively impact strength development. Therefore, it can be concluded that the fresh concrete temperatures measured during both summer and winter castings complied with the relevant standard requirements.

The fundamental mechanical property used for classifying concrete is the 28-day axial compressive strength. The aim of this study was to produce C30/37 grade concrete. Since 15x15x15 cm cube specimens were used for the axial compressive strength tests, it is essential to compare the 28-day axial compressive strengths with the target value of 37 MPa. According to Eurocode 2 (BS EN 1992-1-1:2004+A1:2014), with the use of Type R cement, the concrete is expected to reach approximately 76% of its 28-day axial compressive strength at the end of the 3rd day. Therefore, rather than evaluating the 3-day axial compressive strengths numerically, it is considered more beneficial to examine the percentage of strength gain relative to the 28-day strength. The ratios of the 3-day axial compressive strengths to the expected 28-day axial compressive strength of 37 MPa for all groups are presented in Table 4.

Upon examination of Table 4, it is observed that the summer group specimens reached only 51% of the target axial compressive strength by the 3rd day. This is significantly lower than the expected value of approximately 76% according to Eurocode 2 (BS EN 1992-1-1:2004+A1:2014). It is worth noting that water was added during the production of the summer group specimens in a way that disrupted the mix design, and this low strength gain percentage is believed to be a result of this modification. Similarly, for the Winter-1 group specimens without admixture, Table 4 shows that the 3-day strength development was below the expected 76% according to Eurocode 2 (BS EN 1992-1-1:2004+A1:2014). For the Winter-1 group specimens without admixture, when heating was applied, the strength gain percentage was 68%, whereas without heating, it was 59%. In all other groups, the expected strength gain percentages were achieved. This is a particularly striking result. For concrete cast at temperatures below -15°C, it is evident that heating, in addition to greenhouse sheeting protection, significantly impacts the 3-day strength gain. However, it is clear that in order to achieve the target strength gain percentage specified by Eurocode 2 (BS EN 1992-1-1:2004+A1:2014), the use of accelerating admixtures is necessary for concrete cast at temperatures below -15°C. Furthermore, it is concluded that the use of accelerating admixtures, along with greenhouse sheeting, is more effective than heating during concrete casting at these low temperatures. In cases where accelerating admixtures are used, heating is not necessary as a third protective measure. Under the Winter-1 conditions, with ambient temperatures between +5°C and -15°C, it is observed that by using only greenhouse sheeting concrete achieved 78% of the final strength by the 3rd day. The Winter-1 group specimens with admixture both reached 84% of the target strength, making them the highest strength gaining group. Notably, these specimens were exposed to sunlight for almost half of the 72-hour curing period in the protection tents after casting. The greenhouse effect of the sun/solar exposure is believed to have contributed to the rapid axial compressive strength gain of these specimens.

The primary aim of this study is to propose an approach for estimating early-age (3-day) concrete compressive strength using internal concrete temperature measurement data during winter concrete castings. Based on this proposed approach, the goal is to determine the optimal timing for terminating concrete protection measures and form removal during winter concrete production. Table 3 presents two parameters derived from the internal concrete temperature monitoring data. The first is the internal concrete temperature measured at the end of 72 hours, and the second is the calculated temperature-time factor at the end of 72 hours. The relationship between each of these parameters and the 3-day axial compressive strength was examined separately. The internal temperature of the concrete after 72 hours and the 3-day axial compressive strength were evaluated together, and a graph shown in Fig. 6 was prepared to illustrate this relationship.

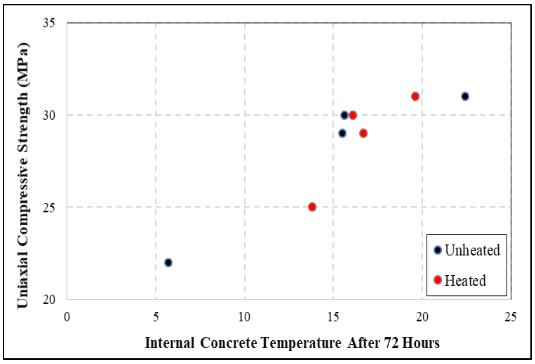

Fig. 6. Internal concrete temperatures and 28-day axial compressive strengths of winter poured concrete samples measured after 72 hours

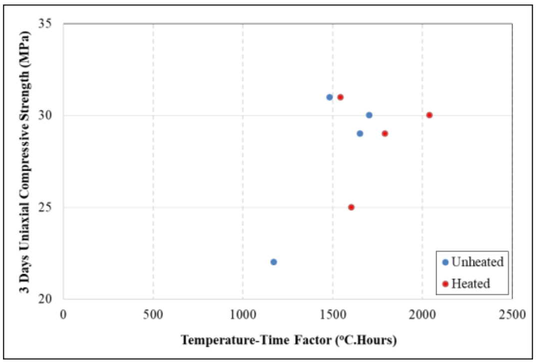

Fig. 7. Temperature-time factor and 3-day axial compressive strength of concrete produced in winter

Upon examining Fig. 6, it can be stated that the internal concrete temperatures at the 72-hour mark and the 3-day axial compressive strengths exhibit a nearly linear relationship, which can be represented by Equation 2 (R^2 = 0.83). In practice, CEMI-42.5R type rapid setting, high-strength cement was used. According to Eurocode 2 (BS EN 1992-1-1:2004+A1:2014), when R-type cement is used, it is expected that 76% of the target axial compressive strength will be achieved by the 72nd hour. This indicates that hydration occurs very intensely during the first 3 days, and the high internal temperatures at the 72-hour mark can be associated with high final strength. Based on this, it is suggested that by measuring the internal concrete temperature of concrete produced with CEMI-42.5R type cement under cold weather conditions as defined by TS1248 (2017), the 3-day axial compressive strength can be estimated using Equation 2.

$$f_{c3} = 0.6T + 19.0 \tag{2}$$

In Equation 2;

f_{c3}: 3-day axial compressive strength of the 15x15x15 cm cube sample, (MPa)

T: Internal concrete temperature measured at the 72-hour mark after casting, (°C)

Another parameter, the temperature-time factor, which was calculated using the temperature data, is presented in Table 3. A graph prepared to examine the relationship between the 3-day axial compressive strength of concrete produced in winter and the temperature-time factor, as a maturity index, is presented in Fig. 7.

Upon examining Fig. 7, it is clear that there is no significant relationship between the 3-day temperature-time factor values and axial compressive strengths of the concrete produced in winter with various protection measures. Since maturity-strength relationships in the relevant literature are generally presented as logarithmic functions, the equation presented in Equation 3 was derived from the data shown in Fig. 7.

$$f_{c3} = 12.6 \ln(M) - 54.5 \tag{3}$$

In Equation 3;

f_{c3}: 3-day axial compressive strength of the 15x15x15 cm cube sample, (MPa)

M: Temperature-time factor calculated at the 72-hour mark after casting, (°C.Hour)

The R^2 value of 0.40 was calculated in the derivation of the equation presented in Equation 3. This value indicates that the model has a relatively weak ability to represent the given data. Calculations were also made to introduce linear, exponential, and polynomial models, and it was observed that the obtained models had a determination coefficient smaller than 0.40. Therefore, it can be stated that a mathematical relationship capable of strongly representing the correlation between the temperature-time factor values and the 3-day axial compressive strength could not be established. It has been concluded that for concrete produced with CEMI-42.5R type cement, with the fresh concrete temperature at the time of casting not lower than +10°C and protected under greenhouse plastic sheeting, the linear expression presented in Equation 2 and the internal concrete temperature at 72 hours can be used to estimate the 3-day cube sample compressive strength.

4. Conclusions

Within the scope of the project titled *"Experimental Investigation of the Flexural Behavior of Reinforced Concrete Beams Cast in Cold Weather"* (TÜBİTAK 1001 – 219M403), full-scale reinforced concrete beams were cast both in summer and winter. Various combinations of protection measures such as greenhouse plastic sheeting cover, the use of setting accelerating admixtures, and external heating applications were implemented. Based on internal concrete temperature monitoring data, this study aimed to estimate the 3-day compressive strength of concrete. The main findings are summarized below:

- According to Eurocode 2 (BS EN 1992-1-1:2004+A1:2014), the target 3-day compressive strength was achieved for concretes cast at ambient temperatures between 5°C and -15°C, provided that the fresh concrete temperature was maintained above +10°C and CEM I 42.5R type cement was used. The only precaution was unheated greenhouse plastic covering.
- For concrete casting at temperatures below -15°C, in order to meet the 3-day compressive strength target set by Eurocode 2 (BS EN 1992-1-1:2004+A1:2014), in addition to maintaining the fresh concrete temperature above +10°C and using CEM I 42.5R type cement, the application of an accelerating admixture alongside greenhouse sheet protection was found to be necessary.
- It was determined that, for concrete cast-in winter conditions, evaluating the internal concrete temperature at the end of 72 hours yielded more meaningful results than using the traditional time-temperature factor in estimating 3-day axial compressive strength. A correlation equation was proposed for this purpose.
- Increasing the number of scientific studies on winter concreting will contribute to knowledge accumulation in this field and provide valuable guidance for practical applications. It is recommended that further studies be conducted under real winter conditions using concrete with diverse properties.

Acknowledgments

This study was supported by the Scientific and Technological Research Council of Türkiye (TÜBİTAK) under the project titled "Experimental Investigation of the Flexural Behavior of Reinforced Concrete Beams Cast in Cold Weather" (TÜBİTAK 1001 – 219M403). The authors would like to express their gratitude to TÜBİTAK for their support.

References

Abd Elaty, M.A.A., Ghazy, M.F., & Ghannam, M.F. (2017). Influence of maturity for concrete containing different cement types on mechanical and durability properties. In *Proceedings of the International Conference on Advances in Structural and Geotechnical Engineering (ICASGE'17)*, Hurghada, Egypt.

ACI PRC-306. (2016). *Guide to cold weather concreting*. American Concrete Institute.

ASTM C1074-19e1. (2019). *Standard practice for estimating concrete strength by the maturity method*. ASTM International. https://doi.org/10.1520/C1074-19E01

CSA A23.1/A23.2. (2019). *Concrete materials and methods of concrete construction / Test methods and standard practices for concrete*. Canadian Standards Association.

Eurocode 2 (BS EN 1992-1-1:2004+A1:2014). (2014). *Design of concrete structures – Part 1-1: General rules for buildings*. British Standards Institution.

Gedik, B. (2020). *Experimental investigation of bond strength–slip relationship under tensile effect in reinforced concrete elements cast in cold weather* (Master's thesis). Erzurum Technical University, Institute of Science, Erzurum, Turkey.

Japan Society of Civil Engineers (JSCE). (2007). *Standard specifications for concrete structures – 2007, materials and construction*. JSCE.

Karhonen, C.J. (1990). *Antifreeze admixtures for cold regions concreting – A literature review* (Special Report No. 90-32). U.S. Army Cold Regions Research and Engineering Laboratory (CRREL).

Karhonen, C.J., Cortez, E.R., & Charest, B.A. (1992). Strength development of concrete cured at low temperature. *Concrete International*, 34–39

Khasikov, S. (2020). Calculation of the payback period for energy-efficient building envelope. *IOP Conference Series: Materials Science and Engineering*, *753*, 042032. https://doi.org/10.1088/1757-899X/753/4/042032

Koç, E., Kaya, K., & Şenel, M.C. (2017). Development of the construction industry sector in Turkey – Basic construction industry indicators. *Nevşehir Journal of Science and Technology*, *6*(2), 643–660

Northeastern Anatolia Development Agency (KUDAKA). (2014). *2014–2023 regional current situation analysis report*. Erzurum, Turkey.

Nassif, A.Y., & Petrou, M.F. (2013). Influence of cold weather during casting and curing on the stiffness and strength of concrete. *Construction and Building Materials*, *44*, 161–167

Neville, A.M. (1997). *Properties of concrete* (4th ed.). Pearson Education Limited.

Nmai, C.K. (1998). Cold weather concreting admixtures. *Cement and Concrete Composites*, *20*(2–3), 121–128

Novatek. (2025, April 29). *U.S. further tightens sanctions screw, targeting Russian Arctic gas projects*. High North News. Retrieved from https://www.highnorthnews.com/en/us-further-tightens-sanctions-screw-targeting-russian-arctic-gas-projects

Okuyucu, D., Kazaz, İ., & Bingöl, A.F. (2023). *Experimental investigation of the flexural behavior of reinforced concrete beams cast in cold weather conditions* (Research Project Report No. TÜBİTAK1001 / 219M403). The Scientific and Technological Research Council of Türkiye (TÜBİTAK), Ankara.

Pushpalal, D., Danzandorj, S., Bayarjavkhlan, N., Nishiwaki, T., & Yamamoto, K. (2022). Compressive strength development and durability properties of high-calcium fly ash incorporated concrete in extremely cold weather. *Construction and Building Materials*, *316*, 125801

Ryou, J. S., & Lee, Y. S. (2012). Properties of early-stage concrete with setting-accelerating tablet in cold weather. *Materials Science and Engineering: A*, *532*, 84–90

Republic of Türkiye Ministry of Agriculture and Forestry, General Directorate of Meteorology, 12th Regional Directorate, Erzurum. (2019). *Statistical meteorological data report*. Erzurum, Turkey.

TS 1247. (2018). *Rules for concrete production, casting and curing (under normal weather conditions)*. Turkish Standards Institution, Ankara.

TS 1248. (2017). *Rules for preparation, casting and curing of concrete (under abnormal weather conditions)*. Turkish Standards Institution, Ankara.

TS 13508. (2012). *Estimation of concrete strength by the maturity method*. Turkish Standards Institution, Ankara.

TS EN 12390-3. (2019). *Testing hardened concrete – Part 3: Compressive strength of test specimens*. Turkish Standards Institution, Ankara.

TS EN 206+A2. (2021). *Concrete – Specification, performance, production and conformity*. Turkish Standards Institution, Ankara.

Zhang, G., Yang, Y., & Li, H. (2020). Calcium-silicate-hydrate seeds as an accelerator for saving energy in cold weather concreting. *Construction and Building Materials*, *264*, 120191

4th International Civil Engineering & Architecture Conference
17-19 May 2025, Trabzon, Türkiye

Effect of the connection shape of cables on behaviour of suspension bridges

Nefya Soysal*[1], Murat Muvafık[2]

[1] Yıldız Technical University, Graduate School of Science and Engineering, 34220 Istanbul, Türkiye
[2] Yüzüncü Yıl University, Department of Civil Engineering, Division of Structures, Van Turkey

Abstract. This paper aims to investigate the effects of suspension cables connected in different ways on the behavior of suspension bridges and to evaluate the results. In this study, 6 existing suspension bridges are modelled, and 10 additional suspension bridges were created by changing the number and diameter of the suspension cables. A total of 16 suspension bridges have been modeled and three-dimensional nonlinear analyses of these models have been performed.The results of Fatih Sultan Mehmet Bridge, 15 July Martyrs Bridge, Osmangazi Bridge, Humber Bridge, Tsing Ma Bridge and Yeoungjong bridges modeled in three dimensions were evaluated. Models FSM_40H, FSM_50H, FSM_60H, FSM_70H and FSM_80H were modeled in three dimensions by taking the Fatih Sultan Mehmet Bridge as an example and changing the number of suspensions in the middle span. Models FSM_50D, FSM_100D, FSM_150D, FSM_200D and FSM_250D were modeled in three dimensions by changing the diameters of the suspension cables in the mid-span.

Keywords: Suspension bridge; Hanger cable shape; Hanger cable number; Hanger cable diameter; Nonlinear static analysis

1. Introduction

Mubuli (2016), In this study, the structural behavior of Fatih Sultan Mehmet Bridge is investigated under self-weight, earthquake and vehicle loads. The cross-sectional effects and displacements of the bridge foundation elements under the effects of both earthquake and vehicle loads are presented in graphs and tables. They concluded that different earthquake acceleration records and different vehicle speeds significantly affect the dynamic behavior of the bridge.

Kartal (2012) modeled three different upper decks, namely rectangular hollow, trapezoidal hollow and circular hollow, using the Csi Bridge program. These models were analyzed under live load. As a result of this study, the stresses and strains in box girder upper decks increase with depth, but this increase is not proportional. It was found that these stresses and strains are at the lowest level in the rectangular section upper deck and the highest level in the circular section upper deck.

Rahwan (2019) carried out comparative two-dimensional and three-dimensional finite element analysis of the 15 July Martyrs Bridge Suspension Bridge with diagonal and vertical suspension systems using the Sap2000 program. First, he analyzed the 15 July Martyrs Bridge Bridge with diagonal suspension cables in two dimensions and three dimensions. Then, he modeled the suspension cables vertically and performed two and three-dimensional analyses. Static and dynamic analyses were performed on the models and all four models were compared. As a result, he stated that vertical cables have a better effect on the performance of suspension bridges.

2. Material and method

A total of 16 suspension bridge models have been created within the framework of this study, based on suspension bridges whose suspension cables are connected in different ways. The models created were analysed in the CsiBridge V.20 program. In all models; the deck width, tower heights, centre and side spans, fixed beams between the towers were kept constant and only the number and diameter of the suspension cables were changed according to the connection types of the suspension cables and the analysis results. The models whose elements' dimensions kept constant were analysed with the same dimensions of the Fatih Sultan Mehmet Bridge constructed in Istanbul in 1988.

As seen in Fig.1, the dimensions of the models used in the bridges the side spans of the bridges were modelled as 210 m, the centre spans as 1090 m, the deck width between the cables as 33.8 m, the deck height as 3 m and the

* Corresponding author, E-posta: nefyasoysal@gmail.com

https://doi.org/10.31462/icearc2025_ce_sme_805

tower heights from the deck level as 110 m. A total of 120 suspension cables of various lengths were used in the centre span. The suspension cables are connected to the deck by rigid links. The distance between the cables is 17.869 m along the x-axis and 33.8 m along the y-axis.

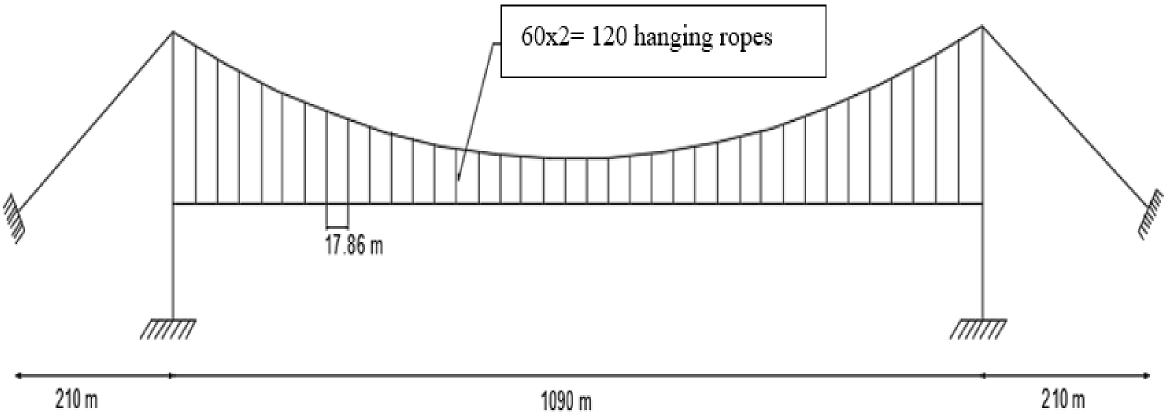

Fig. 1. General x-z view of the Fatih Sultan Mehmet suspension bridge

2.1. Suspension bridges in The World and in Türkiye

Bridges in the world and in our country with suspension ropes connected in different ways and their three-dimensional images are shown in Table 1. The Osmangazi Bridge has suspension cables in the centre span and both spans. Humber Bridge has diagonal cables in both the centre and side spans. Fatih Sultan Mehmet Bridge has vertical cables only in the centre span. 15 July Martyrs Bridge has diagonal cables only in the middle span. Tsing Ma Bridge has suspension ropes in both the centre span and a single side span. Yeoungjong Bridge has the side and centre span cables connected as 2 pairs of cables.

There are various bridges with suspension cables connected differently both in the world and in Turkey. Their three-dimensional images of some of them are shown in Fig. 2. There are suspension cables in the middle span and both side spans of the Osmangazi Bridge as well as of the Humber Bridge. Fatih Sultan Mehmet Bridge has vertical cables only in its central span. Between the mentianed bridges, The July 15 Martyrs Bridge is the only bridge that has diagonal cables only in the middle span. In the Tsing Ma Bridge, there exist suspension cables in the middle span and in only one side span. The side and middle span cables of the Yeoungjong Bridge are connected as 2 pairs of ropes.

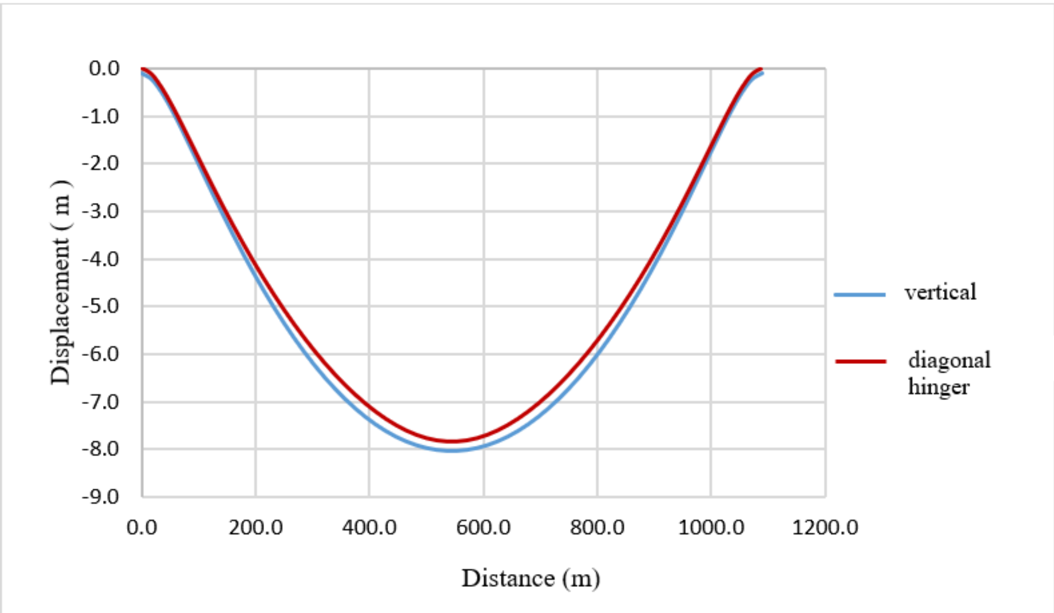

Fig. 2. Comparison of vertical displacements along the deck of the Fatih Sultan Mehmet Bridge and the 15 July Martyrs Bridge Bridge

Table 1. Suspension bridges with suspension cables connected in different shapes and positions

Osmangazi Suspension Bridge		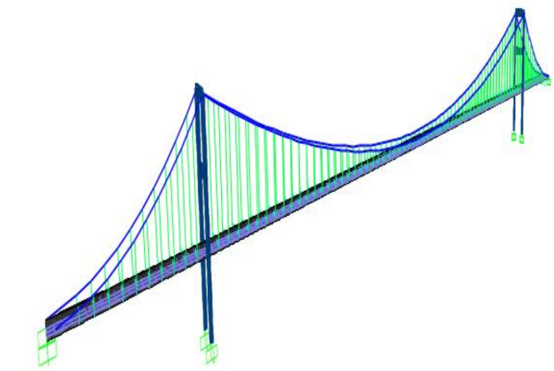
Fatih Sultan Mehmet Suspension Bridge		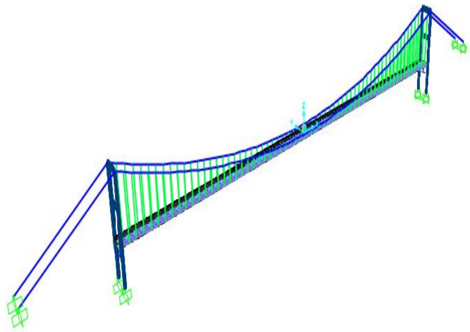
15 July Martyrs Suspension		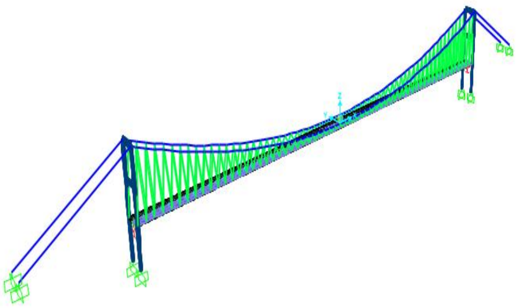
Tsing Ma Suspension Bridge		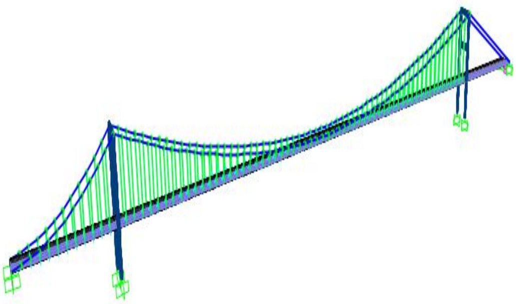

Table 1. Continued

Humber Suspension Bridge		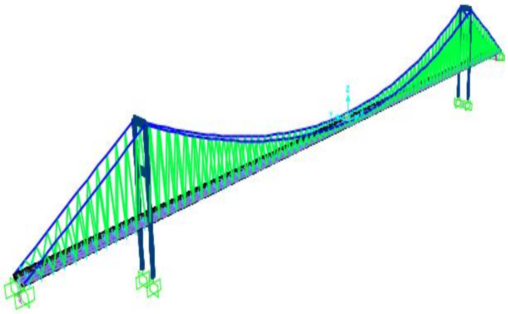
Yeoungjong Suspension Bridge		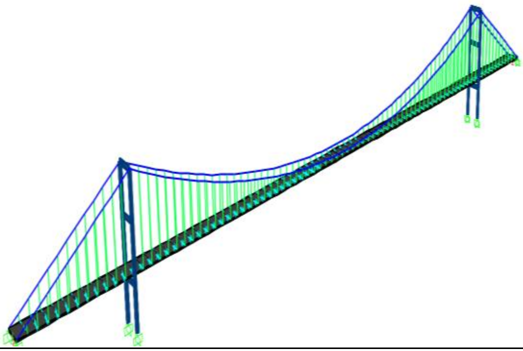

2.2. The effect of the number of suspension cables

In this section, the number of suspension cables in the mid-span was changed and the effect on the main structural system has been investigated. The cross-sectional and dimensional characteristics of the bridge are the same as Fatih Sultan Mehmet Bridge, and the models were created by changing only the number of suspension ropes in the mid-span, and the models were named as FSM_40H, FSM_50H, FSM_60H, FSM_70H and FSM_80H respectively. In this section, 5 suspension bridges with different numbers of cables are modelled.

2.3. The effect of the diameter of suspension cables

In order to investigate the effect of the variation in diameter on the behavior of the structure, 5 different models with different diameters were created. The models have been chosen to have the same characteristics as the towers, decks, main cables and girders in the mid-span of the Fatih Sultan Mehmet Bridge and the only parameter that changes is the diameter of the suspension cables. Therefore, the models are named as given in Table 2 FSM_50D, FSM_100D, FSM_150D, FSM_200D and FSM_250D. Five models with different diameters were created in the CsiBridge V20 Program.

Table 2. Diameters of suspension cables used in suspension bridge

	Diameter(m)	Single hinger Area (m^2)	Double hanging Area (m^2)
FSM_50D	0.05	0.001963	0.003926
FSM_100D	0.1	0.00785	0.0157
FSM_150D	0.15	0.01767	0.03534
FSM_200D	0.2	0.0314	0.0628
FSM_250D	0.25	0.0491	0.0982

Moreover, for investigating whether the number of cables or their diameter is more important for the vertical displacement of suspension bridges. 6 existing suspension bridges were modelled and investigated. 10 additional bridge models were created as a result of the investigations.

3. Conclusion

3.1. Static analysis results

The Fatih Sultan Mehmet Bridge vs The 15 July Martyrs Bridge: The vertical displacement of the Fatih Sultan Mehmet Bridge is 7.88 m at the centre of the span and 67 cm at the apex of the tower. The centre span of the 15 July Martyrs Bridge has a vertical displacement of 7.835 m and a displacement of 69 cm at the top of the tower.

The The Osmangazi Bridge vs The Humber Bridge: It can be seen that the largest vertical displacement occurs in the centre span of Osmangazi Bridge and its value is 7.973 m. The same vertical displacement occurs in the decks in the side span and its value is found to be 1.594 m, 71 cm displacement is observed at the top of the tower. The maximum vertical displacement in the centre span of the Humber Bridge is 7.828 m. The maximum vertical displacement in the side spans is 1.668 m. The displacement at the top of the tower is 71.51 cm.

The The Osmangazi Bridge vs The Yeoungjong Bridge: The number of suspension cables connected to a single point in Yeoungjong Bridge is 4, while the number of suspension cables connected to a single point in Osmangazi Bridge is modelled as 2. As a result, the maximum vertical displacement at the centre span is 7.933 m and the displacement at the top of the tower is 71.59 cm. It can be seen that larger displacements occur in Osmangazi Bridge.

In the models created by increasing the number of suspension ropes, it is seen that the largest vertical displacement at the center span of the deck occurs in the FSM_40A bridge model and its value is 7.92 m. Increasing the number of suspension ropes increases the vertical displacement of the deck by 0.89%. The largest displacement at the top of the tower occurs in the FSM_80A bridge model and is 68.06 cm. The displacement at the top of the tower is 67.91 cm for the bridge model FSM_40A. By increasing the number of suspension cables, the axial force in the suspension cables decreased by 49%, the moments in the deck increased by 3.23% and the axial force in the main cable increased by 0.2%.

In the models created by increasing the suspension diameters, the largest vertical displacement at the centre of the deck occurs in the FSM_50D bridge model and its value is 7.94 m. Increasing the diameter of the suspension cables increases the vertical displacement of the deck by 3.5%. The vertical displacement at the top of the tower is 63 cm for the FSM_50Ç model and 68 cm for the FSM_250D model. Increasing the diameter couses the vertical displacement in the tower to increase by 7.93%. By increasing the diameter of the suspension cables, 13% amount of increments in axial forces in the suspension cables, 33% amount of increments in the moment in the deck and 7.4%. amount of increments in the axial forces in the main cable are observed.

The largest vertical displacement in the decks at the edge span occurs at the Tsing Ma Bridge. On the Tsing Ma Bridge, the vertical displacement is 3.35 m at the edge span without suspension cables.

The results obtained for The Humber Bridge with diagonal (inverted V) cables and those for The Osmangazi Bridge with vertical cables are compared in Fig. 3. It can be seen that there is more vertical displacement in The Osmangazi Bridge.

The vertical displacements of the deck of Osmangazi Bridge and the deck of Tsing Ma Bridge are compared in Fig. 4. It is seen that the vertical displacement of the deck with suspension cables is lower than the vertical displacement of the deck without suspension cables.

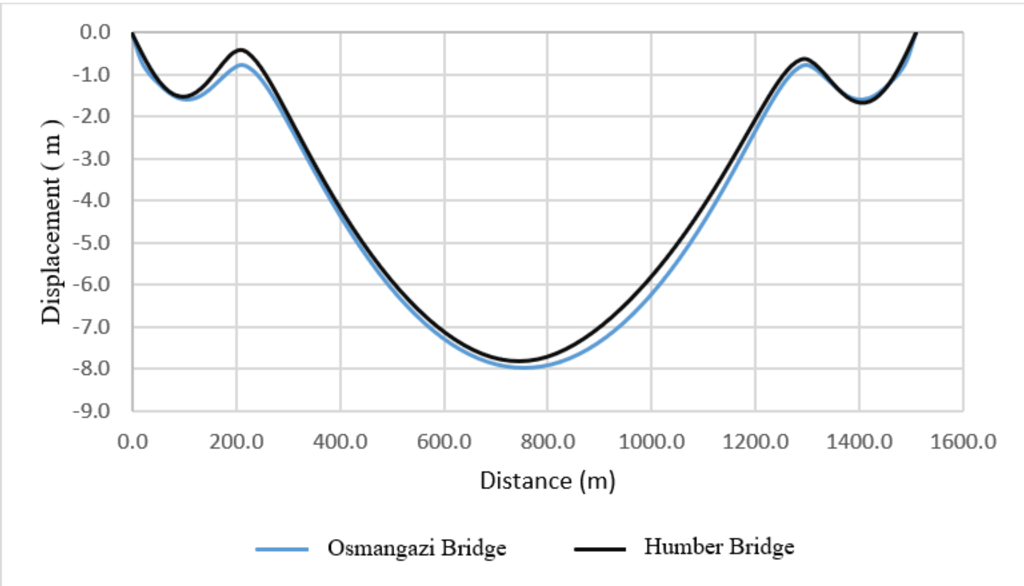

Fig. 3. Comparison of vertical displacements along the deck of The Osmangazi Bridge and The Humber Bridge

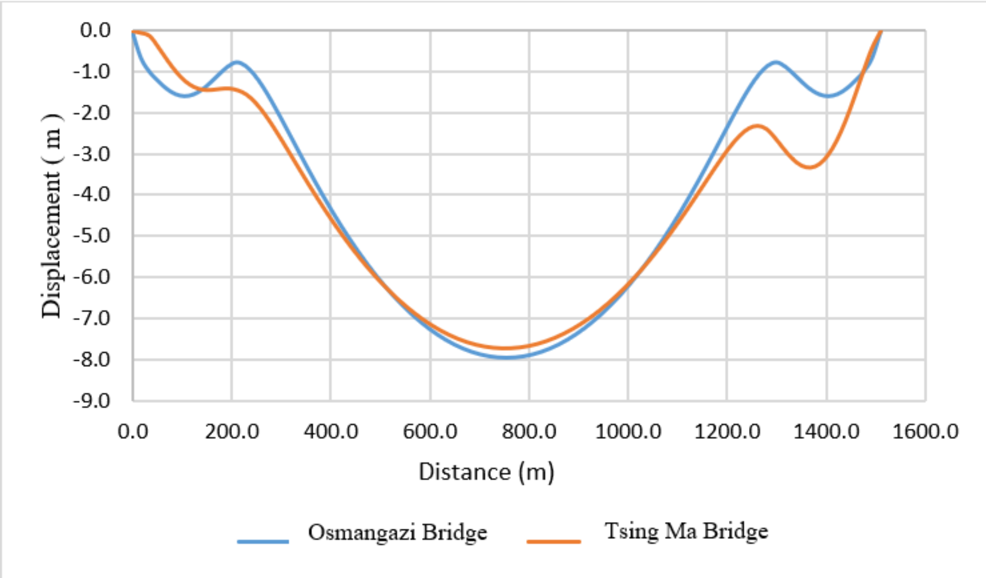

Fig. 4. Comparison of vertical displacements along the deck of Osmangazi Bridge and Tsing Ma Bridge

The versical dislacements obtained for the models FSM_50D, FSM_100D, FSM_150D, FSM_200D and FSM_250D are compared Fig. 5. The maximum vertical displacement of the deck is observed in FSM_50D. The lowest vertical displacement is observed with FSM_250D.

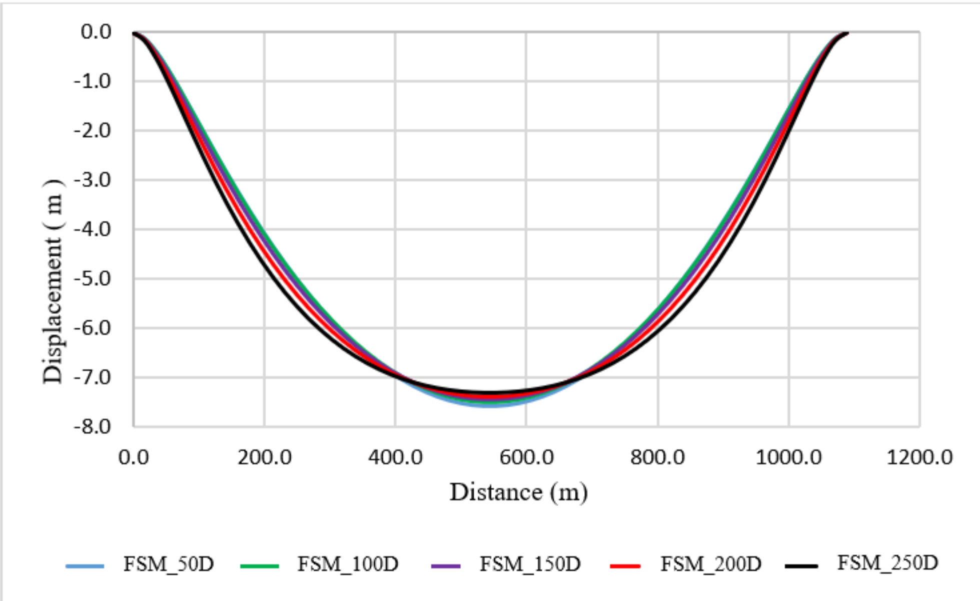

Fig. 5. Comparison of vertical displacements along the deck of FSM_50D, FSM_100D, FSM_150D, FSM_200D and FSM_250D bridges

3.2. Modal analysis results

By comparing the period values of Fatih Sultan Mehmet Bridge with 15 July Martyrs Bridge it can be seen that that the first one is between 11.37 seconds and 2.5 seconds. The period values of the 15 July Martyrs Bridge in the first 20 modes vary between 8.47 seconds and 2.54 seconds. In contrast, the period values of Fatih Sultan Mehmet Bridge are higher.

When comparing the Osmangazi Bridge and the Humber Bridge, it can be seen that the average period values in the first 20 modes of the former vary between 11.65 seconds and 3.08 seconds. The period values in the first 20 modes of the Humber Bridge vary between 8.67 seconds and 5.67 seconds.

It is clear that the largest period value is observed at Tsing Ma Bridge. In the first 20 modes, the period values vary between 12.17 seconds and 4.29 seconds.

It has been shown that the period values of bridges modeled with diagonal (inverted V) suspension cables are lower than the period values of bridges modeled with vertical suspension cables.

Comparison of the modal analysis results of the models created by increasing the number of suspension ropes reveals that there is no significant decrease between FSM_40H and FSM_80H.

Modal analysis of the bridge models created by increasing the suspension diameters reveals a decrease in the modal values. As shown in Fig. 1, the period in the first mode of the FSM_50D model is 11.16 seconds, while the period in the first mode of the FSM_250D model is 9.8 seconds.

4. Conclusions

When the results of the studies carried out in this thesis are analyzed, some suggestions are presented below. It is concluded that vertical suspension cables are more advantageous than diagonal (inverted V) cables, where the way the suspension cable is connected is important in the design phase of suspension bridge models. It is concluded that the effect of suspension cable diameter on the stiffness of the structure is more than the effect of the number of suspension cables. The reason why the moment value of the moment created in the deck due to the increase in mass with the change of suspension cable diameter is higher than the moment value created by the change of suspension cable is the increase in mass. For this reason, it should be more sensitive when deciding the suspension cable diameter. Based on the results of the Tsing Ma bridge, the vertical displacement of the deck with no suspension cable in the edge span is more than 2 times higher than the vertical displacement of the deck with a suspension cable in the edge span, which emphasizes the importance of suspension cables.

If the results obtained from this study are analyzed, some suggestions can be presented as follow:

It has been concluded that the connection type of the suspension cable is important in the design phase of suspension bridge models, and that vertical suspension cables are more advantageous than diagonal (inverted V) cables. It has also been concluded that the effect of the suspension cable diameter on the rigidity of the structure is greater than the effect of the number of suspension cables. The reason why the moment value formed on the deck due to the increase in mass with the change in the suspension cable diameter is higher than the moment value formed by the change in the number of suspension cables is the increase in mass. Therefore, there sould be more sensitive when determining the suspension cable diameter. According to the results of the Tsing Ma Bridge, the vertical displacement obtained in the deck for the bridge model without a suspension cable in the side span is more than 2 times of those obtained in the deck fro the bridge model with a suspension cable in the side span, which emphasizes the importance of suspension cables.

References

AASHTO LRFD Bridge Design Specifications. (2012). American Association of State Highway And Transportation Officals, 5.th Edition.

Abdel-Ghaffar, A.M., & Rubin, L.I. (1983). Lateral earthquake response of suspension bridges. *Journal of Structural Engineering*, *109*(3), 664-675

Adanur, S. (1997). *The dynamic analysis of suspension bridges with geometrically nonlinearity and elastic foundation analogy* (Master's thesis). Karadeniz Technical University, Trabzon, Türkiye (in Turkish)

Adanur, S. (2003). *Geometrically nonlinear deterministic and stochastic analyses of suspension bridges to multiple support sesimic excitations* (Doctoral dissertation). Karadeniz Technical University, Trabzon, Türkiye (in Turkish)

Aktaş, E. (2010). *Design and performance analysis of a prestressed girder bridge* (Master's thesis). Istanbul Technical University , İstanbul, Türkiye. (in Turkish)

Atabey, N.A. (2011). *Static and dynamic analysis of fiber reinforced polymer suspension bridges* (Master's thesis). Karadeniz Technical University, Trabzon, Türkiye. (in Turkish)

Atmaca, B. (2012). *Consturtion stage anaysis of three dimensional cable-stayed bridge* (Master's thesis). Karadeniz Technical University, Trabzon, Türkiye. (in Turkish)

Bhagwat, K.K., Kulkarni, D.K., & Cholappanavar, P. (2017). Parametric study on behaviour of box girder bridges using CSi Bridge. *International Research Journal of Engineering and Technology (IRJET)*, *4*.

Cengiz, A. (2009). *Dynamic response of long span cable stayed bridges under traffic loadings* (Master's thesis). Gazi University, Ankara, Türkiye. (in Turkish)

Cengizoğlu, H. (2006). *The comprasion of the strength of undamaged suspension bridge with current situtaion, one of the rods broke off* (Master's thesis). İstanbul Technical University, İstanbul, Turkiye. (in Turkish)

Denizolgun, F.S. (2017). *Design ans implementation of stream bridge in Kuzey Marmara Highway: Alemdag Stream Bridge* (Master's thesis). İstanbul Technical University, İstanbul, Türkiye. (in Turkish)

Chen, W.F., & Duan, L. (2014). Substructure design. Bridge Engineering Handbook (2nd ed.) CRC Press, Taylor & Francis Group.

Eyüpgiller, M.M. (2017). *Comperative structural analysis of suspension bridges with diagonal and vertical hanger* (Master's thesis). Yıldız Technical University, İstanbul, Türkiye. (in Turkish)
Farhad, A.A. (2018). *The economic comparison of cable stayed bridges and suspension bridges* (Master's thesis). Konya Selcuk University, Konya, Türkiye. (in Turkish)
Ganbat, B. (2008). *Seismic performance evaluation of bridges by using pushover analysis and stergthening of Bayrampasa bridge* (Master's thesis). İstanbul Technical University, İstanbul, Türkiye. (in Turkish)
Gökmen, E. (2015). *Comparative cost analysis of suspension bridges and cable stayed bridges* (Master's thesis). Gazi University, Ankara, Türkiye. (in Turkish)
Gölen, M.S. (2017). *Load sharing methods and comparison in steel bridges and concrete bridges* (Master's thesis). İstanbul Gelişim Universtiy, İstanbul, Türkiye. (in Turkish)
Günaydın, M. (2011). *Determination of structural behavior of suspension bridges considering construction stage and time dependent material properties* (Master's thesis). Karadeniz Technical University, Trabzon, Türkiye. (in Turkish)
Gunaydin, M., Adanur, S., Altunişik, A., & Sevim, B. (2012). Construction stage analysis of fatih sultan mehmet suspension bridge. *Structural Engineering and Mechanics*, *42*(4)
İbrahimoğlu F. (2002). *Researchment of the design and the construction techniques of the suspension bridges by the Lillebaelt and Fatih Sultan Mehmet Bridges examples* (Master's thesis). İstanbul Technical University, İstanbul, Türkiye. (in Turkish)
İldan, K.B. (2018). *Experimental study on the behavior of prestressed a nineteen Parallel Wire Strand (PWS) in suspension bridges under hydrocarbon pool fires* (Doctoral dissertation). Bogazici Universtiy, İstanbul, Türkiye. (in Turkish)
Karslıoğlu, M. (2016). *Investigation of seismic site amplification effects on dynamic behaviour of Osman Gazi Suspension Bridge* (Master's thesis). Yıldız Technical University, İstanbul, Türkiye. (in Turkish)
Kartal, H. (2018). *Comparison of dynamic responses of suspension and cable-stayed bridges having equal center span lenghts* (Doctoral dissertation). Gazi University, Ankara, Turkiye. (in Turkish)
Kartal, H. (2012). *Investigation of the dynamic behaviour of cable - stayed bridges with respect to the earthquake and traffic loads* (Master's thesis). Gazi University, Ankara, Turkiye. (in Turkish)
Mubuli, A. (2016). *Determining the structural behavior of Fatih Sultan Mehmet Suspension Bridge under earthquake loads and vehicle loads* (Master's thesis). Yıldız Technical University, İstanbul, Türkiye. (in Turkish)
Rahwan, B.R. (2019). *Investigation of structural behaviour of Bosporus Suspension Bridge before and after the changing of the hangers* (Master's thesis). Karadeniz Technical University, Trabzon, Türkiye. (in Turkish)
Shinozuka, M., Karmakar, D., Chaudhuri, S.R., & Lee, H. (2009). *Verification of computer analysis models for suspension bridges* (No. CA/UCI-VTB-2009). California. Dept. of Transportation. Division of Research and Innovation.
Soyluk, K. (2002). *Stochastic analysis of cable-stayed bridges subjected to spatially varying ground motions* (Doctoral disserttion). Karadeniz Technical University, Trabzon, Türkiye (in Turkish)
Soyoz, S., Dikmen, U., Apaydin, N., Kaynardag, K., Aytulun, E., Senkardasler, O., & Erdik, M. (2017). System identification of Bogazici suspension bridge during hanger replacement. *Procedia Engineering*, *199*, 1026-1031
Xu, Y.L., & Xia, Y. (2011). *Structural health monitoring of long-span suspension bridges*. CRC Press.
Zhang, X., & Sun, B. (2004). Parametric study on the aerodynamic stability of a long-span suspension bridge. *Journal of wind engineering and industrial aerodynamics*, *92*(6), 431-439
Yetim, M. (2018). *Effect of change in the ratio of the main cable sag depth to main span distance on the normal force generated on the suspended main cable* (Master's thesis). İstanbul Technical University, İstanbul, Türkiye. (in Turkish)
Zengin, E. (2008). *Sturctural analysis and desing of a long span combined cable-stayed suspension bridge crossing the İzmit Bay* (Master's thesis). Middle East Technical University, Ankara, Türkiye. (in Turkish)

4th International Civil Engineering & Architecture Conference
17-19 May 2025, Trabzon, Türkiye

Free vibration analysis of FG-GPLRC straight beams via warping-included mixed FEM

Osman Guner[1], Merve Ermis[*1], Umit N. Aribas[2], Mehmet H. Omurtag[2]

[1] *Kırklareli University, Department of Civil Engineering, 39000 Kırklareli, Türkiye*
[2] *Istanbul Medipol University, Department of Civil Engineering, 34810, Istanbul, Türkiye*

Abstract. This study uses warping-included mixed finite element formulation to investigate the free vibration behavior of transversely functionally graded (FG) straight beams reinforced with graphene nanoplatelets (GPLs). The composite material consists of a polymer matrix reinforced with GPLs, where the volume fraction of the reinforcement varies through the thickness of the beam. The effective elastic modulus is derived using the Halpin-Tsai micromechanical model, which accounts for the geometry and distribution of GPLs within the matrix material. The warping-included mixed finite element formulation is developed based on the Timoshenko beam theory, employing a two-node element with twelve degrees of freedom per node. These degrees of freedom include three displacements, three section rotations, three forces, two bending moments, and one torsional moment, providing a robust framework for accurately modeling the dynamic behavior of the FG-GPL reinforced composite beam. A detailed parametric study examines the influence of GPL weight fraction, material distribution patterns, and boundary conditions on the vibration characteristics of the beam. The results highlight the significant influence of the GPL reinforcement and its distribution on the natural frequencies, providing valuable insights for optimizing the mechanical performance of composite beams in advanced engineering applications.

Keywords: Graphene nanoplatelets reinforced composites; Functionally graded material; Mixed finite element method; Free vibration analysis

1. Introduction

In recent years, composite laminated beams have attracted considerable attention in the fields of materials science and engineering, owing to their exceptional mechanical performance and versatility across various applications. The increasing demand for advanced materials with enhanced mechanical, thermal, and electrical properties has spurred the development of innovative composite structures. Among these, functionally graded materials (FGMs) have emerged as a promising category of composites, specifically designed to fulfill both structural and functional requirements through a gradual variation of material properties in a designated direction.

Functionally graded materials, originally developed in the mid-1980s by Japanese scientists, offer distinct advantages over traditional fiber-reinforced laminated composites, including improved stress distribution and enhanced performance under varying environmental conditions (Long et al. 2016; Ninh et al., 2020). These attributes have made FGMs particularly suitable for aerospace, marine, mechanical, and structural engineering applications. Functionally graded materials are advanced composites where the material properties vary continuously and smoothly with position, offering significant advantages in high-temperature applications and structural optimization (Cong and Duc, 2016). The concept of FGMs involves a gradual variation of material properties, often achieved by varying the volume fraction of the constituent materials (Chakraverty and Pradhan, 2016). This approach eliminates the abrupt interfaces found in traditional composites, reducing stress concentrations and improving the overall structural integrity.

Within the domain of FGMs, functionally graded graphene platelet-reinforced composite (FG-GPLRC) beams have emerged as a notable development. Graphene, known for its outstanding mechanical strength, high electrical conductivity, low density, and nanometric scale, serves as a highly effective reinforcement in composite materials (Ebrahimi et al., 2024; Priyadarshini, 2025; Rangappa et al., 2022). The integration of graphene platelets into FGMs significantly enhances their mechanical and physical properties, thereby improving the performance and durability of composite beams in various engineering applications. Some of the studies related to FG-GPLRC straight beams can be cited as follows: Wu et al. (2017) investigate the dynamic instability of functionally graded

[*] Corresponding author, E-mail: mermis@klu.edu.tr

https://doi.org/10.31462/icearc2025_ce_sme_834

multilayer graphene nanocomposite beams under thermal environments, employing the First-order Shear Deformation Theory. To determine the principal unstable region of FG multilayer GPLRC beams, the study utilizes the differential quadrature method in combination with Bolotin's method. The effective Young's modulus of the GPLRCs is estimated through the Halpin-Tsai micromechanics model. The effects of various parameters, including the distribution pattern, geometry, and dimensions of the GPL nanofillers, as well as the impact of initial static axial load and uniform temperature variation on the dynamic instability behavior, are thoroughly analyzed. The findings demonstrate that the GPL weight fraction and distribution pattern substantially impact the thermal buckling, free vibration, and dynamic instability of FG multilayer GPLRC beams.In contrast, the effects of GPL geometry and dimensions diminish when the width-to-thickness ratio of the GPL exceeds 10^3. Feng et al. (2017) comprehensively examine the linear and nonlinear free vibration behaviors of nanocomposite beams reinforced with non-uniformly distributed GPL reinforcements, employing the Timoshenko beam theory alongside the von Kármán nonlinear strain-displacement relationship. The study demonstrates that incorporating a small amount of GPL into the polymer matrix significantly enhances the natural frequency of the composite beam, highlighting its potential for innovative engineering applications. Furthermore, at the same weight fraction, GPLs characterized by a larger surface area and fewer graphene layers demonstrate superior reinforcement efficiency. Among the four examined GPL distribution patterns, the results indicate that positioning a higher concentration of GPLs near the top and bottom surfaces of the beam most effectively enhances beam stiffness, leading to increased natural frequencies. The study also verifies that a multilayer configuration with ten individual stacked layers adequately represents an ideal FG structure, ensuring a continuous and smooth variation in material properties. Song et al. (2020) investigate the nonlinear free vibration behavior of edge-cracked GPLRC laminated beams resting on a two-parameter elastic foundation under thermal conditions. The study assumes that the GPL nanofillers are randomly oriented and functionally graded in a layer-wise distribution along the beam thickness, with a uniform temperature distribution throughout the beam domain. To estimate the effective material properties of the GPL-reinforced nanocomposite, micromechanical models are utilized. Stress intensity factors are determined using finite element methods. The equations of motion for the cracked GPLRC beams are formulated within the framework of the first-order shear deformation beam theory, incorporating von Kármán-type geometric nonlinearity to account for large deformations. The bending stiffness at the cracked section is evaluated using a massless rotational spring model. To compute the linear and nonlinear natural frequencies, the differential quadrature method is applied. Karamanli and Vo (2021) conduct a comprehensive study on the bending, vibration, and buckling behavior of carbon nanotube-reinforced composite (CNTRC) and GPLRC beams. The governing equations of motion are derived by incorporating both normal and shear deformation effects. To evaluate the displacements, critical buckling loads, and natural frequencies of the beams under various boundary conditions, finite element analysis is utilized. Parametric analyses are performed to investigate the effects of crucial parameters, including the distribution pattern, volume fraction of CNTs, GPL weight fraction, slenderness ratio, and boundary conditions, on the structural performance. Vinh and Son (2022) propose a first-order mixed beam element formulation for analyzing the static bending behavior of functionally graded graphene oxide powder-reinforced composite (FG-GOPRC) beams. The formulation is based on a mixed finite element approach that utilizes the first-order shear deformation theory. The developed beam element consists of two nodes, each with three degrees of freedom, and employs linear shape functions, effectively eliminating shear locking without the need for selective or reduced integration. The study demonstrates that the proposed beam element can accurately predict static bending responses with a minimum number of elements, significantly reducing computational costs. To validate the efficiency and accuracy of the formulation, a comparative analysis is conducted, confirming the superior performance of the new element. Subsequently, the proposed beam element is applied to investigate the static bending behavior of FG-GOPRC beams. Fouaidi et al. (2023) propose a numerical approach that integrates the reproducing kernel particle collocation meshless method with the implicit Newmark time integration scheme to analyze the transient response of porous composite beams reinforced with FG-GOPs resting on elastic foundations. The study considers composite beams subjected to dynamic loads under various boundary conditions, with the elastic foundation modeled using the Winkler–Pasternak foundation model. To model the composite beams reinforced with FG-GOPs, the first-order shear deformation theory is employed. The effective material properties of the porous composite beams are estimated using the Halpin–Tsai homogenization technique and the rule of mixtures, taking into account the effects of porosity. The equations of motion are reformulated in a matrix–vector strong form and solved using the proposed numerical strategy. Aribas et al. (2021, 2022, 2023, 2024) developed a mixed finite element method based on the Timoshenko beam theory to analyze the structural behavior of laminated composite beams, considering the warping effect. This method provides results with engineering accuracy when compared to three-dimensional finite element methods. Furthermore, the mixed FEM, which incorporates the warping effect and is developed based on the Timoshenko beam theory, has been employed by Ermis 2024 to investigate the dynamic behavior of FG-GPLRC straight-axis and curved-axis beams. This study investigates the effect of GPL weight fractions and GPL distribution patterns on the natural frequencies of FG-GPLRC straight beams for different boundary conditions and slenderness ratios using the outcomes of Güner (2025).

2. Mathematcal formulation

2.1 Effective Material Properties of the FG-GPLRC Composite Beam

Nanocomposite materials reinforced with graphene nanoplatelets (GPLs) are obtained by combining polymer matrix material and graphene nanoplatelet material at specific volume fractions. The layered graphene nanoplatelet-reinforced composite beam with a rectangular cross-section, presented in Fig. 1, has a thickness of h and a width of w. This composite beam consists of N_L layers of equal thickness. The thickness of each layer is defined as $h_k=h/N_L$, arranged as k=1, h,…, N_L . In each layer, the GPLs are uniformly distributed within the matrix material. By varying the GPL ratios within the layers, functionally graded GPL-reinforced composite beams are formed.

In this study, the same amount of GPL material is considered with four different distribution types: UD, X, O, and A (Karamanlı and Vo 2021, Ermis 2024). In the uniform distribution (UD) type, the GPLs are homogeneously distributed within the cross-section, while the other distribution types vary along the thickness and exhibit a linear change. In the FG-X type, the upper and lower parts of the cross-section are rich in GPLs, while in the FG-O type, the opposite is true; in this model, the central part of the cross-section is GPL-rich. The FG-A type demonstrates a gradual increase in the GPL content from the top to the bottom of the cross-section.

For the GPL-reinforced nanocomposite beams, where GPLs are assumed to be randomly and homogeneously distributed within each layer, the volume fraction of GPLs in the kth layer for the aforementioned different distribution types can be expressed as follows.

$$
\begin{aligned}
&\text{UD} &&: V_{\mathrm{GPL}}^{(k)} = V_{\mathrm{GPL}},\\
&\text{FD-X} &&: V_{\mathrm{GPL}}^{(k)} = 2V_{\mathrm{GPL}}\left(\left|2k-N_L-1\right|/N_L\right),\\
&\text{FD-O} &&: V_{\mathrm{GPL}}^{(k)} = 2V_{\mathrm{GPL}}\left(1-\left|2k-N_L-1\right|/N_L\right),\\
&\text{FD-A} &&: V_{\mathrm{GPL}}^{(k)} = V_{\mathrm{GPL}}\left(\left(2k-1\right)/N_L\right),
\end{aligned}
\tag{1}
$$

Here, V_{GPL} represents the total volume fraction of GPLs and is calculated using the following formulation:

$$V_{\mathrm{GNL}} = \frac{W_{\mathrm{GNL}}}{W_{\mathrm{GNL}} + \left(\rho_{\mathrm{GNL}}/\rho_{\mathrm{M}}\right)\left(1-W_{\mathrm{GNL}}\right)} \tag{2}$$

ρ_{GPL} and ρ_{M} denote the densities of the GPL and the polymer matrix, respectively. W_{GPL} represents the total weight fraction of GPLs. The uniform and homogeneous dispersion of graphene/graphene derivative materials within the polymer matrix of the nanocomposite layer is valid only for low values of the weight fraction (W_{GPL}). According to Zhao et al. (2020), this value should be less than approximately 1% to 3%, as detailed in the referenced study. The Halpin-Tsai micromechanics model is used to estimate the effective material properties of two-phase nanocomposites (Rafiee et al., 2009). In this micromechanics model, the GPL reinforcement material in each layer is assumed to be randomly oriented and homogeneously distributed within the polymer matrix material. This multiscale material model for the two-phase nanocomposite approximately calculates the effective elastic modulus of the FG-GPL reinforced nanocomposites as follows (Yang et al., 2023)

$$
\begin{gathered}
E_{\mathrm{eff}}^{(k)} = \frac{3}{8}\frac{1+\xi_l\eta_l V_{\mathrm{GPL}}^{(k)}}{1-\eta_l V_{\mathrm{GPL}}^{(k)}}\times E_{\mathrm{M}} + \frac{5}{8}\frac{1+\xi_w\eta_w V_{\mathrm{GPL}}^{(k)}}{1-\eta_w V_{\mathrm{GPL}}^{(k)}}\times E_{\mathrm{M}}\\
\eta_l = \frac{\left(E_{\mathrm{GPL}}/E_{\mathrm{M}}\right)-1}{\left(E_{\mathrm{GPL}}/E_{\mathrm{M}}\right)+\xi_l},\ \eta_w = \frac{\left(E_{\mathrm{GPL}}/E_{\mathrm{M}}\right)-1}{\left(E_{\mathrm{GPL}}/E_{\mathrm{M}}\right)+\xi_w}
\end{gathered}
\tag{3}
$$

Here, E_{GPL} and E_{M} represent the elastic moduli of the GPL and polymer matrix, respectively. The scaled parameters ξ and η are dependent on the geometric characteristics of the GPL reinforcement material, as follows:

$$\xi_l = 2l_{\mathrm{GPL}}/h_{\mathrm{GPL}},\ \xi_w = 2w_{\mathrm{GPL}}/h_{\mathrm{GPL}} \tag{4}$$

Here, l_{GPL}, w_{GPL}, and h_{GPL} represent the length, width, and thickness of the GPLs, respectively. Additionally, the effective material density ρ_{eff} and Poisson's ratio υ_{eff} of the FG-GPL reinforced beam in the kth layer are calculated using the rule of mixtures as follows:

$$
\begin{aligned}
\rho_{\mathrm{eff}}^{(k)} &= \rho_{\mathrm{GPL}} V_{\mathrm{GPL}}^{(k)} + \rho_{\mathrm{M}} \left(1 - V_{\mathrm{GPL}}^{(k)}\right) \\
\upsilon_{\mathrm{eff}}^{(k)} &= \upsilon_{\mathrm{GPL}} V_{\mathrm{GPL}}^{(k)} + \upsilon_{\mathrm{M}} \left(1 - V_{\mathrm{GPL}}^{(k)}\right)
\end{aligned} \tag{5}
$$

Here, υ_{GPL} and υ_{M} denote the Poisson's ratios of the GPL and polymer matrix, respectively.

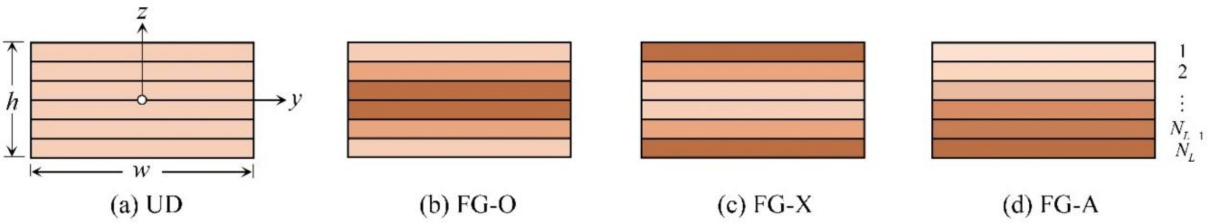

Fig. 1. Cross-sectional view of a functionally graded graphene nanoplatelet (FG-GPL) reinforced composite beam with different distribution models: (a)UD, (b) FG-O, (c) FG-X, (d) FG-A.

2.2. Field Equations

The field equations of spatial curved rods based on the Timoshenko beam theory (Omurtag and Aköz, 1992), and the field equations of FG composite beams through the cross-sectional height can be expressed as follows (Aribas et al. 2022, 2024):

$$
\left.
\begin{aligned}
-\mathbf{F}_{,x} - \mathbf{q} + \rho_{\mathrm{eff}} A \ddot{\mathbf{u}} &= \mathbf{0} \\
-\mathbf{M}_{,x} - \mathbf{i} \times \mathbf{F} - \mathbf{m} + \rho_{\mathrm{eff}} \mathbf{I} \ddot{\mathbf{\Omega}} &= \mathbf{0}
\end{aligned}
\right\} \quad \text{Equations of motion} \tag{6}
$$

$$
\left.
\begin{aligned}
\mathbf{u}_{,x} + \mathbf{i} \times \mathbf{\Omega} - \mathbf{C}_m \mathbf{F} - \mathbf{C}_{mf} \mathbf{M} &= \mathbf{0} \\
\mathbf{\Omega}_{,x} - \mathbf{C}_{fm} \mathbf{F} - \mathbf{C}_f \mathbf{M} &= \mathbf{0}
\end{aligned}
\right\} \quad \text{Constitutive equations} \tag{7}
$$

$$
\left.
\begin{aligned}
-\mathbf{u} + \hat{\mathbf{u}} = \mathbf{0}\,;\; -\mathbf{\Omega} + \hat{\mathbf{\Omega}} = \mathbf{0} \\
\mathbf{F} - \hat{\mathbf{F}} = \mathbf{0}\,;\; \mathbf{M} - \hat{\mathbf{M}} = \mathbf{0}
\end{aligned}
\right\} \quad \text{Boundary conditions} \tag{8}
$$

Here, $\mathbf{u}(u_x, u_y, u_z)$ represents the displacement vector, $\mathbf{\Omega}(\Omega_x, \Omega_y, \Omega_z)$ denotes the cross-sectional rotation vector, $\mathbf{F}(F_x, F_y, F_z)$ is the force vector, and $\mathbf{M}(M_x, M_y, M_z)$ is the moment vector. The parameter ρ_{eff} denotes the effective material density of the composite cross-section, A is the cross-sectional area, and $\mathbf{I}$ represents the moment of inertia vector. The vectors $\mathbf{q}$ and $\mathbf{m}$ represent the distributed force and moment vectors, respectively, while $\ddot{\mathbf{u}}$ and $\ddot{\mathbf{\Omega}}$ indicate the acceleration terms.The terms with a hat (e.g., $\hat{\mathbf{u}}$) denote the known boundary values.

2.3 Functional

Using the potential operator and Gâteaux derivative (Oden & Reddy, 2012; Omurtag & Aköz, 1992), the functional for the free vibration of composite straight beams is obtained in the following form by employing equations (6)-(8). In the free vibration analysis, when harmonic motion is considered, it is evident that the distributed force and moment vectors in equation (6) will be equal to zero, and the acceleration terms can be expressed in the form $\left[\ddot{\mathbf{u}}, \ddot{\mathbf{u}}\right] = -\omega^2 \left[\mathbf{u}, \mathbf{u}\right]$ and $\left[\ddot{\mathbf{\Omega}}, \ddot{\mathbf{\Omega}}\right] = -\omega^2 \left[\mathbf{\Omega}, \mathbf{\Omega}\right]$, where ω is the natural angular frequency as follows:

$$
\left.
\begin{aligned}
\mathbf{I}(\mathbf{y}) = & -\left[\mathbf{u}, \mathbf{F}_{,x}\right] + \left[\mathbf{i} \times \mathbf{\Omega}, \mathbf{F}\right] - \left[\mathbf{M}_{,x}, \mathbf{\Omega}\right] - \tfrac{1}{2}\left[\left(\mathbf{C}_m\right) \mathbf{F}, \mathbf{F}\right] - \tfrac{1}{2}\left[\left(\mathbf{C}_{mf}\right) \mathbf{M}, \mathbf{F}\right] - \tfrac{1}{2}\left[\left(\mathbf{C}_{fm}\right) \mathbf{M}, \mathbf{F}\right] \\
& - \tfrac{1}{2}\left[\left(\mathbf{C}_f\right) \mathbf{M}, \mathbf{M}\right] - \tfrac{1}{2} \rho_{\mathrm{eff}} A \omega^2 \left[\mathbf{u}, \mathbf{u}\right] - \tfrac{1}{2} \rho_{\mathrm{eff}} \omega^2 \left[\mathbf{I} \mathbf{\Omega}, \mathbf{\Omega}\right] + \left\langle \left(\mathbf{F} - \hat{\mathbf{F}}\right), \mathbf{u} \right\rangle_{\sigma} + \left\langle \left(\mathbf{M} - \hat{\mathbf{M}}\right), \mathbf{\Omega} \right\rangle_{\sigma} \\
& + \left\langle \mathbf{F}, \hat{\mathbf{u}} \right\rangle_{\varepsilon} + \left\langle \mathbf{M}, \hat{\mathbf{\Omega}} \right\rangle_{\varepsilon}
\end{aligned}
\right\} \tag{9}
$$

golden light publishing®

2.4 Mixed FEM

The mixed finite element formulation is developed based on a two-node finite element formulation derived from the Timoshenko beam theory. The finite element formulation is derived using the dimensionless coordinate ξ. The linear shape functions are denoted as $\phi_i = 1-\xi$ and $\phi_j = \xi$, where the nodal coordinates are defined as $\xi = 0$, and $\xi = 1$ respectively. The subscripts indicate the nodal points associated with the element. Each node of the linear element has a total of twelve unknowns. These unknowns include three displacements, three rotations, one axial force, two shear forces, one torsional moment, and two bending moments. The total number of degrees of freedom for the element is twenty-four. The natural frequencies of vibration in a structural system can be determined by formulating the problem as a standard eigenvalue problem. Detailed information on the mixed finite element formulation can be found in Omurtag and Aköz (1992) and Eratlı et al. (2016), while detailed information related to the FG beam can be found in Arıbas et al. (2024).

3. Numerical examples

In this study, the free vibration behavior of GPL-reinforced composite beams is investigated under various parameters. In Section 4.1, the effects of different boundary conditions, GPL distribution types, GPL weight ratios, and length-to-height ratios on natural frequency are evaluated. The accuracy of the presented mixed FEM is previously demonstrated in detail in Ermis (2024), hence the focus of this study is on parametric examples presented in Güner (2025). Four different configurations, namely UD, X, O, and A, are considered as GPL distribution types. The GPL weight ratios (W_{GPL}) are set as 0.1%, 0.3%, 0.5%, 1%, 2%, and 3%. According to the literature, to consider the GPL distribution as homogeneous, the GPL weight ratio should not exceed 3% (Zhao et al., 2020). Three different boundary conditions are evaluated: clamped-clamped, clamped-pinned, and clamped-free (see Fig. 2). The length-to-height ratios (L/h) are chosen as 10, 20, 30, and 40, respectively. The height and width of the cross-section are h = 0.4 *m and w* = 0.4 m, respectively. The out-of-plane first natural frequency values of the FG-GPLRC beam with clamped-free, clamped-pinned, and clamped-clamped boundary conditions are presented in Tables 1–3, respectively, for different length-to-height ratios, GPL distribution types, and GPL weight ratios. The material properties of the GPL are $E_{\text{GPL}} = 1.01\,\text{TPa}$, $\upsilon_{\text{GPL}} = 0.186$, $\rho_{\text{GPL}} = 1062.5\,\text{kg/m}^3$, $l_{\text{GPL}} = 2.5\,\mu\text{m}$, $w_{\text{GPL}} = 1.5\,\mu\text{m}$ and $h_{\text{GPL}} = 1.5\,\text{nm}$. The material properties of matrix material are $E_{\text{M}} = 3\,\text{GPa}$, $\upsilon_{\text{M}} = 0.34$, $\rho_{\text{M}} = 1200\,\text{kg/m}^3$. The effective material properties of each layer of the FG-GPLRC beam are obtained by using Eqs. (1)-(5).

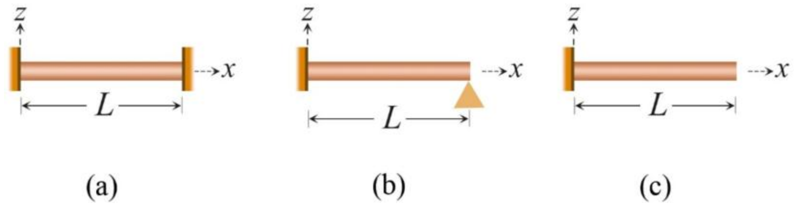

Fig. 2. Boundary conditions (a) clamped-clamped, (b) clamped-pinned, (c) clamped-free

When examining the fundamental natural frequency values (Tables 1–3) of FG-GPLRC beams with clamped-free, clamped-pinned, and clamped-clamped boundary conditions, it is observed that increasing the GPL weight ratio results in a significant increase in natural frequency values for each distribution type and *L*/*h* ratio. This increase shows noticeable differences depending on the material distribution types (UD, FG-X, FG-O, FG-A). In Tables 1–3, for each GPL weight ratio and *L*/*h* ratio, the highest natural frequency value is observed in the X-type distribution, while the lowest frequency value is found in the O-type distribution. This phenomenon can be attributed to the spatial distribution of GPL within the beam cross-section. In the X-type distribution, GPL concentration in the lower and upper regions significantly enhances bending rigidity, while in the O-type distribution, GPL concentration in the central regions is less effective in increasing rigidity. For example (Table 1), in the case of *L*/*h* = 10 with a clamped-free boundary condition, the first mode frequency values for the FG-X distribution are obtained as 7.73 Hz for a 0.1% GPL weight ratio and 25.14 Hz for a 3% GPL weight ratio. Under the same conditions, these values are calculated as 6.86 Hz and 15.81 Hz, respectively, for the FG-O distribution. Additionally, as the length-to-height ratio (*L*/*h*) increases, it is observed that the frequency values decrease for each distribution type and GPL weight ratio. For instance (Table 1), for the X-type distribution and 3% GPL content, the first mode natural frequency value is obtained as 25.14 Hz when *L*/*h* = 10, while it decreases to 1.58 Hz when *L*/*h* = 40. This indicates that the beam stiffness changes inversely with the *L*/*h* ratio.

Table 1. The first out-of-plane natural frequency (Hz) of FG-GPLRC beams with clamped-free boundary condition.

L/h	Distribution type	W_{GPL}					
		% 0.1	% 0.3	% 0.5	%1	%2	%3
10	UD	7.31	8.95	10.33	13.17	17.53	21.01
	FG-X	7.73	9.95	11.76	15.38	20.83	25.14
	FG-O	6.86	7.81	8.66	10.48	13.41	15.81
	FG-A	7.23	8.58	9.66	11.84	15.23	17.98
20	UD	1.83	2.25	2.59	3.31	4.40	5.28
	FG-X	1.94	2.50	2.96	3.87	5.25	6.33
	FG-O	1.72	1.96	2.17	2.63	3.36	3.96
	FG-A	1.82	2.15	2.42	2.97	3.82	4.51
30	UD	0.81	1.00	1.15	1.47	1.96	2.35
	FG-X	0.86	1.11	1.31	1.72	2.33	2.82
	FG-O	0.76	0.87	0.96	1.17	1.49	1.76
	FG-A	0.80	0.96	1.08	1.32	1.70	2.01
40	UD	0.46	0.56	0.65	0.82	1.10	1.32
	FG-X	0.48	0.62	0.74	0.97	1.31	1.58
	FG-O	0.43	0.49	0.54	0.65	0.84	0.99
	FG-A	0.45	0.54	0.60	0.74	0.95	1.13

Table 2. The first out-of-plane natural frequency (Hz) of FG-GPLRC beams with clamped-pinned boundary condition.

L/h	Distribution type	W_{GPL}					
		% 0.1	% 0.3	% 0.5	%1	%2	%3
10	UD	31.06	38.03	43.91	55.99	74.51	89.31
	FG-X	32.74	42.01	49.57	64.73	87.55	105.62
	FG-O	29.26	33.44	37.13	45.03	57.68	68.04
	FG-A	30.81	36.75	41.57	51.37	66.51	78.75
20	UD	7.99	9.79	11.30	14.41	19.18	22.99
	FG-X	8.45	10.87	12.85	16.81	22.76	27.47
	FG-O	7.51	8.55	9.48	11.48	14.69	17.32
	FG-A	7.92	9.44	10.67	13.17	17.03	20.16
30	UD	3.57	4.37	5.05	6.44	8.57	10.27
	FG-X	3.78	4.86	5.75	7.52	10.19	12.30
	FG-O	3.35	3.82	4.23	5.12	6.55	7.72
	FG-A	3.54	4.22	4.76	5.88	7.60	9.00
40	UD	2.01	2.46	2.84	3.63	4.83	5.79
	FG-X	2.13	2.74	3.24	4.24	5.75	6.94
	FG-O	1.89	2.15	2.38	2.88	3.69	4.35
	FG-A	1.99	2.37	2.68	3.31	4.28	5.07

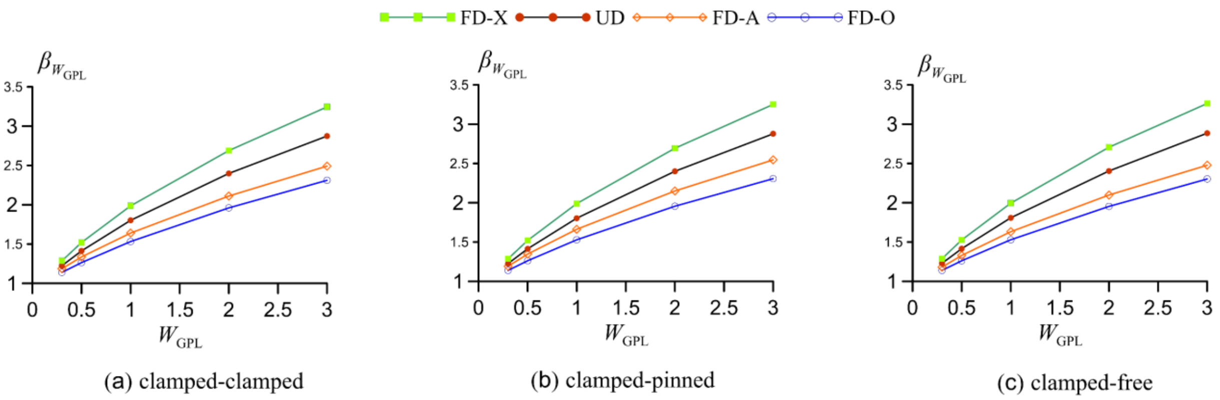

Fig. 3. The effect of GPL weight fraction on the fundamental natural frequency in FG-GPL composite beams for different boundary conditions. (L/h=20, $\beta_{W_{GPL}} = f_{W_{GPL=i}} / f_{W_{GPL}=0.1\%}$ where i = 0.3%, 0.5%, 1%, 2%, and 3%)

Table 3. The first out-of-plane natural frequency (Hz) of FG-GPLRC beams with clamped-clamped boundary condition.

L/h	Distribution type	W_{GPL}					
		% 0.1	% 0.3	% 0.5	%1	%2	%3
10	UD	43.88	53.73	62.03	79.09	105.26	126.17
	FG-X	46.11	59.01	69.53	90.65	122.48	147.70
	FG-O	41.46	47.51	52.84	64.21	82.35	97.18
	FG-A	43.48	51.7	58.36	71.80	92.60	109.43
20	UD	11.52	14.10	16.28	20.76	27.63	33.11
	FG-X	12.16	15.64	18.48	24.15	32.70	39.46
	FG-O	10.83	12.34	13.69	16.59	21.23	25.03
	FG-A	11.40	13.53	15.24	18.70	24.07	28.41
30	UD	5.17	6.32	7.30	9.31	12.39	14.86
	FG-X	5.46	7.03	8.31	10.87	14.72	17.77
	FG-O	4.85	5.52	6.12	7.42	9.49	11.19
	FG-A	5.11	6.07	6.83	8.38	10.78	12.72
40	UD	2.91	3.57	4.12	5.25	6.99	8.38
	FG-X	3.08	3.97	4.69	6.14	8.32	10.04
	FG-O	2.73	3.11	3.45	4.18	5.35	6.30
	FG-A	2.88	3.42	3.85	4.72	6.08	7.17

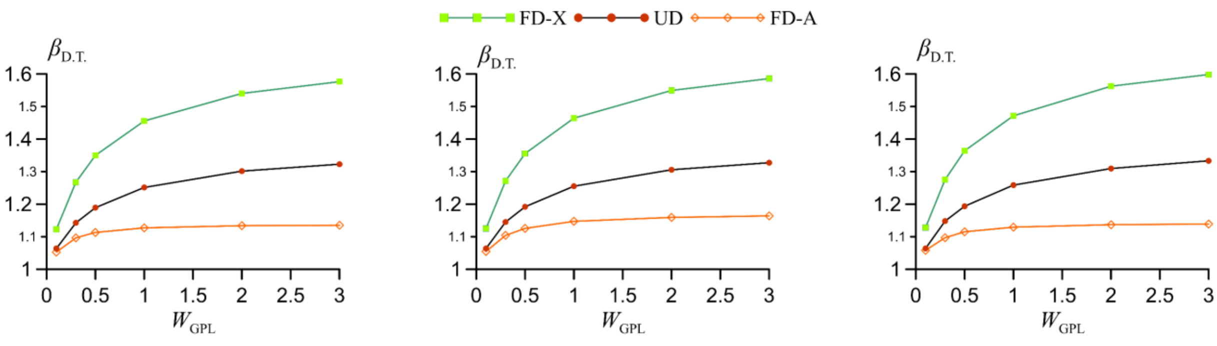

Fig. 4. The effect of GPL distribution type on the fundamental natural frequency in FG-GPL composite beams for different boundary conditions. (L/h=20, $\beta_{D.T.} = f_{D.T.=i} / f_{D.T.=O}$ where $i =$ UD, X, and A.)

3.1 The effect of GPL weight fraction

The effect of the GPL (W_{GPL}) weight fraction on the natural frequency values of the beam is examined through the ratio $\beta_{W_{GPL}}$, calculated using the formula $\beta_{W_{GPL}} = f_{W_{GPL=i}} / f_{W_{GPL}=0.1\%}$ where $i = 0.3\%, 0.5\%, 1\%, 2\%,$ and 3%. In this context, the variations of the $\beta_{W_{GPL}}$ ratio corresponding to the fundamental natural frequency for L/h=20 are presented in Figures 3(a), 3(b), and 3(c) for clamped-clamped, clamped-pinned, and clamped-free boundary conditions, respectively. Similar trends are observed for other L/h ratios (10, 30, and 40). As the GPL amount increases, a noticeable rise in natural frequency values is observed across all three boundary conditions and L/h ratios. This increase is clearly reflected in the rise of the $\beta_{W_{GPL}}$. The increase in the GPL weight ratio leads to a more pronounced enhancement in cross-sectional rigidity in the X distribution, where GPL is concentrated in the lower and upper regions, resulting in higher $\beta_{W_{GPL}}$ ratios for this distribution type. Consequently, in the graphs presented in Figures 3(a)-(c), the highest ratio is obtained for the X distribution, while the lowest values are observed for the O distribution. For example, for L/h = 10 with a 3% GPL ratio under clamped-free boundary conditions, the first natural frequency increases approximately 3.25 times for the X distribution, whereas this increase is only 2.30 times for the O distribution. Under the same conditions, for clamped-pinned boundary conditions, these values are 3.23 and 2.32, respectively, while for clamped-clamped boundary conditions, they are 3.20 and 2.34. Also, as the GPL weight fraction increases, the slope of the increase in $\beta_{W_{GPL}}$ ratios decreases, and this trend is consistent across all three boundary conditions. On the other hand, when the GPL weight ratio is at low levels (e.g., in the range of 0.1%~0.3%), it is noteworthy that the $\beta_{W_{GPL}}$ ratios corresponding to different distribution types are quite close to each other. This indicates that under conditions of low GPL content, the effect of the GPL distribution type on the free vibration frequency remains limited, and the differences between distribution types become less pronounced at these levels. However, as the GPL ratio increases (particularly at values of 1% and above), the differences between the $\beta_{W_{\text{GPL}}}$ ratios of the distribution types become more distinct.

3.2 The effect of GPL distribution type

The effect of the GPL distribution type on the natural frequency values of the beam is examined through the ratio $\beta_{\text{D.T.}}$, calculated using the formula $\beta_{\text{D.T.}} = f_{\text{D.T.}=i} / f_{\text{D.T.}=\text{O}}$ where $i =$ UD, X, and A. The natural frequencies (Tables 1-3) indicate that when the GPL reinforcement is predominantly concentrated in the central region of the beam cross-section (FG-O), the natural frequency values reach their minimum values. Conversely, when the GPL reinforcement is concentrated near the lower and upper surfaces of the cross-section (FG-X), the natural frequency values attain their maximum values. The frequency values corresponding to the UD distribution, representing a homogeneous distribution, and the FD-A distribution, where the GPL reinforcement material exhibits maximum concentration in the lower region and minimum concentration in the upper region, consistently lie between the natural frequencies observed for the FD-X and FD-O distributions across all L/h ratios and boundary conditions. In this context, the variations of the $\beta_{\text{D.T.}}$ ratio corresponding to the fundamental natural frequency for L/h=20 are presented in Figures 4(a), 4(b), and 4(c) for clamped-clamped, clamped-pinned, and clamped-free boundary conditions, respectively. Similar trends are observed for other L/h ratios (10, 30, and 40). At low GPL weight fractions, the effect of the distribution type is more pronounced, whereas this effect tends to diminish as the GPL weight ratio increases. Notably, when the GPL weight ratio exceeds 0.5%, the $\beta_{\text{D.T.}}$ ratio corresponding to the FD-A distribution remains approximately constant at around 1.1.

4. Conclusions

This study presents a comprehensive investigation into the free vibration behavior of transversely FG straight beams reinforced with GPLs using a warping-included mixed finite element formulation. The developed model, based on Timoshenko beam theory, effectively incorporates the warping effects through a two-node element with twelve degrees of freedom per node, providing an accurate representation of the dynamic response of FG-GPLRC beams. The findings can be summarized as follows:

- The results demonstrate that both the GPL weight fraction and the distribution type have a significant impact on the natural frequencies of the beams. Among the considered distribution types, the X-type distribution, where GPLs are concentrated near the top and bottom surfaces, consistently exhibits the highest natural frequency values, while the O-type distribution, with GPLs concentrated in the mid-region, shows the lowest.
- The natural frequencies increase with the GPL content, highlighting the reinforcement efficiency, particularly at higher weight ratios. Additionally, the influence of boundary conditions on the vibration characteristics is significant, indicating the necessity to consider both material distribution and support configurations during the design process.

References

Aribas, U. N., Aydin, M., Atalay, M., & Omurtag, M. H. (2023). Cross-sectional warping and precision of the first-order shear deformation theory for vibrations of transversely functionally graded curved beams. *Applied Mathematics and Mechanics, 44(5)*, 2109–2138. https://doi.org/10.1007/s10483-023-3065-6.

Aribas, U. N., Atalay, M., & Omurtag, M. H. (2024). Warping included mixed finite elements for bending and stresses of functionally graded exact curved beams. *Mechanics of Advanced Materials and Structures.* https://doi.org/10.1080/15376494.2023.2211075.

Aribas, U. N., Ermis, M., & Omurtag, M. H. (2021). The static and stress analyses of axially functionally graded exact super-elliptical beams via mixed FEM. *Archive of Applied Mechanics, 91(12)*, 4783–4796. https://doi.org/10.1007/s00419-021-02033-w.

Aribas, U. N., Ermis, M., Kutlu, A., Eratli, N., & Omurtag, M. H. (2022). Forced vibration analysis of composite-geometrically exact elliptical cone helices via mixed FEM. *Mechanics of Advanced Materials and Structures, 29(8)*, 1456–1474. https://doi.org/10.1080/15376494.2020.1824048.

Chakraverty, S., & Pradhan, K. K. (2016). *Origin and Basics of Functionally Graded Structural Members*. In Elsevier eBooks (p. 7). Elsevier BV. https://doi.org/10.1016/b978-0-12-804228-1.00002-x.

Cong, P. H., & Duc, N. D. (2016). Thermal stability analysis of eccentrically stiffened Sigmoid-FGM plate with metal–ceramic–metal layers based on FSDT. *In Cogent Engineering, 3(1)*, 1182098. Cogent OA. https://doi.org/10.1080/23311916.2016.1182098.

Ebrahimi, F., Ezzati, H., & Najafi, M. (2024). Wave propagation analysis of functionally graded nanocomposite plate reinforced with graphene platelets in presence of thermal excitation. *Acta Mechanica, 235(1)*, 215–234.

Eratli, N., Yilmaz, M., Darilmaz, K., & Omurtag, M. H. (2016). Dynamic analysis of helicoidal bars with non-circular cross-sections via mixed FEM. *Structural Engineering and Mechanics: An International Journal, 57(2)*, 221–238.

Ermis, M. (2024). Warping-included mixed FE approach of beating characteristics in functionally graded graphene platelet-reinforced composite spatially curved beams under harmonic excitation force. *Archive of Applied Mechanics, 94(12)*, 3687–3713. https://doi.org/10.1007/s00419-024-02690-7

Feng, C., Kitipornchai, S., & Yang, J. (2017). Nonlinear free vibration of functionally graded polymer composite beams reinforced with graphene nanoplatelets (GPLs). *Engineering Structures, 140*, 110–119. https://doi.org/10.1016/j.engstruct.2017.02.052

Fouaidi, M., Belfallah, K., Jamal, M., & Belouaggadia, N. (2023). Transient analysis of functionally graded graphene oxide powders-reinforced porous composite beams resting on elastic foundations using the reproducing kernel particle meshless method. *Engineering Analysis with Boundary Elements, 146*, 460–472. https://doi.org/10.1016/j.enganabound.2022.10.029

Güner, O. (2025). Free vibration analysis of functionally graded graphene nanoplatelet-reinforced composite beams using mixed finite element method (Master's thesis, accepted in April 2025, in Turkish). Kirklareli University, Institute of Science and Technology.

Karamanli, A., & Vo, T. P. (2021). Finite element model for carbon nanotube-reinforced and graphene nanoplatelet-reinforced composite beams. *Composite Structures, 264*, 113739. https://doi.org/10.1016/j.compstruct.2021.113739

Long, N. V. D., Quốc, T. H., & Tú, T. M. (2016). Bending and free vibration analysis of functionally graded plates using new eight-unknown shear deformation theory by finite-element method. *International Journal of Advanced Structural Engineering, 8(4)*, 391. https://doi.org/10.1007/s40091-016-0140-y

Ninh, V. T. A., Anh, L. T. N., & Nguyen, D. K. (2020). Free vibration of a 2D-FGSW beam based on a shear deformation theory. *Vietnam Journal of Mechanics*. https://doi.org/10.15625/0866-7136/14817

Oden, J. T., & Reddy, J. N. (2012). *Variational Methods in Theoretical Mechanics*. Springer.

Omurtag, M. H., & Aköz, A. Y. (1992). The mixed finite element solution of helical beams with variable cross-section under arbitrary loading. *Computers & Structures, 43(2)*, 325–331. https://doi.org/10.1016/0045-7949(92)90149-T

Priyadarshini, A., Sutar, M. K., & Pattnaik, S. (2025). Investigation of mechanical properties on functionally graded material reinforced with graphene nanoplatelets for biomedical applications. *Composite Interfaces, 32(2)*, 147–176.

Rafiee, M. A., Rafiee, J., Wang, Z., Song, H., Yu, Z.-Z., & Koratkar, N. (2009). Enhanced mechanical properties of nanocomposites at low graphene content. *ACS Nano, 3(12)*, 3884–3890. https://doi.org/10.1021/nn9010472

Rangappa, S. M., Parameswaranpillai, J., Ayyappan, V., Motappa, M. G., & Siengchin, S. (2022). *Innovations in Graphene-Based Polymer Composites*. Amsterdam, Netherlands: Elsevier Science & Technology.

Song, M., Gong, Y., Yang, J., Zhu, W., & Kitipornchai, S. (2020). Nonlinear free vibration of cracked functionally graded graphene platelet-reinforced nanocomposite beams in thermal environments. *Journal of Sound and Vibration, 468*, 115115. https://doi.org/10.1016/j.jsv.2019.115115

Vinh, P. V., & Son, L. T. (2022). A new first-order mixed beam element for static bending analysis of functionally graded graphene oxide powder-reinforced composite beams. *Structures, 36*, 463–472. https://doi.org/10.1016/j.istruc.2021.12.032

Wu, H., Yang, J., & Kitipornchai, S. (2017). Dynamic instability of functionally graded multilayer graphene nanocomposite beams in thermal environment. *Composite Structures, 162*, 244–254. https://doi.org/10.1016/j.compstruct.2016.12.001

Yang, Z., Hurdoganoglu, D., Sahmani, S., Safaei, B., & Liu, A. (2023). Surface stress size dependency in nonlinear thermomechanical in-plane stability characteristics of FG laminated curved nanobeams. *Engineering Structures, 284*, 115957. https://doi.org/10.1016/j.engstruct.2023.115957

Zhao, S., Zhao, Z., Yang, Z., Ke, L., Kitipornchai, S., & Yang, J. (2020). Functionally graded graphene reinforced composite structures: A review. *Engineering Structures, 210*, 110339. https://doi.org/10.1016/j.engstruct.2020.110339

4th International Civil Engineering & Architecture Conference
17-19 May 2025, Trabzon, Türkiye

Mechanical performance of a flat tie connection system for timber and clay bricks cavity walls: numerical and experimental study

Imane Hammoudi[1], Chaimaa Jaafari[*1], Sebastien Durif[1], Laetitia Bertel[2], Fousia Henzsel[2], Le B. T. Huong[2], Maxime Fiabane[3], Thomas Catterou[3], Maria Saneh[2]

1 INP Clermont Auvergne, CNRS, Institut Pascal, F-63000 Clermont-Ferrand, France
2 Technical Center for Natural Building Materials, CTMNC, 17 rue Letellier, France
3 FCBA, Wood Technological Institute, Allée du Boutaut, 33000 Bordeaux, France

Abstract. Cavity walls are made of an inner wall and an outer wall that could be of different materials separated by an air space and attached to each others using tie systems. In an attempt to reduce environmental impact of structures, cavity walls made of timber and clay bricks appear to be a good alternative to more traditional cavity walls made of concrete and masonry. In France, the design and implementation of such walls are not currently supported by specific standards or guidelines.While the NF DTU 31.2 and NF DTU 20.1 standards previously included provisions for these structures, they were removed in the last revisions due to insufficient experimental data.The Woodstone project funded by MECD aims to study the behavior of walls made of timber and clay bricks in details (stability of the structures under lateral and vertical loadings, waterproofing tests, mechanical behavior of the connections, etc.) in a way to provide more data regarding the behavior of this type of structures for the development of guidelines needed by practioners. As part of the project, several clay bricks walls were built with different ties and brick types. Then the walls were subjected to mechanical stress and their watertightness was assessed. More specifically, this article deals with the efficiency of one type of tie connections that could be used to attach cavity walls made of timber and fired clay bricks. First, the study focuses on the characterization of the considered flat tie type connection under traction (experimental and numerical confrontation). Then the interface between mortar and bricks is modeled to fit experimental shear tests. Finally, the mechanical behavior of connection blocks, comprising two bricks and a mortar layer with an embedded tie, is modeled and validated against experimental data.

Keywords: Ties; Cavity walls; Timber; Fired clay bricks; Interface

1. Introduction:

The use of metal ties in brick masonry dates back to the load-bearing walls of the 19th century, when their design was based mainly on empirical approaches. Introduced in England in the mid-1800s with wrought-iron fasteners, their adoption spread to the USA, where tests revealed that walls bonded with metal ties were more resistant to water penetration than those simply made of masonry. Tie connections gained in popularity with the move away from solid walls to lighter systems, such as cavity walls and double-skin walls. Such evolution in construction practices came with several challenges that had yet to be faced, including frequent shear failures, inappropriate load transfer and a reliance on empirical choices for sizing and spacing of ties in some built cavity walls. While there are several types of existing tie connections in the practice (in terms of materials, size, layout), it is a necessaty to have clear rules and requirements regarding their design to avoid failure due to innaproriate design. In that regard, some building codes such as The Building Code for Masonry Structures (ACI 530 / ASCE 5 / TMS 402-02), also known as the MSJC (MSJC, 2008) provide clear guidelines for their use. Recent scientific articles also deal with the characterization of the behavior of such tie systems. Arslan et al. (2020/2021) for instance published studies regarding the behavior of tie metal connections in double skin walls made of an inner load-bearing brick masonry wall and an outer clay brick cladding, separated by an air gap.

The study by Aslan et al. (2021) is based on observations of damaged buildings, which revealed their vulnerability to out-of-plane failure when the connections between the two walls are insufficient. The study focuses on proposing analytical models for assessing the mechanical resistance associated with the different modes of failure observed in the practice. The study focuses exclusively on hook-zigzag type ties (or mortar ties) embedded

* Corresponding author, E-mail: chaimaa.jaafari@uca.fr

https://doi.org/10.31462/icearc2025_ce_sme_859

in a 10 mm thick mortar joint. Different mortar strengths, air gap lengths and anchor lengths were studied. This study compares analytical results with those obtained experimentally through elementary tests carried out on the ties. The study focuses only on axial loading (compression/tension). Failure modes that were observed are :- In tension : tensile failure of the tie; cone failure in mortar (failure associated with mortar/brick bond); tie/mortar sliding and tie/mortar bond failure - In compression: tie buckling; sliding of tie in the mortar expulsion of mortar cone.

The authors proposed various analytical models to evaluate the resistances associated with each of these failure modes. Following this, Javier Ortega et al. (2022) proposed a numerical model aimed at analyzing and understanding the mechanical behavior of metal ties connecting brick veneer walls to masonry infill walls, particularly under horizontal loads, such as those induced by earthquakes or wind. The work is based on experimental cyclic tension-compression tests carried out on brick-mortar-tie assemblies, during which various failure modes were observed: sliding of the tie, cracking of the mortar and buckling of the metal tie. In France, the design and implementation of double walls are not currently supported by specific standards or guidelines. While the (NF DTU 31.2,2019)and (NF DTU 20.1,2020) standards previously included provisions for these structures, they were removed in the last revisions due to insufficient experimental data. The Woodstone project funded by MECD aims to study the behavior of walls made of timber and clay bricks in details (stability of the structures under lateral and vertical loadings, waterproofing tests, mechanical behavior of the connections, etc.) in a way to provide more data regarding the behavior of this type of structures for the development of guidelines needed by practioners.

More specifically, this article deals with the efficiency of one type of tie connections that could be used to attach cavity walls made of timber and fired clay bricks. First, the study focuses on the characterization of the considered flat tie type under traction (experimental and numerical confrontation). Then the interface between mortar and bricks was modeled to fit experimental shear tests. Finally, the tensile behavior of connection blocks, made of two bricks and a mortar layer with an embedded tie, was modeled and validated against experimental data.

2. Traction of the flat tie system

2.1. Geometry

The studied tie is shown in Fig.1, (Leviat type). It is 19 mm wide and 2 mm thick. It has three round holes aligned horizontally: the first two have a diameter of 12 mm, while the third one has a diameter of 10 mm. These perforations reinforce its anchorage in the masonry. Between the holes and near the edges, 2.5 mm deep notches are symmetrically arranged, to insert the tie into the rail on the one hand, and to improve the positioning and adhesion of the tie in the mortar on the other. A special notch, known as a drop breaker, can be integrated into the flat part. The drop breaker was not present in the ties used for the elementary tests performed. However, its influence on the mechanical behavior of the connection should be accounted for in future parametric sudies since it was part of the ties used in the tested real size cavity walls.

The flat tie under consideration is embedded in mortar on the one hand, and fixed in a rail on the other hand.Fig. 2, shows the geometry of the rail. The rail is fixed to the timber frame using 6 mm diameter screws every 220 mm. The ties are simply inserted into the rail, allowing free movement of the tie along the length of the rail.

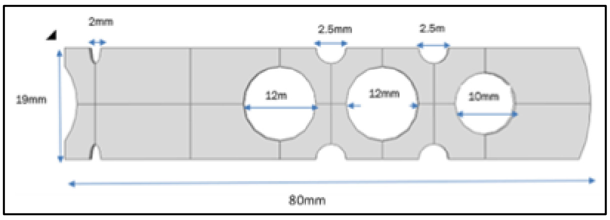

Fig. 1. Flat tie

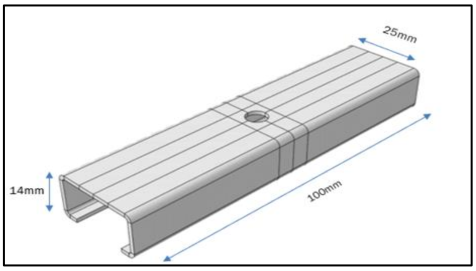

Fig. 2. Rail section

2.2. Material properties of the flat tie

A tensile test was performed on the flat tie. Thanks to a video extensometer, it was possible to track the relative displacement between 2 measuring points positioned around a hole in the tie (Fig.3). These points were then used as reference points to reproduce the test numerically and calibrate the material of the tie. The flat tie was modeled on Abaqus using quadratic volume elements.

A mesh sensivity analysis was carried out to determine the adequate mesh that should be used. Through such analysis, it appeared that a structural hexgonal mesh is appropriate. Two elements across the thickness of the flat tie were used in the numerical model (Fig. 4).

The material's behavior was modeled using an elastic-plastic law with strain-hardening, which accurately accounts for the progressive increase in stress after deformation observed experimentally. Fig. 5, shows the comparison between the numerical model and the experimental results. Table 1., shows the flat tie parameters determined though calibration and Table 2., shows the evolution of stresses with strains used in the numerical model.

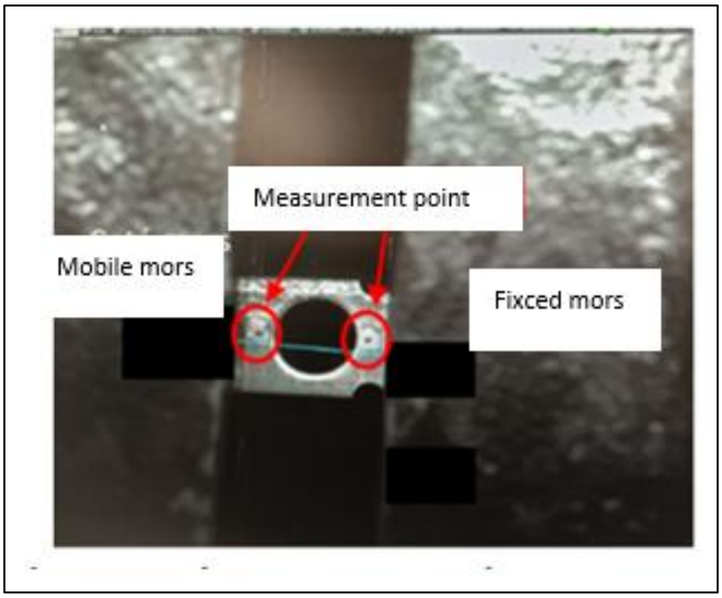

Fig. 3. Experimental set up used to perform the tensile characterization test on the flat tie

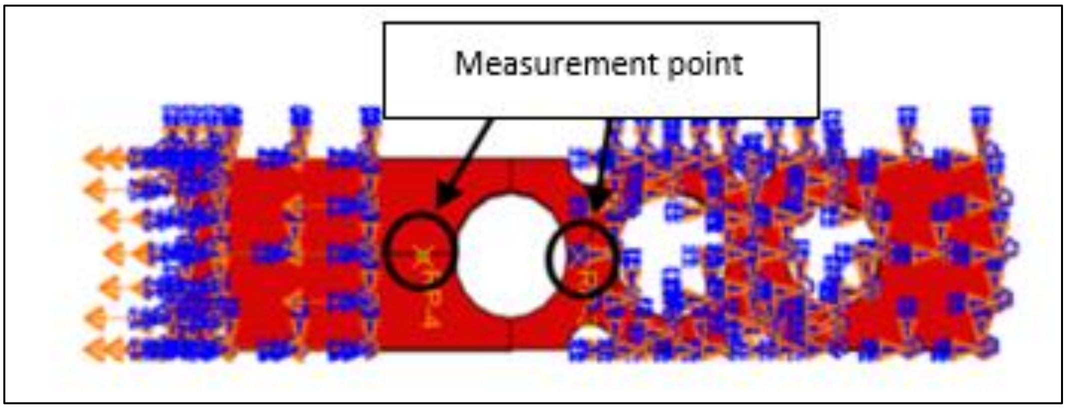

Fig. 4. Numerical model of the tensile test on the flat tie system

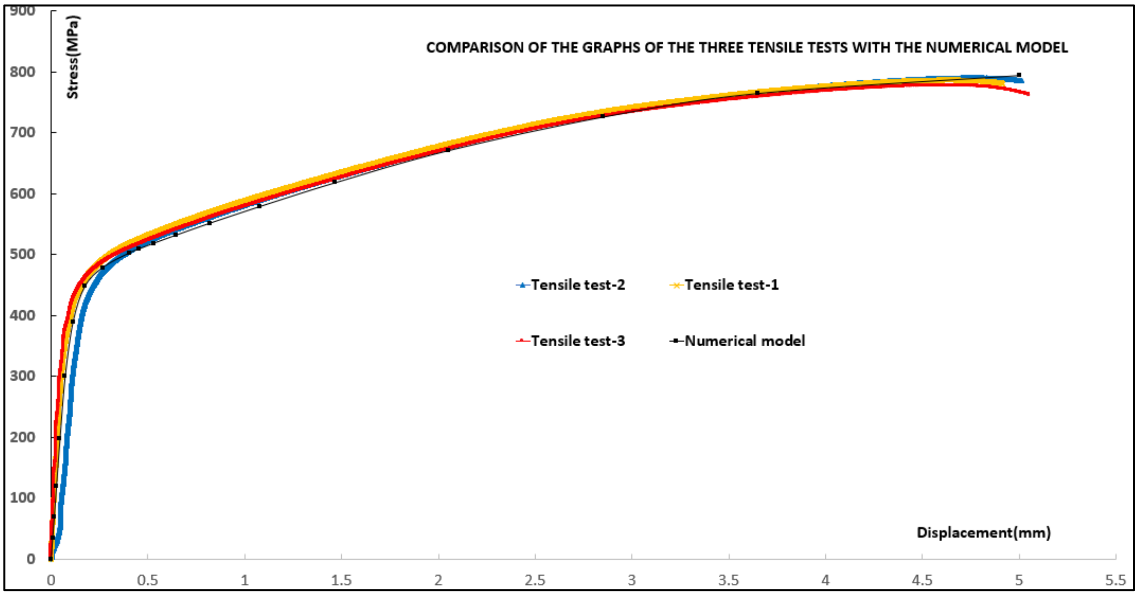

Fig. 5. Comparison of flat tie tensile test with numerical model

Table 1:Flat tie parameters

Young modulus (MPa)	Poisson modulus	Elastic stress (MPa)	Ultimate Stress (MPa)
200000	0.3	382	787

Table 2: Evolution of stresses with strain

Stress (MPa)	Strain (%)
368.43	0.02
516.96	0.023
650.83	1.10
744	0.18
786	0.3

2.3. Flat tie with rail

Another model was developed to study the tensile behavior of the flat tie associated with a metal rail. The objective of this study is to ensure that the model is representative of the specific mode of failure associated with the connection between the rail and the tie. The new model introduces a frictional contact law between the rail and tie, with a steel-to-steel friction coefficient of 0.3 (XP ENV1993-2).

To validate the Finite Element model, tensile tests were carried out on this assembly (Fig. 6,). The objective of the rail-tie tensile test was to determine the maximum force attainable before separation of the rail from the tie. It was observed that, during the tensile test, the tie tended to shift, coming out of the rail on one side and out of alignment on the other side. It was observed that the deformation of the rail largely predominated over the deformation of the tie.

Fig. 6, shows the model of the flat tie with rail. Fig. 7, compares the evolution of force versus displacement given by the finite element model and the 2 performed tests. For this purpose, the displacement used was that obtained between the 2 measurement points specified in Fig.6,. Good agreement can be observed between the model and the tests, with a maximum difference of 5.7%. The numerical model can then be used to study in detail the influence of the rail on the overall behavior of the ties, which appears to have a decisive influence on the system's stiffness and strength. The rail was not used in the tensile tests performed on the tie/brick/mortar complex.

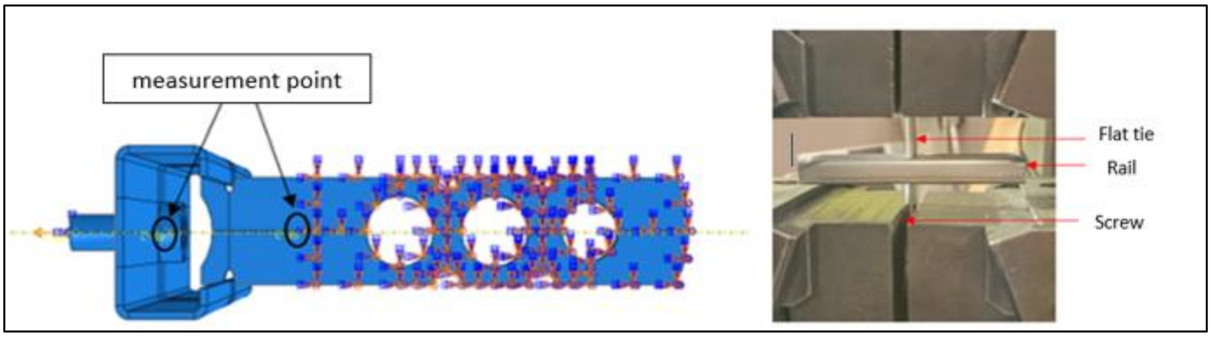

Fig. 6. Modeling the flat tie-rail tensile test ("embedded end versus free end-meshing1mm") and experimental test of the flat tie and rail connection system

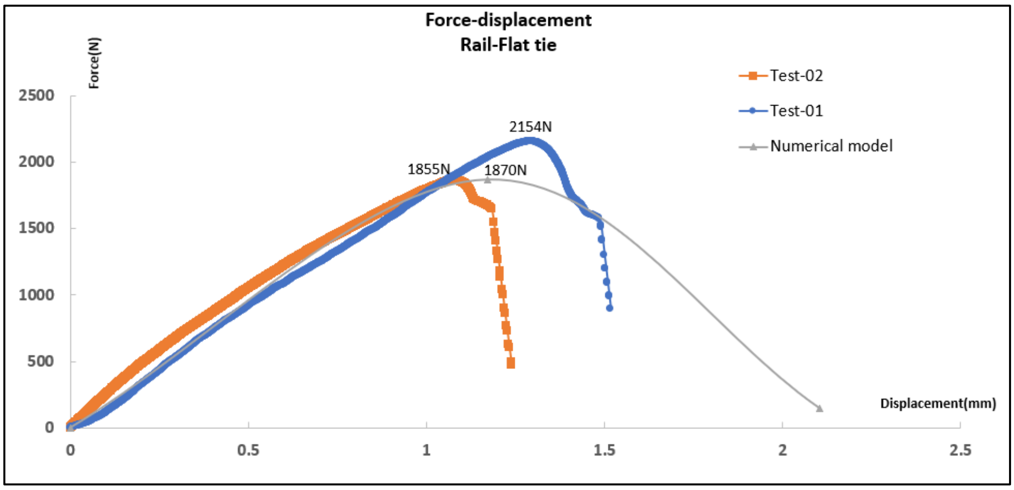

Fig. 7. Modeling the tie-rail tensile test (embedded end versus free end-meshing1mm)

3. Numerical simulation of the experimental Shear tests performed on the mortar/brick complex

3.1. Shear tests protocole

A series of shear tests were performed on mortar/brick complexes. Such tests were used to calibrate the brick to mortar cohesive interface model. Fig. 8, illustrates the experimental tests conducted and summarizes results obtained when testing 10 samples. An important variability was observed in the traction test results performed. It was chosen to model the test giving the minimum shear force (more conservative).

Sample	Failure Load (N)	Shear Strength (MPa)	Standard Error (MPa)	Variability (%)	Average Shear Strength (MPa)
1	27409	0.59			
2	11368	0.36			
3	27041	0.61			
4	13948	0.61			
5	18756	0.42	0.14	31	0.45
6	18207	0.3			
7	16636	0.29			
8	27624	0.62			
9	15952	0.58			
10	27628	0.61			

Fig. 8. Shear tests on bricks-mortar complexes

3.2. Material properties of the Mortar and the bricks

The value of the Young's modulus that was used to numerically simulate the behaviour of the mortar is equal to 3779 MPa. This value was taken from the literature based on the work published by M.A.Dalle (2025) on a similar mortar reference type as the one used in the project. A series of tests were conducted to evaluate both the tensile and compressive strength of the mortar.

For the numerical simulations, a compressive strength of 4.2 MPa and a tensile strength of 11.8 MPa were adopted. These values were obtained from the same literature source as the one used for Young's modulus..The stress versus strain curves for the mortar and its corresponding damage law were determined using a Mazars model, implemented on Matlab.

The curves giving the stress versus strain and damage law are shown in Fig. 9,Fig. 10,. For the plain bricks, the elastic properties were considered based on stress-strain curves provided in the CTTB report of 2006. From these curves, the Young's modulus of two tested bricks similar to those used in the WoodStone project was determined to be approximately equal to 5912 MPa.

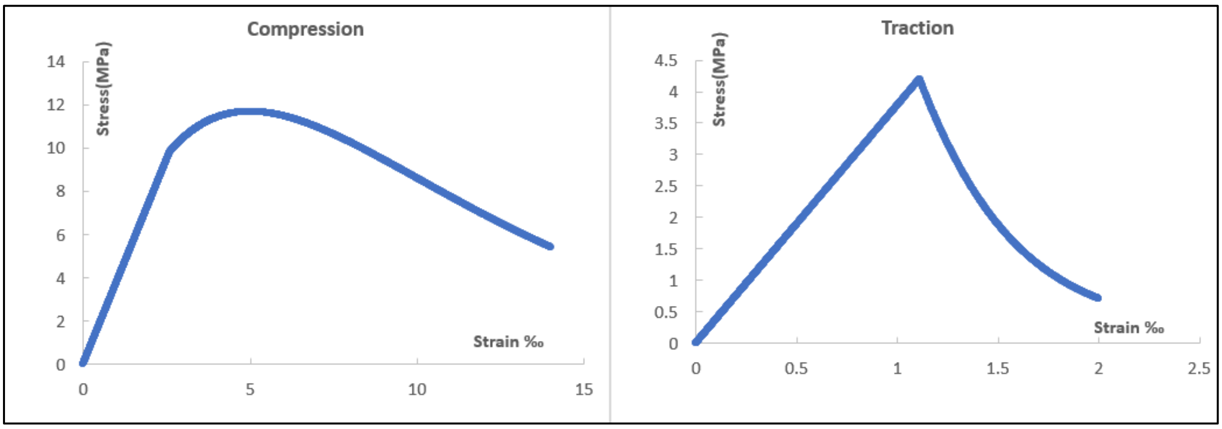

Fig. 9. Stress-strain curves for mortar : Compression and Traction

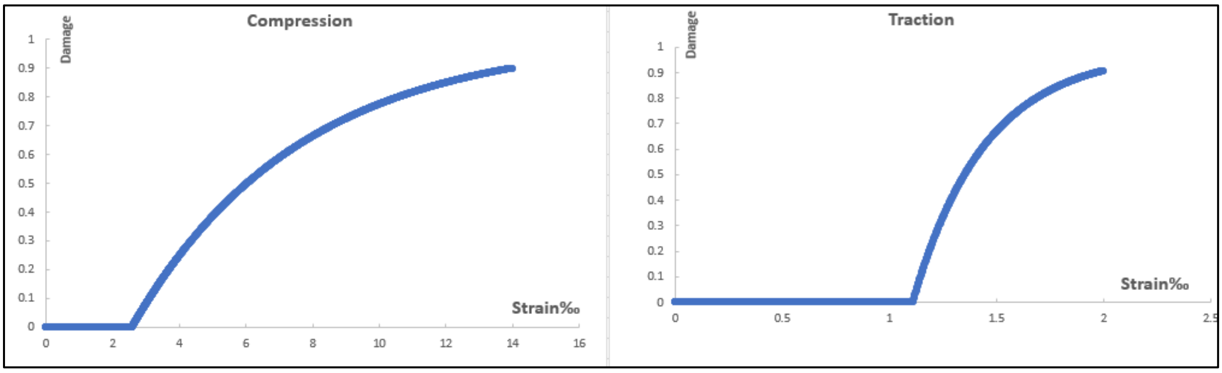

Fig. 10 . Damage of PRB MJ VIF mortar : Compression and Traction

3.3. Cohesive brick-mortar model

The connection between brick and mortar was modeled using a cohesive model at the interface of the two materials. This cohesive model was calibrated based on the shear tests. To account for this variability and assess its impact on the strength of the tie system, the cohesive model was calibrated on the 2 tests giving the maximum and minimum stiffnesses and strengths respectively, as shown in Table 3. To model the brick/mortar/tie complex in section 4, the minimum configuration was used.

This calibration determines 2 parameters of the cohesive model, one associated with tangential stiffness (Kt) and one associated with maximum shear strength (τ_t), corresponding to a limit stress beyond which the cohesive model is no longer active and allows sliding. Fig.11, shows the adequacy of the model for the minimum configuration corresponding to shear test n°2. This configuration is the one that was used later on to simulate the brick/mortar/tie traction test as it is the less conservative.

Table 3. Stiffnesses between brick and mortar

Configuration	Stiffness coefficient (MPa/mm)	Shear strength (MPa)
Minimum	1.1	0.6
Maximum	1.1	0.8

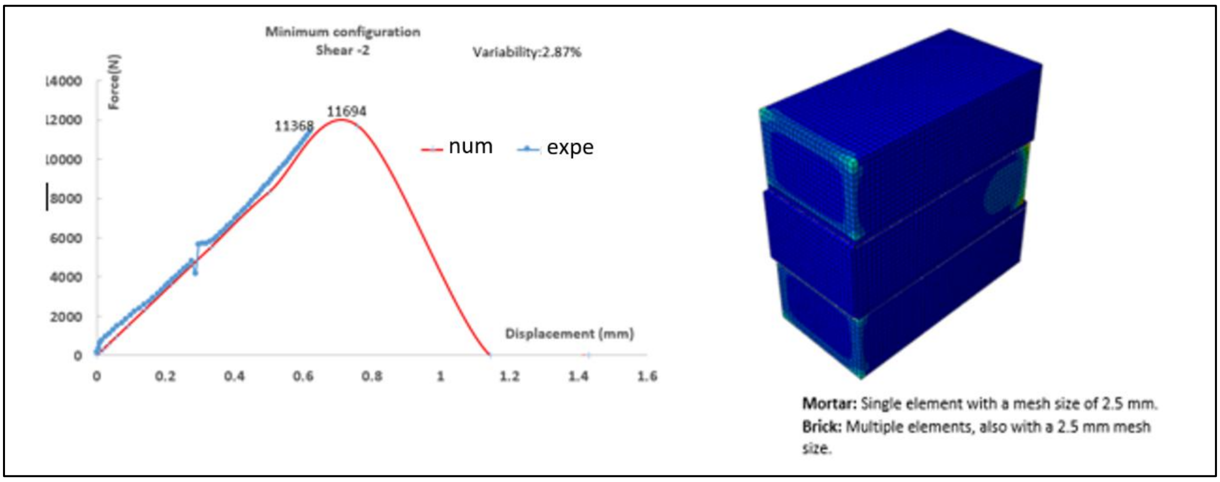

Fig. 11 . Superposition of numerical and experimental shear test

4. Numerical simulation of traction tests performed on Brick-mortar-tie connections:

4.1. Presentation of the model and results

Two solid bricks measuring 220mm × 105mm × 50mm, joined by 5mm-thick mortar were modeled. A flat tie without drain breaker was anchored in the center of the mortar to a depth of 50mm. The objective of this model was to calibrate the cohesive model between the mortar and tie on the basis of the performed tensile tests.

In total, 10 tensile tests with a certain variability were performed. Such variability was accounted for in the simulation by adjusting the properties of the cohesive model. Two experimental graphs were selected to calibrate the model: one corresponding to the configuration giving the weakest results (called minimum properties), corresponding to the tensile test no. 2, and the one giving the strongest results (called maximum properties), corresponding to the tensile test no. 4.

The parameters of the cohesive model for these 2 minimum and maximum configurations are presented in Table 4. The objective of this cohesive model is to take account of the failure between the mortar surrounding the tie and the mortar filling the holes in the tie (mortar balls). Experimentally, the cohesion between tie and mortar results mainly from the mortar passing through the tie. Fig. 12, illustrates the cross-section at tie level, with the mortar balls corresponding to the mortar in the holes.

A separation is observed between the mortar and the brick, as well as between the tie and the mortar. A separation of the mortar balls inside the tie is also visible, as shown in Fig. 12. This phenomenon is similar to that observed in the experimental tests, confirming a good agreement between the two approaches. Fig. 13 , compares the model with the tensile test, considering the 2 minimum and maximum configurations whereas Fig. 14, shows particularly the result obtained in the minimum force case scenario.

Table 4. Stifnesses between brick and mortar

Configuration	Stiffness coefficient (MPa/mm)	Shear strength (MPa)
Minimum	1.3	3.1
Maximum	2	7.5

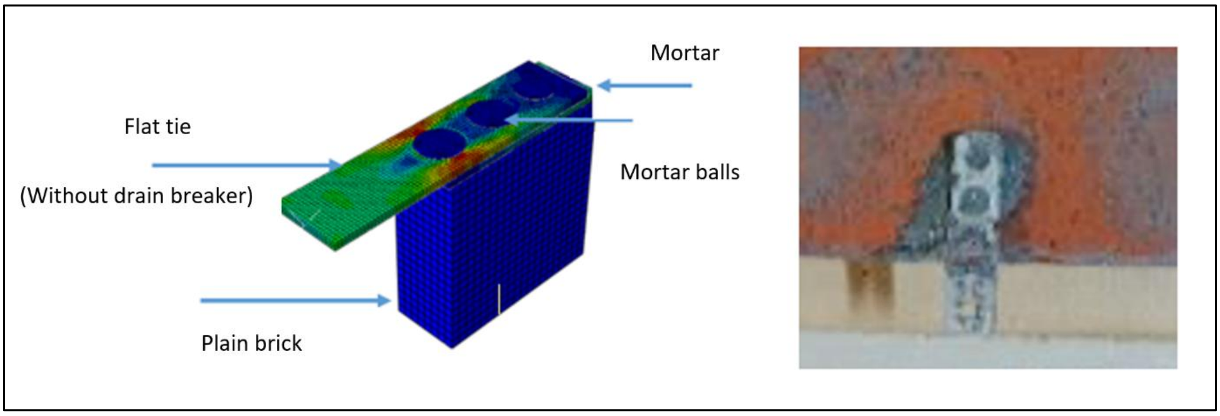

Fig. 12 . Traction test on the Brick-mortar-flat tie complex

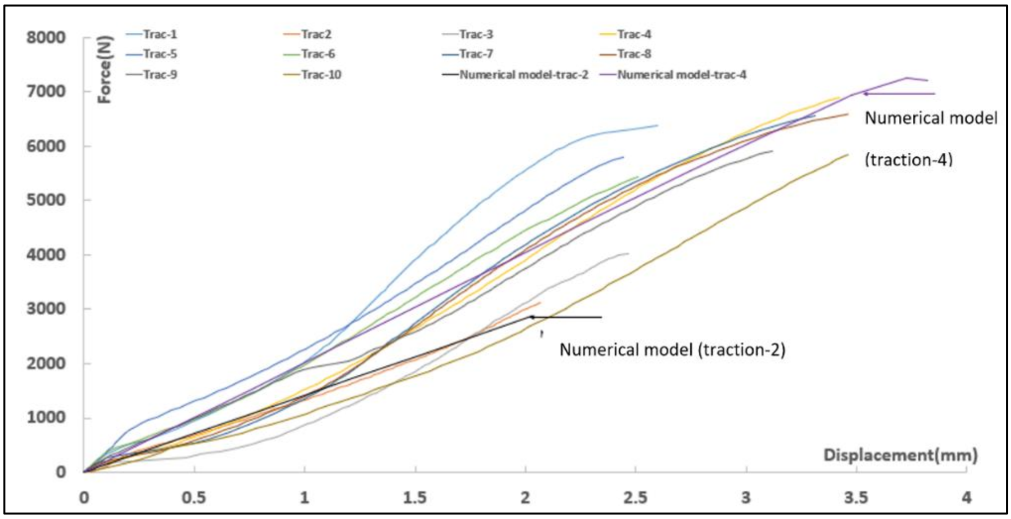

Fig. 13 . Superposition of numerical curves for tensile ytest of complete block(brick-mortar-flat

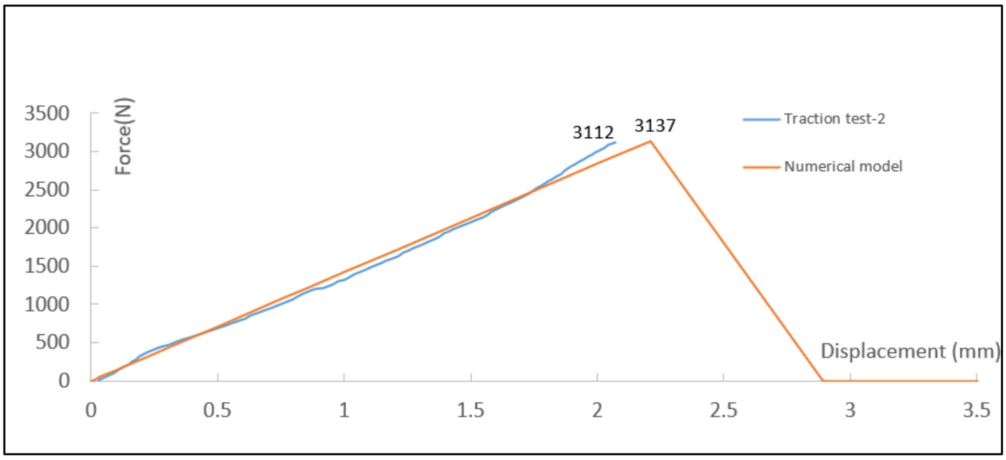

Fig. 14 . Comparison of the tensile test with the numerical model of the complete block(brick-mortar-flat tie) in the case of low forces.

4.2. Parametric analysis: Influence of the variability of the mortar Young modulus value

Additional 3-point bending tests were carried out at the Institut Pascal on mortar prismatic samples (40mm × 40mm × 160 mm) made from the same mix used to make the cavity walls and the small scale connections. The objective was to check the Young modulus value first used in the numerical model developed (based on the literature). It appeared that the mean value found for the Young's modulus is close to the one found in the literature reference : 3504 MPa versus 3779 MPa Table 5., However, an important variability was observed experimentally

Table 5., between testes samples. Therefore a parametric study was conducted to account for the impact of a variability of the mortar Young's modulus value on the behavior of the brick/mortar/tie complex.

Therefore, 3 additional traction tests on brick/mortar/tie connections were modeled by varying the Young modulus value of the mortar to account for its variability determined in experimental tests. The corresponding stress versus strain curves (true values) and damage evolution curves are given in Fig. 15., Fig. 16.

Results presented in the previous subsection were performed using a mortar Young modulus value derived from the literature. The objective of this subsection is to compare this case (referred to as the reference model) with simulated brick/mortar tie connections under traction with the three mortar laws presented in Fig. 16,. The purspose being to assess the sensitivity of the tensile behavior of the brick/mortar/tie connections for different mortar parameters.

Fig. 17, shows the force-elongation curve for the reference model (Young modulus value taken from the literature) and for 3 additional specimens whose mortar law has been modified based on experiments. Table 6, compares the results obtained with the overall calculations.

The mortar model derived from the literature is relatively close to the models derived from testing. Ultimately, the prediction error on maximum force and stiffness is less than 10%.

Table 5. Mortar Young Modulus variability

Function	Young modulus (MPa)	Variability %	Average (MPa)
Test specimen -1	2780	26.44	
Test specimen -2	4579	-21.17	3504
Test specimen -3	3154	15.54	
Reference model	3779		

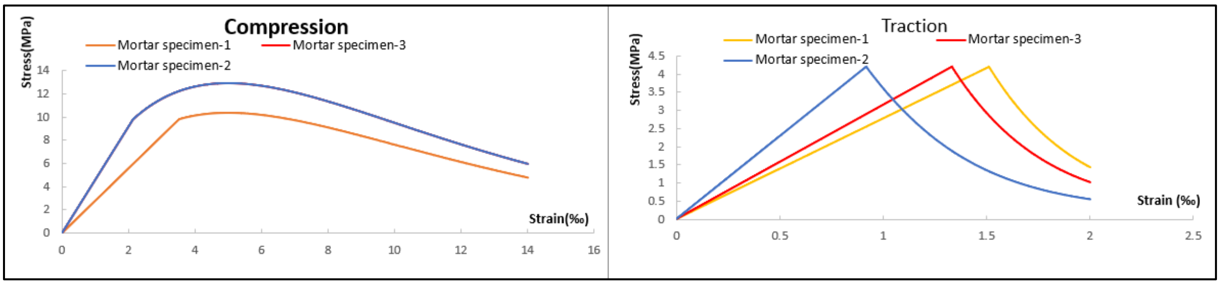

Fig. 15 .Stress versus strain evolutions used in the parametric study (to account for the variability of the mortar): Both in compression and traction

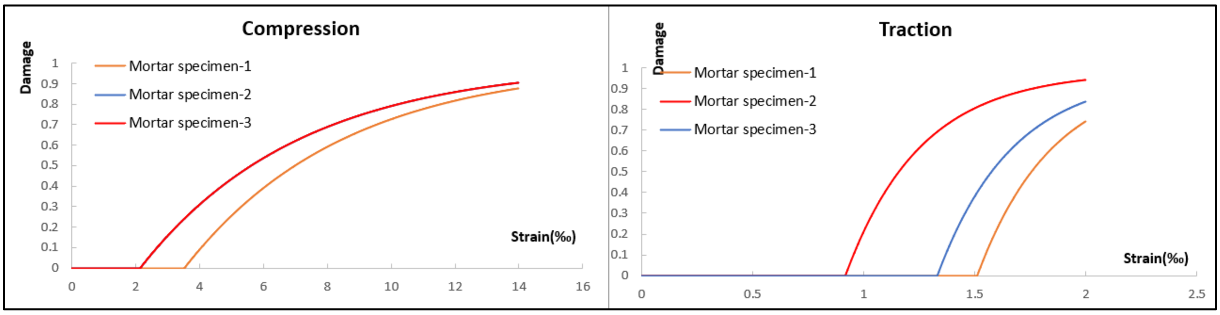

Fig. 16 . Damage evolutions used in the parametric study (to account for the variability of the mortar) : Both in compression and traction

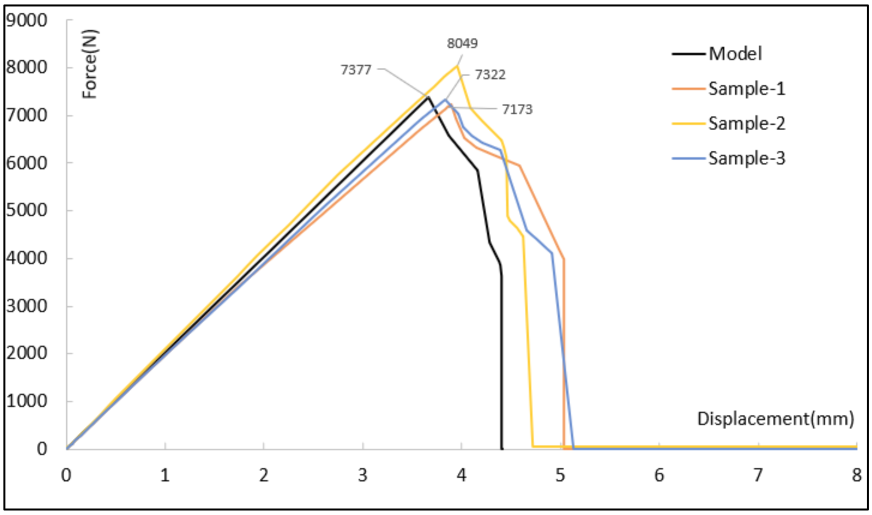

Fig. 17. Traction brick/mortar/tie model with variation of mortar parameters

Table 6. Comparison of the value of the maximum tensile forces and stiffnesses of the three specimens with the reference model

	Force Max(N)	Comparaison with reference model	Stiffnesse (N/mm)	Comparaison with reference model
Test piece-1	7131.94	-3,4%	1873.59	-2.96%
Test piece-2	8049	8,36%	2049.65	6.15%
Test piece-3	7322.45	-0.74%	1921.88	-0.46%
Reference model	7376.83		1930.81	

5. Conclusions

Finite element numerical modeling, developed on Abaqus, has enabled us to realistically represent the mechanical behavior of a flat tie connection system (for timber/brick cavity wall applications). The various components of the system - tie, mortar, brick - were modeled with behavior laws calibrated from experimental tests. Cohesive models were used to simulate the mortar/brick and mortar/tie bounds. Results show a good agreement between simulations and tests.

In particular, the use of cohesive models enabled us to account for failure mechanisms observed at mortar-tie and mortar-brick interfaces. This model has enabled parametric analyses to be carried out, objectifying the sensitivity of tie systems to various variable mortar characteristics. Such parametric study should be extended to account for other sources of variations, such as the presence of a drain breaker and the influence of the rail on the resistance of flat ties and their eccentricities. The developed model could also be used in order to simulate other load case scenarios that were experimentally tested (compression of the brick/mortar tie connection) to account for potential instability scenarios of the tie system (buckling, etc). Other tie types were experimentally tested as part of this project and their behaviour could also be modeled (flat tie with rail, zigzag tie) using the same approach. Models developed for the connection systems (made of brick/mortar and tie) can then be used in order to simulate the behavior of the complete cavity walls that were tested under different load scenarios.

Acknowledgement

Authors would like to thank MECD for the financial support. Many thanks for the Leviat company for providing the ties as well as Briqueterie du Nord and Wienerberger for providing bricks for the project.

References

AFNOR. (2008). *NF DTU 20.1 - Travaux de bâtiment – Ouvrages en maçonnerie de petits éléments - Parois et murs*. Paris, France : AFNOR.

AFNOR. (2019). *NF DTU 31.2 - Travaux de bâtiment - Construction de maisons et bâtiments à ossature en bois*. Paris, France : AFNOR.

AFNOR. (2020). *NF DTU 20.1 - Travaux de bâtiment – Ouvrages en maçonnerie de petits éléments - Parois et murs*. Paris, France : AFNOR.

Arslan, O., Messali, F., Smyrou, E., Bal, İ. E., & Rots, J. G. (2021). Mechanical modelling of the axial behaviour of traditional masonry wall metal tie connections in cavity walls. *Construction and Building Materials, 310*, 125205. https://doi.org/10.1016/j.conbuildmat.2021.125205

Arslan, O., Messali, F., Smyrou, E., Bal, İ. E., & Rots, J. G. (2020). *Numerical modelling of cavity wall metal ties*. In *17th World Conference on Earthquake Engineering*.
Comité Européen de Normalisation. (2000). *XP ENV 1993-2 - Eurocode 3: Calcul des structures en acier et document d'application nationale*. Bruxelles, Belgique : CEN.
CTTB. *Internal report* (2006) . Centre Technique des Tuiles et Briques.
Dalle, M. A. (2022). *Étude multi-échelle du comportement mécanique et au feu des murs en maçonnerie montés aux joints minces* (Thèse de doctorat, INSA de Rennes). Consulté le 28 mars 2025. Retrieved from https://theses.hal.science/tel-04420084
Masonry Standards Joint Committee (MSJC). (2008). *Building code requirements for masonry structures (TMS 402-08/ACI 530-08/ASCE 5-08)*. United States: MSJC.
Ortega, J., Mendes, N., & Vasconcelos, G. (2022). Numerical simulation of the tension–compression behavior of tie connections in brick masonry walls. *CivilEng, 3*(2), 441–455. https://doi.org/10.3390/civileng3020026

ICEARC'25
4th International Civil Engineering & Architecture Conference
17-19 May 2025, Trabzon, Türkiye

Design and analysis of unreinforced and reinforced masonry buildings according to TBEC-2018

Ali Bayburt*[1], Süleyman Adanur[2], Murat Günaydın[2], Ahmet C. Altunışık[2]

[1] *Karadeniz Technical University, Graduate School of Natural and Applied Sciences, Trabzon, Turkiye*
[2] *Karadeniz Technical University, Department of Civil Engineering, 61080 Trabzon, Turkiye*

Abstract. This study investigates the performance of a building model equipped with a tuned liquid damper through a series of shaking table tests under varying excitation directions. To assess directional effects, the model was rotated in 15-degree increments from 0° to 180°, while the excitation direction remained fixed. Acceleration and displacement time histories were recorded for each orientation to evaluate the damper's effectiveness. The results demonstrate that the TLD effectively reduced both accelerations and displacements of the structure. However, its efficiency declined progressively as the excitation angle increased from 0° to 90°.

Keywords: Different excitation direction; Shake table test; Tuned liquid damper; Vibration control

1. Introduction

Masonry structures are structures that constitute a significant portion of the building stock in our country. Although their construction has decreased in developed cities, their construction continues in rural areas and underdeveloped cities. Masonry structures are damaged due to poor ground conditions, construction activities that are not earthquake resistant, and similar reasons. These types of structures that do not have earthquake safety cause loss of life and property. Masonry structures are generally built by economically weak people in rural areas. The fact that masonry structures are seen as structures that do not require engineering services also has a great effect on the formation of earthquake-resistant building stock in our country. Therefore, earthquake-resistant masonry structure design and construction is of vital importance.

The walls of masonry structures are important structures used both as load-bearing and partition walls. Engineered and manufactured walls contribute to the behavior of the masonry building against earthquake forces. The material properties of the masonry units used contribute to the behavior of the structure. Modeling the structure under various loads and monitoring the behavior of the structure with engineering service are of vital importance.

1.1. Masonry building systems

1.1.1. Unreinforced masonry buildings

These are systems where the carrier systems are formed only with masonry units. Carrier walls are formed using masonry units and binding mortar. In the carrier systems of these systems, reinforcement or materials with high ductility are not used. Since the carrier systems exhibit brittle behavior rather than ductile behavior, they have less earthquake safety or resistance to earthquake effects compared to other systems. They can be made of natural stone, adobe, factory brick and concrete briquettes. It is the most common type of masonry structure in our country.

1.1.2. Reinforced masonry buildings

They are obtained by forming masonry walls with reinforcement. They are formed by knitting vertical and horizontal perforated or grooved brick or briquettes with reinforcement and binding mortar. Unreinforced masonry structures formed only from masonry units exhibit more brittle behavior compared to other systems. Supporting these types of structures with reinforcement allows the structures to exhibit more ductile behavior. Placing reinforcements both in the direction and horizontally provides earthquake resistance to the structure in both directions. These types of structures are not very common in our country.

*Corresponding author, E-mail: a.mrburt@gmail.com

https://doi.org/10.31462/icearc2025_ce_sme_875

golden light publishing

2. Code and standards

The first building earthquake regulation was published in Turkey in 1940 after the 1939 Erzincan earthquake. Later, in 1975, the Regulation on Buildings to be Constructed in Disaster Zones was published and entered into force. Since Turkey is an earthquake country and the regulations and standards were insufficient, an earthquake regulation was published again in 1998. In the light of scientific developments, these regulations have been updated and adapted to new techniques. They have been made compatible with international standards and regulations. Before TBEC-2018, many regulations and standards were used for the design of masonry structures in our country. Regulations such as the calculation and construction rules of masonry structures in TS 2510, the 1975 Regulation on Buildings to be Constructed in Disaster Zones, Eurocode-6 and later the 2007 Regulation on Buildings to be Constructed in Earthquake Zones (DBYBHY-2007) were used (Aldemir,2010).

2.1. Masonry building design principles according to TBEC-2018

2.1.1 Number of floors allowed

The number of floors allowed in masonry buildings in the Turkish Building Earthquake Code varies according to the load-bearing systems and earthquake design classes of the buildings (Fig. 1 and 2).

Masonry Building Systems			
Systems with High Ductility Level			
Reinforced Masonry Building	4	2	BYS ≥ 7
Reinforced Concrete Panel Buildings	4	2	BYS ≥ 7
Systems with Limited Ductility Level			
Confined Masonry Building	3	2	BYS = 8
Uneinforced Masonry Building	2.5	1.5	BYS = 8

Fig. 1. Structural System Behavior Coefficient for Building Structural Systems, Excess Strength Coefficient (TBEC,2018)

Building Height Class	Building Height Range Defined According to Building Height Classes and Earthquake Design Classes (m)		
	DTS = 1, 1a, 2, 2a	DTS = 3, 3a	DTS = 4, 4a
BYS = 1	$H_N > 70$	$H_N > 91$	$H_N > 105$
BYS = 2	$56 < H_N \leq 70$	$70 < H_N \leq 91$	$91 < H_N \leq 105$
BYS = 3	$42 < H_N \leq 56$	$56 < H_N \leq 70$	$56 < H_N \leq 91$
BYS = 4	$28 < H_N \leq 42$	$42 < H_N \leq 56$	
BYS = 5	$17.5 < H_N \leq 28$	$28 < H_N \leq 42$	
BYS = 6	$10.5 < H_N \leq 17.5$	$17.5 < H_N \leq 28$	
BYS = 7	$7 < H_N \leq 10.5$	$10.5 < H_N \leq 17.5$	
BYS = 8	$H_N \leq 7$	$H_N \leq 10.5$	

Fig. 2. Building Height Classes and Building Height Ranges Defined According to Earthquake Design Classes (TBEC,2018)

2.1.2. Wall height and thickness

Our regulation states that the effective wall thickness and effective height should be determined according to TS EN 1996-1-1 (Eurocode-6) standards. These standards specify the effective thickness to be taken according to whether the wall is single-layered or double-layered; supported or unsupported.

It is desired that the additional height of the wall be determined according to the same standard. It is desired that these walls be formed with elements that increase the rigidity of the wall, such as floors and horizontal joists, and their rigidity be increased. It is mentioned that the door and window openings and support walls in the wall affect the effective heights of the masonry walls.

2.1.3. Materials

According to the regulation, the void ratios of the masonry units are divided into two. Fig. 3 shows the grouping of the masonry units according to their hole ratios. In these voids, the places where the reinforcement will come and the areas to be filled with mortar will be excluded from the brick void ratio, provided that it does not exceed 15% (TBEC,2018).

Masonry unit type	Grup I	Grup II
Brick	$\alpha \leq \%35$	$\%35 < \alpha \leq \%50$
Concrete	$\alpha \leq \%35$	$\%35 < \alpha \leq \%50$

Fig. 2. Grouping of Masonry Units According to Hole Ratios (TBEC,2018)

The characteristic compressive strengths of masonry load-bearing walls, fk, can be learned from the tests to be carried out as well as from the tests to be carried out on the masonry units. The strengths obtained with the two different methods are shown in Fig. 4 of the code.

Unit	Mortar	Mortar Compressive Strength	Masonry Unit Compressive Strength					
			5	10	15	20	25	30
Grup I	General Purpose Mortar	M10-M20	3.4-4.2	5.5-6.8	7.3-9.0	8.9-11.0	10.4-12.9	11.9-14.6
		M2.5-M9	2.2-3.3	3.6-5.3	4.8-7.1	5.9-8.7	6.9-10.1	7.8-11.5
		M1-M2	1.7-2.1	2.8-3.4	3.7-4.5	4.5-5.5	5.2-6.4	5.9-7.3
Grup II ve Cut Stone		M10-M20	2.8-3.4	4.5-5.5	6.0-7.4	7.3-9.0	8.5-10.5	9.7-12.0
		M2.5-M9	1.8-2.7	3.0-4.4	3.9-5.8	4.8-7.1	5.6-8.3	6.4-9.4
		M1-M2	1.4-1.7	2.3-2.8	3.0-3.7	3.7-4.5	4.3-5.3	4.9-6.0
Brick (Grup I)	Thin Layer Mortar		2.9	5.3	7.5	9.6	11.6	13.5
Brick (Grup II)			2.2	3.5	4.7	5.7	6.7	7.6
Concrete (Grup I),			3.1	5.7	8.0	10.2	12.3	14.4
Concrete (Grup II)			2.6	4.6	6.5	8.3	10.0	11.7

Fig. 3. Characteristic Compressive Strength of Masonry Bearing Walls, fk (MPa) (TBEC,2018)

Characteristic shear strength of walls in masonry structures;

$$f_{vk} = f_{vk0} + 0.4\sigma_d \leq 0.10 f_b \tag{1}$$

It is desired to be calculated as follows. The characteristic compressive strength is desired to be selected as the smaller of the total of 40% of the vertical compressive stress calculated under the joint effect of the characteristic shear strength in the absence of axial stress and the vertical loads multiplied by the load coefficients and earthquake loads, or 10% of the standardized average compressive strength of the masonry unit.

In all masonry building systems given in the regulation, the concrete quality in reinforced concrete components is required to be at least C25. In the calculation of material properties of load-bearing walls, if possible, it is required to obtain it by performing experiments, if it is not possible to perform experiments, the elasticity modulus Eduv is requested to be taken empirically as 750fk and in walls made of reinforced panels as 450fk. Wall shear modulus, Gduv, is calculated by taking 40% of the elasticity modulus.

2.1.4. Design of structures for earthquake

Permitted building heights and building height classes in masonry buildings vary according to earthquake design classes. Permitted building heights, load-bearing system behavior coefficient and strength excess coefficient depending on the building load-bearing systems in the regulation are given in Table 3.3 and Table 4.1 in TBEC-2018.

2.1.5. Modeling techniques of masonry wall elements

According to the regulation, it is stated that the structure should be made according to the principles of Section 4 of the earthquake calculation. After the structure is modeled, the analysis of the structure is required to be made under the effects of vertical and horizontal loads. This analysis should be done using the finite element method or the equivalent bar method.

In the finite element method, the structure can be modeled with 3 different methods. These models are detailed micro modeling, simplified micro modeling or macro modeling (Fig. 5). Detailed micro modeling is used as the closest model to reality. In this method, all units that make up the element are modeled in detail. In simplified micro modeling, the model is made by considering the units that make up the element together. In macro modeling, calculations are made by considering the wall as a whole element.

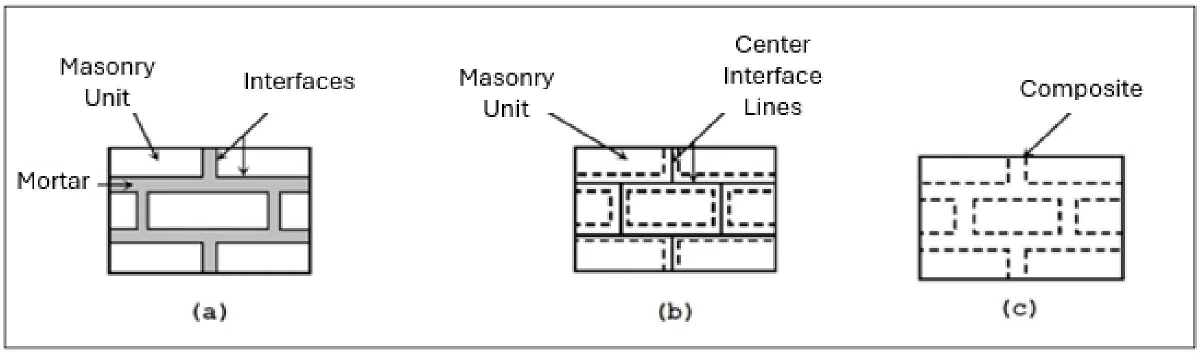

Fig. 5. (a) Detailed micro, (b) Simplified micro, (c) Macro modeling

In the equivalent bar method, the stiffness and elastic properties are applied using the wall's own material properties. The free height of the wall, H, is taken as the distance from the upper floor level to the lower floor level. If there is a joist, the joist lower level is used. Its length is used as the distance between the gaps. The stiffness is calculated with equation (2) assuming that both ends are fixed.

$$k_{duv} = \frac{1}{\left(\frac{H^3}{12E_{duv}I} + \frac{H}{1.2G_{duv}A}\right)} \tag{2}$$

2.1.6. Calculation according to bearing capacity method

According to TBDY-2018, the design force acting on masonry walls under axial load, Ned, is required not to be greater than the vertical load design strength, NRd. Here NRd;

$$N_{Rd} = \lambda A f_d \tag{3}$$

It is calculated by . Here fd is the masonry wall design strength. It is found by dividing the wall characteristic compressive strength by the material strength reduction capacity. The capacity reduction capacity, λ, varies according to the slenderness to slenderness ratio.

Design shear strength for unreinforced masonry walls, VRd;

$$V_{Rd} = f_{vd} t l_e \tag{4}$$

$$V_{Rd} = lt\frac{1.5f_{vd0}}{b}\sqrt{1 + \frac{N_{ed}}{1.5ltf_{vd0}}} \tag{5}$$

It is accepted as the smaller of the two equations calculated with. Here, in the calculation of shear strength, the part of the wall that works under pressure under the effect of bending, lc, is used. There is no calculation related to this length in TBDY-2018.

$$lc = 3\left(\frac{l}{2} - e\right) = 3\left(\frac{l}{2} - \frac{M_{ed}}{N_{ed}}\right) \tag{6}$$

It is calculated with . If the eccentricity is less than l/6, it is taken as l=lc, if it exceeds l/2, it is taken as lc=0. In this case, in-plane overturning occurs.

In order to take the shear reinforcement into account, the horizontal reinforcement must be continuous along the wall. The contribution of the shear reinforcement is VRd2;

$$V_{Rd2} = 0.9A_{sw}f_{yd} \tag{7}$$

$$V_{Rd1+}V_{Rd2} \geq V_{Ed} \tag{8}$$

$$(V_{Ed})/(tl) \leq 2.0MPa \tag{9}$$

Should be. VRd1 is the unreinforced wall design shear strength.

2.1.7. Geometric conditions

The architectural forms of masonry structures must be simple and planned. In masonry buildings consisting of complex wall arrangements, torsional effects are likely to occur under earthquake effects. Therefore, creating T, L, H shaped plans rather than complex plans increases the safety of the structure. In addition, the wall thicknesses and slenderness ratios limited in masonry structures are given in Fig. 6.

Masonry Type	$(t_{ef})_{min}$ *(mm)*	$(h_{ef}/t_{ef})_{max}$
Unreinforced masonry with natural or artifical cut stone	350	9
Unreinforced masonry with other masonry units	240	12
Confined masonry	240	15
Reinforced systems	240	15
Reinforced panel systems	200	15

Fig. 6. Geometric Conditions to be Applied to Masonry Walls Under Shear Force (TBEC,2018)

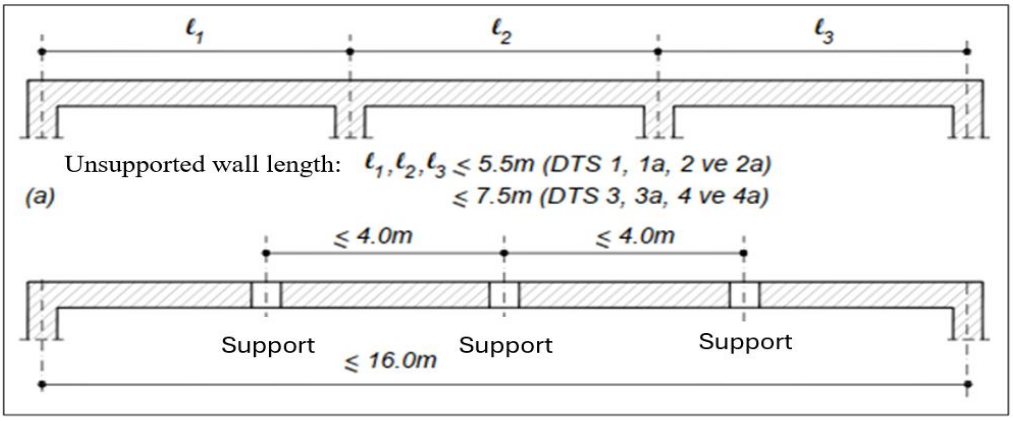

Fig. 7. Maximum Unsupported Length of Walls and Distance Between Vertical Beam (TBEC,2018)

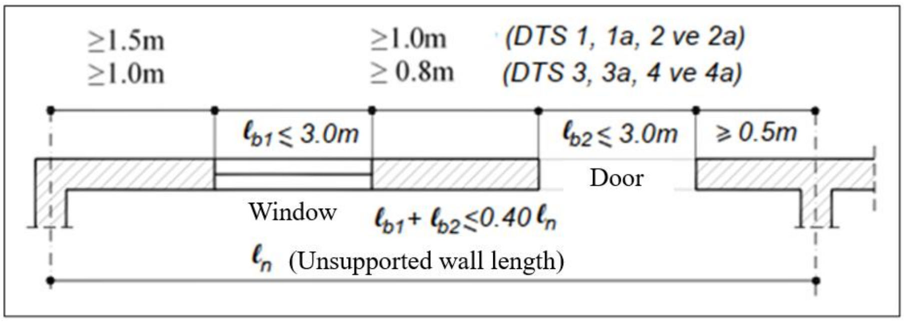

Fig. 8. Permitted Door and Window Openings (TBEC,2018)

3. Studies performed

The floor plan of the masonry building to be used in this study was created as in Fig. 9. These buildings to be used were designed as a lodging structure in Trabzon and Istanbul. These buildings are 2-storey and consist of 2 flats on each floor.

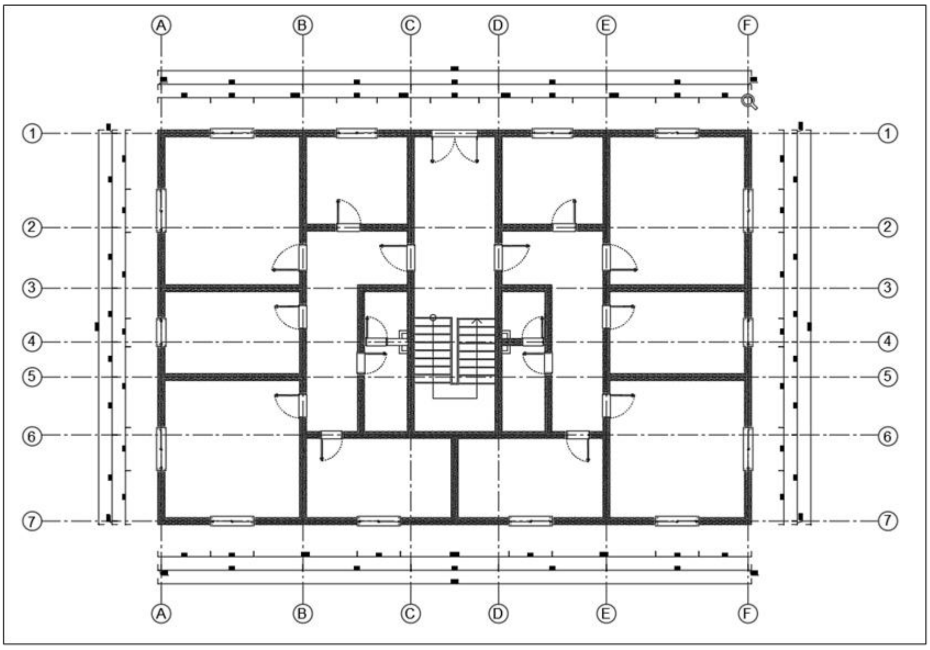

Fig. 9. Masonry Building Floor Plan

The materials to be used in masonry buildings were selected in accordance with the standards and the unit mechanical properties are given in Table 1.

Table 1. Mechanical Properties Of Masonry Building Unit

Definitions	Brick	Concrete
Brick space ratio	<%35	<%35
Group by vacation rate	Grup-1	Grup-1
Brick unit compressive strength (fb)	9 MPa	11 MPa
Mortar compressive strength (fm)	10 MPa	10 MPa
Masonry wall characteristic compressive strength (fk)	5.08 MPa	5.86 MPa
Wall initial shear strength (fvko)	0.3 MPa	0.2 MPa
Modulus of elasticity of walls (E=750*fk)	3810 MPa	4395 MPa
Shear modulus of walls (G=0.40*E)	1524 MPa	1758 MPa
Wall unit specific gravity (γ)	15 kN/m3	18 kN/m3
Masonry wall material coefficient (γ)	2.00	2.00

3.1. Earthquake parameters

In the first calculation, the location of the KTU Civil Engineering Department building in Trabzon was taken into account, and in the second calculation, the location of the YTU Civil Engineering Department building in Istanbul was taken into account. The necessary parameters for the earthquake load calculation taken from the Türkiye Earthquake Hazard Maps Interactive Web Application in these locations are given below (Fig.s 10-12).

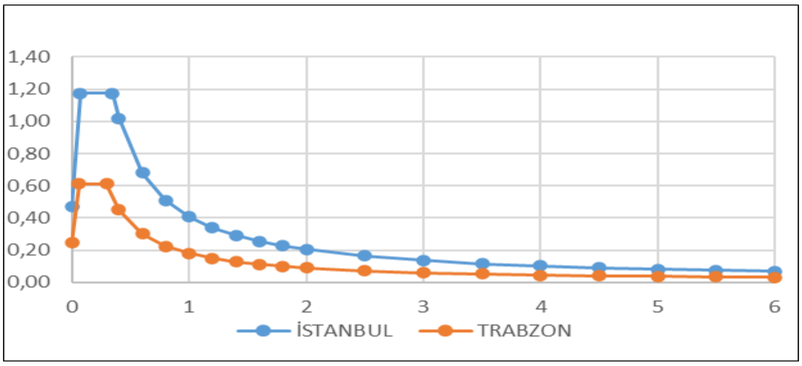

Fig. 10. Horizontal Elastic Design Spectra at Istanbul and Trabzon Locations

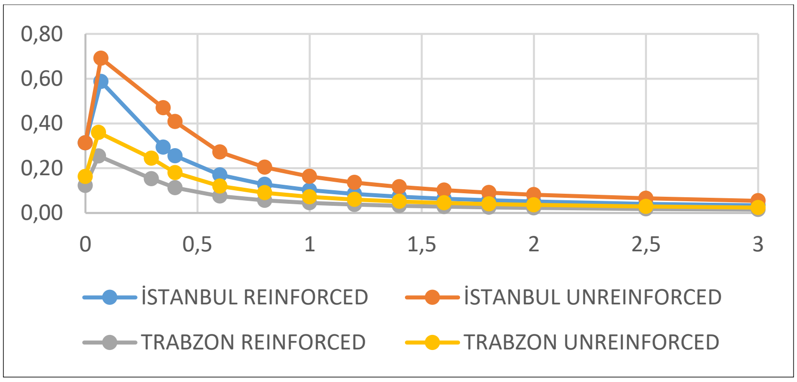

Fig. 11. Reduced Design Acceleration Spectra Used in Calculations

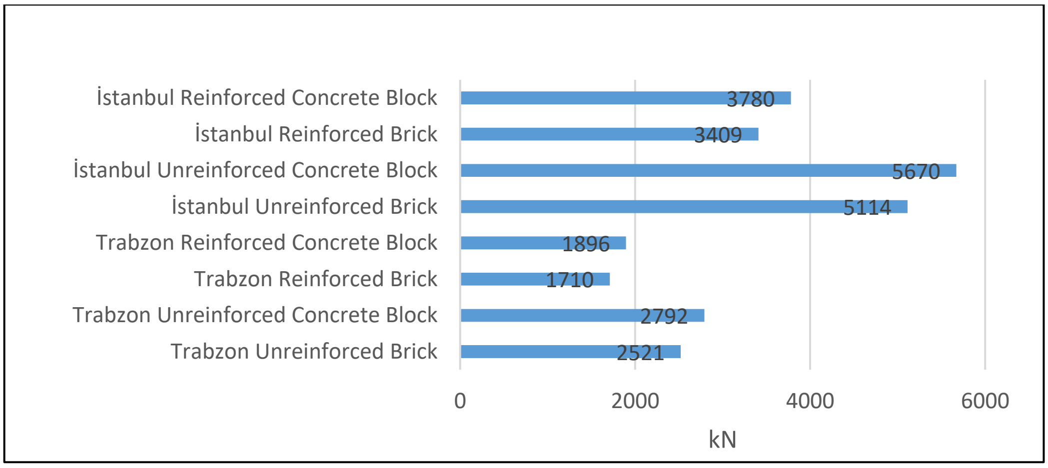

Fig. 12. Earthquake Loads on Buildings Based on Calculations

3.2. Axial capacity control

The axial capacity control of the walls was made according to the envelope function that gives the most unfavorable result of the 1.4G+1.6Q combination and the G+Q+0.2S+Ed(H)+0.3Ed(Z) combination given in the earthquake code. As a result of the calculations, it was determined that the axial capacity of the walls was sufficient (Tables 2 and 3).

Table 2. Trabzon Unreinforced Brick Wall Vertical Load Design Strength Calculation

Wall No	t (m)	L (m)	A (m^2)	hef (m)	tef (m)	(hef/tef)	λ	NRd=λ*A*fd (kN)
DX1	0.29	1.845	0.535	2.60	0.29	8.97	0.8	1087.22
DX2	0.29	3.115	0.903	2.60	0.29	8.97	0.8	1835.61
DX3	0.29	2.015	0.584	2.60	0.29	8.97	0.8	1187.40
DX4	0.29	2.015	0.584	2.60	0.29	8.97	0.8	1187.40
DX5	0.29	3.115	0.903	2.60	0.29	8.97	0.8	1835.61

Table 3. Trabzon Unreinforced Brick Wall Axial Capacity Control

Wall No	NRd=λ*A*fd (kN)	Nd (1.4G +1.6Q)	Nd (Env_Axial_GQE)	Nd (kN)	Situation
DX1	1254.16	148.53	182.93	182.93	OK
DX2	2117.45	254.82	296.39	296.39	OK
DX3	1369.72	168.65	227.28	227.28	OK
DX4	1369.72	168.81	226.61	226.61	OK
DX5	2117.45	255.02	295.07	295.07	OK

3.3. Shear capacity control

The shear capacity control of the walls was calculated by considering the shear force obtained from each of the combinations G+Q+0.2S+Ed(H)+0.3Ed(Z) and the excess strength coefficient D=1.5. In the calculations, lc, specified in TBEC-2018 article 11.4.3, was calculated depending on the ratio (eccentricity) between the length of the wall working under pressure, the in-plane bending moment (M3) acting on the walls and the axial force (P) (Tables 4 and 5). As a result of the calculations, it was determined that the shear capacities of the 1st and 2nd floor walls were sufficient for a thickness of 29 cm.

Table 4. İstanbul Unreinforced Brick Building Calculation Outputs

Wall No	Combination	P	V2	M3
		kN	kN	kN-m
DX1	G+Q+EX+0.3EY+0.3EZ	-35.13	5.01	65.75
DX1	G+Q+EX+0.3EY+0.3EZ	-167.39	-1.42	-84.57
DX1	G+Q+EX-0.3EY+0.3EZ	-35.13	5.01	65.75
DX1	G+Q+EX-0.3EY+0.3EZ	-167.39	-1.42	-84.57
DX1	G+Q-EX-0.3EY+0.3EZ	-35.13	5.01	65.75
DX1	G+Q-EX-0.3EY+0.3EZ	-167.39	-1.42	-84.57
DX1	G+Q-EX+0.3EY+0.3EZ	-35.13	5.01	65.75
DX1	G+Q-EX+0.3EY+0.3EZ	-167.39	-1.42	-84.57
DX1	G+Q+EY-0.3EX+0.3EZ	24.50	8.03	30.18
DX1	G+Q+EY-0.3EX+0.3EZ	-227.03	-4.43	-49.00
DX1	G+Q+EY+0.3EX+0.3EZ	24.50	8.03	30.18
DX1	G+Q+EY+0.3EX+0.3EZ	-227.03	-4.43	-49.00
DX1	G+Q-EY-0.3EX+0.3EZ	24.50	8.03	30.18
DX1	G+Q-EY-0.3EX+0.3EZ	-227.03	-4.43	-49.00
DX1	G+Q-EY+0.3EX+0.3EZ	24.50	8.03	30.18
DX1	G+Q-EY+0.3EX+0.3EZ	-227.03	-4.43	-49.00

Table 5. İstanbul Unreinforced Brick Building Shear Control

VRd1 (kN)	VRd2 (kN)	VRd (kN)	VEd (kN)	D*VEd (kN)	
D. İ. D.	97.10	D. İ. D.	5.01	7.52	NOT OK
87.93	132.08	87.93	1.42	2.13	OK
D. İ. D.	97.10	D. İ. D.	5.01	7.52	NOT OK
87.93	132.08	87.93	1.42	2.13	OK
D. İ. D.	97.10	D. İ. D.	5.01	7.52	NOT OK
87.93	132.08	87.93	1.42	2.13	OK
D. İ. D.	97.10	D. İ. D.	5.01	7.52	NOT OK

Table 5. Continued

87.93	132.08	87.93	1.42	2.13	OK
D. İ. D.	9.24	D. İ. D.	8.03	12.04	NOT OK
125,66	145.12	125.66	4.43	6.65	OK
D. İ. D.	9.24	D. İ. D.	8.03	12.04	NOT OK
125,66	145.12	125.66	4.43	6.65	OK
D. İ. D.	9.24	D. İ. D.	8.03	12.04	NOT OK
125,66	145.12	125.66	4.43	6.65	OK
D. İ. D.	9.24	D. İ. D.	8.03	12.04	NOT OK
125,66	145.12	125.66	4.43	6.65	OK

3.4. Reinforced masonry building reinforcement calculation

In reinforced masonry building design, in accordance with TBEC-2018 article 11.5.7, excessive reinforcements should be formed in masonry walls in a way that they are not less than 0.05% of the gross wall section and not exceed 60 cm intervals. These Extreme reinforcements to be placed should be made inside the Extreme joints or in suitable notches (Tables 6 and 7).

Table 64. İstanbul Reinforced Brick Building Shear Reinforcement Calculation

Wall No	t (m)	L (m)	A (m^2)	Asw(min) (mm^2)	Rebar Diameter (mm)	Number of Rebar	Placed Rebar Area (mm^2)	Rebar Spacing (mm)	VRd3 (kN)
DX1	0.29	1.85	0.535	267.53	10	6	471.24	42	154.80
DX2	0.29	3.12	0.903	451.68	10	6	471.24	42	154.80
DX3	0.29	2.02	0.584	292.18	10	6	471.24	42	154.80
DX4	0.29	2.02	0.584	292.18	10	6	471.24	42	154.80
DX5	0.29	3.12	0.903	451.68	10	6	471.24	42	154.80

Table 7. İstanbul Reinforced Brick Building Shear Control

VRd1 (kN)	VRd2 (kN)	VEd (kN)	(TBEC)11.8 Control	VRd (kN)	D*VEd (kN)	Result
95.84	109.64	23.12	Use	302.24	46.24	OK
105.18	121.87	38.09	Use	311.58	76.17	OK
95.84	109.64	23.12	Use	302.24	46.24	OK
105.18	121.87	38.09	Use	311.58	76.17	OK
95.84	109.64	23.12	Use	302.24	46.24	OK
105.18	121.87	38.09	Use	311.58	76.17	OK
95.84	109.64	23.12	Use	302.24	46.24	OK
105.18	121.87	38.09	Use	311.58	76.17	OK
91.64	103.68	6.80	Use	298.05	13.61	OK
109.38	126.98	21.77	Use	315.78	43.53	OK
91.64	103.68	6.80	Use	298.05	13.61	OK
109.38	126.98	21.77	Use	315.78	43.53	OK
91.64	103.68	6.80	Use	298.05	13.61	OK
109.38	126.98	21.77	Use	315.78	43.53	OK
91.64	103.68	6.80	Use	298.05	13.61	OK
109.38	126.98	21.77	Use	315.78	43.53	OK

3.5. Bending capacity control

In accordance with TBEC-2018 article 11.5.8, minimum vertical reinforcement was placed on the masonry walls, not less than 0.08% of the wall gross cross-sectional area. While placing the reinforcement, the vertical holes of the masonry wall unit were taken into consideration.

The bending calculations of reinforced masonry walls were made in the CSI Col v10.1 program using material models and vertical reinforcement placed in the sections. As a result of the calculations, it was determined that the bending capacities of all walls with the placed reinforcement were sufficient and that there were no pressure failures in the walls before the reinforcement yielded (Fig. 13).

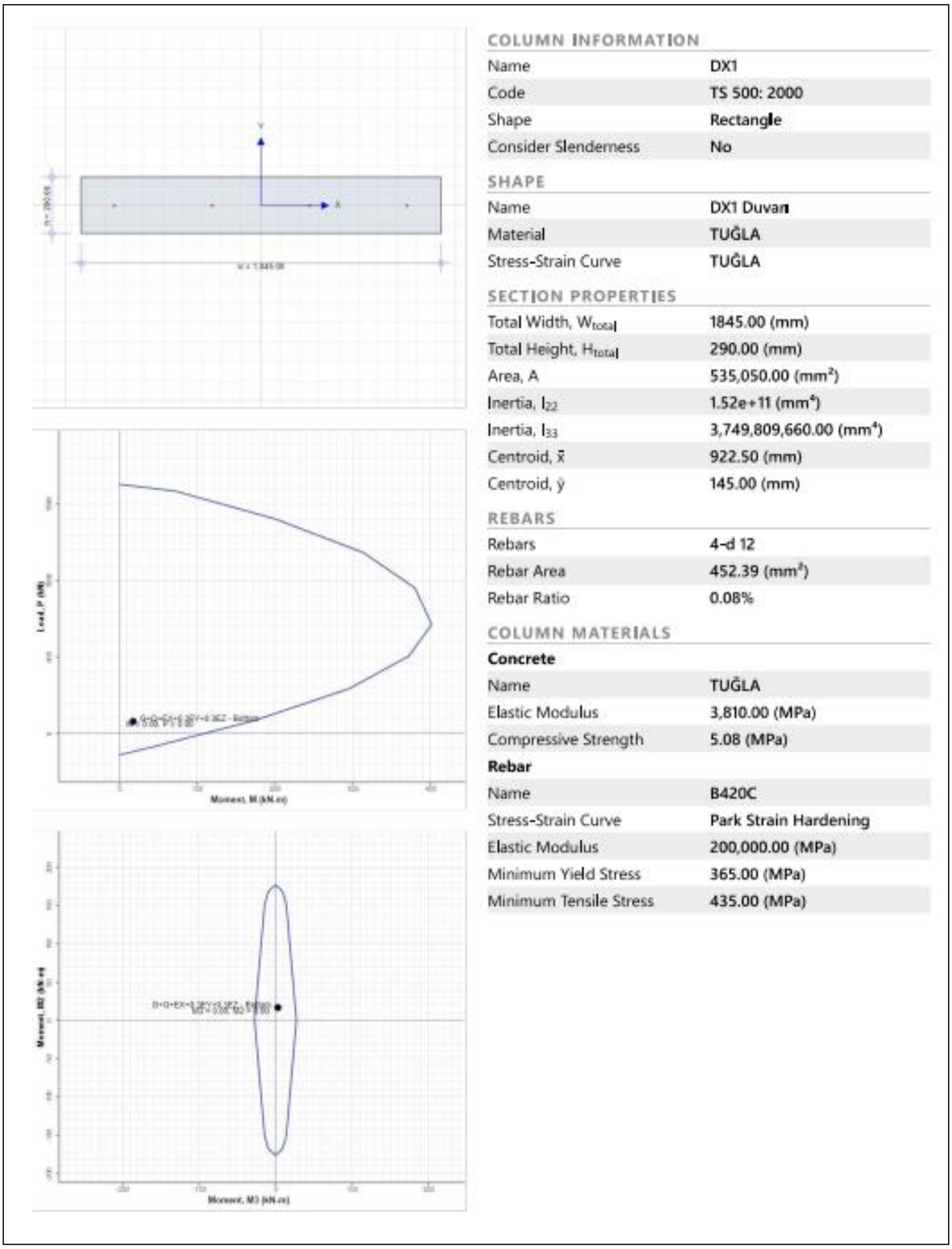

Fig. 13. Bending Capacity Control

4. Conclusions

In the continuation of the study, the Turkish Building Earthquake Code (TBEC-2018) and the codes used before this current code were examined. In addition to the Turkish codes and standards, the Eurocode-6 standard used in the design of masonry structures was also examined. The different types of buildings used in the study were created with the restrictions and standards in the light of these codes. Their designs and controls were made according to the Turkish Building Earthquake Code. These designs and controls were made with the help of various computer programs. ETABS and CSICol applications, which are widely used in building and section analyses, were used in the study.

In the study, buildings with the same architecture but different materials, locations and load-bearing systems were examined and the similarities and differences between them were revealed.

- Firstly, the earthquake parameters and dynamic properties to be used in calculations and designs were examined since they have different locations. In the light of these examinations, the reduced design spectrum acceleration graph obtained from the selected spectra is shown in Fig. 6. Here, it was observed that the acceleration spectra of the Istanbul location data were approximately twice as large as those of the Trabzon location data.

- The effects of the load-bearing system features, i.e. whether the building is unreinforced or reinforced, on the calculation and design of the structure have been examined. The design calculations of masonry buildings with different load-bearing systems in the regulation have been examined and the effects of these differences on the calculation and analysis of the buildings have been examined.
- Of the 8 buildings examined, 4 are made of factory bricks and the other 4 are made of concrete blocks. Material differences make the properties of the buildings different. It was observed that the concrete block building was a heavier building than the factory brick building and this weight was reflected in the base shear forces. The dynamic properties resulting from these material differences were also examined.
- The behavior of the walls under the effect of bending was investigated. Bending controls were performed with the help of auxiliary programs. In accordance with the regulation, it was shown that the reinforcement yielded before the compression failure in the sections. Mutual effect diagrams were created. The capacity ratios of the sections were given.

References

Aslan, A. (2016). Evaluation of Earthquake Performance of Suleymaniye Mosque Depending on Local Soil Conditions. YTU Institute of Science, Department of Civil Engineering, Master Thesis.

Atikoğlu, M. C. (2018). Materıals Propertıes Of Contemporary Solıd Brıcks And Theır Assessment In Reference To The Hıstorıc Brıcks. Mıddle East Technıcal Unıversıty, The Graduate School Of Natural And Applıed Scıences.

Bayülke, N. (2018). Masonry Structures (Stone and Brick). Ankara: TMMOB Chamber of Civil Engineers Ankara Branch.

Büyükgökmen, D. (2001). Reinforced Masonry Structure Design. ITU Institute of Science, Department of Civil Engineering, Master's Thesis.

Çambay, E. (2022). Investigation of the Effectiveness of Rotational Distributed Damage Model in Micro Modeling of Masonry Structures: Eindhoven Walls Example. Firat University, Institute of Science, Department of Civil Engineering.

Er, A. C. (2013). Traditional Blend Brick and Its Production. Journal of Professional Sciences, 61-70.

Erçolak, A. (2021). Shear Tensile Strength of Walls of Masonry Structures. Necmettin Erbakan University, Institute of Science, Department of Civil Engineering, Master's Thesis.

Kuran, F. (2020). An Evaluation on the Masonry Structures Section of the 2018 Turkish Building Earthquake Code. Turkish Journal of Earthquake Research, 47-60.

Kuruşçu, A. O. (2005). Analysis of Masonry Structures. Yıldız Technical University, Institute of Science, Department of Civil Engineering.

Presidency of Disaster and Emergency Management. (2019). *Türkiye earthquake hazard map*. Retrieved from https://tdth.afad.gov.tr/TDTH

Sallıo, N. (2005). Earthquake Inspection and Strengthening of Existing Masonry Structures. Pamukkale University, Institute of Science, Department of Civil Engineering.

Schellback, G. (1970). The İnfluence of Perforation On The Load Bearing Capacity of Hollow Brick Masonry Structures. Proceeding of SIBMAC.

TBDY. (2018). Türkiye Building Earthquake Code, Disaster and Emergency Management Presidency. Ankara.

ICEARC'25
4th International Civil Engineering & Architecture Conference
17-19 May 2025, Trabzon, Türkiye

Numerical simulation of progressive collapse behavior in self-centering precast concrete frames with infill walls

Sameer Alabsi[*1], Fezayil Sunca[2], Suhail Alabsi[1], Ahmet C. Altunışık[1,2]

[1] *Karadeniz Technical University, Department of Civil Engineering, 61080 Trabzon, Türkiye*
[2] *Karadeniz Technical University, Earthquake and Structural Health Monitoring Research Center, 61080 Trabzon, Türkiye*

Abstract. The behavior of progressive collapse in precast post-tensioned concrete frames was investigated through Finite Element Analysis (FEA) using ABAQUS software. The study assessed concrete damage behavior by employing the Concrete Damaged Plasticity (CDP) model available in ABAQUS. This study addressed the finite element analysis of precast concrete frames by making certain assumptions, such as a perfect bond between steel and concrete, and applying the CDP model to define concrete properties. Additionally, for modeling the infill wall, a simplified micro-modeling approach was used. A simplified numerical model was developed, showing strong consistency with both experimental results and detailed simulations. This approach offers a significant reduction in computational time while maintaining an acceptable level of accuracy.

Keywords: Self-centering precast concrete frames; Progressive collapse; Concrete damaged plasticity; Numerical simulation; Micro-modeling

1. Introduction

Public and private buildings of all types are vulnerable to extreme events such as hurricanes, tsunamis, earthquakes, explosions, vehicle impacts, fires, human errors, or even terrorist attacks. These events often result in localized structural damage, which can trigger a full collapse. This phenomenon is known as progressive collapse, a process where localized damage initiates a chain reaction of failures, ultimately leading to the collapse of the entire building or a significant portion of it. Progressive collapses are invariably associated with severe personal and material losses (Ellingwood 2006). The progressive collapse is defined in ASCE (2017) as the spread of an initial local failure from element to element, eventually resulting in the collapse of an entire structure or disproportionately large part of it. The key characteristic here is that the total damage at the end is not proportional to the original cause (Engineers 2017). It was coined following the collapse of Ronan Point tower in 1968 (Pearson and Delatte 2005). The catastrophe was sparked by a gas explosion on the 18th floor of a corner unit, which resulted in the rapid collapse of an external bearing wall that served as the primary structural component for the above flat. Research effort further intensified following the collapse of Alfred P. Murrah building in Oklahoma (1995) (Corley, Sr et al. 1998) due to explosion by a terrorist attack, and the collapse of the World Trade Center Towers (Bažant and Zhou, 2001). Shan and Li (2022) study uses finite element analysis to examine how infill walls affect the progressive collapse resistance of post-tensioned (PT) RC frames under column removal. Results show that while infill walls improve strength, they reduce re-centering capacity and alter failure modes. Factors like tendon arrangement, PT force, and masonry properties significantly influence performance. A design method is proposed for predicting collapse resistance. Meng et. al (2021) analyzes six SF-SPSW substructures under different column failure scenarios to assess progressive collapse resistance. Using a simplified method with Cartesian connectors, it identifies key resistance mechanisms and shows that collapse can be prevented post-failure. Stiffened triangular steel plates enhance capacity, with their design parameters examined. Sasani (2008) evaluates the Hotel San Diego's response to the removal of two exterior columns. Using Finite and Applied Element Methods, it finds the structure resisted collapse with minimal displacement (6.4 mm). Load redistribution occurred mainly through 3D Vierendeel action aided by infill walls. Brittle failure modes and the impact of added loads and wall absence are also analyzed. Li et. al (2016) examines how infill walls affect the progressive collapse of RC frames. Tests on a scaled frame show that infill walls act as compressive struts, increasing strength and stiffness but reducing beam ductility and altering failure modes. Finite element analysis confirms key influencing factors. Brodsky and Yankelevsky (2017) investigates how masonry infill walls help prevent progressive collapse

[*] Corresponding author, E-mail: samkh5537@gmail.com

https://doi.org/10.31462/icearc2025_ce_sme_912

in RC frames during extreme events. Lab tests on half-scale infilled frames without a column show that infill walls significantly boost vertical load resistance—by 280% on average. Masonry type, shear connectors, and improved reinforcement details strongly influence performance and failure modes. Tsai and Huangstudy (2009) investigate models brick-infill panels as compression struts to assess their impact on progressive collapse in an earthquake-resistant RC building. Finite element analysis shows that infill location affects performance—panels near shorter spans reduce beam-end DCR, but may increase axial tension in beams spanning the removed column.

This study aims to contribute a modeling framework for re-centering precast frames, both with and without connections, by introducing several simplifying assumptions to reduce computational demands. The proposed approach is intended to save time and cost when analyzing such systems under column removal scenarios.

2. Proposed numerical model

The modeled frame is based on the experiment conducted by Li et al. (2023). A six-story self-centering precast concrete (PC) frame building was designed based on Chinese codes to study its resistance to progressive collapse. A scaled-down two-story model was tested with three frame types (SCBF, SCIF, SCIF-A), differing mainly in beam span. PC components were preassembled with unbonded prestressed strands and protected by steel jackets and plates. Infill walls used AAC blocks, adjusted to fit around steel joints and bonded with mortar. Two specimens were modeled Specimen SCBF and Specimen SCIF were the two specimens have the same dimensions but Specimen SCBF has no infill wall, while Specimen SCIF consider the effect of infill wall see Fig. 1.

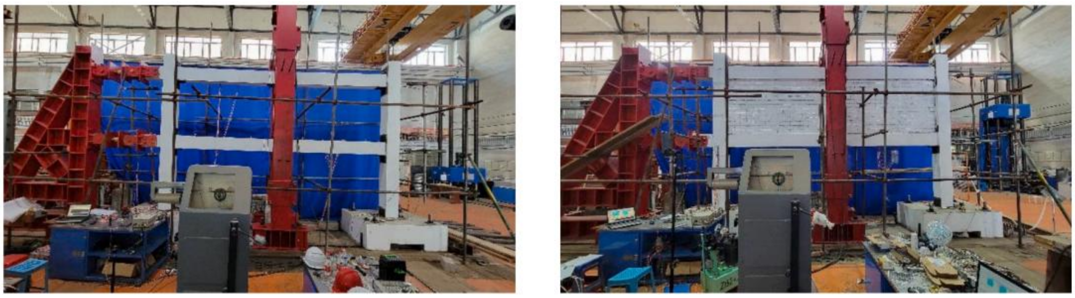

(a) (b)

Fig. 1. Specimens adopted in this study (a) SCBF (b) SCIF (Li, Wang et al. 2023)

The system consists of five main components: precast concrete, reinforcing steel, prestressing strands, steel angles, and bolts.

Fig. 2 show the detailed model of spaciement SCBF. The dimensions of the steel angles are shown in Fig. 4. Two types of steel angles were used: one for connecting the beam to the column, and another for connecting the column to the foundation. The clear concrete cover of all PC members was 20 mm. The infill walls were composed of autoclaved aerated concrete (AAC) blocks with dimension of 285 mm × 90 mm × 90 mm. Table 1 summarize the Properties of modeled specimens. Fig. 6. show dimensions and reinforcement details of specimen SCIF.

Table 1. Properties of test specimens

Test ID	Beam			Column			Infill wall
	Section size (mm)	Net span (mm)	Diameter of strands (mm)	Section size (mm)	Net span (mm)	Diameter of strands (mm)	
SCBF	300×200	2400	2×15.2	300×200	3750	2×15.2	None
SCIF	300×200	2400	2×15.2	300×200	3750	2×15.2	Infilled

All the materials were clearly specified in the experiment) Li et al. (2023). As indicated in the test, the effective prestress of the steel strands used to connect beams to columns, as well as columns to foundations, was $0.65f_{ptk}$ and $0.7f_{ptk}$, respectively. Here, f_{ptk} represents the ultimate strength of the steel strands.

For modeling a detailed configuration (Fig. 3), it is important to account for the interaction among various elements. This can only be achieved by using 3D solid parts and introducing holes in the column and beam elements, as shown in (a) (b)

Fig. 6(a). A frictionless interaction was assumed between the concrete elements (beams and columns) and the strands, as illustrated in (a) (b)

Fig. 6(b). Regarding friction coefficients, a complete tie was used to represent the interaction between bolts and concrete, and a coefficient of 0.75 was adopted for the friction between concrete elements, determined through a sensitivity test.

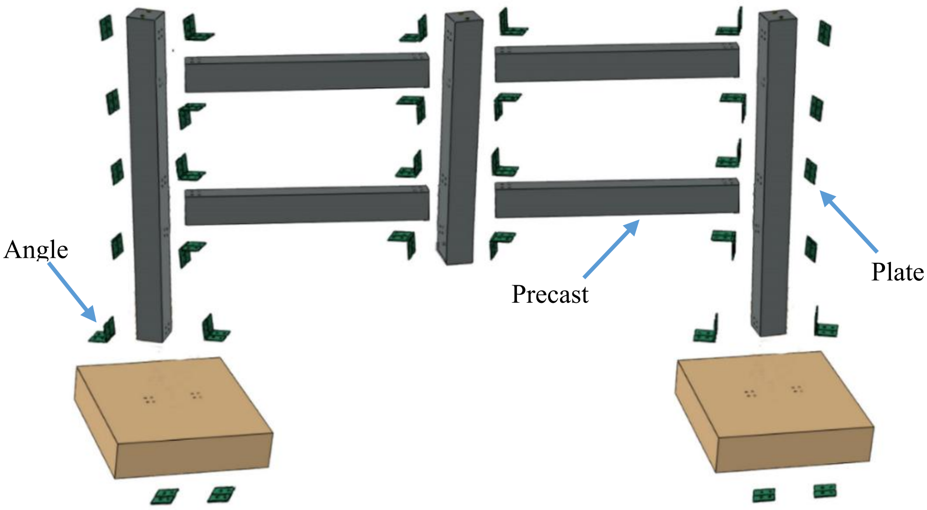

Fig. 2. Precast concrete assembly

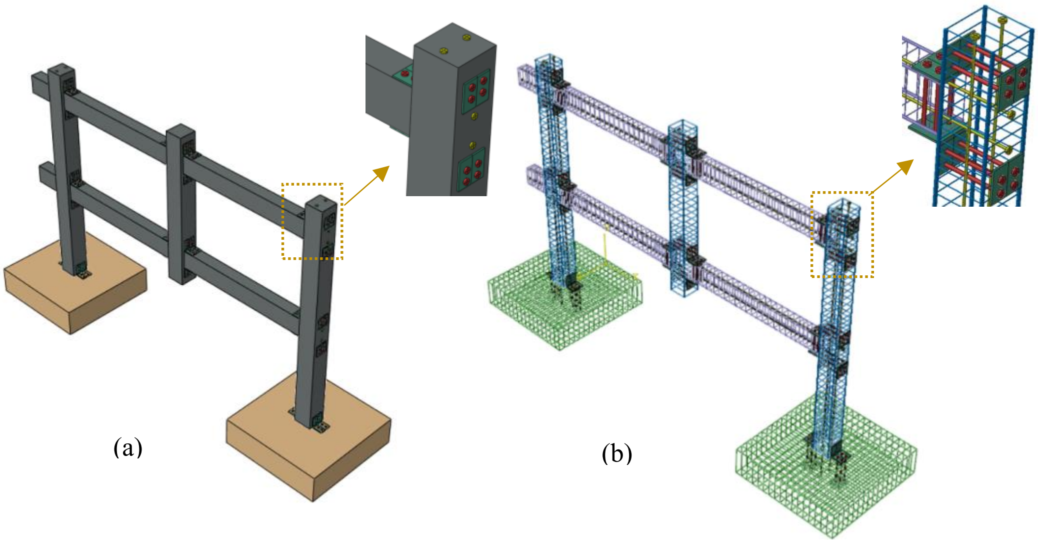

Fig. 3. Detailed modeling (a) Concrete details (b) Steel details

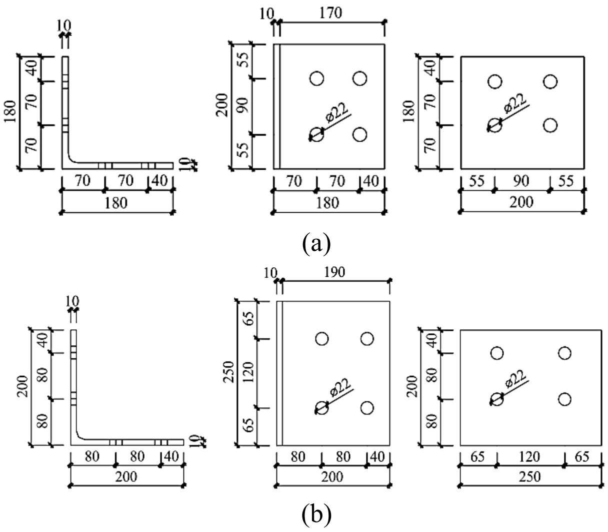

Fig. 4. Dimensions of steel angles (a) steel angle for beam-column joint (b) steel angle for column-foundation join (Unite: mm) (Li, Wang et al. 2023)

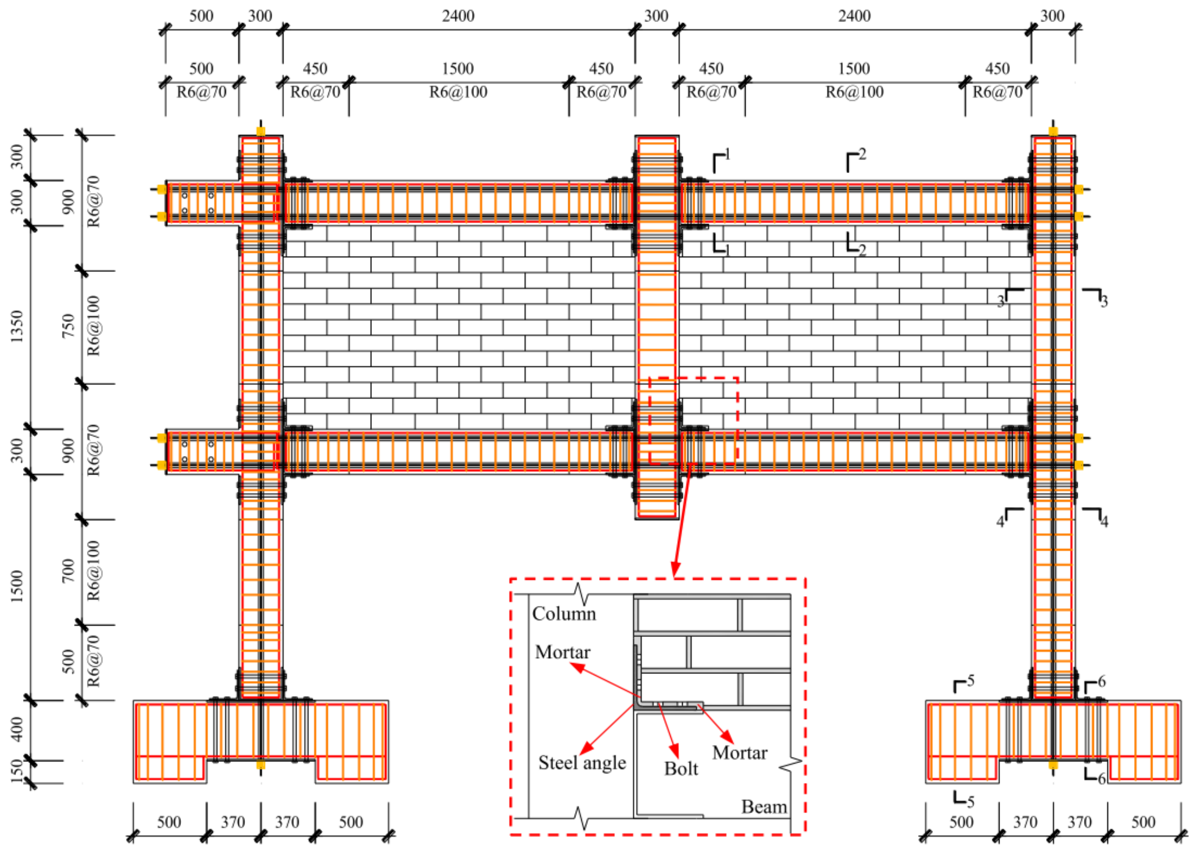

(a)

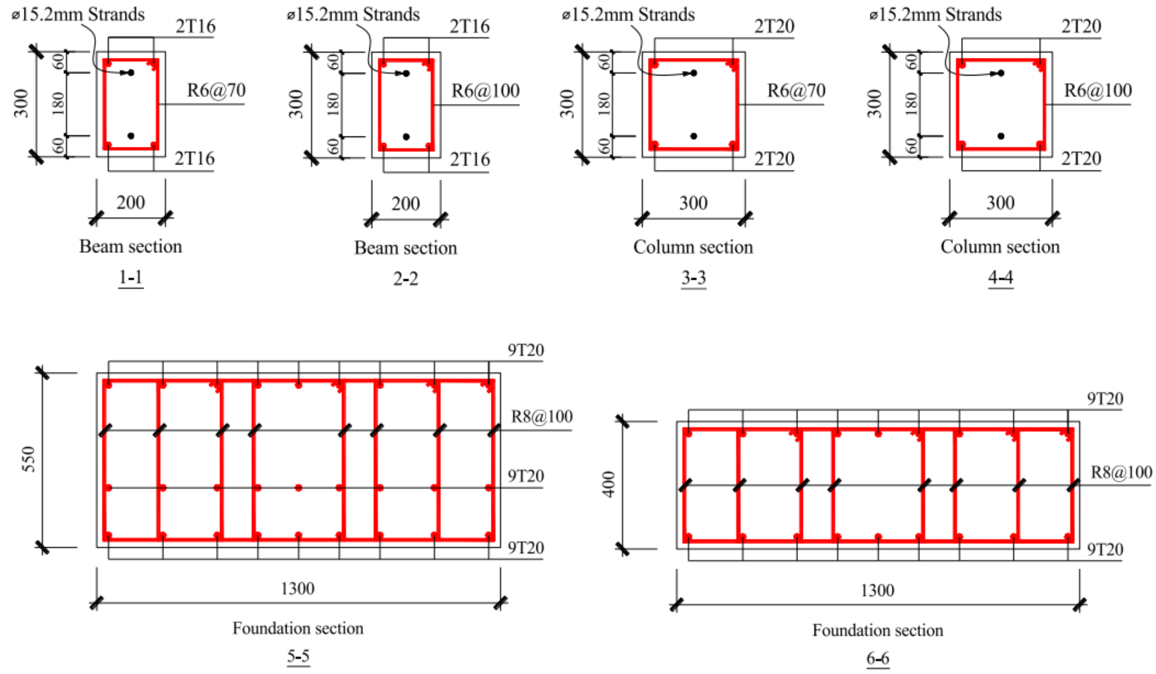

(b)

Fig. 5. Dimensions and reinforcement details of specimen SCIF (a) Speciment SCIF (Unit: mm) (b) Cross sectional of PC members (mm) (Wang, Li et al. 2023)

However, creating a detailed model with numerous small holes requires a finer mesh, which significantly increases computational time. Since accurate analysis depends on mesh refinement, mesh size becomes a critical factor. To address this, simplifications were introduced to reduce computational time. Two models were proposed to streamline the analysis:

The first model included the fixation of the footing without modeling its detailed geometry. Since the experiment did not indicate any separation between the steel components and the bolts, the bolts were omitted for simplification.

The second, more simplified model represented the strand as a wire, with the assumption that the interaction between the strand and concrete was fully embedded. While prestress was included in this model, it assumes the strand is bonded to the concrete, thereby eliminating the re-centering effect. However, this system has proven sufficiently accurate due to the symmetry in the frame's loads and dimensions.

This aforementioned modification had a significant impact on mesh sizing (see Fig. 7). Larger mesh sizes contribute to improved time step stability, thereby reducing computational time. Table 2 presents the computational parameters for the different modeling techniques. For additional simplification, a complete tie between the concrete elements was adopted, as no splitting between them was observed. Because of the geometry complexity of the detailed model an optimazied tetrahedral mesh was employed resulting in a 5mm mesh, in contrast to the other two models where a hexahedral mesh utilized.

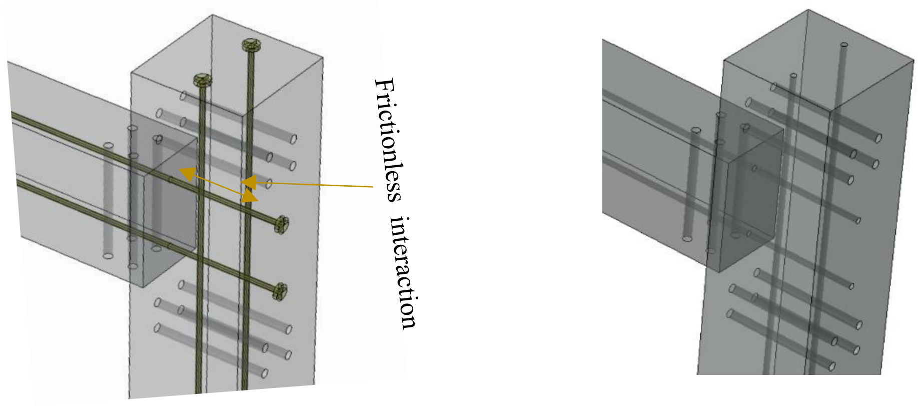

(a) (b)

Fig. 6. Details of connection (a) friction between strand and concrete (b) holes details

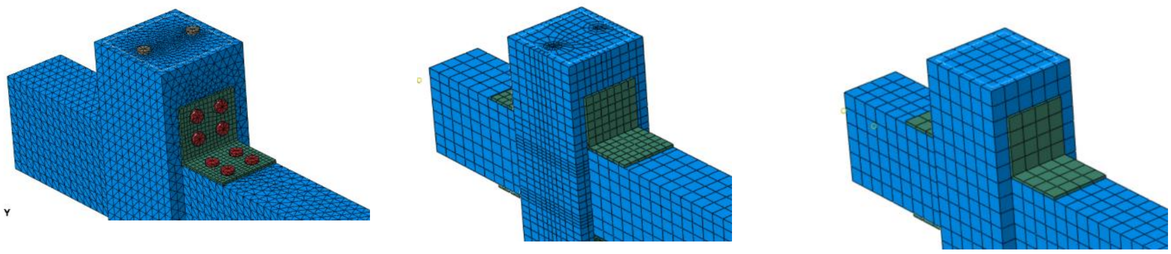

(a) (b) (c)

Fig. 7. Mesh technique (a) tet mesh (b) hex with partitions (c) hex

3. Concrete constitutive model

Based on the experimental data, the compressive strength of the precast concrete was reported as 32.8 MPa. However, the test did not provide the necessary Concrete Damage Plasticity (CDP) parameters. Therefore, the Kent and Park parabolic constitutive model (see Fig. 5) was adopted to estimate the damage parameters under both compression and tension, including crack and inelastic strain values (Hafezolghorani, Hejazi et al. 2017). All the derived parameters are summarized in Table 3. Typically, the uniaxial compressive behavior of concrete can be characterized through experimental testing or by employing well-established constitutive models, such as those proposed by Kent and Park (1971). This model assumes a simplified parabolic curve and sets the ultimate strain consistently at 0.002 for ease of calculations Park and Paulay (1991).

Table 2. Computational parameters for the different modeling techniques

Model technic	Minimum mesh size	Stable Time (s)	Approximate Computational Time by 12 cores for 40s analysis
Detailed Model	5 mm	1.24 e-8	750 hours
Simplified unbonded Model	10 mm	9.99 e-7	120 hours
Simplified bonded Model	50 mm	1.4 e-4	40 hours

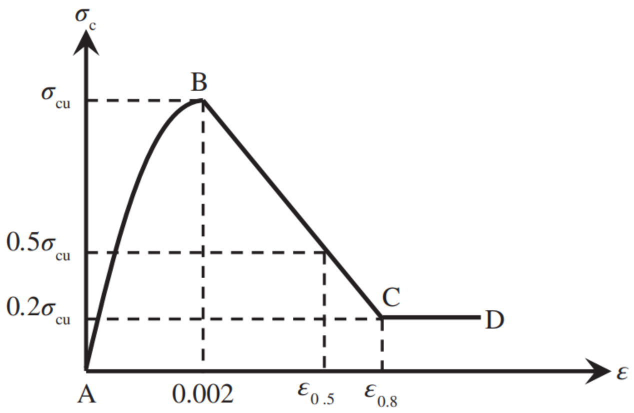

Fig. 8. Kent and Park parabolic constitutive model (Kent and Park 1971)

CDP parameters were adopted according to Mahdi (2023)'s study uses Abaqus to analyze how five CDP parameters affect UHPC beam behavior. The parameters used in the analysis are presented in Table 3.

Table 3. Concrete properties

Elastic Properties of concrete				
Elastic Modulud Ec (Mpa)			Poisson's Ratio	
4700 √fc' =26917.5			0.2	
Compression behavior in concrete			Compression damage in concrete	
Yield Stress (Mpa)		Inelastic Stain	Damage Parameter	Inelastic Stain
19.3		0	0	0
21.81		3.20577E-05	0	3.20577E-05
24.31		7.93412E-05	0	7.93412E-05
26.81		0.000149309	0	0.000149309
32.8		0.000781462	0	0.000781462
27.88		0.001964243	0.15	0.001964243
Tension behavior in concrete			Tension damage in concrete	
Yield Stress (Mpa)		Cracking Stain	Damage Parameter	Cracking Stain
3.28		0	0	0
2.19		0.00024371	0.3333	0.00024371
1.23		0.00059404	0.625	0.00059404
0.55		0.00115761	0.8333	0.00115761
		Concrete Damage Plasticity (CDP)		
Dilation angle,ψ	Eccentricity,e	fb0/fc0	K	Viscosity parameter,μ
38	0.1	1.156	0.667	0.261

4. Infill wall material modeling

In the SCIF specimen experiment, autoclaved aerated concrete (AAC) blocks and mortar with relatively low strength were used. A simplified micro-modeling approach (see Fig. 9) was employed to represent the material behavior at the microstructural level (Abdulla, Cunningham et al. 2017). This technique captures the essential mechanical characteristics of the materials without the computational cost of modeling each individual component in high detail. To accurately simulate the behavior of the infill wall under compression, it is necessary to determine specific mechanical properties. Given that the blocks are composed of AAC, they are well-suited for simulation using the Concrete Damage Plasticity (CDP) model.

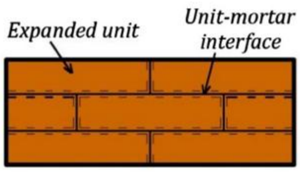

Fig. 9. Simplified micro-model (Lourenço 1997)

4.1. Estimation of interface cohesive parameters

Assuming that the contact stress is distributed uniformly on both the (AAC) blocks and mortar, the equivalent stiffness constants KN and KS are expressed as a function of the elastic and shear moduli of mortar and (AAC) blocks as shown in Eq. (1), and (2) respectively (Lourenço 1997).

$$K_N = \frac{E_b\, E_m}{h_m(E_b - E_m)} \tag{1}$$

$$K_S = \frac{G_b\, G_m}{h_m(G_b - G_m)} \tag{2}$$

Here, h_m represents the mortar thickness, while E_b, G_b, E_m, and G_m denote the elastic and shear moduli of (AAC) blocks and mortar, respectively. The shear stiffness, K_S, is approximately 0.43 times the normal stiffness, K_N, specified as $K_S = 0.43K_N$. This relationship is established through $G_{b,m} = E_{b,m}/2(1 + \nu)$, where ν represents the Poisson's ratios of both (AAC) blocks and mortar, typically assumed to be 0.16. The suggested relationship between the elastic moduli of (AAC) blocks and mortar and their corresponding strength is shown in Eq. (3).

$$E_b = 4467 f_1^{0.22}; \quad E_m = 1057 \tag{3}$$

Where f_1 and f_2 represent the average compressive strengths of the brick and mortar, respectively. According to the experimental results, the average compressive strength of the AAC block and mortar was measured to be 3.96 MPa and 3.44 MPa, respectively. When the compressive strengths of the brick and mortar are nearly equal or very close in value, it may lead to unrealistic estimations of the contact stiffness K_N. To address this issue, the value of the interface stiffness is adjusted as described in Eq. (4).

$$K_N = min\left(\frac{E_b\, E_m}{h_m|E_b - E_m|}, \frac{E_m}{0.5 \times h_m}\right); \qquad K_S = 0.43K_N \tag{4}$$

It indicates that the tensile and shear strength are only related to the strength of mortar, and the shear strength is slightly smaller than the tensile strength. Previous research (Karimi Ghaleh Jough and Golhashem 2020) recommended defining the mean shear strength in finite element (FE) analysis as 1.6 or 1.4 times the mean axial tensile strength i.e., $f_{v,m} = 1.6(\text{or}1.4) \times f_{t,m}$. At present, Eq. (5) is used to determine the peak tensile and shear stresses (Zhou, 2019).

$$T = 0.141\sqrt{f_2}; \qquad S = 2 \times 0.125\sqrt{f_2} \tag{5}$$

All parameters were calculated and summarized in Table 4.

Table 4. Parameters of cohesive contact

Eb (MPa)	Em (MPa)	KS (MPa/ mm)	KN (MPa/ mm)	T (MPa)	S (MPa)
6046.6	2983.9	58910.274	25331.42	0.261	0.464

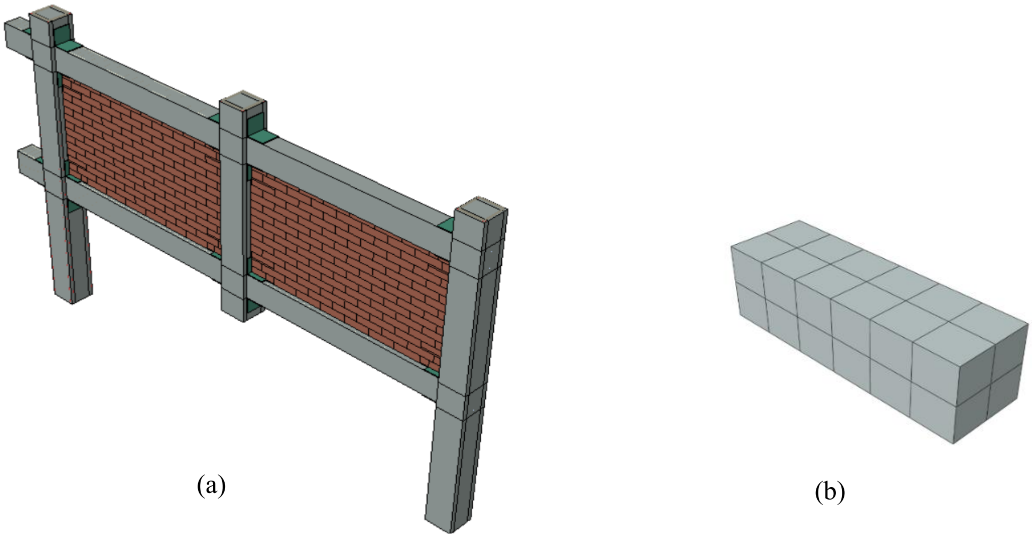

(a) (b)

Fig. 10. Simplified finite element modeling of specimenet SCIF (a) Assemblage Geometry (b) Blocks mesh

4.2. Calibration of Mode I and Mode II ultimate fracture energy release rates of the interface
Determining Mode I and Mode II ultimate fracture energy release rates at an interface, i.e., G_{IC} and G_{IIC} typically involves a combination of experimental testing and numerical analysis. It is important to highlight that a definitive and standardized approach for determining fracture energy has yet to be established. Nonetheless, experimental findings consistently demonstrate that the ultimate fracture energy release rate tends to increase with the enhancement of mortar strength (Van der Pluijm 1999).

Determination methods are calibrated and validated using tension and compression-shear tests on brick-mortar-brick assemblies by (Van der Pluijm 1992), Van der Pluijm (1999). A finite element (FE) model with a 5 mm mesh size was developed. Interface stiffness (K_N and K_S) were computed from existing equations, while peak tensile and shear stresses were derived from test data (Van der Pluijm 1992, Van der Pluijm 1999). G_{IC} and G_{IIC} were then estimated by trial and error. The static and dynamic friction coefficients were taken as 0.7 and 0.6, respectively, following Chinese Code for Design of Masonry Structures (GB 50003- 2011). These parameters are essential for characterizing the fracture behavior of materials and interfaces.

5. Results and comparison

The simplified unbonded model was implemented, and its results showed strong agreement with both the experimental data and the detailed numerical simulations reported by Wang, Li et al. (2023). This was evident in the comparison of the vertical displacement-vertical force diagram for the SCBF and SCIF specimens (Fig. 11). It observed that the initial stiffness predicted by the FE models was slightly higher in some parts and lower in other parts than that obtained from the experimental results. In the case of specimen SCIF, a sudden reduction in load-bearing capacity was previously noted, primarily due to a transverse crack that developed in the left infill wall. This behavior is likely attributed to a minor installation imperfection, which may have caused slight out-of-plane movement of the central column during testing. Such physical irregularities, however, are not represented in the finite element (FE) model which also agreed with Wang, Li et al. (2023)'s simulation. As a result, the FE simulation of specimen SCIF did not exhibit any notable drop in structural resistance. The inclusion of the infill wall significantly enhanced the structural strength of the SCIF specimen, increasing its load-bearing capacity by approximately 90 kN. Additionally, the presence of the wall effectively prevented excessive vertical displacement, contributing to the overall stability of the structure. Moreover, the wall played a crucial role in extending the capacity of the compression arch action. This is evidenced by the sustained vertical force throughout the loading process, in contrast to the SCIF specimen without the wall, which exhibited a drop in vertical force around a displacement of 100 cm, which is an indicator of concrete cracking.

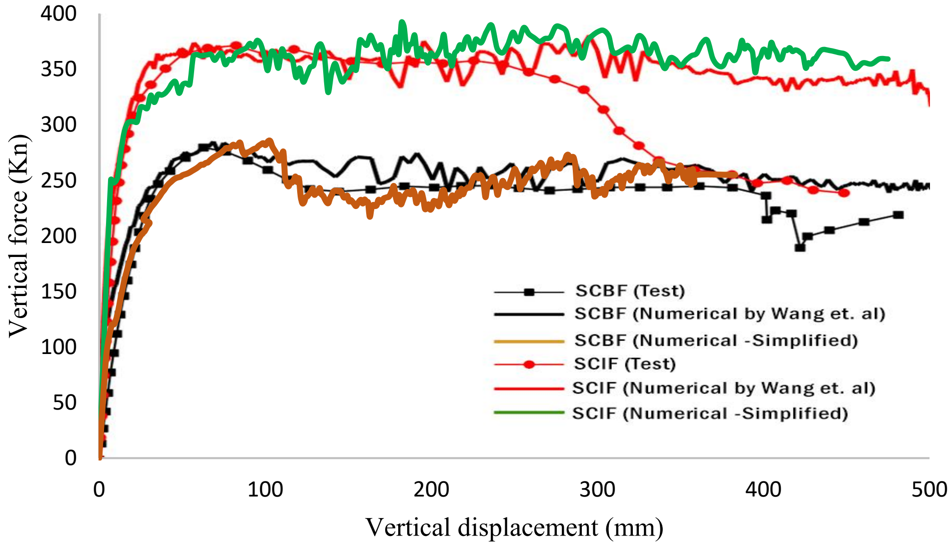

Fig. 11. Vertical applied force versus vertical displacement curves

Also compression damage in concrete compared with that in the experiment for SCBF Specimen Fig. 12 as well as for SCIF Specimen Fig. 13. which shows the final failure mode of the system.

Comparison of horizontal displacements at the exterior join of the right-hand column as illustrated in Fig. 14. As shown in

Fig. 14 the finite element (FE) simulations captured the overall deformation trends observed in both the experimental measurements and the detailed analysis by previous studies. Nonetheless, during the advanced deformation stage, the FE models predicted more pronounced inward movement than the physical tests. This discrepancy is likely due to the omission of strand re-centering effects in the simplified simulation framework.

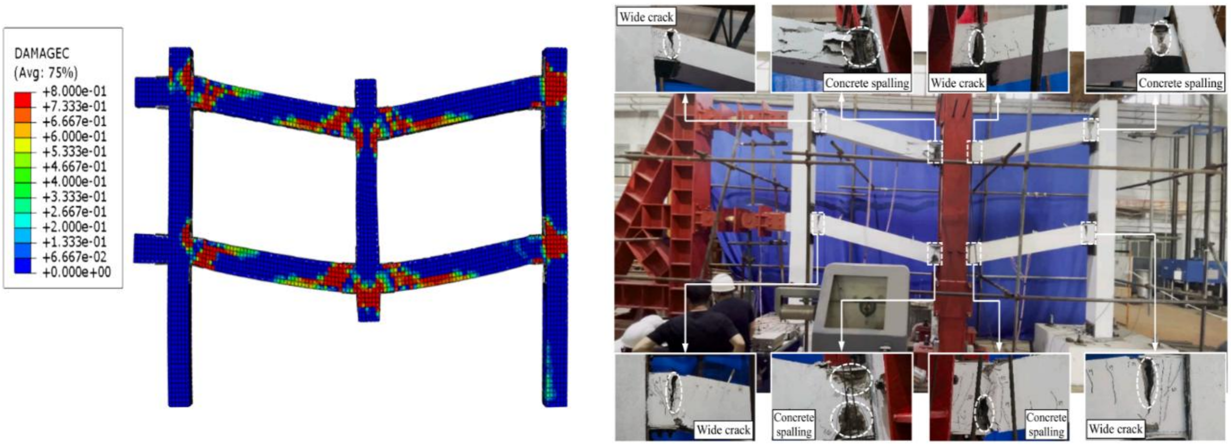

(a) (b)

Fig. 12. Final failure mode of specimen SCBF (a) Abaqus, (b) Experiment

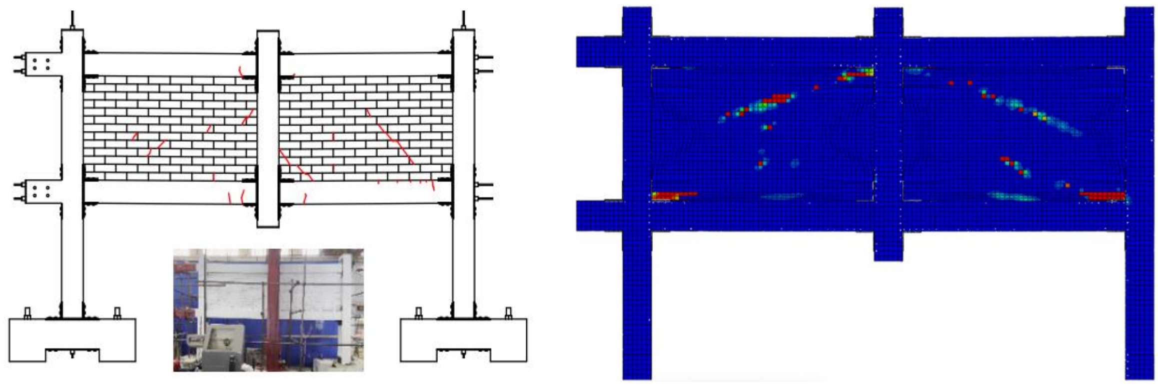

(A) 13.5 mm

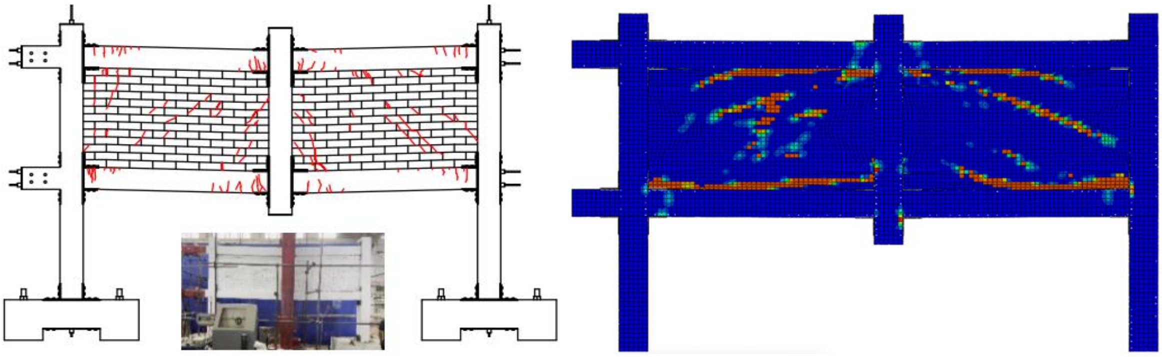

(B) 50.6 mm

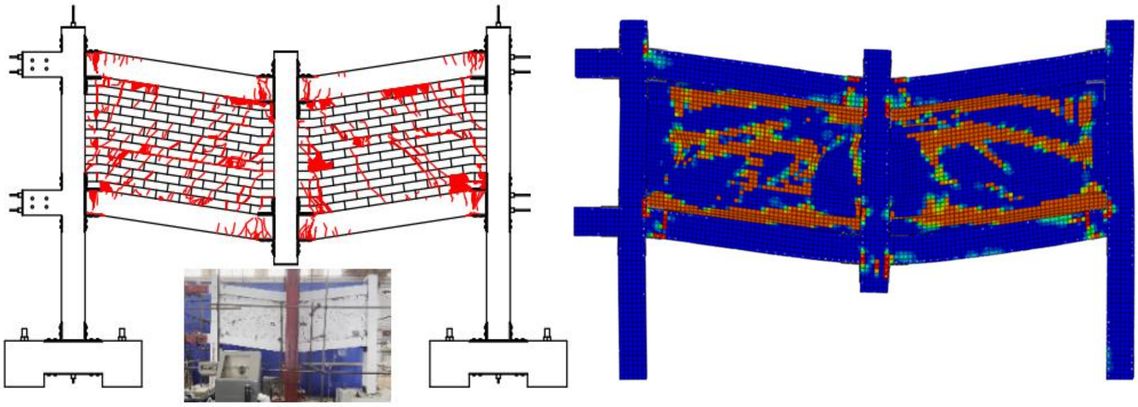

(C) 291.9 mm

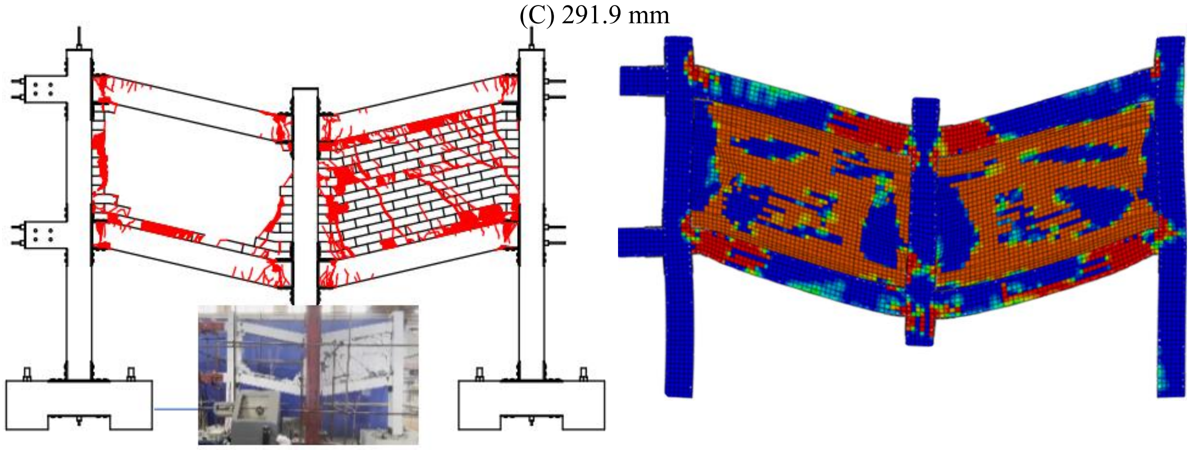

(D) 440 mm

Fig. 13. Crack patterns of infill walls under different vertical displacements in specimen SCIF

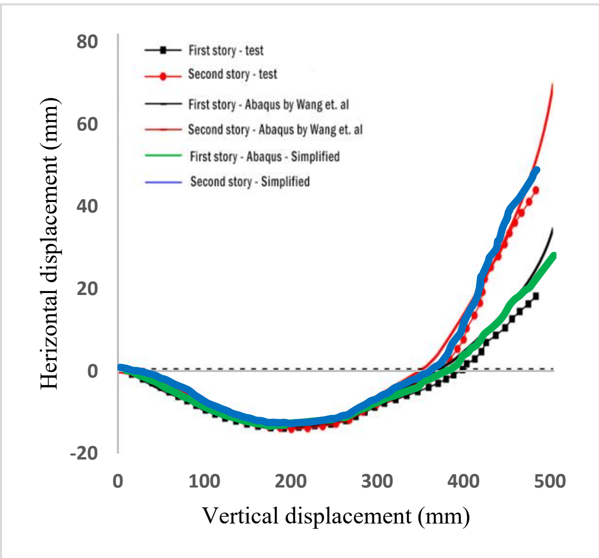

(a)

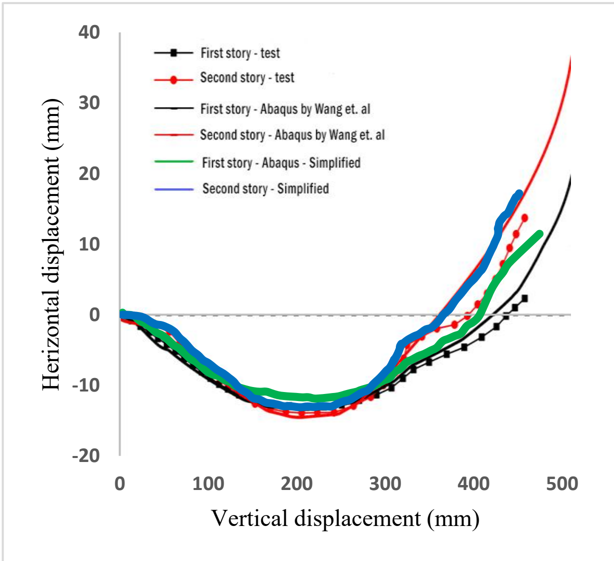

(b)

Fig. 14. Horizontal displacement and vertical displacement diagram (a) SCBF (b) SCIF

6. Conclusions

This study explores a simplified unbonded finite element (FE) modeling approach for simulating the behavior of re-centering precast concrete frames. Aimed at balancing computational efficiency with modeling accuracy, the approach demonstrates strong agreement with both experimental data and detailed numerical analyses. Such simplified models show promise for early-stage structural design and assessment, particularly where computational resources are limited. However, its applicability to non-symmetric geometries and dynamic conditions requires further refinement. The study emphasizes the importance of cohesive interface modeling and realistic damage representation in enhancing the reliability of simplified structural simulations. This study conclude that:

- The inclusion of a structural wall significantly enhances the overall stiffness and load-bearing strength of the frame when compared to a bare frame configuration. This improvement is particularly noticeable under vertical loading conditions, where the wall provides additional resistance to deformation, thereby increasing the structural integrity and stability of the entire system. The wall acts as a crucial component that not only distributes the applied loads more efficiently but also restrains excessive displacements, contributing to better performance under column removal scenario.
- In the case of a symmetric structural system, the observed performance results demonstrate that there is little to no significant difference between the behavior of vertically bonded strands and unbonded strands. This suggests that the inherent symmetry of the structure leads to a uniform distribution of stresses and strains, which in turn mitigates any potential disparities in load transfer mechanisms between different types of vertical strand connections. As a result, both bonded and unbonded vertical strands perform comparably in terms of contributing to the overall structural capacity and deformation characteristics of the system.
- When comparing the structural behavior of a bare frame to that of a frame integrated with a wall element, it becomes evident that the latter configuration possesses a substantially higher capacity to form and sustain compression arches. This increased compression arch capacity is largely attributed to the added confinement and load path continuity provided by the wall, which facilitates more effective development of arching action within the frame. Consequently, the frame with the wall can resist higher compressive forces, reduce shear demand on beam-column joints, and improve the energy dissipation capabilities of the system under extreme loading events.

Acknowledgments
No potential conflict of interest was reported by the author(s).

References

Abdulla, K.F., Cunningham, L.S., & Gillie, M. (2017). Simulating masonry wall behaviour using a simplified micro-model approach. *Engineering Structures, 151*, 349-365

Bažant, Z.P., & Zhou, Y. (2001). Why did the world trade center collapse?—Simple analysis. *International Journal of Structural Stability and Dynamics, 1*(04), 603-615

Brodsky, A., & Yankelevsky, D. (2017). Resistance of reinforced concrete frames with masonry infill walls to in-plane gravity loading due to loss of a supporting column. *Engineering Structures, 140*, 134-150

Corley, W.G., Sr, P.F.M., Sozen, M.A., & Thornton, C.H. (1998). The Oklahoma City bombing: Summary and recommendations for multihazard mitigation. J*ournal of Performance of Constructed Facilities, 12*(3), 100-112

Ellingwood, B.R. (2006). Mitigating risk from abnormal loads and progressive collapse. *Journal of Performance of Constructed Facilities, 20*(4), 315-323

Engineers, A.S.O.C. (2017). Minimum design loads and associated criteria for buildings and other structures, American Society of Civil Engineers.

GB 50003-, M. (2011). Code for design of masonry structures, China Architecture & Building Press Beijing, China.

Hafezolghorani, M., Hejazi, F., Vaghei, R., Jaafar, M.S.B., & Karimzade, K. (2017). Simplified damage plasticity model for concrete. *Structural Engineering International, 27*(1): 68-78

Karimi Ghaleh Jough, F., & Golhashem, M. (2020). Assessment of out-of-plane behavior of non-structural masonry walls using FE simulations. *Bulletin of Earthquake Engineering, 18*(14), 6405-6427

Kent, D.C., & Park, R. (1971). Flexural members with confined concrete. *Journal of the Structural Division, 97*(7), 1969-1990

Li, S., Shan, S., Zhai, C., & Xie, L. (2016). Experimental and numerical study on progressive collapse process of RC frames with full-height infill walls. *Engineering Failure Analysis, 59*, 57-68

Li, S., Wang, H., Liu, H., Shan, S., & Zhai, C. (2023). Experimental study on progressive collapse of self-centering precast concrete frame with infill walls. *Engineering Structures, 294*, 116746

Lourenço, P.J.B.B. (1997). Computational strategies for masonry structures.

Mahdi, A.M. (2023). Impact of failure-surface parameters of concrete damage plasticity model on the behavior of reinforced ultra-high performance concrete beams. *Periodica Polytechnica Civil Engineering, 67*(2), 495-504

Meng, B., Hao, J., & Zhong, W. (2021). Numerical study on the anti-progressive collapse performance of steel frame-steel plate shear wall structures. *Journal of Building Engineering*, *35*, 102049

Park, R., & Paulay, T. (1991). Reinforced concrete structures, John Wiley & Sons.

Pearson, C. & Delatte, N. (2005). Ronan point apartment tower collapse and its effect on building codes. *Journal of Performance of Constructed Facilities, 19*(2), 172-177

Sasani, M. (2008). Response of a reinforced concrete infilled-frame structure to removal of two adjacent columns. *Engineering Structures, 30*(9), 2478-2491

Shan, S., & Li, S. (2022). Progressive collapse mechanisms of post-tensioned reinforced concrete frames considering effect of infill walls. *Engineering Structures, 250*, 113451

Tsai, M.-H., & Huang, T.-C. (2009). Effect of interior brick-infill partitions on the progressive collapse potential of a RC building: linear static analysis results. *Engineering and Technology, 26*, 883-889

Van der Pluijm, R. (1992). Material properties of masonry and its components under tension and shear. In *Proceedings 6th Canadian Masonry Symposium*. 15-17 June 1992, Saskatoon, Canada, University of Saskatchewan.

Van der Pluijm, R. (1999). Out-of-plane bending of masonry: behaviour and strength.

Wang, H., Li, S., & Zhai, C. (2023). Experimental and numerical investigation on progressive collapse of self-centering precast concrete frame with infill walls. *Journal of Building Engineering*, *78*, 107472

Zhou, X. (2019). Discussion on parameters in finite element analysis of mechanical properties of masonry wall based on separation modeling. *Building Structure, 49*(S1), 640-644

4th International Civil Engineering & Architecture Conference
17-19 May 2025, Trabzon, Türkiye

Comparative analysis of optimization algorithms for vibration-based damage detection in laminated composite beams

Sebahat Şimşek*[1], Volkan Kahya[1]

[1] Karadeniz Technical University, Department of Civil Engineering, 61080 Trabzon, Türkiye

Abstract. The increasing application of laminated composite beams as structural load-bearing elements necessitates the understanding of the complex damage mechanisms of such materials and the development of reliable and easy-to-apply methods for timely damage detection. The use of damage detection methods based on vibration data together with robust computational algorithms in such materials appears to be a very good option due to its ease of application. Recent research in this field has accelerated and garnered significant industrial and scientific interest worldwide. However, the practical application of optimization methods in vibration-based damage detection for composites remains limited.In this study, the damage detection problem is solved by optimization based finite element model updating. A general anisotropic composite beam under various damage scenarios is considered. A new objective function based on vibration characteristics is used in the solution. The damage detection results using four different optimization algorithms (HSA, GA, TLBO, PSO) are presented comparatively.

Keywords: Laminated composite beam, Finite element method, Free vibration, Damage detection, Optimization

1. Introduction

Composite materials have been attractive in industrial and engineering applications due to their superior characteristics such as high strength-to-weight ratio, better thermal properties, corrosion resistance, etc. However, they may possess damages either in production or during their service lives. The damages may be in the form of matrix cracking or delamination, which are not generally visible, and may cause failure (Ghobadi, 2017). The visual inspection method or experimental non-destructive methods such as acoustic or ultrasonic methods, magnetic field methods, radiographs, Eddy-current methods, or thermal field methods require the damage is on or near the surface of the structure. They cannot detect internal or hidden damages like matrix cracking and delamination, which are commonly encountered damage types in composite materials (Rao et al., 2015).

Health monitoring and damage detection in engineering structures are currently one of the most interesting research topics and there has been a lot of research in which new methodologies have been developed. Among them, vibration-based damage detection methods are of interest because they are efficient, easy to implement, and cost-effective. Natural frequencies, mode shapes, modal curvature, modal flexibility, frequency response function, and modal strain energy are commonly used damage identification indicators since they will drastically change due to the presence of damage (Avci et al., 2021; Chang et al., 2003; Das et al., 2016; Doebling et al., 1996, 1998; Sinou, 2009).

Finite element (FE) model updating is one of the commonly used approaches in structural damage detection based on vibration data. One way to solve the damage detection problem is to assume it as an unconstraint optimization problem in which an objective function based on vibration characteristics from the actual structure and FE model must be minimized or maximized. Metaheuristic-based algorithms are powerful tools to solve such types of optimization problems. Since they are population-based optimization methods, they can solve the problems by avoiding the local minima trap (Gomes et al., 2018). Regarding the issue of damage detection in laminated composites, there are different kinds of metaheuristic-based optimization algorithms available in the literature. Examples are Genetic Algorithm (GA) (Gomes et al., 2018; He & Hwang, 2007; Pan et al., 2019) and its hybrids with other metaheuristics (Gomes et al., 2019; Tran-Ngoc et al., 2021; Vosoughi & Gerist, 2014), Particle Swarm Optimization (PSO) and its improved variants (Hadi, 2016; Jebieshia et al., 2020; Masoumi et al., 2018; Rao et al., 2015), Differential Evolution Algorithm (DE) (Dinh-Cong et al., 2017; Dinh-Cong et al., 2017; Vo-Duy et al., 2016; Vo-Duy et al., 2016), Cuckoo Search Algorithm (CS) (Khatir et al., 2018), Sunflower Optimization (SFO) (Gomes et al., 2019; Gomes & Giovani, 2020), Jaya Algorithm (Dinh-Cong et al., 2018),

* Corresponding author, E-mail: sebahatkaraca@ktu.edu.tr

https://doi.org/10.31462/icearc2025_ce_sme_926

Lichtenberg Optimization (Pereira et al., 2021), Experience-Based Learning Algorithm (EBL) (Zheng et al., 2020), Lightning Attachment Procedure Optimization (LAPO) (Dinh-Cong et al., 2021) and so on. In these research works, a single- or multi-objective optimization process was used with single-, two- or multi-stage-based damage detection. The use of computational and intelligent techniques for structural health monitoring (SHM) and damage detection with an emphasis on composite materials was discussed in detail by (Gomes et al., 2018).

This study proposes a robust methodology for damage detection in generally laminated composite beams by utilizing optimization-based finite element model updating. The beam is modeled with a thirteen-degrees-of-freedom finite element formulation that can account for extension-bending, bending-torsion, and extension-torsion couplings, as well as Poisson's effect. To address the practical limitation of incomplete modal data, the Guyan reduction technique is applied. The damage detection problem is formulated as an unconstrained optimization task, and the performance of four different optimization algorithms—Harmony Search Algorithm (HSA), Genetic Algorithm (GA), Teaching–Learning-Based Optimization (TLBO), and Particle Swarm Optimization (PSO)—is evaluated comparatively. A parametric study is conducted on anisotropic laminated composite beams with cantilever and clamped boundary conditions under three predefined damage scenarios. The investigation is carried out with and without the inclusion of measurement noise to assess the accuracy and robustness of each method.

2. Theoretical background

2.1. Finite element model

For finite element simulations of the laminated composite beams with general lay-ups, the thirteen-DOFs beam element shown in Fig. 1 is used. This element was derived by the authors previously and applied to various problems of anisotropic composite beams (Kahya et al., 2021, 2022, 2019a, b). The main advantage of the element is being able to capture the bending-extension, bending-torsion, and extension-torsion couplings arising from material anisotropy. Here, a brief formulation of the model is given for the sake of completeness. The detailed formulation can be found in (Kahya et al., 2019a, b).

According to the first-order shear deformation theory (FSDT), the displacement field for an orthotropic lamina is expressed by

$$\begin{aligned} u(x,z,t) &= u_0(x,t) + z\theta(x,t), \\ v(x,z,t) &= z\psi(x,t), \\ w(x,z,t) &= w_0(x,t) \end{aligned} \tag{1}$$

where u, v, and w denote the displacement components in x-, y-, and z- directions, respectively. u_0 and w_0 are the extension and deflection at $z = 0$, θ and ψ are the rotations of the normal to the midplane about the y- and x-axis, respectively. t denotes time.

Assuming the followings for the unknown field variables

$$\begin{aligned} u_0 &= \sum_{i=1}^{3} \Omega_i(x)\, u_i(t), \quad w_0 = \sum_{i=1}^{4} \Psi_i(x)\, w_i(t), \\ \theta &= \sum_{i=1}^{3} \Omega_i(x)\, \theta_i(t), \quad \psi = \sum_{i=1}^{3} \Omega_i(x)\, \psi_i(t) \end{aligned} \tag{2}$$

where $\Omega(x)$ and $\Psi(x)$ are the second and third-order Lagrange polynomials, respectively, and using Lagrange's principle, the equation of motion can be obtained as

$$\mathbf{M}_e \ddot{\mathbf{u}}_e + \mathbf{K}_e \mathbf{u}_e = \mathbf{0} \tag{3}$$

where $\mathbf{M}_e$ and $\mathbf{K}_e$ are, respectively, the elemental mass and stiffness matrices, $\mathbf{u}_e$ and $\ddot{\mathbf{u}}_e$ are the nodal displacement and acceleration vectors, respectively.

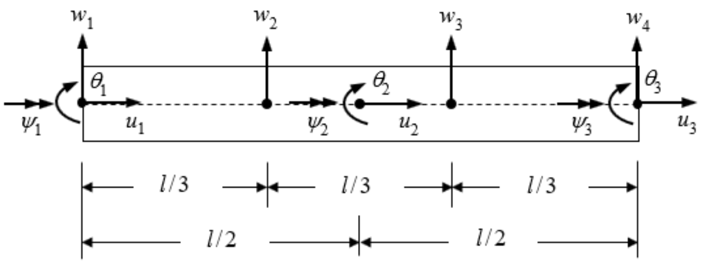

Fig. 1 Thirteen-DOF beam element

A stiffness loss parameter (or damage index) α_e ranging from zero to one is employed to simply assign damage to any element of the structure. This is a frequently preferred way by many researchers in problems related to damage detection, e.g., (Casciati, 2008; Das & Dhang, 2022; Dinh-Cong et al., 2018; Pereira et al., 2021; Ručevskis et al., 2009; Vo-Duy et al., 2016). Note that the elemental mass matrix is assumed to be unchanged due to damage. Thus, for the *e*th damaged element, the elemental stiffness matrix become

$$\mathbf{K}_e^D = (1-\alpha_e)\mathbf{K}_e^U \quad (0 \le \alpha_e \le 1) \tag{4}$$

where the superscripts D and U denote damaged and undamaged states, respectively. The value of stiffness loss parameter one represents full damage, and zero value indicates no damage to the corresponding member.

Based on the above-given assumption for the damage modelling, the global mass and stiffness matrices of the structure can be formed in $\mathbf{M} = \Sigma \mathbf{M}_e^U$ and $\mathbf{K} = \Sigma(1-\alpha_e)\mathbf{K}_e^U$, respectively, by the usual way of FE methodology to constitute the following:

$$\mathbf{M}\ddot{\mathbf{U}} + \mathbf{K}\mathbf{U} = \mathbf{0} \tag{5}$$

where **M** and **K** denote the global mass and stiffness matrices, respectively, and the vector **U** includes the global unknowns. Assuming the solution of Eq. (5) as in the form $\mathbf{U} = \mathbf{\Phi} e^{i\omega t}$ where $i = \sqrt{-1}$ and using it into Eq. (5), the following standard eigenvalue problem is obtained:

$$(\mathbf{K} - \omega^2 \mathbf{M})\mathbf{\Phi} = \mathbf{0} \tag{6}$$

where ω denotes the natural frequency, $\mathbf{\Phi}$ is the corresponding mode shape vector. The non-trivial solution of Eq. (6) will result in the natural frequencies (eigenvalues). Then, the corresponding eigenvectors (mode shapes) can be obtained by the back-substitution.

2.2. Guyan condensation

FE modeling of a structure produces many DOFs that result in the system matrices being comparatively large. However, in an experimental measurement, the vibration data can be extracted by considering only a limited number of DOFs. To compare the vibration data of a large-scale model with that of the measurement for damage detection and structural health monitoring, the full system FE matrices can be reduced by a model-order reduction method. Here, the Guyan method (Guyan, 1965) is preferred because it is the traditional model reduction technique implemented in most commercial finite element analysis software.

Guyan or static condensation uses the stiffness equation (Marinone et al., 2018) as

$$\mathbf{K}_n \mathbf{X}_n = \mathbf{F}_n \tag{7}$$

where $\mathbf{K}_n$ is the stiffness matrix, $\mathbf{X}_n$ is the displacement response vector, and $\mathbf{F}_n$ is the force vector. Eq. (7) can be partitioned into

$$\begin{bmatrix} \mathbf{K}_{aa} & \mathbf{K}_{ad} \\ \mathbf{K}_{da} & \mathbf{K}_{dd} \end{bmatrix} \begin{Bmatrix} \mathbf{X}_a \\ \mathbf{X}_d \end{Bmatrix} = \begin{Bmatrix} \mathbf{F}_a \\ \mathbf{F}_d \end{Bmatrix} \tag{8}$$

where the subscripts a and d denote the active and deleted DOFs, respectively. Assuming the slave force vector $\mathbf{F}_d$ is zero, the second equation of Eq. (8) will result

$$\mathbf{X}_d = -\mathbf{K}_{dd}^{-1}\mathbf{K}_{da}\mathbf{X}_a \tag{9}$$

which gives the following coordinate transformation relation:

$$\mathbf{X}_n = \begin{Bmatrix} \mathbf{X}_a \\ \mathbf{X}_d \end{Bmatrix} = \begin{Bmatrix} \mathbf{I} \\ -\mathbf{K}_{dd}^{-1}\mathbf{K}_{da} \end{Bmatrix} \mathbf{X}_a = \mathbf{T}_G \mathbf{X}_a \tag{10}$$

where **I** is the identity matrix. Using the transformation matrix into the general energy balance formula yields the reduced stiffness and mass matrices as follows (Guyan, 1965; Marinone et al., 2018):

$$\mathbf{K}_a = \mathbf{T}_G^T \mathbf{K}_n \mathbf{T}_G, \quad \mathbf{M}_a = \mathbf{T}_G^T \mathbf{M}_n \mathbf{T}_G \tag{11}$$

where

$$\mathbf{K}_a = \mathbf{K}_{aa} - \mathbf{K}_{ad}\mathbf{K}_{dd}^{-1}\mathbf{K}_{da} \tag{12}$$

$$\mathbf{M}_a = \mathbf{M}_{aa} - \mathbf{K}_{ad}\mathbf{K}_{dd}^{-1}\mathbf{M}_{da} - \mathbf{M}_{ad}\mathbf{K}_{dd}^{-1}\mathbf{K}_{da} + \mathbf{K}_{ad}\mathbf{K}_{dd}^{-1}\mathbf{M}_{dd}\mathbf{K}_{dd}^{-1}\mathbf{K}_{da} \tag{13}$$

Since Guyan reduction is based on the static equilibrium, stiffness is preserved while neglecting the inertia forces. The eigenvalues of the reduced model are always higher than those of the full FE model, and the quality of their approximation depends on the location of preserved DOFs and the mode shape of interest. However, the first few lowest modes include less error and yield relatively accurate results.

3. Damage detection methodology

Vibration-based damage detection methods use the modal parameters as damage diagnostic parameters. An error function called objective function can be defined in terms of the modal parameters from the actual and numerical models. This objective function is minimized or maximized to localize and quantify damages in the structure.

Among modal parameters, natural frequencies are preferred due to their relative insensitivity to ambient noise and ease of measurement. However, using only frequency data often fails to provide sufficient accuracy in damage identification. Therefore, researchers have proposed incorporating mode shapes or mode shape-derived parameters in combination with frequency data. In this study, a new objective function is used and mathematically defined as follows:

$$f(\mathbf{x}) = \sqrt{\frac{1}{nm}\sum_{i=1}^{nm} W_{1i}\left(\frac{\omega_i^{\text{Target}} - \omega_i^{\text{Predicted}}}{\omega_i^{\text{Target}}}\right)^2} \\ + \sum_{i=1}^{nm} W_{2i}\left[1-\text{COMAC}(i)\right]^2 + W_{3i}\frac{\left\|\mathbf{F}^{\text{Target}} - \mathbf{F}^{\text{Predicted}}(x)\right\|_{Fro}}{\left\|\mathbf{F}^{\text{Target}}\right\|_{Fro}} \tag{13}$$

where ω_i^{Target} and $\omega_i^{\text{Predicted}}$ are the ith target and predicted frequencies, respectively nm is the number of modes considered. W_{1i}, W_{2i} and W_{3i} are weighting coefficients. In Eq. (13), COMAC(i) represents the Coordinate Modal Assurance Criterion, and **F** denotes the flexibility matrix. The symbol $\|\cdot\|_F$ indicates the Frobenius norm of a matrix. COMAC is a modified version of the traditional Modal Assurance Criterion, and it quantifies the correlation between two data sets at the coordinate level (Allemang, 2003). This allows for the identification of specific coordinates that disrupt the overall agreement providing a significant advantage in localizing damage. The COMAC is defined as follows:

$$\text{COMAC}(i) = \frac{\sum_{j=1}^{np}\left|(\phi_{ij}^{\text{Target}})^T \phi_{ij}^{\text{Predicted}}\right|^2}{\sum_{j=1}^{np}(\phi_{ij}^{\text{Target}})^2 \sum_{j=1}^{np}(\phi_{ij}^{\text{Predicted}})^2} \quad (i = 1, 2, \ldots, nm) \tag{14}$$

where np denotes the number of measurement coordinates. The elements of the COMAC vector range between 0 and 1, where 0 indicates no correlation and 1 denotes perfect agreement.

The flexibility matrix, which is the inverse of the stiffness matrix, is preferred due to its high sensitivity to damage. It is mathematically expressed as (Pandey & Biswas, 1994):

$$\mathbf{F} = \sum_{i=1}^{nm}\frac{1}{\omega_i^2}\mathbf{\Phi}_i\mathbf{\Phi}_i^T \tag{15}$$

where, ω_i represents the natural frequencies and Φ_i he corresponding mode shapes. The main advantage of the flexibility matrix is that it can be accurately approximated using only a few lower modes.

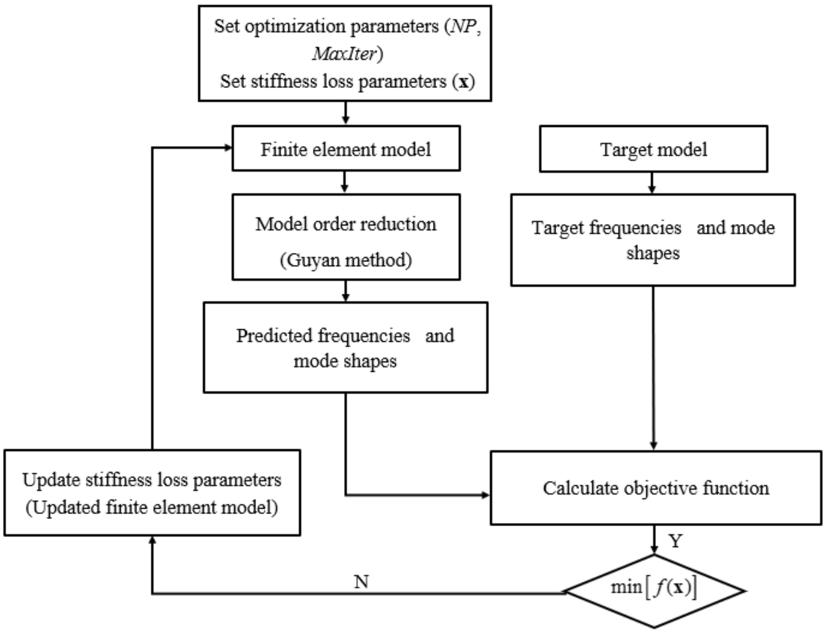

Fig. 2 Flowchart of the proposed damage detection methodology

The damage detection results were obtained using Harmony Search Algorithm (HSA), Genetic Algorithm (GA), Teaching–Learning-Based Optimization (TLBO), and Particle Swarm Optimization (PSO). The theoretical background and implementation details of these algorithms can be found in (Şimşek, 2024). The flowchart illustrating the proposed damage detection methodology is presented in the Fig. 2.

4. Results and discussion

Damage detection results using four different optimization algorithms (HSA, GA, TLBO, PSO) are presented comparatively in this section. The properties of the beam used in the numerical simulations for damage detection are presented in Fig. 3. and Table 1. The beam has a square cross-section with dimensions b = h= 24.5mm and a length of L = 381 mm. The laminated composite beam has a $[30/50]_2$ ply stacking sequence and all layers have equal thickness.

The beam was analyzed under three different damage scenarios, as listed in Table 2. The initial parameters selected for the four optimization algorithms are provided in Table 3. Each scenario was independently executed five times, and the average of the obtained results is presented through tables and figures.

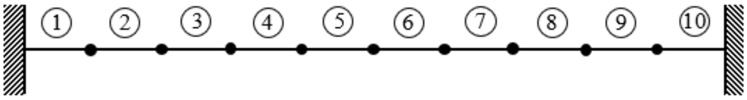

Fig. 3 Finite element model of the beam considered in the parametric study

Tablo 1. Ply material properties used in the parametric study

E_1 (GPa)	$E_2 = E_3$ (Gpa)	$G_{12} = G_{13}$ (Gpa)	G_{23} (Gpa)	ν	ρ (kg/m^3)
144.8	9.65	4.14	3.45	0.30	1389.23

Table 2. Damage scenarios considered in the parametric study using TLBO for damage detection

Damage Scenario	Damaged Elements			Stiffness Reduction. α		
1	3	-	-	0.50		
2	3	4		0.30	0.20	
3	3	4	8	0.30	0.10	0.10

Table 3. Initial parameters considered in the optimization process

Optimization Algorithm	Initial Parameters
HSA	HM = 10, HMCR = 0,9, PAR = 0,25, tol = 10^{-5}, MaxIt = 25000
GA	NP =40, tol = 10^{-5}, MaxIt = 300
PSO	NP =30, tol = 10^{-5}, MaxIt = 100
TLBO	NP =30, tol = 10^{-6}, MaxIt = 500

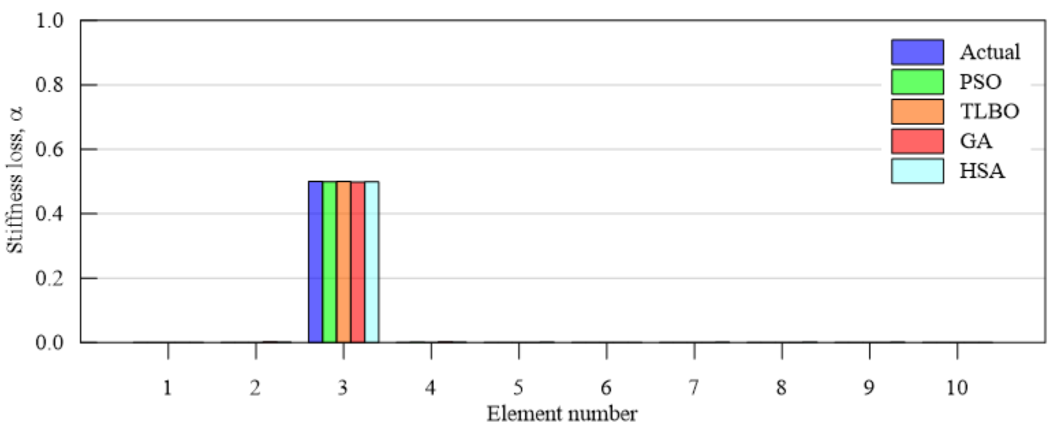

(a) Noise-free

Fig. 4. Damage detection results for Damage-1

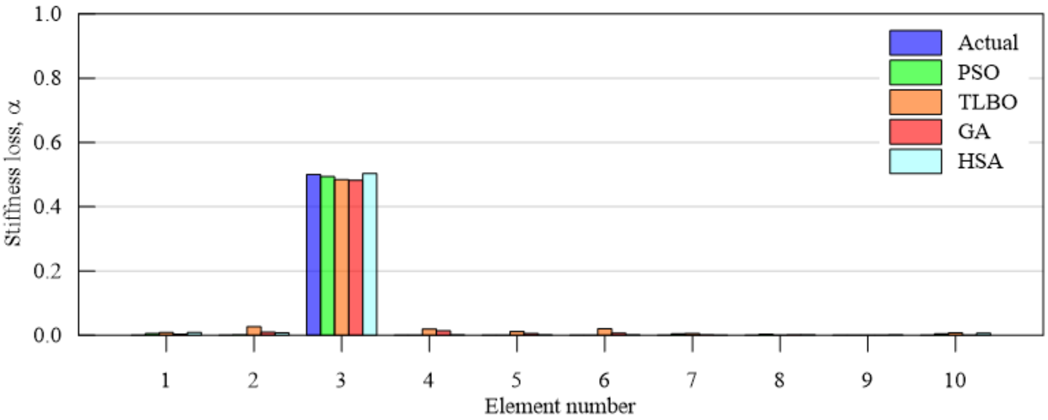

(b) Noise-polluted

Fig. 4. Continued

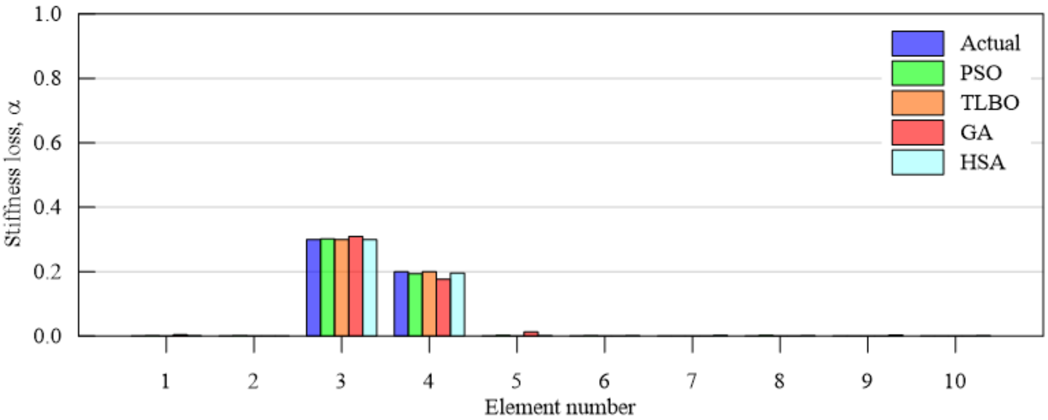

(a) Noise-free

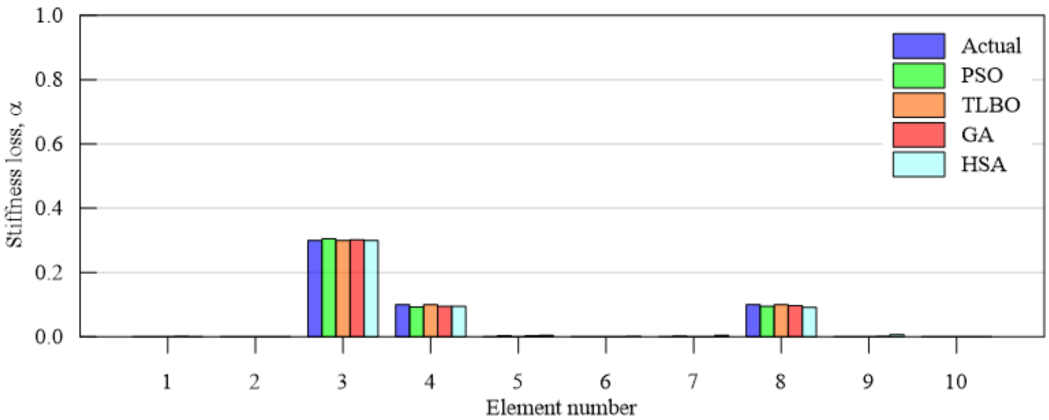

(b) Noise-polluted

Fig. 5. Damage detection results for beam Damage-2

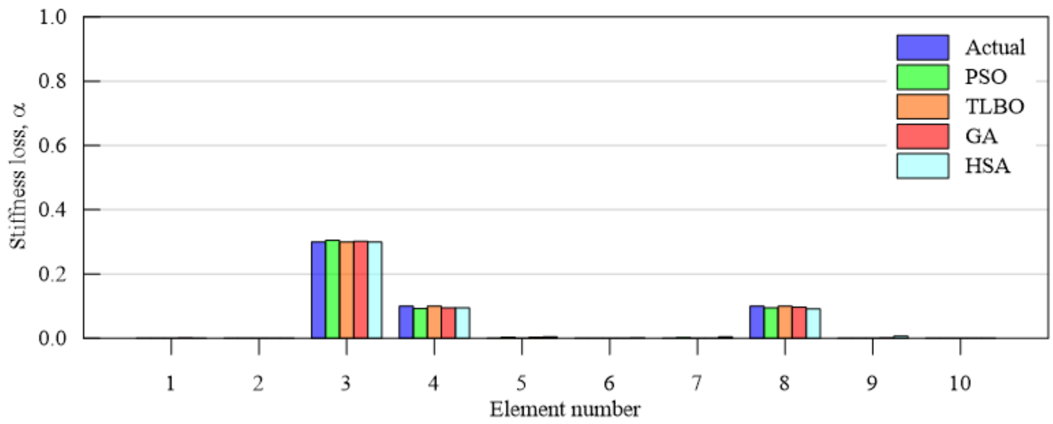

(a) Noise-free

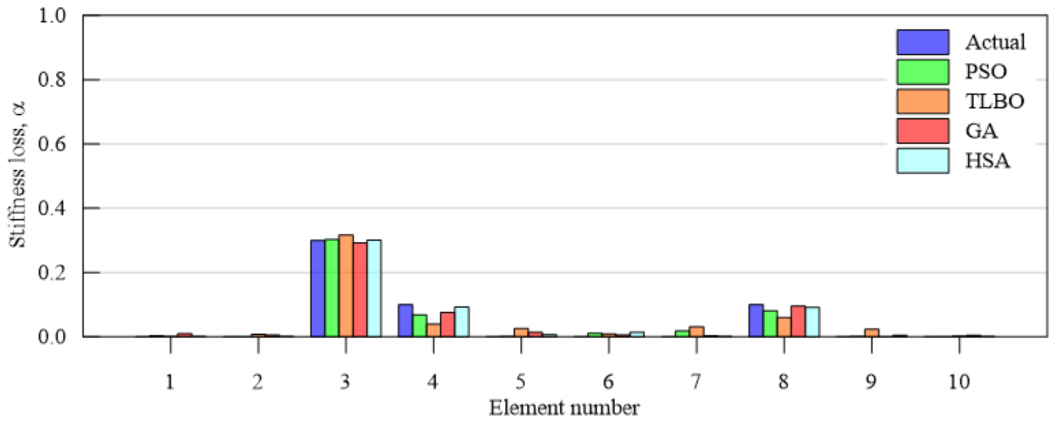

(b) Noise-polluted

Fig. 6. Damage detection results for beam Damage-3

Fig. 4 – Fig. 6 present the damage detection results obtained using four different algorithms for a clamped–clamped laminated composite beam. As can be seen from the figures, in all considered scenarios, the damaged elements were identified with high accuracy under both noise-free and noisy conditions by all four algorithms. Additionally, the influence of noise on the results was observed to be more significant in the Damage-3.

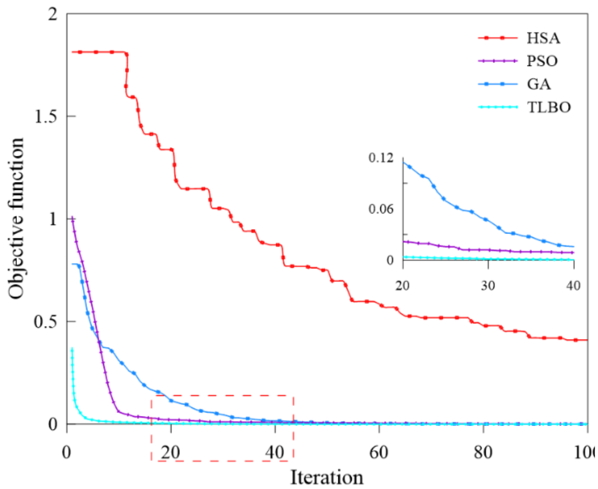

(a)

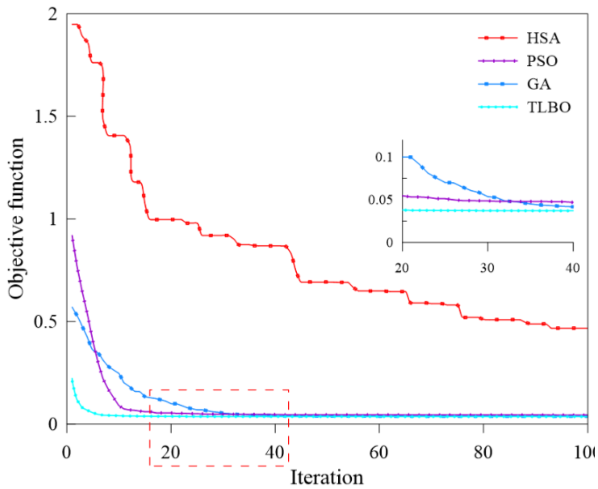

(b)

Fig. 7 Convergence of the objective function in damage detection using four different algorithms for a clamped–clamped $[30/50]_2$ laminated beam (Damage-3)

Fig. 7 illustrates the convergence curves of the objective function for the four algorithms used in Damage-3 of the clamped–clamped laminated composite beam. Since the maximum number of iterations varies among the algorithms, the first 100 iterations were considered to provide a common basis for comparison. As observed in the graphs, under both noise-free and noisy conditions, the convergence curves are ordered from top to bottom as HSA, PSO, GA, and TLBO. TLBO is the fastest converging algorithm, followed by PSO, GA, and HSA, respectively. Although HSA appears to converge much more slowly than the others, all algorithms completed the process in approximately the same computational time. In the noise-free case, the best convergence value (on the order of 10^{-5}) was achieved by TLBO, while under noisy conditions, all algorithms converged to nearly the same value.

Table 4 presents a comparative summary of the damage detection results obtained from five independent runs of four algorithms for Damage Scenario 3 in a clamped–clamped laminated composite beam. According to the table, under noise-free conditions, the TLBO algorithm provides the best convergence to the actual results compared to the other algorithms, with a standard deviation close to zero. When the effect of noise is considered, it can be stated that all four algorithms yield similar results.

Table 4. Comparison of damage detection results obtained using four algorithms for Damage Scenario 3 in a clamped–clamped laminated composite beam

Algorithm	Noise-free				Noise-polluted			
	Variable	Best value	Mean value	Standard deviation	Variable	Variable	Best value	Mean value
HSA	$\alpha_3 = 0.3$	0.2992	0.2999	0.0013	α_3	0.2939	0.3006	0.0151
	$\alpha_4 = 0.1$	0.0995	0.0952	0.0066	α_4	0.1438	0.0922	0.0488
	$\alpha_8 = 0.1$	0.0993	0.0917	0.0054	α_8	0.0706	0.0918	0.0165
	$f(x)$	4.06×10^{-4}	1.22×10^{-3}	5.33×10^{-4}	$f(x)$	2.64×10^{-2}	1.22×10^{-3}	1.03×10^{-2}
GA	$\alpha_3 = 0.3$	0.2971	0.3022	0.00463	α_3	0.2917	0.2917	0.0177
	$\alpha_4 = 0.1$	0.1041	0.0947	0.00924	α_4	0.1235	0.07541	0.0469
	$\alpha_8 = 0.1$	0.0993	0.0972	0.00255	α_8	0.0944	0.09564	0.0092
	$f(x)$	2.04×10^{-4}	4.02×10^{-4}	2.70×10^{-4}	$f(x)$	1.92×10^{-2}	3.79×10^{-2}	1.26×10^{-2}
TLBO	$\alpha_3 = 0.3$	0.2999	0.2999	0.0000	α_3	0.2989	0.3136	0.0272
	$\alpha_4 = 0.1$	0.1000	0.0999	0.0002	α_4	0.0492	0.0411	0.0396
	$\alpha_8 = 0.1$	0.0995	0.0995	0.0002	α_8	0.1116	0.0623	0.0420
	$f(x)$	3.1×10^{-5}	3.7×10^{-5}	0.08×10^{-4}	$f(x)$	2.52×10^{-2}	3.68×10^{-2}	1.28×10^{-2}
PSO	$\alpha_3 = 0.3$	0.3008	0.3045	0.0031	α_3	0.2553	0.3024	0.0268
	$\alpha_4 = 0.1$	0.0952	0.0921	0.0034	α_4	0.1747	0.0678	0.0595
	$\alpha_8 = 0.1$	0.1003	0.0943	0.0047	α_8	0.0781	0.0808	0.0165
	$f(x)$	3.16×10^{-4}	4.82×10^{-4}	1.95×10^{-4}	$f(x)$	3.87×10^{-2}	4.43×10^{-2}	5.82×10^{-3}

Table 5. Comparison of error indices for the clamped–clamped laminated composite beam

Damage	HSA		GA		TLBO		PSO	
Scenario	I_1	I_2	I_1	I_2	I_1	I_2	I_1	I_2
Noise-free								
1	0.1750	0.0037	0.3105	0.0053	0.0019	0.0007	0.1750	0.0037
2	3.9307	0.0077	14.6822	0.0171	0.0630	0.0005	3.9307	0.0077
3	14.9956	0.0078	8.7317	0.0061	0.5500	0.0010	14.9956	0.0078
Noise-polluted								
1	1.2965	0.0196	3.6461	0.0417	3.2367	0.1003	1.2965	0.0196
2	12.7754	0.0457	8.9383	0.0289	9.9151	0.0513	12.7754	0.0457
3	52.1819	0.0369	31.6971	0.0437	101.0293	0.0955	52.1819	0.0369

Performance evaluations were carried out using the following error indices:

$$I_1 = \sum_{i=1}^{nd} \left| \frac{\alpha_i^{\text{actual}} - \alpha_i^{\text{predicted}}}{\alpha_i^{\text{actual}}} \right| \times 100 \tag{16}$$

$$I_2 = \sum_{i=1}^{nel-nd} \alpha_i^{\text{incorrect prediction}} \tag{17}$$

Table 5 shows that the I_2 index values obtained by the TLBO algorithm are closer to zero compared to the other algorithms. As previously mentioned, this indicates that the TLBO algorithm is capable of identifying the damaged elements with high accuracy. When evaluating the I_1 index values, it is observed that under noise-free conditions, TLBO provides the best results for all damage scenarios in the clamped–clamped beam. Under noisy conditions, however, the performance of all four algorithms decreases, and significant error rates occur, particularly in the detection of shallow damages.

4. Conclusions

This study presented a comparative investigation of four different optimization algorithms—HSA, GA, TLBO, and PSO—for vibration-based damage detection in clamped–clamped laminated composite beams. The performance of the algorithms was evaluated under both noise-free and noise-polluted conditions using convergence characteristics, damage localization accuracy, and error indices.

The key conclusions drawn from the results are as follows:

- TLBO algorithm consistently demonstrated the highest accuracy in identifying damaged elements, especially under noise-free conditions, with nearly zero standard deviation in results.
- In all three damage scenarios, TLBO achieved the best convergence of the objective function compared to other algorithms, particularly reaching values on the order of 10^{-5} in the absence of noise.
- Under noisy conditions, although the accuracy of all algorithms decreased, TLBO maintained a relatively better performance than the others.
- The convergence analysis revealed that TLBO was the fastest converging algorithm, followed by PSO, GA, and HSA, respectively.
- The HSA algorithm showed significantly slower convergence but had comparable computational time to the other methods due to fewer internal operations.
- The I_2 error index values for TLBO were the closest to zero in all scenarios, confirming its robustness in both noise-free and noisy environments.
- In shallow damage cases, especially under noise-polluted conditions, all algorithms showed decreased accuracy, with higher error rates observed.

References

Allemang, R. J. (2003). The modal assurance criterion - Twenty years of use and abuse. *Sound and Vibration*, *37*(8), 14–21. http://www.scopus.com/inward/record.url?eid=2-s2.0-0141958862&partnerID=tZOtx3y1

Avci, O., Abdeljaber, O., Kiranyaz, S., Hussein, M., Gabbouj, M., & Inman, D. J. (2021). A review of vibration-based damage detection in civil structures: From traditional methods to Machine Learning and Deep Learning applications. *Mechanical Systems and Signal Processing*, *147*, 107077. https://doi.org/10.1016/j.ymssp.2020.107077

Casciati, S. (2008). Stiffness identification and damage localization via differential evolution algorithms. *Structural Control and Health Monitoring*, *15*(3), 436–449. https://doi.org/10.1002/stc.236

Chang, P. C., Flatau, A., & Liu, S. C. (2003). Review Paper: Health Monitoring of Civil Infrastructure. *Structural Health Monitoring*, *2*(3), 257–267. https://doi.org/10.1177/1475921703036169

Das, S., & Dhang, N. (2022). Damage identification of structures using incomplete mode shape and improved TLBO-PSO with self-controlled multi-stage strategy. *Structures*, *35*, 1101–1124. https://doi.org/10.1016/j.istruc.2021.07.089

Das, S., Saha, P., & Patro, S. K. (2016). Vibration-based damage detection techniques used for health monitoring of structures: a review. *Journal of Civil Structural Health Monitoring*, *6*(3), 477–507. https://doi.org/10.1007/s13349-016-0168-5

Dinh-Cong, D., Dang-Trung, H., & Nguyen-Thoi, T. (2018). An efficient approach for optimal sensor placement and damage identification in laminated composite structures. *Advances in Engineering Software*, *119*(December 2017), 48–59. https://doi.org/10.1016/j.advengsoft.2018.02.005

Dinh-Cong, D., Nguyen-Thoi, T., & Nguyen, D. T. (2021). A two-stage multi-damage detection approach for composite structures using MKECR-Tikhonov regularization iterative method and model updating procedure. *Applied Mathematical Modelling*, *90*, 114–130. https://doi.org/10.1016/j.apm.2020.09.002

Dinh-Cong, D., Vo-Duy, T., Ho-Huu, V., Dang-Trung, H., & Nguyen-Thoi, T. (2017). An efficient multi-stage optimization approach for damage detection in plate structures. *Advances in Engineering Software*, *112*, 76–87. https://doi.org/10.1016/j.advengsoft.2017.06.015

Dinh-Cong, D., Vo-Duy, T., Nguyen-Minh, N., Ho-Huu, V., & Nguyen-Thoi, T. (2017). A two-stage assessment method using damage locating vector method and differential evolution algorithm for damage identification of cross-ply laminated composite beams. *Advances in Structural Engineering*. https://doi.org/10.1177/1369433217695620

Doebling, S. W., Farrar, C. R., & Prime, M. B. (1998). A summary review of vibration-based damage identification methods. *Shock and Vibration Digest*, *30*(2), 91–105. https://doi.org/10.1177/058310249803000201

Doebling, S. W., Farrar, C. R., Prime, M. B., & Shevitz, D. W. (1996). Damage identification and health monitoring of structural and mechanical systems from changes in their vibration characteristics: A literature review. In *Los Alamos National Laboratory*. https://doi.org/10.2172/249299

Ghobadi, A. (2017). Common type of damages in composites and their inspections. *World Journal of Mechanics*, *07*(02), 24–33. https://doi.org/10.4236/wjm.2017.72003

Gomes, G. F., da Cunha, S. S., & Ancelotti, A. C. (2019). A sunflower optimization (SFO) algorithm applied to damage identification on laminated composite plates. *Engineering with Computers*, *35*(2), 619–626. https://doi.org/10.1007/s00366-018-0620-8

Gomes, G. F., de Almeida, F. A., Junqueira, D. M., da Cunha, S. S., & Ancelotti, A. C. (2019). Optimized damage identification in CFRP plates by reduced mode shapes and GA-ANN methods. *Engineering Structures*, *181*(December 2018), 111–123. https://doi.org/10.1016/j.engstruct.2018.11.081

Gomes, G. F., & Giovani, R. S. (2020). An efficient two-step damage identification method using sunflower optimization algorithm and mode shape curvature (MSDBI–SFO). *Engineering with Computers*, *0123456789*. https://doi.org/10.1007/s00366-020-01128-2

Gomes, G. F., Mendéz, Y. A. D., da Cunha, S. S., & Ancelotti, A. C. (2018). A numerical–experimental study for structural damage detection in CFRP plates using remote vibration measurements. *Journal of Civil Structural Health Monitoring*, *8*(1), 33–47. https://doi.org/10.1007/s13349-017-0254-3

Gomes, G. F., Mendéz, Y. A. D., da Silva Lopes Alexandrino, P., da Cunha, S. S., & Ancelotti, A. C. (2018). The use of intelligent computational tools for damage detection and identification with an emphasis on composites – A review. *Composite Structures*, *196*(September 2017), 44–54. https://doi.org/10.1016/j.compstruct.2018.05.002

Guyan, R. J. (1965). Reduction of stiffness and mass matrices. *AIAA Journal*, *3*(2), 380–380. https://doi.org/10.2514/3.2874

Hadi, N. H. (2016). Delamination modeling and assessment for composite laminated plates using particle swarm optimization. *International Journal of Computer Applications*, *134*(1), 31–41.

He, R. S., & Hwang, S. F. (2007). Identifying damage in spherical laminate shells by using a hybrid real-parameter genetic algorithm. *Composite Structures*, *80*(1), 32–41. https://doi.org/10.1016/j.compstruct.2006.02.035

Jebieshia, T. R., Maiti, D. K., & Maity, D. (2020). Frequency-based damage assessment of composite members using unified particle swarm optimization. *International Journal of Aeronautical and Space Sciences*, *21*(1), 63–79. https://doi.org/10.1007/s42405-019-00187-0

Kahya, V., Karaca, S., Okur, F. Y., Altunışık, A. C., & Aslan, M. (2019). Free vibrations of laminated composite beams with multiple edge cracks: Numerical model and experimental validation. *International Journal of Mechanical Sciences*, *159*, 30–42. https://doi.org/10.1016/j.ijmecsci.2019.05.032

Kahya, V., Karaca, S., Okur, F. Y., Altunışık, A. C., & Aslan, M. (2021). Damage localization in laminated composite beams with multiple edge cracks based on vibration measurements. *Iranian Journal of Science and Technology, Transactions of Civil Engineering*, *45*(1), 75–87. https://doi.org/10.1007/s40996-020-00393-x

Kahya, V., Karaca, S., & Vo, T. P. (2019). Shear-deformable finite element for free vibrations of laminated composite beams with arbitrary lay-up. *Steel and Composite Structures*, *33*(4), 473–487. https://doi.org/10.12989/scs.2019.33.4.473

Kahya, V., Şimşek, S., & Toğan, V. (2022). Vibration-based damage detection in anisotropic laminated composite beams by a shear-deformable finite element and harmony search optimization. *Structural and Multidisciplinary Optimization*, *65*(6), 181. https://doi.org/10.1007/s00158-022-03270-5

Khatir, S., Brahim, B., Capozucca, R., & Abdel Wahab, M. (2018). Damage detection in CFRP composite beams based on vibration analysis using proper orthogonal decomposition method with radial basis functions and cuckoo search algorithm. *Composite Structures*, *187*(December 2017), 344–353. https://doi.org/10.1016/j.compstruct.2017.12.058

Marinone, T., Dardeno, T., & Avitabile, P. (2018). Reduced model approximation approach using model updating methodologies. *Journal of Engineering Mechanics*, *144*(3), 04018005. https://doi.org/10.1061/(ASCE)EM.1943-7889.0001422

Masoumi, F., Ghasemi-Ghalebahman, A., & Kokabi, M. J. (2018). Identification of mechanical and damage parameters of composite laminates based on a CPAM method. *Journal of Reinforced Plastics and Composites*, *37*(17), 1114–1128. https://doi.org/10.1177/0731684418793207

Pan, J., Zhang, Z., Wu, J., Ramakrishnan, K. R., & Singh, H. K. (2019). A novel method of vibration modes selection for improving accuracy of frequency-based damage detection. *Composites Part B: Engineering*, *159*, 437–446. https://doi.org/10.1016/j.compositesb.2018.08.134

Pandey, A. K., & Biswas, M. (1994). Damage detection in structures using changes in flexibility. *Journal of Sound and Vibration*, *169*(1), 3–17. https://doi.org/10.1006/jsvi.1994.1002

Pereira, J. L. J., Francisco, M. B., Cunha Jr., S. S. da, & Gomes, G. F. (2021). A powerful Lichtenberg Optimization Algorithm: A damage identification case study. *Engineering Applications of Artificial Intelligence*, *97*(June 2020), 104055. https://doi.org/10.1016/j.engappai.2020.104055

Rao, A. R. M., Lakshmi, K., & Kumar, S. K. (2015). Detection of delamination in laminated composites with limited measurements combining PCA and dynamic QPSO. *Advances in Engineering Software*, *86*, 85–106. https://doi.org/10.1016/j.advengsoft.2015.04.005

Ručevskis, S., Wesolowski, M., & Chate, A. (2009). Vibration-based damage identification in laminated composite beams. *Scientific Journal of Riga Technical University: Construction Science*, *10*, 100–112.

Sebahat Şimşek. (2024). *Tabakalı kompozit kirişlerde titreşim verileri yardımıyla optimizasyon tabanlı hasar tespiti* [Ph.D. Thesis]. Karadeniz Technical University (in Turkish).

Sinou, J.-J. (2009). A review of damage detection and health monitoring of mechanical systems from changes in the measurement of linear and non-linear vibrations. In R. C. Sapri (Ed.), *Mechanical Vibrations: Measurement, Effects and Control* (pp. 643–702). Nova Science Publishers, Inc. http://hal.archives-ouvertes.fr/docs/00/77/93/22/PDF/Sinou_Chapter_13_review_SHM.pdf

Tran-Ngoc, H., Khatir, S., Ho-Khac, H., De Roeck, G., Bui-Tien, T., & Abdel Wahab, M. (2021). Efficient Artificial neural networks based on a hybrid metaheuristic optimization algorithm for damage detection in laminated composite structures. *Composite Structures*, *262*(October 2020), 113339. https://doi.org/10.1016/j.compstruct.2020.113339

Vo-Duy, T., Ho-Huu, V., Dang-Trung, H., Dinh-Cong, D., & Nguyen-Thoi, T. (2016). Damage detection in laminated composite plates using modal strain energy and improved differential evolution algorithm. *Procedia Engineering*, *142*, 181–188. https://doi.org/10.1016/j.proeng.2016.02.030

Vo-Duy, T., Ho-Huu, V., Dang-Trung, H., & Nguyen-Thoi, T. (2016). A two-step approach for damage detection in laminated composite structures using modal strain energy method and an improved differential evolution algorithm. *Composite Structures*, *147*, 42–53. https://doi.org/10.1016/j.compstruct.2016.03.027

Vosoughi, A. R., & Gerist, S. (2014). New hybrid FE-PSO-CGAs sensitivity base technique for damage detection of laminated composite beams. *Composite Structures*, *118*(1), 68–73. https://doi.org/10.1016/j.compstruct.2014.07.012

Zheng, T., Luo, W., Hou, R., Lu, Z., & Cui, J. (2020). A novel experience-based learning algorithm for structural damage identification: simulation and experimental verification. *Engineering Optimization*, *52*(10), 1658–1681. https://doi.org/10.1080/0305215X.2019.1668935

4th International Civil Engineering & Architecture Conference
17-19 May 2025, Trabzon, Türkiye

Relationship between slot gap length and fatigue performance in knife plate connections

Elif Aydın*[1,2], Fatih Alemdar[2]

[1] Istanbul Kultur University, Vocational Schools, 34158 Istanbul, Türkiye
[2] Yildiz Technical University, Faculty of Engineering, Department of Construction, 34220 Istanbul, Türkiye

Abstract. The need for high-rise structures with wide spans is increasing over time and steel construction technology is becoming importance day by day. Steel construction technologies are used in large structural systems, also referred to as mega structures. Therefore, every detail in the design phase is very important and it is necessary to investigate in detail which parameters are affected. In this study, welded connections in knife plate connections, which are frequently used in important projects such as bridges, high-rise structures and airports and can be damaged by repeated fatigue loads, were examined. Analyses were performed using the data of 7 specimens, the experimental studies of which were previously completed and the effect of the variability of the slot gap length between the welded plate and the slot opened in the HSS profile representing the connections under the effect of tensile forces on the fatigue performance was investigated. Tensile capacities were determined and a relationship was tried to be established between the fatigue performance. The results obtained from the experimental study were compared with the ABAQUS finite element analysis results. In addition, the stress range and cycle number were calculated by analytical method and the S-N diagram was determined and compared with the experimental results. It was observed that the experimental results and the finite element and analytical solution results converged.

Keywords: Fatigue; Steel structure; Knife plate connection; S-N diagram; Tensile capacity

1. Introduction

Steel bridges are among the most common civil engineering structures that must be designed for fatigue due to dynamic loads caused by repetitive traffic movements (EN, 1993). The increasing vehicle loads have raised concerns that fatigue-induced damage will become even more critical, highlighting the necessity for a more thorough investigation of connection details in steel bridges. Fatigue, which refers to the process of crack initiation and propagation due to irregular stress effects in steel structural connections can result in unforeseen and sudden failures, potentially leading to progressive collapse over time (Fisher et al., 1998). These fatigue cracks are caused by the repeated application of loads that are individually too small to cause immediate damage (Simulia, 2019).

The focus of this study, knife plate connections, are a commonly used type of connection in steel frame systems to enable joint configurations in structural steel design (Ebrahimi et al., 2019). Due to the repetitive loads occurring in these connections, exposure to fatigue loading is inevitable. Each parameter constituting knife plate connections, which are frequently used in steel structure design, must be investigated in detail. It is particularly important to identify the fundamental causes of fatigue-related problems frequently observed in connection elements in order to provide effective solutions. In this study, finite element analysis (FEA) was employed to develop fast and cost-effective solutions.

Due to the threat fatigue damage poses to structural safety, this process must be thoroughly investigated. The methods used in the fabrication of structural components should be evaluated from multiple perspectives. In this study, the aim is to investigate the effect of slot length on the tensile capacity of welded knife plate connections composed of box profiles, and to examine the relationship between tensile strength and fatigue performance.

In their study, Batistini et al. conducted experiments on knife plate connections of diagonal members fabricated from box sections with uniform slot lengths. Three of the specimens incorporated stress relief holes to reduce stress concentration, while the other three had slits directly welded using the plasma torch method without any drilled holes. The specimens with stress relief holes were classified as AASHTO Category E, with one specimen categorized as D. The remaining specimens without holes were classified under AASHTO Category E'. It was observed that the presence of stress relief holes led to a slight improvement in fatigue life. However, it was also

*Corresponding author, E-mail: elif.aydin@iku.edu.tr

https://doi.org/10.31462/icearc2025_ce_sme_935

found that the connection configuration of the specimens without holes, fabricated using conventional methods, did not significantly affect fatigue life (Battistini et al., 2013).

Willibald et al. aimed to evaluate the tensile issues caused by shear lag in knife plate connections of elliptical and circular profiles according to existing design standards. To this end, they conducted tension and compression tests on 13 slot-type connections, incorporating various parameters such as weld thickness, weld length, and geometric properties of the profiles. Their findings indicated that the shear lag effect plays a critical role in gusset plate connections, and that in the compression-tested specimens, local buckling at the profile ends hindered adequate connection performance. Based on these observations, they proposed recommendations for improvements to current design provisions (Willibald et al., 2006).

Zhao et al. conducted experimental studies to investigate the influence of various parameters on shear lag and the effective utilization of net cross-section in HSS (Hollow Structural Section) members. A total of 30 specimens with different geometries were tested, examining three variables each for knife plate thickness, the L/w ratio, and the slot length between the knife plate and the HSS member. Slot lengths of 5 mm, 25 mm, and 50 mm were used in the experiments. The results indicated that the variation in slot length did not significantly impact shear lag to the extent of producing substantial differences in performance based on plate thickness. Moreover, comparisons of specimens with L/w ratios less than and greater than 1 revealed similar efficiency in the use of the cross-section. The study also demonstrated higher capacity values than those specified in Canadian and American codes, allowing for comparative evaluation (Zhao et al., 2008). However, the effects of fatigue were not considered in this study.

McDonald and Frank conducted experimental studies on welded connections composed of single and double L-shaped profiles in X-type bracing frame systems with varying cross-sectional properties. Their aim was to investigate the effects of gusset plate thickness and weld length on fatigue performance and stress concentration. The test results indicated that specimens with single L profiles and shorter weld lengths exhibited lower fatigue performance. However, weld length and plate thickness were found to have minimal influence on stress concentration (Mc Donald & Frank, 2009).

Liu et al. experimentally examined the effect of the gap left between the slot made in HSS members and the knife plate on the fatigue performance of cross-bracing frame systems. They concluded that the gap between the edge of the slot and the knife plate had negligible influence on fatigue behavior (Liu et al., 2006).

2. Materials and methods

In this study, finite element analyses were conducted using the ABAQUS software for 7 specimens (Liu et al., 2006), for which experimental tests had already been completed, in order to evaluate their tensile and fatigue performance. The results of the analyses were compared with the corresponding experimental data.

A total of 7 test specimens were prepared as shown in Fig. 1, by welding knife plates made of ASTM A36 steel to both ends of 1700 mm-long HSS profiles. The cross-sectional and connection detail information of the 7 specimens is presented in Table 1. In this study, the influence of different gap lengths between the slot and the knife plate on the connection strength and fatigue performance is investigated. As shown in Table 1, this gap length was set to 50 mm, 5 mm, and 0 mm for specimens KPC05, KPC06, and KPC07, respectively. For the remaining specimens (KPC01, KPC02, KPC03, KPC04), the gap length was fixed at 25 mm.

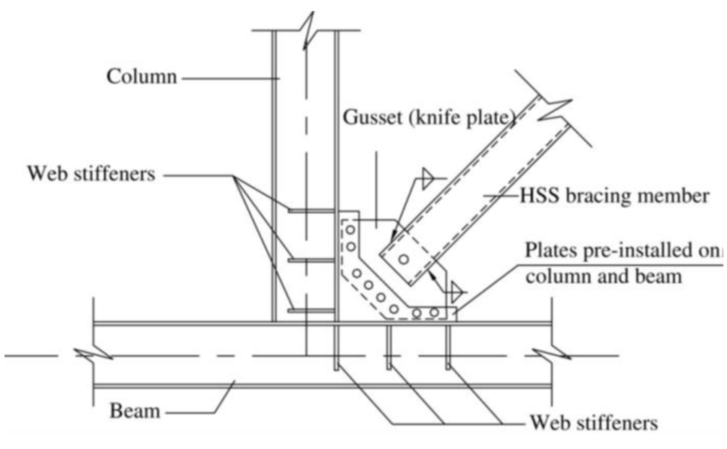

Fig. 1. Knife plate connection detail

Table 1. Test specimens

Specimen no	HSS length	HSS width	HSS thickness	Bolt hole diameter	Knife Plate width	Knife plate length	Knife plate thickness	Weld thickness	Weld length	Slot length
KPC01	1698.63	100.78	6.50	27.02	299.43	409.20	12.93	7.20	149.55	174.89
KPC02	1698.95	101.84	6.51	26.93	300.00	410.55	13.05	7.08	149.35	174.35
KPC03	1699.10	100.40	6.67	27.17	299.75	410.45	13.17	7.13	148.88	174.70
KPC04	1700.95	101.40	6.71	27.02	301.00	411.43	13.09	7.00	151.15	176.20
KPC05	1699.00	101.97	6.80	26.45	299.93	409.58	12.93	6.05	149.75	202.40
KPC06	1699.43	101.03	6.72	26.68	300.73	411.95	12.99	7.31	152.63	155.93
KPC07	1698.90	100.37	6.70	26.89	300.00	411.28	13.00	6.23	152.23	151.85

*All dimensions in mm.

3. Finite element analysis study

Finite element analysis for the 7 experimentally tested specimens was performed using the ABAQUS/Standard software (Simulia, 2018). In the modeling, the specimen length of 1700 mm was reduced to 450 mm, as shown in Fig. 2, to ensure a constant stress distribution along the length. This approach helped avoid excessive data and unnecessary computational time during the analysis.

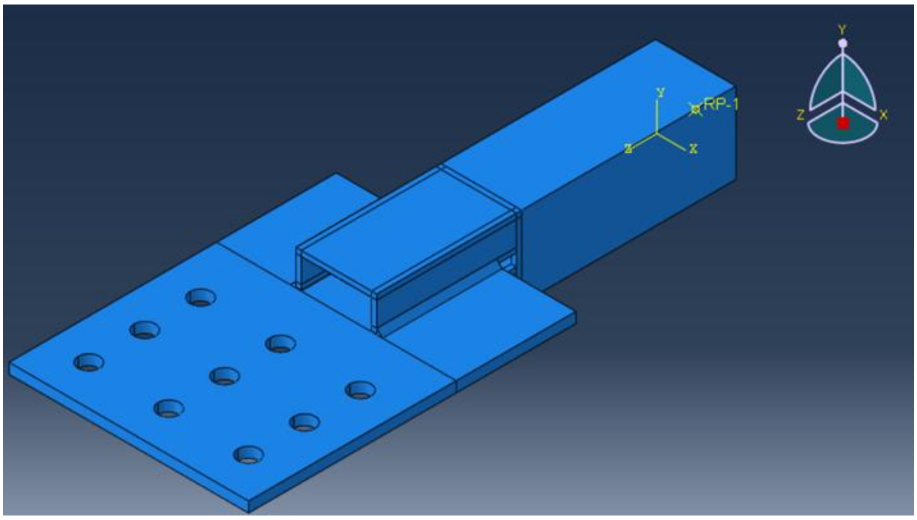

Fig. 2. Finite element model

In the finite element model, the gap lengths between the slit and the knife plate for specimens KPC05, KPC06, and KPC07 are shown in Fig. 3.

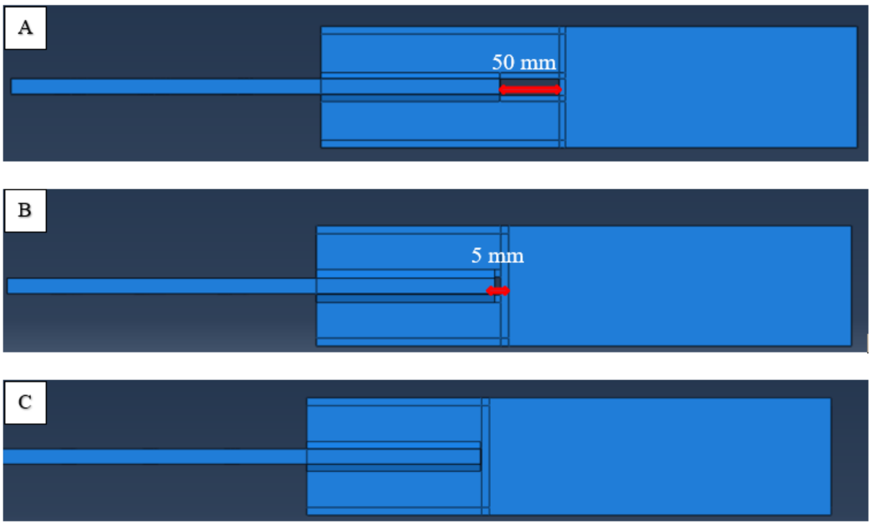

Fig. 3. KPC05 (A), KPC06 (B) ve KPC07 (C) FEM model

The material used is ASTM A36 steel. In ABAQUS, the material definition was provided in both elastic and plastic forms to represent the material's true behavior curve. The material properties are presented in Table 2.

Table 2. Material properties

Properties	Value
Steel	ASTM36
Modulus of Elasticity,E (MPa)	200000
Poisson ratio, ν	0.3

Considering the stress on the bolts, which are the main connection points of the Knife-plate, the bolt holes were divided into two and a pinned boundary condition was defined here. The boundary condition is shown in Fig. 4.

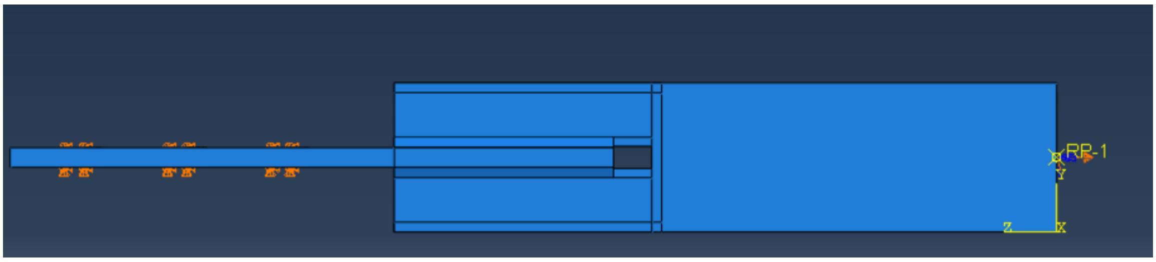

Fig. 4. Loading condition

The yield limit state of the connection was found to be critical and the displacement load corresponding to this condition was determined and 7 mm was given by defining the HSS surface to a reference point as shown in Fig. 5.

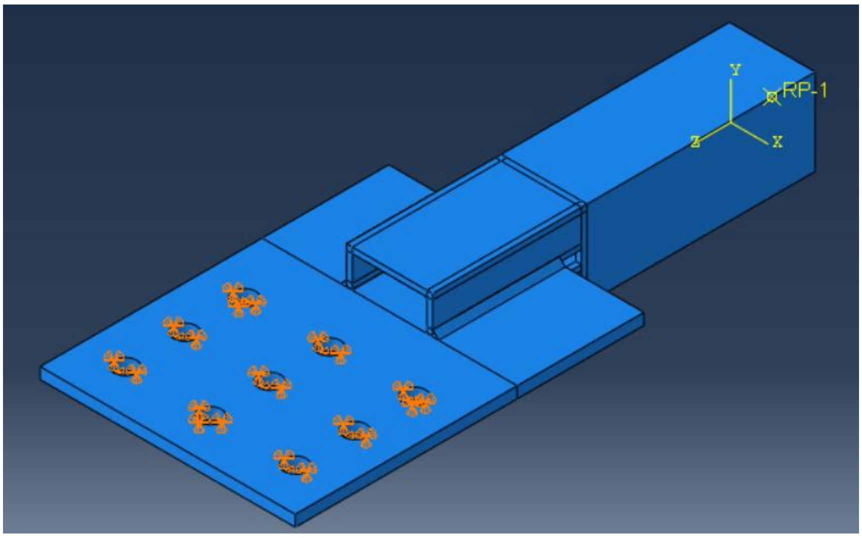

Fig. 5. Boundary condition

The regions where stresses are considered to be critical, including the weld and plate connection area as well as the regions near the weld in the HSS, were divided into smaller elements. As shown in Fig. 6, two types of mesh sizes were used.

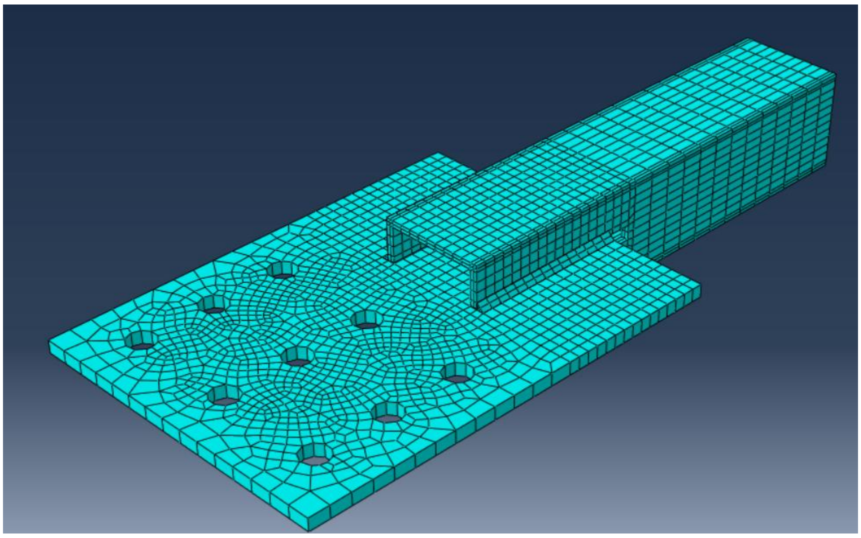

Fig. 6. Mesh configuration

4. Results and discussion

4.1. Finite element analysis results
In this study, the effect of the gap length between the initiation point of the slot in the HSS and the knife plate on both fatigue performance and tensile strength was investigated using 7 specimens subjected to experimental testing.

Table 3. Experimental and FEM comparisons

Specimen	Experimental strength (kN)	FEM strength (kN)	Displacement load for strength in FEM (mm)	Comparison (Experimental /FEM) (%)
KPC01	621	669	6.10	93
KPC02	625	669	6.21	93
KPC03	633	663	4.30	95
KPC04	645	689	6.73	94
KPC05	668	658	7.00	102
KPC06	668	684	4.00	98
KPC07	662	689	5.00	96

Based on the finite element analysis (FEA) results in Table 3, the distance between the slot and the knife plate was found to have no significant impact on the tensile capacity. The numerical results closely matched the experimental data. As confirmed by the experimental study, variations in this distance (50 mm, 5 mm, 0 mm) had minimal effect on fatigue performance. It was concluded that tensile strength and fatigue behavior follow similar patterns, suggesting that fatigue performance can generally be assessed based on this connection detail. The stress distribution from the FEA is shown in Fig. 7.

The strong correlation between experimental and numerical results suggests that parametric studies can be performed quickly and cost-effectively using FEA, eliminating the need for extensive physical testing for every variable. The load–displacemenet responses for specimens KPC05, KPC06, and KPC07 are illustrated in Fig. 8.

Comparisons with the standard specimen KPC01 are provided in the graphs in Fig. 9. The slot length used for KPC01 was 25 mm.

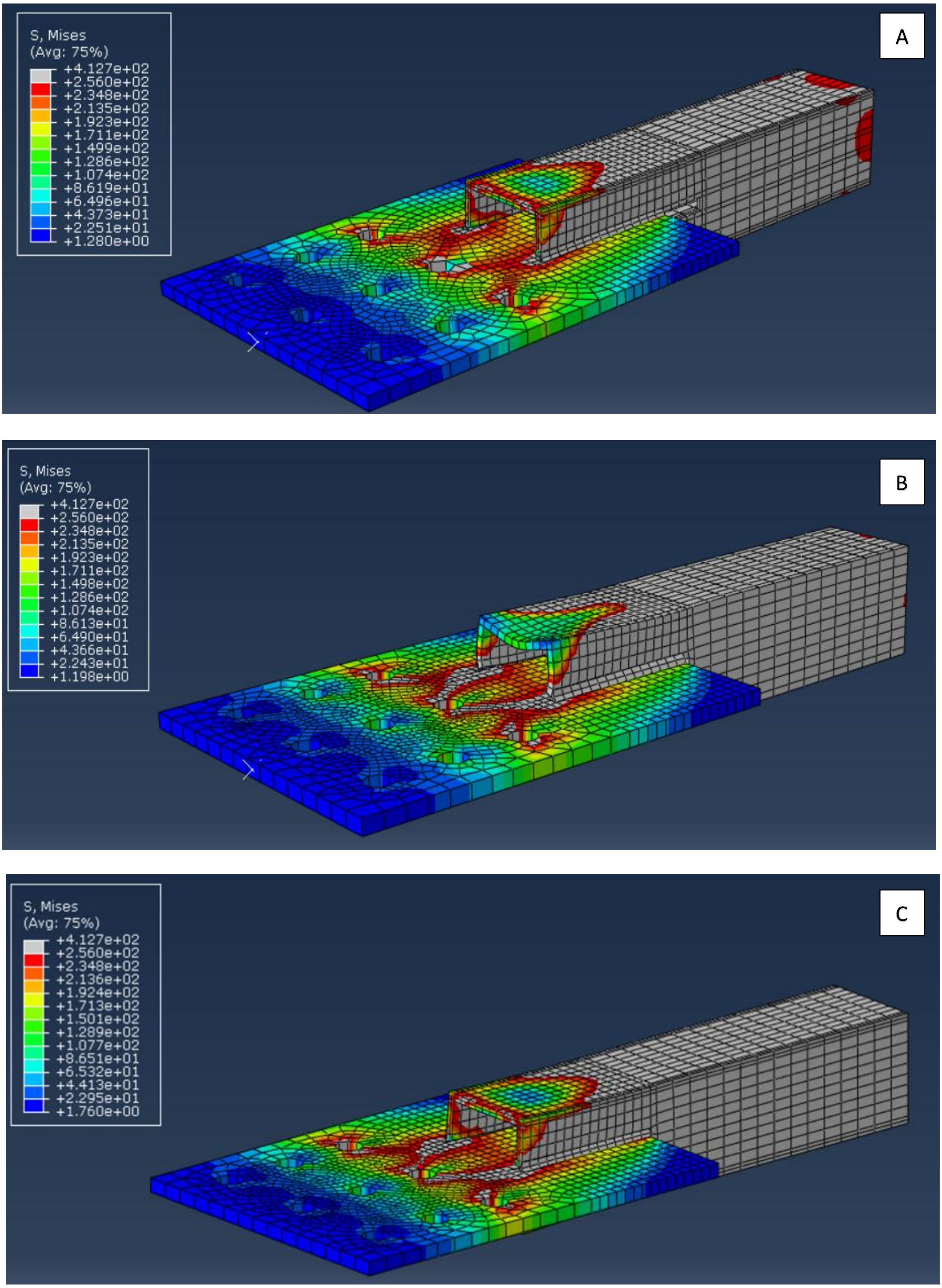

Fig. 7. KPC05 (A), KPC06 (B) ve KPC07 (C) FEM analysis results

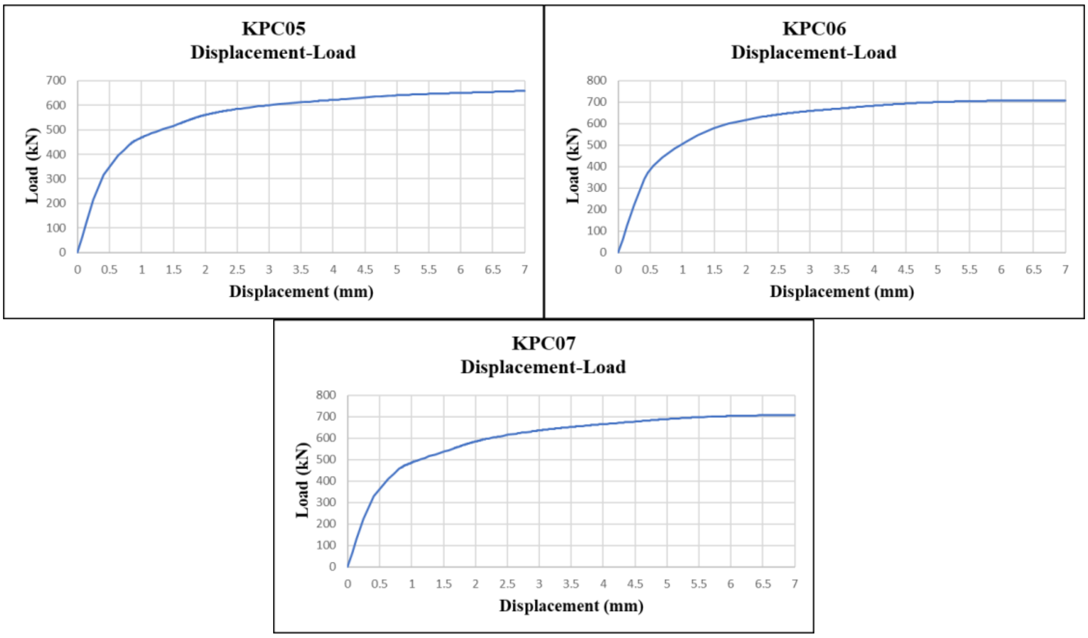

Fig. 8. KPC05, KPC06 ve KPC07 load-displacement curve

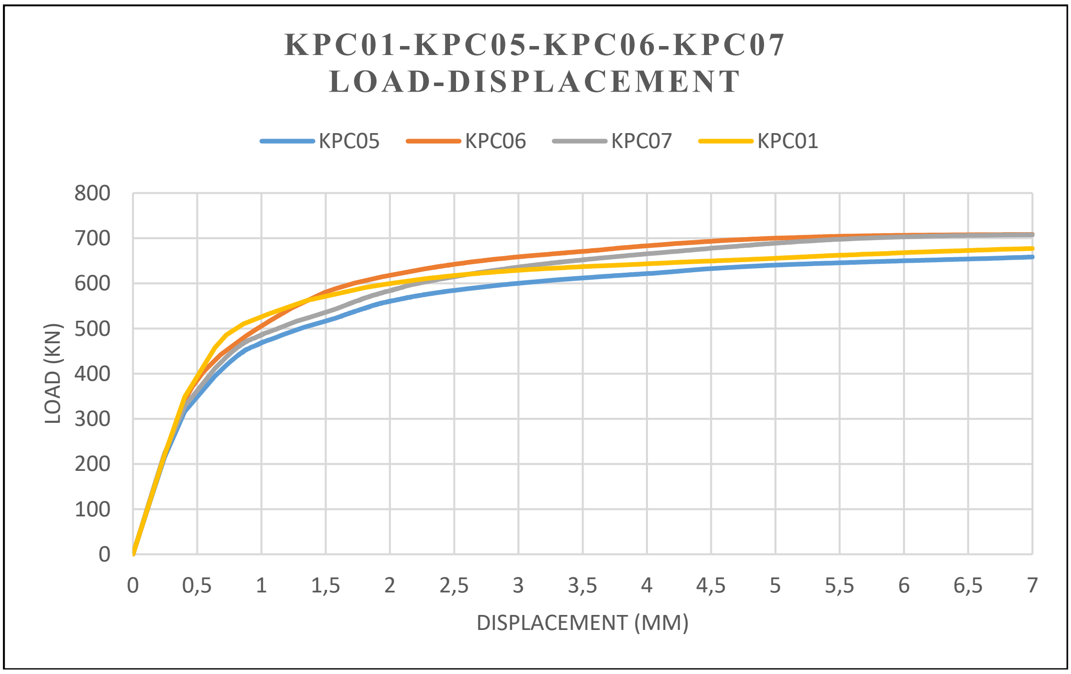

Fig. 9. Relation between KPC01-KPC05-KPC06-KPC07 specimen

4.2. Analytical solution results

Fatigue time calculations according to Paris rule are presented in Table 4. Considering the fact that the results of the experimental study contain many uncertainties, the pattern of change in the number of cycles in the results obtained from finite element analysis and the pattern of change (increase-decrease) in the experimental study are compatible. Fig. 10 shows the cycle number-stress range results obtained from finite element analysis. In addition, for similar stress range values, close fatigue performance was obtained in KPC05-KPC06-KPC07 specimens. According to the analytical calculations, it is seen that the change in slot gap length (0, 5 mm, 25 mm, 50 mm) does not affect the fatigue performance much.

Table 4. FEM results for failure

Specimen	Load range (kN)	Stress range (MPa)	Load/tensile design strength of HSS (%)	Number of cycles to failure (Experimental results)	Number of cycles to failure (FEM results)
KPC01	0-669	0-95	32	104 475	1400209
KPC02	0-669	0-189	64	37 283	177528
KPC03	0-663	0-273	95	8 457	58872
KPC04	0-689	0-231	78	22 570	97243
KPC05	0-658	0-218	75	16 228	115640
KPC06	0-684	0-221	75	18 357	111047
KPC07	0-689	0-225	76	17 260	105134

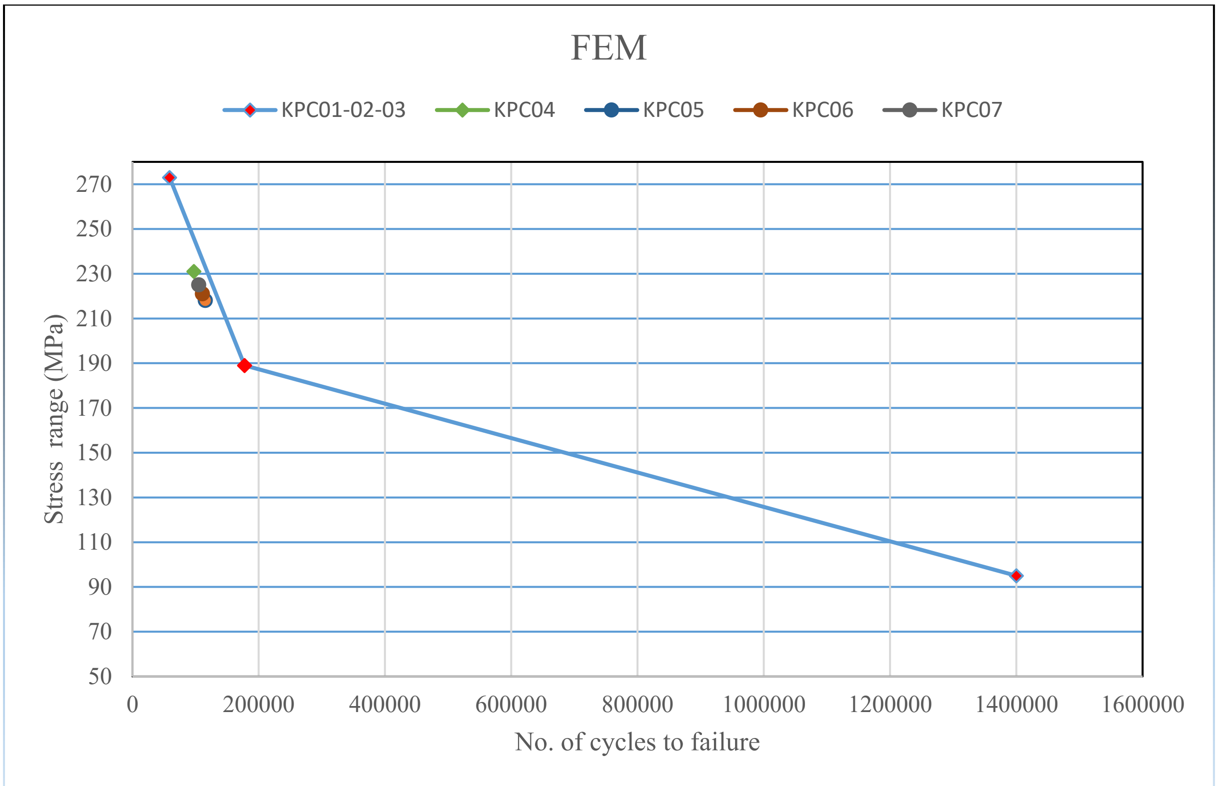

Fig. 10. Stress range vs. number of cycles to failure in FEM model

5. Conclusions

In this study, the effect of slot gap length on the tensile capacity of knife plate connections—a commonly preferred detail in high-rise buildings and bridge structures—was investigated. Finite element analyses were carried out based on a previously conducted experimental study, with the aim of establishing a relationship between tensile capacity and fatigue performance. According to the results obtained:

- It was observed that different slot gap lengths did not significantly affect the tensile capacity.
- A strong correlation of over 90% was observed between the numerical and experimental findings, demonstrating the reliability of the finite element model.
- Although similar tensile capacities were observed across different slot gap lengths, the presence and size of the slot gap play a critical role in achieving a more uniform stress distribution. Properly adjusting this detail may contribute to forming a connection configuration that more accurately represents the behavior of the joint under applied loads.
- Consequently, it can be concluded that while slot gap length has limited influence on ultimate tensile strength, it remains a key parameter in optimizing the structural performance and durability of knife plate connections.
- As a result of the analytical results according to the Paris rule, it was observed that there was no significant difference in fatigue performance between the standard specimens KPC01-KPC02-KPC03-KPC04 and

KPC05 (0), KPC06 (5 mm) and KPC07 (50 mm), where the effect of slot gap length on fatigue performance was investigated.

References

EN 1993-1-9. (2005). Eurocode 3: Design of steel structures - Part 1-9: Fatigue. The European Union.

Fisher, J.W., Kulak, G.L. & Smith, I.F. (1998). A Fatigue Primer for Structural Engineers. National Steel Bridge Alliance.

Simulia. (2019). Fatigue Theory Reference. 3Dexperience.

Ebrahimi, S., Mirghaderi, S.R., & Zahrai, S.M. (2019). Proposed design procedure for gusset plate dimensions and force distribution at its interfaces to beam and column. *Engineering Structures, 178*, 554-572

Battistini, A., Wang, W., Donahue, S., Helwig, T., Engelhardt, M., & Frank, K. (2013). Improved Cross Frame Details for Steel Bridges. Center for Transportation Research at The University of Texas at Austin.

Willibald, S., Packer, J., & Martinez-Saucedo, G. (2006). Behaviour of gusset plate connections to ends of round and elliptical hollow structural section members. *Canadion Journal of Civil Engineering, 33*, 373-383

Zhao, R.G., Huang, R.F., Khoo, H., & Cheng, J. (2008). Experimental study on slotted rectangular and square hollow structural section (HSS) tension connections. *Canadian Journal of Civil Engineering, 35*, 1318-1330

Mc Donald, G., S., & Frank, K., H., (2009). The Fatigue Performance of Angle Cross-Frame Members in Bridges. The University of Texas at Austin, American Institute for Iron and Steel, Report FSEL No: 09-1.

Liu Y., Dawe J., L., & Li, L. (2006). Experimental study of gusset plate connections for tubular bracing. *Journal of Constructional Steel Research, 62*, 132-143

Simulia. (2018). ABAQUS FEA Version 6.14-5. Providence.

ICEARC'25
4th International Civil Engineering & Architecture Conference
15-17 May 2025, Trabzon, Türkiye

Ohmic heating as a novel curing method for enhancing the properties of geopolymer mortars containing waste marble powder

Dilan Tuncer[1], Ekrem D. Sezer[1], Sahin Ekmekci[1], Mucteba Uysal[1], Furkan Sahin[2], Beyza Aygün[*3]

[1] *Yıldız Technical University, Department of Civil Engineering, 34220 Istanbul, Türkiye*
[2] *Nisantası University, Department of Civil Engineering, 34398, Istanbul, Türkiye*
[3] *Istanbul University-Cerrahpasa, Department of Civil Enginering, 34320 Istanbul, Türkiye*

Abstract. In this study, the development of hybrid (Fly Ash (FA)-Ground Granulated Blast Furnace Slag (GBSFS)-Marble powder (MP)) geopolymer mortars/composites was discussed with the aim of providing sustainable alternatives to traditional concrete by using different curing methods. Equal proportions of fly ash and ground granulated blast furnace slag were used as binder materials in geopolymer production. Equal proportions of marble powder and river sand were used as aggregates. In the activation process, it was aimed to improve the mechanical properties by using chemical activators at Na_2SiO_3 + NaOH ratios of 2:1 and 6, 8 and 10M. For this purpose, the effects of different curing processes on the mortars were investigated by applying electrical curing (30V), thermal curing (80°C, 24 hours) and ambient curing (23±2°C, 95% humidity) methods among the curing methods. In this context, physical properties such as unit volume weight, water absorption, void ratio and capillarity and mechanical properties such as pressure and bending strength tests were carried out on the 7th and 28th days. For the series (10M) with the highest average strength, the same tests were repeated by adding 0.5% carbon FIBER by volume. In the results, the compressive strength of the 10M-FIBER-ELECTRIC sample was found to be 30.13 MPa and the bending strength was found to be 7.22 MPa.

Keywords: Geopolymer, Recyling Concrete Aggregate, Curing Methods, Mechanical Properties.

1. Introduction

Concrete, a pillar of contemporary construction and architecture, remains the most prevalent material in global construction activity. The annual use of concrete is currently estimated to exceed ten billion tons and is second only to water in the volume used by humans. This unrivaled dominance is largely a consequence of its beneficial engineering properties such as high compressive strength, ease of mold shape retention, ready availability of raw materials in most geographical locations, low cost of production, and flexibility in tolerating diverse environments and structure conditions. However, the very ubiquity of concrete and especially concrete produced with ordinary Portland cement (OPC) used as the main binding material has generated serious ecological and financial worries. Processing OPC is energy-intensive and depends almost singly upon calcination of raw materials and limestone at temperatures of about 1450°C. This releases enormous amounts of carbon dioxide (CO_2) and contributes almost 7% to the CO_2 emissions of the planet. Further, the energy needed to power these high-temperature processes contributes about 15% to the resultant industrial energy demand of the planet. These statistics of concern have triggered exhaustless research activity aimed at seeking alternative binders that can rival and even surpass traditional cement performance with lessening the ecological impact of traditional cement fabrication. One of the most promising alternatives in this endeavor is geopolymer technology (Malhotra, 2002; Meyer, 2009; Madlool et al., 2011)

Geopolymers constitute a group of amorphous aluminosilicate-based inorganic polymers that set at room temperature or mildly elevated temperatures by the alkali activation of precursors such as metakaolin, zeolite, industrial by-products, and fly ash and ground granulated blast furnace slag (GBFS). geopolymerization process is a sequence of sequential and related steps involving the dissolution of the source of aluminsilicate in a medium of alkaline nature, rearrangement and polycondensation of reactive monomers to oligomers, and resulting in the formation of a set of rigid, polymeric networks based predominantly of Si-O-Al bonds with properties being largely

* Corresponding author, E-mail: beyza.aygun@ogr.iuc.edu.tr

https://doi.org/10.31462/icearc2025_ce_sme_951

golden light publishing

dependent on the Si/Al molar ratio, the type and concentration of the activator of the alkali, the curing regime, and the ratio of water to solid matter. Geopolymer has significant benefits from a sustainability standpoint. Besides having a production carbon footprint up to 80% lower than that of OPC in terms of CO_2 release, geopolymers also use industrial by-flow streams as major feedstocks, hence encouraging material flow recycling and valorization of wastes. Moreover, geopolymers have good chemical resistance, good thermal stability, low shrinkage, and great mechanical properties and hence can be used in various applications such as in construction concrete, refractory fire panels, hazardous waste immobilization, and advanced composites (Luga, 2015; Boyaci, 2018; Sahin et al., 2020; Singh & Middendorf, 2020).

Current research is conducted in this context and aims to develop and examine a high-performance geopolymer mortar that is a promising substitute to conventional cement-based composites. In the current investigation, Class F type fly ash (FA) and GBFS were mixed in similar weight proportions to act as the reactive binding phase. For activating the system, a binary alkaline solution of sodium hydroxide (NaOH) and sodium silicate (Na_2SiO_3) was used. Three different concentrations of NaOH of 6M, 8M, and 10M were used to examine the role of alkalinity in reaction kinetics and material properties. NaOH to Na_2SiO_3 ratio was kept constant at 1:2 by weight in all of the blends to be uniform and comparable in nature. For the filler materials, a 1:1 mixture of marble powder (MP) and river sand was added to take advantage of the fine particle size and chemical inertness of the MP to improve packing density and minimize permeability. Carbon fibers (CFs) were also added to some of the mixes to determine the influence of micro-reinforcement on strength properties. CFs ossess high tensile strength, low density, and chemical stability and can be capable of spanning microcracks and countering brittle modes of failure typically seen in geopolymer matrices. The primary aim of this research is to examine the synergistic impact of molarity change and carbon fiber reinforcement on fresh and hardened properties of geopolymer mortars. An extensive set of tests was employed to assess compressive strength, flexural strength, ultrasonic pulse velocity, water absorption, void percentage, unit weight, and capillarity properties. These tests give not just information about the mechanical strength, but also the durability and long-term performance of the resultant geopolymer mortar. Finally, the results look to add to the literature supporting sustainable construction methods and to pinpoint available routes to de-carbonize the built environment.

2. Materials and methods

2.1. Materials

GBFS was used in the composition of the geopolymer mortar system used in the current experimental study as the main binding component. GBFS with a specific gravity of 2.91 g/cm³ was used in the study and is in correspondence with the general density range of high-calcium slag products. Because of its glassy and amorphous nature and also high reactivity in the presence of alkaline environments, GBFS is most favorable to be used in geopolymerization reaction and in contributing to the development of a resistant aluminosilicate network structure.

Class F was the type of FA used and is a low-calcium type typically recovered from coal combustion operations. It had a relatively low specific gravity of 1.96 g/cm³ because of its relatively low particle size and porosity. GBFS-fly ash synergistic reaction under alkaline activator conditions leads to the formation of a denser microstructure and increased setting times and appreciable thermal stability.

Supplementary filler was also provided in the form of MP to be used in conjunction with the binders. This had a specific gravity of 2.70 g/cm³ and was largely made up of calcium carbonate material. MP was added to the mixture to enhance packing density and lower permeability and also to enhance the surface finish of the set mortar. Its chemical inertness prevents it from disrupting the geopolymerization reaction whilst providing additional physical contributions to the system.

Fine aggregate used was natural river sand with particle size distribution from 0 to 5 mm. Specific gravity of the natural river sand was 2.65 g/cm³ and absorbed water at a rate of 1.2%. These figures reflect a high-quality aggregate to be used in mortar purposes. Pre-washing and drying of sand was performed to eliminate impurities and achieve uniformity. Its gradation curve in Figure 2.1 shows accordance with ASTM C33 standards of fine aggregate in use in structural concrete to assure a good balance of workability and mechanical interlocks in the matrix.

CFs were added as a micro-reinforcement material to enhance the tensile and flexural properties of the mortar. These fibers were of 7 mm length with a density of 1.80 g/cm³ and a specific volume weight of 390 g/l and were added at a dosage of 0.5% by volume to achieve optimal fiber dispersion and bonding without influencing the workability. CFs with high tensile strength, chemical inertness, and good crack-bridging capacity are recognized to enhance the ductility and sustainability of cementitious and geopolymer composites. In the current research, the fibers were evenly distributed into the matrix during the mixing to achieve uniform reinforcement and avoid fiber clustering and segregation problems.

Chemical composition of the main materials—GBFS, FA, and MP—involved in the current research is shown in Table 1 and gives information on the elemental constituents that affect the geopolymerization reaction and the physical-mechanical properties of the resulting geopolymer mortars.

Table 1. Chemical properties of materials

Oxide/Component	GBFS (%)	FA (%)	MP (%)
SiO_2	40.5	57.72	1.12
Al_2O_3	12.8	25.83	0.73
Fe_2O_3	1.1	6.6	0.05
CaO	35.5	1.74	
MgO	5.8	2.44	
SO_3	0.18	0.11	0.56
Na_2O	0.79	0.6	
TiO_2	0.75		
K_2O		3.69	
Ca_2O_3			83.22
Loss of Ignitionn(LOI)	0.03	1.12	14.8

In this study, NaOH was used as the primary alkaline activator and was prepared at molar concentrations of 6 M, 8 M and 10 M. The solutions were dissolved in deionized water for at least 24 h before sample casting to ensure complete dissolution and thermal stabilization. Na_2SiO_3 was used as a secondary activator to increase silicate availability during the geopolymerization process. Synergistic interaction between NaOH and sodium silicate plays an important role in regulating the dissolution kinetics of aluminosilicate precursors and promoting the formation of geopolymeric networks.

Detailed physical and chemical properties of sodium silicate are presented in Table 2, while the compositional properties of sodium hydroxide are given in Table 3.

Table 2. Physical and chemical properties of sodium silicate used in the study

Feature	Na_2O (%)	Si_2O (%)	Intensity (g/ml) (20 °C)	Fe (%)	Heavy Metals (%)
Amount(%)	8.2	27	1.36	≤0.005	≤0.005

Table 3 Chemical properties of sodium hydroxide used in the study

Component	NaOH	Na_2CO3	Cl	SO_4	Al	Fe
Amount (%)	99,1	0,3	<0,01	<0,001	0	0

3. Results and discussion

3.1. Physical properties

Unit volume weight in the 19 tested samples ranged from a low of 2.33 g/cm³ for Sample 19 (10M-Fiber-Electric) to a high of 2.46 g/cm³ in Sample 2 (6M-Thermal). Average unit weight was determined to be 2.393 g/cm³ with a standard deviation of around 0.045 g/cm³. In comparison with the average, Sample 2 registered a positive deviation of +2.8%, and Sample 19 registered a negative deviation of -2.6%. Coefficient of variation (CV) of all the samples was 1.88%, which shows that relatively uniform density levels were observed with small fluctuations depending upon molarity and fiber quantity. Observably, carbon fiber mixes registered an average weight loss of 0.06 g/cm³ compared to fiberless mixes. Weight difference between electric-cured and thermally cured samples at 6M molarity was 0.02–0.04 g/cm³ showing the densifying action of heat treatment (Table 4).

Void ratio values were between 15.91% (Sample 8, 10M-Ambient) and 24.83% (Sample 12, 6M-Electric) with a total range of 8.92%. The mean of all samples was 19.71% with a deviation of 2.76%. Sample 12 was the most porous in deviation from the mean at +25.9%, and Sample 8 at -19.3%. Regression of molarity against the void ratio was linear and negative with $R^2 \approx 0.78$ and demonstrates that higher alkaline concentration leads to a more closely packed matrix. In the comparison of curing methods, electric curing had a mean void ratio of 21.94%, thermal curing 18.38%, and ambient curing 17.69%. This indicates that ambient and thermal curing methods are more effective in reducing the formation of voids at similar molarities. Void ratio was negatively proportional to unit weight ($r = -0.68$) and therefore supported to be inextricably linked with them (Table 5).

Table 4. Unit volume weights of geopolymer mortars

Sample No.	Unit Weight (g/cm^3)
1	2.45
2	2.46
3	2.45
4	2.40
5	2.42
6	2.44
7	2.44
8	2.36
9	2.36
10	2.37
11	2.39
12	2.45
13	2.42
14	2.41
15	2.37
16	2.34
17	2.36
18	2.36
19	**2.33**

Table 5. Void ratio of geopolymer mortars.

Sample No.	Void Ratio (%)
1	19.61
2	19.83
3	20.05
4	17.35
5	17.66
6	18.72
7	18.41
8	**15.91**
9	16.24
10	17.32
11	17.31
12	**24.83**
13	23.45
14	22.79
15	21.62
16	20.94
17	20.99
18	18.02
19	23.78

Water absorption ranged from 8.00% to 13.46%, having a mean of 10.29% and the standard deviation of 1.61%. Sample 12 (6M-Electric) with the highest absorption was +30.8% above the mean and the lowest absorptive Sample 8 (10M-Ambient) was -22.3% below it. Comparison indicated that water absorption was positively correlated with the void ratio (r = +0.82) and negatively correlated with molarity (r = -0.74). This is in accordance with the fact that higher alkaline activation reduces accessible pores and hence water absorption. Electric curing at lower molarity produced the maximum absorption with unformed areas of gels and trapped microvoids. Addition of carbon fiber additives caused hardly any change in water absorption in a direct way, yet it indirectly affected outcomes by changing internal connectivity of the matrix (Table 6).

Table 6. Water absorption rate of geopolymer mortars

Sample No.	Water Absorption (%)
1	9.94
2	10.05
3	10.25
4	8.76
5	8.85
6	9.44
7	9.25
8	8.00
9	8.21
10	8.83
11	8.76
12	13.46
13	12.65
14	12.27
15	11.65
16	11.32
17	11.25
18	9.31
19	13.41

Range in capillary rise was from 5.29 µm (Sample 16, 10M-Electric) to 9.18 µm (Sample 12, 6M-Electric) with an average of 7.14 µm. Standard deviation was 1.15 µm and coefficient of variation was 16.1%. Similar to other properties, with increasing molarity, capillarity decreased. 6M samples had a mean of 8.72 µm and 10M samples had a mean of 6.11 µm—reduced by 29.9%. In comparison of electric-cured samples only, from 9.18 µm at 6M to 5.29 µm at 10M gave evidence of a 42.3% improvement in capillarity. $R^2 = 0.81$ was what regression gave from molarity vs. capillarity that confirmed that concentration of the activator plays a dominant role in controlling water transport routes. Reduced capillarity is translated to increased durability and resistance to water in actual applications, especially in freeze-thaw or coastal conditions (Fig. 1.).

3.2 Mechanical properties

When the compressive strengths of geopolymer mortars were examined, it varied between 9.25 MPa and 22.83 MPa for the 7th day. Maximum compressive strength was observed in sample number 11 (10M-FIBER-THERMAL) and the minimum compressive strength was observed in sample number 7 (10M-AMBIENT). In AMBIENT and THERMAL curings, the compressive strength decreased with increasing molarity. In ELECTRIC curing, the compressive strength increased with increasing molarity and THERMAL curing method showed better performance than other curing methods at all molarities. Carbon fiber showed positive performance for compressive strength in all curing methods. Compressive strength of geopolymer mortars varied between 14.1 MPa and 30.13 MPa for the 28th day. Maximum compressive strength was observed in sample number 12 (10M-FIBER-ELECTRIC) and minimum compressive strength was observed in sample number 3 (6M-FIBER-ELECTRIC). While compressive strength was maximum at 8 M in AMBIENT curing, compressive strength decreased with increasing molarity in THERMAL curing and compressive strength increased with increasing molarity in ELECTRIC curing. In 10M-FIBER, ELECTRIC curing showed better performance than THERMAL and AMBIENT curings. Carbon fiber showed positive performance for compressive strength in all curing methods (Fig. 2.).

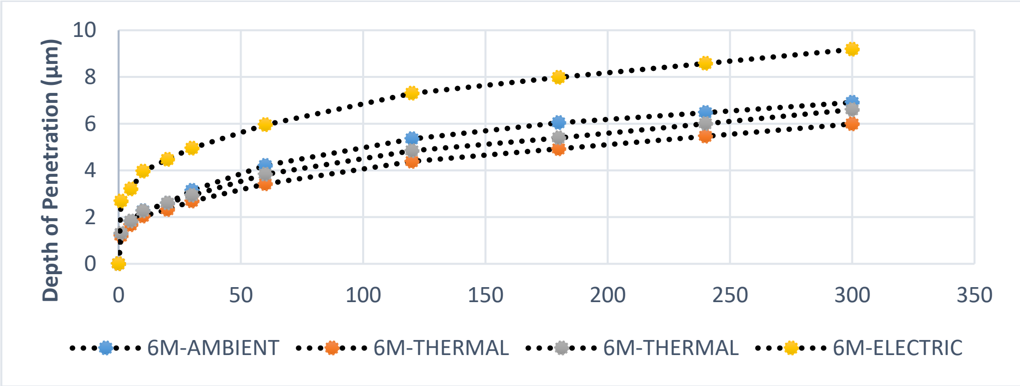

a) (6M)

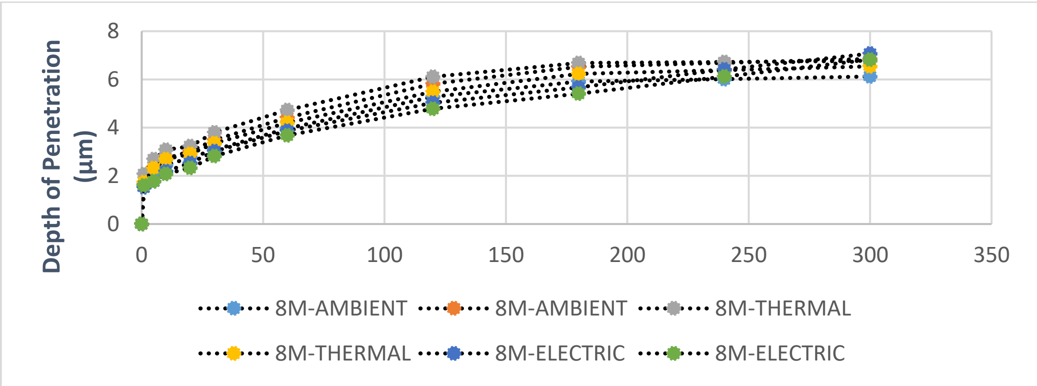

b) (8M)

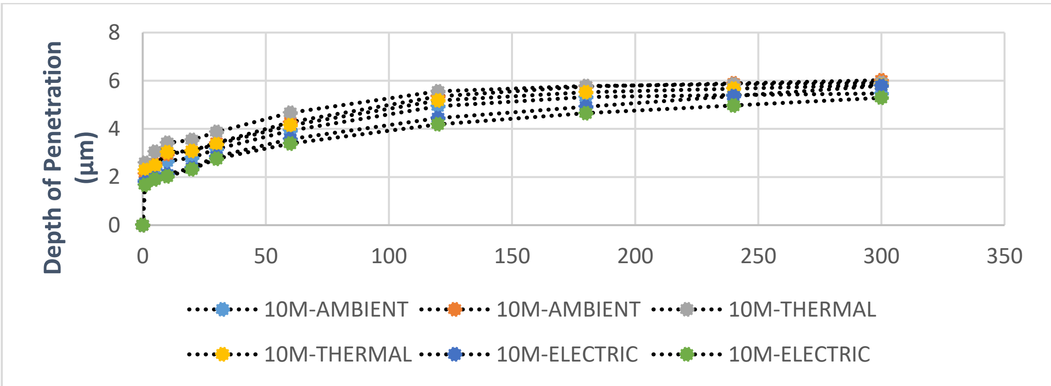

c) (10M)

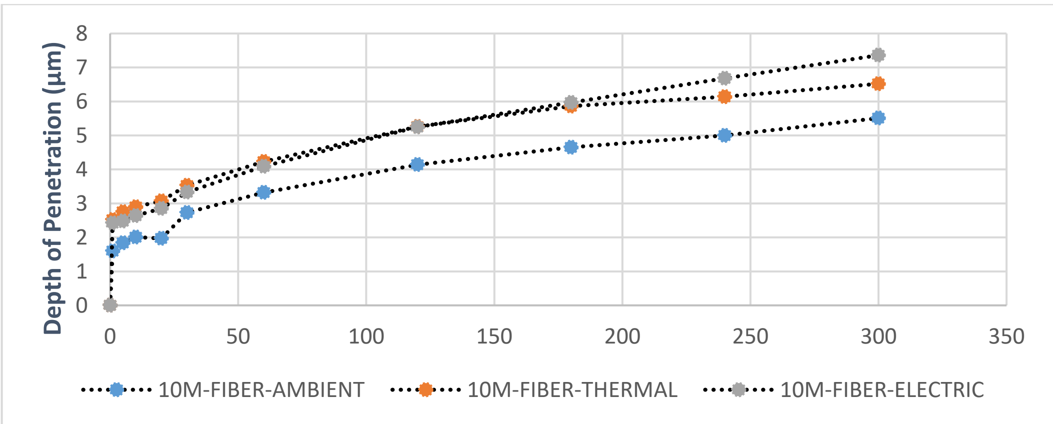

d) (10M FIBER)

Fig. 1. Capillarity test results (6M, 8M, 10 M and 10M-FIBER series).

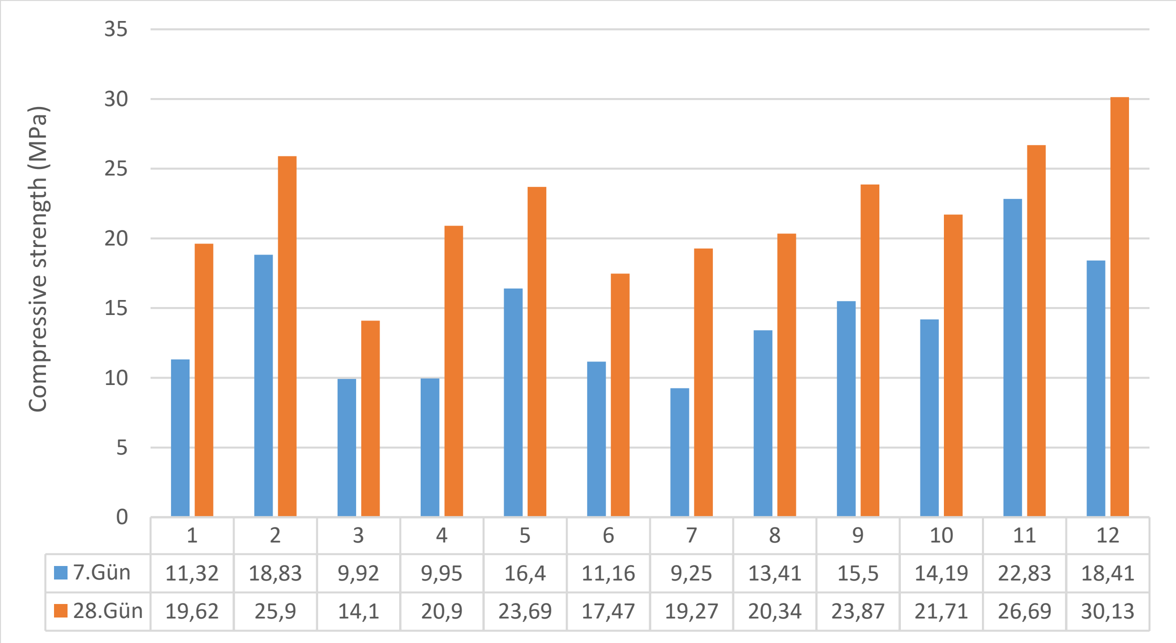

Fig. 2. Compressive strength results (7 and 28d).

Flexural strength of geopolymer mortars varied between 3.19 MPa and 7.08 MPa for day 7. The maximum flexural strength was observed in sample number 12 (10M-FIBER-ELECTRIC) and the minimum flexural strength was observed in sample number 7 (10M-AMBIENT). In AMBIENT and THERMAL curings, flexural strength decreased with increasing molarity, but in ELECTRIC curing, flexural strength increased with increasing molarity and carbon fiber exhibited positive performance for flexural strength in all curing methods. On day 28, flexural strengths were obtained between 3.68 MPa and 7.22 MPa, while the maximum flexural strength was determined in sample number 12 (10M-FIBER-ELECTRIC) and the minimum flexural strength was determined in sample number 3 (6M-FIBER-ELECTRIC). While carbon fiber provided an increase in bending strength similar to compressive strength in all curing methods, almost all of its strength was gained on the 7th day in all curing methods (Fig. 3.).

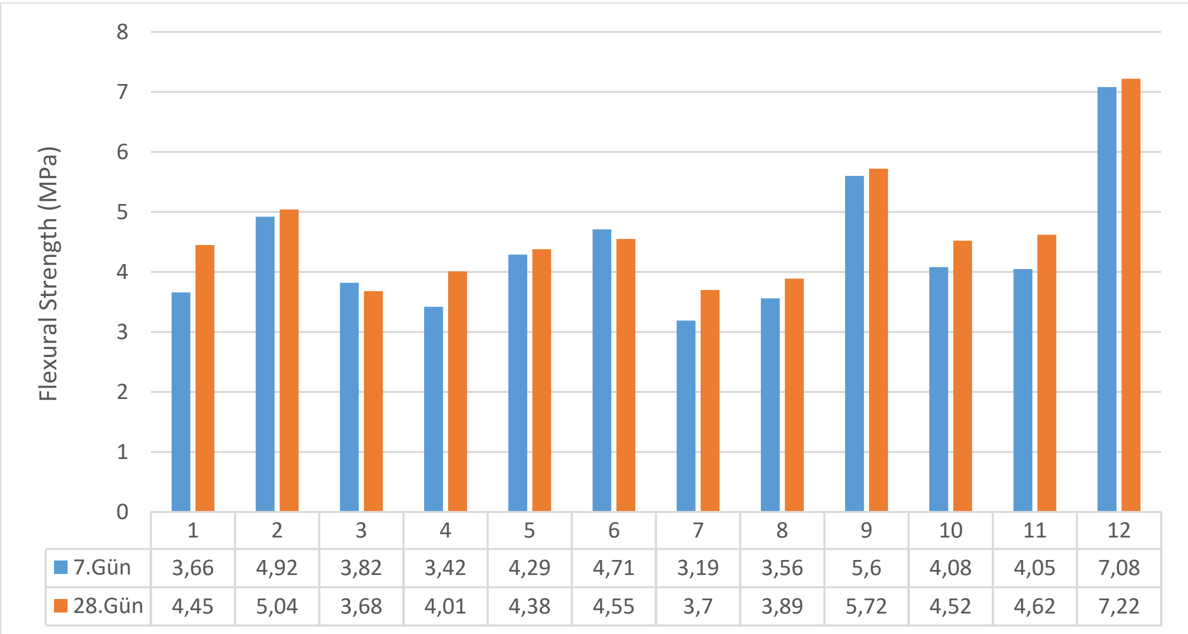

Fig. 3. Flexural strength results (7 and 28d).

4. Conclusions

- 10M-FIBER-ELECTRIC, which reached 7.08 MPa in flexural strength, is the sample that gave the best performance in 7 days.
- 10M-AMBIENT, which reached 3.19 MPa in flexural strength, is the sample that gave the worst performance in 7 days.
- 10M-FIBER-THERMAL, which reached 22.83 MPa in compressive strength, is the sample that gave the best performance in 7 days.
- 6M-ELECTRIC, which reached 9.92 MPa in compressive strength, is the sample that gave the worst performance in 7 days.
- 10M-FIBER-ELECTRIC, which reached 7.22 MPa in flexural strength and 30.13 MPa in compressive strength, is the sample that gave the best performance in 28 days.
- 6M-ELECTRIC, which reached 3.68 MPa in Flexural strength and 14.10 MPa in compressive strength, is the sample that gave the worst performance in 28 days.

References

Boyacı, Ö. (2018). *Geopolymer behavior of different kaolins in metakaolin and spinel structures* (Master's thesis). Dumlupınar University. (In Turkish)

Luga, E. (2015). *Properties of fly ash and blast furnace slag geopolymer mortars* (Doctoral dissertation). Erciyes University. (In Turkish)

Madlool, N. A., Saidur, R., Hossain, M. S., & Rahim, N. A. (2011). A critical review on energy use and savings in the cement industries. *Renewable and Sustainable Energy Reviews, 15*(4), 2042–2060.

Malhotra, V. M. (2002). Introduction: Sustainable development and concrete technology. *Concrete International, 24*(7), 22–27.

Meyer, C. (2009). The greening of the concrete industry. *Cement and Concrete Composites, 31*(8), 601–605.

Singh, B., & Middendorf, B. (2020). Geopolymers as an alternative to Portland cement: A review. *Construction and Building Materials, 237*, 117651. https://doi.org/10.1016/j.conbuildmat.2019.117651

Şahin, F. (2020). *Investigation of mechanical and durability properties of metakaolin-based geopolymer mortars produced with different types of aggregates* (Doctoral dissertation). Istanbul University-Cerrahpaşa. (In Turkish)

Size optimization of truss footbridge using BMR and BWR algorithms

Büşra Yakak[1], Barbaros Atmaca*[1], Hülya Aksoy[1]

[1]*Karadeniz Technical University, Department of Civil Engineering, 61080 Trabzon, Türkiye*

Abstract. Truss footbridges (TFBs) are widely preferred in engineering structures thanks to their features such as light weight and durability. However, material utilization and cost effectiveness are of great importance in the design of these structures. Therefore, size optimization is an important engineering problem in the design of TFBs. In this study, the Best-Mean-Random (BMR) and Best-Worst-Random (BWR) algorithms is proposed for the size optimization of the selected 132-element TFB. The size optimization process is carried out by integrating SAP2000 and MATLAB software using SAP2000's Open Application Programming Interface (OAPI) features. For the size optimization of TFB, the finite element model of the bridge was first created in the SAP2000 program and then the analysis results were transferred to the MATLAB programming language through SAP2000-OAPI. In the optimization process, the BMR and BWR algorithms optimized the size of the bridge elements in each iteration using this data. At each iteration, the structural suitability of the proposed new design was checked by re-analysis with SAP2000 and the optimization process was carried forward in this cycle. As a result, this study reveals that the integration of SAP2000 and MATLAB with the BMR and BWR algorithm provides an effective solution to the size optimization problem of TFBs. As a result of the study, it was seen that the BMR algorithm exhibited a more stable convergence and could produce lighter and therefore more efficient solutions compared to the BWR algorithm.

Keywords: BMR algorithm; BWR algorithm; SAP2000-OAPI; Size optimization; Truss footbridge

1. Introduction

Steel truss footbridges (TFBs) are engineering structures designed in an economical and durable way using triangular truss systems to span wide spans. They are widely used in railway and highway thanks to their advantages such as lightness and high carrying capacity. However, due to the high cost and maintenance requirements of steel materials, optimizing the use of materials in the design process is of great importance. At this point, it is necessary to determine the most suitable sections with engineering calculations and to increase structural performance (Megson, 2019).

Size optimization is a critical engineering problem to increase the cost-effectiveness of steel TFBs and ensure structural safety. Having more than necessary cross-sectional area of steel elements can lead to material waste and additional costs, while insufficient dimensioning can negatively affect structural strength. For this reason, optimization techniques focus on determining the dimensions of steel elements in a way that provides maximum efficiency with minimum material while maintaining the load-carrying capacity.

Although great advances have been made in the field of engineering today, the use of current optimization algorithms in the size optimization of steel TFBs is still not sufficient. Traditional methods usually include analytical solutions based on certain assumptions or numerical approaches with limited iterations, which makes it difficult to reach a global optimum solution in the design process. Especially in large-scale and complex truss systems, traditional optimization methods often get stuck in local minima. In addition, the integration of advanced techniques such as current metaheuristic algorithms into engineering applications is limited. This deficiency causes the cost-effectiveness of steel TFBs not to be fully achieved and ideal solutions in terms of structural performance not to be achieved. Therefore, the more widespread use of current algorithms in dimensional optimization will both increase engineering efficiency and contribute to sustainable design processes.

Farahmand-Tabar and Babaei (2023), developed the multi-verse optimizer (MVO) algorithm based on the multiverse theory and proposed its memory-assisted adaptive version (MAMVO). They showed that it provides superior performance compared to both classical MVO and other algorithms in truss structure optimization problems. Focusing on solving large-scale problems in rod systems, Etaati et al. (2024) integrated the cooperative

* Corresponding author, E-mail: atmaca@ktu.edu.tr

https://doi.org/10.31462/icearc2025_ce_sme_964

coevolutionary marine predators algorithm (CCMPA) with the greedy search (GS) method. This study addressed the problem of performance loss as the scale increases in the literature. Nemati et al. (2024) proposed the connected banking system(CBS) optimization algorithm in solving truss optimum design problems and tested it for both small-scale and large-scale structures and produced competitive results compared to existing methods in the literature. Ugur and Degertekin (2025) proposed the NCSBO algorithm, a new approach developed based on the circulatory system-based optimization (CSBO) algorithm, in order to improve the performance in shape and size optimization of truss structures. In the study, they demonstrated the effectiveness of the NCSBO algorithm in reaching the optimum design.

Structural optimization problems can be difficult to solve with classical deterministic methods due to their complex structure. For this reason, meta-heuristic algorithms have come to the fore in solving these problems, especially in recent years. The aim of this study is to perform the size optimization of the 132-element steel TFB system with minimum weight. In this context, two metaheuristic algorithms found in the literature, Best-Mean-Random (BMR) and Best-Worst-Random (BWR) algorithms, were used. The size optimization process was carried out by integrating SAP2000 (2016) and MATLAB (R2023b) software using SAP2000's Open Application Programming Interface (OAPI) features. First, the three-dimensional finite element model of the bridge was created in SAP2000 program, and then the analysis results were transferred to MATLAB via OAPI. In each iteration, the BMR and BWR algorithms optimized the cross-sections of the bridge elements. Similarly, Atmaca (2021a) and Atmaca (2021b) also performed optimization studies by integrating MATLAB and SAP2000 via OAPI, demonstrating the effectiveness of this approach in determining optimum post-tensioning cable force and minimizing the total cable weight in cable-stayed footbridges.

2. Description of the truss footbridge

In this study, a two-span steel TFB model consisting of 132 elements with 36 nodes is investigated within the scope of the optimum size problem. The elements forming the structural system of the bridge are divided into six main groups as G_1, G_2, G_3, G_4, G_5 and G_6. These groups are lower edge, upper edge, diagonal, middle zone lower edge, middle zone upper edge and middle zone diagonal elements respectively.

The length of each element of the TFB used in the model is 4 m, the total span is 32 m and the vertical height of the system is 4 m. Two different perspectives of the steel bridge, three dimensional and front view, are given in Fig. 1. Each group is defined with different colors and this information is given in detail in Table 1, and the profiles are listed in Table 2.

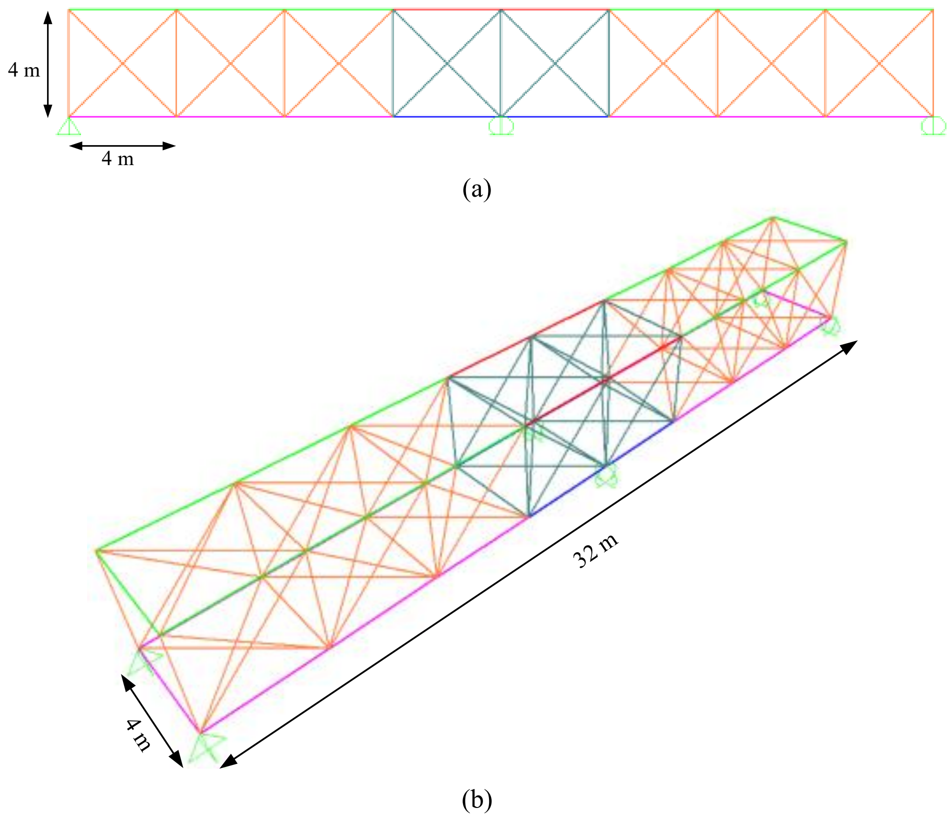

Fig. 1. TFB (a) front view and (b) three-dimensional view

Table 1. Definitions of element groups

Structural group	Assigned color	Number of element
Lower edge		14
Upper edge		14
Diagonal		68
Middle zone lower edge		4
Middle zone upper edge		4
Middle zone diagonal		28

Table 2. Defined steel profile sections

No	TUBO Profile	No	TUBO Profile	No	TUBO Profile
1	D76.1X3.2	9	D139.7X4	17	D298.5X5.9
2	D82.5X3.2	10	D152.4X4	18	D323.9X5.9
3	D88.9X3.2	11	D159X4	19	D355.6X6.3
4	D101.6X3.6	12	D168.3X4	20	D368X6.3
5	D108X3.6	13	D193.7X4.5	21	D406.4X6.3
6	D114.3X3.6	14	D219.1X5	22	D419X7.1
7	D127X4	15	D244.5X5.4	23	D457.2X7.1
8	D133X4	16	D273X5.6		

3. The finite element model of the truss footbridge

The finite element model (FEM) of the steel TFB was created in SAP2000 (Fig. 2). There are 36 nodes, each with six degrees of freedom (DOF). The model is fixed by two nodes at the left end and there is a sliding support at the middle region and right end. The density ρ = 7850 kg/m^3 and the modulus of elasticity E = 2.1x10^{11} kN/m^2.

The external loads applied to the bridge model are dead load (G) and live load (Q). In this context, the dead loads, representing the loads from the slab system of the bridge, were applied to the sub-nodes as 15 kN in the vertical direction. The live load, which represents the temporary loads on the bridge, was defined as 20 kN at the sub-nodes. A total of 30 kN dead load and 40 kN live load were applied to the nodes where two elements connect at each sub-node. In order to evaluate the structural performance of the structure, a linear static analysis was performed and the loading combination was based on G + Q. The data obtained as a result of this analysis formed the basis for determining the optimum cross-sectional dimensions of the bridge elements.

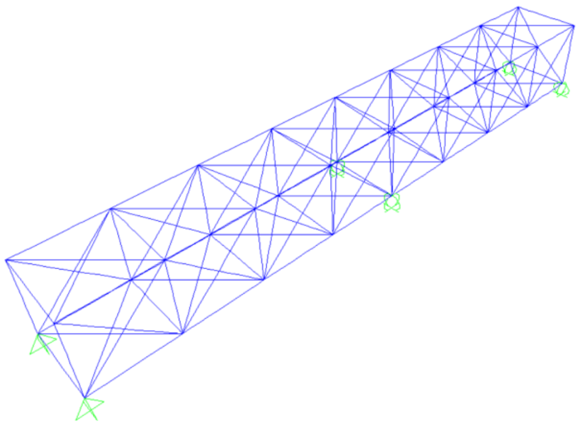

Fig. 2. FEM of the TFB

4. BMR and BWR algorithms

BMR and BWR optimization algorithms that do not include metaphors and algorithm-specific parameters were first developed by Rao and Shah (n.d.). BWR algorithm uses the best, worst and random solutions of the population when addressing a certain problem. On the other hand, BMR algorithm uses the best, average and random solutions of the population.

Let's assume that the objective function is $f(x)$ and for each iteration i there are 'm' design variables and 'n' candidate solutions. $f(x)_{best}$ is the best value among all possible solutions, while $f(x)_{worst}$ is the worst value. The random values for r_1, r_2, r_3, and r_4 can be any value between 0 and 1. U_j and L_j are the jth variable's lower and higher values, respectively. For the k^{th} candidate in the i^{th} iteration, the value of the jth variable is $V_{j,k,i}$. T is a factor that can randomly take either 1 or 2 during an iteration.

BMR algorithm;

$$V'_{j,k,i} = \begin{cases} V_{j,k,i} + r_{1,j,i}\left(V_{j,best,i} - T^{*}V_{j,mean,i}\right) + r_{2,j,i}\left(V_{j,best,i} - V_{j,random,i}\right), if \;\; r_4 > 0.5 \\ U_j - \left(U_j - L_j\right) r_3, \qquad otherwise \end{cases} \tag{1}$$

BWR algorithm;

$$V'_{j,k,i} = \begin{cases} V_{j,k,i} + r_{1,j,i}\left(V_{j,best,i} - T^{*}V_{j,random,i}\right) - r_{2,j,i}\left(V_{j,worst,i} - V_{j,random,i}\right), if \;\; r_4 > 0.5 \\ U_j - \left(U_j - L_j\right) r_3, \qquad otherwise \end{cases} \tag{2}$$

The modified value of $V_{j,k,i}$ is denoted by $V'_{j,k,i}$. For variable j^{th} variable, $V_{j,best,i}$ is the best value of $f(x)$ during the i^{th} iteration, $V_{j,mean,i}$ is the average value and $V_{j,worst,i}$ is the worst value. The value picked at random for the j^{th} variable in the i^{th} iteration is $V_{j,random,i}$.

In this study, two different metaheuristic optimization algorithms, called BMR and BMW, are used to perform the optimum design of a steel TFB by taking into account the structural constraints such as stress and buckling for compression members specified in American Institute of Steel Construction-Allowable Stress Design (AISC-ASD) (1989) standards. In the optimization process, the number of generations was set as 30 and the population size was set as 20.

5. Optimization results

In this study, the optimal design of a TFB system with minimum weight is realized using two different metaheuristic algorithms called BMR and BWR. Five runs were performed for each algorithm and the performances of the algorithms were evaluated based on the results obtained. The convergence behavior of the best solutions obtained during different iterations in the optimization process is examined.

First of all, the convergence graph showing the variation of the best solutions obtained in different runs of the BMR algorithm according to iteration is given in Fig. 3(a). The minimum structure weight, the number of iterations and the number of function evaluations (NFE) obtained in each run of the BMR algorithm are summarized in Table 3. When Fig. 3(a) and Table 3 are analyzed, the total structure weights obtained as a result of five different runs are quite close, ranging from 41.494 kN to 41.970 kN. Run-1 gives the best result with a minimum total structure weight of 41.494 kN. In this run, this solution was reached after only 5 iterations.

Then, the convergence graph showing the change of the best solutions obtained in different runs of the BWR algorithm according to the iteration is given in Fig. 3(b). The minimum structure weight, the number of iterations and NFE obtained in each run of the BWR algorithm are summarized in Table 4. When Fig. 3(b) and Table 4 are examined, it is seen that as a result of five different runs, Run-2 and Run-4 reached the best result in the first iteration and obtained a minimum total structure weight of 42.049 kN.

The selected profiles for six different groups and the weight of each group are shown in Table 5. When this table is examined, the BMR algorithm obtained a lighter weight of approximately 1.32% compared to the BWR algorithm.

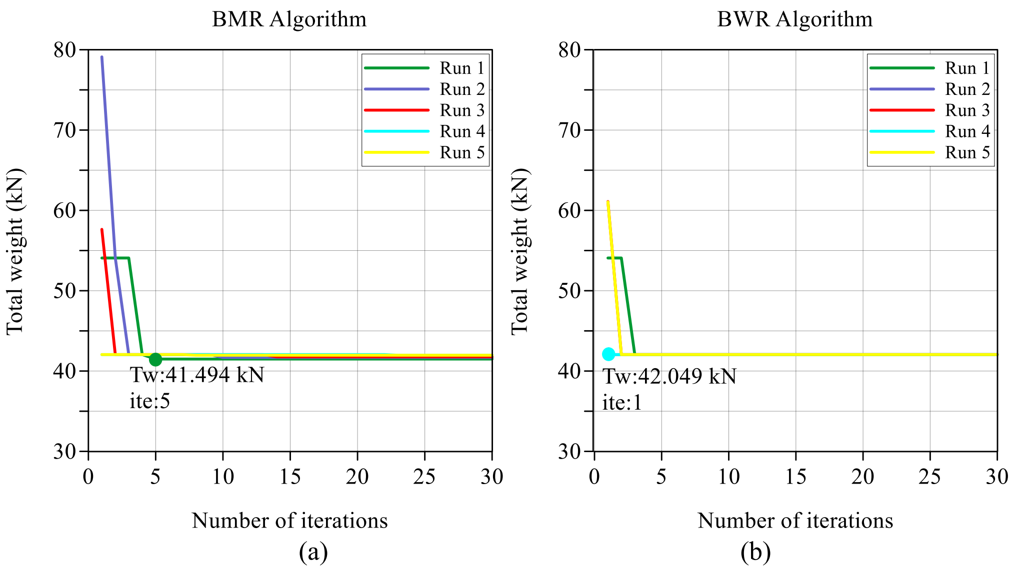

Fig. 3. Convergence graphs of (a) the BMR algorithm and (b) the BWR algorithm

Table 3. Optimization results obtained by the BMR algorithm

Run	G_1	G_2	G_3	G_4	G_5	G_6	Ite.	NFE	Total weight (kN)
Run-1	D82.5X3.2	D82.5X3.2	D88.9X3.2	D88.9X3.2	D88.9X3.2	D88.9X3.2	5	120	41.494
Run-2	D88.9X3.2	D82.5X3.2	D88.9X3.2	D82.5X3.2	D88.9X3.2	D88.9X3.2	10	220	41.692
Run-3	D88.9X3.2	D82.5X3.2	D88.9X3.2	D88.9X3.2	D88.9X3.2	D88.9X3.2	14	300	41.772
Run-4	D88.9X3.2	D88.9X3.2	D88.9X3.2	D88.9X3.2	D82.5X3.2	D88.9X3.2	23	480	41.970
Run-5	D88.9X3.2	D88.9X3.2	D88.9X3.2	D88.9X3.2	D82.5X3.2	D88.9X3.2	8	180	41.970

Table 4. Optimization results obtained by the BWR algorithm

Run	G_1	G_2	G_3	G_4	G_5	G_6	Ite.	NFE	Total weight (kN)
Run-1	D88.9X3.2	D88.9X3.2	D88.9X3.2	D88.9X3.2	D88.9X3.2	D88.9X3.2	3	80	42.049
Run-2	D88.9X3.2	D88.9X3.2	D88.9X3.2	D88.9X3.2	D88.9X3.2	D88.9X3.2	1	40	42.049
Run-3	D88.9X3.2	D88.9X3.2	D88.9X3.2	D88.9X3.2	D88.9X3.2	D88.9X3.2	2	60	42.049
Run-4	D88.9X3.2	D88.9X3.2	D88.9X3.2	D88.9X3.2	D88.9X3.2	D88.9X3.2	1	40	42.049
Run-5	D88.9X3.2	D88.9X3.2	D88.9X3.2	D88.9X3.2	D88.9X3.2	D88.9X3.2	2	60	42.049

Table 5. Comparison of total weights for BMR and BWR algorithms

Groups	Number of elements	BMR algorithm		BWR algorithm	
		TUBO profile	Total weight (kN)	TUBO profile	Total weight (kN)
G_1	14	D82.5X3.2	3.436	D88.9X3.2	3.714
G_2	14	D82.5X3.2	3.436	D88.9X3.2	3.714
G_3	68	D88.9X3.2	23.313	D88.9X3.2	23.313
G_4	4	D88.9X3.2	1.061	D88.9X3.2	1.061
G_5	4	D88.9X3.2	1.061	D88.9X3.2	1.061
G_6	28	D88.9X3.2	9.186	D88.9X3.2	9.186
			41.494		42.049

As a result of the optimization, when the sections obtained from both the BMR algorithm and the BWR algorithm are placed in FEM in SAP2000 and designed according to AISC-ASD, it is seen in Fig. 4 that all sections are sufficient.

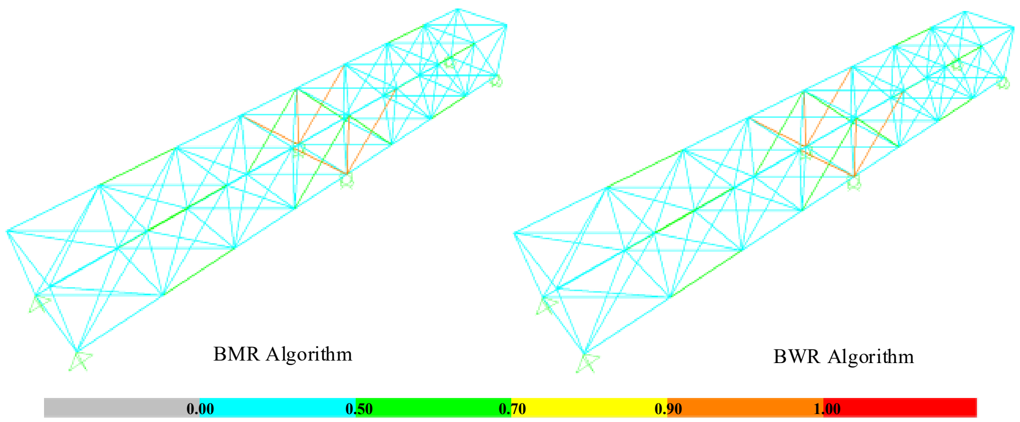

Fig. 4. Design check in SAP2000 according to AISC-ASD

6. Conclusions

In this study, the size optimization of a 132-element steel truss footbridge (TFB) system is performed using two metaheuristic algorithms, Best-Mean-Random (BMR) and Best-Worst-Random (BWR), which are available in the literature. By integrating SAP2000 and MATLAB software through SAP2000's Open Application Programming Interface (OAPI), a three-dimensional finite element model of the bridge was analyzed and in each iteration the algorithms optimized the cross-sections of the bridge elements. For each algorithm, five runs were conducted; the performance comparison was made based on the results obtained and the convergence behavior of the best solutions in the optimization process was examined. Based on this study, the following conclusions were reached:

- The total weights of the bridge obtained with the BMR algorithm in the five runs vary between 41.494 kN and 41.970 kN. This shows that the BMR algorithm exhibits a stable convergence performance.
- With the BWR algorithm, the total weight of the bridge obtained in all five runs was 42.049 kN and did not change at all. This may indicate that the algorithm is stuck to the same local optimum in each run.
- The weight of the best solution obtained with the BWR algorithm (42.049 kN) is higher than the best solution obtained with the BMR algorithm (41.494 kN). This shows that the BMR algorithm performs a more efficient search and can produce better results.

References

AISC-ASD, American Institute of Steel Construction-Allowable Stress Design (1989). Chicago, Illinois.

Atmaca, B. (2021a). Determination of proper post-tensioning cable force of cable-stayed footbridge with TLBO algorithm. *Steel and Composite Structures*, *40*(6), 805–816

Atmaca, B. (2021b). Size and post-tensioning cable force optimization of cable-stayed footbridge. *Structures*, *33*(June), 2036–2049

Etaati, B., Neshat, M., Dehkordi, A.A., Pargoo, N.S., El-Abd, M., Sadollah, A., & Gandomi, A.H. (2024). Shape and sizing optimisation of space truss structures using a new cooperative coevolutionary-based algorithm. *Results in Engineering*, *21*(September 2023), 101859

Farahmand-Tabar, S., & Babaei, M. (2023). Memory-assisted adaptive multi-verse optimizer and its application in structural shape and size optimization. *Soft Computing*, *27*(16), 11505–11527

Nemati, M., Zandi, Y., & Sabouri, J. (2024). Truss sizing optimum design using a metaheuristic approach: Connected banking system. *Heliyon*, *10*(20), e39308

Rao, R.V., & Shah, R. (n.d.). BMR and BWR :Two simple metaphor-free optimization algorithms for solving real-life non-convex constrained and unconstrained problems.

SAP2000. (2016). Computer and Structures.

T.H.G. Megson. (2019). *Structural and Stress Analysis*. Elsevier.

MATLAB (R2023b) (2023). The MathWorks, Inc.

Ugur, I.B., & Degertekin, S.O. (2025). A new approach to circulatory system-based optimization for the shape and sizing design of truss structures. *Applied Sciences (Switzerland)*, *15*(7)

Effect of pre-curing rest period on the compressive strength of calcined marl-based geopolymer mortars

Ayşe Türk[*1], Ülkü S. Keskin[1]

[1] *Konya Technical University, Department of Civil Engineering,42250 Konya, Türkiye*

Abstract. Due to the high greenhouse gas emissions and energy consumption caused by cement production, in recent years, studies have focused on geopolymer concrete produced without the cement. Various precursors are used in alkali-activated geopolymer mixtures. The availability and cost of these precursors is a concern. In addition to providing high strength, it is desired that the precursor used are locally accessible and low-cost. In this study, a low-cost marl obtained from local resources of Konya province is used as a geopolymer precursor. Raw marl was calcined at 800 °C in order to increase its reactivity before being used in mixtures. NaOH and Na_2SiO_3 were used together as activators. The binder dosage of the geopolymer mortar was selected as 675 kg/m^3, water/binder ratio as 0.6, NaOH molarity as 10 M, activator/binder ratio as 1, Na_2SiO_3 ratio as 2.5. In order to investigate the effect of the resting period before thermal curing on the compressive strength of geopolymer mortars, samples with 0 (reference sample), 6, 12 hour, and 1, 3, 7, 14 days resting periods were produced and after resting period samples cured at 80 c for 24 hours. The samples were subjected to compressive strength test on the 28th day.The compressive strength of the samples with all pre-curing rest periods increased compared to the sample cured by direct heat without a resting period. The sample with a 3-day rest period provided the highest strength with a 25% increase compared to the reference mixture.

Keywords: Geopolymer mortar; precursor; calcined marl; thermal curing; pre-curing rest period

1. Introduction

Cement is one of the most produced and consumed products in the world (Scrivener et al., 2018; Fode et al., 2023). It is responsible for approximately 7% of global carbon dioxide emissions due to the high temperatures required in production processes and the consumption of natural resources (Meyer, 2009). Because of this, research has concentrated on figuring out how to use less cement while still preserving the strength and durability required to lower carbon emissions and lessen the consequences of climate change. One of the steps taken in this regard is geopolymer concrete produced without the need for Portland cement. Geopolymers are inorganic polymers formed by the chemical reaction of aluminum and silicon-rich materials (kaolinite, fly ash, slag, metakaolin, clay, etc.) via alkali activator. The selection of binder materials for geopolymer concrete production depends on factors such as availability, cost, and type of application.

There are many parameters affecting the strength of geopolymer concrete and mortars. Studies investigating the effects of factors such as precursor type, activator type, activator amount, curing temperature, curing time on the strength of geopolymer concrete/mortars are frequently encountered in the literature. Most studies have focused on the effects of curing temperature and curing time. However, the time interval between casting and curing (resting period) has rarely been investigated by researchers. In a study examining the effects of the resting period before curing on fly ash geopolymers, it was reported that the resting period increased the reaction products and caused a denser microstructure, thus increasing the mechanical strength. In addition, it has been reported that the water permeability, capillarity coefficient, and porosity of the samples decreased compared to the reference samples (Durak et al., 2021). There are studies reporting that the compressive strength of fly ash-based geopolymers increases with the increase of the pre-resting period up to a certain limit (Harle, 2017; Hardjito et al., 2005). When the effect of the pre-resting period on the properties of metakaolin-based geopolymers was examined, a short resting period initially increased the reaction rate, but decreased the total reaction level. It also increased the porosity and decreased the compressive strength. The extension of the resting period improved the porosity and increased the reaction level, modified the gel structure and densified the matrix (Tian et al., 2024).

There is no study in the literature investigating the effects of pre-resting period on calcined marl-based geopolymers. In this study, marl obtained from local resources of Konya province was calcined and used as

[*] Corresponding author, E-mail: akaroglu@ktun.edu.tr

https://doi.org/10.31462/icearc2025_ce_sme_965

geopolymer precursor. The effects of resting period before curing on the strength of calcined marl geopolymer mortars were investigated.

2. Materials and methods

2.1. Materials

The XRD analysis results of raw marl obtained from local sources in Konya province of Turkey are shown in Figure 1. The semi-quantitative mineralogical analysis results are given in Table 1.

The raw material was first sieved through a 2.36 mm sieve and calcined for 1 hour in a 15 °C/min heat ramp oven after the oven reached 800 °C and left to cool at room temperature. After cooling, it was ground in a ball mill for 1 hour.

CEN standard sand was used as aggregate in the preparation of geopolymer mortars.

The water/binder ratio of all mixtures was selected as 0.6. Sodium hydroxide solutions were prepared by mixing 98% pure solid pellet NaOH with pure water and stored in closed glass jars at room temperature for 24 hours. 2 Module, 40 bome (40% Na_2SiO_3, 60% water) Na_2SiO_3 solution was commercially supplied.

Table 1. Results of Semi-Quantitative Mineralogical Analysis of Marl

Content	Calcite	Mica	Quartz	Feldspar	Smectite	Illite	Kaolinite
Amount (%)	29	23	6	5	17.7	15.5	3.7

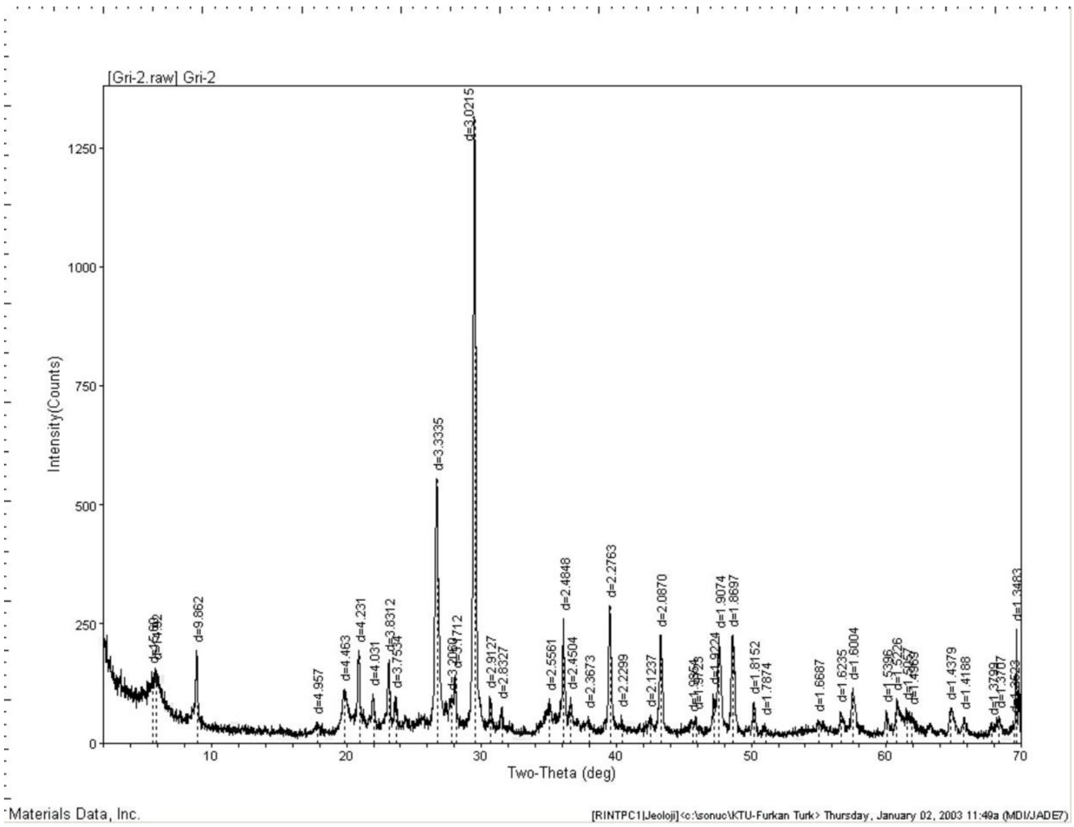

Fig. 1. XRD analysis of raw marl

2.2. Preparing of mixtures

Mixing ratios are presented in Table 2. No additional water was used in the mixtures, the total water/binder ratio included in the mixture from alkali activator solutions was selected as 0.6, binder/sand 0.5, and Na_2SiO_3/NaOH 2.5.

Sodium hydroxide, sodium silicate solutions were first mixed in a separate container and then added to the binder. The mixture was mixed at low speed for 30 seconds. Then sand was added for 30 seconds. Then the mixer was stopped and the container was scraped with a spatula, including all sides and bottom, and rested for 60 seconds. The mortar was mixed again at high speed for the next 60 seconds. After the mixing process of the geopolymer mortars was completed, they were placed into 50x50x50 mm molds. As presented in Table 2, the samples with rest periods of 0 hours (reference), 12 hours, 24 hours, 3 days, 7 days and 14 days were stored at room conditions. At the end of the rest periods, they were cured at 80 °C for 24 hours and stored by wrapping them in a bag until the test day.

Table 2. Mixtures and resting time

Sample	Binder (g)	Sand (g)	NaOH (g)	Na_2SiO_3 (g)	Resting Time (g)	Curing Temperature
R0	675	1350	193	482	0 hour	80 °C
R1/4	675	1350	193	482	6 hours	80 °C
R1/2	675	1350	193	482	12 hours	80 °C
R1	675	1350	193	482	24 hours	80 °C
R3	675	1350	193	482	3 days	80 °C
R7	675	1350	193	482	7 days	80 °C
R14	675	1350	193	482	14 days	80 °C

2.3. Compressive strength test

On the 28th day, the samples were subjected to a compressive strength test. Compressive strength test were carried out according to ASTM C1928 "Standard Test Method for Compressive Strength of Alkali Activated Cementitious Material Mortars" standard. The loading rate was selected to be 0.9 kN/s. Three cube samples were tested for each resting period and average values were obtained.

3. Results and discussion

The compressive strength results of alkali-activated calcined marl-based geopolymer mortar samples, which were subjected to a certain pre-resting period before thermal curing and then subjected to thermal curing at 80 °C for 24 hours, are presented in Figure 2. The compressive strengths of the samples were 32.62, 34.79, 39.83, 40.58, 40.86, 39.79, 38.54 MPa.

An increase in compressive strength was observed with the increase in pre-resting period. Although a slight decrease was observed after the 3-day resting period, the compressive strength increased for all samples compared to the R0 sample without any pre-resting. The compressive strength of the R3 sample increased by 25% compared to the R0 sample. Therefore, it was found that the pre-resting period was important in terms of the strength properties of geopolymer mortars.

The reasons for the strength increase in the samples cured after pre-resting were interpreted as follows in the literature: It was concluded that when there was no resting period before high-temperature curing, the rapidly formed gel covered the undissolved precursor particles and prevented further reactions (Tian et al., 2024). It shows that a pre-resting period at room temperature allowed the reactive species from the precursor material to be effectively dissolved without significant polymerization and condensation. In the presence of effectively dissolved species, heat curing after the pre-rest period causes a rapid and advanced polymerization and condensation process. In addition, geopolymer formation occurs by the interaction of the precursor material with alkaline solutions and heat. The presence of water is very important in this process because water helps the movement of ions and the progress of the reaction. However, water evaporates rapidly during heat curing and the geopolymerization process ends when it evaporates completely. This usually causes the reaction to be incomplete. If the evaporation of water is slowed down and the process is held longer, geopolymerization can be completed. A longer geopolymerization reaction time and slower water evaporation during this period may result in a more efficient geopolymerization process and a geopolymeric product with improved qualities (Durak et al., 2021). Thus, a stronger and higher quality geopolymer can be obtained. In the pre-rest period, time is given for the reaction to take place at room temperature without water evaporation, and it is thought that the strength increases in this way.

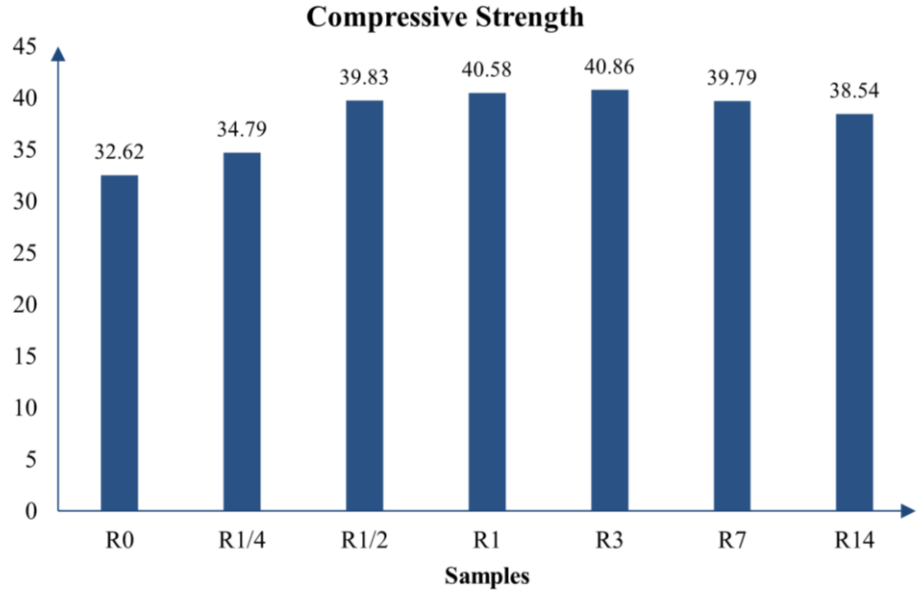

Fig. 2. 28th day compressive strength of samples

It was concluded that the application of pre-curing resting period improves the geopolymerization process and compressive strength. Therefore, it is concluded that resting period is of critical importance in terms of strength properties.

4. Conclusions

This work investigated the influence of pre-curing rest period on calcined marl geopolymer properties, and the main conclusions from the article are:

- A rest period before curing improved the compressive strength of calcined marl geopolymer mortars.
- The compressive strength of the sample with a 3-day resting period increased by 25% compared to the sample directly cured.
- Although some decrease in compressive strength was observed at rest periods longer than 3 days, rest periods up to 14 days exhibited higher compressive strength compared to the reference sample.
- These results are consistent with other studies in the literature.

References

ASTM C1928 "Standard Test Method for Compressive Strength of Alkali Activated Cementitious Material Mortars (Using 2-in. [50 mm] Cube Specimens)"

Durak, U., İlkentapar, S., Karahan, O., Uzal, B., & Atiş, C. D. (2021). A new parameter influencing the reaction kinetics and properties of fly ash based geopolymers: A pre-rest period before heat curing. *Journal of Building Engineering*, *35*, 102023.

Fode, T. A., Jande, Y. A. C., & Kivevele, T. (2023). Effects of different supplementary cementitious materials on durability and mechanical properties of cement composite–Comprehensive review. *Heliyon*, *9*(7).

Hardjito, D., Wallah, S. E., Sumjouw, D. M. J., & Rangan, B. V. (2005). Effect of mixing time and rest period on the engineering of fly ash-based geopolymer concrete. In Proceedings of the Geopolymer 2005 World Congress: Green Chemistry and Sustainable Development Solutions (pp. 145-147).

Harle, S. (2017). Effect of curing period, rest period and mixproportion on geopolymer concrete. Journal of Research in Engineering and Applied Sciences, 2, 105-109.

Meyer, C. (2009). The greening of the concrete industry. Cement and concrete composites, 31(8), 601-605.

Scrivener, K. L., John, V. M., & Gartner, E. M. (2018). Eco-efficient cements: Potential economically viable solutions for a low-CO2 cement-based materials industry. Cement and concrete Research, 114, 2-26.

Tian, X., Shuai, J., Wu, J., Zhong, Q., Liu, Z., & Jin, Z. (2024). Understanding the influence of compressive strength, microstructure, and mechanism for metakaolin-based geopolymer under varying rest periods in the curing process. *Construction and Building Materials*, *427*, 136239.

4th International Civil Engineering & Architecture Conference
17-19 May 2025, Trabzon, Türkiye

The innovations shaping the traffic of future: Autonomous vehicles and smart transportations

Nuriye Kabakuş[1], Nathan W. Mwasembe[*2]

[1] Atatürk University, Department of Emergency Aid and Disaster Management, 25240 Erzurum, Türkiye
[2] Atatürk University, Graduate School of Natural and Applied Sciences, 25240 Erzurum, Türkiye

Abstract. Inside Autonomous vehicle technology, is a revolution that will lead to radical changes in transport systems for the smart cities of the future. In this study, the impacts of autonomous vehicles on traffic safety and urban transport in Turkey are discussed. Based on literature reviews and analyses of existing technologies, the potential of autonomous vehicles in reducing traffic accidents, their capacity to improve the safety of road users and their contribution to sustainable transport goals will be evaluated. In the context of Turkey's specific traffic infrastructure, driver behaviour and legal regulations, problems that may be encountered during the adaptation of autonomous vehicles will be discussed. In this context, the importance of infrastructure adaptation requirements, data sharing and integration, change in driver-passenger habits, public awareness and legal regulations will be emphasised. In addition, Turkey will be compared with other countries in terms of autonomous vehicles. As a result, the impact of autonomous vehicles on urban transport will be evaluated in terms of increasing traffic safety, reducing accident rates and reducing traffic congestion. A multidisciplinary approach will be proposed for the effective management of this process. In addition, it is aimed to contribute to transport policies for the smart city concept in Turkey.

Keywords: Autonomous vehicles; Smart cities; Traffic safety; Urban transport; Sustainability

1. Introduction

Autonomous vehicle technology is one of today's fastest developing and remarkable innovative transportation solutions. Developed by combining advanced technologies such as artificial intelligence, sensors, radar systems and machine learning, autonomous vehicles have the capacity to move safely and effectively without the need for human intervention. With the potential to improve traffic safety, reduce carbon emissions and make transportation systems more efficient, these vehicles are attracting great interest from both the public and private sectors. Research and pilots in different parts of the world show how autonomous vehicles can revolutionize urban transportation, logistics and personal transportation.

There are significant differences between the level of adaptation of autonomous vehicle technologies in Turkey and the world. While investments in this technology have increased in developed countries, some cities have initiated special regulations and infrastructure works for the integration of autonomous vehicles into traffic. For example, countries such as the US, Germany and Japan have accelerated the process of establishing legal frameworks for the testing and use of autonomous vehicles. In Turkey, there is growing interest in autonomous vehicle technology, but applications in this field are mostly limited to academic research and limited-scale pilot projects. For autonomous vehicles to become widespread, key challenges such as infrastructure deficiencies, legal regulations and society's adaptation to this technology need to be overcome.

This study aims to analyze the changes that may occur in our lives with the spread of autonomous vehicles and what needs to be done to adapt to these changes. The main focal points of the research are the transformations in transportation systems, impacts on traffic safety, environmental gains and potential risks. In addition, dimensions such as social acceptance of this technology, economic impacts and infrastructure requirements will also be examined in detail. It will be discussed what role autonomous vehicles can play in Turkey's transportation systems and urban planning and what strategic steps should be taken to take advantage of this technology.

In this context, the aim of this study is not only to assess the potential impacts of autonomous vehicles, but also to provide policy, infrastructure and regulatory recommendations to maximize these impacts. This study, which will be discussed from both national and global perspectives, aims to contribute to future transportation policies.

* Corresponding author, E-mail: mwasembenathan@outlook.com

https://doi.org/10.31462/icearc2025_ce_tra_005

2. Literature review

Autonomous vehicles (AVs) are revolutionizing transportation technologies with their ability to move without human intervention. Thanks to advanced sensors, artificial intelligence (AI) and machine learning algorithms, these vehicles are capable of sensing their environment and making real-time decisions (B, 2023; Pettersson & Karlsson, 2015; Zhao et al., 2018). Rapid advances in sensor technology and machine learning are accelerating the proliferation of autonomous vehicles by increasing the reliability and safety of these systems (Pettersson & Karlsson, 2015; Zhao et al., 2018).

While autonomous vehicles offer significant advantages in terms of traffic safety, environmental sustainability and transportation efficiency, public perception and acceptance of these technologies play a critical role in the adoption process. Research shows that users' biggest concern is safety and demand the highest safety standards for AVs (Bęczkowska, 2023; Kyriakidis et al., 2015). While the perception of risk and trust in technology directly affect the level of acceptance of these vehicles, the lack of experience with autonomous vehicles constitutes a significant obstacle in this process (Raue et al., 2019; Nielsen & Haustein, 2018).

Technological advances have the potential to not only increase individual safety, but also improve overall traffic flow and reduce traffic congestion. Research shows that autonomous vehicles can communicate with each other, enabling more coordinated driving behaviors and leading to improvements in traffic management (Yang et al., 2017; Wang et al., 2017). This can contribute to solving traffic problems without the need to expand road infrastructure (Chen, 2017). Moreover, the integration of autonomous vehicles into public transportation systems can provide advantages such as increasing accessibility and reducing operating costs (Guo, 2023; Ni et al., 2020). However, the integration of autonomous vehicle technology into society is not limited to technical developments. Many critical issues such as legal regulations, ethical issues, and safety verification mechanisms must be addressed in this process (Gao, 2023; Paden et al., 2016). In countries like Turkey, with its unique traffic culture, infrastructure deficiencies, and regulatory needs, the process of adapting to this technology is more complex. Traffic density, behavioral characteristics of drivers and pedestrians, and complex road conditions in Turkey are factors that need to be taken into account for the safe integration of autonomous vehicles.

3. Material-method

The development process of driverless vehicle technology has been systematically categorized by defining certain levels. In this context, the US National Highway Traffic Safety Administration (NHTSA) has conducted studies aimed at standardization in this field by classifying vehicles into various levels according to the characteristics and functionality levels of autonomous elements involved in the production and use stages of automobiles. This classification allows vehicles to be graded according to the scope of the autonomous technologies they incorporate, the level of need for human intervention and their control capabilities in driving environments. This system is an important reference for understanding the technical capabilities of autonomous vehicles and establishing regulatory frameworks. Accordingly, the levels and grades determined for autonomous vehicles are expressed as follows (NHTSA, 2013):

- Level 0: Vehicles without any autonomous system.
- Level 1: Vehicles with at least one of any critical navigation systems that operate independently of each other, not at the driver's discretion.
- Level 2: Vehicles with at least one of any automated driving systems that are under the driver's control and operate independently of each other.
- Level 3: Vehicles that can be expressed as partially driverless vehicles, where the user can use the vehicle in manual mode at any time, as well as switch to autonomous mode when needed.
- Level 4: Fully autonomous vehicles that are completely closed to driver support, managed by fully autonomous systems and in which all driving functions are used by the vehicle itself, and do not allow human intervention.

Fig. 1 shows the different levels of automation that autonomous vehicles are categorized into.

3.1. The impact of autonomous vehicles on future transportation

The future of transportation systems will be shaped by the integration of autonomous vehicles, and this change will have profound impacts on safety infrastructure, technological requirements, environmental impacts and economic outcomes. Fig. 2 shows the potential impact areas of autonomous vehicles.

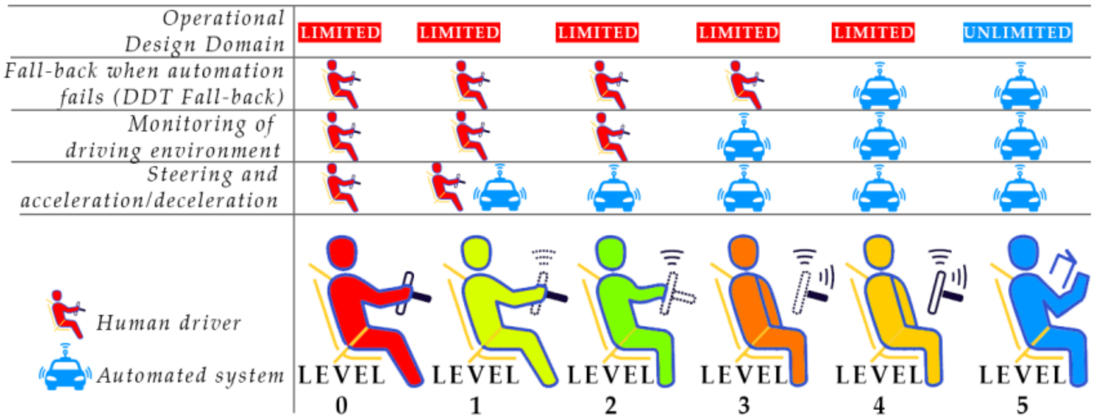

Fig. 1. Levels of driving automation (Kozlowski et. al.,2024)

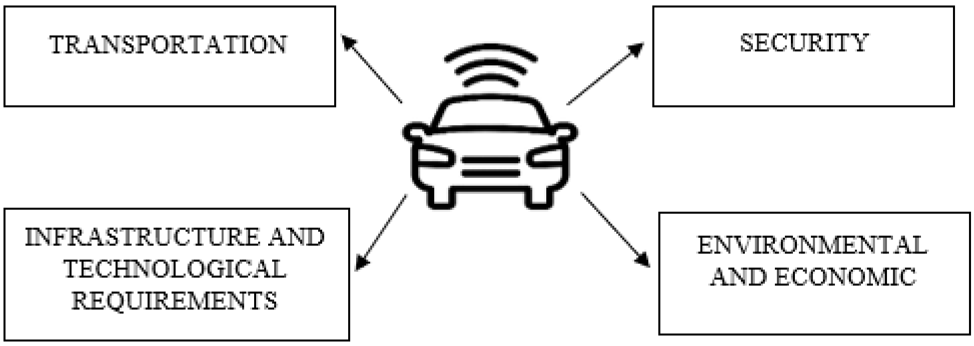

Fig. 2. The impacts of autonomous vehicles on future transportation

3.1.1. The impact of autonomous vehicles on transportation

3.1.1.1. Integration with public transportation
Autonomous minibuses and robotaxi services can be integrated with traditional public transport systems to increase the coverage and efficiency of transportation networks. By facilitating access to areas outside of fixed routes, such applications can support demand for public transport and contribute to lower urban traffic congestion by reducing the use of individual vehicles. They can also improve the user experience by providing solutions to the last mile problem of public transport systems.

3.1.1.2. Passenger and freight transportation
Autonomous vehicle technology has the potential to revolutionize the logistics industry in particular. Autonomous trucks make it possible to reduce human error, optimize fuel consumption and lower operational costs. These developments offer great advantages in terms of shortening delivery times and increasing overall efficiency in the supply chain. In terms of passenger transportation, shared autonomous vehicle models can contribute to sustainable urban transportation by enabling more efficient use of transport capacity.

3.1.1.3. Accessibility and transportation equality
Autonomous vehicles offer important opportunities for individuals with limited access to transportation systems. They can provide an independent and safe transportation alternative, especially for the elderly, people with disabilities and communities that cannot benefit from transportation infrastructure. This can support social participation and access to economic activities by increasing the mobility of individuals who cannot be an active part of social life. This would represent a significant advance in transportation equality.

3.1.1.4. Urban mobility
Autonomous vehicles have an important role in making urban transportation smarter and more sustainable. Thanks to advanced sensor systems and artificial intelligence algorithms, these vehicles can analyze traffic flow in real time and provide a more orderly and safer ride. Contributions such as reducing traffic congestion, reducing the need for parking space and minimizing carbon emissions allow for an improved quality of life in cities. At the

same time, a holistic improvement in urban mobility can be achieved by promoting a more integrated and user-friendly public transport experience.

3.1.2. Impacts on security

3.1.2.1. Decrease in traffic accidents

Autonomous vehicles have the potential to drastically reduce human errors thanks to advanced sensor systems, radars, cameras and AI-supported decision-making mechanisms. Eliminating risks arising from human behavior such as inattention while driving, fatigue, alcohol use, excessive speed, etc. can lead to a significant reduction in the number and severity of traffic accidents. This contributes not only to preventing loss of life, but also to reducing economic losses and the burden on the healthcare system.

3.1.2.2. Pedestrian and bicycle safety

Autonomous vehicle technologies can improve the safety of pedestrians and cyclists in traffic with sensors and advanced detection systems that increase environmental awareness. By recognizing road users earlier and minimizing reaction time, vehicles can greatly reduce the likelihood of collisions. It enables safe driving decisions to be made by analyzing risky situations in advance, especially at intersections, school zones and busy pedestrian crossings. This creates a more inclusive and safer environment for all users of urban transportation.

3.1.2.3. Emergency response

Thanks to their real-time data processing and environmental analysis capabilities, autonomous vehicles can make fast and effective decisions in unexpected dangerous situations. This capability makes it possible to take evasive maneuvers before a potential collision or to anticipate risky situations and implement preventive measures. In addition, it can shorten response times and reduce life risks in times of crisis with features such as giving way to emergency vehicles in traffic jams and automatically notifying authorities in case of an accident.

3.1.2.4. Risks in transition

The transition to fully autonomous systems is critical as a period when manual drivers and autonomous vehicles share the same road network. In this period, behavioral differences between human drivers and AI-based systems can pose significant safety risks. Situations such as unpredictable maneuvers, failure to use signals, and failure to fully comply with traffic rules by human drivers may not be predicted by the algorithms of autonomous vehicles. Therefore, special regulations, infrastructure investments and public awareness-raising practices for mixed traffic environment are of great importance in the transition process.

3.1.3. Infrastructure and technological requirements

3.1.3.1.Intelligent road and traffic systems

In order for autonomous vehicles to operate safely and efficiently, they must be able to communicate with their environment continuously and in real time. At this point, V2V (Vehicle-to-Vehicle) and V2I (Vehicle-to-Infrastructure) communication systems are of great importance. Thanks to these systems, vehicles can reduce accident risks and optimize traffic flow by transmitting information such as speed, location and road conditions to each other. In addition, smart traffic lights, intersections with sensors and digital information boards integrated into the infrastructure support the decision-making processes of autonomous systems and contribute to the creation of a smarter transportation network.

3.1.3.2. Road and lane arrangements

For the sensor systems of autonomous vehicles to function correctly, road markings, signage and traffic signs must be clear and up to standard. Inadequate road markings or poor surface conditions can make it difficult for autonomous systems to navigate and make decisions. Therefore, with the proliferation of autonomous vehicles, road infrastructure needs to be re-evaluated, smart intersection designs and lane arrangements need to be adapted to autonomous driving systems. These investments both increase driving safety and ensure that systems work in harmony.

3.1.3.3. Autonomous vehicle charging and maintenance infrastructure

Autonomous vehicles powered by electric motors require increasing the capacity of existing charging infrastructure. Without widespread and fast charging stations, large-scale deployment of these vehicles will not be possible. Moreover, the complex technological hardware of autonomous systems requires a restructuring of maintenance and repair processes. Unlike traditional vehicle maintenance services, new maintenance protocols need to be developed, such as software updates, sensor calibrations and control of artificial intelligence systems. This leads to the emergence of new areas of specialization in the technical service infrastructure.

3.1.3.4. Digital security and data management

Autonomous vehicles generate and process large amounts of data through sensors, GPS systems and communication networks. This data plays a critical role in both driving decisions and traffic management. However, this also brings security threats such as cyber-attacks and data breaches. Securing autonomous vehicles requires integrating technologies such as strong encryption protocols, authentication systems and cyber firewalls. In addition, transparent and ethical data management policies should be developed on how the data collected is stored, with whom it is shared and for what purposes it is used to protect user privacy.

3.1.4. Environmental and economic impacts

3.1.4.1. Reduced carbon emissions

If the majority of autonomous vehicles are powered by electric systems, this could significantly reduce fossil fuel consumption compared to conventional internal combustion engine vehicles. This can play an important role in combating global warming by contributing to the reduction of carbon emissions from transportation. Moreover, promoting electric autonomous vehicles as part of sustainable transportation policies can facilitate the achievement of national and international environmental goals.

3.1.4.2. Energy efficiency

Artificial intelligence and sensor systems used in autonomous vehicles can analyze traffic density, road conditions and weather conditions to determine the shortest and least energy-intensive routes. In addition, these systems can reduce sudden stop-starts and exhibit more balanced and efficient driving behaviors. When all these factors come together, fuel or energy consumption is minimized, resulting in significant energy savings on both an individual and societal level.

3.1.4.3. Improved air quality in cities

Integrating autonomous vehicle technology with electric systems can directly contribute to improving air quality in urban centers. Reduced particulate matter (PM) and nitrogen oxide (NOx) emissions, especially from diesel-fueled vehicles, can reduce the incidence of respiratory diseases. These improvements can have a positive impact on public health, especially in large and densely populated cities, while increasing environmental comfort levels.

3.1.4.4. Employment and economic transformation

The proliferation of autonomous technologies in the transportation sector may directly affect professions such as taxi, bus and truck drivers. While some jobs may decline over time, employment opportunities may arise in new fields such as software development, artificial intelligence engineering, data analytics, maintenance and hardware services. Managing this structural transformation in a balanced way is important to avoid sudden losses in the labor market and to provide new skills. Hence, the need for vocational training and reskilling programs will increase.

3.1.4.5. Impacts on urban planning

Autonomous vehicles reduce the need for parking spaces, allowing large areas to be reclaimed, especially in urban centers. Areas traditionally reserved for car parking can be transformed into green spaces, pedestrian paths, cycling routes or social spaces. This contributes to making cities more livable and sustainable. Furthermore, road infrastructure can be used more efficiently as autonomous vehicles improve traffic flow, which can open up new opportunities in urban transportation planning.

4. Results

With advancing technologies, transportation systems are undergoing radical changes, and autonomous vehicles are at the center of this transformation. These vehicles, which will shape the traffic of the future, offer many potential advantages such as increasing safety, reducing traffic congestion, improving energy efficiency and increasing accessibility in transportation. However, there are also challenges such as technical inadequacies, high costs, legal and ethical uncertainties. Moreover, while new business models and economic opportunities emerge with the proliferation of this technology, risks such as workforce losses in traditional transportation sectors are also on the agenda. The assessments made in this context show that a balanced and multidimensional approach should be developed in the process of integrating autonomous vehicles into transportation systems. Figure 3 presents the strengths, weaknesses, opportunities and threats of autonomous vehicles.

Strengths

1.Potential to Reduce Traffic Accidents: Autonomous vehicles have a low error rate, potential to reduce accidents.

2. Improving Traffic Flow: Congestion can be reduced through V2V communication and intelligent traffic management.

3. Artificial Intelligence and Technology Development: High engineering competence and rapid technology adoption in Turkey.

4. Environmental Benefits: Route planning that reduces fuel consumption and emissions.

5. Young Population and Technology Aptitude: Younger population is more prone to autonomous vehicles.

Weaknesses

1.Lack of Legislation: Legal regulations are not clear enough.

2.Inadequate Infrastructure: Infrastructure deficiencies, especially the inadequacy of smart signaling systems.

3.User Insecurity: Public perception of technology as unreliable, high risk perception.

4.Lack of Education and Awareness: Insufficient training and awareness for effective use of technology.

5.High Costs: High initial costs.

Opportunities

1. International Collaborations: Joint projects and technology transfer with developed countries.

2.Smart City Projects: Smart city projects in Turkey offer opportunities for autonomous vehicles.

3.Energy Efficiency and Sustainability: Contributing to environmental goals.

4.Local Production Opportunities: Supporting autonomous production with local production vehicles such as TOGG.

5.Tourism and Transportation Transformation: Integrating autonomous vehicles in tourism and transportation.

Threats

1.Cybersecurity Risks: The risk of autonomous vehicles being hacked.

2.Ethical Issues: Ethical decisions to be made in the event of an accident (who to save, etc.).

3.High Implementation Costs: High infrastructure renewal and integration costs.

4.Legal Issues: Uncertainties of liability in autonomous vehicle accidents.

5.Social Acceptance and Resistance: Distrust of the technology and loss of existing jobs.

Fig. 3. Strengths, weaknesses, opportunities and threats of autonomous vehicles

In terms of technological infrastructure, developed countries such as the United States, Germany, and Japan have made significant strides in integrating autonomous vehicles (AVs) and intelligent transportation systems (ITS). These countries have advanced digital infrastructures with the widespread adoption of 5G technology, enabling real-time data exchange and seamless communication between vehicles and infrastructure. Furthermore, high-resolution mapping and sensor systems are widely deployed, allowing for improved navigation and enhanced vehicle autonomy. The communication infrastructure, including Vehicle-to-Vehicle (V2V) and Vehicle-to-Infrastructure (V2I) systems, is well established, facilitating coordinated traffic management and safe AV operation. In contrast, Turkey has initiated the gradual implementation of 5G technology, though it is not yet available across all cities. The development of smart traffic management systems and real-time monitoring is concentrated in major cities, leaving rural areas underserved. Additionally, advancements in mapping technologies and data-sharing infrastructure are ongoing, but there is still considerable work needed to achieve the level of integration seen in more technologically advanced nations.

Developed countries have established detailed regulatory frameworks for the testing and use of autonomous vehicles. For example, in the United States, several states have legal provisions allowing the testing and deployment of AVs on public roads. These regulations also cover crucial aspects such as insurance, data security, and driver responsibility, ensuring a structured and safe deployment of AVs. Japan and Germany have similarly crafted comprehensive laws to accommodate autonomous driving technologies.Turkey, however, is still in the early stages of developing specific regulations for AVs. While there have been some discussions about integrating autonomous vehicles into the national transportation system, there is a lack of established legal guidelines regarding data privacy, safety standards, and the interaction of autonomous vehicles with other road users. As the technology progresses, regulatory frameworks in Turkey will need to be adapted to address these emerging challenges.

In developed countries, public awareness of autonomous vehicles and smart transportation systems is relatively high. Citizens are more inclined to embrace technological innovations, and there is a greater willingness to adapt to the changes brought by autonomous mobility. This readiness facilitates the smoother integration of AVs into the existing transport infrastructure. In Turkey, however, while there is a growing interest in autonomous technologies, public awareness remains limited. Awareness campaigns and educational initiatives are necessary to inform users about the benefits and safety features of AVs. Furthermore, driving behaviors and adherence to traffic laws are crucial factors that may influence the successful integration of autonomous vehicles. In particular, it is essential to foster a driving culture that aligns with the autonomous driving technology's capabilities to ensure smoother transitions to AV-centric transportation systems.

In developed countries, the environmental benefits of autonomous vehicles are becoming increasingly evident. The widespread adoption of electric and autonomous vehicles has contributed to a reduction in carbon emissions, helping to meet climate goals. Additionally, smart transportation systems, such as intelligent traffic management and dynamic pricing, have optimized traffic flow and reduced congestion, further supporting sustainability. Turkey is experiencing a gradual increase in the use of electric vehicles (EVs); however, the adoption rate remains lower compared to that in developed nations. Traffic congestion and air pollution remain significant issues, particularly in major cities like Istanbul and Ankara, where vehicle numbers and emissions continue to rise. The introduction of AUS can play a crucial role in addressing these challenges, offering solutions for traffic management and environmental improvements. By integrating smart systems and promoting electric vehicle use, Turkey can reduce its carbon footprint and improve overall urban mobility.

In conclusion, while Turkey has made strides in developing autonomous and intelligent transportation systems, it still lags behind more advanced nations in terms of technological infrastructure, legal frameworks, and public awareness. The successful integration of autonomous vehicles in Turkey will require a multi-faceted approach, including investment in infrastructure, legal reform, and public education, to fully realize the potential benefits of these innovations in the transportation sector.

5. Conclusion

The rapid development and adoption of autonomous vehicles (AVs) and Intelligent Transportation Systems (ITS) hold immense potential for transforming urban mobility, improving safety, and promoting environmental sustainability. As demonstrated by the comparison between developed countries and Turkey, significant advancements have been made in infrastructure, regulatory frameworks, and public awareness in regions such as the United States, Germany, and Japan. However, Turkey still faces several challenges in fully integrating these technologies into its transportation system.

The integration of autonomous vehicles and smart transportation systems in Turkey is an ongoing process, with progress being made in major urban areas. However, to achieve the full benefits of these technologies, it is essential to address gaps in technological infrastructure, regulatory frameworks, and public awareness. Currently, Turkey's digital and regulatory infrastructure is under development, and its adoption of autonomous vehicles is not as widespread as in other developed countries. While there is interest in electric and autonomous vehicles, there is a need for stronger incentives and a supportive ecosystem to accelerate this transition.

The environmental and traffic management challenges faced by Turkey's rapidly growing urban population can be significantly mitigated by the widespread adoption of AUS and electric vehicles. By optimizing traffic flow, reducing emissions, and promoting sustainable mobility, these technologies can contribute to a more efficient and cleaner transportation system. Suggestions:

- Rapid Expansion of 5G Technology: To facilitate the effective functioning of autonomous vehicles and smart transportation systems, the rapid nationwide rollout of 5G technology should be prioritized. This will support real-time communication, vehicle-to-vehicle (V2V) and vehicle-to-infrastructure (V2I) systems, and enhanced data sharing capabilities.
- Integration of Smart Traffic Management Systems: Investment in smart traffic signalization systems and advanced traffic monitoring infrastructure should be accelerated. This includes the integration of AI-based

solutions that can manage traffic flow dynamically, reduce congestion, and prioritize autonomous vehicles, ultimately leading to smoother and safer traffic conditions.

- Development of Legal and Regulatory Frameworks: Turkey must expedite the development of comprehensive laws and regulations for autonomous vehicles, ensuring that safety standards, insurance policies, and data privacy laws are clearly defined. A national regulatory framework should be established for the testing, deployment, and use of AVs on public roads, taking into account global best practices.
- Public Awareness and Education: To ensure a smooth transition to autonomous and smart transportation systems, it is crucial to raise public awareness. Public information campaigns about the benefits and safety of autonomous vehicles should be launched. Additionally, pilot projects and test drives should be organized in major cities to build trust and familiarity with the technology among the public.
- Promotion of Electric Vehicles (EVs): To enhance environmental sustainability, incentives for electric vehicles should be expanded. Subsidies, tax breaks, and government-supported charging infrastructure would encourage individuals and businesses to adopt EVs, contributing to a reduction in carbon emissions and air pollution.
- Addressing Traffic Congestion: Smart transportation systems, such as dynamic pricing and intelligent route management, should be adopted to optimize traffic flow, reduce congestion, and improve the efficiency of both autonomous and traditional vehicles. Additionally, policies that encourage car-sharing and the use of public transport can help alleviate the strain on urban road networks.
- Collaboration with International Stakeholders: Collaborating with international experts, private sector partners, and research institutions can help accelerate the development of Turkey's autonomous vehicle infrastructure. Learning from the experiences of countries with established AV and AUS systems can guide Turkey in overcoming challenges and maximizing the potential of these technologies.

The future of transportation in Turkey hinges on the integration of autonomous vehicles and intelligent transportation systems. These technologies offer the potential to address traffic congestion, reduce emissions, and improve safety, but achieving these benefits will require concerted efforts across multiple sectors. By investing in technology, legal frameworks, public education, and infrastructure, Turkey can position itself as a leader in smart mobility, ensuring that its transportation system becomes more efficient, sustainable, and inclusive for all citizens.

References

B, T. (2023). Self-driving car. *International Journal of Engineering Technology and Management Sciences, 7*(4), 275–280. https://doi.org/10.46647/ijetms.2023.v07i04.038

Bęczkowska, S. (2023). Autonomous vehicles as viewed by future users in Poland. *Sustainability, 15*(24), 16627. https://doi.org/10.3390/su152416627

Chen, Z. (2017). Traffic flow models for road network with intersections. https://doi.org/10.2991/emim-17.2017.311

Diels, C., & Bos, J. (2016). Self-driving carsickness. *Applied Ergonomics, 53*, 374–382. https://doi.org/10.1016/j.apergo.2015.09.009

Gao, F. (2023). Online safety verification of autonomous driving decision-making based on dynamic reachability analysis. *IEEE Access, 11*, 93293–93309. https://doi.org/10.1109/access.2023.3300423

Guo, S. (2023). Automatic driving model based on machine learning agents. https://doi.org/10.1117/12.2667914

Kozłowski, M., Racewicz, S., & Wierzbicki, S. (2024). Image analysis in autonomous vehicles: A review of the latest AI solutions and their comparison. *Applied Sciences, 14*(18), 8150.

Kyriakidis, M., Happee, R., & Winter, J. (2015). Public opinion on automated driving: Results of an international questionnaire among 5000 respondents. *Transportation Research Part F: Traffic Psychology and Behaviour, 32*, 127–140. https://doi.org/10.1016/j.trf.2015.04.014

National Highway Traffic Safety Administration. (2013). *Preliminary statement of policy concerning automated vehicles*. Washington, DC: U.S. Department of Transportation.

Ni, J., Chen, Y., Chen, Y., Zhu, J., Ali, D., & Cao, W. (2020). A survey on theories and applications for self-driving cars based on deep learning methods. *Applied Sciences, 10*(8), 2749. https://doi.org/10.3390/app10082749

Nielsen, T., & Haustein, S. (2018). On sceptics and enthusiasts: What are the expectations towards self-driving cars? *Transport Policy, 66*, 49–55. https://doi.org/10.1016/j.tranpol.2018.03.004

Othman, K. (2021). Public acceptance and perception of autonomous vehicles: A comprehensive review. *AI and Ethics, 1*(3), 355–387. https://doi.org/10.1007/s43681-021-00041-8

Paden, B., Čáp, M., Yong, S., Yershov, D., & Frazzoli, E. (2016). A survey of motion planning and control techniques for self-driving urban vehicles. *IEEE Transactions on Intelligent Vehicles, 1*(1), 33–55. https://doi.org/10.1109/tiv.2016.2578706

Pettersson, I., & Karlsson, M. (2015). Setting the stage for autonomous cars: A pilot study of future autonomous driving experiences. *IET Intelligent Transport Systems, 9*(7), 694–701. https://doi.org/10.1049/iet-its.2014.0168

Raue, M., D'Ambrosio, L., Ward, C., Lee, C., Jacquillat, C., & Coughlin, J. (2019). The influence of feelings while driving regular cars on the perception and acceptance of self-driving cars. *Risk Analysis, 39*(2), 358–374. https://doi.org/10.1111/risa.13267

Wang, S., Huang, Y., & Sha, Y. (2017). The assessment of traffic with self-driving, cooperating cars. https://doi.org/10.2991/icmeit-17.2017.87

Yang, L., Liu, T., Zhao, X., & Wu, P. (2017). Analysis of the impact of self-driving cars on traffic flow. *DEStech Transactions on Computer Science and Engineering* (AIEA). https://doi.org/10.12783/dtcse/aiea2017/14946

Zhao, J., Liang, B., & Chen, Q. (2018). The key technology toward the self-driving car. *International Journal of Intelligent Unmanned Systems, 6*(1), 2–20. https://doi.org/10.1108/ijius-08-2017-0008

4th International Civil Engineering & Architecture Conference
17-19 May 2025, Trabzon, Türkiye

Investigating the effect of polyamine fatty acid on the moisture sensitivity of warm mix asphalt mixtures

Sepehr Saedi *[1], Mohsen Seyedi[1], Sepanta Naimi[1]

[1] *Altinbas University, Department of Civil Engineering, 34200 Istanbul, Türkiye*

Abstract. The moisture sensitivity of warm mix asphalt (WMA) is a critical factor in the damage process of asphalt pavements. Therefore, using anti-stripping additives to mitigate moisture-induced changes is essential. This study investigated the effect of a Polyamine Fatty Acid (PFA) additive on improving WMAs' moisture sensitivity. To achieve this, various amounts of the additive, specifically 0.2%, 0.25%, 0.3%, 0.35%, and 0.4% by weight of the binder, were incorporated into the mixtures. A series of tests were conducted, including the boiling water test, saturated Marshall stability test, and modified Lottman tensile strength test. The results demonstrated that the additive samples exhibited better moisture resistance under saturated conditions than those without. Notably, the use of 0.35% of this additive significantly enhanced the moisture damage resistance of the prepared mixtures to an acceptable level.

Keywords: Warm mix asphalt**,** Polyamine Fatty Acid , Moisture damage, Stripping, Tensile strength

1. Introduction

The use of warm mix asphalt (WMA) technology has significantly increased in recent years, primarily to protect the environment and reduce energy consumption. However, despite its numerous benefits, WMA is still used less frequently than hot mix asphalt (HMA) due to its comparatively lower performance. One key factor contributing to the lower performance of WMA is its high sensitivity to moisture (Zhang et al., 2025). In challenging weather conditions, stresses are applied to the surface layer, increasing the strain. Inadequate supervision, traffic, and water play a key role in the damage of asphalt concrete coatings. Water causes the loss of adhesion at the contact surfaces between the bitumen and aggregate particles. This type of early adhesion loss is typically referred to as "stripping" in asphalt coatings (Naser et al., 2023). The sensitivity of hot mix asphalts to moisture-induced damage is critical for assessing the vulnerability of the surface layer. When aggregates detach from the asphalt mix, the mix's strength decreases. This reduction in strength can lead to several issues within the layers, including cracking, detachment, and rutting caused by wheel pressure (Kok & Yilmaz 2009). Factors such as the properties of bitumen, characteristics of the aggregate materials, the features of asphalt mixes, quality control during compaction, and the impact of dynamic traffic loads play an important role in creating moisture sensitivity and exacerbating the damage (Hesami et al., 2015).

In surface layer design, there are significant differences between laboratory results and those obtained under real-world conditions. In the lab, mechanical results are generally better than those obtained in real-world conditions. Specifically, with the Marshall compaction method, the volume of voids in practice is usually higher than the volume of voids observed in laboratory tests (Brown & Bitutest 1995).

In a study, lime filler and anti-stripping liquid were tested as materials to prevent stripping in WMA. The findings revealed that the anti-stripping liquid was more effective at reducing stripping compared to lime filler. However, taking into account economic considerations and the necessity to meet technical standards to prevent stripping, the combination of these two materials emerged as the best mixture for achieving optimal performance. This combination is especially recommended in situations where both cost savings and technical efficiency are priorities (Mahdi et al., 2024). The use of the Sasobit Redox additive in various gradations demonstrated its ability to enhance the moisture resistance of WMAs. This improvement is attributed to an increase in the indirect tensile strength (ITS) of the mixtures. Test results indicated that the most significant enhancement in ITS occurred with the addition of 2.5% Sasobit Redox to the gradations (Taher et al., 2024). Research indicates that adding carbon fibers to hot asphalt mixtures increases their resistance to water damage and enhances the ability of bitumen to bind the aggregate materials together. This improvement ultimately boosts the performance and longevity of asphalt concrete (Saedi & Oruc 2020). Studies have shown that Nano-Zycotherm helps make warm mix asphalts

*Corresponding author, E-mail: Sepehr.saedi@altinbas.edu.tr

https://doi.org/10.31462/icearc2025_ce_tra_009

(WMAs) more resistant to moisture, but its impact on rutting failure remains unclear. In contrast, Sasobit improves the strength and stiffness of WMAs and reduces their vulnerability to permanent deformation (Behbahani et al., 2016).

Research has shown that adding Evotherm and paraffin wax is not effective in reducing moisture susceptibility in asphalt mixtures (Yu et al., 2016). The results from Nicholson stripping tests indicate that both nano-bentonite and fatty Arbocel additives significantly improve the adhesion between aggregates and bitumen in Warm Mix Asphalts (WMAs). Consequently, it is recommended that WMAs modified with these additives are particularly effective in resisting stripping, especially in cold and wet regions. Both nano-bentonite and fatty Arbocel enhance the moisture resistance of WMAs. The test results show that the highest Tensile Strength Ratio (TSR) was found in samples containing 0.7% nano-bentonite and 0.3% fatty Arbocel. Although these additives require lower mixing temperatures, which usually increase a mixture's sensitivity to moisture, the inclusion of nano-bentonite and fatty Arbocel effectively counteracts the functional weaknesses associated with moisture-induced damage. This makes them a valuable choice for enhancing the performance of asphalt mixtures in wet conditions (Saedi & Oruc 2020).

2. Materials and methods

2.1. Aggregates

In this study, basalt aggregates were utilized. Table 1 displays the characteristics of both coarse and fine aggregates.

Table 1. Aggregate characteristics

Characteristic	Code	Unit	Results
Coarse Specific gravity	ASTM C-127-15	gr / cm3	2.881
Fine Specific gravity	ASTM C-128-15	gr / cm3	2.747
Filler specific gravity	ASTM C-128-15	gr / cm3	2.887
Los Angeles	ASTM C-131	%	11
water absorb	ASTM C-127-15	%	0.96
Elongated- Flat	ASTM D-4791	%	11.5
Crushed content (two faces)	ASTM D-5821	%	98

2.2. Binder

In this study, the binder used is PG 58-22, produced by Tupras Company. The physical characteristics of the used binder are outlined in Table 2.

Table 2. The physical properties of PG 58-22 binder

Test	Code	Unit	Results
Specific Gravity	ASTM D-70	gr/cm3	1.022
Ductility	ASTM D-113	cm	>100
Viscosity	AASHTO T316	Pa.s	135
Dynamic shear (G*/sin)	AASHTO T315	KPa	60
Flash Point	AASHTO T48	˚C	230

2.3. Polyamine fatty acid

Table 3 presents some physical properties of the additive, including Polyamine Fatty Acid, utilized in this research.

Table 3. The physical properties are additive

	Polyamine Fatty Acid
Physical form	Liquid
Flash Point	Up to 180$^{˚C}$

2.4. Samples provided

The samples tested in this study were cylindrical, with a diameter of 4 inches (101.6 mm) and an approximate height of 2.5 inches (63.5 mm). To prepare the samples, various aggregate components were weighed and mixed in a container before being poured into a Marshall mold. Each side of the mold received 75 blows to simulate heavy traffic conditions. After compaction, the samples were removed from the mold 24 hours later using special jacks and prepared for further testing. Six types of mixtures were prepared: asphalt without additives and asphalt containing 0.2%, 0.25%, 0.3%, 0.35%, and 0.4% by weight of the binder, following the modified Marshall method (Saedi 2024).

2.5. Boiling water test

In this test, we visually assess different levels of stripping after boiling an uncondensed asphalt mixture for 10 minutes. We begin by pouring 500g of water into a container and heating it until it reaches boiling. Next, we add 250g of the uncondensed sample to the boiling water, stirring every three minutes for 10 minutes. After boiling, we let the container cool to room temperature, then pour out the water for further analysis. The mixture is placed on a white surface, and we remove any bitumen that has floated to the water's surface to prevent it from reappearing. Observing the stripped material will help us determine the failure criterion (Fakhri 2021).

2.6. Immersion marshall test

The Immersion Marshall test is used to evaluate the moisture sensitivity of asphalt mixtures. According to AASHTO T-165, the specimens are divided into two distinct groups. Conditioned specimens are immersed in water for 48 hours at a temperature of 60°C, while unconditioned specimens are immersed for 30 minutes at the same temperature. After immersion, the Marshall stability test is performed on both groups of samples. The retained Marshall stability (RMS) is then calculated using Equation (1).

$$RMS\% = \frac{MSconditined}{MSunconditioned} * 100 \tag{1}$$

where, MSconditined is the average Marshall stability of conditioned samples and MSunconditioned is the average Marshall stability of unconditioned samples (Saedi 2024).

2.7. Lottman tensile strength test

Latman has conducted an indirect tensile test to assess the moisture sensitivity of asphalt mixtures under real traffic service conditions. In this test, as outlined in the AASHTO T283 code, one group of samples is tested in a dry condition, while another group is conditioned with moisture before testing. The Indirect Tensile Strength Ratio (TSR) is calculated by comparing the indirect tensile strength of the saturated samples to that of the dry samples (Saedi & Oruc 2022).

$$ITS = \frac{2Pmax}{\pi Dt} \tag{2}$$

$$TSR = (ITS\ wet/ITSdry) \times 100 \tag{3}$$

3. Results and discussion

The results of the experiments were discussed and analyzed based on each case.

3.1. Boiling water

The visual test results are shown in Figure 1. These findings indicate that incorporating modified bitumen with PFA significantly enhances the adhesion strength between the aggregates and the bitumen. It appears that PFA helps form a strong bond, ensuring a more stable connection between the aggregates and the bitumen. Upon closer examination of the results, it is evident that the mixture's resistance to stripping improves as the percentage of PFA increases. This suggests that higher concentrations of PFA contribute to greater durability and performance in WMAs, particularly by enhancing bond stability and reducing the likelihood of stripping under challenging conditions.

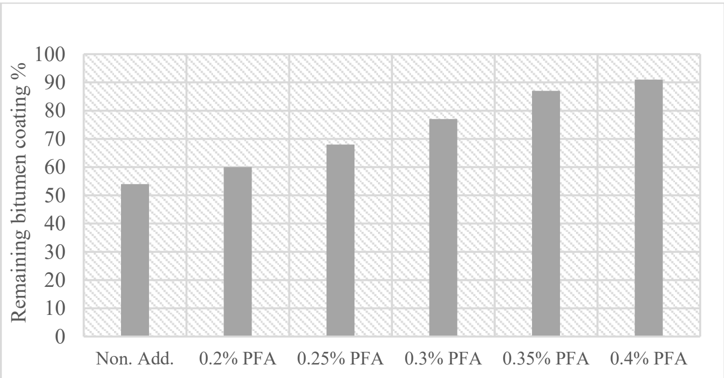

Fig. 1. The result of the boiling water test

3.2. Immersion marshall

Figure 2 presents the findings of the current study. The results indicate that increasing the percentage of PFA up to 0.35% significantly enhances the immersion Marshall value.

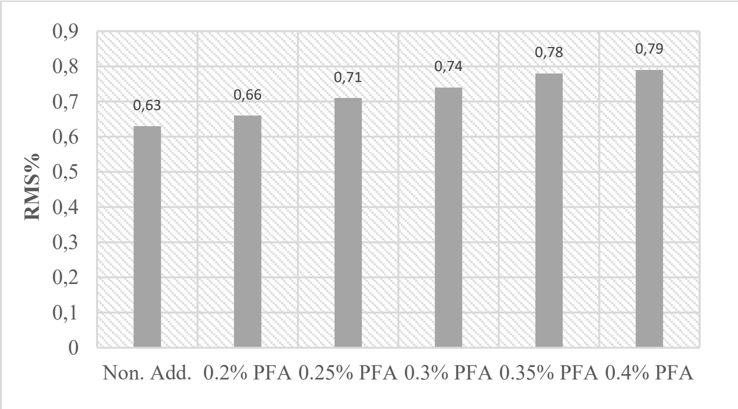

Fig. 2. The results of the Immersion Marshall Test

PFAs exhibit amphiphilic behavior due to the presence of both hydrophilic functional groups, such as amino ($-NH_2$) and carboxyl ($-COOH$) groups, and hydrophobic hydrocarbon chains. These active sites facilitate chemical interactions with mineral surfaces within asphalt mixtures, particularly by forming ionic or covalent bonds with the polar sites on aggregate particles. This molecular interaction significantly enhances the adhesive bonding between the bitumen binder and aggregates, which is critical for the mechanical integrity of the asphalt mixture.
Furthermore, the incorporation of polyamine fatty acids contributes to the formation of a denser and more uniform microstructural matrix. This microstructure acts as a barrier to water penetration, thereby mitigating moisture-induced damage mechanisms such as stripping. The resultant compact texture not only improves resistance to water infiltration but also supports the long-term durability of the mixture. Empirical evaluations, such as the immersion Marshall stability test, indicate a notable improvement in performance under water-saturated conditions for asphalt mixtures containing these additives. This enhancement is particularly relevant for WMAs, which are inherently more susceptible to moisture damage due to reduced mixing temperatures and potential limitations in binder-aggregate interaction. By addressing this vulnerability, polyamine fatty acid additives may contribute to an extended service life and enhanced moisture resistance of WMAs.

3.3 Lottman test
The results of the tensile strength ratio of the samples are shown in Figure 5.

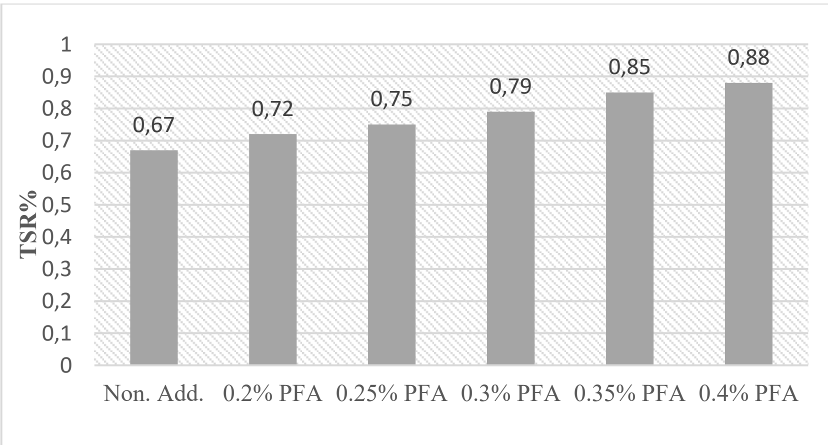

Fig. 3. The results of the Latman test

As shown, the TSR of mixtures with 35% is above 80%, and they all pass the Superpave limit. It can be stated that the FRP additive increases the resistance of the mixtures to moisture. Polyamines affect the tensile strength ratio by improving the chemical bonds between bitumen and mineral aggregates. These additives enhance the asphalt's ability to resist tensile stresses by forming hydrogen and covalent bonds while also preventing the bitumen from overheating and degrading. Additionally, polyamines significantly improve the performance of asphalt in wet conditions by mitigating the negative effects of moisture and other environmental factors. As an additive in warm mix asphalts, polyamine-based amino acid additives positively impact the tensile strength ratio. By improving the adhesion of bitumen to mineral aggregates, reducing asphalt's susceptibility to moisture and temperature variations, and enhancing the overall stability of the asphalt, these additives increase the performance and durability of the asphalt. This is particularly beneficial in areas exposed to harsh weather conditions or heavy traffic, where the use of such additives can substantially extend the lifespan of the asphalt. Therefore, incorporating polyamine amino acids into asphalt mixtures is an effective strategy for enhancing the performance of these materials, which can reduce road and highway maintenance and repair costs.

4. Conclusions

This study aimed to evaluate the effects of Polyamine Fatty Acid additives on the performance of the warm mix asphalts against water damage. Below are the results of the investigation.

- The results of the boiling water test show that the PFA additives fully function as an anti-stripping agent, such that increasing the percentage of this additive in the mixture improves its performance against the stripping phenomenon.
- PFAs help in the densification of warm mix asphalt samples by creating microscopic matrices, and denser samples exhibit better Marshall stability in both dry and saturated conditions.
- The RMS index is one of the important factors in determining the behavior of asphalt mixtures against moisture damage. According to the results, PFAs play a significant role in improving this index. Therefore, it can be said that this type of additive can address the weaknesses of warm mix asphalt mixtures in this regard.
- Based on the results of the Latham test, adding 0.35% of the PFA-containing additive provides the specified acceptance limit for warm mix asphalt mixtures. Therefore, it can be concluded that the optimal amount of this additive in warm mix asphalt mixtures is 0.35%.
- Given that moisture weakness leads to premature failure of warm mix asphalt mixtures, the use of the PFA additive can play a beneficial role in increasing the service life of these types of pavements and reducing maintenance and repair costs.

Acknowledgments

The research described in this paper was not financially supported.

References

Zhang, H., Sui, Y., Gong, M., Li, X., Zhu, H., Liu, Y., & Sun, J. (2025). Temperature control and energy-saving efficiency evaluation of low-energy warm-mix asphalt mixtures with composite additives. *Case Studies in Thermal Engineering*,*65*, 105604.

Naser, S. S. M., Seyedi, M., & Al-Busaltan, S. (2023). Enhancing Stone Mastic Asphalt through the Integration of Waste Paper and Cement Kiln Dust. *Journal of Civil and Hydraulic Engineering*, *1*(1), 23-37.

Kok, B. V., & Yilmaz, M. (2009). The effects of using lime and styrene–butadiene–styrene on moisture sensitivity resistance of hot mix asphalt. *Construction and building materials*, *23*(5), 1999-2006.

Hesami, S., Ameri, M., Goli, H., & Akbari, A. (2015). Laboratory investigation of moisture susceptibility of warm-mix asphalt mixtures containing steel slag aggregates. *International Journal of Pavement Engineering*, *16*(8), 745-759.

Brown, S. F., & BITUTEST. (1995, November). PRACTICAL TEST PROCEDURES FOR MECHANICAL PROPERTIES OF BITUMINOUS MATERIALS. In *Proceedings of the Institution of Civil Engineers-Transport* (Vol. 111, No. 4, pp. 289-297). Thomas Telford-ICE Virtual Library.

Mahdi, N. J., Jehad, A. E., Rajab, O. F., & Akhlaghi, T. (2024, October). Evaluation of the impact of moisture damage on warm mix asphalt containing zeolite and hydrated lime. In *AIP Conference Proceedings* (Vol. 3249, No. 1). AIP Publishing.

Al-Taher, M. G., Sawan, A. M., Attia, M. I. E. S., & Ibrahim, M. F. (2024). Investigating the moisture susceptibility of warm asphalt mixtures modified by sasobit redux (SR). *Innovative Infrastructure Solutions*, *9*(5), 133.

Saedi, S., & Oruc, S. (2020). The influence of SBS, viatop premium and FRP on the improvement of stone mastic asphalt performance. *Fibers*, *8*(4), 20.

Behbahani, H., Ayazi, M. J., & Shojaei, M. H. (2016). Laboratory evaluation of moisture susceptibility and rutting potential of warm mix asphalt mixtures. *Quarterly Journal of Transportation Engineering*, *7*(3), 405-418.

Yu, H., Leng, Z., Dong, Z., Tan, Z., Guo, F., & Yan, J. (2018). Workability and mechanical property characterization of asphalt rubber mixtures modified with various warm mix asphalt additives. *Construction and Building Materials*, *175*, 392-401.

Saedi, S., & ORUÇ, Ş. (2020). The effects of nano bentonite and fatty arbocel on improving the behavior of warm mixture asphalt against moisture damage and rutting.*Civil Engineering Journal-Tehran*, *6*(5).

Saedı, S. Evaluation of the effect of para-aramid and micro-polyolefin fibers on permanent displacement in stone mastic asphalt. *Journal of Sustainable Construction Materials and Technologies*, *9*(2), 106-113.

Fakhri, M. (2021). The effects of nano zinc oxide (ZnO) and nano reduced graphene oxide (RGO) on moisture susceptibility property of stone mastic asphalt (SMA).*Case Studies in Construction Materials*, *15*, e00655.

Saedi, S. (2024). Laboratory investigation of the effect of de-icing solutions on moisture susceptibility of hot mix asphalt with biomass fibers.*Innovative Infrastructure Solutions*,*9*(11), 1-12.

Saedi, S., & Oruc, S. (2022). Investigating the possibility of using roof shingles waste and fibers in stone mastic asphalt pavements. *International Journal of Transportation Engineering*, *9*(3), 681-691.

4th International Civil Engineering & Architecture Conference
17-19 May 2025, Trabzon, Türkiye

The Effect of Chevrons Markings for Tunnel Safety: A Simulator Based Approach

Omer Faruk Ozturk[1], Yusuf Mazlum[2], Emine Coruh[3*], Halim Ferit Bayata[4], Metin Mutlu Aydın[5]

[1] Giresun University, Department of Civil Engineering, 28200 Giresun, Türkiye
[2] Erzincan Binali Yıldırım University, Ilic Dursun Yıldırım Vocational School, 24700 Erzincan, Türkiye
[3*] Gümüşhane University, Department of Civil Engineering, 29100 Gümüşhane, Türkiye
[4] Erzincan Binali Yıldırım University, Department of Civil Engineering, 24002 Erzincan, Türkiye
[5] Ondokuz Mayıs University, Department of Civil Engineering, 55270 Samsun, Türkiye

Abstract. Maintaining a safe following distance is crucial for ensuring driving safety in tunnels, as its violation can increase the likelihood of accidents and disrupt traffic flow. This study examined the impact of a visual marking system known as "chevrons," applied at 50-meter intervals on the asphalt, designed to encourage drivers to maintain proper following distances in tunnel environments. The research was conducted in a driving simulator at the Autonomous Driving Techniques and Driver Behaviour Detection Laboratory at Erzincan Binali Yıldırım University, involving 65 participants. Through simulator-based experiments, driver behavior was evaluated under varying traffic densities and speed limits to assess the effectiveness of the chevron markings. The findings demonstrated that chevron markings positively influenced driver behavior. Drivers showed increased awareness, reduced their speed, and adjusted their following distances more appropriately. Moreover, the markings contributed to lower stress levels and facilitated better decision-making in traffic. These improvements were particularly evident under heavy traffic conditions, where maintaining safe distances is typically more challenging. Overall, the study concluded that chevron markings offer a practical and effective solution for enhancing in-tunnel traffic safety. Their implementation can help reduce accident rates and improve traffic flow, particularly in densely trafficked tunnels. As a low-cost and easy-to-implement strategy, this approach has strong potential for broader application in future tunnel designs and intelligent traffic management systems. The chevron system represents a promising contribution to safer and more sustainable transportation infrastructure.

Keywords: Tunnel safety; Chevrons marking system; Driver behaviour; Traffic flow analysis; Simulator based experiment

1. Introduction

Road transportation represents one of the most essential infrastructure systems facilitating the mobility of individuals, goods, and services on a global scale. However, the safety and sustainability of this system vary considerably depending on road types and environmental conditions. Highway tunnels, with their low illumination, monotonous surroundings, and limited visual cues, create a weak and insufficient visual environment that can lead to visual illusions and impair drivers' ability to accurately perceive their speed (Wan et al., 2018). Driving in enclosed road environments, such as tunnels, requires particular attention and behavioral adaptation from drivers (Ozturk et al., 2024). In this context, various engineering solutions have been developed to enhance driver performance and promote safe driving behavior, especially in physically constrained settings like tunnels. Studies have shown that chevron alignment signs improve drivers' focus on the roadside, reduce stress levels, and contribute to speed reduction in curves, thereby encouraging safer driving behavior in confined spaces (Wu et al., 2013). Fiolić et al. (2023) emphasized that well-designed and properly positioned road markings and signs can significantly improve driver behavior and enhance overall traffic safety. Traffic control devices including pavement markings like chevrons are considered vital components of road safety strategies aimed at influencing driver behavior and enhancing roadway safety (Babić et al., 2020). While vertical chevron signs have been extensively studied, recent research has begun to explore the potential benefits of horizontal chevron markings applied directly to the road surface (Fig. 1).

* Corresponding author, E-mail: coruhemine@gmail.com

https://doi.org/10.31462/icearc2025_ce_tra_029

Fig. 1. Chevron applications in real highways (Mock Theory Test, 2025; Sabre Roads, 2025)

These markings are hypothesized to support following distance awareness and speed adaptation, especially under heavy traffic or low visibility. This represents a novel direction in traffic safety research and forms the foundation of the current study. So this study conducted a simulator-based study to evaluate how horizontal chevron markings influence driver behavior in tunnel environments. Amini et al. (2023) highlighted that driving simulators constitute a robust and reliable method for investigating driver behavior, offering a controlled and replicable environment to examine complex and high-risk scenarios that are impractical to study in real-world traffic conditions.

To investigate the impact of chevron markings on tunnel driving safety, an experimental simulator-based study was conducted at the Autonomous Driving Techniques and Driver Behavior Observation Laboratory of Erzincan Binali Yıldırım University. The sample included 65 participants with diverse backgrounds in age, gender, and driving experience. Each participant engaged in simulated driving scenarios involving tunnel environments with and without chevron markings, under varying traffic densities and speed limits.

2. Literatue review

In the literature, chevron signs are predominantly examined as vertical traffic control devices placed along road edges to warn drivers about upcoming horizontal curves. These vertical signs function as visual cues intended to enhance curve perception and promote speed reduction (Wu et al., 2016). For instance, Zhao et al. (2015) analyzed the impact of chevron alignment signs on driver performance under various roadway geometries and concluded that such signs significantly improved vehicle positioning and speed control on curves. Similarly, Babić et al. (2022) focused on how different chevron color combinations influence driver behavior in simulated rural road environments. Their results showed that all chevron variants reduced driving speeds, with fluorescent and white background signs being the most effective. These findings collectively highlight that the design and placement of vertical chevron signs play a critical role in curve negotiation and road safety, emphasizing the importance of visual contrast and clarity in guiding driver behavior. Research also suggests that properly spaced chevron signs can encourage drivers to reduce their speed when entering and traveling through curves (Srinivasan et al., 2010). In the U.S. studies have primarily examined the influence of chevrons on vehicle dynamics such as speed and lane positioning, as well as on criteria for optimal placement to enhance their effectiveness (Zhao et al., 2015). Zhao et al. (2017) examined the effects of differently colored chevron signs on drivers' visual responses and speeds in order to enhance curve safety under snowy and icy road conditions. Using visual feedback metrics such as fixation duration and pupil size, the study found that proper color selection helped drivers reduce their speed when approaching curves and made it easier for them to perceive road alignment. These findings provide valuable references for highway warning systems and intelligent vehicle design.

A study conducted in Denmark reported that nearly 45% of injury accidents on freeways involve vehicles traveling in the same direction; however, on freeways equipped with chevron markings, fewer rear-end accidents were observed as drivers maintained safer following distances (Greibe, 2010). Another study in Western Australia highlighted that enhanced chevron alignment markers could reduce crashes by up to 47% when combined with other delineation treatments (Palamara et al., 2014). In a study by Helliar-Symons and Butler (1995), French-designed chevron markings were tested on the M1 motorway in the UK, where inverted "V" shaped patterns were applied at 40-meter intervals on the nearside and center lanes. Drivers were instructed via roadside signs to "Keep apart, 2 chevrons." Their findings indicated that these markings contributed to a 56% reduction in accidents compared to control sections. It was also observed that the positive effect on safety extended up to 18 kilometers beyond the start of the chevron-marked area. Although the intervention primarily targeted multi-vehicle collisions, a significant decrease in single-vehicle accidents was also recorded, suggesting that chevron markings may broadly enhance driving behavior and overall roadway safety (Helliar-Symons & Butler, 1995). Merat & Jamson (2013) conducted a simulator-based study following a consultation workshop with highway engineering experts. Based on these workshops, three engineering treatments were selected and implemented: transverse rumble strips, chevron markings, and variable message signs (VMS) (Fig. 2).

Fig. 2. The chevrons (left) rumble strips (middle) and VMS (right) used in the study (Merat & Jamson, 2013)

In the study, chevrons (commonly used in the UK to indicate safe following distances) were applied across all three lanes, with markings spaced every 40 meters over a 3 km section of road. In their study, Merat & Jamson (2013) found that all three low-cost engineering treatments effectively alleviated driver fatigue, with no significant difference in the alerting effects of the treatments. Historically, chevrons in the UK have primarily used to encourage speed reduction, such as on motorways (Helliar-Symons et al., 1995). Voigt & Kuchangi (2009) evaluated the impact of converging chevron pavement markings on speed reduction on freeway-to-freeway connector ramps. They found that the chevron markings effectively reduced vehicle speeds, with a significant reduction of approximately 4 mph observed for heavy trucks. The speed reduction varied based on vehicle class and location along the curve, indicating that chevron markings are an important factor in influencing driver behavior and improving safety on ramp curves. A study conducted in Georgia and New Mexico examined the effects of different curve delineation treatments on vehicle speed and placement on rural two-lane highways. The research found that chevron signs, particularly those with retroreflective materials, played a key role in improving vehicle positioning by reducing encroachment into opposing lanes and shifting vehicles toward the centerline.

While chevrons were part of a broader range of treatments, including post-mounted delineators and raised pavement markers, the findings highlight the importance of chevron markings, especially in enhancing lane positioning and promoting safer driving behaviors. Notably, the chevrons used in this study were vertical signs, and their effectiveness in reducing speed variability and improving curve-following behaviors suggests that clear curve delineation, including chevrons, helps drivers better recognize upcoming curves and adjust their driving accordingly (Zador et al., 1987). Hunter et al. (2014) highlighted that a somewhat nontraditional but potentially effective method to reduce excessive speeds is by altering drivers' perception of a road's traversable speed. One such approach, first proposed in Japan over two decades ago, involves the use of converging chevron pavement markings, which have recently gained increasing attention in the United States. Hunter et al. (2014) found that chevron markings led to significant crash reductions of 76% and 87% in the 20 months after installation, compared to only 15% and 20% reductions at control ramps. These results indicated that the chevrons effectively enhanced safety, prompting the identification of additional sites with high potential for safety improvements. Chevron or herringbone pavement markings have been shown to significantly reduce vehicle speed and improve drivers' lane positioning (Godley et al., 2002; Charlton, 2007a, b). These treatments are also effective in emphasizing perceptual cues at critical locations such as highway curves, ramps, or tunnels, enhancing overall safety (Retting et al., 2000; Gilmore et al., 2013).Wan et al. (2018) conducted an experimental study to examine the influence of sidewall marking angles and lengths on drivers' speed perception in low-luminance highway tunnels, utilizing a three-dimensional tunnel model within a driving simulator. Their findings indicated that appropriately configured sidewall markings led to an overestimation of speed by drivers, thereby increasing sensitivity to speed variations and contributing to the regulation of unintended acceleration. They concluded that this effect could support efforts to reduce speeding behavior and enhance overall driving safety in tunnel environments.

A review of the literature reveals that various chevron applications (including both horizontal and vertical markings) have generally produced positive outcomes in improving driver behavior and enhancing road safety. Vertical chevron signs have been shown to improve curve perception, promote speed reduction, and enhance lane positioning. Horizontal chevron markings have also demonstrated effectiveness in reducing vehicle speeds and influencing drivers' perceptual judgments. However, it is evident that there is a limited number of studies specifically investigating the effects of horizontal chevron markings in tunnel environments, highlighting the need for further research in this area.

3. Material and methods

3.1. Driver properties and driving simulator

In the simulator tests, 65 drivers (14 female, 51male) attended in the driving simulator tests voluntarily (mean age = 38.7 years, SD = 10.3; age range: 21–76). All test drivers held valid driving licenses ranging from 2 to 37 years of experience (mean = 17.9 years). Volunteer drivers were randomly selected from various age and gender groups within the tunnel's surrounding area, minimizing demographic and cultural bias. While some had prior simulator experience, all were familiar with tunnel driving because of the hihgh tunnel roads in Türkiye. An tthical approval was granted by the university's ethics committee for the test with volunteer drivers. In the study, all driving tests took place at the Driving Simulator and Traffic Analysis Laboratory at Erzincan Binali Yıldırım University. The used simulator, based on a Fiat Egea hatchback with operational pedals, steering, and gearbox, integrates visual and audio systems with developed software. The visual output is displayed on a 60° curved screen (8 m × 2.5 m), projecting images of all tunnel environments to match real New Zigana Tunnel conditions given in Fig. 3 (Kircher & Ahlstrom, 2012). Projector calibration was based on real-world luminance measurements to ensure simulation accuracy during the tests.

(a)) (b)

Fig. 3. (a) Inside view and (b) outside view of the developed simulator system

A special simulator software was developed to record and examine driver behavior, including speed, trajectory, and timing. This software has a synchronization ability for vehicle control inputs, projection visuals, and sound at the same time. The developed software and connected system offers full HD visual fidelity with a 60° field of view. Speed and gear indicators are also projected onscreen to supply easy utilization to test drivers, and an in-vehicle camera records driver behavior and surroundings. The driving experiments took place between April and July 2024, with all volunteer drivers. Prior to the test sessions, participants received introductory information about the tunnel route and the simulator system. To help drivers acclimate to the simulator's controls, such as the gears, steering, and braking, each completed a 1 km neutral practice route that included a tunnel segment. This initial session ensured they were comfortable with the system before beginning the main test. After the familiarization run, participants proceeded to drive the 6.3 km test route, completing three separate scenario runs. Before the driving tests, all attendees were fully informed about all audio-visual recordings and simulator system definetly (Fig. 4).

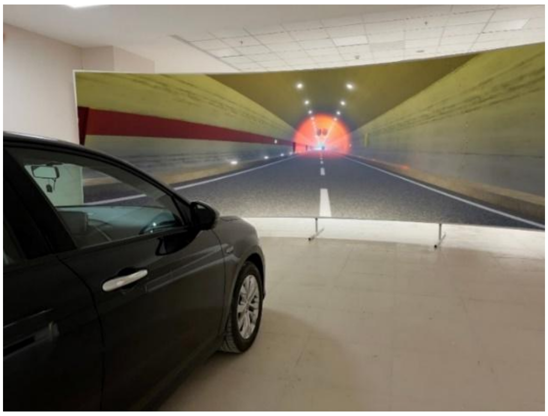

Fig. 4. A typical view of driving simulator platform

3.2. Virtual tunnel design and chevrons

The simulated road was modeled on the Zigana Tunnel in Trabzon, Türkiye, a twin-tube tunnel spanning 29 km (14.5 km per tube), making it Europe's longest and the world's third-longest twin-tube tunnel (General Directorate of Highways, 2024) (Fig. 5). The simulation replicated tunnel infrastructure, including lighting, wall patterns, signage, advertisements, shoulders, emergency lanes, and ventilation shafts. In the developed simulator, the 6.3 km test route featured two lanes in each direction, a posted speed limit of 80 km/h, minor gradients, and a 0.6 km horizontal curve. Weather conditions were set to sunny, and traffic volume was maintained at approximately 500 vehicles/hour, reflecting typical peak-hour conditions observed on examined road site. To match real-world driving conditions, traffic flow remained free of congestion. Tests were conducted in the morning to minimize fatigue effects. Although the simulator lacked lateral motion axes, realism was enhanced through a wide field of view, authentic vehicle controls, realistic sound effects, and detailed 3D environments, including accurate tunnel geometry and traffic simulation. Real roadside photographs were overlaid in the simulation software to create an authentic visual environment. All environmental and infrastructural elements of the Zigana Tunnel were accurately integrated into the virtual scene. Free-flow traffic conditions were consistently applied in all experiments, replicating actual tunnel conditions. The geometric characteristics of the developed virtual scenario is given in Table 1.

Fig. 5. Schematic view of New Zigana Tunnel project

Table 1. Properties of the virtual tunnel

Tunnel Lighting Colour	Lane Number	Lane Width (Left + Right) (m)	Lateral Clearance (Left + Right) (m)	Sidewalk Width (Left + Right) (m)	Interval Between Two Checrons
White	2	3.50 + 3.50	0.50 + 0.50	1.00 + 1.00	50

3.3. Aplication of chevrons in virtual scenario and measurements

In the tunnel road scenario simulated using a driving simulator, chevron markings were applied to evaluate their impact on driver behavior and safety. Chevron patterns, typically used to visually guide drivers and create an illusion of speed, were integrated into the simulated tunnel environment to examine their effectiveness in enhancing lane discipline, reducing vehicle speed, and improving overall spatial awareness. The immersive simulator setup allowed for precise monitoring of driver responses, including changes in speed, steering stability, and lane positioning, under consistent traffic and lighting conditions (Fig. 6).

Fig. 6. Different images for chevron applications in the New Zigana Tunnel

Driving performance was evaluated in three main areas: average vehicle speeds and driver characteristics. Vehicle speeds were continuously recorded at a rate of nine times per second using the simulator software. Upon completing the simulator session, participants filled out a questionnaire capturing demographic information such as gender, age, driving license duration, familiarity with the route etc. Additionally, they provided feedback on the simulator's performance, including the realism of the 3D modeling, the quality of the vehicle controls, and the effectiveness of the sound system.

4. Analysis and results

4.1. Speed analysis

Vehicles' mean spot speeds at entry, exit, and average speeds were collected and analysed to study driving behaviours. The measured standard deviation, mean, minimum, and maximum values of vehicle speeds (km/h) for entry, exit, and average speeds were determined for all 65 drivers.These results are summarized in Table 2.

Table 2. Descriptive statistics for vehicle speed results for examined locations

Vehicle Location in the Tunnel	Vehicle Speeds (km/h)			
	Average	Std. Deviation	Minimum	Maximum
Entrance	98.2	24.3	52	147
Inside	104.2	30.8	40	153
Exit	100.6	28.7	42	150

Table 2 presents descriptive statistics summarizing vehicle speeds measured at three distinct locations within the highway tunnel scenario: entrance, inside, and exit. The results indicate that the average vehicle speed increased from the tunnel entrance (98.2 km/h) to the inside section (104.2 km/h) and then slightly decreased at the exit (100.6 km/h). The highest variability in vehicle speeds was observed inside the tunnel (standard deviation = 30.8 km/h), suggesting that drivers exhibited less consistent behavior in this section. The recorded speed range also indicates substantial variability, with speeds ranging from as low as 40 km/h (inside) to as high as 153 km/h (inside). Such high variations may reflect differences in individual driver perceptions or confidence levels within tunnel environments. Overall, the findings highlight notable speed fluctuations inside the tunnel, which could potentially impact safety and traffic flow efficiency.

A one-way ANOVA Test was conducted to examine the relation average speeds between the tunnel entrance, inside, and exit sections. The statistical analysis using one-way ANOVA shows an F-statistic of approximately 1.15 with a p-value of 0.318. Since the p-value exceeds the common significance level of 0.05, there is no statistically significant difference in average speeds between the tunnel entrance, inside, and exit sections. This indicates that there is no statistically significant difference between average speeds measured at these three locations in the tunnel. Therefore, based on this analysis, the slight variations observed in average vehicle speeds across different tunnel sections appear random and do not reflect meaningful differences in driver behavior or tunnel influence.

4.2. Driver characteristics

Before the driving tests, a detailed survey conducted to measure driver charactersitics of the volunteer participants. According to Fig. 7. The majority of participants hold either a Bachelor's degree or a PhD degree, indicating a generally high educational attainment among drivers in the sample. High School and Master degree holders also constitute noticeable proportions of the sample, reflecting a diverse educational range. Participants with an Associate Degree or Primary School education represent smaller segments of the overall group. This distribution suggests that the study involved a relatively educated participant pool, which could imply that participants were likely capable of adequately understanding simulator instructions and procedures. However, the relatively low representation of primary education participants should be considered when generalizing findings to broader populations.

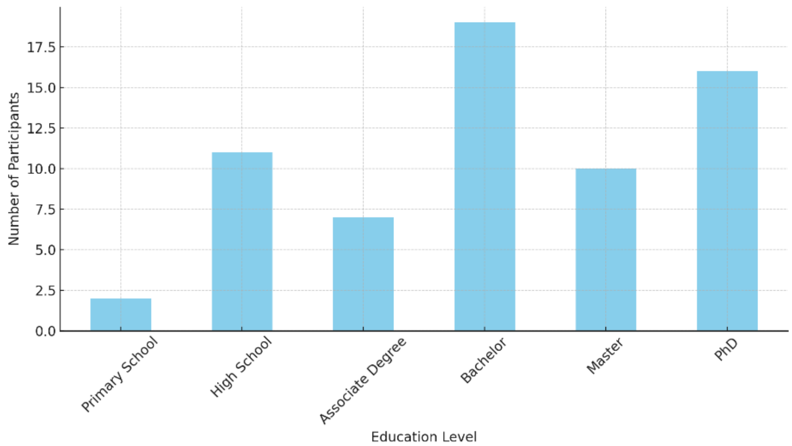

Fig. 7. Distribution of education levels

Fig. 8 also presents the distribution of job types among participants in the driving simulator study. From the Fig. 8, it can be seen that "Academicians" represent the largest job group, suggesting substantial involvement from technically-oriented professionals. Tradesmen and officers also have notable representation, indicating a diverse occupational background among participants. Groups such as Teachers, Workers, and Students appear less frequently, suggesting these occupations are underrepresented in the sample. This occupational diversity may influence the generalizability of the study findings, particularly regarding driving behavior that could be affected by occupational background and experience.

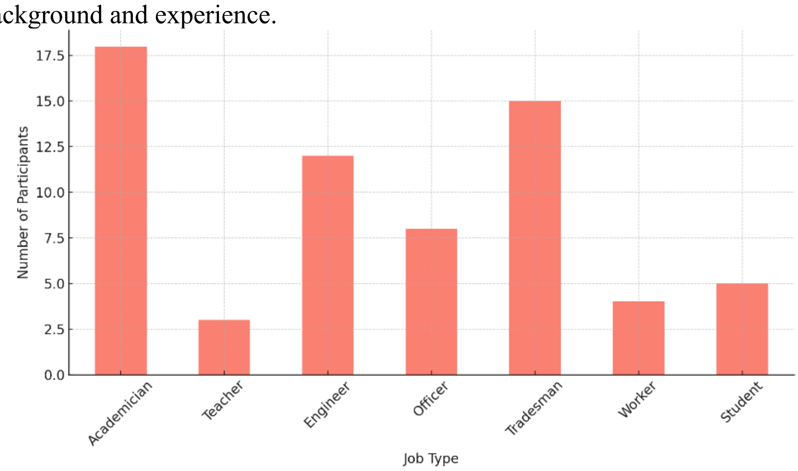

Fig. 8. Distribution of jobs among participants

Fig. 9 illustrates participants' self-reported ability to use a vehicle. The majority identify as having a professional level of ability, followed by those at the intermediate level. Very few participants classified themselves as beginners, and none reported being unable to use a vehicle. This suggests that the sample primarily consists of confident and experienced drivers, which is appropriate for a driving simulator study. However, the lack of novice drivers may limit insights into how less experienced individuals respond to tunnel environments or simulator conditions.

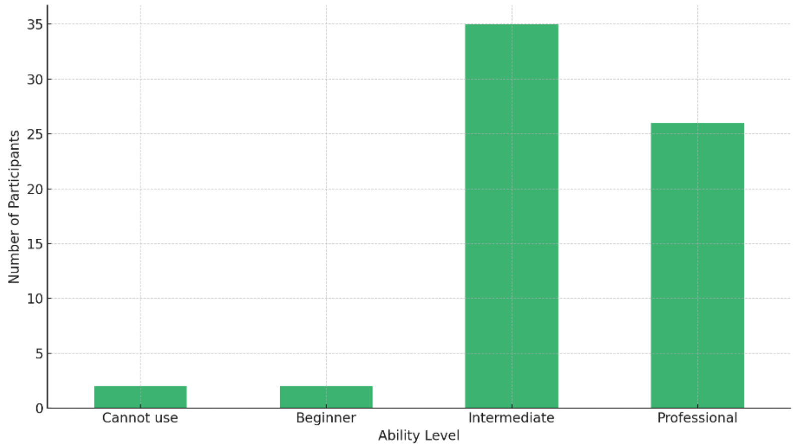

Fig. 9. Participants ability to use a vehicle

Fig. 10 also displays the distribution of driver profiles among participants. The most common profile is moderate, indicating a balanced driving style. This is followed by calm drivers, while aggressive drivers are the least represented. These results suggest that the participant group primarily exhibits controlled and composed driving behavior, which may influence how they respond to different tunnel scenarios in the driving simulator. The relatively low number of aggressive drivers may also limit insights into more risk-prone driving styles.

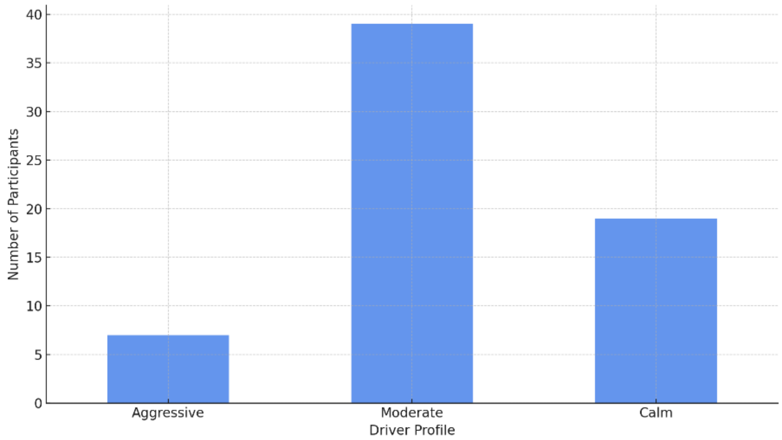

Fig. 10. Distribution of driver profiles

4.3. Driving in the Tunnel

A survey was also conducted to understand the simulator experience and feelings to drive in longer tunnels. Survey results showed that a significant majority of participants (over 80%) had never used a driving simulator before, with a small minority having prior experience or being unsure (Fig. 11a). About 21.5% of participants reported having prior knowledge about the vehicle simulator, while nearly 79% had none (Fig. 11b).

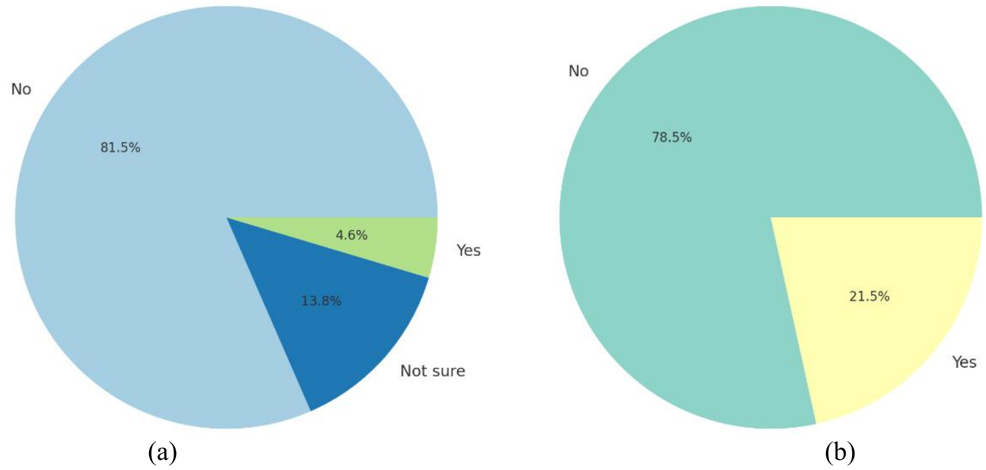

Fig. 11. (a) Driving simulator use before and (b) knowledge about driving simulator

In the survey, some special questions were also asked to particiopants to measure their opinions on driving in longer tunnel and tunnel conditions for New Zigana Tunnel. A majority of participants (~63%) responded “Not sure” about whether road tunnels are adequate in terms of traffic safety, indicating uncertainty or lack of awareness. Only a small fraction felt they were adequate (Fig. 12a). Similarly, most participants (~56%) were unsure about whether tunnels offer proper prior warnings of dangerous areas. A smaller group indicated “Sometimes”, and very few responded positively (Fig. 12b). Over 62% were uncertain if lighting conditions are sufficient, with 28% selecting “Sometimes”, reflecting overall concern or variability in lighting perception (Fig. 12c). Half of the participants (~49%) reported that driving in long tunnels is “sometimes” boring, while ~36% agreed outright, suggesting a need for visual or environmental improvements to enhance driver engagement (Fig. 12d).

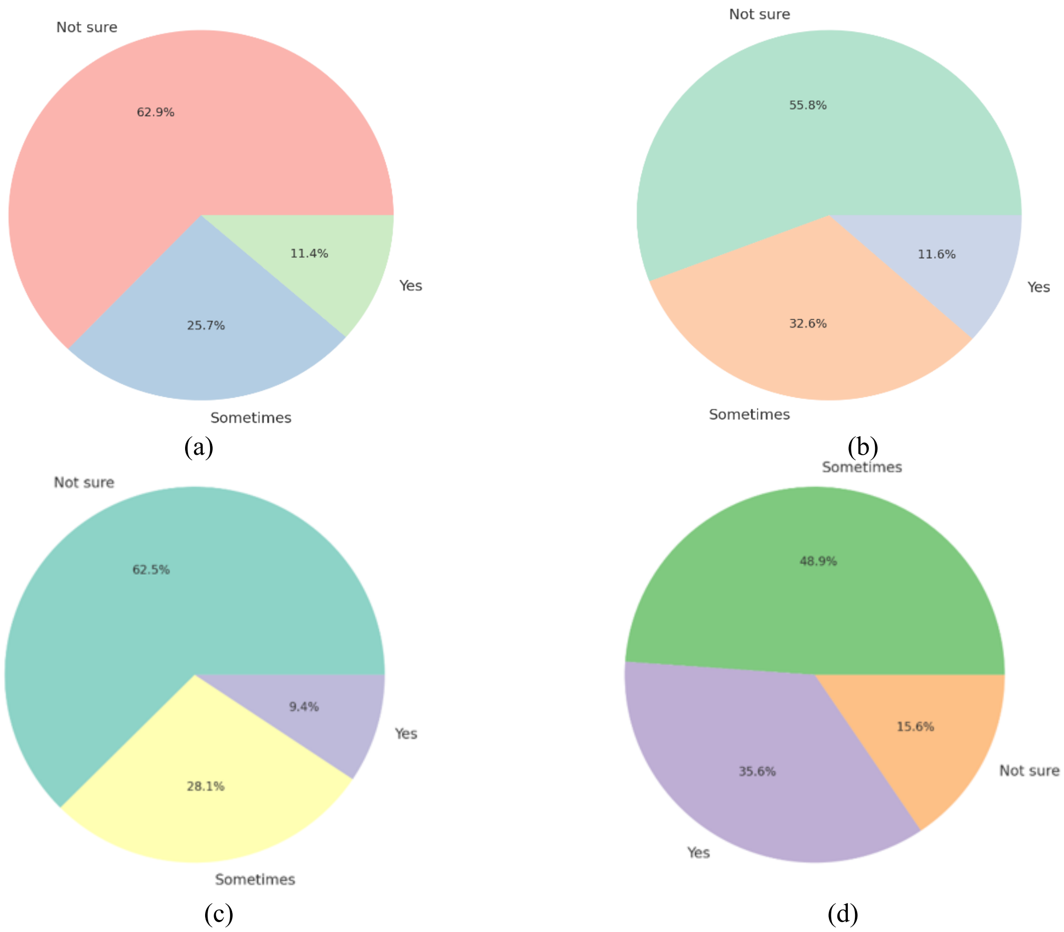

Fig. 12. Adequancy of (a) tunnel safety, (b) warnings, (c) lighting conditions and (d) weathering conditions

4.4. Behaviors and perceptions in the tunnel

A set of behavioral and perceptual questions were posed to participants using a 5-point Likert scale (1 = None, 5 = Very Much), to assess key responses in tunnel. The results are summarized below based on participants' self-reported behavior and perceptions.

Speed Adjustment to Exit the Tunnel: When asked whether they would increase speed to exit the tunnel more quickly, a majority of participants reported moderate to high agreement. Specifically, 25% selected "Much", and 3% selected "Very Much". This trend suggests that psychological factors such as discomfort or impatience may influence acceleration behaviors in longer tunnel sections (Fig. 13a).

Overtaking Heavy Vehicles Within the Tunnel: Participants were also asked if they would accelerate to overtake heavy vehicles inside the tunnel. A strong response was observed in favor of this behavior, with over 50% selecting "Very Much", indicating a substantial proportion of drivers are likely to perform overtaking maneuvers even in enclosed, confined driving conditions—potentially increasing risk if not well regulated (Fig.13b).

Speed Reduction at Tunnel Entrances and Exits for Safety: In contrast to overtaking tendencies, participants overwhelmingly reported that they do reduce speed for safety at tunnel entrance and exit points. Over 50% selected "Very Much", and 3% selected "Much", highlighting a strong adoption of cautious driving practices at critical transitional areas where visibility and reaction time can be compromised (Fig. 13c).

Impact of Digital Stimuli on Driver Attention: A significant number of participants indicated that digital stimuli within tunnels (e.g., digital signage, light strips, projections) effectively attracted their attention. The response "Very Much" was the most selected, with more than half of participants indicating a high level of engagement. This finding supports the potential utility of visual stimuli for guiding driver behavior or enhancing alertness in tunnel environments (Fig. 13d).

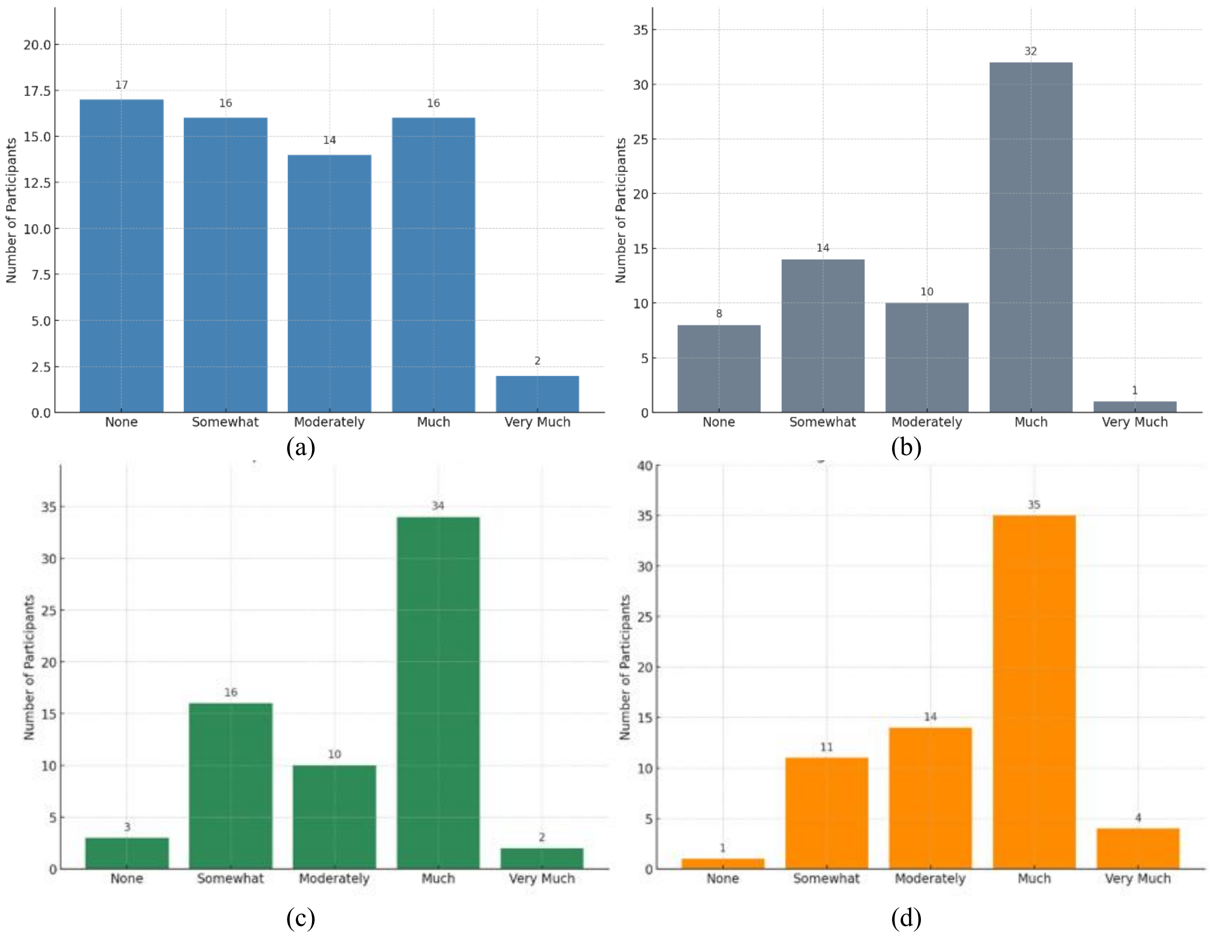

Fig. 13. (a) Increase speed to exit tunnel more faster (b) Increase speed to overtake in the tunnel, (c) Reduce speed at the tunnel entrance/exit and (d) digital stimuli impact

4.5. Awareness of chevron markings on road surfaces

As part of the driving simulator study, participants were asked whether they were familiar with chevron markings, a common road surface feature designed to help drivers maintain safe following distances on main roads. The responses were categorized as either "Yes" (aware) or "No" (not aware), and the distribution was visualized using a pie chart given in Fig. 14. The results revealed that 44% of the participants reported being aware of chevron markings, while 56 % indicated no prior knowledge of their purpose or presence. This relatively balanced distribution suggests that although more than half of the drivers recognized the markings, a significant portion of the sample lacked familiarity with this important traffic safety element. Given that chevron markings are intended to enhance road safety by visually cueing appropriate spacing between vehicles, especially at higher speeds or in complex environments like tunnels, the lack of awareness among a sizable group of drivers may reduce their effectiveness. These findings point to a need for improved public education and awareness campaigns about road safety markings. Incorporating information about chevrons into driver training programs or roadside signage could enhance their impact and support safer driving behavior.This result aligns with previous findings from the study, which highlighted mixed awareness and engagement with visual cues and digital stimuli in tunnels. As such, chevron marking, if properly understood, may serve as an additional, low-cost strategy to influence driver behavior and improve safety in confined or high-risk road environments.

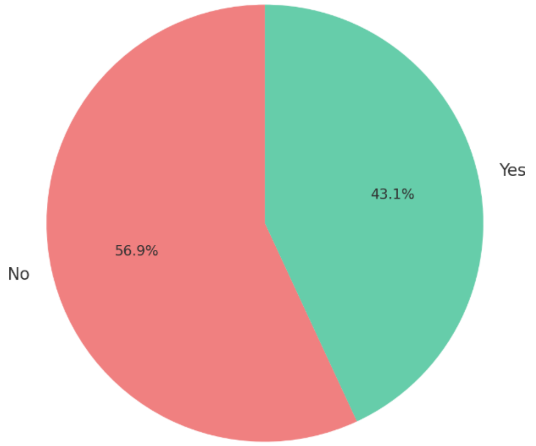

Fig. 14. Awareness of chevron markings on road surfaces in the New Zigana Tunnel

Participants were also asked to rate two statements “It is important for traffic safety to have chevrons showing the vehicle following distance in the tunnel” and “The chevron signs on the the road surface helped me to adjust the following distance.” related to the function and impact of chevron markings using a 7-point Likert scale (1 = Strongly Disagree, 7 = Strongly Agree). The responses to both statements were overwhelmingly positive. The majority of participants selected either “Agree” or “Strongly Agree”, indicating a shared perception that chevron markings are both meaningful and practical (Fig. 15). The first statement underscored the safety significance of chevrons, with participants strongly supporting their presence in tunnels. The second statement confirmed their usefulness in real-time driving behavior, as drivers found chevrons helpful for maintaining appropriate following distances. These findings suggest that chevron markings are not only recognized by many drivers but are also viewed as an effective aid in enhancing safety and spatial awareness in tunnel environments. This supports their wider implementation, particularly in road sections where driver behavior requires subtle guidance through visual means.

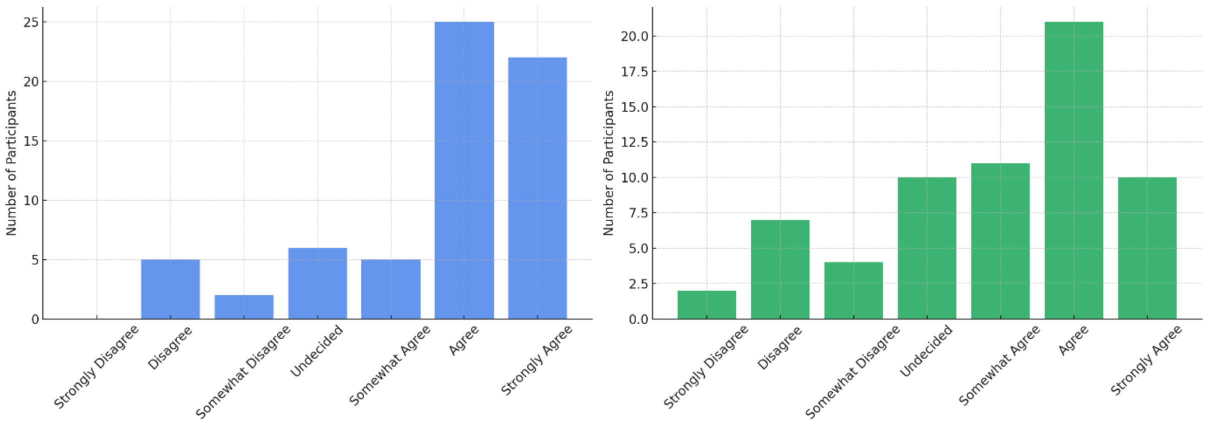

Fig. 15. Perceived effectiveness of chevron markings (a) importance of chevrons for traffic safety and (b) help of chevrons to keep vehicle following distance

5. Conclusions and suggestions

This study examined the effectiveness of chevron road markings in enhancing driving safety within tunnel environments through simulator-based experiments conducted at Erzincan Binali Yıldırım University. Results indicated that chevron markings positively influenced driver behavior by increasing driver awareness, promoting safer following distances, and contributing to speed regulation. Particularly under heavy traffic scenarios, the markings were beneficial in reducing driving stress and supporting improved decision-making. These findings underscore the practical utility of chevrons as a low-cost yet effective measure to enhance traffic safety and operational efficiency within highway tunnels.

Furthermore, survey analyses highlighted drivers' strong support for the use of chevron markings, reflecting substantial perceived benefits in maintaining appropriate following distances. However, a notable portion of participants lacked prior awareness of chevron markings, indicating a potential gap in public knowledge and driver education. This suggests a need for targeted informational campaigns and enhanced signage to maximize the effectiveness of chevron markings. Additionally, the participants' preference for visual stimuli within tunnels suggests complementary strategies such as dynamic visual alerts and enhanced illumination could further improve driver engagement and safety.

In conclusion, horizontal chevron markings demonstrate significant potential as a strategic safety intervention in tunnel environments, positively affecting driver speed, following distance, and overall safety perception. Given their low implementation cost and proven effectiveness, these markings could be widely adopted in current and future tunnel designs and integrated into broader intelligent traffic management systems. Considering the positive impact of chevron markings demonstrated in this simulator-based study, it is suggested that transportation authorities integrate chevron road markings into existing and new tunnel infrastructure, particularly in high-density traffic areas. Further studies should involve real-world trials to validate simulator findings across diverse environmental conditions and demographic groups. Additionally, awareness campaigns and educational initiatives could be implemented to enhance public understanding of chevron markings, thereby maximizing their safety benefits and ensuring drivers consistently adhere to recommended following distances within tunnels.

Acknowledgments

This research described in this paper was financially supported by The Scientific and Technological Research Council of Türkiye (TUBITAK) (Project No: 1002/123M190) and Gümüşhane University Scientific Research Projects Coordination Department (Project No: 22.F5110.02.01 and Project No: 22.E0111.07.01) and Erzincan Binali Yıldırım University Scientific Research Projects Coordination Department (Project No: FBA-2022-813). Authors also thank to TOFAS Turk Automobile Factory Inc..Inc. for their test car support under the Vocational Education Support Programme.

References

Amini, R. E., Al Haddad, C., Batabyal, D., Gkena, I., De Vos, B., Cuenen, A., … Antoniou, C. (2023). Driver distraction and in-vehicle interventions: A driving simulator study on visual attention and driving performance. *Accident Analysis & Prevention, 191*, Article 107195.

Babić, D., Fiolić, M., Babić, D., & Gates, T. (2020). Road markings and their impact on driver behaviour and road safety: A systematic review of current findings. *Journal of Advanced Transportation, 2020*, Article 7843743.

Babić, D., Žebec, M.-S., & Čavka, M. (2022). Effect of chevron design on driver behaviour when encountering and passing through a dangerous curve. *Transportation Research Part F: Traffic Psychology and Behaviour, 86*, 370–383.

Charlton, S. G. (2007a). Delineation effects in overtaking lane design. *Transportation Research Part F: Traffic Psychology and Behaviour, 10*(2), 153–163.

Charlton, S. G. (2007b). The role of attention in horizontal curves: A comparison of advance warning, delineation, and road marking treatments. *Accident Analysis & Prevention, 39*(5), 873–885.

Fiolić, M., Babić, D., Babić, D., & Tomasović, S. (2023). Effect of road markings and road signs quality on driving behaviour, driver's gaze patterns and driver's cognitive load at night-time. *Transportation Research Part F: Traffic Psychology and Behaviour, 99*, 306–318.

General Directorate of Highways. (2024). *Projects – Zigana Tunnel*. Republic of Türkiye Ministry of Transport and Infrastructure. https://www.kgm.gov.tr/Sayfalar/KGM/SiteEng/Projeler/ProjelerDetay.aspx?q=104 (accessed August 25, 2024)

Gilmore, D. K., Bauer, K. M., Torbic, D. J., Kinzel, C. S., & Frazier, R. J. (2013). Treatment effects and design guidance for high-to-low-speed transition zones for rural highways. *Transportation Research Record, 2348*(1), 47–57.

Godley, S. T., Triggs, T. J., & Fildes, B. N. (2002). Driving simulator validation for speed research. *Accident Analysis & Prevention, 34*(5), 589–600.

Greibe, P. (2010). *Chevron markings on freeways: Effect on speed, gap and safety*. Trafitec.

Helliar-Symons, R. D., & Butler, N. R. (1995). *M1 chevron trial—Accident study* (TRL Project Report 118). Transport Research Laboratory.
Hunter, M., Rodgers, M. O., & Pratyaksa, P. (2014). *Safety performance evaluation of converging chevron pavement markings* (Report FHWA-GA-14-1202). Georgia Department of Transportation, Office of Materials & Research; U.S. Department of Transportation, Federal Highway Administration.
Kircher, K., & Ahlstrom, C. (2012). The impact of tunnel design and lighting on the performance of attentive and visually distracted drivers. *Accident Analysis & Prevention, 47*, 153–161.
Merat, N., & Jamson, A. H. (2013). The effect of three low-cost engineering treatments on driver fatigue: A driving simulator study. *Accident Analysis & Prevention, 50*, 8–15.
Mock Theory Test. (n.d.). *ADI theory test: Keep apart two chevrons*. Retrieved March 20, 2025, from
Ozturk, O. F., Mazlum, Y., Aydin, M. M., Coruh, E., & Bayata, H. F. (2024). Performance comparison of various tunnel lighting scenarios on driver lane-changing behaviours in a driving simulator. *Applied Sciences, 14*(23), Article 11319.
Palamara, P., Broughton, M., & Wicks, S. (2014). *Improving curve delineation: A review of the literature and investigation of crashes on midblock curves in Western Australia 2007–2011*. Curtin-Monash Accident Research Centre.
Retting, R. A., McGee, H. W., & Farmer, C. M. (2000). Influence of experimental pavement markings on urban freeway exit-ramp traffic speeds. *Transportation Research Record, 1705*(1), 116–121.
Sabre Roads. (n.d.). *File:M11 – keep apart two chevrons*. Retrieved March 20, 2025, from https://www.sabre-roads.org.uk/wiki/index.php?title=File:M11_-_keep_apart_two_chevrons_-_Geograph_-_2640925.jpg
Srinivasan, R., Persaud, B., Eccles, K. A., Carter, D. L., & Baek, J. (2010). Safety evaluation of curve delineation improvements. *Transportation Research Board 89th Annual Meeting Compendium of Papers*. Paper No. 10-3568.
Voigt, A. P., & Kuchangi, S. P. (2009). *Evaluation of chevron markings on freeway-to-freeway connector ramps in Texas*. Texas Transportation Institute.
Wan, H., Du, Z., Yan, Q., & Chen, X. (2018). Evaluating the effectiveness of speed reduction markings in highway tunnels. *Transport, 33*(3), 647–656.
Wu, Y., Zhao, X., Chen, C., He, J., Rong, J., & Ma, J. (2016). Modeling the influence of chevron alignment sign on young male driver performance: A driving simulator study. *Accident Analysis & Prevention, 95*, 479–486.
Wu, Y., Zhao, X., Rong, J., & Ma, J. (2013). Effects of chevron alignment signs on driver eye movements, driving performance, and stress. *Transportation Research Record, 2365*(1), 10–16.
Zador, P., Stein, H., Wright, P., & Hall, J. W. (1987). Effects of chevrons, post-mounted delineators, and raised pavement markers on driver behavior at roadway curves. *Transportation Research Record, 1114*.
Zhao, W., Xu, L., Xi, S., Wang, J., & Runge, T. (2017). Evaluation of color effects of chevron alignment signs on drivers under snow and ice conditions using visual response sensors. *Sensors, 17*(1), Article 79.
Zhao, X., Wu, Y., Rong, J., & Ma, J. (2015). The effect of chevron alignment signs on driver performance on horizontal curves with different roadway geometries. *Accident Analysis & Prevention, 75*, 226–235.

4th International Civil Engineering & Architecture Conference
17-19 May 2025, Trabzon, Türkiye

Enhancing highway subbase performance with cement-stabilized recylcled concrete aggregate and fly ash

Muhammet Çelik*[1], Yavuz Abut[2], Dilara Yaşar[1]

[1] *Yalova University, Department of Civil Engineering, 77200, Yalova, Türkiye*
[2] *Yalova University, Department of Transportation Engineering, 77200, Yalova, Türkiye*

Abstract. In earthquake-prone countries like Türkiye, it is essential for the building stock to be earthquake-resistant. Therefore, the recycling of structurally compromised buildings is crucial. However, the recycling process generates demolition waste, contributing to environmental pollution, another critical issue. The reuse of demolition waste in line with sustainability principles becomes vital. There is extensive research on the reuse of demolition waste. However, gaps remain in the literature due to variations in waste properties or additives used to enhance the usability of the waste material. This study conducted California Bearing Ratio (CBR) tests to evaluate the use of demolition waste from Yalova Province as a subbase material in road construction. Existing studies often involve recycled concrete aggregate (RCA) combined with virgin aggregate or stabilized with binders like cement, which has a high carbon footprint. In this research, RCA was not mixed with other aggregates; instead, it was enhanced with fly-ash (FA) and cement. By using a low cement ratio, the primary stabilizer was intended to be FA, with cement serving as a supplementary additive. The study intevtigated whether RCA and FA, stabilized with cement, met the CBR requirements for subbase materials according to the Highway Technical Specification. Mixes containing 5%, 7%, and 10% FA and 1% or 2% cement were cured for 7, 14, and 28 days. The results indicated that a 14-day curing period was sufficient for subbase use, while the highest CBR value (216.4%) was achieved with 10% FA and 2% cement after 28 days.

Keywords: California bearing ratio; Fly ash; Highway; Recycled concrete aggregaye; Subbase

1. Introduction

In countries like Türkiye, which are located on active fault lines that can produce earthquakes, the renewal of the building stock is of great importance. Especially the renovation of buildings that have completed their economic life, that have been built without utilizing developing building technologies, without using modern workmanship and materials, and that have been built according to the old period regulations but do not comply with the current regulations is of even greater importance. In Türkiye, especially buildings that do not comply with current regulations carry a great risk. As a result of the risky building inspections of the official authorities, it has been stated that there are 28.6 million buildings in Turkey as of 2023 and approximately 6.7 million of these buildings are high-risk against earthquakes and need to be demolished urgently (ÇŞİDB, 2023).

The renovation of buildings will generate billions of tons of demolition waste. Demolition waste is a problem in many countries with similar problems like Türkiye. If waste is not planned and utilized in accordance with the principle of sustainability, it will pose a problem for the environment. In addition, storage costs constitute another problem (Lu & Tam, 2013). On the other hand, studies have shown that construction waste contains recyclable materials, and some studies have even found that 90% of construction waste can be recycled (Demir, 2009; Eren & Şen, 2023). Research shows that recycled concrete aggregate (RCA) can be used in all layers of highway pavement. Kavussi et al. showed that RCA is used in flexible pavement coating and RCA is suitable for use after a series of processes (Akbaş et al, 2023). Pasandín and Pérez in their review of previous studies on the use of RCA in bituminous hot mixes (BHM) stated that the use of RCA in BHM would be possible, but the properties of RCA would need to be developed or improved (Pasandín & Pérez, 2015). In one of the studies in the literature on the use of RCA in rigid pavements, it was observed that the flexural strength of the rigid pavement increased when rigid pavement produced with RCA reinforced with polyvinyl alcohol polymers (Yaowarat et al., 2017). In another study, Özbakkaloğlu et al. determined the results related to the substitution of different sizes of unused aggregate for the use of RCA in rigid pavements (Ozbakkaloglu et al., 2018). In highway pavements, when the layers are

*Corresponding author, E-mail: muhammet.celik@yalova.edu.tr

https://doi.org/10.31462/icearc2025_ce_tra_071

ordered from top to bottom, the highest strength properties are in the top layers. For this reason, in flexible and rigid pavements, studies have generally tried to improve on RCA or substitute it with virgin aggregates. In the base and subbase layers under the pavement, research on the use of RCA is more common. This is because the standards demand lower durability and strength in these layers than in the pavement layer. The use of RCA as a granular material in sub-base layers is very important for sustainable highway engineering (Park, 2003; Ardalan et al., 2017; Poon et al., 2004). At this point, especially the studies where CBR tests were performed are listed below.

Within the scope of the study, RCA will be examined together with fly ash, another waste material. In the literature, there is a lot of CBR test information about both the studies on subbase and base layers formed by adding RCA and the studies with other wastes. Among the studies examined in the literature, it was observed that the properties of the demolition waste, the differences in the material used as additives, and even the differences in the fly ash content changed the results. As a result of the literature review on the recycling of waste materials and the areas where fly ash is used, the following studies were found: Arulrajah et al. conducted CBR experiments in the laboratory at different time periods using RCA. They compressed the experiments with modified proctor energy at optimum water content. They kept the compressed specimens in water for four days with an additional load of 4.5 kg. The CBR values obtained as a result of the test were determined to be between 118% and 160%. The specimens were found to comply with the 80% values specified in the Australian local state road specifications (Arulrajah et al., 2012). In his master's thesis study, Yazıcı investigated the effect of fly ash on fine sand soils by CBR experiments. He prepared test specimens with different proportions of fly ash (5%, 10%, 15%, 20%, 25%) as well as a fixed proportion of cement added to the sand soil. After 7 days of curing, the CBR value obtained in pure soil was 18%, while this value increased up to 129% with the addition of cement and fly ash. The CBR value of the pure soil with a CBR value of 18% was also compared with the 28-day sample with the addition of fly ash and cement, and the CBR value of the sample increased up to 222%. As it is understood from this, the addition of fly ash as a stabilizer and cement as an activator provided a positive increase in CBR results (Yazıcı, 2023). Demir and Ok conducted CBR tests with recycled concrete aggregates consisting of demolition waste. Ok and Demir determined the optimum water content as 9.7% and also examined the CBR values of the mixtures prepared using 6% and 12% water content. While the CBR value they found with the optimum water content was 99.9%, the CBR value of the mixture with 6% water content was 50% and the CBR value of the mixture with 12% water content was 30%. Within the scope of this study, they concluded that demolition waste of reinforced concrete buildings can be an alternative to natural materials in highway embankment works (Ok & Demir 2018). Tajwar Ahmed et al. conducted CBR tests with a mixture prepared by combining concrete aggregates obtained from an old and demolished building in Hazaribag area of Dhaka with F class fly ash (5%, 10%, 15%). As a result of the experiment, they observed an increase in CBR value with the increase in the proportion of recycled concrete aggregate, while a decrease in CBR value was observed with the substitution of fly ash at certain ratios. They obtained the maximum CBR value by adding 5% fly ash (Ahmet et al., 2024).

In this study, it is planned to construct the subbase standards of the Turkish Republic Highways Technical Specifications (KTŞ) with urban recycling material. There are two different subbase types in the KTŞ (KTŞ, 2023). In the study, the subbase type with type A gradation curve was studied. In addition, fly ash, another waste material, was used in the study to increase (improve) the CBR results of RCA. In order for fly ash to play a more active role as an improver, a reinforcement improver cement additive was used. It is known that the content of fly ash varies according to the source from which it is obtained, and in some cases even differences in time can affect the content. In this study, fly ash utilization rates were selected (5%, 7%, 10%) similar to the values reported in the literature (5%, 10%, 15%). In addition, fly ash was reinforced with cement at 1% and 2% by weight. Thus, the properties of the fly ash were aimed to be activated, i.e. improved, by the cement. The activated fly ash was expected to improve the properties of another waste, RCA, in subbase behavior. The RCA used was taken from a building constructed more than 30 years ago in Yalova province.

2. Materials and methot

In this study, the improvement of RCA using fly ash (FA) for use in highway subbase was investigated. In addition, low cement addition was used for better contribution of fly ash. In the study, the comparison was made by looking at the soaked CBR values.

2.1. Materials

In this study, RCA was obtained from the demolition waste landfill of the ongoing urban transformation projects in Yalova Province. In the literature, there are studies on the improvement of RCA with cement additives and its use in highway pavements. In this study, the use of fly ash as an alternative to cement was investigated. Fly ash, which is the waste of Aksa Akrilik Kimya San.A.Ş. located in Tavşanlı Town of Yalova Province, was selected in accordance with TS EN 450-1 2013 standard (TSE, 2013). All of the FA passes through sieve number 200 and X-ray fluorescence spectrometry (XRF) results for FA are given in Table 1 (compounds with less than 1% are not shown). When the table is examined, it is understood that according to ASTM C618-23, FA is a type F due to its

CaO content (ASTM C618-23, 2023). Some properties of fly ash are also given in Table 2. CEM IV/B class cement from Bursa Beton was supplied for comparison with FA.

Table 1. Fly ash X-ray fluorescence spectrometry (XRF) results.

SiO_2	Al_2O_3	Fe_2O_3	CaO	MgO	K_2O
%57.56	%24.08	%50.94	%5.101	%1.226	%1.408

Table 2. Some properties and standard limits of fly ash.

Analyses	Unit	Results	Standard Limits
Loss on ignition	%	3.73	Category A max.:5.0
Fineness	%	9.41	Tip N max.: 40
Free calcium oxide	%	0.085	Max: 1.5
Reactive calcium oxide	%	1.49	Max.: 10
Chloride	%	0.00733	Max.: 0.1
Sulfuric anhydride	%	0.33	Max.: 3
Particle density	kg/cm^3	2295	Max.: 2500
Expansion	mm		Max.: 10

2.2. Method

In the study, for a gradation within the limits of the sub-base layer determined in the KTŞ, the concrete rubble provided should be separated into different sieve sizes. For this reason, since the crusher in the laboratory was not working at the desired efficiency, the rubble was crushed in a Los Angeles abrasion device. It was then separated into different sieve sizes (Fig. 1). After the crushing and sieving processes were completed, the mixture was prepared in accordance with the KTŞ 2023 subbase standards to be investigated for use in highway subbase and the (TYPE A) granulometry curve was formed as shown in Fig. 2.

Fig. 1. Crushing and Sieving Process

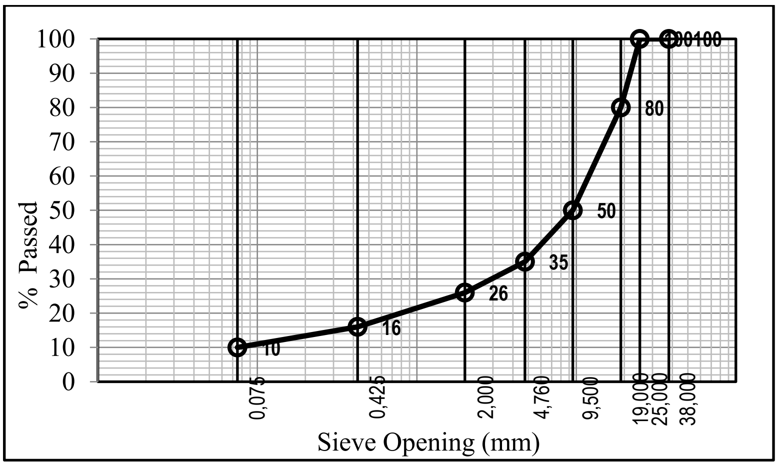

Fig. 2. Granulometric Curve in accordance with KTŞ Type A formed with sieved RCA

In the study, the use of RCA, a waste material, together with FA, another waste material, was investigated, as well as cement was added as a curing material in order to use both together. Experiments were carried out with different mixing ratios. Accordingly, the cement additive was used at 1% and 2% of the total weight of the mixture and fly ash was used at 5%, 7% and 10% of the total weight. While determining these ratios, it was planned to use the granulometric curve determined for the sub-base material in the KTŞ instead of the filler (below 0.075 mm) material. For this reason, 12% filler rate in the mixture was determined as the highest additive rate. These 6 different mixtures were evaluated according to 3 different curing times. In addition, CBR values in case only RCA was used were analyzed. Cement or fly ash was added to the mix as a substitute for the filler material.

In the experimental study, the modified Proctor test was first applied to find the optimum water contents required for the mixtures. At this point, the Modified Proctor test in accordance with TS EN 1900-1 was selected, especially due to the large grain diameter and the need for high energy for compaction (TS 1900-1, 2006). In the second part of the experimental study, soaked CBR tests were performed. CBR tests were determined according to (TS 1900-2, 2006). Three 2.27 kg weights were placed on the CBR specimens soaked in water to represent the pavement. All CBR tests were repeated at least 2 times (Table 3)

Table 3. CBR test lists in the study.

Test Number	Cement (%)	FA (%)	Curing Period (Day)	Test Number	Cement (%)	FA (%)	Curing Period (Day)
1	1	5	0	11	2	7	14
2	1	7	0	12	2	10	14
3	1	10	0	13	1	5	28
4	2	5	0	14	1	7	28
5	2	7	0	15	1	10	28
6	2	10	0	16	2	5	28
7	1	5	14	17	2	7	28
8	1	7	14	18	2	10	28
9	1	10	14	19	0	0	0 (3 Set)
10	2	5	14				

3. Result and discussion

In this study, an observational research followed by an experimental study was conducted. According to the findings obtained:

3.1. Observational research

Observational determinations were made on the RCA collected from the field and brought to the laboratory. As can be seen in Fig. 3 below, aggregates exceeding the maximum grain diameter and even reaching 10 cm in diameter were detected in the aggregate. Flat aggregates were observed in some of the specimens. It is concluded that these aggregates cause a decrease in concrete strength due to their fracture in the direction of flatness. Seashells were found in some of the aggregates. The fact that the seashell is of organic origin, can be easily broken, has a salty structure and the possibility that sea sand was used may have caused the concrete quality to be low. Smoothness was detected on the surfaces of some of the aggregates, and the inability of the cement paste to bond on smooth surfaces was evaluated within the observational findings. It was also observationally determined that some of the concrete pieces were have many voids. It is estimated that these voids are caused by both gradation defects and water/cement ratio defects. Some of the reinforcements were found to be unribbed and rusted during the inspections of the reinforced concrete elements. It was also found that the concrete quality varied between the elements. As a result of these findings, it was determined that the low strength of the concrete from which the RCA used in the experimental study was produced was one of the factors affecting the results.

Fig.3. Samples of concrete pieces collected on the storage area

3.2. Determination of optimum water content

According to TS EN 1900-1, the optimum water content and maximum dry density values obtained as a result of Modified Proctor tests were determined. Accordingly, the optimum water content and maximum dry density of RCA were determined without any additives. Subsequently, the experiment was repeated with fly ash and cement additives, but the experiments were completed by repeating the experiments separately for each fly ash and cement ratio. According to the data obtained, the optimum water content of the specimens containing only RCA was determined as 7.64% and the dry density as 22.74 kN/m³. It was determined that the optimum water level increased as the fly ash content increased, but the dry density decreased. This is an information obtained from similar studies in the literature (Totiç et al., 2019; Çelik Et al., 2024). These results are due to the pozzolanic material and light weight of the fly ash used as an additive. Table 4 shows the optimum water level and maximum dry densities obtained according to the mixture ratios.

Table 4. Results of the modified proctor experiment.

Cement	FA	Opt. Water Con. (%)	Dry Density (kN/m³)
%0	%0	7.64	22.74
%1	%5	7.82	22.58
%1	%7	8.25	22.59
%1	%10	8.33	22.34
%2	%5	8.31	22.41
%2	%7	8.68	22.19
%2	%10	9.17	21.97

3.3. California bearing ratio tests

CBR results obtained using RCA are given below. Accordingly, the specimens prepared from mixtures obtained only from urban recycling materials without any additives were kept in the water pool for 4 days (96 hours) without any curing, and the results of the CBR tests performed afterwards were 11.8%, 40.2% and 7.8%, respectively. The CBR results obtained from recycled aggregate are expected to be low. As a matter of fact, the information obtained about concrete quality in the first determinations also supports this. The reason for the differences of more than 400% between the figures is explained by the fact that aggregate breakage in the area where the CBR piston tries to sink causes low values, and relatively high values are generated when it coincides with solid durable aggregate. In the Technical Specifications of Highways, it is stated that sub-base CBR values should be 30% for Type-A and 50% for Type-B. At this point, it is seen that only one of the three different CBR tests performed exceeded the 30% limit. This shows that the aggregate obtained from recycled concrete does not have a homogeneous strength. After curing for 14 days, the results obtained from the crushing of CBR specimens kept in water for 4 days and the effect of 1% and 2% cement additives and 5,7,10% fly ash are given in Fig. 4. When the cement ratio increased, the CBR value increased approximately 2 times, which is an expected result. It is also observed in other studies that cement ratio gives similar results in highway foundation studies (Seferoğlu et al. 2018; Ai et al., 2024). In all of the results, the CBR value for subbase type A specified in the CTB was achieved, and even the mixtures with 2% cement admixture were found to meet the other foundation and subbase types.

After 28 days of curing and 4 days of soaking in water, the other specimens were subjected to CBR test and the results in Fig. 5 were obtained. When the results are analyzed, it is seen that higher CBR values were obtained compared to 14 days. It is a known fact in the literature that fly ash sets late. At this point, it is understood that the fly ash effect is more at the end of 28 days and increases the CBR results. Similar to the 14-day results, it was observed that 7% fly ash contribution gave the highest values. According to the KTŞ, it was seen that the appropriate conditions for subbase type A were met in all results, and even the desired CBR value (50%) for subbase type B was also met, while 2% cement admixture was able to meet the conditions specified for different foundation types. Fig. 6 shows the deformations of the soil specimens as a result of the test.

The results of the CBR test on the specimens placed directly in the water without curing are given in Table 5. When the results are analyzed, the importance of curing becomes apparent. It is understood that the results are inconsistent and that fly ash and cement content do not reveal a significant relationship on CBR results.

Table 5. CBR results of uncured specimens

	%1 Cement	%2 Cement
FA%5	24.3	100.2
FA%7	11.6	76.4
FA%10	6.6	16.8

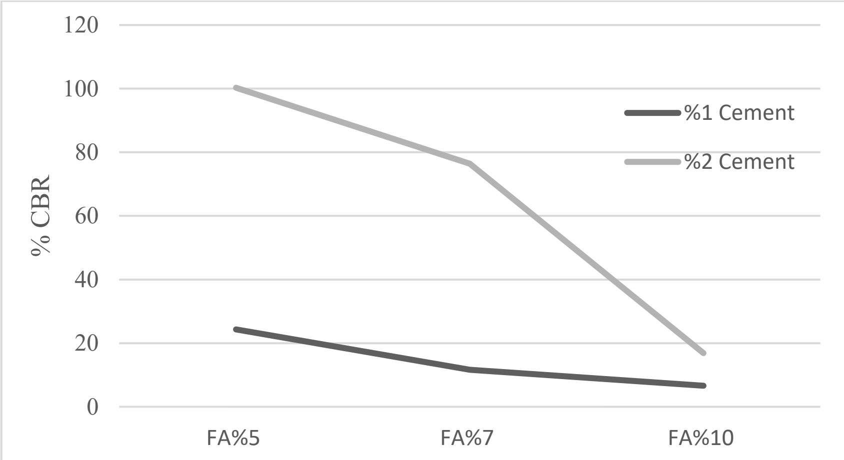

Fig.4. Samples Cured for 14 Days.

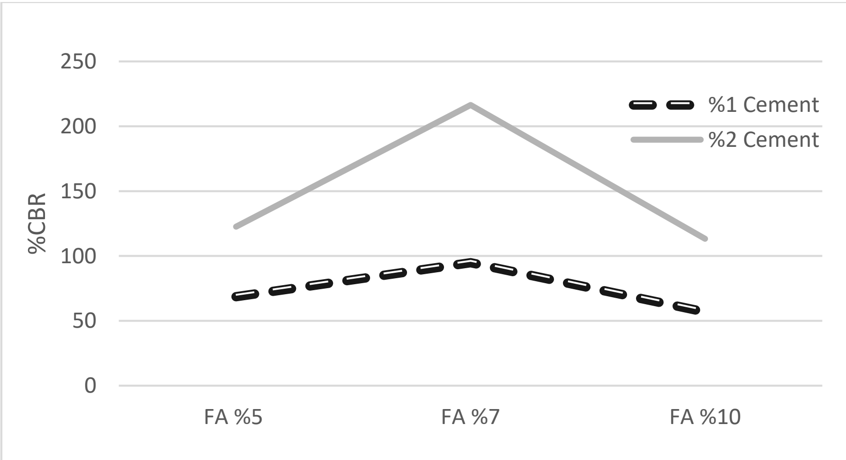

Fig.5. Samples Cured for 28 Days.

Fig.6. Deformations of the specimens after the test

4. Conclusions

As a result of the studies, observational and experimental investigations, the following points were determined:

The properties of the concrete to be used in the production of RCA are very important, and if the RCA does not show the desired properties, if improvement is to be made, the negativities it has should be eliminated. As a matter of fact, the poor quality of the concrete used in the study affected the results.

Aggregates in the range of 9.5-19.5 in the gradation are around 20% by mass. However, it was determined that some of this material obtained by crushing urban transformation waste concrete and separated through sieves is a combination of aggregate and cement paste. The fact that these joints have weak bonds due to various effects and that the CBR piston coincides with these weak bonds caused differences in the CBR test results. In addition, the concentration of coarse-grained materials (without cement paste) consisting only of pure aggregate in the mixture in the lower regions of the CBR piston is predicted as another effect that may cause an increase in the test results.

It was found that fly ash and cement additives made the results more regular, especially the curing treatment made it possible to establish a relationship between the results.

It has been observed that if a 28-day curing is applied, every mixture with fly ash and/or cement additive meets the necessary standards for the sub-base, and that the mixture with 2% cement and 7% fly ash reaches a CBR value of 216.4%

Acknowledgments

This project has been supported by TÜBİTAK under the 2209 code Research Projects Support Program for undergraduate students with the number 1919B012319239

References

Ahmet, T. S., Kabir, M., Zayid, C. Z., Tarık, T., & Mirmotalebi, S. (2024). Improvement of subgrade California bearing ratio (CBR) using recycled concrete aggregate and fly ash. *Hybrid Advances*, *100153*, 743–751. https://doi.org/10.1016/j.hybadv.2024.100153

Ai, X., Yi, J., Pei, Z., Huang, L., Zhou, W., Xu, M., ... & Feng, D. (2024). Micromechanical modeling of cement-treated base materials considering recycled crushed aggregate morphology from construction and demolition waste using three-dimensional discrete element method. *Journal of Testing and Evaluation*, *52*(4), 2219–2231.

Akbaş, M., Ozaslan, B., & Iyisan, R. (2023). Utilization of recycled concrete aggregates for developing high-performance and durable flexible pavements. *Construction and Building Materials*, *407*, 133479. https://doi.org/10.1016/j.conbuildmat.2023.133479

Ardalan, N., Wilson, D., & Larkin, T. (2017). Laboratory performance of recycled concrete aggregate as base-course material. In *Australasian Transport Research Forum (ATRF)*, Auckland, New Zealand.

Arulrajah, A., Piratheepan, J., Ali, M. M. Y., & Bo, M. W. (2012). Geotechnical properties of recycled concrete aggregate in pavement sub-base applications. *Geotechnical Testing Journal*, *35*(5), 743–751.

ASTM C618–23. (2023). *Standard specification for coal fly ash and raw or calcined natural pozzolan for use in concrete*. ASTM International.

Çelik, M., Kuvat, A., Abut, Y., & Ceyhan Erdoğan, M., et al. (2024). Biyokömür ile aktive edilmiş uçucu küllerin zemin stabilizasyonuna yönelik kullanılabilirliğinin incelenmesi. *Journal of Innovative Engineering and Natural Science*, *4*(2), 354–371. https://doi.org/10.61112/jiens.1421364

ÇŞİDB. (2023). *2022 yılı idare faaliyet raporu*. T.C. Çevre, Şehircilik ve İklim Değişikliği Bakanlığı, Ankara.

Demir, İ. (2009). İnşaat yıkıntı atıklarının beton üretiminde kullanımı ve beton özelliklerine etkisi. *Afyon Kocatepe Üniversitesi Fen ve Mühendislik Bilimleri Dergisi*, *9*(2), 105–114.

Eren, Z., & Şen, B. N. (2023). İnşaat ve yıkıntı atıklarının döngüsel ekonomi modeline göre yönetimi. *Uluslararası Gelişim Akademi Dergisi*, *1*(2), 1–10.

Korkmaz, B., Taştan, Ş., Dayıoğlu, A. Y., & Hatipoğlu, M. (2023). Geri dönüştürülebilir atık malzemelerin jeoteknik özelliklerinin karşılaştırmalı olarak incelenmesi. *Erciyes Üniversitesi Fen Bilimleri Enstitüsü Fen Bilimleri Dergisi*, *39*(1), 1–12.

KTŞ. (2023). *Karayolu teknik şartnamesi*. T.C. Ulaştırma ve Altyapı Bakanlığı, Karayolları Genel Müdürlüğü Yayını, Ankara.

Lu, W., & Tam, V. W. Y. (2013). Construction waste management policies and their effectiveness in Hong Kong: A longitudinal review. *Renewable and Sustainable Energy Reviews*, *23*, 214–223. https://doi.org/10.1016/j.rser.2013.03.007

Ok, B., & Demir, A. (2018). Yapım yıkım atıklarının yol temellerinde kullanılabilirliğinin incelenmesi. *Ömer Halisdemir Üniversitesi Mühendislik Bilimleri Dergisi*, *7*(1), 224–236. https://doi.org/10.28948/ngumuh.386621

Ozbakkaloglu, T., Gholampour, A., & Xie, T. (2018). Mechanical and durability properties of recycled aggregate concrete: Effect of recycled aggregate properties and content. *Journal of Materials in Civil Engineering*, *30*(2), 04017275.

Park, T. (2003). Application of construction and building debris as base and subbase materials in rigid pavement. *Journal of Transportation Engineering*, *129*(5), 558–563. https://doi.org/10.1061/(ASCE)0733-947X(2003)129:5(558)

Pasandín, A. R., & Pérez, I. (2015). Overview of bituminous mixtures made with recycled concrete aggregates. *Construction and Building Materials*, *74*, 151–161.

Poon, C. S., Shui, Z. H., & Lam, L. (2004). Effect of microstructure of ITZ on compressive strength of concrete prepared with recycled aggregates. *Construction and Building Materials*, *18*(6), 461–468.

Seferoğlu, A. G., Seferoğlu, M. T., & Akpınar, M. V. (2018). Experimental study on cement-treated and untreated RAP blended bases: Cyclic plate loading test. *Construction and Building Materials*, *182*, 580–587.

Totiç, E., Göktepe, F., & Yaşar, M. (2019). Uçucu kül katkısının killi zeminlerin mekanik özelliklerine etkisi. *Dicle Üniversitesi Mühendislik Fakültesi Mühendislik Dergisi*, *10*(2), 769–778.

TSE. (2013). *TS EN 450-1: Fly ash for concrete – Part 1: Definition, specifications and conformity criteria*. Türk Standardları Enstitüsü.

TS 1900-1. (2006). *İnşaat mühendisliğinde zemin laboratuvar deneyleri – Bölüm 1: Fiziksel özelliklerin tayini*. Türk Standardları Enstitüsü.

TS 1900-2. (2006). *İnşaat mühendisliğinde zemin laboratuvar deneyleri – Bölüm 2: Mekanik özelliklerin tayini – Taşıma oranının tayini*. Türk Standardları Enstitüsü.

Yazıcı, E. (2023). İnce kum zeminlerde uçucu külün zemin özellikleri üzerindeki etkisinin incelenmesi (Yüksek lisans tezi). T.C. Bursa Uludağ Üniversitesi Fen Bilimleri Enstitüsü.

Yaowarat, T., Horpibulsuk, S., Arulrajah, A., Mirzababaei, M., & Rashid, A. S. A. (2017). Compressive and flexural strength of polyvinyl alcohol modified pavement concrete using recycled concrete aggregates. *Journal of Materials in Civil Engineering*. https://doi.org/10.1061/(ASCE)MT.1943-5533.0001914 *(DOI eklenmiştir)*

Object detection methods for vehicle counting: Comparison and optimal approach proposal

Akif Akbulut*[1],Ufuk Kirbaş[1]

[1] Ondokuz Mayıs University, Department of Civil Engineering, 55100 Samsun, Türkiye

Abstract. Object detection and recognition methods have significantly advanced in recent years thanks to developments in artificial intelligence and computer vision. These technologies provide high accuracy and efficiency, particularly in complex tasks such as vehicle counting. Determining the most suitable method for vehicle counting from video footage depends on the dataset used, environmental conditions, and application objectives. Traditional methods rely on predefined features and algorithms, whereas modern approaches, leveraging deep learning-based neural networks, offer more flexible and high-performing solutions. Notably, deep learning models such as You Only Look Once (YOLO), Faster R-CNN, and Mask R-CNN excel in both speed and accuracy for object detection and classification. These methods dynamically analyze by extracting regional features to detect and classify moving objects. During vehicle counting, challenges such as variable lighting conditions, perspective distortions, and background complexity can impact the success of the chosen algorithm. In this context, preprocessing video footage, employing data augmentation techniques, and optimizing hyperparameters for the model are critically important. Additionally, for real-time applications, factors like processing speed and hardware compatibility of the methods must be considered. By evaluating all these factors, selecting the most suitable method for vehicle counting is crucial for achieving accurate results and enhancing the overall system efficiency. This study aims to compare various object detection methods and propose the optimal approach for vehicle counting from video footage.

Keywords: Object detection; Vehicle counting; Deep learning; You Only Look Once; Computer vision

1. Introduction

Deep learning is a machine learning method that enables artificial neural networks to represent data at a higher level through nonlinear transformations and layers. Deep neural networks consist of input and output layers as well as intermediate and hidden layers, allowing the learning process to take place within a multi-layered structure. This multi-layered architecture enhances data processing and improves the model's learning accuracy (Chen et al., 2015). Advances in information technologies enable more efficient big data analysis. Although vehicle classification can be performed based on the sizes of moving objects, the accuracy level of this method is generally lower. However, the use of deep learning techniques provides more reliable and precise results in the vehicle classification process. These approaches significantly improve classification accuracy due to their ability to learn complex patterns (Krizhevsky et al., 2017). Object recognition methods are generally categorized into two main types: single-stage and two-stage approaches. Single-stage approaches prioritize processing speed, focusing on rapid data analysis. Examples of such methods include YOLO (You Only Look Once), SSD (Single Shot Multibox Detector), and RetinaNet. While these techniques offer speed advantages, their accuracy rates are often lower. On the other hand, two-stage methods aim to enhance accuracy at the expense of processing time. Models in this category include Faster R-CNN (Region-based Convolutional Neural Network), Mask R-CNN, and Cascade R-CNN. These models provide higher accuracy but may require greater computational resources (Paperswithcode, 2024). The resolution and characteristics of input images are among the key factors that directly affect the processing speed of object recognition algorithms.

1.1. Single-stage object recognition methods

Single-Stage Object Detection Methods stand out in the object detection process due to their high processing speed and low computational cost. In these methods, object classification and location prediction are performed in a single step. In contrast, traditional two-stage methods first identify potential object regions and then classify these regions, resulting in longer processing times. Single-stage methods complete all these steps at once, providing a

* Corresponding author, E-mail: akbulutakif1461@gmail.com

https://doi.org/10.31462/icearc2025_ce_tra_094

significant advantage, especially in real-time applications. The most notable feature of these methods is their simple architecture and ability to directly predict object bounding boxes and class labels. This makes them widely used in areas such as traffic monitoring in smart city systems, environmental perception in autonomous vehicles, and threat detection in surveillance systems. Additionally, their low computational requirements make them preferable for mobile devices, drones, robotic systems, and augmented reality applications. However, single-stage object detection methods have certain limitations. Compared to two-stage methods, they may suffer some accuracy loss. Performance can particularly decline in detecting small or closely located objects. One of the main reasons for this is that most single-stage methods use a grid-based approach. Dividing an image into specific cells for processing can make it difficult to adequately represent small objects. Furthermore, performing classification and location prediction simultaneously can restrict information sharing, negatively affecting accuracy. Despite these limitations, single-stage methods offer significant advantages in terms of speed, efficiency, and low computational cost. Improvements aimed at increasing their accuracy further expand their application areas, and when combined with deep learning-based approaches, they provide significant enhancements in object detection processes (Zivkovic, 2004).

1.1.1. YOLO (You Only Look Once)

YOLO (You Only Look Once) is an innovative approach that performs the object detection process using a single deep learning model. First developed in 2016 by Joseph Redmon and his team, this method works faster and more efficiently than traditional multi-stage techniques, providing an advantage in real-time applications. YOLO models divide an image into a grid and predict whether an object is present in each cell. Beginning with YOLOv1, this series has continuously improved in terms of accuracy and performance. YOLOv2 introduced anchor box usage, YOLOv3 gained multi-scale detection capability, and YOLOv4 became more efficient with CSPDarknet53 and new activation functions. Although YOLOv5, based on PyTorch, was not an official release, it was widely adopted, while YOLOv7 introduced advanced optimizations for speed and accuracy (Karadağ & Arı, 2023). YOLOv8 builds on the successes of its predecessors, offering high performance in tasks such as object detection, segmentation, tracking, and classification. Its architecture, consisting of backbone, neck, and head components, enhances detection accuracy while maintaining low resource consumption, making it suitable for real-time applications. Developed with support from Ultralytics, YOLOv8 provides various model sizes (YOLOv8n, YOLOv8m, YOLOv8l, YOLOv8x) that adapt to different hardware. The training process can be conducted on platforms like Google Colab, and extended training improves accuracy. The YOLO series has continuously evolved from YOLOv1 to the most recent version, YOLOv12 (Wang & Liao, 2024). YOLO analyzes an image by dividing it into a grid structure and determines whether an object is present in each cell. For detected objects, it simultaneously predicts class labels and bounding box coordinates, ensuring a fast and efficient detection process. Optimized with deep learning techniques and CNN architecture, the model effectively detects objects of different sizes using anchor boxes. YOLO's biggest advantage is its ability to detect multiple objects in a single operation with high speed and accuracy (Kılıç et al., 2022). YOLO is widely used in many fields that require fast and accurate object detection. Autonomous vehicles, traffic monitoring systems, security cameras, robotic systems, and augmented reality applications are among the most common areas where YOLO is preferred. Its speed and accuracy in real-time video processing and object tracking make it a crucial tool. Thanks to its high performance, YOLO has become an indispensable technology in numerous industrial applications. Each new version introduces improvements in speed, accuracy, and efficiency, significantly contributing to the advancement of object detection technology. YOLO's rapid processing time and high accuracy make it an ideal solution, especially for real-time applications. With the continuous development of deep learning techniques and ongoing optimizations, YOLO's impact in the field of object detection continues to grow.

1.1.2. SSD (Single Shot Multibox Detector)

SSD (Single Shot MultiBox Detector) is a single-stage deep learning model that performs object detection quickly and efficiently. Developed in 2016 by Wei Liu and his team, this model differs from two-stage methods like R-CNN by detecting objects directly on the image. SSD predicts objects of different sizes using predefined default boxes and can detect both small and large objects through multi-scale feature maps. This structure enables the model to provide high speed and accuracy, making it highly effective for real-time applications (Malkoçoğlu & Samli, 2023). SSD conducts object detection through a convolutional neural network (CNN)-based structure, extracting features from images and predicting object locations. The model utilizes predefined boxes at each layer to determine the presence and class of objects while optimizing coordinates to enhance the precision of bounding boxes. Being a single-stage model accelerates processing, making it suitable for real-time applications. During training, the discrepancy between predicted values and ground truth labels is minimized to improve model accuracy. SSD's holistic learning approach allows it to generate outputs directly from input data, increasing computational efficiency and enabling successful detection of objects at different scales (Liu et al., 2016). The SSD model offers significant advantages in object detection, including high speed, low computational cost, and multi-object detection capability. Its single-stage structure accelerates processing, making it ideal for real-time applications. It is effectively used in time-sensitive fields such as autonomous vehicle systems, traffic monitoring mechanisms, and security cameras. The model's ability to detect objects of varying scales, from small to large, ensures reliable performance in complex scenes. Compared to other single-stage models like YOLO, SSD achieves similar accuracy levels while requiring less computational power, making it suitable for resource-limited platforms such as embedded systems and mobile devices. SSD is widely used in real-time video processing, facial recognition, traffic monitoring, robot navigation, and augmented reality applications. Its use of multi-scale feature maps, predefined boxes for object prediction, and end-to-end training process helps maintain high accuracy while reducing computational costs. With advancements in deep learning and computer vision, future versions of SSD are expected to offer even higher performance (Liu et al., 2016).

1.1.3. RetinaNet (Retina Network)

RetinaNet was developed in 2017 by Facebook AI Research (FAIR) to optimize the balance between speed and accuracy in object detection. Addressing the class imbalance issue common in traditional single-stage models, RetinaNet achieves high success in object detection tasks. Its most significant innovation is the Focal Loss function. While previous single-stage models like YOLO and SSD excelled in speed, they struggled with detecting small or rare objects. RetinaNet mitigates this issue by assigning greater weight to low-frequency classes, allowing the model to focus more effectively on these objects. This approach enhances accuracy without sacrificing speed, effectively addressing class imbalance. Thanks to its innovative methodology, RetinaNet has become a powerful choice for real-time object detection applications (Lin et al., 2017). RetinaNet operates using a Convolutional Neural Network (CNN)-based architecture for object detection. Leveraging multi-scale feature maps, it successfully detects objects of varying sizes. The model generates predefined default boxes at each location and predicts their class labels and bounding box coordinates. Due to its single-stage nature, it eliminates the need for a separate region proposal step, significantly reducing processing time. The most crucial innovation of RetinaNet is its Focal Loss function. Traditional single-stage models struggle to detect small or rare objects due to class imbalance, but Focal Loss alleviates this problem by emphasizing misclassified examples. This enables the model to achieve high accuracy even with small datasets. Another key component enhancing RetinaNet's performance is the Feature Pyramid Network (FPN). This structure generates multi-level feature maps to better detect objects at different scales—small objects are processed in lower layers, while larger objects are handled in upper layers, ensuring scale-independent accuracy. Additionally, RetinaNet's use of default boxes (anchor boxes) allows for more efficient detection of objects with varying sizes and aspect ratios. With innovations like Focal Loss and FPN, RetinaNet stands out as a model that offers both high speed and accuracy. Its single-stage structure reduces computational cost, making it a strong candidate for real-time object detection applications. Notably, its ability to successfully detect small and rare objects distinguishes it from other single-stage models (Lin et al., 2017).

1.2. Two-stage object detection methods

Two-stage object recognition methods stand out among deep learning-based object detection approaches with high accuracy. These methods aim to achieve more precise results by performing object detection and classification in a two-step process. In the first stage, the potential object locations in the image are determined using a Region Proposal Network (RPN). Then, object classification and bounding box refinement are performed on these detected candidate regions by a second deep network. The major advantage of this method is its ability to provide object detection with high accuracy. Since the candidate regions identified in the first stage only contain parts thought to potentially include an object, the classification process in the second stage becomes more efficient and precise. Particularly in images with complex backgrounds or scenes containing objects with similar features, two-stage object recognition methods reduce false detections and produce more reliable results. This structure is commonly preferred in applications where accuracy in object detection is critical, such as security systems, medical image analysis, and autonomous driving (Türkarslan & HardalAğaç, 2022). Two-stage object recognition methods hold a significant place in the field of object detection due to their ability to achieve high accuracy. However, these models are more costly in terms of processing time due to their two-stage structure. Therefore, they are generally preferred in applications that work with large datasets and require high accuracy. The biggest disadvantage of these methods is that they require more computational power compared to single-stage models. Particularly in real-time applications, long processing times can be a limitation. Nevertheless, the advantages offered by two-stage models, especially in terms of increasing the accuracy of object candidates and enabling more precise classifications, are highly valuable. Successful models like Faster R-CNN have demonstrated that this method can be effectively applied. These models are widely used in scenarios requiring high accuracy, such as medical image analysis, autonomous vehicle systems, and security applications (Türkarslan & HardalAğaç, 2022).

1.2.1. Faster R-CNN

Faster R-CNN has been developed as a model that optimizes both speed and accuracy in object detection. In traditional two-stage methods, object regions are first determined, and then these regions are classified to predict object locations, whereas Faster R-CNN optimizes this process by using the Region Proposal Network (RPN) to make region proposals directly learnable. Previous approaches, such as R-CNN and Fast R-CNN, were inefficient either due to high computational cost or the need for an external region proposal algorithm. However, with the integration of RPN, Faster R-CNN reduces unnecessary computations, enabling end-to-end faster and more accurate object detection. The model, especially preferred in applications requiring high accuracy, has brought a significant innovation to the field of computer vision by making object detection processes more efficient (He et al., 2017). Faster R-CNN divides the object detection task into two main stages: region proposal generation (RPN) and classification and bounding box regression. The first stage, RPN, generates potential object regions for every pixel in the image. This process is carried out using Convolutional Neural Networks (CNN). A sliding window is used over the CNN feature map, associating predefined anchor boxes with each pixel. These anchor boxes provide initial predictions regarding the positions and classes of objects. The second stage involves classifying the regions proposed by RPN and refining the exact locations of each region. In this step, the Fast R-CNN classification and bounding box regression network processes the region proposals generated by RPN. Each proposed region is classified to determine which object it belongs to, and the correct location of the object is predicted through bounding box regression. Thus, Faster R-CNN presents an efficient model that integrates object classification and localization tasks (Girshick, 2015). Faster R-CNN is a model that efficiently performs object detection tasks and contains key components that contribute to its success. The first component, the Region Proposal Network (RPN), generates proposal boxes (region proposals) to detect objects in the image and makes object predictions using anchor boxes associated with each pixel. The second component is the Backbone Network, typically built using deep learning networks such as VGG16 or ResNet; these networks extract important visual features from the image. The RoI Pooling layer ensures that proposal regions of varying sizes are converted into fixed dimensions, allowing each proposal region to produce a fixed-size feature map. Finally, the Classification and Bounding Box Regression stage predicts which object each proposed region belongs to and the precise location of the object. The collaboration of these components allows Faster R-CNN to perform accurate and fast object detection. Its main advantage is significantly reducing processing time by performing object detection in an integrated manner. While traditional methods perform proposal box generation and classification independently, Faster R-CNN integrates these processes, improving both accuracy and processing speed. Additionally, by offering end-to-end training, it allows all model components to be trained simultaneously, optimizing performance. This structure makes Faster R-CNN superior to traditional methods with higher accuracy and faster processing times (Everingham et al., 2010). Faster R-CNN is used in a wide range of applications in object detection and image analysis. In autonomous driving systems, Faster R-CNN can help achieve safe driving by detecting pedestrians, vehicles, and other obstacles, enabling the vehicle to perceive its surroundings. In security systems, it can be effectively used in tasks such as theft detection, facial recognition, and intrusion detection. In industrial automation, robotic systems can use Faster R-CNN for object recognition and placement tasks on production lines. In healthcare, Faster R-CNN can be utilized for anomaly detection in medical images and disease diagnosis. By overcoming the challenges of previous object detection methods, Faster R-CNN has made significant progress in the field of object detection. The Region Proposal Network (RPN) and end-to-end training strategies enhance the model's accuracy and speed, providing a more efficient solution. This innovative model is successfully used in many applications in the field of object detection and is shaping the future of deep learning-based object recognition.

1.2.2. Mask R-CNN

Mask R-CNN is a significant advancement in the fields of object detection and image segmentation, and it is an advanced version of Faster R-CNN. Developed in 2017, this model adds pixel-level object mask prediction to the object detection process. As a result, it not only detects objects but also performs segmentation of the objects at the pixel level, providing more precise and detailed results. In addition to the core components of Faster R-CNN, such as the Region Proposal Network (RPN) and RoI Align layers, Mask R-CNN introduces a structure that predicts a mask for each detected object. This is especially advantageous in applications where accurate object boundary detection is crucial. The primary motivation behind the development of this model is that image segmentation is more complex and challenging than other tasks like object detection. Mask R-CNN improves the object detection structure of Faster R-CNN, which works in three stages, by adding an extra stage that involves classifying pixels. The first stage includes the RPN technique used in Faster R-CNN, where RPN generates potential object regions and identifies key areas. The second major innovation is RoI Align. To avoid the loss of accuracy in the RoI Pooling method, Mask R-CNN uses RoI Align, which provides more accurate feature extraction. The third stage involves the model making three predictions for each proposed region: the classification of the object, its location, and the generation of a pixel-level mask. This allows Mask R-CNN to accurately segment the pixels of each object. Mask R-CNN works with components such as the Backbone Network (using networks like ResNet or ResNeXt), RPN, RoI Align, and the Mask Generation Network. The Backbone Network extracts fundamental features from the image, while RPN detects potential object regions, RoI Align transforms each proposed region into fixed sizes, and the Mask Generation Network generates pixel-level masks for each object.

Mask R-CNN provides high precision in pixel-level accuracy and segmentation tasks and can be adapted to various applications due to its flexible structure. Additionally, the RoI Align feature eliminates sharp edge rounding issues, leading to more precise region predictions. This enhances the model's accuracy, especially in situations where accurate boundary detection of objects is required. These advantages make Mask R-CNN a powerful model in object detection and segmentation. Mask R-CNN is particularly effective in tasks that require high accuracy and reliability. In industrial applications, it is also used in processes such as object separation and classification on production lines, making manufacturing processes more efficient. With innovations added on top of Faster R-CNN, Mask R-CNN combines object detection and segmentation tasks into a powerful model. Thanks to innovations such as RoI Align and pixel-level prediction capabilities, the model offers both precise and comprehensive solutions. Since its development, Mask R-CNN has continued to achieve impressive results in many applications in the field of image analysis and segmentation (Güçlü et al., 2022).

1.2.3. Cascade R-CNN

Cascade R-CNN is a deep learning architecture developed to improve the detection of objects at various scales and complexity in the field of object detection. Traditional object detection methods often require learning both low and high-quality features simultaneously, which has specific limitations. In particular, low Intersection over Union (IoU) threshold values used during object detection can lead to false positive results and missed detections. To overcome this issue, Cascade R-CNN utilizes multiple detection stages sequentially, increasing the IoU threshold at each stage to achieve higher accuracy in object detection. Developed to overcome the limitations of popular object detection models such as Faster R-CNN, Cascade R-CNN uses a staged structure instead of a single-stage detector, offering a more precise learning process at each step. This approach allows the model to detect objects at different scales more accurately and consistently. The mechanism of the model is based on progressively improving the object detection process. Initially, the Region Proposal Network (RPN) identifies potential object regions, which serve as the foundation for subsequent object detection and classification tasks. Then, sequential detectors working with increasing IoU thresholds progressively refine the coarse detections made in the first stage, producing more accurate results. The first detector usually works with a low IoU threshold, identifying object candidates, and subsequent detectors refine these detections to produce more precise outcomes. Each stage corrects the missed or incorrect detections from the previous stage, increasing the accuracy of the model. This structure not only improves object detection but also enhances the precision of classification and bounding box regression, thereby improving the overall performance of the model. Cascade R-CNN consists of various components, including the Region Proposal Network (RPN) used to identify object candidates, Staged Object Detectors that operate with different IoU thresholds at each stage, and a Backbone Network used for feature extraction from the image. Typically, convolutional neural network (CNN)-based architectures like ResNet or ResNeXt are preferred. Additionally, a special loss function is used to optimize the learning process of the model, minimizing the error rate of each detector. One of the key advantages of this model is its ability to increase detection accuracy by working with higher IoU thresholds. The staged structure eliminates low-quality proposals early on, reducing false positive and negative rates and enhancing the reliability of the model. Moreover, the use of detectors with different IoU thresholds allows the model to successfully detect objects at different scales. Finally, the staged learning structure ensures that the model generalizes better on both small and large datasets. Considering all these features, Cascade R-CNN provides a more precise, reliable, and scalable solution in object detection tasks, standing out as an effective method for improving detection accuracy. Cascade R-CNN is effectively used in a wide range of applications. In autonomous vehicles, it helps improve driving safety by accurately detecting traffic signs, pedestrians, and other vehicles. In medical imaging, it provides high accuracy in detecting cancer cells or other anomalies, improving early diagnosis processes. In video surveillance systems, it is effective in detecting people or objects from security camera footage, thus enhancing the effectiveness of security monitoring systems. In industrial inspection, it is used to detect product defects or assembly flaws, strengthening quality control processes. In robotic systems, it enables more precise operation of robotic arms by detecting the positions of objects. Cascade R-CNN is a powerful architecture with high accuracy and generalization capabilities, increasingly gaining significance in both research and industry (Cai & Vasconcelos, 2018).

1.3. Object recognition methods and comparisons

Object recognition is the process of determining the location and type of objects in an image. Deep learning-based approaches have made significant progress in this field. These approaches are generally divided into two categories: single-stage and multi-stage methods. Both methods have certain advantages and limitations, offering features suitable for different application areas. Below, these methods are compared in detail (Aalami, 2020).

1.3.1. Properties of single layer methods

Single-stage methods are an approach that perform object detection and classification directly in a single step. In such models, the entire image is converted into feature maps, and possible objects along with their classes are predicted within the same network structure. Key features of these methods include fast operation, simple architectural structures, and high processing speed. These models are particularly suitable for real-time applications, and their less complex structures facilitate the training process and model design. Examples such as

YOLO (You Only Look Once) and SSD (Single Shot Multibox Detector) are common applications of single-stage methods. The advantages of these methods include providing time efficiency by enabling lower latency and high processing speed per image. Moreover, they are effectively used in areas that require real-time performance, such as autonomous vehicles and robotic systems. Due to their hardware-friendly nature, they can also be easily implemented on mobile devices or embedded systems. However, these methods also have limitations. The single-step process can lead to accuracy issues in detecting small objects or complex scenes. Additionally, in detections with a high IoU (Intersection over Union) threshold, they may cause sensitivity deficiencies such as an increased rate of false positives.

1.3.2. Features of double layer methods

Two-stage methods are an approach that perform object detection and classification in two separate stages. In the first stage, a Region Proposal Network (RPN) identifies potential object regions. In the second stage, these regions are processed in more detail, classified, and the bounding boxes are refined. The main feature of these methods is the analysis of different feature maps in both stages, which leads to higher accuracy. Examples of two-stage methods include models such as Faster R-CNN and Mask R-CNN. Advantages of these methods include high accuracy and improved detection and classification performance through detailed analysis. They also yield better results on small objects and complex scenes. Their flexibility makes them suitable for various applications and allows for optimization with different components. However, two-stage methods also have certain limitations. The two-step structure increases processing time, making them less suitable for real-time applications. In addition, their more complex architecture requires greater computational resources, which can increase training and deployment costs.

1.4. Comparison of single and dual layer object recognition methods

Single-stage object detection models are widely preferred in applications based on real-time image analysis due to their high processing speeds. These models can be effectively used in real-time systems that require low latency (Medium, 2024). Especially in cases such as traffic counting, where a balance between speed and accuracy is crucial, the YOLO model stands out. YOLO reduces the object recognition process to a regression problem, allowing it to simultaneously predict the positions and probabilities of bounding boxes for each class. Unlike two-stage models such as Fast R-CNN, this method enables direct detection without the need to predefine possible object locations. YOLO's ability to analyze all classes in a single operation allows for much faster determination of object positions and attributes compared to traditional methods. As a result of comprehensive research in the literature, a summary table has been created that presents a comparative analysis of single-stage and two-stage object recognition methods in terms of speed, accuracy, complexity, application areas, and hardware requirements. This table reveals that single-stage methods are preferred in real-time systems due to their high speed and low hardware requirements, whereas two-stage methods are used in procedures requiring high precision due to their accuracy and complexity (Table 1).

Table 1. Comparison of single and dual layer object recognition methods

Feature	Single Layer Methods	Double Layer Methods
Speed	High	Low
Accuracy	Middle	High
Complicacy	Low	High
Application Areas	Real Time Systems	Procedures Requiring Precision
Hardware Requirement	Little	Extra

1.5. Selection according to application areas

Single-Stage Methods: These are widely used in areas where speed is crucial, such as video surveillance, autonomous driving, and mobile applications. These methods offer low computational cost and high speed, making them effective in real-time systems. Two-Stage Methods: These are preferred in applications that require high accuracy, such as medical imaging, security analysis, and industrial control. These methods enhance object detection accuracy by performing more detailed analysis. Single-stage and two-stage object recognition methods offer complementary approaches in the field of object detection. While single-stage methods provide speed and ease of processing, two-stage methods are more advantageous in terms of accuracy and precision. Depending on the usage scenario, the strengths and weaknesses of both methods should be evaluated to select the appropriate model. In real-time applications, fast models like YOLO and SSD are preferred, whereas in cases requiring higher accuracy, methods such as Faster R-CNN or RetinaNet stand out (Tan et al., 2021). Considering the scope of real continuous object ranges, the YOLO architecture is implemented more efficiently compared to SSD. The YOLOv3 model, detailed by Redmon and Farhadi (2018), offers higher detection ranges and speed compared to SSD, providing an advantage in real-time applications. Structurally, YOLO has demonstrated better results in object detection with less programming resource usage than SSD (Redmon & Farhadi, 2018). Comprehensive reviews conducted for real-time object detection reveal that the YOLO model provides advantages in terms of both speed and accuracy. In this context, performance evaluation will be conducted using the default models of YOLO, and the model's efficiency and accuracy rates will be analyzed. The tests to be carried out will measure the detection capability of the model under different scenarios, contributing to the determination of the most suitable configuration for real-time applications.

2. Materials and methods

The materials and methods used to evaluate the performance of an object detection model include various elements such as the datasets to be analyzed, evaluation criteria, and hardware and software components employed. In this study, a comparative analysis in terms of accuracy and speed will be conducted for the latest versions of the YOLO family: YOLOv8, YOLOv9, YOLOv10, and YOLOv11. The main objective of the study is to determine how consistent the accuracy (mAP—mean Average Precision) and speed (FPS—Frames Per Second) values reported by the developers are when applied to real-world video scenarios. The datasets used in this study will consist of video data containing various objects under different environmental conditions. The video footage will include both static and dynamic scenes and will be tested at various resolutions and lighting conditions. In this context, the performance of the models under variable conditions will be evaluated. In particular, the balance between speed and accuracy in detecting moving objects will be considered an important criterion. During the evaluation process, both the accuracy and speed values reported by the developers and those obtained through experimental testing will be compared for each model. The YOLOv8 model offers higher accuracy and better overall performance compared to previous versions due to its improved architecture. YOLOv9 is optimized for enhanced performance in detecting small objects and in low-light conditions. YOLOv10 was developed to improve computational efficiency, enabling more effective operation on embedded systems and low-power devices. YOLOv11 aims to set a new standard in both speed and accuracy through deeper neural network structures and advanced data processing techniques. For model comparisons, each version will be run on the same video data, and the results will be evaluated based on specific metrics. Evaluation criteria include mAP, FPS, processing time, false positive rate, and false negative rate. Real-time tests will be conducted on the selected video sets, and each model’s object detection capability will be analyzed. Model outputs will be assessed frame-by-frame in terms of detection accuracy and timing, and cases such as missed objects and false detections will be examined in detail. Python programming language and the PyTorch deep learning library will be used as the software infrastructure. During the testing process, all models will be run in the same environment to minimize variations due to hardware differences. Through this method, the study will reveal how valid the accuracy and speed values reported by the YOLO developers are when applied to real-world video data. The specifications provided by the YOLO developers are shown in Table 2.

In this study, the real-time object detection performance of the YOLOv8, YOLOv9, YOLOv10, and YOLOv11 models will be compared using the fastest versions of each release. In real-time applications, the combined evaluation of parameters such as speed, accuracy, and processing time is of great importance. In this context, different versions of each model will be selected, specifically those optimized for speed. The fastest model in the YOLOv8 family, YOLOv8n, demonstrates highly efficient performance in terms of processing time. In the YOLOv9 series, the YOLOv9t model stands out with its faster processing capabilities, while YOLOv10 and YOLOv11 also offer strong alternatives in terms of both speed and accuracy. Smaller versions such as YOLOv10n and YOLOv11n provide faster processing times, enabling low-latency object detection. The comparison of these models will aid in selecting those that offer high efficiency, particularly for use on low-power devices or in real-time video streams. The evaluation will be based on metrics such as FPS (frames per second), processing time, and accuracy, and the efficiency of each version will be analyzed in detail. Based on the test results, the strengths and weaknesses of each model will be identified, and recommendations will be provided for selecting the most suitable model for various application scenarios. In particular, a detailed analysis will be conducted to determine which version offers the highest performance in real-time systems, and the factors that should be considered in model selection will be evaluated accordingly.

Table 2. YOLO models and their features (Ultralytics, 2025)

Model	size (pixels)	mAPval 50-95	Speed CPU ONNX (ms)	Speed T4 TensorRT10 (ms)	params (M)	FLOPs (B)
YOLOv8l	640	52,9	375,2	9,06	43,7	165,2
YOLOv8m	640	50,2	234,7	5,86	25,9	78,9
YOLOv8n	640	37,3	80,4	1,47	3,2	8,7
YOLOv8s	640	44,9	128,4	2,66	11,2	28,6
YOLOv8x	640	53,9	479,1	14,37	68,2	257,8
YOLOv9c	640	53	-	7,16	25,3	102,1
YOLOv9e	640	55,6	-	16,77	57,3	189
YOLOv9m	640	51,4	-	6,43	20	76,3
YOLOv9s	640	46,8	-	3,54	7,1	26,4
YOLOv9t	640	38,3	-	2,3	2	7,7
YOLOv10x	640	54,4	-	12,2	56,9	160,4
YOLOv10s	640	46,7	-	2,66	7,2	21,6
YOLOv10n	640	39,5	-	1,56	2,3	6,7
YOLOv10m	640	51,3	-	5,48	15,4	59,1
YOLOv10l	640	53,3	-	8,33	29,5	12,3
YOLOv10b	640	52,7	-	6,54	24,4	92
YOLO11x	640	54,7	462,8	11,3	56,9	194,9
YOLO11s	640	47	90	2,5	9,4	21,5
YOLO11n	640	39,5	56,1	1,5	2,6	6,5
YOLO11m	640	51,5	183,2	4,7	20,1	68
YOLO11l	640	53,4	238,6	6,2	25,3	86,9

3. Findings and discussion

In today's computer vision applications, object detection plays a crucial role, especially in areas such as autonomous vehicles, security cameras, and traffic analysis systems. In this context, an experiment was conducted to determine the performance differences between various versions of the YOLO (You Only Look Once) family. In the study, the models YOLOv8n, YOLOv9t, YOLOv10n, and YOLOv11n were applied to the same video footage, and their object detection accuracy and FPS values were compared. To evaluate the performance of the models, a video with a duration of 10 minutes and 20 seconds at 30 FPS was used, and the detections made by each model were examined individually. YOLO models are evolutionary deep learning networks developed to optimize both speed and accuracy in object detection. Different versions of the YOLO family offer enhanced features based on architectural optimizations and improvements. The YOLOv8n model is a relatively lightweight and optimized model suitable for real-time applications. The YOLOv9t model aims to improve accuracy rates through modifications in its deep learning architecture, while the YOLOv10n model offers a structure that requires fewer computational resources while still achieving high accuracy. The YOLOv11n model is the latest version, aiming to overcome the shortcomings of previous versions and achieve higher detection performance. As part of the experimental study, a specific video frame was selected, and the object detection performance of each YOLO model was visualized. During this evaluation, the object categories identified by the models and their detection confidence scores were analyzed. Factors such as whether the models correctly classified vehicles (car, bus, truck, etc.) and the presence of false positives and false negatives were taken into account (Fig. 1).

The image is divided into four sections, each showing a video frame analyzed by a different YOLO model. The objects detected within the same time frame and their corresponding confidence scores are displayed. The differences in object classification and the changes in confidence scores are indicated on the visual. The image includes various vehicle types in traffic, with each vehicle detected by the models at different accuracy levels. YOLOv8n model (a): This model successfully detected cars in traffic and classified a minibus as "bus," with a confidence score of 0.66. Overall, the vehicle detection accuracy is observed to be good. YOLOv9t model (b): This model also detected cars, but it misclassified the minibus as "truck," assigning a confidence score of 0.55. Therefore, this model shows some differences in object classification. YOLOv10n model (c): While generally successful in vehicle detection, this model classified the minibus as "bus" and assigned a confidence score of 0.47. The confidence scores for cars are relatively lower compared to other models, and one car was not detected. YOLOv11n model (d): This model successfully detected cars, but misclassified the minibus as "truck," with a confidence score of 0.49. The confidence scores for car detection showed variability. The analysis of the visual shows that all models were able to detect vehicles in traffic but classified the minibus differently. YOLOv8n and YOLOv10n classified the minibus as "bus," while YOLOv9t and YOLOv11n classified it as "truck." This discrepancy may be due to the dataset used during model training, the model's learning capacity, and updated algorithms. This study compares the object detection performance of different YOLO versions, focusing on accuracy rates and processing speeds for car and bus detection. The evaluation analyzes the frames-per-second (FPS) processing speeds, the number of objects detected, and their alignment with ground truth values for YOLOv8n, YOLOv9t, YOLOv10n, and YOLOv11n models running on a CPU. The detection results and speed values are shown in Table 3.

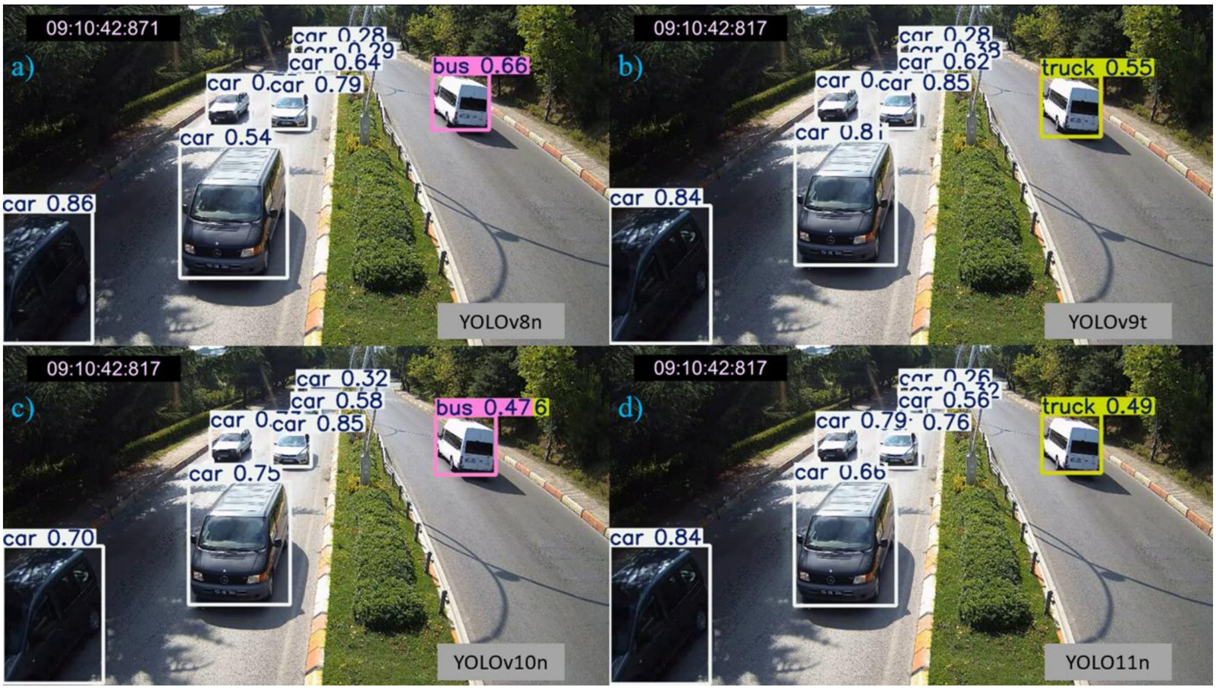

Fig. 1. Object detection confidence scores of different YOLO models within the same time frame

Table 3. YOLO models and performances

Model	FPS CPU	Car		Bus		Accuracy Rate (%)
		Detected	Real	Detected	Real	
YOLOv8n	15,81	220	256	36	36	87,67
YOLOv9t	12,87	217	256	35	36	86,30
YOLOv10n	10,68	223	256	36	36	88,69
YOLO11n	17,78	221	256	36	36	88,01

Based on the results, the model with the highest frames-per-second (FPS) is YOLOv11n, achieving 17.78 FPS. Despite this high FPS, it detected 257 vehicles. The YOLOv8n model, with a processing speed of 15.81 FPS, detected 265 vehicles and achieved an accuracy of 87.67%. The YOLOv9t model, with a lower FPS of 12.87, detected 252 vehicles and achieved an accuracy of 86.30%. The model with the lowest FPS, YOLOv10n, with 10.68 FPS, still achieved the highest accuracy of 88.69% and detected 259 vehicles. In terms of bus detection, all models performed similarly, with the exception of YOLOv9t. All models, except YOLOv9t, correctly detected 36 buses. This indicates that the models showed similar performance in distinguishing larger objects like buses. However, there were significant differences in vehicle detection. Despite its relatively lower FPS, YOLOv10n showed the highest accuracy, indicating that it provided more reliable detection. On the other hand, YOLOv11n achieved the highest FPS, offering an advantage in processing speed, but it did not deliver the best performance in terms of accuracy. These results highlight the need to balance speed and accuracy when selecting a model for object detection. Models with higher FPS may be preferred for real-time applications, while in scenarios where accuracy is critical, models that provide more reliable results with lower FPS might be more suitable. In applications like autonomous driving, traffic management, and security systems, optimizing both the processing speed and accuracy of the model is essential. YOLOv10n offers the best detection performance, while YOLOv11n stands out as the fastest option for real-time applications. Accordingly, the appropriate model should be chosen based on the specific requirements of the application.

4. Conclusion

This study presents a comparative analysis of the object detection performance of the YOLOv8, YOLOv9, YOLOv10, and YOLOv11 models on video data. A comprehensive performance evaluation was conducted by measuring detection accuracy, false positive, and false negative rates in a real-time, multi-frame data stream. The findings indicate that the YOLOv11 model has a higher overall accuracy compared to the other models. However, the YOLOv8 and YOLOv9 models exhibited lower error rates in detecting specific objects. The YOLOv10 model showed moderate accuracy but performed better than other models in certain scenes. These results demonstrate that each model has its own advantages and disadvantages depending on the use case. A more detailed analysis of model performances and testing of updated versions is recommended for future research. Additionally, testing under different angles and variable environmental conditions is crucial for assessing the models' overall detection capabilities. The findings of such studies can help determine which model should be prioritized for real-world applications. In conclusion, this study contributes to understanding the performance of object detection algorithms in video-based analysis, aiding advancements in the field. The analyses conducted are significant for understanding the evolution of object detection technologies and guiding the selection of the most effective model. In the future, it is anticipated that hybrid uses of these models or integration with advanced optimization techniques may further enhance performance.

Acknowledgments

The research described in this paper was financially supported by Ondokuz Mayıs University under the project titled "Karayolu Ağlarında Kurp Kesimlerinde Şerit Disiplininin Sağlanması ve Yol Kapasitesinin Arttırılması Uygulaması" with the project number PYO.MUH.1906.23.004.

The research described in this paper was financially supported by TÜBİTAK under the project titled *"Karayolu Trafiğinde Şerit İhlallerinin Azaltılmasına Yönelik Bir Çözümün Geliştirilmesi"* with the project number 124M818.

References

Aalami, N. (2020). Derin öğrenme yöntemlerini kullanarak görüntülerin analizi. *ESTUDAM Bilişim Dergisi , 1*(1), 5-20

Cai, Z., & Vasconcelos, N. (2018). Cascade R-CNN: High-quality object detection via a cascade of detectors. In *Proceedings of the IEEE Conference on Computer Vision and Pattern Recognition (CVPR)*, 6154–6162

Chen, Y., Yang, X., Zhong, B., Pan, S., Chen, D., & Zhang, H. (2016). CNNTracker: Online discriminative object tracking via deep convolutional neural network. *Applied Soft Computing, 38*, 1088–1098. https://doi.org/10.1016/j.asoc.2015.06.048

Everingham, M., Van Gool, L., Williams, C.K.I., Winn, J. & Zisserman, A. (2010). The PASCAL Visual Object Classes (VOC) Challenge. *International Journal of Computer Vision, 88*(2), 303–338

Girshick, R. (2015). Fast R-CNN. In *2015 IEEE International Conference on Computer Vision (ICCV)*, 1440–1448. https://doi.org/10.1109/ICCV.2015.169

Güçlü, E., Aydın, İ., & Akın, E. (2022). Mask R-CNN algoritmasını kullanarak demiryolu travers eksikliklerinin tespiti için otonom İHA tasarımı. *Fırat Üniversitesi Mühendislik Bilimleri Dergisi, 34*(1), 409-420. https://doi.org/10.35234/fumbd.1039995

Karadağ, B., & Arı, A. (2023). Akıllı mobil cihazlarda YOLOv7 modeli ile nesne tespiti. *Politeknik Dergisi, 26*(3), 1207–1214. https://doi.org/10.2339/politeknik.1296541

Kılıç, Ö.D., Aydemir, M.E., & Özdemir, P.Ö. (2022). Uçak oranlarının sınıflandırılmasında farklı yapay zekâ performanslarının performansı. In *SETSCI Conference Proceedings, 14*, 84–88. https://doi.org/10.36287/setsci.5.2.018

Krizhevsky, A., Sutskever, I., & Hinton, GE (2017). ImageNet Classification with Deep Convolutional Neural Networks. *Communications of the ACM, 60* (6), 84–90

Lin, T., Goyal, P., Girshick, R., He, K., & Dollar, P. (2017). Focal loss for dense object detection. In *Proceedings of the IEEE International Conference on Computer Vision (ICCV)*, 2999–3007

Liu, W., Anguelov, D., Erhan, D., Szegedy, C., Reed, S., Fu, C.-Y., & Berg, A.C. (2016). SSD: Single shot multibox detector. In B. Leibe, J. Matas, N. Sebe, & M. Welling (Eds.), Computer Vision – ECCV 2016 (pp. 21–37). Springer International Publishing https://doi.org/10.1007/978-3-319-46448-0_2

Malkoçoğlu, A.B., & Şamlı, R. (2023). Review on detection of dangerous objects in video data using deep learning methods. *Bilgisayar Bilimleri ve Mühendisliği Dergisi, 16*(1), 60–80 https://doi.org/10.54525/tbbmd.1184322

Medium. (2024, 3 Ekim). Object detection: Speed and accuracy comparison (Faster R-CNN, R-FCN, SSD, FPN, RetinaNet and YOLOv3). Retrieved from https ://jonathan -hui.medium.com /object -detection -speed -and -accuracy -comparisonfaster -r -cnn -r -fcn -ssd -and -yolo -5425656ae359

Paperswithcode. (2024, October 3). *Object detection*. Kodlu Kağıtlar. Retrieved from https://paperswithcode.com/task/object-detection

Redmon, J., & Farhadi, A. (2018). YOLOv3: An incremental improvement. *arXiv preprint*, arXiv:1804.02767 https://arxiv.org/abs/1804.02767

Tan, F.G., Yüksel, A.S., Aydemir, E., & Ersoy, M. (2021). Derin öğrenme teknikleri ile nesne tespiti ve takibi üzerine bir inceleme. *European Journal of Science and Technology, 25*, 159-171. https://doi.org/10.31590/ejosat.878552

Türkarslan, K., & HardalAğaç, F. (2022). Derin öğrenme yöntemleri kullanılarak havadan elde edilen görüntüler üzerinde nesne tespiti. *El-Cezeri Fen ve Mühendislik Dergisi, 9*(4), 1398–1410. https://doi.org/10.31202/ecjse.1135509

Ultralytics. (2025, March 31). *YOLOv11 models documentation*. Ultralytics. Retrieved from https://docs.ultralytics.com/tr/models/yolo11/

Wang, C.-Y., & Liao, H.-Y.M. (2024). YOLO survey, August 2024: YOLOv1 to YOLOv10: The fastest and most accurate real-time object detection systems. *arXiv preprint arXiv:2408.09332v1* https://arxiv.org/abs/2408.09332

Zivkovic , Z. (2004). Improved adaptive Gaussian mixture model for background subtraction. In *Proceedings of the 17th International Conference on Pattern Recognition (ICPR 2004)* (Vol. 2). IEEE https://doi.org/10.1109/ICPR.2004.1333992

4th International Civil Engineering & Architecture Conference
17-19 May 2025, Trabzon, Türkiye

Current methods for determining the thermal properties of asphalt concrete: a comprehensive review

Duygu Demirtürk[1], Hande Işık Öztürk[2], Murat Güler[*2]

[1] Ankara Yıldırım Beyazıt University, Faculty of Engineering and Natural Sciences, Department of Civil Engineering, Ankara, Türkiye
[2] Middle East Technical University, Faculty of Engineering, Department of Civil Engineering, Ankara, Türkiye

Abstract. The thermal properties of asphalt concrete are required for understanding pavement behavior, especially regarding heat absorption, heat transfer, and the susceptibility to volumetric changes caused by temperature fluctuations throughout its service life. However, a standardized testing procedure to determine these properties has not yet been established. Although recent advancements in testing methods show promise, additional research is necessary to address limitations such as strict sample size requirements, long testing durations, and inaccuracies in test setups, which can impact the reliability and applicability of the measurements. To overcome these limitations, this study recognizes the necessity of comprehensively evaluating existing methods for measuring thermal properties, including thermal conductivity and specific heat capacity. It also systematically reviews experimental and numerical approaches from recent literature and assesses their effectiveness in understanding heat transfer mechanisms and their efficiency in practical applications. Previous studies categorized the experimental methods into steady-state and transient methods. Steady-state methods, such as the Guarded Hot Plate (GHP) and Heat Flux Meter (HFM), offer high accuracy but require significant time and careful sample preparation. In contrast, transient methods like the Transient Plane Source (TPS) and Transient Line Source (TLS) facilitate quicker measurements and greater adaptability, with innovations like the modified TPS enhancing the evaluation of various material compositions. Finally, numerical methods have become increasingly utilized as an alternative to address the limitations of experimental techniques. In summary, this study evaluates the existing methods for measuring the thermal properties of asphalt concrete and identifies their strengths, limitations, and potential for enhancement.

Keywords: Thermal properties; Asphalt concrete; Heat Transfer; Steady-state method; Transiet method

1. Introduction

Thermal changes, especially under fluctuating climatic conditions, significantly affect the long-term performance of pavement structures (El-Maaty, 2017; Tiza et al., 2022). This is mainly due to the temperature sensitivity of the asphalt binder. The viscoelastic properties of the asphalt binder change with temperature, causing permanent deformation (rutting) at high temperatures and cracking due to thermal stresses at low temperatures (Adwan et al., 2021; Li et al., 2021). These heat-induced variations directly relate to how heat is absorbed, conducted, and stored in the pavement layers. In asphalt pavements, heat is transferred by three different heat transfer modes: conduction, convection, and radiation. These modes are influenced by parameters such as surface color, roughness, and thermal properties of the asphalt mixture (Shamsaei et al., 2022). Specifically, the coefficient of thermal expansion, thermal conductivity, specific heat capacity, and thermal diffusivity of asphalt concrete are the main factors that define its thermal behaviour. These properties determine the material's capacity to undergo volumetric changes in response to temperature variations and its ability to conduct and absorb heat. Therefore, these properties need to be used as input in research on heat transfer modes in pavement engineering (Mamlouk et al., 2005; Mirzanamadi et al., 2018; Shi, 2014).

Thermal stresses and strains in asphalt concrete are intimately associated with thermal properties, as these properties directly influence the material's expansion or contraction in response to temperature variations (Zhong & Geng, 2009). Additionally, the amount of heat absorbed and retained by asphalt pavements significantly affects their environmental performance, particularly in summer when elevated surface temperatures and traffic loads lead to thermal oxidation and rutting (Abbas & Alhamdo, 2023; Khasawneh et al., 2023). Due to asphalt's dark color and low thermal conductivity, the pavement accumulates heat, increasing the surface temperature and intensifying

[*] Corresponding author, E-mail: gmurat@metu.edu.tr

https://doi.org/10.31462/icearc2025_ce_tra_133

the Urban Heat Island (UHI) effect (Calkins, 2012). Thermal properties of asphalt concrete play a crucial role in predicting pavement surface temperatures, which impact not only structural performance but also frost effects in subgrades and the effectiveness of winter maintenance (Ayasrah et al., 2023; Minhoto et al., 2005). Heat-based self-healing technologies also depend on these properties to activate healing mechanisms within microcracks (Concha & Norambuena-Contreras, 2020; García et al., 2013; Liang et al., 2021). Tools like the Mechanistic-Empirical Pavement Design Guide (MEPDG) incorporate thermal properties as main inputs to simulate long-term performance in pavement design (Ceylan et al., 2009). The cooling rate of pavements during construction is fundamentally governed by their thermal properties, particularly the specific heat capacity and thermal conductivity, and thus, accurate determination of thermal properties is needed to optimize compaction processes (Highter, 1983; Timm et al., 2001). To summarize, accurately measuring the thermal properties of asphalt concrete can be defined as a key to improving pavement design practices, ensuring construction quality, and developing effective maintenance strategies, especially to hedge against urban climate changes and their challenges.

Despite its acknowledged importance, a standard test method for measuring thermal properties of asphalt concrete is still under discussion. Although recent efforts have focused on characterizing thermal behavior using current experimental approaches, further research is required to identify the main influencing parameters and to modify the test procedures. Notably, there is still no comprehensive comparative study that evaluates the suitability, accuracy, and limitations of different measurement techniques. The effect of the testing method used in obtaining the thermal properties is not yet known. Given these concerns, this study aimed to provide a comprehensive review of experimental and numerical methods used to determine the thermal properties of asphalt concrete. The study begins by reviewing commonly applied experimental methods and then presents numerical and simulation-based approaches. It then presents a comparative evaluation of these methods, attempting to reveal their practical advantages and limitations. Finally, the aim is to evaluate the applicability and effectiveness of the techniques used in determining the thermal properties of asphalt concrete, while identifying the methodological procedure and standardization opportunities.

2. Experimental methods for measuring thermal properties

There are some experimental studies in the literature on the development of test methods, the design of special equipment, and the modification of test setups to precisely measure the thermal properties of asphalt concrete. These studies primarily classify measurement techniques into two categories: steady-state and transient methods (Byzyka et al., 2021; Côté et al., 2013; Elkholy et al., 2019; Islam & Tarefder, 2014; Kuvandykova & Bateman, 2013). The following figure presents some of these experimental methods and their related test equipment, as seen in Fig.1.

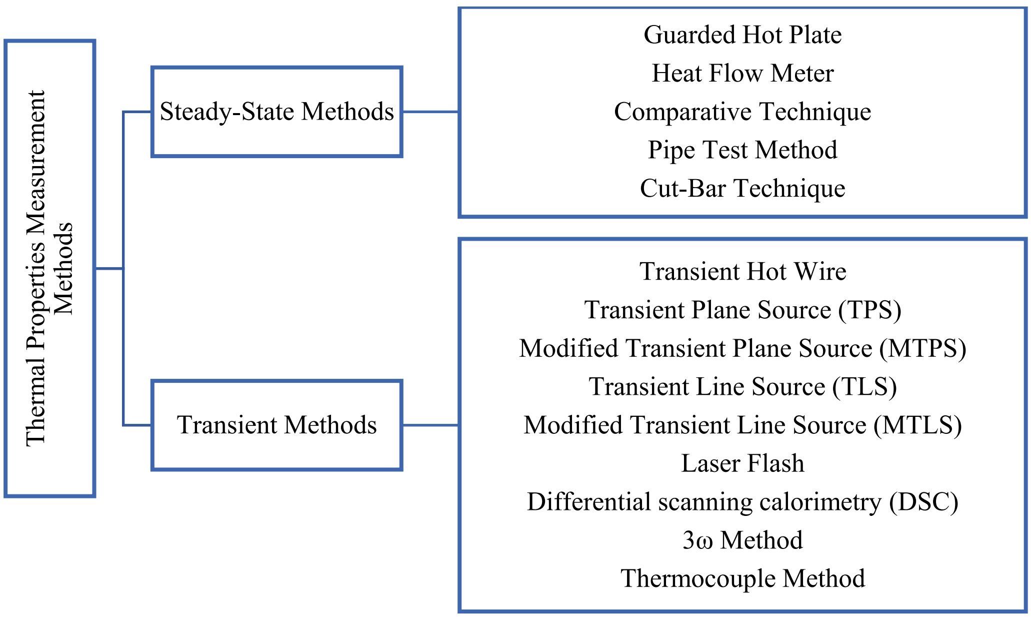

Fig. 1. Methods for measuring thermal properties (Kuvandykova & Bateman, 2013; Palacios et al., 2019)

The thermal conductivity and specific heat capacity of asphalt concrete were generally measured with the steady-state approach when the equilibrium heat flow conditions were provided in the test setup. These studies were mainly structured on one-dimensional heat transfer conditions under constant temperature changes, following Fourier's heat transfer principle (Carlson et al., 2010; Mehling & Cabeza, 2008; Tritt, 2005). Among the most widely adopted standardized procedures were the Guarded Hot Plate (GHP) and Heat Flow Meter (HFM) methods, as defined by ASTM C177-19 and ASTM C518-21, respectively (*Standard Test Method for Steady-State Heat Flux Measurements and Thermal Transmission Properties by Means of the Guarded-Hot-Plate Apparatus*, n.d.; *Standard Test Method for Steady-State Thermal Transmission Properties by Means of the Heat Flow Meter Apparatus*, n.d.). Both techniques can be considered practical approaches, particularly when working with flat and homogeneous specimens, provided that calibration and surface conditions are carefully controlled (Kim et al., 2021; Palacios et al., 2019; Richter et al., 2003). However, because asphalt concrete is a naturally heterogeneous material, applying these standard test procedures to asphalt mixtures is controversial. Nonetheless, alternative setups and modifications have been attempted to overcome the difficulties presented by traditional methods, such as long test durations and stringent sample size requirements.

Among past studies, Mrawira and Luca (2002) developed the UNB k-alpha tester, specifically designed to test small cylindrical samples, including cores extracted from pavements and lab-compacted briquettes (Mrawira & Luca, 2002). In a similar effort to address sample geometry issues, Carlson et al. (2010) developed a cylindrical heating model in which radial heat flow was generated by placing a heat source along the axis of a cylindrical sample, insulated at both ends. This method, which enabled thermal measurements within specimens typically used in mechanical tests, produced repeatable thermal conductivity results (0.896 ± 0.023 W/m·°C) (Carlson et al., 2010). On the other hand, other researchers focused on analytical modeling and enhanced instrumentation. Accordingly, Xu and Solaimanian (2010) tested asphalt concrete samples in a controlled climate chamber. They monitored transient heat transfer to validate a predictive model, eventually reaching steady-state conditions (Xu & Solaimanian, 2010). Meanwhile, Côté et al. (2013) proposed a modified test system using a thermal conductivity cell with brass disks and thermoelectric heat flux meters, as seen in Fig.2. Their study provided consistent measurements across asphalt mixtures with varying aggregate size, bitumen content, and air void ratios (Côté et al., 2013). Hassn et al. (2016a, 2016b) also made a notable contribution to this topic by using the P.A. Hilton B480 HFM system with large slab specimens (306 × 306 × 50 mm³), demonstrating that higher air void content significantly impedes heat flow due to the insulating nature of air (Hassn et al., 2016a, 2016b). In the following, Fig. 2 gives some parts of the experimental setup prepared based on the steady-state principle in the study conducted by Côté et al. (2013).

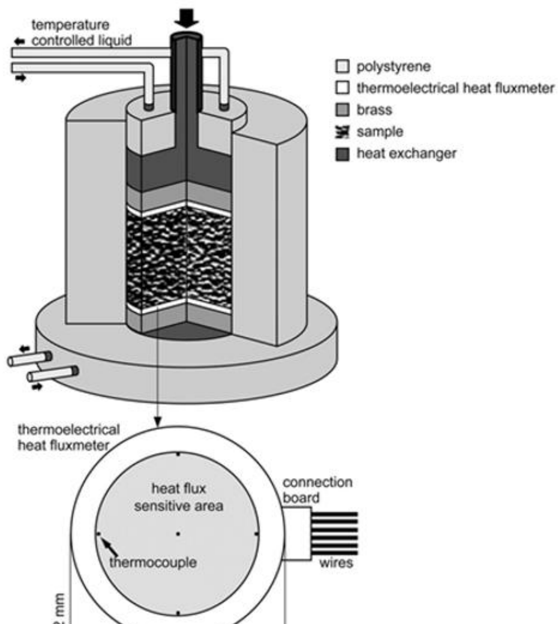

Fig. 2. Heat transfer cell adapted from Côté et al., 2013.

Some studies have also used the steady-state approach to determine specific heat capacity; however, these studies are limited. In the past, specific heat capacity was determined based on the weighted average of the constituent materials (Johnston, 1981; Jordan & Thomas, 1976). These studies were found to be unreliable due to moisture and void variations; more recent approaches are needed to provide better accuracy. Accordingly, Wolfe et al. (1980) and Islam & Tarefder (2014) studied the development of the drop calorimeter method, applying the principle of energy conservation in a steady-state setting. The latter study used a thermally insulated ice box and hot water bath to monitor temperature changes in asphalt samples (See Fig. 3c), directly calculating specific heat capacity under controlled conditions (Islam & Tarefder, 2014; Wolfe et al., 1980). Lastly, Demirtürk et al. (2023) modified the drop calorimeter method. They designed a custom calorimetry-based setup to measure the specific heat capacity of asphalt concrete samples produced in the laboratory under steady-state conditions (See Fig.3a & Fig. 3b). The system consisted of a thermally insulated steel cabinet with a water heating unit, a circulation pump, RTD sensors, and a data acquisition system. Samples pre-conditioned at a known temperature were immersed in heated water, and the temperature changes were recorded until thermal equilibrium was reached. The energy balance between the water and the asphalt specimens was then used to calculate the specific heat capacity. This setup effectively minimized lateral heat losses and allowed for precise thermal measurements in a controlled environment (Demirtürk et al., 2023).

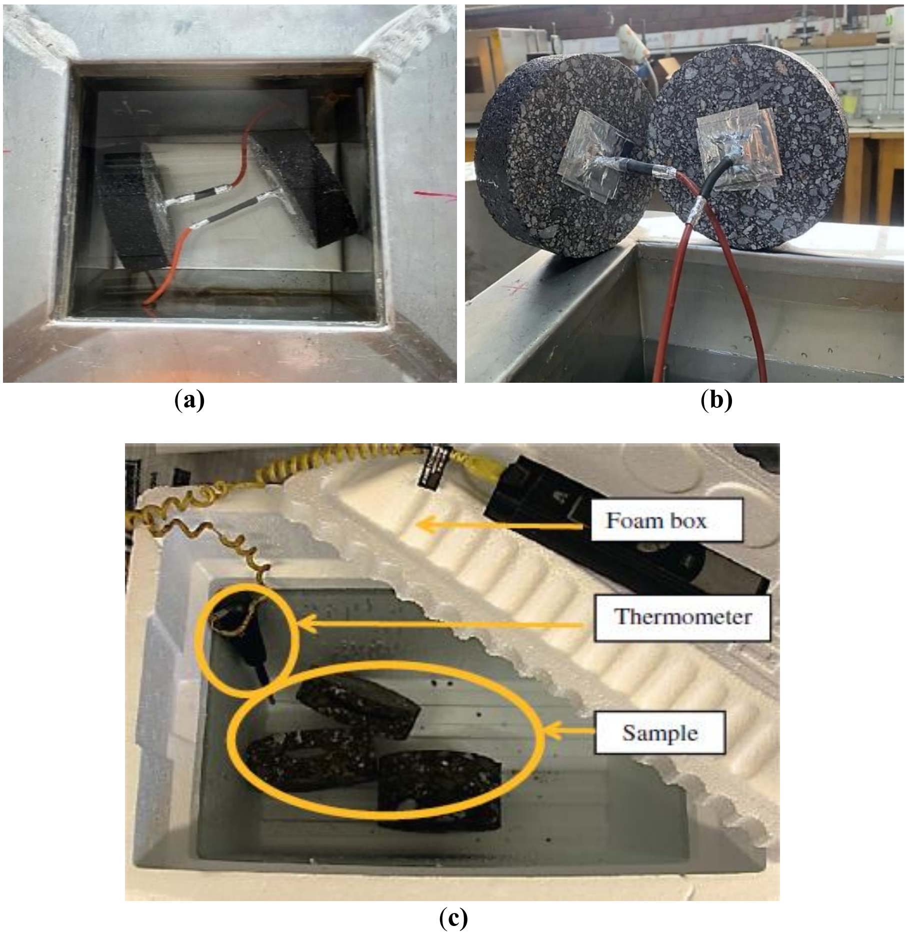

Fig.3. The main parts (a & b) of the test setup developed by Demirtürk et al. (2023) and the specific heat capacity measurement test setup (c) in asphalt concrete developed by Islam & Tarefder (2014).

Traditional one-dimensional steady-state methods may lead to inaccurate and erroneous test results (Zarr, 2010). Therefore, many researchers have tried to investigate and suggest the transient approach-based test methods, which are considered modern and rapid. The reviewed studies applied various transient methods—Transient Line Source (TLS), Transient Plane Source (TPS), and Modified Transient Plane Source (MTPS)—to measure the thermal properties of asphalt concrete. An overview of the equipment and applications related to the TLS, TPS, and MTPS methods is presented in Fig. 4. For example, Byzyka et al. (2021) applied the TLS method to find the effects of aging, temperature, and air voids on the measurement results. Their results indicated that variables, including poor needle-sample contact and drilling residue presence, can cause measurement errors, therefore affecting the reliability of the results (Byzyka et al., 2021). Mirzanamadi et al. (2018) employed the TPS method. They highlighted the importance of sensor size, heating power, and measurement time, revealing inaccuracies when the sensor diameter was too small relative to aggregate size (Mirzanamadi et al., 2018). Chen et al. (2022) and Khasawneh et al. (2023) also used TPS techniques, stressing the significance of good sensor contact (X. Chen et al., 2022; Khasawneh et al., 2023). Demirtürk et al. (2024) also found that thermal conductivity values acquired using the TPS approach were extremely location-dependent, highlighting the importance of numerous measurements to ensure acceptable results in heterogeneous materials (Demirtürk et al., 2024). Petkova-Slipets & Zlateva (2018) introduced the MTPS method, which simplifies measurements and allows field testing without needing identical samples (Petkova-Slipets & Zlateva, 2018). While accuracy depends on sensor-aggregate compatibility, it is stated that transient methods remain popular due to their speed and practicality.

In addition to thermal conductivity measurements, transient approaches have also been required to measure specific heat capacity. In this context, the MTPS method, developed by Mathis Instruments Ltd. in 2004, has emerged as one of the few applicable techniques for measuring the specific heat capacity of asphalt concrete (Petkova-Slipets & Zlateva, 2018). Besides the MTPS method, other commonly used methods include Differential Scanning Calorimetry (DSC) and Modulated Differential Scanning Calorimetry (MDSC). The DSC method provides both quantitative and qualitative data on physical and chemical changes as well as variations in heat capacity. The MDSC method, as an advanced and patent-pending version of DSC, enables the differentiation between reversible and irreversible thermal events (Reading et al., 1994). For example, Hu and Yu (2016) utilized the MDSC method to investigate the thermal behavior of thermochromic asphalt pavements. They reported a specific heat capacity range of 1475–1778 J/(kg·K) for black asphalt coating within the temperature range of –20 to 50 °C (Hu & Yu, 2016). However, a review of previous studies reveals that transient methods such as DSC and MDSC have primarily been applied to bitumen rather than asphalt mixtures. This is mainly due to the incompatibility of asphalt mixture sample sizes with the requirements of transient testing methods. Specifically, in the DSC method, the quantity of sample used in measurement pans is typically limited to around 10–20 mg (Zadshir et al., 2020). Consequently, DSC is most often employed to assess changes in the thermal properties of bitumen (Elkashef et al., 2020; Hosseinnezhad et al., 2019; Zadshir et al., 2020). Accurately measuring the specific heat capacity of asphalt concrete using transient methods remains challenging, and efforts are ongoing to discover and develop new measurement techniques.

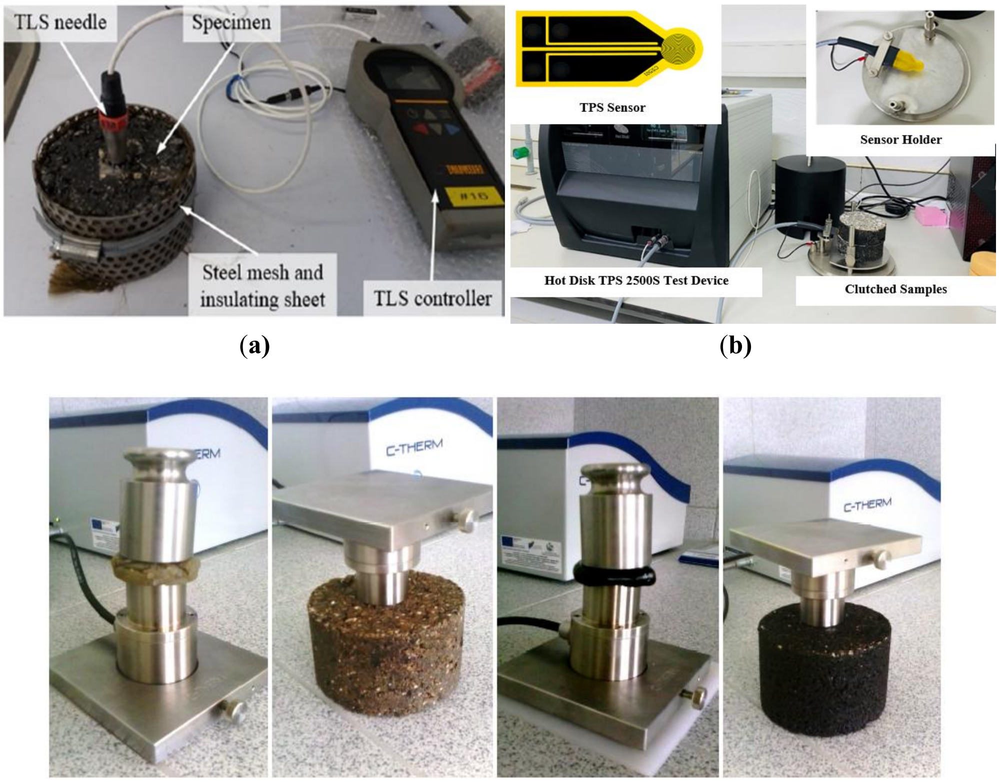

(a) **(b)**

(c)

Fig. 3. (a) Use of the TLS method in asphalt concrete sample (Byzyka et al., 2021), (b) Hot Disk TPS 2500S test device & parts (Demirtürk et al., 2024), and (c) testing different samples with the MTPS (Petkova-Slipets & Zlateva, 2018).

3. Numerical approaches and simulation-based studies

Microstructural modeling should be considered as the first step in applying numerical methods to determine the thermal properties of asphalt concrete and thus, the thermal behavior of asphalt concrete. Two basic techniques are commonly used to create three-dimensional (3D) representations of asphalt mixtures: computer-aided modeling and image-based modeling (Chen et al., 2015b; Wang et al., 2018; Zhang et al., 2017). In recent years, integrated approaches combining multi-scale modeling with mathematical prediction techniques have also been studied to increase the accuracy of thermal property predictions (Ren et al., 2018)

Previous studies, such as Chen et al. (2015b), established a multi-scale 3D microstructure model of asphalt concrete and combined it with Finite Element Analysis (FEA) to improve the simulation accuracy. Asphalt concrete was modeled as a three-phase heterogeneous system in which aggregates and air voids were represented by simplified polyhedral shapes dispersed in the asphalt binder. The FEM applied in the study was based on steady-state heat transfer principles. Constant temperatures were applied to the top and bottom faces of a cubic sample, while the remaining four sides were thermally insulated, maintaining one-dimensional heat flow. The model's predictions of effective thermal conductivity showed strong agreement with experimental data, with relative errors of 4.35% and 8.92% for samples made with crushed gravel and hornfels, respectively (Chen et al., 2015b). In a related study, Chen et al. (2015a) modified the aggregate generation algorithm originally proposed by Wang et al. (1999) to create angular coarse aggregates as polygons with defined elongation ratios. Randomized aggregate distributions were generated using MATLAB and implemented into ABAQUS—the hierarchical multiscale approach for constructing the microstructure. The FEM included three-node linear heat transmission elements and relied on thermal data from Mrawira & Luca (2006) (Chen et al., 2015a; Mrawira & Luca, 2006; Wang et al., 1999). Zhang et al. (2017) used a Voronoi diagram to generate a 3D random microstructure of asphalt mixtures. This method increased modeling efficiency by preventing particle overlap. Using steady-state FEA, it was found that the shape and orientation of the aggregates affected the mixture's thermal conductivity (Zhang et al., 2017). Using a simplified modeling approach, Chu et al. (2020) examined the relationship between the volumetric composition of asphalt mixtures and their thermal conductivity. They introduced a regular row-column model, allowing a more practical simulation of mixture behavior (Chu et al., 2020). As illustrated in Fig. 5a, this 2D model used square four-node elements and assumed conduction as the sole heat transfer mechanism. Despite its simplicity, the model produced results comparable to more complex microstructure-based simulations. Zhao et al. (2020) focused on porous asphalt concrete and utilized X-ray CT scanning to capture its internal structure. A mapped meshing method was used to construct the FEM. Their study performed a transient heat transfer analysis, highlighting the role of air voids in porous mixtures, in contrast to the more uniform structure of dense-graded mixtures (Zhao et al., 2020). Lastly, current developments in numerical modeling have paved the way for inverse methods, which can be particularly useful when direct data inputs are unavailable (Telejko & Malinowski, 2004). These methods rely on known temperature fields to back-calculate thermal properties. Once an appropriate material model is established, inverse techniques can be effectively combined with commercial finite element software to determine the thermal properties of asphalt concrete.

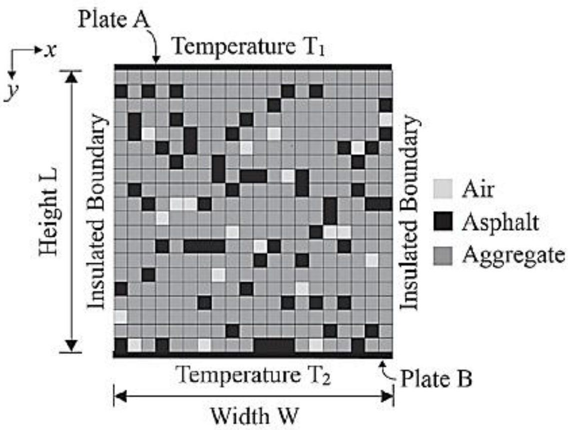

(a)

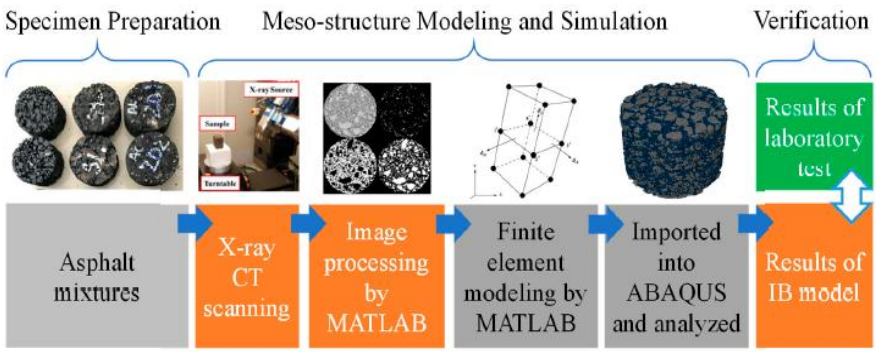

(b)

Fig. 4. (a) 2D row-column representation of asphalt mixture (Chu et al., 2020) and (b) Image-based model development steps (Zhao et al., 2020).

4. Comparative evaluation of current methods

The main purpose of this study is to critically compare experimental and numerical approaches to measure or determine the thermal properties of asphalt concrete. It has been found that the existing methods offer different advantages and limitations. The following points summarize the main differences and practical implications associated with steady-state, transient, and computational techniques in a general framework:

- Studies with steady-state methods have found that they offer high measurement accuracy under controlled conditions but are limited by long test durations and strict sample geometry requirements, making them less practical.
- Transient methods such as TPS and MTPS are significantly faster and more flexible when testing homogeneous materials. However, their accuracy is highly sensitive to sensor-sample contact quality and surface conditions, making their use in heterogeneous materials difficult and questionable.
- While the Guarded Hot Plate (GHP) and Heat Flow Meter (HFM) techniques have been cited as reliable measurements for flat, homogeneous samples, they have often failed to accommodate the irregular geometry of asphalt samples retrieved from the field.
- Specific heat capacity measurements in steady-state setups are limited by humidity and air void variability, while calorimetry-based methods, although promising, still lack standardization and reproducibility.
- Transient methods such as DSC and MDSC are used to measure the specific heat capacity of materials, but these are mainly suitable for bitumen and not for asphalt concrete due to the limited sample volume.
- New steady-state setups, such as the UNB k-alpha tester and cylindrical heat flow systems, offer improved realism for laboratory measurement of thermal properties by increasing compatibility with laboratory-compressed briquettes and in situ cores.
- TPS and TLS methods show broader applicability and adaptability in both laboratory and field environments. However, it is underlined that for valid results, test parameters such as heating power, sensor size, and test duration are necessary for safe and reliable measurement.
- The literature introduces image-based finite element models and inverse numerical techniques as valuable alternatives that provide detailed microstructural analysis and prediction of thermal properties in asphalt concrete, where experimental methods encounter limitations. However, their reliability mostly depends on accurate experimental calibration and high-resolution input or availability of experimental data, which remain critical prerequisites for ensuring model validity.
- Despite considerable progress, existing numerical models often oversimplify material heterogeneity and heat transfer mechanisms, limiting their ability to reproduce the complex thermal reactions observed in real-world pavements accurately.

5. Conclusions

This study tries to compare the current experimental and numerical methods to determine the thermal properties of asphalt concrete. It can be concluded that steady-state and transient techniques offer certain advantages. However, their application to the inherently heterogeneous structure of asphalt mixtures remains challenging. Similarly, although numerical approaches are considered an alternative for determining the thermal properties of asphalt concrete when combined with microstructural analysis, their dependence on simplifying assumptions and the need for experimental calibration alone undermine their reliability. Thus, future research should focus on strengthening the compatibility of testing procedures with the intrinsic variability of asphalt mixtures. Steady-state procedures should be modified to reduce heat loss and improve specimen preparation consistency. Transient approaches, on the other hand, require standardisation with a larger emphasis on sensor-sample interactions and surface conditions. Furthermore, integrating numerical modelling and experimental calibration could offer a more complete understanding of heat transfer mechanisms at different levels. Accordingly, it may be beneficial for new standards to focus on the following recommendations at the first stage:

- Sensor-based measurement systems should use multi-point measurement procedures to capture local thermal property changes.
- Improved calibration protocols should be created for both steady-state and transient setups, considering sample geometry and surface conditions.
- Studies based on integrating numerical models based on microstructural information with robust experimental validation need to be increased and supported.
- Attempts should be made to combine the strengths of existing methods, such as developing hybrid methods that combine steady-state accuracy with the flexibility of transient approaches.

Acknowledgments

This study was conducted by Middle East Technical University Scientific Research Projects (METU-BAP) under the research project GAP-303-2021-10743.

References

Abbas, F. A., & Alhamdo, M. H. (2023). Enhancing the thermal conductivity of hot-mix asphalt. *Results in Engineering*, *17*, 100827. https://www.sciencedirect.com/science/article/pii/S2590123022004972

Adwan, I., Milad, A., Memon, Z. A., Widyatmoko, I., Ahmat Zanuri, N., Memon, N. A., & Yusoff, N. I. M. (2021). Asphalt pavement temperature prediction models: A review. *Applied Sciences*, *11*(9), 3794. https://www.mdpi.com/2076-3417/11/9/3794

Ayasrah, U. B., Tashman, L., AlOmari, A., & Asi, I. (2023). Development of a temperature prediction model for flexible pavement structures. *Case Studies in Construction Materials*, *18*, e01697. https://www.sciencedirect.com/science/article/pii/S2214509522008294

Byzyka, J., Rahman, M., & Chamberlain, D. A. (2021). A laboratory investigation on thermal properties of virgin and aged asphalt mixture. *Construction and Building Materials*, *305*, 124757. https://www.sciencedirect.com/science/article/pii/S0950061821025113

Calkins, M. (2012). *The sustainable sites handbook: A complete guide to the principles, strategies, and best practices for sustainable landscapes*. John Wiley & Sons.

Carlson, J. D., Bhardwaj, R., Phelan, P. E., Kaloush, K. E., & Golden, J. S. (2010). Determining Thermal Conductivity of Paving Materials Using Cylindrical Sample Geometry. *Journal of Materials in Civil Engineering*, *22*(2), 186–195. https://doi.org/10.1061/(ASCE)0899-1561(2010)22:2(186)

Ceylan, H., Coree, B., & Gopalakrishnan, K. (2009). *Evaluation of the mechanistic-empirical pavement design guide for implementation in Iowa*.

Chen, J., Wang, H., & Li, L. (2015a). Determination of Effective Thermal Conductivity of Asphalt Concrete with Random Aggregate Microstructure. *Journal of Materials in Civil Engineering*, *27*(12), 04015045. https://doi.org/10.1061/(ASCE)MT.1943-5533.0001313

Chen, J., Zhang, M., Wang, H., & Li, L. (2015b). Evaluation of thermal conductivity of asphalt concrete with heterogeneous microstructure. *Applied Thermal Engineering*, *84*, 368–374.

Chen, X., Wang, H., Jiang, B., & Venkiteela, G. (2022). Evaluation of Microwave Heating for Potential Applications in Hot In-Place Recycling of Asphalt Pavement. *Transportation Research Record: Journal of the Transportation Research Board*, *2676*(9), 256–268. https://doi.org/10.1177/03611981221086635

Chu, L., He, L., & Fwa, T. F. (2020). Determination of thermal conductivity of asphalt paving mixtures using finite element method. *Construction and Building Materials*, *243*, 118250.

Concha, J. L., & Norambuena-Contreras, J. (2020). Thermophysical properties and heating performance of self-healing asphalt mixture with fibres and its application as a solar collector. *Applied Thermal Engineering*, *178*, 115632.

Côté, J., Grosjean, V., & Konrad, J.-M. (2013). Thermal conductivity of bitumen concrete. *Canadian Journal of Civil Engineering*, *40*(2), 172–180. https://doi.org/10.1139/cjce-2012-0159

Demirtürk, D., Öztürk, H. I., & Güler, M. (2023). Using Calorimetry-Based Method for Measuring Specific Heat Capacity of Asphalt Concrete. *3rd International Civil Engineering and Architecture Congress*, 2031–2040. https://doi.org/10.31462/icearc.2023.tra873

Demirtürk, D., Ozturk, H. I., & Guler, M. (2024). Investigation of the influence of mixture and microstructural properties on the thermal conductivity of asphalt concrete using the transient heat transfer method. *Materials and Structures*, *57*(8), 179. https://doi.org/10.1617/s11527-024-02456-1

Elkashef, M., Elwardany, M. D., Liang, Y., Jones, D., Harvey, J., Bolton, N. D., & Planche, J.-P. (2020). Effect of Using Rejuvenators on the Chemical, Thermal, and Rheological Properties of Asphalt Binders. *Energy & Fuels*, *34*(2), 2152–2159. https://doi.org/10.1021/acs.energyfuels.9b03689

Elkholy, A., Sadek, H., & Kempers, R. (2019). An improved transient plane source technique and methodology for measuring the thermal properties of anisotropic materials. *International Journal of Thermal Sciences*, *135*, 362–374. https://www.sciencedirect.com/science/article/pii/S1290072918305374

El-Maaty, A. E. A. (2017). Temperature change implications for flexible pavement performance and life. *International Journal of Transportation Engineering and Technology*, *3*(1), 1–11.

García, A., Norambuena-Contreras, J., & Partl, M. N. (2013). Experimental evaluation of dense asphalt concrete properties for induction heating purposes. *Construction and Building Materials*, *46*, 48–54.

Hassn, A., Aboufoul, M., Wu, Y., Dawson, A., & Garcia, A. (2016a). Effect of air voids content on thermal properties of asphalt mixtures. *Construction and Building Materials*, *115*, 327–335. https://www.sciencedirect.com/science/article/pii/S0950061816304081

Hassn, A., Chiarelli, A., Dawson, A., & Garcia, A. (2016b). Thermal properties of asphalt pavements under dry and wet conditions. *Materials & Design*, *91*, 432–439. https://www.sciencedirect.com/science/article/pii/S0264127515308546

Highter, W. (1983, June 1). Thermal properties of some asphaltic concrete mixes. *International Air Transportation Conference*. International Air Transportation Conference, Montreal,Canada. https://doi.org/10.2514/6.1983-1598

Hosseinnezhad, S., Zadshir, M., Yu, X., Yin, H., Sharma, B. K., & Fini, E. (2019). Differential effects of ultraviolet radiation and oxidative aging on bio-modified binders. *Fuel*, *251*, 45–56.

Hu, J., & Yu, X. (Bill). (2016). Innovative thermochromic asphalt coating: Characterisation and thermal performance. *Road Materials and Pavement Design*, *17*(1), 187–202. https://doi.org/10.1080/14680629.2015.1068215

Islam, M. R., & Tarefder, R. A. (2014). Determining thermal properties of asphalt concrete using field data and laboratory testing. *Construction and Building Materials*, *67*, 297–306. https://www.sciencedirect.com/science/article/pii/S0950061814003031

Johnston, G. H. (1981). Permafrost: Engineering design and construction. *(No Title)*. https://cir.nii.ac.jp/crid/1130000794354624000

Jordan, P. G., & Thomas, M. E. (1976). *Prediction of cooling curves for hot-mix paving materials by a computer program*. https://trid.trb.org/View/66511

Khasawneh, M. A., Sawalha, A. A., Aljarrah, M. T., & Alsheyab, M. A. (2023). Effect of aggregate gradation and asphalt mix volumetrics on the thermal properties of asphalt concrete. *Case Studies in Construction Materials*, *18*, e01725. https://www.sciencedirect.com/science/article/pii/S2214509522008579

Kim, D., Lee, S., & Yang, I. (2021). Verification of thermal conductivity measurements using guarded hot plate and heat flow meter methods. *Journal of the Korean Physical Society*, *78*(12), 1196–1202. https://doi.org/10.1007/s40042-021-00177-0

Kuvandykova, D., & Bateman, R. (2013). A new transient method to measure thermal conductivity of asphalt. *Thermal Conductivity31/Thermal Expansion*, *19*, 98–107.

Li, L., Yang, L., Lin, Y., & Zhang, X. (2021). A Compressive Review on High- and Low-Temperature Performance of Asphalt Modified with Nanomodifier. *Advances in Materials Science and Engineering*, *2021*(1), 5525459. https://doi.org/10.1155/2021/5525459

Liang, B., Lan, F., Shi, K., Qian, G., Liu, Z., & Zheng, J. (2021). Review on the self-healing of asphalt materials: Mechanism, affecting factors, assessments and improvements. *Construction and Building Materials*, *266*, 120453.

Mamlouk, M. S., Witczak, M. W., Kaloush, K. E., & Hasan, N. (2005). Determination of thermal properties of asphalt mixtures. *Journal of Testing and Evaluation*, *33*(2), 118–126. https://asmedigitalcollection.asme.org/testingevaluation/article/33/2/118/1189302

Mehling, H., & Cabeza, L. F. (2008). *Heat and cold storage with PCM: An up to date introduction into basics and applications*. Springer Berlin Heidelberg. https://doi.org/10.1007/978-3-540-68557-9

Minhoto, M. J. C., Pais, J. C., Pereira, P. A. A., & Picado-Santos, L. G. (2005). Predicting Asphalt Pavement Temperature with a Three-Dimensional Finite Element Method. *Transportation Research Record: Journal of the Transportation Research Board*, *1919*(1), 96–110. https://doi.org/10.1177/0361198105191900111

Mirzanamadi, R., Johansson, P., & Grammatikos, S. A. (2018). Thermal properties of asphalt concrete: A numerical and experimental study. *Construction and Building Materials*, *158*, 774–785. https://www.sciencedirect.com/science/article/pii/S0950061817321220

Mrawira, D. M., & Luca, J. (2002). Thermal Properties and Transient Temperature Response of Full-Depth Asphalt Pavements. *Transportation Research Record: Journal of the Transportation Research Board*, *1809*(1), 160–171. https://doi.org/10.3141/1809-18

Mrawira, D. M., & Luca, J. (2006). Effect of aggregate type, gradation, and compaction level on thermal properties of hot-mix asphalts. *Canadian Journal of Civil Engineering*, *33*(11), 1410–1417. https://doi.org/10.1139/l06-076

Palacios, A., Cong, L., Navarro, M. E., Ding, Y., & Barreneche, C. (2019). Thermal conductivity measurement techniques for characterizing thermal energy storage materials–A review. *Renewable and Sustainable Energy Reviews*, *108*, 32–52. https://www.sciencedirect.com/science/article/pii/S1364032119301625

Petkova-Slipets, R., & Zlateva, P. (2018). Thermal Properties of a New Pavement Material for Using in Road Construction. *Civil and Environmental Engineering*, *14*(2), 99–104. https://doi.org/10.2478/cee-2018-0013

Reading, M., Luget, A., & Wilson, R. (1994). Modulated differential scanning calorimetry. *Thermochimica Acta*, *238*, 295–307. https://www.sciencedirect.com/science/article/pii/S0040603194852154

Ren, Z., Wang, H., Zhang, L., & Chen, C. (2018). Computational Analysis of Thermal Conductivity of Asphalt Mixture Based on a Multiscale Mathematical Model. *Journal of Engineering Mechanics*, *144*(8), 04018064. https://doi.org/10.1061/(ASCE)EM.1943-7889.0001493

Richter, C., Viljoen, H. J., & Van Rensburg, N. F. J. (2003). Effective thermal conductivity estimates of particulate mixtures. *Journal of Applied Physics*, *93*(5), 2663–2670. https://pubs.aip.org/aip/jap/article-abstract/93/5/2663/759676

Shamsaei, M., Carter, A., & Vaillancourt, M. (2022). A review on the heat transfer in asphalt pavements and urban heat island mitigation methods. *Construction and Building Materials*, *359*, 129350.

Shi, X. (2014). *Controlling thermal properties of asphalt concrete and its multifunctional applications* [PhD Thesis]. https://oaktrust.library.tamu.edu/items/a6647ad1-dccd-40b8-8f75-76ec9201a89e

Standard Test Method for Steady-State Heat Flux Measurements and Thermal Transmission Properties by Means of the Guarded-Hot-Plate Apparatus. (n.d.). Retrieved April 21, 2025, from https://store.astm.org/c0177-19.html

Standard Test Method for Steady-State Thermal Transmission Properties by Means of the Heat Flow Meter Apparatus. (n.d.). Retrieved April 21, 2025, from https://store.astm.org/c0518-21.html

Telejko, T., & Malinowski, Z. (2004). Application of an inverse solution to the thermal conductivity identification using the finite element method. *Journal of Materials Processing Technology*, *146*(2), 145–155.

Timm, D. H., Voller, V. R., Lee, E., & Harvey, J. (2001). Calcool: A multi-layer Asphalt Pavement Cooling Tool for Temperature Prediction During Construction. *International Journal of Pavement Engineering*, *2*(3), 169–185. https://doi.org/10.1080/10298430108901725

Tiza, M. T., Jırgba, K., Sanı, H. A., & Sesugh, T. (2022). Effect of thermal variances on flexible pavements. *Journal of Sustainable Construction Materials and Technologies*, *7*(3), 220–230. https://dergipark.org.tr/en/pub/jscmt/article/1136848

Tritt, T. M. (2005). *Thermal conductivity: Theory, properties, and applications*. Springer Science & Business Media.

Wang, H., Wang, C., You, Z., Yang, X., & Huang, Z. (2018). Characterising the asphalt concrete fracture performance from X-ray CT Imaging and finite element modelling. *International Journal of Pavement Engineering*, *19*(3), 307–318. https://doi.org/10.1080/10298436.2017.1347440

Wang, Z. M., Kwan, A. K. H., & Chan, H. C. (1999). Mesoscopic study of concrete I: Generation of random aggregate structure and finite element mesh. *Computers & Structures*, *70*(5), 533–544.

Wolfe, R. K., Heath, G. L., & Colony, D. C. (1980). *University of Toledo Time-Temperature Model Laboratory and Field Validation*. https://trid.trb.org/View/164351

Xu, Q., & Solaimanian, M. (2010). Modeling temperature distribution and thermal property of asphalt concrete for laboratory testing applications. *Construction and Building Materials*, *24*(4), 487–497. https://www.sciencedirect.com/science/article/pii/S095006180900350X

Zadshir, M., Ploger, D., Yu, X., Sangiorgi, C., & Yin, H. (2020). Chemical, thermophysical, rheological, and microscopic characterisation of rubber modified asphalt binder exposed to UV radiation. *Road Materials and Pavement Design*, *21*(sup1), S123–S139. https://doi.org/10.1080/14680629.2020.1736606

Zarr, R. R. (2010). Uncertainty analysis of thermal transmission properties determined by ASTM C177-04. *Journal of Testing and Evaluation*, *38*(2), 151–160. https://asmedigitalcollection.asme.org/testingevaluation/article/38/2/151/1189523

Zhang, L., Wang, H., & Ren, Z. (2017). Computational Analysis of Thermal Conductivity of Asphalt Mixture Using Virtually Generated Three-Dimensional Microstructure. *Journal of Materials in Civil Engineering*, *29*(12), 04017234. https://doi.org/10.1061/(ASCE)MT.1943-5533.0002081

Zhao, Y., Jiang, J., Dai, Y., Zhou, L., & Ni, F. (2020). Thermal property evaluation of porous asphalt concrete based on heterogeneous meso-structure finite element simulation. *Applied Sciences*, *10*(5), 1671. https://www.mdpi.com/2076-3417/10/5/1671

Zhong, Y., & Geng, L. (2009). Thermal stresses of asphalt pavement under dependence of material characteristics on reference temperature. *Mechanics of Time-Dependent Materials*, *13*, 81–91.

4th International Civil Engineering & Architecture Conference
17-19 May 2025, Trabzon, Türkiye

A Comparative analysis of bus rapid transit (BRT) systems: A framework for Sakarya

Süleyman N. A. Şahin[1], Abdurrahman Korkmaz[2], Abdulkadir Özden[1*],

[1]*Sakarya University of Applied Sciences, Department of Civil Engineering, 54050 Sakarya, Türkiye*
[2] *Giresun University, Keşap Vocational School, Department of Menagement and Organization, 28000 Giresun, Türkiye*

Abstract. This study presents a comprehensive comparative analysis of Bus Rapid Transit (BRT) systems across diverse geographic regions and cities across the world. Key performance indicators such as GDP per capita, urban population, system length, and station spacing were examined to uncover the socioeconomic and infrastructural dynamics influencing the efficiency and design of BRT networks. The findings provide a strategic framework for planning and developing BRT systems. According to these indicators, with comparative data analysis and visualization, the current status of Sakarya is shown in a wider perspective. Within this perspective for the most sustainable design for the future and transformation of urban mobility, this system will have a potential to build up the development under the human-centric paradigm. This finding highlights the crucial role of geographic and economic disparities in the design and operation of BRT systems. The significance of this study for Sakarya lies in its ability to serve as a benchmark for planning and developing the city's BRT system. The visualizations and results obtained are used to compare Sakarya with other cities from different regions with similar characteristics and identify the strengths and weaknesses of the future-planned BRT system. This allows for the development of customized BRT system design and improvement strategies for Sakarya and also for the local policy and decision makers.

Keywords: BRT system; Comparative analysis; Transformation; Sustainability; Urban mobility

---

1. Introduction

Since the early 21st century, urbanization and increasing mobility demands have prompted cities worldwide to seek cost-effective and scalable public transportation solutions (Cervero & Kang, 2011; ITDP, 2016). Bus Rapid Transit (BRT) offers a more affordable and flexible alternative to rail-based transit systems, mimicking many of Light Rail System's (LRT) advantages while maintaining lower infrastructure costs (Halimergün et al., 2024; Deng & Nelson, 2011). By incorporating dedicated lanes, traffic signal priority, and enhanced station design, BRT has gained prominence as a sustainable and efficient urban mobility solution.

The growing popularity of BRT worldwide is reflected in its rapid expansion over the past two decades. From the completion of the first BRT system in Curitiba, Brazil in 1974, BRT infrastructure remained relatively modest until the early 2000s (Prestes et al., 2022). However, as cities sought cost-effective transit solutions, BRT corridor development accelerated significantly, reaching over 5,300 km globally by 2021 (BRTDATA, 2025). Despite this growth, North America and Europe lag behind Latin America and East Asia in terms of BRT adoption, as cities in developed economies often prioritize rail-based systems (Cervero & Kang, 2011; Carrigan et al., 2019). In the North and South America, for example, BRT accounts for only 8.2% of total BRT corridor length worldwide, with many systems operating as BRT-lite, lacking dedicated right-of-way infrastructure (ITDP, 2016). This variation in BRT implementation underscores the diverse nature of BRT infrastructure, ranging from full busways with dedicated lanes to mixed-traffic operations, affecting the efficiency, reliability, and attractiveness of these systems (Deng & Nelson, 2011; Ferbrache, 2019).

Beyond mobility benefits, BRT systems have far-reaching implications for economic development, land use, and urban accessibility. Studies show that high-quality transit investments, such as LRT and BRT, can increase property values, attract new businesses, and support transit-oriented development (TOD) (Cervero & Dai, 2014). However, while the positive impact of rail-based transit on property values is well-documented, BRT's effects remain less understood, particularly in the United States and Europe (Deng & Nelson, 2011; Su, 2024). Research

*Corresponding author, Prof., E-mail: aozden@subu.edu.tr

https://doi.org/10.31462/icearc2025_ce_tra_256

in Latin America and East Asia suggests that BRT systems can generate land value premiums ranging from 5% to 10%, especially when integrated with mixed-use development and pedestrian-friendly infrastructure (Suzuki et al., 2015). However, the design and operational characteristics of BRT—such as station spacing, integration with other transport modes, and fare structures—play a crucial role in determining whether BRT can stimulate economic growth and enhance.

Given these global variations in BRT performance and effectiveness, it is essential to conduct comparative analyses that benchmark BRT systems across different geographic and economic contexts. This study aims to evaluate key performance indicators such as system length, urban population, GDP per capita, station spacing, and multimodal integration to understand the factors that drive BRT efficiency (Merkert, 2017). This study aims to clarify and provide a deeper understanding of the public transport network in Sakarya by examining the implementation of a new transit system. The system, which is still under construction, is designed as a BRT network to connect both sides of the city, contributing to the development of more inclusive and sustainable urban environments. Sakarya is a city located in the northwest of Türkiye. As of the end of 2024, its population is 1,110,735, with an annual population growth rate of 16.6 per thousand. The province covers a surface area of 4,817 km², with a population density of 228 people per km². This study was conducted in the most populated districts of Sakarya—Serdivan, Adapazarı, and Erenler—which also serve as the city's central districts (Figure 1). These districts play a significant role in the economic and social structure of Sakarya.

Fig. 1. Location map of study area

By analysing Sakarya's urban characteristics in comparison with global BRT systems, this study aims to uncover both opportunities and challenges in developing a locally adapted BRT strategy that aligns with the city's socioeconomic dynamics and sustainability objectives. The findings offer a strategic roadmap for BRT implementation in Sakarya, providing valuable insights for local policymakers, urban planners, and transit authorities. The discussion delves into how Sakarya's urban mobility strategy can be enhanced by integrating global BRT best practices, culminating in policy recommendations for effective implementation. This paper serves as a strategic background for the planning and development of Sakarya's BRT system, using global benchmarks to inform region-specific solutions.

2. Methodology

BRT systems serve as one of the best examples of urban transportation systems implemented in all continents of the world. In particular, the data of the cities with BRT systems in all continents, especially in this field, are also kept on the web address www.brtdata.org (BRTDATA, 2025). This website, which also has an interactive user interface, is a very useful website for the necessary comparisons and current situation analysis as well as presenting data.

In this study, the data sets of all cities available on this website (Fig. 2) were collected. Infrastructure data for a total of 192 cities were extracted and listed. The data for 191 cities were collected considering basic variables such as GDP, population city, population density by metropolitan area, integration terminals, system length, station spacing and standard fare. In the light of the collected data, it was observed that some cities lacked data in these categories, and for this reason, the number of data to be subjected to analysis was reduced to 151 cities by cleaning the data.

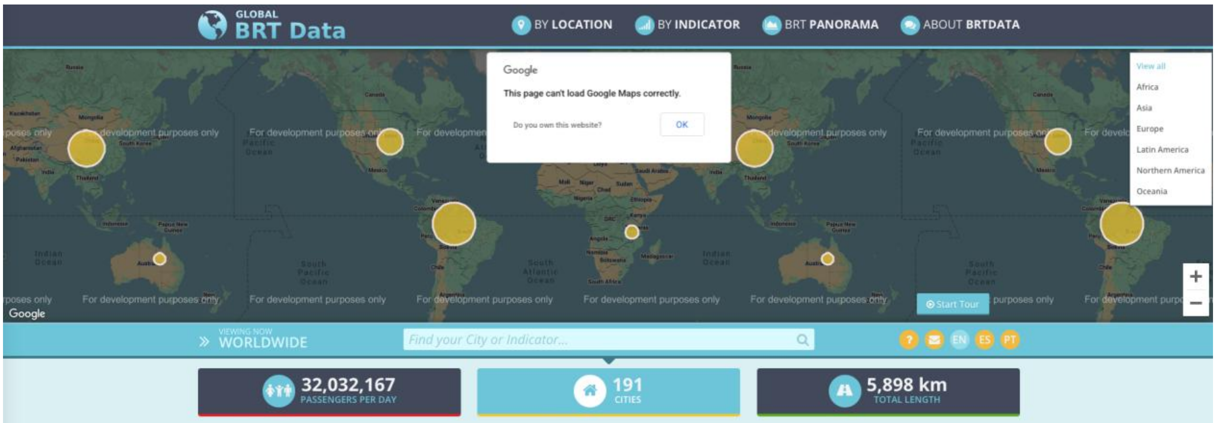

Fig. 2. The general view of www.brtdata.org

However, the data for cities in all these categories are compared using comparative analyses across continents. Since Sakarya will be the second metrobus city in Turkey (Fig. 3), the system length, station spacing and standard fare planned by the metropolitan municipality were added to this dataset and a comparison was made between 152 cities. It should be taken into account that some of the data sets we receive from BRT (www.brtdata.org) are outdated and may produce different results when compared with today's values. The integration terminals and population city categories, which were not found to contribute to the continent-specific comparisons of all these cities, were not included in the analysis. Sakarya data sets are presented in Table 1.

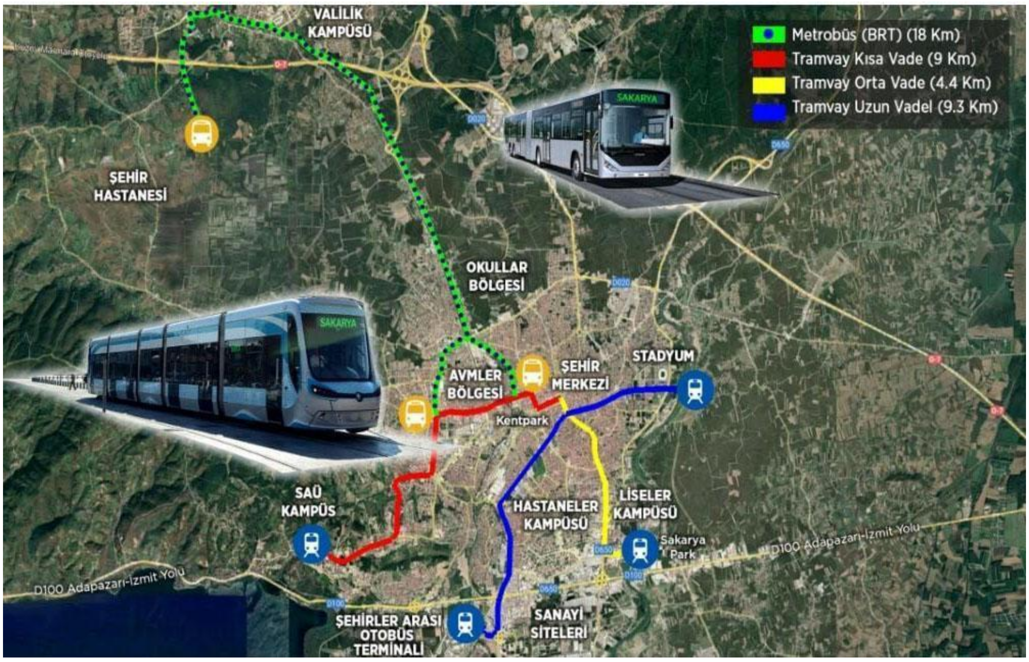

Fig. 3. The general view of www.brtdata.org

These analyses and comparisons have been tested with the current state of the data on www.brtdata. org and have enabled us to see the current status of the BRT system planned to be implemented in Sakarya with all other continents and its current position resulting from the comparisons. It was evaluated in this way that the planned system is at a level that can compete with both Europe and all other continents and that this sustainable public transportation system will come to this city.

Table 1. Sakarya city datasets

Region	Country	City	GDP per capita (US$)	Population density	Standard fare (US$)	System length (km)	Station spacing (m)
Europe	Türkiye	Sakarya	8.171	907	0,31	16	1.300

3. Results

This comparative analysis of BRT systems highlights the critical interplay between economic, demographic, and infrastructural factors. The insights provide valuable guidance for designing equitable and efficient transit systems, emphasizing the importance of context-sensitive approaches in global BRT planning.

The heatmap highlights global disparities in GDP per capita in Figure 4, with economically advanced nations (e.g., North America and Western Europe) exhibiting higher values compared to regions such as Africa and parts of Asia. Turkey's GDP per capita is positioned in the middle range, reflecting its developing economy status. These economic variations have significant implications for the development and sustainability of BRT systems, particularly in funding and affordability

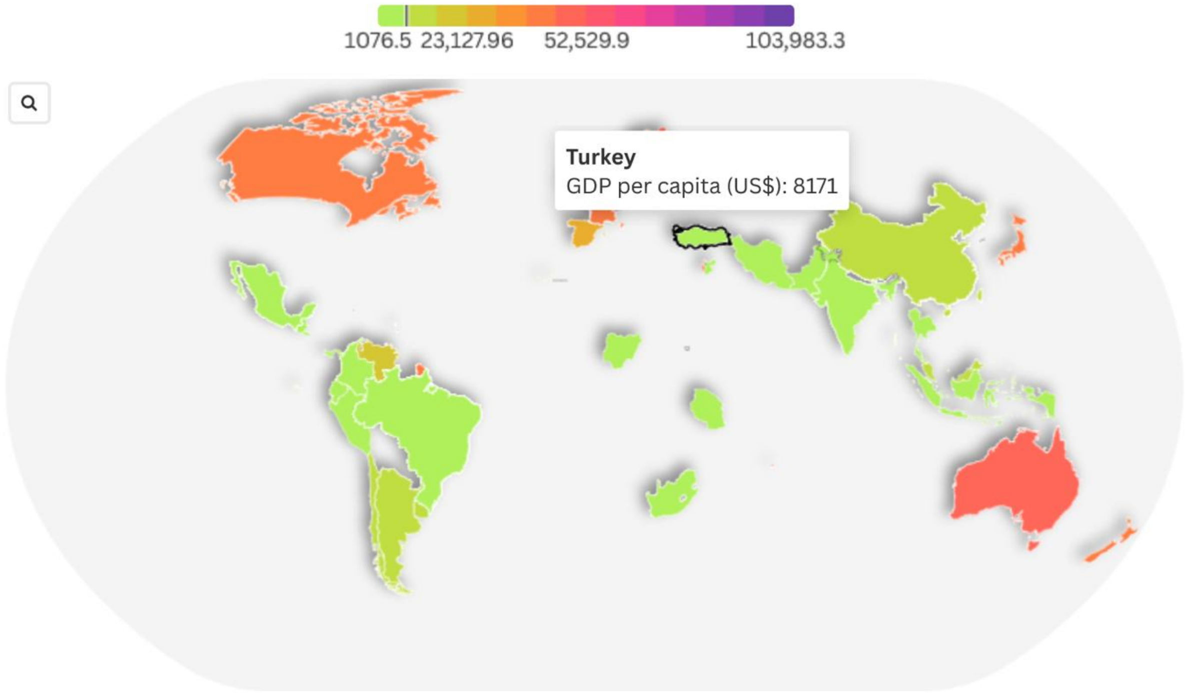

Fig. 4. The global distribution heatmap of GDP (BRTDATA, 2025)

The circular bar chart demonstrates in Figure 5 stark differences in population density across regions. Highly urbanized countries such as India and China showcase significantly higher densities, indicating greater reliance on public transport solutions like BRT systems. In contrast, lower-density regions like Australia suggest a reduced demand for such infrastructure. This underscores the necessity of tailoring BRT designs to the unique urban fabric of each region.

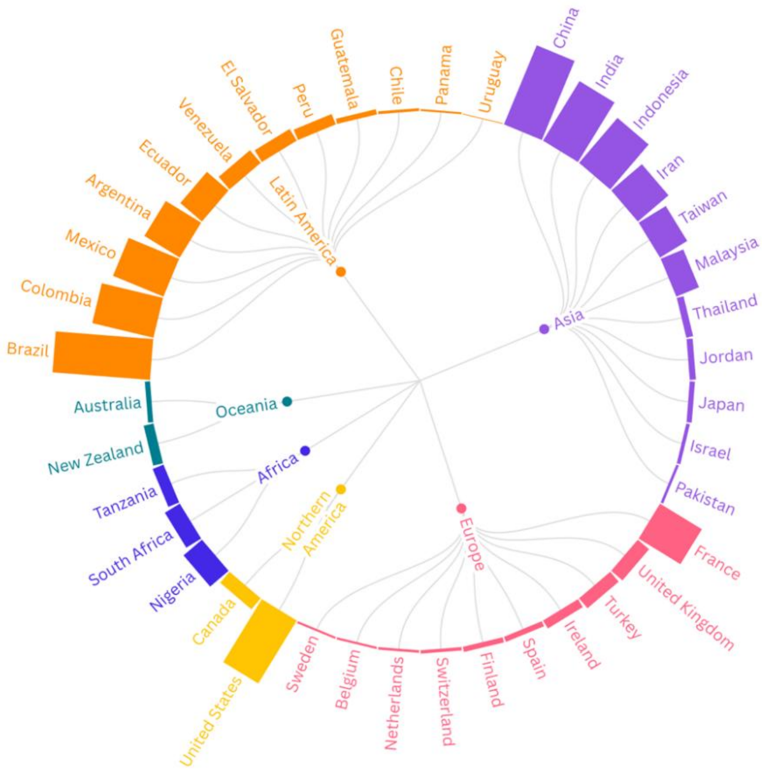

Fig. 5. The population density in metropolitan areas (BRTDATA, 2025)

The visualization of standard fare distribution in Figure 6 reveals considerable variability, with lower fares in developing regions and higher fares in developed economies. This disparity reflects not only differences in economic capacity but also the degree of subsidies provided by governments. The equitable balance between affordability and system sustainability emerges as a key consideration for policymakers.

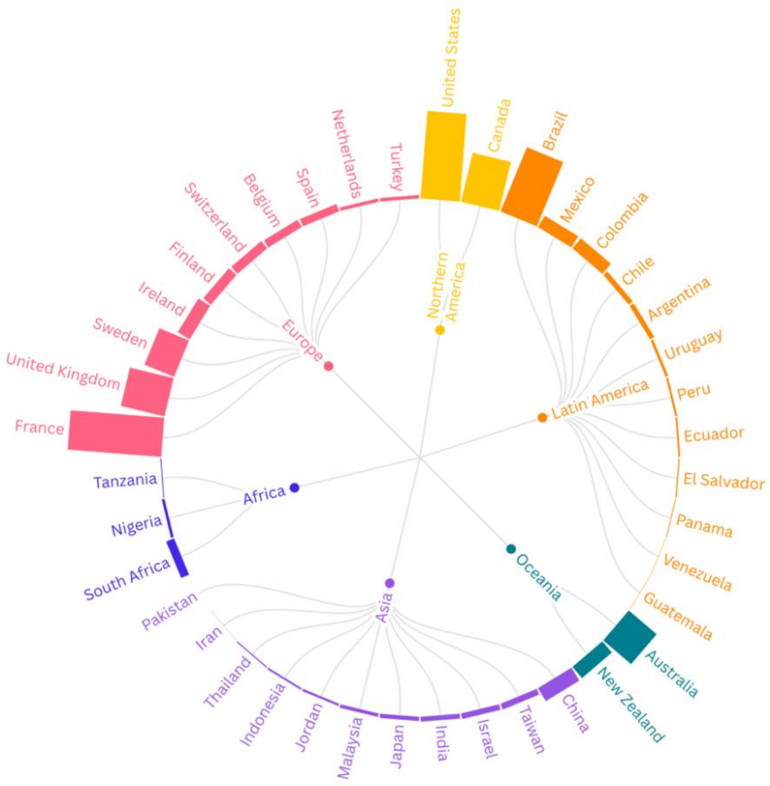

Fig. 6. The standard fare analysis (BRTDATA, 2025)

The scatter plot in Figure 7 reveals a strong correlation between GDP per capita and standard fare, with higher-income regions typically charging higher fares. Sakarya, located within a moderate GDP per capita range, demonstrates a fare structure that aligns with regional norms for affordability. This observation underscores how mid-income regions prioritize public transport affordability to encourage ridership and accessibility. However, notable outliers in the scatter plot highlight the role of subsidies and operational efficiencies in determining fares, suggesting areas for policy innovation in Sakarya's BRT development.

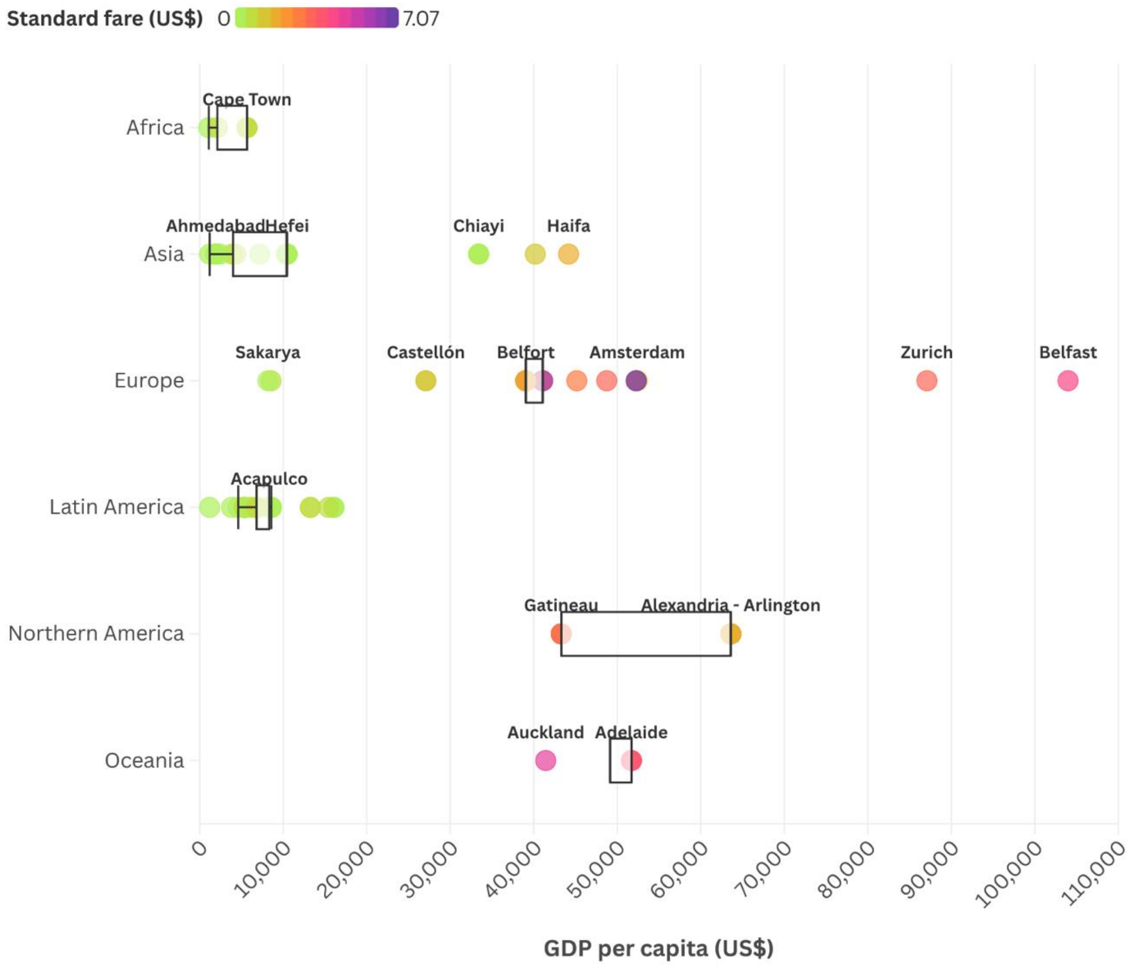

Fig. 7. The GDP per capita vs. standard fare (BRTDATA, 2025)

The relationship between station spacing and population density in Figure 8 indicates divergent strategies across regions, with developed areas favouring longer spacings to enhance travel speed and high-density regions prioritizing shorter distances for accessibility. Sakarya's station spacing aligns with regional averages for Europe, reflecting its focus on balancing commuter convenience and network efficiency. This suggests that Sakarya has adopted a scalable design suitable for its urban density, aligning with broader trends observed in similarly populated regions.

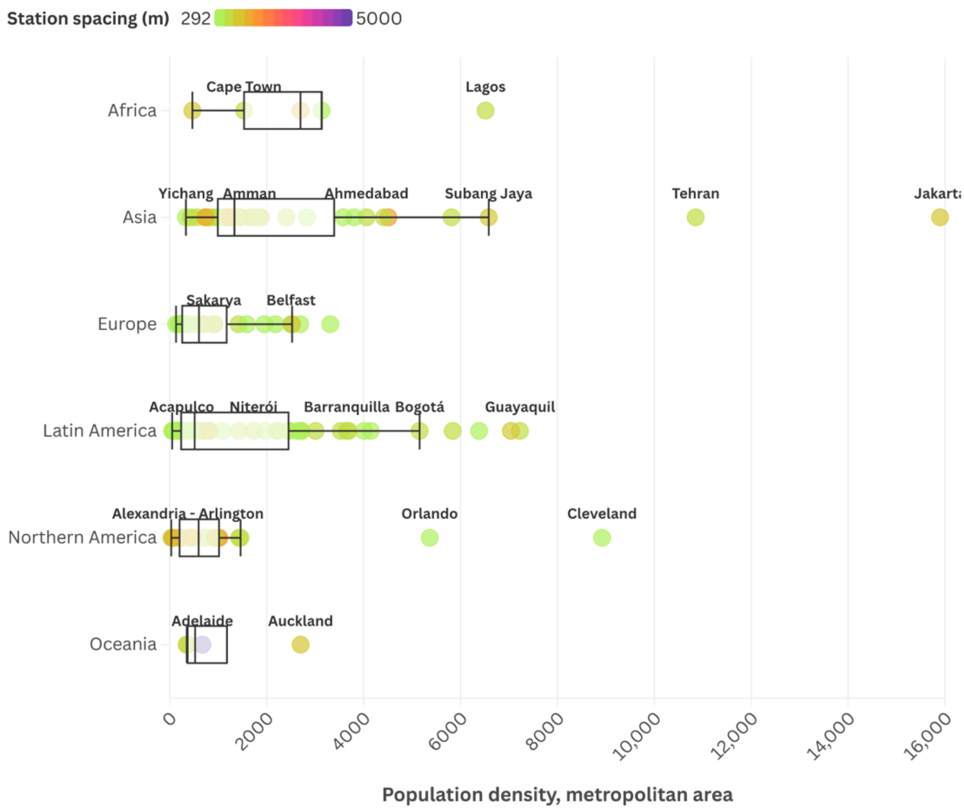

Fig. 8. The station spacing vs. population density (BRTDATA, 2025)

System length varies widely with population density, highlighting the influence of urban sprawl and transit policy on network design. Sakarya represents a developing urban area with a shorter system length, consistent with cities that emphasize efficient coverage in smaller geographic footprints. This design strategy aligns with the global trend of tailoring transit solutions to local urban characteristics, particularly in growing metropolitan areas where system expansion is incremental (Figure 9).

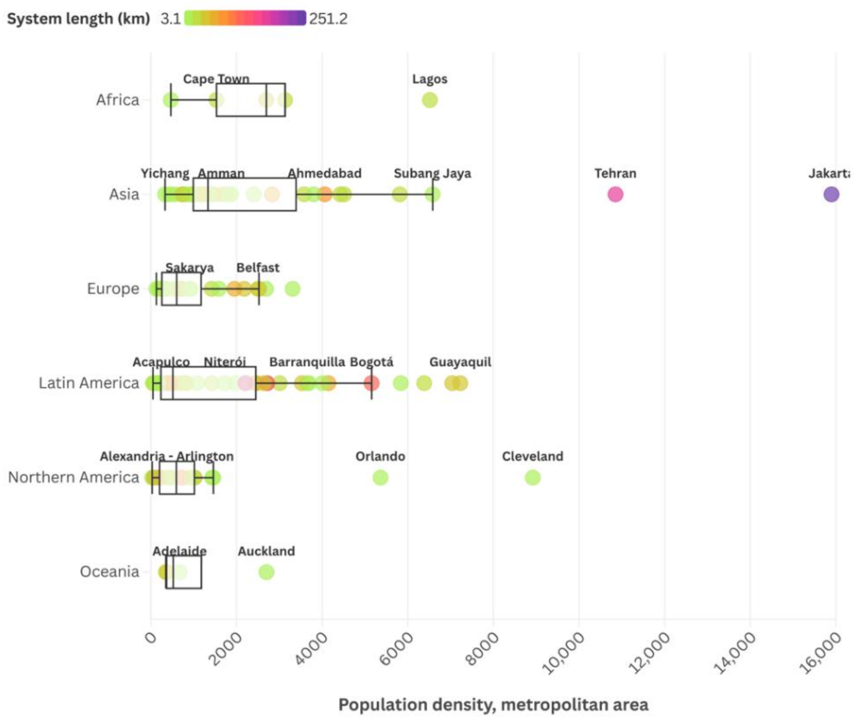

Fig. 9. The system length vs. population density (BRTDATA, 2025)

The violin plot demonstrates in Figure 10, the variability in station spacing across different system lengths. Sakarya lies within a cluster of cities that maintain moderate station spacings relative to their system length, suggesting a balanced approach to network design. By situating itself within the broader Asian and European trend of compact yet effective networks, Sakarya's BRT system appears well-suited to its urban and commuter needs, emphasizing accessibility without compromising operational speed.

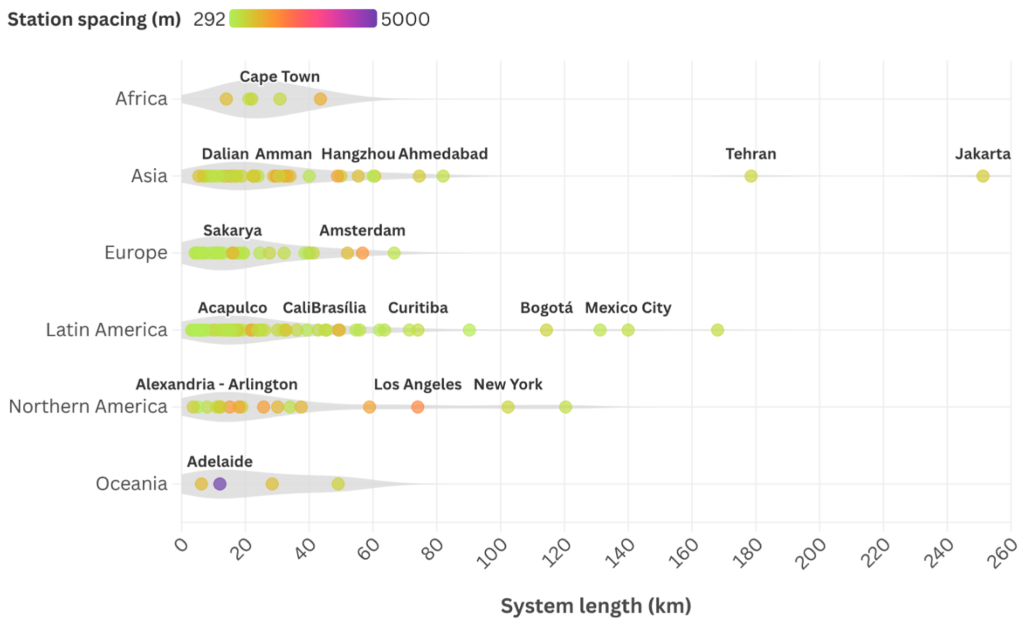

Fig. 10. The station spacing vs system length (BRTDATA, 2025)

The violin plot in Figure 11 examining the trade-off between system length and station spacing highlights distinct regional patterns. Asia and Europe exhibit standardized clustering, with Sakarya fitting neatly into the European cluster. Its positioning reflects a focus on optimizing station distribution to ensure efficient transit coverage within its compact network. This finding reinforces Sakarya's adherence to regional best practices while accommodating the unique demands of its urban landscape.

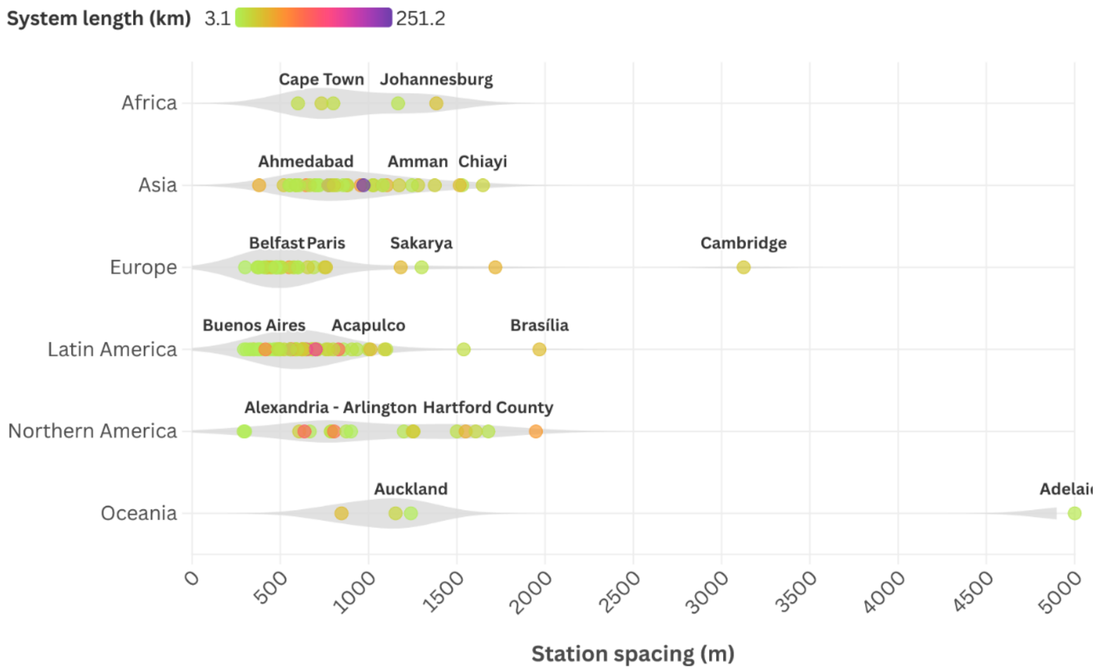

Fig. 11. The system length vs. station spacing (BRTDATA, 2025)

Incorporating Sakarya into the comparative analysis reveals that its BRT system aligns closely with global and regional patterns observed in similar economic and urban contexts. The city exhibits a balanced approach to station spacing and system length, prioritizing accessibility and efficiency in a developing urban environment. By adhering to regional norms while identifying opportunities for innovation, Sakarya's BRT system can serve as a model for scalable, context-sensitive transit solutions in mid-income, high-density areas. This analysis highlights the potential for further aligning local transit policies with global best practices to enhance system performance and sustainability.

4. Conclusions

This comparative analysis of BRT systems provides critical insights into the socioeconomic and infrastructural factors influencing transit system efficiency and accessibility across diverse geographic contexts. By benchmarking Sakarya's planned BRT system against global best practices, this study offers valuable recommendations for its development and operational optimization.

Sakarya's BRT design reflects a tailored alignment with its socioeconomic profile, particularly within the middle GDP per capita range. This ensures affordability for public transport users, a critical factor in fostering accessibility and widespread adoption. Additionally, the city's moderate station spacing and system length highlight a balanced approach that effectively integrates operational efficiency with commuter accessibility. These characteristics are consistent with regional practices observed in Asia, demonstrating Sakarya's adherence to global benchmarks and its commitment to efficient urban mobility. The study also reveals significant regional variations in BRT characteristics. Developed regions prioritize travel speed through longer station spacings, while high-density urban areas focus on shorter spacings to enhance accessibility. Sakarya's station spacing and system length align with European trends, emphasizing a compact and efficient network tailored to its urban density. Furthermore, global insights indicate that financial sustainability and fare affordability are crucial for mid-income cities. Innovative approaches, such as integrating multimodal transit options and optimizing network expansion, are essential for ensuring long-term operational efficiency and resilience.

The most important perspective emerging from this analysis is the necessity of adopting a context-sensitive approach. Sakarya must prioritize strategies that account for its unique urban density, economic constraints, and mobility needs. For example, Adapazarı, as the administrative and commercial center, experiences high daily commuting volumes, requiring efficient transit connections to reduce congestion. Serdivan, home to Sakarya University and a growing student population, demands accessible and affordable public transport solutions, particularly during peak hours. Meanwhile, Erenler, with its expanding residential areas and industrial zones, needs a well-integrated transit network to support both workers and residents. Addressing these specific dynamics involves conducting detailed assessments of local commuting patterns, spatial constraints, and demographic trends to design a sustainable and equitable transit system tailored to Sakarya's needs.

However, there are areas for improvement that could enhance Sakarya's BRT system. Integration with multimodal transit options, such as minibuses, cycling infrastructure, and pedestrian pathways, should be emphasized to ensure seamless connectivity. Investments in digital tools, such as real-time tracking and integrated ticketing systems, would significantly enhance user experience and operational efficiency. Moreover, exploring green energy solutions, such as electric or hybrid buses, could reduce environmental impacts and align with global sustainability goals. Dynamic pricing models and targeted subsidies could further improve fare equity while maintaining financial sustainability. Leveraging urban mobility data and advanced modelling tools would provide valuable insights into optimizing station placement, route design, and frequency management. Regular evaluations of system performance would allow for adaptive improvements and scalability in response to evolving urban demands.

Ultimately, Sakarya's planned BRT system demonstrates the potential to serve as a benchmark for mid-income, high-density cities seeking scalable and sustainable transit solutions. By aligning its policies with global best practices, enhancing integration with multimodal systems, and investing in sustainability and innovation, the city can position itself as a leader in urban mobility. Addressing the identified improvable aspects through a scientific, evidence-based approach will ensure long-term efficiency, equity, and resilience in its transit network.

References

BRTDATA. (2025). https://brtdata.org

Cervero, R., & Dai, D. (2014). BRT TOD: Leveraging transit-oriented development with bus rapid transit investments. *Transport Policy*, *36*, 127–138. https://doi.org/10.1016/j.tranpol.2014.08.001

Cervero, R., & Kang, C. D. (2011). Bus rapid transit impacts on land uses and land values in Seoul, Korea. *Transport Policy*, *18*(1), 102–116. https://doi.org/10.1016/j.tranpol.2010.06.005

Deng, T., & Nelson, J. D. (2011). Recent Developments in Bus Rapid Transit: A Review of the Literature. *Transport Reviews*, *31*(1), 69–96. https://doi.org/10.1080/01441647.2010.492455

Ferbrache, F. (2019). The value of bus rapid transit in urban spaces. In F. Ferbrache (Ed.), *Developing Bus Rapid Transit*. Edward Elgar Publishing. https://doi.org/10.4337/9781788110914.00005

Halimergün, Y., Özden, A., Adahi Şahin, S. N., & Kocaman, H. (2024). Will new tram lines enhance the connectivity and walkability? A case study of Sakarya. *Sustainable Social Development*, *2*(5), 2886. https://doi.org/10.54517/ssd.v2i5.2886

ITDP. (2024). *The BRT Standard 2024*. Institute for Transportation and Development Policy. https://www.itdp.org/publication/the-brt-standard

Merkert, R., Mulley, C., & Hakim, M. M. (2017). Determinants of bus rapid transit (BRT) system revenue and effectiveness – A global benchmarking exercise. *Transportation Research Part A: Policy and Practice*, *106*, 75–88. https://doi.org/10.1016/j.tra.2017.09.010

Prestes, O. M., Ultramari, C., & Caetano, F. D. (2022). Public transport innovation and transfer of BRT ideas: Curitiba, Brazil as a reference model. *Case Studies on Transport Policy*, *10*(1), 700–709. https://doi.org/10.1016/j.cstp.2022.01.031

Su, H. (2024). Comparison and Integration of BRT and Railway Development. *Highlights in Science, Engineering and Technology*, *83*, 217–224. https://doi.org/10.54097/m41bwy05

4th International Civil Engineering & Architecture Conference
17-19 May 2025, Trabzon, Türkiye

Renovating transportation infrastructure in emerging economies: Transforming systems for a sustainable future

Ilgin Gokasar*[1], Ali E. Karaismailoglu[1]

[1] Bogazici University, Department of Civil Engineering, 34342, Istanbul, Turkiye

Abstract. Both industrialized and developing nations have realized in recent years that there are important indicators that infrastructure needs to be updated, especially in urban areas where the need for strong infrastructure is much greater than in less populated areas. At the same time, there are many environmental problems facing the planet, and one of the most urgent ones is global climate change. To address the underlying causes of climate change, almost every country has responded by committing to international accords aimed at modernizing and enhancing infrastructure with eco-friendly solutions. The transportation industry and its infrastructure are a major cause of this problem. In order to build a more resilient and environmentally friendly future, this article looks at the best infrastructure renovation options for the transportation sector in emerging nations that are in line with sustainable development objectives.

Keywords: Sustainability; Transportation infrastructure; Renovation; Emerging economies

1. Introduction

The foundation of human mobility, economic competitiveness, and urban functionality is transportation infrastructure. Emerging countries are battling an unparalleled confluence of environmental deterioration, urban population growth, and the need for mobility in the twenty-first century (World Bank, 2021). Urbanization increases inequality, pollution, and traffic while also putting a burden on the infrastructure that already exists. Older roads, overworked buses, and congested streets are signs of more serious systemic issues in cities throughout Asia, Africa, and Latin America (United Nations Human Settlements Programme, 2020). These challenges are compounded by rising emissions, extreme weather events, and unsustainable fossil fuel dependence (International Energy Agency, 2023).

Amid this context, the transition to sustainable transportation systems has become an international imperative. The United Nations Sustainable Development Goals, especially Goal 11 on sustainable cities and Goal 13 on climate action, frame transportation not just as a logistical concern but as a lever for environmental and social transformation (United Nations, 2015). One of the most viable solutions emerging from global best practices is the widespread deployment of mass rapid transit systems, particularly metro networks and urban rail lines, which have proven to reduce urban emissions, improve commuter safety, and provide equitable access to economic centers (Litman, 2020).

In particular, metro systems provide long-term resilience against climate threats and energy shocks. Metros may transport hundreds of thousands of people every day with little energy intensity and land use, in contrast to road-based alternatives that frequently promote private vehicle ownership or dispersed informal transit (Guerra & Cervero, 2011). A move away from carbon-intensive growth and toward an inclusive, dependable, and environmentally sustainable urbanization vision is reflected in their incorporation into national infrastructure plans (International Renewable Energy Agency, 2022).

Additionally, the growing interdependence of economic systems across continents has elevated the role of urban transportation networks in ensuring the fluidity of trade, employment access, and service delivery. Transport bottlenecks in megacities directly impact GDP by increasing operational costs, hindering logistics, and causing labor inefficiencies (World Bank, 2021). The consequences of inaction are not just economic but also social and environmental, as congestion exacerbates greenhouse gas emissions and reduces productivity (Intergovernmental Panel on Climate Change, 2023).

Therefore, policymakers in emerging economies need to view transportation as a complex socio-technical system with environmental implications rather than just an engineering problem. A new planning paradigm focused on mass public transportation is required due to the pressing need for decarbonization, energy resilience,

* Corresponding author, E-mail: ilgin.gokasar@bogazici.edu.tr

https://doi.org/10.31462/icearc2025_ce_tra_262

and equal access. In this regard, metro systems are a fundamental resource. They are essential to any national sustainability strategy because of their capacity to operate on renewable energy, integrate with land use planning, and lower per capita emissions (United Nations Economic and Social Commission for Asia and the Pacific, 2021).

2. Methodology

This research employs a multidisciplinary approach that combines policy evaluation, energy systems analysis, and literature review. Publications from the Intergovernmental Panel on Climate Change, the World Bank, the United Nations, and the International Energy Agency are cited. Regional insights are provided by case studies from Kenya, India, and Turkiye. In addition to examining sectoral integration with national energy planning and urban development objectives, comparative analysis is employed to identify common difficulties and best practices.

3. Global transportation energy landscape

The use of fossil fuels continues to dominate the global transportation industry. Oil-based energy sources are essential to shipping, aviation, and road transportation. Nearly 77% of all transport energy was used for road transportation as of 2022, with aviation and maritime shipping accounting for a large portion of emissions (International Energy Agency, 2022). Nearly 25% of global CO_2 emissions are caused by this reliance on fossil fuels, which has direct effects on the climate (Intergovernmental Panel on Climate Change, 2023).

Vehicle production systems, port terminals, and gasoline distribution networks are important infrastructure elements. Without major financial investment and policy reform, these systems' inertia makes transformations challenging. However, by adopting sustainable transport models early on, rising economies can also avoid the expensive effects of stranded infrastructure.

4. The case for energy system transformation in transport

Among the most ecological and energy-efficient modes of urban transportation are electrified mass transit systems, especially light rail and metros. These systems provide a zero-emission solution for urban transportation demands when they are fueled by renewable electricity (International Energy Agency, 2022). The utilization of solar and wind energy to power whole transit lines is demonstrated by international examples like the Delhi Metro and Santiago Metro (Delhi Metro Rail Corporation, 2021).

Compared to diesel or compressed natural gas systems, electrified mass transit systems offer long-term operational cost savings in addition to lowering direct emissions. Furthermore, metro systems that run on renewable energy offer a dual climate answer by reducing transportation-related emissions and increasing grid flexibility at the same time. Hybrid strategies that combine modular hydrogen fuel cells, solar photovoltaic microgrids, and battery storage are becoming popular decentralized options for areas where grid dependability is still an issue (Asian Development Bank, 2022).

5. Transportation infrastructure in emerging economies

Existing transportation networks are under tremendous strain as a result of the exponential urbanization occurring in emerging economies. Over the last three decades, the population of cities like Lagos, Jakarta, and Dhaka has more than doubled, but there hasn't been a commensurate increase in transportation infrastructure (World Bank, 2021). The ensuing imbalance between capacity and demand shows up as heavy traffic, protracted commutes, and high transportation expenses. These areas frequently have disjointed and inadequately linked public transportation networks that mostly rely on unofficial minibuses or antiquated diesel bus fleets. These systems lack fare unification, uniform ticketing systems, and coordinated route planning in addition to having scheduling and reliability issues. Consequently, metro infrastructure—despite its efficiency and scalability—remains underfunded, largely due to high initial capital costs, political short-termism, and limited technical capacity at municipal levels.

Rapid motorization is a characteristic that exacerbates this difficulty. Car ownership is rising in emerging economies due to urban development and increased affluence. The use of private vehicles is expected to increase in the absence of robust public transportation options, particularly in middle-class urban areas. The Intergovernmental Panel on Climate Change (2023) estimates that if current trends continue unchecked, transportation-related emissions could triple by 2050. In addition to its effects on the climate, this trend presents serious concerns to public health, air quality, and urban livability, especially in megacities like Delhi, Cairo, and Manila that already have high pollution levels.

Reform initiatives are made more difficult by the institutional environment. In many cities, several entities with conflicting agendas and overlapping powers share responsibility for transportation planning, funding, and operations. This institutional fragmentation leads to delays, redundancy, and suboptimal project outcomes. Furthermore, ineffective budgetary allocations, a lack of procurement openness, and susceptibility to political cycles are frequently the outcomes of inadequate governance structures (United Nations Economic and Social Commission for Asia and the Pacific, 2021).

To achieve meaningful progress, emerging economies must pursue integrated urban planning, wherein transportation is coordinated with housing, land use, and environmental strategies. Successful examples can be found in Curitiba (Brazil) and Ahmedabad (India), where transit-oriented development (TOD) has helped synchronize metro expansion with high-density zoning and walkable neighborhoods. Moreover, sustainable financing mechanisms such as land value capture, congestion pricing, and public-private partnerships can provide stable funding streams for metro investments while promoting equitable cost distribution.

Equally crucial is the emphasis on inclusive design. Vulnerable populations—particularly women, elderly citizens, and persons with disabilities—face disproportionate barriers to mobility. Features such as level boarding, tactile guidance, well-lit stations, and gender-segregated compartments significantly enhance access and safety (United Nations, 2015). When combined with fare affordability programs, these measures can dramatically improve labor force participation and access to essential services like education and healthcare. In this way, well-designed metro systems function not only as infrastructure but as enablers of social equity, economic opportunity, and environmental sustainability.

6. Comparative global case studies

India's Smart Cities Mission advocates for solar-powered electrified metro systems. The metropolises of Bengaluru, Pune, and Delhi have implemented energy recovery and rooftop solar systems (International Renewable Energy Agency, 2022).

The integrated urban rail architecture of Turkey is demonstrated by the Marmaray, Başkentray, and Gaziray projects, which provide dependable substitutes for driving and lower emissions (Republic of Türkiye Ministry of Transport and Infrastructure, 2022).

Kenya's mobility initiatives tackle energy and equality issues by combining solar mini-grids, fare digitization, and indigenous technical capabilities (World Bank, 2021). Rail may service informal settlements, as demonstrated by Medellín's cable metro and hillside access (United Nations Human Settlements Programme, 2020).

7. Conclusion

Expanding electrified metro systems with renewable energy infrastructure must be a strategic priority for rising countries in order to address both the pressing demands of growing urbanization and climate mitigation goals. Metro systems have the twin benefits of high-capacity urban transit and much reduced per capita emissions, in contrast to private vehicle-based options. They offer a scalable and sustainable route to decarbonization when driven by clean electricity, such as that produced by solar, wind, or hydropower. Additionally, urban areas reduce traffic, enhance air quality, and open doors for fair access to services, jobs, and education. In light of the Intergovernmental Panel on Climate Change's (2023) warnings about rising emissions trends, electrifying public transit becomes imperative rather than optional. Additionally, governments can lessen urban sprawl and encourage compact, efficient communities by planning rail corridors in accordance with land use plans and urban density.

But more than just the deployment of infrastructure is required to make this vision a reality. It necessitates long-term institutional transformation, coordinated multi-level governance, and creative financing techniques that can raise both public and private funds. Governments must support regulatory frameworks that facilitate the integration of sustainable energy, promote transit-oriented development, and expedite project approval procedures. By bridging the silos between energy, transportation, and urban development, national urban transport agencies and metropolitan transit authorities can overcome institutional fragmentation, which is frequently a significant obstacle. Meanwhile, the funds required for long-term metro expansion can be unlocked through sustainable financing options including land value capture, green bonds, and performance-based public-private partnerships. In the end, making the switch to sustainable, electrified transportation systems is not only possible, but essential to creating resilient, inclusive, and climate-aligned urban futures.

References

Asian Development Bank. (2022). Financing Sustainable Transport in Asia.

Delhi Metro Rail Corporation. (2021). Annual Sustainability Report.

Food and Agriculture Organization of the United Nations. (2020). The State of Bioenergy Development in Brazil and Southeast Asia.

Guerra, E., & Cervero, R. (2011). Cost of a ride: The effects of densities on fixed-guideway transit ridership and costs. *Journal of the American Planning Association, 77*(3), 267–290.

Hydrogen Europe. (2023). Hydrogen in Rail Applications.

Intergovernmental Panel on Climate Change. (2023). Sixth Assessment Report – Mitigation of Climate Change.

International Energy Agency. (2022). Transport and Environment Outlook 2022.

International Energy Agency. (2023). Energy Efficiency 2023 Report.

International Renewable Energy Agency. (2022). Electrification of Public Transport: Global Trends.

Litman, T. (2020). Evaluating Transportation Land Use Impacts. Victoria Transport Policy Institute.

Republic of Türkiye Ministry of Transport and Infrastructure. (2022). Istanbul Urban Rail Development Strategy.

Sustainable Mobility for All Initiative. (2020). Global Mobility Report 2020.
United Nations. (2015). Transforming Our World: The 2030 Agenda for Sustainable Development.
United Nations Economic and Social Commission for Asia and the Pacific. (2021). Smart Urban Mobility in Asia-Pacific.
United Nations Human Settlements Programme. (2020). World Cities Report.
World Bank. (2021). Electric Mobility and Urban Transport in Emerging Economies.

Usability of the T-Flex in bitumen modification and its effects on physical properties

Erman Çavdar*[1], Aytuğ Kumandaş[2], Neslihan Şahan[3], Ersoy Kabadayı[4], Mahir Kumantaş[1], Şeref Oruç[1]

[1] Karadeniz Technical University, Department of Civil Engineering, 61080 Trabzon, Türkiye
[2] Ondokuz Mayıs University, Department of Civil Engineering, 55139 Samsun, Türkiye
[3] Kırşehir Ahi Evran University, Civil Engineering Department, 40100 Kırşehir, Türkiye
[4] Giresun University, Keşap Vocational School, Department of Construction Technology, 28900 Giresun, Türkiye

Abstract. With the increasing population and traffic volume, the demand for high-performance pavement materials has become necessary. This necessity has encouraged researchers to explore novel additives and materials to enhance bitumen performance. Although various additives have been investigated over the years, recent studies have increasingly focused on sustainable, environmentally friendly, and cost-effective solutions for bitumen modification. Consequently, research on incorporating waste and sustainable materials in bitumen modification has been steadily expanding. This study investigates the applicability of T-Flex, a product of the Tayraş Refinery, for bitumen modification and its effects on physical properties. Accordingly, modified bitumen samples were prepared by adding T-Flex at 5% and 10% by weight of the bitumen, followed by penetration, softening point and rotational viscosity tests. The experimental results revealed that T-Flex addition increased the penetration values and decreased the softening point and penetration index, indicating a softening effect and increased temperature susceptibility of the bitumen. Furthermore, T-Flex significantly reduced the rotational viscosity, improving the workability of the bitumen at mixing and compaction temperatures. These findings suggest that T-Flex can effectively enhance the flexibility and workability of bitumen. However, its use should be optimized depending on application requirements, considering the mechanical performance.

Keywords: Bitumen; Bitumen modification; T-Flex; Penetration; Softening point; Rotational viscosity

1. Introduction

In recent years, increasing environmental awareness has highlighted the importance of utilizing waste materials across various industries. The construction sector has become one of the prominent fields where the use of waste materials has attracted attention. Today, besides being used as building materials, different types of waste materials are also being explored for bitumen modification (Fode et al., 2025; Hu et al., 2025; Minhajuddin & Saha, 2025; Yegane et al., 2025). Researchers have investigated the use of waste plastics (Deb et al., 2025; Javadi et al., 2024), waste rubbers (Blab et al., 2024; Obukhova et al., 2024), other waste polymers (Rashid et al., 2024), waste oils (Çavdar et al., 2024; Kumandaş et al., 2022; Kumandaş et al., 2024), and many other waste materials to modify bitumen, the binder in asphalt pavements.

Waste oils encompass a broad range of materials, including waste cooking oils derived from vegetable oils such as soybean, corn, and cottonseed oils, as well as waste engine oils generated by industries such as chemical manufacturing, production, and automotive sectors. Studies have generally shown that waste oils can effectively improve the workability of bitumen, enhance its low-temperature cracking resistance, increase fatigue resistance, and positively affect aging resistance (Kumandaş et al., 2022; Xu et al., 2023).

Each year, approximately 40 million tons of waste engine oil are produced worldwide (Guo et al., 2025). About 70–80% of this amount is recycled into products like lubricants through centrifugation and distillation processes (Guo et al., 2025). However, 20–30% of waste engine oil cannot be recycled and is known as Re-refined Engine Oil Bottoms (REOB) (Guo et al., 2025). In other words, REOB refers to the residue from refining processes after the removal of metal particles and light compounds, and it has a wide range of sources (Xu et al., 2025).

Although the use of REOB in bitumen modification dates back almost thirty years, its effects on bituminous binder properties have been examined in only a limited number of studies (Karki & Zhou, 2019). Furthermore, the findings reported in the literature are inconsistent, making it difficult to draw a definitive conclusion regarding the

* Corresponding author, E-mail: ermancavdar@ktu.edu.tr

https://doi.org/10.31462/icearc2025_ce_tra_388

influence of REOB on bitumen. While one study (Li et al., 2023) reported that REOB improved the high-temperature performance of bitumen, other studies (Karki & Zhou, 2019; Xu et al., 2021; You et al., 2018) observed the opposite effect. Similarly, one study (You et al., 2018) found that REOB increased the low-temperature cracking susceptibility of bitumen, whereas other studies (Fried & and Castorena, 2024; Karki & Zhou, 2019) indicated that although REOB softened bitumen, its impact on low-temperature performance was not significant. Additionally, while one study (Xu et al., 2021) reported that REOB improved the fatigue life of bitumen, another study (Li et al., 2017) suggested that the addition of small amounts of REOB enhanced the fatigue resistance of bitumen, whereas higher amounts significantly reduced it.

In light of the above, there is a need to further investigate the effects of REOB on bitumen properties. This study aims to examine the impact of REOB on bitumen through experimental methods. For this purpose, a type of REOB known as T-Flex, supplied by Tayraş Company, was incorporated into 50/70 penetration grade bitumen at 5% and 10% by weight to produce modified binders. Subsequently, the properties of both the unmodified and modified bitumens were evaluated through penetration, softening point, and rotational viscosity (RV) tests.

2. Materials and methods

2.1. Materials

2.1.1. Bitumen

The base bitumen used in this study was supplied by the 10th Regional Directorate of the General Directorate of Highways of the Republic of Türkiye and belongs to the 50/70 penetration grade. This grade was selected due to its widespread use across the country and its frequent reference in previous academic studies.

2.1.2. T-Flex

The T-Flex product, supplied by the company Tayraş to the Transportation Laboratory of Karadeniz Technical University (KTU), is recommended in the product information sheet as a bitumen modifier for use in asphalt and roofing applications. Considering its production process, the material is believed to be similar to waste oil products referred to in the literature as "Re-refined Engine Oil Bottom (REOB)." Several properties of the material were identified through tests conducted at the Tayraş refinery and were included in the product information sheet. These properties are presented in Table 1.

Table 1. Properties of T-Flex

Property	Test Method	Value
Appearance	ASTM D4126	Dark Coloured Viscous Liquid
Viscosity @50 °C, cSt	ASTM D4052	<10000
Density @15 °C, kg/lt	ASTM D7042	0.93
Flash Point, °C	ASTM D3278	Min. 200
Pour Point, °C	ASTM D97	-3
Water Content, %	ASTM D95	Max. 0.2
Sulfur Content, %	ICP-OES	1.0

2.1.3. Preparation of T-Flex modified bitumen

In order to produce modified bitumen, certain process parameters must be defined in advance. These include the type of mixer, mixing speed, temperature, duration, and additive dosage. In the literature, studies on the production of REOB-modified bitumen commonly involve manual mixing at approximately 150 °C for a duration of 5 to 15 minutes (Karki & Zhou, 2019; Omari et al., 2016). However, due to the limitations of manual mixing methods, our previous experimental experience has led us to adopt more controlled processing conditions in our own studies (Çavdar et al., 2024; Kumandaş et al., 2022; Kumandaş et al., 2024). The parameters applied in this study are summarized in Table 2.

Table 2. Preparation parameters for T-Flex modified bitumen

Parameter	Value
Type of Mixer	Four-blade mechanical mixer
Mixing Speed	1500 rpm
Mixing Temperature	135±2 °C
Mixing Duration	30 minutes
Additive Dosage	5% and 10%

The liquefied bitumen was transferred into 600 mL beakers and placed on a temperature-controlled hot plate. The temperature of the plate was adjusted to maintain the bitumen at 135±2 °C. Once this target temperature was reached, T-Flex was added at dosages of 5% and 10% by weight. The mixing process was carried out at a constant speed of 1500 rpm for 30 minutes. At the end of this period, the T-Flex modified bitumen samples were prepared and made ready for further analysis. To ensure systematic identification during the experimental process, a sample coding scheme was employed, as presented in Table 3.

Table 3. Description and coding of the tested samples.

Description	Sample Details	Code
Base bitumen	Base Bitumen (Pen 50/70)	B
Control bitumen (base bitumen mixed without T-Flex addition)	Base Bitumen (Pen 50/70) mixed at 135 °C and 1500 rpm, for 30 minutes	CB
5% T-Flex modified bitumen	Base Bitumen (Pen 50/70) + 5% T-Flex: mixed at 135 °C and 1500 rpm, for 30 minutes	T5
10% T-Flex modified bitumen	Base Bitumen (Pen 50/70) + 10% T-Flex: mixed at 135 °C and 1500 rpm, for 30 minutes	T10

2.2. Methods

2.2.1. Penetration test

The penetration test is one of the fundamental methods used to assess the consistency, or in other words, the hardness of bitumen. In this study, the procedure was conducted in accordance with the TS EN 1426 (2025) standard. During the test, a standard needle of specified dimensions is allowed to penetrate the bitumen sample for 5 seconds under a load of 100 grams at a temperature of 25 °C. The depth of penetration, measured in tenths of a millimeter (dmm), represents the penetration value of the sample. This value is widely employed in the classification of bituminous binders, where a higher penetration value indicates a softer material, whereas a lower value reflects a harder consistency.

The needle on the device is carefully aligned with the surface of the bitumen sample and then fixed in position. Subsequently, the needle is released, initiating a 5-second penetration period. The depth of penetration is recorded at the end of this duration. For each sample, three individual measurements are performed, and the average of these values is taken as the final test result. The variation between the individual measurements must remain within the limits specified by the relevant standard.

2.2.2. Softening point test

The softening point test is a method used to evaluate the temperature-dependent viscosity behavior of bitumen. In this study, the procedures were carried out in accordance with the TS EN 1427 (2015) standard. The principle of the test is based on recording the temperature at which a metal ball, placed on a bitumen specimen, travels a specified distance under conditions of steadily increasing temperature. The temperature at which this occurs is defined as the softening point of the bitumen.

In the application of the test, the bitumen sample is first heated until it becomes fluid, then poured into metal rings whose inner surfaces have been coated with a release agent (e.g., petroleum jelly). Once the sample reaches room temperature, any excess bitumen on the edges of the rings is trimmed using a heated spatula. The prepared rings are then placed into the test apparatus, and steel balls are positioned on top of the bitumen samples.

During the test, the apparatus is immersed in a 600 mL beaker filled with distilled water, and the heating rate is adjusted to 5 °C per minute. As the temperature rises, the steel balls gradually push the bitumen downward. The temperature at which each ball reaches the bottom plate is recorded. The test is considered valid only if the difference between the two recorded temperatures does not exceed 1 °C. If the difference exceeds this limit, the test must be repeated. When valid results are obtained, the average of the two temperatures is calculated and reported as the softening point of the bitumen sample.

2.2.3. Penetration index (*PI*)

The penetration index (*PI*) is calculated to assess the temperature susceptibility of bitumen. This parameter is derived using the softening point and the penetration value measured at 25 °C, according to the Equation (1):

$$PI=\frac{1952\text{-}500\times \log Pen25\text{ -}20\times SP}{50\times \log Pen25\text{ -}SP\text{-}120} \tag{1}$$

In this formula, *SP* represents the softening point in °C, while *Pen25* denotes the penetration value measured at 25 °C, expressed in tenths of a millimeter (dmm). As the *PI* value increases, the bitumen is considered to exhibit lower sensitivity to temperature fluctuations, indicating enhanced resistance to rutting at high temperatures and cracking at low temperatures.

2.2.4. Rotational viscosity test

The rotational viscosity of the base and modified bitumen samples was determined using a Brookfield rotational viscometer, in accordance with the TS EN 13302 (2018) standard. The purpose of this test was to evaluate the flow behavior of the samples at elevated temperatures, which are critical for mixing and compaction processes during asphalt pavement construction.

Approximately 8-10 grams of each bitumen sample was carefully poured into aluminum sample chambers. Prior to testing, the samples were heated in an oven at the target test temperatures to ensure thermal equilibrium without causing thermal degradation. The measurements were conducted at five different temperatures: 120 °C, 135 °C, 150 °C, 165 °C, and 180 °C. A spindle (No.21) was used for the measurements, operating at a constant rotational speed of 20 rpm. The viscosity values (in centipoise, cP) were recorded once the system achieved stable torque readings, indicating steady-state conditions. The obtained viscosity data were used to assess the effect of T-Flex addition on the workability of the bitumen samples, especially at typical asphalt mixing and compaction temperatures.

3. Results and discussion

3.1. Penetration test results

Fig. 1 illustrates the penetration values of the base bitumen (B), control bitumen (CB), and T-Flex modified bitumens (T5 and T10). It is observed that the B exhibits a penetration value of 59.8 dmm. After mixing under the specified conditions (135 °C, 1500 rpm, 30 minutes), the CB shows a slight reduction in penetration, suggesting that the mixing process alone leads to a minor hardening of the bitumen.

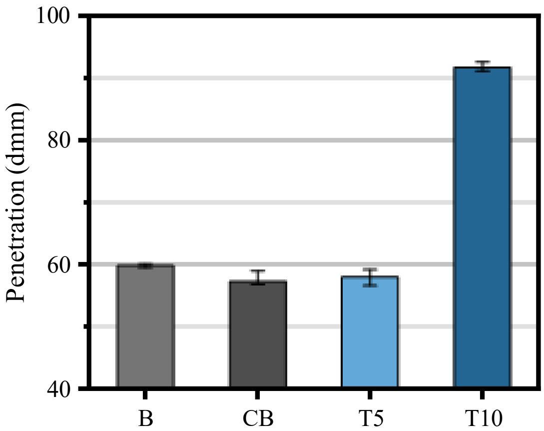

Fig. 1. Penetration test results.

Upon the addition of 5% T-Flex (T5), a marginal increase in penetration is observed compared to the control bitumen, although the value remains close to that of the base bitumen. This indicates that low levels of T-Flex addition have a limited softening effect on bitumen. However, when the T-Flex content is increased to 10% (T10), the penetration value significantly rises, reaching 91.7 dmm. This substantial increase demonstrates that higher T-Flex dosages effectively soften the bitumen, resulting in a material with lower consistency and higher deformability under loading.

3.2. Softening point test results

Fig. 2 presents the softening point values of the B, CB, T5, and T10. The base bitumen exhibits a softening point of 50.3 °C. Following the mixing process (135 °C, 1500 rpm, 30 minutes), the CB shows a slight increase in softening point compared to the base bitumen, indicating a minor hardening effect attributed to mixing.

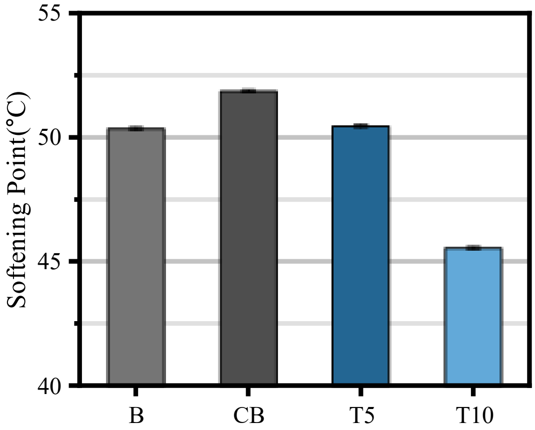

Fig. 2. Softening point test results.

Upon the addition of 5% T-Flex (T5), a slight decrease in the softening point is observed relative to the control sample, suggesting that low levels of T-Flex have a limited softening influence on the bitumen. Nevertheless, the softening point remains relatively close to that of the base bitumen. A significant reduction in the softening point is noted when 10% T-Flex (T10) is incorporated, with the value dropping to 45.5 °C. This substantial decrease confirms that higher T-Flex content significantly lowers the softening point of bitumen, reflecting a considerable reduction in the material's thermal stability at elevated temperatures.

3.3. Penetration index results

Fig. 3 displays the penetration index (PI) values of the B, CB, T5, and T10. The PI is an important indicator reflecting the temperature susceptibility of bituminous binders; lower PI values generally denote higher sensitivity to temperature changes.

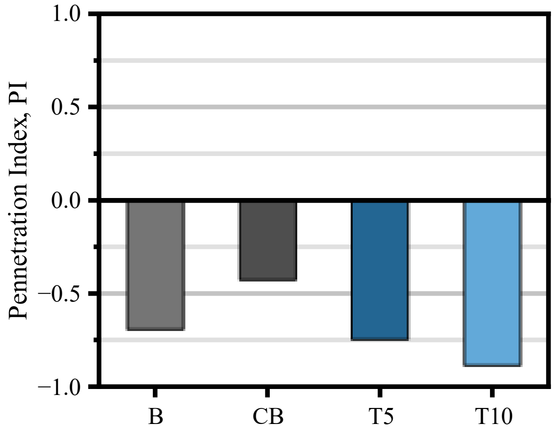

Fig. 3. Penetration indexes.

The B shows a PI value of -0.7, indicating moderate temperature sensitivity. The CB, produced by mixing without T-Flex addition, exhibits a slightly higher PI compared to the base bitumen, suggesting a marginal improvement in temperature resistance due to the mixing process.

In contrast, with the addition of 5% T-Flex (T5), the PI value decreases, indicating that T-Flex addition slightly increases the temperature susceptibility of the bitumen. This trend becomes even more pronounced with the addition of 10% T-Flex (T10), where the PI value drops to -0.88. Such a decrease implies that higher T-Flex content significantly worsens the thermal stability of the bitumen, making it more sensitive to temperature variations.

3.4. Rotational viscosity test results

Fig. 4 shows the rotational viscosity values of the base bitumen (B), control bitumen (CB), and T-Flex modified bitumens (T5 and T10) measured at different temperatures ranging from 120 °C to 180 °C. As expected, the viscosity of all samples decreases with increasing temperature, reflecting the typical thermorheological behavior of bituminous binders.

At 120 °C, the control bitumen (CB) exhibits a slightly higher viscosity compared to the base bitumen (B), indicating that the mixing process without T-Flex addition induces a minor increase in stiffness. However, upon T-Flex modification, especially at 10% addition (T10), a considerable reduction in viscosity is observed at 120 °C compared to both the base and control samples. The T5 sample also shows a viscosity decrease but to a lesser extent than T10.

This viscosity-lowering trend persists across all tested temperatures. At higher temperatures (150 °C, 165 °C, and 180 °C), the viscosity differences among the samples become less pronounced; nonetheless, T10 consistently maintains the lowest viscosity values.

The observed reduction in rotational viscosity due to T-Flex addition, particularly at lower temperatures, confirms the softening effect of T-Flex. Lower viscosities at mixing and compaction temperatures (typically 135–165 °C) are generally beneficial for workability during asphalt production and paving operations. However, excessively low viscosities may raise concerns about the rutting resistance of the final asphalt mixture.

In summary, the addition of T-Flex significantly improves the workability of bitumen by reducing its viscosity, with the magnitude of reduction increasing with higher T-Flex content.

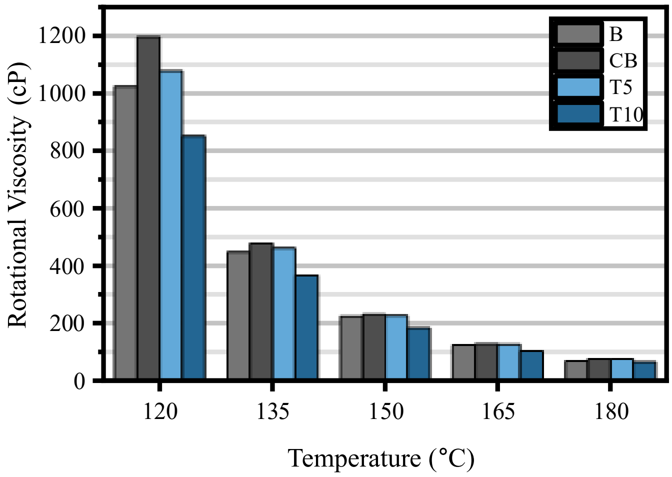

Fig. 4. Rotational viscosity test results.

The experimental findings revealed that the addition of T-Flex, a REOB-derived material, significantly altered the physical and rheological properties of bitumen. The comparison among B, CB, T5, and T10 samples showed that the mixing process alone (CB) resulted in a slight hardening of the bitumen, evidenced by minor changes in penetration and softening point values. However, the incorporation of T-Flex at 5% and 10% (T5 and T10) led to increased penetration values, reduced softening points, and lower penetration indexes, indicating a softening effect and increased temperature susceptibility.

Furthermore, rotational viscosity tests demonstrated a substantial reduction in viscosity with T-Flex addition, particularly at higher temperatures, enhancing the workability of the bitumen during mixing and compaction operations. Among the modified samples, T10 exhibited the most pronounced changes across all measured properties. Overall, the results suggest that REOB-based additives like T-Flex can effectively improve bitumen flexibility and workability but require careful optimization to balance thermal stability and mechanical performance for practical applications.

4. Conclusions

This study investigated the effects of Recycled Engine Oil Bottoms (REOB), commercially known as T-Flex, on the physical and rheological properties of 50/70 penetration grade bitumen. Modified binders were prepared by incorporating T-Flex at 5% and 10% by weight, and their performance was evaluated through penetration, softening point, penetration index (PI), and rotational viscosity tests.

The main findings of the study are as follows:

- The addition of T-Flex increased the penetration values of bitumen, especially at higher contents, indicating a softening effect.
- The softening point of the bitumen decreased with increasing T-Flex content, suggesting reduced thermal stability at elevated temperatures.

- Penetration index (PI) values decreased with T-Flex addition, highlighting an increase in temperature susceptibility, particularly at 10% T-Flex content.
- Rotational viscosity values significantly dropped across all tested temperatures with T-Flex modification, improving the workability of bitumen during mixing and compaction.

Although the use of T-Flex improved the flexibility and workability of bitumen, it also led to increased temperature susceptibility and reduced high-temperature performance. Future research should focus on optimizing the dosage of T-Flex to achieve a balance between workability, flexibility, and thermal stability, as well as investigating the long-term aging behavior and field performance of T-Flex-modified bitumens under various climatic and traffic conditions.

Acknowledgments

The authors would like to sincerely thank Mr. Hakan İMRE for his valuable support in supplying the T-Flex material used in this study. His contribution was essential for the successful completion of the experimental work.

References

Blab, R., Ahmad, J., Shaffie, E., Sidek, N., Mirwald, J., Eberhardsteiner, L., & Hofko, B. (2024). Performance of Crumb Rubber Tire-Modified Bitumen for Malaysian Climate Regions. *Materials (Basel)*, *17*(23).

Çavdar, E., Kumandaş, A., Şahan, N., Kabadayı, E., & Oruç, Ş. (2024). Investigation of Rheological and Physical Properties of SBS and WCO Composite Modified Bitumen. *Turkish Journal of Civil Engineering*, *35*(6).

Deb, S., Kumar, P., & Saboo, N. (2025). Use of Recycled Waste Plastic for Wet Modification of Bitumen. *Journal of Materials in Civil Engineering*, *37*(1), 04024468.

Fode, T. A., Jande, Y. A. C., Kivevele, T., & Rahbar, N. (2025). Effect of waste water bottle and treated sisal fibers on the durability and mechanical properties of concrete. *Scientific Reports*, *15*(1), 7945.

Fried, A., & and Castorena, C. (2024). Understanding recycling agent modification mechanisms through rheological and compositional impacts. *International Journal of Pavement Engineering*, *25*(1), 2444506.

Guo, D., Yang, S., Xu, M., Li, X., Sun, X., Wang, T., An, Y., & Huang, S. (2025). Preparation and performance study of PPA-REOB composite modified bitumen. *Construction and Building Materials*, *468*, 140361.

Hu, X., Chen, X., Yu, J., Cheng, G., Yuan, Y., & Zhang, L. (2025). Physical Properties and Rheological Characteristics of Cigarette Butt-Modified Asphalt Binders. *Coatings*, *15*(2), 170.

Javadi, N. H. S., Hajimohammadi, A., Heydari, S., Chung Ng, J. J. K., Kypreos, J. E., & Khalili, N. (2024). Investigating the applicability of storage stability test for waste plastic modified bitumen: Morphological analyses. *Construction and Building Materials*, *441*, 137451.

Karki, P., & Zhou, F. (2019). Impact of Re-Refined Engine Oil Bottoms on Asphalt Binder Properties. *Journal of Transportation Engineering, Part B: Pavements*, *145*(4), 04019033.

Kumandaş, A., Çavdar, E., Oruç, Ş., Pancar, E. B., & Kök, B. V. (2022). Effect of WCO addition on high and low-temperature performance of RET modified bitumen. *Construction and Building Materials*, *323*, 126561.

Kumandaş, A., Çavdar, E., Şahan, N., Kök, B. V., Pancar, E. B., & Oruç, Ş. (2024). Investigation of Rutting and Low Temperature Cracking Behavior of Reactive Ethylene Terpolymer and Waste Cooking Oil Modified Bitumen. *Turkish Journal of Civil Engineering*, *35*(4), 1-26.

Li, X., Gibson, N., Andriescu, A., & S. Arnold, T. (2017). Performance evaluation of REOB-modified asphalt binders and mixtures. *Road Materials and Pavement Design*, *18*(sup1), 128-153.

Li, X., Guo, D., Xu, M., Guo, C., & Wang, D. (2023). REOB/SBS Composite-Modified Bitumen Preparation and Modification Mechanism Analysis. *Buildings*, *13*(7), 1601

Minhajuddin, A., & Saha, A. (2025). Performance evaluation of geopolymer concrete with waste granite powder as a sustainable alternative to sand. *Journal of Materials Science: Materials in Engineering*, *20*(1), 20.

Obukhova, S., Budkina, A., Korolev, E., & Gladkikh, V. (2024). Impacts of Waste Rubber Products on the Structure and Properties of Modified Asphalt Binder: Part I—Crumb Rubber. *Materials*, *17*(19), 4685.

Omari, I., Aggarwal, V., & Hesp, S. (2016). Investigation of two Warm Mix Asphalt additives. *International Journal of Pavement Research and Technology*, *9*(2), 83-88.

Rashid, S., Mudavath, R., Chandra, H., Shekhar, I., Kumar, P., Srivastava, M., & Kumar, K. (2024). A Review on Virgin or Waste Polymers in Bitumen Modification for Ageing and Rejuvenation. *Chemical Engineering & Technology*, *47*(4), 624-637.

TS EN 1426. (2025). Bitumens and bituminous binders - Determination of needle penetration. In. Ankara: Türk Standardları Enstitüsü.

TS EN 1427. (2015). Bitumen and bituminous binders - Determination of the softening point - Ring and Ball method. In. Ankara: Türk Standardları Enstitüsü.

TS EN 13302. (2018). Bitumen and bituminous binders - Determination of dynamic viscosity of bituminous binder using a rotating spindle apparatus. In. Ankara: Türk Standardları Enstitüsü.

Xu, J., Pei, J., Cai, J., Liu, T., & Wen, Y. (2021). Performance improvement and aging property of oil/SBS modified asphalt. *Construction and Building Materials*, *300*, 123735.

Xu, J., Zhang, B., Gao, J., Yao, Y., Gao, J., & Yu, D. (2025). Long-Term Performance of Oil Recycled Asphalt Binders Based on Fatigue, Moisture Damage, and Oxidation Aging. *Journal of Materials in Civil Engineering*, *37*(5), 04025081.

Xu, N., Wang, H., Wang, H., Kazemi, M., & Fini, E. (2023). Research progress on resource utilization of waste cooking oil in asphalt materials: A state-of-the-art review. *Journal of Cleaner Production*, *385*, 135427.

Yegane, M., Katanalp, B. Y., & Ahmedzade, P. (2025). Effects of using biochar materials obtained from cherry and sour cherry wastes on bitumen modification. *Construction and Building Materials*, *470*, 140609.

You, T., Shi, Y., Mohammad, L. N., & Cooper, S. B. (2018). Laboratory Performance of Asphalt Mixtures Containing Re-Refined Engine Oil Bottoms Modified Asphalt Binders. *Transportation Research Record*, *2672*(28), 88-95.

4th International Civil Engineering & Architecture Conference
17-19 May 2025, Trabzon, Türkiye

Sustainable concrete pavements using pb-zn-cu mining waste and recycled tire steel fibers

Mehmet T. Seferoğlu*[1]

[1] Gümüşhane University, Department of Civil Engineering, 29100 Gümüşhane, Türkiye

Abstract. This study explores the combined use of lead-zinc-copper (Pb-Zn-Cu) mining waste and recycled steel fibers (SF) from waste vehicle tires in concrete pavement mixtures to enhance sustainability and mechanical performance. Traditional concrete pavement samples were prepared using three aggregate sizes (0–5 mm, 5–12 mm, 12–36 mm), with the 0–5 mm portion subsequently replaced by mining waste. Additionally, SFs were incorporated at 0.2%, 0.4%, and 0.6% by volume. Physical tests indicated that porosity and water absorption remained largely unaffected, though slight reductions in porosity were noted with 0.4% and 0.6% SF additions. A strong correlation between porosity and water absorption was observed, particularly at early curing stages. Mechanically, the inclusion of SFs improved compressive and splitting tensile strengths, with the highest compressive strength increase (18.2%) recorded at 0.6% SF after 28 days. The use of mining waste alone decreased strength, whereas the addition of 0.2% SF enhanced the modulus of elasticity by 25% at 7 days and 60% at 28 days. Higher SF contents reduced elasticity, and variations in Poisson's ratio indicated changes in microstructural deformation. The results suggest that combining mine waste with low levels of recycled SF (especially 0.2%) enhances concrete's mechanical and elastic properties without compromising its physical durability. This approach supports the reuse of industrial waste materials and offers an environmentally sustainable solution for concrete pavement applications.

Keywords: Concrete pavement; Mining waste; Recycled vehicle tires; Mechanical properties; Sustainability.

1. Introduction

In recent years, concrete pavement has been widely preferred due to its durability and long service life. However, the conventional materials used in its production pose significant challenges in terms of environmental sustainability. For this reason, the incorporation of waste materials into concrete production has gained importance both to reduce environmental impacts and to promote the efficient use of natural resources. In line with the goals of minimizing environmental impacts and enhancing sustainability in the construction sector, the reuse of waste materials is becoming increasingly critical. The utilization of recyclable industrial and manufacturing wastes in construction materials such as concrete not only reduces the consumption of natural resources but also offers both economic and environmental benefits in terms of waste management.

The uncontrolled disposal of mining wastes into the environment can lead to severe environmental issues such as heavy metal leaching, soil contamination, and water pollution. Furthermore, the disposal of these wastes typically involves high-cost processes. In this context, the use of wastes derived from lead, zinc, and copper mining as alternative binders or aggregates in concrete pavements presents significant potential for sustainable infrastructure solutions. However, the direct utilization of mining wastes in concrete pavement applications has been explored in only a limited number of studies.

Studies on the use of metallic wastes such as lead-zinc-copper (Pb-Zn-Cu) residues in concrete production have shown that these materials can positively affect the mechanical properties of concrete. For example, the partial replacement of conventional materials with up to 50% Pb-Zn slag has led to improvements in both durability and radiological performance. Additionally, these types of wastes have been found to enhance the sulfate resistance of concrete (Kanneboina et al., 2023).

Çullu (2018) reported that replacing limestone aggregate with Pb-Zn mining waste in concrete mixtures—at substitution rates of up to 75%—resulted in reduced porosity and water absorption, increased density, and consequently, improved mechanical performance. Öztürk (2018) incorporated granulated Zn ore slag into concrete by classifying it into two particle size ranges: 5–15 mm and 0–5 mm. Compressive strength tests conducted at 7, 14, and 28 days of curing revealed that the 28-day compressive strength was comparable to that of the reference

* Corresponding author, E-mail: mtseferoglu@gmail.com

https://doi.org/10.31462/icearc2025_ce_tra_397

concrete, while the resulting concrete was lighter in weight. These findings indicate that Zn ore slag can serve as a viable aggregate replacement for producing lightweight concrete without compromising compressive strength. El Machi et al. (2024) investigated the inclusion of Au (gold), Cu, and Fe (iron) ore wastes in concrete mixtures at rates ranging from 10% to 30%. They reported that a 20% substitution with Cu waste resulted in a 12% increase in compressive strength, whereas a 30% replacement with Fe waste led to a 9% decrease in strength.

Nandi et al. (2022) evaluated jarosite, a byproduct of Zn production, for its potential to reduce cement consumption in road construction. Their study concluded that jarosite enhances concrete strength and provides environmental benefits. Similarly, Amrani et al. (2022) used Pb and Zn mining wastes as aggregate replacements in low-traffic pavement applications. A 25% inclusion of these wastes led to an 18% reduction in cost, a 22% decrease in CO_2 emissions, and surface strength that met standard requirements.

Wu et al. (2024) conducted an experimental study on the preparation of cementitious materials using activated Pb-Zn wastes. The study evaluated both the usability and environmental impact of these wastes in cement-based materials. According to the results of the Toxicity Characteristic Leaching Procedure (TCLP) applied to the samples, the leaching of Pb remained well below the Chinese Hazardous Waste Standard limit of 5.0 mg/L, indicating that these materials can be used in an environmentally safe manner. Similarly, Vahdat et al. (2024) demonstrated that Pb-Zn mining wastes can be used as an alternative to aggregates in mortar mixtures, with minimal environmental impact. The findings suggest that the use of such wastes contributes to both environmental sustainability and effective waste management.

In studies specifically focusing on Zn slag, Kotan et al. (2023) reported that replacing cement with 5%, 7.5%, and 10% of Zn slag powder in self-compacting concrete (SCC) mixtures resulted in improved fresh and hardened concrete properties, particularly at the 5% replacement level. The compressive strength was found to be comparable to that of the control mixture. The study confirmed that Zn slag powder enhanced the workability of fresh SCC and achieved compressive strengths equivalent to those of conventional concretes at 28 days.

Today, industrially manufactured steel fibers (SF) are widely used to improve the strength and durability of reinforced concrete structures. These fibers enhance the tensile strain capacity and ductility of concrete, while also preventing crack propagation and positively affecting post-cracking behavior (Su et al., 2023). Although the use of SF increases tensile strength and toughness, some reduction in workability has been observed (Samindi et al., 2019). Recent research has highlighted that steel fibers recovered from waste vehicle tires (RF) can serve as an environmentally friendly and cost-effective alternative to conventional SF.

Şimşek et al. (2021) observed that the addition of fibers reduced the workability and air content of fresh concrete. In hardened concrete, particularly with the inclusion of 80/60 type SF at a dosage of 0.10%, the best performance was achieved in terms of compressive strength, flexural strength, and abrasion resistance. Although increasing the fiber dosage led to improvements in certain mechanical properties, exceeding the optimum level resulted in significant losses in workability. Therefore, the study emphasized the critical importance of selecting the appropriate fiber shape and content to optimize concrete performance.

Waris et al. (2022) reported that a combination of 0.2% SF and 2% rubber fiber resulted in higher compressive and flexural strength compared to concrete containing only rubber fibers. Awal et al. (2018) stated that while strength improved with increasing fiber content, workability decreased. Centonze et al. (2012) emphasized that concrete reinforced with recycled SFs exhibited post-cracking energy absorption and residual strength performance comparable to that of concrete reinforced with industrial SFs. Zeybek et al. (2022) reported that incorporating 1% recycled SFs from waste vehicle tires led to a 25% increase in flexural strength and a 20% increase in tensile strength.

Amin et al. (2023) reported that the addition of 0.75% waste SF increased compressive strength by 13%, flexural strength by 18%, and tensile strength by 20%. Şengül (2016) indicated that the use of 0.75% recycled SF increased compressive strength from 39 MPa to 42 MPa (7.7%) and flexural strength from 5.2 MPa to 6.6 MPa (26.9%). Furthermore, it was found that these fibers significantly enhanced ductility while maintaining post-cracking strength. Domski et al. (2017) reported that waste SFs exhibited 10–20% lower tensile strength performance compared to engineered fibers but showed similar levels of flexural strength. They emphasized that with proper mix design, waste fibers could be effectively utilized. Altun et al. (2007) observed increases in both compressive and tensile strengths with increasing SF content, with a 3% fiber addition resulting in an 18% increase in compressive strength and a 40% increase in tensile strength. However, they also noted that higher fiber dosages negatively impacted workability. Ayhan et al. (2024) used waste SFs as a replacement for aggregates in concrete at volumes of 0.4% and 0.8%. Experimental studies included the production of cylindrical samples (150×300 mm) and beam samples (150×150×600 mm), with tests on compressive strength, flexural strength, and ultrasonic pulse velocity (UPV). The results indicated that the addition of waste vehicle tire steel had no significant effect on compressive strength but improved flexural strength. Moreover, there was a parallel relationship between concrete compressive strength and UPV.

These studies suggest that the use of waste SF in concrete mixtures, with appropriate proportions and distribution, can lead to significant improvements in mechanical properties while also providing an environmentally sustainable contribution. However, there are limited studies in the existing literature on the combined use of Pb-Zn-Cu waste and waste tire SF in concrete mixtures.

In this study, traditional concrete mortar samples will first be prepared. Three different aggregate particle sizes will be used in these samples: 0-5 mm, 5-12 mm, and 12-25 mm. These aggregates will be included in the mixture in specific proportions to examine their effect on the mechanical properties of concrete. This mixture will be considered as the control sample. In the next phase, the 0-5 mm filler portion of the concrete mix will be replaced with Pb-Cu-Zn waste materials. These waste materials will be used in place of traditional filler materials and will be incorporated into the concrete mix. Finally, SF from waste vehicle tires will be added to the concrete mix at volumetric ratios of 2%, 4%, and 6% to prepare samples. The effects of adding these SF on the mechanical behavior of concrete will be investigated. This approach aims to contribute to environmental sustainability while improving the performance of the concrete pavement.

2. Materials and methods

2.1. Materials

2.1.1. Concrete

In this study, CEM I 42.5 R type Portland cement was used. Aggregates with particle sizes of 0-5 mm, 5-12 mm, and 12-25 mm were utilized. The aggregates were sourced from basalt aggregates obtained from a quarry. The concrete mixtures were prepared according to the TS802 standard. Since waste steel fibers were used in the study, the largest aggregate size was ensured to be 22.40 mm according to the TS 10514 (mix proportions and production of fiber-reinforced concrete) standard based on the selected fiber content. For mixtures with a maximum aggregate size of 22.4 mm, the TS 10514 standard recommends a water/cement ratio between 0.35 and 0.50. In this study, the water/cement ratio was set at 0.5 to ensure good mechanical strength and adequate workability of the mixtures.

Plasticizer additive, modified polycarboxylate (PCE) is polymer based and has the appearance of light brown liquid. PCE is a liquid with a density of 1.10+0.02 kg/l and is a highly water-reducing/super plasticizing admixture developed for the ready-mixed concrete and precast industry, where early and final high strength and durability are required, to achieve excellent surface appearance.

2.1.2. Pb-Zn-Cu waste materials

Gümüştaş Pb-Zn-Cu mineralisation located in Süleymaniye Quarter of Gümüşhane province is located in 1/25.000-scale H42-b2 map, and the area consists of Palaeozoic quartz porphyry, Permocarboniferous Gümüşhane Granite (Çoğulu, 1970), Jurassic-Liassic volcanotortulae series (Kandemir, 2004), Lower Cretaceous (Dogger-Malm) massive and stratified limestones (Pelin, 1977) and Upper Cretaceous phyllites and andesitic tuffs, Eocene andesite and basalt lavas and pyroclasts (Tokel, 1972) are surfaced. Mineralisation is observed in the form of veins within the Jurassic-Liassic volcanotortulae series and Lower Cretaceous limestones. The 0-5 mm size range of the waste material used in this study consists mostly of pyrite-bearing limestone and volcanotorture rocks. The maximum aggregate diameter of 30 mm was taken from the mine site and brought to the laboratory and then this material was sieved through a 5 mm sieve and the part between 0-5 mm was used as fine aggregate in the study (Fig. 1).

Fig. 1. The Pb-Zn-Cu mine wastes

2.1.3. Steel fibre from recycled tire

The SFs used in this study were obtained through a mechanical shredding process of waste tires. The diameters of the fibers were measured using an electronic caliper. Since the lengths of the SFs vary due to the mechanical fragmentation process, the lengths are presented as measurement ranges. The aspect ratio of the fibers was calculated by dividing their lengths by their diameters. The images of the SFs are shown in Fig. 1, and physical properties are provided in Table 1. As can be seen in Fig. 2, the SFs have a curled structure and vary in length and diameter.

Fig. 2. The SFs

Table 1. The physical properties of the SFs

	Diameter, mm	Length, mm	Aspect ratio	By weight ratio, %
SF	0,10-0,15	15-35	110-180	40-60

2.1.4. Concrete mix and preparation of test specimens

As the reference sample, a standard concrete mix composed entirely of basalt aggregates, with three different particle size ranges of 0-5 mm, 5-12 mm, and 12-25 mm, was prepared. This control sample was labeled as 'N.' In the control mix, the natural aggregates with a 0-5 mm particle size were replaced with Pb-Zn-Cu mine wastes of the same size. This mix was labeled as "W." By substituting only, the filler-sized aggregates, approximately 45% of the total mix weight was made up of recycled materials.

The recycled SFs were added to the fresh concrete mix to determine their applicability as reinforcement in concrete. Recycled SFs obtained from waste vehicle tires were added to the W mix at volumetric rates of 0.2%, 0.4%, and 0.6%, and the samples were labeled as W-2, W-4 and W-6, respectively. Thus, recycled-based concrete mixes containing both mine wastes and steel fiber additions were obtained.

For each mix, a total of 12 cylindrical samples, six each for 7-day and 28-day curing periods, were prepared. In total, 60 cylindrical concrete samples were produced (Fig. 3) for the N, W, W-2, W-4 and W-6 mixes, and cured in water until the day of testing.

Fig. 3. Concrete samples used in the study

Table 2. Mix design of recycled SF reinforced concrete

Mixture code	Cement, kg/m^3	Water, L/m^3	Aggregate, kg/m^3	SP, kg/m^3	Pb-Zn-Cu wastes (0-5 mm), kg/m^3	SF, %	SF, kg/m^3
N					-	-	-
W						-	-
W-2	350	175	1,744.03	5.25	784.81	2	15.7
W-4						4	31.4
W-6						6	47.1

For each mix, three of the six cylindrical samples underwent non-destructive physical property tests, such as porosity and void ratio. Following these tests, splitting tensile strength tests were performed on the same samples. The remaining three samples were subjected to compressive strength tests, thereby determining mechanical properties such as compressive strength, elastic modulus, and Poisson's ratio. All experimental data obtained were evaluated by calculating the average of the three samples for each test group. The mix proportion of recycled SF reinforced concrete is shown in Table 2.

2.2. Test methods

2.2.1. Physical characteristics

Three samples were taken from each concrete group made with different fiber ratios, and their physical properties were evaluated according to TS EN 12390-7 standard. First, the samples were soaked in water at 23±2 °C until they were fully saturated. Then, the samples were removed from the water, and procedures were carried out to clean the free water on their surfaces and determine their mass in the air. In the next step, the mass of the samples in water was measured using an Archimedean balance. Finally, the samples were dried in an oven at 105°C and left to cool to room temperature. During this process, the mass of the samples in their oven-dried state was determined.

2.2.2. Compressive strength tests

The compressive strength of the concrete samples cured for 7 and 28 days was tested according to BS EN 12390-3. The compressive strengths of both control and fiber-reinforced samples were determined using a uniaxial compressive strength test conducted on standard cylindrical specimens in accordance with BS EN 12390-3. The cylinder samples were prepared with dimensions of 102 × 204 mm. The tests were performed with a loading rate of 0.22 MPa/s, and the average compressive strength was determined by testing three samples for each group.

The determination of the modulus of elasticity and Poisson's ratio was carried out according to ASTM C39. The axial and lateral unit deformations of the specimens were recorded using extensometers on a gauge measuring the change in length and diameter. Poisson's ratio was determined by the ratio of lateral unit deformation to axial unit deformation.

2.2.3. Splitting tensile strength tests

According to ASTM C496 Standard, the splitting tensile strength was tested for each type of sample at 7 and 28 curing days to investigate the effect of fibers on the tensile strength of concrete. The tests were conducted on cylindrical samples of the same size as those used in the compression test, using a material testing system and strain control method. The loading rate was kept constant at 0.04 – 0.06 $N/mm^2.s$, and the peak load was recorded during the test. The splitting tensile strength was calculated using Equation (1), and the tensile strength of each type of concrete was determined by averaging the results of three samples. The splitting tensile strength was calculated as follows:

$$T = \frac{2P}{\pi DL} \tag{1}$$

Where, T = Splitting tensile strength, MPa; P = Peak load at failure point, N; D = Diameter of the cylinder, mm; L = Length of the cylinder, mm.

3. Results and discussion

3.1. Physical properties

When the porosity (v%) and water absorption (m%) results of the 7 and 28-day samples given in Fig. 4 and Fig. 5 are examined, it is observed that the use of mine waste and the addition of waste tyre wire did not cause a significant change in porosity and water absorption values compared to the control sample (N) at both curing times. In 7-day samples, porosity values in W group series showed a slight increase compared to N sample, while no significant difference was detected in water absorption rates. Similarly, although small fluctuations were observed in porosity values in 28-day samples, water absorption values followed a fairly constant course. In particular, the addition of 0.4% and 0.6% waste tyre wire (W-4 and W-6) did not affect the porosity and water absorption performance negatively in both 7 and 28 day samples, and even showed a slight decrease in porosity. These results indicate that the use of mine waste and waste tyre wire does not have a negative effect on the permeability properties of the concrete and microstructural improvements continue at later curing times.

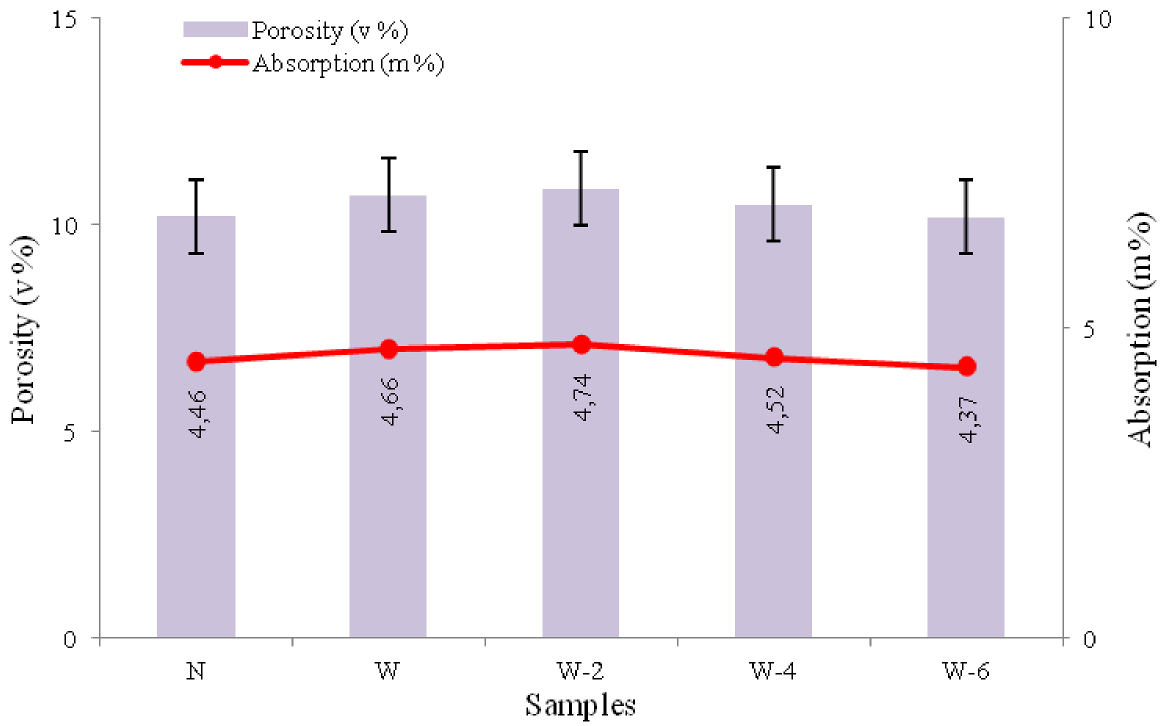

Fig. 4. Physical properties of fibre reinforced concrete with witness and mine waste admixture (7 days)

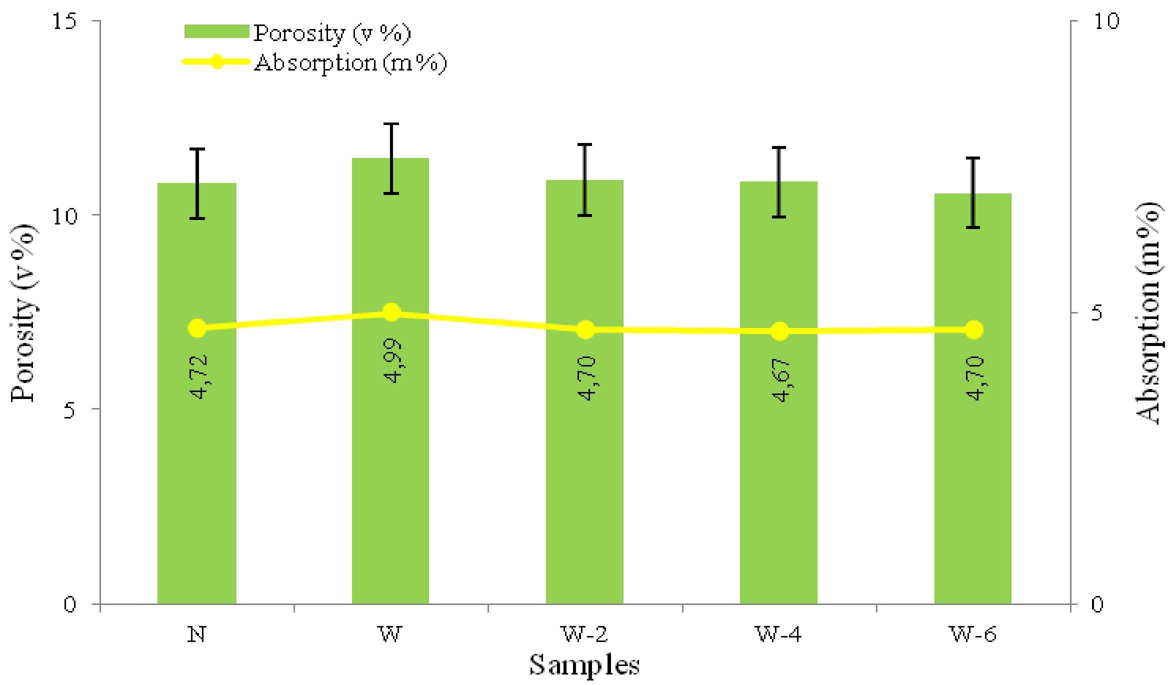

Fig. 5. Physical properties of fibre reinforced concrete with witness and mine waste admixture (28 days)

When the relationship between water absorption (m%) and porosity (v%) given in Fig. 6 and Fig. 7 is analysed, it is seen that there is a positive correlation for both curing times. According to the regression equation (y = 2.0064x

+ 1.3755) determined in the correlation graph of 7-day samples (Fig. 6), the R^2 value is 0.954 and it is understood that there is a very strong linear relationship between water absorption and porosity. This high correlation coefficient indicates that microstructural voids directly affect the water absorption capacity during the early curing period. In the correlation graph of 28-day samples (Fig. 7), the regression equation (y = 2.2611x + 0.1606) and R^2 value was found as 0.8192. This value shows that the correlation has weakened slightly compared to the 7-day samples, but there is still a strong relationship. After 28 days of curing, it can be said that the direct relationship between water absorption and porosity has decreased slightly due to the microstructural development of the specimens and the effect of the organisation of the void structure. In general, it was determined that porosity increased as the water absorption rate increased in both 7 and 28 day samples; therefore, the two parameters are closely related to each other in the evaluation of permeability and durability properties of concrete. The control of porosity, especially at early ages, is critical for the long-term durability of concrete.

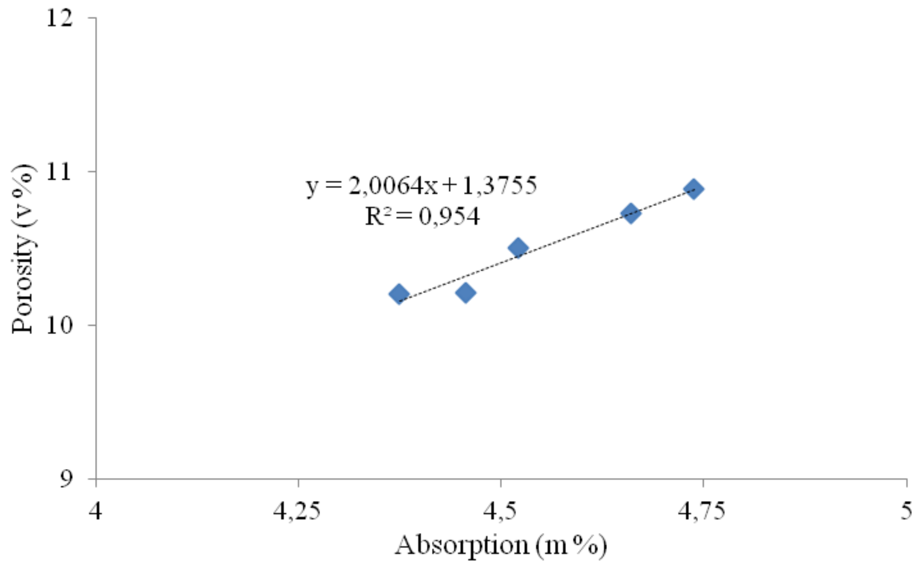

Fig. 6. Porosity-water absorption relationship of fibre concrete with witness and mine waste admixture (7 days)

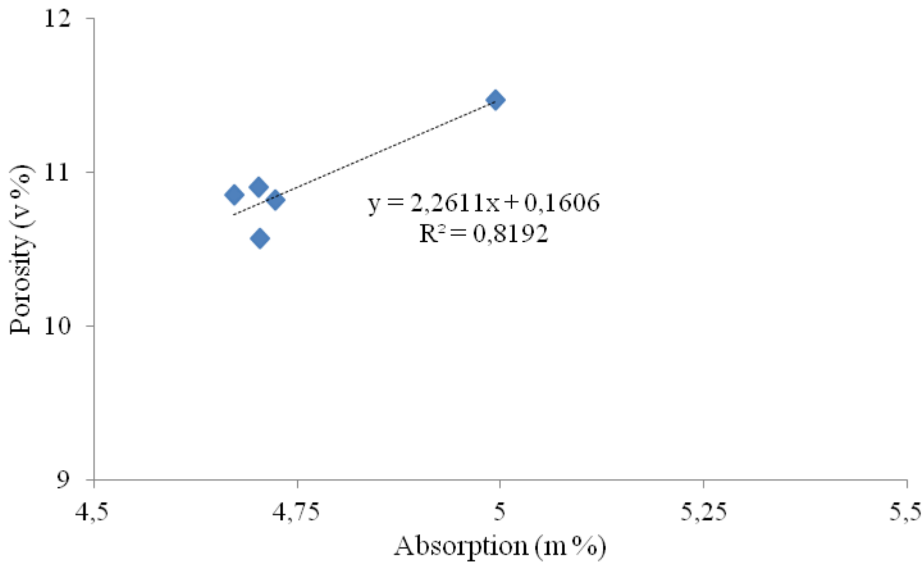

Fig. 7. Porosity-water absorption relationship of fibre concrete with witness and mine waste admixture (28 days)

3.2. Mechanical properties

According to the results presented in Fig. 8 and Fig. 9, the normal concrete (N) specimen exhibited a compressive strength of 18.88 MPa and a splitting tensile strength of 2.92 MPa at 7 days curing time. These values decreased by 20.2% and 5.8% to 15.08 MPa and 2.75 MPa, respectively, for the W specimen using mine waste. On the other hand, the compressive strength increased by 13.7% to 21.47 MPa and the splitting tensile strength increased by 4.1% to 3.04 MPa in specimen W-2 to which 0.2% waste tyre wire was added. The increasing trend continued in W-4 and W-6 specimens; the compressive strength of W-4 specimen was 22.96 MPa (21.6% increase) and W-6 specimen was 22.44 MPa (18.9% increase). At 28 days curing time, the compressive strength of N specimen was 21.99 MPa and the splitting tensile strength was 2.87 MPa. In W specimen, the compressive strength decreased by 18.1% to 18.00 MPa and the splitting tensile strength decreased by 8.4% to 2.63 MPa. However, W-2, W-4 and W-6 specimens increased by 4.0%, 10.1% and 18.2% respectively and reached compressive strength values of 22.87 MPa, 24.21 MPa and 26.00 MPa. The splitting tensile strengths ranged between 2.58-2.83 MPa and the W-6 specimen obtained the highest value of 2.83 MPa with an increase of 2.1%. These findings show that the addition of low proportions (0.2%-0.6%) of waste tyre wire significantly increased the compressive and tensile strengths both at early age and at later curing times, whereas the use of only mine waste decreased the mechanical performance. In particular, 0.6% tyre wire admixture provided 18.2% higher compressive strength compared to normal concrete after 28 days.

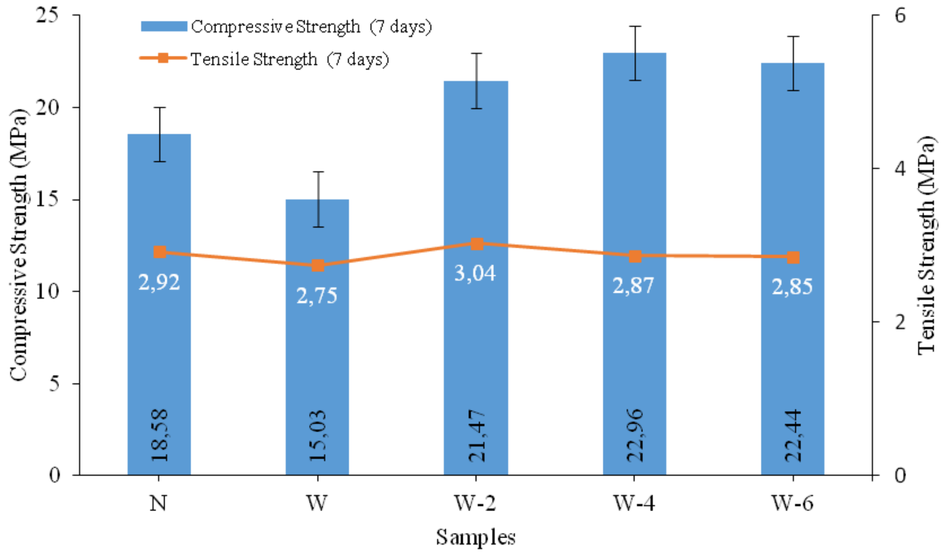

Fig. 8. 7-days compressive and splitting tensile strength of mine waste and waste tyre wire at different replacement ratios (0.2%; 0.4% and 0.6%)

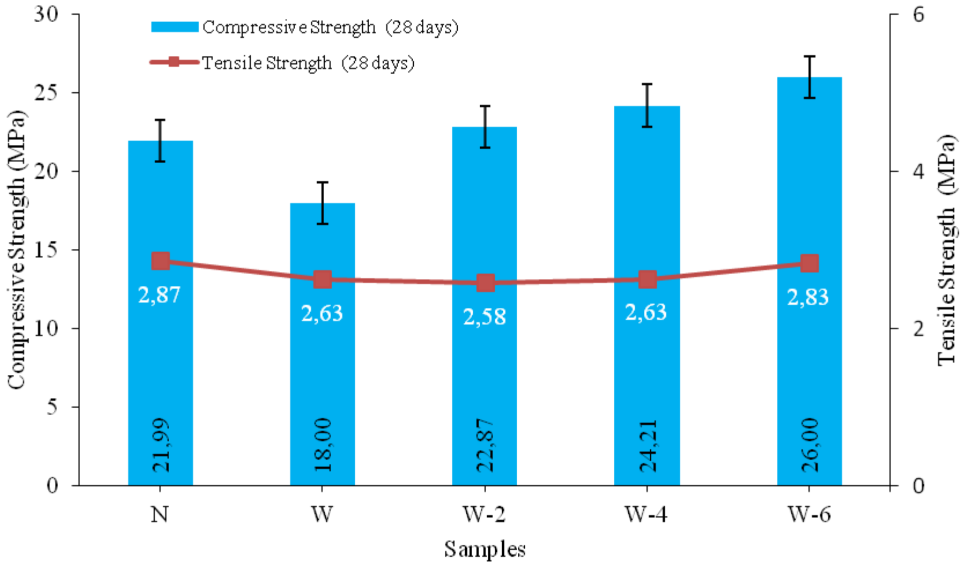

Fig. 9. 28-days compressive and splitting tensile strength of mine waste and waste tyre wire at different replacement ratios (0.2%; 0.4% and 0.6%)

According to the modulus of elasticity and Poisson's ratio results given in Fig. 10 and Fig. 11, the modulus of elasticity of the normal concrete (N) sample was determined as approximately 30 GPa and Poisson's ratio was 0.015 at the end of 7 days of curing. The modulus of elasticity increased by 6.7% to approximately 32 GPa and the Poisson's ratio doubled to 0.03 for specimen W. The modulus of elasticity increased by 25.0% to approximately 40 GPa and the Poisson's ratio increased to 1.3 for specimen W-2 to which 0.2% waste tyre wire was added. In specimens W-4 and W-6, the modulus of elasticity was approximately 32 GPa and 34 GPa, respectively, and the Poisson's ratio was 1.12 and 1.73. At 28 days curing time, a general increase in the modulus of elasticity values was observed. While the modulus of elasticity increased to 50 GPa in sample N, it reached approximately 55 GPa in sample W with a 10% increase. In specimen W-2, the modulus of elasticity increased to approximately 80 GPa, which is a 60% increase compared to normal concrete. Poisson's ratio was determined as 1.81 in this specimen. In specimens W-4 and W-6, the modulus of elasticity was measured at approximately 35 GPa and 38 GPa, respectively, showing a decrease of 30% and 24%, respectively, compared to specimen N. Poisson's ratio decreased to 0.8 in W-4 and increased to 1.03 in W-6. These findings indicate that the addition of 0.2% waste tyre wire significantly increases the modulus of elasticity of concrete with mine waste, whereas higher additions lead to a decrease in the modulus of elasticity. In addition, changes in Poisson's ratio indicate changes in microstructural deformation characteristics within the specimen.

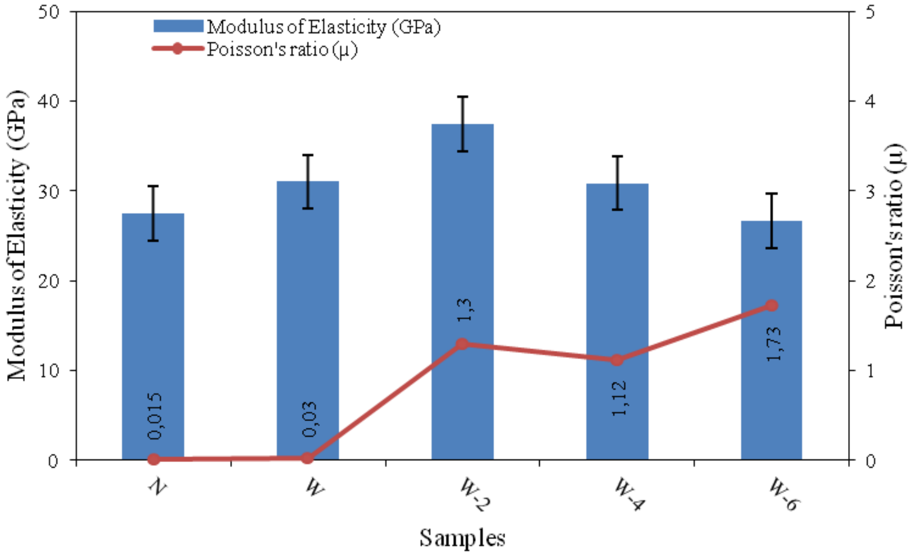

Fig. 10. Elasticity-Poisson relationship of mine waste and waste tyre wire substituted concretes (7 days)

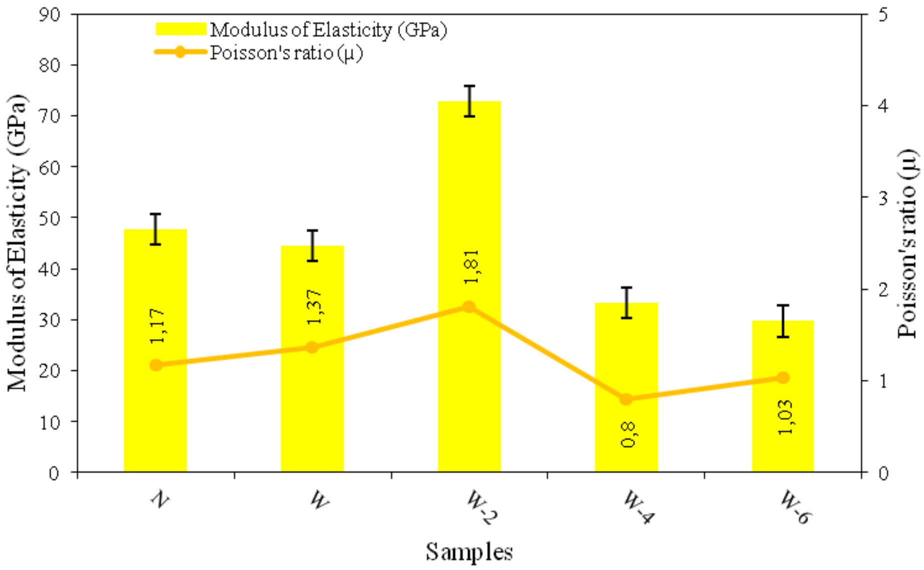

Fig. 11. Elasticity-Poisson relationship of mine waste and waste tyre wire substituted concretes (28 days)

3.3. Discussion

Several studies in the literature have indicated that the incorporation of SFs can enhance the compressive strength of concrete (Li & Li., 2017; Abbas et al., 2018). However, contrasting findings have also been reported, with some researchers concluding that SFs have little to no impact on compressive strength (Papakonstantinou & Tobolski, 2006; Doğruyol et al., 2024). In this study, the physical and mechanical properties of concretes produced using mine waste and waste tyre wire at different ratios (0.2%, 0.4% and 0.6%) were evaluated. In terms of physical properties, it was observed that the addition of mine waste and waste tyre wire at both curing times (7 and 28 days) did not cause a significant change in porosity and water absorption rates compared to the control sample. In particular, it was determined that the addition of 0.4% and 0.6% wire decreased the porosity to a limited extent and did not adversely affect the water absorption performance. The strong positive correlation between water absorption and porosity (R^2 = 0.954 for 7 days, R^2 = 0.8192 for 28 days) was found to be effective on microstructural permeability especially at early ages. In terms of mechanical performance, the addition of 0.2%-0.6% waste tyre wire had an increasing effect on both compressive and splitting tensile strengths. At 7 days curing time, compressive strength of 0.2% wire added specimen increased by 13.7% and at 28 days curing time, compressive strength of 0.6% wire added specimen increased by 18.2%. A decrease in mechanical strength was observed in the specimens where only mine waste was used. In addition, in the modulus of elasticity evaluations, it was determined that the addition of 0.2% wire increased the modulus of elasticity by 25.0% in 7 days and 60% in 28 days; decreases in the modulus of elasticity were recorded at higher wire ratios. The changes in Poisson's ratio values indicate the differentiation in microstructural deformation mechanisms. In general, the use of mine waste and low levels of waste tyre wire has the potential to improve the mechanical performance and modulus of elasticity of concrete while maintaining its physical integrity. In particular, 0.2% tyre wire admixture provided optimum performance enhancement at both early and later curing times, and in this context, made a significant contribution to the sustainable utilisation of environmental wastes in the concrete road industry.

4. Conclusions

This study investigated the physical and mechanical properties of concrete incorporating mine waste and varying proportions (0.2%, 0.4%, and 0.6%) of waste tyre wire. The findings suggest that the inclusion of these materials can contribute to both performance enhancement and sustainable waste utilization in the concrete pavement industry. Physically, the addition of mine waste and tyre wire did not significantly alter porosity or water absorption rates compared to the control specimens at both 7 and 28 days of curing. Notably, wire additions at 0.4% and 0.6% slightly reduced porosity without negatively impacting water absorption. A strong positive correlation between water absorption and porosity was observed, particularly at early curing stages, indicating an influence on microstructural permeability. Mechanically, the incorporation of waste tyre wire enhanced both compressive and splitting tensile strengths, with the most notable increase in compressive strength (18.2%) recorded at 0.6% wire addition after 28 days. Conversely, the use of mine waste alone resulted in decreased strength. The addition of 0.2% wire significantly improved the modulus of elasticity by 25.0% at 7 days and 60% at 28 days while higher wire ratios led to reductions. Variations in Poisson's ratio further reflected changes in microstructural deformation behavior. Overall, the results indicate that the use of mine waste in combination with low levels of waste tyre wire, particularly at 0.2%, can enhance mechanical properties and elastic behavior without compromising physical durability. This approach not only improves concrete performance but also offers a promising pathway for the sustainable reuse of industrial and environmental waste materials in infrastructure applications such as concrete pavements.

References

Abbass, W., Khan, M.I., & Mourad, S. (2018). Evaluation of mechanical properties of steel fiber reinforced concrete with different strengths of concrete. *Construction and Building Materials, 168*, 556-569. https://doi.org/10.1016/j.conbuildmat.2018.02.164

Altun, F., Haktanır, T., & Arı, K. (2007). Effects of steel fiber addition on mechanical properties of concrete and RC beams, *Construction and Building Materials, 21*(3), 654-661. https://doi.org/10.1016/j.conbuildmat.2005.12.006.

Amin, M., Khan, K., Nazar, S., & Deifalla, A. (2023). Application of waste recycle tire steel fibers as a construction material in concrete. *Reviews on Advanced Materials Science, 62*(1), 20220319. https://doi.org/10.1515/rams-2022-0319

Amrani, M., Taha, Y., Kchikach, A., Benzaazoua, M., & Hakkou, R. (2022). Field and economic studies on mine waste: sustainable reuse as aggregates for low traffic pavement structure. *Sustainability, 14*(19), 12540. https://doi.org/10.3390/su141912540

Ayhan, E., Doğruyol, M., Kıpçak, F., & Karaşin A. (2024). Atık taşıt lastik çelik lifinin beton davranışına etkisi. *Düzce University Journal of Engineering, 15*(2), 525–532. https://doi.org/10.24012/dumf.1468070.

ASTM. (1992). Standard specification for chemical admixtures for concrete. ASTM C494-92

ASTM. (2000). Standard test method for density (unit weight), yield, and air content (gravimetric) of concrete. ASTM C138.
ASTM. (2001). Standard test method for slump of hydraulic-cement concrete. ASTM C143.
ASTM. (2017). Standard test method for splitting tensile strength of cylindrical concrete specimens. ASTM C496.
ASTM. (2021). Standard test method for compressive strength of cylindrical concrete specimens. ASTM C39.
ASTM. (2019). Standard test method for abrasion resistance of concrete or mortar surfaces by the rotating-cutter method. ASTM C944.
ASTM. (2022). Standard test method for ultrasonic pulse velocity through concrete. ASTM C597.
ASTM. (2022). Standard test method for measuring the P-wave speed and the thickness of concrete plates using the impact-echo method. ASTM C1383
Awal, A.S.M.A., Yee, L.L., & Hossain, M.Z. (2018). Fresh and hardened properties of concrete containing steel fibre from recycled tire. *Malaysian Journal of Civil Engineering, 25*(1). https://doi.org/10.11113/mjce.v25.15839
Bayer Öztürk, Z. (2018). Agrega olarak çinko madeni cürufu kullaniminin beton basinç dayanimina etkisi. *International Journal of Engineering Research and Development, 10*(2), 144-152. https://doi.org/10.29137/umagd.412093
BS EN. (2009). Testing hardened concrete - Part 3: Compressive strength of test specimens. BS EN 12390-3.
Centonze, G., Leone, M., & Aiello, M.A. (2012). Steel fibers from waste tires as reinforcement in concrete: A mechanical characterization. *Construction and Building Materials, 36*, 46–52. https://doi.org/10.1016/j.conbuildmat.2012.04.088.
Çoğulu, E. (1975). Gümüşhane ve Rize Bölgelerinde Petrolojik ve Jeokronometrik Araştırmalar. *İTÜ Article,* No: 1034, İstanbul.
Çullu, M. (2018). Kurşun-çinko maden artiği kayaçlarla üretilen betonlarin mekanik ve fiziksel özelliklerinin araştirilmasi. *Politeknik Journal, 21*(2), 427-435. https://doi.org/10.2339/politeknik.374053
Doğruyol, M., Ayhan, E., & Karaşin, A. (2024). Effect of waste steel fiber use on concrete behavior at high temperature. *Case Studies in Construction Materials, 20*, 1-14. https://doi.org/10.1016/j.cscm.2024.e03051
Domski, M., Katzer, J., Zakrzewski, M., & Ponikiewski, T. (2017). Comparison of the mechanical characteristics of engineered and waste steel fiber used as reinforcement for concrete. *Journal of Cleaner Production, 158*, 18-28. https://doi.org/10.1016/j.jclepro.2017.04.165.
El Machi, A., El Berdai, Y., Mabroum, S., Safhi, A.e.M., Taha, Y., Benzaazoua, M., & Hakkou, R. (2024). Recycling of mine wastes in the concrete industry: A review. *Buildings, 14*(6), 1508. https://doi.org/10.3390/buildings14061508
Guo, S., Dai, Q., Sun, X., & Sun, Y. (2016). Ultrasonic scattering measurement of air void size distribution in hardened concrete samples. *Construction and Building Materials, 113*, 415-422. https://doi.org/10.1016/j.conbuildmat.2016.03.051
Kandemir, R. (2004). Gümüşhane ve Yakın Yörelerindeki Erken-Orta Jura Yaşlı Şenköy Formasyonu'nun Çökel Özellikleri ve Birikim Koşulları. PhD Thesis, *Karadeniz Technical University*, Trabzon.
Kanneboina, Y.Y., Saravanan, T.J., Kabeer, K.I.S.A., & Bisht, K. (2023). Valorization of lead and zinc slags for the production of construction materials - A review for future research direction. *Construction and Building Materials*, *367*:130314. https://doi.org/10.1016/j.conbuildmat.2023.130314
Kotan, T., Ardahanlı, M., & Özbey, Ö. F. (2023). Atık çinko cüruf tozu katkili kendiliğinden yerleşen betonlarin taze beton ve mekanik özelliklerinin incelenmesi. *Konya Journal of Engineering Science, 11*(2), 518–529. https://doi.org/10.36306/konjes.1174194
Li, Y., & Li, Y. (2017). Experimental study on performance of rubber particle and steel fiber composite toughening concrete. *Construction and Building Materials, 146*, 267-275. https://doi.org/10.1016/j.conbuildmat.2017.04.100
Nandi, S., Ransinchung, G., & Rana, G.B. A sustainable approach towards reducing cement consumption in the road sector using zinc industry waste. *Int. J. Pavement Res. Technol. 15*, 1463–1483 (2022). https://doi.org/10.1007/s42947-021-00101-6
Papakonstantinou, C.G., & Tobolski, M.J. (2006). Use of waste tire steel beads in portland cement concrete. *Cement and Concrete Research, 36*(9), 1686- 1691. https://doi.org/10.1016/j.cemconres.2006.05.015
Pelin, S. (1977). Alucra (Giresun) Güneydoğu Yöresinin Petrol Olanakları Bakımından Jeolojik İncelemesi. *Karadeniz Technical University Article,* 87, 103.
Samindi, S.M., Samarakoon, M.K., Ruben, P., Pedersen, J.W., & Evangelista, L. (2019). Mechanical performance of concrete made of steel fibers from tire waste. *Case Studies in Construction Materials, 11*:e00259. https://doi.org/10.1016/j.cscm.2019.e00259
Su, P., Li, M., Dai, Q., & Wang, J. (2023). Mechanical and durability performance of concrete with recycled tire steel fibers. *Construction and Building Materials, 394*:132287. https://doi.org/10.1016/j.conbuildmat.2023.132287

Şengül, Ö. (2016). Mechanical behavior of concretes containing waste steel fibers recovered from scrap tires. *Construction and Building Materials, 122*, 649-658. https://doi.org/10.1016/j.conbuildmat.2016.06.113.

Şimşek, O., Toklu, K., & Ünal, M.T. (2021). Çelik liflerin geometrik şeklinin ve oranının beton özelliklerine etkisinin araştırılması. *Politeknik Journal, 24*(2), 409-415. https://doi.org/10.2339/politeknik.691640

Tokel, S. (1972). Stratigraphically and Volcanic History of the Gümüşhane Region (NE Turkey). Phd Thesis, University of College, London.

TS. (2016). Design of concrete mixes. TS 802.

TS. (2015). Concrete - steel fiber reinforced - rules for mixing concrete and control. TS 10514.

TS EN. (2019). Concrete - tests for hardened concrete - Part 7: Determination of the density of hardened concrete. ts en 12390-7.

Vahdat, F.R., Ashtari, P., & Dehghani, H. (2024). Sustainable utilization of mine wastes in mortar production as a part of aggregates: A case study on calcareous wastes of Angoran lead and zinc mine. *Environ Sci Pollut Res, 31*, 49300–49316. https://doi.org/10.1007/s11356-024-34401-8

Waris, M.A., us Sahar, U., Akmal, U., Khurram, N., Aslam, F., & Fathi, D. (2022). Coupled effect of waste tire rubber and steel fibers on the mechanical properties of concrete. *Materials Science-Poland, 40*(1), 49-59. https://doi.org/10.2478/msp-2022-0009

Wu, X., Xu, X., Li, S., Li, X., Pei, D., Yang, X., Yu, X., & Zhu, X. (2024). Experimental study on the preparation of cementitious materials through the activation of lead—zinc tailings. *Minerals, 14*(12), 1215. https://doi.org/10.3390/min14121215

Zeybek Ö., Özkılıç Y.O., Çelik A.İ., Deifalla A.F., Ahmad M., & Sabri M.M. (2022). Performance evaluation of fiber-reinforced concrete produced with steel fibers extracted from waste tire. *Front. Mater., 9*:1057128. https://doi.org/10.3389/fmats.2022.1057128.

4th International Civil Engineering & Architecture Conference
17-19 May 2025, Trabzon, Türkiye

Evaluation of the effects of centralized multi-purpose urban transportation stations on land use with a TOD approach

Amir H. Imani[1], Ali Bayati[2], Sadegh Partani*[1], Mehran Mohammadi[1], Seyyed M. Mousavi[3]

[1] *University of Bojnord, Faculty of Engineering, Department of Civil Engineering, Bojnord, Iran*
[2] *Islamic Azad University, Central Tehran Branch, Department of Civil Engineering, Tehran, Iran*
[3] *Research and Education Center, Islamic City Council of Bojnord, Bojnord, Iran*

Abstract. The rapid growth of urban populations has raised the imperative of efficient mass transit systems, and subway lines have emerged as an integral part thereof. Over the years, subway stations have evolved from solely functional transport endpoints to diversified multi-use complexes involving heterogeneous services and facilities and promoting Transit-Oriented Development (TOD). This is an evaluation of the effects on land use caused by central urban multi-purpose transit nodes, which includes how these nodes influence interactions between metro/subway crossing nodes and bus/BRT routes and the growth of private small convenience stores and nearby local taxi fleets. A range of indicators, measures, and variables were isolated to construct an ordered questionnaire whose reliability was guaranteed by Cronbach's alpha. Testing of hypotheses was conducted based on Pearson's correlation coefficient. The results confirm that the integration of mixed-use developments and a range of services within and in the areas of transport hubs significantly enhances their attractiveness, elevates the extent of citizens' involvement, and renders the complexes more utilized. Furthermore, the study highlights the importance of such terminals in spurring localized economic activities, including the growth of private small markets and taxi businesses, thereby promoting the sustainable urban space development. Such observations call for an adoption of a TOD strategy to ensure urban transportation centers maximize functionality and socio-economic impacts.

Keywords: Private transportation system; Socio-economic impacts; Heterogeneous services; Urban land use; TOD

1. Introduction

This urban transportation challenges linked to rapid urbanization and proposes solutions like Transit-Oriented Development (TOD). Integrating transport and land use planning helps cities become more sustainable, efficient, and liveable. Urban population growth has exacerbated traffic congestion and pollution. Traditional public transportation has become inadequate, necessitating sustainable urban transport solutions including metro systems and TOD principles (Curtis & Scheurer, 2021).

Sustainable transport aims to reduce reliance on private vehicles, minimize environmental impacts, and improve accessibility. Strategies include promoting public transport, walking, and cycling, and encouraging compact, mixed-use development (Curtis & Scheurer, 2021)

Metro systems provide fast, clean, and high-capacity transport, reducing dependence on private cars. TOD encourages dense, walkable, mixed-use developments around transit stations, improving urban quality (Calthorpe, 2017). High-quality urban spaces are accessible, attractive, safe, and multifunctional. These spaces promote social interaction, encourage public transport use, and contribute to urban sustainability (Gehl, 2019). Sustainable transport and TOD principles offer a viable pathway for developing resilient cities. Proper integration of transport systems and land-use planning is essential to achieve liveable urban environments (Bertolini, 2020).

Table 1. Comparison of urban transport modes based on speed, capacity, and pollution

Transport Mode	Speed	Capacity	Pollution Level
Bus	Low	Medium	Low
Tram	Medium	Medium-High	Very Low
Metro	High	High	High

*Corresponding author, E-mail: s_partani@ub.ac.ir

https://doi.org/10.31462/icearc2025_ce_tra_563

With the rapid growth of urbanization, public transportation systems, especially metro networks, have gained increasing importance in organizing urban land use.

Transit-Oriented Development (TOD) focuses on increasing density, mixed land use, and enhancing pedestrian accessibility to public transport stations. This study analyses the impact of metro station complexes on land use patterns, emphasizing the case study of Mirdamad Metro Station. Urban rail transport is now recognized as a key tool for sustainable urban development (Cervero, 2016).

Establishing metro station complexes with commercial, residential, administrative, and cultural land uses not only improves the environmental quality of surrounding areas but also reduces energy consumption and reliance on private vehicles (Curtis, 2020). Studies in London (Broadgate and King's Cross stations) show that station complexes integrating commercial spaces and green areas have significantly enhanced land value and environmental quality (Mior, 2002).

In Seoul (Samsung station), the development of administrative and recreational spaces attracted private investment and increased pedestrian traffic around the station (Jamshidzadeh, 1999). Similarly, Stockholm and Paris offer successful examples of connecting transport networks with commercial and leisure centers (Loukaitou-Sideris, 2022).

The TOD approach emphasizes high-density development, mixed land use, improved walkability, and reduced dependence on private vehicles (Newman & Kenworthy, 2021) .Building multifunctional complexes around metro stations attracts investments in residential, commercial, administrative, and recreational projects due to improved accessibility (Knowles, 2022) .In the case of Mirdamad Metro Station in Tehran, developing station complexes can lead to:

- Increased population and economic density around the station
- Improved pedestrian access and service availability
- Reduced local traffic congestion
- Enhanced urban environmental quality

Mirdamad Station, located strategically in northern Tehran, holds high potential for TOD-based development. Creating commercial, administrative, and public spaces in this area can significantly transform surrounding land uses and promote sustainable urban development. International examples such as Ploshchad Metro in Moscow and La Defence Metro Station in Paris have demonstrated how station complexes can effectively revitalize local economies and enhance urban living standards. Developing station complexes around Mirdamad Metro based on TOD principles can significantly improve surrounding land use patterns. Proper integration of commercial, administrative, residential, and cultural spaces will enhance environmental quality and encourage public transportation use. Global experiences demonstrate that with proper planning, station complexes can foster economic and social growth alongside improved urban mobility.

2. Methodology

This study employed a descriptive-analytical research methodology to assess the impacts of metro station complexes on surrounding land use, adopting a Transit-Oriented Development (TOD) framework. The research included two segments: theoretical studies (reviewing global TOD practices and station complexes) and fieldwork (direct observations, data collection, and surveys). The methodology integrated qualitative insights and quantitative analysis to evaluate the spatial impacts of Mirdamad Metro Station. Primary data was collected through direct surveys with 120 randomly selected passengers at Mirdamad Metro Station, authorized by Tehran Metro Co. Secondary data included document reviews and internet searches (Bertolini, 2012).

Key dimensions assessed in three items as following (Table 2):

- Attractiveness and aesthetics
- Activity and functionality
- Security and comfort

Descriptive statistics, correlation analysis (using Pearson coefficients), and regression modelling were applied. Reliability of the questionnaire was assessed through Cronbach's Alpha ($\alpha > 0.7$).

Table 2. Key indicators assessed

Dimension	Indicators	Examples
Attractiveness	Cleanliness, Visual Quality	Public Space Aesthetics
Functionality	Activity Diversity	Restaurants, Shops, Cultural Centers
Security	Lighting, Surveillance	CCTV Cameras, Police Presence

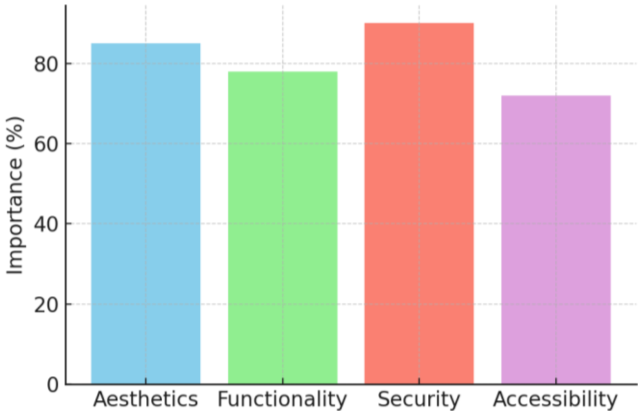

Fig. 1. Respondents' prioritized preferences

The questionnaire covered two sections: current station conditions and user improvement preferences. Sample questions evaluated aspects such as aesthetics, cultural activity presence, and public safety (Cervero, 2021).

After refinement, the Cronbach's Alpha coefficient exceeded 0.7, validating the internal consistency of the survey instrument (Zhang & Xu, 2022).

The analysis revealed strong user preference for diversified amenities (Table 3), enhanced aesthetics, and secure environments around Mirdamad Station, consistent with TOD principles [17]. Regression analysis confirmed that improvements in station complexes significantly influenced surrounding land use changes (Tehran Urban & Suburban Railway Co., 2023).

3. Results and discussion

The study revealed several significant outcomes, summarized in Table 3. Transit-Oriented Development (TOD) focuses on creating vibrant, liveable urban spaces around high-quality public transport stations. Metro stations like Mirdamad in Tehran act as significant catalysts for influencing surrounding land uses (Cervero, 2021). Data was collected via a structured 29-question survey filled by 120 participants, analysed using SPSS software. Both descriptive and inferential statistics were employed.

Table 3. Change in land use indicators after TOD implementation

Indicator	Before TOD (%)	After TOD (%)
Small Commercial Establishments	25	67
Private Vehicle Usage	80	43
Local Taxi Fleet Size	10	41
Pedestrian Traffic	30	78

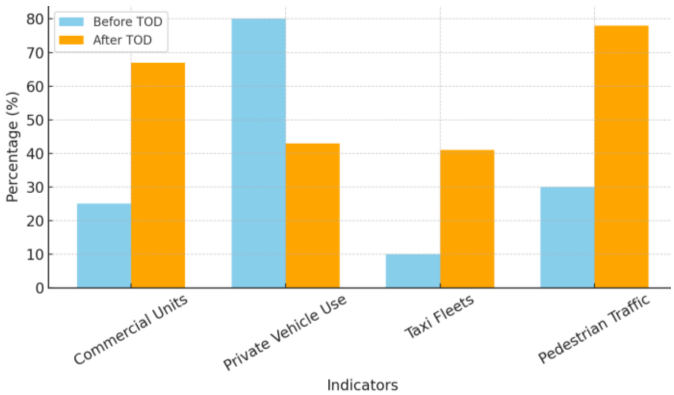

Fig. 2. Comparison of urban indicators before and after TOD

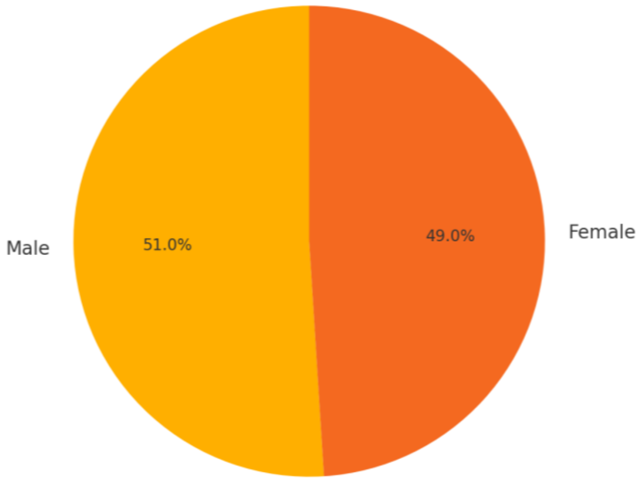

Fig. 3. Gender distribution among participants

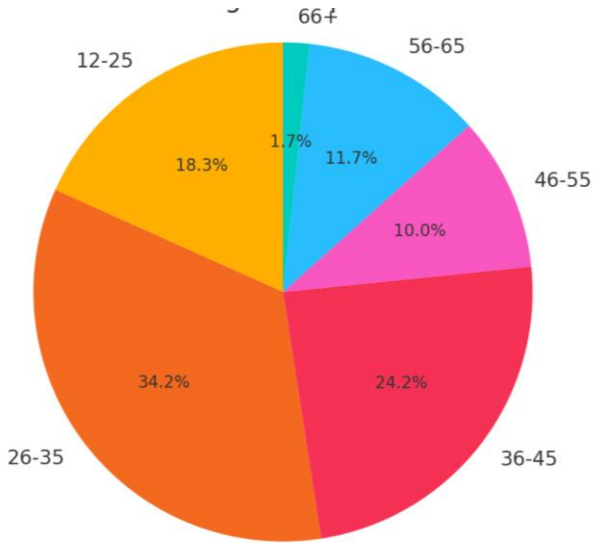

Fig.4. Age group distribution among participants

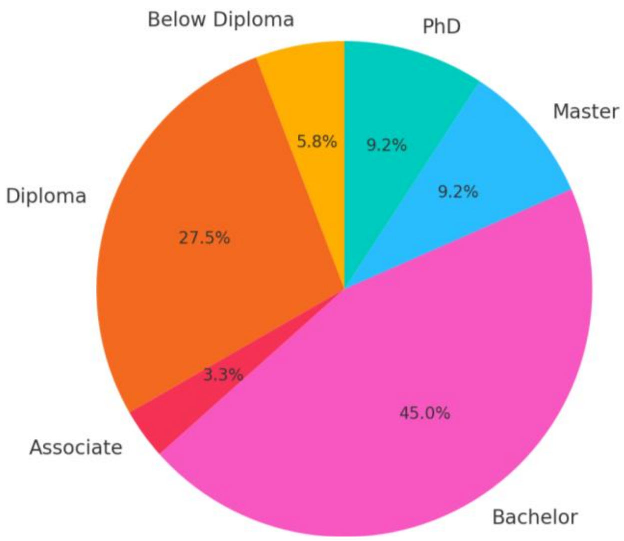

Fig. 5. Education level of participants

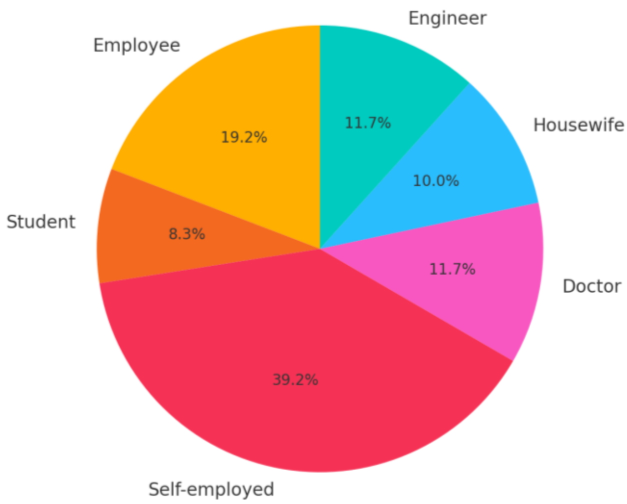

Fig. 6. Occupation of participants

Overall, the majority of respondents were young, educated, and professionally active, which enhances the credibility of the survey results. Survey results indicated positive satisfaction levels regarding cleanliness, lighting, accessibility, and safety measures around the metro station.

The Pearson correlation coefficient ($r=0.611$, $p<0.001$) showed a significant positive relationship between the availability of diverse land uses and station efficiency (Zhang & Xu, 2022). Further analysis indicated strong links between the presence of services and perceived security and attractiveness (Pojani & Stead, 2021).

4. Conclusion

Centralized multi-purpose transit stations are pivotal for modern urban development. Their ability to integrate transportation functions with commercial and social activities promotes sustainable land use, enhances local economies, and contributes to reducing urban sprawl. Policymakers and planners should prioritize TOD strategies to optimize the utility of transportation hubs and foster resilient urban growth. The Mirdamad Metro Station demonstrates that integrated TOD principles can successfully influence urban growth patterns. Authorities are recommended to plan future urban expansions with TOD models in mind (Newman & Kenworthy, 2020).

References

Calthorpe, P. (2017). Urbanism in the Age of Climate Change. Island Press.
Cervero, R. (2016). Transit-oriented development and the urban fabric. In *Sustainable Railway Futures* (pp. 75-94). Routledge.
Cervero, R., Guerra, E., & Al, S. (2021). Transit-oriented development and sustainable communities. Island Press.
Curtis, P. (2020). Planning for public transport accessibility: An international sourcebook. Routledge.
Curtis, R., & Scheurer, J. (2021). Planning for public transport accessibility. Routledge.
Gehl, J. (2019). Cities for people. Island Press.
Jamshidzadeh, M. (1999). The role of Seoul Metro in urban development. Transportation Journal.
Knowles, D. (2022). Transport impacts on land use change in London. *Journal of Transport Geography, 99*.
Loukaitou-Sideris, J. (2022). Transit-oriented development: Lessons from international cases. *Journal of Urban Affairs*.
Mior, A. (2002). Stations and their surroundings in London. Tehran Metro Company.
Newman, P., & Kenworthy, J. (2020). The end of automobile dependence: How cities are moving beyond car-based planning. Island Press.
Newman, P., & Kenworthy, J. (2021). Sustainable urban form and sustainable transport. *Built Environment, 47*(3), 383–397.
Pojani, D., & Stead, D. (2021). Sustainable urban transport in the developing world: Beyond TOD. *Cities, 114*, 103196.
Suzuki, P., Cervero, H., & Iuchi, K. (2013). Transforming cities with transit: Transit and land-use integration for sustainable urban development. The World Bank.
Tehran Urban & Suburban Railway Co. (2023). Annual report 2023. Tehran, Iran.
Vale, M. (2020). Transit-oriented development: Integrating land use and transport. *Urban Policy and Research, 38*(2), 137–151.
Zhao, X., Zhang, X., & Wang, Y. (2020). Metro-induced urban land use changes: Evidence from Beijing. *Cities, 96*.

Zhang, Y., & Xu, C. (2022). Transit-oriented development in high-density cities: Impacts and challenges. *Journal of Urban Studies, 59*(4), 812–829.

4th International Civil Engineering & Architecture Conference
17-19 May 2025, Trabzon, Türkiye

Superhydrophobic surfaces and road pavement applications

Cansu İskender*[1], Halime Solak*[2], Erol İskender[2], Atakan Aksoy[3], Mustafa Taha Aslan[3]

[1*] Avrasya University, Department of Civil Engineering, 61010 Trabzon, Türkiye
[2*] Karadeniz Technical University, Of Faculty of Technology, 61830 Trabzon, Türkiye
[3] Karadeniz Technical University, Department of Civil Engineering, 61080 Trabzon, Türkiye

Abstract. The presence of water, snow, or ice on road surfaces poses a significant threat to road safety. These adverse conditions substantially reduce the friction coefficient between the tires and the road surface. Therefore, prompt measures are necessary to mitigate such risks. To melt ice and snow on pavement surfaces, chemicals such as NaCl, $MgCl_2$, and $CaCl_2$ are often applied. However, these methods carry risks of negatively impacting asphalt pavement performance, vehicles, and infrastructure such as bridges, as well as causing long-term environmental issues. Current literature indicates that the application of superhydrophobic pavements can significantly enhance road safety. In this context, the use of fluoropolymer-based materials containing PTFE, TiO_2, ZnO, SiO_2, Mg-Al LDHs, and nano-CaO has been proposed for incorporation into asphalt mixtures to improve road safety. Superhydrophobic surfaces offer a wide range of functionalities, including water resistance, ice prevention, antibacterial properties, dirt repellence, self-cleaning capabilities, and corrosion resistance. Superhydrophobic pavements are a special type of surface treatment characterized by unique wettability properties, with a water contact angle greater than 150° and a roll-off angle of less than 10°. These surfaces are typically designed by applying low-surface-energy treatments or creating rough surface textures. When applied to road pavements, these features provide significant advantages, such as reduced water accumulation, minimized ice formation, and less damage to the pavement compared to conventional methods. This study provides an overview of superhydrophobic pavement applications and their potential benefits for enhancing road safety.

Keywords: Superhydrophobic pavements; Road safety; Anti-icing agent; De-icing agent.

1. Introduction

The accumulation of water, snow, and ice on pavement surfaces leads to time loss, economic damage, environmental pollution, compromised passenger safety and increased traffic congestion (Segundo et al., 2020). Furthermore, the formation of ice or snow on airport runways often results in flight cancellations, causing personal inconvenience for passengers and financial losses amounting to millions for airline companies and airport operators (Arabzadeh et al., 2016).

The conventional method for removing ice and snow from pavement surfaces involves the application of salts (primarily chloride-based salts such as sodium chloride (NaCl) and calcium chloride ($CaCl_2$) etc.) and chemical compounds. It can deteriorate asphalt pavement performance, accelerate the corrosion of vehicles and critical infrastructure (e.g., bridges) and contribute to significant long-term environmental degradation (Peng et al., 2018). For field applications, deicers are selected based on their effectiveness at freezing temperatures, cost, availability and ease of application on the pavement surface. Their effectiveness in melting ice and snow is defined by the effective temperature, which is the lowest practical temperature at which the deicer can be used; this temperature is relevant for ice melting, anti-icing and other applications. In road deicing and anti-icing operations, chloride-based deicers are commonly used. This is because their costs are lower and they can be obtained easily. Among chloride-based deicers used on roads, NaCl is the most commonly used. The effective temperature for NaCl is 15°F (Nilssen et al., 2018). Below this temperature, NaCl is unable to melt snow and therefore becomes ineffective at extremely low freezing temperatures. However, to enable its use across a wide range of conditions, it is often mixed with other deicers and corrosion inhibitors (Sajid et al., 2021; Abbas et al., 2021). On the other hand, calcium

*Corresponding author, E-mail: cansu.iskender@avrasya.edu.tr

https://doi.org/10.31462/icearc2025_ce_tra_564

chloride is another chloride-based deicer that remains effective at temperatures as low as -25°F, making it suitable for regions experiencing severe winter conditions. It is considered relatively harmless to the environment. However, it has been shown to cause significant deterioration of pavement materials (Wang et al., 2006; Sutter et al., 2006) and is more expensive compared to sodium chloride (Nixon, 2008).

Magnesium chloride is another chloride-based deicer effective at relatively low temperatures (approximately -10°F), and it is widely used for deicing highways and parking lots (Shi et al., 2009). However, it has also been found to be corrosive, cause severe pavement deterioration, and contribute to environmental pollution (Fay & Shi, 2012).

Calcium magnesium acetate (CMA) deicer is less corrosive compared to chloride-based deicers (Peterson, 1995). It is also biodegradable, which makes it somewhat environmentally friendly. However, CMA is not as cost-effective as chloride-based deicers. Moreover, its effectiveness is limited to moderately cold temperatures. Potassium acetate is another acetate-based deicer that works at very low temperatures (-15°F) (Western Transportation Institute, 2017). Like CMA, it is a less corrosive and more environmentally friendly option. For this reason, it is mostly used on airport runways (Shi et al., 2009). The selection of deicers is an important part of the experimental methods adopted in the literature. Different deicers have different properties, which result in varying rates of concrete deterioration.

Due to its high efficiency and low environmental impact, superhydrophobic deicing coating material holds great promise for road pavement applications. Therefore, it is necessary to explore reliable and cost-effective deicing methods to ensure safe driving on pavements under severe weather conditions (Huang et al., 2021). Commonly used deicing methods include the application of chemical products, heating, and the use of superhydrophobic materials. The mechanisms of road deicing methods are generally categorized into passive and active deicing approaches (Cao et al., 2018). Passive deicing methods (e.g., the use of chemical products) are simple and relatively low-cost. However, they tend to be less efficient and often require labor and material-intensive. In addition, they can cause significant damage to the pavement structure. In contrast, active deicing methods offer high efficiency and cause less harm to road structures. However, current active deicing methods used in the market (e.g., heating) are often expensive. The use of superhydrophobic materials as another potential active deicing option is attracting increasing interest due to their simple preparation, cost-effectiveness, and pollution-free properties (Cao et al., 2018). Therefore, utilizing superhydrophobic materials as an anti-icing technology in road pavements is considered an ideal solution due to their numerous advantages (Huang et al., 2021).

In engineering, superhydrophobic coatings are temporarily applied to critical and ice-prone areas, such as intersections and bridge decks, to maintain their anti-icing properties for at least one year before winter. However, the strategies for preparing superhydrophobic coating materials and the testing methods are diverse, and there is a lack of a unified understanding of the anti-icing mechanisms and the performance characteristics of these materials. All of these factors limit the further development of this new anti-icing approach (Li et al., 2023).

2. Superhydrophobic coatings

One of the most common methods for deicing pavements is the use of salts and chemicals. However, these methods have become outdated and insufficient in contemporary practice. Numerous studies have shown that these chemicals significantly affect the performance of asphalt pavement. Furthermore, they contribute to the corrosion of vehicles and deck bridge deck, leading to long-term environmental damage (Munck et al., 2010). In recent years, thermal melting technologies (including liquid heating) (Chen et al., 2011), microwave heating (Tang et al., 2008), thermal cables (Zhou et al., 2011) and electrically conductive roads (Hou et al., 2010) have been widely utilized to prevent the formation of ice layers on road surfaces. However, the high energy consumption of these technologies and their economic inefficiency have limited their development and application (Li et al., 2012). Research indicates that low free energy levels are indicative of a superhydrophobic surface, which reduces the adhesion of ice to the surface (Lin et al., 2013).

Objects with superhydrophobic surfaces were first discovered through the investigation of the lotus leaf's ability to remain clean. The leaf surface is covered with a substance that has low free surface energy and also features a rough structure at the nanoscale. The combination of these two properties has been found to give the lotus leaf surface its superhydrophobic characteristics. As a result, the liquid droplet on the surface makes minimal contact with the surface, as it is trapped in the nanoscale cavities, with air occupying the space. This allows the droplet to remain on the surface with a high contact angle, closely resembling a spherical shape due to surface tension. Additionally, the liquid droplet can roll off the surface at a slight slope. As it rolls, it picks up dirt and dust from the surface, thereby cleaning it. Due to these properties, superhydrophobic/hydrophobic surfaces have the potential for use in a wide range of applications, including self-cleaning, anti-icing, corrosion prevention, anti-fogging, and reducing drag resistance (Kibar, 2016).

The self-cleaning ability of lotus (Nymphaea) leaves was discovered by W. Barthlott et al. in 1997 during their study of the surface structure of lotus leaves, which possess superhydrophobic properties (Barthlott & Neinhuis, 1997).

Various studies have been conducted to investigate the adhesion mechanism of ice on superhydrophobic surfaces (Zhang et al., 2017; Chen et al., 2017). Superhydrophobic coatings can reduce the ice formation area, prevent the development of ice layers, and weaken the adhesive force of ice to surfaces. Additionally, these coatings possess self-cleaning properties and can protect the underlying substrate. Such coatings have been successfully applied in fields such as aerospace (Huang et al., 2019), energy transmission (Peng et al., 2018), marine environments (Ferrari & Benedetti, 2015), and medical applications (Falde et al., 2016). However, the use of superhydrophobic coatings for road surface anti-icing is still in the exploratory stage, and there are limited reports on their applications in road anti-icing engineering (Cui et al., 2024).

Several potential applications of superhydrophobic surfaces, including anti-freezing, anti-corrosion, anti-frosting, anti-icing for photovoltaic cells, power lines, airplanes, ships, anti-friction for submarines, self-cleaning of solar panels and glass windows etc. are illustrated in Fig. 1 (Zhang & Lv, 2015).

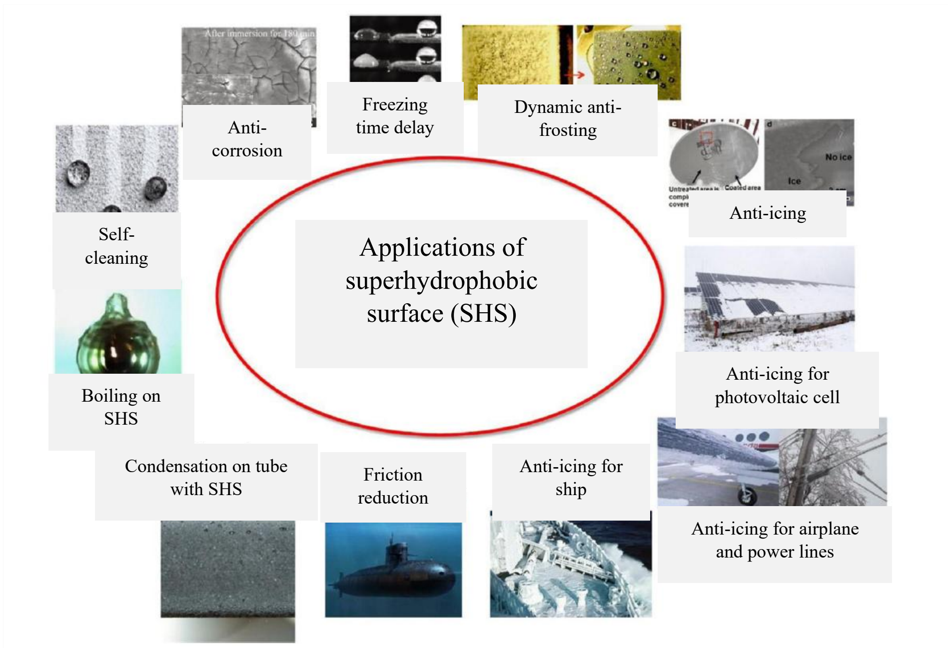

Fig. 1. The potential applications of superhydrophobic surfaces (Hooda et al., 2020).

Asphalt mixtures with photocatalytic properties support air purification through the application of semiconductor materials. Photocatalytic asphalt pavements, when exposed to sunlight in the presence of water and oxygen, degrade organic pollutants as well as SO_2 and NO_x. This effect contributes to both air and surface cleanliness, particularly when oils and greases are adsorbed onto the asphalt surface. Another functionalization process involves enhancing the superhydrophobic capacity. A superhydrophobic asphalt mixture possesses the ability to repel water and prevent ice formation on the surface, which can improve road safety. The self-cleaning capacity associated with superhydrophobicity is based on the fact that water droplets maintain a spherical shape and can easily roll over the surface, carrying away dirt particles (da Rocha Segundo, 2021). A long-term superhydrophobic self-cleaning coating was first developed through the simple mixing of TiO_2 nanoparticles with a fluorinated polysiloxane binder that cures under ambient conditions (Ding et al., 2011).

The superhydrophobic property is achieved when the contact angle is greater than 150° (Zhu et al., 2014). Superhydrophobic coating is a type of coating with special surface wetting properties; the water contact angle is greater than 150° and the rolling angle is less than 10° (Barthlott & Neinhuis, 1997; Pan et al., 2017).

Surfaces with a water contact angle less than 90° are considered hydrophilic, whereas those with a contact angle greater than 90° are defined as hydrophobic. The contact angles of a water droplet on a hydrophilic, hydrophobic and superhydrophobic surfaces are shown in Fig. 2 (Khan et al., 2022).

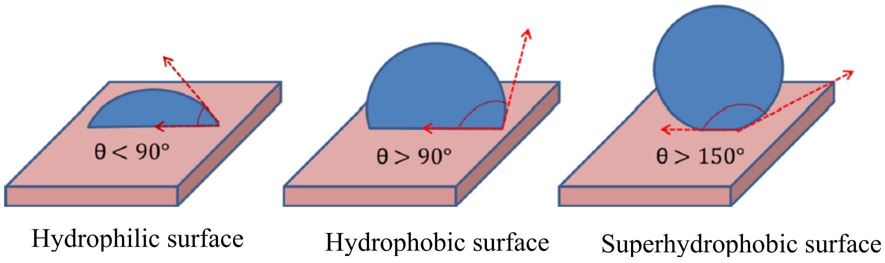

Fig. 2. Schematic illustration of the wettability of surfaces with different water contact angles.

Superhydrophobic properties are typically evaluated using optical and electron-based analyses. The primary method involves measuring the contact angle between water and the surface. As the surface must be rough, the analysis of the microtopography of the surface is important in this respect. Surface roughness is often examined through optical methods, such as optical triangulation-based microtopography. In this case, characterization can be done by evaluating the surface parameters and comparing the materials and processes. In addition, the images obtained with the Scanning Electron Microscope (SEM) are important to understand the microtopographic structure of the surface (Segundo et al., 2020).

One of the factors influencing the hydrophobic treatment is the curing time. In one study, all hydrophobic materials with a curing time of 24 hours exhibited larger contact angles compared to those cured for only 2 hours. Therefore, it can be concluded that curing time has a significant impact on the formation of hydrophobic coatings on asphalt surfaces. On average, longer curing times increased the contact angles by 20 degrees (approximately 18%) (Zakerzadeh et al., 2018).

3. Superhydrophobic coatings preparation methods

Superhydrophobic surfaces are not wetted by water and exhibit low surface energy. These surfaces are typically designed either by applying surface treatments that lower surface energy or by creating a rough surface texture (Segundo et al., 2020).

Superhydrophobicity is generally achieved in two ways: by increasing the roughness of low surface energy materials or by reducing the surface energy of micro- and nano-structured rough surfaces (Li et al., 2023). To describe the wettability of rough surfaces, two main models are commonly used: the Wenzel model (Wenzel, 1936) and the Cassie–Baxter model (Cassie & Baxter, 1944). Fig. 3 presents both the Wenzel and Cassie–Baxter models. The Wenzel model assumes that the liquid completely fills the grooves in the rough surface. In this case, by increasing the roughness of the object, the surface of an initially hydrophilic object becomes more hydrophilic, while the surface of an initially hydrophobic object becomes more hydrophobic. However, the Wenzel model has a shortcoming; it can only be applied to surfaces with uniform chemical composition. Asphalt and various asphalt mixtures are not suitable for this condition. Cassie and Baxter proposed a drop contact model to describe surfaces composed of composites. In this model, it is assumed that the droplets do not fully wet the solid surface, and the rough structure of the surface traps air, thus the droplets remain at the composite phase interface, consisting of solid-liquid and solid-gas phases. This situation aligns with the Cassie-Baxter model (Lafuma & Quéré, 2003).

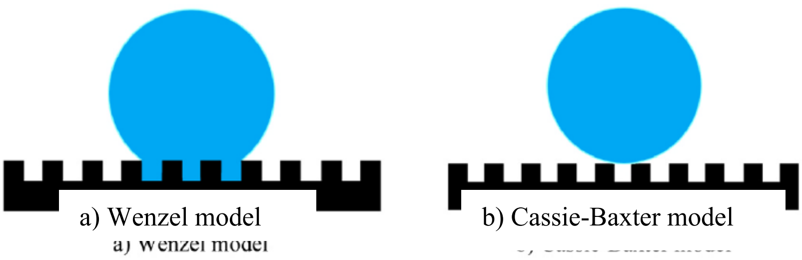

Fig. 3. Wenzel and Cassie-Baxter model

In general, the contact angle and rolling angle are used to evaluate the superhydrophobic capacity of a material (Yao et al., 2010). In order to enhance the performance and service life of the pavement, a nano-TiO_2 superhydrophobic coating (PSC) was prepared on asphalt pavement using waterborne polyurethane and stearic acid-modified nano-TiO_2. The SEM image indicate that the superhydrophobic coating has a rough surface structure. In the contact angle test, the contact angle of the PSC was measured to be 153.5° and the rolling angle was 4.7°. The results indicate that the surface superhydrophobic coating can effectively reduce water damage on asphalt pavement and has a significant impact (Li et al., 2021).

Water-repellent surfaces are typically recognized by their micro or nano roughness and complex morphologies. Another important feature is the replication of the micro-level morphology into what are called nano projections, creating multi-scale roughness. Therefore, the following fabrication techniques are employed to develop the specified characteristics on pseudo-surfaces (Hooda et al., 2020).

- Electrochemical deposition
- Electro-spinning and electro-spraying
- Chemical vapour deposition (CVD)
- Layer-by-layer (LBL) deposition
- Wet-chemical method
- Phase separation technique
- Imprinting technique
- Lithography technique
- Templating technique
- Hydrothermal method
- Sol-gel route
- Mussel-inspired chemistry

The sol-gel, wet chemical, electrochemical deposition, and Mussel-inspired chemistry are recognized as the most efficient, cost-effective, and industrially viable methods for producing superhydrophobic coatings. Therefore, there is a significant need to optimize the control parameters of these techniques in order to develop advanced superhydrophobic coatings for various applications (Hooda et al., 2020).

The superhydrophobic coating fabrication process consists of two steps: synthesis and coating. Commonly used synthesis techniques include etching, isoelectric precipitation, phase separation and the sol-gel method. For road superhydrophobic coatings, the sol-gel method is primarily used, as it meets the cost-effective and large-scale production requirements. On the other hand, the coating process should ensure uniformity and good adhesion to the coating surface. In addition to traditional brush and spray methods, the layer-by-layer (LBL) technique is primarily employed (Li et al., 2023).

The original contact angle of asphalt binder is approximately 100°, which decreases to about 70° after oxidation by thermal treatment. After spraying a superhydrophobic coating on the road surface, it will restore its hydrophobicity. Researchers commonly investigate material selection, material modification and production processes. Polytetrafluoroethylene (PTFE) is a widely used super anti-ice and waterproof material due to its low surface energy properties. PTFE waterproof coatings can enhance the waterproofing and anti-icing properties of airport runways, standard asphalt road surfaces and ordinary cement concrete road surfaces (Cui et al., 2024). Some studies have shown that under optimum spray conditions, PTFE coatings applied using layer-by-layer (LBL) techniques impart remarkable hydrophobic properties, achieving high contact angles of up to 155° (Arabzadeh et al., 2017).

In order to functionalize asphalt mixtures used in road pavements, nano/micro materials such as polytetrafluoroethylene (PTFE), TiO_2 and SiO_2 among others, have been applied to the pavement by spraying. The mixtures are typically characterized by their water contact angle and surface roughness is usually evaluated using optical and electron analysis (Segundo et al., 2020).

A study has proposed a heterogeneous nucleation ice crystal growth model, focusing specifically on the effects of surface roughness and contact angle. The mechanism of ice retention by superhydrophobic materials has been determined using this model and experimentally validated. Experimental results from water contact angle and sliding resistance tests showed that the prepared TiO_2–stearic acid coating material exhibited a contact angle greater than 150° and good sliding resistance. Superhydrophobic coatings are typically prepared with materials that have good inhibitor performance. In this study, superhydrophobic materials were prepared using a hydrothermal method. The reaction between nano-sized titanium dioxide (TiO_2) and stearic acid was synthesized in an anhydrous ethanol environment. Titanium dioxide has a purity of 99.8% and a particle size of 60 nm, with a rutile structure. Stearic acid and anhydrous ethanol are analytical reagents. To prepare the TiO_2–octadecanoic acid composite material, nano TiO_2 powder was first dispersed in pure ethanol by sonication for 1 hour. Then, octadecanoic acid was added to the previous solution. The mixture was homogenized by sonication for 3 hours. The final solution was obtained by stirring with a magnetic stirrer at 70°C for 6 to 12 hours. After that, an additional 60 mL of ethanol was added at 25°C, and the solution was centrifuged for 20 minutes to remove the supernatant. Finally, the TiO_2-OA sample was obtained after being dried at 120°C for 1 hour. The resulting superhydrophobic materials were then applied to asphalt or concrete surfaces by manual brushing or spray method (Huang et al., 2021).

In this study, spraying, dipping and brushing methods were used to determine the optimum preparation method for hydrophobic coatings. In this work, Nano-ZnO, TiO_2 and SiO_2 particles were converted into hydrophobicity with stearic acid. The optimum preparation method for the nanoparticle/epoxy coating was determined to be ultrasonic dispersion and layered spraying. The mass ratio of nanoparticles to stearic acid and the nanoparticle dosage were found to have a significant impact on the contact angle of the hydrophobic coating. If the amount of stearic acid exceeds the optimum value, the hydrophilic carboxyl group of the unreacted stearic acid and the hydrophobic interactions of stearic acid reduce the hydrophobicity of the coating. Furthermore, as the nanoparticle content increases, the aggregation of nanoparticles becomes more pronounced, which complicates the dispersion of nanoparticles and negatively affects the rate of hydrophobicity increase of the coating (Liu et al., 2024).

In a study where modified nano-TiO_2 and waterborne polyurethane were used as the main materials, the spraying method was employed to create a superhydrophobic surface. Compared to the sol-gel method, vapor deposition method, electrochemical method, template method, etc., the coating offers a simple preparation process, low cost, excellent superhydrophobic properties and some wear resistance. Test results demonstrate that it can effectively enhance the road surface's resistance to water damage and extend its service life (Li et al., 2021).

The production of superhydrophobic coatings using the spray coating method has become the subject of many studies due to several advantages, including the ability to be applied to surfaces with different chemical structures, large and irregular surfaces, low production and application costs, the fact that the spray coating method is already used in the coating industry, simplicity of application, not requiring special and high-cost equipment, the ability to be prepared and applied in a short period, ease of application, no need for specially trained personnel, allowing the production of translucent coatings and being user-friendly from the end-user's perspective (Güneş & Fidan, 2022).

One of the major issues encountered in road safety is the slipperiness of the road surface during rain. The presence of water on the road reduces friction on the surface of the pavement. When there is insufficient friction, accidents caused by sliding become inevitable. A common phenomenon during rain is hydroplaning, which refers to the reduction of contact on wet surfaces, leading to the loss of traction. Hydroplaning characteristics are influenced by factors such as water film thickness, tire inflation pressure, pavement texture depth, surface hydraulic properties, and tire tread depth (Zakerzadeh et al., 2021).

In a study investigating the effects of octafluoropentyl methacrylate superhydrophobic coating on hydroplaning risk and water film thickness on asphalt roads, a device simulating rainy conditions on asphalt roads was designed. The water flow rate was measured on coated and uncoated asphalt surfaces with varying degrees of superhydrophobic coating and the hydroplaning speed was calculated. According to the results, the average hydroplaning speeds of vehicles on coated asphalt samples were found to be approximately 1.33 times higher compared to uncoated asphalt samples. Additionally, the results suggest that superhydrophobic coatings could be an innovative method to reduce the hydroplaning risk and decrease the water film thickness on asphalt roads (Zakerzadeh et al., 2021).

One of the main factors for surface superhydrophobicity is the amount of material sprayed. To determine the optimum consumption of superhydrophobic material, the amount sprayed on asphalt samples was experimentally chosen as 50, 100, 150, 200 and 250 grams; this amount was determined for a 0.5 m^2 (0.5 m × 1 m) asphalt surface. In this part of the experiment, the slope was set to 3% and the flow rate was set to 3 lit/min. The surfaces coated with superhydrophobic material need to remain free from contact with any substances for 24 hours to allow the chemical bond between the coating and the asphalt surface to form. The results show that increasing the consumption rate from 50 g to 100 g strongly increases the hydroplaning speed; however, when the consumption rate exceeds 100 g, the hydroplaning speed remains almost constant (Zakerzadeh et al., 2021).

A superhydrophobic coating material typically consists of two main components: a superhydrophobic agent and a coating base (Li et al., 2023). On one hand, an effective and stable superhydrophobic material can be achieved by combining a micro-rough surface (approximately 1 nm to 10^2 nm) (Lin et al., 2013) with a low surface energy (SFE) material (Oliveira et al., 2013), which is considered a key factor in anti-icing strategies (Mahadik et al., 2010). There are two principal fabrication strategies: roughening low-SFE materials, such as by producing polytetrafluoroethylene (PTFE) nanoparticles (Nahvi et al., 2019) or forming a micro-rough surface via hydrolysis and condensation of polymethylhydrosiloxane (PMHS) (Zhang et al., 2021); and using nanomaterials modified with low-SFE substances to generate micro-rough surfaces. Among the successful applications of nanomaterials, nano-SiO_2, which offers high cost-effectiveness, is considered the most suitable option for large-scale highway engineering (Peng et al., 2018; Gao et al., 2018; Soleimani et al., 2021). Additionally, nano-TiO_2, known for its photocatalytic degradation properties, has also attracted significant research interest (Segundo et al., 2022; Huang et al., 2021; Li et al., 2021).

Nanostructures are considered an attractive option for creating nanoscale roughness on solid surfaces, as nanomaterials typically have dimensions in the range of 1–100 nm, allowing them to deposit as layers on surfaces (Goyat et al., 2011). The small size of nanostructures enables them to exhibit unique physical and chemical properties, particularly due to their high specific surface area-to-volume ratios (Goyat et al., 2011). The surface energy of solid surfaces can be reduced by incorporating low surface energy materials onto the surface. This can be achieved in two ways. In the first approach, low surface energy materials are either directly coated onto the surface or first attached to nanostructures, which are then deposited onto the solid surface. In the second approach, both low surface energy and nanoscale roughness are combined, which is particularly beneficial for the development of superhydrophobic surfaces (Chen & Carroll, 2002). It is a well-known concept that rough surfaces exhibit superior hydrophobic properties compared to smooth surfaces (Burkarter et al., 2007).

4. Shortcomings of superhydrophobic coating

There are two major challenges associated with achieving superhydrophobicity on asphalt surfaces. First, the hydrophobic nature of the surface alone is not sufficient to prevent ice adhesion; instead, a truly superhydrophobic surface is required (Arabzadeh et al., 2016). Therefore, it is essential to use a material that is not only compatible with asphalt surfaces (due to the presence of bitumen) but also capable of forming a superhydrophobic layer (Zakerzadeh et al., 2018). The second issue is the high cost of superhydrophobic materials, which makes some of them economically unfeasible for use with asphalt surfaces (Zakerzadeh et al., 2018).

In the development of superhydrophobic surfaces and films, several limitations are encountered, such as the high cost of superhydrophobic materials, the durability of nanostructures, coating stability, issues related to precipitation/condensation, interaction problems and emulsifier/oil wetting issues (Hooda et al., 2020).

To obtain an extraordinary superhydrophobic coating, a high water contact angle is required. Therefore, it is important to have a low-energy surface with water-repellent chemistry and durable micro- and nanoscale topographical features. Typically, achieving all of these challenging experimental parameters simultaneously can be somewhat difficult. For example, some polymers at the nanoscale have nano-textural properties and behave like 'wet noodles'. These polymer strands or 'wet noodles', easily mix and as a result, they stop behaving like a superhydrophobic surface (Bhushan & Jung, 2011).

Current studies show that improving the hydrophobicity of the coating and the adhesion between the coating and the road surface can provide good de-icing performance and durability. However, existing research on the application of hydrophobic materials for road anti-icing is generally limited to laboratory experiments and only a few coating technologies are used, recognized or promoted in physical engineering. The reason for this is that superhydrophobic coating materials are fragile and wear-sensitive, have poor adhesion to the road surface, easily peel off and have poor surface stability, which leads to insufficient durability of their ice and snow melting function (Wu & Chen, 2018); (Zhuo, et al., 2018).

Future studies on superhydrophobic surfaces should focus on improving the durability and stability of superhydrophobic surfaces. In the future, more research is needed on precisely controlling the surface roughness and structure at both small and large scales (Khan et al., 2022).

5. Conclusions

This study aims to examine superhydrophobic coatings, their production methods and general properties. Adverse weather conditions in terms of road safety occur when there is water, snow or ice on the road surface. The presence of these adverse weather conditions significantly reduces the friction coefficient on the road surface. Therefore, it is important to remove them quickly. The application of superhydrophobic coatings, removal of water droplets from the surface or prevention of ice/snow formation makes roads safer. In addition to their water-proof and anti-icing properties, superhydrophobic coatings also provide various benefits such as antibacterial, dirt-repellent, self-cleaning and corrosion protection.

- The ability of coatings to repel water varies depending on the properties of the materials used and the application methods. Superhydrophobic coatings containing PTFE, TiO_2, SiO_2, Mg-Al LDHs and nano-CaO nano/microparticle fluorine polymers have been applied on asphalt mixtures to increase road safety. The relevant literature results show that superhydrophobic asphalt mixtures can significantly increase road safety.
- Although superhydrophobic surfaces have attracted widespread attention in industrial areas, there are some limitations in the development of superhydrophobic coatings. These are; the cost of superhydrophobic materials, durability of nano-features, coating stability, precipitation/condensation problem and interaction problem.

As a result, superhydrophobic coatings are one of the effective methods to reduce the effects of water on road surfaces and there is a need for increased research in this area. Future studies should focus on improving the durability and stability of superhydrophobic surfaces.

References

Abbas, T., Lavadiya, D. N. & Kiran, R. (2021). Exploring the use of polyols, corn, and beet juice for decreasing the freezing point of brine solution for deicing of pavements. *Sustainability*, 13(11), 5765

Arabzadeh, A., Ceylan, H., Kim, S., Gopalakrishnan, K., & Sassani, A. (2016). Superhydrophobic coatings on asphalt concrete surfaces: Toward smart solutions for winter pavement maintenance. *Transportation Research Record,* 2551(1), 10-17

Arabzadeh, A., Ceylan, H., Kim, S., Gopalakrishnan, K., Sassani, A., Sundararajan, S., & Taylor, P. C. (2017). Superhydrophobic coatings on Portland cement concrete surfaces. *Construction and Building Materials*, 141, 393-401.

Barthlott, W., & Neinhuis, C. (1997). Purity of the sacred lotus, or escape from contamination in biological surfaces. *Planta,* 202, 1-8

Bhushan, B., & Jung, Y. C. (2011). Natural and biomimetic artificial surfaces for superhydrophobicity, self-cleaning, low adhesion, and drag reduction. *Progress in Materials Science,* 56(1), 1-108

Burkarter, E., Saul, C. K., Thomazi, F., Cruz, N. C., Roman, L. S., & Schreiner, W. H. (2007). Superhydrophobic electrosprayed PTFE. *Surface and Coatings Technology*, 202(1), 194-198

Cao, Y., Tan, W., & Wu, Z. (2018). Aircraft icing: An ongoing threat to aviation safety. *Aerospace Science and Technology,* 75, 353-385

Cassie, A. B. D., & Baxter, S. (1944). Wettability of porous surfaces. *Transactions of the Faraday Society*, 40, 546-551

Chen, S., & Carroll, D. L. (2002). Synthesis and characterization of truncated triangular silver nanoplates. *Nano Letters,* 2(9), 1003-1007.

Chen, M., Wu, S., Wang, H., & Zhang, J. (2011). Study of ice and snow melting process on conductive asphalt solar collector. *Solar Energy Materials and Solar Cells*, 95(12), 3241-3250

Chen, D., Gelenter, M.D., Hong, M., Cohen, R.E., & McKinley, G.H (2017). Icephobic surfaces ınduced by ınterfacial nonfrozen water. *ACS Appl. Mater. Interfaces*, 9, 4202–4214

Cui, Y., Zhang, L., Xing, C., & Tan, Y. (2024). Anti-icing properties and application of superhydrophobic coatings on asphalt pavement. *Construction and Building Materials*, 419, 135452

Da Rocha Segundo, I. G. (2021). Ecological, photocatalytic, superhydrophobic and self-cleaning asphalt pavement surfaces (Doctoral dissertation, Universidade do Minho (Portugal)).

Ding, X., Zhou, S., Gu, G., & Wu, L. (2011). A facile and large-area fabrication method of superhydrophobic self-cleaning fluorinated polysiloxane/TiO_2 nanocomposite coatings with long-term durability. *Journal of Materials Chemistry,* 21(17), 6161-6164

Falde, E. J., Yohe, S. T., Colson, Y. L., & Grinstaff, M. W. (2016). Superhydrophobic materials for biomedical applications. *Biomaterials,* 104, 87-103

Fay, L. & Shi, X. (2012). Environmental impacts of chemicals for snow and ice control: state of the knowledge. *Water, Air & Soil Pollution*, 223, 2751-2770

Ferrari, M., & Benedetti, A. (2015). Superhydrophobic surfaces for applications in seawater. *Advances in Colloid And Interface Science,* 222, 291-304

Gao, Y., Qu, L., He, B., Dai, K., Fang, Z., & Zhu, R. (2018). Study on effectiveness of anti-icing and deicing performance of super-hydrophobic asphalt concrete. *Construction and Building Materials,* 191, 270-280.

Goyat, M. S., Ray, S., & Ghosh, P. K. (2011). Innovative application of ultrasonic mixing to produce homogeneously mixed nanoparticulate-epoxy composite of improved physical properties. *Composites Part A: Applied Science and Manufacturing,* 42(10), 1421-1431.

Güneş A.H., &Fidan S., (2022). Investigating mechanical strength of epoxy/sio2 superhydrophobic coatings prepared by spray coating method, *Gazi University Journal of Science Part C: Design and Technology*, 10(4), 987-1005.

Hooda, A., Goyat, M. S., Pandey, J. K., Kumar, A., & Gupta, R. (2020). A review on fundamentals, constraints and fabrication techniques of superhydrophobic coatings. *Progress in Organic Coatings,* 142, 105557.

Hou, Z., Li, Z., & Wang, J. (2010). Electrically conductive concrete for heating using steel bars as electrodes. *Journal of Wuhan University of Technology-Mater. Sci. Ed.,* 25(3), 523-526

Huang, X., Tepylo, N., Pommier-Budinger, V., Budinger, M., Bonaccurso, E., Villedieu, P., & Bennani, L. (2019). A survey of icephobic coatings and their potential use in a hybrid coating/active ice protection system for aerospace applications. *Progress in Aerospace Sciences*, 105, 74-97

Huang, K., Liu, J., Wang, J., & Shi, X. (2021). Characterization and mechanism of a new superhydrophobic deicing coating used for road pavement. *Crystals*, 11(11), 1304

Khan, M. Z., Militky, J., Petru, M., Tomková, B., Ali, A., Tören, E., & Perveen, S. (2022). Recent advances in superhydrophobic surfaces for practical applications: A review. *European Polymer Journal*, 178, 111481.

Kibar, A., (2016). Süperhidrofobik ve hidrofobik yüzeyler üzerinde sıvı damlası gaz kabarcığı ve sıvı jeti dinamiğinin incelenmesi. *Pamukkale Üniversitesi Mühendislik Bilimleri Dergisi,* 22(7), 613-619

Lafuma, A., & Quéré, D. (2003). Superhydrophobic states. *Nature Materials*, 2(7), 457-460.

Li, H., Zhao, Y., & Yuan, X. (2012). Anti-icing coatings: From surface chemistry to functional surfaces. *Progress in Chemistry*, 24(11), 2087-2096

Li, H., Lin, X., & Wang, H. (2021). Fabrication and evaluation of nano-TiO_2 superhydrophobic coating on asphalt pavement. *Materials,* 14(1), 211.

Li, Y., Sha, A., Tian, Z., Cao, Y., Li, X., & Liu, Z. (2023). Review on superhydrophobic anti-icing coating for pavement. *Journal of Materials Science*, 58(8), 3377-3400

Lin, J., Chen, H., Fei, T., & Zhang, J. (2013). Highly transparent superhydrophobic organic–inorganic nanocoating from the aggregation of silica nanoparticles. *Colloids and Surfaces A: Physicochemical and Engineering Aspects*, 421, 51-62

Liu, S., Wang, H., & Yang, J. (2024). Influence of preparation methods and nanomaterials on hydrophobicity and anti-ıcing performance of nanoparticle/epoxy coatings. *Polymers*, 16(3), 364.
Mahadik, SA., Kaval,e MS., Mukherjee, SK., & Rao, AV. (2010). Transparent superhydrophobic silica coatings on glass by sol-gel method. *Applied Surface Science*, 257, 333
Munck, I. A., Bennett, C. M., Camilli, K. S., & Nowak, R. S. (2010). Long-term impact of de-icing salts on tree health in the Lake Tahoe Basin: Environmental influences and interactions with insects and diseases. *Forest Ecology And Management,* 260(7), 1218-1229
Nahvi, A., Sadoughi, M. K., Arabzadeh, A., Sassani, A., Hu, C., Ceylan, H., & Kim, S. (2019). Multi-objective Bayesian optimization of super hydrophobic coatings on asphalt concrete surfaces. *Journal of Computational Design and Engineering,* 6(4), 693-704
Nilssen, K., Klein-Paste, A., & Wåhlin, J. (2018). The effect of additives on the low temperature ice-melting capacity of NaCl. *Transportation Research Record*, 2672(12), 158-166
Nixon, W. A. (2008). Economics of using calcium chloride vs. sodium chloride for deicing/anti-icing" (No. TR-488)
Oliveira, NM., Reis, RL., & Mano, JF. (2013). Superhydrophobic surfaces engineered using diatomaceous earth. *ACS Applied Materials & Interfaces,* 5, 4202
Pan, Z., Cheng, F., & Zhao, B. (2017) Bio-inspired polymeric structures with special wettability and their applications: An overview. *Polymers,* 9, 725
Peng, C., Chen, PX., You, ZP., Lv, S., Xu, F., Zhang, W., Yu, J., & Zhang, H. (2018) The anti-icing and mechanical properties of a superhydrophobic coating on asphalt pavement. *Construction and Building Materials*, 190, 83-94
Peng, C., Zhang, H., You, Z., Xu, F., Jiang, G., Lv, S., Zhang, Y., & Yang, H. (2018). Preparation and anti-icing properties of a superhydrophobic silicone coating on asphalt mixture. *Construction and Building Materials*, 189, 227-235
Peng, W., Gou, X., Qin, H., Zhao, M., Zhao, X., & Guo, Z. (2018). Creation of a multifunctional superhydrophobic coating for composite insulators. *Chemical Engineering Journal*, 352, 774-781
Sajid, H. U., Naik, D. L. & Kiran, R. (2021). Improving the ice-melting capacity of traditional deicers. *Construction and Building Materials*, 271, 121527
Segundo, I. R., Landi, S., Freitas, E., Branco, V. C., Costa, M. F., & Carneiro, J. (2020). Superhydrophobic asphalt pavements: surface improvement. In EPJ Web of Conferences, 238, pp. 12012. EDP Sciences.
Segundo, I. R., Zahabizadeh, B., Landi Jr, S., Lima Jr, O., Afonso, C., Borinelli, J., ... & Carneiro, J. O. (2022). Functionalization of smart recycled asphalt mixtures: a sustainability scientific and pedagogical approach. *Sustainability,* 14(1), 573.
Shi, X., Akin, M., Pan, T., Fay, L., Liu, Y., & Yang, Z. (2009). Deicer impacts on pavement materials: ıntroduction and recent developments*. The Open Civil Engineering Journal*, 3
Shi, X., Fay, L., Gallaway, C., Volkening, K., Peterson, M., Pan, T., A. Creighton, C. Lawlor, S. Mumma & Nguyen, T. A. (2009). Evaluation of alternative anti-icing and deicing compounds using sodium chloride and magnesium chloride as baseline deicers, Report No. CDOT-2009-01. Colorado Department of Transportation. Denver, CO.
Soleimani, M., Bagheri, E., Mosaddegh, P., Rabiee, T., Fakhar, A., & Sadeghi, M. (2021). Stable waterborne epoxy emulsions and the effect of silica nanoparticles on their coatings properties. *Progress in Organic Coatings,* 156, 106250.
Sutter, L., Van Dam, T., Peterson, K. R. & Johnston, D. P. (2006). Long-term effects of magnesium chloride and other concentrated salt solutions on pavement and structural portland cement concrete. *Transportation Research Record,* 1979(1), 60-68
Tang, X. W., Jiao, S. J., Gao, Z. Y., & Xu, X. L. (2008). Study of 5.8 GHz magnetron in microwave deicing. *Journal of Electromagnetic Waves and Applications*, 22(10), 1351-1360
Wang, K., Nelsen, D. E. & Nixon, W. A. (2006). Damaging effects of deicing chemicals on concrete materials. *Cement And Concrete Composites*, 28(2), 173-188
Wenzel, R. N. (1936). Resistance of solid surfaces to wetting by water. *Industrial & Engineering Chemistry*, 28(8), 988-994
Western Transportation Institute (2017). Field usage of alternative deicers for snow and ıce control, Report No. TRS 1706. Local Road Research Board. Minnesota Department of Transportation.
Wu, X., & Chen, Z. (2018). A mechanically robust transparent coating for anti-icing and self-cleaning applications. *Journal of Materials Chemistry A,* 6(33), 16043-16052
Yao, X., Xu, L., & Jiang, L. (2010) Fabrication and characterization of superhydrophobic surfaces with dynamic stability. *Advanced Functional Materials*, 20, 3343–3349
Zakerzadeh, M., Abtahi, S. M., Allafchian, A., & Chamani, M. R. (2018). Examining the effect of different super hydrophobic nanomaterials on asphalt pavements. *Construction and Building Materials,* 180, 285-290

Zakerzadeh, M., Abtahi, S. M., Allafchian, A., & Chamani, M. R. (2021). Effectiveness of superhydrophobic material on the hydroplaning risk of asphalt pavements. *International Journal of Pavement Engineering*, 22(12), 1592-1600.

Zhang, P., & Lv F.Y., (2015) A review of the recent advances in superhydrophobic surfaces and the emerging energy-related applications. *Energy,* 82, 1068–1087

Zhang, R., Hao, P., & He, F (2017). Drop ımpact on oblique superhydrophobic surfaces with two-tier roughness. *Langmuir,* 33, 3556

Zhang, Z., Liu, H., Zhang, K., & Zhang, S. (2021). Preparation of super-hydrophobic anti-icing coating for asphalt pavement and evaluation of its anti-Icing properties. *Journal of Materials in Civil Engineering*, 33(3), 04021004.

Zhou, X. M., Yang, Z. J., Chang, C., & Song, G. (2011). Numerical assessment of electric roadway deicing system utilizing emerging carbon nanofiber paper. *Journal of Cold Regions Engineering*, 26(1), 1-15

Zhu, H., Guo, Z., & Liu, W. (2014). Adhesion behaviors on superhydrophobic surfaces. *Chemical Communications,* 50(30), 3900-3913

Zhuo, Y., Håkonsen, V., He, Z., Xiao, S., He, J., & Zhang, Z. (2018). Enhancing the mechanical durability of icephobic surfaces by introducing autonomous self-healing function. *ACS Applied Materials & Interfaces,* 10(14), 11972-11978

4th International Civil Engineering & Architecture Conference
17-19 May 2025, Trabzon, Türkiye

Balancing costs and commuter comfort to enhance urban rail transit performance

Emre Demir*[1]

[1] Antalya Bilim University, Department of Civil Engineering, 07190 Antalya, Türkiye

Abstract. In civil engineering, designing effective public transportation (PT) lines in urban settings necessitates a strategy that takes into account both technological and human-centric aspects. This study measures the effectiveness of new rail transit (RT) stations in a large urban area, focusing on a balanced assessment of costs and benefits. Alongside structural costs and traditional benefits like travel demand and service frequency, this study adds two dimensions: commuter comfort in terms of food accessibility near the stations and the impact of terrain slope, including the amount of stairs around each station. As a case study, a lot of new stations on an RT line are examined in Antalya, Türkiye using a multi-criteria decision-making (MCDM) method. Thus, building costs and the operations to constitute station surroundings, such as cutting slopes and generating steps, are seen as significant cost factors. On the other hand, benefits include higher peak-hour trip volumes, faster average speed of the RT line, more frequent service, and the availability of food options nearby, which improve commuter satisfaction. The results reveal significant differences in station efficiency, demonstrating how design and location considerations influence both operational performance and user comfort. In addition, RT stations with better access to food services and fewer physical barriers have higher scores in efficiency. As a result, this study aims to support the construction of PT systems in developing regions by addressing human-centric concerns with cost-efficiency by implementing an MCDM technique.

Keywords: Public transportation; Rail transit efficiency; Multi-criteria decision-making; Commuter comfort

1. Introduction

Rail transit (RT) systems in urbanized areas serve as essential components of public transportation (PT) networks, significantly contributing to urban accessibility, sustainability, and overall quality of life. In this manner, the planning and effective operation of RT stations are crucial for the success of PT systems in developing areas where transportation demand rises. Therefore, efficient PT planning requires a balance between structural costs and societal benefits which needs an integrated assessment considering both technical performance and human-centric issues together.

While traditional assessments of RT stations often include metrics such as travel demand and structural costs, emerging urban planning patterns emphasize the need to integrate commuter experience into evaluation frameworks. Sustainable and accessible PT systems not only depend on operational efficiency but also on the extent to which they meet the comfort and convenience needs of the road users. In this way, human-centric factors become important in shaping user satisfaction and PT adoption rates. Despite this growing recognition, systematic evaluations that holistically address both cost-efficiency and commuter-centric benefits remain relatively limited. Decision-making processes for station planning and optimization often lack structured, multi-dimensional methodologies. Consequently, there is a critical need for comprehensive assessment frameworks that can guide the design and operation of RT stations in a way that balances technical, financial, and human factors.

This study proposes an evaluative approach that applies the technique for order of preference by similarity to ideal solution (TOPSIS) that is a multi-criteria decision-making (MCDM) methodology, for assessing the performance of newly developed tram stations in Antalya, Türkiye. The research examines 20 tram stations, utilizing six key evaluation criteria: platform type, maximum daily trips during peak hours, average vehicle speed near the station, service frequency, commuter comfort in terms of food accessibility, and the terrain slope around each station. By including commuter comfort indicators (specifically food accessibility and terrain slope) in the evaluation, this study extends beyond traditional infrastructure assessments. Station surroundings, such as the proximity of food services, are treated as important elements influencing user experience. On the cost side, building efforts such as constructions are considered that reflect construction and maintenance challenges.

* Corresponding author, E-mail: emre.demir@antalya.edu.tr

https://doi.org/10.31462/icearc2025_ce_tra_577

The research findings reveal the variations in station efficiency which illustrate how infrastructural design and locational attributes impact functional performance and user satisfaction. For instance, stations with fewer physical barriers and greater food accessibility tend to achieve higher efficiency scores. Therefore, this study contributes to the field of urban transportation planning by offering a balanced and systematic evaluation framework.

A number of studies have looked at factors that influence passenger comfort in urban RT systems. For example, Nordin et al. (2016) investigate noise, vibration, and coach design. They collect input from RT commuters across various rail routes. A methodology for measuring comfort degrees throughout RT rides is presented (Mohammadi et al., 2020), whereas longitudinal acceleration numbers and traveler input are used to estimate traveling comfort in a big metropolitan subway (Ma et al., 2020). Also, a configuration is offered for en route comfort degree based on passenger counts and vehicle position statistics (Roncoli et al., 2023). Several scholars use MCDM approaches to examine the transformation of urban PT systems (Demir, 2024; Kiciński & Solecka, 2018; Li et al., 2019; Görçün, 2021; Zhang et al., 2020). These pieces of art use a variety of factors, including comfort, to assess various settings. Nevertheless, none of these works expressly address comfort at RT stops, especially with regard to nearby services or amenities. Therefore, this study gap in the literature highlights the requirement for more research into the comfort aspects during RT stops.

This study employs the TOPSIS method because the method's ability to handle complex decision-making environments by integrating multiple criteria has made it a popular tool across various areas such as engineering (Celik et al., 2012). The method of TOPSIS was developed as a reliable method within the field of MCDM (Tzeng & Huang, 2011). TOPSIS is based on the notion that the most desired option should be the smallest geometric distance from an ideal solution while remaining the farthest away from a negative-ideal solution. In the context of urban PT systems, TOPSIS has been utilized to evaluate many infrastructural and operational elements (Awasthi et al., 2011; Zhang et al., 2018). Studies apply TOPSIS to select optimal PT routes by considering factors such as travel time, passenger load capacity, operating costs, and environmental impact. Moreover, TOPSIS is a reliable method to address urban mobility challenges by aiding in the selection of optimal locations for transportation infrastructure, through the consideration of different criteria like accessibility, safety, cost, and social equity (de Aquino et al., 2019; Tsao et al., 2025). Recent studies recognize that focusing solely on technical and economic indicators is insufficient for promoting sustainable urban PT. Incorporating variables like food accessibility and physical accessibility (e.g., terrain slope) allows for a more comprehensive understanding of PT performance from a user perspective.

2. Materials and method

The study offers a systematic and holistic approach to assess the performance of RT stations in Antalya, Türkiye. Additionally, the study integrates operational, design, and commuter-centric service dimensions. The analysis uses the TOPSIS method, a widely recognized MCDM technique. The section below elaborates on the steps involved in the TOPSIS methodology, the evaluation criteria employed, and the specific characteristics of the study area.

2.1 TOPSIS methodology

The TOPSIS method is designed to rank alternatives based on their proximity to an ideal solution (Tzeng & Huang, 2011). The key assumption underlying TOPSIS is that the optimal alternative should have the shortest distance to the positive ideal solution and the farthest distance from the negative ideal solution. The method systematically proceeds through six algorithmic steps, each described in detail below:

- Step 1 is to create a decision matrix. The decision matrix is an n x m dimensional matrix produced by the decision maker after identifying the alternatives and assessment criteria. Here, n and m are the numbers of choice options and evaluation measures, respectively.
- Step 2 forms the standard decision matrix which is normalized or regulated. The standard decision matrix is obtained by taking the square root of the sum of squares of the values of each measure in the decision matrix (sum of squares of column values) and dividing the relevant component of the column by this value. If any member of the choice matrix has a value of zero, the corresponding part of the conventional decision matrix has the same value.
- Step 3 is to establish a weighted standard decision matrix. Initially, the weight standards for the assessment criteria are determined. Here, the sum of all weights must be the value of 1. This weighting approach exposes the subjective characteristic of the TOPSIS in decision-making since the weighting process is based on the importance or significance of the criteria. The components of the standard decision matrix are multiplied by their respective weight values to form a matrix called weighted standard decision matrix.
- Step 4 obtains positive ideal and negative ideal or optimum solution values. By means of the weighted standard decision matrix, the sets of positive ideal and negative ideal solutions are obtained for each criterion consistent with the objective of the evaluation criterion of interest. If the evaluation criteria are in terms of benefits, the positive ideal solution is the largest value of the columns of the weighted standard decision matrix, and the negative ideal solution is the smallest value of the columns of the weighted standard decision matrix. If the appraisal criteria are in terms of costs, the positive ideal outcome is the smallest

value of columns of weighted standard decision matrix, and the negative ideal answer is the largest value of columns of standard decision matrix weighted.

- In step 5, the distances to the positive ideal and negative ideal solutions are acquired. The Euclidean methodology is utilized to discover deviations of evaluation criteria for each decision alternative from the positive ideal and negative ideal solution values. Accordingly, distances or distance values are computed for the number of decision options.
- Finally, step 6 calculates the relative closeness coefficients to the optimum or ideal solution. The distances from the positive ideal and the negative ideal answers are accepted to estimate the relative closeness constants of each decision possibility to the ideal result. Relative closeness values are found for each decision option. Further, the share of distance to the negative ideal answer in the entire distance is calculated. Consequently, options of decision are prioritized as close to the value of 1.

2.2 Evaluation criteria

In line with the holistic aim of the study, six evaluation criteria were selected to comprehensively assess RT station performance, which are in the following. Evaluation criterion 1 (EC1) is platform type (PLT), capturing the influence of platform design choices on both construction and long-term maintenance costs. For instance, simple platforms are generally less costly, while elevated or underground structures entail higher financial demands. Secondly, evaluation criterion 2 (EC2) is maximum daily trips at peak hours (MDT), reflecting the level of passenger demand. In this case, higher values are associated with greater station utility and network significance. Thirdly, evaluation criterion 3 (EC3) is average speed of vehicles near the station (ASV), which is an operational indicator reflecting the smoothness of service near each station. For example, higher average speeds suggest efficient operations and minimal congestion, enhancing overall network performance. Then, the fourth evaluation criterion (EC4) is service frequency (SFR), indicating the intervals between successive tram arrivals. Hence, higher frequencies are associated with improved commuter satisfaction and reduced wait times. Moreover, the fifth evaluation criterion (EC5) is commuter comfort for food accessibility (CFA), recognizing the importance of station surroundings. CFA measures the proximity and availability of food options. Therefore, stations with better food access improve commuter comfort and satisfaction. Lastly, evaluation criterion 6 (EC6) is terrain slope around the stations (TSS) because the physical accessibility of a station is influenced by its surrounding terrain. Stations located in areas with steep slopes present challenges for road users with mobility difficulties.

2.3 Study area and data collection

The case study focuses on 20 tram stations located along the recently expanded tram line in Antalya, Türkiye, as of February 2024. The stations include Kadınlar Plajı (D1), Sarısu (D2), Liman (D3), Serbest Bölge (D4), Akdeniz Blv (D5), Konyaaltı (D6), Boğaçay (D7), Gürsu (D8), Altınkum (D9), Konyaaltı Bld (D10), Tıp Merkezi (D11), İl Sağlık Müd. (D12), AVM (D13), Stadyum Piramit (D14), Meltem Defterdarlık (D15), Güllük 100 Yıl (D16), Muratpaşa Cami (D17), Büyükşehir Bld (D18), Yeşilırmak (D19), and Kepez Bld (D20).

Data for each evaluation criterion were collected from available sources provided by the Antalya's available web sources and field observations. Physical site inspections were conducted to assess food accessibility and terrain slope conditions around each station. Moreover, operational data, including MDT, ASV, and SFR, were obtained from the Antalya's available internet sources. Thus, the final decision matrix comprised 20 alternatives which are the stations in this case and six criteria, with standardized and weighted values prepared for TOPSIS analysis created by the decision makers (Table 1). Accordingly, a representative portion of the decision or determination matrix's normalized form and the related main criteria weights obtained are seen in Table 2 and Table 3 respectively. Experts with relevant expertise and knowledge in the related field assign weights to each criterion based on their subjective judgment.

Table 1. A sample of the decision matrix

Station ID	PLT	MDT	ASV	SFR	CFA	TSS
D13	2	4.871	30	8	10	1.5
D14	2	4.988	30	8	1	2.5
D15	6	6.086	30	8	3	1.5
D16	6	6.635	35	12	27	0.5
D17	6	7.224	35	12	21	1.0

Table 2. A sample of the normalized decision matrix

Station ID	PLT	MDT	ASV	SFR	CFA	TSS
D13	0.1257	0.2239	0.2258	0.2141	0.2160	0.3511
D14	0.1257	0.2239	0.2258	0.2141	0.0216	0.5852
D15	0.3772	0.2797	0.2258	0.2141	0.0648	0.3511
D16	0.3772	0.3049	0.2634	0.3212	0.5831	0.1170
D17	0.3772	0.3320	0.2634	0.3212	0.4535	0.2341

Table 3. Main criteria weights obtained

Criterion ID	Criterion	Weight (%)	Rank
PLT	Platform type	25	1
MDT	Maximum daily trips at peak hours	20	2
ASV	Average speed of the vehicle near the station	10	5
SFR	Service frequency	20	2
CFA	Commuter comfort for food accessibility	20	2
TSS	Terrain slope near the station	5	6

3. Results and discussion

The application of the TOPSIS method to evaluate the 20 tram stations in Antalya yielded a ranking of their relative efficiency scores (P-scores) in Table 4. The results demonstrate a differentiation among the stations based on the six evaluation criteria showing the holistic approach of this study.

Table 4. Stations ranking

Station ID	P_score	Rank	Station ID	P_score	Rank
D16	0.68595	1	D6	0.41613	11
D9	0.64930	2	D12	0.41367	12
D17	0.63364	3	D7	0.39514	13
D20	0.63176	4	D14	0.39508	14
D13	0.52305	5	D2	0.35505	15
D11	0.51439	6	D5	0.34287	16
D19	0.48818	7	D1	0.33840	17
D10	0.44313	8	D15	0.31862	18
D8	0.43643	9	D4	0.30462	19
D18	0.42053	10	D3	0.30011	20

The top-performing stations are identified as D16 (Güllük 100. Yıl), D9 (Altınkum), D17 (Muratpaşa Cami), D20 (Kepez Bld), and D13 (AVM), with D16 achieving the highest P-score of 0.68595. These stations not only exhibit operational advantages such as high peak-hour trip volumes and favorable service frequencies but also excel in human-centric aspects such as accessibility to food services and convenient terrain conditions. Therefore, higher performance of those stations demonstrates the importance of designing station environments that are both operationally efficient and user-friendly. Furthermore, only four stations (D16, D9, D17, and D20) achieved a P-score between 0.6 and 0.7 indicating a relatively high level of efficiency within the RT network (Fig. 1). In other words, a limited number of stations optimize the balance between structural investments and commuter satisfaction.

On the other hand, the majority of the stations scored between 0.3 and 0.5 showing substantial room for improvement (Fig. 2). For example, the stations like D3 (Liman), D4 (Serbest Bölge) and D15 (Meltem Defterdarlık), which occupy the lower end of the ranking, may suffer from design inefficiencies, insufficient service frequencies, challenging topographical conditions, or limited access to food amenities. Such deficiencies can adversely affect the utility of many stations. Therefore, some interventions are necessary to elevate the performance of low score stations.

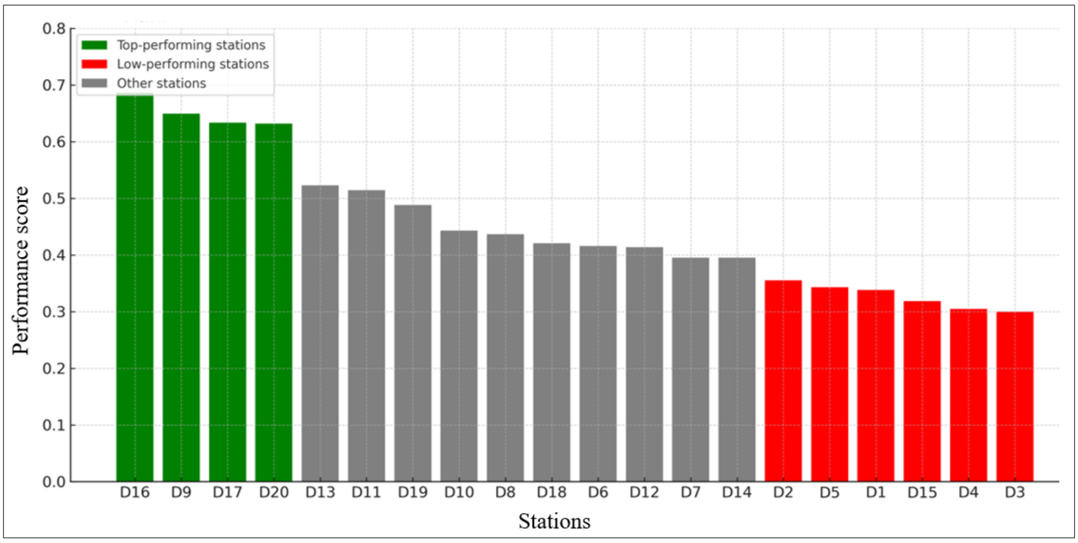

Fig. 1. Performance scores of 20 tram stations assessed, highlighting variations based on operational efficiency and commuter-centric factors

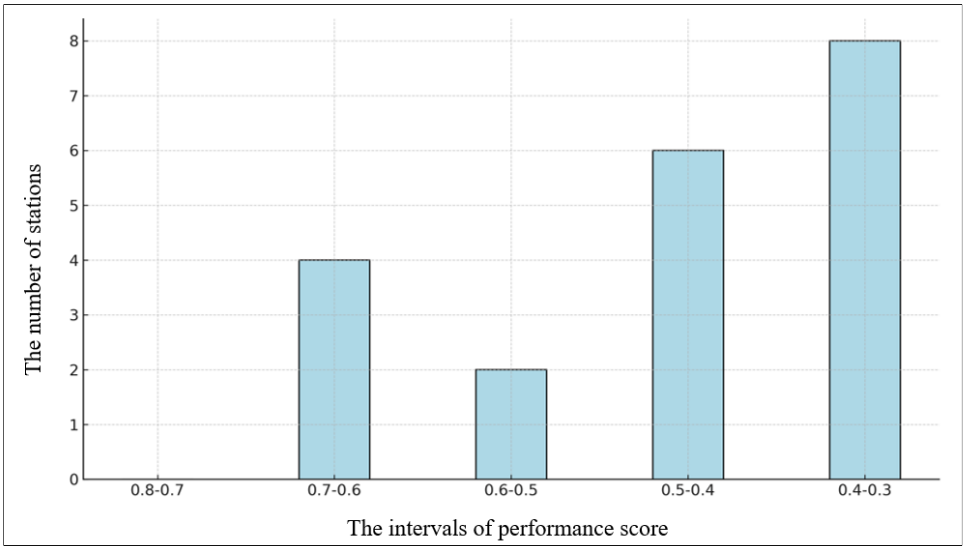

Fig. 2. Distribution of P-score values among the stations

The overall distribution of scores suggests that while a few stations are setting a benchmark for efficiency, there is a general need for network-wide improvements, especially in addressing the human-centric factors that are emphasized in this study. Additionally, the findings in this study validate the significance of integrating both technical and commuter-oriented parameters into RT station performance evaluations. Therefore, the multi-criteria framework provides valuable insights for decision makers aiming to enhance the functionality and attractiveness of urban RT systems, especially in developing cities like Antalya.

4. Conclusions

This study provides actionable insights for optimizing RT systems by aiming to enhance urban livability and promote transportation equity, particularly in developing urban environments. Through the application of the TOPSIS method, a systematic and structured evaluation of 20 tram stations in Antalya, Türkiye, was conducted, offering a replicable framework for improving PT systems in similar contexts.

The analysis reveals that stations D16 and D17 excel due to their high accessibility to food facilities, efficient operations, high service frequencies, and elevated average speeds, although they incur relatively higher platform construction costs. In contrast, RT stations D9, D20, and D13 perform strongly because of their low platform costs, efficient operational metrics, and frequent services. Also, the majority of stations scored between 0.4 and 0.7 which shows a significant room for enhancement across the RT network. Therefore, the results indicate that optimizing station design, improving surrounding amenities, and enhancing service quality may contribute to reliable PT development.

Addressing inefficiencies at underperforming RT stations is essential for improving public satisfaction, operational effectiveness, and the long-term viability of urban PT systems. Importantly, the methodology employed here is highly adaptable and can be applied to other cities globally, offering a structured approach for evaluating and refining urban transportation infrastructure.

By balancing technical performance and human-centric needs, this study supports the broader goal of creating more inclusive, efficient, and commuter-friendly transportation networks worldwide. Thus, the highlights of the research are as follows:

- A holistic TOPSIS-based framework is developed to assess tram station performance in Antalya, Türkiye.
- Both operational efficiency and commuter-centric factors, such as food accessibility and terrain slope, are integrated into the evaluation.
- Stations D16 and D17 excel due to high service frequency, commuter amenities, and operational performance, despite higher platform costs.
- Stations D9, D20, and D13 achieve strong rankings by balancing low construction costs with efficient operations.
- Stations D3, D4 and D15 are identified as the lowest-performing, highlighting the need for targeted improvements in service quality and commuter accessibility.
- The proposed methodology offers a replicable model for improving PT systems in developing cities worldwide.

References

Awasthi, A., Chauhan, S. S., & Omrani, H. (2011). Application of fuzzy TOPSIS in evaluating sustainable transportation systems. *Expert systems with Applications*, *38*(10), 12270-12280.

Celik, E., Gul, M., Gumus, A. T., & Guneri, A. F. (2012). A fuzzy TOPSIS approach based on trapezoidal numbers to material selection problem. *Journal of Information Technology Applications and Management*, *19*(3), 19-30.

de Aquino, J. T., de Melo, F. J. C., Jeronimo, T. D. B., & de Medeiros, D. D. (2019). Evaluation of quality in public transport services: the use of quality dimensions as an input for fuzzy TOPSIS. *International Journal of Fuzzy Systems*, *21*, 176-193.

Demir, E. (2024). Evaluation of Rail Transportation Stops Efficiency in Antalya by Applying Intuitionistic Fuzzy TOPSIS Analysis. *Interdisciplinary Studies on Contemporary Research Practices in Engineering in the 21st Century-VI*, 89.

Görçün, Ö. F. (2021). Evaluation of the selection of proper metro and tram vehicle for urban transportation by using a novel integrated MCDM approach. *Science progress*, *104*(1), 0036850420950120.

Kiciński, M. M., & Solecka, K. (2018). Application of MCDA/MCDM methods for an integrated urban public transportation system–case study, city of Cracow. *Archives of Transport*, *46*(2), 71-84.

Li, J., Xu, X., Yao, Z., & Lu, Y. (2019). Improving service quality with the fuzzy TOPSIS method: a case study of the Beijing rail transit system. *Ieee Access*, *7*, 114271-114284.

Ma, H., Chen, D., & Yin, J. (2020). Riding comfort evaluation based on longitudinal acceleration for urban rail transit—Mathematical models and experiments in Beijing subway. *Sustainability*, *12*(11), 4541.

Mohammadi, A., Amador-Jimenez, L., & Nasiri, F. (2020). A multi-criteria assessment of the passengers' level of comfort in urban railway rolling stock. *Sustainable Cities and Society*, *53*, 101892.

Nordin, N. H., Masirin, M. I. M., Ghazali, M. I., & Azis, M. I. (2016). Passenger rail service comfortability in Kuala Lumpur urban transit system. In *MATEC web of Conferences* (Vol. 47, p. 03011). EDP Sciences.

Roncoli, C., Chandakas, E., & Kaparias, I. (2023). Estimating on-board passenger comfort in public transport vehicles using incomplete automatic passenger counting data. *Transportation Research Part C: Emerging Technologies*, *146*, 103963.

Tsao, H. H., Leu, Y. G., & Chou, L. F. (2025). Developing an Hourly Multi-reservoir Optimization System Adaptable to Extreme Weather Conditions Using Multi-objective Optimization, Fuzzy Logic, and Fuzzy TOPSIS. *International Journal of Fuzzy Systems*, 1-21.

Tzeng, G. H., & Huang, J. J. (2011). *Multiple attribute decision making: methods and applications*. CRC press.

Zhang, X., Liu, H., Xu, M., Mao, C., Shi, J., Meng, G., & Wu, J. (2020). Evaluation of passenger satisfaction of urban multi-mode public transport. *PloS one*, *15*(10), e0241004.

Zhang, X., Zhang, Q., Sun, T., Zou, Y., & Chen, H. (2018). Evaluation of urban public transport priority performance based on the improved TOPSIS method: A case study of Wuhan. *Sustainable cities and society*, *43*, 357-365.

4th International Civil Engineering & Architecture Conference
17-19 May 2025, Trabzon, Türkiye

Samsun E1 bus route analysis: Impacts of urban traffic regulations on public transportation

Dilara D. Erakman*[1], Erhan B. Pancar[1]

[1] *Ondokuz Mayıs University, Department of Civil Engineering, 55100 Samsun, Türkiye*

Abstract. The study focuses on analyzing the impacts of urban traffic regulations on public transportation by examining the E1 bus route in Samsun. The E1 route is a significant public transport corridor connecting the Canik, İlkadım, and Atakum districts and plays a critical role in providing access to Ondokuz Mayıs University Campus. The research addresses the effects of traffic regulations on the efficiency of this route, passenger satisfaction, and overall urban traffic. The study investigates changes in stop usage, travel times, passenger density at stops, and the general performance of the route. Particular attention is given to the impact of tramway extensions and other transportation projects on the E1 line. Data were collected through field studies and numerical analysis methods, and indicators reflecting the current situation were analyzed. Passenger numbers, changes in travel times between stops, and service frequency were thoroughly examined to compare the route's conditions before and after traffic regulations. Additionally, the effects of bus usage on traffic flow in high-demand areas were explored. The primary goal of this research is to develop improvement recommendations aimed at making public transportation systems more attractive by reducing individual car use. It seeks to enhance public transport efficiency, improve user satisfaction, and support environmental sustainability. The findings provide valuable insights for the planning of the Samsun E1 bus route and for implementing urban traffic regulations more effectively. The study aims to contribute significantly to solving urban transportation challenges and improving public transportation systems.

Keywords: Public transport efficiency; Traffic regulations; Traffic impact; Passenger flow; Sustainability

1. Introduction

Transportation refers to various systems and infrastructures that enable the movement of people and goods from one place to another, encompassing different modes such as land, sea, air, and railways. These modes offer various advantages depending on geographical conditions and societal needs, playing a critical role in achieving economic development and social welfare. Efficient and effective transportation systems contribute to the growth of trade volume, a more spatially efficient distribution of the workforce, and the optimization of resource usage. The effective management of transportation systems is a significant tool in reducing urban issues such as traffic congestion, environmental pollution, and energy consumption. Particularly, environmentally friendly and sustainable transportation solutions serve the goals of reducing carbon emissions and increasing energy efficiency. Moreover, the development of transportation infrastructure supports social equity by enhancing the accessibility opportunities of all segments of society within urban areas. Therefore, transportation is considered a multidimensional concept that directly affects not only individuals' daily mobility but also quality of life, economic competitiveness, and sustainable urbanization goals. In this context, public transportation systems play an indispensable role in urban transportation and have become one of the determining factors of quality of life in developed societies. In our country as well, reflecting the social state approach, various improvement efforts have been made in public transportation infrastructures to ensure that citizens can travel safely, quickly, and comfortably. These initiatives, including the expansion of networks of roads, stops, trams, metros, and buses, have aimed to increase the rate of public transportation usage. However, these efforts have been limited in achieving a transformation sufficient to reduce the widespread use of private vehicles. The continued preference for private vehicles can be attributed to several factors, such as the insufficient coverage of public transportation networks across the entire city, the long distances to access stops, low service frequencies, excessive crowding in public transport vehicles, and uncertain waiting times at stops. Additionally, the inability of public transport services to match the comfort level provided by private vehicles constitutes a significant barrier. All these factors make it difficult for individuals to voluntarily prefer public transportation, leading to efficiency losses in urban transportation systems.

* Corresponding author, E-mail: dilaradenizerakman@hotmail.com

https://doi.org/10.31462/icearc2025_ce_tra_656

In this study, the E1 bus line in Samsun province was examined to analyze the effects of urban traffic regulations on public transportation performance. The Samsun E1 line operates between the districts of Canik, İlkadım, and Atakum, serving as a critical transportation corridor, especially for access to the Ondokuz Mayıs University Campus. The research analyzed indicators such as stop usage, travel times, service frequencies, and passenger densities through field studies and quantitative analyses. Based on the findings, the overall performance of the line was evaluated, and the impacts of current traffic regulations on public transportation efficiency were examined. The main objective of the study is to develop strategies that will reduce the use of private vehicles, increase the attractiveness of public transportation, and contribute to environmental sustainability and energy efficiency goals. Based on the findings, suggestions for more effective planning of the Samsun E1 line are presented, contributing to the adoption of a public transportation-oriented approach in urban mobility. In this regard, the study aims to offer valuable contributions to both the literature and practice concerning the rational management of urban transportation and the improvement of public transportation systems.

1.1. Literature review

Public transportation systems in urban areas have been developed to offer sustainable solutions to challenges such as increasing population density, traffic congestion, and environmental concerns. By providing an alternative to private vehicle use, public transportation contributes to enhancing transportation efficiency, reducing environmental impacts, and supporting social mobility (Kaya, 2024). Comprising various modes such as buses, trams, metros, commuter trains, and ferries, public transportation systems are structured according to the geographical and socio-economic conditions of cities, offering different advantages. Among these, bus systems particularly stand out in many cities due to their flexible route structures and low infrastructure costs. The role of public transportation in reducing environmental impacts, alleviating traffic congestion, and addressing socio-economic inequalities has become even more critical today. Numerous studies have emphasized that public transportation is an effective solution for mitigating negative externalities caused by private vehicles, such as carbon emissions, air pollution, and traffic accidents (Culum, 2013). In this context, it is essential to continually improve public transportation systems in terms of accessibility, punctuality, and comfort. The integration of urban traffic regulations with public transportation systems has emerged as an important research area aimed at enhancing transportation efficiency and reducing congestion in cities. Tona, Maraş, and Demir (2024) analyzed intersection densities along Atatürk Boulevard in the Atakum district of Samsun using Geographic Information Systems (GIS) and found that implementing grade-separated intersections and modern roundabouts, particularly in high-density areas such as the Karayolları Intersection, could significantly improve traffic flow. Their findings highlight the importance of intersection improvements on urban main arteries, especially along routes with intense passenger movements like the E1 bus line (Tona, Maraş, & Demir, 2024). Research focusing on the optimization of bus service schedules in urban areas is also closely linked to traffic management. In a study conducted by Polat, Sağbaş, and Dermenci (2024), the optimization of bus services was achieved through linear goal programming methods, targeting reductions in fuel consumption and carbon emissions. Optimizing service schedules not only increases cost-effectiveness but also makes significant contributions to environmental sustainability (Polat, Sağbaş, & Dermenci, 2024). Applying such optimization models to the Samsun E1 line could present considerable opportunities for enhancing both environmental and operational efficiency.

Studies addressing transportation issues on a national scale in Turkey have shown that increasing numbers of motor vehicles have led to major problems such as traffic congestion, insufficient public transportation, and parking shortages (Bostancı & Tanrıvermiş, 2024). Field studies conducted in Ankara suggest that increasing the availability of bicycle lanes, making public transportation more attractive, and ensuring integration between different transportation modes could offer effective solutions to traffic-related problems. These strategies could likewise be beneficial for medium-sized cities like Samsun. Furthermore, an examination of the historical development of urban transportation planning practices in Turkey reveals that a focus on short-term solutions and the insufficient integration of sustainable transportation policies have limited planning effectiveness (Karataş Çifçi & Düzgün, 2024). Therefore, it is crucial to adopt long-term, integrated, and environmentally friendly transportation policies in the planning of major public transportation routes such as the E1 line. Research on demand forecasting and route planning for public transportation systems emphasizes that monitoring passenger movements through electronic systems and applying dynamic planning based on such data can enhance service quality (Ozan, Ceylan, Haldenbilen, & Yaşar, 2010; Arıç Döner, 2012). Implementing passenger movement-based planning on the Samsun E1 line could enable more efficient use of bus capacity and allow the optimization of service frequencies based on actual demand. Finally, a study by Çalışkan (2020) on the effectiveness of bus-priority lanes revealed that such applications significantly reduce travel times for public transportation and positively influence user preferences. Planning bus-priority lanes along specific corridors of the Samsun E1 line could enhance public transportation efficiency while reducing traffic congestion caused by private vehicles. In light of all these findings, it is possible to improve the usage rates of public transportation and achieve a more organized urban traffic flow in Samsun city center through traffic regulations, intersection improvements, service optimizations, and bus-priority applications implemented along the E1 bus line.

2. Materials and methods

When evaluated specifically within the context of Samsun city, the E1 bus line, which is a key component of the public transportation system, provides a connection between the districts of Canik, İlkadım, and Atakum. Extending along the main arteries surrounding the city center, this line experiences high passenger circulation, particularly during commuting hours, and meets a significant portion of the city's internal transportation demand. The buses operating on the E1 line are equipped with advanced technological systems such as large passenger capacities, electronic ticketing systems (Samkart), GPS-based real-time location tracking, digital information displays, and stop announcement systems. Moreover, the selection of environmentally friendly vehicles aims to minimize emissions, thereby supporting environmental sustainability. The implementation of Intelligent Transportation Systems (ITS) in Samsun has made significant contributions to enhancing the efficiency of traffic management and improving the functionality of public transportation systems. Traffic management systems monitor city traffic flow in real-time and allow for dynamic adjustment of traffic lights based on congestion levels (Samsun Metropolitan Municipality, 2023). Supported by sensors and cameras, these systems continuously measure traffic density and direct drivers to alternative routes by detecting potential bottlenecks early. Additionally, smart bus stops enable passengers to track bus arrival times via digital screens, thus allowing for more efficient use of waiting times. GPS-based bus tracking systems also facilitate real-time monitoring of bus locations along their routes, thereby contributing to more reliable operations. Analyses conducted specifically for the E1 line indicate that its extensive network connects key points in the city, frequent services reduce passenger waiting times, and high-capacity buses ensure efficient transportation. However, it has been identified that during morning and evening peak hours, service comfort levels decrease due to overcrowding, service times become irregular due to dependence on urban traffic, journey times are extended because of the long route, and passenger satisfaction is negatively affected by large distances between some stops. Furthermore, during periods of high urban traffic density, prolonged waiting times at traffic lights hinder the timely operation of the line. Over the years, significant structural changes have been made in the city’s transportation systems. Intersection layouts in Samsun have been extensively revised; additional lanes have been added to certain intersections, turning radii of roundabouts have been expanded, and many intersections have been equipped with intelligent traffic management systems. Electronic control systems (EDS) have been established to enhance road safety, and roadside enforcement infrastructure has been strengthened. Bus stops have been upgraded by adding bus bays or expanding existing ones, thus allowing buses to load and unload passengers without disrupting traffic flow. Additional bays have also been created at intersections to support turning movements.

Meanwhile, various changes have occurred within the fleet of the Samsun E1 bus line. At one point, electric buses were introduced but later withdrawn, and articulated buses were incorporated into the fleet instead. Although most vehicles are now newer models, a limited number of older buses remain in operation. Furthermore, with the extension of the tram line to the Ondokuz Mayıs University campus, the campus shuttle bus service was discontinued, and adjustments were made to the organization of public transportation services. Under the scope of bus route modifications, new stops have been added, and the route of the E1 line has been revised over time. Initially comprising 32 stops, the number has increased to 39 following the adjustments. Moreover, the diversification of bus routes serving the E1 corridor has directly influenced stop-based passenger movement. To enhance service quality, measures such as organizing additional services during peak hours, increasing the number of articulated buses, expanding heavily used stops, implementing bus-priority lanes, and granting priority to buses at traffic lights are proposed. In addition, integrating real-time bus tracking systems with mobile applications, installing digital information displays at stops, and increasing infrastructure improvements to facilitate access for disabled individuals are among the measures expected to boost passenger satisfaction. It is further suggested that Samsun could benefit from best practices exemplified by the Munich public transportation system, including integrated ticketing, real-time information dissemination, public transportation-prioritized policies, and environmentally friendly transport infrastructure. The Munich model, with its emphasis on sustainability, integration, and user-oriented transportation principles, serves as a significant example for developing cities like Samsun (Arslan, 2010). In conclusion, enhancing the effectiveness of public transportation in Samsun requires both the optimization of existing routes and the broader integration of intelligent transportation systems. Regular monitoring of heavily used bus lines such as the E1 through systematic data analysis, implementing flexible planning based on emerging needs, and carrying out passenger-oriented improvement initiatives will make substantial contributions to achieving a more sustainable and efficient urban transportation system.

2.1. Characteristics of the E1 (express) bus line

The E1 (Express 1) bus line, operating in Samsun, is an important component of the city's urban public transportation system. Managed by SAMULAŞ Inc., a subsidiary of the Samsun Metropolitan Municipality, the line connects the districts of Canik, İlkadım, and Atakum, operating between Belediye Evleri (Canik) and Ondokuz Mayıs University Faculty of Education (Atakum). The majority of the route runs along Atatürk Boulevard, passing through central locations such as Cumhuriyet Square, Samsun Bus Terminal, and the Atakum coastal area, thus meeting various transportation needs related to work, education, and social activities. The line comprises a total of

44 stops, and a single trip takes approximately 54 minutes. Weekday services operate between 06:15 and 23:00 at intervals of 15–20 minutes, while weekend services operate between 06:35 and 23:00 at intervals of 20–25 minutes; in addition, regular services are also provided during night hours. The vehicles operating on the E1 line are predominantly BMC Procity brand buses, equipped with Euro 6 standard engines, featuring a 6.7-liter engine capacity and 209 kW (284 PS) of power. These buses are fitted with automatic transmissions and have a total passenger capacity of 163, including 39 seated and 124 standing passengers. Currently, a total of eight vehicles are allocated to the E1 (Express 1) line. Seven of these vehicles are newly designed, articulated buses with a length of 18 meters. The other vehicle is an older model 12-meter-long bus, which has a lower passenger capacity compared to the new-generation articulated buses. As part of the service scheduling plan, each bus completes six or seven trips per day on a rotational basis. The E1 line utilizes modern payment systems, including Samkart and mobile payment options, and by offering 24-hour uninterrupted service, it significantly enhances accessibility and safety in urban transportation, thereby playing a critical role in strengthening the effectiveness of public transportation in Samsun.

2.2. E1 (eXPRESS 1) route and service frequency

The E1 (Express 1) bus line operates along a route that begins at the Soğuksu stop in the Canik district of Samsun and extends to the Karadeniz Male Student Dormitory stop in the Atakum district (Fig. 1). This route structure connects the three major central districts of the city: Canik, İlkadım, and Atakum. Starting from Belediye Evleri and continuing along Atatürk Boulevard to the University Junction, the route passes through key business, educational, and social hubs of the city, effectively meeting daily transportation demands. This strategic route selection is one of the key factors supporting the high usage of the line. The service times and frequencies of the E1 bus line are presented in Table 1.

Table 1. Service Times and Frequencies (SAMULAŞ, 2025)

Time Interval	Average Service Interval on Weekdays (minutes)	Average Service Interval on Weekends (minutes)
00:00 - 00:59	60 minutes	60 minutes
01:00 - 01:59	60 minutes	60 minutes
02:00 - 02:59	-	-
03:00 - 03:59	60 minutes	60 minutes
04:00 - 04:59	-	-
05:00 - 05:59	60 minutes	60 minutes
06:00 - 06:59	13 minutes	20 minutes
07:00 - 07:59	10 minutes	20 minutes
08:00 - 08:59	10 minutes	20 minutes
09:00 - 09:59	13 minutes	20 minutes
10:00 - 10:59	13 minutes	22.5 minutes
11:00 - 11:59	15 minutes	20 minutes
12:00 - 12:59	20 minutes	25 minutes
13:00 - 13:59	20 minutes	22.5 minutes
14:00 - 14:59	20 minutes	20 minutes
15:00 - 15:59	20 minutes	25 minutes
16:00 - 16:59	22 minutes	22.5 minutes
17:00 - 17:59	20 minutes	20 minutes
18:00 - 18:59	20 minutes	25 minutes
19:00 - 19:59	20 minutes	22.5 minutes
20:00 - 20:59	20 minutes	20 minutes
21:00 - 21:59	20 minutes	-
22:00 - 22:59	20 minutes	30 minutes
23:00 - 23:59	-	-

Fig. 1. E1 (Express 1) line route (SAMULAŞ, 2025)

The E1 (Express 1) line schedules frequent services on selected corridors to minimize travel time losses and deliver faster service to passengers. Its operational efficiency is enhanced by carefully optimizing the distances between stops. Moreover, the specific stop names and their inter-stop distances play a crucial role in streamlining the line's overall performance. Detailed information on the stop names and distances for the E1 (Express 1) line is provided in Table 2 below.

Table 2. E1 (Express 1) Stop Names and Inter-stop Distances

Stops	Distance Between Stops (m)	Stops	Distance Between Stops (m)
Soğuksu	0	Hanimeli	330
Gazi Giray Sokak	920	Ömürevleri	810
Iğdır Sokak	440	Olimpik Yüzme Havuzu	315
Canik Belediyesi	280	Meteoroloji	480
Belediye Evleri Aktarma	600	Atakent	330
19 Mayıs Stad Kavşağı	115	Yenimahalle	790
Samsunspor	1100	Çankaya	960
Kılıçdede	650	Pelitköy	350
Gar	700	Körfez	640
Cumhuriyet Meydanı	715	Eczaneler	670
Büyük Cami	610	Lojmanlar	730
Gençlik Parkı	930	Hastane Poliklinikler	1020
Samsun Müzesi	670	Tıp Fakültesi	380
Baruthane	1550	Spor Bilimleri Fakültesi	515
Kenan Şara Köprüsü	470	İlahiyat Fakültesi	790
Güzel Sanatlar Fakültesi	580	Sağlık Bilimleri	240
Saski	590	Ziraat Fakültesi	740
Atakum Endüstri Meslek Lisesi	740	Mühendislik Ek Bina	300
Büyükşehir Sanat Merkezi	790	Mühendislik Fakültesi	500
İlkadım Öğrenci Yurdu	550	Fen Edebiyat Fakültesi	320
Mimar Sinan	360	Eğitim Fakültesi	370
Türkiş	1000	Karadeniz Erkek Yurdu	600
Total		26540	

3. Findings and discussion

In this study, data from three different years has been evaluated between the dates of March 9, 2019 - March 20, 2019, March 21, 2022 - April 2, 2022, and March 12, 2025 - March 24, 2025. To capture different segments of the week, measurements were conducted on Monday (start of the week), Wednesday (midweek), and Saturday (weekend), each day at 09:00, 12:00, and 17:00. The route segment between Belediye Evleri and the Faculty of Education was selected as the study area, and passenger boarding and alighting counts, waiting times at stops, and delays at traffic signals were recorded; the average vehicle speeds were also calculated. For the 2025 measurements, boarding and alighting durations were determined in detail. In addition to these quantitative data, field observations were used to identify problematic stops, passenger difficulties, and traffic flow issues at intersections. Thus, the aim was to perform a comprehensive analysis of operational disruptions, passenger service quality, and traffic regulation along the corridor. The collected data including trip-related metrics such as stop and signal waiting times, total trip duration, average speed, and overall time losses were analyzed to assess changes in service performance over the years. Measurements were taken in 2019, 2022, and 2025 on Monday, Wednesday, and Saturday at 09:00, 12:00, and 17:00. Based on these findings, Table 3 was constructed to illustrate the temporal evolution of service performance indicators.

Table 3. Service Performance Indicators and Time Management Data

Service Performance Indicators and Time Management Data	2019	2022	2025
Number of Passengers Using Samkart per Trip	1085	1059	1682
Total Waiting Time at Stops (min)	218.36	8078	12068
Total Waiting Time at Traffic Signals (min)	49.08	2490	5638
Trip Duration (min)	899	861	995
Average Speed (km/h)	37.61	35.24	32.24
Total Time Loss (min)	267.45	176.13	295.1

In 2019, an average of 1,085 passengers were transported per trip, which slightly decreased to 1,059 in 2022. However, by 2025, the number increased significantly to 1,682. During the same period, there were notable increases in the total waiting times at stops and at traffic lights. The total waiting time at stops was 218.36 minutes in 2019, which increased to 8,078 minutes in 2022 and reached 12,068 minutes in 2025. Waiting times at traffic lights followed a similar trend. Examining average speed data, it was found that the speed, which was 37.61 km/h in 2019, decreased to 35.24 km/h in 2022 and further dropped to 32.24 km/h in 2025. Although trip durations decreased slightly in 2022 compared to 2019, they rose again in 2025, reaching 995 minutes. Total time loss was at its lowest level in 2022 but increased significantly in 2025 to 295.10 minutes. These findings indicate that the increase in passenger numbers has negatively impacted trip performance by extending waiting times at stops and traffic lights. The boarding and alighting times, as well as the waiting times at stops, for the E1 bus line stops in Samsun were compared for the years 2019, 2022, and 2025 (Table 4).

The findings indicate that significant changes in stop-based travel behavior occurred over the years. Notably, the Belediye Evleri stop, which recorded zero boardings in 2019, experienced a remarkable increase to 185 boardings by 2025. This growth may be related to route adjustments or changes in local population density. Conversely, the Stad Kavşağı stop saw an 80% decrease in boardings accompanied by a dramatic reduction in waiting times, possibly due to a loss of function at that stop or the emergence of alternative transport options. At the Samsunspor stop, boardings more than doubled, and waiting times increased substantially, suggesting that new developments in the area or shifts in public transport preferences have driven this trend. In the centrally located Cumhuriyet Meydanı stop, boardings decreased while alightings increased, indicating its growing role as a transfer point or final destination. Both the Güzel Sanatlar and Eczaneler stops recorded significant increases in boardings and alightings, along with marked rises in waiting times, implying the emergence of new attraction points around these stops. At some stops, alightings increased even as boardings declined (e.g., Poliklinikler and Tıp Fakültesi), while other stops (e.g., Fen-Edebiyat Fakültesi) experienced decreases in both directions. The most pronounced variations in passenger movements between 2019 and 2025 at each stop are summarized in Table 5.

These findings may indicate changes in the user profile around the stops or shifts in service delivery in the region. Based on the data obtained, it can be concluded that significant spatial and temporal changes have occurred on the Samsun E1 bus line over the years. The sudden increase in boardings at certain stops, such as Belediye Evleri, can be explained by the introduction of new residential areas, route changes, or an increase in the attractiveness of public transportation. In particular, the increase in waiting times should be considered a result of the higher passenger volume at these stops. On the other hand, the dramatic decrease in boardings at stops like Stad Kavşağı suggests a reduction in the need for public transportation in that area, or that passengers have shifted to alternative transportation modes. The decrease in boardings but increase in alightings at Cumhuriyet Meydanı indicates that the stop is being used more as a point of alighting towards the city center. This situation reveals a shift in demand towards central areas in Samsun's transportation network. The increases observed at stops such as Güzel Sanatlar and Eczaneler can be associated with the emergence of new services, educational, or healthcare facilities on a micro scale. Particularly high alightings and low boardings around university campuses (such as the Faculty of Medicine, Dentistry, etc.) suggest that these areas are primary destinations during the day, but the return trips occur on different lines. These data provide valuable information that can be used in decision-making processes such as route optimization, stop-based improvements, and resource allocation based on passenger density in urban transportation planning. Additionally, it has been highlighted that user trends can change over time, indicating the importance of developing data-driven dynamic transportation management policies.

Table 4. Samsun E1 Bus Line Stop-Based Passenger Movements and Waiting Times (2019-2025)

Stop Name	2019 Input	2022 Input	2025 Input	2019 Output	2022 Output	2025 Output	2019 Waiting Time (sec)	2022 Waiting Time (sec)	2025 Waiting Time (sec)
Belediye Evleri	0	33	185	0	0	8	880	554	1036
Stad Kavşağı	186	287	38	0	0	1	4498.74	732	379
Samsunspor	53	81	109	0	0	16	235.58	316	1021
Kılıçdede	70	91	101	3	1	11	354.05	439	501
Gar	52	79	64	2	4	32	299.16	416	442
Cumhuriyet Meydanı	171	106	106	21	22	136	726.44	533	999
Büyük Cami	124	108	170	14	2	71	544.63	434	918
Gençlik Parkı	28	20	26	4	2	17	249.92	196	278
Fener	8	7	6	3	0	7	65.4	54	133
Baruthane	26	33	12	5	11	20	141.14	220	201
Güzel Sanatlar	27	10	54	15	3	39	186.93	95	472
Karayolları (SASKİ)	8	4	18	17	13	45	121.3	102	301
Teknik Lise	69	27	51	46	48	55	388.67	331	511
İlkadım Öğrenci Yurdu	46	60	2	46	27	17	371.57	533	422
Mimar Sinan	13	14	10	29	20	28	211.21	280	290
Türk-İş	74	51	54	70	89	144	423.63	456	465
Ömürevleri	38	23	19	33	53	77	307.97	446	522
Meteoroloji	7	5	11	24	36	56	184.76	164	443
Atakent	34	38	22	59	95	64	327.13	336	260
Yeni Mahalle	19	19	10	35	42	83	302.1	236	277
Pelitköy	7	6	4	25	24	42	233.5	384	371
Eczaneler	1	20	22	36	63	63	185.85	278	565
Lojmanlar	0	0	1	5	3	8	43.62	39	81
Poliklinikler	1	3	2	48	96	69	223.67	331	240
Tıp Fakültesi	4	1	2	59	54	54	267.86	235	209
Diş Hekimliği	0	2	0	54	49	37	223.19	142	147
İktisat (İlahiyat) Fak.	0	0	0	64	49	71	220.22	222	241
Sağlık Fak.	0	0	0	58	20	38	171.39	104	75
Ziraat Fakültesi	0	0	0	67	67	61	236.07	228	185
Mühendislik Fakültesi	0	0	0	88	40	26	246.92	182	240
Fen-Edebiyat Fakültesi	0	0	0	57	29	8	160.56	86	37
Eğitim Fakültesi	0	0	0	98	50	74	180	179	185

Table 5. Summary of the Most Significant Changes (2019–2025)

Stop Name	Summary of Changes
Belediye Evleri	Boardings rose from zero in 2019 to 185 in 2025. Waiting time increased by 17%.
Stad Kavşağı	The number of boardings decreased from 186 to 38 (an 80% decrease). Waiting time significantly decreased.
Samsunspor	Boardings increased from 53 to 109 (a 105% increase). Waiting time quadrupled.
Cumhuriyet Meydanı	Boardings decreased (171 → 106), while alightings increased (21 → 136). Waiting time increased by 37%.
Büyük Cami	Both boardings and alightings increased. Waiting time nearly doubled.
Güzel Sanatlar	Boardings increased from 27 to 54, and alightings rose from 15 to 39. Waiting time increased by 150%.
İlkadım Öğrenci Yurdu	Boardings decreased dramatically (46 → 2). Waiting time fluctuated irregularly.
Türk-İş	Boardings remained stable, while alightings doubled.
Atakent	Boardings decreased by 35%, while alightings slightly increased. Waiting time decreased.
Eczaneler	Boardings increased from 1 to 22, and alightings rose from 36 to 63.
Poliklinikler	Boardings were low, while alightings nearly doubled.
Tıp Fakültesi	Boardings remained very low, while alightings stabilized. Waiting time decreased.
Fen-Edebiyat Fakültesi	There were no boardings, and alightings significantly decreased (57 → 8). Waiting time decreased by 77%.

4. Conclusion

This study was conducted to evaluate the performance of the E1 (Express 1) bus line in Samsun, analyze the effects of urban traffic regulations on public transportation, and reveal the temporal and spatial changes in passenger mobility. Measurements and field observations were made using data from three different years (2019, 2022, and 2025), and it was determined that significant dynamic changes had occurred in the line's operation. Notably, a distinct increase in passenger density was observed, with the number of passengers per trip rising from 1,085 in 2019 to 1,682 in 2025. Additionally, it was found that the waiting times at stops and at traffic lights had significantly increased, average speed had decreased, and total time loss had risen. This situation indicates that the increasing passenger demand and traffic congestion have negatively impacted trip performance. In stop-based analyses, significant increases in passenger boardings and alightings were recorded at stops such as Belediye Evleri, Samsunspor, and Güzel Sanatlar, while severe passenger losses occurred at stops like Stad Kavşağı. These results show that changes in urban dynamics and route adjustments directly reflect on public transportation usage habits. Furthermore, despite technical and operational improvements made on the E1 line, excessive congestion during peak hours and irregularities in trip durations have prevented service quality from reaching the desired level. It is understood that additional structural and managerial adjustments are needed for public transportation to become a strong alternative to individual vehicle use across the city.

Based on the findings, the following recommendations can be made to increase the efficiency of the Samsun E1 bus line and to make public transportation a more effective alternative for urban mobility. To improve the effectiveness of urban transportation and enhance the attractiveness of public transport, various structural and managerial improvements need to be implemented for the Samsun E1 line. Firstly, the establishment of bus-priority lanes in areas with high traffic congestion along the route and the prioritization of public transport vehicles at intersections will help reduce irregularities in trip durations. Additionally, increasing the frequency of trips during periods of high passenger movement and strengthening the existing fleet with high-capacity, new-generation buses will help improve service quality sustainably. Physical expansion efforts should be made at bus stops to reduce waiting times, and infrastructure adjustments for disabled individuals should be implemented considering accessibility criteria. Furthermore, to enable public transport users to obtain real-time information about bus schedules and locations, digital information screens should be placed at stops, and this information should be synchronized with mobile applications to enhance the passenger experience. Regular analysis of passenger mobility data and dynamic route and schedule planning based on these data will also increase operational efficiency. In line with environmental sustainability goals, the inclusion of electric or low-emission vehicles in the fleet should be encouraged, and strategies such as campaigns to promote public transportation usage and integrated ticketing systems should be implemented. Finally, by examining the best practices of integrated transportation policies in Munich's public transport system and adapting them to Samsun, a holistic and user-oriented model for urban transportation can be developed.

References

Kaya, Ö. (2024). Şehir içi ulaşımda sürdürülebilir mikromobilite: Müşteri tercihlerine dayalı bir inceleme. Iğdır Üniversitesi Fen Bilimleri Enstitüsü Dergisi, 14(4), 1576-1589. https://doi.org/10.21597/jist.1491968 (In Turkish)

Culum, C. (2013). *Trafik sinyal sürelerinin optimizasyonu ve çevre kirliliği üzerine etkisinin incelenmesi* (Yüksek lisans tezi, Bahçeşehir Üniversitesi, İstanbul). (In Turkish)

Samsun Büyükşehir Belediyesi. (2024). *Kent İçi Toplu Ulaşım Yönetmeliği*. Samsun: SBB Ulaşım Dairesi Başkanlığı. (In Turkish)

Arslan, O. (2010). Kaliteli Bir Toplu Taşıma Sistemi Nasıl Olmalıdır, Münih Örneği. *TMMOB İnşaat Mühendisleri Odası İstanbul Şubesi 9. Ulaştırma Kongresi*, 16-18. (In Turkish)

Bostancı, S., & Tanrıvermiş, Y. (2024). Türkiye'de kent içi ulaşım sorunları ve çözüm önerileri: Ankara ili örneği. *Kent Akademisi Dergisi, 17*(2), 346-368. https://doi.org/10.35674/kent.1408317 (In Turkish)

Çalışkan, G. (2022). *Kent içi ulaşım ağlarında otobüs öncelikli şeritlerin etkinliğinin araştırılması* (Yüksek lisans tezi). Pamukkale Üniversitesi Fen Bilimleri Enstitüsü, Denizli. (In Turkish)

Arıç Döner, M. (2012). *Otobüsle toplu taşımada yolcu hareketlerinin analizi ile hat planlama; İzmir için bir örnek çalışma* (Yüksek lisans tezi). Bahçeşehir Üniversitesi, İstanbul. (In Turkish)

Polat, U., Sağbaş, A., & Dermenci, M. S. (2022). Sürdürülebilir ulaşım planlaması için şehir içi otobüs hatlarında sefer çizelgeleme optimizasyonu. *Uludağ Üniversitesi Mühendislik Fakültesi Dergisi, 27*(3), 1099. https://doi.org/10.17482/uumfd.848950 (In Turkish)

Karataş Çifçi, G. B., & Düzgün, Ü. A. (2024). Kentsel ulaşım planlamasında arazi kullanımı: Ankara ili örneği. *Kent Araştırmaları Dergisi (Journal of Urban Studies), 16*(45), 1644-1673. https://doi.org/10.31198/idealkent.1539407 (In Turkish)

Tona, A. U., Maraş, E. E., & Demir, V. (2024). Mevcut kavşakların işlevlerinin (yoğunluklarının) CBS ortamında değerlendirilmesi (Samsun- Atakum örneği). *Geomatik, 9*(1), 12-26. https://doi.org/10.29128/geomatik.1258135 (In Turkish)

Ozan, C., Ceylan, H., Haldenbilen, S., & Yaşar, A. B. (2010). Kent içi otobüs taşımacılığında talep tahmini ve fiyat analizleri: Denizli örneği. *Mühendislik Bilimleri Dergisi, 12*(1), 47-61.

Samsun Büyükşehir Belediyesi. (n.d.). *Otobüs hareket saatleri*. Retrieved from https://samsun.bel.tr/icerik/otobus-hareket-saatleri (In Turkish)

Estimation of air pollution indices from road transport in Turkey for 2024 based on fuel types using the IPCC Tier 2 Method

Muhammed Enes Çelebi*[1], Emre Kuşkapan[1]

[1] *Erzurum Technical University, Engineering and Architecture Faculty, Erzurum, Turkey*

Abstract. Road transport is one of the largest sources of greenhouse gas emissions and air pollution on a global scale. Vehicles relying on fossil fuels, in particular, stand out as the primary sources of environmentally harmful pollutants such as CO_2, CO, NO_x, and PM. The amount of emissions varies significantly depending on the fuel type and engine technology. This variation necessitates the detailed and accurate calculation of emissions in efforts to mitigate air pollution. The IPCC Tier 2 methodology is one of the most advanced methods used in this field, enabling more precise evaluations of emissions by taking detailed parameters such as vehicle types, fuel consumption, and engine efficiency into account. In this study, the registered motor vehicle inventory in Turkey for 2024 is analyzed based on fuel types, and air pollution indices caused by road transport are calculated using the IPCC Tier 2 methodology. In line with data from Turkish Statistical Institute, detailed analyses are conducted on fuel consumption, engine technologies, and annual mileage performance of vehicles. Key emission types, including CO_2, CH_4, N_2O, CO, and PM, are calculated, revealing the environmental impacts of Turkey's vehicle fleet. The results highlight the significant share of diesel and gasoline vehicles in greenhouse gas emissions and air pollution in Turkey. Conversely, it is shown that widespread adoption of electric vehicles could substantially reduce emissions from road transport. This study provides actionable insights and solutions for developing sustainable transportation policies and improving air quality, serving as a guide for Turkey to achieve its environmental goals.

Keywords: Air pollution; Road transport; IPCC Tier 2 Method; Emission factors; Fuel types; Sustainable transportation

1. Introduction

Road transport, especially passenger car usage, is considered one of the most significant sources of air pollution worldwide. According to the World Health Organization (WHO) and the European Environment Agency (EEA), a substantial portion of measured urban pollutants such as particulate matter ($PM_{2.5}$), nitrogen dioxide (NO_2), and ozone (O_3) originates from motor vehicles (WHO, 2021; EEA, 2022). Automobiles, particularly those powered by fossil fuel-based internal combustion engines, release considerable amounts of pollutants through exhaust emissions, negatively impacting both environmental quality and human health.

Advanced calculation methods such as the IPCC Tier 2 methodology allow for a more accurate estimation of automobile emissions by differentiating according to fuel types. These methods provide detailed calculations for major pollutants such as carbon dioxide (CO_2), methane (CH_4), nitrogen oxides (NO_x), and particulate matter, considering the different emission profiles of gasoline, diesel, and alternative-fuel vehicles (IPCC, 2006). Such comprehensive approaches play a critical role in the development of air pollution mitigation strategies for countries and cities.

Pollutants such as nitrogen dioxide (NO_2) and particulate matter ($PM_{2.5}$) emitted from automobiles directly contribute to increased rates of respiratory diseases, cardiovascular disorders, and premature deaths. Especially diesel-powered vehicles have significantly higher emission factors for NO_x and PM compared to gasoline-powered vehicles (Kuşkapan, 2024). Studies conducted in Turkey also reveal that a significant portion of measured NO_2 concentrations in major cities can be attributed to automobile emissions and show a strong correlation with traffic density (Coşkun & Oktay, 2020)

Although the use of electric and hybrid vehicles has been increasing in recent years, the share of fossil-fueled automobiles in Turkey's road transport remains quite high as of 2024. This situation leads to the continued contribution of the transport sector to both greenhouse gas emissions and local air pollutants. Particularly during

*Corresponding author, E-mail: muhammed.celebi52@erzurum.edu.tr

https://doi.org/10.31462/icearc2025_ce_tra_704

peak traffic hours, emissions from motor vehicles can seriously impact human health, even with short-term exposure (Anenberg et al., 2019).

In this context, in developing countries like Turkey, monitoring, modeling, and reducing emissions from automobiles are of great importance. Emission estimates conducted using the IPCC Tier 2 methodology provide detailed data categorized by fuel type, forming the scientific basis for strategies such as establishing low-emission zones, promoting public transport, and increasing the use of alternative-fuel vehicles. Thus, it would be possible to improve local air quality while contributing to the fight against climate change.

Vehicle type plays a critical role in determining the amount and type of pollutants emitted. Heavy-duty vehicles, such as trucks and buses, despite being fewer in number compared to passenger cars, contribute disproportionately to air pollution due to their larger engines and higher fuel consumption rates. Moreover, diesel-fueled heavy vehicles are major sources of NO_x and PM emissions, which persist longer in the atmosphere and cause cumulative air quality degradation. Therefore, policies aimed at reducing emissions must consider vehicle type-specific strategies to be effective (Nelson et al., 2008).

Similarly, the type of fuel used in vehicles significantly influences emission profiles. While gasoline engines primarily emit carbon monoxide (CO) and hydrocarbons (HCs), diesel engines are associated with higher NO_x and particulate matter emissions. The adoption of alternative fuels such as compressed natural gas (CNG), liquefied petroleum gas (LPG), and biofuels can lead to a measurable reduction in certain pollutant emissions. However, the overall environmental benefit depends on the life-cycle emissions, including production and distribution stages of these fuels (Yakın and Behçet, 2021).

2. Material and methods

This section details the methodology, data sources and calculation process used to calculate GHG emissions from road transportation in Turkey for 2023. The calculations are based on the most recent methodology developed by the Intergovernmental Panel on Climate Change (IPCC). The main objective of the study is to determine the main GHG emissions from motor vehicles in Turkey. For this purpose, the IPCC Tier 2 approach was preferred, which provides more accurate results due to the availability of country-specific activity data. The methodological framework is based on the "2019 Refinement to the 2006 IPCC Guidelines for National Greenhouse Gas Inventories" (IPCC, 2019). Emission values were calculated according to the Tier 1 and Tier 2 approaches provided by IPCC. While the Tier 1 method requires more superficial data, the Tier 2 method requires more detailed data. Due to the fact that some data for the Tier 2 method are not province-based, calculations were carried out by preferring general data on a country basis.

The activity data forming the basis of emission calculations were obtained from official statistics published by the Turkish Statistical Institute (TÜİK). The main datasets used are; the Energy Market Regulatory Authority Annual Sector Reports (EPDK, 2024) for the Tier 1 method, and the "Vehicle-kilometer Statistics, 2023" (TÜİK, 2023) for the Tier 2 method. The latter includes the numerical distribution of distances traveled by cars registered in Turkey, categorized by fuel type (gasoline, diesel, LPG, hybrid, electric).

The emission factors (CO2, CH4, and N2O) used in the calculations were taken from the 2006 IPCC Guidelines (IPCC, 2006). The selected emission factors are compliant with the Tier 1 and Tier 2 approaches, Turkey's specific conditions, and the vehicle/fuel type breakdowns in the activity data obtained from TÜİK.

According to the IPCC Tier 1 methodology, emissions are calculated by multiplying the amount of fuel sold by a default emission factor.

Tier 1 emmissions of CO2, CH4 and N2O:

$$Emission = \sum_a [Fuel_a \bullet EF_a] \quad (1)$$

Emissions = emission in kg

EF_a = emission factor (kg/TJ)

$Fuel_a$ = fuel consumed, (TJ) (as represented by fuel sold)

a = fuel type a (e.g., diesel, gasoline, natural gas, LPG)

In the Tier 2 methodology, vehicle type and emission control technology are also taken into account.

Tier 2 emmissions of CO_2, CH_4 and N_2O:

$$Emission = \sum_{a,b,c} [Fuel_{a,b,c} \bullet EF_{a,b,c}] \quad (2)$$

Emission = emission in kg.

$EF_{a,b,c}$ = emission factor (kg/TJ)

$Fuel_{a,b,c}$ = fuel consumed (TJ) (as represented by fuel sold) for a given mobile source activity

a = fuel type (e.g., diesel, gasoline, natural gas, LPG)

b = vehicle type

c = emission control technology (such as uncontrolled, catalytic converter, etc)

Calculations were performed separately for all provinces and fuel types, and subsequently, province-based total CO2e emission values were obtained.

Microsoft Excel software was used for data processing, analysis, and calculation processes. It was assumed that all vehicles were actively in traffic throughout the year.

2.1. Scope and limitations

This study covers the CO_2, CH_4, and N_2O emissions originating from gasoline, diesel, and LPG-fueled cars registered in Turkey for the year 2023.

The study has some limitations. Among these are; the average annual distance traveled by cars was not considered separately for each province; instead, the Turkish average was applied to all provinces. When calculating the distribution of registered cars by fuel type, the national percentage distribution for Turkey was assumed to be the same for every province. When calculating CH_4 and N_2O emissions from cars, the vehicle combustion technology was assumed to be Euro 4 and later, taking into account the average age of registered cars (TÜİK, 2024).

3. Results and discussion

According to the Tier 1 and Tier 2 methods in the IPCC standards, the emission values obtained for each province are first proportioned to the surface area of the provinces and then to the population of the provinces. The aim here is to reveal the emission values of the provinces per square meter and per capita. Fig. 1 shows the emission/surface area according to Tier 1 method and Fig. 2 shows the emission/population density maps.

Fig. 1. Emission/surface area density map according to Tier 1 method

Fig. 2. Emission/population density map according to Tier 1 method

Fig. 1 shows that the amount of emissions per surface area in Istanbul is significantly high. After Istanbul, Kocaeli has the highest amount of emissions per surface area. However, the amount of emissions per surface area of this city is about one-third of that of Istanbul. Among the other provinces, Edirne, Bursa, Sakarya, Yalova and Tekirdağ, which are close to Istanbul, have higher emissions per surface area than many other cities. Apart from these, cities such as Gaziantep, Hatay and Ankara have higher values than other cities. Hakkari and Tunceli have the lowest emissions per surface area.

When the emission values of the provinces in Fig. 2 are analyzed according to population, it is seen that the highest value is in Edirne, followed by Bolu, Kırıkkale and Çankırı. Hakkari, Iğdır and Van have the lowest emission values according to population.

Similarly, the analysis was repeated using the Tier 2 methodology, which incorporates more country-specific data such as local fleet characteristics, vehicle kilometers traveled (VKT), and more detailed emission factors reflecting local driving conditions. The resulting maps for Tier 2 emission/surface area and emission/population are presented in Fig. 3 and Fig. 4, respectively.

Fig. 3. Emission/surface area density map according to Tier 2 method

Fig. 4. Emission/population density map according to Tier 2 method

Fig. 3, illustrating Tier 2 emissions per surface area, shows a pattern largely similar to Tier 1, with İstanbul, Kocaeli, İzmir, Ankara and Bursa exhibiting the highest emission densities. These regions are among the most urbanized and industrialized in the country, contributing to concentrated emissions. On the other hand, provinces such as Hakkari, Tunceli, Ağrı, Ardahan, and Şırnak show the lowest emissions per surface area, reflecting lower population and vehicle densities.

When examining emissions per capita (Fig. 4), according to Tier 2 Ankara, Antalya, Muğla, İstanbul and Burdur as having the highest values. These provinces likely have higher vehicle ownership relative to population or frequent intercity transport. Conversely, the lowest per capita emissions in both tiers are consistently observed in Hakkari, Şırnak, Ağrı, Siirt and Bitlis, indicating relatively low motorization rates.

Comparison Between Tier 1 and Tier 2

In addition to spatial patterns, total emissions were also analyzed:

- Tier 1 Total Emissions: 67,063.89 Gg CO_2e
- Tier 2 Total Emissions: 33,581.19 Gg CO_2e
- Overall Reduction: –49.93%
- When the percentage changes on a provincial basis are averaged, the decrease in the Tier 2 method is -61.97%

This substantial reduction highlights the importance of localized data in greenhouse gas inventories. Tier 1's reliance on default emission factors may lead to overestimations, especially in regions with low vehicle ownership or unique driving patterns. In contrast, Tier 2's use of local data yields more accurate and policy-relevant results.

4. Conclusions

This study highlights the critical importance of methodological precision when estimating emissions from road transport, particularly in the context of a country with diverse vehicle usage patterns like Turkey. The comparative application of IPCC Tier 1 and Tier 2 methodologies revealed substantial differences in emission estimates, both in total values and regional distribution. Tier 1, relying on generalized default factors, consistently produced higher emission figures, while Tier 2, grounded in country-specific parameters such as vehicle type, annual mileage, and fuel consumption characteristics, provided more nuanced and locally relevant results.

The findings confirm that emissions are disproportionately concentrated in major metropolitan areas such as İstanbul, Ankara, and İzmir, reflecting dense populations, industrial activities, and high vehicle volumes. In contrast, provinces in Eastern Anatolia, including Hakkari, Şırnak, and Ardahan, demonstrated the lowest emission intensities, underscoring regional disparities in motorization and transport-related environmental impacts.

Importantly, the Tier 2 method yielded a national emission total nearly 50% lower than Tier 1, emphasizing the risk of overestimation when relying solely on generic coefficients. This discrepancy reinforces the necessity for policymakers to prioritize refined calculation methods in national inventories to inform sustainable transport strategies effectively. Furthermore, emission intensity per capita and per surface area varied significantly across provinces, illustrating the multifactorial nature of transport emissions and the need for tailored mitigation measures.

Future research should expand the scope beyond passenger cars to include freight transport and public transit systems, integrating life-cycle assessments where possible. Enhancing the availability and granularity of regional transport data will also be essential to develop more precise and equitable emission reduction strategies. As Turkey advances toward its climate goals, adopting higher-tier IPCC methodologies and aligning transport policies with region-specific realities will be crucial steps in reducing environmental burdens from the road transport sector.

References

Anenberg, S. C., Henze, D. K., Tinney, V., Kinney, P. L., Raich, W., Fann, N., ... & Achakulwisut, P. (2019). Estimates of the global burden of ambient $PM_{2.5}$, ozone, and NO_2 on asthma incidence and emergency room visits. Environmental Health Perspectives, 127(10).

Bıyık, Y., & Civelekoğlu, G. (2020). Calculation of carbon footprint originated from highways in Isparta province. Bilge International Journal of Science and Technology Research, 4(2), 78–87. https://doi.org/10.30516/bilgesci.427359

Coskun, C., & Oktay, Z. (2020). Carbon footprint prediction of vehicle usage in Turkey. Greenhouse Gases: Science and Technology, 10(4), 736-758.

Energy Market Regulatory Authority. (2024). Petroleum market annual report 2023. https://www.epdk.gov.tr/Detay/Icerik/3-0-107/yillik-sektor-raporu

European Environment Agency (EEA). (2022). Air quality in Europe 2022 report. Retrieved from https://www.eea.europa.eu/publications/air-quality-in-europe-2022

Intergovernmental Panel on Climate Change (IPCC). (2006). 2006 IPCC Guidelines for National Greenhouse Gas Inventories. Retrieved from https://www.ipcc-nggip.iges.or.jp/public/2006gl/

Intergovernmental Panel on Climate Change. (2006). Mobile combustion. In 2006 IPCC guidelines for national greenhouse gas inventories: Vol. 2. Energy (pp. 3.1–3.32). Institute for Global Environmental Strategies. https://www.ipcc-nggip.iges.or.jp/public/2006gl/vol2.html

Kuşkapan, E. (2024). An assessment of the relationship between micro-mobility use and air quality in selected cities. Urban Climate, 58, 102180.

Nelson, P. F., Tibbett, A. R., & Day, S. J. (2008). Effects of vehicle type and fuel quality on real world toxic emissions from diesel vehicles. Atmospheric Environment, 42(21), 5291-5303.

Pekin, M. A. (2006). Greenhouse gas emissions produced by transportation sector [Master's thesis, İstanbul Teknik Üniversitesi]. Polen. https://polen.itu.edu.tr/handle/11527/3847

Turkish Statistical Institute. (2025). Motor land vehicles, December 2024 (Publication No. 53463). https://data.tuik.gov.tr/Bulten/Index?p=Motorlu-Kara-Tasitlari-Aralik-2024-53463

Turkish Statistical Institute. (2025). Vehicle-kilometre statistics, 2023 (Publication No. 54055). https://data.tuik.gov.tr/Bulten/Index?p=Tasit-kilometre-Istatistikleri-2023-54055

World Health Organization (WHO). (2021). WHO global air quality guidelines: Particulate matter ($PM_{2.5}$ and PM_{10}), ozone, nitrogen dioxide, sulfur dioxide and carbon monoxide. Retrieved from https://www.who.int/publications/i/item/9789240034228

Yakın, A., & Behçet, R. (2021). Effect of different types of fuels tested in a gasoline engine on engine performance and emissions. International Journal of Hydrogen Energy, 46(66), 33325-33338.

Yalılı Kılıç, M., Dönmez, T., & Adalı, S. (2021). Change in carbon footprint due to fuel consumption in road transport: The case of Çanakkale. Gümüşhane Üniversitesi Fen Bilimleri Dergisi, 11(3), 943–955.

4th International Civil Engineering & Architecture Conference
17-19 May 2025, Trabzon, Türkiye

Comparison of the pavement condition index and riding comfort levels of newly built urban interlocking concrete pavements

Ufuk Kırbaş*[1], Zafer Genç[1], M. Fatih Başoğlu[2]

[1] Ondokuz Mayıs Univesity, Department of Civil Engineering, 55139 Samsun, Türkiye
[2]Tokat Gaziosmanpaşa University, Department of Civil Engineering, 60150 Tokat, Türkiye

Abstract. Interlocking concrete paving coating (Pavements), which can be produced locally in developing countries and offer ease of construction, is frequently used on urban low-traffic roads. In the study, driving at urban speeds (10, 20, 30, 40, and 50 km/h) on a newly completed interlocking concrete paving road network was performed and the vibrations affecting the vehicle interior and the driver from the road surface were measured. The service level of the pavement was determined simultaneously. The measured vibrations were evaluated by the ISO 2631 standard. In addition, a pavement condition index (PCI) study was conducted using the ASTM E2840 standard, which allows evaluation in the range of 0-100. It was determined that there was a close relationship between the PCI values of the superstructure obtained from the irregularities on the interlocking concrete paving surface and the vertical vibrations coming to the vehicle and the driver during the drives at the determined speeds.

Keywords: Interlocking concrete pavement; Urban road; Whole-body vibration; PCI; Comfort

1. Introduction

The first examples of interlocking concrete paving superstructures are found in the Roman Empire. In addition to traditional asphalt and concrete paved roads, the use of interlocking concrete paving pavements is constantly increasing today (Gogoi, 2019).

The use of interlocking paving stones became widespread in the United States from the early 1970s onwards. At that time, the use of interlocking concrete paving stones was relatively slower to enter the market in Africa, Australia and Japan (Shackel, 1979). Interlocking concrete pavement production in North America has doubled every five years since 1980. In 1989, the Interlocking Concrete Pavement Institute (ICPI) was established in the USA (Smith, 1992).

Organizations such as the American Concrete Institute (ACI), the National Concrete Pavement Association (NCPA), the National Ready Mixed Concrete Association (NRMCA), the Asphalt Institute, and the National Asphalt Pavement Association (NAPA) have acted as the voice of their industries. Universities, the Federal Highway Administration (FHWA), the Federal Aviation Administration (FAA), the Transportation Association of Canada (TAC), the American Association of State Highway and Transportation Officials (AASHTO), the American Society for Testing and Materials (ASTM), and the Transportation Research Board (TRB) have helped to sustain the use of asphalt and concrete pavements (Smith, 1992). Between 1998 and 2005, the use of concrete paving stones in the United States increased by an average of 6 million m^2 per year (Hein & Burak, 2007).

Concrete paving has mostly entered the market for aesthetic purposes. However, since aesthetics were not enough for US and Canadian highway engineers, performance data on municipal and industrial projects were needed. In 1990, a list of ideas was published by obtaining the opinions of 22 senior pavement experts to improve existing product features, improve structural design methods, develop maintenance and life cycle information, and create promotional projects. In 1992, 15-16 million m^2 of concrete paving was produced in the USA (Smith, 1992).

Interlocking concrete paving resilient pavers have high resistance to freeze-thaw and de-icing salts, high abrasion and shear resistance, high resistance to temperature-induced deformation, and high resistance to damage from fuel spills and other petroleum products. They can also be designed with excellent drainage properties and are often used to help reduce stormwater runoff. In a typical municipal application, joint sand between individual concrete pavers facilitates the transfer of vehicle wheel loads through shear transfer, and the joints also facilitate controlled crack locations to minimize stress cracking and surface distress. Concrete paving pavers are typically placed on coarse bed sand placed over an untreated aggregate base. They can also be placed over bituminous or

* Corresponding author, E-mail: ufuk.kirbas@omu.edu.tr

https://doi.org/10.31462/icearc2025_ce_tra_754

cement-treated (stabilized) base, asphalt concrete, or Portland cement concrete. The voids between individual paving units are filled with clean, durable, high-quality joint sand (Hein et al., 2007; 2009).

The unevenness of the surface of the pavement layer on the new highways that have been completed or on the highways that have been built before and which are currently in service can affect the driving comfort, safety, fuel economy of the vehicles, etc. affects many factors. The characteristics of the material used (binder type, quality, aggregate type) and external conditions (traffic load, climate, application of materials, etc.) play an important role in the service life of the coating (Kırbaş, 2013).

Since the 1950s, researchers have applied the panel evaluation technique, which requires the evaluation of at least three evaluation experts, to determine the current service level of the superstructures. Although the evaluators are experts in their fields, since objective results cannot always be obtained during human evaluation, mechanical measurement and evaluation techniques were developed in the following process (Hass et al., 1994).

The AASHTO road test (1950-1960) shows that there is a very high correlation between ride comfort and the level of service of the superstructure. It states that vertical vibrations are the most effective factor in determining driver comfort and that the main causes of vertical vibrations are road surface distresss and vehicle origin. The most important element of superstructure performance and therefore ride comfort is the distresss and deformations in the interlocking concrete pavement. Ride comfort is explained by whole body vibration assessment methods in ISO 2631-1 and BS 6841 international standards (Kırbaş, 2021).

2. Materials and methods

2.1. PCI for interlocking concrete paving roads

Interlocking concrete pavement superstructures can be kept in a 25-50 year monitoring program if the relevant procedures are followed and timely maintenance, repair and rehabilitation processes are implemented (Hein & Smith, 2009).

In order to objectively evaluate the service level of the pavements, performance indices such as pavement condition index (PCI), pavement serviceability (PSI), number of rides (RN), ride comfort index (RCI), international roughness index (IRI) that can express the current status with a numerical value have been developed in relation to the surface condition of the pavement. Today, the pavement condition index (PCI), which uses surface distress type inputs, is frequently preferred by authorities, especially in the evaluation of urban pavements. The current condition of the pavement and the vertical vibrations coming to the driver and passengers due to distresss on the pavement surface have a very high correlation (Hein et al., 2009).

Although the types of distress and cut-off values presented in the standard E2840-11 published by ASTM and based on the guide published by ICPI are specific to interlocking concrete pavements, it is based on the same principles as the MicroPAVER/ASTM procedure in terms of selecting sample units, conducting the survey, and using the corrected cut-off value for multiple types of distress (Hein et al., 2009).

Table 1. Types of distress of interlocking concrete pavements (ASTM, 2011)

Distress Number	Description
101	Damaged Pavers
102	Depressions
103	Edge Restraint Damage
104	Excessive Joint Width
105	Faulting
106	Heave
107	Horizontal Creep
108	Joint Sand Loss/Pumping
109	Missing Pavers
110	Patching
111	Rutting

Table 1 includes the distress types and their numbers to be taken into account in the PCI assessment of interlocking concrete paving roads according to the ASTM E2840-11 standard.

The initial design of the pavement is a critical factor in pavement performance and life cycle cost assessment. The service life of a pavement is usually determined during the initial design. The service life takes into account the subgrade, pavement layer materials, thicknesses and expected traffic on the roadway. This service life depends on the environmental and loading conditions of the pavement. By monitoring and rating pavement performance using standard pavement management tools such as the Pavement Condition Index (PCI), it is possible to establish typical pavement performance curves for the pavement (ICPI, 2007).

Table 2. Standard PCI rating scale (ASTM, 2011)

PCI	Verbal Rating
86-100	Good
71-85	Satisfactory
56-70	Fair
41-55	Poor
26-40	Very Poor
11-25	Serious
0-10	Failed

PCI numerical and verbal evaluation scale according to ASTM E2840-11 standard is shown in Table 2. Before PCI assessment, the road route to be measured must be determined. Then, the measurement area information such as street name, road length, lane width, pavement type, etc. are transferred to the survey sheets. Then, the types of distress on the surface are determined. After the type, severity and amount of each distress are determined, the data is processed for PCI evaluation in the paver package program PAVER prepared for this study.

The PCI value obtained can be interpreted as follows depending on the situation. In superstructures with interlocking concrete paving, the minimum serviceability PCI value is accepted as 60. However, in sections with low speed and traffic volume, this value can be reduced to 50 for moderation (Hein & Smith, 2009).

Fig. 1. Top view of Uzunkar Street in Ondokuz Mayıs district of Samsun

Fig. 1 shows the top view of Uzunkar Street. The points on the figure are the location points that the measuring device sends at second intervals while driving. The dots shown represent the measured speeds of 10 km/h. Uzunkar Street is 250 meters long and 6 meters wide. This two-lane road, which has a very low traffic volume, was taken as a single lane for both safety and suitability for use. Observations made at the measurement site generally did not reveal any two-way traffic.

Uzunkar Street has a very smooth road surface as seen in Fig. 2 and is an interlocking concrete paving road whose construction was completed recently. The use of the interlocking concrete paving road on this street means that heavy tonnage vehicles do not use this road and it has a very low traffic volume, which also extends its future service life.

In many studies, it is seen that ride comfort is evaluated with weighted frequency root mean square (a_w) with vertical vibration analysis. In addition, although not very often, the vibration dose value (VDV) parameter is also preferred (Griffin, 2007; Múčka, 2020).

Fig. 2. View of Uzunkar Street with interlocking concrete pavement in Ondokuz Mayıs district of Samsun

2.2. Comfort levels with whole body vibration and vertical acceleration

Research on the problems related to irregularities of pavements has increased significantly in recent years. Highway authorities try to reduce and eliminate irregularities in pavements in order to improve ride comfort on the road network. Irregularities in pavements cause whole body vibration (WBV) of the users during vehicle movement and generally reduce ride comfort (Cantisani & Loprencipe, 2010).

The importance of ride comfort and safety on superstructures with fast traffic flow has been known for many years. However, recent studies have shown that ride comfort depending on pavement conditions also significantly affects road safety on superstructures with low speed limits (Chan et al., 2010; Li et al., 2013). Regression models have been proposed and subjective evaluations have been developed between five objective measurements (hand, hip, foot, back and whole body) to evaluate ride comfort. It has been determined that the highest correlation between objective measurements and subjective evaluations was obtained in the hip (Kırbaş & Karaşahin, 2019).

Vibration measurements should be made with vibration transducers placed between the body and the surface. When a person is sitting in a vehicle, the supportive seat surface, seat back and feet are the areas that perceive vibration (Fig. 3). When we sit, especially on hard ground, there is a bony prominence in the lower back part of the pelvis that comes into contact with the ground. This area is called the ischial tuberosity. Measurements on the supportive seat surface should be made under the ischial tuberosity with a soft, flexible seat cushion (ISO, 1997).

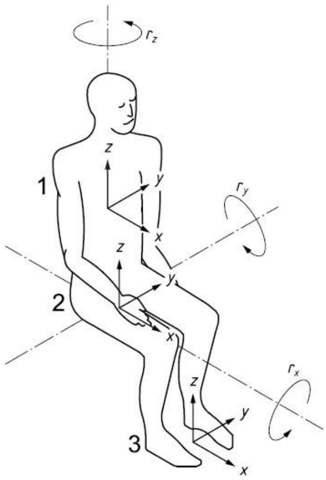

Fig. 3. Translation and rotation axes for TVT of seated driver or passenger (ISO, 1997)

The ISO 2631-1 standard specifies how to determine the effects of vibrations on human comfort, starting from vertical acceleration. In order to determine ride comfort, the standard requires the use of frequency-weighted root mean square RMS accelerations.

$$a_{wz} = \sqrt{\sum_i (W_{k,i} \cdot a_{iz}^{RMS})^2} \quad (1)$$

In formula one, a_{wz} is the weighted vertical frequency acceleration, W_i is the corresponding weighting factor (ISO 2631-1), a_{iz} is the vertical RMS value for the 1/3 octave bandwidth.

Table 3. Comfort levels related to a_{wz} threshold values (ISO, 1997)

a_{wz} Values (m/s^2)	Comfort Levels
<0.315	Not uncomfortable
0.315–0.63	A little uncomfortable
0.5–1	Fairly uncomfortable
0.8–1.6	Uncomfortable
1.25–2.5	Very uncomfortable
>2	Extremely uncomfortable

Table 3 shows the comfort assessment scale according to the ISO 2631-1 standard. Table 3 is used to verbally express the vertical vibration data (a_{wz}) obtained during the rides to investigate comfort levels.

According to the December 2024 data of TÜİK, motor land vehicles, there are more than 31 million land vehicles in Türkiye. 51.9% of these vehicles are automobiles. Therefore, a sedan vehicle in the C segment of the Euro Car classification was used in this study. A brand new car was preferred to minimize errors caused by the vehicle suspension and powertrain.

Fig. 4. C segment automobile and measuring equipment, GPS antenna, datalogger, laptop, seat cushion and vertical accelerometer and power battery

With this equipment (in Fig.4), vibration data will be collected from the interlocking concrete paved roads divided into sections and determined in the field with the accelerometers located on the driver, passenger (front right seat) and ground center axis. The accelerometers used (three pieces) have ±4g, sensitivity 500±15 mV/g feature and can collect 1000 data per second. GPS antenna (<15 m accuracy) can record location data instantly to the computer. Vertical vibration data is recorded on interlocking concrete paved roads with this equipment.

Three runs were made for each speed on the interlocking concrete paving road at speeds of 10, 20, 30, 40 and 50 km/h. With each run, vertical vibration data from three separate points in the vehicle (driver's seat, passenger seat, ground center axis) were recorded as 1000 data per second. At the same time, the position of the GPS antenna measuring vehicle operating simultaneously was recorded as one data per second.

3. Results and discussion

For PCI assessment, the severity and amount of distress types were calculated using specific apparatus from the ASTM standard (3 m ruler, 15 m rope, 1 m ruler, 30-50 cm steel ruler, etc.).

Uzunkar street was taken as a single lane and in the PCI assessment, the lane width used by the vehicle was determined as 3 m. The total length of the road is 250 m. The road section is divided into sample areas at 50-meter intervals, each sample area is 150 m^2 and is within the sample area determination limit of 225 $m^2 \pm 90$ m^2 specified in the ASTM standard. Thus, a PCI evaluation was carried out on Uzunkar Street, consisting of 5 sample areas and an area of 750 m^2 (Fig. 5). Five sample areas constitute one section.

When evaluating PCI, the types, severity and amount of distress were determined and recorded in each sample area. The total amount of each type of distress was divided by the total area of the sample unit at each severity level and multiplied by 100 to obtain the percentage density of each type of distress and severity. Deduct value (DV) was determined for each combination of type of distress and severity from the deduct value curves. Then, after determining the correct deduct value (CDV) value from the deduct curves within the relevant standard, this value was subtracted from 100 to calculate the PCI values of the sample areas. The average of the PCI values of the sample areas also showed the PCI value of Uzunkar Street.

Fig. 5. Uzunkar Street consisting of 5 sample areas

Since Uzunkar Street is a newly constructed road, it was determined that the PCI values of the sample areas were 87 and above. Among the types of distress sought in the PCI assessment of interlocking concrete paved roads on the road surface (Table 1), only 101 and 110 types of distress were found (Fig. 6). While a 110 type distress due to a manhole cover was found in the fourth sample area, the 101 type distresss were quite low and almost did not affect driving comfort.

Fig. 6. Distress types and severities on interlocking paving road pavement

Table 4. Calculated PCI values of sample areas on Uzunkar street

Sample Unit	Types of distress detected	PCI	Verbal Rating	Section PCI	Section Verbal Rating
1	101 (L)	93	Good		
2	101 (L)	93	Good		
3	101 (L), 101 (M)	87	Good	92	Good
4	101 (L), 110 (L)	88	Good		
5	101 (L)	97	Good		

The PCI evaluation is shown in Table 4. As mentioned before, 101 and 110 types of deterioration were encountered. PCI values were found as 93, 93, 87, 88 and 97 according to the numerical order of the sample areas. When the average was taken, it was determined that Uzunkar Street was 92, that is, "good" in terms of road pavement.

Table 5. Vibration data of aw_z according to in-vehicle measurement points of the entire road section

Section ID	Measuring Point	Sample Unit (PCI)	Speed (km/h)/a_{wz} (m/s^2)				
			10	20	30	40	50
Uzunkar Street	Driver's Seat	1 (93)	0.21	0.33	0.43	0.51	0.59
		2 (93)	0.21	0.33	0.43	0.51	0.64
		3 (87)	0.24	0.35	0.49	0.58	0.78
		4 (88)	0.22	0.40	0.48	0.55	0.58
		5 (97)	0.21	0.38	0.39	0.33	0.50
	Average	92	0.22	0.36	0.45	0.50	0.62
	Passenger Seat	1 (93)	0.30	0.44	0.64	0.77	0.80
		2 (93)	0.25	0.43	0.57	0.74	0.97
		3 (87)	0.24	0.45	0.59	0.83	0.96
		4 (88)	0.25	0.50	0.62	0.79	0.88
		5 (97)	0.28	0.52	0.55	0.51	0.79
	Average	92	0.26	0.47	0.60	0.73	0.88
	Center Axle	1 (93)	0.20	0.31	0.48	0.56	0.59
		2 (93)	0.16	0.31	0.42	0.57	0.74
		3 (87)	0.19	0.33	0.48	0.59	0.78
		4 (88)	0.18	0.38	0.43	0.60	0.66
		5 (97)	0.16	0.36	0.40	0.34	0.63
	Average	92	0.18	0.34	0.44	0.53	0.68

Vertical directional (a_{wz}) vibration data were obtained at speeds of 10, 20, 30, 40, 50 km/h with whole body vibration measurement equipment combined and calibrated according to ISO 2631-1 standard. Three rides were made at each speed and the vibration data obtained from the rides were averaged (Table 5).

As seen in Table 5, the vertical vibration data on this interlocking concrete paving road with a high PCI value could not exceed 1 m/s^2. While it was observed that the vibration values increased as the speed increased, the lowest value was determined to be 0.16 m/s^2.

In the table below, the comfort levels of the vertical vibrations obtained from the driver's seat, passenger seat and floor center axis measurement points are verbally evaluated according to Table 3. As can be seen, on an interlocking concrete paving road with a good service level, even at 50 km/h within the urban speed limits, the comfort threshold has not exceeded the expression "fairly uncomfortable". The smoother the road, the higher the driving comfort will be.

Since the service level of the interlocking concrete paving road measured is high, it can be stated that the increase in discomfort in the driver's seat depends on the speed variable (Table 5). If we interpret this increase in discomfort through driving experiences, it can be said that interlocking concrete paving roads consist of fragmented elements and that there is a -x-directional impact (Fig. 3) between the joints on the vehicle's wheel and from there into the vehicle.

Table 6. Comfort levels of Uzunkar Street according to driver's seat, passenger seat and ground center axis

Section ID	Measuring Point	Sample Unit	Speed (km/h)/a_{wz} (m/s^2)				
			10	20	30	40	50
Uzunkar Street (PCI:92)	Driver's Seat	1	Not *	A little *	A little *	A little *	Fairly *
		2	Not *	A little *	A little *	A little *	Fairly *
		3	Not *	A little *	A little *	A little *	Fairly *
		4	Not *	A little *	A little *	A little *	Fairly *
		5	Not *	A little *	A little *	A little *	Fairly *
	Evaluation		Not *	A little *	A little *	A little *	Fairly *
	Passenger Seat	1	Not *	A little *	Fairly *	Fairly *	Fairly *
		2	Not *	A little *	A little *	Fairly *	Fairly *
		3	Not *	A little *	A little *	Fairly *	Fairly *
		4	Not *	A little *	A little *	Fairly *	Fairly *
		5	Not *	A little *	A little *	A little *	Fairly *
	Evaluation		Not *	A little *	A little *	Fairly *	Fairly *
	Center Axle	1	Not *	Not *	A little *	A little *	Fairly *
		2	Not *	Not *	A little *	A little *	Fairly *
		3	Not *	A little*	A little *	A little *	Fairly *
		4	Not *	A little *	A little *	A little *	Fairly *
		5	Not *	A little *	A little *	A little *	Fairly *
	Evaluation		Not *	A little *	A little *	A little *	Fairly *

*Uncomfortable

Table 6 includes verbal vibration assessments for the driver's seat, passenger seat and ground center axle according to sample areas and speeds. When we look at the linear correlation between aw_z and PCI according to the driver's seat, it is seen that the highest correlation is at 30 km/h speed. The lowest correlation is at 20 km/h driving speed. (Table 7).

Table 7. aw_z-PCI linear correlation according to driver seat speed

	10 km/sa	20 km/sa	30 km/sa	40 km/sa	50 km/sa	PCI
10 km/sa	1.000					
20 km/sa	0.334	1.000				
30 km/sa	0.809	0.155	1.000			
40 km/sa	0.500	-0.202	0.895	1.000		
50 km/sa	0.724	-0.382	0.755	0.748	1.000	
PCI	-0.800	-0.154	-1.000	-0.898	-0.747	1.000

When we look at the aw_z-PCI relationship in the passenger seat, it is seen that the 40 km/h measurement speed has a higher relationship. When we look at the awz-PCI relationship in the passenger seat, it is seen that the 40 km/h measurement speed has a higher correlation. Again, as in the driver's seat, it was determined that the 20 km/h speed has a lower correlation than the other speeds (Table 8).

Table 8. aw_z-PCI linear correlation according to passenger seat speed

	10 km/sa	20 km/sa	30 km/sa	40 km/sa	50 km/sa	PCI
10 km/sa	1.000					
20 km/sa	0.085	1.000				
30 km/sa	0.294	-0.331	1.000			
40 km/sa	-0.411	-0.618	0.707	1.000		
50 km/sa	-0.890	-0.519	-0.146	0.588	1.000	
PCI	0.653	0.219	-0.491	-0.865	-0.598	1.000

When we examined the relationship between the vibration data taken from the ground center axis point and PCI, it was determined that the 40 km/h measurement speed on the passenger seat had a higher correlation, while the 20 km/h speed had a lower correlation than the other speeds (Table 9).

Table 9. aw_z-PCI linear correlation according to center axle speed

	10 km/sa	20 km/sa	30 km/sa	40 km/sa	50 km/sa	PCI
10 km/sa	1.000					
20 km/sa	-0.431	1.000				
30 km/sa	0.982	-0.515	1.000			
40 km/sa	0.572	-0.354	0.646	1.000		
50 km/sa	-0.107	-0.265	0.077	0.398	1.000	
PCI	-0.516	-0.013	-0.596	-0.838	-0.535	1.000

As mentioned in the previous sections of the study, taking measurements from the driver's seat using a sitting type accelerometer as in the measuring equipment gives the most accurate results. This is shown in Table 7.

4. Conclusions

As a result of this study in determining the service life and driving comfort levels of newly constructed interlocking concrete paving roads;

- A PCI assessment was carried out to see the serviceability of a newly completed interlocking concrete paving road according to the ASTM E2840 standard. The PCI value of the interlocking concrete paving road consisting of five sample areas was determined as 92 "good".
- On the interlocking concrete paving road section where PCI assessment was made, drives were made with a brand new Euro Car C segment vehicle and vibration measurement data set at urban speed limits of 10, 20, 30, 40, and 50 km/h.
- Whole body vibration data were collected at determined speeds by measurements made from the driver's seat, passenger seat and floor center axis points.
- The comfort levels of the road measured according to the ISO 2631-1 standard were determined.
- When comfort levels were examined, it was determined that "Not uncomfortable" was found at all measurement points at 10 km/h.
- It was determined that "A little uncomfortable" was generally found at 20 and 30 km/h.
- While it was "A little uncomfortable" at 40 km/h except for the passenger seat, it was found that "Fairly uncomfortable" was found at other measurement points.
- At 50 km/h, it was interpreted as "Fairly uncomfortable" at all measurement points.
- When the linear correlation between the awz values taken from the driver's seat, passenger seat and ground center axis and PCI is examined, it is determined that the tightest relationships are when there is a driver and the highest relationship is at the 30 km/h measurement speed in the driver's seat.
- As a result, with this technique, which can be used by institutions and organizations responsible for the construction, maintenance-repair and renewal activities of interlocking concrete paving roads, the current status of interlocking concrete paving roads can be determined and their service life can be extended when necessary.

Acknowledgments

The research described in this paper was financially supported by the Ondokuz Mayıs University/Scientific Research Projects Coordination Unit (BAPKOB) under the grant number [PYO.MUH.1904.23.011].

References

ASTM. (2011). Standart practice for pavement condition index surveys for interlocking concrete roads and parking lots. *ASTM E2840-11. West Conshocken, PA: ASTM International*

Cantisani, G. & Loprencipe, G. (2010). Road rougness and whole body vibration: Evaluation tools and comfort limits. *Journal Of Transportation Engineering, 136*(9), 818-826

Chan, C.Y., Huang, B., Yan, X. & Richards, S. (2010). Investigating effects of asphalt pavement conditions on traffic accidents in tennessee based on the pavement management system (PMS). *Journal of Advanced Transportation, 44*(3), 150-161

Gogoi, R. & Dutta, B. (2019). Maintenance prioritization of interlocking concrete block pavement using fuzzy logic. *International Journal of Pavement Research and Technology, 13*, 168-175

Griffin, M.J. (2007). Discomfort from feeling vehicle vibration. *Vehicle System Dynamics, 45*(7–8), 679-698 https://doi.org/10.1080/00423110701422426

Haas, R., Hudson, W.R., & Zaniewski, J.P. (1994). Modern pavement management. *Malabar, FL: Kriger Publishing Corp.*

Hein, D.K. & Burak, R. (2007). Development of a pavement condition rating procedure for interlocking concrete pavements. *Transportation Association Of Canada Fall 2007 Meeting, Saskatoon, Saskatchewan*

Hein, D.K & Smith, D.R. (2009). Life-cycle cost comparison for municipal road pavements. *9th. international conference on concrete block paving.* Buenos Aires, Argentina

Hein, D.K., Aho, B. & Burak, R. (2009). Development of a pavement condition index procedure for interlocking concretece pavements. *9th. international conference on concrete block paving.* Buenos Aires, Argentina

ICPI. (2007). Standard practice for pavement condition index surveys for concrete block pavement, *Herndon, VA.*

ISO. (1997). Mechanical vibration and shock - evaluation of human exposure to whole-body vibration, part 1: general requirement ISO 2631-1. *Geneva, Switzerland: ISO*

Kırbaş, U. (2013). *Pavement maintenance management system design in urban roads, the case of Turkey (*Doktoral dissertation). İstanbul University, İstanbul, Türkiye (in Turkish)

Kırbaş, U. & Karaşahin, M. (2019). Determination of pavement performance thresholds for comfortable riding on urban roads. *Journal of Testing and Evaluation, 47*(1), 57-77. https://doi.org/10.15220/JTE20170319. ISSN 0090-3973

Kırbaş, U. (2021). Determination of ride comfort thresholds based on international roughness index for asphalt concrete pavements. *International Journal of Pavement Engineering* https://doi.org/10.1080/10298436.2021.2011279

Múčka, P. (2020). Vibration dose value in passenger car and road roughness. *Journal of Transportation Engineering, Part B: Pavements*, *146* (4), 04020064. 1-15

Smith, D.R. (1992). The institutionalization of concrete block pavements in north america. *Concrete Paver Institute. PAVE 92.* Herndon, Virginia, USA

TÜİK, (2025). *Motor land vehicles in Türkiye.* Retrieved from https://data.tuik.gov.tr/Bulten/Index?p=Motorlu-Kara-Tasitlari-Aralik-2024-53463

Tree-based estimation of voids in mineral aggregate in superpave mix design: Feature importance and validation analysis

Duygu Demirtürk[*1], Ömer Mintemur[2]

[1] Ankara Yıldırım Beyazıt University, Faculty of Engineering and Natural Sciences, Department of Civil Engineering, Ankara, Turkey
[2] Ankara Yıldırım Beyazıt University, Faculty of Engineering and Natural Sciences, Department of Software Engineering, Ankara, Turkey

Abstract. Researchers in asphalt mixtures have concentrated on optimizing mix designs to improve performance and meet specified requirements. The accurate estimation of Voids in Mineral Aggregate (VMA) has become a critical topic in this optimization process. Advanced computational techniques, such as LightGBM and XGBoost, have gained prominence due to their reliability and efficiency in handling complex datasets and enhancing VMA prediction accuracy. This study emphasizes the significance of identifying and quantifying critical features in VMA estimation using gradient-boosting algorithms. Permutation importance is proposed as a robust and interpretable method for assessing the influence of each input variable on model performance. This approach evaluates the impact of individual features by measuring how much the model's performance is affected when the values of a specific feature are randomly shuffled. Cross-validation is applied to evaluate the models across multiple data splits to ensure reliability and generalizability. Accordingly, this study computed permutation importance on the different test subsets in the cross-validation approach, enabling the gradient-boosting models to provide more objective and broadly applicable insights into VMA estimation. This methodology yielded feature-importance results that closely aligned with field knowledge, enhancing the interpretability of the models. Specifically, the specific gravity (G_{mb}) of the compacted hot mix asphalt and the bulk specific gravity of the aggregate blend (G_{sb}) were validated as pivotal parameters for VMA estimation, consistent with established empirical formulas. Consequently, this study demonstrates the effectiveness of combining cross-validation with permutation importance in LightGBM and XGBoost models to achieve reliable and consistent feature importance, thereby minimizing biases from individual data splits.

Keywords: Voids in minerals aggregates; Mix design; Gradient-boosting algorithms; Feature importance; Permutation importance

1. Introduction

Asphalt mix design has critical procedures to determine appropriate aggregate gradation and optimum binder content to meet specified volumetric and mechanical requirements (Gardete et al., 2022). It can also be stated that a proper mix design is a critical step in pavement construction, as it directly affects the performance of the pavement during its service life. Well-designed mixtures ensure long-lasting pavements, while poorly designed ones can lead to premature failure. Using empirical methods, traditional asphalt mix design mainly focuses on volumetric properties (e.g., air voids, VMA), which are required by specifications and strongly influence pavement performance. However, there has been a shift toward performance-based approaches to better predict long-term pavement behavior since the late 1990s (Wang, 2019). As a result, developed as part of the Strategic Highway Research Program, the Superpave mix design method was introduced to address the limitations of earlier methods, such as the Marshall and Hveem mix designs (Cooper et al., 2014; Lee et al., 2023). Another important role of the Superpave mix design method is to improve pavement performance by solving common problems such as rutting, thermal cracking, and fatigue cracking.

While this method includes specifications on rutting and fatigue resistance, actual field performance is not directly incorporated into the initial design phase. Moreover, the implementation of the Superpave mix design necessitates extensive experimental procedures, including preparing multiple trial samples and evaluating the volumetric properties associated with the asphalt binder, aggregates, and mixtures. In short, this process requires

[*] Corresponding author, E-mail: ddemirturk@aybu.edu.tr

https://doi.org/10.31462/icearc2025_ce_tra_755

a substantial investment of labour, materials, and financial resources (Liu et al., 2022). In the literature, studies on traditional asphalt mixture design are primarily based on experimental methods and extensive laboratory studies, while recent studies have evolved into optimization-based approaches that are compatible with modern engineering standards and increase performance and efficiency (Hossain & Chen, 2002; Liu et al., 2022; Sebaaly et al., 2018).

According to Hossain and Chen (2002), optimising volumetric properties is very important in designing asphalt mixes because changing one property can directly affect the others. Changing the binder content, for instance, can thin the binder film, raise the VMA, and lower the air voids. This interaction highlights the importance of precise control over volumetric parameters to achieve the desired mix performance. Therefore, they advocated the need for more accurate and practical methods to predict and optimize volumetric properties. Among these volumetric properties, it is obvious that VMA is an important volumetric property in the design of asphalt mixtures (Kandhal & Chakraborty, 1996; Roquier, 2023; Shen & Yu, 2011a). This is because the requirement to meet McLeod's minimum VMA is a critical but often challenging step in Superpave mix design, as it may eliminate cost-effective mixtures with acceptable performance (Hislop & Coree, 2000). Some researchers also underlined that it is overly restrictive and not universally applicable to all asphalt mixtures (Hinrichsen & Heggen, 1996; Mallick et al., 2000). In properly designed mixtures, the VMA value serves as a decisive parameter in preventing the formation of low-performing mixtures. To infer this statement, past studies have investigated the effects of factors such as aggregate grading, nominal maximum aggregate size (NMAS), surface texture, and aggregate shape on the VMA of asphalt mixtures (Pouranian & Haddock, 2018; Prowell et al., 2005).

Shen and Yu (2011) noted that precise prediction of VMA is still a difficult subject due to its complex and nonlinear relationship with aggregate grading and packing behavior, which usually requires iterative and trial-and-error methods. Therefore, they focused on a theoretical method to predict the VMA parameter in hot mix asphalt by analyzing aggregate packing using discrete element modeling (DEM). In the same study, the gradation weighing factor (f_v), was introduced to directly link aggregate gradation to the VMA, enabling faster and more accurate predictions without extensive laboratory testing (Shen & Yu, 2011b). Moreover, in the study, DEM effectively simulated aggregate compaction and structure and produced volumetric results that agreed well with experimental data. However, due to computational constraints, this model excluded particles smaller than 1.18 mm and did not fully replicate actual molding processes, thereby limiting its potential to entirely replace laboratory testing (Dai et al., 2024). Based on the defined deficiencies, researchers increasingly need machine learning (ML) techniques to predict volumetric properties more accurately and efficiently in asphalt mix design (Rahman et al., 2021). In the past, volumetric design parameters, such as VMA, have traditionally been determined using empirical methods and have rarely been the subject of prediction using ML techniques. Nowadays, most ML research-based pavement engineering studies have primarily addressed performance-related outputs such as rutting, fatigue cracking, and dynamic modulus (Eleyedath & Swamy, 2022; Haddad et al., 2022; Krcmarik et al., 2016).

On the other hand, in traditional Superpave mix design, test data is generated through a trial and error approach, and most of it is unused (Liu et al., 2022). ML models can use these data sets to support more efficient data-driven asphalt mix design processes. Rather than relying solely on trial-and-error methods, ML enables optimized decisions regarding aggregate gradation and binder content. For example, Hosseini et al. (2021) offered various ML algorithms, including Artificial Neural Networks (ANNs), Support Vector Regression (SVR), Decision Trees, and Ensemble models, to predict the complex shear modulus and phase angles of modified bitumens. Their study reported optimal dosages and test conditions for different modifiers (e.g., rubber, SBS, PPA), thereby supporting a more rational choice of mix design (Hosseini et al., 2021). Furthermore, the growing availability of comprehensive asphalt mix data has enabled the effective training of ML models to predict volumetric properties (Jweihan et al., 2022; Zavrtanik et al., 2016; Zhang et al., 2021a). Notably, Dai et al. (2024) developed an interpretable ML-based framework that integrates Extreme Gradient Boosting (XGBoost) with SHapley Additive exPlanations (SHAP) analysis to predict and explain the volumetric properties of asphalt mixtures, including air voids and VMA. The approach employed advanced outlier detection, combining Kernel Density Estimation (KDE) and Local Outlier Factor (LOF), significantly enhancing the model's robustness. The study concluded that asphalt content and fine aggregate were the most significant parameters affecting air void content. In contrast, the coarse aggregate ratio had the most significant impact on VMA. The method achieved high prediction accuracy (R^2 = 0.9441 for air voids) and reduced design time by up to 70% (Dai et al., 2024).

In addition, integrating ML models with feature importance techniques such as SHAP or permutation importance, researchers can determine which mix design parameters (e.g., asphalt content, aggregate classification) most influence key volumetric properties. Among these techniques, SHAP, introduced by Lundberg and Lee (2017), has been widely adopted in predictive modeling due to its consistency and ability to quantify feature contributions across a broad range of ML algorithms (Lundberg & Lee, 2017). Liu et al. (2024) applied SHAP to interpret the influence of input variables on the predicted volumetric properties of asphalt mixtures, revealing that asphalt content (P_b) and aggregate bulk specific gravity (G_{sb}) were the most influential factors for both air voids (AV) and maximum theoretical specific gravity (G_{mm}) (Liu et al., 2024). Then, Junaid et al. (2024) applied a Multilayer Perceptron Model (MLP) to predict the dynamic modulus of asphalt mixtures modified with polyethylene. They conducted a feature importance analysis based on the model's internal weights. Their results showed that frequency had the greatest influence on the prediction results, followed by temperature and low-density polyethylene (LDPE) content, demonstrating the effectiveness of neural network-based models in capturing and quantifying feature contributions (Junaid et al., 2024).

Although ML techniques have been used in many studies on observed problems in pavement engineering, the combined use of permutation-based feature importance and cross-validation to estimate VMA has not been studied before. This work focused on this issue by proposing an interpretable approach to improve the accuracy of VMA prediction using advanced gradient boosting algorithms, specifically LightGBM and XGBoost. This study also advocated permutation importance as a reliable and easy-to-understand method for identifying and quantifying the impact of each input variable on VMA. Accordingly, the feature importance was calculated across multiple test sets using a cross-validation strategy to ensure the results were robust and applicable to different data conditions. This helped reduce bias from individual data splits and provided a clearer understanding of the most important variables. Finally, the study compared the model findings with well-known engineering knowledge to confirm the accuracy and practical relevance of the results.

2. Dataset

The data set used in this study belongs to 200 asphalt mixtures collected from previously conducted experimental studies. In this dataset, there are 13 variables, such as asphalt binder content (P_b), theoretical maximum specific gravity (G_{mm}), bulk specific gravity of the compacted mix (G_{mb}), bulk specific gravity of the aggregate blend (G_{sb}), effective asphalt content (P_{be}), effective aggregate specific gravity (G_{se}), air voids (V_a), Voids in Mineral Aggregate (VMA), Voids Filled with Asphalt (VFA), and dust ratio. These features are crucial for evaluating and forecasting the volumetric behavior of hot mix asphalt (HMA). Additionally, Table 1 presents the descriptive statistics of these variables, including the mean, standard deviation, minimum, maximum, and median values.

Additionally, the statistical distributions of selected input and output variables in the asphalt mix design dataset are presented in Fig. 1. The histograms, combined with kernel density estimation curves, provide insight into the data structure of variables such as asphalt binder content (P_b), bulk specific gravities (G_{sb} and G_{mb}), air voids (V_a), Voids in Mineral Aggregate (VMA), and Voids Filled with Asphalt (VFA). Most variables, including P_b, VMA, and VFA, exhibit approximately normal distributions, while others, such as V_a and G_{sb}, display slight skewness or multimodal tendencies. These visual assessments are essential for understanding variable behavior and ensuring the appropriateness of the dataset for predictive modeling.

Table 1. Descriptive statistics of input and output variables used in the asphalt mix design dataset.

Variables	N Total	Mean	Standard Deviation	Sum	Minimum	Median	Maximum
P_b	200	5.53	0.56	1105.26	4.00	5.50	7.00
G_{mm}	200	2.54	0.04	507.61	2.46	2.54	2.63
G_{mb}	200	2.43	0.06	486.30	2.33	2.44	2.55
G_b	200	1.029	0	205.80	1.029	1.029	1.029
G_{sb}	200	2.71	0.05	541.96	2.63	2.69	2.77
P_{ba}	200	0.91	0.44	182.15	0.45	0.69	1.62
P_{be}	200	4.62	0.50	923.11	3.03	4.58	5.80
G_{se}	200	2.78	0.04	555.21	2.69	2.80	2.81
V_a	200	4.20	1.67	839.18	1.22	4.15	7.55
VMA	200	15.23	1.25	3045.48	12.00	15.07	18.12
VFA	200	72.89	9.80	14578.66	48.40	72.78	91.18
Density	200	2431.49	55.83	486298	2329	2437	2550
Dust Ratio	200	0.84	0.13	167.47	0.62	0.82	1.37

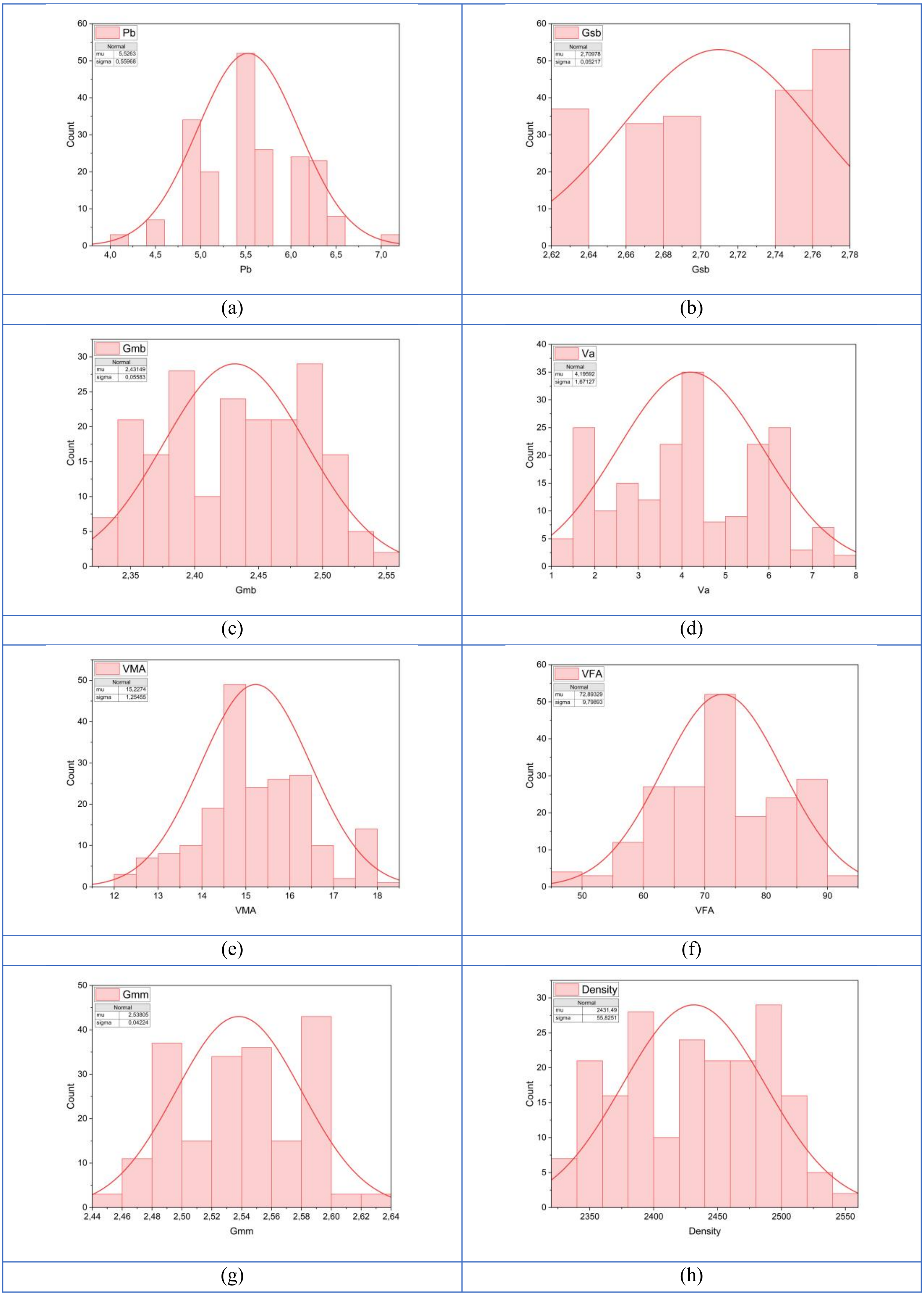

Fig. 1. Histogram and kernel density plots showing the distribution of selected asphalt mix design variables: (a) binder content (P_b), (b) bulk specific gravity of aggregate (G_{sb}), (c) bulk specific gravity of the mixture (G_{mb}), (d) air void content (V_a), (e) voids in mineral aggregate (VMA), (f) voids filled with asphalt (VFA), (g) maximum specific gravity of the mixture (G_{mm}), and (h) mixture density.

3. Methodology

It is widely accepted that, in a high-dimensional feature set, not all features contribute equally to the ML model. Since ML models are often considered black-box models, the contribution of each feature is typically assessed only after the model has been trained. The assessment of each feature's contribution after model training is referred to as feature importance. A typical workflow for constructing an ML model is as follows: A dataset is prepared, then divided into train and test sets (typically 80% for train and 20% for test). The model is trained on the train set and evaluated on the test set. After the modelling part is done, feature importances are calculated. Several methods have been proposed to assess the importance of the feature. One of them is Permutation Feature Importance (PFI) (Kaneko, 2022). The main idea of the PFI is to shuffle the value of feature $\boldsymbol{i}$, which will break down the association between feature $\boldsymbol{i}$ and outcome $\boldsymbol{x}$. Thus, if the ML model relies on the feature $\boldsymbol{i}$, shuffling it results in high error. This will indicate that the feature $\boldsymbol{i}$ is an important feature for the dataset. When the output after permutation does not produce a high error on feature $\boldsymbol{i}$, it indicates that feature $\boldsymbol{i}$ is not important.

However, there is no consensus on using training and test data when assessing feature importance. When constructing the ML model on training data, inevitably, the ML model overfits. For this reason, calculating feature importance on training data will eventually be erroneous, and calculated feature importance will be unimportant. Revealing feature importance on training data only answers the question, "What are the variables that the model uses for prediction?" A figurative example of PFI on both test and train sets on a randomly, non-correlated dataset is given in Fig. 2.

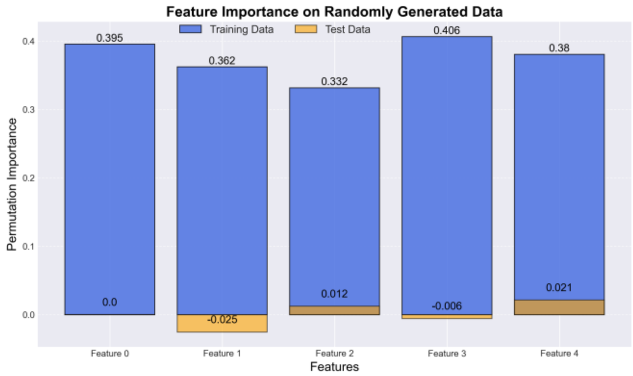

Fig. 2. Feature importance for non-correlated variables.

As seen from Fig. 2, even if the dataset was constructed with no correlation, PFI will assign each feature an importance value, which is obviously incorrect. Moreover, PFI is higher on the train set than the test set, proving the mentioned problem above. The optimal way to calculate the importance of the feature is to let the model be evaluated on unseen data. For this reason, PFI should be calculated on the test set to obtain reliable feature importances. Another important aspect of calculating PFI is to let the model see not only a constant portion of the dataset but also all subsets of the dataset. For this reason, cross-validation (CV) can be considered when calculating PFI. Using the CV approach, the model can see all portions of the data, and by calculating PFI for each test subset of the data, the importance of each feature can be assessed objectively. This study employed K-Fold CV to evaluate an ML model by dividing the dataset into K equal parts (folds). The model is trained on K-1 folds and tested on the remaining fold, repeating this process K times. A classical K-Fold CV as a figure is given in Fig. 3.

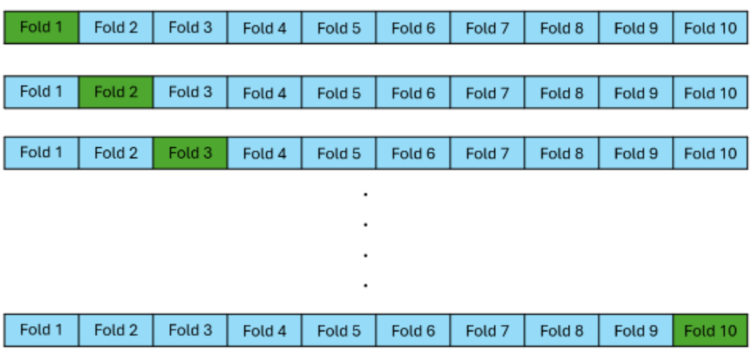

Fig. 3. K-Fold cross validation (K=10).

To objectively evaluate the PFI, we employ two state-of-the-art ML algorithms: Light Gradient Boosting Machine (LightGBM) (Chen et al., 2019) and eXtreme Gradient Boosting (XGBoost) (Ibrahem Ahmed Osman et al., 2021). Both are based on the Gradient Boosting Decision Tree (GBDT) framework, which constructs an ensemble of decision trees, in which each successive tree attempts to correct the errors of its predecessors. Unlike traditional models that learn independently from data, GBDT leverages this sequential learning strategy to produce a more accurate and robust model. LightGBM, developed by Microsoft, introduces a key innovation to enhance the efficiency of GBDT, particularly when dealing with high-dimensional feature spaces. The innovation is Gradient-based One-Side Sampling (GOSS), which improves training speed and accuracy by prioritizing instances with large gradients. Moreover, while traditional GBDT splits nodes based on information gain, GOSS utilizes variance gain as a splitting criterion. XGBoost, another powerful implementation of GBDT, distinguishes itself from LightGBM primarily in its tree construction strategy. Whereas LightGBM grows trees in a leaf-wise manner, focusing on the branch that maximally reduces loss, XGBoost adopts a level-wise approach that grows all branches evenly. In summary, LightGBM and XGBoost are among the most widely adopted gradient boosting frameworks and have been selected as two ML models in this study. The general working mechanism for both LightGBM and XGBoost is presented in Fig. 4.

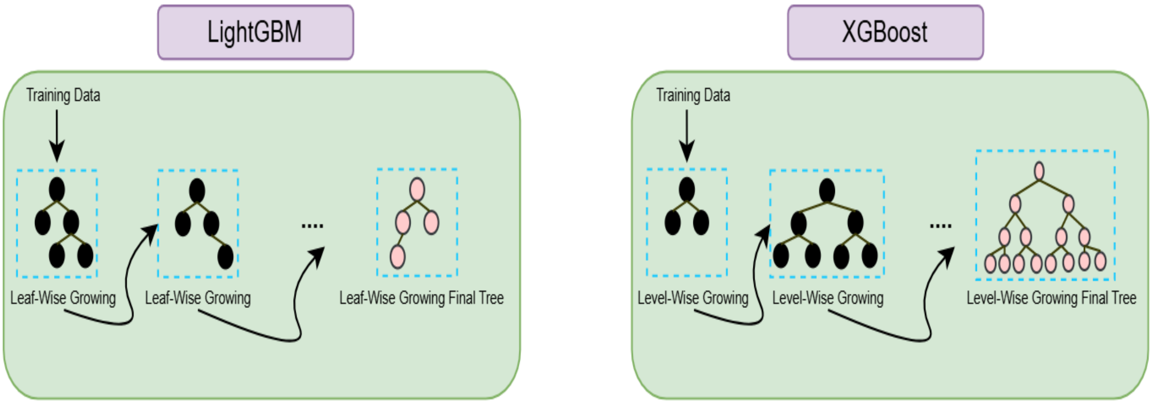

Fig. 4. LightGBM and XGBoost algorithms (Adapted from Chen et al., 2019).

To assess the impact of PFI in both the classical train-test split and K-Fold cross-validation, we divided our experimental setup into two parts. In the first part, the entire dataset was split into 80% for training and 20% for testing, following common practice in the literature. We then applied the two ML models mentioned above and calculated the PFI on the training and test sets. In the second part, we employed K-Fold CV, calculated the PFI for each fold, and then averaged the PFI, in which the ML models were trained on the training fold, and the PFI was computed on the corresponding test fold. Moreover, we calculated the performance metrics of both ML models using the classical train-test split approach and K-Fold CV approach, namely Root Mean Squared Error (RMSE) and Mean Squared Error (MSE). The formula for RMSE and MSE is given in Equations (1) and (2), respectively.

$$RMSE = \sqrt{\sum_{i=1}^{n} \frac{(\hat{y}_i - y_i)^2}{n}} \tag{1}$$

$$MSE = \frac{1}{n}(\hat{y}_i - y_i)^2 \tag{2}$$

Where n represents the total points in the dataset, $\hat{y}_i$ represents the output of the ML model for a specific point (i), and y_i shows the real value of point (i) in the dataset. We selected these error metrics because the problem at hand is essentially a regression task. All experiments were conducted using Python programming language (version 3.8.13). LightGBM and XGBoost were used with their default parameter settings, and no additional optimization techniques were applied.

4. Experimental results

In this section, the study first presents the results using the PFI calculated based on the classical 80%-20% training-test split of the dataset. Accordingly, the PFI results for the LightGBM and XGBoost models are shown in Fig. 5. Additionally, the RMSE and MSE for both ML models are provided in Table 2.

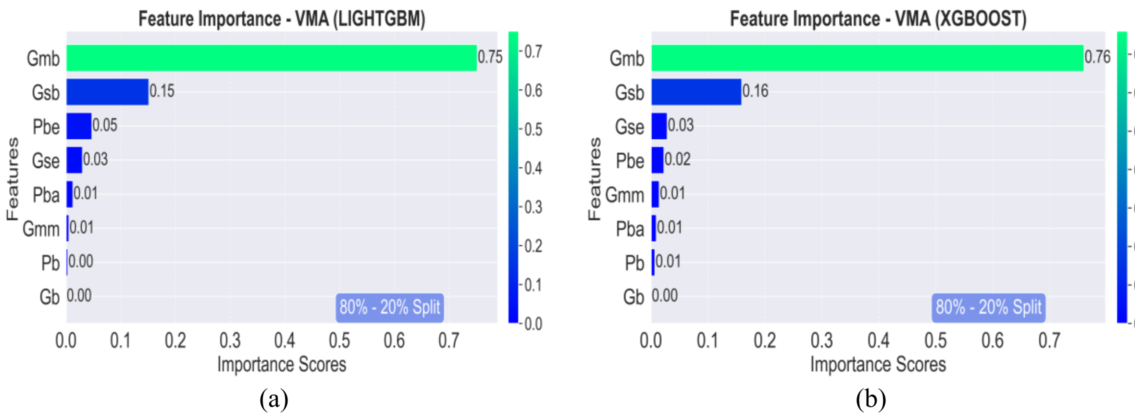

Fig. 5. PFI Scores for Both Models on 80%-20% Split. (a) LightGBM (b) XGBoost

Table 2. Error metrics for 80%-20% split

Error Metric	Train Set		Test Set	
	LightGBM	XGBoost	LightGBM	XGBoost
RMSE	0.2221	0.00021	0.235	0.1155
MSE	0.0493	0.0000047	0.055	0.0133

In the classical 80%-20% split, both ML models consistently identified G_{mb} as the most important feature in the dataset. In other words, the findings indicate that G_{mb} plays the key role in predicting VMA. Additionally, both models agreed that G_{sb} is the second most important feature. However, they diverged in identifying the third most important variable: LightGBM emphasized P_{be}, whereas XGBoost highlighted G_{se}. Regarding predictive performance, both models exhibited significant overfitting under the classical split, as reflected in the error metrics. This is a classical, expected result on small datasets, since in the classical splitting method, ML models do not see all of the dataset and perform poorly on the test set. In this study, XGBoost achieved the lowest RMSE (0.1155) and MSE (0.0133), indicating a more accurate prediction of VMA compared to LightGBM, which recorded higher test errors (RMSE: 0.235, MSE: 0.055). Hence, in terms of both evaluation metrics, XGBoost clearly outperformed LightGBM.

To improve interpretability and mitigate overfitting, we also applied K-fold CV to the dataset and calculated the PFI for each test fold in this study. An average PFI score was then computed for each feature. Similarly, average RMSE and MSE values were obtained for each model under different K values. Accordingly, Fig. 6 presents the PFI values obtained for different values of K in the CV approach.

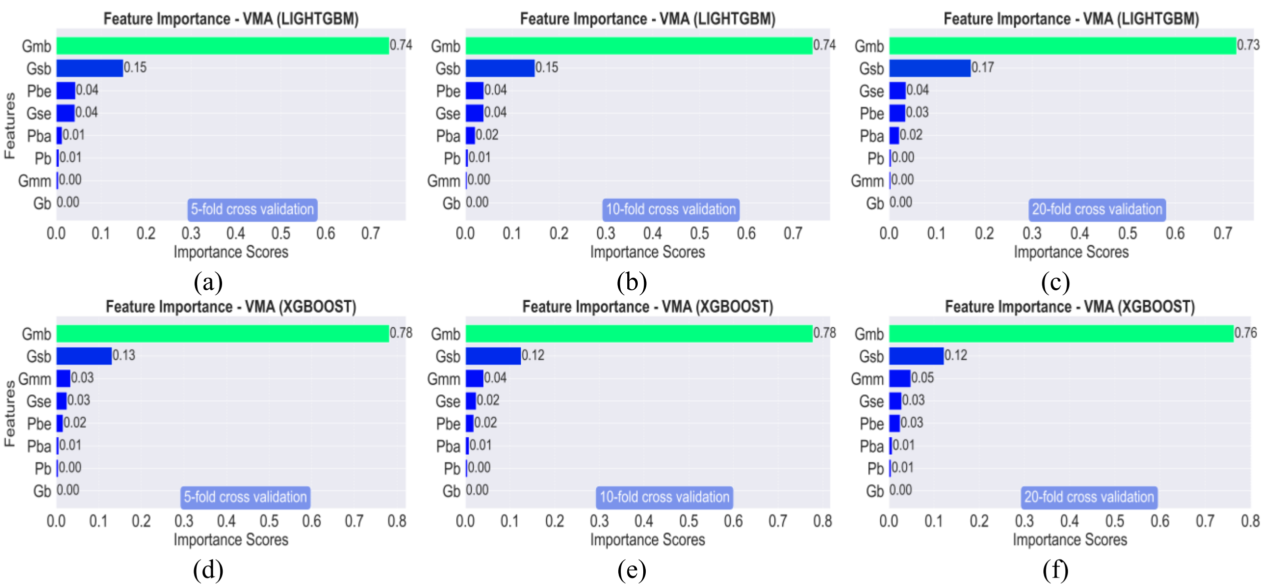

Fig. 6. PFI scores for both models across different K values in cross-validation. (a) LightGBM 5-Fold (b) LightGBM 10-Fold (c) LightGBM 20-Fold (d) XGBoost 5-Fold (e) XGBoost 10-Fold (f) XGBoost 20-Fold.

Similar to the results obtained from the 80%-20% split, both LightGBM and XGBoost consistently found G_{mb} and G_{sb} as the top two influential variables influencing VMA across all folds. However, while LightGBM showed minor variations in ranking the third most important feature depending on the K value (alternating between P_{be} and G_{se}), XGBoost demonstrated a more stable pattern by consistently ranking G_{mm} in third place. This discrepancy implies that XGBoost can pick stronger structural patterns, whereas LightGBM appears more sensitive to data partitioning effects. Especially under CV in XGBoost, G_{mm}'s significance became quite clear despite its minor relevance in the 80%-20% split, therefore highlighting the need for repeated sampling in revealing hidden relationships. On the other hand, the binder specific gravity (G_b) showed negligible importance in both the 80%-20% train-test split and the cross-validation setups (see Fig. 5 and Fig. 6). This is mainly due to two factors. First, as indicated in Table 1, G_b remained constant across all samples (mean = 1.029, SD = 0), providing no variation for the models to learn from. Since ML models rely on feature variability to assess influence, a fixed input like G_b has no predictive contribution. Second, G_b does not appear directly in the theoretical VMA formula, as seen in Equation (3).

$$\mathrm{VMA} = \left(1 - \frac{G_{mb}(1 - P_b)}{G_{sb}}\right) \mathrm{x}100 \tag{3}$$

Given their direct occurrence in Equation (3), G_{mb}, G_{sb}, and P_b are inherently critical in calculating VMA and are likely to emerge as the highest-ranked features in any feature importance analysis. Furthermore, binder-related effects are already captured through P_b and P_{be}, making G_b redundant. These findings hold across both model types (LightGBM and XGBoost) and all CV folds, confirming that the low importance of G_b is both statistically and theoretically well-founded. In short, the observed feature importance rankings strongly align with the analytical VMA equation, where G_{mb}, G_{sb}, and P_b are the primary contributors. Consistently, both LightGBM and XGBoost identified G_{mb} as the dominant feature, followed by G_{sb}, reflecting the structural formulation of the empirical equation. Furthermore, the emergence of features such as G_{mm} and P_{be} in PFI results, despite not being explicitly part of the original formula, suggests that ML models can detect latent interdependencies within mix design parameters. This reinforces the reliability of the PFI method and highlights its potential for both validating known empirical relationships and uncovering additional influential factors in asphalt mix design.

In addition to the PFI scores for both models under various K-fold CV settings, Table 3 presents the corresponding error metrics. The significant disparity between training and test errors indicates that both LightGBM and XGBoost show signs of overfitting over all K values. However, an interesting observation is that LightGBM appears to overfit less than XGBoost. Another insight is that LightGBM's overfitting decreases as the K value increases, suggesting improved generalization with more folds. In contrast, XGBoost does not exhibit this trend. This discrepancy may be attributed to the different feature set that each model emphasizes. To further support these findings, Fig. 7 illustrates the PFI scores computed individually for each fold in the cross-validation process.

In Fig. 7, each bar shows the normalized PFI value of a particular feature for a particular fold, allowing an assessment of the stability of importance ratings over the folds. Across all configurations, G_{mb} consistently maintained the highest normalized importance scores, with relatively low variation between folds. XGBoost shows greater stability across folds, as evidenced by the more tightly clustered importance scores in graphs (b), (d), and (f), indicating lower sensitivity to data partitioning compared to LightGBM. As a result, these fold-wise analyses expose the uncertainty around secondary variables and confirm the stability of important predictors (G_{mb} and G_{sb}). Particularly when calculating PFI, they show even more the importance of cross-validation for feature interpretation as well as for model performance.

Table 3. Error metrics for each K value in the CV approach.

Error Metric	**Train Set**						**Test Set**					
	LightGBM			XGBoost			LightGBM			XGBoost		
	K=5	K=10	K=20	K=5	K=10	K=20	K=5	K=10	K=20	K=5	K=10	K=20
RMSE	0.232	0.225	0.220	0.0023	0.0026	0.002	0.2951	0.288	0.255	0.1408	0.1304	0.1372
MSE	0.054	0.051	0.048	0.000005	0.000007	0.000007	0.090	0.088	0.073	0.0228	0.0195	0.0233

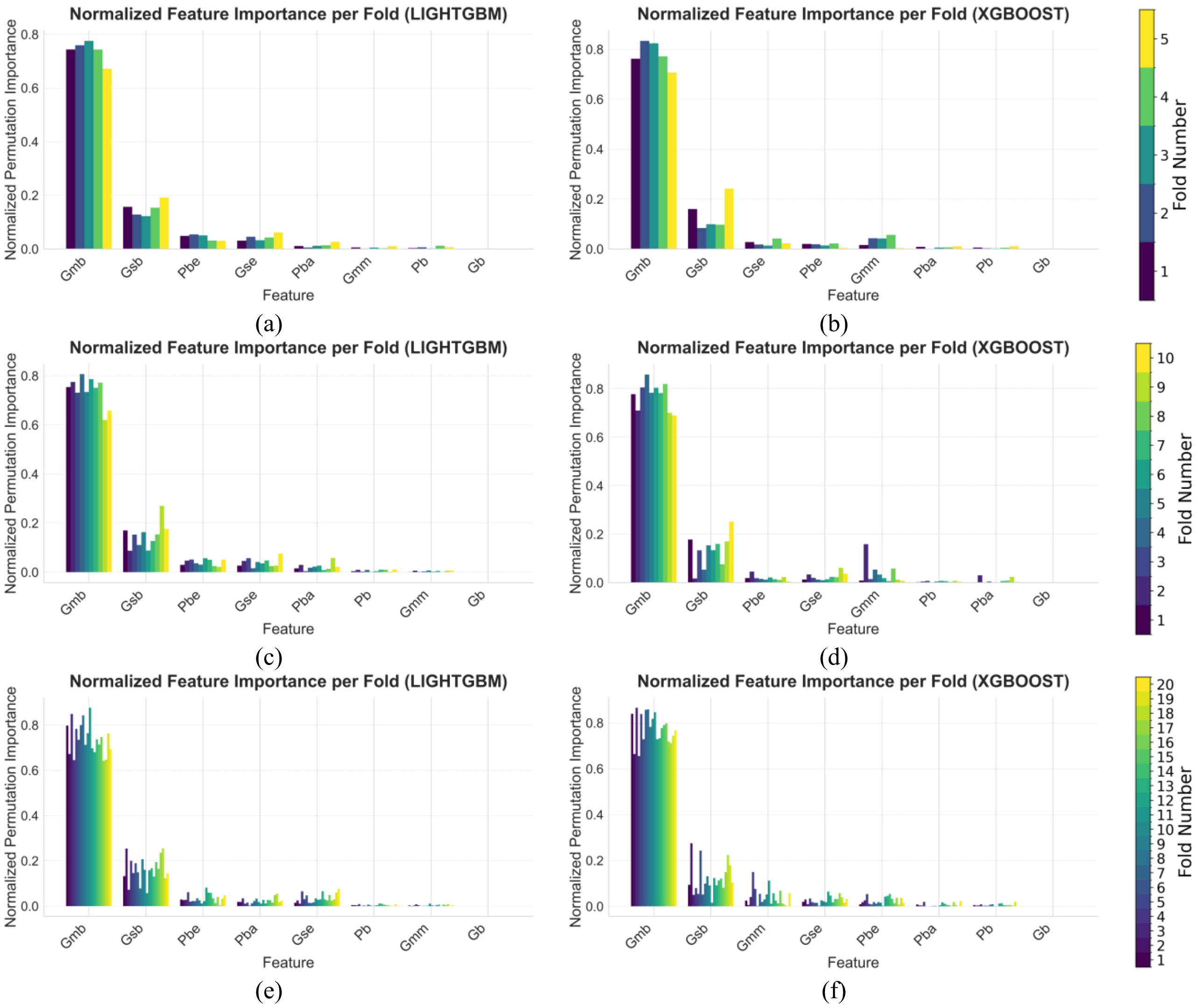

Fig. 7. PFI scores for each fold for each feature. (a) LightGBM 5-Folds (c) LightGBM 10-Folds (e) LightGBM 20-Folds (b) XGBoost 5-Folds (d) LightGBM 10-Folds (f) LightGBM 20-Folds

5. Conclusion

This study tried to test and validate the reliability of interpretable ML methods in engineering problems related to asphalt mixture design, such as VMA estimation. Based on the results, it is possible to reach the following specific findings:

- It is emphasized that reliable identification of the most important input variables is possible by combining K-fold CV with Permutation Feature Importance (PFI).
- XGBoost consistently had lower RMSE and MSE values, indicating higher prediction accuracy. It also had a more stable feature importance distribution across all folds, indicating greater robustness to data partitioning.
- While LightGBM was slightly less accurate overall, it demonstrated lower overfitting and improved generalization as the number of folds increased, indicating its strength in handling small datasets.
- The specific gravity of the compacted mix (G_{mb}) and the aggregate blend (G_{sb}) were consistently ranked as the most important properties, which agrees with the empirical VMA equation. This finding demonstrates the reliability of ML approaches in creating predictive models for engineering problems.
- Variables such as G_{mm} and P_{be} that are not explicitly included in the empirical formula were found to impact the VMA significantly, demonstrating the potential of ML models to uncover hidden relationships.

Acknowledgments

This research did not receive any specific grant from funding agencies in the public, commercial, or not-for-profit sectors.

References

Chen, C., Zhang, Q., Ma, Q., & Yu, B. (2019). LightGBM-PPI: Predicting protein-protein interactions through LightGBM with multi-information fusion. *Chemometrics and Intelligent Laboratory Systems*, *191*, 54–64. https://doi.org/10.1016/j.chemolab.2019.06.003

Cooper, S. B., Mohammad, L. N., Kabir, S., & King, W. (Bill). (2014). Balanced Asphalt Mixture Design through Specification Modification: Louisiana's Experience. *Transportation Research Record: Journal of the Transportation Research Board*, *2447*(1), 92–100. https://doi.org/10.3141/2447-10

Dai, M., Zhang, F., Dai, S., Xing, C., Xiao, S., Lv, H., & Tan, Y. (2024). Optimizing asphalt mix design through predicting volumetric properties using interpretable machine learning. *Powder Technology*, *444*, 119954.

Eleyedath, A., & Swamy, A. K. (2022). Prediction of dynamic modulus of asphalt concrete using hybrid machine learning technique. *International Journal of Pavement Engineering*, *23*(6), 2083–2098. https://doi.org/10.1080/10298436.2020.1841191

Gardete, D., Picado-Santos, L., Capitão, S., & Luzia, R. (2022). Asphalt mix design: Discussion on the bulk specific gravity procedure influence on the results obtained from empirical, volumetric, and performance-based methods. *Construction and Building Materials*, *342*, 127870.

Haddad, A. J., Chehab, G. R., & Saad, G. A. (2022). The use of deep neural networks for developing generic pavement rutting predictive models. *International Journal of Pavement Engineering*, *23*(12), 4260–4276. https://doi.org/10.1080/10298436.2021.1942466

Hinrichsen, J. A., & Heggen, J. (1996). Minimum Voids in Mineral Aggregate in Hot-Mix Asphalt Based on Gradation and Volumetric Properties. *Transportation Research Record: Journal of the Transportation Research Board*, *1545*(1), 75–79. https://doi.org/10.1177/0361198196154500110

Hislop, W. P., & Coree, B. J. (2000). *VMA as a design parameter in hot-mix asphalt*. https://rosap.ntl.bts.gov/view/dot/40406

Hossain, M., & Chen, J. Z. (2002). Optimization of Superpave mixture volumetric properties. *International Journal of Pavement Engineering*, *3*(2), 63–69.

Hosseini, A. S., Hajikarimi, P., Gandomi, M., Nejad, F. M., & Gandomi, A. H. (2021). Optimized machine learning approaches for the prediction of viscoelastic behavior of modified asphalt binders. *Construction and Building Materials*, *299*, 124264.

Ibrahem Ahmed Osman, A., Najah Ahmed, A., Chow, M. F., Feng Huang, Y., & El-Shafie, A. (2021). Extreme gradient boosting (Xgboost) model to predict the groundwater levels in Selangor Malaysia. *Ain Shams Engineering Journal*, *12*(2), 1545–1556. https://doi.org/10.1016/j.asej.2020.11.011

Junaid, M., Jiang, C., Gazder, U., Hafeez, I., & Khan, D. (2024). Evaluation of asphalt mixtures modified with low-density polyethylene and high-density polyethylene using experimental results and machine learning models. *Scientific Reports*, *14*(1), 24601.

Jweihan, Y. S., Alawadi, R. J., Momani, Y. S., & Tarawneh, A. N. (2022). Prediction of marshall test results for dense glasphalt mixtures using artificial neural networks. *Frontiers in Built Environment*, *8*, 949167.

Kandhal, P. S., & Chakraborty, S. (1996). *Evaluation of voids in the mineral aggregate for HMA paving mixtures*. National Center for Asphalt Technology (US). https://rosap.ntl.bts.gov/view/dot/13627

Kaneko, H. (2022). Cross-validated permutation feature importance considering correlation between features. *Analytical Science Advances*, *3*(9–10), 278–287. https://doi.org/10.1002/ansa.202200018

Krcmarik, M., Varma, S., Emin Kutay, M., & Jamrah, A. (2016). Development of Predictive Models for Low-Temperature Indirect Tensile Strength of Asphalt Mixtures. *Journal of Materials in Civil Engineering*, *28*(11), 04016139. https://doi.org/10.1061/(ASCE)MT.1943-5533.0001655

Lee, J.-S., Lee, S.-Y., & Le, T. H. M. (2023). Developing performance-based mix design framework using asphalt mixture performance tester and mechanistic models. *Polymers*, *15*(7), 1692.

Liu, J., Liu, F., & Wang, L. (2024). Acceleration of Superpave Mix Design: Solving Multi-Objective Optimization Problems Using Machine Learning and the Non-Dominated Sorting Genetic Algorithm-II. *Transportation Research Record: Journal of the Transportation Research Board*, *2678*(11), 1863–1886. https://doi.org/10.1177/03611981241246782

Liu, J., Liu, F., Zheng, C., Zhou, D., & Wang, L. (2022). Optimizing asphalt mix design through predicting effective asphalt content and absorbed asphalt content using machine learning. *Construction and Building Materials*, *325*, 126607. https://doi.org/10.1016/j.conbuildmat.2022.126607

Lundberg, S. M., & Lee, S.-I. (2017). A unified approach to interpreting model predictions. *Advances in Neural Information Processing Systems*, *30*. https://proceedings.neurips.cc/paper/2017/hash/8a20a8621978632d76c43dfd28b67767-Abstract.html

Mallick, R. B., Buchanan, M. S., Kandhal, P. S., Bradbury, R. L., & McClay, W. (2000). A rational approach of specifying the voids in the mineral aggregate for dense-graded hot-mix-asphalt. *79th Annual Meeting of the Transportation Research Board*.

Pouranian, M. R., & Haddock, J. E. (2018). Determination of voids in the mineral aggregate and aggregate skeleton characteristics of asphalt mixtures using a linear-mixture packing model. *Construction and Building Materials*, *188*, 292–304. https://doi.org/10.1016/j.conbuildmat.2018.08.101

Prowell, B. D., Zhang, J., & Brown, E. R. (2005). *Aggregate properties and the performance of superpave-designed hot mix asphalt* (Vol. 539). Transportation Research Board.

Rahman, S., Bhasin, A., & Smit, A. (2021). Exploring the use of machine learning to predict metrics related to asphalt mixture performance. *Construction and Building Materials*, *295*, 123585. https://doi.org/10.1016/j.conbuildmat.2021.123585

Roquier, G. (2023). Estimation of voids in a multi-sized mineral aggregate for asphalt mixture using the Theoretical Packing Density Model. *Construction and Building Materials*, *367*, 130302.

Sebaaly, H., Varma, S., & Maina, J. W. (2018). Optimizing asphalt mix design process using artificial neural network and genetic algorithm. *Construction and Building Materials*, *168*, 660–670.

Shen, S., & Yu, H. (2011a). Analysis of Aggregate Gradation and Packing for Easy Estimation of Hot-Mix-Asphalt Voids in Mineral Aggregate. *Journal of Materials in Civil Engineering*, *23*(5), 664–672. https://doi.org/10.1061/(ASCE)MT.1943-5533.0000224

Shen, S., & Yu, H. (2011b). Analysis of Aggregate Gradation and Packing for Easy Estimation of Hot-Mix-Asphalt Voids in Mineral Aggregate. *Journal of Materials in Civil Engineering*, *23*(5), 664–672. https://doi.org/10.1061/(ASCE)MT.1943-5533.0000224

Wang, Y. (2019). *Development of the framework of performance-engineered mixture design for asphalt concrete*. North Carolina State University. https://search.proquest.com/openview/1416a8d6df1073f5b821ff7db6d8a5c1/1?pq-origsite=gscholar&cbl=18750&diss=y

Zavrtanik, N., Prosen, J., Tušar, M., & Turk, G. (2016). The use of artificial neural networks for modeling air void content in aggregate mixture. *Automation in Construction*, *63*, 155–161.

Zhang, W., Khan, A., Huyan, J., Zhong, J., Peng, T., & Cheng, H. (2021). Predicting Marshall parameters of flexible pavement using support vector machine and genetic programming. *Construction and Building Materials*, *306*, 124924.

4th International Civil Engineering & Architecture Conference
17-19 May 2025, Trabzon, Türkiye

Design and estimation of plastic properties of gradations for flexible pavement courses

Mustafa Aytekin*[1]

[1] University of Bahrain, Department of Civil Engineering, 973, Sakhir Campus, Kingdom of Bahrain

Abstract. In the design of flexible pavements, there are several layers that must be designed according to the specifications such as subgrade-improvement, subbase, base, and surface courses. Most of the time, it is needed to use materials that must be blended from several stockpiles to generate an adequate gradation for the courses of flexible pavements within the range that is given by specifications. Also, the liquid limit and plasticity index of the mixture must have specific values given by the specifications. For this purpose, a rational approach and formulation that allows engineers to do the job effectively and faster are developed. In the proposed method, the materials provided from two stockpiles or more without any limitations would be taken into consideration for the design of mixture gradation. Then, the liquid limit and plasticity index of the designed mixture would be estimated accordingly. An "MS-Excel Spread Sheet" has been created and the gradations for all types of requirement given by the specifications can be designed with any number of material stockpiles. A numerical example of the method is also provided.

Keywords: Flexible pavement design; Gradation of materials; Plastic properties of mixture; Rational method; Mix design

1. Introduction

In the design of flexible pavements, there are several layers that must be designed like subgrade-improvement, subbase, base, and surface courses Garber, and Hoel (2015). The materials used in these courses must satisfy the certain properties. For example, the gradation of the materials used in any of these courses should be within a range given by the specifications. Researchers in this subject have studied the impact of aggregate gradation on mixture properties and mixture performance. Thus, many research studies have been conducted for this purpose, Ahmed and Attia (2013), Chen and Liao (2002), El-Basyouny and Mamlouk (1999), Fang, Park, Singuranayo, Chen, and Li (2019), Garcia, V. M., Barros, L., Garibay, et al (2020), Stakton and Bahia (2003). It has been discovered that aggregate gradation strongly influences the rutting resistance of mixtures, and a mixture made with high-quality materials would fail without suitable gradation, Stakton and Bahia (2003). The material specifications should be checked to assure that hydraulic conductivity, strength, load-distribution, and construction stability requirements are met, Al-Saoudi and Kawla (2017). An estimation of the proper proportions of available materials in the field is possible and depends on manual and visual inspections, Reimer (1992). There are a few methods to determine the proper gradation and estimation of the plastic properties of these mixtures in the literature, Mallick and El-Korchi (2013). Even, there is a graphical method to determine the gradation if you will blend only two materials to be blended, Reimer (1992). However, the usage of these methods is not rational. For instance, when more than two material-stockpiles are available to create a mixture for an adequate gradation, the methods are very subjective and time consuming like trial and error method. The trial and error method is still in use, Shakhan and Sengoz (2022).

A new method of the determination of mix gradation is presented in this paper. It is believed that this new method will be very useful while designing a gradation that would be within the zone specified by the standards and/codes.

2. Setting up the specified gradation mixtures

In this paper, a new approach is offered to setup the gradation curve within the zone that is specified by the codes or specifications. The gradation of mixture can be set up from the any number available sources that might be two sources or more with no upper limitation. For example, five different sources have been considered in Example 1.

* Corresponding author, E-mail: maytekin@uob.edu.bh

https://doi.org/10.31462/icearc2025_ce_tra_800

3. Vectors to be created on the design of gradation

In the proposed method, the following vectors must be created first to design of a mixture by blending a number of materials from different stockpiles. Of course, the sieve analyses and gradation of each material that would be blended must be available before starting any calculation. A vector, named as vector O that would have openings of sieves employed in the determination of the gradations, The gradation data for each material should be included in a vector. In other words, the number (n) of the vectors that must be created would be equal to the number of materials in the mixture to be designed. Let's call the gradations vectors as Gi, i = 1 to n. Other vectors are listed below:

MS: selected gradation of the mixture vector, BU: upper boundary of the mixture given by the specification. BL: Lower boundary of the mixture given by the specification. Di: differences of the gradations between the selected gradation (matrix MS) and the materials' gradations to be included in the mixture. DD: summations of absolute differences between the selected gradation and each material that would be included in the mixture. PR: Percentages of absolute differences of each material in matrix DD. MF: Final gradation of the mixture.

The numerical values in PR vector must be arranged from the maximum to minimum values. The values in vector DD must be arranged from minimum to maximum values. Then, the gradation values represented by the minimum value in vector DD must be multiplied by the maximum value of PR vector. Similarly the gradation values represented the maximum value in vector DD must be multiplied by the minimum value of PR vector. The other percentages of the remaining materials must be calculated accordingly.

It seems to be a little bit complicated procedure. However, this procedure is very easy to apply in a spreadsheet like the excel spreadsheet or a software like MATLAB. An example (Example 1) is given here to understand the method more clearly.

4. Plastic properties of the mixture

The plastic properties of the mixture can be estimated by considering percentages of materials in the mixture passing No.40 sieve that has an opening of 0.425mm. The reason for this approach is that the plastic properties of any soil are determined by using the portion of the material passing No.40 sieve. First, the plasticity indexes (PI) and liquid limits (LL) of all materials blended to create the mixture must be known along with their gradations. Example 2 illustrates the estimation of plasticity index, PI, and the liquid limit, LL, of the mixture designed in Example 1.

Example 1: Design a mixture of that the gradation must be between the upper and lower borders given by the code. In Table 1, the openings (sizes) of sieve set, the gradation of soils from five stockpiles are given. Also upper and lower borders are provided.

Solution:

- Step 1: It would be a good approach to plot gradations of all materials in a graph as seen in Fig.1. Then, the upper and lower borders should be plotted on the same graph to see the zone in which the gradation of the mixture would take place as seen in Fig 2. It is obvious that soil 4 should have the largest percentage in the mixture because its gradation is the closest one to the band as seen in Fig 2. Similarly, soil 2 should have the least percentage in the mixture since its gradation is far from the band. First of all, an initial gradation of the mixture to be designed is selected between upper and lower borders for each diameter (Table 2). Then, the differences of gradations between the selected mix-gradation and the gradations of the each material (soil) that would be in the mixture is calculated as seen Table 2. At the bottom of the columns in Table 2, the summations of absolute values of the differences between selected one and each soil is shown.

Table 1**.** Gradations (% finer) of soils and specified range of the mixture to be designed

Sieve Size (mm)	Soil 1	Soil 2	Soil 3	Soil 4	Soil 5	Upper Border	Lower Border
19.000	100	100	100	100	100	100	100
12.500	100	81	100	100	100	100	90
9.500	93	15	100	100	100	90	80
4.750	24	1.7	98.7	95.3	100	75	65
2.360	7.5	1.5	79	77.4	84.5	60	50
1.180	5.8	1.4	57.4	50	57.4	50	35
0.600	5.1	1.3	39.7	31	40.5	30	20
0.300	4.5	1.2	16.9	17.7	29.2	20	10
0.150	3.5	1	6.9	5.7	21.1	15	5
0.075	1.6	0.7	2.8	1.6	14.2	10	0

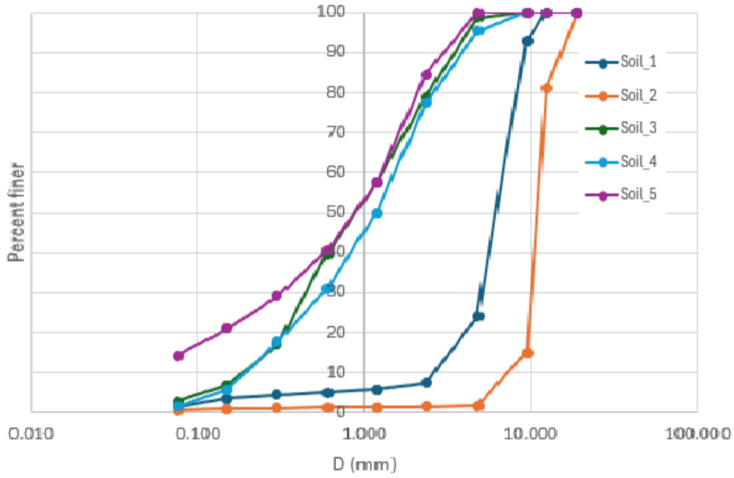

Fig.1. Gradations of five materials that would be in the mixture.

- Step 2. The ratios of the total absolute differences for each soil to the total of all differences will be calculated as follows:
  Soil 1: 176/834.2 = 0.211
  Soil 2: 290.2/834.2 = 0.348
  Soil 3: 117/834.2 = 0.140
  Soil 4: 99.1/834.2 = 0.119
  Soil 5: 151.9/834.2 = 0.182

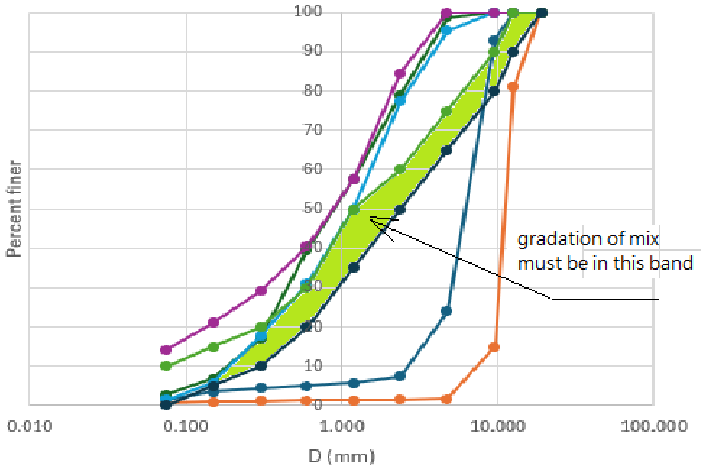

Fig. 2. The zone of gradation of the mixture

Table 2. Selected gradation and its difference with 5-soil gradations

Upper Border	Lower Border	Selected Mix - MS	MS-Soil 1	MS-Soil 2	MS-Soil 3	MS-Soil 4	MS-Soil 5
100	100	100	0	0	0	0	0
100	90	95	-5	14	-5	-5	-5
90	80	85	-8	70	-15	-15	-15
75	65	70	46	68.3	-28.7	-25.3	-30
60	50	50	42.5	48.5	-29	-27.4	-34.5
50	35	40	34.2	38.6	-17.4	-10	-17.4
30	20	25	19.9	23.7	-14.7	-6	-15.5
20	10	15	10.5	13.8	-1.9	-2.7	-14.2
15	5	10	6.5	9	3.1	4.3	-11.1
10	0	5	3.4	4.3	2.2	3.4	-9.2

Table 2 continued

Vector DD= Total absolute differences =	176	290.2	117	99.1	151.9
DT, Total of all absolute differences =	834.2				
Ratios, Vector PR	0.211	0.348	0.140	0.119	0.182
Sum of the ratios	1.00				

*Summation of these ratios must be equal to 1. (0.211+0.348+0.140+0.119+0.182)= 1.00 OK.

- Step 3. The final percentages of the soils that would be in the mixture can be determined as follows:
  a. The smallest ratio among the calculated values (in this example, it is 0.119) is taken the percentage of soil that has the largest sum of absolute differences (in this example it is 290.2-Soil 2). Thus, the percent of Soil 2 in the mixture will be 11.9%.
  b. The largest ratio among the calculated values (in this example, it is 0.348) is taken the percentage of soil that has the smallest sum of absolute differences (in this example it is 99.1-Soil 4). Thus, the percent of Soil 4 in the mixture will be 34.8%
  c. Then, the second largest value of the ratios (in this example, it is 0.211) is taken the percentage of second smaller sum of the absolute differences (it is 117-Soil 3 in this example). Thus, the percent of Soil 3 in the mixture will be 21.1%.

By the same procedure, the percentages of Soil 1, and Soil 5 would be 14,0%, and 18.2%, respectively. The calculated percentages of each soil and the final gradation of the mixture are seen in Table 3.

Table 3. Percentages of the soils in the mixture and the final mixture gradation

% of Soil 1	% of Soil 2	% of Soil 3	% of Soil 4	% of Soil 5	MF Final Mix
14.03	11.88	21.10	34.79	18.21	100.00
14.03	9.62	21.10	34.79	18.21	97.74
13.04	1.78	21.10	34.79	18.21	88.92
3.37	0.20	20.82	33.15	18.21	75.75
1.05	0.18	16.67	26.93	15.39	60.21
0.81	0.17	12.11	17.39	10.45	40.94
0.72	0.15	8.38	10.78	7.37	27.40
0.63	0.14	3.57	6.16	5.32	15.81
0.49	0.12	1.46	1.98	3.84	7.89
0.22	0.08	0.59	0.56	2.59	4.04

It should be shown graphically that the gradation of final mixture takes place within the zone as seen in Fig.3.

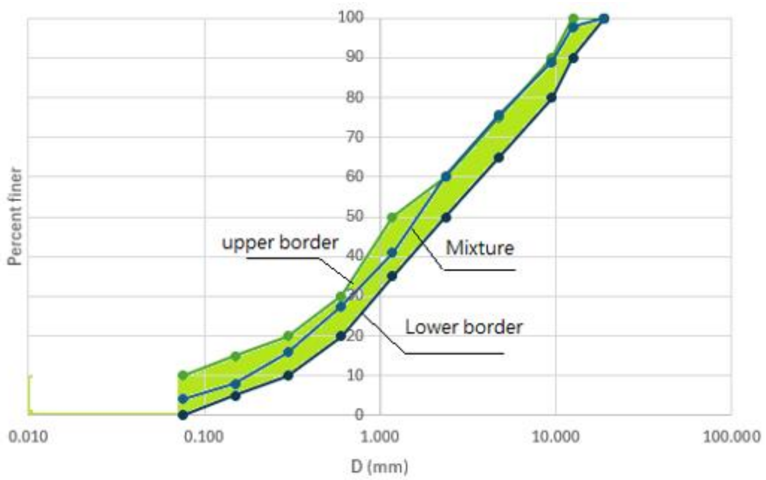

Fig. 3. Designed gradation of the mixture within the borders by blending five materials

Example 2: Estimate the plasticity index, PI, and the liquid limit, LL, of the mixture designed in Example 1 if the PI and LL values of each materials are given as seen Table 4. Estimate the PI, and LL values of the mixture.

Table 4. Plastic properties of the materials used in Example 1.

Materials (Soils)	Plasticity Index, PI	Liquid Limit, LL
Soil 1	3	15
Soil 2	2	10
Soil 3	7	30
Soil 4	8	25
Soil 5	11	31

Solution: As seen in Table 5, the data of the columns from 1 to 3 are readily available. The data of column #4 are taken from Table 3, and column #5 is filled by the data taken from Fig. 1. Column #6 is filled by (column #4 * column #5). Column #7 is filled by (column #6 * 25,25 which is total amount of materials' portions passing No.40 sieve) / 100. Finally, estimated values of the PI ((3×2.78 + 2×0.94 + 7×31.75 + 8×38.57 + 11×25.96)/100 = 8.27) and LL ((15×2.78 + 10×0.94 + 30×31.75 + 25×38.57 + 31×25.96)/100 = 27.73) of the mixture will be calculated.

Table 5. Estimation of the Plasticity Index and Liquid Limit of the mixture in Example 1.

Materials (Soils)	PI	LL	Amount (kg) of each soil in 100kg mix Table 3	% passing No.40 sieve Fig 1	Amount (kg) of each soil passing No.40 in 100kg mixture	% of each soil passing No.40 sieve in mix
Soil 1	3	15	14.03	5	0.70	2.78
Soil 2	2	10	11.88	2	0.24	0.94
Soil 3	7	30	21.10	38	8.02	31.75
Soil 4	8	25	34.79	28	9.74	38.57
Soil 5	11	31	18.21	36	6.56	25.96
Mixture	8.27	27.73	100.0	---	25.25	100.00

In this study, MS-Excel spread sheet has been employed to show readers the details of the calculations. Actually, a MATLAB code might be prepared to get the results only when there is no need to details of the calculations and the procedure.

5. Conclusions

The conclusions drawn from this investigation can be summarized as follows. Once the available methods to set up a specified gradation of mixtures have been evaluated. It is seen that these methos are okay to be employed in the mix design processes but they have several deficiencies like a trial and error approach is used. This might be ended a subjective results and time consuming for the design stages. In this study, it is shown that there is a new approach by which engineers can design the gradation of the mixtures by a more rational method that is proposed and explained with two examples in this study.

References

Ahmed, M. A., & Attia, M. I. E. (2013), Impact of aggregate gradation and type on hot mix asphalt rutting in Egypt. *International Journal of Engineering Research and Applications (IJERA), 3*(4), 2249–2258.

Al-Saoudi, N. K. S., & Kawla, H. H. S. (2017), Hydraulic conductivity of layered compacted granular materials used as pavement foundation. *Proceedings of the 1st GeoMEast International Congress and Exhibition, on Sustainable Civil Infrastructures*, Egypt.

Chen, J.-S., & Liao, M.-C. (2002). Evaluation of internal resistance in hot-mix asphalt (HMA) concrete. *Construction and Building Materials, 16*.

El-Basyouny, M. M., & Mamlouk, M. S. (1999). Effect of aggregate gradation on rutting potential of Superpave mixes. *8th Annual Meeting of the Transportation Research Board*.

Fang, M., Park, D., Singuranayo, J. L., Chen, H., & Li, Y. (2019). Aggregate gradation theory, design and its impact on asphalt pavement performance: A review. *International Journal of Pavement Engineering, 20*(12), 1408–1424.

Garber, N. J., & Hoel, L. A. (2015). *Traffic and highway engineering* (5th ed., SI ed.). University of Virginia: Cengage Learning.

Garcia, V. M., Barros, L., Garibay, J., Abdallah, I., & Nazarian, S. (2020). Effect of aggregate gradation on performance of asphalt concrete mixtures. *Journal of Materials in Civil Engineering, 32*(5), 04020102.

Mallick, R. B., & El-Korchi, T. (2013). *Pavement engineering principles and practice* (2nd ed.). CRC Press, Taylor and Francis Group.

Reimer, D. J. (1992). *Military soil engineering*. Headquarters Department of the Army, Washington, DC. C1, Field Manual 5-410.

Shakhan, M., Topal, A., & Sengoz, B. (2022). Improving flexible pavement performance through suitable aggregate gradation. *Revista de la Construcción. Journal of Construction, 21*(2), 295–308.

Stakton, A. D., & Bahia, H. U. (2003). The effect of fine aggregate angularity, asphalt content and performance graded asphalts on hot mix asphalt performance. *WisDOT Highway Research Study*, Wisconsin Department of Transportation.

4th International Civil Engineering & Architecture Conference
17-19 May 2025, Trabzon, Türkiye

The impact of big data and artificial intelligence on public transportation optimization

Tolga Avci*[1], Ilgin Gokasar[1]

[1] Bogazici University, Department of Civil Engineering, 34342 Istanbul, Türkiye

Abstract. With the rapid development of big data and artificial intelligence, the promising applications have widely and profoundly spread to many fields, such as public transportation. This work surrounds the utilization of big data analytics and artificial intelligence-based solutions in enhancing public transit systems. Through a systematic literature examination, the paper presents a new concept and its role in improving cost structure, increasing operational effectiveness, and satisfaction of the user. The findings indicate that the merger of AI technology with big data allows accurate forecasting of demand, determination of routes and supervision, and conditions which leads to a greater transport system optimization.

Keywords: Big data; Artificial intelligence; Public transportation

1. Introduction

Public transportation infrastructures serve as the engine of urban mobility, facilitating the movement of millions of individuals daily. Still, they also greatly influence the way cities run. This system is essential since it influences commuter behavior, economic activity, and social contacts. Although some would argue that private cars are handier, the benefits of public transportation overall cannot be emphasized. Maintaining and upgrading this infrastructure becomes more crucial, yet as cities develop. Demand for fast, economically priced, environmentally friendly transportation choices rises along with the population living in metropolitan megacities. Public transportation systems do, however, have significant issues even given their significance. These are in the form of schedule, routing, and capacity utilization inefficiencies; traffic congestion during peak travel hours; environmental issues related to high carbon emissions, and increasing passenger needs, which can result in vehicles being very crowded. Conventional approaches to the problem of public transportation are not sufficient enough to justify solutions to these problems. Such methods, although they are quite effective, are indeed becoming more and more ineffective in the context of a dynamic world in which real-time reactions to the situation change are necessary. Big Data is defined as a large amount of data originating from various sources such as ticketing systems, mobile applications, GPSs, social networks, and IoT sensors. The sheer volume, variety, and velocity of this data offer and pose a challenge. If well managed and leveraged, big data has the potential to reveal patterns and insights that can better influence decision-making, operational efficiency, and passenger experience. In public transport, even a lot of potentially different data sources may be considered big data sources, including real-time GPS-based one-commercial vehicle location data, passenger behavior data, supplied by mobile applications, and environmental data collected from IoT devices installed in the transport facility. In contrast, natural intelligence comprises a wide concept of machinery to mimic human intelligence. Concrete examples of machine learning, deep learning, natural language processing, and reinforcement learning. AI can analyze huge data sets efficiently and extremely rapidly, can reveal underlying patterns, and can generate predictions that are impossible to derive manually for humans. Artificial intelligence offers public transportation various advantages, including predictive maintenance and dynamic route optimization as well as other optimization tasks. Paris Metro, for example, has used an artificial intelligence-based predictive maintenance system to boost operational efficiency; the London Underground employs big data analytics to identify areas of congestion and hence improve dependability. Tokyo Metro has also embraced demand forecast artificial intelligence models to maximize passenger flow; in Barcelona, the public transportation system uses deep learning methods to process both past and present data, therefore guaranteeing improved service adaption and efficiency. For now, these real-life applications have been provided in a general manner, but it is possible to find detailed explanations in the later sections of the paper. Integration of big data with AI is one of the most important forces causing the transformation of public transportation systems. These types of technologies enable data-driven decisions, real-time control, and dynamic management. For

* Corresponding author, E-mail: tolga.avci@std.bogazici.edu.tr

https://doi.org/10.31462/icearc2025_ce_tra_870

example, by employing predictive analytics, the demands can be forecasted. The resources can be optimally allocated and disruptions can be more effectively dealt with and responded to by transit agencies. Furthermore, AI-powered systems have a promise to improve customers´ satisfaction by providing more customized suggestions, and by facilitating safer routes with less time at their execution. This paper explores the potential use of big data and AI in optimizing public transport systems and provides an overview of their possible advantages and challenges. This work will highlight the role of data size and artificial intelligence technologies in demand forecasting, route optimization, and improving operational efficiency, drawing on case studies and current literature analysis. Additionally, we will explore the technological, ethical, and infrastructure challenges that come with integrating these technologies into effective transportation systems. The structure of the work is laid out like this: Section 2 explores the various techniques of artificial intelligence that are applied in public transportation, along with the data sources that support them.

Demand prediction approaches are discussed in Section 3 and the approaches used in the AI methods for the demand prediction of passenger demand and how the prediction model can contribute to system efficiency. In Section 4, route and scheduling optimization is addressed, where AI and big data serve as the foundation for dynamic routing and adaptive scheduling. Section 5 discusses the challenges of using big data and AI technology for transit systems, and addresses the possible ways to overcome these challenges. The conclusion reports the results and discusses the direction of future research in this dynamic area.

2. Data sources and AI methodologies

The sources of big data used for common supervision and optimization in public transportation include GPS through its acquisition managers, as well as smart ticketing systems that provide valuable insights. A few devices track the real-time location, speed, and status of public transport vehicles to improve fleet management. Mobile applications provide huge data on users' preferences, ticketing, and traveling behavior, which help in understanding the demand of passengers. Social media sites like X (or formerly, Twitter) and Facebook offer a wealth of information on the public's mood, troubles, and activities that could impact transportation systems. Some of the data that can be easily obtained include passenger counts, travel paths, and peak hours from the ticketing systems which help in making sound demand estimates. The AI approaches used in this area are also as varied as supervised learning for predictive analytics and reinforcement learning for adaptive control systems. For example, neural networks are very effective in demand forecasting while genetic algorithms (The genetic algorithm is a method for solving both constrained and unconstrained optimization problems that is based on natural selection) have been efficient in solving the complex transit network design problem.

Some of the applications of AI are predictive analytics where machine learning models are used to forecast future trends of transit; optimization techniques like linear programming and meta-heuristic (metaheuristic is a higher level procedure or heuristic designed to find, generate, or select a lower level procedure or heuristic (partial search algorithm) that may provide a sufficiently good solution for an optimization problem.) for improving resource management and scheduling; real-time data analysis applied via stream processing systems for decision-making. Using artificial intelligence (AI) and the Internet of Things (IoT), a case study offers a strategy for maximizing energy demand in metropolitan systems. For dynamic energy demand prediction, it employs real-time data from IoT sensors applying machine learning methods such as Random Forests and Neural Networks. Metro operators can thus instantly change energy use, hence increasing efficiency and lowering waste. Using Paris Metro system data, the method was tested; simulations revealed notable energy savings, especially concerning regenerative braking systems (Rziki et al., 2025) and another case study (the London Underground) shows some valuable insights as follows: The London Underground implemented a remote condition monitoring system on the Victoria Line to enhance reliability for 200 million annual passengers. The Underground may now remotely monitor track circuit conditions in real-time by using variable length frequency-driven tuned electrical track circuits and the NI CompactRIO system. By allowing maintenance workers to forecast and stop equipment breakdowns, this proactive method guarantees the least disturbance. With anticipatory alarms provided to operators, the system monitors and analyzes track circuits using over 7,000 data samples every second. This has cut maintenance expenses and greatly increased system efficiency (Etchell et al., 2025).

3. Demand prediction

Effective planning depends on knowing the expected demand ahead of time for public transportation authorities to properly allocate services, lower expenses, and raise passenger satisfaction. For demand forecasting, several techniques (time-series analysis, regression models, and more lately deep learning) have value depending on the availability of certain auxiliary tools. Short-term demand forecasting benefits especially from time-series analysis since it allows one to recognize trends, seasonal fluctuations, and cyclical patterns in past rider data. Patterns from the previous week, the month, or the previous day (simply, any past time) can be analyzed to predict demand with a relatively high accuracy, especially in transit modes, where movement patterns do not escape the predictability. The models are particularly helpful for planning on a daily and weekly level (e.g., rush hours, holidays).

On the other end, for more complex and timely forecasting, deep neural networks. Neural networks, or deep learning models are inherently capable of featuring the dynamic non-linear relationships among multiple covariates features (weather, public events, socio-economic variables, and so on.) that might be influencing passenger movement behavior. These represent approaches that potentially can synthesize data from a variety of sources - for example, real-time ticketing data, GPS information from buses and subways, and social media produce more precise and finely grained predictions of travel demand at different times of day and places. Through consideration of the interaction among various contributors, DNNs (Deep neural networks) provide large improvements in learning about optimal demand peaks, which can guide adaptive changes over time for transit agencies on how to offer their services. Moreover, hybrid models that combine traditional statistical methods with machine learning algorithms or ensemble approaches will enhance the reliability and precision of demand forecasting tools. These hybrid models combine both long-term and current information and therefore can adapt to dynamic environments.

In many fields, demand prediction has practical applications, in the area of public transit management, for instance, dynamic pricing and supply planning are perhaps the most consequential. In dynamic pricing, the fare scheme is made to change in real-time according to the forecast of the demand to enhance off-peak travel and avoid congestion during peak travel periods. For example, travel fares could be lower when the need for transportation is minimal and higher when the usage of transportation is intense, to achieve demand balance and efficient use of transportation resources. This can, moreover, be used as a stimulus to passengers to change travel times and thus relieve overloaded lines so it is possible to increase the efficiency of the system as a whole. Accurate demand forecasting also enables more optimum capacity planning, where the availability of resources such as buses, trains, and drivers is provisioned based on expected peak-hour demand.

Many instances of practical uses shed light on the effects demand prediction driven by artificial intelligence has on public transportation. For instance, a case study on Tokyo Metro offers a simulation model meant to lower passenger congestion and delays during Tokyo Metropolitan Area rush hour. It models train travel times by using daily ticket gate data and on-site inspections, therefore accounting for unplanned events like passenger crowding onto trains. The model shows how demand fluctuations and schedule changes affect travel time and provides ideas for lowering delays. The model showed notable travel time savings during peak hours by modeling several demand scenarios; recommendations for staggered commuting help to further ease congestion (Adachi et al., 2019))

With a target toward lowering congestion and carbon emissions, sustainable mobility projects in Barcelona have greatly enhanced urban transportation. By including real-time data in its public transportation system, the city guarantees correct bus and train schedules; therefore, boosting public transportation usage by 15%. With 6,000 bikes spread across 420 stations, Barcelona's bike-sharing program Biking facilitates 14 million rides yearly, therefore reducing congestion and pollution. Along with incentives like free parking and low-emission zone access, the spread of more than 500 electric vehicle charging stations supports greener transportation and lowers air pollution (Inam, 2024).

4. Route and scheduling optimization

Route and schedule optimization is an important aspect of lowering operating costs and improving passenger experience. AI-driven approaches offer dynamic and flexible solutions. High-tech methods include genetic algorithms, which mimic an evolutionary process to find the best-suited routes taking also into account the constraints of the traffic and the number of passengers, and reinforcement learning, which trains AI agents to update schedules in real-time, based on the interaction with a dynamic transit system, to achieve the highest possible effectiveness under evolving situations. Clustering algorithms are used to partition passenger information into groups according to similar origins and destinations, which allows the optimization of routes to reduce travel time.

Public transportation applications range from dynamic route planning, performed by AI algorithms wherein AI processes override current traffic patterns and demand fluctuations to optimize travel, to Just-in-Time optimization, where the machine learning models reason the optimal departure time delays to reduce passengers queuing times and facilitate those passengers will best utilize the traveling bus, car or train. The Smart Nation Initiative of Singapore is a success tale since it expanded and maximized dynamic bus lines using artificial intelligence. By combining several forms of transportation (buses, trains, bicycles, and ride-sharing services) into a multi-modal network, Singapore has achieved great strides toward public transportation system optimization. This integration lessens transportation congestion, improves accessibility, and lessens environmental impact. Among important projects include the use of real-time data analytics to enhance bus frequencies and schedules, hence increasing on-time performance. Additionally, the city has instituted a vibrant, on-demand bus system whereby users may schedule pick-ups via a smartphone app. These developments show Singapore's will to design a data-driven, sustainable urban mobility system fit for smart city objectives (Chadalawada, R. (2022).

5. Challenges and future considerations in ai-driven public transport and possible ways to overcome these challenges

Still, obstacles exist. Data quality is still a big problem since inadequate or biased datasets could make AI models useless. Particularly concerning the gathering and processing of passenger data, privacy issues call for strong data governance systems and ethical AI values adherence. The deployment of these technologies is also hampered by infrastructure constraints, mainly in areas where public transport is underfunded or obsolete. Breakthroughs in addressing these challenges are best achieved through a multifaceted policy that includes investments in infrastructure, the creation of ethical guidelines, and standardization of data interfaces to enable interoperability among systems.

The paper further identifies the community-private partnership in facilitating faster evolution of technologies and making them sustainable in the process of implementation. Joint work between governments, technology suppliers, and academics can promote innovation, bring down costs, and allow that which is proven to be viable pilot projects to be expanded to general transit systems. Like predictive maintenance on Shanghai Metro Lines and deep learning for capacity optimization at Barcelona, both of which are instances of artificial intelligence producing major innovation if sufficiently funded and supported with experience.

Future studies should concentrate on building transparent, inclusive, scalable artificial intelligence systems. These systems cannot only take into consideration the complexities of urban mobility, but they must also guarantee the accessibility of services to different groups. Further, investigations of hybrid models involving combinations of conventional transportation planning approaches and AI-driven analysis techniques could provide a hybrid solution to the tradeoff between reliability and efficiency.

6. Conclusions

The disruptive capacity of big data and artificial intelligence (AI) in public transportation is becoming more obvious. Through the use of large data sets and state-of-the-art algorithms, transportation systems around the world are now beginning to address legacy problems, such as lack of efficiency, uncertainty in demand changes, and environmental issues. The combination of these technologies makes it possible to do precise demand forecasting, efficient routing, and real-time tracking, all of which lead to operational excellence and better user experience.

A comprehensive review of the literature highlights the significance of data sources such as GPS, IoT devices, ticketing systems, and mobile applications, which provide the foundational inputs for AI algorithms. Complex models able to forecast passenger demand, optimize routes, and dynamically update schedules can be produced using deep learning, genetic algorithms, reinforcement learning, and other artificial intelligence approaches. Case studies (Singapore, Madrid, Tokyo, London, Barcelona) let one realize improvements in passenger experience, traffic performance, and transport efficiency.

Ultimately, the combination of artificial intelligence and large data marks a public transportation framework change. Though the road to completely ideal and, finally sustainable transportation systems is still under development, the knowledge gained from past application and research projects lays a firm foundation for the next developments. Through the remediation of current issues and synergies between stakeholder groups, these technologies can be used to develop smarter, greener, and more resilient transport networks that serve the needs of an urbanizing world.

References

Abduljabbar, R., Dia, H., Liyanage, S., & Bagloee, S. A. (2019). Applications of artificial intelligence in transport: An overview. Sustainability, 11(1), 189. https://doi.org/10.3390/su11010189

Adachi, S., Yoshino, H., Koresawa, M., Parady, G. T., Takami, K., & Harata, N. (2019). A study on train travel time simulation focused on detailed dwell time structure and on-site inspections. https://easychair.org/publications/preprint/hR8F

Chadalawada, R. (2022). Optimizing public transit networks: An exploration of how multi-modal transportation systems can be integrated in smart cities. World Journal of Advanced Research and Reviews, 15(01), 829–841. https://doi.org/10.30574/wjarr.2022.15.1.0630

Etchell, S., Phillips, D., & Ward, B. (2025). London Underground improves reliability for 200 million annual passengers with remote condition monitoring. https://www.ni.com/en/solutions/transportation/case-studies/london-underground-improves-reliability-for-200-million-annual-passengers-with-remote-condition-monitoring

Inam, M. (2024, July 11). Example of a smart city: A case study into Barcelona.

Jović, M., Tijan, E., Marx, R., & Gebhard, B. (2019). Big Data Management in Maritime Transport

Kaffash, S., Nguyen, A., & Zhu, J. (2020). Big data algorithms and applications in intelligent transportation system: A review and bibliometric analysis. International Journal of Production Economics, 231, 107868. https://doi.org/10.1016/j.ijpe.2020.107868.

Rziki, M. H., Hessane, A., Boutahir, M. K., Bourray, H., El Ouadghiri, M. D., & Belkadi, R. (2025). Predictive energy demand and optimization in metro systems using AI and IoT technologies.

4th International Civil Engineering & Architecture Conference
17-19 May 2025, Trabzon, Türkiye

Rheological characterization of BARC-modified asphalt binder via frequency sweep testing

Merve Gülfer Bozdemir*[1], Hacer Yeşilçiçek[2], Şeref Oruç[3]

1 Erzurum Technical University, Department of Civil Engineering, 25050 Erzurum, Turkey
2 Karadeniz Technical University, Faculty of Of Technology, 61830 Trabzon, Turkey
3 Karadeniz Technical University, Department of Civil Engineering, 61080 Trabzon, Turkey

Abstract. Asphalt binders are widely used in road pavements due to their favorable physical and rheological properties. However, increasing traffic volumes and loads, climatic factors, and production defects negatively affect the performance of asphalt pavements. These issues lead to a reduction in service life and a rise in maintenance and repair costs. In this context, polymer additives have been utilized in recent years to improve the rheological properties of asphalt. Nevertheless, the high cost and environmental concerns associated with these additives have highlighted the need for sustainable and cost-effective alternatives. This study investigates the rheological effects of a bio-based additive called Boron Added Rosin Compound (BARC), developed using naturally occurring colophony resin and locally sourced boron oxide. For this purpose, BARC was incorporated into a base binder at concentrations of 0.5%, 1%, and 1.5% by weight. Unaged base and modified binders were tested within a temperature range of 40–70 °C and a frequency range of 0.1–100 rad/s. Master curves were constructed at a reference temperature of 40 °C using the complex modulus (G*) and phase angle (δ) data obtained from frequency sweep tests. The results indicated that the binder containing 1.5% BARC exhibited the highest G* values at low frequencies. Additionally, modified binders demonstrated lower phase angles, indicating more elastic behavior, and showed greater stability with increasing temperature compared to the unmodified binder. These findings suggest that the BARC additive enhances the elasticity of asphalt binders and improves their resistance to rutting.

Keywords: Asphalt binder; Bio-based additive; Boron oxide; Colophony resin; Rheological properties; Frequency sweep.

1. Introduction

The majority of road pavements worldwide are constructed using asphalt binders, which are utilized in various forms due to their physical and rheological properties (J. Zhu, 2014). In recent years, increased traffic loads driven by economic growth and rising living standards, along with environmental and climatic influences and construction-related deficiencies, have negatively affected asphalt pavement performance (H. Wang, 2010; J. Baek, 2010). These deteriorations reduce the service life and ride quality of highways and necessitate earlier-than-planned maintenance and repair interventions, thereby increasing overall costs. Particularly under the influence of growing traffic volumes, asphalt pavements experience various types of distress, such as rutting, fatigue, and cracking at different temperature conditions. To mitigate these forms of deterioration and improve the overall performance of asphalt pavements, various additives are incorporated into asphalt binders through modification techniques (Geçkil, 2008; Arabani et al., 2010; Yıldırım, 2014). A wide range of materials have been utilized for this purpose, including different types of polymers (Yılmaz et al., 2013; Sengoz & Işıkyakar, 2008; Liang et al., 2015; Adeboje et al., 2020), nanomaterials and nanocomposites (Yao et al., 2015; Yusoff et al.,2014; Zhou et al., 2021), bio-based materials (Portugal et al., 2017; Rahman et al., 2014), and waste-derived materials (Gürü et al., 2014;Kumar et al.2018). These modifiers aim to enhance the durability, mechanical performance, and environmental sustainability of asphalt mixtures under varying service conditions.

In modification studies, polymer-based additives are widely used. However, due to their high cost, the requirement for specialized mixing facilities, and their potential to cause environmental pollution, there is a growing need to develop alternative additives that are cost-effective, environmentally friendly, and capable of enhancing asphalt pavement performance. With increasing environmental concerns, the investigation of bio-based

*Corresponding author, E-mail: merve.ozcan@erzurum.edu.tr

https://doi.org/10.31462/icearc2025_ce_tra_875

and biodegradable polymers (molecules) has gained significance, aiming to expand the palette of renewable polymers used in asphalt modification.

Colophony resin, a type of pine resin, has emerged as a suitable renewable modifier due to its chemical compatibility with asphalt binders. Studies have reported that binders modified with resin and resin-based materials exhibit improved resistance to rutting and moisture damage compared to conventional binders, and that resins enhance the flexibility of the binder structure (Yao, 2013).

Boron and its derivatives, which are abundantly available in our country and considered a valuable national resource, are utilized across various industries. Studies on asphalt modification have also indicated that boron can enhance the properties of asphalt binders (Yılmaz, 2016). However, for effective use in asphalt modification, boron must be synthesized with another compatible material before being incorporated into the binder. In this context, a novel modification additive containing bio-based boron and colophony resin has been developed in the laboratory and is referred to as BARC. The objective of this study is to investigate the viscoelastic behavior of asphalt binders modified with BARC through frequency sweep analyses.

2. Materials and method

2.1. Materials

In this study, PG 64-16 asphalt cement (penetration grade 50/70) obtained from the Turkish Petroleum Refinery (Izmit) was used. To determine the properties of the neat asphalt binder, conventional tests listed in Table 1 were conducted.

Table 1. The physical properties of the pure asphalt binder.

Specifications	Value	Standard
Penetration (25 °C, dmm)	56	ASTM D5/D5M-13
Softing point (°C)	50	ASTM D36/D36M-14
Ductility (25 °C, cm)	100 +	ASTM D113-17
Flash point (°C)	249	ASTM D92-18
Specific gravity (g/cm3)	1.028	ASTM D70M-21
Viscosity (135 °C, cP)	500	ASTM D4402M-15
Viscosity (165 °C, cP)	100	ASTM D4402M-15

The BARC additive, possessing the desired consistency and homogeneity, was synthesized in the laboratory through the reaction of boron oxide and colophony resin. The resulting additive is dark in color and solid at room temperature. This synthesized additive can be produced industrially through a relatively short manufacturing process. The general appearance of the boron oxide and resin compound (BARC) synthesized additive is shown in Fig. 1.

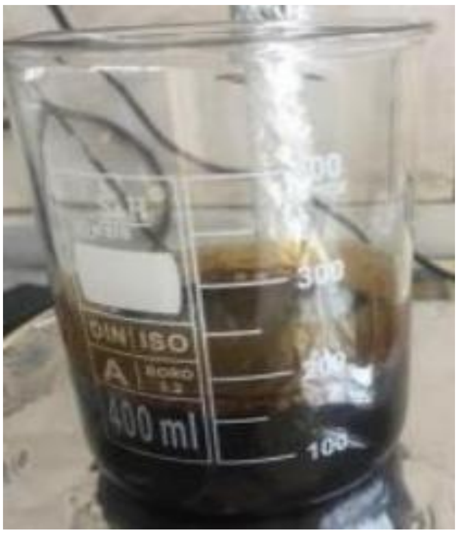

Fig. 1. General Appearance of the Additive

2.1.1. Preparation of modified asphalt binders

According to the 1000 g weight of the pure asphalt binder, synthesized additive was added separately at rates of 0.5%, 1%, 1.5%, and 3% by weight into mixing containers. The modified binders were prepared using a high shear mixer at 150 ± 5 °C and 2000 rpm for 30 minutes. The binders used in this study and their corresponding designations are presented in Table 2.

Table 2. Symbols of Binders Used in the Experiments

Additive (BARC) Content	Symbols
50/70 Asphalt binder	BA
50/70 Asphalt binder + % 0.5 BARC	BA0.5
50/70 Asphalt binder + % 1.0 BARC	BA1.0
50/70 Asphalt binder + % 1.5 BARC	BA1.5
50/70 Asphalt binder + % 3.0 BARC	BA3.0

2.2. Methods

2.2.1. Frequency sweep test

Frequency sweep tests were conducted on pure and modified asphalt binders using a Malvern DSR+ rheometer. The tests were performed at temperature intervals of 5 °C between 10 °C and 30 °C, and 10 °C intervals between 40 °C and 70 °C.

At lower temperatures (10–30 °C), an 8 mm parallel plate with a 2 mm gap was used, while at higher temperatures (40–70 °C), a 25 mm parallel plate with a 1 mm gap was employed (Airey G. D., 2002). The tests were carried out within the linear viscoelastic (LVE) region of the binder using a constant strain level of 0.01%. The frequency range was set between 0.1 and 100 rad/s.

The obtained complex modulus (G*) and phase angle (δ) data were horizontally shifted to a reference temperature of 40 °C using the time-temperature superposition principle (TTSP) with the assistance of the Malvern DSR+ software. As a result, master curves were generated, representing the viscoelastic behavior of the binders over an extended frequency range.

3. Results

Fig. 2 presents the master curves of the complex modulus values for pure and modified binders at the reference temperature of 40 °C. As the frequency (loading rate) increases, the complex modulus values also increase. As shown in the figure, the pure binder exhibits the lowest complex modulus values across the entire frequency range.

At low frequencies, the highest G* values are observed for the binders modified with 3% additive, whereas at high frequencies, all modified binders exhibit similar G* values. The influence of the additive is more pronounced at low frequencies compared to the pure binder, while this effect diminishes as the frequency increases. Among the binders, the one with 1% additive shows the lowest G* values after the pure binder at low frequencies. At high frequencies, the modified binders demonstrate comparable performance.

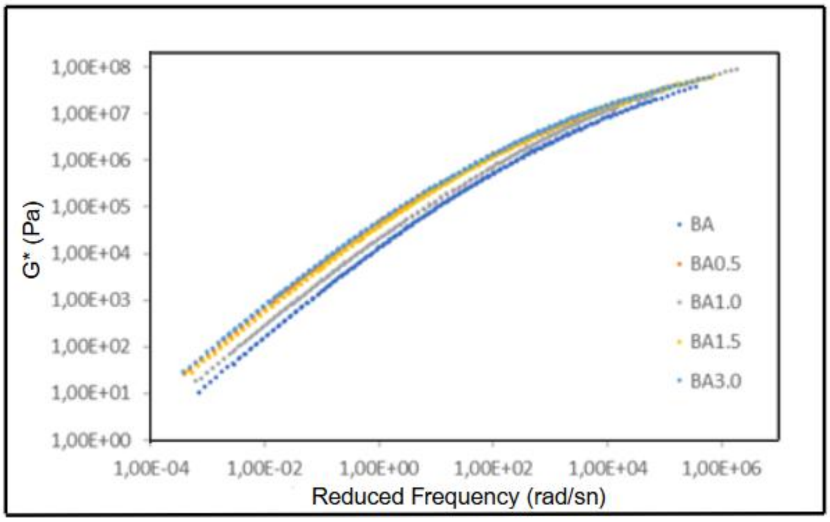

Fig.2. The master curves of G* at a reference temperature of 40 °C for pure and modified binders

Fig. 3 illustrates the variation of phase angle with frequency for pure and modified binders. As seen in the figure, at low frequencies (10^{-3} rad/s), all binders exhibit similar phase angle values. However, beyond a frequency of 0.01 rad/s, the phase angle of the modified binders decreases more significantly compared to the pure binder, indicating a transition toward more elastic behavior.

Among the modified binders, those containing BA0.5 and BA3.0 additives show lower phase angle values. At higher frequencies, the phase angles of the B0.5, BA1.5, and BA3.0 modified binders tend to converge, indicating similar viscoelastic characteristics.

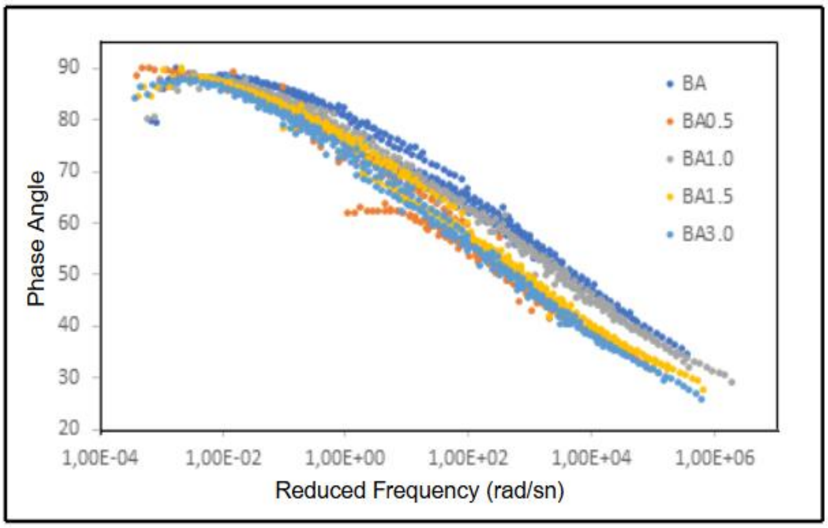

Fig.3. The master curves of phase angle at a reference temperature of 40 °C for pure and modified binders

Fig. 4 presents the changes in elastic and viscous moduli (Cole-Cole diagram) for unmodified and modified binders. As seen in the figure, at low frequencies, the elastic and viscous moduli of both unmodified and modified binders are similar. However, as the frequency increases, the modified binders shift toward the elastic modulus axis, indicating a more elastic behavior.

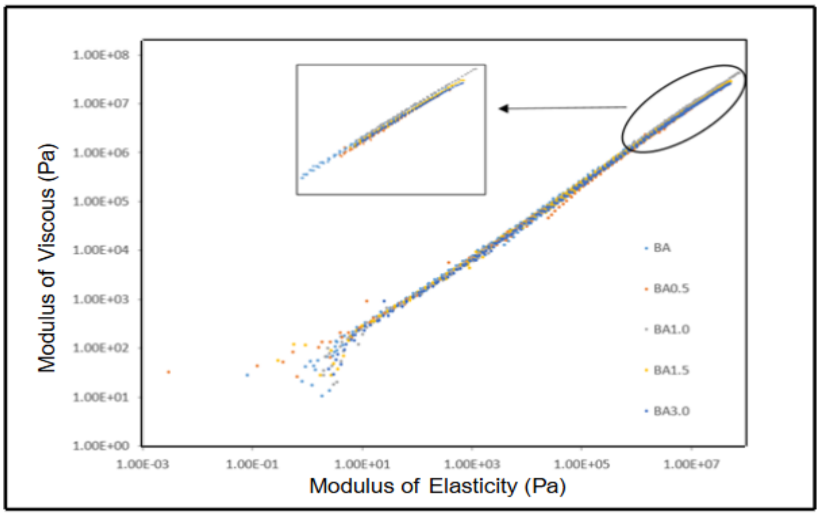

Fig.4. Cole-Cole diagram

4. Conclusions

The BARC additive was produced in a laboratory environment and used for asphalt modification. The rheological behavior of the additive on conventional asphalt binder was investigated, and the findings are summarized below:

- Under low-frequency (high temperature) and high-frequency (low temperature) conditions, the asphalt binder modified with 3% BARC exhibited increased complex modulus values and decreased phase angle values, indicating enhanced elastic behavior of the binder.
- According to the Cole-Cole diagram, the modified binders exhibited a noticeable shift toward the elastic modulus axis, suggesting that the additive contributed to an enhancement in the elastic behavior of the conventional binder.

Acknowledgments
This study was supported by the Scientific Research Projects (SRPU) Unit of Karadeniz Technical University (Project No.: FBA-2020-8788), to which the authors are indebted. The findings and evaluations of the results of this study are not the official opinions of the SRPU.

References

Adeboje, A., Kupolati, W., Sadiku, E., & Ndambuki, J. (2020). Characterization of Modified Crumb Rubber Concrete . International Journal of Sustainable Development and Planning, IIETA,, 15(3).

Arabani, M., Mirabdolazimi, S., & Sasani, A. (2010). The Effect of Waste Tire Thread Mesh on the Dynamic Behaviour of Asphalt Mixtures. Construction and Building Materials, 24, s. 1060-1068.

Geçkil, T. (2008). Siyah Karbonun Bitümlü Sıcak Karışımların Özelliklerine Etkisinin Araştırılması. Fırat Üniversitesi, Fen Bilimleri Enstitüsü,Doktora Tezi, Elazığ.

Gürü, M., Nubuk, M., Arslan, D., Farzanian, S., & Bilici, I. (2014). An Approach To The Usage Of Polyethyleneterephthalate (PET) Waste As Roadway Pavement Material. J. Hazard. Mater., 279, s. 302-310.

Kumar, A., Choudhary, R., Narzari, R., Kataki, R., & Shukla, S. (2018). Evaluation of bio-asphalt binders modified with biochar: a pyrolysis by-product of Mesua ferrea seed cover waste. Cogent Eng., 5, s. 1-15.

J. Zhu, B. B. (2014). Polymer Modification Of Bitumen: Advances And Challenges. Eur. Polym. J., 54, s. 18-38.

J., W., Wang T., H. X., & F., X. (2019). Modelling of rheological and chemical properties of asphalt binder considering SARA fractio. Fuel, 238, s. 320-330.

J. Baek, H. O.-Q. (2010). EffectsOf İnterface Conditions On Reflective Cracking Development İn Hot-Mix Asphalt Overlays. Road Mater. Pavement Des.,, 11(2), s. 307-334.

Liang, M., Liang, P., Fan, W., Qian, C., Xin, X., Shi, J., & Nan G.Z. (2015). Thermo-rheological behavior and compatibility of modified asphalt with various styrene–butadiene structures in SBS copolymers. Mater. Des., 88, s. 177-185.

Portugal, Lucena, L., Lucena, A., & Costa, D. B. (2017). Rheological Performance of Soybean in Asphalt Binder Modification. Road Materials Pavement Design, s. 1-15.

Rahman, Aziz, M., Hainin, M., & Bakar, W. (2014). Impact of Bitumen Binder: Scope of Bio-Based Binder for Construction Of Flexible Pavement. J. Teknol., 70(7), s. 105-109.

Sengoz, B., & Isikyakar, G. (2008). Evaluation of the Properties and Microstructure of SBS and EVA Polymer Modified Bitumen. Construction and Building Materials , 22, s. 1897-1905 .

Yao, K. (2013). Renewable Bio-Based Polymers and Degradable Functional Polymers. Doctoral dissertation.

Yao, H., Dai, Q., & You, Z. (2015). Chemo-physical Analysis and Molecular Dynamics (Md) Simulation of Moisture Susceptibility of Nanohydrated Lime Modified Asphalt Mixtures. Constr. Build. Mater., 101(1), s. 536-547.

Yıldırım, M. (2014). Farklı Doğal Asfaltların Bitüm ve Bitümlü Sıcak Karışımların Özelliklerine Etkisi. Fırat Üniversitesi, Fen Bilimleri Enstitüsü,Yüksek Lisans Tezi,Elâzığ.

Yılmaz, M., Kök, B. V., N., K., & Alataş, T. (2013). Elastomer Türü polimerler İle Modifiye Edilmiş Bitümlü Bağlayıcıların Depolama Stabilitelerinin ve Reolojik Özelliklerinin İncelenmesi. Deü Mühendislik Fakültesi Fen Ve Mühendislik Dergisi, 15(1), s. 67-77.

Yılmaz, B. (2016). Bor içerikli Katkıyla Modifiye Edilen Asfaltın Performans Özelliklerinin Araştırılması. Karadeniz Teknik Üniversitesi, Fen Bilimleri Enstitüsü, Doktora Tezi, Trabzon.

Yusoff, N., Breem, A., Alattug, H., Hamim, A., & Ahmad, J. (2014). The effects of moisture susceptibility and Ageing Conditions on Nano-Silica/Polymer Modified Asphalt Mixtures. Constr. Build. Mater., 72, s. 139-147.

Zhou, H.-Y., Dou, H.-B., & Chen, X.-H. (2021). Rheological Properties of Graphene/Polyethylene Composite Modified Asphalt Binder. Materials, 14, s. 3986.

Comparison of terrain modeling approaches: evaluating software performance in infrastructure projects

Kadir Akgol*[1], Omer Faruk Ozturk[1], Yelda Nur Kara[1]

[1] *Giresun University, Department of Civil Engineering, 28200 Giresun, Türkiye*

Abstract. In highway and various infrastructure projects, terrain models play a crucial role in shaping key stages such as planning, design, and cost estimation. These models are typically generated from x, y, and z coordinate data collected from field surveys and processed using different software tools and modeling techniques. However, ensuring that these models accurately represent real-world terrain conditions often requires expert adjustments, particularly when using automated triangulation or interpolation methods. This study investigates the accuracy and reliability of terrain models generated by two widely used software environments, NetCAD and MATLAB, based on the same reference dataset collected from a complex terrain in Gümüşhane Province, Turkey. The initial triangulated model created in NetCAD exhibited notable discrepancies, which were corrected through expert intervention. In contrast, MATLAB applied various interpolation methods, including Natural Neighbor, Linear, and V4 (biharmonic spline), to produce grid-based terrain models. These models were then compared to the expert-adjusted reference model to assess their performance. The findings reveal that while Natural Neighbor interpolation in MATLAB produced results closer to the reference terrain, even this method showed minor deviations. Moreover, significant differences emerged among interpolation techniques, emphasizing that the choice of modeling method greatly affects terrain representation accuracy. This study underscores the limitations of automated modeling processes and highlights the need for advanced approaches, such as machine learning-based methods, to minimize the need for manual corrections. The results demonstrate the importance of software selection and modeling strategies in achieving accurate terrain models, which are essential for reducing risks and improving decision-making in engineering projects.

Keywords: Terrain modeling; Infrastructure projects; Highway design; Triangulation; Accuracy assessment.

1. Introduction

Terrain modeling processes have critical importance in highway engineering and infrastructure projects in general. A Digital Terrain Model (DTM) is typically established at the initial stage of a project and forms the basis for all subsequent design and engineering calculations (Gigović, 2010). DTM data is utilized in fundamental engineering design phases, including determining the optimal road alignment, generating longitudinal and cross-sectional profiles, and calculating excavation and fill volumes. As each of these steps directly depends on the accuracy of the terrain model, creating an accurate and reliable DTM is crucial for the project's overall success.

Each of these design stages directly relies on the accuracy of the terrain model. If the DTM contains inaccuracies, significant engineering errors may occur, ranging from incorrect route selection to erroneous volume calculations. Indeed, obtaining a precise and reliable terrain model is essential for both the safety and cost-effectiveness of a project (Kaźmierczak, 2013). Having a high-accuracy DTM during the early design phase enables engineers to clearly visualize existing terrain conditions, thereby facilitating safer and more efficient infrastructure designs (Sun et al., 2015).

In the literature, various methods have been developed for terrain modeling in infrastructure projects. The most common approach is the Triangulated Irregular Network (TIN) model, which aims to create surfaces from irregularly distributed points. In this model, scattered X, Y, Z point clouds collected from terrain surveys are interconnected through triangles to define the surface geometry (Thekdi & Lambert, 2012). During the triangulation process, the Delaunay triangulation algorithm is commonly employed, as it enforces the condition that no data points should fall within the circumcircle of any triangle formed. This constraint results in triangles with relatively uniform angles (close to equilateral), thereby preventing the formation of long, thin ("sliver") triangles and significantly improving the representation accuracy of the model (Ma et al., 2015). Delaunay-based TIN models are frequently preferred in digital terrain modeling because they realistically represent abrupt changes

* Corresponding author, E-mail: kadir.akgol@giresun.edu.tr

https://doi.org/10.31462/icearc2025_ce_tra_878

golden light publishing

in slopes and fault lines. Common engineering software like NetCAD typically utilizes TIN/Delaunay triangulation as the default method for terrain modeling (Kidner et al., 2000; Yomralıoğlu, 2005). This method offers distinct advantages, especially in handling irregularly distributed measurement points and effectively representing terrain surfaces with varying levels of detail.

However, several limitations of the triangulation method have been emphasized in the literature. In scenarios involving irregular or sparse data distributions, or complex terrain morphologies, automatically generated TIN models may include incorrectly connected triangles. Specifically, improperly positioned, elongated triangles connecting distant points on the surface may create artificial ridges or depressions, which do not exist in reality. Such inaccuracies can lead to significant errors in engineering calculations, necessitating manual intervention and correction by experts (Zhu et al., 2008). Indeed, some studies have highlighted the unreliability of the initial terrain models automatically generated by software, requiring engineers to manually adjust the triangulation networks to align models with actual terrain conditions (Yeu et al., 2006). These issues indicate that existing commercial software packages may not fully meet expectations for automatic terrain modeling processes, highlighting the necessity of careful consideration before applying their results directly in projects (Darnell et al., 2010). For instance, within NetCAD software, users are advised to set parameters such as minimum and maximum edge lengths during triangulation to prevent the formation of defective triangles (Ren & Liu, 2013). Such precautions aim to minimize triangulation errors during the modeling process.

Alternatively, grid-based modeling and interpolation methods are widely used for terrain modeling purposes (Garnero & Godone, 2014). In this approach, the study area is divided into a regular grid structure at specified intervals, and the elevation value at each grid node is estimated from surrounding measured points through interpolation techniques. Continuous surfaces are generated by calculating elevation values on grid points using various interpolation methods, such as Inverse Distance Weighted (IDW), Kriging, and Natural Neighbor interpolation (Gaffar et al., 2018).

In the literature, several studies have compared the performance and accuracy of different interpolation methods. For instance, in one comparative study, five distinct methods—including IDW, Kriging, and Delaunay triangulation—were applied to the same terrain dataset (Üstüntaş, 2006). The study concluded that Delaunay triangulation generally provides the optimal balance between computational efficiency and accuracy. However, the highest accuracy under certain conditions was achieved by the Kriging interpolation method.

The grid-based approach is particularly preferred for analyses requiring regularly spaced elevation data, such as raster-based hydrological modeling, and offers flexibility in estimating missing data. Programs like MATLAB facilitate the application of these interpolation methods, allowing the generation of a regular grid surface from a set of measured points. For instance, in the MATLAB environment, functions like griddata enable users to create a regularly spaced grid and perform surface interpolation based on point data obtained from software like NetCAD (Gümüş & Şen, 2013). Consequently, it becomes feasible to generate a grid-based terrain model using MATLAB alongside the TIN model created in NetCAD, allowing the comparison of surfaces produced by two different approaches. Indeed, in one practical application, digital terrain data derived from NetCAD was imported into MATLAB, and the surface models produced by both software were evaluated comparatively.

Studies focusing on triangulation errors and discrepancies between different terrain models have revealed significant findings regarding their impact on engineering projects. In particular, deviations in automatically generated models have been shown to cause serious errors in excavation-fill volume calculations and alignment design. As a result, several researchers have conducted comparative analyses of various terrain modeling methods to identify potential inaccuracies inherent in each approach (Liu et al., 2012). However, many of these studies remain limited to specific regions or focus solely on individual methods, leaving a gap in comprehensive evaluations. For instance, only a limited number of studies have directly compared TIN-based and grid-based terrain models against actual field measurements. This gap highlights the continuing need for more reliable terrain modeling in engineering projects.

In conclusion, the appropriate selection of modeling methods and the careful adjustment of model parameters are indispensable for the success of infrastructure projects. Recognizing these challenges, the authors of this study aim to address these gaps in the literature by emphasizing the necessity of accurate terrain modeling. The objective is to comprehensively evaluate the accuracy of terrain models produced by widely used software tools (e.g., NetCAD) and modeling approaches. Specifically, this study compares the TIN-based model generated in NetCAD with the grid-based model produced in MATLAB, using the same real-world terrain dataset. The differences between these models, the sources of potential errors, and their impacts on design processes will be analyzed. In doing so, the study seeks to reveal performance disparities between various terrain modeling methods and to develop recommendations for achieving more reliable results in engineering applications. Ultimately, this research reaffirms the critical role of terrain modeling in infrastructure projects and aims to clearly identify the limitations of current approaches.

2. Methodology

2.1. Selection of reference terrain data for model evaluation

In order to compare the accuracy and performance of terrain modeling methods, it is essential to utilize a reference dataset that has been verified against real-world terrain conditions. For this comparative study, a terrain model located in Alemdar Village, Gümüşhane Province, surrounding a stream bed, was selected as the reference dataset. The primary reason for selecting this area lies in its complex and variable topographic features, which pose significant challenges for accurate terrain modeling. The terrain data, consisting of (X, Y, Z) coordinates, was originally modeled using the triangulation method within the NetCAD software as part of a real-world engineering project.

However, during the course of this project, it was observed that the initial terrain model generated by the software exhibited notable discrepancies from the actual terrain conditions in certain areas. These discrepancies were primarily caused by incorrect triangulation connections formed between inappropriate points on the terrain surface. As a result, manual adjustments were made to the triangulated model by the project team, based on expert judgment, to align the model accurately with the real terrain conditions. This situation clearly highlights the limitations of current commercial software in automatically generating accurate terrain models and underscores the ongoing need for manual intervention.

Consequently, the terrain dataset selected for this study serves as a robust and reliable reference for comparison and analysis due to its validation against actual field conditions and its ability to reflect the potential issues associated with triangulation methods. This ensures that differences between modeling approaches and their potential impacts on engineering projects can be clearly demonstrated.

2.2. NetCAD terrain model

NetCAD is widely used in engineering and surveying projects and offers various methods for terrain modeling processes (Doytsher et al., 2009; Yomralıoğlu, 2005).

2.2.1. Terrain modeling with the triangulation method

For numerical modeling of terrain surfaces, NetCAD typically employs the Triangulated Irregular Network (TIN) approach. In this method, the terrain geometry is digitally defined by forming triangles between irregularly distributed data points with x, y, and z coordinates collected from the field. The triangulation process utilizes the Delaunay triangulation algorithm, which ensures that no other point lies within the circumcircle of any triangle formed. This condition results in triangles with more balanced geometric angles, thereby enhancing the precision of the modeling process.

During Delaunay triangulation, for a given set of data points $P = \{p_1, p_2, \dots, p_n\}$, each triangle is constructed in such a way that no point p_k lies within the circumcircle of any triangle $\Delta(p_i, p_j, p_m)$. This method enables the accurate representation of abrupt slope changes and morphological discontinuities on the terrain surface. Through NetCAD's interface, users can further guide the triangulation algorithm by defining boundary conditions and breaklines specific to the terrain's characteristics.

Nevertheless, although the software provides automated numerical modeling capabilities, it is well-documented that irregular data distributions, varying point densities, and complex morphological features of the terrain can negatively impact the quality of triangulation.

2.2.2. Grid-based modeling and interpolation

An alternative approach to terrain modeling is grid-based methods. In this approach, the study area is divided into a regular grid composed of cells with specified dimensions. The elevation value for each grid cell is estimated through various interpolation techniques, based on the elevation data of surrounding known points.

One of the most commonly used interpolation techniques within this method is the Inverse Distance Weighted (IDW) method. According to this approach, the elevation value z_p of an unknown grid point P is calculated as a weighted average of the elevations from n surrounding known points, as follows:

$$z_p = \frac{\sum_{i=1}^{n} \frac{z_i}{d_i^p}}{\sum_{i=1}^{n} \frac{1}{d_i^p}} \tag{1}$$

In this formula, z_i represents the elevation value of a known point, d_i is the distance between the unknown grid point and the known point, and p is the weighting power parameter, which is typically set to 2. This formulation ensures that points closer to the unknown location have a greater influence on the estimated elevation value.

2.3. MATLAB terrain model
MATLAB typically generates regular grids for terrain modeling and evaluates the obtained GPS data using various interpolation techniques. Among the widely used methods are Natural Neighbor, Linear, and V4 (biharmonic spline) interpolation techniques. Each method offers a different approach for estimating elevation values on the terrain surface and is preferred based on specific use cases (Salekin et al., 2018; Watson, 2013).

2.3.1. Natural neighbor interpolation
In MATLAB, Natural Neighbor interpolation estimates the elevation value of a given point based on the geometric relationships of its nearest neighbors. This method utilizes Voronoi diagrams to define natural neighbors and calculates the elevation of new points according to the area weights of these neighbors. Voronoi cells form equidistant boundaries around each data point in the dataset. The value of a new point located within these boundaries is computed as the area-weighted average of the surrounding natural neighbors. The elevation value z_p of a new point P is calculated using the following formula:

$$z_p = \sum_{i=1}^{n} z_i \frac{A_i}{A} \tag{2}$$

In this equation, z_i represents the elevation value of the neighboring point, A_i denotes the area weight associated with the i^{th} natural neighbor, and A represents the total weight area. This method provides reliable results, especially for irregularly distributed datasets, as it considers the geometric arrangement of nearby points and distributes influence proportionally based on their Voronoi areas.

2.3.2. Linear interpolation
Linear interpolation estimates the unknown elevation value at a given point by applying linear functions between known data points. This method, implemented in MATLAB via the griddata function, first constructs planar triangles in two dimensions from the known data points and then computes the unknown elevation values within each triangle using linear height functions.

The elevation value z_p at a new point $P(x, y)$ is calculated based on the elevation values at the vertices of the triangle that contains the point, using the following equation:

$$z_p(x, y) = a + bx + cy \tag{3}$$

In this equation, the coefficients a, b, c are determined by solving the system of equations based on the three known elevation values at the vertices of the triangle. This approach is computationally efficient; however, it may yield lower accuracy in terrains with complex topographic features, as it assumes linear variation of elevation within each triangle.

2.3.3. V4 interpolation (MATLAB V4 method)
One of MATLAB’s specialized interpolation techniques is the V4 method, which is based on two-dimensional biharmonic spline interpolation. This method is particularly effective for producing smooth and natural surfaces in datasets with irregular structures and complex topographies. The V4 interpolation solves the following biharmonic equation:

$$\nabla^4 z(x, y) = 0 \tag{4}$$

In this equation, ∇^4 represents the biharmonic operator, which ensures that the resulting surface maintains maximum smoothness while fitting the available data points as accurately as possible. This interpolation method is preferred for its ability to maintain surface continuity and smooth transitions. However, it requires greater computational power, especially when applied to dense datasets, due to the complexity of the underlying calculations.

3. Results
In this study, the GPS data obtained from the selected reference terrain were initially imported into NetCAD software, and a terrain model was generated using the triangulation method. The version of this terrain model, which had previously been refined through expert adjustments within the same NetCAD environment as part of an earlier project to better align with actual field conditions, is presented in Fig. 1.

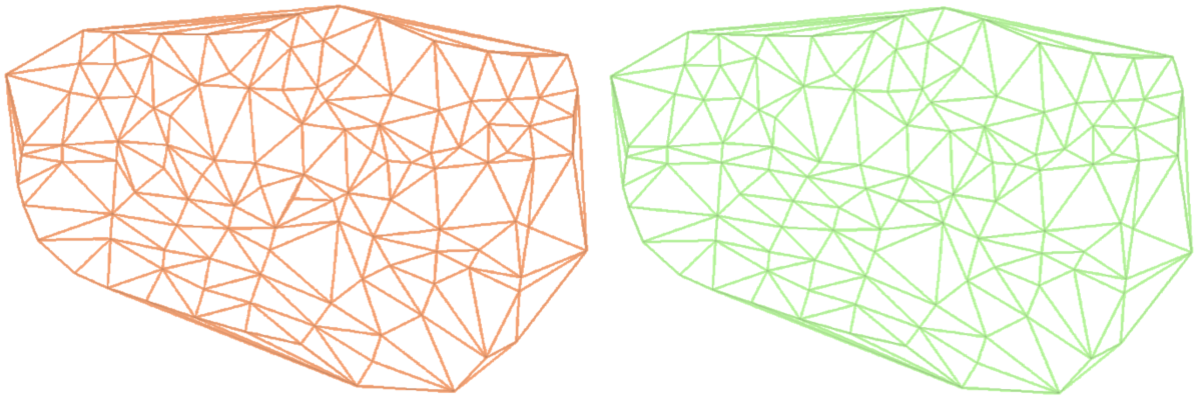

Fig. 1. The original triangulated terrain model generated by NetCAD (orange) and the expert-adjusted terrain model aligned with actual field conditions (green).

Although the models presented in Fig. 1 appear similar at first glance, a closer examination clearly reveals differences at the triangle connection points. These discrepancies in the triangulation connections are subtle enough to escape notice during a quick evaluation by users. However, failing to detect these differences can lead to erroneous calculations in subsequent planning stages and cause unexpected deviations in project costs. The specific area where the differences become more pronounced when the models are overlaid is shown in detail in Fig. 2.

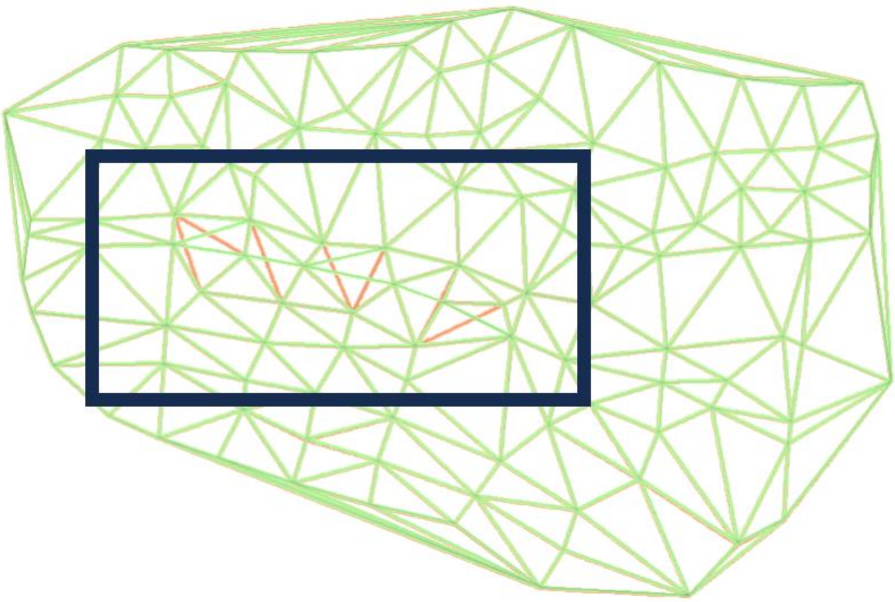

Fig. 2. Detailed view of the triangle connections requiring adjustment in the triangulated model.

If these connections are not adjusted, erroneous contour maps emerge, as illustrated in Fig. 3. When adjustments are made and the model is aligned with actual terrain conditions, the accurate contour map shown in Fig. 4 is obtained. A comparison between the two contour maps reveals that, particularly in the lower sections of the stream bed, artificially curved structures appear in the unadjusted model, whereas the expert-corrected model accurately reflects this area as having a flatter and more natural structure.

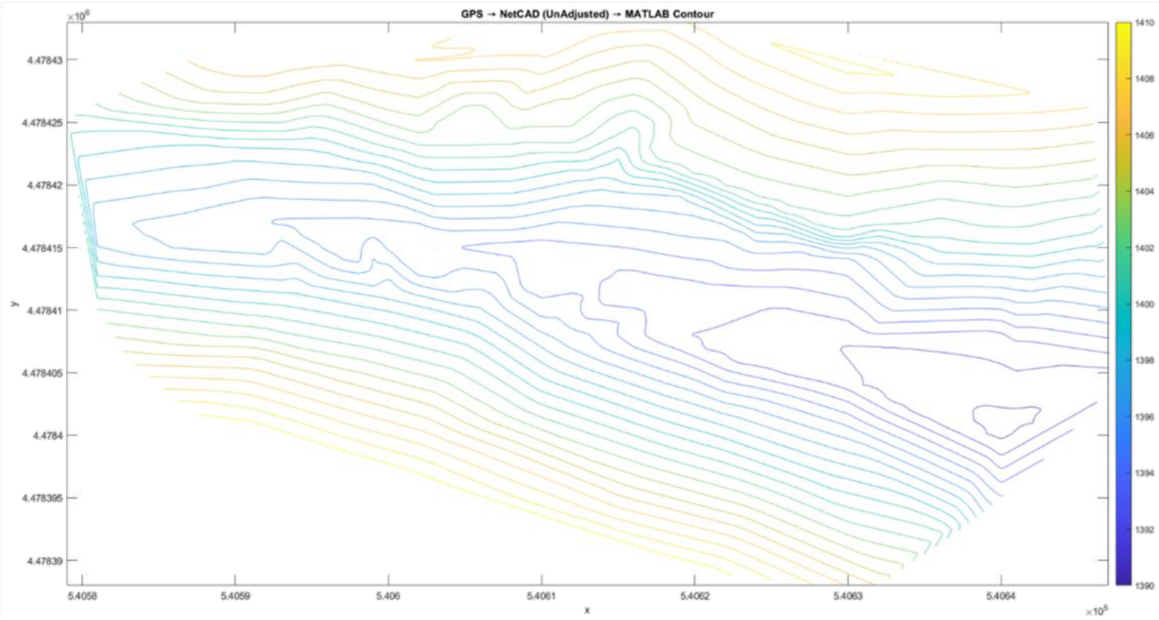

Fig. 3. Contour map generated by NetCAD without expert adjustments.

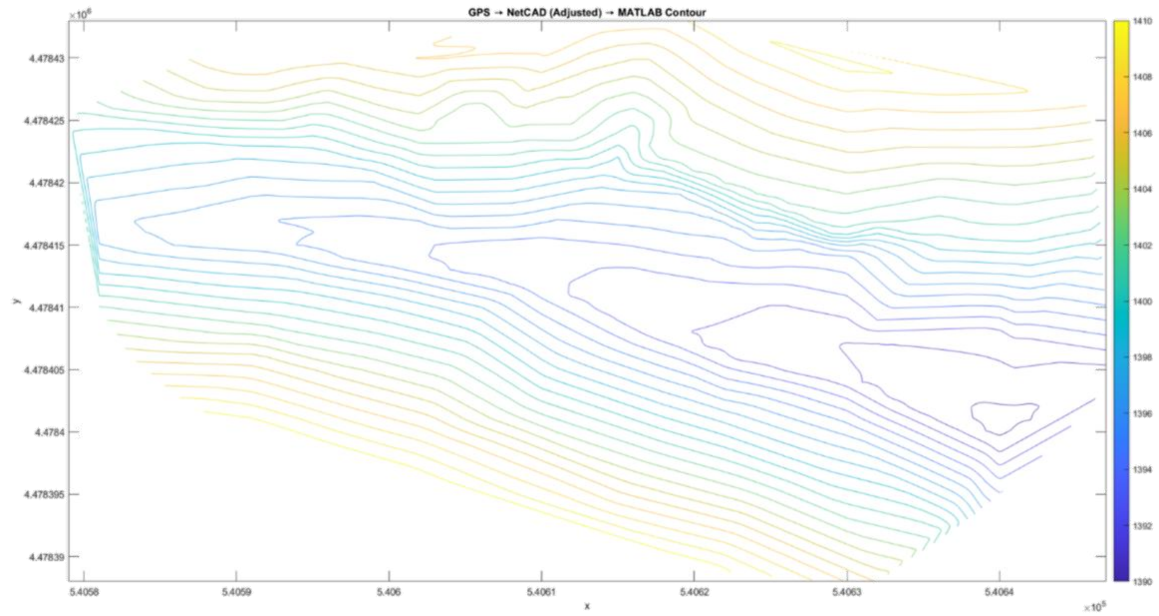

Fig. 4. Contour map adjusted by experts in NetCAD to align with actual terrain conditions.

When comparing the validated contour map in Fig. 4 with the contour map generated by MATLAB using the Natural Neighbor interpolation method (Fig. 5), it is observed that an artificial curvature appears in the lower right section of the stream bed in the MATLAB-generated model. Such errors are difficult to detect and correct without direct comparison to actual terrain data, making field validation an essential step in the modeling process.

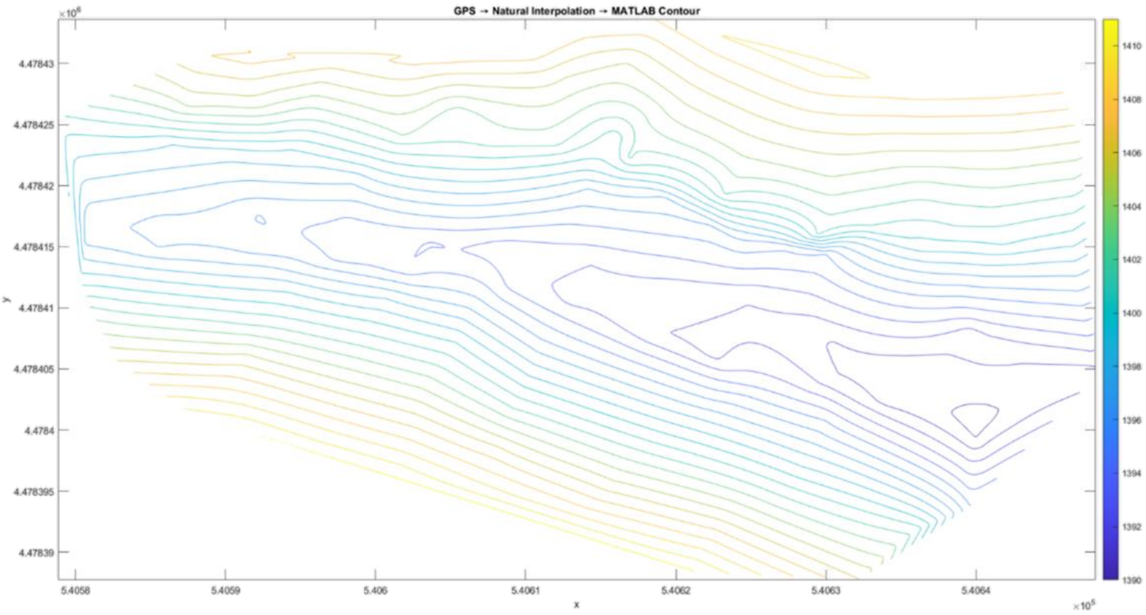

Fig. 5. Contour map generated using the Natural Neighbor interpolation method in MATLAB.

When comparing the terrain models generated by MATLAB using other interpolation methods, notable differences emerge. The terrain model produced using the Linear interpolation method, shown in Fig. 6, exhibits sharper transitions and discontinuities compared to the Natural Neighbor method. Additionally, several erroneous curvatures can be clearly observed in different sections of the model. This demonstrates that even within the same software environment, different interpolation techniques can yield significantly different results.

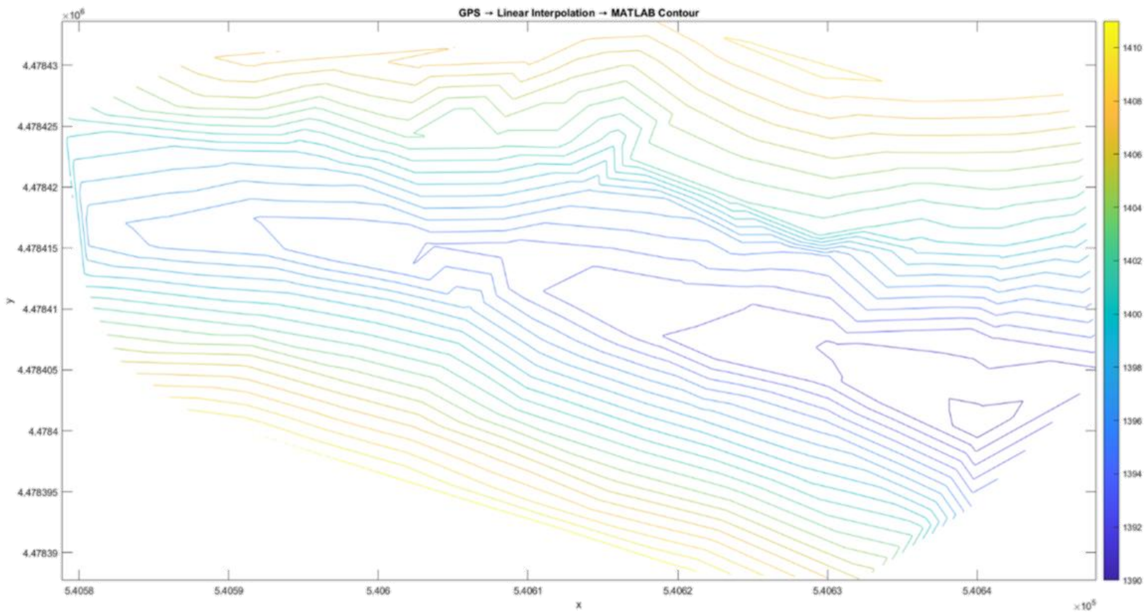

Fig. 6. Contour map generated using the Linear interpolation method in MATLAB.

The contour map produced using MATLAB's V4 interpolation method is presented in Fig. 7. Although this method generates smoother and more continuous contour lines compared to other techniques, it tends to deviate further from actual terrain conditions. Therefore, applying this method in engineering projects that require high precision may lead to significant planning errors.

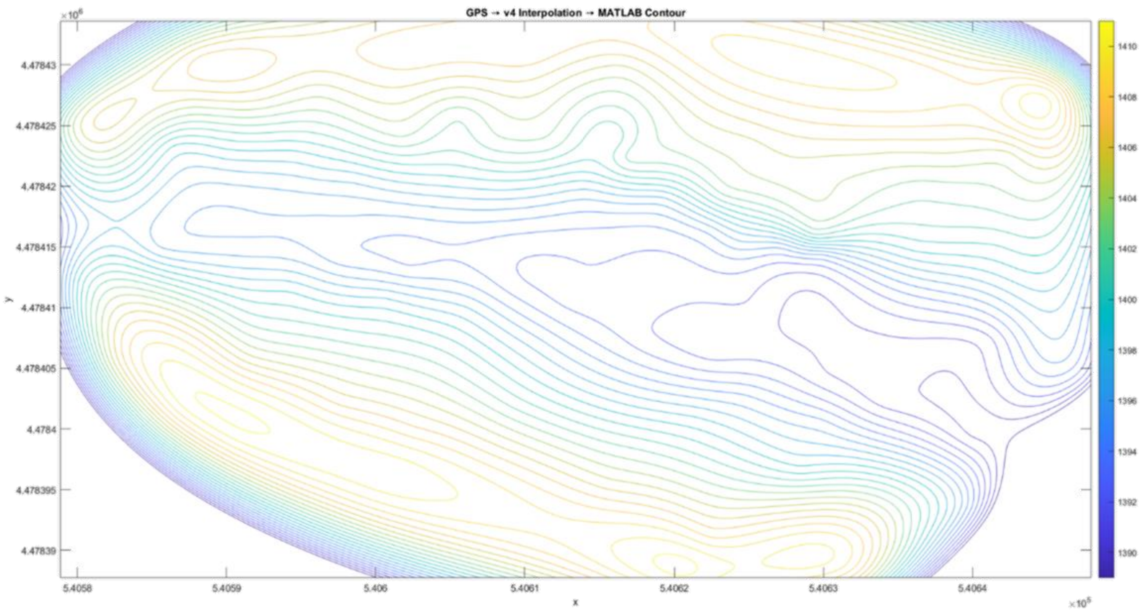

Fig. 7. Contour map generated using the V4 interpolation function in MATLAB.

When the examined terrain models are evaluated as a whole, it is observed that the Natural Neighbor interpolation method in MATLAB provides results that are closer to the actual terrain compared to other methods. However, even this approach contains minor deviations from the real terrain data upon closer inspection. These findings reveal that the accuracy of terrain modeling is significantly influenced by the choice of interpolation methods within existing software tools, emphasizing the need for developing new approaches to achieve more reliable terrain models.

4. Conclusion and recommendations

In this study, the accuracy levels of different software tools and modeling methods used in terrain modeling—an essential process in highway projects—were comparatively analyzed. Various terrain modeling approaches employed by widely used software such as NetCAD and MATLAB were applied to the same reference dataset, and the results were compared.

In the terrain model generated by NetCAD's default triangulation algorithm, connection errors requiring expert intervention were identified. These errors were shown to have the potential to cause planning inaccuracies and unexpected cost deviations in real-world project applications. Although MATLAB's Natural Neighbor interpolation method yielded results closer to the reference model compared to other methods, even this approach failed to produce a fully accurate terrain model.

In engineering applications that demand high precision, such as terrain modeling, even minor discrepancies can lead to significant deviations. In this context, the need for manual intervention during terrain modeling processes in existing software and the limited accuracy of the algorithms employed expose users to potential errors during decision-making processes.

As a result of this study, it is recommended that new-generation modeling approaches be developed as alternatives to conventional interpolation or triangulation methods. These new approaches should aim to achieve higher accuracy without requiring expert intervention. In particular, the applicability of artificial intelligence (AI) and machine learning (ML)-based techniques in this field should be explored, focusing on the development of algorithms capable of producing generalizable results across different terrain types and data distributions. Additionally, it is essential that these advanced modeling approaches be integrated into software environments in an accessible and user-friendly manner for broader adoption by practitioners.

For future research, it is recommended to conduct comprehensive performance analyses of the proposed methods by testing them across different geographical regions and varying data densities. Furthermore, the impact of terrain modeling accuracy on project costs should be quantitatively assessed to support the development of decision-support systems for guiding software selection processes in engineering projects. This study contributes to the understanding of how different terrain modeling approaches affect engineering outcomes and highlights the necessity for more reliable modeling techniques in practice.

References

Darnell, A. R., Lovett, A. A., Barclay, J., & Herd, R. A. (2010). An application-driven approach to terrain model construction. *International Journal of Geographical Information Science*, *24*(8), 1171-1191.

Doytsher, Y., Dalyot, S., & Katzil, Y. (2009). Digital terrain models: a tool for establishing reliable and qualitative environmental control processes. GeoSpatial Visual Analytics: Geographical Information Processing and Visual Analytics for Environmental Security, Trento, Italy.

Gaffar, A. F. O., Malani, R., & Putra, A. B. W. (2018). Prediction of the Topographic Shape of the Ground Surface Using IDW Method through the Rectangular-Neighborhood Approach. 2018 International Symposium on Advanced Intelligent Informatics (SAIN), Yogyakarta, Indonesia.

Garnero, G., & Godone, D. (2014). Comparisons between different interpolation techniques. *The International Archives of the Photogrammetry, Remote Sensing Spatial Information Sciences*, *40*, 139-144.

Gigović, L. J. (2010). Digital models of heights and military application for terrain analysis. *Vojnotehnički glasnik*, *58*(2), 165-178.

Gümüş, K., & Şen, A. (2013). Comparison of spatial interpolation methods and multi-layer neural networks for different point distributions on a digital elevation model. *Geodetski vestnik*, *57*(3).

Kaźmierczak, A. (2013). The Model of the Digital Terrain Map (DTM). *Journal of Applied Computer Science Methods*, *5*, 17-36.

Kidner, D. B., Ware, J. M., Sparkes, A. J., & Jones, C. B. (2000). Multiscale terrain and topographic modelling with the implicit TIN. *Transactions in GIS*, *4*(4), 361-378.

Liu, B., Ding, Y., & Yan, J. (2012). Research on automatic large scale terrain modeling. Asian Simulation Conference, Shanghai, China.

Ma, Y., Hao, Y.-l., & Tian, F.-m. (2015). A novel model of conforming Delaunay triangulation for sensor network configuration. *Abstract and Applied Analysis*, *2015*(1), 1-7.

Ren, G., & Liu, Z. (2013). NetCAD: a network analysis tool for coronary artery disease-associated PPI network. *Bioinformatics*, *29*(2), 279-280.

Salekin, S., Burgess, J. H., Morgenroth, J., Mason, E. G., & Meason, D. F. (2018). A comparative study of three non-geostatistical methods for optimising digital elevation model interpolation. *ISPRS international journal of geo-information*, *7*(8), 300.

Sun, D.-b., Di, Y.-q., & Cui, H.-h. (2015). A real-time vehicle-terramechanics model for visual simulation. International Conference on Materials Engineering and Information Technology Applications (MEITA 2015), Guilin, China.

Thekdi, S. A., & Lambert, J. H. (2012). Decision analysis and risk models for land development affecting infrastructure systems. *Risk Analysis: an international journal*, *32*(7), 1253-1269.

Üstüntaş, T. (2006). Sayısal Arazi Modellerinde Bazı Enterpolasyon Yöntemlerinin Karşılaştırılması. *Selçuk-Teknik Dergisi*, *5*(2), 41-48.

Watson, D. (2013). *Contouring: a guide to the analysis and display of spatial data*. Elsevier.

Yeu, C.-W. T., Lim, M.-H., & Huang, G.-B. (2006). Terrain modeling using machine learning methods. 2006 9th International Conference on Control, Automation, Robotics and Vision, Singapur.

Yomralıoğlu, T. (2005). *Coğrafi bilgi sistemleri: Temel kavramlar ve uygulamalar*. Karadeniz Teknik Üniversitesi.

Zhu, Q., Zhang, Y., & Li, F. (2008). Three-dimensional TIN algorithm for digital terrain modeling. *Geo-spatial Information Science*, *11*(2), 79-85.

4th International Civil Engineering & Architecture Conference
17-19 May 2025, Trabzon, Türkiye

Investigating severity of motorcycle-involved crashes in the context of developing countries

Sina Asgharpour *[1], Kouros Mohammadian[1]

[1] Department of Civil, Material, and Environmental Eng., University of Illinois Chicago, Chicago, IL.

Abstract. Despite special attention to the motorcycle-involved crashes in the safety research, little is known about their pattern in developing countries. The widespread adoption of motorcycles in such regions in tandem with the vulnerability of motorcyclists exacerbates the likelihood of severe crashes. The main objective of this paper is to investigate the underlying factors contributing to the severity of motorcycle-involved crashes through employing crash data between March 2018 to March 2019 in Iran. Firstly, we showed the significance of injury severity of motorcycle-involved crashes among others. In this sense, the data statistics suggest that motorcycle-involved crashes account for 20% of all crashes of which 82% contain injury; however, only 36% of the crashes involving other vehicles (i.e., 80%) has resulted in injury. Subsequently, we focused on eliciting the factors associated with motorcycle crash severity. To this end, we employed a random parameter ordered probit model with heterogeneity in mean to address: 1) the ordinal nature of injury classes (i.e., property-damage-only, injury, and fatal crashes), and 2) unobserved heterogeneity across the crash records. The estimation results indicate that several factors significantly contribute to severe crashes including collision type, road type, spatial, temporal, and motorcycle rider characteristics. According to estimated marginal effects, crashes involving not-at-fault riders and unlicensed riders are the most significant crash types contributing to injury. Finally, upon the insights obtained from the results, we propose safety countermeasures, including 1) strict traffic rule enforcement upon riders and pedestrians, 2) educational programs, and 3) road-specific adjustment policies.

Keywords: Crash data; Motorcycle; Severity; Developing countries

1. Introduction

Motorcycles are a popular transportation mode in many developing and low-income countries owing to their affordability and flexibility on congested roads (Lin & Kraus, 2009). For instance, motorcycles constitute less than 3% of all motorized vehicles in the United States with a per capita income of $56,180 (World Health Organization, 2018). However, in countries such as Pakistan (with a per capita income of $1,510) and Iran (with a per capita income of $6,530), motorcycles account for nearly 74% and 38% of all motorized vehicles, respectively (World Health Organization, 2018). In Tehran, the capital of Iran, there are 3.5 million registered motorcycles, among which 600,000 are used for daily commuting (IRNA, 2021). Despite the prevalence of motorcycles in developing countries, road traffic legislation in these countries is often inadequate noting that only 6% of countries with standard legislation for motorcycles are low-income (World Health Organization, 2018).

The extensive use of motorcycles in developing countries, coupled with inadequate road traffic legislation, poses a significant peril to motorcyclists' safety, leading to a surge in accident injuries and fatalities. Recent evidence suggests that motorcycles are involved in almost 45% of all road accidents in Karachi, Pakistan (Pervez et al., 2021). Furthermore, developing countries, especially Southeast Asia and Africa, account for over 80% of global motorcycle fatalities (World Health Organization, 2018). These statistics highlight the pressing need for effective measures to reduce the injury and fatality risk associated with motorcycle use in developing countries. To this end, identifying the underlying factors influencing the severity of motorcycle crashes can aid in the development of targeted interventions and policies to enhance motorcycle safety.

Despite the high risk of injury associated with motorcycle-involved crashes in developing countries, the existing research on this topic is limited. Furthermore, a review of the literature indicates that studies analyzing motorcycle crash severity in developing countries mostly concentrate on urban areas. This limitation is particularly problematic since motorcycles are often a primary mode in some rural regions, where infrastructure and public transportation options are limited. Therefore, further research is needed to compare the pattern of injury severity

*Corresponding author, E-mail: sasgha3@uic.edu

https://doi.org/10.31462/icearc2025_ce_tra_887

of motorcycle crashes between urban and rural settings in developing countries, identify the underlying factors affecting motorcycle crash severity, and develop targeted policies to improve motorcycle safety in both settings.

This study aims to investigate the severity of injuries associated with motorcycle-involved crashes in Iran, a developing country, with a specific focus on comparing injury severity trends in rural and urban areas. To accomplish this objective, we employ police-reported crash data from Iran spanning from March 2018 to March 2019. Firstly, we demonstrate a marked difference in injury severity between motorcycle-involved and other types of crashes. Subsequently, focusing on motorcycle-involved crashes, we examine injury patterns in urban and rural settings in motorcycle-involved crashes. To identify the factors affecting the injury severity of motorcycle crashes, we estimate two separate Random Parameter Ordered Probit models for urban and rural settings accounting for unobserved heterogeneity. Additionally, we perform a transferability test to determine the need for model separation. By analyzing the estimation results, we identify the factors that impact the injury severity of motorcycle crashes in urban and rural areas.

The findings of this study will have significant implications for policymakers in developing effective policies for motorcycle safety in developing countries. The study will characterize the most significant factors that contribute to injury severity of motorcycle-involved crashes, specific to urban and rural area. These findings can be used to develop targeted interventions to reduce motorcycle-related injuries and fatalities in developing countries. The study will also provide a basis for understanding the differences in injury severity between urban and rural areas. Such insights can be used to develop interventions that are tailored to the specific contexts of rural and urban areas.

The structure of the remainder of this paper is as follows: Section 2 provides a thorough literature review of the analysis of injury severity in motorcycle-involved crashes. Section 3 details the methodology employed in this study. In Section 4, we present descriptive statistics of the dataset used in the analysis, including a comparison of motorcycle crashes to other types of crashes in terms of injury severity. Further, Section 5 reports the results of the analysis and provides a discussion of the findings. In Section 6, policy recommendations resulting from the study are presented. Lastly, Section 7 presents a summary of the study.

2. Literature review

The severity of crashes involving motorcycles has been extensively studied in recent years, and significant efforts have been made to identify the key factors influencing injury severity of these crashes. For instance, among collision characteristics, single and multi-vehicle motorcycle crashes are widely examined and found to be significant (Farid & Ksaibati, 2021; Geedipally et al., 2011; Marizwan et al., 2018; Savolainen & Mannering, 2007; Shaheed & Gkritza, 2014). In this regard, motorcycle-pedestrian (Chen & Fan, 2018; Quddus et al., 2002; Sohrabi et al., 2021; Solagberu et al., 2006) and stationary object collisions (Lin et al., 2003; Shaheed & Gkritza, 2014; Waseem et al., 2019) are usually correlated with severe crashes. Moreover, road type and road geometry (Farid & Ksaibati, 2021; Jones et al., 2013) (e.g., horizontal/vertical curves) are also two paramount factors. Special ambient conditions, such as light level (Geedipally et al., 2011), motorcyclist conspicuity (Wali et al., 2019), and surface condition (M. Haque et al., 2012), are recognized as factors influencing crash severity. Regarding the attributes of a motorcycle rider, young riders are one of the most vulnerable groups, mainly for lack of experience (Das et al., 2018; Farid & Ksaibati, 2021; Halbersberg & Lerner, 2019). Furthermore, human factors, such as helmet use (Shaheed & Gkritza, 2014), alcohol or drug impairment (Shaheed & Gkritza, 2014), and speeding behavior (Shankar & Mannering, 1996), are of special interest. As a summary, Table 1 presents the significant explanatory variables in the reviewed studies of motorcycle accidents from 2003 to 2021.

Various modeling tools are used to assess the impact of different factors on motorcycle crash severity. Lin et al. (Lin et al., 2003) utilized an ordered logit model to ascertain risk factors associated with injury among young riders. Savolainen and Mannering (Savolainen & Mannering, 2007) employed nested and multinomial logit models to assess the contributing factors to the severity of single and multi-vehicle crashes. In addition, Wahab and Jiang (Wahab & Jiang, 2019) utilized machine learning algorithms to investigate risk factors impacting injury severity of motorcycle crashes. Furthermore, Halbersberg and Lerner (Halbersberg & Lerner, 2019) determined factors associated with fatal crashes of young motorcycle riders using the Bayesian network.

In crash data analyses, it is impossible to collect all possible factors affecting the response variable. Therefore, a dataset may always have some unobserved factors. If the unobserved factors are not taken into account, the estimated parameters would be biased and incorrect (Mannering & Bhat, 2014) . This issue is referred to as unobserved heterogeneity which is especially important in police recorded crash data (Mannering et al., 2016). Different approaches are employed in the literature to address this issue. For instance, Rahimi et al. (Rahimi et al., 2020) employed a random parameter random threshold hierarchical ordered probit model to analyze truck-involved crashes. Fountas et al. (Fountas et al., 2021) used a random parameter ordered probit model to study severity of bicycle crashes. Besides, several studies utilized a latent class approach (Eluru et al., 2012; Xie et al., 2012). Comparing latent class and random parameter logit models, Cerwivk et al. (Cerwick et al., 2014) showed that the latent class model has a slightly better fit, while the random parameters model has more accurate predicted probabilities. Meanwhile, unobserved heterogeneity is adequately addressed in the context of motorcycle crashes.

From a few, Shaheed and Gkritza (Shaheed & Gkritza, 2014) used a latent class multinomial logit model to identify dominant severity factors of single-vehicle motorcycle crashes in Iowa. Moreover, Pervez et al. (Pervez et al., 2021) utilized a random parameter ordered logit model to assess the underlying factors associated with motorcycle crash severity in Pakistan.

Motorcycle crashes in developing countries have some distinct characteristics that challenge utilizing policies implemented in developed countries to improve motorcycle-related safety. Lin and Kraus (Lin & Kraus, 2009) identified some of these characteristics, including 1) rapid growth of motorcycle use, 2) roadway environment features (e.g., traffic congestion), 3) poor traffic rules enforcement or inadequate education. Analyzing crash data from Karachi city, Pervez et al. (Pervez et al., 2021) suggested strict enforcement measures to control motorcyclists’ risky behavior and exclusive motorcycles lanes. Additionally, Manan et al. (Marizwan et al., 2018) determined risk factors associated with motorcycle single and multi-vehicle fatal crashes in Malaysia and recommend exclusive lanes for motorcyclists. Despite the studies mentioned above, few works investigate motorcycle crash severity in developing countries compared to developed ones (Lin & Kraus, 2009).

Table 1. Significant explanatory variables in the reviewed studies of motorcycle accidents from 2003 to 2021

Studies (Sorted by Year in Descending Order)	Collision Type	Collision Mode	Road Type	Road Geometry	Land-use	Human Factor	Time of Day	Season	Weather	Surface Condition	Rider’s Fault	Rider’s Gender	Rider’s Age	Rider’s Education	Rider’s License
Pervez et al. (2021)	✓						✓	✓				✓	✓		
Farid & Ksaibati (2021)	✓		✓	✓			✓			✓		✓	✓		
Vajari et al. (2020)	✓				✓		✓		✓	✓		✓	✓		
Shajith et al. (2019)	✓	✓				✓	✓			✓		✓	✓		
Waseem et al. (2019)	✓	✓	✓				✓	✓	✓			✓	✓	✓	
Quddus et al. (2002)	✓		✓				✓	✓		✓		✓	✓		
Halbersberg & Lerner (2019)	✓	✓	✓		✓		✓					✓	✓		
Wahab & Jiang (2019)	✓	✓		✓	✓		✓		✓						
Marizwan et al. (2018)			✓	✓	✓		✓		✓	✓					
Das et al. (2018)	✓	✓	✓	✓			✓		✓		✓		✓		
De Oliveira et al. (2015)												✓	✓	✓	✓
Chichom-Mefire et al. (2015)	✓						✓					✓	✓		
Shaheed & Gkritza (2014)	✓				✓	✓	✓	✓		✓		✓	✓		
Jones et al. (2013)		✓		✓	✓	✓	✓		✓			✓	✓		
Rifaat et al. (2012)		✓	✓			✓	✓	✓				✓			
Haque et al. (2012)							✓			✓					
Geedipally et al. (2011)	✓		✓	✓	✓	✓	✓			✓		✓	✓		
Eustace et al. (2011)		✓		✓	✓	✓	✓	✓	✓			✓	✓		
Oginni et al. (2009)	✓	✓										✓	✓		
Savolainen & Mannering (2007)		✓		✓			✓			✓	✓	✓	✓		
Chang & Yeh (2006)	✓		✓	✓		✓	✓					✓	✓		
Lin et al. (2003)	✓		✓	✓	✓	✓	✓		✓	✓		✓	✓		✓
Iamtrakul et al. (2003)						✓	✓	✓	✓			✓	✓		

3. Method

To investigate the injury severity of crash data, a wide range of econometric models have been employed in the research background. As the most basic models, binary logit/probit (Al-Ghamdi, 2002; Lee & Abdel-Aty, 2008), multinomial logit/probit (Chen & Fan, 2019; Tay et al., 2011), and nested logit models (Holdridge et al., 2005; Patil et al., 2012) have been broadly utilized. Probit models are preferred more than logit models since they assume a normal distribution for error term avoiding the estimation difficulties (Washington et al., 2020). The modeling approaches have become more elaborate over time to incorporate more realistic aspects into injury severity analyses. Mannering and Bhat (Mannering & Bhat, 2014) extensively reviewed the different methods employed in the road safety research.

Ordered probability models have been used to account for the ordinal nature of the injury classes (Mannering & Bhat, 2014). In this sense, ordered logit/probit models have been widely used to estimate injury severity (Khattak et al., 2002; Yasmin & Eluru, 2013; Zhu & Srinivasan, 2011). Ordered models consider a common utility function across all injury classes which can be written as Eq. (1), where i is the observation indicator, U_i represents the utility function of observation i, ϵ_i captures the unobserved factors of observation i (i.e, the error term), and $\mathbf{X_i}$ and $\boldsymbol{\beta}$ are the exogenous variable vector and parameter vector, respectively. In the ordered models, there are $J-1$ cut-off points separating J classes. According to Eq. (2), the probability of being classified into class j equals to the probability of U_i being between two adjacent cut-off points (i.e., C_j and C_{j-1}); where y_i is the discrete class of observation i.

$$U_i = \mathbf{X_i} \cdot \boldsymbol{\beta} + \epsilon_i \qquad ,\forall i = 1, 2, \dots, N \qquad (1)$$

$$\Pr(y_i = j) = Pr\big(C_{j-1} < U_i < C_j\big) \qquad ,\forall i = 1, 2, \dots, N, \ \ \forall = 1, 2, \dots, J \qquad (2)$$

According to Eq. (1) and (2), $\Pr(y_i = j)$ takes the form shown in Eq. (3) in terms of ϵ_i , the random variable signifying the error term. As a solution to Eq. (3), the ordered probit model assumes a normal distribution for ϵ_i (Train, 2003). Consequently, difference of two normally distributed variables also follows a normal distribution. Therefore, $\Pr(y_i = j)$ can be obtained by Eq. (4) where $\Phi(.)$ is the standard normal cumulative density function. Moreover, parameters of $\boldsymbol{\beta}$ and cut-off points are determined through the model estimation process.

$$\Pr(y_i = j|\mathbf{X_i}) = Pr\big(\epsilon_i < C_j - \mathbf{X_i} \cdot \boldsymbol{\beta}\big) - Pr\big(\epsilon_i < C_{j-1} - \mathbf{X_i} \cdot \boldsymbol{\beta}\big) \qquad ,\forall i = 1, 2, \dots, N, \ \ \forall j = 1, 2, \dots, J \qquad (3)$$

$$\Pr(y_i = j) = \Phi\big(C_j - \mathbf{X_i} \cdot \boldsymbol{\beta}\big) - \Phi\big(C_{j-1} - \mathbf{X_i} \cdot \boldsymbol{\beta}\big) \quad ,\forall i = 1, 2, \dots, N, \forall j = 1, 2, \dots, J (\text{if } j = 0 \colon C_j = 0) \qquad (4)$$

Unobserved heterogeneity is one of the essential limitations of the traditional ordered choice models (Fountas & Anastasopoulos, 2017a). Meanwhile, the random parameter models suggest a solution to the unobserved heterogeneity by allowing the parameters to vary across the dataset records. In this regard, a line of the literature has employed random parameter models to estimate crash severity (Fountas & Anastasopoulos, 2017b; Morgan & Mannering, 2011; Ye & Lord, 2014). Moreover, it is highly recommended to take unobserved heterogeneity into consideration in severity analyses of motorcycle crashes (F. Chang et al., 2021; Islam, 2022). In this sense, Islam (Islam, 2021) studied crash severity of single motorcycle crashes in Florida using a random parameter multinomial logit model. Using a similar model, Pervez et al. (Pervez et al., 2021) analyzed severity of motorcycle-involved crashes in Pakistan.

In order to incorporate the unobserved heterogeneity as well as the ordinal nature of the motorcycle crashes, we use a random parameter ordered probit model. In this model, the probability of each injury class is estimated according to Eq. (5) in which the constraint of fixed parameter ordered probit model is relaxed by replacing the $\boldsymbol{\beta}$ in Eq. (4) by $\boldsymbol{\beta_i}$. In Eq. (6), the form of $\boldsymbol{\beta_i}$ is specified where $\boldsymbol{\beta}$ is the vector of parameter mean, $\boldsymbol{\Gamma}$ is a diagonal matrix of standard deviation, and $\mathbf{v_i}$ is normally distributed term with zero mean and unit standard deviation.

$$\Pr(y_i = j) = \Phi\big(C_j - \mathbf{X_i} \cdot \boldsymbol{\beta_i}\big) - \Phi\big(C_{j-1} - \mathbf{X_i} \cdot \boldsymbol{\beta_i}\big) \qquad ,\forall i = 1, 2, \dots, N, \ \ \forall j = 1, 2, \dots, J \qquad (5)$$

$$\boldsymbol{\beta_i} = \boldsymbol{\beta} + \boldsymbol{\Gamma}\mathbf{v_i} \qquad ,\forall i = 1, 2, \dots, N \qquad (6)$$

4. Data

In this section, we present the details of data used in our study. Our data contain nationwide crash information of Iran recorded by traffic authorities from March 2018 to March 2019. Crash injury severity is the dependent variable in our model which is recorded in three categories/classes in the dataset: Property-damage only (PDO), injury (i.e., non-fatal injury), and fatal (i.e., fatal injury). Injury or fatal records refer to crashes in which at least one occupant involved in the crash is injured or died, respectively. Moreover, in this dataset, each record/observation constitutes information of a vehicle involved in a crash as well as the characteristics of the vehicle's driver. The vehicles involved in the same crash are linked to a crash ID. As a result, the crash-specific features (e.g., occurrence time) are identical across the vehicles involved in a crash. More details on the explanatory variables are discussed in section 4.2.

In the following, firstly in section 4.1, we demonstrate the significance of motorcycle-involved crash severity compared to other vehicles using the dataset of all crashes in the country. Subsequently, in section 4.2, we focus on the motorcycle-involved crashes, as a subset of all crashes. The dataset of motorcycle crashes is used for the further analyses in this paper.

4.1. Significance of motorcycle-related severity

As illustrated in Fig. 1, 20% of all accidents are motorcycle-involved. Yet, 82.2% of motorcycle-involved crashes contain injury, whereas this fraction for other vehicles is 35.6% signifying the remarkable share of motorcycle-caused injury. Moreover, motorcycle-involved crashes account for 5% of PDO (12,737 out of 280,948), 38% of injury (93,013 out of 244,659), and 15% of fatal (1,197 out of 7,802) crashes. These statistics are consistent with the background research highlighting the high injury of motorcycle crashes in developing countries in comparison to other vehicle types (Oxley et al., 2013; Salum et al., 2019; Shaker et al., 2014).

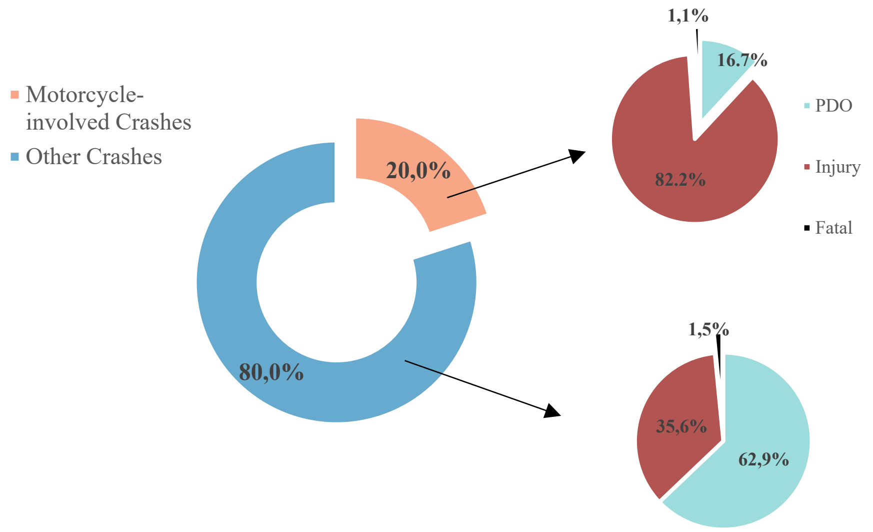

Fig. 1. Distribution of motorcycle-involved vs. other crashes and their corresponding share of PDO, injury, and fatal severity classes

To further elaborate on the significance of injury in motorcycle-involved crashes, we performed Pearson's Chi-square test (Donald, 2015) which captures the degree of association between two categorical variables by mapping associated counts in a cross-tabulated matrix. More specifically, this test measures the difference of counts within matrix cells with respect to uniformly distributed counts based on row and column sums. Chi-square test is defined according to Eq. (7) and (8) where χ^2 is the chi-square statistic, $res_{r,c}$ is the residual value for cell r, c (i.e., row r and column c), $E_{r,s}$ and $O_{r,c}$ represent the uniform and observed counts for cell r, c, respectively. Residual values represent the contribution of each cell to the chi-square statistic.

$$\chi^2 = \sum_{r,c} res_{r,c}^2 \tag{7}$$

$$res_{r,c} = \frac{E_{r,c} - O_{r,c}}{\sqrt{E_{r,c}}}\ , \qquad \forall r, c \tag{8}$$

We utilize the chi-square test to determine the association between vehicle type and severity level. The results indicate statistically significant correlation between these variables. Fig. 2 depicts the associated residual values as well as frequency percentage of each cell. In this chart, size of bubbles represents the residuals quantity associated with each cell. Also, color of the bubbles demonstrates the type of correlation, blue and orange representing positive and negative correlations, respectively. The number in each cell signifies the percentage of crash frequencies in that cell implying that the summation of all cells is 100. According the Fig. 2, the most degree of the association is captured by motorcycle-involved crashes. The residuals of the motorcycle category show a significant positive correlation of this category with injury crashes and a negative correlation with PDO. Even though the highest frequency of injury crashes is related to passenger cars (i.e., 23.8%), among all vehicle types, the motorcycle crashes have the highest positive and negative correlation with injury and PDO crashes, respectively.

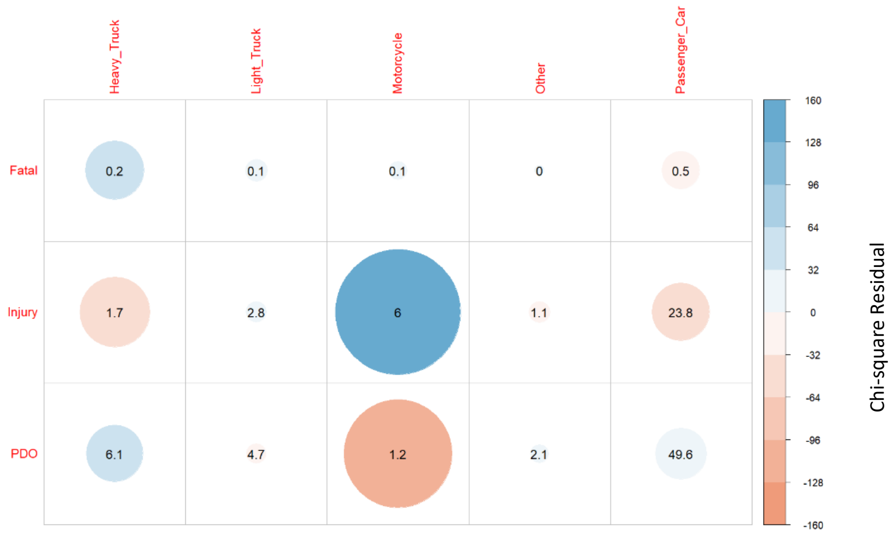

Fig. 2. Chi-Square Test Residual between Crash Severity and Vehicle Types (Size of bubbles is proportional to the residuals and numbers in cells signifies frequency % of them)

4.2. Statistics of the motorcycle dataset

Table 2 shows the descriptive statistics of the motorcycle-involved crashes. In this table, the crash frequency and the associated percentage of explanatory variables are presented cross-tabulated with the dependent variable of our model (i.e., crash severity). Moreover, the summation of frequency percentages in each row over three severity classes is 100%, for instance, there are 29,718 crashes in Motor-vehicle category from which 18.33%, 80.9%, and 0.8% are associated with PDO, injury, and fatal crashes, respectively. Similarly, the summation of percentages in Total column over categories of a variable is 100%.

The explanatory variables of Table 2 can be categorized into four broad groups: 1) collision characteristics (i.e., Collision Type and Collision Mode), 2) road characteristics (i.e., road type and road geometry), 3) spatial and temporal characteristics (i.e., region rain, land-use, season, and time of day), and motorcycle rider's characteristics (i.e., fault status, gender, age, education, license status, and human factors). In the following, details of each variable group are summarily discussed.

About the collision characteristics, collision type variable determines whether the vehicles involved in a motorcycle crash (i.e., motorcycle-vehicle, motorcycle-pedestrian, and two motorcycle) or the type of a single-motorcycle crash (e.g., overturn of a motorcycle without other vehicles involved). In this regard, as the most frequent crash type, motorcycle-vehicles crashes make up 76.5% of all crashes. Moreover, multi-vehicle and multiple categories refer to crashes with more tan two vehicles and compound crash types, respectively. Collision mode specifies the angle of the collision. For instance, front-side refers to a perpendicular collision angle.

Road characteristics group comprises road type and road geometry. Road type signifies the type of the road segment in which a crash occurred. For instance, nearly 67% of the crashes within the dataset took place in urban main streets. Similarly, road geometry specifies presence of a horizontal/vertical curve in proximity of the accident. About the spatial and temporal characteristics, region rain feature states the rain level of the region on average. Since the northern provinces of the country has noticeably high rains, we believe the rain variable in binary format can capture this effect. In a higher resolution, land-use variable specifies the location of the accident belonging to a residential or non-residential area. Furthermore, season and time of day variables are time attributes signifying the season and daytime of the crash, respectively.

Finally, motorcycle rider's variable group includes rider's fault status, their age, gender, education, license status, and human factors. Rider fault specifies the motorcycle rider being whether at-fault of not-at-fault in the crash. Human factors refer to cases that the traffic police detects some behavioral factors associated with the motorcycle rider which potentially led to the accident. In this regard, reckless and/or hurry driving is the most prevalent case of such human factors.

Table 2. Descriptive statistics of motorcycle-involved crashes

Variable		PDO		Injury		Fatal		Total	
	Total	6.486	16.7%	31.926	82.2%	421	1.1%	38.833	100.0%
Collision Type	Motor-Vehicle	5.441	18.3%	24.037	80.9%	240	0.8%	29.718	76.5%
	Two-Motor	506	16.0%	2.599	82.3%	53	1.7%	3.158	8.1%
	Motor-Pedestrian	6	0.3%	2.258	98.5%	29	1.3%	2.293	5.9%
	Overturn	92	5.5%	1.550	92.1%	41	2.4%	1.683	4.3%
	Multi-Vehicle (>2)	243	37.6%	389	60.2%	14	2.2%	646	1.7%
	Multiple	136	28.0%	344	70.8%	6	1.2%	486	1.3%
	Other	62	7.3%	749	88.2%	38	4.5%	849	2.2%
Collision Mode	Front-side	2.047	13.9%	12.541	85.4%	98	0.7%	14.686	37.8%
	Head-on	1.066	16.1%	5.451	82.2%	117	1.8%	6.634	17.1%
	Front-Rear	1.473	26.2%	4.083	72.5%	74	1.3%	5.630	14.5%
	Sideswipe	962	20.7%	3.672	79.0%	16	0.3%	4.650	12.0%
	Other	938	13.0%	6.179	85.4%	116	1.6%	7.233	18.6%
Road Type	Main Street	4.299	16.6%	21.525	82.9%	136	0.5%	25.960	66.9%
	Secondary Street	485	14.0%	2.970	85.4%	21	0.6%	3.476	9.0%
	Main Road	506	16.1%	2.554	81.1%	89	2.8%	3.149	8.1%
	Highway	602	26.8%	1.598	71.1%	47	2.1%	2.247	5.8%
	Secondary Road	313	14.9%	1.714	81.6%	74	3.5%	2.101	5.4%
	Rural Road	196	14.4%	1.120	82.3%	45	3.3%	1.361	3.5%
	Other	85	15.8%	445	82.6%	9	1.7%	539	1.4%
Road Geometry	Flat	6.195	16.7%	30.542	82.3%	368	1.0%	37.105	95.6%
	Horiz./Vert. Curve	291	16.8%	1.384	80.1%	53	3.1%	1.728	4.4%
Regio Rain	Not High Rain	6.325	17.6%	29.220	81.4%	373	1.0%	35.918	92.5%
	High Rain	161	5.5%	2.706	92.8%	48	1.6%	2.915	7.5%
Land-use	Residential	5.181	17.5%	24.240	81.9%	190	0.6%	29.611	76.3%
	Non-residential	1.305	14.2%	7.686	83.3%	231	2.5%	9.222	23.7%
Season	Spring/Summer	3.276	14.3%	19.404	84.6%	263	1.1%	22.943	59.1%
	Fall/Winter	3.210	20.2%	12.522	78.8%	158	1.0%	15.890	40.9%
Time of Day	Day	4.892	18.5%	21.371	80.7%	209	0.8%	26.472	68.2%
	Night	1.409	12.6%	9.573	85.7%	191	1.7%	11.173	28.8%
	Down/Dusk	185	15.6%	982	82.7%	21	1.8%	1.188	3.1%
Rider’s Fault	not at-Fault	2.815	12.2%	20.087	87.0%	177	0.8%	23.079	59.4%
	at-Fault	3.671	23.3%	11.839	75.1%	244	1.5%	15.754	40.6%
Rider’s Gender	Male	6.474	16.7%	31.868	82.2%	420	1.1%	38.762	99.8%
	Female	12	16.9%	58	81.7%	1	1.4%	71	0.2%
Rider’s Age	Under 25	1.740	12.3%	12.182	86.4%	176	1.2%	14.098	36.3%
	26 to 55	4.480	19.9%	17.789	79.2%	197	0.9%	22.466	57.9%
	Over 56	266	11.7%	1.955	86.2%	48	2.1%	2.269	5.8%
Rider’s Education	Secondary School or Less	1.141	14.6%	6.559	84.1%	97	1.2%	7.797	20.1%
	Diploma	4.852	16.6%	24.142	82.4%	316	1.1%	29.310	75.5%
	College/Higher	493	28.6%	1.225	71.0%	8	0.5%	1.726	4.4%
Rider’s License Status	Motorcycle License	4.318	30.8%	9.664	69.0%	30	0.2%	14.012	36.1%
	Not Reported	1.761	11.8%	12.835	86.3%	280	1.9%	14.876	38.3%
	Without License	407	4.1%	9.427	94.8%	111	1.1%	9.945	25.6%
Human Factor	Reckless/Hurry	4.595	19.6%	18.592	79.5%	213	0.9%	23.400	60.3%
	None	1.563	13.9%	9.508	84.8%	137	1.2%	11.208	28.9%
	Rule Ignorance	193	6.1%	2.919	92.4%	46	1.5%	3.158	8.1%
	Other	135	12.7%	907	85.0%	25	2.3%	1.067	2.7%

5. Results

To estimate the model, we used NLOGIT 6 software and the simulation-based maximum likelihood approach. As the simulation process, it is shown that a Halton draw sequence with one tenth of a number of random draws is similarly efficient (Bhat, 2001). On this basis, we used 100 Halton draws to estimate the model. Furthermore, we set 10% significance level as the threshold to consider a parameter whether random or fixed. Moreover, as mentioned in section 3, we considered three injury classes, including PDO, injury, and fatal. As a part of the model specification procedure, we arranged these classes in an increasing order in our model. Accordingly, a positive sign of an estimated coefficient implies that an increase in the associated variable increase the probability of severe classes.

In order to better understand the impact of unobserved heterogeneity, we run both fixed and random parameters ordered probit models. Table 3 shows the overall fitting of these models. According to this table, both fixed and random parameter models are statistically significant. Moreover, two goodness-of-fit measures, ρ^2 and Akaike Information Criterion (AIC), are also presented in this table which are based on Eq. (9) and Eq. (10), respectively (Train, 2003). In these equations, $LL(\hat{\beta})$ and $LL(0)$ stand for the optimal log-likelihood at the estimated parameters and log-likelihood with parameters set to zero, respectively. Further, K represents the number of estimated parameters and N is the dataset size. According to ρ^2 and normalized AIC, the random parameter model has a better fitting compared to the fixed parameter version.

$$\rho^2 = 1 - \frac{LL(\hat{\beta})}{LL(0)} \tag{9}$$

$$AIC = -2LL(\hat{\beta}) + K \cdot \log(N) \tag{10}$$

Table 4 presents the estimation results comprising the coefficients' mean and standard errors for both random and fixed parameter ordered probit models. Additionally, in random parameters model, standard deviations of random parameters' distribution are shown in this table. Accordingly, the parameters without standard deviation are considered fixed across the observation. Furthermore, according to t-test-based statistical significance shown in Table 4, all variables of the random and fixed model have a significance level over 95%, and 90%, respectively.

According to Table 4, significance of random parameters' distribution standard errors demonstrates the advantage of the random parameters model over the fixed parameters model. As discussed, unobserved heterogeneity potentially leads to incorrect parameter estimates in fixed parameters model. This issue can be noticed in Table 4 by comparing estimated parameters of random and fixed parameters models. In most cases, the difference of estimated parameters between random and fixed parameter models is remarkable. For instance, the estimated coefficients for Highway variable for the random model is 0.103 while it is -0.072 for the fixed model. As a result, these differences can lead to incorrect conclusion in case of using the fixed parameter model. Therefore, we will focus on the results of the random parameter model in the remaining of the paper.

As shown in Table 4, if the cut-off point between PDO and injury classes is normalized to zero, 6.619 is the estimated cut-off point of random model between injury and fatal classes. In addition, the statistical significance of the threshold confirms the distinct difference between associated severity classes. Table 5 demonstrates the sample-average marginal effects of the random parameters model signifying the average change in the outcome probabilities as a result of a unit increase in a specific variable. In the following subsections, we interpret the estimation results presented in Table 4 coupled with Table 5.

Table 3. Overall fitting of estimated models

Measure	Random Parameters Ordered Probit	Fixed Parameters Ordered Probit
p-value (Significance)	0.000	0.000
$LL(0)$	-19,765	-19,765
$LL(\hat{\beta})$	-16,971	-17,223
ρ^2	0.141	0.129
$\frac{AIC}{N}$	0.876	0.888

Table 4. Estimation results of the random/fixed parameter ordered probit model

Variable/Parameter		Random Parameters			Fixed Parameters	
		Coefficient Mean	(St. Dev. of Distribution)	Coefficient St. Error	Coefficient Mean	Coefficient St. Error
Thresholds	Cut-off Point 1	Normalized to 0			Normalized to 0	
	Cut-off Point 2	6.619 ***		0.062	5.371 ***	0.050
	Constant	-0.436 ***		0.028	-0.243 ***	0.0233
Collision Type	Motor-Pedestrian	2.038 ***		0.010	1.518 ***	0.054
	Overturn	1.573 ***	(0.643 ***)	0.063	0.909 ***	0.039
	Two-Motor	0.482 ***	(0.911 ***)	0.035	0.179 ***	0.025
Collision Mode	Head-on	0.107 ***	(0.410 ***)	0.024	0.041 **	0.019
	Front-side	0.119 ***		0.023	0.088 ***	0.018
Road Type	Highway	0.103 **	(1.327 ***)	0.043	-0.072 **	0.031
	Main Street	0.063 ***		0.020	0.104 ***	0.017
Land Use	Non-residential	0.648 ***	(1.231 ***)	0.026	0.133 ***	0.017
Region Rain	High Rain Area	0.805 ***	(0.659 ***)	0.048	0.427 ***	0.030
Season	Spring/Summer	0.217 ***		0.017	0.154 ***	0.014
Time of Day	Night	0.227 ***	(0.321 ***)	0.020	0.131 **	0.016
	Down/Dusk	0.482 ***	(1.078 ***)	0.053	0.067 *	0.036
Rider’s Fault	not at-Fault	0.698 ***	(0.296 ***)	0.018	0.487 ***	0.015
Rider’s Age	Under 25	0.245 ***	(0.483 ***)	0.019	0.108 ***	0.015
	Over 56	0.405 ***		0.035	0.311 ***	0.031
Rider’s Education	Secondary School or Less	0.060 ***		0.022	0.046 **	0.018
	College or Higher	-0.313 ***		0.040	-0.239 ***	0.033
Rider’s License Status	without License	0.849 ***		0.024	0.586 ***	0.018
Human Factor	Rule Ignorance	0.505 ***	(0.606 ***)	0.043	0.240 ***	0.028

* 90% significance level, ** 95% significance level, *** 99% significance level

Table 5. Marginal effects of random parameters model

Variables		Severity Class		
		PDO	Injury	Fatal
Collision Type	Motor-Pedestrian	-0.0701	0.0468	0.0233
	Overturn	-0.0608	0.0467	0.0141
	Two-Motor	-0.0466	0.0443	0.0024
Collision Mode	Head-on	-0.0148	0.0144	0.0004
	Front-side	-0.0166	0.0161	0.0005
Road Type	Highway	-0.0140	0.0136	0.0004
	Main Street	-0.0096	0.0094	0.0003
Land Use	Non-residential	-0.0692	0.0661	0.0031
Region Rain	High Rain Area	-0.0577	0.0531	0.0046
Season	Spring/Summer	-0.0337	0.0329	0.0009
Time of Day	Night	-0.0309	0.0299	0.0010
	Down/Dusk	-0.0446	0.0422	0.0024
Rider's Fault	not at-Fault	-0.1195	0.1168	0.0027
Rider's Age	Under 25	-0.0344	0.0334	0.0010
	Over 56	-0.0411	0.0392	0.0019
Rider's Education	Secondary School or Less	-0.0086	0.0084	0.0002
	College or Higher	0.0604	-0.0593	-0.0011
Rider's License Status	without License	-0.0861	0.0818	0.0043
Human Factor	Rule Ignorance	-0.0478	0.0453	0.0025

5.1. Collision characteristics

Collision characteristics are represented by collision type and collision mode (i.e., collision angle) attributes in the estimated model. As shown in Table 4, three collision type variables (i.e., motor-pedestrian, overturn, and two motorcycles), and two collision mode attributes (i.e., head-on, and front-left) turned out to be statistically significant.

Per the results, motor-pedestrian crashes tend to be more severe since their associated coefficient mean is 2.038. According to Table 5, involving in a motor-pedestrian accident decreases the probability of the accident being PDO by 0.70, while increases the likelihood of injury and fatality by 0.0468 and 0.0233, respectively. This outcome is in line with the similar studies in motorcycle crash severity as specified in Shajith et al. (Shajith et al., 2019); Quddus et al. (Quddus et al., 2002); Chen and Fan (Chen & Fan, 2018). Even in minor motorcycle-pedestrian crashes, both sides of the accident (i.e., the rider and the pedestrian) are highly vulnerable which makes them susceptible to higher risks. In addition, the lack of traffic rule regulations in Iran, especially for the pedestrians, is a serious underlying factor contributing to more severe accidents. For instance, no rigorous traffic rules are imposed on pedestrians and motorcycle riders crossing a red light. Also, in congested areas, some riders prefer to take sidewalks instead of the main road, yet there are not enough regulations tackling this risky behavior. This is also in good agreement with Shajith et al. (Shajith et al., 2019) who acknowledged the motorcycle-pedestrian crashes on sidewalks as a noticeable factor affecting crash severity in Sri Lanka.

Overturn Crashes are the other collision type that contributes to increasing the odds of more severe crashes since it has a positive sign in the model. Overturn usually occur as a result of rider's loss of control in critical situations (e.g., slippery surface condition, attempt to avoid hitting other objects). Falling into this crash category raises the probability of injury and fatality by 0.0467 and 0.0141, respectively. This finding is also well in line with the findings of Pervez et al. (Pervez et al., 2021), and Shaheed and Gkritza (Shaheed & Gkritza, 2014), both studying motorcycle crash severity in developing countries. Similarly, overturn has identified as one of the harmful events associated with fatal motorcycle crashes in U.S. between 2004 to 2008 (Daniello & Gabler, 2011).

Furthermore, being involved in two-motorcycle crashes increases the likelihood of fatal and non-fatal injuries by 0.0024 and 0.0443, respectively. An underlying reason for this finding could be the high vulnerability of both motorcycle riders, especially at higher speeds, compared to motorcycle-vehicle crashes. In fact, unlike motor-vehicle accidents, here both sides are unprotected and at high injury risk. Analogous results can also be found in Savolainen and Mannering (Savolainen & Mannering, 2007). Another contributing factor to the significance of this collision type could be the high share of motorcycle use in developing countries which accounts for the relatively high frequency of two motor crashes (i.e., 8.1% of the whole motorcycle-involved accident according to Table 2).

According to the model results, the collision mode also plays a significant role in the severity of a motorcycle crash. In this sense, head-on and front-side motorcycle crashes are positively associated with more severe crashes. Compared to the other modes, a head-on motorcycle crash increases the odds of injury and fatality by 0.0144 and 0.0004, respectively. Head on crashes potentially lead to severe injuries due to the opposite movement direction and high relative speed of vehicles. This finding is also supported by evidence from the literature (Shajith et al. (Shajith et al., 2019); Savolainen and Mannering (Savolainen & Mannering, 2007)). Moreover, front-side crashes also positively affect the probability of more severe motorcycle crashes. It increases the probability of injury by 0.0161 and fatality by 0.005. In this regard, Rifaat et al. (Rifaat et al., 2012) found the front-side crashes significant factor studying the motorcycle crashes in Calgary. From another perspective, front-side motorcycle crashes usually occur at intersections and can be related to gap acceptance behavior of motorcycle riders which is identified as a major safety concern (Pai et al., 2009).

5.2. Road characteristics

The model indicates that the occurrence of a crash in highway segments increases the probability of severe crashes since the associated coefficient has a positive sign. According to Table 5, shifting from another road segments to highway segments increases the probability of injury and fatality by 0.0136 and 0.0004, respectively, whereas reduces the probability of PDO by 0.0140. As an underlying factor, high speed of vehicles (both motorcycles and cars) in highway segments can account for this trend. Similar findings are also reported for motorcycle crash severity in the literature (Farid & Ksaibati, 2021; Geedipally et al., 2011). Moreover, injury severity of crashes at highways has been studied widely due to the high risk of severe crashes (Ebnali et al., 2020; Fountas & Anastasopoulos, 2017a; Mahmud et al., 2021; Yingfeng & Yong, 2009).

Moreover, motorcycle crashes occurring at main streets are positively associated with more severe crashes, according to the results. Happening a motorcycle-involved crash in these road segments increases the probability of injury and fatal accidents by 0.0094 and 0.0003, respectively. Previous research also supports this finding (Marizwan et al., 2018). Fig. 3 illustrates the share of main streets form whole motorcycle crash locations in our dataset (Table 2) implying that motorcycle crashes mostly happen in main streets by far. Furthermore, most of them contain crash injury. The underlying reason can be the ease of access that main streets provide to motorcycles. This factor can also lead to risky and speeding behaviors by motorcycle riders increasing the risk of severe crashes.

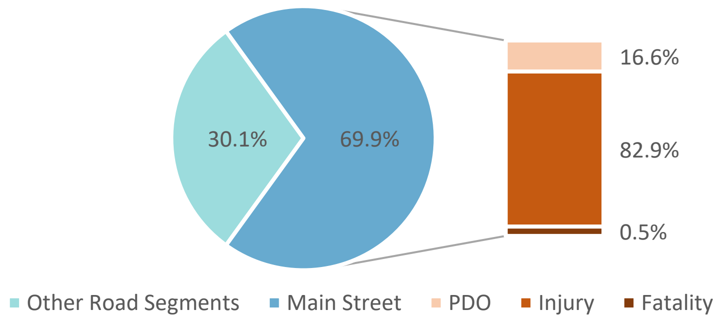

Fig. 3. Percentage of Crashes in the Dataset (by Severity Level) Occurring on Main Streets Compared to Other Road Segments

5.3. Spatial and temporal characteristics

In the estimated model, two spatial factors (i.e., crash location's land use, and region rain features) significantly affect the injury severity. In this regard, non-residential land-use is positively associated with more severe crashes since its estimated coefficient is 0.648. Accordingly, its marginal effect for injury and fatal crashes is 0.0661 and 0.0031, respectively. This trend is in line with a line of the literature (Prato et al., 2018; Zajac & Ivan, 2003) implying that populated and residential areas are associated with less severe crashes. This can be attributed to riders' cautious behavior in these regions. Moreover, crashes occurring in areas of the country with high rains are associated with more severe crashes increasing the probability of injury and fatal crashes by 0.0531 and 0.0046, respectively. In this regard, most of the literature investigated impact of inclement weather on crash severity (Omranian et al., 2018; Tay et al., 2011); however, we focused on the impact of regional climate on crash severity due to the unavailability of day-to-day weather information in our dataset.

About the temporal characteristics, two features turned to be statistically significant: season and time of the day. According to the results, spring/summer category affects crash severity by increasing the probability of injury and fatality by 0.0329 and 0.0009, respectively. This also implies that the base category (i.e., fall/winter) has an inverse effect. This conclusion is in line with Pervez et al. (Pervez et al., 2021). Rifaat at al. (Rifaat et al., 2012) (also truck involved)

A paramount reason for this trend is the different number of motorcycle trips in different seasons. According to Table 2, nearly 60% of motorcycle-involved crashes have occurred in warm seasons. Concerning the time-of-day attribute, night and Down/Dusk time intervals significantly affect the injury severity. Crashes happening at night increase the probability of the injury and fatal crashes by 0.0299 and 0.0010, respectively. Similarly, dawn or dusk variables also contribute to increasing the injury probability by 0.0422 and the fatality probability by 0.0024. These findings are also confirmed by previous research (Abrari Vajari et al., 2020; Marizwan et al., 2018; Pervez et al., 2021; Quddus et al., 2002), and reportedly, due to the drivers' fatigue and poor lighting level (Rowden et al., 2008). Furthermore, the malfunction of motorcycles, specifically the head-light problem, can aggravate this effect which is the direct consequence of non-compulsory maintenance checks and low enforcement in the country.

5.4. Motorcycle rider characteristics

According to the results, five motorcycle rider characteristics in the model have statistically significant impacts on the injury severity: rider's fault status, age, education, license status, and human factor associated with the accident cause.

The results suggest that the likelihood of more severe accidents increases when the motorcycle rider is not at fault. More specifically, shifting rider's status from at-fault to not-at-fault would raise the probability of injury and fatal crashes by 0.1168 and 0.0027, respectively. This result is reasonable considering if a motorcycle rider is at fault, he/she is more aware of the situation and can react quickly. This also means that in not-at-fault cases, motorcyclists have a higher chance of losing their control and balance due to unexpected conditions and become exposed to more severe damages. In this regard, the background research mainly investigated the factors affecting the fault status of the motorcycle rider (M. M. Haque et al., 2009; Schneider et al., 2012) and impact of fault status of motorcycle riders on crash severity is unexplored.

About the age variable, the model indicates that being a younger driver (i.e., aged less than 25 years) increases the probability of injury and fatal by 0.0334 and 0.0010, respectively. According to the literature, this finding could be attributed to the prevalence of unskilled riders and the tendency to disobey the rules at this age group (H. L. Chang & Yeh, 2007; Kashani et al., 2017; Quddus et al., 2002). Furthermore, being an elderly rider (i.e., over 56) also has a negative impact on injury severity by increasing the probability of injury and fatality by 0.0392 and 0.0019, respectively. This increase is even more considerable than that of young riders. The decline in vision, cognitive functioning, inability to react quickly are some challenges putting elderly riders at high risk of severe crashes (CDC, 2020), especially for the motorcycle riders, that on-time reaction and decision-making is of crucial importance. These results are in good agreement with Pervez et al. (Pervez et al., 2021); Quddus et al. (Quddus et al., 2002); and Vajari et al. (Abrari Vajari et al., 2020).

With respect to the education status, it is observed that riders with education levels of secondary school or less are positively associated with severe crashes. Belonging to this category engenders an increase in both injury and fatal crash probabilities by 0.0084 and 0.0002, respectively. Conversely, the negative sign for the college education coefficient implies that crashes in this category tend to be less severe. When a rider has a college or higher education, the probability of PDO increases by 0.0604, whereas the probability of injury and fatal crashes reduces by 0.0593 and 0.0011, respectively. These outcomes depict the positive impact of education on making individuals more disciplined riders. In other words, less educated riders may less adhere to traffic rules (e.g., helmet use, alcohol/drug use, and speeding), as has been emphasized by Waseem et al. (Waseem et al., 2019) and Kashani et al. (Kashani et al., 2017). The reverse correlation between rider's education level and crash severity is also identified in severity of truck-involved crashes (Rahimi et al., 2020).

As the model results suggest, motorcycle riders without a motorcycle license are more likely to involve in a severe crash. Associated marginal effects of this factor are 0.0818, and 0.0043 for injury and fatal crashes, respectively. The result of a decision tree analysis on motorcycle crashes in China revealed that the motorcycle riders without license are significantly associated with high-risk crashes (F. Chang et al., 2019). According to Table 1, license status is not widely included in the literature of motorcycle crash severity analyses; however, our finding is in line with some studies in the context (Kashani et al., 2017; Lin et al., 2003). Moreover, according to Table 2, almost 25% of motorcycle riders in our dataset do not have a valid license. In this regard, strict enforcement is needed to reduce the unlicensed motorcycle driving.

About the human factors associated with accident cause, rule ignorance by motorcycle riders is positively correlated with severe crashes. This factor raises the probability of injury and fatal crashes by 0.0453 and 0.0025, respectively. In our model, rule ignorance refers to traffic rule violation of any type (e.g., not using helmet, impaired by drug/alcohol, etc.) since we do not have access to more detailed information about the violation type. Previous studies confirmed the positive association between rule ignorance and motorcycle crash severity. For instance, alcohol use (Crocker et al., 2010; Rifaat et al., 2012), riding without helmet (Keng, 2005; Rutledge & Stutts, 1993), and traffic signal violation (Salum et al., 2019) are found to be remarkably increasing crash severity.

6. Policy implications

In this section, upon the results of the presented model, we recommend countermeasures to improve the safety of motorcyclists and reduce the number of motorcycle-involved accidents in developing countries. In this sense, we propose three types of applicable policies, including traffic rule enforcement, educational programs, and road-specific adjustments.

According to the model results, unlicensed driving and traffic rule ignorance are among the most influential variables increasing injury severity (i.e., based on the marginal effects). These findings are direct results of a wide gap in traffic rule enforcement upon motorcycle riders. The World Health Organization has assigned an enforcement score of 5 out of 10 to Iran in 2018 (World Health Organization, 2018). For example, helmet use among motorcyclists of Iran is estimated to be 59% (World Health Organization, 2018), whereas this rate in the United States, as a developed country, is at least 71% in the same year (National Highway Traffic Safety Administration, 2020). Further, as underlined in the case of motorcycle-pedestrian crashes, pedestrians are not penalized when violating the traffic rules. It is estimated that nearly 80% of pedestrians in the country do not comply with traffic laws (Aghdam et al., n.d.). These findings highlight the necessity of developing a comprehensive regulation enforcement system for motorcycle riders and pedestrians. According to Table 5, the maximum marginal effect of fatal crashes is related to motorcycle-pedestrian crashes. Accordingly, countermeasures targeting both riders and pedestrians would remarkably boost the safety of these crashes. Similar policy is suggested toward motorcycle crashes in Ghana (Dapilah et al., 2017).

As another countermeasure, the government can provide educational programs on assorted platforms, especially targeting young riders who are more likely to have risky riding behaviors. For instance, programs embedded in the licensing procedures can be effective. Licensing system in Iran lacks oriented educational programs, especially for motorcyclists, and individual's skills are developed as a result of the self-training process. Therefore, embedding educational programs as a prerequisite part of getting a motorcycle license can be substantially effective in the long run. Similar recommendations are also suggested by Chang and Yeh (H. L. Chang & Yeh, 2007) upon motorcycle licensing in Taiwan.

Last but not least, we recommend road-specific adjustments to upgrade the safety of motorcyclists and pedestrians. As mentioned in section 5.2, highway and main street urban road segments are associated with severe crashes. Rider's speeding and unsafe maneuvers due to the lack of traffic control systems may account for this trend. Installing traffic signs can be a general countermeasure to reduce the risk in such roads; however, depending on the condition of the road segments and the volume of motorcycle users, more specific measures can be considered. As shown in Fig. 3, nearly 70% of crashes in our dataset occurred in main streets implying that motorcyclists are more intended to take local streets instead of freeways and highways. Therefore, these road segments require special intention in terms of policy implementation. For instance, in main road segments with high motorcycle volume, a separate exclusive path can be designated to improve the safety of motorcycle riders. In this regard, implementation of exclusive motorcycle lanes in Malaysia has reduced motorcycle deaths by 600% (Radin Umar, 2006).

7. Conclusion

In this paper, we study the characteristics of the injury severity of motorcycle-involved crashes in Iran, as a developing country. In this regard, we employed Iran's crash records from March 2018 to March 2019. Notwithstanding 20% share of motorcycle-involved crashes from all, 82% of them are injury crashes. However, this ratio for the other crashes is nearly 36%. Moreover, the data statistics suggest that motorcycle-involved crashes make up 5% of PDO, 38% of the injury, and 15% of the fatal crashes. Furthermore, Chi-square test results revealed that the highest association between injury crashes and all vehicle types is related to motorcycles.

To determine the contributing factors to the severity of motorcycle-involved crashes, we utilized a random parameter ordered probit model with heterogeneity in mean. We also estimated a fixed parameters version of the model to better understand the impact of unobserved heterogeneity. By comparing the results of the fixed and random models, we showed that the estimated parameters of them are significantly different. As a result, using the fixed parameter models can lead to incorrect conclusions since it does not embed unobserved heterogeneity. Therefore, we focused on the random parameters model to draw conclusions.

The results of the random parameters model suggest that three collision types (motorcycle-pedestrian, overturn, and two-motorcycle crashes) increase the probability of severe crashes. Besides, head-on, and front-side collisions negatively affect severity in the collision angle category. About the road type, collisions taking place in highways and main streets are associated with injury and fatal crashes. About the spatial factors, areas with non-residential land use and provinces with high annual rain increase the crash severity. Three temporal characteristics are found to be significant in increasing the likelihood of severe crashes (spring/summer seasons, night hours, and dawn/dusk hours). Moreover, not-at-fault motorcycle riders are more susceptible to injury and fatal crashes. Moreover, regarding rides' age, under 25 and over 56 aged motorcycle riders are more likely to be involved in severe crashes. About the rider's education, per the results, riders with secondary school or less education are more likely to be categorized in more severe crashes. In contrast, riders with college degrees decrease the probability of severe crashes. Further, riders without a motorcycle license significantly contribute to crash severity increase. Finally, traffic rule ignorance behavior of riders is also found to be influential.

Based on the model's marginal effects, the most effective attribute on fatal crashes is collision type comprising two variables motorcycle-pedestrian and overturn. Being involved in a motorcycle-pedestrian and overturn crashes results in an increase in the probability of fatality by 0.0233 and 0.0141, respectively. About the injury crashes, the most influential variables are related to not-at-fault riders, rule ignorance, all three collision types (motorcycle-pedestrian, overturn, and two-motorcycle crashes), respectively.

As per the research findings, we recommended three countermeasures for safety improvement regarding motorcycle-involved crashes, including traffic rule enforcement, educational programs, and road-specific adjustments. We also highlight the lack of traffic rule enforcement for motorcyclists and pedestrians. The score of traffic law enforcement upon motorcyclists in Iran in 2018 is 5 out of 10 (World Health Organization, 2018), which is consistent with our results.

As a rewarding future extension of our research, we recommend employing more crash severity classes in the context of developing countries. Since the data availability limited our model to consider three injury classes, we were unable to distinguish slight injuries from incapacitating injuries that may have different patterns. This issue is addressed by several studies for developed countries (Abrari Vajari et al., 2020; Eustace et al., 2011; Jones et al., 2013) usually because of the availability of rich and detailed crash databases.

Acknowledgments

There is no funding source for this research.

References

Abrari Vajari, M., Aghabayk, K., Sadeghian, M., & Shiwakoti, N. (2020). A multinomial logit model of motorcycle crash severity at Australian intersections. *Journal of Safety Research*, 73, 17–24. https://doi.org/10.1016/j.jsr.2020.02.008

Aghdam, F. B., Bazargani, H. S., Sarbakhsh, P., Pashaie, T., Ponent, K., & Nicknejad, M. (n.d.). Pedestrians in Iran: Determinants of unsafe traffic behaviors of pedestrians. *Research Square*, 1–11.

Al-Ghamdi, A. S. (2002). Using logistic regression to estimate the influence of accident factors on accident severity. *Accident Analysis & Prevention*, 34(6), 729–741. https://doi.org/10.1016/S0001-4575(01)00073-2

Bhat, C. R. (2001). Quasi-random maximum simulated likelihood estimation of the mixed multinomial logit model. *Transportation Research Part B: Methodological*, 35(7), 677–693. https://doi.org/10.1016/S0191-2615(00)00014-X

CDC. (2020). Older Adult Drivers. Centers for Disease Control and Prevention. Retrieved from https://www.cdc.gov/transportation.

Cerwick, D. M., Gkritza, K., Shaheed, M. S., & Hans, Z. (2014). A comparison of the mixed logit and latent class methods for crash severity analysis. *Analytic Methods in Accident Research*, 3–4, 11–27. https://doi.org/10.1016/j.amar.2014.09.002

Chang, F., Xu, P., Zhou, H., Lee, J., & Huang, H. (2019). Identifying motorcycle high-risk traffic scenarios through interactive analysis of driver behavior and traffic characteristics. *Transportation Research Part F: Traffic Psychology and Behaviour*, 62, 844–854. https://doi.org/10.1016/j.trf.2019.03.010

Chang, F., Yasmin, S., Huang, H., Chan, A. H. S., & Haque, M. M. (2021). Injury severity analysis of motorcycle crashes: A comparison of latent class clustering and latent segmentation based models with unobserved heterogeneity. *Analytic Methods in Accident Research*, 32, 100188. https://doi.org/10.1016/j.amar.2021.100188

Chang, H. L., & Yeh, T. H. (2006). Risk factors to driver fatalities in single-vehicle crashes: Comparisons between non-motorcycle drivers and motorcyclists. *Journal of Transportation Engineering*, 132(3), 227–236. https://doi.org/10.1061/(ASCE)0733-947X(2006)132:3(227)

Chang, H. L., & Yeh, T. H. (2007). Motorcyclist accident involvement by age, gender, and risky behaviors in Taipei, Taiwan. *Transportation Research Part F: Traffic Psychology and Behaviour*, 10(2), 109–122. https://doi.org/10.1016/j.trf.2006.08.001

Chen, Z., & Fan, W. D. (2019). A multinomial logit model of pedestrian-vehicle crash severity in North Carolina. *International Journal of Transportation Science and Technology*, 8(1), 43–52. https://doi.org/10.1016/j.ijtst.2018.10.001

Chichom-Mefire, A., Atashili, J., Tsiagadigui, J. G., Fon-Awah, C., & Ngowe-Ngowe, M. (2015). A prospective pilot cohort analysis of crash characteristics and pattern of injuries in riders and pillion passengers involved in motorcycle crashes in an urban area in Cameroon: Lessons for prevention. *BMC Public Health*, 15(1), 1–8. https://doi.org/10.1186/s12889-015-2290-4

Crocker, P., Zad, O., Milling, T., & Lawson, K. A. (2010). Alcohol, bicycling, and head and brain injury: A study of impaired cyclists' riding patterns. *The American Journal of Emergency Medicine*, 28(1), 68–72. https://doi.org/10.1016/j.ajem.2008.09.011

Daniello, A., & Gabler, H. C. (2011). Fatality risk in motorcycle collisions with roadside objects in the United States. *Accident Analysis & Prevention*, 43(3), 1167–1170. https://doi.org/10.1016/j.aap.2010.12.027

Dapilah, F., Guba, B. Y., & Owusu-Sekyere, E. (2017). Motorcyclist characteristics and traffic behaviour in urban Northern Ghana: Implications for road traffic accidents. *Journal of Transport & Health*, 4, 237–245. https://doi.org/10.1016/j.jth.2016.03.001

Das, S., Dutta, A., Dixon, K., Minjares-Kyle, L., & Gillette, G. (2018). Using deep learning in severity analysis of at-fault motorcycle rider crashes. *Transportation Research Record*, 2672(34), 122–134. https://doi.org/10.1177/0361198118797212

Das, S., Tsapakis, I., & Khodadadi, A. (2021). Safety performance functions for low-volume rural minor collector two-lane roadways. *IATSS Research*. https://doi.org/10.1016/j.iatssr.2021.02.004

De Oliveira, A. L., Petroianu, A., Gonçalves, D. M. V., Pereira, G. A., & Alberti, L. R. (2015). Characteristics of motorcyclists involved in accidents between motorcycles and automobiles. *Revista Da Associacao Medica Brasileira*, 61(1), 61–64. https://doi.org/10.1590/1806-9282.61.01.061

Donald, S. (2015). Your chi-square test is statistically significant: Now what? *Practical Assessment, Research and Evaluation*, 20(8), 1–10.

Ebnali, M., Fathi, R., Lamb, R., Pourfalatoun, S., & Motamedi, S. (2020). Using augmented holographic UIs to communicate automation reliability in partially automated driving. *AutomationXP@CHI*.

Eluru, N., Bagheri, M., Miranda-Moreno, L. F., & Fu, L. (2012). A latent class modeling approach for identifying vehicle driver injury severity factors at highway-railway crossings. *Accident Analysis & Prevention*, 47, 119–127. https://doi.org/10.1016/j.aap.2012.01.027

Eustace, D., Indupuru, V. K., & Hovey, P. (2011). Identification of risk factors associated with motorcycle-related fatalities in Ohio. *Journal of Transportation Engineering*, 137(7), 474–480. https://doi.org/10.1061/(ASCE)TE.1943-5436.0000229

Farid, A., & Ksaibati, K. (2021). Modeling severities of motorcycle crashes using random parameters. *Journal of Traffic and Transportation Engineering*, 8(2), 225–236. https://doi.org/10.1016/j.jtte.2020.01.001

Fountas, G., & Anastasopoulos, P. C. (2017). A random thresholds random parameters hierarchical ordered probit analysis of highway accident injury-severities. *Analytic Methods in Accident Research*, 15, 1–16. https://doi.org/10.1016/j.amar.2017.03.002

Fountas, G., Fonzone, A., Olowosegun, A., & McTigue, C. (2021). Addressing unobserved heterogeneity in the analysis of bicycle crash injuries in Scotland: A correlated random parameters ordered probit approach with heterogeneity in means. *Analytic Methods in Accident Research*, 32, 100181. https://doi.org/10.1016/j.amar.2021.100181

Geedipally, S. R., Turner, P. A., & Patil, S. (2011). Analysis of motorcycle crashes in Texas with multinomial logit model. *Transportation Research Record*, 2265, 62–69. https://doi.org/10.3141/2265-07

Halbersberg, D., & Lerner, B. (2019). Young driver fatal motorcycle accident analysis by jointly maximizing accuracy and information. *Accident Analysis and Prevention*, 129, 350–361. https://doi.org/10.1016/j.aap.2019.04.016

Haque, M., Chin, H. C., & Debnath, A. K. (2012). An investigation on multi-vehicle motorcycle crashes using log-linear models. *Safety Science*, 50(2), 352–362.

Haque, M. M., Chin, H. C., & Huang, H. (2009). Modeling fault among motorcyclists involved in crashes. *Accident Analysis & Prevention*, 41(2), 327–335. https://doi.org/10.1016/j.aap.2008.12.010

Holdridge, J. M., Shankar, V. N., & Ulfarsson, G. F. (2005). The crash severity impacts of fixed roadside objects. *Journal of Safety Research*, 36(2), 139–147. https://doi.org/10.1016/j.jsr.2004.12.005

IRNA. (2021). Occupation of motorcyclists. Islamic Republic News Agency. Retrieved from https://www.irna.ir/news

Islam, M. (2021). The effect of motorcyclists' age on injury severities in single-motorcycle crashes with unobserved heterogeneity. *Journal of Safety Research*, 77, 125–138. https://doi.org/10.1016/j.jsr.2021.02.010

Islam, M. (2022). An analysis of motorcyclists' injury severities in work-zone crashes with unobserved heterogeneity. *IATSS Research*. https://doi.org/10.1016/j.iatssr.2022.01.003

Jones, S., Gurupackiam, S., & Walsh, J. (2013). Factors influencing the severity of crashes caused by motorcyclists: Analysis of data from Alabama. *Journal of Transportation Engineering*, 139(9), 949–956. https://doi.org/10.1061/(ASCE)TE.1943-5436.0000570

Kashani, A. T., Besharati, M. M., & Mohamadian, A. (2017). Analyzing motorcycle crash pattern and riders' fault status at a national level: A case study from Iran. *International Journal of Transportation Engineering*, 5(1), 87–101.

Keng, S.-H. (2005). Helmet use and motorcycle fatalities in Taiwan. *Accident Analysis & Prevention*, 37(2), 349–355. https://doi.org/10.1016/j.aap.2004.09.006

Khattak, A. J., Pawlovich, M. D., Souleyrette, R. R., & Hallmark, S. L. (2002). Factors related to more severe older driver traffic crash injuries. *Journal of Transportation Engineering*, 128(3), 243–249.

Lee, C., & Abdel-Aty, M. (2008). Presence of passengers: Does it increase or reduce driver's crash potential? *Accident Analysis & Prevention*, 40(5), 1703–1712. https://doi.org/10.1016/j.aap.2008.06.006

Lin, M. R., Chang, S. H., Huang, W., Hwang, H. F., & Pai, L. (2003). Factors associated with severity of motorcycle injuries among young adult riders. *Annals of Emergency Medicine*, 41(6), 783–791. https://doi.org/10.1067/mem.2003.186

Lin, M. R., & Kraus, J. F. (2009). A review of risk factors and patterns of motorcycle injuries. *Accident Analysis and Prevention*, 41(4), 710–722. https://doi.org/10.1016/j.aap.2009.03.010

Mahmud, M. S., Gupta, N., Safaei, B., Jashami, H., Gates, T. J., Savolainen, P. T., & Kassens-Noor, E. (2021). Evaluating the impacts of speed limit increases on rural two-lane highways using quantile regression. *Transportation Research Record*, 2675(11), 740–753. https://doi.org/10.1177/03611981211019732

Mannering, F. L., & Bhat, C. R. (2014). Analytic methods in accident research: Methodological frontier and future directions. *Analytic Methods in Accident Research*, 1, 1–22. https://doi.org/10.1016/j.amar.2013.09.001

Mannering, F. L., Shankar, V., & Bhat, C. R. (2016). Unobserved heterogeneity and the statistical analysis of highway accident data. *Analytic Methods in Accident Research*, 11, 1–16. https://doi.org/10.1016/j.amar.2016.04.001

Marizwan, M., Manan, A., Várhelyi, A., Kemal, A., & Hanis, H. (2018). Road characteristics and environment factors associated with motorcycle fatal crashes in Malaysia. *IATSS Research*, 42(4), 207–220. https://doi.org/10.1016/j.iatssr.2017.11.001

Morgan, A., & Mannering, F. L. (2011). The effects of road-surface conditions, age, and gender on driver-injury severities. *Accident Analysis & Prevention*, 43(5), 1852–1863. https://doi.org/10.1016/j.aap.2011.04.024

National Highway Traffic Safety Administration. (2020). Motorcycle helmet use in 2019 - Overall results. U.S. Department of Transportation.

Oginni, F. O., Ajike, S. O., Obuekwe, O. N., & Fasola, O. (2009). A prospective multicenter study of injury profile, severity and risk factors in 221 motorcycle-injured Nigerian maxillofacial patients. *Traffic Injury Prevention*, 10(1), 70–75. https://doi.org/10.1080/15389580802496968

Omranian, E., Sharif, H., Dessouky, S., & Weissmann, J. (2018). Exploring rainfall impacts on the crash risk on Texas roadways: A crash-based matched-pairs analysis approach. *Accident Analysis & Prevention*, 117, 10–20. https://doi.org/10.1016/j.aap.2018.03.030

Oxley, J., Ravi, M. D., Yuen, J., Hoareau, E., & Hashim, H. H. (2013). Identifying contributing factors to fatal and serious injury motorcycle collisions involving children in Malaysia. *Annals of Advances in Automotive Medicine*, 57, 329–336.

Iamtrakul, P., Hokao, K., & Tanaboriboon, Y. (2003). Analysis of motorcycle accidents in developing countries: A case study of Khon Kaen, Thailand. *Journal of the Eastern Asia Society for Transportation Studies*, 5, 147–162.

Pai, C.-W., Hwang, K. P., & Saleh, W. (2009). A mixed logit analysis of motorists' right-of-way violation in motorcycle accidents at priority T-junctions. *Accident Analysis & Prevention*, 41(3), 565–573. https://doi.org/10.1016/j.aap.2009.02.007

Patil, S., Geedipally, S. R., & Lord, D. (2012). Analysis of crash severities using nested logit model—Accounting for the underreporting of crashes. *Accident Analysis & Prevention*, 45, 646–653. https://doi.org/10.1016/j.aap.2011.09.034

Pervez, A., Lee, J., & Huang, H. (2021). Identifying factors contributing to the motorcycle crash severity in Pakistan. *Journal of Advanced Transportation*, 2021. https://doi.org/10.1155/2021/6636130

Prato, C. G., Kaplan, S., Patrier, A., & Rasmussen, T. K. (2018). Considering built environment and spatial correlation in modeling pedestrian injury severity. *Traffic Injury Prevention*, 19(1), 88–93. https://doi.org/10.1080/15389588.2017.1329535

Quddus, M. A., Noland, R. B., & Chin, H. C. (2002). An analysis of motorcycle injury and vehicle damage severity using ordered probit models. *Journal of Safety Research*, 33(4), 445–462. https://doi.org/10.1016/S0022-4375(02)00051-8

Radin Umar, R. S. (2006). Motorcycle safety programmes in Malaysia: How effective are they? *International Journal of Injury Control and Safety Promotion*, 13(2), 71–79. https://doi.org/10.1080/17457300500249632

Rahimi, E., Shamshiripour, A., Samimi, A., & Kouros, A. (2020). Investigating the injury severity of single-vehicle truck crashes in a developing country. *Accident Analysis & Prevention*, 137, 105444. https://doi.org/10.1016/j.aap.2020.105444

Rifaat, S. M., Tay, R., & De Barros, A. (2012). Severity of motorcycle crashes in Calgary. *Accident Analysis & Prevention*, 49, 44–49. https://doi.org/10.1016/j.aap.2011.02.025

Rowden, P., Steinhardt, D., & Sheehan, M. (2008). Road crashes involving animals in Australia. *Accident Analysis & Prevention*, 40(6), 1865–1871. https://doi.org/10.1016/j.aap.2008.08.002

Rutledge, R., & Stutts, J. (1993). The association of helmet use with the outcome of motorcycle crash injury when controlling for crash/injury severity. *Accident Analysis & Prevention*, 25(3), 347–353. https://doi.org/10.1016/0001-4575(93)90028-U

Salum, J. H., Kitali, A. E., Bwire, H., Sando, T., & Alluri, P. (2019). Severity of motorcycle crashes in Dar es Salaam, Tanzania. *Traffic Injury Prevention*, 20(2), 189–195. https://doi.org/10.1080/15389588.2018.1544706

Savolainen, P., & Mannering, F. (2007). Probabilistic models of motorcyclists' injury severities in single- and multi-vehicle crashes. *Accident Analysis & Prevention*, 39(5), 955–963. https://doi.org/10.1016/j.aap.2006.12.016

Schneider, W. H., Savolainen, P. T., Van Boxel, D., & Beverley, R. (2012). Examination of factors determining fault in two-vehicle motorcycle crashes. *Accident Analysis & Prevention*, 45, 669–676. https://doi.org/10.1016/j.aap.2011.09.037

Shaheed, M. S., & Gkritza, K. (2014). A latent class analysis of single-vehicle motorcycle crash severity outcomes. *Analytic Methods in Accident Research*, 2, 30–38. https://doi.org/10.1016/j.amar.2014.03.002

Shajith, S. L. A., Pasindu, H. R., & Ranawaka, R. K. T. K. (2019). Evaluating the risk factors in fatal accidents involving motorcycles: A case study on motorcycle accidents in Sri Lanka. *Engineer: Journal of the Institution of Engineers, Sri Lanka*, 52(3), 33. https://doi.org/10.4038/engineer.v52i3.7363

Shaker, R. H., Eldesouky, R. S., Hasan, O. M., & Bayomy, H. (2014). Motorcycle crashes: Attitudes of motorcyclists regarding riders' experience and safety measures. *Journal of Community Health*, 39(6), 1222–1230. https://doi.org/10.1007/s10900-014-9883-1

Shankar, V., & Mannering, F. (1996). An exploratory multinomial logit analysis of single-vehicle motorcycle accident severity. *Journal of Safety Research*, 27(3), 183–194. https://doi.org/10.1016/0022-4375(96)00010-2

Sohrabi, S., Khodadadi, A., Mousavi, S. M., Dadashova, B., & Lord, D. (2021). Quantifying the automated vehicle safety performance: A scoping review of the literature, evaluation of methods, and directions for future research. *Accident Analysis & Prevention*, 152, 106003. https://doi.org/10.1016/j.aap.2021.106003

Solagberu, B. A., Ofoegbu, C. K. P., Nasir, A. A., Ogundipe, O. K., Adekanye, A. O., & Abdur-Rahman, L. O. (2006). Motorcycle injuries in a developing country and the vulnerability of riders, passengers, and pedestrians. *Injury Prevention*, 12(4), 266–268. https://doi.org/10.1136/ip.2005.011221

Tay, R., Choi, J., Kattan, L., & Khan, A. (2011). A multinomial logit model of pedestrian–vehicle crash severity. *International Journal of Sustainable Transportation*, 5(4), 233–249. https://doi.org/10.1080/15568318.2010.497547

Xie, Y., Zhao, K., & Huynh, N. (2012). Analysis of driver injury severity in rural single-vehicle crashes. *Accident Analysis & Prevention*, 47, 36–44. https://doi.org/10.1016/j.aap.2011.12.012

Yasmin, S., & Eluru, N. (2013). Evaluating alternate discrete outcome frameworks for modeling crash injury severity. *Accident Analysis & Prevention*, 59, 506–521. https://doi.org/10.1016/j.aap.2013.06.040

Ye, F., & Lord, D. (2014). Comparing three commonly used crash severity models on sample size requirements: Multinomial logit, ordered probit, and mixed logit models. *Analytic Methods in Accident Research*, 1, 72–85. https://doi.org/10.1016/j.amar.2013.03.001

Yingfeng, L., & Yong, B. (2009). Highway work zone risk factors and their impact on crash severity. *Journal of Transportation Engineering*, 135(10), 694–701. https://doi.org/10.1061/(ASCE)TE.1943-5436.0000055

Zajac, S. S., & Ivan, J. N. (2003). Factors influencing injury severity of motor vehicle–crossing pedestrian crashes in rural Connecticut. *Accident Analysis & Prevention*, 35(3), 369–379. https://doi.org/10.1016/S0001-4575(02)00013-1

Zhu, X., & Srinivasan, S. (2011). A comprehensive analysis of factors influencing the injury severity of large-truck crashes. *Accident Analysis & Prevention*, 43(1), 49–57. https://doi.org/10.1016/j.aap.2010.07.007

Investigation of rheological properties of asphalt binder modified with TOBO additive

Hacer Yeşilçiçek*[1], Merve Gulfer Bozdemir[2], Seref Oruc[3]

[1*] Karadeniz Technical University, Technology Faculty, Department of Civil Engineering, 61080 Trabzon, Türkiye
[2] Erzurum Technical University, Faculty of Engineering and Architecture, Department of Civil Engineering, 25100 Erzurum, Türkiye
[3] Karadeniz Technical University, Faculty of Engineering, Department of Civil Engineering, 61080 Trabzon, Türkiye

Abstract. The need for bituminous binders is growing daily around the world as a result of the increased demand for transportation brought on by rising living standards, economic development, and population expansion. Significant factors include the depletion of bituminous binders, a byproduct of petroleum refining that are used in the paving layer, the fact that nearly all freight and passenger transportation is done via highways and that a significant portion of it is imported, the decline in all types of maintenance and repair expenses incurred for the paving layer from an economic standpoint, and the improvement of certain characteristics of the current paving layer material. The effects of the new synthesis TOBO additive, which was created by chemically synthesizing tall oil, a by-product of the paper industry, and boron compound, a strategic raw material for industry, on the rheological characteristics of bituminous binders at different temperatures were examined in this study. The rheological characteristics of the binders with additives were assessed using the frequency sweep test after 1% and 3% TOBO were added to the base asphalt binder. The unaged binders underwent frequency sweep tests with a frequency range of 0.1-100 rad/s and 31 frequency values, at test temperatures ranging from 10°C to 70°C (in increments of 10°C). The test results showed that adding TOBO additive to the base asphalt binder reduced the binder's complex modulus (G*) values. Additionally, the asphalt binders with additives behaved more rigidly and were more resistant to rutting, particularly at low frequencies, such as low vehicle speeds or stationary traffic. Every binder showed viscous behavior and comparable phase angle (δ) values. Nevertheless, the modified asphalt binders started to behave more elastically as the frequency value rose, and their phase angle value decreased more than that of the base asphalt binder. Consequently, it was found that the binders modified with TOBO performed better than the base asphalt binder in terms of rheological qualities.

Keywords: Asphalt; Modification; Boron oxide; Rheology

1. Introduction

With the swift expansion of highway networks caused by population growth, the demand for additives to strengthen asphalt binders as well as to maintain and repair asphalt pavements has gradually increased since the beginning. Meanwhile, the supply of refined crude oil for asphalt binder products is becoming increasingly scarce. As a result, to address the lack of raw materials and uncertainties in asphalt binders, experts have concentrated on the development of new generation and future research alternative additives (Colbert et al., 2016).

Researchers and professionals all around the worldwide utilize additives such as polymer-based materials (Li et. al., 2024, Arabani et. al., 2024, Yu et. al., 2023, Zhang et al., 2023, Huang et. al., 2025), rubber (Morea et. al., 2023, Zhang et. al., 2024, Ansari et. al., 2023), bio-oils (Liu et. al., 2025, Huo et al., 2024, Peng et al., 2023), different wastes (Ye et al., 2023, Feng et. al., 2025, Zhang et. al. 2023), waxes (Yuan et. al., 2024, Useche-Castelblanco et. al., 2023), and lastly nanomaterials (Arabani et. al., 2024, Kadhim et. al., 2024, Shafabakhsh et. al., 2020) as asphalt binders. A comprehensive literature study revealed that very few research used boron in asphalt modification (Oruç & Yılmaz, 2016, Oruç et. al., 2016, Oruç et. al., 2022, Yeşilçiçek et. al., 2022, Bozdemir et. al., 2023)

Boron oxide, a boron mineral component found in Turkey, which accounts for around 73% of the worldwide economy, had been used. According to the data gathered from the literature research and early examinations, adding boron oxide singly to the asphalt binder proved inefficient (Oruç & Yilmaz, 2016, Oruç et. al., 2016). Based

*Corresponding author, E-mail: haceryesilcicek@ktu.edu.tr

https://doi.org/10.31462/icearc2025_ce_tra_920

on this, the fact that pine forests constitute 60% of Turkey's wooded lands was reacted with boron oxide utilizing tall oil, a by-product of paper produce with a high quantity of unsaturated fatty acid. As a consequence, TOBO, a novel additive not previously available in the literature (Yeşilçiçek et. al., 2022), was developed using local resources, has a quick manufacturing process, is cheap in cost, and is fully ecologically friendly.

In this investigation, the previously obtained TOBO additive was applied to the asphalt binder at 0%, 1%, and 3% rates to carry out the modification process. To investigate the rheological characteristics of the modified binders, frequency sweep tests were performed across different kinds of temperatures and frequencies.

2. Materials and method

2.1.Materials

This investigation employed 50/70 penetration grade bitumen supplied by Turkish Petroleum Refinery. The characteristics of the base asphalt binder were established using standard test procedures, as indicated in Table 1.

Table 1. Physical properties of the asphalt binder.

Properties	Value	Standard
Penetration (25°C, dmm)	56	ASTM D5/D5M-13
Softening point (°C)	50	ASTM D36/D36M-14
Ductility (25°C, cm)	100 +	ASTM D113-17
Flash point (°C)	249	ASTM D92-18
Viscosity (135°C, cP)	500	ASTM D4402M-15
Viscosity (165°C, cP)	100	ASTM D4402M-15
Viscosity (180°C, cP)	50	ASTM D4402M-15

Previous research show that TOBO can be synthesized successfully in a laboratory setting (Yeşilçiçek et. al., 2022, Bozdemir et. al., 2023). The resulting TOBO additive was shown to have excellent extensibility. Furthermore, it was visually noted that it possessed the requisite homogeneity; the material transitioned from the liquid phase to the solid phase and remained solid at room temperature. Fig. 1 shows a representation of TOBO.

Fig. 1. Visual of the additive.

2.1.1. Preparation of modified asphalt binders

Before adding the TOBO, the base asphalt binder was heated at 150 °C until liquid. TOBO was applied to the asphalt binder at three different rates: 0%, 1%, and 3% of the asphalt weight. Based on promptly test findings and previously literature study [45, 50-53, 64-67], the modification method and ratios were determined to be a high-shear mixer with a rotation speed of 3000 rpm for 30 minutes. After this procedure was done, the modified asphalt binder was ready for testing. Table 2 outlines the description of the asphalt binders.

Table 2. The description of the asphalt binders

Sample content	Code
Asphalt Binder+ % 0 TOBO	BA
Asphalt Binder+ % 1 TOBO	BA1
Asphalt Binder+ % 3 TOBO	BA3

2.2. Method

2.2.1. Characterization of TOBO
TOBO's chemical structure was disclosed by FTIR study and its microstructure by SEM investigation.

2.2.2. Determination of rheological properties of modified binders
The frequency sweep test involves the oscillation of the material at different frequencies under constant strain. Since the frequency is based on the inverse of time, it is possible to evaluate the time-dependent viscoelastic character of a material by changing the oscillation frequency. Since these tests are performed in the linear viscoelastic region, microstructural fingerprinting of the material is provided without compromising the structural integrity (Airey, 2011, Akpolat, 2023).

The Malvern DSR rheometer was used to evaluate base and TOBO-added binders at 10°C increments in the temperature range of 10-70°C. The test was based on a prior research, which used two distinct temperature ranges and test geometries (Hu et. al., 2024). The test was conducted such that the bituminous binders stayed in the linear viscoelastic (LVE) zone. The frequency ranged from 0.1 to 100 rad/s, with 31 possible possibilities to determine. To replicate viscoelastic behavior throughout a large frequency range, master curves of the complex modulus (G*) and phase angle (δ) values were generated using the time-temperature superposition principle (TTSP) at 40°C as the reference temperature.

Within the scope of this research, frequency sweep tests were carried out on unaged binders at 31 various frequencies (0.1-100 rad/s) and 7 different temperatures (10 °C, 20 °C, 30 °C, 40 °C, 50 °C, 60 °C, and 70 °C).

3. Results and discussion

3.1. Structure of the TOBO
Infrared spectroscopy was employed to achieve chemical property changes in the TOBO's functional groups. . The FTIR spectra of TOBO are displayed in Fig. 2. Vinyl C=C-H bonds are detected at 2922 cm^{-1} in the TOBO spectrum, whereas aliphatic C-H tension bonds are found at 2853 cm^{-1}. In TOBO, the deformation bands of CH_3 and CH_2 peaks stay at 1455 cm^{-1} and 1376 cm^{-1}, respectively. The additive exhibits numerous carbonyl peaks (1704 cm^{-1} and 1735 cm^{-1}), while the C=O tension band shrinks significantly. The esteric carbonyl peak (O=C-O-C) in the FT-IR spectrum at 1273 cm^{-1} becomes minor or vanishes in the produced TOBO molecule. This shows that there is an exact change in the ester function, implying that the intended additive was properly produced (Yeşilçiçek et. al., 2022).

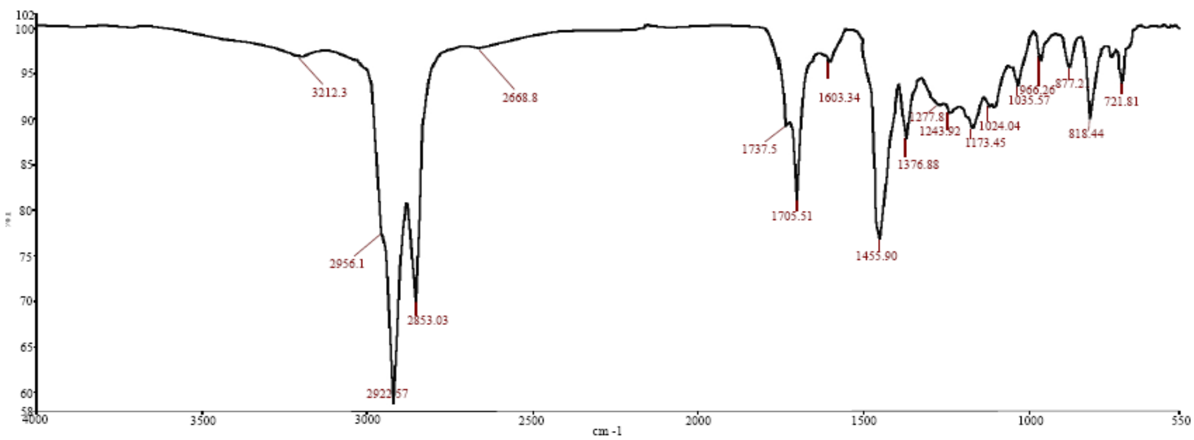

Fig. 2. FT-IR spectrum of TOBO (Yeşilçiçek et. al., 2022).

Fig. 3 displays SEM images of the TOBO additive at magnifications of 958 X (a) and 4.06 K (b). The surface of the tall oil matrix exhibits microscopic bubbles and droplet-like solidified formations, influencing its shape. These forms are believed to be boron oxide (Shadab et. al., 2023). These solid forms in TOBO material are defined as an increase in surface area that will interact with bitumen.

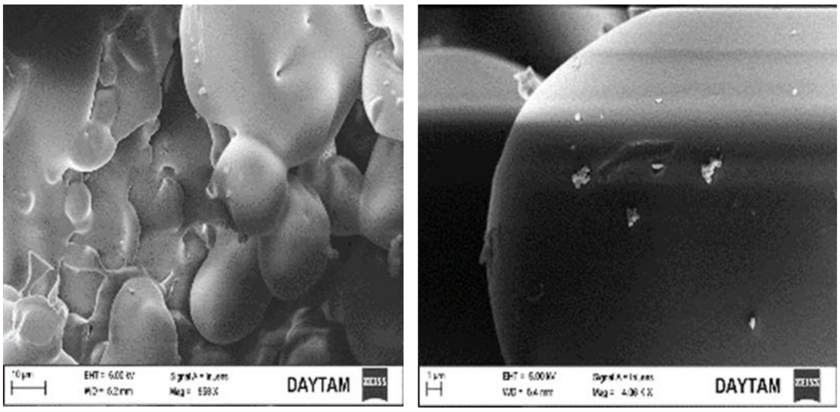

Fig. 3. SEM images of TOBO at different magnifications (Yeşilçiçek et. al., 2022).

3.2. Frequency sweep test results

Fig. 4 shows the change in the complex modulus of asphalt binders with 0%, 1%, and 3% TOBO at different temperatures with frequency, as well as the major curves of the binder with 0%, 1%, and 3% TOBO at 40°C for comparison. According to the figures, complex modulus decrease as temperature increases. Asphalt binders with additives exhibited greater complex modulus values than base asphalt binders at all frequencies and 40°C reference temperature.

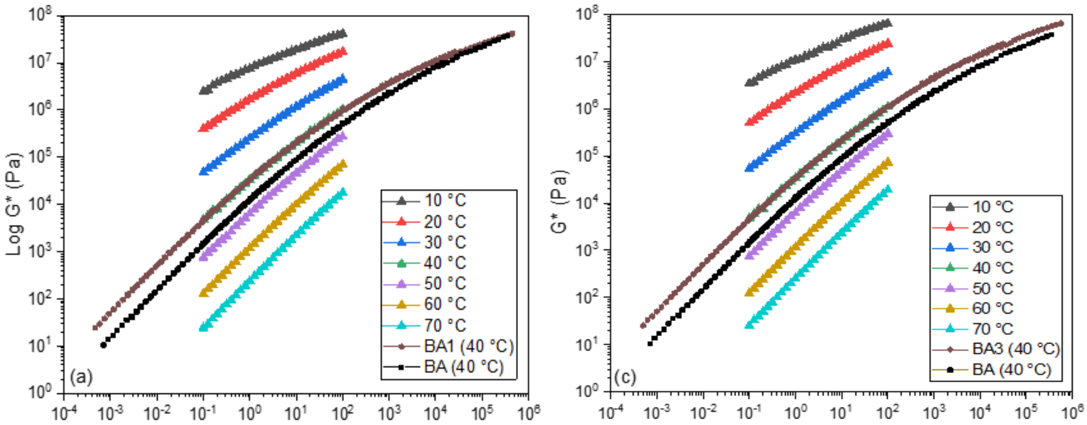

Fig. 4. Variation of complex modules at different temperatures with frequency.

Fig. 5 shows the main curves for all asphalt binders at the reference temperature of 40°C. The figure shows that asphalt binders with 1% and 3% TOBO with addittives have greater complex modulus values than base asphalt binders at all frequencies, indicating more rigid behavior. Asphalt binders with additions displayed more stiff behavior and were more resistant to rutting, particularly at low frequencies, such as low vehicle speeds or stationary traffic. As frequency grew, the complex G* values approached each other. It was discovered that the base asphalt binder had the lowest complex modulus value at all frequency levels. Using 3% additives resulted in the greatest complex modulus values.

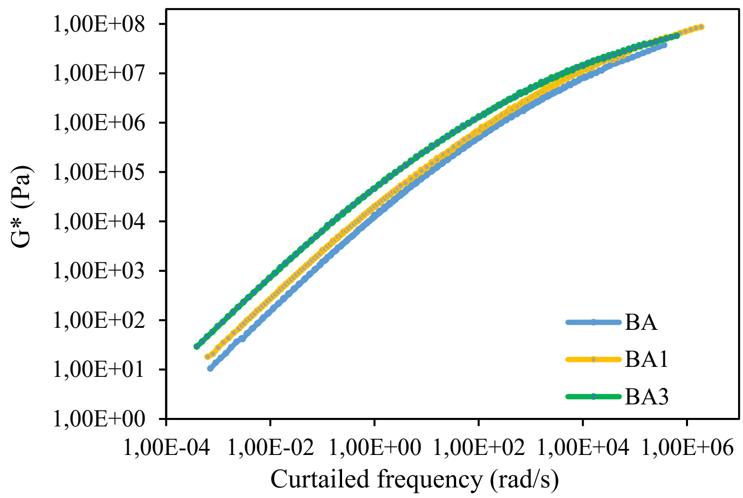

Fig. 5. G* master curves of asphalt binders at 40°C reference temperature.

Fig. 6 depicts how the phase angles of base and modified asphalt binders vary with frequency. As seen in the figure, at low frequencies (low vehicle speed or standstill traffic), all asphalt binders displayed viscous behavior, resulting in identical phase angles. However, when the frequency value grew, the modified binders' phase angle value decreased faster than the base asphalt binder's, and the modified asphalt binders began to behave more elastically.

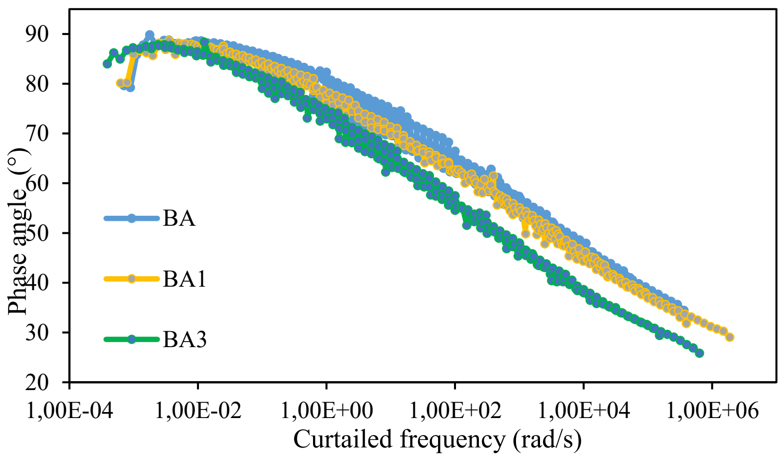

Fig. 6. Phase angle master curves of the connectors at a reference temperature of 40°C

The phase angle related to the complex shear modulus is shown by the Black space diagram (Figure 7). It defines the rheological characteristics of modified bitumens. It is used to assess the veracity of the displayed curve's distinctive time-temperature superposition as well as its simplicity in thermorheological terms (Qin et. al., 2015). In general, an increase in the elastic behavior of the asphalt binder is represented by a low complex modulus and a matching low phase angle value. All asphalt binders performed similarly.In comparison to the base asphalt binder, the rheological data of each modified bituminous binder changes towards the lower phase angle, showing the presence of a network in the additive-bitumen combination (in short, more elastic behavior). As seen in the picture, BA1 and BA3 asphalt binders displayed stronger elastic behavior, resulting in high complex modulus values, particularly at low phase angles. This demonstrates that 1% and 3% ratios will be beneficial in preventing rutting. At higher phase angle values, all binders performed similarly.

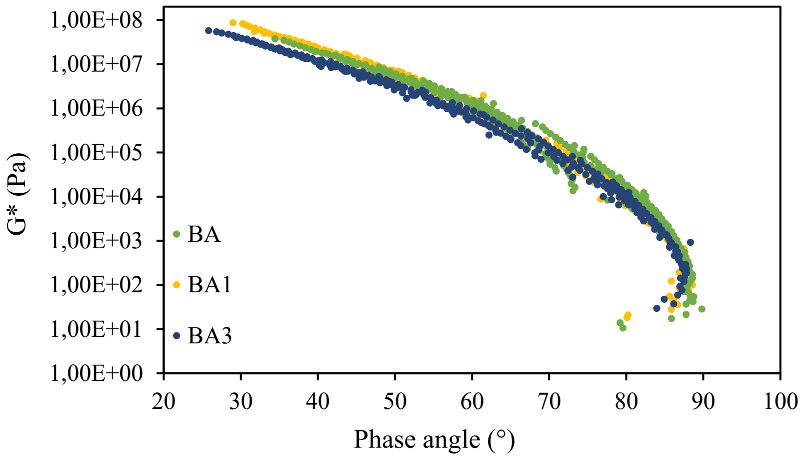

Fig. 7. Black space diagram.

4. Conclusions

The structural characterization of a TOBO additive produced under laboratory situations was the first stage in this investigation. Second, the rheological characteristics of modified binders utilized at certain ratios in bitumen modification were examined. The findings obtained are summarized as follows:

- The FTIR spectrum shows that the C=O tension band of the TOBO additive moves while the esteric carbonyl peak (O=C-O-C) diminishes, showing that the additive is chemically produced.
- When the SEM study is performed, it is discovered that the structure is primarily constituted of tall oil, with little bubbles forming on the surface. It is believed that these solidified forms are boron oxide, and the surface area that interacts with the bitumen rises.
- According to the frequency sweep test, asphalt binders with a high complex modulus and a low phase angle show stronger elastic behavior. This newly synthesized TOBO additive has been shown to have highly positive effects in rutting resistance at rates of 1% and 3%.

References

Airey, G. (2011). 8- Factors affecting the rheology of polymer modified bitumen (PMB). Editor(s): Tony McNally, In Woodhead Publishing Series in Civil and Structural Engineering, Polymer Modified Bitumen, Woodhead Publishing, 238-263.

Akpolat M. (2023). Investigation of the rheological properties of asphalt binders modified with nanomaterial, The European Journal of Research and Development, 3(1), 97-107.

Ansari, A.H., Jakarni, F.M., Muniandy, R., Hassim, S., Elahi, Z., & Mohamed Meftah Ben Zair, M.M.B. (2023). Mechanical performance of cup lump rubber modified asphalt mixtures incorporating polyphosphoric acid. Construction and Building Material, 408(8), 133625.

Arabani, M., Amiri, A., & Hassanjani, M.H. (2024). Utilizing olive pomace oil and the extrusion of SBS and PVC to enhance the physical and rheological characteristics of asphalt binder. Case Studies in Construction Materials, 21, e04097.

Arabani, M., Sadeghnejad, M., Haghanipour, J., & Hassanjani, M.H. (2024). The influence of rice bran oil and nano-calcium oxide into bitumen as sustainable modifiers. Case Studies in Construction Materials, 21, e03458.

Bozdemir, M. G., Oruc, Ş., & Yeşilçiçek, H., (2023). Physical and microstructural properties of new boron resin compound synthesized asphalt. Journal of Materials in Civil Engineering, 35(2).

Colbert, B., Mohd Hasan, M.R., & You, Z.P. (2016). A hybrid strategy in selecting diverse combinations of innovative sustainable materials for asphalt pavements, Journal of Traffic Transportation Engineering (English Edition) 3 (2), 89–103.

Feng, X., Fu, H., Dai, Z., & Li., W. (2025). Study on performance and microscopic mechanism of hydrogen peroxide treated waste crumb rubber modified asphalt. Journal of Traffic and Transportation Engineering (English Edition).

Hu, Y., Omairey, E., Hughes, D., Bailey, H., Watkins, M., Twitchen, J., Airey, G., D. & Anand Sreeram, A. (2024). Recovering the properties of aged bitumen using bio-rejuvenators derived from municipal wastes. Construction and Building Materials, 438, 137268.

Huang, T., Lin, B., Cao, Z., Yi, J., Yu, X., & Qian, G. (2025). Laboratory testing of road performance and mechanism study of SBR/APAO composite modified asphalt and its mixtures. Case Studies in Construction Materials, 22, e04525.

Huo, J., Zhang, X., Liu, F., Liu, Y., Niu, Y., Zhang, N., & Liu, P. (2024). Rejuvenation performance and mechanism of aged SBS modified asphalt rejuvenated by bio-oil based rejuvenators. Construction and Building Materials, 457, 139366.

Kadhim, H.J., Amir Modarres, A., & Al-Busaltan, S. (2024). Rheological and microstructural properties of nano-composite bitumen modified by nano-alumina and low-SBS content. Case Studies in Construction Materials, 20, e03244.

Li, Y., Li, J., Yang, H., Ye, Z., Hu, C. & Shen, S. (2024). Laboratory evaluation of synergistic blending with SBS-modified bitumen and rejuvenator to enhance the performance of recycled bitumen with a high content of RAP materials. Construction and Building Materials, 442, 137675.

Liu, C., Liao, X., Fan, G., Yang, Z., Qin, X., Jie Chen, J., & Lv, S. (2025). Utilization of bio-oil for separation of aged asphalt from reclaimed asphalt pavement: Mechanistic and experimental insights. Construction and Building Materials, 471, 140743.

Morea, F., Nosetti, R., Gonzalez, L., & Sánchez, A. (2023). Performance analysis of non-conventional Stone Mastic asphalt (SMA) elaborated with crumb rubber bitumen or by mean of glass macrofibers addition. Construction and Building Materials, 400, 132654.

Oruç, Ş., & Yilmaz, B., (2016). Improvement in performance properties of asphalt using a novel boron-containing additive. Construction and Building Materials, 123, 207-213.

Oruç, Ş., Yılmaz, B., & Sancak, K., (2016). Effect of boron-containing additives on rheological properties of asphalt binder. Road Materials and Pavement Design , 17(4), 810-824.

Oruç, Ş., Yılmaz, B., & Sancak, K., (2022). Characterization and rheological behavior of asphalt binder modified by a novel cyclic borate ester additive. Construction and Building Materials ,348

Peng, X., Xie, N., Xia, C., Zhou, X., Zhao, P., Ma, S., Zhang, C., & Lv, S. (2024). Laboratory evaluation of different bio-oil recycled aged asphalts: Conventional performances and microscopic characteristics. Journal of Cleaner Production, 428, 139442.

Qin, Q., Farrar, M., Turner, T. F. & Planche, J. (2015). Technical white paper characterization of the effects of wax (Sasobit ®) on asphalt binder, Fundamental Properties of Asphalts and Modified Asphalts III Product: FP 13 By.

Shadab, M., Jirsa, M. & Miryala, M. (2023). Tuning of superconductivity of bulk MgB_2 by ball milling and sieving the boron precursor, Materials Chemistry and Physics, 309, 128348.

Shafabakhsh, G.A., Sadeghnejad, M., Ahoor, B., & Taher, E. (2020). Laboratory experiment on the effect of nano SiO2 and TiO2 on short and long-term aging behavior of bitumen. Construction and Building Materials, 237, 117640.

Useche-Castelblanco, J.S., Reyes-Ortiz, O.J., & Alvarez, A.E. (2023). Application of machine learning models for prediction of rheological properties of wax-modified asphalt binders. Construction and Building Materials, 395, 132352.

Ye, X., Xia, Z., He, C., Li, W., Lin, P., Meng, Y., & Hu, C. (2023). Roles of waste carbon fibers on the efficiency of multiple induction heating healing behavior in asphalt mixture for sustainable infrastructure. Journal of Cleaner Production, 423, 138694.

Yeşilçiçek, H., Oruç, Ş., & Gülfer Bozdemir, M., (2022). Characterization and rheological properties of asphalt binder with a novel tall oil-based boron additive to enhance asphalt performance. Construction and Building Materials , 359.

Yu, D., Yang, E., Zhang, M., Zhang, H., Chen, G., Di, H., Huang, B., & Qiu, Y. (2023). Chemical modification of sustainable bagasse fiber and its absorption mechanism on SBS-modified emulsified bitumen, Construction and Building Materials, 133983.

Yuan, H., Liu, J., Ding, H., Xie, Q., & Qiu, Y. (2024). Evaluation of physical hardening of wax-based warm mix asphalt binders from low-temperature rheological properties. Construction and Building Materials, 419, 135496.

Zhang, H., Ren, S., & Qiu, Y. (2023). Balancing the sustainable component of ethylene-vinyl acetate for achieved better compatibility improvement of wax-based warm mix additives in bitumen. Colloids and Surfaces A: Physicochemical and Engineering Aspects, 675, 132054.

Zhang, J., Cao, W., Li, W., Lou, S., Zhang, W., Hou, Z. (2024). Performance assessment of composite modified bitumen integrated with desulfurized crumb rubber and SBS modifier as waterproofing adhesive layer. International Journal of Adhesion and Adhesives, 134, 103802.

Zhang, J., Chen, M., Wu, S., Chen, D., Zhao, Y., & Zhou, X. (2023). Characteristics of waste dry battery powder and its enhancement effect on the physicochemical properties of asphalt binder. Journal of Cleaner Production, 426, 139090.

4th International Civil Engineering & Architecture Conference
17-19 May 2025, Trabzon, Türkiye

Examining the link between property development and transportation infrastructure

Ilgin Gokasar*[1], Mahmut G. Tülü[1], Volkan Yıldız[1]

[1] *Bogazici University, Department of Civil Engineering, 34342 İstanbul, Türkiye*

Abstract. As cities continue to expand, access to public transportation can play a crucial role in advancing sustainable urban growth and enhancing overall quality of life. In this context, transportation is one of the fundamental criteria that boost the real estate prices. Numerous studies have explored the relationship between transportation investments and real estate markets, highlighting the share of public transportation in shaping urban property values. The studies in the literature suggests that access to efficient public transport could increase economic growth, reduce commuter costs, and enhance urban mobility, making surrounding areas more attractive for both residents and investors. Research further emphasizes that improvements in public transportation networks contribute to rising property values by increasing accessibility, reducing travel time, and stimulating commercial activity. While previous studies have identified key elements of real estate values such as property size, age, location and amenities. This research integrates these factors with a specific focus on public transportation access. Closeness to transportation hubs such as metro stations, bus rapid transit lines, or railway connections, has been shown to have a positive effect on property prices, particularly in densely populated urban centers. A comparative analysis of the literature provides a clearer understanding of how access to public transportation interacts with traditional real estate valuation factors, such as property size, age, location, and amenities. Beyond serving as an academic contribution, this study also offers practical value by enhancing decision-making for real estate professionals and acting as a reference for policymakers in urban planning and transportation investment strategies.

Keywords: Real estate pricing; Transportation; Public transportation; Accessibility

1. Introduction

Since the middle of the 20th century, the world's population has grown by more than three times. With an extra 1 billion people since 2010 and 2 billion since 1998, the world's population increased from an estimated 2.5 billion in 1950 to 8.0 billion in mid-November 2022. Furthermore, 55% of people on Earth already live in cities, and by 2050, that percentage is expected to increase to 68% (United Nations, 2018). Many nations will face difficulties meeting the growing demands of urban populations for housing, infrastructure, employment, and essential services. Without strategic planning and timely investments, many nations may struggle to meet these expanding demands. Consequently, urban development could create an array of complex and multifaceted challenges for cities (McHale et al., 2015). In this context, sustainable urbanization is no longer just an ideal, it has become a pressing necessity for ensuring long-term economic stability, social well-being, and environmental sustainability. As cities grow at an unprecedented pace, there is an urgent need for thoughtful planning strategies that can accommodate rising populations while preserving quality of life.

One of the most critical strategies in achieving sustainable urbanization is the development of efficient public transportation systems. Ensuring the long-term effectiveness and appeal of these systems requires continuous evaluation and improvement. Since businesses must constantly enhance their performance to draw in more customers while planning and providing services in a highly competitive market with limited resources, performance measurement is becoming increasingly popular in the public transportation sector (Georgiadis et al., 2014). As cities grow denser, access to transit becomes a key factor not only in shaping mobility patterns and urban form but also in influencing real estate values. Properties located near transportation hubs often become more desirable due to improved accessibility and reduced travel times, leading to increased demand and higher property prices. Understanding this relationship is essential for managing the spatial and economic outcomes of rapid urban growth.

This study aims to explore in greater depth how access to public transportation influences property values in urban settings. By focusing on this specific relationship, it seeks to uncover the dynamics at play and offer detailed

* Corresponding author, E-mail: ilgin.gokasar@bogazici.edu.tr

https://doi.org/10.31462/icearc2025_ce_tra_948

insights that can support more informed decision-making among policymakers, urban planners, and real estate professionals.

2. Literature review

The literature has a large number of research that look at the factors influencing the real estate market. Because there are so many variables to consider, estimating real estate values has always been a difficult task for scholars. Numerous factors, including infrastructure, immigration, economic stability, social amenities, and demographics, can affect real estate values.

First of all, age distribution and social cohesiveness are two demographic characteristics that might boost economic vitality and raise real estate prices (DellaVigna & Pollet, 2007). For example, future realized excess returns on equities will be little as the baby boom generation retires and moves out of the middle-aged, peak-saving years (Ang & Maddaloni, 2005). In addition, those who live in financial instability throughout their life are more cautious when it comes to investing as a direct result of dramatic occurrences like the Great Depression (Malmendier & Nagel, 2011).

Furthermore, it is acknowledged that economic factors have a significant impact on the real estate market. The real estate market generally exhibits a cyclical pattern characterized by booms, or periods of sharp price increases, which are frequently followed by downturns, in which property values sharply decrease (Smith & Tesarek, 1991). Although well-known economic variables like employment rates and income levels are important, research also suggests that there are other, more subtle economic forces at work. According to Li & Chu (2017) bankers and investors have a substantial impact on Taiwanese market trends through their lending and investment methods, which in turn affects real estate values.

Moreover, according to analytical frameworks, factors such as firm production amenities, worker and household accessibility, legal growth restrictions, and land supply conditions influence long-term office and commercial space rents, with transportation access playing a crucial role in shaping these dynamics (Franco & Cutter, 2022). Besides, findings indicate that the price of real estate is influenced economically by features from various dimensions such as amenities and emotions (Zhao et al., 2022).

Also, environmental factors are yet another crucial component. In addition to the natural beauty, a number of environmental concerns are linked to land use, which means they have an impact on land markets and real estate (Segerson, 2001). According to study conducted in Geneva, Switzerland, environmental quality such as air quality and the presence of green spaces is a major influencer of real estate market success (Din et al., 2001).

In addition, the suburban real estate market is driven by rising demand for construction sites, with property prices mainly influenced by proximity to the city and strong transport links, which notably raise values (Szczepańska, 2021). As cities expand toward their boundaries, nearby suburban areas face increased investment demand, and this process of suburbanization is closely tied to the accessibility provided by transportation networks (Wolny, 2016).

From a similar but different perspective, immigration is another underlooked component of real estate market. Examining how immigration affects real estate markets provides clear insights into the social and economic ramifications of immigration, even though the majority of the literature on immigration concentrates on labor market implications (Scheve & Slaughter, 2004). Although it is commonly believed that immigration to wealthy, established cities raises real estate values, this is not always the case. For instance, an analysis of Miami's rental prices showed a negative relationship between the city's immigration rate and rental prices (Saiz, 2007).

Among the various factors influencing real estate markets, transportation access emerges as a key component also. Although mentioned in broader urban development literature, its direct relationship with property values warrants deeper investigation. Therefore, in the following section, the connection between transportation investments and real estate will be examined in greater detail.

3. Transportation and real estate

Property values are influenced by a number of significant factors, including location demands like accessibility to public transportation (Haider & Miller, 2000). The relationship between transportation infrastructure and real estate markets is a critical dimension of urban development and expansion (Debrezion et al., 2011; Efthymiou & Antoniou, 2013). Transportation systems not only serve as conduits for mobility but also act as catalysts for shaping land use, urban form, and economic activity. Researches have demonstrated that transportation infrastructure in cities and metropolises significantly improves socioeconomic daily activities, individual lifestyles, real estate values, and urban land usage (Aliyu et al., 2018). As cities expand and population densities rise, the spatial relationship between transit accessibility and property values becomes increasingly pronounced.

Public transportation investments such as metro lines, bus stops and rail connections tend to enhance the desirability of nearby locations. For example, it is revealed that impact of bus transportation accessibility on real estate prices showed a positive trend in a Spain-based research (Ibeas et al., 2012). Likewise, it was anticipated that rail transportation would have positive effects if the surrounding area's accessibility and appeal were enhanced (Suhaimi et al., 2021). What’s more, properties within close proximity to major transit hubs often provide higher market values due to increased accessibility, reduced commute times. The reason behind is the fact that Mass transit serves as a primary mode of transportation in many urban areas, and improving access to main transit hubs can enhance city mobility by easing transfers between different modes (Yu et al., 2012, 2013).

From a supply-demand perspective, improved transit access broadens the geographic reach of potential buyers and tenants, thereby intensifying competition for conveniently located properties. In the USA, rent plays a crucial role in property valuation and development decisions, as it reflects economic feasibility, with mobility especially proximity to workplaces or central locations being a key factor influencing rent and shaping urban growth (Benjamin & Sirmans, 1996). On the demand side, individuals and households may be willing to pay a premium for the convenience and cost savings associated with reduced reliance on private vehicles. On the supply side, landowners and developers may respond by intensifying land use near transit corridors, further reinforcing the cycle of investment and value appreciation. To improve both sides, by entering into agreements with transportation corporations, real estate developers may either construct residential properties close to public transit or introduce public transportation into their neighborhood (Wang & Yan, 2011).

Moreover, fixed-guideway transit systems play a key role in reinforcing agglomeration economies, essential drivers of urban economic development, by reducing automobile dependency and enhancing connectivity, thereby unlocking the full potential of densely concentrated economic activity and supporting more sustainable metropolitan growth (Nelson, 2017). At the same time, transportation investments often signal broader governmental commitments to urban revitalization and infrastructure renewal, prompting speculative activity in real estate markets; as a result, perceptions of future accessibility can shape property values and trigger anticipatory shifts in urban form and land use even before construction begins. All things considered, transportation infrastructure serves as both a physical link between locations and a source of income for the real estate market.

3. Policy implications

The findings of this study highlight the strategic importance of integrating transportation planning with real estate development. Policymakers should recognize that investments in public transportation do not only serve mobility goals but also significantly influence urban land values and development patterns. Proximity to well-connected transit hubs increases the attractiveness of surrounding areas, which can guide zoning decisions, infrastructure prioritization, and housing policies.

To maximize the benefits of public transport investments, coordinated planning efforts between transportation authorities, urban planners, and local governments are essential. Using real estate market data in evaluating transit projects can help align mobility improvements with sustainable urban growth objectives. In this way, transportation infrastructure can be leveraged not only to enhance accessibility but also to support long-term goals for livability, economic resilience, and inclusive development. Special attention should also be given to suburban areas, where improved transit access can help manage urban sprawl, reduce car dependency, and promote more balanced regional development.

4. Conclusions

This study examined the connection between public transportation investments and real estate values within the context of rapid urbanization. As cities grow, access to efficient transit systems plays a key role in shaping land use, improving mobility, and enhancing property values. The literature shows that while many factors influence real estate markets, transportation access remains a consistent and powerful driver of value.

Efforts to measure and improve public transport performance further support sustainable urban development by making transit systems more efficient and appealing. Understanding this relationship is essential for policymakers, planners, and stakeholders aiming to create livable, resilient, and well-connected urban environments.

While this study provides valuable insights into the relationship between transportation and real estate, it does not include empirical data or case-specific analysis. Additionally, regional variations, regulatory frameworks, and socio-economic conditions may influence outcomes in ways that are not fully captured here.

Future research could incorporate quantitative methods and spatial data analysis to measure the real-world impacts of transit investments on property values. Comparative studies across different cities or countries would also help clarify how local context shapes the strength and direction of this relationship. Further investigation into equity impacts and the role of transit in shaping affordable housing access would also be valuable in guiding inclusive urban development strategies.

References

Aliyu, A.A., Kemiki, O.A., & Bello, M.U. (2018). Transportation accessibility benefit and the dynamic pattern of real estate prices: emerging literature. *Traektoriâ Nauki = Path of Science, 4*. https://doi.org/10.22178/pos.40-5

Ang, A., & Maddaloni, A. (2005). Do demographic changes affect risk premiums? Evidence from international data. *Journal of Business, 78*(1), 341–379. https://doi.org/10.1086/426528

Benjamin, J., & Sirmans, G.S. (1996). Mass transportation, apartment rent and property values. *Journal of Real Estate Research, 12*(1), 1–8. https://doi.org/10.1080/10835547.1996.12090830
Debrezion, G., Pels, E., & Rietveld, P. (2011). The impact of rail transport on real estate prices: An empirical analysis of the Dutch housing market. *Urban Studies, 48*(5), 997–1015. https://doi.org/10.1177/0042098010371395
DellaVigna, S., & Pollet, J.M. (2007). Demographics and ındustry returns. *The American Economic Review, 97*, 1667–1702. https://www.jstor.org/stable/30034580?seq=1
Din, A., Hoesli, M., & Bender, A. (2001). Environmental variables and real estate prices. *Urban Studies, 38*(11), 1989–2000. https://doi.org/10.1080/00420980120080899
Efthymiou, D., & Antoniou, C. (2013). How do transport infrastructure and policies affect house prices and rents? Evidence from Athens, Greece. *Transportation Research Part A: Policy and Practice, 52*, 1–22. https://doi.org/10.1016/J.TRA.2013.04.002
Franco, S.F., & Cutter, W.B. (2022). The determinants of non-residential real estate values with special reference to environmental local amenities. *Ecological Economics, 201*, 107485. https://doi.org/10.1016/J.ECOLECON.2022.107485
Georgiadis, G., Politis, I., & Papaioannou, P. (2014). Measuring and improving the efficiency and effectiveness of bus public transport systems. *Research in Transportation Economics, 48*, 84–91. https://doi.org/10.1016/J.RETREC.2014.09.035
Haider, M., & Miller, E.J. (2000). Effects of Transportation Infrastructure and Location on Residential Real Estate Values: Application of Spatial Autoregressive Techniques. *Transportation Research Record, 1722*, 1–8. https://doi.org/10.3141/1722-01
Ibeas, Á., Cordera, R., Dell'Olio, L., Coppola, P., & Dominguez, A. (2012). Modelling transport and real-estate values interactions in urban systems. *Journal of Transport Geography, 24*, 370–382. https://doi.org/10.1016/J.JTRANGEO.2012.04.012
Li, L., & Chu, K.H. (2017). Prediction of real estate price variation based on economic parameters. In *Proceedings of the 2017 IEEE International Conference on Applied System Innovation: Applied System Innovation for Modern Technology (ICASI 2017)* (pp. 87–90). https://doi.org/10.1109/ICASI.2017.7988353
Malmendier, U., & Nagel, S. (2011). Depression Babies: Do macroeconomic experiences affect risk taking? *The Quarterly Journal of Economics, 126*(1), 373–416. https://doi.org/10.1093/QJE/QJQ004
McHale, M.R., Pickett, S.T.A., Barbosa, O., Bunn, D.N., Cadenasso, M.L., Childers, D.L., ... & Zhou, W. (2015). The new global urban realm: Complex, connected, diffuse, and diverse social-ecological systems. *Sustainability, 7*(5), 5211–5240. https://doi.org/10.3390/SU7055211
Nelson, A.C. (2017). Transit and real estate rents. *Transportation Research Record, 2651*(1), 22–30. https://doi.org/10.3141/2651-03
Saiz, A. (2007). Immigration and housing rents in American cities. *Journal of Urban Economics, 61*(2), 345–371. https://doi.org/10.1016/J.JUE.2006.07.004
Scheve, K., & Slaughter, M.J. (2004). Economic ınsecurity and the globalization of production. *American Journal of Political Science, 48*(4), 662–674. https://doi.org/10.1111/J.0092-5853.2004.00094.X
Segerson, K. (2001). Real estate and the environment: An introduction. *The Journal of Real Estate Finance and Economics, 22*(2), 135–139. https://doi.org/10.1023/A:1007821311507
Smith, B.A., & Tesarek, W.P. (1991). House prices and regional real estate cycles: Market adjustments in Houston. *Real Estate Economics, 19*(3), 396–416. https://doi.org/10.1111/1540-6229.00559
Suhaimi, N.A., Adi Maimun, N.H., & Sa'at, N.F. (2021). Does rail transport ımpact house prices and rents? *Planning Malaysia, 19*(2), 141–149. https://www.planningmalaysia.org/index.php/pmj/article/view/959/664
Szczepańska, A. (2021). Transport accessibility in a Suburban Zone and ıts ınfluence on the local real estate market: A Case Study of the Olsztyn Functional Urban Area (Poland). *Land, 10*(5), 465. https://doi.org/10.3390/LAND10050465
United Nations. (2018). 68% of the world population projected to live in urban areas by 2050, says UN. https://www.un.org/uk/desa/68-world-population-projected-live-urban-areas-2050-says-un
Wang, X., & Yan, J. (2011). Analysis on public transportation influences on real estate development in East Lansing. *Geo-Spatial Information Science, 14*(1), 73–78. https://doi.org/10.1007/S11806-011-0433-Z
Wolny, A. (2016). Accessibility of Real Estate by Transportation as a Determinant of the Development of Suburban Real Estate Markets-Case Study. *Real Estate Management and Valuation, 24*(1), 5–18. https://doi.org/10.1515/remav-2016-0001
Yu, B., Yang, Z., & Li, S. (2012). Real-time partway deadheading strategy based on transit service reliability assessment. *Transportation Research Part A: Policy and Practice, 46*(8), 1265–1279. https://doi.org/10.1016/J.TRA.2012.05.009
Yu, B., Zhu, H., Cai, W., Ma, N., Kuang, Q., & Yao, B. (2013). Two-phase optimization approach to transit hub location – the case of Dalian. *Journal of Transport Geography, 33*, 62–71. https://doi.org/10.1016/J.JTRANGEO.2013.09.008

Zhao, Y., Ravi, R., Shi, S., Wang, Z., Lam, E.Y., & Zhao, J. (2022). PATE: Property, Amenities, Traffic and Emotions Coming Together for Real Estate Price Prediction. In *Proceedings of the 2022 IEEE International Conference on Data Science and Advanced Analytics (DSAA)*. https://doi.org/10.1109/DSAA54385.2022.10032416

4th International Civil Engineering & Architecture Conference
17-19 May 2025, Trabzon, Türkiye

Streetmeter as a tool for human-centered urban analysis: Expanding the metrics

Ilgin Gokasar*[1], Volkan Yıldız[1]

[1] Bogazici University, Department of Civil Engineering, 34342 İstanbul, Türkiye

Abstract. Quality of life is affected by the design and functionality of urban spaces, particularly streets, which serve as the backbone of daily social and economic interactions. To enhance street quality, streets could be transformed. In this context, street transformation is crucial for improving urban livability, promoting social inclusion and enhancing welfare of the society in general. Measuring street quality requires a multidimensional approach, incorporating metrics such as environmental quality, pedestrian safety, economic impact, gender equality and religious equality. These factors are interlinked and collectively affect urban experiences. This study utilizes Streetmeter, a digital assessment tool, to compare and analyze different streets based on different parameters such as geometry of the road and buildings located on the street. By prioritizing pedestrian mobility over vehicular movement, the study aims to re-examine how we understand the concept of urban planning. This concept is called as human-centered design. This term indicates that streets should be designed for the people who use them daily rather than accommodating vehicles. The findings contribute to policy development by providing data for decision-makers to enhance walkability, safety, and accessibility in urban spaces. Moreover, the study highlights the role of digital tools in fostering public awareness, empowering individuals, and advocating for pedestrian rights. By incorporating objective data into street evaluations, this research supports more equitable and sustainable urban planning approaches. Ultimately, this study emphasizes the importance of designing streets that serve as inclusive, safe, and vibrant public spaces, aligning with contemporary urban development goals and social justice principles.

Keywords: Quality of streets; Street transformation; Streetmeter

1. Introduction

Urban spaces play a fundamental role in shaping the daily experiences of city residents, with streets serving as dynamic environments where social, cultural, and economic interactions unfold. In this context, streets should be seen as communication centers shared by all living entities. They transcend the notion of public utilities, representing more than mere traffic arteries by facilitating the movement of people and things from one location to another (Jacobs, 1993). City streets also serve important urban purposes beyond transportation, such as play and commerce, leisure and social contact, and politics and innovation (Lydon & Garcia, 2015). As cities grow, humankind's perspective to life evolves. This evolvement requires changing our look to streets which will lead to redesign of the streets in a way that increases livability, fosters social inclusion and enhances general welfare. By achieving this transformation, human wellbeing will be prioritized over vehicular efficiency which will help assist the accomplish main goal, human-centered design that could be described as an approach that centers the needs of pedestrians and everyday users. To support this movement of change, the experimentation paradigm is increasingly adopted by citizens and governments seeking to reallocate urban streets from motorized traffic to active transportation and public spaces, facilitating "stationary" operations like play and socialization in pursuit of a vision of "streets for people" rather than "streets for traffic." (Bertolini, 2020). Also there is a consensus that livable streets aim to improve the street's pedestrian character by implementing design elements that reduce the detrimental effects of motor vehicle use on pedestrians and by maintaining a continuous network of pavements (Dumbaugh, 2005).

Measuring the quality of streets requires a comprehensive and multidimensional approach. Factors such as environmental quality, pedestrian safety, economic vibrancy, gender equality, and religious inclusivity must all be considered to accurately capture the lived experience of urban spaces. The perceived spatial quality of urban streets is considered a significant benefit to society (Ye et al., 2019). Also, maintaining air quality is crucial, as urban streets bordered by buildings often trap pollutants, exposing pedestrians, cyclists, drivers, and residents to

* Corresponding author, E-mail: ilgin.gokasar@bogazici.edu.tr

https://doi.org/10.31462/icearc2025_ce_tra_956

concentrations that exceed health standards (Vardoulakis et al., 2003). What's more, an enhanced comprehension of the link between design and safety may help designers in creating secure and habitable streets (Asadi-Shekari et al., 2015). In addition to them, street economics involves offering commercial and artistic goods and services in public spaces without a fixed location, and with around 2 million people working in this sector, the economic use of streets is vital (Sirkeci, 2020). It should also not be overlooked that an important influence on women's spatial behavior stems from the gender distribution of domestic labor and activities taking place outside the home at the household level (Lo & Houston, 2018). Recognizing the interconnectedness of these elements, this study employs Streetmeter, a digital assessment tool, to systematically evaluate and compare streets based on parameters like road geometry and building configurations.

By embracing the principles of human-centered design, this research challenges traditional car-centric models of urban planning. In doing so, it provides valuable data and insights for policymakers, urban designers, and community advocates striving to create safer, more inclusive, and more sustainable streets. Ultimately, this study seeks to contribute to a broader understanding of streets not just as pathways for movement, but as vital spaces for community life, aligned with contemporary goals of urban development, equity, and social justice.

2. Factors that effect quality of streets

Vibrant, sustainable cities and regions depend on well-designed pedestrian spaces. Researchers show that pedestrian-friendly streets improve the public space's social quality, that pedestrian traffic boosts local businesses' bottom lines, and that walking is a sustainable form of transportation that diminishes greenhouse gas emissions (Macdonald et al., 2018).

To achieve better streets, quality assesment is the initial step. Evaluating urban street quality requires a multifaceted strategy. The way people travel, participate, and experience urban life is influenced by the many social and functional systems that make up streets. In this regard, a number of factors significantly influence how inclusive, sustainable, and effective street environments are.

The Streetmeter tool, which assesses streets based on five dimensions such as health, social, economy, mobility, and environment is used in this study. Together, these categories' indicators offer a data-driven evaluation of street performance and livability (Streetmeter, 2025). This study also adds two important but frequently disregarded elements to these dimensions: gender equality and religious inclusivity. In order to include the social and cultural complexities of using public spaces, these dimensions have been added. By incorporating these perspectives, the analysis aims to advance more inclusive street design that takes into account the diverse needs and life experiences of various user groups.

2.1. Health

The health dimension plays a crucial role in evaluating the overall quality of streets, as urban environments have direct impacts on public well-being. Streets designed with health considerations in mind can significantly reduce physical and mental health risks for urban populations. Since individuals spend a significant portion of the day in public urban areas, the design and quality of these areas may have a direct effect on stress levels (Sadeghpoor et al., 2024). In a physical health manner, youth physical activity is directly related to street quality (Kaczynski et al., 2018).

A variety of indicators are used to assess the health-related quality of a street, each contributing to a more comprehensive understanding of how urban design affects residents.

Key metrics include noise level which influences stress and sleep quality since reducing environmental sources of excessive street-level noise should be a top goal for urban planning and public health (McAlexander et al., 2015). To add, the share of active transportation which promotes physical fitness through walking and cycling. Increased active transportation can result from more inclusive pedestrian infrastructure, and this can enhance people's physical health and overall wellness (Georgescu et al., 2024). Another critical factor is the risk of serious traffic injuries that reflect the safety of street users, particularly pedestrians and cyclists. This topic is so important that evidence-based traffic safety principles ought to be taught to all professionals involved in the planning of streets and road networks (Mohan, 2008).

Environmental health is also addressed through air quality indicators such as PM10, PM2.5, and NOx annual means. Streets with poor air quality contribute to an increased risk of asthma attacks, particularly among vulnerable populations such as children and the elderly. Researches shows that an increase in the number of trees can reduce the risk of asthma, thereby improving overall health quality and decreasing the burden of disease, which may also result in economic benefits (Eisenman et al., 2019).

Additionally, greenery's oxygen production represents the environmental contribution of vegetation along streets, offering cleaner air. It is a known fact that one of the beneficial effects of street greenery is the production of oxygen (Nowak et al., 2007). Together, these metrics underscore how the design, infrastructure, and ecological components of a street can profoundly influence public health.

2.2. Social

The social aspect of street quality focuses on how public areas promote inclusion, ease human contact, and strengthen an aura of community. Streets are not only physical corridors but also important locations for social life, where people gather, connect, and participate in everyday urban culture. Research has shown a strong relationship between the quality of the street environment and people's willingness to engage in social interaction (Mehta & Bosson, 2021). Evaluating social factors helps ensure that streets support diverse needs, equitable access, and opportunities for public engagement.

A core metric is the number of people using the space as a meeting place which indicates the social vitality of the street. Not only do streets serve as visual appearances of the community, but they also serve as crucial conduits that connect persons and make movement more efficient (Rahayu et al., 2017).

The presence of safe street spaces reflects how well streets are integrated into surrounding buildings and neighborhoods, enhancing both security and accessibility. Surface illumination is another element, affecting perceptions of safety and the usability of streets during evening hours. The streets are one of the primary locations where stranger harassment persists, which is tragically widespread in today's society and involves behaviors like physical contact, verbal abuse, staring, and stalking (Macmillan et al., 2000).

Physical amenities also play a crucial role in shaping social experiences. The availability and placement of public seating and outdoor dining encourage lingering, interaction, and leisure activities. Significant changes in the material environment (perceived space) could alter people's mobility, accessibility, and general quality of life (lived space), as well as their opportunities for involvement and movement through them (Saphan et al., 2022). These features are particularly important for vulnerable groups such as the elderly and children.

2.3. Economy

The economic dimension of street quality reflects how public spaces contribute to local prosperity, business activity, and property values. When talking about street economy, the first concept to come to mind is street vendors. Although once seen as outdated and nearing extinction, street markets and vending have grown increasingly popular over time (Cross, 2000). However, street’s economic benefits are beyond these open-air markets. Streets that support economic vitality not only benefit individual enterprises but also enhance the overall sustainability of urban areas increasing land value and encouraging community investment. Economic indicators are essential for understanding how spatial design decisions turn into financial outcomes.

One key set of indicators involves value creation: the extent to which streets contribute to residential and office value creation. Good street design can enhance land value by enabling more development and supporting investment in public goods (Hack & Sagalyn, 2011). Well-designed, accessible, and vibrant streets often correlate with increased demand for adjacent properties, reflecting their desirability as places to live or work. For example, Romsey’s annual folk and roots music festival, which activates the town’s medieval streets with performances, food stalls, and pedestrian-only access, illustrates how street environments can attract sustained public interest and enhance the overall desirability of the area (Rust, 2020). Similarly, retail turnover offers insight into the commercial productivity of the street, especially in areas where pedestrian traffic is high.

In terms of public revenue, metrics such as on-street car parking revenue and outdoor dining revenue quantify how street space can be used efficiently to generate income, either through vehicle-related fees or supporting local hospitality businesses. Research indicates that optimizing the prices of street parking spaces can become an important source of income as well as regulating traffic (Xu & Sun, 2024). These revenues can be reinvested in further street improvements or public services.

2.4. Mobility

Mobility is a fundamental component of street quality, as it determines how easily and safely people can move through urban environments. In fact, human mobility in street networks combines both topological jumps between streets and persistent movement along them, but this simplified view overlooks the purposive nature of real-world travel, which is often driven by specific destinations like homes, schools, or workplaces (Jiang et al., 2009). A high quality street supports a balanced, multimodal transportation system that prioritizes accessibility, equity, and efficiency. Streets could serve as public areas for all users when the emphasis is shifted. To add, walking on urban streets with human-centered street designs makes pedestrians feel better (Choi et al., 2016).

Key metrics include safe walking and biking from age which reflect how early children can independently wander streets which can be counted as a strong indicator of safety. Children are involved in road accidents for many different kinds of reasons, majority of which are out of their control (Riaz et al., 2022). Therefore, streets’ design must prioritize the safety of the children.

Passenger capacity and bus speed reveal the efficiency public transit infrastructure, critical for reducing dependence on private vehicles. What’s more, the use of public transportation is frequently promoted as a solution in an era of growing concern over environmental issues, including global warming (Holmgren, 2013). The motor traffic level of service shows the balance between vehicular flow and other modes, informing decisions about traffic calming and space allocation.

Accessibility is further addressed through indicators such as on-street car and bike parking access and wheelchair width ensuring that all users regardless of physical ability or transport mode can access and use the street comfortably. Wheelchair users, like everyone else, require broad mobility to live and work and should have access to a well-connected system of suitable walkways for transportation (Ning et al., 2022). Biking width and pedestrian crossing time also influence safety and ease of movement, particularly at intersections and high-traffic zones.

2.5. Environment

The environment dimension addresses how street design influences ecological sustainability, climate resilience, and the overall environmental health of urban areas. More and more, ecologists, planners, designers, and the general public are worried about how these changes impact day-to-day living and the sustainability of "quality of life" for the generations to come (McPherson et al., 2011). Streets are key interfaces between the built environment and natural systems, and their quality directly affects air quality, heat regulation, water management, and carbon emissions. For instance, in warm climates and especially in Mediterranean towns, it is essential to preserve and care for urban street trees in order to reap the benefits of their microclimate (Coutts et al., 2016). Environmentally responsive street planning contributes to both local well-being and global sustainability goals.

A central set of indicators involves CO_2 emissions which is a major contributor to climate change. Important thing is that it should not be forgotten that alongside CO_2, other greenhouse gases contributing to global warming—such as methane (CH_4), nitrous oxide (N_2O), hydrofluorocarbons (HFCs), perfluorocarbons (PFCs), and sulfur hexafluoride (SF_6)—are also listed in the Kyoto Protocol of 1998 (United Nations, 1998). Streets that prioritize human-centered mobility and greenery can help reduce these levels significantly.

Additionaly, since ancient times, it has been understood that stormwater from constructed places needs to be managed carefully since the pollutants and litter it contains can have an adverse effect on both quantity and quality, affecting both environmental and public health (Barbosa et al., 2012). Stormwater management is addressed in the Streetmeter through two distinct but complementary functions. Stormwater delay refers to the street's capacity to slow down the flow of rainwater. Stormwater cleaning, on the other hand, reflects the street's ability to remove pollutants from runoff before it enters the sewer system or local waterways.

2.6. Gender equality

While often overlooked in traditional urban planning, gender equality is a critical lens through which street quality should be assessed. Particularly when it comes to individuals of different genders, races, and classes, different cultures have varying thresholds for tolerance and acceptance (Rapoport, 1990). This situation results in the fact that public spaces are experienced differently based on gender, particularly in terms of safety, accessibility, and usability. Integrating gender-inclusive design ensures that urban environments are inclusive and supportive of all people, regardless of gender identity. Equity-focused policies, including those addressing gender, can have a broad community impact by helping to shift norms and promote a healthier, more inclusive society (Keippel et al., 2017).

Key considerations include perceived and actual safety, especially during evening or night hours. Factors such as adequate lighting, clear visibility, active frontages, and the presence of diverse users contribute to a sense of security. Streets that are poorly lit or isolated can deter women and girls from using them freely, especially for walking or cycling. It is found in a research that personal security issues for women and gender minorities go beyond the possibility of traffic-related injuries (McAndrews et al., 2023). This finding highlights how depressing the circumstances are.

Accessibility also intersects with gender in terms of caregiving responsibilities. Features like wide, smooth pavements, resting areas, ramps for strollers, and step-free crossings make a significant difference for individuals navigating with children, strollers, or mobility aids. Keep in mind that while both women and men with disabilities face inequality, women with disabilities experience greater challenges due to compounded effects of disability and gender stereotypes that reinforce traditional roles (European Institute for Gender Equality, 2018).

Moreover, the presence of gender-diverse street users, inclusive seating arrangements, and representation in street art or naming can signal cultural recognition and belonging. Local governments have the potential to promote gender equality through arts-based initiatives, as art can highlight inequities, empower women, spark dialogue, and inspire community action (Shearson et al., 2022).

2.7. Religious inclusivity

Religious inclusivity is a vital yet often underrepresented aspect of street design. Even, conflict assessments do not necessarily include an emphasis on faith and religious diversity (Wilkinson & Eggert, 2021). In diverse urban settings, streets should reflect and accommodate the cultural and religious practices of all community members. Policymakers, scholars, practitioners, and local communities must all work together to successfully interpret, protect, manage, and develop the many manifestations of heritage in order to make cities more sustainable (Giliberto, 2023). This not only fosters mutual respect and social cohesion but also ensures that public spaces are welcoming and functional for individuals of varying and beliefs.

Indicators of religious inclusivity in street quality could include the availability and visibility of culturally sensitive amenities. Notably, a empirical research has revealed how parish churches promote interactions that aren't frequently discussed in urban discourse on homophobia and transphobia (Andersson et al., 2011). Additionally, street design should allow for flexible use, such as accommodating increased foot traffic near places of worship during religious events, processions, or peak visitation times. This flexibility is important because religion influences long-standing planning issues, including community formation, public space use, land-use policy, and the placement and architectural style of religious buildings (Mazumdar & Mazumdar, 2013).

Furthermore, representation and recognition in public art, placemaking elements, or the naming of streets and features can foster a sense of belonging among religious groups. Since ancient times, art has drawn inspiration from myth, magic, and religion, maintaining its powerful and sacred appeal (Shusterman, 2008). Thoughtful design choices should therefore be mindful to avoid marginalization or exclusion, particularly in neighborhoods with significant religious or ethnic diversity.

3. Policy implications

The comprehensive evaluation of street quality across multiple dimensions provides a strong foundation for data-informed urban policy. These findings highlight the need for policies that not only address infrastructure and efficiency but also promote equity, inclusion, and sustainability in public space design. Embracing a human-centered design approach is essential to ensure that streets are planned for the people who use them.

Health indicators emphasize the importance of policies that reduce air pollution, noise, and traffic related injuries while promoting active transportation. Public health goals can be advanced through investments in safe, clean, and walkable street environments.

Social indicators highlight the role of streets in building community life. Policymakers should ensure that streets are welcoming and inclusive by supporting features such as seating, lighting, and public gathering areas. These elements foster social interaction and improve perceived safety, especially for vulnerable users.

Economic outcomes demonstrate the potential of well-designed streets to support local commerce and contribute to municipal revenues. Governments should facilitate flexible use of street space, such as outdoor dining and accessible storefronts, while aligning zoning and investment policies to enhance value creation.

Mobility related insights examines the street space from the perspective of active transport and public transport. Decision-makers should make streets easier to access, shorten the time it takes to cross safely, and ensure that people of all ages and abilities can move through them without difficulty.

Environmental considerations, such as stormwater delay and cleaning and temperature regulation, point to the need for streets that contribute to long-term climate resilience and improved urban health. Policy frameworks should incorporate these functions into infrastructure planning and performance standards.

Ensuring gender equality in street design is essential for creating fair and inclusive public spaces. Streets should promote safety, accessibility, and comfort for all genders, recognizing differing mobility needs and caregiving roles. Urban planning regulations should incorporate gender-sensitive principles to make streets more equitable for everyone.

Religious inclusivity is equally important in reflecting the cultural and spiritual diversity of communities. Streets should be designed to respect religious practices, provide space for inclusive use, and avoid elements that may marginalize specific groups.

By bringing all of these dimensions together, governments can create places where every individual feels a sense of belonging.

4. Conclusions

This study has provided a multidimensional evaluation of street quality using Streetmeter, assessing key factors including health, social interaction, economy, mobility, and environmental impact. To broaden the framework, gender equality and religious inclusivity were added as critical dimensions, emphasizing the importance of inclusive and human-centered street design in contemporary urban planning. This approach offers a more comprehensive understanding about function of streets.

This study adds to both academic and policy discussions by providing a clear, data-based way to understand how streets function. It helps decision-makers design urban spaces that are more livable, fair, and responsive to people's needs, while also paying attention to often-overlooked cultural and social aspects of street life.

Limitations of the study include the tool’s focus on numbers and measurable data, which may not fully show people’s personal experiences or the unique details of each street’s context. Additionally, the newly introduced aspects such as gender equality and religious inclusivity are not yet fully supported by standardized metrics within Streetmeter, and their assessment relies in part on qualitative interpretation. The findings may also vary depending cultural context, limiting direct generalizability across all urban settings.

Future work should focus on developing standardized indicators for social inclusivity dimensions, particularly gender and religious equity, to allow for more robust and comparable evaluations. Expanding the study to multiple cities with varying cultural and spatial characteristics could help to improve to software, also. Additionally, integrating participatory research methods such as community workshops, user interviews, and ethnographic observations would help capture lived experiences and bridge the gap between digital assessment and real-world perceptions of street quality.

Acknowledgments
This study is funded by the projects: EN-UAC, Grant Nr: 99950070, https://www.smartmobilityhubs.eu), StreetForum (Transforming streets into accessible urban oases through consensus building with digital and analog tools, EN-UAC Innovation Action). It is also supported by the Scientific and Technological Research Council of Turkey (TUBİTAK) Project number 123N051.

References

Andersson, J., Vanderbeck, R.M., Valentine, G., Ward, K., & Sadgrove, J. (2011). New York encounters: Religion, sexuality, and the city. *Environment and Planning A, 43*(3), 618–633. https://doi.org/10.1068/A43202

Asadi-Shekari, Z., Moeinaddini, M., & Zaly Shah, M. (2015). Pedestrian safety index for evaluating street facilities in urban areas. *Safety Science, 74*, 1–14. https://doi.org/10.1016/j.ssci.2014.11.014

Barbosa, A.E., Fernandes, J.N., & David, L.M. (2012). Key issues for sustainable urban stormwater management. *Water Research, 46*(20), 6787–6798. https://doi.org/10.1016/j.watres.2012.05.029

Bertolini, L. (2020). From "streets for traffic" to "streets for people": Can street experiments transform urban mobility? *Transport Reviews, 40*(6), 734–753. https://doi.org/10.1080/01441647.2020.1761907

Choi, J., Kim, S., Min, D., Lee, D., & Kim, S. (2016). Human-centered designs, characteristics of urban streets, and pedestrian perceptions. *Journal of Advanced Transportation, 50*(1), 120–137. https://doi.org/10.1002/atr.1323

Coutts, A.M., White, E.C., Tapper, N.J., Beringer, J., & Livesley, S.J. (2016). Temperature and human thermal comfort effects of street trees across three contrasting street canyon environments. *Theoretical and Applied Climatology, 124*(1–2), 55–68. https://doi.org/10.1007/s00704-015-1409-y

Cross, J. (2000). Street vendors, and postmodernity: Conflict and compromise in the global economy. *International Journal of Sociology and Social Policy, 20*(1–2), 29–51. https://doi.org/10.1108/01443330010789061

Dumbaugh, E. (2005). Safe streets, livable streets. *Journal of the American Planning Association, 71*(3), 283–300. https://doi.org/10.1080/01944360508976699

Eisenman, T.S., Churkina, G., Jariwala, S.P., Kumar, P., Lovasi, G.S., Pataki, D.E., Weinberger, K.R., & Whitlow, T.H. (2019). Urban trees, air quality, and asthma: An interdisciplinary review. *Landscape and Urban Planning, 187*, 47–59. https://doi.org/10.1016/j.landurbplan.2019.02.010

European Institute for Gender Equality. (2018). *Gender equality needs to reach everyone.* https://eige.europa.eu/sites/default/files/documents/20181612_mh0418229enn_pdf_0.pdf

Georgescu, A.I., Allahbakhshi, H., & Weibel, R. (2024). The impact of microscale street elements on active transport of mobility-restricted individuals: A systematic review. *Journal of Transport & Health, 38*, 101842. https://doi.org/10.1016/j.jth.2024.101842

Giliberto, F. (2023). Religious inequalities, inclusive cities and sustainable development. In *Religious Inequalities* (pp. 181–189). https://library.oapen.org/bitstream/handle/20.500.12657/76368/9781529229066.pdf

Hack, G., & Sagalyn, L.B. (2011). Value creation through urban design. In *Urban Design in the Real Estate Development Process* (pp. 258–281). https://doi.org/10.1002/9781444341188.ch13

Holmgren, J. (2013). The efficiency of public transport operations – An evaluation using stochastic frontier analysis. *Research in Transportation Economics, 39*(1), 50–57. https://doi.org/10.1016/j.retrec.2012.05.023

Jacobs, A.B. (1993). *Great streets.* University of California Transportation Center. https://ideas.repec.org/p/cdl/uctcwp/qt3t62h1fv.html

Jiang, B., Yin, J., & Zhao, S. (2009). Characterizing the human mobility pattern in a large street network. *Physical Review E, 80*(2), 021136. https://doi.org/10.1103/PhysRevE.80.021136

Kaczynski, A.T., Besenyi, G.M., Child, S., Hughey, S.M., Colabianchi, N., McIver, K.L., Dowda, M., & Pate, R.R. (2018). Relationship of objective street quality attributes with youth physical activity: Findings from the Healthy Communities Study. *Pediatric Obesity, 13*(Suppl. 1), 7–13. https://doi.org/10.1111/ijpo.12429

Keippel, A.E., Henderson, M.A., Golbeck, A.L., Gallup, T.L., Duin, D.K., Hayes, S., Alexander, S., & Ciemins, E.L. (2017). Healthy by design: Using a gender focus to influence complete streets policy. *Women's Health Issues, 27*(Suppl. 1), S22–S28. https://doi.org/10.1016/j.whi.2017.09.005

Lo, A. W.T., & Houston, D. (2018). How do compact, accessible, and walkable communities promote gender equality in spatial behavior? *Journal of Transport Geography, 68*, 42–54. https://doi.org/10.1016/j.jtrangeo.2018.02.009

Lydon, M., & Garcia, A. (2015). *Tactical urbanism: Short-term action for long-term change.* Island Press. https://doi.org/10.5822/978-1-61091-567-0

Macdonald, E., Szibbo, N., Eisenstein, W., & Mozingo, L. (2018). Quality-of-service: Toward a standardized rating tool for pedestrian quality of urban streets. *Journal of Urban Design, 23*(1), 71–93. https://doi.org/10.1080/13574809.2017.1340092

Macmillan, R., Nierobisz, A., & Welsh, S. (2000). Experiencing the streets: Harassment and perceptions of safety among women. *Journal of Research in Crime and Delinquency, 37*(3), 306–322. https://doi.org/10.1177/0022427800037003003

Mazumdar, S., & Mazumdar, S. (2013). Planning, design, and religion: America's changing urban landscape. *Journal of Architectural and Planning Research, 30*(3), 221–243. https://www.jstor.org/stable/43031006

McAlexander, T.P., Gershon, R.R.M., & Neitzel, R.L. (2015). Street-level noise in an urban setting: Assessment and contribution to personal exposure. *Environmental Health, 14*, 1–10. https://doi.org/10.1186/s12940-015-0006-y

McAndrews, C., Schneider, R.J., Yang, Y., Kohn, G., Schmitz, A., Elliott, F., Pittner, J., & Purisch, H. (2023). Toward a gender-inclusive complete streets movement. *Journal of Planning Literature, 38*(1), 3–18. https://doi.org/10.1177/08854122221087472

McPherson, E.G., Simpson, J.R., Xiao, Q., & Wu, C. (2011). Million trees Los Angeles canopy cover and benefit assessment. *Landscape and Urban Planning, 99*(1), 40–50. https://doi.org/10.1016/j.landurbplan.2010.08.011

Mehta, V., & Bosson, J.K. (2021). Revisiting lively streets: Social interactions in public space. *Journal of Planning Education and Research, 41*(2), 160–172. https://doi.org/10.1177/0739456x18781453

Mohan, D. (2008). Road traffic injuries: A stocktaking. *Best Practice & Research Clinical Rheumatology, 22*(4), 725–739. https://doi.org/10.1016/j.berh.2008.05.004

Ning, H., Li, Z., Wang, C., Hodgson, M.E., Huang, X., & Li, X. (2022). Converting street view images to land cover maps for metric mapping: A case study on sidewalk network extraction for wheelchair users. *Computers, Environment and Urban Systems, 95*, 101808. https://doi.org/10.1016/j.compenvurbsys.2022.101808

Nowak, D.J., Hoehn, R., & Crane, D.E. (2007). Oxygen production by urban trees in the United States. *Arboriculture & Urban Forestry, 33*(3), 220–226. https://research.fs.usda.gov/treesearch/11485

Rahayu, M.J., Putri, R.A., Rini, E.F., Sulaiman, N., Abdullah, Y.A., & Hamdan, H. (2017). Street as public space – Measuring street life of Kuala Lumpur. *IOP Conference Series: Materials Science and Engineering, 245*, 082025. https://doi.org/10.1088/1757-899x/245/8/082025

Rapoport, A. (1990). *History and precedent in environmental design.* https://books.google.com.tr/books?hl=tr&id=K8zcBwAAQBAJ

Riaz, M.S., Cuenen, A., Polders, E., Akram, M.B., Houda, M., Janssens, D., & Azab, M. (2022). Child pedestrian safety: Study of street-crossing behaviour of primary school children with adult supervision. *Sustainability, 14*(3), 1503. https://doi.org/10.3390/su14031503

Rust, E. (2020). Understanding experiential value creation at small-scale events: A multi-stakeholder perspective. *Journal of Policy Research in Tourism, Leisure and Events, 12*(3), 344–362. https://doi.org/10.1080/19407963.2019.1701811

Sadeghpoor, F., Ranjbar, E., Esmaeilinasab, M., Valiloo, M.H.S., & Nieuwenhuijsen, M.J. (2024). Streets and stress: A pilot study on how quality and design of streets impacts on urban stress. *Health Environments Research and Design Journal, 17*(1), 224–248. https://doi.org/10.1177/19375867231200584

Saphan, L., Pipitone, J.M., Perez-Garcia, E., Vieira, A., & Francisco, R. (2022). Outdoor dining and the transformation of public space in New York City. *Streetnotes, 29*(0). https://doi.org/10.5070/S529059361

Shearson, K., Sonn, C., Ivey, G., Sharples, J., Brasacchio, L., Ms, E.B., & Durkan, B. (2022). *Gender equality through the arts program evaluation.* https://www.vichealth.vic.gov.au/sites/default/files/2023-08/VH_GE-ARTS_evaluation-full%20report_FINAL.pdf

Shusterman, R. (2008). Art and religion. *Journal of Aesthetic Education, 42*(3), 1–18. https://doi.org/10.2307/25160287

Sirkeci, O. (2020). Actors and functions of street economy. In *Global Street Economy and Micro Entrepreneurship* (Vol. 103, pp. 11–28). https://doi.org/10.1108/S1569-375920200000103002

Streetmeter. (2025). *Streetmeter – Home.* https://streetmeter.net/

United Nations. (1998). *Kyoto Protocol to the United Nations Framework Convention on Climate Change.* https://unfccc.int/resource/docs/convkp/kpeng.pdf

Vardoulakis, S., Fisher, B.E.A., Pericleous, K., & Gonzalez-Flesca, N. (2003). Modelling air quality in street canyons: A review. *Atmospheric Environment, 37*(2), 155–182. https://doi.org/10.1016/s1352-2310(02)00857-9

Wilkinson, O., & Eggert, J.P. (2021). *Understanding inclusivity of religious diversity in humanitarian response.* https://doi.org/10.19088/CREID.2021.011

Xu, Z., & Sun, X. (2024). Economic analysis of on-street parking with urban delivery. *Transportation Science.* https://doi.org/10.1287/trsc.2024.0569

Ye, Y., Zeng, W., Shen, Q., Zhang, X., & Lu, Y. (2019). The visual quality of streets: A human-centred continuous measurement based on machine learning algorithms and street view images. *Environment and Planning B: Urban Analytics and City Science, 46*(8), 1439–1457. https://doi.org/10.1177/2399808319828734

4th International Civil Engineering & Architecture Conference
17-19 May 2025, Trabzon, Türkiye

Are public transport ınformation systems equally effective? Insights from local and migrant passengers

Abdulkadir Özden*[1], Hakan Kocaman[2], Yavuz Halimergün[2]

[1] Sakarya University of Applied Sciences, Department of Civil Engineering, 54050 Sakarya, Türkiye
[2] Sakarya University of Applied Sciences, Graduate Education Institute, 54050 Sakarya, Türkiye

Abstract. This study investigates the differences in public transport usage patterns and perceptions of passenger information systems between migrant and non-migrant populations in Türkiye. Based on data collected from 513 participants through face-to-face surveys conducted in the cities of Sakarya and Istanbul, the research adopts a descriptive approach to explore demographic characteristics, transport mode preferences, and satisfaction with digital and on-site information services. The analysis reveals that migrants tend to be younger, more highly educated, and are more likely to use high-capacity transport modes such as metro systems. Interestingly, migrants also report higher satisfaction with information systems, particularly with mobile applications and language accessibility—an unexpected finding considering the generally limited multilingual support in Türkiye's public transport infrastructure. This may reflect positive experiences in cities like Istanbul, where such systems are more developed, as well as comparative perceptions shaped by migrants' countries of origin. Common challenges shared by both groups include long waiting times and concerns about vehicle safety. The study emphasizes the importance of inclusive, technology-supported transport systems and suggests that future research should expand to other cities—both metropolitan and less developed—in order to assess how infrastructure disparities influence public transport accessibility and user satisfaction among diverse urban populations.

Keywords: Public transport; Passenger ınformation systems; Immigirants; Accessibility

1. Introduction

Urban transportation systems play a fundamental role in ensuring social inclusion, economic vitality, and quality of life in modern cities. Efficient and accessible public transport (PT) services not only facilitate daily mobility but also contribute to broader societal goals such as environmental sustainability and social equity. In an increasingly diverse urban landscape, the inclusiveness of transportation systems—encompassing infrastructure, vehicles, information systems, and supporting digital applications—has become a central concern for both local authorities and policymakers.

For transportation systems to serve all segments of society effectively, they must address the needs of diverse user groups, including both native residents and migrants. Public transport inclusiveness is not limited to physical accessibility; it also encompasses the effectiveness of passenger information systems, the clarity of real-time announcements, the user-friendliness of route planning applications, and the availability of multilingual services (Sime & Fox, 2014). For migrants, who may face linguistic, cultural, and informational barriers, the ability to easily access and interpret public transportation information is a critical factor influencing their mobility patterns and integration into urban life (Li et al., 2024; Welsch et al., 2016).

Despite the recognized importance of inclusive transportation design, relatively limited research has focused on comparative analyses of migrants' and non-migrants' experiences with public transport, particularly in Türkiye's urban settings. Understanding the differences and commonalities between these groups can provide valuable insights into how transportation services—and especially digital passenger information systems—can be improved to better serve an increasingly heterogeneous population.

This study aims to contribute to this emerging field by conducting a descriptive analysis of public transport usage patterns among migrants and non-migrants. Based on survey data, the research examines how demographic factors correlate with transport habits, the perceived effectiveness of infrastructure and digital information tools, and the role of passenger information systems in facilitating urban mobility. Through this lens, the study seeks to highlight critical areas for enhancing the inclusiveness of public transportation services in Türkiye.

* Corresponding author, E-mail: aozden@subu.edu.tr

https://doi.org/10.31462/icearc2025_ce_tra_987

2. Literature review

Public transport systems play a crucial role in fostering social inclusion by enhancing accessibility, expanding infrastructure, and integrating digital passenger information tools. Academic research highlights these components as essential for creating equitable transportation networks that cater to the needs of diverse populations, including marginalized groups.

One foundational aspect of social inclusion in public transport is the accessibility of such systems. Saghapour et al. (2016) elaborate on how inadequate access to public transportation can hinder individuals' abilities to engage with various services and activities, leading to social isolation and exacerbating socio-economic disadvantages (Saghapour et al., 2016). This aligns with Yang et al., who advocate for comprehensive accessibility indices that consider various demographic factors to ensure that public transport serves all urban residents effectively (Yang et al., 2019). These infrastructural advancements are critical for building a connected urban environment that facilitates movement for all citizens.

The increasing integration of digital technology into public transport systems has significant implications for social inclusion. Digital tools can disseminate real-time information about services, enhancing the user experience and encouraging public transit usage (Davidsson et al., 2016). Digital maps and applications have been cited as effective means to promote green transportation, encouraging sustainable commuting behaviors among users, particularly in urban settings where congestion and emissions are concerns (Zhang et al., 2024). Furthermore, digital systems can streamline payments and expand access to transport services, making them more appealing to a broader audience, as evidenced by findings from Sener et al., which indicate that prior positive experiences with public transit foster ongoing use intentions (Sener et al., 2019). Research indicates that an integrated and well-structured public transport system enhances social cohesion among diverse communities.

Migrants face numerous barriers when using urban public transport systems, which significantly impacts their ability to integrate and access vital services. These barriers are often categorized into three primary areas: language difficulties, access to information, and navigation challenges. Insufficient proficiency in the local language can impede migrants' understanding of transit systems, leading to confusion and hesitation in using public transport. According to Nteliou et al., language proficiency directly influences the ability of migrants to navigate public facilities, including transport systems, exacerbating issues of exclusion and integration (Nteliou et al., 2021).This lack of understanding can deter them from accessing information necessary for effective public transport use.

Access to relevant information regarding transport options and services is another critical barrier faced by migrants. As indicated by Waitt et al., many migrants lack adequate information about public transport schedules, routes, and payment systems, which can hinder their mobility (Waitt et al., 2016). This situation is often worse in rural areas where public transport services are limited or non-existent (Pilling & Estes, 2016). In metropolitan areas, digital information tools have the potential to alleviate some informational barriers. However, the efficacy of these tools depends on their accessibility and usability for migrants. Studies indicate that many public transportation systems fail to provide multilingual and culturally relevant information, which can further marginalize non-native speakers and create disparities in service usage (Gruer et al., 2021).

Navigating public transport systems poses unique challenges for migrants, particularly those who may be unfamiliar with urban environments. Navigational challenges arise from inadequate signage, the complexity of transit maps, and a lack of user-friendly tools that cater to migrants. As highlighted by Welsch et al., migrants are less likely to own personal vehicles, making them more reliant on buses and trains; however, the unfamiliarity with the transport landscape can deter them from using these services (Welsch et al., 2016). Moreover, the experience of feeling lost or insecure in an unfamiliar environment can deter migrants from fully utilizing public transport systems. This navigation issue is compounded by the fact that many urban transport systems still operate with outdated or insufficient technology that does not accommodate the diverse needs of their users (Welsch et al., 2016).

The effectiveness of passenger information systems and mobile applications in improving public transport accessibility and user experience for diverse populations has garnered considerable attention. Recent studies highlight the various dimensions of how these digital tools facilitate better mobility and enhance the overall user experience across different demographics, including migrants, seniors, and individuals with disabilities. Real-time passenger information systems significantly enhance the user experience by reducing uncertainty and making travel more predictable (Corsar et al., 2018). Similarly, mobile applications have emerged as powerful tools that enhance public transport accessibility. The participatory design approach in creating mobile apps, as discussed by Vollenwyder et al., ensures that the needs of users with disabilities are met by incorporating their feedback into app development (Vollenwyder et al., 2020). This fosters user engagement and enhances the functionality of the digital tools, making transportation more accessible to all demographics. Furthermore, Setiabudi and Tjahyana (2015) demonstrate that hybrid mobile applications can improve public transport user experiences by addressing individual preferences and facilitating better planning through intuitive interfaces.

On the other hand, as migrants become more established within their new environments, their dependency on public transport tends to decrease, indicating a shift towards car ownership as financial stability increases (Blumenberg & Evans, 2010). This transition underscores the dynamic relationship between transportation availability, socio-economic status, and migrant integration processes. Cities that emphasize developing equitable public transport systems are better equipped to handle the influx of diverse populations and foster a sense of community among residents (Sime & Fox, 2014).

The implications of inclusive transport systems extend beyond mere mobility; they also encompass broader social integration. Inclusive transport facilitates access to essential services, such as healthcare and education, thereby enhancing migrants' quality of life and social connectivity (Li et al., 2024). Hence, it is evident that building inclusive public transport frameworks can play a transformative role in enhancing the social fabric of urban environments as they yield benefits not only for migrants but also for non-migrants by creating more interconnected communities.

3. Methodology

This study adopts a descriptive research design to examine public transport usage patterns and perceptions among migrants and non-migrants in Türkiye. The primary objective is to explore how demographic characteristics relate to transport habits and the use of passenger information systems, without applying inferential statistical modeling.

3.1. Data collection

Data were collected through a structured survey instrument administered via face-to-face interviews. The survey was conducted in two major metropolitan cities, Sakarya and Istanbul, in November and December 2024. These locations were selected due to their diverse populations and significant levels of immigration, which provide a rich context for analyzing public transport accessibility and usage patterns among different demographic groups.

A total of 513 valid responses were obtained. Participants were approached in public areas such as transport hubs, community centers, and marketplaces to ensure a diverse representation of public transport users. Participation was voluntary, and respondents were assured of anonymity and confidentiality. The questionnaire included items covering participants' demographic profiles, transportation usage frequency, types of public transport utilized, satisfaction with passenger information systems, and the use of mobile applications related to public transportation.

Survey items consisted of both categorical variables (e.g., gender, age, education level, employment status) and Likert-scale items (ranging from "Strongly Disagree" to "Strongly Agree") that assessed perceptions of accessibility, information availability, and overall service quality.

3.2. Sample characteristics

The sample includes individuals representing a broad range of socio-demographic backgrounds. Respondents were classified into two main groups based on self-reported citizenship status:

• *Non-migrants:* Native Turkish citizens born in Türkiye.

• *Migrants:* Individuals who were either born outside of Türkiye or had migrated within the last 10 years, regardless of their citizenship status.

This classification allows for a comparative descriptive analysis between migrants and non-migrants regarding their transport experiences and informational needs.

3.3. Data analysis

The analysis was exclusively descriptive. Frequencies, percentages, and cross-tabulations were employed to summarize the data across the key demographic and usage variables. Initially, general demographic distributions were examined to outline the profile of respondents. Subsequently, descriptive comparisons were made between migrant and non-migrant groups in terms of transport usage frequency, satisfaction with transport services, and experiences with passenger information systems.

4. Findings and results

The findings of this study provide a descriptive overview of public transport usage patterns, perceptions of passenger information systems, and demographic characteristics among migrants and non-migrants residing in Sakarya and Istanbul in Türkiye. Based on data collected through face-to-face surveys, the results highlight key differences and similarities between these two groups. The analysis focuses on how variables such as gender, age, education level, and household income relate to public transport behavior and access to information systems. By examining these patterns, the study aims to shed light on the inclusiveness of urban mobility services and the extent to which current public transport infrastructures meet the needs of diverse populations. This section first presents the demographic profile of the respondents, followed by a comparative evaluation of public transport usage and satisfaction across migrant and non-migrant groups. Table 1 summarizes the demographic distribution of migrants and non-migrants in the sample, categorized by gender, age, education level, and household income. The table reports both the number and percentage of respondents within each group, providing a basis for understanding the population diversity among public transport users.

Table 1. Demographic characteristics of survey respondents

Category	Migrant	Migrant Percentage	Non-Migrant	Non-Migrant Percentage
Gender				
Male	105	29,91	246	70,09
Female	64	40,25	95	59,75
DNPS	1	33,33	2	66,67
Age				
< 18	13	44,83	16	55,17
18-24	79	50,00	79	50,00
25-34	38	28,15	97	71,85
35-44	27	26,21	76	73,79
45-54	8	14,81	46	85,19
55-64	3	20,00	12	80,00
65+	2	10,53	17	89,47
Education				
Middle school or less	9	8,11	102	91,89
High school	23	17,69	107	82,31
College or above	138	50,74	134	49,26
Household income				
<17,000 TRY	21	70,00	9	30,00
17,000–29,000 TRY	52	52,00	48	48,00
30,000–44,000 TRY	38	26,39	106	73,61
45,000–59,000 TRY	32	25,00	96	75,00
60,000–79,000 TRY	15	19,74	61	80,26
80,000–99,000 TRY	1	5,26	18	94,74
100,000+ TRY	11	68,75	5	31,25

*DNPS: Do not prefer to say

The following Fig. 1 illustrates vehicle ownership status among migrants and non-migrants. A significant disparity is observed between the two groups. While 170 non-migrants reported owning a vehicle, only 33 migrants indicated the same. Conversely, 137 migrants reported not owning a vehicle, compared to 173 non-migrants. This suggests a notably lower rate of vehicle ownership among migrants, potentially reflecting economic disparities, differences in mobility needs, or access to private transportation. Such insights are critical for informing inclusive transportation and mobility policies targeting vulnerable populations.

On the other hand, Fig. 2 presents the distribution of public transport mode preferences among migrant and non-migrant respondents. Among non-migrants, the bus is clearly the most preferred mode, with 252 selections, followed by 224 for minibus, 65 for heavy rail/metro, 42 for tram. In comparison, migrants show a more balanced distribution across multiple modes. While the minibus (99) and bus (98) are the most frequently selected modes by migrants, the heavy rail/metro system also receives notable attention with 30 selections. This indicates that migrants make significant use of both formal and semi-formal systems and tend to diversify their public transport usage more than non-migrants, possibly due to their residential dispersion across urban peripheries and high-density corridors.

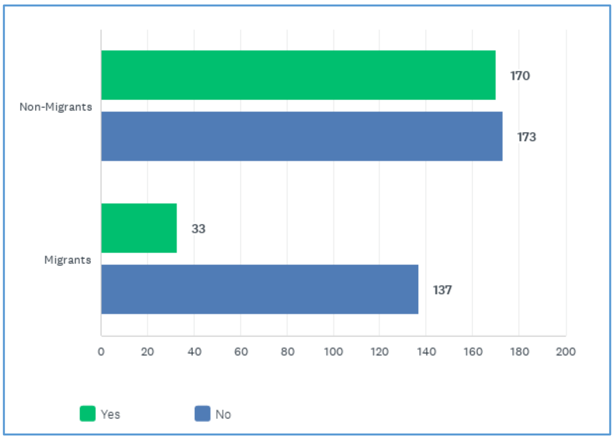

Fig. 1. Vehicle ownership by migration status

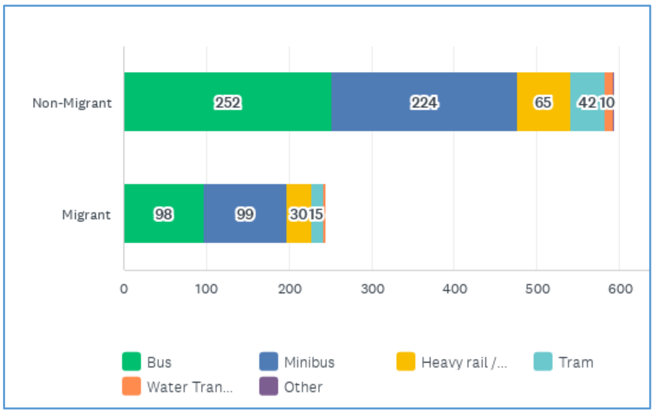

Fig. 2. PT mode/type preference

Fig. 3 compares the attitudes of non-migrant and migrant respondents toward public transport (PT) and associated information systems. Each statement was evaluated using a three-point Likert scale (Agree, Neutral, Disagree), allowing for a visual contrast between the two groups. Overall, both groups exhibit relatively positive perceptions; however, migrant respondents consistently demonstrate slightly higher levels of agreement across most items, indicating a more favorable evaluation of the transport services and digital tools available to them.

Regarding general public transport usage, both groups show high levels of agreement with the statements *"I prefer to use PT in my daily life"* and *"Using PT is cost-effective for me"*. These findings highlight the essential role that public transport plays in the daily routines of both populations. However, the slightly higher agreement among migrants suggests that they may be more reliant on public transport for economic and practical reasons, likely due to lower rates of private vehicle ownership and a greater need for affordable mobility.

Satisfaction with public transport operations—particularly in terms of routes and schedules—also appears to be slightly higher among migrants. Migrant respondents more frequently agree that *"The routes and schedules of PT meet my needs"* and that *"I can easily access up-to-date information about PT schedules."* This may be attributed to their more active use of mobile applications or their greater sensitivity to transport reliability as newcomers navigating unfamiliar environments.

Interestingly, a notable and somewhat unexpected difference between the two groups emerges in their evaluation of passenger information systems. Migrants report higher satisfaction with onboard announcements and the availability of language options compared to non-migrants. This finding is surprising given that passenger information systems in Türkiye are often perceived as inconsistent, with limited multilingual support and uneven technological integration, especially outside major urban centers. However, it is possible that some migrant respondents reside in Istanbul, where relatively advanced and accessible transport infrastructure—including digital displays, audio announcements, and mobile app integration—is more widely available.

Moreover, the higher levels of satisfaction among migrants may also be influenced by their comparative perspective: when contrasted with the public transport environments in their countries of origin, Türkiye's infrastructure—particularly in metropolitan contexts—may represent a notable improvement in terms of clarity, modernity, and accessibility. This contrast could enhance their perception of effectiveness, even if the system still presents gaps from a local policy or universal design standpoint. Therefore, this result underscores not only the importance of localized infrastructure investment, but also how relative expectations and past experiences shape perceived quality among diverse user groups.

In relation to mobile technologies, both groups express strong approval of mobile applications as tools for planning and navigating public transport. Statements such as *"I regularly use PT mobile applications on my smartphone"* and *"I can quickly access PT schedules and route information"* received high agreement from both groups, with slightly greater enthusiasm from migrants. This reinforces the critical role of digital tools in enhancing the public transport experience, especially for users who may depend on real-time information to reduce uncertainty and plan their journeys efficiently.

Despite these generally positive evaluations, certain areas reveal shared challenges. Both groups identify *long waiting times during travel* as a persistent issue. Additionally, non-migrants express more concern regarding the *safety of PT vehicles*, with higher disagreement levels in this item. These findings suggest that while information systems and mobile applications are functioning effectively, there are still operational aspects of the public transport system—particularly reliability and safety—that require attention for all users.

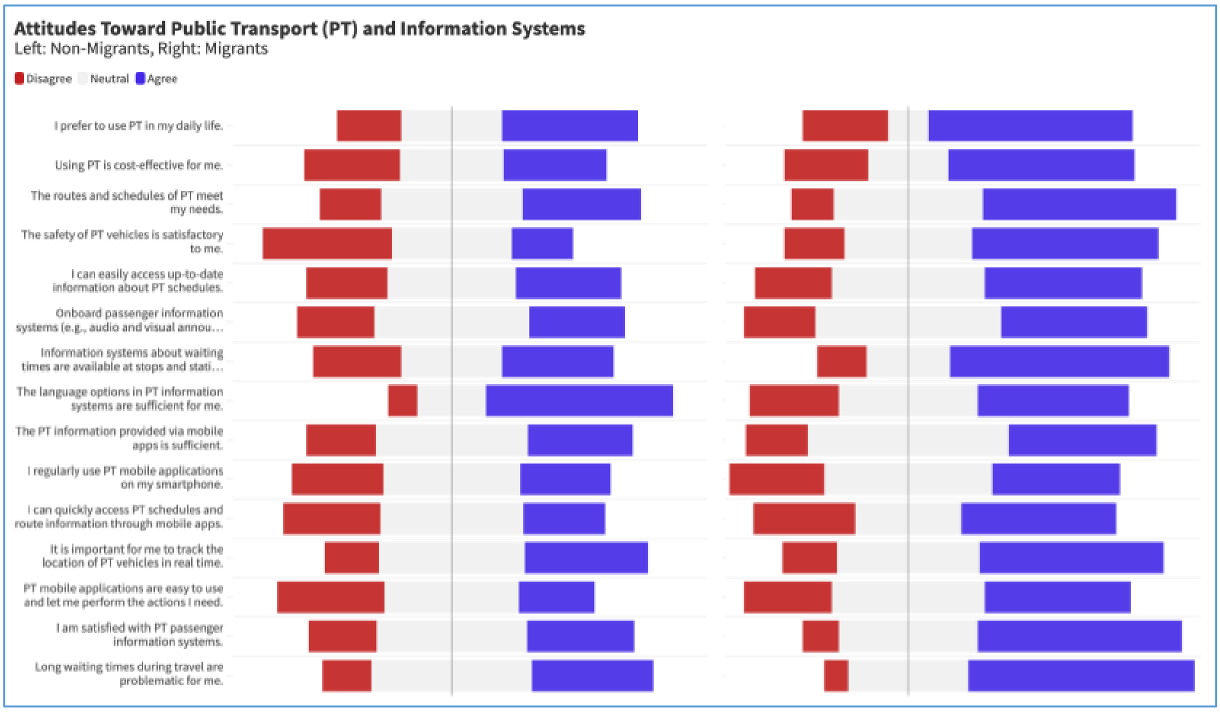

Fig. 3. Comparison of attitudes toward public transport (PT) and passenger information systems among non-migrant and migrant respondents.

5. Conclusion and discussions

This study provided a descriptive analysis of public transport usage patterns and perceptions of passenger information systems among migrant and non-migrant populations in Türkiye. Drawing on data collected through face-to-face surveys conducted in Sakarya and Istanbul, the findings offer valuable insights into how different user groups experience and evaluate urban mobility services.

The demographic analysis revealed that migrants tend to be younger, more likely to have higher educational attainment, and more concentrated in both the lowest and highest income brackets. These findings suggest a heterogeneous migrant population, consisting of both economically vulnerable individuals and highly mobile professionals or students. In contrast, non-migrants were generally spread in various age and income categories, reflecting a more stable, long-settled urban population.

Public transport usage patterns showed that both groups rely heavily on buses and minibuses; however, migrants reported greater use of metro systems, suggesting that they are more engaged with high-capacity and multimodal networks, particularly in metropolitan areas like Istanbul. Migrants also demonstrated slightly higher satisfaction levels with public transport routes, schedule information, and affordability, indicating a relatively positive experience despite broader system-level limitations in Türkiye.

A particularly notable finding was the migrants' more favorable evaluation of passenger information systems, especially in terms of onboard announcements, language accessibility, and mobile applications. This result was somewhat unexpected, given that Türkiye's information systems are often criticized for inconsistency and lack of multilingual support outside of major cities. However, this positive perception may stem from both the higher-quality infrastructure available in cities like Istanbul and a comparative advantage when contrasted with the public transport conditions in migrants' countries of origin. These experiences highlight the role of digital tools and inclusive communication strategies in improving accessibility and reducing uncertainty, particularly for newer or more vulnerable urban residents.

Despite these positive trends, both migrant and non-migrant groups expressed dissatisfaction with waiting times and, to a lesser extent, concerns about vehicle safety. These shared pain points emphasize the ongoing need to improve not only digital and informational infrastructures but also the operational reliability of public transport services.

Future research could build on these findings by expanding the geographical scope beyond Istanbul and Sakarya. While this study offers valuable insights from two urban centers with relatively developed transport infrastructures, it remains important to examine whether similar patterns and perceptions emerge in other parts of Türkiye. Comparative studies that include other metropolitan cities such as Ankara, Izmir, or Bursa, as well as smaller urban centers with less advanced public transport infrastructure, would help determine the extent to which infrastructure quality influences migrant and non-migrant experiences. Moreover, exploring cities with limited multimodal integration or reduced availability of digital information systems could reveal whether satisfaction and accessibility gaps widen under less favorable transit conditions. Such efforts would contribute to a more comprehensive understanding of transport equity and informational inclusion across different urban contexts in Türkiye.

In conclusion, the study underscores the importance of maintaining and expanding inclusive, multimodal, and technology-enhanced transport systems that meet the needs of a diverse urban population. Policymakers should pay particular attention to the mobility challenges of migrants—not only through equitable route and fare planning, but also by ensuring that information systems are accessible, multilingual, and responsive to varying levels of digital literacy. Doing so will support more inclusive, efficient, and resilient public transport networks in Türkiye's rapidly urbanizing contexts.

Acknowledgement

The authors would like to thank all participants who contributed to the survey conducted in Istanbul and Sakarya. Special appreciation is extended to the local institutions and community centers that supported access to respondents during fieldwork. This study was conducted as part of an independent academic research initiative. The authors also acknowledge the use of artificial intelligence-based tools (ChatGPT) for language editing, text structuring, and terminology support during the writing process, which contributed to the clarity and consistency of the manuscript.

References

Blumenberg, E., & Evans, A. (2010). Planning for demographic diversity: The case of immigrants and public transit. *Journal of Public Transportation, 13*(2), 23–45. https://doi.org/10.5038/2375-0901.13.2.2

Corsar, D., Cottrill, C., Beecroft, M., Nelson, J., Papangelis, K., Edwards, P., … & Sripada, S. (2018). Build an app and they will come? Lessons learnt from trialling the GetThereBus app in rural communities. *IET Intelligent Transport Systems, 12*(3), 194–201. https://doi.org/10.1049/iet-its.2016.0216

Davidsson, P., Hajinasab, B., Holmgren, J., Jevinger, Å., & Persson, J. (2016). The fourth wave of digitalization and public transport: Opportunities and challenges. *Sustainability, 8*(12), 1248. https://doi.org/10.3390/su8121248

Gruer, L., Agyemang, C., Bhopal, R., Chiarenza, A., Krasnik, A., & Kumar, B. (2021). Migration, ethnicity, racism and the COVID-19 pandemic: A conference marking the launch of a new global society. *Public Health in Practice, 2*, 100088. https://doi.org/10.1016/j.puhip.2021.100088

Li, J., Li, T., & Wang, W. (2024). Get out of life on the edge: The role of urban public health services on migrants' social integration in China. *Population, Space and Place, 30*(8), e2841. https://doi.org/10.1002/psp.2841

Nteliou, E., Koreman, J., Tolskaya, I., & Kehagia, O. (2021). Digital technologies assisting migrant population overcome language barriers: The case of the easyRights research project. In *Advances in Information and Communication* (pp. 108–124). https://doi.org/10.1007/978-3-030-77889-7_8

Pilling, S., & Estes, L. (2016). Barriers to perinatal care among migrant women farmworkers in northern Ohio. Universal *Journal of Public Health, 4*(2), 47–54. https://doi.org/10.13189/ujph.2016.040201

Saghapour, T., Moridpour, S., & Thompson, R. (2016). Public transport accessibility in metropolitan areas: A new approach incorporating population density. *Journal of Transport Geography, 54*, 273–285. https://doi.org/10.1016/j.jtrangeo.2016.06.019

Sener, I., Lee, K., Durand, C., Oluyomi, A., & Kohl, H. (2019). Intention to use light-rail transit in Houston, Texas, United States: Findings from the Travel-Related Activity in Neighborhoods study. *International Journal of Sustainable Transportation, 14*(12), 944–955. https://doi.org/10.1080/15568318.2019.1663962

Setiabudi, D., & Tjahyana, L. (2015). Android and iOS hybrid applications for Surabaya public transportation route. *International Journal of Science and Engineering Applications, 4*(4), 223–227. https://doi.org/10.7753/ijsea0404.1012

Sime, D., & Fox, R. (2014). Migrant children, social capital and access to services post-migration: Transitions, negotiations and complex agencies. *Children & Society, 29*(6), 524–534. https://doi.org/10.1111/chso.12092

Vollenwyder, B., Buchmüller, E., Trachsel, C., Opwis, K., & Brühlmann, F. (2020). My train talks to me: Participatory design of a mobile app for travellers with visual impairments. In *Design, User Experience, and Usability: Design for Contemporary Interactive Environments* (pp. 10–18). https://doi.org/10.1007/978-3-030-58796-3_2

Waitt, G., Kerr, S., & Klocker, N. (2016). Gender, ethnicity and sustainable mobility: A governmentality analysis of migrant Chinese women's daily trips in Sydney. *Applied Mobilities, 1*(1), 68–84. https://doi.org/10.1080/23800127.2016.1147751

Welsch, J., Conrad, K., & Wittowsky, D. (2016). Exploring immigrants' travel behaviour: Empirical findings from Offenbach am Main, Germany. *Transportation, 45*(3), 733–750. https://doi.org/10.1007/s11116-016-9748-9

Yang, N., Liu, N., Liu, N., Liu, N., & Gan, N. (2019). Comprehensive public transport service accessibility ındex—A new approach based on degree centrality and gravity model. *Sustainability*, *11*(20), 5634. https://doi.org/10.3390/su11205634

Zhang, L., Tao, L., Yang, F., Bao, Y., & Li, C. (2024). Promoting green transportation through changing behaviors with low-carbon-travel function of digital maps. *Humanities and Social Sciences Communications, 11*(1), 1–11. https://doi.org/10.1057/s41599-024-02737-8

Performance of concrete mix incorporating incinerated bottom ash

Handojo Djati Utomo*[1], Li Xiaodong[2]

[1] *School of Architecture and The Built Environment, 500 Dover Road, Singapore 139651*
[2] *Advanced Material Technology Centre, 500 Dover Road, Singapore 139651*

Abstract. Replacing some Microfine Cement (MCEM) with Silica Aerogel (SA), Aerogel Aggregate (AA) and Ash Residue (AR) derived from Incinerated Bottom Ash (IBA) during concrete casting were studied. During fabrication, aerogel materials made from IBA exhibited excellent characteristics, such as low thermal conductivity, low density and high porosity, making it heatproof, hydrophobic, fire resistant and highly absorptive. The SA and AR were added to replace 5% - 30% in volume of MCEM. The compressive strength of the concrete cubes were then tested after 7, 14 and 28 days. The compressive strength of the SA concrete mix were measured ranging from 19.10 MPa to 34.19 MPa, within the same range of normal concrete mix. It was also observed that the compressive strength could reach up to 25.58 MPa after 28 days of casting period when 5% of MCEM being replaced with AA. The average compressive strength of AA concrete mix is higher than those in SA concrete mix but comparable to those in AR concrete mix. Overall, the replacement of MCEM with 5% of AR or AA maintained the same compressive strength of the 100% MCEM concrete mix. In conclusion, the replacement of MCEM with silica aerogel components might reduce the cost of concrete making, while the fabrication of aerogel could minimise the waste disposal to Semakau landfill of Singapore.

Keywords: Compressive strength; Incinerated bottom ash; Micro-Cement; Silica aerogel, Sustainable material

1. Introduction

Singapore is a city-state island that holds a growing population of 5.704 million (2019). In a tiny country where land is scarce, Singapore's only waste landfill, Pulau Semakau, is expected to be completely stocked by 2035. It is essential to divert incineration ash and use it for construction purposes to avoid potential crises for a new landfill (Patra *et al*., 2021). Singapore's garbage is burned in four Waste-to-Energy incinerator plants, 7% of the total burned rubbish is converted into energy, and the remaining 93% generates approximately 600 tonnes of non-incinerable ash, including incinerated bottom ash (IBA) (Tan, 2021). It is predicted that a new landfill with a size equivalent to Pulau Semakau has to be constructed every 25 to 30 years. Such a man-made landfill island is extremely highly-priced, costing about $610 million to create (Murdoch, 2021). Due to this, Singapore has to constantly upgrade and implement new technologies such as more effective incinerators to keep abreast with the demands of waste produced per year. It is also estimated by the World Bank that global waste could grow by 70% by 2050 from 2.01 billion tonnes to 3.40 billion tonnes with the buildup of urbanisation and increasing population. Therefore, it is vital that we implement proper and cost-efficient methods in the treatment of ash and also find ways to create products out of ash such as Silica Aerogel (SA), Aerogel Aggregate (AA) and Ash Residue (AR) to better improve on other aspects of the current materials such as concrete, widely used in the construction and infrastructure industries.

SA has ultralight weight, high porosity with 99% air by volume, low density, and thermal conductivity range (0.002 ~ 0.03 W/mK) lower than still air (0.6 W/mK). The highly porous and flame retardant SA is also superhydrophobic at 99% under normal temperature. The extremely low thermal conductivity which results from the composition of 99% air is the characteristic of the SA that we intend to utilize to improve the fire resistance of concrete. Aerogel is also known as a very strong material. Although a typical SA could hold up to 2000 times its weight in applied force, this only holds when the conditions of the force are gently and uniformly applied (aerogel, 2021). Meanwhile AA and AR could described as a SA derivation and SA by-products during SA fabrication. In this laboratory work, a different concentrations of SA, AA, and AR were added during concreting work to test the compressive strength of the SA, AA and AR concrete mixes.

* Corresponding author, E-mail: han@sp.edu.sg

https://doi.org/10.31462/icearc2025_ce_was_073

golden light publishing

One of the most common cement that is used in the construction industry is Ordinary Portland Cement (OPC). This type of cement is made by combining limestone with other raw ingredients such as argillaceous, calcareous, and gypsum to make powder. It is preferred in places where fast construction is required. This cement is available in the market in three grades namely OPC 33, OPC 43 and OPC 53. After 28 days, these grades show the maximum strength of cement (Civil Digital, 2021).

A part of concreting works, Microfine Cement (MCEM) is widely used in pre-excavation grouting and post excavation grouting, both in drill and blast, and Tunnel Boring Machine (TBM) construction (Stalprotect, 2021). MCEM is a specialized cement that is mainly used in underground construction works such as tunnels, caverns, fixation, water sealing of tunnel walls and water scaling in fractured zones during tunnel construction (Engro-global, 2021). They can provide exceptional advantages and benefits over OPC due to the MCEM's ability to penetrate finer rock fractures. This decreases its rock mass permeability to the required level through the primary grouting operation. The use of MCEM indirectly minimise the need for a secondary microfine grouting or the injection of low viscosity chemical resins. Furthermore, the material is cured into hardened concrete which does not cause pollution to underground soils or water supplies (Cement, 2021). Moreover, it also offers an improvement in rock stability from filling rock discontinuities with its high strength properties. It is also commonly used for stabilisation or consolidation of soils as OPC grains are too coarse. MCEM is a polymer modified cement-based coating possessing more than twice the specific surface area (> 800 m^2/kg) (Engro-global, 2021a) in comparison to OPC (331 m^2/kg) (Aso-cement, 2021) with excellent permeability, strength, and durability properties. There are mainly 3 types of Microfine Cement: MCEM, Prefine 60/80, and RapidSet 150 (Engro-global, 2021). Each of them varies in terms of their specific surface area, cost and application. Despite its greater functionality, there is a huge price difference between MCEM and OPC, resulting in many companies opting for OPC over MCEM. Based on one of SP industry partners, EnGro Corporation Limited, OPC costs SGD 0.12/kg whereas MCEM can costs 5- 6 times more expensive or as much as SGD 0.65/kg.

The main objective is to investigate the compressive strength of concrete mix with replacement of cement by aerogel compound made from IBA. While comparing the compressive strength with a standard, the project aimed to replace MCEM/ OPC with SA, AA and AR as the main cost in concreting works. The secondary objective was to prolong the Semakau landfill in Singapore as it could serve a cheaper alternative by-products.

2. Materials and methods in fabricating aerogels and designing concrete mix

2.1. Fabrication process of SA, AA and AR

Raw IBA, provided by an industry partner, was oven dried to remove the moisture and stench. The raw ash was grinded into finer power size using a ball milling machine at 250 rpm for 30 minutes. Afterwards, the powerised ash is sieved in 300 µm of ASTM Standards by using a sieving machine and the grinded ash is stored in bottled containers. A chemical treatment was then carried out by adding IBA into 30% of HNO_3 and letting it stirred using a magnetic stir bar in a 1 L of glass beaker for 30 minutes to remove unwanted chemicals including metals present in the ash. The magnetic stir bar ensures proper mixing of the process. The solution containing ash is then poured into bottled containers and placed into the centrifuge machine for another 30 minutes to separate the ash from the acid solution. The remaining ash sludge that is settled at the bottom of the bottle container is then washed with deionized water and placed in the centrifuge machine for 30 minutes to remove excess acid that may still be present in the ash. The solution was then disposed of into an acid waste container. The rinsing process was repeated to ensure that the ash sludge is clean and all the acid was washed away. The ash sludge was removed from the bottle container and transfer it onto a weighing boat before placing it in the oven for drying as shown in Fig. 1.

Silica extraction is carried out by using 1 M NaOH solution in stainless steel autoclave at 180°C for 3 hours. After that, the ash was filtered out from the solution to obtain the water glass solution. Filtering of solution is conducted by using a fibre filter paper placed on a vacuum pumping machine. The filter paper and the pumping process was repeated until the solution becoming visibly clear from residue. Lastly, the ash sludge was extracted from the flask and place in the oven for drying. This ash sludge will be used for concrete cube casting known as AR after drying. After obtaining water glass solution. 0.1 M Hydrocloride Acid is then added drop by drop to fabricate silica gel via sol-gel method. In this process, silica gel is smashed and added slowly into triple solution containing trimethylchlorosilane, isopropanol and n-hexane . This step is to make the silica gel hydrophobic. The layer of white gel is then transferred onto a petri dish and put into the oven at 150 °Cfor drying for 1 hour. The SA that was produced after drying will be used for concrete cube casting.

AA was made by cutting the Aerogel Blanket (AB) that purchased from Guangdong Alison Technology (China) into small cubes of 1 cm^3. AB is a product by the combination of fibreglass mixed with SA. AB is known as a good heat and sound insulator. It also inherits most of the characteristics of the SA such as it has low density, ultralight, and hydrophobic. In terms of cost-effectiveness, AA is higher than SA because it only contains about 10% of SA and 90% of fiberglass.

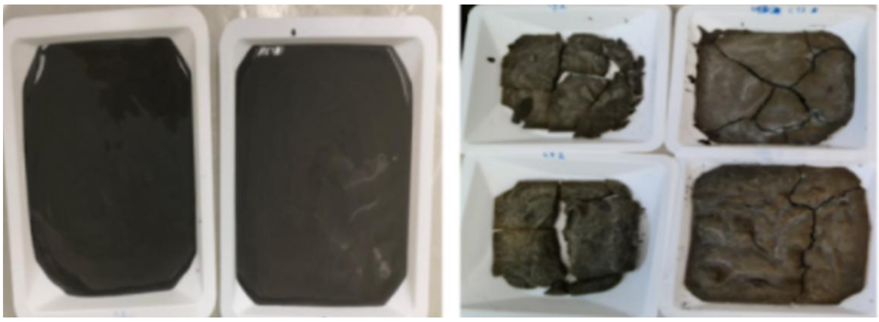

Fig. 1. Ash Sludge Before (left) and After drying (right)

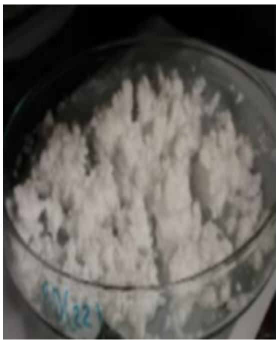

Fig. 2. SA after being over dried

2.2. Design of Concrete Mix

Quantity of SA was calculated in percentage by volume instead of weight since SA and AA has a very low density of 0.100 g/cm^3 and 0.180 g/cm^3 respectively. Table 1 showed the design of 1,000 cm^3 of concrete mix composition with various water/ cement ratios. In details, Table 2 showed an example of the compositions of individual material in making 1,000 cm^3 of SA concrete cubes with water/ cement (W/C) ratio of 0.625. Similar composition was shown in Table 3 for the making of 1,000 cm^3 of AA concrete mix at W/C of 0.65. Quantity of AR was calculated in percentage by weight since the density was similar to MCEM and OPC (density of 0.850 g/cm^3). Table 4 showed the composition of individual material in making 1,000 cm^3 of AR concrete cube.

Table 1. Design of 1,000 cm^3 of concrete mix composition

Coarse Aggregate	1.000 kg
Fine Aggregate	0.770 kg
Cement (MCEM / OPC)	0.400 kg
Type of mix	Water/Cement ratio (W/C
MCEM + Silica Aerogel (SA)	0.625
OPC + Aerogel Aggregate (AA)	0.650
OPC + Ash Residue (AR)	0.700

Table 2. Composition of materials in making 1,000 cm3 of SA concrete cubes at water/cement ratio of 0.625

Item	Material composition			
	MCEM (% in weight)	MCEM (kg) ± 5%	SA Powder (% in Volume)	Mass of SA (g)
100% MCEM	100	0.40	NA	0
95% MCEM + 5% SA	95	0.38	5	2.35
90% MCEM + 10% SA	90	0.36	10	4.70
85% MCEM + 15% SA	85	0.34	15	7.05
80% MCEM + 20% SA	80	0.32	20	9.40
75% MCEM + 25% SA	75	0.30	25	11.75
70% MCEM + 30% SA	70	0.28	30	14.10

Table 3. Composition of materials in making 1,000 cm3 of AA concrete cubes at water/cement ratio of 0.65

Item	Material composition			
	OPC (% in Weight)	OPC (kg)	AA (% in Volume)	AA (g)
100% OPC	100	0.40	NA	0
95% OPC + 5% AA	95	0.38	5	1.14
90% OPC + 10% AA	90	0.36	10	2.29
85% OPC + 15% AA	85	0.34	15	3.43
80% OPC + 20% AA	80	0.32	20	4.57
75% OPC + 25% AA	75	0.30	25	5.72
70% OPC + 30% AA	70	0.28	30	6.86

Table 4. Composition of materials in making 1,000 cm3 of AR concrete cubes at water/cement ratio of 0.7

Item	Material composition			
	OPC (% in Weight)	OPC (kg)	AR (% in Volume)	AR (g)
100% OPC	100	0.40	NA	0
95% OPC + 5% AR	95	0.38	5	20
90% OPC + 10% AR	90	0.36	10	40
85% OPC + 15% AR	85	0.34	15	60
80% OPC + 20% AR	80	0.32	20	80
75% OPC + 25% AR	75	0.30	25	100
70% OPC + 30% AR	70	0.28	30	120

2.3. Concrete Making

SA, AA and AR are weighed using a digital analytical balance based on the required amount calculated in Section 2.2. Steel cube moulds, each with dimension of 10 × 10 × 10 cm^3, were coated with one layer of oil throughout surfaces in contact with concrete to ensure for easy extraction. After weighing the required amount of cement either MCEM or OPC, fine aggregate and coarse aggregate, all the materials are poured into a concrete mixer. Thereafter, SA/AA/AR are added into the mixture and mixed for one minute. Water was poured into the mixture and stir thoroughly until the water is completely mixed with the mixture. After the mixture is thoroughly mixed, half of the mixture was poured into the mould and compacted using a square compacting bar 35 times. The procedure was repeated for the second half of the mixture before smoothening the top surface of the cube with a finishing trowel. The cubes were strored in a dry and well-ventilated area for 1 day. All the screws were on the mould were removed, the samples were extracted and stored in water bath for 7, 14 and 28 days (Fig. 3) before proceeding with compressive testing. All sample were made in duplicate with the total samples being made up to 42 concrete cubes.

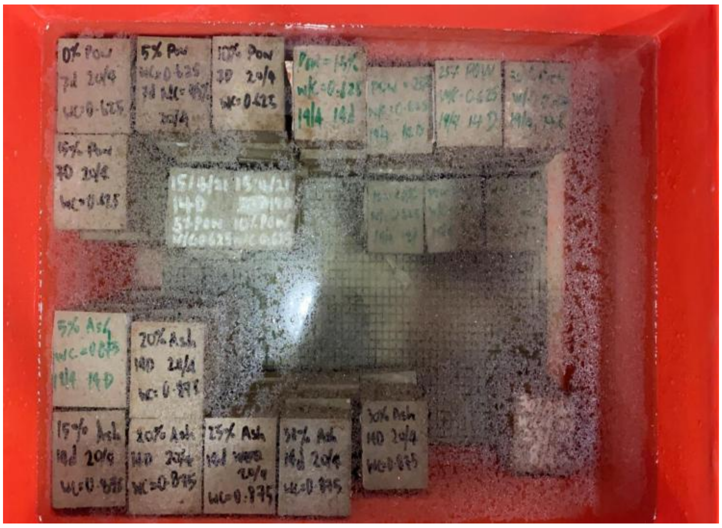

Fig. 3. Storage of concrete cubes in water bath (hydration)

3. Experimental results and discussions

3.1 X-Ray Fluorescence (XRF) scanning result

The elements of raw IBA, SA, AR, MCEM and OPC were analysed and the content was listed in 3.1 to understand the change of elemen composition in each sample of materials. Table 5 indicated that the first 3 main elements in IBA were silica (Si) and calcium (Ca) and iron (Fe), which Si and Ca filled more than 30% of IBA sample. In contrast, Table 6 indicated that Si was successfully embedded in SA (> 90%) to replace other elements, except chloride compound (Cl). It also showed that AR was contained similar composition of elements as extracted in IBA but with Ca compound had tripled up to >30% than those in SA. Table 6 also showed that Ca compound was the main element found in MCEM and OPC at 84.646% and 78.735% respectively.

Table 5. XRF analysis results on raw IBA samples

Elements	Types of IBA sample					
	Top Large-1	Top Large-2	Top Large-3	Top Small-1	Top Small-2	Top Small-3
Si (%)	35.442	36.643	38.184	27.831	32.204	35.743
Ca (%)	34.677	33.339	31.761	42.929	37.923	34.078
Fe (%)	12.459	12.380	11.843	11.376	11.793	12.019
Al (%)	8.274	9.203	9.553	7.624	8.550	9.407
K (%)	4.298	4.232	4.339	4.308	4.288	4.203
Ti (%)	2.109	2.109	2.007	2.340	2.232	2.072
S (%)	0.690	0.690	0.383	1.889	1.277	0..645
Zn (%)	0.504	0.504	0.642	0.471	0.424	0.470
Mn (%)	0.270	0.270	0.258	0.287	0.258	0.252
Cu (%)	0.455	0.455	0.286	0.231	0.301	0.367
Sr (%)	0.166	0.166	0.207	0.201	0.174	0.159
Cr (%)	0.311	0.311	0.289	0.165	0.245	0.330
Zr (%)	0.123	0.123	0.114	0.105	NA	0.106

Table 6. XRF analysis results on SA, AR, MCEM and OPC samples used for concrete casting

Elements	Types of samples							
	SA-1 Top (SA)	SA-2 Mid (SA)	SA-3 Bottom (SA)	CY4-1 0(AR)	CY4-4 0(AR)	CY4-2 0(AR)	MCEM	OPC
Si (%)	94.584	93.312	92.536	33.639	NA	NA	7.349	8.922
Ca (%)	NA	NA	NA	25.146	NA	NA	84.646	78.735
Fe (%)	NA	NA	NA	30.059	NA	NA	4.734	5.073
Al (%)	NA	NA	NA	NA	NA	NA	NA	3.781
K (%)	NA	NA	NA	1.510	NA	NA	0.816	0.705
Ti (%)	NA	NA	NA	5.655	NA	NA	0.363	0.445
S (%)	NA	NA	NA	NA	NA	NA	1.640	1.242
Zn (%)	NA	NA	NA	0.954	NA	NA	NA	0.082
Mn (%)	NA	NA	NA	0.555	NA	NA	0.130	0.157
Mg (%)	NA	NA	NA	NA	NA	NA	NA	0.486
Cu (%)	NA	NA	NA	1.115	NA	NA	NA	0.053
Sr (%)	NA	NA	NA	0.440	NA	NA	0.158	0.236
Cr (%)	NA	NA	NA	0.307	NA	NA	NA	0.045
Zr (%)	NA	NA	NA	0.366	NA	NA	NA	0.038
Ag (%)	NA	NA	NA	0.102	NA	NA	NA	NA
Eu (%)	NA	NA	NA	NA	NA	58.107	NA	NA
Ce (%)	NA	NA	NA	NA	NA	41.893	NA	NA
Mo (%)	NA	NA	NA	NA	0.595	NA	NA	NA
Ba (%)	NA	NA	NA	NA	43.393	NA	NA	NA
Cl (%)	5.416	6.688	7.464	NA	56.012	NA	NA	NA

3.2 Compressive strength measurements

To test the concrete mixes strength, two samples of each mix (different % of MCEM to SA or AA or AR) were casted for 7 days, 14 days and 28 days and the result shown in Fig. 4. The minimum strength of the structural concrete of 2500 psi (17.24 MPa) (ACI, 2021) was used as the baseline compressive strength for the discussion.

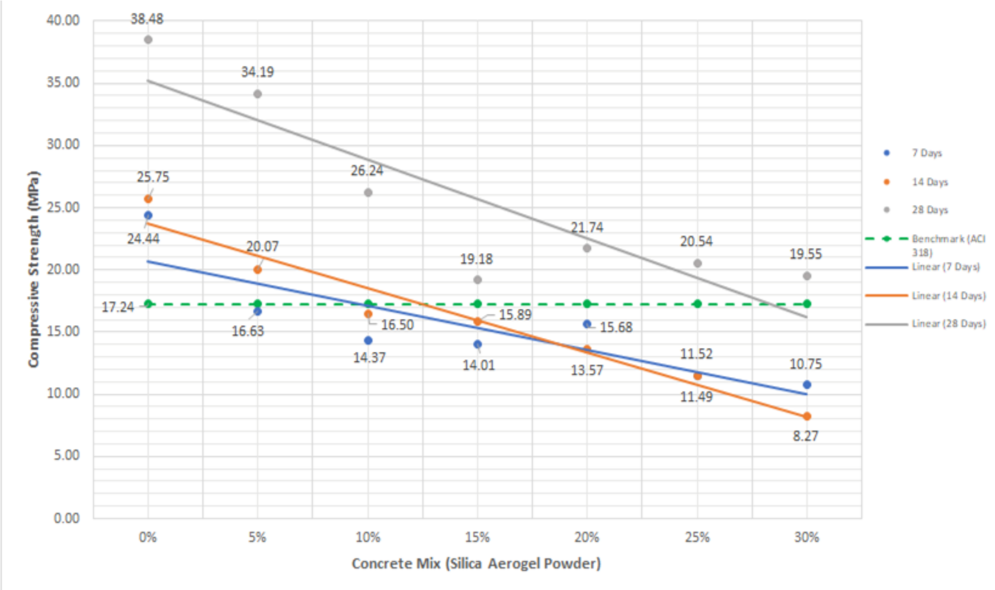

Fig. 4. Compressive strength of SA concrete cubes after 7, 14 and 28 days casting periods

Fig. 4 showed that the percentage of SA in concrete mix increasing from 5% to 30% while the compressive strength of the concrete cubes decreasing quite significantly. The reduction in compressive strengths from 0% to 30% SA content (highest value - lowest value) for casting periods of 28 days, 14 days and 7 days are 18.93 MPa, 17.48 MPa and 13.69 MPa respectively. The replacement of Ca with Si compounds could be the reason for the reduction of the compressive strength, as shown in Table 5 and 6. Hence, the replacement of MCEM with SA in concrete mix without using any binding agents have significantly lowered the compressive strength of concrete.

In constract, the compressive strength of AR in concrete mix decreased insignificantly. Fig. 5 showed that the average compressive strength dropped approximately 3 MPa for the 7, 14 and 28 days after AR replacement in concrete mix from 0% to 30%. This data showed a consistent decreasing trend of compressive strength. Overall, all of the concrete samples reached their maximum compressive strength after 28 days of casting period.

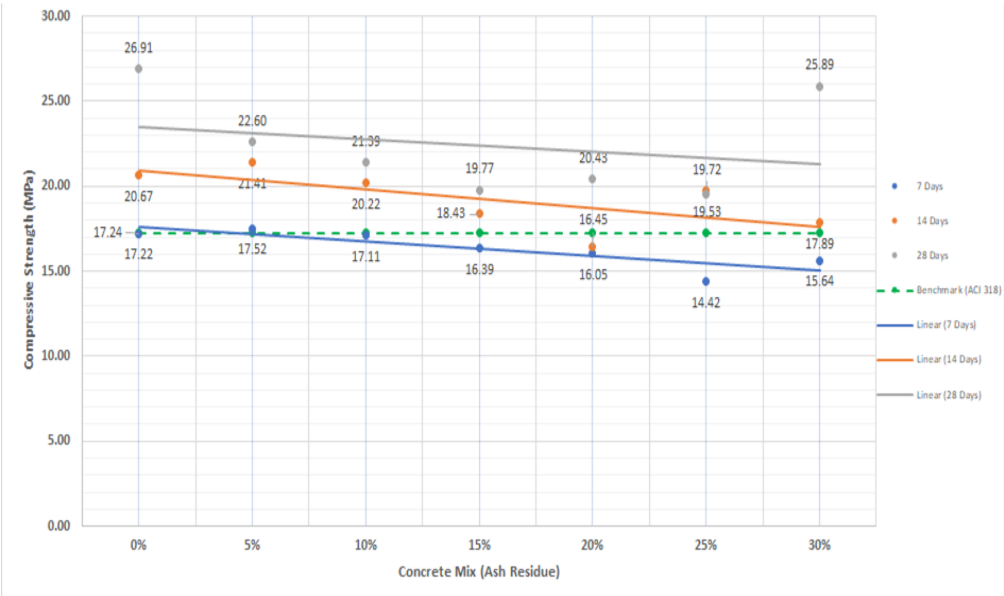

Fig. 5. Compressive strength of AR concrete cubes after 7, 14 and 28 days casting periods

Fig. 6 showed that the range of decrement for samples with different AA replacement in concrete samples was approximately between 0.15- 7.45 MPa. The average compressive strength dropped after replacement of AA from 0% to 30% for 28, 14 and 7 days of casting periods were 5 MPa, 9.2 MPa and 7.5 MPa respectively. During observation, it showed that AA results were more fluctuative than SA as AA was irregular form of aggregates.

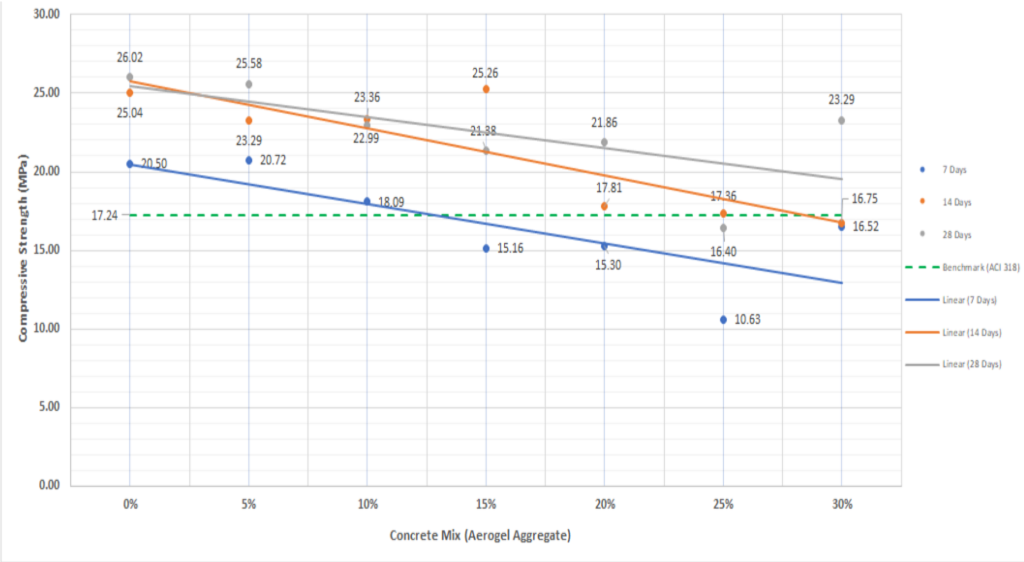

Fig. 6. Compressive strength of AA concrete cubes after 7, 14 and 28 days casting periods

4. Conclusions

In general, IBA derivatives shows a potential by- product material to replace cement in concrete mix based on the compressive strength. The replacement of cement using IBA can eventually prolong the Semakau landfill. Some specific discussions can be detailed as follows:

- The compressive strength of concrete decreased as SA replacement increased. However, the compressive strength of the SA concrete (19.55 - 38.48 MPa) is relatively strong compared to the reference of the average value (20 MPa ~ 40 MPa, ranging from 0.4 ~ 0.6 W/C ratio (The constructor, 2021), considering that the W/C ratio of the SA concrete samples is 0.625 with no additional binding agents were used. However, SA might be not cost-effective for MCEM replacement.
- The AR concrete mix is relatively consistent with the lesser reduction of compressive strength than those SA concrete mix. Therefore, it may be potential to produce concrete with the same compressive strength as 100% cement with the replacement of 5% of cement with AR. The project may reduce the concrete cost more than 5% due to the double effect from zero cost of ash residue and lesser of the waste disposal to Semakau landfill.
- AR and AA possessed most of the characteristics of SA, some being low density, ultralightweight, and hydrophobic. These attributes may lead to new findings such as improved durability, heat resistance or improved noise insulation of concrete.
- MCEM concrete incorporating SA has a potential to be noise and thermal insulator as the two main characteristics of SA. However, based on the result from our experiment, the compressive strength of the concrete could not be maintained well thus the application may be limited to non- structural concretes.

Acknowledgments

The research described in this paper was supported by Singapore Polytechnic Cat A Fund 2025 and FYP funds.

References

ACI. (2021). *An ACI standard building code requirements for structural concrete (ACI 318-19)* [PDF]. https://www.usb.ac.ir/FileStaff/5526_2020-1-25-11-12-7.pdf (Accessed 11 August 2021)

Aerogel.org. (2021). Strong and flexible aerogels. http://www.aerogel.org/?p=1058 (Accessed 28 July 2021)

Aso-cement. (2021). *Ordinary Portland Cement / ASO CEMENT*. http://www.aso-cement.jp/en/products/product_ordinary.html (Accessed 8 May 2021)

Cement, M. (2021). *Microfine Cement - PreFine 60/80 (Microfine Cement)*. Zureli.com. https://www.zureli.com/product/microfine-cement-prefine-6080-microfine-cement (Accessed 8 May 2021)

Civil Digital. (2021). Ordinary Portland Cement (OPC) & Portland Pozzolana Cement (PPC) | Differences. https://civildigital.com/ordinary-portland-cement-opc-portland-pozzolana-cement-ppc-differences/ (Accessed 28 July 2021)

Engro-global. (2021). *MicroFine Cement*. https://engro-global.com/microfine-cement/ (Accessed 26 April 2021)

Engro-global. (2021a). *MicroCem* [Brochure]. https://engro-global.com/wp-content/uploads/Product_Brochure/MicroCem-MFC_brochure_Rev00.pdf (Accessed 8 May 2021)

Patra, S., Whaung, S., & Kwan, W. (2021). Analysis of heavy metals in incineration bottom ash in Singapore and potential impact of pre-sorting on ash quality. *ScienceDirect*. https://www.sciencedirect.com/science/article/pii/S1876610217364743 (Accessed 6 May 2021)
Murdoch, G. (2021). Trash and burn: Singapore's waste problem. *Reuters*. https://www.reuters.com/article/us-waste-singapore-idUSSP9046620080522 (Accessed 6 May 2021)
Stalprotect. (2021). *Normet Microfine Cement* [Brochure]. https://stalprotect.ru/f/normet_microfine_cement_brochure_eng_0.pdf (Accessed 8 May 2021)
Tan, A. (2021). Singapore aims to send one-third less waste to Semakau landfill by 2030: Amy Khor. *The Straits Times*. https://www.straitstimes.com/singapore/environment/spore-aims-to-send-one-third-less-waste-to-semakau-landfill-by-2030-amy-khor (Accessed 6 May 2021)
The Constructor. (2021). Normal concrete vs. high-strength concrete properties and difference. https://theconstructor.org/concrete/normal-high-strength-concrete-properties/17771/ (Accessed 15 May 2021)

4th International Civil Engineering & Architecture Conference
15-17 May 2025, Trabzon, Türkiye

Investigation of filtration performance of recycled asphalt material under different geotextile apparent opening sizes

Emir Yildiz*[1], Ozge Tosunbayraktar[1], Mehmet H. Calım[1], Rumeysa Usta[1], Sabriye B. Ikizler[1], Asli Y. Dayioglu[2], Mustafa Hatipoglu[2]

[1] *Karadeniz Technical University, Department of Civil Engineering, 61080 Trabzon, Türkiye*
[2] *Istanbul Technical University, Department of Civil Engineering, 34469 Istanbul, Türkiye*

Abstract. The rapid depletion of natural resources and the increasing accumulation of waste have become global concerns in terms of environmental sustainability, highlighting the importance of innovative recycling practices. The growing interest in sustainability practices in civil engineering has encouraged the exploration of alternative materials for infrastructure applications. Recycled asphalt pavement (RAP) materials are considered a potential alternative to natural aggregates (NA) due to their ability to reduce environmental pollution, conserve energy, and lower costs. This study examines the filtration and drainage properties of RAP in subgrade drainage systems. Laboratory tests were conducted to evaluate the long-term performance and clogging behavior of RAP-based drainage systems used in combination with nonwoven geotextiles of varying pore sizes. Long-term filtration tests (LFT) were carried out using a specially designed and remanufactured test setup developed by ASTM D5101 standards. In this setup, a constant hydraulic gradient of 0.33 was used. Parameters such as the hydraulic gradient ratio (GR) and the permeability ratio (KR) were monitored to assess the system's functionality under various geotextile apparent opening sizes. This study revealed that RAP materials meet the performance standards required for filtration applications in subgrade drainage systems. These findings suggest that RAP can contribute to waste management and provide more sustainable infrastructure solutions by reducing the reliance on natural aggregates.

Keywords: Recycled asphalt pavement; Geotextile; Filtration; Demolition waste; Sustainability

1. Introduction

The increasing global population, rapid urbanization, and expanding infrastructure demands place significant pressure on natural resources and pose a serious threat to sustainable development. In this context, the volume of construction and demolition (C&D) waste has substantially increased, and the effective management of this waste has become a strategic priority both environmentally and economically (Silva et al., 2017; Edeme & Chibuzo, 2018). Construction and demolition waste includes materials such as concrete, metal, wood, and ceramics, which have the potential to be processed and reused in various infrastructure applications (Lu & Yuan, 2011).

Recent studies have shown that recycling C&D waste within the framework of sustainability principles not only reduces environmental impacts but also generates economic benefits (Tošić et al., 2015; Caro et al., 2024). Accordingly, many countries have developed legal regulations that encourage recycling and have made the separation and reuse of waste at the source mandatory (Purchase et al., 2022; Kim, 2021).

Subsurface drainage systems in road infrastructure are of critical importance for both the service life of the road and vehicle safety. The particle size distribution, permeability coefficient, and long-term filtration behavior of the aggregate materials used in these systems directly affect their performance (Li et al., 2017). However, the use of natural aggregates contributes to environmental degradation and the rapid depletion of natural resources. As sustainability and environmental concerns gain prominence in modern road construction, the use of recycled materials in infrastructure systems has become increasingly widespread. In this regard, reclaimed asphalt pavement (RAP) stands out among C&D wastes as a significant alternative due to its economic advantages, potential to reduce natural resource consumption, and ability to ensure long-term filtration performance (Rout et al., 2023).

Subsurface drainage systems to function effectively, the filter material must have sufficient permeability and be capable of limiting the passage of fine particles. The suitability of RAP as a filter material must be evaluated in terms of its long-term filtration performance. To prevent damage to the drainage structure due to particle movement

*Corresponding author, E-mail: yemir7433@gmail.com

https://doi.org/10.31462/icearc2025_ce_was_312

caused by water flow, the hydraulic properties of the recycled asphalt material must be accurately determined, and the drainage system should be designed accordingly. In recent years, experimental studies on the use of RAP in drainage systems have shown that this material demonstrates adequate hydraulic performance (Dager et al., 2023).

Thanks to its particle structure and drainage properties, reclaimed asphalt pavement (RAP) has the potential to be used as a filter material in road infrastructure. However, the physical and mechanical behaviors of RAP differ from those of natural aggregates, which may limit its use as a standalone material in drainage systems. Therefore, to enhance the long-term filtration performance of RAP, it is often used in combination with nonwoven geotextile materials (Mijica et al., 2020). Nonwoven geotextiles are geosynthetic materials produced by bonding natural or synthetic fibers (usually polypropylene or polyester) through needling, thermal, or chemical methods. Due to their flexible structure, high water permeability, and large pore openings, these materials are widely used in many geotechnical engineering applications (Koerner, 2005; Wu et al., 2020). Nonwoven geotextiles typically serve filtration, drainage, separation, protection, and reinforcement functions. When used with soils that have heterogeneous particle sizes or with alternative aggregates such as reclaimed asphalt, the structural and hydraulic functions of the geotextile are of critical importance (Bouazza, 2002; Tanasă et al., 2022).

The long-term performance of RAP when used in conjunction with nonwoven geotextiles is evaluated using filtration tests conducted according to ASTM D 5101. In these tests, parameters such as the permeability ratio (KR) and gradient ratio (GR) are used to assess the potential for fines accumulation and clogging on the geotextile surface over time (Sariahmetoglu et al., 2020).

In this study, the behavior of RAP material with different geotextile properties in subsurface drainage systems was investigated experimentally. The GR values of the systems exceed the acceptable clogging threshold of 3 within a short period of time. Moreover, a a strong correlation between the geotextile's apparent opening size and the filtration parameters of the system

2. Materials

2.1. Materials

In the modified ASTM D5101 testing configuration, Recycled Asphalt Pavement (RAP) sourced from a decommissioned asphalt surface within the Karadeniz Technical University campus was employed alongside a nonwoven geotextile. The selection of these materials was guided by their potential contribution to the development of sustainable drainage systems. The incorporation of RAP promotes the recycling of construction and demolition debris, thereby enhancing environmental sustainability and resource conservation.

2.1.1. Recycled asphalt pavement (RAP)

In this study, recycled asphalt pavement (RAP) material, obtained from construction and demolition waste, was used in long-term filtration tests. The RAP material was tested according to ASTM D5101 standards. The material was oven-dried and sieved for 24 hours. The sieved RAP aggregate, based on particle sizes, is shown in Fig 1 below. Subsequently, density measurements were taken using a pycnometer (Table 1). Additionally, the Standard Proctor test (ASTM D698-12) was conducted to determine the optimum moisture content and maximum dry unit weight (Table 2). The data obtained from these tests provide insights into the filtration properties of RAP material (Table 3) and its potential for use in subsurface drainage systems.

2.1.2. Geotextile

The combined use of aggregate and geotextile materials has proven to be an effective method, especially in drainage applications. In such systems, the filtration capacity of the geotextile layer directly affects the performance of the entire drainage structure. Therefore, the correct selection of the geotextile material is of critical importance for the long-term efficiency of the drainage system. Determining the geotextile by the soil's particle size distribution and permeability characteristics contributes to the sustainable achievement of the desired filtration performance. In this study, the apparent opening size of the geotextile material used was specified as 0.3 mm (Fig 2) The selected geotextiles are presented in Table 4.

Fig. 1. Different grains of RAP

Table 1. Pycnometer test results

Measurement	Value (g)
Mass of bottle (M1)	37.964
Mass of bottle + dry soil (M2)	71.420
Mass of bottle + dry soil + water (M3)	157.211
Mass of bottle + water (M4)	139.443
Specific Gravity (ρs)	2.13 g/cm³

$$\rho_s = \rho_w \frac{M_2 - M_1}{(M_4 - M_{1)} - (M_3 - M_2)} 2{,}13\ g/cm^3 \tag{1}$$

Table 2. Standart proctor test results

Trial	Water Content (%)	Bulk Density (ρn) (g/cm³)	Dry Density (ρd) (g/cm³)
1	7.0	1.79	1.671
2	9.6	1.92	1.752
3	11.7	1.95	1.746
4	15.8	1.98	1.710
5	29.7	1.95	1.503

Table 3. Properties of RAP

Aggregate Type	Particle Density, ps (g/cm³)	Maximum Dry Unit Weight, γkmax (kN/m³)	Optimum Moisture Content, Wopt (%)
RAP	2.13	17.5	10.5

PS: Particle specific gravity, γkmax: Maximum dry unit weight, Wopt: Optimum moisture content

Table 4. Properties of geotextile

Property	Unit	GT1	GT2	Standard / Test Method
Mass per Unit Area	g/m²	123	400 (±50)	EN ISO 9864
Thickness (at 2 kPa)	mm	1,3	3.5 (±0.5)	EN ISO 9863-1
Tensile Strength	kN/m	-	27 (-3.0)	TS EN ISO 10319
Elongation at Break	%	Min.50	≥ 50	TS EN ISO 10319
Static Puncture Resistance	N	1800	4900 (-300)	EN ISO 12236
Characteristic Opening Size (O90)	mm	0.3	0.077 (±0.025)	EN ISO 12956
Water Permeability (H_{50})	l/(s·m²)	110	55 (±15)	EN ISO 11058

3. Methodology

In this study, a modified experimental setup was developed based on the geotextile-filtration test setup specified in ASTM D 5101 standard, to determine the filtration properties of reclaimed asphalt pavement (RAP). Cylindrical samples with a diameter and height of 150 mm were used in the experimental system. In the sample cell, three manometer connection points were placed at heights of 25 mm, 75 mm, and 125 mm, attached to geotextile layers positioned on opposite sides of the cell. This arrangement enabled a more precise monitoring of the hydraulic gradient variations throughout the sample.

The RAP aggregate, which was dried in an oven, sieved, and classified by particle size, was mixed in the proportions specified in Table 5, and then water was added in the amount determined by the Standard Proctor test to prepare the sample. The geotextile was initially positioned in the central chamber of the three-part system, followed by the sample, which was compacted in five layers. The properties of the placed geotextiles are presented in Fig. 2 and Table 5. Subsequently, the three components of the system were assembled using silicone to ensure proper sealing. The system was then allowed to rest for 24 hours to enable the silicone to cure and guarantee water-tightness. Following this, the system was gradually flooded from the bottom to prevent the loss of particles, facilitating the reduction of air trapped within the sample and ensuring full saturation. Upon completion of the saturation process, water was introduced into the system from top to bottom.

The experimental setup was adjusted to maintain a hydraulic gradient of 0.33, and regular manometer readings and water flow measurements were recorded throughout the day. Based on the collected data, the gradient ratio (GR) and permeability ratio (KR) were calculated, and the relationship between these two parameters was also assessed. The pressure data obtained from manometers placed at different positions within the sample were analyzed using appropriate mathematical equations (Equations 2–5) to determine the gradient ratios.

Table 5. Material percentages to be used according to sieve numbers

Sieve No	10	18	30	40	50	70	100	Pan
% Quantity	10	15	9	14	13	19	10	10

(a) (b)

Fig. 2. Geotextiles (a) GT1 (b) GT2

$$GR_1 = \frac{i_{0-25}}{i_{25-75}} = 2 \times \frac{h_{25} - h_0}{h_{75} - h_{25}} \quad (2)$$

$$GR_2 = \frac{i_{25-75}}{i_{75-125}} = \frac{h_{75} - h_{25}}{h_{125} - h_{75}} \quad (3)$$

$$GR_3 = \frac{i_{0-25}}{i_{25-125}} = 4 \times \frac{h_{25} - h_0}{h_{125} - h_{25}} \quad (4)$$

$$GR_4 = \frac{GR_1 + GR_2}{2} \quad (5)$$

h_0, h_{25}, h_{75}, h_{125} : Manometer readings at different heights
i : hydraulic gradient

According to the ASTM D 5101 Standard, the KR parameter (Equation 6) is defined as the ratio between the permeability coefficient of the aggregate (as expressed in Equation 7) and that of the entire system (as shown in Equation 8) (Sariahmetoğlu et al., 2024).

$$KR = \frac{k_{aggregate}}{k_{system}} \tag{6}$$

$$k_{system} = \frac{Q}{A \times t} \times \frac{1}{i_{system}} \times \frac{\mu_T}{\mu_{20}} = \frac{Q}{A \times t} \times \frac{l}{h_{150} - h_0} \times \frac{\mu_T}{\mu_{20}} \tag{7}$$

$$k_{aggregate} = \frac{Q}{A \times t} \times \frac{1}{(U_{avg} - A_{avg})} \times \frac{\mu_T}{\mu_{20}} \tag{8}$$

k_{system} : The permeability value of the system at 20°C is, (cm/s),
Q : The accumulated flow volume at time t, (cm^3),
i : Hydraulic gradient,
A : Cross-sectional area of the sample, (cm^2),
t : The time required to collect the amount of drained water, Q (s),
μ_T : The viscosity of water at temperature T.
μ_{20} : The viscosity of water at 20°C,
l : The length of the sample,
U_{avg} : The average of the upper manometer readings,
A_{avg} : The average of the lower manometer readings.

Fig 3. Test system

4. Results and discussion

By the ASTM D5101 standard, long-term filtration tests were conducted using reclaimed asphalt pavement (RAP) in combination with two geotextiles of different apparent opening sizes. The tests were performed under a hydraulic gradient of $i = 0.33$, and the experimental results were evaluated based on the Gradient Ratio (GR) and Permeability Ratio (KR) criteria defined in the standard.

According to ASTM D 5101, a GR value equal to 1 indicates no clogging within the system. A GR value greater than 1 signifies the onset of particle migration, leading to increased clogging and reduced flow, while a GR value less than 1 suggests the passage of fine particles through the geotextile, potentially resulting in piping and increased flow within the system. The rapid increase of GR values beyond 3 within a short period of time, indicates that the systems are experiencing significant clogging.

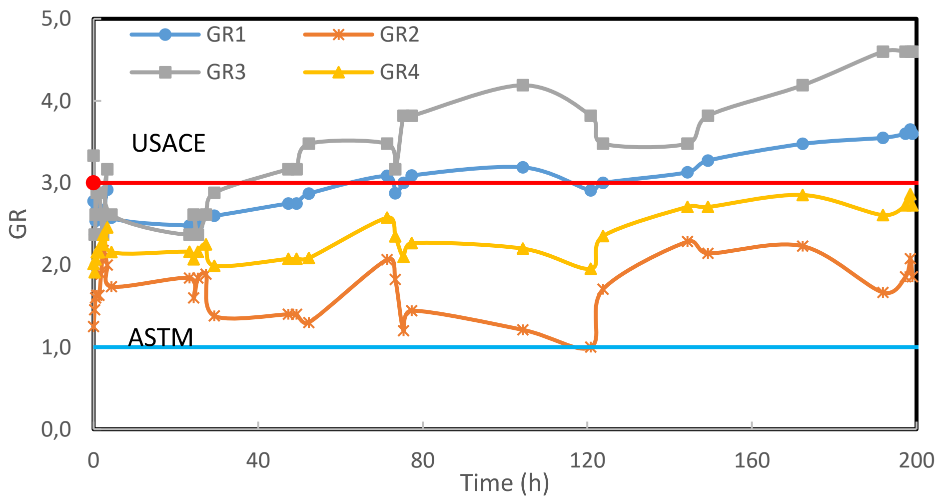

Fig 4. Time-dependent GR values of RAP-GT2

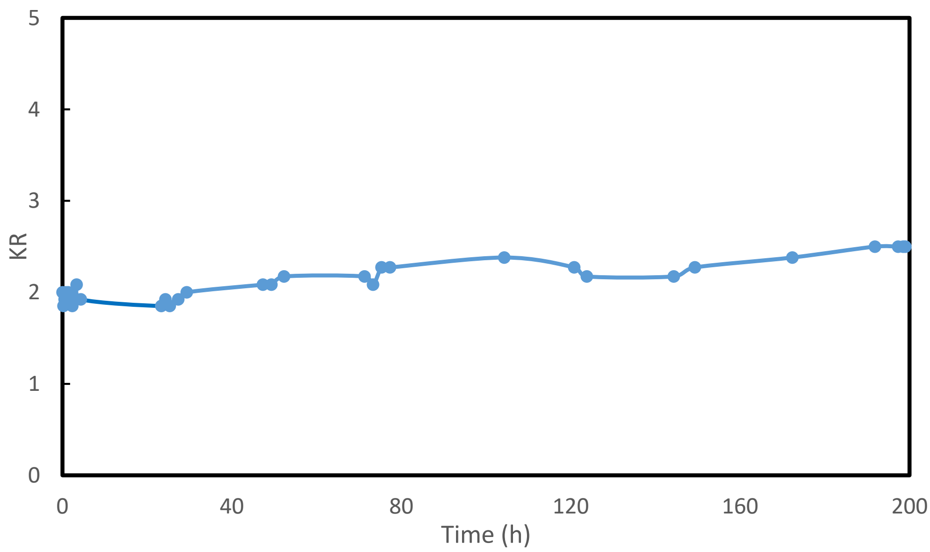

Fig. 5. Time-dependent KR values of RAP- GT2

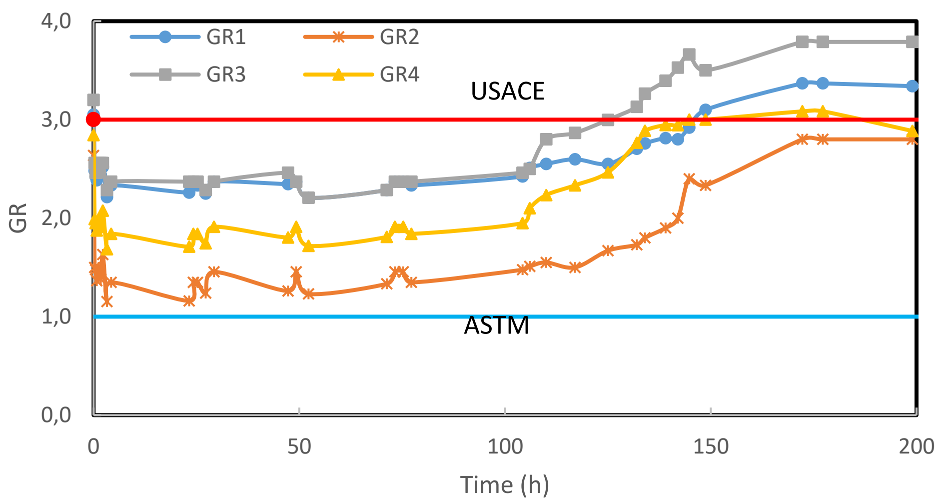

Fig. 6 Time-dependent GR values of RAP- GT1

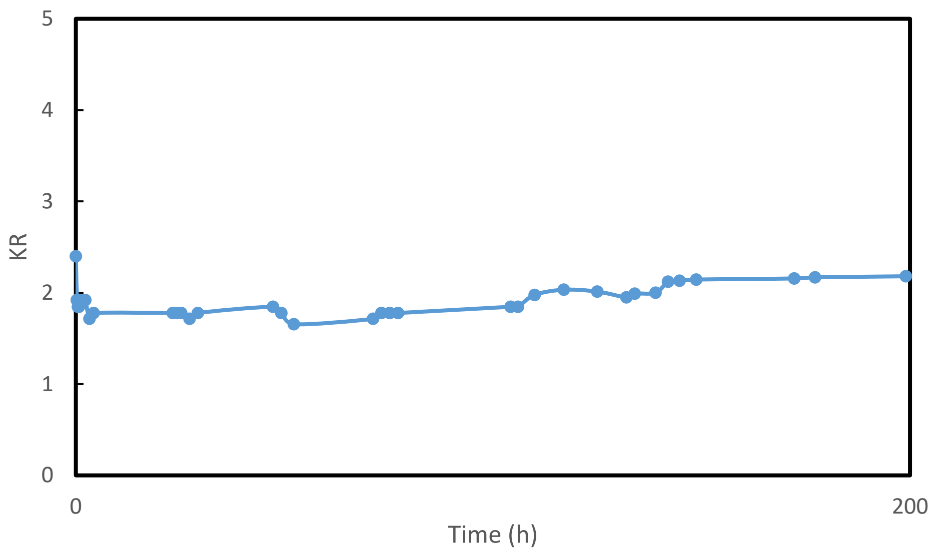

Fig 7. Time-dependent KR values of RAP-GT1

5. Conclusions

Filtration performance of RAP-geotextile system was tested using a enhanced version of long term filtration test apparatus specifically redesigned and manufactured according to ASTM D 5101 standard. Based on experimental data, the following conclusions were obtained:

- GR values exceeding 1 and show an increasing trend, suggesting the migration of fine particle material.
- Rapid increase in GR values beyond the critical threshold of 3 suggests that the system loses its drainage functionality within a relatively short duration
- It is difficult to assert a significant difference in filtration performance between the systems tested with two different geotextiles with different apparent opening sizes. Further research may be conducted by employing geotextiles with a broader spectrum of apparent opening sizes and subjecting the systems to different hydraulic gradients to gain deeper insight into filtration performance

Acknowledgement

We would like to express our gratitude to the Scientific and Technological Research Council of Turkey (TUBITAK) for supporting this study under the 2209-A University Students Research Projects Support Program. We also wish to thank the İstanbul Teknik İnşaat company for kindly providing the geotextile materials used in this research.

References

Bouazza, A. (2002). Geosynthetic Clay Liners. Geotextiles and Geomembranes, 20(1), 3-17.

Caro, D., Lodato, C., Damgaard, A., Cristóbal, J., Foster, G., Flachenecker, F., & Tonini, D. (2024). Environmental and socio-economic effects of construction and demolition waste recycling in the European Union. Science of the Total Environment(908).

Dager, C. H., Morro, R. H., Hubler, JF., & Sample-Lord, K. M. (2023). Review of Geotechnical Properties of Reclaimed Asphalt Pavement for Reuse in Infrastructure. Geotechnics, 21-42.

Edeme, R. K., & Chibuzo, N. P. (2018). Urban Population Growth and Environmental Sustainability in Nigeria. International Journal of Development and Sustainability, 1063–1074.

Kim, J. (2021). Construction and demolition waste management in Korea: recycled aggregate and its application. Clean Technologies and Environmental Policy, 2223–2234 .

Koerner, R. (2005). Designing with geosynthetics (5 b.). Pearson Prentice Hall.

Li, C., Ashlock, J., White, D., & Vennapusa, P. (2017). Permeability and Stiffness Assessment of Paved and Unpaved Roads with Geocomposite Drainage Layers. Applied Sciences, 7(7)(718).

Lu, W., & Yuan, H. (2011). A framework for understanding waste management studies in construction. Waste Management. Waste management, 1252-1260.

Mijica, Z., Dayioglu, A. Y., Hatipoglu, M., & Aydilek, A. H. (2020). Hydraulic and environmental impacts of using recycled asphalt pavement on highway shoulders. Construction and Building Materials, 234.

Purchase, C. K., Al Zulayq, D. M., O'Brien, B. T., Kowalewski, M. J., Berenjian, A., Tariqhaleslami, A.H. & Seifan, M. (2022). Circular Economy of Construction and Demolition Waste: A Literature Review on Lessons, Challenges, and Benefits. Materials, 15 (1), 76.
Rout, M. D., Biswas, S., Shubham, K., & Sinha, A. K. (2023). A systematic review on performance of reclaimed asphalt pavement (RAP) as sustainable material in rigid pavement construction: Current status to future perspective. Journal of Building Engineering, 76.
Sariahmetoglu, A., Iyisan, R., Dayıoglu, A., & Hatipoglu, M. (2020). Geri Kazanılmış Asfalt Malzemenin Uzun Süreli Filtrasyon Performansı. Pamukkale Üniversitesi Mühendislik Bilimleri Dergisi.
Sariahmetoglu, A., Hatipoglu, M., & Yalcin Dayioglu, A. (2024). Comparative Evaluation of the Long-Term Filtration Performance of Recycled Materials in Highway Drainage Systems. Geotechnical Testing Journal(47(1)), 45-64.
Silva, R., De Brito, J., & Dhir, R. (2017). Availability and processing of recycled aggregates within the construction and demolition supply chain: A review. Journal of Cleaner Production, 598-614.
Tanasă, F., Nechifor, M., Ignat, M.-E., & Teacă, C.-A. (2022). Geotextiles—A Versatile Tool for Environmental Sensitive Applications in Geotechnical Engineering. Textiles, 190-208.
Tošić, N., Marinković, S., Dašić, T., & Stanić, M. (2015). Multicriteria optimization of natural and recycled aggregate concrete for structural use. Journal of Cleaner Production, 766-776.
Wu, H., Yao, C., Li, C., Miao, M., Zhong, Y., & Liu, T. (2020). Review of Application and Innovation of Geotextiles in Geotechnical Engineering. Materials, 13(7)(1174).

Production of building blocks using demolished buildings waste and gypsum in Gaza City, Palestine

Saadoon O. Eyada*[1,2], Hasan A. H. Altawil[3,4]

[1] *Senior Engineer, Anbar Health Directorate, Iraqi Ministry of Health, Anbar , Iraq.*
[2] *Doctor of Transportation Engineering, from Konya Technical University, Konya, Turkiye.*
[3] *Msc., Civil Engineering Department, Islamic University, Gaza, Palestine.*
[4] *Doctor of Geotechnical Engineering, Civil Engineering Department, Konya Technical University, Selçuklu, Konya, Turkiye.*

Abstract. Over recent years, Gaza has faced extensive destruction due to military conflicts, resulting in the accumulation of approximately 40 million tons of demolition waste by Israeli aggression. This significant volume of waste poses severe environmental challenges and demands costly, long-term remediation efforts. Addressing this issue, the current study explores the potential for recycling demolition waste into building blocks to support reconstruction efforts in Gaza. With the anticipated restrictions on cement imports, gypsum, known for its lower environmental impact and energy requirements compared to cement, is proposed as a sustainable alternative binder. The study investigates the incorporation of various additives to enhance the mechanical and physical properties of gypsum-based blocks GB. Gypsum is weak against water, therefore, different types of additives are selected to be studied. The experimental program included two stages. In the first stage, gypsum is mixed with water and each type of additive and tested for compressive strength and absorption. The results of the first stage concluded that the Superplastisizer S is the best between the other types of additives, so it is selected to be used in the second stage. In the second stage, S is mixed with gypsum and aggregate produced from buildings demolished waste GA at different ratios and tested for compressive strength and absorption. It is concluded that mixing one part of gypsum with 4 parts of GA with 2% of S and 52% of water can produce the best mix to produce GB which can be cheaper and has lesser adverse effect on the environment.

Keywords: Gaza demolished buildings; Gaza aggregate; Gypsum block; Gypsum-waste aggregate block; waste aggregate

1. Introduction

Concrete blocks are used in different construction applications, such as partition walls, load bearing walls and paving and floor blocks due to their unique feature ability to be molded into different shapes, and strengths for different civil engineering applications (Scholz & Grabowiecki, 2007; Zhu, Yan, & Liang, 2019).

Environmental problems caused by excessive mining and usage of natural resources such as aggregate and cement with approximately 275 MT of aggregate are extracted annually in the UK and this amount can increase by 1% annually (Mo, Alengaram, Jumaat, Yap, & Lee, 2016; Soutsos, Tang, & Millard, 2011a).

Moreover, the huge amount of industrial waste materials are either burnt or landfilled which cause serious environmental pollution and health risks (Karade, 2010) (Xuan, Poon, & Zheng, 2018). Therefore, there is a need to recycle waste materials.

Therefore, efforts to recycle and reuse waste materials have resulted in intensive research works being carried out to incorporate these wastes into concrete blocks. The incorporation of different types of demolition wastes such as recycled concrete, crushed bricks, and concrete slurry waste as aggregate enhanced the properties of concrete blocks such as compressive strength and fire resistance (Hossain, Xuan, & Poon, 2017; Kou, Zhan, & Poon, 2012; Xiao et al., 2013; B. Zhan, 2017; B. Zhan, Poon, & Shi, 2013; B. J. Zhan, Poon, & Shi, 2016).

The European Union (EU) produces about 850 million tons of recycled concrete waste RCW each year, representing 31% of the total waste generated within the EU (Fischer, Werge, & Reichel, 2009).

In Gaza, during 8 months of Israeli aggression, about 40 million tons of buildings demolished waste has been accumulated on sites causing serious environmental risks. Moreover, about 3 years of extensive efforts and costs are needed to get rid of these wastes (According to the UN). According to BBC Newspaper on the internet, by 29

* Corresponding author, E-mail: Saadooneyada@gmail.com

https://doi.org/10.31462/icearc2025_ce_was_351

golden light publishing

Jan 2024, about 61% of buildings in Gaza have been demolished due to the Israeli aggression as shown in Figure 1.

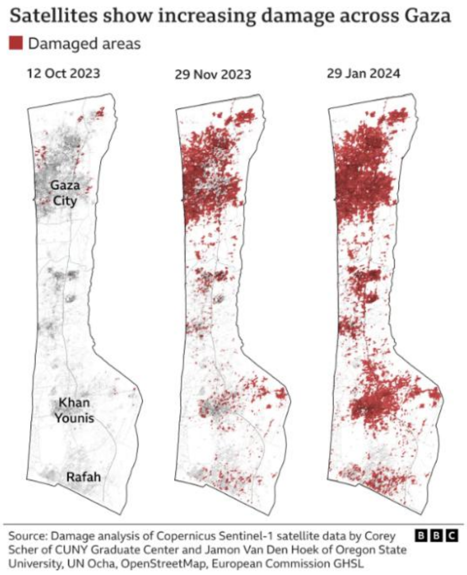

Fig. 1. Damage across Gaza due to Israeli aggression according to BBC Newspaper on internet published on 30 Jan 2024.

1.1 Concrete-waste aggregate block

Generally, researches revealed that the increase in RCW content caused a reduction in the compressive strength of concrete blocks (Pierre Matar & El Dalati, 2011; Sabai, Cox, Mato, Egmond, & Lichtenberg, 2013; Soutsos et al., 2011a; Soutsos, Tang, & Millard, 2011b). The compressive strength of RCW ranged from (5.2 to 10.4 N/mm2) compared to (14.2 N/mm2) for normal concrete with higher porosity (about 7 times) (Sabai et al., 2013).

Soutsos et al. (2011a) noted that the reduction in strength of concrete blocks was more significant when RCW was used as a fine aggregate. . Researchers also concluded that higher cement content is usually required for RCW concrete blocks to overcome the loss in compressive strength (Pierre Matar & El Dalati, 2011; P Matar & El Dalati, 2012; Soutsos et al., 2011a).

Researchers found that using crushed bricks as aggregate in concrete blocks reduced the density and compressive strength while increased water absorption of concrete block (Poon & Chan, 2006; Xiao, Ling, Kou, Wang, & Poon, 2011; Xiao et al., 2013). Xiao et al (2011). They suggested replacement levels of coarse and fine aggregate with crushed bricks to be less than 25% and between 50% and 75%, respectively.

On the other hand, the inclusion of ceramic tile waste and tile polishing waste as a sand replacement seems to have positive contribution to the compressive strength of concrete blocks while, using coarse aggregate decreased the compressive strength of concrete blocks(Penteado, de Carvalho, & Lintz, 2016; Sadek & El Nouhy, 2014).

1.2 Gypsum block

Gypsum is also widely applied in the construction industry due to some properties, such as fire resistance, high sound absorption and good decorative effects. Compared to cement, the temperature for producing gypsum is much lower, resulting in lower energy consumption and CO_2 liberation. Besides that, the gypsum plaster has better volume stability and lesser drying shrinkage than cement paste. However, gypsum has a lower water resistance (Zhang, Mo, Yap, & Tan, 2023).

Gypsum is used for the production of Non-bearing Gypsum Block GB by mixing gypsum with water and some additives to be shaped by special molds. The GB can be used in the construction of partition walls that are not subjected to the effect of moisture and weather.

Different studies were conducted in gypsum composites incorporating different waste streams (gypsum, insulation materials, plastics, wood, ceramic etc.). Pedreño-Rojas et al., conducted a research on recycled gypsum and showed different physical proprieties associated with the commercial gypsum (Pedreno-Rojas, Flores-Colen, De Brito, & Rodríguez-Linán, 2019). San Antonio Gonzalez, analyzed different compounds containing polystyrene waste, resulting in lightweight gypsums with good thermal behavior and resistance to water, while there was a decrease in the surface hardness and compression strength (San-Antonio-González, Merino, Arrebola, & Villoria-Sáez, 2015).

Another study was conducted by Santos Jimenez et al. They incorporated ceramic waste CW into the gypsum matrix. They found that the surface hardness and water absorption improved when less than 50% of CW was incorporated in a gypsum matrix (Jiménez, San-Antonio-González, Merino, Cortina, & Arrebola, 2015).

In general, these research works add one single type of waste and some properties improve, while others worsen. For this reason, more recent publications focus on materials incorporating a mixture of different wastes, in order to seek a synergistic effect and balance the properties obtained. Del Río Merino et al, analyzed the feasibility of adding CW and extruded polystyrene EPS waste from construction sites in two types of gypsums. Blends of gypsum with 50% CW and 1% EPS can be used to produce prefabricated elements or cladding materials (del Rio Merino, Astorqui, Sáez, Jiménez, & Cortina, 2018).

1.3 Objectives

The primary objective of this study is to develop sustainable building blocks using gypsum and recycled concrete waste (RCW) generated from the extensive demolition of buildings in Gaza City. Recognizing the potential restrictions on cement imports, gypsum is proposed as an alternative binder, offering lower environmental impact and production energy. However, given gypsum's inherent vulnerability to moisture, this study aims to enhance its mechanical and absorption properties through the incorporation of various additives.

The research is structured into two stages. In the first stage, the effect of individual additives on compressive strength and water absorption is evaluated to identify the most effective additive. In the second stage, the selected additive is incorporated into gypsum and Gaza aggregate (GA) at varying ratios to determine the optimal mix design. The ultimate goal is to produce building blocks that meet or exceed the Iraqi Standards for Blocks (IRS 1077) while minimizing costs and environmental impact. These findings are anticipated to support reconstruction efforts in Gaza by providing an economical and eco-friendly alternative to conventional building materials.

2.Experimental works.

2.1 Materials

Different types of materials are used for the preparation of mixes. The materials are collected from different sources.

2.1.1 Gaza Aggregate GA

It is impossible during the Israeli aggression against Gaza to collect RCW from demolished buildings. The only way is to simulate GA by collecting data about the most popular RCW in Gaza and the percentage of each portion of RCW. It is found that RCW consists of 80% of concrete waste, 10% of flooring waste and 10% of plastering waste. The data is used to make GA by collecting RCW from demolished buildings in Iraq. The RCW is milled and sieved and used for the preparation of mixes. Figure 2 shows the sieve analysis of GA used in the preparation of mixes used to make GB.

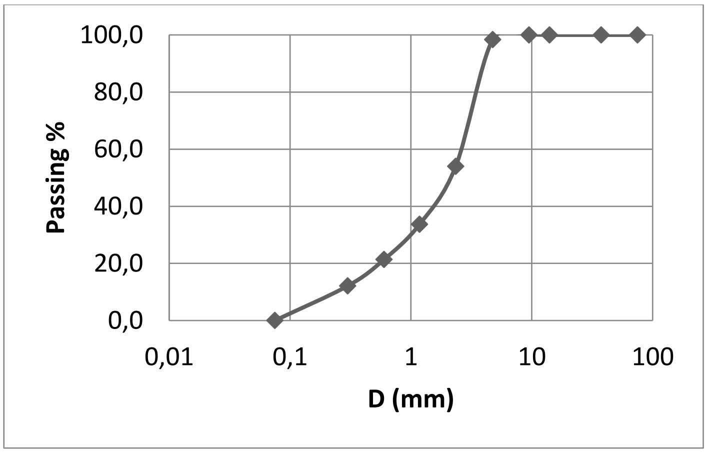

Fig. 2. Sieve analysis test result of GA.

Fig. 3 demonstrates GA before and after milling and sieving. Fig. 4 shows a demolished building in Gaza due to Israeli aggression against civilians.

Fig. 3. GA before and after milling and sieving.

Fig. 4. Destroyed buildings in Gaza due to Israeli aggression

2.1.2 Gypsum

Two types of gypsum are used:

- White Gypsum WG. This type of gypsum is purchased from AlMizan company in Iraq. The WG is pure gypsum with high specifications and it is usually used in finishing and decorative applications.
- Natural Gypsum NG. This type of gypsum is purchased from Alnibaee company in Iraq. the NG is not pure and has impurities such as sand. NG is usually used in layers before finishing to reduce the cost of finishing.

2.1.3 Additives

Superplasticizer S. It is used to increase workability of mixing while reducing the w/c ratio and increasing the compressive strength of concrete. Sika ViscoCrete – 180 GS from Sika company (Germany) is used in the mixes.

Silica Fume SF. It has a positive effect on the compressive strength of concrete so, it is expected that it has the same on the gypsum blend. SF type MegaAdd MS (D) from KONMIX Ltd. company (UAE) is used in mixes.

Citric Acid CA. It has a positive effect on the compressive strength of concrete and it is used as retarder and water reducer. It is locally available in local markets and used with food.

Citric Citrate CC. It has a positive effect on the compressive strength of concrete and it was investigated for use in clinical applications such as Vertebroplasty. CC from Segma company (England) is used to prepare mixes.

Sodium Bicarbonate SB. It is mainly used to produce air bubbles within the structure of the mixes and can reduce the weight of the products. It is locally available in local markets and used with bakeries.

MantuSur MS. It is one of the products of the KONIZMA company (Turkiye). It is used as an insulation plastering material for the outside of the buildings.

Thermostone Waste Tw. It is a byproduct of Thermostone production. It was collected from Thermostone Factory in the Ramadi city (Iraq). Tw was milled and the material passing sieve No.8 (less than 2.36 mm) is used as an additive with gypsum mixes.

Ammonia Am. It is mainly used to produce air bubbles within the structure of the mix and can reduce the weight of the products. It is locally available in local markets and used with bakeries.

River Sand Sa. It is mainly used to reduce the cost and can enhance the strength of the mix. It is purchased from the Ramadi quarry in Iraq. Water w. Tab water is used to prepare mixes.

2.2 Testing program

To study the effect of different types of additives on testing results, a testing program is conducted according to the stages below:

2.2.1 Stage 1

In this stage, gypsum is mixed with each type of additives and tested for compressive strength and absorption. A mold (10x10x10 cm) is used to conduct tests. The gypsum is mixed with additive. The water is added to the mix and blended together and poured into the mold. After 24 hours, the sample is extracted from the mold and left to dry until testing date. Table 1 shows the mixing weights of each type of mix.

Table 1. The mixing weight of each type of mix (Stage 1).

	Material type and weight (gm)											
Mix type	WG	NG	w	Am	MS	Tw	S	CA	CC	SB	SF	Sa
WG-NG-w40-Am 0.6	500	500	666.7	6	-	-	-	-	-	-	-	-
WG-NG-w40-MS10	500	500	666.7	-	100	-	-	-	-	-	-	-
WG-NG-w41-Tw30	300	300	420	-	-	180	-	-	-	-	-	-
WG-NG-w30-S0.6	500	500	428.6	-	-	-	5	-	-	-	-	-
WG-NG-w40-CA0.2-CC0.5	500	500	666.7	-	-	-	-	2	5	-	-	-
WG-NG-w40-SB0.5-CC0.5	500	500	666.7	-	-	-	-	-	5	5	-	-
WG-NG-w40	500	500	666.7	-	-	-	-	-	-	-	-	-
WG-NG-w40-SF10	500	500	666.7	-	-	-	-	-	-	-	100	-
WG-NG-w35-CC0.5	500	500	538.5	-	-	-	-	-	5	-	-	-
WG-NG-w30-S0.6-CC1	500	500	428.6	-	-	-	6	-	10	-	-	-
WG-NG-w40-SB0.5	500	500	666.7	-	-	-	-	-	-	5	-	-
WG-NG-w40-Sa50	250	250	666.7	-	-	-	-	-	-	-	-	500

2.2.2 Stage 2

The results of Stage 1 are used to choose the best additive that makes the best mix in terms of compressive strength and absorption. According to the results of Stage 1, it was found that S is the best additive that when added to the mix satisfied the compressive strength and absorption limits required by the Iraqi standard of block. Accordingly, a mold of (38x18x20 cm) is used to make complete samples of GB to be tested for compressive strength and absorption . First, the gypsum is mixed with additive and GA. The water is added to the mix and blended together and poured into the mold. After 24 hours, the sample is extracted from the mold and left to dry until testing date. Figure 5 shows the samples of GB after extraction from the mold.

Fig. 5. Samples of GB after extraction from the mold (Stage 2)

Table 2 shows the mixing proportions of each type of mix for Stage 2.

Table 2. Mixing proportions of each type of mix (Stage 2).

Material type and proportions				
Mix type	WG	GA	w/WG (ratio)	S (% of WG)
WG1-GA3-w47	1	3	47/53	2
WG1-GA3-w50	1	3	50/50	2
WG1-GA3-w45	1	3	45/55	2
WG1-GA4-w52	1	4	52/48	2
WG1-GA4-w53.5	1	4	53.5/46.5	2

3.Results and discussion

3.1 Results of stage 1.

3.1.1 Compressive strength test results

Compressive strength tests were conducted after 7 days of curing at a constant temperature of 35°C. The results, as illustrated in Figure 6, indicate that reducing water content significantly enhances compressive strength. Among the tested additives, superplasticizer (S), silica fume (SF), thermostone waste (Tw), and insulation material (MS) positively impacted compressive strength, with superplasticizer (S) yielding the highest improvement. Conversely, additives such as ammonia (Am), citric acid (CA), and sodium bicarbonate (SB) exhibited a reduction in compressive strength, likely due to increased porosity and reduced binding efficiency. These findings emphasize the importance of additive selection in achieving the desired mechanical performance.

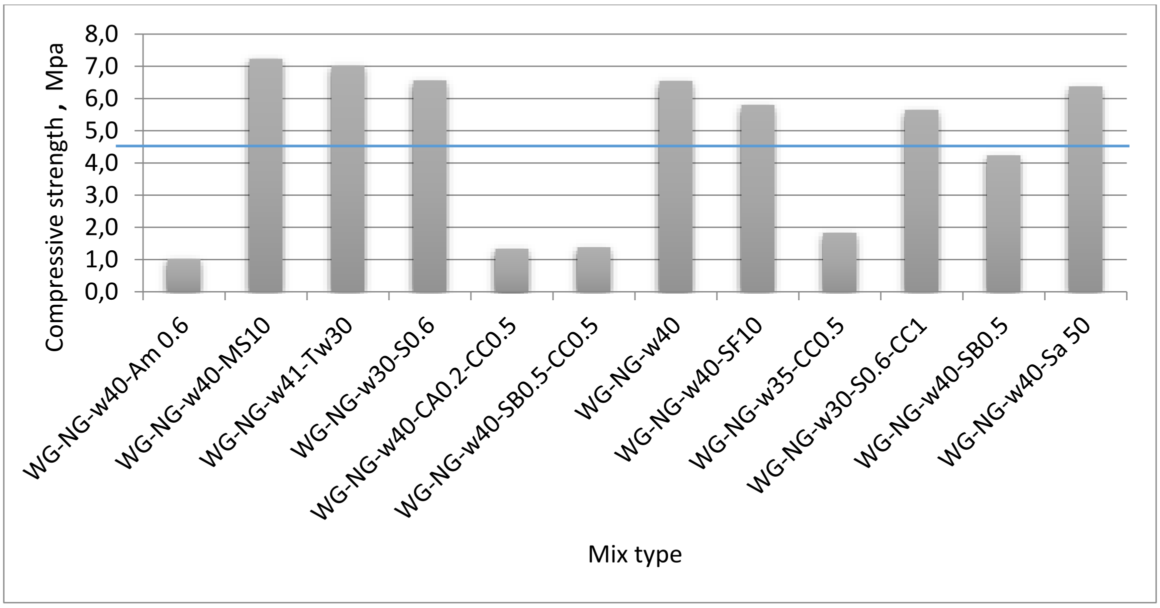

Fig. 6. Results of compressive strength test of samples (Stage 1)

The results of compressive strength cannot be discussed alone since the specifications of GB depend on the limits specified by compressive strength and absorption test together, so the discussion of this stage will be done after discussing the results of the absorption test.

3.1.2 Absorption test results

The test is conducted after 7 days of complete drying at a temperature of (35 Co). The results of test are shown in Fig. 7.

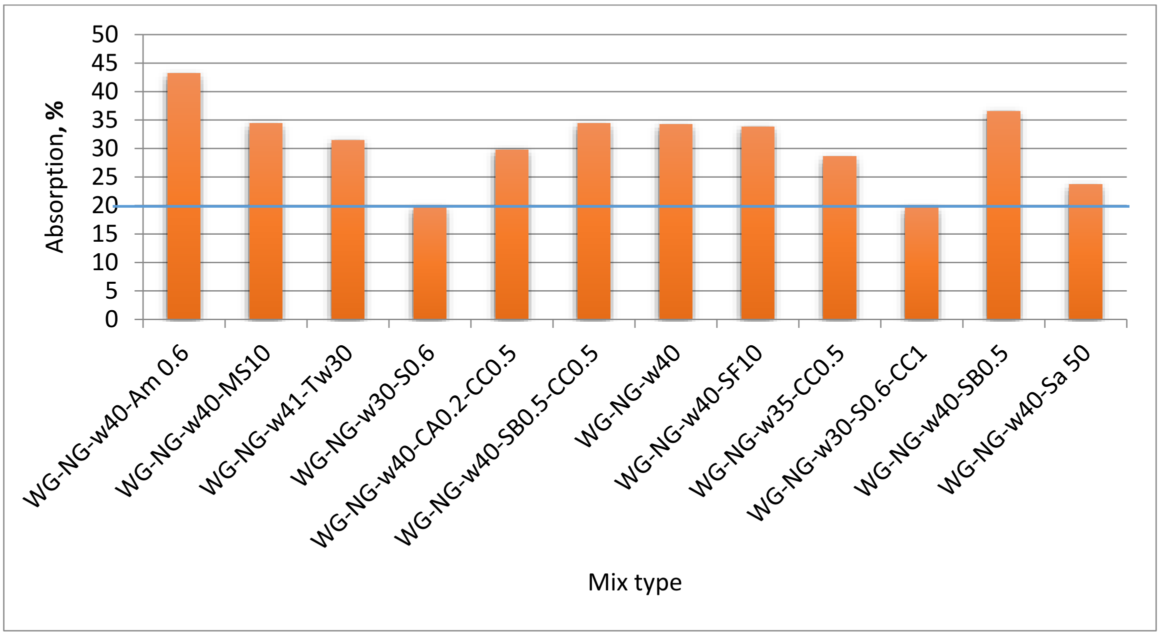

Fig. 7. Results of absorption test of samples (Stage 1)

The results show that only mixes containing (S and SB) are within the limits of Iraqi Specifications of Block (IRS 1077).

When combining the results of compressive strength with the results of absorption, only additive (S) succeeded in achieving the limits required by Iraqi Specifications of Block (IRS 1077) (Institution, 1988).

Accordingly, additive (S) was selected to be used for the preparation of complete GB samples in Stage 2.

3.2 Results of stage 2.

During the second stage, compressive strength and water absorption tests were conducted on gypsum block (GB) samples after 7 days of curing at 35°C. The results, depicted in Figures 8 and 9, reveal key insights into the effects of varying Gaza aggregate (GA) and water content ratios.

3.2.1 Compressive strength test results

Increasing the ratio of GA led to a noticeable reduction in compressive strength. This outcome is attributed to the lower binding capacity of gypsum when combined with higher proportions of aggregate.

- Nevertheless, all tested mixes exceeded the minimum compressive strength requirements set by the Iraqi Standards (IRS 1077).
- A higher gypsum content improved the compressive strength by approximately 100%, emphasizing gypsum's role as a binding agent.
- Reducing the water content from 52% to 45% further enhanced compressive strength by approximately 10%, likely due to the reduction in porosity and improved particle bonding.

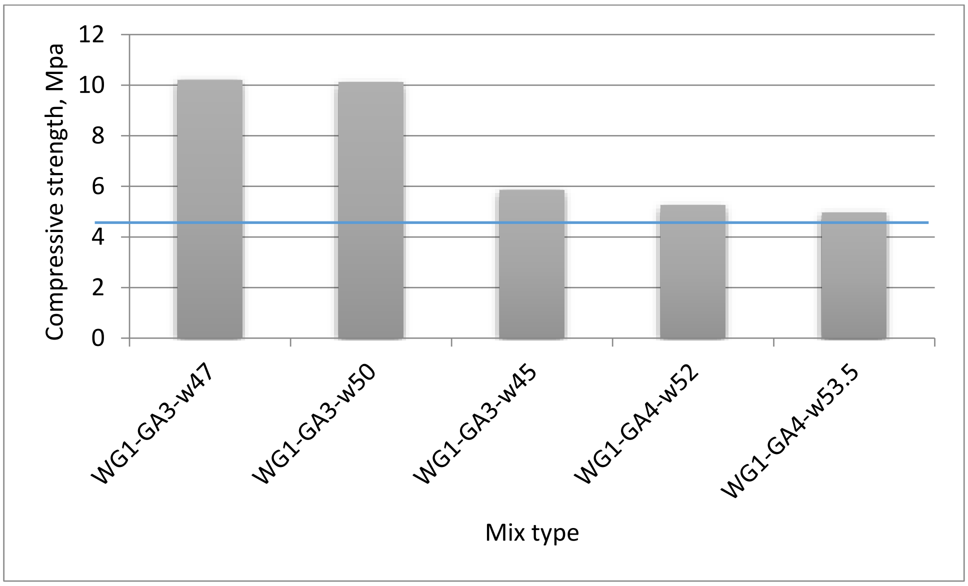

Fig. 8. Results of compressive strength test of GB samples (Stage 2)

3.2.2 Absorption test results

The results indicate that increasing the GA ratio resulted in higher water absorption. This is primarily due to the increased void content and reduced cohesion within the mix. Conversely, higher gypsum content reduced water absorption by filling voids and improving the overall matrix density. Despite the variations, all tested mixes met the minimum absorption requirements according to IRS 1077 standards.

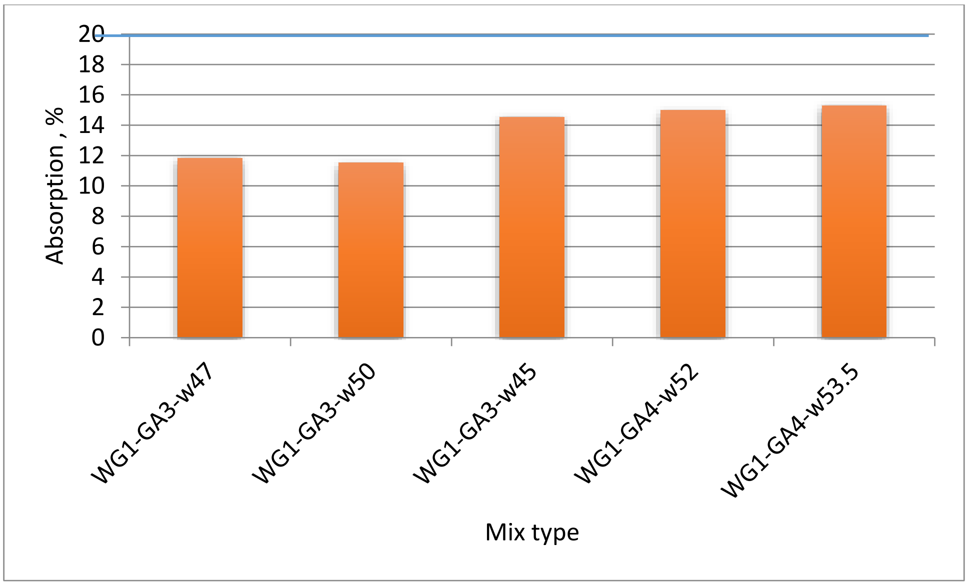

Fig. 9. Results of absorption test of GB samples (Stage 2)

Since all mixes passed the required minimum limits of compressive strength and absorption tests according to Iraqi Specifications of Block IRS1077, the selection of the best mix is based on two principles:

1-The most economic,

2-The less negative environmental effect.

Based on the results, the mix designated as (WG1-GA4-w52) emerged as the most suitable. This mix combines the highest GA content with sufficient gypsum and reduced water, achieving a balance between compressive strength and absorption. Additionally, it offers significant economic and environmental benefits by maximizing the use of demolition waste while minimizing gypsum consumption.

4. Conclusions

This study investigated the feasibility of producing gypsum-based blocks (GB) by incorporating recycled aggregates (GA) from demolition waste. A systematic experimental program was employed to evaluate the effects of various additives on compressive strength and water absorption. The results demonstrated that superplasticizer (S) was the most effective additive, achieving the required standards for both compressive strength and absorption. Furthermore, the optimized mix (WG1-GA4-w52) was identified as the most economical and environmentally friendly solution, with significant potential to reduce waste and reliance on cement in Gaza. Future research could focus on evaluating the long-term durability of these blocks under environmental stressors and exploring their scalability for mass production.

Acknowledgment

We would also like to express our gratitude to the members of the Concrete Laboratory/ Civil Engineering Department/Anbar University for their constructive criticism and valuable feedback, which contributed to enhancing the quality of this research.

Finally, we thank Civil Engineering Department/Anbar University for providing the necessary facilities and resources to conduct my research.

References

del Rio Merino, M., Astorqui, J. S. C., Sáez, P. V., Jiménez, R. S., & Cortina, M. G. (2018). Eco plaster mortars with addition of waste for high hardness coatings. *Construction and Building Materials, 158*, 649–656.

Fischer, C., Werge, M., & Reichel, A. (2009). *EU as a recycling society: Present recycling levels of municipal waste and construction & demolition waste in the EU*.

Hossain, M. U., Xuan, D., & Poon, C. S. (2017). Sustainable management and utilisation of concrete slurry waste: A case study in Hong Kong. *Waste Management, 61*, 397–404.

Institution, I. S. (1988). *Iraqi specifications of block (IRS 1077)* (Vol. 1077). Iraqi Standard Institution.

Jiménez, R. S., San-Antonio-González, A., Merino, M. D. R., Cortina, M. G., & Arrebola, C. V. (2015). Gypsum composites with CDW as raw material. *International Journal of Civil and Environmental Engineering, 9*(7), 835–838.

Karade, S. (2010). Cement-bonded composites from lignocellulosic wastes. *Construction and Building Materials, 24*(8), 1323–1330.

Kou, S.-C., Zhan, B.-J., & Poon, C.-S. (2012). Properties of partition wall blocks prepared with fresh concrete wastes. *Construction and Building Materials, 36*, 566–571.

Matar, P., & El Dalati, R. (2011). Strength of masonry blocks made with recycled concrete aggregates. *Physics Procedia, 21*, 180–186.

Matar, P., & El Dalati, R. (2012). Using recycled concrete aggregates in precast concrete hollow blocks. *Materialwissenschaft und Werkstofftechnik, 43*(5), 388–391.

Mo, K. H., Alengaram, U. J., Jumaat, M. Z., Yap, S. P., & Lee, S. C. (2016). Green concrete partially comprised of farming waste residues: A review. *Journal of Cleaner Production, 117*, 122–138.

Pedreno-Rojas, M. A., Flores-Colen, I., De Brito, J., & Rodríguez-Linán, C. (2019). Influence of the heating process on the use of gypsum wastes in plasters: Mechanical, thermal and environmental analysis. *Journal of Cleaner Production, 215*, 444–457.

Penteado, C. S. G., de Carvalho, E. V., & Lintz, R. C. C. (2016). Reusing ceramic tile polishing waste in paving block manufacturing. *Journal of Cleaner Production, 112*, 514–520.

Poon, C. S., & Chan, D. (2006). Paving blocks made with recycled concrete aggregate and crushed clay brick. *Construction and Building Materials, 20*(8), 569–577.

Sabai, M., Cox, M., Mato, R., Egmond, E., & Lichtenberg, J. (2013). Concrete block production from construction and demolition waste in Tanzania. *Resources, Conservation and Recycling, 72*, 9–19.

Sadek, D. M., & El Nouhy, H. A. (2014). Properties of paving units incorporating crushed ceramic. *HBRC Journal, 10*(2), 198–205.

San-Antonio-González, A., Merino, M. D. R., Arrebola, C. V., & Villoria-Sáez, P. (2015). Lightweight material made with gypsum and extruded polystyrene waste with enhanced thermal behaviour. *Construction and Building Materials, 93*, 57–63.

Scholz, M., & Grabowiecki, P. (2007). Review of permeable pavement systems. *Building and Environment, 42*(11), 3830–3836.

Soutsos, M. N., Tang, K., & Millard, S. G. (2011a). Concrete building blocks made with recycled demolition aggregate. *Construction and Building Materials, 25*(2), 726–735.

Soutsos, M. N., Tang, K., & Millard, S. G. (2011b). Use of recycled demolition aggregate in precast products, phase II: Concrete paving blocks. *Construction and Building Materials, 25*(7), 3131–3143.

Xiao, Z., Ling, T.-C., Kou, S.-C., Wang, Q., & Poon, C.-S. (2011). Use of wastes derived from earthquakes for the production of concrete masonry partition wall blocks. *Waste Management, 31*(8), 1859–1866.

Xiao, Z., Ling, T.-C., Poon, C.-S., Kou, S.-C., Wang, Q., & Huang, R. (2013). Properties of partition wall blocks prepared with high percentages of recycled clay brick after exposure to elevated temperatures. *Construction and Building Materials, 49*, 56–61.

Xuan, D., Poon, C. S., & Zheng, W. (2018). Management and sustainable utilization of processing wastes from ready-mixed concrete plants in construction: A review. *Resources, Conservation and Recycling, 136*, 238–247.

Zhan, B. (2017). *CO_2 curing of concrete blocks containing recycled aggregate* [Doctoral dissertation, The Hong Kong Polytechnic University].

Zhan, B., Poon, C., & Shi, C. (2013). CO_2 curing for improving the properties of concrete blocks containing recycled aggregates. *Cement and Concrete Composites, 42*, 1–8.

Zhan, B. J., Poon, C. S., & Shi, C. J. (2016). Materials characteristics affecting CO_2 curing of concrete blocks containing recycled aggregates. *Cement and Concrete Composites, 67*, 50–59.

Zhang, L., Mo, K. H., Yap, S. P., & Tan, T. H. (2023). Recycled waste glass as fine aggregate in eco-friendly gypsum–cement composite. *Materials Today: Proceedings*. https://doi.org/10.1016/j.matpr.2023.02.010

Zhu, H., Yan, J., & Liang, W. (2019). Challenges and development prospects of ultra-long and ultra-deep mountain tunnels. *Engineering, 5*(3), 384–392.

4th International Civil Engineering & Architecture Conference
17-19 May 2025, Trabzon, Türkiye

Optimizing selective demolition with BIM: A path toward sustainable concrete recycling

Mustafa C. Alp[1], Zeynep Başaran Bundur[*1], Gürşans Güven[2]

[1] Ozyegin University, Department of Civil Engineering, Istanbul, Türkiye
[2] University of Manitoba, Department of Civil Engineering, Winnipeg, Manitoba, Canada

Abstract. The construction industry contributes roughly 39% of the annual global carbon dioxide emissions and is responsible for 35% of global waste generation in landfills due to the demolition of structures. To improve sustainability and material circularity in society, the construction and demolition sector holds a prominent position, particularly in recycling. With the release of EN 197-6 "Recycled Concrete), recycling of construction demolition waste (CDW) becomes more important. An essential step in recycling CDW is the efficiency of selective demolition techniques to maximize resource efficiency. However, major limitations of selective demolition includes increased duration of demolition, labor demand, and cost. This necessity underscores the importance of integrating selective demolition techniques with Building Information Modeling (BIM). This study aims to demonstrate the economic and operational perspective of smart demolition processes by using a BIM-based approach. A six-story residential building was modeled in Autodesk Revit to simulate the selective demolition process. This was followed by simulating the demolition process, enabling the recycling of concrete components. The results indicate that although optimizing the demolition process improves resource efficiency in recycling and enables the valorization of concrete components across various industries, selective demolition is currently an unfeasible option for demolition contractors in the absence of regulations or incentives.

Keywords: BIM (Building Information Modeling); Circular economy; Selective demolishing; Recycled Aggregates (RA)

1. Introduction

The world climate is changing rapidly due to increasing urbanization and industrialization activities, and this causes problems related to climate change. Excessive consumption of natural resources, such as unlimited concrete production, raw material extraction, waste storage, as well as greenhouse gas emissions caused by construction activities are among the main problems that accelerate climate change and environmental degradation. When these adverse effects of cement production are combined with the consumption of raw materials required for concrete production, like aggregate, water, and chemicals; the negative impact of construction activities on the environment increases even more. As a result of factors such as new building and infrastructure construction, demolition, reconstruction or renovation works, expansion of existing buildings, and maintenance activities, a large amount of Construction and Demolition Waste (CDW) is emerging, such as concrete, brick, ceramics, glass, and wood.

CDW represent the most significant waste volume, one-third of the waste generated in the European Union (Deloitte, 2015). Approximately 800 million tons of CDW are produced in Europe every year, and this figure is expected to increase further due to the increasing urban population, the continuous development of economies, and industrialization activities (Deloitte, 2015; Zajac et al., 2022). As a developing country, Türkiye anticipates demolishing or reconstructing 8.2 million buildings over the next two decades (Çalkıvik et al., 2024). Moreover, with the addition of population growth and increased infrastructure needs, CDW volume will be much more than expected. For instance, in the city of Istanbul, many buildings located in different districts of the city need to undergo urban transformation, and all the waste that will be generated due to the demolition of these buildings will be sent to landfills if they are not recycled or reused.

As CDW continues to pose environmental and logistical challenges, strategies such as selective demolition and on-site waste separation have emerged as effective approaches to improve material recovery and reduce landfill use. This way, the performance of waste after recycling can be improved and the recovery of valuable materials such as Recycled Concrete Aggregates (RCA) and Recycled Concrete Fines (RCF) becomes possible. In England, Portugal, and Japan, RCA can be substituted for 20% of the aggregates for new construction (de Andrade Salgado

[*] Corresponding author, Email: zeynep.basaran@ozyegin.edu.tr

https://doi.org/10.31462/icearc2025_ce_was_495

& de Andrade Silva, 2022). Thus, it contributes to the circular economy and creates landfill space (Purnell & Dunster, 2010). Recycling of concrete at the end of the life of a structure can also potentially reduce the depletion of virgin aggregate materials (Purnell & Dunster, 2010). While RCF, generated through concrete recycling, carbon dioxide can be captured under certain conditions through a process known as carbon capture or carbon sequestration. This transformation results in a high value-added material which can be used as a supplementary cementitious material, that contributes to more sustainable construction practices (Zajac et al., 2022).

For successful selective demolition, detailed planning, scheduling, and waste quantification are required. These make selective demolition more environmentally friendly and cost-effective. The efficiency of selective demolition also depends on having a skilled team and using the right equipment. In the selective demolition approach first non-bearing elements (brick walls and insulation material) can be manually dismantled with demolition drills, followed by the dismantling of the walls and insulation, and the concrete elements (structural walls, columns, floors, stairs) can be dismantled starting from the top floor with a jaw excavator and continuing down to the lowest floor (Public Fill Committee Civil, 2004).

To address the growing demands for sustainable construction practices and the limitations of traditional demolition methods; this study proposes to use Building Information Modeling (BIM) to apply selective demolition approaches for optimum material recovery from buildings. This paper investigates the economic benefits of selective demolition practices in construction, through a case study of a six-story residential building located in Istanbul.

2. Materials and methods

To model and simulate the selective demolition process, a 3D model of a six-story residential building was developed using Autodesk Revit 2025. The building model includes one basement level, a ground floor, three typical upper floors, and an attic (Fig. 1). The 3D model was created using the .dwg drawings of the building, and all structural and non-structural elements were modeled following standard design practices. The visual programming plug-in of Revit, namely Dynamo, was utilized to automate the extraction of material quantity take-offs from the BIM model, while Autodesk Navisworks Manage 2025 was used for simulating and scheduling the demolition phases.

Fig. 1. Render of Revit Model

2.1. 3D modeling in Revit

Two L-shaped columns of different sizes were modeled using the Revit Family Editor. Due to varying floor heights across different stories, two additional columns were created to accommodate those levels. Appropriate types and sizes of windows and doors were also added. All model elements were developed at Level of Detail (LOD) 300 (Shin & Song, 2024). Parameters of elements such as length, area, volume, floor levels, and attribute information like material type, material ID were defined. Finally, a custom "task ID" parameter was created in Revit to support the modelling and simulation process in Navisworks.

2.2. Quantity take-off with Dynamo
With the Dynamo visual programming, the quantity take-off process in Revit was automated. Custom scripts were developed to extract quantities and values such as volume, area, floor level, element ID (a custom parameter) and element name. For every element, different code blocks are created in Dynamo. Since the parameter names of floors are different for every material, different parameter names had to be used for Dynamo code blocks to extract the information from the BIM model to Excel. For example, the “Base Constraint” string is used to extract the floor level information of the walls, while the “Base Level” string is used to extract same information for structural columns. The stairs were manually modelled in Revit which allowed the geometry of the stairs to be customized precisely according to the building’s layout and dimensions. Since the geometry of the stairs is different, Revit does not allow the extraction of the volume of stairs with the “Volume” string in Dynamo. Therefore, “Solid Volume” string was used to extract the volume of stairs as seen in Fig.2.

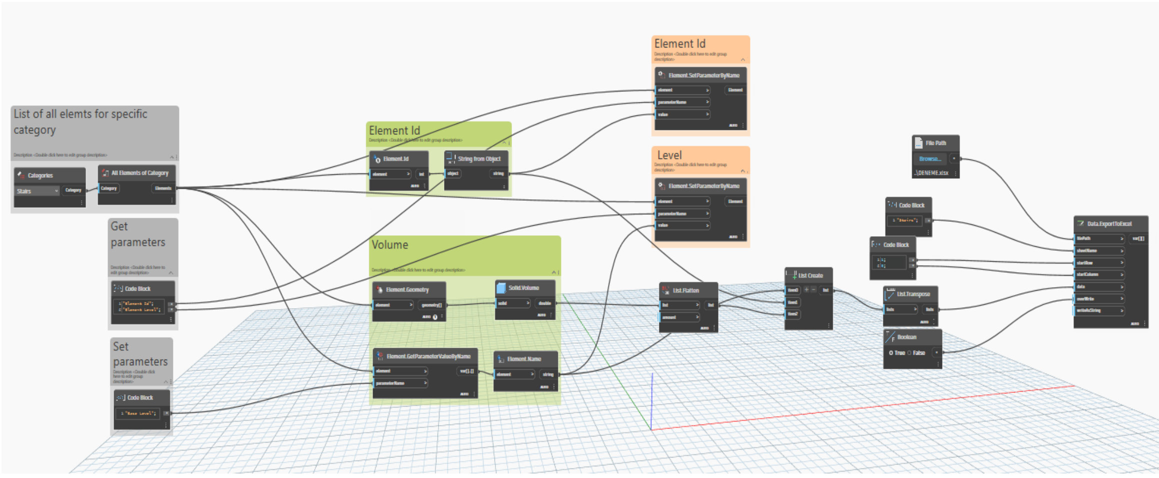

Fig. 2. Dynamo script for extracting information from Revit to Excel for Stairs

2.3. Simulation of the demolition process in Autodesk Navisworks Manage 2025
The completed Revit model was exported in NWC format and imported into Navisworks. Building elements were grouped as “demolition sets” according to their floor level and structural types (e.g., structural walls, walls, columns). Using Excel, a phased demolition schedule was developed and imported into Navisworks, considering the floor sequence from top to bottom, ending with the basement as seen in Fig. 3.

Each demolition phase was linked to a timeline task to simulate the selective demolition process. This 4D simulation provided a visual insight into the sequence and duration of demolition activities.

A new task type was defined in Navisworks to represent the to identify whether the demolition was done manually or with an excavator in the simulation. The demolition schedule prepared in Excel was then exported into Navisworks as a .CSV file, enabling simulation by linking the demolition sets with the custom Task ID parameter created in Revit using “auto-attach” rules.

Active	Name	Status	Planned Start	Planned End	Task Type	Attached
	New Data Source (Root)		3.02.2025 08:00	21.02.2025 18:00		
	Predemolition		N/A	N/A		
	Deconstruction of Doors and Windows of 4. Floor		3.02.2025 08:00	3.02.2025 10:00	Demolish Manual	Sets->Task ID->110
	Deconstruction of Doors and Windows of 3. Floor		3.02.2025 10:00	3.02.2025 12:00	Demolish Manual	Sets->Task ID->110
	Deconstruction of Doors and Windows of 2. Floor		3.02.2025 13:00	3.02.2025 15:00	Demolish Manual	Sets->Task ID->110
	Deconstruction of Doors and Windows of 1. Floor		3.02.2025 15:00	3.02.2025 17:00	Demolish Manual	Sets->Task ID->110
	Deconstruction of Doors and Windows of Ground Floor		3.02.2025 17:00	3.02.2025 18:00	Demolish Manual	Sets->Task ID->110
	Deconstruction of Roof		4.02.2025 08:00	4.02.2025 18:00	Demolish Manual	Sets->Task ID->120
	Deconstruction Wall of 4. Floor		5.02.2025 08:00	5.02.2025 18:00	Demolish Manual	Sets->Task ID->130
	Deconstruction Wall of 3. Floor		6.02.2025 08:00	6.02.2025 18:00	Demolish Manual	Sets->Task ID->140
	Deconstruction Wall of 2. Floor		7.02.2025 08:00	7.02.2025 18:00	Demolish Manual	Sets->Task ID->150
	Deconstruction Wall of 1. Floor		10.02.2025 08:00	10.02.2025 18:00	Demolish Manual	Sets->Task ID->160
	Deconstruction Wall of Ground Floor		11.02.2025 08:00	11.02.2025 18:00	Demolish Manual	Sets->Task ID->170
	Deconstruction Strucral Columns of 4. Floor		17.02.2025 08:00	17.02.2025 10:00	Demolish	Sets->Task ID->180
	Deconstruction Floor of 4. Floor		17.02.2025 10:00	17.02.2025 14:00	Demolish	Sets->Task ID->190
	Deconstruction Stairs of 3. Floor		17.02.2025 14:00	17.02.2025 15:00	Demolish	Sets->Task ID->200
	Deconstruction Strucral Columns of 3. Floor		17.02.2025 15:00	17.02.2025 17:00	Demolish	Sets->Task ID->210
	Deconstruction Floor of 3. Floor		18.02.2025 08:00	18.02.2025 11:00	Demolish	Sets->Task ID->220
	Deconstruction Stairs of 2. Floor		18.02.2025 11:00	18.02.2025 12:00	Demolish	Sets->Task ID->230
	Deconstruction Strucral Columns of 2. Floor		18.02.2025 13:00	18.02.2025 15:00	Demolish	Sets->Task ID->240
	Deconstruction Floor of 2. Floor		18.02.2025 15:00	18.02.2025 18:00	Demolish	Sets->Task ID->250
	Deconstruction Stairs of 1. Floor		19.02.2025 08:00	19.02.2025 09:00	Demolish	Sets->Task ID->260
	Deconstruction Strucral Columns of 1. Floor		19.02.2025 09:00	19.02.2025 11:00	Demolish	Sets->Task ID->270
	Deconstruction Floor of 1. Floor		19.02.2025 11:00	19.02.2025 14:00	Demolish	Sets->Task ID->280
	Deconstruction Stairs of Ground Floor		19.02.2025 14:00	19.02.2025 17:00	Demolish	Sets->Task ID->290
	Deconstruction Strucral Columns of Ground Floor		20.02.2025 08:00	20.02.2025 09:00	Demolish	Sets->Task ID->300
	Deconstruction Floor of Ground Floor		20.02.2025 09:00	20.02.2025 12:00	Demolish	Sets->Task ID->310
	Deconstruction of Stairs of Basement		20.02.2025 13:00	20.02.2025 13:00	Demolish	Sets->Task ID->320
	Deconstruction of Basement Floor Concrete Wall		20.02.2025 13:00	20.02.2025 18:00	Demolish	Sets->Task ID->330
	Deconstruction of Basement Floors Structrual Columns and Curtain Wall		21.02.2025 08:00	21.02.2025 11:00	Demolish	Sets->Task ID->340
	Deconstruction of Foundation		21.02.2025 11:00	21.02.2025 18:00	Demolish	Sets->Task ID->350

Fig. 3. Demolition schedule visualized in Navisworks after importing from Excel

3. Results and discussion

This study models and optimizes the demolition and recycling of a six-story structure in Istanbul, using an integrated BIM-based workflow. By combining various BIM tools, such as Revit, Dynamo, and Navisworks, with Excel, the methodology delivers precise material quantification, demolition scheduling and simulation. It also assists the calculation of waste logistics in a cost-effective manner. This section presents the results and compares the approach to traditional methods, highlighting its environmental and economic advantages.

3.1. Material quantification and demolition scheduling

A Dynamo script extracted detailed material volumes from the BIM model. Custom families created for L-shaped columns and sketch-based stairs ensured accurate calculations. Custom parameters (Task_ID, Element ID) enabled material categorization by floor and type, facilitating waste tracking and recycling analysis.

The BIM model was imported into Navisworks to develop a selective demolition schedule. Non-load-bearing brick walls and insulation were manually dismantled using demolition drills, followed by the C30 concrete elements (structural walls, columns, slabs, stairs) demolished top-down with a jaw excavator. Contractor interviews indicated that three workers could demolish brick walls on one floor in one day, while one worker was needed for dust control using water spraying during excavator operations. The demolition schedule projected 427.56 tons of waste over 10 workdays, including 149.7 tons of C30 concrete waste for the case study building. Daily waste quantities were tracked in Excel. Concrete volumes, extracted from the BIM model using Dynamo, were multiplied by a density factor of 2.3 t/m³ to calculate tonnage. Similarly, brick waste volumes were multiplied by 0.65 t/m³ for tonnage estimation.

3.2. Waste logistics and costs

The amount of waste produced per day was calculated using Dynamo, Naviswork schedule and Excel. A formula was created in Excel so vehicles with three different waste carrying capacities (Cevre Koruma Sube Mudurlugu, 2025)can optimally complete the daily waste transportation at the fewest turns and at the lowest price. Assuming that the waste would be transported from Beyoglu (where the building is located) to Arnavutkoy Waste Disposal Facility, it was multiplied by the fee for 1 ton of CDW transported for 1 kilometer, given by Istanbul Metropolitan Municipality. The distance between the building site and Arnavutkoy Waste Disposal Facility is 28 km. Table 1 presents the total cost of vehicles and related documentation.

Table 1. Cost and logistics data for construction and demolition waste management

Date	Volume	#Truck	Ton	Vehicle Price to Landfill (VPL)	Waste Carry Cost (WCC)	Transport and Acceptance Document (VAD)	TOTAL (VPL+WCC+VAD)
5.02.2025	12.90	1	8.39	3990	906.25	480.00	5376.25
6.02.2025	19.80	2	12.87	6840	1390.99	960.00	9190.99
7.02.2025	20.80	2	13.52	6840	1461.24	960.00	9261.24
10.02.2025	19.60	2	12.74	6840	1376.94	960.00	9176.94
11.02.2025	12.50	1	8.13	3990	878.15	480.00	5348.15
17.02.2025	24.51	2	63.00	7980	6809.04	960.00	15749.04
18.02.2025	27.81	2	71.00	7980	7673.68	960.00	16613.68
19.02.2025	19.02	2	58.00	6840	6268.64	960.00	14068.64
20.02.2025	40.40	3	92.92	11970	10042.79	1440.00	23452.79
21.02.2025	38.00	3	87.00	10830	9402.96	1440.00	21672.96
TOTAL	235.35	20	427.56	74100	46210.68	9600.00	129910.68

3.3. Excavator and labor cost

Excel spreadsheets were created to calculate the number of days the workers would work, and excavators would operate as seen in Table 2. and Table 3. According to the interviews with contractors, demolishing brick walls on one floor would take one day with three workers. Also, after manual demolition, the excavator would start demolition, and that one worker would need to be there to water the concrete to prevent dust on the day the excavator would operate. The interviewed demolition contractors stated that the jaw excavator can demolish approximately 1 to 1.5 floors daily. 3.000 TL per day will be paid to a worker for each working day and the daily rental cost of a jaw excavator including an operator is 50.000 TL. Given that the excavator is scheduled for use over five days, it was determined that commencing demolition at the start of the week would optimize cost efficiency and minimize additional expenses.

Table 2. Workforce schedule and cost summary

Date	Duration	#Workers	Daily Cost (TRY)
4.02.2025	1	3	9000
5.02.2025	1	3	9000
6.02.2025	1	3	9000
7.02.2025	1	3	9000
10.02.2025	1	3	9000
11.02.2025	1	3	9000
17.02.2025	1	1	3000
18.02.2025	1	1	3000
19.02.2025	1	1	3000
20.02.2025	1	1	3000
21.02.2025	1	1	3000
		TOTAL	69000

Table 3. Excavator and workforce cost summary

Date	Excavator	Daily Cost (TRY)
4.02.2025	0	0
5.02.2025	0	0
6.02.2025	0	0
7.02.2025	0	0
10.02.2025	0	0
11.02.2025	0	0
17.02.2025	1	50000
18.02.2025	1	50000
19.02.2025	1	50000
20.02.2025	1	50000
21.02.2025	1	50000
	TOTAL	250000

3.4. Cost analysis

To assess the potential contribution of recycling from the circular economy point of view, the mass of steel extracted from the structural project of the building was multiplied by the sales price of steel scrap obtained from scrap dealers, thereby calculating the revenue generated from the sale of steel waste (Table 4). Subsequently, using a script developed in Dynamo, a material take-off was extracted from the BIM model to determine the quantities of coarse aggregate, fine aggregate, and recycled concrete fines that could be produced from concrete waste by an on-site recycling plant. The percentages of these materials were obtained from a previous study (Shima et al., 2005). Sales prices for the recycled materials were used to calculate the potential revenue from their sales (Table 5).

As the costs associated with the excavator, labour, and waste vehicles for the demolition process had been previously calculated, the total expenses and revenues were aggregated in this step. Subsequently, a financial analysis was conducted to determine the potential profit or loss for demolition contractors, assuming selective demolition is performed, and the materials are sold at the specified prices.

Table 4. Revenue analysis of scrap iron sales

Iron Diameter	Weight(kg)	Total Price (TRY)
6-12 Phi	10327.99	109476.69
14-50 Phi	6982.16	74010.90
	TOTAL	183487.59

Table 5. Revenue analysis of concrete from recycling

Parts of Concrete	%	Ton	Selling Price (TRY)	Total Price (TRY)
Concrete Gross	-	372	-	-
Coarse Aggregate	35%	130	300	39,052
Fine Aggregate	30%	112	300	33,473
RCF	35%	130	1,300	169,224
			TOTAL	241,748

4. Conclusions

The cost analysis indicated that no profit could be generated from the sale of concrete and steel waste resulting from the building's demolition. This result was anticipated prior to the study, given the lack of an established market for recycled construction materials in Türkiye, as well as the absence of supportive regulations and incentive mechanisms. Moreover, the limited adoption of selective demolition practices can be primarily attributed to time and cost constraints. The findings of this study suggest that, with the implementation of appropriate regulations and incentives, demolition contractors may be more inclined to adopt selective demolition methods. Additionally, targeted training programs could enable contractors to carry out selective demolition in a more systematic and safer manner.

The implementation of BIM in this study played a critical role in accurately planning and analyzing selective demolition processes. Additionally, the 4D simulation supported the development of an effective work plan, leading to enhanced overall demolition efficiency for the case study building. Future work will involve consultations with additional demolition contractors to further refine the model. This will be followed by material-specific calculations, such as for recycled concrete waste, bricks, and other recoverable components, to evaluate the contribution of recycling efforts to a circular economy.

Acknowledgments

The authors would also like to thank Ender Bozkurt, and Ali Cimen for their collaboration and for sharing project-related information.

References

Çalkıvik, K., Ergül, N., Soyuer, S., Erbin, B., & Şabap, S. (2024). Kentsel Dönüşüm, Deprem ve Olası Diğer Afetler Sonucunda Oluşan Yıkıntı Atıklarının Yönetimi Rehberi. SKD Türkiye. İstanbul: SKD Türkiye Yayınları. (in Turkish)

Cevre Koruma Sube Mudurlugu. (2025). Cevre-Koruma-Sube-Mudurlugu-2025-YILI-UCRET-TARIFESI-KTE KOYULACAK. (in Turkish)

de Andrade Salgado, F., & de Andrade Silva, F. (2022). Recycled aggregates from construction and demolition waste towards an application on structural concrete: A review. *Journal of Building Engineering, 52*. Elsevier Ltd. https://doi.org/10.1016/j.jobe.2022.104452

Deloitte. (2015). Construction and Demolition Waste Management in Denmark.

Public Fill Committee Civil. (2004). Guidelines for Selective Demolition & On Site Sorting Public Fill Committee Civil Engineering and Development Department. Retrieved from http://www.cedd.gov.hk/eng/services/recycling/index.htm

Purnell, P., & Dunster, A. (2010). Recycling of concrete. In *Management, Recycling and Reuse of Waste Composites* (pp. 569-591). Woodhead Publishing. https://doi.org/10.1016/B978-1-84569-462-3.50020-0

Shima, H., Tateyashiki, H., Matsuhashi, R., & Yoshida, Y. (2005). An advanced concrete recycling technology and its applicability assessment through input-output analysis. *Journal of advanced concrete technology*, *3*(1), 53-67

Shin, J., & Song, J. (2024). Dismantling quantity estimation for nuclear power plant: Scan-to-BIM versus conventional method. *KSCE Journal of Civil Engineering, 28*(5), 1607–1621. https://doi.org/10.1007/s12205-024-0675-6

Zajac, M., Skocek, J., Ben Haha, M., & Deja, J. (2022). CO2 mineralization methods in cement and concrete industry. *Energies*, *15*(10), 3597. https://doi.org/10.3390/en15103597

4th International Civil Engineering & Architecture Conference
17-19 May 2025, Trabzon, Türkiye

The effect of waste foundary sand on mixed-mode I/II fracture behavior of concrete

Mahdi Pakseresht[1], Javad Akbardoost*[1]

[1] Department of Mechanical Engineering, Faculty of Engineering, Kharazmi University, Mofatteh Avenue, P.O. Box 15719-14911, Tehran, Iran.

Abstract. As an important material in civil engineering, concrete contains naturally a large number of cracks and flaws which make the concrete components to be vulnerable against the mechanical loading. Therefore, the fracture behavior of concrete has been extensively investigated by engineers and researchers. On the other hand, the initial resource for constructing concrete has been limited and use of recycled materials such as waste foundry sand has been recently considered as an interesting approach for compensate of this limitation. In this study, the effect of waste foundry sand (WFS) which can be used instead of natural fine aggregate, on the mixed-mode fracture of concrete is assessed. For this purpose, five compositions of concrete with different contents of WFS (0%, 5%, 10%, 15% and 20% weight ratios) were made. Then, single-edge notched beam (SENB) samples were manufactured from these concrete mixtures. After that, the SENB samples were tested by symmetric and asymmetric three-point bending fixture in order to produce the pure mode I and mixed mode I/II loading conditions. The mixed-mode fracture curves obtained from experiments show that the increase of WFS content leads to decrease the mixed-mode fracture resistance of concrete due to microstructure variations. For example, by adding 20% WFS in concrete, the pure mode I fracture resistance decreases 22% relative to the normal concrete. Moreover, it is revealed that decreasing trend for mixed mode loading is more than that for pure mode I.

Keywords: Concrete; Waste foundry sand (WFS); Mixed-mode I/II fracture; Single-edge notched beam (SENB); Cracked sample.

1. Introduction

Concrete is one of the major materials in the construction of buildings, dams, tunnels and other civil projects. Civil researchers and engineers carry out extensively several studies about concrete and its compositions. They are interest to find new methods and sources for constructing the concrete due to the lack of initial sources. In this way, the use of recycled or waste materials is one of the most applicable approaches (Gupta, Siddique, Sharma, & Chaudhary, 2019; Jokar, Khorram, Karimi, & Hataf, 2019; T. Naik, Kraus, Chun, Ramme, & Singh, 2003; T. R. Naik, Kraus, Ramme, & Canpolat, 2012; Pathak & Siddique, 2012; Peighambarzadeh, Asadollahfardi, & Akbardoost, 2020; Pytel, 2014; Smarzewski & Barnat-Hunek, 2016; Smit, Nakum, & Bhogayata, 2014; Xie et al., 2019). One of the wasted material which can be considered in the construction of concrete instead of natural sand, is the foundry sand (FS) and/or waste foundry sand (WFS). The foundry sand (FS) is an important material in the metal casting mold and is often disposed after several casting procedures leading to environmental pollutions. It is reported by Bhardwaj and Kumar (Bhardwaj & Kumar, 2017) that 1.71 million tons and 6-10 million tons of WFS is annually discarded in India and USA, respectively. Thus, employing WFS as partial replacement of concrete sand not only reduces the problems of land-fill shortage and negative environmental pollution, but also can be a competent material for sand replacement and reduces the consumption of natural resources.

It is obvious that each component employed in concrete construction plays an important role in its strength and durability. Hence, the mechanical and chemical properties of the concrete will be changed when the waste materials are used instead of the natural resources and this variation should be assessed in order to use the waste materials appropriately. For example, the effect of FS as an alternative material for fine aggregate (sand) on the density, tensile and compressive strength, flexural strength, workability (slump test) and ultrasonic pulse velocity has been experimentally investigated by Ganesh Prabhu et al. (Ganesh Prabhu, Hyun, & Kim, 2014). They showed that although the flexural, tensile and compressive strengths of concrete with FS are relatively close to those values of the control mixture, FS decreases the workability of concrete. As another example, Singh and Siddique (Singh & Siddique, 2012a) revealed that the use of 5, 10 and 15 % WFS enhances the splitting tensile strength,

*Corresponding author, E-mail: akbardoost@khu.ac.ir

https://doi.org/10.31462/icearc2025_ce_was_529

compressive strength, modulus of elasticity and abrasion resistance. In other study, they (Singh & Siddique, 2012b) showed that partial substitution of WFS increases the value of ultrasonic pulse velocity and decreases chloride ion penetration in concrete.

On the other hand, concrete mixture includes a large number of microcracks which make this quasi-brittle material to be vulnerable to the mechanical loading. These microcracks might change to macro-cracks due to weather conditions, construction procedures or during the service life and lead to reduce significantly the load-bearing capacity of concrete parts. In this way, the concepts of fracture mechanics have been extensively used for assessing the fracture resistance of cracked concrete parts. In fracture mechanics, there are three major modes of loading: 1) mode I or opening mode in which the crack flanks open without any sliding, 2) mode II or in-plane sliding mode in which the crack flanks slide normal to the crack front without any opening or closing, 3) mode III or tearing mode in which the crack flanks slide parallel to the notch front without any opening or closing. Similar to other mechanical properties, the fracture behavior of concrete under different modes should be assessed. As the best of author's knowledge, almost all of the studies dealing with the fracture assessment of recycled concrete have focused only on the recycled aggregate concrete. For example, Kazemian et al. (Kazemian, Rooholamini, & Hassani, 2019) assessed experimentally the fracture behavior of concrete made with treated and untreated recycled coarse aggregates. There is only a study in the literature which investigates the fracture behavior of FS or WFS concrete. Aslani et al. (Aslani, Akbardoost, & Delnavaz, 2021) carried out several fracture tests on single edge notched beam (SENB) made of concrete with different contents of FS and WFS and under pure mode I. They revealed that fracture toughness of concrete reduces by using FS and WFS. This study has been limited on mode I loading the mixed mode I/II loading condition has not been investigated yet. Therefore, in the paper, the effect of WFS on the mixed mode I/II fracture behavior of concrete is studied. To this end, several single-edge notched beam (SENB) specimens were manufactured from concrete with five contents of WFS (0, 5, 10, 15 and 20% WFS). Then, the SENB samples were tested by three-point bend fixture until final fracture. The mixed mode loading conditions is achieved in this study by changing the distance between the bottom supports. The comparison between the experimental results of normal concrete and concrete with WFS is revealed that the mixed mode fracture resistance of concrete decreases by increasing the contents of WFS.

2. Experiments

There are 4 major components for manufacturing concrete: water, cement, fine aggregate (sand) and coarse aggregate (gravel). After mixing these four components in appropriate contents named concrete mix design, the mixture is poured in a mold and then is kept in water for a specific time referred as curing time.

In the present study, portland cement type II from Abyek cement factory (Abyek city in Qazvin province, Iran) was utilized. Water used in the present study for both construction of concrete mix and curing the concrete samples was tap water. The coarse aggregate was the gravel with maximum size of 20 mm determined according to ASTM C136/C136M-2 standard (" ASTM C136/C136M-19," 2019) for the sieve analysis. The fine aggregate was the twice-washed natural sand with a maximum size of 4.7 mm based on ASTM C136/C136M-2 standard (" ASTM C136/C136M-19," 2019) in normal concrete. Also, WFS were extracted from a small metal casting factory in Shahriyar industrial zone in Tehran, Tehran province, Iran. WFS is a by-product from the metal casting factory and is often disposed. The sand, gravel and WFS utilized for constructing the concrete in this study are shown in Fig. 1. Fig. 2 illustrates the gradation curves of sand, gravel and WFS.

Fig. 1: Gravel, sand and WFS utilized for constructing concrete in this study.

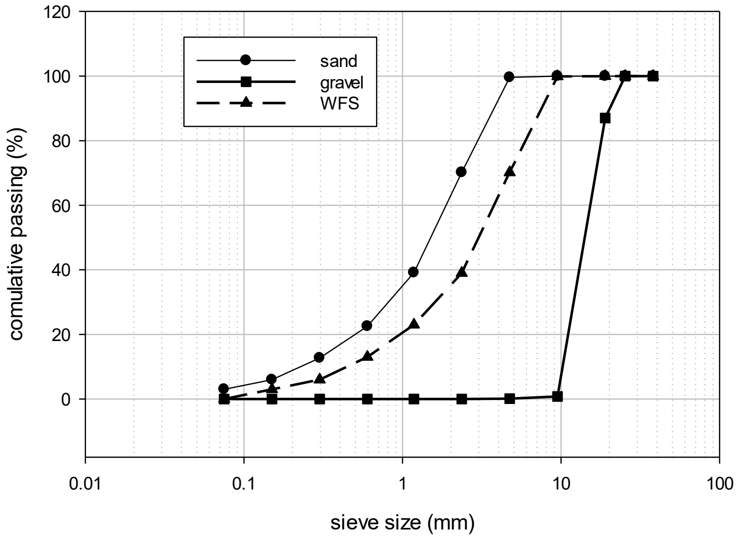

Fig. 2. Gradation of sand, gravel and WFS.

2.2. Mix contents

As mentioned earlier, five mix contents were considered in this study. The first one named as the control sample was made by the natural sand as fine aggregate. In the other samples, 5%, 10%, 15% and 20% weigth ratios of WFS were used instead of the natural sand. All mix contents were made according to the Iranian national mix design. The water-cement ratio (W/C) for all mixtures were constant values of 0.55 weight of cement. Table 1 shows the proportion of each mixture for one cubic meter of concrete. It is necessary to mention that increase of WFS more than 20% leads to decrease the slump and fluidity of concrete due to existence of clayey type fine materials in WFS (Bhardwaj & Kumar, 2017; Siddique & Singh, 2011).

Table 1. Mix proportion for one cubic meter of concretes

Category	Normal concrete	5% WFS	10% WFS	15% WFS	20% WFS
Cement (kg/m^3)	400	400	400	400	400
Sand (kg/m^3)	1000	950	900	850	800
Coarse Gravel (kg/m^3)	320	320	320	320	320
Fine Gravel (kg/m3)	480	480	480	480	480
WFS (kg/m^3)	0	50	100	150	200
Water (kg/m^3)	220	220	220	220	220
W/C	0.55	0.55	0.55	0.55	0.55
Slump (cm)	7	6	4	3	1
Concrete unit weight (kg/m^3)	2345	2356	2345	2343	2348

2.3. Sample preparation and test procedure

The single-edge notched beam (SENB) was utilized in this study for conducting the mixed-mode I/II fracture tests. The SENB specimen is a beam with width w, length L and thickness t. A crack of length a is created artificially in the middle of SENB specimen. Fig. 3 displays a schematic of SENB sample as well as loading condition. As shown, the SENB sample is loaded by a three-point fixture in which the bottom supports have distances S_1 and S_2 from the crack line and the applied load is along the crack line. In order to provide pure mode I loading, the SENB sample is subjected to three-point bending with symmetric distance in bottom supports, i.e. $S_1 = S_2$. The mixed-mode and pure mode II loading conditions are achieved in this sample by moving one of the bottom supports toward the crack. The sample tested in this study has the dimensions of $100\times100\times250$ mm^3 and includes a crack length of 25 mm. Using finite element method for the SENB sample with aforementioned dimensions, it is obtained that pure mode II is provided when S_1=100 mm and S_2=11.5 mm. In addition to pure mode I and pure mode II, two mixed-mode loading conditions were also tested in this study by considering the values of S_2=20 mm and S_2=30 mm.

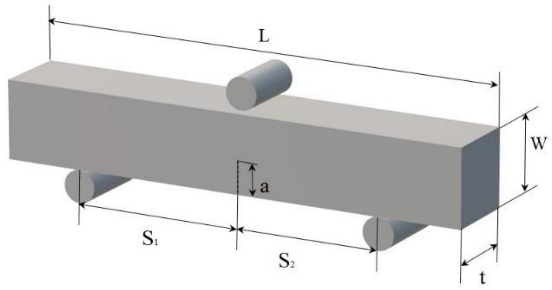

Fig. 3. Schematic of SENB specimen.

Fig. 4. The SENB specimens tested in this study.

After preparing concrete according to compounds given in Table 1, mixtures were poured in the molds with dimensions of 100×100×250 mm^3 for each WFS content. The concrete beams were removed from molds after a day and then were cured in tap water for 28 days. After that, a crack was created in one side of the concrete beams by means of a rotary fret saw with a thin saw blade of 0.3 mm in thickness. The total length of crack was nearly 25 mm for all specimens. Since 4 loading conditions were considered in this study and each test category were repeated four times in order to obtain reliable results, 16 beams were manufactured for each WFS content. Totally, 80 SENB samples were prepared in this study. Fig. 4 shows the all SENB samples prepared for testing in this study.

Finally, the prepared specimens were tested by a universal tension/compression test machine with a load cell capacity of 50 kN under three-point bending condition. Displacement control conditions with a constant cross head speed of 0.5 mm/min was utilized for all specimens. Table 2 shows the values of fracture loads obtained from the fracture experiments. Fig. 5 also displays some broken concrete samples. As seen in this Fig., the onset of fracture for all samples under pure mode II took place from bottom support which is undesirable. This point were observed after testing two SENB samples for each WFS content. Thus, the results obtained from this category and given in Table 2 (the last 10 fracture loads) is not reliable. This is mainly because the bottom support is very close to the crack flank and in materials with relatively low tensile strength such as concrete, the stress concentration generated at the contact point between the roller support and the edge of sample controls the crack path.

3. Results and discussion

In order to assess the mixed-mode fracture behavior of materials, the critical stress intensity factors for mode I and mode II defined respectively by K_{If} and K_{IIf} are often used. These parameters are usually calculated by numerical approaches such as finite element method (FEM). Since there are no values of K_{If} and K_{IIf} for teste SENB sample (SENB sample subjected to three-point bend with asymmetric supports), they were obtained numerically in this study. To this end, a 2D model of the SENB samples with dimensions of 250×100 mm^2 were generated in ABAQUS code. Then, the model was discretized by eigth-node iso- parametric elements. The singular collapsed elements were also used around the crack tip in order to take into account the high stress gradient at the crack tip. After that, loading condition and boundary conditions were set in FE models according to tested samples. Fig. 6 displays a sample of FE model for SENB under mixed mode loading, as well as applied load and boundary conditions. It is noteworthy that the average of fracture loads given in Table 4 were applied in the FE models. After solving process, the values of K_{If} and K_{IIf} were obtained directly from ABAQUS code.

Table 2: The fracture loads obtained from experiments.

Sample Code	% WFS	Fracture Load(N)	S_2(mm)	Average of fracture load (N)	Loading condition
S-0-100-1	0	9557.44	100	9725	Pure mode I
S-0-100-2	0	10410.9	100		
S-0-100-3	0	9436.0	100		
S-0-100-4	0	9495.5	100		
S-5-100-1	5	8836.4	100	8897	
S-5-100-2	5	9252.1	100		
S-5-100-3	5	8891.5	100		
S-5-100-4	5	8606.6	100		
S-10-100-1	10	8453.8	100	8280	
S-10-100-2	10	8262.5	100		
S-10-100-3	10	8382.9	100		
S-10-100-4	10	8022.7	100		
S-15-100-1	15	7734.2	100	8017	
S-15-100-2	15	8299.3	100		
S-15-100-3	15	8493.6	100		
S-15-100-4	15	7542.4	100		
S-20-100-1	20	7254.5	100	7431	
S-20-100-2	20	6179.6	100		
S-20-100-3	20	8082.8	100		
S-20-100-4	20	8207.3	100		
S-0-30-1	0	25221.5	30	24247	Mixed mode I/II
S-0-30-2	0	24209.9	30		Mixed mode I/II
S-0-30-3	0	24364.4	30		Mixed mode I/II
S-0-30-4	0	23190.8	30		Mixed mode I/II
S-5-30-1	5	22414.6	30	21742	Mixed mode I/II
S-5-30-2	5	21660.5	30		Mixed mode I/II
S-5-30-3	5	21395.6	30		Mixed mode I/II
S-5-30-4	5	21498.6	30		Mixed mode I/II
S-10-30-1	10	21119.7	30	20962	Mixed mode I/II
S-10-30-2	10	20932.1	30		Mixed mode I/II
S-10-30-3	10	21071.9	30		Mixed mode I/II
S-10-30-4	10	20726.1	30		Mixed mode I/II
S-15-30-1	15	19986.6	30	19565	Mixed mode I/II
S-15-30-2	15	18507.8	30		Mixed mode I/II
S-15-30-3	15	19339.2	30		Mixed mode I/II
S-15-30-4	15	20424.4	30		Mixed mode I/II
S-20-30-1	20	18298.1	30	18400	Mixed mode I/II
S-20-30-2	20	18474.7	30		Mixed mode I/II
S-20-30-3	20	17661.7	30		Mixed mode I/II
S-20-30-4	20	19166.3	30		Mixed mode I/II

Table 2 Continued

Sample Code	% WFS	Fracture Load(N)	S_2(mm)	Average of fracture load (N)	Loading condition
S-0-20-1	0	36393.9	20		Mixed mode I/II
S-0-20-2	0	39244.9	20	36504	Mixed mode I/II
S-0-20-3	0	35076.9	20		Mixed mode I/II
S-0-20-4	0	35301.3	20		Mixed mode I/II
S-5-20-1	5	32078.7	20		Mixed mode I/II
S-5-20-2	5	31552.6	20	32242	Mixed mode I/II
S-5-20-3	5	31795.4	20		Mixed mode I/II
S-5-20-4	5	33542.7	20		Mixed mode I/II
S-10-20-1	10	28090.9	20		Mixed mode I/II
S-10-20-2	10	30371	20	29714	Mixed mode I/II
S-10-20-3	10	29878.8	20		Mixed mode I/II
S-10-20-4	10	30515.2	20		Mixed mode I/II
S-15-20-1	15	27410.4	20		Mixed mode I/II
S-15-20-2	15	28521.3	20	28181	Mixed mode I/II
S-15-20-3	15	27506	20		Mixed mode I/II
S-15-20-4	15	29286.5	20		Mixed mode I/II
S-20-20-1	20	25534.2	20		Mixed mode I/II
S-20-20-2	20	27388.3	20	23614	Mixed mode I/II
S-20-20-3	20	20056.5	20		Mixed mode I/II
S-20-20-4	20	21477	20		Mixed mode I/II
S-0-5	0	39656.9	11.5	44432	Pure mode II
S-0-6	0	49207	11.5		Pure mode II
S-5-5	5	39465.6	11.5	37978	Pure mode II
S-5-6	5	36489.5	11.5		Pure mode II
S-10-5	10	35477.9	11.5	36841	Pure mode II
S-10-6	10	38203.8	11.5		Pure mode II
S-15-5	15	33778.3	11.5	31505	Pure mode II
S-15-6	15	29231.3	11.5		Pure mode II
S-20-5	20	26151.1	11.5	26358	Pure mode II
S-20-6	20	26564.3	11.5		Pure mode II

a) Pure mode I (S_2=100 mm)

b) Mixed mode (S_2=30 mm)

b) Mixed mode (S2=20 mm)

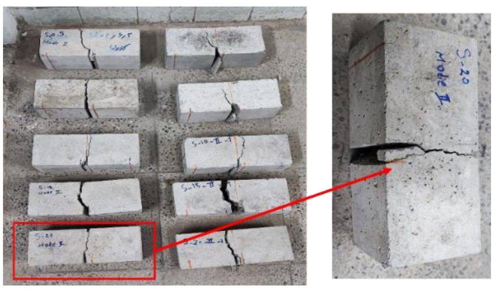

b) Pure mode II (S2=11.5 mm)

Fig. 5. Some broken SENB samples under pure mode I and mixed-mode loading.

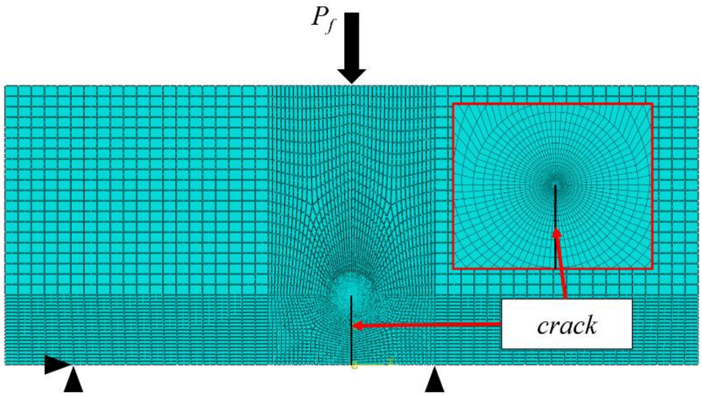

Fig. 6. A sample of FE model for SENB with S_1=100 mm and S_2=30 mm

The values of K_{If} and K_{IIf} obtained from FE analysis are listed in Table 3. Also, Fig. 7 illustrates the mixed mode fracture curves of tested samples with different contents of WFS. It is again mentioned that the values of K_{IIf} for pure mode II loading conditions listed in Table 3 or depicted in Fig. 7 are not reliable due to unreliable fracture loads obtained from experiments. It is observed from this Fig. that the fracture resistance of concrete decreases when the content of WFS becomes more.

Table 3: The values of K_{If} and K_{IIf} for tested SENB samples.

Sample Code	WFS content (%)	S_2 (mm)	Average Fracture Load	K_{If} (MPa.√m)	K_{IIf} (MPa.√m)	Loading condition
S-0-100	0	100	9725	0.757	0.000	Pure mode I
S-5-100	5	100	8897	0.693	0.000	
S-10-100	10	100	8280	0.645	0.000	
S-15-100	15	100	8017	0.624	0.000	
S-20-100	20	100	7431	0.579	0.000	
S-0-30	0	30	24247	0.696	0.215	Mixed mode I/II
S-5-30	5	30	21742	0.624	0.193	
S-10-30	10	30	20962	0.602	0.186	
S-15-30	15	30	19565	0.562	0.173	
S-20-30	20	30	18400	0.528	0.163	
S-0-20	0	20	36504	0.522	0.596	Mixed mode I/II
S-5-20	5	20	32242	0.461	0.527	
S-10-20	10	20	29714	0.425	0.485	
S-15-20	15	20	28181	0.403	0.460	
S-20-20	20	20	23614	0.338	0.386	
S-0-11.5	0	11.5	44432	0.000	1.226	Pure mode II
S-5-11.5	5	11.5	37978	0.000	1.048	
S-10-11.5	10	11.5	36841	0.000	1.017	
S-15-11.5	15	11.5	31505	0.000	0.870	
S-20-11.5	20	11.5	26358	0.000	0.728	

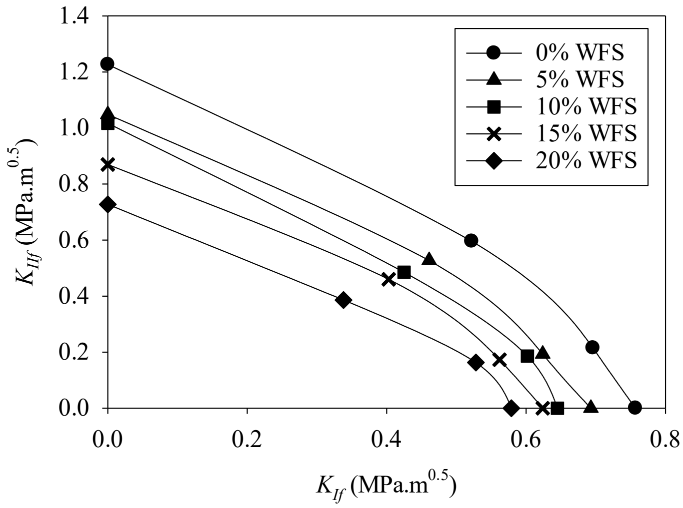

Fig. 7. The mixed mode fracture curves of tested samples with various contents of WFS.

As seen from Fig. 7, when the content of WFS increases from 5% to 20 %, the mode I fracture toughness decreases from 0.757 MPa.√m to 0.579 MPa.√m because WFS reduced coherence between aggregates. Aslani et al. (Aslani et al., 2021) showed previously this point by scanning electron microscopy (SEM) images. This decreasing trend can be observed for mixed-mode I/II behavior of concrete with WFS. Therefore, one can conclude that the existence of WFS leads to reduce the fracture resistance of concrete both in tension and shear.

4. Conclusions

The mixed mode fracture behavior of concrete including WFS was investigated in this study. For this purpose, 80 SENB samples in five contents of WFS (0%, 5%, 10%, 15% and 20%) and 4 mode mixity (pure mode I, 2 mixed-mode loading conditions and pure mode II) were prepared and then were tested by three-point bending fixture with symmetric and asymmetric bottom supports. In order to calculate the critical stress intensity factors K_{If} and K_{IIf} which define the mixed mode fracture resistance of materials, the SENB samples were modeled in a commercial finite element code. The experimental results indicated that the existence of WFS leads to decrease the fracture resistance of concrete both in pure mode I and mixed mode I/II loading (tension and shear). It was also observed in this study that the SENB sample with aforementioned dimensions and loading conditions for pure mode II (i.e. S_2=11.5 mm) is not suitable for pure mode II fracture test. This is mainly because the bottom support is very close to the crack flank and the fracture may initiate from the contact point between the SENB edge and roller of bottom support and then reach the crack flank. While the crack initiation from crack tip is expected in fracture mechanics, this type of fracture path is undesirable.

References

Aslani, M., Akbardoost, J., & Delnavaz, M. (2021). Investigating the effect of the foundry sand and waste foundry sand on the fracture toughness of concrete. *Arabian Journal of Geosciences, 14*(6), 464.

ASTM C136/C136M-19. (2019). *Standard test method for sieve analysis of fine and coarse aggregates*. West Conshohocken, PA: ASTM International.

Bhardwaj, B., & Kumar, P. (2017). Waste foundry sand in concrete: A review. *Construction and Building Materials, 156*, 661–674.

Ganesh Prabhu, G., Hyun, J. H., & Kim, Y. Y. (2014). Effects of foundry sand as a fine aggregate in concrete production. *Construction and Building Materials, 70*, 514–521.

Gupta, T., Siddique, S., Sharma, R. K., & Chaudhary, S. (2019). Behaviour of waste rubber powder and hybrid rubber concrete in aggressive environment. *Construction and Building Materials, 217*, 283–291.

Jokar, F., Khorram, M., Karimi, G., & Hataf, N. (2019). Experimental investigation of mechanical properties of crumbed rubber concrete containing natural zeolite. *Construction and Building Materials, 208*, 651–658.

Kazemian, F., Rooholamini, H., & Hassani, A. (2019). Mechanical and fracture properties of concrete containing treated and untreated recycled concrete aggregates. *Construction and Building Materials, 209*, 690–700.

Naik, T., Kraus, R., Chun, Y., Ramme, B., & Singh, S. (2003). Properties of field manufactured cast-concrete products utilizing recycled materials. *Journal of Materials in Civil Engineering, 15*(4), 400–407.

Naik, T. R., Kraus, R. N., Ramme, B. W., & Canpolat, F. (2012). Effects of fly ash and foundry sand on performance of architectural precast concrete. *Journal of Materials in Civil Engineering, 24*(7), 851–859.

Pathak, N., & Siddique, R. (2012). Effects of elevated temperatures on properties of self-compacting concrete containing fly ash and spent foundry sand. *Construction and Building Materials, 34*, 512–521.
Peighambarzadeh, F., Asadollahfardi, G., & Akbardoost, J. (2020). The effects of using treated wastewater on the fracture toughness of the concrete. *Australian Journal of Civil Engineering*, 1–9.
Pytel, Z. (2014). Evaluation of potential applications of recycled moulding and core sands to production of ceramic building materials. *Ceramics International, 40*(3), 4351–4358.
Siddique, R., & Singh, G. (2011). Utilization of waste foundry sand (WFS) in concrete manufacturing. *Resources, Conservation and Recycling, 55*(11), 885–892.
Singh, G., & Siddique, R. (2012a). Abrasion resistance and strength properties of concrete containing waste foundry sand (WFS). *Construction and Building Materials, 28*(1), 421–426.
Singh, G., & Siddique, R. (2012b). Effect of waste foundry sand (WFS) as partial replacement of sand on the strength, ultrasonic pulse velocity and permeability of concrete. *Construction and Building Materials, 26*(1), 416–422.
Smarzewski, P., & Barnat-Hunek, D. (2016). Mechanical and durability related properties of high performance concrete made with coal cinder and waste foundry sand. *Construction and Building Materials, 121*, 9–17.
Smit, K., Nakum, A., & Bhogayata, A. (2014). Use of used foundry sand in concrete: A state of art review. *International Journal of Research in Engineering and Technology, 3*, 586–589.
Xie, J., Li, J., Lu, Z., Li, Z., Fang, C., Huang, L., & Li, L. (2019). Combination effects of rubber and silica fume on the fracture behaviour of steel-fibre recycled aggregate concrete. *Construction and Building Materials, 203*, 164–173.

Evaluation of crack resistance in asphalt mixtures modified with recycled pet granules at low and intermediate temperatures

Sajed Baradaran[1], M.R.M Aliha[*2,3,5], Mahmoud Ameri[1], Nazife Erarslan[4], Tomasz Sadowski[5]

[1] Department of Civil Engineering, Iran University of Science and Technology (IUST), Narmak, Tehran 16846-13114, Iran
[2] Welding and Joining Research Center, School of Industrial Engineering, Iran University of Science and Technology (IUST), Narmak, 16846-13114, Tehran, Iran
[3]Department of Mechanical Engineering, Gebze Technical University, Kocaeli, 41400, Turkiye
[4]Izmir Democracy University, Engineering Faculty, Civil Engineering Department, Izmir, Turkey
[5]Group of Solid Mechanics, Lublin University of Technology, Nadbystrzycka 40 Str, Lublin 20-216, Poland

Abstract. Amid escalating global concerns over environmental sustainability in civil infrastructure, the pursuit of eco-friendly and durable pavement solutions has gained considerable attention. Among various waste streams, plastic waste presents a significant challenge due to its persistence and environmental impact. Incorporating plastic waste into pavement construction emerges as a promising strategy to mitigate plastic pollution while enhancing the mechanical performance of pavements. Prior research has demonstrated that asphalt binders modified with plastic waste exhibit superior durability, improved deformation resistance, and reduced maintenance demands. This approach aligns with circular economy principles by transforming waste materials into valuable resources, thereby fostering sustainable infrastructure development. In this study, the focus is directed toward improving the cracking resistance of asphalt pavements through the incorporation of chemically recycled polyethylene terephthalate (PET) in granular form. The PET additive, obtained via chemical recycling processes, were blended with a conventional asphalt binder to produce modified cylindrical specimens. Semi-Circular Bending (SCB) samples were subsequently extracted from these specimens to evaluate their fracture properties. SCB tests conducted at three different temperatures (-10°C, 0°C, and +10°C) assessed key fracture parameters, including fracture toughness (K_{IC}) and fracture energy (G_f). The results revealed substantial enhancements in both fracture toughness and energy, indicating improved cracking resistance across varying temperature conditions. These findings underscore the potential of integrating recycled plastic waste into asphalt mixtures as an effective means to advance pavement durability and sustainability.

Keywords: Asphalt pavement; Cracking resistance; Recycling; PET granules; Fracture energy; Fracture toughness

1. Introduction

Cracking represents one of the most prevalent and severe forms of structural distress in asphalt pavements, particularly in regions subject to extreme temperature variations or persistently cold climates. Fluctuations in service temperature significantly affect the viscoelastic properties of asphalt mixtures. At elevated temperatures, bitumen exhibits predominantly viscous behavior, allowing for plastic deformation. Conversely, at intermediate to low temperatures, bitumen becomes increasingly brittle, making the asphalt mixture more susceptible to crack formation (Aliha et al., 2021; Hong et al., 2020; Shahryari et al., 2021; Xiongzhou et al., 2021; Baradaran and Ameri., 2023; Baradaran and Ziaee., 2025). Asphalt pavement cracking can be categorized into several distinct types, including fatigue cracking, which is primarily load-induced; thermal cracking, triggered by temperature fluctuations; longitudinal cracking; and reflective cracking, often associated with differential movement or underlying layer behavior. These cracking types are all fundamentally linked to the fracture resistance of the asphalt materials in the pavement structure. Under traffic loading, pavements are subjected to complex stress states—ranging from tensile (Mode I) to shear (Mode II)—depending on the wheel position and load magnitude. In contrast, environmental temperature changes often induce thermal tensile stresses, which predominantly

[*] Corresponding author, E-mail: mrm_aliha@iust.ac.ir

https://doi.org/10.31462/icearc2025_ce_was_668

promote Mode I fracture opening (Aliha et al., 2015; Fakhri et al., 2018; Uzan & Levenberg, 2001; Zhu et al., 2017; Aliha et al., 2014).

The prediction and analysis of asphalt pavement cracking remain a challenging task for pavement engineers due to the heterogeneous and time-dependent nature of asphalt concrete (Alaswadko et al., 2019; Aliha & Mousavi, 2020). Consequently, ongoing research is devoted to understanding and improving the fracture behavior and resistance of asphalt mixtures. Linear Elastic Fracture Mechanics (LEFM) has been widely employed to characterize crack propagation mechanisms at low and intermediate temperatures, offering a reliable framework for assessing fracture behavior in brittle materials like asphalt under certain conditions (Ameri et al., 2012; Ziari et al., 2020; Fakhri et al., 2020; Motevalizadeh et al., 2020; Saha & Biligiri, 2016). At low temperatures, the stress intensity factor (K) is commonly used as a primary fracture criterion to evaluate the crack initiation resistance of asphalt mixtures (Aliha et al., 2017; Marasteanu et al., 2002; Aliha et al., 2023). At intermediate temperatures, where viscoelastic effects are more pronounced, energy-based parameters such as the critical strain energy release rate (G_c) and fracture energy (G_f) provide more meaningful insights into the material's resistance to cracking (Song et al., 2023; Ameri et al., 2016; Fatemi et al., 2023; Li et al., 2024; Tabasi et al., 2023; Alae et al., 2023). Various fracture test methodologies have been developed and adopted to characterize these properties, including the Single-Edge Notched Beam (SENB), Disk-Shaped Compact Tension (DCT), Edge-Notched Disc Bend (ENDB), and Semi-Circular Bend (SCB) tests, each providing different advantages for characterizing crack propagation and toughness in asphalt mixtures (Wagoner et al., 2005; Wagoner et al., 2006; Aliha et al., 2015; Qiu et al., 2024; Ren et al., 2023; Meng et al., 2024). In parallel with advancements in fracture characterization techniques, there has been a growing global emphasis on adopting eco-friendly and sustainable approaches in the development of construction materials. Utilizing recycled and waste materials not only addresses environmental concerns but also contributes to improving the mechanical resilience of infrastructure, ensuring longer service life and reduced maintenance. This increased focus reflects a strategic shift toward integrating sustainability and durability as complementary objectives in modern civil engineering practices (Baradaran et al., 2023; Baradaran et al., 2024a; Niri et al., 2024; Tareghian et al., 2024; Yazdi et al., 2024; Pargar et al., 2024; Yeganeh et al., 2024; Pournoori et al., 2024; Rajaee et al., 2025a, Rahaee et al., 2025b; Baradaran et al., 2024b).

To mitigate the susceptibility of asphalt mixtures to cracking, considerable research has explored the incorporation of various additives and modifiers into both the asphalt binder and the aggregate matrix. These include recycled and waste materials such as crumb rubber (Bazoobandi et al., 2024; Liang et al., 2024), waste glass (Phan et al., 2024; Yang et al., 2023), steel slag (Zhong et al., 2024; Xu et al., 2024), and waste polyethylene (Baradaran et al., 2024; Ayar et al., 2022). Among these, polyethylene terephthalate (PET) has garnered significant attention due to its abundance and high-value polymer properties. The global rise in PET waste generation, largely due to its widespread application in packaging, bottles, textiles, and industrial products (Salazar-Beltrán et al., 2018; Li et al., 2016), poses an environmental threat as PET is non-biodegradable (Mohammed, 2017). While several advanced methods—such as hydrogenation, glycolysis, methanolysis, and hydrolysis—exist for chemical recycling of PET (Thiounn & Smith, 2020; Ragaert et al., 2017), many are cost-prohibitive on a large scale (Webb et al., 2012). As such, integrating recycled PET into construction materials such as asphalt presents an economically and environmentally favorable solution, contributing to reduced landfill accumulation, lower greenhouse gas emissions, and decreased reliance on non-renewable materials (Sulyman et al., 2016; Yao et al., 2022). Several studies have validated the potential of PET to enhance asphalt performance. In a 2018 study by Leng et al., chemically treated PET-derived additives were incorporated into reclaimed asphalt pavement (RAP) mixtures. Laboratory evaluations using dynamic shear rheometer (DSR), bending beam rheometer (BBR), and moisture susceptibility tests revealed that the modified binders exhibited up to 60% improvement in fatigue resistance compared to traditional mixtures (Leng et al., 2018). In another investigation, Ghabchi et al. (2021) demonstrated that micronized PET (MPET) improved binder-aggregate adhesion, increased viscosity, and significantly enhanced resistance to stripping and cracking in asphalt mixtures. Similarly, research by Ma and Hesp (2022) explored the impact of PET fibers of varying lengths (6 mm and 18 mm) on fracture resistance. Results showed a notable increase (approximately 10%) in fracture energy at 20°C for the 6 mm PET fiber mixture, while the 18 mm fibers yielded even higher resistance across temperature ranges. At 10°C, only the longer fibers contributed to a substantial improvement in fracture toughness, emphasizing the critical role of fiber length in reinforcing asphalt composites. Further supporting these findings, Callomamani et al. (2023) conducted a comparative study on the use of synthetic fibers (PET and aramid) in asphalt mixtures. The inclusion of 0.1% PET fiber and 0.065% aramid fiber led to consistent increases in total fracture energy across all test temperatures, averaging 30% and 40% improvements respectively, thereby confirming the enhanced crack resistance afforded by PET fiber reinforcement.Although the global momentum toward sustainable infrastructure and circular economy practices has intensified in recent years, limited attention has been paid to the fracture behavior of asphalt mixtures modified with recycled polyethylene terephthalate (PET)—especially when PET is utilized in chemically processed forms.

While prior studies have investigated the general mechanical properties and durability improvements offered by PET-modified asphalt, the fracture resistance of such mixtures under critical service conditions remains underexplored. In particular, the impact of temperature-induced brittleness at low and intermediate temperatures—where asphalt pavements are most susceptible to cracking—has not been adequately assessed in the context of chemically recycled PET-based additives. To date, no comprehensive study has investigated the fracture performance of asphalt mixtures incorporating synthesized additives derived from PET granules through chemical recycling techniques. Most existing research has relied on PET in physically treated forms, such as flakes, powders, or short fibers, without considering the significant changes in molecular structure and chemical compatibility that result from recycling processes like aminolysis. Such chemical transformations have the potential to enhance the interaction between PET derivatives and asphalt binder, thereby improving crack resistance through better stress distribution and energy dissipation mechanisms. However, these effects remain largely undocumented in the existing body of literature. Addressing these gaps, the present study aims to assess the fracture resistance of asphalt mixtures modified with a value-added additive synthesized from PET granules via a chemical recycling pathway. Specifically, this research investigates the influence of this additive on crack propagation behavior under pure Mode I fracture conditions at two temperature levels representative of field service extremes: –10°C and 0°C (low temperature) and +10°C (intermediate temperature). Semi-Circular Bend (SCB) specimens were fabricated for each mixture type, including a control (0% PET) and a modified mixture containing 2% chemically recycled PET additive by weight of bitumen. All samples were subjected to Mode I loading using standardized SCB fracture testing procedures to evaluate tensile fracture resistance. By integrating chemically recycled PET into asphalt mixtures and analyzing its effect on low-temperature and intermediate-temperature fracture behavior, this study contributes not only to the scientific understanding of fracture mechanics in modified asphalt systems but also to the broader goal of sustainable construction. The findings are anticipated to inform the development of more resilient pavement materials while offering a practical and environmentally beneficial solution for the reuse of non-biodegradable PET waste in the construction sector.

2. Materials and methods

2.1. Materials

2.1.1. Aggregates

In this study, limestone aggregates were utilized, sourced from a quarry situated in the northeastern region of Tehran Province. The aggregate gradation was carefully selected in accordance with the specifications provided in ASTM D692. The selection process involved a thorough consideration of the standard’s designated upper and lower gradation limits to ensure compliance with the required criteria and to maintain consistency in aggregate quality throughout the experimental procedures. Fig. 1 shows the gradation curve of the limestone aggregate used in this study.

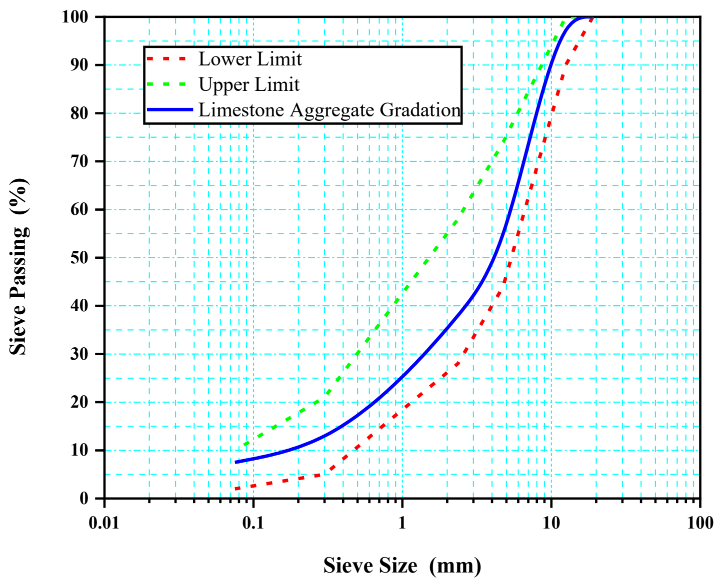

Fig. 1. Gradation curve of limestone aggregate used in this study

2.1.2. Asphalt binder

A conventional penetration-grade 85/100 asphalt binder was employed in this research. This binder was selected due to its common application in road construction and its compatibility with polymeric modifiers. The physical properties of the binder were verified in accordance with ASTM D5 and other relevant standards prior to mixture preparation. The properties of the asphalt binder used in this study are shown in the Table. 1.

Table 1. Physical properties of Pen 85/100 asphalt binder

Properties	Test Method	Result
Specific gravity at 25°C (gr/cm^3)	ASTM D70	1.011
Softening point (R&B) (°C)	ASTM D36	46
Penetration, at 25°C (0.1 mm)	ASTM D5	96
Ductility, at 25°C (cm)	ASTM D113	100
Rotational viscosity at 135°C (mPa.s)	ASTM D4402	250

2.1.3. Polyethylene terephthalate (PET)

Polyethylene terephthalate (PET), a widely used thermoplastic polyester, is a major contributor to global plastic waste due to its extensive application in consumer packaging—particularly in single-use beverage bottles. Owing to its non-biodegradable nature, PET poses persistent environmental challenges, with approximately 70% of PET waste being either incinerated for energy recovery or disposed of in landfills. In contrast, only about 26% undergoes mechanical recycling, and a mere 4% is chemically recycled, highlighting the underutilization of advanced recycling techniques. In response to this imbalance, innovative strategies are being pursued to repurpose PET waste into value-added materials with practical engineering applications. PET was utilized in its granular form in this study, as illustrated in Fig. 2.

Fig. 2. Granular form of PET used in this study

2.2. Methods

2.2.1. Additive derived from recycling of PET

Chemical recycling of polyethylene terephthalate (PET) is recognized as a sustainable alternative to conventional disposal methods, offering the potential to convert post-consumer plastic waste into high-value materials (Shojaei et al., 2020). Among the various chemical recycling techniques, aminolysis was selected in this study due to its efficiency and suitability for producing asphalt-modifying additives. Aminolysis involves the cleavage of PET's ester linkages through a reaction with primary amines—such as methylamine, ethylamine, ethanolamine, allylamine, and hydrazine—in an aqueous environment. Compared to alcohol-based methods like glycolysis, aminolysis proceeds more rapidly, as amines act as stronger nucleophilic agents and organic bases that accelerate polymer chain degradation (Gupta et al., 2019). In this research, triethylenetetramine (TETA) was selected as the aminolysis reagent due to its high reactivity and multifunctional amine structure. The process was initiated by combining PET granules—used as the polymer feedstock in this study—with TETA in a weight ratio of 2:1 (PET:TETA). The mixture was introduced into a two-necked round-bottom flask equipped with a reflux condenser and magnetic stirrer. The aminolysis reaction was conducted at 140°C for 6 hours under a continuous nitrogen gas atmosphere to prevent oxidation and ensure reaction stability. Upon completion of the reaction, the system was subjected to vacuum conditions to facilitate the recovery of by-products such as low-molecular-weight polyamines and glycols. The residue remaining in the flask was a yellowish solid at room temperature, which was collected and designated as the PET-derived additive. After that this additive in dosages of 0%, 1% was blended with virgin asphalt binder by a low-shear mixer at 1000 rpm for 50 minutes at 140°C.

2.2.2. SCB samples

In this study, cylindrical specimens were fabricated according to each mixture type. A gyratory compactor was used to manufacture cylindrical specimens 150 mm in height and 150 mm in diameter with 7±0.5% air voids in accordance with the AASHTO TP124-16 specification. The air void content for each specimen was confirmed, using AASHTO T 166, to fall within the target range. The mean air void content for test specimens was 7%. To achieve this target range, 20 mm of the upper and 20 mm of the bottom section of the cylindrical specimen were cut, and the core of the cylindrical specimen was used to obtain semi-circular bending (SCB) specimens with 150 mm in diameter and 50 mm in thickness. after that, a notch, 2 mm wide and 15 mm deep, was made in the center of the SCB specimens.

2.2.3. Fracture toughness

Fracture toughness under Mode I loading is a critical parameter in fracture mechanics that characterizes a material's resistance to crack propagation under tensile stress conditions. Mode I, also referred to as the opening mode, occurs when the applied load acts perpendicular to the plane of the crack, causing the crack surfaces to separate. The Mode I fracture toughness is commonly denoted by the stress intensity factor K_{IC}. This parameter is essential for understanding the fracture performance of brittle or quasi-brittle materials, such as asphalt mixtures at low service temperatures. It reflects the material's ability to resist crack initiation and growth under tensile loading and is influenced by factors such as temperature, loading rate, and material heterogeneity. A higher value of Mode I fracture toughness indicates a greater resistance to crack growth, making it a key indicator for durability and long-term performance. The Mode I fracture toughness was calculated in this study using Equation (1) based on the observed test parameters.

$$K_{IC}(SCB) = \frac{F_{cr}}{2Rt}\sqrt{\pi a}\,Y_1\left(\frac{a}{D},\frac{2S}{D}\right) \quad (1)$$

In the context of fracture mechanics, Y_I represents the geometric shape factor for Mode I loading, while R and t denote the radius and thickness of the SCB specimen, respectively. The parameter a refers to the notch depth, and F_{cr} indicates the maximum load applied during the fracture test. The values of Y_I (for Mode I) is functions of the relative crack length a/D and the loading span ratio 2S/D, where D is the specimen diameter and S is the distance from the center of the specimen to each support. These geometric factors can be determined either through finite element analysis (FEM) or by referencing analytical plots developed by M.R. Ayatollahi and M.R.M. Aliha (Ayatollahi, M. R., & Aliha, M. R. M., 2007). Fig. 3 illustrates the specimen geometry and loading configuration for the SCB test under Mode I conditions. In this study, a loading rate of 2 mm/min was employed to evaluate the fracture behavior of different asphalt mixture types. Tests were conducted at low and intermediate temperatures (–10°C, 0°C, and +10°C) to simulate critical field conditions. As shown in Fig. 4, the loading configuration consists of a conventional three-point bending fixture, where the load F_{cr} is applied vertically at the top of the specimen, while the specimen is symmetrically supported by two bottom supports spaced at a distance S from the center crack, creating a stable bending setup for crack propagation analysis.

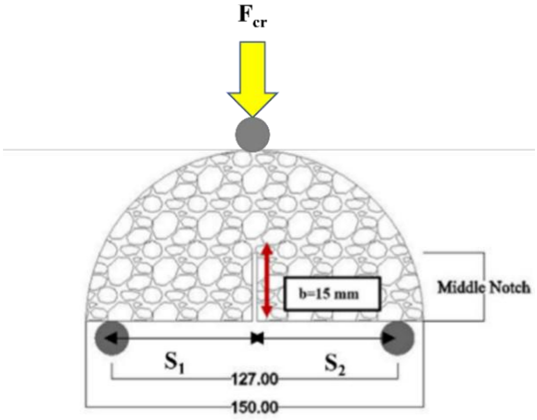

Fig. 3. Configuration of the three-point bending fixture and geometry of the SCB specimen

2.2.4. Fracture energy

Fracture energy is a fundamental parameter in characterizing the fracture behavior of materials within the framework of fracture mechanics. It represents the energy required to initiate and propagate a crack to failure and has been widely recognized as a reliable indicator for evaluating the crack resistance of various materials. Theoretically, fracture energy corresponds to the area under the load–displacement curve obtained from a fracture test, quantifying the total energy absorbed by the material during crack development—from initiation to complete separation. This energy metric is sensitive to changes in material composition, temperature, and other physical conditions, which directly influence the material's capacity to absorb and dissipate energy (Aliha et al., 2010; Razmi et al., 2018). In this study, fracture energy was determined using Equation (2).

$$G_f = \frac{W_f}{A_{ligamnet}} \quad , \quad A_{ligamnet} = (R - a) \times t \tag{2}$$

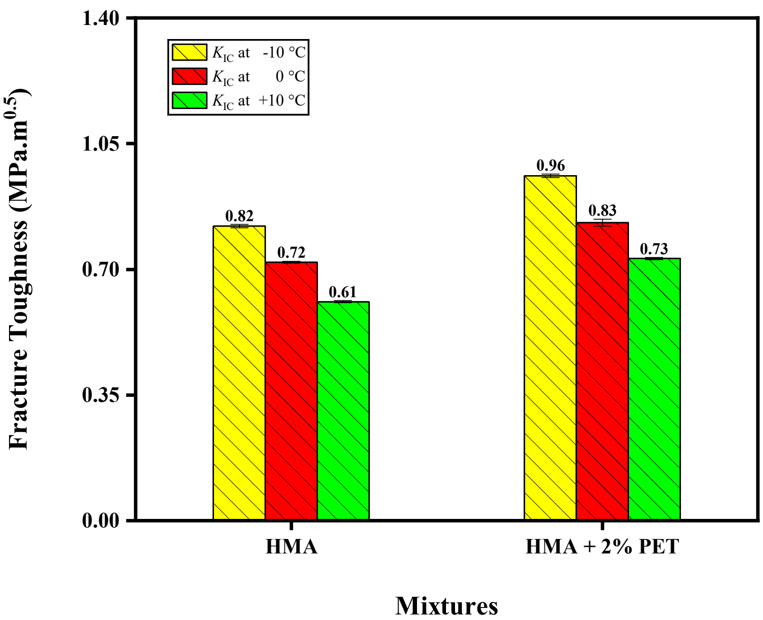

Fig. 4. Fracture Toughness (K_{IC}) values of mixtures at different temperatures

3. Results and discussions

3.1. Evaluation of fracture toughness

Fig. 4 illustrates the fracture toughness values of asphalt mixtures evaluated at three distinct temperatures -10°C, 0°C, and +10°C. The experimental results clearly demonstrate that incorporating a 2% additive derived from chemically recycled polyethylene terephthalate (PET) granules significantly improves the fracture toughness of hot mix asphalt (HMA) pavements across all tested conditions. Specifically, at –10°C, the fracture toughness of the PET-modified mixture increased by 17.1% compared to the unmodified control. Similarly, enhancements of 15.3% and 19.7% were observed at 0°C and +10°C, respectively. These findings underline the effectiveness of PET additives in enhancing the low-temperature cracking resistance of asphalt pavements, which is critical for maintaining performance in cold climates. According to the previous, The enhancement in asphalt mixture performance observed with the incorporation of polyethylene terephthalate (PET) additives can be fundamentally ascribed to complex chemical interactions between the PET molecules, asphalt binder, and mineral aggregates. At the molecular scale, the efficacy of PET additives is rooted in their unique chemical architecture, notably the presence of functional groups such as amines, which actively participate in chemical bonding with both binder constituents and aggregate surfaces.

These molecular interactions critically reinforce the cohesion and structural integrity of the asphalt composite. A key determinant of PET additive performance lies in the abundance and spatial configuration of these amine groups. Their reactive nature facilitates robust chemical linkages, and any variation in their number or orientation significantly modulates the additive's interaction dynamics with asphalt components, thereby influencing the overall mechanical properties of the mixture. Moreover, the balance between hydrocarbon chain length and the density of amine groups within the PET molecular framework further governs its performance characteristics. Longer hydrocarbon chains are hypothesized to enhance adhesive interactions with the binder matrix, while a higher concentration of amine groups promotes compatibility and chemical bonding within the asphalt system. Striking the optimal balance between these molecular features is pivotal for maximizing binder performance, particularly its resistance to stress-induced microcracking. Emerging research underscores that PET additives amplify key intermolecular forces within the asphalt matrix, such as hydrogen bonding and van der Waals interactions. These enhanced molecular forces contribute to improved cohesion and mechanical stability, fostering the formation of a more intricate and resilient molecular network. The interaction of amine groups within this network enhances critical mechanical properties, including elasticity, tensile strength, and ductility—essential for withstanding environmental stresses and repetitive traffic loading. Additionally, the incorporation of PET additives aligns with broader findings on amine-functionalized modifiers, which are known to augment the binder's capacity for mechanical energy absorption and dissipation. This mitigates crack initiation and propagation under cyclic loading conditions, thus prolonging pavement lifespan and enhancing reliability across diverse climatic and operational environments.

In conclusion, PET additives represent a highly promising approach for advancing asphalt mixture performance. By strategically engineering their molecular structure—optimizing the amine group density, spatial orientation, and hydrocarbon chain length—the reinforcing effects of PET can be fine-tuned to deliver superior durability and crack resistance. This positions PET additives as critical enablers in the formulation of next-generation, high-performance asphalt composites designed for long-term serviceability (Baradaran et al., 2025; Baradaran et al., 2024; Xu et al., 2022).

3.2. Evaluation of fracture energy

The other important fracture parameter investigated in this study was fracture energy. Fracture energy value results for mixtures at -10°C, 0°C, and +10°C are shown in Fig. 5. Based on the results it can be seen adding PET additive can increase fracture energy of asphalt pavement which is indicated PET additive can improve cracking resistance of asphalt pavement. For instance, by adding 2% PET additive to the HMA mixture at +10°C, G_f value is increased by 43.4%. This improvement is observed at other temperatures. For example, at -10°C and 0°C G_f values are increased by 72.5% and 59.3%, respectively. The enhancement of fracture energy in asphalt pavements through the incorporation of recycled PET additives has been consistently validated by multiple studies (Baradaran et al., 2024; Ma & Hesp, 2022; Baradaran, Aliha, Maleki, & Underwood, 2024; Baradaran & Aliha, 2025; Saleh, Ahmed, Moghaddam, & Hashemian, 2024). These findings suggest that asphalt mixtures modified with PET-TETA additives require substantially more energy to propagate cracks, thereby improving the material's resistance to fracture. Several critical factors have been identified in previous research as significantly influencing the fracture energy and cracking behavior of asphalt mixtures.

One key factor is the optimal spatial arrangement of coarse aggregates within the ligament area. Proper distribution of aggregates ensures effective stress dispersion, reducing the likelihood of premature crack initiation and propagation (Stewart, Oputa, & Garcia, 2018; Airey, Hunter, & Collop, 2008). Another fundamental element is the cohesion within the soft asphalt matrix (SAM), the binder-rich zone that integrates the aggregates. The mechanical integrity of this matrix is essential for maintaining the mixture's structural strength and resistance to cracking (Aliha, Fazaeli, Aghajani, & Nejad, 2015). Additionally, the inclusion of various additives or binder modifiers has been shown to enhance both the chemical and physical properties of asphalt binders, thereby improving their fracture resistance (Pirmohammad, Amani, & Shokorlou, 2020; Pirmohammad, Shokorlou, & Amani, 2020; Alkuime, Tousif, Kassem, & Bayomy, 2020; Ghoroghi, Haghighatpour, Aliha, & Berto, 2023). Environmental conditions further impact the cracking performance of asphalt pavements. Processes such as freeze-thaw cycles and temperature-induced expansion and contraction subject the material to repeated stress, influencing its durability and long-term fracture behavior (Haghighatpour & Aliha, 2022; Ziari, Aliha, Moniri, & Saghafi, 2020). The current research focuses on the modification of asphalt binders using amine-functionalized compounds, particularly PET-TETA, derived from chemically recycled PET. Recent evidence indicates that PET-TETA significantly strengthens the bond between the asphalt binder and mineral aggregates (Baradaran et al., 2024; Baradaran & Aliha, 2025). This improvement is attributed to intensified intermolecular interactions within the binder matrix, particularly hydrogen bonding and van der Waals forces, which enhance cohesive strength and molecular stability. These interactions result in stronger adhesion at the binder–aggregate interface, promoting a more durable and resilient bond. The increased bonding strength provided by PET-TETA also leads to an improved elastic response in the asphalt mixture under mechanical loading. This enhanced elasticity translates into greater ductility, a critical factor for resisting crack initiation and propagation. Ductility improvements directly contribute to the elevation of fracture energy—a key parameter defining the material's capacity to absorb energy before failure. By augmenting the ductility and elastic properties of the asphalt mixture, PET-TETA facilitates higher fracture energy levels, making the material more resilient to cracking under mechanical and environmental stresses. This increase in fracture energy is a primary contributor to the superior cracking resistance observed in PET-TETA-modified asphalt mixtures, as corroborated by numerous studies (Baradaran et al., 2024; Ma & Hesp, 2022; Baradaran et al., 2024; Baradaran & Aliha, 2025; Xu et al., 2022). In conclusion, the integration of PET-TETA into asphalt formulations represents a promising strategy for enhancing pavement durability. Through the reinforcement of binder-aggregate interactions and the improvement of mechanical properties such as ductility and fracture energy, PET-TETA-modified mixtures exhibit superior performance in resisting cracking and sustaining long-term mechanical integrity.

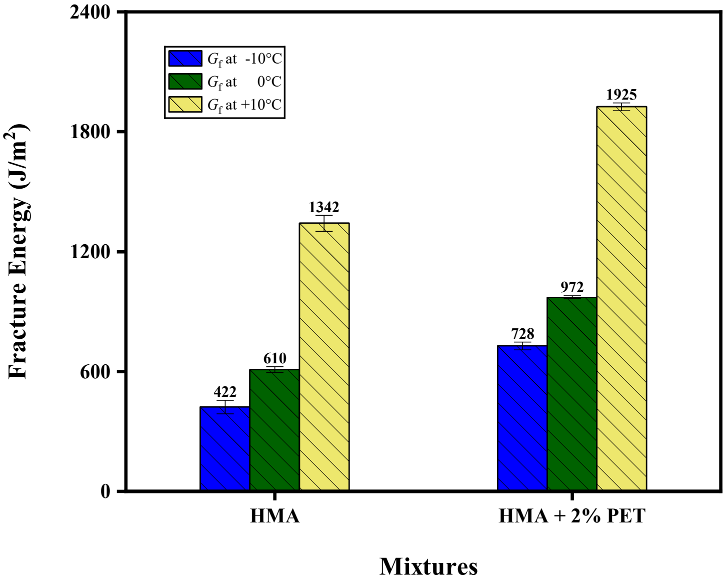

Fig. 5. Fracture Energy (G_f) values of mixtures at different temperatures

4. Conclusions

This study investigated the fracture resistance of asphalt mixtures modified with chemically recycled polyethylene terephthalate (PET) in granular form, focusing on enhancing performance at low and intermediate temperatures. The PET granules, processed via aminolysis into an amine-functionalized additive, were incorporated at a dosage of 2% by weight of bitumen to assess their influence on asphalt fracture behavior. The experimental findings clearly demonstrated that the inclusion of granular PET-derived additives significantly improved both fracture toughness (K_{IC}) and fracture energy (G_f) across the tested temperatures (-10°C, 0°C, +10°C). Enhancements of up to 19.7% in fracture toughness and 72.5% in fracture energy were observed, indicating superior resistance to crack initiation and propagation in the modified mixtures. These improvements are largely attributed to the amine-functional groups present in the chemically recycled PET additive, which enhance the binder-aggregate interaction and improve the mixture's elasticity and ductility. The research highlights the potential of chemically recycled PET granules as an effective modifier for asphalt pavements, offering not only enhanced mechanical performance but also contributing to environmental sustainability by repurposing plastic waste. Utilizing PET in granular form provides a practical and scalable method for integrating recycled materials into pavement construction.

Acknowledgements

This work was partially supported (T.Sadowski) and funded under the grant "Subvention for Science" by the Ministry of Science and Higher Education of the Republic of Poland - project No. FD-20/IL-4/046. M.R. M. Aliha acknowledges the Polish National Agency for Academic Exchange (Grant No. ULAM NAWA BNI/ULM/2024/1/00180/UO/00001) for visiting scientists on sabbatical leave to visit Lublin University of Technology, Poland

References

Airey, G.D., Hunter, A.E., & Collop, A.C. (2008). The effect of asphalt mixture gradation and compaction energy on aggregate degradation. *Construction and Building Materials, 22*(5), 972-980

Alae, M., Xu, L., Cao, Z., Xu, X., & Xiao, F. (2023). Fatigue and intermediate-temperature cracking performance of rejuvenated recycled asphalt binders and mixtures: A review. *Journal of Cleaner Production, 384*, 135587

Alaswadko, N., Hassan, R., Meyer, D., & Mohammed, B. (2019). Probabilistic prediction models for crack initiation and progression of spray sealed pavements. *International Journal of Pavement Engineering, 20*(1), 1-11

Aliha, M.M., Behbahani, H., Fazaeli, H., & Rezaifar, M.H. (2014). Study of characteristic specification on mixed mode fracture toughness of asphalt mixtures. *Construction and Building Materials, 54*, 623-635

Aliha, M.R.M., & Mousavi, S.S. (2020). Sub-sized short bend beam configuration for the study of mixed-mode fracture. *Engineering Fracture Mechanics, 225*, 106830

Aliha, M.R.M., Ayatollahi, M.R., Smith, D.J., & Pavier, M.J. (2010). Geometry and size effects on fracture trajectory in a limestone rock under mixed mode loading. *Engineering Fracture Mechanics, 77*(11), 2200-2212

Aliha, M.R.M., Bahmani, A., & Akhondi, S. (2015). Determination of mode III fracture toughness for different materials using a new designed test configuration. *Materials & Design, 86*, 863-871

Aliha, M.R.M., Fazaeli, H., Aghajani, S., & Nejad, F.M. (2015). Effect of temperature and air void on mixed mode fracture toughness of modified asphalt mixtures. *Construction and Building Materials, 95*, 545-555

Aliha, M.R.M., Razmi, A., & Mansourian, A. (2017). The influence of natural and synthetic fibers on low temperature mixed mode I+ II fracture behavior of warm mix asphalt (WMA) materials. *Engineering Fracture Mechanics, 182*, 322-336

Aliha, M.R.M., Zalnezhad, M., & Haghighatpour, P.J. (2023). Fracture toughness of colored slurry seal at low temperatures and different loading Modes: Comparative study with warm and hot mix asphalt materials. *Construction and Building Materials, 409*, 133786

Aliha, M.R.M., Ziari, H., Sobhani Fard, E., & Jebalbarezi Sarbijan, M. (2021). Heterogeneity effect on fracture parameters of a multilayer asphalt pavement structure containing a top-down crack and subjected to moving traffic loading. *Fatigue & Fracture of Engineering Materials & Structures, 44*(5), 1349-1371

Alkuime, H., Tousif, F., Kassem, E., & Bayomy, F.M. (2020). Review and evaluation of intermediate temperature monotonic cracking performance assessment testing standards and indicators for asphalt mixes. *Construction and Building Materials, 263*, 120121

Ameri, M., Mansourian, A., Pirmohammad, S., Aliha, M.R.M., & Ayatollahi, M.R. (2012). Mixed mode fracture resistance of asphalt concrete mixtures. *Engineering Fracture Mechanics, 93*, 153-167

Ayar, P., Baradaran, S., & Abdipour Vosta, S. (2022). A review on the effect of various additives on mechanical properties of stone mastic asphalt (SMA). *Road, 30*(110), 57-86

Ayatollahi, M.R., & Aliha, M.R.M. (2007). Wide range data for crack tip parameters in two disc-type specimens under mixed mode loading. *Computational materials science, 38*(4), 660-670

Baradaran, M.S., Aftabi Sani, A., & Abrishami, S. (2024a). Application of differential transform method for solving free-surface seepage problem of one-dimensional porous media. *Ferdowsi Civil Engineering*, *37*(1), 1-18

Baradaran, M.S., Qazanfari, R., & Baradaran, S. (2023). Study of soil reinforcement in the east of Mashhad using glass granule. *Materials research express*, *10*(5), 055202

Baradaran, S., & Aliha, M.R.M. (2025). Mode I and Mode II fracture assessment of green asphalt pavements containing plastic waste and RAP at low and intermediate temperature. *Results in Engineering*, *25*, 103734

Baradaran, S., & Ameri, M. (2023). Investigation of rutting failure in asphalt mixtures and its improvement strategies. *Road*, *31*(114), 53-70

Baradaran, S., & Ziaee, S.A. (2025). Review of the Mechanical Properties of Asphalt Pavement Reinforced with Natural Plant Fibers as an Eco-Friendly Solution in Pavement Engineering. *Road*.

Baradaran, S., Aliha, M.R.M., Maleki, A., & Underwood, B.S. (2024). Fracture properties of asphalt mixtures containing high content of reclaimed asphalt pavement (RAP) and eco-friendly PET additive at low temperature. *Construction and Building Materials*, *449*, 138426

Baradaran, S., Rahimi, J., Ameri, M., & Maleki, A. (2024b). Mechanical performance of asphalt mixture containing eco-friendly additive by recycling PET. *Case Studies in Construction Materials, 20*, e02740

Bazoobandi, P., Mousavi, S.R., Karimi, F., Karimi, H.R., Ghasri, M., & Aliha, M.R.M. (2024). Cracking resistance of crumb rubber modified green asphalt mixtures, using calcium carbonate nanoparticles and two by-product wax-based warm mix additives. *Construction and Building Materials, 424*, 135848

Callomamani, L.A.P., Bala, N., & Hashemian, L. (2023). Comparative analysis of the impact of synthetic fibers on cracking resistance of asphalt mixes. *International Journal of Pavement Research and Technology, 16*(4), 992-1008

Fakhri, M., Kharrazi, E.H., & Aliha, M.R.M. (2018). Mixed mode tensile–In plane shear fracture energy determination for hot mix asphalt mixtures under intermediate temperature conditions. *Engineering Fracture Mechanics, 192*, 98-113

Fakhri, M., Siyadati, S.A., & Aliha, M.R.M. (2020). Impact of freeze–thaw cycles on low temperature mixed mode I/II cracking properties of water saturated hot mix asphalt: An experimental study. *Construction and Building Materials, 261*, 119939

Farahinia, E., Sheikhi, M., Amirhossein, D.T.Q., Rajaee, A., Ghodratnama, M., Banihashem, S.M., & Pournoori, P. (2024). Experimental and numerical exploration of mechanical properties of sawdust concrete due to the addition of waste glass powder. *International Journal of Sustainable Building Technology and Urban Development*, *15*(3), 328-353

Fatemi, S., Zarei, M., Ziaee, S.A., Shad, R., Saadatjoo, S.A., & Tabasi, E. (2023). Low and intermediate temperatures fracture behavior of amorphous poly alpha olefin (APAO)-modified hot mix asphalt subjected to constant and variable temperatures. *Construction and Building Materials, 364*, 129840

Ghabchi, R., Dharmarathna, C.P., & Mihandoust, M. (2021). Feasibility of using micronized recycled Polyethylene Terephthalate (PET) as an asphalt binder additive: A laboratory study. *Construction and Building Materials, 292*, 123377

Ghoroghi, S.S., Haghighatpour, P.J., Aliha, M.R.M., & Berto, F. (2023). Comparative cracking resistance-cost study for the hot mix asphalt (HMA) mixtures made of natural and recycled asphaltic materials. *Fatigue & Fracture of Engineering Materials & Structures, 46*(11), 4199-4217

Gupta, P., & Bhandari, S. (2019). Chemical depolymerization of PET bottles via ammonolysis and aminolysis. In Recycling of polyethylene terephthalate bottles (pp. 109-134). *William Andrew Publishing*.

Haghighatpour, P.J., & Aliha, M.R.M. (2022). Assessment of freezing and thawing cycle (FTC) effects on mixed mode I/III fracture toughness and work of fracture of HMA asphalt mixtures. *Theoretical and Applied Fracture Mechanics, 118*, 103261

Hong, R.B., Wu, J.R., & Cai, H.B. (2020). Low-temperature crack resistance of coal gangue powder and polyester fibre asphalt mixture. *Construction and Building Materials, 238*, 117678

Leng, Z., Sreeram, A., Padhan, R.K., & Tan, Z. (2018). Value-added application of waste PET based additives in bituminous mixtures containing high percentage of reclaimed asphalt pavement (RAP). *Journal of Cleaner Production, 196*, 615-625

Li, A., Song, W., & Zhou, L. (2024). Investigation of the fracture performance of reclaimed asphalt mixture at the intermediate temperature using multi-parameters. *Construction and Building Materials, 412*, 134872

Li, W.C., Tse, H.F., & Fok, L. (2016). Plastic waste in the marine environment: A review of sources, occurrence and effects. *Science of the Total Environment, 566*, 333-349

Liang, Y., Harvey, J.T., & Wu, R. (2024). Evaluation of the laboratory aging of field-blended crumb rubber modified binder. *Construction and Building Materials, 423*, 135849

M. Ameri, S. Nowbakht, M. Molayem, et al. (2016). Investigation of fatigue and fracture properties of asphalt mixtures modified with carbon nanotubes, Fatigue Fract. *Eng. M., 39*(7), 896–906

Ma, J., & Hesp, S.A. (2022). Effect of recycled polyethylene terephthalate (PET) fiber on the fracture resistance of asphalt mixtures. *Construction and Building Materials, 342*, 127944

Marasteanu, M.O., Dai, S., Labuz, J.F., & Li, X. (2002). Determining the low-temperature fracture toughness of asphalt mixtures. *Transportation Research Record, 1789*(1), 191-199

Meng, Y., Chen, J., Kong, W., Wang, Z., Lu, Y., & Chen, P. (2024). Research on the influence of parameters on the fracture performance of the large stone asphalt mixture based on the semi-circular bending test. *Construction and Building Materials, 422*, 135720

Mohammed, A.A. (2017). Flexural behavior and analysis of reinforced concrete beams made of recycled PET waste concrete. *Construction and Building Materials, 155*, 593-604

Motevalizadeh, S.M., Sedghi, R., & Rooholamini, H. (2020). Fracture properties of asphalt mixtures containing electric arc furnace slag at low and intermediate temperatures. *Construction and Building Materials, 240*, 117965

Niri, S.R., Akhtarpour, A., Daliri, F., & Baradaran, M.S. (2024). Experimental investigation of dewatering silty tailings using electrokinetic method. *Canadian Geotechnical Journal*.

Pargar, J., Akhtarpour, A., & Baradaran, M.S. (2024). An unsaturated soil mechanics-based numerical and experimental method to assess soil settlement due to ground water level rise. *Transportation Infrastructure Geotechnology*, *11*(5), 3621-3646

Phan, T.M., Ma, H.J., & Park, D.W. (2024). Evaluation on performance of rubber tire powder and waste glass modified binder as crack filling materials using 3D printing technology. *Construction and Building Materials*, *416*, 135225

Pirmohammad, S., Amani, B., & Shokorlou, Y.M. (2020a). The effect of basalt fibres on fracture toughness of asphalt mixture. *Fatigue & Fracture of Engineering Materials & Structures, 43*(7), 1446-1460

Pirmohammad, S., Shokorlou, Y. M., & Amani, B. (2020b). Laboratory investigations on fracture toughness of asphalt concretes reinforced with carbon and kenaf fibers. *Engineering Fracture Mechanics, 226*, 106875

Pournoori, P., Davarpanah T.Q., A., Rajaee, A., Ghodratnama, M., Abrishami, S., & Masoodi, A.R. (2024). Experimental exploration of fracture behavior (pure mode III) in eco-friendly steel fiber-reinforced self-compacting concrete with waste tempered glass as coarse aggregates. *Scientific Reports*, *14*(1), 9043

Qiu, J., Tabasi, E., Hammoud, A., Benjeddou, O., Zarei, M., & Khordehbinan, M.W. (2024). Determining the fracture stiffness of modified Hot and Warm Mix Asphalt using semi-circular bending (SCB) geometry. *Theoretical and Applied Fracture Mechanics, 129*, 104237

Ragaert, K., Delva, L., & Van Geem, K. (2017). Mechanical and chemical recycling of solid plastic waste. *Waste management, 69*, 24-58

Rajaee, A., Talebi, N., & Abrishami, S. (2025a). The impacts of freeze-thaw cycles on polypropylene fiber-reinforced clayey soil stabilized with alkali-activated fly ash. *Case Studies in Construction Materials*

Rajaee, A., Sadeghzadeh, M., Shekhi, M., & Yousefi, M. (2025b). Enhancing the Mechanical Properties of Sawdust Concrete with Silica Fume, Metakaolin, and Marble Powder. *Journal of Civil Aspects and Structural Engineering*, *2*(1), 1-13

Razmi, A., & Mirsayar, M.M. (2018). Fracture resistance of asphalt concrete modified with crumb rubber at low temperatures. *International Journal of Pavement Research and Technology, 11*(3), 265-273

Ren, X., Ma, J., & Hesp, S.A. (2023). Another look at the semi-circular bend test for the performance ranking of hot mix asphalt. *Construction and Building Materials, 395*, 132367

Saha, G., & Biligiri, K.P. (2016). Fracture properties of asphalt mixtures using semi-circular bending test: A state-of-the-art review and future research. *Construction and Building Materials, 105*, 103-112

Salazar-Beltrán, D., Hinojosa-Reyes, L., Palomino-Cabello, C., Turnes-Palomino, G., Hernández-Ramírez, A., & Guzmán-Mar, J.L. (2018). Determination of phthalate acid esters plasticizers in polyethylene terephthalate bottles and its correlation with some physicochemical properties. *Polymer Testing, 68*, 87-94

Shahryari, N., Keymanesh, M.R., & Aliha, M.R.M. (2021). Specimen type effect on measured low-temperature fracture toughness of asphalt concrete. *Fatigue & Fracture of Engineering Materials & Structures, 44*(2), 551-567

Shojaei, B., Abtahi, M., & Najafi, M. (2020). Chemical recycling of PET: A stepping-stone toward sustainability. *Polymers for Advanced Technologies, 31*(12), 2912-2938

Song, W., Zou, X., Wu, H., & Yang, F. (2023). Energy evolution in fracture process of hot mix asphalt containing reclaimed asphalt pavement and rejuvenator. *Theoretical and Applied Fracture Mechanics, 124*, 103809

Stewart, C.M., Oputa, C.W., & Garcia, E. (2018). Effect of specimen thickness on the fracture resistance of hot mix asphalt in the disk-shaped compact tension (DCT) configuration. *Construction and Building Materials*, *160*, 487-496

Sulyman, M., Haponiuk, J., & Formela, K. (2016). Utilization of recycled polyethylene terephthalate (PET) in engineering materials: A review. *International Journal of Environmental Science and Development, 7*(2), 100

Tabasi, E., Zarei, M., Mobasheri, Z., Naseri, A., Ghafourian, H., & Khordehbinan, M.W. (2023). Pre-and post-cracking behavior of asphalt mixtures under modes I and III at low and intermediate temperatures. *Theoretical and Applied Fracture Mechanics, 124*, 103826

Tareghian, B., Baradaran, M.S., & Akhtarpour, A. (2024). The effect of sand-crumb rubber mixture treatment on the seismic response of a low-rise building located on liquefiable soil. *Discover Geoscience*, *2*(1), 11

Thiounn, T., & Smith, R.C. (2020). Advances and approaches for chemical recycling of plastic waste. *Journal of Polymer Science, 58*(10), 1347-1364

Uzan, J., & Levenberg, E. (2001). Strain measurements in asphalt concrete specimens towards the development of a fracture model. *International Journal of Pavement Engineering, 2*(4), 243-258

Wagoner, M.P., Buttlar, W.G., & Paulino, G.H. (2005). Development of a single-edge notched beam test for asphalt concrete mixtures. *Journal of Testing and Evaluation, 33*(6), 452-460

Wagoner, M.P., Buttlar, W.G., Paulino, G.H., Blankenship, P., Roque, R., Rongzong, W., ... & Gibson, N. (2006). Laboratory testing suite for characterization of asphalt concrete mixtures obtained from field cores. In *Asphalt Paving Technology: Association of Asphalt Paving Technologists-Proceedings of the Technical Sessions* (Vol. 75, pp. 815-852)

Webb, H.K., Arnott, J., Crawford, R.J., & Ivanova, E.P. (2012). Plastic degradation and its environmental implications with special reference to poly (ethylene terephthalate). *Polymers, 5*(1), 1-18

Xiongzhou, Y., Yuze, T., Qinglin, L., Song, L., Qianwen, D., & Aliha, M.R.M. (2021). KIc and KIIc measurement for hot mix asphalt mixtures at low temperature: Experimental and theoretical study using the semicircular bend specimen with different thicknesses. *Fatigue & Fracture of Engineering Materials & Structures, 44*(3), 832-846

Xu, H., Chen, A., Wu, S., Li, Y., Li, J., Zhu, Y., ... & Feng, J. (2024). Mechanism of asphalt concrete reinforced with industrially recycled steel slag from the perspectives of adhesion and skeleton. *Construction and Building Materials, 424*, 135899

Xu, X., Chen, G., Wu, Q., Leng, Z., Chen, X., Zhai, Y., ... & Peng, C. (2022). Chemical upcycling of waste PET into sustainable asphalt pavement containing recycled concrete aggregates: Insight into moisture-induced damage. *Construction and Building Materials, 360*, 129632

Xu, X., Chu, Y., Luo, Y., Wu, Q., Chen, X., & Shu, S. (2022). Value-added use of waste PET in rubberized asphalt materials for sustainable pavement. *Applied sciences, 12*(2), 871

Yang, Q., Fan, Z., Yang, X., Hao, L., Lu, G., Fini, E.H., & Wang, D. (2023). Recycling waste fiber-reinforced polymer composites for low-carbon asphalt concrete: The effects of recycled glass fibers on the durability of bituminous composites. *Journal of Cleaner Production, 423*, 138692

Yao, L., Leng, Z., Lan, J., Chen, R., & Jiang, J. (2022). Environmental and economic assessment of collective recycling waste plastic and reclaimed asphalt pavement into pavement construction: A case study in Hong Kong. *Journal of Cleaner Production, 336*, 130405

Yazdi, A.N., Akhtarpour, A., Abdalhusein, M.M., & Baradaran, M.S. (2024). Experimental investigation of the volume change of a swelling clay and its improvement. *Transportation Infrastructure Geotechnology*, *11*(3), 1008-1031

Yeganeh, N., Akhtarpour, A., Bazaz, J.B., & Baradaran, M.S. (2024). Analysis of the Soil-Structure Interaction for a High Rise Building Adjacent to Deep Excavation. *Iranian Journal of Engineering Geology*, *17*(1)

Zhong, T., Zheng, Y., Chen, Z., Yao, L., Zhang, W., Zhu, Y., & Fu, L. (2024). Utilization of steel slag as coarse aggregate and filler in stone mastic asphalt (SMA) mixture: Engineering performance, environmental impact and economic benefits analysis. *Journal of Cleaner Production*, 141891

Zhu, Y., Dave, E.V., Rahbar-Rastegar, R., Daniel, J.S., & Zofka, A. (2017). Comprehensive evaluation of low-temperature fracture indices for asphalt mixtures. *Road Materials and Pavement Design, 18*(sup4), 467-490

Ziari, H., Aliha, M.R.M., Moniri, A., & Saghafi, Y. (2020). Crack resistance of hot mix asphalt containing different percentages of reclaimed asphalt pavement and glass fiber. *Construction and Building Materials, 230*, 117015

Utilization of juniper seed waste as a lightweight aggregate in SCMs-based cementitious composites: Effects on physical and mechanical properties

Damla N. Celik*[1], Tugba Yildizli[2]

[1] Gazi University, Department of Civil Engineering, 06500 Ankara, Türkiye
[2] Delft University of Technology, Faculty of Civil Engineering and Geosciences, 2628 CN, Delft, The Netherlands

Abstract. Juniperus species are globally significant due to their extractive components and applications in medicine and pharmacology. Juniperus trees, widely distributed in Turkey, provide essential oils that are traditionally used as antiseptics, anti-inflammatory agents, and antibacterial remedies. However, large quantities of juniper seeds are discarded as waste after oil extraction. This study investigates the potential of using juniper seed waste as lightweight aggregate in SCM-based cementitious composites to reduce the unit weight of mixtures. The juniper seeds (JSA) were volumetrically replaced with No.1 aggregates at 10%, 20% and 30% levels, while 40% level was found to be unstable. Two experimental groups were prepared with cement partially replaced by 70% fly ash (FA) or ground granulated blast furnace slag (GBFS). Tests were conducted to assess fresh, physical and mechanical properties. FA-based mixtures showed lower fluidity at higher JSA content compared to GBFS-based ones. Due to the high JSA porosity, water absorption increased from 1.23% to 15.83% at 30% replacement. The dry unit weight decreased by up to 35%, 10% JSA replacement reducing the weight to 1.83 g/cm³ and 1.63 g/cm³ in FA and GBFS mixtures, respectively. The mechanical performance declined as JSA content increased, due to the lower strength of JSA compared to conventional aggregates. However, a 10% JSA replacement maintained moderate performance, achieving splitting tensile strengths of 1.22 MPa and 1.00 MPa and compressive strengths of 18.40 MPa and 13.22 MPa for FA and GBFS, respectively. The results suggest that a 10% JSA replacement is optimal for lightweight concrete applications.

Keywords: Juniperus seed waste, Lightweight concrete, Waste management, Mineral addition, Water absorption

1. Introduction

Concrete is the most widely used material in the world after water due to its advantages, such as easy production, low cost, abundance of raw materials, ease of access, and modification of performance properties (Celik et al., 2024). Thus, it is known that 60% of the materials used in the construction of a building come from concrete (Aytekin & Mardani-Aghabaglou, 2022). According to the U.S. Geological Survey published in January 2025, 4.0 Gt of cement is produced globally (Geological Survey, 2025). This amount of Portland cement (PC) is assumed to be combined with over 26 Gt of concrete, approximately 19 Gt of aggregates, and 2-3 Gt of fresh water (J. Li et al., 2019; Vahidi et al., 2024). Although concrete's raw materials are essentially natural, it is responsible for approximately 7-8% of global CO_2 emissions because of the extreme consumption of cement-related products. Therefore, the global cement and concrete sector published Net zero progress report in 2025 committing to produce net zero concrete by 2050 (Cement Industry Net Zero Progress Report, 2025). However, the production and consumption of cement are expected to increase by 43–72% by 2050, with rising demand concentrated in economically-developing regions such as India, Africa, Southeast Asia and Latin America (Fry, 2013). Reducing the number of raw materials used in concrete production is crucial for minimizing environmental impact and promoting the efficient use of natural resources. One of the key strategies for reducing the environmental impact of concrete is to decrease the amount of PC used in its composition. The incorporation of supplementary cementitious materials (SCMs) is an effective approach to achieve this. A range of materials, including fly ash (FA), ground granulated blast furnace slag (GBFS), rice husk ash, silica fume, metakaolin, red mud, bottom ash, and agricultural waste ashes, are employed as supplementary cementitious materials (SCMs). Among these, FA and GGBFS are especially preferred due to their significant availability as industrial by-products(Çelik et al., 2023; Demircan et al., 2021; Yahyaee Nojoukambari et al., 2023). FA, one of the commonly used SCMs, is a by-product

* Corresponding author, E-mail: damlanur.celik@gazi.edu.tr

https://doi.org/10.31462/icearc2025_ce_was_871

of coal-fired thermal power plants, with an estimated global annual production of approximately 750 million tons (Wang et al., 2025). GBFS is another widely used SCM, produced as a by-product of iron and steel manufacturing, with around 394 million tons generated annually worldwide (L. Li et al., 2023). In addition to their high production volumes, FA and GBFS can replace up to 50% of PC in cementitious systems without compromising performance (Mehta & Monteiro, 2006). Research studies have demonstrated that the replacement of PC with FA and GGBFS enhances both the fresh and hardened properties of concrete. These SCMs chemically react with the hydration products of cement, particularly calcium hydroxide (CH), thereby refining and densifying the microstructure (Demircan et al., 2021; Naresh & Saravanan, 2022). In addition to the microstructural improvements, the use of SCMs enhances mechanical performance and significantly reduces the risk of durability-related issues such as sulfate attack, alkali-silica reaction (ASR), and chloride ion penetration, especially at higher replacement levels. Furthermore, SCMs contribute to lower overall production costs, improved long-term performance, and a notable reduction in carbon emissions (Berryman et al., 2005; Ifzaznah et al., 2024; Wang et al., 2025).

Another important strategy to reduce the environmental impact of concrete is to minimize the number of conventional aggregates used in its composition. A very effective approach to achieve this is the replacement of recycled aggregates with conventional ones. The use of recycled aggregates reduces the need for waste disposal, conserves natural resources and lowers the overall cost of concrete mixtures (Cheng & Khasani, 2024). Recycled concrete, recycled plastic, and recycled ceramic are the predominant types of recycled aggregates, mainly due to their high availability as construction by-products. In addition to these materials, various other waste materials have also been investigated for potential use as aggregates in concrete mixtures (Abbas & Qureshi, 2025; Cheng & Khasani, 2024; Huang et al., 2025). Juniper seed is one of the alternative waste materials used as aggregate in concrete. Juniperus species are globally recognized for their bioactive extractive components and are widely utilized in the fields of medicine and pharmacology. Juniper trees and their primary product, juniper seeds, are broadly distributed in Turkey and valued for their essential oils, which have traditionally been employed for their antiseptic, anti-inflammatory, and antibacterial properties (Ayşegül, 2018; Güvendiren, 2015; Judžentienė, 2019). Following oil extraction, large quantities of juniper seeds are discarded as waste, creating potential for their utilization in two distinct applications within concrete mixtures: as recycled aggregates and as supplementary cementitious materials. Once the oil is extracted, the residual juniper seed can be directly used as a lightweight aggregate due to its low density. Alternatively, when used as a biofuel, the resulting ash can serve as a SCM, contributing to sustainable concrete production. However, juniper seed has been rarely used in the construction sector in the literature. Celik et al. (2023) investigated the use of juniper seed ash as a SCM to obtain high-strength mortars. The performance of the mixtures was compared with the conventional SCMs. SCMs replaced cement at a ratio (wt%) of 7.5%, 12.5% and 17.5%. According to experimental results, JSA improved the flowability of the mortar mixture and reduced the unit weight due to its low density and porous structure. In terms of mechanical performance, a small amount of JSA slightly reduced the compressive strength of the mortar. However, long-term compressive strength results were higher than those of RHA-modified mortars (Celik et al., 2023). To date, the use of juniper seeds as a lightweight aggregate has not been reported in the literature. This study aims to investigate the feasibility of using juniper seeds as a partial replacement for No.1 coarse aggregates in concrete mixtures at varying replacement levels. The fresh, physical and mechanical properties of mixtures were evaluated. Additionally, the economic and environmental benefits of concretes incorporating juniper seed aggregates (JSA) were assessed and compared with those of conventional concrete.

2. Materials and method

2.1. Materials

In mixtures, CEM I 52.5 R type cement was used as main binder, which concordant with both EN 197-1 (EN 197-1, 2012) and ASTM C150 (ASTM C150, 2010) standards. To reduce PC usage, FA and GBFS were preferred as SCMs. F class FA was selected in line with the ASTM C618 standard (ASTM C618-22, 2025). GBFS was chosen which concordant with ASTM C989 standard (ASTM C989, 2024). The physical properties and chemical compositions of binders are given in Table 1.

Table 1. The physical properties of aggregate types

Properties	Coarse aggregate			Fine aggregate
Gradation	No.2	No.1	Juniper seed aggregate	Crushed-sand
Specific gravity	2.66	2.64	0.65	2.77
Fineness modulus	-	-	-	3.36
Water absorption (%)	1.1	0.89	15.03	0.75
Dmax(mm)	22.4	11.2	11.2	4

Table 2. The physical properties and chemical compositions of cement and SCMs

Type	Cement	FA	GBFS
CaO	68.4	5.1	39.8
SiO_2	19.1	56.6	35.7
Al_2O_3	6.4	24.6	8.1
Fe_2O_3	0.3	7.7	1.7
SO_3	2.5	0.6	0.3
MgO	1.5	1.6	12.7
Na_2O	0.4	0.6	0.4
K_2O	0.8	0.8	0.5
Cl	<0.1	<0.1	<0.1
Specific gravity	3.14	2.33	2.84
Specific surface area* (cm^2/g)	3350	3870	4400
LOI**	1.3	3.8	2.6

*Blaine method. **Loss on ignition.

Fig. 1. Juniper seed particles

For concrete mix design, No.1 and No.2 type coarse aggregate and crushed-sand type fine aggregate were preferred. In order to reduce the amount of coarse aggregate and lower the weight of the concrete, the juniper seed aggregate was replaced with No.1 type coarse aggregates (Fig. 1). The physical properties of the aggregates are given in Table 1. The particle size distribution of the various types of aggregates is shown in Fig. 2.

2.2. Mixture proportions and preparation

The mixture proportions of cementitious composites used in this study are given in Table 3. The mix design of cementitious composites was completed according to TS EN 802 standard (TS EN 802, 2016). Two groups of mixtures were prepared with cement partially replaced by 70% FA or GBFS. SCMs are replaced with PC at 70% by weight of cement in mixtures. The w/c ratio was kept at 0.40 for all mixtures. In order to investigate the potential use of juniper seed waste as a lightweight aggregate in SCMs-based cementitious composites, JSA were volumetrically replaced with No.1 type aggregates at ratios of 10%, 20%, and 30% with a 40% replacement proving unstable.

A total of 8 mixtures were produced in this study, including two reference mixtures containing only FA and GBFS. In order to obtain cementitious composites, aggregate types except for JSA were first mixed for 3 minutes. Afterwards, the total amount of binder (cement + SCMs) was added to the mixture within 1 minute and mixing continued for 3 minutes. Then, total amount of mixing water was added to the mixture within 1 minute and mixing continued for 5 minutes until a homogenous mixture obtained. Finally, the total amount of JSA was added to the mixture and mixed for 1 minute to avoid damaging juniper seed aggregate particle, resulting in the final mixture. As a result of the procedure, the fresh mixture was placed into oiled molds without the application of vibration. The samples were removed from their molds after 24 hours. All samples were air-dried for 7 days, followed by moist curing for 21 days. The samples were coded as shown constituents of mixture. For instance, the mixture coded as "FA-20% JSA" was produced using fly ash as the cement replacement material and 20% JSA replaced with No1.type aggregate.

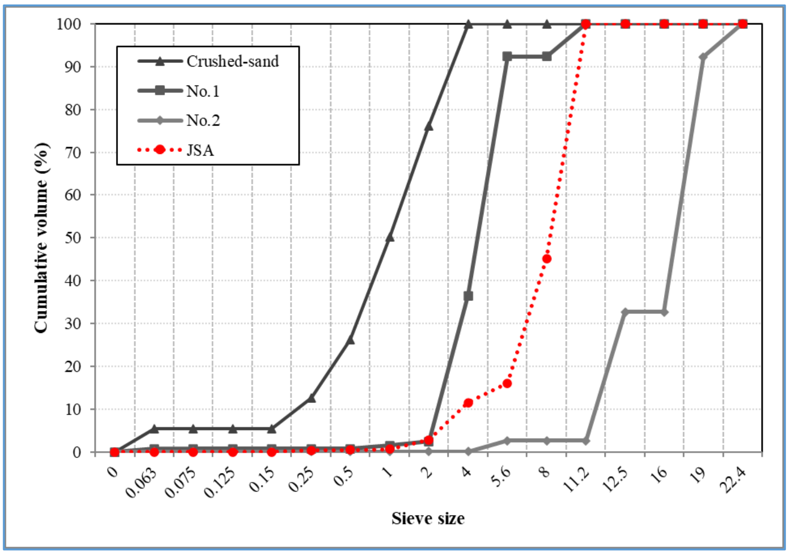

Fig. 2. The particle size distribution of the types of aggregates

Table 3. Quantities of materials used in mixtures (kg/m^3)

Mix ID	Cement	FA	GBFS	No.2	No.1	JSA	Crushed-sand	Water
FA-reference	1580	3700	0	1170	3120	0	3510	2100
FA-10% JSA	1580	3700	0	820	1640	550	2460	2100
FA-20% JSA	2260	5280	0	900	1200	1200	2710	3000
FA-30% JSA	2260	5280	0	730	490	1470	2200	3000
GBFS-reference	1580	0	3700	1180	3150	0	3550	2100
GBFS-10% JSA	1580	0	5280	1180	2370	790	3550	2100
GBFS-20% JSA	2260	0	5280	910	1210	1210	2730	3000
GBFS-30% JSA	2260	0	5280	740	490	1480	2220	3000

2.3. Tests

The fresh, mechanical, and physical properties were evaluated for the performance of SCMs-based cementitious composites. Each test results was obtained by averaging at least three samples.

2.3.1. Fresh properties

In order to determine the consistency of the developed composites, flow diameters of mixtures were measured according to ASTM C1437 standard (ASTM C1437, 2020).

2.3.2. Mechanical properties

The mechanical performance of the proposed composites was evaluated by measuring splitting tensile strength and compressive strength after 28d of curing. The splitting tensile strength test was conducted according to ASTM C496 standard from Q100*200mm cylindrical samples (ASTM C496, 2017). The compressive strength test was applied according to ASTM C39 standard from 100*100*100mm cube samples (ASTM C39-05, 2005).

2.3.3. Physical properties

The water absorption and hardened unit weight tests were conducted in compliance with ASTM C642 standard (ASTM C642, 2022). The physical properties were then determined on cube samples with an edge length of 100 mm after 28 days.

2.3.4. Transport properties

Capillary water absorption was measured according to EN 1015-18 standard (EN 1015-18, 2002). The transport properties were then tested using 100*100*100mm cube samples after 28d of curing.

3. Results and discussion

3.1.1. Fresh properties

The effect of the JSA replacement in SCMs-based cementitious composites on fluidity is shown in Fig. 3. According to the test results, the flow diameter of reference samples varied based on the type of SCM. In FA-group samples, a larger flow diameter was observed than in the GBFS-group. One of the main reasons is the spherical structure of FA particles, which creates a ball effect and improves fluidity. Additionally, the structure of FA reduces friction between fine aggregates (Banerjee & Chakraborty, 2016; Memphis, 1996). Replacing 70% of the cement with FA significantly affected fluidity. The beneficial effect of FA on fluidity was observed at higher levels in comparison to GBFS. Increasing the replacement ratio of JSA with No.1 type aggregates negatively affected flowability. One of the main reasons for this is the high-water absorption capacity of JSA (Demircan et al., 2021). Although the water content in the mixture was adjusted in the design according to the water absorption capacity of JSA, a higher replacement content negatively affected the flow diameters, regardless of the SCM type. Interestingly, the GBFS-reference mixture had a lower flow diameter than the JSA utilized at different ratios. This is due to the improvement of fluidity due to the reduction of frictional forces between GBFS and the aggregates. Among the JSA-used mixtures, the best results were obtained in the FA-10 and GBFS-10 samples with 19 cm and 20 cm, respectively.

3.1.2. Mechanical properties

The effect of the JSA replacement in SCMs-based cementitious composites on compressive strength and splitting tensile strength is shown in Fig. 4. The 28-day strength results indicated that different strength values were measured for the reference samples depending on the SCM type. The FA-reference mixture exhibited the highest compressive strength at 56.85 MPa, while the GBFS-reference mixture recorded a compressive strength of 37.05 MPa. The results for splitting tensile strength were also similar to those for compressive strength. As the JSA replacement ratio increased, the splitting tensile and compressive strengths of the mixtures were significantly negatively affected. The compressive strength decreased by 75% with 30% of JSA replacement compared to the reference mixtures. This decrease can be explained by the low density and high porous structure of the JSA particles. The strength results indicate that the strength of JSAs is lower than that of conventional aggregates. In the FA-group, a moderate compressive strength of 18.40 MPa was achieved with the replacement of 10% JSA.

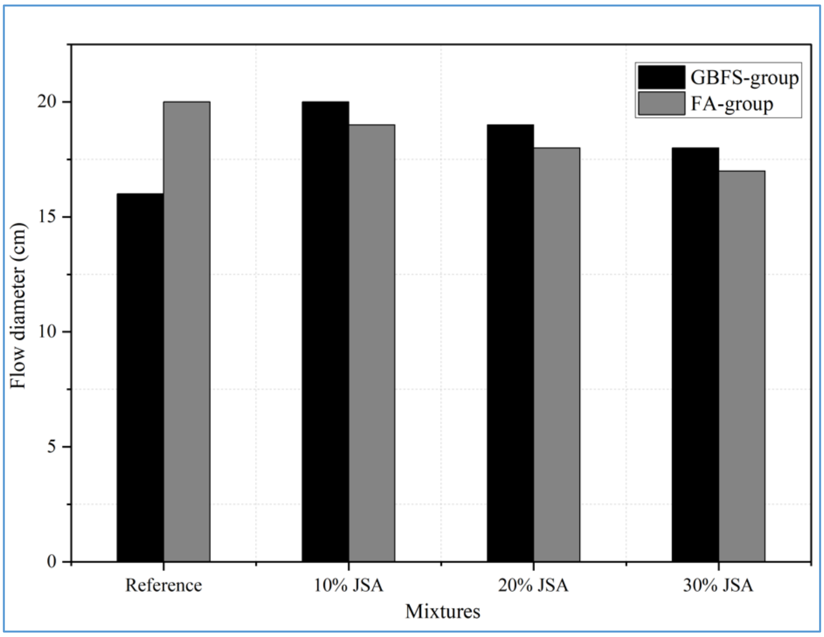

Fig. 3. Flow diameters of mixtures

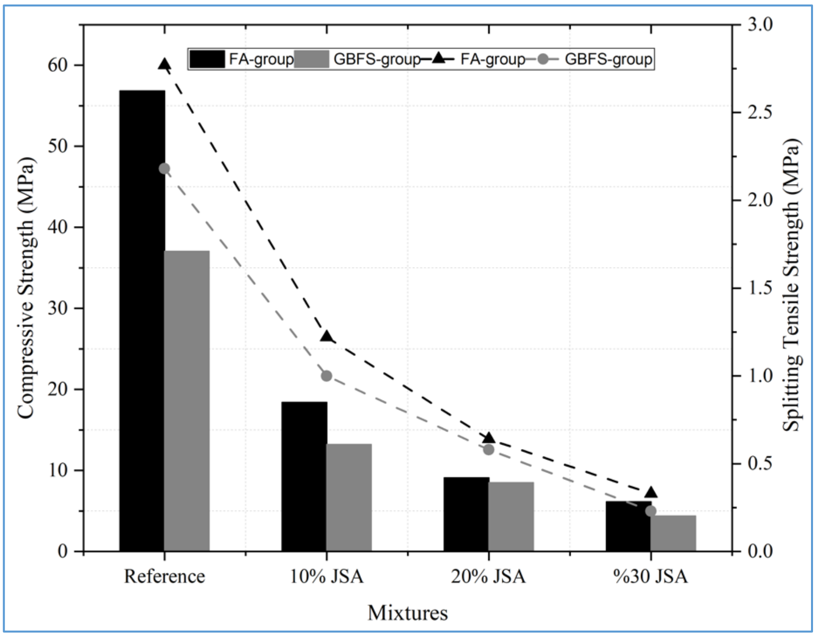

Fig 4. Mechanical properties of mixtures

3.1.3. Physical and transport properties

The effect of the JSA replacement in SCMs-based cementitious composites on physical properties is shown in Fig. 5. According to the test results, similar dry unit weight values were measured among SCM types. Fig. 5-a shows the highest dry unit weights were measured from reference samples. The dry unit weights decreased significantly with the higher JSA content. In the mixtures with the highest JSA replacement level, the dry unit weight decreased by 30% in the FA-group and by 35% in the GBFS-group. The differences arose from the low density of JSA compared to conventional aggregates. With a 10% replacement of JSA, dry unit weights were measured at 1.83 g/cm³ for the FA group and 1.63 g/cm³ for the GBFS group, respectively. Fig. 5-b shows the similar water absorption values for reference samples. The use of SCM resulted in a denser microstructure, whereby the water absorption level of the reference mixtures remained at 1.3%. However, the values for water absorption increased parabolically with the higher JSA content in both groups. Water absorption increased by up to 15 times with the 30% addition of JSA in the FA group, while it increased by 12 times in the GBFS group with the same JSA content. The reason for this increase is that JSAs have a higher level of water absorption compared to conventional aggregates. The lowest water absorption was observed with 10% JSA replacement, recorded as 3% for the FA group and 6% for the GBFS group, respectively.

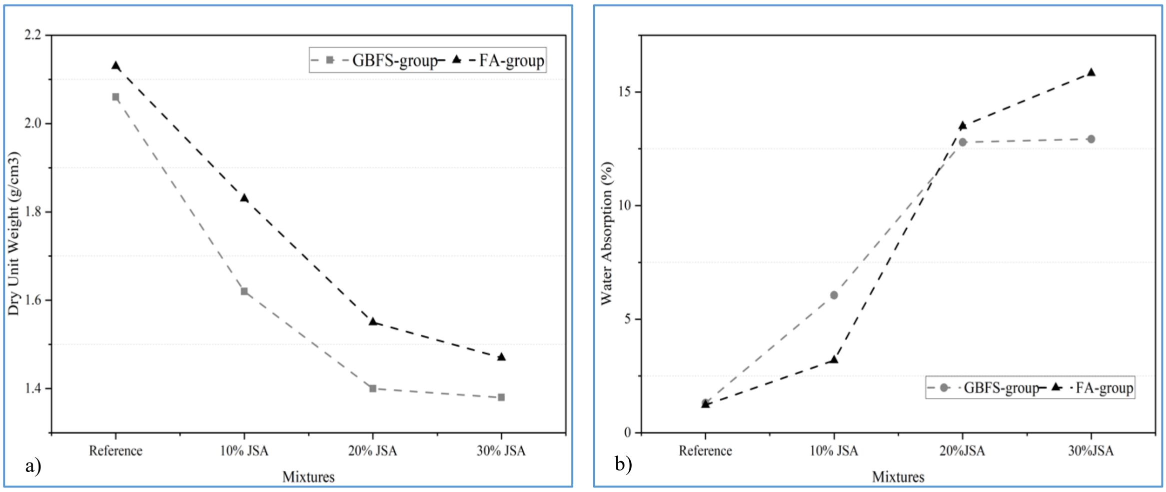

Fig 5. The physical properties of mixtures a) Dry unit weights b) Water absorption

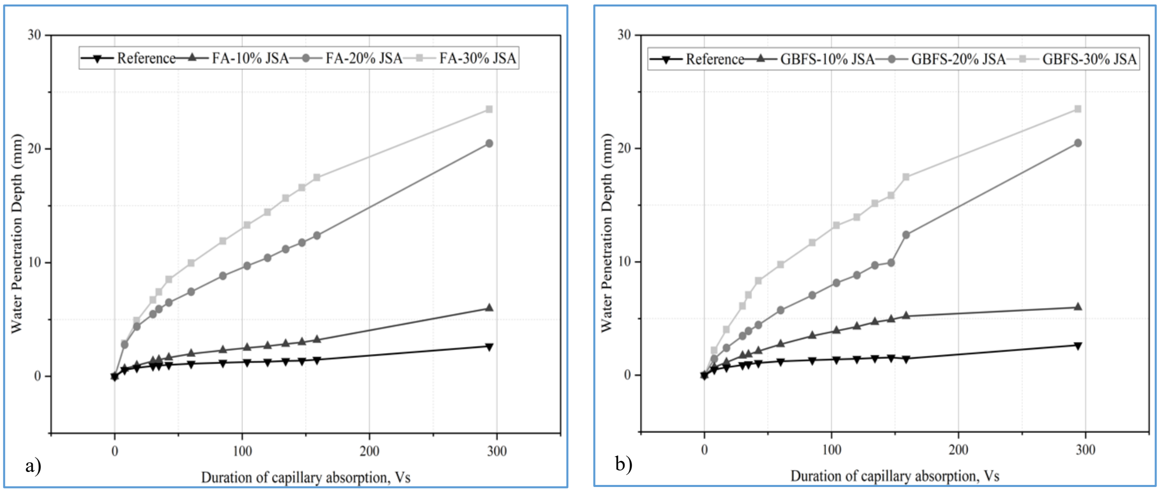

Fig 6. The water penetration depth of mixtures a) FA-group b) GBFS-group

The effect of the JSA replacement in SCMs-based cementitious composites on transport properties is illustrated in Fig. 6. The results of 2-day test, the water absorption depths were measured at 2.66 and 2.71 mm for FA and GBFS-reference mixtures, respectively. The water absorption depths increased continuously with the higher JSA content in both groups. With 30% of the JSA replacement, the water absorption depth increased up to 8 times regardless of the SCM type. Among the mixtures, the water absorption depth increased by 2 to 3 times with a 10% addition of JSA compared to the reference mixture, but it remains the most optimal rate among the other displacement ratios. The main reason for the high-water absorption depth in a short time is the high porous structure and significant water absorption capacity of JSAs.

4. Conclusion

This study investigates the use of juniper seed waste as a lightweight aggregate in SCM-based cementitious composites. The fresh properties, mechanical properties and physical properties are examined in relation to the JSA replacement ratio with natural coarse aggregate. Based on the results and discussion, the main conclusions are as follows:

- Increasing the replacement ratio of JSA with No.1 type aggregates negatively affected flowability due to the high-water absorption capacity of JSA. Among the JSA-used mixtures, the best results were obtained in the FA-10 and GBFS-10 samples with 19 cm and 20 cm, respectively.
- In terms of mechanical strength, the FA-reference mixture exhibited the highest compressive strength at 56.85 MPa, while the GBFS-reference mixture recorded a compressive strength of 37.05 MPa.
- Due to the low density and high porous structure of the JSA particles, the splitting tensile and compressive strengths of the mixtures were significantly negatively affected with increasing the JSA replacement ratio. Moderate strength was obtained with a 10% of JSA usage in the FA-group.
- The dry unit weights significantly decreased with the higher JSA content. In the mixtures with the highest JSA replacement level, the dry unit weight decreased by 30% in the FA-group and by 35% in the GBFS-group. With a 10% JSA replacement, the dry unit weight was measured as 1.83 g/cm^3 in the FA mixture and 1.63 g/cm^3 in the GBFS mixture, respectively.
- Water absorption values increased parabolically with the higher JSA content in both groups.
- With 30% of the JSA replacement, the water absorption depth increased by up to 8 times regardless of the SCM type. The replacement of 10% JSA resulted in water absorption of 3% in the FA group and 6% in the GBFS group, indicating the most favorable performance among all replacement ratios.

In conclusion, optimum fluidity and mechanical properties were obtained when 10% by volume of No.1 type aggregates were replaced with JSA, regardless of the SCM type. However, the water absorption values of the mixtures were 2 to 3 times higher than those of reference mixtures due to the high-water absorption capacity of JSA. On the other hand, the significant reduction in the dry unit weight of mixtures indicates the possible use of JSA as a lightweight aggregate.

Acknowledgments

The authors would like to express their sincere gratitude to Zekai Yıldızlı for his valuable insights, constructive suggestions, and support in providing materials for this study.

References

Abbas, S. N., & Qureshi, M. I. (2025). Effect of recycled plastic aggregates on mechanical and durability properties of concrete: A review. *Materials Chemistry and Physics: Sustainability and Energy*, *3*, 100016. https://doi.org/10.1016/j.macse.2025.100016

ASTM C39-05. (2005). *Standard test method for compressive strength of cylindrical concrete specimens*: In *ASTM Standards,* West Concshohocken.

ASTM C150. (2010). Standard Specification for Portland Cement. In *ASTM Standards:* West Concshohocken. https://doi.org/10.1520/C0150

ASTM C496. (2017). *Standard Test Method for Splitting Tensile Strength of Cylindrical Concrete Specimens*: In *ASTM Standards,* West Concshohocken.

ASTM C618-22. (2025). *Standard Specification for Coal Fly Ash and Raw or Calcined Natural Pozzolan for Use in Concrete*: In *ASTM Standards,* West Concshohocken.

ASTM C642. (2022). *Standard Test Method for Density, Absorption, and Voids in Hardened Concrete*: In *ASTM Standards,* West Concshohocken.

ASTM C989. (2024). *Standard Specification for Slag Cement for Use in Concrete and Mortars*: In *ASTM Standards,* West Concshohocken.

ASTM C1437. (2020). *Standard Test Method for Flow of Hydraulic Cement Mortar*: In *ASTM Standards,* West Concshohocken.

Ayşegül, K. K. (2018). The morphological properties of leaves, cones, seeds of some juniperus species native to Turkey. *Communications Faculty of Science University of Ankara Series C Biology Geological Engineering and Geophysical Engineering*, *27*(1), 61–84. https://doi.org/10.1501/commuc_0000000192

Aytekin, B., & Mardani-Aghabaglou, A. (2022). Sustainable Materials: A Review of Recycled Concrete Aggregate Utilization as Pavement Material. *Transportation Research Record*, *2676*(3), 468–491. https://doi.org/10.1177/03611981211052026

Banerjee, S. & Chakraborty, J. (2016). Replacement of Cement by Fly Ash in Concrete. *International Journal of Civil Engineering*, *3(8),* https://doi.org/10.14445/23488352/IJCE-V3I8P110

Berryman, C., Zhu, J., Jensen, W., & Tadros, M. (2005). High-percentage replacement of cement with fly ash for reinforced concrete pipe. *Cement and Concrete Research*, *35*(6), 1088–1091. https://doi.org/10.1016/j.cemconres.2004.06.040

Celik, D. N., Belendir, U., Ardoga, M. K., Yildirim, G., & Sahmaran, M. (2024). High-conductivity cementitious composites suited for flooring applications: Effect of mixing methods and utilization rates of conductive materials. *Journal of Building Engineering*, *87.* https://doi.org/10.1016/j.jobe.2024.109010

Celik, D. N., Demircan, R. K., Shi, J., Kaplan, G., & Durmuş, G. (2023). The engineering properties of high strength mortars incorporating juniper seed ash calcined at different temperatures: Comparison with other SCMs. *Powder Technology*, *422*. https://doi.org/10.1016/j.powtec.2023.118474

Cement Industry Net Zero Progress Report 2024/25. (2025 April 5). *Global Cement and Concrete Association*. Retrieved from https://gccassociation.org/cement-industry-net-zero-progress-report-2024-25/

Cheng, M. Y., & Khasani, R. R. (2024). An innovative moment balanced inference engine for predicting recycled concrete aggregate strength and minimizing mixture CO_2 emissions. *Construction and Building Materials*, *441*. https://doi.org/10.1016/j.conbuildmat.2024.137482

Demircan, R. K., Kaplan, G., & Çelik, D. N. (2021). High temperature resistant restoration mortar with fly ash and GGBFS. *Journal of Sustainable Cement-Based Materials*, 1–32. https://doi.org/10.1080/21650373.2021.1992682

EN 197-1. (2012). Composition, specifications and conformity criteria for common cements. In *European Standards.*

EN 1015-18. (2002). Methods of test for mortar for masonry - Part 18: Determination of water absorption coefficient due to capillary action of hardened mortar. In *European Standards.*

Fry, M. (2013). Cement, carbon dioxide, and the "necessity" narrative: A case study of Mexico. *Geoforum*, *49*, 127–138. https://doi.org/10.1016/j.geoforum.2013.06.003

Geological Survey, U. (2025). *Mineral commodity summaries 2025*. https://doi.org/10.3133/mcs2025

Güvendiren, A. D. (2015). *Molecular Phylogenetic Analyses of Juniperus L. Species in Turkey and Their Relations with Other Junipers Based on cpDNA* [The Degree of Doctor of Philosophy]. Natural and Applied Sciences of Middle East Technical University.

Huang, H., Zhong, Y., Yang, C., Chen, M., Wang, A., Chen, J., Zhuang, H., & Wang, Y. (2025). Experimental study and prediction model analysis for creep behaviour of recycled ceramic aggregate concrete-filled square-shaped steel tube. In *Structures* (Vol. 75). Elsevier Ltd. https://doi.org/10.1016/j.istruc.2025.108674

Ifzaznah, H. H. H., Güllü, A., Memiş, S., Yaprak, H., Gencel, O., & Ozbakkaloglu, T. (2024). Performance, cost, and ecological assessment of fiber-reinforced high-performance mortar incorporating pumice powder and ground granulated blast furnace slag as partial cement replacement. *Journal of Cleaner Production*, *476*. https://doi.org/10.1016/j.jclepro.2024.143720
Judžentienė, A. (2019). Juniperus communis L.: A review of volatile organic compounds of wild and cultivated common juniper in Lithuania. In *Chemija*, *30(3),* pp. 184–193. https://doi.org/10.6001/chemija.v30i3.4053
Li, J., Zhang, W., Li, C., & Monteiro, P. J. M. (2019). Green concrete containing diatomaceous earth and limestone: Workability, mechanical properties, and life-cycle assessment. *Journal of Cleaner Production*, *223*, 662–679. https://doi.org/10.1016/j.jclepro.2019.03.077
Li, L., Xie, J., Zhang, B., Feng, Y., & Yang, J. (2023). A state-of-the-art review on the setting behaviours of ground granulated blast furnace slag- and metakaolin-based alkali-activated materials. In *Construction and Building Materials*, *368*. https://doi.org/10.1016/j.conbuildmat.2023.130389
Memphis. (1996). Fly ash, Slag, silica fume, and natural Pozzolans. *Design and Control of Concrete Mixtures*, *54048*, 57–72.
Naresh, B., & Saravanan, M. (2022). Experimental study of replacement of cement with ground granulated blast furnace slag. *Materials Today: Proceedings*, *62*, 3493–3496. https://doi.org/10.1016/j.matpr.2022.04.302
TS EN 802. (2016). Design of concrete mixes. Türk Standartları, Ankara (in Turkish).
Vahidi, A., Mostaani, A., Teklay Gebremariam, A., Di Maio, F., & Rem, P. (2024). Feasibility of utilizing recycled coarse aggregates in commercial concrete production. *Journal of Cleaner Production*, *474*. https://doi.org/10.1016/j.jclepro.2024.143578
Wang, Y., Liu, Z., Takasu, K., & Suyama, H. (2025). A study on the workability of self-compacting mortar with blast furnace slag as sand replacement supplemented by fly ash. *Construction and Building Materials*, *465*. https://doi.org/10.1016/j.conbuildmat.2025.140252
Yahyaee Nojoukambari, T., Sadrmomtazi, A., & Kohani Khoshkbijari, R. (2023). Influence of Feldspar and Ground Granulated Blast-furnace slag as a partial cement replacement on mechanical properties and thermal durability and environmental impacts of cement mortars. *Journal of Cleaner Production*, *398*. https://doi.org/10.1016/j.jclepro.2023.136074

Keyword Index

D

E

F

G

H

I

J

K

L

M

N

O

P

Q

R

S

T

U

V

W

X

Y

Z

The Proceedings of the 4th International Civil Engineering and Architecture Conference includes all the accepted and presented papers, compiled in two volumes:

Volume 1: Civil Engineering, comprising 303 papers under major categories such as Structural Mechanics, Earthquake Engineering, Hydraulics & Fluid Mechanics, Geotechnics & Soil Mechanics, Transportation, Structural Materials, Hydrology & Water Resources, Construction Management, and Waste Management.

Volume 2: Architecture, featuring 118 papers grouped under topics such as Architectural Philosophy, Design & Practice, Architecture, Conservation & Restoration, Urban Planning & Landscape, Architectural Engineering, and Interior Design.

We are sincerely grateful to all authors for their valuable contributions. The papers included in these volumes were rigorously reviewed by field experts, and only those that were accepted and presented at the conference have been published. We extend our deepest appreciation to the reviewers for their meticulous evaluations, which significantly contributed to the quality of this publication.

KTU 1955 KARADENIZ TECHNICAL UNIVERSITY

KARADENİZ TEKNİK ÜNİVERSİTESİ Deprem ve Yapı Sağlığı Uygulama ve Araştırma Merkezi UYGAR

dynamic academy®

golden light publishing®

ISBN: 978-605-81854-9-4

9 786259 616001